Synthesis of (±)-15-thia-15-deoxy-PGE_1 methyl ester[1]

HERBERT L. HOLLAND, ELAREF S. RATEMI, AND (IN PART) LUIS CONTRERAS[2]
Department of Chemistry, Brock University, St. Catharines, ON L2S 3A1, Canada

Received January 25, 1993

This paper is dedicated to Professor David B. MacLean

HERBERT L. HOLLAND, ELAREF S. RATEMI, and (in part) LUIS CONTRERAS. Can. J. Chem. **72**, 1 (1994).

The 15-thia-15-deoxy analogue of prostaglandin E_1 methyl ester has been prepared by the zirconocene chloride mediated conjugate addition of an *n*-pentyl ethynyl sulfide derived anion to an appropriately substituted cyclopentenone. Similar methodology has also been used to prepare other 3-(3′-thia-1′-octenyl)-cyclopentanones.

HERBERT L. HOLLAND, ELAREF S. RATEMI et (in part) LUIS CONTRERAS. Can. J. Chem. **72**, 1 (1994).

On a préparé l'analogue 15-thia-15-désoxy de l'ester méthylique de la prostaglandine E_1 en procédant à une addition conjuguée, catalysée par le chlorure de zirconocène, d'un anion dérivé du sulfure d'éthynyle et de *n*-pentyle à une cyclopenténone substituée d'une façon appropriée. On a utilisé une méthodologie semblable pour préparer d'autres 3-(3′-thia-1′-octényl)cyclopentanones.

[Traduit par la rédaction]

Can. J. Chem. Downloaded from www.nrcresearchpress.com by 195.246.54.202 on 09/08/12
For personal use only.

The synthesis of natural prostaglandins and structurally modified prostanoids has a long and extensive history (see, for example, refs. 1–3). One of the long-term goals in the production of modified prostaglandins has been the suppression or reduction of the normally rapid metabolic deactivation of these compounds (for an overview of PG activity and metabolism, see ref. 4); in this regard, the significance of C-15 in prostanoid metabolism is apparent from the rapid oxidation of the 15-hydroxyl group of natural PG's by the enzyme 15-hydroxyprostaglandin dehydrogenase, and modification of the molecule at or close to C-15 has indeed been productive in the development of longer term physiologically active prostanoids (5–7).

As a part of this endeavour, prostanoids modified by the presence of heteroatoms in place of ring or side-chain carbons have also been investigated, resulting in the synthesis of compounds incorporating, for example, sulfur atoms in both side chains (8, 9). However, there have been no reports to date of the preparation of prostanoids, such as **11**, containing sulfur at the metabolically important C-15 position. In view of this fact, we have undertaken the synthesis of a structurally modified prostanoid incorporating sulfur in place of C-15.

The 15-deoxy-15-thia analogue of PGE_1 methyl ester (**11**) was chosen as the synthetic target in view of the central position occupied by the PGE series in prostaglandin biochemistry (1), and also the comparative difficulty in simple construction of the PG_1 (as opposed to the PG_2) skeleton (10, 11). Thus, any synthetic method for **11** based on a conjugate addition approach should be in principle applicable to its PGE_2 analogue, via Noyori's "three-component coupling" method (11), whereas the reverse is not necessarily true. It is our intention in further studies to investigate both chemical and enzymatic methods for the oxidation of **11** at the 15 position, hence the choice of a 15-deoxy analogue as the initial synthetic target.

The essential feature of our synthetic approach is the conjugate addition of a 3-thia-alkenyl anion equivalent, corresponding to the lower side chain of the final product, to a suitably substituted cyclopentenone, such as **6** (Scheme 1). To establish the viability of this approach, it was necessary first to demonstrate that this addition would proceed with stereospecific formation of a product having *E* geometry about the double bond, and to this end the addition of a terminal anion equivalent of *E*-3-thia-1-octene (**14**) (12) to cyclopentenone (**1**), giving the 3-substituted cyclopentanone **7** (Scheme 2, line 1), was first investigated.

Of the methods available for the in situ generation of a terminal anion equivalent of *E*-3-thia-1-octene, the most successful was found to be that based on 3-thia-1-octyne (**13**), via generation of the higher order cuprate complex **14** (Scheme 3) using Schwartz's reagent (zirconocene hydride chloride) (12–14). Prepared using this methodology, the cyclopentanone **7**, obtained in 70% yield, clearly possessed *E* geometry about the olefinic bond based on an observed coupling constant of 16 Hz between the two olefinic hydrogens (12).

Addition of the complex **14** to a protected 4-hydroxycyclopentenone **3** (Scheme 2, line 3) proceeded in 55% yield to give product **9**. The 2-substituted cyclopentenones **4** and **6**, prepared as outlined in Scheme 1, were also used for the conjugate addition reaction of Scheme 2 (lines 4 and 6, respectively), and gave the corresponding *trans*-2,3-dialkyl cyclopentanones **10** and **12**. The synthesis of **4** by the route of Scheme 1 in an overall yield of 38% from 2-carboethoxycyclopentanone represents an improvement in both yield and utility on a similar route originally developed by Bagli et al. (10% overall yield) (15, 16). The preparation of the alcohol **5** in 62% yield from **4** by the allylic hydroxylation procedure of Baraldi et al. (17) is also superior to the previously reported method for this conversion stated to proceed in 40% yield (18).

When addition of **14** to the 2,4-disubstituted cyclopentenone **6** was carried out, giving the protected 15-thiaprostanoid **12** in 60% yield, careful control of the reaction conditions was found to be essential; when the reaction was carried out at –78°C, product formation was very slow (less than 10% conversion in 6 h, whereas stereoisomeric product mixtures were obtained at temperatures above –40°C. The all-*trans* relative stereochemistry of the ring substituents of the final product **11**, obtained following deprotection of **12**, was confirmed by analysis of both ^{1}HMR and ^{13}CMR spectra; a close correspondence of the resonance positions of the relevant carbons (C-8, -11, and -12; 54.6, 55.5, and 72.2 ppm) with the corresponding carbons of PGE_1

[1]This paper commemorates the professional career of our mentor, David B. MacLean, on the occasion of his retirement and elevation to the position of Professor Emeritus at McMaster University, Hamilton, Ontario.

[2]On leave from the Department of Chemistry, University of Venezuela, Caracas, Venezuela.

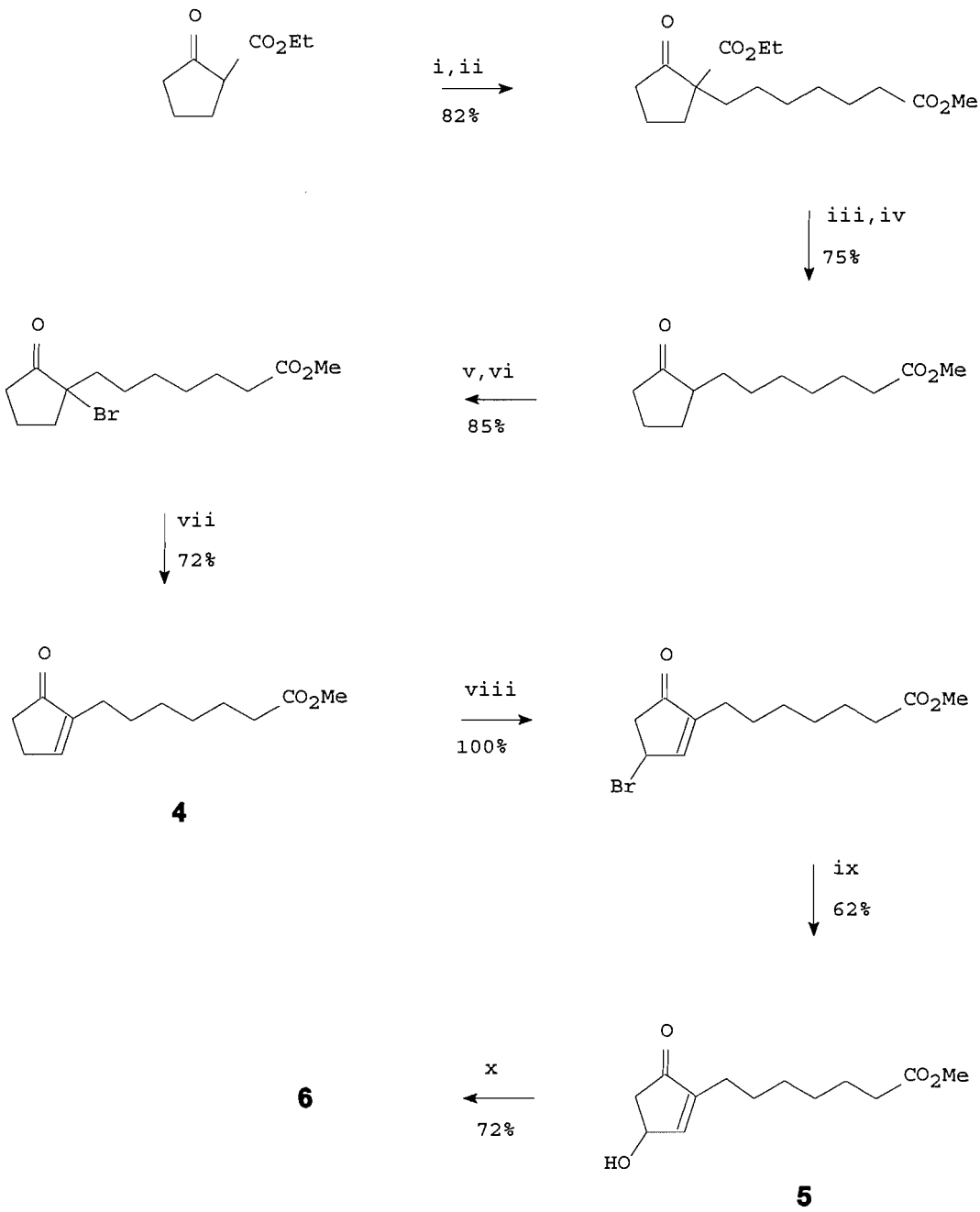

SCHEME 1: i, NaH/DME; ii, methyl 7-bromoheptanoate; iii, H^+; iv, *p*-toluenesulfonic acid/MeOH; v, Ac_2O/H^+; vi, Br_2; vii, $LiBr/Li_2CO_3$; viii, NBS; ix, H_2O/dioxane; x, DHP/H^+

(54.2, 54.6, and 71.6 ppm) and other closely related compounds of known *trans* stereochemistry was observed, together with a similar correspondence of the appropriate hydrogen resonance positions and coupling constants of **11** deduced from 2D ^{1}HMR analysis (19–21). This finding is consistent with the observation that the *trans* product is formed in similar conjugate additions of hydrocarbon-derived anion equivalents to substituted cyclopentenones (13, 14).

The production of **11** by the synthetic route outlined in the accompanying scheme provides an efficient method for the construction of 15-thiaprostanoids. The availability of intermediates, such as **5**, in chiral form (22) opens the possibility of synthesis of chiral 15-thia-PGE derivatives. Preliminary studies of the biological activity of **11** are currently being undertaken.

Experimental

Apparatus, materials, and methods

Melting points were determined on a Kofler heating stage and are uncorrected. Infrared spectra were recorded with an Analect 6260FX spectrometer. Proton NMR spectra were recorded at 200 MHz and carbon NMR spectra at 50.3 MHz (JMOD mode) with a Bruker AC200 spectrometer using deuteriochloroform as solvent and chloroform as internal standard. Mass spectra were obtained with a Kratos concept IS mass spectrometer in EI or CI mode (isobutane) as indicated. Thin-layer chromatography was performed on Merck silica gel 60F-254 and preparative column chromatography using 230–400 mesh silica gel (Merck 9385 or equivalent). HPLC analysis was carried out using a Perkin Elmer Series 3 chromatograph.

Can. J. Chem. Downloaded from www.nrcresearchpress.com by 195.246.54.202 on 09/08/12
For personal use only.

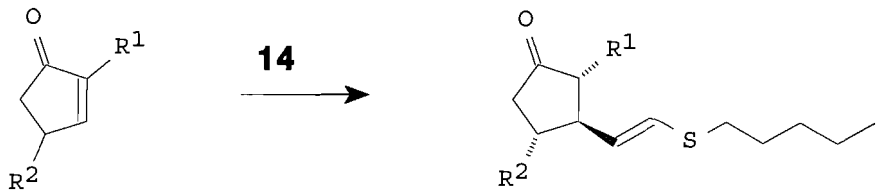

1	**7**	$R^1 = R^2 = H$
2	**8**	$R^1 = H$, $R^2 = OH$
3	**9**	$R^1 = H$, $R^2 = OSiEt_3$
4	**10**	$R^1 = (CH_2)_6CO_2CH_3$, $R^2 = H$
5	**11**	$R^1 = (CH_2)_6CO_2CH_3$, $R^2 = OH$
6	**12**	$R^1 = (CH_2)_6CO_2CH_3$, $R^2 = OTHP$

SCHEME 2

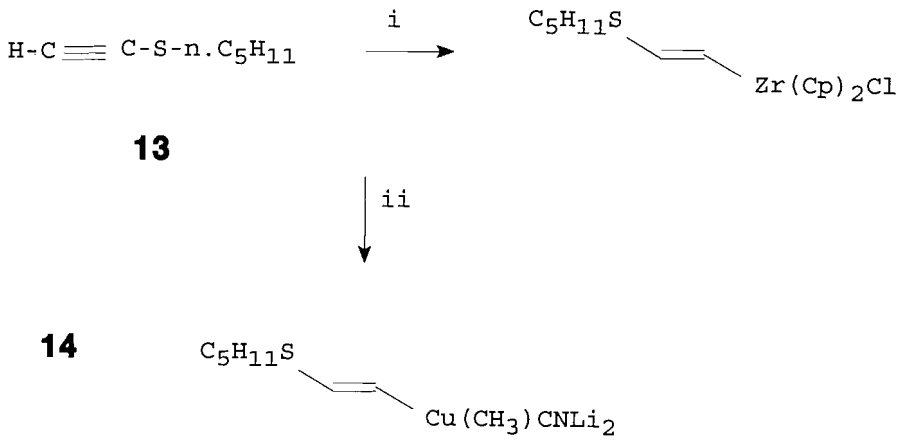

SCHEME 3: i, Cp_2ZrHCl; ii, MeLi/CuCN

4-Hydroxycyclopent-2-enone (2)

This was prepared as described (23) by acid-catalyzed rearrangement of furfuryl alcohol to give, following chromatography (elution with hexane:ethyl acetate, 3:2), the title compound in 45% yield; R_f 0.34 (ethyl acetate); IR ν_{max}: 1720, 3425 cm^{-1}; ^{1}HMR δ: 2.21 (1H, dd, J = 2, 16 Hz, H-5), 2.72 (1H, dd, J = 6, 12 Hz, H-5), 5.02 (1H, m, H-4), 6.19 (1H, d, H-2), and 7.64 (1H, dd, H-3) ppm; ^{13}CMR δ: 43.4 (C-5), 69.2 (C-4), 133.7 (C-2), 164.2 (C-3), 207.2 (C-1) ppm; MS (EI) *m/z* (%): 98(88), 97(34), 80(3), 70(67), 55(77), 43(100).

4-Triethylsilyloxycyclopent-2-enone (3)

Triethylsilyl chloride (3 g) was added to a solution of the hydroxyketone **2** (1.47 g) in dry pyridine (20 mL). The mixture was stirred at ambient temperature for 30 min, then heated at 55°C for 45 min, cooled, diluted with water (40 mL), and extracted with dichloromethane. The extract was dried and evaporated to give an oil, which was chromatographed (ethyl acetate:hexane, 2:3) to give the title compound (2.92 g) as a pale yellow oil; R_f 0.66 (ethyl acetate: hexane 3:7); IR ν_{max}: 1590, 1720 cm^{-1}; ^{1}HMR δ: 0.65 (6H, q, CH_3CH_2-Si), 0.97 (9H, t, CH_3CH_2-Si), 2.22 (1H, m, H-5), 2.68 (1H, dd, J = 6, 16 Hz, H-5), 4.99 (1H, m, H-4), 6.15 (1H, dd, J = 1.1, 5.7 Hz, H-2), and 7.46 (dd, J = 2.2, 5.6 Hz, H-3) ppm; ^{13}CMR δ: 4.3 (3C), 6.2 (3C), 44.6 (C-5), 70.2 (C-4), 134.0 (C-2), 163.3 (C-3), and 205.6 (C-1) ppm; MS (EI) *m/z* (%): 212(3), 183(100), 155(35), 127(43), 125(73).

2-Carboethoxy-2-(6′-methoxycarbonylhexyl)-cyclopentanone

2-Carboethoxycyclopentanone (49.5 g) was added over 35 min to a stirred suspension of sodium hydride (8.1 g) in dry DME (320 mL), with the reaction temperature being maintained at 25°C. When gas evolution was complete, methyl 7-bromoheptanoate (70.7 g) was added, and the resulting mixture then refluxed under argon for 26 h. The mixture was cooled and filtered, the solids washed with ether, and the combined filtrate and washings evaporated. The resulting residue was added to water (200 mL) and the mixture acidified (10% HCl). Extraction with ether followed by drying and evaporation of the extract gave an orange oil (80 g) that, following chromatography (hexane:-ethyl acetate, 1:1), gave the title compound (75 g) as a colourless oil; R_f 0.45 (ethyl acetate:hexane 3:1); IR ν_{max}: 1730, 1748 cm^{-1}; ^{1}HMR included signals at δ: 1.24 (3H, t, OCH_2CH_3), 2.25 (2H, t, CH_2CO_2), 3.67 (3H, s, OCH_3), 4.17 (2h, q, OCH_2CH_3) ppm; ^{13}CMR δ: 13.9 (CH_3), 19.4, 24.4, 24.6, 28.6, 29.3, 32.6, 33.5, 33.8, 37.7, 51.2 (OCH_3), 61.1 (OCH_2), 64.0 (C-2), 170.9, 173.9, and 214.6 (C-1) ppm.

2-(6′-Methoxycarbonylhexyl)-cyclopentanone

A mixture of the above diester (65.5 g), acetic acid (195 mL), water (273 mL), and H_2SO_4 (77 mL) was heated under reflux for 20 h. The cooled mixture was then treated with 10% sodium bicarbonate (250 mL), and extracted with ether. The extract was washed (2 × 400 mL water followed by 400 mL 10% $NaHCO_3$), dried, and evaporated. Distillation of the residue (159–163°C, 0.09 Torr; 1 Torr = 133.3 Pa)

Can. J. Chem. Downloaded from www.nrcresearchpress.com by 195.246.54.202 on 09/08/12
For personal use only.

afforded a clear oil (R_f 0.3 (ethyl acetate:hexane 1:1); IR ν_{max}: 1710, 1748, 3102 cm^{-1}), which was esterified using dry methanol (250 mL), benzene (800 mL), and *p*-toluenesulfonic acid (1 g), refluxing in a Dean–Stark apparatus for 7 h. Conventional work-up gave the title ester (37 g), bp 120–125°C, 0.7 Torr (lit. (24) bp 135–140°C, 0.4 Torr); R_f 0.55 (ethyl acetate:hexane 4:1); IR ν_{max}: 1739, 1745 cm^{-1}; ^{1}HMR δ: 1.22–1.32 (8H, m), 1.55–1.98 (6H, m), 3.67 (3H, s, OCH_3); ^{13}CMR δ: 20.5, 24.7, 27.1, 28.7, 29.0, 29.4 (2C), 33.8, 37.9, 48.8 (C-2), 51.1 (OCH_3), 173.9, 221.0 ppm; MS (EI) *m/z* (%): 226(5), 195(9), 143(5), 97(9), 84(100).

1-Acetoxy-2-(6′-methoxycarbonylhexyl)-cyclopentene

A stirred solution of the above ester (28.2 g) and *p*-toluenesulfonic acid (270 mg) in acetic anhydride (57 mL) was heated while the acetic acid that formed was fractionally distilled. The original volume was maintained by periodic addition of acetic anhydride. When no more acetic acid distilled, the mixture was briefly heated to 140°C, then cooled and poured onto a stirred ice-cold mixture of saturated $NaHCO_3$ (400 mL) and hexane (300 mL). The organic phase was removed, dried, and evaporated, and the residue distilled to give a colourless oil (28.6 g, bp 81–85°C, 0.07 Torr); R_f 0.6 (ethyl acetate:hexane 4:1); IR ν_{max}: 1698, 1742 cm^{-1}; ^{1}HMR δ: 1.25–1.40 (6H, m), 1.61 (2H, m), 1.93 (4H, m), 2.14 (3H, s, $COCH_3$), 2.28 (4H, m), 2.45 (2H, m), 3.67 (3H, s, OCH_3) ppm; ^{13}CMR δ: 19.7, 20.6 (CH_3CO), 24.8, 26.2, 26.8, 28.8, 28.9, 30.9, 31.0, 33.9, 51.3 (OCH_3), 126.5 (C-2), 143.9 (C-1), 168.7, 174.1 ppm; MS (EI) *m/z* (%): 268(5), 194(100), 166(30), 123(33), 97(76), 84(37).

2-Bromo-2-(6′-methoxycarbonylhexyl)-cyclopentanone

A 500-mL 3-neck flask was fitted with a mechanical stirrer and two dropping funnels, cooled in ice, and charged with calcium carbonate (9 g) and chloroform (100 mL). To this cooled and stirred mixture were added simultaneously over 15 min a solution of the above enol acetate (22.5 g) in chloroform (10 mL) and a solution of bromine (13.4 g) in carbon tetrachloride (10 mL). The mixture was stirred at 5°C for a further 30 min, and the organic layer was then separated, washed (5% sodium thiosulphate, water, then saturated NaCl), dried, and evaporated at <40°C to yield the desired bromoketone, which was used directly in the next step without further manipulation.

*2-(6′-Methoxycarbonylhexyl)-cyclopent-2-enone (**4**)*

The crude bromoketone prepared as above (25.5 g) was added to an anhydrous, refluxing, and well-stirred mixture of LiBr (16.5 g) and Li_2CO_3 (16.5 g) in DMF (200 mL) under argon. The mixture was refluxed for a further 30 min, then cooled, poured into water (1 L), acidified (10% HCl), and extracted with ether. The ether extract was washed (water, saturated NaCl), dried, and concentrated to give an oil, which after distillation gave 13.5 g of the title compound, bp 95°C, 0.05 Torr (lit. (24) bp 145–150°C, 0.2 Torr); R_f 0.4 (ethyl acetate:hexane 1:1); IR ν_{max}: 1633, 1703, 1736 cm^{-1}; ^{1}HMR δ: 1.30–1.66 (8H, m), 2.16 (2H, m), 2.56 (2H, m), 3.66 (3H, s, OCH_3), 7.33 (1H, m, H-3) ppm; ^{13}CMR δ: 24.6, 24.8, 26.3, 27.5, 28.8, 28.9, 34.0, 34.5, 51.4 (OCH_3), 146.3 (C-2), 157.3 (C-3), 174.1, 209.9 ppm; MS (EI) *m/z* (%): 224(13), 193(43), 150(53), 123(42), 109(75), 96(100).

2-(6′-Methoxycarbonylhexyl)-4-bromocyclopent-2-enone

A stirred mixture of the above ketone (6 g), *N*-bromosuccinimide (freshly crystallized from water, 5.52 g), and 2,2-azadiisobutyronitrile (19 mg) in carbon tetrachloride (25 mL) was heated under reflux, and the reaction monitored by ^{1}HMR (appearance of peaks at δ 5.01, (H-4), 7.59 (H-3) ppm). After 5 h, the mixture was cooled to 5°C and filtered. The solids were washed with cold CCl_4 (3 × 20 mL), and the combined organic phase was washed (water, 5% sodium thiosulphate), dried, and evaporated to give 8.47 g of an orange oil, which was used directly in the next step.

*2-(6′-Methoxycarbonylhexyl)-4-hydroxycyclopent-2-enone (**5**)*

The crude bromoketone (above) was refluxed in aqueous dioxane (80 mL, 1:1) for 2.5 h. The reaction mixture was then cooled, the solvent evaporated, and the residue extracted with chloroform (4 × 40 mL). The extract was dried, evaporated, and purified by chromatography (10% stepwise elution from benzene to ethyl acetate) to give the title compound, 4.0 g, mp 46–48°C (lit. (25) mp 48–49°C); R_f 0.2 (ethyl acetate:hexane 3:7); IR ν_{max}: 1630, 1695, 1735 cm^{-1}; ^{1}HMR δ: 1.26–1.64 (8H, m), 2.13–2.36 (5H, m), 2.80 (1H, dd, J = 6, 14 Hz), 3.67 (3H, s, OCH_3), 3.45–3.95 (1H, br s, OH), 4.93 (1H, m, H-4) ppm; ^{13}CMR δ: 24.3, 24.7, 27.1, 28.7, 28.8, 34.0, 44.8, 51.4 (OCH_3), 68.4 (C-4), 147.0 (C-3), 155.9 (C-2), 174.0, 206.3 ppm; MS (EI) *m/z* (%): 240(2), 222(33), 190(89), 163(33), 111(48), 95(100).

*2-(6′-Methoxycarbonylhexyl)-4-(tetrahydropyranyloxy)cyclopent-2-enone (**6**)*

One drop of concentrated hydrochloric acid was added to a stirred mixture of the hydroxyester **5** (3.2 g) and dihydropyran (3.28 g), and the resulting mixture stirred at room temperature for 4 h. The solution was then diluted with ether, washed (saturated $NaHCO_3$ followed by saturated NaCl), dried, and evaporated to give an oil, 4.52 g, which was purified by chromatography (10% stepwise gradient elution from hexane to ethyl acetate) to give **6** (3.1 g), R_f 0.75 (ethyl acetate:hexane 3:1), IR ν_{max}: 1720, 1740 cm^{-1}; ^{1}HMR included signals at δ: 3.66 (3H, s, OCH_3), 3.85 (2H, m, $COCH_2$), 4.83–4.91 (2H, m, HC-O-CH), and 7.26 (1H, m, H-3) ppm; ^{13}CMR δ: 19.8, 24.4, 24.7, 25.3, 27.1, 28.7, 28.9, 30.8, 33.9, 42.2/43.2, 51.3, 62.7, 72.9/73.0, 98.4/98.6, 148.0/148.2, 153.5/155.3, 174.1, and 205.8/206.1 ppm; MS (EI) *m/z* (%): 324(0.2), 293(1), 223(12), 191(25), 163(22), 85(100).

*Preparation of the alkenyl cuprate complex **14***

All manipulations were performed in flame-dried apparatus under an argon atmosphere. A 50-mL 2-neck flask equipped with a low-temperature thermometer, magnetic stirrer bar, and a septum was charged with a solution of ethynyl *n*-pentyl sulfide (**13**, 61 mg) (12) in dry THF (3 mL). To this was added solid zirconocene hydride chloride (130 mg), and the mixture stirred until a yellow solution formed (ca. 30 min). This solution was cooled to –70°C, and then treated with methyllithium (0.75 mL, 1.4 M in ether). The resulting mixture was allowed to reach –50°C for 5 min, then recooled to –70°C.

Concurrently, copper(I) cyanide (43 mg) was placed in a 25-mL 2-neck flask fitted with a septum, low-temperature thermometer, and a magnetic stirrer bar. Tetrahydrofuran (2 mL) was added and the resulting slurry cooled to –70°C, then treated with methyllithium (0.38 mL, 1.4 M in ether). The mixture was allowed to reach –50°C, stirred until clear, recooled to –70°C, then cannulated into the alkenyl zirconocene solution, keeping both solutions at –70°C. The flask containing the cyanocuprate was washed with 1 mL of THF, and the washing cannulated as above. The resulting mixture was maintained at –50°C for 30 min, then cooled to –70°C in readiness for the conjugate addition reaction.

*3-(E-3′-Thia-1′-octenyl)cyclopentanone (**7**)*

A solution of cyclopent-2-enone (**1**) (0.25 mmol) in dry THF (2 mL) was added at –70°C to the reagent **14**, prepared as described above. The stirred mixture was allowed to reach –50°C and maintained at that temperature for 5 h. It was then cooled to –70°C and quenched with the addition of saturated ammonium chloride:ammonium hydroxide (9:1, 20 mL). Vigorous stirring of the mixture for 30 min produced a deep blue aqueous layer and a pale yellow organic layer, which was separated. The aqueous layer was extracted with ether (3 × 25 mL), and the combined organic extracts washed (saturated ammonium chloride:ammonium hydroxide, 9:1), dried, filtered through Celite, and evaporated. The residue was purified by chromatography (5% stepwise elution from hexane to ethyl acetate) to give the title compound in 70% yield; R_f 0.5 (ethyl acetate:hexane 1:4); IR ν_{max}: 1740 cm^{-1}; ^{1}HMR included signals at δ: 0.92 (3H, t, H-8′), 1.25–1.39 (8H, m, CH_2′s), 6.24 (1H, d, J = 16 Hz, H-2′), and 6.46 (dd, J = 6, 16 Hz, H-1′) ppm; ^{13}CMR δ: 13.8, 21.7, 22.3, 29.1, 30.9, 37.8, 39.2, 43.8, 54.0, 132.6, 141.0, and 216.4 ppm; MS (EI) *m/z* (%): 212(66), 141(64), 109(57), 91(32), 85(100); HRMS M^+: 212.1257; calcd. for $C_{12}H_{20}OS$: 212:1235.

Can. J. Chem. Downloaded from www.nrcresearchpress.com by 195.246.54.202 on 09/08/12
For personal use only.

Can. J. Chem. Downloaded from www.nrcresearchpress.com by 195.246.54.202 on 09/08/12
For personal use only.

trans-*2-(6′-Methoxycarbonylhexyl)-3-(*E*-3″-thia-1″-octenyl)-cyclopentanone (**10**)*

Conjugate addition of the complex **14** to 2-(6′-methoxycarbonylhexyl)-cyclopent-2-enone (**4**) as described above gave, following chromatography, the title compound in 62% isolated yield; R_f 0.55 (ethyl acetate:hexane 3:2); IR ν_{max}: 1740 cm^{-1}; ^{1}HMR included signals at δ: 0.90 (3H, t, H-8″), 1.1–1.8 (12H, m), 6.16 (1H, d, J = 16 Hz, H-2″) and 6.46 (dd, J = 6.5, 16 Hz, H-1″) ppm; ^{13}CMR δ: 13.8, 22.1, 24.7, 26.4, 27.7, 28.8, 29.0, 30.5, 30.6, 33.9, 35.7, 41.0, 43.6, 51.2, 54.0, 127.4, 131.9, 174.0, and 219.4 ppm; MS (EI) *m/z* (%): 354(0.4), 290(41), 259(28), 258(31), 230(17), 147(64), 92(100); HRMS M^+: 354.2245; calcd. for $C_{20}H_{34}O_3S$: 354:2228.

trans-*3-(*E*-3′-Thia-1′-octenyl)-4-triethylsilyloxycyclopentanone (**9**)*

Conjugate addition of the complex **14** to 4-triethylsilyloxycyclopent-2-enone (**3**), as described above gave, following chromatography (elution with hexane:ethyl acetate 7:3), the title compound in 55% isolated yield; R_f 0.54 (ethyl acetate:hexane 3:7); IR ν_{max}: 1742 cm^{-1}; ^{1}HMR included signals at δ: 0.56 (6H, q, CH_3CH_2Si), 0.92 (12H, t, CH_3CH_2Si and H-8′), 4.02 (1H, q, H-4), 5.51 (1H, dd, J = 7.5, 15 Hz, H-1′), and 6.11 (d, J = 15 Hz, H-2′) ppm; ^{13}CMR δ: 4.7(3C), 6.7(3C), 13.9, 22.6, 28.7, 28.9, 29.8, 41.7, 42.6, 53.5, 74.0, 127.3, 131.4, and 214.5 ppm; MS (EI) *m/z* (%): 342(8), 313(26), 271(14), 258(14), 249(24), relative to 183(100). HRMS M^+: 342.2035; calcd. for $C_{18}H_{34}O_2SSi$: 342.205.

trans-*2-(6′-Methoxycarbonylhexyl)-3-(*E*-3″-thia-1″-octenyl)-4-tetrahydropyranyloxycyclopentanone (**12**)*

Addition of the cuprate complex **14** to 2-(6′-methoxycarbonylhexyl)-4-(tetrahydropyranyloxy)-cyclopent-2-enone (**6**) (80 mg) as described above, followed by chromatography of the product (5% stepwise elution from hexane to ethyl acetate), gave **12** (80 mg, 60%) as a pale yellow oil, R_f 0.5 (ethyl acetate:hexane 1:4), which was used directly in the next step.

trans-*2-(6′-Methoxycarbonylhexyl)-3-(*E*-3″-thia-1″-octenyl)-4-hydroxycyclopentanone, (±)-15-thia-15-deoxy-PGE$_1$ methyl ester (**11**)*

A solution of the tetrahydropyranyl ether **12** (75 mg) in acetic acid:water:THF (4:2:1, 7 mL), was stirred at room temperature for 24 h. The yellow mixture was then neutralized by the addition of solid sodium bicarbonate and worked up with ether. The ethereal extract was washed with saturated $NaHCO_2$, dried, and evaporated to yield 39 mg of material, which after purification by chromatography (10% stepwise elution from benzene to ethyl acetate) gave (±)-15-thia-15-deoxy-PGE$_1$ methyl ester (**11**) (22 mg); R_f 0.3 (chloroform:methanol 97.3); IR ν_{max}: 1746, 3392 cm^{-1}; ^{1}HMR (PG numbering) δ: 0.92 (3H, t, H-20), 1.30–1.40 (8H, m, CH_2′s), 1.57–1.66 (7H, m, CH_2′s), 1.88 (1H, br s, OH), 2.0 (1H, m, H-8), 2.16–2.49 (2H, m, including H-12 as dd at 2.40), 2.30 (2H, t), 2.71 (2H, t), 2.78 (2H, dd), 3.67 (3H, s, OCH_3), 4.05 (1H, q, H-11), 5.45 (1H, dd, J = 8, 16 Hz, H-13), and 6.18 (1H, d, J = 14 Hz, H-14) ppm; ^{13}CMR (PG numbering) δ: 13.9 (C-20), 22.2 (C-19), 24.8 (C-3), 26.6 (C-7), 27.6 (C-6), 28.9, 29.0, 29.3 (C-4, -5, -17), 30.9 (C-18), 32.6 (C-16), 34.0 (C-2), 46.0 (C-10), 51.4 (OCH_3), 54.6 (C-8), 55.5 (C-12), 72.2 (C-11), 127.2 (C-13), 128.1 (C-14), 174.1 (C-1), and 214.3 (C-9) ppm; MS (CI) *m/z* (%): 371(1.5), 352(0.4), 306(1), 279(15), 241(11), 167(27), 149(85), 129(100); HPLC (15 × 0.46 cm ODS2-C_{18} column, chloroform eluent, 1.5 mL/min, UV_{254} detection): single peak at retention time 7.5 min.

Acknowledgments

This work was supported by grants from the Natural Sciences and Engineering Council of Canada (to H.L.H.) and a studentship from the Government of Libya (to E.S.R.). We are also grateful to Mr. T. Jones for help with the acquisition of spectral data.

1. R.F. Newton and S.M. Roberts. Prostaglandins and thromboxanes. Butterworth Scientific Press, London. 1982.
2. M. Suzuki, Y. Morita, H. Koyano, M. Koga, and R. Noyori. Tetrahedron, **46**, 4809 (1990).
3. R.F. Newton and S.M. Roberts. Tetrahedron, **36**, 2163 (1980).
4. N.A. Nelson, R.C. Kelly, and R.A. Johnson. Chem. Eng. News, **60**, 30 (1982).
5. R. Noyori, M. Suzuki, S. Kurozumi, and T. Kawagishi. Eur. Pat. Appl. 0103445, Chem. Abstr. **101**, 130497g (1984).
6. J.E. Pike and D.R. Morton. *In* Chemistry of the prostaglandins and leukotrienes. Raven Press, New York. 1985. p. 291.
7. P.W. Collins, E.Z. Dajani, R. Pappo, A.F. Gasiecki, R.G. Bianci, and E.M. Woods. J. Med. Chem. **20**, 1152 (1977).
8. S. Kurozumi, T. Toru, M. Kobayashi, and Y. Hashimoto. Synth. Commun. **7**, 169 (1977).
9. L. Novak, P. Kolonits, C. Szantay, J. Aszodi, and M. Kajtar. Tetrahedron Lett. **38**, 153 (1982).
10. M. Suzuki, F. Suzuki, T. Kawagishi, V. Morita, and R. Noyori. Isr. J. Chem. **24**, 118 (1984).
11. M. Suzuki, A. Yanagisawa, and R. Noyori. J. Am. Chem. Soc. **107**, 3348 (1985); R. Noyori and M. Suzuki. Angew. Chem. Int. Ed. Engl. **23**, 847 (1984).
12. H.L. Holland, L. Contreras, and E.S. Ratemi. Synth. Comm. **22**, 1473 (1992).
13. B.H. Lipshutz and E.L. Ellsworth. J. Am. Chem. Soc. **112**, 7440 (1990).
14. K.A. Babiak, J.R. Behlaing, J.H. Dygos, K.T. McLaughlin, J.S. Ng, V.J. Kalish, S.W. Kramer, and R.L. Shone. J. Am. Chem. Soc. **112**, 7441 (1990).
15. J.F. Bagli, T. Bogri, and R. Deghenghi. Tetrahedron Lett. 465 (1966).
16. J.F. Bagli and T. Bogri. J. Org. Chem. **37**, 2132 (1972).
17. P.G. Baraldi, A. Barco, S. Benetti, G.P. Pollini, D. Simoni, and V. Zanirato. Tetrahedron, **43**, 4669 (1987).
18. A.F. Kluge, K.G. Untch, and J.H. Fried. J. Am. Chem. Soc. **94**, 7827 (1972).
19. J.P. Marino, R. Fernandez de la Pradilla, and E. Laborde. J. Org. Chem. **52**, 4898 (1987).
20. E. Breitmaier and W. Voelter. Carbon-13 NMR spectroscopy. VCH Publishers, Weinheim. 1987. p. 467.
21. H.L. Holland, F.M. Brown, P.C. Chenchaiah, and J.A. Rao. Can. J. Chem. **68**, 282 (1990).
22. C.J. Sih, J.B. Heather, G. Peruzzotti, P. Price, R. Sood, and L.F.H. Lee. J. Am. Chem. Soc. **97**, 865 (1975).
23. Japanese Patent 56-86128 to Teijin Ltd.; Chem. Abstr. **96**, 6257t (1979).
24. L. Novak and C. Szantay. Synthesis, 353 (1974).
25. P.G. Baraldi, P.G. Polini, D. Simoni, and V. Zanirato. Synthesis, 781 (1986).

Nucleoside intermediates in blasticidin S biosynthesis identified by the in vivo use of enzyme inhibitors

STEVEN J. GOULD[1]

Departments of Chemistry and of Biochemistry and Biophysics, Oregon State University, Corvallis, OR 97331-4003, U.S.A.

JINCAN GUO AND ANJA GEITMANN

Department of Biochemistry and Biophysics, Oregon State University, Corvallis, OR 97331-4003, U.S.A.

AND

KARL DEJESUS

Department of Chemistry, Oregon State University, Corvallis, OR 97331-4003, U.S.A.

Received March 9, 1993

This paper is dedicated to Professors Ian Spenser and David B. MacLean

STEVEN J. GOULD, JINCAN GUO, ANJA GEITMANN, and KARL DEJESUS. Can. J. Chem. **72**, 6 (1994).

Intermediates in the biosynthesis of blasticidin S and its nucleoside co-metabolites were detected by altering fermentation conditions. Inhibitors of specific types of biochemical reactions that were expected to be involved in blasticidin biosynthesis were fed to *Streptomyces griseochromogenes*, in some cases with the inclusion of large quantities of the primary precursors of blasticidin S. The types of reactions and inhibitors used were (1) transaminase (aminooxyacetic acid and 2-methylglutamate), (2) amidotransferase (azaserine and 6-diazo-5-oxo-L-norleucine), (3) arginine biosynthesis (arginine hydroxamate), and (4) methyltransferase (ethionine). These manipulations apparently distorted the pools of precursors and (or) intermediates, and led to substantial accumulations of three known, previously minor, metabolites of *S. griseochromogenes*, cytosylglucuronic acid, pentopyranine C, and demethylblasticidin S, and of two new ones, pentopyranone and isoblasticidin S. New cytosyl metabolites were detected by HPLC with photodiode array detection. Fermentations to which arginine hydroxamate and cytosine had been added also produced three aberrant metabolites that were derived from pentopyranone and arginine hydroxamate.

STEVEN J. GOULD, JINCAN GUO, ANJA GEITMANN et KARL DEJESUS. Can. J. Chem. **72**, 6 (1994).

En modifiant les conditions de fermentation, on a pu détecter les intermédiaires dans la biosynthèse de la blasticidine S et de ses cométabolites nucléosidés. Des inhibiteurs de réactions biochimiques spécifiques attendues dans la biosynthèse de la blasticidine ont été données au *Streptomyces griseochromogenes*, dans certains cas avec inclusion de grandes quantités de précurseurs primaires de la blasticidine S. Les types de réactions et d'inhibiteurs utilisés sont : (1) la transaminase (acide aminooxyacétique et le 2-méthylglutamate); (2) amidotransférase (azasérine et 6-diazo-5-oxo-L-norleucine); (3) biosynthèse de l'arginine (hydroxamate d'arginine) et (4) méthyltransférase (éthionine). Ces manipulations ont apparemment modifié la répartition des précurseurs et (ou) des intermédiaires et ont conduit à des accumulations importantes de trois métabolites connus, mais antérieurement mineurs, du *S. griseochromogenes*, l'acide cytosylglucoronique, la pentopyranine C et la démethylblasticidine S, ainsi que deux nouveaux métabolites, la pentopyranone et l'isoblasticidine S. Grâce à la CLHP avec une photodiode comme détecteur, on a pu mettre en évidence la présence de nouveaux métabolites cytosylés. Les fermentations réalisées avec des substrats dans lesquels de l'hydroxamate d'arginine et de la cytosine avaient été ajoutés ont aussi conduit à la formation de trois métabolites aberrants dérivés de la pentopyranone et de l'hydroxamate d'arginine.

[Traduit par la rédaction]

Blasticidin S, an antifungal antibiotic produced by *Stretomyces griseochromogenes* first isolated by Takeuchi et al. in 1958, is used commercially for the control of *Piricularia oryzae* (rice blast) (1). Chemical degradation (2–5) and X-ray diffraction studies (6, 7) yielded the nucleoside structure **1**. Since then, a number of structurally related nucleoside antibiotics have been characterized, including gougerotin (8), mildiomycin (9), bagougeramines A and B (10), arginomycin (11), and antibiotic Sch 36605 (12).

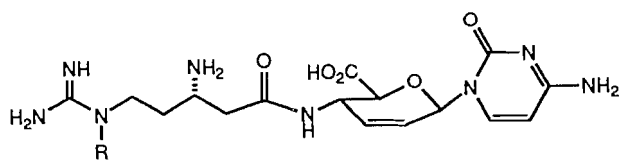

1, R = CH_3
20, R = H

Blasticidin S is composed of *N*-methyl-L-β-arginine, **2** (blasticidic acid), and an unusual nucleoside (cytosinine), **3**. Seto et al. (13) had established that cytosine, **4**, D-glucose, **5**, L-α-arginine, **6**, and methionine, **7**, are the primary precursors (Scheme 1). We first became interested in the biosynthesis of **1** because of the potential relevance of our studies (14) on the L-β-lysine unit of another nucleoside antibiotic, streptothricin F, to the origin of the L-β-arginine moiety embedded in **1**. Indeed, both β-amino acids proved to be derived by 2,3-aminomutase reactions in which an intramolecular migration of nitrogen from C-2 to C-3 and a companion migration of the 3-pro*R* hydrogen to the 2-pro*R* position takes place (15, 16).

Feedings with [1-^{2}H]- and [2,3,4,6,6-$^2H_5$]-D-glucoses, used to probe the biosynthesis of the cytosinine moiety, revealed that the carbinol hydrogens H-1, -2, and -3 were retained in **1**, but that H-4 was lost. Retention of H-2 and H-3 indicated that the deoxygenations at these positions could not occur by simple dehydrations (17).

Efforts to incorporate more advanced putative intermediates proved inconclusive. We now report these results, as well as those of a subsequent program of feeding *inhibitors* of specific

[1]Author to whom correspondence may be addressed.

Can. J. Chem. Downloaded from www.nrcresearchpress.com by 203.198.23.82 on 09/08/12
For personal use only.

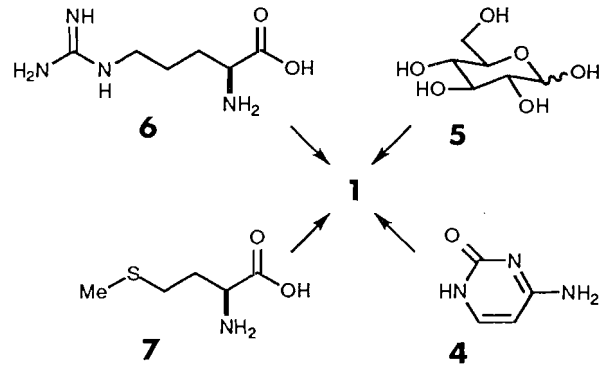

SCHEME 1

types of biochemical reactions that were expected to be involved in the biosynthesis of **1**. The latter approach successfully led to the identification of the roles of a number of intermediates in the metabolic matrix that includes the biosynthesis of **1**.

Experimental

General

[1-^{2}H]-D-Glucose was obtained from Cambridge Isotope Laboratories. Other organic chemicals were obtained from either Aldrich or Sigma Chemical Company.

*Preparation of [1-^{14}C]-blastidic acid, 2*a

A sample of [1″-^{14}C]-**1** hydrochloride (485 mg, 1.06 mmol, 5.97 × 10^6 dpm/mmol) was dissolved in 6 N HCl (10 mL), and stirred at room temperature for 6 h (these conditions caused significant decomposition of **3**). The mixture was neutralized to pH 4.0 and applied to an anion exchange column (Amberlite, IRA-410, 100 mesh, OH–, 2.5 cm × 30 cm), and the initial effluent immediately loaded onto a cation exchange column (Amberlite, IRC-50, 50 mesh, H^+, 2.5 cm × 20 cm). This was washed first with H_2O to neutrality and then with 0.5 N HCl until the eluates no longer contained **2***a*. The HCl eluate was concentrated by rotary evaporation at ambient temperature, and the remaining solution was lyophilized. Recrystallization of the lyophilized residue from EtOH gave pure **2***a* dihydrochloride (234 mg, 5.97 × 10^6 dpm/mmol, 85% yield).

*Preparation of [1′-^{14}C]-cytosinine, 3*a

A sample of [1′-^{14}C]-**1** hydrochloride (320 mg, 0.70 mmol, 3.85 × 10^6 dpm/mmol) was dissolved in 3 N H_2SO_4 (10 mL), and heated to 90°C for 40 h (18). The mixture was neutralized with $BaCO_3$ to pH 4.0, and the precipitate was removed by centrifugation at 3000 × *g* for 10 min. The supernatant was applied to an anion exchange column (Amberlite, IRA-410, 100 mesh, OH–, 2.5 cm × 30 cm), and the initial effluent discarded. The column was washed with H_2O (ca. 100 mL) to pH < 9 and then eluted with 0.5 N HCl. Fractions of ca. 20 mL were collected and monitored for **3** by HPLC (see conditions below; t_R = 3.4 min). Appropriate fractions were lyophilized and the crude product was recrystallized from H_2O–acetone to obtain pure **3***a* (69.4 mg, 3.54 × 10^6 dpm/mmol, 40% yield).

*Feeding [1′-^{14}C]-cytosinine, 3*a

A sample of **3***a* (9.3 × 10^5 dpm) was dissolved in deionized H_2O (10 mL) and fed sterilely by filtering through a Gelman membrane filter (Product No. 4192, pore size 0.2 μm) into a 200 mL production culture (synthetic medium) (18) 42 h after inoculation with a seed culture. After an additional 80 h, the fermentation was bioassayed (95 mg of **1** had been produced) and worked up as previously described (16) to yield 29.0 mg of pure **1**. Liquid scintillation counting revealed that this material was not radioactive.

*Feeding [1′-^{14}C]-blastidic acid, 2*a

A sample of **2***a* (1.1 × 10^6 dpm) was dissolved in deionized H_2O (10 mL) and fed sterilely in two equal portions to a 200 mL production culture (synthetic medium) 48 and 72 h after inoculation with a seed culture. After an additional 72 h, the fermentation was bioassayed (122 mg of **1** had been produced) and worked up as previously described to yield 29.4 mg of pure **1**. Liquid scintillation counting revealed that this material was not radioactive.

β-N-*Acetylcytosyl-2′,3′,4′,6′-tetrabenzoylglucose, 10*

N-Acetylcytosine (19) (215 mg, 1.40 mmol) and $Hg(CN)_2$ (783 mg, 3.10 mmol) were suspended in 6 mL of nitromethane in a dry 50-mL round-bottom flask. A distillation head was attached, the mixture heated, and ca. 1 mL of solvent was distilled. At this point, the heat was removed and α-1-bromotetrabenzylglucose (20) (923 mg, 1.40 mmol) in CH_2Cl_2 (1 mL) was added dropwise from the top of the distillation head. An additional aliquot of nitromethane (1 mL) was added, and the mixture once again heated at reflux. After 4.5 h, the yellow suspension was cooled to 0°C and filtered. The solid was washed with cold nitromethane, 30% aqueous KI, water, and EtOH. After standing overnight, a second crop could be recovered from the filtrate, and this was washed as described above. The combined solids were recrystallized from DMF–water to give 567 mg (77%): mp 250°C (dec.); IR: 1778, 1739, 1717 cm^{-1}; ^{1}H NMR (TFA-d_1) δ: 8.72 (d, 1H, *J* = 7.8 Hz), 8.02 (d, 2H, *J* = 7.6 Hz). 7.93 (d, 2H, *J* = 7.4 Hz), 7.85 (d, 2H, *J* = 7.6 Hz), 7.81 (d, 2H, *J* = 7.6 Hz), 7.69–7.61 (m, 3H), 7.55 (t, 1H, *J* = 7.6 Hz), 7.49–7.32 (m, 9H), 6.74 (bm, 1H), 5.56 (d, 1H, *J* = 9.0 Hz), 6.41 (t, 1H, *J* = 9.5 Hz), 6.15 (t, 1H, *J* = 9.6 Hz), 5.93 (t, 1H, *J* = 9.2 Hz), 4.87 (dd, 1H, *J* = 12.4, 1.9 Hz), 4.81–4.73 (m, 2H), 2.43 (s, 3H); ^{13}C NMR (TFA-d_1) δ: 178.54, 178.36, 172.63, 171.76, 171.59, 162.24, 161.54, 155.83, 154.05, 149,58, 148.34, 138.25, 138.03, 137.82, 137.61, 132.58, 132.45, 131.61, 131.53, 131.36, 130.39, 129.53, 129.01, 99.57, 85.96, 78.29, 76.60, 75.24, 71.96, 65.64, 25.93. Anal. calcd. for $C_{40}H_{13}N_3O_{11}$: C 67.52; H 1.84, N 5.91; found: C 67.60, H 1.70, N 5.84.

β-N-*Acetylcytosyl-2′,3′,4′,6′-tetrabenzoyl[1-^{2}H]glucose, 10*a

Using the same procedure, α-1-bromotetrabenzoyl[1-^{2}H]glucose (618 mg, 0.94 mmol), *N*-acetylcytosine (148 mg, 0.96 mmol), and $Hg(CN)_2$ (5.34 mg, 2.11 mmol) yielded 474 mg (66%) of **10***a*: ^{1}H NMR lacked the δ: 6.56 doublet, and the δ 5.93 triplet was a doublet (*J* = 9.5 Hz); ^{13}C NMR δ: 85.96 (bt).

β-*Cytosylglucose, 8*

Sodium (2 mg, 0.08 mmol) in a 25-mL round-bottom flask was washed with hexane, dried in a stream of N_2, and reacted with MeOH (2 mL) under a N_2 atmosphere. **10***a* (423 mg, 0.58 mmol) was added, followed by an additional 2 mL MeOH. The suspension was stirred at room temperature (RT) for 25 h, diluted with CH_2Cl_2 (10 mL), cooled to 0°C, and centrifuged. The resulting hygroscopic solid was dissolved in water and lyophilized to yield a fluffy white solid (113 mg, 71%) that had to be protected from moisture: ^{1}H NMR (D_2O) δ: 7.07 (d, 1H, *J* = 7.6 Hz), 6.06 (d, 1H, *J* = 7.7 Hz), 4.05 (d, 1H, *J* = 9.1 Hz), 3.90 (dd, 1H, *J* = 12.5, 2.0 Hz), 3.77 (dd, 1H, *J* = 12.5, 5.2 Hz), 3.72 (dd, 1H, *J* = 9.0, 9.1 Hz), 3.67 (t, 1H, *J* = 8.8 Hz), 3.65–3.61 (m, 1H), 3.53 (dd, 1H, *J* = 9.3, 9.2 Hz); ^{13}C NMR (D_2O) δ: 167.53, 159.45, 143.43, 98.51, 84.76, 80.20, 77.82, 72,75, 70.70, 62.09. Anal. calcd. for $C_{10}H_{15}N_3O_6$: C 43.96, H 5.53, N 15.39; found: C 43.90, H 5.62, N 15.11.

β-*Cytosyl[1-^{2}H]glucose, 8*a

Using the same quantities, **10***a* was deprotected to yield **8***a* (105 mg, 66%): ^{1}H NMR lacked the δ 4.05 doublet and the δ 3.72 triplet was now a doublet (*J* = 9.0 Hz); ^{13}C NMR δ: 85.76 (bt).

Culture maintenance, fermentation, and bioassay conditions

Standard culture maintenance, fermentation, and bioassay conditions have been described previously (16).

Inhibitor/precursor feedings

Inhibitors and precursors were added as sterile-filtered (pore size 0.2 μm) aqueous solutions at 50 h after inoculation of production

Can. J. Chem. Downloaded from www.nrcresearchpress.com by 203.198.23.82 on 09/08/12
For personal use only.

broths (100 mL in 500-mL Erlenmeyer flasks). The quantities of additives were cytosine 30 mg, arginine 200 mg, methionine 200 mg, aminooxyacetic acid 40 mg, 2-methylglutamate 50 mg, arginine hydroxamate 200 mg, 6-diazo-5-oxo-L-norleucine 30 mg, azaserine 31 mg, ethionine 50 mg.

HPLC analysis

For each experiment, 0.5 mL samples were taken at the times noted in the tables, centrifuged 10 min (Eppendorf microfuge), and either immediately analyzed or stored at –20°C. Twenty microlitre aliquots were injected for each analysis. The conditions for analytical HPLC (Waters Assoc. model 600E) were C_{18} RadialPak^R column, 0.8 cm × 10 cm (Waters Assoc. 4 μm packing), eluted with 95% H_2O, 5% CH_3CN, 0.15% TFA, 1.1 mL/min, with a Waters model 990+ photodiode array detector scanning the region 200–300nm. Chromatograms were printed out for absorption at 275 nm.

Results and discussion

A retrobiogenetic analysis fragmented **1** into **2** or β-arginine, itself, and **3**. The reconstruction of **1** from **2** and **3** by a mycelial suspension of *S. griseochromogenes* had been reported (18), but was not reproducible (private communication, H. Seto), and had been tested without the benefit of isotope labels. We, therefore, produced blasticidin S samples from biosynthetic incorporations of [1-^{14}C]arginine and [1-^{14}C]glucose, and hydrolyzed each to yield [1-^{14}C]-**2***a* and [1′-^{14}C]-**3***a*, respectively. Each was fed to cultures of *S. griseochromogenes*, and the blasticidin S produced by each was isolated and purified (16). However, neither sample was radioactive (Scheme 2) and, furthermore, much of the radioactivity had remained in the broth at the end of the fermentations.

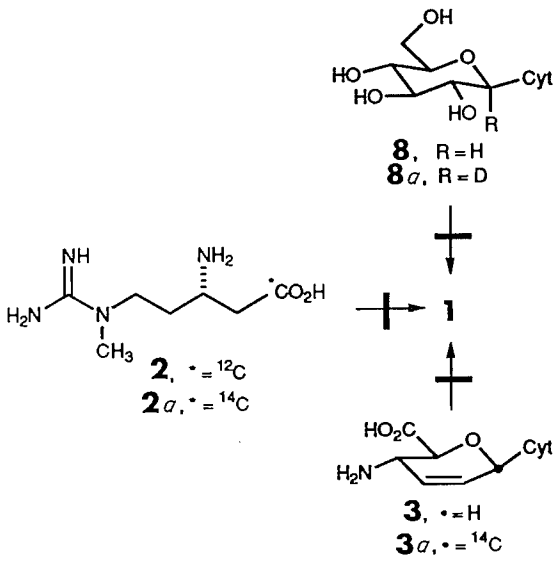

SCHEME 2

We next tested cytosylglucose, **8**, as the first nucleoside intermediate. To test this, [1′-^{2}H]-**8***a* was synthesized as shown in Scheme 3. [1-^{2}H]-D-Glucose, **5***a*, was converted to the 1-bromotetrabenzoate (20) **9***a* and coupled with *N*-acetylcytosine (19) using standard Hg^{2+} catalysis (19). Methoxide then fully deprotected **10***a* to yield **8***a*. In the undeuterated series, a 9.1 Hz coupling between the H-1′ and H-2′ NMR resonances confirmed that the β anomer had been obtained. A sample of **8***a* (100 mg) was fed to a culture of *S. griseochromogenes*, but ^{2}H NMR analysis of the derived **1** failed to show any incorporation of deuterium (Scheme 2).

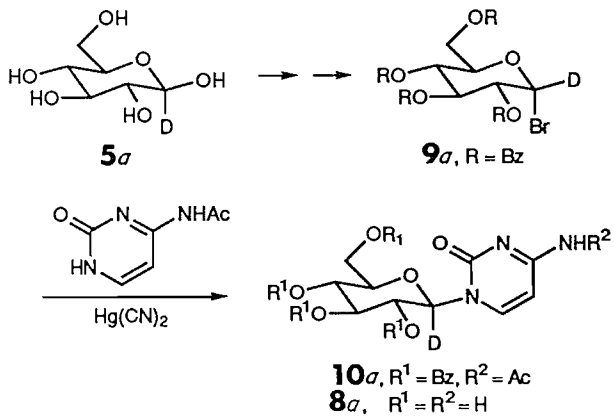

SCHEME 3

Numerous permutations on the same types of biochemical reactions could be proposed for the biosynthesis of **1** from the known precursors. Since each hypothetical sequence involved numerous intermediates, and in view of the negative results described above, it was clear that alternative approaches to conventional feeding experiments were needed to overcome potential permeability problems and to avoid the synthesis of a large number of putative, but incorrect, intermediates. A novel approach was adopted that altered fermentation conditions in order to block potential biosynthetic steps. This was done by feeding inhibitors of specific types of biochemical reactions, and in some cases large quantities of primary precursors were included. These manipulations were expected to distort the biosynthetic precursor pools and force the accumulation of biosynthetic intermediates or new metabolites in the fermentation broth.

Although this empirical approach lacks control over the effects an inhibitor may have at other points in the cellular metabolism, selective inhibition of secondary metabolism with little stress on primary metabolism seemed possible because in most cases the timings of bacterial growth and antibiotic production are well differentiated (21). In comparison with attempting to develop blocked mutants, this approach appeared to offer greater flexibility in selecting the inhibition points.

The selection of inhibitors for these studies was based on three assumptions: (*a*) the 4′-amino group is introduced after the formation of the cytosine glycosidic bond, (*b*) the nucleoside portion is coupled to the β-amino acid portion at a relatively late stage, and (*c*) δ-*N*-methylation occurs late in the overall pathway. Attention was therefore focused on blocking three potential biosynthetic points. These points, and the specific inhibitors tested, were (*a*) blocking transamination with transaminase inhibitors (aminooxyacetic acid (AOAA), **11** (22–24), and 2-methylglutamate (MeGlu), **12** (25)) or amidotransferase inhibitors (azaserine, **13** (26), and 6-diazo-5-oxo-L-norleucine (DON), **14** (27)); (*b*) blocking the availability of L-α-arginine with a L-α-arginine biosynthetic inhibitors (L-arginine hydroxamate (ArgH), **15** (28, 29), and **12**); and (*c*) blocking *N*-methylation with a methyltransferase inhibitor (L-ethionine (Eth), **16** (30, 31)).

To maximize both the effect and selectivity of the inhibitors, it was necessary to first determine the relative timing of bacterial growth and production of **1** (BS) so that inhibitors were fed at the onset of BS production. A synthetic medium (18) was chosen for production broths to simplify the interpretation of the inhibitor results. It was found that the bacteria entered log

Can. J. Chem. Downloaded from www.nrcresearchpress.com by 203.198.23.82 on 09/08/12
For personal use only.

Can. J. Chem. Downloaded from www.nrcresearchpress.com by 203.198.23.82 on 09/08/12
For personal use only.

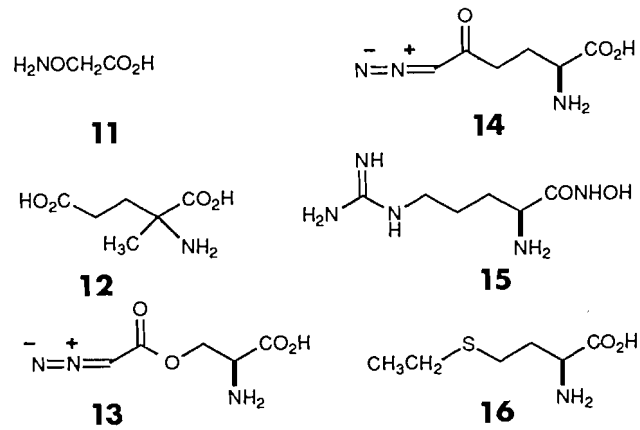

phase right after inoculation of production broths with the seed culture, and reached stationary phase within 84–96 h. **1** was first detected between 50 and 60 h after inoculation, and the accumulation typically lasted for 5 days. Therefore, inhibitors were fed at 50 h. Production of **1** and its related metabolities was initially assayed 168 h later. HPLC conditions were developed that separated authentic samples of **1**, blasticidin H, **17** (32), and pentopyranine C (PPNC), **18** (33, 34), and a photodiode array detector was used to easily identify new cytosine-containing metabolites.

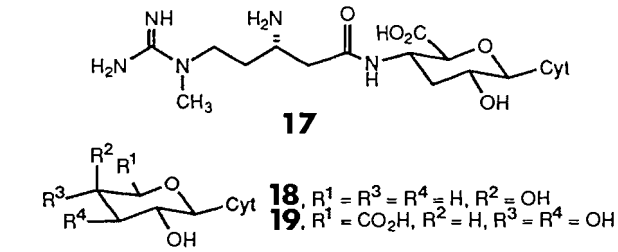

The amounts of inhibitors initially used were comparable to those used in the literature, and some were subsequently adjusted according to the information obtained during the feeding experiments. In several preliminary feedings of either **11** or **15**, the production of two cytosyl metabolites was stimulated as much as 200–300% over a control broth, while the production of **1** was inhibited by 50–70%. One of these metabolites had an HPLC retention time identical to that of authentic **18**, while the other was considerably more polar. Further studies demonstrated that when cytosine was co-fed with either **11** or **15**, production of these two new metabolites was increased dramatically (Fig. 1). These were then purified and identified by NMR spectroscopy. The less polar compound was indeed **18**. The other, which was found to bind to both anion and cation exchange resins, indicating an acid, was identified as cytosylglucuronic acid (CGA), **19**. This compound had previously been isolated in milligram quantities from hundreds of litres of fermentation broth (35). In these latter inhibitor feedings, accumulation of a third new component was also slightly stimulated (ca. 2-fold). Purification by HPLC provided enough material for its identification by ^{1}H NMR spectroscopy as demethylblasticidin S (DeMeBS), **20** (36). Only a slight elevation for **20** was observed with ethionine when assayed at 168 h, although there was also a noticeable decrease in the amount of **1**.

With these initial successes, a more systematic study was developed to examine the effects of **11**, **15**, and **16**, as well as of

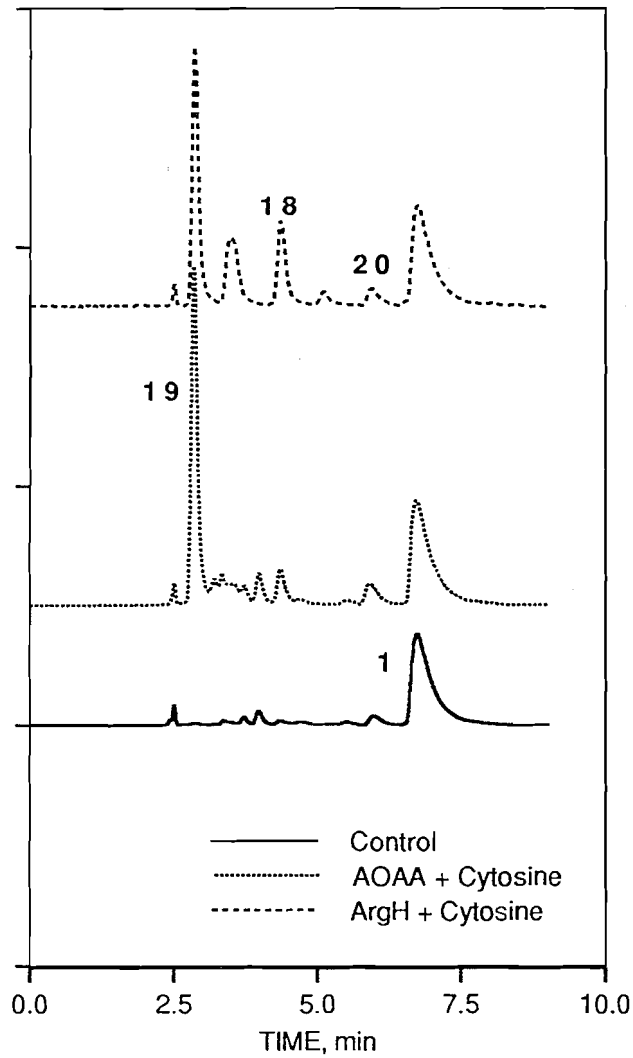

FIG. 1. HPLC of *Streptomyces griseochromogenes* fermentations with and without the addition of cytosine and the enzyme inhibitors aminooxyacetic acid (AOAA), **11**, or arginine hydroxamate (ArgH), **15**. See Experimental for conditions.

12, **13**, and **14**. Some of these inhibitors were also co-fed with the primary precursors cytosine, arginine, and methionine. Fermentations with each inhibitor were assayed at 12 h intervals for the first 4 days, and then daily for the next 3. A number of these were repeated on two or three occasions and, although the absolute amounts varied from one set of fermentations to another (each set was inoculated from the same seed culture for consistency), the relative levels of metabolites were similar. The more significant effects of the inhibitors on CGA (**19**), PPNC (**18**), DeMeBS (**20**), and BS (**1**) production are presented in Tables 1–3. Several trends were apparent, and are summarized as follows.

Feeding the primary precursors **4**, **6**, and **7** (data for the latter two not shown) had a stimulatory effect on the production of all four compounds assayed. Cytosine, which had been incorporated almost quantitatively into **1** as a radiolabeled tracer (13), had a much stronger effect than the other precursors. This was especially true for production of **19**, which was increased 30-fold at 96 h and 71-fold at 168 h. Co-feeding the precursors cytosine and arginine had an additive effect, and was the best

Can. J. Chem. Downloaded from www.nrcresearchpress.com by 203.198.23.82 on 09/08/12
For personal use only.

TABLE 1. The effects of cytosine and of enzyme inhibitors on the production of *S. griseochromogenes* metabolites at 96 h

Additive(s)[a]	CGA (**19**)[b]	PPNC (**18**)[B]	DeMeBS (**20**)[b]	BS (**1**)[b]
Cytosine (**4**)	30.5	10.6	1.5	1.1
AOAA (**11**)	1.9	2.0	0.5	0.6
MeGlu (**12**)	5.6	2.2	0.6	0.5
ArgH (**15**)	1.4	11.9	<0.2	0.4
DON (**14**)	1.2	1.1	0.9	0.8
Azaserine (**13**)	0.7	1.1	1.0	0.9
Ethionine (**16**)	4.1	1.5	2.5	0.6
AOAA/MeGlu	2.1	3.1	0.4	0.3
ArgH/MeGlu	3.1	11.0	0.5	0.2

[a]For amounts fed, see Experimental.
[b]Relative concentration compared to production by a control fermentation to which nothing had been added.

TABLE 2. The effects of enzyme inhibitors on the production of *S. griseochromogenes* metabolites at 120 h

Additive(s)[a]	(**19**)[b]	(**18**)[B]	(**20**)[b]	(**1**)[b]
11	2.4	2.0	0.7	0.8
12	7.0	1.8	1.1	0.7
15	1.1	10.1	<0.1	0.5
14	1.5	1.4	1.0	0.9
13	0.5	1.3	0.9	0.9
16	3.1	2.0	0.8	1.0
11/12	2.8	4.5	0.5	0.5
15/12	2.2	2.7	0.7	0.3

[a]For amounts fed, see Experimental.
[b]Relative concentration compared to production by a control fermentation to which nothing had been added.

TABLE 3. The effects of cytosine and of enzyme inhibitors on the production of *S. griseochromogenes* metabolites at 168 h

Additive(s)[a]	(**19**)[b]	(**18**)[B]	(**20**)[b]	(**1**)[b]
4	70.6	6.4	3.5	1.6
11	3.3	3.2	0.7	0.7
12	7.5	2.1	1.0	0.6
15	1.6	1.9	0.4	0.6
14	1.5	1.4	0.0	0.9
13	0.5	1.2	0.9	0.9
16	3.4	1.7	1.2	0.7
11/12	4.5	2.2	0.4	0.6
15/12	4.1	12.1	0.7	0.4

[a]For amounts fed, see Experimental.
[b]Relative concentration compared to production by a control fermentation to which nothing had been added.

condition for accumulation of **20** (data not shown), presumably by overwhelming the pool of *S*-adenosyl-L-methionine.

Aminooxyacetic acid, **11**, substantially inhibited the production of **1** and **20** while moderately stimulating the production of **18** and **19**. In contrast, the glutamine-dependent amidotransferase inhibitors **13** and **14** showed much milder effects. The effect of **11** also appeared to be quite specific, since its inhibitory effect on the production of **1** could not be relieved by methionine, arginine, or β-arginine.

2-Methylglutamate had effects similar to those of **11**. At 96 h its effects on **18, 20**, and **1** were similar, although it enhanced **19** substantially more. At later time points, the inhibition of **20** was no longer noticeable, but the enhancement of **19** was even more pronounced. These effects were most likely due both to its action as a glutamate/PLP-dependent transaminase inhibitor and as an inhibitor of glutamate biosynthesis; the latter effect would indirectly inhibit arginine biosynthesis. While the effects of arginine hydroxamate, **15**, were very similar to those of **11**, it was particularly efficient, especially in the presence of added cytosine, in stimulating production of **18** (ca. 17-fold at 168 h).

Although in the initial study ethionine, **16**, showed hardly any effect on **20** after 168 h, assay at the earlier times now showed that **16** caused a transitory increase of **20** and decrease of **1**. The production of **20** was highest after 96 h, and decreased afterwards. Possibly **16** was degraded after longer periods of incubation. Nevertheless, the effect of **16** was consistent with our previous proposal that δ:-*N*-methylation occurs at a late stage in the pathway (16).

The effects of these metabolic inhibitors and primary precursors were next examined in fermentations in the standard complex medium (16), which normally produced much more of **1**. Although higher dosages of inhibitors were needed to bring about a comparable extent of inhibition, the same patterns of inhibition and stimulation were observed on the production of all four metabolites (data not shown). By using this system, substantial quantities of **19, 18**, and **20**, which were originally produced only in trace amounts, could now be easily purified (as much as 1.5 g/L of CGA) from a relatively small fermentation (typically 1 L). In addition to the four compounds already identified, HPLC analysis of the crude fermentation broth obtained from the complex medium supplemented by 1.0 g/L of **4** and 2.0 g/L of **15** revealed several new components. Photodiode array detection showed that at least five of those new components had UV spectra characteristic of the cylosine glycosides. Large-scale fermentations under these conditions allowed isolation of sufficient quantities of each to characterize them spectroscopically as **21–25** (37).

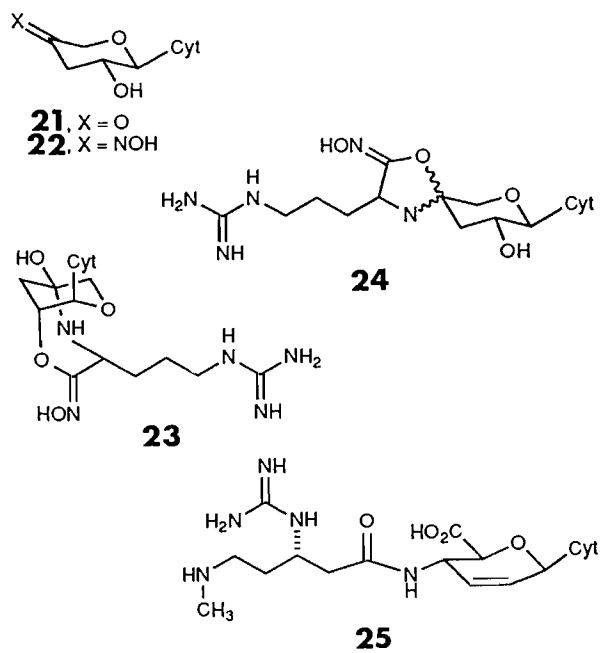

The in vivo use of specific enzyme inhibitors with *S. griseochromogenes* fermentations has led to the accumulation of four otherwise very minor metabolites, including one (**21**) that had

not been previously detected. This has led to an intimate view into the individual biochemical steps that lead to blasticidin S and the metabolic matrix that includes related cytosyl nucleosides. With these large accumulations now possible, **19** was confirmed as the first nucleoside intermediate (38) and CGA synthase, the first prokaryotic glucuronosyltransferase, was isolated and purified (39), demethylblasticidin S was shown to be the last intermediate in the overall pathway by its enzymatic conversion to **1** (40), and the mechanism and stereochemistry of C-3′ deoxygenation was established (41).

Nucleoside antibiotics comprise a large and structurally diverse group of microbial metabolites (42). Considering their numbers and significant biological activities, the sparsity of biosynthetic studies is at first surprising. However, real or anticipated permeability barriers have probably been significant impediments (42). Indeed, many of the most definitive studies have focused on the appendages to the nucleoside sugar (42–44). The in vivo use of specific enzyme inhibitors, which has proved so rewarding in the present study, is likely to be effective with other such "converging" pathways, where individual subpathways can be targeted. We are currently investigating the effects of additional inhibitors on blasticidin biosynthesis, as well as exploring the utility of this approach in probing further into the biosynthesis of streptothricin F.

Acknowledgements

Dr. Y. Miyazaki, Kaken Chemical Co., Ltd., Japan, is thanked for providing a culture of *S. griseochromogenes* and the recipe for the standard growth medium ("complex medium"). Professor H. Seto is thanked for authentic samples of blasticidin H and pentopyranine C. Mr. P.C. Prabhakaran is thanked for preparation of the arginine- and glucose-labeled samples of blasticidin S. This work was supported by Public Health Service Research Grant GM 32110 to S.J.G.

1. S. Takeuchi, K. Hirayama, K. Ueda, H. Sakai, and H. Yonehara. J. Antibiot. Ser. A, **11**, 1 (1958).
2. J.J. Fox and K.A. Watanabe. Tetrahedron Lett. 897 (1966).
3. H. Yonehara and N. Otake. Tetrahedron Lett. 3785 (1966).
4. N. Otake, S. Takeuchi, T. Endo, and H. Yonehara. Agric. Biol. Chem. **30**, 126 (1966).
5. N. Otake, S. Takeuchi, T. Endo, and H. Yonehara. Agric. Biol. Chem. **30**, 132 (1966).
6. S. Onuma, Y. Nawata, and Y. Saito. Bull. Chem. Soc. Jpn. **36**, 1091 (1966).
7. V. Swaminathan, J.L. Smith, M. Sundaralingam, C. Coutsogeorgopoulos, and G. Kartha. Biochim. Biophys. Acta, **655**, 335 (1981).
8. T. Kanzaki, E. Higashide, H. Yamamoto, M. Shibata, K. Nakazawa, H. Iwasaki, T. Takewaka, and A. Miyake. J. Antibiot. Ser. A, **15**, 93 (1962).
9. S. Harada and T. Kishi. J. Antibiot. **31**, 519 (1978).
10. A. Takahashi, D. Ikeda, H. Naganawa, Y. Okami, and H. Umezawa. J. Antibiot. **39**, 1041 (1986).
11. A.D. Argoudelis, L. Baczynskyj, M.T. Kuo, A.L. Laborde, O.K. Sebek, S.E. Truesdell, and F.B. Shilliday. J. Antibiot. **40**, 750 (1987).
12. R. Cooper, M. Conover, and M. Patel. J. Antibiot. **41**, 123 (1988).
13. H. Seto, I. Yamaguchi, N. Otake, and H. Yonehara. Argic. Biol. Chem. **32**, 1292 (1968).
14. S.J. Gould and T.K. Thiruvengadam. J. Am. Chem. Soc. **103**, 6752 (1981).
15. T.K. Thiruvengadam, S.J. Gould, D.J. Aberhart, and H.J. Lin. J. Am. Chem. Soc. **105**, 5470 (1983).
16. P.C. Prabhakaran, N.T. Woo, P. Yorgey, and S.J. Gould. J. Am. Chem. Soc. **110**. 5785 (1988).
17. S.J. Gould, C.H. Tann, P.C. Prabhakaran, and L.R. Hillis. Bioorg. Chem. **16**, 258 (1988).
18. H. Yonehara and N. Otake. Antimicrob. Agents Chemother. 855 (1965).
19. K.A. Watanabe, M.P. Kotick, and J.J. Fox. J. Org. Chem. **35**, 231 (1970).
20. R.K. Ness, H.G. Fletcher, Jr., and C.S. Hudson. J. Am. Chem. Soc. **72**, 2200 (1950).
21. J.F. Martin and A.L. Demain. Microbiol. Rev. **44**, 230 (1980).
22. D.P. Wallach and N.J. Crittenden. Biochem. Pharmacol. **5**, 323 (1961).
23. D.G. Brunk and D. Rhodes. Plant Physiol. **87**, 447 (1988).
24. A.R. Khomutov, A.G. Gabibov, E.N. Khurs, E.A. Tolosa, A.M. Shuster, E.V. Goryachenkova, and R.M. Khomutov. *In* Biochemistry of Vitamin B_6: Proceedings of the 7th International Congress on Chemical and Biological Aspects of Vitamin B_6 Catalysis. *Edited by* T. Korpela and P. Christen. International Union of Biochemistry Symposium. Birkhauser Verlag, Basel, Boston. 1987. pp. 317–320.
25. B.S. Sukhareva, H.C. Dunathan, and A.E. Braunstein, FEBS Lett. **15**, 241 (1971).
26. O. Kurashashi, M. Nodawatanabe, Y. Toride, T. Takenouchi, K. Akashi, Y. Morinaga, and H. Enei. Agric. Biol. Chem. **51**, 1791 (1987).
27. T. Kida and H. Shibai. Agric. Biol. Chem. **49**, 3231 (1985).
28. K. Nakayama and H. Yoshida. Agic. Biol. Chem. **36**, 1675 (1972).
29. S. Baumberg and A. Mountain, J. Gen. Microbiol. **130**, 1247 (1984).
30. S. Simmonds, E.B. Keller, J.P. Chandler, and V. Duvigneaud. J. Biol. Chem. **183**, 191 (1960).
31. S.L. Neidleman, E. Bienstock, and R.E. Bennett. Biochim. Biophys. Acta, **71**, 199 (1963).
32. H. Seto and H. Yonehara. J. Antibiot. **30**, 1022 (1977).
33. H. Seto. Agric. Biol. Chem. **37**, 2415 (1973).
34. H. Seto, N. Otake, and H. Yonehara. Agric. Biol. Chem. **37**, 2421 (1973).
35. H. Seto, K. Furihata, and H. Yonehara. J. Antibiot. **29**, 595 (1976).
36. H. Seto and H. Yonehara. J. Antibiot. **30**, 1019 (1977).
37. J. Guo and S.J. Gould. Phytochemistry, **31**, 1239 (1993).
38. J. Guo and S.J. Gould. J. Am. Chem. Soc. **113**, 5898 (1991).
39. S.J. Gould and J. Guo. J. Bacteriol. In press.
40. S.J. Gould and J. Guo. Bioorg. Med. Chem. Lett. **1**, 497 (1991).
41. S.J. Gould and J. Guo. J. Am. Chem. Soc. **114**, 10176 (1992).
42. K. Isono. J. Antibiot. **41**, 1711 (1988).
43. R.J. Parry, V. Bornemann, and R. Subramanian. J. Am. Chem. Soc. **111**, 5819 (1989).
44. S. Miyakoshi, H. Haruyama, T. Shioiri, S. Takahashi, A. Torikata, and M. Yamazaki. J. Antibiot. **45**, 394 (1992).

Can. J. Chem. Downloaded from www.nrcresearchpress.com by 203.198.23.82 on 09/08/12
For personal use only.

Direct NMR evidence for the equivalent participation of L-phenylalanine and L-tyrosine in the biosynthesis of the intermolecular Diels–Alder type adducts of prenylchalcone and prenylated 2-arylbenzofuran in *Morus alba* cell cultures[1]

YOSHIO HANO AND TARO NOMURA[2]
Faculty of Pharmaceutical Sciences, Toho University, 2-2-1, Miyama, Funabashi, Chiba 274, Japan

AND

SHINICHI UEDA[2]
Faculty of Pharmaceutical Sciences, Kyoto University, Sakyo-ku, Kyoto 606-01, Japan

Received June 21, 1993

This paper is dedicated to Professors Ian Spenser and David B. MacLean.

YOSHIO HANO, TARO NOMURA, and SHINICHI UEDA. Can. J. Chem. **72**, 12 (1994).

L-[3-^{13}C]Phenylalanine and L-[3-^{13}C]tyrosine were administered to *Morus alba* cell cultures, to produce intermolecular Diels–Alder type adducts of a prenylchalcone and a 2-arylbenzofuran such as chalcomoracin (**1**) as well as the adducts of two molecules of prenylchalcones such as kuwanon J (**2**) in high yields. The ^{13}C NMR spectra of **1** and **2** isolated from the cultures revealed that both amino acids were incorporated intact into chalcomoracin (**1**) and kuwanon J (**2**). This is the first example of direct NMR evidence for the almost equivalent incorporation of phenylalanine and tyrosine into the shikimate metabolites. This finding suggests the participation of a biosynthetic route from phenylalanine via *trans*-cinnamate to *p*-coumarate and from tyrosine to *p*-coumarate in this plant.

YOSHIO HANO, TARO NOMURA et SHINICHI UEDA. Can. J. Chem. **72**, 12 (1994).

On a introduit de la L-[3-^{13}C]phénylalanine et de la L-[3-^{13}C]tyrosine à des cultures de cellules *Morus alba* et il y a production, avec des rendements élevés, d'adduits de type Diels–Alder intermoléculaires d'une molécule de prénylchalcone avec un 2-arylbenzofurane, comme la chalcomoracine (**1**), et des adduits avec deux molécules de prénylchalcones, comme la kuwanone J (**2**). Les spectres RMN du ^{13}C des composés **1** et **2** révèlent que les deux acides aminés sont incorporés intacts dans ces composés. Ceci est le premier exemple de preuve RMN directe pour l'incorporation pratiquement équivalente de la phénylalanine et de la tyrosine dans des métabolites de l'acide shikimique. Ces résultats suggèrent que dans cette plante, il y a participation d'une voie biosynthétique permettant de transformer avec autant de facilité la phénylalanine et la tyrosine en *p*-coumarate alors que la transformation de la phénylalanine se fait par le biais d'un *trans*-cinnamate.

[Traduit par la rédaction]

Introduction

In previous papers (1–3), we reported the biosynthesis of optically active intermolecular Diels–Alder type adducts such as chalcomoracin (**1**) (4, 5) and kuwanon J (**2**) (6) with the aid of *Morus alba* cell cultures having a high pigment productivity (5). Many other possible biosynthetic Diels–Alder type constructions have also been reported (7–31). An experiment with administration of ^{13}C-labelled acetate to the cell cultures demonstrated that **1** and **2** are composed of two cinnamoylpolyketide-derived skeletons (1). Administration of the *O*-methylated precursory chalcones revealed that **1** and **2** are biosynthesized through an intermolecular Diels–Alder type cycloaddition reaction between a prenyl portion of the prenylchalcone as a diene and an α,β-unsaturated bond of the chalcone skeleton as a dienophile (2). Further administration experiments with [2-^{13}C]-labelled acetate demonstrated that the isoprenyl unit of **1** was labelled with ^{13}C in a different way from that of β-sitosterol co-occurring in the cell cultures (3). Although the ^{13}C-labelling pattern of β-sitosterol was consistent with that observed in the case of *Rabdosia japonica* tissue cultures (32), the prenyl unit of **1** was labelled with ^{13}C only at the two successive carbons corresponding to the starter acetate unit for the biosynthesis of mevalonate. This phenomenon implies that the ^{13}C-labelled acetate incorporated into the prenyl unit of **1** was not intact, but one reorganized through at least two passages of the tricarboxylic acid (TCA) cycle (1, 3).

Regarding the biosynthesis of **1** and **2**, recent findings obtained through the administration of ^{13}C-labelled glucose and glycerol revealed that the starter acetate unit is formed directly from the glycolysis, whereas the second and the third acetate units for mevalonate are formed by way of the pentosephosphate cycle (33).

This paper describes clear-cut NMR evidence for the equivalent participation of two aromatic amino acids, L-phenylalanine and L-tyrosine, in the biosynthesis of chalcomoracin (**1**) and kuwanon J (**2**).

Results and discussion

Both chalcomoracin (**1**) and kuwanon J (**2**) are composed of two molecules of cinnamoylpolyketide-derived skeletons (1). In the administration experiment with L-[3-^{13}C]phenylalanine to the *M. alba* cell cultures, a high ^{13}C-enrichment from the amino acid was observed at the C-3 and C-5″ positions of **1** (Fig. 1) as well as at the C-β and C-5″ positions of **2**. The ^{13}C-incorporation on the basis of enriched signal intensity was 33%. This finding indicates that the two cinnamoyl units in **1** and **2** originate from L-phenylalanine. An analogous experiment with L-[3-^{13}C]tyrosine also showed the same ^{13}C-labelling pattern as in the case of L-[3-^{13}C]phenylalanine. The ^{13}C-incorporation was 18%. Both L-tyrosine and L-phenylalanine are thus precursory to the prenylchalcones and prenylated arylbenzofurans in *M. alba* cell cultures.

Transformation of L-phenylalanine into L-tyrosine by direct

[1]Dedicated to Ian Spenser and David MacLean with appreciation and respect for their imaginative contributions on natural product chemistry.

[2]Authors to whom correspondence may be addressed.

Can. J. Chem. Downloaded from www.nrcresearchpress.com by 203.198.23.82 on 09/08/12
For personal use only.

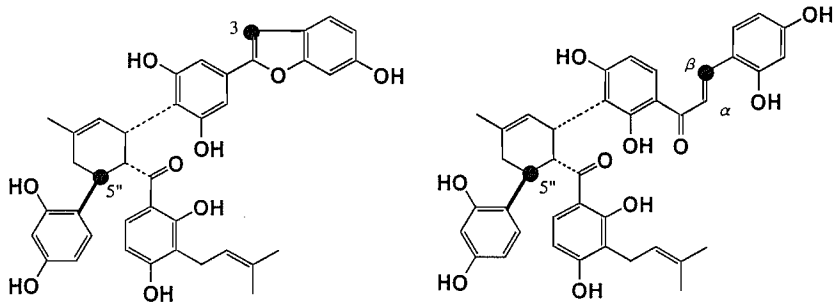

1 2

FIG. 1. ^{13}C labelling patterns of **1** and **2** in the administration experiments with L-[3-^{13}C]phenylalanine and L-[3-^{13}C]tyrosine. ●: ^{13}C-labelled positions.

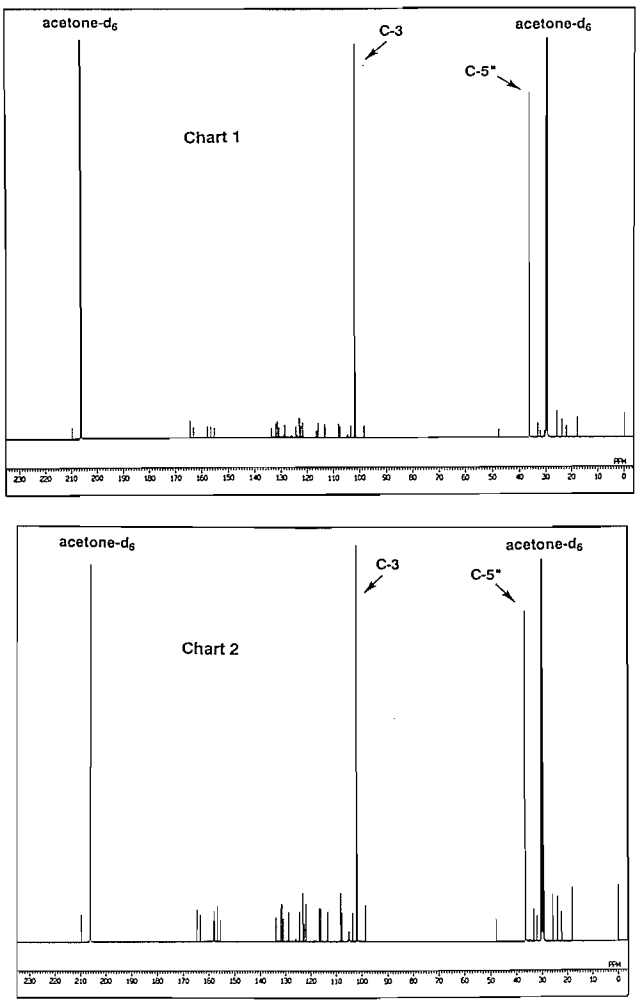

FIG. 2. Proton noise-decoupled ^{13}C NMR spectra. Chart 1: L-[3-^{13}C]phenylalanine-derived chalcomoracin (**1**); Chart 2: L-[3-^{13}C]tyrosine-derived chalcomoracin (**1**).

hydroxylation has been well established in mammal cells (34). An enzyme system isolated from spinach leaves also hydroxylated L-phenylalanine into L-tyrosine (35). In higher plants, however, direct conversion of L-phenylalanine into L-tyrosine has been rare (36).It has also been reported that the overlapping of the secondary metabolites from L-phenylalanine with those from L-tyrosine is restricted, because of the presence of two independent metabolic pathways for these aromatic amino acids in the biosynthesis of rosmarinic acid in *Mentha arvensis* and *Mentha piperita* (37). L-Phenylalanine has been known to be converted to *trans*-cinnamate, which, in turn, is subjected to 4-hydroxylation giving rise to *p*-coumarate through the action of cinnamate 4-hydroxylase in higher plants (38). The present study suggests that both L-phenylalanine and L-tyrosine are converted into *p*-coumarate, which is conclusively converted to chalcomoracin (**1**) and kuwanon J (**2**) in *M. alba* cell cultures.

Experimental

Materials and instruments

L-[3-^{13}C]Phenylalanine (99 at.% ^{13}C) and L-[3-^{13}C]tyrosine (99.8 at.% ^{13}C) were purchased from Isotec Inc., U.S.A. Wakogel C200 and B-5F (Wako Pure Chem. Osaka, Japan) were used for column chromatography and preparative thin-layer chromatography (TLC), respectively. The NMR data were recorded on a JEOL JNM EX-400 FTNMR spectrometer using $(CD_3)_2CO$ as a solvent and TMS as an internal standard. HPLC was carried out with an SSC (Senshu Scientific Co. Ltd., Tokyo) high-pressure liquid chromatograph with a UV detector using a Senshu Pak Silica-4251-N column (10 mm ϕ × 250 mm).

Administration experiment with L-[3-^{13}C]-phenylalanine

The induction of *M. alba* callus tissues from the seedlings or the leaves of a mulberry tree was described previously (5). The *M. alba* cells, placed in 10 300-mL flasks, were suspended each in 100 mL of sterilized water to which a 10% ethanol solution (10 mL) of L-[3-^{13}C]phenylalanine (137.9 mg) containing two drops of Tween 80 was added. After incubation of the cell suspension for 1 week in the dark at 25°C, the cells were harvested and lyophilized. The lyophilized cells (3.27 g) were extracted with methanol. Concentration of the methanol extract in vacuo gave a residue (0.39 g), which was extracted with acetone. The acetone extract was concentrated (0.23 g) and chromatographed on silica gel (70 g) using chloroform with increasing content of acetone as solvent. Combined fractions (0.02 g) eluted with chloroform–acetone (2:1) were subjected to preparative TLC (hexane–acetone 1:1), followed by HPLC (Senshu Pak Silica-4251-N, 10 mm ϕ × 250 mm) eluted with ether, to yield chalcomoracin (**1**, 11 mg) and kuwanon J (**2**, 2 mg), respectively.

Administration experiment with L-[3-^{13}C]tyrosine

L-[3-^{13}C]Tyrosine (116.0 mg) was administered to *M. alba* cell cultures and worked up in an analogous way to the experiment with L-[3-^{13}C]phenylalanine, giving rise to chalcomoracin (**1**, 11 mg) and kuwanon J (**2**, 2 mg), respectively.

1. Y. Hano, T. Nomura, and S. Ueda. Chem. Pharm. Bull. **37**, 554 (1989).
2. Y. Hano, T. Nomura, and S. Ueda. J. Chem. Soc. Chem. Commun. 610 (1990).
3. Y. Hano, A. Ayukawa, T. Nomura, and S. Ueda. Naturwissenschaften, **79**, 180 (1992).
4. M. Takasugi, S. Nagao, T. Masamune, A. Shirata, and K. Takahashi. Chem. Lett. 1573 (1980).

Can. J. Chem. Downloaded from www.nrcresearchpress.com by 203.198.23.82 on 09/08/12
For personal use only.

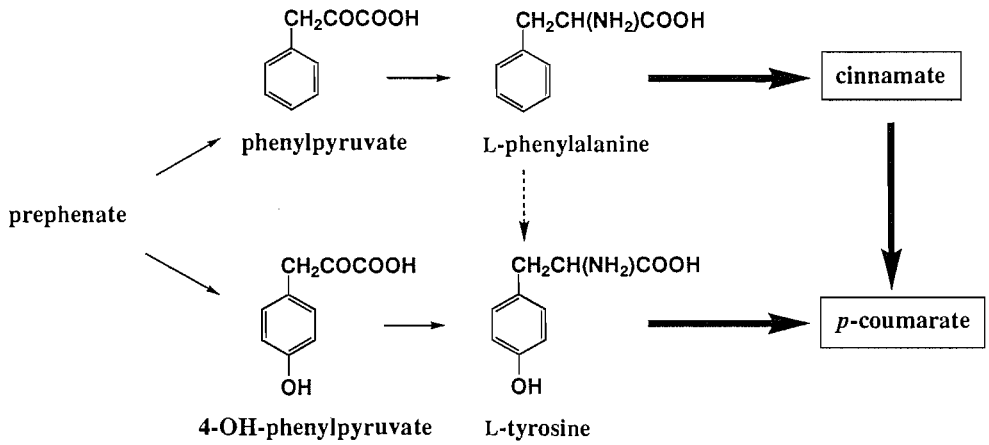

SCHEME 1. The shikimate pathway leading to *p*-coumarate from L-phenylalanine and L-tyrosine.

5. S. Ueda, T. Nomura, T. Fukai, and J. Matsumoto. Chem. Pharm. Bull. **30**, 3042 (1982).
6. J. Ikuta (nee Matsumoto), T. Fukai, T. Nomura, and S. Ueda. Chem. Pharm. Bull. **34**, 2471 (1986).
7. S. Ito and Y. Hirata. Tetrahedron Lett. 2557 (1972).
8. S. Seo, U. Sankawa, Y. Ogihara, Y. Iitaka, and S. Shibata. Tetrahedron, **29**, 3721 (1973).
9. W. Hofheinz and P. Schoenholzer. Helv. Chim. Acta, **60**, 1367 (1977).
10. A.C. Bazan and J.M. Edwards. Tetrahedron, **34**, 3005 (1978).
11. W.M. Bandaranayake and J. E. Banfield. J. Chem. Soc. Chem. Commun. 902 (1980).
12. D.E. Cane and C. Yang. J. Am. Chem. Soc. **106**, 784 (1984).
13. H. Oikawa, A. Ichihara, and S. Sakamura. J. Chem. Soc. Chem. Commun. 814 (1984).
14. W.R. Roush, S.M. Peseckis, and A.E. Walts. J. Org. Chem. **49**, 3429 (1984).
15. R.N. Moore, G. Bigam, J.K. Chan, A.M. Hogg, T.T. Nakashima, and J.C. Vederas. J. Am. Chem. Soc. **107**, 3694 (1985).
16. D.E. Cane and C. Yang. J. Antibiot. **38**, 423 (1985).
17. A. Ichihara, M. Miki, H. Tazaki, and S. Sakamura. Tetrahedron Lett. **28**, 1175 (1987).
18. H. Oikawa, A. Ichihara, and S. Sakamura. J. Chem. Soc. Chem. Commun. 600 (1988).
19. R.M. Williams, E.Kwast, H.Coffman, and T. Glinka. J. Am. Chem. Soc. **111**, 3064 (1989).
20. I. Messana, F. Ferrari, J. Francisco de Mello, and M. do Carmo Mesquita de Araujo. Heterocycles, **29**, 683 (1989).
21. H. Oikawa, T. Yokota, A. Ichihara, and S. Sakamura. J. Chem. Soc. Chem. Commun. 1282 (1989).
22. H. Oikawa, T. Yokota, A. Ichihara, and S. Sakamura. J. Chem. Soc. Chem. Commun. 1284 (1989).
23. J. Kobayashi, M. Tsuda, T. Murayama, H. Nakamura, Y. Ohizumi, M. Ishibashi, M. Iwamura, T. Ohta, and S. Nozoe. Tetrahedron, **46**, 5579 (1990).
24. J.A. Marco, J.F. Sanz, E. Falco, J. Jakupovic, and J. Lex. Tetrahedron, **46**, 7941 (1990).
25. C. Chen and D.J. Hart. J. Org. Chem. **55**, 6236 (1990).
26. I. Messana, F. Ferrari, F. Delle Monache, R.A. Yunes, J.B. Calixto, and T. Biognin. Heterocycles, **32**, 1287 (1991).
27. H. Oikawa, Y. Murakami, and A. Ichihara. J. Chem. Soc. Perkin Trans. 1, 2949 (1992).
28. H. Oikawa, Y. Murakami, and A. Ichihara. J. Chem. Soc. Perkin Trans. 1, 2955 (1992).
29. I.C. Parsons, A.I. Gray, T.G. Hartley, and P.G. Waterman. Phytochemistry, **33**, 479 (1993).
30. D.E. Cane, W. Tan, and W.R. Ott. J. Am. Chem. Soc. **115**, 527 (1993).
31. W.A. Carroll and P.A. Grieco. J. Am. Chem. Soc. **115**, 1164 (1993).
32. S. Seo, A. Uomori, Y. Yoshimura, K. Takeda, H. Seto, Y. Ebizuka, H. Noguchi, and U. Sankawa. J. Chem. Soc. Perkin Trans. 1, 2407 (1988).
33. Y. Hano, A. Ayukawa, T. Nomura, and S. Ueda. Tennen Yuki Kagobutsu Toronkai Koen Yoshishu, 34th 1992. Symposium papers of the 34th Symposium on the chemistry of natural products, Tokyo, October 1992. pp. 780–787.
34. A.R. Moss and P. Schoenheimer. J. Biol. Chem. **135**, 415 (1940).
35. P.M. Nair and L.C. Vining. Phytochemistry, **4**, 401 (1965).
36. U. Weis and J.M. Edwards. The biosynthesis of aromatic compounds. John Wiley & Sons, New York. 1980. p. 144.
37. B.E. Ellis and G.H.N. Towers. Biochem. J. **118**, 291 (1970).
38. H.G. Teutsch, M.P. Hasenfratz, A. Lesot, C. Stoltz, J.-M. Garnier, J.-M. Jetsch, F. Durst, and D. Werck-Reichhart. Proc. Natl. Acad. Sci. U.S.A. **90**, 4102 (1993).

Can. J. Chem. Downloaded from www.nrcresearchpress.com by 203.198.23.82 on 09/08/12
For personal use only.

Oxidative radical cyclization to pyrroles under reducing conditions. Reductive desulfonylation of α-sulfonylpyrroles with tri-*n*-butyltin hydride[1,2]

YULIA ANTONIO, MA. ELIZABETH DE LA CRUZ,[3] EDVIGE GALEAZZI, AND ANGEL GUZMAN
Syntex, S.A. de C.V., División de Investigación, Apartado Postal 517, 62000 Cuernavaca, Morelos, México

AND

BRIAN L. BRAY,[4] ROBERT GREENHOUSE, LILIA J. KURZ, DAVID A. LUSTIG, MICHAEL L. MADDOX, AND JOSEPH M. MUCHOWSKI[5]
Syntex Research, Institute of Organic Chemistry, 3401 Hillview Ave., Palo Alto, CA 94304, U.S.A.

Received January 18, 1993

This paper is dedicated to Professor David B. MacLean

YULIA ANTONIO, MA. ELIZABETH DE LA CRUZ, EDVIGE GALEAZZI, ANGEL GUZMAN, BRIAN L. BRAY, ROBERT GREENHOUSE, LILIA J. KURZ, DAVID A. LUSTIG, MICHAEL L. MADDOX, and JOSEPH M. MUCHOWSKI. Can. J. Chem. **72**, 15 (1994)

1-(2-Bromobenzyl)-2-alkanesulfonylpyrroles (**1***c*, **1***d*) and 1-(4-bromobutyl)-2-methylsulfonfylpyrrols (**8**) undergo oxidative radical cyclization with partial or complete reductive desulfonylation to the pyrrolizidine derivatives **5** and **9** by an AIBN initiated reaction with tri-*n*-butyltin hydride. These cyclizations are suggested to proceed via a pseudo $S_{RN}1$ process involving radical addition to the α position of the pyrrole nucleus not bearing the sulfonyl group. Reductive removal of the alkylsulfonyl moiety is proposed to occur in a second process after completion of the oxidative radical cyclization. The site of the radical addition is supported by deuterium labelling studies. Consistent with the timing of the loss of the sulonyl group is that 2-alkysulfonylpyrroles **11** are reductively desulfonylated under the same conditions that effect the oxidative radical cyclizations.

YULIA ANTONIO, MA. ELIZABETH DE LA CRUZ, EDVIGE GALEAZZI, ANGEL GUZMAN, BRIAN L. BRAY, ROBERT GREENHOUSE, LILIA J. KURZ, DAVID A. LUSTIG, MICHAEL L. MADDOX et JOSEPH M. MUCHOWSKI. Can. J. Chem. **72**, 15 (1994)

Lorsqu'ils sont soumis à une réaction initiée par l'AIBN et l'hydrure de tri-*n*-butylétain, les 1-(2-bromobenzyl)-2-alcanesulfonylpyrroles (**1***c*,**1***d*) et les 1-(4-bromobutyl)-2-méthylsulfonylpyrroles (**8**) subissent une cyclisation radicalaire oxydante accompagnée d'une désulfonylation réductrice partielle ou complète conduisant aux dérivés pyrrolizidine **5** et **9**. Il y a des indications à l'effet que ces cyclisations se produisent par le biais d'un processus pseudo $S_{RN}1$ impliquant une addition radicalaire sur la position α du noyau du pyrrole ne portant pas le groupe sulfonyle. Il est suggéré que l'élimination réductrice de la portion alkylsulfonyle se produit au cours d'un deuxième processus, après la cyclisation radicalaire oxydante. Le site de l'addition radicalaire est en accord avec les études de marquage au deutérium. En accord avec la séquence des réactions, il faut noter que les 2-alkylsulfonylpyrroles (**11**) sont désulfonylés d'une façon réductrice dans les conditions conduisant aux cyclisations radicalaires réductrices.

[Traduit par la rédaction]

Several years ago we embarked on a research program, the objective of which was to study the reactions of pyrroles with alkyl and aryl radicals. Although both radical addition and radical substitution reactions of pyrrole derivatives had been reported at that time (1, 2), only arylation had been systematically studied and was of preparative significance (see ref. 1 for a summary of these studies). Recently, Gravel et al. (3) and we (4–6) have reported synthetically useful examples of oxidative radical substitution of pyrrole derivatives in the intra- (3, 4, 6) and intermolecular (5) modes. This article describes our first studies on the intramolecular addition of radicals, generated with tri-*n*-butyltin hydride, to the pyrrole nucleus.

The radical species **2** (Scheme 1) were first selected for study based on the synthetic accessibility[6] of the precursor bromo compounds **1**. It was expected that the allylic radicals **3** generated by the cyclization of **2** would be converted into the dihydro compounds **4** by capture with tri-*n*-butyltin hydride. A closely related radical cyclization to C-2 of indoles has recently been reported by Ziegler and Jeroncic (7). When a solution of equimolar amounts of the bromo compound **1***a* and tri-*n*-butyltin hydride in benzene containing catalytic AIBN was heated at reflux temperature under flood lamp irradiation,[7] 1-benzylpyrrole (**6***a*) was the sole product formed (Table 1). In contrast, slow addition (syringe pump) of tri-*n*-butyltin hydride to the bromoaldehyde **1***b*, under conditions otherwise identical to those used for **1***a*, gave a mixture of two products. The minor material was the reductive debromination product **6***b*, while the major one (43%) was the pyrrole **5***b*, the product of oxidative radical cyclization. This compound was formed even though the reaction was conducted in degassed solution under an inert atmosphere!

The sulfone analog **1***c* of **1***a* was next examined, since such a strong electron-withdrawing substituent ($\sigma_m = 0.60$ for SO_2Me (8)) should decrease the SOMO–LUMO energy difference and accelerate the cyclization process (9) versus that of **1***a* and **1***b* ($\sigma_m = 0.35$ for CHO). Indeed, when **1***c* was subjected to the tri-*n*-butyltin hydride/AIBN reaction in boiling benzene, two new compounds were rapidly formed in 47 and 18% yields, respectively (35% recovered **1***c*, Table 1). The minor component of the

[1]This paper is dedicated to Professor David B. MacLean, an excellent chemist, a true Canadian, a gentleman of the first order, and a friend, in recognition of and admiration for his contributions to organic chemistry.

[2]Contribution no. 857 from the Syntex Institute of Organic Chemistry.

[3]A portion of this research was completed by M. E. De La Cruz in partial fulfillment for a Licienciatura de Quimico Farmaceutico Biologo at the Universidad Autonoma de Chiapas, Tapachula, Chiapas, Mexico.

[4]Syntex Research Postdoctorate Fellow, 1987–1989.

[5]Author to whom correspondence may be addressed.

[6]The syntheses of this and the other starting materials referred to herein are straightforward and are described in detail in the experimental section.

[7]The reactions were considerably slower in the absence of flood lamp irradiation.

Can. J. Chem. Downloaded from www.nrcresearchpress.com by 203.198.23.82 on 09/08/12
For personal use only.

TABLE 1. Oxidative radical cyclization of pyrrole derivatives

Starting material	Methods[a]	Equiv. Bu_3SnH	Time (h)[b]	% Yield (products)
1*a*	A	1.1	48	70(**6***a*)
1*b*	A	1	57(24)	43(**5***b*), <10(**6***b*)
1*c*	B	1.1	8.5	45(**5***a*), 18(**6***c*), 35(**1***c*)
1*c*	B	2.2	5(4)	64(**5***a*), 28(**6***c*)
1*d*	B	1.2	41	47(5a), 53(1d)
7*a*	B	2.1	24	59(7b)
8*a*	B	2	24(5)	60(9a), 7(9b), 17(10a)
8*b*	B	2	40(4)	24(9c), 40(9d), <5(10b), 20(8b)

[a]Method A = heating at reflux + flood lamp irradiation. Method B = heating at reflux.
[b]The number in parentheses is the time elaspsed during the syringe pump addition of tri-*n*-butyltin hydride while the first number refers to the total reaction time, which includes the number in parentheses.

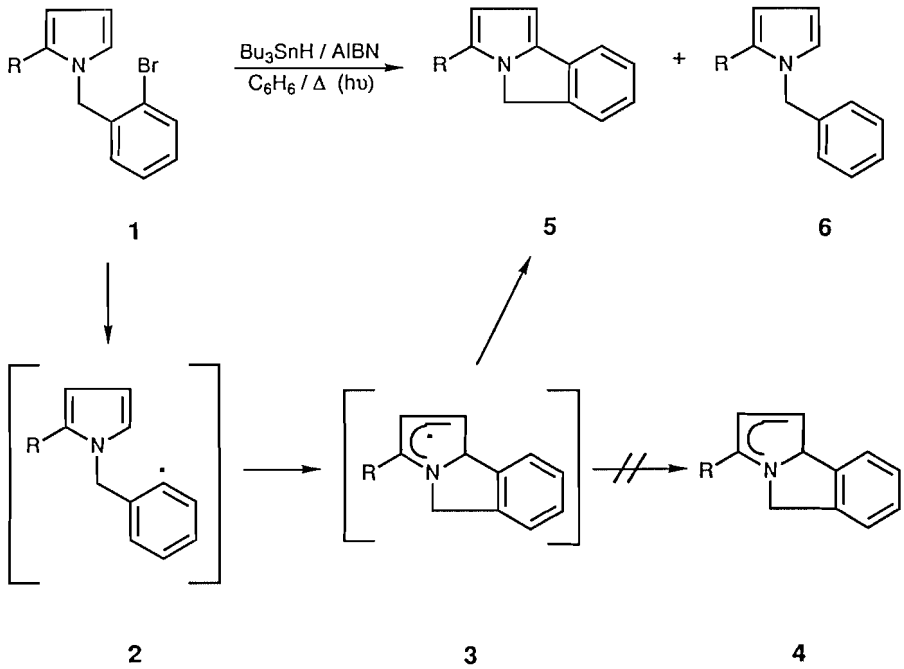

a, R = H
b, R = CHO
c, R = SO_2Me
d, R = $SO_2C_6H_4Me$

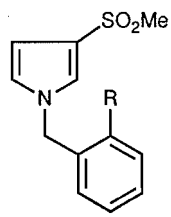

7*a*, R = Br
b, R = H

SCHEME 1

mixture was the reductively dehalogenated material **6***c*, but the major product was not the expected tricyclic sulfone **5***c*. The spectroscopic and microanalytical data were, however, fully consistent with structure **5***a*, the formal reductive desulfonylation product of **5***c*! When the reaction was effected with 2 equivalents of tri-*n*-butyltin hydride, **1***c* was consumed in <5h and **5***a* and **6***c* were isolated in 64 and 28% yields, respectively. Although the reactions were not studied in detail, compound **5***a* was also obtained from the *p*-tolylsulfone **1***d* but not from the 3-methylsulfonyl derivative **7***a*. Only the debrominated sulfone **7***b* was formed in the latter case.

The oxidative radical cyclization could also be effected with alkyl radical species. Thus, reaction of 1-(4-bromobutyl)-2-methylsulfonylpyrrole (**8***a*, Scheme 2) with 2 equivalents of tri-

Can. J. Chem. Downloaded from www.nrcresearchpress.com by 203.198.23.82 on 09/08/12
For personal use only.

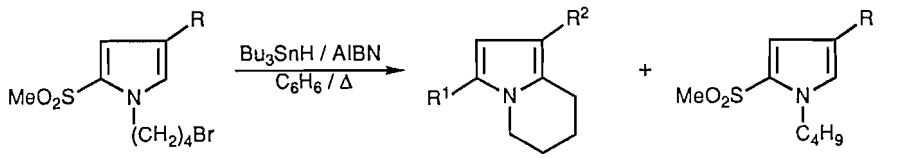

8*a*, R = H
b, R = COPh

9*a*, $R^1 = R^2 = H$
b, $R^1 = MeSO_2$, $R^2 = H$
c, $R^1 = H$, $R^2 = COPh$
d, $R^1 = MeSO_2$, $R^2 = COPh$

10*a*, R = H
b, R = COPh

SCHEME 2

n-butyltin hydride, as for **1***c*, gave the known (10) pyrrolopyridine derivative **9***a* (60%), a small amount of the corresponding sulfone **9***b*, and the reductively debrominated compound **10***a* (Table 1). The 4-benzoyl congener **8***b* of **8***a* gave an analogous mixture of products except that now the major bicyclic product was the sulfone **9***b*.

The formation of compounds **9***b* and **9***d* suggested that the sulfones might be intermediates in the generation of the reductively desulfonylated products. Consistent with this supposition, 1-benzyl-2-methylsulfonylpyrrole (**11***a*, Scheme 3 and Table 2) was reduced to 1-benzylpyrrole (**12***a*) in over 70% yield by 1 equivalent of tri-*n*-butyltin hydride. In fact, this process has some degree of generality as shown by the data in Table 2. The reductive desulfonylation of arylsulfonyl compounds under such mild conditions is totally unprecedented; this type of reduction has only been reliably accomplished by various heterogeneous nickel based reagents (11). The process described herein seems, however, to be restricted to 2-sulfonylpyrroles, since both 1-benzyl-3-methylsulfonylpyrrole (**7***b*, Scheme 1) and diphenylsulfone were unaffected under the above conditions.[8,9]

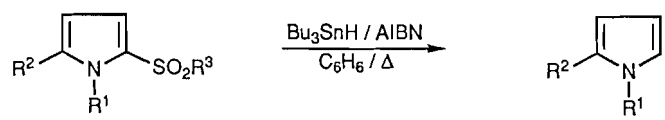

11 **12**

SCHEME 3

The radical cyclizations in which compounds **5***a*, **5***b*, and **9***a*–**9***d* were formed are particularly intriguing since no apparent oxidant is present nor were products indicative of disproportionation processes observed. With regard to the sulfone-derived radicals, it was shown that an ipso addition process with subsequent loss of $RSO_2^{\cdot}$ was not a significant pathway for aromatization since compound **13** (Scheme 4) labelled with deuterium at C-5 (and partially deuterated at C-3,4)[10] gave a 5*H*-pyrrolo[2,1]isoindole **19** with at least 88%[11] loss of this deuterium atom by nmr, i.e., cyclization via **17** and not **15**.[12]

What then is the mechanism by which the radicals **3** (Scheme 1) and the related species from **8** (Scheme 2) are oxidized to the aromatic systems? We suggest, with the deuterium-labelled substrate **13** (Scheme 4) serving as an example, that tri-*n*-butyltin hydride functions as a base, removing the relatively acidic deuteron from the cyclic radical **16** to produce a radical anion **17**. **17** then undergoes single electron transfer with the starting material to give the radical **14** and the primary product **18**, which is subsequently reduced to **19**. Such a pseudo $S_{RN}1$ mechanism has recently been proposed by Bowman et al. (12) to rationalize various oxidative cyclizations in radical reactions, using tri-*n*-butyltin hydride, that they and others have observed.

Experimental

The melting points were determined in a Mel-Temp or a Buchi 510 melting point apparatus and are not corrected. The infrared spectra were measured with a Nicolet 5 PC FT, a Perkin–Elmer 1720, or a Perkin–Elmer 1420 infrared spectrophotometer. The ^1H nmr spectra were measured with a Varian EM-360, a Varian EM-390, a Varian Gemini-200, a Bruker WM 300, or a Bruker AM 500nmr spectrometer in deuteriochloroform and are expressed as parts per million from internal tetramethylsilane. When exchangeable protons were present, the data are given for deuterium oxide exchanged spectra. Those nmr spectra not found in the experimental section can be obtained from the Depository of Unpublished Data.[13] The high-resolution mass spectra were obtained with a Finnigan MAT 311A mass spectrometer on samples that were at least 95% pure as judged by nmr spectrometry.

The terms "worked up in the usual manner" or "the usual work-up" signify that the extract was dried over anhydrous magnesium or sodium sulfate and evaporated in vacuo.

1-(2-Bromobenzyl)pyrrole (1a)

Pyrrole (3.0 g, 44.8 mmol) was added portionwise to a stirred sus-

[8]Alkyl-2-pyrrolylsulfoxides undergo both desulfinylation and deoxygenation under these conditions, e.g., 1-benzyl-2-acetyl-5-methylsulfinylpyrrole was converted into 1-benzyl-2-acetylpyrrole (45%) and 1-benzyl-2-acetyl-5-methylthiopyrrole (14% (M. E. de la Cruz and Y. Antonio, unpublished data)).

[9]We have no data regarding the mechanism of this process.

[10]The method by which deuterium was introduced at C-5 of **13** (see experimental section) also resulted in partial deuteration (ca. 65% by nmr) at C-3,4.

[11]The nmr spectrum of **19** also showed that a small amount (10.5%) of the deuterium label was still present at C-3. This may imply a minor incursion of the ipso aromatization process or that partial scrambling of the label had occurred. Consistent with scrambling is that the nmr of **19** also showed ca. 25% loss of the label from C-1,2, although it is not obvious how such scrambling could occur. The mass spectrum shows that 0.90 ± 0.02 D was lost during the formation of **19** from **13** (note that 0.94 D was present originally at C-5 in **13** by nmr).

[12]**Note added in proof:** In contrast, Caddick et al. (26) have recently reported that the radicals derived from 1-halo-2-*p*-toluenesulfonylindoles (Bu_3SnH/AIBN) cyclize at C-2 to produce species that aromatize by loss of the *p*-toluenesulfonyl radical (i.e., by an addition–elimination process).

[13]These spectra can be purchased from: The Depository of Unpublished Data, Document Delivery, CISTI, National Research Council Canada, Ottawa, ON K1A 0S2, Canada.

Can. J. Chem. Downloaded from www.nrcresearchpress.com by 203.198.23.82 on 09/08/12
For personal use only.

TABLE 2. Synthesis of pyrroles **12** by reductive desulfonylation of 2-pyrrolylsulfones **11** with tri-*n*-butyltin hydride

Starting material	R^1	R^2	R^3	Time (h)	Equivalents Bu_3SnH	Equivalents AIBN	Solvent for tlc	Product[a] (%)	Recovered starting material
11*a*	$PhCH_2$	H	Me	22	1.1	0.4	CH_2Cl_2–hexane (1:4)	**12***a*[b] (73)	13
11*b*	$PhCH_2$	H	Ph	7	2.2	0.66	CH_2Cl_2–hexane (1:4)	**12***a* (84)	13
11*c*	$PhCH_2$	CHO	Me	5	2.2	0.66	Hexane–EtOAc (7:3)	**12***b*[c] (40)	8
11*d*	H	COMe	Me	17	2.2	0.66	Hexane–EtOAc (4:1)	**12***c*[d] (58)	—
11*e*	Me	COMe	Me	5	2.2	0.66	CH_2Cl_2	**12***d*[e] (64)	—
11*f*	$PhCH_2$	COMe	Me	6	2.2	0.66	Hexane–EtOAc (7:3)	**12***e* (62)	—
11*g*	Me	COPh	Me	9	3.3	0.99	Hexane–EtOAc (85:15)	**12***f* (52)	31
11*h*	$PhCH_2$	COPh	Me	14	2.2	0.66	Hexane–EtOAc (9:1)	**12***g* (36)	—

[a]Identity of known compounds established by direct comparison with authentic specimens.
[b]Reference 23.
[c]Reference 22.
[d]Reference 24.
[e]Reference 25.

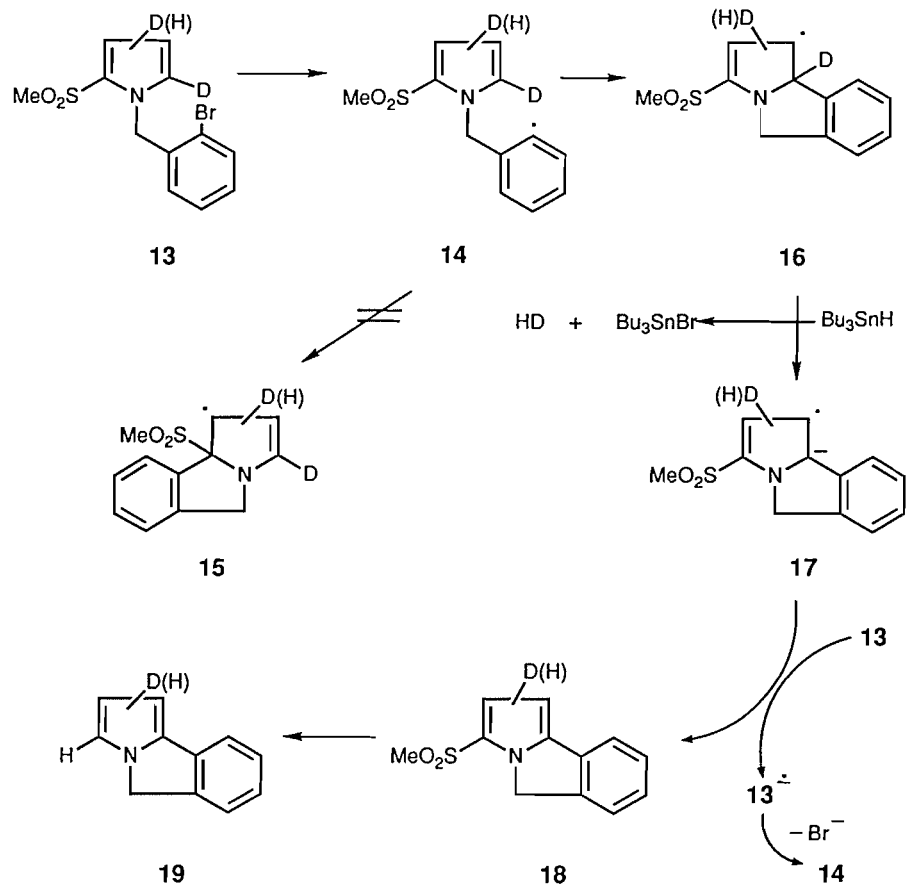

SCHEME 4

pension of sodium hydride (60% in mineral oil, 2.0 g, 50 mmol) in anhydrous dimethylformamide (100 mL) at 0°C (nitrogen atmosphere). Stirring was then continued at room temperature until hydrogen evolution had ceased (0.25 h). 2-Bromobenzyl bromide (10.0 g, 40 mmol) was added all at once and after 2 h the reaction mixture was poured into water and the product was extracted into ether. The extract was washed with water and after the usual work-up the crude product was purified by distillation to give an oil (8.7 g, 92%), bp 107–109°C/1 Torr (1 Torr = 133.3 Pa). Anal. calcd. for $C_{11}H_{10}BrN$: C 55.96, H 4.27, N 5.93; found: C 55.87, H 4.63, N 6.18.

*1-(2-Bromobenzyl)pyrrole-2-carboxaldehyde (**1**b)*

This compound was prepared from equimolar quantities of pyrrole-2-carboxaldehyde and 2-bromobenzyl bromide under conditions otherwise identical to those described for **1***a*. After crystallization from ethyl acetate, pure **1***b* (72% yield) had mp 90–92°C. Anal. calcd. for $C_{12}H_{10}BrNO$: C 54.56, H 3.81, N 5.30; found: C 54.34, H 3.79, N 5.04.

*1-(2-Bromobenzyl)-2-methylsulfonylpyrrole (**1**c)*

2-Methylthiopyrrole (13) was alkylated with 2-bromobenzyl bromide as described for **1***b*. The crude product (not characterized) from a 16 mmol reaction was dissolved in dichloromethane (400 mL) and the solution was cooled to 0°C. *m*-Chloroperbenzoic acid (80 wt.%, 7.1 g, 33 mmol) was added with stirring, and after 1 h the reaction mixture was washed with saturated sodium bicarbonate solution, dried over

Can. J. Chem. Downloaded from www.nrcresearchpress.com by 203.198.23.82 on 09/08/12
For personal use only.

Can. J. Chem. Downloaded from www.nrcresearchpress.com by 203.198.23.82 on 09/08/12
For personal use only.

anhydrous potassium carbonate, and the solvent was removed in vacuo. Crystallization of the crude product from hexane – ethyl acetate gave pure **1***c* (3.6 g, 71%), mp 102–103°C; nmr (300)δ: 2.90 (s, 3H, SO_2Me) 5.53 (s, 2H, CH_2), 6.30 (dd, 1H, $J_{3,4}$ = 4.0 Hz, $J_{4,5}$ = 2.7 Hz, H-4), 6.67 (, 1H, H-6′), 6.85 (t, 1H, H-5), 7.03 (dd, 1H, $J_{3,5}$ = 1.9 Hz, $J_{3,4}$ = 4.0 Hz, H-3), 7.18 (m, 1H, H-4′ or H-5′), 7.27 (m, 1H, H-5′ or H-4′), 7.61 (dd, 1H, J_o = 7.8 Hz, J_m = 1.4 Hz, H-3′). Anal. calcd. for $C_{12}H_{12}BrNO_2S$: C 45.87, H 3.85, N 4.45; found: C 45.82, H 3.90, N 4.38.

*1-(2-Bromobenzyl)-2-(4-methylphenylsulfonyl)pyrrole (**1**d)*

1-(2-Bromobenzyl)pyrrole (**1***a*) was reacted with an equilmolar amount of *p*-toluenesulfinylchloride (14) in the presence of triethylamine as described by Carmona et al. (15, Method C). The crude 1-(2-bromobenzyl)-2-(4-methylphenylsulfinyl)pyrrole from a 19.6 mmol reaction was then oxidized to the sulfone with *m*-chloroperbenzoic acid (37 mmol) as described for **1***c*. The crude product on crystallization from hexane – ethyl acetate gave pure **1***d* (5.0 g, 65%), mp 141–142°C. Anal. calcd. for $C_{18}H_{16}BrNSO_2$: C 55.40, H 4.13, N 3.59; found: C 55.58, H 4.21, N 3.52.

*1-(2-Bromobenzyl)-3-methylsulfonylpyrrole (**7**a)*

2-Methylthiopyrrole was alkylated with 2-bromobenzyl bromide as described for the synthesis of **1***c* and the crude 1-(2-bromobenzyl)-2-methylthiopyrrole (4.0 g, 14 mmol) was dissolved in dichloromethane (75 mL) and cooled to 0°C. *m*-Chloroperbenzoic acid (80%, 2.9 g, 14 mmol) was added to the stirred solution and after 1 h the reaction mixture was worked up as described for **1***c*. The crude 1-(2-bromobenzyl)-2-methylsulfinylpyrrole was dissolved in dichloromethane (50 mL), *p*-toluenesulfonic acid monohydrate (2.6 g) was added, and the solution was stirred at 25°C for 1.5 h. The solution was washed with saturated aqueous sodium bicarbonate solution and water, and then it was worked up in the usual manner. The product was purified by flash chromatography on silica gel using hexane – ethyl acetate – triethylamine (1:1:0.05) to elute pure 1-(2-bromobenzyl)-3-methylsulfinylpyrrole (2.1 g, 50%) as a solid that had mp 75–77°C after crystallization from hexane – ethyl acetate. Anal. calcd. for $C_{12}H_{12}BrNOS$: C 48.33, H 4.05, N 4.69; found: C 48.30, H 4.11, N 4.58.

m-Chloroperbenzoic acid (80 wt.%, 0.60 g, 2.8 mmol) was added to a stirred solution of the above sulfoxide (0.83 g, 2.8 mmol) in dichloromethane (20 mL) at 25°C. After stirring for 2 h at 25°C, the reaction mixture was worked up as for **1***c* to give material that was purified by flash chromatography on silica gel using hexane – ethyl acetate to elute pure **7***a* (0.70 g, 80%) as a solid that on crystallization from hexane – ethyl acetate had mp 122–124°C; nmr (300)δ: 2.81 (s, 3H, SO_2Me), 5.16 (s, 2H, CH_2), 6.54 (dd, 1H, $J_{2,5}$ = 1.8 Hz, $J_{4,5}$ = 2.6 Hz, H-5), 6.80 (t, 1H, H-4), 6.89 (dd, 1H, H-6′), 7.11 (t, 1H, H-2), 7.19 (td, 1H, H-5′), 7.27 (td, 1H, H-4′), 7.59 (dd, 1H, H-3′). Anal. calcd. for $C_{12}H_{12}BrNO_2S$: C 45.87, H 3.85, N 4.45; found: C 45.88, H 3.83, N 4.55.

*1-(4-Bromobutyl)-2-methanesulfonylpyrrole (**8**a)*

A solution of 2-methylthiopyrrole (1.5 g, 13 mmol) in anhydrous DMF (10 mL) was added to a stirred suspension of sodium hydride (60% in mineral oil, 0.58 g, 15 mmol) in dry DMF (100 mL) at 0°C. When hydrogen evolution had ceased (0.5 h), a solution of 1,4-dibromobutane (14.0 g, 66 mmol) in dry DMF (20 mL) was added and the reaction mixture was stirred for 3 h at room temperature. The reaction mixture was poured into water, and the product was extracted into ether. The ether extract was washed successively with water and saturated aqueous sodium chloride solution, and it was then worked up as usual. The crude 1-(4-bromobutyl)-2-methylthiopyrrole was then oxidized to the sulfone with *m*-chloroperbenzoic acid (29 mmol) as described for **1***c*. The crude product was purified by flash chromatography on silica gel using hexane – ethyl acetate (12:1 to 3:1) to elute **8***a* (2.3 g, 61%) as an oil; nmr (300)δ: 1.76–2.10 (m, 4H, CH_2CH_2), 3.11 (s, 3H, SO_2Me), 3.42 (t, 2H, *J* = 6.4 Hz, CH_2Br), 4.26 (t, 2H, *J* = 7.1 Hz, NH_2), 6.23 (dd, 1H, $J_{3,4}$ = 3.58 Hz, $J_{4,5}$ = 3.03 Hz, H-4), 6.89 (m, 2H, H-3, 5). Anal. calcd. for $C_9H_{14}BrNO_2S$: C 38.58, H 5.04, N 4.99; found: C 38.70, H 5.17, N 5.00.

*1-(4-Bromobutyl)-2-methanesulfonyl-4-benzoylpyrrole (**8**b)*

Bromine (5.6 g, 35 mmol) was added dropwise to methanol (25 mL) at –40°C, and this cold solution was added dropwise to a stirred slurry of potassium thiocyanate (7.1 g, 74 mmol) in methanol (25 mL) at –78°C. After 20 min at this temperature, this mixture was added to a stirred solution of 3-benzoylpyrrole (ref. 16, 6.0 g, 35 mmol) in methanol at –78°C. The reaction mixture was warmed to –40°C and after 0.5 h it was poured into water. The product was extracted into ethyl acetate, the extract was washed sucessively with saturated aqueous solutions of sodium bisulfite and sodium chloride, and then it was worked up as usual. Crystallization of the crude product from hexane – ethyl acetate gave pure 2-thiocyano-4-benzoylpyrrole (5.0 g, 63%) mp 180–181°C. Anal. calcd. for $C_{12}H_8N_2OS$: C 63.13, H 3.53, N 12.27; found: C 63.02, H 3.63, N 12.28.

A solution of sodium hydroxide (3.1 g, 78 mmol) in 50% aqueous methanol (30 mL) was added to a stirred solution of the above thiocyanate (7.4 g, 32 mmol) and methyl iodide (5.5 g, 39 mmol) in methanol (40 mL) at 0°C. The solution was then stirred at room temperature for 1.5 h and poured into water. Solid sodium bisulfite was added to bring the solution to pH 6, and the product was extracted into ether. The ether extract was washed with saturated sodium choloride solution and then worked up in the usual manner. The crude product was purified by flash chromatography on silica gel using hexane – ethyl acetate to elute pure 2-methylthio-4-benzoylpyrrole (5.4 g, 77%) as a solid that was used without further characterization in the next step.

A suspension of potassium carbonate (1.5 g, 11 mmol) in acetonitrile (25 mL) containing 2-methylthio-4-benzoylpyrrole (1.5 g, 6.9 mmol) and 1,4-dibromobutane (7.8 g, 36 mmol) was stirred at reflux temperature for 22 h. The cooled mixture was diluted with ethyl acetate (125 mL), then washed with water and saturated sodium chloride solution. After the usual work-up, the crude product was purified by flash chromatography on silica gel using hexane – ethyl acetate (4:1) to give pure 1-(4-bromobutyl)-2-methylthio-4-benzoylpyrrole (1.5 g, 60%), which was used directly in the next step.

A solution of Oxone (3.9 g, 6.3 mmol) in water (30 mL) was added all at once to a stirred solution of the above bromo compound (1.5 g, 4.2 mmol) in methanol (60 mL). The resulting slurry was stirred at room temperature for 3 h and then poured into water. The product was extracted into ethyl acetate; the extract was washed with saturated sodium chloride solution and then worked up as usual. The crude product was purified by flash chromatography on silica gel using hexane – ethyl acetate (3:1 to 1:1) to elute **8***b* as a solid (1.2 g, 73%), mp 99–100°C; nmr (300)δ: 1.90–2.16 (m, 4H, CH_2CH_2), 3.17 (s, 3H, SO_2Me), 3.45 (t, 2H, *J* = 6.34 Hz, CH_2Br), 4.33 (t, 2H, *J* = 7.33 Hz, CH_2N), 7.34 (d, 1H, *J* = 1.96 Hz, H-5), 7.47–7.62 (m, 4H, H-3, 3′, 4′, 5′), 7.83 (m, 2H, H-2′, 6′). Anal. calcd. for $C_{16}H_{18}BrNO_3S$: C 50.00, H 4.72, N 3.64; found: C 49.90, H 4.74, N 3.56.

*1-Benzyl-2-methylsulfonylpyrrole (**11**a)*

2-Methylthiopyrrole was alkylated with benzylchloride in the same manner as described for the synthesis of **1***b* to give 1-benzyl-2-methylthiopyrrole in 90% yield. This compound was converted into the sulfone **11***b* by oxidation with *m*-chloroperbenzoic acid (3.8 equiv., 2 h) as described for the synthesis of **1***c*. The crude product was purified by column chromatography on silica gel using hexane – ethyl acetate (4:1) to give pure **11***a* (67% yield), which had mp 62–63°C; nmr (200)δ: 2.56 (s, 3H, SO_2Me), 5.47 (s, 2H, CH_2), 6.28, (dd, 1H, $J_{3,4}$ = 3.63 Hz, $J_{4,5}$ = 2.95 Hz, H-4), 6.98 (m, 2H, H-3, 5), 7.12–7.17 (m, 2H, H-2′, 6′), 7.29–7.41 (m, 3H, H-3′, 4′, 5′). Anal. calcd. for $C_{12}H_{13}NO_2S$: C 61.25, H 5.57, N 5.95; found: C 61.46, H 5.54, N 5.97.

*1-Benzyl-2-phenylsulfonylpyrrole (**11**b)*

This compound was prepared from 2-phenylsulfonylpyrrole (17) and benzyl chloride in the manner described for the synthesis of **1***b*. Compound **11***b* was obtained as a solid (96% yield) that, after crystallization from dichloromethane–hexane, had mp 128–129°C. Anal.

Can. J. Chem. Downloaded from www.nrcresearchpress.com by 203.198.23.82 on 09/08/12
For personal use only.

calcd. for $C_{17}H_{15}NO_2S$: C 68.66, H 5.08, N 4.71; found: C 68.48, H 4.98, N 4.67.

*1-Benzyl-2-methylsulfonylpyrrole-5-carboxaldehyde (**11**c)*

A mixture of 2-methylthiopyrrole-5-carboxaldehyde (ref. 18, 2.30 g, 16.3 mmol), benzyl chloride (2.68 g, 21.2 mmol), and anhydrous potassium carbonate (11.2 g, 81.4 mmol) in dry DMF (23 mL) was stirred at room temperature for 16 h. The reaction mixture was poured into water, the product was extracted into ethyl acetate, and the extract was washed with water. After the usual work-up, 1-benzyl-2-methylthiopyrrole-5-carboxaldehyde was obtained as an oil (3.57 g, 95% yield); ir (film): 1657 cm^{-1}; nmr (200)δ: 2.35 (s, 3H, MeS), 5.71 (s, 2H, CH_2), 6.30 (d, 1H, J = 4.2 Hz, H-3), 7.00 (d, 1H, J = 4.2 Hz, H-4), 7.08–7.14 (m, 2H, H-2′, 6′), 7.22–7.34 (m, 3H, H-3′, 4′, 5′), 9.44 (s, 1H, CHO). Exact Mass calcd. for $C_{13}H_{13}NOS$: 231.0718; found: 231.0711.

The above sulfide was oxidized to the sulfone **11***c* with *m*-chloroperbenzoic acid (3 equiv., 4 h) as described for the synthesis of **1***c*. The crude product was purified by column chromatography on neutral alumina (Fluka, Act 11) using hexane – ethyl acetate (4:1) to elute **11***c* as a solid (46% yield) that had mp 60–62°C after crystallization from dichloromethane–methanol; ir ($CHCl_3$): 2824, 1682, 1327, 1217, cm^{-1}; nmr (200)δ: 2.58 (s, 3H, SO_2Me), 6.08 (s, 2H, CH_2), 6.95–7.19 (m, 4H, H-3, 4, 2′, 6′), 7.20–7.45 (m, 3H, H-3′, 4′, 5′), 9.85 (s, 1H, CHO). Anal. calcd. for $C_{13}H_{13}NO_3S$: C 59.30, H 4.98, N 5.32; found: C 59.40, H 4.99, N 5.33.

*2-Acetyl-5-methylsulfonylpyrrole (**11**d)*

Phosphorous oxychloride (12.7 g, 82.7 mmol) was added, with stirring under argon, to *N*-acetylmorpholine (10.9 g, 84.4 mmol) at –5°C. The reaction mixture was then stirred at 1 h at room temperature, cooled to 0°C, and a solution of 2-methylthiopyrrole (8.00 g, 70.7 mmol) in anhydrous 1,2-dichloroethane (25 mL) was added. The reaction mixture was stirred for 0.5 h at room temperature and then added cautiously to a solution of sodium carbonate (15 g) in water (160 mL). The two-phase mixture was stirred vigorously at reflux temperature for 2 h and, after cooling to room temperature, the organic phase was separated and combined with a dichloromethane extract of the aqueous phase. The organic phase was washed with saturated salt solution and after the usual work-up the crude product was purified by column chromatography on silica gel using hexane – ethyl acetate (9:1) to elute 2-acetyl-5-methylthiopyrrole as a solid (7.5 g, 68% yield). After crystallization from dichloromethane–hexane, this material had mp 79–81°C; ir ($CHCl_3$): 3437, 3263, 1641, cm^{-1}; nmr (200)δ: 2.41 (s, 3H, MeS or MeCO), 2.47 (s, 3H, MeCO or MeS), 6.24 (d, 1H, J = 3.93 Hz, H-4), 6.87 (d, 1H, J = 3.93 Hz, H-3). Anal. calcd. for C_7H_9NOS: C 54.16, H 5.84, N 9.02; found: C 54.20, H 5.85, N 8.99.

The above sulfide was oxidized to the sulfone **11***d* with *m*-chloroperbenzoic acid (3 equiv., 4 h) as described for **11***c* except that the solid product (90% yield) was eluted from the alumina column with dichloromethane. After crystallization from dichloromethane–hexane, compound **11***d* had mp 119–120°C; ir ($CHCl_3$): 3406, 3269, 1672, 1323, 1188 cm^{-1}; nmr (200)δ: 2.52 (s, 3H, MeCO), 3.18 (s, 3H, $MeSO_2$), 6.90 (q, 2H, J = 4.03, H-3, 4). Anal. calcd. for $C_7H_9NO_3S$: C 44.90, H 4.84, N 7.48; found: C 45.00, H 4.81,N 7.50.

*1-Methyl-2-acetyl-5-methylsulfonylpyrrole (**11**e)*

2-Acetyl-5-methylthiopyrrole was N-methylated using methyl iodide (5 equiv.) in the presence of potassium carbonate (10 mol equiv.) in DMF as described above (see synthesis of **11***c*). 1-Methyl-2-acetyl-5-methylthiopyrrole was obtained as an oil (96% yield); ir (film): 1651 cm^{-1}; nmr (200)δ: 2.39 (s, 3H, MeS or MeCO), 2.42 (s, 3H, MeCO or MeS), 3.96 (s, 3H, NMe), 6.20 (d, 1H, J = 4.23 Hz, H-4), 6.95 (s, 1H, J = 4.23 Hz, H-3). Exact Mass calcd. for $C_8H_{11}NOS$: 169.0561; found: 169.0559.

The above sulfide was oxidized to the sulfone **11***e* exactly as described for the synthesis of **11***d*. Chromatographically pure **11***e* was obtained as a solid (92% yield) that, after crystallization from dichloromethane–hexane, had mp 104–105°C; ir (KBr): 1681, 1307, 1147 cm^{-1}; nmr (200)δ: 2.54 (s, 3H, MeCO), 3.17 (s, 3H, $MeSO_2$), 4.23 (s, 3H, NMe), 6.94 (q, 2H, J = 4.34 Hz, H-3, 4). Anal. calcd. for $C_8H_{11}NO_3S$: C 47.74, H 5.50, N 6.96; found: C 47.83, H 5.51, N 6.90.

*1-Benzyl-2-acetyl-5-methylsulfonylpyrrole (**11**f)*

2-Acetyl-5-methylthiopyrrole was N-benzylated exactly as described above (see synthesis of **11***c*). 1-Benzyl-2-acetyl-5-methylthiopyrrole was obtained as an oil (91% yield). Exact Mass calcd. for $C_{14}H_{15}NOS$: 245.0874; found: 245.0878.

The above sulfide was oxidized to the sulfone **11***f* exactly as described for **11***c*, except that the product was eluted from the alumina column as a solid (83% yield) with hexane – ethyl acetate (85:15). After crystallization from dichloromethane–hexane **11***f* had mp 99–100°C. Anal. calcd. for $C_{14}H_{15}NO_3S$: C 60.62, H 5.45, N 5.05; found: C 60.59, H 5.38, N 5.03.

*1-Methyl-2-benzoyl-5-methylsulfonylpyrrole (**11**g)*

2-Benzoyl-5-methylsulfonylpyrrole (13) was N-methylated using methyl iodide (10 equiv.) in the presence of potassium carbonate (6 equiv.) in DMF as described for the synthesis of **11***c*. Crystallization of the crude product from dichloromethane–methanol gave a solid (64% yield), mp 89–90°C. Anal. calcd. for $C_{13}H_{13}NO_3S$: C 59.29, H 4.95, N 5.31; found: C 59.38, H 5.00, N 5.41.

*1-Benzyl-2-benzoyl-5-methylsulfonylpyrrole (**11**h)*

2-Benzoyl-5-methylsulfonylpyrrole (13) was N-benzylated as described above (see synthesis of **11***c*). Crystallization of the crude product from dichloromethane–methanol gave a solid (60% yield), mp 124–125°C. Anal. calcd. for $C_{19}H_{17}NO_3S$: C 67.23, H 5.05, N 4.12; found: C 67.42, H 4.98, N 4.00.

*Deuterated 1-(2-bromobenzyl)-2-methylsulfonylpyrrole (**13**)*

This compound was not prepared in the manner described above for the protio compound **1***c*. Instead, a synthesis of **13** was devised based on 1-phenylsulfonylpyrrole (19) as the starting material. The synthesis of **13** was carried out in parallel with that of the nondeuterated congener, for which the experimental details are given below.

1-Phenylsulfonylpyrrole (10.0 g) was added in one portion to deuteriotrifluoroacetic acid (prepared by addition of trifluoroacetic anhydride (52.2 mL) to deuterium oxide (20.0 mL, 99.9% D) at 0°C) with stirring (nitrogen atmosphere) at room temperature.[14] After 21 h, the solution was poured into a two-phase mixture of ether and excess saturated aqueous sodium bicarbonate solution. The organic phase was then worked up in the usual way to give deuterated 1-phenylsulfonylpyrrole (10.0 g), which showed 94.0% D (1.88 D) at C-2,5 and 67.6% D (1.32 D) at C-3,4 as determined from a comparison of the nmr signals (300) at δ 7.16 and 6.30 with the benzenoid multiplets at δ 7.48–7.62 and 7.84–7.87. Mass spectral analysis (molecular ions) showed an isotopic composition of 2.4% D_1, 19.5% D_2, 45.1% D_3, and 33.0% D_4 (3.09 D).

The thiocyanation of 1-phenylsulfonylpyrrole was carried out exactly as described by Kakushima and Frenette (20) for the thiocyanation of 1-(4-methylphenylsulfonyl)pyrrole. The crude product was subjected to purification by flash chromatography on silica gel using hexane – ethyl acetate (9:1) as the eluting solvent. A minor (9%) amount of a less polar material, which was 1-phenylsulfonyl-2-thiocyano-5-chloropyrrole, was obtained as an unstable oil. Exact Mass calcd. for $C_{11}H_7ClN_2O_2S_2$: 297.9637; found: 297.9637. The major (70%), more polar product was 1-phenylsulfonyl-2-thiocyanopyrrole, a solid with mp 74–76°C. Anal. calcd. for $C_{11}H_9N_2O_2S_2$: C 49.98, H 3.05, N 10.60; found: C 49.64, H 3.12, N 10.50.

Methyl iodide (1.6 g, 11.3 mmol) and 1 N sodium hydroxide solution (11.4 mL) was added to a stirred solution of 1-phenylsulfonyl-2-thiocyanopyrrole (1.0 g, 3.8 mmol) in methanol (40 mL) at room temperature. After 20 min, the reaction mixture was poured into dilute hydrochloric acid and the product was extracted into dichloromethane.

[14] We thank Dr. R. Frenette, Merck Frosst Canada Inc., Pointe Claire/Dorval, Quebec, for providing us with information regarding this deuteration reaction.

Can. J. Chem. Downloaded from www.nrcresearchpress.com by 203.198.23.82 on 09/08/12
For personal use only.

After the usual work-up, 1-phenylsulfonyl-2-methylthiopyrrole was obtained as a solid (0.97 g, 100% yield) that, after crystallization from dichloromethane–methanol, had mp 91.5–92°C. Anal. calcd. for $C_{11}H_{11}NO_2S_2$: C 52.15, H 4.38, N 5.53; found: C 52.08, H 4.37, N 5.66.

1-Phenylsulfonyl-2-methylthiopyrrole was oxidized to the sulfone with *m*-chloroperbenzoic acid (2 equiv., 1 h) as described for the synthesis of **1***c*. The crude product was purified by column chromatography on Act II neutral alumina using dichloromethane to elute 1-phenylsulfonyl-2-methylsulfonylpyrrole as a solid (91% yield) that, after crystallization from ether – methylene chloride, had mp 133–134°C. Anal. calcd. for $C_{11}H_{11}NO_4S_2$: C 46.30, H 3.89, N 4.91; found: C 46.23, H 3.68, N 5.12.

Sodium hydroxide (1 mL, 1 N) was added to a solution of 1-phenylsulfonyl-2-methylsulfonylpyrrole (0.300 g, 1.05 mmol) in methanol (25 mL) and the mixture was warmed briefly to give a clear solution. The solution was left at room temperature for 0.5 h and then evaporated to dryness in vacuo. Water was added to the residue and the product was extracted into dichloromethane. After the usual work-up, 2-methylsulfonylpyrrole (0.153 g, 100% yeild) was obtained as a solid identical to an authentic specimen (13, 21).

Tetra-*n*-butylammonium bromide (0.30 g), 2-bromobenzylbromide (0.30 g), and 50% sodium hydroxide (1 mL) were added to a solution of 2-methylsulfonylpyrrole (0.153 g) in dichloromethane (25 mL) and the resulting mixture was vigorously stirred at room temperature for 2 h. Additional dichloromethane was added, and the organic phase was separated and worked up in the usual manner. The crude product was purified by column chromatography on silica gel using hexane – ethyl acetate to elute 1-(2-bromobenzyl)-2-methylsulfonylpyrrole (**1***c*) as a solid (0.224 g, 68% yeild) identical to a specimen prepared as described previously. The deuterated compound **13** prepared in the same way had 93.7 ± 3.2% D (0.94 D) at C-5 and 60.7 ± 0.3% D (1.21 D) at C-3,4 as determined by comparison of the integrals for the nmr multiplets of the pyrrole protons to those of the benzenoid multiplets centered at δ 6.67, 7.18, and 7.61. Mass spectral analysis (molecular ions) showed an isotopic composition of 3.5% D_0, 19.5% D_1, 43.5% D_2, and 31.9% D_3.

Oxidative radical cyclizations

*(a) Method A. 5H-Pyrrolo[2,1-a]isoindole-3-carboxaldehyde (**5**b)*

A solution of tri-*n*-butyltin hydride (0.529 g, 1.82 mmol) and azobisisobutyronitrile ((AIBN), 0.040 g) in dry, degassed benzene (10 mL) was added with a syringe pump to a solution of compound **1***b* (0.480 g, 1.82 mmol) in dry, degassed benzene (30 mL), which was irradiated with a 150-W flood lamp and heated at reflux (argon atmosphere) over a 24 h period. The reaction mixture was then heated at reflux while irradiating for an additional 33 h. The solvent was removed in vacuo, the residue was dissolved in ethyl acetate (20 mL), saturated aqueous potassium fluoride (10 mL) was added, and the mixture was agitated vigorously for 2 h. The mixture was filtered, poured into water, and extracted with ether. After the usual work-up, the crude product was purified by flash chromatography on silica gel using hexane – ethyl acetate (8:1) to elute the products. The major product (0.143 g, 43% yield) **5***b* was obtained as a solid together with a very minor amount (≤5%) of the known, oily 1-benzylpyrrole-2-carboxaldehyde (**6***b* (22)). Recrystallization of **5***b* from ethyl acetate gave a solid, mp 128–129°C; ir (KBr): 1653 cm^{-1}; nmr (300)δ: 5.23 (s, 2H, CH_2), 6.48 (d, 1H, J = 4.09 Hz, H-1), 7.10 (d, 1H, J = 4.09 Hz, H-2), 7.35 (td, 1H, J_o = 7.3 Hz, J_m = 1.2 Hz, H-7 or H-8), 7.42 (t, 1H J_o = 7.3 Hz, H-8 or H-7), 7.51 (d, 1H, J_o = 7.3 Hz, H-9), 7.66 (d, 1H, J_o = 7.3 Hz, H-6), 9.59 (s, 1H, CHO). Anal. calcd. for $C_{12}H_9NO$: C 78.67, H 4.95, N 7.64; found: C 78.49, H 5.06, N 7.32.

*(b) Method B. 5H-Pyrrolo[2,1-a]isoindole (**5**a)*

A solution of tri-*n*-butyltin hydride (1.0 g, 3.5 mmol) and AIBN (0.050 g) in dry, degassed benzene (20 mL) was added by syringe pump over a 4 h period to a solution of **1***c* (0.50 g, 1.6 mmol) in dry, degassed benzene (50 mL, argon atmosphere) at reflux temperature. The solution was heated at reflux for a further 1 h and then worked up as described above for the synthesis of **5***b*. The product mixture was separated by flash chromatography on silica gel using hexane–dichloromethane (6:1 to 3:1) to elute **5***a* (0.15 g, 64%) and 1-benzyl-2-methylsulfonylpyrrole (**6***c*, 0.10 g, 28%) as solids. Crystallization of **5***a* from hexane – ethyl acetate gave material with mp 86–88°C; nmr (300)δ: 4.89 (s, 2H, CH_2), 6.27 (m, 1H, $J_{1,2}$ = 3.54 Hz, $J_{1,3}$ = 1.08 Hz, $J_{1,5}$ = 0.5 Hz, H-1), 6.33 (q, 1H, $J_{1,2}$ = 3.54 Hz, $J_{2,3}$ = 2.59 Hz, H-2), 6.93 (m, 1H, $J_{1,3}$ = 1.08 Hz, $J_{2,3}$ = 2.59 Hz, $J_{3,5}$ = 0.6 Hz, H-3), 7.12 (td, 1H, $J_{7,8}$ = $J_{8,9}$ = 7.5 Hz, $J_{6,8}$ = 1.1 Hz, H-8), 7.26–7.73 m, 2H, H-7, 9), 7.46 (m, 1H, H-6). Anal. calcd. for $C_{11}H_9N$: C 85.13, H 5.84, N 9.02; found: C 84.95, H 5.89, N 9.00.

Crystallization of the sulfone **6***c* from hexane – ethyl acetate gave a solid, mp 68°C. Anal. calcd. for $C_{12}H_{13}NO_2S$: C 61.25, H 5.57, N 5.95; found: C 61.46, H 5.64, N 6.05.

*1-Benzyl-3-methylsulfonylpyrrole (7*b)

Obtained from **7***a* by method B except that additional portions of AIBN were added after 5 and 8 h of reflux. The product was purified by flash chromatography on silica gel (hexane – ethyl acetate (2:1 to 1:2)) to give a solid (59% yield) that had mp 94–95°C after crystallization from hexane – ethyl acetate; nmr (500)δ: 3.06 (s, 3H, SO_2Me), 5.07 (s, 2H, CH_2), 6.52 (m, 1H, H-4 or H-5), 6.71 (m, 1H, H-5 or H-4), 7.16 (m, 2H, H-2′, 6′), 7.26 (m, 1H, H-2), 7.35 (m, 3H, H-3′, 4′, 5′). Anal. calcd. for $C_{12}H_{13}NO_2S$: C 61.25, H 5.57, N 5.95; found: C 61.54, H 5.64, N 5.81.

*5,6,7,8-Tetrahydropyrrolo[1,2-a]pyridine (**9**a) and 3-methylsulfonyl-5,6,7,8-tetrahydropyrrolo[1,2-a]pyridine (**9**b)*

Reaction of **8***a* with tri-*n*-butyltin hydride as in method B (see also Table 1) gave a mixture that was separated by flash chromatography on silica gel (hexane–dichloromethane (8:1) to hexane–dichloromethane –ethyl acetate (1:1:1)).

The known (10) 5,6,7,8-tetrahydropyrrolo[1,2-*a*]pyridine (**9***a*) was obtained as an oil (60% yield); nmr (300)δ: 1.79–1.96 (m, 4H, C-6,7-CH_2CH_2), 2.77 (t, 2H, J = 6.2 Hz, C-8-CH_2), 3.93 (t, 2H, J = 6.1 Hz, C-5-CH_2), 5.82 (dd, 1H, $J_{1,2}$ = 3.39 Hz, $J_{1,3}$ = 1.76 Hz, H-1), 6.12 (t, 1H, H-2), 6.51 (dd after decoupling C-8-CH_2, 1H, $J_{1,3}$ = 1.76 Hz, $J_{2,3}$ = 2.65 Hz, H-3).

3-Methylsulfonyl-5,6,7,8-tetrahydropyrrolo[1,2-*a*]pyridine was obtained as an oil; nmr (300)δ: 1.79–2.05 (m, 4H, C-6,7-CH_2CH_2), 2.83 (t, 2H, J = 6.5 Hz, C-8-CH_2), 3.08 (s, 3H, SO_2Me), 4.22 (t, 2H, J = 6.1 Hz, C-5-CH_2), 5.93 (d, 1H, $J_{1,2}$ = 4.00 Hz, H-2), 6.88 (d, 1H, $J_{1,2}$ = 4.00 Hz, H-2). Exact Mass calcd. for $C_9H_{13}NO_2S$: 199.0667; found: 199.0670.

1-*n*-Butyl-2-methylsulfonylpyrrole (**10***a*) was obtained as an oil (17% yield). Anal. calcd. for $C_9H_{15}NO_2S$: C 53.70, H 7.51, N 6.96; found: C 53.78, H 7.91, N 7.10.

*1-Benzoyl-5,6,7,8-tetrahydropyrrolo[1,2-a]pyridine(**9**c) and 1-benzoyl-3-methylsulfonyl-5,6,7,8-tetrahydropyrrolo[1,2-a]pyridine (**9**d)*

Reaction of **8***b* with tri-*n*-butyltin hydride as in method B (see Table 1), except that an additional quantity of AIBN was added after 22 h total reflux, gave a mixture that was separated by flash chromatography on silica gel (hexane – ethyl acetate 4:1 to 1:1).

Compound **9***c* was obtained as a solid (24% yield) that, after crystallization from hexane–ether, had mp 75–76°C; ir (KBr): 1597 cm^{-1}; nmr (300)δ: 1.84–2.04 (m, 4H, C-6,7-CH_2CH_2), 3.17 (t, 2H, J = 6.40 Hz, C-8-CH_2), 3.98 (t, 2H, J = 5.96 Hz, C-5-CH_2), 6.41 (d, 1H, J = 3.05 Hz, H-2 or H-3), 6.47 (d, 1H, J = 3.05 Hz, H-3 or H-2), 7.40–7.51 (m, 3H, H-3′, 4′, 5′), 7.78 (dd, 2H, J_o = 8.0 Hz, J_m = 1.5 Hz, H-2′, 6′). Anal. calcd. for $C_{15}H_{15}NO$: C 79.97, H 6.71, N 6.22; found: C 79.90, H 6.79, N 6.16.

Compound **9***d* was obtained as a solid (40% yield) that, after crystallization from hexane–ether, had mp 164–166°C; ir (KBr): 1636, 1310, 1121 cm^{-1}; nmr (300)δ: 1.87–2.12 (m, 4H, C-6,7-CH_2CH_2), 3.12 (s, 3H, SO_2Me), 3.26 (t, 2H, J = 6.5 Hz, C-8-CH_2), 4.30 (t, 2H, J = 6.6 Hz, C-5-CH_2), 7.17 (s, 1H, H-2), 7.43–7.62 (m, 3H, H-3′, 4′, 5′), 7.74–7.77 (m, 2H, H-2′, 6′). Anal. calcd. for $C_{16}H_{17}NO_3S$: C 63.34, H 5.65, N 4.62; found: C 63.11, H 5.69, N 4.63.

Compound **10***b* was obtained as an oil (<5% yield). Anal. calcd. for $C_{16}H_{19}NO_3S$: C 62.92, H 6.27, N 4.59; found: C 63.06, H 6.46, N 4.35.

*Deuterated 5H-pyrrolo[2,1-a]isoindole (**19**)*

The oxidative radical cyclization of **13** was effected in the same manner as described for the conversion of **1***c* to **5***a*. Two reactions were run in duplicate (0.50 g scale) and gave deuterated **5***a* (i.e., **19**) in essentially the same yields as obtained for the undeuterated congener. Compound **19** had 10.5 ± 1.8% D at C-3 and 47.4 ± 5.2% D (0.95 D) at C-1 and C-2 as determined by comparison of the integrals (500 MHz) for the pyrrole protons to the total integral for the benzenoid protons. Mass spectral analysis showed an isotopic composition of 24.1 ± 0.6% D_0, 41.1 ± 0.5% D_1, and 34.8 ± 9.1% D_2. Thus the total loss of D by nmr was1.10 D (46.5%) vs. 0.90 D (44.5%) by mass spectrometry.

*Reduction of 2-sulfonylpyrroles (**11**) with tri-*n*-butyltin hydride*

A solution of the sulfone in anhydrous benzene (3–20 mL/mmol substrate) containing the appropriate amounts of tri-*n*-butyltin hydride and AIBN (see Table 2) was heated at reflux temperature in an argon atmosphere for the time specified in Table 2. The solvent was removed in vacuo and the residue was purified by preparative thin-layer chromatography on silica gel using the solvent system shown in Table 2. Known compounds were characterized by direct comparison with authentic specimens (see Table 2); new compounds are listed below.

*1-Benzyl-2-acetylpyrrole (**12**e)*

Oil; ir ($CHCl_3$): 1651 cm^{-1}; nmr (200)δ: 2.41 (s, 3H, Me), 5.58 (s, 2H, CH_2), 6.19 (dd, 1H, $J_{3,4}$ = 4.05 Hz, $J_{4,5}$ = 2.56 Hz, H-4), 6.90 (dd, 1H, $J_{3,5}$ = 1.75 Hz, $J_{4,5}$ = 2.56 Hz, H-5), 7.01 (dd, 1H, $J_{3,4}$ = 4.05 Hz, $J_{3,5}$ = 1.75 Hz, H-3), 7.09–7.13 (m, 2H, H-2′, 6′), 7.22–7.30 (m, 3H, H-3′, 4′, 5′). Anal. calcd. for $C_{13}H_{13}NO$: C 78.36, H 6.57, N 7.03; found: C 78.32, H 6.78, N 6.95.[15]

*1-Methyl-2-benzoylpyrrole (**12**f)*

Oil; ir ($CHCl_3$): 1615 cm^{-1}; nmr (200)δ: 4.03 (s, 3H, Me), 6.15 (m, 1H, H-4), 6.75 (m, 1H, H-3), 6.92 (m, 1H, H-5), 7.51 (m, 3H, H-3′, 4′, 5′), 7.83 (m, 2H, H-2′, 6′). Anal. calcd. for $C_{12}H_{11}NO$: C 77.81, H 5.99, N 7.56; found: C 77.85, H 6.11, N 7.23.[15]

*1-Benzyl-2-benzoylpyrrole (**12**g)*

Oil; ir ($CHCl_3$): 1625 cm^{-1}; nmr (200) δ: 5.71 (s, 2H, CH_2), 6.23 (m, 1H, H-4), 6.77 (m, 1H, H-3), 7.04 (m, 1H, H-5), 7.15–7.61 (m, 8H), 7.73 (m, 2H). Anal. calcd. for $C_{18}H_{15}NO$: C 82.73, H 5.78, N 5.36; found: C 82.71, H 6.04, N 5.38.[15]

[15]This microanalytical data is taken from the B.Sc. thesis of C. Gonzalez, Universidad Autonoma del Estado de Mexico, Escuela de Ciencias Quimicas, Toluca, Mexico, 1985. We are very grateful to Mr. Gonzalez for providing us with these elemental analyses.

1. H.J. Anderson and C.E. Loader. *In* Pyrroles. Part one. The synthesis and the physical and chemical aspects of the pyrrole ring. *Edited by* R.A. Jones. John Wiley & Sons, New York. 1990. pp. 446–448.
2. M. Aiura and Y. Kanaska. Chem. Pharm. Bull. **23**, 2835 (1975).
3. D. Gravel, J. Rancourt, and E. Ghiro. The Third Chemical Congress of North America. Toronto, Ont., Canada, June 5–10, 1988. Abstract ORGN 421.
4. I-S. Cho, S. Jaime, and J.M. Muchowski. 74th Canadian Chemical Conference. Hamilton, Ont., Canada, June 2–6, 1991. Abstract 673.
5. I-S. Cho and J.M. Muchowski. Synthesis, 567 (1991).
6. D.R. Artis, I-S. Cho, and J.M. Muchowski. Can. J. Chem. **70**, 1838 (1992).
7. F.E. Ziegler and L.D. Jeroncic. J. Org. Chem. **56**, 3479 (1991).
8. C. Hansch, S.H. Unger, D. Nikaitani, and E. Lein. J. Med. Chem. **16**, 1207 (1973).
9. B. Giese. *In* Radicals in organic synthesis: formation of carbon–carbon bonds. Pergamon Press, Oxford. 1986. pp. 14–17.
10. J.M. Patterson, J. Brasch, and P. Drenchko. J. Org. Chem. **27**, 1652 (1962).
11. S. Becker, Y. Fort, and P. Caubère. J. Org. Chem. **55**, 6194 (1990), and references cited therein.
12. W.R. Bowman, H. Heaney, and B.M. Jordan. Tetrahedron, **47**, 10119 (1991).
13. F. Franco, R. Greenhouse, and J.M. Muchowski. J. Org. Chem. **47**, 1682 (1982).
14. F. Kurzer. Org. Synth. Collect. Vol. **IV**, 937 (1963).
15. O. Carmona, R. Greenhouse, R. Landeros, and J. M. Muchowski. J. Org. Chem. **45**, 5336 (1980).
16. M. Kakushima, P. Hamel, R. Frenette, and J. Rokach. J. Org. Chem. **48**, 3214 (1983).
17. J. Desales, R. Greenhouse, and J.M. Muchowski. J. Org. Chem. **47**, 3668 (1982).
18. S. Gronowitz, A.B. Hoernfeldt, and R.A. Hoffman. J. Org. Chem. **26**, 2615 (1961).
19. E.P. Papadopoulos and N.F. Haidar. Tetrahedron Lett. 1721 (1968); J.W.F. Wasley and K. Chan. Synth. Commun. **3**, 303 (1973).
20. M. Kakushima and R. Frenette. J. Org. Chem. **49**, 2025 (1984).
21. R.K. Olsen and H.R. Snyder. J. Org Chem. **28**, 3050 (1963).
22. R.A. Jones, C.F. Candy, and P.H. Wright. J. Chem. Soc (C), 2563 (1970); H.J. Anderson and S.J.Griffiths. Can. J. Chem. **45**: 2227 (1967).
23. C.F. Candy and R.A. Jones. J. Org. Chem. **36**, 3993 (1971).
24. R. Schiff. Ber. Dtsch. Chem. Ges. **10**, 1500 (1877).
25. G. Ciamician and M. Dennstedt. Ber. Dtsch. Chem. Ges. **17**, 2944 (1877).
26. S. Caddick, K. Aboutayab, and R. West. Synlett, 231 (1993).

Can. J. Chem. Downloaded from www.nrcresearchpress.com by 203.198.23.82 on 09/08/12
For personal use only.

Heteroatom-directed lateral lithiation: synthesis of isoquinoline derivatives from *N*-(*tert*-butoxycarbonyl)-2-methylbenzylamines[1,2]

ROBIN D. CLARK,[3] JAHANGIR,[3] AND JAMES A. LANGSTON
Institute of Organic Chemistry, Syntex Research, Palo Alto, CA 94304, U.S.A.

Received May 27, 1993

This paper is dedicated to Professor David B. MacLean

ROBIN D. CLARK, JAHANGIR, and JAMES A. LANGSTON. Can. J. Chem. **72**, 23 (1994).

Methodology for the preparation of isoquinoline derivatives from *N*-(*tert*-butoxycarbonyl)-2-methylbenzylamines (**1**) was developed. Conversion of **1** to the dilithio species followed by condensation with DMF afforded Boc-3-hydroxy-1,2,3,4-tetrahydroisoquinolines **3**, which could be dehydrated to 1,2-dihydroisoquinolines **4**. Hydrogenation of dihydro compounds **4** afforded the corresponding tetrahydroisoquinolines **5**. Treatment of the dilithio species from **1** with *N*-methoxy-*N*-methylamides afforded ketones **14**, which were converted to 3-substituted dihydro-isoquinoline **15**, tetrahydroisoquinolines (**16, 17**), or isoquinolines (**20**).

ROBIN D. CLARK, JAHANGIR et JAMES A. LANGSTON. Can. J. Chem. **72**, 23 (1994).

On a développé une méthodologie pour la préparation de dérivés isoquinoléines à partir de *N*-(*tert*-butoxycarbonyl)-2-méthylbenzylamines (**1**). La conversion des composés **1** en dérivés dilithiés suivie par une condensation avec le DMF conduit aux Boc-3-hydroxy-1,2,3,4-tétrahydroisoquinoléines (**3**) qui peuvent être soumises à une déshydratation conduisant aux 1,2-dihydroisoquinoléines (**4**). L'hydrogénation des composés dihydro **4** fournit les tétrahydroisoquinoléines correspondantes (**5**). Le traitement des espèces dilithiées des produits **1** avec des *N*-méthoxy-*N*-méthylamides conduit aux cétones **14** qui peuvent être transformées en dihydroisoquinoléines substituées (**15**), en tétrahydroisoquinoléines (**16** et **17**) et en isoquinoléines (**20**) en position 3.

[Traduit par la rédaction]

A number of heterocycle-forming annelations based on heteroatom-facilitated lateral lithiation reactions have recently been reported and these procedures offer useful alternatives to the more classical syntheses of important heterocycles, for example, indole (1) and isoquinoline (2) derivatives. We have described preliminary results on a synthesis of tetrahydroisoquinolines that was based on the lateral lithiation of *N*-(*tert*-butoxycarbonyl)-2-methylbenzylamine (**1***a*) (3). In this paper, we report details of that work and extensions that provide routes to a variety of substituted dihydroisoquinolines, tetrahydroisoquinolines, and isoquinolines.

Prior to our initial investigations, it had been demonstrated that *N*-benzylbenzamide underwent deprotonation at the α(benzylic) position (in addition to NH deprotonation) (4) and that *N*-pivaloylbenzylamine underwent both *ortho* and α-lithiation (5). It was subsequently reported that Boc-benzylamine was cleanly dilithiated to afford the *N*-α-dilithio species (6). However, based on the facility with which various toluenes undergo heteroatom-facilitated lateral lithiation (1, 7), we felt it likely that the methyl group of **1***a*, rather than the α position, would be the second site of deprotonation. In the event, treatment of **1***a* with two equivalents of *sec*-butyllithium at ca. –40°C gave the red-orange dilithio species **2***a* as evidenced by the formation of Boc-3-hydroxytetrahydroisoquinoline **3***a* as the sole product upon treatment with DMF (Scheme 1). We subsequently demonstrated that the Boc-phenylethylamine homolog of **1***a* also undergoes lateral lithiation under the same conditions and that only when the *N*-Boc group is extended by an additional methylene (phenylpropylamine derivative) does α-deprotonation become a competing, albeit minor, process (8).

Results of the application of this methodology to the synthesis of tetrahydroisoquinolines with substitutents at the 4-position or in the aromatic ring are presented in Scheme 2. The 3-hydroxy derivatives **3** obtained by DMF quench of the dilithio species **2** were isolable by crystallization and (or) silica gel chromatography and underwent rapid dehydration to the rather unstable 1,2-dihydroisoquinolines **4** upon brief treatment with HCl in THF. The dihydro compounds were hydrogenated to afford 1,2,3,4-tetrahydroisoquinolines **5**.

Several of the entries in Scheme 2 warrant further comment. Ring-halogenated tetrahydroisoquinolines, as exemplified by entries **5***b–d*, are not readily accessible by classical syntheses, for example, the Bischler–Napieralski (9) and Pictet–Spengler (10) procedures, which generally involve cyclizations onto electron-rich aromatic rings. Entry **1***f* demonstrated that lateral lithiation was the predominant pathway despite the presence of a 5-methoxy group that, in principle, could have induced competing ring (*ortho*) deprotonation at the 6-position. Entries **1***g–i* indicated a limitation of the methodology as 2-alkyl substituents other than methyl proved to be significantly more difficult to deprotonate, even when longer reactions times, higher temperatures, and the stronger base *tert*-BuLi were employed. This phenomenon was previously noted in the case of the related Boc-2-alkylanilines (1). An obvious exception is **1***j*, in which the additional phenyl group enhances the acidity of the methylene protons. With substrate **1***i*, the decreased rate of lateral lithiation allowed metalation *ortho* to the methoxy group in the appended aromatic ring to become a competing process.

The requisite benzylamines for the preparation of Boc derivatives **1***a–i* were either commercially available (**1***a*) or were, in general, prepared in straightforward fashion (Experimental). The preparation of the tetrasubstituted example **1***d*, which exemplifies several additional aspects of *ortho* and lateral lithiation methodology, is shown in Scheme 3. A previous report

[1]Dedicated to Professor D.B. MacLean in recognition of his outstanding contributions to natural product and alkaloid chemistry, which have encompassed isolation, structure determination, and synthesis. One of us (J) was fortunate enough to have obtained his doctoral training under D.B.M.'s mentorship. The work presented in this paper was inspired by the lateral metalation technology developed in Professor MacLean's laboratory for the synthesis of isoquinoline alkaloids.

[2]Contribution no. 880 from the Institute of Organic Chemistry.

[3]Authors to whom correspondence may be addressed.

Can. J. Chem. Downloaded from www.nrcresearchpress.com by 195.246.54.202 on 09/08/12
For personal use only.

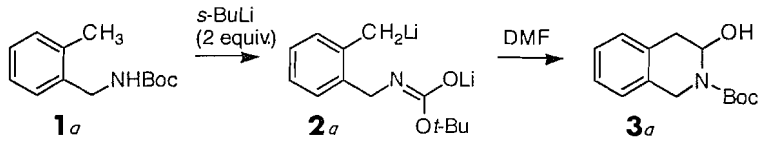

1a **2a** **3a**

SCHEME 1

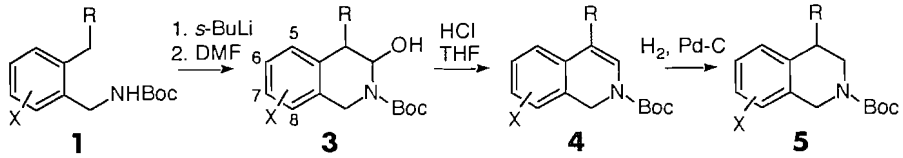

1 **3** **4** **5**

			% Yield		
entry	R	X in **3**,**4**,**5**	**3**	**4**	**5**
a	H	H	78	95	95
b	H	5-F	72	-[a]	79[b]
c	H	8-Cl	80	-	76[c]
d	H	6-Cl, 8-$CH(CH_3)_2$	97	95	95
e	H	6-OMe	65		
f	H	6,7-$(OMe)_2$	60		
g	$CH_2CH_2CH_3$	H	-	<20	
h	CH_2Ph	H	-	42	90
i	CH_2(3-OMe)Ph	H	-	<20	
j	Ph	H	-	71[c]	

[a]Intermediate was not isolated. [b]Yield from **3**. [c]Yield from **1**.

SCHEME 2

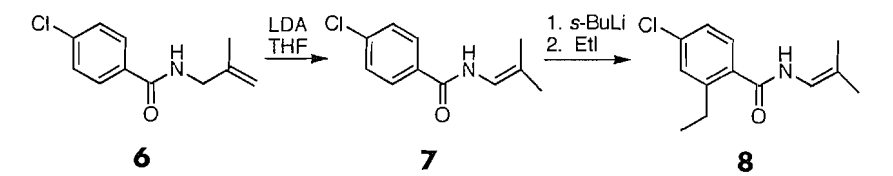

6 **7** **8**

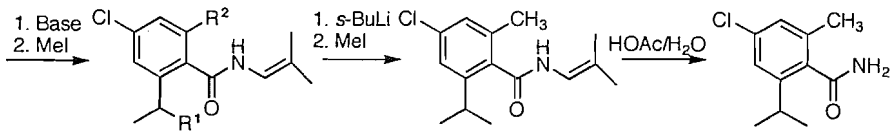

9 R^1 = Me R^2 = H
10 R^1 = H R^2 = Me

Base	**9** (%)	**10** (%)
n-BuLi	70	30
s-BuLi	70	30
t-BuLi	40	60
LiTMP	100	0

11

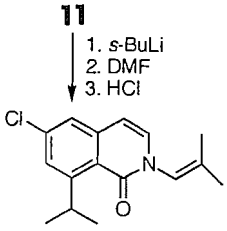

13

12

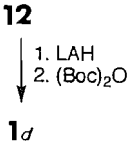

1d

SCHEME 3

Can. J. Chem. Downloaded from www.nrcresearchpress.com by 195.246.54.202 on 09/08/12
For personal use only.

Can. J. Chem. Downloaded from www.nrcresearchpress.com by 195.246.54.202 on 09/08/12
For personal use only.

from these laboratories introduced the 1-propenyl group for protection of benzamides in *ortho* lithiation reactions (11). One drawback of this methodology is that a mixture of *cis/trans* propenyl isomers is obtained, which complicates further synthetic steps. To obviate this inconvenience, in the present work we used the symmetric 2-methyl-1-propenyl group. Thus, benzamide **7** was obtained in quantitative yield by the lithium diisopropylamide (LDA)-induced isomerization (12) of the 2-methylallylbenzamide **6**. *ortho* Lithiation of **7** followed by treatment with iodoethane furnished the 2-ethyl derivative **8**. Attempts to effect lateral lithiation of **8** using organolithium bases were complicated by competing *ortho* lithiation as evidenced by formation of **9** and **10** upon treatment of the lithiated species with iodomethane (Scheme 3). However, it was found that lateral lithiation was the exclusive pathway when lithium 2,2,6,6-tetramethylpiperidide (LiTMP) was used as the base. LiTMP was superior to LDA, which gave only lateral metalation but with incomplete (ca. 70%) conversion. The superiority of LiTMP over LDA was also recently demonstrated in the lateral lithiation of *o*-tolualdehyde cyclohexylimine (13).

Compound **9**, with the 2-position effectively blocked to further metalation by the isopropyl group, was then subjected to the third consecutive lithiation reaction in the sequence to afford **11** after methylation. The 2-methyl-1-propenyl group was removed by acid hydrolysis to give the primary benzamide **12**, which was converted to **1***d*. We note in passing that **11** afforded the isoquinolone **13** upon lateral lithiation and treatment with DMF followed by dehydration with HCl (14). However, attempts to remove the *N*-protecting group from **13** with strong acid resulted in decomposition.

Acylation of dianion **2***a* was efficiently accomplished by treatment with *N*-methoxy-*N*-methylamides (15) to afford key intermediates **14***a–d* for the preparation of 3-substituted dihydro and tetrahydroisoquinolines (Scheme 4). Brief exposure of these ketones to a catalytic amount of trifluoroacetic acid in CH_2Cl_2 gave the Boc-1,2-dihydroisoquinolines **15**, which could be catalytically reduced to the corresponding Boc-protected tetrahydroisoquinolines **16**. Alternatively, the Boc group of **14** could be removed with trifluoroacetic acid, and reduction of the intermediate imine with sodium borohydride in ethanol afforded tetrahydroisoquinolines **17**. Several of the 3-substituted tetrahydroisoquinolines thus obtained were set up for additional ring closure reactions (Scheme 5). Deprotection of **16***b* with TFA followed by neutralization gave hexahydro-2*H*-benzo[*b*]quinolizine **18** and Pictet–Spengler reaction of **17***d* afforded the tetrahydro-5*H*-dibenzo[*b,g*]quinolizine **19**.

In addition to providing access to 3-substituted tetrahydroisoquinolines, the dihydroisoquinolines **15** can also serve as precursors to the corresponding isoquinolines. Thus, deprotection of **15***a* with TFA followed by treatment with iodine and KOAc in ethanol (16) afforded 3-butyl isoquinoline **20** (Scheme 6). Whereas the Reissert reaction (17) affords 1-substituted derivatives, 3-substituted isoquinolines are not readily accessible from classical isoquinoline syntheses, for example, the Pomeranz–Fritsch synthesis (18). Another versatile route for the preparation of 3-substituted isoquinolines based on the lateral lithiation of tolualdehyde imines has recently been reported (19).

A variant on the preparation of certain 3-substituted tetrahydroisoquinolines is shown in Scheme 7. Condensation of dianion **2***a* with veratraldehyde afforded adduct **21**, which cyclized to Boc-3(3,4-dimethoxyphenyl)tetrahydroisoquinoline **23** upon treatment with a catalytic amount of trifluoroacetic acid in CH_2Cl_2. This cyclization appears to require the presence of the 4-methoxy group, presumably through stabilization of the intermediate carbonium ion, as the corresponding unsubstituted phenyl congener **22** failed to cyclize under similar (or more strongly acid) conditions. In an attempt to prepare 3,3-disubstituted tetrahydroisoquinolines, the benzophenone and cyclohexanone adducts **24** and **26**, respectively, were similarly treated

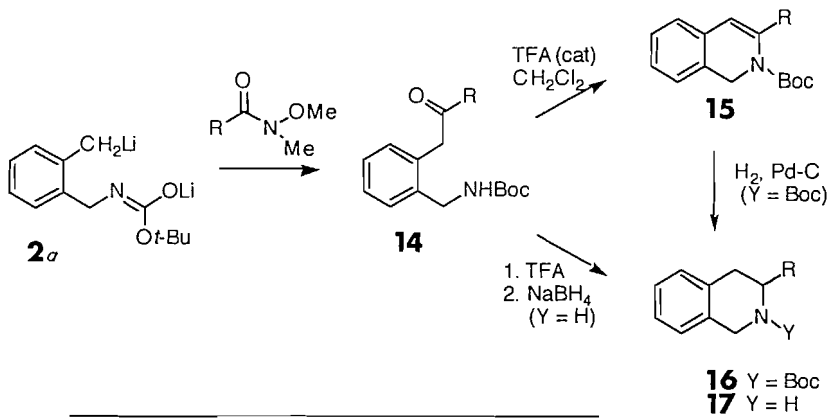

entry	R	%yield 14	15	16	17
a	$CH_2CH_2CH_2CH_3$	94	92	-[a]	92
b	$CH_2CH_2CH_2CH_2Cl$	95	92	98	-[b]
c	Ph	79	94		
d	CH_2(3,4-$(OMe)_2$Ph)	45	99	90	81

[a]Not isolated. [b]See Scheme 5.

SCHEME 4

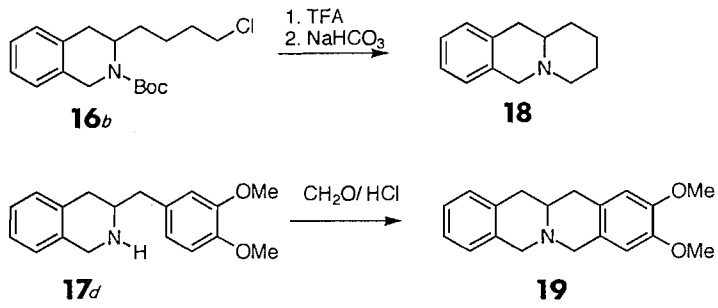

SCHEME 5

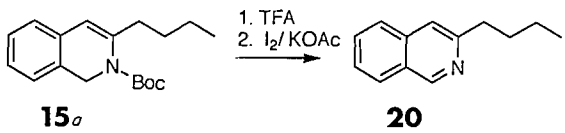

SCHEME 6

with trifluoroacetic acid in CH_2Cl_2. However, **24** underwent almost immediate dehydration to stilbene **25** whereas **26** proved resistant to either cyclization or dehydration. Under strongly acidic conditions (neat trifluoroacetic acid or HCl in THF), the Boc group of **26** was removed while the tertiary alcohol remained intact.

In summary, the methodology reported herein can be used to prepare a variety of derivatives of the isoquinoline ring system. As has been amply demonstrated with heteroatom-directed *ortho* lithiation technology (7), Boc-directed *lateral* lithiations also can be used to synthesize compounds that might otherwise be difficult to prepare by classical means. Thus, lateral lithiation of **1** was used to prepare halogen-substituted tetrahydroisoquinolines and 3-substituted tetrahydroisoquinolines and isoquinolines. Applications to the preparation of more complex isoquinolines and isoquinoline-containing ring systems are underway and will be reported in due course.

Experimental

General information

Melting points were determined on a Thomas–Hoover capillary apparatus and are uncorrected. Thin-layer chromatography (tlc) was performed using Analtech silica gel GF glass plates. Medium-pressure chromatography (mpc) was performed with 230–400 mesh Merck Kieselgel. Microanalysis were carried out by the Syntex Analytical Department.

Proton (^1H) nmr spectra were recorded at 300 MHz on a Bruker WM 300 spectrometer in $CDCl_3$ or Me_2SO-d_6 solution referenced to internal tetramethylsilane (TMS). Chemical shifts, quoted as δ values, were measured in relation to TMS. Infrared (ir) spectra were run on a Nicolet 5 PC FT infrared spectrophotometer. Mass spectra were recorded with an Atlaswerke CH-7 spectrometer. High-resolution mass spectra (hrms) were obtained with a Finnigan MAT 311A mass spectrometer.

All lithiation reactions were carried out under an inert atmosphere (nitrogen or argon). THF was dried by distillation from Na–benzophenone under a nitrogen atmosphere immediately prior to use. "Usual work-up" refers to addition of aqueous NH_4Cl solution to the reaction mixture, extraction with EtOAc, washing the extract with water and brine, drying over Na_2SO_4, and evaporation on a rotary evaporator.

Typical procedure for the preparation of Boc-2-alkylanilines ***1****:* N-*(*tert*-butoxycarbonyl)-1-methylbenzylamine* **1a**

Di-*tert*-butyl dicarbonate (37 g, 170 mmol) was added to a cold (ice-bath) solution of 2-methylbenzylamine (Aldrich Chem. Co.) (20 g, 165

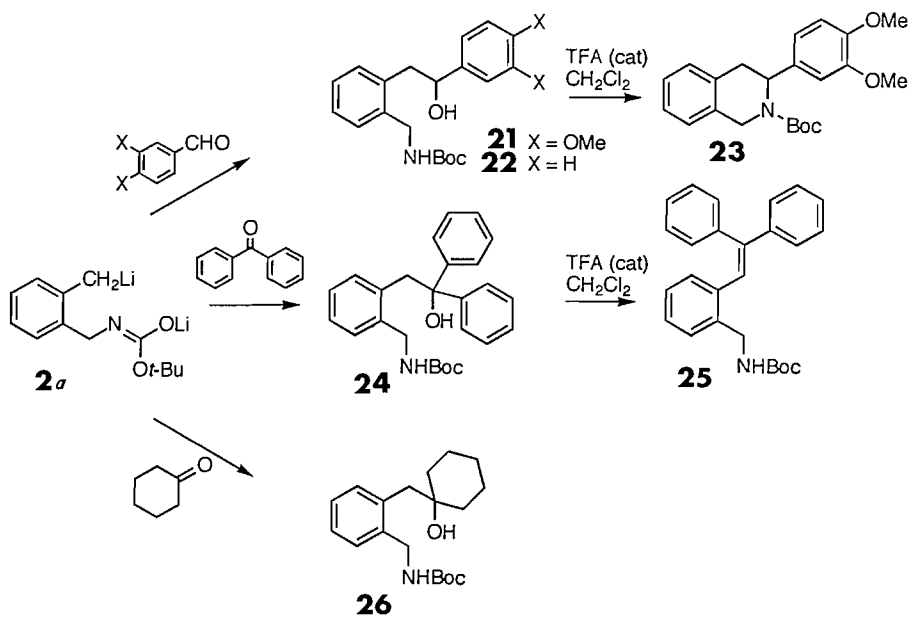

SCHEME 7

Can. J. Chem. Downloaded from www.nrcresearchpress.com by 195.246.54.202 on 09/08/12
For personal use only.

Can. J. Chem. Downloaded from www.nrcresearchpress.com by 195.246.54.202 on 09/08/12
For personal use only.

mmol) in THF (250 nmL). The resulting solution was stirred at room temperature for 4 h and was then concentrated in vacuo to a semi-solid. Crystallization from hexane (cooling in a Dry Ice – acetone bath) afforded **1***a* as a white solid (32 g, 88%); mp 50–51°C; ^{1}H nmr ($CDCl_3$) δ: 1.46 (s, 9H), 2.32 (s, 3H), 4.32 (d, 2H, J = 5.6 Hz), 4.70 (br m, 1H, NH), 7.18 (m, 4H); ms(EI), *m/z*(relative intensity): 221(5)M^+, 165(99), 164(79), 150(34), 120(16), 105(47), 104(100), 57(29). Anal. calcd. for $C_{13}H_{19}NO_2$: C 70.56, H 8.65, N 6.33; found: C 70.50, H 8.61, N 6.40.

The following compounds were similarly prepared.

N-*(*tert*-Butoxycarbonyl)-3-fluoro-2-methylbenzylamine* **1**b

This was prepared from 3-fluoro-2-methylbenzoic acid (Aldrich Chem. Co.) by conversion to the amide, LAH reduction, and reaction with di-*tert*-butyl dicarbonate; mp 69–70°C. Anal. calcd. for $C_{13}H_{18}FNO_2$: C 65.25, H 7.58, N 5.85; found: C 65.17, H 7.59, N 5.87.

N-*(*tert*-Butoxycarbonyl)-2-chloro-6-methylbenzylamine* **1**c

This was prepared from 2-chloro-6-methylbenzonitrile (Aldrich Chem. Co.) by reduction (borane–methylsulfide) and reaction with di-*tert*-butyl dicarbonate; mp 69–70°C. Anal. calcd. for $C_{13}H_{18}ClNO_2$: C 61.05, H 7.09, N 5.48; found: C 61.11, H 7.09, N 5.51.

N-*(*tert*-Butoxycarbonyl)-4-chloro-2-(2-propyl)-6-methylbenzylamine* **1**d

This was prepared from compound **12**, the preparation of which is described below; mp 69–70°C. Anal. calcd. for $C_{16}H_{24}ClNO_2$: C 64.52, H 8.13, N 4.70; found: C 64.79, H 8.23, N 4.82.

N-*(*tert*-Butoxycarbonyl)-4-methoxy-2-methylbenzylamine* **1**e

This was prepared from 4-methoxy-*o*-toluic acid by conversion to the amide, reduction with LAH, and reaction with di-*tert*-butyl dicarbonate; mp 79–80°C. Anal. calcd. for $C_{14}H_{21}NO_3$: C 66.90, H 8.42, N5.57; found: C 66.95, H 8.78, N 5.61.

N-*(*tert*-Butoxycarbonyl)-4,5-dimethoxy-2-methylbenzylamine* **1**f

This was prepared from 4,5-dimethoxy-*o*-toluic acid by conversion to the amide, reduction with LAH, and reaction with di-*tert*-butyl dicarbonate; mp 63–65°C. Anal. calcd. for $C_{15}H_{23}NO_4$: C 64.03, H 8.24, N 4.98; found: C 64.01, H 8.54, N 5.01.

N-*(*tert*-Butoxycarbonyl)-2-(1-*n*-butyl)benzylamine* **1**g

This was prepared by alkylation of the dilithio species **2***a* (see below) with 1-iodopropane; mp 46–48°C. Anal. calcd. for $C_{16}H_{25}NO_2$: C 71.45, H 9.00, H 5.95; found: C 71.64, H 9.17, N 5.54.

N-*(*tert*-Butoxycarbonyl)-2-(2-phenylethyl)benzylamine* **1**h

This was prepared from 2-bibenzylcarboxylic acid (Aldrich Chem. Co.) by conversion to the amide, reduction with LAH, and reaction with di-*tert*-butyl dicarbonate; mp 124–125°C. Anal. calcd. for $C_{20}H_{25}NO_2$: C 77.13, H 8.10, N 4.50; found: C 77.19, H 8.12, N 4.60.

N-*(*tert*-Butoxycarbonyl)2-((3-methoxyphenyl)ethyl)benzylamine* **1**i

This was prepared by alkylation of the dilithio species **2***a* with 3-methoxybenzyl chloride; mp 62–64°C. Anal. calcd. for $C_{21}H_{27}NO_3$: C 73.87, H 7.97, N 4.10; found: C 73.64, H 7.95, N 4.38.

N-*(*tert*-Butoxycarbonyl)-2-(phenylmethyl)benzylamine* **1**j

This was prepared from α-phenyl-*o*-toluic acid (Aldrich Chem. Co.) by conversion to the amide, reduction with LAH, and reaction with di-*tert*-butyl dicarbonate; mp 77–78°C. Anal. calcd. for $C_{19}H_{23}NO_2$: C 76.74, H 7.79, N 4.71; found: C 76.76, H 7.72, N 4.90.

General procedure for lithiation of **1** *followed by trapping with DMF*

A solution of the *N*-(*tert*-butoxycarbonyl)-2-methylbenzylamine **1***a* (5 mmol) in THF (10 mL) was cooled in an acetone–Dry Ice bath to ca. –60°C (internal temperature) and a solution of *sec*-BuLi (8.5 mL, 1.3 M in cyclohexane, 11 mmol) was added over a period of several minutes at such a rate as to maintain the internal temperature at ca. –30°C. The resulting bright orange solution was stirred for 5–10 min and DMF (0.58 mL, 7.5 mmol) was added. The now colorless reaction mixture was quenched with saturated aqueous NH_4Cl. The mixture was diluted with ether, washed with water and brine, and dried ($NaSO_4$). Removal of solvent in vacuo gave the crude product **3**, which was purified by crystallization (**3***a*, hexane) or mpc (**3***b*, **3***c*, **3***e*, **3***f*, EtOAc–hexane). Compounds **3***d* and **3***g–j* were used in the next step without purification.

The yields for the following compounds are given in Scheme 2.

*2-(*tert*-Butoxycarbonyl)-3-hydroxy-1,2,3,4-tetrahydroisoquinoline* **3**a: mp 97–98°C; ir (KBr): 3600–3200, 1682 cm^{-1}; ^{1}H nmr ($CDCl_3$) δ: 1.52 (s, 9H), 2.98 (dd, 1H, J = 4.3, 15.4 Hz), 3.06 (dd, 1H, J = 4.3, 15.4 Hz), 3.65 (br s, 1H, OH), 4.46 (d, 1H, J = 15.7 Hz), 4.54 (d, 1H, J = 15.7 Hz), 5.80 (br m, 1H), 7.20 (m, 4H); ms (EI), *m/z* (% relative intensity)): 249 (3)M^+, 193 (38), 175 (44), 130 (32), 104 (100), 57 (96). Anal. calcd. for $C_{14}H_{19}NO_3$: C 67.45, H 7.68, N 5.62; found: C 67.57, H 7.82, N 5.79.

*2-(*tert*-Butoxycarbonyl)-5-fluoro-3-hydroxy-1,2,3,4-tetrahydroisoquinoline* **3**b: mp 137–138°C; ir (KBr): 3650–3200, 1668 cm^{-1}; ^{1}H nmr ($CDCl_3$) δ: 1.51 (s, 9H), 2.97 (dd, 1H, J = 4.2, 16.4 Hz), 3.13 (dd, 1H, J = 4.2, 16.4 Hz), 3.45 (br s, 1H, OH), 4.35 (d, 1H, J = 16.2 Hz), 4.63 (d, 1H, J = 16.2 Hz), 5.92 (br m, 1H), 6.95 (m, 2H), 7.18 (m, 1H); ms (EI) *m/z* (% relative intensity): 267 (5)M^+, 211 (23), 193 (32), 167 (12), 148 (22), 122 (65), 57 (100). Anal. calcd. for $C_{14}H_{18}FNO_3$: C 62.91, H 6.79, N 5.24; found: C 63.01, H 6.76, N 5.24.

*2-(*tert*-Butoxycarbonyl)-8-chloro-3-hydroxy,1,2,3,4-tetrahydroisoquinoline* **3**c: mp 105–106°C; ir (KBr): 3660–3200, 1670 cm^{-1}; ^{1}H nmr ($CDCl_3$) δ: 1.53 (s, 9H), 2.95 (dd, 1H, J = 3.7, 15.8 Hz), 3.10 (dd, 1H, J = 3.7, 15.8 Hz), 3.30 (br s, 1H, OH), 4.45 (d, 1H, J = 17.0 Hz), 4.70 (d, 1H, J = 17.0 Hz), 5.90 (m, 1HO, 7.14 (m, 2H), 7.27 (m, 1H); ms (EI), *m/z* (% relative intensity): 285 (7)M^+ + 2, 283 (18)M^+, 229 (6), 227 (18), 211 (12), 209 (32), 192 (12), 164 (16), 148 (22), 138 (44), 57 (100). Anal. calcd. for $C_{14}H_{18}ClNO_3$: C 59.26,H 6.40, N 4.94; found: C, 58.98, H 6.34, N 4.92.

*2-(*tert*-Butoxycarbonyl)-3-hydroxy-6-methoxy-1,2,3,4-tetrahydroisoquinoline* **3**e: Oil; ir (neat): 3650–3150, 1693 cm^{-1}; ^{1}H nmr ($CDCl_3$) δ: 1.52 (s, 9H), 2.95 (dd, 1H, J = 4.3, 15.4 Hz), 3.05 (dd, 1H, J = 4.3, 15.4 Hz), 3.80 (s, 3H), 4.44 (2, 2H), 5.75 (br s, 1H), 6.87 (m, 2H), 7.08 (m, 1H); ms (EI), *m/z* (% relative intensity): 279 (5)M^+, 222 (50), 204 (15), 160 (100), 134 (32). Exact Mass (hrms) calcd. for $C_{15}H_{21}NO_4$: 279.147; found: 279.147.

*2-(*tert*-Butoxycarbonyl)-6,7-dimethoxy-3-hydroxy-1,2,3,4-tetrahydroisoquinoline* **3**f: mp 142–143°C; ir (KBr): 3640–3110, 1678 cm^{-1}; ^{1}H nmr ($CDCl_3$) δ: 1.52 (s, 9H), 2.90 (dd, 1H, J = 3.9, 15.5 Hz), 3.02 (dd, 1H, J = 3.9, 15.5 Hz), 3.40 (br s, 1H, OH), 3.87 (s, 3H), 3.88 (s, 3H), 4.43 (m 2H), 5.80 (br m, 1H), 6.69 (s, 1H), 6.73 (s, 1H). Anal. calcd. for $C_{16}H_{23}NO_5(0.25\ H_2O)$: C 61.23, H 7.60, N 4.46; found: C 61.56, H 7.70, N 4.50; Exact Mass (hrms) calcd. for $C_{16}H_{23}NO_5$: 309.158; found: 309.158.

General procedure for dehydration of 3-hydroxy-1,2,3,4-tetrahydroisoquinolines **3**

To a solution of compound **3** (2 mmol) in THF (20 mL) was added 5 drops of concentrated HCl. The reaction mixture was stirred for 10 min at room temperature and then quenched with solid Na_2CO_3. The mixture was filtered and the filter cake was washed with EtOAc. The combined filtrate was evaporated in vacuo to afford the crude 1,2-dihydroisoquinoline **4**. Compounds **1***a* and **1***j* were isolated by mpc (EtOAc–hexane). Compounds **4***b,c,h* were used in the next step without purification. Yields for the following compounds are given in Scheme 2.

*2-(*tert*-Butoxycarbonyl)-1,2-dihydroisoquinoline* **4**a: Isolated as an unstable oil: ^{1}H nmr ($CDCl_3$) δ: 1.52 (s, 9H), 4.80 (br s, 2H), 5.66 (br d, 1H, J = 7.0 Hz), 6.80–7.19 (m, 5H).

*2-(*tert*-Butoxycarbonyl)-1,2-dihydro-4-phenylisoquinoline* **4**j: mp 96–98°C; ir (KBr): 1704 cm^{-1}; ^{1}H nmr ($CDCl_3$) δ: 1.53 (s, 9H), 4.85 (s, 2H), 6.87–7.20 (m, 5H), 7.40 (m, 5H); ms (EI), *m/z* (% relative intensity): 307 (12)M^+, 251 (100), 206 (60). Anal. calcd. for $C_{20}H_{21}NO_2$: C 78.14, H 6.89, N 4.56; found: C 77.99, H 6.81, N 4.52.

Can. J. Chem. Downloaded from www.nrcresearchpress.com by 195.246.54.202 on 09/08/12
For personal use only.

General procedure for hydrogenation of 1,2-dihydroisoquinolines ***4*** *to 1,2,3,4-tetrahydroisoquinolines* ***5***

The 1,2-dihydroisoquinoline **4** (2 mmol) was dissolved in EtOAc (25 mL), 20% $Pd(OH)_2$ (100 mg) was added, and the mixture was hydrogenated in a Parr apparatus for ca. 12 h at 50 psi (1 psi = 6.9 kPa). The catalyst was removed by filtration through Celite and the filtrate was evaporated in vacuo to afford the crude tetrahydroisoquinoline **5**, which was purified by mpc (EtOAc–hexane). Yields for the following compounds are given in Scheme 2.

2-(tert-Butoxycarbonyl)-1,2,3,4-tetrahydroisoquinoline **5**a: mp 35–36°C; this material was identical to an authentic sample prepared from 1,2,3,4-tetrahydroisoquinoline.

2-(tert-Butoxycarbonyl)-5-fluoro-1,2,3,4-tetrahydroisoquinoline **5**b: mp 39–40°C; ir (KBr): 1698 cm^{-1}; ^1H nmr ($CDCl_3$) δ: 1.48 (s, 9H), 2.81 (t, 2H, J = 5.9 Hz), 3.65 (t, 2H, J = 5.9 Hz), 4.58 (s, 2H), 6.88 (m, 2H), 7.14 (m, 1H); ms (EI), *m/z* (% relative intensity): 251 (5)M^+, 195 (50), 194 (100), 178 (23), 150 (43), 122 (17), 57 (79). Anal. calcd. for $C_{14}H_{18}FNO_2$: C, 66.91, H 7.61, N 5.28; found: C 66.86, H 7.61, N 5.28.

2-(tert-Butoxycarbonyl)-8-chloro-1,2,3,4-tetrahydroisoquinoline **5**c: mp 42–43°C; ir (KBr): 1692 cm^{-1}; ^1H nmr (300 MHz, $CDCl_3$) δ: 1.50 (s, 9H), 2.83 (t, 2H, J = 5.6 Hz), 3.64 (t, 2H, J = 5.6 Hz), 4.58 (s, 2H), 7.09 (m, 2H), 7.22 (m, 1H); ms (EI), *m/z* (% relative intensity): 210 (37)M^+, 194 (11), 168 (10), 168 (33), 138 (17), 103 (7), 57 (100). Anal. calcd. for $C_{14}H_{18}ClNO_2$: C 62.80, H 6.78, N 5.23; found: C 62.80, H 6.76, N 5.23.

2-(tert-Butoxycarbonyl)-6-chloro-8-(2-propyl)-1,2,3,4-tetrahydroisoquinoline **5**d: mp 60–63°C; ir (KBr): 1697 cm^{-1}; ^1H nmr ($CDCl_3$) δ: 1.22 (d, 6H, J = 6.7 Hz), 1.47 (s, 9H), 2.81 (t, 2H, J = 5.7 Hz), 3.02 (br m, 1H), 3.60 (t, 2H, J = 5.7 Hz), 4.56 (s, 2H), 6.97 (d, 1H, J = 2.1 Hz), 7.10 (d, 1H, J = 2.1 Hz); ms(EI), *m/z* (% relative intensity): 309 (1)M^+, 254 (40), 252 (100), 236 (10), 218 (10), 208 (21), 180 (14), 57 (78). Anal. calcd. for $C_{17}H_{24}ClNO_2$: C 66.12, H 7.51, N 4.54; found: C 66.25, H 7.92, N 4.48.

2-(tert-Butoxycarbonyl)-4-(phenylmethyl)-1,2,3,4-tetrahydroisoquinoline **5**h: Oil; for characterization this was deprotected with trifluoroacetic acid in CH_2Cl_2 followed by conversion to the HCl salt to afford *4-(phenylmethyl)-1,2,3,4-tetrahydroisoquinoline hydrochloride*; mp 179–180°C; ir (KBr): 3630–3260 cm^{-1}; ^1H nmr (Me_2SO-d_6) δ: 2.99 (m, 2H), 3.12 (dd, 1H, J = 5.2, 12.8 Hz), 3.25 (dd, 1H, J = 4.7, 13.6 Hz), 3.46 (m, 1H), 4.23 (AB quartet, J_{AB} = 16.2 Hz), 7.30 (m, 8H), 7.48 (d, 1H, J = 7.0 Hz), 9.80 (br s, NH_2^+). Anal. calcd. for $C_{16}H_{18}ClN$: C 73.97, H 6.99, N 5.39; found: C 73.82, H 6.97, N 5.26.

N-*(2-Methyl-1-propenyl)-4-chlorobenzamide* ***7***

Benzamide **6** was prepared from 4-chlorobenzoyl chloride and 2-methylallylamine hydrochloride (CH_2Cl_2, Et_3N) in 97% yield; mp 111–112°C. Anal. calcd. for $C_{11}H_{12}ClNO_3$: C 63.01, H 5.77, N 6.68; found: C 62.96, H 5.76, N 6.61.

A solution of *n*-BuLi (44 mL, 2.5 M in hexane, 110 mmol) was added to a solution of diisopropylamine (15.4 mL, 110 mmol) in THF (200 mL) at –60°C and the resulting solution was stirred at this temperature for 5 min. A solution of amide **6** (10.5 g, 50 mmol) in THF (50 mL) was slowly added and the mixture was stirred at ca. –60°C for 1 h and then allowed to warm to –10°C over a period of 45 min. Saturated aqueous NH_4Cl solution was added and the reaction mixture was then partitioned between EtOAc and water. The EtOAc was washed with water and brine, dried (Na_2SO_4), and evaporated. Crystallization of residue from EtOAc–hexane gave amide **7** (26.5 g, 89%); mp 129–130°C; ir (KBr): 3600–3200, 1638 cm^{-1}; ^1H nmr ($CDCl_3$) δ: 1.71 (d, 3H, J = 1.3 Hz), 1.78 (d, 3H, J = 1.1 Hz), 6.74 (m, 1H), 7.35 (br s, 1H, NH), 7.43 (d, 2H, J = 8.5 Hz), 7.74 (d, 2H, J = 8.5 Hz); ms (EI), *m/z* (% relative intensity): 211 (11) M+2, 209 (32)M^+, 194 (14), 141 (37), 139 (100), 113 (7), 111 (15). Anal. calcd. for $C_{11}H_{12}ClNO$: C 63.01, H 5.77, N 6.68; found: C 62.76, H, 5.73, N, 6.60.

N-*(2-Methyl-1-propenyl)-4-chloro-2-ethylbenzamide* ***8***

To a –70°C solution of amide **7** (7.0 g, 33.4 mmol) in THF (100 mL) was added a solution of *sec*-BuLi (56.5 mL, 1.3 M in cyclohexane, 73.4 mmol) and the resulting dark solution was stirred at –70°C for 30 min. The temperature of the solution was allowed to slowly rise to –30°C over 30 min and the mixture was then cooled back to –70°C. Iodoethane (4 mL, 50 mmol) was added and the mixture was allowed to warm to 0°C. Aqueous NH_4Cl solution was added and the mixture was extracted with EtOAc. The extract was washed with water and brine, dried (Na_2SO_4), and evaporated. Crystallization of the residue from hexane afforded compound **8** (6.94 g, 87%); mp 86–87°C; ir (KBr): 3600–3200, 1640 cm^{-1}; ^1H nmr ($CDCl_3$) δ: 1.26 (t, 3H, J = 7.6 Hz), 1.66 (d, 3H, J = 1.0 Hz), 1.78 (d, 3H, J = 1.0 Hz), 2.81 (q, 2H, J = 7.6 Hz), 6.70 (m, 1H), 7.13 (m, 1H, NH), 7.22 (dd, 1H, J = 2.0, 8.1 Hz), 7.29 (d, 1H, J = 2.0 Hz), 7.33 (d, 1H, J = 8.1 Hz). Anal. calcd. for $C_{13}H_{16}ClNO$: C 65.68, H 6.79, N 5.89; found: C 65.53, H 6.81, N 5.60.

N-*(2-Methyl-1-propenyl)-4-chloro-2-(2-propyl)benzamide* ***9***

To a stirred solution of 2,2,6,6-tetramethylpiperidine (17.8 mL, 105 mmol) in THF (150 mL) at –60°C was added *n*-BuLi (65.7 mL, 1.6 M in hexane, 105 mmol). After 10 min, the LiTMP solution was treated dropwise with a solution of amide **8** (10.0 g, 42 mmol) in THF (150 mL). After stirring the deep purple solution at –60°C for 1 h, the temperature was allowed to slowly rise to –10°C over a 1 h period and the reaction was then quenched by addition of NH_4Cl solution. The mixture was extracted with EtOAc (300 mL) and the extract was successively washed with water, 1 N HCl, water, and brine. The EtOAc was dried (Na_2SO_4) and evaporated to give amide **9** (10.0 g, 94%); mp 110–111°C; ir (KBr): 3700–3180, 1640 cm^{-1}; ^1H nmr ($CDCl_3$) δ: 1.25 (d, 6H, J = 6.9 Hz), 1.64 (s, 3H), 1.77 (s, 3H), 3.34 (hept, 1H, J = 6.9 Hz), 6.70 (m, 1H), 7.00 (br d, 1H, NH), 7.19 (dd, 1H, J = 2.0, 8.2 Hz), 7.26 (d, 1H, J = 8.2 Hz), 7.35 (d, 1H, J = 2.0 Hz); ms (EI), *m/z* (% relative intensity): 253 (7)M+2, 251 (22)M^+, 183 (34), 181 (100), 165 (32), 146 (7), 128 (14). Anal. calcd. for $C_{14}H_{18}ClNO$: C 66.79, H 7.21, N 5.56; found: C 66.47, H 7.25, N 5.44.

N-*(2-Methyl-1-propenyl)-4-chloro-6-methyl-2-(2-propyl)benzamide* ***11***

To a stirred solution of amide **9** (2.0 g, 8.0 mmol) in THF (20 mL) at –60°C was added a solution of *sec*-BuLi (15.3 mL, 1.3 M in cyclohexane, 19.9 mmol). The reaction mixture was stirred at –60°C for 1 h and at –30°C for an additional hour. The solution was cooled to –60°C and treated with iodomethane (0.74 mL, 11.9 mmol). Aqueous NH_4Cl was added and the mixture was extracted with EtOAc and worked up as in the previous example to afford amide **11** (1.7 g, 81%) after crystallization from cyclohexane; mp 101–103°C; ir (KBr): 3620–3200, 1628 cm^{-1}; ^1H nmr ($CDCl_3$) δ: 1.23 (d, 6H, J = 6.8 Hz), 1.61 (s, 3H), 1.77 (s, 3H), 2.30 (s, 3H), 2.98 (hept, 1H, J = 6.9 Hz), 6.72 (m, 1H), 6.88 (br d, 1H, NH), 7.05 (d, 1H, J = 1.9 Hz), 7.14 (d, 1H, J = 1.9 Hz; ms EI), *m/z* (% relative intensity): 267 (7)M^++2, 265 (20)M^+, 197 (35), 195 (100), 181 (10), 177 (20). Anal. calcd. for $C_{15}H_{20}ClNO$: C 67.78, H 7.59, N 5.27; found: 67.67, H 7.54, N 5.32.

4-Chloro-6-methyl-2-(2-propyl)benzamide ***12***

A solution of amide **11** (4.1 g, 15.5 mmol) in acetic acid (20 mL), water (20 mL), and concentrated HCl (1 mL) was heated at 80°C for 24 h. The cooled reaction mixture was concentrated in vacuo, diluted with water, and extracted with EtOAc. The EtOAc extract was washed with 5% Na_2CO_3 solution, water, and brine, dried (Na_2SO_4), and evaporated. Crystallization of the residue from EtOAc–hexane gave benzamide **12** (3.1 g, 95%); mp 138–140°C; ir (KBr): 3600–3300, 1643 cm^{-1}; ^1H nmr ($CDCl_3$) δ: 1.24 (d, 6H, J = 6.9 Hz), 2.33 (s, 3H), 3.07 (hept, 1H, J = 6.9 Hz), 5.77 (br s, 1H, NH), 6.31 (br s, 1H, NH), 7.03 (d, 1H, J = 1.5 Hz), 7.13 (d, 1H, J = 1.5 Hz); ms (EI), *m/z* (% relative intensity): 213 (31)M+2, 211 (93)M^+, 196 (61), 194 (100), 181 (32), 179 (83), 115 (46). Anal. calcd. for $C_{11}H_{14}ClNO$: C 62.42, H 6.67, N 6.62; found: C 62.54, H 6.66, N 6.32.

6-Chloro-2-(2-methyl-1-propenyl)-8-(2-propyl)-1(2H)-isoquinolone ***13***

This compound was prepared in 96% yield from **11** according to the procedures described in ref. 11; mp 91–93°C (EtOAc–hexane); ir

Can. J. Chem. Downloaded from www.nrcresearchpress.com by 195.246.54.202 on 09/08/12
For personal use only.

(KBr): 1651 cm^{-1}; ^1H nmr ($CDCl_3$) δ: 1.29 (d, 6H, J = 6.9 Hz), 1.68 (d, 3H, J = 1.1 Hz), 1.89 (d, 3H, J = 1.4 Hz), 4.84 (hept, 1H, J = 6.9 Hz), 6.35 (d, 1H, J = 7.3 Hz), 6.50 (m, 1H), 6.97 (d, 1H, J = 7.3 Hz), 7.31 (d, 1H, J = 2.1 Hz), 7.37 (d, 1H, J = 2.1 Hz); ms (EI), *m/z* (% relative intensity): 277 (36)M+2, 275 (100)M^+, 262 (95), 260 (100), 220 (22), 218 (40), 206 (17), 204 (33). Anal. calcd. for $C_{16}H_{18}ClNO$: C 69.68, H 6.58, N 5.08; found: C 69.63, H 6.67, N 5.47.

*General procedure for the preparation of ketones **14** by condensation of dianion **2**a with* N-*methoxy*-N-*methylamides*

Amide **1***a* was converted to dianion **2***a* as described above and treated at –60°C with the requisite *N*-methoxy-*N*-methylamide (prepared as described in ref. 1). The reaction mixture was allowed to warm to –30°C over a 0.5 h period and was then quenched by addition of NH_4Cl solution and worked up by EtOAc extraction to afford ketones **14***a–d*. Purification was by mpc (EtOAc–hexane). Yields for the following compounds are given in Scheme 4.

*1-[2-((*tert-*Butoxycarbonyl)aminomethyl)phenyl]-2-hexanone **14**a*: mp 66–67°C; ir (KBr): 3660–3200, 1713, 1686 cm^{-1}; ^1H nmr ($CDCl_3$) δ: 0.90 (t, 3H, J = 7.3 Hz), 1.40 (m, 2H), 1.44 (s, 9H), 1.59 (m, 2H), 2.51 (t, 2H, J = 7.5 Hz), 3.80 (s, 2H), 4.24 (d, 2H, J = 5.7 Hz), 4.88 (br m, 1H, NH), 7.11 (m, 1H), 7.25 (m, 2H), 7.31 (m, 1H); ms (EI), *m/z* (% relative intensity): 249 (19)M^+, 231 (25), 189 (21), 187 (26), 104 (100), 85 (41), 57 (65). Anal. calcd. for $C_{18}H_{27}NO_3$: C 70.79, H 8.91, N 4.59; found: C 70.79, H 8.97, N 4.65.

*1-[2-((*tert-*Butoxycarbonyl)aminomethyl)phenyl]-6-chloro-2-hexanone **14**b*: mp 47–48°C; ir (KBr): 3350, 1713, 1686 cm–^{1}; ^1H nmr ($CDCl_3$) δ: 1.45 (s, 9H), 1.75 (m, 4H), 2.56 (t, 2H, J = 6.7 Hz), 3.50 (m, 2H), 3.81 (s, 2H), 4.24 (d, 2H, J = 5.8 Hz), 4.85 (br m, 1H, NH), 7.10 (m, 1H), 7.25 (m, 2H), 7.32 (m, 1H); ms (EI), *m/z* (% relative intensity): 283 (15), 265 (28), 223 (34), 222 (34), 104 (100), 91 (29), 57 (45). Anal. calcd. for $C_{18}H_{26}ClNO_3$: C 63.61, H 7.71, N 4.12; found: C 63.66, H 7.84, N 3.72.

*2-[2-((*tert-*Butoxycarbonyl)aminomethyl)phenyl]-1-phenylethanone **14**c*: mp 110–112°C; ir (KBr): 3720–3160, 1686 cm^{-1}; ^1H nmr ($CDCl_3$) δ: 1.35 (s, 9H), 4.28 (d, 2H, J = 5.6 Hz), 4.41 (s, 2H), 4.89 (br m, 1H, NH), 7.15 (m, 1H), 7.28 (m, 2H), 7.35 (m, 1H), 7.49 (m, 2H), 7.59 (m, 1H), 8.04 (m, 2H); ms (EI), *m/z* (% relative intensity): 325 (1)M^+, 269 (7), 268 (7), 251 (10), 208 (30), 105 (100). Anal. calcd. for $C_{20}H_{23}NO_3$: C 73.82, H 7.12, N 4.30; found: C 73.89, H 7.15, N 4.40.

*3-[2-((*tert-*Butoxycarbonyl)aminomethyl)phenyl]-1-(3,4-dimethoxyphenyl)-2-propanone **14**d*: mp 90–91°C; ir (KBr): 3660–3220, 1719, 1684 cm^{-1}; ^1H nmr (300 MHz, $CDCl_3$) δ: 1.45 (s, 9H), 3.73 (s, 2H),3.84 (s, 3H), 3.85 (s, 3H), 3.89 (s, 3H), 4.18 (d, 2H, J = 5.8 Hz), 4.82 (br m, 1H, NH), 6.70 (m, 1H), 6.75 (m, 1H), 6.83 (m, 1H), 7.02 (m, 1H), 7.23 (m, 3H); ms (EI), *m/z* (% relative intensity): 399 (33)M^+, 343 (8), 299 (75), 282 (74), 254 (20), 151 (100). Anal. calcd. for $C_{23}H_{29}NO_5$: C 69.15, H 7.32, N 3.51; found: C 69.04, H 7.39, N 3.74.

*General procedure for cyclization of ketones **14** to dihydroisoquinolines **15***

A solution of ketone **14** (10 mmol) in CH_2Cl_2 (25 mL) at 0°C was treated with trifluoroacetic acid (0.75 mL) and the mixture was stirred with warming to room temperature over a 0.5 h period. Additional CH_2Cl_2 (50 mL) was added and the mixture was washed with saturated $NaHCO_3$ and dried (Na_2SO_4). Evaporation afforded the crude product (**15**), which could be purified by mpc (EtOAc–hexane) or used directly in subsequent reactions. Yields for the following compounds are given in Scheme 4.

*2-(*tert-*Butoxycarbonyl)-1-(1-*n*-butyl)-1,2-dihydroisoquinoline **15**a*: Oil; ir (neat): 1700 cm^{-1}; ^1H nmr ($CDCl_3$) δ: 0.94 (t, 3H, J = 7.2 Hz), 1.38 (m, 2H), 1.48 (s, 9H), 1.51 (m, 2H), 2.66 (t, 2H, J = 7.0 Hz), 4.67 (s, 2H), 6.04 (s, 1H), 7.04 (m, 1H), 7.18 (m, 3H); ms (EI), *m/z* (% relative intensity): 287 (18)M^+, 231 (100), 189 (25), 186 (54), 156 (13), 145 (21), 143 (35), 57 (68). Anal. calcd. for $C_{18}H_{25}NO_2$: C 75.22, H 8.77, N 4.87; found: C 75.02, H 8.73, N 5.06.

*2-(*tert-*Butoxycarbonyl)-3-(4-chloro-1-*n*-butyl)-1,2-dihydroisoquinoline **15**b*: Oil; ir (neat): 1701 cm^{-1}; ^1H nmr ($CDCl_3$) δ: 1.48 (s, 9H), 1.70 (m, 2H), 1.85 (m, 2H), 2.70 (t, 2H, J = 7.7 Hz), 3.57 (t, 2H, J = 6.4 Hz), 4.67 (s, 2H), 6.05 (s, 1H), 7.04 (m, 1H), 7.18 (m, 3H); ms (EI), *m/z* (% relative intensity): 321 (20)M^+, 267 (47), 265 (96), 222 (26), 221 (34), 220 (64), 186 (17), 184 (20), 57 (100). Anal. calcd. for $C_{18}H_{24}ClNO_2$: C 66.35, H 7.44, N 4.28; found: C 66.38, H 7.13, N 4.41.

*2-(*tert-*Butoxycarbonyl)-1,2-dihydro-3-phenylisoquinoline **15**c*: mp 105–106°C; ir (KBr): 1704 cm^{-1}: ^1H nmr ($CDCl_3$) δ: 1.05 (s, 9H), 4.89 (s, 2H), 6.43 (s, 1H), 7.18–7.40 (m, 7H), 7.50 (m, 1H); ms (EI), *m/z* (% relative intensity): 307 (11)M^+, 251 (43), 206 (100), 128 (7), 57 (43). Anal. calcd. for $C_{20}H_{21}NO_2$: C 78.14, H 6.89, N 4.56; found: C 77.94, H 6.91, H 6.91, N 4.54.

*2-(*tert-*Butoxycarbonyl)-1,2-dihydro-3-(3,4-dimethoxyphenylmethyl)isoquinoline **15**d*: Waxy solid; ir (KBr): 1701 cm^{-1}; ^1H nmr (300 MHz, $CDCl_3$) δ: 1.45 (s, 9H), 3.85 (s, 3H), 3.88 (s, 3H), 3.95 (s, 2H), 4.60 (s, 2H), 6.07 (s, 1H), 6.82 (m, 3H), 7.17 (m, 4H); ms (EI), *m/z* (% relative intensity): 381 (4)M^+, 325 (44), 280 (100), 57 (30). Exact Mass (hrms) calcd. for $C_{23}H_{27}NO_4$: 381.194; found: 381.194.

*General procedure for the catalytic hydrogenation of **15***

A mixture of dihydroisoquinoline **15** (10 mmol) and 20% $Pd(OH)_2$ (0.7 g) in EtOAc (30 mL) was hydrogenated for 12 h at ca. 45 psi. The catalyst was removed by filtration and evaporation of the filtrate afforded crude **16**, which was purified by mpc (**16***b*) (EtOAc–hexane) or used directly in a subsequent reaction (**16***d*).

*2-(*tert-*Butoxycarbonyl)-3-(4-chloro-1-*n*-butyl)-1,2,3,4-tetrahydroisoquinoline **16**b*: Oil; ir (neat): 1690 cm^{-1}; ^1H nmr ($CDCl_3$) δ: 1.20–1.50 (m, 4H), 1.45 (s, 9H), 1.75 (m, 2H), 2.63 (d, 1H, J = 15.9 Hz), 3.19 (dd, 1H, J = 5.8, 15.9 Hz), 3.50 (t, 2H, J = 6.6 Hz), 4.20 (br d, 1H, J = 17.2 Hz), 4.50 (br d, 1H, J = 17.2 Hz), 4.83 (m, 1H), 7.15 (m, 4H); ms (EI), *m/z* (% relative intensity): 266 (42)$M^+ - C_4H_9$, 232 (26), 176 (100), 132 (39). Anal. calcd. for $C_{18}H_{26}ClNO_2$: C 66.75, H 8.10, N 4.32; found: C 66.92, H 8.15, N 4.32.

*3-*n*-Butyl-1,2,3,4-tetrahydroisoquinoline **17**a*

A solution of ketone **14***a* (1.07 g, 3.5 mmol) in CH_2Cl_2 (5 mL) was cooled in an ice-bath and trifluoroacetic acid (3 mL) was added. The mixture was stirred at room temperature for 1 h and was then concentrated in vacuo. The residue was dissolved in EtOH (10 mL) and the resulting solution was cooled in an ice-bath. $NaBH_4$ (0.5 g, 13 mmol) was slowly added in small portions and the mixture was stirred with warming to room temperature over 1 h. Aqueous 5% HCl (30 mL) was added and the mixture was basified with NH_4OH and extracted with CH_2Cl_2. The CH_2Cl_2 was dried (Na_2SO_4) and evaporated to give **17***a* as an oil that was homogeneous by tlc (5% MeOH–CH_2Cl_2); ^1H nmr ($CDCl_3$) δ: 0.93 (t, 3H, J = 6.9 Hz), 1.30–1.55 (m,6H), 1.86 (br s, 1H, NH), 2.50 (dd, 1H, J = 10.5, 16.2 Hz), 2.80 (dd, 1H, J = 3.9, 16.2 Hz), 2.85 (m, 1H), 4.06 (AB quartet, 2H, J_{AB} = 16.0 Hz), 6.96–7.12 (m, 4H); ms (EI), *m/z* (% relative intensity): 189 (4)M^+, 188 (3), 133 (16), 132 (100), 130 (21), 104 (18).

Hydrochloride salt: mp 149–151°C (EtOH–Et_2O). Anal. calcd. for $C_{13}H_{20}ClN$: C 69.16, H 8.93, N 6.20; found: C 68.93, H 8.87, N 6.32.

*3-(3,4-Dimethoxyphenyl)methyl-1,2,3,4-tetrahydroisoquinoline **17**d*

Crude **16***d* (0.80 g, 2.1 mmol), obtained as above, was dissolved in CH_2Cl_2 (10 mL) and trifluoroacetic acid (2 mL) was added. The resulting solution was allowed to stand at room temperature for 48 h. Additional CH_2Cl_2 (50 mL) was added and the mixture was washed (carefully) with aqueous $NaHCO_3$, dried (Na_2SO_4), and evaporated. Purification by mpc (3% MeOH–CH_2Cl_2, 0.5% NH_4OH) afforded **17***d* (0.48 g, 81%); mp 99–100°C; ir (KBr): 3650–3250 cm^{-1}; ^1H nmr ($CDCl_3$) δ: 2.57–2.90 (m, 4H), 3.12 (m, 1H), 3.88 (s, 6H), 4.03 (s, 2H), 6.81 (m, 3H), 6.96–7.14 (m, 4H); ms (EI), *m/z* (% relative intensity): 152 (8) $M^+ - C_9H_{10}N$, 132 (100). Anal. calcd. for $C_{18}H_{21}NO_2$(0.2 H_2O): C 75.32, H 7.52, N 4.88; found: C 75.32, H 7.27, N 4.88.

*1,3,4,6,11,11a-Hexahydro-2*H*-benzo[*b*]quinolizine **18***

A solution of **16***b* (0.25 g, 0.77 mmol) in CH_2Cl_2 (10 mL) was treated with trifluoroacetic acid (1 mL) and the resulting mixture was stirred at room temperature for 2 h. The mixture was concentrated in vacuo, saturated $NaHCO_3$ solution was added, and the mixture was extracted three times with EtOAc. The EtOAc extract was washed with water and brine, dried (Na_2SO_4), and evaporated. Purification of the

Can. J. Chem. Downloaded from www.nrcresearchpress.com by 195.246.54.202 on 09/08/12
For personal use only.

residue by mpc (5% MeOH–CH_2Cl_2, 0.1% NH_4OH) afforded compound **18** (0.14 g, 94%); mp 42–43°C (lit. (20) mp 46–47°C); HCl salt, mp 252–254°C. Anal. calcd. for $C_{13}H_{18}ClN$: C 69.78, H 8.11, N, 6.26; found: C 69.37, H 8.00, N 6.23.

2,3-Dimethoxy-7,12,12a,13-tetrahydro-5H-dibenzo[b,g]quinolizine ***19***

A suspension of **17***d* (0.10 g, 0.35 mmol) in water (1 mL) was treated with concentrated HCl (3 drops) and 37% aqueous formaldehyde (0.6 mL) and the resulting solution was stirred at 95°C for 1 h. After dilution with water (10 mL), the mixture was basified with NH_4OH and extracted with EtOAc. The EtOAc extract was washed with water and brine, dried (Na_2SO_4), and evaporated. Purification by mpc (3% MeOH–CH_2Cl_2, 0.5% NH_4OH) gave **19** (0.09 g, 89%); mp 176–177°C; ^1H nmr ($CDCl_3$) δ: 2.72 (dd, 1H, J = 5.0, 16.8 Hz), 2.80 (dd, 1H, J = 5.0, 16.8 Hz), 2.92 (dd, 1H, J = 5.0, 16.8 Hz), 3.03 (dd, 1H, J = 5.0, 16.8 Hz), 3.23 (m, 1H), 3.78 (d, 1H, J = 15.5 Hz), 3.82 (d, 1H, J = 15.5 Hz), 3.84 (s, 3H), 3.85 (s, 3H), 3.97 (d, 1H, J = 15.5 Hz), 4.04 (d, 1H, J = 15.5 Hz), 6.55 (s, 1H), 6.58 (s, 1H), 7.10 (m, 4H); ms (EI), *m/z* (% relative intensity): 295 (42)M^+, 164 (100). Anal. calcd. for $C_{19}H_{21}NO_2$: C 77.26, H 7.17, N 4.74; found: C 77.15, H 7.20, N 4.85.

*3-*n*-Butylisoquinoline* ***20***

A solution of dihydroisoquinoline **15***a* (1.0 g, 3.5 mmol) in CH_2Cl_2 (2.5 mL) was treated with trifluoroacetic acid (2.5 mL) and the resulting mixture was stirred at room temperature for 15 min. The solution was concentrated in vacuo and the residue was dissolved in EtOH (20 mL). To this solution was added KOAc (0.98 g, 10 mmol) and I_2 (1.0 g, 4 mmol) and the mixture was heated under reflux for 2 h. The mixture was cooled to room temperature, diluted with aqueous NH_4OH, and extracted with EtOAc. The EtOAc was washed with aqueous $NaHSO_3$, water, and brine, dried (Na_2SO_4), and evaporated. Purification by mpc (2% MeOH–CH_2Cl_2) afforded **20** as a colorless oil. The ^1H nmr spectrum of this material was identical to that reported in ref. 19. The HCl salt had mp 202–203°C (EtOH–Et_2O).

*2-[2-((*tert*-Butoxycarbonyl)aminomethyl)phenyl]-1-(3,4-dimethoxyphenyl)ethanol* ***21***

A solution of anion **2***a*, prepared from **1***a* (0.50 g, 2.26 mmol) in THF (10 mL) as previously described, was treated with a solution of veratraldehyde (0.42 g, 2.49 mmol) in THF (2 mL) at –60°C. The reaction mixture was stirred at that temperature for 30 min and then worked up as usual to afford alcohol **21** (0.58 g, 66%) after mpc (40% EtOAc–hexane); mp 99–100°C; ir (KBr): 3600–3110, 1694 cm^{-1}; ^1H nmr ($CDCl_3$) δ: 1.45 (s, 9H), 2.15 (br m, 1H, OH), 3.00 (dd, 1H, J = 8.5, 13.9 Hz), 3.10 (dd, 1H, J = 4.7, 13.9 Hz), 3.87 (s, 3H), 3.88 (s, 3H), 4.34 (d, 2H, J = 5.2 Hz), 4.87 (dd, 1H, J = 4.7, 8.4 Hz), 5.09 (br m, 1H,NH), 6.83 (d, 1H, J = 8.7), 6.92 (m, 2H), 7.17–7.32 (m, 4H); ms (EI), *m/z* (% relative intensity): 387 (6)M^+, 221 (9), 167 (100), 166 (73), 139 (24), 104 (50), 57 (34). Anal. calcd. for $C_{22}H_{29}NO_5$: C 68.19, H 7.54, N 3.62; found: C 68.17, H 7.44, N 3.55.

*2-(*tert*-Butoxycarbonyl)-(3-(3,4-dimethoxyphenyl))-1,2,3,4-tetrahydroisoquinoline* ***23***

A solution of **21** (0.25 g, 0.65 mmol) in CH_2Cl_2 (10 mL) was treated with trifluoroacetic acid (0.5 mL) and the resulting mixture was stirred at room temperature for 0.5 h. The usual work-up afforded **25** (0.21 g, 87%) after mpc (30% EtOAc–hexane); mp 58–60°C; ir (neat): 3570–3200, 1690 cm^{-1}; ^1H nmr (300 MHz, $CDCl_3$) δ: 1.43 (s, 9H), 3.06 (dd, 1H, J = 3.4, 15.7 Hz), 3.31 (dd, 1H, J = 6.1, 15.8 Hz), 3.68 (s, 3H), 3.78 (s, 3H), 4.23 (d, 1H, J = 16.4 Hz), 4.80 (d, 1H, J = 16.4 Hz), 5.44 (m, 1H), 6.67 (m, 3H), 7.13 (m, 4H); ms (EI), *m/z* (% relative intensity): 369 (21)M^+, 313 (33), 268 (40), 252 (24), 175 (40), 131 (19), 104 (29), 57 (36), 43 (100). Anal. calcd. for $C_{22}H_{27}NO_4$: C 71.52, H 7.37, N 3.79; found: C 71.51, H 7.51, N 3.63.

*2-[2-((*tert*-Butoxycarbonyl)aminomethyl)phenyl]-1,1-diphenylethanol* ***24***

A solution of dianion **2***a*, prepared from **1***a* (1.1 g, 5.0 mmol) in THF (10 mL) as described above, was treated with a solution of benzophenone (1.0 g, 5.5 mmol) in THF (5 mL) at –60°C. The reaction mixture was stirred at –60°C for 30 min and was then allowed to warm to 0°C. The usual work-up afforded alcohol **24** (1.2 g, 60%) after crystallization from hexane; mp 117–118°C; ir (KBr): 3600–3200, 1701 cm^{-1}; ^1H nmr ($CDCl_3$) δ: 1.42 (s, 9H), 1.95 (br m, 1H, OH), 3.69 (s, 2H), 4.18 (br s, 2H), 4.80 (br m, 1H, NH), 6.63 (d, 1H, J = 7.5 Hz), 6.96 (t, 1H, J = 7.5 Hz), 7.14 (t, 1H, J = 7.5 Hz), 7.25 (m, 7H), 7.37 (m, 4H); ms (EI), *m/z* (% relative intensity): 403 (4)M^+, 347 (5), 312 (5), 269 (7), 221 (12), 183 (100), 165 (45), 105 (38), 104 (33). Anal. calcd. for $C_{26}H_{29}NO_3$: C 77.39, H 7.25, N 3.47; found: C 77.63, H 7.33, N 3.60.

*2-[2-((*tert*-Butoxycarbonyl)aminomethyl)phenyl]-1,1-diphenylethylene* ***25***

A solution of **24** (0.2 g, 0.5 mmol) in CH_2Cl_2 (5 mL) was treated with trifluoroacetic acid (0.75 mL) and the resulting mixture was stirred at room temperature for 15 min. Anhydrous K_2CO_3 (1.0 g), and CH_2Cl_2 (25 mL) were added and the mixture was filtered. Evaporation of the filtrate afforded compound **25** (0.16 g, 83%) after crystallization from hexane; mp 106–108°C; ir (KBr): 3620–3200, 1688 cm^{-1}; ^1H nmr ($CDCl_3$) δ: 1.40 (s, 9H), 4.34 (d, 2H, J = 5.8 Hz), 4.63 (br m, 1H, NH), 6.88–7.40 (m, 15H); ms (EI), *m/z* (% relative intensity): 385 (26)M^+, 329 (36), 284 (70), 268 (100), 57 (68). Anal. calcd. for $C_{26}H_{27}NO_2$: C 81.00, H 7.06, N 3.63; found: C 81.25, H 7.06, N 3.81.

*1-[(2-((*tert*-Butoxycarbonyl)aminomethyl)phenyl)methyl]cyclohexan-1-ol* ***26***

Condensation of dianion **2***a* with cyclohexanone as described for the preparation of **25** afforded alcohol **26** in 50% yield after crystallization from hexane; mp 82–83°C; ir (KBr): 3600–3200, 1680 cm^{-1}; ^1H nmr ($CDCl_3$) δ: 1.20 (m, 2H), 1.40–1.65 (m, 9H), 1.45 (s, 9H), 2.81 (s, 2H), 4.40 (br d, 2H, J = 5.0 Hz), 5.20 (br m, 1H, NH), 7.18 (m, 3H), 7.32 (m, 1H). Anal. calcd. for $C_{19}H_{29}NO_3$: C 71.44, H 9.15, N 4.38; found: C 71.47, H 9.21, H 4.52.

Acknowledgment

We thank Dr. J.M. Muchowski for stimulating discussions in regard to this work.

1. R.D. Clark, J.M. Muchowski, L.E. Fisher, L.A. Flippin, D.B. Repke, and M. Souchet. Synthesis, 871 (1991), and references cited therein.
2. R.D. Clark and Jahangir. *In* Trends in organic chemistry. Vol. 3. *Edited by* J. Menon. Council of Scientific Research Integration, Trivandrum, India. 1992. pp. 65–92.
3. R.D. Clark and Jahangir. Heterocycles, **32**, 1699 (1991).
4. A.N. Tischler and M.H. Tischler. Tetrahedron Lett. 3 (1978).
5. G. Simig and M. Schlosser. Tetrahedron Lett. **29**, 4277 (1988).
6. A.M. Kanazawa, A. Correa, J.-N. Denis, M.-J. Luche, and A.E. Greene. J. Org. Chem. **58**, 255 (1993).
7. V. Snieckus. Chem Rev. **90**, 879 (1990).
8. R.D. Clark and Jahangir. Tetrahedron, **49**, 1351 (1993).
9. W.M. Whaley and T.R. Govindachari. Org. React. **6**, 74 (1951).
10. W.M. Whaley and T.R. Govindachari. Org. React. **6**, 151 (1951).
11. L.E. Fisher, J.M. Muchowski, and R.D. Clark. J. Org. Chem. **57**, 2700 (1992).
12. A.N. Tischler and M.H. Tischler. Tetrahedron Lett. 3407 (1978).
13. L.A. Flippin, J.M. Muchowski, and D.S. Carter. J. Org. Chem. **58**, 2463 (1993).
14. R.S. Mali, B.K. Kulkarni, and K. Schankaran. Synthesis, 329 (1982).
15. S. Nahm and S.M. Weinreb. Tetrahedron Lett. **22**, 3815 (1981).
16. M. Sainsbury, D.W. Brown, S.F. Dyke, R.D.J. Clipperton, and W.R. Tonkyn. Tetrahedron, **26**, 2239 (1970).
17. F.D. Popp. Adv. Heterocycl. Chem. **24**, 187 (1979).
18. W.J. Gensler. Org. React. **6**, 191 (1951).
19. L.A. Flippin and J.M. Muchowski, J. Org. Chem. **58**, 2631 (1993).
20. J.M. Paton, P.L. Pauson, and T.S. Stevens. J. Chem. Soc.(C), 2130 (1969).

Mechanistic studies on diamine oxidase: oxidation of α,ω-diamines does not involve an enamine intermediate[1]

STEPHEN S. GAVIN, ANGELA M. EQUI, AND DAVID J. ROBINS[2]
Department of Chemistry, University of Glasgow, Glasgow G12 8QQ, U.K.

Received June 4, 1993

This paper is dedicated to Professor Ian Spenser

STEPHEN S. GAVIN, ANGELA M. EQUI, and DAVID J. ROBINS. Can. **72**, 31 (1994).

Three β,β,β′,β′-$^2H_4$-labelled α,ω-diamines were synthesized and incubated with pea seedling diamine oxidase. The aminoaldehydes formed by oxidative deamination cyclized to the corresponding imines, which were trapped with benzoylacetic acid. In all three cases the acetophenone derivatives produced were shown by NMR and mass spectrometry to contain four deuterium atoms. The retention of all four deuterium atoms demonstrates that oxidative deamination of α,ω-diamines catalyzed by pea seedling diamine oxidase does not involve an enamine intermediate as previously suggested.

STEPHEN S. GAVIN, ANGELA M. EQUI et DAVID J. ROBINS. Can. **72**, 31 (1994).

On a synthétisé trois β,β,β′,β′-$^2H_4$-α,ω-diamines et on les a incubées avec de la diamine oxydase de la semence de pois. Les trois aminoaldéhydes qui se forment par désamination oxydante se cyclisent en imines correspondantes que l'on peut piéger à l'aide d'acide benzoylacétique. Dans les trois cas, on a démontré, par RMN et par spectrométrie de masse, que les dérivés acétophénones qui se forment contiennent toutes quatre atomes de deutérium. La rétention des quatre atomes de deutérium démontre que, contrairement à ce qui avait été suggéré antérieurement, la désamination oxydante des α,ω-diamines catalysée par la diamine oxydase de la semence de pois n'implique pas d'intermédiaire énamine.

[Traduit par la rédaction]

Introduction

Decarboxylation of basic α-amino acids such as ornithine and lysine followed by the oxidative deamination of the resulting diamines, putrescine (**1**) and cadaverine (**2**), respectively, are key steps in amino acid metabolism and the biosynthesis of many alkaloids (1). Naturally occurring polyamines such as **1** also have an important function in the control of growth and proliferation processes (2). Putrescine is formed by decarboxylation of L-ornithine catalyzed by L-ornithine decarboxylase. The stereochemistry of this process was studied by several groups of workers (3–7). An analogous process operates on the homologue L-lysine, which leads to cadaverine on decarboxylation with L-lysine decarboxylase. Again this process was shown to proceed with retention of configuration (6–9). The next step in the metabolism of the diamines **1** and **2** is oxidative deamination to the corresponding aldehydes **5** and **6** catalyzed by diamine oxidase (DAO, EC 1.4.3.6) (Scheme 1). The stereochemistry of these processes was studied extensively by Spenser and co-workers (3, 10) and by other groups of workers (9, 11). DAO catalyses the removal of the 1-*pro-S* hydrogen from **1** and **2**.

A series of *N*-alkylputrescines was tested as substrates of DAO by Frydman et al. (12). With the surprising exception of *N*-methylputrescine, these diamines were shown to be oxidized to the corresponding aminoaldehydes. We repeated this work using an improved kinetic assay procedure, and demonstrated that *N*-methylputrescine was in fact a good substrate for pea seedling and pig kidney DAO (13). A range of derivatives of **1** and **2** was synthesized and assayed as substrates for these DAOs by several groups (14–16). Recently we obtained enzyme kinetic data for the DAO-catalyzed oxidation of α,ω-diamines with chain lengths ranging from 2 to 12. The highest V_{max} values were observed for chain lengths of 5 (**2**), 4 (**1**), and 6 (**3**), which together with the K_m data suggested that after initial attachment of one end of the substrate to the enzyme, the other end might also become attached to the enzyme thus creating a cyclic conformation (17). In their work on DAO, Frydman et al. (12) noted that 1,3-dimethylputrescine was a very poor substrate for the pea seedling and pig kidney DAO. They suggested that oxidation of putrescine (**1**) proceeds via an enamine intermediate (**4**) formed by abstraction of hydride from C-2 of putrescine (presumably tautomerism and hydrolysis of the resulting imine then produces the aldehyde). They postulated that 1,3-dimethylputrescine sterically hinders the formation of the enamine intermediate (**4**) thus accounting for its poorness as a substrate for DAO. We decided to test this hypothesis by preparing some α,ω-diamines containing deuterium labels at appropriate positions, so that the loss or retention of deuterium in the diamines during oxidative deamination catalyzed by DAO could be followed by NMR and mass spectrometry.

Results and discussion

DAO can be easily isolated and partially purified from pea seedlings (18). The cyclic imine **7** generated by the DAO-catalyzed oxidation of putrescine (**1**) can be trapped by reaction with benzoylacetic acid to form the substituted acetophenone **8**, which can be isolated and characterized (Scheme 1) (19). The corresponding derivatives (**9** and **10**) were also prepared for spectroscopic characterization (15, 20, 21). Three different ^2H-labelled α,ω-diamines were prepared for this study of the mechanism of DAO action. [2,2,3,3-$^2H_4$]Putrescine (**11**) dihydrochloride containing 98 ± 2% $^2H_4$ was made from succinonitrile by exchanging the protons for deuterium atoms followed by reduction and acidification in a modification of a published procedure (22). Samples of [2,2,4,4-$^2H_4$]cadaverine (**12**) dihydrochloride and [2,2,5,5-$^2H_4$]-1,6-diaminohexane (**13**) dihydro-

[1]This paper is dedicated to Professor Ian Spenser, an acknowledged expert in the determination of the stereochemistry of enzymic reactions and the elucidation of biosynthetic pathways to alkaloids. For several years our two groups published almost simultaneously but independently on the same aspects of the biosynthesis of pyrrolizidine and quinolizidine alkaloids and his thoroughness and attention to detail were always most impressive.

[2]Author to whom correspondence may be addressed.

Can. J. Chem. Downloaded from www.nrcresearchpress.com by 195.246.54.202 on 09/08/12
For personal use only.

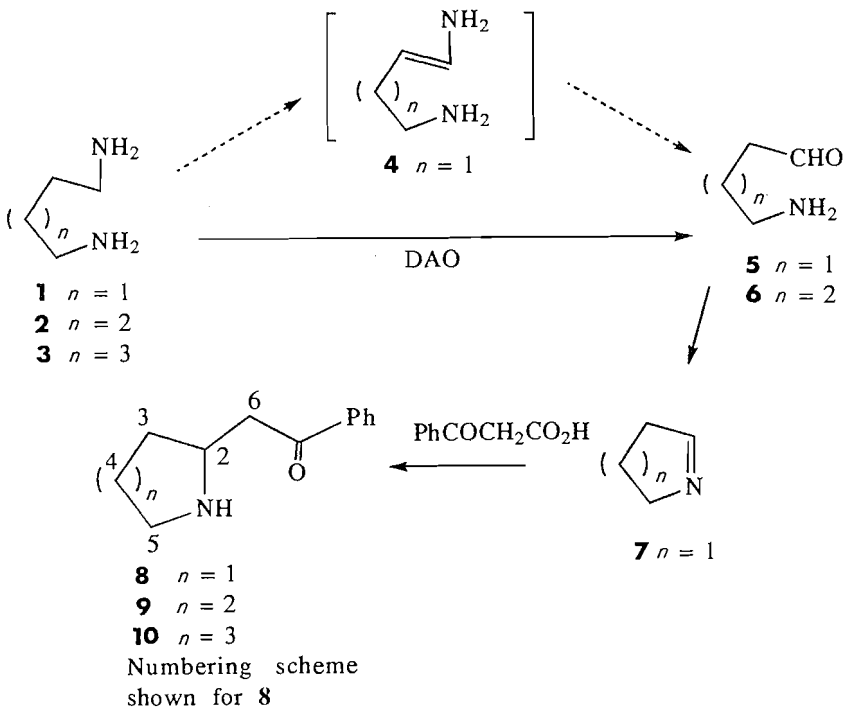

SCHEME 1

chloride were prepared in an analogous manner with $^2H_4$ contents of 96 ± 2% and 93 ± 2%, respectively.

Incubation of the tetradeuteriated putrescine (**11**) with DAO for one day at pH 7 in phosphate buffer in the presence of catalase and benzoylacetic acid gave 2-pyrrolidin-2-ylacetophenone in 76% yield. The product was purified by preparative TLC and the purity was checked by HPLC. The $^2H_4$ content of this product (**14**) was estimated to be 96 ± 2% by analysis of the integrals for the protons in the ^1H NMR spectrum of **14**. The signals observed for the protons at the 3- and 4-positions in **8** were barely visible in the ^1H NMR spectrum of **14** at δ1.3–1.9 and the protons at the 5-position of **14** were observed as an AB system. The signals for the 2-H and the 6-H protons were also greatly simplified to an ABX system. Furthermore, in the ^2H NMR spectrum of **14** four separate signals each with about the same intensity were observed. Finally, in unlabelled **8**, peaks were visible in the mass spectrum at *m/e* 190 and 189 (M^+), whereas in the labelled product (**14**) the major isotopic species were at *m/e* 194 and 193.

When the tetradeuteriated cadaverine (**12**) dihydrochloride was treated with DAO in a similar fashion, the corresponding piperidinylacetophenone (**15**) was obtained in 70% yield. Comparison of the ^1H NMR spectra of labelled and unlabelled material indicated that the $^2H_4$ content of **15** was 97 ± 2%. The protons at the 4-position in **15** were present as an AB system and signals for the 3-H and 5-H protons were absent. Signals for the remaining five protons overlapped each other. Four separate signals were observed with approximately the same intensity in the ^2H NMR spectrum of **15**. The mass spectrum of **15** in the molecular ion region contained peaks that were four mass units higher than those in the unlabelled material (**9**).

Finally incubation of [2,2,5,5-$^2H_4$]-1,6-diaminohexane (**13**) dihydrochloride with DAO as in the previous two cases afforded a sample of the seven-membered derivative (**16**) in 75% yield. The region δ 1.0–1.6 in the ^1H NMR spectrum of **16** integrated for four protons compared to eight in the corresponding spectrum for **10**. The ^2H NMR spectrum of **16** contained a broad unresolved band at δ 1.0–1.8. The $^2H_4$ content of **16** was estimated to be 94 ± 2% and comparison of the mass spectra of **10** and **16** in the molecular ion region confirmed the presence of the $^2H_4$-labelled species.

Thus enzyme-catalyzed oxidative deamination of specifically tetradeuteriated samples of **11**, **12**, and **13** by pea seedling DAO and trapping of the products using benzoylacetic acid produces acetophenone derivatives **14**, **15**, and **16**, which are almost entirely tetradeuteriated. Indeed no loss of deuterium was detected in any of these conversions within experimental error. From these results it is clear that oxidation of α,ω-diamines catalyzed by DAO cannot involve an enamine intermediate. (Observation of overall retention of deuterium by removal of deuteride from C-2 of the diamine and replacement of C-2 by the same deuterium in protonated form during tautomerism of the enamine (**4**) to the imine does not seem a likely process.)

Experimental

Melting points were measured with a Kofler hot-stage apparatus and are uncorrected. Organic solutions were dried with anhydrous Na_2SO_4, and solvents were removed under reduced pressure below 40°C. NMR spectra were obtained on a Bruker WP200-SY spectrometer operating at 200 MHz for ^1H, 50 MHz for ^{13}C, and 30.72 MHz for ^2H. EIMS were obtained on Kratos MS 12 or MS 902 instruments. Thin-layer chromatography was carried out on silica gel GF_{254} plates of 0.25 mm thickness developed with chloroform–methanol–concentrated ammonia (80:19:1), and the bases were located by the modified Dragendorff reagent (23). HPLC was performed on a Spectra-Physics SP8800 system with a reverse phase 5 μm ODS-Hypersil column (150 × 4.6 mm) using MeOH–H_2O (70:30) and a flow rate of 3.5 mL min^{-1}.

General procedure for the synthesis of [$^2H_4$]-labelled dinitriles

Deuterium oxide (35 mL, 99.3 at.% ^2H), 1,4-dioxane (10 mL), and diazabicyclo[5.4.0]undec-7-ene (364 mg, 4.56 mmol) were added to

Can. J. Chem. Downloaded from www.nrcresearchpress.com by 195.246.54.202 on 09/08/12
For personal use only.

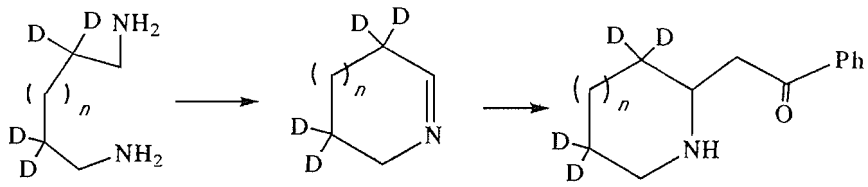

11 $n = 0$
12 $n = 1$
13 $n = 2$

14 $n = 0$
15 $n = 1$
16 $n = 2$

SCHEME 2

the dinitrile (45.6 mmol). The mixture was stirred and heated at reflux for 24 h. The reaction mixture was cooled and the solvent was removed in vacuo to yield an amorphous solid. The solid was dissolved in 1 M HCl and the acidic solution was extracted with chloroform (5 × 25 mL). The organic extracts were dried (Na_2SO_4), filtered, and the solvent was removed in vacuo to yield an amorphous white solid, which was recrystallised from hot benzene. This process was repeated to obtain [$^2H_4$] incorporations of 93–98%.

[2,2,3,3-$^2H_4$]Succinonitrile: 2.87 g (75%); IR ($CHCl_3$) ν: 3010, 2250, 1460, 1070 cm^{-1}; ^{13}C NMR ($CDCl_3$) δ: 116.4 (2 × CN) ppm; MS *m/e(I)*: 84 (M^+) (6), 82 (15), 56 (100), 54 (68), 42 (66). HRMS, Exact Mass calcd. for $C_4D_4N_2$: 84.0625; found: 84.0617.

[2,2,4,4-$^2H_4$]Glutaronitrile: 3.22 g (72%); IR ($CHCl_3$) ν: 2990, 2880, 2250, 1450, 1050 cm^{-1}; ^1H NMR ($CDCl_3$) δ: 2.15 (s, 2H) ppm; ^{13}C NMR ($CDCl_3$) δ: 33.1 (CH_2), 116.4 (2 × CN) ppm; MS *m/e(I)*: 98 (M^+) (6), 96 (8), 70 (100), 46 (65), 38 (75), 28 (64). HRMS, Exact Mass calcd. for $C_5H_2D_4N_2$: 98.0782; found: 98,0780.

[2,2,5,5-$^2H_4$]Adiponitrile: 3.57 g (70%); IR ($CHCl_3$) ν: 3005, 2990, 2250, 1450, 1070 cm^{-1}; ^1H NMR ($CDCl_3$) δ: 1.80 (s, 4H) ppm; ^{13}C NMR ($CDCl_3$) δ: 27.7 (2 × CH_2), 116.4 (2 × CN) ppm; MS *m/e(I)*: 112 (M^+) (6), 110 (1), 86 (9), 61 (69), 55 (60), 44 (100), 28 (75). HRMS, Exact Mass calcd. for $C_6H_4D_4N_2$: 112.0939; found: 112.0940.

General procedure (24) for the synthesis of [$^2H_4$]-labelled diamine dihydrochloride salts

An oven-dried flask containing a septum-capped inlet and a magnetic stirring bar was equipped with a 12-in. Vigreux column. The flask was charged with the [$^2H_4$]-labelled dinitrile (15 mmol) and dry THF (1.5 mL) and brought to reflux under an atmosphere of nitrogen. Then borane – dimethyl sulphide complex in THF (16 mL, 32 mmol) was added dropwise over a period of 10 min. The dimethyl sulphide distilled off and was collected. This gave a clear residue, which was left for 15 min and then allowed to cool to room temperature. 6 M HCl (18 mL, 41 mmol) was added dropwise. The reaction mixture was then heated under reflux for 30 min. The resultant clear solution was cooled to 0°C giving a white precipitate (boric acid). The solution was filtered, and the filtrate was concentrated to approximately 5–10 mL giving a second precipitate of boric acid. The solution was again filtered, and the filtrate was evaporated to dryness giving a creamy white solid of diamine dihydrochloride. The solid was crystallized from 95% aqueous ethanol.

*[2,2,3,3-$^2H_4$]Putrescine (**11**) dihydrochloride:* 1.36 g (55%); IR (KBr disc) ν: 3075, 3025, 2010, 1605, 1473, 1395, 1335, 1170, 1145 cm^{-1}; ^1H NMR (D_2O) δ: 2.85 (br s 4H) ppm; ^{13}C NMR (D_2O, dioxane) δ: 23.9 (quintet, 2 × CD_2), 39.6 (2 × CH_2) ppm. Anal. calcd. for $C_4H_{10}D_4N_2Cl_2$: C 29.10, H 6.12, D 4.87, N 16.97%; found: C 29.08, H 6.20, D 4.90, N 16.98%.

*[2,2,4,4-$^2H_4$]Cadaverine (**12**) dihydrochloride*: 1.61 g (60%); IR (KBr disc) ν: 3080, 2000, 1600, 1475, 1160, 1145 cm^{-1}; ^1H NMR (D_2O) δ: 1.25 (br s 2H), 2.79 (br s, 4H) ppm; ^{13}C NMR (D_2O, dioxane) δ: 23.1 (C-3), 26.3 (quintet, C-2 and C-4), 39.8 (C-1 and C-5) ppm. Anal. calcd. for $C_5H_{12}D_4N_2Cl_2$: C 33.52, H 6.70, D 4.47, N 15.64%; found: C 33.61, H 6.73, D 4.48, N 15.72%.

*[2,2,5,5-$^2H_4$]-1,6-Diaminohexane (**13**) dihydrochloride:* 1.65 g (57%); IR (KBr disc) ν: 3080, 3020, 2000, 1600, 1475, 1175, 1145 cm^{-1}; ^1H NMR (D_2O) δ: 1.25 (s, 4H), 2.83 (s, 4H) ppm; ^{13}C NMR (D_2O, dioxane) δ: 25.7 (C-3 and C-4), 26.6 (quintet, C-2 and C-5), 40.1 (C-1 and C-6) ppm. Anal. calcd. for $C_6H_{14}D_4N_2Cl_2$: C 37.31, H 7.25, D 4.14, N 14.51%; found: C 37.30, H 7.26, D 4.02, N 14.54%.

Benzoylacetic acid

This was prepared as described (19) (75%) and used without purification; IR (Nujol) ν: 2500–3100 (acid OH), 1750 (CO) cm^{-1}; ^1H NMR ($CDCl_3$) δ: 3.99 (s, 2H), 7.35–7.55 (m, 3H), 7.95 (dd, 2H) ppm.

General procedure for oxidative deamination of diamines using diamine oxidase and the subsequent coupling with benzoylacetic acid (19)

A solution of benzoylacetic acid (320 mg, 1.96 mmol), diamine dihydrochloride (0.1 M aqueous solution, 20 mL), and 0.02 M sodium phosphate buffer (pH 7, 7 mL) was prepared. The pH was adjusted to 7. Catalase (0.2 mg) and pea seedling DAO purified to step four (18) (300 μL, enzyme activity ca. 1200 units per mg) were added. The solution was incubated on a shaker at 25°C for 24 h. The pH of the reaction mixture was monitored and readjusted to neutrality as necessary. The solution was then acidified with dilute sulphuric acid and washed with diethyl ether (4 × 30 mL). The aqueous solution was basified with concentrated ammonia and extracted with chloroform (3 × 30 mL). The combined organic extracts were dried (Na_2SO_4), filtered, and evaporated to dryness under reduced pressure to yield an oily product. The products were purified by preparative TLC and the purity of each isolated product was checked by HPLC.

*2-Pyrrolidin-2-ylacetophenone (**8**) (19):* 229 mg (61%) (from putrescine dihydrochloride), R_f 0.40, R_t 2.85 min, IR (film) ν: 3680, 3020, 2400, 1680, 1635, 1600, 1525, 1215 cm^{-1}; ^1H NMR ($CDCl_3$) δ: 1.30–1.90 (m, 4H), 2.35 (br s, NH), 3.0–3.7 (m, 5H), 7.35–7.60 (m, 3H), 7.93 (dd, 2H) ppm; ^{13}C NMR ($CDCl_3$) δ: 23.9 (C-4),30.7 (C-3), 41.9 and 45.1 (C-5 and C-6), 55.2 (C-2), 128.1 (2 × Ar-C), 128.6 (2 × Ar-C), 133.4 (Ar-C), 136.2 (Ar-C), 197.7 (C=O) ppm; MS *m/e(I)*: 190 ($M^+ + 1$) (4), 189 (M^+) (28), 188 ($M^+ - 1$) (9), 170 (19), 105 (45), 84 (21), 70 (100). HRMS, Exact Mass calcd. for $C_{12}H_{15}NO$: 189.1154; found: 189.1155.

*2-Piperidin-2-ylacetophenone (**9**) (15):* 350 mg (87%) (from cadaverine dihydrochloride), R_f 0.43, R_t 2.73 min, IR (film) ν: 3690, 3020, 2400, 1685, 1600, 1520, 1215, 1020, 930 cm^{-1}; ^1H NMR ($CDCl_3$) δ: 1.3–1.75 (m, 6H), 2.68 (m, 1H), 3.03–3.14 (m, 4H), 3.43 (br s, NH), 7.35–7.51 (m, 3H), 7.92 (dd, 2H) ppm; ^{13}C NMR ($CDCl_3$) δ: 24.4 (C-4), 25.5 (C-5), 32.1 (C-3), 45.0 and 46.6 (C-6 and C-7), 52.8 (C-2), 128.0 (2 × Ar-C), 128.5 (2 × Ar-C), 133.2 (Ar-C), 136.8 (Ar-C), 199.1 (C=O) ppm; MS *m/e(I)*: 204 ($M^+ + 1$) (3), 203 (M^+) (18), 202 ($M^+ - 1$) (25), 186 (3), 105 (53), 98 (10), 84 (100), 77 (26), 43 (57). HRMS, Exact Mass calcd. for $C_{13}H_{17}NO$: 203.1310; found: 203.1289.

*2-Hexahydroazepin-2-ylacetophenone (**10**) (15):* 213 mg (50%) (from 1,6-diaminohexane dihydrochloride), R_f 0.40, R_t 2.70 min, IR (film) ν: 3670, 3010, 2395, 1680, 1600, 1515, 1215, 1015, 925 cm^{-1}; ^1H NMR ($CDCl_3$) δ: 0.9–1.6 (m, 8H), 2.09 (br s, NH), 2.3–2.7 (m, 3H),

Can. J. Chem. Downloaded from www.nrcresearchpress.com by 195.246.54.202 on 09/08/12
For personal use only.

2.95–3.00 (m, 1H), 7.21–7.48 (m, 3H), 7.85 (dd, 2H) ppm; ^{13}C NMR ($CDCl_3$) δ: 25.4 (C-5), 27.2 (C-4), 30.9 (C-6), 36.5 (C-3), 46.2 and 46.9 (C-7 and C-8), 55.2 (C-2), 128.2 (2 × Ar-C), 128.5 (2 × Ar-C), 133.0 (Ar-C), 136.8 (Ar-C), 199.0 (C=O) ppm; MS *m/e*(*I*): 218 ($M^+ + 1$) (3), 217 (M^+) (18), 216 ($M^+ - 1$) (4), 200 (2), 113 (3), 105 (100), 98 (14), 43 (66). HRMS, Exact Mass calcd. for $C_{14}H_{19}NO$: 217.1466; found: 217.1470.

*[3′,3′,4′,4′-$^2H_4$]-2-Pyrrolidin-2-ylacetophenone (**14**):* 323 mg (76%) (from [2,2,3,3-$^2H_4$]-putrescine dihydrochloride), R_f 0.42, R_t 2.87 min, IR (film) ν: 3690, 3020, 2400, 1680, 1620, 1600, 1520, 1420, 1215, 1020, 930 cm^{-1}; ^1H NMR ($CDCl_3$) δ: 2.98 and 3.04 (AB system *J* ca. 10 Hz, 2H), 3.4 and 3.6 (AB part of ABX system, J_{AB} ca. 7 Hz, 2H), 3.9 (X part of ABX system, 1H), 4.00 (br s, NH), 7.45 (m, 3H), 7.94 (dd, 2H) ppm; ^{13}C NMR ($CDCl_3$) δ: 44.2 and 45.7 (C-5 and C-6), 54.5 (C-2), 127.9 (2 × Ar-C), 128.0 (2 × Ar-C), 133.1 (Ar-C), 136.7 (Ar-C), 199.1 (C=O) ppm; ^2H NMR ($CHCl_3$) δ: 1.38, 1.72, 1.79, 1.96 ppm; MS *m/e*(*I*): 194 ($M^+ + 1$) (5), 193 (M^+) (19), 192 ($M^+ - 1$) (15), 174 (10), 105 (45), 88 (13), 74 (100), 73 (38). HRMS, Exact Mass calcd. for $C_{12}H_{11}D_4NO$: 193.1404; found: 193.1404.

*[3′,3′,5′,5′-$^2H_4$]-2-Piperidin-2-ylacetophenone (**15**):* 284 mg (70%) (from [2,2,4,4-$^2H_4$]-cadaverine dihydrochloride), R_f 0.42, R_t 2.85 min, IR (film) ν: 3690, 3020, 2400, 1680, 1600, 1525, 1420, 1220, 1015, 930 cm^{-1}; ^1H NMR ($CDCl_3$) δ: 1.4 and 1.8 (AB system, *J* ca. 13 Hz, 2H), 2.52 (br s, NH), 2.66 (d, *J* = 11.6 Hz, 1H), 2.99–3.14 (m, 4H), 7.40–7.59 (m, 3H), 7.94 (dd, 2H) ppm; ^{13}C NMR ($CDCl_3$) δ: 24.2 (C-4), 45.5 and 46.6 (C-6 and C-7), 52.5 (C-2), 127.9 (2 × Ar-C), 128.5 (2 × Ar-C), 133.1 (Ar-C), 136.9 (Ar-C), 199.5 (C=O) ppm; ^2H NMR ($CHCl_3$) δ: 1.35, 1.49, 1.61, 1.68 ppm; MS *m/e*(*I*): 208 ($M^+ + 1$) (3), 207 (M^+) (17), 206 ($M^+ - 1$) (16), 190 (4), 105 (70), 88 (100), 77 (54), 43 (10). HRMS, Exact Mass calcd. for $C_{13}H_{13}D_4NO$: 207.1561; found: 207.1558.

*[3′,3′,6′,6′-$^2H_4$]-2-Hexahydroazepin-2-ylacetophenone (**16**):* 327 mg (75%) (from [2,2,5,5-$^2H_4$]-1,6-diaminohexane dihydrochloride), R_f 0.38, R_t 2.69 min, IR (film) ν: 3680, 3015, 1680, 1600, 1525, 1215, 1020, 930 cm^{-1}; ^1H NMR ($CDCl_3$) δ: 1.17–1.67 (m, 4H), 2.21 (br s, NH), 2.38–2.73 (m, 3H), 3.05 (dd, 1H), 3.15 (m, 1H), 7.41–7.55 (m, 3H), 7.93 (dd, 2H) ppm; ^{13}C NMR ($CDCl_3$) δ: 25.2 (C-5), 27.0 (C-4), 46.2 and 46.8 (C-7 and C-8), 55.0 (C-2), 128.0 (2 × Ar-C), 128.5 (2 × Ar-C), 133.0 (Ar-C), 137.2 (Ar-C), 199.7 (C=O) ppm; ^2H NMR ($CHCl_3$) δ: 1.0–1.8 ppm; MS *m/e*(*I*): 222 ($M^+ + 1$) (2), 221 (M^+) (18), 220 ($M^+ - 1$) (6), 215 (11), 117 (8), 105 (100), 102 (8), 77 (94), 43 (55). HRMS, Exact Mass calcd. for $C_{14}H_{15}D_4NO$: 221.1717; found: 221.1716.

Acknowledgements

We are grateful to Dr. D.S. Rycroft and Mr. J. Gall (Glasgow) for running the NMR spectra and Mr. A. Ritchie for the mass spectra. We thank Ms. I.K.M. Freer for technical assistance in the enzyme preparations and the Science and Engineering Research Council for Earmarked Studentships to S.S.G. and A.M.E.

1. K. Mothes, H.R. Schutte, and M. Luckner (*Editors*). Biochemistry of alkaloids. VCH Publishers, Deerfield Beach, Fla. 1985.
2. D.R. Walters. Biologist, **34**, 73 (1987).
3. I.D. Wigle, L.J.J. Mestichelli, and I.D. Spenser. J. Chem. Soc. Chem. Commun. 662 (1982).
4. G.R. Orr, S.J. Gould, A.E. Pegg, J.E. Seely, and J.K. Coward. Bioorg. Chem. **12**, 252 (1984).
5. Y. Asada, K. Tanizawa, K. Nakamura, M. Moriguchi, and K. Soda. J. Biochem. (Tokyo), **95**, 277 (1984).
6. D.J. Robins. Phytochemistry, **22**, 1133 (1983).
7. G.R. Orr and S.J. Gould. Tetrahedron Lett. **23**, 3139 (1982).
8. A.R. Battersby, R. Murphy, and J. Staunton. J. Chem. Soc. Perkin Trans. 1, 449, (1982).
9. H.J. Gerdes and E. Leistner. Phytochemistry, **18**, 771 (1979).
10. E. Leistner and I.D. Spenser. J. Chem. Soc. Chem. Commun. 378 (1975); J.C. Richards and I.D. Spenser. J. Am. Chem. Soc. **100**, 7402 (1978); Tetrahedron, **39**, 3549 (1983).
11. A.R. Battersby, J. Staunton, and M.C. Summers. J. Chem. Soc. Perkin Trans. 1, 1052 (1976).
12. R.B. Frydman, O. Ruiz, M. Kreisel, and U. Bachrach. FEBS Lett. **219**, 380 (1987).
13. A. Cooper, A.M. Equi, S.K. Ner, A.B. Watson, and D.J. Robins. Tetrahedron Lett. **30**, 5167 (1989).
14. A.M. Equi, A.M. Brown, A. Cooper, S.K. Ner, A.B. Watson, and D.J. Robins. Tetrahedron, **47**, 507 (1991).
15. J.E. Cragg, R.B. Herbert, and M.M. Kgaphola. Tetrahedron Lett. **31**, 6907 (1990).
16. E. Santaniello, A. Manzocchi, P.A. Biondi, C. Secchi, and T. Simonic. J. Chem. Soc. Chem. Commun. 803 (1984).
17. A.M. Equi, A. Cooper, and D.J. Robins. J. Chem. Res. (S), 94 (1992).
18. J.M. Hill. Methods Enzymol. **17B**, 730 (1971).
19. J.E. Cragg, R.B. Herbert, F.B. Jackson, C.J. Moody, and I.T. Nicholson. J. Chem. Soc. Perkin Trans. 1, 2477 (1982).
20. R.B. Herbert, E. Knagg, H.M. Organ, V. Pasupathy, and D.S. Towlson. Heterocycles, **25**, 409 (1987).
21. G. Baxter, J.C. Melville, and D.J. Robins. Synlett, 359 (1991).
22. J. Rana and D.J. Robins. J. Chem. Soc. Perkin Trans. 1, 983 (1986).
23. R. Munier and M. Macheboef. Bull. Soc. Chim. Biol. **33**, 846 (1951).
24. R.C. Brown, Y.M. Choi, and S. Narasimhan. Synthesis, 605 (1981).

Can. J. Chem. Downloaded from www.nrcresearchpress.com by 195.246.54.202 on 09/08/12
For personal use only.

Photochemistry of a model lignin compound. Spin trapping of primary products and properties of an oligomer

L.R.C. BARCLAY,[1] G.R. CROMWELL, AND J.W. HILBORN

Department of Chemistry, Mount Allison University, Sackville, NB Canada E0A 3C0

Received April 21, 1993

This paper is dedicated to Professor David B. MacLean

L.R.C. BARCLAY, G.R. CROMWELL, and J.W. HILBORN. Can. J. Chem. **72**, 35 (1994).

α-Guaiacoxylacetoveratrone, 1, was selected as a model of a lignin structure component for photolysis and free radical spin trapping studies. The 3,4-dimethoxyphenacyl radical, Ar-COĊH$_2$, 2, thermally generated from α-bromoacetoveratrone with trimethyltin, was spin trapped by phenyl-*tert*-butylnitrone (PBN), and the spin-trapped radical identified by ESR and mass spectroscopy. Spin trapping by PBN of radical photoproducts from 1 gave a mixture of trapped radicals, according to ESR. These were separated as their hydroxylamines and identified by liquid chromatography/mass spectroscopy (LC/MS) under chemical ionization (CI) conditions. This LC/MS (CI) method identified the same phenacyl fragment, 2 (reduced), as well as a fragment tentatively attributed to a spin-trapped guaiacoxyl radical, chemically reduced to the hydroxylamine. Extended direct photolysis of 1 yields colored paramagnetic oligomers. The synthesis of 1-(3,4-dimethoxyphenyl)-2-(4-hydroxy-3-methoxyphenyl-ethanone(10), a rearranged, recombination photoproduct of 1, is described. A pathway for formation of oligomers as unstable dimers of 10 is presented.

L.R.C. BARCLAY, G.R. CROMWELL et J.W. HILBORN. Can. J. Chem. **72**, 35 (1994).

On a choisi l'α-guaïacoxylacétovératrone, **1**, comme modèle d'un composant de la structure de la lignine pour des études de photolyse et de piégeage de spin de radicaux libres. On a piégé le radical 3,4-diméthoxyphénacyle (Ar-COĊH$_2$, **2**), obtenu d'une façon thermique à partir de l'α-bromoacétovératrone et du triméthylétain, par la phényl-*tert*-butylnitrone (PBN) et on a identifié le radical piégé par RPE et par spectrométrie de masse. Selon la RPE, le piégeage de spin par le PBN des photoproduits radicalaires du composé **1** conduit à des mélanges de radicaux piégés. On les a séparé sous la forme d'hydroxylamines et on les a identifiés par chromatographie liquide/spectrométrie de masse (CL/SM) dans des conditions d'ionisation chimique (IC). Ce méthode de CL/SM (IC) a permis d'identifier le même fragment phénacyle, **2**, réduit, ainsi qu'un fragment attribué d'une façon préliminaire à un radical guaïacoxyle piégé, réduit chimiquement en hydroxylamine. Une photolyse directe plus longue du composé **1** fournit des oligomères paramagnétiques colorés. On décrit la synthèse de la 1-(3,4-diméthoxyphényl)-2-(4-hydroxy-3-méthoxyphényl)éthanone (**10**), un photoproduit de recombinaison réarrangé du produit **1**. On présente une voie possible pour la formation d'oligomères comme dimères instables du composé **10**.

[Traduit par la rédaction]

Introduction

Lignin is structurally a very complex polymer; however, known structural units are involved. Consequently, monomeric compounds, such as α-guaiacoxylacetoveratrone (**1**) and similar compounds, have been studied by different groups (1–6) as appropriate models for the photochemistry of lignin-type molecules, since they contain some structural features common in lignin. The chemistry of free radicals from photolysis of model lignin compounds like **1** is expected to provide important insights into the nature and inhibition of undesirable photoyellowing of papers from mechanical wood pulps containing lignin.

Considerable evidence on the photochemistry of lignin-type models like **1** supports a mechanism involving homolytic β-cleavage to give carbon and phenoxyl radicals (e.g., **2** and **3**; see Scheme 1). There is recent evidence to show that the photoyellowing process is linked to free radical autoxidation induced by initially formed carbon-centred and (or) phenoxyl radicals (7). The inhibition of photoyellowing has traditionally concentrated on the inhibition of processes subsequently initiated by radical reactions (8). On the other hand, it should be possible to *trap* the radicals initially formed *before* further reactions occur. This paper reports on our initial results using compound **1** as a model system chosen because information is available on its photochemistry.

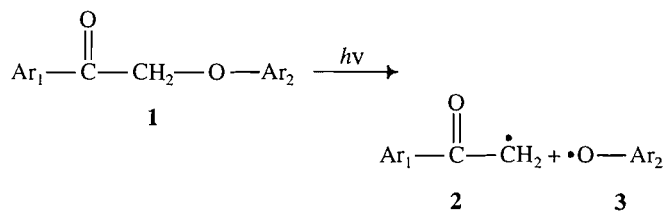

Ar_1 = 3,4-dimethoxyphenyl; Ar_2 = 2-methoxyphenyl

SCHEME 1

The objectives of this study are (1) to determine if spin trapping by phenyl *tert*-butylnitrone (PBN) can be used to intercept radicals initially formed such as **2** and **3** before radical rearrangements and (or) recombinations occur; (2) to study the properties of colored oligomers, which also form on photolysis of **1** (1–3), and (3) to synthesize a phenolic rearranged-recombination isomer of **1** and study how its free radical chemistry is related to colored oligomers and presumably to the photoyellowing of lignin itself.

Results

1. Spin trapping the 3,4-dimethoxyphenacyl radical (**2**)

(a) Thermal generation of 2. Characterization of the spin adduct by LC/MS

We are unaware of any previous spin trapping studies of phenacyl-type radicals. Consequently, it was desirable to explore the spin trapping method using PBN on phenacyl and

[1]Author to whom correspondence may be addressed.

Can. J. Chem. Downloaded from www.nrcresearchpress.com by 203.198.23.82 on 09/08/12
For personal use only.

Can. J. Chem. Downloaded from www.nrcresearchpress.com by 203.198.23.82 on 09/08/12
For personal use only.

3,4-dimethoxyphenacyl (**2**) radicals that were generated thermally. For this independent characterization of the PBN-trapped **2** radical, we first generated type **2** radicals by bromine atom abstraction from α-bromoacetophenone and α-bromoacetoveratrone using photochemically generated trimethyltin radicals (9) in the presence of the spin trap, PBN. Photolyses of equimolar mixtures of hexamethylditin, α-bromoacetophenone (or α-bromoacetoveratrone), and PBN results in a typical 1:1:1 triplet of doublets identical for both systems with a_N = 14.8 G, a^{β}_H = 4.6 G, and g = 2.0059, and assigned to the phenacyl (or 3,4-dimethoxyphenacyl)-PBN radicals, **4**, **5**

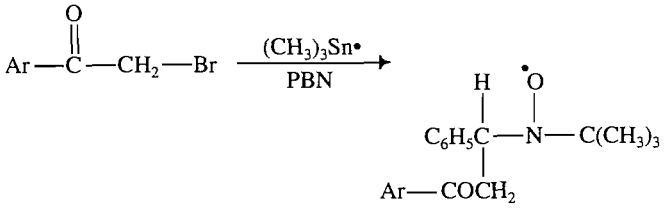

4 Ar = C_6H_5-
5 Ar = 3,4-dimethoxyphenyl

The mixture from the spin trapping experiment was separated by PREP-TLC using 95:5 V/V methylene chloride – ethyl acetate and the paramagnetic component, located at R_f = 0.35, showed the typical ESR spectrum when subjected to LC/MS analysis. The major component at t_R = 1.57 min gave the MS shown in Fig. 1. This spectrum is consistent with the assigned structure for the 3,4-dimethoxyphenacyl-PBN radical (**5**). The highest mass ion observed, m/z = 357, isthe protonated molecular ion $[M + H]^+$. Such $[M + H]^+$ ions are common in LC/MS using protic solvents due to proton transfer from the solvent (10). Significant fragment ions and assignments are m/z = 269 (5.2%), $C_6H_5\overset{(+)}{C}HCH_2COC_6H_3(OCH_3)_2$; m/z = 180 (33%), $(CH_3O)_2C_6H_3\overset{(+)}{C}OCH_3$; m/z = 165 (100%), $(CH_3O)_2C_6H_3\overset{(+)}{C}O$; and m/z = 77 (36%), $C_6H_5^{(+)}$.

(b) Spin trapping during photolysis of α-guaiacoxylacetoveratrone (1)

Photolysis in benzene of a 4:1 molar ratio of **1** to PBN at 254 nm (where the respective molar absorptivities are 3800 and 2500) resulted in an intense ESR signal. The spectrum appears to contain a mixture of radicals, the major component having the same properties (measured a_N = 14.8 G, a^{β}_H = 4.6 G, g = 2.0059) as the 3,4-dimethyoxyphenacyl-PBN radical trapped above in (*a*). Attempts to separate the component radicals by TLC for LC/MS characterization were not successful.

The spin trapping experiment during photolysis of **1** was repeated and hydrazobenzene was added to the ESR sample. This immediately quenched the ESR signals. The products were separated by PREP-TLC as before in (*a*). Two new bands were separated, at R_f = 0.33 and 0.25. The former band (R_f = 0.33) was extracted into benzene and a portion of this extract treated with PbO_2. The resulting ESR spectrum was identical to that of the original 3,4-dimethoxyphenacyl-PBN (3,4-DMP-PBN) trapped radical. The remainder of this benzene extract was analyzed by LC/MS in the chemical ionization (CI) mode using methane as the ionization gas. This produced only two major peaks in the spectrum. A peak at m/z = 359 corresponds to the

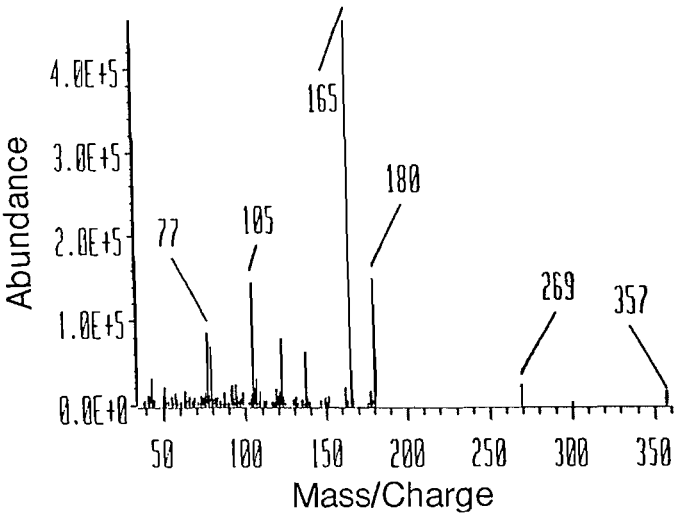

FIG. 1. Particle beam LC/MS spectrum of separated paramagnetic component from photolysis of α-bromoacetoveratrone with PBN and hexamethylditin in benzene.

$[M + 2H]^+$ ion, assigned to the parent [3,4-DMP-PBN-OH + $2H]^+$, and one at m/z = 181 assigned to the $[3,4\text{-DMP} + 2H]^+$ fragment ion. The LC/MS (CI) analysis of the second TLC band (R_f 0.25) also showed only two peaks, at m/z = 303 and 125. The peak at m/z = 303 corresponds to a trapped [quaiacoxyl-PBN-OH + $2H]^+$ species and the peak at m/z = 125 corresponds to a fragmentation forming an ionized guaiacoxyl fragment $[CH_3OC_6H_5OH + H]^+$ and a neutral PBN-OH fragment.

2. Oligomer formation from the photolysis of 1

Extended photolysis of **1** was carried out to obtain sufficient amounts of oligomeric material for analyses. For example, irradiation of a 7.45 × 10^{-3} M solution of **1** in benzene for 6 days gave a yellow-orange solution. Chromatography of the crude product on silica gel separated starting material **1** and other known compounds (6) in early fractions. Oligomeric material was isolated from a strongly adsorbed dark red band, which typically yielded 23 wt.% of a brown solid.

Oligomers have been reported before from the photolysis of **1** (1–3). It is not clear, however, if the same type of oligomer is formed from photolysis of **1** by different methods. The most prominent property of the oligomer formed in this photolysis of **1** is its strong and persistent paramagnetism, which has not been reported on previously. It exhibits a broad, single ESR signal in both the solid state and in solution. The signal intensity increases on ultraviolet irradiation but the signal does not decay entirely even on long standing. The g value (2.0036) is consistent with a radical on carbon adjacent to oxygen. Attempts to obtain resolved ^1H or ^{13}C NMR spectra were unsuccessful due to the strong paramagnetism. Other properties of this oligomer are outlined in Table 1.

3. Synthesis of a phenolic isomeric recombination compound of 1. Oligomer formation

The unusual paramagnetic properties of the oligomer can be accounted for by a structure formed from a weakly bonded dimer of a phenolic recombination product from **1** that readily dissociates into phenoxyl radicals. This postulate is consistent with the (GPC) molecular weight (a dimer requires 604), and

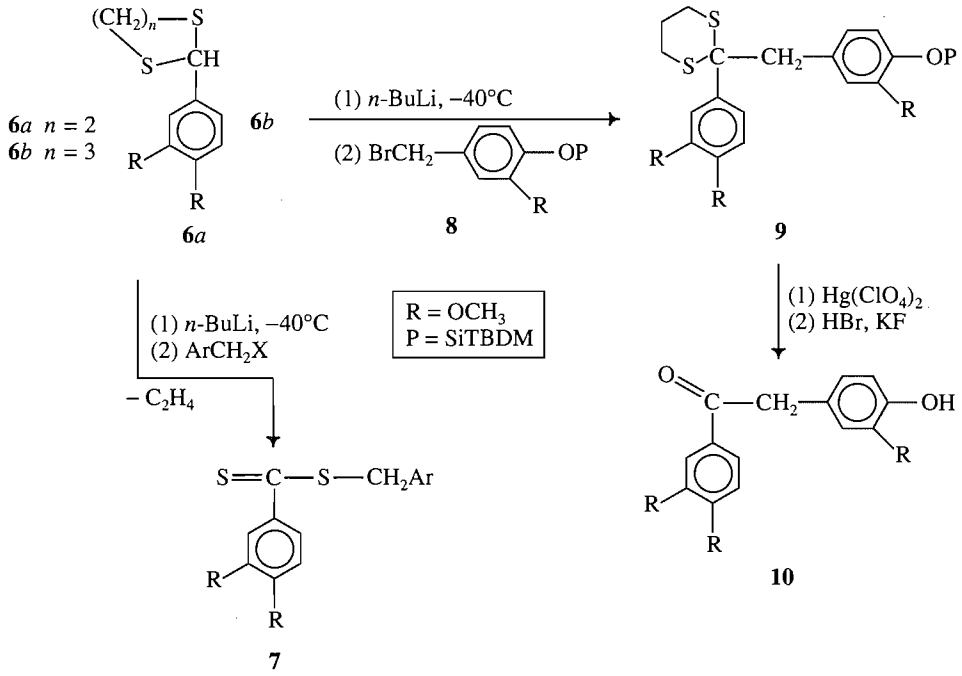

SCHEME 2

TABLE 1. Properties of oligomer from photolysis of α-guaiacoxylacetoveratrone (**1**)

Color:	Light-brown solid, red solution in benzene
Melting point:	196–200°C
Mol.Wt.:	622, number average from GPC[2]
Mass spectrum:	base peak at m/z = 165, under EI conditions, 3,4-$(CH_3O)_2C_6H_3{}^+CO$ fragment, the highest mass observed (using isobutaneCI) at m/z = 359 [fragment + H], peak at m/z = 303, assigned to "phenolic fragment" + H (see Part 3 below)
Infrared spectrum (KBr):	3423 cm^{-1} (broad) -OH (H-bonded), 1670 C=O (conjugated), 1595 and 1515 (aromatic), 1269 (strong) -O-CH_3

the spectroscopic properties (Table 1). The mass spectrum did not show a parent ion. However, the base peak under chemical ionization conditions (i-C_4H_9) at m/z = 303 is attributed to [fragment + H]$^+$ where the [fragment] is assigned to dissociation of the "dimer". We therefore undertook a complete synthesis of a phenolic isomeric recombination compound of **1**, 1-(3,4-dimethoxyphenyl)-2-(4-hydroxy-3-methoxyphenyl)ethanone (**10**), Scheme 2, to study its free radical chemistry, in particular its relationship to oligomer formation

Our initial attempts on the synthesis of **10** starting with the 3,4-dimethoxyphenyldithiolane **6***a*, resulted instead in formation of an interesting side product, the 3,4-dimethoxydithiobenzyl ester **7**, as the only new compound in 55% isolated yield. The reported Friedel-Crafts method for the synthesis of **10** (2) was not successful in our hands.

A successful synthesis of **10** was accomplished by starting with 2-(3,4-dimethoxyphenyl)-1,3-dithiane (**6***b*). The carbanion generated from **6***b* was reacted with 4-[(*tert*-butyldimethylsilyl)oxy]-3-methoxybenzyl bromide (**8**) to give the diprotected compound (**9**) in 70% yield. Removal of the protecting groups in two steps yielded the desired phenol, **10**, in 60% yield from **9**.

The synthetic phenol (**10**) gave the expected spectroscopic properties (Experimental, Preparation of **10**), and it appears to be the same as the compound reported by Castellan and coworkers (2). Solutions of this phenol rapidly became colored (orange-red) on exposure to air and light. Treatment of a benzene solution of **10** with the thermal azo initiator di-*tert*-butylhyponitrite (DBHN) at 37°C gave an orange solution that exhibited a broad persistent ESR signal similar to that observed for the oligomer, and TLC on the product mixture from **10** contained material with the same R_f as the oligomer formed on photolysis of **1**. Irradiation of a solution of **10** in benzene also gave the same persistent signal. ESR spectra of the oligomer and photolysis of **10** are given in Fig. 2.

Discussion

1. Spin trapping and mass spectroscopy analyses

The spin trapping of thermally generated 3,4-dimethoxyphenacyl radical, **2**, indicates that the PBN trapping competes against other known reactions such as rearrangement–decarbonylation, well known for phenacyl itself (11, 12), and recombination reactions (6). On the other hand, photolysis of **1** in the pressence of PBN gave a mixture of trapped radicals according to ESR studies. Evidence from the LC/MS(CI) of the reaction mixture separated after hydrazobenzene reduction together with regeneration of the same ESR spectrum on lead dioxide oxidation demonstrates that the substituted phenacylradical, **2**, is also spin trapped under photolysis conditions.

The LC/MS spectrum (Fig. 1) of the spin-trapped 3,4-DMP-PBN radical (**5**) provides a useful confirmation of its structure.

[2]The gel permeation chromatography was carried out at the PAPRICAN Laboratory, Pointe Claire, Quebec. The value of 622 is known to be high due to adsorption onto the gel.

Can. J. Chem. Downloaded from www.nrcresearchpress.com by 203.198.23.82 on 09/08/12
For personal use only.

Can. J. Chem. Downloaded from www.nrcresearchpress.com by 203.198.23.82 on 09/08/12
For personal use only.

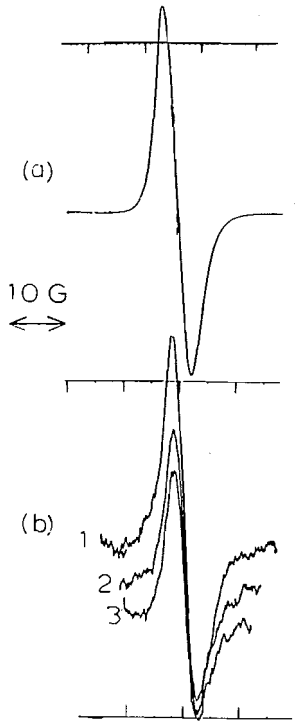

FIG. 2. ESR spectra: (*a*) oligomers separated from photolysis of **1**; (*b*) from irradiation of synthetic phenol, **10**, in ESR probe; 1, signal with light on; 2, light off; 3, light off 1.5 h; spectra recorded in benzene.

The parent ion was observed as $[M + H]^+$ at $m/z = 357$. We can assign this to the protonated parent molecule

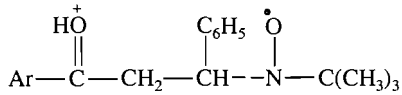

Then the peak at $m/z = 269$ is assigned to fragmentation giving

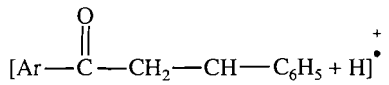

due to loss of $(CH_3)_3CNO$. The peak at $m/z = 180$ is attributed to fragmentation giving $[(CH_3O)_2\text{-}C_6H_3\text{-}COCH_2 + H]^+$ and that at $m/z = 165$ (the base peak) to $(CH_3O)_2\text{-}C_6H_3\text{-}CO^+$. The fragment at $m/z = 105$ could not be assigned with certainty but is probably due to fragmentation and rearrangement giving the $C_6H_5\text{-}\overset{H}{\overset{+}{C}}CH_3$ ion. Although we were unable to separate the *initial* mixture of trapped radicals from photolysis of **1** with PBN for mass spectroscopic analysis, the derived hydroxylamines were separated by preparative TLC. Their mass spectra obtained under "softer" CI conditions, using methane as the ionization gas, were remarkably simple. The component corresponding to spin trapping of the 3,4-dimethoxyphenacyl radical (established by PbO_2 oxidation back to the radical observed before) now gave only two major peaks in the higher mass range, at $m/z = 359$ and 181. The peak at $m/z = 359$ is assigned to the parent molecule

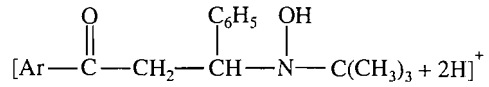

Ions corresponding to $[M + 2H]^+$ may appear unusual but they have been observed before in such LC/MS as those of nucleotide bases (13) and, more significantly to this study, in ion–molecule reactions of acyl spin adducts of PBN as proposed below (14):[3]

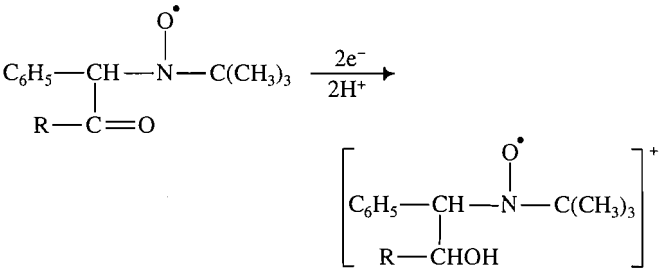

In our case, the fragment at $m/z = 181$ is assigned to $[(CH_3O)_2\text{-}C_6H_3\text{-}COCH_2 + 2H]^+$.

The LC/MS under CI conditions of the second component can be attributed to spin trapping and reduction of a PBN-trapped guaicoxyl radical, such as:

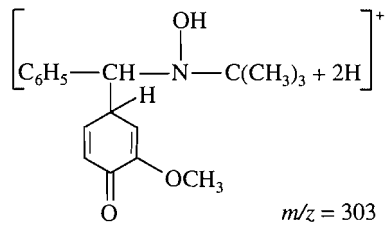

$m/z = 303$

In this event, the fragment at $m/z = 125$ corresponds to a fragment ion of the type $[CH_3OC_6H_4OH + H]^+$. There does not appear to be a precedent for spin trapping of phenoxyl radicals so these assignments are tenuous until independent evidence is obtained.

*2. The recombination phenolic compound (**10**) and colored oligomer formation*

Initial attempts to synthesize the phenolic compound, **10**, from the 1,3-dithiolane, ***6a***, resulted instead in an unexpected fragmentation reaction (Scheme 1). We suggest that the facile (–40°C) elimination of ethylene occurs via a stabilized cyclic six-electron transition state, for example:

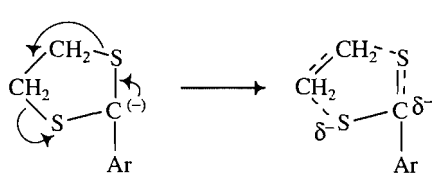

followed by nucleophilic displacement of the resulting dithiobenzoate anion on added benzyl halide. We were unaware initially that a similar reaction had been reported for a synthesis

[3] This equation does not imply the mechanism for the ion–molecule reaction.

of aromatic dithioesters (15, 16). However, the procedure used before (15) involved elevated temperatures (150°C) over an extended time. Our results indicate that dithiobenzyl ester can be prepared under much milder conditions. It is expected that the dithiane protecting group in a six-membered ring (**6***b*, $n = 3$) would resist this elimination since a stable cyclic aromatic transition state is not available. So this reaction gives the required compound **9**, which is readily deprotected to give the desired phenol, **10**.

Treatment of the synthetic phenol under a variety of conditions (direct irradiation, heating with a thermal azo initiator, or oxidation with lead dioxide) all resulted in a broad persistent ESR signal comparable to that observed in the oligomer itself. These results can be explained by a dimeric structure of the oligomer that is in thermal equilibrium with a paramagnetic species as proposed in Scheme 3.

Experimental

General procedure

Melting points were measured on a Gallenkamp melting point apparatus and are uncorrected. Proton and carbon-13 nuclear magnetic resonance (^1H and ^{13}C NMR) spectra were obtained in $CDCl_3$ with TMS as an internal standard on either a Nicolet NB 360 or a Bruker AC 250 spectrometer and are recorded in ppm. Electron paramagnetic resonance (EPR) spectra were run on a Varian E3 EPR spectrometer to obtain hyperfine coupling constants and *g*-values. These measurements were typically run at a microwave frequency of 9.5 GHz, centre field 3400 gauss (G) with a 100 G sweepwidth. Mass spectra were obtained on a Hewlett Packard 5988A GC/LC/MS instrument using an HP 5890 Series II gas chromatograph and a Series 1050 HPLC both recorded using an ionization potential of 70 eV. The liquid chromatograph used an HP MOS Hypersil 5 μm 100 × 2.1 mm column with 80:20 Me-OH:H_2O as solvent for the analysis. An HP 59980A particle beam LC/MS interface was used for insertion into the ion source. Infrared spectra were obtained on a Perkin Elmer 1420 infrared spectrophotometer. Microanalysis were by Desert Analytics, Tuscon, Arizona.

Vanillin, acetophenone, 3,4-dimethoxyacetophenone, imidazole, *tert*-butyldimethlsilyl chloride, sodium borohydride, lithium bromide, trimethylsilyl chloride, ammonium chloride, sodium chloride, sodium bicarbonate, 3,4-dimethoxybenzaldehyde, benzyl chloride, 1,3-propanedithiol, 1,2-ethanedithiol, hexamethylditin, *p*-toluenesulfonic acid, phenyl-lithium, and *n*-butyllithium were obtained from Aldrich Chemical Co. and were used without purification. *N-tert-Butyl*-α-phenylnitrone (PBN) from Aldrich was sublimed before use. Potassium fluoride was obtained from B & A Specialty Chemicals Division. Hydrobromic acid (48%) was obtained from the Fisher Scientific Company. Mercuric perchlorate ($Hg(ClO_4)_2$) was prepared using the method described in the literature (17).

The preparative TLC was done using Kieselgel 60 $PF_{254+366}$ silica gel, and normal TLC for monitoring of reactions was done using Merck DC-Plastikfolien Kieselgel $60F_{254}$ silica gel sheets.

THF was distilled from CuCl and then from $LiAlH_4$ and kept over molecular sieves. Benzene was distilled and kept over molecular sieves prior to use. The other solvents for this study were obtained from either the Aldrich Chemical Co. or the BDH Chemical Co. and were distilled prior to use. Photolyses with PBN spin trap were carried out in a Rayonet Reactor using 350-nm lamps through Pyrex or at 254 nm in quartz tubes. Extended photolyses of **1** to form oligomers were done in a 400-mL immersion well using a 400-W Hanovia mercury medium-pressure lamp through Pyrex during a continual purge with argon.

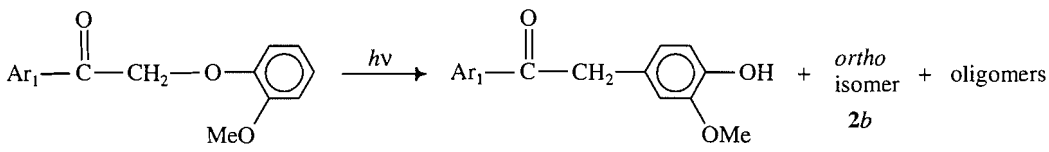

1

Ar_1 3,4-dimethoxyphenyl

10

Synthetic **10**

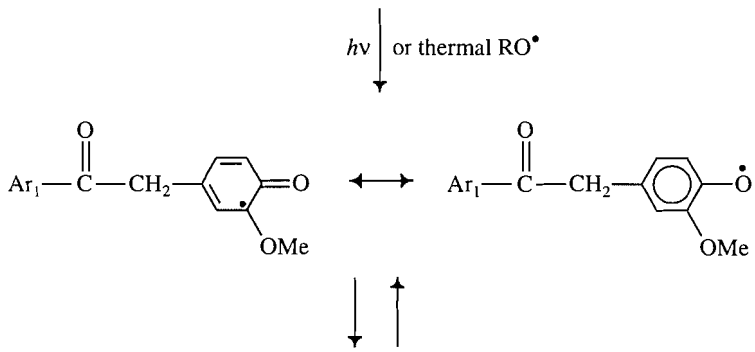

Proposed oligomer:

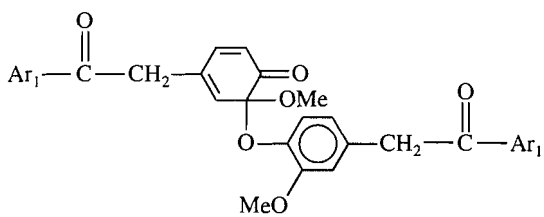

SCHEME 3

Can. J. Chem. Downloaded from www.nrcresearchpress.com by 203.198.23.82 on 09/08/12
For personal use only.

Can. J. Chem. Downloaded from www.nrcresearchpress.com by 203.198.23.82 on 09/08/12
For personal use only.

Syntheses

Preparation of α-bromoacetoveratrone and α-bromoacetophenone

The α-bromoacetoveratrone and α-bromoacetophenone were prepared by the reported method (18). The ^{1}H NMR and GC/MS were consistent with their structures.

*Preparation of α-(2-methoxyphenoxy)acetoveratrone (**1**)*

Compound **1***a* was synthesized by the reported procedure (19) and the crude material was recrystallized four times from methanol; mp 92–93°C.

*Preparation of α-phenoxyacetophenone (**1**b)*

This compound was prepared by the reported procedure (19) and the crude material recrystallized from hexane; mp 70–71°C (lit. (5) mp 71–72°C). The product gave the expected mass spectrum.

*Preparation of 4-[(*tert*-butyldimethylsilyl)oxy]-3-methoxybenzaldehyde*

To a 50-mL round-bottom flask was added 2.0 g (0.013 mol) of vanillin, and it was dissolved in 10 mL of DMF under argon. To this solution was added 2.2 g (0.032 mol) of imidazole and, once it had dissolved, 2.4 g (0.016 mol) of *tert*-butyldimethylsilyl chloride was added. The reaction was stirred overnight after which water was added (20 mL) and it was extracted with ether (2 × 30 mL). The organic layer was washed with saturated $NaHCO_3$ solution, followed with a brine, and finally with water. The ether layer was dried ($MgSO_4$), filtered, and distilled under reduced pressure to give a colourless oil; 2.1 g, 61%; bp 136–138°C (1.5 Torr; 1 Torr = 133.3 Pa). IR and ^{1}H NMR were comparable to that given in the literature (20). ^{13}C NMR δ: 191.0, 127.6, 126.3, 120.7, 110.0, 108.7, 56.1, 55.5, 25.6, 18.5, –4.6; GC/MS, *m/z*: 251 (2, $M^+ - CH_3$), 210 (16), 209 (86), 194 (100), 193 (38), 165 (10), 163 (10), 73 (16).

*Preparation of 4-[(*tert*-butyldimethylsilyl)oxy]-3-methoxybenzyl alcohol*

The above aldehyde (1.20 g, 4.5×10^{-3} mol) was dissolved in 15 mL of absolute alcohol and sodium borohydride (0.25 g, 6.6×10^{-3} mol) was added. After stirring for 4 h water was added (40 mL), and the product was then extracted with ether (3 × 40 mL). The ether layer was washed with water (2 × 10 mL), then dried ($MgSO_4$), filtered, and rotoevaporated to yield a colourless oil; 1.04 g, 86%; bp 176–178°C (2.0 Torr). IR and ^{1}H NMR were comparable to those given in the literature (20). ^{13}C NMR δ: 151.0, 144.5, 134.5, 120.8, 119.5, 111.1, 63.5, 55.4, 25.7, 18.5, –4.7; GC/MS, *m/z*: 238 (15), 212 (9), 211 (60), 197 (15), 196 (100), 195 (10), 179 (16), 167 (28), 151 (8).

*Preparation of 4-[(*tert*-butyldimethylsilyl)oxy]-3-methoxybenzyl bromide (**8**)*

The procedure used was that outlined previously (20). The crude product was purified by column chromatography on silica gel by elution with hexane:ethyl acetate (5%). IR and ^{1}H NMR are in agreement with those given in the literature (20).

*Preparation of 2-(3,4-dimethoxyphenyl)-1,3-dithiolane (**6**a)*

The procedure used to prepare this compound is that outlined in ref. 15; mp 64–66°C (lit. (15) mp 62–65°C); IR (CCl_4): 2996, 2932, 2834, 1592, 1512, 1463, 1417, 1264, 1138, 1030 cm^{-1}; ^{1}H NMR δ: 7.11 (d, 1H, J = 1.8 Hz), 7.05 (dd, 1H, J_1 = 8.0 Hz, J_2 = 1.8 Hz), 6.78 (d, 1H, J = 8.1 Hz), 5.64 (s, 1H, CHSS), 3.90 (s, 3H, OCH_3), 3.87 (s, 3H, OCH_3), 3.52–3.49 (m, 2H), 3.37–3.32 (m, 2H); GC/MS *m/z*: 242 (82, M^+), 214 (32), 213 (21), 211 (17), 199 (15), 183 (100), 182 (36), 181 (55), 138 (15), 95 (14).

*Formation of 3,4-dimethoxybenzenecarbodithioic acid benzyl ester (**7**)*

To a 50-mL three-necked round-bottom flask equipped with a low-temperature thermometer, argon inlet, and a condenser was added 1.00 g (4.1×10^{-3} mol) of 2-(3,4-dimethoxyphenyl)-1,3-dithiolane (**6***a*). To this was added 15 mL of anhydrous THF and the dithiolane was completely dissolved. The solution was then cooled to –80°C. After 5 min 2.38 mL of a 1.8 M solution of phenyllithium was added and allowed to stir for 2 h. Then 0.54 mL (4.0×10^{-3} mol) of benzyl chloride was added and the temperature was allowed to warm to –40°C for 30 min after which it was allowed to warm to room temperature. After 6 h at room temperature, the solution was worked up as described previously (21). The crude compound was column chromatographed using 80:20 hexane:CH_2Cl_2 as eluent. Yield 0.70 g (2.3×10^{-4} mol, 55%) red solid, mp 62–63°C; IR (KBr): 2957, 1590, 1512, 1461, 1411, 1335, 1266, 1143, 1048, 1022, 760 cm^{-1}; ^{1}H NMR δ:7.75 (dd, 1H, J_1 = 8.5 Hz, J_2 = 2.1 Hz), 7.68 (d, 1H, J = 2.1 Hz), 7.39–7.29 (m, 5H), 6.79 (1H, J = 8.5 Hz), 4.58 (s, 2H), 3.91 (s, 3H, OCH_3), 3.90 (s, 3H, OCH_3); ^{13}C NMR[4] δ: 220.7 (q, CSS), 143.3 (q), 148.5 (q), 137.7 (q), 135.1 (q), 129.3, 128.7, 127.7, 120.2, 110.5, 109.9, 56.1 (OCH_3), 56.0 (OCH_3), 42.0 (CH_2-S); GC/MS, *m/z*: 304 (14, M^+), 182 (10), 181 (100), 137 (19), 91 (46). Anal. calcd. for $C_{16}H_{16}S_2O_2$: C 63.13, H 5.30; found: C 62.76, H 5.17.

*Preparation of 2-(3,4-dimethoxyphenyl) 1,3-dithiane (**6**b)*

To a 200-mL round-bottom flask was added 4.0 g (2.4×10^{-2} mol) of 3,4-dimethoxyphenylbenzaldehyde and 140 mL of dry benzene. To this was added 2.70 g (2.50 mL, 2.5×10^{-2} mol) of 1,3-propanedithiol and a catalytic amount of *p*-toluenesulfonic acid. The mixture was refluxed with a Dean–Stark trap for 4 h and then allowed to cool. The benzene layer was washed with 1 M sodium hydroxide solution, followed by a wash with water. The benzene was dried ($MgSO_4$), filtered, and rotoevaporated to yield an oil. The oil was recrystallized from diethyl ether to give white needles: yield 4.3 g, 70%, mp 94–96°C (lit. (22) mp 99–101°C). The ^{1}H NMR and MS were in agreement with the literature values (23). IR (KBr): 2965, 2945, 2896, 2840, 1603, 1588, 1513, 1465, 1261, 1138, 1020, 764 cm^{-1}; ^{13}C NMR δ:149.0, 131.7, 120.0, 111.0, 110.7, 55.9, 55.9, 51.2, 32.2, 25.1.

*2-(3,4-Dimethoxyphenyl)-2-{4-[(*tert*-butyldimethyldilyl)oxy]-3-methoxylbenzyl}-1,3-dithiane (**9**)*

Into an oven-dried 50-mL three-necked flask was added 0.53 g (2.07×10^{-3} mol) of the dithiane (**6***b*). Then 15 mL of anhydrous THF was added and the dithiane was stirred until it dissolved. The flask was next cooled to –40°C under an argon atmosphere when *n*-BuLi was added (2.5 M solution in hexanes) until complete conversion of the dithiane into the carbanion was accomplished (monitored by deuterium exchange using D_2O). The carbanion solution was then transferred quickly to a cold dropping funnel and the benzyl bromide, **8**, (0.70 g, 2.1×10^{-3} mol) in 5 mL of dry THF in a separate dropping funnel was added dropwise simultaneously into a magnetically stirred three-necked flask with 30 mL of THF at –40°C under an argon atmosphere. The solution was stirred and kept at –40°C for 5 h and then allowed to warm to room temperature overnight. The reaction mixture was rotoevaporated to remove the THF, and then treated with a saturated NH_4Cl solution and extracted with chloroform. The organic layer was dried over $MgSO_4$, filtered, and rotoevaporated to yield the crude oil, which was then column chromatographed (eluent: CH_2Cl_2) to give the pure silyl protected thioketal (**9**). Yield 0.75 g, 70%, mp 100–102°C; IR (KBr):2950, 2932, 2854, 1601, 1596, 1512, 1461, 1235, 1133, 1026, 908 cm^{-1}; ^{1}H NMR δ:7.28–7.24 (m, 2H), 6.77 (d, 1H, J = 9.0 Hz), 6.61 (d, 1H, J = 7.9 Hz), 6.28 (dd, 1H, J_1 = 8.0 Hz, J_2 = 1.6 Hz), 6.05 (bs, 1H), 3.90 (s, 3H), 3.75 (s, 3H), 3.51 (s, 3H), 3.16 (s, 2H), 2.77–2.58 (m, 4H), 1.98–1.95 (m, 2H), 0.96 (s, 9H), 0.10 (s, 6H); ^{13}C NMR δ:149.6, 148.4, 147.8, 143.8, 132.7, 127.7, 123.3, 122.2, 119.6, 114.8, 112.9, 110.4, 59.9, 55.9, 55.8, 55.1, 51.3, 27.6, 25.7, 25.2, 18.4, –4.7; GC/MS, *m/z*: 256 (13), 255 (100), 181 (15). Anal. calcd. for $C_{26}H_{38}S_2O_4Si$: C 61.62, H 7.56; found: C 61.42, H 7.70.

*Preparation of 1-(3,4-dimethoxyphenyl)-2-{4-[(*tert*-butyldimethylsilyl)oxy}-3-methoxylphenyl} ethanone*

The deprotection step is a modification of a literature procedure (24). The protected silyl thioketal, **9** (0.35 g, 6.9×10^{-4} mol), was dissolved in 3 mL of THF and 0.5 mL of water was added. To this solu-

[4] For ^{13}C NMR, q refers to quaternary carbons.

tion was added 0.14 g (1.4×10^{-2} mol) of $CaCO_3$ and this was allowed to stir at room temperature for 5 min, after which 0.5 mL of a 2.5 M aqueous solution of $Hg(ClO_4)_2$ was added slowly over 10 min. The solution was stirred for 1 h and then 30 mL of ether was added and the mixture filtered. The solvents were removed to leave the crude ketone, which was chromatographed (eluent: CH_2Cl_2) to obtain pure ketone, mp 129–130°C; IR (KBr):2935, 2860, 1675, 1587, 1517, 1462, 1290, 1153, 1024, 923, 787 cm^{-1}; ^1H NMR δ: 7.65 (dd, 1H, $J_1 = 8.4$ Hz, $J_2 = 2.0$ Hz), 7.56 (d, 1H, $J = 2.0$ Hz), 6.87 (d, 1H, $J = 8.4$ Hz), 6.80–6.69 (m, 3H), 4.16 (s, 2H, $COCH_2$), 3.94 (s, 3H, OCH_3), 3.91 (s, 3H, OCH_3), 3.77 (s, 3H, OCH_3), 0.98 (s, 9H, $C(CH_3)_3$), 0.13 (s, 6H, Si $(CH_3)_2$); ^{13}C NMR δ: 196.7(C=O), 153.2, 151.0, 149.0, 143.9, 129.8, 128.4, 123.5, 121.6, 120.9, 113.1, 110.7, 109.9, 56.0, 55.9, 55.5, 45.0, 25.7, 18.4, −4.6. GC/MS, *m/z*: 360 (12), 359 (47), 179 (21), 166 (10), 165 (100), 73 (18). Anal. calcd. for $C_{23}H_{32}O_5Si$: C 66.31, H 7.74; found: C 66.26, H 7.57.

*Preparation of 1-(3,4-dimethoxyphenyl)-2-(4-hydroxy-3-methoxyphenyl) ethanone (**10**)*

The desilylation procedure used was that given in ref. 25. The silyl protected ketone (0.050 g, 1.2×10^{-4} mol) was dissolved in 1 mL of anhydrous DMF and then 0.014 g (2.4×10^{-4} mol) of potassium fluoride was added followed by 1 drop of 48% hydrobromic acid. The solution was stirred for 24 h and the reaction was monitored by TLC (eluent: CH_2Cl_2). Work-up was as described in the reference and the crude material should not be column chromatographed but recrystallized from CH_2Cl_2:hexane. The pure material should be kept from light and heat sources due to the ease of colouration; mp 118–120°C (lit. (2) mp 119–119.5°C); IR (KBr): 3427 (O-H, 2935, 1667 (C=O), 1594, 1514, 1465, 1455, 1268, 1149, 1023, 880, 802, 771 cm^{-1}; ^1H NMR δ: 7.66 (dd, 1H, $J_1 = 8.4$ Hz, $J_2 = 2.1$ Hz), 7.55 (d, 1H, $J = 2.0$ Hz), 6.84–6.89 (m, 2H), 6.77 (s, 2H), 5.67 (bs, 1H, OH), 4.16 (s, 2H), 3.93 (s, 3H), 3.91 (s, 3H), 3.84 (s, 3H); ^{13}C NMR[4] δ: 196.7 (C=O), 153.3 (q), 149.1 (q), 146.6 (q), 144.6 (q), 129.7 (q), 126.8 (q), 123.5, 122.2, 114.5, 111.7, 110.7, 110.0, 56.0 (OCH_3), 55.9, 55.9 (2 × OCH_3), 44.8 (CH_2). GC/MS, *m/z*: 302 (6, M^+), 166 (10), 165 (100), 137 (14), 79 (10), 77 (10).

Acknowledgements

Support of this research by the Mechanical and Chemimechanical Wood-Pulps Network, part of Canada's Networks of Centres of Excellence is gratefully acknowledged. One of us (G.R.C.) received a Graduate Scholarship funded by DuPont and PAPRICAN and the Ira Puddington Fund (Mount Allison). The ^1H and ^{13}C NMR were determined at the Atlantic Regional Magnetic Resonance Centre, Dalhousie University, Halifax, N.S.

1. A. Castellan, J.H. Zhu, N. Colombo, and A. Nourmamade. J. Photochem. Photobiol. A: **58**, 263 (1991).
2. C. Vanucci, P. Fornier de Violet, H. Bouas-Laurent, and A. Castellan. J. Photochem. Photobiol. A: **41**, 251 (1988).
3. A. Castellan, N. Colombo, C. Cucuphat, and P. Fornier de Violet. J. Photochem. Photobiol. A: **43**, 179 (1989).
4. W.U. Palm and H. Dreeskamp. J. Photochem. Photobiol. A: Chem. **52**, 439 (1990).
5. J.C. Netto-Ferreira, I.G.J. Avellar, and J.C. Scaiano. J. Org. Chem. **55**, 89 (1990).
6. J.A. Schmidt, A.B. Berinstain, F. DeRege, C. Heitner, L.J. Johnston, and J.C. Scaiano. Can. J. Chem. **69**, 104 (1991).
7. I.A. Shkrob, M.C. Depew, and J.K.S. Wan. Res. Chem. Intermed. **17**, 271 (1992).
8. J.A. Schmidt and C. Heitner. J. Wood Chem. Technol. **11**, 397 (1991).
9. D. Griller, L.R.C. Barclay, and K.U. Ingold. J. Am. Chem. Soc. **97**, 6151 (1975).
10. E.G. Janzen, P.H. Krygsman, D.A. Lindsay, and D.L. Haire. J. Am. Chem. Soc. **112**, 8279 (1990).
11. G. Brunton, H.C. McBay, and K.U. Ingold. J. Am. Chem. Soc. **99**, 4447 (1977).
12. N.J. Turro, I.R. Gould, and B.H. Baretz. J. Phys. Chem. **87**, 531 (1983).
13. C.R. Blakely, J.J. Carmody, and M.L. Vestal. J. Am. Chem. Soc. **102**, 5933 (1980).
14. P.H. Krygsman. Ph.D. Dissertation, University of Guelph, Guelph, Ont. March 1990.
15. N.C. Gonnella, M.V. Lakshmikantham, and M.P. Cava. Synth. Commun. **9**, 17 (1979).
16. S.R. Ramadas, P.S. Srinivasan, J. Ramachandran, and V.V.S.K. Sastry. Synthesis, 605 (1983).
17. Nouveau traité de chimie minerale. Vol. V. Maggon, Paris. 1962. p. 741.
18. H. Erdtman and B. Leopold. Acta Chem. Scand. **3**, 1358 (1949).
19. E. Adler, B.O. Lingren, and U. Saeden. Sven. Papperstidn. **55**, 245 (1952).
20. S.B. Singh and G.R. Pettit. Synth. Commun. **17**, 877 (1987).
21. D. Seebach and E.J. Corey. J. Org. Chem. **40**, 231 (1975).
22. H. Ramuz. Arzneim.-Forsch. **28**, 2048 (1978).
23. M.D. Rozwadowska and M. Chrzanowska. Tetrahedron, **41**, 2885 (1985).
24. R. Bernardi and D. Ghiringhelli. J. Org. Chem. **52**, 5021 (1987).
25. A.K. Sinhababu, M. Kawase, and R.T. Borchardt. Synthesis, 710 (1988).

Can. J. Chem. Downloaded from www.nrcresearchpress.com by 203.198.23.82 on 09/08/12
For personal use only.

The synthesis and some chemical reactions of a 5a-methyl 2*H*-naphtho[1,8-*bc*]furan[1]

PATRICIA A. BURNS, NICHOLAS J. TAYLOR, AND RUSSELL RODRIGO[2]

Guelph–Waterloo Centre for Graduate Work in Chemistry, University of Waterloo, Waterloo, ON N2L 3G1, Canada

Received June 24, 1993

This paper is dedicated to Professors David B. MacLean and Ian Spenser

PATRICIA A. BURNS, NICHOLAS J. TAYLOR, and RUSSELL RODRIGO. Can. J. Chem. **72**, 42 (1994).

A synthesis of the tricycle **19** has been completed in 14% overall yield from guaiacol. Several chemical transformations of this compound including its reduction to an octahydro naphtho[1,8-*bc*]furan and conversion to the hitherto unknown azuleno-[8,1-*bc*]furan ring system are described.

PATRICIA A. BURNS, NICHOLAS J. TAYLOR et RUSSELL RODRIGO. Can. J. Chem. **72**, 42 (1994).

Utilisant le guaïacol comme produit de départ on a réalisé une synthèse du tricycle **19** avec un rendement global de 14%. On décrit plusieurs transformations chimiques de ces composés, y compris sa réduction en un octahydro naptho[1,8-*bc*]furane et sa conversion dans le système cyclique de l'azuléno[8,1-*bc*]furane inconnu jusqu'à maintenant.

[Traduit par la rédaction]

Can. J. Chem. Downloaded from www.nrcresearchpress.com by 84.22.46.98 on 09/08/12
For personal use only.

The 2*H*-naphtho[1,8-*bc*]furan structural unit occurs at various oxidation levels in some terpenes and fungal metabolites. Its 5a-methyl (angular methyl) derivative **1** is a particularly important target for synthetic chemists because the development of an efficient general method for the preparation of **1** and closely related tricycles will be a significant step towards the synthesis of many natural products such as the pentacyclic marine quinones **2** and **3** (1), the fungal metabolites of *Gliocladium virens* **4** and **5** (2), and *Penicillium wortmanni* **6** (3). Some synthetic activity in this area has already been recorded by Kanematsu et al. (4) who applied their "furan transfer" protocol to prepare **7** in 6.3% yield from α-furyl methanol. In addition, both Xestoquinone **2** and Halenaquinone **3** have been synthesized in low yields (5) but in these instances the naphtho-[1,8-*bc*]furan unit was generated after the aromatic rings A and B had been attached. Very recently an oxidized variant, the furanocyclohexadienone lactone **8**, has been prepared (6) as part of a synthetic program directed at Wortmannin. We now report some of our synthetic work in this area.

The benzofuran ester **9** prepared from 2-methoxy-5-methylphenol as previously described (7) was saponified and the resulting acid **10** was converted to the diazoketone **11** through the acid chloride. All of several attempts to cyclize this material to the desired tricycle **12** via cationic intermediates with trifluoroacetic acid or boron trifluoride (8), or via carbenoids with rhodium(II) acetate (9) or silver oxide, failed to provide any isolable and identifiable product.[3] It was therefore apparent that the angular methyl group had to be introduced by different methods. The benzofuran **13**, prepared as described earlier (7) in 33% overall yield from 2-methoxyphenol, was subjected to one-carbon chain homologation in 63% yield by the Arndt–Eistert sequence to produce the acid **17** through the usual intermediates **14–16**. Intramolecular Friedel–Crafts cyclization to **18** was easily accomplished by either polyphosphoric acid (PPA) at 90°C (81%) or trifluoroacetic acid – trifluoroacetic anhydride (TFA–TFAA) in dry methylene chloride at 25°C (87%). Birch reduction[4] with potassium/liquid ammonia/*tert*-butanol followed by methylation (4.5 equiv. lithium bromide, followed by methyl iodide in THF–water) gave a 76% yield of the desired 5a-methylated-2*H*-naphthofuran **19**. The addition of the lithium bromide to exchange the potassium enolate for the lithium is necessary to preserve the selectivity of the methylation step. Without it, methylation on both sides of the C-5 carbonyl group was observed. The loss of the methoxyl group *para* to the C-5 carbonyl was not unexpected (10). The 200-MHz ^{1}H NMR spectrum of the product shows only one signal for the 5a methyl group at 1.36 ppm and no evidence could be found for the existence of more than one diastereomer in the product. The *cis* configuration at C-2a,5a was assigned to this product by the examination of models and was confirmed by an X-ray structure of a crystalline derivative (vide infra). This synthetic route provides the angularly methylated 2*H*-naphthofuran in 14% overall yield from 2-methoxyphenol. Although this was a reasonably efficient process there appeared to be room for improvement in the fact that the methoxyl group of the starting material was lost in the Birch reduction step and a great increase in efficiency would be possible if *o*-iodophenol, a commercial material, was used instead of guaiacol. The tedious *o*-iodination procedure necessary with the latter could then be avoided. Thus the benzofuran ester **20** was prepared from *o*-iodophenol as before (7) in two steps in 61% yield and homologated by the same Arndt–Eistert protocol to the ester **21** in 52% yield (32% overall from *o*-iodophenol). Unfortunately every attempt made, and a great many were tried, to cyclize the ester **21**, the acid **22**, or diazoketone **23** failed. All acidic reagents in Friedel–Crafts reactions, carbenoids, as well as the use of a Cu(I) triflate-promoted cyclization of a selenate ester **24** (11) failed. Mild conditions returned the starting material and forcing ones caused its destruction. The requirement for a *para*-methoxy group in a similar intramolecular Friedel–Crafts cyclization has been noted previously (12). In the hope that the benzofuran might cyclize better than the dihydrobenzofuran **22**, the methyl ester of the latter was dehydrogenated quantitatively with dichlorodicyanobenzoquinone (DDQ) in dioxan and saponified to provide the acid **25**. Friedel–Crafts cyclization with PPA or through the acid chloride with aluminum chloride was again not successful. The cyclopentanone **26** was the only isolable product (20% yield).

The chemical properties of **19** were investigated next. Attempts were made to deoxygenate the carbonyl group at C-5. Initially the thioketal – Raney Ni desulfurization and the tosylhydrazone–hydride reduction (13) were contemplated. How-

[1]Dedicated to Professors David MacLean and Ian Spenser for their outstanding contributions to Organic Chemistry.

[2]Author to whom correspondence may be addressed.

[3]G. Weeratunga and R. Rodrigo, unpublished results.

[4]For a recent review of the Birch reduction see ref. 10*b*.

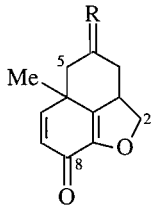

1 (R = H, H)
7 (2,2*a* dehydro R = H, H)
12 (R = O)

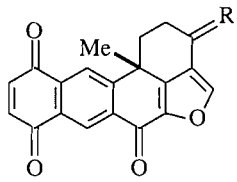

2 (R = H, H) Xestoquinone
3 (R = O) Halenaquinone

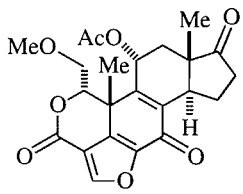

6 Wortmannin

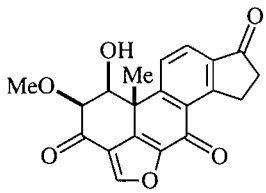

4 Viridin

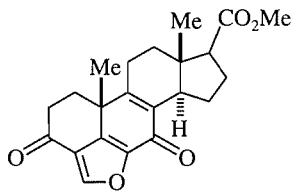

5 Virone

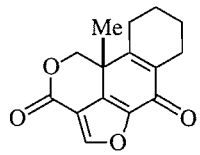

8

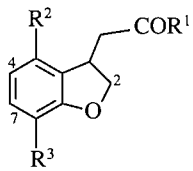

9 (R^1 = OEt, R^2 = Me, R^3 = OMe)
10 (R^1 = OH, R^2 = Me, R^3 = OMe)
11 (R^1 = CHN_2, R^2 = Me, R^3 = OMe)
13 (R^1 = OEt, R^2 = H, R^3 = OMe)
14 (R^1 = OH, R^2 = H, R^3 = OMe)
15 (R^1 = CHN_2, R^2 = H, R^3 = OMe)
20 (R^1 = OEt, R^2 = R^3 = H)
23 (R^1 = CHN_2, R^2 = R^3 = H)

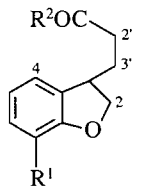

16 (R^1 = R^2 = OMe)
17 (R^1 = OMe, R^2 = OH)
21 (R^1 = H, R^2 = OMe)
22 (R^1 = H, R^2 = OH)
24 (R^1 = H, R^2 = SeMe)
25 (R^1 = H, 2,3-dehydro, R^2 = OH)

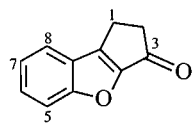

26

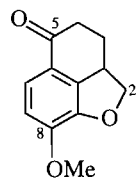

18

19

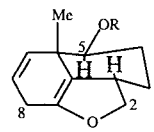

27 (R = H)
31 (R = Me)

ever, neither derivative could be obtained under the usual conditions but extensive decomposition of **19** took place instead. Reduction of the C-5 carbonyl group with sodium borohydride in ethanol could be accomplished in 93% yield to provide the alcohol **27** with the hydroxyl group in an apparently equatorial orientation ($J_{4,5}$ = 4.4 and 11.1 Hz). Attempts were now made to prepare the bromide or tosylate Treatment of the alcohol **27** with carbon tetrabromide and triphenylphosphine in methylene chloride or with 1,2-bis(triphenylphosphino) ethane tetrabromide (14) in the same solvent resulted in a complex mixture of products. Tosyl chloride in the presence of dimethylaminopyridine at 0°C also provoked decomposition. A recent report (15) suggests that even neopentyl alcohols can be deoxygenated efficiently by conversion to the 2,4,6-trichlorophenoxy thiocarbonyl ester followed by treatment with tributyl tin hydride. When this method was applied to **27**, extensive decomposition again resulted and the ^{1}H NMR spectrum of the product mixture showed aromatic absorption. An attempt was then made to prepare an imidazole thioester. Treatment of **19** with thiocarbonyldiimidazole in refluxing THF produced a 48% yield of a material identified as the azulenofuran **28**. The 250-MHz ^{1}H NMR spectrum showed the presence of three vinyl protons at 5.53 (1H) and 6.14 (2H) ppm. Irradiation of the former produced a clean AB pattern for H-6 and H-7 at 6.14 ppm. The proton at C-2a was found at 3.08 ppm as a multiplet that was coupled to a doublet at 2.91 ppm (H-8b) and to the protons at C-2 and C-3. The ^{13}C NMR spectrum was also in accord with this structure. No report could be found in the literature of the preparation or natural occurrence of this simple tricyclic system. It must arise in this instance by participation of the enol ether oxygen in displacing the imidazole ester at C-5 (Scheme 1). This proposal is supported by the fact that the 8a,8b-dihydro derivative of **27** (vide infra) when treated with thiocarbonyldiimidazole did provide the thioimidazole ester **29** in 65% yield.

In view of the presence of a carbonyl group in the natural products **2–6** at a position corresponding to C-8 of **19** it was decided to attempt oxidation at this allylic methylene group. Various chromium(VI) species (e.g., PDC, CrO_3 – dimethyl pyrazole (DMP)), DDQ, and allylic bromination with *N*-bromosuccinimide (NBS) caused decomposition, and the mixtures of products obtained showed aromatic signals in their ^{1}H NMR spectra. Thus in both the allylic bromination and DDQ oxidations the dihydrobenzofuran carboxylic acid **30** was obtained and characterized, in yields of 74 and 31%, respectively. Its formation is rationalized in Scheme 2 (X = Br or a positive charge). The first step (also the rate-determining step) in oxidations with quinones is generally believed to be hydride abstraction from the substrate; the cation (or ion pair) subsequently goes on to product(s). Since it appeared that the combination of positive centres at the C-5 and C-8 led to ring-opening

Can. J. Chem. Downloaded from www.nrcresearchpress.com by 84.22.46.98 on 09/08/12
For personal use only.

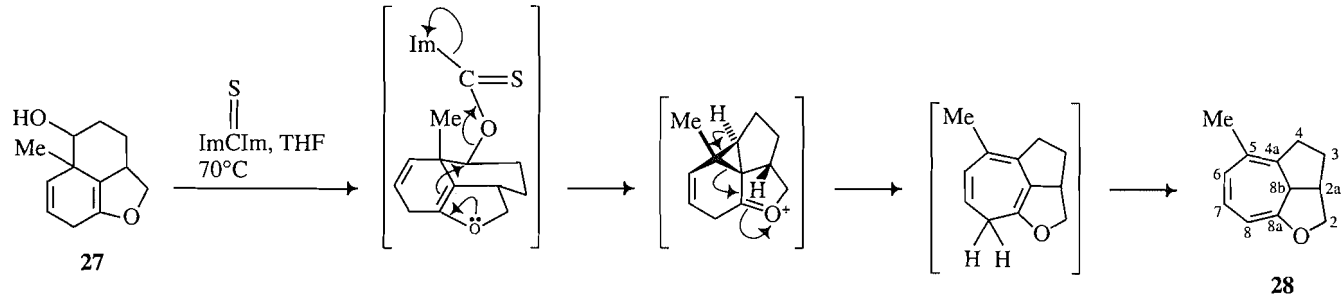

SCHEME 1. The ring expansion of **27**

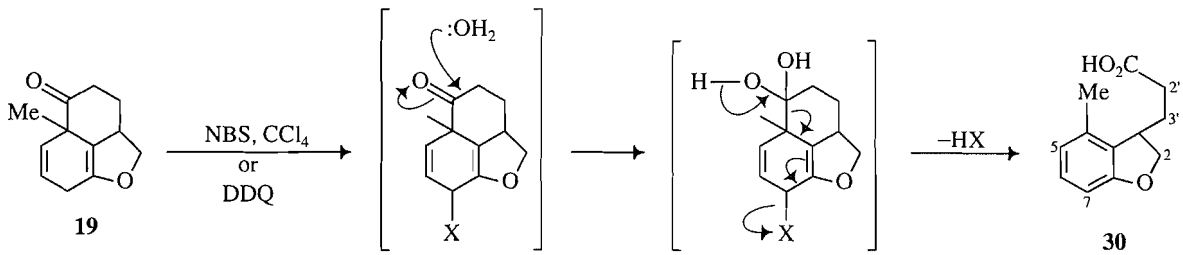

(X = Br or a positive charge)

SCHEME 2. The aromatization of **19**

and aromatization, the C-5 methyl ether **31** was prepared from the alcohol **27** in 82% yield by successive treatment with *n*-BuLi in THF–HMPA at −78°C and using excess methyl iodide. Every attempt at oxidation of this compound with various Cr(VI) and Ce(IV) reagents, DDQ, and NBS led to decomposition and the production of mixtures displaying aromatic signals in the ^{1}H NMR spectra.

Isobenzofurans are among the most reactive dienes known (16) and have been shown (17) to react even with cyclohexene to provide adducts in good yield. The isobenzofuran **33** (18), generated in situ with glacial acetic acid from the hydroxyphthalan **32**, was reacted with **19** in refluxing carbon tetrachloride for 2h. A crystalline product obtained in 50% yield displayed ^{1}H NMR signals consistent with the presence of both the methoxylated benzene ring and the tricyclic dienophile **19**. However, the vinyl protons of the 6,7 double bond were still present in the NMR spectrum of this compound at 5.19 (dd, H-7, $J_{6,7}$ = 10, $J_{7,8}$ = 3.65 Hz) and 5.98 ppm (dd, H-6, $J_{6,7}$ = 10 and $J_{6,8}$ = 1.7 Hz), suggesting that the reaction had taken place at C-8 and that the product **34** was not a Diels–Alder adduct. When dissolved in ethanol and stirred for 20 min with one drop of concentrated hydrochloric acid, a new crystalline material **35** was formed in 80% yield. An X-ray structure (Fig. 1) of this compound confirmed that it was derived from the expected product of reaction at C-8 of **19**, and established the relative stereochemistry of **19** to be *cis* at C-2a and C-5a as surmised previously. The formation of **34** and **35** is rationalized in Scheme 3 as an acid-catalysed aldol condensation between the oxonium ion **36** and enol ether **37** produced from **32** and **19**, respectively, in the acidic conditions employed, followed by rearrangement to the benzoxepin.

At this stage it appeared that any transformation of **19** into a synthon useful for the natural products would require the elimination of the C-5 oxygen and the C_{8a}—C_{8b} double bond. This objective was achieved as follows: the alcohol **27** was generated (but not isolated) as before and then reduced further with

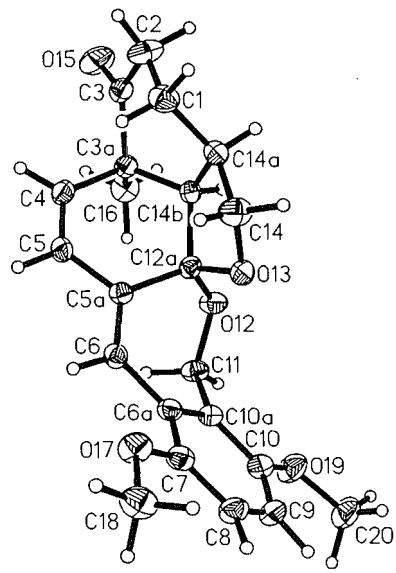

FIG. 1. Molecular plot of the X-ray crystallographic structure of **35**.

sodium cyanoborohydride in acidified solution to provide the alcohol **38** in 78% yield in a "one-pot" process. The relative stereochemistry of this alcohol is not evident from the ^{1}H NMR spectrum but it is assumed to be all *cis* at C-2a, 5a, 8a, and 8b from the X-ray structure of **35** and the well-known preference of 6/5 ring junctions for *cis* fusion. Deoxygenation of the alcohol could be achieved by radical procedures through several different intermediates. The imidazole thioester **29** could be obtained in 65% yield upon refluxing with thiocarbonyldiimidazole in benzene, the trichlorophenoxy thioester **39** in 23% yield by treatment with trichlorophenoxythiocarbonyl chloride in acetonitrile with a catalytic amount of dimethylaminopyridine, the xanthate **40** in 79% yield by reaction with *n*-butyl-

Can. J. Chem. Downloaded from www.nrcresearchpress.com by 84.22.46.98 on 09/08/12
For personal use only.

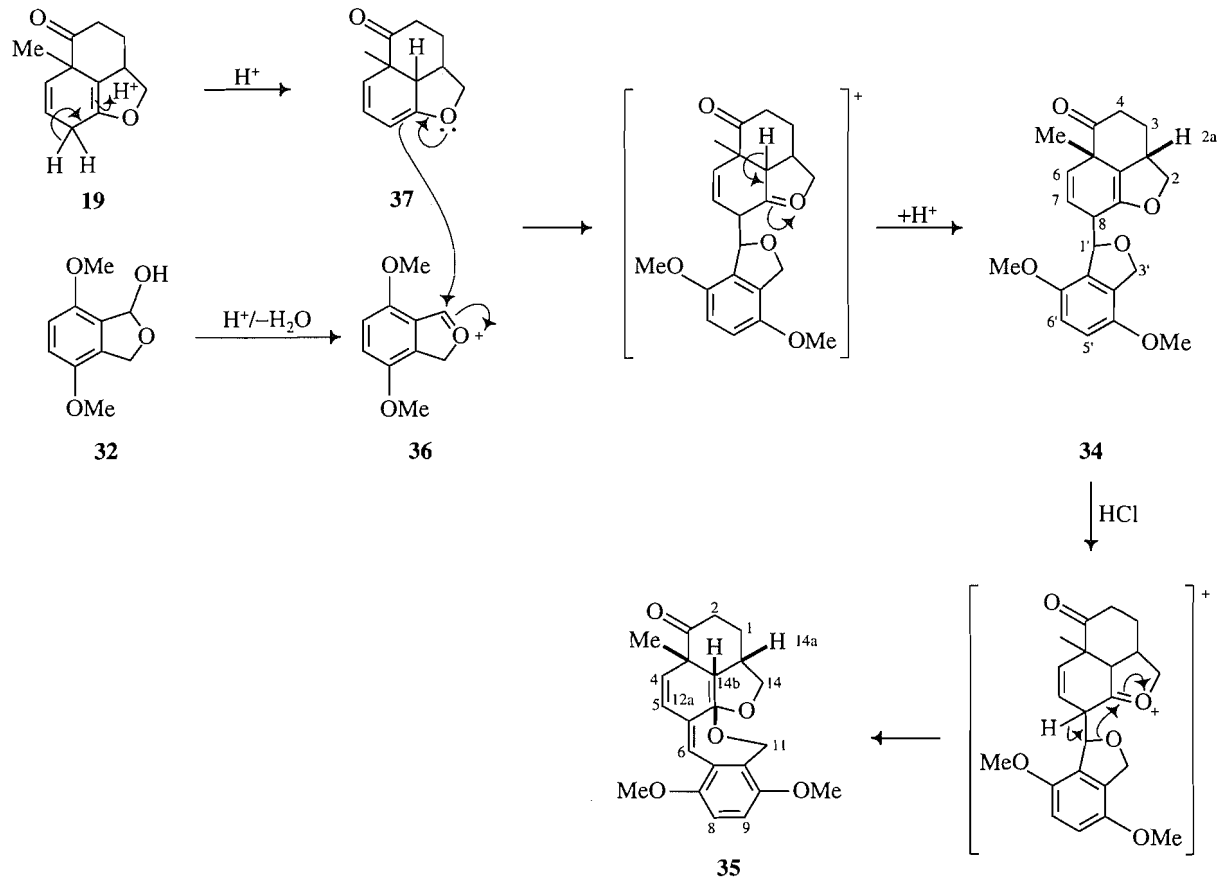

SCHEME 3. Aldol condensation of enol ether **37** with oxonium ion **36**

lithium at −78°C followed by carbon disulfide at 0°C and methyl iodide at 25°C. Preparation of the bromide, however, with CBr_4 and triphenylphosphine was unsuccessful. All three thio derivatives could be deoxygenated to **41** with tri-*n*-butyltin hydride and azobis isobutyro nitrile (AIBN) in refluxing toluene but the xanthate gave the best yield (69% in this step and 43% from **19**). Thus **41** is available from 2-methoxyphenol in 4.7% overall yield. No other diastereomer was detectable in the product but the *cis* stereochemistry at C-8a, 8b is to be expected for this 6/5 ring fusion. With the dihydro compound in hand, several attempts at allylic oxidation at C-8 were made. Various chromium(VI) reagents ($Cr(CO)_6$ and 90% *tert*-butyl hydroperoxide, dimethylpyrazole CrO_3, PCC), selenium dioxide with and without *tert*-butyl hydroperoxide, palladium(II) acetate and manganese dioxide, and DDQ all failed to oxidize the allylic methylene group. In many cases starting material was returned, but the PCC and DMP·CrO_3 oxidations of **41** gave 35% and 21% yields, respectively, of the γ-lactone **42**. Such oxidations of tetrahydrofurans to γ-lactones with Cr(VI) reagents are not unknown (19). Allylic bromination with NBS under various conditions was not successful and no method could be found to achieve allylic oxidation at C-8 of this tricyclic system. The final attempt to use **41** as a synthon depended on whether its unactivated double bond would undergo a Diels–Alder reaction with the reactive isobenzofuran **33**. This was tested by heating the precursor **32** in *p*-xylene with cyclohexene at 140°C with a catalytic amount of *p*-toluic acid for 36h. A 6:1 mixture of *endo*:*exo* adducts **43** was obtained in a total yield of 53%. The same conditions were then employed with **41** as the dienophile

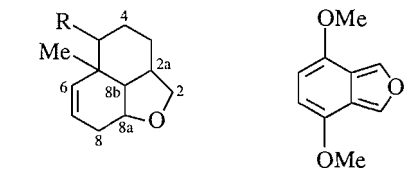

29 (R = O-CS-Im)
38 (R = OH)
39 (R = O-CS-$C_6H_2Cl_3$)
40 (R = O-CS-SMe)
41 (R = H)

33

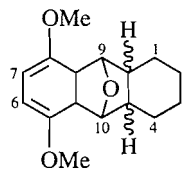

43

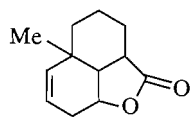

42

but no cycloaddition products could be found even when heating was conducted in a sealed tube placed in refluxing xylene for 5 days. The starting material **41** was recovered from these reactions, indicating the lower reactivity of its cyclohexene double bond towards cycloaddition. The isobenzofuran was produced as before, but polymerized in the absence of a sufficiently reactive dienophile. High pressure is perhaps one way of forcing this reaction to occur but, even if it does, a satisfactory yield cannot realistically be expected and the requirement for several further transformations detracts from the value of this route to the marine quinones. Other approaches to the natural products **2–6** are being explored at present. They show some

Can. J. Chem. Downloaded from www.nrcresearchpress.com by 84.22.46.98 on 09/08/12
For personal use only.

promise of success and these results will be reported in due course.

Experimental

Melting points were determined on a Fischer Mel-Temp unit and are uncorrected. IR spectra were recorded on a Perkin Elmer 983 or a Bomem MB-100 Fourier Transform spectrophotometer. ^1H and ^{13}C NMR spectra were recorded on Bruker AM-250, AC-200, or WP-80 spectrometers at the field strengths specified. Chemical shifts are reported in δ (ppm) and coupling constants (*J*) in hertz. Mass spectra were obtained on a Kratos MS 890 (at the Guelph MS Centre) or on a VG ZAB-E or VG 7070 spectrometer (at the S.W. Ontario Regional MS Centre at Hamilton). The EI and CI modes were used for ionization. Elemental analyses were performed by M-H-W Laboratories, Phoenix, Ariz.

*2-(2,3-Dihydro-7-methoxybenzo[*b*]furan-3-yl)acetic acid* ***14***

To a solution of ester **13** (5.50g, 23.3 mmol) in MeOH (100 mL) was added 50 mL of 10% NaOH and the resulting mixture was stirred for 5h at room temperature. The solution was cooled in ice and acidified with 2 N HCl. Extraction with EtOAc (3 × 50 mL) followed by washing the combined organic layers with water (2 × 50 mL) and drying (Na_2SO_4) provided 4.30g of crude product upon removal of the solvent under reduced pressure. The solid was recrystallized from Et_2O–hexane to give 4.00g (82%) of **14** as colourless plates; mp 99–100°C (lit. (20) mp 101–103°C); IR ($CHCl_3$): 3500–2500 (br), 3024, 1711, 1620, 1593, 1492, 1282, 723 cm^{-1}; ^1H NMR (250 MHz, $CDCl_3$) δ: 2.77 (AB of an ABX system, J_{AB} = 17.0, J_{AX} = 5.1, J_{BX} = 9.6, $\Delta\nu$ = 50.7, 2H, $CHCH_2CO_2H$), 3.88 (s, 3H, OMe), 3.87–3.94 (m, 1H, H-3), 4.35 (dd, $J_{2\alpha,2\beta}$ = 9.3, $J_{3,2\beta}$ = 6.4, 1H, H-2β), 4.83 (t, $J_{2\beta,2\alpha} = J_{3,2\alpha}$ = 9.3, 1H, H-2α), 6.76–6.88 (m, 3H, H-4, H-5, and H-6), 11.05 (br s, exchanged with D_2O, 1H, OH); LRMS (EI) *m/e*: 208 (87, M^+), 190 (11), 177 (20), 161 (13), 149 (100), 131 (13), 121 (55), 103 (12), 91 (36), 77 (19), 68 (16), 51 (14). Anal. calcd. for $C_{11}H_{12}O_4$: C 63.45, H 5.81; found C 63.37, H 5.83.

*1-Diazo-3-(2,3-dihydro-7-methoxybenzo[*b*]furan-3-yl)-2-propanone* ***15***

To a solution of oxalyl chloride (1.42 mL, 16.3 mmol) in benzene (50 mL) at room temperature was added a mixture of acid **14** (2.00g, 9.61 mmol) and pyridine (0.85 mL, 11 mmol) in benzene (40 mL) dropwise over 30 min. The resulting solution was stirred an additional 30 min, then filtered to remove pyridinium hydrochloride. The filtrate was concentrated in vacuo with the aid of a drying tube on the aspirator to prevent the ingress of moisture. Any remaining solvent was removed under high vacuum. The acid chloride thus obtained was not purified but taken up in benzene (20 mL) and added dropwise to an ice-cold solution of diazomethane. The solution was stirred at 0°C for 2h and slowly allowed to warm to room temperature. The mixture was stirred for 15h to allow excess diazomethane to evaporate. The Et_2O was removed in vacuo and the resulting yellow solid was recrystallized from Et_2O to provide 1.93g (87%) of **15** as yellow needles; mp 96.5–97.5°C; IR ($CHCl_3$): 3007, 2961, 2111, 1732, 1640, 1492, 1283, 1196, 951 cm^{-1}; ^1H NMR (250 MHz, $CDCl_3$) δ: 2.55–2.84 (m, 2H, $CHCH_2COCHN_2$), 3.86 (s, 3H, OMe), 3.90–4.00 (m, 1H, H-3), 4.28 (dd, $J_{2\alpha,2\beta}$ = 9.2, $J_{3,2\beta}$ = 6.1, 1H, H-2β), 4.80 (t, $J_{2\beta,2\alpha} = J_{3,2\alpha}$ = 9.2, 1H, H-2α), 5.26 (br s, 1H, $COCHN_2$), 6.73–6.85 (m, 3H, H-4, H-5, and H-6); LRMS (EI) *m/e*: 232 (19, M^+), 222 (13), 204 (15), 173 (12), 161 (34), 149 (55), 133 (9), 121 (100), 103 (10), 91 (56), 77 (32), 65 (16). Anal. calcd. for $C_{12}H_{12}N_2O_3$: C 62.06, H 5.21; found: C 62.28, H 5.34.

*Methyl 3-(2,3-dihydro-7-methoxybenzo[*b*]furan-3-yl)propionate* ***16***

Diazo ketone **15** (6.78 g, 29.6 mmol) was dissolved in MeOH (250 mL) and Ag_2O (7.54 g, 32.5 mmol) was added. The reaction mixture was stirred at room temperature for 2h, then filtered and concentrated. Flash chromatography of the crude oil on silica (40% EtOAc–hexanes eluent) afforded 6.49 g (93%) of **16** as a pale yellow oil. IR (neat): 2951, 1736, 1618, 1592, 1492, 1279, 1199, 773, 734 cm^{-1}, ^1H NMR (250 MHz, $CDCl_3$) δ: 1.88–2.15 (m, 2H, 2 × H-3′), 2.30–2.42 (m, 2H, 2 × H-2′), 3.44–3.56 (m, 1H, H-3), 3.67 (s, 3H, CO_2Me), 3.87 (s, 3H, ArOMe), 4.28 (dd, $J_{3,2\beta}$ = 5.8, $J_{2\alpha,2\beta}$ = 9.0, 1H, H-2β), 4.68 (t, $J_{3,2\alpha} = J_{2\beta,2\alpha}$ = 9.0, 1H, H-2α), 6.74–6.84 (m, 3H, H-4, H-5, H-6); LRMS (EI) *m/e*: 236 (78, M^+), 205 (18), 176 (15), 162 (100), 149 (97), 131 (13), 121 (59), 103 (11), 91 (77), 78 (20), 65 (17), 51 (16). Anal. calcd. for $C_{13}H_{16}O_4$: C 66.09, H 6.83; found: C 65.96, H 6.62.

*3-(2,3-Dihydro-7-methoxybenzo[*b*]furan-3-yl)propionic acid* ***17***

To ester **16** (3.03 g, 12.9 mmol) dissolved in THF (60 mL) was added 20 mL of 10% NaOH and the solution was stirred for 22h at room temperature. The solution was concentrated in vacuo and EtOAc (50 mL) was added. The solution was acidified with 2 N HCl and the layers separated. The aqueous layer was further extracted with EtOAc (2 × 50 mL). The organic extracts were combined, dried (Na_2SO_4), and the solvent removed under reduced pressure. Flash chromatography (silica, 50% Et_2O–hexanes eluent) followed by recrystallization from Et_2O – petroleum ether gave 2.5 g (87%) of **17** as colourless plates; mp 63–64°C; IR ($CHCl_3$): 3500–2500, 3023, 2942, 1708, 1618, 1491, 1278, 1197, 952 cm^{-1}; ^1H NMR (200 MHz, $CDCl_3$) δ: 1.88–2.17 (m, 2H, 2 × H-3′), 2.38–2.48 (m, 2H, 2 × H-2′), 3.46–3.60 (m, 1H H-3), 3.87 (s, 3H, OMe), 4.30 (dd, $J_{3,2\beta}$ = 5.6, $J_{2\alpha,2\beta}$ = 9.1, 1H, H-2β), 4.69 (t, $J_{3,2\alpha} = J_{2\beta,2\alpha}$ = 9.1, 1H, H-2α), 6.74–6.88 (m, 3H, H-4, H-5, H-6), 10.75 (br s, exchanged with D_2O, 1H, OH); LRMS (EI) *m/e*: 222 (77, M^+), 208 (2), 189 (4), 176 (5), 162 (41), 149 (100), 131 (9), 121 (59), 103 (97), 91 (25), 77 (16), 65 (8). Anal. calcd. for $C_{12}H_{14}O_4$: C 64.85, H 6.35; found: C 65.00, H 6.37.

*8-Methoxy-2,2a,3,4,tetrahydronaphtho[1,8-*bc*]furan-5-one* ***18***

To acid **17** (4.00 g, 18.0 mmol) in CH_2Cl_2 (140 mL) was added trifluoroacetic acid (1.66 mL, 21.6 mmol) and trifluoracetic anhydride (3.05 mL, 21.6 mmol). The reaction mixture was stirred for 5 h. Water (75 mL) was added and the layers separated. The aqueous layer was extracted with CH_2Cl_2 (3 × 75 mL) and the organic layers combined, dried (Na_2SO_4), and concentrated in vacuo to provide a solid that was recrystallized from EtOAc–hexane to give 3.21 g (87%) of **18** as colourless plates. The same compound was prepared utilizing PPA as follows: phosphorus pentoxide (20.83 g, 0.147 mol) was combined with 85% orthophosphoric acid (16.67 mL, 0.145 mol) and heated at 160–165°C for 5h. Acid **17** (0.50 g, 2.2 mmol) was added to the PPA at 90°C and heated for 1 h, then cooled and poured into ice. The mixture was extracted with CH_2Cl_2 (3 × 50 mL) and the organic layer was washed with 10% K_2CO_3 (75 mL) and water (2 × 75 mL), then dried (Na_2SO_4) and concentrated; 0.37 g (81%) of **18** was obtained after recrystallization from EtOAc–hexanes; mp 114–115°C; IR (neat): 2999, 2941, 1670, 1616, 1600, 1274, 1099, 914, 803cm^{-1}; ^1H NMR (200 MHz, $CDCl_3$) δ: 1.93 (qd, $J_{4\alpha,3\beta} = J_{2a,3\beta} = J_{3\alpha,3\beta}$ = 12.7, $J_{4\beta,3\beta}$ = 4.6, 1H, H3β), 2.37 (dtd, $J_{3\beta,3\alpha}$ = 12.7, $J_{2a,3\alpha} = J_{4\alpha,3\alpha}$ = 4.6, $J_{4\beta,3\alpha}$ = 2.6, 1H, H-3α), 2.65 (AB of an ABMX system, J_{AB} = 17.6 J_{AX} = 2.6, J_{AM} = 4.6, J_{BM} = 12.7, J_{BX} = 4.6, $\Delta\nu$ = 29, 2H, 2 × H-4), 3.64–3.83 (m, 1H, H-2a), 3.96 (s, 3H, OMe), 4.17 (dd, $J_{2a,2\beta}$ = 11.9, $J_{2\alpha,2\beta}$ = 8.6, 1H, H-2β), 4.95 (t, $J_{2a,2\alpha} = J_{2\beta,2\alpha}$ = 8.6, 1H, H-2α), 6.83 (d, *J* = 8.5, 1H, H-7), 7.42 (d, *J* = 8.5, 1H, H-6); LRMS (EI) *m/e*: 204 (100, M^+), 190 (15), 176 (72), 162 (29), 148 (32), 134 (28), 119 (46), 105 (26), 91 (34), 77 (21), 51 (13). Anal. calcd. for $C_{12}H_{12}O_3$: C 70.58, H 5.92; found: C 70.42, H 6.09.

*2,2a,3,4,5,5a-Hexahydro-5a-methyl-8*H*-naphtho[1,8-*bc*]furan-5-one* ***19***

To freshly distilled liquid ammonia (50 mL) at −78°C was slowly added a solution of **18** (0.500 g, 2.45 mmol) and *t*-BuOH (0.76 mL, 8.1 mmol) in THF (5 mL). Potassium metal (0.431 g, 11.0 mmol) was added in small pieces. The resulting dark blue solution was stirred for 30 min. A solution of LiBr (0.957 g, 11.0 mmol) in THF (3 mL) was added dropwise with stirring. The colourless mixture was stirred a further 30 min, then MeI (0.183 mL, 2.94 mmol) and aqueous THF (1:1, 2.1 mL) were added simultaneously. The cooling bath was removed and the ammonia allowed to evaporate. Water (75 mL) was added and

Can. J. Chem. Downloaded from www.nrcresearchpress.com by 84.22.46.98 on 09/08/12
For personal use only.

Can. J. Chem. Downloaded from www.nrcresearchpress.com by 84.22.46.98 on 09/08/12
For personal use only.

the mixture extracted with Et_2O (3 × 50 mL). The ether extracts were washed with water (75 mL) and brine (75 mL), dried (Na_2SO_4), and evaporated to dryness. The residue was purified by column chromatography (silica, 30% EtOAc–hexanes eluent) to give 354 mg (76%) of **19** as a colourless oil. IR (neat): 2957, 2925, 2886, 1705, 1450, 1389, 1329, 1201, 1069, 1010, 944, 934, 720 cm^{-1}; ^1H NMR (200 MHz, $CDCl_3$) δ: 1.36 (s, 3H, Me), 1.53–1.74 (m, 1H, H-3β), 2.07–2.20 (m, 1H, H-3α), 2.27–2.38 (ddd, $J_{4\alpha,4\beta}$ = 14.5, $J_{3\alpha,4\beta}$ = 3.0, $J_{3\beta,4\beta}$ = 4.0, 1H, H-4β), 2.56–2.66 (ddd, $J_{4\beta,4\alpha}$ = 14.5, $J_{3\beta,4\alpha}$ = 5.4, $J_{3\alpha,4\alpha}$ = 1.0, 1H, H-4α), 2.70–2.76 (m, 2H, 2 × H-8), 3.25–3.37 (m, 1H, H-2a), 4.08 (dd, $J_{2\alpha,2\beta}$ = 9.3, $J_{2a,2\beta}$ = 4.7, 1H, H-2β) 4.51 (t, $J_{2\beta,2\alpha}$ = $J_{2a,2\alpha}$ = 9.3, 1H, H-2α), 5.85 (AB of ABXX′, J_{AB} = 10.0, J_{AX} = 2.1, J_{BX} = 3.3, Δν = 42, 2H, H-6, H-7); LRMS (EI) *m/e*: 190 (28, M^+), 162 (61), 134 (78), 119 (100), 105 (27), 91 (47), 77 (18), 65 (11), 55 (11). Anal. calcd. for $C_{12}H_{14}O_2$: C 75.76, H 7.42; found: C 75.68, H 7.34.

*2-(2,3-Dihydrobenzo[*b*]-furan-3-yl)acetic acid*

To a solution of ester **20** (4.09, 19.8 mmol) in 60 mL THF and 30 mL MeOH was added 40 mL of 10% aqueous NaOH. The mixture was stirred at room temperature for 5h, then acidified with 2 N HCl and extracted with EtOAc (3 × 75 mL). The combined organics were washed with brine (75 mL) and dried (Na_2SO_4). Concentration in vacuo provided a yellow solid that was recrystallized from Et_2O–hexane to afford 3.00 g (91%) of the acid as colourless plates; mp 100–101°C; IR ($CHCl_3$): 3400–2500, 1709, 1596, 1481, 1217, 965 cm^{-1}; ^1H NMR (200 MHz, $CDCl_3$) δ: 2.76 (AB of an ABX system, J_{AB} = 17.0, J_{AX} = 5.3, J_{BX} = 9.4, Δν = 40.7, $CHCH_2CO_2H$), 3.83–3.92 (m, 1H, H-3), 4.28 (dd, $J_{3,2\beta}$ = 6.3, $J_{2\alpha,2\beta}$ = 9.1, 1H, H-2β), 4.76 (t, $J_{3,2\alpha}$ = $J_{2\beta,2\alpha}$ = 9.1, 1H, H-2α), 6.79–6.91 (m, 2H, H-5, H-7), 7.12–7.20 (m, 2H, H-4, H-6), 10.20 (br s, exchanged with D_2O, 1H, OH); LRMS (EI) *m/e*: 178 (51, M^+), 147 (4), 131 (14), 119 (100), 91 (72), 77 (13), 65 (10), 51 (10). Anal. calcd. for $C_{10}H_{10}O_3$: C 67.41, H 5.66; found: C 67.30, H 5.60.

*1-Diazo-3(2,3-dihydrobenzo[*b*]furan-3-yl)-2-propanone **23***

To a solution of oxalyl chloride (1.48 mL, 17.0 mmol) in benzene (50 mL) at room temperature was added a mixture of this acid (1.78 g, 10.0 mmol) and pyridine (0.89 mL, 11 mmol) in benzene (40 mL) dropwise over 30 min. The resulting solution was stirred an additional 30 min, then filtered to remove pyridine hydrochloride. The filtrate was concentrated to dryness while protecting from the entry of moisture by employing a drying tube on the aspirator. Any remaining solvent was removed under high vacuum. The acid chloride thus obtained was not purified but taken up in 20 mL of benzene and added dropwise at 0°C to the solution of diazomethane prepared previously. The solution was allowed to warm to room temperature and stirred for 15h to allow excess diazomethane to evaporate. The Et_2O was removed in vacuo and the resulting yellow solid was subjected to flash chromatography (silica, 40% EtOAc–hexanes eluent) to yield 1.69 g (84%) of **23** as a yellow oil. IR (neat): 3093, 2893, 2106, 1727, 1638, 1481, 1460, 1373, 1232, 1137, 962, 745 cm^{-1}; ^1H NMR (250 MHz, $CDCl_3$) δ: 2.61–2.83 (m, 2H, $CHCH_2COCHN_2$), 3.90–397 (m, 1H, H-3), 4.21 (dd, $J_{2\alpha,2\beta}$ = 9.1, $J_{3,2\beta}$ = 6.0, 1H, H-2β), 4.74 (t, $J_{2\beta,2\alpha}$ = $J_{3,2\alpha}$ = 9.1, 1H, H-2α), 5.24 (br s, 1H, $COCHN_2$), 6.77–6.88 (m, 2H, H-5, H-7), 7.10–7.16 (m, 2H, H-4, H-6); LRMS (EI) *m/e*: 202 (2, M^+), 192 (4), 174 (19), 145 (7), 131 (51), 119 (60), 103 (7), 91 (100), 77 (12), 65 (18), 55 (13). Anal. calcd. for $C_{11}H_{10}N_2O_2$: C 65.34, H 4.98; found: C 65.53, H 5.00.

*Methyl 3-(2,3-dihydrobenzo[*b*]furan-3-yl)propionate **21***

Silver(I) oxide was prepared as follows: silver nitrate (4.50 g, 26.5 mmol) was dissolved in water (45 mL) and concentrated aqueous NaOH was added until the solution was basic. The brown precipitate of Ag_2O was filtered and rinsed with several portions of water (4 × 50 mL), then acetone (4 × 50 mL), then diethyl ether (4 × 50 mL). The solid was dried under high vacuum for several hours. Diazo ketone **23** (1.25 g, 6.18 mmol) was dissolved in MeOH (40 mL) and Ag_2O (1.58, 6.80 mmol) was added. The reaction mixture was stirred at room temperature for 2h, then was filtered and the filtrate was concentrated in vacuo. The resulting crude oil was chromatographed on silica (40% EtOAc/hexanes eluent) to provide 1.09 g (86%) of **21** as a colourless oil. IR (neat): 2950, 1734, 1609, 1481, 1229, 1170, 1017, 752 cm^{-1}; ^1H NMR (200 MHz, $CDCl_3$) δ: 1.87–2.17 (m, 2H, 2 × H-3′), 2.34–2.43 (m, 2H, 2 × H-2′), 3.43–3.51 (m, 1H, H-3), 3.68 (s, 3H, OMe), 4.22 (dd, $J_{3,2\beta}$ = 5.8, $J_{2\alpha,2\beta}$ = 8.9, 1H, H-2β), 4.61 (t, $J_{2\beta,2\alpha}$ = $J_{3,2\alpha}$ = 8.9, 1H, H-2α), 6.77–6.90 (m, 2H, H-5, H-7), 7.09–7.20 (m, 2H, H-4, H-6); LRMS (EI) *m/e*: 206 (51, M^+), 175 (11), 146 (7), 132 (100), 131 (77), 119 (77), 91 (79), 77 (8), 65 (12), 51 (6), 45 (46). Anal. calcd. for $C_{12}H_{14}O_3$: C 69.89, H 6.84; found: C 69.64, H 6.67.

*3-(2,3-Dihydrobenzofuranyl) propionic acid **22***

This acid was prepared in 90% yield by the hydrolysis of ester **21** in THF–methanol (10:1) with 2 M sodium hydroxide for 3h at room temperature.[3]

*Methyl 3-(2,3-dihydrobeno[*b*]furan-3-yl)propioselenate **24***

In a dry box, $AlMe_3$ (12.5 mL of a 2 M solution in toluene, 25.0 mmol) was added to a flask containing selenium metal (2.05 g, 26.0 mmol). The mixture was refluxed for 2h, at which time it was cooled to room temperature and the unreacted Se was allowed to settle from the solution. A portion of this solution (1.34 mL, 2.67 mmol) was transferred to a solution of methyl ester **21** (0.500 g, 2.43 mmol) in 5 mL of argon-degassed CH_2Cl_2 at 0°C. The mixture was stirred at 0°C for 30 min, then allowed to warm to room temperature over 30 min. To the yellow solution was added sodium sulfate decahydrate (1 g) and the mixture was stirred for 20 min. The solution was extracted with Et_2O (3 × 20 mL) and the organic layer was dried (Na_2SO_4) and concentrated to provide 0.58 g (89%) of selenol ester **24** as a yellow oil. IR (neat): 3020, 2986, 1732, 1602, 1500, 1420, 1220, 1201, 1132, 1055, 906, 796 cm^{-1}; ^1H NMR (80 MHz, $CDCl_3$) δ: 1.85–2.40 (m, 2H, 2 × H-3′), 2.25 (s, 3H, Me), 2.53–2.82 (m, 2H, 2 × H-2′), 3.28–3.71 (m, 1H, H-3), 4.21 (dd, $J_{2\alpha,2\beta}$ = 8.9, $J_{3,2\beta}$ = 6.1, 1H, H-2β), 4.61 (t, $J_{2\beta,2\alpha}$ = $J_{3,2\alpha}$ = 8.9, 1H, H-2α), 6.68–6.95 (m, 2H, H-5, H-7), 7.05–7.28 (m, 2H, H-4, H-6); LRMS (EI) *m/e*: 269 (75, M^+), 254 (10), 175 (15), 163 (100), 119 (16), 103 (11), 91 (77), 78 (16), 65 (12), 51 (18). Anal. calcd. for $C_{12}H_{14}O_2Se$: C 53.54, H 5.24; found: C 53.62, H 5.16.

*Methyl 3-benzo[*b*]furan-3-yl)propionate*

To ester **21** (1.00 g, 4.85 mmol) in dry dioxane (25 mL) was added a solution of DDQ (1.32 g, 5.82 mmol) in dioxane (15 mL). The mixture was refluxed for 4h, then cooled. The solid was filtered off and washed with benzene (20 mL), then chloroform (20 mL). The filtrate and washings were combined and concentrated under reduced pressure. The benzofuran ester (0.999 g, 100%) was obtained as a colourless oil after flash chromatography (silica, 30%, EtOAc–hexanes eluent). IR (neat): 2951, 1738, 1452, 1167, 1094, 857, 747 cm^{-1}; ^1H NMR (200 MHz, $CDCl_3$) δ: 2.67–2.75 (m, 2H, 2 × H-3′), 2.98–3.06 (m, 2H, 2 × H-2′), 3.68 (s, 3H, OMe), 7.19–7.33 (m, 2H, H-5, H-7), 7.43–7.57 (m, 3H, H-2, H-4, H-6); LRMS (EI) *m/e*: 204 (61, M^+), 173 (6), 145 (55), 131 (100), 115 (24), 103 (9), 91 (9), 77 (14), 63 (9), 51 (7), 45 (12). Anal. calcd. for $C_{12}H_{12}O_3$: C 70.58, H 5.92; found: C 70.49, H 5.78.

*3-(Benzofuran-3-yl)propionic acid **25***

To the foregoing ester (0.999 g, 4.89 mmol) dissolved in THF (30 mL) with a few drops of MeOH was added 10 mL of 10% NaOH. The solution was stirred at room temperature for 22h. The mixture was concentrated in vacuo and EtOAc (50 mL) added. This was acidified with 2 N HCl and the layers were separated. The aqueous layer was further extracted with EtOAc (2 × 50 mL) and the combined organics were washed with brine and dried (Na_2SO_4). Evaporation of the solvent followed by recrystallization from ether–hexanes gave 0.77 g (83%) of **25** as a colourless solid; mp 106–108°C; IR ($CHCl_3$): 3400–2500, 1710, 1451, 1284, 1118, 858 cm^{-1}; ^1H NMR (250 MHz, $CDCl_3$) δ: 2.75–2.81 (m, 2H, 2 × H-3′), 3.00–3.06 (m, 2H, 2 × H2′), 7.21–7.33 (m, 2H, H-5, H-7), 7.45 (s, 1H, H-2), 7.45–7.56 (m, 2H, H-4, H-6); LRMS (EI) *m/e*: 190 (58, M^+), 178 (7), 145 (29), 131 (100), 119 (15), 115 (14), 103 (9), 91 (14), 77 (14), 63 (6), 51 (5). Anal. calcd. for $C_{11}H_{10}O_3$: C 69.47, H 5.30; found: C 69.64, H 5.33.

Can. J. Chem. Downloaded from www.nrcresearchpress.com by 84.22.46.98 on 09/08/12
For personal use only.

2,3-Dihydro-1H-cyclopenta[b]benzofuran-3-one ***26***

Polyphosphoric acid was prepared by combining phosphorus pentoxide (0.85 g, 6.0 mmol) with 85% orthophosphoric acid (0.559 mL, 8.17 mmol) and heating at 85°C for 30 min. The acid **25** (0.100 g, 0.526 mmol) was added to the PPA and the mixture was heated at 90°C for 1h. The dark purple solution was cooled to 60°C and poured into ice water. Extraction with Et_2O (3 × 25 mL) was followed by washing the ether extracts with 20% NaOH (50 mL) and water (2 × 25 mL). The organic layer was dried (Na_2SO_4) and concentrated to give 13 mg (14%) of **26** after flash chromatography (silica, 10% EtOAc–hexanes eluent). The basic layer was acidified with 2 N HCl and extracted with EtOAc (2 × 25 mL). The organics were washed with brine (50 mL), dried (Na_2SO_4), and the solvent was removed to provide 76 mg of an orange polymeric material that was not characterized. **26** could be recrystallized from Et_2O–hexanes to afford colourless needles; mp 145–146°C; IR ($CHCl_3$): 3003, 2929, 1688, 1590, 1442, 1394, 1043, 820 cm^{-1}; ^1H NMR (250 MHz, $CDCl_3$) δ: 3.00–3.09 (m, 4H, 2 × H-2, 2 × H-1), 7.35 (td, J = 7.9, J = 1.1, 1H, H-7), 7.48–7.61 (m, 2H, H-5, H-6), 7.71 (d, J = 7.9, 1H, H-8); LRMS (EI) *m/e*: 172 (100, M^+), 144 (28), 115 (68), 89 (8), 63 (10); HRMS calcd. for $C_{11}H_8O_2$: 172.05242; found: 172.05240.

2,2a,3,4,5,5a-Hexahydro-5-hydroxy-5a-methyl-8H-naphtho[1,8-bc]furan ***27***

To **19** (450 mg, 2.37 mmol) in EtOH (20 mL) at 0°C was added $NaBH_4$ (24.2 mg, 0.639 mmol). After stirring for 1h at 0°C, water (10 mL) was added and the EtOH was removed under reduced pressure. The aqueous residue was extracted with EtOAc (3 × 20 mL) and the organic extracts were washed with water (50 mL), dried (Na_2SO_4), and concentrated in vacuo. The pale yellow oil was chromatographed (silica, 30% Et_2O–hexanes) to afford 424 mg (93%) of **27** as a colourless oil. IR (neat): 3439 (br), 2931, 1633, 1443, 1389, 1330, 1197, 1062, 1028, 1002, 948, 917, 729 cm^{-1}; ^1H NMR (200 MHz, $CDCl_3$) δ: 1.11 (s, 3H, Me), 1.14–1.32 (m, 1H, H-3β), 1.47–1.79 (m, 2H, H-3α and H-4β), 1.83–1.95 (m, 1H, H-4α), 2.70–2.75 (m, 2H, 2 × H-8), 2.84–2.98 (m, 1H, H-2a), 3.46 (dd, $J_{4\alpha,5}$ = 4.4, $J_{4\beta,5}$ = 11.1, 1H, H-5), 3.96 (dd, $J_{2\alpha,2\beta}$ = 9.1, $J_{2a,2\beta}$ = 5.2, 1H, H-2β), 4.42 (t, $J_{2a,2\alpha} = J_{2\beta,2\alpha}$ = 9.1, 1H, H-2α), 5.75 (AB of ABXX′, J_{AB} = 9.9, J_{AX} = 2.1, J_{BX} = 3.3, Δν = 42, 2H, H-6, H-7); LRMS (EI) *m/e*: 192 (52, M^+), 177 (5), 159 (18), 148 (8), 133 (100), 119 (11), 105 (31), 91 (22), 77 (15), 65 (7). Anal. calcd. for $C_{12}H_{16}O_2$: C 74.96, H 8.39; found: C 74.88, H 8.41.

2a,3,4,8b-Tetrahydro-5-methyl-2H-azuleno[8,1-bc]furan ***28***

To a solution of **27** (70 mg, 0.36 mmol) in THF (2 mL) was added 1,1′-thiocarbonyldiimidazole (0.144 g of 90% technical grade, 0.728 mmol) and the mixture was stirred at 70°C for 3h. The solution was cooled to 25°C and water (10 mL) added. The mixture was extracted with CH_2Cl_2 (3 × 10 mL) and the organic extracts were combined and washed sequentially with 2 N HCl (10 mL), saturated $NaHCO_3$ (10 mL), and water (10 mL). The organic layer was dried (Na_2SO_4) and the solvent removed under reduced pressure to provide an oil, which was subjected to flash chromatography (silica, 20% Et_2O–hexanes eluent) to give 30 mg (48%) of **28** as a pale yellow oil. IR (neat): 2952, 2883, 1640, 1534, 1450, 1368, 1178, 777, 744 cm^{-1}; ^1H NMR (200 MHz, $CDCl_3$) δ: 1.39–1.60 (m, 1H, H-3), 1.84 (s, 3H, Me), 2.11–2.24 (m, 1H, H-3), 2.39–2.53 (m, 1H, H-4), 2.61–2.70 (dd, $J_{3,4}$ = 7.4, $J_{4\alpha,4\beta}$ = 15.5, 1H, H-4), 2.91 (d, $J_{2a,8b}$ = 8.6, 1H, H-8b), 3.01–3.14 (m, 1H, H-2a), 4.08 (dd, $J2a,2\beta$ = 1.3, $J_{2\alpha,2\beta}$ = 8.8, 1H, H-2β), 4.36 (dd, $J_{2a,2\alpha}$ = 5.7, $J_{2\beta,2\alpha}$ = 8.8, 1H, H-2α), 5.53 (dd, $J_{8b,8}$ = 1.4, $J_{7,8}$ = 6.2, 1H, H-8), 6.14 (AB of an ABX system, J_{AB} = 11.3, J_{AX} = 6.1, Δν = 19.7, 2H, H-6, H-7); ^{13}C NMR (50 MHz, $CDCl_3$) δ: 19.89, 31.99, 33.05, 43.96, 49.61, 76.42, 94.43, 125.67, 127.21, 128.25, 132.10, 155.28; LRMS (EI) *m/e*: 174 (91, M^+), 159 (7), 146 (85), 145 (100), 131 (23), 115 (16), 105 (16), 91 (22), 77 (17), 62 (18); HRMS calcd. for $C_{12}H_{14}O$: 174.1044; found 174.1041. Anal. calcd. for $C_{12}H_{14}O$: C 82.72, H 8.10; found: C 82.51, H 7.97.

Attempted dehydrogenation of ***19****, synthesis of 3-(2,3-dihydro-4-methylbenzol[b]furan-3-yl)propanoic acid* ***(30)***

To ketone **19** (118 mg, 0.621 mmol) in dry dioxane (3.5 mL) was added DDQ (0.141 g, 0.621 mmol) and the mixture refluxed for 7h. The solution was cooled and the solid was filtered off. The solid was washed with benzene and the filtrate was concentrated. Flash chromatography (silica, 40% Et_2O–hexanes eluent) afforded an orange oil that appeared as several spots on TLC. NMR analysis of this material revealed the absence of any vinylic protons and the presence of aromatic protons. This material was rechromatographed to furnish 40 mg (31%) of **30** as a colourless solid that could be recrystallized from Et_2O–hexanes.

Attempted bromination of ***19****, synthesis of* ***30***

To **19** (50 mg, 0.26 mmol) in CCl_4 (3 mL) was added freshly recrystallized NBS (50 mg, 0.27 mmol) and the mixture was heated at 60°C for 20 min. The succinimide was seen floating on top of the solution. The flask was cooled in ice and the solution was filtered. The filtrate was concentrated in vacuo. Flash chromatography (silica, 30% EtOAc–hexanes) provided 40 mg (74%) of **30**; mp 85.5–86°C; IR ($CHCl_3$): 3400–2500, 2931, 1709, 1596, 1453, 1244, 710, 649 cm^{-1}; ^1H NMR (250 MHz, $CDCl_3$) δ: 1.82–2.11 (m, 2H, 2 × H-3′), 2.31 (s, 3H, Me), 2.28–2.47 (m, 2H, 2 × H-2′), 3.47 (m, 1H, H-3), 4.33 (dd, $J_{2\alpha,2\beta}$ = 9.1, $J_{3,2\beta}$ = 3.1, 1H, H-2β), 4.49 (t, $J_{2\beta,2\alpha} = J_{3,2\alpha}$ = 9.1, 1H, H-2α), 6.63 (d, J = 7.8, 1H, H-5 or H-7), 6.67 (d, J = 7.8, 1H, H-5 or H-7), 7.04 (t, J = 7.8, 1H, H-6); LRMS (EI) *m/e*: 206 (36, M^+), 146 (15), 133 (100), 105 (46), 84 (25), 49 (38). Anal. calcd. for $C_{12}H_{14}O_3$: C 69.89, H 6.84; found: C 69.95, H 6.91.

2,2a,3,4,5,5a-Hexahydro-5-methoxy-5a-methyl-8H-naphtho[1,8-bc]furan ***(31)***

To a solution of **27** (172 mg, 0.895 mmol) and HMPA (171 μL, 0.980 mmol) in dry THF (4 mL) at −78°C was added *n*-BuLi (0.615 mL of a 1.6 M solution in hexanes, 0.98 mmol) dropwise. The solution was stirred at −78°C for 1h. MeI (0.111 mL, 1.77 mmol) was added and the solution allowed to warm to 25°C and stirred for 1h. Water (10 mL) was added and the organic solvents evaporated off under reduced pressure. The aqueous residue was extracted with EtOAc (3 × 10 mL). The organic extracts were combined, washed with brine (20 mL), dried (Na_2SO_4), and concentrated in vacuo. Flash chromatography (silica, 10% EtOAc–hexanes eluent) afforded 152 mg (82%) of methyl ether **31** as a colourless oil. IR (neat): 2933, 2885, 1668, 1582, 1202, 1098, 1000, 955, 932, 729 cm^{-1}; ^1H NMR (200 MHz, $CDCl_3$) δ: 1.09 (s, 3H, Me), 1.15–1.50 (m, 2H, 2 × H-3), 1.84–1.97 (m, 2H, 2 × H-4), 2.70–2.74 (m, 2H, 2 × H-8), 2.84–3.01 (m, 1H, H-2a), 2.94 (dd, $J_{4\beta,5\beta}$ = 3.7, $J_{4\alpha,5\beta}$ = 7.4, 1H, H-5), 3.96 (dd, $J_{2\alpha,2\beta}$ = 9.1, $J_{2a,2\beta}$ = 5.4, 1H, H-2β), 4.42 (t, $J_{2a,2\alpha} = J_{2\beta,2\alpha}$ = 9.1, 1H, H-2α), 5.60 (dt, $J_{8,7}$ = 3.3, $J_{6,7}$ = 9.9, 1H, H-7), 5.88 (dt, $J_{7,6}$ = 9.9, $J_{8,6}$ = 2.1, 1H, H-6); LRMS (EI) *m/e*: 206 (45, M^+), 189 (16), 173 (19), 159 (23), 145 (36), 133 (100), 119 (12), 105 (34), 91 (22), 77 (14), 65 (7). Anal. calcd. for $C_{13}H_{18}O_2$: C 75.71, H 8.80; found: C 75.52, H 8.65.

8-(4′,7′-Dimethoxy-1′,3′-dihydro-1′-benzo[c]furanyl)-2,2a,3,4,5,5a-hexahydro-5a-methyl-8H-naphtho[1,8-bc]furan-5-one ***34***

To a solution of **19** (200 mg, 1.05 mmol) and **32** (103 mg, 0.525 mmol) in CCl_4 (3 mL) was added AcOH (30 μL, 0.53 mmol) and the solution was refluxed for 2h. Saturated aqueous $NaHCO_3$ (5 mL) was added and the mixture was extracted with CCl_4 (3 × 5 mL). The organic extracts were combined, washed with brine (10 mL), dried (Na_2SO_4), and concentrated in vacuo. The crude material was subjected to flash chromatography (silica, 10% EtOAc–hexanes eluent) to afford 90 mg (50%) of **34**, which was recrystallized from Et_2O as colourless plates; mp 177–179° C; IR ($CHCl_3$): 3001, 2929, 1702, 1500, 1310, 1258, 1090, 1049, 953, 796, 713 cm^{-1}; ^1H NMR (200 MHz, $CDCl_3$) δ: 1.41 (s, 3H, Me), 1.57–1.75 (m, 1H, H-3β), 2.09–2.22 (m, 1H, H-3α), 2.33 (dt, $J_{4\alpha,4\beta}$ = 14.7, $J_{3\beta,4\beta} \approx J_{3\alpha,4\beta}$ = 3.4, 1H, H-4β), 2.65 (td, $J_{4\beta,4\alpha} = J_{3\beta,4\alpha}$ = 14.7, $J_{3\alpha,4,\alpha}$ = 5.4, 1H, H-4α), 3.36–3.51 (m, 1H, H-2a), 3.59–3.60 (m, 1H, H-8), 3.77 (s, 3H, OMe), 3.78 (s, 3H, OMe), 4.13 (dd, $J_{2\alpha,2\beta}$ = 9.2, $J_{2a,2\beta}$ = 5.2, 1H, H-2β), 4.66 (t, $J_{2a,2\alpha} = J_{2\beta,2\alpha}$ = 9.2, 1H, H-2α), 5.00–5.01 (m, 2H, 2 × H3′), 5.19 (dd, $J_{6,7}$ = 10.0, $J_{8,7}$ = 3.65, 1H, H-7), 5.61–5.63 (m, 1H, H-1′), 5.98 (dd, $J_{7,6}$ = 10.0, $J_{8,6}$ = 1.7, 1H, H-6), 6.71 (s, 2H, H-6′, H-5′); ^{13}C NMR (50

Can. J. Chem. Downloaded from www.nrcresearchpress.com by 84.22.46.98 on 09/08/12
For personal use only.

MHz, $CDCl_3$) δ: 25.71, 33.51, 37.79, 39.40, 39.82, 41.41, 50.65, 55.61, 72.95, 75.03, 82.73, 109.93, 110.32, 113.05, 122.79, 128.36, 129.53, 132.01, 148.01, 148.47, 150.01, 211.75; LRMS (EI) *m/e*: 368 (21, M^+), 340 (2), 179 (100), 145 (10), 121 (4), 91 (5), 77 (2); HRMS calcd. for $C_{22}H_{24}O_5$: 368.1623; found: 368.1620.

(3aα,12aS, 14aα,* 14bα)-(±)-*1,2,3a,14,14a,14b-Hexahydro-7,10-dimethoxy-3a-methyl-3*H,*11*H-*benz[*c*]*isobenzofuro[7,1*-ij*][1]-benzoxepin-3-one **35***

To a solution of **34** (50 mg, 0.14 mmol) in EtOH (2 mL) was added 1 drop of concentrated HCl and the solution was stirred at room temperature for 20 min. Water (5 mL) was added and the solution was extracted with $CHCl_3$ (3 × 10 mL). The organic extracts were combined, dried, and concentrated in vacuo. The crude solid was recrystallized from Et_2O to provide 40 mg of **35** as yellow prisms; mp 139.5–140.5° C; IR ($CHCl_3$): 3002, 2937, 1705, 1481, 1461, 1262, 1090, 1046, 953, 798, 715 cm^{-1}; ^1H NMR (200 MHz, $CDCl_3$) δ: 1.28 (s, 3H, Me), 1.81–2.14 (m, 2H, 2 × H-1), 2.26–2.79 (m, 4H, 2 × H-2, H-14a, H-14b), 3.46 (dd, $J_{14\alpha,14\beta}$ = 8.9, $J_{14a,14\beta}$ = 5.4, 1H, H-14β), 4.27 (s, 3H, OMe), 4.32 (s, 3H, OMe), 4.01 (dd, $J_{14\alpha,14\beta}$ = 8.9, $J_{14a,14\alpha}$ = 7.6, 1H, H-14α), 4.88 (AB q, J_{AB} = 13.9, Δν = 65, 2H, 2 × H-11), 5.62 (d, $J_{4,5}$ = 9.8, 1H, H-5), 6.47 (dd, $J_{4,5}$ = 9.8, *J4,14b* = 0.7, 1H, H-4), 6.78 (s, 2H, H-8 and H-9), 7.01 (s, 1H, H-6); LRMS (EI) *m/e*: 368 (44, M^+), 340 (6), 297 (8), 269 (100), 226 (10), 179 (30), 149 (21), 115 (19), 91 (31), 77 (31), 55 (56), 44 (52), 41 (70). HRMS calcd. for $C_{22}H_{24}O_5$: 368.1623; found: 368.1618.

*X-ray structure determination summary of **35***

Crystals of **35** ($C_{22}H_{24}O_5$) are triclinic, space-group $P\bar{1}$ with *a* = 9.411 (2), *b* = 9.694 (2), *c* = 11.478(3) Å, α = 99.92 (2)°, β = 113.50 (2)°, γ = 97.88 (2)° , *V* = 921.1 (4) $Å^3$; Mol. Wt. 368.4, *Z* = 2, D_c = 1.328 g/ cm^3, *F*(000) = 392, μ (MoKα) = 0.93 cm^{-1}.

Data were collected on a colourless prism of dimensions 0.42 × 0.40 × 0.32mm mounted on a Nicolet–Siemens P3m/V diffractometer at 295 K. Data were collected by the ω -scan method to a 2θ-maximum of 50° . From a total of 3265 absorption corrected (ψ-scan) independent reflections measured, 2439 with $F > 6\sigma(F)$ were considered observed and used in the structure solution and refinement. The structure was solved by direct methods (Siemens SHELXTL PLUS) and refined by full-matrix least-squares methods to *R* and *wR* values of 4.24 and 4.04%; the weighting scheme used was $w^{-1} = \sigma^2(F)$. Full details have been deposited as supplementary material.[5]

*5-Hydroxy-5a-methyl-2,2a,3,4,5,5a,8,8a-octahydro-2*H*-naphtho-[1,8-*bc*]furan **38***

To a solution of **27** (80 mg, 0.42 mmol) and $NaBH_3CN$ (27 mg of a 95.7% grade, 0.42 mmol) in EtOH (2 mL) was added one drop of bromocresol green – methyl red indicator. The solution was cooled to 0° C. One drop of concentrated HCl was added to maintain the yellow colour of the solution. The solution was warmed to 25°C and HCl was added a drop at a time as the solution turned blue. The mixture was stirred for 3.5h. Water (10 mL) was added and the EtOH was removed by evaporation under reduced pressure. The aqueous residue was extracted with EtOAc (3 × 10 mL). The organic extracts were combined, washed with water (25 mL), dried (Na_2SO_4), and concentrated in vacuo. Flash chromatography on silica (30% Et_2O–hexanes eluent) afforded 66 mg (82%) of **38** as a colourless oil.

*Direct reduction of **19** to **38***

Compound **19** (1.13 g, 5.94 mmol) and $NaBH_4$ (60.7 mg, 1.61 mmol) were allowed to react according to the procedure given above except that after 1h at 0°C the bromocresol green – methyl red indicator was added and the previous procedure was followed. After flash chromatography on silica (10% Et_2O–hexanes eluent), 0.886 g (78%) of **38** was obtained. IR (neat): 3415 (br), 2934, 2872, 1455, 1060, 1002, 941, 909, 732 cm^{-1}; ^1H NMR (200 MHz, $CDCl_3$) δ : 1.13 (s, 3H, Me), 1.44–1.83 (m, 5H, 2 × H-3, 2 × H-4, H-8b), 1.95–2.09 (m, 1H, H-8α), 2.25–2.45 (m, 1H, H-2a), 2.51 (dtd, $J_{8\alpha,8\beta}$ = 15.7, $J_{8a,8\beta} = J_{7,8\beta}$ = 5.7, $J_{6,8\beta}$ = 0.9, 1H, H-8β), 3.61 (dd, $J_{2\alpha,2\beta}$ = 8.4, $J_{2a,2\beta}$ = 1.2, 1H, H-2β), 3.69–3.72 (q, 1H, $J_{4,5}$ = 11.1, 4.4, H-5), 3.89 (ddd, $J_{8b,8a}$ = 9.9, $J_{8\alpha,8a}$ = 11.4, $J_{8\beta,8a}$ = 5.6, 1H, H-8a), 4.03 (dd, $J_{2\beta,2\alpha}$ = 8.4, $J_{2a,2\alpha}$ = 6.1, 1H, H-2α), 5.70 (AB of an ABMX system, J_{AB} = 9.8, J_{BX} = 5.7, J_{BM} = 1.8, J_{AX} = 2.8, J_{AM} = 0.9, Δν = 39.6, 2H, H-6, H-7); ^{13}C NMR (50 MHz, $CDCl_3$) δ: 19.65, 28.20, 30.11, 32.60, 34.63, 41.60, 53.28, 73.08, 73.81, 74.90, 123.12, 136.54; LRMS (EI) *m/e*: 194 (27, M^+), 176 (38), 161 (22), 145 (31), 135 (38), 119 (24), 108 (54), 93 (100), 79 (59), 69 (47). Anal. calcd. for $C_{12}H_{18}O_2$: C 74.19, H 9.34; found: C 74.39, H 9.08.

*5a-Methyl-2a,3,4,5,5a,8,8a,8b-octahydro-2*H*-naphtho[1,8-*bc*]-furanyloxythiocarbonyl-1-imidazole **29***

Alcohol **38** (200 mg, 1.03 mmol) and 1,1′-thiocarbonyldiimidazole (408 mg, 2.06 mmol) were refluxed in benzene (8 mL) for 5h. The solution was cooled to 25°C and the benzene removed under reduced pressure. Water (20 mL) was added to the residue and the mixture extracted with CH_2Cl_2 (3 × 20 mL). The organic layer was washed with 2 N HCl (25 mL), saturated aqueous $NaHCO_3$ (25 mL), and water (50 mL), then dried (Na_2SO_4) and concentrated in vacuo. Flash chromatography (silica, 50% Et_2O–hexanes eluent) provided a pale yellow solid, which was recrystallized from $CHCl_3$–hexanes to give 202 mg (65%) of **29** as colourless cubes; mp 152–154° C; IR (neat): 2934, 2879, 1458, 1380, 1330, 1319, 1277, 1233, 979, 738 cm^{-1}; ^1H NMR (250 MHz, $CDCl_3$) δ: 1.34 (s, 3H, Me), 1.60–1.81 (m, 3H, 2 × H-3, H-8b), 1.85–2.15 (m, 3H, 2 × H-4, H-8α), 2.39–2.51 (m, 1H, H-2a), 2.58 (dt, $J_{8\alpha,8\beta}$ = 16.2, $J_{7,8\beta} = J_{8a,8\beta}$ = 5.3, 1H, H-8β), 3.67 (dd, $J_{2a,2\beta}$ = 1.3, $J_{2\alpha,2\beta}$ = 8.6, 1H, H-2β), 3.98 (ddd, $J_{8\alpha,8a}$ = 11.5, $J_{8b,8a}$ = 10.0, $J_{8\beta,8a}$ = 5.3, 1H, H-8a), 4.08 (dd, $J_{2\beta,2\alpha}$ = 8.6, $J_{2a,2\alpha}$ = 6.1, 1H, H-2α), 5.53–5.64 (m, 3H, H-5, H-6, H-7), 7.05 (dd, *J* = 1.0, 1H, H-4′ or 5′), 7.63 (dd, *J* = 1.5, *J* = 1.0, 1H, H-4′ or 5′), 8.34 (t, *J* = 1.0, 1H, H-2′); LRMS (EI) *m/e*: 304 (32, M^+), 271 (7), 177 (100), 159 (8), 147 (10, 131 (9), 117 (11), 105 (20), 95 (21), 91 (24), 81 (34), 67 (35). HRMS calcd. for $C_{16}H_{20}N_2O_2S$: 304.1245; found: 304.1235.

*5a-Methyl-2a,3,4,5,5a,8,8a,8b-octahydro-2*H*-naphtho[1,8-*bc*]-furanyl-5-oxy-2,4,6-trichlorophenoxythiocarbonate **39***

To a solution of alcohol **38** (100 mg, 0.515 mmol) in benzene (2.5 mL) was added pyridine (42μ L, 0.52 mmol) and *N*-hydroxysuccinimide (12 mg, 0.10 mmol). Trichlorophenoxythiocarbonyl chloride (156 mg, 0.566 mmol) in benzene (2.5 mL) was added to the solution and the mixture was refluxed for 20h. The solution was filtered to remove any pyridine hydrochloride and the solvent was evaporated under reduced pressure. Water (10 mL) was added to the residue and this was extracted with EtOAc (3 × 10 mL). The organic layer was washed with water (25 mL), dried (Na_2SO_4), and concentrated in vacuo. Flash chromatography (silica, 20% EtOAc–hexane eluent) provided 48 mg (48%) of alcohol starting material and 49 mg (22%, 42% based on recovered starting material) of **39**. This was recrystallized from Et_2O–hexanes; mp 102–103° C; IR ($CHCl_3$): 2938, 2875, 1773, 1568, 1451, 1330, 1233, 1176, 1130, 1054, 1004, 820, 804, 756 cm^{-1}; ^1H NMR (250 MHz, $CDCl_3$) δ: 1.24 (s, 3H, Me), 1.53–2.16 (m, 6H, 2 × H-3, 2 × H-4, H-8b, H-8α), 2.32–2.50 (m, 1H, H-2a), 2.51–2.62 (m, 1H, H-8β), 3.65 (dd, $J_{2\alpha,2\beta}$ = 8.5, $J_{2a,2\beta}$ = 1.0, 1H, H-2β), 3.95 (ddd, $J_{8\alpha,8a}$ = 11.5, $J_{8b,8a}$ = 9.9, $J_{8\beta,8a}$ = 5.2, 1H, H-8a), 4.06 (dd, $J_{2\beta,2\alpha}$ = 8.5, $J_{2a,2\alpha}$ = 6.2, 1H, H-2α), 5.30 (dd, $J_{4,5}$ = 4.1, $J_{4,5}$ = 11.5, 1H, H-5), 5.60–5.70 (m, 2H, H-6, H-7), 7.39 (s, 2H, 2 × ArH); LRMS (EI) *m/e*: 434 (17, M^+), 194 (11), 178 (17), 177 (100), 147 (12), 105 (20), 81 (36), 67 (44), 45 (26). Anal. calcd. for $C_{19}H_{19}Cl_3O_3S$: C 52.61, H 4.41; found: C 52.88, H 4.78.

[5]Tables of crystal data, atomic coordinates, bond lengths and angles, anisotropic displacement factors, and observed and calculated structure factors can be purchased from: The Depository of Unpublished Data, Document Delivery, CISTI, National Research Council Canada, Ottawa, ON K1A 0S2, Canada.

Tables of crystal data, atomic coordinates, and bond lengths and angles have also been deposited with the Cambridge Crystallographic Data Centre, and can be obtained on request from The Director, Cambridge Crystallographic Data Centre, University Chemical Laboratory, 12 Union Road, Cambridge, CB2 1EZ, U.K.

Can. J. Chem. Downloaded from www.nrcresearchpress.com by 84.22.46.98 on 09/08/12
For personal use only.

Methyl-5a-methyl-2a,3,4,5,5a,8,8a,8b-octahydro-2H-naphtho[1,8-bc]furanyl-5-xanthate ***40***

Compound **38** (564 mg, 2.90 mmol) was dissolved in dry THF (15 mL) and cooled to −78° C. *n*-BuLi (2.37 mL of a 1.6 M solution in hexanes, 3.80 mmol) was added dropwise to this solution and the mixture stirred at −78°C for 30 min, then at 0°C for 20 min. Dry carbon disulfide (0.263 mL, 4.37 mmol) was added dropwise and the reactin mixture was stirred at 0°C for 40 min. Iodomethane (0.727 mL, 11.6 mmol) was added and the solution stirred at 0°C for 20 min, then at 25°C for 30 min. The solution was poured into ice water (50 mL) and extracted with EtOAc (3 × 40 mL). The EtOAc layer was washed with saturated aqueous NH_4Cl (75 mL), and brine (75 mL), then dried (Na_2SO_4). Concentration in vacuo followed by flash chromatography (silica, 10% EtOAc–hexanes) afforded 0.652 g (79%) of **40** as a colourless oil. IR (neat): 2932, 2870, 1452, 1369, 1216, 1055, 1010, 968, 728 cm^{-1}; ^1H NMR (250 MHz, $CDCl_3$) δ: 1.29 (s, 3H, Me), 1.55–2.08 (m, 6H, 2 × H-3, 2 × H-4, H-8b, H-8α), 2.33–2.52 (m, 2H, H-2a, H-8β), 2.56 (s, 3H, SMe), 3.64 (dd, $J_{2\alpha,2\beta}$ = 8.6, $J_{2a,2\beta}$ = 1.4, 1H, H-2β), 3.96 (ddd, $J_{8\alpha,8a}$ = 11.5, $J_{8b,8a}$ = 9.9, $J_{8\beta,8a}$ = 5.3, 1H, H-8a), 4.06 (dd, $J_{2\beta,2\alpha}$ = 8.6, $J_{2a,2\alpha}$ = 6.1, 1H, H-2α), 5.58–5.68 (m, 3H, H-5, H-6, H-7); LRMS (EI) *m/e*: 284 (20, M^+), 251 (5), 237 (5), 177 (100), 159 (20), 133 (14), 117 (19), 105 (29), 91 (36), 81 (36), 79 (20), 67 (37), 55 (16), 41 (20). Anal. calcd. for $C_{14}H_{20}O_2S_2$: C 59.12, H 7.09; found: C 59.01, H 7.01.

5a-Methyl-2a,3,4,5,5a,8,8a,8b-octahydro-2H-naphtho[1,8-bc]furan ***41***

To a solution of xanthate **40** (620 mg, 2.18 mmol) in dry toluene (15 mL) at 90°C was added a solution of *n*-Bu_3SnH (1.99 mL, 7.19 mmol) and AIBN (221 mg) dropwise over 30 min. The solution was stirred an additional 30 min at 90° C, then cooled to 25° C. The solvent was removed by concentrating in vacuo and the residue chromatographed (silica, 100% hexane then 50% CH_2Cl_2–hexanes eluent) to provide 268 mg (69%) of **41**. IR (neat): 2927, 2868, 1459, 1365, 1060, 1006, 938, 724 cm^{-1}; ^1H NMR (200 MHz, $CDCl_3$) δ: 1.11 (s, 3H, Me), 1.31–1.72 (m, 7H, 2 × H-3, 2 × H-4, 2 × H-5, H-8b), 2.00 (ddd, $J_{8\alpha,8\beta}$ = 15.3, $J_{8a,8\alpha}$ = 10.1, $J_{7,8\alpha}$ = 1.5, 1H, H-8α), 2.26–2.39 (m, 1H, H-2a), 2.42–2.55 (m, 1H, H-8β), 3.62 (dd, $J_{2\alpha,2\beta}$ = 8.3, $J_{2a,2\beta}$ = 1.3, 1H, H-2β), 3.89 (ddd, $J_{8\alpha,8a}$ = 11.1, $J_{8a,8b}$ = 10.1, $J_{8\beta,8a}$ = 5.2, 1H, H-8a), 4.04 (dd, $J_{2\beta,2\alpha}$ = 8.3, $J_{2a,2\alpha}$ = 6.1, 1H, H-2α), 5.45–5.46 (m, 2H, H-6, H-7); ^{13}C NMR (50 MHz, $CDCl_3$) δ: 20.99, 26.82, 28.51, 32.64, 34.48, 35.12, 50.80, 65.92, 73.60, 74.41, 121.30, 139.54; LRMS (EI) *m/e*: 178 (68, M^+), 163 (20), 147 (34), 134 (36), 119 (27), 105 (43), 91 (66), 82 (100), 69 (65), 55 (32), 41 (72); HRMS calcd. for $C_{12}H_{18}O$: 178.1358; found: 178.1347.

5a-Methyl-2a,3,4,5,5a,8,8a,8b-octahydro-2H-naphtho[1,8-bc]furan-2-one ***42***

Chromium trioxide (438 mg, 4.38 mmol) was suspended in 5 mL of dry CH_2Cl_2 at −20°C and 3,5-dimethylpyrazole (421 mg 4.36 mmol) was added in one portion. After stirring at −20°C for 15 min, **41** (65 mg, 0.36 mmol) in CH_2Cl_2 (1 mL) was added and the mixture was stirred for 4h at −23°C. NaOH (3 mL of a 5 M solution) was added and the mixture was stirred at 0°C for 1 h. The layers were separated and the organic layer was washed with 0.5 N HCl (10 mL) to remove the DMP. The CH_2Cl_2 layer was subsequently washed with water (2 × 10 mL), and brine (10 mL). After drying (Na_2SO_4) and concentrating in vacuo, flash chromatography (silica, ether–hexane 1:1) provided 40 mg (62%) of starting material and 15 mg of **42** as a colourless oil. IR (neat): 2933, 2862, 1780, 1449, 1196, 1160, 1037, 1010, 967, 726 cm^{-1}; ^1H NMR (200 MHz, $CDCl_3$) δ: 1.09 (s, 3H, Me), 1.39–1.71 (m, 6H, 2 × H-3, 2 × H-4, 2 × H-5), 1.88–2.04 (m, 2H, H-8, H-8b), 2.23 (ddd, $J_{8,8}$ = 14.9, $J_{8a,8}$ = 10.4, $J_{7,8}$ = 0.9, 1H, H-8), 2.71–2.52 (m, 2H, H-8, H-2a), 4.53 (td, $J_{8a,8\alpha} \approx J_{8a,8b} \approx$ 11.0, $J_{8a,8\beta}$ = 5.3, 1H, H-8a), 5.50–5.51 (m, 2H, H-6, H-7); LRMS (EI) *m/e*: 192 (42, M^+), 177 (5), 164 (12), 148 (33), 133 (100), 119 (31), 106 (68), 91 (96), 79 (63), 67 (34), 55 (29), 41 (58).

5,8-Dimethoxy-1,2,3,4,4a,9,9a,10-octahydro-9,10-epoxyanthracene ***43***

To a solution of **32** (150 mg, 0.765 mmol) in dry *p*-xylene (1.5 mL) was added dry cyclohexene (387μ L, 3.82 mmol) and toluic acid (11 mg, 0.076 mmol). The mixture was heated at 140°C for 36h. The solvent was removed under reduced pressure and the residue was subjected to flash chromatography (neutral alumina, 50% CH_2Cl_2–hexanes eluent) to provide 105 mg (53%) of a 6:1 mixture of *endo* and *exo* isomers of **43**. This mixture was recrystallized from Et_2O to provide colourless needles; mp 75–76° C; IR ($CHCl_3$): 3106, 2937, 2864, 1500, 1461, 1297, 1256, 1091, 985, 894, 846, 797 cm^{-1}; ^1H NMR (200 MHz, $CDCl_3$) δ, *exo* isomer: 1.18–1.70 (m, 10H, 2 × H-1, 2 × H-2, 2 × H-3, 2 × H-4, H-4a, H-9a), 3.79 (s, 6H, 2 × OMe), 5.10 (s, 2H, H-9, H-10), 6.63 (s, 2H, 2 × ArH); *endo* isomer: 0.20–0.38 (m, 2H, H-4a, H-9a), 1.18–1.70 (m, 6H, 2 × H-2, 2 × H-3, H-4, H-1), 2.33–2.48 (m, 2H, H-1, H-4), 3.78 (s, 6H, 2 × OMe), 5.42 (d, *J* = 4.8, 2H, H-9, H-10), 6.65 (s, 2H, 2 × ArH); LRMS (EI) *m/e*: 260 (4, M^+), 242 (4) 227 (3), 201 (1), 178 (100), 163, (54), 135 (4), 115 (3), 92 (3), 77 (3), 67 (2), 41 (2). Anal. calcd. for $C_{16}H_{20}O_3$: C 73.82, H 7.74; found: C 73.61, H 7.73.

Acknowledgement

We thank the Natural Sciences and Engineering Research Council of Canada (NSERC) for support of this work.

1. D.M. Roll, P.J. Scheuer, G.K. Matsumoto, and J. Clardy. J. Am. Chem. Soc. **105**, 6177 (1983); H. Nakamura, J. Kobayashi, M. Kobayashi, Y. Ohizumi, and Y. Hirata. Chem. Lett. 713 (1985); F.J. Schmitz and S.J. Bloor. J. Org. Chem. **53**, 3922 (1988).
2. M.M. Blight and J.F. Grove. J. Chem. Soc. Perkin Trans. 1, 1317 (1986).
3. J. MacMillan, T.J. Simpson, and S.K. Yeboah. J. Chem. Soc. Chem. Commun. 1063 (1972); T.J. Petcher, H.P. Weber, and Z. Kis. J. Chem. Soc. Chem. Commun. 1061 (1972).
4. K. Kanematsu, S. Soejima, and G. Wang. Tetrahedron Lett. **32**, 4761 (1991).
5. N. Harada, T. Sugioka, H. Uda, and T. Kuriki. J. Org. Chem. **55**, 3158 (1990); N. Harada, T. Sugioka, Y. Ando, H. Uda, and T. Kuriki. J. Am. Chem. Soc. **110**, 8483 (1988).
6. C.A. Broka and B. Ruhland. J. Org. Chem. **57**, 4888 (1992).
7. G. Weeratunga, A. Jaworska-Sobiesiak, S. Horne, and R. Rodrigo. Can. J. Chem. **65**, 2019 (1987).
8. A.B. Smith and R.K. Dieter. Tetrahedron, **37**, 2407 (1981).
9. M.P. Doyle. Chem. Rev. **86**, 919 (1986).
10. (*a*) J.M. Brown, T.M. Cresp and L.N. Mander. J. Org. Chem. **42**, 3984 (1978); (*b*) J.M. Hook and L.N. Mander. Nat. Prod. Rep. **37**, 35 (1986).
11. A.P. Kozikowski and A. Ames. J. Am. Chem. Soc. **102**, 860 (1980).
12. L.N. Mander. Synlett, 134 (1991).
13. G.W. Kabalka and S.T. Summers. J. Org. Chem. **46**, 1217 (1981).
14. S.P. Schmidt and D.W. Brooks. Tetrahedron Lett. **28**, 767 (1987).
15. D.H.R. Barton and J.C. Jaszberenyi. Tetrahedron Lett. **30**, 2619 (1989).
16. R. Rodrigo. Tetrahedron, **44**, 2093 (1988).
17. B.M.M. Sadeghy and B. Rickborn. J. Org. Chem. **48**, 2237 (1983).
18. B.A. Keay and R. Rodrigo. Tetrahedron, **40**, 4597 (1984).
19. D.H. Boschelli, R.M. Scarborough, Jr., and A.B. Smith III. Tetrahedron Lett. **22**, 19 (1981).
20. P. Bravo, C. Ticozzi, and A. Gentile. Gazz. Chim. Ital. **14**, 89 (1984).

Isolation and characterization of an UDPG-dependent glucosyltransferase activity from *Rauwolfia serpentina* Benth. cell suspension cultures[1]

RALF LUTTERBACH, CARL MICHAEL RUYTER, AND JOACHIM STÖCKIGT[2]

Johannes Gutenberg-Universität Mainz, Institute of Pharmacy, Department of Pharmaceutical Biology, Staudinger Weg 5, D-55099 Mainz, Germany

Received June 2, 1993

This paper is dedicated to Professor Ian Spenser

RALF LUTTERBACH, CARL MICHAEL RUYTER, and JOACHIM STÖCKIGT. Can. J. Chem. **72**, 51 (1994).

From cell suspension cultures of *Rauwolfia serpentina* Benth. a new enzyme activity was isolated and its properties determined. The enzyme is a soluble protein and catalyzes the transfer of a glucose moiety from UDPG to a wide variety of phenolic compounds with *p*-nitrophenol as one of the best substrates (K_m = 1.21 mM, UDPG = 0.54 mM). In contrast to the membrane-bound UDPG: vomilenine-21-OH-β-D-glucosyltransferase from *Rauwolfia serpentina* cells, this enzyme is not able to glucosylate indole alkaloids. The enzyme activity has been detected in 14 callus cultures belonging to 10 different plant families.

RALF LUTTERBACH, CARL MICHAEL RUYTER et JOACHIM STÖCKIGT. Can. J. Chem. **72**, 51 (1994).

On a isolé une nouvelle activité enzymatique à partir de cultures d'une suspension de cellules du *Rauwolfia serpentina* Benth. et on en a déterminé les propriétés. L'enzyme est une protéine soluble et elle catalyse le transfert d'une unité de glucose du UDPG à grande variété de composés phénoliques parmi lesquels le *p*-nitrophénol est l'un de ses meilleurs substrats (K_m = 1,21 mM, UDPG = 0,54 mM). Par opposition au UDPG lié à la membrane, la vomilénine-21-OH-β-D-glyucosyltransférase isolé de cellules de *Rauwolfia serpentina*, cet enzyme ne peut effectuer la glcosylation des alcaloïdes de l'indole. On a pu détecter l'activité enzymatique dans 14 cultures de callus appartenant à 10 familles différentes de plantes.

[Traduit par la rédaction]

Introduction

As reported previously, cell cultures of *Rauwolfia serpentina* (L.) Benth. ex Kurz contain a highly specific membrane-bound UDPG:[3] vomilenine glucosyltransferase (EC 2.4.1.-), which is responsible for the formation of the glucoalkaloid raucaffricine (1). In contrast to this we have found, in soluble protein extracts of *Rauwolfia* cells, high glucosyltransferase activities that catalyse preferentially the glucosylation of aromatic hydroxyl groups of a number of structurally diverse compounds. In this paper we describe the isolation and properties of this transferase activity.

Experimental

Materials and methods

Plant cell suspension cultures

Rauwolfia serpentina cells were cultivated under standard conditions in LS medium (2) as described recently (3). After a growth period of 7 days, cells were harvested, frozen with liquid nitrogen, stored at –25°C, and used as an enzyme source.

Enzyme isolation and enrichment

The cultured *Rauwolfia* cells (1 kg FW) to be used as the enzyme source were frozen with liquid nitrogen and homogenized for 2 min using a Braun-Starmix and 1.4 L Tris-HCl buffer (0.1 M, pH 8.5, 10 mM BME, 10 mM KCl, 1 mM EDTA). The mixture was stirred for 30 min at 4°C, filtered through cheesecloth, and centrifuged (20 min, 4500 × *g*). The supernatant (2.07 g protein) was subjected to ammonium sulphate precipitation (30–70% saturation) resulting in 1.58 g crude enzyme (27.7 nkat/g). The protein was dissolved in 230 mL of 0.2 M Tris-HCl buffer (pH 7.5, 10 mM BME) and dialyzed for 12 h against the same buffer at 0.02 M. The supernatant of centrifuged protein solution (11000 × *g*) was transferred to a DEAE DE 52 column. Fractionation of the protein (10 mL/fraction) was achieved with a linear gradient from 0 to 0.5 M KCl (20 mM Tris-HCl, pH 8.5, 10 mM BME) at a flow rate of 1 mL/min. Fractions 13–18 were combined and contained 174 mg protein (107 nkat/g) with a 7-fold enrichment. After concentration of the enzyme solution to 2.5 mL, the protein was subjected to gel chromatography (Fractogel 55 S, column 2.5 × 80 cm, and the above-mentioned buffer with a flow rate of 20 mL/h). Fractions (each 5 mL) 29, 30, and 31 were combined and contained 36 mg of the transferase (156 nkat/g) with a 10-fold enrichment. Proteinconcentrations were determined as previously reported (4).

Enzyme assays

For the determination of the enzyme activities dependent on culture conditions, temperature variation, kinetic data, and enzyme enrichment an HPLC assay with PNP as substrate was used. In a total volume of 0.25 mL (0.1 M Tris-HCl, pH 7.5) the enzyme solution was incubated for 30 min at 37°C in the presence of 1 mM PNP and excess of UDPG (2 mM). After addition of 0.75 mL MeOH containing 0.1 mg/mL dansyl-threonine as an internal standard, the precipitated protein was centrifuged off and the PNP-β-D-glucoside formed was quantitatively determined in the supernatant under the following conditions: HPLC column, LiChrocart^R supersphere 100 (RP-18), 4 × 125 mm; mobile phase, acetonitrile – KPi buffer (6.66 g KH_2PO_4, 2.8 mL 83% H_3PO_4 to 1 L, pH 2.3) = 38:62 under isocratic conditions; 1 mL/min flow; detection at 300 nm. Retention time of PNP-β-D-glucoside was 1.4 min. For the determination of the substrate specificity of the transferase an assay based on the TLC analysis of the appropriate radioactive glucosides from UDP-[^{14}C]-glucose (11.7 GBq/mmol) was employed.

A standard incubation mixture contained, in a volume of 0.15 mL (0.2 M Tris-HCl, pH 7.5), the appropriate substrate (2 mM), 0.5 mM UDP-[^{14}C]-G (4.625 KBq), and about 0.4 mg of a prepurified enzyme (1.8-fold). After incubation of the mixture for 2 h at 37°C, 0.3 mL MeOH was added, the mixture was centrifuged as above, and 10 µL of the mixture was chromatographed on TLC plates (Merck G/UV_{254}, 0.2 mm) in the solvent system EtOAc–MeOH–H_2O (7:2:1). The yield of ^{14}C-labelled glucosides formed was calculated after TLC scanning using a Rita 3200 instrument (Raytest).

Results

An enzyme with glucosylating activity could be isolated from *Rauwolfia* cell suspensions that were grown under stan-

[1]Dedicated to Professor Ian Spenser for his outstanding contributions in the field of biosynthesis of natural products.

[2]Author to whom correspondence may be addressed.

Can. J. Chem. Downloaded from www.nrcresearchpress.com by 203.198.23.82 on 09/08/12
For personal use only.

dard conditions, transforming PNP into its ß-D-glucoside in the presence of UDPG. The transferase reaction was completely dependent on the presence of active protein. The reaction showed normal Michaelis–Menten kinetics for PNP (Fig. 1) and UDPG (Fig. 2). The double reciprocal plots of enzyme activity and substrate concentration gave linear relationships (Figs. 1 and 2). The apparent K_m values were found to be 1.21 mM for PNP (V_{max} = 40 pkat) and 0.54 mM for UDPG (V_{max} = 26.9 pkat). When the enzyme activity was measured at different pH, the optimum activity was found between pH 7.3 and 7.8. The enzyme tolerated a relatively broad pH range, with half-maximum activity at pH 6.5 and pH 8.3 (Fig. 3). The optimum temperature of the reaction was 37°C.

Dependency of the transferase activity on cell growth and nutrition medium

The enzyme activity in crude protein extracts of cells that were grown in 1 L LS medium increased with cell growth. After 4 days 18 nkat and 6.5 g DW were recorded, after 6 days 48 nkat and 10.6 g DW, and after 10 days 78 nkat and 18.3 g DW. During this growth period the total protein isolated from the cells by the standard procedure increased from 188 mg to 746 mg/L medium. The maximum value for the specific activity of the transferase (171 pkat/mg protein) could be measured on the fifth day of cell growth. When the protein and transferase content was determined after 7 days under constant conditions (inoculum per litre of medium corresponded to 2.2 g DW), the cultured cells in MS (5) and LS medium showed highest total and specific enzyme activities of 9 nkat/L (7.5 pkat/mg protein) and 7 nkat/L (5.5 pkat/mg protein), respectively. Significantly lower values were observed when cells were grown in APII or Ringe medium (6, 7).

Stability of the enzyme

When a crude soluble protein extract was stored at 4°C, the enzyme activity decreased after 2 days to 90% of the original activity and after 5 days 50% of the activity could still be measured, but after 2 weeks no transferase activity was detected. If the enzyme extract was frozen in the presence of 20% glycerol, 95% of the original enzyme activity was retained after 3 months of storage.

Transferase stability in the presence of organic solvents

To test the stability of the enzyme in relation to the organic solvent required to dissolve water-insoluble substrates, a range of solvents was tested.

The enzyme best tolerated DMSO and MeOH, 50% of the enzyme activity being retained at 22% and 14%, respectively. EtOH, DMF, and THF decreased the transferase activity to 50% at much lower concentrations, viz. 8%, 4%, and 3%, respectively.

Substrate and co-substrate specificity

The substrate specificity of the transferase activity was investigated using a broad variety of phenolic compounds (Table 1). Standard incubation conditions for substrates were used and results are summarized in Table 1. Three of the substrates, HQ (108%), ß-naphthol (120%), and thymol (140%), were more efficiently accepted as substrate when compared to PNP (100%) and MNP (101%). When PNP was used as substrate only TDPG showed a significant donor activity for glucose (18.5% relative activity), as compared with UDPG (100% relative activity). When different UDP-activated sugars were employed as substrate only UDP-glucuronic acid showed a very slight activity of 2.5% of UDPG.

Taxonomic distribution of the transferase activity in a variety of callus cultures

When the taxonomic occurrence of the enzyme was determined, we observed a very broad distribution. Using a selection of callus cultures as sources of the crude enzyme, we found the transferase in 14 different cultures belonging to 10 different plant families. For PNP as substrate only three cultures exceeded the enzyme activity of the *Rauwolfia* cells. For niclosamide as substrate, 10 cultures showed higher enzyme activities than the controls (*Rauwolfia* cells). Thymol was best glucosylated exclusively by a protein extract obtained from *R. serpentina* cells.

Discussion

We recently isolated and characterized a glucosyltransferase named UDPG: vomilenine-21-ß-D-glucosyltransferase (EC 2.4.1.-) from cell suspension cultures of *R. serpentina* Benth. (1). This enzyme catalyzes the formation of the glucoalkaloid raucaffricine, which is the major alkaloidal compound in these cells.

During these investigations we also detected other glucosylating enzyme activities, which did not transform the aglycone of raucaffricine but did glucosylate a range of phenolic compounds. To understand these transformations more precisely and to search our cell cultures for high glucosylating activities, we investigated this enzyme further. Two assays could be employed, one an HPLC-based method, and the other based on the radioactive ^{14}C-UDPG and TLC separations. Both methods allowed relatively fast and sensitive analyses for glucosylating enzymes. Having established these test systems, we searched and investigated our *Rauwolfia* cultures, which had been grown in a variety of different nutrition media, in order to find the conditions for optimum enzyme formation.

In fact, the transferase activity depends significantly on the nutrition medium used, ranging from 9 nkat/L in MS medium or 7 nkat/L in LS medium down to about 1.5 nkat/L in Ringe medium. Because we have continuously cultivated our *Rauwolfia* cells for many years in LS medium, we used the cell material grown under these conditions for enzyme isolation. In contrast to the membrane-bound UDPG-dependent vomilenine-glucosyltransferase, this transferase is a soluble protein that therefore can be simply enriched (10-fold) by ammonium sulphate precipitation and two-step column chromatography. When the enzyme was incubated with UDPG in the presence of PNP, the appropriate PNP-ß-D-glucoside was synthesized. This transferase reaction was absolutely dependent on the presence of active protein and proceeded best at a pH of 7.5, in contrast to the enzymatic vomilenine-glucoside biosynthesis showing an optimum at pH 6.3 (1).

The relatively high K_m value points to a rather low affinity of the enzyme towards the substrate PNP. This result is not surprising as PNP cannot be the natural substrate for this enzyme. At the present time the endogenous substrate of the transferase is not known. From broader substrate studies that included a number of phenolic compounds one can conclude that the enzyme has a relatively unspecific substrate acceptance because many of the phenolic compounds bearing hydroxy groups were glucosylated (Table 1). One must, however, keep in mind that the

Can. J. Chem. Downloaded from www.nrcresearchpress.com by 203.198.23.82 on 09/08/12
For personal use only.

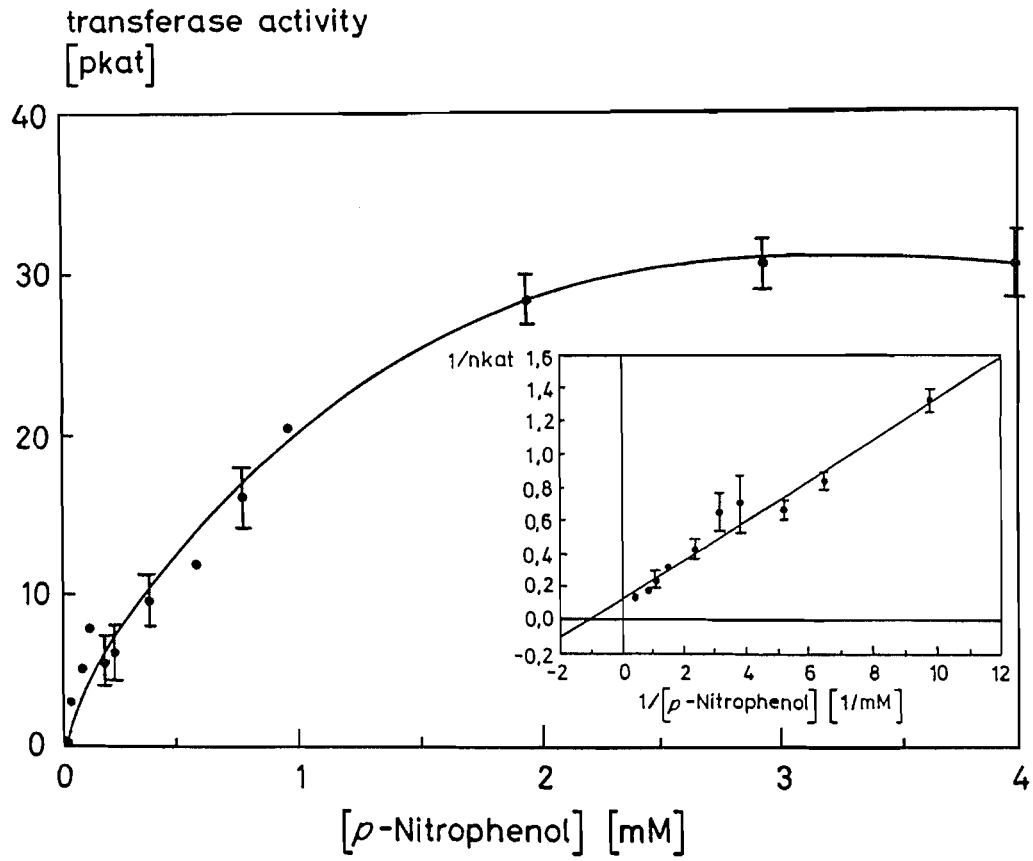

FIG. 1. The effect of the concentration of *p*-nitrophenol on the reaction rate of the PNP-glucosyltransferase activity; K_m = 1.21 mM, V_{max} = 40 pkat.

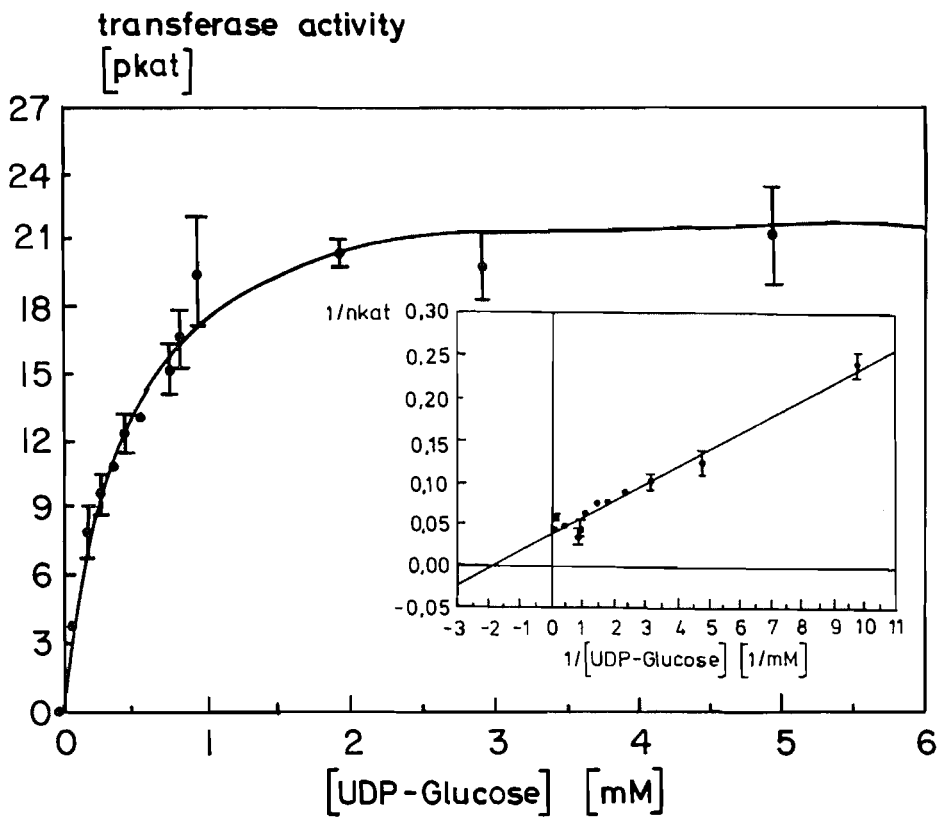

FIG. 2. The effect of the concentration of UDPG on the reaction rate of the PNP-glucosyltransferase activity; K_m = 0.54 mM, V_{max} = 26.9 pkat.

Can. J. Chem. Downloaded from www.nrcresearchpress.com by 203.198.23.82 on 09/08/12
For personal use only.

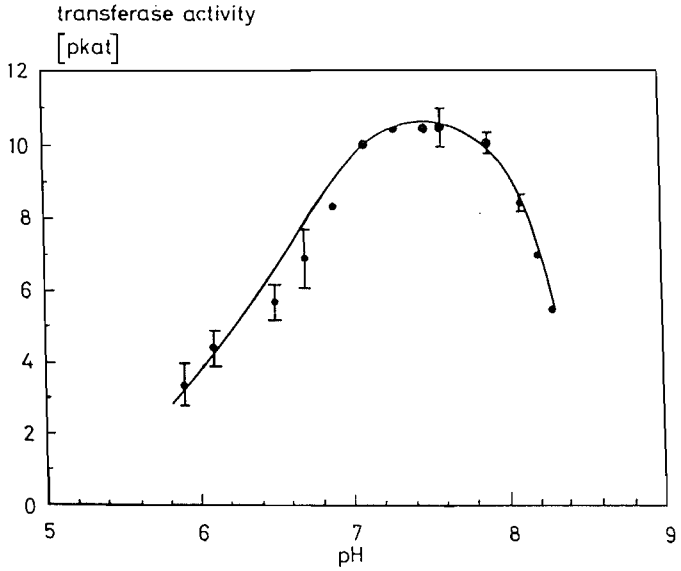

FIG. 3. The effect of pH on the PNP-glucosyltransferase activity. The assays were performed in presence of 0.49 mg enzyme and 0.2 mM KPi buffer.

studies on substrate specificity were carried out with a very crude enzyme preparation and, therefore, the possible occurrence of other glucosyltransferases in the extracts cannot be excluded. Clarification of this point must be deferred until the enzyme has been purified to homogeneity.

Like several glucosyltransferases already described, this enzyme has no great affinity for the nucleotide part of a number of nucleotide-activated glucoses. Based on the relative enzyme activity, UDP-glucose was the most efficient co-substrate but TDP-glucose was also accepted as co-substrate to an extent of 18.5%. All the other glucose nucleotides investigated exhibited nearly no effect (<1% relative activity), which is in agreement with, for example, the *p*-hydroxybenzoate glucosyltransferase or the flavonol glucosyltransferase described previously (8, 9). The sugar part of the co-substrate seems to be very important, because UDP-galactose, -mannose, or -xylose were not accepted by the enzyme. One of our future aims is to employ this enzyme on a preparative scale to glycosylate a variety of useful

TABLE 1. Substrate specificity of the transferase activity from *Rauwolfia* cell suspensions

Substrate	Relative enzyme activity (%)
p-Nitrophenol	100
m-Nitrophenol	101
o-Nitrophenol	75
p-Cresol	33
m-Cresol	34
o-Cresol	14
Vanillin	56
p-Hydroxybenzaldehyde	49
p-Hydroxyacetophenone	23
p-Hydroxyanisol	19
Phenol	14
Resorcin	41
Hydroquinone	108
β-Naphthol	120
Thymol	146
o-Coumaric acid	43
m-Coumaric acid	9
p-Coumaric acid	<1
2,5-Dinitrophenol	9
2,4-Dinitrophenol	<1
Dihydrocaffeic acid	10
Eugenol	30
Niclosamide	57

TABLE 2. Taxonomic distribution of the glucosyltransferase activity in callus cultures of a broad variety of plant families

Family	Plant	Substrate (specific conversion, %)		
		PNP	Thymol	Niclosamide
Apocynaceae	*Rauwolfia serpentina* (L.) Benth.	100	100	100
Apocynaceae	*Rauwolfia mannii* Stapf	89	28	329
Boraginaceae	*Cordia abyssinica*	<1	<1	<1
Boraginaceae	*Echium pininana* Webb et Bert.	<1	<1	<1
Cactaceae	*Notocactus mammulosus* (Lem.) Berger	68	57	73
Cactaceae	*Rebutia albispina*	48	23	55
Chenopodiaceae	*Spinacia oleracea*	67	<1	156
Convolvulaceae	*Convolvulus arvensis* L.	107	28	66
Epacridaceae	*Pentachondra pumulia*	<1	<1	<1
Fabaceae	*Cytisus purpureus* Scop.	120	42	96
Lamiaceae	*Hyptis lanceolata*	<1	<1	<1
Lamiaceae	*Plectranthus purpuratus* Harv.	<1	<1	<1
Liliaceae	*Harworthia turgida* Haw.	87	13	395
Polygonaceae	*Rheum franzenbachii*	53	28	143
Rosaceae	*Malus domestica Borkh.*	32	98	350
Rubiaceae	*Coprosma baueri* Endl.	<1	<1	194
Rubiaceae	*Conostomium natalense*	80	67	335
Rubiaceae	*Gardenia posoquerioides*	80	13	215
Rubiaceae	*Psychotria kirkii*	111	28	349
Rutaceae	*Ruta chalepensis*	61	84	186

Can. J. Chem. Downloaded from www.nrcresearchpress.com by 203.198.23.82 on 09/08/12
For personal use only.

compounds and thus to enhance their water solubility. A first attempt could be the taenicide niclosamide, which was efficiently transformed by the described enzyme here. To enhance the concentration of such substrates it was necessary to test the solvent tolerance of the enzyme. Of the several water-soluble solvents investigated, DMSO proved to be the solvent most tolerated by the enzyme, permitting about 10–22% DMSO with retained transferase activities of 50–80%. Obviously DMSO seems to be the solvent of choice to generate glucosides from water-insoluble substrates. All other solvents such as MeOH, EtOH, or THF were much more inhibiting to the enzyme.

We have also investigated the taxonomic distribution of this enzyme by testing a number of different callus cultures. In fact, the transferase activity was found in many cultures, indicating that it is a rather unspecific transferase. We detected it in 14 callus systems of 10 plant families (Table 2). Although this material will now be used to develop preparative scale glucosylation of different substrates, the current enzyme needs to be purified to confirm the broad substrate acceptance or to discover whether several transferases, each responsible for a glucosylation of small groups of phenols, are present in the tissue and cell cultures investigated.

[3]Abbreviations: BME, ß-mercaptoethanol; DEAE, diethylaminoethyl; DMSO, dimethyl sulphoxide; DW, dry weight; EtOAc, ethyl acetate; EtOA, ethanol; FW, fresh weight; HQ, hydroquinone; kat, katal (1 U = 16.67 nkat); MeOH, methanol; MNP, *m*-nitrophenol; PNP, *p*-nitrophenol; TDPG, thymidine-5′-diphosphate glucose; THF, tetrahydrofuran; UDPG, uridine-5′-diphosphate glucose.

Acknowledgements

We thank Prof. Dr. W. E. Court (Mold/Wales) for his kind help in preparing the English version of this manuscript. We also thank Dr. M. Schumacher (DSM GmbH, Braunschweig) for cell material. Our thanks are also due to the Deutsche Forschungsgemeinschaft (Bonn – Bad Godesberg) and to the Fonds der Chemischen Industrie (Frankfurt/Main) for financial support.

1. C.M. Ruyter and J. Stöckigt. Helv. Chim. Acta, **74**, 1707 (1991).
2. E.M. Linsmaier and F. Skoog. Physiol. Plant. **18**, 100 (1965).
3. C.M. Ruyter, H. Schübel, and J. Stöckigt. Z. Naturforsch. C: Biosci. **43**, 479 (1988).
4. M.M. Bradford. Anal. Biochemistry, **72**, 248 (1976).
5. T. Murashige and F. Skoog. Physiol. Plant. **15**, 473 (1962).
6. H. Schübel, C.M. Ruyter, and J. Stöckigt. Phytochemistry, **28**, 491 (1989).
7. F. Ringe. Z. Pflanzenphysiol. **76**, 462 (1972).
8. A. Bechthold, U. Berger, and L. Heide. Arch. Biochem. Biophys. **288**, 39 (1991).
9. J. Heilemann and D. Strack. Phytochemistry, **30**, 1773 (1991).

Can. J. Chem. Downloaded from www.nrcresearchpress.com by 203.198.23.82 on 09/08/12
For personal use only.

Rearrangements of tricyclic ketones: [3.3.3]propellane formation via a γ-enolate revealed in an approach to the pentalenene skeleton through β-enolization[1]

HEMANT A. PATEL,[2] J.B. STOTHERS, AND S.E. THOMAS
Department of Chemistry, University of Western Ontario, London, ON N6A 5B7, Canada

Received May 31, 1993

This paper is dedicated to Professor David B. MacLean in recognition of his contributions to chemistry

HEMANT A. PATEL, J.B. STOTHERS, and S.E. THOMAS. Can. J. Chem. **72**, 56 (1994).

The known isomerization of the tricyclo[5.3.1.$0^{1,5}$]- to the [6.3.0.$0^{1,5}$]undecane skeleton by β-homoenolization led to examination of 2,9,9-trimethyl-6-methoxymethyltricyclo[5.3.1.$0^{1,5}$]undecanone (**6**) as a potential precursor for the synthesis of pentalenene, a naturally occurring sesquiterpenoid, utilizing a β-enolate rearrangement as a key step. While the anticipated rearrangement of **6** occurs, it is a minor process. The major rearrangement product arises by generation of a γ-enolate intermediate from a tricyclic enone formed by loss of methanol from **6**. This constitutes a new route to [3.3.3]propellanes and provides a third example of γ-enolate rearrangement. Structures of the products were established primarily from their ^{1}H and ^{13}Cmr spectra.

HEMANT A. PATEL, J.B. STOTHERS et S.E. THOMAS. Can. J. Chem. **72**, 56 (1994).

L'isomérisation connue du squelette tricyclo[5.3.1.$0^{1,5}$]undécane en tricyclo[6.3.0.$0^{1,5}$]undécane par β-homoénolisation a conduit à examiner l'utilité de la 2,9,9-triméthyl-6-méthoxytricyclo[5.3.1.$0^{1,5}$]undécanone (**6**) comme précurseur potentiel dans la synthèse du pentalènène, un sesquiterpénoïde naturel, en utilisant le réarrangement β-énolique comme étape clé. Même si le réarrangement désiré du produit **6** se produit, il s'agit d'un processus mineur. Le produit majeur de réarrangement provient d'un intermédiaire γ-énolique formé à partir de l'énone tricyclique **6**, par la perte de méthanol. Cette réaction constitue une nouvelle voie de préparation des [3.3.3]propellanes et fournit un troisième exemple d'un réarrangement γ-énolique. Les structures des produits ont été principalement déterminées à partir de leurs spectres rmn du ^{1}H et du ^{13}C.

[Traduit par la rédaction]

Introduction

Over the past 15 years, several naturally occurring sesquiterpenoids with various angular triquinane carbon skeletons have been discovered (1). These compounds have attracted attention as targets for synthesis not only because of their inherently interesting structures but also since some possess biological activity. Two examples having the tricyclo[6.3.0.0]undecane ring system are pentalenene (**1**) (2) and isocomene (**2**) (3). Pentalenene is the biosynthetic precursor of the pentalenolactones (4), antibiotic metabolites produced by several *Streptomyces* species, and it has been synthesized by several groups through a variety of routes (1, 5). Isocomene cooccurs with the first carbocyclic propellane to be found in nature, modhephene (**3**) (6). Several syntheses of these fascinating structures have been described: isocomene (1, 7) and modhephene (8).

Our interest in the potential of β-enolate rearrangement as a preparative route to less accessible polycyclic carbon skeletons has led to a synthesis of the linear triquinane, hirsutene (9), and to the generation of the angular triquinane ring system through the rearrangement **4** → **5** (10). From this finding, we became interested in devising a sequence leading to **1** from an appropriate analog of **4**. To this end, ketone **6** was selected as a suitable compound for an initial investigation, with the interconversion **6** → **7** envisaged as the key step. We found that this reaction indeed occurs, but only as a minor process. The major rearrangement involves an unsaturated derivative of **6** and leads to the generation of a [3.3.3]propellane. We wish to describe here the results of our study of the behavior of **6** under typical homoenolization conditions (*t*-BuO^{-}/*t*-BuOH/185°C).

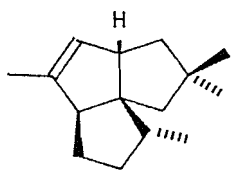

1

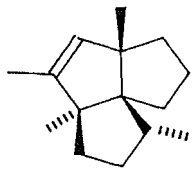

2

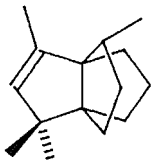

3

Results

Syntheses

The sequence employed for the preparation of ketone **6** is given in Scheme 1. The key step involves a well-known intramolecular Diels–Alder reaction (11) to furnish the [5.2.1.0] skeleton, which is then readily expanded to the required [5.3.1.0] system of **6**. The reaction of 2-methyloxetane (12) with methyl propargyl ether (13), as described by Yamaguchi et al. (14), gave 7-methoxyhept-5-yn-2-ol (**8**) in 88% yield. Hydrogenation of **8** over the Lindlar catalyst afforded 7-methoxy-*cis*-hept-5-en-2-ol (**9**) in 93% yield. Tosylation of **9** and condensation of this tosylate with sodium cyclopentadiene fur-

[1]Part 146 of the series ^{13}Cmr studies; for Part 145 see ref. 33.
[2]Present address: Malti-Chem Research Centre, Nandesari, India.

Can. J. Chem. Downloaded from www.nrcresearchpress.com by 203.198.23.82 on 09/08/12
For personal use only.

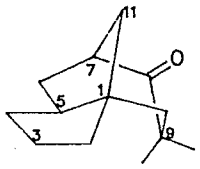

4

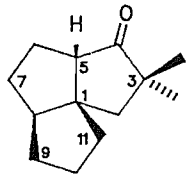

5

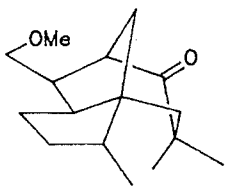

6

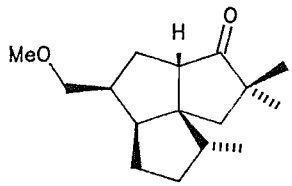

7

nished a 5:3 mixture of two trienes in 84% yield.The ^{13}Cmr spectrum contained four methylene signals for each component, with only that at δ_C 68.0 (-CH_2O-) common to both, showing that **10** and its 3′-isomer were present. The cyclopentadienyl methylene proton bands, δ 2.925 (m, $\nu_{1/2}$ 4.5 Hz) and δ 2.845 (m, $\nu_{1/2}$ 4.1 Hz) with relative intensities of 5:3, respectively, indicated that **10** was the major component. In any event, the assignment was not critical since the intramolecular Diels–Alder cycloaddition proceeded in 82% yield to the desired [5.2.1.0] olefin **11** as a 2:1 mixture of the 2-epimers.

An excellent analogy for the transformation of **9** to **11** has been described by Breitholle and Fallis in the report of their synthesis of cedrol and cedrene (15). Their key step was the intramolecular Diels–Alder reaction of 1,5-dimethyl-4-hexenyl-2′-cyclopentadiene, prepared from sodium cyclopentadiene and 1,5-dimethyl-4-hexenyl tosylate. Although they obtained a single alkylcyclopentadiene isomer, in contrast to our results, they stressed that the Diels–Alder conditions may alter the equilibrium mixture of these isomers and, consequently, all

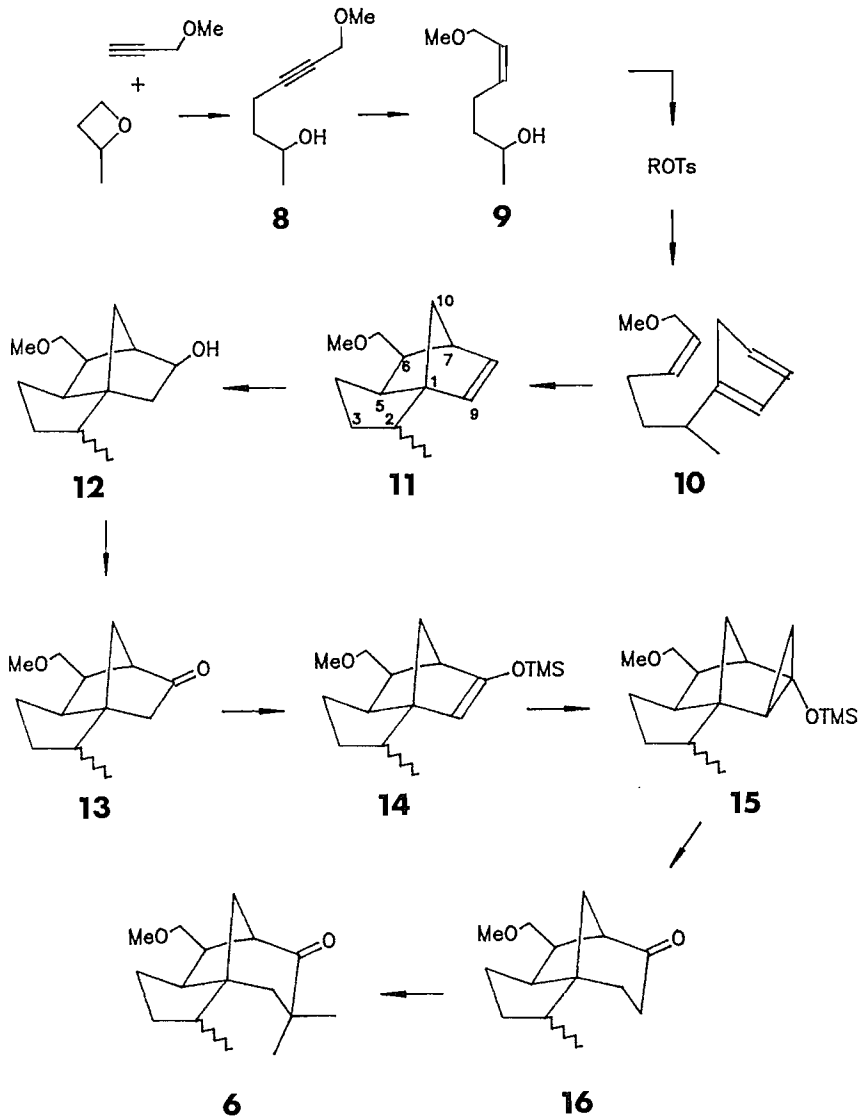

SCHEME 1

Can. J. Chem. Downloaded from www.nrcresearchpress.com by 203.198.23.82 on 09/08/12
For personal use only.

TABLE 1. 2-Methyl and skeletal methylene ^{13}C shieldings for **6**, **11–14**, and **16**[a]

Compound	Epimer	2-Me	C-3	C-4	C-9	C-10	C-11
11	Major	20.0	37.2	25.1		49.3	
	Minor	17.2	34.8	23.3		42.8	
12	Major	18.9	36.4	23.8	41.8	36.0	
	Minor	15.9	34.4	22.1	43.1	29.3	
13	Major	18.7	36.1	24.2	46.3	39.1	
	Minor	15.6	33.6	22.4	46.9	32.8	
14	Major	19.9	36.3	24.9		47.7	
	Minor	16.9	34.3	23.1		41.2	
16	Major	16.3	36.1	25.2	35.4	32.0	41.7
	Minor	14.7	(33.8)	23.3	34.7	36.0	(33.9)
6[b]	Major	16.3	35.7	24.9		46.9	38.6
	Minor	14.6	33.1	23.5		49.1	31.1

[a]In ppm from TMS for $CDCl_3$ solutions; values in parentheses may be reversed.
[b]Full data are given in Table 3; for the others, see Experimental.

possible intramolecular cycloaddition products should be considered. They concluded that the formation of the [5.2.1.0] skeleton would be expected to be strongly favored, as was observed in their case and in the present study. The isomeric internal Diels–Alder structures were excluded by the nmr spectra of the products in each of these studies. A second feature of this cycloaddition is the lack of a simple method to control the stereochemisty at C-2. In their synthesis of the cedrane skeleton, Breitholle and Fallis obtained a 1:1 mixture of the 2-epimers of the Diels–Alder cycloadduct but a 2:1 mixture of the 2-epimers of **11** was found in this work.

Hydroboration of **11** with $Siam_2BH$ in THF proceeded smoothly to give **12** in 74% yield; this was subsequently oxidized with pyridinium chlorochromate (16) to furnish **13** in 95% yield. Ring expansion to the desired [5.3.1.0] ring system was accomplished in a three-step sequence that had been demonstrated for several polycyclic ketones (17). Conversion of **13** to enol ether **14** (90%), cyclopropanation of **14** to **15** (81%), and ketonization in 88% yield gave **16** as a 2:1 epimeric mixture. Dimethylation of **16** with $MeI/NaNH_2/Et_2O$ proceeded in 80% yield to furnish **6**, as a 2:1 mixture of the 2-epimers, for our homoenolization experiments.

Consideration of the methylene shieldings in the ^{13}C spectra of these compounds led to a rational stereochemical assignment for the 2-methyl group in these epimeric pairs. Specific assignments for the individual carbons in **11–14** were made by comparing the shift data with the results for the compounds lacking the 2- and 6-substituents (10). The shifts for the 2-methyl and the skeletal methylene carbons in **11–14** are collected in Table 1.

In each of the sets of three methylene signals for **11** and **14**, those near 35 and 24 ppm could be readily assigned to C-3 and C-4, respectively, by comparison with the data for **17** and **18**. While the corresponding signals for the latter appear near 25 and 33 ppm, respectively, the 2-methyl group in **11** and **14** will deshield C-3 by ca. 9 ppm through its β-effect and the *exo*-6 methylene group will shield C-4 appreciably because these carbons are *syn*-periplanar. As a result, the C-3 and C-4 shieldings are reversed in **11** and **14**. The shifts for the third methylene signal, arising from C-10, differ by 6.5 ppm for each pair of epimers, which must reflect the orientation of the 2-methyl group. This group is either *syn* or *anti* to C-10 in the two epimers and, in the *syn* form, will exert a shielding effect thereon because of the relatively small dihedral angle relating the two centres. Analogous trends are also found for **12** and **13**

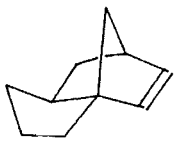

17

18

(see Table 1). A consistent difference of ca. 3 ppm is observed for the 2-methyl carbons in each epimeric mixture. In each pair, the minor form exhibits the more shielded 2-methyl and C-10 signals, and we can conclude, therefore, that the epimer having an *anti*-2-methyl group is predominant in each of these mixtures.

Assignments for these carbons in **6** and **16** are included in Table 1. These were also made by comparisons with the data for **4** and the parent ketone for which unequivocal assignments were available (10). For the two epimers of **6**, the C-11 shieldings differ by 7.5 ppm and, consequently, we can conclude that the desired *anti*-2-methyl epimer is the major form.

Homoenolization experiments

With the epimeric mixture of **6** in hand, we proceeded with our examination of its behavior under homoenolization conditions. After treatment of **6** with *t*-BuO^-/*t*-BuOH at 185°C for periods ranging from 24 to 240 h, we obtained neutral products in 53–80% yields by pentane extraction. Extraction of the aqueous phase after it was acidified furnished a single acidic product in 17–41% yields. The neutral fraction contained five major tlc spots; samples of each spot were examined by ^{13}Cmr to find that only partial separation had been achieved. Gas–liquid chromatographic (glc) analysis showed that the product contained two groups of components, a group of four having distinctly shorter retention times than a second group of three. The relative proportion of the first group slowly increased with reaction time, constituting ca. 75% of the neutral product after 240 h.

In the second group, two of the bands appeared to arise from two poorly resolved compounds and one, which slowly decreased with time, was easily shown to be the starting material. The first of the three bands was more symmetric and increased slowly to contain ~7% of the total neutral product after 240 h. ^{13}C spectra of samples collected by preparative glc indicated the presence of two closely related compounds in a 10:1 ratio. The major component, having a molecular formula

Can. J. Chem. Downloaded from www.nrcresearchpress.com by 203.198.23.82 on 09/08/12
For personal use only.

TABLE 2. ^{13}C shieldings for **5**, **7**, and *epi*-**7**[a]

Carbon	**5**	**7**	*epi*-**7**	Carbon	**5**	**7**	*epi*-**7**
1	55.5	58.3	58.1	9	33.3	22.8	24.7
2	50.9	43.5	49.5	10	27.0	35.0	35.6
3	47.5	47.5	47.5	11	43.2	44.1	44.9
4	225.9	225.6	225.6	3-CH_3	24.7	24.7	25.6
5	60.2	58.2	55.1		26.6	26.4	27.1
6	29.6	31.8	34.6	7-CH_2		74.0	73.7
7	33.4	42.3	42.6	11-CH_3		17.4	14.9
8	53.3	53.3	52.0	OCH_3		59.0	58.9

[a]In ppm from TMS for $CDCl_3$ solutions.

TABLE 3. ^{13}C shieldings for **6**, **19**–**21**[a]

	6		**19**		**20**		**21**	
Carbon	Major	Minor	Major	Minor	Major	Minor	Major	Minor
1	54.9	56.6	54.6	57.0	54.8	55.5	58.6	58.7
2	41.0	41.1	40.6	41.2	41.3	41.8	41.8	37.6
3	35.7	33.1	36.5	33.0	33.5	32.2	36.7_3	36.6_7
4	24.9	23.5	25.1	23.2	32.1	31.3	21.6	21.9
5	43.7	44.7	47.5	47.1	50.1	51.9	154.1	153.0
6	48.1	48.2	37.8	38.7	154.9	155.9	126.7	127.3
7	56.2	55.1	49.0	48.0	61.3	61.1	66.4	65.0
8	217.3	217.5	80.0	80.1	214.5	214.5	215.2	215.0
9	42.1	42.3	35.2	35.3	43.1	43.2	43.0	43.3
10	46.9	49.1	47.3	50.2	46.9	48.9	39.0	40.7
11	38.6	31.1	42.3	33.9	40.5	33.3	45.2	47.2
2-CH_3	16.3	14.6	16.8	15.2	17.1	14.1	13.9	16.5
9-CH_3	31.3	31.2_7	24.1	24.0	30.2	30.1	30.7_6	30.8_0
	31.4	31.2_2	35.3	35.0	32.7	32.5	34.0	33.9
6-CH_2X	73.4	73.3	75.0	75.1	108.7	108.5	13.2	13.5
CH_3O	58.5	58.4	58.7	58.7				

[a]In ppm from TMS for $CDCl_3$ solutions.

of $C_{16}H_{26}O_2$ by precise mass measurement, is an isomer of **6** with a cyclopentanone ring to judge from its carbonyl absorption (1730 cm^{-1}, δ_C 225.6); this is quite different from that for **6** (1700 cm^{-1}, δ_C 217.3, 217.5). From nmr spectra, the major compound was identified as **7**, accompanied by small amounts of its *syn*-2-methyl epimer. These were anticipated to form by β-enolate rearrangement of **6**. The results from $^{13}C\{^1H\}$ and $^1H\{^1H\}$ correlation spectra allowed complete assignments for the ^{13}C signals arising from **7**. Three ^{13}C methyl signals at δ_C 24.7, 26.4, and 59.0 correlated with ^1H singlets at δ 1.02, 1.06, and 3.28, respectively, while the highest field peak at δ_C 17.4 correlated with the proton doublet (δ 0.98, J = 7.0 Hz, 11-Me) coupled to H-11 (δ 1.98, m), which, in turn, is coupled to the 10-methylene protons near 1.4 and 1.6 ppm; these patterns correlate with the ^{13}C peaks, δ_C 44.1 (C-11) and 35.0 (C-10), respectively. An AX pattern, δ 2.17, δ 1.45, J_{AX} = 14.1 Hz, was readily assigned to the 2-methylene protons, which correlated with the methylene signal at δ_C 43.5 (C-2). The lowest field ^1H methine pattern at δ 2.28 (bd, J = 9.1 Hz), coupled to a methylene group near δ 1.4 and 2 .0, served to identify C-5 and -6, δ_C 58.2 and 31.8, respectively. The fourth methylene carbon signal, δ_C 22.8, arises from C-9. The ^{13}C data are collected in Table 2 with those for the minor component, *epi*-**7**, and **5**. From these data, it is clear that C-9 is strongly shielded by the methylene carbon on C-7, as expected since these are *syn*-periplanar. The shifts for C-2 in **7** and for C-5 in *epi*-**7** differ markedly from the corresponding shieldings in **5**. In **7**, C-2 is shielded by 7.4 ppm and C-5 by 5.1 ppm in *epi*-**7** relative to the values for **5**. This must reflect the orientation of the 11-methyl group and is only consistent with **7** bearing an *anti*-11-methyl group, i.e., *syn*-periplanar to C-2.

Preparative glc provided samples of the third band, which was found to contain a 2:1 mixture of alcohols. The ^{13}C spectrum showed these to be closely related to the starting material, LAH reduction of which gave an identical mixture. Therefore, these must be **19**; the ^{13}C data are listed in Table 3. Reduction of **6** was puzzling because the carbonyl group is unaffected under these conditions in the vast majority of ketones so far examined (18). To our knowledge, the only exceptions are 3-phenyl-6,6-dimethylcyclohexanone and its cycloheptanone analog from which small amounts of alcohols are formed under these conditions (19); but these are rather different systems.

For Bands 1–4 in order of increasing retention time in the first group, samples for characterization were obtained by preparative glc. Each was a mixture of epimers, but the relative proportions in two of these samples differed markedly from that of the initial ketone. All were found to have lost the methoxyl group and to contain one double bond. Band 3 constituted about 5% of the neutral product from short runs, while Band 2 was prominent in all samples, exhibiting a maximum of ~30% (72 h) and then decreasing to about 8%. Band 1 grew slowly to constitute about 45% of the total neutral product after 240 h, whereas Band 4 was a minor component in each of the product mixtures.

Can. J. Chem. Downloaded from www.nrcresearchpress.com by 203.198.23.82 on 09/08/12
For personal use only.

Can. J. Chem. Downloaded from www.nrcresearchpress.com by 203.198.23.82 on 09/08/12
For personal use only.

Band 3, which showed little change in relative intensity with time, consisted of a 2:1 epimeric mixture of ketones, each component of which gave rise to nmr signals for three methyl groups and those for an exocyclic methylene group. This showed that the methoxyl group had been lost, while the carbonyl absorption (δ_C 214.5) indicated that no major skeletal change had occurred. An identical mixture was prepared from the initial ketone by treatment with NaI/Me_3SiCl in MeCN (20), to replace the methoxyl group with iodide, followed by reaction with base to eliminate HI. Thus, this product was assigned structure **20** with which the ^{13}Cmr data are fully consistent; these may be compared with those for **6** (see Table 3). The replacement of C-6 with an sp^2 carbon produced marked shifts for C-5, C-6, C-7, and C-11, as expected, and the -3 ppm shift for the carbonyl signal is consistent with the formation of a β,γ-enone (21).

Band 2, a major product in the early neutral samples, was found to contain a 4:1 mixture of epimeric ketones from its ^{13}Cmr spectrum. It is isomeric with **20**, having a molecular formula of $C_{15}H_{22}O$ by precise mass measurement. The nmr spectrum of each epimer included signals for four C-methyl groups, one of which is olefinic (δ_H 1.57, δ_C 13.2, 13.5), together with those for two nonprotonated sp^2 carbons (δ_C 126.7, 154.1 and 127.3, 153.0). As in **20**, the carbonyl absorption at δ_C 215.0 and 215.2 indicated that no major skeletal change was involved. This product, therefore, was assigned structure **21** on the basis of the ^{13}C data (see Table 3).

Since **20** and **21** must be related through a common allylic anion, additional evidence for these structures was sought by examination of the behavior of **20** in strong base. After treatment of **20** at 130°C with *t*-BuO–/*t*-BuOH for 24 h, the neutral fraction contained only **20** and **21** in a 4:1 ratio, and after 72 h this ratio was 1:1. This confirmed that **20** and **21** differ only in the position of the olefinic bond. For the neutral product, the

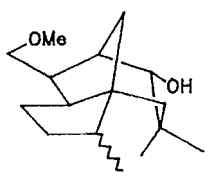

19

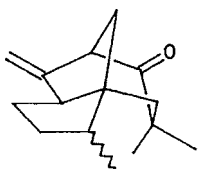

20

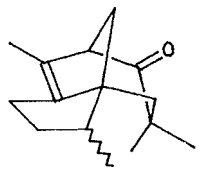

21

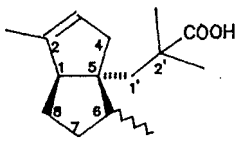

22

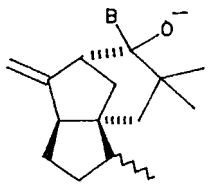

23

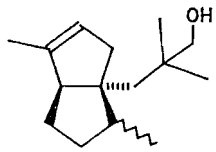

24

yields were 51 (24 h) and 43% (72 h) and, for the acid, 38 and 46%, respectively. The ^{13}C spectrum of the acidic product was virtually identical to that for the acidic fraction from the homoenolization experiments with **6**. Both contained two sets of 15 signals, ascribable to a pair of epimeric acids. The proportions of these acids differed slightly in the two cases, with a slight excess of one in the runs with **6**, but essentially equal proportions from **20** and **21**. From the ^{13}C spectra, each has a trisubstituted double bond, four methyl groups, of which one is olefinic, four methylene, two methine, and two quaternary carbons, as well as the carboxyl group. These data are consistent with structure **22**, which can arise from **20** and (or) **21** through Haller–Bauer cleavage after addition at the carbonyl carbon by the alkoxide base, collapse of which could generate an allylic anion (see **23**). Although this is one of a number of possible isomers, differing only in the position of the double bond, **22** must be the most stable. It may be noted that earlier studies had shown that *tert*-butyl esters do not survive under these reaction conditions and the corresponding acids are isolated. Assignment of the ^{13}C signals for the **22** epimers was made by comparison with the data for several model compounds (22) and by heteronuclear $^{13}C\{^1H\}$ correlation spectra. The ^{13}C data are collected in Table 4 and the ^{1}H data are in the experimental section.

The spectra of samples from Band 4 were strikingly similar to those exhibited by **22**, except that the carboxyl signals were replaced by those for hydroxymethyl carbons. Identical spectra were recorded for samples obtained by LAH reduction of **22**. Thus, this product is **24**; the ^{13}C data are collected in Table 4. The stereochemistry of the 6-methyl group in each epimeric pair **22** and **24** was revealed by the large difference found for the C-1′ shieldings. The upfield signal must arise from the *exo* epimer in which the 6-methyl is *syn*-periplanar to C-1′. Thus, these mixtures **22** and **24** contained a small excess of the *exo* epimer.

Band 1 increased slowly with reaction time to represent about 45% of the total neutral product after 240 h. Its ^{13}C spectrum revealed the presence of two epimers, in a 10:1 ratio, which gave rise to carbonyl absorption (1730 cm^{-1}, δ_C 224.0, 225.0) indicative of cyclopentanone rings. Exact mass measurement gave a molecular formula of $C_{15}H_{22}O$. For each of the two epimers, the ^{13}C spectrum included signals for two olefinic carbons of a trisubstituted double bond, and those for four methyl, of which one is olefinic, four methylene, one methine, and **three** quaternary carbons. With the ^{1}H, $^1H\{^1H\}$, and $^{13}C\{^1H\}$ COSY

TABLE 4. ^{13}C shieldings for the *exo*- and *endo*-6-methyl isomers of **22** and **24**[a]

	22		24			22		24	
Carbon	*exo*	*endo*	*exo*	*endo*	Carbon	*exo*	*endo*	*exo*	*endo*
1	55.5	59.1	58.9	56.3	2-CH_3	14.9	15.3	15.4	15.6
2	143.6	141.7	143.6	142.7	6-CH_3	13.0	14.3	14.2	14.5
3	121.0	123.7	124.1	121.7	1′	41.1	50.1	39.9	48.1
4	43.3	39.3	43.8	39.2	2′	53.8	55.4$_5$	54.6	56.1
5	42.3	42.4	36.2	37.2	2′-CH_3	24.1	26.7	25.0	25.4
6	46.3	44.1	46.5	45.4		29.4	27.4	26.1	25.6
7	32.7	32.9	32.7	32.9	COOH	186.2	186.4		
8	27.8	28.9	28.1	29.2	CH_2OH			74.0	73.5

[a]In ppm from TMS for $CDCl_3$ solutions.

TABLE 5. ^1H and ^{13}Cmr data for **25** and *epi*-**25**[a]

	25			*epi*-25	
	^1H	^{13}C		^{13}C	
Position	In $CDCl_3$	In $CDCl_3$	In C_6H_6	In $CDCl_3$	In C_6H_6
1	—	76.7	76.7		77.3
2	—	224.0	221.7	225.0	222.3
3	—	48.5	48.3	47.4	47.2
4	1.556 [13.5] 1.650 [13.5]	42.8	42.8	49.7	49.8
5	—	56.8	56.9	58.5	58.5
6	2.370 [2.2, 2.4, 17.0] 2.454 [2.2, 2.4, 17.0]	46.6	46.7	41.2	41.4
7	5.080 [1.4, 2.2]	123.7	123.5	126.1	125.9
8	—	143.0	143.5	140.7	141.2
9	1.42 [6.0, 12.5, 12.5] 2.02 [6.8, 12.5]	35.1	35.3	34.5	34.7
10	~1.0 [m] ~1.6 [m]	33.6	33.7	33.5	33.8
11	~1.65 [m]	47.2	47.4	45.5	45.7
3-CH_3	0.974	25.2	25.5	27.9	28.0
	1.053	27.0	27.0	28.6	28.6
8-CH_3	1.67 [1.4, 2.4]	12.9	13.0	13.1	13.2
11-CH_3	0.976 [6.4]	12.0	12.0	13.7	13.7

[a]Shieldings in ppm from internal TMS; ^1H–^1H couplings in Hz listed within square brackets.

spectra, all protons of the major component were assigned and correlated with the carbon signals; from these data three structural subunits were identified.

The olefinic methyl protons (δ 1.67) exhibited allylic coupling to the olefinic proton (J = 1.5 Hz) and homoallylic coupling to a pair of methylene protons (J = 2.4 Hz) with which the olefinic proton is coupled (J = 2.2 Hz). These interactions, confirmed by decoupling, established the presence of a -CH_2-CH=C(CH_3)- unit. Methyl protons (δ 0.976, d, J = 6.4 Hz) coupled to a methine proton, which is also coupled to one of a pair of contiguous methylene groups, revealed a -$(CH_2)_2$-CH(CH_3)- unit. A $^{13}C\{^1H\}$ flock spectrum (23) showed that the methyl protons giving rise to singlets at δ 0.974 and 1.053 are both vicinally coupled to a methylene carbon whose protons appear as an AB pattern (δ 1.556, 1.650, J_{AB} = 13.5 Hz). Thus, a -$CH_2C(CH_3)_2$- unit was identified. The combination of these three units with the two quaternary centres and the carbonyl led to the propellene structures **25** and *epi*-**25** for these compounds. The ^1H and ^{13}C results for **25** are given in Table 5 with the ^{13}C results for *epi*-**25**. Within the strong proton spectrum of **25**, only the signals for H-7 (δ 5.24), the 3- and 11-methyl groups (δ 1.031, s; 1.073, s; 0.945, d, J = 6.4 Hz), and an AB system (1.71, 1.98, J = 13.7 Hz) for *epi*-**25** were easily discerned. Further, this AB system was correlated with the δ_C 49.7 signal in the $^{13}C\{^1H\}$ COSY spectrum, thereby identifying C-4 in *epi*-**25**. Since the C-4 shieldings will depend on the orientation of the 11-methyl group and C-4 absorbs at δ_C 42.8 in **25**, we conclude that the 11-methyl is *syn*-periplanar to C-4 in **25**, in which C-4 is shielded by –7 ppm. The C-6 shieldings also support this assignment, since these exhibit the opposite trend. The shift of +5.4 ppm for C-6 in **25** is consistent with an *anti*-periplanar relationship to the 11-methyl group.

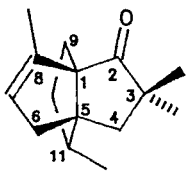

25

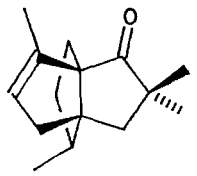

epi-**25**

Can. J. Chem. Downloaded from www.nrcresearchpress.com by 203.198.23.82 on 09/08/12
For personal use only.

TABLE 6. Composition[a] of the product mixtures from **6**

Time (h)	Neutral Fraction[b]							Acid fraction
	6	**7**	**19**	**20**	**21**	**24**	**25**	**22**
24	42	8	3	2	21	<2	2	17
72	10	5	7	5	30	3	7	25
120	8	6	6	2	20	8	12	31
144	7	5	5	3	20	6	15	34
240	2	7	5	<2	8	6	24	41
120[c]	8	8	8	5	27	4	10	20
240[c]	6	10	10	<1	12	2	15	36

[a]Given as the proportion, on a % molar basis, of isolated product.
[b]Estimated from a combination of glc and ^{13}Cmr data.
[c]Results from runs with the pure major epimer (see text).

The composition of the product mixtures from the experiments with **6** are listed in Table 6. These data include the results for a few runs with pure samples of the major epimer of **6**, small quantities of which were obtained by repeated chromatography over silica. The latter data confirmed that the major component in each epimeric mixture arose from the major epimer of **6**.

To shed more light on the sequence of formation of the neutral products, samples of **21** were treated with *t*-BuO$^-$/*t*-BuOH. The neutral fraction, isolated in 85% yield after 100 h at 150°C, was found to be virtually identical to the starting material, according to the ^{13}C spectra. At 185°C, glc analysis showed that **21** was transformed slowly to **25** and *epi*-**25** together with small amounts of unidentified neutral material. The mixture of propellenones constituted ca. 25 and 60% of the neutral fraction after 50 and 150 h, respectively. From the results of the experiments with **20** and **21**, it became clear that the sequence is **20** → **21** → **25** + *epi*-**25**. In principle, each of these is prone to Haller–Bauer cleavage leading to **22** since this process will generate an allylic carbanion, as noted above (see **23**). The results indicate, however, that **20** is the most susceptible to this cleavage, and the propellenones the least. It can be noted that **24** was not found in the products from the experiments with **20** or **21**.

Discussion

By analogy with our earlier findings for **4** (10, 24), we would anticipate β-proton abstraction from **6** at C-6 and -11 to generate the β-enolates **26** and **27**, or equivalent species, respectively. Cleavage of these β-enolates can proceed by either, or both, of two modes: *a* and *b* in Scheme 2. Path *a* regenerates starting material and *b* leads to rearranged product. For the corresponding β-enolates from **4**, the cleavage is unidirectional, since **5** is the only rearranged product (10) and H/D exchange was observed at C-6 but not at C-11 (24). The isolation of **7** and *epi*-**7** showed that proton abstraction proceeded at C-11 in **6** to form **27**, or its equivalent, with subsequent opening to the tricyclo[6.3.0.0]undecanone skeleton. In agreement with earlier results for **4**, there was no evidence of formation of the [4.3.2.0] system **28**, but, in sharp contrast, rearrangement to **7** is not a major mode of reaction for **6**.

Four neutral products from **6** lack the methoxyl group and contain an olefinic bond. This can be envisaged to involve an E1cB process through an "open" β-enolate, such as **29**, leading to **20**, as shown in Scheme 2. It should be noted that β-enolates are commonly depicted as cyclopropoxide ions as a convenient symbolism. Although results for many β-enolate rearrangements are readily accommodated by these species, the cyclopropoxide form may be a representation of the transition state between rapidly equilibrating "open" forms. Precise definition of β-enolates is difficult. In any event, isomerization **20** → **21** would involve abstraction of H-5, generating the allylic carbanion **30**, and protonation at the incipient methyl carbon to form **21**. Our data provide permissive evidence that **21** is the more stable. Introduction of the double bond through loss of the methoxyl renders both **20** and **21** susceptible to Haller–Bauer cleavage because collapse of the intermediates **31***a* and **31***b*, formed by addition of alkoxide ion at the carbonyl carbon, will give an allylic anion. The isolation of **22** indicates that the isomers differing only in the position of the double bond must be less stable.

Although the original objective of this study was doomed by the disappointingly low yields found for the interconversion **6** → **7**, the unexpected finding that **25** is the major rearrangement product was a welcome surprise for two reasons. The isolation of **25** not only illustrates a new route to the [3.3.3]propellane skeleton but it also provides an example of γ-enolate rearrangement, since its formation is readily rationalized in terms of **32**, or an equivalent species, formed from **20** and **21**, as outlined in Scheme 3. Cleavage of **32** by path *b* leads to **33**, which will equilibrate with **25** (*epi*-**25**) under the strongly basic conditions. Since **33** was not detected in the neutral product mixtures, this equilibrium clearly favors the skeleton having the endocyclic double bond.

Since the discovery that a ketonic carbonyl group can activate proton abstraction from carbons other than those to which it is directly bonded (25), the vast majority of the reported cases involve β-enolate formation (18). However, ^{1}H/^{2}H exchange studies have shown that γ-enolization occurs in a few systems (18), but rearrangement had been observed in only two cases (26, 27). Thus, the formation of **25** from **20** and **21** is a third example of γ-enolate rearrangement.

Although both **20** and **21** may undergo β-enolization to form tricyclo[6.3.0.0]undecenones **36***a–c*, it is conceivable that these were destroyed by Haller–Bauer cleavage to **22** (see Scheme 4).

The fate of **21** is distinctly different from that of its simpler analog **34**, which we had investigated earlier (28). The major neutral product from **34** was **35**, showing that the anticipated β-enolization at C-8 produced the [3.3.0] skeleton, but subsequent reduction of the olefinic bond had not been anticipated. Furthermore, the rest of the neutral product consisted of compounds having a *tert*-butoxyl group, showing that the addition of *t*-BuO– to the double bond in **34** is a competitive process. None of the products that would arise by the corresponding processes with **21** was detected.

An analogous competitive reduction process has been encountered in one other study in which it was found that **37** is reduced to **38** (27) under these conditions. We have ascribed the formation of both **35** and **38** to single electron transfer from *tert*-butoxide anion to the conjugated carbonyl group. A distinctly different reduction process was recently observed (19) in another homoenolization study in which it was found that **39** is reduced slowly to the corresponding alcohol. We suggested that this process may be initiated by formation of **40** through homolytic cleavage of the more substituted bond in the cyclic β-enolate formed from **39**, by analogy with the observation that **41** and **42** are in rapid equilibrium (29) and the fact that an oxy anion substituent has a significant weakening effect on the adjacent bonds (30). In any event, other reduction processes must be operative in the present system to produce **19** and **24**.

Can. J. Chem. Downloaded from www.nrcresearchpress.com by 203.198.23.82 on 09/08/12
For personal use only.

Can. J. Chem. Downloaded from www.nrcresearchpress.com by 203.198.23.82 on 09/08/12
For personal use only.

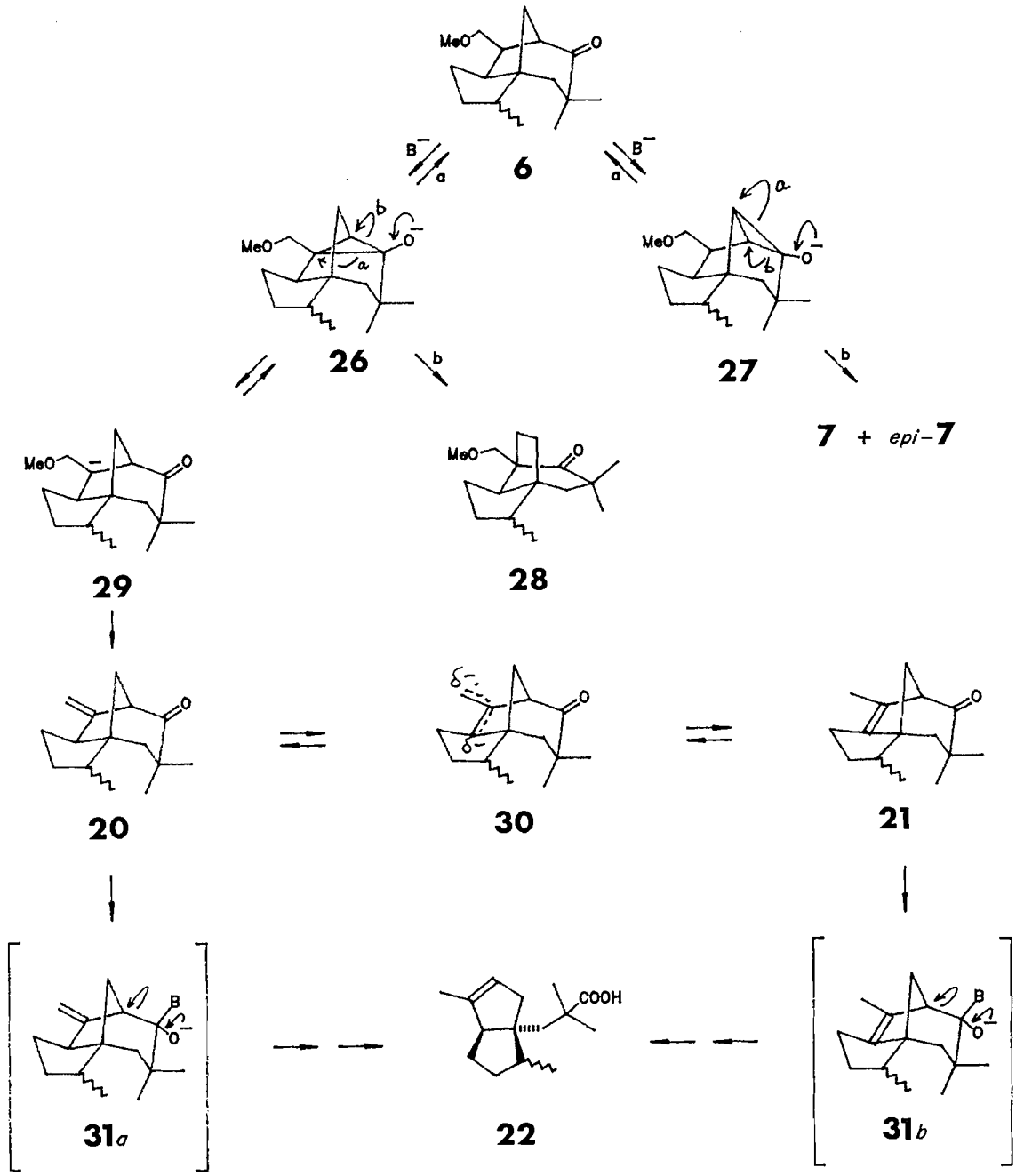

SCHEME 2

Alcohol **19** must arise simply from reduction of the carbonyl group in **6**. This process can be attributed to hydride transfer from the methoxide ion formed through the E1cB elimination in anion **29** (Scheme 2). The failure to detect formaldehyde is not surprising since it would have been easily lost during the work-up.

Alcohol **24** is a minor component in all of the neutral product mixtures from **6**, but was not found in the products obtained upon the same treatment of **20** or **21**. This observation leads us to suggest that its formation is triggered by hydride transfer from methoxide ion to the carbonyl group in **20** and (or) **21**. Subsequent cleavage of the resultant alkoxide through a retro-aldol reaction, as outlined in Scheme 5, would yield bicyclic aldehyde **43**, which could undergo a Cannizzaro reaction to give equimolar quantities of **22** and **24**. From the experiments with **20** and **21** as starting material, there is no doubt that **22** is primarily generated by their Haller–Bauer cleavage.

Experimental

Gas–liquid chromatography (glc) was carried out on a Varian 3300 instrument using a column of 5% SE-30 on Chromosorb W 80-100. Thin-layer chromatography (tlc) was done on Kiesel gel 60 F_{254} plates and flash chromatography (FC) columns were prepared as described in the literature (31). Tetrahydrofuran (THF) and ether were distilled from Na/benzophenone just before use. Pyridine, *tert*-butyl alcohol, diisopropylamine, and trimethylamine were distilled from CaH_2 and stored over 4A molecular sieves.

Can. J. Chem. Downloaded from www.nrcresearchpress.com by 203.198.23.82 on 09/08/12
For personal use only.

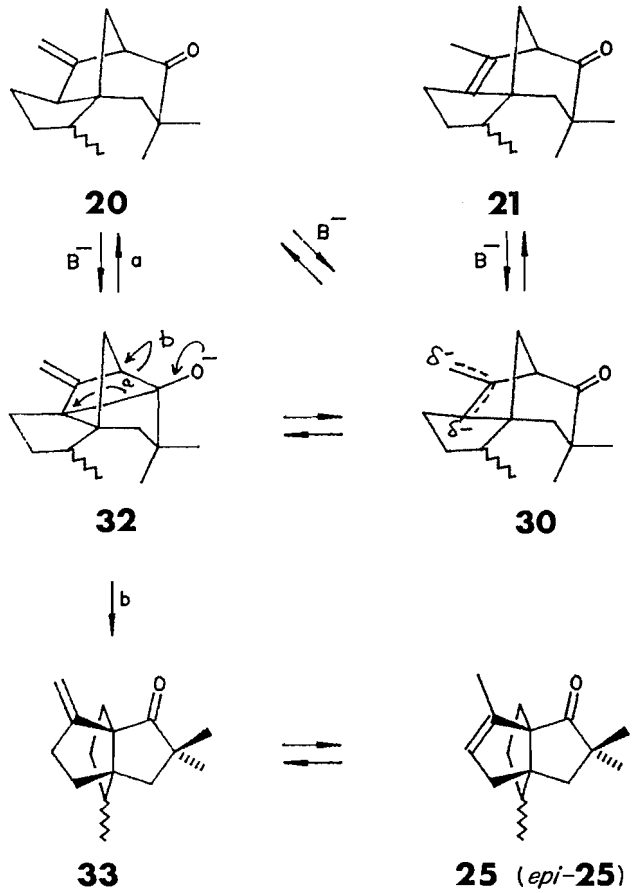

SCHEME 3

Infrared spectra were recorded with either a Beckman 4250 instrument or a Bruker/IBM FTIR 32 spectrophotometer. Mass spectra were obtained with either a Varian MAT-311A or a Finigan MAT 8230 instrument at 70 eV for routine spectra and at 20 eV for exact mass measurements.

Proton and carbon nmr spectra of each compound were obtained with Varian XL-200 (^{1}H) and XL-300 (^{13}C) spectrometers. The number of protons bonded to each carbon was found by recording either the APT or DEPT spectrum. Correlation spectra were obtained using the programs of the Varian software, $^1H\{^1H\}$ and $^{13}C\{^1H\}$ spectra with the HOMCOR and HETCOR sequences, while long-range $^{13}C\{^1H\}$ correlations were revealed with spectra recorded using the FLOCK sequence (23). While full assignments for the ^{13}Cmr spectra are presented, the fact that most of the compounds were obtained as C-2 epimeric mixtures precluded complete analysis of their ^{1}Hmr spectra, thereby limiting definitive assignments to those listed.

7-Methoxy-5-heptyn-2-ol (8)

To a stirred solution of methyl propargyl ether (13) (3.5 g, 0.05 mol) in THF (100 mL) under dry nitrogen was added *n*-BuLi (19.2 mL, 2.6 M in hexane) at –78°C. Stirring was continued for 20 min, before the sequential addition of 2-methyloxetane (12) (1.8 g, 0.025 mol) and $BF_3{\cdot}Et_2O$ (7.5 mL) at –78°C. This mixture was stirred at –78°C for 0.5 h before it was allowed to warm to room temperature and diluted with saturated NH_4Cl solution. After the product was extracted with ether (3 × 60 mL), the extracts were washed with brine, 10% $NaHCO_3$ solution, and brine again, before drying over anhydrous Mg_2SO_4. Removal of the solvent furnished a yellow oil. Distillation was attempted but led to decomposition; thus, the product was purified by FC (EtOAc – petroleum ether, 40:60) to furnish alcohol **8** (3.1 g, 88% yield); ir ($CDCl_3$): 3640, 3480 (OH), 2840 (OMe), 2240 (C≡C), 1090 (C—O) cm^{-1}; ^{1}Hmr ($CDCl_3$) δ: 1.10 (d, 3H, J = 6.1 Hz, H-1), 1.55 (dt, 2H, J = 6.1, 7.2 Hz, H-3), 2.25 (tt, 2H, J = 2.1, 7.2 Hz, H-4) 2.48 (s, OH), 3.26 (s, 3H, OMe), 3.81 (tq, 1H, J = 6.1, 6.1 Hz, H-2), 3.97 (t, 2H, J = 2.1 Hz, H-7); ^{13}Cmr ($CDCl_3$) δ: 23.2, 57.2 (2 × CH_3), 15.2, 37.5, 60.0 (3 ×

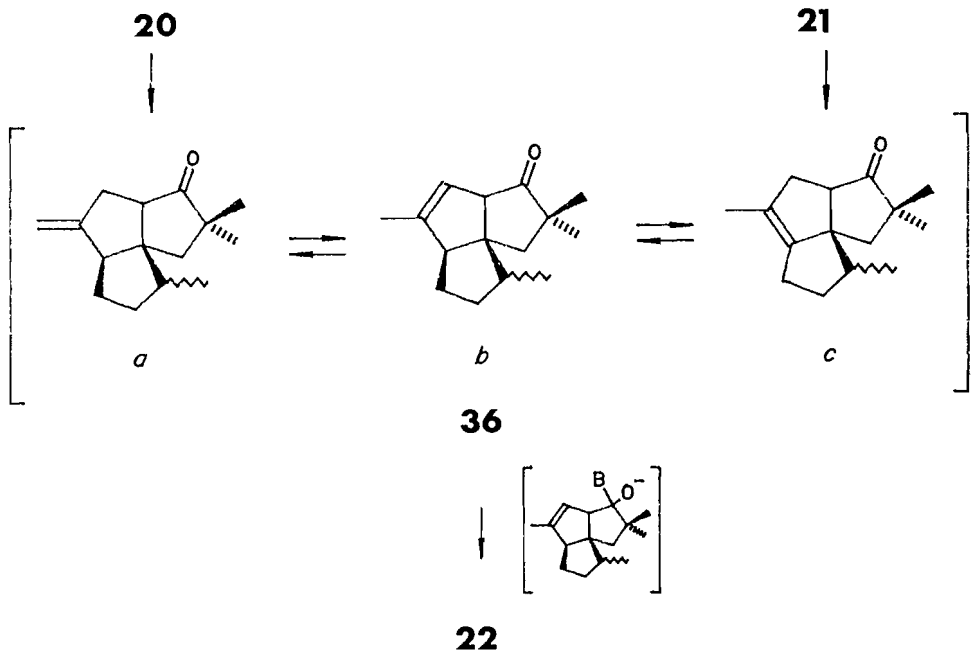

SCHEME 4

Can. J. Chem. Downloaded from www.nrcresearchpress.com by 203.198.23.82 on 09/08/12
For personal use only.

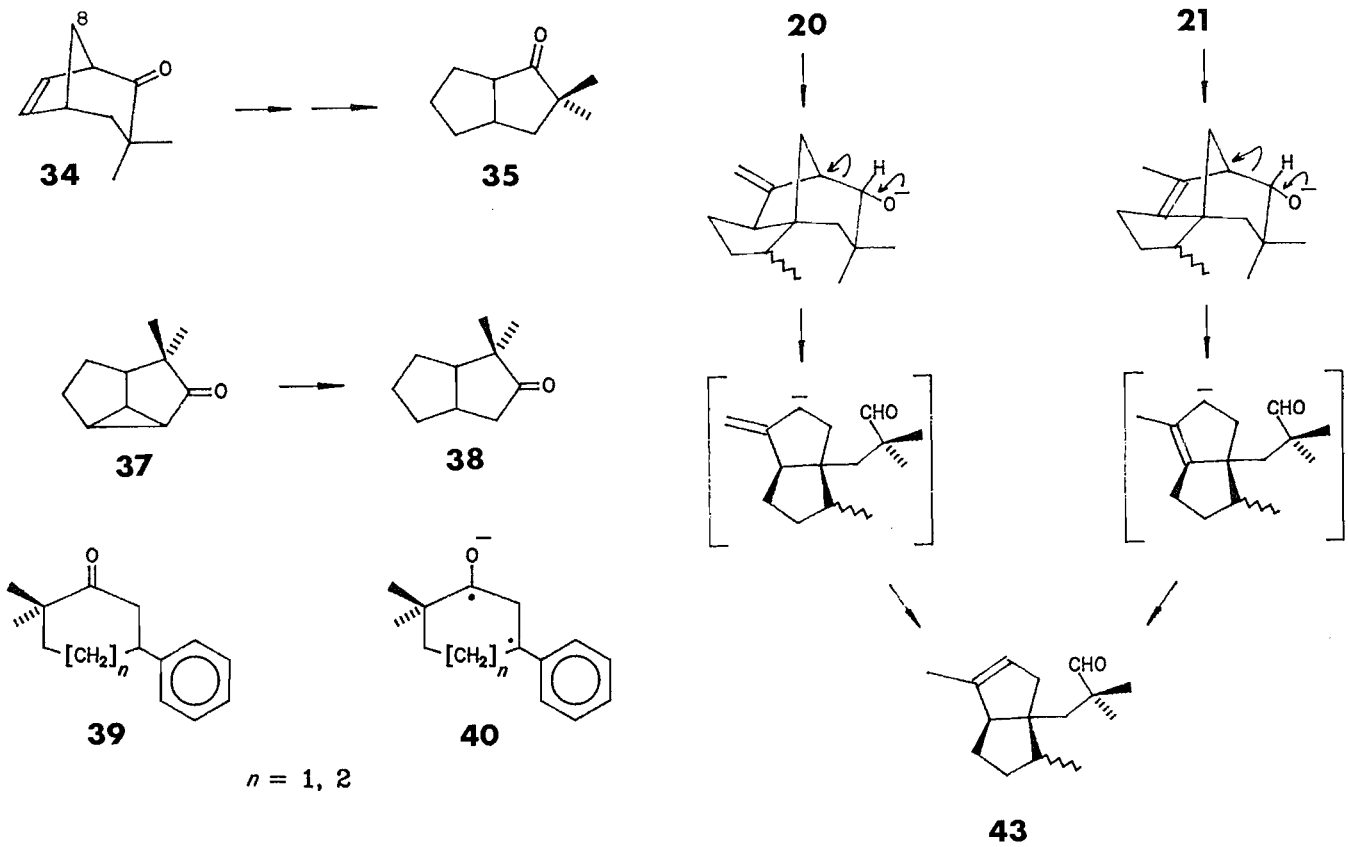

SCHEME 5

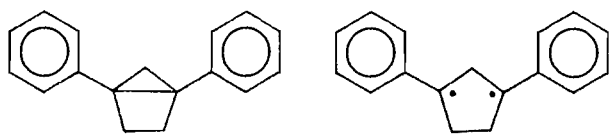

41 42

CH_2), 66.6 (CH), 75.9, 86.5 (C≡C). Exact Mass calcd. for $C_7H_{10}O$ (M – 32): 110.0732; found: 110.0736.

7-Methoxy-cis-*5-hepten-2-ol (9)*

A solution of alcohol **8** (0.67 g, 4.72 mmol) in THF – petroleum ether (20:80, 60 mL) containing 0.4 mL of pyridine and the Lindlar catalyst (135 mg) was hydrogenated at –15°C until one equivalent of H_2 was taken up. The progress of the reaction was also monitored by tlc. When the reaction was deemed complete, the catalyst was removed by filtration and the solvent evaporated. The residue was taken up in ether (100 mL) and the ethereal solution washed with 3% aqueous HCl and brine before drying over anhydrous $MgSO_4$. Evaporationof the solvent afforded **9** as a yellow oil (0.61 g, 93%): ir ($CHCl_3$): 3640, 3450 (OH), 3045 (=CH), 2840 (OMe), 1450 (C=C), 1100 (C—O) cm^{-1}; ^{1}Hmr ($CDCl_3$) δ: 1.08 (d, 3H, J = 6.3 Hz, H-1), 1.35–1.50 (m, 2H, H-3), 2.05–2.25 (m, 2H, H-4), 2.80 (bs, 1H, OH), 3.24 (s, 3H, OMe), 3.70 (tq, 1H, J = 6.3, 6.4 Hz, H-2), 3.8–4.0 (m, 2H, H-7), 5.4–5.6 (m, 2H, H-5,6); ^{13}Cmr ($CDCl_3$) δ: 23.3, 57.8 (2 × CH_3), 23.8, 28.4, 67.8 (3 × CH_2), 66.5 (CH), 125.8, 134.0 (2 × HC=). Exact Mass calcd. for $C_7H_{12}O$ (M – 32): 112.0888; found: 112.0892.

1-Methyl-6-methoxy-cis-*4-hexenyl-2′-cyclopentadiene (10)*

To a stirred solution of **9** (1.44 g, 10 mmol) in dry pyridine (12 mL), at ice-bath temperature, was added *p*-toluenesulfonyl chloride (2.87 g, 15 mmol) in small portions. The reaction mixture was then stirred at 0°C for 2 h and placed in a refrigerator for 12 h. The mixture was neutralized with ice-cold 30% aqueous HCl solution before extraction with ether (3 × 30 mL). The combined extracts were washed with water, 3% aqueous HCl, 5% aqueous $NaHCO_3$ solution, and brine before drying over anhydrous $MgSO_4$. Removal of the ether gave the desired tosylate of **9** (2.85 g, 96%) as a thick oil; ir ($CHCl_3$): 3040 (=CH), 2835 (OMe), 1580 (Ph), 1440 (C=C), 1180 (-SO_3R) cm^{-1}; ^{1}Hmr ($CDCl_3$) δ: 1.20 (d, 3H, J = J.6 Hz, H-1), 1.45–1.7 (m, 2H, H-3), 1.8–2.1 (m, 2H, H-4), 2.39 (s, 3H, aryl-Me), 3.25 (s, 3H, OMe), 3.83 (d, 2H, H-7), 4.56 (tq, 2H, J = 6.5, 7.5 Hz, H-2), 5.3–5.5 (m, 2H, H-5,6), 7.3, 7.7 (AA′BB′ system of aryl CH's); ^{13}Cmr ($CDCl_3$) δ: 20.7, 21.5, 57.9 (3 × CH_3), 23.1, 36.3, 67.9 (3 × CH_2), 79.8 (CH), 127.0, 131.5 (2 × CH=), 127.6, 129.7 (2 × 2 aryl CH), 134.4, 144.5 (2 × aryl C).

Sodium sand was prepared by vigorously stirring sodium metal (0.345 g) in refluxing xylene (20 mL) under nitrogen. The xylene was decanted and the sodium sand washed with THF (2 × 20 mL). To a stirred suspension of the sand in 10 mL of THF was added freshly distilled cyclopentadiene in several portions until the sodium was consumed (ca. 3h). The resulting deep red-purple solution was then cooled in an ice-bath. A solution of the tosylate (2.98 g, 1 mmol) in THF (10 mL) was added slowly over 30 min and the reaction mixture was stirred overnight. The resulting light brown mixture was diluted with brine and then extracted with ether (3 × 50 mL). The combined extracts were washed with brine before drying over anyhdrous $MgSO_4$. Evaporation of the solvent left a dark brown oil, which was purified by FC (Et_2O – petroleum ether, 10:90) to give **10** as a light yellow oil (1.60 g, 84%); ir ($CHCl_3$): 3060, 3025 (=CH), 2840 (OMe), 1450 (C=C), 1105 (C—O) cm^{-1}; ^{1}Hmr ($CDCl_3$) δ: 1.06 (d, J = 6.8 Hz, 1-Me), 1.4–1.6 (m, H-2), 2.00 (m, H-3), 2.55 (m, H-1), 2.845 (m) and 2.925 (m) (int. ratio 3:5, =CCH_2C=′s), 3.28 (s, OMe), 5.4–5.6 (m, H-4, 5), 5.8–6.4 (m's, =CH's); ^{13}Cmr ($CDCl_3$) δ: (major component): 20.2, 57.7_6 (2 × CH_3), 25.4, 36.1, 40.9, 68.0 (4 × CH_2), 33.7 (CH), 124.8, 126.0, 133.0, 133.6, 133.7 (5 × =CH), 151.9 (sp^2-C); (minor component): 21.2, 57.8_1 (2 × CH_3), 25.4_6, 37.1, 40.6, 68.0 (4 × CH_2), 34.6 (CH), 125.6, 126.0, 130.4, 132.1, 133.4 (5 × =CH), 154.5 (sp^2-C). Exact Mass calcd. for $C_{13}H_{20}O$: 192.1514; found; 192.1514.

Can. J. Chem. Downloaded from www.nrcresearchpress.com by 203.198.23.82 on 09/08/12
For personal use only.

2-Methyl-exo-*6-methoxymethyltricyclo[5.2.1.0^{1,5}]dec-8-ene (**11**)*

Xylene (50 mL) was heated to reflux under nitrogen with stirring before the slow addition of triene **10** (1.92 g, 10 mmol) in xylene (50 mL) over the course of an hour. Heating under reflux was continued for 24 h before the xylene was removed under vacuum at 45–50°C (bath temperature) to furnish a dark oil. This Diels–Alder product was purified by FC (EtOAc – petroleum ether, 2.5:98.5) to give a 2:1 mixture of the 2-epimers of **11** (1.57 g, 82%) as a faintly yellow liquid, bp 90°C/0.2 Torr (Kugelrohr distillation; 1 Torr = 133.3 Pa); ir ($CHCl_3$): 3035 (=CH), 2820 (OMe), 1450 (C=C) cm^{-1}. ^{1}Hmr ($CDCl_3$) δ: (major epimer): 1.03 (d, 3H, J = 7.0 Hz, 2-Me), 2.70 (m, 1H, H-7), 3.31 (s, 3H, OMe), 3.2–3.35 (m, 2H, CH_2OMe), 6.03 ("t", 1 H, J ca. 6 Hz, H-8), 6.21 (d, 2H, J = 6.1 Hz, H-9); (minor epimer): 0.92 (d, 3H, J = 6.7 Hz, 2-Me), 2.70 (m, 1H, H-7), 3.27 (s, 3H, OMe), 6.08 (m, 2H, H-8,9); ^{13}Cmr ($CDCl_3$) δ: (major epimer): 20.0, 58.8, (2 × CH_3), 25.1, 37.2, 49.3, 75.6 (4 × CH_2), 32.5, 41.2, 46.1, 46.5 (4 × CH), 66.1 (quat C), 136.6, 138.1 (2 × CH=); (minor epimer): 17.2, 58.8 (2 × CH_3), 23.3, 34.8, 42.8, 75.6 (4 × CH_2), 33.3, 41.8, 46.3, 47.5 (4 × CH), 67.5, (quat C), 137.2, 140.3 (2 ×CH=). Exact Mass calcd. for $C_{13}H_{20}O$: 192.1514; found 192.1515.

2-Methyl-exo-*6-methoxymethyltricyclo[5.2.1.0^{1,5}]decan-8-one (**13**)*

To a stirred solution of BH_3·Me_2S (1.14 g, 15 mmol) in THF (30 mL) at 0°C under nitrogen was added 2-methyl-2-butene (2.1 g, 30 mmol) and stirring was continued at 0–10°C for 2 h. To this clear solution of $Siam_2BH$ was slowly added a solution of the tricyclic olefin **11** (0.96 g, 5 mmol) in THF (2 mL) over 20 min. Stirring was continued at 0° to –5°C for 4 h before the reaction mixture was left to stand with stirring overnight without cooling. The mixture was cooled as the excess $Siam_2BH$ was destroyed by the slow addition of cold water (0.4 mL) before the addition of 3 M aqueous NaOH (5 mL). Hydrogen peroxide (30%, 5.0 mL) was then added cautiously at room temperature and the mixture was allowed to stand for 24 h with stirring. After dilution with brine (20 mL), the reaction mixture was extracted with ether (3 × 45 mL). The combined extracts were washed with brine until neutral, 10% aqueous Na_2SO_3 solution (2 × 25 mL), and again with brine until the washings gave a negative peroxide test, before drying over anhydrous $MgSO_4$. Evaporation of the ether gave a viscous oil that was purified by FC (EtOAc – petroleum ether, 40:60) to yield alcohol **12** as a colorless, thick oil (0.81 g, 74%); ir ($CHCl_3$): 3630, 3470 (OH), 3020 (=CH), 2830 (OMe), 1465 (C=C), 1110 (C—O) cm^{-1}; ^{1}Hmr ($CDCl_3$) δ (major epimer): 0.81 (d, 3H, J = 7.0 Hz, 2-Me), 3.1–3.24 (m, 2H, 6-CH_2O-), 3.25 (s, 3H, OMe), 3.85 (m, 1H, H-7); (minor epimer): 0.89 (d, 3H, J = 6.6 Hz, 2-Me); ^{13}Cmr ($CDCl_3$) δ (major epimer): 18.9, 58.6 (2 × CH_3), 23.8, 36.0, 36.4, 41.8, 73.8 (5 × CH_2), 33.6, 40.8, 47.9, 49.1, 75.2 (5 × CH), 58.9 (quat C); (minor epimer): 15.9, 58.6 (2 × CH_3), 22.6, 29.3, 34.4, 43.1, 73.8 (5 × CH_2), 34.3, 41.3, 49.1, 49.8, 75.3 (5 × CH), 60.3 (quat C). Exact Mass calcd. for $C_{13}H_{22}O_2$: 210.1619; found: 210.1623. A solution of **12** (0.21 g, 1 mmol) in CH_2Cl_2 (2 mL) was added to a stirred suspension of PCC (0.322 g, 1.5 mmol), NaOAc (0.028 g, 0.34 mmol), and Celite (300 mg) in CH_2Cl_2 (10 mL). This reaction mixture was stirred for 3.5 h at room temperature before the addition of ether and filtration through a short column of silica. The solvent was then evaporated and the residue purified by Kugelrohr distillation to yield **13** as a 2:1 mixture of 2-epimers (0.197 g, 95%), bp 110–115°C/0.2 Torr; ir ($CHCl_3$): 3040 (=CH), 2820 (OMe), 1740 (C=O), 1105 (C—O) cm^{-1}; ^{1}Hmr ($CDCl_3$) δ (major epimer): 0.86 (d, 3H, J = 7.1 Hz, 2-Me), 3.24 (s, 3H, OMe), 3.2–3.3 (m, 2H, -CH_2O-); (minor epimer): 0.92 (d, 3H, J = 6.5 Hz, 2-Me), 3.24 (s, 3H, OMe); ^{13}Cmr ($CDCl_3$) δ (major epimer): 18.7, 58.5 (2 × CH_3), 24.2, 36.1, 39.1, 46.3, 72.6 (5 × CH_2), 34.5, 39.2, 47.8, 55.7 (4 × CH), 58.9 (quat C), 217.4 (C=O); (minor epimer): 15.6, 58.5, (2 × CH_3), 22.4, 32.8, 33.6, 46.9, 72.6 (5 × CH_2), 34.6, 40.0, 49.2, 55.3 (4 × CH), 60.0 (quat C), 217.5 (C=O). Exact Mass calcd. for $C_{13}H_{20}O_2$: 208.1463; found: 208.1463.

2-Methyl-exo-*6-methoxymethyltricyclo[5.3.1.0^{1,5}]undecan-8-one (**16**)*

A solution of **13** (208 mg, 1 mmol) in THF (1.0 mL) was added under N_2 at –70°C to a stirred solution of LDA (diisopropylamine (172 mg, 1.7 mmol), THF (2.5 mL), and *n*-BuLi (0.58 mL, 5.6 M in hexane) at –70°C, 20 min). Stirring at –70°C was continued for 1 h before the addition of quenching solution prepared by centrifugation of a mixture of TMSCl (333 mg, 3.1 mmol), Et_3N (42 mg, 0.42 mmol), and THF (1.0 mL) in a nitrogen-purged tube. After the reaction mixture was stirred at –70°C for another hour, it was allowed to warm to room temperature and, after 2 h, was diluted with saturated aqueous $NaHCO_3$ solution; the product was extracted with ether (3 × 25 mL). These extracts were washed with brine and then dried over $MgSO_4$. Removal of the solvent afforded a yellow oil that was purified by Kugelrohr distillation to yield colorless **14** as a mixture of 2-epimers (251 mg, 90%): bp 110°C/0.2 Torr; ir ($CHCl_3$): 3060 (=CH), 2820 (OMe), 1625 (C=C), 1105 (C—O), 860 ($SiCH_3$) cm^{-1}; ^{1}Hmr ($CDCl_3$) δ (major epimer): 0.15 (s, 9H, $SiMe_3$), 0.95 (d, 3H, J = 6.6 Hz, 2-Me), 3.30 (s, 3H, OMe), 3.25–3.40 (m, 2H, -CH_2O-), 4.87 (d, 1H, 0.6 Hz, H-9); (minor epimer): 0.15 (s, 9H, $SiMe_3$), 0.90 (d, 3H, J = 6.0 Hz, 2-Me), 3.30 (s, 3H, OMe), 4.68 (d, 1H, J = 0.6 Hz, H-9); ^{13}Cmr ($CDCl_3$) δ (major epimer): 0.0 (3), 19.9, 58.8 (5 × CH_3), 24.9, 36.3, 47.7, 75.4 (4 × CH_2), 33.2, 40.8, 48.9, 50.4, 107.6 (5 × CH), 65.1, 161.7 (2 × C); (minor epimer): 0.0 (3), 16.9, 58.8 (5 × CH_3), 23.1, 34.3, 41.2, 75.4 (4 × CH_2), 33.8, 41.4, 50.1, 50.6, 109.2 (5 × CH), 66.3, 161.9 (2 × C). Exact Mass calcd. for $C_{16}H_{28}O_2Si$: 280.1859; found: 280.1861.

Methylene iodide (456 mg, 1.7 mmol) was added to Zn/Ag couple (195 mg, 3.0 mmol) in ether (1.0 mL) and the mixture was warmed until refluxing occurred without external heating. When refluxing ceased, more ether (0.5 mL) was added and the mixture stirred for 1 h at room temperature. Trimethylsilyl enol ether **14** (280 mg, 1.0 mmol) in Et_2O (1.5 mL) was added and the mixture was heated under gentle reflux overnight. After cooling to 0°C, pyridine (320 mg, 4.05 mmol) and pentane (7.0 mL) were added with vigorous stirring. The precipitate that formed was removed by filtration and washed several times with pentane. The combined washings were concentrated at room temperature to furnish a light yellow oil which, upon FC (Et_2O – petroleum ether, 20:80), gave the cyclopropanated **15** as a colorless oil (237 mg, 81%); ir ($CHCl_3$): 3050 (cyclopropyl CH), 2820 (OMe), 1100 (C—O), 860, 840 (C—O—Si) cm^{-1}; ^{1}Hmr ($CDCl_3$) δ: 0.11 (s, 9H, $SiMe_3$), 0.45–0.95 (m, 3H, cyclopropyl H's), 0.92 (d, 3H, J = 7.0 Hz, 2-Me), 3, .29 (s, 3H, OMe); ^{13}Cmr ($CDCl_3$) δ (major): 0.9 (3), 19.4, 58.5 (5 × CH_3), 10.5$_4$, 24.0, 32.5, 36.6, 74.2$_5$ (5 × CH_2), 22.3, 33.0, 40.2, 47.1, 49.3 (5 × CH), 60.2, 60.7 (2 quat C); (minor): 0.9 (3), 16.5, 58.5 (5 × CH_3), 10.5, 22.2, 25.6, 34.1, 74.3 (5 × CH_2), 24.4, 35.1, 40.3, 46.8, 50.5 (5 × CH), 60.2, 60.6 (2 quat C). Exact Mass calcd. for $C_{17}H_{30}O_2Si$: 294.2015; found: 294.2011.

To a solution of **15** (294 mg, 1.0 mmol) in MeOH (2.1 mL), stirring at 0°C, was added 0.42 mL of 3 M aqueous NaOH solution. Stirring was continued for 3 h before the mixture was allowed to stand in the refrigerator for 24 h. After removal of the methanol at 40°C under vacuum, the mixture was diluted with brine (5 mL) and extracted with ether (4 × 5 mL). The combined extracts were washed with brine before drying over anhydrous $MgSO_4$. Evaporation of the solvent gave a faintly yellow oil, which upon FC (Et_2O – petroleum ether, 40:60) furnished the desired tricyclic ketone **16** (194 mg, 88%) as a 2:1 mixture of the 2-epimers; ir ($CHCl_3$): 1700 (C=O), 1090 (C—O) cm^{-1}; ^{1}Hmr ($CDCl_3$) δ: 0.85 (d, 3H, J = 7.0 Hz, 2-Me), 2.55 (bd, 1H, J = 5 Hz, H-7), 3.22 (s, 3H, OMe), 3.15–3.35 (m, 2H, -CH_2O-); ^{13}Cmr ($CDCl_3$) δ (major epimer): 16.3, 58.5 (2 × CH_3), 25.2, 32.0, 35.4, 36.1, 41.7, 73.1 (6 × CH_2), 40.1, 43.2, 49.8, 57.1 (4 × CH) 53.9 (quat C), 213.2 (C=O); (minor epimer): 14.7, 58.5 (2 × CH_3), 23.3, 33.8, 33.9, 34.7, 36.0, 73.1 (6 × CH_2), 40.9, 44.5, 48.7, 55.6 (4 × CH), 56.1 (quat C), 213.4 (C=O). Exact Mass calcd. for $C_{14}H_{22}O_2$: 222.1620; found: 222.1617.

*2,9,9-Trimethyl-6-methoxymethyltricyclo[5.3.1.0^{1,5}]undecan-8-one (**6**)*

Ketone **16** (222 mg, 1.0 mmol) in Et_2O (1 mL) was added dropwise to a vigorously stirred suspension of $NaNH_2$ (211 mg, 5.4 mmol) in Et_2O (2.5 mL) at room temperature under nitrogen and the mixture was refluxed gently with stirring for 3.5 h before cooling to room temperature. Methyl iodide (0.4 mL, 6.5 mmol) was slowly added and the

Can. J. Chem. Downloaded from www.nrcresearchpress.com by 203.198.23.82 on 09/08/12
For personal use only.

reaction mixture was refluxed overnight with vigorous stirring. After a second addition of methyl iodide (0.14 mL, 2.25 mmol), the mixture was refluxed for an additional 2.5 h before cooling to room temperature. Water (2 mL) was added and the product extracted with ether (3 × 15 mL). The combined extracts were washed with brine and then dried over anhydrous $MgSO_4$. After removal of the solvent, the product was purified by Kugelrohr distillation to yield **6** as a 2:1 mixture of epimers (201 mg, 80%): bp 120–125°C/0.1 Torr; ir ($CHCl_3$): 1700 (C=O), 1105 (C—O) cm^{-1}; ^{1}Hmr ($CDCl_3$) δ (major epimer): 0.85 (d, 3H, J = 7.2 Hz, 2-Me), 1.07 (s, 3H, 9-Me), 1.12 (s, 3H, 9-Me), 3.25 (s, 3H, OMe), 3.15–3.35 (m, 2H, -CH_2O-); (minor): 0.86 (d, 3H, J = 6.5 Hz, 2-Me), 1.07 (s, 3H, 9-Me), 1.12 (s, 3H, 9-Me), 3.24 (s, 3H, OMe); ^{13}Cmr: see Table 3. Exact Mass calcd. for $C_{16}H_{26}O_2$: 250.1933; found: 250.1926.

*Alcohol (**19**)*

A sample of the epimeric mixture **6** (20 mg, 0.08 mmol) in Et_2O (1 mL) was slowly added to a cooled suspension of LAH (10 mg, 0.25 mmol) in Et_2O (2 mL). After the addition, the mixture was stirred at room temperature for 1 h before the cautious addition of a few drops of water to destroy excess LAH. The mixture was acidified with 5% aqueous HCl (2 mL) and the product extracted with ether. The extracts were washed with saturated $NaHCO_3$ solution, brine, and water before drying over anhydrous $MgSO_4$. Evaporation of the ether afforded lightly colored **19** (18.5 mg, 91%); ir (film): 3550 cm^{-1}; ^{1}Hmr ($CDCl_3$) δ: 0.82 (d, 6H, J = 6.8 Hz, 2-Me), 0.990 (s, 6H, 9-Me, major), 1.012 (s, 6H, 9-Me, minor), 3.1–3.3 (m, 4H, 2 × -CH_2O-), 3.28 (s, 6H, 2 ×MeO), 3.45 (m, 2H, 2 × -CH(OH)-); ^{13}Cmr: see Table 3. Exact Mass calcd. for $C_{16}H_{28}O_2$: 252.2089; found: 252.2094.

*2,9,9-Trimethyl-6-methylenetricyclo[5.3.1.0^{1,5}]undecan-8-one (**20**)*

Sodium iodide (270 mg, 1.8 mmol) was added to a solution of the epimeric mixture **6** (433 mg, 1.7 mmol) in dry acetonitrile (10 mL) under argon. A solution of trimethylsilyl chloride (0.7 mL, 600 mg, 5.4 mmol) in CH_3CN (0.7 mL) was very slowly added with stirring. As the reaction proceeded a yellow color developed and gradually intensified. The progress of the reaction was monitored at 0.5 h intervals by tlc and, after 3 h, the starting material had been consumed. The reaction mixture was diluted with water and extracted with ether. The combined extracts were washed with 10% aqueous $NaHCO_3$ solution, 10% sodium thiosulfate solution, water, and brine before drying over $MgSO_4$. Removal of the solvent gave a crude product that was purified by FC (Et_2O – hexane, 20:80) to give the expected 6-iodomethylene derivative (395 mg, 67%) and the analogous alcohol (80 mg. 20%), both as 2:1 epimeric mixtures. These were identified by ^{13}Cmr; the spectrum of the iodides had distinctive signals near δ_C 8 for the -CH_2I groups.

*2-Methyl-6-iodomethyl-**4***: ir (film): 1705 cm^{-1}; ^{1}Hmr ($CDCl_3$) δ: 0.85 (d, 3H, J = 6.7 Hz, 2-Me minor), 0.88 (d, 3H, J = 7.0 Hz, 2-Me major), 1.121 (s, 6H, 9-Me), 1.165 (s, 6H, 9-Me), 3.0–3.3 (m, 6-CH_2I); ^{13}Cmr ($CDCl_3$) δ (major epimer): 16.4, 31.5$_1$, 31.5$_4$ (3 × CH_3), 8.2$_7$, 24.7, 35.8, 37.9, 46.5 (5 × CH_2), 41.4, 47.8, 50.0, 59.7 (4 × CH), 42.2, 55.5 (2 × C), 217.1 (C=O); (minor epimer): 14.6, 31.3, 31.4$_6$ (3 × CH_3), 8.2$_3$, 23.3, 30.3, 33.1, 42.2 (5 × CH_2), 41.3, 48.8, 49.9, 58.4 (4 × CH), 42.5, 57.1 (2 × C), 217.4 (C=O).

*2-Methyl-6-hydroxymethyl-**4***: ir (film): 1703, 3443 cm^{-1}; ^{1}Hmr ($CDCl_3$) δ: 0.874 (d, 3H, J = 7.1 Hz, 2-Me major), 0.886 (d, 3H, J = 6.6 Hz, 2-Me minor) 1.107 (s, 6H, 9-Me), 1.155 (s, 6H, 9-Me), 3.4–3.7 (m, -CH_2O-); ^{13}Cmr ($CDCl_3$) δ (major epimer): 16.3, 31.4, 31.5 (3 × CH_3), 24.8, 35.9, 38.4, 46.8, 63.4 (5 × CH_2), 40.9, 46.6, 48.3, 55.8 (4 × CH), 42.2, 54.8 (2 × C), 218.7 (C=O); (minor epimer): 14.6, 31.2, 31.3 (3 × CH_3),23.3, 30.8, 33.2, 49.1, 63.1 (5 × CH_2), 40.9, 47.6, 48.2, 54.6 (4 × CH), 42.5, 56.6 (2 × C), 219.0 (C=O).

Under dry nitrogen, a 1 M solution of potassium *tert*-butoxide in anhydrous *tert*-butyl alcohol (2 mL) was added to the mixture of iodides (312 mg, 0.9 mmol) and the solution was stirred at 50°C for 2 h, after which time tlc indicated that the iodide had been consumed. The mixture was diluted with water and the product extracted with ether. The combined extracts were washed with cold water until neutral, then with brine before drying over $MgSO_4$. Evaporation of the solvent afforded a colorless oil (184 mg, 94%) that gave ^{13}Cmr spectra (Table 3) that were identical to those obtained for **20**, isolated from the neutral homoenolization product; ir (liquid film): 1700 cm^{-1}; ^{1}Hmr ($CDCl_3$) δ: 0.849 (d, 3H, J = 7.0 Hz, 2-Me major), 0.857 (d, 3H, J = 6.7 Hz, 2-Me minor), 1.064 (s, 6H, 9-Me), 1.096 (s, 6H, 9-Me), 4.80 and 5.05 (multiplets, =CH_2). Exact Mass calcd. for $C_{15}H_{22}O$: 218.1671; found: 218.1674.

Homoenolization experiments

Our standard procedures for homoenolization experiments (32) were followed as outlined for **6**. To a solution of *t*-BuO–/*t*-BuOH (1.27 M, H_2O content <250 μg/mL) was added **6**, to obtain a solution that was 0.26 M in ketone. Aliquots (0.35 mL) were transferred to a series of 5-mL predried, thick-walled glass tubes; these tubes were then degassed and sealed before immersion in a Blue M constant high-temperature oil-bath at 185 ±1°C. These tubes were removed after intervals of several hours, cooled before opening, and the contents collected by washing with water and pentane. The neutral organic products were isolated by pentane extraction (3 × 15 mL) and the combined extracts dried over anhydrous magnesium sulfate. The aqueous layer was acidified with 10% aqueous HCl solution (10 mL) before ether extraction (3 × 15 mL) to recover any acidic organic products. The combined ether extracts were dried over magnesium sulfate.

To identify the acidic products, the oily residue obtained upon removal of the ether was examined by ^{13}Cmr. These data led to structure **22**, as described in the text; ^{1}Hmr ($CDCl_3$) δ (major epimer): 0.878 (d, 3H, J = 6.4 Hz, 6-Me), 1.148 (s, 3H, 2′-Me), 1.18 (s, 3H, 2′-Me), 1.56 (bs, 3H, 2-Me), δ1.47 (m, 1H, H-6), 1.417 (d, 1H, J = 14.6, Hz, H-1′), 1.887 (d, 1H, J = 14.6 Hz, H-1′), 2.01 (dm, 1H, J = 16.5 Hz, H-4), 2.199 (dm, 1H, J = 16.5 Hz, H-4), 2.56 (bd, 1H, J δ 9 Hz, H-1), 4.94 (m, 1H, H-3); (minor epimer): 0.837 (d, 3H, J = 6.6 Hz, 6-Me), 1.18 (s, 3H, 2′-Me), 1.206 (s, 3H, 2′-Me), 1.56 (bs, 3H, 2-Me), δ 1.67 (m, 1H, H-6), 1.711 (d, 1H, J = 14.7 Hz, H-1′), 1.968 (d, 1H, J = 14.7 Hz, H-1′), 1.819 (dm, 1H, J = 17 Hz, H-4), 2.219 (dm, 1H, J = 17 Hz, H-4), 2.61 (bd, 1H, J δ 9 Hz, H-1), 5.06 (m, 1H, H-3); ^{13}Cmr: see Table 4. Exact Mass calcd. for $C_{15}H_{24}O_2$: 236.1776; found: 236.1770.

*3,3,8,11-Tetramethyl[3.3.3]propell-8-en-2-one (**25**)*

The neutral product exhibiting the shortest retention time on glc analysis was assigned structure **25** as discussed in the text; ir (liquid film): 1730 cm^{-1}; ^{1}H and ^{13}Cmr data are listed in Table 5. Exact Mass calcd. for $C_{15}H_{22}O$: 218.1671; found: 218.1670.

*2,6,9,9-Tetramethyltricyclo[5.3.1.0^{1,5}]undec-5-en-8-one (**21**)*

The second band found by glc analysis was assigned structure **21** as discussed in the text; ir (liquid film): 1701 cm^{-1}; ^{1}Hmr ($CDCl_3$) δ: 0.86 (d, 3H, J = 7.0 Hz, 2-Me minor), 0.88 (d, 3H, J = 6.5 Hz, 2-Me major), 1.12 (s, 6H, 9-Me), 1.13 (s, 6H, 9-Me), 1.56 (bs, 3H, 6-Me major), 1.57 (bs, 3H, 6-Me minor), 2.95 (bm, 1H, H-7); the ^{13}Cmr data are collected in Table 3. Exact Mass calcd. for $C_{15}H_{22}O$: 218.1671; found: 218.1674.

*2,6-Dimethyl-5-(3′-hydroxy-2′,2′-dimethylpropyl)bicyclo[3.3.0]oct-2-ene (**24**)*

The fourth glc band was found to contain a mixture of alcohols that was shown to be **24** as noted in the text; ir (liquid film): 3355 cm^{-1}; ^{1}Hmr ($CDCl_3$) δ: 0.85 (d, 3H, J = 6.2 Hz, 6-Me minor), 0.87 (d, 3H, J = 6.6 Hz, 6-Me major), 0.927 (s, 12H, 2′-Me), 1.61 (bs, 6H, 2-Me), 5.03 (m, 1H, H-3 minor), 5.15 (m, 1H, H-3 major); ^{13}Cmr: see Table 4. Exact Mass calcd. for $C_{15}H_{26}O$: 222.1981; found: 222.1981.

*3,3,11-Trimethyl-7-methoxymethyltricyclo[6.3.0.0^{1,5}]undecan-4-one (**7**)*

The fifth glc band was assigned structure **7** on the basis of its physical data; ir (liquid film): 1730 cm^{-1}; ^{1}Hmr: see text; ^{13}Cmr: see Table 2. Exact Mass calcd. for $C_{16}H_{26}O_2$: 250.1933; found: 250.1935.

Acknowledgements

We are grateful for the continued financial support of the Natural Sciences and Engineering Research Council of Canada and acknowledge the assistance of Dr. S. Peiris with preliminary examination of the β-enolization step. We thank Professor E.W. Warnhoff for valuable discussion and comments.

1. T. Hudlicky, G. Sinai-Zingde, M.G. Natchus, B.C. Ranu, and P. Papadopolous. Tetrahedron, **43**, 5685 (1987), and references therein.
2. Y. Ohfune, H. Shirahama, and T. Matsumoto. Tetrahedron Lett. 2869 (1976).
3. L.H. Zalkow, R.N. Harris, D. Van Derveer, and J.A. Bertrand. J. Chem. Soc. Chem. Commun. 456 (1977).
4. D.E. Cane and A.M. Tillman. J. Am. Chem. Soc. **105**, 122 (1983); D.E. Cane, J.S. Oliver, P.H.M. Harrison, C. Abell, B.R. Hubbard, C.T. Kane, and R. Lattman. J. Am. Chem. Soc. **112**, 4513 (1990).
5. Y-J. Wu and D.J. Burnell. J. Chem. Soc. Chem. Commun, 764 (1991); S. Zhao, G. Mehta, and P. Helquist. Tetrahedron Lett. **32**, 5753 (1991), and references therein.
6. L.H. Zalkow, R.N. Harris, and D. Van Derveer. J. Chem. Soc. Chem. Commun. 420 (1978).
7. L. Fitjer, A. Kanschik, and M. Majewski. Tetrahedron Lett. **29**, 5525 (1988), and references therein.
8. G.K. Sha, T-S. Jean, and D.C. Wang. Tetrahedron Lett. **31**, 3745 (1990), and references therein.
9. B.A. Dawson, A.K. Ghosh, J.L. Jurlina, A.G. Ragauskas, and J.B. Stothers. Can. J. Chem. **62**, 2521 (1984).
10. J.L. Jurlina, H.A. Patel, and J.B. Stothers. Can. J. Chem. **62**, 1159 (1984).
11. A.G. Fallis. Can. J. Chem. **62**, 183 (1984).
12. F. Sondheimer and R.B. Woodward. J. Am. Chem. Soc. **75**, 5438 (1953).
13. W. Reppe and Mitarbeiter. Liebigs Ann. Chem. **596**, 1 (1955).
14. Y. Yamaguchi, Y. Nobayashi, and I. Hirao. Tetrahedron Lett. 5121 (1983).
15. E.G. Breitholle and A.G. Fallis. J. Org. Chem. **43**, 1964 (1978).
16. E.J. Corey and J.W. Suggs. Tetrahedron Lett. 2647 (1975).
17. V. Patel, A.J. Ragauskas, and J.B. Stothers. Can. J. Chem. **64**, 1440 (1986).
18. N.H. Werstiuk. Tetrahedron, **39**, 205 (1983).
19. W. Sifton, J.B. Stothers, and S.E. Thomas. Can. J. Chem. **70**, 1274 (1992).
20. G.A. Olah, S.C. Narang, B.G.B. Gupta, and R. Malhotra. J. Org. Chem. **44**, 1247 (1979).
21. J.B. Stothers, J.R. Swenson, and C.T. Tan. Can. J. Chem. **53**, 581 (1975).
22. J.K. Whitesell and M.A. Minton. Stereochemical analysis of alicyclic compounds by C-13 nmr spectroscopy. Chapman and Hall, London. 1987. pp. 137–147.
23. W.F. Reynolds, S. McLean, M. Perpick-Dumont, and R.G. Enriquez. Magn. Reson. Chem. **27**, 162 (1989).
24. J.L. Jurlina, H.A. Patel, S. Peiris, and J.B. Stothers. Magn. Reson. Chem. **25**, 109 (1987).
25. A. Nickon and J.B. Lambert. J. Am. Chem. Soc. **84**, 4604 (1962); **88**, 1905 (1966).
26. R. Howe and S. Winstein. J. Am. Chem. Soc. **87**, 915 (1965); T. Fukunaga. J. Am. Chem. Soc. **87**, 917 (1965); T. Fukunaga and R.A. Clement. J. Org. Chem. **42**, 270 (1977).
27. A.K. Cheng, A.K. Ghosh, and J.B. Stothers. Can. J. Chem. **62**, 1385 (1984).
28. G.A. Antoniadis, M.T. Clements, S. Peiris, and J.B. Stothers. Can. J. Chem. **65**, 1557 (1987).
29. F.D. Coms and D.A. Dougherty. J. Am. Chem. Soc. **111**, 6894 (1989); W. Adams, H. Platsch, and J. Wirz. J. Am. Chem. Soc. **111**, 6896 (1989).
30. M.L. Steigerwald, W.A. Goddard III, and D.A. Evans. J. Am. Chem. Soc. **101**, 1994 (1979).
31. W.C. Still, M. Kahn, and A. Mitra. J. Org. Chem. **43**, 2923, (1978).
32. A.L. Johnson, J.B. Stothers, and C.T. Tan. Can. J. Chem. **53**, 212 (1975).
33. D.J. Muir and J.B. Stothers. Can. J. Chem. **71**, 1290 (1993).

Can. J. Chem. Downloaded from www.nrcresearchpress.com by 203.198.23.82 on 09/08/12
For personal use only.

Some routes to C2-alkoxymethyl hex-2-enopyranosides[1]

GORDON WONG AND BERT FRASER-REID[2]

Paul M. Gross Chemical Laboratory, Duke University, Durham, NC 27708, U.S.A.

Received February 22, 1993

This paper is dedicated to Professors David B. MacLean and Ian Spenser

GORDON WONG and BERT FRASER-REID. Can. J. Chem. **72**, 69 (1994).

Several procedures for installing a C2 alkoxy group at C2 of a hex-2-enopyranoside have been investigated. The one that is most convenient for large-scale preparation begins with a 2-keto pyranoside, which is converted into the corresponding *exo* methylene derivative. An S_N2' rearrangement is effected with thionyl chloride, and the resulting primary allylic chloride is displaced with sodium benzylate.

GORDON WONG et BERT FRASER-REID. Can. J. Chem. **72**, 69 (1994).

On a examiné diverses méthodes d'introduire un groupe alcoxyle en position C2 d'un hex-2-énopyranoside. Celle qui semble la plus appropriée pour des préparations sur une haute échelle fait appel à un 2-cétopyranoside qui est transformé en dérivé exométhylène correspondant. On effectue ensuite un réarrangement S_N2' à l'aide du chlorure de thionyle avant de déplacer le chlorure allylique primaire qui en résulte avec du benzylate de sodium.

[Traduit par la rédaction]

A recent report from our laboratory described a route to the *trans*-decalin core, symbolized by **1***a*, via an intramolecular Diels–Alder (IMDA) reaction of a hex-2-enopyranoside of type **2** (1). This approach to **1** seemed attractive since all of the functional groups represented by labels **A** → **G** could be installed in, or derived from, precursor **2** (1). The success of the early venture, with preparation of a key intermediate for forskolin (1), prompted us to explore more expeditious methods for obtaining **2**. Use of a normal hexose precursor would require attaching carbon substituents at C1 and C2 of the pyranose precursor. In the reported synthesis (1), the latter had proved to be more problematic, and we therefore examined alternative methods. In doing so we have been mindful that in many naturally occurring terpenes the angular C19 methyl group, which corresponds to the C2 substituent of **2**, is functionalized (3) and hence provisions for this possibility ought to be made. The alkoxymethyl analog **2***b* was conceived as a valuable synthon. Its precursor would be alkene **3***b*. In this manuscript, we describe our efforts to prepare alkenes related to **3***b*.

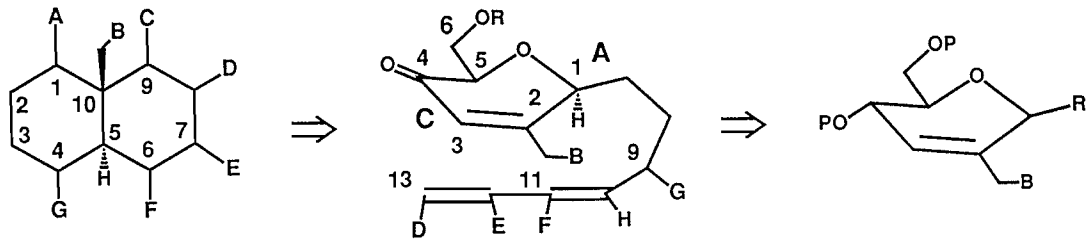

1
a B= H
b B= OR'
Terpenoid numbering

2
a B= H
b B= OR'
Sugar numbering

3
a B= H
b B= OR'

In our recent work (1), the Corey–Winter reductive elimination strategy (3) had proven to be the method of choice for the preparation of C2-CH_3 alkenes of type **3***a*. Accordingly, our initial approaches to the alkoxymethyl analog **3***b* were undertaken with this reaction in mind. A particularly encouraging feature of the prototype study was the fact that the Corey–Winter reaction had succeeded with both diastereomeric *cis*- and *trans*-diol precursors of **3***a* (1). In the light of this precedent, the known uloside **4***a* (4), seemed a plausible starting material whose reaction with an alkoxymethyl anion would provide the required C2-functionalized carbon.

Benzyloxymethyl magnesium chloride (5) was tested first, but problems were encountered with its preparation from commercially available benzyloxymethyl chloride and also with its lack of stability. The lithio analog, obtained most conveniently by treating benzyloxymethyl tributylstannane with butyllithium as described by Still (6) was successful, giving the expected adduct **5***a* along with substantial amounts of the product from silyl migration, both of which underwent desilylation without event to give **5***b* in 74% overall yield. A more direct route to **5***b* arose from addition of an excess of the benzyloxymethyllithium to the known 3-*O*-acetyl uloside **4***b* (7).

In contrast to the previously described (2) results for the C2-CH_3 analog **3***a*, treatment of **5***b* with thiocarbonyl diimidazole gave nearly equal amounts of the corresponding thionocarbonate **8** and its uncyclized precursor, which could be partially pro-

[1]This paper is dedicated to Professors Dave MacLean and Ian Spenser with grateful thanks for their many kindnesses and help when one of us (B.F.R) was at the then fledgling University of Waterloo.

[2]Author to whom correspondence may be addressed.

Can. J. Chem. Downloaded from www.nrcresearchpress.com by 195.246.54.202 on 09/08/12
For personal use only.

Can. J. Chem. Downloaded from www.nrcresearchpress.com by 195.246.54.202 on 09/08/12
For personal use only.

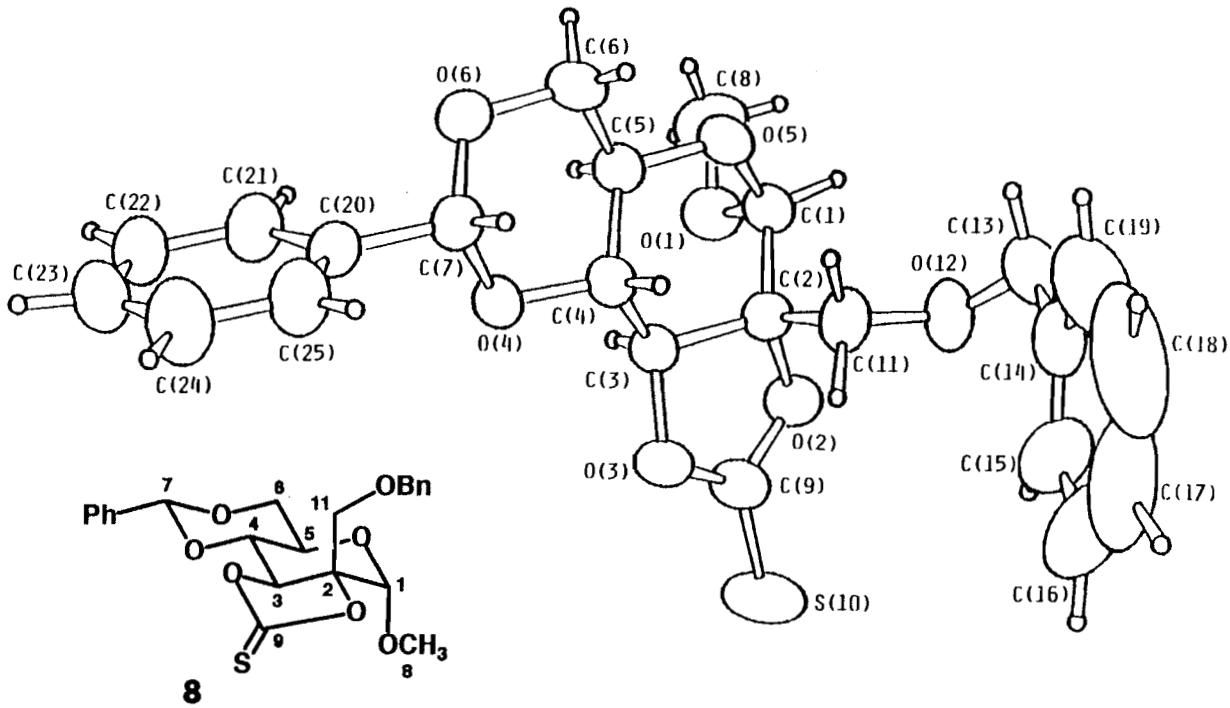

FIG. 1.ORTEP diagram (50% probability ellipsoids) showing the crystallographic atom numbering scheme and solid-state conformation of **8**. Small circles represent hydrogen atoms.

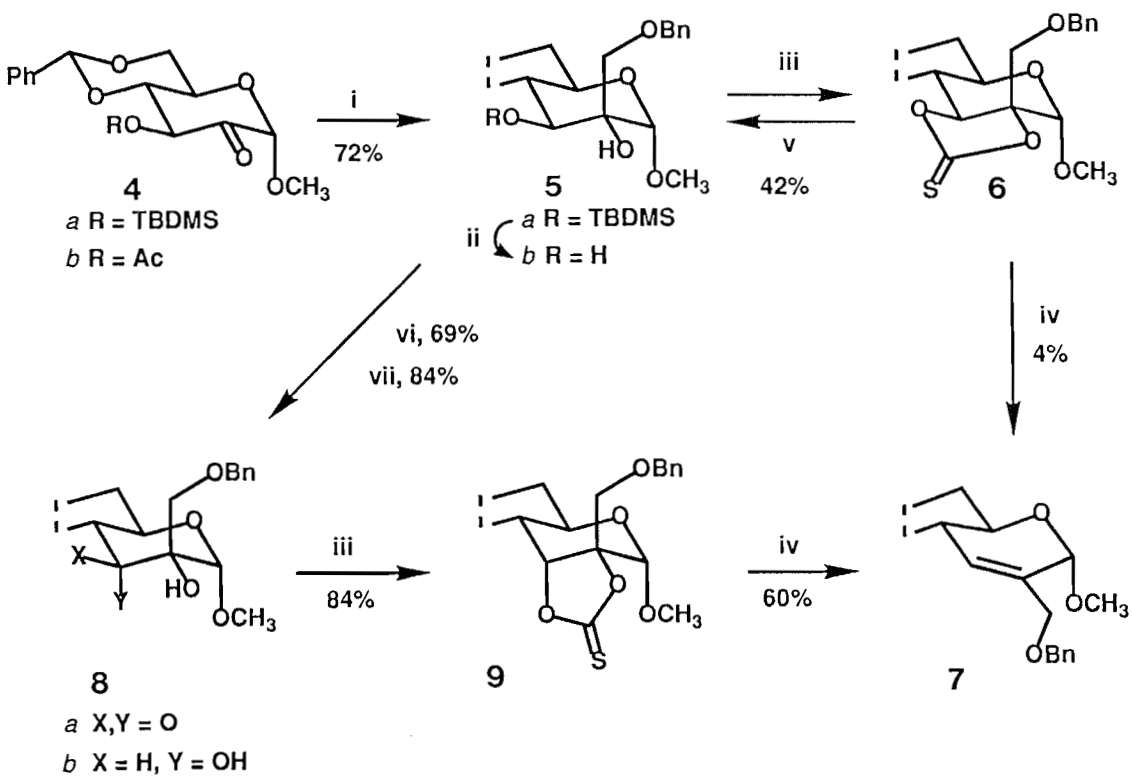

(i) Bu_3SnCH_2OBn, *n*BuLi, THF; (ii) TBAF,THF; (iii) $(im)_2C{=}S$, toluene; (iv) $P(OMe)_3$
(v) 1,3-dimethyl-2-phenyl-1,2-diazaphospholidene; (vi) Dess-Martin periodinane,CH_2Cl_2; (vii) $NaBH_4$, MeOH

SCHEME 1

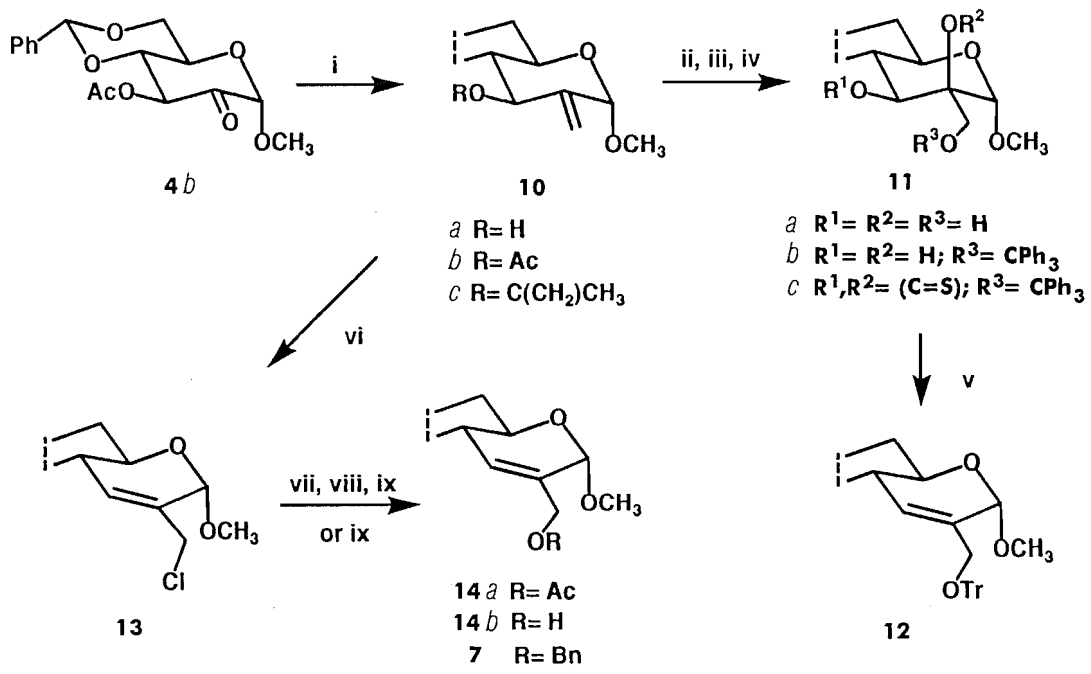

(i) Cp_2TiCl_2 $AlMe_3$ gave **10***a* (75%), **10***b* (10%), **10***c* (5%); (ii) OsO_4, Et_4NOH, *t*-BuOOH, *t*-BuOH, THF, 30%; (iii) TrCl, DMAP, pyridine, 80%; (iv) NaH, CS_2, nBu_4NI CH_3I, 88%; (v) $P(OMe)_3$, 59%; (vi) $SOCl_2$, pyridine, THF; (vii) KOAc, HMPA, 51% from **10***b*; (viii) NaOMe, 64%; (ix) NaH, BnBr, THF, 81%; (x) NaOH, Bu_4NHSO_4, BnOH, CH_2Cl_2/water 19:1, ultrasound 4 days, 54% from **10***b*.

SCHEME 2

cessed to give **8** by prolonged treatment in toluene under reflux. The structure **8** was confirmed by the X-ray crystal structure shown in Fig. 1.[3]

By comparison with the corresponding C2-CH_3 analogue used earlier (2), the reaction of **8** was disappointing in that treatment with trimethylphosphite gave the desired alkene **10** in only 4% yield. Use of 1,3-dimethyl-2-phenyl-1,2-diazaphospholidene as recommended by Corey and Hopkins (8) was even more discouraging in that the only course of reaction with this reagent was regeneration of diol **5***b*.

There should be fewer problems with formation and reaction of this *cis*-fused thionocarbonate and hence the diol **5***b* was processed with this objective in mind. Oxidation to ketone **11***a* was best effected with the Dess–Martin reagent (9) and sodium borohydride reduction led to **11***b* without event. As expected, the thionocarbonate **12** was now obtained without complication, and reductive elimination to **10** proceeded in 60% yield. Thus although it involves one more step, the route via **12** was slightly higher yielding overall, and much easier operationally than that via **8**.

The results with **8** and **12** showed that the *cis*-fused thionocarbonate better underwent reductive elimination, in spite of the lack of preference that we had found in the earlier work (1). It was therefore of interest to see how the alternative *cis* analog (i.e., the *manno* counterpart) would fare. A C2-*exo* methylene derivative was seen as a plausible precursor since dihydroxylation should occur from the ß face.

Some deacetylation would be expected to accompany olefination of **4***b* with methylenetriphenylphosphorane, and hence an alternative route was examined. Tebbe's reagent (10) reacts with the carbonyl groups of ketones and esters, but the enol ether resulting from the latter would be readily hydrolysed. In the event, the best procedure turned out to be to treat **4***b* with 2.5 equivalents of Tebbe's reagent, which gave the allylic alcohol **10***a* as the major product and the corresponding acetate **10***b* as the minor. A third product, obtained in 4% yield, was assigned as the enol ether **10***c* since it decomposed to **10***a* on standing.

Dihydroxylation of **10***a* gave the triol **11***a*, which was processed to give the thionocarbonate **11***c*. Reductive elimination to **12** proceeded in virtually the same yield (59%) as had the diastereomer **9**.

The allylic alcohol **10***a* offered yet another alternative route to the desired alkene via S_N2' rearrangement. Indeed this was accomplished by treating **10***a* with thionyl chloride to give the 2-alkene **13**. Acetolysis then afforded **14***a* in 50% overall yield from **10***a*. Saponification to **14***b*, followed by benzylation, then gave the previously described alkene **7**. Alternatively, alkene **7** could be obtained directly from the chloride **13** in a yield of 54% by a process involving nucleophilic displacement with benzylate ion under phase transfer conditions (11).

In summary, four routes to the generalized hex-2-enopyranoside **3***b* have been examined: (*i*) **4***a* → **5** → **8** → **9** → **7**; (*ii*) **4***b* →

[3]Crystallographic data for **1** have been deposited and can be purchased from: The Depository of Unpublished Data, Document Delivery, CISTI, National Research Council Canada, Ottawa, ON K1A 0S2, Canada.

The ORTEP diagram, crystallographic data, tables of H-atom coordinates and of bond lengths and angles for **1** have also been deposited with the Cambridge Crystallographic Data Centre, and can be obtained on request from The Director, Cambridge Crystallographic Data Centre, University Chemical Laboratory, 12 Union Road, Cambridge, CB2 1EZ, U.K.

Can. J. Chem. Downloaded from www.nrcresearchpress.com by 195.246.54.202 on 09/08/12
For personal use only.

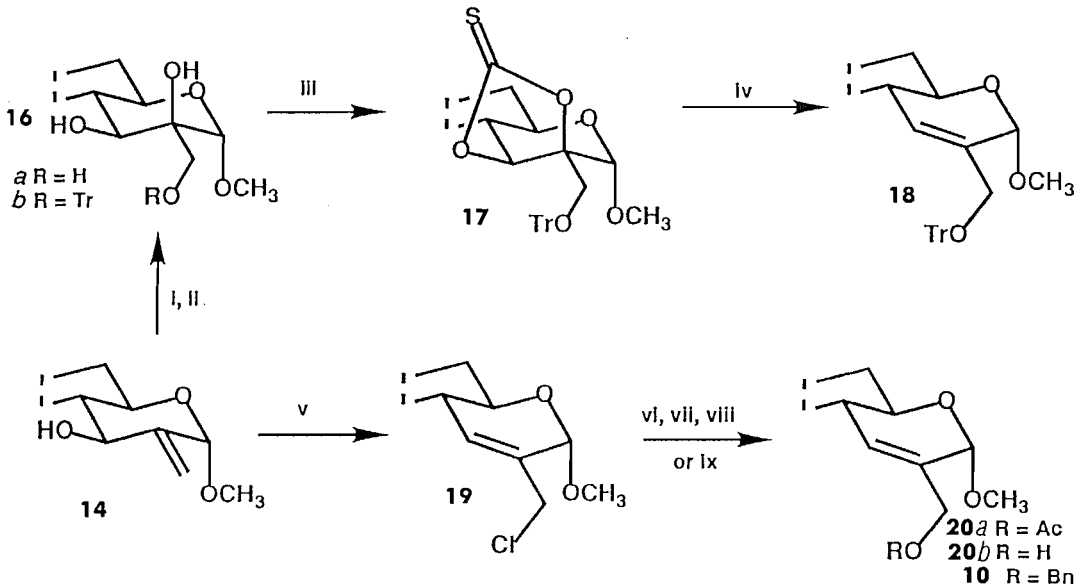

(i) OsO_4, Et_4NOH, *t*-BuOOH, *t*-BuOH, THF, 30%; (ii) TrCl, DMAP, pyridine, 80%; (iii) NaH, CS_2, nBu_4NI CH_3I, 88%; (iv) $P(OMe)_3$, 59%; (v) $SOCl_2$, pyridine, THF; (vi) KOAc, HMPA, 51% from **13**; (vii) NaOMe, 64%; (viii) NaH, BnBr, THF, 81%; (ix) NaOH, Bu_4NHSO_4, BnOH, CH_2Cl_2/water 19:1, ultrasound 4 days, 54% from **13**.

SCHEME 3

10 → **11** → **12**; (*iii*) **4***b* → **13** → **14** → **7**; and (*iv*) **4***b* → **13** → **7**. The last is the most direct but, for large-scale preparations, the need for prolonged ultrasonication could present practical problems and, in such cases, route (*iii*) may be more attractive, particularly since the intermediates are crystalline. Routes (*i*) and (*ii*) are seen as second choices to (*iv*) and (*iii*), respectively.

Experimental

*Methyl 4,6-*O*-benzylidene-2-*C*-benzyloxymethyl-*α*,*D*-glucopyranoside* **5**b*, and its 3-*O*-tert-butyldimethysilymethyl derivative* **5**a

To (benzyloxymethyl)tributylstannane (7) (1.30 g, 3.16 mmol) and two crystals of 2,2-dipyridyl in dry THF (10 mL), cooled to –78°C under a stream of argon, was added *n*BuLi (1.35 mL, 2.06 M in hexane, 2.79 mmol) dropwise with stirring. The appearance of a red color indicated an excess of *n*BuLi; a few drops of the stannane were then added to dissipate the color. After stirring for 20 min, a cooled solution (–78°C) of ketone **4***a* (5) (714 mg, 1.81 mmol) in dry THF (10 mL) was added by cannula and stirring was continued for 1 h. The reaction was quenched by the addition of brine and diluted with ether, warmed to room temperature, and separated. The aqueous layer was extracted with ether (×2) and the combined extracts were washed with brine and dried over anhydrous Na_2SO_4. Flash chromatography (2–15% EtOAc –petroleum ether) gave **5***a* (674 mg, 72%) and the product of silyl migration (12%) as oils. For **5***a*: R_f 0.40 (20% EtOAc –petroleum ether); $[\alpha]_D^{20}$ +9.3 (*c* 1.00, $CHCl_3$); ^1H NMR (300 MHz, $CDCl_3$) δ: 0.03, 0.06 (s, 6H, $(CH_3)_2Si$), 0.82 (s, 9H, $(CH_3)_3CSi$), 2.69 (s, 1H, OH), 3.44 (s, 3H, OCH_3), 3.45 (d, 1H, *J* = 9.6 Hz, C*H*′HOBn), 3.65–3.85 (m, 4H, H4, H5, H6a, O*H*′HOBn), 4.01 (d, 1H, $J_{3,4}$ = 9.5 Hz, H3), 4.26 (dd, 1H, $J_{5,6e}$ = 4.2 Hz, $J_{6a,6e}$ = 9.5 Hz, H6e), 4.59, 4.63 (d, 2H, *J* = 12.4 Hz, PhCH_2O), 4.90 (s, 1H, H1), 5.46 (s, 1H, PhC*H*), 7.30–7.50 (m, 10 H, aromatic). ^{13}C NMR δ: 18.4, 25.9 (TBDMS), 55.6 (q, OCH_3), 62.5 (d, C5), 69.0 (t, Ph*C*H_2), 69.1 (t, C6), 73.8 (t, *C*H_2OCH_2Ph), 76.0 (s, C2), 80.7 (d, C4), 100.7 (d, C1), 101.7 (d, Ph*C*H), 126.1–137.9 (aromatic). MS *m/z*: 516 (M^+). Anal. calcd. for $C_{28}H_{40}O_7Si$: C 65.07, H 7.82; found: C 64.88, H 7.81.

*Methyl 4,6-*O*-benzylidene-2-*C*-benzyloxymethyl-*α*,*D*-glucopyranoside* **5**b

(*a*) Compound **5***a* (292 mg, 0.57 mmol) in dry THF (35 mL) was stirred with tetra-*n*-butylammonium fluoride (0.68 mL, 1.0 M in THF, 0.68 mmol) overnight. Evaporation of the solvent and flash chromatography (20–70% EtOAc –petroleum ether) gave **5***b* (200 mg, 88%) as an oil: R_f 0.48 (70% EtOAc – petroleum ether); $[\alpha]_D^{20}$ +27.3 (*c* 1.00, $CHCl_3$); ^1H NMR (300 MHz, $CDCl_3$) δ: 2.82, 2.97 (s, 2H, OH), 3.44 (s, 3H, OCH_3), 3.51 (t, $J_{3,4} = J_{4,5}$ = 9.9 Hz, H4), 3.71, 3.87 (d, 2H, *J* = 10.0 Hz, CH_2OBn), 3.71 (t, 1H, $J_{5,6a} = J_{6a,6e}$ = 9.9 Hz, H6a), 3.83 (td, 1H, $J_{5,6e}$ = 4.4 Hz, H5), 4.09 (d, 1H, H3), 4.25 (dd, 1H, H6e), 4.59, 4.62 (d, 2H, *J* = 12.0 Hz, PhCH_2), 4.80 (s, 1H, H1), 5.47 (s, 1H, Ph C*H*), 7.30–7.50 (m, 10H, aromatic). ^{13}C NMR δ: 55.8 (q, OCH_3), 62.8 (d, C5), 69.0 (t, C6), 69.4 (t, Ph*C*H_2), 72.9 (d, C3), 74.0 (t, *C*H_2OBn), 75.5 (s, C2), 79.7 (d, C4), 100.5 (d, C1), 102.1 (d, Ph*C*H), 126.4–137.5 (aromatic). MS *m/z*: 402 (M^+). Anal. calcd. for $C_{22}H_{26}O_7$: C 65.65, H 6.52; found: C 65.43, H 6.54.

(*b*) Compound **6** (13 mg, 0.03 mmol) in 1,3-dimethyl-2-phenyl-1,3-diazaphospholidine (18 mg, 0.09 mmol) was stirred under a stream of argon at 40°C for 12 h. Flash chromatography (30–50% EtOAc – petroleum ether) gave diol **5***b* (5 mg, 42%).

*Methyl 4,6-*O*-benzylidene-2-*C*-benzyloxymethyl-2,3-*O*-thionocarbonyl-*α*,*D*-glucopyranoside* **6**

Diol **5***b* (98 mg, 0.24 mmol) and 1,1′-thiocarbonyldiimidazole (90 mg, 0.51 mmol) in toluene (4 mL) were heated to reflux under a stream of argon for 12 h. Evaporation of the solvent and flash chromatography (10–70% EtOAc – petroleum ether) gave **6** (57 mg, 53%) as a white solid and the uncyclized, C-3 imidazoyl-*N*-thionocarbonyl derivative (44%) as an oil. For **6**: R_f 0.29 (30% EtOAc – petroleum ether); $[\alpha]_D^{20}$ –9.6 (*c* 1.00, $CHCl_3$); mp 158°C (recrystallized from methylene chloride – petroleum ether). ^1H NMR (300 MHz, $CDCl_3$)δ 3.51 (s, 3H, OCH_3), 3.68–3.72 (m, 4 H, H4, H6a, CH_2OBn), 4.02–4.10 (m, 1H, H5), 4.21–4.30 (m, 1H, H6e), 4.57, 4.64 (d, 2H, *J* = 12.2 Hz, PhCH_2O), 5.06 (d, 1H, $J_{3,4}$ = 11.0 Hz, H3), 5.07 (s, 1H, H1), 5.50 (s, 1H, PhC*H*), 7.30–7.50 (m, 10H, aromatic). ^{13}C NMR δ: 56.4 (q, OCH_3), 66.4 (d, C5), 68.3 (t, Ph*C*H_2), 69.0 (t, C6), 74.2 (t, *C*H_2OBn), 77.5 (d, C3), 79.8 (d, C4), 87.4 (s, C2), 98.5 (d, C1), 101.4 (d, Ph*C*H), 126.0–136.9 (aromatic), 190.2 (s, C=S). Structure confirmed by X-ray crystallography.

*Methyl 4,6-*O*-benzylidene-2-*C*-benzyloxymethyl-*α*,*D*-*erythro*-hex-2-enopyranoside* **7**

(*a*) Thionocarbonate **6** (32 mg, 0.07 mmol) was dissolved in trimeth-

Can. J. Chem. Downloaded from www.nrcresearchpress.com by 195.246.54.202 on 09/08/12
For personal use only.

Can. J. Chem. Downloaded from www.nrcresearchpress.com by 195.246.54.202 on 09/08/12
For personal use only.

ylphosphite (3 mL) and heated to reflux under a stream of argon for 12 h. Evaporation of the solvent and flash chromatography (0–20% EtOAc – petroleum ether) gave **7** (1 mg, 4%) as a white solid: R_f 0.56 (20% EtOAc – petroleum ether); $[\alpha]_D^{20}$ +84.7 (*c* 0.71, $CHCl_3$); mp 110°C. ^{1}H NMR (300 MHz, CDl_3) δ: 3.43 (s, 3H, OCH_3), 3.77–3.96 (m, 3H, H5, H6a, C*H*$_2$OBn), 4.10–4.22 (m, 2H, H4, CH_2OBn), 4.30 (dd, 1H, $J_{5,6e}$ = 3.0 Hz, $J_{6a,6e}$ = 8.9 Hz, H6e), 4.46, 4.55 (d, 2H, *J* = 12.0 Hz, PhC*H*$_2$O), 4.92 (s, 1H, H1), 5.57 (s, 1H, PhC*H*), 6.09 (br s, 1H, H3), 7.30–7.50 (m, 10H, aromatic). ^{13}C NMR δ: 56.3 (q, OCH_3), 64.3 (d, C5), 69.5 (t, C6), 70.0 (t, Ph*C*H$_2$), 72.5 (t, *C*H$_2$OBn), 75.5 (d, C4), 96.8 (d, C1), 102.3 (d, Ph*C*H), 129.2 (d, C3), 136.0 (s, C2), 126.3–137.4 (aromatic). Anal. calcd. for $C_{22}H_{24}O_5$: C 71.71, H 6.58; found: C 71.72, H 6.66.

(*b*) Compound **9** (20 mg, 0.05 mmol) was dissolved in trimethylphosphite (2 mL) and heated to reflux under a stream of argon for 18 h. The solvent was partially evaporated. Flash chromatography (5–15% EtOAc – petroleum ether) gave **7** (10 mg, 60%).

(*c*) Compound **14***b* (28 mg, 0.10 mmol) in dry THF (2 mL) was stirred with NaH (7 mg, 60% dispersion in oil, 0.17 mmol) under a stream of argon for 2 h. Tetra-*n*-butylammonium iodide (catalytic amount) and benzyl bromide (0.02 mL, 24 mg, 0.14 mmol) were added and the reaction stirred overnight. The mixture was diluted with brine, extracted with ether (×3), and the combined extracts washed with brine (×2) and dried over Na_2SO_4. Flash chromatography (5–15% EtOAc – petroleum ether) gave **7** (30 mg, 81%).

(*d*) To allylic chloride **13** (synthesized as below from allylic alcohol **10***b* (68 mg, 0.24 mmol)) in methylene chloride (3 mL) was added water (2 mL), benzyl alcohol (0.03 mL, 31 mg, 0.29 mmol), NaOH (60 mg, 1.5 mmol), and tetrabutylammonium hydrogen sulfate (98 mg, 0.29 mmol). The mixture was placed under a stream of argon and subjected to ultrasonication for 4 days. The mixture was diluted with CH_2Cl_2 and water then separated. The aqueous layer was extracted with CH_2Cl_2 (×2), and the combined extracts were washed with brine and dried over Na_2SO_4. Flash chromatography (5–15% EtOAc – petroleum ether) gave **7** (49 mg, 54% from **10***b*).

*Methyl 4,6-*O*-benzylidene-2-*C*-benzyloxymethyl-2,3-thionocarbonyl-*α*,*D*-allopyranoside* ***9***

To diol **5***b* (62 mg, 0.15 mmol) in dry methylene chloride (3 mL) was added Dess–Martin periodinane (9) (140 mg, 0.33 mmol) and the reaction mixture was stirred overnight at room temperature under a stream of argon. Methylene chloride, saturated $NaHCO_3$, and $Na_2S_2O_3$ solutions were added and stirring was continued for 30 min. The layers were separated and the organic layer dried over Na_2SO_4. Flash chromatography (10–50% EtOAc – petroleum ether) gave **8***a* (44 mg, 71%) as an oily solid: R_f 0.60 (70% EtOAc – petroleum ether); ^{1}H NMR (300 MHz, $CDCl_3$) δ: 3.39 (s, 3H, OCH_3), 3.74 (t, 1H, $J_{5,6a}$ = $J_{6a,6e}$ = H6a), 3.74 (br s, 1H, OH), 3.75, 3.99 (d, 2H, *J* = 10.6 Hz, C*H*$_2$OBn), 3.97 (td, 1H, $J_{4,5}$ = 10.0 Hz, $J_{5,6e}$ = 4.6 Hz, H5), 4.19 (d, 1H, H4), 4.32 (dd, 1H, $J_{6a,6e}$ = 10.0 Hz, H6e), 4.43, 4.70 (d, 2H, *J* = 12.2 Hz, PhC*H*$_2$O), 4.73 (s, 1H, H1), 5.38 (s, 1H, PhC*H*), 7.30–7.50 (m, 10H, aromatic). ^{13}C NMR δ: 55.9 (q, OCH_3), 66.0 (d, C5), 69.5 (t, C6), 72.8 (t, Ph*C*H$_2$), 73.7 (t, *C*H$_2$OCH$_2$Ph), 81.3 (d, C4), 82.6 (s, C2), 102.0 (d, Ph*C*H), 103.8 (d, C1), 126.4–137.2 (aromatic), 198.4 (s, C3). Ketone **8***a* (44 mg, 0.11 mmol) in methanol (2 mL) was stirred with sodium borohydride (2 mg, 0.05 mmol) under a stream of argon for 1 h. The reaction was quenched with a few drops of acetic acid and the solvent evaporated. The mixture was dissolved in ethyl acetate, washed with saturated $NaHCO_3$ solution (×2) and brine (×2), and dried over Na_2SO_4. Flash chromatography (30–70% EtOAc – petroleum ether) gave **8***b* (39 mg, 88%) as an oil: R_f 0.48 (70% EtOAc – petroleum ether); ^{1}H NMR (300 MHz, $CDCl_3$) δ: 3.44 (s, 3H, OCH_3), 3.57 (br s, 2H, C*H*$_2$OBn), 3.64 (t, 1H, $J_{5,6a}$ = $J_{6a,6e}$ = 10.0 Hz, H6a), 4.10 (td, 1H, $J_{4,5}$ = 10.0 Hz, $J_{5,6e}$ = 5.1 Hz, H5), 4.24 (br s, 1H, H3), 4.31 (dd, 1H, H6e), 4.45 (s, 1H, H1), 4.53, 4.71 (d, 2H, *J* = 12.2 Hz, PhC*H*$_2$O), 5.44 (s, 1H, PhC*H*), 7.30–7.50 (m, 10H, aromatic). ^{13}C NMR δ: 56.6 (q, OCH_3), 57.7 (d, C5), 69.3 (t, C6), 69.5 (d, C3), 71.6 (t, Ph*C*H$_2$), 73.2 (s, C2), 73.7 (t, *C*H$_2$OBn), 77.1 (d, C4), 101.6 (d, C1), 102.0 (d, Ph*C*H), 126.1–137.7 (aromatic). Compound **8***b* (39 mg, 0.10 mmol) and 1,1-thiocarbonyldiimidazole (36 mg, 0.20 mmol) in dry toluene (2 mL) was heated to reflux under a stream of argon overnight. Flash chromatography (10–50% EtOAc – petroleum ether) gave **9** (36 mg, 84%) as a white solid: R_f 0.47 (50%EtOAc – petroleum ether) $[\alpha]_D^{20}$ +131.3 (*c* 1.00, $CHCl_3$); mp 186°C. ^{1}H NMR (300 MHz, $CDCl_3$ δ: 3.42 (s, 3H, OCH_3), 3.63–3.75 (m, 3H, H4, H6a, C*H*$_2$OBn), 3.85 (d, 1H, *J* = 11.7 Hz, C*H*$_2$OBn), 4.21 (td, 1H, $J_{4,5}$ = $J_{5,6a}$ = 10.1 Hz, $J_{5,6e}$ = 5.2 Hz, H5), 4.34 (dd, 1H, $J_{6a,6e}$ = 10.1 Hz, H6e), 4.53 (s, 1H, H1), 4.58, 4.65 (d, 2H, *J* = 12.0 Hz, PhC*H*$_2$O), 5.15 (d, 1H, $J_{3,4}$ = 3.4 Hz, H3), 5.52 (s, 1H, PhC*H*), 7.30–7.50 (m, 10H, aromatic). ^{13}C NMR δ: 56.2 (q, OCH_3), 57.1 (d, C5), 67.5 (t, Ph*C*H$_2$), 68.8 (t, C6), 74.0 (t, *C*H$_2$OBn), 74.1 (d, C3), 78.7 (d, C4), 86.9 (s, C2), 98.2 (d, C1), 102.8 (d, Ph*C*H), 126.4–136.6 (aromatic), 191.4 (s, C=S). Anal. calcd. for $C_{23}H_{24}O_7S$: C 62.14, H 5.45, S 7.21; found: C 62.21, H 5.48, S, 7.12.

*Methyl 4,6-*O*-benzylidene-2-*C*-methylene-α,D-arabino-hexopyranoside,* ***10****a, and its 3-*O*-acetyl derivative* ***10****b*

The use of Tebbe's reagent was adapted from the published procedure 10*b*. In a dry box, titanocene dichloride (1.4, 5.62 mmol) was added to an oven-dried flask that was then closed with a septum. The flask was removed from the dry box and the septum wrapped with parafilm. Trimethyl aluminium (5.62 mL, 2 M in toluene, 11.24 mmol) was added and the methane gas generated was allowed to escape through the needle of a cannula that was then removed. The red solution was stirred for 4 days. Methane gas was vented once a day. Ketoacetate **4***b* (820 mg, 2.54 mmol) in THF (5 mL) was added by syringe and the solution stirred for 1 h. The septum was removed and anhydrous ether (5 mL) was added. Sixteen drops of 1 M $NaOH_{(aq)}$ was added over a period of 1 h and the stirring continued overnight. Ether and anhydrous Na_2SO_4 were added and stirring continued for 1 h. The mixture was filtered through Celite (eluted with a copious quantity of ether) and the solvent evaporated. Flash chromatography (0–40% EtOAc – petroleum ether) gave **10***b* (73 mg, 10%) and **10***a* (530 mg, 75%). A high R_f material was also obtained and was assigned as **10***c* since it rearranged on standing to give **10***a* (29 mg; 4%).

10*a*: R_f 0.41 (30% EtOAc – petroleum ether); $[\alpha]_D^{20}$ +54.3 (*c* 1.05, $CHCl_3$); mp 178°C. ^{1}H NMR (300 MHz, $CDCl_3$) δ: 1.62 (s, 1H, OH), 2.63 (d, 1H, J_{LR} = 3.0 Hz, OH), 3.40 (s, 3H, OCH_3), 3.45 (t, 1H, $J_{3,4}$ = $J_{4,5}$ = 10.0 Hz, H4), 3.74 (t, 1H, $J_{5,6}$ = $J_{6a,6e}$ = 10.0 Hz, H6a), 4.00 (td, 1H, $J_{5,6e}$ = 4.9 Hz, H5), 4.30 (dd, 1H, H6e), 4.62 (dd, 1H, J_{LR} = 2.0 Hz, H3), 5.03 (s, 1H, H1), 5.21, 5.43 (d, 2H, *J* = 1.5 Hz, =CH$_2$), 5.54 (s, 1H, PhC*H*), 7.32–7.52 (m, 5H, aromatic). ^{13}C NMR δ: 54.8 (q, OCH_3), 63.3 (d, C5), 69.1 (d, C3), 69.5 (t, C6), 84.2 (d, C4), 102.0 (d, Ph*C*H), 103.1 (d, C1), 112.2 (t, =CH$_2$), 126.3–137.2 (aromatic), 142.9 (s, C2). MS *m/z*: 278 (M^+). Anal. calcd. for $C_{15}H_{18}O_5$: C 64.73, H 6.53; found: C 64.85, H 6.50.

10*b*: R_f 0.44 (30% EtOAc – petroleum ether); $[\alpha]_D^{20}$ +54.5 (*c* 1.10, $CHCl_3$); mp 100°C. ^{1}H NMR (300 MHz, $CDCl_3$) δ: 2.16 (s, 3H, OAc), 3.41 (s, 3H, OCH_3), 3.62 (t, 1H, $J_{3,4}$ = $J_{4,5}$ = 10.0 Hz, H4), 3.76 (t, 1H, $J_{5,6a}$ = $J_{6a,6e}$ = 10.0 Hz, H6a), 4.11 (td, 1H, $J_{5,6e}$ = 4.8 Hz, H5), 4.31 (dd, 1H, H6e), 5.04 (s, 1H, H1), 5.07, 5.18 (d, 2H, *J* = 2.2 Hz, =CH$_2$), 5.52 (s, 1H, PhC*H*), 5.88 (dt, 1H, J_{LR} = 2.2 Hz, H3), 7.32–7.52 (m, 5H, aromatic). ^{13}C NMR δ: 20.8 (q, OAc), 54.7 (q, OCH_3)m 63.7 (d, C5), 69.0 (t, C6), 70.5 (d, C3), 81.3 (d, C4), 101.5 (d, C1), 102.9 (d, Ph*C*H), 111.9 (t, =CH$_2$), 126.1–137.7 (aromatic). Anal. calcd. for $C_{17}H_{20}O_6$: C 63.73, H 6.31; found: C 63.56, H 6.34.

*Methyl 4,6-*O*-benzylidene-2-*C*-hydroxymethyl-α,D-mannopyranoside,* ***11****a*

To **10***a* (490 mg, 1.76 mmol) in THF (10 mL) and *t*-BuOH (10 mL) were added tetraethylammonium hydroxide (0.26 mL, 54 mg, 20 wt.% in water, 0.36 mmol), tertiary butyl hydroperoxide (0.76 mL, 504 mg, 70%, 5.6 mmol), and osmium tetroxide (0.08 mL, 2.5 wt.% in *t*-BuOH, 0.007 mmol) and the solution was stirred at room temperature overnight. More Et_4NOH (0.2 mL), *t*-BuOOH (0.7 mL), and OsO_4 (0.08 mL) were added and the reaction was stirred for 7 h, with periodic additions of Et_4NOH to maintain the basicity of the solution (monitored with pH paper). Aqueous sodium bisulfite solution (10 mL of 10%) was added and stirring was continued for 30 min. Most of the

Can. J. Chem. Downloaded from www.nrcresearchpress.com by 195.246.54.202 on 09/08/12
For personal use only.

organic solvent was removed by rotary evaporatory (very mild heat), the mixture diluted with brine, extracted with methylene chloride (×3), and the combined extracts washed with brine and dried over Na_2SO_4. Flash chromatography (5:45:45 EtOH:EtOAc:petroleum ether) gave **11***a* (200 mg, 36%) as a solid: R_f 0.17 (70% EtOAc – petroleum ether); $[\alpha]_D^{20}$ +79.6 (*c* 1.00, $CHCl_3$); mp 102°C. ^{1}H NMR (300 MHz, $CDCl_3$) δ: 3.37 (s, 1H, OCH_3), 3.57, 3.75 (d, 2H, *J* = 11.8 Hz, C*H*$_2$OH), 3.75–3.88 (m, 2H, H4, H5), 3.91 (t, 1H, $J_{5,6a} = J_{6a,6e}$ = 9.3 Hz, H6a), 4.07 (d, 1H, $J_{3,4}$ = 9.5 Hz, H3), 4.26 (dd, 1H, $J_{5,6e}$ = 3.4 Hz, H6e), 4.56 (s, 1H, H1), 5.54 (s, 1H, PhC*H*), 7.30–7.50 (m, 5H, aromatic). ^{13}C NMR δ: 55.3 (q, OCH_3), 63.0 (d, C5), 65.3 (t, CH_2OH), 68.8 (t, C6), 70.0 (d, C3), 74.4 (s, C2), 79.4 (d, C4), 102.2 (d, Ph*C*H), 103.1 (d, C1), 126.4–137.3 (aromatic). Anal. calcd. for $C_{15}H_{20}O_7 \cdot 0.4\ H_2O$: C 76.57, H 6.33; found: C 76.46, H 6.62.

Methyl 4,6-O-benzylidene -2-C-triphenylmethoxymethyl-2,3-O-thionocarbonyl-α,D-mannopyranoside ***11****b*

Compound **11***a* (90 mg, 0.29 mmol) and triphenylmethyl chloride (125 mg, 0.43 mmol) in dry pyridine (3 mL) were stirred with a catalytic amount of DMAP at 100°C for 2 h. Evaporation of the solvent and flash chromatography (0–20% EtOAc – petroleum ether) gave **11***b* (148 mg, 80%) as an oil: R_f 0.23 (30% EtOAc – petroleum ether); ^{1}H NMR (300 MHz, $CDCl_3$) δ: 3.32 (s, 1H, OCH_3), 3.44, 3.47 (d, 2H, *J* = 9.5 Hz, C*H*$_2$OTr), 3.76–3.95 (m, 4H, H3, H4, H5, H6a), 4.27 (m, 1H, H6e), 4.76 (s, 1H, H1), 5.55 (s, 1H, PhC*H*), 7.20–7.50 (m, 20 H, aromatic). ^{13}C NMR δ: 55.3 (q, OCH_3), 62.7 (d, C5), 66.1 (t, *C*H$_2$OTr), 69.0 (t, C6), 70.5 (d, C3), 75.4 (s, C2), 79.5 (d, C4), 87.2 (s, Ph_3C), 102.1 (d, C1), 102.2 (d, Ph*C*H), 126.3–143.4 (aromatic). To **11***b* (122 mg, 0.22 mmol) in dry THF (3 mL) under a stream of argon was added NaH (25 mg, 60% dispersion in oil, 0.62 mmol), followed by tetra-*n*-butylammonium iodide (catalytic amount) and carbon disulfide (0.04 mL, 0.68 mmol), and the reaction was stirred for 15 min. Methyl iodide (0.04 mL, 0.66 mmol) was added and the reaction stirred overnight. Saturated NH_4Cl (0.4 mL) was added and the mixture was diluted with ether, washed with brine (×2), and dried over Na_2SO_4. Flash chromatography (5–25% EtOAc – petroleum ether) gave **11***c* (116 mg, 88%) as an oil: R_f 0.48 (30% EtOAc – petroleum ether); $[\alpha]_D^{20}$ –5.1 (*c* 1.02, $CHCl_3$); ^{1}H NMR (300 MHz, $CDCl_3$) δ: 3.26 (s, 3H, OCH_3), 3.30, 3.39 (d, 2H, *J* = 11.0 Hz, C*H*$_2$OTr), 3.70 (td, 1H, $J_{4,5} = J_{5,6a}$ = 9.8 Hz, $J_{5,6e}$ = 4.4 Hz, H5), 3.78 (t, 1H, $J_{6a,6e}$ = 9.8 Hz, H6a), 3.84 (dd, 1H, $J_{3,4}$ = 7.1 Hz, H4), 4.31 (dd, 1H, H6e), 4.69 (d, 1H, H3), 4.98 (s, 1H, H1), 5.57 (s, 1H, PhC*H*), 7.20–7.50 (m, 20 H, aromatic). ^{13}C NMR δ: 55.9 (q, OCH_3), 58.8 (d, C5), 65.2 (t, *C*H$_2$OTr), 68.7 (t, C6), 79.1 (d, C4), 81.9 (d, C3), 87.6 (s, Ph_3C), 89.2 (s, C2), 98.1 (d, C1), 101.9 (d, Ph*C*H), 126.1–143.0 (aromatic), 189.8 (s, C=S). Anal. calcd. for $C_{35}H_{32}O_7S \cdot 0.5\ H_2O$: C 69.39, H 5.50; found: C 69.64, H 5.63.

Methyl 4,6-O-benzylidene-2-C-triphenylmethoxymethyl-α,D-erythro-hex-2-enopyranoside ***12***

Compound **11***c* (92 mg, 0.15 mmol) in $P(OMe)_3$ (3 mL) was heated to reflux under a stream of argon for 18 h. Partial evaporation of the solvent and flash chromatography (0–10% EtOAc – petroleum ether) gave **12** (47 mg, 59%) as an oil: R_f 0.45 (15% EtOAc – petroleum ether); $[\alpha]_D^{20}$ +45.7 (*c* 1.00, $CHCl_3$); ^{1}H NMR (300 MHz, $CDCl_3$) δ: 3.35 (s, 3H, OCH_3), 3.65 (br s, 1H, C*H*$_2$OTr), 3.81 (t, 1H, $J_{5,6} = J_{6a,6e}$ = 10.2 Hz, H6a), 3.87 (td, 1H, $J_{4,5}$ = 10.2 Hz, $J_{5,6e}$ = 3.8 Hz, H5), 4.16–4.23 (m, 1H, H4), 4.27–4.33 (m, 1H, H6e), 4.88 (s, 1H, H1), 5.59 (s, 1H, Ph*C*H), 6.18 (br s, 1H, H3), 7.20–7.50 (m, 20H, aromatic). ^{13}C NMR δ: 56.0 (q, OCH_3), 63.6 (t, *C*H$_2$OTr), 64.3 (d, C5), 69.5 (t, C6), 75.7 (d, C4), 86.9 (s, Ph_3C), 97.1 (d, C1), 102.3 (d, Ph*C*H), 125.4 (d, C3), 126.4–136.4 (aromatic), 137.5 (s, C2). Anal. calcd. for $C_{34}H_{32}O_5 \cdot 0.7\ H_2O$: C 76.57, H 6.33; found: C 76.46, H 6.62.

Methyl 4,6-O-benzylidene-2-C-hydroxymethyl-α,D-erythro-hex-2-enopyranoside ***14***b

To **10***a* (510 mg, 1.83 mmol) in dry THF (150 mL) were added pyridine (1.3 mL, 16 mmol) and thionyl chloride (1 mL, 13.7 mmol), and the mixture was stirred overnight under a stream of argon. It was then diluted with ether, washed with brine (×2), saturated $NaHCO_3$ (×2), brine (×2), and dried over Na_2SO_4 to give crude **13** as a slightly brown solid: R_f 0.67 (20% EtOAc – petroleum ether); ^{1}H NMR (300 MHz, $CDCl_3$) δ: 3.48 (s, 3H, OCH_3), 3.75–4.36 (m, 6H, H4, H5, H6a, H6e, CH_2Cl), 5.03 (s, 1H, H1), 5.56 (s, 1H, PhC*H*), 6.13 (s, 1H, H3), 7.30–7.50 (m, 5H, aromatic). ^{13}C NMR δ: 44.5 (t, CH_2Cl), 56.5 (q, OCH_3), 64.2 (d, C5), 69.3 (t, C6), 75.3 (d, C4), 96.2 (d, C1), 102.2 (d, Ph*C*H), 129.2 (d, C3), 135.2 (s, C2), 126.3–137.2 (aromatic). To crude **13** in HMPA (20 mL) was added potassium acetate (180 mg, 1.83 mmol) and the mixture was stirred overnight under argon. It was then diluted with brine, extracted with ether (×4), and the combined extracts were washed with saturated $NaHCO_3$ (×2), and dried over Na_2SO_4. Flash chromatography (2–10% EtOAc – petroleum ether) gave **14***a* (298 mg, 51% from **10***a*) as a white solid: R_f 0.41 (30% EtOAc – petroleum ether); ^{1}H NMR (300 MHz, $CDCl_3$) δ: 2.06 (s, 3H, OAc), 3.45 (s, 3H, OCH_3), 3.80 (t, 1H, $J_{5,6a} = J_{6a,6e}$ = 10.5 Hz, H6a), 3.85 (td, 1H, $J_{4,5} = J_{5,6e}$ = 3.7 Hz, H5), 4.11–4.19 (m, 1H, H4), 4.26–4.34 (m, 1H, H6e), 4.55, 4.60 (d, 2H, *J* = 13.4 Hz, C*H*$_2$OAc), 4.86 (s, 1H, H1), 5.56 (s, 1H, PhC*H*), 6.09 (br s, 1H, H3), 7.30–7.50 (m, 5H, aromatic). ^{13}C NMR δ: 20.9 (q, OAc), 56.3 (q, OCH_3), 63.7 (t, CH_2OAc), 64.1 (d, C5), 69.4 (t, C6), 75.3 (d, C4), 96.7 (d, C1), 102.3 (d, PhCH), 126.3–137.3 (aromatic), 128.0 (d, C3), 133.9 (s, C2), 170.6 (s, C=O). Compound **14***a* (250 mg, 0.78 mmol) in MeOH (15 mL) was stirred with a catalytic amount of sodium methoxide (1 M in MeOH) for 2 h. Dowex 50X8-100 acidic ion exchange reagent (prewashed in MeOH) was added and the mixture stirred for 15 min. The mixture was filtered and the solvent removed. Flash chromatography (30–50% EtOAc – petroleum ether) gave **14***b* (139 mg, 64%) as a white solid: R_f 0.31 (50% EtOAc – petroleum ether); $[\alpha]_D^{20}$ +98.5 (*c* 1.00, $CHCl_3$); mp 146°C. ^{1}H NMR (300 MHz, $CDCl_3$) δ: 3.47 (s, 1H, OCH_3), 3.80 (t, 1H, $J_{5,6a} = J_{6a,6e}$ = 10.4 Hz, H6a), 3.84 (td, 1H, $J_{5,6e}$ = 3.4 Hz, H5), 4.09–4.19 (m, 3H, H4, CH_2OH), 4.28–4.33 (m, 1H, H6e), 4.91 (s, 1H, H1), 4.57 (s, 1H, PhCH), 6.06 (br s, 1H, H3), 7.30–7.50 (m, 5H, aromatic). ^{13}C NMR δ: 56.2 (q, OCH_3), 63.2 (t, CH_2OAc), 64.3 (d, C5), 69.4 (t, C6), 75.4 (d, C5), 97.5 (d, C1), 102.3 (d, PhCH), 126.3–137.6 (aromatic), 126.8 (d, C3), 137.6 (s, C2). Anal. calcd. for $C_{15}H_{18}O_5$: C 64.73, H 6.53; found: C 64.65, H 6.57.

Acknowledgements

We are grateful to the National Science Foundation (CHE 892003) for support of this work. We thank Professor A.T. McPhail of the Crystal Structure Center, Duke University, for the X-ray crystallographic analysis of **6**.

1. R. Tsang and B. Fraser-Reid. J. Org. Chem. **57**, 1065 (1992).
2. T.A. van Beek, and Ae de Groot. Recl. Trav. Chim. Pays-Bas, **105**, 513 (1986); J. R. Hansoon. Nat. Prod. Rep. **7**, 347 (1990), and references therein.
3. E.J. Corey, and R.A.E. Winter. J. Am. Chem. Soc. **85**, 2677 (1963).
4. D.B. Tulshian, R. Tsang, and B. Fraser-Ried. J. Org. Chem. **49**, 2347 (1984).
5. B. Castro. Bull Soc. Chim. Fr. (S), 1533 (1967).
6. W.C. Still. J. Am. Chem. Soc. **100**, 1481 (1978).
7. Y. Kondo, N. Kashimura, and K. Onodera. Agric. Biol. Chem. **38**, 2553 (1974).
8. E.J. Corey and P.B. Hopkins. Tetrahedron Lett. **23**, 1979 (1982).
9. D.B. Dess and J.C. Martin. J. Org. Chem. **48**, 4155 (1983).
10. (*a*) F.N. Tebbe, G.W. Parshall, and G.S. Reddy. J. Am. Chem. Soc. **100**, 3611 (1978); (*b*) S. H. Pine, G. Kin, and V. Lee. Org. Synth. **69**, 72 (1990).
11. (*a*) A. McKillop, J.-C. Fiauld, and R.P. Hug. Tetrahedron, **30**, 1379 (1974); (*b*) W. Oppolzer, H. Bienaymé, and A. Genevois-Borella. J. Am. Chem. Soc. **113**, 9660 (1991).

Site-directed mutagenesis of farnesyl diphosphate synthase; effect of substitution on the three carboxyl-terminal amino acids

TANETOSHI KOYAMA, KAZUHIRO SAITO, AND KYOZO OGURA[1]
Institute for Chemical Reaction Science, Tohoku University, Sendai, Miyagi 980, Japan

AND

SHUSEI OBATA AND AYUMI TAKESHITA
R & D Planning Division, Toyota Motor Corporation, Toyota-cho, Toyota, Aichi 471, Japan

Received June 9, 1993

This paper is dedicated to Professor Ian Spenser

TANETOSHI KOYAMA, KAZUHIRO SAITO, KYOZO OGURA, SHUSEI OBATA, and AYUMI TAKESHITA. Can. J. Chem. **72**, 75 (1993).

Site-directed mutation was introduced into the gene for the farnesyl diphosphate synthase of *Bacillus stearothermophilus*. To investigate the significance of the three C-terminal amino acids, where arginine is completely conserved throughout the farnesyl diphosphate synthases of prokaryotes and eukaryotes, three kinds of mutant enzymes, R295V, D296G, and H297L, which have replacements of arginine-295 with valine, aspartate-296 with glycine, and histidine-297 with leucine, respectively, were overproduced and purified to homogeneity. All of the three mutant enzymes showed similar catalytic activities to that of the wild-type enzyme, indicating that the basic amino acids including the conserved arginine in the C-terminal region are not essential for catalytic function. They were also similar to the wild-type enzyme with respect to pH optima, thermostability, reaction product, and kinetic parameters for allylic substrates. However, their K_m values for isopentenyl diphosphate are approximately twice that of the wild type.

TANETOSHI KOYAMA, KAZUHIRO SAITO, KYOZO OGURA, SHUSEI OBATA et AYUMI TAKESHITA. Can. J. Chem. **72**, 75 (1993).

On a introduit une mutation dirigée sur un site du gène de la synthase de la diphosphate de farnésyle du *Bacillus stearothermophilus*. Dans le but d'évaluer l'importance des trois acides aminés du terminal-C où l'arginine est complètement conservé au cours dans tous les synthases de la diphosphate de farnésyle des procaryotes et des eucaryotes, on a surproduit et purifié jusqu'à homogénéité trois types d'enzymes mutants, les R295V, D296G et H297L dans lesquels on a respectivement remplacé l'arginine-295 par la valine, l'aspartate-296 par de la glycine et l'histidine-297 par de la leucine. Les trois enzymes mutants présentent chacun des activités catalytiques similaires à celles de l'enzyme de type sauvage; ceci indique que les acides aminés basiques, y compris l'arginine conservé dans la région du terminal-C ne sont pas essentiels pour la fonction catalytique. Pour les substrats allyliques, elles sont aussi semblables à l'enzyme de type sauvage en ce qui a trait au pH optimal, à la thermostabilité, au produit réactionnel et aux paramètres cinétiques. Toutefois, leurs valeurs de K_m pour le diphosphate d'isopenténylé sont approximativement deux fois plus grandes que celle de l'enzyme de type sauvage.

[Traduit par la rédaction]

Introduction

Prenyltransferases catalyze the condensation of isopentenyl diphosphate (IPP) with allylic diphosphates to synthesize prenyl diphosphates with various chain lengths and stereochemistries (1, 2). They are extremely interesting from the mechanistic viewpoint in that they catalyze the repetition of stereospecific condensation of IPP with allylic diphosphates to give products with chain lengths determined by the specificities of the individual enzymes (3, 4).

Farnesyl diphosphate (FPP) synthase (EC 2.5.1.10) is one of the prenyltransferases and it occupies a central point in isoprenoid chain elongation pathways. It catalyzes the condensations of IPP with dimethylallyl diphosphate (DMAPP) and with geranyl diphosphate (GPP) to produce FPP as the ultimate reaction product as shown in Scheme 1 (1). Comparison of the primary structures of prenyltransferases, including FPP synthase (5–9), geranylgeranyl diphosphate (GGPP) synthase (10), and hexaprenyl diphosphate (HPP) synthase (11), from a wide range

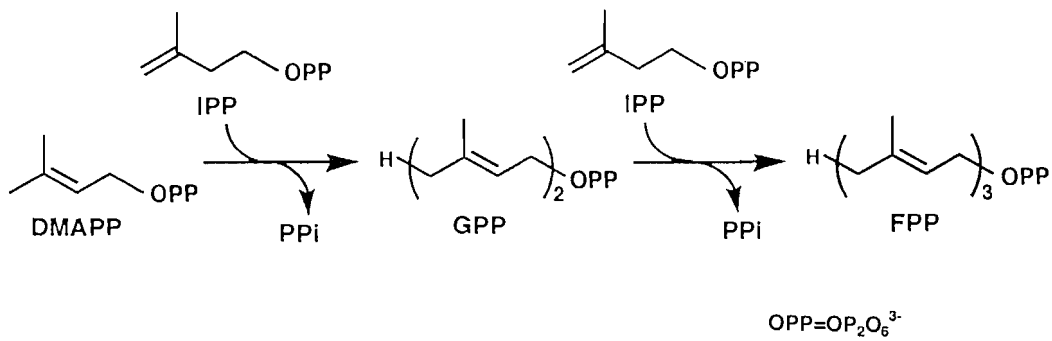

SCHEME 1. Reaction catalyzed by FPP synthase.

[1]Author to whom correspondence may be addressed.

Can. J. Chem. Downloaded from www.nrcresearchpress.com by 195.246.54.202 on 09/08/12
For personal use only.

Can. J. Chem. Downloaded from www.nrcresearchpress.com by 195.246.54.202 on 09/08/12
For personal use only.

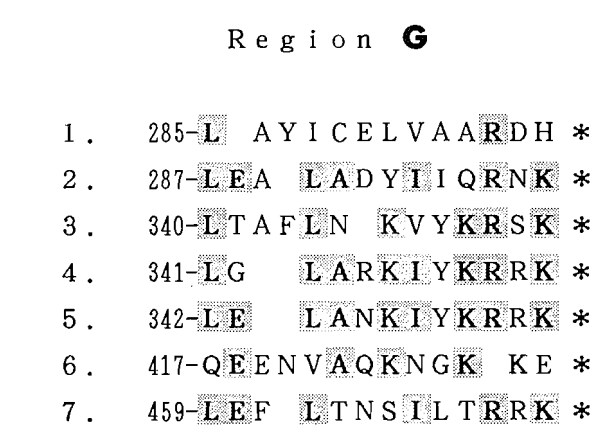

FIG. 1. Amino acid sequence alignment of Region **G** (C-terminal) within various prenyltransferases. Numbers attached to the left of the sequences indicate the position of the first amino acid displayed. Shaded areas indicate amino acids conserved in at least four out of the seven enzymes. 1, FPP synthase from *B. stearothermophilus* (9); 2, FPP synthase from *E. coli* (8); 3, FPP synthase from yeast (6); 4, FPP synthase from rat (5); 5, FPP synthase from human (7); 6, GGPP synthase from *N. crassa* (10); 7, HPP synthase from yeast (11).

of organisms has revealed the presence of seven conserved regions (9). These include regions characterized as rich in highly conserved aspartate and arginine residues. Site-directed mutagenesis studies carried out by Marrero et al. (12) using rat FPP synthase have recently shown that one of the highly conserved aspartate residues in Domain II (Region **F**) is essential for catalytic function while another one can be replaced with glutamate without significant change in catalytic properties. However, the significance of the highly conserved arginine residues remained unknown. Among the seven conserved regions in FPP synthases there are four highly conserved arginines in Regions **A**, **B** (two residues), and **G**. This paper describes the result of studies carried out, using the FPP synthase of *Bacillus stearothermophilus*, in an attempt to explore the role of the conserved arginine residue that occupies the third position from the carboxyl terminus. It also reports the effects of mutagenesis in the penultimate and the carboxyl terminus residues.

Experimental procedures

Materials

[1-^{14}C]IPP (1.95 TBq/mol) was purchased from Amersham Corp. Nonlabeled IPP, DMAPP, and GPP were the same preparations as used in the previous work (4). Restriction enzymes and other DNA-modifying enzymes were purchased from Takara Shuzo Co., Ltd. and Toyobo Co., Ltd. unless otherwise stated.

Site-directed mutagenesis

To introduce mutations in the structural gene for the FPP synthase of *B. stearothermophilus*, a *Bam*HI/*Hin*dIII DNA fragment from the clone pΔ1a (9) was subcloned into pTZ18R (Toyobo) yielding pEX47. Then single-stranded DNA templates were isolated with a helper phage, M13KO7 (13). Site-directed mutagenesis was conducted with uracil-enriched single-stranded DNA according to the procedure described by Kunkel et al. (14), and a series of mutated plasmids, pMu18, pMu88, and pMu84, were obtained. The nucleotide sequences of the mutagenic oligonucleotides are given in Fig. 2. The introduction of mutation was confirmed by sequencing the whole nucleotide sequence using the dideoxy chain-termination method (15) with a DNA sequencer (Applied Biosystems, model 373A).

Construction of expression vector systems for mutated FPP synthase

The *Nco*I/*Hin*dIII fragment of each of the three kinds of pMu plasmids into which a series of mutation had been introduced was ligated into the *Nco*I/*Hin*dIII site of pTrc99A (Pharmacia) to construct a series of recombinant plasmids, pEX121, pEX125, and pEX134 (Fig. 3).

Overproduction and purification of mutated FPP synthase

Each of the series of expression plasmids, pEX121, pEX125, and pEX134, was transformed into *E. coli* JM105, and the overnight culture of *E. coli* JM105 harboring the pEX plasmid in L-B medium (13) containing 50 μg/mL of ampicillin was inoculated into a 250-fold volume of M9YG medium (M9 salt (13) with 0.2% glycerol and 0.2% yeast extract) with 50 μg/mL of ampicillin. The *E. coli* cells were incubated at 30°C to an OD_{600} of 0.6–0.8, then isopropyl-ß-thiogalactopyranoside (IPTG) was added to a final concentration of 1 mM. The incubation was continued for additional 3 h at 30°C.

The mutated enzymes were purified essentially according to our previous paper, including heat treatment of the cell-free extracts followed by two chromatographic steps (9). The fractions of the mutated FPP synthases were analyzed for purity by sodium dodecyl sulfate – polyacrylamide gel electrophoresis (SDS–PAGE) (14%, ref. 16) with Coomassie Brilliant Blue staining, and fractions that proved to be homogeneous were used for further characterization. All of the mutated FPP synthases, R295V, D296G, and H297L, showed similar chromatographic properties to those of the wild-type enzyme during the purification procedure described above (data not shown).

FPP synthase assay

The enzyme activity was measured by determination of the amount of [1-^{14}C]IPP incorporated into butanol-extractable polyprenyl diphosphates (9). In a standard experiment, the incubation mixture contained, in a final volume of 1.0 mL, 50 mM Tris-HCl buffer of pH 8.5, 50 mM $MgCl_2$, 50 mM NH_4Cl, 5 mM KF, 50 mM 2-mercaptoethanol, 25 μM DMAPP or GPP, 25 μM [1-^{14}C]IPP (specific activity 37 GBq/mol), and a suitable amount of enzyme protein. After incubation at 55°C for 15 min, the reaction products were immediately extracted with 1-butanol. The butanol layer was washed with water and an aliquot of the extract was counted for radioactivity.

Product analysis

After enzymatic reaction at 55°C, the radioactive prenyl diphosphate in the reaction mixture was hydrolyzed to the corresponding alcohol with potato acid phosphatase according to the method of Fujii et al. (17).

The hydrolysate was extracted with pentane and analyzed by reversed phase thin-layer chromatography with LKC-18 (Whatman) in a solvent system of acetone–water (19:1). The positions of authentic standards were visualized with iodine vapor, and the distribution of radioactivity was detected.

Results

Effect of arginine specific reagents on FPP synthase activity

It has been shown that prenyltransferases such as the FPP synthases of pig liver (18) and human (19), undecaprenyl diphosphate synthase of *Lactobacillus plantarum* (20), and the HPP synthase of *Micrococcus luteus* B-P 26 (21) are sensitive to arginine-specific reagents.

To characterize the recombinant FPP synthase of *B. stearothermophilus*, we examined the effect of arginine-specific reagents, 2,3-butanedione and 1,2-cyclohexanedione, and found that both of these reagents strongly inhibited the enzyme with an I_{50} of approximately 5 mM.

Production of FPP synthase mutants

To examine the role of the conservative arginine residue in Region **G**, site-directed mutations were introduced in *B. stearothermophilus* FPP synthase. Figure 2 shows the C-terminal sequences of *B. stearothermophilus* FPP synthase and its mutated enzymes along with the sequences of mutagenic oligonucleotides.

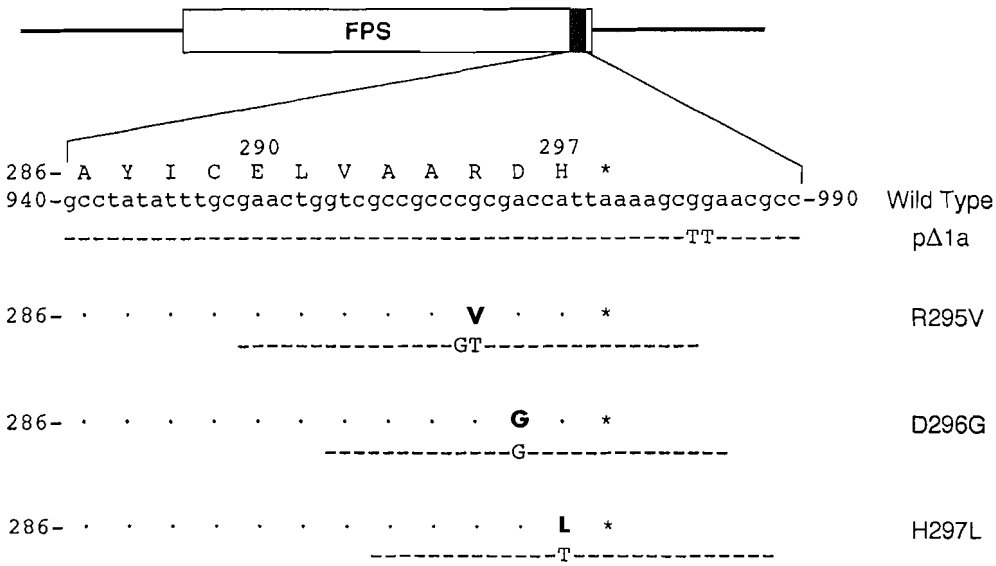

FIG. 2. Schematic presentation of wild-type and mutant FPP synthase gene sequences corresponding to the Region **G** (C-terminal). The nucleotide sequence of FPP synthase of *B. stearothermophilus* for residues 940–990 is shown. The sequences of mutagenic oligonucleotides are aligned underneath the wild-type sequence as well as that of pΔ1a corresponding to the FPP synthase gene (FPS). Nucleotides identical to those in the wild type are indicated by *dashes*, and altered nucleotides are indicated by *capital letters*. All mutant genes have been sequenced to verify point mutations. Amino acid sequences are also shown above the corresponding nucleotides. Dots indicate amino acids identical to those in the wild type.

The arginine residue at position 295, which is completely conservative in Region **G**, was changed to valine in order to produce a less basic mutant (R295V). The aspartic acid at 296 was replaced with glycine so that the C-terminal region was made less acidic (D296G). Substitution of leucine for the histidine at the C-terminus was made to prepare a mutant having a less basic C-terminal region (H297L).

To construct overexpression systems for these mutants, we employed plasmid pΔ1a, in which *Nco*I and *Hin*dIII sites were introduced immediately upstream and downstream, respectively, of the open reading frame of the *B. stearothermophilus* FPP synthase gene (9). The *Bam*HI/*Hin*dIII DNA fragment from pΔ1a was subcloned into pTZ18R and then oligonucleotide-mediated mutagenesis was conducted into the resulting plasmid, pEX47, to obtain a series of the mutated plasmids, pMu18, pMu88, and pMu84.

The *Nco*I/*Hin*dIII fragment of each of the pMu plasmids was ligated into the *Nco*I/*Hin*dIII site of pTrc99A, and expression plasmids pEX121, pEX125, and pEX134 were obtained. After transformation of *E. coli* JM105 with these plasmids, the FPP synthase mutants R295V, D296G, and H297L were overproduced and purified essentially according to the procedure for the production of wild-type recombinant FPP synthase (9). This procedure yielded proteins that gave a single band on SDS–PAGE, and the purities were judged, by staining with Coomassie Brilliant Blue, to be better than 95%.

Kinetic analysis of FPP synthase mutants

Kinetic parameters of the purified FPP synthase mutants are listed in Table 1. All the mutant enzymes showed catalytic activities comparable to that of the wild-type enzyme. H297L, especially was even better than the wild type in terms of specific activity and V_{max}. Even R295V, in which the highly conserved arginine had been replaced with valine, showed more than half the specific activity of the wild type. The K_m values of the mutant enzymes for IPP are approximately twice that of the wild type.

Effect of pH

The mutant enzymes showed similar pH–activity profiles to that of the wild-type enzyme, having pH optima around pH 8–8.5.

Thermostability

The mutant enzymes exhibited similar thermostabilities to that of the wild type, retaining enough activity even after heating at 60°C for at least 50 min.

Reaction product

Product analysis revealed that (all-*E*)-farnesyl diphosphate (FPP) was exclusively synthesized by all the mutant enzymes (data not shown).

Discussion

To study the significance of the conserved arginine residue in the C-terminal region, we carried out oligonucleotide-mediated mutagenesis and prepared three kinds of mutants of *B. stearothermophilus* FPP synthase, R295V, D296G, and H297L.

All these mutant enzymes showed FPP synthase activity, and their properties were similar to those of the wild-type enzyme. In other words, none of the three amino acid residues in the C-terminal region (Region **G**) is essential for enzyme activity. It is noteworthy, however, that the K_m values of the mutated enzymes for IPP are approximately twice as large as those of the wild-type enzyme, while those for the allylic substrates, DMAPP and GPP, are similar to those of the wild-type enzyme. These results suggest the possibility that the C-terminal region occupies a position that weakly affects the IPP binding site.

The specific activity of R295V is about half that of the wild type, while the other two mutants show values comparable to that of the wild type. Therefore, the arginine residue that is completely conserved at the third position from the C-terminus seems more important for enzymatic activity than the other two residues. Preference for the basic nature of the C-terminal region is also suggested by the observation that the replacement

Can. J. Chem. Downloaded from www.nrcresearchpress.com by 195.246.54.202 on 09/08/12
For personal use only.

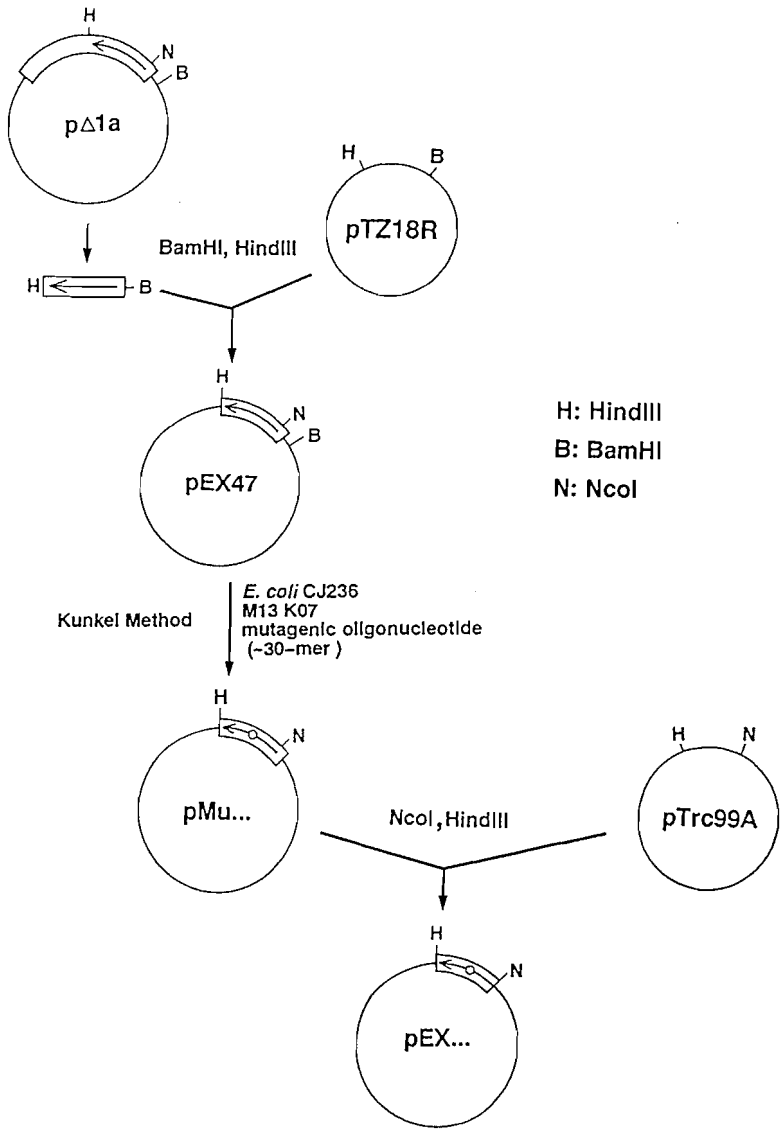

FIG. 3. Schematic diagram of construction of the plasmids. Restriction sites; H, *Hin*dIII; B, *Bam*HI; N, *Nco*I. The arrows indicate the coding region of the FPP synthase and open circles on the arrow indicate the point-mutated sites.

of the penultimate aspartate with glycine improved the V_m/K_m values for both DMAPP and GPP. However, it is surprising that the replacement of the C-terminal histidine with leucine is the most effective of the three in improving the enzymatic activity with respect to both specific activity and the V_m/K_m values for the allylic substrates.

It is interesting that the arginine residue conserved at the third position from the C-terminus is not essential for catalytic activity. However, this observation might not be surprising in view of the fact that the corresponding position is occupied by lysine and alanine in the GGPP synthases of *Nurospora crassa* (10) or *Erwinia herbicola* (22) and of *Erwinia uredovora* (23), respectively.

One or both of the arginine residues forming the RRG motif in Region **B** must be essential and responsible for the inhibition by arginine-specific reagents, because this motif is conserved not only in FPP synthases but also in GGPP synthases and HPP synthase.

According to the recent results of site-directed mutagenesis by Marrero et al. (12) in the aspartate-rich domain II, which is equivalent to Region **F** of *B. stearothermophilus* FPP synthase, the first aspartate is involved in the catalysis by the enzyme. These authors found that when the first aspartate in domain II was replaced with glutamate, the K_m value for IPP increased 23-fold but the K_m value for GPP did not change. This tendency is somewhat similar to our result in that the K_m values of the mutant enzymes for IPP increase while those for allylic substrates do not change significantly. Namely, the binding affinity for IPP is affected more easily by amino acid substitution than that of the allylic substrates. The C-terminal region might be located in a space in such a way that it affects the binding of IPP, though to a lesser extent than in the case of Region **F**.

To elucidate the reaction mechanism of prenyltransferase in more detail, it is indispensable to obtain information about its three-dimensional structure as well as data for the effect of site-directed mutagenesis on the catalytic function of the enzyme. Although crystallization of the FPP synthase of avian liver was reported by Reed and Rilling, no crystallographic information was available (24). As we recently succeeded in crystallization

Can. J. Chem. Downloaded from www.nrcresearchpress.com by 195.246.54.202 on 09/08/12
For personal use only.

TABLE 1. Kinetic parameters of mutant FPP synthases

Enzyme	Specific Activity[c]	DMAPP		GPP		IPP[a]		IPP[b]	
		K_m[d]	V_{max}[c]	K_m[d]	V_{max}[c]	K_m[d]	V_{max}[c]	K_m[d]	V_{max}[c]
Wild type	1600 ± 310	13.0 ± 2.8	1750 ± 150	6.4 ± 0.1	3210 ± 10	5.8 ± 0.8	1080 ± 50	14.3 ± 0.9	3560 ± 430
R295V	1070 ± 320	16.6 ± 2.0	990 ± 80	6.2 ± 0.1	1710 ± 20	16.4 ± 1.4	720 ± 40	21.2 ± 2.9	1560 ± 260
D296G	1800 ± 340	14.6 ± 1.5	2630 ± 190	5.1 ± 1.4	2800 ± 200	15.8 ± 3.8	1990 ± 270	19.6 ± 1.6	3310 ± 100
H297L	2140 ± 190	11.0 ± 0.1	1800 ± 50	5.2 ± 0.6	3260 ± 30	15.3 ± 0.1	2010 ± 10	21.4 ± 3.0	3810 ± 220

Each value represents the mean ±SD of three determinations.
[a]For the reaction with DMAPP.
[b]For the reaction with GPP.
[c]In nmol of [1-^{14}C]IPP converted to FPP per minute per milligram of the enzyme.
[d]In μM.

of the wild-type FPP synthase of *B. stearothermophilus* (25), X-ray diffraction studies are now in progress.

Acknowledgment

This work was supported in part by Grant-in-Aid on Priority Areas 03236103 from the Ministry of Education, Science, and Culture of Japan.

1. C.D. Poulter and H.C. Rilling. *In* Biosynthesis of isoprenoid compounds. Vol. 1. *Edited by* S.L. Spurgeon and J.W. Porter. John Wiley & Sons, New York. 1982. pp. 161–224.
2. J.A. Glomset, M.H. Gelb, and C.C. Farnsworth. Trends Biochem. Sci. **15**, 139 (1990).
3. M. Ito, M. Kobayashi, T. Koyama, and K. Ogura. Biochemistry, **26**, 4745 (1987).
4. S. Ohnuma, T. Koyama, and K. Ogura. J. Biol. Chem. **266**, 23706 (1991).
5. C.F. Clarke, R.D. Tanaka, K. Svenson, M. Wamsley, A.M. Fogelman, and P.A. Edwards. Mol. Cell. Biol. **7**, 3138 (1987).
6. M.S. Anderson, J.G. Yarger, C.L. Burck, and C.D. Poulter. J. Biol. Chem. **264**, 19176 (1989).
7. D.J. Wilkin, S.Y. Kutsunai, and P.A. Edwards. J. Biol. Chem. **265**, 4607 (1990).
8. S. Fujisaki, H. Hara, Y. Nishimura, K. Horiuchi, and T. Nishino. J. Biochem. (Tokyo), **108**, 995 (1990).
9. T. Koyama, S. Obata, M. Osabe, A. Takeshita, K. Yokoyama, M. Uchida, T. Nishino, and K. Ogura. J. Biochem. (Tokyo), **113**, 355 (1993).
10. A. Carattoli, N. Romans, P. Ballario, G. Morelli, and G. Macino. J. Biol. Chem. **266**, 5854 (1991).
11. M.N. Ashby and P.A. Edwards. J. Biol. Chem. **265**, 13157 (1990).
12. P.F. Merrero, C.D. Poulter, and P.A. Edwards. J. Biol. Chem. **267**, 21873 (1992).
13. J. Sambrook, E.F. Fritsch, and T. Maniatis. *In* Molecular cloning: a laboratory manual. 2nd ed. Cold Spring Harbor Laboratory, Cold Spring Harbor, N.Y. 1989.
14. T.A. Kunkel, J.D. Roberts, and R.A. Zakour. Methods Enzymol. **154**, 367 (1987).
15. F. Sanger, S. Nicklen, and A.B. Coulson. Proc. Natl. Acad. Sci. U.S.A. **74**, 5463 (1977).
16. U.K. Laemmli. Nature, **227**, 680 (1970).
17. H. Fujii, T. Koyama, and K. Ogura. Biochim. Biophys. Acta, **712**, 716 (1982).
18. G.F. Barnard and G. Popják. Biochim. Biophys. Acta, **617**, 169 (1980).
19. G.F. Barnard and G. Popják. Biochim. Biophys. Acta, **661**, 87 (1981).
20. J.D. Muth and C.M. Allen. Arch. Biochem. Biophys. **230**, 49 (1984).
21. I. Yoshida, T. Koyama, and K. Ogura. Biochim. Biophys. Acta, **995**, 138 (1989).
22. G. Sandmann and N. Misawa. FEMS Microbiol. Lett. **90**, 253 (1992).
23. S.K. Math, J.E. Hearst, and C.D. Poulter. Proc. Natl. Acad. Sci. U.S.A. **89**, 6761 (1992).
24. B.C. Reed and H.C. Rilling. Biochemistry, **14**, 50 (1975).
25. H. Nakane, T. Koyama, S. Obata, M. Osabe, A. Takeshita, T. Nishino, K. Ogura, and K. Miki. J. Mol. Biol. **233**, 787 (1993).

Can. J. Chem. Downloaded from www.nrcresearchpress.com by 195.246.54.202 on 09/08/12
For personal use only.

Biosynthesis of pyrrolizidine alkaloids: putrescine and spermidine are essential substrates of enzymatic homospermidine formation

FRANK BÖTTCHER, DIETRICH OBER, AND THOMAS HARTMANN[1]

Institut für Pharmazeutische Biologie der Technischen Universität, D-38106 Braunschweig, Germany

Received June 8, 1993

This paper is dedicated to Professor Ian D. Spenser

FRANK BÖTTCHER, DIETRICH OBER and THOMAS HARTMANN. Can. J. Chem. **72**, 80 (1994).

sym-Homospermidine, the first pathway-specific intermediate of pyrrolizidine alkaloid (PA) biosynthesis, is formed from two moles of putrescine in an NAD^+-dependent reaction catalyzed by homospermidine synthase (HSS). In the overall process catalyzed by HSS, NAD^+ seems to function as hydride acceptor in the first part of the reaction and subsequently as hydride donor in the second part. This was proved with chirally C1-deuterated putrescines. Both a bacterial HSS (isolated from *Rhodopseudomonas viridis*) and the enzyme from PA-producing *Eupatorium cannabinum* transformed (*R*)-[1-^{2}H]putrescine and (*S*)-[1-^{2}H]-putrescine into homospermidine with a 100% retention of deuterium. Studies with deuterated and ^{14}C-labeled substrates revealed that in the presence of putrescine spermidine is a substrate of HSS. The putrescine semialdehyde moiety of spermidine is combined with putrescine and 1,3-diaminopropane is released. Kinetic studies with plant HSS documented that the putrescine semialdehyde moiety of spermidine is incorporated into homospermidine with the same affinity (K_m) and activity (V_{max}) as putrescine. Plant HSS is highly specific for putrescine and spermidine; spermidine is not a substrate in the absence of putrescine. It is suggested that in the biosynthesis of homospermidine and thus PAs, one of the two C4 units is derived from spermidine and the other one from putrescine. A scheme of the HSS-catalyzed reaction is proposed that fully accounts for the enzymatic data and the results of previous tracer studies. Bacterial HSS is less substrate specific and not as well adapted as plant HSS to accept spermidine as a substrate.

FRANK BÖTTCHER, DIETRICH OBER et THOMAS HARTMANN. Can. J. Chem. **72**, 80 (1994).

La *sym*-homospermidine, le premier intermédiaire spécifique à une voie de biosynthèse des alcaloïdes de la pyrrolizidine (AP), se forme à partir de deux molécules de putrescine dans une réaction qui dépend du NAD^+ et qui est catalysée par la synthase de l'homospermidine (SHS). Dans le processus global catalysé par la SHS, le NAD^+ semble agir comme un accepteur d'hydrure dans la première partie de la réaction et comme donneur d'hydrure dans la deuxième partie. Ceci a été prouvé à l'aide de putrescines chirales, deutérées en C1. La SHS bactérienne (isolée du *Rhodopseudomonas viridis*) et l'enzyme provenant du *Eupatorium cannabinum* produisant des AP transforment tous les deux la (*R*)-[1-^{2}H]putrescine et la (*S*)-[1-^{2}H]putrescine en homospermidine avec 100% de rétention du deutérium. Des études avec des substrats deutérés et marqués au ^{14}C ont révélé que, en présence de putrescine, la spermidine est un substrat de la SHS. La portion semialdéhyde de la putrescine présente dans la spermidine se combine avec la putrescine et du 1,3-diaminopropane est libéré. Des études cinétiques avec de la SHS de plante ont permis de confirmer que la portion semialdéhyde de la putrescine présente dans la spermidine s'incorpore dans l'homospermidine avec la même affinité (K_m) et la même activité (V_{max}) que la putrescine. La SHS de plante est très spécifique pour la putrescine et la spermidine; la spermidine n'est pas un substrat en l'absence de putrescine. On suggère que dans la biosynthèse de l'homospermidine, et donc dans celle des AP, l'une des deux unités en C4 provient de la spermidine alors que l'autre provient de la putrescine. On propose un schéma pour la réaction catalysée par la SHS qui explique complètement les données enzymatiques et les résultats d'études antérieures à l'aide de marqueurs. La SHS bactérienne est moins spécifique aux substrats et elle n'est pas aussi bien adaptée que la SHS de plante pour accepter la spermidine comme substrat.

[Traduit par la rédaction]

Introduction

Biosynthesis of retronecine, the basic moiety of many pyrrolizidine alkaloids (PAs), has independently been studied by I. D. Spenser using *Senecio vulgaris* and by D.J. Robins using *Senecio isatideus* (for review see refs. 1–3). Extensive tracer experiments carried out in the two laboratories confirmed that retronecine is derived from putrescine via a symmetrical intermediate such as *N*-(4-aminobutyl)-1,4-diaminobutane (*sym*-homospermidine) (4–7). Recently we found homospermidine synthase (HSS) to be the first enzyme of the alkaloid specific pathway (8). HSS catalyzes in an NAD^+-dependent reaction the formation of homospermidine from two moles of putrescine. Free Δ^1-pyrroline as an intermediate in homospermidine formation could be excluded. The enzyme that has previously been reported to occur in the bacterium *Rhodopseudomonas viridis* (9) and the legume *Lathyrus sativus* (10) was purified and characterized from root cultures of *Eupatorium cannabinum* and *Senecio* spec. (Asteraceae) (8).

Here we report that HSS from PA-producing plant sources uses spermidine with high efficiency instead of putrescine as donor of the 4-aminobutanyl moiety that is combined with the second mole of putrescine. The bacterial enzyme is also able to use spermidine, but less efficiently.

Results

Incorporation of chiral deuterated putrescines into homospermidine

In the overall reaction catalyzed by HSS, NAD^+ functions as electron acceptor in the first part of the reaction (oxidative deamination) and as electron donor in the second part (hydrogenation of the intermediate imine):

$$2 \times H_2N\text{-}(CH_2)_4\text{-}NH_2 + NAD^+ \rightarrow H_2N\text{-}(CH_2)_3\text{-}CH{=}N\text{-}(CH_2)_4\text{-}NH_2$$

$$+ NH_3 + NADH + H^+ \rightarrow H_2N(CH_2)_4\text{-}NH\text{-}(CH_2)_4\text{-}NH_2 + NAD^+$$

Kinetic studies suggest that the NAD^+-mediated hydride transfer may proceed enzyme-bound without external exchange (8). To prove this we incubated partially purified HSS of *Rhodopseudomonas viridis* (bacterial HSS) and *Eupatorium*

[1]Author to whom correspondence may be addressed.

Can. J. Chem. Downloaded from www.nrcresearchpress.com by 195.246.54.202 on 09/08/12
For personal use only.

Can. J. Chem. Downloaded from www.nrcresearchpress.com by 195.246.54.202 on 09/08/12
For personal use only.

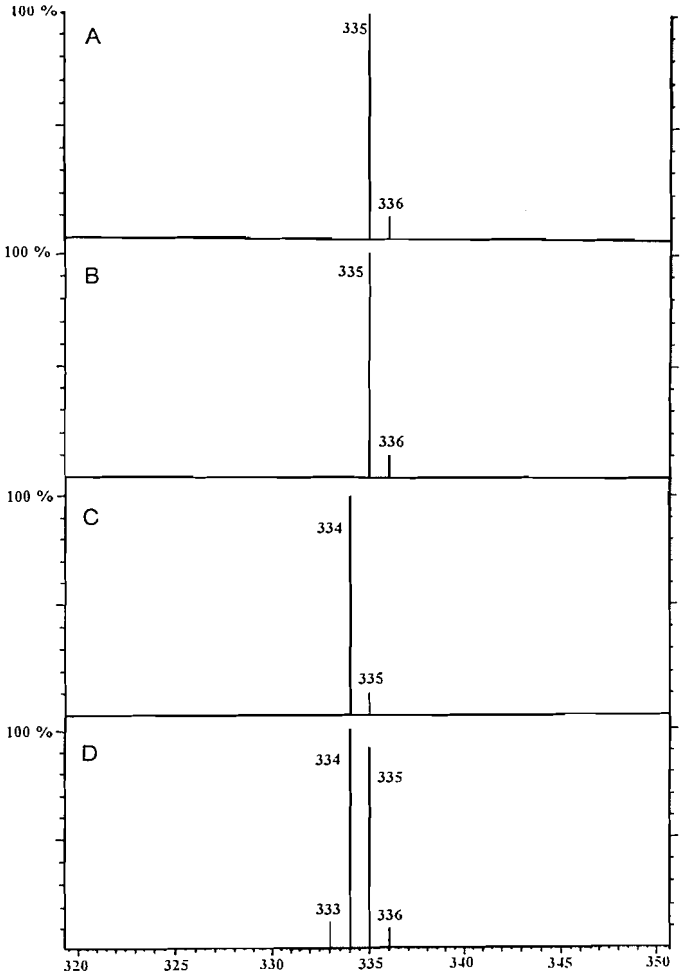

FIG 1. GC–MS analysis of *sym*-homospermidine (analyzed as the *N*-Carbomethoxy(NCM) derivative) synthesized by homospermidine synthase (HSS) incubated with chirally deuterated putrescines as substrates. M^+ (*m/z* 335) = incorporation of $2 \times {}^2H$; M^+ (*m/z* 334) = incorporation of $1 \times {}^2H$; M^+ (*m/z* 333) = undeuterated *sym*-homospermidine. *A*: Bacterial HSS incubated with (*R*)-[1-^{2}H]putrescine as substrate; *B*: bacterial HSS incubated with (*S*)-[1-^{2}H]putrescine as substrate; *C*: plant HSS incubated with (*S*)-[1-^{2}H]putrescine as substrate (in the presence of 0.5 mM spermidine added as stabilizing agent); *D*: bacterial HSS incubated with (*S*)-[1-^{2}H]putrescine in the presence of equimolar amounts of spermidine.

cannabinum (plant HSS), respectively, with (*R*)-[1-^{2}H]putrescine and (*S*)-[1-^{2}H]putrescine as substrates in the presence of NAD^+. GC–MS analysis of the *N*-carbomethoxy(NCM) derivatives of the homospermidine formed shows that with the bacterial enzyme the two deuterated substrates were incorporated into homospermidine without any loss of tracer (Fig. 1, *A* and *B*), i.e., occurrence of M^+ 335 (incorporation of $2 \times {}^2H$) and absence of M^+ 333 (undeuterated homospermidine) and M^+ 334 in the mass spectra.

Unexpectedly, under comparable experimental conditions the plant enzyme gave completely different results (Fig. 1*C*). M^+ 334 (incorporation of $1 \times {}^2H$) became the most dominant fragment. The result was essentially the same with either of the chirally deuterated putrescines. In comparison to bacterial HSS, the only difference was that the enzyme assay with plant HSS was achieved in the presence of 0.5 mM spermidine, which is needed to stabilize the enzyme (8). Addition of spermidine to the assay with bacterial HSS also leads to the appearance of the mass fragment M^+ 334 (Fig. 1*D*). This was the first indication that in the presence of putrescine spermidine is incorporated into homospermidine.

TABLE 1. Efficiency of bacterial and plant HSS to incorporate (*R*)-[1-^{2}H]putrescine into homospermidine in the presence of increasing proportions of spermidine

Substrates[a] [^{2}H]put:spd	% [1-^{2}H]putrescine incorporated (putrescine units)[b] *R. Viridis*	*E. cannabinum*
100: 0	100 (2.00)	
95: 5		97 (1.94)
83:17		63 (1.26)
75:25	88 (1.75)	58 (1.16)
60:40	81 (1.62)	57 (1.14)
48:52	74 (1.48)	
42:58		56 (1.12)

[a]Assay concentration of putrescine plus spermidine: 3.0 mM (bacterial enzyme); 0.25 mM (plant enzyme).

[b]100% = the two putrescine moieties of homospermidine are derived exclusively from putrescine; in parentheses are proportions of the two putrescine moieties in homospermidine derived from putrescine.

Incorporation of "spermidine-bound" putrescine into homospermidine

Incubation of bacterial HSS with a putrescine–spermidine mixture revealed that with increasing amounts of spermidine the incorporation of the "spermidine-bound" putrescine moiety into homospermidine increased. This was established by application of [1-^{2}H]putrescine (Table 1) as well as [^{14}C]putrescine and [^{14}C]spermidine, respectively. In the presence of equimolar concentrations of the two substrates, ca. 25% of the homospermidine formed was derived from spermidine (Table 1). The same results were obtained with plant HSS; the efficiency of spermidine incorporation, however, was considerably higher (Table 1).

Substrate specificity and proposed reaction mechanism of HSS

Bacterial and plant homospermidine synthases have been described as enzymes that catalyze reactions which are highly specific for putrescine as substrate (8–10). Reinvestigation of the substrate specificity revealed, indeed, that putrescine cannot be substituted by homologous diamines if offered as sole substrate (Table 2). If, however, homologous diamines such as 1,3-diaminopropane, cadaverine, or 1,6-diaminohexane are offered in the presence of putrescine, bacterial HSS produces, in addition to homospermidine, low but significant amounts of the respective homologous polyamines (Table 2). On the contrary, plant HSS was virtually unable to catalyze these side reactions. With the two enzymes, however, spermidine was found to be an efficient substrate in the presence of putrescine. The 160% turnover with plant HSS is due to the stabilizing effect of spermidine on the enzyme protein (8). If spermidine is offered as sole substrate or in the presence of diamines different from putrescine, no turnover was found with plant HSS, except the formation of trace amounts of 1,3-diaminopropane. On the other hand, the bacterial enzyme produces homospermidine, putrescine, and diaminopropane upon feeding of spermidine as sole substrate. In the presence of spermidine and various putrescine analogues, small amounts of the respective homologous polyamines are formed, as well as homospermidine.

The mechanism for the HSS-catalyzed reaction, illustrated in Scheme 1, accounts for the data given here and described pre-

TABLE 2. Substrate specificity of bacterial and plant homospermidine synthases

Substrate(s) (1 mM each)	Product(s) formed or expected to be formed	*R. viridis* (%)[a]	*E. cannabinum* (%)[a]
1,3-Diaminopropane	*N*-(3-Aminopropyl)-1,3-diaminopropane	—	—[d]
Putrescine[b]	*sym*-Homospermidine	100	100
Cadaverine[b]	*N*-(5-Aminopentyl)-1,5-diaminopentane	—	—
Putrescine[b] + 1,3-diaminopropane	*sym*-Homospermidine	5	51
	Spermidine	2	—
Putrescine[b] + cadaverine[b]	*sym*-Homospermidine	56	89
	N-(4-Aminobutyl)-1,5-diaminopentane	6	—
Putrescine[b] + 1,6-diaminohexane	*sym*-Homospermidine	54	95
	N-(4-Aminobutyl)-1,6-diaminohexane	5	—
Putrescine[b] + 1,7-diaminoheptane	*sym*-Homospermidine	63	100
	N-(4-Aminobutyl)-1,7-diaminoheptane	tr	—
Spermidine[b]	*sym*-Homospermidine	10	—
	1,3-Diaminopropane	+[c]	tr[c]
	Putrescine	4	—
Spermidine[b] + Putrescine[b]	*sym*-Homospermidine	73	160
	1,3-Diaminopropane	+[c]	+[c]
Spermidine[b] + cadaverine[b]	*sym*-Homospermidine	5	—
	N-(4-Aminobutyl)-1,5-diaminopentane	6	—
	1,3-Diaminopropane	+[c]	tr[c]
Spermidine[b] + 1,6-diaminohexane	*sym*-Homospermidine	6	—
	N-(4-Aminobutyl)-1,6-diaminohexane	<1	—
	1,3-Diaminopropane	+[c]	tr[c]

[a]Activities with putrescine as substrate were set 100% (i.e., bacterial HSS, 33 nmol/h and assay; plant enzyme, 1.8 nmol/12 h and assay). Quantification by radio HPLC; identity proved by GC–MS.

[b]Applied as ^{14}C-labeled substrates; in assays with two substrates (e.g., spermidine + putrescine where both substrates were available as labeled compounds, two assays were performed with, alternatively, one applied as tracer.

[c]Unequivocally identified by GC–MS; quantification not possible due to lack of radioactivity.

[d]— = not detectable, neither by radio HPLC nor GC–MS; tr = traces.

viously (8–10). We assume two binding sites, one for each of the two putrescine molecules. At site A (Scheme 1, I), which may bind either putrescine or spermidine, the NAD^+-dependent oxidativedeamination takes place. Ammonia is released if putrescine is the substrate and 1,3-diaminopropane if spermidine is the substrate. The semialdehyde formed is proposed to remain enzyme-bound, possibly linked as Schiff's base to a protein amino group (e.g., an ϵ-NH_2 group of a lysine residue) (Scheme 1, II/III). Site B specifically binds putrescine, which is suggested to react with the enzyme-bound semialdehyde by transaldimination (Scheme 1, III/IV) to yield an imine as enzyme-bound intermediate. Finally the imine is reduced at the expense of NADH and the homospermidine released (Scheme 1, IV/V). The two enzymes are assumed to bind either putrescine or spermidine to site A and putrescine to site B. In contrast to plant HSS, the bacterial enzyme also accepts some homologous diamines as substrates to some extent (Table 2), and may even bind spermidine in a manner such that putrescine is released as product in the course of the oxidative deamination, as indicated by the detection of both free putrescine and homospermidine (Table 2).

Substrate kinetics of HSS

The results documented in Tables 1 and 2 suggest that there are differences between the two enzymes in respect to their efficiency in using spermidine as substrate in addition to putrescine. Comparative kinetic studies were performed to manifest the role of the two substrates. In each case the incorporation of increasing concentrations of either putrescine or spermidine into homospermidine was measured in the presence of a constant level of the respective other substrate. To be well above the K_m values of putrescine, concentrations of 1 mM and 0.1 mM, respectively, were chosen for the bacterial and the plant enzymes. The Hanes plots show linear behaviour so that the K_m and V_{max} could be calculated for the two substrates (Fig. 2, Table 3). The kinetic data show that in the case of bacterial HSS putrescine is the better substrate for binding site A (Scheme 1, Fig. 2*A*, *C*). The K_m value for putrescine as sole substrate is six times lower than the K_m values for putrescine in the presence of spermidine and for spermidine in the presence of putrescine (Table 3). Furthermore V_{max} and V_{max}/K_m for spermidine are about 10 times lower than the comparable values for putrescine in the presence of spermidine. Although in the presence of the respective other substrate putrescine and spermidine bind to the enzyme with almost the same affinity, the turnover of the latter is much lower.

The situation is quite different with plant HSS. In comparison to bacterial HSS, its substrate affinity is much higher and the K_m and V_{max} values of the two substrates are almost identical (Fig. 2, Table 3). The latter indicates that spermidine not only binds to plant HSS with the same affinity as putrescine but shows also the same reactivity (Table 3).

Discussion

Homospermidine is the first intermediate of the alkaloid-specific pathway leading to PAs (8, 11). Tracer studies have shown

Can. J. Chem. Downloaded from www.nrcresearchpress.com by 195.246.54.202 on 09/08/12
For personal use only.

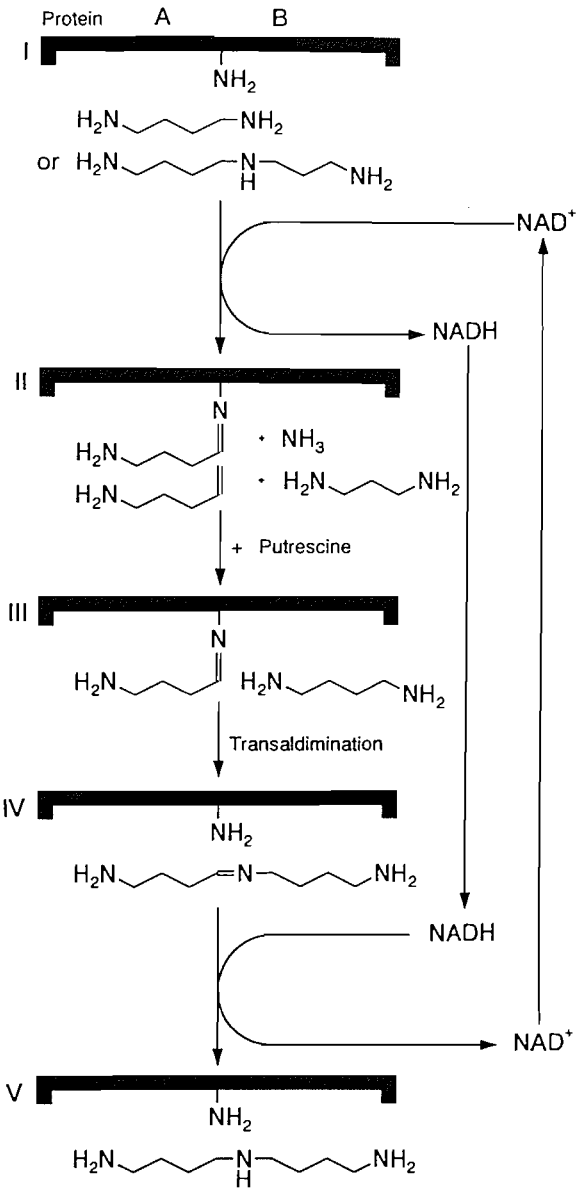

SCHEME 1. Proposed reaction mechanism for homospermidine synthase. A and B are two assumed binding sites.

that labeled free putrescine and the labeled diaminobutane moiety of spermidine are incorporated into PAs with equal efficiency (12–14). Because in PA-producing root cultures of *Senecio vulgaris* putrescine and spermidine exist in a highly dynamic state and are rapidly interconverted, it has been suggested that spermidine is incorporated into PAs via free putrescine (15). The enzymatic data presented here indicate that both free putrescine and "spermidine-bound" putrescine are directly incorporated into homospermidine and thus into the necine base of PAs. If we take into account the steady-state concentrations of putrescine and spermidine (i.e., 70–120 μM and 30–100 μM, respectively, on a fresh weight basis) in growing root cultures of *Senecio* and *Eupatorium* (8) we can assume that the incorporation of the two substrates is around 1:1, i.e., binding site A (Scheme 1) may be almost completely occupied by spermidine (see Table 1). The biosynthetic mechanism suggested here on the basis of enzymatic studies is, except for one deviation (see below), compatible with previous isotope tracer studies that established the symmetrical putrescine as an essential intermediate of necine biosynthesis (1–7). In fact, by tracer studies, even with sophisticated labeled precursors, it would not be possible to distinguish whether a putrescine moiety of homospermidine or a necine base is derived from free putrescine or is incorporated via spermidine.

The experiments with chirally ^{2}H-labeled putrescines proved that the ^{2}H is completely retained in the conversion of each of the (*R*)- and the (*S*)-[1-^{2}H]putrescine into homospermidine, as must be predicted from the mechanism of HSS. This is not fully in agreement with the plant tracer experiments carried out by Grue-Sorensen and Spenser (16) and Rana and Robins (17) who, in convincing experiments, followed the fate of chirally 1-^{2}H-labeled putrescines into the necine base (i.e., retronecine) formed, and analyzed the ^{2}H retention by means of ^{2}H NMR. These authors (Spenser, Robins and co-workers) found retention of 69% and 68%, respectively, of ^{2}H at the carbons that are affected in the formation of homospermidine (i.e., adjacent to the secondary amino group) if (*S*)-[1-^{2}H]putrescine was fed. When (*R*)-[1-^{2}H]putrescine was fed the retention was100%. Because the authors expected a diamine oxidase to be involved, which is known to remove stereospecifically the *pro-S* hydrogen from the methylene group of the primary amine, the predicted retention with (*S*)-[1-^{2}H]putrescine should be 50%. The authors explained the observed differences by the operation of an intramolecular deuterium isotope effect in the enzymatic oxidations involved. From our own results, one should expect a 100% retention. For the HSS reaction catalyzed with putrescine as sole substrate we were unable to detect any significant isotope effect. But it could be that this is associated with the incorporation of the 4-aminobutanyl moiety of spermidine into homospermidine or that it occurs at the stage of spermidine rather than homospermidine formation. Studies to resolve this are in progress in our laboratory.

Finally we have to put forward the question, why do plants substitute free putrescine at least partly by spermidine as biosynthetic precursor of PAs? Polyamines such as spermidine have been implicated in many plant growth and developmental processes (18). On the other hand, we know that in *Senecio* root cultures PA biosynthesis is functionally and spatially related to root growth; PAs do not show any significant degradation or turnover but their concentration in a growing root system is kept constant (15, 19). Thus, a direct metabolic linkage of PA biosynthesis to spermidine may offer a control mechanism to adjust the rate of PA biosynthesis to growth velocity.

Experimental

Preparation of bacterial homospermidine synthase (HSS)

Rhodopseudomonas viridis (DSM 134) was obtained from the German Collection of Microorganisms and Cell Cultures (DSM Braunschweig, Germany). The strain was cultured anaerobically in the medium given in ref. 20 in screw-capped 500-mL flasks in the light at 20–27°C. The cultures were harvested at the beginning of the stationary growth phase (ca. 7 days). The cells collected by centrifugation were treated twice with cold (–18°C) acetone in a Waring blender (30 s). Acetone-treated cells were collected by filtration under reduced pressure, air-dried, and ground in a mortar. The "acetone powder" (AP) retained HSS activity without loss for months if stored dry at –18°C.

For HSS preparation 1 g AP was suspended in 20 mL standard buffer (50 mM KH_2PO_4, 2 mM dithioerythritol (DTE), pH 8.5 adjusted with 5 M NaOH), stirred for 30 min at 4°C, and centrifuged, and the supernatant was desalted via a Sephadex G-50 column. The desalted extract was further purified by affinity chromatography via a spermidine-CH

Can. J. Chem. Downloaded from www.nrcresearchpress.com by 195.246.54.202 on 09/08/12
For personal use only.

Can. J. Chem. Downloaded from www.nrcresearchpress.com by 195.246.54.202 on 09/08/12
For personal use only.

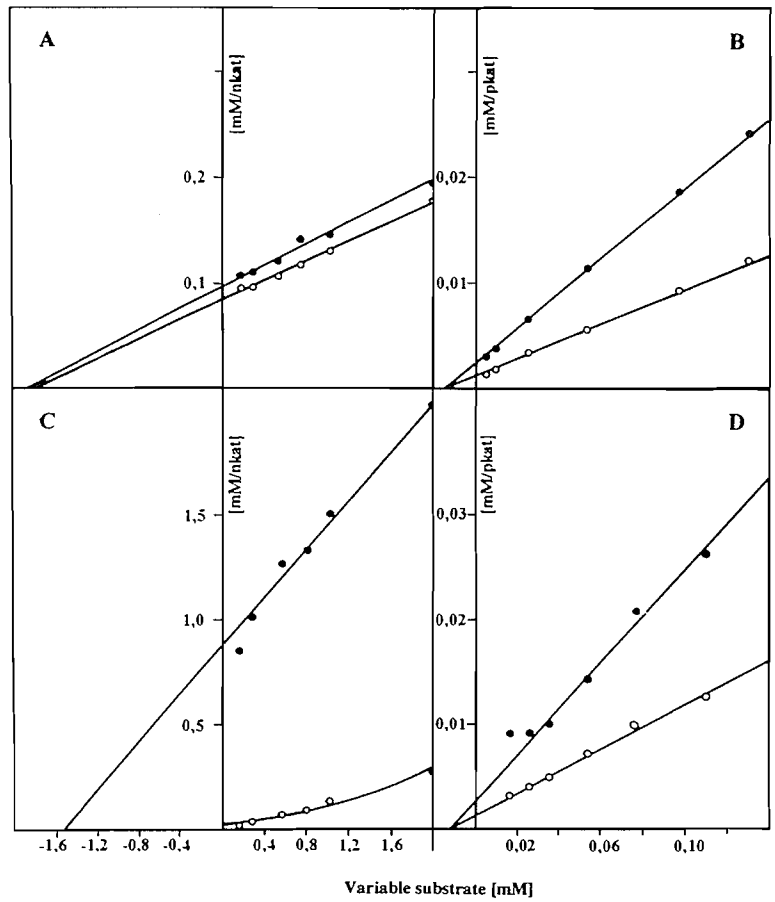

FIG. 2. Substrate kinetics (Hanes plots) of bacterial (*A*, *C*) and plant homospermidine synthase (HSS) (*B*, *D*). *A* and *B*: putrescine as variable substrate in the presence of fixed 1.0 mM (*A*) and 0.1 mM (*B*): spermidine; *C* and *D*: spermidine as variable substrate in the presence of fixed 1.0 mM (*C*) and 0.1 mM (*D*) putrescine. ●—● incorporation of the variable substrate into homospermidine; ○—○ total homospermidine (incorporation of variable plus fixed substrate).

TABLE 3. Substrate kinetics of bacterial and plant homospermidine synthases (HSS). The incorporation of the radioactively labeled variable substrate into homospermidine was determined in the presence of the respective unlabeled second substrate at the concentrations indicated

Substrate	app. K_m(mM)	V_{max}[a]	V_{max}/K_m
R. viridis HSS			
Putrescine	0.26	22	84.6
At 1 mM spermidine:			
Putrescine	1.7	17	10.0
At 1 mM putrescine:			
Spermidine	1.5	1.6	1.1
E. cannabinum HSS			
Putrescine[b]	0.013	14.5	1115
At 0.1 mM spermidine:			
Putrescine	0.015	11.0	733
At 0.1 mM putrescine:			
spermidine	0.012	8.8	733

[a]Bacterial HSS = nkat/mg protein; plant HSS = pkat/mg protein; K_m and V_{max} were calculated on the basis of the incorporation of the respective substrate into homospermidine.

[b]Residual spermidine concentration of the enzyme preparation <0.01 mM.

Sepharose 4B batch column (20 mL bed volume). The gel was equilibrated with 300 mL standard buffer, then 20 mL enzyme extract was mixed with the gel, and after 20 min elution was started. After washing, the column with standard buffer HSS activity was eluted with standard buffer supplemented with a mixture of spermidine plus putrescine (100 mM each). The active fractions were collected and desalted via Sephadex G 50 to remove the spermidine and putrescine. HSS activity remains stable for at least several weeks if kept cool at 4°C; the specific activity of HSS was about 10–20 nkat/mg protein.

Preparation of plant homospermidine synthase (HSS)

Enzyme preparations were obtained from root cultures of *Eupatorium cannabinum* following a four-step protocol: (1) preparation of a crude extract; (2) desalting via a Sephadex G 50 column; (3) ca. 10-fold concentration of the desalted crude extract by ultrafiltration; (4) protein separation by gel filtration via a Superdex TM 200 "high load" column. The whole procedure was the same as described previously (8). The preparation was immediately used for enzymatic studies due to the instability of plant HSS; the specific activity was about 10 pkat/mg protein. If spermidine-free enzyme preparations were required, extracts were desalted via PD-10 columns (Pharmacia) and the desalted eluate, which still contained residual spermidine up to 0.01 mM, was used immediately for enzyme assays.

Enzyme assays

(1) Bacterial HSS

The standard assay contained, in a total volume of 125 µl standard buffer, pH 8.5 1.0 mM [^{14}C]putrescine (0.05 µCi/assay), 0.2 mM NAD^+, and further additives as indicated. Assays were incubated for 10–60 min at 37°C. Formation of labeled homospermidine was followed quantitatively by radio TLC or radio HPLC as described previously (8).

(2) Plant HSS

Standard assays were performed and analyzed as described in ref. 8, except that the addition of 0.5 mM spermidine as protective agent was omitted.

Preparations of the two enzymes were essentially free of interfering enzyme activities such as diamine or polyamine oxidases or other enzymes that utilize either putrescine or spermidine.

HPLC analysis of polyamines

The various polyamines that were formed or were expected to be formed as reaction products of bacterial or plant HSS were separated by HPLC as benzoyl derivatives according to refs. 8 and 21. An RP-18 column (Nucleosil 25 cm, 4 mm i.d.; Macherey & Nagel) was applied. Elution: isocratically using the solvent system MeCN–H_3PO_4(1.5%) (40:60); parallel detection: (*a*) UV 230 nm, (*b*) radio monitoring. The retention times (R_t; min) for the polyamines in investigations were as follows: 1,3-diaminopropane, 5.2; putrescine, 5.5; cadaverine, 6.4; 1,6-diaminohexane, 8.7; spermidine, 8.4; *sym*-homospermidine, 9.5; *N*-[4-aminobutyl]-1,5-diaminopentane, 9.5; *N*-[4-aminobutyl]-1,6-diaminohexane, 16.3.

Identification of the reaction products of HSS

For unequivocal identification the reaction products were analyzed as *N*-carbomethoxy derivatives (NCM derivatives) by GC–MS (22). An aliquot (1.0 mL) of the aqueous enzymatic reaction was mixed with 20 µL of methyl chloroformate medium and left standing at room temperature for 15 min. The amine NCM derivatives were extracted into diethyl ether (3 × 1 mL each). The extracts were combined and the solvent evaporated. The residue was dissolved in 10–25 µL dichloromethane prior to GC–MS analysis. GC–MS: Carlo Erba 5160 gas chromatography equipped with 30 m × 0.32 mm fused-silica column (DB-1); conditions, injector 250°C, split-ratio 1:20, injection volume 1–2 µL, carrier gas He 0.75 bar (1 bar = 100 kPa), detector FID; the capillary column was directly coupled to a quadrupole mass spectrometer Finnigan MAT 4515. EI mass spectra were recorded at 40 eV. The NCM derivatives of the following diamines (applied as substrates) and polyamines (formed as products) were identified (see Table 2) by their Kovats indices (RI), and M_r (M^+): 1,3-diaminopropane, RI 1485, [M^+] *m/z* 190; putrescine, RI 1622, [M^+] *m/z*, 204; cadaverine, RI 1727, [M^+] *m/z* 218; 1,6-diaminohexane, RI 1838, [M^+] *m/z 232;* spermidine, RI 2365, [M^+] *m/z* 319; *sym*-homospermidine, RI 2467, [M^+] *m/z* 333; *N*-[4-aminobutyl]-1,5-diaminopentane, RI 2570, [M^+] *m/z* 347; *N*-[4-aminobutyl]-1,6-diaminohexane, RI 2678, [M^+] *m/z* 361.

The same GC–MS procedure was applied to analyse the deuterium incorporation.

Radiochemicals and deuterated putrescines

[1,4-^{14}C]Putrescine (108 mCi mmol^{-1}), [^{14}C]spermidine (*N*-(3-aminopropyl)-[1,4-^{14}C]tetramethylene-1,4-diamine) (109 mCi mmol^{-1}), and L-[U-^{14}C]lysine (312 mCi mmol^{-1}) were purchased from Amersham Braunschweig). [U-^{14}C]Cadaverine was prepared from labelled lysine by application of L-lysine decarboxylase (Sigma, Heidelberg).

(*S*)-[1-^{2}H]Putrescine (97% $^2H_1$ species) and (*R*)-[1-^{2}H]putrescine (99% $^2H_1$ species) were prepared according to the method described in ref. 23.

Acknowledgements

The financial support of the Deutsche Forschungsgemeinschaft (DFG) and Fonds der chemischen Industrie is gratefully acknowledged. The authors wish to thank Dr. L. Witte for the GC–MS analysis.

1. I.D. Spenser. Pure Appl. Chem. **57**, 453 (1985).
2. D.J. Robins. Chem. Soc. Rev. **18**, 375 (1989).
3. D.J. Robins. Experientia, **47**, 1118 (1991).
4. H.A Khan and D.J. Robins. J. Chem. Soc. Chem. Commun. 146 (1981)
5. H.A. Khan and D.J. Robins. J. Chem. Soc. Chem. Commun. 554 (1981)
6. G. Grue-Sorensen and I.D. Spenser. J. Am. Chem. Soc. **103**, 3208 (1981).
7. G. Grue-Sorensen and I.D. Spenser. Can. J. Chem. **60**, 643 (1982).
8. F. Böttcher, R.D. Adolph, and T. Hartmann. Phytochemistry, **32**, 679 (1993).
9. G.H. Tait. Biochem. Soc. Trans. **7**, 199 (1979).
10. K.S. Srivenugopal and P. R. Adiga. Biochem. J. **189**, 553 (1980).
11. D.J. Robins. J. Chem. Soc. Chem. Commun. 1289 (1982).
12. D.J. Robins and J.R. Sweeney. J. Chem. Soc. Chem. Commun. 120 (1979).
13. D.J. Robins and J.R. Sweeney. J. Chem. Soc. Perkin Trans. 1, 3083 (1981).
14. T. Hartmann and G. Toppel. Phytochemistry, **26**, 1639 (1987).
15. T. Hartmann, H. Sander, R.D. Adolph, and G. Toppel. Planta, **175**, 82 (1988).
16. G. Grue-Sorensen and I.D. Spenser. J. Am. Chem. Soc. **105**, 7401 (1983).
17. J. Rana and D.J. Robins. J. Chem. Soc. Perkin Trans. 1, 983 (1986).
18. P.T. Evans and R.L. Malmberg. Annu. Rev. Plant Physiol. Plant Mol. Biol. **40**, 235 (1989).
19. H. Sander and T. Hartmann. Plant Cell, Tissue Organ Cult. **18**, 19 (1989).
20. K.A. Malik. J. Microbiol. Methods, **1**, 343 (1983).
21. J.W. Redmond and A. Tseng. J. Chromatogr. **170**, 479 (1979).
22. P. Husek, Z.H. Huang, and C.C. Sweely. Anal. Chim. Acta, **259**, 185 (1992).
23. J.C. Richards and I.D. Spenser. Can. J. Chem. **60**, 2810 (1982).

Can. J. Chem. Downloaded from www.nrcresearchpress.com by 195.246.54.202 on 09/08/12
For personal use only.

Investigations of the biosynthesis of the phytotoxin coronatine[1]

RONALD J. PARRY,[2] SUNIL V. MHASKAR, MING-TEH LIN, ALAN E. WALKER, and ROBSON MAFOTI
Department of Chemistry, Wiess School of Natural Sciences, Rice University, Houston, TX 77251, U.S.A.

Received May 31, 1993

This paper is dedicated to Professors Ian Spenser and David B. MacLean

RONALD J. PARRY, SUNIL V. MHASKAR, MING-TEH LIN, ALAN E. WALKER, and ROBSON MAFOTI. Can. J. Chem. **72**, 86 (1994).

The biosynthesis of the phytotoxin coronatine has been investigated by administration of isotopically labeled precursors to *Pseudomonas syringae* pv. *glycinea*. The structure of coronatine contains two moieties of distinct biosynthetic origin, a bicyclic, hydrindanone carboxylic acid (coronafacic acid) and a cyclopropyl α-amino acid (coronamic acid). Investigations of coronafacic acid biosynthesis have shown that this compound is a polyketide derived from three acetate units, one butyrate unit, and one pyruvate unit. The two carbonyl oxygen atoms of coronafacic acid were found to be derived from the oxygen atoms of acetate. Additional experiments are described that rule out some possible modes for assembly of the polyketide chain. Coronamic acid is shown to be derived from L-isoleucine via the intermediacy of L-alloisoleucine. Examination of the mechanism of the cyclization of L-alloisoleucine to coronamic acid revealed that the formation of the cyclopropane ring takes place with the removal of only two hydrogen atoms from the amino acid, one at C-2 and the other at C-6. The nitrogen atom at C-2 of L-alloisoleucine is shown to be retained. On the basis of these observations, a mechanism is postulated for the cyclization reaction that involves the diversion of an enzymatic hydroxylation reaction into an oxidative cyclization. Finally, a precursor incorporation experiment with deuterium-labeled coronamic acid demonstrated that free coronamic acid can be efficiently incorporated into coronatine. This observation indicates that the cyclization of L-alloisoleucine to coronamic acid can occur before formation of the amide bond between coronafacic acid and coronamic acid.

RONALD J. PARRY, SUNIL V. MHASKAR, MING-TEH LIN, ALAN E. WALKER et ROBSON MAFOTI. Can. J. Chem. **72**, 86 (1994).

On a étudié la biosynthèse de la phytotoxine coronatine en administrant des précurseurs marqués au *Pseudomonas syringae* pv. *glycinea*. La structure de la coronatine contient deux portions d'origines biosynthétiques différentes : un acide hydrindanone carboxylique bicyclique (l'acide coronafacique) et un acide cyclopropylique α-aminé (l'acide coronamique). Des études sur la biosynthèse de l'acide coronafacique ont montré que ce composé est un polycétide dérivé de trois unités acétique, d'une unité butyrique et d'une unité pyruvique. On a trouvé que les deux atomes d'oxygène carbonyles de l'acide coronafacique sont dérivés des atomes d'oxygène de l'acide acétique. On décrit des expériences additionnelles qui permettent d'éliminer un certain nombre de modes d'assemblage de la chaîne polycétide. On démontre que l'acide coronamique est dérivé de la L-isoleucine par le biais de la L-alloisoleucine comme intermédiaire. L'examen du mécanisme de cyclisation de la L-alloisoleucine en acide coronamique a révélé que la formation du cyclopropane se produit avec l'enlèvement de seulement deux atomes d'hydrogène à partir de l'acide aminé, l'un en C-2 et l'autre en C-6. On a démontré que l'atome d'azote en C-2 de la L-alloisoleucine est conservé. Sur la base de ces observations, on propose un mécanisme pour la réaction de cyclisation qui implique la transformation d'une réaction enzymatique d'hydroxylation en une cyclisation oxydante. Finalement, une expérience d'incorporation d'un précurseur avec de l'acide coronamique marqué au deutérium a permis de démontrer que l'acide coronamique libre peut être incorporé efficacement dans la coronatine. Cette observation indique que la cyclisation de la L-alloisoleucine en acide coronamique peut se produire avant la formation de la liaison amide entre l'acide coronafacique et l'acide coronamique.

[Traduit par la rédaction]

Introduction

Coronatine (**1**) is a phytotoxin of novel structure that is produced by many pathovars of *Pseudomonas syringae*, including pv. *atropurpurea* (1,2), pv. *glycinea* (2,3), pv. *tomato* (4), and pv. *morsprunorum* (2). Infection of the host plants by these bacteria induces chlorosis on the leaves due to the production of coronatine(1,2). In addition, coronatine distorts leaf growth, inhibits root elongation, and causes hypertrophy when applied to the cut surface of potato tubers (5,6). Treatment of plant tissues with coronatine has been shown to stimulate the production of ethylene, and it has been hypothesized that the biological effects of coronatine on plant tissues are due to this stimulative effect (7).

Coronatine can be hydrolyzed to yield two components, the bicyclic acid (**2**), which is called (+)-coronafacic acid, and the cyclopropyl amino acid **3**, which has been dubbed (+)-coronamic acid (Fig. 1). The structure and absolute stereochemistry of coronafacic acid were elucidated by X-ray crystallographic analysis of its 7a epimer (1). The absolute stereochemistry of coronamic acid has been determined by X-ray analysis of its *N*-acetyl derivative (8). The structures of **2** and **3** suggest they should have distinct biosynthetic origins. The results of detailed

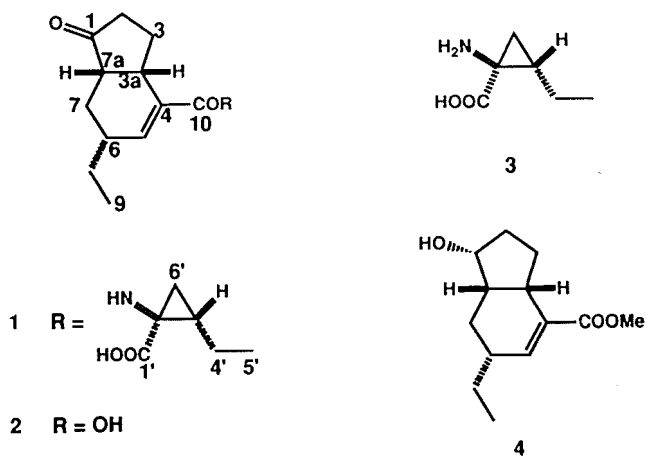

FIG. 1. Structures of coronatine, coronafacic acid, and coronamic acid.

[1]The author is pleased to dedicate this article to Professors Ian Spenser and David MacLean for their friendship, counsel, and many contributions to natural products chemistry.

[2]Author to whom correspondence may be addressed.

Can. J. Chem. Downloaded from www.nrcresearchpress.com by 195.246.54.202 on 09/08/12
For personal use only.

Can. J. Chem. Downloaded from www.nrcresearchpress.com by 195.246.54.202 on 09/08/12
For personal use only.

TABLE 1. Carbon-13 chemical shifts for methyl ester of coronafacic acid (**2**)

Carbon atom	Shift (ppm)[a]	Carbon atom	Shift (ppm)[a]
1	220.5	7	25.8
2	38.1	7a	46.6
3	28.1	8	27.8
3a	36.2	9	11.2
4	131.3	10	167.3
5	144.2	11	51.7
6	37.7		

[a]Shifts were measured in deuterochloroform at 75.47 MHz.

investigations of the biosynthesis of coronafacic acid and coronamic acid will now be described.[3]

Results and discussion

Investigations of coronafacic acid (**2**) and coronamic acid (**3**) biosynthesis were carried out by administration of labeled precursors to liquid cultures of *Pseudomonas syringae* pv. *glycinea* strains PDDCC 4182 and 4180. These strains produce both coronafacic acid and coronatine when grown in Hoitink–Sinden medium (2). Compounds **1** and **2** were isolated from the culture broth as their methyl esters, after treatment with diazomethane.

Coronafacic acid

To elucidate the biosynthesis of coronafacic acid, it was necessary to assign the resonances present in its ^{13}C NMR spectrum. The complete assignment (Table 1) required the use of several techniques. Treatment of methyl coronafacate with D_2O/DCl led to the disappearance of the ^{13}C signal for C-2 from the noise-decoupled spectrum due to exchange of the hydrogens at C-2 for deuterium. Reduction of methyl coronafacate with lithium tri-*tert*-butoxyaluminum hydride yielded a single alcohol (**4**) (Fig. 1) in which the ^{13}C NMR signals for C-2 and C-7a were shifted upfield to 31.05 and 42.28 ppm, respectively. The hydroxyl group in **4** was assigned the α configuration on the basis of the assumption that the reagent will approach from the less-hindered face of the coronafacate skeleton.

Precursor incorporation experiments also provided a very powerful tool for assignment. The structure of coronafacic acid suggested that the compound was likely to be a polyketide. Therefore, sodium (1-^{13}C)-, (2-^{13}C)-, and (1,2-$^{13}C_2$)acetate were administered to *P. syringae* cultures. The results of these experiments (Table 2, expts. 1–3) clearly indicated that five molecules of acetate were incorporated into **2**. The positions of the labels and their connectivities were unequivocally established by a ^{13}C COSY analysis (10,11) of the methyl coronafacate derived from doubly ^{13}C-labeled acetate.

Since the incorporation experiments with ^{13}C-labeled sodium acetate indicated that C-1 and C-10 of the coronafacate moiety are derived from C-1 of an acetate unit, an experiment was carried out to determine whether or not the carbonyl oxygen atoms present at C-1 and C-10 are derived from the oxygen atoms of acetate. Administration of sodium (1-^{13}C, $^{18}O_2$)acetate yielded a sample of methyl coronatine in which the ^{13}C NMR signals for C-1 and C-10 exhibited upfield ^{18}O isotope-induced shifts of ca. 0.05 and 0.03 ppm, respectively (Table 2, expt. 4). One can therefore conclude that the carbonyl oxygens present at C-1 and C-10 of coronatine are derived from the oxygens atoms of an acetate unit (12).

The presence of an ethyl side chain in coronafacic acid suggested that butyrate might also serve as a specific precursor of this compound, since butyrate has been found to be the source of the ethyl side chains that are present in a number of polyketide antibiotics (13). This expectation was confirmed by administration of sodium (1-^{13}C)butyrate to *P. syringae* and isolation of a sample of methyl coronafacate that exhibited a 38% enrichment at C-5 (Table 2, expt. 5).[4]

The incorporation experiments with labeled acetate demonstrated that two carbon atoms of the coronafacate acid skeleton, C-3 and C-3a, are not derived from acetate. Glycine, glycerol, and pyruvate were therefore evaluated as sources of these carbon atoms. Of these compounds, only pyruvic acid appeared to be specifically incorporated. Administration of sodium (1-^{13}C)-, (2-^{13}C)-, and (3-^{13}C)pyruvate revealed the somewhat surprising fact that C-3 and C-3a of coronafacate are derived from C-2 and C-3 of pyruvate, respectively (Table 2, expts. 6–8). In these experiments, the remaining carbon atoms of coronafacate exhibited a labeling pattern consistent with the partial degradation of pyruvate to acetate. The intact incorporation of C-2 and C-3 of pyruvate into coronafacate was confirmed by administration of (2,3-$^{13}C_2$)pyruvate followed by analysis of the resulting labeled coronafacate by a ^{13}C COSY experiment (Table 2, expt. 9). The COSY experiment revealed the presence of ^{13}C–^{13}C connectivity between C-3 and C-3a, as well as the connectivities expected from degradation of the doubly labeled pyruvate to doubly labeled acetate.

Although the results of preceding experiments reveal the origin of all of the carbon atoms of the skeleton of coronafacic acid, they do not define the starting point for assembly of the polyketide chain, nor do they provide any insight into the mechanism for incorporation of pyruvate into the coronafacate skeleton. A potential solution to both these uncertainties is provided by the hypothesis shown in Scheme 1. This hypothesis postulates that pyruvate serves as the starter unit and that the first step in the assembly of the polyketide chain involves the condensation of acetyl or malonyl CoA with pyruvate to yield the mono CoA ester of citramalic acid (**5**). The plausibility of this hypothesis is enhanced by the fact that both (+)-(*S*) and (–)-(*R*) forms of citramalic acid have been reported to occur naturally (14,15), although the biosynthetic origins of citramalate have apparently never been examined. Initially, we decided to prepare the appropriate mono *N*-acetylcysteamine (NAC) ester of (^{13}C)-labeled (*S*)-citramalate for evaluation as a precursor. The NAC ester was utilized because the NAC esters of a number of polyketide intermediates have been successfully incorporated intact into polyketide natural products (16). The NAC ester of (5-^{13}C)-(*S*)-citramalate (**6**) was synthesized from l-malic acid as shown in Scheme 2*a*. The key steps in the synthesis make use of chemistry reported by Seebach et al. (17) and Schwab and Klassen (18). Unfortunately, administration of **6** to the coronatine fermentation yielded methyl coronafacate that exhibited no

[3]Portions of this work have been the subject of preliminary communications (9).

[4]In initial studies of coronafacate biosynthesis (ref. 9), an incorporation experiment with (1-^{13}C)butyrate failed to show enrichment. The reasons for this behavior are unclear.

TABLE 2. Incorporation of precursors into the coronafacic acid moiety (**2**) of coronatine

Expt.	Precursor	Labeling pattern
1	Sodium (1-^{13}C)acetate	C-1, C-5, C-7, C-8, C-10
2	Sodium (2-^{13}C)acetate	C-2, C-4, C-6, C-7a, C-9
3	Sodium (1,2-$^{13}C_2$)acetate	Connectivities between C-1, C2; C-4, C-10; C-5, C-6; C-7, C-7a; C-8, C-9
4	Sodium (1-^{13}C, $^{18}O_2$)acetate	Upfield isotope shifts of 0.05 ppm at C-1, 0.03 ppm at C-10
5	Sodium (1-^{13}C)butyrate	C-5
6	Sodium (1-^{13}C)pyruvate	No enrichment
7	Sodium (2-^{13}C)pyruvate	C-3; C-1, C-5, C-7, C-8, C-10
8	Sodium (3-^{13}C)pyruvate	C-3a; C-2, C-4, C-6, C-7a, C-9
9	Sodium (2,3-$^{13}C_2$)pyruvate	Connectivities between C-3, C-3a; C-1, C-2;C-4, C-10; C-5, C-6; C-7, C-7a; C-8, C-9
10	Ethyl (3-^{13}C)acetoacetate	C-8
11	Ethyl (2,3-$^{13}C_2$)acetoacetate	Connectivity between C-6, C-8 ($^1J_{CC}$ = 33.9 Hz)
12	Ethyl (2,3-$^{13}C_2$)-3-ketohexanoate	C-5
13	*N*-Acetylcysteamine ester of (2,3-$^{13}C_2$)-3-ketohexanoate	C-5

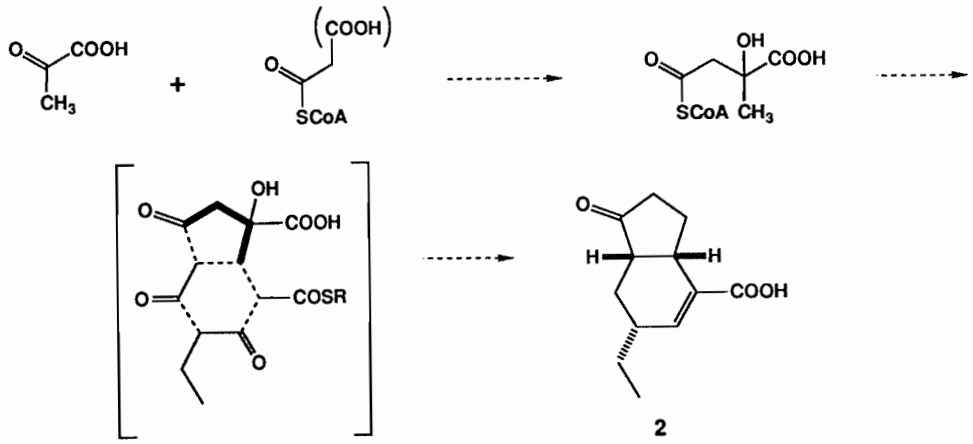

SCHEME 1

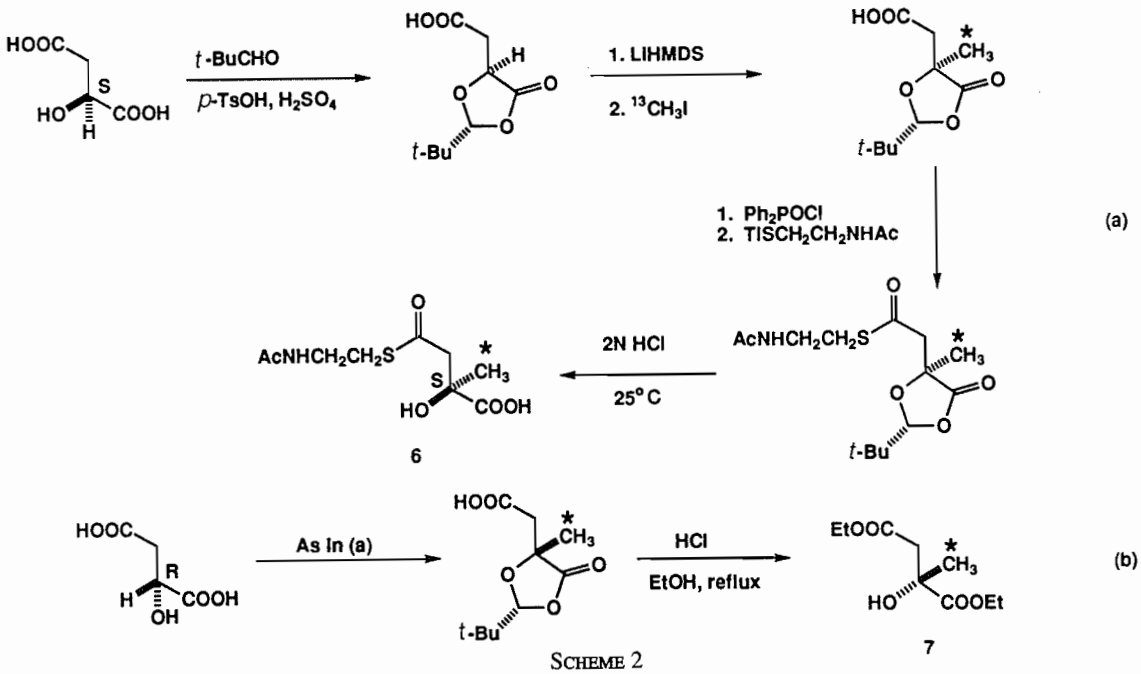

SCHEME 2

Can. J. Chem. Downloaded from www.nrcresearchpress.com by 195.246.54.202 on 09/08/12
For personal use only.

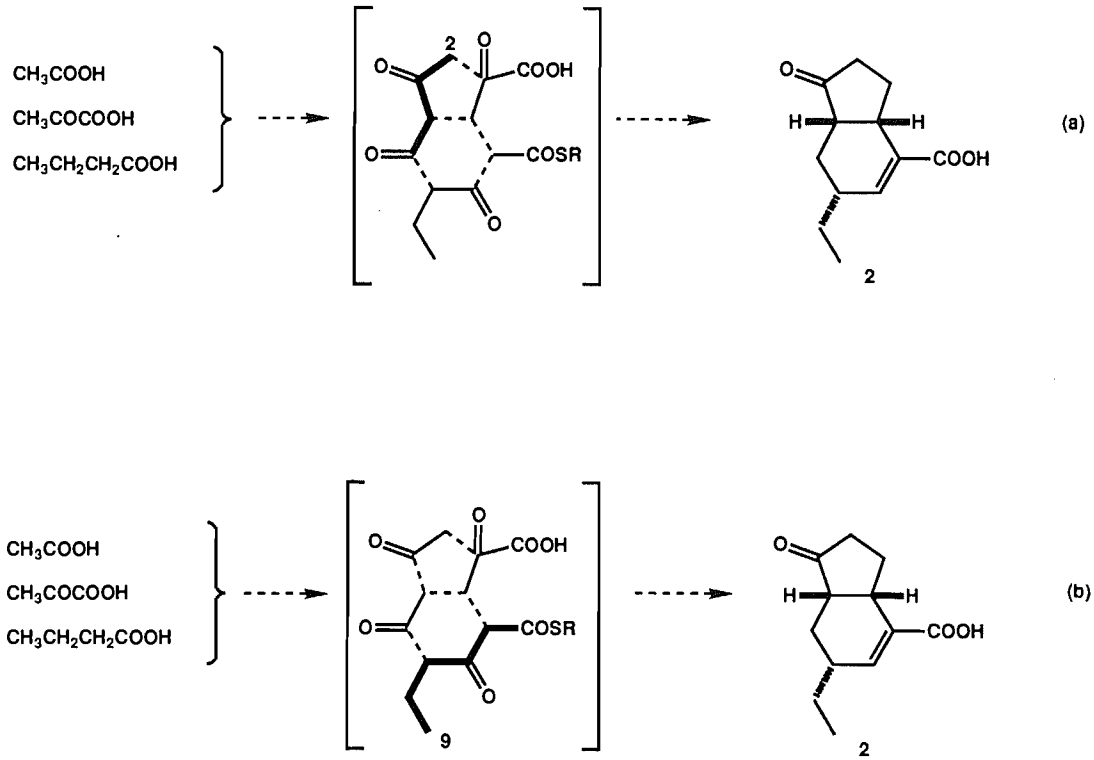

SCHEME 3

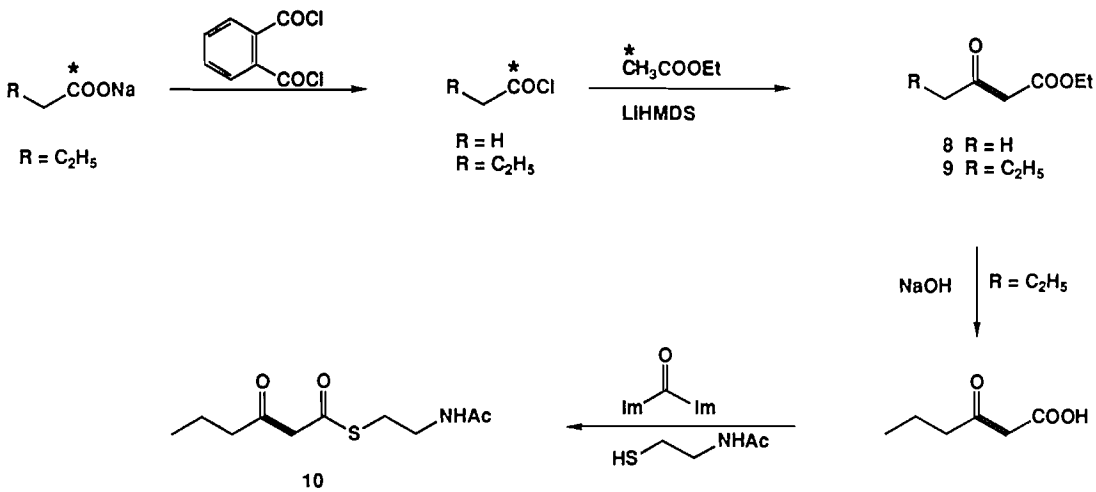

SCHEME 4

evidence of enrichment, not even that resulting from catabolism of the precursor to yield (2-^{13}C)acetate (data not shown). It therefore appeared necessary to examine the (*R*) form of citramalic acid as a precursor. For this purpose, the diethyl ester of (5-^{13}C)-(*R*)-citramalate (**7**) was synthesized (Scheme 2*b*) and evaluated. The diethyl ester was employed since no evidence of catabolism had been observed with the (*S*) precursor **6**. In the event, compound **7** also yielded methyl coronafacate that showed no signs of ^{13}C enrichment (data not shown). The results of these two experiments suggest that the hypothesis for polyketide assembly shown in Scheme 1 is incorrect. Although these observations indicate that pyruvate is not incorporated into coronafacate via the intermediacy of citramalate, they do not rule out the possibility that some metabolite of pyruvate serves as a starter unit. For example, pyruvate could be converted to phosphoenolpyruvate, which could then condense with malonyl CoA to yield a mono CoA ester of itaconic acid. The potential role of itaconic acid in coronafacate biosynthesis remains to be evaluated.

An alternative mode for assembly of the polyketide skeleton of coronafacic acid that can be envisioned proceeds from C-2 of the skeleton, with acetate serving as the starter unit and pyruvate serving as the terminating unit (Scheme 3*a*). If this hypothesis were correct, then a thiol ester of acetoacetic acid should be the intermediate resulting from the first polyketide condensation step. Investigations of this hypothesis were initiated by administering commercial ethyl (3-^{13}C)acetoacetate to *P. syringae*. The results of this experiment were quite unexpected: the isolated methyl coronafacate exhibited 27% enrichment at C-8, with no other detectable enrichments (Table 2, expt. 10)! This

Can. J. Chem. Downloaded from www.nrcresearchpress.com by 195.246.54.202 on 09/08/12
For personal use only.

Can. J. Chem. Downloaded from www.nrcresearchpress.com by 195.246.54.202 on 09/08/12
For personal use only.

observation was confirmed by the synthesis (Scheme 4) and administration of ethyl (2,3-$^{13}C_2$)acetoacetate (**8**). In this instance, the resulting methyl coronafacate exhibited ^{13}C–^{13}C coupling between C-6 and C-8, but no trace of ^{13}C–^{13}C coupling was apparent between C-1 and C-7a (Table 2, expt. 11). Three conclusions can be drawn from these two precursor incorporation experiments. First, ethyl acetoacetate does not appear to be significantly catabolized to acetate by *P. syringae*. Second, ethyl acetoacetate is incorporated intact into the butyrate-derived portion of the coronafacate skeleton. Finally, since no coupling appears between C-1 and C-7a in the coronafacate derived from doubly labeled acetoacetate, the polyketide assembly process does not appear to begin at C-2 of the coronafacate skeleton. Consequently, the polyketide assembly mode hypothesized in Scheme 3*a* is probably not correct. The efficient and intact incorporation of ethyl acetoacetate observed in experiments 10 and 11 is quite remarkable since it is usually necessary to administer thiol esters of polyketide intermediates in order to observe intact incorporation (16). Furthermore, Vederas and co-workers (19) have reported that even the thiol esters of *acetate*-derived polyketide intermediates tend to be completely degraded unless special measures are taken.

A third mode of polyketide assembly that can be considered for coronafacate is one in which the assembly proceeds from C-9 of the coronafacate skeleton, with acetate serving as the starter unit (Scheme 3*b*). This hypothesis is consistent with the results obtained from the ethyl acetoacetate experiments, but it requires the rather unorthodox insertion of a pyruvate unit into the middle of the growing polyketide chain. If polyketide assembly indeed begins at C-9, then a thiol ester of 3-ketohexanoate should be an intermediate in the assembly process. Emboldened by the results with ethyl acetoacetate, we therefore synthesized ethyl (2,3-$^{13}C_2$)-3-ketohexanoate (**9**) (Scheme 4) and administered it to the coronatine fermentation. The results from this experiment provided a sharp contrast to those observed with ethyl acetoacetate, since the methyl coronafacate exhibited a 35% enrichment at C-5, but no ^{13}C coupling to C-4 was apparent (Table 2, expt. 12). Curiously, no significant enrichments were present at those carbons expected to be derived from C-2 of acetate. This may reflect the fact that the amount of acetate generated by catabolism of this precursor would be significantly less than the amount that was administered when acetate was used as a precursor. In any case, the labeling pattern indicates that the ethyl (2,3-$^{13}C_2$)-3-ketohexanoate had been catabolized to give (1-^{13}C)butyrate, which was then incorporated into coronafacate. Much the same result was observed when the NAC ester of (2,3-$^{13}C_2$)-3-ketohexanoate (**10**) was synthesized (Scheme 4) and evaluated as a precursor (Table 2, expt. 13). These observations can be interpreted in one of two ways: either 3-ketohexanoate is not an intermediate in coronafacate biosynthesis and the polyketide assembly does not proceed from C-9 (Scheme 3*b*) or 3-ketohexanoate is so readily catabolized by *P. syringae* that its intact incorporation into methyl coronafacate cannot be observed under the usual fermentation conditions.

Coronamic acid

The structure and absolute configuration of coronamic acid (**3**) suggest that the compound could be derived from L-isoleucine (**11**) via the intermediacy of L-alloisoleucine (**12**) (Scheme 5). This hypothesis was evaluated by administration of commercial (1-^{13}C)-L-isoleucine and (1-^{13}C)-L-alloisoleucine to *P. syringae*, followed by isolation of coronatine methyl ester. The results of these experiments (Table 3, expts. 1,2) demonstrated

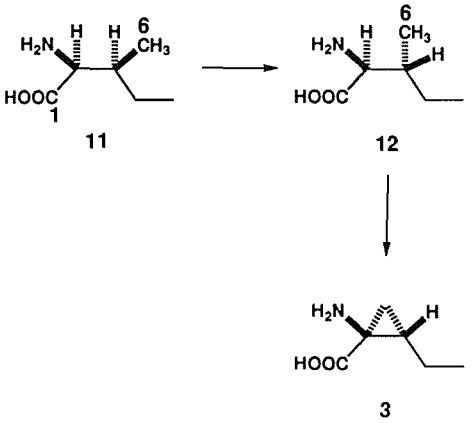

SCHEME 5

that both of these amino acids are specific precursors, and, furthermore, they indicated that L-alloisoleucine is more efficiently incorporated than L-isoleucine. Since the formation of the cyclopropane ring of coronamic acid by cyclization of L-alloisoleucine would constitute a highly unusual process, it appeared important to verify that the methyl group of the amino acid (C-6) is indeed the source of the cyclopropane bridge. This was accomplished by administration of a mixture of (6-^{13}C)-DL-isoleucine and (6-^{13}C)-DL-alloisoleucine synthesized according to Scheme 6 to the coronatine fermentation. The ^{13}C NMR spectrum of the resulting coronatine methyl ester clearly showed that the cyclopropane bridge is derived from the methyl group of isoleucine (Table 3, expt. 3). These observations set the stage for more detailed investigations of the mechanism of the cyclization process.

The first mechanistic probe utilized a mixture of (6-^{13}C, 6-$^2H_3$)-DL-isoleucine and (6-^{13}C, 6-$^2H_3$)-DL-alloisoleucine prepared from (^{13}C, $^2H_3$)methyl iodide (Scheme 6) as a precursor. Examination of the ^{13}C NMR spectrum of the coronatine methyl ester obtained in this experiment while carrying out simultaneous ^1H and ^2H decoupling revealed the presence of a new ^{13}C resonance shifted upfield by 0.59 ppm relative to the signal for C-6′ of coronatine. The magnitude of the upfield isotopic shift indicates that two deuterium atoms are located at C-6′ (20). The conversion of L-alloisoleucine to coronamic acid therefore proceeds with the removal of one hydrogen atom from C-6 of the amino acid. It is also noteworthy that the level of ^{13}C incorporation observed in this experiment (Table 3, expt. 4) was dramatically lower than that observed when no deuterium was present at C-6 (Table 3, expt. 3). This difference in incorporation efficiency is presumably due to the operation of a substantial deuterium isotope effect.

The loss of only one hydrogen atom from C-6 of L-alloisoleucine during coronamic acid formation rules out the intermediacy of species with a C-6 oxidation level higher than that of an alcohol. Putative intermediates with the appropriate oxidation level would therefore include 3-methylene-L-norvaline and 6-hydroxy-L-alloisoleucine. The possible intermediacy of the former amino acid was evaluated by means of a precursor incorporation experiment with [L-^{14}C, 3-^3H]-L-alloisoleucine. The synthesis of L-alloisoleucine carrying the appropriate isotopic labels was accomplished using modifications of chemistry devised by Oppolzer et al. (21) (Scheme 7). Administration of a mixture of the labeled amino acids to *P. syringae* generated a sample of coronatine methyl ester that was purified chromato-

TABLE 3. Incorporation of precursors into the coronamic acid moiety (**3**) of coronatine

Expt.	Precursor ($^3H/^{14}C$)	Percent enrichment or incorporation	Labeling pattern
1	(1-^{13}C)-L-Isoleucine	9	C-1′
2	(1-^{13}C)-L-Alloisoleucine	60	C-1′
3	(6-^{13}C)-DL-Isoleucine + (6-^{13}C)-DL-alloisoleucine	31	C-6′
4	(6-^{13}C, 6-$^{2}H_3$)-DL-Isoleucine + (6-^{13}C, 6-$^{2}H_3$)-DL-alloisoleucine	0.5	^{13}C and 2 D at C-6′
5	[1-^{14}C, 3-^{3}H]-L-Alloisoleucine (3.89)	1.8	$^3H/^{14}C$ = 3.67 (94% ^{3}H retention)
6	(2-^{13}C, ^{15}N)-DL-Isoleucine + (2-^{13}C, ^{15}N)-DL-alloisoleucine	7.8% ^{13}C 2.4% ^{15}N	Connectivity between C-2′ and ^{15}N ($^1J_{CN}$ = 12 Hz)
7	(4-$^{2}H_1$, 5-$^{2}H_1$)-DL-Coronamic acid	ca. 32%	1 D at C-4′, 1 D at C-5′

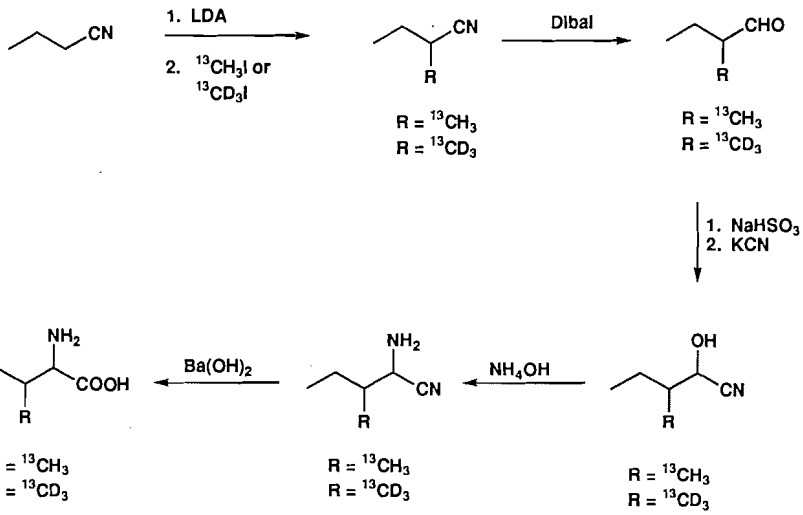

SCHEME 6

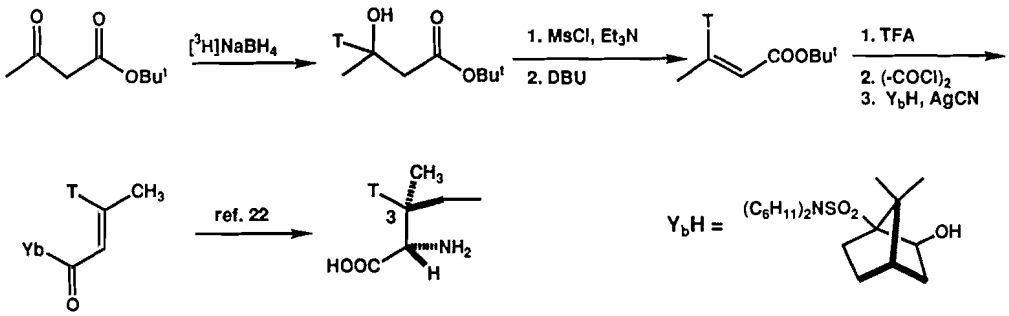

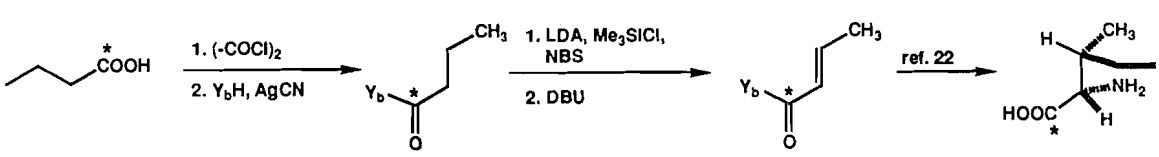

SCHEME 7

Can. J. Chem. Downloaded from www.nrcresearchpress.com by 195.246.54.202 on 09/08/12
For personal use only.

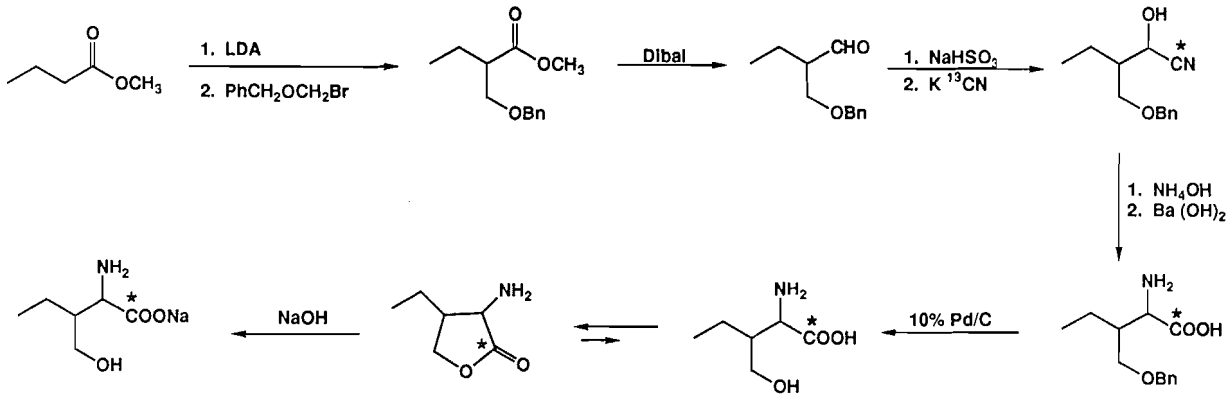

SCHEME 8

graphically and then reduced to the corresponding alcohol with lithium tri-*tert*-butoxyaluminum hydride. The radioactive alcohol was subjected to additional chromatography in order to remove any lingering radiochemical impurities. Comparison of the $^{3}H/^{14}C$ ratio in the doubly labeled alcohol with that in the doubly labeled alloisoleucine (Table 3, expt. 5) clearly shows that alloisoleucine is cyclized to coronamic acid without significant loss of the hydrogen atom present at C-3. The intermediacy of 3-methylene-L-norvaline in the cyclization process is thereby ruled out. To evaluate the potential intermediacy of 6-hydroxy-L-alloisoleucine in coronamate biosynthesis, a mixture of (1-^{13}C)-6-hydroxy-DL-isoleucine and (1-^{13}C)-6-hydroxy-DL-alloisoleucine was synthesized as shown in Scheme 8. Since the NMR spectrum of this mixture of amino acids indicated that they exist as the γ-lactones, the compounds were administered both in the lactone form and as the ring-opened sodium salts prepared by treatment of the lactones with one equivalent of sodium hydroxide. Both forms of the hydroxy amino acids failed to exhibit incorporation into coronatine (data not shown).

Another question to be addressed with respect to the mechanism of cyclization of L-alloisoleucine to coronamic acid concerns the fate of the nitrogen atom present at C-2 of the amino acid, i.e., one may inquire whether the cyclization process requires the loss of the α-amino group. This question was answered by means of an incorporation experiment with a mixture of (2-^{13}C, ^{15}N)-DL-isoleucine and (2-^{13}C, ^{15}N)-DL-alloisoleucine synthesized according to Scheme 9. When this mixture of amino acids was supplied to *P. syringae*, the resulting coronatine displayed a total ^{13}C enrichment at C-2′ of about 7.8%, of which 2.4% exhibited coupling to ^{15}N (Table 3, expt. 6). One can therefore conclude that the cyclization reaction proceeds without obligatory loss of the amino group of L-alloisoleucine.

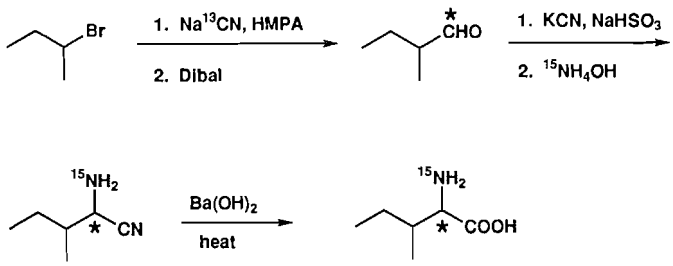

SCHEME 9

The fact that the total ^{13}C enrichment exceeds the ^{15}N enrichment indicates that some loss of ^{15}N from the mixture of doubly labeled amino acids occurs in vivo. This loss might be associated with the conversion of L-isoleucine to L-alloisoleucine since one mechanism for this epimerization reaction could involve the intermediacy of an α-keto acid.

Coronatine is accompanied in the fermentation broth of *P. syringae* by a number of congeners, including *N*-coronafacoyl-L-valine (22), *N*-coronafacoyl-L-isoleucine (23), and *N*-coronafacoyl-L-alloisoleucine (23). The co-occurrence of these congeners has led to the suggestion that the formation of the cyclopropane ring of coronamic acid may take place after formation of the amide bond between L-isoleucine or L-alloisoleucine and coronafacic acid (22). If this hypothesis were correct, then *P. syringae* might not possess the capability of utilizing free coronamic acid for the biosynthesis of coronatine. Information bearing on this aspect of coronatine biosynthesis was obtained by carrying out an incorporation experiment with (4-$^{2}H_1$, 5-$^{2}H_1$)-DL-coronamic acid, which was synthesized as outlined in Scheme 10. The synthesis makes use of a coronamic acid synthesis reported by Baldwin et al. (24). Analysis of the resulting coronatine methyl ester by ^{13}C NMR revealed the presence of two triplets at 13.0 and 20.0 ppm, which could be assigned to C-5′ and C-4′ of coronatine methyl ester, respectively. The center of each triplet was shifted upfield by ca. 0.25 ppm relative to the resonance positions of C-4′ and C-5′ in unlabeled coronatine methyl ester, thereby indicating that one deuterium atom was present at C-4′ and at C-5′. Analysis of the same sample of coronatine methyl ester by ^{2}H NMR revealed the presence of deuterium resonances at 1.00 and 1.65 ppm. Integration of these two absorptions with respect to an internal benzene standard indicated a deuterium incorporation of ca. 32% at both C-4′ and C-5′ (Table 3, expt. 7). Consequently, it appears that coronamic acid is a highly efficient precursor of coronatine.

The results of the experiments summarized in Table 2 limit the number of mechanisms that can be envisioned for the oxidative cyclization of L-alloisoleucine to coronamic acid. The available evidence is consistent with the possibility that this cyclization is related to the oxidative cyclizations observed in the biosynthesis of isopenicillin N (25), deacetoxycephalosporin C (25), and clavaminic acid (26). Based upon the analogy provided by these processes, one could postulate that the formation of coronamic acid proceeds by the mechanism outlined in Scheme 11. The cyclization could be initiated by reac-

Can. J. Chem. Downloaded from www.nrcresearchpress.com by 195.246.54.202 on 09/08/12
For personal use only.

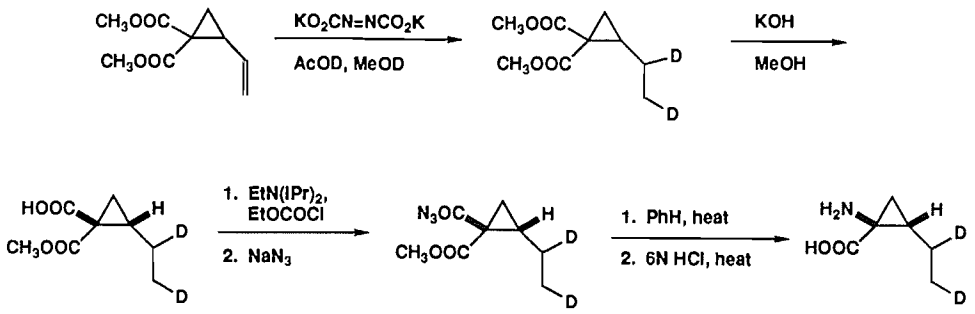

SCHEME 10

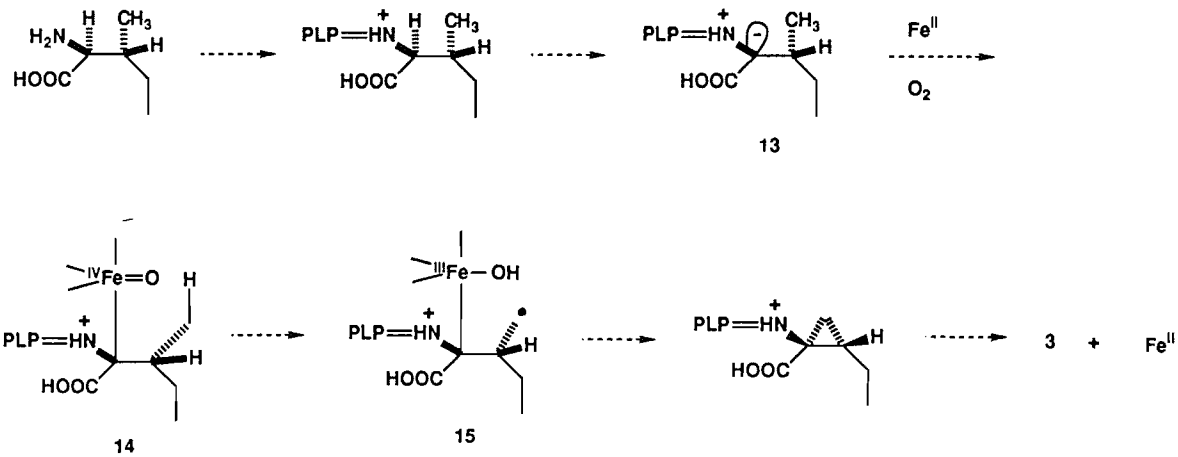

SCHEME 11

tion of L-alloisoleucine with pyridoxal phosphate (PLP) to yield a Schiff base, which could then be deprotonated to give the α-carbanion (**13**).[5] This carbanion could then react with a ferryl species formed from ferrous iron and molecular oxygen to yield the intermediate **14**. In this step, the carbanion would mimic the role of the thiol group or hydroxyl group in the isopenicillin N and clavaminate cyclizations, respectively. The next stage of the cyclization would involve abstraction of a hydrogen atom from the C-6 methyl group by the iron-oxo species to yield a carbon radical (**15**), which then collapses to give the PLP adduct of coronamic acid. Hydrolysis of the PLP adduct would finally yield free coronamic acid.

In conclusion, investigations of the biosynthesis of coronatine by means of precursor incorporation experiments have revealed that the biosynthesis of this phytotoxin possesses some novel features. The derivation of the coronafacic acid moiety of coronatine from C-2 and C-3 of pyruvate, as well as acetate and butyrate, appears to be unprecedented. Likewise, the formation of the coronamic acid moiety of coronatine by cyclization of L-alloisoleucine appears to involve a mechanism for cyclopropane ring formation that has not been previously encountered in Nature. A more detailed understanding of the biochemical processes underlying coronatine biosynthesis is likely to require the application of both chemistry and molecular biology to the solution of this problem.

[5]Since some amino acid epimerases do not require a cofactor to generate a carbanion at the α position of an amino acid, it is conceivable that the formation of a carbanion at the α position of L-alloisoleucine may be cofactor independent. See ref. 27.

Experimental

General procedures

Proton nuclear magnetic resonance spectra were taken on either a JEOL FX-90Q (90 MHz), an IBM AF300 (300 MHz), or a Bruker AC250 (250 MHz) spectrometer. Chemical shifts are given in parts per million downfield from tetramethylsilane (0.0 ppm) for spectra taken in $CDCl_3$. In other organic solvents, the solvent itself was used as the reference. In D_2O the water signal (4.80 ppm) was used as reference. Carbon-13 NMR spectra were taken on the same three instruments at 22.5, 75.45, and 62.89 MHz, respectively. Methanol (49.0 ppm) or *p*-dioxane (66.5 ppm) were used as an internal reference when D_2O was the solvent. Deuterium NMR spectra were obtained with the IBM AF300 instrument at 46.07 MHz. Deuterium-depleted water was used both as solvent and as reference. Benzene was added as a standard for the calculation of ^2H enrichment. Mass spectra were run on Finnigan 3300 and CEC 111021-110B mass spectrometers. Infrared spectra were recorded on a Nicolet 205 FT-IR spectrophotometer. All melting points were taken on a Fisher–Johns melting point apparatus and are uncorrected. Preparative thin-layer chromatography was accomplished using 0.75-mm layers of Merck silica gel, type PF-254. Analytical TLC was carried out using glass plates precoated with Cellulose F or Merck silica gel, type 60, F-254. Cellulose plates were visualized with short-wavelength ultraviolet light or by spraying with a 2% solution of ninhydrin in ethanol and heating. Silica gel plates were visualized with short-wavelength ultraviolet light, iodine vapor, or phosphomolybdic acid. Flash chromatography was carried out using silica gel, type 60A, 230–400 mesh as the stationary phase. Cellulose column chromatography utilized Merck microcrystalline cellulose. Coronatine and coronafacic acid production were monitored by high-pressure liquid chromatography (HPLC) on a Whatman octadecylsilane reversed-phase column (4.6 mm i.d. × 25 cm, 5 μm) using a Spectraphysics SP model 8700 solvent delivery system. Microbiological media for slants, agar plates, and fermentation broths were either pur-

Can. J. Chem. Downloaded from www.nrcresearchpress.com by 195.246.54.202 on 09/08/12
For personal use only.

Can. J. Chem. Downloaded from www.nrcresearchpress.com by 195.246.54.202 on 09/08/12
For personal use only.

chased from Difco or prepared from the appropriate reagents. Fermentations were performed using a New Brunswick G-25R rotary shaker. The shaker was connected to a Forma Scientific CH/P 2067 circulating water bath in order to carry out fermentations of *P. syringae* at 18°C. Slants were either grown at room temperature or incubated at 30°C. Measurement of radioactivity was carried out with a Beckmann LS-3801 liquid scintillation counter.

Materials

Authentic samples of coronafacic acid and of coronatine were obtained as a gift from Dr. R.E. Mitchell. All reagents and compounds were purchased from Aldrich Chemical Co., Fluka, ICN, and sigma Chemical Co. and were purified, where necessary, by standard techniques. Radiolabeled compounds were purchased from Amersham Life Sciences. Stable isotopically labeled compounds were generally purchased from Cambridge Isotope Laboratories. (1-^{13}C)-l-Isoleucine and (1-^{13}C)-l-alloisoleucine were purchased from Tracer Technologies, Inc. (Somerville, Mass.). Unless otherwise stated, all reactions were performed under a dry nitrogen atmosphere.

Organism and fermentation

Pseudomonas syringae pv. *glycinae* (PDDCC no. 4182) was obtained from the Culture Collection of Plant Diseases Division of the New Zealand Department of Scientific and Industrial Research; *P. syringae* pv. *glycinae* (PDDCC no. 4180) was a gift from Professor Carol Bender of Oklahoma State University. The organism was maintained on mannitol–glutamate yeast agar slants which consisted of mannitol 1%, sodium L-glutamate 0.2%, KH_2PO_4 0.05%, NaCl 0.02%, $MgSO_4 \cdot 7H_2O$ 0.02%, yeast extract 0.025%, agar 1.5%, pH adjusted to 7.0 with dilute sodium hydroxide. For long-term storage, the organism was preserved by lyophilization in mist desiccans (28). For fermentation, *P. syringae* growing on one mannitol slant was suspended in 1.0 mL of sterile water and the suspension used to inoculate 100 mL of seed medium, which consisted of yeast extract (500 mg), glucose (500 mg), $MgSO_4 \cdot 7H_2O$ (20 mg), KH_2PO_4 (410 mg), K_2HPO_4 (360 mg), dissolved in 100 mL water with the pH adjusted to 6.8. The inoculated seed medium was incubated at 25°C, 250 rpm, for 24 h. After 24 h, the seed medium was used to inoculate 10 1-L flasks each containing 200 mL of production medium (10 mL of inoculum per flask). Production medium consisted of two solutions: (A) glucose (20.0 g), $MgSO_4 \cdot 7H_2O$ (0.4 g), KH_2PO_4 (8.2 g), K_2HPO_4 (7.2 g), dissolved in 2.0 L of water, and adjusted to pH 6.8 with 1 N NaOH. This solution was sterilized by autoclaving at 121°C for 20 min. After this solution had cooled to room temperature, 1 mL of solution (B) consisting of NH_4Cl (2.0 g) and biotin (2.0 mg) dissolved in 10 mL water was added to each production medium flask through a sterile filter. The inoculated fermentation flasks were incubated at 18°C, 200 rpm, and monitored for coronatine and coronafacic acid production by HPLC using 28% acetonitrile in H_2O containing 0.05% trifluoroacetic acid (flow rate = 1.5 mL/min, R_T = ca. 7 min for coronafacic acid, ca. 12 min for coronatine). The HPLC analysis indicated that coronatine production usually begins on day 1 and reaches a maximum after 5 days.

Isolation of methyl coronafacate and methyl coronatine

After 5 days the cells were removed by centrifugation at 8000 rpm for 40 min. The supernatant broth was filtered through glass wool, and stirred with a mixture of activated charcoal (20 g) and Celite (20 g) for 30 min before being loaded into a column and washed with 400 mL of distilled water. The column was then eluted with ca. 300 mL of acetone. The acetone elutant was concentrated fivefold, adjusted to pH 2.5 with 2.5 M H_2SO_4, and vigorously extracted three times with ethyl acetate. The combined ethyl acetate extracts were dried over anhydrous $MgSO_4$, filtered through Celite, and concentrated in vacuo. The acidic residue was dissolved in 2.0 mL methanol and treated with excess diazomethane. The excess diazomethane was blown off in the hood under a stream of nitrogen and the methanol removed in vacuo. The residue was further purified by preparative thin-layer chromatography (0.75 mm noncommercial silica gel plates, eluant 10% isopropanol in hexane). To obtain an adequate purification, it was necessary to develop the plate two or three times. This yielded, on average, 10 mg of coronatine as its methyl ester derivative and 4–6 mg of the methyl ester of coronafacic acid.

Administration of labeled precursors to P. syringae *pv.* glycinea

Precursors were pulse fed to the producing organism 24, 48, and 72 h after initiation of the fermentation. Both stable and radiolabeled precursors were dissolved in a suitable volume of Milli-Q water or ethanol and administrated to the fermentation flasks through a sterile Millipore filter (pore size 0.22 μm). In experiments employing precursors labeled with stable isotopes, about 100 mg were fed each day.

Synthesis of labeled precursors

*Synthesis of (5-^{13}C)-*N*-acetylcysteamine ester of* (S)*-citramalic acid (**6**)*

*A. Synthesis of (methyl-^{13}C)-(2S, 5S)-2-(*tert*-butyl)-5-(methoxycarbonyl)-5-(methyl)-1,3-dioxolan-4-one.* The ^{13}C-labeled dioxolane acid was prepared from L-malic acid and (^{13}C)methyl iodide using the procedure of Seebach et al. (17).

B. Synthesis of N*-acetylcysteamine ester of (methyl-^{13}C)-(2S, 5S)-2-(*tert*-butyl)-5-(methoxycarbonyl)-5-(methyl)-1,3-dioxolan-4-one.* The labeled dioxolane acid prepared in step A (375.0 mg, 1.74 mmol) was dissolved in 7.5 mL of dry CH_2Cl_2. *N*-Methylmorpholine (194.4 mg, 1.92 mmol) was then added at room temperature. The reaction mixture was cooled to –20°C for 15 min and diphenylphosphinic chloride (438 mg, 1.92 mmol) was then added. The reaction mixture was then stirred at room temperature for 20 min. Ether (10 mL) was added to the mixture and the precipitated *N*-methylmorpholine hydrochloride was removed by filtration. The salt was then washed with ether (3 × 30 mL) and the combined ether portions were washed with 15 mL of 10% $NaHCO_3$ and then with brine. After drying of the organic phase over anhydrous $MgSO_4$, the solvent was removed to furnish a thick oil, which was dissolved in dry THF (57 mL). The resulting solution was cooled in an ice bath to –3 to –4°C. A suspension of the thallium salt of *N*-acetylcysteamine in THF (19.8 mL, 1.92 mmol), prepared by the method of Schwab et al. (18), was added quickly, with vigorous stirring. The bright yellow reaction mixture was then stirred at –2 to –4°C for 18 h under an inert atmosphere. The solvent was removed from the reaction mixture and the residue redissolved in ether and filtered through Celite. The filtrate was taken to dryness in vacuo to give a thick, yellowish oil (835 mg). This oil was chromatographed on Florisil. Gradient elution with an ethyl acetate – hexane mixture furnished the product (401 mg) in 73% yield: ^{1}H NMR (250 MHz, $CDCl_3$) δ: 0.94 (s, 9H), 1.47 (d, $^1J_{CH}$ = 127.5 Hz, 3H), 1.97 (s, 3H), 2.9–3.5 (m, 6H), 5.17 (s, 1H), 5.8–6.0 (bs, 1H); ^{13}C NMR (62.89 MHz, $CDCl_3$) δ: 19.7 (enriched) ppm.

*C. (5-^{13}C)-*N*-acetylcysteamine ester of* (S)*-citramalic acid (**6**).* The 1,3 dioxolane NAC ester prepared in step B (254 mg, 0.8 mmol) was hydrolyzed with 2 N HCl (5.4 mL) at room temperature for 48 h under an argon atmosphere. The aqueous acid was then removed under reduced pressure, and remaining traces of HCl removed by twice adding water, which was then removed in vacuo. This procedure afforded the product as a colorless viscous oil (168 mg) in 84% yield: ^{1}H NMR (250 MHz, $CDCl_3$) δ: 1.45 (d, $^1J_{CH}$ = 125 Hz, 3H), 1.94 (s, 3H), 2.9–3.5 (m, 4H); ^{13}C NMR (62.89 MHz, $CDCl_3$) δ: 21.7 (enriched), 25.6, 28.1, 38.5, 52.3 ppm.

Synthesis of (5-^{13}C)-(R)*-citramalic acid diethyl ester (7)*

(*methyl*-^{13}C)-(2*R*, 5*R*)-2-(*tert*-Butyl)-5-(methoxycarbonyl)-5-(methyl)-1, 3-dioxolan-4-one (202 mg, 1 mmol), prepared (17) from D-malic acid using $^{13}CH_3I$, was dissolved in 30.0 mL of dry ethanol. Dry HCl gas was bubbled through the solution for 5 h. An exothermic reaction ensued. The reaction mixture was thenrefluxed for 18 h, after which time the ethanol was removed in vacuo. Column chromatography on silica gel furnished 161 mg of the diethyl ester of (*methyl*-^{13}C)citramalic acid in 79% yield: ^{1}H NMR (250 MHz, $CDCl_3$) δ: 1.24 (t, 3H), 1.29 (t, 3H), 1.42 (d, $^1J_{C-H}$ = 130 Hz, 3H), 2.67 (d, *J* = 15.6 Hz, 1H), 2.97 (d, *J* = 15.6 Hz, 1H), 4–4.35 (m, 4H); ^{13}C NMR (62.89 MHz, $CDCl_3$) δ: 14.09, 26.29 (enriched), 44.20, 60.83, 61.94, 103.5, 170.5, 175.5 ppm.

Can. J. Chem. Downloaded from www.nrcresearchpress.com by 195.246.54.202 on 09/08/12
For personal use only.

Synthesis of (2,3-$^{13}C_2$)ethyl acetoacetate (8)

A solution of LiHMDS in THF (10.5 mL, 10.5 mmol) was cooled to –78°C under dry nitrogen, and (2-^{13}C)ethyl acetate (440 mg, 5.0 mmol) was added to it. The solution was then stirred for 30 min to allow generation of the ester anion. To this mixture was then added (1-^{13}C)acetyl chloride (354 mg, 4.5 mmol) dissolved in dry THF (0.4 mL). The mixture was stirred at –78°C for 30 min. To this mixture 24 mL of 2 N HCl was added at the same temperature. The reaction was brought to room temperature over 2 h. It was then further acidified to pH 3 with 2 N HCl. The acidic solution was extracted with ether (3 × 4 mL). The combined ethereal extracts was dried over $MgSO_4$. Solvent removal and Kugelrohr distillation furnished 351 mg of (2,3-$^{13}C_2$)ethyl acetoacetate in 60% yield: ^{1}H NMR (250 MHz) δ: 1.28 (t, 3H), 2.27 (d, J_{CH} = 7.5 Hz, 3H), 3.45 (dd, J_{CH} = 130 Hz, $^2J_{CH}$ = 7.5 Hz, 2H), 4.19 (q, 2H); ^{13}C NMR (62.89 MHz, $CDCl_3$) δ: 14.01, 30.01, 50.14 (d, J = 38.4 Hz, enriched), 61.30, 167.5, 200.6 (d, J = 38.4 Hz, enriched) ppm.

Synthesis of (2,3-$^{13}C_2$)ethyl 3-ketohexanoate (9)

The compound was prepared from (2-^{13}C)ethyl acetate and (1-^{13}C)butyryl chloride following the procedure employed to synthesize doubly labeled ethyl acetoacetate. The yield was 69%: ^{1}H NMR (300 MHz, $CDCl_3$) δ: 0.92 (t, 3H), 1.28 (t, 3H), 1.5–1.75 (m, 2H), 2.45–2.6 (q, 2H), 3.63 (dd, $^1J_{CH}$ = 131.3 Hz, $^2J_{CH}$ = 6.3 Hz, 2H), 4.1–4.25 (q, 2H); ^{13}C NMR (75.45 MHz, $CDCl_3$) δ: 49.28 (d, J = 37.7 Hz, enriched), 202.83 (d, J = 37.7 Hz, enriched) ppm.

Synthesis of the N*-acetylcysteamine ester of (2,3-$^{13}C_2$)-3-ketohexanoate (10)*

A. Synthesis of (2-3-$^{13}C_2$)-3-ketohexanoic acid. Hydrolysis of ethyl (2,3-$^{13}C_2$)-3-ketohexanoate (**9**) was carried out at room temperature by stirring the ester (1.29 g, 8.2 mmol) with aqueous sodium hydroxide (0.82 g in 10 mL H_2O) for 20 h. The reaction mixture was doubly diluted with water and the pH adjusted to 12. The alkaline solution was then extracted with ether (3 × 30 mL) to remove neutral compounds. The aqueous phase was then acidified with 1 N HCl to pH 2. The free ß-keto acid was then extracted with $CHCl_3$ (3 × 80 mL) and the chloroform extracts dried over anhydrous Na_2SO_4. Removal of the $CHCl_3$ at room temperature furnished colorless crystals of the ß-keto acid (669 mg, 61% yield): ^{1}H NMR (250 MHz, $CDCl_3$) δ: 0.95 (t, 3H), 1.5–1.8 (m, 2H), 2.5–2.65 (q, 2H), 3.51 (dd, J = 13 Hz, J = 2.5 Hz, 2H).

B. Synthesis of the N*-acetylcysteamine ester of (2,3-$^{13}C_2$)-3-ketohexanoate (10).* 1,1′-Carbonyldiimidazole (488 mg, 3 mmol) was added to a solution of (2,3-$^{13}C_2$)-3-ketohexanoic acid (325 mg, 2.5 mmol) in dry acetonitrile (7.2 mL) at –5°C. The mixture was stirred for 1.5 h below 0°C, and a solution of freshly prepared *N*-acetylcysteamine (353 mg, 2.7 mmol) in dry acetonitrile (0.5 mL) was then added. The resulting mixture was stirred for another 1 h at the same temperature. The solvent was then removed in vacuo and residue dissolved in 15 mL water. This aqueous solution was extracted with ethyl acetate (3 × 50 mL), the combined extracts dried over anhydrous sodium sulfate, and the solvent was removed in vacuo to give 200 mg of residue. This residue was purified by flash chromatography on silica gel. Gradient elution with a mixture of ethyl acetate and hexane furnished nearly pure fractions of the ester. Traces of *N*-acetylcysteamine were removed from these fractions by preparative TLC to give 161 mg of the product in 28% yield: ^{1}H NMR (250 MHz, $CDCl_3$) δ: 0.93 (t, 3H), 1.5–1.75 (m, 2H), 1.98 (s, 3H), 2.4–2.6 (q, 2H), 2.9–3.15 (t, 2H), 3.35–3.55 (t, 2H), 3.71 (dd, $^1J_{CH}$ = 119.8 Hz, $^2J_{CH}$ = 5.2 Hz, 2H); ^{13}C NMR (62.89 MHz, $CDCl_3$) δ: 57.18 (d, J = 36.5 Hz, enriched), 202.15 (d, J = 36.5 Hz, enriched) ppm; HRMS, calcd. for $^{13}C_2C_8H_{17}NO_3S$: 233.0996; found (M^+): 233.0996; calcd. for $^{13}C_3C_7H_{17}NO_3S$: 234.1030; found (M + 1): 234.1028.

Synthesis of a mixture of (6-^{13}C)-DL-isoleucine and (6-^{13}C)-DL-alloisoleucine

The first synthesis developed for the preparation of these labeled amino acids involved the alkylation of the anion of *n*-butyl butyrate with (^{13}C)methyl iodide followed by diisobutyl aluminum hydride (DIBAL) reduction of the resulting ester to yield the corresponding aldehyde. Since difficulties were encountered with overreduction in the DIBAL step, an alternative synthetic route was devised. This is the one outlined below.

A. (5-^{13}C)-2-Methylbutyronitrile. *n*-Butyronitrile (2.0 g, 28.9 mmol) was added dropwise to a stirred solution of commercially available lithium diisopropylamide (3.71 g, 34.7 mmol) in 50 mL of dry THF at –78°C.The resulting yellow solution was stirred at –78°C for 30 min before (^{13}C)methyl iodide (4.13 g, 28.9 mmol) was added. The reaction mixture was stirred at –78°C for a further 1 h and then allowed to warm to 0°C over 3.5 h. The reaction mixture was quenched at 0°C by the addition of saturated aqueous NH_4Cl (30 mL). The THF was removed in vacuo and the residue extracted with CH_2Cl_2. The combined organic extracts were washed with water, saturated NaCl, dried over $MgSO_4$, filtered, and concentrated at atmospheric pressure. This gave 2.5 g of crude (5-^{13}C)-2-methylbutyronitrile as a pale yellow liquid, ^{1}H NMR (250 MHz, $CDCl_3$) δ: 1.0–1.1 (m, 3H), 1.35 (dd, $^1J_{CH}$ = 125 Hz, $^3J_{HH}$ = 7.9 Hz, 3H), 1.65–1.8 (m, 2H), 3.5–3.65 (m, 1H); ^{13}C NMR (62.89 MHz, $CDCl_3$) δ: 11.35, 17.58 (enriched), 26.58, 27.56, 77.0 ($CDCl_3$), 122.91.

B. (5-^{13}C)-2-Methylbutyraldehyde. Diisobutyl aluminum hydride (DIBAL) (37.2 mL, 37.2 mmol) was added dropwise to a stirred solution of (5-^{13}C)-2-methylbutyronitrile (2.5 g, 29.8 mmol) in dry CH_2Cl_2 (50 mL) at room temperature. The reaction mixture was stirred at room temperature for 1 h and quenched by cautiously adding 5% aqueous H_2SO_4. The aqueous and organic layers were separated and the aqueous layer extracted with CH_2Cl_2. The combined organic extracts were dried over $MgSO_4$, filtered through Celite, and concentrated at atmospheric pressure. This gave 2 g of crude (5-^{13}C)-2-methyl butyraldehyde.

C. (6-^{13}C)-2-Hydroxy-3-methylvaleronitrile. Ethanol (50 mL) was added to a solution of (5-^{13}C)-2-methylbutyraldehyde and sodium bisulfite (3.53 g, 34.6 mmol) in water (50 mL) until the solution became homogeneous and clear. The solution was stirred at room temperature for 1 h before potassium cyanide (1.99 g, 30.6 mmol) was added and the reaction mixture stirred at room temperature for 3 h. The ethanol was then removed in vacuo and the aqueous residue extracted with ether. The combined ether extracts were washed with water, saturated NaCl, dried over $MgSO_4$, filtered, and concentrated in vacuo. This gave 2.3 g of crude (6-^{13}C)-2-hydroxy-3-methylvaleronitrile.

D. (6-^{13}C)-2-Amino-3-methylvaleronitrile. The crude cyanohydrin from the previous step was dissolved in concentrated NH_4OH (34.6 mL) and ethanol (30 mL) was added until the solution became homogeneous and clear. The reaction mixture was then stirred at room temperature for 18 h. The ethanol was removed in vacuo and the aqueous residue extracted with ether. The combined ether extracts were washed with water, saturated NaCl, dried over $MgSO_4$, filtered, and concentrated in vacuo. This gave 1.7 g of the crude aminonitrile.

E. (6-^{13}C)-DL-Isoleucine/(6-^{13}C)-DL-alloisoleucine. The crude aminonitrile was dissolved in water (100 mL) and barium hydroxide (19.3 g, 61 mmol) added. The reaction mixture was then heated at reflux for 18 h. After cooling to room temperature, the solution was filtered and the filtrate taken to dryness. The solid white residue was redissolved in water (50 mL). This solution was treated twice with solid $(NH_4)_2CO_3$ to remove any remaining barium as insoluble barium carbonate. The filtrate was stirred in a water bath at 60–65°C for 1 h before being finally concentrated in vacuo. This gave 0.5 g of the crude amino acid mixture as a white solid. The remaining impurities were removed by repeated cellulose column chromatography (eluant: *n*-butanol:HOAc:H_2O (BAW), 4:1:2). This gave 169 mg (4.5% from *n*-butyronitrile) of the pure amino acid mixture as a flaky white solid: ^{1}H NMR (250 MHz, D_2O) (ca. 1:1 mixture of isoleucine and alloisoleucine) δ: 0.85 (dd, $^3J_{HH}$ = 6.9 Hz, $^1J_{CH}$ = 125.3 Hz, 3H, one diastereomer), 1.00 (t, $^3J_{HH}$ = 6.25 Hz, 3H), 1.25 (dd, $^3J_{HH}$ = 7.5 Hz, $^1J_{CH}$ = 125.9 Hz, 3H, other diastereomer), 1.36–1.50 (m, 2H), 2.04–2.12 (m, 1H), 3.69 (dd, $^3J_{HH}$ = 3.95 Hz, $^3J_{CH}$ = 3.92 Hz, 1H, one diastereomer), 3.76 (dd, $^3J_{HH}$ = 5.92 Hz, $^3J_{CH}$ = 5.90 Hz, 1H, other diastereomer); ^{13}C NMR (62.89 MHz, D_2O) δ: 11.14, 11.21, 13.42 (enriched), 14.79 (enriched), 24.56, 25.61, 35.70, 35.99, 58.58, 59.66, 174.3, 175.2 ppm.

Can. J. Chem. Downloaded from www.nrcresearchpress.com by 195.246.54.202 on 09/08/12
For personal use only.

Synthesis of a mixture of (6-^{13}C,$^{2}H_3$)-DL-isoleucine and 6-^{13}C,$^{2}H_3$)-DL-alloisoleucine

The synthesis of this mixture of labeled amino acids was carried out in the same manner as described for the preparation of the (6-^{13}C)-labeled compounds, except that (6-^{13}C, 6-$^{2}H_3$)methyl iodide was substituted for (6-^{13}C)methyl iodide. From 2.4 g of *n*-butyronitrile (34.3 mmol), 185 mg (4.1% yield) of a mixture of (6-^{13}C,$^{2}H_3$)-DL-isoleucine and (6-^{13}C,$^{2}H_3$)-DL-alloisoleucine was obtained as a flaky white solid: ^{1}H NMR (250 MHz, D_2O) (ca. 1:1 mixture of isoleucine and alloisoleucine) δ: 0.9–1.1 (m, 3H), 1.3–1.6 (m, 2H), 3.69 (dd, $^3J_{HH}$ = 3.95 Hz, $^3J_{CH}$ = 3.92 Hz, 1H), 3.76 (dd, $^3J_{HH}$ = 5.92 Hz, $^3J_{CH}$ = 5.90 Hz, 1H); ^{13}C NMR (62.89 MHz, D_2O) δ: 11.14, 11.21, 13.42 (enriched septet), 14.79 (enriched septet), 24.56, 25.61, 35.70, 35.99, 58.58, 59.66, 174.3, 175.2 ppm.

Synthesis of [3-^{3}H]-L-alloisoleucine

A. [3-^{3}H]-tert-Butyl 3-hydroxybutyrate. Unlabeled sodium borohydride (9 mg) was added to a stirred solution of *tert*-butyl acetoacetate (600 mg, 3.8 mmol) in dry ethanol (2.7 mL) at 0°C. The solution was stirredat 0°C for 15 m in and [^{3}H]sodium borohydride (100 mCi, specific activity 500 mCi/mmol) added. The reaction mixture was then stirred at 0°C for 30 min. The ice bath was removed and the mixture stirred at room temperature overnight. The reaction mixture was then cooled at 0°C, a further 65 mg of unlabeled sodium borohydride was added, and the reaction mixture was stirred at 0°C for 15 min and then at room temperature for 2 h. The ethanol was removed in vacuo, water was added, and the pH of the solution was adjusted to 5 with glacial acetic acid. The aqueous layer was extracted with ethyl acetate and the combined organic extracts were dried over anhydrous $MgSO_4$, filtered, and concentrated in vacuo. The clear residual oil was further purified by Kugelrohr distillation in vacuo (0.1 Torr). This gave 0.439 g (72%) of [3-^{3}H]-*tert*-butyl 3-hydroxybutyrate: bp 60–65°C at 0.1 Torr (1 Torr = 133.3 Pa); radiochemical yield, 11.1%; specific activity, 0.025 m Ci/mg: ^{1}H NMR (250 MHz, $CDCl_3$) δ: 1.2 (d, 3H), 1.4 (s, 9H), 2.4 (s, 3H), 3.1 (s, -OH), 3.9–4.2 (m, 2H); HRMS, calcd. for $C_8H_{16}O_3$: 160.1099; found (M^+): 160.1095; calcd. for $^{13}C_1C_7H_{16}O_3$: 161.1132; found (M + 1): 161.1129.

B. [3-^{3}H]-tert-Butyl 3-mesyloxybutyrate. Triethylamine (338 mg, 3.34 mmol) was added to a stirred solution of [3-^{3}H]-*tert*-butyl 3-hydroxybutyrate (0.435 g, 271 mmol) in 16 mL dry CH_2Cl_2 at room temperature. The solution was stirred at room temperature for 10 min, cooled in an ice bath to 0°C, and methanesulfonyl chloride (0.382 g, 3.34 mmol) added dropwise. After stirring at room temperature for a further 1 h, the reaction mixture was carefully poured into 1 M $NaHCO_3$ and the aqueous and organic layers separated. The aqueous layer was further extracted with CH_2Cl_2 and the combined organic extracts washed once with water, dried over anhydrous $MgSO_4$, filtered, and concentrated. The residual oil was further purified by Kugelrohr distillation. This gave [3-^{3}H]-*tert*-butyl 3-mesyloxybutyrate, 0.622 g (96%): ^{1}H NMR (250 MHz, $CDCl_3$) δ: 1.4 (s, 9H), 1.5 (s, 3H), 2.5–2.7 (m, 2H), 3.0 (s. 3H), 5.0–5.2 (m, 1H); HRMS, calcd. for $C_8H_{15}O_2$: 143.0690; found (M^+ – MsO): 143.0694; calcd. for $^{13}C_1C_7H_{15}O_2$: 144.0724; found (M + 1 – MsO): 144.0718.

C. [3-^{3}H]-trans-Crotonic acid. 1,8-Diazabicyclo[5.4.0]undec-7-ene (DBU) (796 mg, 5.23 mmol) was added dropwise to a stirred solution of [3-^{3}H]-*tert*-butyl 3-mesyloxybutyrate (622 mg, 2.6 mmol) in 25 mL dry CH_2Cl_2. The reaction mixture was stirred at room temperature for 24 h before being quenched by the addition of 20 mL of 1 M acetic acid. The aqueous layer was extracted with CH_2Cl_2 and the combined organic extracts washed with water, dried over anhydrous $MgSO_4$, filtered, and concentrated in vacuo. The residual oil was purified by Kugelrohr distillation. This gave 0.37 g (2.6 mmol) of [3-^{3}H]-*tert*-butyl crotonate: ^{1}H NMR (90 MHz, $CDCl_3$) δ: 1.5 (s, 9H), 1.82 (dd, $^3J_{HH}$ = 7.7 Hz, $^4J_{HH}$ = 2.5 Hz, 3H), 5.74 (dd, $^3J_{HH}$ = 16.7, $^4J_{HH}$ = 2.5 Hz, 1H), 6.7–7.0 (m, 1H); HRMS, calcd. for $C_8H_{14}O_2$: 142.0993; found (M^+): 142.0994; calcd. for $^{13}C_1C_7H_{14}O_2$: 143.1027; found (M + 1): 143.1028.

The tritiated *tert*-butyl crotonate was dissolved in 25 mL of freshly distilled benzene and *p*-toluenesulfonic acid (84 mg, 0.44 mmol) added. The flask was fitted with a Dean–Stark trap and condenser and the whole heated at reflux for 1 h. The reaction mixture was cooled to room temperature and the benzene removed in vacuo. The white, crystalline solid was further purified by passage through a CC-4 silica gel column (15 g, eluant 5%–20% ethyl acetate – hexane). This gave 0.189 g (84%) of [3-^{3}H]-*trans*-crotonic acid as a white solid: ^{1}H NMR (90 MHz, $CDCl_3$) δ: 1.90 (dd, $^3J_{HH}$ = 7.7 Hz, $^4J_{HH}$ = 2.6 Hz, 3H), 5.82 (dd, $^3J_{HH}$ = 16.7 Hz, $^4J_{HH}$ = 2.6 Hz, 1H), 6.7–7.1 (m, 1H).

D. [3-^{3}H]-(+)-10′-Dicyclohexylsulfamoyl-L-isobornyl crotonate. Oxalyl chloride (290 mg, 2.29 mmol) was added dropwise to a stirred solution of [3-^{3}H]crotonic acid (190 mg, 2.20 mmol) in 10 mL dry benzene at room temperature. The solution was stirred at room temperature for 24 h and then at 40°C for 1 h. Silver cyanide (294 mg, 2.20 mmol) and (+)-10-dicyclohexylsulfamoyl-L-isoborneol (665 mg, 1.67 mmol) were added, the flask fitted with a reflux condenser, and the mixture heated at reflux for 72 h. After 72 h no chiral auxillary remained as shown by TLC analysis (SiO_2, 15% ethyl acetate – hexane). The reaction mixture was cooled to room temperature, filtered through Celite, and the benzene removed in vacuo. The residue was purified by flash chromatography (eluant 5%–20% ethyl acetate – hexane). This gave 232 mg (29.8%) of [3-^{3}H]-(+)-10-dicyclohexylsulfamoyl-L-isobornyl crotonate: ^{1}H NMR (300 MHz, $CDCl_3$) δ: 0.85 (s, 3H), 1.0 (s, 3H), 1.05–2.15 (m, 30H), 2.68 (d, *J* = 12.9 Hz, 1H), 3.1–3.35 (m, 3H), 5.05 (d, *J* = 8.6 Hz, 1H) 5.83 (d, *J* = 17.2 Hz, 1H), 6.8–7.03 (m, 1H); ^{13}C NMR (75.47, $CDCl_3$) δ: 17.86, 19.98, 20.39, 25.06, 26.34, 26.95, 29.77, 32.68, 39.33, 44.45, 49.03, 49.38, 53.56, 57.29, 77.87, 123.27, 143.69, 164.78, 205.5 ppm.

E. [3-^{3}H]-(3R)-(+)-10′-Dicyclohexylsulfamoyl-L-isobornyl-3-methylpentanoate. Ethyllithium (1.09 mmol) was added dropwise to a stirred solution of tetra-(tri-*n*-butylphosphine) copper(I) iodide (29) (424 mg, 0.27 mmol) in 7 mL dry ether at –78°C. The solution was stirred at –78°C for 30 min before boron trifluoride etherate (154 mg, 1.09 mmol) was added. After stirring at –78°C for a further 30 min, the tritiated isobornyl crotonate (225 mg, 0.49 mmol) was added as a solution in 2 mL ether/1 mL THF and the reaction mixture stirred for 2 h at –78°C. After 2 h the reaction mixture was quenched by the addition of 7 mL of saturated aqueous NH_4Cl and the aqueous layer extracted with ether. *m*-Chloroperoxybenzoic acid (245 mg, 1.42 mmol) was added to the combined ether extracts and the solution stirred for 10 min, filtered through Celite, and washed with 1 M NaOH until colorless. The ether extracts were further dried over anhydrous $MgSO_4$, filtered, and concentrated in vacuo. The residue was purified by flash chromatography (SiO_2, elutant 5%–20% ethyl acetate –hexane). This gave [3-^{3} H]-(+)-10-dicyclohexylsulfamoyl-L-isobornyl-3-methylpentanoate, 173 mg (71.5%) as a white solid: ^{1}H NMR (300 MHz, $CDCl_3$) δ: 0.85 (s, 6H), 0.93 (d, 3H), 1.00 (s, 3H), 1.05–2.4 (m, 32H), 2.55–2.7 (d, *J* = 14 Hz, 1H), 3.1–3.4 (m, 3H), 4.85–4.95 (dd, *J* = 5.1 Hz, *J* = 3.8 Hz, 1H); ^{13}C NMR (75.45 MHz, $CDCl_3$) δ: 11.25, 19.23, 19.93, 20.42, 25.13, 26.45, 26.97, 29.37, 30.09, 31.81, 32.71, 39.71, 41.85, 44.42, 49.06, 49.22, 53.63, 57.39, 78.34 ppm.

F. [3-^{3}H]-(2R, 3R)-2-Bromo-(+)-10′-dicyclohexylsulfamoyl-L-isobornyl-3-methylpentanoate. Butyllithium (0.595 mmol) was added dropwise to a stirred solution of diisopropylamine (60 mg, 0.595 mmol) in 6 mL dry THF between 0°C and –10°C. The solution was stirred for 30 min before being cooled to –78°C. A solution of the ester prepared under *E* was added in 4 mL of dry THF and the whole stirred at –78°C for 1 h. Trimethylsilyl chloride (105.8 mg, 0.974 mmol) was added and the reaction mixture stirred for 45 min before carefully recrystallized and dried *N*-bromosuccinimide (105.9 mg, 0.595 mmol) was added. The reaction mixture was stirred at –78°C for 5 h. After 5 h the reaction was quenched by the addition of aqueous NH_4Cl. The aqueous layer was extracted with ether; the combined extracts were washed with water and brine, dried over anhydrous $MgSO_4$, filtered, and concentrated in vacuo. The residue was purified by flash chromatography (SiO_2, eluant 4%–20% ethyl acetate – hexane). This gave 118 mg of the tritiated bromide as a white solid: ^{1}H NMR (90 MHz, $CDCl_3$) δ: 0.85 (s, 6H), 1.0 (s, 6H), 1.1–2.2 (m, 30H), 2.5–2.8 (d, *J* = 14 Hz, 1H), 3.0–3.6 (m, 3H), 4.0–4.22 (d, *J* = 7.6 Hz, 1H), 4.8–5.1 (m, 1H).

Can. J. Chem. Downloaded from www.nrcresearchpress.com by 195.246.54.202 on 09/08/12
For personal use only.

G. [3-^{3}H]-(2S, 3R)-2-Azido-(+)-10′-dicyclohexylsulfamoyl-L-isobornyl-3-methylpentanoate. DMF (3 mL) was added to a mixture of sodium azide (30.7 mg, 0.472 mmol) and the tritiated bromo ester (90.3 mg, 0.157 mmol) prepared under *F*, and the reaction was stirred at room temperature for 3 days with periodic monitoring by TLC (SiO_2, 10% ethyl acetate – hexane). After 3 days the reaction mixture was quenched with water and extracted with ether. The combined ether extracts were washed with water and saturated sodium chloride. They were then dried over anhydrous $MgSO_4$, filtered, and concentrated in vacuo. The residue was purified by flash chromatography (SiO_2, eluant 5%–15% ethyl acetate – hexane). This gave 72 mg (85%) of the tritiated azide: ^{1}H NMR (90 MHz, $CDCl_3$) δ: 0.75–1.00 (m, 12H), 0.95 (s, 3H), 1.0–2.2 (m, 31H), 2.4–2.7 (d, J = 14 Hz, 1H), 2.9–3.4 (m, 3H), 4.8–5.1 (m, 1H).

H. [3-^{3}H]-(2S, 3R)-2-Amino-(+)-10′-dicyclohexylsulfamoyl-L-isobornyl-3-methylpentanoate. A mixture of the tritiated azide from procedure *G* (72.1 mg, 0.133 mmol) and 5% palladium – barium sulfate catalyst (50.4 mg) in 5 mL absolute ethanol was stirred at room temperature for 24 h under hydrogen at atmospheric pressure. After 24 h the reaction mixture was filtered through Celite to remove the catalyst and the residue washed with $CHCl_3$. The filtrate was concentrated in vacuo and the residue purified by flash chromatography (SiO_2, 5%–50% ethyl acetate – hexane). This gave 53 mg (78%) of [3-^{3}H]-2-amino-(+)-dicyclohexylsulfamoyl-L-isobornyl-3-methylpentanoate: ^{1}H NMR (90 MHz, $CDCl_3$) δ: 0.75–1.2 (m, 12H), 1.2–2.2 (m, 30H), 2.5–2.9 (dd, J = 14 Hz, 1H), 2.95–3.5 (m, 3H), 3.8–4.1 (d, J = 3.8 Hz, 1H), 4.8–5.1 (m, 1H).

I. [3-^{3}H]-L-Alloisoleucine. A mixture of the tritiated amino ester prepared under *H* (53.3 mg, 0.103 mmol) and barium hydroxide (57.5 mg, 0.18 mmol) in 4 mL of water and 2 mL of ethanol was heated at reflux for 24 h. After 24 h the reaction mixture was cooled to room temperature, filtered through Celite, and concentrated in vacuo. The residue was redissolved in 10 mL water and treated with 8 mg $(NH_4)_2CO_3$. The milky white solution was filtered and concentrated before being redissolved in water and treated with a second batch of $(NH_4)_2CO_3$. The solution was filtered one more time to remove any remaining $BaCO_3$ and then stirred in a water bath at 60–65°C for 1 h. The water was then removed in vacuo and the white residue purified by flash chromatography (cellulose, eluant butanol:acetic acid:water (BAW) 12:3:5). This gave 13 mg (95%) of [3-^{3}H]-L-alloisoleucine whose specific activity was 11 μCi/mg: ^{1}H NMR (250 MHz, D_2O) δ: 1.0 (m, 6H), 1.3–1.5 (m, 2H), 1.9–2.1 (m, 1H), 3.6 (d, J = 0.36 Hz, 1H), 4.9 (s, D_2O); ^{13}C NMR (75.46 MHz, D_2O) δ: 11.17, 13.43, 25.65, 35.78, 58.58, 174.89 ppm.

Synthesis of [1-^{14}C]-L-alloisoleucine

A. [1-^{14}C]-(+)-10′-Dicyclohexylsulfamoyl-L-isobornyl butyrate. [1-^{14}C]Butyric acid (44 mg, 0.5 mmol) and oxalyl chloride (46 μL, 0.52 mmol) were allowed to react in 1 mL of dry benzene for 18 h at room temperature. The reaction mixture was then heated to 42°C for 30 min. After cooling to room temperature, (+)-10-dicyclohexylsulfamoyl-l-isoborneol (150 mg, 0.38 mmol) and AgCN (134 mg, 1.0 mmol) were added to the crude acid chloride along with 0.5 mL of dry benzene. The mixture was heated to gentle reflux for 48 h. The silver salts were removed by filtration through Celite and the filtrate evaporated in vacuo to give a residue that was chromatographed on silica gel to furnish the coupling product (131 mg) in 56% yield with a specific activity of 8.1 μCi/mg: ^{1}H NMR (90 MHz, $CDCl_3$) δ: 0.85 (s, 3H), 0.95 (t, 6H), 1.04–2.4 (m, 31H), 2.64 (d, J = 14 Hz, 1H), 2.95–3.4 (m, 3H), 4.8–5.04 (m, 1H). HRMS, calcd. for $C_{26}H_{45}NO_4S$: 467.3069; found (M^+): 467.3076; calcd. for $^{13}C_1C_{25}H_{45}NO_4S$: 468.3103; found (M + 1): 468.3110.

B. [1-^{14}C]-(+)-10′-Dicyclohexylsulfamoyl-L-isobornyl-2-bromobutyrate. Under a nitrogen atmosphere, diisopropylamine (290 mg, 2.9 mmol) in dry THF (45 mL) was cooled to 0°C and *n*-BuLi (1.1 mL, 2.6 M in hexane, 2.9 mmol) was added. After stirring at 0°C for 30 min, the reaction mixture was cooled to –78°C before a solution of the radioactive ester prepared in step *A* (808 mg, 1.7 mmol) in dry THF (15 mL) was added. The colorless reaction mixture was stirred at –78°C for 1 h before trimethylsilyl chloride (0.565 mL, 4.4 mmol) was added. After stirring for an additional 45 min at –78°C, recrystallized *N*-bromosuccinimide (518.7 mg, 2.82 mmol) in dry THF (22 mL) was added. The resulting cloudy yellowish reaction mixture was stirred at –78°C for 5 h and then quenched with water. After the usual aqueous work-up, the crude product was purified by flash chromatography on silica gel to furnish pure bromide (762 mg) in 81% yield: ^{1}H NMR (90 MHz, $CDCl_3$) δ: 0.85 (s, 3H), 1.0 (s, 3H), 1.04–2.4 (m, 32H), 2.8 (d, J = 14 Hz, 1H), 2.9–3.5 (m, 3H), 4.15 (dd, J = 5.8 Hz, 1H), 4.8–5.1 (m, 1H); ^{13}C NMR (75.47 Hz, $CDCl_3$) δ: 11.83, 19.80, 20.24, 24.91, 26.19, 26.76, 28.55, 30.20, 32.03, 33.03, 39.04, 44.06, 49.08, 49.27, 49.59, 53.36, 57.12, 79.91, 167.5 ppm; HRMS, calcd. for $C_{26}H_{44}NO_4BrS$: 545. 2174; found (M^+): 545.2171; calcd. for $^{13}C_1C_{25}H_{44}NO_4BrS$: 546.2208; found (M + 1): 546.2216.

C. [1-^{14}C]-(+)-10′-Dicyclohexylsulfamoyl-L-isobornyl crotonate. The radioactive bromide prepared in part *B* (762 mg, 1.37 mmol) was allowed to react with DBU (823 mg, 5.49 mmol) in 46 mL of dry benzene at reflux under nitrogen for 18 h. The resulting yellowish brown reaction mixture was worked up by addition of 1 M $NaHCO_3$ and water in succession. After drying the organic phase, the solvent was removed in vacuo and the residue purified by flash chromatography on silica gel to afford the pure crotonyl ester (468 mg) in 72% yield: ^{1}H NMR (300 MHz, $CDCl_3$) δ: 0.85 (s, 3H), 1.0 (s, 3H), 1.05–2.15 (m, 30H), 2.68 (d, J = 12.9 Hz, 1H), 3.1–3.35 (m, 3H), 5.05 (d, J = 8.6 Hz, 1H) 5.83 (d, J = 17.2 Hz, 1H), 6.8–7.03 (m, 1H); ^{13}C NMR (75.47 MHz, $CDCl_3$) δ: 17.86, 19.98, 20.39, 25.06, 26.34, 26.95, 29.77, 32.68, 39.33, 44.45, 49.03, 49.38, 53.56, 57.29, 77.87, 123.27, 143.69, 164.78, 205.5 ppm.

D. [1-^{14}C]-L-Alloisoleucine. The [^{14}C]-labeled crotonate ester prepared in part *C* was converted into [1-^{14}C]-L-alloisoleucine using the same sequence of reactions that was employed to convert [3-^{3}H]-(+)-10-dicyclohexylsulfamoyl-L-isobornyl crotonate into [3-^{3}H]-L-alloisoleucine. The specific activity of the resulting [1-^{14}C]-L-alloisoleucine was 7.5 μCi/mg.

Synthesis of a mixture of (2-^{13}C,^{15}N)-DL-isoleucine and (2-^{13}C,^{15}N)-DL-alloisoleucine

A. (1-^{13}C)-2-Methylbutyronitrile. (^{13}C)Sodium cyanide (2.0 g, 40.8 mmol) was added to a solution of 2-bromobutane (3.72 g, 27.2 mmol) in 50 mL HMPA at room temperature. The reaction mixture was stirred at room temperature for 48 h and then connected via a U-tube, cooled in liquid nitrogen, to a vacuum pump and distilled at room temperature. This gave 0.913 g (40%) of (1-^{13}C)-2-methylbutyronitrile as a colorless liquid: ^{1}H NMR (250 MHz, $CDCl_3$) δ: 1.05 (s, 3H), 1.3 (s, 3H), 1.55 (m, 2H), 2.5–2.65 (m, 1H); ^{13}C NMR (62.89 MHz, $CDCl_3$) δ: 11.347, 11.392, 26.585, 27.237, 26.266, 27.464, 122.914 (enriched) ppm.

B. (1-^{13}C)-2-Methylbutyraldehyde. DIBAL (13.4 mL, 13.4 mmol) was added dropwise to a stirred solution of (1-^{13}C)-2-methylbutyronitrile (0.913 g, 11 mmol) in dry CH_2Cl_2 (25 mL) at room temperature. After 1.5 h the reaction mixture was cautiously poured into 5% H_2SO_4 (50 mL) and the aqueous and organic layers separated. The aqueous layer was further extracted with dichloromethane and the combined organic extracts were dried over anhydrous $MgSO_4$, filtered, and concentrated by distillation at atmospheric pressure. The crude (1-^{13}C)-2-methylbutyraldehyde distilled at 90–92°C: ^{1}H NMR (250 MHz, $CDCl_3$) δ: 0.9–1.0 (t, 3H), 1.1–1.15 (t, 3H), 1.3–1.8 (m, 2H), 2.2–2.35 (m, 1H), 9.25–9.95 (d, $^1J_{CH}$, J = 40.9 Hz, 1H).

C. (2-^{13}C)-2-Hydroxy-3-methylvaleronitrile. Ethanol was added to a stirred solution of (1-^{13}C)-2-methylbutyraldehyde (0.95 g, 11 mmol) and sodium bisulfite (1.3 g, 12.5 mmol) in water (10 mL) until the solution became homogenous and clear. After stirring at room temperature for 1 h, potassium cyanide (0.73 g, 11.2 mmol) was added and the reaction mixture stirred at room temperature for 3 h. The ethanol was removed in vacuo and the aqueous layer extracted with ether. The combined ether extracts were washed with water, and with saturated NaCl. They were then dried over $MgSO_4$, filtered, and concentrated in vacuo. This gave 0.76 g (61%) of crude (2-^{13}C)-2-hydroxy-3-methyl valeronitrile.

Can. J. Chem. Downloaded from www.nrcresearchpress.com by 195.246.54.202 on 09/08/12
For personal use only.

D. (2-^{13}C, ^{15}N)-2-Amino-3-methylvaleronitrile. Ethanol was added to a solution of (2-^{13}C)-2-hydroxy-3-methylvaleronitrile (0.76 g, 6.72 mmol) in (^{15}N)ammonium hydroxide (4.1 mL of a 3.3 N solution) until the solution became homogenous and clear. The reaction mixture was stirred at room temperature for 18 h, the ethanol removed in vacuo, and the aqueous layer extracted with ether. The combined ether extracts were washed with water, saturated NaCl, dried over $MgSO_4$, filtered, and concentrated. This gave 0.72 g of crude (2-^{13}C, ^{15}N)-2-amino-3-methylvaleronitrile.

E. Mixture of (2-^{13}C, ^{15}N)-DL-isoleucine and (2-^{13}C, ^{15}N)-DL-alloisoleucine. Barium hydroxide (8.2 g, 26 mmol) was added to a solution of (2-^{13}C, ^{15}N)-2-amino-3-methylvaleronitrile (0.721 g, 6.32 mmol) in water (50 mL). The flask was fitted with a reflux condenser and the mixture refluxed for 18 h. The reaction mixture was then cooled to room temperature, filtered through Celite, and the filtrate treated twice with $(NH_4)_2CO_3$ to remove barium as insoluble barium carbonate. The resulting clear filtrate was stirred at 60–65°C in a water bath for 1 h and finally concentrated in vacuo. Chromatography of the residue on a cellulose column (eluant BAW 12:3:5) gave 0.35 g (42%) of doubly labeled amino acid as a white solid: ^{1}H NMR (250 MHz, $CDCl_3$) δ: 0.6–0.75 (m, 6H), 1.0–1.25 (m, 2H), 1.65–1.85 (m, 1H), 3.4 (ddd, $^1J_{CH}$ = 162 Hz, $^3J_{HH}$ = 25 Hz, $^2J_{NH}$ = 6.4 Hz, 1H); ^{13}C NMR (62.89 MHz, $CDCl_3$) δ: 11.23, 11.29, 13.46, 14.82, 22.83, 24.61, 25.63, 35.99, 58.50, 58.59, 59.58, 59.67 (doublet, $^1J_{CN}$ = 68 Hz), 180.62 ppm.

Synthesis of (5-$^2H_1$, 6-$^2H_1$)-DL-coronamic acid

A. (6-$^2H_1$, 7-$^2H_1$)-1,1-Dicarbomethoxy-2-ethylcyclopropane. A flame-dried and cooled 1000-mL three-necked round-bottomed flask, fitted with a reflux condenser and dropping funnel, was charged with 1,1-dicarbomethoxy-2-vinylcyclopropane (1.0 g, 5.43 mmol) (30) and dipotassium azodicarboxylate (31) (68.9 g, 355 mmol) in 100 mL methanol-O-*d*. Acetic acid-O-*d* (30.1 mL) was added dropwise. The original deep yellow solution turned pale yellow and the methanol began to reflux. The acetic acid was added at such a rate as to maintain reflux. Once the addition was complete, the reaction mixture was stirred at room temperature. After 2.5 h the pale yellow solution had become white. After stirring for 5.5 h the reaction mixture was transferred to a 500-mL round-bottomed flask and the methanol removed in vacuo. The residue was dissolved in water (50 mL) and extracted with ether. The combined ether extracts were washed with 1 N $NaHCO_3$, water, and brine, dried over anhydrous $MgSO_4$, filtered, and concentrated in vacuo. The residue was purified by flash chromatography (SiO_2, elutant 5%–15% ethyl acetate – hexane). This gave 0.8 g (80%) of (6-$^2H_1$, 7-$^2H_1$)-1,1-dicarbomethyoxy-2-ethylcyclopropane as a clear liquid: ^{1}H NMR (250 MHz, $CDCl_3$) δ: 0.9 (m, 2H), 1.2–1.3 (m, 1H), 1.3–1.5 (m, 2H), 1.8–2.0 (m, 1H), 3.7 (s, 3H), 3.8 (s, 3H).

B. (6-$^2H_1$, 7-$^2H_1$)-1-Carboxy-1-carbomethoxy-2-ethylcyclopropane. Potassium hydroxide (0.25 g, 4.4 mmol) was added to a stirred solution of (6-$^2H_1$,7-$^2H_1$)-1,1-dicarbomethoxy-2-ethylcyclopropane in methanol (18 mL) at room temperature. The reaction mixture was stirred at room temperature for 4 days. The methanol was removed in vacuo and the residue dissolved in water (20 mL). The aqueous layer was extracted with ethyl acetate and the combined ethyl acetate extracts washed with brine, dried over $MgSO_4$, filtered, and concentrated in vacuo. This gave 0.41 g (85%) of (6-$^2H_1$, 7-$^2H_1$)-2-carboxy-1-carbomethoxy-2-ethylcyclopropane as a clear liquid, ^{1}H NMR (250 MHz, $CDCl_3$) δ: 0.95 (m, 2H), 1.4–1.7 (m, 1H), 1.7–1.8 (m, 1H), 1.9–2.15 (m, 2H), 3.7 (s, 3H).

C. (5-$^2H_1$, 6-$^2H_1$)-DL-Coronamic acid. Ethyl chloroformate (0.68 mL, 7.1 mmol) was added dropwise to a stirred solution of (6-$^2H_1$,7-$^2H_1$)-1-carboxy-1-carboxymethyl-2-ethylcyclopropane (0.41 g, 2.35 mmol) and *N*-ethyldiisopropylamine (0.82 mL, 4.72 mmol) in acetone (5 mL) at 0°C. The solution was stirred at 0°C for 30 min, a solution of sodium azide (0.76 g, 11.82 mmol) in water (5 mL) was added, and the reaction mixture was stirred at 0°C for 2 h. The acetone was removed in vacuo and the aqueous layer extracted with ethyl acetate. The combined ethyl acetate extracts were washed with water and saturated NaCl, dried over $MgSo_4$, filtered, and concentrated in vacuo. This gave 0.45 g of the crude acyl azide as a pale yellow oil. The crude acyl azide was dissolved in toluene (6 mL) and heated at reflux for 30 min. The reaction mixture was cooled to roomtemperature, and the toluene removed in vacuo. The brown residual oil was dissolved in 6 N HCl (6 mL) and the solution refluxed for 6 h. The solution was cooled to room temperature and the acid removed in vacuo. The residue was redissolved in water (7 mL) and loaded onto a strongly acidic ion-exchange resin (Dowex 50W-X8, H^+-form, 15 mL). After washing the column with water, the amino acid fraction was eluted with 2 N NH_4OH (60 mL) and concentrated in vacuo. This gave 0.250 g (40%) of (5-$^2H_1$, 6-$^2H_1$)-DL-coronamic acid as a pale yellow solid: TLC (cellulose, BAW, 4:1:2, R_f = 0.69); ^{1}H NMR (300 MHz, D_2O) δ: 0.75 (m, 2H), 1.15 (d, $^3J_{HH}$ = 1.2 Hz, 2H), 1.3–1.4 (m, 1H), 1.4–1.5 (m, 1H); ^{13}C NMR (62.89 MHz, D_2O) δ: 12.44 (t, $^1J_{CD}$ = 19 Hz), 17.05, 19.57 (t, $^1J_{CD}$ = 20 Hz), 27.61, 39.85, 174.11 ppm.

Synthesis of a mixture of (1-^{13}C)-6-hydroxy-DL-isoleucine and (1-^{13}C)-6-hydroxy-DL-alloisoleucine

A. Methyl 2-benzyloxymethylbutanoate. A solution of *n*-BuLi (2.04 M in hexane, 5.5 mL) was added with stirring to a solution of diisopropylamine (1.11 g, 11.0 mmol) in dry THF (20 mL) at 0°C. The resulting solution was stirred at 0°C for 30 min, then cooled to –78°C before adding methyl butanoate (1.05 g, 10.3 mmol). After the ester addition, the reaction mixture was stirred at –78°C for 1 h, and bromomethyl benzyl ether[6] (2.27 g, 11.3 mmol) was then added. Stirring at –78°C was continued for 30 min, after which time the reaction was allowed to warm to room temperature and then quenched with excess saturated aqueous NH_4Cl solution. The resulting mixture was concentrated in vacuo and ether (10 mL) was added. The organic phase was washed with 1 N HCl (3 × 20 mL), separated, and dried over $MgSO_4$. Removal of the ether in vacuo gave the crude product, which was purified by flash chromatography (SiO_2, 15% EtOAc in hexane) to yield 1.39 g (61%) of a yellowish oil: ^{1}H NMR (90 MHz, $CDCl_3$) δ: 0.90 (t, *J* = 7 Hz, 3H), 1.45–1.76 (m, 2H), 2.50–2.88 (m, 1H), 3.53–3.59 (m, 2H), 3.69 (s, 3H), 4.50 (s, 2H), 7.30 (s, 5H); ^{13}C NMR (22.5 MHz, $CDCl_3$) δ: 11.49, 21.96, 47.53, 51.43, 70.56, 73.03, 127.55, 128.27, 138.16, 174.85 ppm.

B. 2-Benzyloxymethylbutanal. A solution of DIBAL (5.3 mL, 1.0 M in CH_2Cl_2) was added with stirring to a solution of methyl 2-benzyloxymethylbutanoate (1.16 g, 5.22 mmol) in dry CH_2Cl_2 (20 mL) chilled to –78°C. The resulting solution was stirred at –78°C for 1 h and then quenched with excess saturated aqueous NH_4Cl. The reaction mixture was then warmed to room temperature and the aluminum salts solubilized by addition of 1 N HCl (30 mL). The organic layer was separated, washed with brine (10 mL), dried ($MgSO_4$), and concentrated in vacuo. The crude aldehyde was purified by flash chromatography (SiO_2, 15% EtOAc in hexane) to yield 845 mg (84%) of a colorless oil: ^{1}H NMR (90 MHz, $CDCl_3$) δ: 0.93 (t, *J* = 7 Hz, 3H), 1.45–1.90 (m, 2H), 2.32–2.65 (m, 1H), 3.64–3.71 (m, 2H), 4.50 (s, 2H), 7.31 (s, 5H), 9.69 (d, *J* = 2 Hz, 1H); ^{13}C NMR (22.5 MHz, $CDCl_3$) δ: 11.29, 18.97, 53.58, 68.22, 73.23, 127.55, 127.68, 128.40, 137.96, 203.93 ppm; MS [EI], *m/z*: 121, 116, 107 ($C_7H_7O^+$, base peak), 106, 105, 91.

C. Mixture of (1-^{13}C)-6-benzyloxy-L-isoleucine and (1-^{13}C)-6-benzyloxy-DL-alloisoleucine. 2-Benzyloxymethylbutanal (530 mg, 2.76 mmol) was added to a solution of sodium bisulfite (370 mg) in water (10 mL). Ethanol was then added with stirring until the mixture became homogeneous. The resulting solution was stirred at room temperature for 1 h, at which time (^{13}C)-KCN (184 mg, 2.83 mmol) was added. Stirring of the reaction mixture was then continued for 3 h. The solution was then concentrated in vacuo and the concentrated mixture extracted with ether. After removal of the ether, the residue was suspended in concentrated NH_4OH (10 mL) and ethanol added until the mixture was homogeneous. The resulting solution was stirred overnight at room temperature. The solution was again concentrated in vacuo and the concentrated mixture extracted with ether. Removal of the ether yielded a residue, which was added to a solution of $Ba(OH)_2 \cdot 8H_2O$ (2.25g, 7.14 mmol) in water (10 mL) and the mixture

[6]Prepared using gaseous HBr instead of gaseous HCl following the procedure of Conner et al. (32).

refluxed overnight. The white precipitate was filtered off and washed twice with hot water. The filtrate was concentrated in vacuo and then treated with solid ammonium carbonate (400 mg). The solution was boiled for 10 min and the precipitated $BaCO_3$ was removed by filtration. The filtrate was then treated again with solid ammonium carbonate. This process was repeated until no white precipitate formed. Finally, the clear solution was boiled to destroy excess ammonium carbonate and then taken to dryness in vacuo. The residue was purified by flash chromatography (SiO_2, 25% MeOH in $CHCl_3$) to afford 160 mg (25%) of a mixture of (1-^{13}C)-6-benzyloxy-DL-isoleucine and (1-^{13}C)-6-benzyloxy-DL-alloisoleucine as a yellowish oil: ^{1}H NMR (90 MHz, D_2O) δ: 0.64–0.94 (m, 3H), 1.16–1.56 (m, 2H), 2.04–2.40 (m, 1H), 3.42–3.56 (m, 2H), 4.09 (d, J = 3.6 Hz, 1H), 4.40 (s, 2H), 7.28 (s, 5H); ^{13}C NMR (22.5 MHz, D_2O, *p*-dioxane ref.) δ: 10.94, 19.66, 20.44, 40.87, 55.18, 69.49, 73.07, 128.44, 128.76, 175.1 (enriched) ppm.

D. Mixture of (1-^{13}C)-6-hydroxy-DL-isoleucine and (1-^{13}C)-6-hydroxy-DL-alloisoleucine. A mixture of (1-^{13}C)-6-benzyloxy-DL-isoleucine and (1-^{13}C)-6-benzyloxy-DL-alloisoleucine 332 mg, 1.40 mmol) was dissolved inmethanol (35 mL), 10% Pd/C (143 mg) and concentrated HCl (3 drops) were added, and the suspension was stirred under H_2 at atmospheric pressure for 24 h. The catalyst was then removed by filtration and the solution taken to dryness. The residue was purified by column chromatography (cellulose, BAW 6:1:1) to yield a mixture of the free amino acids weighing 70 mg (39%). On standing in aqueous solution at room temperature, this mixture was converted into a mixture of the corresponding γ-lactones: TLC (cellulose, BAW 6:1:1), R_f = 0.49 for free amino acids, R_f = 0.33 for lactonized amino acids; spectral data for the lactones: ^{1}H NMR (90 MHz, D_2O) δ: 0.96 (t, J = 7.5 Hz, 3H), 1.20–1.96 (m, 2H), 2.08–2.72 (m, 1H), 3.49 (d, J = 11 Hz, 1H), 3.89–4.10 (m, 1H), 4.33–4.65 (m, 1H); ^{13}C NMR (22.5 MHz, D_2O, *p*-dioxane ref.) δ: 11.13, 18.55, 42.17, 57.26, 61,95, 180.25 (enriched) ppm; HRMS, calcd. for $C_6H_{11}NO_2$: 129.07897; found (M^+): 129.07895; calcd. for $^{13}C_1C_5H_{11}NO_2$: 130.08232; found (M + 1): 130.08205.

Acknowledgments

We thank the National Institutes of Health (GM26569) and The Robert A. Welch Foundation (C-729) for financial support, Dr. R.E. Mitchell for authentic samples of coronatine and coronafacic acid, Professor Carol Bender, for *P. syringae* strain PDDCC no. 4180 and for suggestions concerning the maintenance of the strain, and Dr. Alan Kook for running complex NMR experiments.

1. A. Ichihara, K. Shiraishi, H. Sata, S. Sakamura, K. Nishiyama, R. Sakai, A. Furusaki, and T. Matsumoto. J. Am. Chem. Soc. **99**, 636 (1977).
2. R.E. Mitchell. Physiol. Plant Pathol. **20**, 83 (1982).
3. R.E. Mitchell and H. Young. Phytochemistry, **17**, 2028 (1978).
4. R.E. Mitchell, C. Hale, and J. Shanks. Physiol. Plant Pathol. **23**, 315 (1983).
5. R. Sakai. Ann. Phytopath. Soc. Jpn. **46**, 499 (1980).
6. S.S. Gnanamanickam, A.N. Starratt, and E.W.B. Ward. Can. J. Bot. **60**, 645 (1982).
7. J.S. Kenyon and J.G. Turner. Plant Physiol. **100**, 219 (1992).
8. A. Ichihara, K. Shiraishi, S. Sakamura, A. Furusaki, N. Hashiba, and T. Matsumoto. Tetrahedron Lett. 365 (1979).
9. R.J. Parry, and R. Mafoti. J. Am. Chem. Soc. **108**, 4681 (1986); R.J. Parry, M-T. Lin, A.E. Walker, and S. Mhaskar. J. Am. Chem. Soc. **113**, 1849 (1991).
10. W. Aue, E. Bartholdt, and R. Ernst. J. Chem. Phys. **64**, 2229 (1976).
11. R. Freeman. J. Magn. Reson. **44**, 542 (1981).
12. J.C. Vederas. J. Am. Chem. Soc. **102**, 374 (1980); J.M. Risley and R.L. Van Etten. J. Am. Chem. Soc. **102**, 6699 (1980).
13. R.B. Herbert. *In* The biosynthesis of secondary metabolites. 2nd ed. Chapman and Hall, New York. 1989. pp. 55–58.
14. P.A. Stadler, A.J. Frey, and A. Hofmann. Helv. Chim. Acta, **46**, 2300 (1963).
15. A.C. Hulme. Biochim. Biophys. Acta, **14**, 36 (1954).
16. D.E. Cane, W. Tan, and W.R. Ott. J. Am. Chem. Soc. **115**, 527 (1993), and references cited therein.
17. D. Seebach, R. Naef, and G. Calderari. Tetrahedron, **40**, 1313 (1984).
18. J.M. Schwab and J. Klassen. J. Am. Chem. Soc. **106**, 7217 (1984).
19. Y. Yoshizawa, Z. Li, P. Reese, and J.C. Vederas. J. Am. Chem. Soc. **112**, 3212 (1990).
20. C.R. Hutchinson. J. Nat. Prod. **45**, 27 (1982).
21. W. Oppolzer, R. Pedrosa, and R. Moretti. Tetrahedron Lett. **27**, 831 (1986); W. Oppolzer and P. Dudfield. Tetrahedron Lett. **26**, 5037 (1985); W. Oppolzer, C. Chapuis, and G. Bernardinelli. Tetrahedron Lett. **25**, 5885 (1984).
22. R.E. Mitchell. Phytochemistry, **23**, 791 (1984).
23. R.E. Mitchell and H. Young. Phytochemistry, **24**, 2716 (1985).
24. J.E. Baldwin, R. Adlington, and B. Rawlings. Tetrahedron Lett. **26**, 481 (1985).
25. J.E. Baldwin and E.P. Abraham. Nat. Prod. Rep. **5**, 129 (1988).
26. S.P. Salowe, E.N. Marsh, and C.A. Townsend. Biochemistry, **29**, 6499 (1990).
27. K.A. Gallo and J.R. Knowles. Biochemistry **32**, 3981 (1993), and references cited therein.
28. S.P. Lapage, J.E. Shelton, and T.G. Mitchell. *In* Methods in microbiology. Vol. 3A. *Edited by* J.R. Norris and D.W. Robbins. Academic Press, New York. 1970. p. 131.
29. G.B. Kauffman and L.A. Teter. *In* Inorganic syntheses. Vol. VII. *Edited by* J. Kleinberg. McGraw–Hill, New York. 1963. pp. 9–12.
30. K. Burgess. J. Org. Chem. **52**, 2046 (1987).
31. J.A. Berson, W.J. Libbey, and M.S. Pooman. J. Am. Chem. Soc. **91**, 5567 (1969).
32. D.S. Conner, G.W. Klein, G.N. Taylor, R.K. Boeckman, Jr., and J.B. Medwid. *In* Organic synthesis, Coll. Vol. VI. *Edited by* W.E. Noland. Wiley and Sons, New York. 1988. pp. 101–103.

Can. J. Chem. Downloaded from www.nrcresearchpress.com by 195.246.54.202 on 09/08/12
For personal use only.

Septatisine, a novel diterpenoid alkaloid from *Aconitum septentrionale* Koelle

BALAWANT S. JOSHI, HANAA M. SAYED, SAMIR A. ROSS, HARIDUTT K. DESAI, AND S. WILLIAM PELLETIER[1]
Institute for Natural Products Research and Department of Chemistry, The University of Georgia, Athens, GA 30602-2556, U.S.A.

PING CAI AND JOHN K. SNYDER[1]
Department of Chemistry, Boston University, Boston, MA 02215, U.S.A.

AND

ARNE J. AASEN
Department of Pharmacy, University of Oslo, P.O. Box 1068, Blindern 0316, Oslo, Norway

Received June 14, 1993

This paper is dedicated to Professors David B. MacLean and Ian Spenser.

BALAWANT S. JOSHI, HANAA M. SAYED, SAMIR A. ROSS, HARIDUTT K. DESAI, S. WILLIAM PELLETIER, PING CAI, JOHN K. SNYDER, and ARNE J. AASEN. Can. J. Chem. **72**, 100 (1994).

Septatisine **3**, an atisane-type diterpenoid alkaloid, was isolated from the roots of *Aconitum septentrionale* Koelle. Its structure was established on the basis of homonuclear ^{1}H COSY, LRCOSY, NOESY, DNOE, fixed-evolution HETCOR, and selective INEPT techniques.

BALAWANT S. JOSHI, HANAA M. SAYED, SAMIR A. ROSS, HARIDUTT K. DESAI, S. WILLIAM PELLETIER, PING CAI, JOHN K. SNYDER et ARNE J. AASEN. Can. J. Chem. **72**, 100 (1994).

On a isolé la septatisine (**3**), un alcaloïde diterpénoïdique du type de l'atisane, à partir des racines de l'*Aconitum septentrionale* Koelle. On a déterminé sa structure à l'aide de techniques INEPT sélectives, HETCOR à évolution déterminée et de COSY, LRCOSY, NOESY et DNOE homonucléaires du ^{1}H.

[Traduit par la rédaction]

Can. J. Chem. Downloaded from www.nrcresearchpress.com by 203.198.23.82 on 09/08/12
For personal use only.

About a hundred years ago, the presence of alkaloids was noted in *Aconitum septentrionale* (1). Subsequently, more than 24 norditerpenoid alkaloids (C_{19}) have been isolated by Marion et al. (2), Yunusov and co-workers (3–5), and from our own laboratories (6–9). Only two diterpenoid alkaloids (C_{20}) of the hetisane type, septentriosine **1**, and 2-acetylseptentriosine **2**, were isolated from the roots (10, 11). We report herein the isolation and structure determination of a new atisane-type diterpenoid alkaloid (C_{20}) designated as septatisine **3**.

The molecular formula $C_{22}H_{31}NO_3$ of septatisine **3**, deduced from elemental analysis, was confirmed by hr-eims (70 eV, *m/z* 357.2287, M^+; calcd. for $C_{22}H_{31}NO_3$, 357.2304). This formula requires eight units of unsaturation, one of which was quite clearly accounted for by a terminal, and presumably exocyclic, methylene unit as indicated by the ^{1}H and ^{13}C nmr spectra: δ 4.94 (dd, J = 2.6, 1.2 Hz); 4.83 (dd, J = 2.1, 1.2 (Hz); δ 157.9 (s), 103.8 (t). This leads to the conclusion that septatisine is a diterpenoid (C_{20}) alkaloid with two additional carbons and the remaining seven units of unsaturation elaborated by a polycyclic system. The appearance of an isolated dimethylene proton coupled spin system in the homonuclear COSY (COSY) spectrum (δ 3.78 (ddd, J = 13.6, 12.1, 6.9 Hz), 3.56 (ddd, J = 13.6, 8.6, 2.2 Hz), 3.03 (ddd, J = 12.4, 12.1, 8.6 Hz), 2.81 (ddd, J = 12.4, 6.9, 2.2 Hz)) with the corresponding carbons located by a heteronuclear COSY (fixed evolution HETCOR) (12) spectrum (δ 61.7, 51.5), indicated that these two "additional" carbons were attached to the nitrogen[2] forming an ethanolamino grouping.

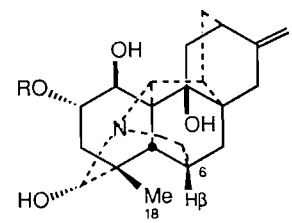

1 R = H
2 R = Ac

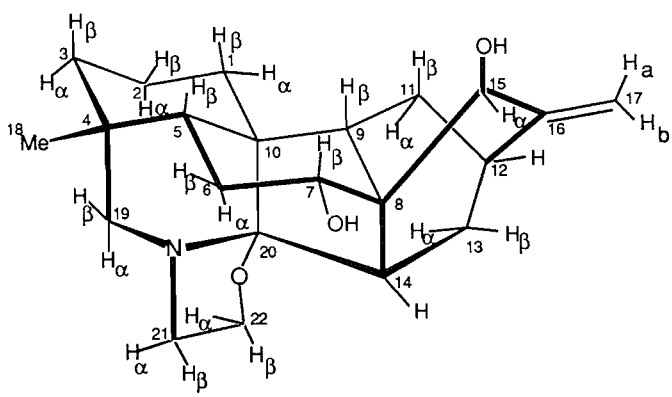

3 Septatisine

[1]Authors to whom correspondence may be addressed.

[2]Even with the fixed-evolution HETCOR, no correlations were observed between the H22 protons and C22, though this assignment was unambiguous as all other correlations were apparent.

Of the three most likely candidate diterpene alkaloidal skeleta, the atisane (**A**), veatchine (**B**), and hetisane (**C**) types, the hetisane skeleton was considered unlikely because the tertiary amino functionality allowed for no realistic option to attach the two "additional" carbons of the C_{22} formula. The veatchine skeleton was ruled out on the basis of the experiment to be described, and the atisane structure with one additional unit of unsaturation (C14/C20 bridge) was confirmed by spectroscopic methods.

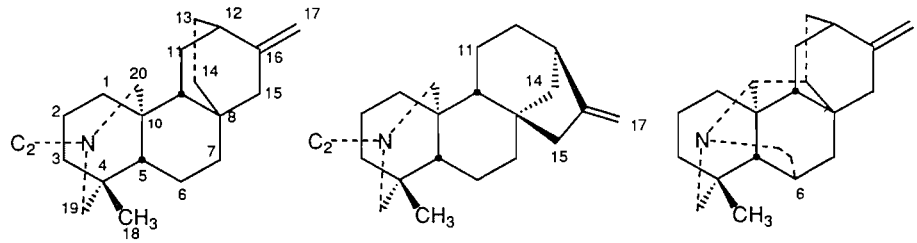

A B C

Weak coupling between both vinylic methylene protons (H17a and H17b) with a carbinol proton (δ 4.49 br s) was observed in the COSY spectrum, as well as in the long-range COSY spectrum (LRCOSY, Δ = 0.25 s). Given the exocyclic nature of the double bond, this could only be allylic coupling, and therefore a secondary alcohol functionality was considered to be located at C15 (^{13}C: δ 68.7 from the fixed-evolution HETCOR spectrum). The methine nature of this carbinol carbon was confirmed by an APT experiment. That this oxygenated carbon was an alcohol and not part of an ether was shown by COSY and the LRCOSY spectra in which the doublet at δ 1.90 (J = 5.8 Hz, exchangeable with D_2O), indicated coupling with H15. In later spectra this resonance apparently broadened and moved downfield to the overlapped region at δ 2.0 with no coupling with H15 observed in the COSY spectra. Apparently the appearance of this OH resonance was very sensitive to the water concentration in the nmr sample.

No coupling was observed between either H17 and any other proton in either the COSY or LRCOSY spectra, but the second allylic position, H12, was located by a selective INEPT experiment. Saturation of the upfield H17 resonance, later shown to be H17a by nOe studies, resulted in an enhancement of a methine carbon (δ 34.5), which must therefore be C12. The fixed-evolution HETCOR spectrum enabled assignment of the proton attached to this methine carbon as a broad singlet (H12: δ 2.20). In the COSY spectrum, this broad singlet showed coupling with three other protons, which were three of the four members of two different methylene groups (H11α, H11ß, and H13α). Coupling with these methylene protons was partially obscured by overlap with other resonances, but the frequencies were sufficiently distinct that they could be resolved for identification. No coupling was observed between H12 and the fourth methylene proton of these two pairs in the COSY spectrum, but was readily apparent in the LRCOSY spectrum (Δ = 0.25 s, H13ß: δ 1.36 (dddd, J = 13.4, 12.2, 2.2, 2.0 Hz)). This latter resonance, which was cleanly resolved in the ^{1}H nmr spectrum, was most easily confirmed as one of the methylene pair adjacent to C12 from the HETCOR spectrum by its one-bond coupling with the same carbon as H13α (δ 27.4). The stereochemical assignments of all methylene pairs of protons were from nOe studies (vide infra).

These observations required that the exocyclic double bond be flanked by a secondary alcohol and a methine carbon, the latter of which was adjacent to two methylene carbons. This requirement can be met by both the atisane and veatchine skeleta with the secondary alcohol group at C15. Two APT experiments, one with a defocusing delay of 8 ms (optimal for $^1J_{1H,13C}$ = 125 Hz for detection of all carbons and the second with a defocusing delay of 4 ms for detection of quaternary carbons (13) (carbons with $^1J_{1H,13C}$ = 125 Hz are nulled) revealed that **3** contained one methyl carbon (δ 28.6), nine methylenes (δ 19.6, 27.4, 29.2, 30.2, 32.3, 41.3, 51.5, 57.3, and 61.7), six methines (δ 34.5, 44.0, 46.6, 49.6, 68.7, and 70.1), and four quaternary carbons (δ 34.4, 47.1, 50.0, and 104.6) in addition to the two sp^2 hybridized carbons (δ 103.8, t; 157.9, s). The downfield quaternary carbon at δ 104.6 indicated the presence of a carbinolamine.

These results account for 29 hydrogens, and the remaining two hydrogens required by the molecular formula must be present as two alcohol functionalities. The third oxygen must therefore be in a cyclic ether. (The sole methyl group can be assigned to C18, and since there is no way to terminate a chain with an oxygenated methine or quaternary carbon, a cyclic ether must be present.)

In both the atisane and hetisine structures, the basic skeleta, the exocyclic double bond, and the cyclic ether account for seven of the eight units of unsaturation. The remaining unit must therefore arise from an additional bridge in the basic alkaloidal skeleton. Location of this bridge in principle should have been possible from knowledge of the spin systems mapped by the COSY spectrum. This effort was stymied, unfortunately, by serious signal overlap in the ^{1}H nmr spectrum (and therefore also in the COSY) in all solvents examined. These solvents included $CDCl_3$, CH_2Cl_2, CD_3OD, Py-d_5, and C_6D_6, as well as titrations of **3** in $CDCl_3$ with Py-d_5, and C_6D_6.

The atisane skeleton with a C14/C20 bridge, as well as location of the carbinolamine-anchored cyclic ether, was established through selective INEPT studies. As mentioned above, one of the two "additional" carbons of the C_{22} formula was considered to be the nitrogenated terminus of an ethanolamine group. In addition, in the ^{1}H nmr spectrum an AB system typical for a C19 methylene group in C_{20} diterpene alkaloids appeared (δ 2.58, 2.35, J_{AB} = 11.4 Hz; ^{13}C: 57.3). This result indicated that nitrogen was bonded to two methylene groups and the quaternary carbinolamine carbon. Saturation of the downfield H19, later shown to be H19ß by nOe studies, resulted in the enhancement of the other nitrogenated methylene carbon of the "additional" C_2 unit, the methyl carbon assigned as C18, and two quaternary carbons: δ 34.4 and 104.6. The upfield quaternary carbon resonance could be assigned to C4 on the basis of its chemical shift, and downfield resonance to the carbinola-

Can. J. Chem. Downloaded from www.nrcresearchpress.com by 203.198.23.82 on 09/08/12
For personal use only.

Can. J. Chem. Downloaded from www.nrcresearchpress.com by 203.198.23.82 on 09/08/12
For personal use only.

mine carbon, which must be C20 since no other carbons can be attached to the nitrogen. If C20 is a carbinolamine carbon and is nonprotonated, then this must be the site of the additional bridge in the diterpene skeleton.[3]

In another selective INEPT experiment, saturation of the well-resolved methylene proton vicinal to H12 (δ 1.36, later assigned to H13ß) also resulted in an enhancement of the quaternary carbinolamine carbon C20, as well as an enhancement of the vinyl C16 carbon, confirming the location of this methylene group three bonds removed from the double bond. A polarization transfer from a methylene proton adjacent to the allylic C12 position is possible only in the atisane skeleton, and only with a C14/C20 bridge. (In principle, the veatchine skeleton with a C11/C20 bridge forming a cyclobutane ring would also account for this observation, with the H13 now as the allylic methine and H12 as the well-resolved methylene proton being saturated in the selective INEPT experiment. Such a structure, however, is quite incompatible with the carbon chemical shifts and is considered highly unlikely.)

With establishment of the basic carbon framework as the atisane skeleton with a C14/C20 bridge, all that remained was location of the fourth oxygenated carbon, location of the cyclic ether, determination of the stereochemistry of the alcohol functions, and then completion of the proton and carbon resonance assignments. The final oxygenated carbon was located at C7 by selective INEPT experiments as well. Saturation of H15, easily assigned by the allylic coupling with both H17a and H17b as discussed above, resulted in an enhancement of this oxygenated carbon. A reciprocal enhancement of C15 was observed upon saturation of the carbinol proton attached to this remaining oxygenated carbon (δ 4.21, dd, J = 8.7, 7.7 Hz).[4] The only possible site for a secondary carbinal carbon within three bonds of H15 in the atisane skeleton with a C14/C20 bridge is at C7. Location of the final oxygenated carbon at C7 requires that the H5 through H7 spin system be -CH-CH_2-CH-, and the H1 through H3 system be a trimethylene unit. The COSY spectrum clearly indicated that H7 was coupled to two other protons, one of which was a cleanly resolved multiplet (δ 2.28, ddd, J = 13.4, 13.3, 8.7 Hz, H6α) while the second proton, which also coupled with H6α, appeared in an overlapped portion of the spectrum (δ 2.10, overlapped with H11 and H1α). These two protons were the C6 methylene pair as shown by the fixed evolution HETCOR spectrum (δ 32.3). Both the C6 methylene protons in turn coupled to one other methine proton, also overlapped, but which could be resolved through extensive decoupling experiments (δ 1.25). The HETCOR spectrum located the carbon of this methine proton at δ 46.6, typical for C5 and completing the C5 through C7 ^{1}H and ^{13}C assignments.

The C1 through C3 system was considered to be an unsubstituted trimethylene sequence by appearance of a methylene carbon at δ 19.6, typical for C2 in structurally analogous terpenoid systems with nonoxygenated C1 and C3 methylene carbons as in spirasines (14), and in nominine and its derivatives (15). Since C12 was vicinal to two methylenes (C11 and C13), C6, C19, and the "additional" C2 unit were all methylenes, only three methylene carbons and no other substituents are to be accounted for in the formula, and these methylenes must be C1 through C3. In a selective INEPT experiment, saturation of a cleanly resolved multiplet (δ 0.90, ddd, J = 13.3, 13.3, 5.4 Hz) resulted in an enhancement of the carbinolamine carbon C20, as well as another quaternary carbon (δ 47.1, assigned as C10), and one of the three remaining methylene carbons (δ 41.3, C3). This proton was therefore assigned as H1ß (stereochemical assignment on the basis of coupling constants), with its methylene partner H1α located in the fixed evolution HETCOR spectrum (^{13}C: δ 30.2) in an overlapped region of the proton spectrum at δ 2.2 (overlapped with H6ß). In the COSY spectrum, H1ß showed coupling with H1α as well as with a second proton, also overlapped (δ 1.45). Coupling to a third proton (δ 1.55) was much weaker. In the same COSY spectrum H1α showed coupling with this third proton (δ 1.55, overlapped with one of the H11 protons), but not with the second proton as coupled with H1ß. The HETCOR spectrum nevertheless revealed that these two new protons were a methylene pair, and therefore these must be the C2 methylene protons (^{13}C: δ19.6). In the LRCOSY spectrum, mutual coupling between all protons of this vicinal pair of methylenes was observed. In a similar manner the C3 methylene protons and carbon were assigned. Thus, in the ^{1}H nmr spectrum a resolved multiplet (δ 1.11, ddd, J = 13.2, 13.2, 5.1 Hz and therefore assigned as H3ß) showed coupling with one of the C2 methylene protons (the same one that showed strong coupling with H1ß in the COSY spectrum) assigned to H2α on the basis of *trans*-diaxial coupling and nOe studies (vide infra). From the fixed evolution HETCOR experiment, H3α was located in an overlapped region of the spectrum at δ 1.25 (overlapped with H5). The C3 resonance was identical to the methylene carbon enhanced by saturation of H1ß in the earlier mentioned selective INEPT experiment. Thus, the C1 through C3 trimethylene subunit was confirmed.

The sole remaining question of the basic skeleton of **3** was the location of the cyclic ether. Of the three possibilities (C7/C20, C7/C22, and C20/C22), the first could be easily ruled out on the basis of strain. A C7/C20 ether linkage would have required that all four bonds to C20 be on the same face of a plane and this would be impossible for a tetrahedral carbon. A C7/C22 ether would also have involved considerable strain as well as severe steric interactions, most notably between the H21 protons and H6α and H22 and H14. Finally, several nOe spectra strongly favored the C20/C22 ether: a strong nOe observed in the 2D-nOe spectrum between H19α and H2α is incompatible with a C7/C22 ether linkage but is in excellent agreement with the C20/C22 linkage as these two protons only lie an estimated 1.45 Å apart. (Selective INEPT experiments to detect a polarization transfer from either one of the C22 methylene protons to C20 were unsuccessful. This was not surprising since the dihedral angle between C20 and either of the H22 protons is about 120° and therefore only small coupling between these nuclei would be expected.)

With the skeletal assignment **3** finished, all that remained to complete the structure assignment was determination of the stereochemistry of the C7 and C15 alcohol functions. The axial nature of the H7 proton was suggested by its coupling constants with the C6 methylene protons. This was confirmed by the observation of an nOe between H7 and H9 in both the 2D-nOe

[3]In this experiment an enhancement of C10 was also observed (δ 47.1). This enhancement may be the result of the reinforcement (additivity) of scalar coupling via two comparable four-bond pathways. Since we can not unambiguously state that this is the reason, this long-range heteronuclear coupling is not included in Table 3.

[4]The enhancement of C15 upon saturation of H7 was 180° out-of-phase with the enhancements of C8 and C14. Presumably this phase distortion (which is not uncommon) arises from significant differences in the heteronuclear coupling constants.

TABLE 1. Proton and carbon nmr chemical shift assignments[a]

Position	^{13}C (m)[b]	^{1}H[c]
1	30.2 (t)	1α: 2.20 (overlapped with H6β)
		1β: 0.90 (ddd, J = 13.3, 13.3, 5.4 Hz)
2	19.6 (t)	2α: 1.55 (overlapped with H11β)
		2β: 1.45 (overlapped with H9)
3	41.3 (t)	3α: 1.25 (overlapped with H5)
		3β: 1.11 (ddd, J = 13.2, 13.2, 5.1 Hz)
4	34.4 (s)	—
5	46.6 (d)	1.25 (overlapped with H3α)
6	32.3 (t)	6α: 2.28 (ddd, J = 13.4, 13.3, 8.7 Hz)
		6β: 2.10 (overlapped with H1α and H11α)
7	70.0 (d)	4.21 (dd, J = 8.7, 7.7 Hz)
8	50.0 (s)	—
9	44.0 (d)	1.45 (overlapped with H2β)
10	47.1 (s)	—
11	29.2 (t)	11α: 2.10 (overlapped with H6β)[d]
		11β: 1.55 (overlapped with H2α)
12	34.5 (d)	2.20 (brs)
13	27.4 (t)	13α: 1.98 (overlapped with H14)
		13β: 1.36 (dddd, J = 13.4, 12.2, 2.2, 2.0 Hz)
14	49.6 (d)	2.01 (overlapped with H13α)
15	68.7 (d)	4.49 (brs)
16	157.9 (s)	—
17	103.8 (t)	17a: 4.83 (dd, J = 2.1, 1.2 Hz)
		17b: 4.94 (dd, J = 2.6, 1.2 Hz)
18	28.6 (q)	1.00 (s)
19	57.3 (t)	19α: 2.35 (d_{AB}, J = 11.4 Hz)
		19β: 2.58 (d_{AB}, J = 11.4 Hz)
20	104.6 (s)	—
21	51.5 (t)	21α: 2.81 (ddd, J = 12.4, 6.9, 2.2 Hz)
		21β: 3.03 (ddd, J = 12.4, 12.1, 8.6 Hz)
22	61.7 (t)	22α: 3.78 (ddd, J = 13.6, 8.6, 2.2 Hz)
		22β: 3.56 (ddd, J = 13.6, 8.6, 2.2 Hz)

[a]Spectra were recorded in $CDCl_3$.
[b]Carbon multiplicities were determined by two APT experiments using defocusing delays of 8 and 4 ms (see text).
[c]"o" overlapped; chemical shifts from cross sections in HETCOR spectrum, coupling constants from extensive decoupling experiments.
[d]H11α and H11β were tentatively assigned on the basis of W-coupling between H13β and H11β as observed in the expended COSY spectrum.

and DnOe spectra, requiring that the C7 hydroxyl group be α-oriented. In addition, nOe's between H7 and H5 and H6ß were also observed in the DnOe spectrum, confirming the ß orientation of H7.

A DnOe experiment upon saturation of H15 revealed an nOe with H14 and a weaker nOe with H13ß. Though H14 and H13α were overlapped in the ^{1}H nmr spectrum, the assignment of the nOe to H14 was clear since an nOe was also observed with this same resonance upon saturation of H21ß. Furthermore, an nOe between H15 and H13α is highly unlikely given the extreme distance between these two protons (4.31 Å). Thus, H14, H15, and H21ß all lie on the same face of the molecule.

Other nOe's observed in the 2D-nOe or DnOe spectra enabled completion of the proton assignments. Thus, an nOe from the C18 methyl protons to H19ß, which in turn showed an nOe with H21α, distinguished the nitrogenated C19 and C21 methylene protons. The H21α proton showed an nOe with its *gem* partner, H21ß, which in turn had an nOe with H22ß as well as with H14; H22ß showed nOe's with its *gem* partner, H22α, as well as with H13α, thereby distinguishing the C13 and the C22 methylene protons. (The H14 and H13α resonances were overlapped and in principle the nOe's observed in the 2D-nOe between H21ß and H14, and those between H22ß and H13α, could have been H21ß with H13α and H22ß with H14. Molecular modelling clearly showed that this is unlikely since H14 is significantly closer to H21ß than H13α, 2.32 vs. 3.48 Å, while H22ß is closer to H13α than H14, 2.41 vs. 3.43 Å). In addition, an nOe between H12 and H17a distinguished the exocyclic methylene pair of protons.

The axial protons of the methylene pairs at C1, C3, and C6 (H1ß, H3ß, and H6α) were well resolved and could be assigned as axial on the basis of their coupling constants (Table 1). In addition, H19α showed nOe's with H2α and H3α in the 2D-nOe spectrum. (While the resonance of H2α was overlapped with one of the H11 protons, and H3α was partially overlapped with that of H5, the resolution was sufficient to assign H2α and H3α. Furthermore, an nOe between H19α and either H5 or any of the H11 protons is impossible). Thus, the methylene protons of C1, C2, C3, and C6 were distinguished, leaving only those of C11 unassigned. This last methylene pair was tentatively distinguished on the basis of W-coupling between H13ß with the higher field partner, assigned as H11ß, observed in the COSY spectrum. It must be stressed, however, that this assignment is tentative and made only on the basis that H11ß and H13ß have a near-perfect "W" relationship in molecular models.

Table 2 lists all observed nOe's with the estimated distances

Can. J. Chem. Downloaded from www.nrcresearchpress.com by 203.198.23.82 on 09/08/12
For personal use only.

Can. J. Chem. Downloaded from www.nrcresearchpress.com by 203.198.23.82 on 09/08/12
For personal use only.

TABLE 2. The nOe's observed with estimated internuclear distances[a]

nOe (method)[b]	Estimated distance (Å)
17a–12 (2D-nOe)	2.44
7–9 (2D-nOe)	2.46
22α–22β (2D-nOe)	1.83
22β–21β (2D-nOe)	2.32
22β–13α (2D-nOe)	2.41
21β–21α (2D-nOe)	1.83
21β–14 (2D-nOe)	2.32
21α–19β (2D-nOe)	2.10
19β–18 (2D-nOe)	2.36
19β–19α (2D-nOe)	1.82
19α–2α (2D-nOe)	1.45
19α–3α (2D-nOe)	2.58
6α–18 (2D-nOe)	2.50
7–5 (DnOe)	2.79
7–6β (DnOe)	2.43
15–13β (DnOe)	3.05
15–14 (DnOe)	2.86

[a]Internuclear distances estimated from MM2 calculations.
[b]The nOe's listed as (DnOe) either were not observed or were obscured by overlap in the 2D-nOe spectrum. All nOe's observed in the 2D-nOe experiment were also observed in the DnOe.

TABLE 3. Long-range (two- and three-bond) heteronuclear $^1H/^{13}C$ scalar couplings[a]

^1H Saturated	Enhanced ^{13}C
H1β	C3, C10, C20
H7	C8, C14, C15
H12	C9, C16
H13β	C16, C20
H15	C7, C8, C16, C17
H17a	C12
H18	C3, C4, C19
H19β	C4, C18, C20, C21

[a]From selective INEPT experiments.

between protons as predicted by MM2 calculations. Table 3 lists the long-range two- and three-bond heteronuclear $^1H/^{13}C$ couplings as observed from selective INEPT experiments.

It is noteworthy that septatisine **3** is the only example of an atisane-type diterpenoid alkaloid in which the C20 carbon of the oxazolidine ring is bridged with C14. In the case of atisine, the oxazolidine ring gives rise to a mixture of two inseparable epimers differing in configuration at C20 (16).

Experimental

General procedures

Melting points are corrected and were determined on a Thomas–Kofler hot stage equipped with a microscope and polarizer. The nmr spectra were recorded on a Varian XL-400 spectrometer (93.94 kG, 400 MHz for ^1H, 100 MHz for ^{13}C). The nmr sample of septatisine was 4 mg dissolved in 0.05 mL $CDCl_3$. Residual $CHCl_3$ and $^{13}CDCl_3$ were used as internal references (^1H: δ 7.24, ^{13}C: δ 77.0) for ^1H and ^{13}C nmr, respectively. The pulse sequences employed in the one- and two-dimensional nmr experiments were the standard Varian software, version 6.1c, except the fixed-evolution HETCOR pulse sequence, which was added to the Varian nmr pulse sequence library based on Reynold's program (17). An evolution time fixed at 0.020 s was employed for the-fixed evolution HETCOR, with a refocusing delay of 0.0019 s ($1/4J$, J = 130 Hz). The hrms spectrum was recorded on a Finnigan MAT 90 instrument (ei, 40 eV); eims was recorded on a Finnigan Quadrupole 4023 mass spectrometer.

Nuclear magnetic resonance multipulse sequences

One-dimensional ^1H nmr spectra were recorded with a spectral window of 4000 Hz and an acquisition time of 2.0 s, giving a digital resolution of 0.5 Hz per point. The spectral window and the acquisition time for one-dimensional ^{13}C nmr spectra were 20 000 Hz and 0.5 s, respectively, giving a digital resolution of 2.0 Hz per point. The ^{13}C multiplicities were assigned by APT experiment. The APT experiment was performed with a spectral window of 20 000 Hz, an acquisition time of 0.5 s, and a defocusing delay of 0.008 s, optimized for one-bond heteronuclear coupling of 125 Hz, in order to get better phased subspectra. A second APT experiment edited for detection of quaternary carbons only was performed with the same spectral window and acquisition time, but with a defocusing delay of 0.004 s (13). Long-range (two and three bond) heteronuclear ^1H, ^{13}C couplings were detected with one-dimensional selective INEPT experiments. The selective INEPT spectra were recorded with the excitation and refocusing delays optimized for different long-range heteronuclear coupling constants according to the formulae $\tau = 1/2J$ and $\delta = 1/3J$, respectively (18).

Isolation of septatisine 3

The basic fraction **C** (0.65 g) (9) was chromatographed on an Al_2O_3 rotor, and eluted with a gradient of hexane, Et_2O, and MeOH. Twelve fractions (50 mL each) were collected. Fractions 11 and 12 collected with 5% and 10% MeOH in Et_2O were combined and the residue (15.1 mg) was purified on a preparative tlc plate (Al_2O_3; 20 cm × 20 cm, 1 mm thick) to afford septatisine **3** (9.2 mg), mp 129–130°C; $[\alpha]^{19}_d$ +30.55 (*c* 0.37, $CHCl_3$); eims: *m/z* 357 (M^+, 33%), 340(70), 329(15), 314(20), 300(6), 286(13), 274(37), 55(50), 41(100). Anal. calcd. for $C_{22}H_{31}NO_3$: C 74.0, H 8.7, N 3.9%; found: C 74.4, H 9.2, N 3.9.

1. H. Rosendahl. Arb. Pharmakol. Inst. Dorpat, **11**, 1 (1895); J. Pharm. Chim. **4**, 262 (1896).
2. L. Marion, L. Fonzes, C. Wilkins, Jr., J. Boca, F. Sandberg, R. Thorsen, and E. Linden. Can. J. Chem. **45**, 969 (1967).
3. S. Usmanova, V. Telnov, M. Yunusov, N. Abdullaev, A. Shreter, and G. Filippova. Khim. Prir. Soedin. 879 (1987).
4. V. Telnov, M. Yunusov, N. Abdullaev, and M. Zhamierashvili. Khim. Prir. Soedin. 556 (1988).
5. E. Sirotenko and Y. Rashkes. Khim. Prir. Soedin. 532 (1989).
6. S.W. Pelletier, R. Sawhney, and A. Aasen. Heterocycles, **12**, 377 (1979).
7. S.W. Pelletier, N. Mody, and R. Sawhney. Can. J. Chem. **57**, 1652 (1979).
8. S. Ross, S.W. Pelletier, and A. Aasen. Tetrahedron, **48**, 1183 (1992).
9. H. Sayed, H. Desai, S. Ross, S.W. Pelletier, and A. Aasen. J. Nat. Prod. **55**, 1595 (1992).
10. B. Joshi, H. Desai, S.W. Pelletier, E. Holt, and A. Aasen. J. Nat. Prod. **51**, 265 (1988).
11. S. Ross, B. Joshi, S.W. Pelletier, M.G. Newton, and A. Aasen. J. Nat. Prod. **56**, 424 (1993).
12. W. Reynolds, S. McLean, M. Perpick-Dumont, and R. Enriquez. Magn. Reson. Chem. **26**, 1068 (1988).
13. M. Bendall, D. Doddrell, and D. Pegg. J. Am. Chem. Soc. **103**, 4603 (1981).
14. F. Sun, X. Liang, and D. Yu. J. Nat. Prod. **51**, 50 (1988).
15. S. Sakai, I. Yamamato, K. Hotoda, K. Yamaguchi, N. Aimi, E. Yamanaka, J. Haginawa, and T. Okamoto. Yakugaku Zasshi, **104**, 22 (1984).
16. S.W. Pelletier, N. Mody, H. Desai, J. Finer-Moore, J. Nowacki, and B. Joshi. J. Org. Chem. **48**, 1787 (1983).
17. (*a*) W. Reynolds, D. Hughes, M. Perpick-Dumont, and R. Enriquez. J. Magn. Reson. **64**, 304 (1985); (*b*) M. Perpick-Dumont and R. Enriquez. Magn. Reson. Chem. **26**, 358 (1988).
18. A. Bax. J. Magn. Reson. **57**, 314 (1984).

Biosynthesis of tetraponerine-8, a defence alkaloid of the ant *Tetraponera* sp.[1]

B. RENSON, P. MERLIN, D. DALOZE, AND J. C. BRAEKMAN[2]

Laboratory of Bio-organic Chemistry, CP 160/7, Faculty of Sciences, University of Brussels, 50 Av. F. Roosevelt, 1050 Brussels, Belgium

AND

Y. ROISIN[3] AND J. M. PASTEELS

Laboratory of Animal and Cellular Biology, CP 160/12, Faculty of Sciences, University of Brussels, 50 Av. F. Roosevelt, 1050 Brussels, Belgium

Received March 23, 1993

This paper is dedicated to Professors David B. MacLean and Ian Spenser

B. RENSON, P. MERLIN, D. DALOZE, J.C. BRAEKMAN, Y. ROISIN, and J.M. PASTEELS. Can. J. Chem. **72**, 105 (1994).

The administration of sodium [1-^{14}C] and [2-^{14}C] acetate, L-[U-^{14}C] glutamic acid, γ-amino [U-^{14}C] butyric acid, L-[U-^{14}C] ornithine hydrochloride, and [1,4-^{14}C] putrescine dihydrochloride to *Tetraponera* sp. ants resulted in the formation, for each feeding experiment, of labelled tetraponerine-8 (**2**). The distribution of radioactivity into **2** was established by chemical degradation. The results obtained favor the hypothesis that the pyrrolidine ring of tetraponerine-8 is derived from L-glutamic acid via L-ornithine and putrescine, while the 12-carbon chain is derived from the combination of six acetate units.

B. RENSON, P. MERLIN, D. DALOZE, J.C. BRAEKMAN, Y. ROISIN et J.M. PASTEELS. Can. J. Chem. **72**, 105 (1994).

L'administration de [1-^{14}C] et [2-^{14}C] acétate de sodium, d'acide L-[U-^{14}C] glutamique, d'acide γ-amino [U-^{14}C] butyrique, de L-[U-^{14}C] ornithine·HCl et de [1,4-^{14}C] putrescine·2HCl à des fourmis de l'espèce *Tetraponera* sp. conduit à l'isolement de tétraponérine-8 radioactive. La distribution de l'activité au sein de la molécule a été déterminée par dégradation chimique. Les résultats obtenus confortent l'hypothèse que le cycle pyrrolidine de la tétraponérine-8 se construit à partir de l'acide L-glutamique via la L-ornithine et la putrescine. La chaîne à 12 atomes de carbone se formerait quant à elle par condensation de six unités acétate.

Introduction

The tetraponerines are a group of tricyclic alkaloids isolated from the venom of the Neo Guinean ant *Tetraponera* sp. (1, 2). These insecticidal substances are 5-alkyldecahydro-pyrido-[1,2-*c*]pyrrolo[1′,2′-*a*] pyrimidines (**1**)[4] differing from each other by the length of the alkyl chain and (or) by the configuration of the cyclic junctions. Such a skeleton is new among natural products. The biosynthetic pathway to the tetraponerines is therefore a matter of particular interest.

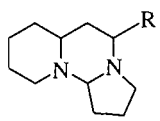

1

The aim of the present paper is to shed light on the biosynthetic pathway of the tetraponerine ring system as represented by tetraponerine-8 (**2**), the major constituent of the ant's venom. To this end, we have developed a degradation procedure for **2**, which would allow us to locate radioactivity after administration of ^{14}C-labelled compounds to *Tetraponera* sp. workers to test the likelihood of hypothetical biosynthetic pathways.

Results and discussion

First of all, we needed adequate supplies of **2** to develop a degradation scheme of this alkaloid as well as to serve as carrier for labelled samples of **2** obtained from each feeding experiment. This was achieved by preparing (±)-tetraponerine-8, utilizing the stereoselective total synthesis we recently reported (3, 4).

To evaluate the distribution of label in **2**, the sequence of reactions shown in Fig. 1 was used. The N17—C5 bond[5] could be cleaved selectively by catalytic hydrogenation in the presence of hydrochloric acid. Treatment of the resulting diamine **3** with methanesulfonyl chloride furnished the sulfonamide **4**. Pyrolysis of the tetraalkylammonium hydroxide **5**, obtained by quaternization of **4** with methyl iodide followed by conversion into hydroxide using an anion exchange resin, led to a mixture from which olefin **6** (27–46%) and *N*-methylpyrrolidine (**7**; 25–47%) could be isolated. Interestingly, of the four possible isomeric olefins that might theoretically result from the elimination of *N*-methylpyrrolidine, only isomer **6** (E Δ^9) was obtained. This suggests that the elimination is stereoselective and proceeds preferentially through a E2 *syn* elimination taking place from a *syn*-periplanar conformation (5, 6). The elimination is also regioselective. The absence of a detectable amount of $\Delta^{9(12)}$ isomers can be explained by the influence of the sulfonamide group that renders the C-10 protons of **5** more acidic than the C-12 protons. The volatile *N*-methylpyrrolidine was trapped in liquid nitrogen and converted into its oxalate. The latter could be recrystallized repeatedly without difficulties whereas the corresponding hydrochloride was too hygroscopic to be purified to constant activity by recrystallization. Olefin **6** was further cleaved by oxidation with the mixture $NaIO_4$–$KMnO_4$ (7) into *N*-mesylpipecolic acid and caproic acid, which were purified by chromatography as their *p*-bromophenacyl esters **8** and **9**, respectively.

[1]King Leopold III Biological Station, Laing Island, Contribution no. 266.

[2]Author to whom correspondence may be addressed.

[3]Research Associate, Fonds National de la Recherche Scientifique (FNRS).

[4]IUPAC numbering.

[5]For convenience, tetraponerine-8 and all its degradation products have been numbered according to ref. 1.

Can. J. Chem. Downloaded from www.nrcresearchpress.com by 195.246.54.202 on 09/08/12
For personal use only.

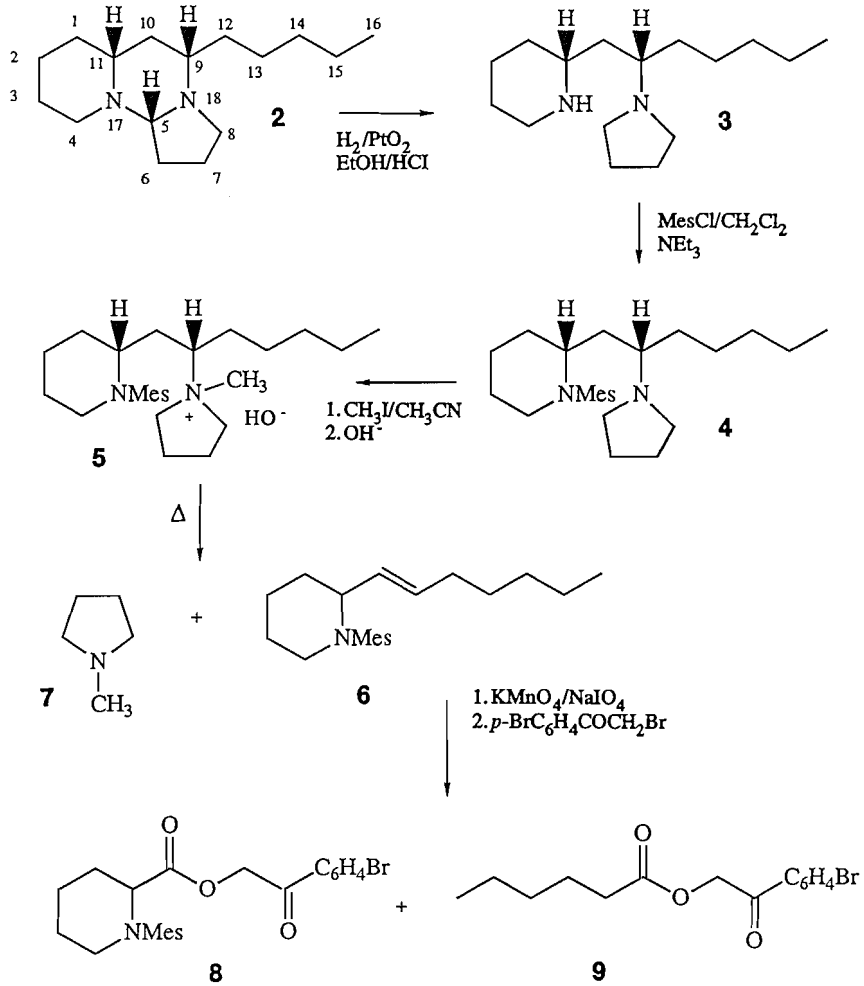

FIG. 1. Degradation of tetraponerine-8.

Insofar as structural relationships can be considered as a guide to biogenesis, the $C_{16}N_2$ skeleton of tetraponerine-8 might be thought to originate by condensation between either a suitably functionalized polyacetate chain such as **10** and putrescine (Fig. 2, pathway A), or a suitably functionalized 2-alkylpiperidine such as **11** and γ-aminobutyric acid (Fig. 2, pathway B). To test these alternative hypotheses, tracer experiments were performed by feeding *Tetraponera* sp. ants with aqueous solutions of sodium [1-^{14}C] and [2-^{14}C] acetate, L-[U-^{14}C] glutamic acid, γ-amino [U-^{14}C] butyric acid, L-[U-^{14}C] ornithine hydrochloride, and [1,4-^{14}C] putrescine dihydrochloride, respectively. A summary of the results of these experiments is presented in Table 1. Each experiment yielded radioactive tetraponerine-8, which was isolated as described in the experimental section. Before applying the degradation scheme of Fig. 1, inactive **2** was added as carrier to each isolated sample. These were then divided in two parts, each of which was separately degraded. After isolation of labelled sulfonamide **4**, inactive **4** was added as carrier and the resulting diluted sample was flash chromatographed repeatedly until constant activity was reached. The relative specific activities measured for the different degradation products are listed in Table 2 for the two replicates.

Sodium [2-^{14}C] acetate proved to be much more efficiently utilized than sodium [1-^{14}C] acetate for the formation of tetraponerine-8. This phenomenon is readily understood when one considers the fate of the carbon atoms of acetic acid when it enters the tricarboxylic acid cycle (8). The samples of tetraponerine-8 derived from the [1-^{14}C] and [2-^{14}C] acetate feeding experiments yielded olefin **6** (corresponding to carbon atoms C-1 to C-4 and C-9 to C-16) and *N*-methylpyrrolidine (**7**, corresponding to carbon atoms C-5 to C-8), which contained about 2/5 and 3/5 of the activity of intact tetraponerine-8, respectively. This suggests that acetate enters into both parts of the molecule by two independent pathways, its incorporation into **7** being more efficient than into olefin **6**. Moreover, within experimental error, the activity of olefin **6** is equally divided between the pipecolic acid moiety (corresponding to carbon atoms C-1 to C-4 and C-10 and C-11) and the caproic acid moiety (corresponding to carbon atoms C-12 to C-16 and C-9), suggesting that the 12-carbon linear chain of tetraponerine-8 might be formed by a linear combination of acetate units.

The results of feeding experiment 3 showed that the pattern of incorporation of activity from L-[U-^{14}C] glutamic acid into the tetraponerine skeleton was similar to that of acetate except that the incorporation into the pyrrolidine moiety was still more efficient than into olefin **6**. This could be explained by admitting that L-glutamic acid is an intermediate between acetate and the pyrrolidine ring moiety of tetraponerine-8 and that this precursor, after having been catabolized into acetate, is also incorporated into the 12-carbon linear chain of tetraponerine-8. It is well known that the two-carbon fragment at the oxidation level

Can. J. Chem. Downloaded from www.nrcresearchpress.com by 195.246.54.202 on 09/08/12
For personal use only.

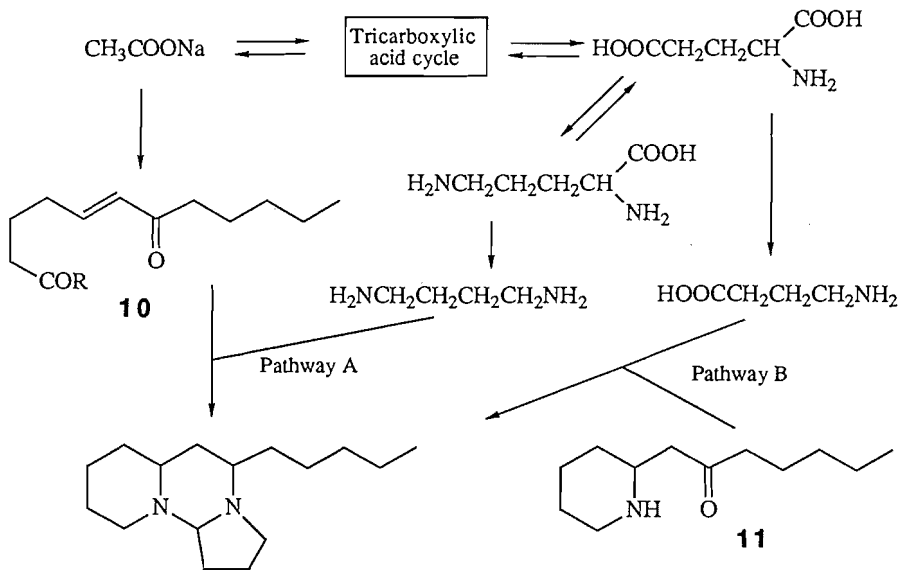

FIG. 2. Hypothetical biosynthetic scheme of tetraponerine-8.

TABLE 1. Incorporation of labelled compounds into tetraponerine-8

Experiment n°	Compound administered	Total activity administered (μCi)	Number of ants fed	Isolated amount of **2** (mg)	Specific activity of **2** (μCi/μmol)	Incorporation (%)
1	Na[1-^{14}C] acetate	150	850	2.0	9.32×10^{-3}	0.05
2	Na[1-^{14}C] acetate	50	400	4.3	8.88×10^{-3}	0.31
3	L-[U-^{14}C] Glutamic acid	50	780	1.7	9.68×10^{-3}	0.13
4	γ-amino[U-^{14}C] butyric acid	50	1150	5.2	3.50×10^{-3}	0.14
5	L-[U-^{14}C] Ornithine HCl	50	1560	5.3	3.09×10^{-2}	1.31
6	[1,4-^{14}C] Putrescine·2HCl	50	1700	6.4	3.95×10^{-2}	2.02

TABLE 2. Observed distribution of label within the degradation products of **2** (each experiment has been duplicated)

Experiment n°	**6** RSA[a]	**7** RSA[a]	**8** RSA[b]	**9** RSA[b]
1	35/34	54/54	52/33	44/36
2	44/42	55/50	43/44	54/56
3	27/24	77/83	64/40	45/74
4	48/45	55/50	45/48	46/49
5	14/16	81/79	64/58	61/55
6	0/0	87/105	—	—

[a]Relative specific activity (%; sulfonamide **4** = 100).
[b]Relative specific activity (%; olefin **6** = 100).

of acetate is derivable from glutamic acid by degradation via α-ketoglutarate and the tricarboxylic acid cycle (9). Moreover, according to classical biogenetic concepts, the pyrrolidine ring of a variety of alkaloids is derived from L-ornithine, which is metabolically interconvertible with L-glutamic acid (10, 11).

Thus, the observed mode of incorporation of these three precursors into tetraponerine-8 is consistent with the hypotheses outlined in Fig. 2. At this stage of the work it was not yet possible to distinguish between the two alternative pathways of incorporation of L-glutamic acid into tetraponerine-8. This demanded additional feeding experiments with γ-amino [U-^{14}C] butyric acid, L-[U-^{14}C] ornithine hydrochloride, and [1,4-^{14}C] putrescine dihydrochloride.

The labelling pattern that was observed after incorporation of γ-aminobutyric acid (experiment 4) was almost identical to that obtained with acetate. This indicates that this acid does not serve as a true intermediate but suffers degradation to acetate. Indeed, γ-aminobutyric acid could enter the tricarboxylic acid ring via succinic semialdehyde and succinic acid (11). Conversely, the results of feeding experiments 5 and 6 were particularly informative. Indeed, L-ornithine and putrescine not only entered the tetraponerine skeleton with high incorporation, and putrescine better than L-ornithine, but the pyrrolidine moiety also contained most of the labelling of intact tetraponerine-8. Such a distribution of the activity led to the inference that these two metabolites serve as specific precursors for the pyrrolidine ring of tetraponerine-8.

It is well established that, in plants, L-ornithine and L-glutamic acid are readily interconverted reversibly while the formation of putrescine from L-ornithine by the action of the enzyme ornithine decarboxylase is an irreversible process (11).

Can. J. Chem. Downloaded from www.nrcresearchpress.com by 195.246.54.202 on 09/08/12
For personal use only.

Can. J. Chem. Downloaded from www.nrcresearchpress.com by 195.246.54.202 on 09/08/12
For personal use only.

Such pathways seem also to occur in the poison gland of *Tetraponera* sp. since, on incorporation of labelled L-ornithine or L-glutamic acid, some residual activity (15% and 25%, respectively) was recovered in the 12-carbon linear chain, indicating that a certain amount of these amino acids had been catabolized to acetate via the tricarboxylic acid cycle. On the other hand, no residual label could be detected in the carbon atoms of the 12-carbon linear chain after feeding labelled putrescine. All these results support pathway A of the biosynthetic scheme depicted in Fig. 2.

Nothing is known about the precise structure of the 12-carbon intermediate that combines with putrescine to furnish tetraponerine-8. It might be an acid (**10**, R = OH) or an aldehyde (**10**, R = H) similar to **10**. The latter can be regarded either as an oxidized derivative of lauric acid or as a degradation product resulting from the cleavage of, for example, an 18-carbon polyunsaturated fatty acid. Such processes of fracture are well documented and are known to proceed through cleavage of peroxidic fatty acids by a lyase to form aldehydes (11, 12).

In the plant kingdom, the couple ornithine/putrescine is the precursor of the atoms of the pyrrolidine ring of many alkaloids, e.g., the pyrrolizidine alkaloids, nicotine, hygrine, and some tropane alkaloids (10, 11, 13). The results we have presented here demonstrate that such a biogenetic pathway also takes place in the ant *Tetraponera* sp. It is the first time that this has been evidenced in the animal kingdom. Further feeding experiments are in progress to refine the biosynthetic scheme depicted in Fig. 2 (pathway A) and to investigate the biosynthesis of the other tetraponerines present in the defence secretion.

Experimental

General methods

The ^1H and ^{13}C nmr spectra were recorded in $CDCl_3$ at 250 and 62.8 MHz, respectively, using a Bruker WM 250 spectrometer. Chemical shifts are quoted in δ values downfield from internal TMS. Data are reported as follows: chemical shift (multiplicity (s = singlet, d = doublet, t = triplet, m = multiplet, br = broad), coupling constants in hertz, integration, assignment). The ir spectra were taken with a Bruker IFS 25 instrument. Electron impact mass spectra were recorded on a VG Micromass 7070 F spectrometer. Gas chromatographic (gc) analyses were carried out on a Varian 3700 apparatus using a PDMS capillary column (25 m) and tlc on neutral aluminium oxide $60F_{254}$ (type E; Merck) or silica gel Sil G/UV_{254} (0.25 mm; Macherey–Nagel) precoated plates. Silica gel column chromatographies were performed on silica gel 60 columns (0.04–0.063 mm; Macherey–Nagel) by the flash technique (14) or on Lobar pre-packed columns (size A (240-10); Lichroprep Si 60 (0.04–0.063 mm)). Alumina chromatographies were carried out on neutral aluminium oxide columns (Macherey–Nagel). Radioactive compounds were assayed in a Packard Tri-Carb 1600 TR liquid scintillation analyser using as solvent MeOH (100 μL) with Packard Insta-Gel liquid scintillation cocktail (10 mL). Triplicate samples of each compound were counted under comparable conditions of quenching.

Incorporation experiments

Tetraponera sp. ants (about 1000 per batch) were collected near Bogia along the North coast of Papua New Guinea. Hollow twigs housing ants were kept in 50 × 35 cm plastic trays. Water was provided ad libitum. After 3 days of starvation, the ants were fed with 1 mL of an aqueous solution of sucrose (1 M) containing the labelled precursor. They were killed 10 days later by dropping them into vials containing methanol. The extraction of the alkaloids and the purification of tetraponerine-8 (**2**) were performed as described in ref. 2. The results obtained from the different feeding experiments are reported in Table 1.

Degradation of tetraponerine-8

Each labelled sample of tetraponerine-8 was degraded in duplicate. Results of both replications are presented in Table 2.

Conversion of tetraponerine-8 (2) into sulfonamide 4

Typically, tetraponerine-8 (14.9 mg) was dissolved in ethanol (15 mL), HCl (12.5 N, 0.2 mL) and PtO_2 (7.5 mg) were added, and the mixture was stirred during 1 h under an atmosphere of hydrogen. The catalyst was filtered off and the solution evaporated to dryness in vacuo. The solid residue was dissolved in CH_2Cl_2 and the resulting organic phase was washed with an aqueous solution of NaOH (2 N) and evaporated to dryness. The resulting oil was dissolved in dry CH_2Cl_2 (7 mL), triethylamine (158 μL) and mesyl chloride (56 μL) were added at –78°C, and the solution was then allowed to warm up to room temperature. After evaporation of the solvent the residue was dissolved in CH_2Cl_2 (10 mL), and the organic phase was washed with an aqueous solution of ammonia (1.25%) and evaporated to dryness in vacuo. The resulting yellowish oil was then chromatographed over alumina (eluent: CH_2Cl_2–AcOEt 8:2). This yielded pure sulfonamide **4** (10.9 mg, yield: 55%). Spectral properties of **4**: ir (NaCl film): 2860 and 2796 (Bohlmann bands), 1326 and 1146 (SO_2 asymmetric and symmetric stretchings) cm^{-1}; ^1H nmr: 0.89 (t, 7, 3H, H_3C-16), 1.3–1.8 (m, 16H, CH_2), 1.95 (br s, 4H, H_2C-6 + H_2C-7), 2.05 (m, 1H, HC-9), 2.88 (s, 3H, SO_2CH_3), 2.41–2.77 (m, 4H, H_2C-5 + H_2C-8), 3.06 (ddd, 13/13/3, 1H, HaxC-4), 3.70 (brd, 1H, HeqC-4), 4.13 (m, 1H, HC-11); ^{13}C nmr: 14.0 (C-16), 18.6 (C-2), 22.6 (C-15), 23.7 (C-6, C-7), 25.2 and 25.7 (C-3, C-14), 28.4 (C-13), 30.2, 32.0 and 32.3 (C-1, C-10, C-12), 40.7 (C-4), 40.8 (-SO_2CH_3), 49.7 (C-11), 50.5 (C-5 + C-8), 60.9 (C-9); ms *m/z*: 330 ($M^{+\cdot}$, 1%), 259 ($M^{+\cdot} - C_5H_{11}\cdot$, 34), 162 ($M^{+\cdot} - C_{11}H_{22}N\cdot$, 100), 154 ($M^{+\cdot} - C_7H_{14}NO_2S\cdot$, 89), 98 ($C_6H_{12}N^+$, 5), 84 ($C_5H_{10}N^+$, 9), 70 ($C_4H_8N^+$, 5).

Hofmann degradation

Typically, freshly distilled methyl iodide (25 μL) was added to a solution of sulfonamide **4** (9.2 mg) in acetonitrile (0.5 mL) and the mixture stirred at room temperature for 3 h. After evaporation of the solvent, the solid residue was dissolved in MeOH (1 mL) and the solution eluted with water through a strongly basic anion exchanger column (Amberlite IRA-400, OH^-). The fractions containing the tetraalkylammonium hydroxyde **5** (positive Dragendorff and phenolphthalein tests) were combined and evaporated to dryness under vacuum. The residual yellowish oil was then pyrolyzed at 170°C for 3 h. The volatile components were caught in a liquid nitrogen trap, dissolved in acetone, and analyzed by capillary gc (CPWAX 52B, 120°C). The chromatogram showed a major peak whose retention time was identical (coinjection) to that of an authentic sample of *N*-methylpyrrolidine. Oxalic acid (2.5 mg) was then added to the acetone solution. After evaporation of the solvent, the resulting solid was recrystallized from acetone; this furnished *N*-methylpyrrolidine oxalate (2.3 mg, yield: 47%, mp 99–100°C). Flash chromatography of the solid residue of pyrolysis over silica gel (eluent: hexane–AcOEt 8:2) furnished olefin **6** (3 mg, yield: 41%). Spectral properties of **6**: ir (NaCl film): 1334 and 1146 (SO_2 asymmetric and symmetric stretchings) cm^{-1}; ^1H nmr (C_6D_6): 0.88 (t, 7, 3H, HC-16), 1.10–1.60 (m, 12H, CH_2), 1.87 (dt, 6/7, 2H, H_2C-12), 2.31 (s, 3H, SO_2CH_3), 2.56 (ddd, 13/13/2, 1H, HaxC-4), 3.50 (br d, 1H, HeqC-4), 4.52 (m, 1H, HC-11), 5.42 (ddt, 15.5/7/<1, 1H, HC-10), 5.55 (ddt, 15.5/0.5/6, 1H, HC-9); ^{13}C nmr (C_6D_6): 14.0 (C-16), 19.0 (C-2), 22.5 (C-15), 25.6 (C-3), 28.8 (C-13), 31.0, 31.4 and 32.4 (C-1, C-12, C-14), 38.7 (-SO_2CH_3), 41.4 (C-4), 55.0 (C-11), 125.6 (C-9), 134.9 (C-10); ms *m/z*: 259 ($M^{+\cdot}$, 8%), 188 ($M^{+\cdot} - C_5H_{11}\cdot$, 42), 180 ($M^{+\cdot} - CH_3SO_2\cdot$, 96), 162 ($M^{+\cdot} - C_7H_{13}\cdot$, 100), 84 ($C_5H_{10}N^+$, 36).

Lemieux – von Rudloff oxydation of 6

Typically, olefin **6** (2.9 mg) was dissolved in freshly distilled dioxane (3 mL); aqueous solutions of K_2CO_3 (3.8×10^{-2} M, 1 mL), $NaIO_4$ (0.1 M, 1 mL), and $KMnO_4$ (1.7×10^{-3} M, 1 mL) were added and the mixture was stirred at room temperature. The evolution of the reaction was monitored by tlc. After 24 h, 1 mL of each solution was added again. The reaction was complete after 80 h. The mixture was evaporated to dryness and the residue dissolved in CH_2Cl_2 (5 mL). The organic phase was washed with an aqueous solution of HCl (1 N) and evaporated to dryness. The residue was dissolved in MeOH (1 mL) and

the pH adjusted to 8.5 by adding dropwise a methanolic solution of KOH (0.01 N). The resulting solution was again evaporated to dryness and the residue dissolved into freshly distilled acetonitrile; *p*-bromophenacyl bromide (8 mg) and dicyclohexano-18-crown-6 ether (0.6 mg) were added and the mixture was refluxed for 1 h. The residue obtained after evaporation of the solvent was flash chromatographed on a silica gel column (eluent: toluene–AcOEt 99:1). This yielded *p*-bromophenacyl caproate (2.3 mg, yield: 65%) and *p*-bromophenacyl *N*-mesylpipecolate (2.7 mg, yield: 60%) successively. Spectral properties of **8**: ir (NaCl film): 1748 (ester C=O stretching), 1704 (arylketone C=O stretching), 1586 (phenyl C=C stretching), 1326 and 1148 (SO_2 asymmetric and symmetric stretchings) cm^{-1}; ^1H nmr: 1.20–2.00 (m, 5H, CH_2), 2.37 (br d, 1H, HeqC-1), 2.93 (s, 3H, SO_2CH_3), 3.28 (ddd, 12/12/3, 1H, HaxC-4), 3.73 (br d, 1H, HeqC-4), 4.92 (dd, 3.5/<1, 1H, HC-11), 5.29 (d, 16.5, 1H, OCH), 5.47 (d, 16.5, 1H, OCH'), 7.65 and 7.77 (aromatic protons); ms *m/z*: 406/404 ($[M + H]^+$), 326/324 ($M^{+\cdot} - CH_3SO_2\cdot$), 206 ($C_7H_{12}NO_4S^+$), 190 ($C_7H_{12}NO_3S^+$), 185/183 ($C_7H_4OBr^+$), 162 ($C_6H_{12}NO_2S^+$), 157/155 ($C_6H_4Br^+$), 84 ($C_5H_{10}N^+$). Spectral properties of **9**: ir (NaCl film): 1744 (ester C=O stretching), 1700 (arylketone C=O stretching), 1586 (phenyl C=C stretching) cm^{-1}; ^1H nmr: 0.91 (t, 7, 3H, H_3C-16), 1.26 –1.42 (m, 4H, H_2C-15 + H_2C-14), 1.70 (m, 2H, H_2C-13), 2.48 (t, 7.5, 2H, H_2C-12), 5.27 (s, 2H, OCH_2), 7.63 and 7.78 (aromatic protons); ms *m/z*: 314/312 ($M^{+\cdot}$), 216/214 ($M^{+\cdot} - C_6H_{10}O\cdot$), 200/198 ($M^{+\cdot} - C_6H_{10}O_2\cdot$), 185/183 ($C_7H_4OBr^+$), 157/155 ($C_6H_4Br^+$).

Acknowledgements

This investigation was supported by grants from the Belgian Fund for joint Basic Research (Grants no. 2.4513.90 and 2.4558.92). One of us (B.R.) thanks the "Institut pour l'Encouragement de la Recherche Scientifique dans l'Industrie et l'Agriculture" (IRSIA) for financial support. We acknowledge the help of Mr. M. Leponce with the feeding experiments. We would also like to thank Dr. R. Ottinger for the nmr spectra and Mr. C. Moulard for the mass spectra.

1. J.C. Braekman, D. Daloze, J. M. Pasteels, P. Vanhecke, J. P. Declercq, V. Sinnwell, and W. Francke. Z. Naturforsch. **42c**, 627 (1987).
2. P. Merlin, J.C. Braekman, D. Daloze, and J. M. Pasteels. J. Chem. Ecol. **14**, 517 (1988).
3. P. Merlin, J.C. Braekman, and D. Daloze. Tetrahedron Lett. **29**, 1691 (1988).
4. P. Merlin, J.C. Braekman, and D. Daloze. Tetrahedron, **47**, 3805 (1991).
5. D.S. Bailey and W. H. Saunders. J. Am. Chem. Soc. **92**, 6904 (1970).
6. M. Pankova, J. Sicher, and J. Zavada. J. Chem. Soc. Chem. Commun. 394 (1967).
7. R.U. Lemieux and E. von Rudloff. Can. J. Chem. **33**, 1701 (1955).
8. E. Leete and J.O. Olson. J. Am. Chem. Soc. **94**, 5472 (1972).
9. A.L. Lehninger. Biochemistry. Worth Publishers, New York. 1981.
10. I.D. Spenser. *In* Comprehensive biochemistry. Vol 20. *Edited by* M. Florkin and E. H. Stotz. Elsevier, Amsterdam. 1968. p. 231.
11. M. Luckner. Secondary metabolism in microorganisms, plants and animals. Springer-Verlag, Berlin. 1990.
12. L. Crombie, D.O. Morgan, and E.H. Smith. J. Chem. Soc. Perkin Trans. 1, 567 (1991).
13. K. Mothes, H.R. Schutte, and M. Luckner (*Editors*). Biochemistry of alkaloids. VCH, Berlin. 1985.
14. W.C. Still, M. Kahn, and A. Mitra. J. Org. Chem. **43**, 2923 (1978).

Can. J. Chem. Downloaded from www.nrcresearchpress.com by 195.246.54.202 on 09/08/12
For personal use only.

Synthesis of (2*S*,4*S*)- and (2*S*,4*R*)-[5,5,5-$^2H_3$] leucine from (*R*)-pulegone[1]

RICHARD K. HILL,[2] CLAUDIO ABÄCHERLI, AND SANJI HAGISHITA
Department of Chemistry, University of Georgia, Athens, GA 30602, U.S.A.

Received June 14, 1993

This paper is dedicated to Professors Ian Spenser and David B. MacLean

RICHARD K. HILL, CLAUDIO ABÄCHERLI, and SANJI HAGISHITA. Can. J. Chem. **72**, 110 (1994).

Beginning with (*R*)-pulegone, a CD_3 group attached to the stereogenic center containing CH_3 has been created by conversion to citronellal-1-*d*, exchange of the acidic hydrogens at C-2 by deuterium, and decarbonylation with Wilkinson's catalyst. Oxidation to isovaleric acid-d_3 and conversion to leucine by standard procedures gave the (2*S*,4*S*) and (2*R*,4*S*) diastereomers (**10** and **12**) of [5,5,5-$^2H_3$]leucine.

RICHARD K. HILL, CLAUDIO ABÄCHERLI et SANJI HAGISHITA. Can. J. Chem. **72**, 110 (1994).

Utilisant la (*R*)-pulégone comme produit de départ, on a créé un groupe CD_3 attaché au centre stéréogénique contenant le CH_3 par une transformation du produit de départ en citronellal-1-*d* suivie d'un échange des hydrogènes acides en C-2 par du deutérium et finalement d'une décarbonylation à l'aide du catalyseur de Wilkinson. Une oxydation en acide isovalérique-d_3 suivie de sa transformation en leucine par des techniques standard conduit aux diastéréoisomères (2*S*,4*S*) et (2*R*,4*S*) (**10** et **12**) de la [5,5,5-$^2H_3$]leucine.

[Traduit par la rédaction]

Can. J. Chem. Downloaded from www.nrcresearchpress.com by 84.22.46.98 on 09/08/12
For personal use only.

The amino acid leucine is a biosynthetic precursor of a number of varied natural products. The impetus of this paper is the existence and projected study of biosynthetic pathways in which one of the methyl groups of leucine is functionalized; examples (Scheme 1) include (*a*) dehydrogenation of one methyl to yield the isopropenyl moiety of acacipetalin and related cyanolipids (1); (*b*) oxidation of one methyl to afford *erythro* 4-methylglutamic acid in seedlings of *Gleditsia triacanthos* (2); and (*c*) bond formation between one methyl and nitrogen to provide the *trans*-4-methylproline unit of the monamycin antibiotics in *Streptomyces jamaicensis* (3).

These enzymatic oxidations of the leucine methyl group pose an interesting stereochemical question. The two methyl groups are diastereotopic, and consequently enzymatic attack is likely to be specific for just one methyl in each biosynthetic pathway. Experimental investigations to test such questions (4) require samples of leucine specifically labelled in either the *pro-R* or *pro-S* methyl. Indeed, an elegant study by Fuganti and coworkers (5) used a specifically ^{13}C-labelled leucine for incorporation into the C_5-isoprenoid units of echinuline and flavoglaucine.

Three synthetic routes to specific ^{13}C-methyl-labeled leucine samples have been published. In the first, Fuganti and co-workers (5) began with the enantiomers of [1-^{13}C]2-methyl-4-phenylbutanoic acid to incorporate ^{13}C stereospecifically into the *pro-R* and *pro-S* methyls of leucine. Later, Stevens and coworkers (6) prepared (2*S*,4*S*)-[5-^{13}C]leucine enzymatically from either ^{13}C-labeled acetolactate or (2*S*,3*S*)-[4-^{13}C]valine in cultures of an *Escherichia coli* strain. Finally, Aberhart and Weiller (7) also prepared a ^{13}C-labeled leucine from specifically labeled valine, by a chemical route.

Leucine "chirally" labelled with deuterium in one of the methyls has not been reported. While the methods used for $^{13}CH_3$-leucine would certainly be amenable to the preparation of CD_3-leucine, we considered that it would be advantageous in preparing this material to begin with a naturally occurring substance of high optical purity in which the "difficult" stereogenic center at C-4 is already present. One member of the "chiral pool" that appeared attractive is citronellal. Natural citronellal, however, has been shown to possess considerably less than 100% enantiomeric purity (8) and so, following the example of Overberger and Kaye (8*c*), (*R*)-(+)-pulegone was selected as an alternative source of the stereogenic center at C-5. The reaction scheme chosen to convert pulegone to optically pure leucine-5,5,5-d_3 is shown in Scheme 2.

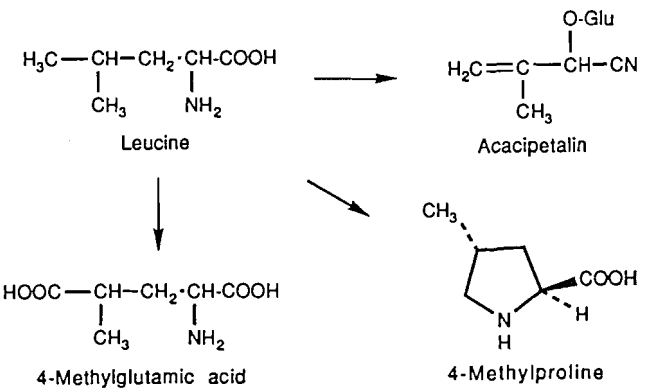

SCHEME 1. Enzymatic transformations of a leucine methyl group.

(*R*)-Pulegone **1** was converted to (*R*)-citronellic acid **2** (R = H) by the published procedure (8*c*, 9). Reduction of the methyl ester **2** (R = CH_3) with lithium aluminum deuteride gave citronellol-1,1-d_2 **3**, which could be oxidized by pyridinium chlorochromate to citronellal-1-*d* **4**. The acidic hydrogens at C-2 were exchanged for deuterium by several exchanges with Na_2CO_3 in D_2O–CH_3OD, leading to citronellal-1,2,2-d_3 **5**.

In the key step, decarbonylation of the aldehyde was achieved with Wilkinson's catalyst, affording (6*S*)-[7,7,7-$^2H_3$]-2,6-dimethyl-2-heptene **6**, in which the pivotal asymmetric center containing methyl and trideuteriomethyl has been introduced with unambiguous configuration and conservation of the enantiomeric purity of pulegone. The double bond of **6** was oxidized by the Lemieux–Rudloff procedure (10) to (4*S*)-[5,5,5-$^2H_3$]-4-methylpentanoic acid **7**. The amino group was intro-

[1]Dedicated to two Canadian grandmasters of natural products and biosynthesis, Ian Spenser and David McLean, in recognition of their distinguished and fruitful careers.

[2]Author to whom correspondence may be addressed.

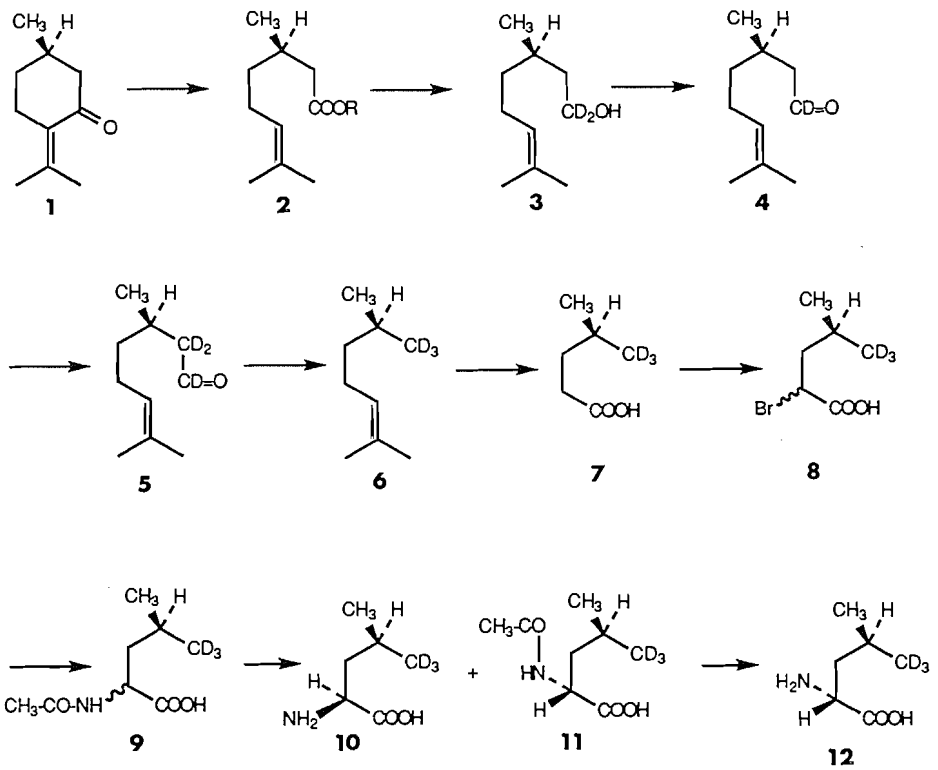

SCHEME 2. Conversion of (*R*)-pulegone to leucine-d_3.

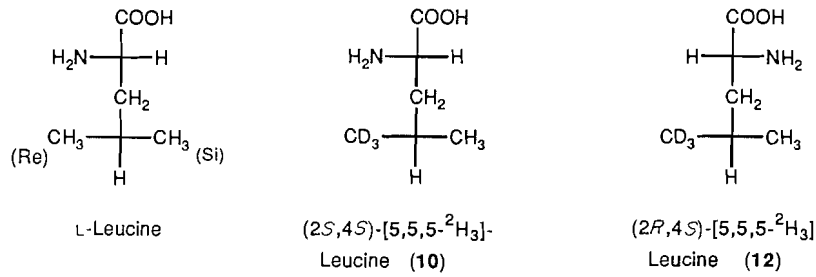

FIG. 1. Fischer projections of labeled leucines.

duced in the usual way by α-bromination followed by ammonolysis, and the amino acid was resolved by hog kidney acylase-catalyzed hydrolysis of the *N*-acetyl derivative **9**. This reaction yielded the (2*S*,4*S*) diastereomer **10** of leucine-5-d_3, and acid hydrolysis of the recovered amide **11** gave the (2*R*,4*S*) diastereomer **12**.

NMR spectra

Although the diastereomeric methyls of leucine cannot be differentiated in proton NMR spectra taken in D_2O or in acid solution, addition of base resolves the methyl signals into two distinct doublets, one centered at δ 0.701 and one at 0.718 ppm,[3] with a coupling constant of 6.1 Hz. This allows the diastereomeric purity of the synthetic samples to be analyzed.

The ^1H NMR spectrum of our synthetic (2*S*,4*S*)-[5,5,5-$^2H_3$]leucine **10** showed only the three-proton doublet at δ 0.718, while (2*R*,4*S*)-[5,5,5-$^2H_3$]leucine **12** showed only the doublet at δ 0.701 ppm, confir ming the stereochemical purity at C-4. Additional confirmation came from the ^2H NMR spectrum of **12**, which showed only a single CD_3 signal.[4] Finally, the ^{13}C NMR spectrum of **12** in alkaline solution showed only the upfield methyl signal at −45.17 ppm (relative to dioxan), while L-leucine displays two methyl signals at −45.05 and −43.89 ppm. The downfield methyl signal essentially disappears from the spectrum as a result of the broadening by three deuterium atoms (11).

These results demonstrate that in both the proton and carbon NMR spectra of leucine taken in alkaline solution, the upfield methyl signal is due to the *pro-S* methyl group (more appropriately, using the nomenclature of Prelog and Helmchen (12), the Re methyl group), while the downfield methyl signal is due to the *pro-R*, or Si, methyl. These methyls are identified in the Fischer projections shown in Fig. 1.

These conclusions seem to differ from those of Fuganti and co-workers (5), who assigned the upfield NMR signal to the *pro-R* methyl. The source of the difference lies in the stereochemical designators, not in actual configurations, since we come to the same conclusion in terms of structural formulae.

[3]The spectra were taken on samples dissolved in D_2O containing NaOH, using dioxan as an internal reference; the hydrogen δ values cited have been converted to the TMS scale by adding 3.57 (the chemical shift of dioxan relative to TMS) to the observed values.

[4]We thank Dr. Andrew Evans, JEOL, for his assistance in obtaining the deuterium NMR spectrum.

Can. J. Chem. Downloaded from www.nrcresearchpress.com by 84.22.46.98 on 09/08/12
For personal use only.

The configuration at C-4 is erroneously assigned in ref. 5, where it appears that the Cahn–Ingold–Prelog rules were used incorrectly (13).[5]

This investigation has provided a source of two diastereomers of CD_3-leucine of fixed configuration at C-4, which should prove useful in biosynthetic studies of enzymatic reactions involving attack at a leucine methyl.

Experimental

NMR spectra were recorded on a JEOL PTF-100 spectrometer; samples were dissolved in $CDCl_3$, using TMS as an internal standard unless otherwise noted. Optical rotations were measured on a Perkin–Elmer 141 polarimeter in a 1-dm tube at the sodium D line. IR spectra were recorded on a Perkin–Elmer 257 spectrometer. Melting points are uncorrected.

(R)-(+)-Citronellic acid (**2**, R = H) was prepared from (+)-pulegone (Aldrich Chemical Co., $[\alpha]_D^{25}$ +21.5 (neat)) as described by Plesek (9) and Overberger and Kaye (8*c*). The twice-distilled acid had $[\alpha]_D^{25}$ +7.73 (neat). The infrared and NMR spectra were identical with those reported. The *methyl ester* (**2**, R = CH_3), bp 115°C (15 Torr; 1 Torr = 133.3 Pa) was prepared from diazomethane and had $[\alpha]_D^{25}$ +4.99 (neat) (lit. (9) $[\alpha]_D^{25}$ +5.45 (neat)).

(R)-[1,1-$^2H_2$]Citronellol (**3**) was prepared by reduction of methyl citronellate with lithium aluminum deuteride in THF, as described for the reduction of citronellic acid with lithium aluminum hydride (8, 9). The alcohol showed $[\alpha]_D^{25}$ +4.54 (neat) (lit. (9) $[\alpha]_D^{25}$ +5.37 (neat) for the unlabeled alcohol). IR (neat): 3330 (OH), 2910, 2200 and 2090 (C-D), 1450, 1375, 970, 825 cm^{-1}. NMR ($CDCl_3$) δ: 5.2 (1H, t, J = 6.0 Hz), 2.75 (1H, s), 1.73 (3H, s), 1.66 (3H, s), 0.93 (3H, d, J = 5.5 Hz), 2.5–1.0 (m). ^{13}C NMR δ: 131.13, 124.85, 60.17 (m, J = 22 Hz, CD_2OH), 39.75, 37.37, 29.32, 25.72, 25.60, 19.63, 17.68.

(R)-[1-$^2H_1$]Citronellal (**4**)

A solution of 9.75g of **3** in dry CH_2Cl_2 was added to a stirred suspension of 20.33g of pyridinium chlorochromate and 1.5g of sodium acetate in 75 mL of CH_2Cl_2. The mixture warmed slightly, turned black, and deposited a tarry material. After 2.5h at room temperature the solution was diluted with 200 mL ether, decanted from the gummy residue, and the residue was washed with several portions of warm ether until it became granular. The combined organic phases containing suspended fines were filtered through a 2 × 20 cm column of silica gel; the eluate was concentrated at reduced pressure and distilled at 105°C (1 Torr), giving 7.22g of the aldehyde. Redistillation gave 6.71g of citronellal, $[\alpha]_D^{25}$ +10.08 (neat); Pino and O'Donnell (8*a*, *b*) calculate rotations of +16.4 and +15.9 for the unlabeled aldehyde. IR (neat): 2910, 2070 (C-D), 1715, 1450, 1375, 1092, 825 cm^{-1}. NMR ($CDCl_3$)δ: 5.16 (1H, t, J = 7.0 Hz), 1.70 (3H, s), 1.62 (3H, s), 1.0 (3H, d, J = 6.0 Hz), 2.4–1.0 (m).

(R)-(+)-[1,2,2-$^2H_3$]Citronellal (5)

A solution containing 1.5g of **4**, 180 mg of anhydrous sodium carbonate, 8.0 mL of CH_3OD, and 2 mL of D_2O was refluxed for 15 min with exclusion of moisture, then distilled at atmospheric pressure to remove the solvents. Fresh CH_3OD (6.0 mL) was added and the mixture was again refluxed for 15 min and concentrated, then 5 mL CH_3OD and 1 mL D_2O were added and refluxed for 15 min. The mixture was concentrated, diluted with 4.0 mL of D_2O, and extracted with ether (3 × 50 mL). After drying and removal of the ether, the residue was distilled in a kugelrohr at 0.5 Torr and 105°C, giving 964 mg of **5**, $[\alpha]_D^{25}$ +12.67 (neat). IR (neat): 2915, 2090, 2040, 1710, 1450, 1375, 1085, 830 cm^{-1}. NMR (acetone-d_6) δ: 5.12 (1H, t, J = 6 Hz), 2.05 (3H, m), 1.66 (3H, s), 1.60 (3H, s), 1.4–1.1 (m), 0.95 (3H, d, J = 6.3 Hz). A barely discernible trace of the C-2 and C-1 protons was seen.

[5]The Standard Sub-rules for sequence ordering (p. 391) specify that higher atomic number precedes lower, and that this rule must be followed to exhaustion before considering atomic mass. Thus, $^{12}CH_2CH(NH_2)COOH$ must precede $^{13}CH_3$.

(S)-[5,5,5-$^2H_3$]-4-Methylpentanoic acid (7)

(a) Decarbonylation

A solution of 3.50g of **5** in 5.0 mL of freshly distilled benzonitrile was added to a suspension of 20g of tris(triphenylphosphine)rhodium chloride in 75 mL of benzonitrile, and the mixture was stirred and heated at 150–160°C under nitrogen for 1.5 h. The flask was then equipped for simple distillation and two fractions were collected, the first at bp 170–183°C, and a second of bp 190–200°C. Each was redistilled in a kugelrohr; the fraction of boiling range 145–160°C (1.79g) was mostly alkene **6**, contaminated with benzonitrile, but since further fractionation did not effect complete separation, this impure material was used in the next step. NMR ($CDCl_3$) δ: 5.2 (1H, poorly resolved triplet), 1.72 (3H, s), 1.63 (3H, s), 0.93 (3H, d, J = 5.0 Hz), 2.2–0.8 (m).

(b) Oxidation

A solution of 1.50g of impure **6** in 20 mL of acetone was added to a mixture of 10.8g of $NaIO_4$ and 3.4g of K_2CO_3 in 40 mL of water at 0°C. After 10 min, a solution of 375 mg of $KMnO_4$ in 12 mL of water was added dropwise, and the mixture was stirred overnight. The mixture was washed with ether (50 mL), acidified to Congo Red, shaken with sodium thiosulfate solution to remove the iodine, then extracted with ether (3 × 50 mL). The extracts were dried and concentrated, and the residue was distilled in a kugelrohr at 200°C, affording 351 mg of **7**. IR (neat): 2975, 2930, 2200 and 2055 (C-D), 1710, 1410, 1280, 1050, 930 cm^{-1}. NMR ($CDCl_3$) δ: 11.33 (1H, s), 2.38 (2H, t, J = 7.0 Hz), 1.57 (3H, m), 0.90 (3H, d, J = 5.5 Hz). The anilide, needles after recrystallization from hexane, had mp 108°C, (lit. (14) mp 109.5–110.5°C).

(2RS, 4S)-[5,5,5-$^2H_3$]-N-Acetylleucine (9)

(a) Bromination (cf. ref. 15)

To 500 mg of **7** and 900 mg of Br_2 was added a crystal of I_2 and 2 drops of PCl_3, and the mixture was stirred overnight at 60°C under a water-cooled condenser. Another drop of PCl_3 and 100 mg Br_2 were added and the mixture was heated 2 h at 100–110°C. The mixture was cooled, dissolved in 8 mL of saturated $NaHCO_3$ solution, washed with ether, acidified to Congo Red with 50% H_2SO_4, and extracted with ether (3 × 10 mL). After drying and concentration, distillation of the residue in a kugelrohr gave 525 mg of the bromoacid **8**, bp 135–140°C (15 Torr).

(b) Amination

A solution of the bromoacid (525 mg) in 12 mL of 27% NH_4OH was tightly stoppered and kept 9 days at room temperature. After concentration at reduced pressure to remove excess ammonia, the residue was acidified with 6 N HCl to Congo Red, washed with ether (2 × 30 mL), and concentrated to a small volume at reduced pressure. The residue was applied to a cation exchange resin column (1.5 × 15 cm, Bio-Rad AG 50W X4 200–400 mesh, H^+ form); the column was rinsed with 3 volumes of water and eluted with 1 N HCl. The fractions containing leucine hydrochloride were concentrated at reduced pressure, taken up in a small volume of water, and applied to a column of Dowex 1 X5, 20–50 mesh, anion exchange resin in the formate form. The column was eluted with water, eluting leucine (475 mg) immediately after the void volume.

(c) Acetylation

A solution of 193 mg of the crude leucine-d_3 in 2 mL of boiling glacial acetic acid was treated with 150 mg of acetic anhydride, refluxed for 5 min, and allowed to cool to room temperature over 2 h. Concentration left an oily residue, which partly crystallized on standing overnight in a desiccator. Warm acetone was added, the mixture was filtered, and the filtrate was concentrated to an oil that was taken up in 4 mL of boiling water. On cooling and seeding, a crop of 74 mg of crystals was collected, mp 156–160°C (lit. (16) mp 157–159°C for nondeuterated *N*-acetylleucine). A second crop of 32 mg was obtained by extraction of the filtrate with ethyl acetate, concentration, and crystallization from water.

Can. J. Chem. Downloaded from www.nrcresearchpress.com by 84.22.46.98 on 09/08/12
For personal use only.

Enzymatic resolution

A solution of 105 mg of **9** in 10 mL of water, adjusted to pH 7.4 with 0.5 N LiOH and 0.1 N acetic acid, was incubated with 2.3 mg of hog kidney Acylase I (Sigma, specific activity 1800 units/ mg) at 37°C for 140 min, at which time the pH was 7.0. Another 2.6 mg of the enzyme was added and incubation continued for 2 h. The mixture was heated to boiling for 30 s and quickly cooled in ice, filtered, and the pH was adjusted to 5.0 with dilute acetic acid. After concentrating to 2.5 mL, the solution was passed through a 1 × 12 cm column of BioRad AG 50W X4 (H^+) ion exchange resin and eluted with 5 volumes of water. The first two 10- mL fractions contained amide **11**, which was recrystallized from water to give 55 mg of (2*R*,4*S*)-[5,5,5-$^2H_3$]-*N*- acetylleucine, mp 179–181°C (lit. (17) mp 185°C for *N*-acetyl-D-leucine), $[\alpha]_D^{20}$ +21.9 (*c* 1 in 96% ethanol); *N*-acetyl-D-leucine is reported (17) to have $[\alpha]_D^{20}$ −21.3.

Elution of the ion-exchange column was continued with 1 N HCl; concentration of the first three acidic fractions gave the crystalline hydrochloride of **10**, which was taken up in 4 mL of water and applied to a column (1 × 10 cm) of Dowex 1 X8 resin (formate form). Slow elution with water, stopping when the eluate became acidic, and lyophilization of the eluate gave a solid residue, which was recrystallized from 80% ethanol to give 20 mg of (2*S*,4*S*)-[5,5,5-$^2H_3$]leucine (**10**), $[\alpha]_D^{20}$ +12.2 (*c* 0.45 in 6 N HCl); the rotation of L-leucine under these conditions was +14.4.

*(2R,4S)-5,5,5-$^2H_3$]Leucine **12***

Hydrolysis of **11** in refluxing 2 N HCl for 2h, followed by ion-exchange chromatography as described for **10**, gave **12**, $[\alpha]_D^{20}$ −12.8 (*c* 0.47 in 6 N HCl).

NMR spectra of labelled leucines

Proton NMR spectra were run on samples of 3.0 mg leucine and 12 mg NaOH in 0.60 mL of D_2O, using dioxane as an internal reference. Chemical shifts were converted to usual values, relative to TMS, by adding 3.57, the chemical shift of dioxane in D_2O.

Acknowledgment

This study was supported by a research grant from the National Institutes of Health, to whom the authors express their appreciation.

1. D.S. Seigler. Prog. Phytochem. **4**, 83 (1977).
2. P.J. Peterson and L. Fowden. Phytochemistry, **11**, 663 (1972).
3. V. Arroyo, M.J. Hall, C.H. Hassall, and K. Yamasaki. J. Chem. Soc. Chem. Commun. 845 (1976).
4. R.K. Hill. *In* Bioorganic chemistry. Vol. II. *Edited by* E.E. van Tamelen. Academic Press, New York. 1978. p. 111; R.J. Parry. *In* Bioorganic chemistry. Vol. II. *Edited by* E.E. van Tamelen. Academic Press, New York. 1978. p. 247.
5. R. Cardillo, C. Fuganti, D. Ghiringhelli, P. Grasselli, and G. Gatti. J. Chem. Soc. Chem. Commun. 474 (1977).
6. (*a*) S.R. Sylvester and C.M. Stevens. Biochemistry, **18**, 4529 (1979); (*b*) S.R. Sylvester, S.Y. Yan, and C.M. Stevens. Biochemistry, **20**, 5609 (1981).
7. D.J. Aberhart and B.H. Weiller. J. Labelled Compd. Radiopharm. **20**, 663 (1983).
8. (*a*) F. Clandelli and P. Pino. Ric. Sci. Parte 2: sez. A: **A4** (5), 694 (1965); (*b*) G.W. O'Donnell and M.D. Sutherland. Aust. J. Chem. **19**, 525 (1966); (*c*) C.G. Overberger and H. Kaye. J. Am. Chem. Soc. **89**, 5640 (1967).
9. J. Plesek. Chem. Listy, **50**, 1854 (1956); Chem. Abstr. **51**, 4314 (1957); R. Lukes, A. Zobacova, and J. Plesek. Croat. Chem. Acta, **29**, 201 (1957); Chem. Abstr. **53**, 17898 (1959).
10. (*a*) R.E. Lemieux and E. Von Rudloff. Can. J. Chem. **33**, 1701 (1955); (*b*) E. Von Rudloff. Can. J. Chem. **33**, 1714 (1955).
11. M.J. Garson and J. Staunton. Chem. Soc. Rev. **8**, 539 (1979).
12. V. Prelog and G. Helmchen. Helv. Chim. Acta, **55**, 2581 (1972).
13. R.S. Cahn, C. Ingold, and V. Prelog. Angew. Chem. Int. Ed. Engl. **5**, 385 (1966).
14. A.W. Crossley and W.H. Perkin, Jr. J. Chem. Soc. **73**, 16 (1898).
15. H. Hauptmann, P.T. Adams, and B.M. Tolbert. J. Am. Chem. Soc. **74**, 2423 (1952).
16. E. Fischer. Chem. Ber. **34**, 433 (1901).
17. S.M. Birnbaum, L. Levintow, R.B. Kingsley, and J.P. Greenstein. J. Biol. Chem. **194**, 455 (1952).

Can. J. Chem. Downloaded from www.nrcresearchpress.com by 84.22.46.98 on 09/08/12
For personal use only.

Preparation of (2*R*,3*S*)-ß-hydroxy-α-amino acids by use of a novel *Streptomyces* aldolase as a resolving agent for racemic material

RICHARD B. HERBERT[1] AND BARRIE WILKINSON
School of Chemistry, The University, Leeds LS2 9JT, U.K.

AND

GEORGE J. ELLAMES
Department of Chemical Development, Sterling Winthrop Pharmaceuticals Research Division, Sterling Winthrop Research Centre, Alnwick, Northumberland NE66 2JH, U.K.

Received July 26, 1993

This paper is dedicated to Professors Ian Spenser and David B. MacLean

RICHARD B. HERBERT, BARRIE WILKINSON, and GEORGE J. ELLAMES. Can. J. Chem. **72**, 114 (1994).

A unique aldolase, which was isolated from *Streptomyces amakusaensis*, is used to catalyse a reverse aldol reaction on representative racemic ß-hydroxy-α-amino acids (**3–6**) to give samples of the (2*R*,3*S*)-(D-*threo*)-enantiomers with excellent enantiomeric purity.

RICHARD B. HERBERT, BARRIE WILKINSON et GEORGE J. ELLAMES. Can. J. Chem. **72**, 114 (1994).

On a utilisé un enzyme unique, une aldolase isolée du *Streptomyces amakusaensis*, pour catalyser une réaction aldolique inverse sur des acides ß-hydroxy-a-aminés racémiques représentatifs (**3–6**); on obtient ainsi des énantiomères (2*R*,3*S*)-(D-*thréo*) avec une excellent pureté énantiomérique.

[Traduit par la rédaction]

β-Hydroxy-α-amino acids are important compounds. They are found both as naturally occurring compounds in their own right, for example, *threo*-β-hydroxyhistidine (1), and also as constituents of a range of antibiotics (refs. 2, 3, and refs. cited in ref. 4), for example, vancomycin (2). The synthesis of these amino acids is thus of importance, an importance which is increased by their use as intermediates in the synthesis of natural products, for example, β-lactams (5–7). It follows that the provision of these β-hydroxy-α-amino acids by synthesis has value and this is enhanced if they can be synthesized in homochiral form.

The synthesis of these amino acids has been achieved by a number of chemical methods (8). We have found one of these methods to have particular value (9) and have used it for the synthesis of (2*S*,3*R*)- and (2*R*,3*S*)-3-(4-hydroxyphenyl)serine, **1** and **3**, respectively, and (2*S*,3*R*)- and (2*R*,3*S*)-3-phenylserine, **2** and **4**, respectively (10); we have used these compounds here as reference materials.

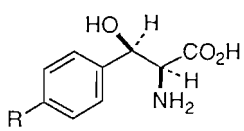

1 R = OH
2 R = H

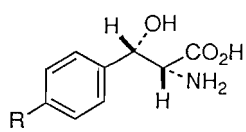

3 R = OH
4 R = H
5 R = Br
6 R = NO_2

There has been very limited success in the use of enzymes for the chiral synthesis of β-hydroxy-α-amino acids (4, 11, 12). However, we have recently isolated (10) a novel aldolase from cultures of *Streptomyces amakusaensis* (ATCC 23876) that catalyses the conversion of β-hydroxy-α-amino acids (**7**) into the corresponding aldehyde (**8**) plus glycine (**9**) [Scheme 1]. The aldolase is easily isolated, is stable, shows broad substrate tolerance, is highly selective for *threo* stereochemistry and, where examined, is stereospecific for the (2*S*,3*R*) configuration (as **1**).

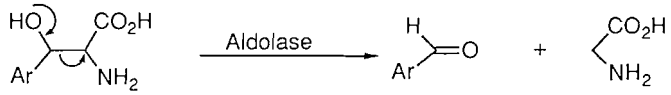

7 **8** **9**

SCHEME 1

Such a list of properties augers well for applications in synthesis and we report here on the use of the aldolase to prepare, very economically, four typical aromatic compounds of this type with (2*R*,3*S*) stereochemistry. This is an approach that we believe can find wide routine application.

Our current approach has been to synthesize, by straightforward chemical means, racemic *threo*-β-hydroxy-α-amino acids and this is then followed by enzyme-catalyzed resolution. The racemic *threo* isomer, which is thermodynamically favoured, is generally obtained as the major, if not exclusive, product of chemical synthesis. Incubation of this material with the aldolase results in lysis of the (2*S*,3*R*) isomer (as **1**) leaving the antipodal compound unchanged. The (2*R*,3*S*)-β-hydroxy-α-amino acid (as **3**) is then simply isolated by ion exchange chromatography.

The four compounds, (2*R*,3*S*)-3-(4-hydroxyphenyl)serine (**3**), (2*R*,3*S*)-3-phenylserine (**4**), (2*R*,3*S*)-3-(4-bromophenyl) serine (**5**), and (2*R*,3*S*)-3-(4-nitrophenyl)serine (**6**), were obtained in excellent isolated yield (74–82%). The enantiomeric purities of **4–6** were assayed through ^{1}H nmr examination of the corresponding *N*-camphanoyl derivatives. First, the *N*-camphanoyl derivatives of racemic material were examined in each case. Two sets of clearly separated signals were seen for the α and β protons of the amino acid moieties. Second, in the case of

[1]Author to whom correspondence may be addressed.

Can. J. Chem. Downloaded from www.nrcresearchpress.com by 195.246.54.202 on 09/08/12
For personal use only.

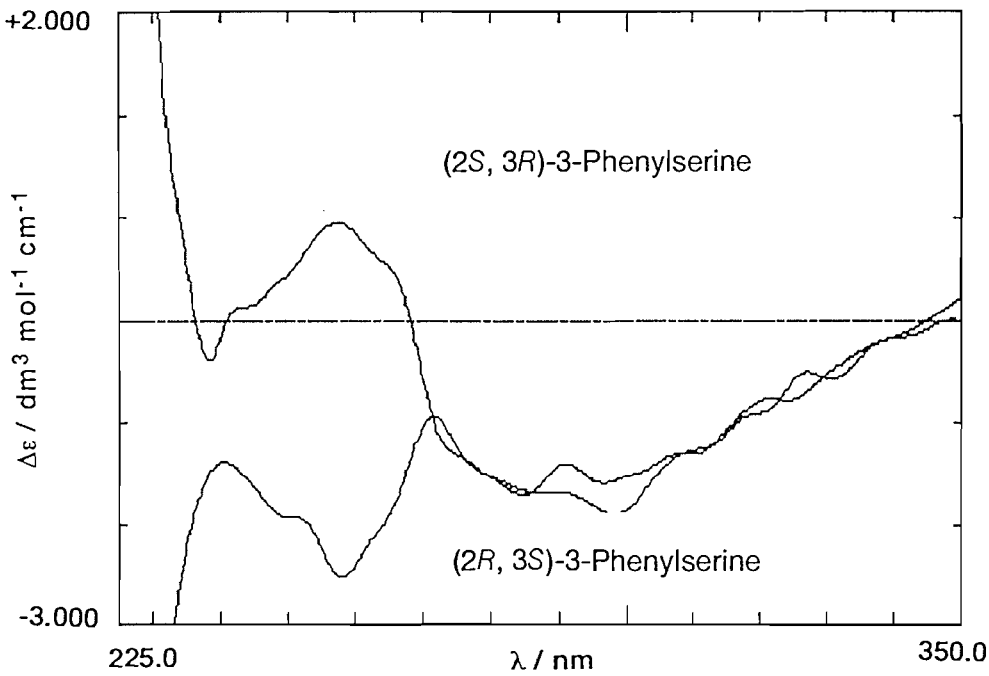

FIG. 1. CD spectra of (2*S*,3*R*)-3-phenylserine (**2**) synthesized according to ref. 9 and (2*R*,3*S*)-3-phenylserine (**4**) obtained by aldolase resolution, which was superimposable on synthetic **4**.

the aldolase-resolved compounds **4–6** only one set of signals could be discerned in each case, i.e., signals for a single stereoisomer. Within the limits of the nmr method we conclude, therefore, that the aldolase-resolved compounds are enantiomerically pure (>95%).

The chemically synthesized homochiral phenylserines **2** and **4** were converted into their *N*-camphanoyl derivatives, which were examined by ^{1}H nmr. They gave complementary signals for the α and β protons that corresponded to those of the racemate. Importantly, the data for the *N*-camphanoyl derivative of the (2*R*,3*S*) isomer (**4**) were identical to those of the aldolase-generated 3-phenylserine derivative. Further identity was seen in the CD spectra of the latter when compared to synthetic (2*R*,3*S*)-3-phenylserine (**4**) (Fig. 1); synthetic (2*S*,3*R*) material gave a spectrum of opposite sign. The foregoing results clearly show, in confirmation of earlier results (10), that the *S. amakusaensis* aldolase catalyses a stereospecific reverse aldol reaction on compounds of type **7** (Scheme 1) and that this reaction occurs exclusively with ß-hydroxy-α-amino acids having (2*S*,3*R*) stereochemistry.

We were unsuccessful in preparing the *N*-camphanoyl derivative of 3-(4-hydroxyphenyl)serine. Our estimation of the optical purity of the aldolase-generated (2*R*,3*S*) isomer is >92%, which is based on its optical rotation compared to those of chemically synthesized **1** and **3**.

The aldolase was simply obtained by sonication of *S. amakusaensis* cells and the protein was then partially purified; full details allowing the routine use of this enzyme are given in the Experimental. We have not yet defined the substrate limits of the aldolase but our results (10) indicate that they are wide. We have found aldolase activity to be present in cultures of two other *Streptomyces* species, which indicates that a family of enzymes exists.[2] This has ramifications for metabolism and also for applications in synthesis since individual family members may have different substrate preferences.

[2]D.R. Evans, R.B. Herbert, and B. Wilkinson. Unpublished results.

Experimental

Apparatus and general procedures were as published (13, 14) except as specified below. Optical rotations were measured on an Optical Activity AA-1000 automatic ranging polarimeter with a pathlength of 25 mm. Sonication of *Streptomyces amakusaensis* was performed using an Ultrasonics A180G apparatus. An MSE high-speed 18 centrifuge was used for centrifugation, which was carried out below 4°C. High-performance liquid chromatography was performed using a Varian 5000 LC pump, Hewlett Packard 1050 UV detector, Hewlett Packard HP 3396 integrator, Polymer Laboratories PLRP-S 8 μm, 100 Å, 250 × 4.6 mm reverse phase column eluting with H_2O:MeCN (1:1) at 1 mL min^{-1}. Reversed phase tlc was conducted using Whatman $LKC_{18}F$ reversed phase plates visualized by uv and (or) ninhydrin (0.2% in ethanol).

Preparation and purification of the Streptomyces amakusaensis *aldolase*

Streptomyces amakusaensis (ATCC 23876) was grown in ISP growth medium (1L) until tuberin production began (15). The cells were centrifuged at 10 000 *g* for 15 min, washed with 0.05 M sodium phosphate buffer (500 ml, pH 7.3) containing 0.1 mM dithiothreitol (DTT), 0.1 mM phenylmethylsulfonyl fluoride (PMSF), and 0.1 mM EDTA. The mixture was centrifuged at 10 000 *g* for 15 min. The cells were suspended in buffer (150 mL), sonicated below 10°C (40 microns, 2 × 30 s pulses) and centrifuged at 10 000 *g* for 15 min.

Ammonium sulfate (20 g) was added to the supernatant solution, the mixture was stirred at room temperature for 15 min and centrifuged at 10 000 *g* for 15 min. Ammonium sulfate (40 g) was added to the resulting supernatant solution and the procedure repeated. The resulting pellet was dissolved in the above buffer (20 mL) and the mixture dialysed twice against a 20-fold excess of the above buffer. DEAE–Sephadex-A50 ion exchange resin was prepared as described previously (4) and the dialysed enzyme solution was chromatographed using a 0.05–0.3 M sodium phosphate (pH 7.3) concentration gradient; the buffer contained 0.1 mM DTT, 0.1 mM PMSF, and 0.1 mM EDTA. The active

Can. J. Chem. Downloaded from www.nrcresearchpress.com by 195.246.54.202 on 09/08/12
For personal use only.

Can. J. Chem. Downloaded from www.nrcresearchpress.com by 195.246.54.202 on 09/08/12
For personal use only.

fractions were combined (70–100 mL) and precipitated by addition of ammonium sulfate (60 g/100 mL) and stirred at room temperature for 15 min. The mixture was centrifuged at 10 000 *g* for 15 min and the resulting pellet dissolved in 0.01 M sodium phosphate (20 mL, pH 7.3) containing 0.1 mM DTT and 0.1 mM EDTA and the solution was dialysed twice against a 20-fold excess of the same buffer. The resulting solution was diluted to 30 mL using the same buffer and was assayed as 1050 units of enzyme activity; 35 units mg^{-1} protein.

Enzyme assay

Streptomyces amakusaensis aldolase solution (0.5 mL) was added to a solution of composition 0.01 M sodium phosphate, 40 mM *threo*-3-(4-hydroxyphenyl)serine, and 0.1 mM pyridoxal 5-phosphate at pH 7.3 (4.5 mL). This solution was incubated at 25°C and assayed by hplc for production of 4-hydroxybenzaldehyde. One unit of enzyme activity is that amount of enzyme required to convert 1 μmol of *threo*-3-(4-hydroxyphenyl)serine into 1 μmol of 4-hydroxybenzaldehyde in 1 min at 25°C.

Synthesis of substrates

(a) Racemic-threo-*β-hydroxy-α-amino acids*

These were synthesized following literature methods, and were crystallized until no *erythro* isomer was detectable by proton nmr.

(threo)-*3-(4-Bromophenyl)serine (as* ***5****) (cf. ref. 16).* 4-Bromobenzaldehyde (3.49 g, 18.9 mmol), glycine (708 mg, 9.4 mmol), and KOH (1.06 g, 18.9 mmol) were dissolved in ethanol (70 mL) and the mixture was stirred at room temperature for 5 h. The Schiff's base product was hydrolysed using 2 M HCl (20 mL) with warming. The precipitate that formed on cooling was removed by filtration. The filtrate was washed with $CHCl_3$ (2 × 10 mL). The aqueous solution was neutralised with concentrated NH_3 and the resulting precipitate was collected and recrystallized from water–ethanol. Yield 67%; mp 184–186°C (dec.); ^{1}H nmr (300 MHz) δ(*d*-TFA): 7.57 (2H, d, 8.4 Hz, Ar), 7.30 (2H, d, 8.4 Hz, Ar), 5.63 (1H, d, 3.3 Hz, ß-H), 4.58 (1H, d, 3.3 Hz, α-H). Anal. calcd. for $C_9H_{10}NO_3Br$: C 41.5, H 3.8, N 5.4, Br 30.5; found: C 41.5, H 3.9, N 5.4, Br 30.7.

(threo)-*3-(4-Hydroxyphenyl)serine (as* ***3****) (cf. ref. 16).* Yield 50%; mp 196–198°C (dec.); ^{1}H nmr (300 MHz) δ(*d*-TFA): 7.32 (2H, d, 8 Hz, Ar), 7.02 (2H, d, 8 Hz, Ar), 5.75 (1H, d, 3.3 Hz, β-H), 4.57 (1H, d, 3.3 Hz, α-H). Anal. calcd. for $C_9H_{11}NO_4$: C 56.6, H 5.8, N 7.3; found: C 56.7, H 6.0, N 7.1.

(threo)-*3-Phenylserine (as* ***4****) (cf. ref. 16).* Yield 62%; mp 184–186°C (dec.); ^{1}H nmr (300 MHz) δ(*d*-TFA): 7.42 (5H, m, Ar), 5.75 (1H, d, 3.3 Hz, β-H), 4.70 (1H, d, 3.3 Hz, α-H). Anal. calcd. for $C_9H_{11}NO_3$: C 59.7, H 6.1, N 7.7; found: C 59.9, H 6.3, N 7.7.

(threo)-*3-(4-Nitrophenyl)serine (as* ***6****) (cf. ref. 17).* Yield 40%; mp 173–175°C (dec.); ^{1}H nmr (300 MHz) δ(*d*-TFA): 8.33 (2H, d, 8.6 Hz, Ar), 7.72 (2H, d, 8.6 Hz, Ar), 5.76 (1H, d, 3.3 Hz, β-H), 4.68 (1H, d, 3.3 Hz, α-H). Anal. calcd. for $C_9H_{10}N_2O_5$: C 47.8, H 4.5, N 12.4; found: C 48.1, H 4.3, N 12.5.

(b) Optically active β-hydroxy-α-amino acids serving as reference compounds

The compounds (2*S*,3*R*)- and (2*R*,3*S*)-3-(4-hydroxyphenyl)serine, **1** and **3**, respectively, were synthesized by adaption of a published procedure (9). This involved condensing the (*R*) isomer of the glycine equivalent **10**, or its enantiomer, with 4-benzyloxybenzaldehyde. Hydrolysis of the product **11** obtained from **10** afforded the amino acid **3**; the isomer **1** was obtained similarly from the enantiomer of **10**. The corresponding 3-phenylserines **2** and **4** were obtained as previously reported (9). The imidazolidinone **10** and its enantiomer were obtained from Fluka Chemicals.

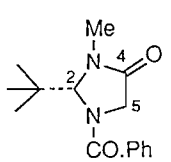

10

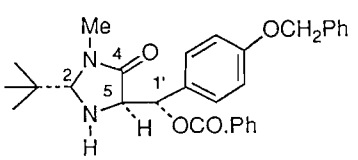

11

*(2S, 5R, 1'S)-1'-Benzoyloxy-1'-(4-benzyloxyphenyl)-2-(*tert-*butyl)-3-methylimidazolidin-4-one (****11****) (cf. ref. 9).* (*R*)-1-Benzoyloxy-2-(*tert*-butyl)-3-methylimidazolidin-4-one (**10**) (246 mg, 0.94 mmol) was dissolved in dry THF (10 mL) and cooled to –78°C. LDA in THF (0.73 M, 1.5 mL, 1.15 mmol) was added and the resulting solution cooled to –100°C for 30 min. To this solution was added 4-benzyloxybenzaldehyde (320 mg, 1.5 mL) in THF (5 mL) and the reaction mixture was stirred at –100°C for 10 min. After this time half-saturated ammonium chloride (10 mL) was added. After warming to room temperature this mixture was extracted with ether (3 × 10 mL), dried over $MgSO_4$, and evaporated. The residual yellow gum was purified by flash silica chromatography eluting with DCM:MeOH (40:1). The resulting product was crystallized from ether. Yield 75%; mp 95–97°C; $[\alpha]_D^{25}$ –30.7 (*c* 0.61, $CHCl_3$); ^{1}H nmr (300 MHz) δ ($CDCl_3$): 8.02 (2H, d, 7.1 Hz, Ar), 7.53–7.25 (10H, m, Ar), 6.93 (2H, d, 3 Hz, Ar), 6.30 (1H, d, 2.2 Hz, H-C(1')), 4.98 (2H, s, CH_2), 4.15 (1H, d, 1.9 Hz, H-C(2)), 4.06 (1H, d, 2.2 Hz, H-C(5)), 2.84 (3H, s, N-CH_3), 1.97 (1H, s, NH), 0.91 (9H, s, ^{t}Bu). Anal. calcd. for $C_{29}H_{32}N_2O_4$: C 73.7, H 6.8, N 5.9; found: C 73.5, H 6.6, N 6.4.

*(2R, 5S, 1'R)-1'-Benzoyloxy-1'-(4-benzyloxyphenyl)-2-(*tert-*butyl)-3-methylimidazolidin-4-one (cf. ref. 9).* Yield 63%; mp 97–99°C; $[\alpha]_D^{25}$ +30.7 (*c* 0.63, $CHCl_3$); ^{1}H nmr (300 MHz) δ ($CDCl_3$): 8.03 (2H, d, 7.1 Hz, Ar), 7.56–7.24 (10H, m, Ar), 6.93 (2H, d, 3 Hz, Ar), 6.32 (1H, d, 2.2 Hz, H-(C1')), 4.99 (2H, s, CH_2), 4.15 (1H, d, 2.0 Hz, H-C(2)), 4.06 (1H, d, 2.2 Hz, H-(C5)), 2.86 (3H, s, N-CH_3), 1.99 (1H, s, NH), 0.90 (9H, s, ^{t}Bu). Anal. calcd. for $C_{29}H_{32}N_2O_4$: C 73.7, H 6.8, N 5.9; found: C 73.2, H 6.8, N 5.8.

*(2S, 5R, 1'S)-1'-Benzoyloxy-2-(*tert-*butyl)-3-methyl-1'-phenylimidazolidin-4-one (cf. ref. 9).* Yield 63%; mp 151–154°C; $[\alpha]_D^{25}$ –27.9 (*c* 0.1, $CHCl_3$); ^{1}H nmr (300 MHz) δ ($CDCl_3$): 8.03 (2H, dd, 1.7 and 8.5 Hz, Ar), 7.60–7.27 (8H, m, Ar), 6.33 (1H, d, 2.8 Hz, H-C(1')), 4.18 (1H, d, 2 Hz, H-C(2)), 4.06 (1H, d, 2.9 Hz, H-C(5)), 2.89 (3H, s, N-CH_3), 2.08 (1H, d, NH), 0.95 (9H, s, ^{t}Bu). Anal. calcd. for $C_{22}H_{26}N_2O_3$: C 72.1, H 7.2, N 7.6; found: C 72.5, H 7.3, N 7.8.

*(2R, 3S, 1'R)-1'-Benzoyloxy-2-(*tert-*butyl)-3-methyl-1'-phenylimidazolidin-4-one (cf. ref. 9).* Yield 60%; mp 151–152°C; $[\alpha]_D^{25}$ +24.0 (*c* 0.1, $CHCl_3$); ^{1}H nmr (300 MHz) δ ($CDCl_3$): 8.03 (2H, dd, 1.7 and 8.5 Hz, Ar), 7.60–7.27 (8H, m, Ar), 6.33 (1H, d, 2.8 Hz, H-C(1')), 4.18 (1H, d, 2 Hz, H-C(2)), 4.06 (1H, d, 2.9 Hz, H-C(5)), 2.89 (3H, s, N-CH_3), 2.08 (1H, d, NH), 0.95 (9H, s, ^{t}Bu). Anal. calcd. for $C_{22}H_{26}N_2O_3$: C 72.1, H 7.2, N 7.6; found: C 72.3, H 7.2, N 7.6.

*(2R, 3S)-(D-*threo*)-3-(4-Hydroxyphenyl)serine (****3****).* Compound **11** (250 mg, 0.58 mmol) was refluxed in 6 M HCl (10 mL) for 8 h. To this was added 5% palladized charcoal (10 mg) and the mixture stirred under hydrogen at atmospheric pressure and room temperature for 1 h. The resulting mixture was filtered through Celite and the filtrate evaporated to a small volume. This was purified using Dowex 50X8-400 ion exchange resin, eluting first with water until neutrality and then using 10% ammonia solution (100 mL). The resultant product was crystallized from water–ethanol. Yield 30%; mp 198–202°C (dec.); $[\alpha]_D^{25}$ +38 (*c* 0.1, H_2O); ^{1}H nmr (300 MHz) δ (*d*-TFA): 7.24 (2H, d, 8 Hz, Ar), 7.06 (2H, d, 8 Hz, Ar), 5.75 (1H, d, 3.3 Hz, ß-H), 4.57 (1H, d, 3.3 Hz, α-H). Anal. calcd. for $C_9H_{11}NO_4$: C 56.6, H 5.8, N 7.3; found: C 56.8, H 6.3, N 7.2.

*(2S, 3R)-(L-*threo*)-3-(4-Hydroxyphenyl)serine (****1****).* Yield 33%; mp 197–200°C (dec.); $[\alpha]_D^{25}$ –36 (*c* 0.1, H_2O); ^{1}H nmr (300 MHz) δ (*d*-TFA): 7.24 (2H, d, 8 Hz, Ar), 7.07 (2H, d, 8 Hz, Ar), 5.76 (1H, d, 3.3 Hz, ß-H), 4.53 (1H, d, 3.3 Hz, α-H). Anal. calcd. for $C_9H_{11}NO_4$: C 56.6, H 5.8, N 7.3; found: C 56.9, H 6.2, N 7.3.

*(2R, 3S)-(D-*threo*)-3-Phenylserine (****4****).* Yield 40%; mp 183–186°C (dec.); $[\alpha]_D^{25}$ +32 (*c* 0.1, H_2O); ^{1}H nmr (300 MHz) δ (*d*-TFA): 7.42 (5H, m, Ar), 5.75 (1H, d, 3.5 Hz, ß-H), 4.70 (1H, d, 3.5 Hz, α-H). Anal. calcd. for $C_9H_{11}NO_3$: C 59.3, H 6.1, N 7.7; found: C 59.5, H 6.2, N 7.8.

*(2S, 3R)-(L-*threo*)-3-Phenylserine (****2****).* Yield 35%; mp 184–186°C (dec.); $[\alpha]_D^{25}$ –31.5 (*c* 0.1, H_2O); ^{1}H nmr (300 MHz) δ (*d*-TFA): 7.42 (5H, m, Ar), 5.75 (1H, d, 3.5 Hz, ß-H), 4.71 (1H, d, 3.5 Hz, α-H). Anal. calcd. for $C_9H_{11}NO_3$: C 59.3, H 6.1, N 7.7; found C 59.2, H 6.1, N 7.6.

Can. J. Chem. Downloaded from www.nrcresearchpress.com by 195.246.54.202 on 09/08/12
For personal use only.

General procedure for the resolution of β-hydroxy-α-amino acids

The amino acid (2 mmol) was dissolved in 0.01 M sodium phosphate buffer (10 mL, pH 7.3) and methanol (5 mL). To this was added a mixed solution containing 0.2 mol pyridoxal 5-phosphate (2 mL) and *S. amakusaensis* enzyme solution (5 mL). The reaction mixture was incubated at 25°C for 8–10 h. The reaction was terminated by addition of 10% TFA (1 mL) and the mixture was centrifuged at 10 000 *g* for 15 min. The resulting supernatant was evaporated, dissolved in water (5 mL), and purified by ion exchange chromatography on Dowex 1-X8-400 resin eluting first with distilled water (50 mL) and then with a gradient of aqueous acetic acid (0.1–0.5 M). The product obtained after evaporation of the solvent was crystallized from water/ethanol.

(2R, 3S)-(D-threo)-3-(4-Hydroxyphenyl)serine (3). Yield 79%; mp 197–199°C (dec.); $[\alpha]_D^{25}$ +35.5 (*c* 0.5, H_2O); ^1H nmr (300 MHz) δ (*d*-TFA): 7.24 (2H, d, 8 Hz, Ar), 7.07 (2H, d, 8 Hz, Ar), 5.76 (1H, d, 3.3 Hz, ß-H), 4.53 (1H, d, 3.3 Hz, α-H); *m/z*, FAB: 198 $(m + 1)^+$.

(2R, 3S)-(D-threo)-3-Phenylserine (4). Yield 82%; mp 183–185°C (dec.); $[\alpha]_D^{25}$ +32.5 (*c* 0.5, H_2O); ^1H nmr (300 MHz) δ (*d*-TFA): 7.42 (5H, m, Ar), 5.76 (1H, d, 3.5 Hz, ß-H), 4.70 (1H, d, 3.5 Hz, α-H), *m/z*, FAB: 182 $(m + 1)^+$.

(2R, 3S)-(D-threo)-3-(4-Bromophenyl)serine (5). Yield 80%; mp 184–186°C (dec.); $[\alpha]_D^{25}$ +27 (*c* 0.3, H_2O); ^1H nmr (300 MHz) δ (*d*-TFA): 7.57 (2H, d, 8.4 Hz, Ar), 7.30 (2H, d, 8.4 Hz, Ar), 5.63 (1H, d, 3.3 Hz, β-H), 4.68 (1H, d, 3.3 Hz, α-H); *m/z*, FAB: 262 ($(m + 1)^+$, 100), 260 ($(m + 1)^+$, 84).

(2R, 3S)-(D-threo)-3-(4-Nitrophenyl)serine (6). Yield 74%; mp 174–176°C (dec.); $[\alpha]_D^{25}$ +27 (*c* 0.5, H_2O); ^1H nmr (300 MHz) δ (*d*-TFA): 8.33 (2H, d, 8.6 Hz, Ar), 7.72 (2H, d, 8.6 Hz, Ar), 5.76 (1H, d, 3.3 Hz, ß-H), 4.68 (1H, d, 3.3 Hz, α-H); *m/z*, FAB: 227 $(m + 1)^+$.

Measurement of Optical Purity

(a) The CD determinations were carried out using equimolar solutions in water of the chemically synthesized (2*S*,3*R*)-(L-*threo*)-3-phenylserine (**2**) and the (2*R*,3*S*)-(D-*threo*)-3-phenylserine (**4**) obtained by enzyme resolution and synthesis.

(b) General procedure for preparing N-camphanoyl derivatives of β-hydroxy-α-amino acids

A solution of β-hydroxy-α-amino acid (0.15 mmol) and sodium hydroxide (0.15 mmol) in water (0.5 mL) was added to (–)-camphanic acid chloride (0.15 mmol) in toluene (0.5 mL) and the mixture was shaken vigorously for 3 h at room temperature. The resulting mixture was washed with $CHCl_3$ (2 × 2 mL) and then acidified to pH 2. This was extracted with $CHCl_3$ (3 × 2 mL), dried over $MgSO_4$, and evaporated to dryness. The resulting white solid was assayed by proton nmr.

(c) The ^1H nmr analysis of resolved materials

The nmr spectra were obtained at 300 MHz in $CDCl_3$. Only a single set of lines was apparent for the material produced by enzymic resolution, i.e., the material appeared to be homochiral. Relevant data is given below.

N-(–)-Camphanoyl-(2R,3S)-(D-threo)-3-phenylserine. Resolved material: 4.94 (1H, dd, 1.8 and 9.0 Hz, α-H), 5.51 (1H, d, 1.8 Hz, ß-H); additional signals for racemate: 5.01 (0.5H, dd, 1.8 and 9.0 Hz, α-H), 5.59 (0.5H, d, 1.8 Hz, ß-H).

N-(–)-Camphanoyl-(2R,3S)-(D-threo)-3-(4-bromophenyl)serine. Resolved material: 4.95 (1H, dd, 1.8 and 8.2 Hz, α-H), 5.48 (1H, d, 1.8 Hz, ß-H); additional signals for racemate: 4.99 (0.5H, dd, 1.8 and 8.2 Hz, α-H), 5.47 (0.5H, d, 1.8 Hz, ß-H).

N-(–)-Camphanoyl-(2R,3S)-(D-threo)-3-(4-nitrophenyl)serine. Resolved material: 5.04 (1H, dd, 1.2 and 8.7 Hz, α-H), 5.64 (1H, d, 1.2 Hz, ß-H); additional signals for racemate: 5.10 (0.5H, dd, 1.2 and 8.7 Hz, α-H), 5.66 (0.5H, d, 1.2 Hz, ß-H).

The signals for the α-protons in the above showed coupling (8–9 Hz) to vicinal NH. These collapsed on standing in MeOD.

Acknowledgments

We are grateful for financial support of a CASE studentship (to B.W.) from the Science and Engineering Research Council (SERC) and Sterling Winthrop Pharmaceuticals Research Division. We thank Dr. Ian White, Department of Biochemistry and Molecular Biology, Leeds University, for assistance in enzyme purification and Miss Rebecca A. Robbins for CD spectra.

1. D.K. Hancock, B. Coxon, S.Y. Wang, E. White V, and D.J. Reeder. J. Chem. Soc. Chem. Commun. 468 (1993).
2. D.H. Williams. Acc. Chem. Res. 364 (1984).
3. B.W. Bycroft (*Editor*). Dictionary of antibiotics and related substances. Chapman and Hall, London. 1988.
4. A. Saeed and D.W. Young. Tetrahedron, **48**, 2507 (1992).
5. M.J. Millar. Acc. Chem. Res. **19**, 49 (1986).
6. R. Labia and C. Morin. J. Antibiot. **37**, 1103 (1984).
7. D.M. Floyd, A.W. Fritz, J. Phiscec, E.R. Weaver, and C.M. Cimarusti. J. Org. Chem. **47**, 5160 (1984).
8. R.M. Williams. Synthesis of optically active α-amino acids. Pergamon Press, Oxford. 1989.
9. D. Seebach, E. Juaristi, D.D. Miller, C. Schikli, and T. Weber. Helv. Chim. Acta, **70**, 237 (1987).
10. R. B. Herbert, B. Wilkinson, G. J. Ellames, and E. K. Kunec. J. Chem. Soc. Chem. Commun. 205 (1993).
11. B.T. Lotz, C.M. Gasparski, K. Peterson, and M.J. Miller. J. Chem. Soc. Chem. Commun. 1107 (1990); R. Chênevert, M. Letourneau, and S. Thiboutot. Can. J. Chem. **68**, 980 (1990).
12. M. Kato, T. Morikawa, and T. Miyoshi. Jpn. Kokai Tokkyo Koho, JP.02207793. 17 Aug. 1990; Chem. Abstr. **114**, 162455 (1991).
13. K.M. Cable, R.B. Herbert, A.R. Knaggs, and J. Mann. J. Chem. Soc. Perkin Trans. 1, 595 (1991).
14. R.B. Herbert and A.R. Knaggs. J. Chem. Soc. Perkin Trans. 1, 103 (1992).
15. K.M. Cable, R.B. Herbert, and J. Mann. J. Chem. Soc. Perkin Trans. 1, 1593 (1987).
16. W.A. Bolhofer. J. Am. Chem. Soc. **76**, 1322 (1954).
17. R. Weichert. Ark. Kemi, **25**, 231 (1966).

Cyclization of farnesyl diphosphate to pentalenene. Orthogonal stereochemistry in an enzyme-catalyzed $S_{E'}$ reaction[1]

DAVID E. CANE[2] AND STEVEN W. WEINER

Department of Chemistry, Box H, Brown University, Providence, RI 02912, U.S.A.

Received July 13, 1993

This paper is dedicated to Professor Ian D. Spenser

DAVID E. CANE and STEVEN W. WEINER. Can. J. Chem. **72**, 118 (1994).

Pentalenene synthase catalyzes the cyclization of farnesyl diphosphate (**1**) to the sesquiterpene hydrocarbon pentalenene (**4**). Separate incubations of (4*S*,8*S*)-[4,8-$^3H_2$, 4,8-$^{14}C_2$]farnesyl diphosphate (**1***a*) and (4*R*,8*R*)-[4,8-$^3H_2$, 4,8$^{14}C_2$]farnesyl diphosphate (**1***b*) with pentalenene synthase isolated from *Streptomyces* UC5319 and analysis of the derived labeled pentalenenes, **4***a* and **4***b*, respectively, by chemical degradation established that H-8*si* of FPP was lost upon cyclization to pentalenene. Consideration of the plausible conformations of the enzymatic cyclization intermediates indicates that the electrophilic allylic addition–elimination ($S_{E'}$) reaction in which the C-4,5 bond of pentalenene is formed involves an orthogonal relationship between the C—C bond being formed and the C—H bond that is ultimately broken.

DAVID E. CANE et STEVEN W. WEINER. Can. J. Chem. **72**, 118 (1994).

La pentalènène synthase catalyse la cyclisation du diphosphate de farnésyle (**1**) en hydrocarbure sesquiterpénique pentalènène (**4**). Des incubations séparées des diphosphates de (4*S*,8*S*)-[4,8-$^3H_2$, 4,8-$^{14}C_2$]farnésyle (**1***a*) et de (4*R*,8*R*)-[4,8$^3H_2$, 4,8-$^{14}C_2$]farnésyle (**1***b*) avec la pentalènène synthase isolée de *Streptomyces* UC5319 et une analyse des pentalènènes marqués, **4***a* et **4***b* respectivement, par une dégradation chimique a permis d'établir que le H-8*si* du diphosphate de farnésyle est perdu lors de la cyclisation en pentalènène. Une considération des conformations plausibles des intermédiaires enzymatiques de la cyclisation indique que la réaction électrophile d'addition–élimination allylique ($S_{E'}$), au cours de laquelle se forme la liaison C-4,5 du pentalènène, implique une relation orthogonale entre la liaison C—C qui se forme et la liaison C—H qui sera finalement brisée.

[Traduit par la rédaction]

The formation of carbon–carbon bonds by the electrophilic attack of carbenium ions on double bonds is one of the most important reactions in the biosynthesis of hundreds of isoprenoid metabolites, including linear polyprenols (dolichols, ubiquinones), cyclic terpenes (mono-, sesqui-, and diterpenes), and steroids and other triterpenes (cholesterol, α-amyrin) (1). Although this process has considerable precedent in solution phase chemistry and much is known about the physical organic chemistry of carbenium ions themselves, the enzymatic reactions remain poorly understood, both with respect to the means by which such reactive species are manipulated and stabilized by protein catalysts and the manner in which enzymes exercise regiochemical and stereochemical control over such reactions (2).

One particularly important subclass of these electrophilic reactions involves the quenching of positive charge resulting from the initial addition to the double bond by the removal of one of the original allylic protons. This allylic addition–elimination formally corresponds to an $S_{E'}$ process. Cornforth and Popjak have shown that the key chain elongation step of polyprenol biosynthesis, typified by the farnesyl diphosphate (FPP, 1) synthase reaction, involves a pair of net *syn* allylic addition–elimination reactions (3). (Scheme 1). By contrast, the closely analogous prototropic rearrangement of isopentenyl diphosphate (IPP, 2) to dimethylallyl diphosphate (DMAPP, 3) has been shown to occur with net *anti* stereochemistry (4). In more recent studies of the cyclization of farnesyl diphosphate (1) to the sesquiterpene hydrocarbon pentalenene (4), we have shown that the initial $S_{E'}$ reaction takes place with net *anti* stereochemistry (5) (Scheme 2). Overton has described model experiments in which an intramolecular $S_{E'}$ reaction was shown to proceed with clean *syn* stereochemistry (6), in contrast to arguments based on MO theory that had predicted a preferred *anti* pathway (7). On the other hand, the possibility could not be excluded that the observed stereochemistry might have resulted from a conformational bias in the substrate rather than from a stereoelectronic imperative. Since that time, there have been several documented examples of (predominant) *anti* stereochemistry in the mechanistically related alkylative or prototropic desilylation of allylsilanes (8). The divergent stereochemical course of various biological allylic addition–elimination reactions suggests that the precise position of substrates relative to enzymic bases may be more important to the outcome than an inherent physicochemical preference for one or the other stereochemistry. To explore this issue further, we have examined a second $S_{E'}$ reaction in the cyclization of FPP to pentalenene.

Pentalenene synthase is a soluble, monomeric enzyme of M_r 42.5 kDa obtained from *Streptomyces* UC5319 (9). A divalent metal cation, either Mg^{2+} or Mn^{2+}, is the only cofactor required. Extensive studies carried out in this laboratory support at mechanism in which FPP, folded as illustrated in Scheme 2, is initially cyclized to humulene (**5**), which undergoes further cyclization initiated by reprotonation at C-10 (5, 10). Consistent with this mechanistic and stereochemical model is the demonstration that cyclization of FPP takes place with net inversion of configuration at C-1 (5). Electrophilic attack on the *si* face of the C-10, 11 double bond is followed by removal the H-9*si* proton. The proton that is removed does not undergo exchange with the medium, but is redonated to the *re* face of the C-9,10 double bond of the intermediate humulene, leading to formation of the protoilludyl cation **6** (5, 10). Following a 1,2-hydride shift, the resultant cation **7** attacks the remaining double bond, leading, after loss of one of the original H-8 protons of FPP, to formation of pentalenene (**4**). We now report experiments which establish that this latter $S_{E'}$ reaction proceeds with neither *syn* nor *anti*

[1] Dedicated with great affection and warm admiration to Professor Ian D. Spenser.

[2] Author to whom correspondence may be addressed.

Can. J. Chem. Downloaded from www.nrcresearchpress.com by 195.246.54.202 on 09/08/12
For personal use only.

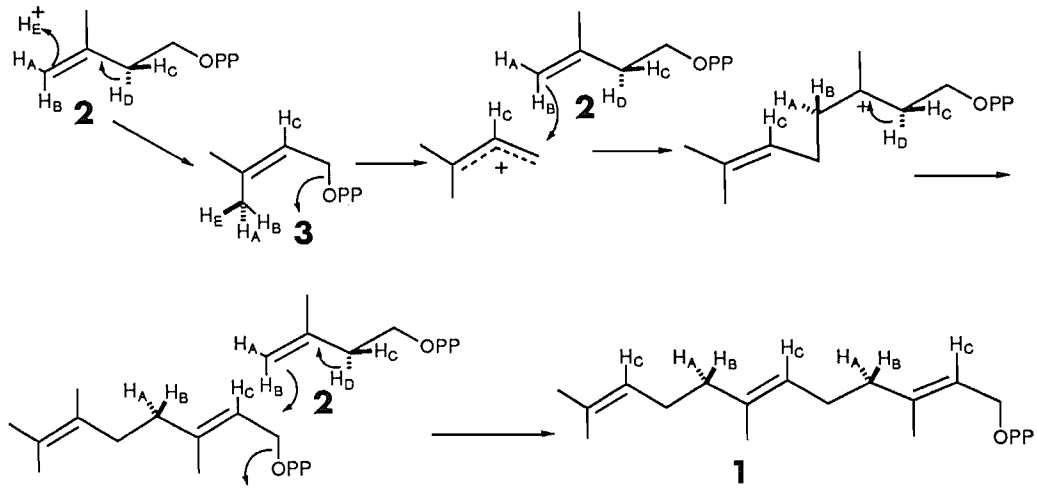

SCHEME 1

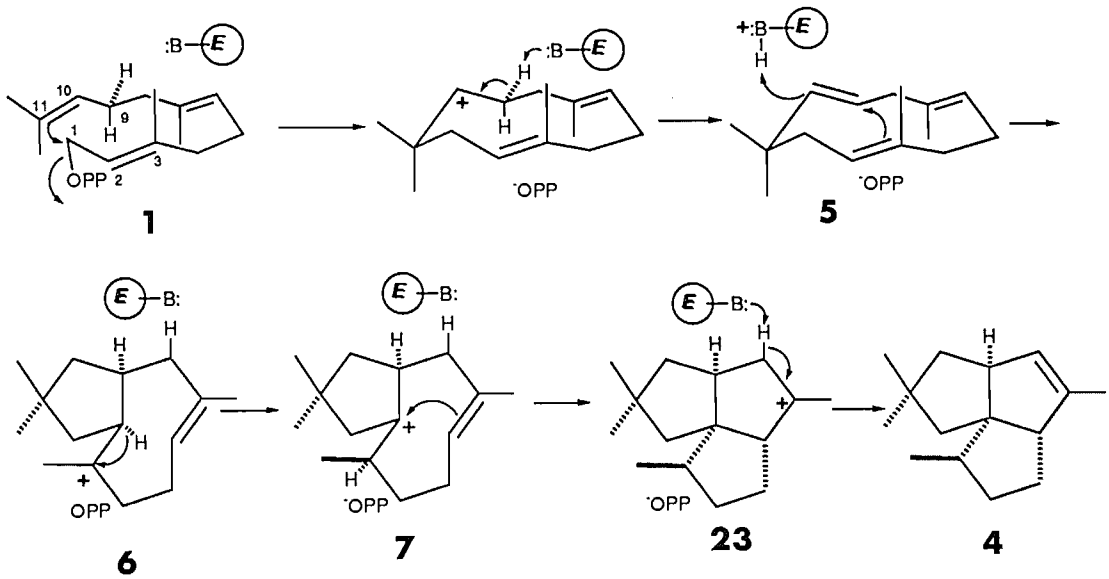

SCHEME 2

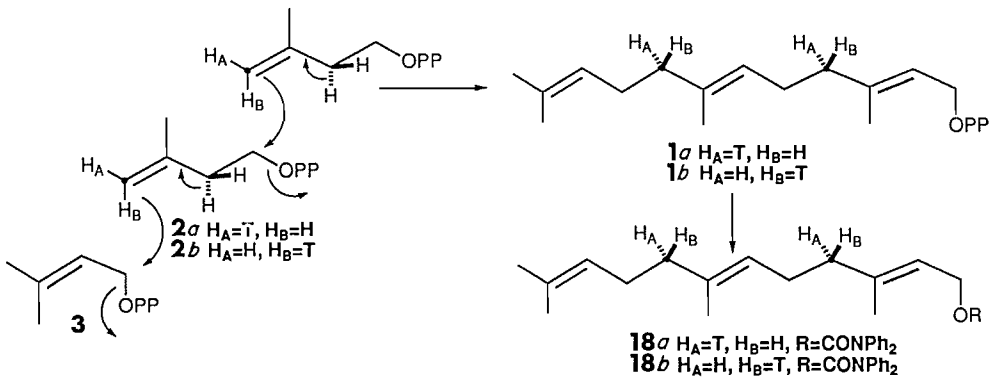

SCHEME 3

stereochemistry but involves a, presumably stepwise, orthogonal electrophilic addition – allylic proton elimination (11).

Results

The stereochemical course of the final deprotonation step was determined by incubation of samples of FPP, stereospecifically tritiated at C-8, with pentalenene synthase obtained from *Streptomyces* UC5319. The requisite labeled samples of FPP could be conveniently prepared by incubation of DMAPP and stereospecifically tritiated IPP with avian liver prenyl transferase (Scheme 3). Thus, condensation of DMAPP (**3**) and *E*-[4-^{3}H]IPP (**2***a*) was expected to afford (4*S*,8*S*)-[4,8-$^3H_2$]FPP

Can. J. Chem. Downloaded from www.nrcresearchpress.com by 195.246.54.202 on 09/08/12
For personal use only.

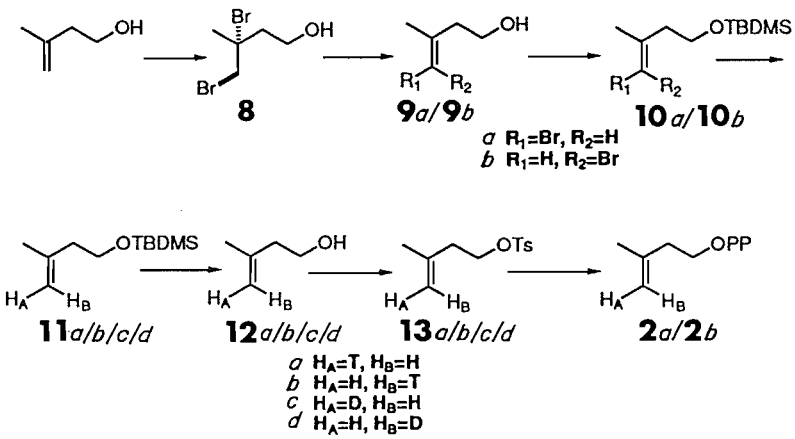

SCHEME 4

(**1***a*), whereas DMAPP (**3**) and *Z*-[4^{3}H]IPP (**2***b*) would yield (4*R*,8*R*)-[4,8-$^3H_2$]FPP (**1***b*) (3). The required samples of IPP labeled with tritium at either the 4*E* or 4*Z* positions were themselves prepared by a modification of the method of Ogura and coworkers (12), initially using deuterium in order to optimize both the incorporation of label and the degree of stereospecificity (Scheme 4).

Bromination (3, 12) of isopentenyl alcohol yielded the corresponding dibromide **8** in 92% yield. Dehydrobromination of **8** with 5 M methanolic KOH gave a 4:1 mixture of *E*- and Z-4-bromo-3-methyl-3-buten-1-ol, **9***a* and **9***a*, respectively, which were separated by flash chromatography on silica gel followed by medium pressure liquid chromatography (MPLC) on silica gel and converted into their respective *tert*-butyldimethylsilyl ethers **10***a* and **10***b* by treatment with *tert*-butyldimethylsilylchloride ((TBDMSCl) and imidazole in DMF. Metallation of **10***a* and **10***b* with 2.2 equivalents of *tert*-butyllithium at −78°C followed by quenching of the resulting bright yellow solution with trifluoroacetic acid 1-*d* (99.8 at.% *d*) at −78°C afforded stereospecifically deuterated isopentenyl *tert*-butyldimethylsilyl ethers **11***c* and **11***d*, respectively. Desilylation of **11***c* and **11***d* with tetra(*n*-butyl)ammonium fluoride (TBAF) in THF followed by treatment of the corresponding 4*E*- and 4*Z*-deuterated isopentenols, **12***c* and **12***d*, and *p*-toluenesulfonyl chloride in pyridine, yielded the tosylates **13***c* and **13***d* in 20% average overall yield from **10***a* and **10***b*. The individual steps of silylation and tosylation were achieved with yields of 80–93% and 80–100%, respectively. **13***c* was 96% deuterated, based on integration of the ^{1}H NMR signals for the *Z* and *E* olefinic protons at δ 4.67 and 4.78. Integration of the two olefinic signals in the ^{2}H NMR spectrum of **13***c* showed the *E*- to *Z*-deuterium ratio to be 92:8. By similar analysis, tosylate **13***d* was found to contain 85% deuterium, exclusively in the expected *Z* geometry.

Having worked out conditions for efficient and stereospecific labeling, both *E*- and *Z*-[4-^{3}H]-3methyl-3-buten-1-yl tosylates, **13***a* and **13***b*, were synthesized following the procedure outlined in Scheme 4, using tritiated trifluoroacetic acid (45 μCi/μmol).[3] Radiolabeled tosylates **13***a* (21.9 μCi/μmol) and **13***b* (41.2 μCi/μmol) were obtained in 34% and 23% overall yield, respectively, from the *tert*-butyldimethylsilyl ethers **11***a* and **11***b*. **13***a* and **13***b* were each converted to the corresponding samples of IPP, **2***a* and **2***b*, upon treatment with tris(tetra-(*n*-butyl)ammonium) hydrogen pyrophosphate in acetonitrile (13).

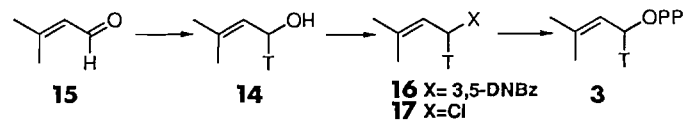

SCHEME 5

[1-^{3}H]DMAPP (**3**) was prepared from [1-^{3}H]dimethylallyl alcohol (**14**), readily obtained by reduction of 3-methyl-2-butenal (**15**) with sodium borotritide in methanol (Scheme 5). Unlabeled carrier dimethylallyl alcohol was added, and a portion of the isotopically diluted alcohol was derivatized as the 3,5-dinitrobenzoate **16**, which was recrystallized to constant specific activity (0.29 nCi/μmol). Treatment of **14** with triphenylphosphine in hexachloroacetone (HCA) (14) generated the allylic chloride **17**, which was converted to [1-^{3}H]-**3** with tris(tetra(*n*-butyl)ammonium)hydrogen pyrophosphate in acetonitrile (13).

For the prenyl transferase-catalyzed preparation of stereospecifically tritiated FPP, **2***a* and **2***b* were each mixed with commercially available [4-^{14}C]IPP. An equimolar mixture of *E*-[4-^{3}H, 4-^{14}C]IPP (**2***a*) (337 μM) and DMAPP (**3**) was incubated with avian liver prenyl transferase to give (4*S*,8*S*)-[4,8-$^3H_2$, 4,8-$^{14}C_2$]FPP (**1***a*) (3, 12).[4] Under similar conditions an equimolar mixture of *Z*-[4-^{3}H, 4-^{14}C]IPP (**2***b*) (309 μM) and DMAPP (**3**) yielded (4*R*,8*R*)-[4,8-$^3H_2$, 4,8-$^{14}C_2$]FPP (**1***b*). **1***a* and **1***b* were each purified by successive Sephadex G-25 gel filtration, C-18 reverse phase HPLC (16), and DEAE–Sephadex anion exchange chromatography. Since the ^{3}H specific activities of **2***a* and **2***b* were each greater than that of **3** by at least a factor of 10^6, the contribution of **3** to the measured ^{3}H/^{14}C ratio in **1***a* and **1***b* was negligible. The precise ^{3}H/^{14}C ratios for **1***a* and **1***b* were determined by hydrolysis of small samples of each

[3]Tritiated trifluoroacetic acid is conveniently prepared by reaction of trifluoroacetic anhydride with tritiated water.

[4]IPP can exhibit substrate inhibition by competing with DMAPP or geranyl diphosphate for binding to the allylic substrate region of the active site (cf. ref. 15). To minimize this problem, IPP and DMAPP are incubated at equimolar concentrations, rather than in the 2:1 ratio required by the stoichiometry of the FPP synthase reaction.

Can. J. Chem. Downloaded from www.nrcresearchpress.com by 195.246.54.202 on 09/08/12
For personal use only.

TABLE 1. Enzymatic cyclization of (4*S*,8*S*)-[4,8-$^3H_2$, 4,8-$^{14}C_2$]FPP (**1***a*) and (4*R*,8*R*)-[4,8-$^3H_2$, 4,8-$^{14}C_2$]FPP (**1***b*) to pentalenenes **4***a* and **4***b* and determination of the distribution of label

Compound	^{14}C specific activity (pCi/μmol)	$^3H/^{14}C$	Atom ratio	Compound	^{14}C specific activity (pCi/μmol)	$^3H/^{14}C$	Atom ratio
1*a*		6.02±0.01[a]	2:2	**1***b*		6.95±0.11[b]	2:2
19*a*	899±34	3.17±0.02	1.05:2	**19***b*	580±6	6.64±0.04	1.91:2
21*b*	831±7	2.99±0.05	0.99:2	**20***b*	569±25	6.58±0.04	1.89:2
				21*b*	555±9	3.46±0.06	1.00:2

[a]Based on recrystallization of farnesyl diphenylurethane **18***a*.
[b]Based on recrystallization of farnesyl diphenylurethane **18***b*.

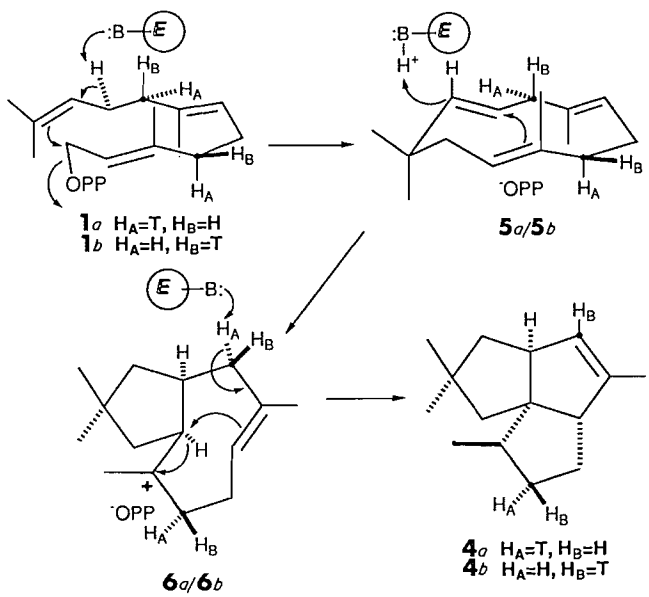

SCHEME 6

labeled FPP with acid phosphatase, followed by the addition of unlabeled carrier *trans,trans*-farnesol and treatment with *N,N*-diphenyl carbamoyl chloride in pyridine (17) to give the diphenylurethanes **18***a* and **18***b*, respectively. **18***a* and **18***b* were each recrystallized to constant $^3H/^{14}C$ ratio, specific activity, and melting point (Scheme 3 and Table 1).

When (4*R*,8*R*)-[4,8-$^3H_2$, 4,8-$^{14}C_2$]FPP, **1***b* ($^3H/^{14}C$ 6.95 ± 0.11), was incubated with crude pentalenene synthase obtained from cell-free extracts of *Streptomyces* UC5319, the resulting **4***b* retained 95% of the original tritium label, based on the $^3H/^{14}C$ ratio of the derived pair of diastereomeric *cis* 6,7-diols (10) **19***b* (β isomer) ($^3H/^{14}C$ 6.64 ± 0.04) and **20***b* (α isomer) ($^3H/^{14}C$ 6.58 ± 0.04), obtained after dilution of the enzymatically generated product with synthetic (±)-pentalenene (18) followed by treatment with osmium tetraoxide in pyridine (Scheme 7 and Table 1). The site of tritiation was established by hydroboration–oxidation followed by PCC oxidation (10) to give 7-keto pentalenane **21***b* ($^3H/^{14}C$ 3.46 ± 0.06). The isotope ratio found in the ketone was roughly half that of both **19***b* and **20***b* as well as 7-hydroxypentalenane (**22***b*), indicating that half the tritium label resided at C-7 of pentalenene (**4***b*) (Table 1).

In a complementary set of experiments, (4*S*,8*S*)-[4,8-$^3H_2$, 4,8-$^{14}C_2$]FPP (**1***a*) ($^3H/^{14}C$ 6.02 ± 0.01) was cyclized to pentalenene (**4***a*) by incubation with crude pentalenene synthase (Scheme 6). After dilution with unlabeled (±)-pentalenene, the derived product was converted to the corresponding mixture of diastereomeric diols **19***a* and **20***a* (Scheme 7). The β isomer **19***a* was recrystallized to constant specific activity, $^3H/^{14}C$ ratio (3.17 ± 0.02), and melting point. These results indicated that 53% of the original tritium label had been retained in the enzymatically generated pentalenene. Hydroboration–oxidation followed by oxidation with PCC as before yielded 7-keto pentalenane (**21***a*) of essentially unchanged $^3H/^{14}C$ ratio (2.99 ± 0.05). These results established that H-8*si* of FPP was lost upon cyclization to pentalenene.

Discussion

Having identified which of the two diastereotopic H-8 protons of FPP is lost in the formation of pentalenene, it is possible to analyze the overall stereochemical course of the final electrophilic allylic addition–elimination reaction, which leads to formation of 4. From the absolute configuration of pentalenene (9, 10), it is evident that the cyclization of cation **7** involves attack on the *si* face of the *trans*-6,7 double bond (FPP numbering, Scheme 8). The *p* orbitals of **7** must be aligned in a parallel orientation for the electrophilic reaction to occur and allow formation of the carbon–carbon σ bond. In principle, formation of the new double bond in pentalenene could involve removal of either of the original allylic protons, H_A or H_B. If H_B (H*re*) were removed, the *p* orbital of the pentalenyl cation 23 would only have to rotate 30° in order to achieve the necessary parallel alignment with the C-H_B σ bond (Scheme 8). Since in fact H_A (H*si*) is removed, this *p* orbital must instead undergo a rotation of 90° prior to the final deprotonation. The final $S_{E'}$ reaction in the enzymic conversion of FPP to pentalenene cannot therefore be described as proceeding with either net *syn* or net *anti* stereochemistry. Intially, both H_A and H_B are *anti* to the newly formed carbon–carbon σ bond. When H_A (corresponding to H-8*si* of FPP) is eventually removed after internal bond rotations, it is actually *orthogonal* to the newly formed 5,6 σ bond of pentalenene.

Although a rotation of only 30° would have sufficed for proper overlap of the vacant *p*-orbital of **22** with the adjacent β proton, why then is a rotation of 90° required for deprotonation to occur? The most likely explanation is that the stereochemistry of deprotonation is determined by the relative positioning of the substrate and the relevant enzymic base. Intriguingly, this final deprotonation occurs immediately adjacent to the sites of deprotonation and reprotonation involved in the formation and further cyclization of the presumed humulene intermediate (5, 10). While the three C—H bonds in question, H-8*si* of FPP (H_A of **7**), H-9*si* of FPP, and H-1*re* of pentalenene are not parallel to each other, they do extend in the same general direction in the various intermediates (5, 10). It is tempting to speculate, therefore, that there is in fact a *single base* at the active site of pen-

Can. J. Chem. Downloaded from www.nrcresearchpress.com by 195.246.54.202 on 09/08/12
For personal use only.

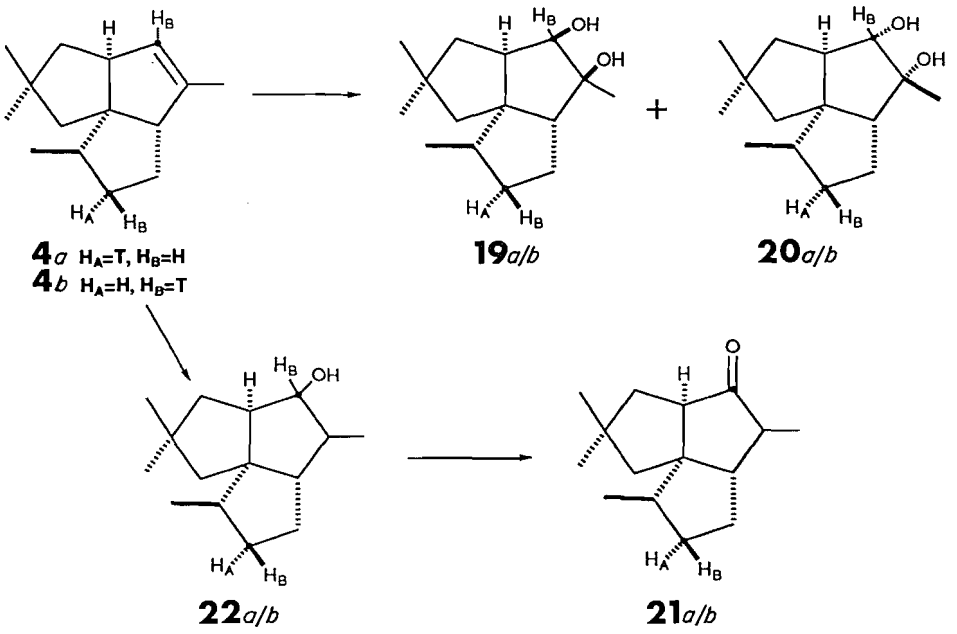

SCHEME 7

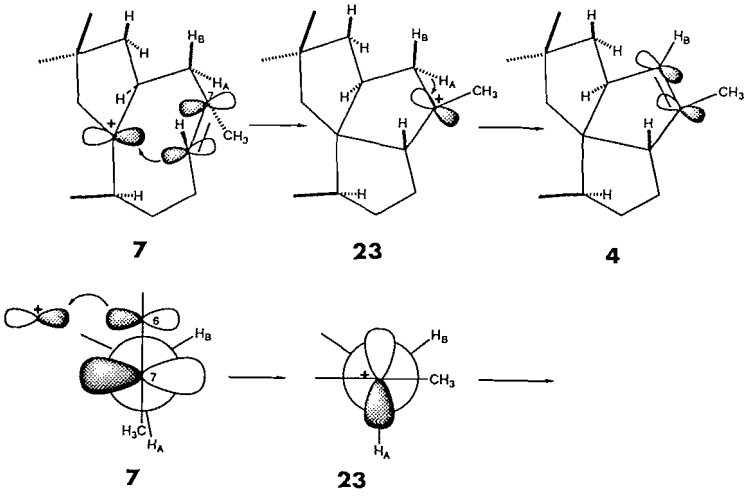

SCHEME 8

talenene synthase that is responsible for deprotonation, reprotonation, and deprotonation at C-9, C-10, and C-8 of the original farnesyl skeleton. We recently succeeded in cloning the relevant structural gene for pentalenene synthase and in obtaining high-level expression of recombinant cyclase in *Escherichia coli* (19). It should therefore be possible to test these predictions directly and to obtain additional insights into the mechanism and stereochemistry of the enzymatic conversion of farnesyl diphosphate to pentalenene.

Experimental

Materials and methods

Melting points were measured on a Thomas–Hoover capillary melting point apparatus and are uncorrected. Proton Fourier transform NMR spectra were routinely obtained at 250 MHz on a Bruker WM250 spectrometer, or at 400 MHz on a Bruker AM-400 spectrometer. Chemical shifts were referenced with respect to TMS at $\delta = 0$ or with respect to HOD at $\delta = 4.60$. ^{13}C NMR spectra were obtained at 100 MHz with broadband ^{1}H decoupling and chemical shifts were referenced with respect to the center of the triplet of $CDCl_3$ at $\delta = 77.0$. ^{2}H NMR spectra were obtained at 61 MHz, and chemical shifts were referenced with respect to $CDCl_3$ at $\delta = 7.24$. Infrared spectra were recorded on a Perkin–Elmer 1600 series FTIR spectrometer. Liquid films were scanned between sodium chloride plates. Radioactive samples were counted for both ^{3}H and ^{14}C activity by dissolving the sample in 5 mL Packard Opti-Fluor liquid scintillation fluid and measuring the activity on a Beckman LS 5801 liquid scintillation counter. For

Can. J. Chem. Downloaded from www.nrcresearchpress.com by 195.246.54.202 on 09/08/12
For personal use only.

Can. J. Chem. Downloaded from www.nrcresearchpress.com by 195.246.54.202 on 09/08/12
For personal use only.

determining specific activities and isotope ratios, the activity was measured to within a standard deviation of ±1%. Lyophilization of aqueous samples was achieved at (7–10) × 10^{-3} Torr (1 Torr = 133.3 Pa) on a Labconco lyophilizer. Centrifugation at 4°C was performed in a Sorvall RC-5 refrigerated centrifuge. Measurements of pH were obtained using a Corning pH/ion meter 150, which was calibrated with pH 4.01 and pH 7.41 buffers. Nanopure water was obtained from a Barnstead NANOpure II apparatus. Radiochemicals were purchased from ICN Radiochemical division (Costa Mesa, Calif.) and other chemicals were routinely purchased from Aldrich (Milwaukee, Wis.). Routine flash chromatography was performed on EM-Science Silica Gel 60 (particle size 40–63 μm, 200–400 mesh), and thin-layer chromatography (TLC) was routinely performed on Kieselgel-60 precoated silica gel plates. For reactions that required anhydrous conditions, glassware was routinely oven dried at 110°C, then cooled either under an atmosphere of dry nitrogen, or in a desiccator containing calcium sulfate (Drierite). Ether and THF were dried and distilled from sodium – benzophenone ketyl. Pentane, hexane, and methylene chloride were distilled from calcium hydride. Pyridine was distilled from calcium hydride and stored over KOH.

E- *and Z-4-Bromo-3-methyl-3-buten-1-ol (**9**a and **9**b) (3, 12)*

To 3,4-dibromo-3-methyl-buten-1-ol (**8**) (5.0 g, 19.4 mmol), prepared as previously described (3, 12), was added 5 M KOH in MeOH (25% excess) at 0°C under a slight positive pressure of nitrogen. The white milky reaction mixture was allowed to stir for 2 h at 25°C, then ether (5–10 mL) was added and the mixture was dried over anhydrous $MgSO_4$ and filtered. The filter cake was washed with several small portions of ether and the combined filtrates were neutralized with a few drops of glacial acetic acid. Solvent was removed via rotovap leaving 2.68 g of a yellow oil (83.9% crude yield). Partial separation of the *E* and *Z* isomers of **9** was achieved by flash chromatography on silica gel (2:1 v:v hexane:ethyl acetate). From the flash column, pure *E* isomer **9***a* could be separated from a mixture of *E* and *Z* isomers (1.51 g, 47.1% yield. A mixture of the *E* and *Z* isomers (223 mg, 1.35 mmol) was loaded onto a size B Lobar medium pressure column prepacked with Si 60 silica gel (particle size 40–63 μm) and eluted with 9:1 v:v hexane:ethyl acetate (5 mL/min, 20 psi (1 psi = 6.9 kPa)). The effluent was monitored by TLC (1:1 v:v hexane:ethyl acetate, visualized by *p*-anisaldehyde). The *Z* isomer **9***b*, R_f = 0.33, was obtained as a colorless oil (55 mg, 335 μmol) in 25% yield. ^{1}H NMR (250 MHz, $CDCl_3$) δ: 1.85 (s, 3H, CH_3), 2.53 (t, *J* = 6.7 Hz, 2H, CH_2CH_2O), 3.78 (t, *J* = 6.7 Hz, 2H, CH_2O), 6.01 (s, 1H, C*H*=C). The *E* isomer **9***a*, R_f = 0.29, was obtained as a colorless oil (142 mg, 860 μmol) in 64% yield. ^{1}H NMR (250 MHz, $CDCl_3$) δ: 1.83 (s, 3H, CH_3), 2.38 (t, *J* = 6.2 Hz, 2H, CH_2CH_2O), 3.72 (t, *J* = 6.3 Hz, 2H, CH_2O), 6.01 (s, 1H, C*H*=C).

E-*4-Bromo-3-methyl-3-buten-1-yl*-tert-*butyldimethylsilyl ether (**10**a)*

To a solution of *E*-4-bromo-3-methyl-3-buten-1-ol (**9***a*) (249 mg, 1.51 mmol) in 10 mL dry DMF were added imidazole (1.07 g, 15.3 mmol) and *tert*-butyldimethylsilyl chloride (Aldrich, 904 mg, 5.99 mmol). The reaction mixture was shaken vigorously for 5 min, effecting a complete consumption of starting material. To the reaction mixture was added 20 mL ether, followed by washing with 3 × 20 mL water. The aqueous layer was saturated with brine and back-extracted with ether. The ether layer was dried over anhydrous $MgSO_4$, and solvent was removed via rotovap. The colorless residue was purified by flash chromatography on silica gel (hexane, followed by 99:1 v:v hexane:ethyl acetate) to afford **10***a* as a colorless oil (391 mg,1.40 mmol) in 93% yield. IR (neat, cm^{-1}): 3074, 2954, 2929, 2896, 2857, 2738, 1632, 1472, 1431, 1408, 1381, 1361, 1288, 1256, 1213, 1161, 1105, 1006, 956, 939, 836, 775, 713, 662. ^{1}H NMR (250 MHz, $CDCl_3$) δ: 0.02 (s, 6H, $(CH_3)_2Si$), 0.86 (s, 9H, $(CH_3)_3CSi$), 1.78 (s, 3H, CH_3), 2.29 (t, *J* = 6.6 Hz, 2H, CH_2CH_2OSi), 3.66 (t, *J* = 6.6 Hz, 2H, CH_2OSi), 5.92 (s, 1H, C*H*=C). ^{13}C NMR (100 MHz, $CDCl_3$) δ: −5.4, 18.2, 19.4, 25.9, 41.4, 61.2, 102.7, 138.9. MS (CI^+/CH_4) (M + 1) (^{79}Br): 279. HRMS, calcd. for $C_{11}H_{23}OSiBr$: 279.0773; found: 279.0791.

Z-*4-Bromo-3-methyl-3-buten-1-yl*-tert-*butyldimethylsilyl ether (**10**b)*

To a solution of *Z*-4-bromo-3-methyl-3-buten-1-ol (**9***b*) (61 mg, 372 μmol) in 1 mL dry DMF were added imidazole (122 mg, 1.74 mmol) and *tert*-butyldimethylsilyl chloride (222 mg, 1.48 mmol, Aldrich). The reaction was carried out as described for the *E* isomer **10***a*. **10***b* was obtained as a colorless oil (81 mg, 290 μmol) in 78% yield. ^{1}H NMR (250 MHz, $CDCl_3$) δ: 0.04 (s, 6H, $(CH_3)_2Si$), 0.87 (s, 9H, $(CH_3)_3CSi$), 1.61 (s, 3H, CH_3), 2.42 (t, *J* = 6.9 Hz, 2H, CH_2CH_2OSi), 3.70 (t, *J* = 6.9 Hz, 2H, CH_2OSi), 5.90 (s, 1H, C*H*=C).

E-*[4-^{2}H]-3-Methyl-3-buten-1-yl*-tert-*butyldimethylsilyl ether (**11**c) (12)*

An oven-dried, nitrogen-cooled flask was charged with *E*-4-bromo-3-methyl-3-buten-1-yl-*tert*butyldimethylsilyl ether **10***a* (93 mg, 332 μmol), which had been dried at atmospheric pressure in a desiccator containing P_2O_5 for 12 h prior to use. Dry *N,N,N′,N′* tetramethylethylenediamine (TMEDA, 0.20 mL) and 1.5 mL dry ether were added via syringe. The reaction mixture was cooled to −78°C before the addition of *tert*-butyllithium (0.43 mL, 1.7 M in pentane, 731 μmol) via syringe. Upon addition of *tert*-butyllithium, the colorless solution turned bright yellow. After 5 min the reaction mixture was quenched with trifluoroacetic acid 1-*d* (Aldrich, 99.8 at.% *d*, 100 μL, 1.3 mmol). After an additional 5 min, the reaction mixture was warmed to 0°C, and 2 mL sodium phosphate buffer, pH 7.0, was added. The reaction mixture was warmed to room temperature and was extracted with 3 × 3 mL ether. The ether extract was washed with brine and solvent was removed via rotovap. The colorless oily residue was purified by flash chromatography on silica gel (5 g, hexane, then 99:1 v:v hexane:ethyl acetate), and solvent was removed in vacuo to afford 39 mg of a colorless oil (58% crude yield). ^{1}H NMR (250 MHz, $CDCl_3$) δ: 0.03 (s, 6H, $(CH_3)_2Si$), 0.87 (s, 9H, $(CH_3)_3CSi$), 1.71 (s, 3H, CH_3), 2.21 (t, *J* = 7.0 Hz, 2H, CH_2CH_2OSi), 3.69 (t, *J* = 7.0 Hz, 2H, CH_2OSi), 4.66 (s, 1H, C*H*=C), 4.73 (s, 0.04 H, 4*Z*-C*H*=C). In addition, the following impurity peaks, each integrating to ca. 0.1 H, were present: 0.12 (s), 1.06 (s), 1.52 (s, H_2O), 1.65 (s), 1.69 (s), 2.10 (t), 2.45 (t), 3.61 (dt).

E-*[4-^{2}H]-3-Methyl-3-buten-1-yl-tosylate (**13**c)*

To the TBDMS ether **11***c* (39 mg, 0.19 mmol, assuming 100% purity) was added tetra(*n*-butyl)ammonium fluoride (TBAF, 1.0 M in THF, 400 μL, 0.40 mmol), and the reaction mixture was allowed to stir for 15 min. Then 1 mL water was added and the mixture was extracted with 5 × 2 mL CH_2Cl_2. The organic layer was washed with brine and dried over anhydrous Na_2SO_4. The organic layer was then concentrated to a volume of <1 mL by simple distillation of the solvent using a Vigreux column. Pyridine (1 mL) and *p*-toluenesulfonyl chloride (*p*-TsCl, recrystallized, 241 mg, 1.16 mmol) were added and the solution was stirred under nitrogen for 13 h. Solvent was partially removed via rotovap and the residual mixture was cooled to 0°C, mixed with 2 mL distilled water, and extracted with 2 × 3 mL ether. The organic layer was washed successively with 10% $NaHCO_3$ and saturated $CuSO_4$:$5H_2O$, and the aqueous washings were back- extracted with ether. The combined organic layers were washed successively with water and brine and then dried over anhydrous Na_2SO_4. Solvent was removed via rotovap and the residue was purified by flash chromatography on silica gel (5 g, 98:2 v:v hexane: ethyl acetate). **13***c* was obtained as a colorless oil (7 mg, 29 μmol) in 24% yield from **11***c*. (Unlabeled isopentenyl tosylate was obtained in 35% overall yield from pure, unlabeled isopentenyl-*tert*-butyldimethylsilyl ether, using the above procedure.) ^{1}H NMR (250 MHz, $CDCl_3$) δ: 1.54 (s, H_2O), 1.64 (s, 3H, CH_3), 2.33 (t, *J* = 6.8 Hz, 2H, CH_2CH_2OTs), 2.43 (s, 3H, ArCH_3), 4.10 (t, *J* = 6.9 Hz, 2H, CH_2OTs), 4.64 (s, 1H, C*H*=C), 4.75 (s, 0.04 H, 4*E*-C*H*=C), 7.30 (d, *J* = 8.0 Hz, 2H, Ar*H*), 7.76 (d, *J* = 8.3 Hz, 2H, Ar*H*). ^{2}H NMR (61 MHz, $CHCl_3$) δ: 4.71 (small br s), 4.83 (s). The ratio of areas of resonances at 4.83 and 4.71 in the ^{2}H NMR spectrum was 92:8.

Z-*[4-^{2}H]-3-Methyl-3-buten-1-yl*-tert-*butyldimethylsilyl ether (**11**d) (12)*

To an oven-dried, nitrogen-cooled flask charged with *Z*-4-bromo-

Can. J. Chem. Downloaded from www.nrcresearchpress.com by 195.246.54.202 on 09/08/12
For personal use only.

3-methyl-3-buten-1-yl-*tert*-butyldimethylsilyl ether **10***b* (23 mg, 83 μmol), which had been dried at room temperature and at atmospheric pressure in a desiccator containing P_2O_5 for 12 h prior to use, was added dry TMEDA (80 μL) and 0.5 mL dry ether. The reaction mixture was cooled to −78°C before the addition of *tert*-butyllithium (0.11 mL, 1.7 M in pentane, 187 μmol) via dry syringe. Upon addition of *tert*-butyllithium, the reaction mixture became a bright yellow color. After 5 min, the reaction was quenched with trifluoroacetic acid 1-*d* (99.8 at.% *d*, Aldrich, 48 μL, 636 μmol). The product was isolated and purified in a manner completely analogous to that described for **11***c* to give a colorless oil (16 mg, 81 μmol if 100% pure) in 98% crude yield. The product was not analyzed by ^{1}H NMR at this point, but was used as is for making the tosylate **13***d*.

*Z-[4-^{2}H]-3-Methyl-3-buten-1-yl-tosylate (**13**d)*

To crude **11***d* (16 mg, 81 μmol) was added TBAF (1.0 M in THF, 160 μL, 160 μmol). The reaction was allowed to proceed for 10 min, after which 1 mL water was added. The aqueous solution was saturated with sodium chloride and extracted with 5 × 2 mL ether. Concentration of the ether extract and conversion to the tosylate **13***d* was carried out as described for the preparation of **13***c*. Purification by flash chromatography on silica gel (5 g, 98:2 v:v hexane:ethyl acetate) afforded **13***d* as a colorless oil (3 mg, 12 μmol) in 15% overall yield from **10***b*. ^{1}H NMR (250 MHz, $CDCl_3$) δ: 1.54 (s, 2H, H_2O), 1.63 (s, 3H, CH_3), 2.33 (t, J = 6.9 Hz, 2H, CH_2CH_2OTs), 2.43 (s, 3H, ArCH_3), 4.11 (t, J = 6.9 Hz, 2H, CH_2OTs), 4.64 (s, 0.14 H, 4*Z*-C*H*=C), 4.75 (s, 1H, C*H*=C), 7.31 (d, J = 8.0 Hz, 2H, Ar*H*), 7.76 (d, J = 8.3 Hz, 2H, Ar*H*). ^{2}H NMR (61 MHz, $CHCl_3$) δ: 4.74 (s), 7.28 (s, $CDCl_3$).

*Z-[4-^{3}H]-3-Methyl-3-buten-1-yl tosylate (**13**b)*

To a solution of *Z*-4-bromo-3-methyl-3-buten-1-yl-*tert*-butyldimethylsilyl ether (**10***b*) (80 mg, 288 μmol, dried over P_2O_5) in 1.5 mL dry ether was added 0.20 mL dry TMEDA. The reaction mixture was cooled to −78°C under a slight positive pressure of nitrogen, and *tert*-butyllithium (0.38 mL, 1.7 M in pentane, 0.65 mmol) was added. A bright yellow color was immediately observed. Within 5 min, the reaction mixture was rapidly quenched with 60 μL (89 mg, 780 μmol) of tritiated trifluoroacetic acid (45 μCi/μmol) at −78°C. After an additional 5 min, the reaction mixture was warmed to 0°C and 2 mL of sodium phosphate buffer, pH 7.0, were added. The product, **11***b*, was isolated as described for **11***c*. The desilylation of **11***b* with TBAF (1.0 M in THF, 600 μL, 600 μmol) and the tosylation of crude alcohol **12***b* using 0.5 mL dry pyridine and *p*-TsCl (recrystallized, 297 mg, 1.56 mmol) were carried out as described for the preparation of **13***d*. Counting of an aliquot indicated a total activity for **13***b* of 6.01 × 10^9 dpm (2.73 mCi). The tosylate was recovered in 23% chemical yield (16 mg, 66 μmol, 41.2 μCi/μmol) from **10***b*. ^{1}H NMR (250 MHz, $CDCl_3$) δ: 1.64 (s, 3H, CH_3), 2.33 (t, J = 6.8 Hz, 2H, CH_2CH_2OTs), 2.43 (s, 3H, ArCH_3), 4.10 (t, J = 6.9 Hz, 2H, CH_2OTs), 4.66 (s, 1H, *Z*-C*H*), 4.77 (s, 1H, *E*-C*H*), 7.31 (d, J = 8.0 Hz, 2H, Ar*H*), 7.77 (d, J = 8.5 Hz, 2H, Ar*H*).

E-*[4-^{3}H]-3-Methyl-3-buten-1-yl tosylate (**13**a)*

E-4-Bromo-3-methyl-3-buten-1-yl-*tert*-butyldimethylsilyl ether **10***a* (82 mg, 292 μmol, dried over P_2O_5) was metallated at −78°C with *tert*-butyllithium (0.42 mL, 1.7 M in pentane, 0.71 mmol) in TMEDA–ether and quenched with tritiated trifluoroacetic acid (45 mCi/mmol, 85 μL, 127 mg, 1.11 mmol) as described for the preparation of **11***c*. Desilylation of **11***c* with TBAF (1.0 M in THF, 600 μL, 600 μmol) gave the alcohol **12***a*, which was converted in the usual manner to the corresponding tosylate **13***a* (26 mg, 107 μmol, 21.9 μCi/μmol) in 34% chemical yield from **10***a*. ^{1}H NMR (250 MHz, $CDCl_3$) δ: 1.64 (s, 3H, CH_3), 2.33 (t, J = 6.8 Hz, 2H, CH_2CH_2OTs), 2.43 (s, 3H, ArCH_3), 4.10 (t, J = 6.9 Hz, 2H, CH_2OTs), 4.66 (s, 1H, *Z*-C*H*), 4.77 (s, 1H, *E*-C*H*), 7.31 (d, J = 8.0 Hz, 2H, Ar*H*), 7.77 (d, J = 8.5 Hz, 2H, Ar*H*).

E-*[4-^{3}H]-3-Methyl-3-buten-1-yl diphosphate (**2**a) (**13**)*

To a solution of *E*-[4-^{3}H]-3-methyl-3-buten-1-yl tosylate **13***a* (2 mg, 8 μmol, 21.9 μCi/μmol) in 200 μL dry acetonitrile was added tris(tetra(*n*-butyl)ammonium) hydrogen pyrophosphate (101 mg, 112 μmol). The reaction was carried out for 2 h at room temperature under nitrogen, after which the reaction mixture was partitioned between 1 mL hexane and 1 mL water. The two layers were vortexed and a 10-μL aliquot of each layer was counted for ^{3}H activity. By comparison of the ^{3}H activity of the aqueous layer ((4.11 ± 0.04) × 10^4 dpm) with that of the hexane layer ((1.63 ± 0.07) × 10^3 dpm), it was determined that pyrophosphorylation had gone to 96% completion. Solvent was removed by passing a stream of nitrogen over the surface of the liquid, followed by drying at high vacuum, and the white solid residue was taken up to 1 mL 0.05 M triethylammonium bicarbonate, pH 8.0. This solution was applied to a DEAE–Sephadex anion exchange column previously equilibrated with 0.05 M triethylammonium bicarbonate at 4°C. The product was eluted using a linear gradient of 0.05–1.0 M triethylammonium bicarbonate. A total of 67 fractions (250 drops perfraction) was collected and a 10-μL aliquot of every other fraction was counted for radioactivity. Fractions 29–33 were combined and lyophilized at (5–10) × 10^{-3} Torr. Two 5-mL portions of 1.0 M ammonium hydroxide were added and the resulting solution was lyophilized each time to near dryness. The fluffy white solid was then taken up in 2 mL isopropanol:acetonitrile:0.1 M ammonium bicarbonate (4.5:2.5:3.0, v:v:v) and the solution was applied to a flash column of EM-Avicel Microcrystalline Cellulose (1.5 cm × 10 cm) previously equilibrated with 4 column volumes of the above elution buffer. The column was run at room temperature, a total of 60 fractions (3 mL each) was collected, and a 20-μL aliquot of every other fraction was counted for radioactivity. Fractions 5–19 were combined, a few drops of 1.0 M ammonium hydroxide were added, and the solution was concentrated to about half its original volume via rotovap over a period of 1 h. A few drops of 1.0 M ammonium hydroxide were added after approximately 30 min to keep the solution slightly basic. Acetonitrile and isopropanol were completely removed from the concentrated solution via SpeedVac over a period of 2 h, during which time a few drops of 1.0 M ammonium hydroxide was added intermittently. The resulting aqueous solution was lyophilized to dryness, then taken up in 5 mL 0.2 M ammonium hydroxide. **2***a*, total ^{3}H activity 3.51 × 10^8 dpm (160 μCi, 7.28 μmol), 92% yield from **13***a*. ^{1}H NMR (250 MHz, D_2O/NH_4OD) δ: 1.60 (s, 3H, CH_3), 2.22 (t, J = 6.6 Hz, 2H, CH_2CH_2OPP), 3.69 (dt, $J_1 = J_2$ = 6.5 Hz, 2H, CH_2OPP), 4.60 (H_2O very intense, obscuring the olefinic protons).

*Z-[4-^{3}H]-3-Methyl-3-buten-1-yl diphosphate (**2**b) (**13**)*

13*b* (6 mg, 25 μmol, 41.2 μCi/μmol) in 400 μL dry acetonitrile was reacted with tris(tetra(*n*-butyl)ammonium) hydrogen pyrophosphate (202 mg, 223 μmol) for 6 h at room temperature. The product was isolated and purified as described for **2***a* to give **2***b*, which was taken up in 10 mL 0.1 M ammonium hydroxide. Total ^{3}H activity 6.52 × 10^8 dpm (294 μCi, 7.13 μmol), 29% overall yield from **13***b*. ^{1}H NMR (250 MHz, D_2O/NH_4OD) δ: 1.60 (s, 3H, CH_3), 2.22 (t, J = 6.6 Hz, 2H, CH_2CH_2OPP), 3.69 (dt, $J_1 = J_2$ = 6.5 Hz, 2H, CH_2OPP), 4.60 (H_2O very intense, and obscuring the olefinic protons).

*[1-^{3}H]-3-Methyl-3-buten-1-ol (**14**)*

To a solution of 3-methyl-2-butenal (**15**) (15 mg, 180 μmol, Aldrich) in 250 μL methanol at 0°C, was added $NaBH_3T$ in methanol (316.7 μCi/μmol, 50 μCi/μL, 5 μL, 0.79 μmol), and the reaction was allowed to proceed at 0°C for 1 h. Unlabeled $NaBH_4$ was added (15 mg, 385 μmol), and the reaction was allowed to proceed for an additional 5–10 min, followed by the dropwise addition of 5% HCl (1 mL). The aqueous solution was extracted with 6 × 1 mL pentane. The combined pentane extracts were filtered through a Pasteur pipet containing anhydrous $MgSO_4$ into a flask charged with unlabeled carrier 3-methyl-2-buten-1-ol (516 mg, 5.99 mmol). Solvent was removed via rotovap for 5–10 min. The alcohol was stored at −10°C. ^{1}H NMR analysis of a sample of **14** prepared under the same conditions with unlabeled $NaBH_4$ indicated the absence of any 1,4 reduction.

The corresponding crystalline 3,5-dinitrobenzoate ester derivative **16**, which was obtained by reaction of a portion of the tritiated alcohol

Can. J. Chem. Downloaded from www.nrcresearchpress.com by 195.246.54.202 on 09/08/12
For personal use only.

(152 mg, 1.76 mmol) and 3,5-dinitrobenzoyl chloride (423 mg, 1.97 mmol) in dry pyridine (1.5 mL) for 3.5 h, was recrystallized to constant specific activity (2.28×10^3 dpm ^{3}H/mg, 0.29 nCi/μmol) and mp (67.5–69.0°C) from benzene–hexane. ^{1}H NMR (250 MHz, $CDCl_3$) δ: 1.55 (br, H_2O), 1.81 (s, with fine splitting, 6H, CH_3), 4.95 (d, J = 7.4 Hz, 2H, CH_2O), 5.49 (t with splitting, J = 7.4 Hz, 1H, C*H*=C), 9.17 (s with fine splitting, 2H, Ar*H*), 9.21 (s with fine splitting, 1H, Ar*H*).

*[1-^{3}H]-3-Methyl-2-buten-1-yl diphosphate (**3**) (13, 14)*

To a solution of [1-^{3}H]-3-methyl-2-buten-1-ol (**14**) (200 mg, 2.32 mmol, 0.29 nCi/μmol) in hexachloroacetone (1.7 mL, 975 mg, 3.68 mmol) at 0°C was added triphenylphosphine (645 mg, 2.46 mmol) in small portions over a period of 10 min. The reaction was allowed to proceed at room temperature for 20 min. Analysis of the reaction mixture by TLC (1:1 v:v hexane:ethyl acetate) showed that the alcohol had been completely consumed. The resulting thick dark brown slurry was cooled to −78°C, and the reaction flask was attached to a flash distillation apparatus. While the receiver flask was kept at room temperature, the distillation system was evacuated to 0.01–0.02 Torr for 1–2 min, then closed to the vacuum pump but kept under vacuum. The receiver flask was cooled to −78°C and the reaction flask was warmed to room temperature. The flash distillation proceeded for 1 h, at which time the system was bled to the atmosphere. When the reaction was carried out on unlabeled alcohol, the recovered 1-chloro-3-methyl-2-butene was analysed by ^{1}H NMR (250 MHz, $CDCl_3$) δ: 1.55 (br, <1H, H_2O), 1.73 (d, J = 11.2 Hz, 6H, $CH_3 \times 2$), 4.07 (d, J = 8.0 Hz, 2H, CH_2Cl), 5.44 (t, with fine splitting, J = 8.0 Hz, 1H, C*H*=C). Also present were two impurity peaks: 2.17 (s, 0.2 H), and 6.74 (s, 0.03 H). The labeled chloride **17**, without any further purification or analysis, was taken up in 1 mL dry acetonitrile and tris(tetra(*n*-butyl)ammonium) hydrogen pyrophosphate (1.60 g, 1.77 mmol) was added. The reaction proceeded at room temperature for 12 h. Analysis of an aliquot of the reaction mixture partitioned between 1 mL water and 1 mL hexane showed that the reaction had only gone to two-thirds completion. The volatile components of the reaction mixture were evaporated with a stream of nitrogen and the resulting thick brown oil was dissolved in 1 mL 0.05 M triethylammonium bicarbonate, pH 8.0, and then extracted with 3 × 1 mL hexane to remove any unreacted allylic chloride. A stream of nitrogen was passed over the aqueous layer to remove any traces of hexane. The aqueous solution was applied to a DEAE–Sephadex anion exchange column equilibrated with 0.05 M triethylammonium bicarbonate at 4°C. The product was eluted by a linear gradient of 0.05–1.0 M triethylammonium bicarbonate pH 8.0. A total of 52 fractions (250 drops each) was collected and a 100-μL aliquot of every other fraction was counted for radioactivity. Fractions 25–30 were combined and lyophilized to near dryness. Two portions of ammonium hydroxide (5 mL, 1.0 M) were added and each time the solution was lyophilized to near dryness. The white solid residue was taken up in 2 mL isopropanol:acetonitrile:0.1 M ammonium bicarbonate (4.5:2.5:3.0, v:v:v) and applied to a flash column of cellulose (1.5 cm × 8 cm) previously equilibrated with the same elution buffer. A total of 36 fractions (3 mL each) was collected and fractions 4–12 were combined. Solvent was removed successively by rotovap, SpeedVac, and lyophilization just to dryness. Intermittently, a few drops of 1 M ammonium hydroxide were added to keep the pH slightly basic. The recovered **3** was taken up in 2 mL 0.25 M ammonium hydroxide. Total ^{3}H activity 1.21×10^5 dpm (54.5 μCi, 190 μmol), 8% overall yield from the alcohol. ^{1}H NMR (250 MHz, D_2O/ND_4OD) δ: 1.37 (s, 3H, CH_3), 1.41 (s, 3H, CH_3), 4.09 (dd, $J_1 = J_2$ = 6.7 Hz, 2H, CH_2OPP), 5.09 (t with fine splitting J = 7.2 Hz, 1H, C*H*=C).

*(4R,8R)-[4,8-$^3H_2$,4,8-$^{14}C_2$]FPP (**1**b) (11)*

A mixture of *Z*-[4-^{3}H]-IPP (**2***b*, 41.2 μCi/μmol, 80.4 nCi/μL, 513 μL, 1.00 μmol), [4-^{14}C]IPP (47.9 μCi/μmol, 20 nCi/μL, 400 μL, 0.17 μmol), and [1-^{3}H]DMAPP (**3**, 0.29 nCi/μmol, 12.9 nmol/μL, 1.17 μmol) in 2.40 mL 20 mM Tris-HCl, pH 7.72, containing 10 mM $MgCl_2.6H_2O$ and 7 mM DTT, was incubated in a total volume of 3.8 mL with avian liver prenyl transferase (400 μL) that had been purified by literature methods (20) through the DE-52 step to a specific activity of 43.5 nmol min^{-1} (mg protein)$^{-1}$ (13.0 pmol min^{-1} μL^{-1}). The concentration of each substrate in the incubation mixture was 307 μM. A 20-μL aliquot of the mixture was counted for activity: ^{3}H 5.84×10^5 dpm, ^{14}C 9.55×10^4 dpm. After 2 h at 30°C, two separate 20-μL aliquots of the incubation mixture were withdrawn. One aliquot was mixed with 500 μL 1:1 v:v EtOH:6 N HCl and extracted with 1 mL hexane. The hexane layer was filtered through a Pasteur pipet column of silica gel, and the silica gel column was washed with 1 mL ether. The ether–hexane eluate (acid labile, hexane-extractable) was counted for radioactivity: ^{3}H 2.09×10^5 dpm, ^{14}C 2.97×10^4 dpm. The other aliquot was mixed with 500 μL 1:1 v:v EtOH:H_2O and extracted with 1 mL hexane. The hexane layer was filtered through a Pasteur pipet column of silica gel, and the column of silica gel was washed with 1 mL ether. The ether–hexane eluate (blank) was counted for radioactivity: ^{3}H 1.10×10^4 dpm, ^{14}C 1.63×10^3 dpm. Based on ^{14}C activity, 30% of the IPP has been turned over by the enzyme. After 2.5 h of incubation, the reaction mixture was applied to a column (20 cm × 2.5 cm) of Sephadex G-25 (100–300 μm bead size) swollen in Eluant One (see below). A total of 48 fractions (2–3 mL each) was collected, and a 10-μL aliquot of every other fraction was counted for activity. Fractions 14–36 were combined and stored at 4°C until further purification. The preparation of the various buffers for C-18 Reverse Phase HPLC (12) was as follows:

Solution A: $(n\text{-Bu})_4NHSO_4$ (6.8 g) and K_2HPO_4 (5.5 g) in nanopure water (100 mL) adjusted to pH 8.0. The solution was vacuum filtered through a Millipore HA filter.

Solution B: 10 mL solution A diluted with 490 mL nanopure water and vacuum filtered through a Millipore HA filter.

Solution C: 10 mL solution A diluted with 490 mL HPLC-grade methanol. The precipitated phosphate was removed by vacuum filtration through a Millipore FH filter. The filtrate was then diluted with 1470 mL Millipore FH-filtered methanol.

Eluant One: a mixture of solution C with solution B in a ratio of 15:85 v:v filtered by suction through a Millipore GV filter.

Eluant Two: a mixture of solution C with solution B in a ratio of 70:30 v:v filtered by suction through a Millipore FH filter.

Fractions 14–36 in Eluant One were loaded onto a Waters C-18 μ-Bondapak reverse phase HPLC column in a Z-module. The column was developed at 1.5 mL/min for 5 min using 100% Eluant One followedby a linear gradient up to 100% Eluant Two over a period of 15.4 min. The column was run with a flow rate of 1.5 mL/min using 100% Eluant Two for an additional 30 min. A total of 84 fractions of 50 drops each was collected. A 10-μL aliquot of every other fraction was counted for radioactivity. Fractions 37–43 were combined, mean retention time 28 min, corresponding to the retention time of [1-^{3}H]FPP used as a standard. Fractions 37–43 were loaded onto a column of DEAE–Sephadex previously swollen and equilibrated with 0.05 M triethylammonium bicarbonate pH 8.0 at 4°C. A linear gradient was established with 1.0 M triethylammonium bicarbonate pH 8.0. A total of 70 fractions of 250 drops each was collected. A 10-μL aliquot of every other fraction was counted for activity. Fractions 39–44 were combined, and the sample lyophilized almost to dryness at a pressure of $(7–10) \times 10^{-3}$ Torr. The residue was taken up in ca. 9 mL of 0.1 M ammonium hydroxide and lyophilized almost to dryness. Finally, the residue was taken up in ca. 5 mL 0.1 M ammonium hydroxide and lyophilized just to dryness. The sample was taken up in 1 mL 0.05 M ammonium hydroxide. **1***b*, total ^{3}H activity 9.60×10^6 dpm (9% radiochemical yield, based on [4-^{3}H]IPP (**2***b*)).

*(4S,8S)-[4,8-$^3H_2$,4,8-$^{14}C_2$]FPP (**1**a)*

A mixture of *E*-[4-^{3}H]-IPP (**2***a*, 21.9 μCi/μmol, 39.9 nCi/μL, 548 μL, 1.0 μmol), [4-^{14}C]IPP (47.9 μCi/μmol, 20 nCi/μL, 218 μL, 0.09 μmol), and [1-^{3}H]DMAPP (**3**, 0.29 nCi/μmol, 12.9 nmol/μL, 1.08 μmol) in 1.95 mL 20 mM Tris-HCl, pH 7.72, containing 10 mM $MgCl_2.6H_2O$ and 7 mM DTT, was incubated with avian liver prenyl transferase (400 μL) in a total volume of 3.20 mL at 30°C for 2.5 h. The concentration of each substrate was 339 μM. The desired product, (4*S*,8*S*)-[4,8-$^3H_2$,4,8-$^{14}C_2$]FPP (**1***a*), was separated by successive

Can. J. Chem. Downloaded from www.nrcresearchpress.com by 195.246.54.202 on 09/08/12
For personal use only.

Sephadex G-25, C-18 reverse phase HPLC, and DEAE–Sephadex anion exchange chromatography as described above for **1***b* (10% radiochemical yield, based on [4-^{3}H]IPP (**2***a*)).

*(4*R,*8*R*)-[4,8-$^3H_2$,4,8-$^{14}C_2$]Farnesyl diphenylurethane (**18**b) (17)*

An aliquot of a dilute solution of (4*R*,8*R*)-[4,8-$^3H_2$, 4,8-$^{14}C_2$]FPP (**1***b*, 6.39×10^2 dpm ^{3}H/μL, 150 μL, total ^{3}H = 9.55×10^4 dpm) was taken up in NaOAc/HOAc buffer, pH 5.5, and incubated with acid phosphatase (Sigma, 8.5 mg) at 30°C for 3.5 h. Subsequently 1 mL EtOH was added, followed by unlabeled *trans,trans*-farnesol (Aldrich, 50 mg, 225 μmol) in 2 mL hexane. The mixture was extracted, and the hexane layer was filtered through a Pasteur pipet containing anhydrous $MgSO_4$. The mixture was further extracted with 5×2 mL hexane. Each hexane extract was filtered through anhydrous $MgSO_4$. Solvent was removed via rotovap. The residue was then taken up in 2 mL hexane and a 20-μL aliquot had ^{3}H 7.57×10^2 dpm, ^{14}C 1.11×10^2 dpm, corresponding to a total ^{3}H activity of 7.57×10^4 dpm (80% radiochemical yield from **1***b*). The radioactive farnesol was dissolved in 1 mL dry pyridine and reacted with *N,N*-diphenyl carbamoyl chloride (recrystallized from hexane, 205 mg, 882 μmol). The mixture was heated on an oil bath at 104°C for 11 h. The reaction mixture was cooled to room temperature and 1 mL water was added, followed by extraction with 5×2 mL ether. The ether extracts were washed with three portions of saturated $CuSO_4.5H_2O$ to remove the pyridine, and the $CuSO_4$ layer was back-extracted with ether. The combined ether extracts were washed with brine and dried over anhydrous $MgSO_4$. Solvent was removed via rotovap. The residue was purified by flash chromatography on silica gel (5 g, 98:2 v:v hexane:ethyl acetate) to give **18***b* as a white solid (74 mg, 178 μmol) in 80% yield. ^{1}H NMR (250 MHz, $CDCl_3$) δ: 1.59 (s, 6H, $CH_3 \times 2$), 1.67 (s, 6H, $CH_3 \times 2$), 1.93–2.10 (m, 8H, CH_2, at C4, C5, C8, and C9), 4.69 (d, J = 6.8 Hz, 2H, CH_2O), 5.08 (bt, J = 6.7 Hz, 2H, C*H*=C, at C6 and C10), 5.33 (bt, J = 6.9 Hz, 1H, C*H*=C at C2), 7.15–7.35 (m, 10H, Ar*H*). **18***b* was recrystallized 4 times from methanol to constant specific activity, isotope ratio, and mp. ^{3}H/^{14}C 6.95 ± 0.10, mp 60.5–61.0°C (lit. (17) mp 61–62°C), 174 ± 0.4 pCi ^{3}H/μmol and 25.2 ± 0.5 pCi ^{14}C/μmol. From the isotope ratio and the specific activity of the diphenylurethane, the ^{3}H specific activity of *Z*-[4-^{3}H, 4-^{14}C]IPP (**2***b*) was calculated to be 36.7 μCi/μmol, and the ^{3}H specific activity of (4*R*,8*R*)-[4,8-$^3H_2$, 4,8-$^{14}C_2$]FPP (**1***b*) was calculated to be 73.3 μCi/μmol.

*(4*S*,8*S*)-[4,8-$^3H_2$, 4,8-$^{14}C_2$]Farnesyl diphenylurethane (**18**a) (17)*

An aliquot of a solution of (4*S*,8*S*)-[4,8-$^3H_2$, 4,8-$^{14}C_2$]FPP (**1***a*) was converted to the corresponding (4*S*,8*S*)-[4,8-$^3H_2$, 4,8-$^{14}C_2$]farnesyl diphenylurethane (**18***a*) as described above for **18***b*. The diphenylurethane was recrystallized 4 times from methanol to constant specific activity, isotope ratio, and mp. ^{3}H/^{14}C 6.02 ± 0.01, 104 ± 1 pCi ^{3}H/μmol, 17.6 ± 0.5 pCi ^{14}C/μmol, mp 60.5–61.5°C (lit. (17) mp 61–62°C). Based on the isotope ratio and the specific activity of the diphenylurethane, the ^{3}H specific activity of *E*-[4-^{3}H, 4-^{14}C]IPP (**2***a*) was calculated to be 20.4 μCi/μmol, and the ^{3}H specific activity of (4*S*,8*S*)-[4,8-$^3H_2$, 4,8-$^{14}C_2$]FPP (**1***a*)was calculated to be 40.7 μCi/μmol.

Isolation of pentalenene synthase from Streptomyces *UC5319 (5, 9, 10)*

A vegetative medium consisting of Pharmamedia (2.5 g) and Bactodextrose (2.5 g) in 100 mL nanopure water, pH adjusted to 7.2, in a 500-mL flask was inoculated with spores of *Streptomyces* UC5319 and the culture incubated at 26°C at 300 rpm for 1 day and at 28°C at 300 rpm for an additional 1.5 days. A 40-mL portion of this 2.5-day-old vegetative culture was used to inoculate a production culture containing NaCl (8 g), $CaCO_3$ (5 g), Casein (acid type) (16.68 g), Bactodextrose (13.32 g), molasses (10 g), and Dextrin (corn type 3) (80 g) in 4 L nanopure water, pH adjusted to 7.2, in a 8-L cylindrical flask. The culture was shaken at 30 cycles/min at 32°C with continuous aeration (10 psi) for 2.5 days, then aeration was discontinued and the culture shaken at 30 cycles/min at 32°C for an additional 24 h. The contents of the flask were centrifuged (GS 3 rotor, 7500 rpm, 10 100 × *g*) at 4°C for 20 min and the mycelial pellet was suspended in 1.0 M KCl and recentrifuged at 10 100 × *g* at 4°C. The supernatant was decanted from the mycelial pellet. The above procedure was repeated successively with 0.8 M NaCl, nanopure water, and breaking buffer. The breaking buffer consisted of 50 mM K_2HPO_4, 10% glycerol (by volume), 1 mM EDTA – Na_2 in nanopure water. This solution was degassed in vacuo with vigorous stirring for 45 min, then chilled to 4°C, the pH adjusted to 7.2, and β-mercaptoethanol was added to a final concentration of 5 mM. The mycelial pellet was resuspended in 200 mL of breaking buffer, and phenylmethylsulfonyl fluoride (PMSF) (3.5 mg PMSF/1 mL acetone, 5 μL, final concentration 0.5 μM) was added. The resulting cell suspension was poured into a 350mL polycarbonate chamber containing a 100-ML volume of glass beads (0.5 mm diameter). Breaking buffer was added to barely cover the surface of the beads and air bubbles were removed with a glass stirring rod before the suspension was poured. The polycarbonate chamber was cooled with an ice-water jacket, and the cells were broken in a Biospec bead beater under a 15 s on/15 s off cycle for 6 min. The beads and the cellular debris were removed by centrifugation (GS 3 rotor, 7500 rpm, 10 100 × *g*) at 4°C for 20 min. The supernatant was decanted into a glass jar and stored at 4°C. Pentalenene synthase activity was assayed with [1-^{3}H]FPP (8.0 μM, 5.0×10^5 dpm/10 μL, 56.3 μCi/μmol, 10 μL, 4.0 nmol), in 480 μL 20 mM Tris buffer, pH 8.2, containing 10 μL of the cell-free extract. The mixture was incubated at 30°C for 10 min, then extracted with 1.5 mL hexane. The hexane extract was filtered through a Pasteur pipet of silica gel and the silica gel was washed with an additional 1.5 mL hexane. The hexane eluate was counted for radioactivity: ^{3}H 6.94×10^3 dpm corresponding to pentalenene synthase activity in crude cell-free extracts of 5.5 nmol/mL cell-free extract per 10 min.

*Preparative-scale cyclization of (4*R,*8*R*)-[4,8-$^3H_2$, 4,8$^{14}C_2$]FPP (**1**b) to pentalenene (**4**b)*

A mixture of (4*R*,8*R*)-[4,8-$^3H_2$, 4,8-$^{14}C_2$]FPP (**1***b* 73.3 μCi ^{3}H/μmol, 9.59×10^4 dpm ^{3}H/10 μL, 700 μL, 41.2 nmol, final concentration 5.9 μM), Tris pH 8.2 (4.90 mL), and cell-free extract (1.40 mL), was incubated at 30°C for 2 h. The incubation was quenched after 2 h by addition of 3 mL ethanol along with 99 mg synthetic (±)-pentalenene in 10 mL of pentane. The mixture was extracted and the pentane layer was filtered through silica gel. The aqueous phase was further extracted with 2×10 mL pentane and each pentane extract was passed through the silica gel column. Counting of an aliquot indicated a total ^{3}H activity of 2.59×10^6 dpm and ^{14}C activity of 4.10×10^5 dpm (39% radiochemical yield). The solution was concentrated to ca. 2 mL by rotovap and stored at −10°C until further use.

*Enzymatic cyclization of (4*S,*8*S*)-[4,8-$^3H_2$, 4,8-$^{14}C_2$]FPP (**1**a) to pentalenene (**4**a)*

A mixture of (4*S*,8*S*)-[4,8-$^3H_2$, 4,8-$^{14}C_2$]FPP (**1***a*, 40.7 μCi ^{3}H/μmol, 3.29×10^4 dpm ^{3}H/10 μL, 1.20 mL, 43.7 nmol, final concentration 7.3 μM), Tris pH 8.2 (3.6 mL), and cell-free extract of *Streptomyces* UC5319 (1.20 mL) was incubated at 30°C for 2 h. After addition of carrier (±)-pentalenene (49 mg), the cyclization product was isolated as described above: total ^{14}C activity 2.49×10^5 dpm (39% radiochemical yield). The pentane extracts were concentrated to ca. 2 mL by rotovap and stored at −10°C until further use.

*6,7-Dihydroxypentalenane (**19**b) and (**20**b) (10)*

A 1.50-mL portion of a solution of pentalene (**4***b*) (74 mg, 363 μmol) derived from (4*R*,8*R*)-[4,8-$^3H_2$, 4,8-$^{14}C_2$]FPP (**1***b*) was converted to the corresponding mixture of diastereomeric *cis*-6,7-diols **19***b* and **20***b* as previously described (10). The resulting diastereomers were separated by fractional recrystallization from CH_2Cl_2–hexane and each diastereomer was recrystallized to constant activity (**19***b*, ^{3}H $(3.85 \pm 0.02) \times 10^3$ pCi/μmol, ^{14}C $(5.80 \pm 0.06) \times 10^2$ pCi/μmol; **20***b*, ^{3}H $(3.74 \pm 0.18) \times 10^3$ pCi/μmol, ^{14}C $(5.69 \pm 0.25) \times 10^2$ pCi/μmol), and isotope ratio (Table 1) (**19***b* mp 147–148°C (lit. (9) mp 145–146°C); **20***b* mp 75–76.5°C (lit. (9, 10) mp 74.5–75°C)).

*Conversion of pentalenene derived from (4*R,8R*)-[4,8-$^3H_2$, 4,8-$^{14}C_2$]-FPP (**1**b) to 7-hydroxypentalenane (**22**b) (9, 10)*

A 500-μL aliquot of a pentane solution of pentalenene (25 mg, 120 μmol) derived from **1***b* was converted to 7-hydroxypentalenane (**22***b*) in 64.0% yield as previously described (9, 10).

*7-Ketopentalenane (**21**b) (9, 10)*

Oxidation of **22***b* with PCC as previously described (10) gave the corresponding ketone **21***b*. $^3H/^{14}C$ 3.46 ± 0.11, ^3H (1.92 ± 0.02) × 10^3 pCi/μmol, ^{14}C (5.55 ± 0.09) × 10^2 pCi/μmol (Table 1).

*6,7-Dihydroxypentalenanes (**19**a and **20**a)*

19*a* and **20***a* were prepared from pentalenene (**4***a*) derived from (4*S*,8*S*)-[4,8-$^3H_2$, 4,8-$^{14}C_2$]FPP (**1***a*) by procedures identical to those described above. The individual diastereomers were separated by fractional recrystallization and the β diastereomer (**19***a*) was recrystallized to constant activity (^3H (2.84 ± 0.09) × 10^3 pCi/μmol, ^{14}C (8.99 ± 0.34) × 10^2 pCi/μmol) and isotope ratio (Table 1); mp 147–148°C (9).

*Conversion of pentalenene derived from (4*S,8S*)-[4,8-$^3H_2$, 4,8-$^{14}C_2$]-FPP (**1**a) to 7-hydroxypentalenane (**22**a)*

The conversion of pentalenene (**4***a*) (10 mg, 49 μmol), derived from **1***a*, to **22***a* was carried out as described above.

*Preparation of 7-ketopentalenane (**21**a)*

21*a* was prepared from the corresponding alcohol **22***a* as described above. ^3H (2.49 ± 0.02) × 10^3 pCi/μmol, ^{14}C (8.31 ± 0.07) × 10^2 pCi/μmol (Table 1).

Acknowledgments

This work was supported by a grant from the National Institutes of Health, GM22172. We would like to thank Dr. John S. Oliver for provision of the sample of partially purified avian prenyl transferase.

1. J.W. Cornforth. Angew. Chem. **7**, 903 (1968).
2. D.E. Cane. Ciba Found. Symp. **171**, Secondary Metabolites: Their Function and Evolution. Ciba Foundation, London. 1992.
3. J.W. Cornforth, R.H. Cornforth, C. Donninger, and G. Popjak. Proc. R. Soc. Lond. B, **163**, 492 (1966); J.W. Cornforth, R.H. Cornforth, G. Popjak, and L. Yengoyan. J. Biol. Chem. **241**, 3970 (1966).
4. (*a*) J.W. Cornforth, K. Clifford, R. Mallaby, and G.T. Phillips. Proc. R. Soc. Lond. B, **182**, 277 (1972); (*b*) C.D. Poulter and H.C. Rilling. *In* Biosynthesis of isoprenoid compounds. Vol. 1. *Edited by* J.W. Porter and S.L. Spurgeon. Wiley, New York. 1981. pp. 161–224.
5. D.E. Cane, C. Abell, R. Lattman, C.T. Kane, B.R. Hubbard, and P.H.M. Harrison. J. Am. Chem. Soc. **110**, 4081 (1988); D.E. Cane, J.S. Oliver, P.H.M. Harrison, C. Abell, B.R. Hubbard, C.T. Kane, and R. Lattman. J. Am. Chem. Soc. **112**, 4513 (1990).
6. K.H. Overton. Chem. Soc. Rev. **8**, 447 (1979).
7. (*a*) K. Fukui. Tetrahedron Lett. 2427 (1965); K. Fukui and H. Fujimoto. Bull. Chem. Soc. Jpn. **39**, 2116 (1966); (*b*) N.T. Ahn. Chem. Commun. 1089 (1968); (*c*) S.D. Kahn, C.F. Pau, A.R. Chamberlin, and W.J. Hehre. J. Am. Chem. Soc. **109**, 650 (1987).
8. (*a*) V.G. Matassa, P.R. Jenkins, A. Kümin, L. Damm, J. Schreiber, D. Felix, E. Zass, and A. Eschenmoser. Isr. J. Chem. **29**, 321 (1989); (*b*) M.J.C. Buckle, I. Fleming, and S. Gil. Tetrahedron Lett. **33**, 4479 (1992); (*c*) T. Hayashi, M. Konishi, H. Ito, and M. Kumada. J. Am. Chem. Soc. **104**, 4962 (1982); J. Am. Chem. Soc. **104**, 4963 (1982); (*d*) H.-J. Wetter and P. Scherrer. Helv. Chim. Acta, **66**, 118 (1983).
9. D.E. Cane and C. Pargellis. Arch. Biochem. Biophys. **254**, 421 (1987); D.E. Cane and A.M. Tillman. J. Am. Chem. Soc. **105**, 122 (1983).
10. D.E. Cane, C. Abell, and A.M. Tillman. Bioorg. Chem. **12**, 312 (1984).
11. D.E. Cane, C. Abell, P.H.M. Harrison, B.R. Hubbard, C.T. Kane, R. Lattman, J.S. Oliver, and S.W. Weiner. Phil. Trans. R. Soc. B, **332**, 123 (1991).
12. M. Ito, M. Kobayashi, T. Koyama, and K. Ogura. Biochemistry, **26**, 4745 (1987).
13. V.J. Davisson, A.B. Woodside, T.R. Neal, K.E. Stremler, M. Muehlbacher, and C.D. Poulter.J. Org. Chem. **51**, 4768 (1986); V.J. Davisson, T.M. Zabriskie, and C.D. Poulter. Bioorg. Chem. **14**, 46 (1986).
14. R.M. Magid, O.S. Fruchey, W.L. Johnson, and T.G. Allen. J. Org. Chem. **44**, 359 (1979).
15. F.M. Laskovics, J.M. Krafcik, and C.D. Poulter. J. Biol. Chem. **254**, 9458 (1979); F.M. Laskovics and C.D. Poulter. Biochemistry, **20**, 1893 (1981).
16. P. Beyer, K. Kreuz, and H. Kleinig. Methods Enzymol. **111**, 248 (1985).
17. R. Bates, D.M. Gale, and B.J. Gruner. J. Org. Chem. **28**, 1086 (1962).
18. S. Misumi, T. Ohtsuka, Y. Ohfune, K. Sugita, H. Shirahama, and T. Matsumoto. Tetrahedron Lett. 31 (1979); Y. Ohfune, H. Shirahama, and T. Matsumoto. Tetrahedron Lett. 2869 (1976).
19. D.E. Cane, J.-K. Sohng, C.R. Lamberson, S.M. Rudnicki, Z. Wu, M.D. Lloyd, J.S. Oliver, and B.R. Hubbard. Biochemistry. In press.
20. B.C. Reed and H.C. Rilling. Biochemistry, **14**, 50 (1975).

Can. J. Chem. Downloaded from www.nrcresearchpress.com by 195.246.54.202 on 09/08/12
For personal use only.

Macleanine, a unique type of dinitrogenous Lycopodium alkaloid[1]

WILLIAM A. AYER[2] AND YU-TING MA
Chemistry Department, University of Alberta, Edmonton, AB T6G 2G2, Canada

JIA-SEN LIU AND MEI-FEN HUANG
Shanghai Institute of Materia Medica, Academia Sinica, 319 Yueyang Road, Shanghai 200031, China

AND

L. WAYNE SCHULTZ AND JON CLARDY
Chemistry Department, Baker Laboratory, Cornell University, Ithaca, NY 14853-1301, U.S.A.

Received May 20, 1993

This paper is dedicated to Professor David B. MacLean

WILLIAM A. AYER, YU-TING MA, JIA-SEN LIU, MEI-FEN HUANG, L. WAYNE SCHULTZ, and JON CLARDY. Can. J. Chem. **72**, 128 (1994).

The structure of macleanine, a unique type of Lycopodium alkaloid, was deduced from its spectroscopic (especially ^1H and ^{13}C nuclear magnetic resonance) properties and from biogenetic considerations. The structure was verified by an X-ray crystallographic study of the hydroperchlorate.

WILLIAM A. AYER, YU-TING MA, JIA-SEN LIU, MEI-FEN HUANG, L. WAYNE SCHULTZ et JON CLARDY. Can. J. Chem. **72**, 128 (1994).

On a déduit la structrure de la macleanine, un type unique d'alcaloïde du *Lycopodium*, en se basant sur ses propriétés spectroscopiques (spécialement la résonance magnétique nucléaire du ^1H et du ^{13}C) et sur des considérations biogénétiques. On a vérifié la structure par une étude de diffraction des rayons X sur son perchlorate.

[Traduit par la rédaction]

Introduction

The discovery that the dinitrogenous Lycopodium alkaloid huperzine A (**1**) (1) is a potent acetylcholinesterase inhibitor (2) has stimulated renewed interest in this group of alkaloids (3). Huperzine A (**1**) is isolated from the Chinese folk medicinal plant *Huperzia serrata* (= *Lycopodium serrata*) (1) and has been shown to be identical with the alkaloid selagine, which had previously been isolated from *L. selago* and incorrectly assigned structure **2** (4, 5). Huperzine A is reported to increase efficiency for learning and memory in animals (1) and to show promise in the treatment of Alzheimer's disease and myasthenia gravis (6–8). Repeated chromatography of the mother liquors from a large-scale isolation of huperzine A (50 kg of *H. serrata*) (9) led to the isolation of a new alkaloid (17 mg) $C_{16}H_{26}N_2$ (**3**), which represents a unique structural type among the Lycopodium alkaloids.[3] We suggest the name macleanine for this alkaloid, in honor of D.B. MacLean, a pioneer in the field of Lycopodium alkaloids (10).

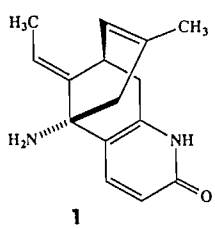

1

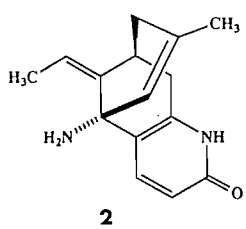

2

[1]Presented in part at the Symposium on Natural Products Chemistry, 74th Canadian Chemical Conference, Hamilton, Ontario, June 1991.
[2]Author to whom correspondance may be addressed.
[3]For a summary of the known structural types see refs. 3 and 9.

Results and discussion

The molecular formula $C_{16}H_{26}N_2$ for macleanine was established by high-resolution electron impact mass spectrometry (hreims) and confirmed by chemical ionization mass spectrometry (cims). The hreims shows the molecular ion as the base peak and, aside from the $M^+ - 15$ peak, the fragmentation pattern is quite different from that of previously reported Lycopodium alkaloids, many of which have very characteristic fragmentation patterns (11). Since the ^{13}C nmr spectrum and the ir spectrum of macleanine show no evidence for the presence of double bonds, the molecule must be pentacyclic. The ir spectrum does show NH absorption (3260 cm^{-1}), although the compound does not react with acetic anhydride–pyridine at room temperature. Since the ^{13}C nmr gives evidence for 25 carbon-bound hydrogens, and the ^1H nmr shows a single exchangeable hydrogen, one nitrogen is tertiary and the other is secondary. The lowest field signal in the ^{13}C nmr, a singlet at δ 84.9, suggests that one carbon in the molecule is attached to both nitrogens.

^1H–^1H COSY experiments indicate the presence of three isolated spin systems, one representing the hydrogens on carbons 14, 15, 16, 8, 7, and 6 and initiated at the easily recognizable signal for the C-16 methyl hydrogens, another representing the C-9, C-10, and C-11 methylenes originating at the C-9 H's at δ 3.40 and 2.95, and a third originating at the C-1 H's (δ 4.30 and 2.75) and extending along C-2, C-3, and C4. The signal for H-5 appears as a broad singlet at δ 3.20, which shows correlation with H-4 (δ 1.80) and H-6 (δ 1.20 and 1.85), and thus connects two of the spin systems. The dihedral angles between H-5 and the hydrogens on C-4 and C-6 in **3** are approximately 90°. An HMQC experiment established that the proton at δ 3.20 is located on a nitrogen-bearing carbon (δ 58.9). The ^1H and ^{13}C nmr spectra and relevant COSY, HMQC, and HMBC data are summarized in Table 1.

Can. J. Chem. Downloaded from www.nrcresearchpress.com by 195.246.54.202 on 09/08/12
For personal use only.

TABLE 1. The nmr spectral data for macleanine (**3**)

Position	δ_C ($CDCl_3$, 90 MHz)	δ_H ($CDCl_3$, 360 MHz)[a]	$2D^1H^{-1}H$ COSY correlations (400 MHz)	HMQC correlations (500/125 MHz)	HMBC correlations (500/125 MHz)
1	53.2, t	H_β 4.30, ddd (19, 12, 6) H_α 2.75, m	2.75, 2.55, 1.75 4.30, 2.55, 1.75	4.30, 2.75	2.10, 1.90
2	22.2, t	H_β 2.55, m H_α 1.75, m*	4.30, 2.75, 1.75, 1.90, 2.10 2.55, 2.75, 4.30, 2.10, 1.90	2.55, 1.75	4.30, 2.10
3	25.8, t	H_β 2.10, m* H_α 1.90, m*	1.90, 1.75, 2.55 2.10, 1.75, 2.55, 1.80	2.10, 1.90	4.30
4	52.7, d	H 1.80, m*	3.20, 1.90	1.80	1.20, 1.90, 1.95, 2.10
5	58.9, d	H 3.20, brs	1.80, 1.20, 1.85	3.20	
6	37.1, t	H_β 1.20, dd (12, 3) H_α 1.85, m*	3.20, 1.85, 1.90 1.20, 3.20, 1.90	1.20, 1.85	
7	41.5, d	H 1.90, m*	1.20, 1.10, 1.45, 1.85	1.90	3.20, 1.85, 1.95
8	32.1, t	H_{exo} 1.10, ddd (13, 13, 3) H_{endo} 1.45, dddd (13, 3, 2, 2)	1.45, 1.75, 1.90 1.10, 1.90, 1.75, 2.60	1.10, 1.45	1.20
9	50.3, t	H_β 3.40, ddd (14, 14, 4, 4) H_α 2.95, ddd (14, 2, 2)	2.95, 2.10, 1.80 3.40, 2.10, 1.80	3.40, 2.95	4.30
10	17.8, t	H_β 2.10, m* H_α 1.80, m*	1.80, 1.95, 2.95, 3.40 2.10, 1.95, 3.40, 2.95	2.10, 1.80	
11	22.3, t	H_β 1.95, m* H_α 1.95, m*	1.80, 2.10 1.80, 2.10	1.95	
12	47.9, s				3.20, 1.95, 1.85
13	84.9, s				3.20, 1.75, 1.80, 2.60
14	35.9, t	H_{endo} 2.60, ddd (13, 2, 2) H_{exo} 1.70, dd (13, 6)	1.70, 1.45, 1.75 2.60, 1.75	2.60, 1.70	
15	23.2, d	H_{endo} 1.75, m*	0.99, 2.60, 1.70, 1.10, 1.45	1.75	
16	21.2, q	H 0.99, d (6)	1.75	0.99	
NH		H 10.95, brs			

[a]An asterisk denotes overlapping signals.

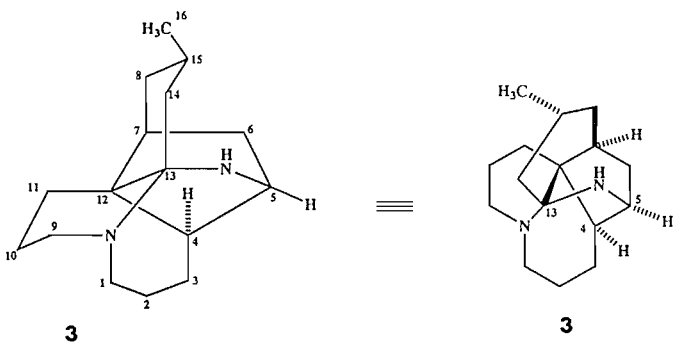

At this stage, biogenetic reasoning suggested structure **3** as a possibility for macleanine. All Lycopodium alkaloids known to date possess functionality at C-5 (3, 10, 11). Fawcettimine (**4**) (Scheme 1) readily forms a transannular carbinolamine (**4***a*) (3, 12). We reasoned that if the C-5 carbonyl group of fawcettimine underwent reductive amination to **5**, and this formed the internal immonium ion **6** (the *trans* C—N double bond is in an eight-membered ring), transannular cyclization would lead to structure **3**. An HMBC experiment demonstrated that H-5 is three-bond coupled to the carbon (C-13) bearing the two nitrogens and another quaternary carbon (C-12) as well as to C-7 (see Table 1). It is not coupled to either C-1 or C-9, excluding C-3 as a possible location of the second nitrogen.

To unambiguously establish structure **3**, a crystalline perchlorate was prepared. Macleanine itself gives twinned crystals. A computer-generated perspective drawing of the final X-ray model of macleanine (**3**) is shown in Fig. 1. The absolute stere-

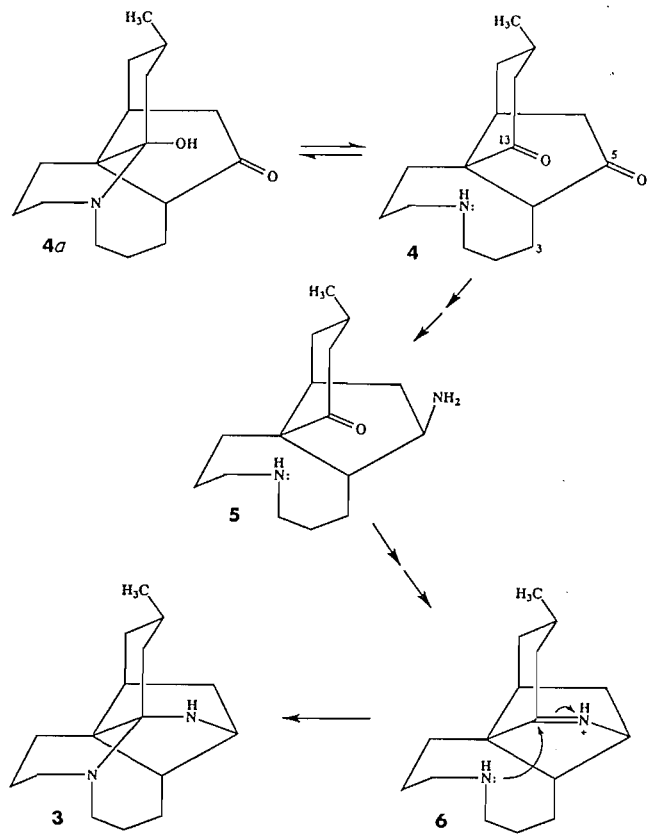

SCHEME 1

Can. J. Chem. Downloaded from www.nrcresearchpress.com by 195.246.54.202 on 09/08/12
For personal use only.

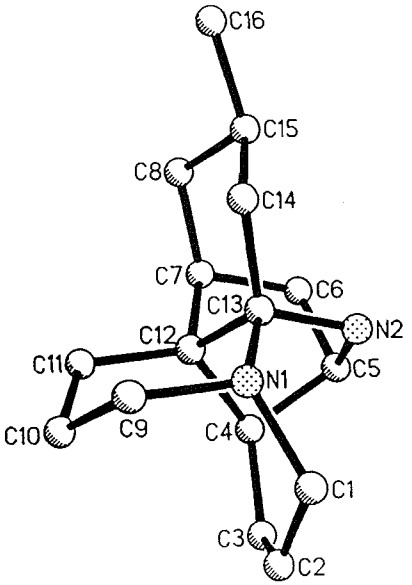

FIG. 1. A computer-generated perspective drawing of one of the independent molecules of macleanine (**3**) hydroperchlorate (anion omitted). The absolute configuration was determined from the anomalous scattering of the chlorine. Hydrogens are omitted for clarity.

ochemistry was determined by the absolute structure method (SHELXTL PLUS implementation) using the anomalous scattering from the chlorine atoms. The crystals contained two crystallographically independent molecules, but the polycyclic arrays of both had the same conformation. The six-membered carbocyclic ring and the piperidine ring containing N-1 have chair conformations, and the piperidine ring containing N-2 is in a boat conformation. The five-membered ring is in an envelope conformation with C-4 as the flap atom. The seven-membered ring is in an approximately pseudochair conformation. The X-ray structure unequivocally confirms structure **3** and shows that the absolute configuration fits the "normal" Lycopodium alkaloid pattern.

The possibility that macleanine (**3**) is an artefact of the isolation procedure seems remote since formation of intermediate **5** from a fawcettimine-type precursor would require a reductive process. Addition of ammonia to a C-13 carbonyl followed by displacement of a leaving group from C-5 (reduced), although not ruled out, seems unlikely.

The pentacyclic alkaloid **3** represents a new structural type among the Lycopodium alkaloids.

Experimental

Isolation of macleanine (3)

The total crude alkaloids from 50 kg of *Huperzia serrata* (= *Lycopodium serratum*) where isolated as previously described (9) and the pyridone alkaloid fraction was obtained by extraction with 0.5% aqueous NaOH. This fraction was chromatographed several times over silica gel (eluent 1–4% methanol in $CHCl_3$). The fractions that followed huperzine A (**1**) were further chromatographed over silica gel, eluting with acetone, then with acetone–methanol (40:1, 20:1, 10:1). The fraction eluted with acetone–methanol (10:1) provided macleanine (**3**, 17 mg), mp ~300°C (dec.), $[\alpha]_D$ + 12.5 (*c* 0.24, $CHCl_3$); ir ν_{max}: 3240 cm^{-1}; ^1H nmr, see Table 1; ^{13}C nmr, see Table 1; hreims, *m/z* calcd. for $C_{16}H_{26}N_2$ (M^+): 246.2095; found; 246.2098 (100), 231 (7), 218 (37), 204 (24), 203 (17), 190 (10), 176 (26), 174 (23), 160 (14), 148 (14), 134 (17), 122 (16), 70 (42); cims (reagent gas ammonia): 247 ($M + H^+$, 100), 493 ($2M + H^+$).

Macleanine hydroperchlorate

Macleanine (**3**, 5 mg) in methanol was treated dropwise with methanolic perchloric acid (prepared by diluting 70% perchloric acid (1 mL) with methanol (9 mL)) to pH ~5.5. The crystalline perchlorate obtained (5 mg) was recrystallized from methanol–ether to give colorless crystals, mp 195–197°C. It crystallized as flat plates in the monoclinic space group $P2_1$ with $a = 8.244(1)$, $b = 15.226(2)$, $c = 3.853(2)$ Å and $\beta = 96.07(1)°$. The asymmetric unit contained two molecules of the perchlorate salt with empirical formula $C_{16}H_{27}ClN_2O_4$. A hemisphere of data — a Friedel redundant data set — for all reflections with $2\theta \leq 116°$ was collected using CuKα radiation (1.54178 Å). Of the 4706 independent reflections measured, 3630 (77%) were judged observed ($|F_o| \geq 4\sigma(F_o)$). The data set contains Friedel pairs. The data were corrected for absorption using a semi-empirical absorption correction. The structure was solved uneventfully using direct methods and refined using full-matrix least-squares techniques. The final model had anisotropic nonhydrogen atoms and isotropic riding hydrogens, and refinement converged to a standard crystallographic discrepancy index of 6.63% for the observed data. The absolute configuration was determined by an absolute structure refinement, and that refinement converged to an index of 1.03 ± 0.05 for the absolute stereochemistry shown. Refinement with η fixed at 1.0 of the structure and its enantiomer gave *R*-values of 0.085 and 0.095, respectively, a statistically significant difference (13). Archival X-ray data have been deposited with the Cambridge Crystallographic Data Centre.[4]

Acknowledgements

We thank the Natural Sciences and Engineering Research Council for financial support. We also thank T.T. Nakashima for his help with the nmr measurements and Drs. H. Orszanska and L. Trifonov for their assistance and interest. The Cornell group acknowledges support from the National Institutes of Health (J.C.) and an NIH Biotechnology Training Grant (L.W.S.). One of us (W.A.A.) thanks David MacLean for his friendship and his common interest in the Lycopodium alkaloids over the past thirty-some years.

1. J-S. Liu, Y-L. Zhu, C-M. Yu, Y-Z. Zhou, Y-Y. Han, F-W. Wu, and B-F. Qui. Can. J. Chem. **64**, 837 (1986).
2. X-C. Tang, Y-F. Han, X-P. Chen, and X-D. Zhu. Acta Pharmacol. Sin. **7**, 507 (1986).
3. W.A. Ayer. Nat. Prod. Rep. **8**, 455 (1991).
4. Z. Valenta, H. Yoshimura, E.F. Rogers, M. Ternbah, and K. Wiesner. Tetrahedron Lett. No. 10, 26 (1960).
5. W.A. Ayer, L.M. Browne, H. Orszanska, Z. Valenta, and J.S. Liu. Can. J. Chem. **67**, 1538 (1989).
6. Y-C. Cheng, C-Z. Lu, Z-L. Ying, W-Y. Ni, C-L. Zhang, and G-W. Sang. New Drugs Clin. Remed. **5**, 2560 (1986).
7. R-W. Zhang, X-C. Tang, Y-Y. Han, G-W. Sang, Y-D. Zhang, Y-X. Ma, C-L. Zhang, and RM. Yang. Acta Pharmacol. Sin. **12**, 250 (1991).
8. A.P. Kozikowski, Y. Xia, R. Reddy, W. Tuckmantel, I. Hanin, and X-C. Tang. J. Org. Chem. **56**, 4636 (1991).
9. J-S. Liu, C-M. Yu, Y-Z. Zhou, Y-Y. Han, F-W. Wu, B-F. Qi, and Y-L. Zhu. Huaxue Xuebao, **44**, 1035 (1986).
10. D.B. MacLean. *In* The alkaloids. Vol. 26. *Edited by* A. Brossi. Academic Press, New York. 1985. Chap. 5.
11. D.B. MacLean. *In* The alkaloids. Vol. 10. *Edited by* R.F. Manske. Academic Press, New York. 1968. pp. 377–379.
12. C.H. Heathcock, T.A. Blumenkopf, and K.M. Smith. J. Org. Chem. **54**, 1548 (1989).
13. W.C. Hamilton. Acta Crystallogr. **18**, 502 (1965).

[4]Tables of crystal data, atomic coordinates, bond lengths and angles, anisotropic displacement coefficients, and H-atom coordinates have been deposited with the Cambridge Crystallographic Data Centre, and can be obtained on request from The Director, Cambridge Crystallographic Data Centre, University Chemical Laboratory, 12 Union Road, Cambridge, CB2 1EZ, U.K.

Can. J. Chem. Downloaded from www.nrcresearchpress.com by 195.246.54.202 on 09/08/12
For personal use only.

Biosynthesis of the indolizidine alkaloid cyclizidine: incorporation of singly and doubly labelled precursors[1]

FINIAN J. LEEPER,[2] SUSAN E. SHAW, AND PADMA SATISH (NÉE PADMANABHAN)
University Chemical Laboratory, Lensfield Road, Cambridge CB2 1EW, U.K.

Received June 10, 1993

This paper is dedicated to Professor Ian Spenser

FINIAN J. LEEPER,[2] SUSAN E. SHAW, and PADMA SATISH (NÉE PADMANABHAN). Can. J. Chem. **72**, 131 (1994).

Incorporation of $CH_3{}^{13}C^{18}O_2Na$ and $CD_3CH_2{}^{13}CO_2Na$ into the indolizidine alkaloid cyclizidine **1**, produced by *Streptomyces* species NCIB 11649, shows that the oxygen attached to C-2 is derived intact from acetate and that the cyclopropyl ring is derived from a single intact propionate unit. However, the level and stereochemistry of the incorporation of deuteriated sodium propionate indicates that it undergoes unexpected modification during incorporation into the cyclopropyl ring.

FINIAN J. LEEPER,[2] SUSAN E. SHAW et PADMA SATISH (NÉE PADMANABHAN). Can. J. Chem. **72**, 131 (1994).

L'incorporation de $CH_3{}^{13}C^{18}O_2Na$ et de $CD_3CH_2{}^{13}CO_2Na$ dans l'alcaloïde de l'indolizidine, la cyclizidine **1**, produite par du *Streptomyces* de l'espèce NCIB 11649, comporte un oxygène attaché en position C-2 qui est dérivé d'une façon intacte de l'acétate alors que le noyau cyclopropyle est dérivé d'une unité intacte de propionate. Toutefois, le degré et la stéréochimie de l'incorporation du propionate de sodium deutéré indique qu'il subit une modification inattendue au cours de son incorporation dans le noyau cyclopropyle.

[Traduit par la rédaction]

Introduction

Cyclizidine **1** is an indolizidine alkaloid produced by *Streptomyces* species NCIB 11649. Its isolation and structure determination by NMR spectroscopy and X-ray crystallography were first reported in 1982 (1). Intriguingly, a very similar indolizidine alkaloid, indolizomycin **2**, was subsequently isolated from a strain created by protoplast fusion of two different *Streptomyces* species, neither of which produced any similar compounds (2). Cyclizidine is especially unusual because, to our knowledge, a monosubstituted cyclopropyl ring has only been reported in one other pair of natural products, the monoterpenes **3** and **4** (3). The biosynthetic pathway to cyclizidine is therefore of particular interest.

We previously established that cyclizidine **1** is derived from acetate and propionate units in a polyketide fashion as shown in Scheme 1 (4). Thus incorporation of $^{13}CH_3{}^{13}CO_2Na$ labelled four pairs of carbons (C-12/C-13, C-2/C-3, C-7/C-8, and C-5/C-6) and $CH_3CH_2{}^{13}CO_2Na$ labelled three carbons (C-14, C-10, and C-8a). As expected, $CD_3CH_2CO_2Na$ labelled the two methyl groups (C-9 and C-17) and two hydrogens on C-16 of the cyclopropyl ring.[3] We describe here further labelling studies that help to define possible mechanism(s) of formation of the five- and three-membered rings of cyclizidine.

Results and discussion

Incorporation of sodium [1-^{13}C,$^{18}O_2$]acetate

One possible mechanism for the formation of the five-membered ring is nucleophilic attack by the nitrogen atom on a 2,3-epoxide, as shown in Scheme 2(*a*). This mechanism would mean that the oxygen atom attached to C-2 in cyclizidine is derived from dioxygen. Alternative mechanisms could be proposed in which this oxygen atom is derived from the acetate precursor. To test this, $CH_3{}^{13}C^{18}O_2Na$ was synthesized starting with $K^{13}CN$ (5). Reaction with methyl iodide gave $CH_3{}^{13}CN$, which was hydrolysed in situ using ^{t}BuOK/$H_2{}^{18}O$. A portion of the labelled acetate was converted into its *p*-phenylphenacyl ester for analysis by NMR and MS, which showed ca. 90% ^{13}C and 75% ^{18}O per labelled site.

The ^{13}C NMR spectrum of cyclizidine derived from $CH_3{}^{13}C^{18}O_2Na$ showed a strong (ca. 6%) ^{13}C enrichment at the expected sites (C-12, C-2, C-7, and C-5). C-12 appeared in the spectrum as a singlet while the other three carbons gave multiplets (Fig. 1): C-7 showed a singlet flanked by a low intensity doublet (J 4 Hz) due to long-range coupling to C-5 in molecules in which both carbons are labelled (peak heights indicated that approximately one third of the molecules that had ^{13}C at C-7 also had ^{13}C at C-5); C-5 showed a singlet flanked by a low-intensity doublet and an even lower intensity triplet (each J ~4 Hz), the latter due to molecules in which C-2, C-5, and C-7 are all labelled; C-2 (δ 86.1) gave a pattern of peaks that could only be interpreted as two singlets (Δδ 0.02 ppm) each flanked by doublets (J ~4 Hz) due to coupling to C-5. The separation of the two singlets is in the range expected (6) for the isotopic shift due to ^{18}O singly bonded to ^{13}C and we can conclude that they represent ^{13}C–^{16}O and ^{13}C–^{18}O at C-2. The ratio of the peaks was ca. 40:60 (after allowing for the contribution of natural abundance to the ^{13}C–^{16}O peak). As the initial sodium acetate had 75% ^{18}O per site, it is evident that there has been some loss of ^{18}O but the majority has been retained intact at C-2.

The retention of ^{18}O from [^{18}O]acetate at C-2 of cyclizidine eliminates mechanisms involving a 2,3-epoxide such as shown in Scheme 2(a). Such an epoxide would be generated by epoxidation of a 2,3-double bond and the oxygen atom would thus derive from dioxygen and not be retained intact from the acetate precursor. Indeed the 7,8-epoxide seems to have been made in this way as the lack of any shifted peak for C-7 indicates that during the biosynthesis it has lost the ^{18}O that was originally attached at this position. While this experiment does not give any direct information about the origin of the oxygen atom attached to C-1, it is clear that the 1,2-diol is not derived by attack of water on a 1,2-epoxide. Hence it is likely that this oxygen atom is introduced either by hydroxylation at C-1 or by

[1] Dedicated to Prof Ian Spenser, who introduced one of us (F.J.L.) to biosynthesis, studying quinolizidine alkaloids, and was an excellent teacher of correct biosynthetic methods. The project described here arose from a desire to continue work on similar compounds, but in order to avoid competing on the quinolizidine (6,6) or pyrrolizidine (5,5) ring systems an indolizidine (6,5) alkaloid was chosen instead.

[2] Author to whom correspondence may be addressed.

[3] We are here defining C-16 to be the cyclopropyl carbon derived from C-3 of propionate and C-15 to be derived from C-2 of propionate.

Can. J. Chem. Downloaded from www.nrcresearchpress.com by 195.246.54.202 on 09/08/12
For personal use only.

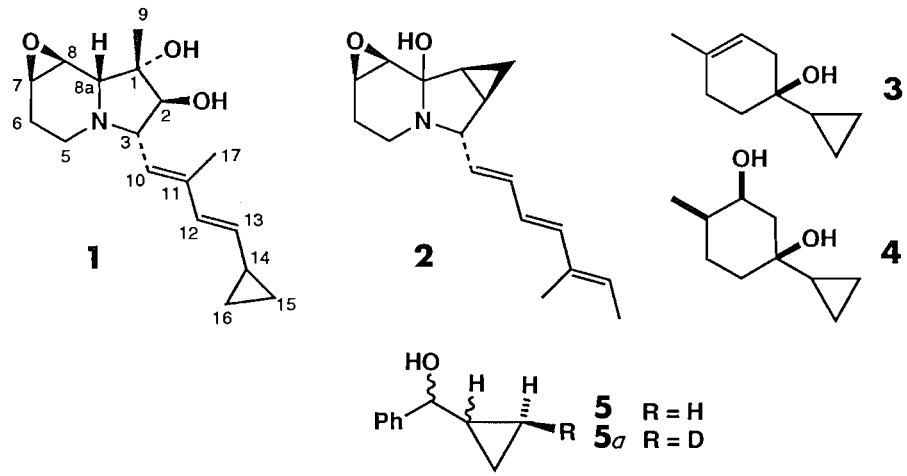

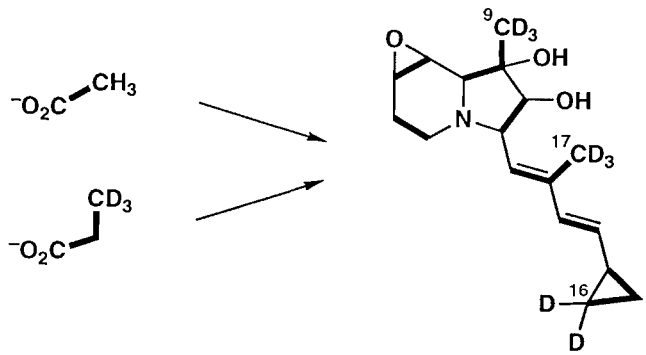

SCHEME 1. The incorporation of acetate and propionate units into cyclizidine.

epoxidation of a 1,8a double bound followed by nucleophilic attack by the nitrogen atom at C-8a, forming the six-membered ring as shown in Scheme 2(b).

Incorporation of sodium [1-^{13}C,3,3,3-$^{2}H_3$]propionate

In a previous communication (4), we reported that the ^{2}H NMR spectrum of cyclizidine derived from $CD_3CH_2CO_2Na$ shows incorporation into the two methyl groups, C-9 (δ 1.34) and C-17 (δ 1.76), and into two sites on C-16 of the cyclopropyl ring (δ 0.76 and 0.40), see Scheme 1. However, an unexpected feature of the spectrum (Fig. 2*a*) was that the deuterium incorporation per labelled site at C-16 was approximately half the level observed at each of the two methyl groups. To understand this phenomenon, it was necessary to determine whether this was due to exchange of these deuterium atoms for protium or due to a reduced level of incorporation of the whole C_3 unit. It was decided to test this by incorporation of $CD_3CH_2{}^{13}CO_2Na$; on formation of the cyclopropane ring, the deuteriated carbon should become attached to the ^{13}C atom and thus cause a detectable β-shift. The precursor was synthesized by treatment of $CH_3{}^{13}CO_2CH_2Ph$ with LDA followed by CD_3I and then hydrogenolysis of the resulting $CD_3CH_2{}^{13}CO_2CH_2Ph$.

In the ^{13}C NMR spectrum of the cyclizidine derived from this precursor three peaks were enhanced as expected. C-10 and C-8a appeared as singlets but C-14 showed a small natural abundance peak at δ 14.23 and shifted peaks 0.09 and 0.19 ppm upfield. These shifts are of the size expected (7) for isotopic shifts due to β-deuterium atoms and the peaks are therefore assigned to ^{13}C—CHD and ^{13}C—CD_2 respectively (Fig. 3). This observation of isotopic shifts proves that all three carbon atoms of the cyclopropane ring are indeed derived intact from a single propionate molecule, as had been previously assumed. The ratio of the intensities of the shifted peaks was ca. 1:6 (CHD:CD_2), indicating that little if any exchange had occurred at this site. As no significant exchange of deuterium has occurred, the low incorporation of deuterium in the cyclopropane ring must be due to low incorporation of the whole propionate unit. In confirmation of this, it was noticeable that the total area of the peaks corre-

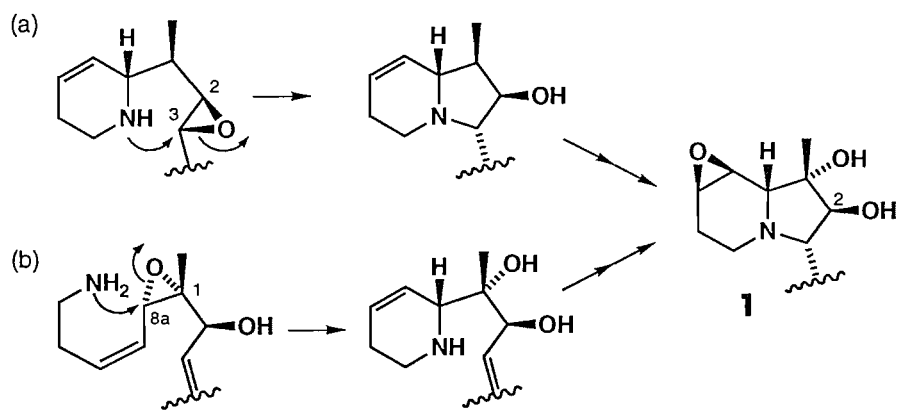

SCHEME 2. Possible mechanisms for formation of the five- and six-membered rings of cyclizidine.

Can. J. Chem. Downloaded from www.nrcresearchpress.com by 195.246.54.202 on 09/08/12
For personal use only.

Can. J. Chem. Downloaded from www.nrcresearchpress.com by 195.246.54.202 on 09/08/12
For personal use only.

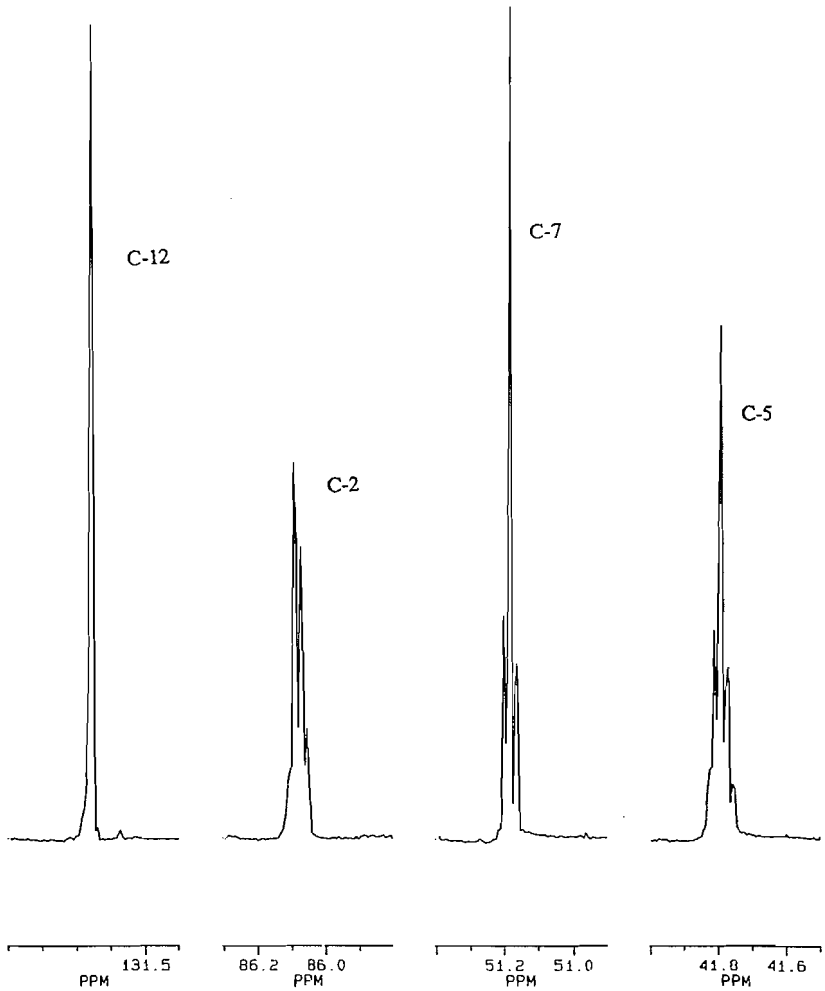

FIG. 1. Four regions, containing the enriched peaks, from the ^{13}C NMR spectrum of cyclizidine **1** derived from $CH_3{}^{13}C^{18}O_2Na$.

sponding to C-14 was about half the area of the other enriched peaks (C-10 and C-8a) whereas in the natural abundance ^{13}C spectrum all three peaks have comparable areas.

The lowered incorporation of propionate into the cyclopropyl ring appears to be due to the deuterium atoms, as undeuteriated $CH_3CH_2{}^{13}CO_2Na$ showed approximately equal incorporation into the three labelled sites of cyclizidine (4). The obvious conclusion is that there is an isotope effect for the reaction which removes the hydrogen atom from this methyl group. However, if the molecule at this stage is already committed to the biosynthesis of cyclizidine, it would be expected that the incorporation of the deuteriated precursor would only be delayed, not prevented. Therefore the final level of incorporation would not be significantly affected. If, on the other hand, the propionate unit is not already committed to the biosynthesis of cyclizidine, it would be expected that the incorporation of the deuteriated precursor into cyclizidine would be lowered as the deuteriated molecules could be diverted down a different pathway.

It was of importance to our experiments on the stereochemistry of propionate incorporation into the cyclopropyl ring that we determine whether C-3 of the propionate ends up as the pro*R* or pro*S* methylene group. In cyclizidine itself there is a very small difference in the ^{13}C chemical shifts of these two methylene groups but there is no way of telling which peak is which. In the proton NMR spectrum there is no discernible difference between the hydrogen atoms on the two adjacent carbon atoms. However, from our previous work (8) we knew that all four methylene protons are well separated in the proton NMR spectrum of phenyl cyclopropyl carbinol **5**. Furthermore these proton signals had been rigorously assigned (see Fig. 4*a*) on the basis of NOE and shift reagent results and by synthesis of a stereospecifically deuteriated form **5***a*.

Therefore a quantity of cyclizidine **1***a* derived by incorporation of $CD_3CH_2CO_2Na$ (synthesized in the same way as the corresponding ^{13}C-labelled material described above) was degraded by the sequence of reactions shown in Scheme 3 to give phenyl cyclopropyl carbinol **5***b*, initially as a racemate. This had to be resolved because if the deuterium atoms occupy the positions of H_A and H_B in one enantiomer then they will occupy the positions of H_C and H_D in the other (see structures in Fig. 4). Hence all four sites would show deuterium labelling.

The racemic alcohol was resolved by formation of the diastereoisomeric (1*S*)-camphanate esters **6**, which were separated by HPLC. Alkaline hydrolysis of the separate diastereoisomers gave back the enantiomeric alcohols (*S*)-**5***b* and (*R*)-**5***b*. The first eluted diastereoisomer had previously been assigned to the (*S*) alcohol and the second eluted one to the (*R*) alcohol on the basis of the chemical shifts of the Mosher's esters (8). This assignment has now been confirmed by an X-ray crystal structure of the latter diastereoisomer, which clearly shows its

Can. J. Chem. Downloaded from www.nrcresearchpress.com by 195.246.54.202 on 09/08/12
For personal use only.

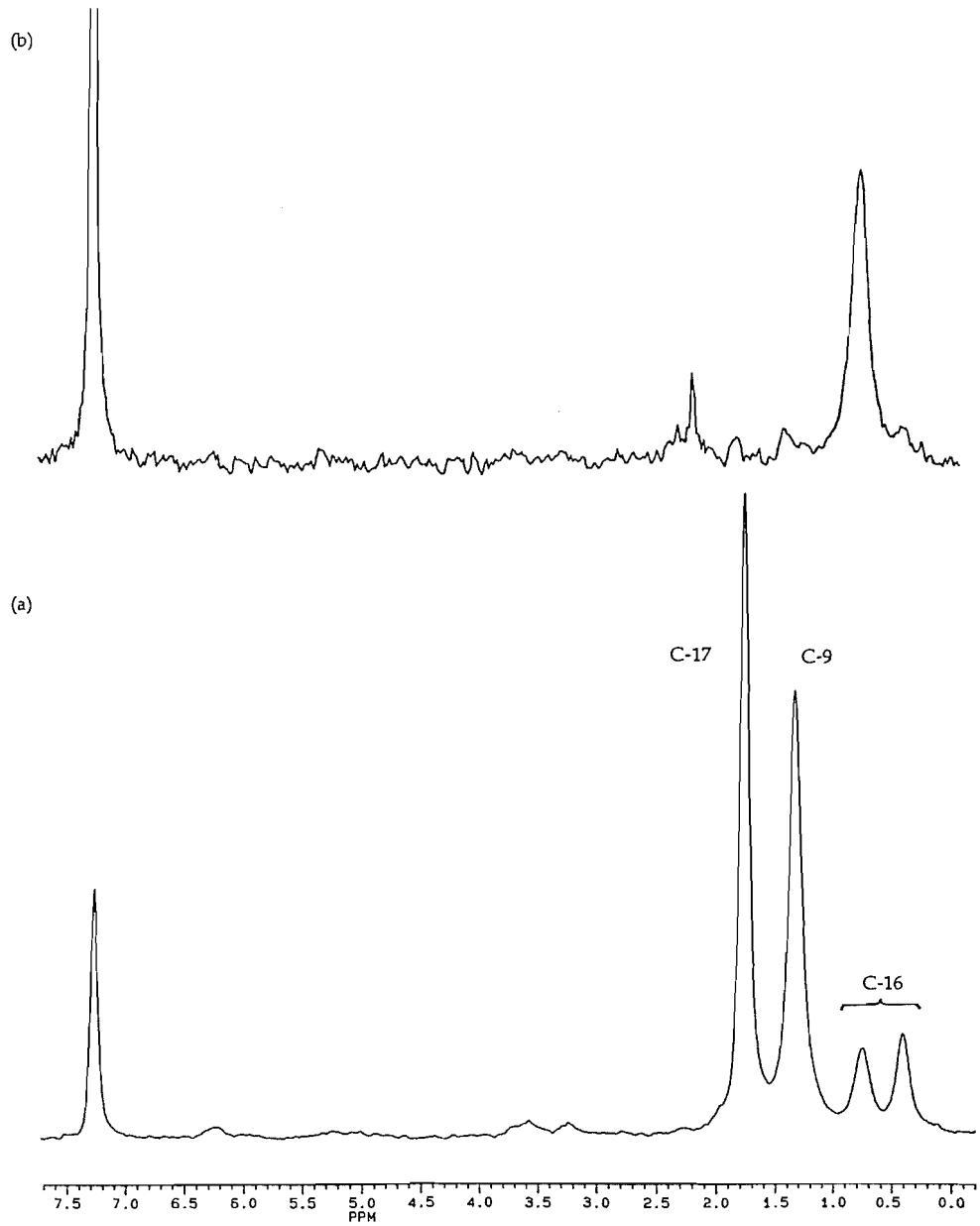

FIG. 2. ^2H NMR spectra of cyclizidine **1** derived from (*a*) $CD_3CH_2CO_2Na$ and (*b*) $CH_3CD_2CO_2Na$. The peaks at δ7.25 in both spectra are due to solvent ($CHCl_3$) and the small peak at δ 2.15 in (*b*) is due to some residual $CH_3CD_2CO_2Na$.

stereochemistry relative to that of the camphanate moiety (Fig. 5).

Partial deuterium NMR spectra of the separate enantiomers, (*S*)-**5***b* and (*R*)-**5***b*, derived from the deuteriated propionate are shown in Figs. 4*b* and 4*c*.[4] It can be seen that just two of the four methylene protons are deuteriated in each enantiomer, H_A and H_B in the (*R*) enantiomer and H_C and H_D in the (*S*) enantiomer. In each enantiomer this corresponds to the pro*S* methylene group. It is thus the pro*S* methylene on the cyclopropyl ring of cyclizidine that is C-16, i.e., derived from C-3 of propionate.

Incorporation of sodium [2-$^2H_2$]propionate

In accord with the established mechanisms of polyketide biosynthesis, it would be expected that the cyclopropyl ring of cyclizidine, being the chain-starter unit, would be derived direct from propionyl CoA, whereas the other propionate-derived units would be incorporated via methylmalonyl CoA. To test this, the incorporation of $CH_3CD_2CO_2Na$ was investigated. If the propionyl CoA is incorporated directly, one would expect retention of both deuterium atoms in the cyclopropane ring of cyclizidine. The deuteriated propionate precursor was made by exchange of the α protons of propionic acid in concentrated D_2SO_4.

Surprisingly, however, on incorporation of the $CH_3CD_2CO_2Na$ into cyclizidine, the ^2H NMR spectrum showed that deuterium was incorporated into only one of the positions on C-15 (δ 0.76) and not into the other position (δ 0.40), Fig. 2(*b*). This position was shown to be the one *cis* to the proton on C-14 by ^1H NOE experiments. As $CD_3CH_2CO_2Na$ has been shown to label the pro*S* methylene group in the cyclopropyl ring of

[4]In addition to the peaks shown in Fig. 4, a small peak was also observed at δ 1.2 for each enantiomer. This is due to deuterium in the cyclopropylmethine position, a result of biosynthetic scrambling of the label into position 14 of cyclizidine.

Can. J. Chem. Downloaded from www.nrcresearchpress.com by 195.246.54.202 on 09/08/12
For personal use only.

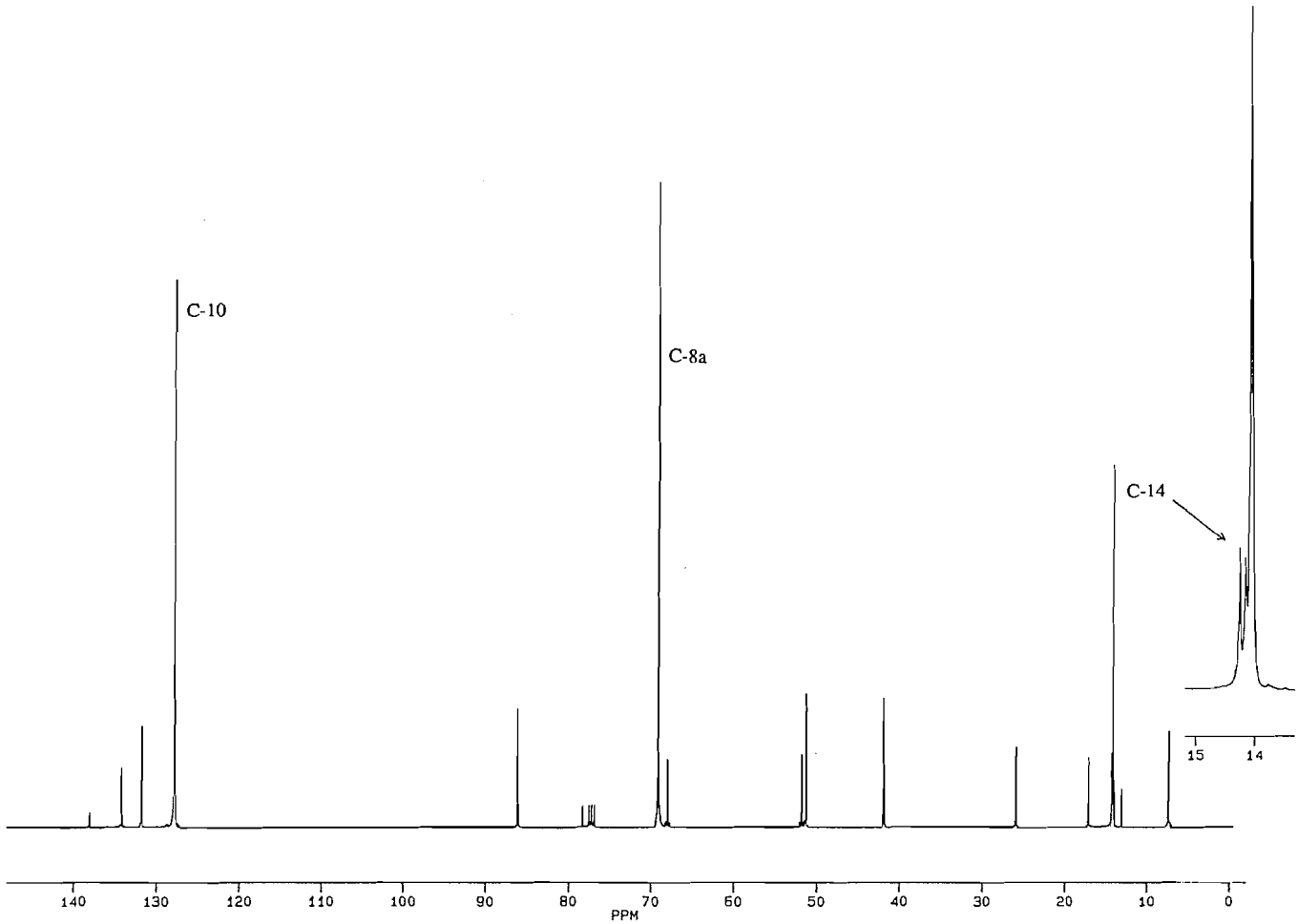

FIG. 3. ^{13}C NMR spectrum of cyclizidine **1** derived from $CD_3CH_2{}^{13}CO_2Na$.

cyclizidine, it can be assumed that $CH_3CD_2CO_2Na$ labels the pro*R* methylene, as shown in structure **1***b*, Scheme 4. Thus it can be seen that the retained deuterium atom is in the pro*R* position on this particular methylene group.

To determine which deuterium atom of the $CH_3CD_2CO_2Na$ is lost and which retained, (2*R*)- and (2*S*)-CH_3CHDCO_2Na were made by treatment of (2*S*)- and (2*R*)-2-bromopropionic acids with lithium triethylborodeuteride (9). The enantiomeric purities of the resulting monodeuteriated propionate salts were estimated at 96% *R* and 93% *S*, respectively, on the basis of the ^1H NMR spectra of their esters with methyl (*S*)-mandelate (10).

Each monodeuteriated propionate salt was mixed with sodium [1-^{14}C]propionate and fed to the organism. The samples of cyclizidine isolated from the two experiments showed comparable levels of ^{14}C (13 and 17% specific incorporation) but only (2*S*)-CH_3CHDCO_2Na showed any incorporation of deuterium by ^2H NMR spectroscopy. Again the only significant peak in the ^2H NMR spectrum was at δ 0.76. A rough estimate of the deuterium enrichment (obtained by comparing the peak areas for the enriched position and for the natural abundance ^2H signal from the solvent, $CHCl_3$) was 3%. When compared with the ^{14}C incorporation, this indicates that even the (2*S*)-[2-^2H]-propionate had exchanged ca. 80% of its deuterium during the biosynthetic process. The most unusual feature of this incorporation of deuterium, however, is that the deuterium atom in the pro*S* position of the propionate precursor ends up in the pro*R* position of its methylene group in cyclizidine, an overall inversion of configuration (see Scheme 4).

As explained above, the loss of any deuterium from C-2 of propionate was unexpected as propionyl CoA **7** was the assumed starter unit for the polyketide chain assembly. However, rapid and reversible carboxylation of the propionyl CoA **7** could occur to give (*S*)-methylmalonyl CoA **8** and this process is known (11) to result in loss of the pro*R* hydrogen atom (see Scheme 5). Reversible interconversion of (*S*)- and (*R*)-methylmalonyl CoA **9**, catalyzed by methylmalonyl CoA epimerase, results in the loss of the remaining hydrogen atom on C-2 (12) and this could then account for the observed partial loss of the pro*S* deuterium atom. These reversible enzymic reactions cannot, however, explain the observed inversion of configuration.

A biosynthetic pathway that could explain the inversion of configuration upon incorporation of (2*S*)-CH_3CHDCO_2Na into cyclizidine is outlined in Scheme 6. This scheme envisages that dehydrogenation of the propionate unit could occur at the stage of propionyl CoA (or later) with loss of the pro*R* hydrogen atom at C-2. Michael addition of HX (where X could be OH or some other leaving group) to the acrylyl unit could then occur with the hydrogen being added in the pro*S* position at C-2, thus achieving the inversion of configuration. The leaving group X could subsequently be involved in formation of the cyclopropane ring, possibly with simultaneous formation of the five-membered ring as shown in the step **10** → **11**.

Can. J. Chem. Downloaded from www.nrcresearchpress.com by 195.246.54.202 on 09/08/12
For personal use only.

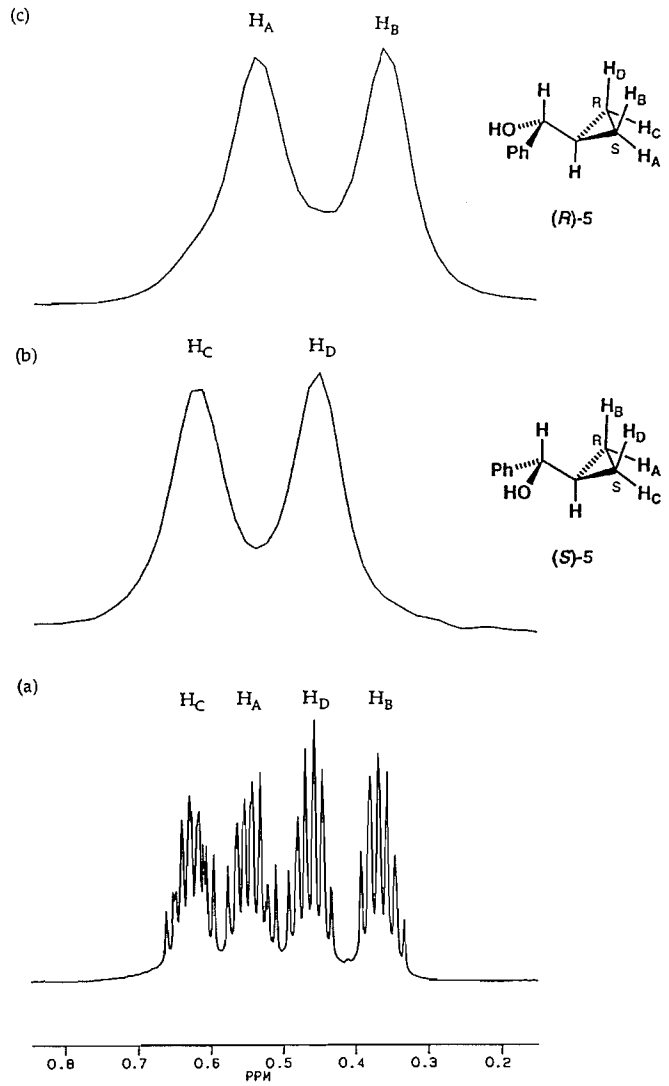

FIG. 4. (*a*) Part of the ^1H NMR spectrum of cyclopropyl phenyl carbinol **5**; assignments are as described in ref. 8. (*b*) and (*c*) Parts of the ^2H NMR spectra of (*S*)- and (*R*)-cyclopropyl phenyl carbinols **5***b* from degradation of cyclizidine **1***a* derived from $CD_3CH_2CO_2Na$.

The dehydrogenation of acyl CoA thioesters and then hydration of the resulting enoyl CoA thioesters to give β-hydroxyacyl CoA thioesters are well-known steps in the β-oxidation of fatty acids. An early study of short-chain acyl CoA dehydrogenase (13) reported that propionyl CoA is dehydrogenated at a reasonable rate but a later study (14) found only a very low rate. Other authors, however, have reported a propionyl CoA dehydrogenase that is involved in the interconversion of lactate and propionate (15). The acyl CoA dehydrogenases studied so far (16, 17) have catalyzed the antiperiplanar removal of the pro-2*R* and pro-3*R* hydrogen atoms, which is the stereochemistry required in our hypothesis. However, the stereochemistry of propionyl CoA dehydrogenase specifically has not been determined.

The enoyl CoA hydratase (crotonase) involved in fatty acid oxidation has been shown to hydrate acrylyl CoA (18) but it performs a *syn* addition of water to crotonyl CoA, giving (*S*)-3-hydroxybutyryl CoA with addition of the pro-*R* proton at C-2 (19, 20). Our hypothesis requires the opposite stereochemistry. However, in fatty acid biosynthesis the corresponding reaction does involve the pro-*S* proton of (*R*)-3-hydroxybutyryl ACP and in addition there are at least two reports of organisms that contain two different enoyl CoA hydratases for the conversion of crotonyl CoA into the (*R*) and (*S*) epimers of 3-hydroxybutyryl CoA (21, 22). It seems quite possible, therefore, that acrylyl CoA is hydrated in our cyclizidine-producing organism with addition of a proton in the pro-*S* position at C-2.

The pathway outlined in Scheme 6 is consistent with all the evidence currently available. It also provides an explanation of why the double bonds in the side chain of cyclizidine are within acetate- or propionate-derived units rather than between them as is more normal in polyketides. Furthermore, the isotope effect expected for the dehydrogenation of [3,3,3-$^2H_3$]propionyl CoA would explain why this precursor is incorporated better into the other two propionate-derived units than into the cyclopropyl ring of cyclizidine.

As yet the pathway shown in Scheme 6 is only one of several possibilities. Incorporation experiments with labelled acrylate and 3-hydroxypropionate are planned to test the proposal. However, the results presented in this paper do require that some unexpected reactions occur that cause the inversion of configuration at C-2 of the propionate unit destined to be the

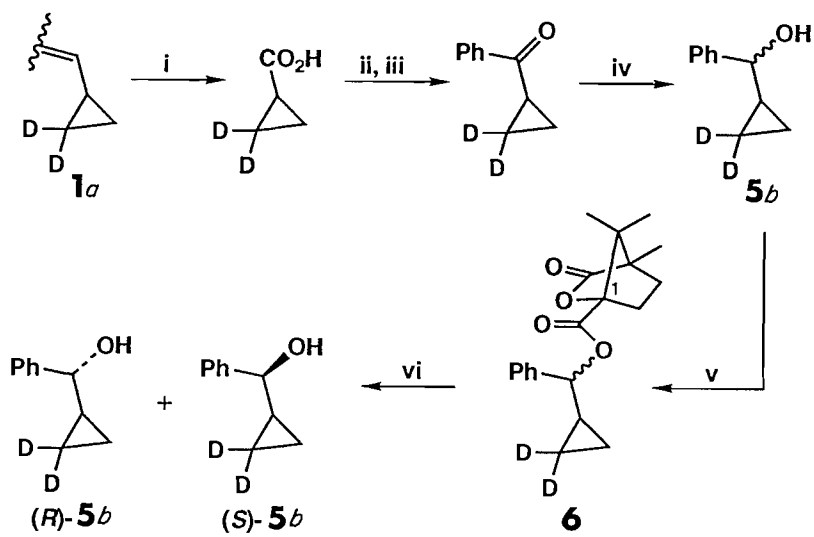

SCHEME 3. Reagents: i, CrO_3, H^+; ii, $(COCl)_2$; iii, PhH, $AlCl_3$; iv, $NaBH_4$; v, (1*S*)-camphanyl chloride, DMAP; vi, separate, then NaOH.

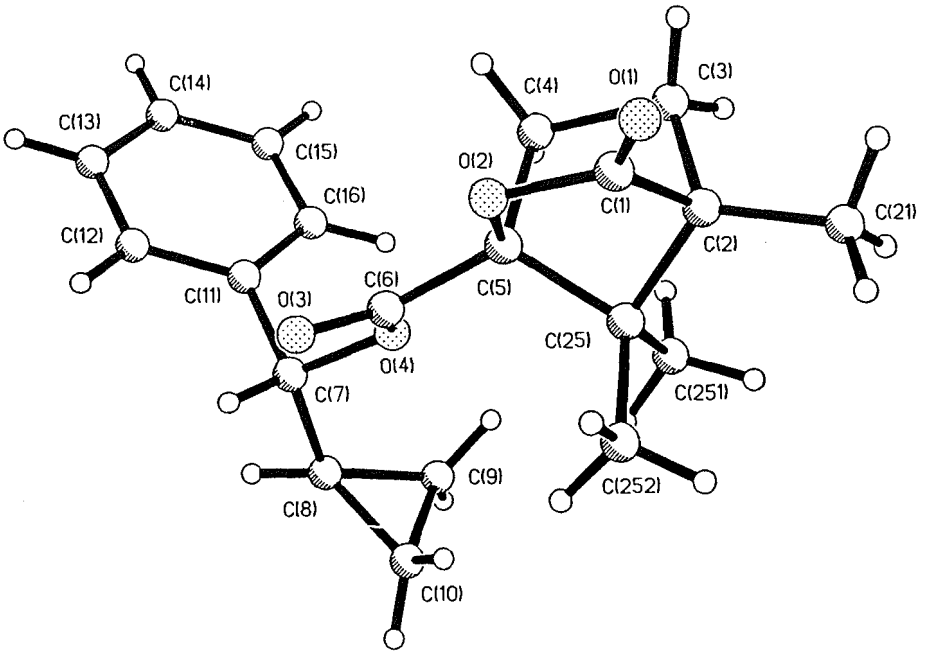

FIG. 5. X-ray crystal structure of the camphanate ester **6** eluted second on HPLC (courtesy of Dr. P.R. Raithby).

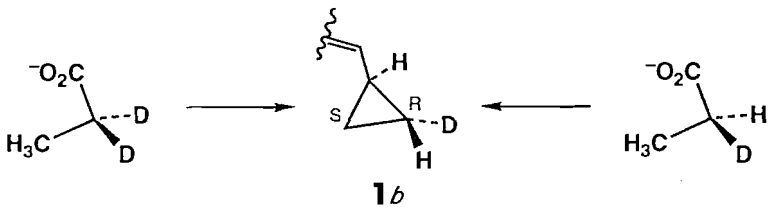

1*b*

SCHEME 4. The incorporation of 2-deuteriopropionates into cyclizidine.

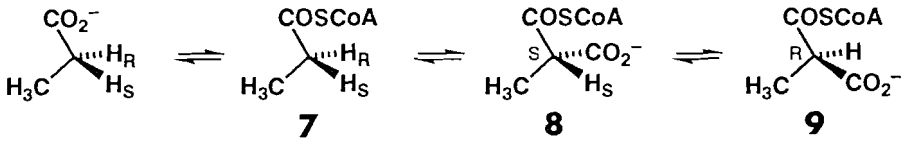

7 **8** **9**

SCHEME 5

cyclopropyl ring of cyclizidine. We feel that the pathway presented is the simplest explanation available.

Experimental methods

Melting points were determined on a Reichert Kofler hot-stage apparatus and are uncorrected. Ultraviolet spectra were recorded on a Uvikon 810 spectrophotometer. Infrared spectra were measured with a Perkin–Elmer 297 spectrometer using a polystyrene standard. Proton NMR spectra were recorded on Bruker WP-80 (80 MHz), WM-250 (250 MHz), and AM-400 (400 MHz) spectrometers, using the solvent signal as the standard. All spectra were recorded in deuteriochloroform unless otherwise stated. Deuterium NMR spectra were obtained on either the Bruker WM-250 (38 MHz) or the AM-400 spectrometer (61 MHz). Carbon NMR spectra were recorded on the Bruker WM-250 (62.5 MHz) or the AM-400 (100 MHz) spectrometer and the deuteriated solvent signal was again used as a standard; all spectra are proton noise decoupled unless otherwise stated. Mass spectra were recorded on AEI MS30 and MS50 spectrometers using electron impact ionization except where indicated. Optical rotations were measured for neat liquids on a Perkin–Elmer SP 241 polarimeter.

Flash column chromatography was carried out using Merck Kieselgel 60 (230–400 mesh). Analytical thin-layer chromatography (TLC) was carried out on commercially prepared plates, coated to a thickness of 0.25 mm with Merck Kieselgel GF_{254}. Preparative layer chromatography (PLC) was carried out on larger plates (20 ×20 cm) coated with the same silica gel (1 mm thick).

Radioactive counting was carried out with Packard Tri-Carb 2000CA scintillation analyser. Approximately, 1 mg of sample was weighed accurately and dissolved in an appropriate scintillant solution (either aqueous or toluene, 10 mL).

Organic solutions that had been in contact with water were dried with sodium sulphate unless otherwise stated. Removal of solvents in vacuo was carried out at water pump pressure on a Buchi rotary evaporator at 30°C, unless mentioned otherwise. All solvents were distilled before use. Standard procedures were used to purify all reagents and to dry solvents where indicated.

Production and isolation of cyclizidine 1

The *Streptomyces* strain NCIB 11649 was grown on Czapek dox agar slopes containing 2% yeast (at pH 7) and incubated at 27°C for 7 days. For cyclizidine production, 10 250-mL conical flasks each con-

Can. J. Chem. Downloaded from www.nrcresearchpress.com by 195.246.54.202 on 09/08/12
For personal use only.

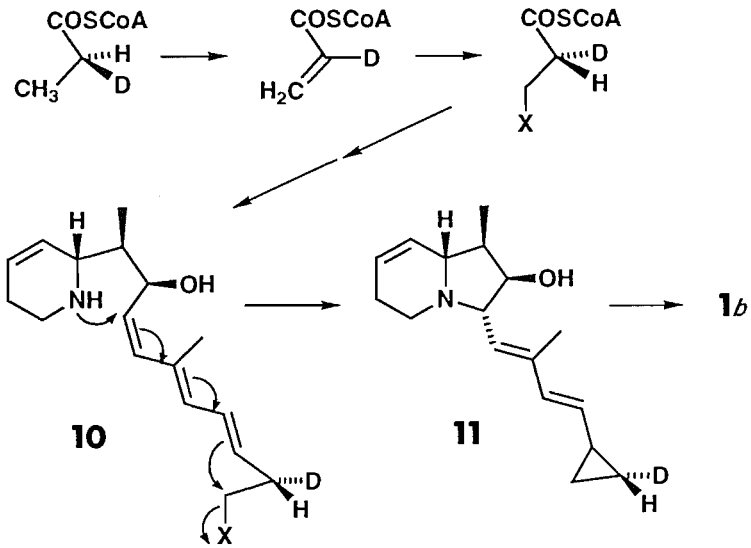

SCHEME 6. A proposed mechanism for formation of the three- and five-membered rings of cyclizidine.

taining 100 mL of M15 medium were inoculated either from the slopes or from a previous liquid culture. The M15 medium was made up of the following: glucose (30 g), calcium carbonate (2.5 g), sodium chloride (5.0 g), bacteriological peptone (1.0 g), Lab LEMCO (5.0 g), and minor elements concentrate (1.0 mL), made up to 1 L with distilled water. The minor elements concentrate used was made up as follows: ferrous sulphate heptahydrate (1.0 g), copper sulphate pentahydrate (0.45 g), zinc sulphate heptahydrate (1.0 g), manganese sulphate tetrahydrate (0.1 g), and potassium molybdate (0.1 g), made up to 1 L with distilled water and clarified by the addition of a few drops of concentrated hydrochloric acid.

The inoculated flasks were incubated at 24°C in the dark, with shaking at 300 rpm. After 5 days of continuous shaking, the whole broth was adjusted to pH 7 and extracted with ethyl acetate (4 × 1000 mL). The combined organic layers were dried and evaporated in vacuo to give a crude yellow gummy solid with a strong mousy odour. PLC, eluting with ethyl acetate and then recrystallization from chloroform–hexane gave cyclizidine as a colourless odourless powder (up to 80–100 mg), mp 179–180°C (lit. (1) mp 176–178°C); R_f 0.41 (ethyl acetate); IR ($CHCl_3$):3450 (br, OH), 1640 (w, C=C), 950 (s, =C-H) cm^{-1}; UV (EtOH): 240, 260 nm (sh); MS: 291 (M^+), 217, 188, 161 (100%), 150, 98, 91, 56. ^1H and ^{13}C NMR were as reported previously (4). Anal. calcd. for $C_{17}H_{25}NO_3$: C 70.05, H 8.65, N 4.81%; M, 291.1834; found: C 70.06, H 8.81, N 4.76%; M^+, 291.1827.

For incorporation experiments, the precursor (250 mg) was dissolved in distilled water (10 mL) and 0.5 mL of this solution was injected into each of the 10 culture flasks twice, 24 and 36 h after inoculation.

Synthesis of sodium [1-^{13}C,$^{18}O_2$]acetate (5)

A mixture of methyl iodide (1.22 mL, 19.66 mmol), potassium [1-^{13}C]cyanide (1.3 g, 19.66 mmol), and [^{18}O]water (0.1 mL, 5 mmol) in dry methanol (6 mL) was heated at reflux under argon for 22 h and then distilled by vacuum transfer. [^{18}O]Water (0.9 mL, 40 mmol) and potassium *tert*-butoxide (2.2 g, 19.66 mmol) were added to the distillate and the mixture was heated at reflux under argon for 48 h. The solvents were removed in vacuo and the residue acidified with 30% aqueous phosphoric acid. The liquid was distilled into a second flask by vacuum transfer and made just alkaline with 10% aqueous sodium hydroxide. The solvents were removed in vacuo and the residue was dried in a vacuum oven for 2 h at 150°C to give the doubly labelled acetate salt as a white solid (0.668 g, 7.9 mmol, 40%); ^{13}C NMR (100 MHz, H_2O) δ: 25.63 (d, J_{CC} 52 Hz, CH_3), 164.09 (s, $^{13}C^{18}O_2$), 164.12 (s, $^{13}C^{18}O^{16}O$), and 164.15 (s, $^{13}C^{16}O_2$). Integration of these peaks gave ca. 58% $^{13}C^{18}O_2$, 34% $^{13}C^{18}O^{16}O$, and 7% $^{13}C^{16}O_2$.

4-Phenylphenacyl[1-^{13}C,$^{18}O_2$]acetate (5)

To a mixture of α-bromo-4-phenylacetophenone (47 mg, 0.173 mmol) and sodium [1-^{13}C,$^{18}O_2$]acetate (7 mg, 0.086 mmol) was added 18-crown-6 (2 mg), acetonitrile (1 mL), and benzene (1 mL). The solution was heated at reflux for 4 h, then evaporated in vacuo. PLC, eluting with ethyl acetate – hexane (2:8) gave the labelled phenylphenacyl acetate as a solid (14 mg, 0.054 mmol, 62%), mp 109–110°C (lit. (5) mp 110°C); R_f 0.67 (ethyl acetate – hexane, 2:3); ^1H NMR (400 MHz, $CDCl_3$) δ: 2.24 (3H, d, J_{CH} 7 Hz, $^{13}COCH_3$), 5.36 (2H, d, J_{CH} 4.4 Hz, $^{13}COOCH_2$), 7.41 (1H, m, *p*-Ar*H*ArCO), 7.48 (2H, m, *m*-Ar*H*ArCO), 7.51 (2H, d, *J* 8.5 Hz, *m*-Ar*H*CO), 7.63 (2H, m, *o*-Ar*H*ArCO), and 7.91 (2H, d, *J* 8.5 Hz, *o*-Ar*H*CO); HRMS: M^+ 259.1055. $C_{12}{}^{13}CH_{14}O^{18}O_2$ requires M, 259.1045. The spectrum also showed ca. 10% of the compound without the ^{13}C label; MS: 259 ($^{13}C^{18}O_2$, 98%), 258 ($^{12}C^{18}O_2$, 8), 257 ($^{13}C^{18}O^{16}O$, 60), and 255 ($^{13}C^{16}O_2$, 5).

Benzyl[1-^{13}C]acetate

To a stirred solution of [1-^{13}C]acetic acid (0.25 g, 4.1 mmol) in dry dichloromethane (5 mL) under argon, was added a solution of benzyl alcohol (0.47 mL, 4.5 mmol) in dry dichloromethane (5 mL) followed by a catalytic amount of 4-dimethylaminopyridine (3 mg). The mixture was cooled to 0°C and dicyclohexylcarbodiimide (0.95 g, 4.62 mmol) was added. The mixture was stirred at 0°C for 15 min and then at room temperature for 4 h, after which time TLC (10% methanol in dichloromethane) showed no acetic acid present. The precipitated urea was filtered off and washed with a small volume of dichloromethane (10 mL). The combined filtrate and washing were evaporated in vacuo. Flash column chromatography, eluting with ether–hexane (1:1), gave the labelled benzyl acetate as an oil (0.60 g, 4.0 mmol, 97%); R_f: 0.5 (ether–hexane, 1:1); IR (CH_2Cl_2): 1705 (s, C=O) and 1600 (s, Ar) cm^{-1}; ^1H NMR (90 MHz, $CDCl_3$) δ: 2.1 (3H, d, J_{CH} 7 Hz, ^{13}C-CH_3), 5.1 (2H, d, J_{CH} 3 Hz, Ar-CH_2), and 7.25 (5H, s, Ar-*H*); ^{13}C NMR (100 MHz, $CDCl_3$) δ: 21.1 (d, J_{CC} 59 Hz, CH_3), 66.3 (s, Ar-CH_2), 128.24, 128.55 (s, *C*H aromatic), 135.92 (s, *C* aromatic), and 170.88 (s, ^{13}C=O, enriched signal); MS: 151 (M^+, 5%), 108 ($M^+ - CH_3CO$, 100), 91 (C_7H_{7+}, 55).

Benzyl[1-^{13}C,3,3,3-$^2H_3$]propionate

n-Butyllithium (1.6 M in hexane, 2.5 mL, 4.0 mmol) was added dropwise to a stirred solution of diisopropylamine (0.56 mL, 4.0 mmol) in dry tetrahydrofuran (8 mL) maintained at –78°C under an argon atmosphere. After 30 min the reaction mixture was warmed to 0°C for 15 min and then cooled to –78°C for 10 min. Benzyl[1-^{13}C]-acetate (0.6 g, 4.0 mmol) was then added dropwise and the solution was stirred for 30 min. Trideuteriomethyl iodide (1.0 g, 7.0 mmol) was

Can. J. Chem. Downloaded from www.nrcresearchpress.com by 195.246.54.202 on 09/08/12
For personal use only.

Can. J. Chem. Downloaded from www.nrcresearchpress.com by 195.246.54.202 on 09/08/12
For personal use only.

added to the solution at –78°C and it was then allowed to warm up gradually to room temperature. After 16 h the reaction was quenched with saturated aqueous ammonium chloride (20 mL) and extracted with dichloromethane (3 × 15 mL). The combined extracts were dried and evaporated in vacuo. Flash column chromatography, eluting with ether–hexane (1:9), followed by distillation gave the labelled benzyl propionate as an oil (0.38 g, 2.3 mmol, 58%); bp 125°C at 10 Torr (1 Torr = 133.3 Pa); R_f: 0.59 (ether–hexane, 1:1); IR ($CDCl_3$): 1680 (C═O) and 1450 (C═O) cm^{-1}; ^1H NMR (90 MHz, $CDCl_3$) δ: 2.29–2.41 (2H, m, ^{13}C-CH_2-CD_3), 5.11 (2H, d, J_{CH} 3.1 Hz, Ar-CH_2), and 7.34 (5H, s, Ar-*H*); ^{13}C NMR (100 MHz, $CDCl_3$) δ: 27.3 (d, J_{CC} 57 Hz, CH_2CD_3), 66.0 (s, Ar-CH_2), 128.07, 128.16, 128.54 (phenyl *C*H), 136.11 (phenyl *C*), and 174.32 (^{13}C═O enriched); ^2H NMR (61 MHz, $CHCl_3$) δ: 1.13 (s, CD_3); MS: 168 (M^+, 24%), 108 (100), 91 (C_7H^{7+}, 99); HRMS: M^+, 168.1055; $C_9{}^{13}CH_9{}^2H_3O_2$ requires M, 168.1056.

Sodium[1-^{13}C,3,3,3-$^2H_3$]propionate

Benzyl [1-^{13}C,3,3,3-$^2H_3$]propionate (0.35 g, 2 mmol) was dissolved in methanol and hydrogenated over 10% palladium on charcoal (3 mg). The catalyst was filtered off and the acid was converted to the sodium salt by addition of 10% aqueous sodium hydroxide (0.8 mL, 2 mmol). The methanol was evaporated and the residue dissolved in water (15 mL) and extracted with ether (3 × 20 mL). The aqueous layer was evaporated in vacuo to give sodium [1-^{13}C,3,3,3-$^2H_3$]propionate as a solid (0.38 g, 3.8 mmol, 92%). IR (Nujol): 2220 (m, C—D), 1550 cm^{-1} (m, COO^-); ^1H NMR (400 MHz, CD_3OD) δ: 2.13 (2H, d, J_{CH} 5.8 Hz, CH_2) (the absence of any significant methyl proton signal at δ 1.1 ppm indicated >95% deuteration); ^{13}C NMR (100 MHz, CD_3OD) δ: 31.62 (d, J_{CC} 51 Hz, CH_2-CD_3) and 184.01 (s, ^{13}C═O enriched); ^2H NMR (61 MHz, H_2O) δ: 0.84 (s, CD_3).

Kuhn–Roth degradation of cyclizidine

Chromic acid solution was prepared by dissolving chromium trioxide (20.6 g) in water (60 mL) and concentrated sulphuric acid (17.6 mL). Cyclizidine **1** (41 mg, 0.14 mmol) was heated at reflux with chromic acid solution (10 mL) and steam distillation carried out. The distillate (80 mL) was made alkaline (pH 8–9) by the dropwise addition of aqueous sodium hydroxide using pH paper as an indicator. The aqueous phase was washed with ether (2 × 20 mL), evaporated in vacuo, and dried at 150°C for 2 h to give a mixture of sodium acetate and sodium cyclopropanecarboxylate (0.043 g) as a solid.

Conversion of sodium cyclopropanecarboxylate into phenyl cyclopropyl carbinol

Oxalyl chloride (0.25 mL, 2.77 mmol) was added to a stirred suspension of sodium cyclopropanecarboxylate (0.1 g, 0.9 mmol) in dry dichloromethane (0.5 mL) under argon at 0°C. After 30 min at 0°C and 30 min at room temperature, aluminium chloride (0.148 g, 1.1 mmol) and dry benzene (4 mL) were added. The mixture was heated at reflux for 30 min, then cooled, poured into ice-cold 3 M hydrochloric acid (10 mL), and extracted with dichloromethane (4 × 20 mL). The combined organic extracts were washed with water (2 × 20 mL) and then saturated brine (2 × 20 mL), dried, and evaporated in vacuo. Flash column chromatography, eluting with dichloromethane–hexane (6:4), gave a mixture of cyclopropyl phenyl ketone and benzophenone (0.367 g) as an oil. The two compounds could not be separated by column chromatography and so were taken on to the next reaction as a mixture.

The mixture of ketones (0.367 g) was dissolved in dry methanol (3 mL) and cooled to 0°C. Sodium borohydride (0.113 g, 2.99 mmol) was added and the solution was stirred at 0°C for 10 min and at room temperature for 30 min, then diluted with water (5 mL) and extracted with dichloromethane (4 × 20 mL). The combined extracts were dried and evaporated in vacuo. Flash column chromatography, eluting with ether–hexane (3:7), gave cyclopropyl(phenyl)methanol (97 mg, 0.655 mmol, 71% from the sodium salt) as an oil; R_f: 0.29 (dichloromethane); IR (CH_2Cl_2): 3550 (OH), 3040 (CH), 1603 (Ar) cm^{-1}; ^1H NMR (400 MHz, $CDCl_3$) δ: 0.36, 0.45, 0.54, 0.62 (each 1H, m, cyclopropyl C-*H*), 1.16 (1H, m, COC*H*), 2.41 (1H, bs, O*H*), 3.97 (1H, d, *J* 8.3 Hz, C*H*OH), and 7.35 (5H, m, Ar*H*).

(R,S)-Cyclopropyl(phenyl)methyl (1S)-camphanate

To a stirred solution of the alcohol **5** (83 mg, 0.56 mmol) in dry dichloromethane under argon was added 4-dimethylaminopyridine (17 mg, 0.14 mmol), triethylamine (130 mg, 1.3 mmol), and (1*S*)-camphanyl chloride (158 mg, 0.73 mmol). The mixture was stirred at room temperature for 16 h, then poured into water (5 mL) and extracted with dichloromethane (3 × 15 mL). The combined organic extracts were dried and evaporated in vacuo. PLC, eluting continuously with ether–hexane (3:7), gave the diastereoisomeric camphanate esters (93 mg, 0.28 mmol, 50%); R_f: 0.18 (ether–hexane, 3:7); IR (CH_2Cl_2); 1800 and 1750 (C═O) cm^{-1}; UV (CH_2Cl_2): 256 nm; MS: 328 (M^+, 13%), 300 ($M^+ - C_2H_4$, 23), 131 (C_3H_5CHPh, 100); HRMS: M^+, 328.1701; $C_{20}H_{24}O_4$ requires M, 328.1674.

Separation of the two diastereoisomers was carried out on a Kontron semi-preparative column (50 cm ×8 mm) packed with 5 μm Spherisorb S5W silica, eluting with ethyl acetate – hexane (5:95) at 2.7 mL/min with detection by UV absorption at 264 nm.

(S)-Cyclopropyl(phenyl)methyl (1S)-camphanate was eluted first as an oil; ^1H NMR (400 MHz, CD_3COCD_3) δ: 0.36–0.70 (4H, m, cyclopropyl C-*H*), 0.89 and 1.05 (9H, 2 × s, camphanyl CH_3), 1.41 (1H, m, C*H*-C-O), 1,61, 1.93, 1.95, and 2.45 (each 1H, each m, camphanyl CH_2), 5.51 (1H, d, *J* 8.9 Hz, C*H*Ph), and 7.47 (5H, m, Ar*H*).

(R)-Cyclopropyl(phenyl)methyl (1S)-camphanate was eluted second and was recrystallized from ether–hexane; ^1H NMR (400 MHz, CD_3COCD_3) δ: 0.50–0.70 (4H, m, cyclopropyl C-*H*), 0.89, 1.06, and 1.14 (9H, 3 × s, camphanyl CH_3), 1.41 (1H, m, C*H*-C-O), 1.61, 1.93, 1.95, and 2.45 (each 1H, each m, camphanyl CH_2), 5.51 (1H, d, *J* 8.9 Hz, C*H*Ph), and 7.47 (5H, m, Ar-*H*). The other spectral data are the same as for the mixture of diastereoisomers.

Hydrolysis of the camphanates

The (*S*)-cyclopropyl(phenyl)methyl (1*S*)-camphanate (21 mg, 0.064 mmol) was heated at reflux with 10% methanolic potassium hydroxide (2 mL) for 1 h. The methanol was evaporated in vacuo, water (1 mL) was added, and the mixture was extracted with ether (3 × 10 mL). The combined organic layers were dried and evaporated in vacuo to yield the optically active alcohol (10 mg, 100%); spectroscopic data were as given above for the racemic alcohol.

The (*R*)-cyclopropyl(phenyl)methyl ester was hydrolysed similarly.

Preparation of the (R)-3,3,3-trifluoro-2-methoxy-2-phenylpropionate esters

A solution of the cyclopropyl phenyl carbinol (1.1 equiv.) in the minimum amount of dry dichloromethane was added to a solution of (*R*)-3,3,3-trifluoro-2-methoxy-2-phenylpropionic acid (1 equiv.) in the same solvent (2 mL) under argon. 4-Dimethylaminopyridine (2–4 mg) was then added. The mixture was cooled in ice, treated with dicyclohexylcarbodiimide (1.1 equiv.), and stirred at 0°C for 5–10 min and at room temperature for 4 h. The precipitated urea was filtered off and washed with a small volume of dichloromethane (1–2 mL) and the filtrate was evaporated. The residue was redissolved in dichloromethane, filtered again, evaporated, and purified by PLC to give the Mosher's ester (26%); IR ($CHCl_3$): 1730 (m, C═O), 1590 (w, Ar) cm^{-1}; MS: 364 (M^+), 224, 131; HRMS: M^+, 364.1281; $C_{20}H_{19}F_3O_3$ requires M, 364.1281.

The ester from the (*S*) alcohol gave ^1H NMR (250 MHz, $CDCl_3$) δ: 0.55–0.87 (4H, m, cyclopropyl CH_2-CH_2), 1.4 (1H, m, CH-C-O), 3.59 (3H, s, OCH_3), 5.36 (1H, d, *J* 9.2 Hz, CHOCO), 7.34 (10H, m, 2 × Ph).

The ester from the (*R*) alcohol gave ^1H NMR (400 MHz, $CDCl_3$) δ: 0.55–0.87 (4H, m, cyclopropyl CH_2-CH_2), 1.4 (1H, m, CH-C-O), 3.5 (3H, s, OCH_3), 5.5 (1H, d, *J* 9.2 Hz, CHOCO), 7.34 (10H, m, 2 × Ph).

Degradation of cyclizidine obtained after incorporation of sodium [3,3,3-$^2H_3$]propionate

Cyclizidine (228 mg, 0.78 mmol), obtained after incorporation of sodium [3-$^2H_3$]propionate, was subjected to Kuhn–Roth degradation as described above to give a mixture of sodium acetate and sodium cyclopropanecarboxylate (0.164 g) as a solid.

The salts (0.164 g) were converted as above into the cyclopropyl

Can. J. Chem. Downloaded from www.nrcresearchpress.com by 195.246.54.202 on 09/08/12
For personal use only.

phenyl ketone and then reduced to give the racemic cyclopropyl phenyl carbinol (46.4 mg, 0.31 mmol, 40% from cyclizidine).

The (1*S*)-camphanate esters (54 mg, 0.16 mmol, 53%) were prepared and separated by HPLC and each diastereoisomer was hydrolysed to give the optically active alcohol as described above. For the (*R*) alcohol, ^{2}H NMR (61 MHz, $CHCl_3$) δ: 0.36, 0.54, and 1.21. For the (*S*) alcohol, ^{2}H NMR (61 MHz, $CHCl_3$) δ: 0.46, 0.63, and 1.22.

Sodium [2-$^2H_2$]propionate

Deuteriated concentrated sulphuric acid (3 mL) was added dropwise to sodium propionate (0.5 g, 5 mmol) at 0°C under nitrogen. The mixture was then heated at 120°C for 20 min, then cooled in ice and deuterium oxide (3 mL) added. The solution was then poured into iced water (30 mL) and extracted thoroughly with ether (5 × 10 mL). The combined extracts were dried, concentrated in vacuo to a volume of 2 mL, redissolved in methanol (2 mL), and titrated with 10% aqueous sodium hydroxide until slightly alkaline, using phenolphthalein as indicator. The aqueous solution was evaporated to dryness and the residue dried in vacuo at 120°C to give the deuteriated sodium salt (0.2 g, 40%); IR (Nujol): 1550 (m, COO^-) cm^{-1}; ^{1}H NMR (80 MHz, NaOD/D_2O) δ: 1.6 (3H, br m, CH_3), 2.7 (ca. 0.3H, br m, residual CH_2); ^{2}H NMR (61 MHz, H_2O) δ: 2.3 (br s, CD_2).

(R)- and (S)-2-Bromopropionic acids

A solution of alanine (3.6 g, 0.04 mol) and potassium bromide (28.5 g, 0.24 mol) in cold 1.25 M aqueous sulphuric acid (288 mL, 0.36 mol) was treated with sodium nitrite (7.5 g, 0.11 mol) over 30 min at 0°C. After 1 h, ether (50 mL) was added and the mixture was warmed to room temperature and stirred for an additional hour. The two layers were separated, and the aqueous layer was thoroughly extracted with ether (4 × 50 mL). The combined organic extracts were dried over calcium chloride and evaporated in vacuo. The residue was distilled under vacuum to give the bromoacid.

(*S*)-2-Bromopropionic acid (3.0 g, 50%) was obtained from (*S*)-(+)-alanine; bp 66–68°C at 1 Torr (lit. (9) bp 70°C at 1 Torr); $[\alpha]_D$ –40.65 (neat) (lit. (9) $[\alpha]_D$ –45.2); IR (thin film): 3100 (br, COOH), 1710 (s, C=O) cm^{-1}; ^{1}H NMR (80 MHz, $CDCl_3$) δ: 1.8 (3H, d, *J* 7 Hz, CH_3), 4.4 (1H, q, *J* 7 Hz, CHBr), 9.5 (1H, br, COOH); MS: 154 and 152 (M^+), 110 and 108 ($M^+ - CO_2$), 109 and 107 (M^+ – COOH); HRMS: M^+, 151.9472; $C_3H_5{}^{79}BrO_2$ requires M, 151.9472.

(*R*)-2-Bromopropionic acid (2.5 g, 41%) was obtained from (*R*)-(–)-alanine; $[\alpha]_D$ +41.76 (neat) (lit. (9) $[\alpha]_D$ +44.2). Other data were the same as for the (*S*) isomer.

Sodium (R)-[2-^{2}H]propionate

A solution of 1 M lithium triethylborodeuteride in tetrahydrofuran (26 mL, 26 mmol, Aldrich Superdeuteride) was added to a solution of (*S*)-bromopropionic acid (1.25 g, 8 mmol) in dry tetrahydrofuran (2.5 mL), at 0°C. The stirred mixture was heated at reflux for 2 h and then stirred at room temperature for 18 h. The mixture was then cooled in ice, diluted with water (10 mL), and concentrated to 25 mL. A mixture of hydrogen peroxide (100 vol) and 2 M aqueous sodium hydroxide (1:1) was added until effervescence ceased. The resulting solution was washed with ether (3 × 15 mL), acidified to pH 3 with 1 M sulphuric acid, and steam distilled. The acidic distillate was made just alkaline with 1 M sodium hydroxide, using phenolphthalein as indicator, and evaporated to dryness in vacuo to yield sodium (*R*)-[2-^{2}H]propionate (0.38 g, 50%); IR (Nujol): 2180 (w, C-D), 1540 (COO^-) cm^{-1}; ^{1}H NMR (80 MHz, D_2O) δ: 1.15 (3H, dt, $J_{H\text{-}H}$ 7.6 Hz, $J_{H\text{-}D}$ 1.1 Hz, CH_3), 2.25 (1H, qt, $J_{H\text{-}H}$ 7.6 Hz, $J_{H\text{-}D}$ 2.2 Hz, CHD).

Sodium (S)-[2-^{2}H]propionate (0.43 g, 55%) was prepared in the same way from (*R*)-2-bromopropionic acid. All data were the same as for the (*R*) isomer.

(S)-Methoxycarbonyl(phenyl)methyl (R)-[2-^{2}H]propionate

A solution of sodium (*R*)-[2-^{2}H]propionate (90 mg, 0.9 mmol) in water (2 mL) was acidified to pH 6 with dilute hydrochloric acid and extracted thoroughly with ether (5 × 3 mL). The combined extracts were dried and the solvent was distilled off at atmospheric pressure to yield (*R*)-[2-^{2}H]propionic acid (50 mg, 74%).

The acid (30 mg, 0.4 mmol) was dissolved in dry dichloromethane (1 mL) and the mandelate ester (39 mg, 44%) was prepared as in ref. 10; IR (thin film): 2150 (w, C—D), 1740 (s, C=O), 1050 (m, C—O) cm^{-1}; ^{1}H NMR (250 MHz, $CDCl_3$) δ: 1.2 (3H, d, *J* 7.5 Hz, CH_3), 2.43 (1H, qt, $J_{H\text{-}H}$ 7.5 Hz, $J_{H\text{-}D}$ 2.3 Hz, CH_SD), 3.7 (3H, s, $COOCH_3$), 5.9 (1H, s, CH-O), 7.4 (5H, m, ArH); ^{2}H NMR (61 MHz, $CHCl_3$) δ: 2.53 (s, CHD); MS: 223 (M^+); HRMS: M^+, 223.0955; $C_{12}H_{13}{}^2HO_4$ requires M, 223.0951.

(S)-Methoxycarbonyl(phenyl)methyl (S)-[2-^{2}H]propionate

(*S*)-[2-^{2}H]propionic acid (30 mg, 0.4 mmol) obtained from sodium (*S*)-[2-^{2}H]propionate as above was converted to the corresponding mandelate ester (47 mg, 53%) as before; ^{1}H NMR (250 MHz, $CDCl_3$) δ: 1.2 (3H, d, *J* 7.5 Hz, CH_3), 2.53 (1H, qt, $J_{H\text{-}H}$ 7.5 Hz, $J_{H\text{-}D}$ 2.3 Hz, CDH_R), 3.7 (3H, s, $COOCH_3$), 5.9 (1H, s, CH-O), 7.4 (5H, m, ArH); ^{2}H NMR (61 MHz, $CHCl_3$) δ: 2.47 (s, CHD); MS: 223 (M^+); HRMS: M^+, 223.0955; $C_{12}H_{13}{}^2HO_4$ requires M, 223.0951.

Incorporation of sodium (S)-[1-^{14}C,2-^{2}H]propionate into cyclizidine

Sodium [1-^{14}C]propionate (5 μCi) and sodium (*S*)-[2-^{2}H]propionate (250 mg, 2.6 mmol, 4.22×10^6 dpm/mmol) were dissolved in distilled water (10 mL) and fed to the organism as described earlier. The cyclizidine obtained (40 mg, 0.14 mmol, 2.2×10^6 dpm/mmol, specific incorporation 51%, 17% per labelled site) was dissolved in chloroform (1.5 g, 14 mmol) and the ^{2}H NMR spectrum recorded. The peak areas of the signals due to deuterium at natural abundance (0.016%) in the chloroform and in cyclizidine (at δ 0.76 ppm) were in the ratio of 1:2. Thus the ^{2}H incorporation in cyclizidine is approximately $(0.016 \times 2 \times 14)/0.14 = 3.2\%$.

Incorporation of sodium (R)-[1-^{14}C,2-^{2}H]propionate

Sodium (*R*)-[1-^{14}C,2-^{2}H]propionate (5 μCi, 250 mg) was fed to the organism as for the (*S*)-isomer. The cyclizidine obtained (40 mg, 0.14 mmol, 1.7×10^6 dpm/mmol, specific incorporation 39%, 13% per labelled site) showed no significant incorporation of deuterium by ^{2}H NMR spectroscopy.

Acknowledgements

We would like to thank Dr. P. R. Raithby for determining the crystal structure, Dr. D.H. Williams for help with some of the ^{2}H NMR experiments, and the Cambridge Commonwealth Trust and the Science and Engineering Research Council (SERC) for studentships to P.S. and S.E.S. respectively.

1. A.A. Freer, D. Gardner, D. Greatbanks, J.P. Poyser, and G.A. Sim. J. Chem. Soc. Chem. Commun. 1160 (1982).
2. S. Gomi, D. Ikeda, H. Nakamura, H. Naganawa, F. Yamashita, K. Hotta, S. Kondo, Y. Okami, H. Umezawa, and Y. Iitaka. J. Antibiot. **37**, 1491 (1984).
3. P. Monaco, L. Previtera, and L. Mangoni. Phytochemistry, **21**, 2408 (1982).
4. F.J. Leeper, P. Padmanabhan, G.W. Kirby, and G.N. Sheldrake. J. Chem. Soc. Chem. Commun. 505 (1987).
5. D.E. Cane, T.-C. Liang, and H. Hasler. J. Am. Chem. Soc. **103**, 5962 (1981).
6. J.C. Vederas. J. Am. Chem. Soc. **102**, 374 (1980); J.M. Risley and R.L. Van Etten. J. Am. Chem. Soc. **102**, 4609 (1980).
7. C. Abell and J. Staunton. J. Chem. Soc. Chem. Commun. 856 (1981).
8. F.J. Leeper and P. Padmanabhan. Tetrahedron Lett. **30**, 5017 (1989).
9. W.L.F. Armarego, B.A. Milloy, and W. Pendergast. J. Chem. Soc. Perkin Trans. 1, 2229 (1976).
10. D. Parker. J. Chem. Soc. Perkin Trans. 2, 83 (1983).
11. D.J. Prescott and J.L. Rabinowitz. J. Biol. Chem. **243**, 1551 (1968).
12. R. Mazumder, T. Sasakawa, Y. Kaziro, and S. Ochoa. J. Biol. Chem. **237**, 3065 (1962).

13. D.E. Green, S. Mii, H.R. Mahler, and R.M. Bock. J. Biol. Chem. **206**, 1 (1954).
14. L. Shaw and P.C. Engel. Biochem J. **218**, 511 (1984); **218**, 521 (1984).
15. R.D. Kuchta and R.H. Abeles. J. Biol. Chem. **260**, 13181 (1985).
16. K. Saito, A. Kawaguchi, Y. Seyama, T. Yamakawa, and S. Okuda. J. Biochem. **90**, 1697 (1981).
17. D.J. Aberhart and C.-H. Tann. J. Am. Chem. Soc. **102**, 6380 (1980).
18. G. Rendina and M.J. Coon. J. Biol. Chem. **225**, 523 (1957).
19. D.J. Aberhart and C.-H. Tann. J. Chem. Soc. Perkin Trans. 1, 939 (1979).
20. P. Willadsen and H. Eggerer. Eur. J. Biochem. **54**, 247 (1975).
21. G.J. Moskowitz and J.M. Merrick. Biochemistry, **8**, 2748 (1969).
22. J.K. Hiltunen, P.M. Palosaari, and W.-H. Kunau. J. Biol. Chem. **264**, 13536 (1989).

Can. J. Chem. Downloaded from www.nrcresearchpress.com by 195.246.54.202 on 09/08/12
For personal use only.

Mild hydrolysis or alcoholysis of amides. Ti(IV) catalyzed conversion of primary carboxamides to carboxylic acids or esters[1,2]

LAWRENCE E. FISHER,[3] JOAN M. CAROON, S. RUSSELL STABLER, SCOTT LUNDBERG, SHAHID ZAIDI, CAROLE M. SORENSEN, MARK L. SPARACINO, AND JOSEPH M. MUCHOWSKI

Syntex Research, 3401 Hillview Avenue, P.O. Box 10850, Palo Alto, CA 94304, U.S.A.

Received May 21, 1993

This paper is dedicated to Professor David B. MacLean

LAWRENCE E. FISHER, JOAN M. CAROON, S. RUSSELL STABLER, SCOTT LUNDBERG, SHAHID ZAIDI, CAROLE M. SORENSEN, MARK L. SPARACINO, and JOSEPH M. MUCHOWSKI. Can. J. Chem. **72**, 142 (1994).

Reaction of primary amides (e.g., **1***a* or **6–13**) or *O*-methylhydroxamates (**1***b* and **1***c*) with a catalytic amount of $TiCl_4$ and one equivalent of aqueous HCl converts these compounds in good yields to carboxylic esters (when an alcohol is used as solvent) or to carboxylic acids (when 9 : 1 dioxane : H_2O is used as solvent). These conversions are chemoselective for primary amides: mono- and dialkyl amides are not affected by the reaction conditions. The hydrolysis conditions described do not compromise the stereochemical integrity of an adjacent chiral center. This is exemplified by the hydrolysis of naproxen amide (**34**) to naproxen (**33**) without detectable racemization as determined by chiral HPLC.

LAWRENCE E. FISHER, JOAN M. CAROON, S. RUSSELL STABLER, SCOTT LUNDBERG, SHAHID ZAIDI, CAROLE M. SORENSEN, MARK L. SPARACINO et JOSEPH M. MUCHOWSKI. Can. J. Chem. **72**, 142 (1994).

La réaction des amides primaires (par exemple **1***a* ou **6–13**) ou des *O*-méthylhydroxamates (**1***b* ou **1***c*) avec une quantité catalytique de $TiCl_4$ et un équivalent de HCl aqueux permet de transformer ces composés, avec d'excellents rendements, en esters carboxyliques (lorsqu'on utilise un alcool comme solvant) ou en acides carboxyliques (lorsqu'on utilise un mélange 9 : 1 dioxane : eau comme solvant). Ces transformations sont chémosélectives pour les amides primaires; les mono- et dialkyl amides ne sont pas affectés par les conditions des réactions. Les conditions d'hydrolyse décrites ne compromettent pas l'intégrité stéréochimique d'un centre chiral adjacent. Pour démontrer cette assertion, on présente comme exemple l'hydrolyse de la naproxenamide (**34**) en naproxen (**33**) qui, d'après une CLHP chirale, se fait sans racémisation détectable.

[Traduit par la rédaction]

We have shown that the *O*-methyl hydroxamic acid moiety is an efficient, easy to prepare *ortho*lithiation directing group for aryl and toluyl systems (1).[4] In addition, we demonstrated that reduction of the *O*-methyl hydroxamic acids to carboxamides could be efficiently accomplished with two equivalents of titanium(III) chloride in alcoholic solution (2). With aqueous (but not anhydrous) titanium(III) chloride it was noted that after prolonged reaction times some of the carboxamide was converted into the carboxylic ester corresponding to the alcohol used. Since Ti(III) chloride had no effect on the primary amide it was assumed that Ti(IV), formed as a consequence of the reduction of the hydroxamate, was the agent responsible for promoting the alcoholysis of the amide. Not only was this supposition found to be correct, it was also shown that the alcoholysis was catalytic in Ti(IV).[5] This paper describes optimized conditions for effecting the Ti(IV) catalyzed conversion of primary amides (**1***a*, **6–13**) to the corresponding carboxylic acids or esters. Also described herein are conditions for the Ti(IV) catalyzed alcoholysis and hydrolysis of *O*methylphenylacetohydroxamate (**1***b*) and *O*-methylbenzylhydroxamate (**1***c*).

Depending on whether an aqueous or alcoholic solvent is used, treatment of N-unsubstituted carboxamides with a catalytic amount of titanium(IV) chloride and one equivalent of aqueous hydrochloric acid converts this class of compounds into the corresponding carboxylic acids or esters. Thus, heating the carboxamide in a solution of the appropriate alcohol containing 10 mol% aqueous $TiCl_4$ and one molar equivalent of hydrochloric acid gave the corresponding esters in good yields (Table 1; refs. 2–15). The carboxylic acids were obtained when 10% aqueous dioxane was used as the solvent (Table 2; refs. 2–20). Not surprisingly, ester-amides **11** and **12** were both hydrolyzed completely to diacids when subjected to the aqueous hydrolysis conditions. Treatment of *O*-methylhydroxamates **1***b* and **1***c* with $TiCl_4$ also resulted in alcoholysis (in alcohol with one molar equivalent of hydrochloric acid, Table 1) or hydrolysis (in 10%aqueous dioxane, Table 2). Although these reactions did proceed in the absence of added aqueous hydrochloric acid, addition of one molar equivalent of aqueous HCl increased the rate considerably. Neither of these reactions proceeded appreciably, however, in the absence of Ti(IV).

Titanium(IV) alkoxides also catalyze the transformation of primary carboxamides to esters. For example, $Ti(OMe)_4$, $Ti(OEt)_4$, and $Ti(OiPr)_4$, in the appropriate alcohol as solvent, catalyze the conversion of **1***a* to the methyl, ethyl, and isopropyl esters **2**, **3**, and **4**, respectively. These results would suggest that the Ti(IV) species involved in the alcoholysis reaction probably is not $TiCl_4$, but rather some intermediate $Ti(Cl)_x(OR)_y$ complex. The Lewis acids boron trifluoride etherate, tin(IV) chloride, and silicon(IV) chloride (12) also catalyze these transformations, although with less efficiency than titanium(IV) chloride (Table 1).

N-Alkyl and *N,N*-dialkyl carboxamides are not affected under the conditions that transform unsubstituted carboxamides to esters or acids. For example, when monoethyl amide **35***a* or diethyl amide **35***b* are subjected to the reaction conditions that successfully converted **1** to **2** or **3**, they were recovered quanti-

[1]Dedicated to Professor David MacLean in recognition of his contributions to the fields of Natural Products and Organic Chemistry.

[2]Contribution No. 879 from the Syntex Institute of Organic Chemistry.

[3]Author to whom correspondence may be addressed.

[4]Titanium trichloride has also been shown to reduce *N*-oxides and oximes (2*b*) and nitro groups (2*c*).

[5]A 1 M solution of $TiCl_4$ in either toluene or CH_2Cl_2 was used (Aldrich).

Can. J. Chem. Downloaded from www.nrcresearchpress.com by 195.246.54.202 on 09/08/12
For personal use only.

TABLE 1. Ti(IV), Si(IV), Sn(IV) and BF_3-OEt_2 catalyzed amide alcoholysis

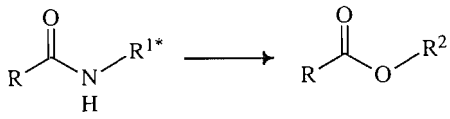

*R^1 = OCH_3 for entries

1*a*, **1***b* and H for all others

Reactant	R	Ref.[a]	Reagent	Solvent[b]	Time (h)	Product	R^2	Yield (%)	MP (°C)(Sol)	Lit MP (°C)	Ref.[c]
1*a*	$CH_2C_6H_5$	2, 3	$TiCl_4$	MeOH	3	**2**	CH_3	86	218–220 (MeOH)	220	3, 10
1*a*	$CH_2C_6H_5$	2, 3	$TiCl_4$	EtOH	17	**3**	C_2H_5	92	224–226 (EtOH)	226	3
1*a*	$CH_2C_6H_5$	2, 3	$TiCl_4$	i-PrOH	22	**4**	i-C_3H_7	87	BP 62 (0.3 Torr)	BP 65 (0.3 Torr)	3, 10
1*b*	$CH_2C_6H_5$	2, 3	$TiCl_4$	MeOH	16	**2**	CH_3	91	218–220 (MeOH)	220	3
1*b*	$CH_2C_6H_5$	2, 3	$TiCl_4$	EtOH	3	**3**	C_2H_5	85	224–226 (EtOH)	226	11
1*c*	C_6H_5	2, 3	$TiCl_4$	EtOH	48	**14**	C_2H_5	81	BP 210	BP 212	4
6	C_6H_5	4	$TiCl_4$	EtOH	36	**14**	C_2H_5	78	BP 210	BP 212	4
7	C-C_6H_{11}	5	$TiCl_4$	MeOH	26	**15**	CH_3	<10[d]	—	—	—
8	C_4H_9	—	$TiCl_4$	EtOH	25	**16**	C_2H_5	<10[d]	—	—	—
9	$CH(C_6H_5)_2$	6	$TiCl_4$	EtOH	40	**17**	C_2H_5	52	56 (hex–Et_2O)	58	12
10	$C_{15}H_{31}$	7	$TiCl_4$	EtOH	12	**18**	C_2H_5	74	28–30 (pentane)	26–28	7
11	4-$CH_3O_2CC_6H_4$	8	$TiCl_4$	EtOH	14	**19**	C_2H_5	76	BP 139–140	BP 140–142	13
12	$C_2H_5O_2C(CH_2)_3$	9	$TiCl_4$	EtOH	10	**20**	C_2H_5	90	BP 214	BP 230	14
13	4-$CH_3OC_6H_4$	8	$TiCl_4$	EtOH	11	**21**	C_2H_5	69	BP 262	BP 269	15
1*a*	$CH_2C_6H_5$		$TiCl_4$	EtOH	12	**3**	C_2H_5	93			
1*a*	$CH_2C_6H_5$		$SiCl_4$	MeOH	16	**2**	CH_3	49			
1*a*	$CH_2C_6H_5$		$SnCl_4$	MeOH	14	**2**	CH_3	41			
1*a*	$CH_2C_6H_5$		BF_3–OEt_2	EtOH	10	**2**	C_2H_5	38			
1*a*	$CH_2C_6H_5$		$Ti(OCH_3)_4$	MeOH	15	**3**	CH_3	73			
1*a*	$CH_2C_6H_5$		$Ti(OEt)_4$	EtOH	17	**2**	C_2H_5	81			
1*a*	$CH_2C_6H_5$		$Ti(Oi\text{-}Pr)_4$	i-PrOH	19	**4**	i-C_3H_7	79			

[a]Preparation of reactant.
[b]Reactions were performed under refluxing conditions.
[c]Physical properties citation.
[d]Products are quite volatile.

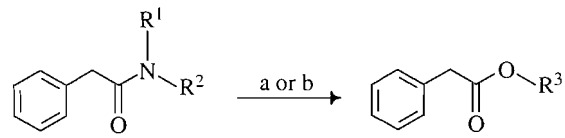

1*a*, $R^1 = R^2 = H$
1*b*, **1***c*,† $R^1 = OCH_3$, $R^2 = H$
35*a*, R^1 = Et, $R^2 = H$
35*b*, $R^1 = R^2$ = Et

2, R^3 = Me
3, R^3 = Et
4, R^3 = iPr
5, $R^3 = H$

†See entry **1***c*, Table 1.

a. $TiCl_4$ (10 mol%), molar equiv. HCl, 1 molar equiv. H_2O, solvent, reflux
b. $Ti(OR)_4$ (10 mol%), 1 molar equiv. HCl, 1 molar equiv. H_2O, solvent, reflux
For entries **35***a* and *b*, only starting amide was recovered after prolonged treatment using reaction conditions "a"

SCHEME 1

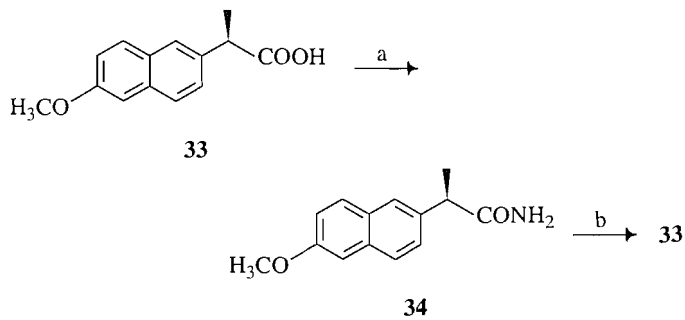

a. 1. $(ClCO)_2$, EtOAc, $NaHCO_3$, 2. NH_4OH
b. $TiCl_4$ (10 mol%), 1 molar equiv. HCl, 9:1 dioxane: H_2O, reflux

SCHEME 2

tatively, even after prolonged (>48 h) reaction times (Scheme 1).[6]

Traditional methods to hydrolyze primary carboxamides usually require strongly basic or acidic conditions (21*b*, *c*). Under these conditions, a chiral center adjacent to the carbonyl group can be racemized. $TiCl_4$ catalyzed hydrolysis of naproxen amide (**34**) (synthesized from naproxen (**33**) via the acid chloride (22) to naproxen (**33**) (Scheme 2) occurred without detectable racemization, as determined by HPLC. This implies that the mechanism of hydrolysis does not involve enolization of the carbonyl group.

In conclusion, this study has shown that catalytic $TiCl_4$ and $Ti(OR)_4$ in the presence of aqueous HCl efficiently converts unsubstituted carboxamides to esters or acids. Two *O*-methyl hydroxamic acids are also shown to be converted to esters or acids by these conditions. Further, the hydrolysis reaction is

[6]A mild three-step method for tertiary amide hydrolysis has been reported (21*a*).

Can. J. Chem. Downloaded from www.nrcresearchpress.com by 195.246.54.202 on 09/08/12
For personal use only.

TABLE 2. $TiCl_4$ catalyzed amide hydrolysis

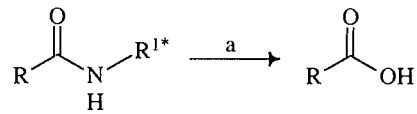

*R^1 = OCH_3 for entries

1*b*, **1***c* and H for all others

Reactant	R	Ref.[b]	Reagent	Solvent	Time (h)	Product	Yield[c] (%)	MP (°C)(Sol)	Lit. MP (°C)	Ref.[d]
1*a*	$CH_2C_6H_5$	2, 3	$TiCl_4$	9:1 Diox.:H_2O	20	**25**	87	74–76 (Tol)	76	16
1*b*	$CH_2C_6H_5$	2, 3	$TiCl_4$	9:1 Diox.:H_2O	17	**25**	91	74–76 (Tol)	76	16
1*c*	C_6H_5	2, 3	$TiCl_4$	9:1 Diox.:H_2O	24	**26**	79	28–31 (EtOAc)	30–32	5
6	C_6H_5	4	$TiCl_4$	9:1 Diox.:H_2O	15	**27**	85	119–120 (H_2O)	121–122	17
7	C_6H_{11}	5	$TiCl_4$	9:1 Diox.:H_2O	19	**26**	86	29–32 (EtOAc)	30–32	5
9	$CH(C_6H_5)_2$	6	$TiCl_4$	9:1 Diox.:H_2O	24	**28**	92	143–146 (EtOAc)	147–149	12
10	$C_{15}H_{31}$	7	$TiCl_4$	9:1 Diox.:H_2O	22	**29**	87	63–63 (Hex)	63–64	7
11	4-$CH_3O_2CC_6H_4$	8	$TiCl_4$	9:1 Diox.:H_2O	21	**30**[e]	78	>285	>300	18
12	$C_2H_5O_2C(CH_2)_3$	9	$TiCl_4$	9:1 Diox.:H_2O	20	**31**[f]	90	88–89 (acetone)	95–96	19
13	4-$CH_3OC_6H_4$	10	$TiCl_4$	9:1 Diox.:H_2O	19	**32**	93	180–184 (EtOAc)	183	20

[a]All reactions carried out in the following manner: approximately 1 molar in substrate in a mixture of 9:1 dioxane: H_2O, approximately 0.1 molar equiv. $TiCL_4$, approximately 1 molar equiv. aqueous HCl. This mixture was heated under reflux for the time specified in Table 2.
[b]Preparation of reactant.
[c]Isolated yields.
[d]Physcial properties citation.
[e]Terephthalic acid.
[f]Glutaric acid.

mild enough to leave adjacent chirality uncompromised, presenting an advantage over traditional, more vigorous, hydrolysis methods.

Experimental section

Melting points are uncorrected. All compounds reported are known and referenced where they appear in the tables. Determinations of enantiomeric purity were performed by analysis by direct HPLC using a Spectra-Physics 8800 ternary pump, Spectra-Physics SP8780 autosampler, and a Spectra Physics Spectra 100 variable wavelength detector connected to a Chiral-AGP column. The following conditions were used: column: Chiral AGP, 100 × 4.0 mm, 5 μm; mobile phase: 99.5% 4 mM NaH_2PO_4 + Na_2HPO_4 pH 7.0, 0.5% 2-PrOH;low rate: 0.8 mL/min; temperature: ambient; detection: 262 nm (22).

Optical rotations were measured on a JASCO DIP-360 instrument.

*General method for the syntheses of primary carboxamides or O-methylphenylacetohydroxamate (**1**b) or methylbenzylhydroxamate (**1**c)*

To a stirred solution of carboxylic acid in methylene chloride (CH_2Cl_2) at 0°C was added oxalyl chloride (2 molar equiv.) and *N,N*-dimethylformamide (DMF, 1 drop). The mixture was allowed to warm to room temperature and subsequently the CH_2Cl_2 was removed in vacuo. The residue was dissolved in CH_2Cl_2, cooled to 0°C, and treated with either NH_4OH (excess, to give the primary amide) or methoxylamine hydrochloride (1 equiv., and Et_3N, 2 equiv., to give the *O*-methyl hydroxamic acid). The reaction mixture was allowed to warm to room temperature and was shaken with 1 M HCl. The organic layer was separated and dried with Na_2SO_4, filtered, and the solvent was removed in vacuo to give the product.

*General method for the titanium(IV) chloride mediated alcoholysis of primary carboxamides or Omethylphenylacethydroxamate (**1**b) or methylbenzylhydroxamate (**1**c)*

To a solution of carboxamide or *O*-methyl hydroxamic acid (1 equiv.) in the appropriate alcohol (approximately 1 M in substrate) was added aqueous $TiCl_4$ (0.1 molar equiv.) and aqueous HCl (1 molar equiv.). The reaction mixture was then brought to reflux for the specified amount of time (Table 1). After being allowed to cool to room temperature, the reaction mixture was poured onto ice–H_2O and brought to neutrality with 1 M NaOH. Extraction with ethyl acetate (EtOAc), removal of water with Na_2SO_4, filtration again, and finally removal of solvent in vacuo gave the ester. If necessary, the product was recrystallized from the appropriate solvent.

*General method for the titanium(IV) chloride mediated conversion of primary carboxamides or Omethylphenylacethydroxamate (**1**b) or methylbenzylhydroxamate (**1**c) to carboxylic acids*

To a solution of carboxamide or *O*-methyl hydroxamic acid (1 equiv.) in 9:1 dioxane:H_2O(approximately 1 M in substrate) was added aqueous $TiCl_4$ (0.1 molar equiv.) and aqueous HCl (1 molar equiv.). The reaction mixture was then brought to reflux for the specified amount of time (Table 2). After being cooled to room temperature, the reaction mixture was poured onto ice–H_2O. Extraction with EtOAc, removal of water with Na_2SO_4, filtration again, and finally removal of solvent in vacuo gave the acid. If necessary, the product was recrystallized from the appropriate solvent.

General method for the Lewis acid mediated alcoholysis of primary carboxamides

To a solution of carboxamide (1 equiv.) in EtOH (approximately 1 M in amide) was added $SiCl_4$, $SnCl_4$, or BF_3_Et_2O (0.1 molar equiv.). To this mixture was added aqueous HCl (1 molar equiv.). The reaction mixture was then brought to reflux for the specified amount of time (Table 1). After being allowed to cool to room temperature, the reaction mixture was poured onto ice–H_2O and brought to neutrality with 1 M NaOH. Extraction with EtOAc, removal of water with Na_2SO_4, filtration again, and finally removal of solvent in vacuo gave the ester. If necessary, the product was recrystallized from the appropriate solvent.

General method for the $Ti(OR)_4$ mediated alcoholysis of primary carboxamides

To a solution of carboxamide (1 equiv.) in EtOH (approximately 1

Can. J. Chem. Downloaded from www.nrcresearchpress.com by 195.246.54.202 on 09/08/12
For personal use only.

M in amide) was added $Ti(OMe)_4$, $Ti(OEt)_4$, or $Ti(OiPr)_4$ (0.1 molar equiv.). To this mixture was added aqueous HCl (1 molar equiv.). The reaction mixture was then brought to the temperature specified for each entry in Table 1 for the specified amount of time. After being allowed to cool to room temperature, the reaction mixture was poured onto ice–H_2O and brought to neutrality with 1 M NaOH. Extraction with EtOAc, removal of water with Na_2SO_4, filtration, and finally removal of solvent in vacuo gave the ester. If necessary, the product was recrystallized from the appropriate solvent.

*6-Methoxy-α-methyl-2-naphthaleneacetamide (**34**)*

To a stirred solution of 6-methoxy-α-methyl-2-naphthaleneacetic acid (**33**) (27.4 g, 0.12 mol) in EtOAc (400 mL) and aqueous $NaHCO_3$ (400 mL of a 1 M solution) at 0°C was added oxalyl chloride (20.7 mL, 0.24 mol). The reaction mixture was allowed to warm to room temperature. The layers were allowed to separate and the organic layer was dried with Na_2SO_4, filtered, and evaporated in vacuo. The residue was redissolved in CH_2Cl_2 (450 mL), cooled to 0°C, and treated dropwise with NH_4OH (50 mL of a 37% aqueous solution). The reaction mixture was allowed to warm to room temperature and was carefully acidified with HCl (1 M) to pH 4. The organic layer was separated and dried with Na_2SO_4, filtered, and the solvent was removed in vacuo to give crude **34**. Recrystallization (acetone–hexane) gave crystalline **34** (26.1 g, 95%); mp 173–176°C (acetone–hexane) (lit. (22) mp 172–175°C); $[\alpha]^{25}_D$ + 20 (*c* 1, $CHCl_3$) (lit. (22) $[\alpha]^{25}_D$ + 20.2 (*c* 1, $CHCl_3$).

*6-Methoxy-α-methyl-2-naphthaleneacetic acid (naproxen) (**33**)*

To a solution of **34** (2.3 g, 0.01 mol) in 9:1 dioxane:H_2O (10 mL) was added aqueous $TiCl_4$ (1 mL, 1 M in $TiCl_4$, in CH_2Cl_2 or toluene) and aqueous HCl (1 mL of a 1 M solution). The reaction mixture was then brought to reflux for 15 h. After cooling to room temperature, the reaction mixture was poured onto ice–H_2O. Extraction with EtOAc, removal of water with Na_2SO_4, filtration again, and finally removal of solvent in vacuo gave the acid **33** as a solid that was crystallized from acetone–hexane (2.21 g, 96%; mp 153–155°C (acetone–hexane) (lit. (22) mp 154–155°C); $[\alpha]^{32}_D$ +66 (*c* 1, $CHCl_3$) (lit. (22) $[\alpha]^{25}_D$ + 66 (*c* 1, $CHCl_3$). Serially increasing injections of **33** (0.2–0.5 mg) dissolved in the mobile phase (1–5 μL) showed that **33** was 99.0% (*S*)-6-methoxy-α-methyl-2-naphthaleneacetic acid (22). This is compared to a USP batch that was shown to be 99.2% (*S*)-6-methoxy-α-methyl-2-naphthaleneacetic acid.

1. L.E. Fisher, J.M. Caroon, Jahangir, S.R. Stabler, S. Lundberg, and J.M. Muchowski. J. Org. Chem. **58**, 3643 (1993).
2. (*a*) P.G. Mattingly and M.J. Miller. J. Org. Chem. **45**, 410 (1980); (*b*) G.H. Timms and E. Wildsmith. Tetrahedron Lett. 195 (1971); (*c*) J.E. McMurry and J. Melton. J. Org. Chem. **38**, 4367 (1973); J.E. McMurry. Acc. Chem. Res. 281 (1974).
3. B. Radszewski. Ber. Dtsch. Chem. Ges. **2**, 207 (1869).
4. J.H. Hall and M.R. Gisler. J. Org. Chem. **42**, 1133 (1977).
5. O. Aschan. Liebigs Ann. Chem. **271**, 231 (1892).
6. A.N. Meldrum and W.E.S. Turner. J. Chem. Soc. **97**, 1605 (1910).
7. F. Krafft and B. Stauffer. Ber. Dtsch. Chem. Ges. **15**, 1728 (1882).
8. E. Dyer and H. Scott. J. Am. Chem. Soc. **79**, 672 (1957).
9. W.J. Bailey and W.G. Carpenter. J. Org. Chem. **29**, 1252 (1964).
10. M.F. Semmelhack, B.P. Chong, R.D. Stauffer, T.D. Rogerson, A. Chong, and L.D. Jones. J. Am. Chem. Soc. **97**, 2507 (1975).
11. G.G. Smith, L. Mutter, and G.P. Todd. J. Org. Chem. **42**, 44 (1977).
12. L. Hellerman, M.L. Cohn, and R.E. Hoen. J. Am. Chem. Soc. **50**, 1716 (1928).
13. E.M. Panov, K. Frybakova, and K.A. Kocheshkov. J. Org. Chem. USSR (Engl. Transl.), **8**, 2408 (1972).
14. C.K. Ingold. J. Chem. Soc. **119**, 329 (1921).
15. D. Kahovec and I. Kohlrausch. Z. Phys. Chem. abt. B: **38**, 119 (1937).
16. H. Thoms and R. Beckstroem. Ber. Dtsch. Chem. Ges. **34**, 1021 (1901).
17. P. Schorygin. Ber. Dtsch. Chem. Ges. **41**, 2723 (1908).
18. A. Baeyer. Liebigs Ann. Chem. **245**, 103 (1888).
19. H. Simon, G. Heubach, W. Bitterlich, and H. Gleinig. Chem. Ber. **98**, 3692 (1965).
20. J. Mirov, E. Zavarini, and J.G. Bicho. J. Pharm. Sci. **51**, 1131 (1962).
21. (*a*) M.P. Sibi, K. Shankaran, B.I. Alo, W.R. Hahn, and V. Snieckus. Tetrahedron Lett. 2933 (1987); (*b*) C. O'Connor. Q. Rev. Chem. Soc. **24**, 553, and references therein; (*c*) R.H. DeWolfe and R.C. Newcomb. J. Org. Chem. **36**, 3870 (1971), and references therein.
22. J.F. Fried and I.J. Harrison. U.S. Patent 3,978,124 (1976).

Can. J. Chem. Downloaded from www.nrcresearchpress.com by 195.246.54.202 on 09/08/12
For personal use only.

Stereoselective total synthesis of the marine sesterterpenoid (±)-palauolide

EDWARD PIERS[1] AND JOHN S.M. WAI

Department of Chemistry, University of British Columbia, 2036 Main Mall, University Campus, Vancouver, BC, V6T 1Z1, Canada

Received June 14, 1993

This paper is dedicated to Professors David B. MacLean and Ian D. Spenser

EDWARD PIERS and JOHN S.M. WAI. Can. J. Chem. **72**, 146 (1994).

A total synthesis of the antimicrobial, structurally unusual sesterterpenoid (±)-palauolide (**1**) is described. Methylenecyclohexane annulation of 3,6-dimethyl-2-cyclohexen-1-one (**4**) afforded a mixture of the bicyclic ketones **7** and **9** in a ratio of 94:6. Stereoselective conversion of this mixture into the phosphorodiamidate **46** was achieved via a five-step reaction sequence. Reduction of **46** with Li in $MeNH_2$ gave the bicyclic substance **47**, which was readily transformed in seven steps into the α,β-unsaturated aldehyde **54**. Subjection of **54** to a Julia olefin synthesis, employing reagent **56**, gave the furan **58**. Photooxygenation of **58** provided (±)-palauolide (**1**).

EDWARD PIERS et JOHN S.M. WAI. Can. J. Chem. **72**, 146 (1994).

On décrit une synthèse totale du (±)-palauolide (**1**), un sesquiterpénoïde antimicrobien de structure inhabituelle. L'annellation du méthylènecyclohexane avec la 3,6-diméthylcyclohex-2-én-1-one (**4**) fournit les cétones bicycliques **7** et **9** dans un rapport de 94 : 6. On a réalisé la transformation stéréosélective de ce mélange en phosphorodiamidate **46** par une séquence réactionnelle de cinq étapes. La réduction de **46** par du Li dans la $MeNH_2$ fournit le composé bicyclique **47** qui peut être facilement transformé, en sept étapes, en aldéhyde α,β-insaturé **54**. Lorsqu'on soumet le composé **54** à une synthèse d'oléfine de Julia, en utilisant le réactif **56**, on obtient le furane **58**. Une photooxygénation du composé **58** conduit au (±)-palauolide (**1**).

[Traduit par la rédaction]

Introduction

In 1982, Sullivan and Faulkner (1) isolated a new natural product from the methanolic extract of a mixture of sponges collected from Palau, Western Caroline Islands. This substance, which displays notable antimicrobial activity against *Bacillus subtilis* and *Staphylococcus aureus*, was named palauolide and was shown (1) to be a sesterterpenoid possessing the novel constitution and relative configuration depicted in structural formula **1**. Prior to the isolation of palauolide, the carbon skeleton present in this substance had not been encountered in natural product chemistry. However, it is appropriate to note that, structurally, palauolide (**1**) is closely related to the very large family of *trans*-clerodane diterpenoids, which share the basic carbon framework shown in **2** (2). The substituted γ-hydroxybutenolide moiety present in **1**, which is derived from an additional isoprene unit, is probably responsible for the observed biological activity of this natural product. We report in this paper a total synthesis of racemic palauolide (**1**).[2]

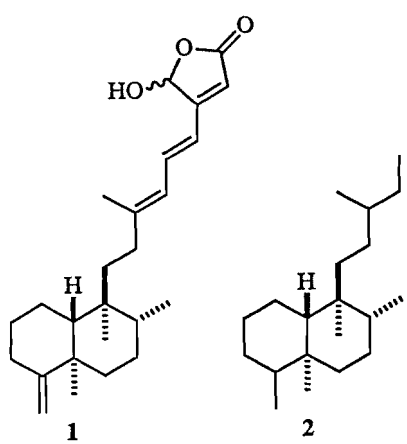

1 **2**

[1]Author to whom correspondence may be addressed.

[2]For a preliminary account of this work, see ref. 3.

Results and discussion

(a) Conversion of 3,6-dimethyl-2-cyclohexen-1-one (4) into the bicyclic nitriles 11 and 12

At the outset of this synthetic endeavor, it was evident that the methylenecyclohexane annulation method developed previously in our laboratory (4) should serve as an effective vehicle for the preparation of the substituted bicyclo[4.4.0]decane portion of the palauolide structure. The necessary substrate for this process, 3,6-dimethyl-2-cyclohexen-1-one (**4**) was readily prepared by alkylation (lithium diisopropylamide (LDA), tetrahydrofuran (THF); MeI) of 3-methyl-2-cyclohexen-1-one (**3**) (see Scheme 1). Copper(I)-catalyzed conjugate addition of 2-(5-chloro-1-pentenyl)magnesium bromide (**5**)[3] to the enone **4** in the presence of $BF_3 \cdot Et_2O$ (4) provided the substituted cyclohexanone **6** (mixture of epimers, ratio ~2:1).

Exposure of **6** to *t*-BuOK in *t*-BuOH at 30°C for 12 h provided, in 89% yield, two bicyclic ketones in a ratio of approximately 94:6. A sample of each of these substances was obtained by subjecting the mixture to column chromatography on silica gel impregnated with 25% silver nitrate. In the ^1H nmr spectra of the two ketones, the angular methyl groups give rise to 3-proton singlets at δ 0.87 (major isomer) and 1.31 (minor isomer). On this basis, it is possible to conclude that the major and minor products are *trans*-fused and *cis*-fused, respectively (see ref. 6).

Since the intramolecular alkylation was carried out under conditions that would equilibrate the two stereogenic centers adjacent to the carbonyl function, four diastereomeric products **7–10** could have been produced. On the basis of conformational analyses, it is clear that, of the two possible *trans*-fused isomers, **7** is more stable than **8**, while in the case of the *cis*-fused substances, **9** is of lower energy than **10**. Therefore, it was concluded that the two products derived from methylenecyclo-

[3]This reagent was derived by sequential treatment of 5-chloro-2-trimethylstannyl-1-pentene (prepared via a procedure modified from that reported earlier (5), see Experimental) with MeLi and $MgBr_2$–etherate in THF at −78°C (4).

Can. J. Chem. Downloaded from www.nrcresearchpress.com by 203.198.23.82 on 09/08/12
For personal use only.

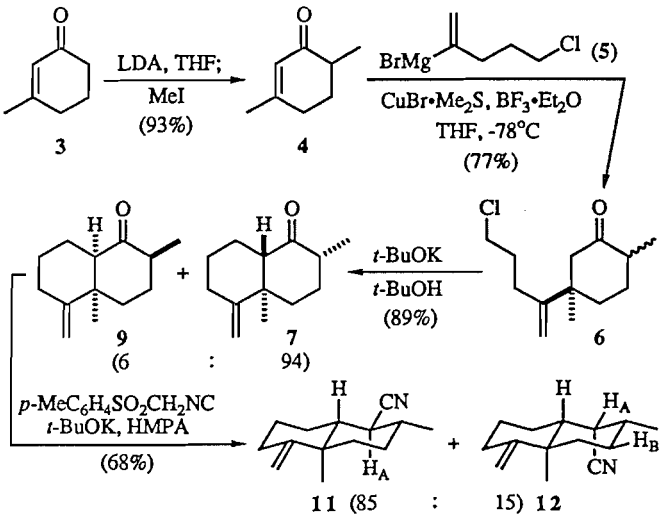

SCHEME 1

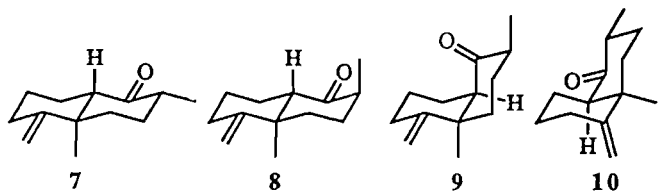

hexane annulation of **4** are the ketones **7** (major) and **9** (minor) (see Scheme 1).

Each of the three stereogenic centers of the ketone **7** possesses the correct relative configuration for an eventual synthesis of (±)-palauolide (**1**). At this stage of the synthesis, the carbonyl function of **7** was to be used as a handle for the introduction of the necessary appendages at this center. To this end, the 94:6 mixture of **7** and **9** was treated with (*p*-toluenesulfonyl)methyl isocyanide (TOSMIC) (**7**) and *t*-BuOK in dry *t*-BuOH–hexamethylphosphoramide (HMPA) (45°C, 88 h). This process produced a mixture of two epimeric nitriles in a ratio of about 85:15. Column chromatography of a portion of this mixture on 4:1 silica gel – silver nitrate allowed the isolation of a pure sample of each product. On the basis of ^{1}H nmr spectral data, these two substances were assigned structures **11** (major) and **12** (minor). In the spectra of **11** and **12**, the protons H_A give rise to a triplet (δ 2.08, J = 11.5 Hz) and a triplet of doublets (δ 2.60, J = 4.5, 1.3 Hz[4]). The coupling constants show clearly that H_A in **11** and **12** are axially and equatorially oriented, respectively. Furthermore, the angular methyl group of **12**, which bears a 1,3-diaxial relationship with the nitrile function, would be expected to resonate at lower field than the corresponding methyl in **11**. This was found to be the case. In the ^{1}H nmr spectra of **11** and **12**, the angular methyl functions produce singlets at δ 0.96 and 1.24, respectively.

It is interesting to note that the base-promoted reaction of the mixture of **7** and **9** with TOSMIC did not produce any nitrile products possessing *cis*-fused six-membered rings. This observation is in accord with reports (see, for example, ref. 8) that a *trans*-fused bicyclo[4.4.0]decan-2-one usually reacts faster with nucleophiles than the corresponding *cis*-fused isomer. Therefore, under conditions in which the two ketones are in equilibrium (as in the conversion of **7** and **9** into **11** and **12**), the

[4]It is likely that this small coupling constant arises from weak, long-range w-coupling between H_A and H_B in **12**.

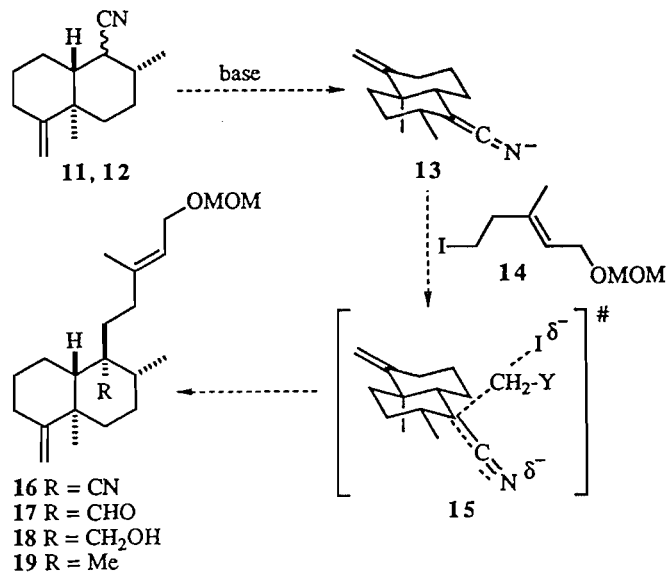

SCHEME 2

products are often those derived mainly or even solely from the *trans*-fused substrate.

*(b) Attempted preparations of the substituted bicyclo[4.4.0]-decanes **19** and **34**. Unsuccessful approaches to the synthesis of (±)-palauolide (**1**)*

An initially investigated approach to the synthesis of (±)-palauolide (**1**) is outlined in general terms in Scheme 2. Treatment of the mixture of nitriles **11** and **12** with a suitable base would provide the anion **13**. Alkylation of the latter species with the electrophile **14** (MOM = CH_2OMe) would be expected to proceed preferentially via a transition state that can be (simplistically) represented by **15**. The alternative transition state, involving approach of **14** from the "bottom" face of **13**, would be notably destabilized by a steric interaction between the incoming electrophile and the angular methyl group present in **13**. Subjection of the expected alkylation product **16** to appropriate reduction procedures would provide the aldehyde **17** and (or) the alcohol **18**. Successful reductive deoxygenation of **17** or **18** would produce **19**, which possesses a functional group (allylic OMOM) suitable for use as a "handle" for the introduction of the functionalized butenolide unit present in the target compound **1**.

The required alkylating agent **14** was prepared from 3-butyn-1-ol (**20**) as summarized in Scheme 3. Reaction of **20** with *t*-BuMe_2SiCl–imidazole in *N,N*-dimethylformamide (DMF), followed by sequential treatment of the resultant ether **21** with MeLi and $ClCO_2Et$ in THF, gave the α,β-acetylenic ester **22**. Stereoselective conversion of **22** into the (*Z*)-β-trimethylstannyl α,β-unsaturated ester **23** was effected by reaction of the former substance with lithium (trimethylstannyl)(phenylthio)cuprate (9) in THF (−40°C, 9 h; NH_4Cl, H_2O) (10). Reduction of **23** and subsequent reaction of the resultant alcohol **24** with $MeOCH_2Cl$ in the presence of i-Pr_2NEt in CH_2Cl_2 produced the diether **25**. Transmetallation (MeLi, THF, −78°C) of the vinyltrimethylstannane function of **25** (11), followed by reaction of the resultant vinyllithium species with MeI, provided the (*E*) alkene **26**. Conversion of **26** into the required iodide **14**, via intermediates **27** and **28**, involved standard functional group interconversions.

Treatment of the 85:15 mixture of **11** and **12** (vide supra)

Can. J. Chem. Downloaded from www.nrcresearchpress.com by 203.198.23.82 on 09/08/12
For personal use only.

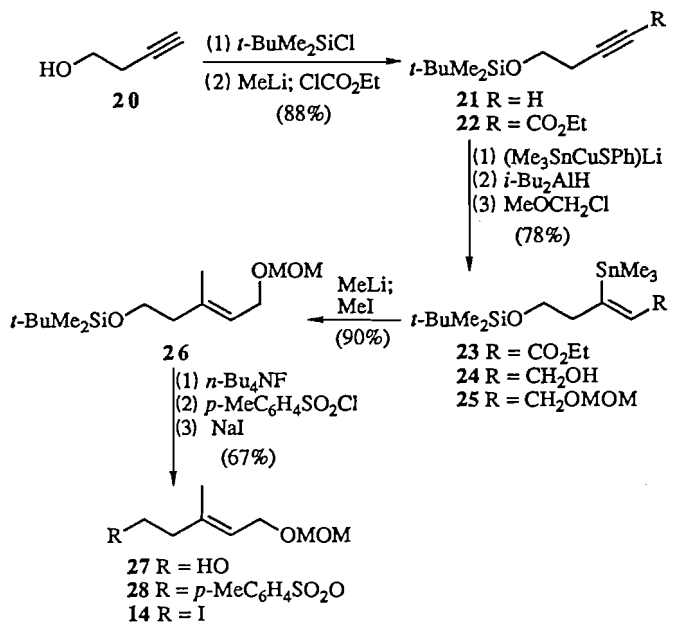

SCHEME 3

with LDA in THF–HMPA[5] at 0°C, followed by addition of the iodide **14**, produced a single alkylation product **16** (70%, 92% based on recovered starting materials), accompanied by the starting materials **11** and **12** (23%, ratio ~2:3, respectively) (eq. [1]). Also isolated was a small amount of the (volatile) diene **29**. Although this material was not fully characterized, its ^{1}H nmr spectrum showed the presence of the CH_2OMOM moiety, the vinyl methyl group, and four olefinic protons (δ 6.43 (dd, J = 11, 17 Hz, H_C), 5.63 (br t, J = 7 Hz, H_D), 5.23 (d, J = 17 Hz, H_B), 5.05 (d, J = 11 Hz, H_A). Thus, it is evident that, in the reaction of the iodide **14** with the nitrile anion derived from **11** + **12**, there is a competition between substitution and elimination. Nevertheless, the required product **16** could be isolated in good yield and, obviously, the recovered nitrile substrates could be recycled.

In the ^{1}H nmr spectrum of the alkylation product **16**, the angular methyl group gives rise to a singlet at δ 1.27, indicating that this moiety is in a 1,3-diaxial relationship with the CN function. Thus, strong evidence for the expectation (vide supra) that the alkylation reaction would proceed stereoselectively in the required sense was readily available.

When the nitrile **16** was treated with excess i-Bu_2AlH in PhH, Et_2O, THF, or 1,2-dimethoxyethane (DME) at room temperature, no reduction occurred and the substrate was recovered intact. On the other hand, reaction of **16** with i-Bu_2AlH in DME at 60°C for 6 h, followed by (sluggish) acid hydrolysis (HOAc, H_2O, THF, room temperature, 12 h) of the hindered imine function, provided the required aldehyde **17** in 87% yield (eq. [2]).

Treatment of **17** with hydrazine (10 equiv.) in MeOH (reflux, 24 h) provided the corresponding hydrazone **30** (ir 3250 cm^{-1}, broad) in good yield. However, although reductive conversion of the latter material into the required product **19** was attempted under a variety of conditions, these efforts did not produce synthetically useful results. For example, reaction of **30** with KOH

[5]Model studies, involving attempted alkylation of **11** + **12** with n-BuI, showed that treatment of the mixture of nitriles with LDA in THF, *in the absence of HMPA*, failed to deprotonate the equatorial nitrile **11** at an appreciable rate.

[1]
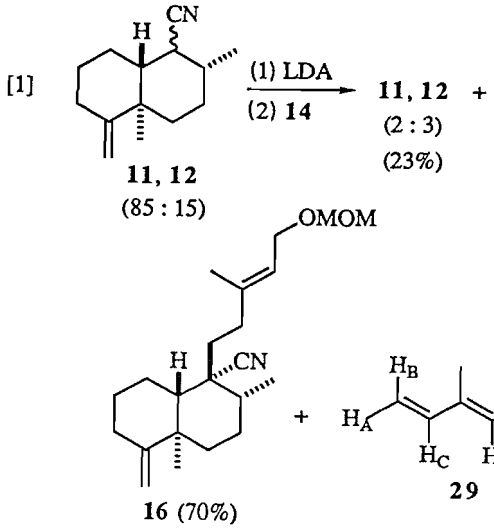

[2]
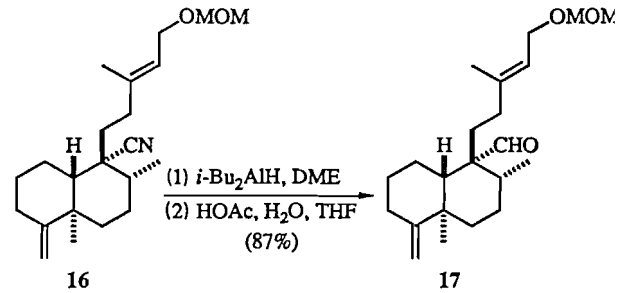

in diethylene glycol (DEG) at 210°C for 3 h produced two products, the chromatographically more polar, desired substance **19** (10% yield) and the less polar triene **31** (45% yield). The ^{1}H nmr spectrum of compound **19** exhibits the expected signals (δ 4.63, OCH_2O; 3.37, OCH_3; 1.66, vinyl Me) due to the OMOM- containing side chain. Resonances due to the exocyclic olefinic hydrogens and three methyl groups (δ 4.51, br s; 1.05 (s), 0.82 (d, J = 6 Hz), 0.74 (s)) are also present. These data, along with the fact that the latter set of signals have chemical shifts identical with those reported (1) for the corresponding functions of palauolide, provided strong evidence for the conclusion that the minor product derived from treatment of **30** with base possesses the constitution and relative configuration shown in **19**.

The ^{1}H nmr spectrum of the major product **31** is also in full accord with the structural assignment. The pertinent data are shown in conjunction with the structural formula (see **31**).

When a solution of the hydrazone **30** in DEG containing K_2CO_3 was heated slowly from 110 to 180°C, analyses (tlc) of aliquots of the reaction mixture indicated that substrate conversion began when the temperature reached ~160°C. Furthermore, both products **19** (minor) and **31** (major) appeared simultaneously. Application of an alternative method, involving reaction of the hydrazone **30** with t-BuOK in dimethyl sulfoxide (DMSO) (12) gave the triene **31** as the only isolated product, albeit in mediocre yield (36%).

Conversion of compound **17** into the hydrazone alcohol **33** was accomplished via a two-step reaction sequence involving Me_2BBr-mediated cleavage of the OMOM function (CH_2Cl_2, −78°C) (13), followed by reaction of the resultant alcohol aldehyde **32** with hydrazine in refluxing MeOH. Unfortunately, treatment of **33** with KOH or K_2CO_3 in DEG at 170°C for ~3 h again afforded, in each case, the triene **31** as the major product. Thus, all attempts to effect an efficient synthesis of the desired

Can. J. Chem. Downloaded from www.nrcresearchpress.com by 203.198.23.82 on 09/08/12
For personal use only.

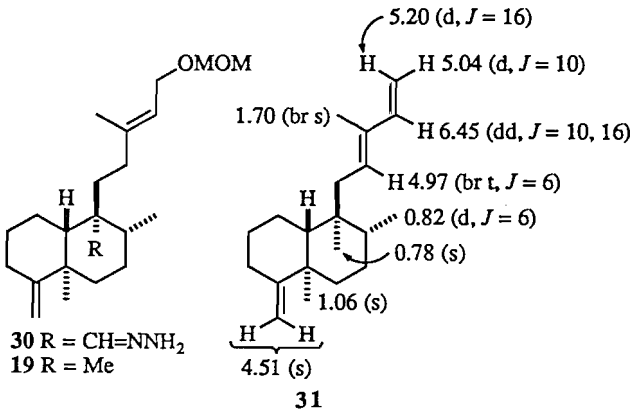

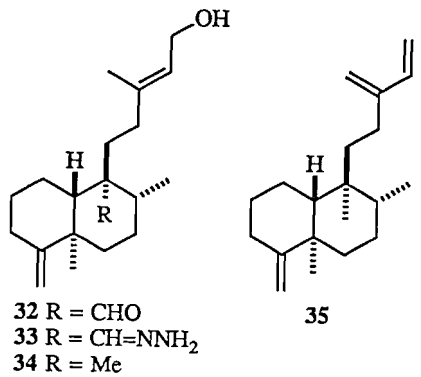

intermediates **19** or **34** by base-mediated reduction of the hydrazones **30** or **33** failed.

The results summarized above showed that the reduction–elimination reactions leading from the hydrazones **30** and **33** to the triene **31** are, with respect to the elimination processes, highly site-selective. In none of the reactions outlined above could the (possible) alternative triene **35** be detected in the reaction product. This selectivity can, perhaps, be best rationalized by postulating that the diene **31** is derived via an intramolecular elimination process involving the intermediacy of the anion **36** derived from the hydrazones **30** or **33** (see Scheme 4). Thus, although protonation of **36** on the H_2C^* group (see **36**) by the solvent would produce the desired products (**19** or **34**), a competitive, internal elimination process via a five-centered cyclic transition state would produce the diene **31**.

The synthetic difficulties associated with the endeavours outlined above led to attempts to prepare **19** or **34** by reduction of the phosphorodiamidate derivatives **38** or **39** (see Scheme 5). To that end, reduction of the aldehyde **17**, followed by sequential treatment of the derived alcohol **37** with *n*-BuLi (DME-*N,N,N′,N′*-tetramethylethylenediamine (TMEDA), room temperature), $Me_2NP(O)Cl_2$, and Me_2NH (0°C) (14) provided the required substrate **38**. Cleavage (Me_2BBr, CH_2Cl_2, −78°C, ref. 13) of the MOM ether function of **38** gave **39**.

Reduction (0°C, 30 min) of **38** with Li in $EtNH_2$ containing *t*-BuOH (15) gave, in 75% yield, the diene **40**. When the reductive process was carried out at −48°C for 15 min, the crude product consisted of a mixture of the starting material **38** and the phosphorodiamidate **41**. Thus, it appears that reductive cleavage of the allylic OMOM function is more facile than reduction of the CH_2-$OP(O)(NMe_2)_2$ moiety. Unfortunately, treatment of the substrate **39** under similar reductive conditions (Li, $EtNH_2$, *t*-BuOH, 0°C) also produced primarily the diene **40**.

The ^1H nmr spectrum derived from the diene **40** is in full

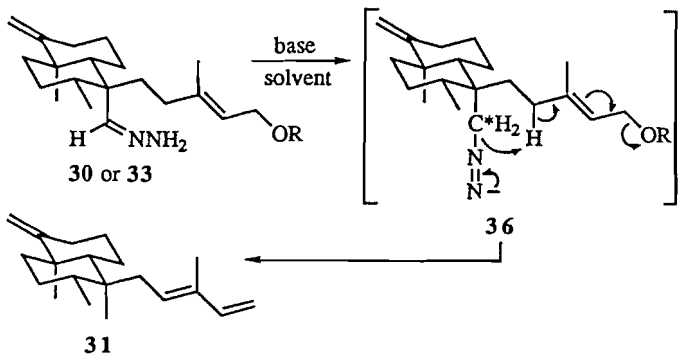

SCHEME 4

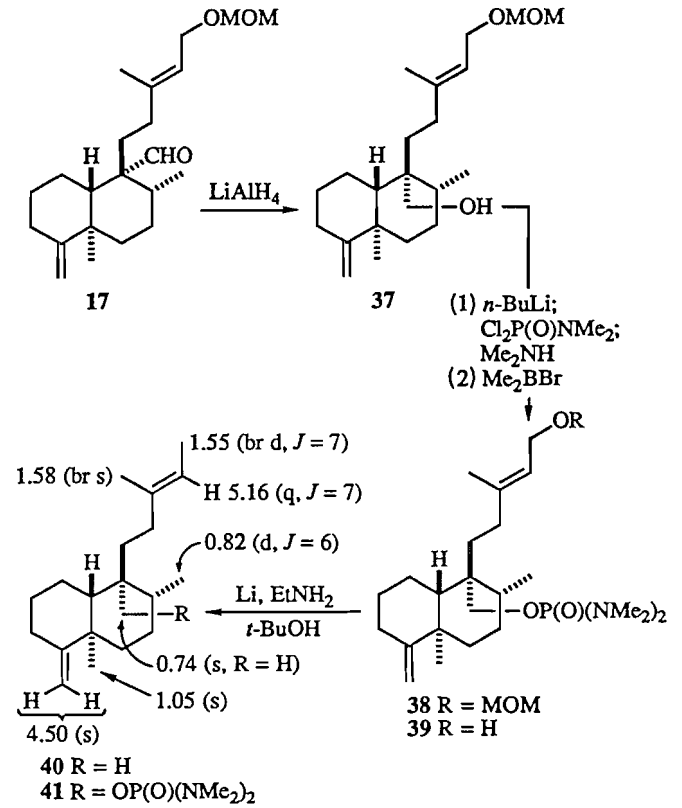

SCHEME 5

accord with the assigned structure. Some of the pertinent chemical shift data are portrayed in conjunction with the structural formula (see **40**).

(c) Completion of a total synthesis of (±)-palauolide (1)

In view of the fact that the work summarized above did not result in a successful approach to the synthesis of (±)-**1**, an alternative, less convergent route had to be developed. Explicitly, it appeared that alkylation of the nitriles **11** and **12** had to be performed with a reagent structurally more simple than the homoallylic iodide **14**. The electrophile that was selected was the iodide **42** (16), which was readily prepared from 3-chloro-1-propanol as shown in eq. [3].

[3] 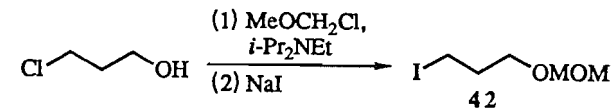

Can. J. Chem. Downloaded from www.nrcresearchpress.com by 203.198.23.82 on 09/08/12
For personal use only.

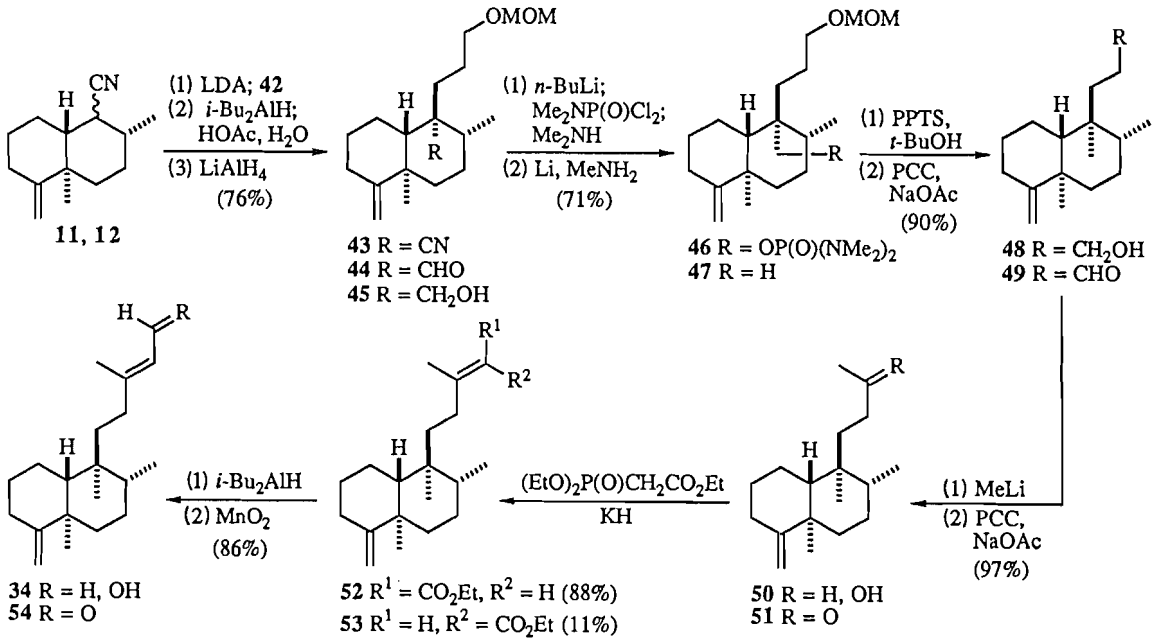

SCHEME 6

Conversion of the mixture of nitriles **11** and **12** into the bicyclic α,β-unsaturated aldehyde **54** is outlined in Scheme 6. Treatment of the anion derived from **11** and **12** with the iodide **42** provided, in nearly quantitative yield, the alkylation product **43**. As expected (vide supra), this reaction proceeded in a completely stereoselective manner. Conversion of **43**, via the intermediates **44** and **45**, into the phosphorodiamidate **46** was achieved efficiently by use of reagents and reaction conditions similar to those employed earlier for the preparation of **38** from **16**.

Subjection of substance **46** to conditions (Li, $EtNH_2$, *t*-BuOH, 0°C, 10 min) normally used (15) for reductive removal of the $OP(O)(NMe_2)_2$ moiety produced a 1:1 mixture of the desired product **47** and the bicyclic ether **55**[6] in which the carbon–carbon double bond on the bicyclic substructure had also been reduced (eq. [4]). When the reduction reaction was carried out at −10°C for 5 min, the ratio of products (**47**:**55**) improved to 2:1 and, when a more dilute solution of Li in $EtNH_2$ was employed, the product ratio was beneficially altered to ~25:1. However, reproduction of the latter result on a larger scale proved to be problematic. Fortunately, after additional experimentation, it was found that reduction (−20°C, 10 min) of **46** with Li in dry *methylamine* in the *absence* of *t*-BuOH provided, chemoselectively and reproducibly, the desired substance **47** in very good yield (Scheme 6). Thus, a suitably substituted bicyclo[4.4.0]decane, possessing the correct relative configuration at each of the four stereogenic centers, had been prepared stereoselectively and efficiently from the dimethylcyclohexenone **4**.

Treatment of the MOM ether **47** with pyridinium *p*-toluenesulfonate (PPTS) in *t*-BuOH (17) at 70°C for 12 h gave the alcohol **48** in 91% yield. A straightforward sequence of reactions, involving oxidation of **48** with pyridinium chloro-

[4]

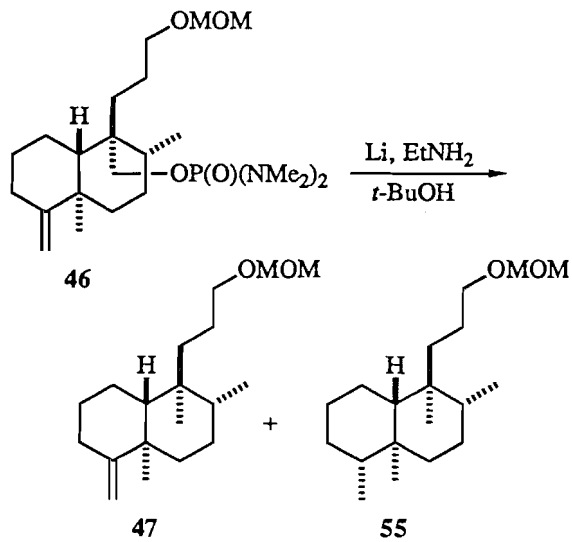

chromate (PCC) in CH_2Cl_2 (18), addition of MeLi to the acquired aldehyde **49**, and oxidation (PCC) of the resultant mixture of epimeric alcohols **50**, produced, in excellent yield, the methyl ketone **51**. It should be noted that compound **51** has also been prepared by Sharma and Grayen (19) via a synthetic route very different from that described above. The ^1H nmr and ir spectral data reported (19) for this material agree very well with those derived from our intermediate.

Reaction of the ketone **51** with the potassium salt of triethyl phosphonoacetate in THF at room temperature produced, highly efficiently, a mixture of two geometrically isomeric α,β-unsaturated esters in a ratio of ~9:1. Fortunately, these substances were readily separated by column chromatography on silica gel. The expectation (20) that the major product, which was isolated in 88% yield, possesses the *E* configuration was confirmed by ^1H nmr spectroscopy. Thus, the vinyl methyl group of the *E* isomer **52**, being *cis* to the CO_2Et group, would be expected to give rise to a ^1H nmr signal at lower field than the resonance of the vinyl methyl function of the *Z* isomer **53**. In

[6]The configuration of the newly introduced secondary methyl group is assumed to be as shown in **55**. Presumably, dissolving metal reduction of the exocyclic double bond of **46** would lead to the more stable (equatorial Me group) of the two possible diastereomeric products. A pure sample of **55** could be obtained by reduction of **46** with Li–$EtNH_2$–*t*-BuOH at 0°C for 20 min (see Experimental).

Can. J. Chem. Downloaded from www.nrcresearchpress.com by 203.198.23.82 on 09/08/12
For personal use only.

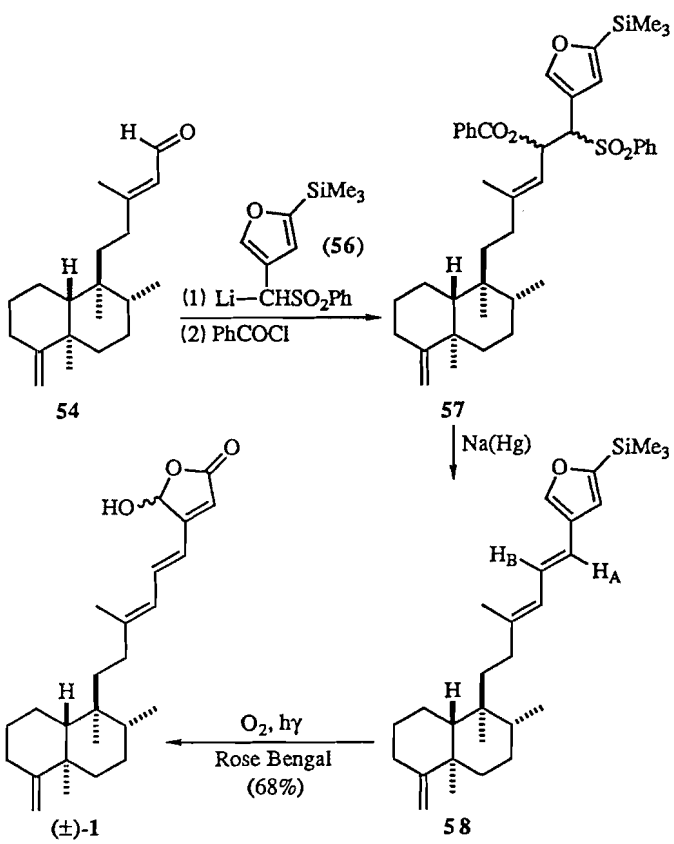

SCHEME 7

fact, the ^{1}H nmr spectra of the major and minor products exhibit vinyl methyl signals at δ 2.14 (d, J = 1.5 Hz) and 1.85 (d, J = 1.3 Hz), respectively.

Reduction (i-Bu_2AlH, THF) of the ester **52**, followed by oxidation (MnO_2, hexane) of the resultant allylic alcohol **34**, gave the α,β-unsaturated aldehyde **54**. In the ^{1}H nmr spectrum of **54**, the formyl proton and the adjacent olefinic hydrogen give rise to a doublet and a broad doublet (J = 8 Hz) at δ 9.97 and 5.86, respectively.

Completion of the total synthesis of racemic palauolide (**1**) was achieved as summarized in Scheme 7. Conversion of the α,β-unsaturated aldehyde **54** into the functionalized furan **58** was conveniently carried out by use of the Julia olefin synthesis (21). The reagent **56** required for this transformation was prepared as shown in eq. [5]. Thus, treatment of 4-chloromethyl-

[5] 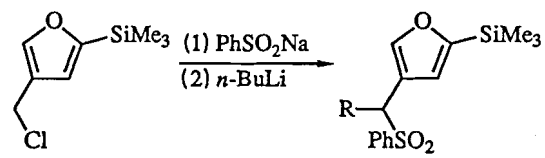

59 **60** R = H, **56** R = Li

2-trimethylsilylfuran (**59**) (22) with $PhSO_2Na$ in DMF at 80–90°C afforded the sulfone **60** in 72% yield. Reaction of the latter substance with n-BuLi in THF at −78°C provided a solution of reagent **56**.

Treatment (THF, −78°C) of the aldehyde **54** with reagent **56**, followed by reaction of the resultant alkoxide with benzoyl chloride (−78°C to room temperature) provided **57** as a mixture of diastereomers. Immediate reduction of this material with sodium amalgam in MeOH–THF at −20°C and subsequent chromatographic purification of the resultant crude product gave the furan **58** in 51% overall yield. The ^{1}H nmr spectrum of this intermediate shows that the coupling constant J_{AB} (see structural formula **58**) is 16 Hz, thus confirming that the newly introduced carbon–carbon bond possesses the expected (21) E configuration.

The final step for the synthesis of the target compound **1** was based on a method reported by Katsumura et al. (23). Thus, photosensitized oxygenation of **58**[7] in MeOH–CH_2Cl_2 at −78°C, followed by appropriate work-up and product purification, afforded (±)-palauolide (**1**), a pale yellow oil, in 68% yield. The spectral data derived from this material are in full accord with the structural assignment and the ^{1}H nmr spectrum was found to be in excellent agreement with that of natural palauolide.[8]

Conclusion

The work outlined above constitutes the first reported synthesis of the sesterterpenoid (±)-palauolide (**1**). Overall, the preparation of this biologically active, structurally unusual natural product was accomplished via a 17-step sequence of reactions, starting from 3,6-dimethyl-2-cyclohexen-1-one (**4**). Of particular note in this synthesis are (*a*) the efficient methylenecyclohexane annulation of **4** to produce the functionalized bicyclic ketone **7**; (*b*) the highly stereoselective alkylation of the mixture of nitriles **11** and **12** to afford **43**; (*c*) deoxygenation of the alcohol **45** via reduction of the phosphorodiamidate **46** with lithium in methylamine; (*d*) conversion of the α,β-unsaturated aldehyde **54** into the furan-triene **58** by use of a Julia olefin synthesis; and (*e*) oxidation of **58** with singlet oxygen to afford (±)-palauolide (1).

Experimental

General information

Distillation temperatures, which refer to short-path (Kugelrohr) distillations, and melting points are uncorrected. Proton nuclear magnetic resonance (^{1}H nmr) spectra were recorded on $CDCl_3$ solutions. Signal positions (δ values) were measured relative to the Me_4Si resonance (internal standard) or the $CHCl_3$ signal (δ 7.25). Tin–proton coupling constants (J_{Sn-H}) are given as an average of the ^{117}Sn and ^{119}Sn values. For compounds containing the Me_3Sn function, high-resolution mass spectrometric measurements are based on ^{120}Sn and were measured on the (M^+ − Me) peak (25). Gas–liquid chromatography (glc) was performed on instruments equipped with flame ionization detectors and 25 m × 0.21 mm fused silica columns coated with cross-linked SE-54. Thin-layer chromatography (tlc) was carried out with commercial aluminum-backed silica gel plates (E. Merck, type 5554). Flash chromatography (26) and conventional column chromatography were accomplished with 230–400 and 70–230 mesh silica gel (E. Merck), respectively, unless otherwise indicated. Silica gel impregnated with $AgNO_3$ was prepared as follows. To a stirred solution of 12.5 g of

[7]After completion of our work (3), Kernan and Faulkner (24) reported that oxidation of 3-alkylfurans with singlet oxygen in the presence of a hindered amine base (e.g., i-Pr_2NEt) provides good yields of 3-alkyl-4-hydroxybutenolides. Therefore, it appears that the overall conversion of **54** into (±)-**1** could have been carried out successfully by initial use of a reagent similar in structure to **56**, but with the Me_3Si function replaced by a hydrogen. Obviously, such a reagent would be less expensive and more easily prepared than **56**.

[8]We are very grateful to Professor D.J. Faulkner for a copy of the ^{1}H nmr spectrum of natural palauolide.

Can. J. Chem. Downloaded from www.nrcresearchpress.com by 203.198.23.82 on 09/08/12
For personal use only.

$AgNO_3$ in 100 mL of distilled water was added 50 g of 70–230 mesh silica gel. Most of the water was removed under reduced pressure (20 Torr; 1 Torr = 133.3 Pa) and the residual material was dried over Drierite for ~16 h at room temperature under reduced pressure (0.02 Torr), with protection from light. Reagents and solvents were purified and dried using standard methods. Aqueous NH_4Cl–NH_4OH (pH 8) refers to a solution prepared by addition of aqueous NH_4OH (58%, ~50 mL) to saturated aqueous NH_4Cl (~950 mL).

Note: Unless otherwise stated, all reactions were carried out under an atmosphere of dry argon in flame-dried glassware.

Note: All compounds for which high-resolution mass measurements are given exhibited clean ^1H nmr spectra.

*3,6-Dimethyl-2-cyclohexen-1-one (**4**)*

To a cold (−78°C), stirred solution of LDA (42 mmol) in dry THF (50 mL) was added, dropwise, 3-methyl-2-cyclohexen-1-one (**3**) (4.5 mL, 40 mmol) and the mixture was stirred at −78°C for 30 min. Iodomethane (5 mL, 80 mmol) was added to the resultant white slurry and the mixture was allowed to warm gradually to room temperature and then was stirred overnight. The mixture was diluted with pentane and water. The phases were separated and the aqueous layer was extracted twice with pentane. The combined organic extracts were washed once with 2 N hydrochloric acid and three times with brine and then were dried ($MgSO_4$) and concentrated. Distillation (40–42°C/0.02 Torr; lit. (27) bp 95–100°C/22 Torr) of the remaining oil gave 4.6 g (93%) of the cyclohexenone **4**, a colorless oil that was homogeneous by glc analysis and exhibited ir (neat): 3031, 1672, 1635 cm^{-1}; ^1H nmr (80 MHz) δ: 5.83 (m, 1H), 3.72 (m, 1H), 2.50–1.40 (m, 4H), 1.96 (br s, 3H), 1.13 (d, 3H, J = 7 Hz).

5-Chloro-2-trimethylstannyl-1-pentene

To a cold (−78°C), stirred solution of $Me_3SnCu{\cdot}Me_2S$ (9) (80 mmol) in dry THF (500 mL) was added 5-chloro-1-pentyne (6.4 mL, 60 mmol) and the mixture was stirred at −78°C for 6 h. Acetic acid (3.4 mL, 60 mmol) was added and stirring was continued for 10 min. Aqueous NH_4Cl–NH_4OH (pH 8) and petroleum ether were added; the vigorously stirred mixture was opened to the atmosphere, and was allowed to warm to room temperature. The phases were separated and the blue aqueous layer was extracted twice with petroleum ether. The combined organic extracts were washed once with aqueous NH_4Cl–NH_4OH (pH 8) and twice with brine and then were dried ($MgSO_4$) and concentrated. Column chromatography (450 g silica gel, petroleum ether) of the residual liquid and distillation (80–85°C/25 Torr) of the acquired oil provided 9.6 g (62%) of the title compound, a colorless oil that displayed spectra identical with those recorded previously (5).

*5-(2-(5-Chloro-1-pentenyl))-2,5-dimethylcyclohexanone (**6**)*

To a cold (−78°C) solution of 5-chloro-2-trimethylstannyl-1-pentene (1.7 g, 6.4 mmol) in dry THF (50 mL) was added a solution of MeLi (6.6 mmol) in Et_2O. After the mixture had been stirred at −78°C for 20 min, solid $MgBr_2$–etherate (1.7 g, 6.6 mmol) was added in one portion and the milky solution was stirred for an additional 20 min. Solid $CuBr{\cdot}Me_2S$ (0.28 g, 1.4 mmol), $BF_3{\cdot}Et_2O$ (0.71 mL, 5.8 mmol), and 3,6-dimethyl-2-cyclohexen-1-one (0.75 mL, 5.3mmol) were added sequentially. After the bright yellow mixture had been stirred at −78°C for 3 h, aqueous NH_4Cl–NH_4OH (pH 8) was added. The vigorously stirred mixture was opened to the atmosphere and was allowed to warm to room temperature. The phases were separated and the blue aqueous layer was extracted twice with petroleum ether. The combined organic extracts were washed (once with pH 8 aqueous NH_4Cl–NH_4OH, twice with brine), dried ($MgSO_4$), and concentrated. Distillation (88–89°C/0.02 Torr) of the residual oil produced 0.93 g (77%) of **6** as a colorless oil that, on the basis of analyses by glc and ^1H nmr spectroscopy, consisted of a 2:1 mixture of epimers. This material exhibited ir (neat): 3098, 1705, 1640, 905 cm^{-1}; ^1H nmr (80 MHz) δ: 4.93 (br s, alkene protons of major isomer), 4.80 (m, alkene protons of minor isomer), 3.59 (br t, 2H), 2.90–1.20 (m, 11H), 1.15 (s, tertiary Me of minor isomer), 1.05 (d, J = 7 Hz, secondary Me of major isomer), 1.03 (s, tertiary Me of major isomer), 1.00 (d, J = 7 Hz, secondary Me of minor isomer). Exact Mass calcd. for $C_{13}H_{21}{}^{35}ClO$: 228.1281; found: 228.1276.

(1S,3R*,6R*)-3,6-Dimethyl-7-methylenebicyclo[4.4.0]decan-2-one (**7**) and (1R*,3S*,6R*)-3,6-dimethyl-7-methylenebicyclo-[4.4.0]decan-2-one (**9**)*

To a solution of *t*-BuOK (6.2 g, 55 mmol) in dry *t*-BuOH (40 mL) was added a solution of the chloro ketone **6** (6.3 g, 27 mmol) in *t*-BuOH (10 mL) and the solution was stirred at 30°C for 12 h. The solution was cooled and neutralized with 2 N hydrochloric acid. The mixture was extracted three times with petroleum ether. The combined organic extracts were washed three times with brine, dried ($MgSO_4$), and concentrated. Distillation (80–85°C/0.02 Torr) of the residual oil afforded 4.6 g (89%) of a colorless oil. Analysis of this material by glc showed that it consisted of a mixture of the two diastereomers **7** and **9** in a ratio of about 94:6, respectively. Column chromatography of 220 mg of this mixture on silica gel impregnated with 25% silver nitrate (25 g, 25:1 petroleum ether – Et_2O), followed by distillation of the acquired oils, gave 170 mg of the *trans* ketone **7** and ~4 mg of the less polar *cis* ketone **9**.

Compound **7** displayed ir (neat): 3086, 1713, 1638, 895, 876 cm^{-1}; ^1H nmr (400 MHz) δ: 4.70 (br s, 2H), 2.40–2.04 (m, 5H), 1.96 (dt, 1H, J = 4, 13 Hz), 1.90–1.78 (m, 2H), 1.69–1.50 (m, 3H), 1.32–1.15 (m, 1H), 0.99 (d, 3H, J = 6 Hz), 0.87 (s, 3H). Exact Mass calcd. for $C_{13}H_{20}O$: 192.1514; found: 192.1515.

Compound **9** showed ir (neat): 3084, 1708, 1639, 894, 874 cm^{-1}; ^1H nmr (400 MHz) δ: 4.74, 4.63 (br s, br s, 1H each), 2.39–2.25 (m, 4H), 2.17–2.08 (m, 2H), 1.92–1.55 (m, 6H), 1.31 (s, 3H), 0.98 (d, 3H, J = 6 Hz). Exact Mass calcd. for $C_{13}H_{20}O$: 192.1514; found: 192.1517.

(1R,2S*,3R*,6R*)-2-Cyano-3,6-dimethyl-7-methylenebicyclo[4.4.0]decane (**11**) and (1R*,2R*,3R*,6R*)-2-cyano-3,6-dimethyl-7-methylenebicyclo[4.4.0]decane (**12**)*

To a cold (0°C) solution of (*p*-toluenesulfonyl)methyl isocyanide (2.9 g, 15 mmol) in dry HMPA (17 mL) was added solid *t*-BuOK (4 g, 36 mmol) and the solution was stirred for 15 min. Dry *t*-BuOH (0.47 mL, 5 mmol) and a mixture of the ketones **7** and **9** (96:4, 960 mg, 5 mmol) were added and the mixture was stirred at room temperature for 1 h and at 45°C for 88 h. The mixture was cooled and poured into cold 1 N hydrochloric acid (40 mL). The mixture was extracted three times with petroleum ether and the combined organic extracts were washed once with water, twice with aqueous $CuSO_4$, and twice with brine and then were dried ($MgSO_4$) and concentrated. Flash chromatography (40 g silica gel, 19:1 petroleum ether – Et_2O) of the crude material and distillation (65–68°C/0.02 Torr) of the acquired liquid gave 690 mg (68%) of a colorless oil that consisted (glc analysis) of a mixture of the epimeric nitriles **11** and **12** (ratio ~85:15, respectively). Column chromatography of 100 mg of this material on silica gel impregnated with 25% silver nitrate (55 g, 25:1 petroleum ether – Et_2O) gave samples of each of the isomers.

The initially eluted, minor substance **12** exhibited ir (neat): 3070, 2225, 1638, 998, 895 cm^{-1}; ^1H nmr (400 MHz) δ: 4.61 (t, 1H, J = 1.5 Hz), 4.56 (br s, 1H), 2.60 (td, 1H, J = 4.5, 1.3 Hz), 2.41 (tdt, 1H, J = 1.5, 5, 14 Hz), 2.16 (br d, 1H, J = 14 Hz), 2.00–1.87 (m, 2H), 1.75–1.30 (diffuse m, 8H), 1.24 (s, 3H), 1.14 (d, 3H, J = 6.4 Hz). Exact Mass calcd. for $C_{14}H_{21}N$: 203.1674; found: 203.1676.

The more polar, major isomer **11** displayed ir (neat): 3070, 2225, 1638, 998, 895 cm^{-1}; ^1H nmr (400 MHz) δ: 4.68 (t, 1H, J = 1.7 Hz), 4.62 (br s, 1H), 2.36 (br t, 1H, J = 12 Hz), 2.17 (br d, 1H, J = 12 Hz), 2.08 (t, 1H, J = 11.5 Hz), 2.00–1.85 (m, 2H), 1.78–1.25 (diffuse m, 8H), 1.17 (d, 3H, J = 6.2 Hz), 0.96 (s, 3H). Exact Mass calcd. for $C_{14}H_{21}N$: 203.1674; found: 203.1676.

*Ethyl 5-tert-butyldimethylsiloxy-2-pentynoate (**22**)*

A solution of 3-butyn-1-ol (**20**) (3.8 mL, 50 mmol), *t*-$BuMe_2SiCl$ (9 g, 60 mmol), and imidazole (8.5 g, 125 mmol) in dry DMF (17 mL) was stirred at room temperature for 12 h. Aqueous $NaHCO_3$ was added and the mixture was extracted three times with petroleum ether. The

Can. J. Chem. Downloaded from www.nrcresearchpress.com by 203.198.23.82 on 09/08/12
For personal use only.

Can. J. Chem. Downloaded from www.nrcresearchpress.com by 203.198.23.82 on 09/08/12
For personal use only.

combined extracts were washed twice with brine, dried ($MgSO_4$), and concentrated. Distillation (55–60°C/0.15 Torr) of the remaining oil gave 9 g (98%) of the silyl ether **21** (ir (neat): 3300, 2100, 1110, 632 cm^{-1}; ^1H nmr (80 MHz) δ: 3.72 (t, 2H, J = 7 Hz), 2.37 (dt, 2H, J = 2.5, 7 Hz), 1.92 (t, 1H, J = 2.5 Hz), 0.90 (s, 9H), 0.07 (s, 6H)), which was used directly for the next reaction.

To a cold (−78°C), stirred solution of **21** (9.2 g, 50 mmol) in dry THF (180 mL) was added a solution of MeLi (55 mmol) in Et_2O. After the solution had been stirred at −78°C for 10 min and at −20°C for 1 h, $ClCO_2Et$ (5.7 mL, 60 mmol) was added and the mixture was stirred at −20°C for 1 h and at room temperature for 1 h. The reaction mixture was diluted with Et_2O, was washed (twice with aqueous $NaHCO_3$, twice with brine), dried ($MgSO_4$), and concentrated. Distillation (75–78°C/0.02 Torr) of the residual oil yielded 11.5 g (90%) of the pentynoate **22**, a colorless oil that displayed ir (neat): 2230, 1705, 1250, 1110, 1080 cm^{-1}; ^1H nmr (80 MHz) δ: 4.20 (q, 2H, J = 7 Hz), 3.76 (t, 2H, J = 7 Hz), 2.52 (t, 2H, J = 7 Hz), 1.28 (t, 3H, J = 7 Hz), 0.90 (s, 9H), 0.07 (s, 6H). Exact Mass calcd. for $C_{12}H_{21}O_3Si$ (M^+ − Me): 241.1260; found: 241.1256.

*Ethyl (Z)-5-*tert*-butyldimethylsiloxy-3-trimethylstannyl-2-pentenoate (23)*

To a cold (−20°C), stirred solution of $Me_3SnSnMe_3$ (2.6 mL, 12 mmol) in dry THF (120 mL) was added a solution of MeLi (13 mmol) in Et_2O. The pale yellow solution was stirred at −20°C for 20 min and then solid PhSCu (28) (2.1 g, 12 mmol) was added. The red solution was stirred at −20°C for 15 min and then was cooled to −78°C. A solution of the pentynoate **22** (2.6 g, 10 mmol) in dry THF (5 mL) was added and the mixture was stirred at −78°C for 15 min and at −40°C for 9 h. Aqueous NH_4Cl–NH_4OH (pH 8) (~5 mL) and petroleum ether were added and the mixture was allowed to warm to room temperature. More petroleum ether was added to the slurry until the organic phase became nearly colorless. The mixture was filtered and the phases were separated. The organic phase was washed twice with brine, dried ($MgSO_4$), filtered through a short pad of Florisil, and concentrated. Distillation (91–95°C/0.02 Torr) of the residual oil gave 3.8 g (91%) of the *Z* ester **23**, a colorless liquid that displayed ir (neat): 1700, 1600, 1110, 1052 cm^{-1}; ^1H nmr (80 MHz) δ: 6.40 (t, 1H, J = 1 Hz, $^3J_{Sn-H}$ = 120 Hz), 4.18 (q, 2H, J = 7 Hz), 3.63 (t, 2H, J = 6.5 Hz), 2.63 (br t, 2H, J = 6.5 Hz), 1.28 (t, 3H, J = 7 Hz), 0.90 (s, 9H), 0.18 (s, 9H, $^2J_{Sn-H}$ = 53 Hz), 0.04 (s, 6H). Exact Mass calcd. for $C_{15}H_{31}O_3Si^{120}Sn$ (M^+ − Me): 407.1063; found: 407.1058.

*(Z)-5-*tert*-Butyldimethylsiloxy-3-trimethylstannyl-2-penten-1-ol (24)*

To stirred solution of the ester **23** (3.8 g, 9 mmol) in dry THF (90 mL) at −78°C was added a solution of *i*-Bu_2AlH (27 mmol) in hexanes. After the mixture had been stirred at −78°C for 1 h and at 0°C for 1 h, it was treated with saturated aqueous NH_4Cl (1.6 mL) and then was diluted with Et_2O. The mixture was stirred at room temperature for 5 min, was dried ($MgSO_4$), and then was filtered through a plug of Florisil and concentrated. Distillation (104–105°C/0.02 Torr) of the remaining liquid afforded 3.3 g (96%) of the alcohol **24**, a colorless oil that exhibited ir (neat): 3350, 1621, 1090, 1010 cm^{-1}; ^1H nmr (80 MHz) δ: 6.26 (br t, 1H, J = 6 Hz), 4.08 (t, 2H, J = 6 Hz, collapsed to a d on addition of D_2O), 3.57 (t, 2H, J = 7 Hz), 2.43 (t, 2H, J = 7 Hz), 1.18 (t, 1H, J = 6 Hz, exchanged with D_2O), 0.89 (s, 9H), 0.19 (s, 9H, $^2J_{Sn-H}$ = 53 Hz), 0.05 (s, 6H). Exact Mass calcd. for $C_{13}H_{29}O_2Si^{120}Sn$ (M^+ − Me): 365.0958; found: 365.0959.

*(Z)-5-*tert*-Butyldimethylsiloxy-1-methoxymethoxy-3-trimethylstannyl-2-pentene (25)*

To a cold (−20°C) solution of the alcohol **24** (3.3 g, 8.7 mmol) and i-Pr_2NEt (2.3 mL, 13 mmol) in dry CH_2Cl_2 (25 mL) was added $MeOCH_2Cl$ (1 mL, 13 mmol) and the mixture was stirred at room temperature for 12 h. The mixture was concentrated and the residual mixture was triturated four times with petroleum ether. The combined organic extracts were concentrated and the residue was filtered through a short column of silica gel (75 g, elution with 9:1 petroleum ether – Et_2O). Concentration of the combined eluate and distillation (90–93°C/0.02 Torr) of the remaining liquid provided 3.3 g (90%) of the diether **25**, a colorless oil that showed ir (neat): 1100, 1040 cm^{-1}; ^1H nmr (80 MHz) δ: 6.21 (t, 1H, J = 6 Hz), 4.63 (s, 2H), 4.01 (d, 2H, J = 6 Hz), 3.58 (t, 2H, J = 7 Hz), 3.38 (s, 3H), 2.45 (t, 2H, J = 7 Hz), 0.91 (s, 9H), 0.20 (s, 9H, $^2J_{Sn-H}$ = 53 Hz), 0.06 (s, 6H). Exact Mass calcd. for $C_{15}H_{33}O_3Si^{120}Sn$ (M^+ − Me): 409.1220; found: 409.1228.

*(E)-5-*tert*-Butyldimethylsiloxy-1-methoxymethoxy-3-methyl-2-pentene (26)*

To a cold (−78°C), stirred solution of the vinylstannane **25** (3.3 g, 7.8 mmol) in dry THF (65 mL) was added a solution of MeLi (8.5 mmol) in Et_2O and the solution was stirred at −78°C for 30 min. Iodomethane (1.2 mL, 20 mmol, freshly passed through a plug of basic alumina) was added and the mixture was stirred at −78°C for 90 min. The mixture was diluted with petroleum ether, was washed three times with brine, dried ($MgSO_4$), and concentrated. Distillation (81–83°C/0.02 Torr) of the residual oil gave 2 g (90%) of the alkene **26**, a colorless liquid that displayed ir (neat): 2725, 1100, 1050 cm^{-1}; ^1H nmr (80 MHz) δ: 5.36 (br t, 1H, J = 7 Hz), 4.61 (s, 2H), 4.04 (d, 2H, J = 7 Hz), 3.68 (t, 2H, J = 7 Hz), 3.35 (s, 3H), 2.23 (t, 2H, J = 7 Hz), 1.69 (br s, 3H), 0.88 (s, 9H), 0.03 (s, 6H). Exact Mass calcd. for $C_{12}H_{25}OSi$ (M^+ − OMOM): 213.1674; found: 213.1671.

(E)-5-Methoxymethoxy-3-methyl-3-penten-1-ol (27)

To a stirred solution of *n*-Bu_4NF (20 mmol) in dry THF (35 mL) at room temperature was added a solution of the diether **26** (2 g, 7.2 mmol) in dry THF (5 mL). After the solution had been stirred for 40 min, it was diluted with Et_2O, washed three times with brine, dried ($MgSO_4$), and concentrated. Distillation (81–83°C/0.02 Torr) of the remaining oil provided 1.1 g (98%) of the homoallylic alcohol **27**, a colorless oil that exhibited ir (neat): 3400, 1040, 922 cm^{-1}; ^1H nmr (80 MHz) δ: 5.48 (br t, 1H, J = 7 Hz), 4.65 (s, 2H), 4.11 (d, 2H, J = 7 Hz), 3.73 (t, 2H, J = 6.5 Hz), 3.40 (s, 3H), 2.30 (t, 2H, J = 6.5 Hz), 1.72 (br s, 4H, changes to a br s, 3H, upon addition of D_2O). Exact Mass calcd. for $C_6H_{11}O_2$ (M^+ − OMOM): 115.0759; found: 115.0762.

(E)-5-Iodo-1-methoxymethoxy-3-methyl-2-pentene (14)

A solution of the alcohol **27** (0.84 g, 5.3 mmol), *p*-$MeC_6H_4SO_2Cl$ (1.2 g, 6.3 mmol), and 4-*N*,*N*-dimethylaminopyridine (0.77 g, 6.3 mmol) in dry CH_2Cl_2 (15 mL) was stirred at room temperature for 12 h. The mixture was diluted with Et_2O, washed with saturated aqueous $NaHCO_3$ and brine, dried ($MgSO_4$), and concentrated. Flash chromatography (75 g silica gel, 1:1 petroleum ether – Et_2O) of the residual material yielded 1.2 g (75%) of the *p*-toluenesulfonate **28**, a rather unstable oil that was used directly for the next reaction.

To a solution of **28** (1.2 g, 3.8 mmol) in dry DMF (8 mL) was added solid NaI (1 g, 6.6 mmol) and the mixture was stirred at room temperature, with protection from light, for 4 days. Water was added and the mixture was extracted three times with pentane. The combined extracts were washed twice with brine, dried ($MgSO_4$), and concentrated. Distillation (48–51°C/0.02 Torr) of the remaining oil yielded 945 mg (91%) of the iodide **14**, a colorless oil that was stored over copper dust in a freezer. Compound **14** exhibited ir (neat): 1040 cm^{-1}; ^1H nmr (80 MHz) δ: 5.41 (br, t, 1H, J = 7 Hz), 4.63 (s, 2H), 4.07 (d, 2H, J = 7 Hz), 3.38 (s, 3H), 3.23 (t, 2H, J = 8 Hz), 2.58 (t, 2H, J = 8 Hz), 1.68 (br s, 3H). Exact Mass calcd. for $C_8H_{15}IO_2$: 270.0116; found: 270.0111.

(1S,2R*,3R*,6R*)-2-Cyano-2-((E)-5-methoxymethoxy-3-methyl-3-pentenyl)-3,6-dimethyl-7-methylenebicyclo[4.4.0]decane (16)*

To a stirred solution of LDA (1.2 mmol) in dry THF (10 mL) at 0°C was added sequentially dry HMPA (0.34 mL, 2 mmol) and a solution of a mixture of the nitriles **11** and **12** (200 mg, 0.98 mmol, 85:15, respectively) in 1 mL of dry THF and the mixture was stirred for 15 min. To the resultant yellow solution was added the iodide **14** (0.35 g, 1.3 mmol). The solution was allowed to warm to room temperature and was stirred overnight. The mixture was diluted with petroleum ether (50 mL), was washed sequentially with water, aqueous $CuSO_4$, and brine (× 2), and then was dried ($MgSO_4$) and concen-

Can. J. Chem. Downloaded from www.nrcresearchpress.com by 203.198.23.82 on 09/08/12
For personal use only.

trated. Flash chromatography (35 g silica gel, 3:1 petroleum ether – Et_2O) of the residual oil gave 47 mg of a 2:3 mixture of the nitriles **11** and **12** and 250 mg (70%, 92% based on recovered starting materials) of the nitrile **16**, a colorless oil that displayed ir (neat): 2227, 1671, 1638, 1150, 1103, 1045, 895 cm^{-1}; ^1H nmr (400 MHz) δ: 5.35 (t, 1H, $J = 6.5$ Hz)), 4.62 (s, 2H), 4.60, 4.55 (s, s, 1H each), 4.05 (d, 2H, $J = 6.5$ Hz), 3.38 (s, 3H), 2.40 (br dt, 1H, $J = 5$, 13.5 Hz), 2.14 (br dd, 1H, $J = 4$, 13.5 Hz), 2.00–1.82 (m, 5H), 1.8–1.5 (m, 9H), 1.68 (s, 3H), 1.27 (s, 3H), 1.11 (d, 3H, $J = 6$ Hz). Exact Mass calcd. for $C_{22}H_{35}NO_2$: 345.2668; found: 345.2668.

(1S,2R*,3R*,6R*)-2-Formyl-2-((E)-5-methoxymethoxy-3-methyl-3-pentenyl)-3,6-dimethyl-7-methylenebicyclo[4.4.0]decane (**17**)*

To a stirred solution of the nitrile **16** (170 mg, 0.49 mmol) in dry DME (7 mL) at room temperature was added a solution of *i*-Bu_2AlH (2 mmol) in hexanes and the mixture was heated at 60°C for 6 h. The cooled mixture was poured cautiously into cold water and the resultant mixture was neutralized with 1 N hydrochloric acid. The mixture was extracted three times with Et_2O and the combined extracts were washed with brine, dried ($MgSO_4$), and concentrated. The residual oil was dissolved in a mixture of THF, HOAc, and water (4 mL, 3:1:0.15 by volume) and the solution was stirred at room temperature for 12 h. The mixture was concentrated under reduced pressure (0.02 Torr), the residual material was dissolved in Et_2O, and the solution was washed (aqueous $NaHCO_3$, brine), dried ($MgSO_4$), and concentrated to provide the aldehyde **17** (150 mg, 87%), a colorless oil that displayed one spot on tlc analyses and showed ir (neat): 1713, 1671, 1637, 1149, 893 cm^{-1}; ^1H nmr (400 MHz) δ: 9.98 (s, 1H), 5.36 (t, 1H, $J = 7$ Hz), 4.62 (s, 2H), 4.58 (br s, 2H), 4.06 (d, 2H, $J = 7$ Hz), 3.37 (s, 3H), 2.27 (br dt, 1H, $J = 5$, 13 Hz), 2.12 (br d, 1H, $J = 13$ Hz), 2.0–1.1 (diffuse m, 14H), 1.69 (s, 3H), 1.03 (d, 3H, $J = 7$ Hz), 0.96 (s, 3H). Exact Mass calcd. for $C_{22}H_{36}O_3$: 348.2664; found: 348.2658.

(1S,2R*,3R*,6R*)-2-(Hydroxymethyl)-2-((E)-5-methoxymethoxy-3-methyl-3-pentenyl)-3,6-dimethyl-7-methylenebicyclo[4.4.0]-decane (**37**)*

To a solution–suspension of $LiAlH_4$ (16 mg, 0.42 mmol) in dry Et_2O (3 mL) was added a solution of the aldehyde **17** (99 mg, 0.28 mmol) in dry Et_2O (1 mL) and the mixture was stirred at room temperature for 1 h. Solid $Na_2SO_4 \cdot 10H_2O$ was added in small portions until gas evolution ceased. The mixture was filtered and the collected material was washed three times with Et_2O. Concentration of the filtrate gave 92 mg (93%) of the alcohol **37**, a colorless oil that displayed ir (neat): 3469 (br), 1669, 1635, 1150, 1103, 1043, 892 cm^{-1}; ^1H nmr (400 MHz) δ: 5.47 (t, 1H, $J = 7$ Hz), 4.63 (s, 2H), 4.52 (br s, 2H), 4.06 (d, 2H, $J = 7$ Hz), 3.80, 3.70 (dd, dd, 1H each, $J = 6$, 12 Hz; each signal collapses to a d, $J = 12$ Hz, on D_2O addition), 3.38 (s, 3H), 2.27 (br dt, 1H, $J = 4$, 14 Hz), 2.11 (br d, 1H, $J = 14$ Hz), 1.93–1.40 (diffuse m, 12H), 1.71 (s, 3H), 1.27–1.11 (m, 2H), 1.06 (s, 3H), 1.02 (t, 1H, $J = 6$ Hz, exchanges with D_2O), 0.94 (d, 3H, $J = 6.5$ Hz). In a nOe difference experiment, irradiation at δ 1.06 (angular Me group) caused enhancement of the signals at 3.80 and 3.70. Exact Mass calcd. for $C_{21}H_{35}O_2$ ($M^+ - OMe$): 319.2637; found: 319.2636.

*Preparation of the phosphorodiamidate **38***

To a stirred solution of the alcohol **37** (23 mg, 66 μmol) in a mixture of DME (1 mL) and TMEDA (0.25 mL) at 0°C was added a solution of *n*-BuLi (73 μmol) in hexanes and the mixture was stirred at room temperature for 30 min. $Me_2NP(O)Cl_2$ (40 μL, 0.32 mmol) was added and the mixture was stirred at room temperature for 12 h. The mixture was cooled to 0°C and dry Me_2NH (1 mL) was added and stirring was continued for 2 h at 0°C. The mixture was diluted with Et_2O, washed twice with brine, and then was dried ($MgSO_4$) and concentrated. Column chromatography (2 g silica gel, 10:1 Et_2O–acetone) of the residual material gave 23 mg (71%) of the phosphorodiamidate **38**, a colorless liquid that exhibited ir (neat): 1667, 1634, 1224, 1041, 994, 891 cm^{-1}; ^1H nmr (270 MHz) δ: 5.34 (t, 1H, $J = 6.8$ Hz), 4.63 (s, 2H), 4.53 (s, 2H), 4.06 (d, 2H, $J = 6.8$ Hz), 4.00 (br m, 2H), 3.39 (s, 3H), 2.69, 2.66 (br s, br s, 6H each), 2.30–1.10 (diffuse m, 16H), 1.70 (s, 3H), 1.08 (s, 3H), 0.93 (d, 3H, $J = 6$ Hz).

*3-Iodo-1-methoxymethoxypropane (**42**)*

To a cold (−20°C), stirred solution of 3-chloro-1-propanol (8.4 mL, 0.1 mol) and i-Pr_2NEt (28 mL, 0.16 mol) in dry CH_2Cl_2 (200 mL) was added chloromethyl methyl ether (11.4 mL, 0.15 mol) and the mixture was stirred at room temperature for 12 h. The mixture was diluted with CH_2Cl_2, was washed three times with 1 N hydrochloric acid, once with saturated aqueous $NaHCO_3$, twice with brine, and then was dried ($MgSO_4$). The solution was concentrated by distillation of the solvent at atmospheric pressure through a 10 cm Vigreux column. Distillation (73–80°C/15 Torr) of the residual oil gave 11 g (80%) of 3-chloro-1-methoxymethoxypropane. A solution of the latter material in dry acetone (150 mL) containing sodium iodide (47 g, 0.32 mol) was stirred at 60°C for 30 h. The mixture was diluted with petroleum ether, filtered, and concentrated by distillation of the solvent through a Vigreux column (10 cm) at atmospheric pressure. Distillation (80–85°C/15 Torr) of the remaining oil yielded 13 g (70%) of the iodide **42** (16), a colorless oil that was stored over copper dust under an argon atmosphere in a freezer. This material displayed ^1H nmr (80 MHz) δ: 4.63 (s, 2H), 3.60 (t, 2H, $J = 6$ Hz), 3.40 (s, 3H), 3.30 (t, 2H, $J = 6$ Hz), 2.05 (quintet, 2H, $J = 6$ Hz).

(1S,2R*,3R*,6R*)-2-Cyano-2-(3-methoxymethoxypropyl)-3,6-dimethyl-7-methylenebicyclo[4.4.0]decane (**43**)*

To a cold (0°C), stirred solution of LDA (1.5 mmol) in a mixture of dry THF (11 mL) and dry HMPA (0.4 mL, 2.2 mmol) was added a solution of a mixture of the nitriles **11** and **12** (230 mg, 1.1 mmol, 85:15, respectively) in dry THF (~1 mL) and the solution was stirred at 0°C for 15 min. The iodide **42** (350 mg, 1.5 mmol) was added and the mixture was stirred at 0°C for 30 min and at room temperature for 1 h. The solution was diluted with petroleum ether, was washed once with 1 N hydrochloric acid, twice with aqueous $CuSO_4$, and twice with brine and then was dried ($MgSO_4$), filtered through a small pad of Florisil, and concentrated. Removal of traces of solvent (vacuum pump, 0.02 Torr) afforded 340 mg (99%) of the nitrile **43**, a colorless oil that was homogeneous by tlc and glc analyses and showed ir (neat): 2228, 1638, 1153, 1112, 1039, 921, 894 cm^{-1}; ^1H nmr (400 MHz) δ: 4.59 (br s, 3H, (1 alkene H and OCH_2O)), 4.55 (br s, 1H), 3.43 (t, 2H, $J = 6$ Hz), 3.35 (s, 3H), 2.34 (br dt, 1H, $J = 5$, 12 Hz), 2.14 (br d, 1H, $J = 12$ Hz), 2.00–1.20 (diffuse m, 14H), 1.27 (s, 3H), 1.11 (d, 3H, $J = 6$ Hz). Exact Mass calcd. for $C_{19}H_{31}NO_2$: 305.2355; found: 305.2356.

(1S,2R*,3R*,6R*)-2-Formyl-2-(3-methoxymethoxypropyl)-3,6-dimethyl-7-methylenebicyclo[4.4.0]decane (**44**)*

To a stirred solution of the nitrile **43** (340 mg, 1.1 mmol) in dry DME (11 mL) was added a solution of i-Bu_2AlH (4.4 mmol) in hexanes and the solution was warmed at 60°C for 6 h. The cooled mixture was poured cautiously into cold water and the resultant mixture was neutralized with 1 N hydrochloric acid and then was extracted three times with Et_2O. The combined extracts were washed (brine), dried (Na_2SO_4), and concentrated. The residual oil was dissolved in a mixture of THF, HOAc, and water (8 mL, 1:1:0.15 by volume) and the solution was stirred at room temperature for 12 h. The solvent was removed under reduced pressure (vacuum pump, 0.02 Torr), the residual material was dissolved in Et_2O, and the resultant solution was washed (aqueous $NaHCO_3$; brine), dried ($MgSO_4$), and concentrated to afford 290 mg (85%) of the aldehyde **44**, a colorless oil that displayed ir (neat): 1713, 1636, 1153, 1112, 1039, 921, 893 cm^{-1}; ^1H nmr (400 MHz) δ: 9.52 (s, 1H), 4.60 (s, 2H), 4.58 (br s, 2H), 3.50 (t, 2H, $J = 6$ Hz), 3.35 (s, 3H), 2.26 (br dt, 1H, $J = 5$, 12 Hz), 2.11 (br d, 1H, $J = 12$ Hz), 1.95–1.10 (diffuse m, 14H), 1.02 (d, 3H, $J = 6$ Hz), 0.98 (s, 3H). Exact Mass calcd. for $C_{19}H_{32}O_3$: 308.2351; found: 308.2359.

(1S,2R*,3R*,6R*)-2-(Hydroxymethyl)-2-(3-methoxymethoxypropyl)-3,6-dimethyl-7-methylenebicyclo[4.4.0]decane (**45**)*

To a solution–suspension of $LiAlH_4$ (70 mg, 1.8 mmol) in dry Et_2O (10 mL) was added an ethereal solution of the aldehyde **44** (280 mg,

Can. J. Chem. Downloaded from www.nrcresearchpress.com by 203.198.23.82 on 09/08/12
For personal use only.

0.9 mmol) and the mixture was stirred at room temperature for 1 h. Solid $Na_2SO_4 \cdot 10H_2O$ was added in small portions to the stirred mixture until gas evolution ceased. The mixture was filtered and the collected material was washed three times with Et_2O. Concentration of the combined filtrate, followed by removal of last traces of solvent (vacuum pump, 0.02 Torr), afforded 250 mg (91%) of the alcohol **45**, a colorless oil that displayed ir (neat): 3462 (br), 1635, 1152, 1111, 1039, 921, 891 cm^{-1}; ^1H nmr (400 MHz) δ: 4.62 (s, 2H), 4.51 (br s, 2H), 3.78, 3.70 (d, d, 1H each, J = 12 Hz in each case), 3.51 (t, 2H, J = 6.5 Hz), 3.37 (s, 3H), 2.26 (br dt, 1H, J = 5, 12 Hz), 2.10 (br d, 1H, J = 12 Hz), 1.87 (br d, 1H, J = 12 Hz), 1.70–1.10 (diffuse m, 14H), 1.06 (s, 3H), 0.94 (d, 3H, J = 6 Hz). Exact Mass calcd. for $C_{19}H_{34}O_3$: 310.2508; found: 310.2509.

Preparation of the phosphorodiamidate ***46***

A solution of *n*-BuLi (0.77 mmol) in hexanes was added to a stirred solution of the alcohol **45** (220 mg, 0.7 mmol) in a mixture of dry DME (6 mL) and dry TMEDA (1.5 mL) at 0°C. After the mixture had been stirred for 15 min, $Me_2NP(O)Cl_2$ (0.45 mL, 3.6 mmol) was added and the solution was stirred at room temperature for 12 h. The mixture was cooled to 0°C, anhydrous Me_2NH (10 mL) was added, and stirring at 0°C was continued for 2 h. The solution was diluted with Et_2O, was washed twice with brine, dried ($MgSO_4$), and concentrated. Column chromatography (10 g silica gel, 10:1 Et_2O–acetone) of the residue, followed by removal of solvent from the acquired liquid (0.02 Torr), gave 270 mg (88%) of the phosphorodiamidate **46**, a colorless liquid that showed ir (neat): 1635, 1305, 1215, 1152, 1111, 1037, 920, 888 cm^{-1}; ^1H nmr (400 MHz) δ: 4.60 (s, 2H), 4.51 (s, 2H), 4.00, 3.95 (dd, dd, 1H each, J = 4, 12 Hz), 3.48 (t, 2H, J = 6 Hz), 3.35 (s, 3H), 2.66, 2.64 (d, d, 6H each, J = 4 Hz), 2.26 (br dt, 1H, J = 5, 12 Hz), 2.11 (br d, 1H, J = 12 Hz), 1.9–1.1 (diffuse m, 14H), 1.06 (s, 3H), 0.93 (d, 3H, J = 6 Hz). Exact Mass calcd. for $C_{23}H_{45}N_2O_4P$: 444.3117; found: 444.3119.

(1R,2R*,3R*,6R*)-2-(3-Methoxymethoxypropyl)-2,3,6-trimethyl-7-methylenebicyclo[4.4.0]decane (**47**)*

Dry liquid $MeNH_2$ (7 mL) was condensed into a cold (−78°C) flask containing Li metal (9 mg, 1.3 mmol) and the mixture was stirred at −30°C for 30 min. To the resultant dark blue solution was added a solution of the phosphorodiamidate **46** (99 mg, 0.2 mmol) in dry Et_2O (~0.5 mL) and the mixture was stirred at −20°C for 10 min. The mixture was treated cautiously with aqueous NH_4Cl (10 mL) and the resultant mixture was extracted three times with Et_2O. The combined extracts were washed (brine), dried ($MgSO_4$), and concentrated. Column chromatography (4 g silica gel, 20:1 petroleum ether – Et_2O) of the residual material gave 48 mg (81%) of the MOM ether **47**, a colorless oil that displayed ir (neat): 1636, 1147, 1112, 1078, 1039, 922, 891 cm^{-1}; ^1H nmr (400 MHz) δ: 4.60 (s, 2H), 4.49 (br s, 2H), 3.44 (t, 2H, J = 6 Hz), 3.36 (s, 3H), 2.28 (br dt, 1H, J = 5, 13.5 Hz), 2.09 (br d, 1H, J = 13.5 Hz), 1.87 (br d, 1H, J = 12 Hz), 1.63–1.00 (diffuse m, 13H), 1.04 (s, 3H), 0.80 (d, 3H, J = 6 Hz), 0.73 (s, 3H). Exact Mass calcd. for $C_{19}H_{34}O_2$: 294.2559; found: 294.2557.

(1S,2S*,3R*,6S*,7R*)-2-(3-Methoxymethoxypropyl)-2,3,6,7-tetramethylbicyclo[4.4.0]decane (**55**)*

Dry liquid $EtNH_2$ (1 mL) was condensed into a cold (−78°C) flask containing Li metal (11 mg, 0.29 mmol) and the mixture was stirred at 0°C for 20 min. A solution of the phosphorodiamidate **46** (13 mg, 29 μmol) and dry *t*-BuOH (0.11 mmol) in dry THF (0.5 mL) was added and the mixture was stirred at 0°C for 20 min. The mixture was treated with aqueous NH_4Cl (5 mL) and the resultant mixture was extracted three times with Et_2O. The combined extracts were washed (brine), dried ($MgSO_4$), and concentrated. Column chromatography of the residual material on silica gel (1 g, 15:1 petroleum ether – Et_2O) gave 7 mg (80%) of the ether **55**, a colorless oil that showed ir (neat): 1463, 1383, 1151, 1112, 1039 cm^{-1}; ^1H nmr (400 MHz) δ: 4.62 (s, 2H), 3.46 (t, 2H, J = 7 Hz), 3.37 (s, 3H), 1.8–0.8 (diffuse m, 17H), 0.78 (d, 3H, J = 7 Hz), 0.77 (s, 3H), 0.73 (d, 3H, J = 7 Hz), 0.70 (s, 3H). Exact Mass calcd. for $C_{19}H_{36}O_2$: 296.2715; found: 296.2707.

(1R,2S*,3R*,6R*)-2-(3-Hydroxypropyl)-2,3,6-trimethyl-7-methylenebicyclo[4.4.0]decane (**48**)*

A stirred mixture of the MOM ether **47** (65 mg, 0.22 mmol) and PPTS (0.55 g, 2.2 mmol) in *t*-BuOH (5 mL) was heated at 70°C for 12 h. The solvent was removed from the cooled mixture under reduced pressure (0.02 Torr) and the residual material was triturated three times with dry Et_2O. The combined organic solution was filtered and concentrated. Column chromatography (1 g silica gel, 7:3 petroleum ether – Et_2O) of the residue gave 50 mg (91%) of the alcohol **48**, a colorless oil that exhibited ir (neat): 3319 (br), 1635, 1055, 891 cm^{-1}; ^1H nmr (400 MHz) δ: 4.50 (br s, 2H), 3.57 (t, 2H, J = 6 Hz), 2.29 (br dt, 1H, J = 5, 12 Hz), 2.10 (br d, 1H, J = 12 Hz), 1.87 (br d, 1H, J = 12 Hz), 1.65–1.00 (diffuse, 14H), 1.05 (s, 3H), 0.80 (d, 3H, J = 6 Hz), 0.75 (s, 3H). Exact Mass calcd. for $C_{17}H_{30}O$: 250.2296; found: 250.2295.

(1R,2S*,3R*,6R*)-2-(2-Formylethyl)-2,3,6-trimethyl-7-methylenebicyclo[4.4.0]decane (**49**)*

To a stirred solution–suspension of PCC (70 mg, 0.32 mmol) and anhydrous NaOAc (5 mg, 61 μmol) in dry CH_2Cl_2 (5 mL) was added a solution of the alcohol **48** (60 mg, 0.24 mmol) in dry CH_2Cl_2 (0.5 mL). After the mixture had been stirred at room temperature for 1 h, it was diluted with dry Et_2O and then was filtered through a short pad of Florisil. Concentration of the filtrate gave 58 mg (99%) of the aldehyde **49**, a colorless oil that showed ir (neat): 1728, 1635, 892 cm^{-1}; ^1H nmr (400 MHz) δ: 9.74 (t, 1H, J = 2 Hz, 4.50 (br s, 2H), 2.30–2.16 (m, 3H), 2.10 (br d, 1H, J = 12 Hz), 1.88 (br d, 1H, J = 12 Hz), 1.70–1.15 (m, 11H), 1.05 (s, 3H), 0.81 (d, 3H, J = 6 Hz), 0.79 (s, 3H). Exact Mass calcd. for $C_{17}H_{28}O$: 248.2140; found: 248.2145.

(1R,2S*,3R*,6R*)-2-(3-Oxo-butyl)-2,3,6-trimethyl-7-methylene-bicyclo[4.4.0]decane (**51**)*

To a cold (0°C), stirred solution of the aldehyde **49** (22 mg, 88 μmol) in dry Et_2O (1 mL) was added a solution of MeLi (0.28 mmol) in Et_2O and the mixture was stirred at room temperature for 3 h. Solid $Na_2SO_4 \cdot 10H_2O$ was added in small portions until evolution of gas ceased. The mixture was diluted with Et_2O and filtered. Concentration of the filtrate gave a mixture of the epimeric alcohols **50** (ir (neat): 3349 (br); Exact Mass calcd. for $C_{18}H_{32}O$: 264.2453; found: 264.2455), which was used directly for the next reaction.

A solution of **50** in dry CH_2Cl_2 (~0.3 mL) was added to a solution–suspension of PCC (31 mg, 0.14 mmol) and anhydrous NaOAc (3 mg, 36 μmol) in dry CH_2Cl_2 (1 mL) and the mixture was stirred at room temperature for 1 h. The mixture was diluted with Et_2O and then was filtered through a short pad of Florisil. Concentration of the filtrate gave 22 mg (97%) of the ketone **51**, a colorless oil that displayed ir (neat): 1718, 1635, 891 cm^{-1}; ^1H nmr (400 MHz) δ: 4.51 (br s, 2H), 2.28 (br dt, 1H, J = 5, 12 Hz), 2.13 (s, 3H), 2.21–2.05 (m, 1H), 1.88 (br d, 1H, J = 12 Hz), 1.65–1.10 (diffuse m, 13H), 1.05 (s, 3H), 0.80 (d, 3H, J = 7 Hz), 0.78 (s, 3H). Exact Mass calcd. for $C_{18}H_{30}O$: 262.2297; found: 262.2298.

(1R,2S*,3R*,6R*)-2-((E)-4-Ethoxycarbonyl-3-methyl-3-butenyl)-2,3,6-trimethyl-7-methylenebicyclo[4.4.0]decane (**52**) and the corresponding Z isomer **53***

To a stirred suspension of KH (~30 mg, ~0.75 mmol) in dry THF (3 mL) at room temperature was added $EtO_2CCH_2P(O)(OEt)_2$ (140 μL, 0.7 mmol) and the mixture was stirred for 30 min. A solution of the ketone **51** (17 mg, 65 μmol) in dry THF (0.5 mL) was added and the mixture was stirred at room temperature for 15 h. Solid $Na_2SO_4 \cdot 10H_2O$ was added; the mixture was diluted with Et_2O, and then was filtered through a pad of Celite. Concentration of the filtrate provided an oil that, on the basis of analysis by tlc and glc, consisted of a mixture of two compounds in a ratio of about 9:1. Column chromatography of this material on silica gel (2 g, 50:1 petroleum ether – Et_2O) gave 2 mg (10%) of the first-eluted *Z* ester **53** and 19 mg (88%) of the chromatographically more polar *E* ester **52**.

Compound **53** showed ir (neat): 1718, 1648, 1151, 890 cm^{-1}; ^1H nmr (400 MHz) δ: 5.60 (br s, 1H), 4.50 (br s, 2H), 4.12 (q, 2H, J = 7.5 Hz), 2.55 (br dt, 1H, J = 4,12 Hz), 2.32, 2.24 (br ddd, br ddd, 1H each,

J = 5, 12, 12 Hz in each case), 2.11 (br d, 1H, J = 12 Hz), 1.90 (m, 1H), 1.85 (d, 3H, J = 1.5 Hz), 1.74–1.22 (diffuse m, 11H), 1.25 (t, 3H, J = 7.5 Hz), 1.05 (s, 3H), 0.85 (d, 3H, J = 6 Hz), 0.73 (s, 3H). Exact Mass calcd. for $C_{22}H_{36}O_2$: 332.2715; found: 332.2721.

The *E* ester **52** displayed ir (neat): 1718, 1646, 1148, 892 cm^{-1}; ^1H nmr (400 MHz) δ: 5.63 (br s, 1H), 4.51 (br s, 2H), 4.14 (q, 2H, J = 7.5 Hz), 2.29 (br dt, 1H, J = 5, 13.5 Hz), 2.14 (d, 3H, J = 1.5 Hz), 2.15–2.07 (m, 1H), 2.02–1.78 (m, 3H), 1.66–1.22 (m, 11H), 1.28 (t, 3H, J = 7.5 Hz), 1.05 (s, 3H), 0.81 (d, 3H, J = 6 Hz), 0.74 (s, 3H). Exact Mass calcd. for $C_{22}H_{36}O_2$: 332.2715; found: 332.2715.

(1R,2S*,3R*,6R*)-2-((E)-5-Hydroxy-3-methyl-3-pentenyl)-2,3,6-trimethyl-7-methylenebicyclo[4.4.0]decane (**34**)*

To a cold (−78°C), stirred solution of the ester **52** (19 mg, 57 μmol) in dry Et_2O (1 mL) was added a solution of i-Bu_2AlH (0.25 mmol) in hexanes. After the solution had been stirred at −78°C for 1 h and at 0°C for 2 h, it was treated with saturated aqueous NH_4Cl (0.1 mL) and then was diluted with Et_2O. The mixture was stirred at room temperature for 5 min and then was dried ($MgSO_4$) and filtered through a pad of Florisil. Concentration of the filtrate gave 16 mg (98%) of the allylic alcohol **34**, a colorless oil that displayed ir (neat): 3327 (br), 1636, 1000, 891 cm^{-1}; ^1H nmr (400 MHz) δ: 5.37 (t, 1H, J = 8 Hz), 4.50 (br s, 2H), 4.12 (d, 2H, J = 8 Hz), 2.29 (br dt, 1H, J = 5, 13.5 Hz), 2.10 (br d, 1H, J = 13.5 Hz), 1.93–1.18 (diffuse m, 15H), 1.65 (br s, 3H), 1.03 (s, 3H), 0.81 (d, 3H, J = 6 Hz), 0.72 (s, 3H). Exact Mass calcd. for $C_{20}H_{34}O$: 290.2610; found: 290.2614.

(1R,2S*,3R*,6R*)-2-((E)-4-Formyl-3-methyl-3-butenyl)-2,3,6-trimethyl-7-methylenebicyclo[4.4.0]decane (**54**)*

A solution of the allylic alcohol **34** (15.8 mg, 55 μmol) in hexane was added to MnO_2 (70 mg) and the suspension was stirred at room temperature for 3 h. The mixture was filtered through a pad of Celite and the collected material was washed four times with dry Et_2O. Concentration of the combined filtrate afforded 14 mg (88%) of the aldehyde **54**, a colorless oil that showed ir (neat): 1676, 1633, 1611, 1195, 891 cm^{-1}; ^1H nmr (270 MHz) δ: 9.97 (d, 1H, J = 8 Hz), 5.86 (br d, 1H, J = 8 Hz), 4.51 (br s, 2H), 2.16 (d, 3H, J = 0.8 Hz), 2.4–1.1 (diffuse m, 16H), 1.06 (s, 3H), 0.81 (d, 3H, J = 6 Hz), 0.77 (s, 3H). Exact Mass calcd. for $C_{20}H_{32}O$: 288.2453; found: 288.2446.

*4-(Phenylsulfonylmethyl)-2-trimethylsilylfuran (**60**)*

A stirred mixture of 4-(chloromethyl)-2-trimethylsilylfuran (**59**) (22) (0.56 g, 2.95 mmol), $PhSO_2Na$ (0.58 g, 3.5 mmol), and dry DMF (2.5 mL) was heated at 80–90°C for 2.5 h. The cooled solution was diluted with Et_2O, was washed twice with brine, and then was dried ($MgSO_4$), filtered, and concentrated. Column chromatography of the residual material on neutral alumina (activity III, 20 g, 1:4 petroleum ether – Et_2O) gave 0.62 g of the sulfone **60**, an oil that displayed ir (neat): 1681, 1587, 1479, 1448, 1310, 1251, 1152 cm^{-1}; ^1H nmr (80 MHz) δ: 7.8–7.3 (m, 6H), 6.45 (s, 1H), 4.15 (s, 2H), 0.25 (s, 9H). Exact Mass calcd. for $C_{14}H_{18}O_3SiS$: 294.0746; found: 294.0744.

(1R,2S*,3R*,6R*)-2-((E,E)-6-(2-Trimethylsilyl-4-furyl)-3-methyl-3,5-hexadienyl)-2,3,6-trimethyl-7-methylenebicyclo[4.4.0]-decane (**58**)*

To a cold (−78°C), stirred solution of the sulfone **60** (25.5 mg, 87 μmol) in dry THF (0.9 mL) was added a solution of *n*-BuLi (~80 μmol) in hexanes and the solution was stirred for 20 min. A solution of the aldehyde **54** (10 mg, 35 μmol) in ~0.3 mL of dry THF was added and the solution was stirred at −78°C for 3 h. Freshly distilled PhCOCl (10 μL, 87 μmol) was added and the reaction mixture was allowed to warm to room temperature over a period of 1.5 h. The solution was diluted with Et_2O, was washed once with saturated aqueous $NaHCO_3$, twice with brine, and then was dried ($MgSO_4$) and concentrated. The remaining oil was dissolved in a 3:1 mixture of dry THF and dry MeOH (1 mL) and the solution was cooled to −20°C. Sodium amalgam (4%, 23 mg) was added and the mixture was stirred at −20°C for 2 h. Additional amalgam (13 mg) was added and stirring was continued for 1 h. The mixture was diluted with pentane, was washed twice with brine, and then was dried ($MgSO_4$) and concentrated. Column chromatography of the residue on neutral alumina (activity III, 2 g, 50:1 pentane – Et_2O) gave 7.5 mg (51%) of compound **58**, a clear liquid that showed ir (neat): 1635, 1250, 891, 844 cm^{-1}; ^1H nmr (400 MHz) δ: 7.58 (s, 1H), 6.76 (s, 1H), 6.56 (dd, 1H, J = 10, 16 Hz), 6.30 (d, 1H, J = 16 Hz), 5.89 (d, 1H, J = 10 Hz), 4.50 (br s, 2H), 2.30 (br dt, 1H, J = 5, 13.5 Hz), 2.12 (br d, 1H, J = 13.5 Hz), 1.97–1.20 (diffuse m, 14H), 1.80 (s, 3H), 1.05 (s, 3H), 0.82 (d, 3H, J = 6 Hz), 0.74 (s, 3H), 0.27 (s, 9H). Exact Mass calcd. for $C_{28}H_{44}OSi$: 424.3161; found: 424.3161.

*(±)-Palauolide (**1**)*

A solution of the furan **58** (7.5 mg, 17 μmol) and a catalytic amount of Rose Bengal (~1.7 μmol) in a 10:3 mixture of MeOH and CH_2Cl_2 was cooled to −78°C. While a stream of oxygen was bubbled through the solution, the latter was irradiated for 8 min with a halogen–tungsten lamp (650 W, 110 V, operated at 50 V) through an aqueous sodium nitrite filter (74 g per L of H_2O). The solution was purged with argon and then was allowed to stand at room temperature in the dark for 3 h. Removal of the solvent and column chromatography (1.5 g silica gel, 7:3 hexane–EtOAc) of the residual material gave 4.5 mg (68%) of (±)-palauolide (**1**), which exhibited ir (neat): 3340 (br), 1757, 1634, 1614, 890 cm^{-1}; ^1H nmr (400 MHz) δ: 7.14 (dd, 1H, J = 11, 15.5 Hz), 6.29 (d, 1H, J = 15.5 Hz), 6.23 (d, 1H, J = 8.5 Hz, collapses to a singlet on addition of D_2O), 5.97 (d, 1H, J = 11 Hz), 5.87 (s, 1H), 4.51 (br s, 2H), 2.30 (br dt, 1H, J = 5, 13.5 Hz), 2.12 (br d, 1H, J = 13.5 Hz), 2.07–1.10 (diffuse m, 15H), 1.88 (s, 3H), 1.06 (s, 3H), 0.82 (d, 3H, J = 6 Hz), 0.75 (s, 3H). Exact Mass calcd. for $C_{25}H_{36}O_3$: 384.2664; found: 384.2660.

Acknowledgement

We are grateful to the Natural Sciences and Engineering Research Council of Canada for financial support.

1. B. Sullivan and D.J. Faulkner. Tetrahedron Lett. **23**, 907 (1982).
2. A.T. Merritt and S.V. Ley. Nat. Prod. Rep. **9**, 243 (1992).
3. E. Piers and J.S.M. Wai. J. Chem. Soc. Chem. Commun. 1342 (1987).
4. E. Piers and B.W.A. Yeung. J. Org. Chem. **49**, 4567 (1984); E. Piers, B.W.A. Yeung, and F.F. Fleming. Can. J. Chem. **71**, 280 (1993).
5. E. Piers and J.M. Chong. Can. J. Chem. **66**, 1425 (1988).
6. R.K. Boeckman, Jr. and S.M. Silver. Tetrahedron Lett. 3497 (1973).
7. O.H. Oldenziel, D. van Leusen, and A.M. van Leusen. J. Org. Chem. **42**, 3114 (1977).
8. J.A. Marshall, M.T. Pike, and R.D. Carroll. J. Org. Chem. **31**, 2933 (1966); J.A. Marshall and A.R. Hochstetler. J. Am. Chem. Soc. **91**, 648 (1969); C.H. Heathcock and R. Ratcliffe. J. Am. Chem. Soc. **93**, 1746 (1971); J.D. Godfrey and A.G. Schultz. Tetrahedron Lett. **35**, 3241 (1971); G.H. Posner and G.L. Loomis. J. Org. Chem. **38**, 4459 (1973); L.A. Burk and M.D. Soffer. Tetrahedron, **32**, 2083 (1976).
9. E. Piers, H.E. Morton, and J.M. Chong. Can. J. Chem. **65**, 78 (1987).
10. E. Piers, J.M. Chong, and H.E. Morton. Tetrahedron, **45**, 363 (1989).
11. E. Piers and R.T. Skerlj. J. Org. Chem. **52**, 4421 (1987).
12. D.J. Cram and M.R.V. Sahyun. J. Am. Chem. Soc. **84**, 1734 (1962).
13. Y. Guindon, H.E. Morton, and C. Yoakim. Tetrahedron Lett. **24**, 3969 (1983); Y. Guindon, C. Yoakim, and H.E. Morton, J. Org. Chem. **49**, 3912 (1984).
14. H.-J. Liu, S.P. Lee, and W.H. Chan. Can. J. Chem. **55**, 3797 (1977).
15. R.E. Ireland, D.C. Muchmore, and U. Hengartner. J. Am. Chem. Soc. **94**, 5098 (1972).
16. V. Pouzar, S. Vasickova, P. Drasar, I. Cerny, and M. Havel. Collect. Czech. Chem. Commun. **48**, 2423 (1983).

Can. J. Chem. Downloaded from www.nrcresearchpress.com by 203.198.23.82 on 09/08/12
For personal use only.

17. H. Monti, G. Leandri, M. Klos-Ringuet, and C. Corriol. Synth. Commun. **13**, 1021 (1983).
18. E.J. Corey and J.W. Suggs. Tetrahedron Lett. 2647 (1975).
19. A.S. Sharma and A.K. Grayen. Tetrahedron, **41**, 4581 (1985).
20. J. Boutagy and R Thomas. Chem. Rev. **74**, 87 (1974).
21. P.J. Kocienski. Phosphorus Sulfur, **24**, 97 (1985); M. Julia. Pure Appl. Chem. **57**, 763 (1985); B.M. Trost. Bull. Chem. Soc. Jpn. **61**, 107 (1988).
22. D. Goldsmith, D. Liotta, M. Saindane, L. Waykole, and P. Bowen. Tetrahedron Lett. **24**, 5835 (1983); S.P. Tanis and D.B. Head. Tetrahedron Lett. **25**, 4451 (1984).
23. S. Katsumura, K. Hori, S. Fujiwara, and S. Isoe. Tetrahedron Lett. **26**, 4625 (1985).
24. M.R. Kernan and D.J. Faulkner. J. Org. Chem. **53**, 2773 (1988).
25. H.G. Kuivila, K.-H. Tsai, and D.G.I. Kingston. J. Organomet. Chem. **23**, 129 (1970).
26. W.C. Still, M. Kahn, and A. Mitra. J. Org. Chem. **43**, 2923 (1978).
27. J. Dreux. Bull. Soc. Chim. Fr. 1443 (1954).
28. G.H. Posner, D.J. Brunelle, and L. Sinoway. Synthesis, 662 (1974).

Can. J. Chem. Downloaded from www.nrcresearchpress.com by 203.198.23.82 on 09/08/12
For personal use only.

Molecular recognition XIII. The binding of the H-type 2 human blood group determinant by a winged bean (*Psophocarpus tetragonolobus*) acidic lectin[1]

RAYMOND U. LEMIEUX,[2] MING-HUI DU,[3] AND ULRIKE SPOHR[4]
Department of Chemistry, University of Alberta, Edmonton, AB T6G 2G2 Canada

AND

SHREETA ACHARYA AND AVADHESHA SUROLIA
Molecular Biophysics Unit, Indian Institute of Science, Bangalore-560012, India

Received August 18, 1993

This paper is dedicated to Professor David B. MacLean

Can. J. Chem. Downloaded from www.nrcresearchpress.com by 195.246.54.202 on 09/08/12
For personal use only.

RAYMOND U. LEMIEUX, MING-HUI DU, ULRIKE SPOHR, SHREETA ACHARYA, and AVADHESHA SUROLIA. Can. J. Chem. **72,** 158 (1994).

The winged bean acidic lectin (WBA II) binds the H-type 2 human blood group related trisaccharide (α-L-Fuc-(1c → 2b)-β-D-Gal-(1b → 4a)-β-D-GlcNAc-OMe, **1**). Interactions that importantly contribute to the specificity of the complex formation are provided by CH_2-6b, OH-4b, OH-3b, and OH-2c of **1**. On the basis of the relative activities of the monodeoxy and mono-*O*-methyl derivatives of **1**, the hydroxyl groups at the 3a, 6a, and 4c positions become located at the periphery of the combining site, whereas the CH_3O-1a, NHAc-2a, and CH_3-5c groups are more remote from the protein surface and fully exposed to bulk water. Whereas the WBA II lectin marginally recognizes the H-type 1 related trisaccharide (α-L-Fuc-(1c → 2b)-β-D-Gal-(1b → 3a)-β-D-GlcNAc-OMe, **23**), the de-*N*-acetyl derivative (**24**) is bound 3.4 times more strongly than **1**. This and other results, which are related to changes in interaction between the ligand and the apron of the combining site, are attributed to changes in hydration that lead to enthalpy–entropy compensation. In certain cases, the interactions are found to stabilize the complex.

RAYMOND U. LEMIEUX, MING-HUI DU, ULRIKE SPOHR, SHREETA ACHARYA et AVADHESHA SUROLIA. Can. J. Chem. **72,** 158 (1994).

La lectine acide de la fève ailée (WBA II) se lie au trisaccharide (α-L-Fuc-(1c → 2b)-β-D-Gal-(1b → 4a)-β-D-GlcNAc-OMe, **1**, relié au groupe sanguin humain H-type 2. Les interactions qui contribuent d'une façon importante à la spécificité de la formation du complexe sont fournies par le CH_2-6b, le OH-4b, le OH-3b et le OH-2c du composé **1**. En se basant sur les activités relatives des dérivés monodésoxy et mono-*O*-méthyl du composé **1**, les groupes hydroxyles aux positions 3a, 6a et 4c se trouvent localisés à la périphérie du site de combinaison alors que les groupes CH_3O-la, NHAc-2a et CH_3-5c se trouvent à des positions plus éloignées de la surface de la protéine et pleinement exposées à l'eau de la solution. Alors que la lectine de la fève ailée ne reconnaît que marginalement le trisaccharide α-L-Fuc-(1c → 2b)-β-D-Gal-(1b → 3a)-β-D-GlcNAc-OMe, **23**, relié au groupe H-type 1, le dérivé dés-*N*-acétylé **24** se lie 3,4 fois plus fortement que le composé **1**. Ce résultat et d'autres qui sont reliés aux changements dans l'interaction entre le coordinat et le tablier du site qui se combine sont attribués aux changements dans l'hydratation qui conduit à une compensation enthalpie–entropie. Dans certains cas, on a trouvé que les interactions stabilisent le complexe.

[Traduit par la rédaction]

Introduction

In 1985, Kortt (1) reported the isolation of three acidic lectins (I, II, III) (p*I* ≃ 5.5) from the seeds of winged bean (*Psophocarpus tetragonolobus*). These proved to be dimeric glycoproteins of molecular weight approximately 54000. Although the agglutinations of trypsinized human type A, B, or O (H) erythrocytes by these lectins were inhibited by D-galactose derivatives and D-galactose-containing di- and trisaccharides, the inhibitions were very weak. Accordingly, it was concluded that the lectins may recognize a complex carbohydrate determinant not represented by the sugar structures that were examined (1). More recently (2), affinity chromatography provided an electrophoretically homogeneous preparation, termed WBA II, which was found to possess an affinity for a dog-intestine H-fucolipid. Indeed, it was subsequently shown (3) that the affinity for 2′-fucosyllactose (α-L-Fuc-(1 → 2)-β-D-Gal-(1 → 4)-α,β-D-Glc) is 13 times greater than that for the H-disaccharide (α-L-Fuc-(1 → 2)-α,β-D-Gal). Since the 2′-fucosyllactose is bound 14 times more strongly than an H (type 1)-related pentasaccharide (α-L-Fuc(1 → 2)-β-D-Gal-(1 → 3)-β-D-GlcNAc-(1 → 3)-β-D-Gal-(1 → 4)-α,β-D-Glc), it was anticipated that WBA II would have a strong affinity for the H-type 2 blood group-determinant, namely, α-L-Fuc-(1 → 2)-β-D-Gal-(1 → 4)-β-D-GlcNAc (**1**).

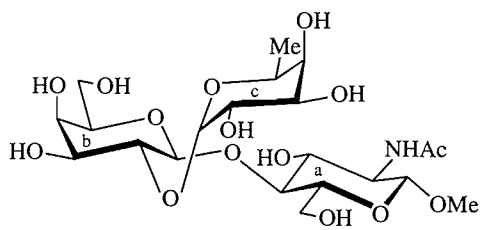

H-type 2-OMe (**1**)

A purpose of this communication is to confirm the affinity of the WBA II lectin for the type 2 trisaccharide (**1**). Mainly, however, we wish to report the delineation of the surface of **1** that is recognized by WBA II using our recently published method, which is based on the determination of the effects on binding of both deoxygenation and *O*-methylation at each of the various

[1] For the previous publication in this series, see ref. 7 .
[2] Author to whom correspondence may be addressed.
[3] University of Alberta Postdoctoral Fellow, 1992–1993.
[4] Research Associate, 1984–1988, 1991–1993.

TABLE 1. Thermodynamic parameters (in kcal /mol at 298 K) for the binding of the H-type 2-β-OMe trisaccharide (**1**) and congeners by the WBA II lectin

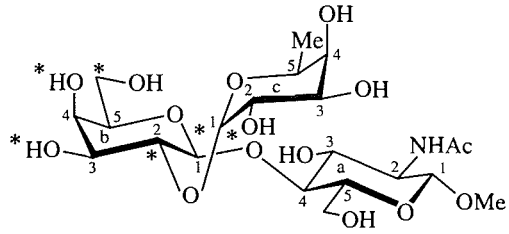

Compound	Substitutional change: Position	Substitutional change: New substituent	$-\Delta G^0$	$\Delta\Delta G^0$	$-\Delta H^0$	$T\Delta S^0$	$\Delta\Delta H^0$	$\Delta(T\Delta S^0)$
1	None	—	6.2	0	5.4	0.8	0	0
2	1a	$O(CH_2)_8COOMe$	—	−0.3[a]	—	—	—	—
3	2a	OH	6.4	−0.2	6.0	0.5	−0.6	−0.3
4	3a	H	6.3	−0.1	11.9	−5.4	−6.5	−6.2
5	3a	OMe	5.2	1.0	4.1	−1.0	1.3	−1.8
6	5a	Me	6.2	0	7.9	−1.7	−2.5	−2.5
7	5a	CH_2OMe	6.1	0.1	7.7	−2.0	−2.3	−2.8
8	5a	H[b]	5.6	0.6	8.9	−3.3	−3.5	−4.1
9	5b	Me	—	1.3[a]	—	—	—	—
10	5b	CH_2OMe	6.1	0.1	9.5	−3.6	−4.1	−4.4
11	5b	H	Inactive	—	—	—	—	—
12	4b	H	Inactive	—	—	—	—	—
13	4b	OMe	Inactive	—	—	—	—	—
14	3b	H	—	1.8[a]	—	—	—	—
15	3b	OMe	Inactive	—	—	—	—	—
16	2c	H	—	1.2[a]	—	—	—	—
17	2c	OMe	Inactive	—	—	—	—	—
18	3c	H	—	1.4[a]	—	—	—	—
19	3c	OMe	—	1.6[a]	—	—	—	—
20	4c	H	6.5	−0.3	1.5	5.0	3.9	4.2
21	4c	OMe	6.7	−0.4	1.3	5.3	4.1	4.5
22	5c	H	—	0.2[a]	—	—	—	—
36	5a	$CH_2NHCOCMe_3$	7.2	−1.0	3.9	3.3	1.5	2.5

[a]Radioimmunoassay.
[b]OH at position 2a.

hydroxyl positions (4). On the basis of this information the changes in the thermodynamic parameters caused by various structural modifications are examined in terms of the observed enthalpy–entropy compensations. As was found in several other cases (5–7), the surface of **1** that is recognized by WBA II is relatively small and polyamphiphilic.

Discussion

The thermodynamic parameters for the binding of **1** and its various congeners by the WBA II lectin (reported in Table 1) were calculated from the association constants at various temperatures in the range 15–30°C. These were determined by measuring the changes in the intensity of fluorescence on competing the binding of the oligosaccharide with *N*-dansyl-D-galactosamine as previously described (3). These data are presented in Table 2 and Fig. 1 and are considered to be sufficiently significant for the purposes of this communication, especially in view of the quality of Fig. 2. To present differential changes in free energy for inhibitions that were too weak to measure using the immunofluorescence assay, values are reported in Table 1 that were obtained using a radioimmunoassay.

TABLE 2. Association constants for the interaction of the H-type 2-OMe (**1**) trisaccharide and its congeners reported in Table 1

Compound	$K_a \times 10^4$, M^{-1}: 288 K	293 K	298 K
1	5.3	5.0	3.6
3	7.2	6.3	5.0
4[a]	—	5.4	4.2
5	0.96	0.67	0.68
6	6.6	4.4	3.6
7	5.3	5.0	3.1
8	2.2	1.6	1.3
10	2.6	2.2	1.5
20	6.2	5.5	5.5
21	9.0	8.1	8.3
24	8.3	6.2	5.0
36[b]	25	20	20

[a]$K_a = 2.9 \times 10^4$ M^{-1} at 303 K.
[b]$K_a = 27 \times 10^4$ M^{-1} and 26×10^4 M^{-1} at 290 K and 296 K, respectively.

Can. J. Chem. Downloaded from www.nrcresearchpress.com by 195.246.54.202 on 09/08/12
For personal use only.

Can. J. Chem. Downloaded from www.nrcresearchpress.com by 195.246.54.202 on 09/08/12
For personal use only.

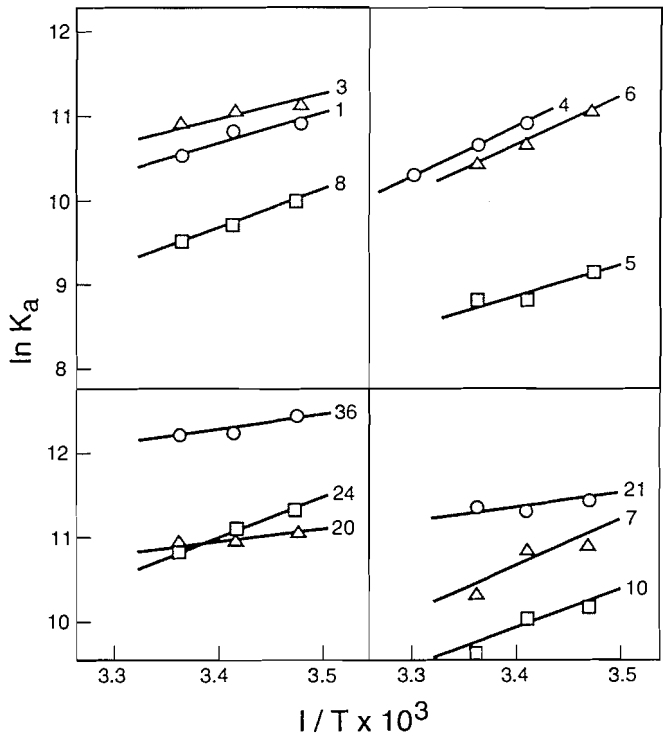

FIG. 1. van't Hoff plots of the data presented in Table 2.

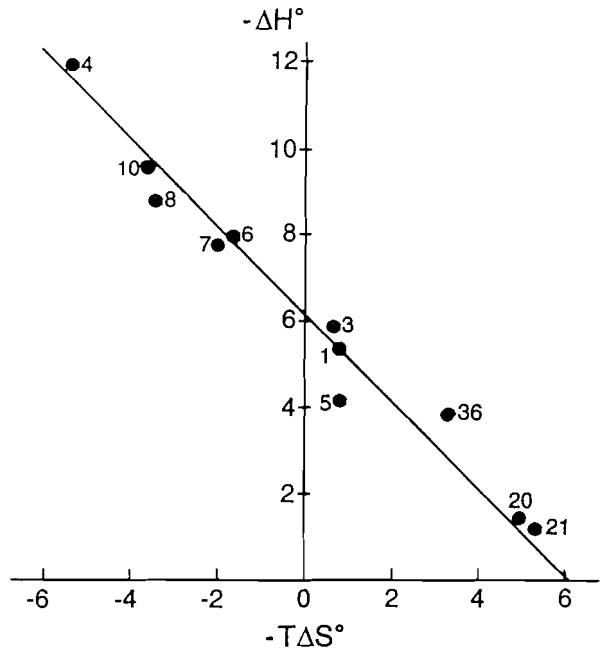

FIG. 2. Plots of the thermodynamic parameters for the binding of the WBA II lectin with **1** and the various congeners of **1** listed in Table 1. The line through the plots was arbitrarily drawn with a slope of one to illustrate the enthalpy–entropy compensation.

The projection formula for **1** provides an indication of its conformational preference (8, 9) that is adequate for an appreciation of the inhibition data presented in Table 1. That is, an examination of the inhibition data at once indicates that the recognition of **1** by the lectin is largely restricted to a series of contiguous groups (indicated by asterisks in Table 1) that extend from the 6b substituent of the β-D-Gal unit to the 2c substituent of the α-L-Fuc unit. It is seen that although changes in structure about the β-D-GlcNAc residue produced relatively minor effects on the extent of the binding reaction, a variety of changes in the other two sugar units strongly decreased the activities, in several cases to such low levels that these are declared as inactive. The plots in Fig. 2 of the thermodynamic parameters, reported in Table 1, show that the expected enthalpy–entropy compensation phenomenon (10) was observed with an overall precision within ±0.5 kcal/mol. As previously discussed (6, 10) these compensating changes are expected to arise mainly from structural changes in the hydration shells about the position of the change in the structure of the congener both in solution and in the complex with the lectin. A discussion of these data best begins by examining the relative effects of monodeoxygenation and of mono-*O*-methylation at each of the eight hydroxyl groups of **1**.

Although deoxygenation at the 3a position to produce compound **4** strongly affected the thermodynamic parameters, the change caused only a negligible differential change in free energy. Since the 3a-*O*-methyl derivative (**5**) showed appreciable activity ($\Delta\Delta G^0$ = 1.0 kcal/mol), it is concluded that, in the complex, the 3a hydroxyl of **1** remains in contact with the aqueous phase. The major compensating changes (−6.5 and −6.2 kcal/mol) in the thermodynamic parameters that were observed for the 3a-deoxy derivative (**4**) are expected to arise from the changes in the hydration shells about the 3a position, both as the reagent and in the complex, as the result of the change from the hydrophilic 3a-OH group of **1** to the hydrophobic 3a-H group of **4**. The less hydrophilic and larger 3a-OMe group of **5** causes smaller incremental changes in the thermodynamic parameters than for **4**. Similarly, both deoxygenation and *O*-methylation at the 6a position to yield **6** and **7** resulted in little change in potency of binding. Since these changes in structure caused relatively small changes in the thermodynamic parameters, the 6a-OH group likely resides in the complex at an appreciable distance from the periphery of the combining site. The effects of other changes at the 6a position will be discussed in connection with Table 3. It is particularly noteworthy that the substitution of the 5a-methyl group of **6** by hydrogen to form **8** caused only a 0.6 kcal/mol change in ΔG^0. The substantial decrease in enthalpy ($\Delta\Delta H^0$ = −3.5 kcal/mol) was compensated by a corresponding strong decrease in entropy. Therefore, it is apparent that the 5a-methylene group of the GlcNAc unit does not come into direct contact with the combining site.

The hydroxyl group at the 6b position of the Gal unit appears to remain in contact with the aqueous phase in view of the low but readily discernible potencies of both the 6b-deoxy and 6b-*O*-methyl derivatives (**9** and **10**, respectively). However, the 6b-methylene group participates in the complementarity required for effective recognition since the 6b-*nor* derivative (**11**) of **9** is highly inactive.

The axial 4b-hydroxyl group is surely involved in a strong polar interaction deep in the combining site since both deoxygenation and *O*-methylation at this position led to the inactive congeners, **12** and **13**. On the other hand, deoxygenations at both the 3b and 2c positions provided weakly active compounds (**14** and **16**, respectively). It is expected, therefore, that these hydroxyl groups are near the periphery of the combining site and in contact with water once the complex is formed. However, since both their *O*-methyl derivatives, **15** and **17**, are essentially inactive, it is concluded for reasons previously presented (4) that, in the complex, the 3b- and 2c-hydroxyl groups

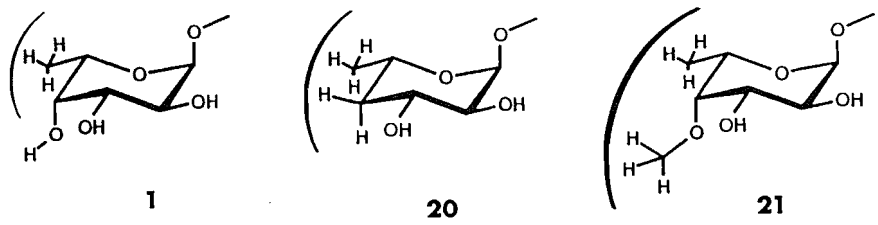

FIG. 3. The changes in hydrophobicity of the group about the 4c position of the fucosyl residue of the H-type 2-OMe trisaccharide (**1**) on preparing the congeners **20** and **21** (Table 1). It is seen that there exists a relationship between the sizes of the hydrophobic groups and the increases in entropy ($T\Delta S$ = 0.8 (**1**), 5.0 (**20**), 5.3 (**21**)) as is to be expected on the basis of hydrophobic effects (11). It is to be noted that, in the trisaccharide, these regions are surrounded by polar groups and, therefore, are amphiphilic in character.

TABLE 3. Effects on binding[a] of structural changes at positions of the H-type 2-β-OMe (**1**) that remain in the aqueous phase in the complex with the WBA II lectin

Compound	Substitutional change(s)		Relative potency	$\Delta\Delta G^0$ kcal/mol
	Position(s)	New substituent(s)		
1	—	None	100	0
4	3a	H	97	0.02
5	3a	OMe	8	1.5
27[b]	3a	O-α-L-Fuc	Inactive	—
28	2a, 3a	H, H	57	0.33
29	2a, 3a, 5aO_r	H, H, CH_2	53	0.37
6	5a	Me	88	0.08
30	2a, 3a, 5a	H, H, Me	59	0.31
31	2a, 3a, 5a, 5aO_r	H, H, Me, CH_2	49	0.42
7	5a	CH_2OMe	112	−0.07
32	5a	CH_2F	125	−0.13
33	5a	CH_2Cl	224	−0.48
34	5a	CH_2NH_2	176	−0.33
35	5a	CH_2NHAc	96	0.03
36	5a	$CH_2NHCOC(Me)_3$	446	−0.88

[a]Radioimmunoassay (13).
[b]Y human blood group determinant.

are hydrogen bonded to amino acid residues at the periphery of the combining site. In contrast, the 3c-hydroxyl group must come to reside near the periphery of the combining site but to remain bonded to water since both the 3c-deoxy (**18**) and 3c-*O*-methyl (**19**) derivatives provide readily discernible inhibition.

The high potencies of both the 4c-deoxy and 4-*O*-methyl derivatives of **1** (**20** and **21**, respectively) indicate that the 4c-hydroxyl group remains in the aqueous phase. The near 4 kcal/mol decreases in enthalpy for both these congeners is noteworthy. In both cases, the change was from a hydrophilic hydroxyl to a hydrophobic methoxy group, one smaller and the other much larger. It is likely coincidental that these changes should cause very similar changes in the thermodynamic parameters. In contrast to all the other reactions presented in Table 1, which are all enthalpy driven, both these complexations are entropy driven. Clearly, therefore, the binding of the 4c-hydroxyl group to water molecules importantly stabilizes the complex and it is apparent that the stability of the hydration shell over the oligosaccharide part that remains exposed to water also contributes to the stability of the complex. Evidently, the region about the 4c position of **1** in the complex is not as favorable for the organization of water molecules to provide so-called "flickering clusters" (11) as for **20** and **21**. The large increases in entropy that accompany the formation of the latter complexes must largely arise from the release of water molecules from over the larger hydrophobic features of the α side of the c-fucosyl unit as is displayed in Fig. 3. These data, therefore, leave no doubt that hydrophobic effects play roles in these associations. It is to be noted, however, that these effects may be associated with the release of water from polyamphiphilic surfaces, as was postulated by Beierbeck and Lemieux (12).

Although the data presented in Table 1 indicate little direct involvement of the β-D-GlcNAc unit in the binding of **1**, as seen in Table 4, both the H-type 1-β-OMe (**23**) and H-disaccharide-β-OMe (**25**) are very weak inhibitors as compared to **1**. Since *N*-deacetylation of **23** to produce the amine **24** caused a 150-fold increase in potency (a decrease of 2.9 kcal/mol in differential change in free energy), it is apparent that the combining site cannot readily accommodate the acetyl group of **23**. As was seen above when discussing the relative potencies of **6** and **8**, the 5a-Me group of **6** does not importantly come into contact with the protein. Likely, therefore, the amino group of **25** encounters a hydrophilic environment with which it is much more compatible for hydration of the complex than is the hydrophobic 5a-methyl group of **6**. It may have been expected that the so-called H-disaccharide (**25**) would be bound more strongly than the H-type 1 trisaccharide **24**. That this proved to not be the case may well be importantly related to changes in

Can. J. Chem. Downloaded from www.nrcresearchpress.com by 195.246.54.202 on 09/08/12
For personal use only.

TABLE 4. Comparisons of the binding[a] by the WBA II lectin of the H-type 2 and H-type 1 human blood group determinants and partial structures

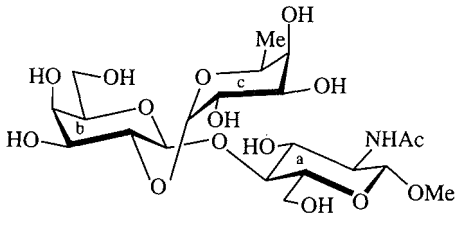

1

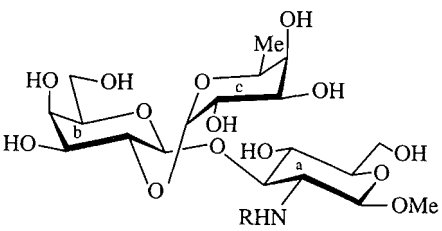

23, 24

	Compound	Relative potency	$\Delta\Delta G^0$, kcal/mol
1	H-type 2-β-OMe	100	0
23	H-type 1-β-OMe (R = Ac)	2.4	2.2
24	De-*N*-Ac-H-type 1-β-OMe (R = H)	341	−0.7
25	α-L-Fuc-(1c → 2b)-β-D-Gal-OMe	3.3	2.0
26	β-D-Gal-(1b → 4a)-β-D-GlcNAc-OMe	0.5	3.1

[a]Radioimmunoassay (13).

the stabilities of the various hydration shells. The very low activity of **26** may be in large part due to the lack of a substituent at the 2b position of the β-D-Gal unit. For example, *N*-acetyl-D-galactosamine is 5.2 times more potent than D-galactose (3).

The relative potencies of **1** and a number of congeners (**27** to **36**) involving changes in the β-DGlcNAc unit are reported in Table 3. On the basis of the foregoing discussion, all the structural changes were made at positions that remain in the aqueous phase once the complex has formed. Therefore, it is expected that all the effects noted on binding arise at least in part from changes in hydration both of the congener prior to complexation and of the complex itself.

It is seen (Table 3) that all the deoxygenated products are well entertained in terms of complex formation. Indeed, as seen for compound **31**, the replacement in **1** of the ring oxygen by methylene and the hydroxyl groups at positions 2a, 3a, and 6a by hydrogen led to only a 0.42 kcal/mol differential change in free energy. Evidently, therefore, the binding of **31** caused little change in the strength of the hydration of binding since the organization of water molecules over its large hydrophobic surface was not affected. However, as seen from the potencies of compounds **32–36**, changes in the substituent at the 6a position can have an effect. This is not surprising since the 6a-methylene group is surely not far from the periphery of the combining site and there exists freedom of rotation about the 5a-carbon to 6a-carbon bond. Therefore, at least two energetically favorable orientations of the 6a substituent can be offered by hydration, namely, the two with *syn*-clinal relationships to the ring oxygen. It is apparent that one of these orientations can provide favorable noncovalent interactions with the apron of the combing site since some of the structural changes substantially improve the strength of binding. This is especially so for the substitution of the acetyl group of **35** by a pivaloyl group to form **36**. Evidently the more hydrophobic and larger *tert*-butyl group of **36** encounters a complementary hydrophobic region on the apron of the combining site. In our experience to date, all structural changes in an epitope that involved groups that become bound by the receptor below the periphery of its combining site have resulted in inactive compounds. It is apparent, therefore, that efforts to improve the binding of an epitope should concentrate on causing stronger interaction with the apron of the combining site. That this is not always the case is illustrated by the relative potencies of compounds **5** and **27**. It is apparent that any substituent at position 3a that is larger than a hydroxyl group causes an adverse nonbonded interaction with the protein. It is to be noted in this regard that the methylation of the OH-3a to form **5** caused a 1 kcal change in free energy that was not well compensated by a change in entropy. This result is likely related, at least in part, to a loss of complementarity and not only to a change in hydration. Similar considerations apply to the binding of **36**, except that in this instance the substituent brought on a much greater increase in complementarity which stabilizes the complex by 0.88 kcal/mol.

Experimental

The isolation of the winged bean acidic lectin was carried out as described recently (2). The thermodynamic parameters were determined by fluorescence substitution titration at three different temperatures, as described previously (3). The radioimmunoassays were performed according to a published procedure (13). The plastic tubes were coated using a solution of WBA-II (100 μg/mL) in 0.1 N phosphate. The artificial antigen ([α-L-Fuc-(1 → 2)-β-D-Gal-(1 → 4)-β-D-GlcNAc-O$(CH_2)_8$CONH]$_{16}$-BSA-^{125}I) provided about 200000 cpm/100 μL. In the absence of inhibitor the lectin-coated tubes acquired about 35–45% of these counts.

Except for the mono-*O*-methyl derivatives of **1** that are presented in Table 1, the syntheses of the various other congeners used in this study have already been reported (6, 7, 14). The mono-*O*-methyl derivatives were prepared following procedures similar to those used for the synthesis of *O*-methyl derivatives of the Lewis b tetrasaccharide (4). These syntheses will be reported in connection with a study of the binding of **1** by the lectin I of *Ulex europaeus*.[5]

Acknowledgements

This research was supported by the Natural Sciences and Engineering Research Council of Canada (Grant A-172 to R.U.L.) and a prize from the Pharmaceutical Manufacturers

[5]M.-H. Du, U. Spohr, and R.U. Lemieux. Manuscript in preparation.

Can. J. Chem. Downloaded from www.nrcresearchpress.com by 195.246.54.202 on 09/08/12
For personal use only.

Association of Canada to R.U.L. A.S. acknowledges financial support from the Department of Science and Technology, Government of India.

1. A. Kortt. Arch. Biochem. Biophys. **236**, 544 (1985).
2. S.R. Patanjali, S.U. Sajjan, and A. Surolia. Eur. J. Biochem. **252**, 625 (1988).
3. S. Acharya, S.R. Patanjali, S.U. Sajjan, B. Gopalakrishnan, and A. Surolia. J. Biol. Chem. **265**, 11586 (1990).
4. P.V. Nikrad, H. Beierbeck, and R.U. Lemieux. Can. J. Chem. **70**, 241 (1992).
5. R.U. Lemieux. Chem. Soc. Rev. **18**, 347 (1989).
6. U. Spohr, E. Paszkiewicz-Hnatiw, N. Morishima, and R.U. Lemieux. Can. J. Chem. **70**, 254 (1992).
7. R. Cromer, U. Spohr, D.P. Khare, J. LePendu, and R.U. Lemieux. Can. J. Chem. **70**, 1511 (1992).
8. H. Thøgersen, R.U. Lemieux, K. Bock, and B. Meyer. Can. J. Chem. **60**, 44 (1982).
9. R.U. Lemieux and K. Bock. Arch. Biochem. Biophys. **221**, 125 (1983).
10. R.U. Lemieux, L.T.J. Delbaere, H. Beierbeck, and U. Spohr. Ciba Found. Symp. **158**, 231 (1991).
11. H.S. Frank and W.-Y. Wen. Discuss. Faraday Soc. **24**, 133 (1957).
12. H. Beierbeck and R.U. Lemieux. Can. J. Chem. **68**, 820 (1990).
13. U. Spohr, O. Hindsgaul, and R.U. Lemieux. Can. J. Chem. **63**, 2644 (1985).
14. E. Petrakova, U. Spohr, and R.U. Lemieux. Can. J. Chem. **70**, 233 (1992).

Can. J. Chem. Downloaded from www.nrcresearchpress.com by 195.246.54.202 on 09/08/12
For personal use only.

Synthesis, characterization, and enzymic conversion of nonhydrolysable analogues of propionylcoenzyme A

YIMIN ZHAO, MARTINA MICHENFELDER, AND JÁNOS RÉTEY[1]

Lehrstuhl Biochemie im Institut für Organische Chemie der Universität Karlsruhe, Richard-Willstätter-Allee, D-76128 Karlsruhe, Germany

Received July 27, 1993

This paper is dedicated to Professor Ian D. Spenser

YIMIN ZHAO, MARTINA MICHENFELDER, and JÁNOS RÉTEY. Can. J. Chem. **72**, 164 (1994).

We describe the synthesis of three novel analogues of propionyl-coenzyme A, in which the sulfur atom has been replaced by methylene, ethylene, and thiomethylene, respectively. All three analogues, propionyl-dethia(carba)-CoA (**1**), propionyl-dethia-(dicarba)-CoA (**2**), and *S*-(2-oxobutanyl)-CoA (**3**) were characterized by ^1H and ^{31}P NMR spectroscopy and FAB mass spectrometry. Propionyl-CoA–oxaloacetate transcarboxylase from *Propionibacterium shermanii* accepted the novel analogues as substrates and carboxylated them to the corresponding methylmalonyl-CoA analogues (**4–6**). The latter were further converted into the succinyl-CoA analogues by the coenzyme-B_{12}-dependent methylmalonyl-CoA mutase from the same organism. The succinyl-CoA analogues, succinyl-dethia(carba)-CoA (**7**), succinyl-dethia(dicarba)-CoA (**8**), and 4-carboxy(2-oxobutanyl)-CoA (**9**) were obtained on a preparative scale and their Michaelis constants (K_m) with methylmalonyl-CoA mutase were determined to be 0.136, 2.20, and 0.132 mM, respectively (K_m for succinyl-CoA is 0.025 mM). The V_{max} values for **7**, **8**, and **9** are 1.1, 0.013, and 0.0047 μmol min^{-1} U^{-1}, respectively (V_{max} for succinyl CoA is 1.0). The utility of the novel coenzyme A analogues in enzyme mechanistic studies is discussed.

YIMIN ZHAO, MARTINA MICHENFELDER, et JÁNOS RÉTEY. Can. J. Chem. **72**, 164 (1994).

On décrit la synthèse de trois nouveaux analogues du propionyl-coenzyme- A dans lesquels l'atome de soufre a été remplacé respectivement par un méthylène, un éthylène et un thiométhylène. On a caractérisé les trois analogues, le propionyl-déthia(carba)-CoA (**1**), le propionyl-déthia(dicarba)-CoA (**2**) et le *S*-(2-oxo-butanyl)-CoA (**3**) par spectroscopie RMN du ^1H et du ^{31}P et par spectrométrie de masse FAB. La propionyl-CoA–oxaloacétate transcarboxylase du *Propionibacterium shermanii* accepte les nouveaux analogues comme substrats et par carboxylation les transforme en analogues méthylmalonyl- CoA correspondants (**4–6**). Par la suite, on a transformé ces derniers en analogues succinyl-CoA en les soumettant à la méthylmalonyl-CoA mutase dépendante du coenzyme-B_{12} provenant du même organisme. On a obtenu les analogues succinyl-CoA, succinyl-déthia(carba)-CoA (**7**), succinyl-déthia(dicarba)-CoA (**8**) et 4-carboxy(2-oxobutanyl)-CoA (**9**) à une échelle préparative et on a déterminé que leurs constantes de Michaelis (K_m) avec la méthylmalonyl-CoA mutase sont respectivement 0,136, 2,20 et 0,132 mM (K_m de la succinyl-CoA est égale à 0,025 mM). Les valeurs de V_{max} pour les composés **7**, **8** et **9** sont respectivement 1,1, 0,013 et 0,0047 μmol min^{-1} U^{-1} (V_{max} pour le succinyl-CoA est égal à 1,0). On discute de l'utilité des nouveaux analogues du coenzyme A dans des études mécanistiques d'enzymes.

[Traduit par la rédaction]

Introduction

Coenzyme A esters play important roles as substrates or regulators of a great number of enzymic reactions including carboxylation–decarboxylations, Claisen-type or aldol-type condensations, thioclastic cleavage, reductions, dehydrogenations, hydration–dehydrations, acylations, isomerizations, and epimerizations. While in some of these reactions the thiolester bond is cleaved, in others it is retained in the product(s). Under neutral and alkaline conditions thiolesters can spontaneously hydrolyse, which may complicate mechanistic studies. In 1978 Stewart and Wieland (1) synthesized a nonhydrolysable analogue of acetyl-CoA, acetonyldethia-CoA (acetyl-CH_2CoA), in which the sulfur had been replaced by methylene. This analogue turned out to be a powerful inhibitor of some enzymic reactions (1, 2), and an allosteric effector of others (2). It was a good substrate for the biotin-enzyme acetyl-CoA carboxylase (3).

Following our interest in the mechanism of propionic acid metabolism, we prepared three different analogues of propionyl-CoA, namely propionyl-dethia(carba)-CoA **1**, propionyl-dethia(dicarba)-CoA **2**, and 2oxobutanyl-CoA **3**. We describe here the syntheses and spectroscopic characterization of these three analogues, as well as their behaviour in some enzymic reactions. A short communication on compound **1** appeared earlier (4).

Results

*Synthesis of propionyl-dethia(carba)-coenzyme A(**1**)*

Following the strategy applied for the total synthesis of coenzyme A (5) and of acetyldethia(carba)CoA (1), the preparation of two key intermediates, propionyl-dethia(carba)pantetheine-4-phosphate (**10**) and adenosine-2′,3′ cyclophosphate 5′ phosphomorpholidate (**11**), was envisaged (Scheme 1). Michael addition of nitromethane to ethylvinylketone gave 1-nitro-4-oxo-hexane (**12**) in 50% yield. After protection of the keto function as the 1,3-dioxolane (**13**, 80%), the nitro group was reduced with Raney nickel to furnish 2-(3-aminopropyl)-2-ethyl-1,3-dioxolane (**14**) in 82% yield. Condensation of the latter with 4-nitrophenyl benzyloxycarbonyl-β-alanine (**15**) (6, 7) resulted in 2-[3-(*N*-benzyloxycarbonyl-β-alanyl)-aminopropyl]-2-ethyl-1,3-dioxolane (**16**, 64.5%). Removal of the *N*-benzyloxycarbonyl protecting group by catalytic hydrogenation was followed, without isolating the intermediate **17**, by condensation in the melt with (−)(*R*)-pantolactone. Two subsequent filtrations, first through a Dowex 50 W × 4 (H^+), then through a Dowex 2 × 8 (^-OH) column, removed the protecting ketal group and afforded propionyl-dethia(carba)pantetheine **18** in 50% yield (based on **16**). Phosphorylation of **19** was carried out with cyanoethylphosphate in analogy to the procedure of Stewart and Wieland (1) and yielded propionyl-dethia(carba)pantetheine-

[1]Author to whom correspondence may be addressed. Tel.: 0049 721 608 2092, Fax: 0049 721 608 4823.

Can. J. Chem. Downloaded from www.nrcresearchpress.com by 195.246.54.202 on 09/08/12
For personal use only.

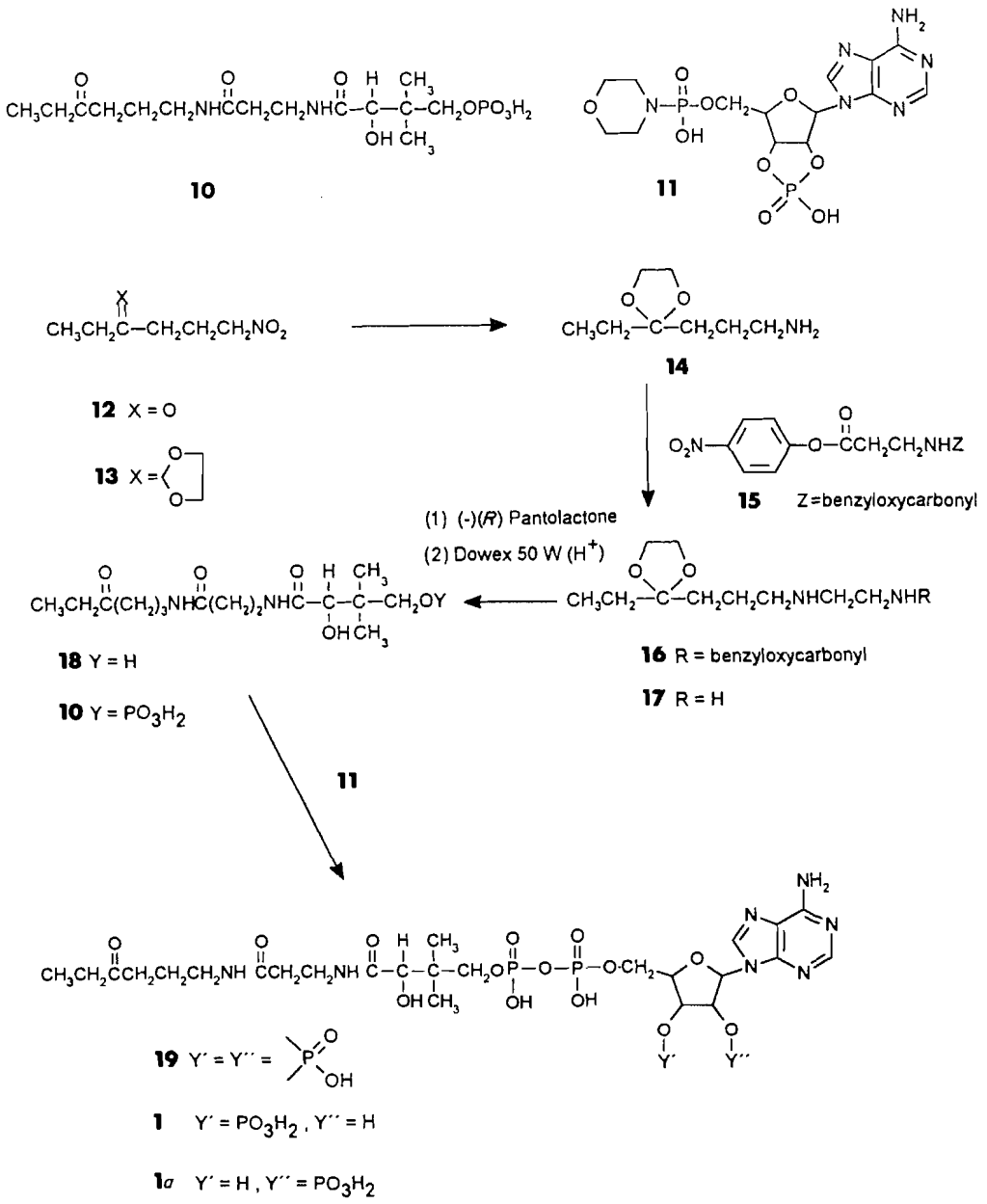

SCHEME 1

4-phosphate (**10**, 42%). Adenosine-2′,3′-cyclophosphate-5′-phosphomorpholi- date (**11**) was prepared according to one of the methods described by M. Yoshikawa et al. (8), Nikawa et al. (3), or A. Simoncsits and J. Tomasz (9). Compound **11** was first described by Moffat and Khorana (5).

Having the two key intermediates **10** and **11** in hand, their condensation to the coenzyme-A analogue could be realized. Acid hydrolysis of the product (**19**) led to a mixture (41%), which was partially separated to propionyl-CH_2CoA (**1**) and propionyl-CH_2-isoCoA (**1***a*) by DEAE cellulose chromatography using a linear LiCl gradient. The final preparation of **1** still contained ~9% **1***a* and was charaterized by ^{1}H and ^{31}P NMR spectroscopy.

Synthesis of propionyl-dethia(dicarba)-coenzyme A **2**

Except for the initial steps, the same method was used as described for analogue **1** (Scheme 2). In the first step the anion of cyanoacetic acid ethylester was added to ethylvinylketone to yield 2-cyano-5-oxoheptanoic acid ethylester (35%). Protection of the keto group afforded 2-(3-cyano-3-carbethoxyethyl)-2-ethyldioxolane (**21**) (83%). The carbethoxy group was removed by heating **21** in a solution of sodium chloride in dimethyl sulfoxide and water to furnish 2-(3-cyanopropyl)-2-ethyldioxolane (**22**) in 69% yield. Reduction of **22** with $LiAlH_4$ gave 2-(4-aminobutyl)-2-ethyldioxolane (**23**) (76%), which was treated further as described for its lower homologue (**14**). This analogous synthesis yielded, after chromatographic separation, propionyl-CH_2CH_2-CoA (**2**) and propionyl-CH_2CH_2-isoCoA (**2***a*) in similar quantities. Both were characterized by ^{1}H and ^{31}P NMR spectroscopy and **2** also by FAB mass spectrometry.

Synthesis of S*-(2-oxobutyl)-coenzyme A (3)*

Compound **3** was synthesized by reaction of coenzyme A

Can. J. Chem. Downloaded from www.nrcresearchpress.com by 195.246.54.202 on 09/08/12
For personal use only.

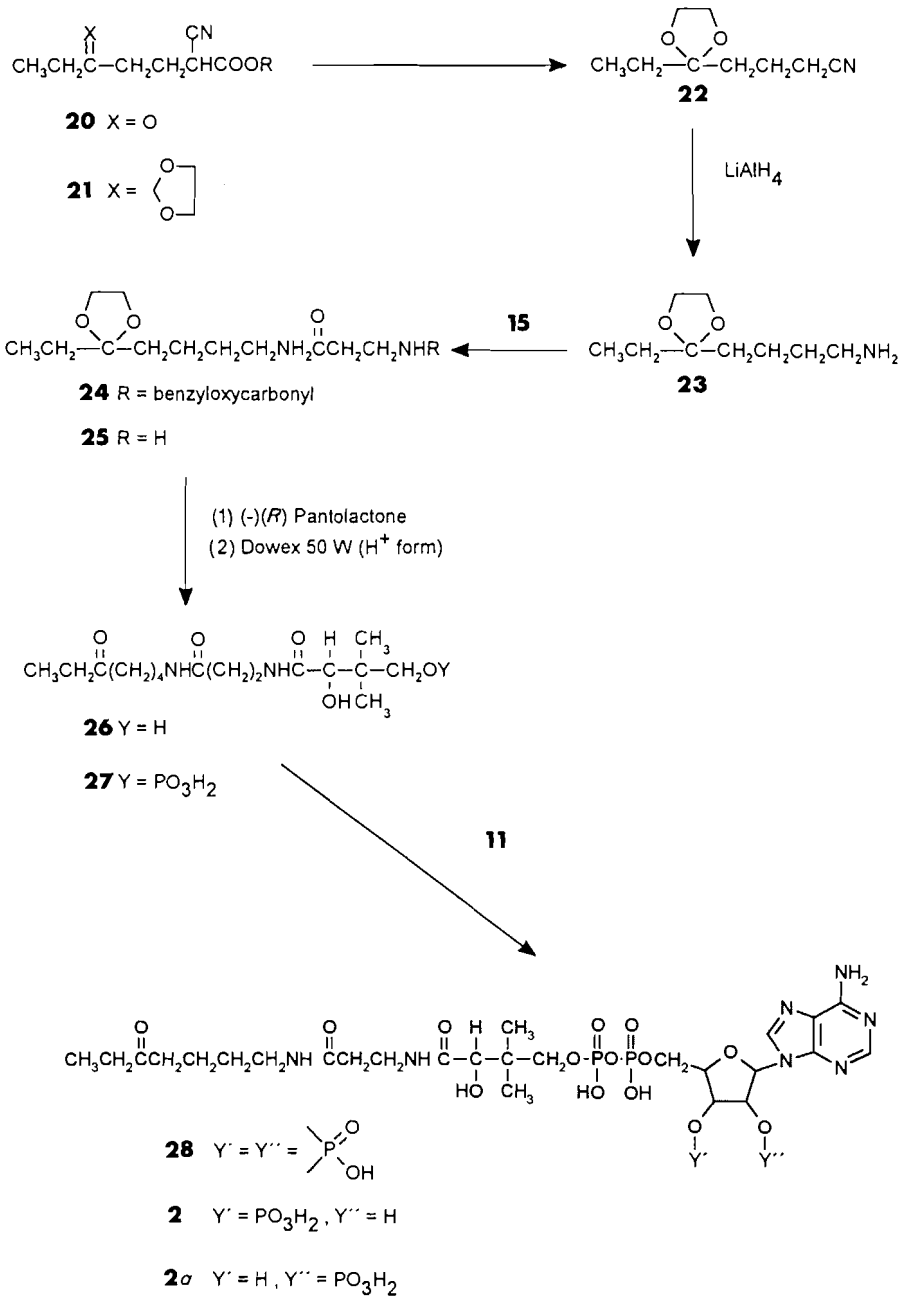

SCHEME 2

with an excess of 1-bromo-2-butanone. After work-up and chromatography as described for analogues **1** and **2** the product was characterized by FAB mass spectrometry and ^{1}H and ^{31}P NMR spectroscopy. Both measurements were consistent with the anticipated structure **3** (see Experimental).

*Conversion and kinetic behaviour of the propionyl-coenzyme A analogues **1**, **2**, and **3** with transcarboxylase*

Propionyl-CH_2-CoA **1**, propionyl-CH_2CH_2 CoA **2**, and *S*-(2-oxobutyl)-CoA **3** were carboxylated to the corresponding methylmalonyl derivatives **4**, **5**, and **6** by incubation with propionyl-CoA–oxaloacetate transcarboxylase from *Propionibacterium shermanii* in the presence of oxaloacetate, lactate dehydrogenase, and NADH. The reaction is summarized in eq. [1]

[1] propionyl-X-CoA + oxaloacetate + NADH + H^+ $\xrightarrow[\text{lactate dehydrogenase}]{\text{transcarboxylase}}$ methylmalonyl-X-CoA + lactate + NAD^+

Additions of lactate dehydrogenase and NADH were necessary to push the equilibrium to the right. After precipitation of the products with acetone, the centrifuged pellets were dried, dissolved in deuterium oxide, and their ^{1}H NMR spectra recorded. All signals could be assigned to the expected structures (see Experimental). Upon prolonged incubation in deuterated phosphate buffer ($p^2H = 7.1$) the methyl doublet at 1.20 ppm slowly changed and was eventually converted into a singlet. This was a measure for the $H/^2H$ exchange rate of the α proton of the methylmalonyl moiety.

Can. J. Chem. Downloaded from www.nrcresearchpress.com by 195.246.54.202 on 09/08/12
For personal use only.

Can. J. Chem. Downloaded from www.nrcresearchpress.com by 195.246.54.202 on 09/08/12
For personal use only.

TABLE 1. Comparison of the K_m and V_{max} values of propionyl-S-CoA and its analogues **1**, **2**, and **3** and in the transcarboxylase reaction

Substrate	K_m (mM)	V_{max} (μmol min^{-1} U^{-1})
$CH_3CH_2\overset{O}{\overset{\|}{C}}S\text{-CoA}$	0.047	1
$CH_3CH_2\overset{O}{\overset{\|}{C}}CH_2\text{-CoA}$	0.15	0.5
$CH_3CH_2\overset{O}{\overset{\|}{C}}CH_2CH_2\text{-CoA}$	0.14	0.025
$CH_3CH_2\overset{O}{\overset{\|}{C}}CH_2S\text{-CoA}$	0.44	0.020

TABLE 2. Comparison of the K_m and V_{max} values of succinyl-S-CoA and its analogues **7**, **8**, and **9** in the methylmalonyl-CoA mutase reaction and the length of X in succinyl-X-CoA (*d*)

Substrate	*d* (Å)	K_m (mM)	V_{max} (μmol min^{-1} U^{-1})
$HOOCCH_2CH_2\overset{O}{\overset{\|}{C}}S\text{-CoA}$	2.75	0.025	1.0
$HOOCCH_2CH_2\overset{O}{\overset{\|}{C}}CH_2\text{-CoA}$	2.48	0.136	1.1
$HOOCCH_2CH_2\overset{O}{\overset{\|}{C}}CH_2CH_2\text{-CoA}$	3.83	2.20	0.013
$HOOCCH_2CH_2\overset{O}{\overset{\|}{C}}CH_2S\text{-CoA}$	4.16	0.132	0.0047

The kinetic measurements with **1**, **2**, and **3** were carried out according to the published assay method (11). The K_m and V_{max} values were determined by the method of Lineweaver–Burk (11) and are listed in Table 1.

*Conversion of the propionyl-coenzyme A analogues **1**, **2**, and **3** into the corresponding succinyl derivatives **7**, **8**, and **9** with an enzyme cocktail*

On an analytical scale, the reaction sequence was monitored directly in the NMR tube. In separate experiments each of the analogues, i.e., propionyl-CH_2-CoA **1**, propionyl-CH_2CH_2-CoA **2**, or *S*-(2-oxobutanyl)-CoA **3**, was dissolved in deuterated phosphate buffer. The reaction was initiated by addition of a lyophilized enzyme mixture consisting of methylmalonyl-CoA mutase, epimerase, and transcarboxylase (12) (eq. [2]).

[2] propionyl-X-CoA + oxaloacetate $\xrightarrow[\text{epimerase, mutase}]{\text{transcarboxylase}}$ succinyl-X-CoA + pyruvate

Conversions of the analogues to their succinyl derivatives could be followed by ^1H NMR spectroscopy. On a preparative scale, the same reactions were carried out in aqueous (nondeuterated) phosphate buffer. After chromatography of the products on a DE-32 column, essentially pure succinyl-CoA analogues, i.e., succinyl-CH_2-CoA (**7**), succinyl-CH_2CH_2-CoA (**8**), and *S*-(2-oxo-4-carboxybutyl)-CoA (**9**), were obtained and characterized by ^1H and ^{31}P NMR spectroscopy.

The K_m and V_{max} values of **7**, **8**, and **9**, as substrates of methylmalonyl-CoA mutase, were determined by the usual spectrophotometrical assay (10, 12) and by using the method of Lineweaver–Burk (11). The results are summarized in Table 2.

Discussion

The synthesis of the novel propionyl-CoA analogues **1**, **2**, and **3** was carried out by conventional methods. While in the case of **1** and **2** a strategy similar to that used for the total synthesis of coenzyme A (5) was applied (Schemes 1, 2), **3** was available by a much simpler procedure involving the reaction of 1-brom-2-butanone with commercial coenzyme A.

Comparison of the geometry of the new analogues with that of natural propionyl-S-CoA is of interest (Table 2). Whereas the C—C bond is shorter than the C—S bond, in propionyl-CH_2CH_2-CoA **2** we have a slightly longer and in propionyl-CH_2-S-CoA **3** a substantially longer CoA chain, respectively.

It is noteworthy that all three propionyl-CoA analogues are substrates of the propionyl-CoA–oxaloacetate transcarboxylase (Table 1). Since acetyl-CH_2CoA was carboxylated by acetyl-CoA carboxylase (3) it was not surprising that its propionyl homologue **1** was also a transcarboxylase substrate. The longer CoA chain has a relatively small effect on K_m but a larger one on V_{max}. In all cases it is possible to carry out the enzymic carboxylation on a preparative scale and to spectroscopically characterize the products.

Prolonged observation of the ^1H NMR spectrum of **1** permitted determination of the spontaneous $^1H/^2H$ exchange rate of the α proton in the methylmalonyl moiety. With a half lifetime of 140 min at p^2H^2 7.1, it was somewhat faster than the value of $t/2 = 480$ min at p^2H^2 7.1 reported for methylmalonyl-thiolester (13).

The enzymically produced methylmalonyl-CoA analogues **4**, **5**, and **6** were also accepted as substrates by the coenzyme B_{12}-dependent methylmalonyl-CoA mutase. In the presence of the transcarboxylase, the epimerase, and the mutase, the propionyl-CoA analogues **1**, **2**, and **3** were converted in one pot into the corresponding succinyl-CoA analogues **7**, **8**, and **9** on a preparative scale. These nonhydrolysable succinyl derivatives were used as substrates to determine the kinetic constants of the mutase reaction (Table 2).

A comparison of the K_m values reveals that both the length of the CoA chain and the presence of sulfur is important. Succinyl-CH_2CH_2-CoA (**8**) has the lowest affinity for the mutase, while succinyl-CH_2S-CoA has only a slightly higher K_m than succinyl-S-CoA. Interestingly, the shorter the CoA chain, the higher the V_{max} value.

The novel, nonhydrolysable, propionyl, methylmalonyl, and succinyl-CoA analogues may be useful in mechanistic and structural studies of the corresponding enzymes by ESR, NMR, and CD spectroscopy as well as by X-ray crystallography.

Experimental

Equipment

^1H NMR, ^{31}P NMR, mass and IR spectra were recorded with the following instruments: Bruker WH 250 or AM 400, Bruker WH 300,

[2]The p^2H was determined in deuterium oxide.

Can. J. Chem. Downloaded from www.nrcresearchpress.com by 195.246.54.202 on 09/08/12
For personal use only.

Varian MAT CH-5 or Finnigan MAT 90, and Beckman IR-8, respectively.

For enzyme assays a Perkin Elmer 550A (UV–vis) spectrometer was used. Melting points were determined in a Büchi apparatus according to Dr. Tottoli.

For HPLC separations a Merck–Hitachi instrument was used.

Materials

Ethylvinylketone, cyanoethylphosphate, β-alanine, (−)-(*R*)-pantolactone, phosphorus oxychloride, and coenzyme B_{12} were products of Fluka (Buchs, Switzerland). Trimetaphosphate, 5′-AMP, and 2′(3′)-AMP were from Sigma (St. Louis, U.S.A.), and DE-32 cellulose from Whatman (Maidstone, England). Coenzyme A, lactate dehydrogenase, NAD^+, and NADH were from Boehringer (Mannheim, Germany). Methylmalonyl-CoA mutase, propionyl-CoA–oxaloacetate transcarboxylase and methylmalonyl-CoA epimerase were isolated from *Propionibacterium shermanii* (10, 12).

Syntheses

1-Nitro-4-oxo-hexane (12) was synthesized as described for the 5-methyl derivative (14): 1 g (11.9 mmol) ethyl vinyl ketone yielded 0.87 g (5.95 mmol) **12** (50%). ^{1}H NMR ($CDCl_3$, 250 MHz) δ: 1.06 (t, J = 8.3 Hz, 3H), 2.26 (quint, J = 7.8 Hz, 2H), (quart, J = 8.3 Hz, 2H), 2.58 (t, J = 7.8 Hz, 2H), 4.43 (t, J = 7.8 Hz, 2H).

*2-(3-Nitropropyl-)2-ethyl-1,3-dioxolane (**13**)* was obtained in analogy to the 2-isopropyl derivative (14); 0.66 g (4.5 mmol) **12** yielded 0.8 g (3.57 mmol) **13** (80%). ^{1}H NMR ($CDCl_3$, 250 MHz) δ: 0.91 (t, J = 8.3 Hz, 3H), 1.65 (quart, J = 8.3 Hz, 2H), 1.73 (m, 2H), 2.11 (quint, J = 7.5 Hz, 2H), 3.95 (s, 4H), 4.41 (t, J = 7.5 Hz, 2H).

*2-(3-Aminopropyl-2-ethyl-1,3-dioxolane (**14**)* was synthesized as described for the 2-isopropyl derivative (14). Starting from 5.75 g (30.5 mmol) **13** we obtained 4.0 g (25 mmol) **14** (82%). ^{1}H NMR ($CDCl_3$, 250 MHz) δ: 0.93 (t, J = 8.3 Hz, 3H), 1.35 (s, 2H), 1.55 and 1.68 (m, 6H), 2.70 (t, J = 7.8 Hz, 2H), 3.98 (s, 4H).

*2-(3-[(N-Benzyloxycarbonyl-β-alanine)-aminopropyl)-2-ethyl-1,3-dioxolane (**16**)* was obtained in analogy to the 2-isopropyl derivative (14). Reaction of 1 g (6.28 mmol) **14** with 2.18 g (6.3 mmol) 4-nitrophenyl benzyloxycarbonyl-β-alanine (**15**) afforded 1.47 g (4.06 mmol) **16** (64.5%); mp 56–57°C; IR (KBr): 3320 (s), 3080 (w), 2980 (s), 2960 (s), 2880 (m), 1685 (s), 1635 (s), 1545 (s), 1460 (w), 1430 (w), 1370 (w), 1335 (m), 1265 (m), 1240 (m), 1190 (w), 1160 (w), 1135 (w), 1070 (m), 910 (w), 750 (w), 690 (m) cm^{-1}. ^{1}H NMR ($CDCl_3$, 250 MHz) δ: 0.91 (t, J = 8.3 Hz, 3H), 1.65 (m, 6H), 2.41 (t, J = 5.85 Hz, 2H), 3.26 (quart, J = 6.4 Hz, 2H), 3.5 (quart, J = 5.85 Hz, 2H), 3.95 (s, 4H), 5.08 (s, 2H), 5.46 (s, 1H), 5.78 (s, 1H), 7.33 (s, 5H), MS (T_d 130°C, 70 eV, *m/e*): 56 (14%), 57 (62), 65 (10), 69 (17), 70 (10), 73 (23), 77 (22), 79 (43), 86 (42), 91 (85), 96 (10), 97 (13), 98 (19), 99 (23), 101 (100), 102 (15), 107 (29), 108 (37), 113 (18), 130 (49), 139 (10), 142 (23), 227 (31), 335 (11), M^+ = 364 (6). Anal. calcd.: C 62.6, H 7.74, N 7.68; found: C 62.2, H 7.96, N 7.74%.

*Propionyl-dethia(carba)pantetheine (**18**)* was synthesized as described for the isobutanoyl derivative (14): 0.854 g (2.34 mmol) **16** yielded 370 mg (1.16 mmol) **18** (50%). IR (film): 3320 (s), 3100 (w), 2990 (s), 2970 (s), 1710 (s), 1650 (s), 1640 (s), 1570 (s), 1550 (s), 1530 (s), 1470 (m), 1440 (m), 1380 (m), 1360 (m), 1300 (m), 1250 (w), 1080 (m), 1050 (m), 880 (w) cm^{-1}. ^{1}H NMR (D_2O, 250 MHz) δ: 0.78 (s, 3H), 0.81 (s, 3H), 0.90 (t, J = 7.9 Hz, 3H), 1.63 (quint, J = 7.7 Hz, 2H), 2.4 (m, 6H), 3.05 (t, J = 7.7 Hz, 2H), 3.36 (AB system, J = 12 Hz, 2H), 3.41 (m, 2H), 3.86 (s, 1H). MS (T_d 160°C, 70 eV, *m/e*): 57 (43%), 58 (13), 71 (100), 72 (24), 86 (24), 98 (22), 99 (30), 100 (13), 115 (26), 116 (26), 157 (13), M^+ 1 = 317 (<1%).

*Propionyl-dethia(carba)pantetheine-4′-phosphate (**10**)* was obtained as described for the isobutanyl derivative (14). Reacting 637 mg (1.98 mmol) **18** with 1 g (2.63 mmol) cyanoethylphosphate (6) we obtained 470 mg (0.83 mmol) **10** (42%). IR (KBr): 3360, (s), 2940 (m), 1710 (m), 1655 (s), 1545 (m), 1450 (w), 1380 (w) 1245 (w), 1080 (s), 990 (s) cm^{-1}. ^{1}H NMR (D_2O, 250 MHz) δ: 0.83 (s, 3H), 0.98 (s, 3H), 1.0 (t, J = 9 Hz, 3H), 1.73 (quint, J = 6.5 Hz, 2H), 2.5 (m, 6H), 3.16 (t, J = 6.5 Hz, 2H), 3.52 (t, J = 5.5 Hz, 2H), 3.74 (m, 2H), 4.10 (s, 1H). ^{31}P NMR (D_2O, H_3PO_4 ext.) δ: 6.2 (s).

*Propionyl-dethia(carba) coenzyme A (**1**)* was prepared as described for its isobutanoyl analogue (14). Starting from 141.5 mg (0.25 mmol) **10** and 298.4 mg (0.62 mmol) adenosine-2′,3′ cyclophosphate-5′-phosphomorpholidate (**11**) we obtained a 48 mg (0.05 mmol) mixture of **1** and propionyl-dethia(carba) isocoenzyme A (**1***a*); 23 mg of this mixture was rechromatographed on a DE 32 cellulose column (2.2 ×30 cm) with an LiCl gradient (14). The first eluted peak contained **1***a* (8.0 mg, 8.3 μmol) while **1** appeared in the second peak (8.3 mg, 8.6 μmol). ^{1}H NMR of **1** (D_2O, pD = 3, 250 MHz) δ: 0.60 (s, 3H), 0.70 (s, 3H), 0.83 (t, J = 6.8 Hz, 3H), 1.51 (quint, J = 6.6 Hz, 2H), 2.32 (m, 6H), 2.91 (t, J = 6.6 Hz, 2H), 3.30 (t, J = 7.0 Hz, 2H), 3.60 (ABX system, J = 12 Hz, J = 5 Hz, 2H), 3.90 (s, 1H), 4.1 (m, 2H), 6.09 (d, J = 8.3 Hz, 1H), 8.18 (s, 1H), 8.43 (s, 1H). ^{31}P NMR (D_2O, 121.48 MHz, H_3PO_4 ext.) δ: = −7.89 (m), 2.7 (s).

*2-(3-Cyano-3-carbethoxyethyl)-2-ethyldioxolane (**21**)*

2-Cyano-5-oxoheptanoic acid ethylester (15) (9.4 g, 48 mmol) in benzene (25 mL) in the presence of 4.2 mL (75 mmol) ethyleneglycol and 0.2 g toluene sulfonic acid was refluxed for 6 h. The reaction water was removed continuously by a separatory funnel. After neutralization with 2% NaOH (15 mL), the resulting solution was washed with water, then dried with anhydrous K_2CO_3. Distillation of the product yielded 9.6 g (40 mmol) **21** (83%); bp 135°C/1.0 Torr (1 Torr = 133.3 Pa). ^{1}H NMR ($CDCl_3$, 250 MHz) δ: 0.92 (t, J = 7.5 Hz, 3H), 1.34 (t, J = 7.1 Hz, 3H), 1.65 (quart, J = 7.5 Hz, 2H), 1.84 (t, J = 6.7 Hz, 2H), 2.06 (m, 2H), 3.66 (t, J = 6.7 Hz, 1H), 3.97 (s, 4H), 4.30 (quart, J = 7.1 Hz, 2H). MS (T_d 130°C, 70 eV, *m/e*): 87 (15%), 101 (100), 124 (7), 154 (3), 198 (12), 212 (32), M^+ + 1 = 241 (21). Anal. calcd.: C 59.73, H. 7.94, N 5.80; found: C 59.87, H 8.07, N 5.68%.

*2-(3-Cyanopropyl)-2-ethyl-1,3-dioxolane (**22**)*

To 7.8 g (32 mmol) **21** dissolved in dimethyl sulfoxide (2.5 mL) were added 1.89 g NaCl and water (1.18 mL). The stirred mixture was heated to 180°C for 7 h. After cooling, water (80 mL) was added and the resulting solution was extracted 5 times with 40-mL portions of ether. The combined extracts were dried with anhydrous $MgSO_4$. Distillation of the product yielded 3.7 g (22 mmol, 69%) **22**; bp 95°C/0.85 Torr. ^{1}H NMR (CD_3Cl, 250 MHz) δ: 0.92 (t, J = 7.5 Hz, 3H), 1.64 (quart, J = 7.5 Hz, 2H), 1.78 (m, 4H), 2.42 (m, 2H), 3.97 (s, 4H). MS (T_d 100°C, 70 eV, *m/e*): 57 (55%), 68 (32), 96 (50), 101 (100), 110 (10), 140 (96), 154 (14), M^+ = 169 (6). Anal. calcd.: C 63.88, H 8.93, N 8.27; found: C 63.95, H 8.97, N 8.14%.

*2-(4-Aminobutyl)-2-ethyl-1,3-dioxolane (**23**)*

To a suspension of 1 g $LiAlH_4$ in 20 mL dry ether a solution of 3.12 g (18 mmol) **22** in 25 mL dry ether was introduced under stirring (1 h). After 4 h reflux ice was added. Work-up afforded 2.4 g (13.8 mmol) **23** (76%); bp 110°C/0.75 Torr. ^{1}H NMR ($CDCl_3$, 250 MHz) δ: 0.90 (t, J = 7.5 Hz, 3H), 1.52 (m, 4H), 1.66 (m, 4H), 2.72 (t, J = 6.8 Hz, 2H), 3.97 (s, 4H). MS (T_d 100°C, 70 eV, *m/e*): 56 (23%), 57 (26), 73 (5), 82 (10), 84 (5), 101 (100), 102 (5), 128 (12), 144 (18), M^+ = 173 (<1). Anal. calcd.: C 62.39, H 11.05, N 8.08; found: C 62.33, H 11.15, N 7.97%. The following compounds (**24**, **25**, **26**, **27**, and **2**) were prepared as described for the lower homologues **16**, **18**, **10**, and **1**.

*2-(4-[(N-Benzyloxycarbonyl-β-alanine)-aminobutyl]-2-ethyl-1,3-dioxolane **24***

Educts: 11.5 g (66 mmol) **23**, 22.7 g (66 mmol) **15**. Yield: 21 g (55 mmol) **24** (83%); mp 48–50°C. ^{1}H NMR ($CDCl_3$, 250 MHz) δ: 0.90 (t, J = 7.5 Hz, 3H), 1.43 (m, 4H), 1.63 (m, 4H), 2.41 (t, J = 5.6 Hz, 2H), 3.27 (quart, J = 5.6 Hz, 2H), 3.52 (quart, J = 5.6 Hz, 2H), 3.93 (s, 4H), 5.12 (s, 2H), 5.54 (s, 1H), 5.62 (s, 1H), 7.38 (s, 5H). MS (T_d 130°C, 70 eV *m/e*: 57 (9%), 91 (56), 101 (100), 144 (12), 227 (4), 333 (5), 349 (15), M^+ = 378 (4). Anal. calcd.: C 63.4, H 7.99, N 7.40; found: C 63.86, H 8.41, N 7.37%.

*Propionyl-dethia(dicarba)-pantetheine **26***

Educts: 5.7 g (15 mmol) **24**, 2.2 g (17 mmol) (−)-(*R*)-pantolactone.

Can. J. Chem. Downloaded from www.nrcresearchpress.com by 195.246.54.202 on 09/08/12
For personal use only.

Yield: 2.5 g (7.5 mmol) **26** (50%); mp 57–59°C. ^{1}H NMR (D_2O, 250 MHz) δ: 0.90 (s, 3H), 0.95 (s, 3H), 1.03 (t, J = 7.5 Hz, 3H), 1.56 (m, 4H), 2.57 (t, J = 6.4 Hz, 2H), 2.66 (m, 4H), 3.27 (t, J = 6.4 Hz, 2H), 3.56 (AB, J = 12 Hz, 2H), 3.63 (m, 2H), 4.10 (s, 1H). MS (T_d 130°C, 70 eV, *m/e*: 57 (41%), 71 (100), 100 (26), 113 (26), 130 (37), 171 (16), 200 (25), 227 (12), 258 (7), 282 (3), M^+ = 330 (0.2). Anal. calcd.: C 58.16, H 9.15, N 8.48; found: C 57.66, H 9.32, N 8.51%.

Propionyl-dethia(dicarba)-pantetheine-4′-phosphate (27)

Educts: 0.9 g (2.7 mmol) **26**, 2.2 g (6.6 mmol) cyanoethylphosphate (6). Yield: 0.59 g (1.1 mmol) **27** (41%). ^{1}H NMR (D_2O, 250 MHz) δ: 0.90 (s, 3H), 0.95 (s, 3H), 1.03 (t J = 7.5 Hz, 3H), 1.56 (m, 4H), 2.57 (t, J = 7.1 Hz, 2H), 2.66 (m, 4H), 3.27 (t, J = 7.1 Hz, 2H), 3.56 (AB, J = 12 Hz, 2H), 3.63 (t, J = 7.1 Hz, 2H). ^{31}P NMR (D_2O, 121.49 MHz, H_3PO_4 ext.) δ: 5.0 (s). FAB-MS: 55 (81%), 70 (29), 113 (52), 154 (42), 229(100), 294 (56), 319 (26), 370 (39), 451 (15), 529 (10), $M^+ + 2$ = 547 (18). Anal. calcd.: C 45.51, H 6.92, N 6.63; found: C 45.24, H 7.18, N 6.54%.

Propionyl-dethia(dicarba)-coenzyme A (2)

Educts: 0.52 g (0.95 mmol) **27**, 1.194 g (2.48 mmol) **11**. Yield: 0.102 g (0.12 mmol) mixture of **2** and **2***a*. After separation on DE-32 cellulose (see **1** and ref. 14): 38 mg (0.045 mmol) **2***a* and 40 mg (0.048 mmol) **2**. ^{1}H NMR (D_2O, 400 MHz) δ: 0.74 (s, 3H), 0.86 (s, 3H), 0.97 (t, J = 7.5 Hz, 3H), 1.45 (m, 4H), 2.43 (t, J = 6.2 Hz, 2H), 2.51 (m, 4H), 3.10 (t, J = 6.0 Hz, 2H), 3.46 (t, J = 6.0 Hz, 2H), 3.66 (ABX, J_1 = 11.2 Hz, J_2 = 5.4 Hz, 2H), 4.00 (s, 1H), 4.22 (s, 2H), 4.40 (m, 1H), 4.64 (m, 1H), 6.18 (d, 1H), 8.26 (s, 1H), 8.56 (s, 1H). ^{31}P NMR (D_2O, 121.49 MHz, H_3PO_4 ext.) δ: −0.3 (s), −15.1 (d, J = 21.9 Hz), −15.6 (d, J = 21.9 Hz). FAB-MS of **2**, *m/e*: 832 (M^+ + 1) (calcd. 831.458).

S-*2-Oxobutyl-coenzyme A* ***3*** was synthesized by reacting, under argon, 25 mg (32 μmol) coenzyme A (Li_3-salt) in 2.5 mL 0.04 M Li_2CO_3 solution with 25 mg (166 μmol) 1-bromo-2-butanone dissolved in 5 mL ethanol. After 12 h the solution was added dropwise to 150 mL acetone and the precipitate collected by centrifugation. The product was purified by chromatography on DE-32 cellulose (see **1** and ref. 14). Yield: 13 mg (15 μmol, 47%). ^{1}H NMR (D_2O, 400 MHz) δ: 0.72 (s, 3H), 0.86 (s, 3H), 0.98 (t, J = 7.5 Hz, 3H), 2.42 (t, J = 6.2 Hz, 2H), 2.57 (t, J = 6.4 Hz, 2H), 2.63 (quart, J = 7.5 Hz, 2H), 3.28 (t, J = 6.2 Hz, 2H), 3.44 (t, J = 6.4 Hz, 2H), 3.65 (ABX, 2H), 3.97 (s, 1H), 4.20 (m, 2H), 4.54 (m, 2H), 6.13 (d, J = 6.2 Hz, 1H), 8.24 (s, 1H), 8.54 (s, 1H). FAB-MS *m/e*: 862 (M^+ + 1) (calcd. 861.363).

*Ezymatic carboxylation of the propionyl-coenzyme A analogues **1**, **2**, and **3** to the methylmalonyl-coenzyme A analogues **4**, **5**, and **6***

In a typical experiment 10 μmol propionyl-CoA analogue was incubated with 30 μmol oxaloacetate, 12 μmol NADH, 6 U propionyl-CoA–oxaloacetate transcarboxylase, and 5 U lactate dehydrogenase in 5 mL potassium phosphate buffer (0.05 M, pH 7.2) for 3 h at room temperature. For chromatographic purification see propionyl-CoA analogues. Yield: ca. 5 μmol (50%). ^{1}H NMR of **4** (D_2O, 250 MHz) δ: 0.73 (s, 3H), 0.88 (s, 3H), 1.21 (d, J = 7.5 Hz, 3H), 1.71 (quint, J = 6.6 Hz, 2H), 2.45 (t, J = 7.4 Hz, 2H), 2.65 (m, 2H), 3.13 (t, J = 6.6 Hz, 2H), 3.45 (t, J = 7.4 Hz, 2H), 3.55 (m, 1H), 3.66 (unresolved ABX, 2H), 4.00 (s, 1H), 4.25 (m, 2H), 6.20 (d, J = 6.2 Hz, 1H), 8.28 (s, 1H), 8.58 (s, 1H). ^{1}H NMR of **5** (D_2O, 250 MHz) δ: 0.74 (s, 3H), 0.86 (s, 3H), 1.24 (d, J = 7.6 Hz, 3H), 1.50 (m, 4H), 2.45 (t, 2H), 2.63 (m, 2H), 3.15 (t, 2H), 3.48 (t, 2H), 3.57 (m, 1H), 3.70 (ABX, unresolved, 2H), 4.02 (s, 1H), 4.25 (s, 2H), 4.58 (m, 1H), 6.20 (d, J = 6.2 Hz, 1H), 8.29 (s, 1H), 8.59 (s, 1H). ^{1}H NMR of **6** (D_2O, 250 MHz) δ: 0.74 (s, 3H), 0.87 (s, 3H), 1.28 (d, J = 7.5 Hz, 3H), 2.49 (t, J = 6.2 Hz, 2H), 2.64 (t, J = 6.4 Hz, 2H), 3.34 (t, J = 6.2 Hz, 2H), 3.48 (t, J = 6.4 Hz, 2H), 3.67 (unresolved ABX, 2H), 3.78 (quart, 1H), 4.01 (s, 1H), 4.25 (m, 2H), 4.60 (m, 1H), 6.22 (d, J = 6.2 Hz, 1H), 8.33 (s, 1H), 8.58 (s, 1H).

*Enzymatic carboxylation and isomerization of the propionyl-coenzyme A analogues **1**, **2**, and **3** to the succinyl-coenzyme A analogues **7**, **8**, and **9***

In a typical experiment 4 μmol propionyl-CoA analogue was incubated with 16 μmol oxaloacetate, 20 μg coenzyme B_{12}, and a mixture of propionyl-CoA–oxaloacetate transcarboxylase, methylmalonyl-CoA epimerase, and methylmalonyl-CoA mutase, 1 U of each, in 2 mL of potassium phosphate buffer (0.2 M, pH 6.8) for 12 h at room temperature. The reaction was terminated at 0°C with 0.1 M perchloric acid (→ pH 3). After removal of the precipitated proteins by centrifugation the pH of the solution was adjusted to 6 with 2 M K_2CO_3. Removal of the crystalline potassium perchlorate was followed by lyophilization. Yield: ca. 40%. ^{1}H NMR of **7** (D_2O, 250 MHz) δ: 0.55 (s, 3H), 0.72 (s, 3H), 1.50 (quint, J = 5.8 Hz, 2H), 2.25 (m, 3H), 2.40 (t, J = 5.8 Hz, 2H), 2.53 (d, J = 6.2 Hz, 2H), 2.95 (t, J = 5.8 Hz, 2H), 3.30 (t, J = 6.8 Hz, 2H), 3.53 (ABX, J = 12 Hz, J_{HP} = 6 Hz, 2H), 3.86 (s, 1H), 4.10 (m, 2H), 6.06 (d, J = 7.5 Hz, 1H), 8.15 (s, 1H), 8.43 (s, 1H). ^{1}H NMR of **8** (D_2O, 400 MHz) δ: 0.75 (s, 3H), 0.86 (s, 3H), 1.48 (m, 4H), 2.46 (m, 4H), 2.75 (t, 2H), 3.08 (t, 2H), 3.44 (t, 2H), 3.65 (unresolved ABX, 2H), 3.97 (s, 1H), 4.20 (m, 2H), 4.54 (m, 1H), 6.15 (d, J = 6.2 Hz, 1H), 8.24 (s, 1H), 8.54 (s, 1H). ^{1}H NMR of **9** (D_2O, 400 MHz) δ: 0.72 (s, 3H), 0.86 (s, 3H), 2.46 (m, 4H), 2.58 (t, J = 6.4 Hz, 2H), 2.84 (t, J = 7.2 Hz, 2H), 3.30 (t, J = 6.2 Hz, 2H), 3.46 (t, J = 6.4 Hz, 2H), 3.65 (unresolved ABX, 2H), 3.97 (s, 1H), 4.20 (m, 1H), 6.13 (d, J = 6.2 Hz, 1H), 8.24 (s, 1H), 8.54 (s, 1H).

Acknowledgements

We thank Ms. Ingeborg Merkler for enzyme purifications. Financial support from the Deutsche Forschungsgemeinschaft and the Fonds der Chemischen Industrie is gratefully acknowledged.

1. C.J. Stewart and T. Wieland. Liebigs Ann. Chem. 57 (1978).
2. H.P. Blaschkowski, J. Knappe, and T. Wieland. FEBS Lett. **98**, 81 (1971).
3. J. Nikawa, S. Numa, T. Shiba, C.J. Stewart, and T. Wieland. FEBS Lett. **91**, 144 (1978).
4. M. Michenfelder and J. Rétey. Angew. Chem. **98**, 337 (1986); Angew. Chem. Int. Ed. Engl. **25**, 366 (1986).
5. J.G. Moffat and H.G. Khorana. J. Am. Chem. Soc. **83**, 649 (1961); **83**, 663 (1961).
6. M. Bergmann and L. Zervas. Ber. Dtsch. Chem. Ges. **65**, 1192 (1932); G.M. Tener. J. Am. Chem. Soc. **83**, 159 (1961).
7. M. Manning and V. du Vigneaud. Biochemistry, **4**, 1884 (1965).
8. M. Yoshikawa, T. Kato, and T. Takensishi. Bull. Chem. Soc. Jpn. **42**, 3505 (1969).
9. A. Simoncsits and J. Tomasz. Biochim. Biophys. Acta, **395**, 74 (1975).
10. H.G. Wood, B.E. Jacobson, B. Gerwin, and D.B. Northrop. Methods Enzymol. **13**, 215 (1969).
11. H. Lineweaver and D. Burke. J. Am. Chem. Soc. **56**, 658 (1934).
12. B. Zagalak, J. Rétey, and H. Sund. Eur. J. Biochem. **44**, 529 (1974).
13. P. Overath, G.M. Kellerman, and F. Lynen. Biochem. Z. **335**, 500 (1962).
14. G. Brendenlberger and J. Rétey. Isr. J. Chem. **29**, 195 (1989).
15. T.A. Spencer, M.D. Newton, and S.W. Baldwin. J. Org. Chem. **29**, 787 (1962).

The formation of corydaline and related alkaloids in *Corydalis cava* in vivo and in vitro

MARTINA RUEFFER, WOLFGANG BAUER, AND MEINHART H. ZENK

Lehrstuhl für Pharmazeutische Biologie der Universität, Karlstrasse 29, 80333 Munich, Germany

Received June 28, 1993

This paper is dedicated to Professors David B. MacLean and Ian D. Spenser

MARTINA RUEFFER, WOLFGANG BAUER, and MEINHART H. ZENK. Can. J. Chem. **72,** 170 (1994).

The biosynthesis of corydaline and thalictricavine has been investigated by application of [8-^{3}H]-labelled palmatine and berberine to *Corydalis cava* bulb tissue. In both cases, high incorporation into the respective (14*R*,13*S*)corydaline and -thalictricavine was observed. (*S*)-[14-^{3}H, 8-^{14}C]Scoulerine was also transferred into corydaline with all of the tritium being lost, indicating that a redox reaction had taken place in the transition of the (14*S*) to the (14*R*) product. A partly enriched protein fraction catalyzed the reduction of both protoberberine precursors to the 7,8-dihydro intermediate, which was subsequently methylated at C-13 at the expense of *S*-adenosylmethionine (SAM) and reduced at C-14 by a B-type reaction with NADPH as reductant. The identity of the product was unequivocally established by NMR, MS, and CD measurements. This biosynthetic route is in full agreement with previously published predictions based on in vivo experiments.

MARTINA RUEFFER, WOLFGANG BAUER et MEINHART H. ZENK. Can. J. Chem. **72,** 170 (1994).

On a étudié la biosynthèse de la corydaline et de la thalictricavine en appliquant de la palmatine et de la berbérine marquées au [8-^{3}H] à des tissus bulbaires de *Corydalis cava*. Dans les deux cas, on a observé une incorporation élevée dans les (14*R*,13*S*)-corydaline et -thalictricavine respectives. La (*S*)-[14-^{3}H, 8-^{14}C]scoulérine se transforme aussi en corydaline avec une perte des trois atomes de tritium; ceci indique qu'il se produit une réaction rédox lors de la transformation du produit (14*S*) en produit (14*R*). Une fraction partiellement enrichie en protéines catalyse la réduction des deux précurseurs protoberbérines en un intermédiaire 7,8-dihydrogéné qui est ultérieurement méthylé en C-13 aux dépens de la *S*-adénosylméthionine (SAM) et réduit en C-14 par une réaction de type B à l'aide NADPH qui agit comme réducteur. On a déterminé sans ambiguïté l'identité du produit en faisant appel à des mesures de RMN, de SM et de DC. Cette voie de biosynthèse est en parfait accord avec les prédictions publiées antérieurement et qui étaient basées sur des expériences in vivo.

[Traduit par la rédaction]

The biosynthesis of select alkaloids of the protoberberine type has been clarified at the enzyme level using plant cell cultures both from the *Berberidaceae* and the *Ranunculaceae* (1–3). These alkaloids, formed from two molecules of tyrosine, posed an interesting biosynthetic problem, in that tyrosine labelled both the isoquinoline "upper" and the benzyl "lower" portion of the benzylisoquinolines, while the more immediate, dihydroxylated precursors DOPA or dopamine unpredictably labelled only the "upper" half of these molecules (4). This question was elegantly and expertly posed again more recently (5). This intriguing problem was solved when it could be demonstrated that the trihydroxylated (*S*)-norcoclaurine but not the tetrahydroxylated (*S*)-norlaudanosoline is the precursor of the benzylisoquinoline alkaloids (6). (*S*)-Norcoclaurine is derived from the enzyme-catalyzed stereoselective condensation of dopamine with *p*-hydroxyphenylacetaldehyde (1). The biosynthetic pathway to berberine is now completely known also at the enzyme level (1–3). One of the remaining questions was, however, by which mechanism the (*R*)-configurated tetrahydroprotoberberine molecules are formed. It was found that a highly stereoselective and reversible enzyme system using NADPH and protoberberine alkaloids as substrates reduced the C ring of protoberberines to yield the (*R*)-configurated tetrahydroprotoberberines (7). The hitherto claimed precursor role of (*R*)-reticuline (8) in the biosynthesis of these alkaloids is incorrect.

Corydalis cava is a rich source of benzylisoquinoline alkaloids and variously modified molecules (9), among them (+)-corydaline (10, 11). The structure of this compound had been elucidated (12, 13) and the stereochemistry of both asymmetric centers was solved (14). This alkaloid is of biosynthetic interest because it belongs to the (14*R*) series of the tetrahydroprotoberberines and, in addition, contains a rare one-carbon unit as methyl group at C-13.

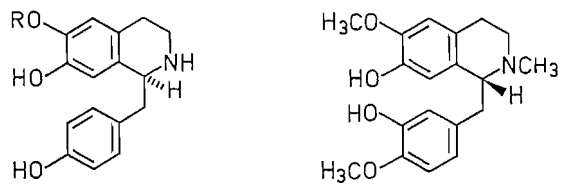

(*S*)-Norcoclaurine: R = H
(*S*)-Coclaurine: R = CH_3

(*R*)-Reticuline

In an admirable set of experiments, MacLean, Spenser, and co-workers (5, 15) first found that corydaline was synthesized along the protoberberine route with its C-methyl group being supplied by methionine (15). Later, the important observation was made that palmatine and not (*R,S*)-tetrahydropalmatine was the immediate precursor of corydaline (15). Some uncertainty, however, remained as to the true intermediates and precursors of this alkaloid. We now set out to clarify at the enzyme level the route by which this (*R*)-configurated, C-methylated alkaloid is formed in the genus *Corydalis*. First, the incorporation experiments reported by Holland et al. (5) were repeated but, instead of *C. solida*, differentiated plants of *C. cava*, which contain (14*R*,13*S*)-thalictricavine (16) and (14*R*,13*S*)-tetrahydrocorysamine (17), in addition to (14*R*,13*S*)-corydaline (11), were used. Coptisine, palmatine, and berberine, all tritium-labelled in the 8-position, were separately supplied to bulbs of *C. cava* and, after being metabolized, the corresponding C-methylated end products were isolated. High relative incorporation rates of 24–38% were observed (Table 1). These data confirm and extend the previous results obtained with a different plant species by Holland et al. (5). The above incorporation experiment was

[1]Author to whom correspondence may be addressed. Telephone (089) 59 02-244, Telefax (089) 59 02-611.

Can. J. Chem. Downloaded from www.nrcresearchpress.com by 203.198.23.82 on 09/08/12
For personal use only.

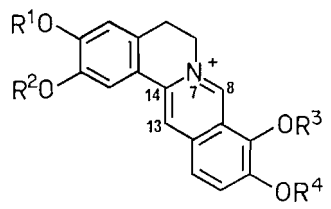

Berberine : $R^1 + R^2 = -CH_2-$; $R^3 = CH_3$; $R^4 = CH_3$
Columbamine : $R^1 = CH_3$; $R^2 = H$; $R^3 = CH_3$; $R^4 = CH_3$
Coptisine : $R^1 + R^2 = -CH_2-$; $R^3 + R^4 = -CH_2-$
Dehydroscoulerine : $R^1 = CH_3$; $R^2 = H$; $R^3 = H$; $R^4 = CH_3$
Jatrorrhizine : $R^1 = H$; $R^2 = CH_3$; $R^3 = CH_3$; $R^4 = CH_3$
Palmatine : $R^1 = R^2 = R^3 = R^4 = CH_3$

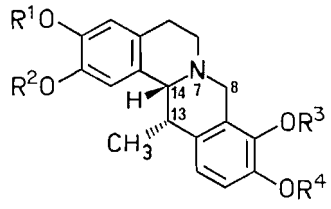

Corydaline : $R^1 = R^2 = R^3 = R^4 = CH_3$
Tetrahydrocorysamine : $R^1 + R^2 = -CH_2-$; $R^3 + R^4 = -CH_2-$
Thalictricavine : $R^1 + R^2 = -CH_2-$; $R^3 = CH_3$; $R^4 = CH_3$

TABLE 1. Feeding of [8-^{3}H]protoberberines to *Corydalis cava* bulb tissue

Substrate	Product isolated	Total activity (dpm)	Product specific activity (dpm/μmol)	Relative incorporation (%)
Coptisine[a]	Tetrahydrocorysamine	9.60×10^5	3.07×10^6	32
Palmatine[a]	Corydaline	5.47×10^5	5.0×10^5	24
Berberine[a]	Thalictricavine	9.65×10^5	1.1×10^5	38

[a]Specific activity: 3.33×10^4 Bq/μmol; a total of 1.85×10^5 Bq was fed.

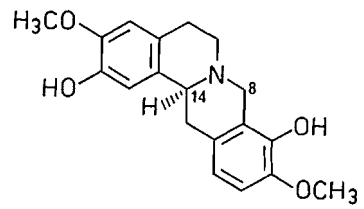

(*S*)-Scoulerine

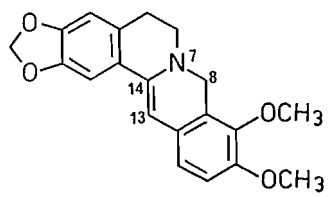

7,8-Dihydroberberine

repeated using a mixture of (*S*)-[14-^{3}H]scoulerine and (*S*)-[8^{14}C]scoulerine, the $^3H/^{14}C$ ratio being 9.8:1. (+)-Corydaline was isolated from the tissue, diluted with unlabelled carrier corydaline, and recrystallized 6 times. Constant specific activity was attained already after the fourth recrystallization. A 2.6% relative incorporation of (*S*)-scoulerine into corydaline was found and the initial $^3H/^{14}C$ ratio of 9.8:1 was lowered to 0.01:1. This indicated clearly that the tritium label was almost completely removed from position 14 of the (*S*)-scoulerine molecule and substantiated the previously found reversal of configuration from (*S*) to (*R*) by an oxido-reduction process as established for the formation of (*R*)-tetrahydroprotoberberines from protoberberines (7).

Since the *C. cava* tissue obviously has a high metabolic potential to convert protoberberines into the corydaline-type compounds, a cell-free system was tested to produce corydaline in vitro. A crude homogenate was prepared from *C. cava* bulbs, and was freed of contaminating low molecular weight compounds by treatment with Sephadex G 25. Unlabelled palmatine was incubated with NADPH and [C^{3}H$_3$]SAM in the presence of *C. cava* crude protein extract at pH 7.5. As shown in Fig. 1*A*, under these conditions a product was formed that had the same R_f value as authentic corydaline. Almost all radioactive SAM had been converted to this product. In control experiments either using heat-denatured enzyme (Fig. 1*B*) or omitting NADPH (Fig. 1*C*), no reaction occurred. In addition, the newly formed product had the same R_f value as corydaline in several other TLC solvent systems. To ascertain the identity of this product, the compound was diluted with unlabelled corydaline (calculated specific activity 1.5×10^4 dpm/μmol), and recrystallized 6 times to yield a specific activity of 1.06×10^4 dpm/μmol. This experiment proved that corydaline was indeed formed under the conditions given in Fig. 1. Extension of this type of experiment showed that neither (*R*)- nor (*S*)-tetrahydropalmatine could serve as acceptor for the activated methyl group of SAM, and verified the in vivo experiments of Holland et al. (5) with regard to the precursorship of palmatine at the in vitro level.

To obtain more insight into this rather complex reaction of reduction and C-methylation, we attempted to partially purify the corresponding enzyme. Since in preliminary experiments it was found that berberine was the best substrate, this substance was used for further experiments, (+)-thalictricavine being the end product of the reaction. The purification of the catalytic activity was carried out using 40 g of deep-frozen cells. Alkaloids and other low molecular weight material were removed from the protein solution by passage through an XAD column. The eluate was loaded directly onto a DEAE-Sephacel column and the enzyme eluted with KCl. The pooled fractions were chromatographed on a hydroxyapatite column at pH 6.5. The enzyme did not bind to this column but was eluted with the washthrough. This protein solution was subjected to affinity

Can. J. Chem. Downloaded from www.nrcresearchpress.com by 203.198.23.82 on 09/08/12
For personal use only.

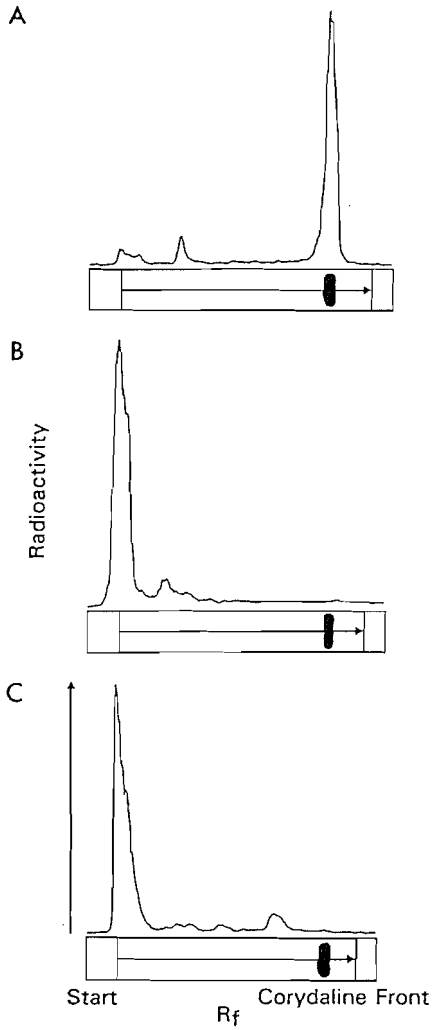

FIG. 1. Radioscan of an incubation mixture after TLC separation consisting of *A*: 25 nmol palmatine, 1 μmol NADPH, 27 pmol [C^3H_3]SAM (5×10^6 dpm), 860 μg *Corydalis cava* protein, in a total volume of 460 μL 50 mM KPO_4^{2-} buffer, pH 7.5; *B*: as in *A*, but with heat-denatured protein; *C*: as in A but without NADPH.

chromatography employing an SAH-AH Sepharose 4B matrix. Elution of the enzyme was achieved with KCl. This procedure yielded a 54-fold purified enzyme with 32% yield based on the crude homogenate. The purification procedure is summarized in Table 2. The enzyme is a cytosolic protein; no evidence for its occurrence in an organelle could be found. The enriched enzyme showed a pH optimum at 8.0 and a temperature optimum at 37°C (Figs. 2*A* and *B*). The M_r of the enzyme was determined by gel permeation HPLC (using appropriate marker proteins) and showed a distribution coefficient that corresponds to a M_r of 56 000, assuming a globular shape of the protein. Lineweaver–Burk plots showed apparent K_M values of 5 μM for berberine, 16 μM for NADPH, and 2.7 μM for SAM as substrates. Using the same three substrates, a K_i value of 2.6 μM was determined for SAH, which demonstrates that this homocysteine derivative, a reaction product, is a potent inhibitor of the methyltransferase reaction.

The product of the reaction was rigorously identified by physical methods. Large-scale standard incubations (total of 300 mL) were performed with [$^{13}CH_3$]SAM and a DEAE prepurified enzyme fraction. After 5 h of incubation at 37°C the mixture was passed through an XAD column that adsorbed the alkaloids. The column was washed thoroughly with distilled water and subsequently eluted with methanol. The eluate was evaporated and subjected to NMR analysis. Figure 3 shows a section of the NMR spectrum depicting clearly the ^{13}C-enriched carbon atom, which is attached to C-13 of thalictricavine (Fig. 3*B*). An aliquot of the enzymic reaction product was subjected to mass spectrometry (EI-mode) and yielded a mass peak at 354 *m/z* (Fig. 4*B*), one mass unit more than the unlabelled reference (Fig. 4*A*), as expected. Furthermore, a prominent benzylic fragment of *m/z* 179 was observed, which represents the D ring of corydaline with the $^{13}CH_3$ group originating from SAM attached to it (Fig. 4*B*). No doubt, the reaction product is thalictricavine. To ascertain the correct stereochemistry of the thalictricavine formed, a CD spectrum of the enzyme-synthesized product was recorded. The CD spectrum of this compound shown in Fig. 5 is identical with that one published previously (14). The enzyme-synthesized product is therefore (+)-thalictricavine, identical with that compound previously isolated from various *Corydalis* species (5, 10–13, 15, 16).

Finally, the substrate specificity of this enzyme was of considerable interest. Employing the reductive enzyme assay in the presence of [C^3H_3]SAM, NADPH, and various alkaloidal substrates using a 50-fold purified enzyme, the results shown in Table 3 were obtained. All protoberberines tested so far, except dehydroscoulerine, served as methyl group acceptor to varying degrees. Fully substituted protoberberines possessing no free OH group (berberine, palmatine) were the best substrates, followed by alkaloids having one unsubstituted OH group (columbamine, jatrorrhizine). The tetrahydroprotoberberines were completely inactive. Dehydroscoulerine was absolutely inactive in this system. This is in accord with the previously found reductase (7), which also is almost inactive with this substrate. It is most likely that this reductase, which operates in two steps (7), first reducing the 7,8 double bond and subsequently the 13,14 double bond, to yield the (*R*)-tetrahydroprotoberberines, is identical with that needed for (+)-thalictricavine biosynthesis. The assumption that this very enzyme is involved in thalictricavine biosynthesis is supported by the fact that 7,8-dihydroberberine serves indeed as an excellent substrate for the methyltransferase with concomitant reduction to the (*R*)-configurated (+)-thalictricavine (Table 3). Presuming that the previously found reductase (7) is involved in (+)-thalictricavine formation, the hydrogen transfer from NADP^{3}H should also follow a B-type reaction. Incubation of berberine in the presence of SAM and either 4A-^{3}H-NADPH or 4B-^{3}H-NADPH (18) under optimal conditions, and isolation of the (+)- thalictricavine formed, clearly showed that absolutely no tritium was transferred from 4A-^{3}H-NADPH, while 48.8% of the radioactivity of the 4B-^{3}H-NADPH was found in thalictricavine. This clearly demonstrated that the reductase involved is a B-type enzyme and most likely identical with the (*R*)-specific reductase found previously in *C. cava* (7). The (*R*)- or (*S*)-tetrahydroprotoberberines do not serve as acceptors for the methyl group of SAM.

The biosynthesis of (+)-corydaline and congeners has now been worked out at the enzyme level. The protoberberine molecule is enzymically reduced by a specific dehydrogenase (7) to a 7,8-dihydro derivative. This intermediate (which can also be supplied in a synthetic form) acts at C-13 as an acceptor for the

Can. J. Chem. Downloaded from www.nrcresearchpress.com by 203.198.23.82 on 09/08/12
For personal use only.

TABLE 2. Purification of *S*-adenosylmethionine: protoberberine-13C-methyltransferase from 40 g *Corydalis cava* cultivated cells

Purification step	Total activity (pkat)	Total protein (mg)	Specific activity (pkat/mg)	Yield (%)	Purification factor (×)
Crude extract	261	440.0	0.6	100	1.0
XAD-2	240	242.0	1.0	92	1.7
DEAE-Sephacel	153	43.3	3.5	58	5.8
Hydroxyapatite	118	16.0	7.4	45	12.3
SAH-AH Sepharose 4B	84	2.6	32.3	32	53.8

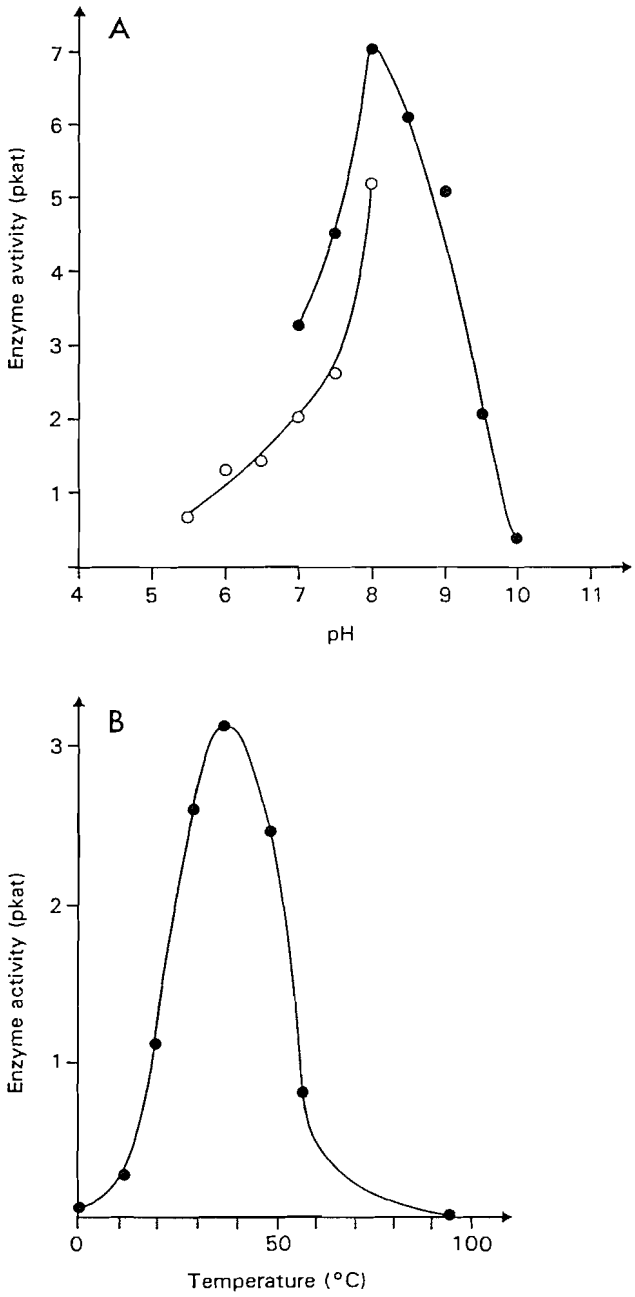

FIG. 2. *A*: pH profile of the catalytic activity of the 50-fold enriched enzyme system yielding thalictricavine using standard incubation mixtures with 100 μM each of (●—●) Tris-HCl buffer; (○—○) KPO_4^{2-} buffer, at 37°C. *B*: Temperature profile using the standard incubation assay at pH 8.0.

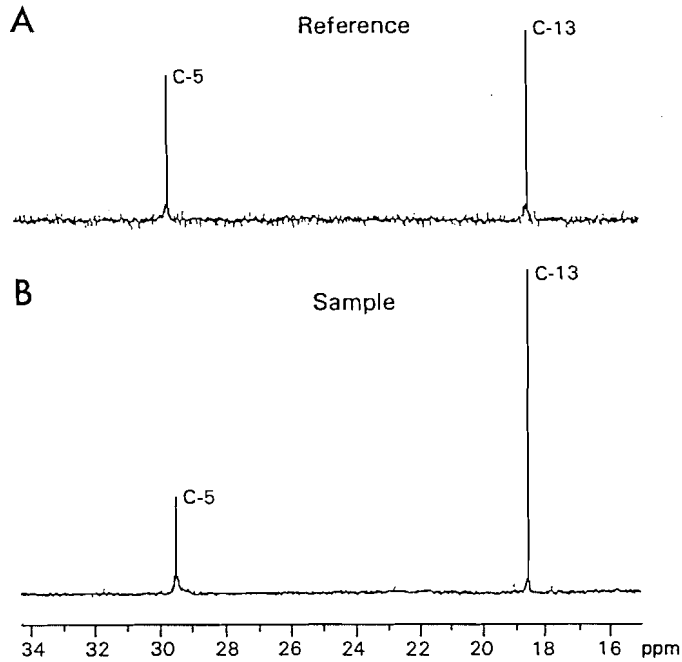

FIG. 3. Partial proton-decoupled ^{13}C NMR spectra of thalictricavine. *A*: unlabelled reference compound; *B*: enzyme product formed by transfer of the methyl group from [$^{13}CH_3$]SAM.

SAM-derived methyl group, and is subsequently reduced in a B-type reaction at the expense of NADPH to yield the (14*R*,13*S*)-(+)-corydaline-type molecule. The course of reaction is depicted in Scheme 1. It is most rewarding to see that the prediction of MacLean and Spenser and co-workers (5, 15) based entirely on in vivo feeding experiments and theoretical considerations could be verified by the results given here, which were obtained in vitro.

Experimental

Plant material

Plants of *Corydalis cava* were grown in pots in the greenhouse of this institute. Plant cell cultures of *Corydalis cava* were cultivated in 1-L Erlenmeyer flasks containing 250 mL Linsmaier and Skoog medium (19) over a period of 7 days at 23°C on a gyratory shaker (100 rpm) at 750 lux. The cells were then harvested by suction filtration, frozen in liquid nitrogen, and stored at −20°C.

Reference alkaloids

Thalictricavine, corydaline, and tetrahydrocorysamine were a kind gift of Prof. Slavik (Brno). Berberine and scoulerine were purchased from Roth (Karlsruhe). Coptisine and palmatine were donated by Dr. T. Tanahashi (Kobe). 7,8-Dihydroberberine was synthesized according to ref. 20.

Can. J. Chem. Downloaded from www.nrcresearchpress.com by 203.198.23.82 on 09/08/12
For personal use only.

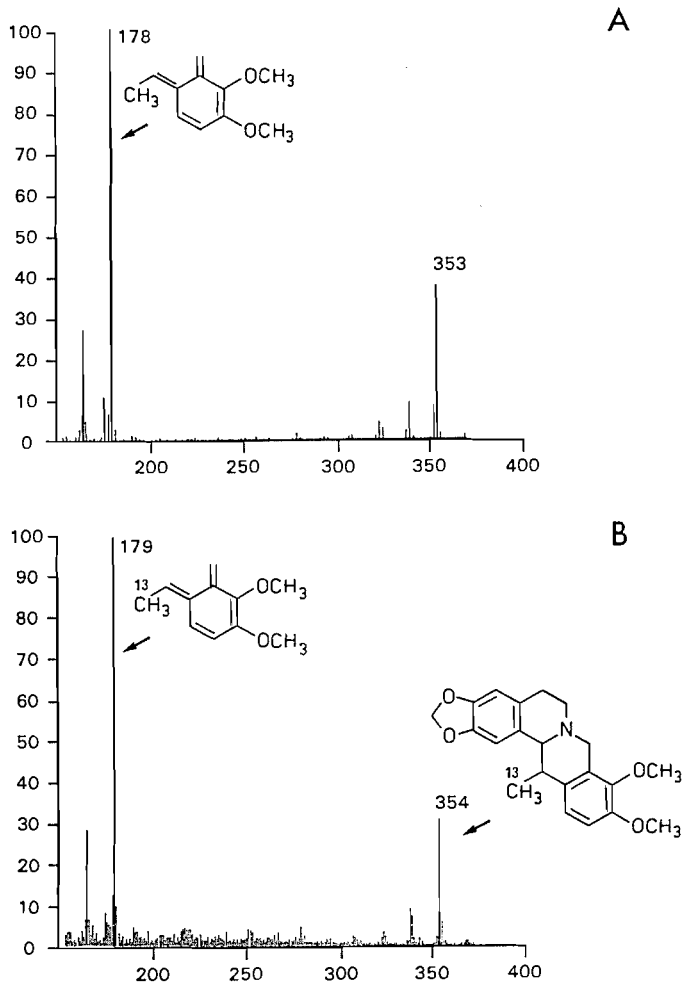

FIG. 4. Partial mass spectra (chemical ionization; isobutane) of thalictricavine. *A*: unlabelled reference compound; *B*: enzymic product formed by transfer of the methyl group from [$^{13}CH_3$]SAM.

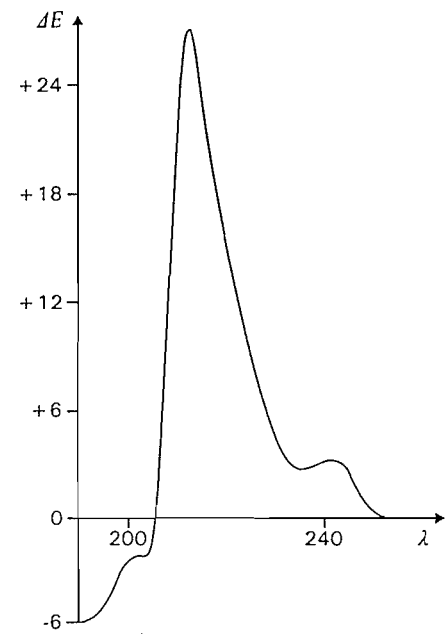

FIG. 5. CD spectrum of enzymically formed thalictricavine (concentration: 0.92 mg/2 mL methanol). Note positive value at 236 nm and 206 nm, negative at 192 nm analogous to (+)-corydaline (14).

TABLE 3. Substrate specificity of *S*-adenosylmethionine: protoberberine-13C-methyltransferase

Substrate[a]	Product formed (pmol)	Relative activity (%)
Berberine	900	100
Dihydroberberine	837	93
(*R,S*)-Canadine	0	0
Columbamine	243	27
Coptisine	189	21
Dehydroscoulerine	0	0
Jatrorrhizine	603	67
Palmatine	837	93

[a]The respective substrate (10 nmol) and 1 pkat of the enzyme were added to the standard assay and incubated for 15 min at 30°C.

Labelled chemicals

[C^3H_3]Methionine (3.15×10^9 Bq/μmol) was purchased from Amersham (U.K.) and transformed to *S*-adenosyl-(L)-methionine (SAM) by SAM-synthetase, isolated from *Escherichia coli* EWH 47 according to ref. 21. [$^{13}CH_3$]SAM was synthesized by the same procedure using [$^{13}CH_3$]methionine. Stereospecifically labelled 4A- and 4B-^{3}NADPH were synthesized according to the method of Moran et al. (18). [8-^{3}H]-Labelled coptisine, palmatine, and berberine were synthesized by simultaneous reduction of all three protoberberines with NaB^3H_4 and reoxidation of the corresponding (*S*)-tetrahydroprotoberberines was performed with (*S*)-tetrahydroprotoberberine oxidase (22). (*S*)-[8-^{14}C]Scoulerine was synthesized enzymatically in a two-step reaction by incubating (*S*)-norreticuline and [$^{14}CH_3$]SAM, first with *S*-adenosylmethionine:coclaurine-*N*-methyltransferase (23) and then with the berberine bridge enzyme (24). (*S*)-[14-^{3}H]Scoulerine was produced by incubation of (*R,S*)-[1-^{3}H]reticuline with the berberine bridge enzyme (24).

Application experiments

Young bulbs of *Corydalis cava* were cut into small pieces of 0.5 g fresh weight and incubated in 1 mL Knop's nutrient solution with berberine, coptisine, or palmatine (each 7.83×10^4 Bq/μmol). After extraction with methanol the labelled alkaloids were purified on TLC plates in three solvent systems: (1) ethyl acetate:2-butanone:formic acid:H_2O (50:30:10:10), R_f thalictricavine = 0.89, R_f corydaline = 0.86, R_f tetrahydrocorysamine = 0.94; (2) cyclohexane:diethylamine (9:1), R_f thalictricavine = 0.63, R_f corydaline = 0.55, R_f tetrahydrocorysamine = 0.71; (3) dioxane:cyclohexane:diethylamine (10:20:0.5), R_f thalictricavine 0.84, R_f corydaline = 0.75, R_f tetrahydrocorysamine = 0.77.

Enzyme assay

Berberine (10 nmol), 1 nmol [C^3H_3]SAM (20 000 cpm), and 100 nmol NADPH were incubated with 20 μmol KPO_4^{2-} buffer (pH 8.0) and 0.1–1 mg protein in a total volume of 250 μL for 30 min at 37°C (standard incubation mixture). The reaction was stopped by the addition of 200 μL sodium carbonate buffer (pH 9.5) and the reaction product extracted with 400 μL isoamyl alcohol for 10 min in a rotary shaker. After centrifugation (3 min in an Eppendorf centrifuge) the radioactivity of a 200-μL aliquot was determined in a scintillation counter.

Enzyme purification

Corydalis cava deep-frozen cultivated cells (40 g) were ground with a chilled mortar and pestle in 80 mL 10 mM KPO_4^{2-} buffer (pH 6.5, 10 mM β-mercaptoethanol) for 15 min, filtered through four layers of cheesecloth, and centrifuged for 10 min at 20 000 × *g*. The supernatant was passed through an XAD-2 column (Serva, Heidelberg, 2.5 cm × 20 cm) to remove the alkaloids and pumped onto a DEAE column (DEAE-Sephacel, Pharmacia, 2.5 cm × 25 cm, equilibrated with the extraction buffer) at a flow rate of 1 mL/min. Elution was per-

Can. J. Chem. Downloaded from www.nrcresearchpress.com by 203.198.23.82 on 09/08/12
For personal use only.

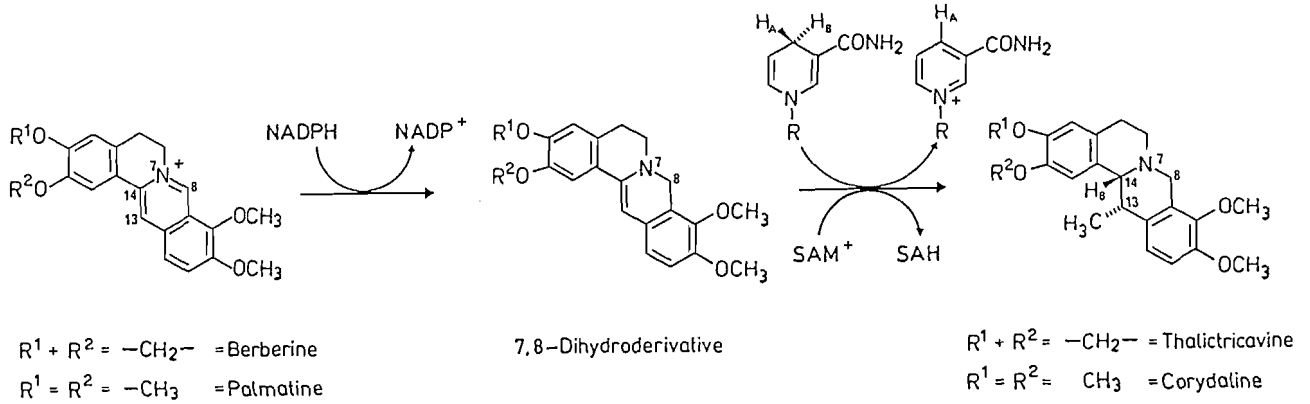

SCHEME 1

formed with a gradient from 0–1 M KCl over 8 h in fractions of 2.5 mL. The active fractions (98–115) were combined (57 mL) and pumped onto a hydroxyapatite column (Biorad, 1 cm × 15 cm, equilibrated with 10 mM KPO_4^{2-} buffer, pH 6.5, 10 mM β-mercaptoethanol) at a flow rate of 0.3 mL/min. The enzyme did not bind to the column but was eluted with the washthrough in 55 mL. This solution was slowly (0.2 mL/min) loaded onto an SAH-AH-Sepharose column (Pharmacia 1 cm × 5 cm, equilibrated with 10 mM KPO_4^{2-} buffer, pH 7.5, 10 mM β-mercaptoethanol) and eluted with a linear gradient up to 1 M KCl in 4 h. Fractions of 1.5 mL were collected. Enzyme activity was eluted with 1 M KCl in 7.5 mL.

Product identification

For identification of the product, four of the following large-scale assays were prepared: 10 mmol KPO_4^{2-} buffer, pH 8.5, 1 μmol [$^{13}CH_3$]SAM, 10 μmol berberine, 50 μmol NADPH, 50 μmol NADP, 50 μmol glucose-6-phosphate, 5 units glucose-6-phosphate-dehydrogenase (Serva, Heidelberg), and 75 mL enzyme solution (DEAE- eluate, 100 mg protein) in a total volume of 250 mL. After incubation (5 h at 37°C) the mixtures were passed through an XAD-2 column (2 cm × 10 cm) and the alkaloids eluted with methanol. After concentration under a stream of nitrogen, the product was purified by TLC (Macherey & Nagel, Polygram SIL G/UV 254, solvent system cyclohexane:diethylamine (9:1), R_f thalictricavine = 0.6, R_f SAM = 0.0), eluted with methanol, and subjected to mass spectrometry (MS 80 RFA, Kratos, EI, 70 eV) and ^{13}C NMR (in deuterated methanol–DMSO, AM, 360, Bruker). The CD spectrum was measured in ethanol with a CD-6 (Jobin-Yvon) instrument.

Stereospecificity of H-transfer from 4A- and 4B-^{3}H-NADPH

To test the stereospecificity of the reduction reaction 100 000 cpm 4A- or 4B-^{3}H-NADPH (18) (1.63×10^8 Bq/μmol), 10 nmol berberine, and 1 nmol SAM were incubated with 0.2 pkat of the enzyme in 50 μmol KPO_4^{2-} buffer, pH 8.0, at 30°C for 1 h. The reaction product was purified by TLC (cyclohexane:diethylamine (9:1), R_f thalictricavine = 0.6) and eluted with methanol. Scintillation counting of the methanol eluate showed no incorporation with 4A-^{3}H-NADPH, but with 4B-^{3}H-NADPH 48775 cpm (48.8%) could be detected in thalictricavine.

Acknowledgements

We thank Dr. T.M. Kutchan for her linguistic help in the preparation of this manuscript. This work was supported by SFB 145 of the Deutsche Forschungsgemeinschaft, Bonn, and by the Fonds der Chemischen Industrie.

1. M.H. Zenk, M. Rueffer, T.M. Kutchan, and E. Galneder. Ciba Found. Symp. **137**, 213 (1988).
2. W. Bauer, R. Stadler, and M.H. Zenk. Bot. Acta, **105**, 370 (1992).
3. M.J. Müller and M.H. Zenk. Planta Med. **58**, 524 (1992).
4. I.D. Spenser. Comp. Biochem. **20**, 231 (1968).
5. H.L. Holland, P.W. Jeffs, T.M. Capps, and D.B. MacLean. Can. J. Chem. **57**, 1588 (1979).
6. R. Stadler and M.H. Zenk. Liebigs Ann. Chem. 555 (1990).
7. W. Bauer and M.H. Zenk. Tetrahedron Lett. **32**, 487 (1991).
8. D.S. Bhakuni, S. Jain, and S. Gupta. Tetrahedron, **39**, 455 (1983).
9. J. Slavik and L. Slavikova. Collec. Czech. Chem. Commun. **44**, 2261 (1979).
10. Wackenroder. Kastner's Archiv, **8**, 423 (1828).
11. H. Wicke. Liebigs Ann. Chem. **137**, 274 (1866).
12. C.K. Yu, D.B. MacLean, R.G.A. Rodrigo, and R.H.F. Manske. Can. J. Chem. **48**, 3673 (1970).
13. S. Naruto and H. Kaneko. J. Pharm. Soc. Jpn. **92**, 1017 (1972).
14. G. Snatzke, J. Hrbek, Jr., L. Hruban, A. Horeau, and F. Santavy. Tetrahedron, **26**, 5013 (1972).
15. H.L. Holland, M. Castillo, D.B. MacLean, and I.D. Spenser. Can. J. Chem. **52**, 2818 (1974).
16. R.H.F. Manske. J. Am. Chem. Soc. **75**, 4928 (1953).
17. H. Kaneko and S. Naruto. J. Pharm. Soc. Jpn. **91**, 101 (1971).
18. R.G. Moran, P. Sartori, and V. Reich. Anal. Biochem. **138**, 196 (1984).
19. E.M. Linsmaier and F. Skoog. Physiol. Plant. **18**, 100 (1965).
20. J.W. Elliot. J. Heterocycl. Chem. **4**, 639 (1967).
21. G.D. Markham, E.W. Hafner, C.W. Tabor, and H. Tabor. J. Biol. Chem. **255**, 9082 (1980).
22. M. Amann, N. Nagakura, and M.H. Zenk. Tetrahedron Lett. **25**, 953 (1984).
23. T. Frenzel and M.H. Zenk. Phytochemistry, **29**, 3491 (1990).
24. P. Steffens, N. Nagakura, and M.H. Zenk. Phytochemistry, **24**, 2577 (1985).

Can. J. Chem. Downloaded from www.nrcresearchpress.com by 203.198.23.82 on 09/08/12
For personal use only.

Use of aromatic thia fatty acids as active site mapping agents for a yeast Δ^9 desaturase[1]

PETER H. BUIST[2] AND DALE M. MARECAK

Ottawa–Carleton Chemistry Institute, Department of Chemistry, Carleton University, 1125 Colonel By Drive, Ottawa, ON K1S 5B6, Canada

Received June 23, 1993

This paper is dedicated to Professors David B. MacLean and Ian D. Spenser

PETER H. BUIST and DALE M. MARECAK. Can. J. Chem. **72**, 176 (1994).

The Δ^9 desaturating system of *Saccharomyces cerevisiae* can sulfoxidize methyl *S*-benzyl-8-mercaptooctanoate as well as its naphthyl analogue but the corresponding isomers where sulfur is bonded to the aromatic ring do not function as substrates. We have accounted for these results in terms of a conformational model. We have also accumulated some evidence that suggests that dealkylation of these thia analogues does not compete with sulfoxidation. Our recently discovered chiral shift reagent (*S*)-(+)-α-methoxyphenylacetic acid (MPAA) can be used to determine the optical purity and absolute configuration of all sulfoxides prepared in this work.

PETER H. BUIST et DALE M. MARECAK. Can. J. Chem. **72**, 176 (1994).

Le système de la *S. cerevisiae* qui provoque une désaturation en Δ^9 peut provoquer une sulfoxydation du *S*-benzyl-8-mercaptooctanoate de méthyle et de son analogue naphtylé; toutefois, les isomères correspondants dans lesquels le soufre est lié au noyau aromatique ne peuvent pas agir comme substrats. On explique ces résultats en fonction d'un modèle conformationnel. On a aussi accumulé des données qui suggèrent que la désalkylation des ces thia analogues n'est pas en compétition avec leur sulfoxydation. On peut utiliser le réactif chiral que nous avons récemment découvert, l'acide (*S*)-(+)-α-méthoxyphénylacétique (MPAA) pour déterminer la pureté optique et la configuration absolue des tous les sulfoxydes préparés au cours de ce travail.

[Traduit par la rédaction]

Introduction

As a class of reactions, irreversible biooxidations involving oxygen – transition metal complexes are poorly understood from a mechanistic point of view. A particularly mysterious biological reaction is the dehydrogenation (desaturation) of stearoyl CoA to give oleyl CoA. The enzyme responsible for

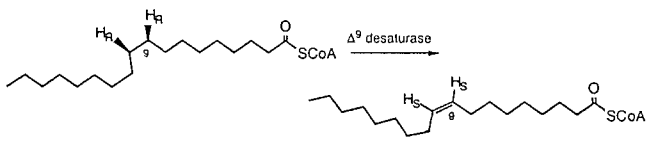

catalyzing this process is typically an iron-containing protein, which binds molecular oxygen and receives the necessary reducing equivalents from NADH via an intermediary electron transfer protein (1). A fresh perspective on the mechanism of desaturation has recently surfaced following the observation that a well-known hydroxylating enzyme system, rat liver cytochrome P_{450}, is also capable of acting as a dehydrogenase with certain substrates (2). Thus dehydrogenation and hydroxylation appear to be part of a single reaction manifold in which the ionization potential (I.P.) of the putative radical intermediate controls the choice of oxidative pathway (3) (see Scheme 1).We have proposed[3] that desaturases lower the I.P. of the carbon radical through the use of a neighbouring negatively charged protein residue such as a carboxylate to stabilize the incipient carbocation.

A logical consequence of this mechanistic scheme is that the Δ^9 desaturase of *Saccharomyces cerevisiae* should be able to oxygenate the appropriate sulfide analogues, presumably via a mechanism involving a radical cation intermediate (*4a,b*) (see Scheme 2). We have shown recently that thia fatty acid analogues (**1–4**) are indeed converted to chiral sulfoxides with high enantioselectivity (5). During the course of this investigation, we were somewhat puzzled by the fact that the apparent ratio of 9-sulfoxidation:10-sulfoxidation varied from ca. 2:1 in favour of the 9-thia compound for the dialkyl series (compounds **1**, **2**) to ca. 10:1 in the benzyl series (compounds **3**, **4**). Since **3** and **4**

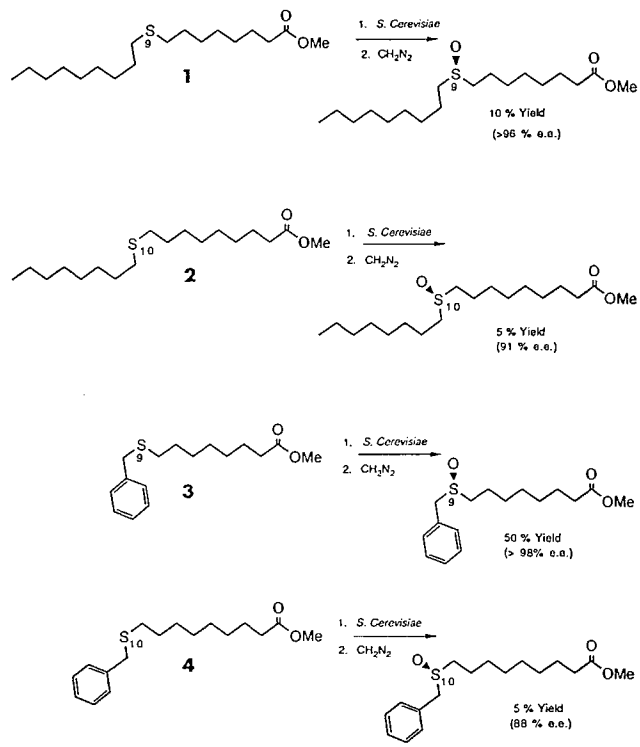

[1]This paper is dedicated to Prof. David MacLean who supervised my (phb) Ph. D. studies with extraordinary patience, indulgence, and compassion. I am also greatly indebted to Prof. Ian Spenser who triggered my interest in bioorganic chemistry.

[2]Author to whom correspondence may be addressed.

[3]P.H. Buist and J.S. Wright. Unpublished results.

Can. J. Chem. Downloaded from www.nrcresearchpress.com by 203.198.23.82 on 09/08/12
For personal use only.

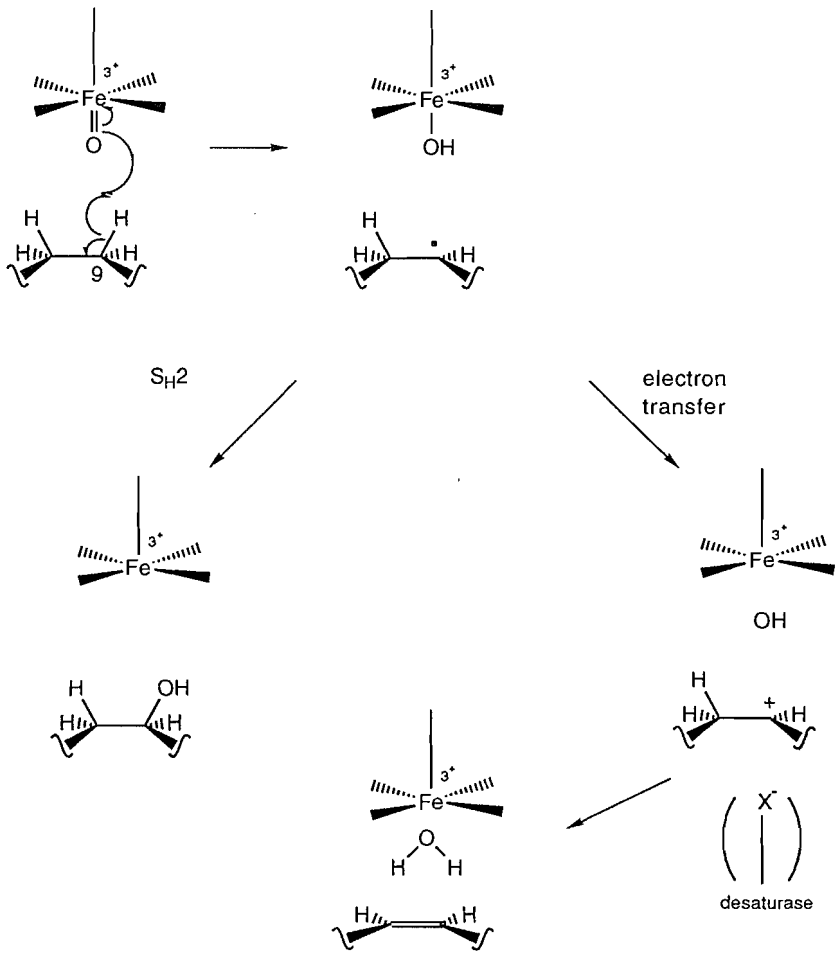

SCHEME 1

have different overall chain lengths, we decided to examine pairs of aromatic thia substrates of equivalent chain length. In this paper, we present the somewhat surprising results of this investigation.

Results and discussion

Aromatic sulfides (**5–8**) were synthesized and administered to *S. cerevisiae* using standard methodology (5). The culture medium was extracted and analyzed for the presence of the corresponding sulfoxide. Racemic sulfoxide reference standards were prepared by oxidation of the corresponding sulfide using one equivalent of MCPBA.

We fully expected **5** to be a better substrate for sulfoxidation than **4**, not only because it has the same overall chain length as our best substrate (**3**) but also because its ionization potential is lower than that of **4**. (The I.P. of ethyl phenyl sulfide is 7.88 eV while that of benzyl methyl sulfide is 8.42 eV (6)). It was therefore most surprising to find that this compound yielded the corresponding sulfoxide in very low yield (3%) and in racemic form. The stereochemical analysis of the sulfoxide product was carried out in a straightforward manner by examining the effect of (*S*)-(+)-α-methoxyphenylacetic acid (MPAA) on the ^{1}H NMR resonances of the C-9 hydrogens using methodology we developed recently (5).

Since desaturase-mediated sulfoxidation normally occurs with high enantioselectivity, we conclude that sulfoxidation of **5** was due entirely to an autoxidative process. This was confirmed by the feeding of a chain-shortened analogue (**6**), which cannot be a substrate of desaturase due to severe steric problems in an active site that force stearoyl CoA into a *cisoid* conformation at C-9,10 (vide infra). Once again, a small amount of racemic sulfoxide (3% yield) was isolated. It is interesting to note that prior to our studies, the only report (7) of a baker's yeast-mediated sulfoxidation was that of an aryl sulfide (**9**), which yielded a 5% yield of racemic sulfoxide! The unsaturated fatty acids present in yeast cells as well as the lower I.P. of the conjugated sulfide would be expected to enhance this autooxidation process.[4]

The apparent unsuitability of **5** as a substrate for our desaturase stimulated a further study in which we examined the desaturase-mediated oxidation of a pair of naphthyl analogues of equivalent chain length (**7**, **8**). As anticipated, the naphthyl compound (**7**) gave rise to optically active sulfoxide, albeit in reduced yield (10%, 13%; 2 separate incubations) and with lower e.e. (75 ± 3%). The stereochemical analysis of this sulfoxide was carried out in two ways — using (*R*)-(−)-*N*-3,5-dinitrobenzoyl-α-methylbenzylamine (8) and MPAA (5) as chiral shift reagents. As shown in Fig. 1, addition of the former reagent to a racemic sample of sulfoxide resulted in the production of a singlet for the ^{1}H NMR resonances, due to the C-10

[4] K.U. Ingold. Personal communication.

Can. J. Chem. Downloaded from www.nrcresearchpress.com by 203.198.23.82 on 09/08/12
For personal use only.

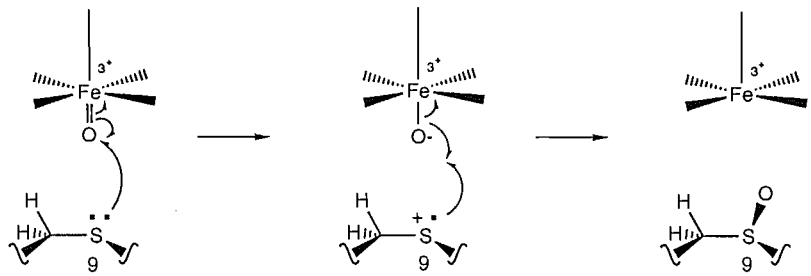

SCHEME 2

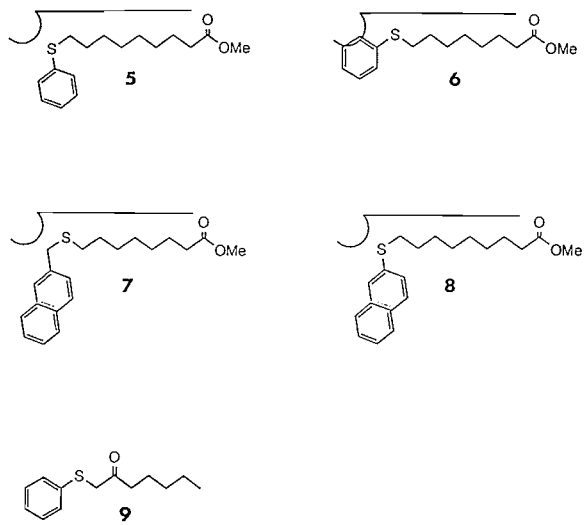

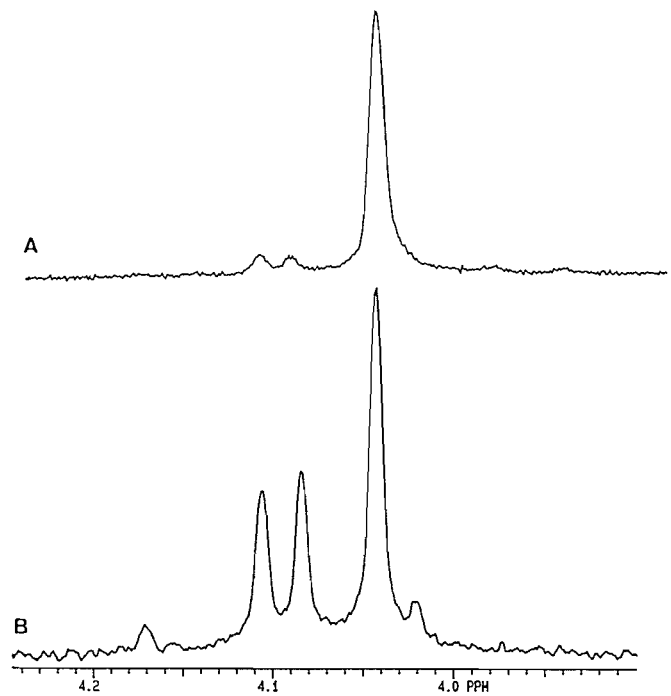

FIG. 1. Effect of addition of 3 equiv. of (*R*)-(−)-*N*-3,5-dinitrobenzoyl-α-methylbenzylamine on ^{1}H NMR (200 MHz) resonances due to the C-10 methylene protons of (*A*) sulfoxide produced from **7** by diverted desaturation and (*B* racemic sulfoxide produced from **7** by treatment with MCPBA.

methylene protons of one enantiomer, and an AB quartet for the corresponding ^{1}H NMR resonances of the other enantiomer. Also, signals due to the methylene protons as far away as C-2 were split by the shift reagent. This behaviour is in marked contrast to that of the benzyl analogue (**3**), which we reported on earlier (5). We assign the "*S*" absolute configuration to the major enantiomer in our biological sample assuming our MPAA-binding model, which we recently developed, is correct (5). According to this model, the resonances due to the C-10 methylene protons of the minor enantiomer are shifted upfield relative to the corresponding signals of the major enantiomer (see Figs. 2 and 3). We do not have a good explanation for the fact that the % e.e. of the biological sulfoxide derived from **7** is reduced relative to that observed for biological sulfoxides derived from **1–4**. It should be mentioned at this point that the amount of sulfoxide derived from autoxidation is usually very small (<1%) for dialkyl sulfides.

In marked contrast to the behaviour of **7**, which is obviously a reasonable substrate for the yeast desaturase, the *S*-napthyl isomer (**8**) yielded only traces of sulfoxide product as determined by TLC comparison with an authentic standard. In this case, insufficient material was isolated to allow stereochemical analysis.

Clearly both **5** and **8** are not being oxidized to sulfoxide by the yeast desaturase, even though the sulfur atom should be accessible to the enzymatic oxidant. It occurred to us that our sulfides may be undergoing chain cleavage as well as or, indeed, instead of, oxygenation (see Scheme 3). It is known (4*a*) that cytochrome P_{450} can dealkylate certain benzylic sulfides; since desaturases normally carry out an elimination reaction, one might expect deprotonation of the radical cation intermediate derived from sulfides to be a viable alternative to oxygenation. Thus, for example, cleavage of **7** would release 2-naphthaldehyde, which would be reduced by the yeast cells to the corresponding alcohol. Indeed, addition of 2-naphthaldehyde to a growing yeast culture at a level corresponding to 0.2% cleavage of substrate followed by extraction in the normal way gave rise to 2-naphthalenemethanol, which was easily detectable by TLC (R_f 0.22, silica gel, 25% EtoAc–hexane, UV detection). Similarly, a limit of detection for 2-naphthalenethiol corresponding to 1% cleavage of **8** was established. However, examination of extracts from all incubations carried out to date involving aromatic thia analogues failed to turn up any evidence that these sulfides are undergoing a cleavage process.

The failure of **5** and **8** to act as substrates of the Δ^9 desaturase of *S. cerevisiae* is striking. The most likely explanation for this phenomenon is as follows: We assume that the desaturase active site is constructed in such a way that C-8, C-9, C-10, and C-11 of stearoyl CoA are forced to adopt a *cisoid* coplanar conformation corresponding to that of the product olefin. This assumption is strengthened by the fact that oleyl CoA but not its

Can. J. Chem. Downloaded from www.nrcresearchpress.com by 203.198.23.82 on 09/08/12
For personal use only.

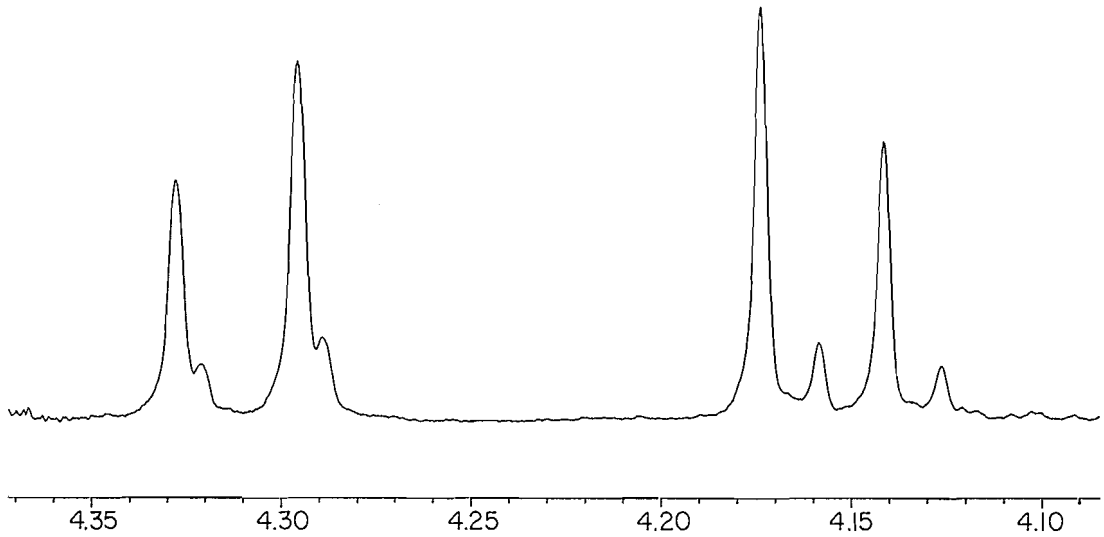

FIG. 2. Effect of addition of 3 equiv. of (*S*)-(+)-α-methoxyphenyl acetic acid on ^{1}H NMR (400 MHz) resonances due to the C-10 methylene protons of sulfoxide produced from **7** by diverted desaturation.

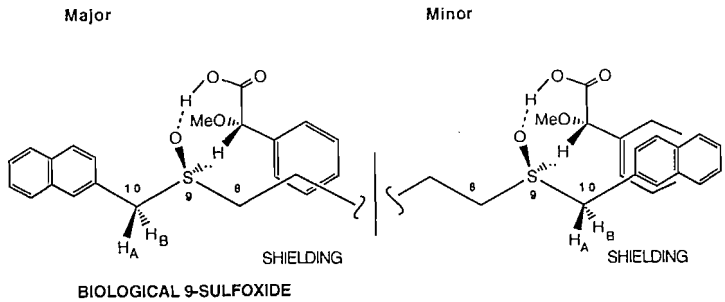

FIG. 3. Binding model for the interaction of (*S*)-(+)-α-methoxyphenyl acetic acid with the two enantiomers of the sulfoxide derived from **7**.

trans isomer shows strong product inhibition in a closely related purified in vitro system(9). To fit into the active site pocket, the 9-benzyl compound (**3**) must tilt its aromatic ring nearly 90°, as shown in Fig. 4, to avoid repulsive interactions between the *ortho* aromatic hydrogen and the hydrogens of the C-8 methylene. Oxidation at sulfur can now proceed. However, for the 10-S-phenyl substrate (**5**), this conformational requirement would be a significant stumbling block during formation of the resonance-stabilized sulfur radical cation. Such resonance stabilization requires a coplanar aromatic ring, which is clearly not achievable in a *cisoid* conformation (see Fig. 4).

Alternatively, **5** may not be able to adopt proper conformation for binding to the enzyme. An abundance of physical and chemical evidence (10) (UV spectra, C—S bond shortening, and C—S—C bond angle widening, decreased nucleophilicity of sulfur atom) suggests that the $3sp^3$–$2p\pi$ interaction between the sulfur atom and the phenyl ring is significant, although the extent to which this effect blocks rotation around the S—C (phenyl) bond is not known. There may in fact be a distinct preference for the π system of the aromatic ring to align with one of the lone pairs of the sulfur atom.

Similar argumentation can be advanced for the two naphthyl systems.

Conclusion

The results presented above point to the strict geometric requirements of the Δ^9 desaturase active site and are helping us to design future mechanistic probes and alternate substrates. In addition, further studies are indicated to determine more accurately the dynamics of a sterically congested aryl sulfide system.

Materials and methods

General methods

All NMR spectra were obtained using dilute $CDCl_3$ solutions at the frequency indicated. All chiral shift experiments involving sulfoxides were carried out using $CDCl_3$ that had been treated with $MgSO_4$ and Woelm basic alumina. Chemical shifts are expressed in ppm and are referenced to tetramethylsilane.

Mass spectra were obtained by direct probe using a VG 7070 E mass spectrometer operating in the Cl (isobutane) mode. Flash chromatography using silica gel (230–400) mesh was used to purify substrates and sulfoxide products isolated from the feeding experiments. Analytical TLC was performed using Merck glass plates precoated with silica G/UV 254. Visualization of UV-inactive materials was accomplished by using a combination of I_2 vapour followed by a water spray.

Unless otherwise stated, all reagents and starting materials were purchased from Aldrich Chemical Company and used without purification. Chiral materials were used without improving their optical purity. All air- and moisture-sensitive reactions were performed under N_2. Unless otherwise noted, organic extracts were shaken with saturated NaCl, dried over Na_2SO_4, and evaporated on a rotary evaporator.

Synthesis of substrates

Aryl thia fatty acids were synthesized by adding the thiophenol to

Can. J. Chem. Downloaded from www.nrcresearchpress.com by 203.198.23.82 on 09/08/12
For personal use only.

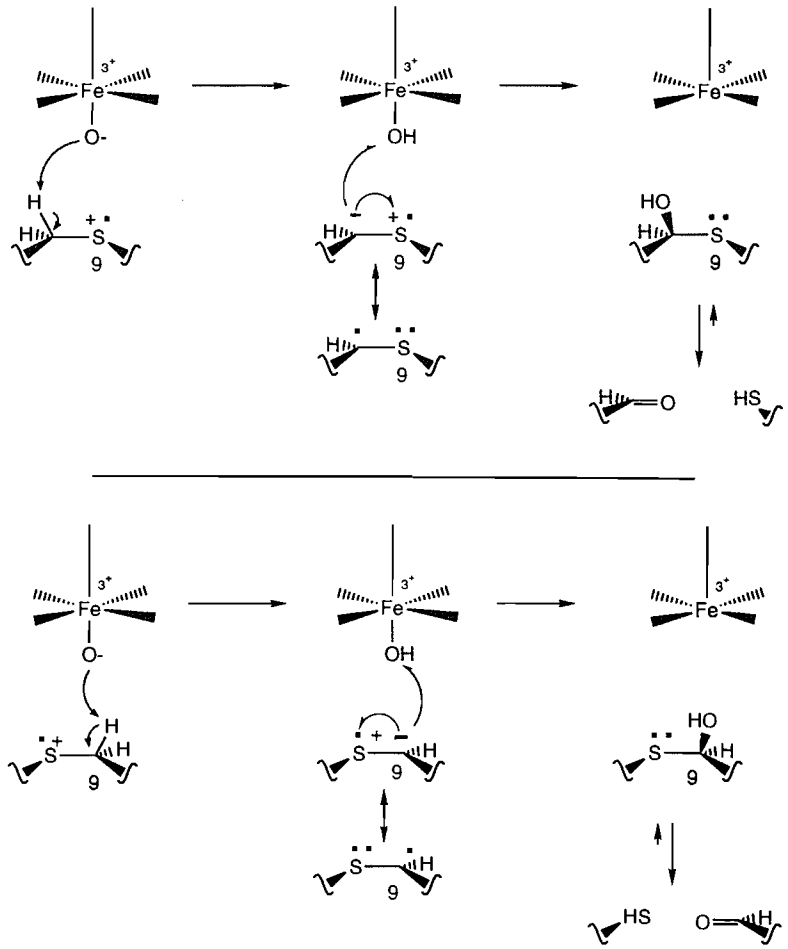

SCHEME 3

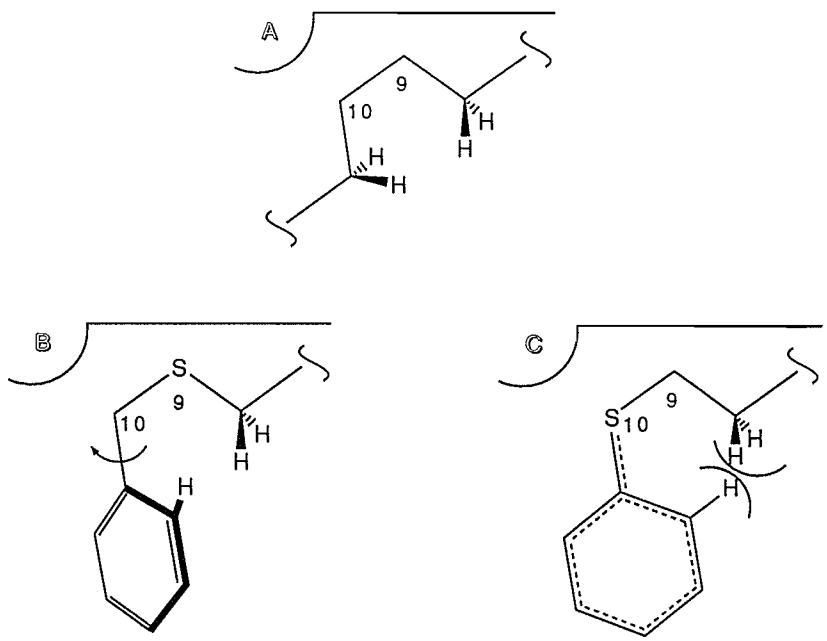

FIG. 4. Active site model for binding of substrates to Δ^9 desaturase: (*A*) *cisoid* conformation of parent substrate, stearoyl CoA; (*B*) *cisoid* conformation of **3** with a tilted aromatic ring; (C) *cisoid* conformation of resonance-stabilized radical cation of **5** showing steric interference between *ortho* hydrogen of aromatic ring and hydrogens at C-8.

Can. J. Chem. Downloaded from www.nrcresearchpress.com by 203.198.23.82 on 09/08/12
For personal use only.

Can. J. Chem. Downloaded from www.nrcresearchpress.com by 203.198.23.82 on 09/08/12
For personal use only.

an alcoholic solution of the appropriate ω-bromo fatty acid in the presence of two equivalents of sodium hydroxide (11). **7** was prepared by alkylating the dilithio salt of 8-mercaptooctanoic acid with 2-(bromoethyl)naphthalene (12). The crude carboxylic acid products were methylated with BF_3–MeOH (13) and purified by flash chromatography (4% EtOAc–hexane) to give colourless low-melting solids or liquids.

A. Methyl S-Phenyl-9-mercaptononanoate (5)

Thiophenol (0.54 g, 4.9 mmol) and 8-bromooctanoic acid (1.1 g, 5.0 mmol) was added to a solution of KOH (0.87 g, 16 mmol) in ethanol (50 mL) and the resultant solution was gently refluxed for 15 h. The solution was concentrated to 10 mL in vacuo, acidified, and extracted with CH_2Cl_2 to yield a crude solid product (1.25 g) which was methylated using 10% BF_3–MeOH (13) to give a pale brown oil (1.30 g). This material was purified by flash chromatography (4% EtOAc–hexane) to give a colourless solid (1.17 g, 89% isolated yield): mp 29–30°C; ^{1}H NMR (200 MHz) δ: 7.1–7.35 (5H, m, phenyl), 3.66 (3H, s, C(O)OC*H*$_3$), 2.91 (2H, t, SC*H*$_2$CH$_2$), 2.3 (2*H*, t, CH$_2$C(O)OCH$_3$), 1.57–1.68 (4H, m, SC*H*$_2$CH$_2$CH$_2$, C*H*$_2$CH$_2$C(O)OCH$_3$), 1.29–1.5 (8H, br s, (C*H*$_2$)$_3$); MS *m/e*: 281 ((M + 1)$^+$), 249 ((M − OCH$_3$)$^+$). Anal. calcd. for $C_{16}H_{24}O_2S$: C 68.53, H 8.63, S 11.43; found: C 68.27, H 9.03, S 11.03.

B. Methyl S-Phenyl-8-mercaptooctanoate (6): mp 12–18°C; ^{1}H NMR (200 MHz) δ: 7.1–7.35 (5H, m, phenyl), 3.65 (3H, s, C(O)OC*H*$_3$), 2.90 (2H, t, SC*H*$_2$CH$_2$), 2.28 (2*H*, t, C*H*$_2$C(O)OCH$_3$), 1.56–1.67 (4H, m, SC*H*$_2$CH$_2$CH$_2$, C*H*$_2$CH$_2$C(O)OCH$_3$), 1.2–1.5 (6H, br s, (C*H*$_2$)$_3$); MS *m/e*: 267 ((M + 1)$^+$), 235 ((M − OCH$_3$)$^+$). Anal. calcd. for $C_{15}H_{22}O_2S$: C 67.63, H 8.32, S 12.04; found: C 67.47, H 8.69, S 11.98.

C. Methyl 10-(2-naphthyl)-9-thiadecanoate (7): mp 23–26°C; ^{1}H NMR (200 MHz) δ: 7.68 (1H, s, 1-naphthyl), 7.76–7.82 (3H, m, naphthyl), 7.42–7.51 (3H, m, naphthyl), 3.65 (3H, s, C(O)OC*H*$_3$), 3.85 (2H, s, C$_{10}$H$_7$ CH$_2$S), 2.39 (2H, t, SC*H*$_2$CH$_2$), 2.26 (2*H*, t, C*H*$_2$C(O)OCH$_3$), 1.46–1.63 (4H, m, SC*H*$_2$CH$_2$CH$_2$, C*H*$_2$CH$_2$C(O)OCH$_3$), 1.2–1.5 (6H, br s, (C*H*$_2$)$_3$); MS *m/e*: 331 ((M + 1)$^+$), 299 ((M − OCH$_3$)$^+$). Anal. calcd. for $C_{20}H_{26}O_2S$: C 72.69, H 7.93, S 9.70; found: C 72.54, H 7.82, S 9.74.

D. Methyl S-(2-naphthyl)-9-mercaptononanoate (8): mp 36–37°C; ^{1}H NMR (200 MHz) δ: 7.7–7.8 (4H, m, naphthyl), 7.38–7.49 (3H, m, naphthyl), 3.67 (3H, s, C(O)OC*H*$_3$), 3.02 (2H, t, SC*H*$_2$CH$_2$), 2.3 (2*H*, t, C*H*$_2$C(O)OCH$_3$), 1.50–1.75 (4H, m, SC*H*$_2$CH$_2$CH$_2$, C*H*$_2$CH$_2$C(O)OCH$_3$), 1.2–1.5 (8H, br s, (C*H*$_2$)$_3$); MS *m/e*: 331 ((M + 1)$^+$), 299 ((M − OCH$_3$)$^+$). Anal. calcd. for $C_{20}H_{26}O_2S$: C 72.69, H 7.93, S 9.70; found: C 72.82, H7.96, S 9.71.

Synthesis of sulfoxide products

Racemic sulfoxides were prepared by treating sulfides with one equiv. of MCPBA (Lancaster) at 0°C in CH_2Cl_2 for 1 h. Contaminating sulfone and sulfide were removed by flash chromatography (60% EtOAc–hexane) to give colorless oils or low-melting solids. The analytical data obtained for these compounds are as follows.

A. (±)-Methyl S-*Phenyl-9-mercaptononanoate* S-*oxide:* oil, ^{1}H NMR (200 MHz) δ: 7.5–7.65 (5H, m, phenyl), 3.66 (3H, s, C(O)OC*H*$_3$), 2.78 (2H, t, S(O)C*H*$_2$CH$_2$), 2.29 (2*H*, t, CH$_2$C(O)OCH$_3$), 1.57–1.68 (4H, m, SC*H*$_2$CH$_2$CH$_2$, C*H*$_2$CH$_2$C(O)OCH$_3$), 1.5–1.8 (8H, br s, (C*H*$_2$)$_3$); MS *m/e*: 297 ((M + 1)$^+$), 265 ((M − OCH$_3$)$^+$). Anal. calcd. for $C_{16}H_{24}O_3S$: C 64.83, H 7.82; found: C 64.59, H 8.16.

B. (±)-Methyl S-*Phenyl-8-mercaptooctanoate* S-*oxide:* oil, ^{1}H NMR (200 MHz) δ: 7.47–7.35 (5H, m, phenyl), 3.65 (3H, s, C(O)OC*H*$_3$), 2.76 (2H, t, S(O)C*H*$_2$CH$_2$), 2.27 (2*H*, t, C*H*$_2$C(O)OCH$_3$), 1.50–1.75 (4H, m, SC*H*$_2$CH$_2$CH$_2$, C*H*$_2$CH$_2$C(O)OCH$_3$), 1.2–1.5 (6H, br s, (C*H*$_2$)$_3$); MS *m/e*: 283 ((M + 1)$^+$), 251 ((M − OCH$_3$)$^+$). Anal. calcd. for $C_{15}H_{22}O_3S$: C 63.80, H 7.85; found: C 63.37, H 7.85.

C. (±)-Methyl 10-(2-naphthyl)-9-thiadecanoate S-*oxide:* mp 74–78°C; ^{1}H NMR (200 MHz) δ: 7.74–7.89 (4H, m, naphthyl), 7.35–7.52 (3H, m, napthyl), 4.13 (2H, AB q, J_{AB} = 12.8 Hz, C$_{10}$H$_7$ C*H*$_2$S(O)), 3.65 (3H, s, C(O)OC*H*$_3$), 2.58 (2H, t, SC*H*$_2$CH$_2$), 2.26 (2*H*, t, C*H*$_2$C(O)OCH$_3$), 1.5–1.8 (4H, m, SC*H*$_2$CH$_2$CH$_2$, C*H*$_2$CH$_2$C(O)OCH$_3$), 1.2–1.5 (6H, br s, (C*H*$_2$)$_3$); MS (CI, iso) *m/e*: 347 ((M + 1)$^+$), 315 ((M − OCH$_3$)$^+$). Anal. calcd. for $C_{20}H_{26}O_3S$: C 69.32, H 7.56; found: C 69.36, H. 7.68.

D. (±)-Methyl S-*(2-naphthyl)-9-mercaptononanoate:* mp 36–37°C; ^{1}H NMR (200 MHz) δ: 7.7–7.8 (4H, m, naphthyl), 7.38–7.49 (3H, m, naphthyl), 3.67 (3H, s, C(O)OC*H*$_3$), 3.02 (2H, t, SC*H*$_2$CH$_2$), 2.3 (2*H*, t, C*H*$_2$C(O)OCH$_3$), 1.50–1.75 (4H, m, SC*H*$_2$CH$_2$CH$_2$, C*H*$_2$CH$_2$C(O)OCH$_3$), 1.2–1.5 (8H, br s, (C*H*$_2$)$_3$); MS (CI, iso) *m/e*: 347 ((M + 1)$^+$), 315 ((M − OCH$_3$)$^+$). Anal. calcd. for $C_{20}H_{26}O_3S$: C 69.32, H 7.56, S 9.25; found: C 69.37, H. 7.58, S 9.03.

Biological synthesis of sulfoxides using S. cerevisae

A typical incubation was carried out as follows: The strain of baker's yeast used in this experiment was wild-type *Saccharomyces cerevisae*, no. ATTC 12341. Cultures were grown in YPD medium (1.0% yeast extract, 2.0% bactopeptone, 2.0% D-glucose), at 30°C in a rotary incubator shaker set at 150 rpm. Starter culture (4 mL) containing 5×10^8 cells was used to inoculate 300 mL of sterile medium in a 1-L Erlenmeyer flask.

A 50-mg portion of thia fatty acid methyl ester was added as a solution (5% w/v) in absolute ethanol to each culture flask, and the inoculated cultures were then incubated for 24 h to give a final cell density of 3×10^{10} cells/flask. The addition of exogenous fatty acid did not affect the growth of the organism with respect to control cultures.

Culture media was collected by centrifugation (6000 × *g*, 10 min); the supernatant was brought to 1.5 M in NaCl, acidified to pH 1.5 with 3 M HCl, and then extracted with CH_2Cl_2 (2 × 30 mL), $CHCl_3$ (2 × 30 mL), CCl_4 (1 × 30 mL). The combined organic extracts were dried over anhydrous Na_2SO_4 (8 g, 4 h). The decanted solution was evaporated in vacuo to give a crude residue, which was methylated using an ethereal diazomethane solution. (The sulfoxide product is excreted from the cells as the free acid.) TLC analysis of the extract was carried out on silica gel plates (80% EtOAc–hexane) Purification of the sulfoxide product was performed by flash chromatography (silica gel, 65% EtOAc–hexane).

Biologically produced sulfoxides were compared with the authentic synthetic standards on the basis of ^{1}H NMR, R_f, and MS data.

Acknowledgement

We wish to thank the Natural Sciences and Engineering Research Council of Canada (NSERC) for a postgraduate scholarship to D.M. and for financial support of this work.

1. H. Cook. *In* Biochemistry of lipids and membranes. *Edited by* D.E. Vance and J.E. Vance. The Benjamin Cummings Publishing Co. Ltd., Menlo Park, Calif. 1985. pp, 191–203.
2. P.R. Ortiz de Montellano. Trends Pharmacol. Sci. **10**, 354 (1989).
3. J.R. Collins, D.L. Camper, and G.H. Loew. J. Am. Chem. Soc. **113**, 2736 (1991).
4. (*a*) Y. Watanabe, T. Iyanagi, and S. Oae. Tetrahedron Lett. **21**, 3685 (1980); (*b*) F.P. Guengerich and T.L. Macdonald. Acc. Chem. Res. **17**, 9 (1984).
5. P.H. Buist and D.M. Marecak. J. Am. Chem. Soc. **114**, 5073 (1992).
6. J.B. Pedley and J. Rylance. Computer analysed thermochemical data: organic and organometallic compounds. Vol. 1. University of Sussex, Brighton, U.K. 1977.
7. R.L. Crumbie, B.S. Deol, J.E. Nemorin, and D.D. Ridley. Aust. J. Chem. **31**, 1965 (1978).
8. M.N. Deshmukh, E. Dunach, S. Juge, and H.B. Kagan. Tetrahedron Lett. **25**, 3467 (1984).
9. H.G. Enoch, A. Catala, and P. Strittmatter. J. Biol. Chem. **251**, 5095 (1976).
10. W. Tagaki. *In* Organic chemistry of sulfur. *Edited by* S. Oae. Plenum Press, New York. 1977. pp. 245–251.
11. N.S. Kishore, T. Lu, L.J. Knoll, A. Katoh, D.A. Rudnick, P.P. Mehta, B. Devads, M. Kuhn, J.L. Atwood, S.P. Adams, G.W. Gokel, and J.I. Gordon, J. Biol. Chem. **266**, 8835 (1991).
12. P.H. Buist, H.G. Dallmann, R.R. Rymerson, and P.M. Seigel, Tetrahedron Lett. **28**, 857 (1987).
13. L.D. Metcalfe and A.A. Schmitz. Anal. Chem. **33**, 363 (1961).

Biosynthesis of naphthomycin A in *Streptomyces collinus*[1]

JONATHAN P. LEE

Department of Chemistry, The Ohio State University, Columbus, OH 43210, U.S.A.

SHENG-WAN TSAO AND CHING-JER CHANG

Department of Medicinal Chemistry and Pharmacognosy, School of Pharmacy and Pharmacal Sciences, Purdu University, West Lafayette, IN 47907, U.S.A.

AND

XIAN-GUO HE AND HEINZ G. FLOSS[2]

Department of Chemistry, The Ohio State University, Columbus, OH 43210, U.S.A., and Department of Medicinal Chemistry and Pharmacognosy, School of Pharmacy and Pharmacal Sciences, Purdue University, West Lafayette, IN 47907, U.S.A.

Received May 27, 1993

This paper is dedicated to Professor Ian D. Spencer

JONATHAN P. LEE, SHENG-WAN TSAO, CHING-JER CHANG, XIAN-GUO HE, and HEINZ G. FLOSS. Can. J. Chem. **72**, 182 (1994).

The biosynthesis of naphthomycin A (**1**) in *Streptomyces collinus* was studied in feeding experiments with single and multiple ^{13}C-labeled precursors followed by ^{13}C NMR analysis of the labeling and ^{13}C–^{13}C coupling patterns in the product. The results indicate that **1** is assembled via the polyketide pathway from 3-amino-5-hydroxybenzoic acid (**2**) as the starter unit (mC_7N unit) plus seven propionate and six acetate chain extension units. **2** is synthesized via the shikimate pathway by a process that attaches the nitrogen to the carbon derived from C1 of erythrose 4-phosphate, consistent with a new branch of the shikimate pathway recently discovered to operate in the biosynthesis of the mC_7N unit of rifamycin B.

JONATHAN P. LEE, SHENG-WAN TSAO, CHING-JER CHANG, XIAN-GUO HE et HEINZ G. FLOSS. Can. J. Chem. **72**, 182 (1994).

On a étudié la biosynthèse de la naphtomycine A (**1**) dans le *Streptomyces collinus* en procédant à des expériences au cours desquelles on a fourni des précurseurs comportant des marqueurs au ^{13}C simples ou multiples alors que l'on a suivi le marquage par une analyse RMN du ^{13}C et par les patrons de couplage ^{13}C–^{13}C dans le produit. Les résultats indiquent que le produit **1** s'assemble par le biais d'une voie impliquant la formation d'un polycétide à partir de l'acide 3-amino-5-hydroxybenzoïque (**2**) (unité mC_7N) et des sept unités propioniques et six chaînes acétiques agissant comme extensions. Le composé **2** est synthétisé par une voie impliquant l'acide shikimique, par un processus que attache un azote au carbone dérivé du C1 4-phosphate d'érythrose; ceci est en accord avec une nouvelle branche de la voie shikimique découverte récemment et qui est impliquée dans la biosynthèse de l'unité mC_7N de la rifamycine B.

[Traduit par la rédaction]

Naphthomycin A (**1**), first isolated from *Streptomyces collinus* Tü 105 by Balerna et al. (1), is a naphthalenic ansamycin (2, 3) antibiotic that contains an unusually large number of carbon atoms, 23, in its ansa chain. Its constitutional formula was first proposed by Williams (4) and later revised by Rinehart and coworkers (5). The structure was subsequently confirmed by X-ray crystallography, which, together with chemical degradations, also established the absolute configuration (6). Naphthomycin A co-occurs with a number of congeners (1, 7, 8) and is structurally related to actamycin (8, 9) and the naphthoquinomycins (10). Unlike other ansamycins, **1** is active against Gram-positive bacteria and its mode of action is different from that of other naphthalenic ansamycins, which generally inhibit bacterial RNA polymerase. Its action is antagonized by vitamin K and by sulfhydryl compounds like cysteine (1).

In this paper we report the results of studies on the biosynthesis of naphthomycin A that show that its formation probably follows a pathway similar to that previously demonstrated for rifamycin S (11–13), geldanamycin (14, 15), actamycin (9, 16), and ansatrienin (13, 17, 18).

Results and discussion

The origin of the carbon framework of both the naphthoquinoid nucleus and the macrocyclic ansa bridge of naphthomycin A was studied in shake cultures of *S. collinus* Tü 105 by feeding ^{13}C-labeled precursors followed by ^{13}C NMR analysis of the product. These experiments were preceded by preliminary studies in which the same compound labeled with ^{14}C was fed to evaluate its general level of incorporation (data not shown). On the basis of time course studies of naphthomycin A formation, the labeled precursors were added to production cultures at 24 h after inoculation, and incubation was continued for an additional 40–55 h. Naphthomycin A could be isolated from the culture broth in yields of about 70 mg/L by extraction of the acidified broth with ethyl acetate and purification by column chromatography on Sephadex LH-20, followed by preparative thin-layer chromatography on silica gel.

The analysis of the products from these experiments for their ^{13}C distribution is reliant upon assignment of the signals in the ^{13}C NMR spectrum of **1**. Naphthomycin A gives a ^{13}C NMR spectrum with 40 well-resolved signals (Table 1). Based upon chemical shift theory the spectrum was divided into four regions: 202–165 ppm, with five carbonyl atoms; 165–120 ppm, 20 aromatic-olefinic methine or quaternary carbon atoms; 80–30 ppm, eight methylene, methine, or alkoxy carbon atoms; and 25–10 ppm, seven methyl carbon atoms. The proton-coupled spectrum distinguished C31 with no observable proton coupling and C28 with a single coupling ($J_{C28-H27}$ =

[1]This paper is dedicated to Professor Ian Spenser, one of the early pioneers of biosynthetic studies and a role model in his commitment to intellectual and experimental rigor and honesty.

[2]Author to whom correspondence may be addressed at the Department of Chemistry, BG-10, University of Washington, Seattle, WA 98195, U.S.A. Fax: (206)543-8318.

Can. J. Chem. Downloaded from www.nrcresearchpress.com by 195.246.54.202 on 09/08/12
For personal use only.

TABLE 1. ^{13}C chemical shifts of **1** and relative ^{13}C abundances in **1** derived from ^{13}C-labeled precursors

Carbon no.	Chemical shift (ppm)	Relative ^{13}C abundances[a] of **1** from: Sodium [1-^{13}C]acetate	Sodium [2-^{13}C]acetate	[1-^{13}C]propionate	[7-^{13}C]-**2**
1	170.0	—[b]	—	16[b]	
2	133.3	—	4.1	—	
3	128.3	4.2	1.0	—	
4	124.4	1.0	5.5	—	
5	131.7	3.6	—	—	
6	127.3	1.0	4.7	—	
7	140.0	2.0	1.6	36	
8	46.0	1.3	3.5	—	
9	73.4	3.5	1.0	—	
10	42.5	1.0	6.8	—	
11	202.6	1.9	—	15[b]	
12	137.9	—	1.9	—	
13	142.0	3.5	1.0	—	
14	37.2	1.0	5.8	—	
15	72.9	4.5	1.0	—	
16	137.8	1.0	6.4	—	
17	133.9	2.0	—	44	
18	41.8	0.9	4.0	—	
19	77.9	2.4	2.1	42	
20	34.9	0.9	3.4	—	
21	148.0	2.0	1.6	41	
22	139.1	1.3	3.1	—	
23	199.5	2.8	1.0	—	
24	123.6	—	2.7	—	
25	159.9	0.8	—	20[b]	
26	133.5	0	3.2	—	
27	131.5	1.0	—	—	64
27a	123.5	—	—	—	
28	179.5	—	—	—	
29	134.3	—	—	—	
30	137.3	—	—	—	
31	179.0	—	—	—	
31a	134.4	—	0.9	—	
32	20.4	1.0	3.8	—	
33	17.3	1.1	5.2	—	
34	11.1	1.3	4.5	—	
35	16.5	1.0	4.0	—	
36	10.4	1.4	4.5	—	
37	12.0	1.3	4.5	—	
38	16.4	0.9	4.5	—	

[a]Natural abundance = 1.0.
[b]Enriched, quantitation subject to large error.

4.6 Hz) from C1, C11, and C23, which all demonstrated multiple and complex proton couplings. The remaining signals in the spectrum demonstrated mixtures of complex first- and second-order coupling patterns and could not be further assigned by this method. DEPT (19) experiments were conducted, resulting in the further assignment of 10 signals in the congested aromatic-olefinic region as methine and the remaining 10 as quaternary carbon atoms. In addition, two signals were assigned to the methylene carbon atoms C10 and C14. The further analysis of the spectrum relied on 2D NMR spectroscopy, particularly a 2D-INADEQUATE (20) experiment on a sample of **1** obtained by feeding [U-$^{13}C_3$]glycerol. This analysis identified coupled, and hence connected, sets of two and three carbon atoms. Combining these data with connectivities obtained from 2D ^{13}C–proton heteronuclear correlation experiments (normal and long-range, HETCOR (21) and COLOC (22)) and 2D proton–proton homonuclear correlation experiments (normal and long-range COSY (23, 24)), we were able to observe connectivities from individual biosynthetically intact units of two or three ^{13}C atoms to their attached protons, and then to either ^{13}C atoms of adjacent intact units or their attached protons. This allowed the complete assignment of both the carbon (Table 1) and proton (Table 2) NMR spectra of naphthomycin A; these assignments are consistent with literature data on closely related compounds (7*b*, 10).

With these assignments at hand we proceeded to probe the biosynthetic origin of **1**. Based on analogy to other ansamycins (9, 11, 14) it was assumed that carbon atoms 1 through 26 and their attached methyl groups are of polyketide origin, whereas the quinoid ring and the attached nitrogen atom and C27 repre-

Can. J. Chem. Downloaded from www.nrcresearchpress.com by 195.246.54.202 on 09/08/12
For personal use only.

TABLE 2. Proton chemical shift assignments for naphthomycin A

Proton no.	δ (ppm)	Proton no.	δ (ppm)
3 (a)[a]	6.73	18 (b)	2.15
4 (a)	6.24	19 (d)	3.10
5 (a)	6.05	20 (b)	2.75
6 (a)	6.65	21 (a)	6.03
7 (a)	5.48	27 (a)	8.00
8 (b)	2.28	32 (e)	2.16
9 (b)	3.73	33 (e)	1.15
10 (c)	2.30	34 (c)	1.72
13 (a)	6.75	35 (e)	0.95
14 (c)	2.10	36 (e)	0.75
15 (d)	3.90	37 (e)	1.97
16 (a)	5.40	38 (e)	2.43
17 (a)	5.45		

[a]Key: (a) aromatic-olefinic methine; (b) alkyl methine; (c) methylene; (d) alkoxyl; (e) metnyl.

sent a mC_7N unit of non-polyketide origin. The branching methyl groups in other ansamycins, as in the majority of bacterial polyketides, arise from the incorporation of propionate instead of acetate units; their formation by methylation of a polyacetate chain, as in boromycin (25) and aplasmomycin (26), seems to be the exception. Hence we decided to feed [1-^{13}C]propionate and [1-^{13}C] and [2-^{13}C]acetate.

In the feeding experiment with propionate, 770 mg of sodium [1-^{13}C]propionate and 25 μCi of sodium [1-^{14}C]propionate (specific radioactivity ~2.7 μCi/μmol) were combined in an aqueous solution and pulse fed to seven 100-mL shake cultures starting 24 h after inoculation at 12 h intervals. Fifteen milligrams of **1** was isolated after 72 h and the specific incorporation of ^{14}C was 213%. The ^{13}C NMR spectrum of this sample (Table 1) showed many slightly enriched signals, but seven signals were rather highly enriched. These were carbon atoms 1, 7, 11, 17, 19, 21, and 25, i.e., all the carbon atoms expected to arise from C1 of propionate if proprionate units are incorporated into the polyketide chain to give rise to the branching methyl groups.

The feeding of sodium [1-^{13}C]acetate (600 mg) with 25 μCi of sodium[1-^{14}C]acetate (specific radioactivity ~5 μCi/μmol) was carried out analogously, and 19.3 mg of **1** was isolated with a specific incorporation of ^{14}C of 50%. The ^{13}C NMR spectrum of this sample (Table 1) contained 11 significantly enriched signals (1.9–4.5 times natural abundance). Five of these signals were identical to those enriched by [1-^{13}C]proprionate and six (carbon atoms 3, 5, 9, 13, 15, and 23) were uniquely labeled. Similarly, 840 mg of sodium [2-^{13}C]acetate and 25 μCi of sodium[2-^{14}C]acetate (specific radioactivity ~3.7 μCi/μmol) was fed, resulting in 12 mg of **1** being isolated with a 40% specific incorporation of ^{14}C. The ^{13}C NMR spectrum of this sample (Table 1) contained 21 signals that were significantly enhanced (1.9–6.8 times natural abundance). None of these carbon atoms, except C19, were significantly labeled in the two previous feeding experiments. The enhanced signals included those for C4, C6, C10, C14, C16, and C24, the carbon atoms expected to arise from C2 of acetate if acetate units were incorporated directly into the polyketide chain. In addition, in every propionate-derived unit the carbon atoms expected to arise from C3 and C2 of propionate were labeled; small enrichments were sometimes also seen in the carbon atoms corresponding to C1 of proprionate. The appearance of ^{13}C from acetate in moieties derived from propionate is easily rationalized by acetate metabolism through the citric acid cycle to succinate and ultimately to methylmalonyl-CoA. In both acetate feedings six enriched signals were detected that did not appear in propionate-derived moieties. It was therefore concluded that, as expected, six acetate and seven proprionate units, in the form of malonyl-CoA and methylmalonyl-CoA, respectively, are condensed to form the major portion of the skeleton of **1**, i.e., the entire framework except the mC_7N unit (Fig. 1).

The origin of the mC_7N unit of ansamycin antibiotics, e.g., rifamycin (11, 27, 28), geldanamycin (14,15), or ansatrienin (13, 17) is related to the shikimate pathway, whereas the mC_7N units found in acarbose and validamycin (29) or manumycin-type (30) antibiotics have different origins unrelated to the shikimate pathway. To shed light on the origin of the mC_7N unit in **1** we employed multiple ^{13}C labeling ("bond labeling") using [U-$^{13}C_3$]glycerol, a highly diagnostic general precursor of actinomycete secondary metabolites.

[U-$^{13}C_3$]Glycerol (432 mg, 99% ^{13}C) and unlabeled glycerol (837 mg) were mixed and fed to 10 100mL cultures of *S. collinus* to give 51 mg of **1**. In the ^{13}C NMR spectrum of this material all signals except for that of C29 were enriched and coupled either to one or two additional ^{13}C nuclei. C29 was possibly enriched, but definitely showed no coupling to any other carbon atom. Using a 2D-INADEQUATE experiment we were able to detect nine intact assemblies of three ^{13}C atoms and six intact units of two ^{13}C atoms, which were all mutually discrete (Table 3). In addition, several of the coupling patterns for intact units of three ^{13}C atoms were found to be superimposed upon overlapping patterns for two intact units of two ^{13}C atoms, e.g., signals for C38–C26–C25 were superimposed on signals for C38–C26 and C26–C25 (also overlapping).

The appearance of coupling between each pair of carbon atoms in the acetate-derived units of the polyketide moiety is expected, based on the well-known metabolic sequence glycerol → dihydroxyacetone phosphate → phosphoenolpyruvate (PEP) → pyruvate → acetyl-coenzyme A. The appearance of intact assemblies of three coupled ^{13}C atoms in the propionate-derived units, in addition to overlapping pairs of coupled carbon atoms, implies that in *S. collinus* PEP or pyruvate must be carboxylated to oxalacetate which, by action of malate dehydrogenase, fumarase, and succinate dehydrogenase, give rise to succinate labeled contiguously in C1, C2, and C3. Activation to the CoA ester and rearrangement by methylmalonyl-CoA mutase will then produce two species of methylmalonyl-CoA, one labeled contiguously in C1, C2, and C3 and the other in C2 and C3. However, the appearance of two coupled carbon atoms in C1 and C2 of the propionate units without coupling to C3 is not as easily rationalized.

In the mC_7N unit, two intact assemblies of three coupled ^{13}C atoms were detected, C27–C27a–C28 and C31a–C31–C30, while C29 was not observed to be coupled to any other ^{13}C. This pattern is typical of shikimate pathway metabolites and results from conversion of glycerol via dihydroxyacetone phosphate and phosphoglyceraldehyde into hexose phosphates containing two coupled three-carbon units ((C1–C2–C3 and C4–C5–C6). Transketolase then generates erythrose 4-phosphate still containing one intact three-carbon unit in C2–C3–C4 but with no coupling to C1, which condenses with another intact three-carbon unit in the form of PEP. Thus, the shikimate pathway origin of the mC_7N unit in **1** is clearly established.

The groups of Rickards (16, 31), Ghisalba and Nüesch (28, 32), and Rinehart (33) have established 3-amino-5-hydroxy-

Can. J. Chem. Downloaded from www.nrcresearchpress.com by 195.246.54.202 on 09/08/12
For personal use only.

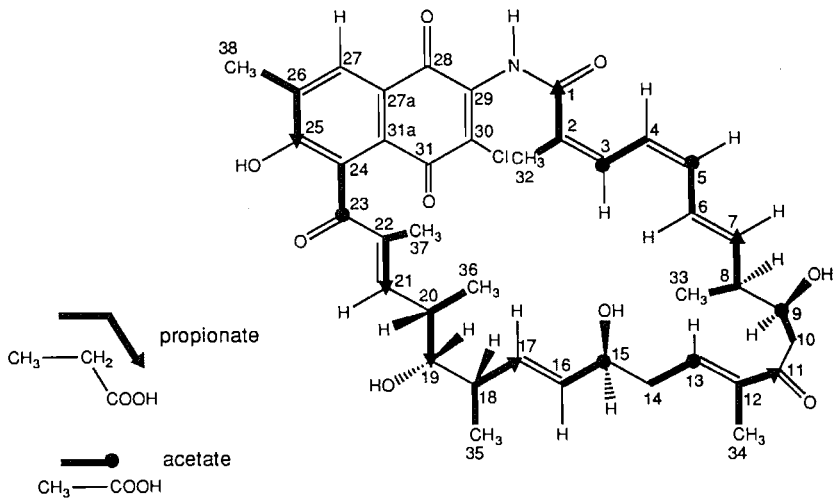

FIG. 1. Origin of naphthomycin A from one mC_7N, six acetate, and seven propionate units.

TABLE 3. Intact assemblies of two and three carbon atoms incorporated into **1** without C—C bond cleavage from [U-$^{13}C_3$]glycerol

(a) Intact three-carbon units

Carbon atoms involved	Coupling constants (Hz)
C28, C27a, and C27	59, 60
C38, C26, and C25	49, 65
C31a, C31, and C30	60, 59
C37, C22, and C21	46, 71
C36, C20, and C19	37, 38
C35, C18, and C17	33, 43
C34, C12, and C11	45, 51
C33, C8, and C7	35, 42
C32, C2, and C1	43, 63

(*b*) Unique intact two-carbon units[a]

Carbon atoms involved	Coupling constant (Hz)
C24 and C23	54
C16 and C15	46
C14 and C13	42
C10 and C9	40
C6 and C5	55
C4 and C3	55

[a]Additional pairs of coupled carbons were detected which coincided with intact three-carbon assemblies.

benzoic acid (**2**) as the proximate precursor of the shikimate pathway-derived mC_7N units of rifamycin, actamycin, ansamitocin, mitomycin, geldamycin, and streptovaricin, and we have shown that **2** is also a specific precursor of the mC_7N unit of ansatrienin A (17). In contrast, the mC_7N unit of pactamycin is derived from 3-aminobenzoic acid rather than **2** (34). To probe whether **2** is the precursor of the mC_7N unit of **1** we synthesized both [7-^{13}C]- and [7-^{14}C]-**2** by the procedure of Rickards and co-workers (35). A mixture of 362 mg [7-^{13}C]-**2** (99 atom% ^{13}C) and 5 μCi [7-^{14}C]-**2** (specific radioactivity 0.35 μCi/μmol) was fed to 12 100mL cultures of *S. collinus* to give 7.2 mg of labeled **1**. The specific incorporation of ^{14}C was 64%. The NMR spectrum of this sample showed only one highly enriched signal at 131.5 ppm corresponding to C27. From these data it was concluded that **2** is a specific and highly efficient precursor of the mC_7N unit of **1**.

The identification of **2** as a specific precursor of the mC_7N unit of ansamycins and mitomycins does not answer the question of how this molecule is generated through the shikimate pathway. This question is particularly intriguing since neither shikimic acid itself (14, 18, 27, 36) nor an earlier pathway intermediate, dehydroquinic acid (37), is incorporated into the mC_7N unit. At least in one case, ansatrienin A, it was shown that this is not due to lack of cell permeability to the precursor, because ^{13}C-shikimic acid labeled another part of the molecule, but not the mC_7N unit (18). Thus the formation of **2** must branch off from the main pathway at an earlier stage. Another intriguing feature is the finding, in the cases of the mitomycins (37) geldanamycin (15) and ansatrienin A (38), that the nitrogen atom of the mC_7N unit is attached to the carbon atom corresponding to C5, not C3, of a shikimate-equivalent moiety. The same conclusion is reached about the mC_7N unit of **1** from the results of the [U-$^{13}C_3$]glycerol experiment presented above. Since C29 shows no coupling whereas C31 is the center of a coupled three-carbon assembly, C29 corresponds to C5 and C31 to C3 of shikimate or dehydroshikimate, i.e., the nitrogen in this case is similarly attached to the C5-equivalent carbon atom.

Recent work from this laboratory (13) has shed some light on the mode of formation of **2** by demonstrating that cell-free extracts of the rifamycin producer, *Nocardia mediterranei*, efficiently convert 3,4-dideoxy-4-amino-D-*arabino*-heptulosonic acid 7-phosphate (aminoDAHP, **3**), but not DAHP, and 5-deoxy-5-amino-3-dehydroshikimic acid (aminoDHS, **4**) into **2**. The enzyme catalyzing the aromatization of **4** into **2** has recently been purified to homogeneity and the gene encoding it has been cloned.[3] These findings lend considerable support to the pathway shown in Fig. 2 for the formation of **2**. All the results of the present study are consistent with and support such a pathway also for the formation of the mC_7N unit of **1**.

In summary, the results of this study indicate that the carbon framework of **1** is assembled by the polyketide pathway from a shikimate pathway-derived starter unit, **2**, presumably as its coenzyme A thioester, and chain extension by seven propionate

[3]C.-G. Kim and H.G. Floss. Unpublished work.

Can. J. Chem. Downloaded from www.nrcresearchpress.com by 195.246.54.202 on 09/08/12
For personal use only.

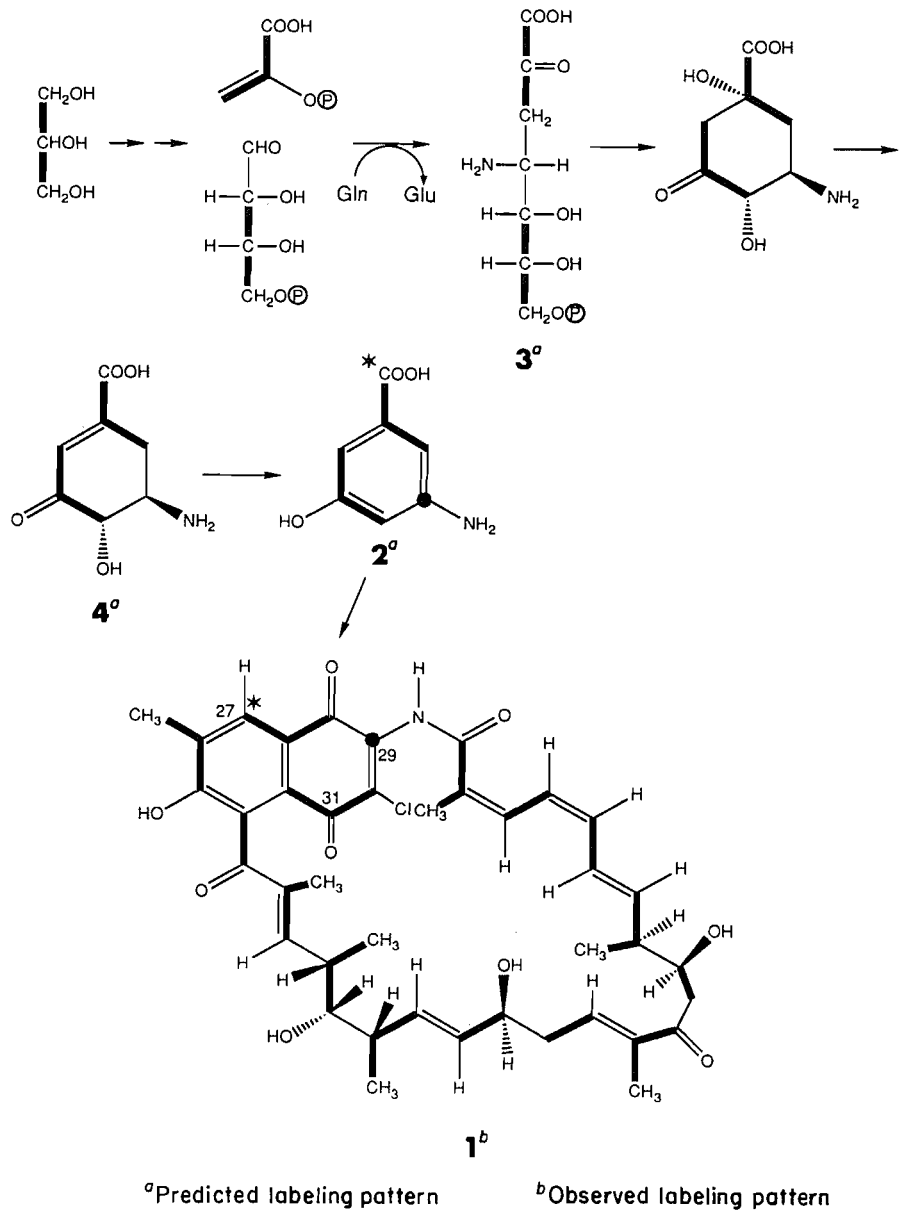

FIG. 2. ^{13}C–^{13}C coupling pattern observed in **1** after feeding [U$^{13}C_3$]glycerol, and proposed mode of formation of the mC_7N unit.

(methylmalonyl-CoA) and six acetate (malonyl-CoA) units. The terminal unit of the polyketide chain that in **1**, uniquely among the naphthomycins, is distinguished by a methyl group at C2, is also derived from propionate rather than by methylation of an acetate-derived moiety. All the labeling patterns in the mC_7N unit are consistent with its formation by a new branch of the shikimate pathway recently demonstrated in rifamycin biosynthesis, which involves amino analogs of the normal pathway intermediates.

Experimental section

Materials

Chemicals were obtained from Aldrich Chemical Co., Alfa Products, or Eastman Organic Chemicals and were of reagent grade or of the highest grade commercially available. Radiolabeled compounds were purchased from NEN or Amersham. Sodium [1-^{13}C] and [2-^{13}C]acetate and sodium [1-^{13}C]propionate were obtained from MSD Isotopes. [U-$^{13}C_3$]Glycerol was synthesized from K^{13}CN (99 at.% ^{13}C) and [1,2-$^{13}C_2$]acetic acid (99 at.% ^{13}C), both provided by the Los Alamos Stable Isotope Resource, via diethyl malonate and diethyl 2-acetoxymalonate as previously described (39). [7-^{14}C] and [7-^{13}C]-**2** were synthesized from 3-bromo-5-nitroanisole and Cu^{14}CN, respectively, by the procedure of Herlt et al. (35). The culture of *S. collinus* Tü 105 as well as full-fat soybean meal (Schoenenberger, Magstadt, Germany) were a gift of Prof. H. Zähner, Tübingen. Reference samples of naphthomycins were provided by Prof. A. Zeeck, Göttingen.

General methods

^{13}C NMR spectra were recorded on Varian XL200, Bruker WM-300, and Bruker AM 500 nuclear magnetic resonance spectrometers operating at 50.1, 75.5, and 125.1 MHz, respectively. High-field ^1H NMR spectra and H:C heteronuclear correlation spectra were recorded at 500.12 MHz (proton frequency) on a Bruker AM 500 instrument. Chemical shifts are given relative to Me_4Si as an internal standard or were adjusted to the Me_4Si scale by reference to the solvent, CHD_2COCD_3, resonance at δ_H 2.04 ppm or the $(CD_3)_2CO$ resonance at δ_C 29.5 ppm.

Preparative thin-layer chromatography was performed on 1.0 mm 20 × 20 cm silica gel 60F-254 plates supplied by Brinkmann. Column chromatography was performed on a 3.2 × 50 cm column of Sephadex

Can. J. Chem. Downloaded from www.nrcresearchpress.com by 195.246.54.202 on 09/08/12
For personal use only.

LH-20 supplied by Sigma. Radioactivity determinations were carried out by liquid scintillation counting on a Beckman LS-7500 spectrometer using AQUASOL® Universal LSC Cocktail (NEN). Counting efficiencies were determined with [^{14}C]toluene as an internal standard.

Fermentation

Streptomyces collinus Tü 105 was maintained as a frozen spore suspension in 20% glycerol. The spores were prepared from agar slants (0.4% yeast extract, 1% malt extract, 0.4% glucose, 2% agar in distilled water, pH adjusted to 7.4) grown at 30°C for 7–10 days. The spore suspensions were used to inoculate production cultures of 100 mL sterile medium (1 g full-fat soy bean meal, 2 g glucose, 100 mL tap water) in 500 mL baffled Erlenmeyer flasks, which were inoculated at 27–28°C on a New Brunswick G-25 orbital shaker at 300 rpm for 64–79 h. Labeled precursors were added as Millipore filter-sterilized solutions 24 h after inoculation either in one portion or several portions in 12 h intervals.

Isolation of ***1***

At the end of the fermentation 2% Hyflo Super Cel® was added to the culture broth followed by filtration through filter paper on a Buchner funnel. The filtrate was brought to pH 4 with 1.0 N HCl and extracted with 3 × 50 mL of ethyl acetate per production flask. The solids on the filter were washed extensively with 500 mL of methanol and the methanol was evaporated under reduced pressure. Water (10 mL) was added to the residue and the suspension was extracted with 3 × 75 mL of ethyl acetate. The two ethyl acetate extracts were combined and evaporated under reduced pressure. The crude extract was chromatographed on a Sephadex LH-20 column with methanol as solvent. The **1**-containing fractions were combined and evaporated to dryness under reduced pressure. The residue was triturated with ethyl acetate and the solution applied to a preparative silica gel plate, which was developed with ethyl acetate:benzene, 4:1. The **1**-containing band was scraped from the plate and the product eluted from the silica gel with ethyl acetate. The ethyl acetate solution was evaporated to a dark oil under reduced pressure. The oil was held under vacuum for 46 h and solidified when the pressure was below 0.1 Torr (1 Torr = 133.3 Pa). Yields ranged from 50 to 220 mg/L.

Acknowledgements

We are indebted to Prof. H. Zähner, Tübingen, for providing the culture of *S. collinus* as well as valuable advice, to Prof. A. Zeeck, Göttingen, for reference compounds, and to the Los Alamos Stable Isotope Resource, supported by NIH (grant RR02231) and USDOE/OHER, for the supply of ^{13}C-labeled synthetic starting materials. Financial support of this work by the NIH through research grant Al 20264 is also gratefully acknowledged.

1. M. Balerna, W. Keller-Schierlein, C. Martius, and H. Zähner. Arch. Mikrobiol. **65**, 303 (1969).
2. K.L. Rinehart, Jr. and L.S. Shields. Forschr. Chem. Org. Naturst. **33**, 231 (1976).
3. W. Wehrli. Topics Current Chem. **72**, 21 (1977).
4. T.H. Williams. J. Antibiot. **28**, 85 (1975).
5. P.V. Deshmukh, K. Kakinuma, J.J. Ameel, K.L. Rinehart, Jr., P.F. Wiley, and L.H. Li. J. Am. Chem. Soc. **98**, 879 (1976).
6. M. Brufani, L. Cellai, and W. Keller-Schierlein. J. Antibiot. **32**, 167 (1979).
7. (*a*) W. Keller-Schierlein, M. Meyer, A. Zeeck, M. Damberg, R. Machinek, H. Zähner, and G. Lazar. J. Antibiot. **36**, 484 (1983); (*b*) T. Muklopadhyay, C.M.M. Franco, G.C.S. Reddy, B.N. Ganguli, and H.W. Fehlhaber. J. Antibiot. **37**, 9480 (1985).
8. M.S. Allen, I.A. MacDonald, and R.W. Rickards. Tetrahedron Lett. 1145 (1981).
9. I.A. McDonald and R.W. Rickards. Tetrahedron Lett. 1149 (1981).
10. J. Mochizuki, E. Kobayashi, K. Furihata, A. Kawaguchi, H. Seto, and N. Otake. J. Antibiot. **39**, 157 (1986).
11. R.J. White and E. Martinelli. FEBS Lett. **49**, 233 (1979).
12. O. Ghisalba and J. Nüesch. J. Antibiot. **34**, 64 (1981).
13. C.-G. Kim, A. Kirschning, P. Bergon, Y. Ahn, J.J. Wang, M. Shibuya, and H.G. Floss. J. Am. Chem. Soc. **114**, 4941 (1992).
14. R.D. Johnson, A. Haber, and K.L. Rinehart, Jr. J. Am. Chem. Soc. **96**, 3316 (1974); A. Haber, R.D. Johnson, and K.L. Rinehart, Jr. J. Am. Chem. Soc. **99**, 3541 (1977).
15. K.L. Rinehart, Jr., M. Potgieter, and D.A. Wright. J. Am. Chem. Soc. **104**, 2649 (1982).
16. J.J. Kibby, I.A. McDonald, and R.W. Rickards. J. Chem. Soc. Chem. Commun. 768 (1980).
17. T.-S. Wu, J. Duncan, S.-W. Tsao, C.-j. Chang, P.J. Keller, and H.G. Floss. J. Nat. Prod. **50**, 108 (1986).
18. R. Casati, J.M. Beale, and H.G. Floss. J. Am. Chem. Soc. **109**, 8102 (1987).
19. D.M. Doddrell, D.T. Pegg, and M.R. Bendrall. J. Magn. Reson. **48**, 323 (1982).
20. A. Bax, R. Freeman, and T.A. Frenkiel. J. Am. Chem. Soc. **103**, 2102 (1981).
21. G. Bodenhausen and R. Freeman. J. Am. Chem. Soc. **100**, 320 (1978).
22. H. Kessler, C. Griesinger, J. Zarbock, and H.R. Loosli. J. Magn. Reson. **57**, 331 (1984).
23. A. Bax, R. Freeman, and L. Morris. J. Magn. Reson. **42**, 164 (1981).
24. A. Bax and R. Freeman. J. Magn. Reson. **44**, 542 (1981).
25. T.S.S. Chen, C.-j. Chang, and H.G. Floss. J. Org. Chem. **46**, 2661 (1981).
26. T.S.S. Chen, C.-j. Chang, and H.G. Floss. J. Am. Chem. Soc. **103**, 4565 (1981).
27. A. Karlson, G. Sartori, and R. White. Eur. J. Biochem. **47**, 51 (1974).
28. O. Ghisalba. Chimia, **39**, 79 (1985).
29. U. Degwert, R.v. Hülst, H. Pape, R.E. Herrold, J.M. Beale, P.J. Keller, J.P. Lee, and H.G. Floss. J. Antibiot. **40**, 855 (1987); T. Toyokuni, W.-Z. Jin, and K.L. Rinehart, Jr. J. Am. Chem. Soc. **109**, 3481 (1987).
30. R. Thiericke, A. Zeeck, A. Nakagawa, S. Omura, R.E. Herrold, S.T.S. Wu, J.M. Beale, and H.G. Floss. J. Am. Chem. Soc. **112**, 3979 (1990).
31. M.G. Anderson, J.J. Kibby, R.W. Rickards, and J.M. Rothschild. J. Chem. Soc. Chem. Commun. 1277 (1980); K. Hatano, S. Akijama, M. Asai, and R.W. Rickards. J. Antibiot. **35**, 1415 (1982); A.M. Becker, A.J. Herlt, G.L. Hilton, J.J. Kibby, and R.W. Rickards. J. Antibiot. **36**, 1323 (1983).
32. O. Ghisalba, H. Fuhrer, W. Richter, and S. Moss. J. Antibiot. **34**, 58 (1981); P. Traxler and O. Ghisalba. J. Antibiot. **35**, 1361 (1982).
33. A.L. Staley and K.L. Rinehart. J. Antibiot. **44**, 218 (1991); and references therein.
34. D.D. Weller and K.L. Rinehart, Jr. J. Am. Chem. Soc. **100**, 6757 (1978).
35. A.J. Herlt, J.J. Kibby, and R.W. Rickards. Aust. J. Chem. **34**, 1319 (1981).
36. G.S. Besanzon and L.C. Vining. Can. J. Biochem. **49**, 911 (1971).
37. U. Hornemann, J.J. Eggert, and D.P. Honor. J. Chem. Soc. Chem. Commun. 11 (1981).
38. J.J. Wang. Ph.D. Dissertation, The Ohio State University, 1989.
39. D.G. Ott. *In* Synthesis with stable isotopes of C, N and O. Wiley, New York. 1981. pp. 33–35, 37; A.W. Murray and D.L. Williams. *In* Organic synthesis with isotopes. Interscience, New York. 1958. pp. 780–781.

Can. J. Chem. Downloaded from www.nrcresearchpress.com by 195.246.54.202 on 09/08/12
For personal use only.

Overexpression of a plant cysteine synthase gene and biosynthesis of a plant specific metabolite, β-(pyrazol-1-yl)-L-alanine, in *Escherichia coli*[1]

KAZUKI SAITO,[2] REIKO KANDA, MAKOTO KUROSAWA, AND ISAMU MURAKOSHI
Faculty of Pharmaceutical Sciences, Chiba University, Yayoi-cho 1-33, Inage-ku, Chiba 263, Japan

Received June 1, 1993

This paper is dedicated to Professor Ian D. Spencer

KAZUKI SAITO, REIKO KANDA, MAKOTO KUROSAWA, and ISAMU MURAKOSHI. Can. J. Chem. **72**, 188 (1994).

Cysteine synthase (EC 4.2.99.8) in higher plants is responsible for biosynthesis of not only cysteine but also some nonprotein amino acids such as β-(pyrazol-1-yl)-L-alanine. The cDNA of a cysteine synthase from spinach (*Spinacia oleracea*) was inserted into pET8c (=pET3d) under the transcriptional control of strong T7 promoter to yield an overexpression vector pCEK1. The amount of the exogenous cysteine synthase was increased up to 40% of the total soluble protein of *Escherichia coli* transformed with pCEK1. β-(Pyrazol-1-yl)-L-alanine, a specific metabolite in plants of the Cucurbitaceae, was biosynthesized by overexpressed cysteine synthase from pyrazole in the presence of *O*-acetyl-L-serine and serine, in vitro and in vivo, respectively. The present study provides the system for mechanistic investigation of biosynthesis of cysteine and biogenetically related β-substituted alanines at molecular genetic level.

KAZUKI SAITO, REIKO KANDA, MAKOTO KUROSAWA et ISAMU MURAKOSHI. Can. J. Chem. **72**, 188 (1994).

La cystéine synthase (EC 4.2.99.8) des plantes supérieures n'est pas uniquement responsable de la biosynthèse de la cystéine, mais aussi de quelques acides aminés non protéiniques comme la β-(pyrzol-1-yl)-L-alanine. On a inséré la cADN d'une cystéine synthase provenant d'épinards (*Spinacia oleracea*) dans le pET8c (=pET3d) sous le contrôle transcriptionnel du puissant promoteur T7 pour obtenir un vecteur de sur expression pCEK1. On a augmenté la quantité de cystéine synthase exogène jusqu'à 40% de la protéine soluble totale d'*Escherichia coli* transformé par du pCEK1. Utilisant une cystéine synthase surexprimée, on a biosynthétisé la β-(pyrzol-1-yl)-L-alanine, un métabolite spécifique dans les cucurbitacées, à partir de pyrazole en présence de *O*-acétyl-L-sérine et de sérine respectivement in vitro et in vivo. L'étude actuelle fournit le système qui permet de faire l'étude du mécanisme de biosynthèse de la cystéine et des alanines β-substituées biogénétiquement apparentées au niveau génétique moléculaire.

[Traduit par la rédaction]

Introduction

Nonprotein amino acids form a large group of plant secondary products (1). Some nonprotein β-substituted alanines show interesting biological activities, such as neuroactive and antimycotic activities, which are potentially useful for pharmaceutical research and development (Table 1) (2). These β-substituted alanines are formed from *O*-acetyl-L-serine (OAS) as a common precursor (Fig. 1). These reactions are catalyzed by cysteine synthase (CSase) (*O*-acetyl-L-serine (thiol)-lyase, EC 4.2.99.8) or by specific enzymes distinct from CSase, depending on the products formed: β-(pyrazol-1-yl)-L-alanine (β-PA) (3) and mimosine (4) are biosynthesized by CSases; willardiine is produced by the enzyme(s) different from CSase (5).

Little is known about the precise reaction mechanism of these pyridoxal phosphate-dependent enzymes and the molecular mechanism determining the substrate specificity governing formation of these structurally diverse compounds, since the enzymatic activity is usually very low in plant cells and only a limited amount of purified enzyme preparation is available for mechanistic study. Therefore, it is a prerequisite for further study to establish an overexpression system of genes for plant biosynthetic enzymes in heterologous cells such as *Escherichia coli*.

Recently, we isolated cDNA clones encoding CSases in spinach (*Spinacia oleracea*) (6, 7), which can utilize pyrazole as a substrate to form β-PA as well as H_2S to form cysteine. In the present study, we established an overexpression system of a cDNA of spinach CSase in *E. coli* by using a pET vector based on a T7 polymerase expression system. β-PA, a plant-specific secondary product, was biosynthesized by the action of exogenous CSase in vitro and in vivo.

Results and discussion

The *Nco*I fragment containing a full-length cDNA encoding a spinach CSase was obtained from an expression plasmid pKM1 (6). This 1.2-kb fragment was ligated into the *Nco*I site of pET8c (=pET3d) just under the ϕ10 promoter sequence of T7 DNA to yield overexpressing plasmids pCEK1 and pCEK2, with sense and antisense orientation, respectively, with respect to the promoter (Fig. 2). The expression system, pET system, employed in this study is based on the strong ϕ10 promoter in the pET plasmid by combination with lysogenic T7 RNA polymerase gene and suitable for overexpression of a heterologus gene in *E. coli* (8). The expression of T7 RNA polymerase gene is controlled by the *lacUV5* promoter, which is inducible by isopropyl β-D-thiogalactoside (IPTG). The plasmids, pCEK1 and pCEK2, were transferred into *E. coli* BL21 (DE3, pLysE) or overexpression.

The total soluble proteins of *E. coli* transformed with the expression plasmids were analyzed by SDS–polyacrylamide gel electrophoresis (PAGE) and subsequent dye staining (Fig. 3A). The protein bands corresponding to the spinach CSase A of 35 kDa were evident in the extract of transformant with the overexpressing vector, pCEK1, but not in that of the antisense pCEK2. The amount of CSase A was increased maximally up to 40% of the total soluble protein of *E. coli* (pCEK1). The corresponding band in *E. coli* NK3, a cysteine auxotrophic mutant, transformed with pKM1, a vector with transcriptional control of *lacZ* promoter for an exogenous gene, is evidently not accumulated in the crude protein extract by this dye staining. This is

[1]This paper is dedicated to Professor Ian D. Spenser for his outstanding contribution to the biosynthesis of nitrogen-containing natural products.

[2]Author to whom correspondence may be addressed. Telephone: +81-43-290-2906/2905; FAX: +8143-290-2905.

Can. J. Chem. Downloaded from www.nrcresearchpress.com by 195.246.54.202 on 09/08/12
For personal use only.

TABLE 1. Naturally occurring nonprotein β-substituted alanines formed from OAS in plants

Name	Structure	Source genus	Biological activity
β-(Pyrazol-1-yl)-L-alanine	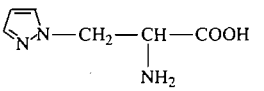	*Citrullus*	
β-(Isoxazolin-5-on-2-yl)-L-alanine	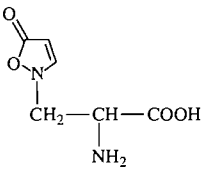	*Pisum, Lathyrus, Lens*	Antimycotic
L-Quisqualic acid	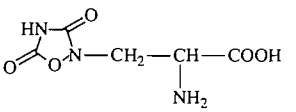	*Quisqualis*	Neuroexcitatory (Glu receptor agonist), vermicide
L-Mimosine	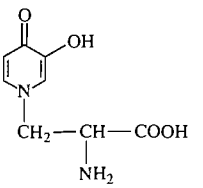	*Mimosa, Leucaena*	Depilatory, thyrotoxic
L-Willardiine	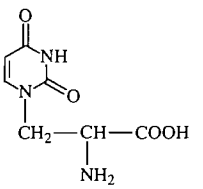	*Pisum, Acacia, Fagus*	Neuroactive

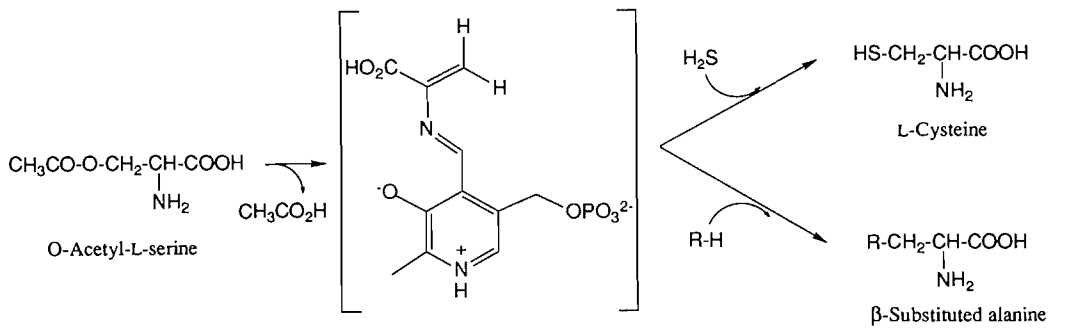

FIG. 1. Biosynthetic pathway of cysteine and nonprotein β-substituted alanines from OAS as a precursor. These amino acids are biosynthesized from OAS via an aminoacryl adduct of amino acid and pyridoxal phosphate as a common intermediate. The reactions are catalyzed by either isoenzyme of CSase or specific synthase distinct from CSase.

certainly due to the low expression level of exogenous cDNA by pKM1 compared with that by pCEK1.

The accumulation of immunoreactive and functionally active translation product of the cDNA was demonstrated by Western blot analysis and CSase enzymatic assay of the extracts of *E. coli* (Fig. 3B). The immunoreactive polypeptide of 35 kDa was detected in the protein extract of *E. coli* transformed with pCEK1 and pKM1 using antibody against CSase A. The concentration of CSase protein was higher in the pCEK1 transformant than in the pKM1 cell. The high enzymatic activity of CSase was also detected in the extracts of these *E. coli* transformants.

The purified CSase from spinach has been reported to have the ability to catalyze the formation of β-PA from pyrazole and OAS (9). However, that enzyme preparation was still a mixture of CSase A and CSase B. The cloned and overexpressed CSase A in *E. coli* was examined to determine whether this isoform could catalyze the formation of β-PA (Table 2). The overexpression plasmid, pCEK1, was able to synthesize β-PA from pyrazole and OAS. Low but substantial activities were also detected in the cell extracts transformed with pCEK2 and pKM1. These activities were presumably due to the bacterial endogenous CSases of *E. coli* BL21 and to the *lacZ*-driven expression of cDNA in pKM1.

The overexpression system in *E. coli* was applied to biosynthesis of β-PA in vivo (Fig. 4). The production of β-PA in vivo by *E. coli* culture was achieved only when both serine and pyrazole were fed to the culture medium, whereas feeding only

Can. J. Chem. Downloaded from www.nrcresearchpress.com by 195.246.54.202 on 09/08/12
For personal use only.

Can. J. Chem. Downloaded from www.nrcresearchpress.com by 195.246.54.202 on 09/08/12
For personal use only.

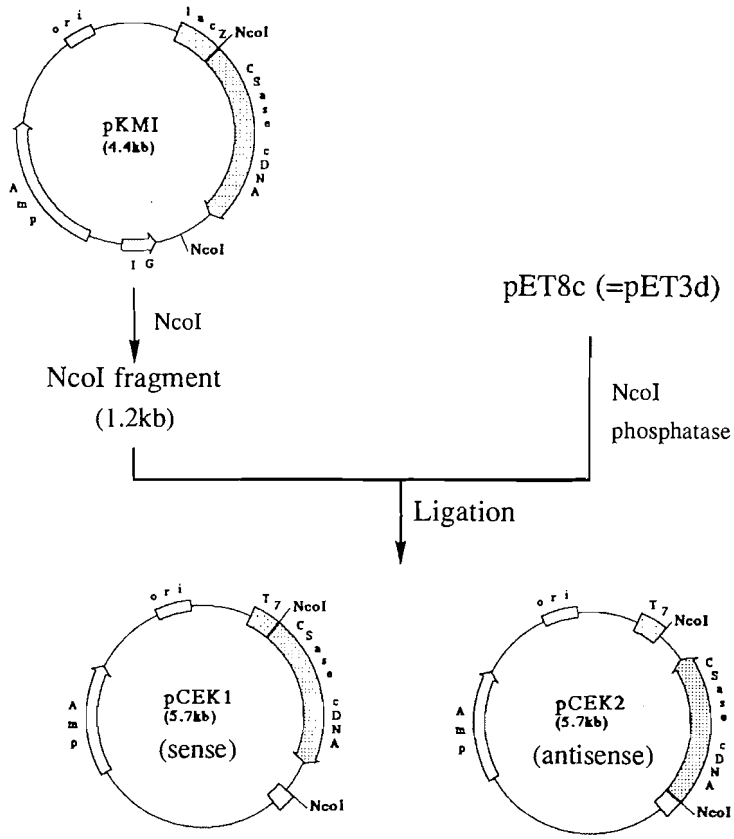

FIG. 2. Construction of a pET-derived vector for overexpression of CSase cDNA. The 1.2-kb *Nco*I fragment of pKM1 containing a full-length cDNA of spinach CSase A was ligated into phosphatase-treated *Nco*I site of pET8c (=pET3d) to afford overexpression vectors, pCEK1 and pCEK2, with sense and antisense orientations, respectively. In the 1.2-kb *Nco*I fragment, the first ATG codon was placed inside of 5′-*Nco*I restriction site. The *Nco*I fragment contained the 3′-untranslated region of 277 bp length including 22-bp poly(A) tail.

pyrazole did not result in the production of β-PA. These results suggested that the supply of OAS was strictly controlled in the *E. coli* cells; the metabolic flow from serine to OAS, however, could be enhanced to some extent by feeding of high concentration of serine. Any other transformants with pCEK2, pKM1, and a control plasmid, pTV118N, failed to produce a detectable amount of β-PA in vivo. This study is one of the first successful examples to show that a plant-specific product was biosynthesized in vivo by expression of cDNA for biosynthetic enzyme in heterologous cells.

Recently, we identified the functional Lys residue, responsible for the binding of pyridoxal phosphate cofactor, in deduced amino acid sequence of CSase A by site-directed mutagenesis experiments (10). By employing directed mutagenesis, it would be interesting to clarify the region determining substrate specificity, the tertiary enzyme structure responsible for the stereochemical course of the reaction, and the essential amino acid sites for protein–protein interaction of the complex of CSase and serine acetyltransferase for supply of OAS (11). The present investigation provides the experimental system for such further research into the biosynthetic enzymes of β-substituted alanines at the molecular genetic level and also represents the first example of production of a plant-specific metabolite by DNA strategy in *E. coli* cells.

Experimental section

Plasmid construction

General method of DNA engineering followed was that of Sambrook et al. (12). The expression plasmid, pKM1, was a derivative of pTV118N (Takara, Kyoto) and contained a full-length cDNA encoding CSase A isolated from *S. oleracea* (6) under the transcriptional control of *lacZ* promoter. The initial ATG codon was engineered to be placed inside of *Nco*I restriction site by oligonucleotide-directed mutagenesis. The *Nco*I fragment (1.2 kb) harboring the full-length cDNA was ligated by using a ligation kit (Takara, Kyoto) into the phosphatase-treated *Nco*I site of an expression vector pET8c (=pET3d) (8) to yield the overexpression vectors, pCEK1 and pCEK2, with sense and antisense orientations, respectively.

Culture of E. coli *transformants and expression of the cDNA*

A cysteine auxotrophic *E. coli* NK3 (Δ*trpE5 leu-6 thi hsdR hsdM*$^+$ *cysK cysM*) lacking endogenous CSase loci was transformed with pKM1. The overexpression vectors, pCEK1 and pCEK2, were transferred into *E. coli* BL21 (DE3, pLysE) in which lysogenic T7 RNA polymerase gene was placed under the *lacUV5* promoter for induction by IPTG. Transformed *E. coli* was precultured in LB medium (12) supplemented with carbenicillin (Cb) (100 mg/L) with continuous rotary shaking at 37°C for 3 h; IPTG (1 mM) was added to induce the expression and incubation was continued for 3 h.

Protein extraction and analysis by SDS–PAGE and Western blotting

Escherichia coli cells cultured in 10 mL LB-Cb medium were harvested by centrifugation at 1000 × *g* (3000 rpm, Hitachi RPR 20-2 rotor) for 15 min at 4°C. The pellet was suspended in 1 mL of homogenizing buffer (200 mM potassium phosphate (pH 8.0), 0.5 mM EDTA, 10 mM 2-mercaptoethanol, and 250 mM sucrose) and sonicated for 15 s, four times, at 100 W in an ice-water bath. The resulting solution was centrifuged at 15 000 g (11 000 rpm, RPR 20-2 rotor) for 15 min at 4°C. The supernatant was used as a soluble protein extract

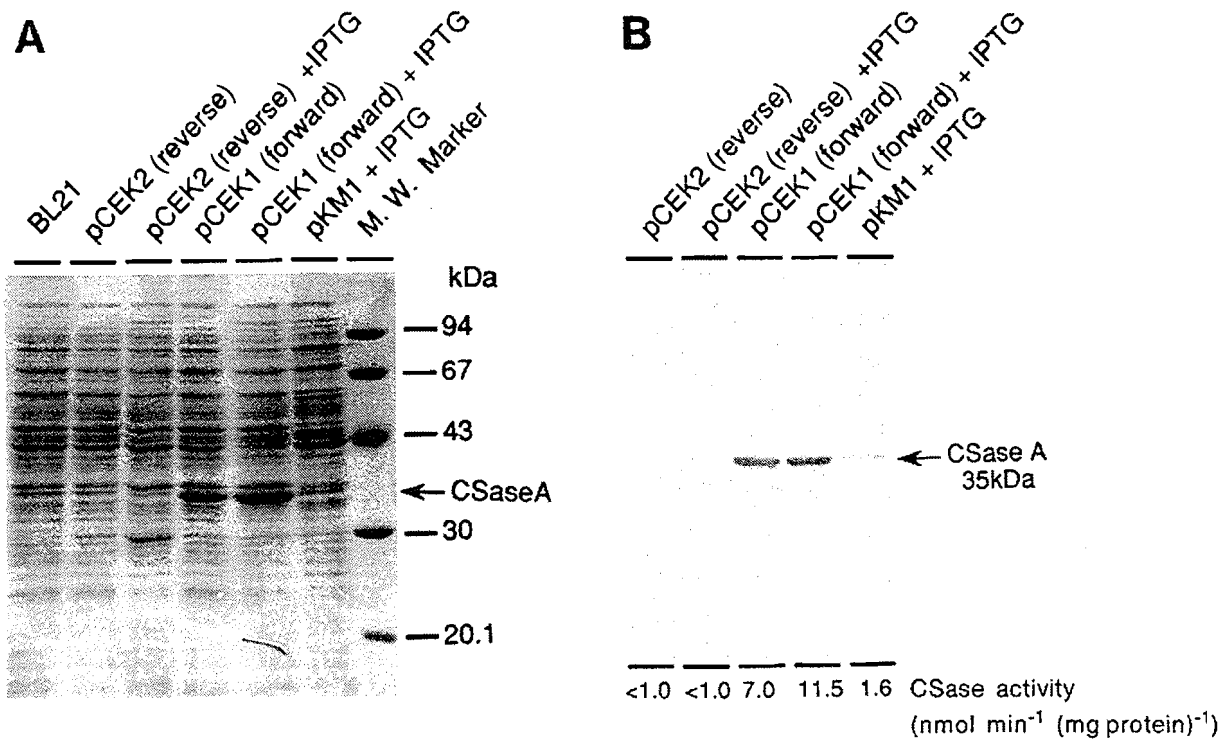

FIG. 3. (*A*) SDS–PAGE and Coomassie brilliant blue staining of the soluble protein in *E. coli* transformants. Twenty micrograms of total soluble proteins of (left to right) *E. coli* BL21 (DE3, pLysE), transformed BL21 (pCEK2), IPTG-induced BL21 (pCEK2), transformed BL21 (pCEK1), IPTG-induced BL21 (pCEK1), IPTG-induced *E. coli* NK3 transformed with pKM1, and the molecular weight marker (Pharmacia) were separated in 12% acrylamide gel (14). Proteins were stained with the blue dye. (*B*) Wester blot analysis and assay of CSase activity in *E. coli* transformants. The total soluble proteins (2.5 μg) of (left to right) *E. coli* BL21 (pCEK2), IPTG-induced BL21 (pCEK2), BL21 (pCEK1), IPTG-induced BL21 (pCEK1), and IPTG-induced *E. coli* NK3 (pKM1) were separated in 12% SDS–PAGE and transblotted onto a Nylon filter (Immobilon P, Millipore). Immunoreactive proteins against rabbit anti-CSase A were visualized by peroxidase staining using 3,3′-dimethylaminobenzidine as a developer. Enzymatic activity of CSase in the soluble protein extracts was determined as described in the experimental section.

TABLE 2. Formation of β-PA in vitro by the protein extracts of *E. coli* transformants from OAS and pyrazole

Plasmid/host *E. coli*	β-PA formation (nmol min^{-1} (mg $protein^{-1}$))
pCEK1/BL21 (DE3, pLysE)	89.0±12
pCEK2/BL21 (DE3, pLysE)	2.9±0.5
pKM1/NK3	8.6±1.5
pTV118N/NK3	Not detectable

for SDS–PAGE, Western blotting, and enzymatic assay. Protein was determined by the method of Bradford (13).

SDS–PAGE was carried out in 12% acrylamide gel by the standard method of Laemmli (14). The molecular weight marker kit (Pharmacia) was used for calibration. Protein was stained with Coomassie brilliant blue dye using a "Quick CBB" kit supplied by Wako (Kyoto).

For Western blot analysis, proteins separated by SDS–PAGE were electrochemically transferred onto Immobilon P membrane (Millipore) with a semidry transblot apparatus (Atto, Tokyo). Proteins blotted onto the membrane were reacted with rabbit antiserum raised against purified CSase A from spinach with 1:1000 dilution. The immunoreactive proteins were visualized by peroxidase staining using 3,3′-diaminobenzidine as a developer as reported previously (15).

In vitro assay for the formation of cysteine and β-PA

The reaction mixture contained 50 mM potassium phosphate (pH 8.0), 6.25 mM OAS, 5 mM H_2S or 50 mM pyrazole, and enzyme preparation corresponding to 2–50 μg of protein in a final volume 0.5 mL. Incubation was carried out at 30°C for 10–30 min.

For the assay of cysteine formation, reaction was terminated with the addition of 0.1 mL of 7.5% trichloroacetic acid and treated with acid ninhydrin reagent at 100°C for 10 min. The absorption was measured at 560 nm in the resulting solution due to cysteine–ninhydrin adduct.

For the assay of β-PA formation, the reaction mixture was acidified with 1 N HCl and filtered through a 0.45-μm membrane filter. The concentration of β-PA was determined with an automatic amino acid analyzer (Hitachi 835-10) using standard operating conditions as described (3).

Biosynthesis of β-PA in vivo of E. coli *culture*

After *E. coli* was precultured in 10 mL LB-Cb medium for 1.5 h at 37°C, IPTG (1 mM), serine (50 mM), and pyrazole (50 mM) were added in the culture medium and incubation was continued. An aliquot of 1 mL was taken every hour from the mixture and was centrifuged at 1000 × *g* for 15 min to separate cells and medium. The cells were broken by sonication, and the resulting solution was acidified by HCl and filtered. The concentration of β-PA in the cells was determined by an automatic amino acid analyzer as reported (3).

Acknowledgements

The authors thank Dr. F. Ikegami for useful suggestions. This research was supported, in part, by Grants-in-Aid for Scientific Research from the Ministry of Education, Science and Culture, Japan; from the Research Foundation for Pharmaceutical Sciences, Japan; from the Shourai Foundation; and from the Naito Foundation.

Can. J. Chem. Downloaded from www.nrcresearchpress.com by 195.246.54.202 on 09/08/12
For personal use only.

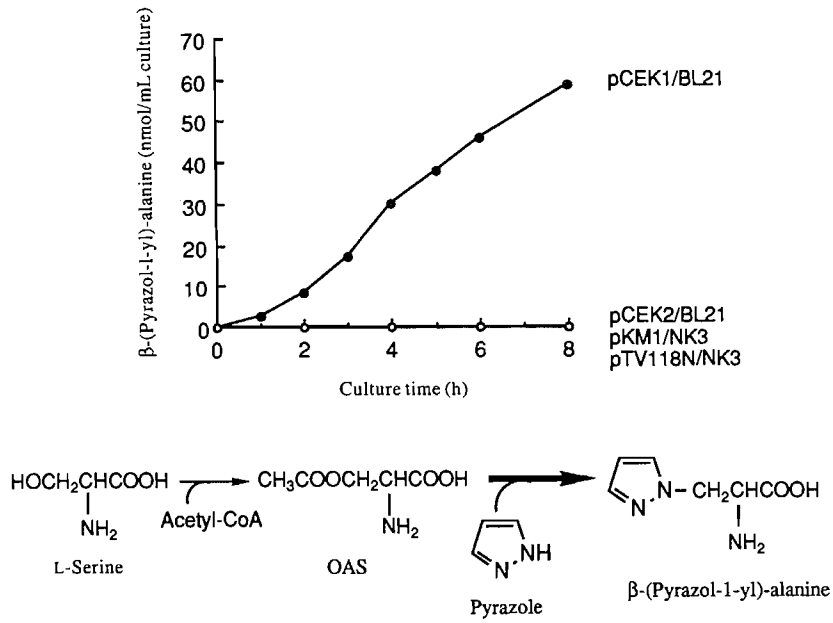

FIG. 4. Biosynthesis of β-PA in vivo by an over expression system in *E. coli*. Transformed *E. coli* was precultured in LB-Cb medium at 37°C for 1.5 h; IPTG (1 mM), pyrazole (50 mM), and serine (50 mM) were added to the culture medium and incubation was continued for an additional 8 h. The accumulation of β-PA in the aliquot of cells was determined by an amino acid analyzer.

1. G.A. Rosenthal. Plant nonprotein amino and imino acids, biological, biochemical and medicine. Academic Press, New York. 1982.
2. S. Hunt. *In* Chemistry and biochemistry of the amino acids. *Edited by* G.C. Barrett. Chapman and Hall, London. 1985. pp. 55–138.
3. F. Ikegami, M. Kaneko, H. Kamiyama, and I. Murakoshi. Phytochemistry, **27**, 697 (1988).
4. F. Ikegami, M. Mizuno, M. Kihara, and I. Murakoshi. Phytochemistry, **29**, 3461 (1990).
5. F. Ikegami, M. Kaneko, F. Lambein, Y.-H. Kuo, and I. Murakoshi. Phytochemistry, **26**, 2699 (1987).
6. K. Saito, N. Miura, M. Yamazaki, H. Hirano, and I. Murakoshi. Proc. Natl. Acad. Sci. U.S.A. **89**, 8078 (1992).
7. K. Saito, K. Tatsuguchi, I. Murakoshi, and H. Hirano. FEBS Lett. **324**, 247 (1993).
8. F.W. Studier, A.H. Rosenberg, J.J. Dunn, and J.W. Dubendorff. Methods Enzymol. **185**, 60 (1990).
9. I. Murakoshi, F. Ikegami, and M. Kaneko. Phytochemistry, **24**, 1907 (1985).
10. K. Saito, M. Kurosawa, and I. Murakoshi. FEBS Lett. **328**, 111 (1993).
11. M. Droux, J. Martin, P. Sajus, and R. Douce. Arch. Biochem. Biophys. **295**, 379 (1992).
12. J. Sambrook, E.F. Fritsch, and T. Maniatis. Molecular cloning, a laboratory manual. 2nd ed. Cold Spring Harbor Laboratory Press, New York. 1989.
13. M.M. Bradford. Anal. Biochem. **72**, 248 (1976).
14. U.K. Laemmli. Nature, **227**, 680 (1970).
15. K. Saito, M. Noji, S. Ohmori, Y. Imai, and I. Murakoshi. Proc. Natl. Acad. Sci. U.S.A. **88**, 7041 (1991).

Can. J. Chem. Downloaded from www.nrcresearchpress.com by 195.246.54.202 on 09/08/12
For personal use only.

Lupin alkaloids 6. Stereochemistry of bis-quinolizidine alkaloids with γ-oxo-α,β-enamine system

TADEUSZ BRUKWICKI, WALERIA WYSOCKA,[1] AND BARBARA NOWAK-WYDRA
Faculty of Chemistry, A.Mickiewicz University, Grunwaldzka 6, PL 60-780 Poznań, Poland

Received May 26, 1993

This paper is dedicated to Professor Ian D. Spenser

TADEUSZ BRUKWICKI, WALERIA WYSOCKA, and BARBARA NOWAK-WYDRA. Can. J. Chem. **72**, 193 (1994).

^{1}H NMR, ^{1}H,^{1}H and ^{1}H,^{13}C COSY, and 2D *J*-resolved spectra of multiflorine (**1**) and 13α-hydroxymultiflorine (**2**) in $CDCl_3$ were taken. Some erroneously determined chemical shifts in **1** were corrected and for the first time signals in **2** were assigned. Most of the coupling constants in **1** and **2** were established. A coupling constant of H7–H17β and chemical shifts for H17β, C14, and C8 were used to define the conformational equilibrium of boat or chair forms in the C rings, in **1** and **2** in solution. The results obtained confirm the previous findings based on chemical shifts of C12: ca. 75 and 70% of the "boat" conformer in **1** and **2**, respectively, at room temperature. Of all the criteria used, the H7–H17β coupling constant seems to be least sensitive to the influence of substituents at rings A and D. From the Haasnoot equation, torsion angles of HCCH in regions of molecular geometry featuring low sensitivity to conformational changes were calculated. The hydroxyl group at position 13α has a slight influence on the geometry of ring D.

TADEUSZ BRUKWICKI, WALERIA WYSOCKA et BARBARA NOWAK-WYDRA. Can. J. Chem. **72**, 193 (1994).

On a enregistré les spectres de RMN du ^{1}H, les spectres COSY du ^{1}H,^{1}H et ^{1}H,^{13}C et les spectres résolus de *J* en 2-D de la multiflorine (**1**) et de la 13α-hydroxymultiflorine (**2**) dans le $CDCl_3$. On a corrigé quelques déplacements chimiques du composé **1** qui comportaient des erreurs et on a, pour la première fois identifié les signaux du composé **2**. On a établi la plupart des constantes de couplage des composés **1** et **2**. On a utilisé une constante de couplage de H7–H17β, des déplacements chimiques de H17β et de C14 et de C8 pour définir l'équilibre conformationnelle des formes bateau ou chaise des cycles C dans les composés **1** et **2** en solution. Les résultats obtenus confirment les premières observations basées sur les déplacements chimiques du C12 : environ 75 et 70% de conformère «bateau» dans les composés **1** et **2** respectivement, à la température de la pièce. De tous les critères utilisés, la constante de couplage H7–H17β semble être la moins sensible à l'influence des substituants sur les cycles A et D. On a calculé, à partir de l'équation de Haasnoot, les angles de torsion HCCH dans les régions de géométrie moléculaire caractérisant la faible sensibilité aux changements conformationnels. Le groupe hydroxy en position 13α a une légère influence sur la géométrie du cycle D.

[Traduit par la rédaction]

Introduction

We recently published the ^{13}C NMR spectra of multiflorine (**1**) and 13α-hydroxymultiflorine (**2**), alkaloids of *Lupinus albus* that have a labile *trans-cis* bis-quinolizidine skeleton and contain a γ-oxo-α,β-enamine system in ring A (1). According to these spectra, compounds **1** and **2** proved to exist in a conformational equilibrium of forms differing in the conformation of ring C (Fig. 1). This was the first attempt at quantitative analysis of a conformational equilibrium in bis-quinolizidine alkaloids.

In this paper, we have extended our studies on the equilibrium by applying ^{1}H NMR spectroscopy. We have assumed that in the bis-quinolizidine systems conformational changes affect primarily the coupling constants H7–H17β and chemical shifts of H17β, which directly reflect changes in the conformation of ring C. Thus their application would allow us not only to verify the data obtained by ^{13}C NMR, but also to facilitate (or even in some cases make possible) the calculation of contributions of particular conformers in compounds whose substituents at ring D or in its vicinity induce changes in the chemical shifts of C12 and C14, or in some three-ring compounds.

Determination of coupling constants would enable us also to examine the effect of the 13α-hydroxyl group on the ^{1}H NMR spectrum, as well as to determine the geometry of those fragments of the molecules which do not differ significantly in their structure in the two basic conformers of **1** and **2**. To this end, a modified version of the Karplus equation can be used (3).

^{1}H NMR chemical shifts of **1** have been recently published by Takamatsu et al. (4). However, we found some of their assignments to be erroneous, and thus decided to carry out our own investigation.

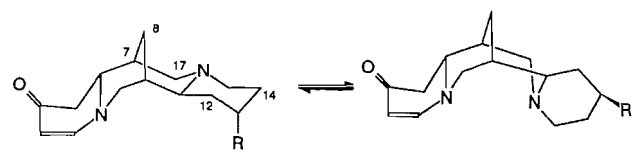

1, R = H; **2**, R = OH

FIG. 1. Conformational equilibrium in multiflorine (**1**) and 13α-hydroxymultiflorine (**2**).

Results

Complete assignment of the ^{1}H NMR signals of multiflorine (**1**) and 13α-hydroxymultiflorine (**2**) has been achieved (Table 1) by the analysis of HOMO or HETERO COSY (^{1}H,^{1}H and ^{13}C,^{1}H respectively) and 2D *J*-resolved spectra as well as by a thorough analysis of the integration of the 1.2–1.9 ppm fragment.

Inaccuracies in Takamatsu's results (4) derive partly from inappropriate differentiation between some α and β protons. It is obvious that the pseudotriplets at 2.68 ppm clearly observed in the spectrum may come only from an axial H5α, which has two large coupling constants of a similar value (geminal and axial–axial), and not from H5β, as was given in ref. 4.[2] A more

[1]Author to whom correspondence may be addressed. FAX: 48 61 658008; e-mail: Tabru@PLPUAM11.Bitnet.

[2]Takamatsu, however, correctly differentiated between H5α and H5β in multiflorine *N*-oxide!

Can. J. Chem. Downloaded from www.nrcresearchpress.com by 195.246.54.202 on 09/08/12
For personal use only.

Can. J. Chem. Downloaded from www.nrcresearchpress.com by 195.246.54.202 on 09/08/12
For personal use only.

TABLE 1. ^{1}H chemical shifts[a] of multiflorine (**1**) and 13α-hydroxymultiflorine (**2**) in $CDCl_3$ (ppm from TMS)

Proton no.	Multiflorine	13α-Hydroxymultiflorine	Effect of hydroxyl group[b]
2	6.85	6.86	
3	4.96	4.97	
5α(ax)	2.68	2.68	
5β(eq)	2.16	2.16	
6	3.46	3.48	
7	2.04	2.05	
8pro*S*	2.20	2.19	
8pro*R*	1.28	1.32	
9	1.65	1.61	
10α(eq)	3.19	3.25	
10β(ax)	3.14	3.16	
11 (ax)	2.06	2.63	0.57 γ_{ax}
12α(eq)	1.46	1.55	0.09 β_{eq}
12β(ax)	1.51	1.79	0.28 β_{ax}
13α(ax)	1.32	(OH) 1.8	
13β(eq)	1.78	4.18	2.40 α
14α(eq)	1.49	1.55	0.06 β_{eq}
14β(ax)	1.58	1.90	0.32 β_{ax}
15α(ax)	2.16	2.67	0.51 γ_{ax}
15β(eq)	2.81	2.60	−0.21 γ_{eq}
17α(psax)	2.37	2.45	
17β(pseq)	2.92	2.96	

[a]Accuracy of measurement 0.01 ppm.
[b]Difference of chemical shifts of the respective protons in **2** and **1**.

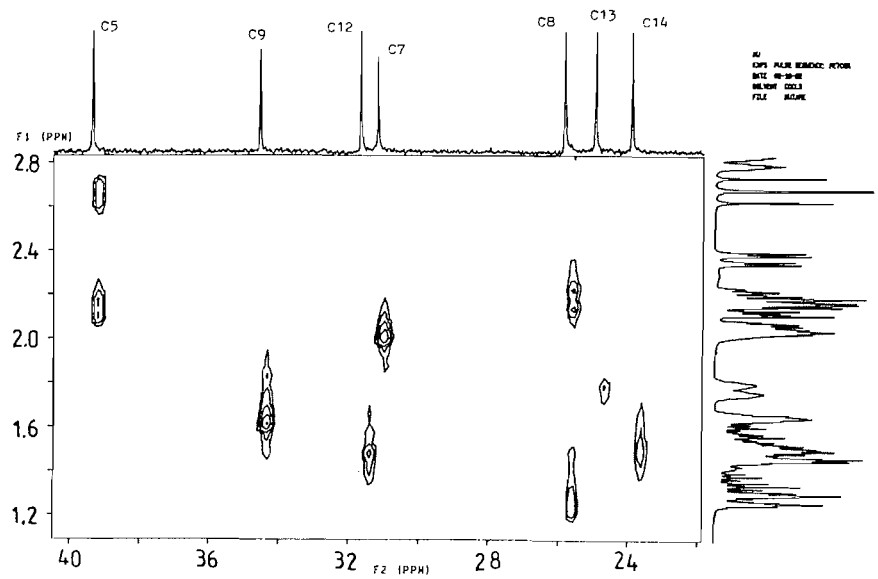

FIGURE 2 BRUKWICKI ET AL. V93-39-GN 1&N

FIG. 2. High-field fragment of ^{1}H, ^{13}C heteronuclear shift correlation (HETCOR) spectrum of multiflorine (**1**).

complex issue is the assignment of signals of protons at C12 and C14. We have taken more precise spectra only for the controversial range concerned. As follows from the ^{1}H,^{13}C COSY spectrum of fragments 22–40 ppm / 1.2–3.5 ppm (Fig. 2), signals of all protons at C12 and C14 are localized close to each other, with those at C12 slightly upfield. A similar conclusion can be drawn from analysis of the ^{1}H,^{1}H COSY spectrum (Fig. 3): the group of cross-peaks attributed to both H12 coupled with H11 is localized slightly upfield of the groups of cross-peaks attributed to both H14 coupled with H15eq and H15ax. More information is provided by an appropriate fragment of the 2D *J*-resolved spectrum (Fig. 4). It clearly exhibits two axial signals of three large coupling constants: at 1.58 ppm and at 1.51 ppm. A sum of the coupling constants for the signals at 1.58 ppm is 46 Hz, which is in agreement with that expected for H14ax, while that for the signal at 1.51 ppm is only 39.6 Hz, which agrees with the fact that H12ax has one less vicinal coupling. The sum of the coupling constants for the signal at 1.49 ppm is 30 Hz, which is rather large for an equatorial proton yet acceptable for H14eq, which has one geminal, two equatorial–equatorial, two

Can. J. Chem. Downloaded from www.nrcresearchpress.com by 195.246.54.202 on 09/08/12
For personal use only.

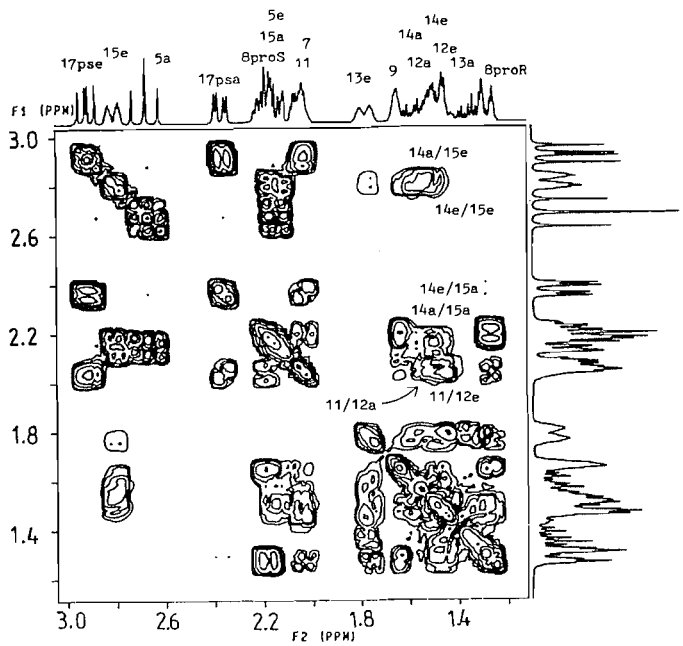

FIG. 3. The 1.2–3.0 ppm fragment of the COSY-45 spectrum of multiflorine (**1**).

equatorial–axial, and one long-range coupling of the W type. The signal of H12eq has one less equatorial–equatorial coupling. Scrutiny of the integration in the 1D NMR spectrum within the 1.2–1.85 ppm fragment allows us to assign the low-intensive and less well-developed signal at 1.46 ppm in the 2D *J*-resolved spectrum to H12eq. Unfortunately, we cannot determine the values of the coupling constants for this proton, probably because its signal is not first order.

In conclusion, contrary to Takamatsu's findings (4), we do not see the second signal in the 1.58–1.60 ppm region, yet we can see two signals within the range 1.50–1.45 ppm; as well, we arrange the axial and equatorial signals differently, as presented in Table 2.

Analogously, on the basis of the results of HOMO and HETERO COSY ($^1H,^1H$ and $^{13}C,^1H$, respectively) and 2D *J*-resolved spectra, we have assigned the ^1H NMR spectrum of 13α-hydroxymultiflorine (**2**). Values of the chemical shifts are given in Table 1.

In both compounds considered, the $^1H,^1H$ coupling constants were in part determined directly from 1D ^1H NMR or from 2D *J*-resolved spectra. In some cases we relied on the spectrum of multiflorine in another solvent (benzene[3]). Some of the *J*-constants are not, however, first order. Although they are mostly geminal, they can also affect the vicinal ones. The coupling constants determined for multiflorine are given in Table 3 (with the appropriate notes), and those for 13α-hydroxymultiflorine in Table 4.

Discussion

Conformational equilibrium

Bis-quinolizidine alkaloids with a sparteine skeleton (**3**) may assume one of two conformations, which differ in the form of ring C: in the boat **b** and the chair **c**. Usually, compounds exist as mixtures of both conformers. Compounds whose structure resembles the structure of those studied and in which the equilibrium is clearly shifted towards one of the forms may serve as models of the pure conformers (2). In sparteine, almost 100% of the molecules adopt the **3b** conformation, whereas 5,6-didehydromultiflorine (**4**) was used as a model compound for a chair conformer. In our previous paper, a comparison of the chemical shifts of C12 indicated that **1** and **2** assume 74 and 67% of a boat conformer, respectively. We also discussed the reasons for such a proportion in the conformational equilibrium (1).

Now, ^1H NMR spectra supply us with new criteria for establishing conformational equilibrium: a coupling constant H7–H17β and a chemical shift of H17β. In sparteine, the coupling constant H7–H17β is 10.8 Hz (both in benzene solution (5) and in $CDCl_3$[4]), while in 5,6-didehydromultiflorine it is 2.7 Hz.[4] As follows from appropriate values found for **1** and **2** (Tables 3 and 4), the contribution of the boat conformer in mixtures of the two conformers both in **1** and **2** is equal to 75 and 70%, respectively.

In chloroform solution, the chemical shifts of sparteine and 5,6-didehydromultiflorine were found to be 2.70 and 3.36 ppm, respectively. Following Eliel's method (2*b*) and applying appropriate values for **1** and **2** (Table 1), we determined the contribution of the boat form in multiflorine and 13α-hydroxymultiflorine to be 67 and 61%, respectively. The reason why these values differ slightly from the others in Table 5 seems to be the shielding effect of ring A, in particular, in the model compound **4**. For the same reason, chemical shifts of C17, C11, and H11 cannot be of use in the determination of the conformational equilibrium in **1** and **2**.

The presently available $^1H,^{13}C$ COSY spectra enabled us to realize that previously we had erroneously assigned signals of C13 and C14 in multiflorine (1). (Correct data were recently published also by Mohamed et al. (6)). Thus, by applying a procedure identical to that in ref. 1, from the chemical shifts of C14 in **1** and **2** we calculated the contribution of the boat conformer: 70 and 68%, respectively. For C8, we obtained similar results: 70 and 69%, yet they may be affected by ring A. The percent contribution of the boat conformer in multiflorine (**1**) and in 13α-hydroxymultiflorine (2), determined via different methods, is shown in Table 5.

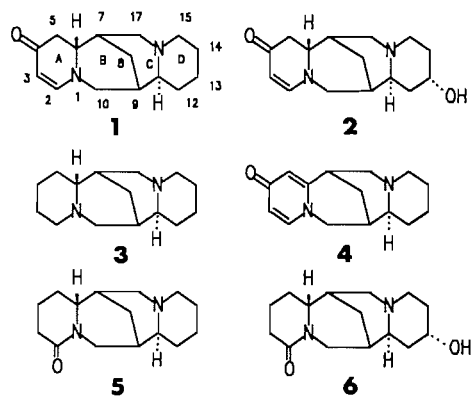

The similarity of values established by using different criteria (Table 5) testifies to the correctness of the applied method of determining the conformational equilibrium. The most reliable are the data obtained in cases where the chemical shift or cou-

[3]The preliminary assignment of signals was done in cooperation with Dr. J. Thiel.

[4]Our studies.

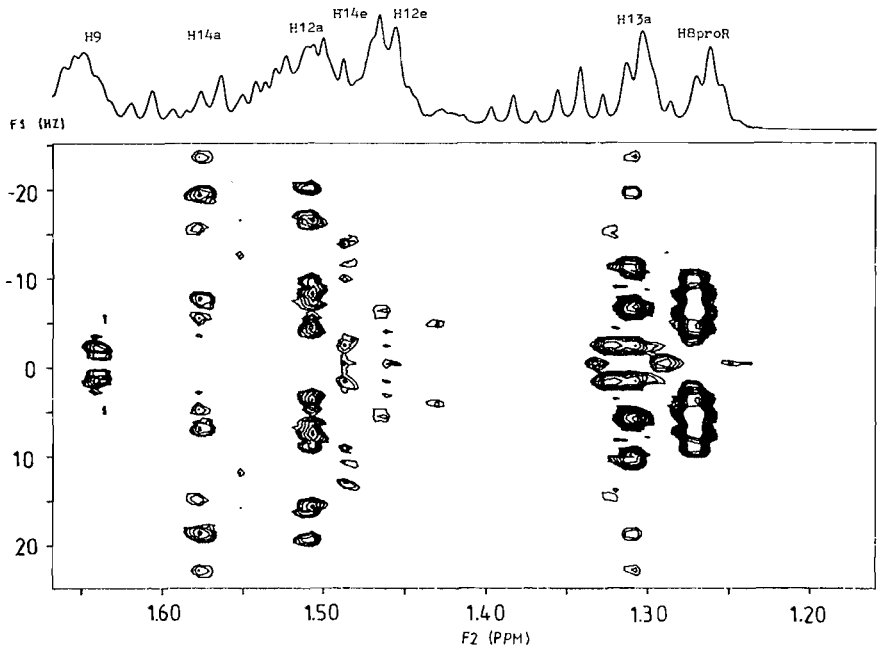

FIG. 4. High-field fragment of 2D *J*-resolved spectrum of multiflorine (**1**).

TABLE 2. Signals of the ^{1}H NMR spectra of multiflorine (**1**) whose assignment in the present paper differs from that in the paper by Takamatsu et al. (4)

Proton no.	Chemical shifts, ppm from TMS	
	According to Takamatsu	This paper
5α (ax)	2.16	2.68
5β (eq)	2.68	2.16
12α (eq)	1.58	1.46
12β (ax)	1.47	1.51
14α (eq)	1.60	1.49
14β (ax)	1.51	1.58

pling constant involved in a given criterion are not affected by any other factors except for the conformational change (or their influence is negligible), while the difference in the corresponding values in model compounds is rather significant. For both of the alkaloids studied, such a criterion is $J_{7-17\beta'}$ and for multiflorine also $\delta_{C(12)}$.

It should be noticed that in all the cases considered the population of the boat conformer in 13α-hydroxymultiflorine is slightly lower than in multiflorine, thus this result is by no means accidental. This can be accounted for by the contribution of a hydroxyl group in an intermolecular hydrogen bond, as we postulated earlier (1).

It is also worth mentioning that in the ^{1}H,^{1}H COSY spectrum of **1** and **2** a weak coupling of H8pro*R* with H17α occurs. Besides, the signal of H17α in the spectrum of **2** is coupled with one of the signals within the range in which the signals originating from protons 5α, 11, 15α, and 15β are observed. This coupling must be the one between H17α and H11. In the COSY spectrum of multiflorine such a coupling might be masked by the cross-peak H7/H17α, as in the 1D ^{1}H NMR spectrum the H11 signal overlaps the signal of H7. Such couplings can be explained best by the significant contribution of a "chair" conformer in which the H8pro*R* and H17α, as well as H11 and H17α, are coplanar.

Geometry of molecules

Table 6 lists torsion angles HCCH calculated for multiflorine (**1**) and 13α-hydroxymultiflorine (**2**) from the Haasnoot equation (3) and X-ray diffraction data for **1** (7), lupanine (**5**) (8), and 13α-hydroxylupanine (**6**) (10) with the typical geometry of methylene groups taken into account (11). In the case of some angles, in particular those that belong to rings B and D in **1** and **2**, agreement between results obtained via the two methods is satisfactory. Some of the observed discrepancies may be due to difficulty in determination of the coupling constant.

The reason why the value of the H5βC5C6H6 angle is smaller than expected is that in the Haasnoot equation for three substituents the effect of the neighboring carbonyl oxygen has not been taken into account. The other discrepancies may be explained by the presence of the conformational equilibrium. Especially large is the difference in the value of the H7C7C17H17β angle calculated by either NMR or X-ray methods and it made us apply $J_{7-17\beta}$ to determine the conformational equilibrium. Conformational changes also exert a slight influence on coupling constants involving the two H8 (more on those from flagpole H8pro*S*) and H11.

Unfortunately, we do not have a good set of model compounds, whose structures would be resolved by X-ray studies, to be applied in examining the influence of the axial hydroxyl group on the geometry of ring D. Rings B, C, and D in compounds **1** and **2** have structures quite similar to those in lupanine (**5**) and 13α-hydroxylupanine (**6**). Lupanine has a boat conformation of ring C both in the solid (8) and in solution (9) (more precisely, the conformational equilibrium in solution is heavily shifted towards conformer **5b**; cf. ref. 1, footnote b), whereas 13α-hydroxylupanine (as well as **2** (1)) as a solid has a chair conformation of ring C (11), and in solution the conformational equilibrium in **6** is clearly shifted towards the dominance of a boat conformation (9). However, in both conformers of **6** the

Can. J. Chem. Downloaded from www.nrcresearchpress.com by 195.246.54.202 on 09/08/12
For personal use only.

TABLE 3. Coupling constants (Hz) in multiflorine (**1**)

	Coupling constant					
	^2J	$^3J_{aa}$	$^3J_{ac}$	$^3J_{ee}$	^4J (w)	Other
2–3						7.5[b]
3–5β						1.1[b]
5α–5β	16.4[c]					
5α–6		16.0[b]				
5β–6			5.2[b]			
6–7			2.5[b]			
7–8 pro*S*				4.3[c,d]		
7–8 pro*R*			2.0[b]			
7–17α			3.4[b]			
7–17β				8.8[b]		
8 pro*S*–8 pro*R*	12.8[b]					
8 pro*S*–9				4.3[c,d]		
8 pro*R*–9			3.2[c]			
9–10α				2.0[a,b,f]		
9–10β			3.0[a,b,f]			
10α–10β	12.0[a,e]					
10α–8 pro*S*					1.7[c]	
9–11			2.6[a,b,d]			
11–12α			2.6[a,b,d]			
11–12β		12.3[a,b]				
12α–12β	11.8[c,e]					
12α–13α			4.2[b,d,f]			
12α–14α					1.4[c,f]	
12α–13β				3.9[c,f]		
12β–13α		13.4[b,f]				
12β–13β			3.6[c,f]			
13α–13β	12.9[b]					
13α–14α			4.2[b,d]			
13α–14β		12.3[b]				
13β–14α			3.6[c]			
13β–14β			3.9[c,f]			
13β–15β						
14α–14β	12.8[c,e]					
14α–15α			3.0[a,b]			
14α–15β				3.4[c]		
14β–15α		12.3[c]				
14β–15β			3.7[b]			
15α–15β	12.2[b]					
17α–17β	11.8[b]					

[a]In benzene.
[b]Determined directly from the 1D ^{1}H NMR.
[c]Determined from the 2D *J*-resolved spectrum, accuracy estimated as < ±0.6 Hz.
[d]The value could be averaged.
[e]Non-first order.
[f]Could be affected by a non-first-order coupling.

Can. J. Chem. Downloaded from www.nrcresearchpress.com by 195.246.54.202 on 09/08/12
For personal use only.

value of the HCCH torsion angles in the C12C13C14 region should not be much different, as suggested by a similarity of values for the corresponding torsion angles determined from X-ray diffraction for **5** and **6** (8, 10) for a geometry typical of the methylene group (11) (Table 6). Not all HCCH torsion angles in **1** and **2** were satisfactorily determined from NMR spectra, yet the data compiled in Table 6 indicate a surprising agreement between the torsion angles involving protons at C12, C13, and C14 determined via NMR for **2** and those established from X-ray diffraction for **1**. It can be observed therefore that in **2** the axial hydroxyl group only slightly affects the geometry of the nearest surroundings.

In contrast, an α-hydroxyl group exerts a significant effect on the chemical shift of protons in ring D (Table 1). This effect is similar to that resulting from a comparison of 5α,17α-pregnan-2-one with its 3α,6α-dihydroxy derivative (12): α, 2.48 ppm; β-ax, 0.27 ppm; β-eq, 0.09 ppm; γ-ax, 0.47 ppm; and γ-eq, −0.28 ppm. This effect in **1** and **2** testifies to a similar conformation of both these compounds. It is worth stressing that chemical shifts of protons H12 and H14 proposed by Takamatsu et al. (4) show a worse agreement between the effect of the hydroxyl group in **2** and that observed in the above mentioned steroid compounds.

Conclusions

1. All ^{1}H chemical shifts and most coupling constants in multiflorine and 13α-hydroxymultiflorine were determined.

2. Precise analysis of ^{1}H NMR (coupling constants and inte-

TABLE 4. Coupling constants (Hz) in 13α-hydroxymultiflorine (**2**)

	Coupling constant					
	^2J	$^3J_{aa}$	$^3J_{ae}$	$^3J_{ee}$	^4J (w)	Other
2–3						7.5[a]
5α–5β	16.4[a]					
5α–6		16.0[a]				
5β–6			5.3[a]			
6–7			2.6[a]			
7–8 pro*S*				4.3[a]		
7–8 pro*R*			2.4[a,c]			
7–17α			3.4[a]			
7–17β				8.4[a]		
8 pro*S*–8 pro*R*	12.9[a]					
8 pro*S*–9				2.2[a]		
8 pro*R*–9			2.4[a,c]			
9–10α				2.1[a,e]		
9–10β			3.2[a,e]			
10α–10β	12.1[a,d]					
9–11			2.9[a,c]			
11–12α			2.9[a,c]			
11–12β		12.3[a]				
12α–12β						
12α–13β				2.8[a,c]		
12β–13β			2.8[a,c]			
13β–14α			2.8[a,c]			
13β–14β				2.8[a,c]		
14α–14β	13.5[b,d]					
14α–15α						
14α–15β						
14β–15α		16.0[b]				
14β–15β						
15α–15β	12.5[a]					

[a]Determined directly from 1D ^{1}H NMR.
[b]Determined from the 2D *J*-resolved spectrum, accuracy estimated as < ±0.6 Hz.
[c]The value could be averaged.
[d]Non-first order.
[e]Could be affected by a non-first-order coupling.

TABLE 5. Percent of the "boat" conformer in multiflorine (**1**) and 13α-hydroxymultiflorine (**2**) in ca. 5% solution in $CDCl_3$ at room temperature

Method	Criterion	Multiflorine (**1**)	13α-Hydroxymultiflorine (**2**)
^{1}H NMR	$J_{7-17\beta}$	75	70
	$\delta_{H(17\beta)}$	67	61
^{13}C NMR	$\delta_{C(12)}$(1)	74	67
	$\delta_{C(14)}$	70	68
	$\delta_{C(8)}$	70	69

gration), ^{1}H,^{1}H and ^{1}H,^{13}C COSY, 2D *J*-resolved spectra, and the effect of the axial hydroxyl group enabled us to correct the assignment of signals of the 5α, 5β, 12α, 12β, 14α, and 14β protons proposed by Takamatsu et al. (4).

3. The method of studying the conformational equilibrium was extended to include the coupling constant H7–H17β and chemical shift of H17β in the ^{1}H NMR spectrum. In the case of **2**, these new criteria allow us to avoid the application of a correction for the effect of hydroxyl group necessary in the previously published method (1). Likewise, the method of quantitative determination of the equilibrium was extended by some new criteria using the ^{13}C NMR spectra.

4. All the applied criteria give comparable results. Slightly lower values for the population of the boat conformer when a chemical shift of H17β is the considered criterion are caused by the effect of ring A.

5. Torsion angles in **1** calculated from the Haasnoot equation (3) for molecules in solution in the region with geometry slightly sensitive to conformational changes are close to the corresponding angles in the solid determined by X-ray studies.

6. HCCH torsion angles calculated from the Haasnoot equation for 13α-hydroxymultiflorine in solution are in agreement with those in multiflorine. The axial hydroxyl group does not significantly affect the geometry of ring D.

Experimental

Multiflorine (**1**) and 13α-hydroxymultiflorine (**2**) were isolated from *Lupinus albus* seeds (cv. BAC) (13, 14).

Can. J. Chem. Downloaded from www.nrcresearchpress.com by 195.246.54.202 on 09/08/12
For personal use only.

TABLE 6. Some dihedral angles HCCH in multiflorine (**1**), 13α-hydroxymultiflorine (2), lupanine (5), and 13α-hydroxylupanine (**6**)

Dihedral angle	Multiflorine NMR	Multiflorine X-ray (7)	13α-Hydroxymultiflorine NMR	Lupanine X-ray (8)[a]	13α-Hydroxylupanine X-ray (10)[a,c]
H5αC5C6H6	~180	167.6	~180	161.6	
H5βC5C6H6	43	48.95	42.5	43.6	
H6C6C7H7	−63.5	−60.4	−59	−62.6	
H7C7C8H8pro*R*	67.5	65.7	64	62.2	
H7C7C8H8pro*S*	−51	−55.3	−51	−58.0	
H8pro*R*C8C9H9	−60	−60.7	−64	−59.1	
H8pro*S*C8C9H9	51	60.2	66	61.1	
H9C9C10H10α	−65	−68.2	−64	−64.2	
H9C9C10H10β	56	51.0	55	53.7	
H9C9C11H11	111.5	113.9	109	117.2	
H7C7C17H7α	−119	−122.2	−119	−120.1	
H7C7C17H7β	15	−2.7	19	−2.4	
H11C11C12H12α	−64.5	−56.4	−59	−59.4	−59.1
H11C11C12H12β	147.5	175.6	~180	177.0	−178.3
H12αC12C13H13α	53.5	53.2	—	54.7	(54.9)[d]
H12αC12C13H13β	−53	−66.4	−68.5	−64.1	−65.7
H12βC12C13H13α	167.5	172.4	—	172.3	(174.2)[d]
H12βC12C13H13β	57.5	52.7	51	53.5	53.5
H13αC13C14H14α	−53.5	−52	—	−54.0	(−54.4)[d]
H13αC13C14H14β	~180	171.9	—	−172.5	(−174.5)[d]
H13βC13C14H14α	56.5	67.5	68.5	64.8	66.0
H13βC13C14H14β	−55.5	−52.1	−51	−53.7	−53.9
H14αC14C15H15α	60	56.35		58.0	52.9
H14αC14C15H15β	−56.5	−61.55		−60.2	−66.3
H14βC14C15H15α	164.5	175.95		176.5	173.0
H14βC14C15H15β	57	58.05		58.3	53.7

[a]With the typical geometry of the CH_2 group (11).
[b]Computed by Dr. U. Rychlewska.
[c]Computed by Dr. A. Katrusiak.
[d]Angles involving the OH group.

All NMR spectra were recorded at ambient temperature on a Varian Gemini 300 spectrometer operating at 300.075 and 75.462 MHz for ^1H and ^{13}C, respectively. The spectra were obtained in $CDCl_3$ and chemical shifts were referenced to internal TMS for ^1H data and $CDCl_3$ for ^{13}C data ($\delta_C(^{13}CDCl_3) = 77.0$).

The 2D $^1H,^1H$ COSY, the $^1H,^{13}C$ COSY (HETCOR), and 2D homonuclear ^1H *J*-resolved NMR spectra were obtained using standard Varian programs.

The accuracy of coupling constant measurements from 2D *J*-resolved spectra is estimated as ±0.6 Hz.

1. W. Wysocka and T. Brukwicki. J. Mol. Struct. **265**, 143 (1992).
2. (*a*) H. Günther. NMR-Spektroskopie. G. Thieme Verlag, Stuttgart. 1983. pp. 225–226; (*b*) E.L. Eliel. Chem. Ind. (London), 568 (1959).
3. C.A.G. Haasnoot, F.A.A.M. de Leuve, and C. Altona. Tetrahedron, **36**, 2783 (1980).
4. S. Takamatsu, K. Saito, S. Ohmiya, and I. Murakoshi. Heterocycles, **32**, 1167 (1991).
5. W.M. Gołebiewski. Magn. Reson. Chem. **24**, 105 (1986).
6. M.H. Mohamed, K. Saito, I. Murakoshi, H.A. Kadry, T.I. Khalifa, and H.A. Ammar. J. Nat. Prod. **53**, 1578 (1990).
7. M. Kubicki and T. Borowiak. Acta Crystallogr. Sect. C: Cryst. Struct. Commun. **C45**, 1045 (1989).
8. H. Doucerain, A. Chiaroni, and C. Riche. Acta Crystallogr. Sect. B: Struct. Crystallogr. Cryst. Chem. **B32**, 3213 (1976).
9. M. Wiewiórowski, O.E. Edwards, and M.D. Bratek-Wiewiórowska. Can. J. Chem. **45**, 1447 (1967); J. Skolik, P.J. Krueger, and M. Wiewiórowski. Tetrahedron, **24**, 5439 (1968).
10. Z. Kaluski, J. Garbarczyk, A.I. Gusiev, Yu.T. Struchkov, J. Skolik, and M. Wiewiórowski. Bull. Acad. Pol. Sci. Ser. Sci. Chim. **25**, 347 (1977).
11. G.M. Sheldrick. SHELX 76. Program for crystal structure determination. Univ. of Cambridge, Cambridge, England. 1976.
12. D.N. Kirk, H.C. Toms, Ch. Douglas, K.A. White, K.E. Smith, Sh. Latif, and R.W.P. Hubbard. J. Chem. Soc. Perkin Trans. 2, 1567 (1990).
13. W. Wysocka and T. Brukwicki. Planta Med. **54**, 522 (1988).
14. W. Wysocka and T. Brukwicki. Planta Med. **57**, 579 (1991).

Can. J. Chem. Downloaded from www.nrcresearchpress.com by 195.246.54.202 on 09/08/12
For personal use only.

The potential role of fatty acid initiation in the biosynthesis of the fungal aromatic polyketide aflatoxin B_1[1]

SUSAN W. BROBST AND CRAIG A. TOWNSEND[2]

Department of Chemistry, The Johns Hopkins University, Charles and 34th Streets, Baltimore, MD 21218, U.S.A.

Received July 21, 1993

This paper is dedicated to Professor Ian D. Spenser

SUSAN W. BROBST and CRAIG A. TOWNSEND. Can. J. Chem. **72**, 200 (1994).

Earlier work in this laboratory has shown the intact incorporation of [1-^{13}C]hexanoate into averufin (**1**), a key intermediate in aflatoxin B_1 biosynthesis. Parallel experiments with equimolar amounts of [1-^{13}C]butyrate, [1-^{13}C]-3-oxo-octanoate, and [1-^{13}C]-5-oxo-hexanoate gave no detectable specific incorporation of heavy isotope but low and equivalent background incorporation comparable to [1-^{13}C]acetate. Three of these potential intermediates in polyketide formation were reexamined as their corresponding *N*-acetylcysteamine (NAC) thioesters. The NAC thioester of [1-^{13}C]hexanoic acid gave a remarkably high 22% intact incorporation while the NAC thioester of [1-^{13}C]-3-oxo-octanoic acid afforded nearly 5% when an equimolar amount was administered to the producing organism *Aspergillus parasiticus* (ATCC 24551). In contrast, the NAC thioester of [1-^{13}C]butyric acid showed no selective enrichment of averufin. This negative result was tested further in a more sensitive experiment with the NAC thioester of [2,3-$^{13}C_2$]butyric acid. No $^1J_{CC}$ coupling was detectable, indicating an incorporation efficiency of <0.1%. [1-^{13}C,$^{18}O_2$]Hexanoate was prepared and gave a 53% retention of ^{18}O relative to the ^{13}C internal standard in keeping with previous experiments with [1-^{13}C,$^{18}O_2$]acetate. It is concluded from these data that the initial C_6 segment of polyketide biosynthesis is unlikely to arise by β-oxidation of a higher fatty acid but more probably is generated by a specialized fatty acid synthase (FAS) that provides this unit either separately to the polyketide synthase (PKS) or as part of a larger FAS/PKS fusion. While these two physical arrangements cannot be distinguished by these experiments, both must accommodate comparatively efficient exchange of the NAC thioesters of both hexanoic and 3-oxo-octanoic acid, but not the NAC thioester of butyric acid.

SUSAN W. BROBST et CRAIG A. TOWNSEND. Can. J. Chem. **72**, 200 (1994).

Des travaux antérieurs effectués dans notre laboratoire ont démontré que le [1-^{13}C]hexanoate s'incorpore d'une façon intacte dans l'avérufine (**1**), un intermédiaire clé dans la biosynthèse de l'aflatoxine B_1. Des expériences parallèles avec des quantités équimoléculaires de [1-^{13}C]butyrate, de [1-^{13}C]-oxo-octanoate et de [1-^{13}C]-5-oxo-hexanoate n'ont pas permis de détecter d'incorporation spécifique de l'isotope lourd; seulement des incorporations faibles, équivalentes au bruit de fond, comparables à celle du [1-^{13}C]acétate. On a réexaminé trois de ces intermédiaires potentiels dans la formation du polycétides sous la forme de thioesters de la *N*-acétylcystéamine (NAC). Lorsqu'on administre des quantités équimoléculaires à l'organisme *Aspergillus parasiticus* (ATCC 24551) qui les produit, le thioester de la NAC de l'acide [1-^{13}C]hexanoïque conduit à une incorporation intacte étonnante de 22% alors que le thioester de la NAC de l'acide [1-^{13}C]-3-oxo-octanoïque en fournit environ 5%. Par opposition, le thioester de la NAC de l'acide [1-^{13}C]butyrique ne présente pas d'enrichissement sélectif de l'avérufine. On a évalué ce résultat négatif plus à fond à l'aide d'une expérience sensible impliquant le thioester de la NAC de l'acide [2,3-$^{13}C_2$]butyrique. On n'a pas observé de couplage $^1J_{CC}$; ce résultat indique que l'efficacité de l'incorporation est inférieure à 0,1%. On a préparé du [1-^{13}C,$^{18}O_2$]hexanoate et il conduit à une rétention de 53% du ^{18}O par rapport au ^{13}C agissant comme référence interne; ce résultat est en accord avec les expériences antérieures avec du [1-^{13}C,$^{18}O_2$]acétate. Sur la base de ces données on conclut que le segment initial en C_6 de la synthèse du polycétide ne provient probablement pas d'une oxydation β d'un acide gras de poids moléculaire plus élevé, mais qu'il est vraisemblablement généré par une synthase d'acide gras spécialisée (FAS) qui fournit cette unité soit d'une façon séparée par rapport à la synthase de polycétide (PKS) ou dans le cadre d'une fusion plus large FAS/PKS. Alors que l'on ne peut pas distinguer entre ces deux arrangements physiques sur la base des expériences réalisées, les deux doivent toutefois accommoder un échange efficace des thioesters de la NAC des acides tant hexanoïque que 3-oxo-octanoïque, mais pas de l'acide butyrique.

[Traduit par la rédaction]

In 1982 we made the unexpected and intriguing observation that [1-^{13}C]hexanoate incorporated label intact into averufin (**1**), a central intermediate in the biosynthesis of the potent mycotoxin aflatoxin B_1 (**2**). The efficiency of linear fatty acid utilization in these whole-cell experiments was 3–4% at C-1′. The specific incorporation was seen in a background of ca. 0.5% at all carboxyl-derived carbons throughout the molecule. This nonspecific labeling is due to β-oxidation of the hexanoate to [1-^{13}C]acetyl CoA and secondary incorporation of the latter in accord with the conventional view of polyketide biosynthesis (1). This experiment was followed by a series under the same experimental conditions in which *equimolar* amounts of [1-^{13}C]butyrate, [1-^{13}C]-5-oxo-hexanoate, and [1-^{13}C]-3-oxo-octanoate were tested. In each instance no intact incorporation of these potential substrates could be detected by ^{13}C{^{1}H}NMR spectroscopy. Only degradation to [1-^{13}C]acetyl CoA was seen and secondary incorporation of heavy isotope as above, comparable to that observed from [1-^{13}C]acetate itself (2).

While in bacteria and plants polyketide starter units have been demonstrated from low molecular weight branched acids (derived from transamination and oxidative decarboxylation of the homologous amino acids (see for example ref. 3)) and propionate (4), exceptions are few to the general observation that "extra" carbon atoms in fungal polyketides are derived from methionine (5). The classic exception to this general rule is the perturbation of orsellinic acid biosynthesis in *Penicillin baarnense* reported by Mosbach in which added propionate gave rise to the appearance of homoorsellinate (6). Similarly, Steyn's group determined that the C_3 primer of aurovertin B (7) and

[1] This paper is dedicated to Professor Ian Spenser and a career of accomplishment in natural products chemistry.

[2] Author to whom correspondence may be addressed. Tel.: (410) 516-7444. Fax: (410) 516-8420.

Can. J. Chem. Downloaded from www.nrcresearchpress.com by 203.198.23.82 on 09/08/12
For personal use only.

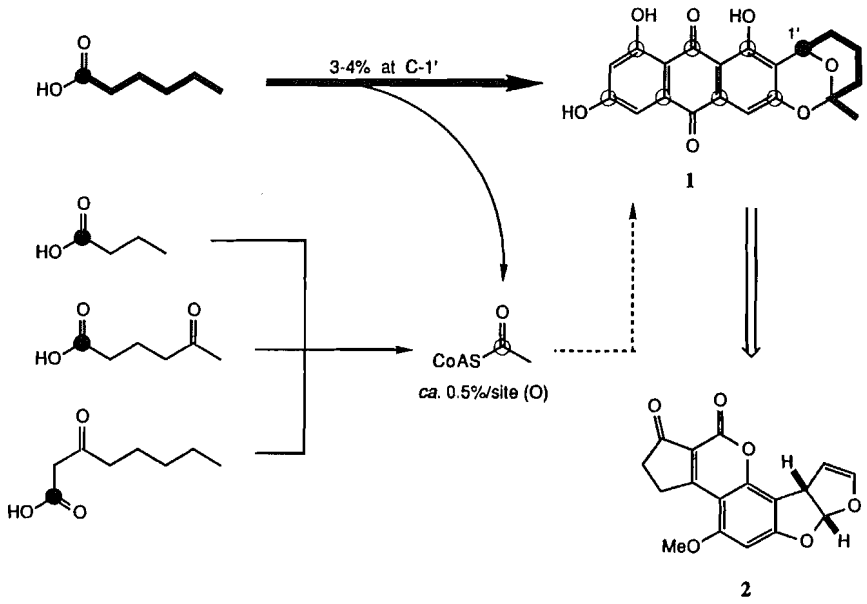

1

2

SCHEME 1

asteltoxin (8) can arise either by direct incorporation of propionate or by the net utilization of acetate and a C_1 unit from methionine.

The suggestion that fatty acids could initiate polyketide biosynthesis was made by Birch more than 30 years ago (9). Yet, apart from two examples that can be recalled from plants (butyrate into margaspidin (10) and octanoate into coniine (11)), failed incorporations of fatty acids, when reported, have been the general rule (see for example ref. 12). The utilization of hexanoate in the biosynthesis of the fungal metabolite averufin, therefore, was an important experimental step forward in the understanding of polyketide biosynthesis. Report of these results (1, 2) was soon followed by the incorporation of acetoacetate into nonactin (13) and octanoate into the chain-terminating unit of fungichromin (14). Successes, however, were limited. Attempts to demonstrate the intact incorporation of free acids derived from linking together of two or three ketide units into macrolides, polyethers, and other secondary metabolites were completely unsuccessful (15, 16). The earlier, crucial finding of Lynen (17) that *N*-acetylcysteamine (NAC) thioesters could substitute for the corresponding CoA thioesters to load biosynthetic intermediates onto fatty acid synthase (FAS) was recalled at this time by the NMR studies of Schwab et al. (18) examining the inhibition of β-hydroxydecanoylthioester dehydrase by the NAC thioester of 3-decynoic acid (19). Testing of potential polyketide intermediates as their NAC thioesters (15, 16) came as a methodological breakthrough that has since been successfully applied in a number of systems and has experimentally secured the central idea of processivity in polyketide chain elongation (see for example ref. 20).

Questions remained, however, from our first experiments. Why was butyrate not detectably incorporated if hexanoate gave a readily observable enrichment? Should one expect that 3-oxo-octanoate, derived by the addition of the first clearly polyketide C_2 unit to a saturated primer, might be successfully incorporated? It could be the case that both of these putative intermediates were utilized but at such low levels that they could not be experimentally detected above natural abundance by single-site ^{13}C-labeling methods. In the hope of achieving greater sensitivity in these experiments, a series of NAC thioesters were prepared and examined for their incorporation into averufin.

The mixed anhydride method of Kass and Brock (21) using freshly prepared *N*-acetylcysteamine (22) gave the NAC thioesters of [1-^{13}]butyric acid and [1-^{13}C]hexanoic acid in 70–80% yields. This approach is summarized in Scheme 2. [2,3-$^{13}C_2$]Butyric acid was prepared by reaction of the dianion of [2-^{13}C]acetic acid and [1-^{13}C]iodoethane in the presence of added HMPA (23). [1-^{13}C]Hexanoic acid was synthesized according to the protocol of Cane et al. from 1-iodopentane and K^{13}CN (24). The yields of the latter two acids were greater than 80%.

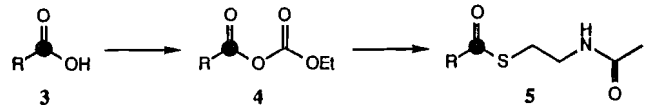

3 4 5

SCHEME 2

Benzyl [1-^{13}C]acetate (25) was treated with lithium hexamethyldisilazide followed by hexanoyl chloride to give the β-ketoester **7** (R = CH_2Ph) in 77% yield. Hydrogenolysis proceeded smoothly to afford the known acid **7** (R = H) (26). Not unexpectedly, thioesterification using the method of Kass and Brock (21) did not take place owing presumably to the self-condensation of the mixed anhydride **4** under the reaction conditions. Literature precedent (27) notwithstanding, attention was turned toward DCC-activated coupling in the presence of 4-dimethylaminopyridine (28). The NAC thioester **8** of 3-oxo-octanoic acid was obtained in about 70% yield as a crystalline solid.

The NAC thioesters of [1-^{13}C]acetic acid, [1-^{13}C]butyric acid, [1-^{13}C]hexanoic acid, and [1-^{13}C]-3-oxo-octanoic acid were administered in equimolar amounts to cell suspensions of *Aspergillus parasiticus* under carefully controlled conditions as was done earlier with the carboxylic acids (1, 2). Freshly prepared mycelial pellets were weighed into 12 250-mL Erlenmeyer flasks (10 g per flask) containing 100 mL of a replacement medium (29). The ^{13}C-labeled thioesters were

Can. J. Chem. Downloaded from www.nrcresearchpress.com by 203.198.23.82 on 09/08/12
For personal use only.

TABLE 1. Incorporation of ^{13}C-labeled carboxylic acids (X = OH) and their corresponding *N*-acetylcysteamine thioesters (X = NAC) into averufin by mycelial suspensions of *A. parasiticus* (ATCC 24551)

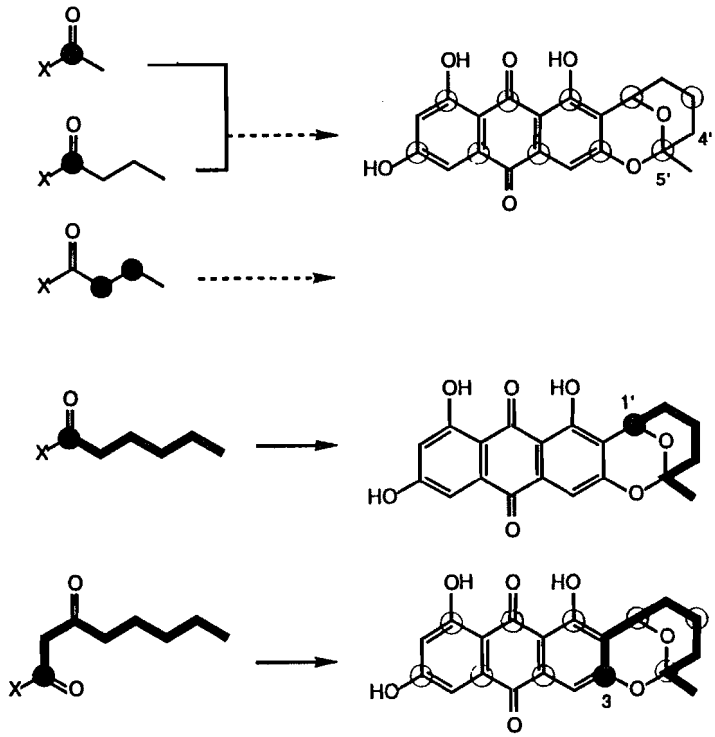

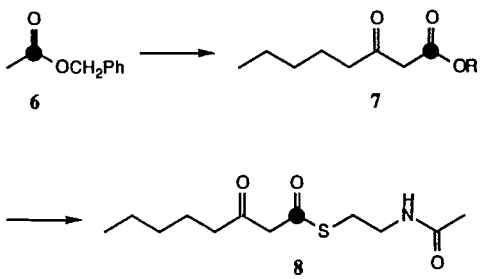

SCHEME 3

apportioned equally among the shaken cultures in acetone solution and, after 48 h, the averufin produced was isolated and purified for $^{13}C\{^1H\}$NMR analysis. The results from the free acids and corresponding NAC thioesters are shown in Table 1.

The sites and levels of isotopic enrichment were determined by comparison to averaged signal intensities at natural abundance. The results were striking in their clarity. [1-^{13}C]-Hexanoate, which as its free acid had given a 3–4% incorporation, as its NAC thioester gave a remarkably high 22% specific incorporation superimposed once again on a ca. 0.5% secondary incorporation from [1-^{13}C]acetyl CoA. [1-^{13}C]-3-Oxo-octanoate, which previously had given no detectable incorporation as its free acid, now showed a 4.7 ± 0.7% enhancement of the resonance for C-3 (30) within the anthraquinone nucleus of averufin when incorporated as its NAC thioester. While substantially lower in efficiency than the NAC thioester of [1-^{13}C]hexanoic acid, this result suggested successful linking of the apparent aliphatic starter with the first C_2 unit at the keto oxidation state. In contrast, the NAC thioester of [1-^{13}C]butyric acid showed no convincing enrichment of the averufin side chain. More sensitive analysis using the NAC thioester of [2,3-$^{13}C_2$]butyric acid revealed no intact incorporation of a C_4 unit measurable as $^1J_{CC}$ coupling between C-4′ and C-5′. The detection limit of this analysis correlated to an incorporation rate of <0.1% given the high signal/noise ratio of the NMR spectrum obtained. Therefore, apart from the intact incorporations shown by the labeled NAC thioesters of hexanoic acid and 3-oxo-octanoic acid, *all* of the tested substrates gave low extents of enrichment comparable to those from [1-^{13}C]acetate or its NAC thioester at carboxyl-derived centers throughout averufin.

Based on these observations, several conclusions can be drawn about the first steps of aflatoxin biosynthesis. First, it could be supposed that a 1,3,6,8-tetrahydroxyanthraquinone **9**, a known natural product from a related *Aspergillus* (31), and a C_6 fatty acid/CoA ester **10** are separately generated and joined to form norsolorinic acid (**11**, Scheme 4), the first anthraquinone intermediate of aflatoxin biosynthesis (32). This possibility can be eliminated on symmetry grounds. Thus, while **9** is symmetrical, its labeling pattern from [1,2-$^{13}C_2$]acetate in **11** is not (30, 33). A Friedel–Crafts-like reaction of this sort is unprecedented in natural product biosynthesis and, if it were to occur, it would require condensation in a non-random manner on the synthase-bound anthraquinone prior to its release from the protein. Owing as well to the inherently poor reactivity of anthraquinones to electrophilic addition, this possibility seems highly unlikely. Moreover, it would not accommodate the specific incorporation of the NAC thioester of [1-^{13}C]-3-oxo-octanoic acid.

Second, it could be visualized that a polyketide synthase (PKS) responsible for assembling norsolorinic acid (**11**) may selectively and with high affinity bind hexanoyl CoA arising

Can. J. Chem. Downloaded from www.nrcresearchpress.com by 203.198.23.82 on 09/08/12
For personal use only.

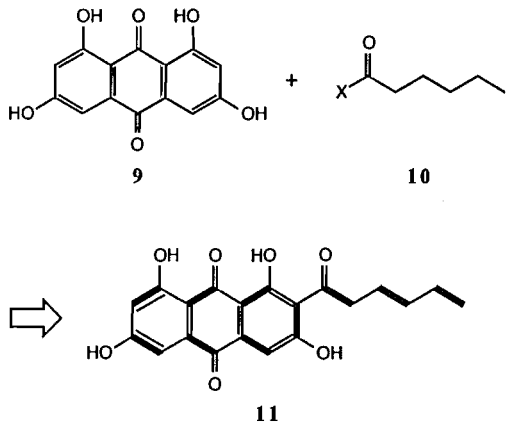

SCHEME 4

from normal fatty acid degradation (2). This possibility is probably not likely. [1-^{13}C,$^{18}O_2$]Acetate was incorporated into averufin and shown to label every oxygen except that at C-10, which was derived from molecular oxygen ($O^{\S}$, Scheme 5) (34). Some exchange of acetate-bound oxygen isotope was observed, as is commonly the case in experiments of this sort, to give an incorporation of 40% at C-1′, that carbon corresponding to C-1 of a potential hexanoyl starter. While 60% of the oxygen at this ^{13}C-labeled site was not accounted for in this experiment, the comparable levels of heavy isotope uptake at this and other sites in averufin suggest that β-oxidation cannot be the source of the first six carbons. Oxygen incorporation through this latter mechanism would be from the aqueous medium, not from acetate. Moreover, given the efficiency with which the NAC thioester of hexanoic acid is incorporated when supplied exogenously, it seems unlikely that hexanoyl CoA ester produced intracellularly could not compete with the already poor incorporation of administered labeled acetate (0.5–1% per site) and, thus, reduce the observed labeling of both isotopes at C-1′. Such a reduction is not evident.

To examine this implication more closely, a sample of [1^{13}C,$^{18}O_2$]hexanoate was prepared by extension of Cane's method (24) and administered to mycelial suspensions of *A. parasiticus*. ^{13}C{^{1}H}NMR analysis of the isolated averufin (**12**, Scheme 5) showed a 53% incorporation of ^{18}O relative to the ^{13}C internal standard at C-1′, as evidenced by the relative proportion of a 0.027 ppm upfield-shifted resonance (for an overview of this method see ref. 35). Therefore, both [1-^{13}C,$^{18}O_2$]-acetate and [1-^{13}C, $^{18}O_2$]hexanoate label C-1′ and its attached oxygen with high and comparable efficiencies.

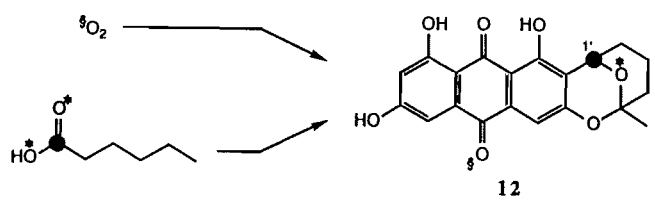

SCHEME 5

In view of these arguments we are led to the following interpretation of the data. The hexanoyl unit is likely prepared by a specialized FAS that releases, for example, hexanoyl CoA, hexanoyl ACP, or channels this unit in an enzyme complex with the PKS to lead on to norsolorinic acid. Alternatively, but indistinguishable by the information presently available, the FAS and PKS are part of one large polyprotein such that the saturated C_6 unit is never released, for example, as a CoA ester, yet can fairly readily exchange with exogenously supplied thioester to load the C_6 site for further PKS elaboration with malonyl CoA. Recent disclosures of the organization and proposed function of the erythronolide genes (36) could be cited to favor this latter view. Nonetheless, the role of a specialized FAS, whether a separately expressed enzyme or part of a larger fusion to give a multifunctional protein, accommodates the "starter effect" noted by Chandler and Simpson on incorporation of diethyl [2-^{13}C]malonate into averufin (37), and, indeed, the slightly increased levels of secondary acetate incorporation detected at C-5′ in the present experiments (ca. 0.7%). Moreover, stereochemical experiments of the enoyl thioester reductase steps resulting in formation of both the averufin side chain and the fatty acids of *A. parasiticus* show a common configurational outcome (38) in contrast to polyketide natural products from other fungi (39). Purification of the protein or proteins responsible for norsolorinic acid synthesis and determination of the genetic organization and expression of the gene or genes that encode them are of considerable interest. As experiments advance to this stage, it may be possible to answer why the NAC thioesters of hexanoic acid and 3-oxo-octanoic acid can be utilized so efficiently in the biosynthesis while the corresponding thioester of butyric acid cannot.

Experimental

General synthetic methods

Melting points were determined in open capillaries using a Thomas–Hoover apparatus and are uncorrected. IR spectra were recorded on a Perkin–Elmer model 599B or a Series 1600 FTIR spectrometer. Proton NMR spectra were obtained using a Varian CFT-20 spectrometer fitted with a probe to operate at 80 MHz or, as indicated, a Varian XL-400 spectrometer operating at 400 MHz. Unless otherwise noted, chemical shifts (δ) are reported downfield of tetramethylsilane as an internal standard. ^{13}C NMR spectra were recorded using a Varian XL-400 spectrometer operating at 100 MHz with the chemical shifts given from deuteriochloroform (δ_C 76.89) or d_6-DMSO (δ_C 39.69) as internal reference. Mass spectra were obtained through the services of mass spectrometry facilities in the Department of Chemistry at Johns Hopkins University (VG Micromass 70-S). Elemental combustion analyses were carried out by Galbraith Laboratories, Inc. (Knoxville, Tenn.).

Analytical thin-layer chromatography was performed on Analtech GHLF Uniplate glass plates coated with silica gel (0.25 mm) containing a fluorescent indicator, and using the mobile phase noted. Column chromatography was conducted on Merck Silica Gel 60 (230–400 mesh), using the column size and mobile phase indicated. Flash column chromatography was conducted under 60 Torr (1 Torr = 133.3 Pa) pressure with silica gel 60, size finer than 0.063 mm (E. Merck).

Dry tetrahydrofuran (THF) and dry ether were distilled from sodium benzophenone ketyl prior to use. Hexamethylphosphoric triamide (HMPA) was distilled under reduced pressure from calcium hydride and stored over molecular sieves (4 Å) under nitrogen. All other reagents were of reagent grade or purified further as indicated.

Biological procedures: strains and culture conditions

The averufin-accumulating mutant *Aspergillus parasiticus* ATCC 24551 was maintained on slants of potato dextrose agar (Difco) plus 0.5% yeast extract. Plates subcultured from these slants were grown for 7 days in the dark before use.

The growth medium used for cultivation of the organisms in submerged culture in shaken flasks was the minimum mineral medium (A&M) of Adye and Mateles (40). The replacement medium (RM) was the nitrogen-free resting cell medium of Hsieh and Mateles (29) containing various amounts of glucose.

Can. J. Chem. Downloaded from www.nrcresearchpress.com by 203.198.23.82 on 09/08/12
For personal use only.

Can. J. Chem. Downloaded from www.nrcresearchpress.com by 203.198.23.82 on 09/08/12
For personal use only.

Shaken cultures were incubated in cotton-stoppered Erlenmeyer flasks in the dark at 28°C and the indicated revolutions/min in a New Brunswick Scientific model G-25-K gyrotary incubator shaker; static cultures were grown in cotton-stoppered Erlenmeyer flasks or Fernbach flasks at 28°C in the dark. For inoculation of liquid cultures, a 7-day-old plate culture was flooded with a 0.85% saline solution (9 mL) containing 0.5% Tween (1 mL) and a 5-mm inoculating loop was used to generate a suspension of spores; the suspension was transferred to a tube containing the saline solution (9 mL) and mixed well to produce a suspension of ca. 10^6 conidiospores per 1 mL.

All broths, slants, and equipment were sterilized at 125°C/20 psi (1 psi = 6.9 kPa) for 20 min prior to inoculation.

N-(2-Mercaptoethyl)acetamide (N-acetylcysteamine)

The procedure of Kass and Brock was used (21). A three-necked 250-mL round-bottomed flask equipped with a pH electrode and argon inlet was charged with *N,S*-diacetylcysteamine (2.09 g, 13.0 mmol; prepared by the method of Schwab and Klassen (22)) and 70 mL of water. The solution was cooled to 0°C and solid potassium hydroxide (2.43 g, 43.3 mmol) was added. The reaction mixture was stirred 1 h at room temperature, and the solution was adjusted to pH 7, saturated with NaCl, and extracted three times with dichloromethane. The combined organic extracts were dried over anhydrous sodium sulfate and concentrated in vacuo to give *N*-acetylcysteamine (1.42 g, 91% yield) as a clear, colorless oil that was prepared just prior to use. ^{1}H NMR (400 MHz, $CDCl_3$) δ: 6.2–5.8 (m, 1H, NH), 3.43 (dt, J = 6, 6 Hz, 2H, -CH_2NH-), 2.71 (dt, J = 8, 6 Hz, 2H, -CH_2SH), 2.00 (s, 3H, CH_3CO), 1.34 (t, J = 8 Hz, SH).

General procedure for preparing NAC thioesters (21)

To a flame-dried three-necked round-bottomed 250-mL flask equipped with magnetic stirring bar and argon inlet was added 50 mL of dry THF and the carboxylic acid **3** (2.5 mmol). The solution was cooled to 0°C and triethylamine (0.35 mmol, 0.25 g, 2.5 mmol) followed by ethyl chloroformate (0.24 mL, 0.27 g, 2.5 mmol) was added and stirred 1 h at 0°C under argon. To a second three-necked 100-mL round-bottomed flask equipped with magnetic stirring bar, potassium hydroxide (1.4 g, 25 mmol) and 40 mL of water were added and stirred until the KOH had dissolved. Diacetylcysteamine (1.2 g, 7.5 mmol) was dissolved in the alkaline solution and allowed to stir at room temperature for 1 h. The pH was then adjusted to 7.8 with 6 N HCl and the solution was added via syringe to the mixed anhydride **4** at 0°C. If the mixture was cloudy, sufficient water was added to maintain a homogeneous solution. The pH was adjusted to 8.0 with 1 N NaOH and maintained at that pH throughout the reaction. The solution was allowed to stir for 1 h at room temperature, was acidified to pH 3.0 with 6 N HCl, and then was saturated with NaCl. The mixture was extracted three times with ether. The combined organic extracts were washed with 5% $NaHCO_3$ and brine and were dried over magnesium sulfate. Filtration and concentration in vacuo gave a clear colorless semisolid. TLC visualization under shortwave UV showed one spot (6:1 dichloromethane:acetone). Spray I followed by Spray II showed magenta spots indicating thioesters and (or) disulfides.

Spray I (sodium nitroprusside (41): 1.5 g of sodium nitroferricyanide, 5 mL of 2 N HCl, 95 mL of absolute methanol, and 10 mL of concentrated ammonium hydroxide (28%). Filter after mixing the above reagents together.

Spray II (methanolic sodium hydroxide): 2 g of NaOH, 5 mL of distilled water, and 95 mL of absolute methanol.

Dipping (spraying) a TLC plate with Spray I showed free thiols (here any residual *N*-acetylcysteamine). Taking the same TLC plate and dipping it in Spray II showed thioesters and disulfides as magenta spots on a yellow background. Dipping in ether intensifies the spots if weak (41). Purification by flash chromatography (20 g, 230–400 mesh, 6:1 dichloromethane:acetone) afforded the *N*-acetyl-*S*-acylcysteamines **5** as white solids. Other data are listed separately for each compound below.

[1-^{13}C]Butanethioic acid S-*[2-(acetylamino)ethyl]ester*

The compound was prepared from [1-^{13}C]butyric acid by acidification of the sodium salt (0.29 g, 2.6 mmol. 90 at% ^{13}C). The NAC thioester was obtained in 73% yield as a white solid, mp 21–23°C (lit. (42) mp 21–23°C). R_f = 0.25 (6:1 dichloromethane:acetone, visualized with Sprays I and II). IR($CHCl_3$): 3448, 3330, 3008, 2969, 2936, 2875, 1673, 1521, 1463, 1440, 1408, 1373, 1360, 1266, 1236, 1221, 1174, 1150, 1114, 1040 cm^{-1}; ^{1}H NMR (400 MHz, $CDCl_3$) δ: 5.9–5.8 (m, 1H, NH), 3.44 (dt, J = 6, 6 Hz, 2H, -CH_2NH-), 3.03 (t, J = 6.6 Hz, 2H, -CH_2S-), 2.55 (dt, J = 7.5, 5.8 Hz, 2H, -C$H_2{}^{13}$CO-), 1.96 (s, 3H, CH_3CO-), 1.73–1.6 (m, 2H, -CH_2CH_3), 0.96 (t, J = 7.3 Hz, 3H, -CH_3); EIMS, *m/z* (relative intensity) (unlabeled material): 189 (M^+, 2), 161 (4), 130 (18), 119 (75), 118 (30), 102 (14), 86 (27), 71 (70), 60 (98), 43 (100). Exact Mass (unlabeled material): 189.0825; calcd. for $C_8H_{15}NO_2S$: 189.0824.

[1-^{13}C]Hexanethioic acid S-*[2-(acetylamino)ethyl]ester*

[1-^{13}C]Hexanoic acid (0.29 g, 2.5 mmol) gave the corresponding NAC thioester in 79% yield as a white solid, mp 43–45°C. R_f = 0.56 (6:1 dichloromethane:acetone, visualized by Sprays I and II). IR ($CHCl_3$): 3450, 3330, 3007, 2959, 2930, 2870, 1672, 1520, 1463, 1440, 1407, 1373, 1360, 1266, 1234, 1221, 1210, 1174, 1147, 1120, 1040 cm–^{1}; ^{1}H NMR (400 MHz, $CDCl_3$) δ: 6.0–5.9 (m, 1H, NH), 3.43 (dt, J = 6, 6 Hz, 2H, -CH_2NH-), 3.02 (t, J = 6.6 Hz, 2H, -CH_2S-), 2.57 (dt, J = 7.3, 5.8 Hz, 2H, -$CH_2{}^{13}$CO-), 1.97 (s, 3H, CH_3CO-), 1.71–1.63 (m, 2H, -CH_2CH_2CO-), 1.33–1.28 (m, 4H, -$CH_2CH_2CH_3$), 0.90 (t, J = 7 Hz, 3H, -CH_3); EIMS, *m/z* (relative intensity) (unlabeled material): 217 (M^+, 1), 161 (1), 158 (8), 132 (7), 119 (78), 118 (23), 102 (11), 99 (40), 86 (17), 76 (15), 72 (26), 71 (39), 60 (85), 55 (12), 43 (100). Exact Mass (unlabeled material): 217.1139; calcd. for $C_{12}H_{21}NO_2S$: 217.1137.

Dicyclohexylcarbodiimide-activated esterification of carboxylic acids (28)

To a flame-dried 10-mL three-necked round-bottomed flask equipped with magnetic stirring bar and argon inlet was added the carboxylic acid (2.5 mmol), 3 mL dichloromethane, 10 mol% dimethylaminopyridine, and *N*-acetylcysteamine (8.5 mmol) in 2 mL of dichloromethane. The mixture was cooled to 0°C and DCC (2.5 mmol) was added. The reaction mixture was stirred at 0°C for 5 min and then warmed to room temperature, at which time dicyclohexylurea (DCU) precipitated. After stirring for 3.5 h at room temperature, the reaction mixture was filtered through Celite to remove DCU and was concentrated in vacuo, providing a yellow semisolid. Purification by flash chromatography (19 g silica, 230–400 mesh, 6:1 dichloromethane: acetone) gave the *N*-acetyl-*S*-cysteamine thioesters as white solids. Other data are listed below for each compound.

[1-^{13}C]Ethanethioic acid S-*[2-(acetylamino)ethyl]ester*

[1-^{13}C]Acetic acid (0.25 g, 4.09 mmol, 99 at% ^{13}C) and one equivalent of *N*-acetylcysteamine were combined to give the NAC thioester (0.56 g, 85% yield) as a clear colorless oil. R_f = 0.36 (6:1 dichloromethane:acetone, visualized by Spray I followed by Spray II). ^{1}H NMR (80 MHz, $CDCl_3$) δ: 6.5–6.25 (m, 1H, NH), 3.40 (dt, J = 6, 6 Hz, -CH_2NH-), 3.06 (t, J = 6.7 Hz, 2H, -CH_2S-), 2.35 (d, J = 6.2 Hz, 3H, $CH_3{}^{13}$CO-), 1.96 (s, 3H, CH_3CONH).

[2,3-$^{13}C_2$]Butanethioic acid S-*[2-(acetylamino)ethyl]ester*

[2,3-$^{13}C_2$]Butyric acid (2.66 mmol) yielded the NAC thioester (250 mg, 50% yield) as a white solid, mp 21–23°C (lit. (42) mp 21–23°C). ^{1}H NMR (400 MHz, $CDCl_3$) δ: 6.5–6.27 (m, 1H, NH), 3.42 (dt, J = 6, 6 Hz, 2H, -CH_2NH-), 3.03 (t, J = 6.5 Hz, 2H, -CH_2S-), 2.56 ($^1J_{CH}$ = 124 Hz, $^2J_{CH}$ = 4.7 Hz, $^3J_{HH}$ = 7.4 Hz, 2H, -$^{13}CH_2$CO-), 1.98 (s, 3H, CH_3CO-), 1.68 ($^1J_{CH}$ = 123 Hz, $^2J_{CH}$ = 4.2 Hz, $^3J_{HH}$ = 7.4 Hz, 2H, -$^{13}CH_2CH_3$), 0.95 ($^2J_{CH}$ = 4.7 Hz, $^3J_{CH}$ = 4.4 Hz, $^3J_{HH}$ = 7.4 Hz, 3H, -CH_3).

[1-^{13}C]-3-Oxo-octanoic acid S-*[2-(acetylamino)ethyl]ester*

[1-^{13}C]-3-Oxo-octanoic acid (0.398 g, 2.5 mmol) afforded the NAC thioester in 69% yield as a white solid, mp 86–89°C. IR ($CHCl_3$): 3450, 3330, 3004, 2960, 2933, 2870, 1721, 1672, 1613, 1524, 1464,

Can. J. Chem. Downloaded from www.nrcresearchpress.com by 203.198.23.82 on 09/08/12
For personal use only.

1440, 1407, 1365, 1266, 1233, 1217, 1177, 1101, 1087, 1040 cm^{-1}; ^{1}H NMR (400 MHz, $CDCl_3$) δ: 6.75–6.25 (m, 1H, NH), 3.70 (d, J = 6.2 Hz, -^{13}CH_2CO-), 3.42 (dt, J = 6, 6 Hz, 2H, -CH_2NH-), 3.13 (t, J = 6.4 Hz, -CH_2S-), 2.53 (t, J = 7.3 Hz, 2H, -CH_2CO-), 1.99 (s, 3H, CH_3CO-), 1.75–1.25 (m, 6H, -$CH_2CH_2CH_2$-), 0.90 (t, J = 6.8 Hz, CH_3CH$_2$-); EIMS *m/z* (relative intensity) (unlabeled material): 259 (1), 200 (1), 141 (25), 119 (80), 118 (19), 102 (2), 99 (32), 86 (12), 84 (50), 76 (10), 72 (23), 71 (19), 69 (31), 60 (94), 56 (15), 44 (20), 43 (64), 41 (24), 30 (100). Exact Mass (unlabeled material): 259.1248; calcd. for $C_{12}H_{21}NO_3S$: 259.1242.

[1-^{13}C]Hexanoic acid (24)

To a 25-mL three-necked round-bottomed flask equipped with nitrogen inlet, magnetic stirring bar, and reflux condenser were added MeOH (6.3 mL), H_2O (0.24 mL), 1-iodopentane (3.27 mL, 4.97 g, 25.1 mmol), and potassium [^{13}C]cyanide (1.63 g, 24.6 mmol, 99% ^{13}C). The mixture was allowed to heat to reflux for 48 h. The hexanenitrile (assume 24.6 mmol) was distilled directly into a 50-mL round-bottomed flask at 55°C (15 Torr) as a clear colorless liquid. Water (0.95 mL, 53 mmol) and 29.5 mL of 0.85 M potassium *tert*-butoxide (25 mmol) in *tert*-butanol were added; the solution was heated to reflux for 48 h under nitrogen and was then cooled to room temperature, affording a white precipate. The residue obtained upon evaporation of the solvent was redissolved in water and acidified with 10% aqueous HCl to pH 2. The aqueous solution was extracted with ether three times. The organic layers were combined and washed with water, brine, and were dried over anhydrous magnesium sulfate. Filtration and concentration in vacuo gave a clear yellow liquid. The liquid was purified by Kugelrohr distillation at 85°C to give [1^{13}C]hexanoic acid as a clear colorless liquid (2.35 g, 80% yield). ^{1}H NMR (400 MHz, $CDCl_3$) δ: 2.33 (dt, J = 7.3, 5.8 Hz, 2H, CH_2^{13}CO-), 1.80–1.50 (m, 2H, -CH_2CH$_2$^{13}CO-), 1.50–1.25 (m, 4H, CH_2CH_2CH$_3$), 0.90 (t, J = 7 Hz, 3H, -CH_3).

[1-^{13}C,$^{18}O_2$]Hexanoic acid, sodium salt

The method used was similar to that for preparing analogously labeled sodium propionate by Cane et al. (24). To a flame-dried 25-mL round-bottomed flask equipped with nitrogen inlet, magnetic stirring bar, and reflux condenser were added methanol (3.8 mL), H_2^{18}O (98% ^{18}O, 0.15 mL), 1-iodopentane (1.98 mL, 15.19 mmol), and potassium [^{13}C]cyanide (99% ^{13}C, 0.99 g, 15.03 mmol). The mixture was heated to reflux for 48 h. After cooling, the mixture was distilled into a 50-mL round-bottomed flask for direct hydrolysis of the nitrile. To the latter flask, equipped with magnetic stirring bar, reflux condenser, and nitrogen inlet, were added 0.85 M potassium *tert*-butoxide in *tert*-butanol (17.8 mL, 15.13 mmol) and H_2^{18}O (98% ^{18}O, 0.64 mL, 32 mmol). The product was obtained as described above to give [1-^{13}C,$^{18}O_2$]hexanoic acid as a colorless liquid (0.78 g, 45% yield). Water (10 mL) and 1 N NaOH (6.7 mL) were added to the carboxylic acid. The mixture was stirred for 30 min at room temperature and then concentrated in vacuo to give a white solid, mp 260°C (dec.). ^{1}H NMR (400 MHz, D_2O) δ: 2.19 (dt, J = 7.3, 5.9 Hz, 2H, -CH_2 ^{13}C$^{18}O_2$), 1.61–1.54 (m, 2H, -CH_2CH$_2$^{13}C$^{18}O_2$), 1.37–1.26 (m, 4H, -CH_2CH_2CH$_3$), 0.89 (t, J = 7.1 Hz, 3H, -CH_3); ^{13}C NMR (100 MHz, D_2O, partial) δ: 183.07 (^{13}C$^{16}O_2$), 183.04 (^{13}C^{16}O^{18}O), 183.01 (^{13}C$^{18}O_2$). Estimation of isotope content of the acid by ^{13}C NMR was 17.9% (^{13}C,$^{16}O_2$), 45.6 (^{13}C,^{16}O,^{18}O), and 36.5 (^{13}C,$^{18}O_2$). The mass spectrum gave the isotopic cluster (M + Na^+) as follows: EIMS *m/z* (unlabeled): 161 (100), 162 (7.03), 163 (1.03), 164 (0.02), 165 (0.32) and 166 (0.03); (labeled): 161 (6.96), 162 (39.99), 163 (8.3), 164 (100), 165 (10.73), 166 (81.4), and 167 (4.54). From these data it can be shown that the contributions of labeled materials are as follows: 18.1% (^{13}C$^{16}O_2$), 45.4% (^{13}C^{16}O^{18}O), and 36.5% (^{13}C$^{18}O_2$).

*Benzyl [1-^{13}C]acetate (**6**) (25)*

To a flame-dried 10-mL round-bottomed flask equipped with reflux condenser, argon inlet, and magnetic stirring bar were added sodium [1-^{13}C]acetate (99% ^{13}C, 0.80 g, 9.64 mmol), methyl ethyl ketone (3 mL), benzylchloride (1.02 mL, 1.12 g, 8.87 mmol), and triethylamine (0.04 mL, catalytic). The heterogeneous mixture was heated to a vigorous reflux for 8.5 h. At this time water was added to dissolve the salt and the aqueous and organic layers were separated. The aqueous phase was extracted with dichloromethane and the organic layers were combined, washed with brine, and dried over anhydrous magnesium sulfate. Filtration and concentration in vacuo provided 1.32 g of **6** as a clear colorless liquid (98% yield). ^{1}H NMR (80 MHz, $CDCl_3$) δ: 7.35 (s, 5H, phenyl), 5.11 (d, J = 3.2 Hz, 2H, C_6H_5CH_2-), 2.10 (d, J = 6.9 Hz, 3H, CH_3^{13}CO-).

Benzyl [1-^{13}C]-3-oxo-octanoate (7, R = CH_2Ph)

To a 50-mL flame-dried three-necked round-bottomed flask containing a nitrogen inlet and magnetic stirring bar were added 13 mL of dry THF and 18.3 mL (18.3 mmol) of lithium hexamethyldisilazide (1.0 M in THF). The stirred solution was cooled to −78°C and benzyl [1-^{13}C]acetate **6** (1.26 mL, 8.7 mmol) was added, followed in 30 min by hexanoyl chloride (1.2 mL, 8 mmol). After 35 min, 2 N hydrochloric acid (13 mL) was added at −78°C and the reaction was allowed to warm to room temperature and stir 35 min more. The mixture was poured into water and extracted with ethyl acetate three times. Concentration of the dried organic extract in vacuo afforded a yellow oil. Purification by flash chromatography (80 g silica, 230–400 mesh, 10:1 hexane:ethyl acetate) provided 1.54 g of product **7** (R = CH_2Ph) as a clear colorless oil (77% yield). R_f = 0.55 (10:1 hexane:ethyl acetate). ^{1}H NMR (80 MHz, $CDCl_3$) δ: 7.35 (s, 5H, phenyl), 5.17 (d, J = 3.3 Hz, 2H, $C_6H_5CH_2$-), 3.47 (d, J = 7.4 Hz, 2H, -^{13}COCH_2CO-), 2.49 (t, J = 7.2 Hz, 2H, -CH_2CO-), 1.75–1.25 (m, 6H, -$CH_2CH_2CH_2$-), 0.87 (virtually coupled triplet, 3H, -CH_3).

[1-^{13}C]-3-Oxo-octanoic acid (7, R = H)

To a 250-mL Parr bottle were added benzyl [1-^{13}C]-3-oxo-octanoate (1.54 g, 9.67 mmol), ethyl acetate (10 mL), and 10% palladium on carbon (100 mg). Debenzylation was carried out under hydrogen at 40 psi for 12 h. The catalyst was removed by filtration through Celite and washed with 1:1 ethyl acetate: ethanol. Concentration in vacuo provided [1-^{13}C]-3-oxooctanoic acid as a while solid (0.89 g, 90% yield), mp 73–74°C (lit. (26) mp 73–74°C). R_f = 0.07 (10:1 hexane: ethyl acetate, visualized with bromocresol green.). ^{1}H NMR (400 MHz, $CDCl_3$) δ: 3.47 (d, J = 7.4 Hz, 2H, -^{13}COCH_2CO-), 2.49 (t, J = 7.2 Hz, 2H, CH_2CO-), 1.75–1.25 (m, 6H, -$CH_2CH_2CH_2$-), 0.87 (t, J = 7 Hz, 3H, CH_3).

[2,3-$^{13}C_2$]Butanoic acid (23)

To a flame-dried 50-mL round-bottomed flask equipped with reflux condenser, magnetic stirring bar, and argon inlet were added THF (9.5 mL) and diisopropylamine (1.99 mL, 1.44 g, 14.2 mmol). After cooling to 0°C, [2-^{13}C]acetic acid (99% ^{13}C, 0.37 mL, 6.37 mmol) was added dropwise giving a milky white suspension, which became homogeneous after the addition of three equivalents of HMPA (3.3 mL, 19.11 mmol). The resulting solution was heated for 2 h at 50°C to facilitate dianion formation. After cooling to room temperature, [1-^{13}C]-1-iodoethane (99% ^{13}C, 500 mg, 3.18 mmol) was added slowly via syringe and the alkylation was allowed to proceed for 12 h. The product was isolated by acidification with ice-cold 10% HCl and extraction with ether. The combined organic layers were washed three times with 10% HCl, water, and brine. The organic extract was dried over anhydrous sodium sulfate, filtered, and concentrated to obtain the crude product as an orange liquid. Any ethyl esters formed in the reaction were saponified with 1 N NaOH and extracted with ether. The aqueous layer was acidified to pH 2 with 2 N HCl and was extracted back into ether. The ether extract was washed with water, brine, and was dried over anhydrous sodium sulfate. Filtration and concentration in vacuo gave a pale yellow liquid, which was Kugelrohr distilled (50°C, 15 Torr) to give a colorless liquid (0.24 g, 85% yield based on 1-iodoethane). ^{1}HNMR (400 MHz, $CDCl_3$) δ: 2.32 ($^1J_{CH}$ = 124 Hz, $^2J_{CH}$ = 4.7 Hz, $^3J_{HH}$ = 7.4 Hz, 2H, -^{13}CH_2CO-), 1.65 ($^1J_{CH}$ = 123 Hz, $^2J_{CH}$ = 4.2 Hz, $^3J_{HH}$ = 7.4 Hz, 2H, -^{13}CH_2CH$_3$), 0.95 ($^2J_{CH}$ = 4.7 Hz, $^3J_{CH}$ = 4.4 Hz, $^3J_{HH}$ = 7.4 Hz, 3H, -CH_3).

Can. J. Chem. Downloaded from www.nrcresearchpress.com by 203.198.23.82 on 09/08/12
For personal use only.

Incorporation of sodium [1-^{13}C,$^{18}O_2$]hexanoate into averufin

Four 500-mL portions of A&M medium (40) contained in 2-L Erlenmeyer flasks were inoculated and allowed to shake at 175 rpm at 28°C in the dark for 48 h. The mycelial pellets were filtered on cheesecloth and rinsed with RM (1.62 g glucose/L) (29). Ten grams each (wet weight) was resuspended in 100 mL of RM contained in each of 12 250-mL Erlenmeyer flasks. Sodium [1^{13}C,$^{18}O_2$]hexanoate (178 mg, 1.25 mmol, 14.9 mg per flask) was dissolved in 24 mL of H_2O and filtered through a sterile 0.2-μm membrane and 2 mL of the filtrate was pipetted into each flask. The flasks were allowed to shake 48 h at 28°C in the dark. The mycelial pellets were filtered on cheesecloth and rinsed with water. The collected mycelial pellets were steeped in acetone and filtered. The acetone extract was concentrated to ca. 300 mL and was extracted four times with ether until the ether layer was nearly colorless. The combined organic extracts were washed with water and brine, and were dried over anhydrous sodium sulfate. Filtration and concentration in vacuo gave an orange solid. Purification by flash chromatography (18 g silica, 230–400 mesh, 97:3 $CHCl_3$:MeOH) gave 59 mg of averufin as an orange solid. ^{13}C NMR (100 MHz, $CDCl_3$ with five drops d_6-DMSO) δ: 188.81 (C-9), 180.99 (C-10), 164.67 (C-6), 164.30 (C-8), 159.71 (C-3), 158.34 (C-1), 134.53 (C-11), 132.86 (C-14), 115.63 (C-2), 109.06 (C-5), 108.57 (C-12), 108.15 (C-13), 107.99 (C-7), 107.5 (C-4), 100.53 (C-5′), 66.32 (C-1′), 35.33 (C-4′), 27.33 (C-6′), 26.9 (C-2′), 15.43 (C-3′); δ: 66.324 (C-1′–^{16}O), 66.297 (C-1′–^{18}O).

Enrichment of averufin labeled with both ^{13}C and ^{18}O was determined to be 31.5% based on peak areas in the NMR spectrum. EIMS gave *m/z* (unlabeled) 368 (100), 369 (22.4), 370 (5.1), 371 (1.2), and 372 (0.02); and for the labeled compound 369 (100), 369 (25.2), 370 (5.8), 371 (2.7), and 372 (1.3). From these data it can be shown that the contributions of labeled species are as follows: 67.7% (^{13}C,^{16}O) and 32.3% (^{13}C,^{18}O). To determine the incorporation of doubly labeled hexanoate into averufin, an assumption was made about the utilization of the hexanoate fed. Of the three peaks integrated in the ^{13}C NMR spectrum of [1-^{13}C,$^{18}O_2$]hexanoate, half of the area of the peak corresponding to ^{13}C,^{16}O,^{18}O-labeled material was used since statistically only half of the oxygens could be retained in the conversion to averufin. With this in mind a corrected figure of 59.3% was obtained for the maximum ^{13}C,^{18}O-enrichment that could be observed in averufin. Dividing the 31.5% enrichment actually obtained for the [^{13}C,^{18}O]-averufin by 59.3% gave 53% retention of ^{18}O in averufin relative to the ^{13}C internal standard.

Administration of NAC thioesters to ATCC 24551

A common procedure was used to test the incorporation of all the NAC thioesters. Mycelial pellets were prepared as above and resuspended in 12 250-mL Erlenmeyer flasks containing 100 mL each of RM. The ^{13}C-labeled NAC thioester was dissolved in 24 mL of acetone and 2 mL was pipetted into each flask. The flasks were allowed to shake 48 h at 28°C in the dark at 175 rpm. The mycelial pellets were then filtered on cheesecloth and rinsed with distilled water. The averufin produced was isolated as above.

Administration of [1-^{13}C]ethanethioic acid S-*[2(acetylamino)-ethyl]ester*

The yield of averufin was 8 mg. The estimation of incorporation by ^{13}C NMR was 0.3% at C-5′. EIMS *m/z* (unlabeled): 368 (100), 369 (22.4), 370 (5.1), and 371 (1.2); (labeled): 368 (100), 369 (26.6), 370 (7.9), and 371 (3.5). The mass spectrum (EI) indicated that the overall level (for 10 sites) of carbon-13 in the molecule was 3.8% above natural abundance.

Administration of [1-^{13}C]butanethioic acid S-*[2(acetylamino)-ethyl]ester*

The yield of averufin was 11.6 mg. Estimation of incorporation by ^{13}C NMR was 0.36% at C-3′ (however, see below). EIMS *m/z* (unlabeled): 368 (100), 369 (22.4), and 370 (5.1); and for the labeled compound: 368 (100), 369 (27.0), and 370 (6.8). The mass spectrum indicated that the level of carbon-13 was 4.4% above natural abundance (for 10 sites).

Administration of [2,3-$^{13}C_2$]butanethioic acid S-*[2(acetylamino)-ethyl]ester*

The yield of averufin was 25 mg. A ^{13}C NMR spectrum showed no intact incorporation of the thioester, as evidenced by the lack of coupling at a detection limit of <0.1% between C-4′ (δ 35.78) and C-5′ (δ 100.9).

Administration of [1-^{13}C]hexanethioic acid S-*[2(acetylamino)-ethyl]ester*

The yield of averufin was 18 mg. Estimation of incorporation by ^{13}C NMR spectroscopy was 22% at C-1′ by peak height analysis compared to natural abundance. EIMS *m/z* (unlabeled): 368 (100), 369 (22.4), 370 (5.1), and 371 (1.2); and for the labeled compound: 368 (100), 369 (62.8), 370 (25.7), and 371 (7.5). From these data it can be shown that the level of enrichment (M + 1) by mass spectrometry was 26%.

Administration of [1-^{13}C]-3-oxo-octanoic acid S-*[2(acetylamino)-ethyl]ester*

Estimation of incorporation by ^{13}C NMR spectroscopy gave 4.7 ± 0.7% at C-3 compared to natural abundance. Incorporation was ca 0.7% per site at alternating carbons, giving a total of 7% secondary incorporation due to acetate. EIMS gave *m/z* (unlabeled): 368 (100), 369 (22.4), 370 (5.1), and 371 (1.2); (labeled): 368 (100), 369 (35.1), 370 (10.5), and 371 (2.8). The level of enrichment (M + 1) estimated by mass spectrometry was 10.9% in the entire molecule.

Acknowledgments

Professor J.W. Bennett is thanked for kindly providing the averufin-accumulating mutant used in this work. We are grateful to the National Institutes of Health (ES01670) for their support of this work, and to the National Science Foundation for grant awards that enabled purchase of the major analytical instrumentation used (NMR: RR01934 and PCM 83-03176; MS: RR02318).

1. C.A. Townsend and S.B. Christensen. Tetrahedron, **39**, 3575 (1983).
2. C.A. Townsend, S.B. Christensen, and K. Trautwein. J. Am. Chem. Soc. **106**, 3868 (1984).
3. G. Albers-Schonberg, B.H. Arison, J.C. Chabala, A.W. Douglas, P. Eskola, M.H. Fisher, A. Lusi, H. Mrozik, J.L. Smith, and R.L. Tolman. J. Am. Chem. Soc. **103**, 4216 (1981); M. Ono, H. Mishima, Y. Takiguchi, M. Terao, H. Kobayashi, S. Iwasaki, and S. Okunda. J. Antibiot. **36**, 991 (1983); F. Drawert and J. Beier. Phytochemistry, **15**, 1695 (1976).
4. W.D. Ollis, I. Sutherland, R.C. Codner, J.J. Gordon, and G.A. Miller. Proc. Chem. Soc. 347 (1960); R.C. Paulick, M.L. Casey, and H.W. Whitlock. J. Am. Chem. Soc. **98**, 3370 (1976); G.T. Carter, A.A. Fantini, J.C. James, D.B. Borders, and R.S. White. Tetrahedron Lett. **25**, 255 (1984); H. Grisebach, H. Achenbach, and M. Grisebach. Naturwissenschaften, **47**, 206 (1960); A.J. Birch, E. Pride, R.W. Richards, P.J. Thompson, J.D. Dutcher, D. Perlman, and C. Djerassi. Chem. Ind. (London), 1245 (1960); P.G. Manwaring, R.W. Richards, G. Gaudiano, and V. Nicolella. J. Antibiot. **22**, 545 (1969); S. Omura, A. Nakagawa, H. Takeshima, J. Miyazawa, and C. Kitao. Tetrahedron Lett. 4503 (1975); S. Omura, H. Takeshima, H. Nakagawa, and J. Miyazawa. J. Antibiot. **29**, 316 (1976).
5. W.B. Turner and D.C. Aldrich. Fungal Metabolites II. Academic Press, London. 1983.
6. K. Mosbach. Acta Chem. Scand. **18**, 1591 (1964).
7. P.S. Steyn, R. Vleggaar, and P.L. Wessels. J. Chem. Soc. Chem. Commun. 1041 (1979); J. Chem. Soc. Perkin Trans. 1, 1298 (1981).

8. P.S. Steyn and R. Vleggaar. J. Chem. Soc. Chem. Commun. 977 (1984).
9. A.J. Birch. Proc. Chem. Soc. 3 (1962).
10. P.G. Gordon, A. Penttila, and H.M. Fales. J. Am. Chem. Soc. **90**, 1376 (1968).
11. E. Leete and J.O. Olson. J. Chem. Soc. Chem. Commun. 1651 (1970); E. Leete. J. Am. Chem. Soc. **92**, 3835 (1970).
12. B. Cross and P. Hendley. J. Chem. Soc. Chem. Commun. 124 (1975); S.W. Tanenbaum and S. Nakajima. Biochemistry, **11**, 4226 (1969); J. Gellerman, W. Anderson, and H. Schlenk. Lipids, **9**, 722 (1974).
13. C. Clark and J.A. Robinson. J. Chem. Soc. Chem. Commun. 1568 (1985).
14. P.H. Harrison, H. Noguchi, and J.C. Vederas. J. Am. Chem. Soc. **108**, 3833 (1986); H. Noguchi, P.H. Harrison, K. Arai, T.T. Nakashima, L.A. Trimble, and J.C. Vederas. J. Am. Chem. Soc. **110**, 2938 (1988).
15. S. Yue, J.S. Duncan, Y. Yamamoto, and C.R. Hutchinson. J. Am. Chem. Soc. **109**, 1253 (1987).
16. D.E. Cane and C.-C. Yang. J. Am. Chem. Soc. **109**, 1255 (1987).
17. F. Lynen. Fed. Proc. **20**, 941 (1961).
18. J.M. Schwab, W.-B. Li, C.-K. Ho, C.A. Townsend, and G.M. Salituro. J. Am. Chem. Soc. **106**, 7293 (1984); **108**, 5309 (1986).
19. L.R. Kass and K. Bloch. Proc. Natl. Acad. Sci. U.S.A. **58**, 1168 (1967); G.M. Helmcamp, Jr. and K. Bloch. J. Biol. Chem. **244**, 6014 (1969).
20. Z.M. Spavold and J.A. Robinson. J. Chem. Soc. Chem. Commun. 4 (1988); D.E. Cane and W.R. Ott. J. Am. Chem. Soc. **110**, 4840 (1988); Y. Yoshizawa, Z. Li, P.B. Reese, and J.C. Vederas. J. Am. Chem. Soc. **114**, 3212 (1990); Z. Li, F.M. Martin, and J.C. Vederas. J. Am. Chem. Soc. **114**, 1531 (1992); J. Staunton and A.C. Sutkowski. J. Chem. Soc. Chem. Commun. 1110 (1991); A. Jacobs, J. Staunton, and A.C. Sutkowski. J. Chem. Soc. Chem. Commun. 1113 (1991); J.A. O'Neill, T.J. Simpson, and W.L. Willis. J. Chem. Soc. Chem. Commun. 738 (1993).
21. L.R. Kass and D.J.H. Brock. Methods Enzymol. **14**, 696 (1969).
22. J.M. Schwab and J.B. Klassen. J. Am. Chem. Soc. **106**, 7217 (1984).
23. P.E. Pfeffer, L.S. Silbert, and J.M. Chirinko, Jr. J. Org. Chem. **37**, 451 (1972).
24. D.E. Cane, H. Hasler, and T.C. Liang. J. Am. Chem. Soc. **103**, 5960 (1981).
25. H.E. Hennis, J.P. Easterly, L.R. Collins, and L.R. Thompson. Ind. Eng. Chem. Prod. Res. Dev. **6**, 193 (1967).
26. R. Locquin. Bull. Soc. Chim. Fr. **108**, 595 (1904).
27. J.R. Grunwell and D.L. Foerst. Synth. Commun. **7**, 251 (1977).
28. B. Neises and W. Steglich. Angew. Chem. **17**, 522 (1978).
29. M.T. Lin, D.P.H. Hsieh, R.C. Yao, and J.A. Donkersloot. Biochemistry, **12**, 5167 (1973).
30. C.P. Gorst-Allman, K.G.R. Pachler, P.S. Steyn, P.L. Wessels, and DeB. Scott. J. Chem. Soc. Perkin Trans. 1, 2181 (1977).
31. Y. Berger. Phytochemistry, **19**, 2779 (1980).
32. D.P.H. Hsieh, M.T. Lin, R.C. Yao, and R. Singh. J. Agric. Food Chem. **24**, 1170 (1976); P.S. Steyn, R. Vleggaar, and P.L. Wessels. S. Afr. J. Chem. **34**, 12 (1981).
33. C.P. Gorst-Allman, K.G.R. Pachler, P.S. Steyn, P.L. Wessels, and DeB. Scott. J. Chem. Soc. Chem. Commun. 916 (1976).
34. J.C. Vederas and T.T. Nakashima. J. Chem. Soc. Chem.Commun. 183 (1980).
35. J.C. Vederas. Nat. Prod. Rep. **4**, 277 (1987).
36. J. Cortes, S.F. Haydock, G.A. Roberts, D.J. Bevitt, and P.F. Leadlay. Nature, **348**, 176 (1990); S. Donadio, M.J. Staver, J.B. McAlpine, S.J. Swanson and L. Katz. Science, **252**, 675 (1991); D.J. Bevitt, J. Cortes, S.F. Haydock, and P.F. Leadlay. Eur. J. Biochem. **204**, 39 (1992); D. Donadio and L. Katz. Gene, **111**, 51 (1992).
37. I.M. Chandler and T.J. Simpson. J. Chem. Soc. Chem. Commun. 17 (1987).
38. C.A. Townsend, S.W. Brobst, S.E. Ramer, and J.C. Vederas. J. Am. Chem. Soc. **110**, 318 (1988).
39. M. Gonzalez-De-La-Parra and C.R. Hutchinson. J. Am. Chem. Soc. **108**, 2448 (1986); P.B. Reese, B.J. Rawlings, S.E. Ramer, and J.C. Vederas. J. Am. Chem. Soc. **110**, 316 (1988); B.J. Rawlings, P.B. Reese, S.E. Ramer, J.C. Vederas. J. Am. Chem. Soc. **111**, 3382 (1989).
40. J.C. Adye and R.I. Mateles. Biochim. Biophys. Acta, **86**, 418 (1964).
41. E.R. Stadtman. Methods Enzymol. **3**, 931 (1957).
42. J.C. Sheehan and C.W. Beck. J. Am. Chem. Soc. **77**, 4875 (1955).

Can. J. Chem. Downloaded from www.nrcresearchpress.com by 203.198.23.82 on 09/08/12
For personal use only.

Heterocyclic analogs of nucleosides: synthesis and biological evaluation of some 1-(3-thianyl)uracil and 9-(3-thianyl)adenine derivatives[1]

PHILIP G. HULTIN AND WALTER A. SZAREK[2]
Department of Chemistry, Queen's University, Kingston, ON K7L 3N6, Canada

Received May 11, 1993

This paper is dedicated to Professor David B. MacLean

PHILIP G. HULTIN and WALTER A. SZAREK. Can. J. Chem. **72**, 208 (1994).

The 1-(3-thianyl)uracil (**9**) and 9-(3-thianyl)adenine (**14**) nucleoside analogs have been prepared from the key intermediate, (±)-(3β,5β)-3-amino-5-(hydroxymethyl)thiane (**6**). Analog **9** was converted into a mixture of diastereomeric sulfoxides (**10**) that afforded, by a Pummerer reaction, a mixture of (±)-1-{(2′β,3′β,5′β)-2′-acetoxy-5′-(acetoxymethyl)thian-3′-yl}-2,4(1*H*,3*H*)-pyrimidinedione (**11***a*) and its 6′-β isomer (**11***b*). The EI mass spectra of the nucleoside analogs are discussed. The uracil nucleoside analogs have been evaluated also for their anti-HIV and antitumor activities.

PHILIP G. HULTIN et WALTER A. SZAREK. Can. J. Chem. **72**, 208 (1994).

On a préparé le 1-(3-thianyl)uracile (**9**) et la 9-(3-thianyl)adénine (**14**), des analogues de nucléosides, à partir de l'intermédiaire clé, (±)-(3β,5β)-3-amino-5-(hydroxyméthyl)thiane (**6**). On a transformé l'analogue **9** en un mélange de sulfoxydes diastéréoisomères (**10**) qui, par réaction de Pummerer, conduit à un mélange de la (±)-1-{(2′β,3′β,5′β)-2′-acétoxy-5′-(acétoxyméthyl)thian-3′-yl}-2,4(1*H*,3*H*)-pyrimidinedione (**11***a*) et son isomère 6′-β (**11***b*). On discute des spectres de masse en IE des analogues de nucléoside. On a aussi évalué les analogues nucléoside de l'uracile pour leurs activités anti-HIV et antitumorale.

[Traduit par la rédaction]

Introduction

Nucleoside analogs have received much attention as a result of their antiviral (1) and antitumor (2) activities. Interest in replacement of the carbohydrate moiety by other heterocycles was recently stimulated by the announcement of the potent anti-HIV activity of the 1,3-oxathiolanyl nucleoside BCH-189 by Belleau and co-workers (3). The chemistry and biological activity of 1,3-oxathiolanyl (4), 1,3-dioxolanyl (5), oxolanyl (6), thiolanyl (7), and pyrrolidinyl (8) nucleosides have been reported by several groups. Nucleosides derived from 1,4- dioxane, 1,4-oxathiane, and 1,4-oxazine have also been prepared and their antiviral activities determined (9).

We have published the results of studies of the synthesis, structure, and antitumor activities of nucleoside analogs having 1,4-oxathianyl, 1,4-dithianyl, 1,4-dioxanyl, 1,4-oxazinyl, 1,4-thiazinyl, and 1,3-thiazolidinyl groups replacing the sugar ring (10). As part of this ongoing project, we wished to prepare the 3-thianyl nucleosides **9**, **10**, and **14**, and to determine their activities against HIV and a variety of human cancers. It was anticipated that **9**, **10**, and **14** would have antitumor properties similar to those of our earlier six-membered heterocyclic analogs, but that they should prove to be more stable *in vivo* since the base ring is not attached by a glycosidic linkage.

Results and discussion

Since our analogs do not involve a glycosidic linkage, the pyrimidine- or purine-ring system had to be constructed on an aminothiane already possessing the desired *cis* stereochemistry. *cis*-3-Amino-5-(hydroxymethyl)thiane (**6**) was prepared as shown in Scheme 1 from the known bicyclic lactam **1** (11). This lactam was prepared as a racemate, and, consequently, our analogs were also racemic; however, **1** can be obtained in optically pure form from a microbiological resolution (12), and is available commercially now in both enantiomeric forms.[3]

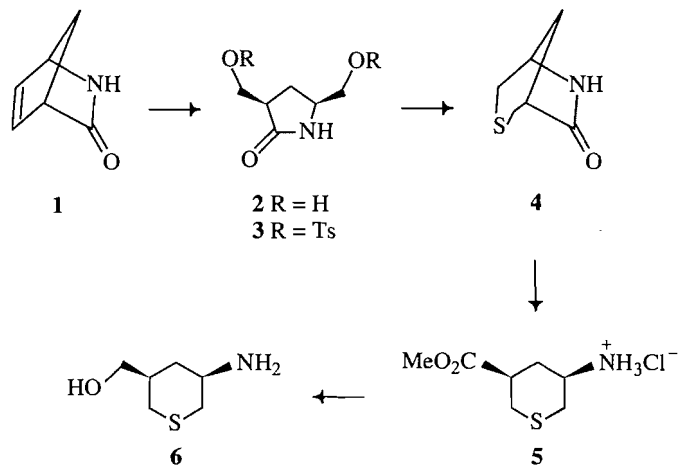

SCHEME 1

Ozonolysis of **1** followed by reduction with sodium borohydride afforded the diol **2**, which was converted directly into ditosylate **3** (57.5% overall). Double displacement with sodium sulfide in hot *N*,*N*-dimethylformamide gave the bicyclic thianelactam **4**, in 68% yield after recrystallization, with the required *cis*-3,5 stereochemistry in place. The lactam was esterified using methanol containing concentrated aqueous hydrochloric acid. It is noteworthy that initial attempts to perform this reaction under anhydrous conditions were unsuccessful, but that addition of even a small amount of water promoted a facile, complete conversion of **4** into **5**. The crystalline amino alcohol **6** then could be obtained in 93% yield by reduction with lithium borohydride.

Synthesis of uracil derivatives

Preparation of the uridine analogs **9** and **10** is shown in Scheme 2. The required acylisocyanate **7** was made by a literature method (13), and condensed with **6** in *N*,*N*-dimethylformamide–benzene in the cold, to afford the acylurea derivative **8** in 78% yield. Cyclization was effected by brief boiling in 2 N

[1]This paper is gratefully dedicated to Professor David B. MacLean, teacher and colleague of one of us (W.A.S.).

[2]Author to whom correspondence may be addressed.

[3]Enzymatix Inc., Rosedale, NY 11422, U.S.A.

Can. J. Chem. Downloaded from www.nrcresearchpress.com by 195.246.54.202 on 09/08/12
For personal use only.

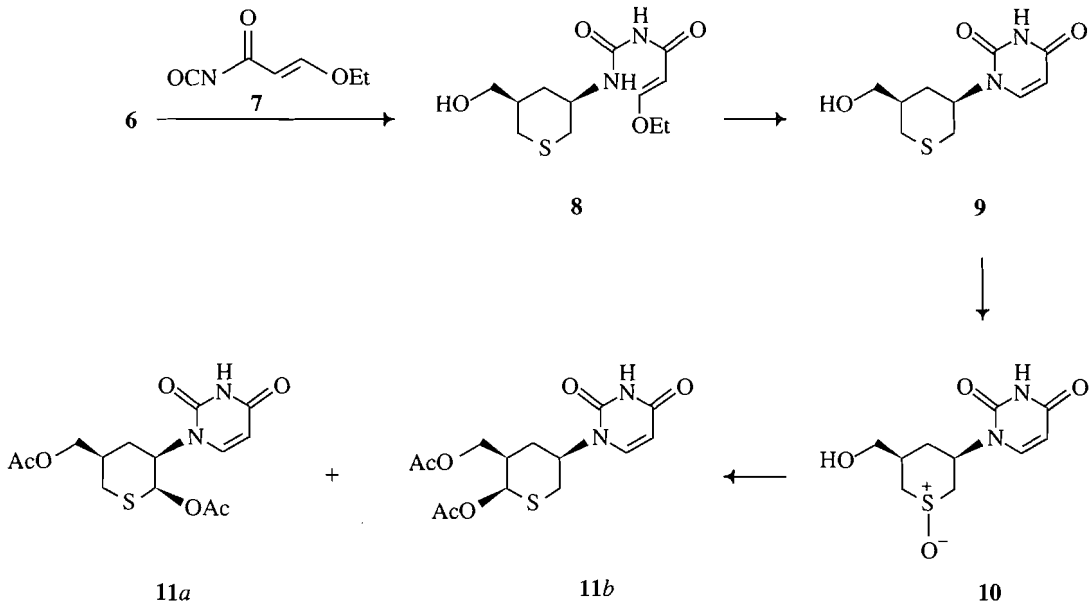

SCHEME 2

sulfuric acid, to give the nucleoside analog **9** as a crystalline solid.

We also wished to prepare the sulfoxide **10**. Treatment of **9** with sodium metaperiodate in ice-cold water gave **10** as an unresolvable mixture of diastereomers. Although the ^{1}H nmr spectrum of **10** was complicated by overlap of all the signals, even at 400 MHz, assignment of the signals attributable to the major and minor products was possible using a COSY experiment. The major product was identified as the axial sulfoxide by the downfield shift of the ^{1}H NMR signals of the axial protons, H-3′ and H-5′, relative to those of the minor product, as well as by the smaller chemical-shift differences between the signals of the geminal-proton pairs, H-2′$_{ax}$/H-2′$_{eq}$ and H-6′$_{ax}$/H-6′$_{eq}$ (see ref. 14). Because of signal overlap, nmr integration could not be used to estimate the axial:equatorial ratio of **10**. Treatment of **10** with *tert*-butyldimethylsilyl chloride provided the corresponding primary silyl ether derivative, in whose nmr spectrum the signals of the vinylic H-5 protons of the major and minor components were well separated. Integration of these signals allowed the axial:equatorial ratio of **10** to be estimated as 12:5.

We explored the use of the Pummerer reaction to install oxygen functionality at C-6′ of our analog. Treatment of **10** with hot acetic anhydride in the presence of *p*-toluenesulfonic acid afforded a 1:1 mixture of regioisomeric products **11***a*,*b* in 65% yield, which co-eluted on silica gel chromatography. The products were identified as 2′- and 6′-axial acetoxy derivatives by ^{1}H nmr spectroscopy in deuterated pyridine solution, which showed no axial–axial couplings for the thioketal-type protons. Partial purification of the 2′-acetoxy isomer **11***a* was achieved by recrystallization from *N*,*N*-dimethylformamide–isobutanol; this sample was useful for achieving a complete assignment of the ^{1}H nmr spectrum. Because of the difficulty in effecting separation of **11***a* and **11***b*, and the low solubility of these compounds, further elaboration of them was not pursued.

Synthesis of adenine derivatives

As shown in Scheme 3, **6** was condensed with 5-amino-4,6-dichloropyrimidine in 1-butanol at reflux temperature (11), to give **12** (88%). The purinyl ring was completed by treatment

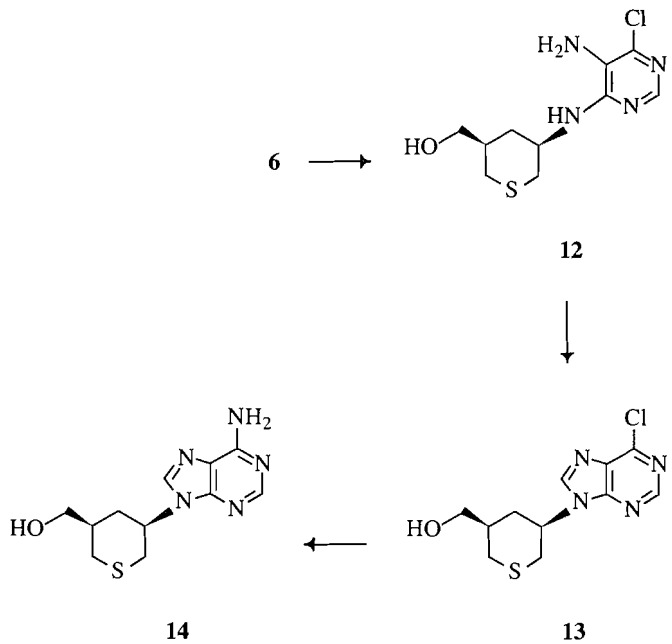

SCHEME 3

with triethyl orthoformate under acid catalysis, followed by brief exposure to 0.5 N hydrochloric acid (15); chloropurine derivative **13** precipitated from solution in 64% yield. Subsequent displacement of chloride by methanolic ammonia in a glass bomb at 75°C gave the desired analog (**14**) of adenosine in 41% yield after recrystallization from 2-propanol.

Anti-HIV and antitumor assays

Nucleoside analogs **9** and **10** were submitted to the U.S. National Cancer Institute (N.C.I.) for anti-HIV screening by the soluble-formazan assay in human T4 lymphocytes (16). The IC_{50} value for each compound was found to be $>10^{-3}$ M in this system. These compounds were screened also by N.C.I. against a panel of human leukemia, lung cancer, colon cancer, CNS

Can. J. Chem. Downloaded from www.nrcresearchpress.com by 195.246.54.202 on 09/08/12
For personal use only.

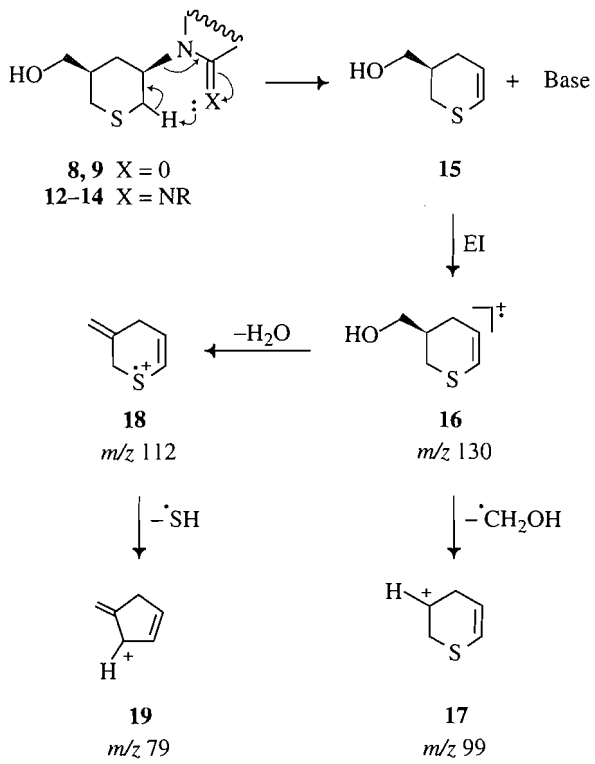

SCHEME 4

cancer, melanoma, ovarian cancer, and renal cancer cell cultures; analog **9** displayed weak activity (GI_{50} 5.6×10^{-5} M) against CNS cancer SNB-75 cells, but **9** and **10** were inactive otherwise ($GI_{50} > 10^{-4}$ M) in this assay. In none of these tests was any significant toxicity observed.

Compounds **9**, **10**, and **11***a* were screened also against HIV in MT-4 T-cells, by both reverse transcriptase assay and indirect immunofluorescence detection of viral p24 antigen.[4] No significant anti-HIV activity was found in these tests.

Mass-spectral observations

Routine EI mass spectra revealed an interesting common fragmentation for the thiane derivatives **8**, **9**, and **12–14**. These molecules afforded weak or no molecular ions, and their spectra displayed a sequence of major fragments at *m/z* 130, 112, 99, and 79. This pattern can be explained by a facile *thermal* elimination promoted by Lewis-basic atoms in the substituent side chain, as shown in Scheme 4. A mechanism of this type has recently been proposed by Lafortune et al. (17) to explain the fragmentation of thymidine in SIMS-TOF mass spectrometry. Subsequent electron-impact ionization of the neutral unsaturated product **15** then affords the observed fragments. The molecular formulas of all the proposed fragments have been determined by high-resolution measurements. A transformation of the type **18** → **19** was observed previously in the spectrum of methyl vinyl sulfide (18), which ejects sulfhydryl radical to give allyl cation by alkyl migration.

The thermal character of the initial elimination is suggested by the absence of any fragment ions characteristic of McLafferty or similar reactions of $M^{+\cdot}$. It is also supported by the behavior of the urea **8** under hot- and cold-injection conditions. This compound may produce fragments at *m/z* 99 by two pathways. High-resolution measurements showed the presence of a 1:1 mixture of ion **17** and acylium ion $[C_5H_7O_2]^+$ when the injection probe was heated, while only the product $[C_5H_7O_2]^+$, arising from direct electron-impact ionization of intact **8**, was observed on cold injection.

The Pummerer product **11** appears to fragment by a similar pathway, but competing loss of HOAc complicates analysis of the spectrum. Interestingly, the sulfoxide **10** gives a strong molecular ion and no fragments related to the sequence of Scheme 4, despite the enhanced acidity of its C-2′ protons.

Experimental

The ^{1}H nmr spectra were recorded on a Bruker AM-400 or AC-F 200 spectrometer at 400.136 or 200.132 MHz. The signals due to residual protons in the deuterated solvents indicated were used as internal standards. Chemical shifts are reported in ppm (δ) downfield from the position of tetramethylsilane (TMS). The symbols s (singlet), d (doublet), t (triplet), q (quartet), m (multiplet), and br (broadened) are used to describe the multiplicity and shape of the signals. The ^{13}C nmr spectra were obtained at 100.6 MHz on the AM-400 spectrometer or at 50.323 MHz on the AC-F 200 spectrometer. The JMOD spin-echo sequence (19) was used to aid in peak identification. Chemical shifts in ppm (δ) downfield from the position of TMS were measured using the solvent signals as internal standards, except for spectra measured in D_2O, where 1,4-dioxane-H_8 (δ 66.5) (20) was added as a standard.

EI mass spectra were recorded on a VG Micromass 7070F mass spectrometer at an ionizing voltage of 70 eV, or on a VG Analytical ZAB-E mass spectrometer, and CI spectra were recorded using NH_3 at ~1 Torr (133.3 Pa) as reagent gas; data are given as *m/z* (% relative intensity). The exact masses were determined under EI conditions. Except where noted, the high-resolution measurements were performed by peak matching using perfluorokerosene as a reference standard, at a resolution of ~4000.

Melting points were determined using a Fisher–Johns apparatus, and are uncorrected. Flash chromatography was performed on Kieselgel 60 (230–400 mesh), and thin-layer chromatography (TLC) was performed on glass plates coated with Kieselgel 60.

The homogeneity of the products was established on the basis of chromatographic, spectroscopic (^{1}H and ^{13}C nmr), and melting-point determinations.

(±)-(3β,5β)-3,5-Bis(p-toluenesulfonyloxymethyl)-1-aza-2-oxocyclopentane (3)

A solution of freshly recrystallized lactam **1** (see ref. 11) (8.2 g, 75 mmol) in dry methanol (300 mL) was purged with oxygen, while being cooled to −60°C in a Dry Ice – acetone bath. Ozone was passed through the solution at −60°C, until TLC analysis (0.5% methanol in ethyl acetate as eluant) and the presence of the blue color of an excess of ozone indicated completion. The temperature of the solution was allowed to rise to −30°C over 20 min, while the excess of ozone was purged with a stream of oxygen. Sodium borohydride (2.84 g, 75 mmol) was added slowly, while the temperature rose to −5°C. Stirring was continued for 1 h, and then Dowex-50 (H^+) ion-exchange resin was added to bring the apparent pH to 5. The mixture was filtered and the filtrate was concentrated. The residual oil was evaporated several times from methanol, and then left overnight on a vacuum pump, to provide diol **2** as a solid (10.01 g, 92%). A sample recrystallized from methanol–ether had mp 91–92°C; ^{1}H nmr (D_2O, 400 MHz) δ: 1.67 (1H, ddd, $J_{4\alpha,4\beta}$ = 13 Hz, J_{vic} = 9 Hz, $J_{vic'}$ = 7 Hz, H-4α), 2.31 (1H, ddd, $J_{4\beta,4\alpha}$ = 13 Hz, J_{vic} = 10 Hz, $J_{vic'}$ = 8 Hz, H-4β), 2.74 (1H, m, H-3), 3.46 (1H, dd, J_{gem} = 12 Hz, $J_{to\,5}$ = 6 Hz, 5-CH_2OH), 3.63 (1H, dd, J_{gem} = 12 Hz, $J_{to\,5}$ = 4 Hz, 5-CH_2OH), 3.68 (1H, dd, J_{gem} = 11 Hz, $J_{to\,3}$ = 5 Hz, 3-CH_2OH), 3.76 (1H, dd, J_{gem} = 11 Hz, $J_{to\,3}$ = 6 Hz, 3-CH_2OH), 3.70–3.80 (1H, m, H-5); ms (EI): 114 (M − CH_2OH)$^+$

[4]We thank Dr. Mark A. Wainberg of the Lady Davis Institute for Medical Research at The Sir Mortimer B. Davis-Jewish General Hospital, Montreal, for conducting these assays.

Can. J. Chem. Downloaded from www.nrcresearchpress.com by 195.246.54.202 on 09/08/12
For personal use only.

Can. J. Chem. Downloaded from www.nrcresearchpress.com by 195.246.54.202 on 09/08/12
For personal use only.

(100%), 96 (M − CH_2OH − H_2O)$^+$ (80.4%), 84 (M − CH_2O − CH_2OH)$^+$ (36.2%); ms (CI): 146 (M + H)$^+$ (100%), 163 (M + NH_4)$^+$ (6.4%), 291 (2M + H)$^+$ (2%). Exact Mass calcd. for $C_5H_8NO_2$ (M − CH_2OH)$^+$: 114.0555; found (hrms): 114.0551.

Without further purification, **2** (9.929 g, 68.4 mmol) was dissolved in freshly distilled, dry pyridine (200 mL) under an argon atmosphere. 4-Dimethylaminopyridine (0.852 g, 6.97 mmol) was added, and the mixture was cooled in an ice–water bath. *p*-Toluenesulfonyl chloride (28.7 g, 150.5 mmol) was added in several portions, and the mixture was stirred for 1 h. The pyridine was then evaporated under vacuum at 35°C. The residue was dissolved in ethyl acetate (200 mL), and the solution was washed successively with water (50 mL), a saturated aqueous solution of copper sulfate (50 mL), and water (50 mL). The combined aqueous layers were extracted with dichloromethane (50 mL), and the combined organic layers were dried ($MgSO_4$) and concentrated. Flash chromatography (ethyl acetate as eluant) of the residue afforded a sample of **3** (19.4 g, 57.5% overall), which was recrystallized from ethyl acetate; mp 131–132°C; ^{1}H nmr ($CDCl_3$, 200 MHz) δ: 1.62 (1H, ddd, $J_{4\alpha,4\beta}$ = 13.3 Hz, J_{vic} = 9 Hz, J_{vic} = 7 Hz, H-4α), 2.38 (1H, ddd, $J_{4\beta,4\alpha}$ = 13.3 Hz, J_{vic} = 9.6 Hz, J_{vic} = 7.3 Hz, H-4β), 2.43 (3H, s, ArCH_3), 2.45 (3H, s, ArCH_3), 2.61–2.81 (1H, m, H-3), 3.78–3.96 (2H, m, H-5 and 5-C*H*OTs), 4.06 (1H, m, 5-C*H*OTs), 4.08 (1H, dd, J_{gem} = 9.9 Hz, $J_{to\ 3}$ = 6 Hz, 3-C*H*OTs), 4.20 (1H, dd, J_{gem} = 9.9 Hz, $J_{to\ 3}$ = 3.7 Hz, 3-C*H*OTs), 6.21 (1H, br s, NH), 7.33 (2H, d, *J* = 8.4 Hz, aromatic), 7.36 (2H, d, *J* = 8.4 Hz, aromatic), 7.73 (2H, d, *J* = 8.4 Hz, aromatic), 7.78 (2H, d, *J* = 8.4 Hz, aromatic); ^{13}C nmr ($CDCl_3$, 50 MHz) δ: 21.72 (2 × Ar*C*H$_3$), 26.04 (C-4), 40.81 (C-3), 50.91 (C-5), 69.06 (*C*H_2OTs), 72.21 (*C*H_2OTs), 128.00 (4 × *meta*-aromatic C's), 130.02 (2 × *ortho*-aromatic C's), 130.19 (2 × *ortho*-aromatic C's), 132.23 (2 × *para*-aromatic C's), 132.26 (2 × *para*-aromatic C's), 145.23 (aromatic *C*-S), 145.51 (aromatic *C*-S), 174.26 (C-2). Anal. calcd. for $C_{20}H_{23}NO_7S_2$: C 52.97, H 5.11, N 3.09, S 14.14; found: C 52.81, H 5.13, N 3.13, S 13.88.

(±)-3-Thia-6-aza-7-oxobicyclo[3.2.1]octane (4)

To a solution of ditosylate **3** (17.0 g, 37.5 mmol) in *N*,*N*-dimethylformamide (300 mL) was added sodium sulfide nonahydrate (10.8 g, 45 mmol), and the mixture was stirred at 90°C for 45 min. Heating was stopped, and the solvent was evaporated in vacuo. The residue was taken up in acetone (100 mL), and the resulting suspension was filtered. The filtrate was concentrated to produce an oil that deposited a solid on standing under vacuum. The solid product was collected by filtration and washed with a small amount of ethyl acetate. The filtrate was concentrated and the residue was chromatographed (gradient elution using 0% → 4% methanol in ethyl acetate) to afford further product. The combined solids were recrystallized from ethyl acetate – hexanes to give **4** (3.67 g, 68%); mp 198–200°C (sealed capillary); ^{1}H nmr ($CDCl_3$, 400 MHz) δ: 1.73 (1H, dd, $J_{8ax,8eq}$ = 11.6 Hz, $J_{8ax,5}$ = 1.5 Hz, H-8_{ax}), 2.37 (1H, m, H-8_{eq}), 2.52 (1H, br dd, $J_{2eq,2ax}$ = 12.8 Hz, $J_{2eq,1}$ = 4.5 Hz, H-2_{eq}), 2.59–2.69 (2H, m, H-4_{eq} and H-5), 2.96 (1H, dd, $J_{4ax,4eq}$ = 12 Hz, $J_{4ax,5}$ = 1.5 Hz, H-4_{ax}), 3.03 (1H, d, $J_{2ax,2eq}$ = 12.8 Hz, H-2_{ax}), 3.98 (1H, br dd, $J_{1,8eq}$ = 5.8 Hz, $J_{1,2eq}$ = 4.5 Hz, H-1), 6.31 (1H, br s, NH); ^{13}C nmr (D_2O, 100 MHz) δ: 25.69 (C-4), 30.04 (C-2), 35.76 (C-8), 39.87 (C-5), 50.83 (C-1), 181.51 (C-6). An analytical sample was obtained by sublimation at 0.2 Torr and 110°C. Anal. calcd. for C_6H_9NOS: C 50.32, H 6.34, N 9.78, S 22.39; found: C 50.36, H 6.29, N 9.78, S 22.79.

(±)-(3β,5β)-3-Amino-5-(methoxycarbonyl)thiane hydrochloride (5)

A solution of lactam **4** (3.00 g, 20.95 mmol) in methanol (50 mL) was treated with concentrated hydrochloric acid (0.25 mL), and the mixture was heated at reflux temperature for 12 h. Heating was stopped, and the solvent was evaporated. The residual solid was recrystallized from isoamyl alcohol. The product crystals were washed with ether and dried in vacuo at 110°C to give **5** (4.05 g, 91%); mp 167–168°C; ^{1}H nmr (DMSO-d_6, 400 MHz) δ: 1.49 (1H, apparent q, J_{app} = 12 Hz, H-4_{ax}), 2.30 (1H, br d, $J_{4eq,4ax}$ = 12 Hz, H-4_{eq}), 2.51 (1H, dd, $J_{2ax,2eq}$ = 13.5 Hz, $J_{2ax,3}$ = 12 Hz, H-2_{ax}), 2.61 (1H, dd, $J_{6ax,6eq}$ = 13 Hz, $J_{6ax,5}$ = 12 Hz, H-6_{ax}), 2.70–2.83 (3H, m, H-2_{eq}, H-5 and H-6_{eq}), 3.26 (1H, m, H-3), 3.64 (3H, s, OCH_3), 8.50 (3H, br s, NH_3^+); ^{13}C nmr (DMSO-d_6, 100 MHz) δ: 28.17 (C-6), 29.34 (C-4), 32.11 (C-2), 43.18 (C-5), 49.12 (C-3), 51.98 (OCH_3), 172.50 (C=O). Anal. calcd. for $C_7H_{13}NO_2S$·HCl: C 39.71, H 6.67, N 6.62, S 15.14; found: C 39.78, H 6.65, N 6.59, S 15.87.

(±)-(3β,5β)-3-Amino-5-(hydroxymethyl)thiane (6)

A stirred suspension of **5** (3.5 g, 16.5 mmol) in dry oxolane (40 mL) was treated with a 2 M solution of lithium borohydride in oxolane (15 mL, 30 mmol). The resulting clear solution was heated at reflux temperature for 2 h. The reaction mixture was cooled, methanol (25 mL) was added slowly, and then concentrated hydrochloric acid was added dropwise until the solution was acidic to pH paper; the solvents were evaporated. The residue was dissolved in methanol (50 mL) and the solution was evaporated; the residue was then dissolved in concentrated aqueous ammonia (70 mL). The solution was continuously extracted with chloroform overnight. The dried ($MgSO_4$) extracts were concentrated to yield **6** as a solid (2.27 g, 93%). An analytical sample was obtained by recrystallization from dichloromethane–hexanes; mp 124–125°C; ^{1}H nmr ($CDCl_3$, 400 MHz) δ: 0.85 (1H, apparent q, J_{app} = 12 Hz, H-4_{ax}), 1.55 (3H, br s, OH and NH_2), 1.93–2.04 (2H, m, H-4_{eq} and H-5), 2.23 (1H, dd, $J_{2ax,2eq}$ = 13 Hz, $J_{2ax,3}$ = 12 Hz, H-2_{ax}), 2.33 (1H, dd, $J_{6ax,6eq}$ = 13 Hz, $J_{6ax,5}$ = 10 Hz, H-6_{ax}), 2.56–2.65 (2H, m, H-2_{eq} and H-6_{eq}), 2.98 (1H, dddd, $J_{3,2ax}$ = 12 Hz, $J_{3,4ax}$ = 12 Hz, $J_{3,4eq}$ = 3.5 Hz, $J_{3,2eq}$ = 3 Hz, H-3), 3.45 (1H, dd, J_{gem} = 11 Hz, $J_{to\ 5}$ = 7 Hz, CH_2OH), 3.53 (1H, dd, J_{gem} = 11 Hz, $J_{to\ 5}$ = 6 Hz, CH_2OH); ^{13}C nmr ($CDCl_3$, 50 MHz) δ: 30.16 (C-4), 36.75 (C-6), 38.80 (C-2), 42.32 (C-5), 50.73 (C-3), 67.06 (CH_2OH); ms (EI): 147 (M$^+$) (24.4%), 116 (M − CH_2OH)$^+$ (7.3%), 104 (M − C_2H_5N)$^+$ (12.8%), 86 (M − CH_2SCH_3)$^+$ (100%). Exact Mass calcd. for $C_6H_{13}NOS$: 147.0719; found (hrms): 147.0707. Anal. calcd. for $C_6H_{13}NOS$: C 48.95, H 8.90, N 9.51, S 21.77; found: C 48.80, H 8.91, N 9.31, S 23.12.

(±)-trans-*3-Ethoxy*-N-*[N'-[(3'β,5'β)-5'-(hydroxymethyl)thian-3'-yl]-carbamoyl]propenamide (8)*

Following the procedure of Shealy and O'Dell (13*a*), silver cyanate was dried at 100°C and <1 Torr in the dark for 2 h. A solution of amine **6** (1.47 g, 10 mmol) in dry, distilled *N*,*N*-dimethylformamide (50 mL) was dried over 3 Å molecular sieves under an argon atmosphere until needed. All glassware was dried overnight at 140°C, and assembled while hot, under an argon atmosphere.

A suspension of silver cyanate (4.5 g, 30 mmol) in dry benzene (20 mL) was heated at reflux temperature for 30 min, under an argon atmosphere. A solution of *trans*-3-ethoxypropenoyl chloride (13*b*) (2.00 g, 15 mmol) in dry benzene (10 mL) was added using a syringe, and the mixture was boiled for 45 min. Heating and stirring were stopped, and the suspended solids were allowed to settle for 2 h.

The solution of amine **6** was transferred to a dry flask by cannula, under argon pressure, and cooled to −60°C. A 20-mL portion (~10 mmol) of the acyl isocyanate solution was removed with a syringe, and was added dropwise to the amine over 15 min. The temperature was raised quickly to −30°C. Stirring was continued as the mixture warmed gradually to 23°C overnight. The solvent was then evaporated under high vacuum, and the residue was re-evaporated from ethanol (50 mL). Traces of solvent were removed on the vacuum pump, and the solid product was recrystallized from 95% ethanol to afford **8** (2.26 g, 78%); mp 171–172°C; IR ν_{max} (KBr): 3510 (sh, OH), 3310, 3230 (sh, NH), 2980 (vinyl CH), 1700, 1670, 1605 (s, C=O), 1530, 1510 (C=C) cm^{-1}; ^{1}H nmr ($CDCl_3$, 400 MHz) δ: 1.11 (1H, apparent q, J_{app} = 12 Hz, H-4_{ax}), 1.37 (3H, t, *J* = 7 Hz, CH_3), 1.56 (1H, br s, OH), 2.00–2.13 (2H, m, H-4_{eq} and H-5), 2.29 (1H, dd, $J_{2ax,2eq}$ = 13 Hz, $J_{2ax,3}$ = 11 Hz, H-2_{ax}), 2.43 (1H, dd, $J_{6ax,6eq}$ = 12.5 Hz, $J_{6ax,5}$ = 11 Hz, H-6_{ax}), 2.64 (1H, br d, $J_{2eq,2ax}$ = 13.5 Hz, H-2_{eq}), 2.87 (1H, ddd, $J_{6eq,6ax}$ = 13 Hz, $J_{6eq,5}$ = 2 Hz, $J_{6eq,2eq}$ ~1.5 Hz, H-6_{eq}), 3.48 (1H, dd,

[5]For the Exact Mass determinations of peaks at *m/z* 99 and 79 in compounds **8** and **9**, peak matching to $C_2H_6O_2$ = 74.03678 and CH_2Cl_2 = 83.9536 was used for calibration.

Can. J. Chem. Downloaded from www.nrcresearchpress.com by 195.246.54.202 on 09/08/12
For personal use only.

J_{gem} = 10.5 Hz, $J_{to\ 5}$ = 7 Hz, CH_2OH), 3.55 (1H, dd, J_{gem} = 10.5 Hz, $J_{to\ 5}$ = 5.5 Hz, CH_2OH), 3.96 (2H, q, J = 7 Hz, OCH_2CH$_3$), 3.92–4.05 (1H, m, H-3), 5.32 (1H, d, J = 12 Hz, C(O) CH=), 7.64 (1H, d, J = 12 Hz, =CHO), 8.69 (1H, d, $J_{to\ 3}$ = 7.5 Hz, CHN*H*C=O), 9.35 (1H, br s, C(O)NHC(O)); ^{13}C nmr ($CDCl_3$, 100 MHz) δ: 14.45 (CH_3), 30.25 (C-4), 33.26 (C-6), 35.46 (C-2), 42.29 (C-5), 49.24 (C-3), 67.19 (O*C*H$_2$CH$_3$), 67.45 (CH_2OH), 97.80 (=*C*C(O)N), 154.32 (NC(O)N), 162.86 (=CHO), 168.19 (=C*C*(O)N); ms (EI): 288 (M^+) (2.5%), 159 ($C_6H_{11}N_2O_3$)$^+$ (68.7%), 130 ($C_6H_{10}OS$)$^+$ (64.4%), 112 (C_6H_8S)$^+$ (22.4%), 99 (O=CC=COEt)$^+$ and (C_5H_7S)$^+$ (83.9%), 79 (C_6H_7)$^+$ (13.2%), 71 (C_4H_7O)$^+$ (100%). Exact Mass calcd. for $C_{12}H_{20}N_2O_4S$: 288.1149; found (hrms): 288.1145. Exact Mass calcd. for $C_5H_7O_2$: 99.0446; found (hrms)[5]: 99.0453. Exact Mass calcd. for C_5H_7S: 99.0268; found (hrms)[5]: 99.0275. Exact Mass calcd. for C_6H_7: 79.0548; found (hrms)[5]: 79.0541. Anal. calcd. for $C_{12}H_{20}N_2O_4S$: C 49.98, H 6.99, N 9.71, S 11.12; found: C 49.73, H 6.82, N 9.62, S 11.37.

*(±)-1-{(3′β,5′β)-5′-(Hydroxymethyl)thian-3′-yl}-2,4(1H,3H)-pyrimidinedione (**9**)*

Enol ether **8** (1.90 g, 6.59 mmol) was suspended in a mixture of concentrated sulfuric acid (4 mL) and water (20 mL), and the reaction mixture was heated at reflux temperature for 30 min. The resulting solution was cooled, and neutralized with 1 M sodium hydroxide. The water was evaporated, and the residue was extracted with 95% ethanol (3 × 75 mL). The extracts were filtered and the filtrate was concentrated to afford a glass. Re-evaporation from toluene–ethanol gave **9** as a powder, which was dried in vacuo (1.53 g, 96%); mp 178–179°C; IR ν_{max} (KBr): 3430 (br, OH), 3176 (NH), 3044 (vinyl C-H), 1687 (C=O) cm^{-1}; ^{1}H nmr (DMSO-d_6, 400 MHz) δ: 1.48 (1H, apparent q, J_{app} = 12 Hz, H-4′$_{ax}$), 1.76 (1H, br d, $J_{4'eq,4'ax}$ = 12 Hz, H-4′$_{eq}$), 1.88 (1H, m, H-5′), 2.23 (1H, dd, $J_{6'ax,6'eq}$ = 12 Hz, $J_{6'ax,5'}$ = 12 Hz, H-6′$_{ax}$), 2.54 (2H, br d, J_{app} = 13 Hz, H-2′$_{eq}$ and H-6′$_{eq}$), 2.88 (1H, dd, $J_{2'ax,2'eq}$ = 12 Hz, $J_{2'ax,3'}$ = 12 Hz, H-2′$_{ax}$), 3.19–3.31 (2H, m, CH_2OH), 4.50 (1H, m, H-3′), 4.68 (1H, dd, J_{vic} = 5 Hz, J_{vic} = 5 Hz, OH), 5.56 (1H, d, $J_{5,6}$ = 8 Hz, H-5), 7.70 (1H, d, $J_{6,5}$ = 8 Hz, H-6), 11.12 (1H, br s, NH); ^{13}C nmr (DMSO-d_6, 100 MHz) δ: 29.27 (C-4′), 30.25 (C-6′), 33.31 (C-2′), 43.51 (C-5′), 54.32 (C-3′), 65.35 (CH_2OH), 101.27 (C-5), 141.93 (C-6), 150.69 (C-2), 163.08 (C-4); ms (CI): 485 (2M + H)$^+$ (2%), 260 (M + NH_4)$^+$ (10.5%), 243 (M + H)$^+$ (100%), 131 ($C_6H_{10}OS$ + H)$^+$ (34.1%); ms (EI): 130 ($C_6H_{10}OS$)$^+$ (100%), 112 (C_6H_8S)$^+$ (28.5%), 99 (C_5H_7S)$^+$ (32.9%), 79 (C_6H_7)$^+$ (57%). Exact Mass calcd. for $C_6H_{10}OS$: 130.0452; found (hrms): 130.0452. Exact Mass calcd. for C_6H_8S: 112.0347; found (hrms): 112.0339 (pyrimidinedione $C_4H_4N_2O_2$ requires 112.0273). Exact Mass calcd. for C_5H_7S: 99.0268; found (hrms)[5]: 99.0270. Exact Mass calcd. for C_6H_7: 79.0548; found (hrms)[5]: 79.0541. Anal. calcd. for $C_{10}H_{14}N_2O_3S\cdot\frac{1}{2}H_2O$: C 47.80, H 6.02, N 11.15, S 12.76; found: C 47.88, H 5.68, N 11.07, S 12.98.

*(±)-1-{(3′β,5′β)-5′-(Hydroxymethyl)thian-3′-yl}-2,4(1H,3H)-pyrimidinedione S-oxide (**10**)*

To a solution of sulfide **9** (1.00 g, 4.13 mmol) in water (30 mL) at 0°C was added sodium periodate (0.929 g, 4.34 mmol) in a minimum amount of water, and the reaction mixture was stirred for 1 h. An excess of solid sodium bisulfite was added with cooling, and the solution was evaporated. The solid residue was dried in vacuo, and extracted with methanol (3 × 30 mL). The extracts were filtered, the filtrate was evaporated, and the residue was chromatographed by gravity on flash-grade silica, using a chloroform–methanol gradient (10% → 20%) as eluant. No separation of sulfoxide diastereomers was observed. Evaporation of the combined product fractions afforded a glassy oil, which was dissolved in water. The solution was freeze-dried, to afford **10** as an amorphous powder (0.732 g, 69%); mp > 155°C; IR ν_{max} (KBr): 3404 (br, OH), 1685 (C=O), 1101 (S=O) cm^{-1}; ^{1}H nmr (D_2O, 400 MHz) major (axial S=O) diastereomer δ: 1.72 (1H, apparent q, J_{app} = 12 Hz, H-4′$_{ax}$), 1.93 (1H, br d, $J_{4'eq,4'ax}$ = 12 Hz, H-4′$_{eq}$), 2.38 (1H, dd, $J_{6'ax,6'eq}$ = 13.5 Hz, $J_{6'ax,5'}$ = 13 Hz, H-6′$_{ax}$), 2.50 (1H, m, H-5′), 2.92 (1H, dd, $J_{2'ax,2'eq}$ = 14 Hz, $J_{2'ax,3'}$ = 14 Hz, H-2′$_{ax}$), 3.04 (br d, $J_{6'eq,6'ax}$ = 13.5 Hz, H-6′$_{eq}$), 3.18 (1H, m, H-2′$_{eq}$), 3.45–3.56 (2H, m, CH_2OH), 4.96 (1H, m, H-3′), 5.71 (1H, d, $J_{5,6}$ = 8 Hz, H-5), 7.52 (1H, d, $J_{6,5}$ = 8 Hz, H-6); minor (equatorial S=O) diastereomer δ: 1.60 (1H, apparent q, J_{app} = 12 Hz, H-4′$_{ax}$), 1.84 (1H, br d, $J_{4'eq,4'ax}$ = 12 Hz, H-4′$_{eq}$), 1.88–1.98 (1H, m, H-5′), 2.44 (1H, dd, $J_{6'ax,6'eq}$ = 12 Hz, $J_{6'ax,5'}$ = 12 Hz, H-6′$_{ax}$), 2.96 (1H, dd, $J_{2'ax,2'eq}$ = 12 Hz, $J_{2'ax,3'}$ = 12 Hz, H-2′$_{ax}$), 3.45–3.56 (3H, m, CH_2OH and H-6′$_{eq}$), 3.63 (1H, br d, $J_{2'eq,2'ax}$ = 12 Hz, H-2′$_{eq}$), 4.53 (1H, m, H-3′), 5.72 (1H, d, $J_{5,6}$ = 8 Hz, H-5), 7.55 (1H, d, $J_{6,5}$ = 8 Hz, H-6); ^{13}C nmr (D_2O, 100 MHz) major (axial S=O) diastereomer δ: 31.34 (C-5′), 31.87 (C-4′), 45.98 (C-6′), 48.05 (C-3′), 52.31 (C-2′), 64.80 (CH_2OH), 102.20 (C-5), 143.71 (C-6), 151.71 (C-2), 166.12 (C-4); minor (equatorial S=O) diastereomer δ: 31.34 (C-4′), 33.30 (C-5′), 45.41 (C-6′), 50.01 (C-3′), 51.35 (C-2′), 64.39 (CH_2OH), 102.29 (C-5), 143.10 (C-6), 151.55 (C-2), 166.05 (C-4). Exact Mass calcd. for $C_{10}H_{14}N_2O_4S$: 258.0675; found (hrms): 258.0666. Anal. calcd. for $C_{10}H_{14}N_2O_4S\cdot H_2O$: C 43.47, H 5.84, N 10.14, S 11.60; found: C 43.51, H 5.54, N 10.13, S 11.80.

Treatment of **10** with *tert*-butyldimethylsilyl chloride afforded the corresponding silyl ether derivative (TLC: **10**, R_f = 0.26; silyl ether, R_f = 0.76; using 8:2 (v/v) chloroform–methanol as eluant). The ^{1}H nmr signals attributable to H-5 in the two diastereomers of this derivative were separated sufficiently at 400 MHz (Δδ = 0.098 ppm) to show the diastereomer ratio to be 12:5.

*(±)-1-{(2′β,3′β,5′β)-2′-Acetoxy-5′-(acetoxymethyl)thian-3′-yl}-2,4(1H,3H)-pyrimidinedione (**11**a)*

A mixture of sulfoxide **10** (200 mg, 0.77 mmol), acetic anhydride (15 mL), and *p*-toluenesulfonic acid (cat.) was heated in an oil bath at 100°C under a nitrogen atmosphere for 2.5 h. The excess of acetic anhydride was evaporated under vacuum. The dried residue was adsorbed on a small amount of silica gel, applied to a silica gel column, and chromatographed using a gradient of chloroform–methanol (0% → 2%) as eluant. All of the product fractions could be seen on TLC analysis, using 2% (v/v) methanol in chloroform as eluant, to contain two components (R_f = 0.17 and 0.23) in approximately equal proportions. Evaporation of these fractions afforded a mixture of **11***a* (2′-β) and its 6′-β isomer **11***b* (171 mg, 65%). Recrystallization of this material from isobutanol–*N*,*N*-dimethylformamide effected a partial resolution, affording 22 mg (8.3%) of an 8:1 mixture of **11***a*:**11***b*; ^{1}H nmr (pyridine-d_5, 400 MHz) δ: 1.83 (1H, br d, $J_{4'eq,4'ax}$ = 12.3 Hz, H-4′$_{eq}$), 2.01 (3H, s, CH_3-11′), 2.04 (3H, s, CH_3-9′), 2.16 (1H, apparent q, J_{app} = 12.4 Hz, H-4′$_{ax}$), 2.45 (1H, m, H-5′), 2.53 (1H, br d, $J_{6'eq,6'ax}$ = 13.4 Hz, H-6′$_{eq}$), 2.76 (1H, dd, $J_{6'ax,6'eq}$ = 13.2 Hz, $J_{6'ax,5'}$ = 11.9 Hz, H-6′$_{ax}$), 4.07 (1H, dd, J_{gem} = 11.0 Hz, $J_{to\ 5'}$ = 6.8 Hz, CH_2OAc), 4.12 (1H, dd, J_{gem} = 11.0 Hz, $J_{to\ 5'}$ = 5.9 Hz, CH_2OAc), 5.32 (1H, ddd, $J_{3',4'ax}$ = 13.2 Hz, $J_{3',2'}$ = 2.4 Hz, $J_{3',4'eq}$ = 3.5 Hz, H-3′), 5.89 (1H, d, $J_{5,6}$ = 8.1 Hz, H-5), 6.44 (1H, d, $J_{2',3'}$ = 2.4 Hz, H-2′), 7.66 (1H, d, $J_{6,5}$ = 8.1 Hz, H-6); ^{13}C nmr (pyridine-d_5, 50 MHz) δ: 20.65 (C-9′ and C-11′), 26.17 (C-4′), 27.94 (C-6′), 40.15 (C-5′), 56.76 (C-3′), 67.66 (C-7′), 71.34 (C-2′), 102.14 (C-5), 141.18 (C-6), 152.26 (C-2), 164.09 (C-4), 169.38 (C-10′), 170.67 (C-8′); ms (EI): 342 (M^+) (3.8%), 282 (M − HOAc)$^+$ (20.1%), 230 (M − pyrimidinedione)$^+$ (13.2%), 222 (M − 2HOAc)$^+$ (28.5%), 113 (pyrimidinedione + H)$^+$ (100%): Exact Mass calcd. for $C_{14}H_{18}N_2O_6S$: 342.0886; found (hrms): 342.0887.

*(±)-5-Amino-6-chloro-4-{[(3′β,5′β)-5′-(hydroxymethyl)thian-3′-yl]-amino}pyrimidine (**12**)*

According to the method of Daluge and Vince (11), a solution of amino alcohol **6** (250 mg, 1.7 mmol), 5-amino-4,6-dichloropyrimidine (563 mg, 3.44 mmol), and triethylamine (1.2 mL, 8.5 mmol) in *n*-butanol (10 mL, dried over 3 Å molecular sieves) was heated at reflux temperature in a nitrogen atmosphere for 24 h. The mixture was cooled, and the solvent was evaporated. The residue was adsorbed on a small amount of silica gel, and applied to a silica gel column. Elution with ethyl acetate afforded **12** as a yellowish solid (412 mg, 88%); mp 177–178°C; ^{1}H nmr (DMSO-d_6, 400 MHz) δ: 1.10 (1H, apparent q,

[6]The overlapping signals at δ 151.20 ppm could be separated by addition of ~20% (v/v) of benzene-d_6 to the sample.

Can. J. Chem. Downloaded from www.nrcresearchpress.com by 195.246.54.202 on 09/08/12
For personal use only.

J_{app} = 12.5 Hz, H-4′$_{ax}$), 1.79–1.94 (1H, m, H-5′), 1.94 (1H, br d, $J_{4'eq,4'ax}$ = 12 Hz, H-4′$_{eq}$), 2.22 (1H, dd, $J_{6'ax,6'eq}$ = 13 Hz, $J_{6'ax,5'}$ = 12 Hz, H-6′$_{ax}$), 2.31 (1H, dd, $J_{2'ax,2'eq}$ = 12.5 Hz, $J_{2'ax,3'}$ = 11 Hz, H-2′$_{ax}$), 2.56 (1H, br d, $J_{6'eq,6'ax}$ = 13 Hz, H-6′$_{eq}$), 2.80 (1H, br d, $J_{2'eq,2'ax}$ = 12.5 Hz, H-2′$_{eq}$), 3.20–3.35 (2H, m, CH_2OH), 4.05–4.16 (1H, m, H-3′), 4.61 (1H, dd, $J_{to\ CH_2O}$=5.5 Hz, $J_{to\ CH_2O}$ = 5.0 Hz, OH), 5.05 (2H, br s, ArNH_2), 6.71 (1H, d, $J_{to\ 3'}$ = 7.0 Hz, ArN*H*CH), 7.74 (1H, s, H-2); ^{13}C nmr (DMSO-d_6, 100 MHz) δ: 29.83 (C-4′), 32.22 (C-2′), 35.06 (C-6′), 42.70 (C-5′), 50.22 (C-3′), 65.63 (C-7′), 123.45 (C-4), 136.95 (C-5), 145.54 (C-2), 150.73 (C-6); ms (EI): 274 (^{35}Cl M$^+$) (3%), 146 ($C_4H_5N_4{}^{37}Cl)^+$ (33%), 144 ($C_4H_5N_4{}^{35}Cl)^+$ (100%), 130 ($C_6H_{10}OS)^+$ (11.1%), 112 ($C_6H_8S)^+$ (3.9%), 99 ($C_5H_7S)^+$ (5%), 79 ($C_6H_7)^+$ (10.7%); ms (CI): 277 (^{37}Cl M + H)$^+$ (38.2%), 275 (^{35}Cl M + H)$^+$ (100%). Exact Mass calcd. for $C_{10}H_{15}N_4OSCl$: 274.0655; found (hrms): 274.0653.

*(±)-6-Chloro-9-[(3′β,5′β)-5′-(hydroxymethyl)thian-3′-yl]purine (**13**)*

A solution of **12** (275 mg, 1 mmol), triethyl orthoformate (5 mL), and concentrated hydrochloric acid (0.3 mL) was stirred at 23°C for 1.75 h (see ref. 15). The excess of the orthoformate was evaporated, the last traces being removed under high vacuum. The residue was dissolved in 0.5 M hydrochloric acid (7 mL), and the solution was stirred for 1 h. A white precipitate formed that was isolated by filtration and found to be **13** (183 mg, 64%). The product could be crystallized from water and dried at 78°C and 0.1 Torr; mp 173–174°C; ^{1}H nmr (DMSO-d_6, 400 MHz) δ: 1.90 (1H, apparent q, J_{app} = 12 Hz, H-4′$_{ax}$), 2.01 (1H, m, H-5′), 2.10 (1H, br d, $J_{4'eq,4'ax}$ = 12.2 Hz, H-4′$_{eq}$), 2.38 (1H, dd, $J_{6'ax,6'eq}$ = 13.2 Hz, $J_{6'ax,5'}$ = 11.2 Hz, H-6′$_{ax}$), 2.65 (1H, br d, $J_{6'eq,6'ax}$ = 13.2 Hz, H-6′$_{eq}$), 2.86 (1H, br d, $J_{2'eq,2'ax}$ = 12.7 Hz, H-2′$_{eq}$), 3.22 (1H, dd, $J_{2'ax,2'eq}$ = 12.7 Hz, $J_{2'ax,3'}$ = 11.6 Hz, H-2′$_{ax}$), 3.29 (1H, dd, J_{gem} = 10.7 Hz, $J_{to\ 5'}$ = 6.5 Hz, CH_2OH), 3.33 (1H, dd, J_{gem} = 10.7 Hz, $J_{to\ 5'}$ = 5.5 Hz, CH_2OH), 4.20–4.60 (1H, br, OH), 4.80 (1H, m, H-3′), 8.75 (1H, s, H-8), 8.76 (1H, s, H-2); ^{13}C nmr (DMSO-d_6, 50 MHz)[6] δ: 29.43 (C-4′), 31.22 (C-2′), 34.34 (C-6′), 42.97 (C-5′), 55.08 (C-3′), 65.22 (C-7′), 130.96 (C-5), 145.63 (C-8), 149.05 (C-4), 151.20 (C-2 and C-6); ms (EI): 285 (M + H)$^+$ (4%), 157 (^{37}Cl purine + H)$^+$ (26.9%), 155 (^{35}Cl purine + H)$^+$ (83.8%), 130 ($C_6H_{10}OS)^+$ (100%), 112 ($C_6H_8S)^+$ (39.3%), 99 ($C_5H_7S)^+$ (27.7%), 79 ($C_6H_7)^+$ (46.4%); ms (CI): 287 (^{37}Cl M + H)$^+$ (38.6%), 285 (^{35}Cl M + H)$^+$ (100%), 251 (M − H_2S + H)$^+$ (6.4%), 131 ($C_6H_{10}OS$ + H)$^+$ (11.6%). Exact Mass calcd. for $C_{11}H_{14}N_4OSCl$ (M + H)$^+$: 285.0577; found (hrms): 285.0577.

*(±)-6-Amino-9-[(3′β,5′β)-5′-(hydroxymethyl)thian-3′-yl]purine (**14**)*

Chloropurine **13** (100 mg, 0.35 mmol) was suspended in methanol (3 mL) in a Pyrex tube. The suspension was cooled to −78°C and anhydrous ammonia was bubbled in until the solution volume was increased to ~5 mL. The tube was sealed, and heated at 75°C for 40 h. The solvent was evaporated under a stream of nitrogen to leave **14** as a solid, which was recrystallized from isopropanol and dried over potassium hydroxide at 0.1 Torr and 61°C (38 mg, 41%); mp 213–215°C; ^{1}H nmr (DMSO-d_6 + D_2O, 400 MHz) δ: 1.81 (1H, apparent q, J_{app} = 12 Hz, H-4′$_{ax}$), 1.90–2.07 (2H, m, H-4′$_{eq}$ and H-5′), 2.34 (1H, dd, $J_{6'ax,6'eq}$ = 12 Hz, $J_{6'ax,5'}$ = 12 Hz, H-6′$_{ax}$), 2.62 (1H, br d, $J_{6'eq,6'ax}$ = 12 Hz, H-6′$_{eq}$), 2.77 (1H, br d, $J_{2'eq,2'ax}$ = 12 Hz, H-2′$_{eq}$), 3.15 (1H, dd, $J_{2'ax,2'eq}$ = 12 Hz, $J_{2'ax,3'}$ = 12 Hz, H-2′$_{ax}$), 3.21–3.36 (2H, m, CH_2OH), 4.63 (1H, m, H-3′), 8.16 (1H, s, H-8), 8.25 (1H, s, H-2); ^{13}C nmr (DMSO-d_6, 100 MHz)[7] δ: 29.55 (C-4′), 31.66 (C-2′), 34.76 (C-6′), 43.06 (C-5′), 54.24 (C-3′), 65.30 (CH_2OH), 118.80 (C-5), 139.34 (C-8), 148.86 (C-4), 151.62 (C-2), 155.39 (C-6); ms (EI): 266 (M + H)$^+$ (2%), 136 (adenine + H)$^+$ (100%), 130 ($C_6H_{10}OS)^+$ (15.3%), 112 ($C_6H_8S)^+$ (7.7%), 99 ($C_5H_7S)^+$ (12.4%), 79 ($C_6H_7)^+$ (16.2%); ms (CI): 266 (M + H)$^+$ (100%), 136 (adenine + H)$^+$ (8.2%). Exact Mass calcd. for $C_{11}H_{16}N_5OS$ (M + H)$^+$: 266.1076; found (hrms): 266.1079.

[7]The signal attributable to C-8 at δ 139.34 ppm was prone to saturation. Accordingly, this spectrum was acquired using a power-gated sequence employing a 3-μs pulse and a 10-s relaxation delay between pulses.

Acknowledgements

We thank the Natural Sciences and Engineering Research Council of Canada for financial support of this work, and Professor D.B. MacLean of McMaster University for the mass spectra.

1. R.K. Robins. *In* Antiviral drug development. A multidisciplinary approach. *Edited by* E. De Clercq and R.T. Walker. Plenum Press, New York, NY. 1988. pp. 11–36
2. (*a*) M. MacCoss and M.J. Robins. *In* The chemistry of antitumour agents. *Edited by* D.E.V. Wilman. Blackie & Son Ltd., Glasgow and London. 1990. pp. 261–298; (*b*) R.K. Robins and G.D. Kini. *In* The chemistry of antitumour agents. *Edited by* D.E.V. Wilman. Blackie & Son Ltd., Glasgow and London. 1990. pp. 299–321.
3. (*a*) H. Soudeyns, X.J. Yao, Q. Gao, B. Belleau, J.L. Kraus, Nguyen Ba Nghe, B. Spira, and M.A. Wainberg. Antimicrob. Agents Chemother. **35**, 1386 (1991); (*b*) B. Belleau, P. Belleau, and Nguyen Ba Nghe. Eur. Pat. Appl. EP 382,526, 16 Aug. 1990, US Appl. 308,101, 08 Feb. 1989; Chem. Abstr. **114**, 43492b (1989); (*c*) Chem. Eng. News, **67**, 7 (June 26, 1989).
4. (*a*) W.-B. Choi, L.J. Wilson, S. Yeola, D.C. Liotta, and R.F. Schinazi. J. Am. Chem. Soc. **113**, 9377 (1991); (*b*) C.K. Chu, J.W. Beach, L.S. Jeong, B.G. Choi, F.I. Comer, A.J. Alves, and R.F. Schinazi. J. Org. Chem. **56**, 6503 (1991); (*c*) J.-K. Kraus and G. Attardo. Synthesis, 1046 (1991).
5. (*a*) B. Belleau, D. Dixit, and Nguyen Ba Nghe. Eur. Pat. Appl. EP 337,713, 18 Oct. 1989, US Appl. 179,615, 11 Apr. 1988; Chem. Abstr. **112**, 198359w (1988); (*b*) D.W. Norbeck, S. Spanton, S. Broder, and H. Mitsuya. Tetrahedron Lett. **30**, 6263 (1989).
6. (*a*) M.J. Bamford, D.C. Humber, and R. Storer. Tetrahedron Lett. **32**, 271 (1991); (*b*) D.M. Huryn, B.C. Sluboski, S.Y. Tam, L.J. Todaro, and M. Weigele. Tetrahedron Lett. **30**, 6259 (1989).
7. M.F. Jones, S.A. Noble, C.A. Robertson, and R. Storer. Tetrahedron Lett. **32**, 247 (1991).
8. K.E. Ng and L.E. Orgel. J. Med. Chem. **32**, 1754 (1989).
9. (*a*) A. Van Aerschot, G. Janssen, and P. Herdewijn. Bull. Soc. Chim. Belg. **99**, 769 (1990); (*b*) E.J. Prisbe. J. Med. Chem. **29**, 2445 (1986).
10. (*a*) D.M. Vyas and W.A. Szarek. Carbohydr. Res. **30**, 225 (1973); (*b*) W.A. Szarek, D.M. Vyas, and B. Achmatowicz. J. Heterocycl. Chem. **12**, 123 (1975); (*c*) W.A. Szarek, D.M. Vyas, and B. Achmatowicz. Tetrahedron Lett. 1553 (1975); (*d*) B.M. Pinto, D.M. Vyas, and W.A. Szarek. Can. J. Chem. **55**, 937 (1977); (*e*) M. Iwakawa, B.M. Pinto, and W.A. Szarek. Can. J. Chem. **56**, 326 (1978); (*f*) L.J.J. Hronowski and W.A. Szarek. J. Med. Chem. **25**, 522 (1982); (*g*) W.A. Szarek, B.M. Pinto, and M. Iwakawa. Can J. Chem. **63**, 2149 (1985).
11. S. Daluge and R. Vince. J. Org. Chem. **43**, 2311 (1978).
12. S.J.C. Taylor, A.G. Sutherland, C. Lee, R. Wisdom, S. Thomas, S.M. Roberts, and C. Evans. J. Chem. Soc. Chem. Commun. 1120 (1990).
13. (*a*) Y.F. Shealy and C.A. O'Dell. J. Heterocycl. Chem. **13**, 1015 (1976); (*b*) G. Shaw and R.N. Warrener. J. Chem. Soc. 153 (1958).
14. (*a*) A.B. Foster, T.D. Inch, M.H. Qadir, and J.M. Webber. J. Chem. Soc. Chem. Commun. 1086 (1968); (*b*) J.B. Lambert and R.G. Keske. J. Org. Chem. **31**, 3429 (1966).
15. R. Vince and M. Hua. J. Med. Chem. **33**, 17 (1990).
16. O.W. Weislow, R. Kiser, D. Fine, J. Bader, R.H. Shoemaker, and M.R. Boyd. J. Natl. Cancer Inst. **81**, 577 (1989).
17. F. Lafortune, G.W. Buchko, F.E. Hruska, K.L. Sadana, K.G. Standing, and J.B. Westmore. Nucleosides, Nucleotides, **11**, 1305 (1992).
18. R.G. Gillis and J.L. Occolowitz. Tetrahedron Lett. 1997 (1966).
19. C. Le Cocq and J.-Y. Lallemand. J. Chem. Soc. Chem. Commun. 150 (1981).
20. R.M. Silverstein, G.C. Bassler, and T.C. Morrill. Spectrometric identification of organic compounds. 4th ed. Wiley, New York. 1981. p. 269.

Absolute stereochemistry of (−)-camoensine and (−)-camoensidine in *Maackia* species[1]

HAJIME KUBO AND SHIGERU OHMIYA[2]

Faculty of Pharmaceutical Sciences, Hoshi University, Ebara 2-4-41, Shinagawa-ku, Tokyo 142, Japan

AND

ISAMU MURAKOSHI

Faculty of Pharmaceutical Sciences, Chiba University, Yayoi-cho 1-33, Inage-ku, Chiba 263, Japan

Received June 4, 1993

This paper is dedicated to Professor Ian D. Spenser

HAJIME KUBO, SHIGERU OHMIYA, and ISAMU MURAKOSHI. Can. J. Chem. **72**, 214 (1994).

It was demonstrated that the attack of Grignard reagents such as methyl-, allyl-, and 3,3-dimethoxypropyl magnesium bromides on 11,12-dehydrocytisine occurs on the α-face, to give the corresponding 11α-alkylcytisine. (−)-Camoensine and (−)-camoensidine were synthesized from (−)-cytisine via the Grignard reaction. The absolute stereochemistry of the above alkaloids was confirmed to be 7*R*, 9*R*, 11*R* and 6*S*, 7*R*, 9*R*, 11*R*, respectively.

HAJIME KUBO, SHIGERU OHMIYA et ISAMU MURAKOSHI. Can. J. Chem. **72**, 214 (1994).

On a démontré que l'addition de réactifs de Grignard, comme les bromures de méthyl-, allyl- et 3,3-diméthoxypropylmagnésium, sur la 11,12-déhydrocytisine se produit par la face α et qu'elle conduit aux 11α-alkylcytisines. Faisant appel à une addition de Grignard, on a synthétisé la (−)-camoensine et la (−)-camoensidine à partir de la cytisine. On a confirmé que les configurations absolues des alcaloïdes mentionnés plus haut sont respectivement 7*R*, 9*R*, 11*R* et 6*S*, 7*R*, 9*R*, 11*R*.

[Traduit par la rédaction]

Lupin alkaloids occur mainly in the Papilionoideae of the family Leguminosae, such as the genera *Sophora* (1), *Euchresta* (2), and *Thermopsis* (3). Most lupin alkaloids contain a quinolizidine ring system, while a few, such as kuraramine (**1**) and ammodendrine (**5**) (4) contain piperidine ring(s) as structural units.

We have found that *Maackia* species (Leguminosae) accumulate atypical alkaloids such as maackiamine (**2**) (5), tashiromine (**3**) (6), and (−)-camoensidine (**4**) (7). These compounds are structurally related to typical lupin alkaloids but they differ in that they contain a pyrrolidine ring in place of a piperidine ring or an indolizidine ring system instead of a quinolizidine ring system. For example, **2**, **3**, and **4**, respectively, correspond to the typical lupin alkaloids, ammodendrine (**5**), epilupinine (**6**), and (−)-lupanine (**7**) (Scheme 1). *Camoensia* species (Leguminosae) accumulate indolizidine-type alkaloids such as (−)-leontidine (**10**), (−)-camoensine (**8**), (−)-camoensidine (**4**), etc. but do not contain quinolizidine-type alkaloids (8, 9), while in *Maackia* species the two types of alkaloids occur together (5–7). Comparison of the absolute stereochemistry of the two types of alkaloids is of interest in connection with their biosynthesis.

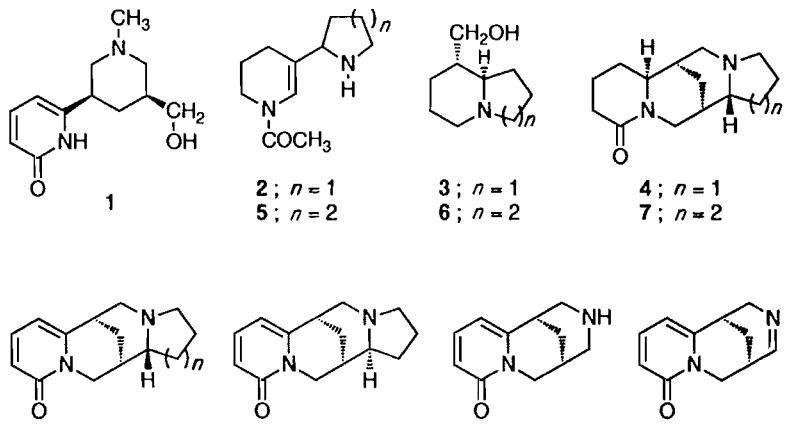

SCHEME 1

Santamaria and Khuong-Huu (8) reported the absolute stereochemistry of the tetracyclic indolizidine-type of alkaloids (−)-camoensine (**8**) and (−)-camoensidine (**4**), which were isolated from *Camoensia maxima*. Their assignments were based on that of (−)-leontidine (**10**), which had been isolated from *Leontice* species (Berberidacea) by Iskandarov et al. (11). The stereochemistry of (−)-leontidine (**10**) had, in turn, been assigned to be 7*R*, 9*R*, 11*R* by reference to (−)-cytisine (**11**), the absolute configuration of which is known (10). (−)-Leontidine

[1]This paper is dedicated to Professor Ian Spenser in honour of his career contributions to chemistry.

[2]Author to whom correspondence may be addressed.

Can. J. Chem. Downloaded from www.nrcresearchpress.com by 195.246.54.202 on 09/08/12
For personal use only.

TABLE 1. ^{1}H NMR data for 11α-alkylcytisine **13–15** (δ in ppm, *J* in Hz)[a]

H	13	14	15
3	6.46, dd, 9.2, 1.2	6.45, dd, 8.5, 1.2	6.45, dd, 9.2, 1.8
4	7.29, dd, 9.2, 6.7	7.30, dd, 8.5, 6.7	7.29, dd, 9.2, 6.7
5	5.98, dd, 6.7, 1.2	5.98, dd, 6.7, 1.2	5.99, dd, 6.7, 1.8
7	2.84, m,	2.87, m	2.83, m
8_{endo}	1.77, dm, 13.4	1.78, dm, 11.6	2.0–1.5, m
8_{exo}	2.23, dm, 13.4	2.12, dm, 11.6	2.15, dm, 13.4
9	2.14, m	2.26, m	2.17, m
10α	3.92, dd, 15.9, 6.7	3.94, dd, 15.9, 6.7	3.92, dd, 15.3, 6.1
10β	4.15, d, 15.9	4.13, d, 15.9	4.13, d, 15.3
11	3.24, ddm, 7.3, 7.3	3.03, dd, 6.7, 6.7	2.91, dd, 9.0, 4.9
13α	2.74, ddd, 12.8, 2.4, 2.4	2.75, ddd, 12.2, 2.4, 2.4	2.71, dm, 12.2
13β	3.32, dd, 12.8, 2.4	3.24, dd, 12.2, 2.4	3.22, dd, 12.2, 2.4
Others	1.31, d, 7.3, Me	5.76, ddd, 17.1, 10.4, 5.5, -CH=	2.0–1.5, m, $-CH_2-CH_2-$
		5.09, m, $=CH_2$	3.34, s, OMe × 2
		2.54, m, $-CH_2-$	4.40, t, $-CH(O-)_2$
		2.33, m, $-CH_2-$	

[a]Spectra were run in $CDCl_3$.

TABLE 2. ^{13}C NMR data for **11**, **13**, **14**, and **15**[a]

C	11(13)	13	14	15
2	163.6	163.9	163.6	163.6
3	116.5	117.4	117.2	116.8
4	138.7	139.2	138.8	138.8
5	104.9	105.3	104.8	104.9
6	151.2	151.7	151.1	151.0
7	35.5	35.2	35.2	35.2
8	26.2	20.9	21.2	21.2
9	27.7	32.1	30.1	30.9
10	49.7	47.4	47.6	47.5
11	52.9	54.2	58.3	58.6
13	53.9	51.2	51.3	51.2
Others		17.5, Me	135.6, -CH=	104.5, -CH<
			107.0, $=CH_2$	53.1, OMe
			35.0, $-CH_2-$	52.8, OMe
				30.0, $-CH_2-$
				25.0, $-CH_2-$

[a]Spectra were run in $CDCl_3$.

was synthesized (11) from (−)-cytisine, via a Grignard reaction of 11,12-dehydrocytisine (**12**) with allyl magnesium bromide giving 11-allylcytisine (11), which was then cyclized to (−)-leontidine (**10**). However, questions of the absolute configuration of (−)-leontidine (**10**) and (−)-camoensidine (**4**) remain, especially that of the stereochemistry at C-11: (1) the synthesis of **10** via the Grignard reaction demands an attack by the Grignard reagent from the more hindered side; (2) the ^{13}C NMR spectrum reported (9) for (−)-camoensidine (**4**) is not in agreement with that of **4** isolated from *Maackia* species, the relative stereochemistry of which was nevertheless established as **4** (7). We therefore reinvestigated the Grignard reaction of 11,12-dehydrocytisine (**12**) with some alkyl magnesium halides, from a stereochemical standpoint. One of the Grignard adducts obtained, 11α-(3,3-dimethoxypropyl)cytisine (**15**), was transformed to (−)- camoensidine (**4**) via (−)-camoensine (**8**) and hence the absolute stereochemistry of **4** and **8** was determined. The results obtained are reported here.

11,12-Dehydrocytisine (**12**) was obtained in 40% yield by treatment of 12-chlorocytisine, derived from (−)-cytisine, with KOH–MeOH. The position of the imine group was assigned as the $C_{(11)}$-$N_{(12)}$ by ^{1}H NMR decoupling experiments: The signal due to the C-9 proton (δ 2.90) was simplified by selective irradiation of the C-10β proton (δ 4.33) and of the C-11 imine proton (δ 7.86).

Dehydrocytisine **12** was reacted with the Grignard reagents, methyl magnesium bromide, allyl magnesium bromide, and 3,3-dimethoxypropyl magnesium bromide, in THF to give the corresponding 11-alkylcytisines (**13–15**) in 60, 23, and 24% yields, respectively.

The products were shown to be 11α-alkylcytisines by nuclear Overhauser effect (NOE) experiments and analysis of the ^{1}H NMR and ^{13}C NMR spectra. Assignments were based on decoupling experiments and ^{1}H–^{1}H and ^{1}H–^{13}C correlation spectroscopy (COSY), taking into account the assignments for (−)-cytisine and its derivatives (Tables 1 and 2). The signals of the H-13α (δ 2.74) and the H-8_{exo} (δ 2.23) protons of 11-methylcytisine (**13**) were enhanced by irradiation at the CH_3-11 signal (δ 1.31). This indicates that the C-ring of **13** possesses a chair conformation and that the CH_3-11 group is oriented axially (Scheme 2). Hence, the absolute configuration of the C-11 of **13** must be *R*. This result is supported by observa-

Can. J. Chem. Downloaded from www.nrcresearchpress.com by 195.246.54.202 on 09/08/12
For personal use only.

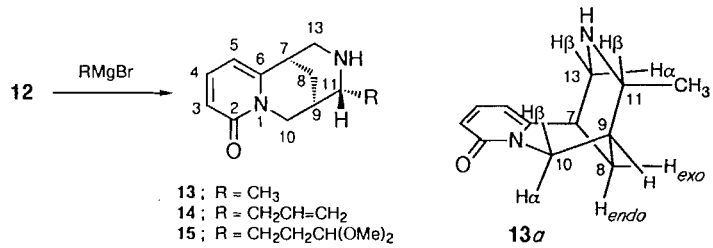

SCHEME 2

tion of an NOE between the C-10β and C-11 protons and of higher field chemical shifts of the C-8 and C-13 carbons in the ^{13}C NMR spectrum of **13** in comparison with those of cytisine (**11**) (Table 2).

The ^1H NMR and ^{13}C NMR spectra of 11-allylcytisine (**14**) and 11α-(3,3-dimethoxypropyl)cytisine (**15**) showed very similar patterns to that of 11-methylcytisine (**13**) (Tables 1 and 2), indicating that they have the same absolute stereochemistry. This was confirmed by an enhancement of the signal due to the C-11 proton (δ 3.03 for **14**, δ 2.91 for **15**) in NOE experiments, on irradiation of the signal of the C-10β proton (δ 4.13 for **14**, δ 4.13 for **15**). The above results demonstrate that the attack of the Grignard reagents on 11,12-dehydrocytisine (**12**) takes place from the α-face.

Treatment of 11-(3,3-dimethoxypropyl)cytisine (**15**) with 10% – HCl-Zn gave a tetracyclic α-pyridone-type alkaloid in 85% yield. This compound was identical with (−)-camoensine (**8**) isolated from *Camoensia maxima* and *C. brevicalyx* (^{13}C NMR and $[\alpha]_D$) (9). The absolute stereochemistry of (−)-camoensine (**8**) is therefore 7*R*, 9*R*, 11*R*, which was the same as that of the typical lupin alkaloid, (−)-anagyrine (**9**).

Catalytic hydrogenation of (−)-camoensine (**8**) with PtO_2 in AcOH yielded a tetracyclic piperidone-type alkaloid in 95% yield. This compound was identical with an authentic sample of (−)-camoensidine (**4**) isolated from *Maackia* species.[3] Thus, the absolute configuration of (−)-camoensidine (**4**) is 6*S*, 7*R*, 9*R*, 11*R*, which is the same as that of (−)-lupanine (**7**).

The above assignments are in agreement with the results obtained by Santamaria and Khuong-Huu (8) but different from those of Iskandarov et al. (11). It would appear that epimerization at C-11 occurs in the course of the cyclization of 11-allylcytisine (**14**) to (−)-leontidine (**10**) in the Iskandarov synthesis.

It is of interest from a biosynthetic and chemotaxonomic point of view that the structurally related alkaloids, (−)-lupanine (**7**) and (−)-camoensidine (**4**), coexist in the same plant and have the same absolute stereochemistry. Further investigation of the absolute configuration of tashiromine and maackiamine is being undertaken in our laboratories.

Experimental

The following equipment was used to obtain physical data: infrared spectra, Hitachi 215 grating infrared spectrometer; ^1H and ^{13}C NMR spectra, JEOL JNM-GSX 270 spectrometer with tetramethylsilane (TMS) as an internal standard; optical rotations, Jasco DIP-181 polarimeter; EIMS, JEOL D-300 spectrometer. Column chromatography was carried out with Kiesel gel 60 (230–400 mesh, Merck). Thin-layer chromatography (TLC) was performed on 0.25 mm precoated silica gel (60 F_{254}, Merck), and spots were detected by exposure to I_2 vapor or spraying with Dragendorff's reagent.

11,12-Dehydrocytisine ***12***

Dehydrocytisine **12** was prepared from (−)-cytisine (**11**) by the procedure reported by Bohlmann et al. (12). **12**, δ_H ($CDCl_3$): 7.86 (1H, m, 11-H), 7.25 (1H, dd, J = 9.2, 6.7 Hz, 4-H), 6.39 (1H, dd, J = 9.2 and 1.8 Hz, 3-H), 6.01 (1H, dd, J = 6.7, 1.8 Hz, 5-H), 4.33 (1H, ddd, J = 15.3, 1.2, 1.2 Hz, 10β-H), 3.93 (1H, dddm, J = 18.3, 3.7, 3.7 Hz, 13-H), 3.76 (1H, ddm, J = 18.3, 1.8 Hz, 13-H), 3.56 (1H, dd, J = 15.3, 5.5 Hz, 10α-H), 3.12 (1H, m, 7-H), 2.90 (1H, m, 9-H), 2.12 (1H, dm, J = 13.5 Hz, 8-H), 1.90 (1H, dm, J = 13.5 Hz, 8-H).

11α-Methylcytisine ***13***

A solution of methyl magnesium bromide (1 mmol) in THF (2 mL) was added at room temperature with stirring under argon to a solution of **12** (5.2 mg, 0.028 mmol) in dry THF (3 mL). After stirring for 8 h, the reaction mixture was quenched by addition of H_2O, made basic with concentrated NH_4OH and extracted three times with CH_2Cl_2. The combined CH_2Cl_2 extracts were dried and evaporated to dryness in vacuo. The residue was purified by silica gel column chromatography using CH_2Cl_2–MeOH (20:1) to yield 11α-methylcytisine **13** (3.3 mg, 60%) as a colourless oil. **13**, $[\alpha]_D^{20}$ −108.7 (*c* 1.0, EtOH); *m/z*(%): 204 (M^+, 100), 160 (34), 148 (55), 147 (78), 146 (80), 134 (22), 96 (60), 58 (93).

11α-Allylcytisine ***14***

A solution of allyl magnesium bromide (10 mmol) in THF was added at room temperature with stirring under argon to a suspension of the hydrochloride of **12** (203 mg, 0.90 mmol) in dry THF (10 mL). After stirring for 8 h, the reaction mixture was treated with H_2O (3 mL), made alkaline with concentrated NH_4OH and then extracted three times with CH_2Cl_2. The combined extracts were dried and concentrated in vacuo. The residue was separated by silica gel column chromatography with CH_2Cl_2–MeOH (20:1) to give 11α-allylcytisine **14** (48 mg, 23%) as a colourless oil. **14**, $[\alpha]_D^{20}$ −94.7 (*c* 1.0, EtOH); *m/z*(%): 230 (M^+, 64), 189 (9), 169 (23), 148 (38), 147 (63), 146 (41), 134 (21), 84 (100).

11α-(3,3-Dimethoxypropyl)cytisine ***15***

A solution of 3,3-dimethoxypropyl magnesium bromide (2 mmol) in dry THF was added at room temperature with stirring under argon to a solution of **12** (88.4 mg, 0.47 mmol) in dry THF (5 mL). The reaction mixture was stirred for 60 h, treated with H_2O (5 mL), made alkaline with concentrated NH_4OH, and then extracted three times with CH_2Cl_2. The combined extracts were dried and evaporated to dryness

[3]The question of the ^{13}C NMR spectrum of (−)-camoensidine isolated from Camoensia brevicalyx (9) remains.

Can. J. Chem. Downloaded from www.nrcresearchpress.com by 195.246.54.202 on 09/08/12
For personal use only.

in vacuo. The residue was separated by silica gel column chromatography with CH_2Cl_2–MeOH (20:1) to give 11α-(3,3-dimethoxypropyl)-cytisine **15** (26 mg, 23%) as a colourless oil, together with unchanged starting **12** (26 mg). **15**, $[\alpha]_D^{20}$ −34.8 (*c* 0.06, EtOH); ν_{max} ($CHCl_3$)/cm^{-1}: 3370 (NH), 1640 (C=O); HRMS for $C_{16}H_{24}N_2O_3$, calcd.: 292.1786; found: 292.1779; *m/z*(%): 292 (M^+, 10), 277 (17), 261 (13), 245 (7), 229 (84), 189 (100), 160 (21), 148 (25), 147 (20), 146 (44), 114 (84), 82 (39).

(−)-Camoensine **8**

Zinc dust (100 mg) was added to a solution of **15** (26.9 mg) in 5% HCl and the mixture was stirred for 2 h. The inorganic precipitate was filtered off. The filtrate was made alkaline with concentrated NH_4OH and extracted three times with CH_2Cl_2. The combined CH_2Cl_2 extracts were dried and evaporated to dryness in vacuo. The product was purified by column chromatography on silica gel using CH_2Cl_2–MeOH – 25% NH_4OH (90:9:1) to give **8** (18.0 mg, 85%) as a colourless oil. **8**, $[\alpha]_D^{20}$ −112.9 (*c* 0.5, $CHCl_3$) (lit. (6) $[\alpha]_D$ −108 (*c* 1.0, $CHCl_3$)); ν_{max} ($CHCl_3$)/cm^{-1}: 2930 (CH), 1650 (C=O); δ_H (C_6D_6): 6.81 (1H, dd, *J* = 9.0, 6.8 Hz, 4-H), 6.54 (1H, dd, *J* = 9.0, 1.5 Hz, 3-H), 5.44 (1H, dd, *J* = 6.8, 1.5 Hz, 5-H), 4.24 (1H, dm, *J* = 15.4 Hz, 10β-H), 3.63 (1H, dd, *J* = 15.4, 6.1 Hz, 10α-H), 2.42 (1H, m, 11-H), 2.42 (1H, ddd, *J* = 12.2, 8.8, 8.8 Hz, 14-H), 2.32 (1H, ddd, *J* = 12.2, 8.8, 2.2 Hz, 14-H), 2.26 (1H, ddd, *J* = 10.3, 3.4, 2.0 Hz, 16-H), 2.19 (1H, m, 7-H), 2.08 (1H, dd, *J* = 10.3, 2.4 Hz, 16-H), 1.61 (1H, m, 9-H), 1.51 (1H, m), 1.27–1.08 (4H, m), 0.93 (1H, dm, *J* = 13.2 Hz, 8-H); δ_C ($CDCl_3$): 163.7 (2-C), 150.8 (6-C), 138.9 (4-C), 116.9 (3-C), 104.9 (5-C), 66.1 (11-C), 55.1 (16-C), 55.0 (10-C), 51.8 (14-C), 35.1 (7-C), 29.1 (9-C), 25.3 (12-C), 21.4 (8-C), 20.9 (13-C) (lit. (9) δ_C 164.1 (2-C), 151.4 (6-C), 139.2 (4-C), 117.2 (3-C), 105.2 (5-C), 66.3 (11-C), 55.3 (16-C), 55.1 (10-C), 51.9 (14-C), 35.2 (7-C), 29.2 (9-C), 25.4 (12-C), 21.4 (8-C), 20.9 (13-C)]; HRMS for $C_{14}H_{18}N_2O$, calcd.: 230.1419; found: 230.1420; *m/z*(%): 230 (M^+, 34), 160 (7), 146 (11), 122 (7), 84 (100), 60 (34).

(−)-Camoensidine **4**

A solution of **8** (8 mg) in AcOH (3 mL) was hydrogenated over PtO_2 (7 mg) at atmospheric pressure at ambient temperature for 8 h. The catalyst was filtered off and the filtrate was evaporated to dryness in vacuo. The residue was purified by silica gel column chromatography with CH_2Cl_2–MeOH – 25% NH_4OH (43:6:1) to yield an oily product (8 mg), which was identical with (−)-camoensidine (**4**) isolated from *Maackia* species (co-TLC, co-HPLC, MS, ^{13}C NMR, $[\alpha]_D$).

1. S. Ohmiya, K. Higashiyama, H. Otomasu, J. Haginiwa, and I. Murakoshi. Phytochemistry, **20**, 1997 (1981); K. Saito, N. Arai, T. Sekine, S. Ohmiya, H. Kubo, H. Otomasu, and I. Murakoshi. Planta Medica, **56**, 487 (1990); S. Takamatsu, K. Saito, S. Ohmiya, N. Ruangrungsi, and I. Murakoshi. Phytochemistry, **30**, 3793 (1991).
2. S. Ohmiya, H. Otomasu, J. Haginiwa, and I. Murakoshi. Chem. Pharm. Bull. **28**, 546 (1980); I. Murakoshi, E. Kidoguchi, M. Nakamura, J. Haginiwa, S. Ohmiya, K. Higashiyama, and H. Otomasu. Phytochemistry, **20**, 1725 (1981).
3. K. Saito, S. Takamatsu, I. Murakoshi, S. Ohmiya, and H. Otomasu. J. Nat. Prod. **52**, 1032 (1989); K. Saito, S. Takamatsu, S. Ohmiya, H. Otomasu, M. Yasuda, Y. Kano, and I. Murakoshi. Phytochemistry, **27**, 3715 (1988).
4. I. Murakoshi, E. Kidoguchi, J. Haginiwa, S. Ohmiya, K.Higashiyama, and H. Otomasu. Phytochemistry, **20**, 1407 (1981).
5. K. Saito, T. Yoshino, T. Sekine, S. Ohmiya, H. Kubo, H. Otomasu, and I. Murakoshi. Phytochemistry, **28**, 2533 (1989).
6. S. Ohmiya, H. Kubo, H. Otomasu, K. Saito, and I. Murakoshi. Heterocycles, **30**, 537 (1990).
7. S. Ohmiya, H. Kubo, Y. Nakaaze, K. Saito, I. Murakoshi, and H. Otomasu. Chem. Pharm. Bull. **39**, 1123 (1991); K. Saito, S. Tsai, S. Ohmiya, H. Kubo, H. Otomasu, and I. Murakoshi. Chem. Pharm. Bull. **34**, 3982 (1986).
8. J. Santamaria and F. Khuong-Huu. Phytochemistry, **14**, 2501 (1975).
9. P.G. Waterman and D.F. Faulkner. Photochemistry, **21**, 215 (1982).
10. S. Okuda, H. Kataoka, and K. Tsuda. Chem. Pharm. Bull. **13**, 491 (1965).
11. S. Iskandarov, R.A. Shaimardarov, and S.Y. Yunusov. Khim. Prir. Soedin. **7**, 631 (1971).
12. F. Bohlmann, E. Winterfeldt, H. Overwien, and H. Pagel. Chem. Ber. **95**, 944 (1962).
13. F. Bohlmann and R. Zeisberg. Chem. Ber. **108**, 1043 (1975).

Can. J. Chem. Downloaded from www.nrcresearchpress.com by 195.246.54.202 on 09/08/12
For personal use only.

Reactions of the ambident super-electrophile series: the 2-(nitroaryl)-4,6-dinitrobenzotriazole 1-oxides with isopropoxide ion. Pathways of decomposition of the anionic σ-adducts[1]

JULIAN M. DUST[2]

Department of Chemistry, Sir Wilfred Grenfell College, Corner Brook, NF A2H 6P9, Canada

AND

ERWIN BUNCEL[2]

Department of Chemistry, Queen's University, Kingston, ON K7L 3N6, Canada

Received June 30, 1993

This paper is dedicated to Professors David B. McLean and Ian D. Spenser

JULIAN M. DUST and ERWIN BUNCEL. Can. J. Chem. **72**, 218 (1994).

To elucidate the reactivity of super-electrophiles such as 4,6-dinitrobenzofuroxan as compared to normal electrophiles such as 1,3,5-trinitrobenzene, reaction of isopropoxide ion ($iPrO^-$) with a series of ambident super-electrophiles was studied by 400 MHz ^1H nuclear magnetic resonance spectroscopy. The 2-(nitroaryl)-4,6-dinitrobenzotriazole 1-oxides, **1–3**, possess both a super-electrophilic (C-7) site and a normal electrophilic (C-1′) site. Nucleophiles can demonstrate selectivity for attack at C-7, which leads to formation of persistent anionic σ-adducts (Meisenheimer complexes), as compared to C-1′, which leads to N-2:C-1′ bond scission. The most reactive substrate, 2-(2′,4′,6′-trinitrophenyl)-4,6-dinitrobenzotriazole 1-oxide (Pi-DNBT, **1**) was found to be the least selective substrate in C-7 adduct formation, while 2-(2′,4′-dinitrophenyl)- and 2-(4′-nitrophenyl)-4,6-dinitrobenzotriazole 1-oxides (DNP-DNBT, **2**, and NP-DNBT, **3**, respectively) showed increasing selectivity towards $iPrO^-$, in turn. These results are discussed on the basis of overall selectivity for C-7 adduct formation and the relative selectivity of $iPrO^-$ as compared to methoxide and *tert*-butoxide ions. The conclusions are illustrated using comparative energy profiles. In terms of pathways for decomposition of the adducts, the C-7 adducts decompose via dissociation back to substrate and nucleophile and, thence, through C-1′ adduct formation to the scission products. However, for **1**, the C-7 adduct **1***a* has now been found to decompose to 7-isopropyl-2-picryldinitrobenzotriazole, **1***c*. The possible mechanism of this formal internal redox will be discussed.

JULIAN M. DUST et ERWIN BUNCEL. Can. J. Chem. **72**, 218 (1994).

Afin d'évaluer la réactivité des super-électrophiles, comme le 4,6-dinitrobenzofuroxane, par rapport à celle d'électrophiles normaux, comme le 1,3,5-trinitrobenzène, on a utiliser la résonance magnétique nucléaire du ^1H à 400 MHz pour étudier la réaction de l'ion isopropylate ($iPrO^-$) avec une série de superélectrophiles ambidents. Les 2-(nitroaryl)-4,6-dinitrobenzotriazole 1-oxydes, **1–3**, possèdent un site superélectrophile (C-7) ainsi qu'un site électrophile normal (C-1′).Les nucléophiles permettent de démontrer une sélectivité pour l'attaque en C-7 qui conduit à la formation d'adduits σ anioniques persistants (complexes de Meisenheimer) alors que l'attaque en C-1′ conduit à une scission de la liaison N-2:C-1′. On a trouvé que le substrat le plus réactif, la 2-(2′,4′,6′-trinitrophényl)-4,6-dinitrobenzotriazole 1-oxyde (Pi-DNBT, **1**), est le substrat le moins sélectif pour la formation d'un adduit en C-7 alors que les 2-(2′,4′-dinitrophényl)- et 2-(4′-nitrophényl)-4,6-dinitrobenzotriazole 1-oxydes (respectivement la DNP-DNBT, **2**, et NP-DNBT, **3**) présentent chacune une sélectivité de plus en plus grande vis-à-vis du $iPrO^-$. On discute de ces résultats en fonction de la sélectivité globale de la formation d'adduits en C-7 et la sélectivité relative du $iPrO^-$ comparée à celles des ions méthylate et *tert*-butylate. On illustre les conclusions en utilisant des profils d'énergie. En termes de chemins réactionnels conduisant à la décomposition des adduits, les adduits en C-7 se décomposent par le biais d'une dissociation redonnant le substrat et le nucléophile et, en conséquence, aux produits de scission par la formation d'un adduit en C-1′. Toutefois, pour le composé **1**, on a maintenant trouvé que l'adduit en C-7, **1***a*, se décompose en 7-isopropyl-2-picryldinitrobenzotriazole, **1***c*. On discute du mécanisme possible de cette réaction rédox interne formelle.

[Traduit par la rédaction]

We have been concerned with studies of super-electrophiles, a class of heteroaromatic compounds that show exalted reactivity with nucleophiles in formation of σ-bonded anionic (Meisenheimer) complexes (1). These are typified by 4,6-dinitrobenzofuroxan (DNBF), much as conventional electron-deficient aromatics are well represented by 1,3,5-trinitrobenzene (TNB) (1–6). A straightforward comparison suffices to demonstrate the enhanced reactivity of these compounds as compared to normal electrophiles. Thus, the forward rate constant for formation of the methoxide adduct of DNBF, DNBF·OMe^-, is 265-fold larger than the corresponding rate constant for formation of the methoxide adduct of TNB, TNB·OMe^-, while the equilibrium constant for formation of the DNBF·OMe^- adduct is 9.1×10^8 times larger than the constant for TNB·OMe^- formation (2, 7). Moreover, DNBF reacts quantitatively at room temperature with such weak carbon nucleophiles as aniline (8) or 1,3,5-trimethoxybenzene (9) to give Meisenheimer C-adducts that are formally products of electrophilic aromatic substitution of the respective benzene rings. In fact, we have used the reaction of DNBF with indole, 2-methylindole, and 1,2,5-trimethylpyrrole to quantify the electrophilicity of DNBF and have shown that *DNBF is more electrophilic than such strong electrophiles as the 4-nitrobenzenediazonium cation and the proton* (10). On these grounds, DNBF and related compounds may be justifiably termed super-electrophiles.

One of our approaches to understanding the exalted reactivity of super-electrophiles has been to design novel ambident substrates, comprising the 2-(nitroaryl)-4,6-dinitrobenzotriazole 1-oxide family, **1–3** (*8b*, 11–14), that contain both types of electrophilic sites. In common with DNBF, the series possesses a

[1]Part 11 in series on heteroaromatic super-electrophiles in anionic σ-adduct formation and part 50 in series on anionic σ-complexes; part 49, ref. 26.

[2]Authors to whom correspondence may be addressed.

Can. J. Chem. Downloaded from www.nrcresearchpress.com by 195.246.54.202 on 09/08/12
For personal use only.

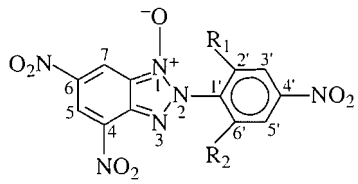

1 Pi—DNBT $R_1 = R_2 = NO_2$
2 DNP—DNBT $R_1 = NO_2$, $R_2 = H$
3 NP—DNBT $R_1 = R_2 = H$

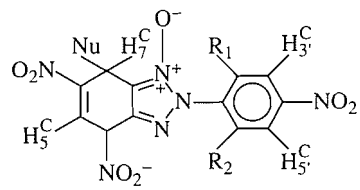

1*a* Pi—DNBT · Nu^-
2*a* DNP—DNBT · Nu^-
3*a* NP—DNBT · Nu^-

super-electrophilic centre at C-7, but also a second electrophilic centre, C-1′, analogous to that in picryl derivatives. The initial result of C-7 attack for the 2-(nitroaryl)-4,6-dinitrobenzotriazole 1-oxide series, as outlined in Scheme 1 (Path a), is formation of a relatively persistent C-7 σ-bonded anionic adduct, **1***a*–**3***a*. The ultimate products of nucleophilic reaction with **1–3** are the substituted nitroaromatics **5–7**, and the 4,6-dinitrobenzotriazole 1-oxyanion, $DNBT^-$, **4**, which arise from attack on the conventional electrophilic C-1′ site (Path b) with formation of the metastable Meisenheimer adducts **1***b*–**3***b*, followed by their ready decomposition in an overall S_NAr displacement (15). Hence for the series **1–3**, reaction at C-7 as compared to C-1′ provides a direct measure of selectivity (k_1 vs. k_2) for complex formation at the C-7 vs. the C-1′ site, as well as insight into the factors affecting the super-electrophilicity of the C-7 position, while avoiding the difficulties inherent in comparing the electrophilicity of two different molecules.

In fact, a broad range of selectivities has been demonstrated for various members of the 2-(nitroaryl)-4,6-dinitrobenzotriazole 1-oxide family. The initial determination of the super-electrophilicity of the C-7 site was based, for example, on the comparatively high electrophilicity shown by the C-7 site of **1** (2-(picryl)-4,6-dinitrobenzotriazole 1-oxide, Pi-DNBT) towards ethanethiol (8*b*); the reactivity of TNB (1–7) and that of DNBF (10, 15*a*, 16, 17) provided benchmarks for comparison. This conclusion has been extended to the other members of the series, **2** and **3**, on the basis of reactivity with phenoxide ion. With this ambident (C- and O-) nucleophile, **1** yields only the products of N-2:C-1′ bond cleavage (**4** and picryl phenyl ether) (8*b*, 11), although formation of a transient C-7 O-adduct could be postulated as arising from an initial rapid equilibrium. However, the observation of C-7 phenoxide C-adducts of **2** and **3** (in a statistical *ortho*:*para* ratio of 2:1) demonstrates the super-electrophilicity of this site, as well as the decreased tendency for N-2:C-1′ bond rupture that follows from the progressive

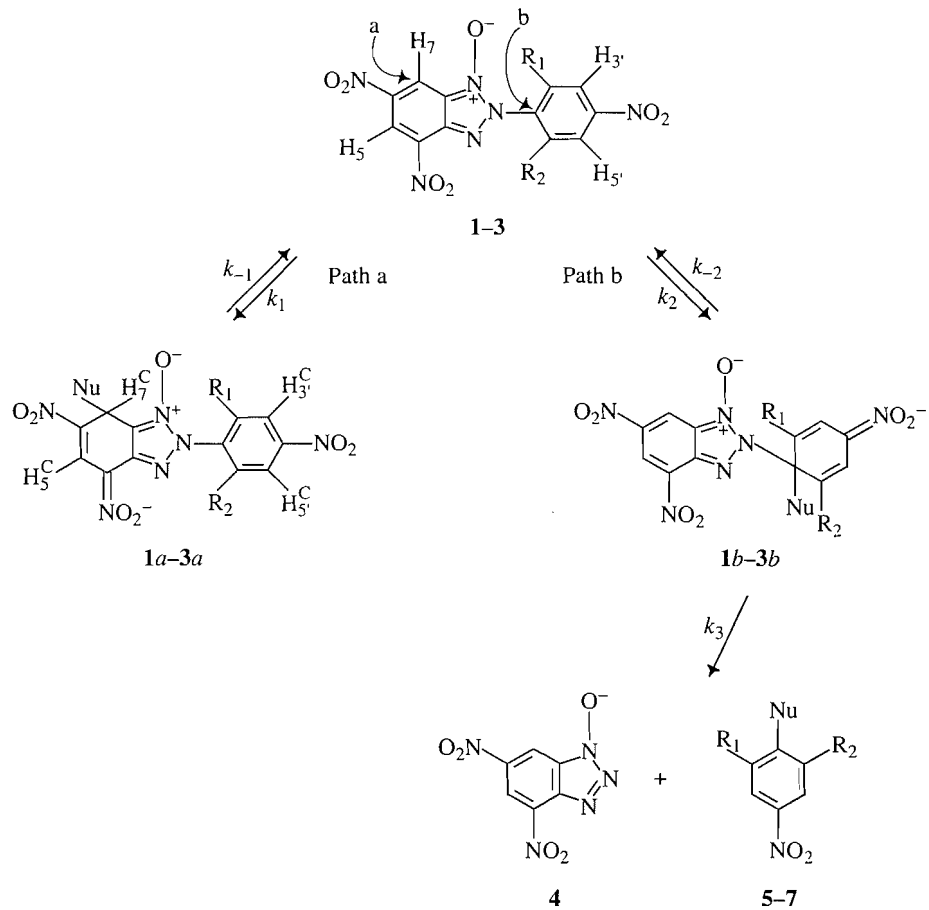

SCHEME 1

Can. J. Chem. Downloaded from www.nrcresearchpress.com by 195.246.54.202 on 09/08/12
For personal use only.

TABLE 1. The ^{1}H nmr characteristics of the C-7 adducts of **1–3**

Adduct, RO^-	Chemical shifts, ppm (J = Hz)						
	OR	H_7^C	H_5^C	$H_{6'}^C$	$H_{5'}^C$	$H_{3'}^C$	$H_{2'}^C$
1*a*, MeO^-	3.256 (s, CH_3)	6.042 (s)	8.761 (s)		9.302 (s)	9.302 (s)	
1*a*, $iPrO^-$	[a]	6.047 (s)	[b]		9.294 (s)	9.294 (s)	
1*a*, OH^-[c]	6.210 (d, OH ca. 7)	5.989 (d, ca. 7)	8.652 (s)		9.286 (s)	9.286 (s)	
2*a*, $iPrO^-$	4.078 (m, ca. 7 C*H*)	5.992 (s)	8.725 (s)	8.171 (d, 8.81)	8.767 8.745 (d,d 8.81 2.50)	8.892 (d, 2.50)	
2*a*, OH^-[c,d]	6.070 (d, OH ca. 6)	5.964 (d, ca. 6)	8.674 (s)	8.133 (d, 9.10)	[e]	[e]	
3*a*, $iPrO^-$	[a]	6.039 (s)	8.696 (s)	8.343	8.446 (A_2X_2 d,d 9.04)	8.446	8.343

[a]Signals obscured by peaks due to one of the following: substrate, **4**, RO^- or ROH.
[b]Peaks obscured by H_5 signal of **4**.
[c]Full assignment based on control experiment, ref. 20*b*.
[d]C-7 DNP–DNBT·OH^- adduct assigned by comparison to other systems (1, 14). Also see footnote 3.
[e]Obscured by corresponding signals of C-7 DNP-DNBT·$OPri^-$ adduct.

TABLE 2. The extent of formation of the $iPrO^-$ adducts of **1–3** (**1***a*, **2***a*, **3***a* and **1***b*, **2***b*, **3***b*)

Substrate	Time, min	% C-7	% C-7 OH^-	Total % C-7	% **1***c*[a]	% C-1′[b]	% Conversion
1	4[c]	6.6	0	6.6	3.7	31.0	41.3
1	30	2.6	0	2.6	9.8	35.9	48.3
1	60	0	0	0	12.1	47.3	59.4
2	61[c]	41.2	11.8	53.0		0	53.0
3	7[c]	18.2	0	18.2		0	18.2
3	35	18.0	0	18.0		0	18.0

[a]7-Isopropyl-2-picryl-4,6-dinitrobenzotriazole (**1***c*, OR = OPr*i*) based on the assumption that the 9.240 singlet represents the two protons of the picryl ring.
[b]% C-1′ = **4** = **5–7** = % **1***b*–**3***b*.
[c]Earliest time of observation at which the spectrum was well resolved and at which quantification would be made.

decrease in the number of NO_2 groups attached to the 2-nitroaryl moiety (13).

Most recently, our comparative study of the selectivity shown by methoxide and *tert*-butoxide towards the C-7 and C-1′ sites indicated the importance of steric factors in determining the degree of regioselectivity in adduct formation with these substrates (14). A greater percentage of C-7 adduct was found to form with MeO^- than with $tBuO^-$ under equimolar conditions, while with an excess of alkoxide MeO^- also was more reactive towards the C-1′ site than was $tBuO^-$. Taken together, $tBuO^-$ was found to be the more selective nucleophile in attack at C-7, in accord with the lesser reactivity of the nucleophile. Reaction at both sites was shown to be governed primarily by steric hindrance, as measured by E_s (Taft's steric substituent constant (18)), rather than by basicity as a measure of the nucleophilicity of the attacking nucleophile (19).

In the present paper we report the results of our 400 MHz ^{1}H nmr study of the reaction of the full series of 2-(nitroaryl)-4,6-dinitrobenzotriazole 1-oxides with iso-propoxide ($iPrO^-$). The behaviour of $iPrO^-$ in reaction with **1–3** would be expected to be intermediate between that found for MeO^- and $tBuO^-$ since its basicity and steric bulk both lie in between these two alkoxides. As such, the present study completes a consistent series of alkoxides. However, some of the behaviour found prompted a reinvestigation of the reaction of methoxide ion with **1**. This distinctive behaviour will be highlighted, while other features of the reactivity of $iPrO^-$ will be discussed in relation to the other alkoxides and the regioselectivity considerations that have already proven useful in examination of these systems (8, 12–15).

Results

The reactions of substrates **1–3** with iso-propoxide (iPrOK) were studied by 400 MHz ^{1}H nmr spectrometry. Chemical shifts (ppm relative to TMS or CD_2HSOCD_3 present in the $(CD_3)_2SO$ solvent) and coupling constants (Hz) for all observed complexes, **1***a*, **2***a*, and **3***a*, are listed in Table 1; integrals support the assignments made. An internal integration standard (1,4-dibromobenzene, DBB) permitted calculation of the concentrations of all observable species at any given time (13) and forms the basis of the extent of formation data tabulated (Table 2). Experiments were carried out under a variety of concentration regimes: equimolar and two to five equivalents of iPrOK.

Reaction of Pi-DNBT (1) with iPrOK

(a) Equimolar $iPrO^-$ conditions

Injection of 1 equivalent of iPrOK in 2-propanol (3.00 M) into a solution of Pi-DNBT in $(CD_3)_2SO$ (final concentration 2.58×10^{-2} M) led to initial broadening and a decrease in intensity of the signals due to **1**, concomitant with appearance of small signals ascribable to the C-7 adduct, **1***a*. These peaks appear at 9.294 (s, $H_{3',5'}^C$) and 6.047 (s, H_7^C). The H_5^C peak is obscured by resonances of **4** that are present even in the initial spectrum (acquired within 4 min). Comparison with the H_5^C signals of related adducts (8, 11–14) shows that these peaks are typically found between 8.6 and 8.8 ppm; the protons (H_5 and H_7) of the leaving group, **4**, are found in the same region, depending upon the degree of protonation. In this case, the signals that represent **4** are centred at 8.719 and 8.697. Picrate anion, $PicO^-$, is also found in the initial spectrum (8*b*, 11–14).

Can. J. Chem. Downloaded from www.nrcresearchpress.com by 195.246.54.202 on 09/08/12
For personal use only.

Can. J. Chem. Downloaded from www.nrcresearchpress.com by 195.246.54.202 on 09/08/12
For personal use only.

In some repetitions of this experiment peaks were also noted at 9.286 (s), 8.652 (s), 6.210 (ill-resolved d, J ca. 7), and 5.989 (d, J ca. 7), ascribed to $H^c_{3',5'}$, H^c_5, O*H*, and H^c_7, respectively, of the C-7 Pi-DNBT adduct (**1***a*, Nu = OH). This assignment rests on separate experiments with **1** and OH^-.[3]

The presence of both $DNBT^-$ and $PicO^-$ signifies that displacement, presumably via the C-1′ adduct, **1***b*, has occurred along with formation of the C-7 adduct, **1***a*. However, isopropyl picrate, **5**, was not detected in this system as the result of overlap of the peaks of **5** with signals of other species present. (Separately prepared **5** has peaks at 9.103 (s, $H_{3,5}$), 4.496 (septet, J = 6.11, C*H* methine), and 1.253 (d, J = 6.11, CH_3).) Reaction of **5** with OH^- or $iPrO^-$, via S_N2 or S_NAr pathways for OH^- or via S_N2 displacement for $iPrO^-$, could generate $PicO^-$ and account for the lack of observation of **5** in the system.

A control experiment shows that the C-7 Pi-DNBT·OP*ri*$^-$ complex, **1***a*, is acid labile; peaks due to **1***a* disappear from the spectrum upon introduction of trifluoroacetic acid (TFA). This behaviour was found previously for alkoxide O-adducts but not phenoxide C-adducts of **1–3** (8, 11–14) and constitutes further support for the assignment of these resonances to the O-centred C-7 adduct, **1***a*.

Interestingly, from the first spectrum onwards the system includes an unknown singlet at 9.240. This peak increases in intensity as the reaction is monitored. Its assignment will be discussed below.

Thus, the sequence of changes observed in the reaction was as follows: initial formation of the C-7 adduct, **1***a* (Nu = OP*ri*), accompanied by evidence of N-2:C-1′ bond rupture via **1***b* and the appearance of the species responsible for the 9.240 singlet. The C-7 adduct rapidly declines in concentration (Table 2) and its signals cannot be detected after 1 h of observation. At that point the system contains $PicO^-$, **4**, and the unknown species.

(b) Excess $iPrO^-$ conditions (3 equivalents)

The initial spectrum from the reaction of **1** with an excess of iPrOK contains no signals for **1** or **5**, but prominent signals for **4** and $PicO^-$ are present. Moreover, a singlet at 8.715 can be assigned to $H_{3,5}$ of the 1,1 $iPrO^-$ adduct of isopropyl picrate, **5**, on the basis of a control experiment in which **5** was treated with an excess of $iPrO^-$ (3 equiv.) in $(CD_3)_2SO$. In the initial spectrum peaks were observed for the 1,1 adduct, as well as for its 1,3 regioisomer at 8.400 (br s, H_5) and 6.272 (br s, H_3) (22). The 1,3 $iPrO^-$ adduct of **5** rapidly gives way to the 1,1 adduct.

In summary, reaction of an excess of iPrOK with **1** results in relatively clean displacement to give **5**, which reacts further with $iPrO^-$ to yield the observed 1,1 adduct of isopropyl picrate. Significantly, the unknown peak at 9.240, observed under equimolar reaction conditions, is not present in this concentration regime.

*(c) Reinvestigation of the reaction of **1** with MeOK*

As previously reported (11, 12), reaction of **1** with MeO^- follows Scheme 1. However, in the present study peaks are also noted at 9.237 and 8.310 (both singlets, 2H:1H) that increase in intensity in tandem with the decline in the intensity of the peaks due to **1***a* (Nu = OMe) and along with growth in the signals of **4** and $PicO^-$.

Comparison of the Pi-DNBT,$iPrO^-$ and MeO^- reaction systems suggests that these peaks (i.e., 9.240 in the former and the 9.237, 8.310 set in the latter system) represent similar species, products that arise from a pathway not described by Scheme 1.

Observation of the signals of the C-7 Pi-DNBT·OH^- adduct in some experiments rules out this species as a candidate for the unknown resonances (20*b*). However, an overall process of deoxygenation has been observed in the reaction of MeO^- with the related 4-nitrobenzofuroxan (21), yielding a 7-alkoxy derivative and (or) a 7-oxyanion of 4-nitrobenzofurazan. Partly on the basis of this comparison, the signals of the unknown species are tentatively assigned to the respective 7-alkoxy-2-(picryl)-4,6-dinitrobenzotriazole, **1***c*. Accordingly, the signal found at 9.240 in the Pi-DNBT,$iPrO^-$ system and at 9.237 in the Pi-DNBT,MeO^- system could belong to the ring protons ($H_{3',5'}$) of **1***c* (where OR = OP*ri* or OMe, as required). It should be noted that these signals would not be expected to differ significantly as a function of the attached alkoxyl group of **1***c*.

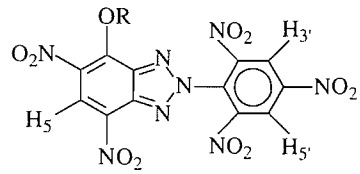

1*c*

Conversely, the slight difference suggests that two separate but similar species are present in the two reaction systems, rather than the 7-oxyanion of 2-(picryl)-4,6-dinitrobenzotriazole alone. In the Pi-DNBT,MeO^- system another singlet was observed at 8.310 and may reasonably be ascribed to H_5 of **1***c*.

Deoxygenation of related benzotriazole 1-oxides has been reported in a number of systems, even under very mild conditions (23). For example, 2-(4′-fluorophenyl)-4,6-dinitrobenzotriazole 1-oxide was noted to undergo deoxygenation to the corresponding benzotriazole simply by heating the material to reflux in ethanol (24). Consequently, it is important to note that the signals found in the Pi-DNBT reaction systems do not correspond to the anticipated resonances of 2-(picryl)-4,6-dinitrobenzotriazole, the product of direct deoxygenation of **1**, i.e., it would exhibit a pair of doublets for H_5 and H_7 of the dinitrobenzotriazole moiety.

*Reaction of DNP-DNBT (**2**) with iPrOK*

(a) Equimolar $iPrO^-$ conditions

The broadened and diminished resonances of DNP-DNBT, **2**, are joined by new signals 5 min after the reagents are mixed and the first spectrum recorded. These signals can be assigned to the C-7 DNP-DNBT·OP*ri*$^-$ complex, **2***a*: 8.892 (d, J = 2.50, $H^c_{3'}$) 8.767 and 8.745 (d,d, J = 8.81, 2.50, $H^c_{5'}$), 8.725 (s, H^c_5), 8.171 (d, J = 8.81, $H^c_{6'}$), and 5.992 (s, H^c_7). These peaks are not quantifiable until later when partly overlapping signals become resolved (Table 2). A partly resolved multiplet can be seen at 4.078 (J ca. 7) and can be attributed to the methine proton of the attached iPrO group of **2***a*, but the methyl signals are not detected and are likely obscured by the large 1.260 doublet due to the methyls of iPrOK and iPrOH. The C-7 DNP-DNBT·OH^- complex (**2***a*, Nu = OH) is identified by the observation of a series of peaks including doublets at 6.071 and 5.964 (J ca. 6 for both) due to O*H* and H^c_7, as well as a singlet at 8.674 that corresponds to H^c_5.[3] Note that the adduct **2***a* (Nu = OH) was observed previously in the DNP-DNBT,OR^- reaction system (13, 14, 20). In accord with these assignments the signals are found to

[3]E. Buncel and R.A. Manderville, unpublished data. See ref. 20*b*.

Can. J. Chem. Downloaded from www.nrcresearchpress.com by 195.246.54.202 on 09/08/12
For personal use only.

disappear upon acidification with TFA. Simultaneously, the resonances assigned to **2** increase in intensity (12–14).

No significant N-2:C-1′ bond cleavage had occurred in this system even after monitoring the reaction for 4 h.

(b) Excess iPrO⁻ conditions (2 equivalents)

Five minutes after mixing, the ^{1}H nmr spectrum of the reaction mixture of 3 equivalents iPrOK with **2** consists of broad, unresolved humps. With time these resolve to reveal signals ascribable to **4** and peaks due to the other scission product: 2,4-dinitrophenyl isopropyl ether, **6**.

Therefore, the reaction system using 2 equivalents of iPrOK was examined. In this case, the initial spectrum obtained shortly after mixing contains resonances assigned to the C-7 adduct, **2***a* (Nu = iPrO). Peaks are also noted that are attributed to the DNP-DNBT·OH⁻ adduct, **2***a* (Nu = OH).

Under these conditions the signals due to the C-7 DNP-DNBT·OPr*i*⁻ adduct, **2***a*, were still dominant in the spectrum even after 3 days had elapsed. Smaller resonances ascribed to **4** and to the ether, **6**, could be noted. The signals of **6** were in fair agreement with those of separately prepared **6**, i.e., 8.696 (d, J = 2.68, H_3), 8.436 and 8.415 (d,d, J = 9.31, 2.68, H_5), 7.604 (d, J = 9.31, H_6), 5.022 (septet, J = 6.00, C*H* methine), and 1.345 (d, J = 6.00, CH_3's).

There was no evidence for formation of adducts derived from **6**. Nor was 2,4-dinitrophenoxide ion (or the phenol) observed in the system over the 3 day period of examination.

Reaction of NP-DNBT (5) with iPrOK

(a) Equimolar iPrO⁻ conditions

Signals, albeit small ones, are observed upon mixing equimolar iPrOK in 2-propanol with NP-DNBT, **3**, in $(CD_3)_2SO$. These weak signals, acquired within 5 min, contrast with the intense resonances due to free **3**. No peaks due to the isopropyl ether, **7**, that would result from N-2:C-1′ bond scission, could be seen in the initial spectrum or in subsequent spectra obtained at intervals over the next 5 h.

The signals due to the C-7 adduct, **3***a*, are located at 8.696 (s, H^c_5), 8.343 and 8.446 (d,d, J = 9.04, $H^c_{2',6'}$ and $H^c_{3',5'}$), and 6.039 (s, H^c_7) (Table 1). Upon acidification with TFA the signals listed above disappear, as expected for acid-labile O-centred Meisenheimer adducts (12–14).

(b) Excess iPrO⁻ conditions (3 and 5 equivalents)

The spectrum recorded after injection of 3 equivalents of iPrOK contains small broad resonances due to **3**, along with more prominent peaks attributable to the C-7 NP-DNBT·OPr*i*⁻ adduct, **3***a*.

At longer times (ca. 2 h) small peaks appear that are ascribed to the isopropyl ether, **7**. The full assignment is only possible at longer times when the spectrum becomes completely resolved. The signals of **7** are found at 8.175 and 7.113 (A_2X_2 d,d, J = 9.01, $H_{3,5}$ and $H_{2,6}$), 4.802 (septet, J = 6.01, C*H* methine), and 1.306 (d, J = 6.01, CH_3's). Simultaneous with the appearance of the peaks due to **7**, resonances that correspond to **4** are also noted. However, even after 2 days had elapsed **3***a* was the dominant species; **3***a* and **7** were found in a ratio of 2:1 at this point.

Addition of 5 equivalents of iPrO⁻ to the solution of **3** leads to a very rapid cleavage reaction. The only peaks visible in the first spectrum are those ascribable to the ether, **7**, and to **4**.

Discussion

1. Reaction pathways

Scheme 1 describes the main reactions of nucleophiles with the members of this family of ambident electrophiles: 2-(2′,4′,6′-trinitrophenyl)-, 2-(2′,4′-dinitrophenyl)-, and 2-(4′-nitrophenyl)-4,6-dinitrobenzotriazole 1-oxides, i.e., Pi-DNBT, **1**, DNP-DNBT, **2**, and NP-DNBT, **3**, respectively. Generally, then, attack of a nucleophile (Nu) including iPrO⁻ at C-7 of **1–3** generates a C-7 anionic σ-complex, **1***a*–**3***a*, respectively, whereas attack at C-1′ leads to irreversible formation of the anionic nucleofuge, DNBT⁻, **4**, and a 1-Nu-$(NO_2)_n$-benzene derivative, **5–7**, presumably via the corresponding C-1′ adduct, **1***b*–**3***b*. The spectroscopic parameters for the C-7 adducts are summarized in Table 1. The pathway whereby these persistent C-7 adducts arise is designated Path a in Scheme 1, while the latter route is designated Path b. Comparison of the selectivity for a given path supplies important information on the nature of these super-electrophiles, and these selectivity considerations for the series, **1–3**, will be dealt with below (Sect. 3).

From another perspective Path b constitutes a route for the decomposition of the C-1′ adduct. The inability to observe the C-1′ adducts in this or related systems (11–15, 20) is consistent with rapid and effectively irreversible decomposition of these adducts to **4** and the ethers, **5–7**, and is the only pathway available for decomposition of the C-1′ adduct, if the reversion to substrate (rate constant, k_{-2}) can be ignored. Note that DNBT⁻, **4**, is a resonance-stabilized anion and would be expected to be a good leaving group and that decomposition of the C-1′ adduct by N-2:C-1′ bond scission releases the steric congestion about this bond. The removal of substrate and nucleophile from the system via Path b drives the breakdown of the C-7 adduct (k_{-1}). We previously derived kinetic equations for the disappearance of the C-7 adduct predicated upon the assumption that the rate coefficient for formation of the C-1′ adduct, k_2, is rate determining (13, 14). Observation of the C-7 adduct would require a relatively high stability for the C-7 adduct as compared to the C-1′ adduct (larger K_1 than K_2) as well as a slower formation of the C-1′ adduct (lower k_2 than k_1) relative to formation of the C-7 adduct.

Spectroscopic evidence suggests that another pathway exists for decomposition of the C-7 adduct of Pi-DNBT, **1***a*. Thus, **1** reacts with iPrO⁻ not only via Paths a and b but also to give the 7-isopropyl ether of picryl 4,6-dinitrobenzotriazole, **1***c*, a product of formal internal redox. Similar evidence is found in the reaction of **1** with MeO⁻ where the corresponding ether can be tentatively identified. This suggests the generality of this competitive sequence for **1**. However, neither DNP-DNBT, **2**, nor NP-DNBT, **3**, shows this behaviour.

Moreover, the cleavage product in the reaction of Pi-DNBT, **1**, with iPrO⁻, i.e., isopropyl picrate, **5**, is arguably almost as electrophilic as the picryl moiety of **1** and, so, reacts with iPrO⁻ under the excess concentration regime. Picryl ethers such as **5** generally react with alkoxides to give a kinetically preferred 1,3 adduct that gives way with time to the thermodynamically more stable 1,1 adduct (25). When an excess of iPrO⁻ was used in the reaction with **1** the only Meisenheimer adduct detected was the 1,1 adduct of **5**. Cleavage of **1** was complete and the only other product detected was **4**, the DNBT⁻ leaving group. A separate control experiment confirmed the regioselectivity in this system (i.e., 1,3 → 1,1 isomerization), a pattern of behaviour that we recently defined as K3T1 (25*a*, 26). In the reaction of **1** with an excess of iPrO⁻, therefore, rearrangement of the kinetically favoured 1,3 adduct to the 1,1 adduct was complete at the time of first observation.

In contrast to the behaviour of **1**, no Meisenheimer complexes were formed from the isopropyl ethers, **6** and **7**. Instead,

Can. J. Chem. Downloaded from www.nrcresearchpress.com by 195.246.54.202 on 09/08/12
For personal use only.

under excess $iPrO^-$ conditions relatively clean cleavage of the N-2:C-1′ bond of **2** and **3** occurs as the dominant process yielding the ethers, **6** and **7**, which are unreactive, notably even when 5 equivalents of $iPrO^-$ are allowed to react with **3**.

2. Mechanism of formation of the 7-alkoxy-2-picryl-4,6-dinitrobenzotriazole

In the reaction of **1** with either equimolar MeO^- or $iPrO^-$ the spectroscopic data are consistent with formation of a 7-alkoxy-2-picryl-4,6-dinitrobenzotriazole, **1***c* (OR = OMe or OiPr). These ethers apparently form along with C-7 adduct formation in the respective systems and constitute an alternate decomposition pathway for **1***a*. Formally, **1***c* (OR = OPr*i*) can be viewed as the result of nucleophilic attack at C-7 of **1** followed by an internal redox of the C-7 adduct, **1***a*, involving deoxygenation of the *N*-oxide. Interestingly, when the reactions are performed with an excess of alkoxide, **1***c* does not form. Also pertinent is the observation that over time the signals assignable to **1***c* increase in intensity as those of the corresponding C-7 complex, **1***a*, decline. Note that the scission products, **4** and the ether **5**, also increase in concentration at the expense of the C-7 adduct but, even after all **1***a* has disappeared from the system, unmodified substrate remains.

It appears that the 7-alkoxy-2-picryl-4,6-dinitrobenzotriazoles do not arise from starting substrate alone, but from the C-7 adducts. (Pi-DNBT left in $(CD_3)_2SO$ alone slowly reacts to yield picrate ion and **4**; no products of deoxygenation are detected.) In the Pi-DNBT,RO^- systems formation of **1***c* is competitive with N-2:C-1′ bond scission under the equimolar regime, but scission alone is detected with excess nucleophile, suggesting that while the rate of the scission process is dependent on the concentration of available nucleophile (cf. k_2 in Scheme 1), the deoxygenation process is not.

The mechanism previously advanced to account for the formation of the related 7-methoxy-4-nitrobenzofurazan from the C-7 methoxide adduct of 4-nitrobenzofuroxan is consistent with the observations in the present system (21). As applied to the reaction of **1** with $iPrO^-$, formation of the C-7 adduct, **1***a* (Nu = iPrO), is followed by internal transfer of the sp^3-bound proton to the *N*-oxide oxygen. Deoxygenation was demonstrated recently in the reaction of aryloxides with 4-nitrobenzofuroxan (27), where it was pointed out that the internal proton transfer step is analogous to the Cope reaction (28). In a subsequent step, hydroxide is ejected to yield the ether, **1***c* (Scheme 2). Note that after C-7 adduct formation, which may be regarded as a pre-equilibrium step, the internal proton transfer step and the expulsion of hydroxide from the nitronate anion are both visualized as unimolecular steps. Therefore, whether the proton transfer or the expulsion of OH^- is taken to be rate determining, use of an excess of nucleophile would not affect the overall rate.

Alternatively, an intermolecular process may operate.[4] In this case **1***a* is first protonated at the *N*-oxide oxygen. The C-7 site is then deprotonated, followed by expulsion of the OH^- from N-1. The lack of formation of **1***c* under excess $iPrO^-$ conditions could, then, result from difficulty in protonation of the *N*-oxide under these alkaline conditions. Although also consistent with the data in the present study, we favour the intramolecular mechanism (Scheme 2) previously found in related systems (21, 27).

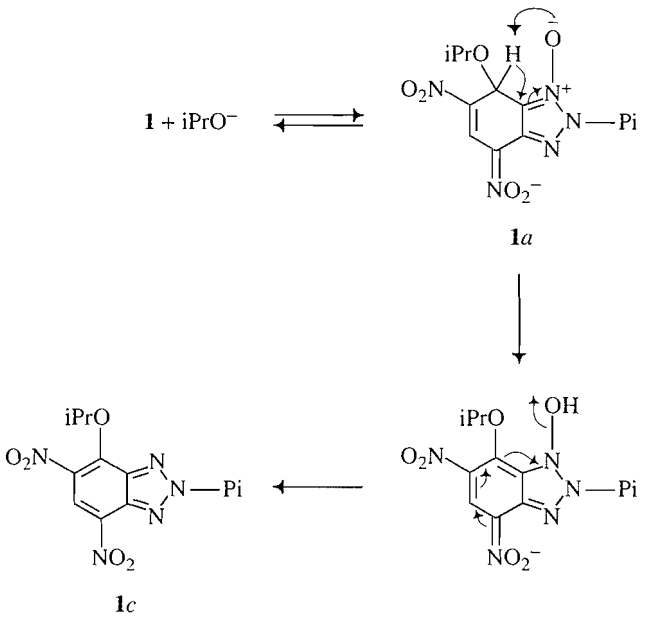

SCHEME 2

3. Selectivity considerations

We previously analysed the reactions of 2-nitroaryl-4,6-dinitrobenzotriazole 1-oxides, **1–3**, on the basis of qualitative selectivity arguments (8, 13, 14) where selectivity (*S*) was defined as the ratio of the forward rate constants for formation of the C-7 as compared to C-1′ adduct. Since the constant for C-7 adduct formation is designated k_1 for **1–3** and k_2 represents the forward rate constant for formation of the C-1′ adducts (Scheme 1), hence $S = k_1/k_2$.

In comparing the series of electrophiles, the percentage of adducts formed (% C-7, % C-1′, Table 2) under selective equimolar conditions serves as a guide to the selectivity for the C-7 position since the ratio of the products must partly reflect the magnitudes of the rate-determining coefficients (k_1, k_2) involved. Clearly, the product ratios must also reflect the relative stabilities of the respective complexes. Two other factors also hinder a more quantitative analysis. First, the data were obtained at somewhat different times due to the initial broadness found in the reaction of **2** with $iPrO^-$.[5] Secondly, the intervention of OH^- in the reaction of **2** and the competitive deoxygenation of the C-7 adduct in the reaction of **1** preclude a more exact determination of the selectivity. However, because the origin of **1***c* requires formation of the C-7 adduct (vide supra), the percentage of **1***a* formed in the Pi-DNBT,$iPrO^-$ reaction system may be taken as the sum of **1***a* and **1***c* (Table 2).

With these limitations it is nonetheless apparent that **2** and **3** are more selective C-7 electrophiles than is **1**. Thus, reaction of **1** with $iPrO^-$ leads to formation of the products of both Paths a and b, visible in the first spectrum, and the C-7 adduct is *not* the dominant species. The selectivity indicated by the ratio of percentages of adducts (% C-7/% C-1′ = 10.3/31.0 = 0.33) is low. Under similar conditions **2** reacts to give a long-lived C-7

[4]We thank a referee for this suggestion.

[5]We previously attributed the broadness found in the spectra of **2** reacting with nucleophiles to the intervention of minor competitive free radical pathways. It should be noted that the substrates are structurally similar to the well-known nitrone spin traps (29). Even low concentrations of radicals could be trapped and persist, giving rise to paramagnetic broadening (30, 31).

adduct, **2***a*, and a C-7 adduct due to OH^- attack; no products attributable to N-2:C-1′ bond scission are present. The contrast between these two systems is even more striking when the spectra obtained for both at ca. 1 h are compared (Table 2). At this time no C-7 adduct remains in the system involving **1**, while the reaction of **3** with $iPrO^-$ is similar to that of **2**. After 7 min 18.2% of **3** has been converted into the C-7 adduct, **3***a*, while only 6.6% of **1***a* is found in the Pi-DNBT system at 4 min, a ratio of 2.75 in favour of the C-7 NP-DNBT·OPr*i*$^-$ adduct, **3***a*.

The comparison between **2** and **3** is more problematic. Using the % C-7/% C-1′ guide to selectivity, it could be concluded that both substrates are equally selective since no products derived from C-1′ attack are observed in either reaction system. It is also clear that a higher percentage of C-7 adduct is formed in the reaction of $iPrO^-$ with **2** than with **3** (41.2% **2***a* vs. 18.2% **3***a*), suggesting that **3** is less selective in C-7 adduct formation than **2**. However, the overall reactivity (as measured by the total percentage conversion, Table 2) also declines in going from **1** to **3**; at 35 min only 18% of **3** has reacted (**3***a* alone), while at 30 min 48% of **1** has reacted. This general decline in reactivity for **3** as compared to **1** or **2** may mask the selectivity of **3**.

In the reaction of phenoxide as an oxygen-centred nucleophile with **2** and **3** the latter was found to be more selective (13) and it seems reasonable on this basis to assign greater selectivity to **3** than to **2**. It is significant that when **2** was treated with a 3-fold excess of $iPrO^-$ scission was complete within the time required for the spectrum to resolve, while similar treatment of **3** yields only **3***a* and *unreacted* **3**, and even after 2 days **3***a* is the major species present. In fact, 5 equivalents of nucleophile are needed to cause clean cleavage of the N-2:C-1′ bond.

It could be argued that the relatively low percentage of C-7 adduct formed from **1** initially (6.6% **1***a* within 4 min of mixing) as compared to the higher amounts of **2***a* and **3***a* formed, indicates that C-7 of **1** is much less electrophilic than C-7 of **2** or **3** and that increasing C-7 electrophilicity accounts for increasing selectivity in going from **1** to **3**. Such a proposition is, however, untenable. Although the C-7 site of **1–3** is remote from the 2-nitroaryl substituent, the electrophilicity of the C-7 site will be modified as successive electron-withdrawing NO_2 groups are removed from the nitroaryl moiety, but this should result in *declining electrophilicity at C-7*. However, as NO_2 groups are removed from the nitroaryl ring the C-1′ site should become even less reactive. It is moot as to whether a decrease in inductive electron withdrawal from C-1′ (reduced positive charge density in the starting state) or reduced stability of the C-1′ adduct (reduced ability to delocalize negative charge in the final state) accounts for the expected decline in reactivity; which effect applies depends upon the position of the transition state (32). Therefore, progressive removal of NO_2 groups from the 2-nitroaryl moiety will have a larger effect on reactivity at the proximate C-1′ site than at the distant C-7 site. The trend in selectivity is primarily due to the decline in reactivity at C-1′ that is only slightly mitigated by the decline in electrophilicity of the C-7 position in proceeding from **1** to **3**.

The percent conversion (Table 2) is a measure of the overall reactivity of the substrates. Thus, at 1 h 59% of **1** has been converted to products, while the total conversion for **2** at ca. 1 h is 53%. The corresponding conversion of **3** would be expected to be around 18% at 1 h, unchanged from the degree of conversion found at 7 min and at 35 min. Therefore, while selectivity for C-7 attack by $iPrO^-$ increases from **1** to **2** and to **3**, in turn, the overall reactivity of the substrates is decreasing in the same order. The most selective substrate is the least reactive one (33).

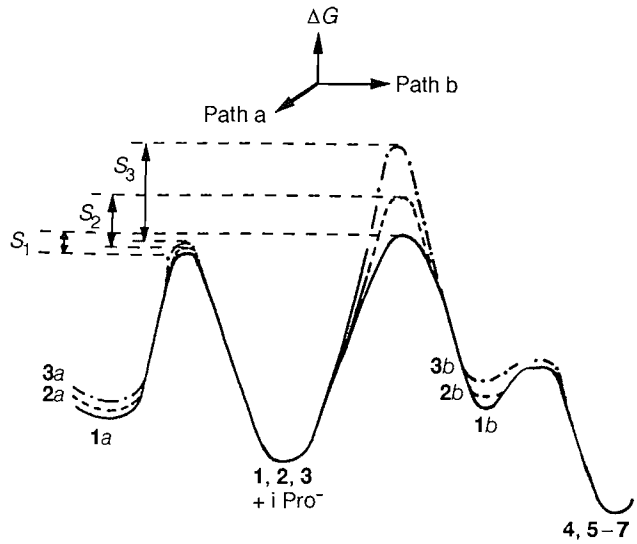

FIG. 1. Attack by $iPrO^-$ at C-7 of the substrate, **1–3**, gives rise to the adducts, **1***a* (solid line), **2***a* (broken line), and **3***a* (dot and dash line) and is shown as the left-hand branch of the energy profile (Path a, Scheme 1). The right-hand branch (Path b) indicates the energetics involved in attack at C-1′ of the substrates, which yields the metastable C-1′ adducts, **1***b*–**3***b*. These C-1′ adducts decompose by N-2:C-1′ bond rupture to yield $DNBT^-$, **4**, and the respective isopropyl nitroaryl ethers, **5–7**. The selectivity, *S*, for a given substrate is shown as the energy gap between the respective activation barrier heights for attack at C-7 (k_1) and C-1′ (k_2).

In our recent study of the reaction of MeO^- and $tBuO^-$ with **2**, it was found that the reactivity and selectivity of the alkoxides was governed primarily by steric hindrance. *tert*-Butoxide proved to be more selective than methoxide (14) even though attack at C-7 was less favourable for $tBuO^-$ than for MeO^-. It is notable, then, that with **2** MeO^- forms 83.5% C-7 adduct (62 min), $tBuO^-$ forms 27.6% C-7 adduct (67 min), and $iPrO^-$, which is intermediate in steric bulk, falls nicely in between by forming 41.2% of **2***a* (61 min).

4. Comparative energy profiles

It has proven useful in previous studies to combine selectivity and other information gleaned from the reactions of **1–3** to construct comparative energy – reaction coordinate diagrams to describe the overall behaviour of the electrophiles in these systems (13, 14).

In constructing such profiles it is expedient to assume that the inherent stability of each member of the series is equal. Given the structural similarities of **1–3** this seems to be an acceptable first approximation. Therefore, Fig. 1 describes attack at the C-7 site (left-hand branch; Path a, Scheme 1) as compared to C-1′ attack (right-hand branch; Path b). Since the deoxygenation reaction (Scheme 2) is restricted to **1** and since competitive OH^- attack at C-7 is only significant with **2**, these processes have been omitted from the profiles.

In the Path a portion of the composite profile, the activation barrier for C-7 attack has been shown to increase slightly for **2** (broken line) as compared to **1** (solid line) and for **3** (dot and dash line) as compared to **2**, in accord with the influence of stepwise removal of NO_2 groups from the 2-nitroaryl ring. This

Can. J. Chem. Downloaded from www.nrcresearchpress.com by 195.246.54.202 on 09/08/12
For personal use only.

Can. J. Chem. Downloaded from www.nrcresearchpress.com by 195.246.54.202 on 09/08/12
For personal use only.

same inductive effect would be expected to impact on the stability of the resultant C-7 adducts; **3***a* would be expected to be slightly less stable than **2***a* and so on for **1***a*.

In assessing selectivity on the comparative energy profile, Path b is of greater importance since the major effects on selectivity involve the activation barrier for attack at C-1′. Here the kinetic barrier rises more abruptly as each NO_2 group is removed from the 2-nitroaryl ring.

Although isopropyl picrate, **5**, can react further in the presence of excess $iPrO^-$, unlike the isopropyl ethers **6** and **7**, all the ethers that arise from N-2:C-1′ scission are shown as having equal stability.

Examination of both branches of the energy profile clearly shows that the activation barriers for Path a attack at C-7 are lower than those for C-1′ attack, in agreement with the known super-electrophilicity of the C-7 site (8–14). Selectivity can be seen to arise mostly from the variation in the C-1′ kinetic barrier; the selectivity of **1**, for example (S_1), is shown as the difference in barrier heights for C-7 versus C-1′ reaction. Concordant with the discussion of selectivity (vide supra) the energy gap represented by S_3 is larger than that for S_2, which is larger than that for selectivity, S_1.

Conclusions

In the first comparison of reaction of a single alkoxide, $iPrO^-$, with the full series of 2-(nitroaryl)-4,6-dinitrobenzotriazole 1-oxides, **1–3**, we have shown that selectivity for C-7 complex formation increases in going from **1** to **3**. Such selectivity is largely the result of the increasing energetic cost of attack at C-1′ that follows from the stepwise removal of stabilizing nitro groups from the 2-nitroaryl moiety. This selectivity and other aspects of the relative energetics of the C-7 and C-1′ adducts are summarized using a composite energy profile (Fig. 1).

While confirming Paths a and b (Scheme 1) as the general routes for reaction of nucleophiles with the ambident electrophiles, **1–3**, we have also presented evidence for formation of 7-isopropyl-2-(2′,4′,6′-trinitrophenyl)-4,6-dinitrobenzotriazole, **1***c*, the product of formal internal redox involving the $iPrO^-$ C-7 adduct of Pi-DNBT, i.e., **1***a* (Scheme 2). Thus, the C-1′ adducts can all decompose to $DNBT^-$, **4**, and the isopropyl ethers, **5–7**, via Path b. The C-7 adducts decompose back to substrate and nucleophiles (and, hence, to the C-1′ adducts and on). However, for **1***a* an additional pathway for decomposition exists: formation of a 7-alkoxy-2-picryl-4,6-dinitrobenzotriazole, **1***c*.

Experimental

2-Propanol (HPLC grade, Caledon) was dried by reflux with and distillation from CaH_2 (34). $(CD_3)_2SO$ (Merck) was dried with 4A molecular sieves as recommended by Burfield and Smithers (35). All other solvents were obtained from commercial sources and purified as described previously (14). The alkoxide solution (iPrOK ca. 3 M) was prepared by dissolution of freshly cut potassium metal in the purified 2-propanol, under N_2, in a nitrogen-filled drybox; the solution was standardized against standard HCl (14). Isopropyl picrate, **5**, was prepared by the method of Farmer (36), yield: 3.7%, mp 92–94°C (lit. (37) mp 95°C). The isopropyl ether of 2,4-dinitrobenzene, **6**, was made by the procedure of Whalley (38) by reaction of 2,4-dinitrofluorobenzene (Aldrich) with 2-propanol in the presence of triethylamine, yield (after recrystallization from aqueous 2-propanol): 37%, mp 55–56°C (lit. (38) mp 56°C). Melting points were determined with a Thomas–Hoover melting point apparatus and are uncorrected.

The Bruker AM-400 MHz nmr spectrometer was adjusted as previously reported (13, 14). Samples of the substrates, **1–3** (final concentration: ca. 0.02 M), were prepared from stock solutions in dry $(CD_3)_2SO$ by injection into Wilmad PP-507 nmr tubes, which contained dry $(CD_3)_2SO$ and 1,4-dibromobenzene as an internal integration standard. Reaction was initiated by injection of a calculated amount of the isopropoxide solution and spectra were recorded at various intervals as described previously (12–14).

Acknowledgements

Support of this research in the form of a grant from the Principal's Research Fund of Sir Wilfred Grenfell College (J.M.D.) and from the Natural Sciences and Engineering Research Council (E.B.) are gratefully acknowledged. We thank Mr. F. Wild for the technical graphics that appear in this paper and thank referees for their helpful comments.

1. E. Buncel, M.R. Crampton, M.J. Strauss, and F. Terrier. Electron deficient aromatic– and heteroaromatic–base interactions. The chemistry of anionic sigma complexes. Elsevier, Amsterdam. 1984.
2. F. Terrier. Chem. Rev. **82**, 77 (1982).
3. G.A. Artamkina, M.P. Egorov, and I.P. Beletskaya. Chem. Rev. **82**, 427 (1982).
4. M.J. Strauss. Acc. Chem. Res. **7**, 181 (1974).
5. C.F. Bernasconi. MTP Int. Rev. Sci. Org. Chem. Ser. 1. **3**, 33 (1973).
6. E. Buncel. The chemistry of functional groups. Supplement F. The chemistry of amino, nitro and nitroso compounds. *Edited by* S. Patai. Wiley, London. 1982.
7. C.F. Bernasconi. J. Am. Chem. Soc. **92**, 4682 (1970).
8. (*a*) M.J. Strauss, R.A. Renfrow, and E. Buncel. J. Am. Chem. Soc. **105**, 2473 (1983); (*b*) E. Buncel, R.A. Renfrow, and M.J. Strauss. J. Org. Chem. **52**, 488 (1987).
9. J.C. Halle, M.P. Simonnin, M.J. Pouet, and F. Terrier. Tetrahedron Lett. **26**, 1307 (1985).
10. F. Terrier, E. Kizillian, J.C. Halle, and E. Buncel. J. Am. Chem. Soc. **114**, 1740 (1992).
11. R.A. Renfrow, M.J. Strauss, S. Cohen, and E. Buncel. Aust. J. Chem. **36**, 1843 (1983).
12. E. Buncel, J.M. Dust, K.T. Park, R.A. Renfrow, and M.J. Strauss. *In* Nucleophilicity. *Edited by* J.M. Harris and S.P. McManus. Adv. Chem. Ser. 215. American Chemical Society, Washington, D.C. 1987. pp. 369–384.
13. E. Buncel and J.M. Dust. Can. J. Chem. **66**, 1712 (1988).
14. J.M. Dust and E. Buncel. Can. J. Chem. **69**, 978 (1991).
15. (*a*) F. Terrier. Nucleophilic aromatic displacement. The influence of the nitro group. Organic Nitro Chem. Ser. VCH, New York. 1991; (*b*) J. Miller. Nucleophilic aromatic substitution. Elsevier, Amsterdam. 1968.
16. (*a*) F. Terrier, F. Millot, and W.P. Norris. J. Am. Chem. Soc. **98**, 5888 (1976); (*b*) F. Terrier, A.P. Chatrousse, and F. Millot. J. Org. Chem. **45**, 2666 (1980); (*c*) M.J. Strauss, A. DeFusco, and F. Terrier. Tetrahedron Lett. **22**, 1945 (1981); (*d*) C. Deicha and F. Terrier. J. Chem. Res. S, 312 (1981).
17. (*a*) W.P. Norris, R.J. Spear, and R.W. Read. Aust. J. Chem. **36**, 297 (1983); (*b*) W.P. Norris, A. Chafin, R.J. Spear, and R.W. Read. Heterocycles, **22**, 174 (1984).
18. J. March. Advanced organic chemistry. Reactions, mechanisms and structure. 3rd ed. Wiley, New York. 1985. pp. 245–250.
19. F.G. Bordwell, T.A. Cripe, and D.L. Hughes. *In* Nucleophilicity. *Edited by* J.M. Harris and S.P. McManus. Adv. Chem. Ser. 215. American Chemical Society, Washington, D.C. 1987. pp. 137–153.
20. (*a*) J.M. Dust. Ph.D. Thesis, Queen's University, 1987; (*b*) R.A. Manderville. Ph.D. Thesis, Queen's University, 1992.
21. E. Buncel, N. Chuaqui-Offermanns, B.K. Hunter, and A.R. Norris. Can. J. Chem. **55**, 2852 (1977).
22. M.R. Crampton, B. Gibson, and F.W. Gibson. J. Chem. Soc. Perkin Trans. 2, 91 (1979).

23. S.S. Joshi and D.S. Deorha. J. Ind. Chem. Soc. **38**, 41 (1961).
24. A. Prakash, R. Prabha, and I.R. Gambhir. J. Inst. Chem. (India), **43**, 214 (1971).
25. (*a*) E. Buncel, J.M. Dust, A. Jonczyk, R.A. Manderville, and I. Onyido. J. Am. Chem. Soc. **114**, 5610 (1992), and references therein; (*b*) A.D.A. Alaruri and M.R. Crampton. J. Chem. Res. M, 2157 (1980); (*c*) C.F. Bernasconi. J. Am. Chem. Soc. **93**, 6975 (1971); (*d*) M.P. Simonnin, M.J. Pouet, and F. Terrier. J. Org. Chem. **43**, 855 (1978); (*e*) R.A. Foster, C.A. Fyfe, P.H. Emslie, and M.I. Foreman. Tetrahedron, **23**, 227 (1967); (*f*) K.L. Servis. J. Am. Chem. Soc. **89**, 1508 (1967); (*g*) J. Am. Soc. Chem. **87**, 5495 (1965).
26. R.A. Manderville and E. Buncel. J. Am. Chem. Soc. **115**, 8985 (1993).
27. R.A. Manderville and E. Buncel. J. Chem. Soc. Perkin Trans. 2, 1887 (1993).
28. J. March. Advanced organic chemistry. Reactions, mechanisms and structure. 3rd ed. Wiley, New York. 1985. p. 909.
29. E.G. Janzen. Acc. Chem. Res. **4**, 31 (1971); Can. J. Chem. **60**, 1379 (1982).
30. J.K.M. Sanders and B.K. Hunter. Modern nmr spectroscopy. Oxford University Press, Oxford. 1987. p. 221.
31. V.F. Starichenko, V.A. Ryabinin, and S.M. Shein. Zh. Strukt. Khim. **15**, 138 (1974).
32. G.S. Hammond. J. Am. Chem. Soc. **59**, 96 (1955).
33. (*a*) E. Buncel and H. Wilson. J. Chem. Educ. **64**, 475 (1987); (*b*) E. Buncel, C. Chuaqui, and H. Wilson. J. Org. Chem. **45**, 3621 (1980).
34. D.D. Perrin, W.L.F. Armarego, and D.R. Perrin. Purification of laboratory chemicals. 2nd ed. Pergamon, Oxford. 1980.
35. D.R. Burfield and R.H. Smithers. J. Org. Chem. 43, 3966 (1978).
36. R.C. Farmer. J. Chem. Soc. 3425 (1959).
37. A. Cooney and M.R. Crampton. J. Chem. Soc. Perkin Trans. 2, 1973 (1984).
38. W.B. Whalley. J. Chem. Soc. 2241 (1950).

Can. J. Chem. Downloaded from www.nrcresearchpress.com by 195.246.54.202 on 09/08/12
For personal use only.

ortho and remote metalation – cross coupling strategies. Total synthesis of the naturally occurring fluorenone dengibsinin and the azafluoranthene alkaloid imeluteine[1]

J.-M. Fu, B.-P. Zhao, M.J. Sharp, and V. Snieckus[2]

Guelph–Waterloo Centre for Graduate Work in Chemistry, Department of Chemistry, University of Waterloo, Waterloo, ON N2L 3G1, Canada

Received October 26, 1993

This paper is dedicated to Professors David B. MacLean and Ian D. Spenser

J.-M. Fu, B.-P. Zhao, M.J. Sharp, and V. Snieckus. Can. J. Chem. **72**, 227 (1994).

The total synthesis of the naturally occurring fluorenone, dengibsinin (**7***a*), and the azafluoranthene alkaloid, imeluteine (**30***e*), is described. Using combined *ortho* metalation – cross coupling sequences that terminate in Friedel–Crafts (**18***b* → **6***d*) and remote metalation (**21***a,b* → **6***c,d*) reactions, the synthesis of fluorenone dimethyl ethers **6***c* and **6***d* is reported. **6***c* and **6***d* were shown not to be identical to dengibsinin dimethyl ether and dengibsin dimethyl ether, respectively, derived from the natural products. This work, together with synthetic and structural evidence from Sargent and Talapatra, led to the reassignment of structures for dengibsinin (**7***a*) and dengibsin (**7***b*). Using the metalation – cross coupling approach, the synthesis of the reassigned dengibsinin (**7***a*) is presented. Two alternate unsuccessful approaches to imeluteine are briefly described (**31** + **32** and **33** + **34**). The successful approach incorporates the remote metalation – double cyclization, **43** → **44**, as the key step.

J.-M. Fu, B.-P. Zhao, M.J. Sharp et V. Snieckus. Can. J. Chem. **72**, 227 (1994).

On décrit la synthèse totale de la fluorénone d'origine naturelle, dengibsinine (**7***a*), et de l'alcaloïde azafluoranthène, imélutéine (**30***e*). Faisant appel à des séquences de métallation *ortho* et de couplage croisé qui se terminent par des réactions de Friedel–Crafts (**18***b* → **6***d*) et des réactions de métallation à des sites éloignés (**21***a,b* → **6***c,d*) on a réalisé la synthèse des éthers diméthyliques (**6***c* et **6***d*) de la fluorénone. On a démontré que ces deux éthers ne sont pas identiques aux éthers diméthyliques de la dengibsinine et de la dengibsine obtenues respectivement à partir de produits naturels. Ces résultats ainsi que les données de structure obtenues par Sargent et Talapatra conduisent à une réattribution des structures de la dengibisinine (**7***a*) et de la dengibsinine (**7***b*). Utilisant l'approche de métallation – couplage croisé, on a réalisé la synthèse de la molécule réassignée comme structure de la dengibisinine (**7***a*). On décrit brièvement deux essais infructueux (**31** + **32** et **33** + **34**) de synthèse de l'imélutéine. L'approche qui a réussi comporte, comme étape clé, une métallation avec double cyclisation.

[Traduit par la rédaction]

During the course of work aimed to establish synthetic links between the Directed *ortho* Metalation (DoM) strategy (1) and transition metal catalyzed cross-coupling reactions (2), the concept of the complex induced proximity effect (CIPE) was unified and brought into prominence by Beak and Meyers (3) and by Klumpp (4). This concept defines pathways in which functional group – reagent preequilibrium complexation is a significant event prior to subsequent irreversible, and necessarily intramolecular, reaction at a proximate site. While CIPE is undoubtedly of broader mechanistic value (3), it has been most notably invoked in organolithium transformations to rationalize formation of (*a*) surprising kinetic in lieu of expected thermodynamic products and (*b*) substantial accelerations of normally unfavorable reactions. As a consequence, it has created new opportunities in the design of regio- and stereo-specific reactions. In contemplating the X-ray structure of a 2,6-diphenyl benzamide,[3] we reasoned that such complexation and entropic factors may induce remote metalation in **1** (Scheme 1) as a function of H_1/H_2 hydrogen relative acidities to give species **2**, which could cyclize to fluorenone **3** in an intramolecular version of the classical amide–RLi condensation reaction. Such a reaction would constitute an anionic Friedel–Crafts equivalent with the following advantages over the latter process: (*a*) mild conditions, which would tolerate greater functional group diversity; (*b*) regioselectivity dictated by the availability of directed metalation groups (DMGs) in the aromatic ring in which the incipient carbanion is generated, i.e., **2**, X = OMe; (*c*) complementarity, i.e., **2** → **3** vs. **1** → **4**, X = OMe; and (*d*) chemoselectivity, i.e., avoidance of dibenzopyranone product **5** in acid-sensitive oxygenated systems **1**, Y = OPG (see below). Herein we report[4] the application of this remote aromatic metalation concept for the construction of the naturally occurring fluorenone dengibsinin (**7***a*) and the azafluoranthene alkaloid, imeluteine (**30***e*). In a sequel,[3] we shall present general methodological results on the Suzuki cross-coupling reaction for precursor teraryls **1** and the corresponding biaryls (6) and their remote metalation-induced cyclization to substituted fluorenones, condensed fluorenones, and azafluorenones (5*a*).

Synthesis of dengibsinin (7*a*)

In 1985, Talapatra et al. (7) reported on the structural elucidation of two fluorenones isolated from *Dendrobium gibsonni* Lindl, an Indian Orchidaceae endemic to the Sikkim Himalayas, Khasia mountains, and Burma, which is used as an epiphytic herb. These natural products, named dengibsinin and dengibsin, were assigned structures **6***a* and **6***b*, respectively, on the basis of ^{1}H NMR spectra of the parent compounds, their dimethyl ether, and their diacetate derivatives. These, at that time,[5] unique structures stimulated retrosynthetic analysis according to the remote aromatic metalation strategy (Scheme 1). During the course of our efforts, the structures of dengibsinin and dengibsin were revised by Sargent (9) to **7***a* and **7***b*, respectively, on the basis of reinterpretation of the spectral data and synthesis of the misassigned **6***a* and **6***b*, their respective

[1]Dedicated to Dave MacLean and Ian Spenser, two scholars who tenaciously enhanced the traditions and set new standards in Canadian organic chemistry.

[2]Author to whom correspondence may be addressed. Telephone:519-888-4007, FAX: 519-746-5884.

[3]J.-m. Fu, B.-p. Zhao, M.J. Sharp, N.J. Taylor, and V. Snieckus. Manuscript in preparation.

[4]For preliminary communications, see ref. 5.

[5]Recently, a highly oxygenated benzofluorenone was isolated from *Streptomyces murayamaensis*: see ref. 8.

Can. J. Chem. Downloaded from www.nrcresearchpress.com by 195.246.54.202 on 09/08/12
For personal use only.

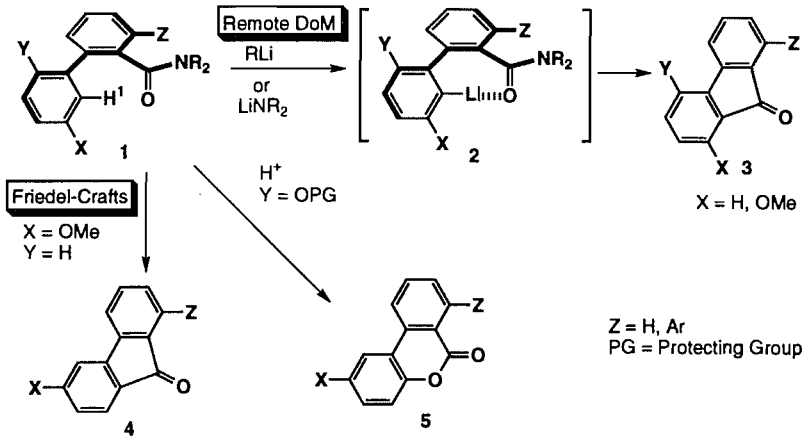

SCHEME 1

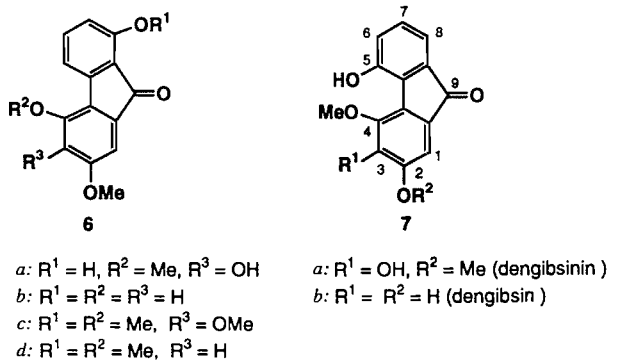

dimethyl ethers, **6***c* and **6***d*, and the natural products themselves. On the basis of additional IR data and reinterpretation of ^{1}H NMR spectra, Talapatra et al. (10) also reassigned the structures of dengibsinin (**7***a*) and dengibsin (**7***b*).

In efforts undertaken prior to knowledge of structural revision, "dengibsin" (**6***b*) was targeted by retrosynthetic analysis (Scheme 2) aimed to take advantage of the developed cross-coupling methodology of benzamide boronic acids with aryl halides (**10** + **11**) (6), the associated general synthesis of dibenzopyranones (→ **9**) (11), and, ultimately, a Friedel–Crafts cyclization to form dengibsin (**8** → **6***b*). The synthesis was initiated by metalation–boronation of the readily available *ortho*-anisamide **12** (Scheme 3) to give the corresponding boronic acid **13**, which, without purification, was subjected to cross coupling with **14**, prepared from the known 2-bromo-4-methoxyphenol, to afford the biaryl **15** in good yield. Quantitative conversion of **15** into the dibenzopyranone **16** was achieved under refluxing acetic acid conditions. Ring opening – phenol protection was effected by dissolution of **16** in 50% NaOH solution followed by slow addition of benzyl bromide and dimethyl sulfate to yield biaryls **17***a* and **17***b*, respectively. Adaptation of the Gassman "anhydrous hydroxide" procedure (12) led smoothly to the carboxylic acids **18***a* and **18***b*. Although treatment of **18***a* with TFAA "returned" the dibenzopyranone **16** in high yield, the use of these conditions on **18***b* provided **6***d* in 16% yield, the major product again being the pyranone **16**. The physical and spectral properties of compound **6***d* did not correspond to dengibsin dimethyl ether but agreed closely with **6***d*, which was unambiguously synthesized (see below). Facile dealkylative cyclizations of biaryls to dibenzopyranones analogous to the conversion **18** → **16** were noted previously (13) and attributed to the proximity of the 2,2′-reacting groups. Sargent

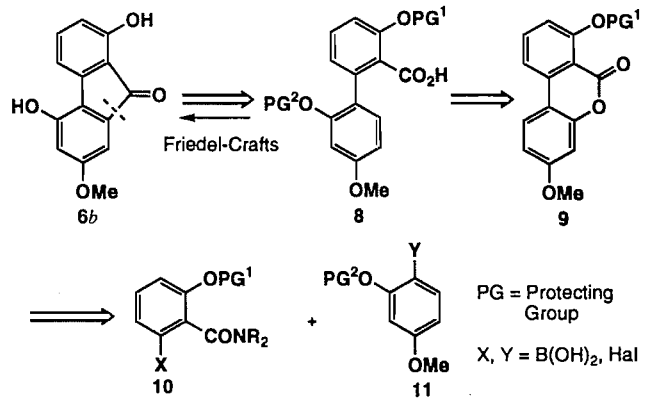

SCHEME 2

encountered similar by-products in his syntheses of dengibsinin (**7***a*) and dengibsin (**7***b*) (9). These and other discouraging results in our Friedel–Crafts cyclization attempts were superseded by the discovery of the remote metalation route to fluorenones.[3]

Towards this end, the requisite biary amides **21***a* and **21***b* (Scheme 4) were rapidly prepared by Suzuki cross coupling of *o*-anisamide boronic acid **13** with aryl bromides **20***a* and commercial **20***b*, respectively, both of which are also easily accessible from commercial products. Concurrent optimization of remote metalation conditions[3] led to the choice of LDA and allowed conversion of **21***a* and **21***b* into the fluorenones **6***c* and **6***d*, respectively, in good yields. Physical and spectral data of these materials were in agreement with those reported for the **6***c* and **6***d* synthesized by Sargent (9) and, in the case of **6***d*, with the compound obtained by TFAA cyclization (Scheme 3) but not with those of dengibsinin dimethyl ether and dengibsin dimethyl ether. With these results in hand, we turned to retrosynthetic analysis of the revised structures **7***a* and **7***b* for the naturally occurring fluorenones.

Of the two strategic bonds in **7** (Scheme 5) for anionic cyclization, dissection leading to most profitable convergence dictates consideration of the key amide **22**, which, upon scission of the biaryl bond, retrogrades in a cross-coupling mode to the aryl boron **23** and aryl halide **24** derivatives. Previous experience (5*a* and footnote 3) suggested the use of boronate ester (**23**, R = alkyl), aryl iodide (**24**, X = I), and anhydrous conditions for circumventing problems of competitive protodeboronation in the sterically hindered cross coupling to the tri-*ortho*-substituted biaryl **22**. Towards this end, the boronate ester **26** (Scheme

Can. J. Chem. Downloaded from www.nrcresearchpress.com by 195.246.54.202 on 09/08/12
For personal use only.

Can. J. Chem. Downloaded from www.nrcresearchpress.com by 195.246.54.202 on 09/08/12
For personal use only.

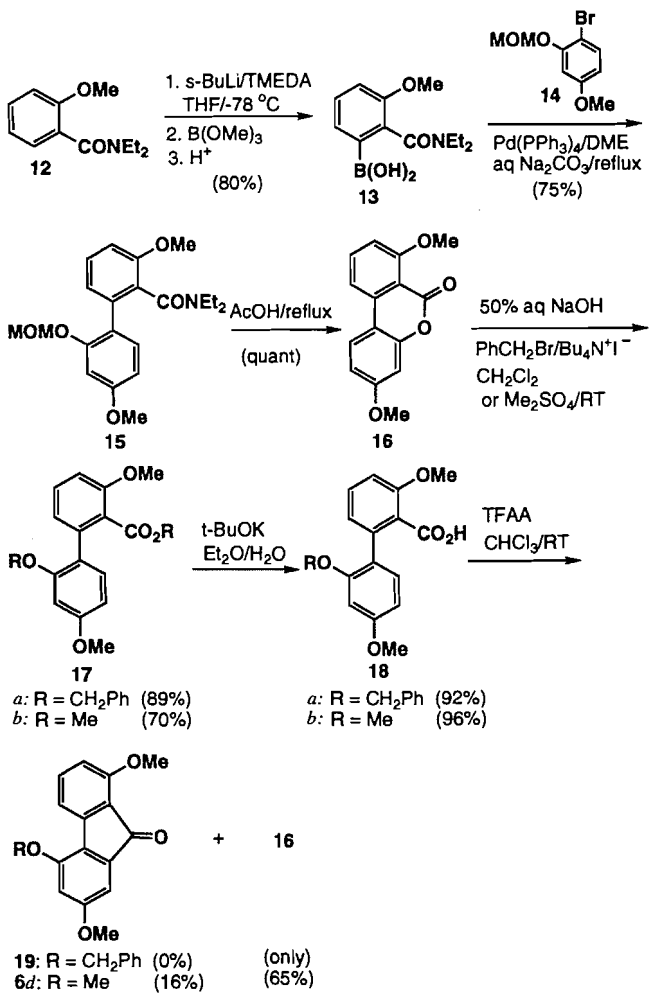

SCHEME 3

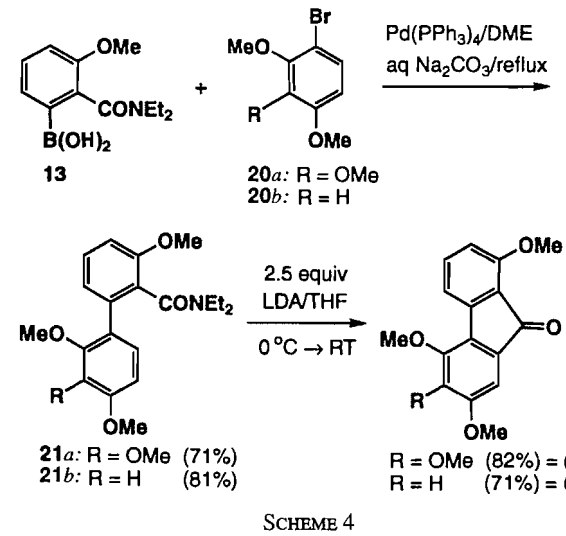

SCHEME 4

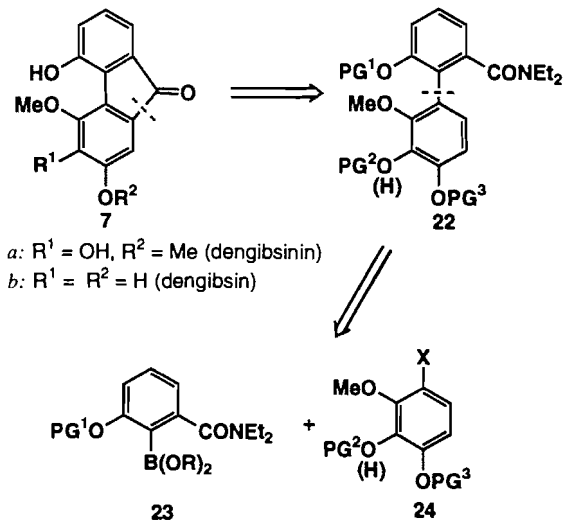

SCHEME 5

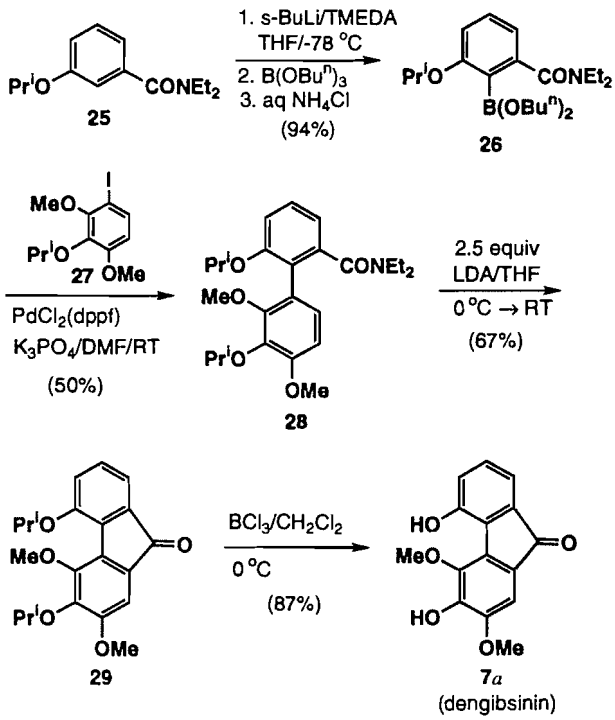

SCHEME 6

6) was prepared in high yield from *m*-isopropoxybenzamide **25** and the aryl iodide **27** partner was obtained in two steps from 2,6-dimethoxyphenol by sequential isopropylation and electrophilic iodination. A thorough investigation of anhydrous conditions was undertaken (Table 1) which indicated that (*a*) the toxic thallium carbonate (14) was an inefficient base compared to potassium phosphate (entry 1), (*b*) DMF is a superior solvent compared to THF (entries 2, 7 vs. 4, 5), and (*c*) $PdCl_2$(dppf) is the catalyst of choice (entries 6, 7). The optimum mildest conditions (entry 7) were based on those reported by Suzuki and co-workers (15) during the course of our studies on highly hindered aryl–aryl coupling reactions.

The key biphenylamide **28** thus obtained in modest yield was subjected to the LDA-induced cyclization conditions and led smoothly to the fluorenone **29**, which, upon treatment with boron trichloride following the excellent procedure of Sala and Sargent (16), afforded dengibsinin (**7***a*) whose physical and spectroscopic properties were shown to be identical to those reported for the natural product (7, 9). The total synthesis of dengibsinin was thus achieved in about eight steps and 27% overall yield based on **25**, which may be compared to the ten-step 1.3% overall yield based on 2-hydroxy-3,4-dimethoxylbenzoic acid reported by Sargent (9) and our earlier

TABLE 1. Conditions for the cross coupling reaction of aryl boronate **26** with aryl halide **27**

Entry	Catalyst	Solvent	Temperature, °C	Base	Yield, %
1	$Pd(PPh_3)_4$	DMF	130–140	Tl_2CO_3	11
2	$Pd(PPh_3)_4$	DMF	110–110	K_3PO_4	50
3	$Pd(PPh_3)_4$	DME	Reflux	K_3PO_4	30
4	$Pd(PPh_3)_4$	THF	Reflux	K_3PO_4	13
5	$PdCl_2$(dppf)	THF	Reflux	K_3PO_4	35
6	$PdCl_2$(dppf)	DMF	60–70	K_3PO_4	48
7	$PdCl_2$(dppf)	DMF	RT	K_3PO_4	50

approach (Scheme 3), both of which suffer from deficiencies in regiochemistry.

Numerous attempts to apply this strategy to the total synthesis of dengibsin (**7***b*) failed (17) for a variety of reasons before an alternate remote metalation route was successfully executed (18).

Synthesis of imeluteine (30*e*)

The biosynthetically intriguing azafluoranthenes (**30**, Scheme 7) make up a small group of alkaloids (19), the earliest members of which, rufescine (**30***d*) and imeluteine (**30***e*) were isolated by Cava et al. (20) 20 years ago from *Abuta rufescens*

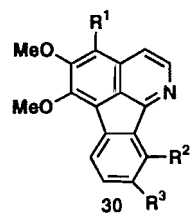

	R^1	R^2	R^3	Name
a:	H	H	H	Triclisine
b:	H	H	OH	Telitoxine
c:	OMe	H	OH	Norrufescine
d:	OMe	H	OMe	Rufescine
e:	OMe	OMe	OMe	Imeluteine

SCHEME 7

and *A. imene* (Menispermaceae). Subsequently, two biogenetically related tropoloisoquinoline alkaloids were also isolated from the same family by Menachery and Cava (21*a*; see also 21*b*). A decade ago, Patel and MacLean (22) reported, as an initial foray towards the synthesis of the azafluoranthene alkaloids, the preparation of a tetrahydro-tetramethoxy analogue in 17% overall yield using both DoM and an interesting lactam Bischler–Napieralski cyclization. Synthetic efforts to date on the azafluoranthene alkaloids have resulted in routes based on Pschorr cyclization and inverse electron demand Diels–Alder strategies to telitoxine (**30***b*), rufescine (**30***d*), and imeluteine (**30***e*) (19). The parent ring system, 3,4-dihydro-2-azafluoranthene, was first prepared by Campbell and Reid (23) proceeding from oxidative cleavage of fluoranthene. Subsequently, this compound has been found as a significant pollutant in coal tar (24), city air (25), and cigarette smoke (26). A successful route to the tropoloisoquinoline alkaloids has defied efforts to date.[6]

In view of the readily discernable fluorenone substructure, the azafluoranthene alkaloids appeared opportune targets for application of the combined metalation (*ortho* and remote) – cross-coupling strategy. The initial efforts were focussed on a

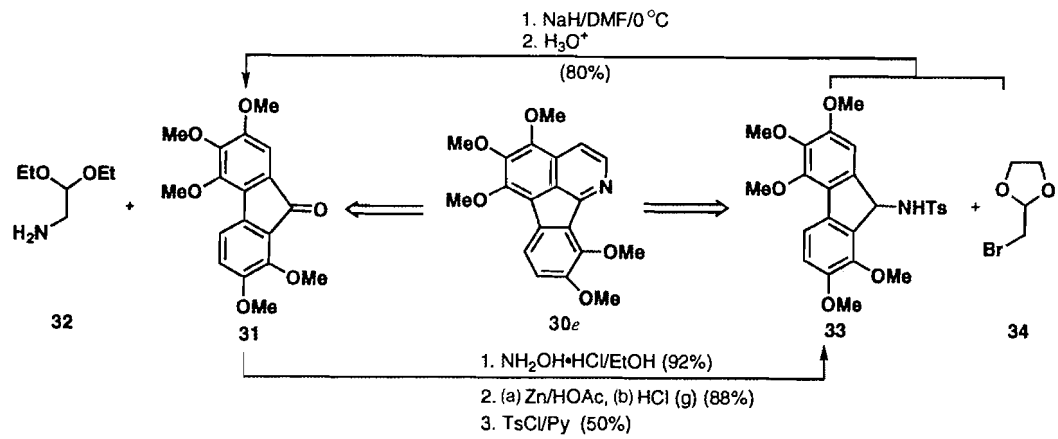

SCHEME 8

retrosynthetic analysis (Scheme 8) based on imeluteine (**30***e*) as the target and ultimate heteroanellation via a Bobbitt modification of the Pomeranz–Fritsch reaction (27), using the pentamethoxyfluoreonone **31** and aminoacetaldehyde diethyl acetal **32** as precursors. The fluoreone **31** was rapidly and efficiently procured (Scheme 9) by cross coupling of the DoM-derived benzamide boronic acid **35** with the methoxylated bromobenzene **20***a* to give the biaryl amide **36** followed by LDA-mediated remote metalation–cyclization. Despite a previous ominous report by Buck[7] concerning the failure to obtain a Schiff base from the reaction of a substituted fluorenone with **32**, we undertook a series of studies to effect the condensation of **31** with **32**. Under a variety of acid-catalyzed conditions, either starting fluorenone (TsOH (28), BF_3·Et_2O (29)) was recovered or decomposition ($TiCl_4$ (30)) occurred. An alternate heteroannelation

[6]M.P. Cava, personal communication.

[7]K.T. Buck. Unpublished observation, see ref. 19.

Can. J. Chem. Downloaded from www.nrcresearchpress.com by 195.246.54.202 on 09/08/12
For personal use only.

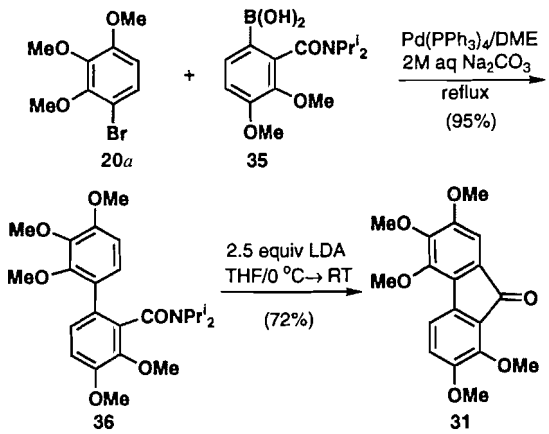

SCHEME 9

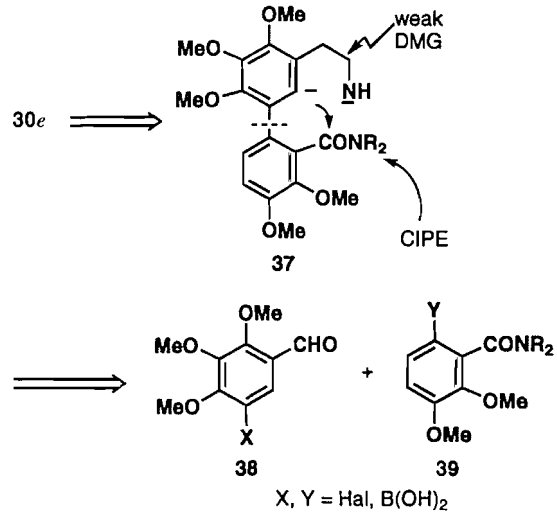

SCHEME 10

approach was based on a recent isoquinoline synthesis starting with benzyl bromide and *N*-tosyl aminoacetaldehyde dimethyl acetal (31). Inverting the condensation partners of this model led to the retrosynthetic consideration of 9-*N*-tosylaminofluorene **33** and the bromoacetal **34** as the precursors. While **33** was conveniently prepared in three steps from fluorenone **31** (Scheme 8), its condensation with **34** under NaH/DMF conditions (32) led to toluenesulfinate elimination and hydrolysis to return **31** in high yield, a result which has precedent (33).

These discouraging results prompted a completely different retrosynthetic analysis of imeluteine (Scheme 10) based on the key intermediate biaryl **37** in which the ethylamino tether is poised for an intramolecular heteroannelation subsequent to the remote metalation–cyclization step. In this analysis, the known weak-DMG effect of the ethylamino group (34) could be envisaged to further facilitate the CIPE-mediated remote metalation process. The biaryl **37** was envisaged to arise from the benzaldehyde **38** and benzamide **39** partners in which the former is ready for classical chain extension methodology.

To initiate this attack on imeluteine, the bromobenzaldehyde **40** (Scheme 11), available by two direct routes in 68% overall yield (see experimental section), was cross coupled with the previously prepared (Scheme 8) benzamide boronic acid **35** to furnish the biaryl aldehyde **41** in high yield. Chain extension by condensation with nitromethane (35) afforded the nitrostyrene **42**, which, upon reduction with LAH (35), smoothly led to the phenethylamine **43** without complications of amide reduction due to its sterically hindered nature (36). Exposure of **43** to excess LDA was rewarded by the formation of dihydroimeluteine **44**, albeit in low yield. To conclude the synthesis, **44** was subjected to dehydrogenation conditions (35) to furnish imeluteine (**30***e*) whose identity with the natural product was established following the usual criteria. The synthesis, effected in five steps and 13% overall yield, compares favorably with that reported (15 steps, 4.9% overall yield (37), five steps, 14.3% overall yield (20*a*)).

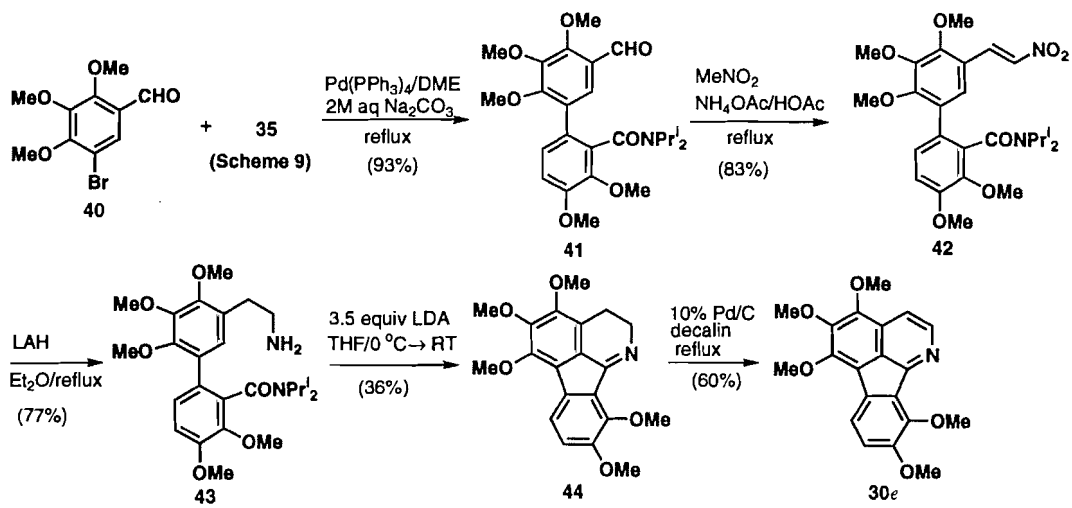

SCHEME 11

Conclusions

Using the concept of CIPE-induced (3, 4) remote metalation in combination with directed *ortho* metalation and cross coupling strategies (Scheme 1), a general approach to substituted and condensed fluorenones has been developed.[3] As reported herein, this integrated approach leads to relatively fast and effi-

Can. J. Chem. Downloaded from www.nrcresearchpress.com by 195.246.54.202 on 09/08/12
For personal use only.

Can. J. Chem. Downloaded from www.nrcresearchpress.com by 195.246.54.202 on 09/08/12
For personal use only.

cient assemblies of two diverse natural products, dengibsinin (Scheme 6) and imeluteine (Scheme 11). In the former, a problematical classical Friedel–Crafts approach (Scheme 3) has been overcome by the use of the remote metalation–cyclization step (Scheme 5), which occurs under mild LDA conditions. In the latter, the DoM – cross coupling tactics allow the rapid construction of an appropriate biaryl intermediate in which the amide serves as a linchpin in the subsequent one-pot formation of two rings that is initiated by the remote metalation process (Scheme 10). Both syntheses illustrate a new methodology for fluorenone ring formation, which constitutes an anionic equivalent of the Friedel–Crafts process and which, by virtue of its mild conditions and regioselectivity, may complement and (or) supersede that classical method for the synthesis of condensed fluorenones.

Experimental section

General procedures

Melting points were determined on a Buchi SMP-20 apparatus and are uncorrected. IR spectra were recorded on a Perkin–Elmer 983 or on a BOMEM MB-100 infrared spectrophotometer in neat, $CHCl_3$, or KBr pellet form. ^1H NMR and ^{13}C NMR spectra were recorded on a Bruker AM-250 or on an AC-200 instrument with tetramethylsilane as internal standard unless otherwise stated. Mass spectra (MS) were determined on a high-resolution Varian MAT-CH7 instrument at 70 eV. Microanalyses were performed by M-H-W Laboratories, Phoenix, Ariz. All compounds were purified by column chromatography and crystallization or distillation.

Tetrahydrofuran and diethyl ether were freshly distilled from sodium benzophenone ketyl under nitrogen prior to use. DME was used directly without purification. *n*-BuLi, *s*-BuLi, and *t*-BuLi were purchased from Aldrich Chemical Co., as solution in hexane, cyclohexane, and pentane, respectively. They were stored in resealable containers and titrated periodically against 2,5-dimethoxybenzyl alcohol (38). Diisopropylamine (DIA) and *N,N,N′,N′*-tetramethylethylenediamine (TMEDA) were dried over and distilled from CaH_2 and stored under argon. LDA was always freshly prepared by stirring a 1:1 mixture of DIA and *n*-BuLi at 0°C for 10 min. All commercial materials were purchased from Aldrich Chemical Co. or Lancaster Synthesis Ltd. Palladium catalyst was prepared according to literature procedures (39) and stored in sealed containers in a refrigerator.

All the reactions were performed in oven-dried glassware under argon, using syringe – septum cap techniques. The "−78°C" temperature designated is approximate as achieved by a Dry Ice – acetone bath. The phrase "standard work-up" refers to addition of water, extraction with CH_2Cl_2, washing the organic extract with brine solution, drying (Na_2SO_4), filtration, and evaporation to dryness in vacuo. Flash chromatography was carried out using Merck silica gel 60 (0.04–0.06 mm) purchased from BDH Chem. Co. Canada with EtOAc–hexane as eluent unless otherwise specified.

Synthesis of tertiary benzamides

The following benzamides were prepared by the standard thionyl chloride – dialkylamine reaction.

N,N-*Diethyl 2-methoxybenzamide* (***12***): bp 90–95°C/0.1 Torr (lit. (11) bp 105–106°C/0.25 Torr; 1 Torr = 133.3 Pa).

N,N-*Diisopropyl 2,3-dimethoxybenzamide*: mp 107–108°C (hexane–EtOAc) (lit. (11) mp 107–108°C).

N,N-*Diethyl 3-isopropoxybenzamide* (***25***)

A mixture of *N,N*-diethyl 3-hydroxybenzamide (17.1 g, 88.4 mmol), K_2CO_3 (18.8 g, 136 mmol), KI (22.6 g, 136 mmol), and 2-bromopropane (12.8 mL, 136 mmol) in acetonitrile (300 mL) was heated at 80°C for 48 h. After cooling, the mixture was subjected to filtration and the filtrate was evaporated to dryness in vacuo. Standard work-up followed by flash chromatography (1:1) afforded 16.18 g (78%) of **25**, bp 160–163°C/4 Torr; IR (neat) ν (max): 1636 cm^{-1}; ^1H NMR ($CDCl_3$) δ: 7.22–7.32 (m, 1H), 6.87–6.94 (m, 3H), 4.55 (sept, J = 6.1 Hz, 1H), 3.15–3.70 (br, 4H), 1.34 (d, J = 6.1 Hz, 6H), 1.00–1.30 (br, 6H); MS *m/z* (rel. intensity): 235 (M^+, 42), 192 (77), 164 (23), 163 (44) 121 (100); HRMS calcd. for $C_{14}H_{21}NO_2$: 235.1573; found: 235.1568.

Preparation of boronic acids

A solution of the benzamide (1 mmol), dissolved in anhydrous THF (2 mL) was added dropwise to a solution of a 1:1 *s*-BuLi (1.1 mmol) – TMEDA (1.1 mmol) complex in anhydrous THF (3 mL) at −78°C. The resulting mixture was stirred at −78° for 1 h and treated with $B(OMe)_3$ (2–3 mmol) followed by warming to ambient temperature over 4 h. Saturated aqueous NH_4Cl solution (2 mL) was added and THF was removed in vacuo. The residue was subjected to standard work-up to afford the crude product, which was used in cross coupling reactions without further purification.

2-N,N-*Diethylcarboxamido-3-methoxyphenyl boronic acid* (***13***): see ref. 11.

2-N,N-*Diisopropylcarboxamido-3,4-dimethoxyphenyl boronic acid* (***35***): see ref. 11.

Di-n-*butyl B-[2-isopropoxy-6-(*N,N-*diethylcarboxamido)phenyl] boronate* (***26***)

A solution of **25** (4.707 g, 20.0 mmol) in THF (20 mL) was added dropwise to a stirred solution of *s*-BuLi (16.92 mL of 1.30 M solution, 22.0 mmol) and TMEDA (3.32 mL, 2.557 g, 22.0 mmol) in THF (80 mL) at −78°C. The resulting solution was stirred at −78°C for 2 h and treated with tributyl borate (18.4 g, 80.0 mmol), followed by stirring below −40°C for an additional 4 h. The reaction was quenched with NH_4Cl solution at −40°C. Standard work-up followed by short-path distillation afforded 7.324 g (94%) of **26**, bp 150–155°C/0.01 Torr; IR (neat) ν (max): 1628 cm^{-1}; ^1H NMR ($CDCl_3$) δ: 7.25 (dd, J = 7.8, 1.1 Hz, 1H), 6.90–6.81 (m, 2H), 4.55 (sept, J = 6.1 Hz, 1H), 3.84 (t, J = 6.6 Hz, 4H), 3.68–3.13 (m, 4H), 1.53 (m, 4H), 1.33–1.31 (d, J = 6.1 Hz, 6H), 1.47–1.10 (m, 10H), 0.89 (t, J = 7.2 Hz, 6H); MS *m/z* (rel. intensity): 390 (M^+, 6), 348 (52), 322 (22), 318 (33), 280 (100), 265 (26), 262 (21), 192 (20), 163 (41), 121 (60); HRMS calcd. for $C_{22}H_{38}BNO_4$: 390.2896; found: 390.2828.

Preparation of aryl halides

4-Bromo-3-(methoxymethoxy)anisole (***14***)

2-Bromo-5-methoxyphenol was prepared using a literature procedure (40), bp 102–104°C/30 Torr (lit. (41) bp 150°C/25 Torr); ^1H NMR ($CDCl_3$) δ: 7.30 (d, J = 8.0 Hz, 1H), 6.63 (d, J = 2.5 Hz, 1H), 6.39 (dd, J = 8.0, 2.5 Hz, 1H), 3.73 (s, 3H), 3.54 (s, 1H). A solution of 2-bromo-5-methoxyphenol (4.8 g, 24 mmol) in DMF (50 mL) was added dropwise to a suspension of NaH (1.2 g, 50% in oil, 25 mmol) in DMF (100 mL) at 0°C and the light gray mixture was stirred at 0°C for 1 h. To the mixture was added dropwise chloromethyl methyl ether (3.8 mL, 50 mmol) and the whole was allowed to warm to room temperature and poured into a 5% NaOH solution (100 mL). Extraction with Et_2O followed by standard work-up and distillation afforded 5.35 g (90%) of **14**, bp 83–85°C/0.1 Torr; IR ($CHCl_3$) ν (max): 1590, 1483 cm^{-1}; ^1H NMR ($CDCl_3$) δ: 7.40 (d, J = 8.8 Hz, C5-H), 6.75 (d, J = 2.6 Hz, 1H, C2-H), 6.39 (dd, J = 8.8, 2.6 Hz, 1H, C6-H), 5.22 (s, 2H), 3.77 (s, 3H), 3.51 (s, 3H); MS *m/z* (rel. intensity): 248 (M^+, 95), 246 (M^+, 100), 218 (60), 216 (59). Anal. calcd. for $C_9H_{11}O_3Br$: C 43.75, H 4.49; found: C 43.92, H 4.61.

1-Bromo-2,3,4-trimethoxybenzene (***20***a)

A mixture of 1,2,3-trimethoxybenzene (24.0 g, 142 mmol) and *N*-bromosuccinimide (25.4 g, 142 mmol) in CCl_4 (350 mL) was stirred at room temperature for 12 h and concentrated in vacuo. Standard work-up followed by distillation afforded 31.9 g (91%) of **20***a*, bp 117–120°C/3.5 Torr (lit. (42) bp 97°C/0.5 Torr); ^1H NMR ($CDCl_3$) δ:

Can. J. Chem. Downloaded from www.nrcresearchpress.com by 195.246.54.202 on 09/08/12
For personal use only.

7.20 (d, J = 9.0 Hz, 1H), 6.59 (d, J = 9.0 Hz, 1H), 3.90 (s, 3H), 3.88 (s, 3H), 3.85 (s, 3H).

1-Iodo-3-isopropoxy-2,4-dimethoxybenzene (27)

To a suspension of 2-isopropoxy-1,3-dimethoxybenzene (9) (4.691 g, 23.9 mmol) and silver trifluoroacetate (5.279 g, 23.9 mmol) in $CHCl_3$ (20 mL) was added a solution of iodine (6.067 g, 23.9 mmol) in $CHCl_3$ (180 mL) dropwise. The resulting mixture was stirred at room temperature for 3 h and subjected to filtration. The filtrate was washed with dilute Na_2SO_3 solution. Standard work-up followed by flash chromatography (1:5) afforded 7.37 g (96%) of **27**, bp 100–102°C/0.02 Torr; ^{1}H NMR ($CDCl_3$) δ: 7.40 (d, J = 8.8 Hz, 1H), 6.49 (d, J = 8.8 Hz, 1H), 4.42 (sept, J = 6.2 Hz, 1H), 3.87 (s, 3H), 3.82 (s, 3H), 1.29 (d, J = 6.2 Hz, 6H); MS *m/z* (rel. intensity): 322 (M^+, 22), 280 (100), 265 (25); HRMS calcd. for $C_{11}H_{15}IO_3$: 322.0067; found: 322.0063.

5-Bromo-2,3,4-trimethoxybenzaldehyde (40)

Following a literature procedure (43), **40** was prepared in two steps in 68% overall yield. In an alternative procedure, a mixture of 2,3,4-trimethoxybenzaldehyde (0.216 g, 1.1 mmol) and Br_2 (0.194 g, 1.21 mmol) in acetic acid (2 mL) was stirred at room temperature for 12 h. Standard work-up followed by flash chromatography (1:5) afforded 0.200 g (67%) of **40**, oil (lit. (43) bp 172–178°C/10 Torr); ^{1}H NMR ($CDCl_3$) δ: 10.23 (s, 1H), 7.78 (s, 1H), 4.04 (s, 3H), 4.01 (s, 3H), 3.93 (s, 3H); MS *m/z* (rel. intensity): 376 (M^+, 98), 274 (100).

Cross coupling reaction to biaryls

A mixture of $Pd(PPh_3)_4$ (0.05 mmol) and aryl halide or aryl triflate (1 mmol) in DME (5 mL) was stirred at room temperature for 5 min. To this mixture was added dropwise in sequence a solution of arylboronic acid (1.5 mmol) dissolved in the minimum amount of EtOH (1 mL) and an aqueous solution of 2 M Na_2CO_3 (2 mL). The resulting mixture was heated under reflux for 12 h, cooled, and the solid was removed by filtration. The filtrate was evaporated to dryness and the residue was washed with Et_2O. Standard work-up followed by flash chromatography afforded the biaryl product.

N,N-*Diethyl 3,4′-dimethoxy-2′-(methoxymethoxy)-2-biphenylcarboxamide (15)*

4-Bromo-3-methoxymethoxyanisole **14** (2.90 g, 12.0 mmol) was coupled with **13** (4.00 g, 16.0 mmol) in the presence of $Pd(PPh_3)_4$ (0.48 g, 0.48 mmol) to afford, after standard work-up followed by flash chromatography (1:1), 3.80 g (75%) of **15**, bp 170–175°C/0.05 Torr; IR ($CHCl_3$) ν (max): 1614 cm–^{1}; ^{1}H NMR ($CDCl_3$) δ: 7.30–7.20 (m, 2H), 6.90 (m, 2H), 6.75 (d, J = 2.4 Hz, 1H), 6.53 (dd, J = 8.5, 2.3 Hz, 1H), 5.09 (s, 2H), 3.85 (s, 3H), 3.79 (s, 3H), 3.39 (s, 3H), 3.16 (m, 2H), 2.88 (m, 2H), 0.89 (t, J = 7.1 Hz, 3H), 0.74 (t, J = 7.1 Hz, 3H); MS (CI) *m/z* (rel. intensity): 373 (M^+, 24), 358 (29), 301 (58), 271 (100). Anal. calcd. for $C_{21}H_{27}NO_5$: C 67.54, H 7.29, N 3.75; found: C 67.47, H 7.29, N 4.09.

N,N-*Diethyl 3,2′,3′,4′-tetramethoxybiphenyl-2-carboxamide (21*a)

2,3,4-Trimethoxybromobenzene **20***a* (5.68 g, 23.0 mmol) was coupled with **13** (7.53 g, 30.0 mmol) in the presence of $Pd(PPh_3)_4$ (1.06 g, 0.92 mmol) to afford, after standard work-up followed by flash chromatography (1:4), 6.11 g (71%) of **21***a*, mp 93–95°C (cyclohexane); IR (KBr) ν (max): 1623 cm^{-1}; ^{1}H NMR ($CDCl_3$) δ: 7.32 (dd, J = 8.1, 7.9 Hz, 1H, C5-H), 7.04 (d, J = 8.6 Hz, 1H, C6′-H),6.88–6.94 (m, 2H), 6.64 (d, J = 8.6 Hz, 1H, C5′-H), 3.86 (s, 3H), 3.85 (s, 3H), 3.84 (s, 3H), 3.72 (s, 3H), 2.79–3.31 (m, 4H), 0.97 (t, J = 7.1 Hz, 3H), 0.77 (t, J = 7.1 Hz, 3H); MS *m/z* (rel. intensity): 373 (M^+, 62), 342 (67), 302 (34), 301 (100), 300 (24), 283 (35), 271 (40), 255 (22). Anal. calcd. for $C_{21}H_{27}NO_5$: C 67.54, H 7.29, N 3.75; found: C 67.91, H 7.42, N 3.77.

N,N-*Diethyl 3,2′,4′-trimethoxybiphenyl-2-carboxamide (21*b)

2,4-Dimethoxybromobenzene **20***b* (1.023 g, 4.71 mmol) was coupled with **13** (1.558 g, 6.20 mmol) in the presence of $Pd(PPh_3)_4$ (0.268 g, 0.23 mmol) to afford, after standard work-up followed by flash chromatography (1:4), 1.306 g (81%) of **21***b*, mp 104–106°C (hexane–CH_2Cl_2); IR (KBr) ν (max): 1623 cm^{-1}; ^{1}H NMR ($CDCl_3$) δ: 7.33–7.26 (m, 2H), 6.93 (d, J = 8.7 Hz, 1H, C6-H), 6.88 (d, J = 8.3 Hz, 1H, C4-H), 6.50–6.45 (m, 2H), 3.84 (s, 3H), 3.80 (s, 3H), 3.72 (s, 3H), 3.22–3.11 (m, 1H), 2.96–2.70 (m, 3H), 0.89 (t, J = 7.1 Hz, 3H), 0.74 (t, J = 7.1 Hz, 3H); MS *m/z* (rel. intensity): 343 (M^+, 56), 271 (100), 243 (23). Anal. calcd. for $C_{20}H_{25}NO_4$: C 69.95, H 7.34, N 4.08; found: C 70.68, H 7.11, N 3.74.

N,N-*Diethyl 2′,4′-dimethoxy-6,3′-diisopropoxybiphenyl-2-carboxamide (28)*

A mixture of $PdCl_2$(dppf) (0.073 g, 0.10 mmol), 2,4-dimethoxy-3-isopropoxy-iodobenzene **27** (0.328 g, 1.02 mmol), **26** (0.474 g, 1.21 mmol), and anhydrous K_3PO_4 (0.509 g, 2.40 mmol) in anhydrous DMF (10 mL) was stirred at room temperature for 30 h and poured onto crushed ice. Extraction with EtOAc, drying (Na_2SO_4), and evaporation to dryness in vacuo followed by flash chromatography (1:4) afforded 0.220 g (50%) of **28**, bp 170–175°C/0.01 Torr; IR (neat) ν (max): 1636 cm^{-1}; ^{1}H NMR ($CDCl_3$) δ: 7.28 (dd, J = 8.0, 8.0 Hz, 1H, C4-H), 7.03–6.85 (m, 3H), 6.62 (d, J = 8.6 Hz, 1H, C5′-H), 4.39–4.29 (m, 2H), 3.89 (s, 3H), 3.83 (s, 3H), 3.34–3.23 (m, 2H), 2.81–2.60 (m, 2H), 1.30 (d, J = 6.1 Hz, 6H), 1.22 (d, J = 6.1 Hz, 3H), 1.16–0.80 (m, 6H), 0.69 (t, J = 7.0 Hz, 3H); MS *m/z* (rel. intensity): 429 (M^+, 59), 387 (20), 356 (53), 344 (20), 315 (24), 314 (22), 273 (55), 249 (20), 248 (100), 241 (51), 213 (26); HRMS calcd. for $C_{25}H_{35}NO_5$: 429.2517; found: 429.2504.

N,N-*Diisopropyl-2′,3,3′,4,4′-pentamethoxybiphenyl-2-carboxamide (36)*

2,3,4-Trimethoxybromobenzene (1.73 g, 7.0 mmol) was coupled with **35** (2.98 g, 10.0 mmol) in the presence of $Pd(PPh_3)_4$ (0.410 g, 0.35 mmol) to afford 2.88 g (95%) of **32**, mp 170–171°C (hexane–EtOAc); IR ($CHCl_3$) ν (max): 1615 cm^{-1}; ^{1}H NMR ($CDCl_3$) δ: 7.26 (d, J = 8.7 Hz, 1H, C6′-H), 7.09 (d, J = 8.5 Hz, 1H, C6-H), 6.92 (d, J = 8.5 Hz, 1H, C5-H), 6.62 (d, J = 8.7 Hz, 1H, C5′-H), 3.92 (s, 3H), 3.89 (s, 3H), 3.86 (s, 3H), 3.84 (s, 3H), 3.83 (s, 3H), 3.59 (sept, J = 6.6 Hz, 1H), 3.24 (sept, J = 6.8 Hz, 1H), 1.51 (d, J = 6.8 Hz, 3H), 1.19 (d, J = 6.8 Hz, 3H), 1.02 (d, J = 6.6 Hz, 3H), 0.63 (d, J = 6.6 Hz, 3H); ^{13}C NMR ($CHCl_3$) δ: 166.6, 153.1, 151.6, 151.4, 145.0, 141.9, 135.6, 134.2, 126.7, 126.5,125.4, 110.9, 106.4, 61.5, 60.9, 60.5, 56.0, 55.6, 50.6, 45.3, 23.0, 20.7, 20.4, 20.2, 19.7; MS *m/z* (rel. intensity): 431 (M^+, 40), 400 (77), 331 (100); HRMS calcd. for $C_{24}H_{33}NO_6$: 431.2335; found: 431.2305.

2′-N,N-*Diisopropylcarboxamido-3′,4′,2,3,4-pentamethoxybiphenyl-5-formaldehyde (41)*

5-Bromo-2,3,4-trimethoxybenzaldehyde (**40**) (2.20 g, 8.00 mmol) was coupled with 2-*N,N*-diisopropylcarboxamido-3,4-dimethoxyphenylboronic acid (**35**) (3.22 g, 10.4 mmol) in the presence of $Pd(PPh_3)_4$ (0.44 g, 0.40 mmol) to afford 3.41 g (93%) of **41**, mp 110–112°C (EtOAc); IR ($CHCl_3$) ν (max): 1681, 1622 cm^{-1}; ^{1}H NMR ($CDCl_3$) δ: 10.23 (s, 1H, CHO), 7.57 (s, 1H, C6′-H), 7.02 (d, J = 8.5 Hz, 1H, C6-H), 6.92 (d, J = 8.5 Hz, 1H, C5-H), 4.03 (s, 3H), 3.93 (s, 3H), 3.90 (s, 3H), 3.87 (s, 3H), 3.86 (s, 3H), 3.67 (sept, J = 6.6 Hz, 1H), 3.27 (sept, J = 6.8 Hz, 1H), 1.49 (d, J = 6.8 Hz, 3H), 1.11 (d, J = 6.8 Hz, 3H), 1.06 (d, J = 6.6 Hz, 3H), 0.87 (d, J = 6.6 Hz, 3H); ^{13}C NMR ($CHCl_3$) δ: 188.6, 166.2, 157.7, 152.1, 145.6, 145.0, 134.9, 133.9, 129.9, 128.7, 127.9, 126.4, 124.1, 111.2, 62.3, 61.5, 60.9, 55.7, 50.8, 45.4, 21.0, 20.5, 20.1, 19.6; MS *m/z* (rel. intensity): 459 (M^+, 33), 428 (50), 359 (100); HRMS calcd. for $C_{25}H_{33}NO_7$: 459.2248; found: 459.2249.

*Friedel–Crafts approach to the putative dengibsin dimethyl ether (6*d)

*3,7-Dimethoxy-6*H*-dibenzo[*b,d*]pyran-6-one (16)*

Amide **15** (4.00 g, 10.7 mmol) was dissolved in glacial acetic acid (20 mL) and the solution was heated under reflux for 4 h, cooled, and poured onto ice water. Standard work-up followed by flash chromatography (1:2) afforded 1.98 g (97%) of **16**, mp 159–160°C (hexane–

Can. J. Chem. Downloaded from www.nrcresearchpress.com by 195.246.54.202 on 09/08/12
For personal use only.

CH_2Cl_2); IR ($CHCl_3$) ν (max): 1726 cm^{-1}; ^1H NMR ($CDCl_3$) δ: 7.89 (d, J = 8.8 Hz, 1H), 7.69 (t, J = 8.1 Hz, 1H), 7.57 (d, J = 8.0, 1H), 6.98 (d, J = 8.2 Hz, 1H), 6.80–6.70 (m, 2H), 4.03 (s, 3H), 3.86 (s, 3H); MS *m/z* (rel. intensity): 256 (M^+, 100), 227 (73). Anal. calcd. for $C_{15}H_{12}O_2$: C 70.31, H 4.72; found: C 70.09, H 4.56.

*Benzyl-2′-benzyloxy-3,4′-dimethoxy-2-biphenylcarboxylate (**17**a)*

According to a modification of a literature procedure (44), a 50% NaOH aqueous solution (25 mL) was added (0.5 mL/min) to a solution of **16** (1.00 g, 3.9 mmol), benzyl bromide (3.34 g, 19.5 mmol), and tetra-*n*-butylammonium iodide (7.20 g, 19.5 mmol) in CH_2Cl_2 (25 mL). The resulting mixture was stirred at room temperature until no **16** could be detected by TLC. The organic layer was separated. Standard work-up followed by flash chromatography (1:1) afforded 1.58 g (89%) of **17***a*, bp 220–225°C/0.05 Torr; IR ($CHCl_3$) ν (max): 1724 cm^{-1}; ^1H NMR ($CDCl_3$) δ: 7.25–7.18 (m, 10H), 7.08 (d, J = 8.0 Hz, 1H), 7.05–6.95 (m, 2H), 6.88 (d, J = 8.4 Hz, 1H), 6.40 (m, 2H), 5.05 (s, 2H), 4.85(s, 2H), 3.84 (s, 3H), 3.73 (s, 3H); MS *m/z* (rel. intensity): 454 (M^+, 13), 346 (12), 241 (10), 91 (100). Anal. calcd. for $C_{29}H_{26}O_5$: C 76.63, H 5.77; found: C 76.59, H 5.85.

*Methyl 3,2′,4′-trimethoxy-2-biphenylcarboxylate (**17**b)*

According to a modification of a literature procedure (44), compound **16** (0.200 g, 0.78 mmol) was dissolved in a minimum amount of dimethyl sulfate (2 mL) and 50% NaOH solution was added dropwise until the starting material was no longer observable by TLC. 50% NaOH solution (5 mL) was then added, and the mixture stirred for 6 h to hydrolyze the excess dimethyl sulfate. Standard work-up followed by flash chromatography (1:1) afforded 0.170 g (70%) of **17***b*, mp 113.5–114°C (hexane–CH_2Cl_2); IR ($CHCl_3$) ν (max): 1725 cm^{-1}; ^1H NMR ($CDCl_3$) δ: 7.36 (t, J = 7.9, 1H), 7.11 (d, J = 8.9 Hz, 1H), 6.95–6.85 (m, 2H), 6.49 (m, 2H), 3.85 (s, 3H), 3.82 (s, 3H), 3.71 (s, 3H), 3.60 (s, 3H); MS *m/z* (rel. intensity): 302 (M^+, 100), 271 (92), 179 (45). Anal. calcd. for $C_{17}H_{18}NO_5$: C 67.54, H, 6.00; found: C 67.35, H 5.94.

*2′-Benzyloxy-3,4′-dimethoxy-2-biphenyl carboxylic acid (**18**a)*

Following the Gassman method (12), to a stirred suspension of potassium *tert*-butoxide (1.06 g, 9.45 mmol) in dry diethyl ether (5 mL) at 0°C was added water (0.048 mL) via syringe and the slurry was stirred for 5 min. Compound **17***a* (0.540 g, 1.19 mmol) was added, the ice bath was removed, and the reaction mixture was stirred at room temperature until **17***a* could not be observed by TLC. The reaction was quenched by adding ice-water until two clear layers formed. The aqueous layer was separated and acidified with concentrated HCl. The acidified solution was extracted with Et_2O to afford 0.390 g (92%) of **18***a*, mp 149–150°C (hexane–CH_2Cl_2); IR ($CHCl_3$) ν (max): 1723 cm^{-1}; ^1H NMR ($CDCl_3$) δ: 7.30–7.05 (m, 7H), 6.87 (d, J = 7.8 Hz, 1H), 6.85 (d, J = 8.1 Hz, 1H), 6.45–6.35 (m, 2H), 4.94 (s, 2H), 3.79 (s, 3H), 3.68 (s, 3H); MS *m/z* (rel. intensity): 364 (M^+, 15), 256 (42), 227 (21), 91 (100). Anal. calcd. for $C_{22}H_{20}O_5$: C 72.52, H 5.53; found: C 72.29, H 5.43.

*3,2′,4′-Trimethoxy-biphenyl-2-carboxylic acid (**18**b)*

Following the above procedure, compound **17***b* (0.087 g, 0.29 mmol) was converted into **18***b* (0.080 g, 96%) as a clear colourless oil, IR ($CHCl_3$) ν (max): 1740, 1700 cm^{-1}; ^1H NMR ($CDCl_3$) δ: 7.39 (t, J = 8.0, 1H), 7.15 (d, J = 8.2 Hz, 1H), 6.92–6.90 (m, 2H), 6.53 (dd, J = 8.3, 2.3 Hz, 1H, C5′-H), 6.46 (d, J = 2.3 Hz, 1H, C2′-H), 3.90 (s, 3H), 3.83 (s, 3H), 3.65 (s, 3H), CO_2H undetected; MS *m/z* (rel. intensity): 288 (M^+, 100), 257 (91), 242 (26); HRMS calcd. for $C_{16}H_{16}O_5$: 288.0998; found: 288.0995.

*2,4,8-Trimethoxyfluoren-9-one (**6**d)*

TFAA (0.5 mL) was added dropwise to a solution of **18***b* (0.080 g, 0.28 mmol) in $CHCl_3$ (5 mL) at room temperature. After stirring for 4 h, the solution was poured into ice water. Standard work-up followed by flash chromatography (1:1) afforded, besides **16** (0.047 g, 65%), product **6***d* (0.012 g, 16%), mp 141–143°C (hexane–CH_2Cl_2) (lit. (9) mp 137–139°C); IR (KBr) ν: 1697 cm^{-1}; ^1H NMR ($CDCl_3$) δ: 7.36 (dd, J = 7.7, 7.4 Hz, 1H, C6-H), 7.33 (d, J = 7.4 Hz, 1H, C5-H), 6.85 (d, J = 2.0 Hz, 1H, C1-H), 6.69 (dd, J = 7.7 Hz, 1H, C7-H), 6.54 (d, J = 2.0 Hz, 1H, C3-H), 3.96 (s, 3H), 3.92 (s, 3H), 3.85 (s, 3H). These spectral data were in accord with those reported (9) for synthetic **6***d* prepared as described below.

Remote metalation reactions to fluorenones

*2,3,4,8-Tetramethoxyfluoren-9-one (**6**c)*

To a solution of LDA (1.25 mmol) in THF (2 mL) was added a solution of **21***a* (0.188 g, 0.50 mmol) in THF (1 mL) at 0°C. The resulting mixture was stirred at room temperature for 10 h. Standard work-up followed by flash chromatography (1:6) afforded 0.124 g (82%) of **6***c*, mp 151–153°C (hexane–CH_2Cl_2) (lit. (9) mp 154–155°C); IR (KBr) ν (max): 1689 cm^{-1}; ^1H NMR ($CDCl_3$) δ: 7.40 (dd, J = 7.8, 7.3 Hz, 1H, C6-H), 7.34 (dd, J = 7.3, 1.4 Hz, 1H, C5-H), 7.06 (s, 1H, C1-H), 6.76 (dd, J = 7.8, 1.4 Hz, 1H, C7-H), 4.00 (s, 3H), 3.97 (s, 3H), 3.94 (s, 3H), 3.92 (s, 3H). These spectral data were in accord with those reported (9) for synthetic **6***c* prepared by a different method.

*2,4,8-Trimethoxyfluoren-9-one (**6**d)*

To a solution of LDA (1.25 mmol) in THF (2 mL) was added the solution of **21***b* (0.172 g, 0.50 mmol) in THF (1 mL) at 0°C. The mixture was stirred at room temperature overnight. Standard work-up followed by flash chromatography (1:6) afforded 0.096 g (71%) of **6***d*, mp 141–143°C (hexane–CH_2Cl_2) (lit. (9) mp 137–139°C); IR (KBr) ν: 1697 cm^{-1}; ^1H NMR ($CDCl_3$) δ: 7.36 (dd, J = 7.7, 7.4 Hz, 1H, C6-H), 7.33 (d, J = 7.4 Hz, 1H, C5-H), 6.85 (d, J = 2.0 Hz, 1H, C1-H), 6.70 (dd, J = 7.7, 1.3 Hz, 1H, C7-H), 6.54 (d, J = 2.0 Hz, 1H, C3-H), 3.96 (s, 3H), 3.92 (s, 3H), 3.85 (s, 3H). These spectral data were in accord with those reported (9) for synthetic **6***d* prepared by a different method.

*1,2,5,6,7-Pentamethoxyfluoren-9-one (**31**)*

To a solution of LDA (2.5 mmol) was added a solution of **36** (0.431 g, 1 mmol) in THF (2 mL) at 0°C and the mixture was allowed to warm to room temperature over 10 h. Standard work-up followed by flash chromatography (1:2) afforded 0.236 g (72%) of **31**, mp 128–130°C (MeOH); IR ($CHCl_3$) ν (max): 1706 cm^{-1}; ^1H NMR ($CDCl_3$) δ: 7.35 (d, J = 8.0 Hz, 1H, C4-H), 7.02 (s, 1H, C8-H); 6.86 (d, J = 8.0 Hz, 1H, C3-H), 4.07 (s, 3H), 3.98 (s, 3H), 3.95 (s, 3H), 3.90 (s, 3H), 3.87 (s, 3H); ^{13}C NMR ($CDCl_3$) δ: 190.4, 153.7, 153.0, 149.0, 148.6, 147.8, 135.7, 130.2, 129.5, 125.0, 117.9, 116.8, 103.9, 61.9, 60.9, 60.4, 56.3; MS *m/z* (rel. intensity): 330 (M^+, 100), 315 (20); HRMS calcd. for $C_{18}H_{18}O_6$: 330.1098; found: 330.1097.

*Synthesis of Dengibsinin (7*a*)*

*2,4-Dimethoxy-3,5-diisopropoxyfluoren-9-one (**29**)*

To a solution of LDA (5.98 mmol) in THF (8 mL) was added a solution of **28** (1.028 g, 2.39 mmol) in THF (4 mL) at 0°C and the mixture was stirred at room temperature for 8–10 h. Standard work-up followed by flash chromatography (1:4) afforded 0.569 g (67%) of **29**, mp 132–134°C (hexane); IR (KBr) ν (max): 1703 cm^{-1}; ^1H NMR δ: 7.26 (dd, J = 6.9, 1.4 Hz, 1H, C8-H), 7.16 (dd, J = 8.2, 6.9 Hz, 1H, C7-H), 7.10 (s, 1H, C1-H), 7.05 (dd, J = 8.2, 1.4 Hz, 1H, C6-H), 4.50–4.74 (m, 2H), 3.88 (s, 3H), 3.86 (s, 3H), 1.42 (d, J = 6.1 Hz, 6H), 1.35 (d, J = 6.1 Hz, 6H); MS *m/z* (rel. intensity): 356 (M^+, 25), 272 (100), 257 (32). Anal. calcd. for $C_{21}H_{24}O_5$: C 70.77, H 6.79; found: C 71.03, H 6.94.

*2,4-Dimethoxy-3,5-dihydroxyfluoren-9-one (**7**a, dengibsinin)*

To a solution of **29** (0.035 g, 0.10 mmol) in CH_2Cl_2 (3.4 mL) at 0°C was added boron trichloride (2 mL of 1.0 M solution in CH_2Cl_2, 2.00 mmol). The resulting mixture was stirred for 1.5 h at 0°C and quenched with saturated NH_4Cl solution at 0°C. Standard work-up followed by flash chromatography (1:4) afforded 0.023 g (87%) of **7***a*, mp 218–220°C (hexane–CH_2Cl_2) (lit. (9) mp 225–227°C); IR (KBr) ν (max): 3259, 1688 cm^{-1}; ^1H NMR δ: 9.14 (s, 1H, C5-OH), 7.19 (dd,

Can. J. Chem. Downloaded from www.nrcresearchpress.com by 195.246.54.202 on 09/08/12
For personal use only.

J = 7.0, 1.9 Hz, 1H, C8-H), 7.17 (dd, J = 7.4, 7.0 Hz, 1H, C7-H), 7.10 (s, 1H, C1-H), 6.99 (dd, J = 7.4, 1.9 Hz, 1H, C6-H), 6.15 (br, 1H, C3-OH), 4.14 (s, 3H), 3.96 (s, 3H); MS *m/z* (rel. intensity): 272 (M^+, 100), 257 (35). These data were in good agreement with those reported for synthetic (9) and natural (7, 10) dengibsinin.

*Synthesis of imeluteine (**30**e)*

N-*Tosyl-9-amino-1,2,5,6,7-pentamethoxyfluorene (**33**)*

A mixture of **31** (0.28 g, 0.845 mmol) and $NH_2OH{\cdot}HCl$ (0.118 g, 1.7 mmol) in 70% aqueous EtOH (10 mL) was refluxed for 5 h. After cooling, the mixture was diluted with water (10 mL) and subjected to filtration. Recrystallization of the crude product from EtOH yielded 0.270 g (92%) of 1,2,5,6,7-pentamethoxyfluoren-9-one oxime, mp 214–216°C (EtOH); IR ($CHCl_3$) ν (max): 3400–2700 cm^{-1}; ^1H NMR ($CDCl_3$) δ: 10.92 (s, 1H, OH, exchangeable with D_2O), 7.99 (s, 1H, C8-H), 7.56 (d, J = 8.2 Hz, 1H, C4-H), 6.90 (d, J = 8.2 Hz, 1H, C3-H), 4.01 (s, 3H), 4.00 (s, 3H), 3.96 (s, 3H), 3.95 (s, 3H), 3.93 (s, 3H); ^{13}C NMR ($CDCl_3$) δ: 153.0, 152.0, 151.7, 148.4, 145.7, 144.8, 133.1, 126.9, 126.7, 126.5, 118.3, 113.7, 109.9, 61.0, 60.5, 60.4, 56.4, 56.2; MS *m/z* (rel. intensity): 345 (M^+, 100), 329 (51); HRMS calcd. for $C_{18}H_{19}NO_6$: 345.1212; found: 345.1221.

Zinc dust (1.16 g, 17.8 mmol) was added in small portions to a stirred solution of 1,2,5,6,7-pentamethoxyfluoren-9-one oxime (1.226 g, 3.55 mmol) in a mixture of glacial HOAc (5 mL) and water (0.25 mL). The mixture was refluxed for 2 h and allowed to cool to room temperature. Water (5 mL) was added, the mixture was filtered, and the residue was washed with 5% HOAc (2 mL). The combined filtrate was mixed with an equal amount of concentrated HCl, and the mixture was kept at 0°C for 12 h. The solid was collected by filtration, washed with cold concentrated HCl, and dried to yield 1.15 g (88%) of 9-amino-1,2,5,6,7-pentamethoxyfluorene hydrochloride, which was converted into its tosylate. A mixture of 9-amino-1,2,5,6,7-pentamethoxyfluorene hydrochloride (0.200 g, 0.55 mmol) and tosyl chloride (0.114 g, 0.6 mmol) in pyridine (3 mL) was stirred at room temperature for 12 h. Et_2O (20 mL) was added, and the resulting mixture was washed in sequence with water, 0.5 N aqueous HCl, and water. Concentration to dryness afforded **33** (0.130 g, 50%), mp 103–105°C (hexane–Et_2O); IR ($CHCl_3$) ν: 3383, 1582 cm^{-1}; ^1H NMR ($CDCl_3$) δ: 7.91 (d, J = 8.2 Hz, 2H, C3′5′-H), 7.50 (d, J = 8.3 Hz, 1H, C4-H), 7.35 (d, J = 8.2 Hz, 2H, C2′,6′-H), 6.99 (s, 1H, C8-H), 6.88 (d, J = 8.3 Hz, 1H, C3-H), 5.44 (d, J = 7.5 Hz, 1H, C9-H), 4.84 (d, J = 7.5 Hz, 1H, NH, exchangeable with D_2O), 3.97 (s, 3H), 3.89 (s, 3H), 3.84 (s, 3H), 3.79 (s, 3H), 3.45 (s, 3H), 2.45 (s, 3H); ^{13}C NMR ($CDCl_3$) δ: 153.3, 151.5, 146.4, 143.3, 142.7, 139.5, 138.6, 133.8, 133.4, 129.6, 128.6, 127.6, 127.1, 117.6, 113.8, 105.7, 77.2, 61.0, 60.5, 60.2, 57.3, 56.1, 21.5; MS *m/z* (rel. intensity): 485 (M^+, 100), 330 (50); HRMS calcd. for $C_{25}H_{27}NO_7S$: 485.1501; found: 485.1500.

N,N-*Diisopropyl 5′-(E-2-nitroethyl)-2′,3,3′,4,4′-pentamethoxybiphenyl-2-carboxamide (**42**)*

A mixture of **41** (4.62 g, 10.6 mmol), nitromethane (1.45 mL, 25.1 mmol), glacial HOAc (5 mL), and NH_4OAc (0.775 g, 10.06 mmol) was refluxed for 2 h. After cooling, the mixture was poured onto crushed ice and the whole was extracted with ether. The extract was dried (Na_2SO_4), filtered, and evaporated to dryness in vacuo. Flash chromatography (1:1) afforded 4.2 g (83%) of **42**, mp 174–176°C (EtOAc); IR ($CHCl_3$) ν (max): 1716, 1616 cm^{-1}; ^1H NMR ($CDCl_3$) δ: 8.14 (d, J = 13.7 Hz, 1H, CH=*CH*NO_2), 7.71 (d, J = 13.7 Hz, 1H, *CH*=CHNO_2), 7.51 (s, 1H, C6′-H), 7.05 (d, J = 8.4 Hz, 1H, C6-H), 6.93 (d, J = 8.4 Hz, 1H, C5-H), 3.99 (s, 3H), 3.93 (s, 3H), 3.91 (s, 3H), 3.90 (s, 3H), 3.86 (s, 3H), 3.57 (sept, J = 6.6 Hz, 1H), 3.22 (sept, J = 6.8 Hz, 1H), 1.50 (d, J = 6.8 Hz, 3H), 1.09 (d, J = 6.8 Hz, 3H), 1.04 (d, J = 6.6 Hz, 3H), 0.65 (d, J = 6.6 Hz, 3H); ^{13}C NMR ($CDCl_3$) δ: 175.1, 166.8, 155.2, 154.0, 152.3, 146.1, 145.2, 137.5, 133.9, 128.7, 127.6, 125.3, 118.4, 111.3, 61.6, 61.2, 60.7, 55.8, 50.9, 45.6, 20.7, 20.5, 20.1, 20.0; MS *m/z* (rel. intensity): 502 (M^+, 25), 471 (100), 402 (52); HRMS calcd. for $C_{26}H_{34}N_2O_8$: 502.2306; found: 502.2300.

N,N-*Diisopropyl 5′-(2-aminoethyl)-2′,3,3′,4,4′-pentamethoxybiphenyl-2-carboxamide (**43**)*

To a well-stirred suspension of $LiAlH_4$ (1.5 g, 41 mmol) in ether (20 mL) was added dropwise a solution of **42** (4.12 g, 8.24 mmol) in THF (10 mL) and the mixture was refluxed for 6 h. Excess of $LiAlH_4$ was decomposed by dropwise addition of ice-cold 6 N HCl with cooling. The aqueous layer was separated, basified with 28% NH_4OH solution, and the whole was extracted with Et_2O (30 mL). The organic phase was dried (Na_2SO_4), and purged with HCl gas to afford 3.41 g (77%) of **43** hydrochloride, mp 160–163°C; IR ($CHCl_3$) ν (max): 3308, 1620 cm^{-1}; ^1H NMR ($CDCl_3$) δ: 7.09 (s, 1H, C6′-H), 7.06 (d, J = 8.6 Hz, 1H, C6-H), 6.92 (d, J = 8.6 Hz, 1H, C5-H) 3.92 (s, 3H), 3.88 (s, 3H), 3.87 (s, 3H), 3.86 (s, 3H), 3.83 (s, 3H), 3.58 (sept, J = 6.6 Hz, 1H), 3.23 (sept, J = 6.8 Hz, 1H), 2.88 (t, J = 6.3 Hz, 2H), 2.70 (m, 2H), 1.50 (d, J = 6.8 Hz, 3H), 1.43 (br s, 2H, exchangeable with D_2O), 1.15 (d, J = 6.8 Hz, 3H), 1.02 (d, J = 6.6 Hz, 3H), 0.65 (d, J = 6.6 Hz, 3H); MS (CI) *m/z* (rel. intensity): 474 (M^+ + 1, 100); HRMS calcd. for $C_{26}H_{38}N_2O_6$ + H: 475.2808; found: 475.2787.

*3,4-Dihydroimeluteine (**44**)*

To a solution of LDA (2.2 mmol) in THF (5 mL) was added a solution of **43** (0.285 g, 0.605 mmol) in THF (1 mL) at 0°C. The mixture was stirred for 10 h. Standard work-up followed by flash chromatography (2:1) afforded 0.076 g (36%) of **44**, mp 105–106°C (MeOH) (lit. (20*a*) mp 105–106°C); IR ($CHCl_3$) ν (max): 1644 cm^{-1}; ^1H NMR ($CDCl_3$) δ: 7.44 (d, J = 8.1 Hz, 1H, C7-H), 6.89 (d, J = 8.1 Hz, 1H, C8-H), 4.03 (s, 3H), 3.96 (s, 3H), 3.95 (s, 3H), 3.90 (s, 3H), 3.87 (s, 3H), 4.24 (t, J = 8.0 Hz, 2H), 2.75 (t, J = 8.0 Hz, 2H); MS *m/z* (rel. intensity): 355 (M^+, 69), 326 (44).

*Imeluteine (**30**e)*

A solution of **44** (0.040 g, 0.113 mmol) in freshly distilled decalin (4 mL) was refluxed at 200–220°C for 3 h under argon in the presence of 10% Pd/C (20 mg). After cooling, Et_2O was added and the catalyst was collected by filtration. Evaporation of the filtrate to dryness followed by flash chromatography (1:2) afforded 0.024 g (60%) of imeluteine (**30***e*), mp 145–146°C (MeOH) (lit. (20*a*) mp 146–147°C); IR ($CHCl_3$) ν (max): 1581 cm^{-1}; ^1H NMR ($CDCl_3$) δ: 8.68 (d, J = 6.0 Hz, 1H, C2-H), 7.63 (d, J = 8.0 Hz, 1H, C7-H), 7.60 (d, J = 6.0 Hz, 1H, C3-H), 6.94 (d, J = 8.0 Hz, 1H, C8-H), 4.18 (s, 3H), 4.11 (s, 3H), 4.10 (s, 3H), 4.04 (s, 3H), 3.95 (s, 3H); ^{13}C NMR ($CDCl_3$) δ: 158.0, 153.1, 150.6, 149.9, 148.4, 147.1, 144.5, 131.9, 126.2, 124.1, 122.1, 119.6, 113.6, 113.1, 62.1, 61.4, 61.3, 56.5; MS *m/z* (rel. intensity): 353 (M^+, 100), 324 (77). These data are in full accord with those reported for synthetic (20*a*, 37) and natural product (20*b*) samples of imeluteine.

1. V. Snieckus. Chem. Rev. **90**, 879 (1990).
2. M.A.F. Brandao, A.B. de Oliveira, and V. Snieckus. Tetrahedron Lett. **34**, 2437 (1993).
3. P. Beak, and A.I. Meyers. Acc. Chem. Res. **19**, 356 (1986).
4. G.W. Klumpp. Recl. Trav. Chim. Pays-Bas, **105**, 1 (1986).
5. (*a*) J.-m. Fu, B.-p. Zhao, M.J. Sharp, and V. Snieckus. J. Org. Chem. **56**, 1683 (1991); (*b*) B.-p. Zhao and V. Snieckus.Tetrahedron Lett. **32**, 5277 (1991).
6. M.J. Sharp and V. Snieckus. Tetrahedron Lett. **26**, 5997 (1985).
7. S.K. Talapatra, S. Bose, A.K. Mallik, and B. Talapatra. Tetrahedron, **41**, 2765 (1985).
8. M.C. Cone, C.R. Melville, M.P. Gore, and S.J. Gould. J. Org. Chem. **58**, 1058 (1993).
9. M.V. Sargent. J. Chem. Soc. Perkin Trans. 1, 2553 (1987).
10. S.K. Talapatra, S. Bose, S. Chakraborty, and B. Talapatra. Indian J. Chem. **27B**, 250 (1988).
11. B.I. Alo, A. Kandil, P.A. Patil, M.J. Sharp, M.A. Siddiqui, V. Snieckus, and P.D. Josephy. J. Org. Chem. **56**, 3763 (1991).
12. P.G. Gassman and W.N. Schenk. J. Org. Chem. **42**, 918 (1977).
13. H.G. Rule and E. Bretscher. J. Chem. Soc. 925 (1927).
14. Y. Hoshino, N. Miyaura, and A. Suzuki. Bull. Chem. Soc. Jpn. **61**, 3008 (1988).

15. T. Oh-e, N. Miyaura, and A. Suzuki. Synlett, 221 (1990).
16. T. Sala and M.V. Sargent. J. Chem. Soc. Perkin Trans. 1, 2593 (1979).
17. J.-m. Fu. Ph.D. Thesis, University of Waterloo, 1990.
18. W. Wang and V. Snieckus. J. Org. Chem. **57**, 424 (1992).
19. K.T. Buck. Alkaloids, **23**, 301 (1984).
20. (*a*) M.P. Cava and K.T. Buck. J. Am. Chem. Soc. **94**, 5931 (1972); (*b*) M.P. Cava, K.T. Buck, I. Noguchi, M. Srinivasan, M.G. Rao, and A.I. daRocha. Tetrahedron, **31**, 1667 (1975).
21. (*a*) M.D. Menachery and M.P. Cava. Heterocycles, **14**, 943 (1980); (*b*) H. Morita, K. Matumoto, K. Takeya, H. Itokawa, and Y. Iitaka. Chem. Pharm. Bull. Jpn. **41**, 1418 (1993).
22. H.A. Patel and D.B. MacLean. Can. J. Chem. **61**, 7 (1983).
23. N. Campbell and K.F. Reid. J. Chem. Soc. 4743 (1958).
24. J.M. Schmitter, I. Ignatiadis, and G. Guiochon. J. Chromatogr. **248**, 203 (1982).
25. M.W. Dong, I. Schmeltz, E. Jacobs, and D. Hoffmann. J. Anal. Toxicol. **2**, 21 (1978).
26. M.W. Dong, D.C. Locke, and D. Hoffmann. Environ. Sci. Technol. **11**, 612 (1977).
27. (*a*) I. Noguchi and D.B. MacLean. Can. J. Chem. **53** 126 (1975); (*b*) S.F. Dyke and E.P. Tiley. Tetrahedron, **31**, 561 (1975).
28. T.J. Schwan. U.S. patent no. 3 971 788 (1976); Chem. Abstr. **85**, 192589y (1976).
29. M.E. Taylor and T.L. Fletcher. J. Org. Chem. **26**, 940 (1961).
30. H. Weingarten, J.P. Chupp, and W.A. White. J. Org. Chem. **32**, 3446 (1967).
31. D.L. Boger, C.E. Brotherton, and M.D. Kelley. Tetrahedron, **37**, 3977 (1981).
32. R.J. Sundberg and H.F. Russell. J. Org. Chem. **38**, 3324 (1973).
33. J.B. Hendrickson, D.D. Sternbach, and K.W. Bair. Acc. Chem. Res. **10**, 306 (1977).
34. R.L. Vaulx, F.N. Jones, and C.R. Hauser. J. Org. Chem. **30**, 58 (1965).
35. S. Kubota, T. Masui, E. Fujita, and M. Kupchan. J. Org. Chem. **31**, 516 (1966).
36. X. Wang. Ph.D. Thesis, University of Waterloo, 1992.
37. D.L. Boger and C.E. Brotherton. J. Org. Chem. **49**, 4050 (1984).
38. M.R. Winkle, J.M. Lansinger, and R.C. Ronald. J. Chem. Soc. Chem. Commun. 87 (1980).
39. D.R. Coulson. Inorg. Synth. **13**, 121 (1972); T. Hayashi, M. Konishi, Y. Kobori, M. Kumada, T. Higuchi, and K. Hirotsu. J. Am. Chem. Soc. **106**, 158 (1984).
40. D.C. Schlegel, C.D. Tipton, and K.L. Rinehart. J. Org. Chem. **35**, 849 (1970).
41 G.P. Rice. J. Am. Chem. Soc. **48**, 3125 (1926).
42. W. Baker, A.W.B. Kirby, and L.V. Montgomery. J. Chem. Soc. 2876 (1932).
43. L.R. Worden, K.D. Kaufman, P.J. Smith, and G.N. Widiger. J. Chem. Soc. (C), 227 (1970).
44. L.F. Fieser. J. Am. Chem. Soc. **51**, 2471 (1929).

Can. J. Chem. Downloaded from www.nrcresearchpress.com by 195.246.54.202 on 09/08/12
For personal use only.

Diastereoselectivity in the synthesis of D-glycero-D-aldoheptoses by 2-trimethylsilylthiazole homologation from hexodialdo-1,5-pyranose derivatives

NAVEEN K. KHARE,[1] RAMESH K. SOOD,[2] AND GERALD O. ASPINALL[3]

Department of Chemistry, York University, North York, Toronto, ON M3J 1P3, Canada

Received May 20, 1993

This paper is dedicated to Professors David B. MacLean and Ian D. Spenser

NAVEEN K. KHARE, RAMESH K. SOOD, and GERALD O. ASPINALL. Can. J. Chem. **72**, 237 (1994).

An exploration of the synthesis of D-*glycero*-D-*altro*-heptose, a constitutent of O antigen chains in lipopolysaccharides from *Campylobacter jejuni* serotypes O:23 and O:36 led to a study of the 2-trimethylsilylthiazole homologation procedure for heptose synthesis. In contrast to the diastereoselective formation of a 1,2:3,4-di-*O*-isopropylidene-D-*glycero*-α-D-*galacto*-heptopyranose derivative from 1,2:3,4-di-*O*-isopropylidene-α-D-*galacto*-hexodialdo-1,5-pyranose, methyl 2,3,4-tri-*O*-benzyl-D-hexodialdo-1,5-pyranosides with the *gluco* and *manno* configurations showed no preference for the formation of compounds with the D-*glycero* configuration. Attempts to achieve high diastereoselectivity in the conversion of L-*glycero* into the D-*glycero* isomers by oxidation at C-6 followed by reduction with L-selectride were unsuccessful with the thiazole adducts, but the desired products were formed in similar reactions of methyl 2,3,4-tri-*O*-benzyl-7-*O*-*tert*-butyldimethylsilyl-D-heptopyranosides. The approach to homologation in the *altro* series was thwarted by epimerization at C-5 in the attempted formation of methyl 2,3,4-tri-*O*-benzyl-α-D-*altro*-hexodialdo-1,5-pyranoside. The successful synthesis of methyl D-*glycero*-α-D-*altro*-heptopyranoside from methyl α-D-glucopyranoside was achieved by homologation followed by configurational alteration from the D-*gluco* to the D-*altro* series.

NAVEEN K. KHARE, RAMESH K. SOOD et GERALD O. ASPINALL. Can. J. Chem. **72**, 237 (1994).

Une exploration de la synthèse du D-*glycéro*-D-*altro*-heptose, un constituant des chaînes O antigéniques des lipopolysaccharides des sérotypes O:23 et O:36 du *Campylobacter jejuni* a conduit à étudier la possibilité d'utiliser la procédure d'homologation du 2-triméthylsilylthiazole pour réaliser la synthèse d'heptoses. Par opposition à la formation diastéréosélective d'un dérivé 1,2:3,4-di-*O*-isopropylidène-D-*glycéro*-α-D-*galacto*-heptopyranose à partir 1,2:3,4-di-*O*-isopropylidène-α-D-*galacto*-hexodialdo-1,5-pyranose, les 2,3,4-tri-*O*-benzyl-D-hexodialdo-1,5-pyranosides de méthyles avec des configurations *gluco* et *manno* ne présentent aucune préférence pour la formation de composés avec la configuration D-*glycéro*. Les essais effectués sur des adduits thiazoles dans le but d'obtenir une grande diastéréosélectivité lors de la conversion des isomères L-*glycéro* en D-*glycéro* par le biais d'une oxydation en C-6 suivie par une réduction à l'aide de L-sélectride se sont avérés vains; toutefois, les produits désirés se forment lors de réactions semblables avec des 2,3,4-tri-*O*-benzyl-7-*O*-*tert*-butyldiméthylsilyl-D-heptopyranosides de méthyle. L'approche à l'homologation dans la série *altro* ne peut être réalisée à cause d'une épimérisation en C-5 lorsqu'on essaie de former le 2,3,4-tri-*O*-benzyl-α-D-*altro*-hexodialdo-1,5-pyranoside de méthyle. On a réalisé la synthèse du D-*glycéro*-α-D-*altro*-heptopyranoside de méthyle à partir de l'α-D-glucopyranoside de méthyle en procédant à une homologation suivie d'une modification de configuration de la série D-*gluco* à D-*altro*.

[Traduit par la rédaction]

Introduction

L-*glycero*-D-*manno*-Heptose is a commonly encountered component of the core region of lipopolysaccharides (LPS) on Gram-negative bacteria (1). In view of the immunological importance of this region of LPS structure considerable attention has been directed to efficient methods for the preparation of derivatives of the sugar for incorporation into synthetic oligosaccharides (2–6). Methods of choice have been those involving a one-carbon extension from benzyl (**1**) or methyl (**2**) 2,3,4-tri-*O*-benzyl-α-D-*manno*-hexodialdo-1,5-pyranoside of which that involving reaction with (phenyldimethylsilyl)magnesium chloride (**4**) proceeds with high diastereoselectivity to give derivatives of L-*glycero*-D-*manno*-heptose from which glycosides of the parent sugar may be readily obtained. In a recent study of the O antigen chains of LPSs of *Campylobacter jejuni* serotypes O:23 and O:36 unusual heptose sugars were found as four variants with the same configurationally unusual *altro* ring configuration (7). LPS preparations all contained trisaccharide, -3-β-D-GlcNAc-(1→3)-α-D-Gal-(1→2)-α-Hep 1-, repeating units with the same linkages and anomeric configurations, but with the heptose residue present in varying proportions as 6-deoxy-D-*altro*-heptose (8) and 6-deoxy-3-*O*-methyl-D-*altro*-heptose (unpublished synthesis with G.V. Reddy), for which enantiomeric configurations have been confirmed, and D-*glycero*-D-*altro*-heptose and 3-*O*-methyl-D-*glycero*-D-*altro*-heptose or their respective enantiomers. In view of the close structural, and presumably also biosynthetic, relationship between the four variants it was highly probable that all had the α-D-*altro* ring configuration. It was still necessary to confirm the absolute configurations of the two latter sugars through the synthesis of defined reference compounds before making preparative quantities for oligosaccharide assembly. The only reported C-6 homologation of a D-hexodialdo-1,5-pyranose derivative proceeding with high diastereoselectivity for the formation of the D-*glycero* product is that reported by Dondoni et al. (5, 6) using 2-(trimethylsilyl)thiazole (TMSthiazole) as a one-carbon synthon in reaction with 1,2:3,4-di-*O*-isopropylidene-α-D-*galacto*-hexodialdo-1,5-pyranose (**3**). This procedure therefore seemed worthy of exploration for the synthesis of D-*glycero*-D-*altro*-heptose derivatives. Two alternative overall strategies seemed possible starting from D-glucopyranose derivatives: (A) 2,3-inversion to gain entry into the D-altropyranose series, followed by C-6 homologation; and (B)

[1]On leave of absence from the Department of Chemistry, Lucknow University, Lucknow, India, 1991–1992.

[2]Present address: Univax Biologicals Inc., 12280 Wilkins Ave., Rockville, MD 20852, U.S.A.

[3]Author to whom correspondence may be addressed.

Can. J. Chem. Downloaded from www.nrcresearchpress.com by 203.198.23.82 on 09/08/12
For personal use only.

TABLE 1. Gas chromatographic analysis of heptitol acetates

Parent sugar	Relative retention times[a] of heptitol acetates with respect to Glucitol hexaacetate	Galactitol hexaacetate
L-*glycero*-D-*manno*-Heptose	1.90	2.08
D-*glycero*-D-*manno*-Heptose	1.65	1.80
L-*glycero*-D-*gluco*-Heptose	2.07	2.26
D-*glycero*-D-*gluco*-Heptose	1.75	1.90
L-*glycero*-D-*galacto*-Heptose	2.06	2.28
D-*glycero*-D-*galacto*-Heptose	1.90	2.08
D-*glycero*-D-*altro*-Heptose	1.47	1.61
3-*O*-Methyl-D-*glycero*-D-*altro*-heptose	1.52	1.66

[a]Gas chromatography using program A.

C-6 homologation in the D-glucopyranose series, followed by 2,3-inversion of the D-*glycero*-D-*gluco*-heptopyranose product. In the event unexpected problems were encountered in both proposed routes. Route A was rejected at an early stage when it was observed that oxidation of methyl 2,3,4-tri-*O*-benzyl-α-D-altropyranoside to give the dialdohexo-1,5-pyranoside was accompanied by substantial epimerization at C-5 with formation of the corresponding β-L-*galacto* derivative. Route B ultimately proved successful for the preparation of the desired heptoses but no diastereoselectivity was observed in the C-6 homologation reaction. We report herein syntheses of these heptoses in confirmation of their absolute configurations, but discuss first diastereoselectivity in the TMSthiazole homologation together with experiments related to the C-5 epimerization accompanying oxidation at C-6 of both altrose and galactose derivatives.

Results and discussion

Configurational assignments for heptose derivatives epimeric at C-6

All homologations were performed and the thiazole adducts were converted into heptose derivatives as described by Dondoni et al. (5, 6) and *O*-debenzylated. Since all 10 diastereomeric heptitol heptaacetates are separable by gas–liquid chromatography (glc) (9) (see Table 1 for examples now reported), formation of these derivatives by hydrolysis of glycosides, reduction, and acetylation was the simplest method for distinguishing the pairs of D-*glycero*/L-*glycero* epimers that may result from C-6 homologations. Other, sometimes quantitatively dominant, compounds are produced in varying amounts due to accompanying 1,6- and (or) 1,7-anhydroheptose formation under hydrolysis conditions, as in the case of D-*glycero*-D-*altro*-heptose (7). In the example reported by Dondoni et al. (5, 6), the absolute configuration at C-6 of the thiazole adduct, (6*S*)-1,2:3,4-di-*O*-isopropylidene-6-(2-thiazolyl)-α-D-*galacto*-hexo-1,5-pyranose (**4**), formed as the sole product from 1,2:3,4-di-*O*-isopropylidene-D-*galacto*-hexodialdo-1,5-pyranose (**3**), was established by conversion into a previously characterized D-*glycero*-α-D-*galacto*-heptose derivative (10). However, derivatives of defined configuration from rarely encountered heptoses are unlikely to be available for comparison. Furthermore for the compounds of present interest, we have found that the differences in nmr parameters for C-6 and H-6 in epimeric heptose derivatives are insufficiently consistent to provide a basis for configurational assignments.

Diastereoselectivity in C-6 homologation of mannose and glucose derivatives

With access to heptitol heptaacetates derived from L-*glycero*- and D-*glycero*-D-*manno*-heptoses for comparison, the TMSthiazole homologation reaction was examined as an alternative to the above-mentioned homologation of **1** with (phenyldimethyl)silylmethylmagnesium chloride, which had been used in the preparation of derivatives of L-*glycero*-D-*manno*-heptose with high diastereoselectivity (3, 4). Diastereoselectivity in homologation was first examined for methyl 2,3,4-tri-*O*-benzyl-α-D-*manno*-hexodialdo-1,5-pyranoside (**2**), prepared as required on Swern oxidation (11) of methyl 2,3,4-tri-*O*-benzyl-α-D-mannopyranoside with oxalyl chloride and methyl sulfoxide. Reaction of **2** with TMSthiazole gave the chromatographically separable 6-(2-thiazolyl)-derivatives (**5** and **6**) in respective yields of 55 and 37%. Conversion of **5** and **6** into the respective methyl 2,3,4-tri-*O*-benzylheptopyranosides (**7** and **8**), in four steps with overall yields of 60–70%, by successive *N*-methylation, reduction with $NaBH_4$, hydrolysis in the presence of $HgCl_2$, and reduction again with $NaBH_4$. Since this research was completed Dondoni et al. (12) have reported an improved procedure for the thiazole to formyl deblocking protocol. Configurational assignments for **7** and **8** were made by conversion into L-*glycero*- and D-*glycero*-D-*manno*-heptitol heptaacetates.

TMSthiazole homologation of the hexodialdo-1,5-pyranoside (**9**) formed on oxidation of methyl 2,3,4-tri-*O*-benzyl-α-D-glucopyranoside was next explored with very similar results to those in the mannose series. Reaction of **9** with TMSthiazole furnished a mixture of 6-(2-thiazolyl) derivatives from which **10** and **11** were obtained in chromatographically pure form in yields of 54 and 18%. These compounds were converted into the corresponding methyl 2,3,4-tri-*O*-benzylheptopyranosides **12** and **13**, as described above, and thence after *O*-debenzylations into the respective methyl glycosides **14** and **15**. Compounds **14** and **15** (and similarly others elsewhere) were converted into their acetylated derivatives **16** and **17** to provide satisfactory elemental analyses and to give well-dispersed one-dimensional ^1H nmr spectra for structural assignments. Relative configurations were assigned after conversion of **14** and **15** into heptitol heptaacetates that were indistinguishable on glc from those derived respectively from L-*glycero*- and D-*glycero*-D-*gluco*-heptitols.

Configurational inversions at C-6 of heptose derivatives

In the light of the preceding results attention was turned to the

Can. J. Chem. Downloaded from www.nrcresearchpress.com by 203.198.23.82 on 09/08/12
For personal use only.

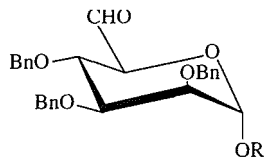

1 R = Bn
2 R = Me

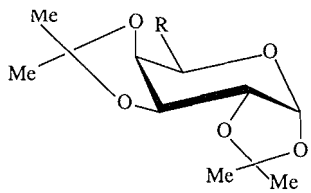

3 R = -CHO
4 R = 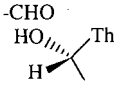

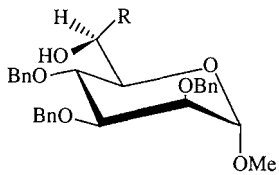

5 R = Th
7 R = CH_2OH
21 R = $CH_2OTBDMS$

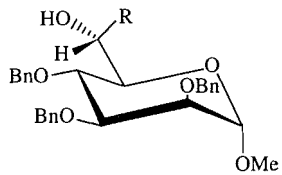

6 R = Th
8 R = CH_2OH

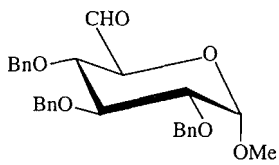

9

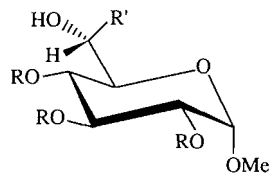

11 R = Bn; R' = Th
13 R = Bn; R' = CH_2OH
15 R = H; R' = CH_2OH
17 R = Ac; R' = CH_2OAc
20 R = Bn; R' = $CH_2OTBDMS$
30 R = Bn; R' = $CH_2OTBDPS$
31 R = H; R' = $CH_2OTBDPS$

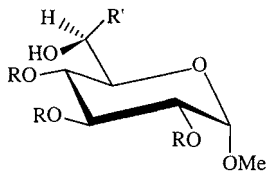

10 R = Bn; R' = Th
12 R = Bn; R' = CH_2OH
14 R = H; R' = CH_2OH
16 R = Ac; R' = CH_2OAc
19 R = Bn; R' = $CH_2OTBDMS$

Th = Thiazolyl =

TBDMS = *tert*-butyldimethylsilyl
TBDPS = *tert*-butyldiphenylsilyl

possibility of achieving a high-yield conversion of L-*glycero* into the epimeric D-*glycero* compounds. Dondoni et al. (13) have described inversion of configuration at C-6 of the (2-thiazolyl) derivative **4** by oxidation to the 6-ulose followed by stereoselective reduction with L- or K-selectride to give the (6*R*) epimer (**18**).

With formation of the L-*glycero* compound **7** as the major product of TMSthiazole homologation in the *gluco series* the possibility of achieving improved overall yields of D-*glycero*-D-*gluco*-heptose derivatives by configurational inversions at C-6 was examined for three derivatives. The 6-(2-thiazolyl) derivative **10** was oxidized with periodinane (14) and the resulting 6-ulose, without purification, was treated with L-selectride to regenerate a mixture of thiazolyl derivatives **10** and **11**, now in the proportions of 2:3. Alternative methods for the configurational inversion were explored for 7-*tert*-butyldiphenylsilyl (TBDPS) and 7-*tert*-butyldimethylsilyl (TBDMS) derivatives of **12** and **13**. In the case of a preliminary experiment performed on TBDPS derivatives from an unresolved mixture of **12** and **13**, Swern oxidation (11) to give the 6-ulose followed by reduction with L-selectride gave back derivatives of **12** and **13** in the same proportions. Samples of the respective TBDMS derivatives (**19** and **20**) of **12** and **13** were prepared so that the reduction of the 6-ulose could be monitored, and complete conversion of **19** to **20** was achieved when **19** was submitted to the oxidation–reduction sequence. A single product was detected by tlc as reduction of the 6-ulose with L-selectride proceeded, but when the reaction mixture was quenched with alkaline hydrogen peroxide, a mixture of products was formed. The chromatographic mobilities of these substances indicated retention of a silyl substituent. Since treatment of these substances with tetrabutylammonium fluoride gave **13** as the sole product, it is probable that intramolecular silyl migration, from O-7 to O-6, had taken place.

In the *manno* series, preparation of the TBDMS derivative **21** from **7** was followed by Swern oxidation (11) to the 6-ulose, reduction with L-selectride, and *O*-desilylation to give the D-*glycero* epimer **8** as the only detectable product and in 80% isolated yield.

Diastereoselectivity in C-6 homologation of altrose and galactose derivatives

Treatment of methyl 2,3,4-tri-*O*-benzyl-α-D-altropyranoside with oxalyl chloride and methyl sulfoxide gave a mixture of hexodialdo-1,5-pyranosides, as judged by the appearance of two aldehydic protons in the ^1H nmr spectrum and, most prominently in the ^{13}C nmr spectrum, of two sets of resonances assignable to ring carbons of the expected methyl 2,3,4-tri-*O*-benzyl-α-D-*altro*-hexodialdo-1,5-pyranoside (**22**) and the C-5 epimer, methyl 2,3,4-tri-*O*-benzyl-β-L-*galacto*-hexodialdo-1,5-pyranoside (**23**) in the approximate ratio of 1:4. The correctness of this conclusion was confirmed by reduction of the mixture of hexodialdo-1,5-pyranosides with $NaBH_4$ followed by acetylation to give a mixture of methyl 6-*O*-acetyl-2,3,4-tri-*O*-benzyl-hexopyranosides in the somewhat altered ratio of 2:3 with glc retention times coincident with those of standard α-D-altrose and β-D-galactose derivatives. Confirmation of the L-*galacto* configuration for the main component was obtained by *O*-debenzylation of the mixture of tri-*O*-benzyl glycosides followed by hydrolysis and conversion of the resulting reducing sugars into acetates of chiral 2-butyl glycosides (15). These results confirmed that epimerization at C-5 had occurred, leading to the formation of the β-L-*galacto* isomer as the major component of the mixture of hexodialdo-1,5-pyranosides. Mixtures of **22** and **23** in the same proportions were obtained on oxidation of methyl 2,3,4-tri-*O*-benzyl-α-D-altropyranoside with periodinane (14), indicating that the epimerization was not just a base-catalyzed reaction promoted by the use of triethylamine in the Swern oxidation.

A rapid interconversion of **22** and **23**, with the composition of isomers on further reaction dependent on the relative rates of formation of different products, was indicated in the above-mentioned reduction to give stereoisomeric products in changed proportions. In an exploration of the stereochemical consequences of the C-6 homologation with TMSthiazole, reaction of the mixture of **22** and **23** gave only one detectable product, which was assigned the structure methyl (6*R*)-2,3,4-tri-*O*- benzyl-6-(2-thiazolyl)-β-L-galactopyranoside (**24**) on the basis of the following evidence. The ^{13}C nmr spectra of **24** and the derived methyl 2,3,4-tri-*O*-benzyl-L-*glycero*-

Can. J. Chem. Downloaded from www.nrcresearchpress.com by 203.198.23.82 on 09/08/12
For personal use only.

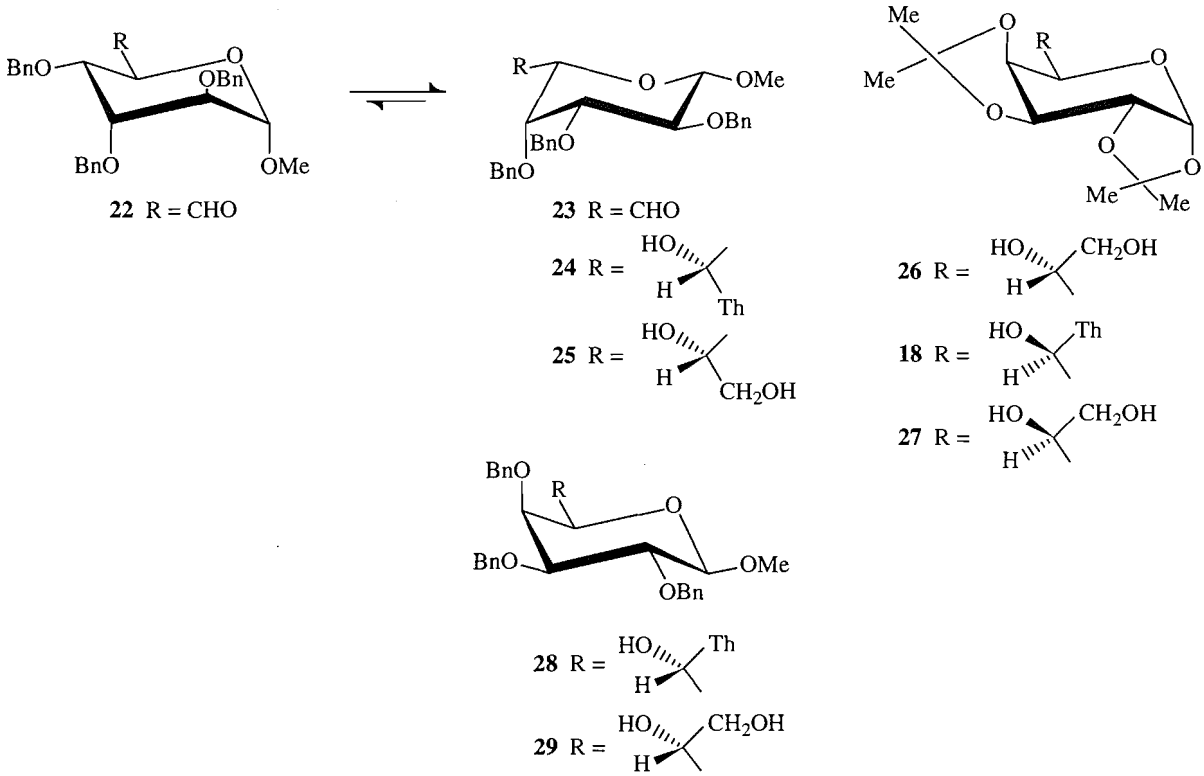

β-L-*galacto*-heptopyranoside (**25**) showed resonances for carbon atoms of the β-*galacto* ring configuration and none for those of the α-*altro* configuration. *O*-Debenzylation of **25** followed by hydrolysis, reduction, and acetylation gave a single heptitol heptaacetate coincident on glc with that formed from the enantiomeric L-*glycero*-D-*manno*-heptose (= D-*glycero*-D-*galacto*-heptose) and therefore confirmed the relative configuration of the chiral centres.

The reversibility of the *altro–galacto* interconversion was also examined in the formation of hexodialdo-1,5-pyranose derivatives in the more accessible D-galactose series. In a reexamination of the oxidation of 1,2:3,4-di-*O*-isopropylidene-α-D-galactopyranose as reported by Dondoni et al. (5, 6), the ^1H and ^{13}C nmr spectra of the corresponding hexodialdo-1,5-pyranose (**3**) showed only the *galacto* isomer with no trace of the *altro* derivative. TMSthiazole homologation likewise gave only the reported (6*S*)-1,2:3,4-di-*O*-isopropylidene-6-(2-thiazolyl)-α-D-galactopyranose (**4**). In confirmation of this observation, independent evidence for the configurational assignments at C-6 in **4** and in its C-6 epimer (**18**) was obtained by their conversions into 1,2:3,4-di-*O*-isopropylidene-D-*glycero*-D- *galacto*-heptopyranose (**26**) and the corresponding L-*glycero*-D- *galacto* compound (**27**), and thence into heptitol heptaacetates that were identical (gc) to samples prepared from the corresponding D-*glycero*-D-*galacto*-heptose and L-*glycero*-D-*gluco*- heptose (= L-*glycero*-D-*galacto*-heptose).

As expected, a parallel series of oxidation and TMSthiazole homologation reactions starting from methyl 2,3,4-tri-*O*-benzyl-β-D-galactopyranoside afforded compounds enantiomeric with those described above that were derived from methyl 2,3,4-tri-*O*-benzyl-α-D-altropyranoside. Comment here is restricted to a few salient points and details are given later. Oxidation of the D-galactopyranoside gave the corresponding mixture of *galacto* and *altro* dialdohexopyranosides in the ratio of 3:1 and, as expected, only a single product (**28**) with the D-*glycero*-α-D-*galacto* configuration was isolated from the ensuing TMSthiazole homologation. Although there were small differences in the magnitudes of the optical rotations of **28** and the corresponding methyl 2,3,4-tri-*O*-benzylheptopyranoside **29**, compared with those of the L-*galacto* compounds **24** and **25**, the enantiomeric pairs were chromatographically indistinguishable and ^1H and ^{13}C nmr spectra showed no significant differences.

The stereoselectivity of configurational inversion at C-6 of **28** by oxidation and subsequent reduction with L-selectride was also examined. Two fractions were separated by preparative tlc and the structures of the products, which were obtained in insufficient quantity and purity for elemental analysis, were established from nmr spectra data and conversions to the corresponding heptitol heptaacetates. The nmr spectra of the derivative from the first fraction showed the presence of a single component with the *galacto* configuration, and further processing furnished L-*glycero*-D-*galacto*-heptitol heptaacetate derived from the product of C-6 inversion. The ^{13}C nmr spectrum of the second fraction showed the presence of compounds with α-*altro* and β-*galacto* configurations, and further processing of the fraction afforded a mixture of two heptitol heptaacetates. Comparison of their glc retention times with those of reference compounds with the D-*glycero*-D-*galacto* and the D-*glycero*-D-*altro* configurations showed that the second fraction of the oxidation–reduction sequence consisted of the product from unchanged starting compound **28** and only one of two possible products arising from epimerization at C-5 of the 6-ulose, that with the L-*glycero*-L-*altro* configuration.

Synthesis of derivatives of D-glycero-D-altro-*heptose*

The preceding studies of C-6 homologations of D-hexodialdo-1,5-pyranose derivatives provided abundant evidence that route B is the only practical strategy for the synthesis of D-*glycero*-D-*altro*-heptose derivatives and ruled out any reac-

Can. J. Chem. Downloaded from www.nrcresearchpress.com by 203.198.23.82 on 09/08/12
For personal use only.

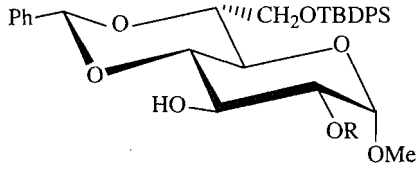

32 R = H
33 R = Ts

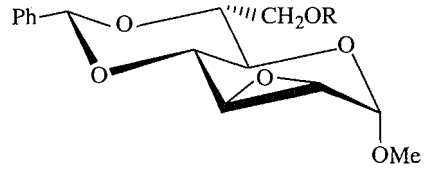

34 R = TBDPS
35 R = H

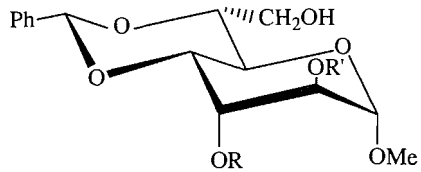

36 R = R' = H
37 R = R' = Ac
40 R = Me; R' = H
41 R = Me; R' = Ac

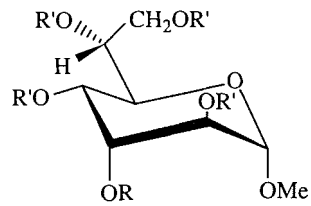

38 R = R' = H
39 R = R' = Ac
42 R = Me; R' = H
43 R = Me; R' = Ac

tions involving carbonyl groups at C-6 of compounds having the *altro* ring configuration. Methyl 7-*tert*-butyldiphenylsilyl-D-*glycero*-α-D-*gluco*-heptopyranoside (**31**) was best prepared by *O*-silylation of methyl glycoside **15**, since silylation of **13** to give the TBDPS derivative (**30**) followed by hydrogenolysis was accompanied by ~25% *O*-desilylation. Reaction of **31** with benzaldehyde dimethylacetal in the presence of catalytic amounts of *p*-toluenesulfonic acid gave the 4,6-*O*-benzylidene derivative **32**. Several methods for the preparation of methyl 2,3-anhydro-4,6-*O*-benzylidene-D-*glycero*-α-D-*manno*-heptopyranoside (**35**) were explored. In the course of these experiments samples of the 2-tolylsulfonyl ester **33** and the *O*-silyl epoxide **36** were obtained in adequate purity for structural characterization by nmr but not for elemental analysis. These samples were of value in monitoring the procedure of Hicks and Fraser-Reid (16) in which treatment of **32** with sodium hydride and tosyl imidazole led to the formation in a single operation of a derivative with the desired 2,3-anhydro-*manno* configuration but this reaction was accompanied by *O*-desilylation to give the epoxide **35**. The initially formed tosyl ester **33** was rapidly converted into the silylated epoxide **34**, but by the time all starting material (**32**) had reacted, much **34** had undergone *O*-desilylation. Prolongation of the reaction led to complete conversion into the epoxide **35**. This further reaction turned out to be advantageous since the 7-*O*-silyl expoxide (**34**) proved to be quite unreactive under normal conditions of epoxide opening. The *O*-desilylated epoxide **35** underwent normal diaxial opening on reaction with aqueous sodium hydroxide to yield methyl 4,6-*O*-benzylidene-D-*glycero*-α-D-*altro*-heptopyranoside (**36**), and *O*-debenzylidenation gave methyl D-*glycero*-α-D-*altro*-heptopyranoside (**38**). The nmr data for the respective acetylated derivatives (**37** and **39**) of these two compounds supported the *gluco* to *altro* configurational change. Confirmation of the relative configuration was obtained by hydrolysis of the glycoside **38**, followed by reduction to give the heptitol and a mixture of 1,6- and 1,7-anhydroheptoses, whose acetylated derivatives were coincident on glc with those derived from the *C. jejuni* O:36 LPS (7). A sample of the heptose was converted into the (*R*)- and (*S*)-2-butyl glycosides whose acetylated derivatives were identical (glc) with those similarly derived from the polysaccharide, thus confirming the absolute configuration of the naturally occurring sugar as D-*glycero*-D-*altro*-heptose. In like manner, methoxide opening of epoxide **35** afforded methyl 4,6-*O*-benzylidene-3-*O*-methyl-D-*glycero*-D-*altro*-heptopyranoside (**40**) and the derived compounds **41–43** were characterized in the same way as for compounds **36–38**. Conversion of a sample of methyl glycoside **41** into (*R*)- and (*S*)-2-butyl glycosides followed by acetylation for glc comparison with those derived from the *C. jejuni* O:23 LPS (7) confirmed that the naturally occurring heptose was 3-*O*-methyl-D-*glycero*-D-*altro*-heptose.

In summary, these studies have shown that the high diastereoselectivity observed by Dondoni et al. (5, 6) in the C-6 homologation of a hexodialdo-1,5-pyranose derivative using 2-trimethylsilylthiazole as a one-carbon synthon is restricted to the galactose series. The unidirectional attack at the *si* face of the 6-aldehyde in this series is presumably governed by the steric effect of the axial oxygen substituent at C-4. No such stereoselectivity was found with glucose and mannose derivatives. In the galactose series a further observation was made that might have escaped attention if experiments had not also been performed in the altrose series. Oxidation of methyl 2,3,4-tri-*O*-benzyl-α-D-altropyranoside was accompanied by epimerization at C-5 with the formation of an equilibrium mixture of 5-epimeric hexodialdo-1,5-pyranosides favouring the β-L-*galacto* isomer **23** over the α-D-*altro* isomer **22** in the ratio of 3:1. In the opposite direction, oxidation of the enantiomeric β-D-galactoside gave the corresponding mixture of products with the α-L-altropyranoside as the minor component. For the monocyclic methyl 2,3,4-tri-*O*-benzyl hexopyranosides, rapid equilibration may be presumed with product composition on further reaction being kinetically determined. Thus rapid and irreversible reduction with sodium borohydride gave back a mixture of hexopyranosides in approximately the same proportions from glc analysis as indicated by nmr for the hexodialdo-1,5-pyranosides. In contrast the TMSthiazole addition, of presumably reversible character, gave a single detectable product with the β-*galacto* ring configuration. In the D-series high diastereoselectivity, as reported by Dondoni et al. (5, 6), led to the formation of the 6-(*S*) thiazolyl derivative **28** and thence of the D-*glycero*-D-*galacto*-heptopyranoside **29**. In reexamining the preparation of 1,2;3,4-di-*O*-isopropylidene-α-D-*galacto*-hexodialdo-1,5-pyranose (**3**), nmr showed no evi-

Can. J. Chem. Downloaded from www.nrcresearchpress.com by 203.198.23.82 on 09/08/12
For personal use only.

Can. J. Chem. Downloaded from www.nrcresearchpress.com by 203.198.23.82 on 09/08/12
For personal use only.

dence for epimerization at C-5 in this conformationally more rigid fused ring derivative. The enolization mechanism for epimerization would require the adoption of a trigonal carbon at C-5 with energetically unfavourable conformational changes in the fused ring system. It is noteworthy that no evidence was obtained for C-5 epimerization in the preparation of hexodialdo-1,5-pyranosides in the mannose and glucose series.

The conversion of (6*S*)- (**4**) into the epimeric (6*R*)-1,2;3,4-di-*O*-isopropylidene-6-(2-thiazolyl)-α-D-galactopyranose (**18**) by oxidation to the thiazolyl heptose-6-ulose followed by stereoselective reduction with L-selectride (5, 6) appeared to establish in principle a route for conversion of D-*glycero*- to the 6-epimeric L-*glycero*-D-heptopyranose derivatives. In our hands this stereoselectivity is not general and seems to be restricted to the conformationally rigid fused ring system in **18** where reduction of the thiazolyl heptose-6-ulose would require unidirectional attack on the *re* face at C-6 analogous to that on the *si* face of the hexodialdo-1,5-pyranose **3** in the formation of thiazolyl derivative **4**. Reaction starting from the (6*S*)-(2-thiazolyl)-β-D-galactopyranoside **28** gave a mixture of products that could be converted into derivatives of D-*glycero*- and L-*glycero*-β-D-galactopyranosides, and L-*glycero*-α-L-altropyranosides. The analogous reaction sequence with the corresponding thiazolyl derivatives in the glucose and mannose series showed no stereoselectivity. Stereoselective reductions were achieved here, but in the *opposite direction* when the heptoside-6-uloses from the severely hindered 7-TBDMS L-*glycero*-α-D-*manno*- (**19**) and α-D-*gluco*- (**20**) heptopyranosides were treated with L-selectride.

In reaching our initial objective, that of developing a synthesis of D-*glycero*-D-*altro*-heptose to confirm the absolute configuration of the O antigen constituent in the LPS of *C. jejuni* serotype O:36, the C-6 homologation was achieved first with the formation of derivatives of D-*glycero*-D-*gluco*-heptose. The well-known series of transformations from D-glucopyranosides to D-altropyranosides with inversions at C-2 and C-3 presented unexpected difficulties in the formation, and subsequent ring opening, of the intermediate 2,3-anhydro-*manno*-heptose derivative bearing a 7-*O*-TBDMS substituent until that protecting group could be removed after its purpose had been served.

Experimental

General methods

The following solvents were dried and purified by distillation over the reagents specified in parentheses: dichloromethane (phosphorus pentoxide), oxolane (lithium aluminum hydride), methanol (magnesium–iodine), toluene (sodium). Light petroleum (bp 30–60°C) and ethyl acetate used as chromatographic solvents were freshly distilled immediately before use. Acetonitrile, *N,N*-dimethylformamide, and methyl sulfoxide were purchased already dried and glass-distilled. Evaporations were conducted under diminished pressure at <40°C. Thin-layer chromatography (tlc) was conducted on plates coated with Silica Gel $60F_{254}$ (Merck). Optical rotations were measured with a Perkin–Elmer 141 polarimeter, for solutions in $CHCl_3$ at ~20°C unless otherwise stated.

^1H, ^{13}C (often in the JMODXH mode), and 2D ^1H nmr spectra were recorded with a Bruker AM 300 spectrometer. Solutions in chloroform-*d* were referenced to internal tetramethylsilane as internal reference. Solutions in D_2O were referenced to internal acetone (δ_H 2.17 ppm and δ_C 30.5 ppm). Chemical shifts and coupling constants are first-order values and assignments in ^1H nmr spectra on the basis of double resonance or COSY experiments are specified in parentheses. Spectra are reported only in sufficient detail to substantiate chemical changes effected and for configurational assignments. The following characteristic resonances were observed consistently and are not cited individually other than when the groups were first incorporated: for thiazolyl derivatives at δ_H ~ 7.7 (H-4′) and 7.3 (H-5′), and δ_C ~171 (C-2′), 142 (C-4′) and 119 (C-5′), for benzyl ethers at δ_H ~ 7.4–7.2 (Ph-H) and 5.0–4.8 (CH_2Ph), and δ_C ~137 and 127 (aromatic C) and 75–72 (Ph-CH_2); and for *O*-isopropylidene derivatives at δ_H 1.5–1.3 ($(CH_3)_2C$), and δ_C ~108 ($(CH_3)_2C$) and 26–24 ($(CH_3)_2C$). The glc analyses were carried out on a Hewlett–Packard model 5890 A chromatograph. Separations were performed using a DB-23 (30 m × 0.25 mm) column with the following programs: (A) for alditol acetates, isothermally at 220°C unless specified at 200°C; (B) for 2-butyl glycoside acetates, 200°C (10 min), 200° → 240°C at 2°/min. Microanalyses were by Canadian Microanalytical Service, Ltd., Delta, B.C.

Preparations of hexodialdo-1,5-pyranose derivatives

Typical oxidations were performed by the addition of freshly distilled methyl sulfoxide (0.23 mL, 3 mmol) in dichloromethane (4 mL) to oxalyl chloride (1.2 mL, 2.4 mmol) in dichloromethane (10 mL) at −60°C. After 5 min substrate (~0.5 g, 1 mmol) in dichloromethane was added dropwise. After 30 min the reaction was quenched by the addition of triethylamine (2 mL) in dichloromethane (5 mL), and the solution was allowed to rise to room temperature, washed twice with water, dried, and concentrated. Completeness of reaction was checked by tlc for disappearance of initial substrate and, if necessary, by nmr (appearance of an aldehydic proton singlet at δ ~9.7 in the ^1H spectrum, appearance of aldehydic carbonyl resonance at δ ~198, and disappearance of C-6 resonance of substrate at δ ~62 in the ^{13}C spectrum). The hexodialdo-1,5-pyranose derivative was used directly without further purification in the TMSthiazole homologation reaction.

*Addition of 2-(trimethylsilyl)thiazole to methyl 2,3,4-tri-*O*-benzyl-α-D-manno-hexodialdo-1,5-pyranoside 2*

2-(Trimethylsilyl)thiazole (0.4 mL) was added to **2** (from methyl 2,3,4-tri-*O*-benzyl-α-D-mannopyranoside (17) (0.5 g)) in dichloromethane (10 mL) at 0°C under nitrogen. The mixture was kept at 0°C overnight and then at room temperature for 3 h. Solvents were evaporated, and the residue in oxolane (10 mL) was treated with 1 M tetrabutylammonium fluoride (2.8 mL) for 30 min. Solvent was partly evaporated and the residue was treated with aqueous sodium hydrogen carbonate and extracted with ethyl acetate. The extract was dried, concentrated, and chromatographed on silica gel (dichloromethane containing 3% of acetone) to give, in order of elution, **5** (320 mg, 55%) and **6** (216 mg, 37%). Methyl (6*R*)-2,3,4-tri-*O*-benzyl-6-(2-thiazolyl)-α-D-mannopyranoside (**5**) had $[\alpha]_D$ +29 (*c* 1.0); ^1H nmr, δ: 5.33 (s, 1H, H-6), 4.64 (s, 1H, H-1), 3.04 (s, 3H, OCH_3); ^{13}C nmr, δ_C: 99.3 (C-1), 80.1, 74.7, 74.2, 73.6, 70.3 (C-2 to C-6), 54.7 (OCH_3). Anal. calcd. for $C_{31}H_{33}NO_6S$: C 67.98, H 6.07, N 2.55, S 5.85; found: C 67.96, H 5.98, N 2.55, S 5.85. Methyl (6*S*)-2,3,4-tri-*O*-benzyl-6-(2-thiazolyl)-α-D-mannopyranoside (**6**) had $[\alpha]_D$ +31 (*c* 1.0); ^1H nmr, δ: 5.39 (d, 1H, $J_{5,6}$ 3.4 Hz, H-6), 4.75 (d, 1H, $J_{1,2}$ 1.7 Hz, H-1), 3.28 (s, 3H, OCH_3); ^{13}C nmr, δ_C: 98.9 (C-1), 80.1, 75.1, 74.6, 73.8, 72.3 (C-2 to C-6), 54.9 (OCH_3). Anal. calcd. for $C_{13}H_{33}NO_6S$: C 67.98, H 6.07, N 2.55, S 5.85; found: C 67.75, H 6.00, N 2.55, S 5.85.

*Methyl 2,3,4-tri-*O*-benzyl-L-glycero- (7) and methyl 2,3,4-tri-*O*-benzyl-D-glycero- (8) α-D-manno-heptopyranoside*

Formyl deblocking from the thiazole ring and subsequent reduction were carried in four successive steps. (1) Compounds **5** and **6** (150 mg, 0.27 mmol each) were separately treated with methyl iodide (0.17 mL, 2.7 mmol) in boiling acetonitrile (7 mL) for 24 h. (2) After removal of solvent, the residues in methanol (5 mL) were each treated with $NaBH_4$ (21 mg, 2 equiv.) at −10°C for 30 min, after which acetone (2 mL) was added to destroy excess of hydride. Solvent was evaporated, the residue were treated with saturated aqueous NaCl and extracted into ethyl acetate, and the extracts were concentrated. (3) The separate residues in acetonitrile (0.4 mL) were added to solutions of

Can. J. Chem. Downloaded from www.nrcresearchpress.com by 203.198.23.82 on 09/08/12
For personal use only.

$HgCl_2$ (90 mg, 1.2 equiv.) in acetonitrile–water (4:1, 5 mL), and the solutions were stirred at room temperature for 15 min. Reaction mixtures were filtered, and the filtrates were concentrated. The residues were treated with saturated aqueous NaCl, extracted with chloroform, and the extracts were concentrated. (4) $NaBH_4$ (21 mg each, 2 equiv.) was added portionwise during 30 min to the crude aldehydic products in methanol (10 mL) at room temperature. Acetic acid – water (1:1) was added dropwise to each solution to destroy excess of hydride and bring the solutions to pH 7, the respective solutions were concentrated, and the residues were chromatographed on silica gel.

Methyl 2,3,4-tri-*O*-benzyl-L-*glycero*-α-D-*manno*-heptopyranoside (**7**) (82 mg, 61%), formed from **5**, was eluted with dichloromethane containing 6% of acetone and had $[\alpha]_D$ +25 (*c* 1.0) (lit. $[\alpha]_D$ +30 (18), $[\alpha]_D$ +23 (19)); ^{1}H nmr, δ: 4.65 (s, 1H, H-1), 4.11 (t, 1H, $J_{3,4} \sim J_{4,5} \sim$ 9.5 Hz, H-4), 3.94 (m, 1H, H-6), 3.84 (dd, 1H, $J_{2,3}$ 3.0 Hz, $J_{3,4}$ 9.4 Hz, H-3), 3.80–3.60 (m, 3H, H-2, H-7), 3.55 (dd, 1H, $J_{5,6}$ 1.4 Hz, $J_{4,5}$ 9.7 Hz, H-5); ^{13}C nmr, δ_C: 99.5 (C-1), 80.0, 74.5, 74.3, 72.5, 69.4 (C-2 to C-6), 65.0 (C-7) (lit. (17, 18) for similar nmr data).

Methyl 2,3,4-tri-*O*-benzyl-D-*glycero*-α-D-*manno*-heptopyranoside (**8**) (76 mg, 57%), formed from **6**, was eluted with dichloromethane containing 4% of acetone and had $[\alpha]_D$ +35 (*c* 1.0); ^{1}H nmr, δ: 4.68 (d, 1H, $J_{1,2}$ 2.1 Hz, H-1), 4.02 (t, 1H, $J_{3,4} \sim J_{4,5} \sim$ 9.3 Hz, H-4), 3.93 (m, 2H, H-3, H-6), 3.80–3.63 (m, 4H, H-2, H-5, H-7); ^{13}C nmr, δ_C: 99.0 (C-1), 80.5, 76.9, 74.4, 72.5, 71.1 (C-2 to C-6), 62.9 (C-7) (lit. (20) for similar data).

Samples of **7** and **8** were each hydrogenolyzed in ethanol over palladium 5% on charcoal, the resulting methyl glycosides were hydrolyzed, and the heptoses were reduced and acetylated. The glc analysis showed the formation, respectively, of heptaacetates of L-*glycero*-D-*manno*-heptitol and D-*glycero*-D-*manno*-heptitol.

*Addition of 2-(trimethylsilyl)thiazole to methyl 2,3,4-tri-*O*-benzyl-α-D-gluco-hexodialdo-1,5-pyranoside* **9**

Treatment of **9** (from methyl 2,3,4-tri-*O*-benzyl-α-D-glucopyranoside (21) (18 g, 38.8 mmol)) in dichloromethane (125 mL) with TMSthiazole (6.5 mL, 39.2 mmol) with subsequent processing, as described for **2**, afforded a mixture of **10** and **11** that was chromatographed on silica gel (light petroleum – ethyl acetate, 2:1). Methyl (6*R*)-2,3,4-tri-*O*-benzyl-6-(2-thiazolyl)-α-D-glucopyranoside (**10**) (11.57 g, 54.3%) had mp 110–112°C, and $[\alpha]_D$ +35 (*c* 1.0); ^{1}H nmr, δ: 5.24 (bs, 1H, H-6), 4.48 (d, 1H, $J_{1,2}$ 3.4 Hz, H-1), 4.16 (m, 1H, H-5), 4.06 (t, 1H, *J* 9.3 Hz, H-3 or H-4), 3.77 (t, 1H, *J* 9.6 Hz, H-4 or H-3), 3.51 (dd, 1H, $J_{1,2}$ 3.5 Hz, $J_{2,3}$ 9.5 Hz, H-2); ^{13}C nmr, δ_C: 98.1 (C-1), 81.9, 79.6, 76.9, 72.4, 69.8 (C-2 to C-6). Anal. calcd. for $C_{31}H_{33}NO_6S$: C 67.98, H 6.07, N 2.55, S 5.85; found: C 67.77, H 5.89, N 2.53, S 6.05.

Methyl (6*S*)-2,3,4-tri-*O*-benzyl-6-(2-thiazolyl)-α-D-glucopyranoside (**11**) (3.84 g, 18%) had $[\alpha]_D$ +33 (*c* 1.0); ^{1}H nmr, δ: 5.30 (d, 1H, $J_{5,6}$ 3.5 Hz, H-6), 4.60 (d, 1H, $J_{1,2}$ 3.8 Hz, H-1), 4.11 (dd, 1H, $J_{5,6}$ 3.5 Hz, $J_{4,5}$ 10 Hz, H-5), 4.04 (t, 1H, *J* 9.2 Hz, H-3 or H-4), 3.67 (t, 1H, *J* 9.4 Hz, H-4 or H-3), 3.43 (dd, 1H, $J_{1,2}$ 3.4 Hz, $J_{2,3}$ 9.5 Hz, H-2); ^{13}C nmr, δ_C: 97.8 (C-1), 82.0, 79.9, 78.6, 72.4, 71.9 (C-2 to C-6). Anal. calcd. for $C_{31}H_{33}NO_6S$: C 67.98, H 6.07, N 2.55, S 5.85; found: C 67.89, H 5.93, N 2.50; S 6.20.

Methyl 2,3,4-tri-*O*-benzyl-L-*glycero*-α-D-*gluco*-heptopyranoside (**12**) (4.5 g, 71%), formed from **10** (7 g), as described for **7** and **8**, was eluted with dichloromethane containing 8% of acetone and had $[\alpha]_D$ +53 (*c* 1.0); ^{1}H nmr, δ: 4.54 (d, 1H, $J_{1,2}$ 3.5 Hz, H-1), 3.97–3.50 (m, 7H, H-2 to H-7′); ^{13}C nmr, δ_C: 97.4 (C-1), 81.1, 79.0, 76.5, 69.9, 68.3 (C-2 to C-6), 64.0 (C-7). Anal. calcd. for $C_{29}H_{34}O_7$: C 70.42, H 6.92; found: C 70.49, H 7.06.

Methyl 2,3,4-tri-*O*-benzyl-D-*glycero*-α-D-*gluco*-heptopyranoside (**13**) (1.1 g, 71%), formed from **11** (2 g), as described for **7** and **8**, was eluted with dichloromethane containing 8% of acetone and had $[\alpha]_D$ +55 (*c* 1.0); ^{1}H nmr, δ: 4.53 (d, 1H, $J_{1,2}$ 3.4 Hz, H-1), 4.05–3.50 (m, 7H, H-2 to H-7′); ^{13}C nmr, δ_C: 97.7 (C-1), 82.1, 80.2, 79.7, 72.6, 69.8 (C-2 to C-6), 62.8 (C-7). Anal. calcd. for $C_{29}H_{34}O_7$: C 70.42, H 6.92; found: C 70.41, H 6.82.

Methyl L-*glycero*-α-D-*gluco*-heptopyranoside (**14**) (40 mg), from hydrogenolysis of **12** (100 mg) in ethanol (50 mL) over palladium 5% on charcoal, had mp 153–155°C, $[\alpha]_D$ +157 (*c* 1.0 MeOH); ^{1}H nmr (D_2O), δ: 4.73 (d, 1H, $J_{1,2}$ 3.66 Hz), 3.32 (s, 3H, OCH_3). The derived pentaacetate (**16**) had $[\alpha]_D$ +86 (*c* 1.0); ^{1}H nmr, δ: 5.46 (t, 1H, $J_{2,3} \sim J_{3,4} \sim$ 9.8 Hz, H-3 or H-4), 5.27 (m, 1H, H-6), 5.04 (t, 1H, $J_{3,4} \sim J_{4,5} \sim$ 9.8 Hz, H-4 or H-3), 4.99 (d, 1H, $J_{1,2}$ 3.7 Hz, H-1), 4.90 (dd, 1H, $J_{1,2}$ 3.7 Hz, $J_{2,3}$ 10 Hz, H-2), 4.29 (dd, 1H, $J_{6,7}$ 5.7 Hz, $J_{7,7'}$ 11.2 Hz, H-7), 4.21 (dd, 1H, $J_{6,7'}$ 7.5 Hz, $J_{7,7'}$ 11.2 Hz, H-7′), 4.08 (dd, 1H, $J_{5,6}$ 2.0 Hz, $J_{4,5}$ 10.2 Hz, H-5), 3.40 (s, 3H, OCH_3), 2.12, 2.08, 2.05, 2.01, 2.00 (5 s, 15H, $OCOCH_3$). Anal. calcd. for $C_{18}H_{26}O_{12}$: C 49.76, H 6.03; found: C 49.56, H 5.86.

Methyl D-*glycero*-α-D-*gluco*-heptopyranoside (**15**) (20 mg), from hydrogenolysis of **13** (60 mg) in ethanol (25 mL) over palladium 5% on charcoal, had $[\alpha]_D$ +107 (*c* 1.0, MeOH); ^{1}H nmr (D_2O), δ: 4.72 (d, 1H, $J_{1,2}$ 3.4 Hz), 3.35 (s, 3H, OCH_3). The derived pentaacetate (**17**) had $[\alpha]_D$ +127 (*c* 1.0); ^{1}H nmr, δ: 5.44 (t, 1H, *J* 10.1 Hz, H-3 or H-4), 5.22–5.17 (overlapping ddd, 1H, $J_{5,6}$ 2.8 Hz, $J_{6,7}$ 4.1 Hz, $J_{6,7'}$ 7.2 Hz, H-6), 5.08 (dd, 1H, *J* 9.2 and 10.2 Hz, H-4 or H-3), 4.94 (d, 1H, $J_{1,2}$ 3.6 Hz, H-1), 4.84 (dd, 1H, $J_{1,2}$ 3.7 Hz, $J_{2,3}$ 10.3 Hz, H-2), 4.36 (dd, 1H, $J_{7,7'}$ 11.8 Hz and $J_{6,7}$ 4.0 Hz, H-7a), 4.19 (dd, 1H, $J_{7,7'}$ 11.8 and $J_{6,7'}$ 7.23 Hz, H-7′), 4.01 (dd, 1H, $J_{5,6}$ 2.8 Hz, $J_{4,5}$ 10.1 Hz, H-5), 3.40 (s, 3H, OCH_3), 2.12, 2.08, 2.05, 2.01, 2.00 (5 s, 15H, $OCOCH_3$). Anal. calcd. for $C_{18}H_{26}O_{12}$: C 49.76, H 6.03; found: C 49.57, H 5.92.

Methyl glycosides **14** and **15** were hydrolyzed, and the heptoses were reduced and acetylated. The glc analysis showed the formation, respectively, of heptaacetates of L-*glycero*-D-*gluco*-heptitol and D-*glycero*-D-*gluco*-heptitol.

*Configurational inversions at C-6 of derivatives of methyl 2,3,4-tri-*O*-benzyl-L-*glycero*-α-D-*gluco*-heptopyranoside by an oxidation–reduction sequence*

(A) Thiazolyl derivative **10** (3.7 g, 6 mmol) in dichloromethane (10 mL) was added to periodinane (3.4 g, 8 mmol) at 0°C and the solution was kept for 30 min at 0°C and then at room temperature for 3.5 h. The solution was diluted with ether (100 mL) and poured with stirring into saturated aqueous $NaHCO_3$ (75 mL) containing $Na_2S_2O_3 \cdot 5H_2O$, and shaken for 5 min. The organic layer was separated, washed successively with saturated aqueous $NaHCO_3$, water, and aqueous sodium chloride, dried, and concentrated. L-Selectride (1 M in oxolane, 14 mL) was added to the resulting syrup (3.7 g) in oxolane at −78°C and stirred for 1 h. The reaction was quenched with a solution of aqueous 10% NaOH (20 mL) and 30% hydrogen peroxide (10 mL), and the mixture was stirred at room temperature for 2 h. Solvents were evaporated, the mixture was extracted with ethyl acetate, and the extract was washed with saturated aqueous NaCl, dried, and concentrated. Column chromatography, as above, furnished **10** (1.6 g) and **11** (1.4 g), characterized by tlc and their ^{1}H and ^{13}C nmr spectra, and incompletely separated mixture (0.5 g).

(B) Methyl glycoside (**12**) (4 g, 8 mmol) in *N,N*-dimethylformamide (30 mL) containing imidazole (1.2 g, 17.8 mmol) was treated with *tert*-butyldimethylsilyl chloride (1.34 g, 8.8 mmol) for 1 h at room temperature. The solution was diluted with ether, washed with water, dried, and concentrated. The product was chromatographed on silica gel (light petroleum – ethyl acetate, 2:1) to yield methyl 2,3,4-tri-*O*-benzyl-7-*O*-*tert*-butyldimethylsilyl-L-*glycero*-α-D-*gluco*-heptopyranoside (**19**) (4.9 g, 99%), $[\alpha]_D$ +7.4; ^{1}H nmr, δ: 4.52 (d, 1H, $J_{1,2}$ 3.47 Hz, H-1), 3.26 (s, 3H, OCH_3), 0.82 (s, 9H, $(CH_3)_3Si$), −0.012, −0.014 (2 s, 6H, CH_3Si). Anal. calcd. for $C_{35}H_{48}O_7Si$: C 69.04, H 7.94; found: C 69.00, H 7.85.

Methyl 2,3,4-tri-*O*-benzyl-7-*O*-*tert*-butyldimethylsilyl-D-*glycero*-α-D-*gluco*-heptopyranoside (**20**), similarly prepared as a reference sample, had $[\alpha]_D$ +11 (*c* 1.0); ^{1}H nmr, δ: 4.56 (d, 1H, $J_{1,2}$ 3.4 Hz, H-1), 3.37 (s, 3H, OCH_3), 0.85 (s, 9H, $(CH_3)_3Si$), 0.00 (2 s, 6H, CH_3Si). Anal. calcd. for $C_{35}H_{48}O_7Si$: C 69.04, H 7.94; found: C 68.94, H 7.74.

Oxidation of **19** (4.9 g, 7.9 mmol) with oxalyl chloride (9 mL, 18 mmol) and methyl sulfoxide (1.63 mL, 24.5 mmol) as described above and monitored by tlc afforded the 6-ulose, which was treated directly in oxolane (30 mL) with L-selectride (1 M in oxolane, 16 mL). After 30 min tlc showed the formation of an altered product with the mobility of **20** and only trace amounts of **19**. When the reaction was

Can. J. Chem. Downloaded from www.nrcresearchpress.com by 203.198.23.82 on 09/08/12
For personal use only.

quenched with alkaline hydrogen peroxide, tlc showed the formation of modified products without loss of silyl substituent. *O*-Desilylation (22) on treatment of the mixture in oxolane (30 mL) with tetrabutylammonium fluoride (1 M in oxolane, 15 mL) gave **13** (3.6 g, 90%), $[\alpha]_D$ +55 (*c* 1.0), identical (tlc, ^1H and ^{13}C nmr, and diastereomeric purity by conversion to the heptitol heptaacetate for glc analysis) to the previously prepared sample.

Configurational inversion at C-6 of methyl 2,3,4-tri-O-benzyl-L-glycero-α-D-manno-heptopyranoside by oxidation–reduction

Methyl heptoside **7** (47 mg, 0.09 mmol) in *N,N*-dimethylformamide (3 mL) containing imidazole (14 mg, 0.2 mmol) was treated with *tert*-butyldimethylsilyl chloride (16 mg, 0.1 mmol) for 4 h at room temperature. Thin-layer chromatography showed that reaction was incomplete, and further TBDMS (16 mg) and imidazole (14 mg) were added and reaction was continued for another 2 h. The solution was diluted with ether, washed with water, dried, concentrated, and chromatographed on silica gel (light petroleum – ethyl acetate, 3:1) to give methyl 2,3,4-tri-*O*-benzyl-7-*O*-*tert*-butyldimethylsilyl-L-*glycero*-α-D-*manno*-heptopyranoside (**21**) (53 mg, 90%), $[\alpha]_D$ +24 (*c* 1.0); ^1H nmr, δ: 4.56 (d, 1H, $J_{1,2}$ 2.78 Hz, H-1), 3.22 (s, 3H, OMe), 0.83 (s, 9H, $(CH_3)_3Si$), 0.00, −0.01 (2 s, 6H, CH_3Si). Anal. calcd. for $C_{35}H_{48}O_7Si$: C 69.04, H 7.94; found: C 68.92, H 7.97.

Oxidation of **21** (40 mg, 0.06 mmol) with oxalyl chloride (184 μL) and methyl sulfoxide (33 μL) in dichloromethane at −78°C, as described above and monitored by tlc, afforded the 6-ulose, which was treated directly in oxolane (5 mL) with L-selectride (1 M in oxolane, 136 μL) for 1 h. The reaction was quenched by the addition of alkaline hydrogen peroxide (10% aqueous NaOH and 30% H_2O_2, 2:1) to give a mixture of compounds that was treated with tetrabutylammonium fluoride (1 M in oxolane, 133 μL). The residue was chromatographed on silica gel to give **8** (26 mg, 80%), $[\alpha]_D$ +33 (*c* 1.0), as the sole detectable product, which was indistinguishable (tlc, ^1H and ^{13}C nmr) from the previous sample, and was further characterized by conversion into D-*glycero*-D-*manno*-heptitol heptaacetate (glc analysis). Treatment of the above-mentioned 6-ulose with sodium borohydride in methanol gave configurationally altered silyl ether (DDManHep) and **21** (LDManHep) in the approximate ratio of 9:1.

Oxidation of methyl 2,3,4-tri-O-benzyl-α-D-altropyranoside and addition of 2-(trimethylsilyl)thiazole to the resulting hexodialdo-1,5-pyranoside mixture

Methyl 2,3,4-tri-*O*-benzyl-α-D-altropyranoside (23) (250 mg, 0.53 mmol) was oxidized with oxalyl chloride (0.6 mL, 1.2 mmol) and methyl sulfoxide (0.11 mL, 1.43 mmol), as described previously, and gave a mixture of products (**22** and **23**) as indicated by the appearance of two aldehydic protons in the ^1H nmr spectrum at δ 9.76 and 9.59 in the approximate ratio of 1:4. The ^{13}C nmr spectrum showed inter alia two sets of resonances in the same relative proportions corresponding to those of ring carbon atoms of methyl glycosides having the β-galactopyranose (δ_C 104.6 (C-1), 80.8, 78.8, 78.5, and 74.7 (C-2 to C-5)) and α-altropyranose (δ_C 101.1 (C-1), 75.8, 74.6, 74.0, and 71.5 (C-2 to C-5)) configurations. Part of the mixture was reduced with $NaBH_4$ in methanol. One portion of the reduction product was acetylated and gc analysis on column B showed the presence of two components with the retention times of 6-*O*-acetyl-2,3,4-tri-*O*-benzyl derivatives of methyl β-D-galactopyranoside and methyl α-D-altropyranoside in the approximate ratio of 3:2. Another portion of the reduction product was *O*-debenzylated for hydrolysis, followed by (*a*) reduction and acetylation to give the corresponding mixtures of galactitol and altritol hexaacetates, and (*b*) glycosidation with (*R*)- and (*S*)-2-butanol and acetylation to give products with the retention times (glc on a DB-5 (15 m × 0.25 mm) column, 230°C (5 min), 230° → 260°C, 2°/min, 260°C) of derivatives of L-galactose and D-altrose.

2-TMSthiazole (0.12 mL was added to the remaining mixture of hexodialdo-1,5-pyranosides **22** and **23** (150 mg) as described previously, and chromatography on silica gel (light petroleum – ethyl acetate, 2:1) gave methyl (6*R*)-2,3,4-tri-*O*-benzyl-6-(2-thiazolyl)-β-L-galactopyranoside (**24**) (103 mg, 59%), $[\alpha]_D$ −4 (*c* 1.0); ^1H nmr, δ: 4.26 (d, 1H, $J_{1,2}$ 7.7 Hz, H-1), 3.87 (dd, 1H, $J_{1,2}$ 7.7 Hz, $J_{2,3}$ 9.7 Hz, H-2), 3.53 (s, 3H, OCH_3); ^{13}C nmr, δ_C: 105.2 (C-1), 81.8, 79.3, 75.9, 73.8, 70.1 (C-2 to C-6), 57.4 (OCH_3). Anal. calcd. for $C_{31}H_{33}NO_6S$: C 67.98, H 6.07, N 2.55; found: C 67.82, H 6.15, N 2.55.

Methyl 2,3,4-tri-*O*-benzyl-L-*glycero*-α-L-*galacto*-heptopyranoside (**25**) (50 mg, 74%), formed from **24** (75 mg), as described for **7** and **8**, was chromatographed on silica gel with dichloromethane containing 8% of acetone and had $[\alpha]_D$ +13 (*c* 1.0); ^1H nmr, δ: 4.24 (d, 1H, $J_{1,2}$ 7.6 Hz, H-1), 3.51 (s, 3H, OCH_3); ^{13}C nmr, δ_C: 105.0 (C-1), 82.1, 79.5, 74.0, 71.9, 69.1 (C-2 to C-6), 63.8 (C-7). Anal. calcd. for $C_{29}H_{34}O_7$: C 70.42, H 6.92; found: C 70.28, H 6.94.

A sample of **25** was hydrogenolyzed in ethanol over palladium 5% on charcoal, the resulting methyl glycoside was hydrolyzed, and the heptose was reduced and acetylated. The glc analysis showed the formation, respectively, of a heptitol heptaacetate with the retention time of the corresponding derivative of L-*glycero*-D-*manno*-heptitol (= enantiomer of L-*glycero*-L-*galacto*-heptitol).

*2-(Trimethylsilyl)thiazole homologation of 1,2:3,4-di-O-isopropylidene-α-D-galacto-hexadialdo-1,5-pyranose **3** and configurational inversion of product **4** at C-6*

A solution in dichloromethane (10 mL) of compound **3** (1 g, 3.84 mmol), from oxidation of 1,2:3,4-di-*O*-isopropylidene-α-D-galactopyranose with oxalyl chloride and methyl sulfoxide showed ^{13}C nmr, δ_C: 199.0 (CHO), 108.3 (C-1), 95.5, 72.5, 70.9, 69.7 (C-2 to C-5), and was reacted with TMS thiazole (0.72 mL, 4.37 mmol), as described previously, and silica gel chromatography (light petroleum – ethyl acetate, 2:1) furnished (6*S*)-1,2:3,4-di-*O*-isopropylidene-6-(2-thiazolyl)-α-D-galactopyranose (**4**) (780 mg, 60%), mp 178–180°C (lit. (6) mp 170–172°C), $[\alpha]_D$ −67 (*c* 1.0); ^1H nmr, δ: 5.57 (d, 1H, $J_{1,2}$ 4.9 Hz, H-1), 5.14 (d, 1H, $J_{5,6}$ 7.9 Hz, H-6), 4.65 (dd, 1H, $J_{2,3}$ 2.3 Hz, H-2), 4.54 (dd, 1H, $J_{4,5}$ 1.3 Hz, H-4), 4.33 (dd, 1H, H-2), 4.10 (dd, 1H, H-5); ^{13}C nmr, δ_C: 96.2 (C-1), 70.7, 70.4, 70.3, 69.4, 68.0 (C-2 to C-6).

1,2:3,4-Di-*O*-isopropylidene-D-*glycero*-α-D-*galacto*-heptopyranose (**26**) (182 mg, 72%), formed from **4** (300 mg), as described for **7** and **8**, was chromatographed on silica gel (dichloromethane containing 10% of acetone) and had $[\alpha]_D$ −57 (*c* 1.0); ^1H nmr: δ: 5.50 (d, 1H, $J_{1,2}$ 4.9 Hz, H-1), 4.63 (dd, 1H, $J_{2,3}$ 2.3 Hz, $J_{3,4}$ 7.9 Hz, H-3), 4.46 (dd, 1H, $J_{4,5}$ 1.6 Hz, H-4), 4.30 (dd, 1H, H-2), 3.88–3.68 (m, 4H, H-5, 6, 7, 7′); ^{13}C nmr, δ_C: 96.2 (C-1), 70.7, 70.6, 70.5, 69.9, 67.3 (C-2 to C-6), 63.8 (C-7). Anal. calcd. for $C_{13}H_{22}O_7$: C 53.78, H 7.64; found: C 53.46, H 7.74. Compound **26** was hydrolyzed, and the resulting heptose was reduced and acetylated. The glc analysis showed the formation, respectively, of the heptaacetate of D-*glycero*-D-*galacto*-heptitol (= L-*glycero*-D-*manno*-heptitol).

Thiazole adduct **4** (49 mg) was oxidized with oxalyl chloride and methyl sulfoxide and the product, without further purification, was reduced with L-selectride, as reported by Dondoni et al. (13), and the isolated (6*R*)-1,2:3,4-di-*O*-isopropylidene-6-(2-thiazolyl)-α-D-galactopyranose (**18**) (30 mg, 60%) had mp 102–104°C (lit. (13) mp 98–100°C); ^1H nmr, δ: 5.57 (d, 1H, $J_{1,2}$ 4.8 Hz, H-1), 5.34 (d, 1H, $J_{5,6}$ 4.8 Hz, H-6), 4.63 (dd, 1H, $J_{2,3}$ 2.4 Hz, $J_{3,4}$ 8.0 Hz, H-3), 4.46 (dd, 1H, $J_{4,5}$ 1.6 Hz, H-4), 4.32 (dd, 1H, H-2), 4.15 (dd, 1H, H-5); ^{13}C nmr, δ_C: 96.4 (C-1), 72.4, 71.9, 70.9, 70.8, 69.8 (C-2 to C-6).

1,2:3,4-Di-*O*-isopropylidene-L-*glycero*-α-D-*galacto*-heptopyranose (**27**) (13 mg, 63%), formed from **18** (25 mg), as described for **7** and **8**, was chromatographed on silica gel (dichloromethane containing 10% of acetone) and had mp 98–100°C, $[\alpha]_D$ −41 (*c* 1.0); ^1H nmr, δ: 5.59 (d, 1H, $J_{1,2}$ 5.0 Hz, H-1), 4.62 (dd, 1H, $J_{2,3}$ 2.3 Hz, $J_{3,4}$ 7.9 Hz, H-3), 4.36–4.33 (m, 2H), 3.79–3.77 (m, 4H); ^{13}C nmr, δ_C: 96.4 (C-1), 71.6, 71.3, 70.8, 70.5, 67.5 (C-2 to C-6), 62.4 (C-7). Anal. calcd. for $C_{13}H_{22}O_7$: C 53.78, H 7.64; found: C 53.93, H 7.63. Compound **27** was hydrolyzed, and the resulting heptose was reduced and acetylated. The glc analysis showed the formation of the heptaacetate of L-*glycero*-D-*galacto*-heptitol (= L-*glycero*-D-*gluco*-heptitol).

Oxidation of methyl 2,3,4-tri-O-benzyl-β-D-galactopyranoside and addition of 2-(trimethylsilyl)thiazole to the resulting hexodialdo-1,5-pyranoside mixture

Methyl 2,3,4-tri-*O*-benzyl-β-D-galactopyranoside (24) (1.09 g,

Can. J. Chem. Downloaded from www.nrcresearchpress.com by 203.198.23.82 on 09/08/12
For personal use only.

2.3 mmol) was oxidized with oxalyl chloride (2.4 mL, 4.8 mmol) and methyl sulfoxide (0.47 mL, 6.1 mmol), as described previously, and gave a mixture of products corresponding to enantiomers **22** and **23**, as indicated by the appearance of two aldehydic protons in the ^{1}H nmr spectrum at δ 9.68 and 9.53 in the approximate ratio of 1:6. The ^{13}C nmr spectrum showed inter alia two sets of resonances in the same relative proportions corresponding to those of ring carbon atoms of methyl glycosides having the β-galactopyranose (δ_C 104.6 (C-1), 80.8, 78.8, 78.5, and 74.7 (C-2 to C-5)) and α-altropyranose (δ_C 101.1 (C-1), 75.8, 74.6, 74.0, and 71.5 (C-2 to C-5)) configurations. A portion of the mixture was reduced with $NaBH_4$ in methanol, the reduction product was acetylated, and glc analysis on column B showed the presence of components with the retention times of 6-*O*-acetyl-2,3,4-tri-*O*-benzyl derivatives of methyl β-D-galactopyranoside and methyl α-D-altropyranoside in the approximate ratio of 3:1. 2-TMSthiazole (0.45 mL) was added to the remaining mixture of hexodialdo-1,5-pyranosides (950 mg) was described previously, and chromatography on silica gel (light petroleum – ethyl acetate, 2:1) gave methyl (6*S*)-2,3,4-tri-*O*-benzyl-6-(2-thiazolyl)-β-D-galactopyranoside (**28**) (853 mg, 76%), $[\alpha]_D$ +2.5 (*c* 1.0); ^{1}H nmr, δ: 4.20 (d, 1H, $J_{1,2}$ 7.6 Hz, H-1), 3.46 (s, 3H, OCH_3); ^{13}C nmr, δ_C: 104.7 (C-1), 81.4, 78.9, 75.8, 73.5, 69.3 (C-2 to C-6), 56.9 (OCH_3). Within experimental limits these spectra were identical to those of the enantiomer **24**. Anal. calcd. for $C_{31}H_{33}NO_6S$: C 67.98, H 6.07, N 2.55; found: C 67.92, H 6.14, N 2.53.

Methyl 2,3,4-tri-*O*-benzyl-D-*glycero*-α-D-*galacto*-heptopyranoside (**29**) (220 mg, 60%), formed from **28** (407 mg), as described for **7** and **8**, was eluted from silica gel with dichloromethane containing 5% of acetone and had mp 101–103°C and $[\alpha]_D$ −18 (*c* 1.0); ^{1}H nmr, δ: 4.21 (d, 1H, $J_{1,2}$ 7.6 Hz, H-1), 3.47 (s, 3H, OCH_3); ^{13}C nmr, δ_C: 104.8 (C-1), 81.9, 79.3, 73.8, 72.4, 69.0 (C-2 to C-6), 63.6 (C-7). Anal. calcd. for $C_{29}H_{34}O_7$: C 70.42, H 6.92; found: C 70.41, H 6.88. A sample of **29** was hydrogenolyzed in ethanol over palladium 5% on charcoal, the resulting methyl glycoside was hydrolyzed, and the heptose was reduced and acetylated. The glc analysis showed the formation of a heptitol heptaacetate with the retention time of the corresponding derivative of L-*glycero*-D-*manno*-heptitol (= enantiomer of L-*glycero*-L-*galacto*-heptitol).

Configurational inversions at C-6 and C-5 of methyl (6S)-2,3,4-tri-O-benzyl-6-(2-thiazolyl)-β-D-galactopyranoside (28)

Thiazolyl derivative **28** (85 mg, 0.15 mmol) was oxidized as described previously with oxalyl chloride (0.175 mL, 0.35 mmol) and methyl sulfoxide (0.03 mL, 0.45 mmol). The product (84 mg), without purification, was reduced with L-selectride (0.3 mL, 0.33 mmol) in oxolane. The resulting syrup was separated by preparative layer chromatography (multiple development in light petroleum – ether–methanol, 14:6:1) to give two main fractions.

Fraction 1 (15 mg) had $[\alpha]_D$ +5 (*c* 1.0); ^{1}H nmr, δ: 5.25 (d, 1H, $J_{5,6}$ 3.58 Hz, H-6), 4.22 (d, 1H, $J_{1,2}$ 7.7 Hz, H-1), 3.84 (d, 1H, $J_{2,3}$ 9.7 Hz and $J_{1,2}$ 7.7 Hz, H-2), 3.52 (dd, 1H, $J_{2,3}$ 9.7 Hz and $J_{3,4}$ 2.8 Hz, H-3), 3.41 (s, 3H, OCH_3); ^{13}C nmr, δ_C: 105.1 (C-1), 81.9, 79.1, 75.9, 75.6, 72.4 (C-2 to C-5), 57.0 (OCH_3). The sequence of operations, formyl deblocking, *O*-debenzylation, hydrolysis, reduction, and acetylation, gave a single heptitol heptaacetate coincident on glc analysis (column A) with the corresponding derivative from L-*glycero*-D-*galacto*-heptose. The ^{13}C nmr spectrum of fraction 2 (39 mg) showed the presence of signals assignable to anomeric C-1 resonances of compounds with β-galacto (δ_C 104.3) and α-altro (δ_C 99.6) ring configurations and, without individual specifications, to two sets of carbon atoms 2 to 6. Formyl deblocking furnished a mixture of methyl tri-*O*-benzyl heptopyranosides whose ^{13}C nmr spectrum likewise showed anomeric carbon resonances at δ_C 105.1 and 100.5 consistent with the presence of β-*galacto* and α-*altro* configurational isomers together with two sets of other carbon resonances. This mixture of compounds was *O*-debenzylated by formic acid with 5% palladium on charcoal as catalyst, hydrolyzed, reduced, and acetylated. The glc analysis (column A) showed the presence of two heptitol heptaacetates coincident with those from D-*glycero*-D-*galacto*-heptose and D-*glycero*-D-*altro*-heptose.

Conversion of methyl D-glycero-D-gluco-heptopyranoside into methyl D-glycero-D-altro-heptopyranoside derivatives

Methyl 2,3,4-tri-*O*-benzyl-7-*O*-*tert*-butyldiphenylsilyl-D-*glycero*-α-D-*gluco*-heptopyranoside (**30**) was prepared as described for **19** and had $[\alpha]_D$ +9 (*c* 1.0); ^{1}H nmr, δ: 7.63–7.10 (m, 25H, Ph-H), 4.61 (d, 1H, $J_{1,2}$ 3.60 Hz, H-1), 3.24 (s, 3H, OCH_3), 1.05 (s, 9H, $(CH_3)_3Si$) Anal. calcd. for $C_{45}H_{52}O_7Si$: 73.73, H 7.15; found: C 73.45, H 7.04.

Similarly, silylation of methyl D-*glycero*-α-D-*gluco*-heptopyranoside (**15**) (2 g, 8.9 mmol) followed by chromatography on silica gel (dichloromethane–methanol, 9:1) afforded methyl 7-*O*-*tert*-butyldiphenylsilyl-D-*glycero*-α-D-*gluco*-heptopyranoside (**31**) (2.9 g, 71%), $[\alpha]_D$ +59 (*c* 1.0, methanol); ^{1}H nmr, δ: 7.68–7.32 (m, 10H, Ph-H), 4.61 (d, 1H, $J_{1,2}$ 3.6 Hz, H-1), 3.24 (s, 3H, OCH_3). Exact Mass calcd. for $C_{24}H_{34}O_7Si$ + H: 463.2135; found: 463.2152; calcd. for $C_{24}H_{34}O_7Si$ + Na: 485.1941; found: 485.1971.

A solution of **31** (1 g, 2.16 mmol), benzaldehyde dimethyl acetal (0.67 mL, 2 equiv., 3.9 mmol), and *p*-toluenesulfonic acid (50 mg) in toluene (50 mL) was kept at 30°C for 1 h under reduced pressure (aspirator), to ensure removal of methanol. Solid $NaHCO_3$ was added, the solution was concentrated, the residue was partitioned between dichloromethane and water, and the organic layer was dried and concentrated. The residue was chromatographed on silica gel (dichloromethane containing 1% of methanol) to give methyl 4,6-*O*-benzylidene-7-*O*-*tert*-butyldiphenylsilyl-D-*glycero*-α-D-*gluco*-heptopyranoside (**32**) (913 mg, 76%), $[\alpha]_D$ +94 (*c* 1.0); ^{1}H nmr, δ: 7.60–7.22 (m, 15H, Ph-H), 5.57 (s, 1H, C*H*Ph), 4.69 (d, 1H, $J_{1,2}$ 3.10 Hz, H-1), 3.34 (s, 3H, OCH_3), 1.03 (s, 9H, $(CH_3)_3Si$). Exact Mass calcd. for $C_{31}H_{38}O_7Si$ + H: 551.2465; found: 551.2465.

Compound **32** (630 mg, 1.14 mmol) was added to sodium hydride (55 mg, 2 equiv.) in *N*,*N*-dimethylformamide (10 mL) and the mixture was stirred for 30 min. *N*-Tosylimidazole (280 mg, 1.1 equiv.) was added and the mixture was stirred at room temperature for 4 days. Thin-layer chromatography showed the successive formation after 1 h of 2-*O*-tosyl derivative (**33**) and *O*-silyl epoxide (**34**), and, after 24 h, complete reaction of **32** and conversion of **33** into **34**, but now the appearance of *O*-desilylated epoxide (**35**). After 84 h conversion of **34** into **35** was complete. The reaction mixture was poured into ice-water, the product was extracted with dichloromethane, and the organic layer was washed with water, concentrated, and chromatographed on silica gel (light petroleum – ethyl acetate, 9:1) to give methyl 2,3-anhydro-4,6-*O*-benzylidene-D-*glycero*-α-D-*manno*-heptopyranoside (**35**) (236 mg, 70%), $[\alpha]_D$ +20 (*c* 1.0); ^{1}H nmr (including ^{1}H–^{1}H COSY), δ: 7.52–7.25 (m, 5H, Ph-H), 5.69 (s, 1H, C*H*Ph), 4.92 (d, 1H, H-1), 3.49 (d, 1H, $J_{2,3}$ 3.7 Hz, H-3), 3.34 (s, 3H, OCH_3), 3.18 (d, 1H, $J_{2,3}$ 3.7 Hz, H-2), 1.03 (s, 9H, $(CH_3)_3Si$). Anal. calcd. for $C_{15}H_{18}O_6$: C 61.21, H 6.16; found: C 61.16, H 6.18.

The ^{1}H nmr spectrum of **33** showed inter alia resonances at δ 7.8–7.2 (m, 14H, Ph-H), 5.57 (s, 1H, acetal C*H*Ph), 4.83 (d, 1H, $J_{1,2}$ 3.7 Hz, H-1), 4.39 (dd, 1H, $J_{1,2}$ 3.8 Hz, $J_{2,3}$ 9.4 Hz, H-2), 4.16 (t, 1H, $J_{2,3} \sim J_{3,4}$ = 9.3 Hz, H-3), 3.31 (s, 3H, OCH_3), 2.43 (s, 3H, CH_3-$C_6H_4SO_2$), 1.03 (s, 9H, $(CH_3)_3C$). On acetylation the resonance of H-3 is shifted to δ 5.60. The ^{1}H nmr spectrum of **34** showed inter alia resonances at δ 7.7–7.2 (m, 10H, Ph-H), 5.66 (s, 1H, acetal C*H*Ph), 4.89 (s, 1H, H-1), 3.51 (d, 1H, $J_{2,3}$ 3.7 Hz, H-3), 3.40 (s, 3H, OCH_3), 3.17 (d, 1H, $J_{2,3}$ 3.7 Hz, H-2), 1.06 (s, 9H, $(CH_3)_3C$).

Compound **35** (151 mg) was heated at 100°C in 1 M aqueous sodium hydroxide for 12 h. Liquid–liquid extraction of the solution with chloroform afforded methyl 4,6-*O*-benzylidene-D-*glycero*-α-D-*altro*-heptopyranoside (**36**) (140 mg, 87%), which crystallized from ether–methanol and had mp 209–211°C, $[\alpha]_D$ +92 (*c* 1.0, methanol); ^{1}H nmr (D_2O), δ: 7.55–7.42 (m, 5H, Ph-H), 5.85 (s, 1H, Ph-C*H*), 4.67 (s, 1H, H-1), 3.35 (s, 3H, OMe); ^{13}C nmr, δ: 129.4, 128.2, 126.0 (aromatic C), 101.4 (Ph-*C*H), 101.0 (C-1), 79.0, 74.3, 69.5, 67.5, 58.3 (C-2 to C-6), 60.1 (C-7), 54.7 (OCH_3). Anal. calcd. for $C_{15}H_{22}O_7$: C 57.68, H 6.45; found: C 57.34, H, 6.33. Acetylation of **36** under standard conditions afforded the tri-*O*-acetyl derivative **37**, which had $[\alpha]_D$ +92 (*c* 1.0); $[\alpha]_D$ +55 (*c* 1.0); ^{1}H nmr (1 D with decoupling and ^{1}H–^{1}H COSY), δ: 7.47–7.26 (m, 5H, Ph-H), 5.23 (1H, br s, H-3), 5.00 (d, 1H, $J_{2,3}$ 2 Hz, H-2), 4.60 (s, 1H, H-1), 4.49 (d, 1H, $J_{7,7'}$ 12 Hz, H-7), 4.27

(dd, 1H, $J_{7,7'}$ 12 Hz, $J_{6,7'}$ 5 Hz, H-7'), 4.06 (m, 3H, H-4, H-5, H-6), 3.36 (s, 3H, OMe), 2.14, 2.12, 2.10 (3 s, 9H, OAc).

O-Benzylidene compound **36** (110 mg) was heated in acetic acid – water (4:1) for 2 h at 80°C and concentration of the solution gave methyl D-*glycero*-α-D-*altro*-heptopyranoside (**38**) (70 mg, 86%), $[\alpha]_D$ +68 (*c* 1.0, methanol); ^{1}H nmr (D_2O), δ: 4.61 (s, 1H, H-1), 3.24 (s, 3H, OMe); ^{13}C nmr, δ_C: 100.4 (C-1), 70.8, 70.0, 69.4, 69.1, 65.0 (C-2 to C-6), 61.3 (C-7), 55.0 (OCH_3). The penta-*O*-acetyl derivative **39** had $[\alpha]_D$ +50 (*c* 1.0); ^{1}H nmr (1 D with decoupling and ^{1}H–^{1}H COSY), δ: 4.94 (dd, 1H, $J_{1,2}$ 1.7 Hz, $J_{2,3}$ 4.1 Hz, H-2), 4.62 (d, 1H, $J_{1,2}$ 1.3 Hz, H-1), 4.43 (dd, 1H, $J_{7,7'}$ 12 Hz, $J_{6,7}$ 3.8 Hz, H-7), 4.18 (dd, 1H, $J_{7,7'}$ 12 Hz, $J_{6,7'}$ 7.2 Hz, H-7'), 3.40 (s, 3H, OMe), 2.13, 2.12, 2.10, 2.07, 2.05 (5 s, 15H, OAc); ^{13}C nmr, δ_C: 99.2 (C-2), 69.8, 69.4, 67.3, 66.6, 65.8 (C-2 to C-6), 61.9 (C-7), 55.6 (OCH_3). Anal. calcd. for $C_{18}H_{26}O_{12}$: C 49.76, H 6.03; found: C 49.83, H 5.95.

Hydrolysis of methyl heptoside (**38**), followed by treatment of the product with $NaBH_4$ and acetylation, gave products that were coincident on gc with the heptitol heptaacetate formed from the O:36 glycan with accompanying 1,6- and 1,7-anhydroheptose tetraacetates. Further samples of the hydrolyzate were converted into glycoside acetates on reaction with (*R*)- and (*S*)-2-butanol followed by acetylation. Comparison (gc on column A) of these glycoside acetates with those similarly derived from the hydrolysate of the O:36 glycan showed that the natural heptose was D-*glycero*-D-*altro*-heptose.

Anhydro glycoside **35** (34 mg) was boiled with methanolic 2 M sodium methoxide (10 mL) for 16 h. Solvent was evaporated and the residue in dichloromethane was washed successively with water, saturated NaCl, and again water, dried, concentrated, and chromatographed on silica gel (light petroleum – ethyl acetate, 4:1, later 2:1) to give methyl 4,6-*O*-benzylidene-3-*O*-methyl-D-*glycero*-α-D-*altro*-heptopyranoside (**40**) (28 mg, 74%), $[\alpha]_D$ +81 (*c* 1.0); ^{1}H nmr, δ: 7.52–7.26 (m, 5H, Ph-H), 5.67 (s, 1H, Ph-C*H*), 4.60 (s, 1H, H-1), 3.58, 3.41 (2 s, 6H, OMe). Acetylation of **40** gave the di-*O*-acetyl derivative **41**, $[\alpha]_D$ +45 (*c* 0.5); ^{1}H nmr (1 D with decoupling and ^{1}H–^{1}H COSY), δ: 7.52–7.26 (m, 5H, Ph-H), 5.67 (s, 1H, Ph-C-*H*), 5.09 (d, 1H, $J_{2,3}$ 2.5 Hz, H-2), 4.58 (s, 1H, H-1), 4.47 (dd, 1H, $J_{7,7'}$ 12 Hz, $J_{6,7}$ 1.7 Hz, H-7), 4.26 (dd, 1H, $J_{7,7'}$ 12 Hz, $J_{6,7}$ 5.9 Hz, H-7'), 4.15 (t, 1H, $J_{4,5} \sim J_{5,6} \sim$ 9.6 Hz, H-5), 4.05–3.99 (m, 1H, H-6), 3.95 (dd, 1H, $J_{4,5}$ 9.5 Hz, $J_{3,4}$ 2.9 Hz, H-4), 3.71 (t, 1H, *J* 2.4 Hz, H-3), 3.58, 3.39 (2 s, 6H, OMe), 2.14, 2.09 (2 s, 6H, OAc); ^{13}C nmr, δ_C: 137.2 (quat. aromatic C), 129.2, 128.3, 126.4 (aromatic C), 101.9 (Ph-*C*-H), 99.4 (C-1), 77.5, 76.3, 75.6, 70.0, 60.1 (C-2 to C-6), 63.2 (C-7), 59.2, 55.8 (2 OCH_3). Anal. calcd. for $C_{20}H_{26}O_9$: C 58.51, H 6.38; found: C 58.24, H 6.35.

Hydrolysis of **40** (27 mg) in acetic acid – water (4:1) for 1 h at 80°C gave methyl heptoside (**42**) (18 mg), $[\alpha]_D$ +92 (*c* 1.0, methanol), which was converted into the acetylated derivative (**43**), $[\alpha]_D$ +86 (*c* 1.0); ^{1}H nmr (1 D with decoupling and ^{1}H–^{1}H COSY), δ: 5.33 (ddd (apparent quintet), 1H, $J_{5,6} = J_{6,7'} \sim$ 3.8 Hz, H-6), 5.11 (dd, 1H, $J_{3,4}$ 3.5 Hz, $J_{4,5}$ 9.1 Hz, H-4), 5.04 (dd, 1H, $J_{1,2}$ 1.7 Hz, $J_{2,3}$ 4.5 Hz, H-2), 4.60 (s, 1H, H-1), 4.43 (dd, 1H, $J_{6,7}$ 3.6 Hz, $J_{7,7'}$ 12.0 Hz, H-7), 4.28 (dd, 1H, $J_{4,5}$ 9.1 Hz, $J_{5,6}$ 4.0 Hz, H-5), 4.18 (dd, 1H, $J_{6,7'}$ 7.4 Hz, $J_{7,7'}$ 12.0 Hz, H-7'), 3.66 (t, 1H, $J_{2,3} = J_{3,4} \sim$ 3.9 Hz, H-3), 3.45, 3.40 (2 s, 6H, OCH_3), 2.14, 2.13, 2.10, 2.05 (4 s, 12H, OAc). Anal. calcd. for $C_{17}H_{26}O_{11}$: C 50.24, H 6.45; found: C 50.44, C 6.47.

Hydrolysis of methyl heptoside (**42**), followed by treatment of the product with $NaBH_4$ and acetylation, gave products that were coincident on gc with the *O*-methylheptitol hexaacetate formed from the O:23 glycan with accompanying 1,6- and 1,7-anhydro-3-*O*-methylheptose triacetates. Further samples of the hydrolyzate were converted into glycoside acetates on reaction with (*R*)- and (*S*)-2-butanol followed by acetylation. Comparison (gc on column A) of these glycoside acetates with those similarly derived from the hydrolysate of the O:23 glycan showed that the natural heptose was 3-*O*-methyl-D-*glycero*-D-*altro*-heptose.

Acknowledgements

We thank the Natural Sciences and Engineering Research Council of Canada for financial support through its strategic and research grants programs. We thank Dr. A.G. McDonald for assistance in glc analyses, and Dr. C.P.J. Glaudemans (National Institutes of Health, Bethesda, Maryland) for reference samples.

1. L. Kenne and B. Lindberg. *In* The polysaccharides. Vol. 2. *Edited by* G.O. Aspinall. Academic Press, New York. 1983. pp. 287–363.
2. K. Dziewiszek and A. Zamojski. Carbohydr. Res. **150**, 163 (1986).
3. G.J.P.H. Boons, P.A.M. Van der Klein, G.A. Van Der Marel, and J.H. Van Boom. Recl. Trav. Chim. Pays-Bas, **107**, 507 (1988).
4. G.J.P.H. Boons, G.A. Van Der Marel, and J.H. Van Boom. Tetrahedron Lett. **30**, 229 (1989).
5. A. Dondoni, G. Fantin, M. Fogagnolo, and A. Medici. Tetrahedron, **43**, 3533 (1987).
6. A. Dondoni, G. Fantin, M. Fogagnolo, A. Medici, and P. Pedrini. J. Org. Chem. **54**, 693 (1989).
7. G.O. Aspinall, A.G. McDonald, and H. Pang. Carbohydr. Res. **231**, 13 (1992).
8. G.O. Aspinall, A.G. McDonald, and R.K. Sood. Can. J. Chem. **72**, 247 (1994).
9. R. Young and G.A. Adams. Can. J. Chem. **44**, 32 (1966).
10. S.J. Danishefsky, W.H. Pearson, D.F. Harvey, C.J. Maring, and J.P. Springer. J. Am. Chem. Soc. **107**, 1256 (1985).
11. K. Omura and D. Swern. Tetrahedron, **34**, 1651 (1978).
12. A. Dondoni, A. Marra, and D. Perrone. J. Org. Chem. **58**, 275 (1993).
13. A. Dondoni, G. Fantin, M. Fogagnolo, A. Medici, and P. Pedrini. J. Org. Chem. **54**, 702 (1989).
14. D.B. Dess and J.C. Martin. J. Org. Chem. **48**, 410 (1983).
15. G.J. Gerwig, J.P. Kamerling, and J.F.G. Vliegenthart. Carbohydr. Res. **62**, 349 (1978).
16. D.R. Hicks and B. Fraser-Reid. Synthesis, 203 (1974).
17. H.B. Boren, K. Eklind, P.J. Garegg, B. Lindberg, and A. Pillotti. Acta Chem. Scand. **26**, 4143 (1972).
18. G.J.P.H. Boons, G.A. Van Der Marel, J.T. Poolman, and J.H. Van Boom. Recl. Trav. Chim. Pays-Bas, **108**, 339 (1989).
19. P.J. Garegg, S. Oscarson, and M. Szönyi. Carbohydr. Res. **205**, 125 (1990).
20. G.J.P.H. Boons. Ph.D. Thesis, University of Leiden, The Netherlands, 1991.
21. A. Lipták, I. Jodal, and P. Nanasi. Carbohydr. Res. **44**, 1 (1975).
22. S. Hanessian and P. Lavallée. Can. J. Chem. **53**, 2975 (1975).
23. R. Julina and A. Vasella. Helv. Chim. Acta, **68**, 819 (1985).
24. P.A.J. Gorin. Carbohydr. Res. **101**, 13 (1982).

Can. J. Chem. Downloaded from www.nrcresearchpress.com by 203.198.23.82 on 09/08/12
For personal use only.

Syntheses of methyl glycosides of 6-deoxyheptoses

GERALD O. ASPINALL,[1] ARMANDO G. MCDONALD,[2] AND RAMESH K. SOOD[3]

Department of Chemistry, York University, North York, Toronto, ON M3J 1P3, Canada

Received May 20, 1993

This paper is dedicated to Professors David B. MacLean and Ian D. Spenser

GERALD O. ASPINALL, ARMANDO G. MCDONALD, and RAMESH K. SOOD. Can. J. Chem. **72**, 247 (1994).

Methyl α-D-glycopyranosides of 6-deoxy-D-*altro*-heptose, 6-deoxy-D-*manno*-heptose, and 6-deoxy-D-*talo*-heptose have been prepared. Displacements of methyl 2,3,4-tri-*O*-benzylhexopyranoside 6-trifluoromethanesulfonates with potassium cyanide, followed by reduction of the resulting heptopyranosidurononitriles with diisobutylaluminum hydride, hydrolysis of the imine, further reduction with sodium borohydride, and catalytic *O*-debenzylation, give the corresponding methyl 6-deoxyheptopyranosides. Configurational change at C-4 of methyl 6-deoxy-7-*O*-*tert*-butyldiphenylsilyl-α-D-*manno*-heptopyranoside to give the *talo* isomer was effected by oxidation followed by stereoselective reduction. ^{1}H nuclear magnetic resonance data of the glycosides, and gas chromatography of acetylated glycosides of (*R*)- and (*S*)-2-butanol serve to establish ring and enantiomeric configurations of the parent sugars when these are encountered as constituents of lipopolysaccharides or extracellular carbohydrate polymers, as in *Campylobacter* species.

GERALD O. ASPINALL, ARMANDO G. MCDONALD et RAMESH K. SOOD. Can. J. Chem. **72**, 247 (1994).

On a préparé les α-D-glycopyranosides de méthyle des 6-désoxy-α-D-*altro*-heptose, 6-désoxy-D-*manno*-heptose et 6-désoxy-D-*talo*-heptose. Les déplacements des 6-trifluorométhanesulfonates des 2,3,4-tri-*O*-benzylhexopyranosides de méthyle par le cyanure de potassium, suivis par la réduction des heptopyranosidurononitriles par l'hydrure de diisobutylaluminium, une hydrolyse de l'imine, une nouvelle réduction par le borohydrure de sodium et finalement une *O*-débenzylation catalytique conduit aux 6-désoxyheptopyranosides de méthyles correspondants. Pour effectuer un changement de configuration en C-4 du 6-désoxy-7-*O*-*tert*-butyldiphénylsilyl-α-D-*manno*-heptopyranoside de méthyle dans le but d'obtenir l'isomère *talo*, on a procédé à une oxydation suivie par une réduction sélective. On a fait appel aux données de la résonance magnétique nucléaire du ^{1}H des glycosides et à la chromatographie gazeuse des glycosides acétylés par les (*R*)- et (*S*)-2-butanol pour établir la grandeur des cycles et les configurations énantiomères des sucres parents rencontrés comme constituants des lipopolysaccharides ou comme hydrates de carbones polymériques extracellulaires, comme dans les espèces *Campylobacter*.

[Traduit par la rédaction]

Introduction

6-Deoxyheptoses are rare constituents of bacterial polysaccharides, and until very recently only two examples had been reported, 6-deoxy-D-*galacto*-heptose as a component sugar of the *Yersinia (Pasteurella) pseudotuberculosis* type II A lipopolysaccharide (LPS) (1), and 6-deoxy-D-*altro*-heptose as a constituent of the polysaccharide antigen from the Gram-positive *Eubacterium saburreum*, strain L 49 (2). In a series of investigations on the lipopolysaccharides from *Campylobacter* species further examples have been found. The O antigen chains in LPS from *C. jejuni* serotypes O:23 and O:36 have been shown to contain units of four closely related types, →3)-β-D-Glc*p*NAc-(1 → 3)-α-D-Gal*p*-(1 → 2)-α-*altro*-Hep*p*-(1-, in which the variable heptose residues differed in the presence or absence of deoxygenation at C-6 and methylation at O-3 (3), but were of unspecified enantiomeric configurations. One of the variants was 6-deoxy-α-*altro*-heptose, but of different ring size from that from the *E. saburreum* polysaccharide. From another *Campylobacter* strain, *C. coli* serotype O:30, a water-soluble extracellular antigenic polymer has been characterized as a teichoic acid-like structure with a poly(ribitol phosphate) backbone with pendant glycobiosyl units, 6-d-Hep*p*-(1 → 3)-β-D-Glc*p*NAc-(1-. As with the 6-deoxy-α-*altro*-heptose, the relative configuration of this deoxyheptose constituent was established by nmr correlation spectroscopy and shown to be β-*talo* (4), but without designation of absolute configuration. In both instances it was necessary to synthesize reference compounds of defined enantiomeric configuration from which to provide, separately, diastereomeric mixtures of (*R*)- and (*S*)-2-butyl glycoside acetates (5) for comparison with the corresponding derivatives from the polysaccharide constituents.

Garegg, Lindberg, and co-workers (6, 7) have reported syntheses of 6-deoxyheptoses with the D-*manno* and D-*galacto* configurations by homologations at C-6 of the corresponding methyl 2,3,4-tri-*O*-benzyl-hexodialdo-1,5-pyranosides by reaction with methoxymethylenetriphenylphosphorane, but with rather unsatisfactory yields. We describe here an alternative approach with the cyanide displacement of 2,3,4-tri-*O*-benzyl-α-D-glycopyranoside 6-sulfonate esters used by Baer et al. (8) in the preparation of 6-deoxy-D-*gluco*-heptopyranosidurononitriles, followed by a two-step reduction involving treatment with diisobutylaluminum hydride (DIBAH), hydrolysis of the resulting imine, and further reduction with sodium borohydride. In the event this proved to be a fortunate choice for the synthesis of the *altro* derivative since, as reported in the accompanying paper (9), the attempted formation of the α-D-*altro*-hexodialdo-1,5-pyranoside by oxidation of methyl 2,3,4-tri-*O*-benzyl-α-D-altropyranoside (**1**) (10) was accompanied by configurational inversion at C-5 with the formation of the corresponding β-L-*galacto* derivative as the major product.

Results and discussion

Altrose derivative **1** was converted into the trifluoromethanesulfonate for immediate displacement by cyanide to give the 6-deoxyheptosidurononitrile **2**. Two-step reduction of **2** with DIBAH, with hydrolysis of the imine and further treatment with sodium borohydride, afforded methyl 2,3,4-tri-*O*-benzyl-6-deoxy-α-D-*altro*-heptopyranoside (**3**) in adequate yield, and

[1]Author to whom correspondence may be addressed.

[2]Present address: Forest Research Institute, Private Bag 3020, Rotorua, New Zealand.

[3]Present address: Univax Biologicals Inc., 12280 Wilkins Ave., Rockville, MD 20852, U.S.A.

Can. J. Chem. Downloaded from www.nrcresearchpress.com by 195.246.54.202 on 09/08/12
For personal use only.

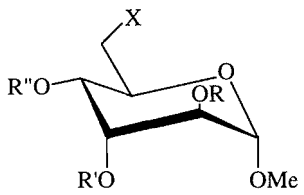

1 R = R' = R" = Bn; X = OH
2 R = R' = R" = Bn; X = CN
3 R = R' = R" = Bn; X = CH_2OH
4 R = R' = R" = H; X = CH_2OH
5 R = R' = R" = Ac; X = CH_2OAc

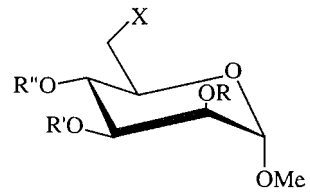

6 R = R' = R" = Bn; X = OH
7 R = R' = R" = Bn; X = CN
8 R = R' = R" = Bn; X = CH_2OH
9 R = R' = R" = H; X = CH_2OH
10 R = R' = R" = Ac; X = CH_2OAc
11 R = R' = R" = H; X = $CH_2OTBDPS$

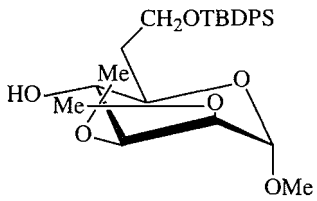

12 TBDPS = *tert*-butyldiphenylsilyl

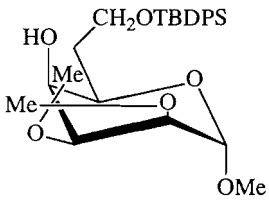

13

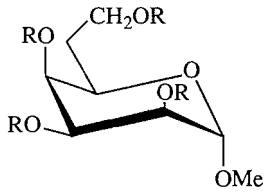

14 R = H
15 R = Ac

thence, by catalytic hydrogenolysis over palladium on carbon, methyl 6-deoxy-α-D-*altro*-heptopyranoside (**4**). For further analytical and spectroscopic characterization a portion of **4** was converted into the tetra-*O*-acetyl derivative (**5**). Hydrolysis of a sample of methyl glycoside **4** followed by reduction and acetylation furnished the 6-deoxyheptitol hexaacetate, which was indistinguishable by gas–liqud chromatography (glc) from the component in the *C. jejuni* serotypes O:23 and O:36 polysaccharide hydrolyzates (3).

In identical manner methyl 2,3,4-tri-*O*-benzyl-α-D-mannopyranoside (**6**) (6) was converted successively into the 6-deoxyheptosidurononitrile (**7**), methyl 2,3,4-tri-*O*-benzyl-6-deoxy-α-D-*manno*-heptopyranoside (**8**), the parent methyl glycoside (**9**), and for further characterization the tetra-*O*-acetyl derivative (**10**) of **9**. The previously prepared (6) methyl 6-deoxy-α-D-*manno*-heptopyranoside (**8**) served as a convenient starting material for the synthesis of the C-4 epimer with the *talo* configuration. Protection of O-7 in **8** as the *tert*-butyldiphenylsilyl derivative **11** was followed by isopropylidenation with 2,2-dimethoxypropane in acetone to give methyl 6-deoxy-2,3-di-*O*-isopropylidene-7-*O*-*tert*-butyldiphenylsilyl-α-D-*manno*-heptopyranoside (**12**). The key step in the overall transformation was the Swern oxidation (dimethyl sulfoxide – oxalyl chloride) (11) from which reaction the intermediate deoxyheptosid-4-ulose was immediately treated with sodium borohydride. The reduction proceeded with high diastereoselectivity, only traces of the *manno* starting material (**12**) being detected in the reaction product, and the desired *talo* isomer (**13**) was isolated in chromatographically and spectroscopically homogeneous form in 85% yield. The configurational change at C-4 was confirmed by changes in the ^1H nmr spectrum, notably at H-4, which showed coupling constants $J_{3,4}$ = 9.2 Hz and $J_{4,5}$ = 9.4 Hz. Deprotection of **13** afforded methyl 6-deoxy-α-D-*talo*-heptopyranoside (**14**), which was further characterized as the tetra-*O*-acetate (**15**).

Hydrolysis of **14** and conversion of the reducing sugar into the 6-deoxyheptitol hexaacetate gave a derivative that was indistinguishable by glc from that formed from the 6-deoxyheptose constituent of the *C. coli* O:30 carbohydrate polymer. It was then observed that the three diastereomeric 6-deoxyheptitol hexaacetates could not be differentiated on glc columns. However, hydrolysis of the methyl glycosides **4**, **9**, and **14**, followed by glycosidation with (*R*)- and (*S*)-2-butanol and acetylation, gave in each case equilibrium mixtures of 2-butyl glycoside tetraacetates whose identities were established by chemical ionization (ci) glc-ms. These sets of derivatives served two purposes. The primary purpose was to distinguish the mixtures formed *either* from each of the enantiomeric alcohols and a given sugar anantiomer *or* from an enantiomerically pure alcohol and each sugar enantiomer (Table 1). Thus the reactions of sugars in polysaccharide hydrolyzates with a chiral 2-butanol gave the corresponding mixtures of chiral glycosides whose retention times defined the enantiomeric sugars of immediate interest as 6-deoxy-D-*altro*-heptose from *Campylobacter jejuni* serotype O:23 (3) and 6-deoxy-D-*talo*-heptose from the teichoic acid-like polymer from *C. coli* serotype O:30 (4). In addition the retention times of at least some of the components from each set of 2-butyl glycoside tetraacetates from diastereomeric sugars were sufficiently different to distinguish the parent 6-deoxyheptoses.

The ^1H nmr data were obtained from 1D spectra and, with the aid of ^1H COSY correlations, resonances were assigned for individual carbon-bound protons for the methyl glycosides **4**, **9**, and **14** (Table 2), and the corresponding tetraacetates **5**, **10**, and **15** (Table 2). The vicinal coupling constants $J_{n,n+1}$ were in accord with all glycoside derivatives in the $^4C_1$ conformation. A long-range W coupling between H-2 and H-4 was detected in the COSY spectra of **15**. The observation of such a coupling had been a key factor in the assignment of the *talo* configuration for the 6-deoxyheptose constituent of *C. coli* polymer (4).

Experimental

General procedures

Unless otherwise stated, experimental methods and spectroscopic analyses were performed as described in the previous paper (9).

Derivatives of 6-deoxyheptoses for glc and glc–ms analysis

(*a*) Methyl 6-deoxyheptopyranosides were hydrolyzed in 1 M trifluoroacetic acid for 4 h at 100°C, and the hydrolyzates were concen-

Can. J. Chem. Downloaded from www.nrcresearchpress.com by 195.246.54.202 on 09/08/12
For personal use only.

TABLE 1. The glc retention times of (*R*)- and (*S*)-2-butyl glycoside tetra-*O*-acetates of 6-deoxyheptoses

Parent sugar configuration	Retention times (min)[a]							
	(*R*)-2-Butyl glycosides				(*S*)-2-Butyl glycosides			
6-Deoxy-D-*altro*-	18.57	20.25	20.37	21.68	18.38	20.34	20.65	21.96
6-Deoxy-D-*manno*-	17.59	19.85	19.95	21.54	17.19	19.69	20.23	
6-Deoxy-D-*talo*-	18.73	20.22	22.74		19.29	19.94	22.62	

[a]Gas–liquid chromatography was performed on a narrow bore DB-23 (30 m × 0.25 mm) column, 200°C (10 min), 200° → 240°C at 2°/min.

TABLE 2. The ^{1}H nmr chemical shift data (ppm) and vicinal coupling constants (Hz) for methyl 6-deoxy-α-D-heptopyranosides **4**, **9**, and **14**, and their respective 2,3,4,7-tetra-*O*-acetyl derivatives **5**, **10**, and **15**[a]

Sugar ring configuration	H-1 ($J_{1,2}$)	H-2 ($J_{2,3}$)	H-3 ($J_{3,4}$)	H-4 ($J_{4,5}$)	H-5	H-6 ($J_{5,6}$)	H-6′ ($J_{5,6'}$)	H-7
altro (**4**)	4.54 (2.9)	3.73 (2.4)	3.85 (3.1)	3.67 (8.4)	3.96	1.95 (2.9)	1.75 (10.3)	3.74
manno (**8**)	4.65 (1.5)	3.87 (3.4)	3.67 (9.5)	3.45 (9.7)	3.60	2.06 (2.4)	1.67 (7.8)	3.57
talo (**14**)	4.77 (bs)	3.78 (~1)	3.79 (3.3)	3.72 (~1)	3.91	1.93 (9.9)	1.75 (4.2)	3.67
altro (**5**)	4.58 (~1)	4.94 (3.9)	5.21 (3.5)	5.00 (9.5)	4.17	1.97 (3.0)	1.78 (7.5)	4.27
manno (**10**)	4.65 (1.5)	5.24 (3.4)	5.31 (10.0)	5.12 (9.9)	3.87	1.90 (2.9)	1.83	4.23
talo (**15**)	4.77 (1.1)	5.10 (2.5)	5.29 (3.5)	5.21 (<2)	4.13	2.01 (12.2)	1.78 (3.2)	4.22

[a]Resonances of methyl glycoside and *O*-acetyl protons are omitted.

trated and converted into 6-deoxyheptitol hexaacetates for glc analysis (12).

(*b*) Hydrolyzates were converted in chiral 2-butyl glycoside tetraacetates as described by Gerwig et al. (5) for glc analysis. The identities of the desired chiral glycosides were confirmed by ci glc–ms.

*Methyl 2,3,4-tri-*O*-benzyl-6-deoxy-*α*-D-*altro*-heptopyranosyluronononitrile 2*

Triflic anhydride (0.79 mL, 4.68 mmol) was added to a solution of 2,6-di-*tert*-butylpyridine (1.16 mL, 5.1 mmol) in dry dichloromethane at −15°C and, after stirring for 10 min, a solution of **1** (1.08 g) in dry dichloromethane was added dropwise and the mixture was stirred at −15°C for 1 h. The solution was poured into aqueous 5% sodium hydrogen carbonate, the organic layer was separated, dried, and concentrated. The residual syrup in acetonitrile:water (9:1, 30 mL) was treated with potassium cyanide (0.24 g, 3.68 mmol) for 2.5 h at room temperature, the solution was concentrated, and the residue was dissolved in ethyl acetate, washed successively with 1 M HCl, aqueous saturated $NaHCO_3$, and water, dried, and concentrated. The residual syrup was chromatographed on silica gel (light petroleum – ethyl acetate, 3.5:1) to give compound **2** (0.9 g, 82%), $[\alpha]_D$ +85 (*c* 1.35); ir ν_{max}: 2250 (C≡N) cm^{-1}; ^{1}H nmr δ: 4.68–4.26 (m, 8H, H-1, H-5, 3 × CH_2Ph), 3.81 (t, 1H, H-2), 3.71 (d, 1H, H-3), 3.61 (3.61 (dd, 1H, $J_{3,4}$ 3.0 Hz, $J_{4,5}$ 9.66 Hz), 3.42 (s, 3H, OMe), 2.80 (dd, 1H, $J_{5,6}$ 3.08 Hz, $J_{6,6'}$ 16.7 Hz, H-6), and 2.5 (dd, 1H, $J_{5,6'}$ 8.3 Hz, H-6′). Anal. calcd. for $C_{29}H_{31}NO_5$: C 73.55, H 6.59, N 2.95; found: C 73.83, H 6.45, N 2.93.

*Methyl 2,3,4-tri-*O*-benzyl-6-deoxy-*α*-D-*altro*-heptopyranoside 3*

DIBAH (1 M in hexane, 0.73 mL) was added to a solution of **2** (0.314 g, 0.66 mmol) in dry toluene (5 mL) at 0°C; after 30 min a further quantity of DIBAH solution (0.2 mL) was added and reaction was terminated after 10 min by the addition of methanol (0.5 mL) followed by aqueous 2 M HCl (0.5 mL). The mixture was stirred for 45 min and filtered, the aqueous layer in the filtrate was extracted with ether, and the combined organic layers were washed with 2 M HCl, aqueous saturated $NaHCO_3$, and water, dried, and concentrated. Sodium borohydride (10 mg) was added to the residual syrup in methanol (5 mL); the solution was stirred at room temperature for 30 min before excess of hydride was destroyed by the addition of acetone, evaporated to dryness, and then evaporated again (×3) with methanol. The residue in ethyl acetate was washed successively with aqueous 2 M HCl, saturated $NaHCO_3$, and water, dried, and concentrated to a syrup that was chromatographed on silica gel (light petroleum – ethyl acetate, 2:1) to give **3** (0.168 g, 53%), $[\alpha]_D$ +87 (*c* 0.8); ^{1}H nmr δ: 4.67–4.26 (m, 8H, H-1, H-5, and 3 × CH_2Ph), 3.83–3.69 (m, 4H, H-2,3,7,7′), 3.56 (dd, 1H, $J_{3,4}$ 3.1 Hz, $J_{4,5}$ 9.2 Hz, H-4), 3.39 (s, 3H, OMe), 3.17 (t, 1H, exchanged with D_2O, OH), 2.13–2.05 (m, 1H, H-6), and 1.79 (m, 1H, H-6′). Anal. calcd. for $C_{29}H_{34}O_6$: C 72.78, H 7.16; found: C 72.68, H 7.21.

Methyl 6-deoxy-α-D-altro-heptopyranoside 4 and the tetra-O-acetyl derivative 5

Compound **3** (75 mg, 0.15 mmol) in ethanol (5 mL) was hydrogenolyzed over palladium 5% on carbon for 72 h. Filtration of the mixture and concentration of the filtrate afforded **4** (30 mg), $[\alpha]_D$ +100 (*c* 1.98, water); ^{13}C nmr (D_2O) δ_C: 100.6 ($^1J_{C,H}$ 166.9 Hz, C-1), 58.3 (C-7), 55.7 (OMe), 32.7 (C-6). Acetylation of a sample of **4** followed by chromatography on silica gel (light petroleum – ethyl acetate, 2.5:1) furnished tetraacetate **5**, which gave a single peak on glc (program A, isothermal at 200°C), $R_{[Me\ Ac_4\ \alpha\text{-D-}Manp]}$ 1.33, $[\alpha]_D$ +77 (*c* 1.01); ^{13}C nmr δ_C: 170.8, 169.9, 169.6, 169.2 (4 × CH_3CO), 98.5 ($^1J_{C,H}$ 167.3 Hz, C-1), 60.3 (C-7), 55.4 (OMe), 30.2 (C-6), 20.8, 20.75, 20.7, 20.6 (4 ×

Can. J. Chem. Downloaded from www.nrcresearchpress.com by 195.246.54.202 on 09/08/12
For personal use only.

CH_3CO). Anal. calcd. for $C_{16}H_{24}O_{10}$: C 51.05, H 6.42; found: C 51.13, H 6.41.

Methyl 2,3,4-tri-O-benzyl-6-deoxy-α-D-manno-heptopyranosyluruononitrile 7

Conversion of compound **6** (4.03 g, 8.68 mmol) into the triflate ester, and thence by reaction with potassium cyanide, as described for **2**, yielded **7** (2.43 g, 59%), $[\alpha]_D$ +44 (*c* 1.35); ir ν_{max}: 2240 (C≡N) cm^{-1}; ^1H nmr δ: 4.70 (s, 1H, H-1), 3.87 (dd, 1H, $J_{3,4}$ 8.9 Hz, H-3), 3.79 (dd, 1H, $J_{2,3}$ 2.8 Hz, H-2), 3.76 (dd, 1H, $J_{4,5}$ 9.1 Hz, H-4), 3.74 (dd, 1H, $J_{5,6}$ 5.5 Hz, $J_{5,6'}$ 2.9 Hz, H-5), 3.34 (s, 3H, OMe), 2.74 (dd, 1H, $J_{6,6'}$ 16.4 Hz, H-6), and 2.5 (m, 1H, H-6′). Anal. calcd. for $C_{29}H_{31}NO_5$: C 73.55, H 2.95, N 2.95; found: C 73.21, H 6.53, N 2.81.

Methyl 2,3,4-tri-O-benzyl-6-deoxy-α-D-manno-heptopyranoside 8

Reduction of **7** (1.8 g, 3.8 mmol) with DIBAH, as described for the preparation of **3**, yielded **8** (0.91 g, 50%), $[\alpha]_D$ +31 (*c* 1.8) (lit. (6) $[\alpha]_D$ +39); ^1H nmr δ: 4.66 (d, $J_{1,2}$ 1.8 Hz, H-1), 3.86 (dd, 1H, $J_{3,4}$ 9.0 Hz, H-3), 3.79 (dd, 1H, $J_{2,3}$ 2.8 Hz, H-2), 3.76 (m, 2H, H-5, H-7), 3.75 (dd, 1H, $J_{4,5}$ 8.8 Hz, H-4), 3.30 (s, 3H, OMe), 2.10 (m, 1H, H-6), and 1.84 (m, 1H, H-6′). Anal. calcd. for $C_{29}H_{34}O_6$: C 72.78, H 7.16; found: C 72.42, H 7.13.

Methyl 6-deoxy-α-D-manno-heptopyranoside 9 and the tetra-O-acetyl derivative 10

Hydrogenolysis of **8** (0.91 g, 1.90 mmol), as described for the conversion of **3** into **4**, afforded **9** (0.33 g, 84%); ^{13}C nmr (D_2O) δ_C: 100.9 ($^1J_{C,H}$ 170.2 Hz, C-1), 58.4 (C-7), 54.8 (OMe), 33.4 (C-6). Acetylation of a sample of **9** followed by chromatography on silica gel (light petroleum – ethyl acetate, 2.5:1) furnished tetraacetate **10**, which gave a single peak on glc (program A, isothermal at 200°C), $R_{[Me\ Ac_4\ \alpha\text{-D-Man}p]}$ 1.29, $[\alpha]_D$ +59 (*c* 1.65) (lit. (6) $[\alpha]_D$ +62); ^{13}C nmr δ_C: 170.8, 169.9, 169.85, 169.8 (4 × CH_3CO), 98.4 ($^1J_{C,H}$ 172.4 Hz, C-1), 60.2 (C-7), 55.0 (OMe), 30.4 (C-6), 20.8 (2C), 20.7, 20.6 (4 × CH_3CO). Anal. calcd. for $C_{16}H_{24}O_{10}$: C 51.05, H 6.42; found: C 51.30, H 6.33.

Methyl 6-deoxy-7-O-tert-butyldiphenylsilyl-α-D-manno-heptopyranoside 11

Imidazole (0.26 g, 2.4 equiv.) and *tert*-butyldiphenylsilyl chloride (0.523 g, 1.2 equiv.) were added successively to compound **10** (0.33 g, 1.59 mmol) in *N,N*-dimethylformamide (5 mL) and the mixture was stirred at 25°C for 16 h. Dichloromethane was added to the mixture, and the solution was washed with water, dried, concentrated, and chromatographed on silica gel (light petroleum – ethyl acetate, 1:4) to give **11** (0.446 g, 63%), $[\alpha]_D$ +43 (*c* 1.5); ^1H nmr δ: 7.66, 7.44–7.25 (m, 10H, aromatic), 4.64 (d, 1H, $J_{1,2}$ 0.9 Hz, H-1), 3.92 (dd, 1H, $J_{2,3}$ 3.3 Hz, H-2), 3.84 (m, 2H, H-7), 3.80 (dd, 1H, $J_{3,4}$ 8.8 Hz, H-3), 3.70 (dd, 1H, $J_{5,6}$ 4.2 Hz, H-5), 3.60 (dd, 1H, $J_{4,5}$ 9.4 Hz, H-4), 3.27 (s, 3H, OMe), 2.11 (m, 1H, H-6), 1.75 (m, 1H, H-6′), and 1.04 (s, 9H, *tert*-butyl). Exact Mass calcd. for $C_{24}H_{34}O_6Si$ + H: 447.2203; found: 447.2182.

Methyl 6-deoxy-2,3-O-isopropylidene-7-O-tert-butyldiphenylsilyl-α-D-manno-heptopyranoside 12

A solution of compound **11** (0.411 g, 9.21 mmol) in acetone (5 mL) containing 2,3-dimethoxypropane (0.4 mL) and *p*-toluenesulfonic acid (5 mg) was stirred at 25°C for 1 h. The reaction was quenched by the addition of $NaHCO_3$ (20 mg), the mixture was concentrated, and the residue in dichloromethane was washed successively with aqueous $NaHCO_3$ and water, dried, and concentrated. The residue was chromatographed on silica gel (light petroleum – ethyl acetate, 4:1) to give **12** (0.391 g, 87%), $[\alpha]_D$ +22 (*c* 1.05); ^1H nmr δ: 7.66, 7.45–7.26 (m, 10H, aromatic), 4.85 (s, 1H, H-1), 4.13 (dd, 1H, $J_{3,4}$ 9.2 Hz, H-3), 4.12 (dd, 1H, $J_{2,3}$ ~3 Hz, H-2), 3.85 (m, 2H, H-7), 3.73 (m, 1H, H-5), 3.60 (t, 1H, $J_{4,5}$ 9.4 Hz, H-4), 3.33 (s, 3H, OMe), 2.03 (m, 1H, H-6), 1.83 (m, 1H, H-6′), 1.53, 1.36 (2s, each 3H, $C(CH_3)_2$), 1.06 (s, 9H, *tert*-butyl). Exact Mass calcd. for $C_{27}H_{38}O_6Si$ + H: 487.2516; found: 487.2490. Anal. calcd. for $C_{27}H_{38}O_6Si$: C, 66.69, H 7.88; found: C 66.86, H 7.86.

Methyl 6-deoxy-2,3-O-isopropylidene-7-O-tert-butyldiphenylsilyl-α-D-talo-heptopyranoside 13

A solution of **12** (0.361 g, 0.74 mmol) in dichloromethane (5 mL) was added dropwise to a stirred mixture of Me_2SO (0.23 mL, 3.24 mmol) in dichloromethane (4 mL) and oxalyl chloride (1.2 mL, 0.24 mmol) in dichloromethane (10 mL) at −78°C, at which temperature the mixture was kept for 45 min. The reaction was quenched by the addition of triethylamine (2 mL) in dichloromethane (5 mL); it was stirred for 30 min at −78°C and then brought slowly to 20°C. The solution was diluted with dichloromethane (20 mL) and washed three times with water, dried, and concentrated. The residual 4-ulose was reduced by stirring with sodium borohydride (56 mg, 2 equiv.) in methanol (10 mL) at 25°C for 90 min. Excess of hydride was destroyed by the addition of acetone, the mixture was concentrated, evaporated with methanol (×3), and the residue was chromatographed on silica gel (light petroleum – ethyl acetate, 4:1) to give **13** (0.306 g, 85%), $[\alpha]_D$ +27 (*c* 0.82); ^1H nmr δ: 7.68–7.62, 7.46–7.26 (m, 10H, aromatic), 4.94 (s, 1H, H-1), 4.22 (dd, 1H, $J_{3,4}$ 5.1 Hz, H-3), 4.05 (dd, 1H, $J_{2,3}$ 6.7 Hz, H-2), 4.01 (t, 1H, $J_{4,5}$ 4.9 Hz, H-4), 3.88 (m, H, H-7), 3.79 (m, 1H, H-7′), 3.57 (d, 1H, $J_{5,6}$ <2 Hz, H-5), 3.38 (s, 3H, OMe), 2.04 (m, 1H, H-6), 1.81 (m, 1H, H-6′), 1.58, 1.38 (2s, each 3H, $C(CH_3)_2$), and 1.05 (s, 9H, *tert*-butyl). Exact Mass calcd. for $C_{27}H_{38}O_6Si$ + H: 487.2516; found: 487.2534. Anal. calcd. for $C_{27}H_{38}O_6Si$: C, 66.69, H 7.88; found: C 66.46, H 7.74.

Methyl 6-deoxy-α-D-talo-heptopyranoside 14

A solution of **13** (0.246 g, 5.06 mmol) in oxolane (5 mL) was treated with 1 M tetrabutylammonium fluoride in oxolane (1.4 mL) at 25°C for 30 min and concentrated. The residue was treated with aqueous saturated $NaHCO_3$ (20 mL), the mixture was extracted with ethyl acetate, and the extract was dried and concentrated. The residual product was heated in aqueous 2 M acetic acid (5 mL) at 80°C for 2 h, and the solution was concentrated. A solution of the residue in water was extracted with dichloromethane, and the aqueous layer was concentrated to a syrup that was chromatographed on silica gel (methanol–dichloromethane, 1:9) to give **14** (90 mg, 86%), $[\alpha]_D$ +84 (*c* 3.0, water); ^{13}C nmr (D_2O) δ_C: 101.6 ($^1J_{C,H}$ 171.3 Hz, C-1), 58.3 (C-7), 55.0 (OMe), 33.0 (C-6). Acetylation of a sample of **9** followed by chromatography on silica gel (light petroleum – ethyl acetate, 2.5:1) furnished tetraacetate **15**, which gave a single peak on glc (program A, isothermal at 200°C); $R_{[Me\ Ac_4\ \alpha\text{-D-Man}p]}$ 2.25, $[\alpha]_D$ +81 (*c* 1.02); ^{13}C nmr δ_C: 170.7, 170.3, 169.9, 169.5 (4 × CH_3CO), 99.4 ($^1J_{C,H}$ 172.2 Hz, C-1), 60.4 (C-7), 55.1 (OMe), 29.9 (C-6), 20.8, 20.7, 20.6, 20.5 (4 × CH_3CO). Anal. calcd. for $C_{16}H_{24}O_{10}$: C 51.05, H 6.42; found: C 50.87, H 6.28.

Acknowledgements

We thank the Natural Sciences and Engineering Research Council of Canada for financial support through its strategic and research grants programs. We thank Dr. Henrianna Pang and her associates for accurate mass determinations and for the ci glc–ms experiments.

1. C.C. Hellerqvist, B. Lindberg, K. Samuelsson, and R.R. Brubaker. Acta Chem. Scand. **26**, 1389 (1972).
2. J. Hoffman, B. Lindberg, J. Lönngren, and T. Hofstad. Carbohydr. Res. **47**, 261 (1976).
3. G.O. Aspinall, A.G. McDonald, and H. Pang. Carbohydr. Res. **231**, 13 (1992).
4. G.O. Aspinall, A.G. McDonald, H. Pang, L.A. Kurjanczyk, and J.L. Penner. J. Biol. Chem. **268**, 18321 (1993).
5. G.J. Gerwig, J.P. Kamerling, and J.F.G. Vliegenthart. Carbohydr. Res. **62**, 349 (1978).
6. H.B. Borén, K. Eklind, P.J. Garegg, B. Lindberg, and A. Pilotti. Acta Chem. Scand. **26**, 4143 (1972).
7. K. Eklind, P.J. Garegg, B. Lindberg, and A. Pilotti. Acta Chem. Scand. **28**, 260 (1974).
8. H.H. Baer, R.L. Breton, and Y. Shen. Carbohydr. Res. **200**, 377 (1990).

Can. J. Chem. Downloaded from www.nrcresearchpress.com by 195.246.54.202 on 09/08/12
For personal use only.

9. N.K. Khare, R.K. Sood, and G.O. Aspinall. Can. J. Chem. **72**, 237 (1994).
10. R. Julina and A. Vasella. Helv. Chim. Acta, **68**, 819 (1985).
11. K. Omura and D. Swern. Tetrahedron, **54**, 1651 (1978).
12. J.H. Sawardeker, J.H. Sloneker, and A. Jeanes. Anal. Chem. **37**, 1602 (1967).

Can. J. Chem. Downloaded from www.nrcresearchpress.com by 195.246.54.202 on 09/08/12
For personal use only.

NMR and molecular modeling study of active and inactive taxol analogues in aqueous and nonaqueous solution[1]

HOWARD J. WILLIAMS, A. IAN SCOTT,[2] AND REINER A. DIEDEN
Center for Biological NMR, Department of Chemistry, Texas A&M University, College Station, TX 77843-3255, U.S.A.

AND

CHARLES S. SWINDELL,[2] LISA E. CHIRLIAN, MICHELLE M. FRANCL, JULIA M. HEERDING, AND NANCY E. KRAUSS
Department of Chemistry, Bryn Mawr College, 101 North Merion Avenue, Bryn Mawr, PA 19010-2899, U.S.A.

Received June 9, 1993

This paper is dedicated to Professor David B. MacLean and Ian D. Spenser

HOWARD J. WILLIAMS, A. IAN SCOTT, REINER A. DIEDEN, CHARLES S. SWINDELL, LISA E. CHIRLIAN, MICHELLE M. FRANCL, JULIA M. HEERDING, and NANCY E. KRAUSS. Can. J. Chem. **72**, 252 (1994).

The conformations of the biologically active taxol analogs Taxotere®, **3R**, **4R**, and **4S**, and the biologically inactive analog **3S** were evaluated in $CDCl_3$ and DMSO–water solution using ^1H NMR coupling constant and NOESY data and molecular modeling. The solution structures of Taxotere® were very similar to those detected previously for taxol. The A-ring side chain conformations of analogs **3** and **4** could not be defined with the same precision as had been possible for taxol, but the conformational possibilities could be significantly limited by the data. Analogs **3R**, **4R**, and **4S** (but not **3S**) can mimic the dominant conformation of taxol in chloroform, but no logical relationship between biological activity and aqueous solution conformation could be detected.

HOWARD J. WILLIAMS, A. IAN SCOTT, REINER A. DIEDEN, CHARLES S. SWINDELL, LISA E. CHIRLIAN, MICHELLE M. FRANCL, JULIA M. HEERDING et NANCY E. KRAUSS. Can. J. Chem. **72**, 252 (1994).

Faisant appel aux constantes de couplage en RMN du ^1H obtenues pour des solutions de $CDCl_3$ ou aqueuses de DMSO, à des données NEOSY et à de la modélisation moléculaire, on a évalué les conformations des analogues biologiquement actifs du taxol, les Taxotere® **3R**, **4R** et **4S**, et de l'analogue biologiquement inactif **3S**. Les structures du Taxotere® en solution sont très semblables à celles détectées antérieurement pour le taxol. Les conformations de la chaîne latérale du cycle A des analogues **3** et **4** n'a pas été déterminée avec la précision qui avait été possible pour le taxol; toutefois, les possibilités conformationnelles ont pu être sérieusement limitées par les données. Les analogues **3R**, **4R** et **4S** (mais pas le **3S**) peuvent reproduire la conformation dominante du taxol dans le chloroforme; toutefois, on ne peut détecter aucune relation logique entre l'activité biologique et la conformation en solution aqueuse.

[Traduit par la rédaction]

Introduction

The diterpenoid antineoplastic drug taxol (1, 2) is distinct from other anti-mitotic agents, such as the vinca alkaloids, in that it promotes the assembly and inhibits the disassembly of microtubules, both in vitro and in vivo (3). Whereas the structure–activity profile that is emerging[3] hints at an intriguing interaction between taxol and its microtubular binding site(s), there is currently available no molecular-level structural information on the taxol–microtubule complex.[4]

Recent spectroscopic and molecular modeling studies (6) have been effective in determining the conformations of the flexible taxol A-ring side chain in hydrophobic and hydrophilic media as a preliminary step toward filling this gap. In hydrophobic media, taxol was found to adopt mainly the A-ring side chain H-C2′-C3′-H *gauche* conformation observed in the solid state structure of Taxotere®, with the alternative H-C2′-C3′-H *gauche* conformation (having the 2′-OH hydrogen bonded to the 4-OAc group) being a minor but detectable species by vibrational circular dichroism spectroscopy. NOESY data indicated little interaction between the A-ring side chain and the diterpenoid portion of the structure in hydrophobic media and suggested the side chain to be rather extended (6*e*). In hydrophilic media, however, the A-ring side chain H-C2′-C3′-H *anti* conformation was found by ^1H NMR spectroscopy to be dominant and the side chain was shown through NOESY experiments to interact more strongly with the diterpenoid substructure in a more compact, somewhat globular conformation (6*e*).

Therefore, the question arose as to whether these conformational features could be related to the biological activities of the taxol analogs Taxotere® (7), the baccatin III *R*- and *S*-*N*-benzoylisoserine esters **3R** and **3S**, and the baccatin III *R*- and *S*-phenyllactate esters **4R** and **4S**, respectively (8). Previously, **3R** and **3S** were shown to possess divergent microtubule assembly activities, **3R** being "active" and **3S** inactive, whereas **4R** and **4S** were essentially equally active. Herein, we provide NMR and molecular modeling data on the solution conformations of these compounds in both hydrophobic and hydrophilic media.

Results

Although in Taxotere® (**2**) the acetoxy group at C-10 is replaced by a hydroxyl group, a structural alteration known to have little effect on biological activity, the main difference between taxol (**1**) and the five analogs studied consists of changes in the C-13 side chain substitution pattern and in the configuration at C2′. In Taxotere® (**2**) the side chain benzamide is replaced by an *O*-*tert*-butylcarbamate group, whereas analogs **4** are lacking it altogether; in analogs **3**, the 3′-Ph is absent. Taxotere®, **3R**, and **4R** have the natural *R* configuration at C2′,

[1]Dedicated to the careers of Dave MacLean and Ian Spenser whose love of natural products and elegant experimental work have enriched the field with so many structural and biosynthetic discoveries.

[2]Authors to whom correspondence may be addressed.

[3]For a recent review see ref. 4*a*; for additional recent developments, ref. 4*b*.

[4]A preliminary photo affinity labeling report has appeared (5).

Can. J. Chem. Downloaded from www.nrcresearchpress.com by 195.246.54.202 on 09/08/12
For personal use only.

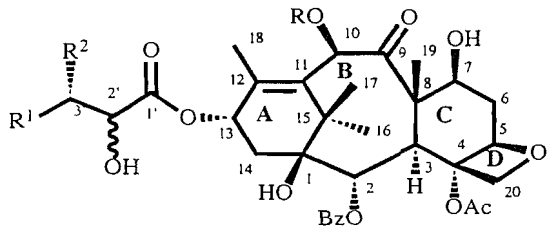

1 R = Ac; R^1 = Ph; R^2 = BzO_2CNH; 2'*R* Taxol
2 R = H; R^1 = Ph; R^2 = $tBuO_2CNH$; 2'*R* Taxotere
3R R = Ac; R^1 = H; R^2 = BzO_2CNH; 2'*R*
3S R = Ac; R^1 = H; R^2 = BzO_2CNH; 2'*S*
4R R = Ac; R^1 = Ph; R^2 = H; 2'*R*
4S R = Ac; R^1 = Ph; R^2 = H 2'*S*

FIG. 1. Structures for compounds studied, with numbering system.

while **3S** and **4S** have the *S* configuration. Configurational variation at C2′ is of interest because the 2′-OH plays an essential role in the structure–activity profile of taxol.

Our earlier (6*e*) experiments with taxol indicated that its conformation, as judged by the side chain coupling constants and nOe's observed, was quite invariant for solutions in DMSO-d_6 or D_2O:DMSO, 3:7 (v/v), as hydrophilic solvent systems. Obtaining high-quality spectra in pure water solution is difficult due to solubility problems, making extensive 2-D studies impractical, so DMSO–H_2O solvent mixtures were used for these experiments.

The NMR spectral properties for compounds **2–4** in the above media are assembled in Tables 1–4. Corresponding molecular modeling studies are summarized in Tables 5–14.[5] Due to the close resemblance of the different spectra to each other and to that of taxol **1**, in most cases the signals were readily assigned and COSY spectra were essentially used for confirmation. However, the NOESY data were essential for the confirmation of the assignments of the different methyl groups and especially for the determination of spatial relationships between different protons.

Taxotere® (2)

In $CDCl_3$, the characteristic triplet of H13 at 6.19δ shows COSY cross-peaks with the $H14_{\alpha,\beta}$ doublet at 2.25δ as well as the singlet of Me18 at 1.89δ. Correlations with $H20_\alpha$ (4.30δ and H2 (5.66δ) identify the signal at 3.89δ as H3. $H20_\alpha$ is coupled to $H20_\beta$ (4.16δ), which is overlapping with H7. The latter shows couplings to $H6_\alpha$ (2.57δ) and $H6_\beta$ (1.85δ, under Me18) and H5 (4.92δ), the latter correlated to $H6_\alpha$ and $H6_\beta$. Finally, the NH signal (5.41δ) is coupled to H3′ (5.24δ), which shows a cross-peak to H2′ at 4.60δ. A correlation between this signal and the broad peak at 3.35δ identifies the latter as OH2′.

The NOESY spectrum shows nOe's equivalent to those observed earlier for taxol (6*e*) and permits the assignment of the remaining methyl groups: Me16 (1.11δ) and Me17 (1.21δ) are differentiated through their dipolar couplings to H2 and H13, respectively. H2 exhibits an nOe cross-peak to Me19 (1.73δ) while H10 is correlated to Me18. However, with the exception of an nOe between *o*-OBz and $H20_\alpha$, no dipolar couplings between side chain protons and the large ring system are observed.

[5]Tables 5–14 may be purchased from: The Depository of Unpublished Data, Document Delivery, CISTI, National Research Council Canada, Ottawa, Canada K1A 0S2.

TABLE 1. Chemical shift data for compounds **2–4** in $CDCl_3$ (δ, ppm)

^1H	δ **2**	δ **3R**	δ **3S**	δ **4R**	δ **4S**
2	5.66	5.60	5.60	5.57	5.59
3	3.89	3.75	3.79	3.69	3.75
5	4.92	4.91	4.91	4.87	4.89
6α	2.57	2.50	2.51	2.47	2.50
6β	1.85	1.81	1.82	1.80	1.82
7	4.20	4.39	4.39	4.32	4.36
10	5.18	6.24	6.25	6.18	6.22
13	6.19	6.16	6.16	6.10	6.16
14α	2.25	2.30	2.27	2.07	2.26
14β	2.25	2.22	2.16	2.07	2.11
16	1.11	1.08	1.08	1.07	1.08
17	1.21	1.18	1.18	1.19	1.18
18	1.89	1.80	1.95	1.67	1.79
19	1.73	1.61	1.62	1.53	1.61
20α	4.30	4.26	4.25	4.22	4.23
20β	4.16	4.09	4.09	4.07	4.09
OAc-4	2.36	2.39	2.33	2.16[b]	2.21[b]
OAc-10	—	2.18	2.18	2.18[b]	2.19[b]
o-Bz-2	8.08	8.01	8.00	8.01	7.99
m-Bz-2	7.48	7.42	7.42	7.45	7.43
p-Bz-2	7.59	7.56	7.56	7.58	7.56
2′	4.60	4.44	4.42	4.46	4.44[d]
3′a	5.24	3.84	3.99	3.08	3.22
3′b	—	3.84	3.79	3.04	2.96
NH	5.41	6.54	6.54	—	—
o-Ph-3′	7.35	—	—	7.15	7.23
m-Ph-3′	7.35	—	—	7.26	7.29
p-Ph-3′	7.31	—	—	7.2[c]	7.23
o-NHBz	—	7.70	7.70	—	—
m-NHBz	—	7.38	7.36	—	—
p-NHBz	—	7.47	7.47	—	—
1-OH	—	—	—	—	—
7-OH	—	—	—	—	—
2′-OH	—	3.35	—	—	—
10-OH	—	—	—	—	—
t-Bu	1.32	—	—	—	—

By analogy with the major chloroform solution conformer observed for taxol (6) and in agreement with the results of Dubois et al. (6*f*), we propose that Taxotere® adopts to a large degree low-energy conformer **6** (Table 5; Fig. 2). Conformer **6** is very similar to the conformer exhibited by Taxotere® in the solid state (9). It is consistent with hydrogen bonding between the 2′-OH and the side chain ester carbonyl oxygen detected for taxol by vibrational circular dichroism (VCD), a technique sensitive to chiral environments near hydrogen bonds (10), and for analogs **3** and **4** in chloroform solution[6] (see below) and which seems very likely to obtain for Taxotere® in the same solvent. The low value for $J_{H2'-H3'}$ calculated for **6** must be increased by a degree of rotational averaging to that observed experimentally for Taxotere® in chloroform (4.5 Hz).

In DMSO–D_2O solution, NMR assignments are also straightforward, and the Ph-group protons are also well resolved. The two protons $H14_\alpha$ and $H14_\beta$ (1.86 and 1.70δ) show COSY cross-peaks to H13 (5.83δ). H2 (5.39δ) and H3 (5.64δ) are correlated as well. $H6_\alpha$ (2.24δ) and $H6_\beta$ (1.60δ) show cross-peaks to each other as well as to the broad multiplet at 4.0δ, resulting from the overlapping signals of H7, $H20_\alpha$, and

[6]T.B. Freedman, Syracuse University. Personal communication (1993).

Can. J. Chem. Downloaded from www.nrcresearchpress.com by 195.246.54.202 on 09/08/12
For personal use only.

TABLE 2. Coupling constants for compounds **2–4** in $CDCl_3$ (*J*, Hz)

^{1}H *J*	*J* **2**	*J* **3R**	*J* **3S**	*J* **4R**	*J* **4S**
2–3	7.1	7.1	7.1	7.0	7.0
5–6α	9.5	9.6	9.6	10.6	7.6
5–6β	—	1.5	2.2	2.9	2.0
6α–6β	14.7	14.6	14.8	14.7	14.9
6α–7	6.5	6.8	6.7	6.7	6.8
6β–7	—	10.7	10.9	10.9	10.8
13–14α	8.5	9.2	7.9	8.9	7.6
13–14β	8.5	9.2	7.9	8.9	7.6
13–18	—	s[a]	s	s	s
14α–14β	15.5	15.5	15.4	—	15.3
20α–20β	8.4	8.5	8.4	8.5	8.4
o–*m*OBz	7.7	6.8	7.8	8.4	8.0
o–*p*OBz	s	s	s	s	s
m–*p*OBz	7.6	7.2	7.5	7.5	7.4
2′–3′a	4.5	4.5	3.4	5.9	4.4
2′–3′b	—	4.5	5.4	6.1	8.1
3′–NH	9.3	5.9	5.9	—	—
3′a–3′b	—	n[a]	14.0	13.6	14.0
o–*m*Ph	—	—	—	8.4	7.2
o–*m*Ph	—	—	—	s	s
m–*p*Ph	—	—	—	7.6	7.6
o–*m*NBz	—	6.8	7.5	—	—
o–*p*NBz	—	s	1.3	—	—
m–*p*NBz	—	7.2	7.2	—	—

[a]Abbreviations are s: small (≤1.5 Hz); n: not determined.

TABLE 3. Chemical shift data for compounds **2–4** in D_2O:DMSO-d_6, 3:7 (v/v) (δ, ppm)

^{1}H	δ **2**[a]	δ **3R**	δ **3S**	δ **4R**	δ **4S**
2	5.39	5.42	5.42	5.38	5.40
3	3.64	3.63	3.68	3.55	3.61
5	5.07	4.91	4.92	4.86	4.90
6α	2.24	2.32	2.62	2.29	2.33
6β	1.60	1.63	1.62	1.61	1.63
7	4.00	4.07	4.05	4.03	4.03
10	4.51	6.28	6.27	6.23	6.23
13	5.83	5.97	5.92	5.93	5.92
14α	1.86	2.15	2.27	1.84	2.19
14β	1.70	2.14	2.16	1.84	2.06
16	0.96	1.00	1.00	1.00	0.99
17	0.98	1.02	1.00	0.97	0.99
18	1.72	1.80	1.79	1.73	1.54
19	1.50	1.46	1.46	1.44	1.46
20α	3.98	3.99	4.02	3.95	4.00
20β	4.00	3.95	3.98	3.95	3.97
OAc-4	2.19	2.21	2.26	2.07	2.18
OAc-10	—	2.07	2.07	1.92	2.07
o-Bz-2	7.96	7.88	7.94	7.90	7.94
m-Bz-2	7.61	7.46	7.51	7.58	7.52
p-Bz-2	7.70	7.62	7.63	7.68	7.63
2′	4.31	4.32	4.41	4.40	4.38
3′a	4.80	3.63	3.66	2.96	3.06
3′b	4.78	3.50	3.57	2.90	2.90
NH	7.45	—	6.58	—	—
o-Ph-3′	7.28	—	—	7.14	7.20
m-Ph-3′	7.35	—	—	7.28	7.27
p-Ph-3′	7.17	—	—	7.16	7.19
o-NHBz	—	7.72	7.73	—	—
m-NHBz	—	7.39	7.43	—	—
p-NHBz	—	7.46	7.48	—	—
OH1	—	—	—	—	—
OH7	—	—	5.07	—	—
OH2′	—	—	5.90	—	—
OH10	—	—	—	—	—
t-Bu	1.34	—	—	—	—

[a]In 100% DMSO-d_6.

$H20_\beta$. H7 is further coupled to a broad signal at 5.02δ, which is therefore attributed to OH7. For the side chain, the doublet at 7.45δ is correlated to H3′ (4.78δ), which in turn is correlated to H2′ (4.31δ), which itself is correlated to OH2′ (5.9δ).

These assignments are confirmed and completed by the NOESY data. H13 exhibits nOe's to Me18 (1.72δ) and Me17 (0.98δ). H2 is dipolarly coupled to H10 (4.51δ), H20 (4.0δ), H3, H19 (1.50δ), and Me16 (0.96δ). H5 shows cross-peaks with H7, H3, and Me18. H7 is dipolarly coupled to OH7, Me19, and H3, which in turn shows cross-peaks to OAc4, $H14_\alpha$, Me18, and Me19. Finally, H10 exhibits nOe correlations to Me17 and Me18.

Most interesting are nOe's observed between the side chain and the ring system protons. H3′ shows cross-peaks to $H6_\alpha$, OAc4, and $H6_\beta$, while H2′ exhibits dipolar couplings to OAc4 and Me18. Combined with the increase in $J_{H2'-H3'}$, these data indicate that Taxotere® undergoes a striking conformational change in hydrophilic solvent. With the exception of the OAc4 interaction, this favors low-energy conformer **12** and the nOe involving H3′ and 4-OAc must arise from contributions made by alternative conformers. However, as observed previously for taxol (6*e*), Taxotere® shows a pronounced preference in this solvent for *anti* H-C2′-C3′-H conformer **12** that is distinctly different from that observed in the solid state and in chloroform solution.

*Baccatin III 13-(*R*-N-Benzoylisoserinate) (**3R**)*

In $CDCl_3$, assignments are straightforward. The two diastereotopic hydrogens $H3'_a$ and $H3'_b$ overlap near 3.84δ while H3 is nearby at 3.75δ. The NOESY spectrum confirms the methyl group assignments through the cross-peaks observed between H13–Me17, H13–Me18, and H2–Me16, H2–Me19. The most interesting nOe observed is a weak correlation between H2′ and OAc4.

The two $J_{H2'-H3'}$ values for **3R** in $CDCl_3$, both 4.5 Hz, are significantly higher than that observed for taxol (2.7 Hz). These values could reflect a single predominant conformation for **3R** having appropriate side chain C2′H—C3′H_2 dihedral angles, or, more likely, increased side chain bond rotational mobility in **3R**, which would equalize and raise the two diastereotopic $J_{H2'-H3'}$ values from that observed for taxol in the same solvent. Indeed, modeling fails to identify a conformation consistent with the former scenario, whereas the observation for **3R** in $CDCl_3$ solution of a side chain – diterpenoid skeleton nOe interaction involving the H2′ and 4-OAc (not observed for taxol or Taxotere® in $CDCl_3$) is consistent with the latter. A study of **3R** in chloroform employing VCD indicates a hydrogen bond between the 2′-OH and the side chain ester carbonyl oxygen (9), thus placing the focus on conformers **18**, **19**, and **22** (Table 7). Therefore, it seems likely that **3R** in $CDCl_3$ is conformationally heterogeneous, but that low-energy conformer **19**, analogous in its side chain torsion angles to the major taxol conformer in $CDCl_3$ and possessing low $J_{H2'-H3'}$ values, is a significant contributor.

In DMSO–H_2O solution, the different signals are again easily attributed to the corresponding hydrogen atoms. Interest-

Can. J. Chem. Downloaded from www.nrcresearchpress.com by 195.246.54.202 on 09/08/12
For personal use only.

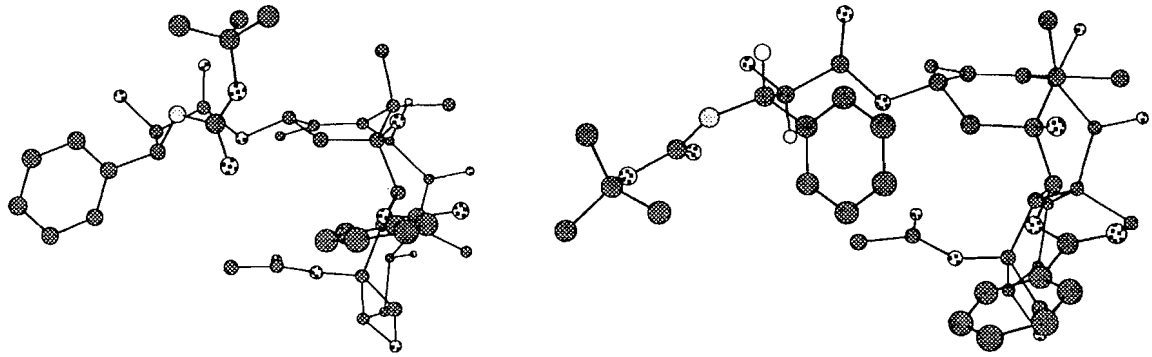

Taxotere Conformer 6 **Taxotere Conformer 12**

FIG. 2. Major Taxotere® conformations.

TABLE 4. Coupling constants for compounds **2–4** in D_2O: DMSO-d_6, 3:7 (v/v) (J, Hz)

^1H J	J **2**	J **3R**	J **3S**	J **4R**	J **4S**
2–3	7.11	7.0	7.0	7.3	7.0
5–6α	9.0	9.0	8.8	10.0	10.0
5–6β	s[a]	s	s	s	s
6α–6β	14.6	14.3	13.0	13.4	13.1
6α–7	—	7.0	6.5	6.5	6.5
6β–7	—	10.7	9.4	8.4	13.1
13–14α	8.5	8.8	8.9	8.9	8.6
13–14β	8.5	8.8	8.4	8.9	8.6
13–18	—	s	s	—	—
14α–14β	—	n	n	n	n
20α–20β	8.3	8.4	8.4	n	8.4
o–*m*OBz	7.5	7.4	7.7	7.8	8.0
o–*p*OBz	s	s	s	s	s
m–*p*OBz	7.3	7.3	7.1	7.4	7.7
2′–3′a	8.6	5.7	6.3	6.3	5.6
2′–3′b	8.6	6.1	6.1	8.2	8.0
3′–NH	8.0	5.7	—	—	—
3′–*o*–Ph	—	—	—	—	—
3′a–3′b	−14.1	n	13.1	13.8	13.9
o–*m*Ph	—	—	7.5	7.3	7.3
o–*p*Ph	—	—	s	s	s
m–*p*Ph	—	—	7.8	7.6	7.6
o–*m*NBz	—	7.3	7.6	—	—
o–*p*NBz	—	s	s	—	—
m–*p*NBz	—	7.2	7.6	—	—

[a]Abbreviations are s: small (≤1.5 Hz); n: not determined.

ingly, inspection of the NOESY spectrum reveals dipolar interactions between H2′ and OAc4, H2′, and Me18, as well as between $H3'_\beta$ and OAc4. The magnitudes of the two $J_{H2'-H3'}$ values detected for **3R** in this medium are closely similar and consistent with rotational averaging about C2′—C3′. Molecular modeling implicates as major contributors low-energy conformers **23–25** (Table 8). These conformers place those protons that are dipolar coupled (H2′ and 4OAc, H2′ and Me18, and H3′ and 4-OAc) in reasonable proximity (within 2.8–4.2 Å). Conformer **27**, which is very similar in its A-ring side chain torsional characteristics to the major aqueous taxol conformer (6*e*), is not inconsistent with the nOe data. However, its high relative energy makes it unlikely to be a significant contributor to the mix of conformers exhibited by **3R** in this solvent.

*Baccatin III 13-(*S*-N-benzoylisoserinate) (**3S**)*

In $CDCl_3$, except for a few chemical shift changes (see, for example H2–H2′, H3–$H3'_a$–$H3'_b$, Me18–Me19), the spectrum resembles very closely that of **3R** and the assignments are therefore straightforward. The NOESY spectrum gives the usual correlations between H10 and Me18, H13 and Me17, H2 and Me19 as well as H2 and Me16, permitting the assignment of the methyl groups, but does not indicate any proximity between the side chain and the baccatin-III ring system.

The somewhat divergent $J_{H2'-H3'}$ values observed for **3S** in chloroform suggest a less conformationally mobile side chain. Again, VCD measurements point to the importance of hydrogen bonding between the 2′-OH and the side chain ester carbonyl oxygen, as in conformers **29**, **31**, and **34** (Table 9). Of these three, a mixture of low-energy conformers **29** and **31** is most consistent with the $J_{H2'-H3'}$ values detected for **3S** since the pro-*R* and pro-*S* H3′ are calculated to exhibit large and small $J_{H2'-H3'}$ values, respectively, in **29**, and vice versa in **31**. Conformational averaging of $J_{H2'-H3'}$ in this way is consistent with the experimental data.

In DMSO–H_2O, the spectra resemble those of **3R** quite closely, and the assignments are straightforward. The most interesting nOe observed is the one between H2′ and OAc4, indicating some proximity between the side chain and the ring system as was observed for **3R**. As in the case of **3R** in this solvent mixture, the two $J_{H2'-H3'}$ values of **3S** are essentially identical in magnitude and consistent with rotational averaging about C2′—C3′. Three of the conformers in Table 10, **36**, **38**, and **39**, show close contacts (2.8–3.2 Å) between the dipolar coupled H2′ and 4-OAc protons. Of those, **39** is somewhat reminiscent of the major aqueous taxol conformer in its disposition of the benzamide group, but its high relative energy would appear to reduce its contribution to the conformer equilibrium of **3S** in aqueous DMSO.

*Baccatin III 13-(*R*-3-phenyllactate) (**4R**)*

In $CDCl_3$, peaks are again readily assigned. It is striking that the two acetate groups, OAc4 and OAc10, generally separated by about 0.2 ppm in **1**, **2**, **3R**, and **3S**, fall almost into a single line for this compound (2.16 and 2.18δ). The most remarkable feature of the spectrum, however, is the NOESY cross-peak between *m*-Ph and Me17 protons, suggesting some over-the-top interaction between the side chain and the ring system.

As in the case of **3R** in $CDCl_3$, **4R** exhibits $J_{H2'-H3'}$ values

Can. J. Chem. Downloaded from www.nrcresearchpress.com by 195.246.54.202 on 09/08/12
For personal use only.

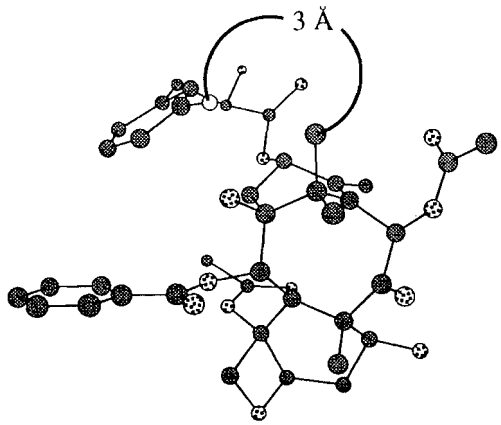

FIG. 3. Possible structure, which brings 3′ Ph into close proximity with Me17.

that are essentially equivalent in magnitude and indicative of rotational averaging. VCD measurements detect hydrogen bonding between the 2′-OH and the side chain ester carbonyl oxygen (11).Thus, **4R** in chloroform probably is a conformational mixture of **42**, **43**, and **45** (Table 11). Consistent with this degree of side chain mobility is the observation of an nOe interaction between the *meta* 3′-Ph protons and those on the 17-Me. Modeling failed to identify stable conformations with appropriately small distances between these protons, but it seems likely that **4R** can reside briefly in conformations related to **42** and **43** that bring these protons into close contact (see Fig. 3).

In DMSO–H_2O, assignments are again straightforward but the NOESY spectrum exhibits *no* dipolar correlations between the side chain and the ring system. The only evidence for some conformational changes occurring, besides the absence of the *m*-Ph and Me17 crosspeak observed in $CDCl_3$, is that the two acetate groups are again moved apart by 0.15 ppm (2.07 and 1.92δ, respectively). This hydrophilic medium appears to impart a degree of rotational restriction about C2′—C3′, as evidenced by more divergent $J_{H2'-H3'}$ values. The failure to detect nOe interactions between the *meta* 3′-Ph protons and those of Me17 in this medium suggests a generally globular conformation with the A-ring side chain wrapped within the concave region of the diterpenoid skeleton. These considerations together with the analogy of the major aqueous conformer observed for taxol point to conformer **47** as an important contributor to the description of **4R** in polar medium.

Baccatin III 13-(S-3-phenyllactate) (4S)

General aspects of the spectra of **4S** in $CDCl_3$ are similar to those of **4R**, and signals for the two OAc groups again occur at almost the same chemical shift (2.21 and 2.19δ). The major difference between the two spectra is that the H3′ protons are well separated ($\delta(H3'_a) = 3.22$, $\delta(H3'_b) = 2.96$) for the *S* epimer, while in the *R* epimer they form a tight AB system at 3.08 and 3.04δ as was observed earlier for **3R** and **3S**. In the NOESY spectrum the usual cross-peaks are observed, as well as couplings between the *m*-Ph and Me17 protons.

The $J_{H2'-H3'}$ values for **4S** in $CDCl_3$ are the most divergent among analogs **3** and **4**, and suggest the greatest degree of side chain C2′—C3′ rotational immobilization. Molecular modeling and the usual observation by VCD of hydrogen bonding between the 2′-OH and the side chain ester carbonyl oxygen (11) for **4S** in chloroform solution point to conformers **53**, **54**, and **55**. Of these three, conformers **53** and **55** possess the appropriate small–large combination of $J_{H2'-H3'}$ values that arise from the diastereotopic H3′ and, on that basis, must predominate. In principle, stereospecific isotopic replacement of the diastereotopic H3′'s would allow a choice to be made between dominant contributions by **53** or **55** since in **53** it is the pro-*R* H3′ that is expected to exhibit the larger $J_{H2'-H3'}$ whereas in **55** the pro-*S* H3′ is expected to do likewise. In the absence of this information, one can only say that it is *either* conformer **53** *or* conformer **55** which contributes most importantly to the description of **4S** in chloroform, but not both. Analog **4S** in chloroform resides at least briefly (as does **4R**) in conformations that bring the *meta* 3′-Ph and the 17-Me into close contact notwithstanding the loss of side chain rotational freedom evidenced by $J_{H2'-H3'}$, as indicated by the observation of appropriate NOESY signals.

In DMSO–H_2O three striking changes are noted in the spectra: the signals corresponding to the two acetate groups separate to 2.18 and 2.07δ, the triplet of H13 is shielded by 0.25 ppm, and the NOESY crosspeak between *m*-Ph and Me17 disappears, as observed before for **4R**. Among analogs **3** and **4** in this medium, it is again **4S** which exhibits the most divergent $J_{H2'-H3'}$ values, suggestive of the greatest degree of C2′—C3′ rotational preference. Like **4R**, **4S** fails to exhibit the nOe interaction between the *meta* 3′-Ph protons and those on the 17-Me that it did in chloroform solution. This suggests a globular conformation like the one detected for taxol in aqueous solution and suggested for **4R** in this solvent. However, without additional experimental data — especially data in which diastereotopic H3′ is involved in the larger $J_{H2'-H3'}$ — it is impossible to decide which is dominant among conformers **60–62**, and **64** (Table 14; those that have appropriately divergent $J_{H2'-H3'}$ values). It is tempting to dismiss **64** based on its high relative energy.

Discussion

We (8) and the French team (11) have speculated about the bound ligand conformation recognized by the microtubular taxol binding site that might be implicated by the taxol (**1**) and Taxotere® (**2**) solution conformations. Such speculation can form the basis of preliminary taxol analog design efforts. Previously, the focus was on the Taxotere® solid state structure (12) that is comparable to the major chloroform solution structures of both Taxotere® and taxol. The taxol aqueous dimethyl sulfoxide structure is an alternative candidate (6*e*). However, until better structural information on the microtubular taxol binding site and the taxol–microtubule complex is available, the question of whether it is the taxol conformation in hydrophobic (i.e., chloroform solution) or hydrophilic (i.e., aqueous dimethyl sulfoxide solution) media, *or neither*, that is recognized by microtubules will remain debatable. This caveat notwithstanding, it is a useful exercise, at this time, to compare the solution conformations accessible to taxol analogs **3** and **4** to those accessible to taxol, with a view toward suggesting an explanation for the spectrum of biological activity exhibited by **3** and **4**.

One of the most important solution conformational differences between taxol and Taxotere®, and analogs **3** and **4**, is that **3** and **4** clearly have more mobile A-ring side chains. This is manifested by **3S**, **4R**, and **4S** in chloroform solution in A-ring side chain – diterpenoid skeleton nOe interactions not observed for **1** and **2**, and, to varying degrees, by **3R** and **4R** in chloro-

Can. J. Chem. Downloaded from www.nrcresearchpress.com by 195.246.54.202 on 09/08/12
For personal use only.

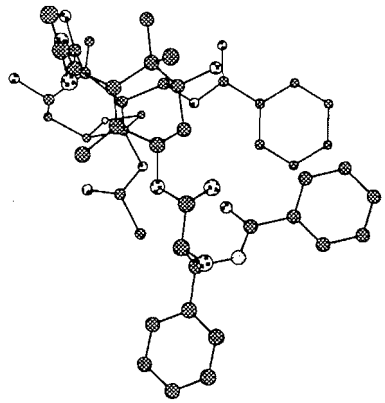

Major Taxol Chloroform Solution Conformer

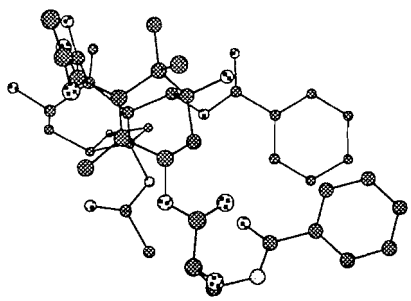

Conformer 19 for 3R

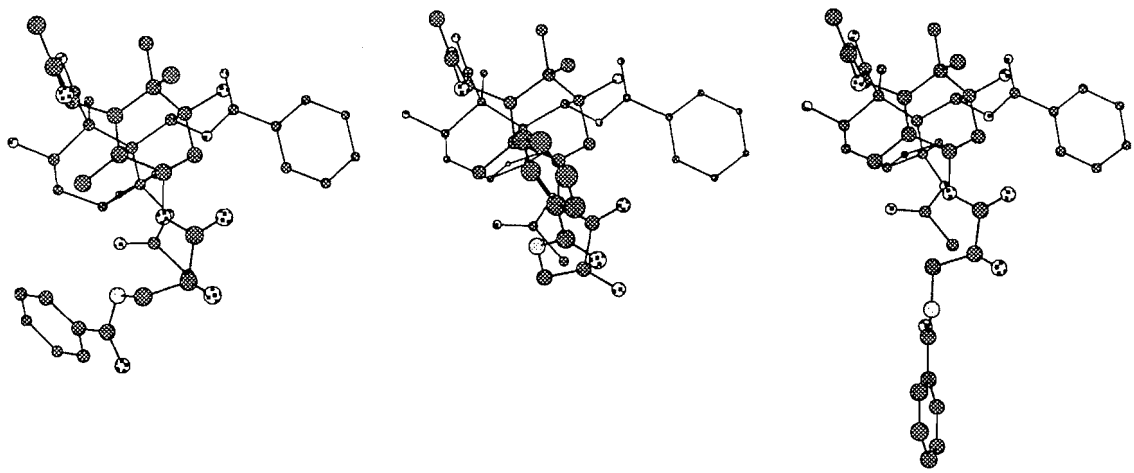

Conformers 29, 31, and 34, respectively, for 3S

FIG. 4. Conformations for **3R** and **3S** in chloroform for comparison with the corresponding taxol structure.

form solution and by **3R** and **3S** in aqueous dimethyl sulfoxide solution in rotationally averaged $J_{H2'-H3'}$ values. For this reason and, in some cases, because the available experimental data are insufficient to choose among conformers suggested by molecular modeling, more equivocation is necessary in specifying solution structures for **3** and **4** than for **1** and **2**. Of analogs **3** and **4**, **4S** appears to possess the most rotationally restricted A-ring side chain in both chloroform and aqueous dimethyl sulfoxide solution. Perhaps not coincidentally, **4S** is also the most biologically active among taxol analogs **3** and **4**.

Figure 4 indicates how conformer **19**, accessible to **3R**, mimics the relevant substructure of the major chloroform solution conformer for taxol, whereas none of the candidate conformers for biologically inactive **3S** in chloroform project the benzamide similarly. Likewise, Fig. 5 shows how the accessible phenyllactate side chain of conformer **45** of **4R** in chloroform overlays onto the corresponding part of the taxol chloroform conformer. As noted above, it is impossible, based on the available data, to choose between conformers **53** and **55** for **4S** in chloroform solution. However, the similar projection of the 3′-Ph in **55** and in the major taxol chloroform conformer and the dissimilar projection of the same group in **53** are striking.

Can. J. Chem. Downloaded from www.nrcresearchpress.com by 195.246.54.202 on 09/08/12
For personal use only.

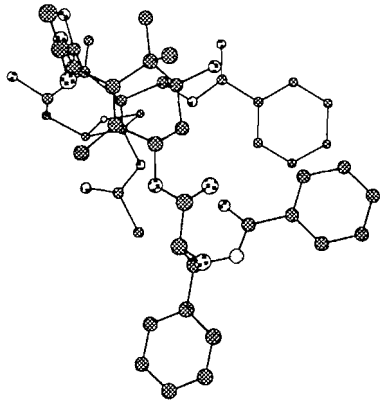

Major Taxol Chloroform Solution Conformer

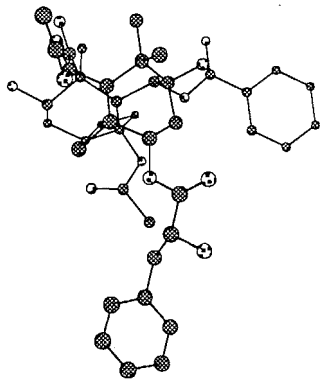

Conformer 45 for 4R

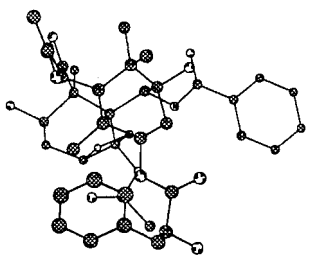

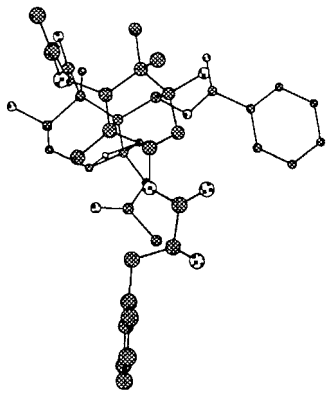

Conformers 53 and 55, respectively, for 4S

FIG. 5. Conformations for **4R** and **4S** in chloroform for comparison with the corresponding taxol structure.

In contrast, there is no consistently logical comparison between the major taxol aqueous solution conformer and the dominant aqueous conformers of analogs **3** and **4**. For example, Fig. 6 demonstrates that the A-ring side chain of high-energy conformer **27** for **3R** best mimics the respective taxol substructure in this medium. Likewise, high-energy conformer **39** of **3S** projects its A-ring side chain in the same manner as taxol. Thus, as one might expect, biologically inactive **3S** does not compare well conformationally to taxol in aqueous media, but neither does biologically active **3R**. The A-ring side chain of aqueous conformer **47** for biologically active taxol analog **4R** (Fig. 7), which appears to be an important contributor to its conformational equilibrium, compares very well to the appropriate part of the taxol aqueous conformer. Again, however, it is difficult to detect conformational similarities between taxol and **4S**, the most active of analogs **3** and **4**. The best candidate is low-energy conformer **61**, which orients its 3′-Ph group appropriately, but at the expense of misdirecting its 2-OH group.

Can. J. Chem. Downloaded from www.nrcresearchpress.com by 195.246.54.202 on 09/08/12
For personal use only.

Can. J. Chem. Downloaded from www.nrcresearchpress.com by 195.246.54.202 on 09/08/12
For personal use only.

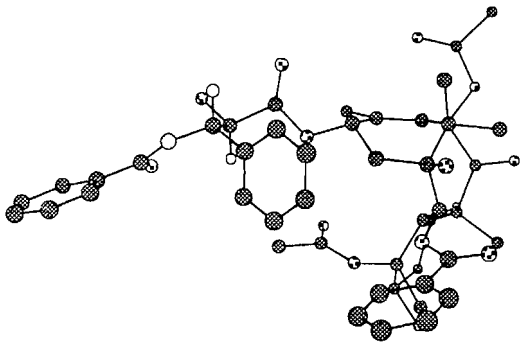

Major Taxol Aqueous Solution Conformer

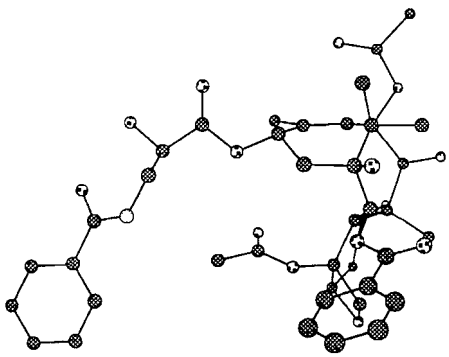

Conformer 27 for 3R

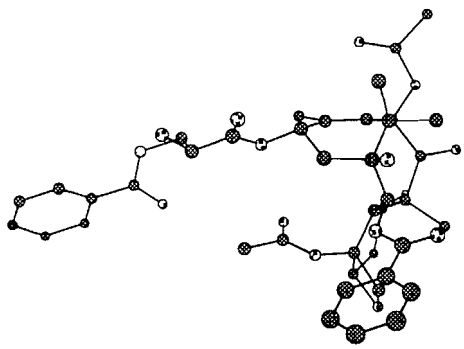

Conformer 39 for 3S

FIG. 6. Conformations for **3R** and **3S** in aqueous solution for comparison with the corresponding taxol structure.

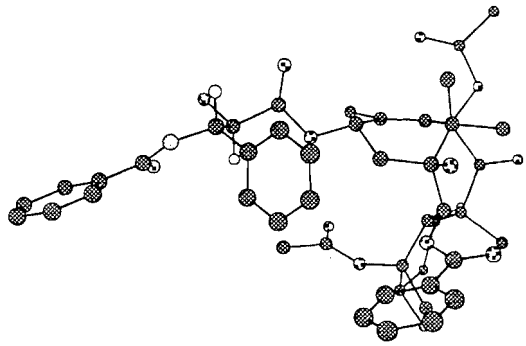

Major Taxol Aqueous Solution Conformer

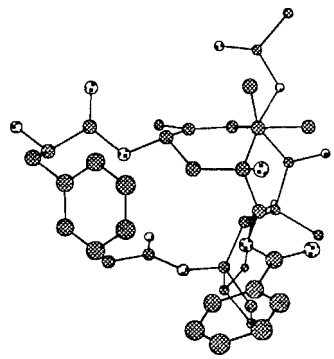

Conformer 47 for 4R

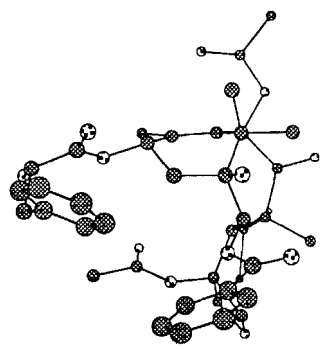

Conformer 61 for 4S

FIG. 7. Conformations for **4R** and **4S** in aqueous solution for comparison with the corresponding taxol structure.

The correspondence of the chloroform conformers with biological activity and the failure to detect a similar relationship between the aqueous conformers of taxol, Taxotere®, and analogs **3** and **4** suggest that the conformation of taxol in hydrophobic media (i.e., in chloroform in the present study) is related to the conformation of taxol at its microtubular binding site. This notion is not unreasonable given the hydrophobicity of taxol itself, and a similar effect seen in peptides during binding in which the hydrophilic conformation only slightly influences binding conformation at a hydrophobic active site has been referred to as "hydrophobic collapse" (13). However, the evaluation of this hypothesis awaits data on the features of tubulin and microtubules responsible for recognition of taxol, and on the ligand–protein complex. These studies are now in progress.

Experimental

Source of the chemicals studied

Taxotere® **2** was a gift from Rhone-Poulenc Rorer, Centre de Recherche de Vitry Alfortville, Quai Jules Guesde 13, BP 14, f94404 Vitry-sur-Seine, France. Taxol analogs **3R**, **3S**, **4R**, and **4S** were prepared as previously described.

NMR studies

^{1}H NMR spectroscopy was performed either at 500 MHz on a Varian Unity 500 equipped with a Sun data system or a Bruker AM-500 with an ASPECT 3000 data system, or at 300 MHz on a Bruker WM-300 spectrometer with an ASPECT 2000 data system. Spectra were taken at room temperature except as noted, and NOESY spectra were acquired in DMSO–water solution at 30°C. ^{1}H chemical shifts are referenced to tetramethylsilane for the $CDCl_3$ samples (δ(TMS) =

0.00) and to dimethyl sulfoxide for the DMSO-containing samples (δ(DMSO-d_5 = 2.49)).

1D-Spectra were taken with 16k data points (0.4 Hz/point), while the 2D experiments were performed with matrix sizes of 1k × 0.256k for COSY spectra and 2k × 0.512k for NOESY spectra. NOESY experiments were performed using mixing times of 0.6 s. Off-line spectral work-up and some NOESY-conformational studies were performed on a Silicon Graphics Iris Indigo workstation using SYBYL-TRIAD software from Tripos Associates.

Molecular modeling

Internal coordinate Monte Carlo conformational searching (13) was carried out on a Silicon Graphics 4D/35 workstation using MacroModel (14) (version 3.1) with the included version of the MM2 force field (15) and the Still chloroform and water continuum solvation models (16). The inspection and analysis of the conformational data were facilitated by the use of SYBYL (version 5.5, Tripos Associates). All taxane starting structures were generated from the Taxotere® crystal structure coordinates (9). Tables 5–15 listing conformational types determined with dihedral angles and calculated coupling constants have been deposited and are available from the National Research Council of Canada (see footnote 5). Additional details of our modeling and conformer analysis protocol that led to the characteristic taxol analog conformers in Tables 5–14 are described in ref. 6*e*. Coordinates for given structures may be obtained by e-mail from cswindel@cc.brynmawr.edu.

Acknowledgements

Support from the National Institutes of Health to A.I.S. (GM32596) and to C.S.S. (CA55139) is gratefully acknowledged. N.E.K. thanks the United States Department of Education for a GAANN fellowship and R.A.D. thanks NATO for a fellowship. We are grateful to Dr. J.W. Clader, Shering-Plough Research, for his MacroModel–SYBYL interface.

1. M.C. Wani, H.L. Taylor, M.E. Wall, P. Coggon, and A.T. Mcphail. J. Am. Chem. Soc. **93**, 2325 (1971).
2. (*a*) W.P. McGuire, E.K. Rowinsky, N.B. Rosenchein, F.C. Grumbine, D.S. Ettinger, D.K. Armstrong, and R.C. Donehower. Ann. Intern. Med. **111**, 273 (1989); (*b*) F.A. Holmes, R.S. Walters, R.L. Theriault, A.D. Forman, L.K. Newton, M.N. Raber, A.U. Buzdar, D.K. Frye, and G.N. Hortobagyi. J. Natl. Cancer Inst. **83**, 1797 (1991); (*c*) A.I. Einzig, H. Hochster, P.H. Wiernik, D.L. Trump, J.P. Dutcher, E. Garowski, J. Sasloff, and T.J. Smith. Invest. New Drugs, **9**, 59 (1991).
3. (*a*) P.B. Schiff, J. Fant, and S.B. Horwitz. Nature, **277**, 665 (1979); (*b*) P.B. Schiff and S.B. Horwitz. Proc. Natl. Acad. Sci. U.S.A. **77**, 1561 (1980); (*c*) J.J. Manfredi and S.B. Horwitz. Pharmacol. Ther. **25**, 83 (1984); (*d*) S.B. Horwitz, L. Lothstein, J.J. Manfredi, W. Mellado, J. Parness, S.N. Roy, P.B. Schiff, L. Sorbara, and R. Zeheb. Ann. N. Y. Acad. Sci. **466**, 733 (1986); (*e*)S.B. Horwitz, P.B. Schiff, J. Parness, J.J. Manfredi, W. Mellado, and S.N. Roy. *In* The cytoskeleton. *Edited by* T.W. Clarkson, P.P. Sager, and T.L.M. Syversen. Plenum Press, New York. 1986; (*f*) E.K. Rowinsky, L.A. Casenave, and R.C. Donehower. J. Natl. Cancer Inst. **82**, 1247 (1990).
4. (*a*) D.G.I. Kingston. Pharmac. Ther. **82**, 1247 (1991); (*b*) L.L. Klein. Tetrahedron Lett. **34**, 2047 (1993); (*c*) S.-H. Chen, C. Fairchild, S.W. Mamber, and V. Farina. J. Org. Chem. **58**, 2927 (1993); (*d*) S.H. Chen, J.-M. Wei, and V. Farina. Tetrahedron Lett. **34**, 3205 (1993).
5. S. Rao, S.B. Horwitz, and I Ringel. J. Natl. Cancer Inst. **84**, 785 (1992).
6. (*a*) G.N. Chmurny, B.D. Hilton, S. Brobst, S.A. Look, K.M. Witherup, and J.A. Beutler. J. Nat. Prod. **55**, 414 (1992). (*b*) J.K. Baker. Spectrosc. Lett. **25**, 31 (1992); (*c*) C.J. Falzone, A.J. Benesi, and J.T.J. Lecomte. Tetrahedron Lett. **33**, 2254 (1992); (*d*) B.D. Hilton, G.N. Chmurny, and G.M. Musckik. J. Nat. Prod. **55**, 1157 (1992); (*e*) H.J. Williams, A.I. Scott, R.A. Dieden, C.S. Swindell, L.E. Chirlian, M.M. Francl, J.M. Heerding, and N.E. Krauss. Tetrahedron. **49**, 6545 (1993); (*f*) J. Dubois, D. Guénard, F. Guéritte-Voegelein, N. Guedira, P. Potier, B. Gillet, and J.-C. Beloeil. Tetrahedron. **49**, 6533 (1993).
7. (*a*) F. Lavelle, C. Fizames, F. Guéritte-Voegelein, D. Guénard, and P. Potier. Proc. Am. Assoc. Cancer Res. **30**, 2254 (1989); (*b*) M.C. Bissery, D. Guénard, F. Guéritte-Voegelein, and F. Lavelle. Cancer Res. **51**, 4845 (1991).
8. C.S. Swindell, N.E. Krauss, S.B. Horwitz, and I. Ringel. J. Med. Chem. **34**, 1176 (1991).
9. F. Guéritte-Voegelein, D. Guénard, L. Mangatal, P. Potier, J. Guilhem, M. Cesario, and C. Pascard. Acta Crystallogr. Sect. C: Cryst. Struct. Commun. **C46**, 781 (1990).
10. D.M. Gigante, T.B. Freedman, C.S. Swindell, L.E. Chirlian, M.M. Francl, N.E. Krauss, and J.M. Heerding. J. Am. Chem. Soc. Submitted.
11. (*a*) F. Guéritte-Voegelein, D. Guénard, F. Lavelle, M.-T. Le Goff, L. Mangatal, and P. Potier. J. Med. Chem. **34**, 992 (1991); (*b*) D. Guénard, F. Guéritte-Voegelein, and P. Potier. Acc. Chem. Res. **26**, 160 (1993).
12. M. Saunders, K.N. Houk, Y.-D. Wu, W.C. Still, M. Lipton, G. Chang, and W.C. Guida. J. Am. Chem. Soc. **112**, 1419 (1990).
13. (*a*) D.H. Rich. J. Cell. Biochem. **17C**, 203 (1993); (*b*) R.A. Wiley and D.H. Rich. Med. Res. Rev. **3**, 327 (1993).
14. F. Mohamadi, N.G.J. Richards, W.C. Guida, R. Liskamp, M. Lipton, C. Caufield, G. Chang, T. Hendrickson, and W.C. Still. J. Comput. Chem. **11**, 440 (1990).
15. (*a*) N.L. Allinger. J. Am. Chem. Soc. **99**, 8127 (1977); (*b*) J.T. Sprague, J.C. Tai, Y. Yuh, and N.L. Allinger. J. Comput. Chem. **8**, 581 (1987); (*c*) T. Liljefors, J.C. Tai, S. Li, and N.L. Allinger. J. Comput. Chem. **8**, 1051 (1987).
16. W.C. Still, A. Tempczyk, R.C. Hawley, and T. Hendrickson. J. Am. Chem. Soc. **112**, 6127 (1990).

Can. J. Chem. Downloaded from www.nrcresearchpress.com by 195.246.54.202 on 09/08/12
For personal use only.

COMMUNICATION/COMMUNICATION

Evidence for the pathway to pantothenate in plants[1]

CAROL E. JONES
University Chemical Laboratory, Lensfield Road, Cambridge CB2 1EW, England, and Department of Plant Sciences, University of Cambridge, Downing Street, Cambridge CB2 3EA, England
JANE E. DANCER
Schering Agrochemicals Ltd., Chesterford Park, Saffron Walden, Essex, CB10 1XL, England
ALISON G. SMITH
Department of Plant Sciences, University of Cambridge, Downing Street, Cambridge CB2 3EA, England
AND
CHRIS ABELL[2]
University Chemical Laboratory, Lensfield Road, Cambridge CB2 1EW, England

Received July 12, 1993

This paper is dedicated to Professor Ian Spenser

CAROL E. JONES, JANE E. DANCER, ALISON G. SMITH, and CHRIS ABELL. Can. J. Chem **72**, 261 (1994).

A protocol to separate the intermediates on the biosynthetic pathway to pantothenate on HPLC is described. Feeding experiments with L-[U-^{14}C]valine to pea leaf disks result in incorporation of radioactivity into 2-ketoisovalerate, ketopantoyl lactone, and pantoyl lactone, providing the first experimental evidence that the biosynthetic pathway to pantothenate is the same in plants and bacteria.

CAROL E. JONES, JANE E. DANCER, ALISON G. SMITH et CHRIS ABELL. Can. J. Chem **72**, 261 (1994).

On décrit un protocole pour séparer, par CLHP, les intermédiaires dans la biosynthèse du pantothénate. Des expériences impliquant l'addition de L-[U-^{14}C]valine à des disques de feuilles de pois provoquent l'incorporation de la radioactivité dans le 2-cétoisovalérate, dans la cétopantanoyl lactone et dans la pantanoyl lactone; ces résultats procurent la première preuve expérimentale que la voie de la biosynthèse du pantothénate est la même avec les plantes et avec les bactéries.

[Traduit par la rédaction]

Pantothenate **4** (vitamin B_3) is the precursor of coenzyme A. Studies to establish the biosynthetic pathway have been carried out in microorganisms, but pantothenate must also be produced in plants. In this paper we describe the first experimental evidence that the same pathway to pantothenate is used in plants and bacteria.

The biosynthesis of pantothenate in microorganisms has been shown to involve three steps (Scheme 1) (1, 2). The first committed step is the formation of ketopantoate **2** from α-ketoisovalerate (**1**, α-KIVA) catalysed by the enzyme ketopantoate hydroxymethyltransferase (KPHMT). This enzyme has been purified to homogeneity from *Escherichia coli* (3), and recently the *E. coli panB* gene, which codes for KPHMT, has been cloned, sequenced, and overexpressed (4).

Ketopantoate **2** is reduced to pantoate **3** by ketopantoate reductase. Low levels of enzyme activity have been detected in *E. coli*, *Saccharomyces cerevisiae* (5), *Salmonella typhimurium* (6), and *Pseudomonas maltophilia* 845 (7). Ketopantoyl lactone reductase, which reduces the corresponding lactone **5** of pantoate, has been found in *S. cerevisiae* (8) and bacteria (5). The conversion of pantoate **3** to pantothenate **4** involves the condensation of pantoate with ß-alanine and is catalysed by pantothenate synthetase. The *E. coli* enzyme has been purified (9).

The only evidence for the operation of the pathway to pantothenate in plants has been the isolation of a ketopantoate auxotroph of *Datura innoxia* P. Mill, thought to be unable to convert α-KIVA **1** to ketopantoate **2** (10). We set out to establish the biosynthetic pathway to pantothenate in plants. Our initial approach was to assay for KPHMT (3, 11) and ketopantoate reductase activity (7, 12) in crude homogenates of plant sources believed to be rich in coenzyme A, including broad beans and cauliflower florets, as well as in pea leaves. However, none of the assays with plant preparations reproducibly showed enzyme activity, suggesting that the levels of activity were below the sensitivity threshold of the assays being used. These results were not surprising as previous attempts to detect enzyme activity in plants had been unsuccessful (10).

This failure prompted us to use an alternative approach of feeding pea seedlings a radioactive precursor and looking for conversion into pathway intermediates. L-[U-^{14}C]Valine **8** was used as it is readily deaminated *in vivo* to give α-KIVA **1**, the first putative intermediate on the pantothenic acid pathway. Complications were anticipated as valine will be readily incorporated into protein, and α-KIVA will also be incorporated into leucine **12** (Scheme 1).

It was necessary to find an analytical system to resolve the potential intermediates on the pantothenate pathway from one another, and from related compounds that could be derived from α-KIVA on the pathway to leucine. A series of standards consisting of compounds derived from α-KIVA on the pantothenate and leucine pathways were therefore assembled. DL-2,3-Dihydroxyisovalerate **7**, the precursor of 2-ketoisovaleric acid, was prepared by the bis-hydroxylation of 3,3-dimethylacrylic acid (13). Ketopantoyl lactone **5** was synthesized by the bro-

[1]This paper is dedicated to Professor Ian Spenser on the occasion of his non-retirement.

[2]Author to whom correspondence may be addressed.

Can. J. Chem. Downloaded from www.nrcresearchpress.com by 195.246.54.202 on 09/08/12
For personal use only.

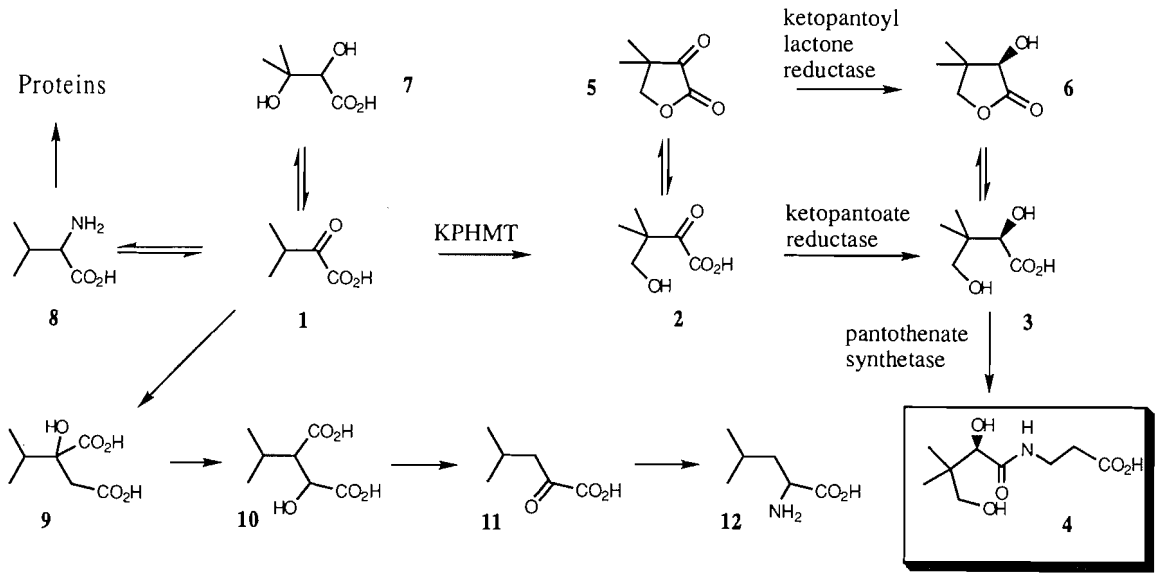

SCHEME 1. The biosynthetic pathway from α-KIVA to pantothenate as established for microorganisms. The scheme also shows the alternative fates of L-[U-^{14}C]valine in an in vivo feeding experiment.

mine oxidation of pantoyl lactone **6** (14). Pantoyl lactone **6**, α-KIVA **1**, 2-isopropylmalate **9**, and 2-ketoisocaproate **11** were all purchased commercially.

It was found that the pantothenate intermediates were well resolved by HPLC on a Bio Rad Organic Acids containing a strong cation-exchange resin. The lactone forms of ketopantoate and pantoate were analysed since these are formed under the acidic conditions used (8). Pantothenate is degraded to pantoyl lactone in acid and so cannot be detected intact under these conditions. The pantothenate pathway standards were also well resolved from the leucine pathway standards 2-isopropylmalate **9** and 2-ketoisocaproate **11**, as well as DL-2,3-dihydroxyisovalerate **7**. An HPLC trace of a mixture of these compounds is shown in Fig. 1*A*.

Having found a method to resolve the potential intermediates on the pantothenate pathway, attention was turned towards finding feeding conditions. L-[U-^{14}C]Valine was first fed to 14-day-old pea seedlings to establish the level of uptake through the exposed xylem. After 4 h, 15% of the valine was taken up and 45% of this was incorporated into protein. Less than 0.01% of the radioactivity was found in the fractions expected to contain intermediates on the pantothenate pathway. This prompted us to attempt an alternative feeding regimen.

To increase the incorporation of valine, the radiolabel was fed in a vacuum infiltration experiment to pea leaf disks. The first differentiated leaves from 2-week-old peas were cut with a cork borer to give disks (15), and floated on a solution containing L-[U-^{14}C]valine (16). The leaf disks were initially placed under vacuum to remove air bubbles that might interfere with the uptake of label. The vacuum was then released and the disks illuminated for several hours to enhance transpiration. In these experiments approximately 50% of the L-[U-^{14}C]valine was taken up, with 0.3% of the radioactivity ending up in the organic acids fraction.

The organic acids fraction was analysed by HPLC, monitoring the elution of compounds from the column using a radioactivity detector. The radioactivity trace for peas fed for 4 h is shown in Fig. 1*B*. Based on the retention times found for authentic standards, the peak at 10–11 min corresponds to α-KIVA **1** and the peak between 15 and 16 min to ketopantoyl lactone **5**. This peak increased in relative intensity from 3 to 4 h and then decreased so that it was barely visible after 24 h. The small peak at 23 min corresponds to pantoyl lactone **6**. There are several small peaks between 12 and 14 min in all traces that have the same retention time as some of the leucine pathway standards. A large unidentified peak at 8–9 min was seen in all traces. The same pattern of peaks was observed in HPLC traces from feedings after 3, 4, 5, and 24 h, although the relative intensity of the peaks varied, depending on the feeding time. The exact correspondence of the retention times of the peaks due to radioactivity and those for the authentic standards suggests that radioactivity from L-[U-^{14}C]valine is being incorporated into these compounds.

The incorporation of radioactivity from L-[U-^{14}C]valine into α-KIVA **1**, ketopantoyl lactone **5**, and pantoyl lactone **6** (which could derive from pantoate **3** or pantothenate **4**) demonstrates that these compounds are formed in plants and provides compelling evidence that the pathway to pantothenate in plants is similar to that in microorganisms. The fractionation protocol described in this paper should provide a handle, which has until now been elusive, to study the pathway to pantothenate in plants and to approach the isolation of the individual plant enzymes. This result complements the recent report of the purification of pantothenate kinase from spinach, where an HPLC protocol to look at phosphorylated intermediates on the common pathway between pantothenate and coenzyme A was described (17).

Experimental

HPLC elution conditions

DL-2,3-Dihydroxyisovaleric acid was prepared by the bis-hydroxylation of 3,3-dimethylacrylic acid (13). Ketopantoyl lactone was synthesized by the bromine oxidation of pantoyl lactone (14). Pantoyl lactone, α-KIVA (as the sodium salt), and 2-isopropylmalate were all purchased from Aldrich Chemical Co., Dorset, U.K. 2-Ketoisocaproate (as the sodium salt) was purchased from the Sigma Chemical Co., Dorset, U.K.

Can. J. Chem. Downloaded from www.nrcresearchpress.com by 195.246.54.202 on 09/08/12
For personal use only.

Can. J. Chem. Downloaded from www.nrcresearchpress.com by 195.246.54.202 on 09/08/12
For personal use only.

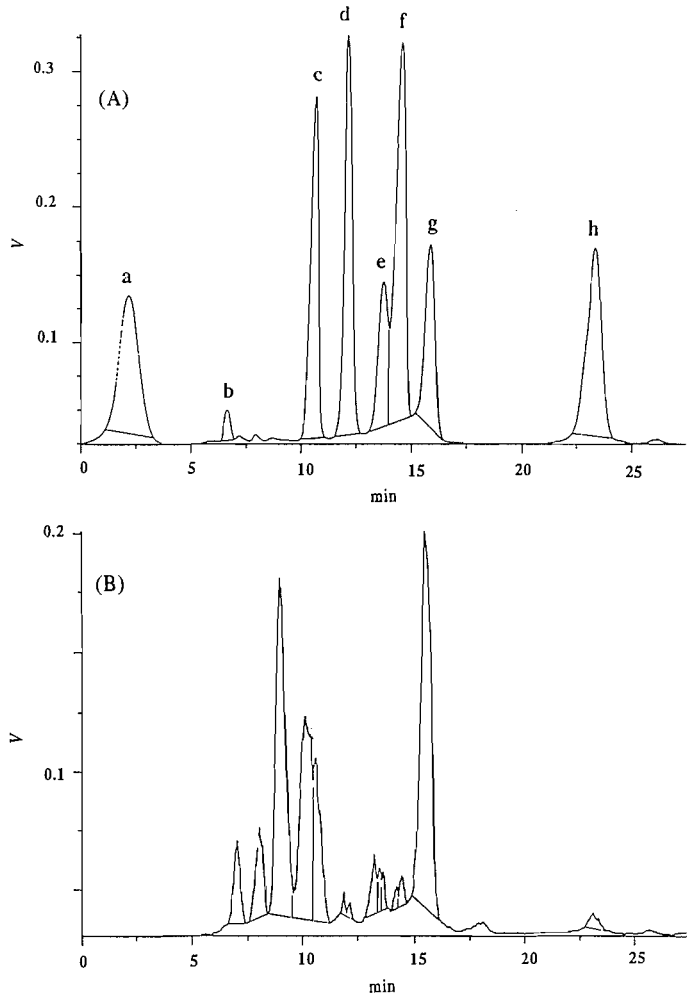

FIG. 1. (*A*) HPLC trace of a mixture of standards. Detection is by UV absorbance at 225 nm. Peaks a and b are due to unidentified impurities, peak c: α-KIVA **1**; d: dihydroxyisovalerate **7**; e: 2-isopropylmalate **9**; f: α-ketoisocaproate **11**; g: ketopantoyl lactone **5**; h: pantoyl lactone **6**. (*B*) HPLC trace of the organic acids fraction from the 4 h feeding experiment with L-[U-^{14}C]valine to pea leaf disks (four experiments combined). The ordinate measures radioactivity detected by a Reeve model 970 radioactivity detector fitted with a heterogeneous flow cell. All HPLC were run on a Bio-Rad Organic Acids column (300 × 7.8 mm) eluting with 4 mM sulphuric acid at a flow rate of 0.6 mL/min.

Standards (10–50 μg) or the fraction from the Sephadex SP-C-25-H^+ column from feeding experiments (10–150 μl) were analysed by HPLC on an organic acids column (Bio-Rad Laboratories Ltd., Hertfordshire, U.K.) (300 × 7.8 mm) containing Aminex HPX-87H resin. Samples were eluted with 4 mM sulphuric acid at a flow rate of 0.6 mL/min. Elution of samples from the column was monitored by UV absorbance at 225 nm and by radioactivity detection using a Reeve model 970 radioactivity detector (Reeve Analytical, Glasgow, U.K.), fitted with a heterogeneous flow cell. Retention times were found to vary by up to ±1 min over a period of months, so the column was calibrated with standards each time samples from feeding experiments were analysed.

Valine uptake by pea shoots

Pea seedlings (14 days old) were harvested and placed in a solution of 10 μL L-[U-^{14}C]valine (474 MBq/mmol, 85 kBq/mL) made up to 1 mL with distilled water. The stems were immediately recut under the surface. After 2 h the shoot was cut above the liquid surface and ground in a mortar with 1 mL distilled water. The sample was centrifuged for 5 min in a microfuge and the supernatant counted.

Valine feeding of pea leaf disks

Leaf disks (6 mm) were prepared from 14-day-old peas (*Pisum sativum* var Onward) using a cork borer, and were floated on distilled water before use. Leaf disks (seven per sample) were put in a small vial containing 100 μL L-[U-^{14}C]valine (10.4 GBq/mmol, 1.85 MBq/mL) and 400 μL distilled water. The vial was placed under vacuum for 15 min and illuminated by a bright light. The vacuum was slowly released and the samples left for 3–24 h. The supernatant was then carefully removed and the leaf disks washed three times with 5 mL distilled water. The disks were transferred to a mortar containing liquid nitrogen and 300 μL of an aqueous solution of authentic pathway standards (sodium 2-ketoisovalerate (60 μg), ketopantoyl lactone (120 μg), and pantoyl lactone (240 μg)) and ground to a fine powder. A solution of 0.4 M perchloric acid (1.5 mL) was added and the sample allowed to thaw before centrifuging in a microfuge for 5 min. The supernatant was applied to an Accubond SPE column® (Fisons Scientific Equipment, Loughborough, U.K.) to remove phenolic compounds. The column had been previously washed with 2 mL methanol and 2 mL 0.4 M perchloric acid. The sample was eluted in 4 mL 0.4 M perchloric acid, and the pH adjusted to 8–9 with 1 M KOH before evaporating to dryness. The resulting residue was resuspended in 300 μL distilled water and the pH adjusted to 7 with 0.1 M HCl.

Amino acids were removed by applying a 250 μL aliquot of the sample to a column of Sephadex SP-C-25-H^+ (18) (Sigma Chemical Co., Dorset, U.K.) prepared in a disposable Pasteur pipette to a bed height of 4 cm. The column had been previously equilibrated with 1.5 mL 7% formic acid, then rinsed with distilled water to neutral pH. The organic acids fraction was eluted with 1.5 mL distilled water, adjusted to pH 8 with 1 M KOH, and evaporated to dryness. It was resuspended in 250 μL 4 mM sulphuric acid and an aliquot (150 μL) analysed by HPLC. The amino acid fraction was eluted from the SP Sephadex column with 3 mL distilled water followed by 4.5 mL 0.3 M ammonium hydroxide.

Acknowledgements

We thank Schering Agrochemicals and the Science and Engineering Research Council (SERC) for a CASE Award to C.E.J. We thank J. B. Pillmoor, S. G. Foster, and K. Wright for their interest in this research.

1. W. K. Maas and H. J. Vogel. J. Bacteriol. **65**, 388 (1953).
2. G. M. brown and J. M. Williamson. Adv. Enzymol. **53**, 345 (1982).
3. J. H. Teller, S. G. Powers, and E. E. Snell. J. Biol. Chem. **251**, 3780 (1976).
4. C. E. Jones, J. M. Brook, D. Buck, C. Abell, and A. G. Smith. J. Bacteriol. **175**, 2125 (1993).
5. H. L. King and D. R. Wilken. Fed. Proc. **31**, 476 (1972).
6. D. A. Primerano and R. O. Burns. J. Bact. **153**, 259 (1983).
7. S. Shimizu, M. Kataoka, M. C. Chung, and H. Yamada. J. Biol. Chem. **263**, 12077 (1988).
8. H. L. King, R. E. Dyar, and D. R. Wilken. J. Biol. Chem. **249**, 4689 (1974).
9. K. Miyatake, Y. Nakano, and S. Kitaoka. Methods Enzymol. **62**, 215 (1979).
10. S. V. Sahi, P. K. Saxena, G. D. Abrahams, and J. King. J. Plant Physiol. **133**, 277 (1988).
11. T. Nash. Biochem. J. **55**, 416 (1953).
12. D. R. Wilken, H. L. King, and R. E. Dyar. Methods Enzymol. **62**, 209 (1979).
13. E. A. Cioffi, K. J. Shaw, W. F. Bailey, and C. M. Berg. Anal. Biochem. **104**, 485 (1980).
14. I. Ojima, T. Kogure, and Y. Yoda. Org. Synth. **63**, 18 (1985).
15. S. A. Boffey. *In* Radioisotopes in biology; a practical approach. *Edited by* R. J. Slater. IRL Press, Oxford. 1990. p. 127.
16. J. V. Possingham and J. W. Smith. J. Exp. Bot. **23**, 1050 (1972).
17. K. L. Falk and D. J. Guerra. Arch. Biochem. Biophys. **301**, 424 (1993).
18. R. J. Redgwell. Anal. Biochem. **107**, 44 (1980).

Allyldimethylsilyl triflate: a self-catalyzed silyl nucleophile[1]

MICHAEL A. BROOK[2] AND GRANT D. CROWE
Department of Chemistry, McMaster University, 1280 Main St. W., Hamilton, ON, L8S 4M1 Canada

AND

HENK HIEMSTRA
Laboratorium voor Organische Scheikunde, Universiteit van Amsterdam, Nieuwe Achtergracht 129, 1018 WS, Amsterdam, The Netherlands

Received May 6, 1993

This paper is dedicated to Professor David B. MacLean

MICHAEL A. BROOK, GRANT D. CROWE, and HENK HIEMSTRA. Can. J. Chem. **72**, 264 (1994).

Allyldimethylsilyl triflate **2** may be prepared by a protiodesilylation reaction between diallyldimethylsilane and triflic acid. This compound possesses both a silyl-substituted carbon nucleophile and the Lewis acid necessary for activation of an electrophile. Upon exposure to an aromatic aldehyde (e.g., *p*-$MeOC_6H_4CHO$), the homoallylic alcohol **4** is formed in good yield. The synthetic advantages of the intramolecular Cope-type cyclization reaction are discussed.

MICHAEL A. BROOK, GRANT D. CROWE et HENK HIEMSTRA. Can. J. Chem. **72**, 264 (1994).

On a préparé le triflate d'allyldiméthylsilyle (**2**) par une réaction de protiodésilylation entre le diallyldiméthylsilane et l'acide triflique. Ce composé possède à la fois un carbone substitué par un silyle qui peut agir comme nucléophile et l'acide de Lewis nécessaire à l'activation d'un électrophile. Mis en présence d'un aldéhyde aromatique (par exemple *p*-$MeOC_6H_5CHO$), l'alcool homoallylique **4** se forme avec un bon rendement. On discute des avantages en synthèse de la réaction de cyclisation intramoléculaire de type Cope.

[Traduit par la rédaction]

Introduction

The combination of silicon-based nucleophiles (enol silyl ethers, allylsilanes, vinylsilanes, etc.) and Lewis acid activated electrophiles is a powerful synthetic method for the construction of carbon–carbon bonds (1). Silyl nucleophiles react with a variety of electrophiles including carbonyl compounds, and, additionally, with those such as acetals and tertiary alkyl halides (2), "S_N1 electrophiles," which won't react with the usual organometallic reagents. For most of these reactions, stoichiometric or excess quantities of the Lewis acid "catalyst" are required.

Trimethylsilyl trifluoromethanesulfonate ($Me_3SiOSO_2CF_3$, TMSOTf)(3) is a very strong, monodentate Lewis acid (4) "catalyst" that will activate a variety of heteroatom-bearing electrophiles stoichiometrically, including carbonyl compounds (1) and imines (5). However, a more appealing combination is that of silyl enol ethers, carbonyl compounds, and TMSOTf, in which case the Lewis acid is truly catalytic (6). The carbon analogue of a silyl enol ether, an allylsilane, reacts much less efficiently with carbonyl compounds (acetals generally yield better results) and only in unusual cases may TMSOTf be successfully used catalytically (7).

We were interested in developing an allylsilane reagent which, by virtue of an intra- rather than an intermolecular coupling reaction with an electrophile, would be more efficient and which would ultimately require only catalytic amounts of a Lewis acid. It seemed possible that an allylsilyl triflate might possess these properties, particularly as the reaction with an aldehyde, for example, should be an intramolecular Cope-type cyclization (Scheme 1). If so, the potential exists for enhanced control of relative stereochemistry (bold bond, if R″ ≠ H). We report herein the feasibility of preparing allylsilyl triflates by the addition of triflic acid to diallylsilanes **1** and, subsequently, the reactivity of these species **2** towards carbonyl compounds.

Results and discussion

Preparation of the allylsilyl triflate

Allylsilanes readily react with electrophiles to give, usually (addition reactions have in some cases been observed: ref. 8), an S_E2' reaction involving loss of the silicon. With diallyldimethylsilane **1** as starting material, it was possible with triflic acid to cleave only one of the two allyl groups leading to **2** (Scheme 2). Depending on the conditions used, other products were also ob-tained. There was always a small amount of $Me_2Si(OTf)_2$ **5** formed. Changes in the reaction procedure (particularly solvent and temperature changes) could minimize but not completely suppress this. Any traces of water were manifested by the formation of isopropoxysilanes **6**, which, after subsequent complete hydrolysis of the reaction mixture, gave 2-propanol and **7**.[3]

In the hope of preparing completely pure **2**, a ligand redistribution reaction was attempted. In the silicone industry, the met-

[1]It is a great pleasure to dedicate this communication to Dave MacLean and to thank him for his support, friendship, and our scientific collaboration.

[2]Author to whom correspondence may be addressed. Natural Sciences and Engineering Research Council University Research Fellow, 1985–1995.

[3] ^1H NMR ($CDCl_3$, 200 MHz) **2**, δ: 0.49 (s, 6H), 1.92 (d, 2H, J = 8.2 Hz), 5.05 (m, 2H), 5.76 (apparent sextet, 1H, J = 8.2 Hz); **5**, δ: 0.87 (s, 6H); **6**, δ: 0.56 (s, 6H), 1.53 (d, 6H, J = 5.5 Hz), 1.73 (d, 2H, J = 6.8 Hz), 4.99 (m, 2H), 5.22 (sept, 1H, J = 5.5 Hz), 5.60 (m, 1H); $TfOMe_2SiOiPr$, δ: 0.56 (s, 6H), 1.53 (d, 6H, J = 6.2 Hz), 5.23 (sept, 1H, J = 6.2 Hz). Hydrolysis of the reaction mixture containing **2** led to the same product that results from the hydrolysis of $Me_2(H_2C{=}CH\text{-}CH_2)SiCl$, the known (9) disiloxane **7** $(H_2C{=}CH\text{-}CH_2SiMe_2)_2O$.

Can. J. Chem. Downloaded from www.nrcresearchpress.com by 203.198.23.82 on 09/08/12
For personal use only.

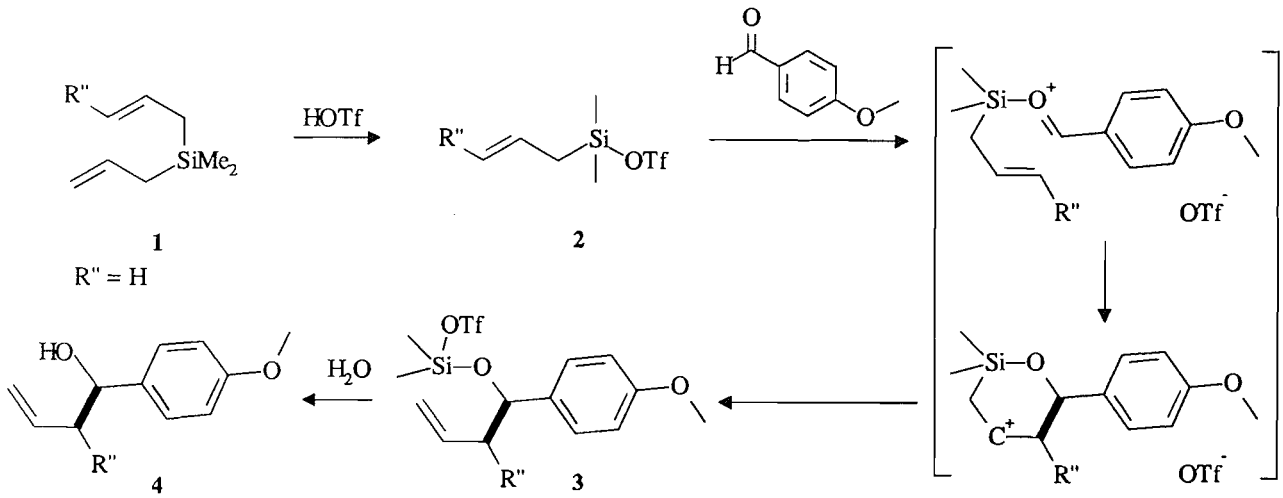

SCHEME 1

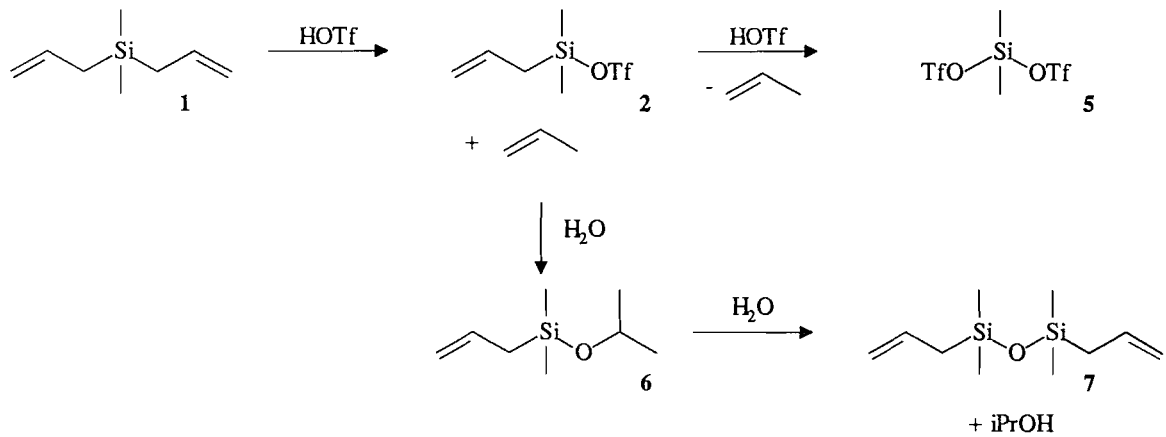

SCHEME 2

athesis of groups on silicon is an important preparative method, the efficiency of which depends upon the relative lability of the groups to be exchanged. For example, while halogens and alkoxy groups will redistribute without catalysts, less labile groups such as H and SiR_3 require weak catalysts such as $R_4N^+X^-$ salts, and unactivated alkyl groups require strong Lewis acids such as $AlCl_3$ (10). Although we expected that the silyl triflate would act as its own Lewis acid catalyst, a reaction between the ditriflate **5** and starting material **1** after refluxing at 61°C for 2 h led to a mixture of **1**, **5**, and **2**[4] (1:1:2, Scheme 3). We have yet to determine whether this represents the equilibrium mixture or whether longer reaction times, higher temperatures, or stronger catalysts[4] are required to force the equilibrium completely to the right.

Reaction of 2 with electrophiles

The normal mechanism for electrophilic attack at allylsilanes[5] is *anti*-S_E2' (7) in which case the silyl group does not directly interact with the electrophile·Lewis acid complex **8** (Fig. 1). To determine if the proposed cyclic transition state (Scheme 1) was reasonable, we examined three conformers as the carbenium ion goes from an "open" structure **9**, via a proposed structure on the reaction path in which the allyl terminus and carbonyl carbon distance is constrained **10** (α = 2.5 Å), to a fully cyclized, β-silyl stabilized cation **11**. Molecular models[6] indicate that a relatively small energy cost is associated with constraining the system in a ring (steric energy **10** = 16.6 kcal/mol, arising primarily from van der Waals terms) when compared to the acyclic minimum (steric energy **9** = 9.3 kcal/mol). More interestingly, the calculated torsional angles between the C—Si bond and the developing *p* orbital of ϕ = 12° and 38°, for **10** and **11**, respectively, are nearly optimal (0°) for the β-effect (12), a factor that will serve to stabilize the (developing) cyclic β-silyl carbocation and compensate for any increased van der Waals interactions. From these results, and in analogy with related radical six-ring cyclizations (13), the proposal of a cationic Cope-type cyclization seems reasonable.

With the allylsilyl triflate in hand, we examined its reactivity towards carbonyl electrophiles. Upon exposure of the solution

[4]If stronger catalysts are required, the redistribution technique would not be appropriate for our purposes. We want to have only one, **intramolecular** Lewis acid catalyst present and, furthermore, wish to avoid separating the hydrolytically unstable triflates from other Lewis acidic materials.

[5]In certain circumstances, when steric bulk interferes with *anti* attack (11*a*) or with electronwithdrawing groups such as fluorine on silicon (11*b*), *syn* attack of the electrophile may be observed.

[6]The structure was modeled using PCMODEL (Serena software, Bloomington, Indiana) with the parameters provided for C^+ "transition state" atoms.

Can. J. Chem. Downloaded from www.nrcresearchpress.com by 203.198.23.82 on 09/08/12
For personal use only.

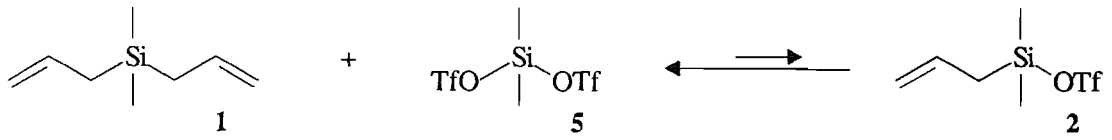

SCHEME 3

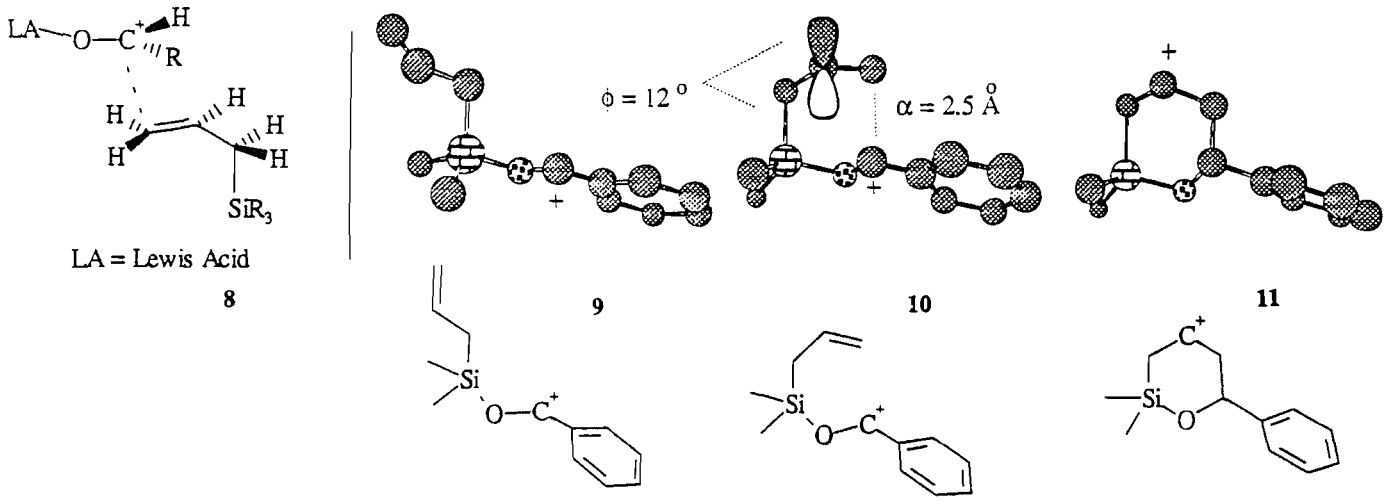

FIG. 1. **8**: Normal open *anti* approach of a Lewis acid activated aldehyde to an allylsilane. **9**: Minimized acyclic intermediate. **10**: Intramolecular *syn* approach, minimized with constraint α = 2.5 Å (resultant ϕ Si—C—C—p orbital = 12°). **11**: Fully cyclized structure (resultant ϕ Si—C—C—p orbital = 38°).

of **2** in $CHCl_3$ to *p*-$MeOC_6H_4CHO$, subsequent work-up,[7] and chromatography, the desired product **4** (14) was isolated in 78% yield (Scheme 1). While other aromatic aldehydes react similarly (PhCHO, 68% (15)), no reaction was observed with ketones such as cyclohexanone as the electrophile source.[8]

We performed a kinetic study to differentiate between an intermolecular, second-order reaction between the allylsilane component and a Lewis acid activated ketone and the proposed first-order, intramolecular cyclization reaction. The reaction between benzaldehyde and the allylsilyl triflate at −62°C in $CDCl_3$ was shown to be first order, consistent with the hypothesis of a cyclic transition state.[9]

Conclusion

Using diallylsilyl compound **1**, it is possible to perform sequential electrophilic addition, desilylation, substitution reactions. The first, with triflic acid, leads to the formation of a silyl nucleophile **2**, which, since it bears a triflate group, is also Lewis acidic. Thus, the addition of a second electrophile, an aldehyde, results in a Cope-type, self-catalyzed condensation giving **4**. In addition to the potential diastereoselective benefits that should arise from a cyclic transition state in the second reaction (Scheme 1, R″ ≠ H), it may be possible to develop related systems in which the active Lewis acidic silyl triflate is present in true catalytic rather than in stoichiometric quantities. Our examination of these questions and the reactivity of other carbon electrophiles will be reported in due course.

Acknowledgment

We gratefully acknowledge the financial support of this research by the Natural Sciences and Engineering Research Council of Canada, and thank the Netherlands' Organisation for the Advancement of Pure Research (NWO) for providing a Visiting Scientist Fellowship to M.A.B.

[7]Typical experimental procedure: To **1** (0.2 mL, 1.0 mmol) in $CHCl_3$ (4 mL) under N_2 at −78°C was added TfOH (0.08 mL, 0.95 mmol). After 45 min, *p*-$MeOC_6H_4CHO$ (0.11 mL, 0.9 mmol) was added. After 2 h, the solution was allowed to warm to 0°C, during which time the solution colour changed from yellow to blue-purple. Following quenching with $NaHCO_3$ solution and extraction with ether, **4** was isolated following flash chromatography (Et_2O: petroleum ether 2:5).

[8]We have not determined whether the reaction does not occur or whether silylation of the enol takes place (3). In the latter case, after hydrolysis, the cyclohexanone would be recovered.

[9]This interpretation is predicated on the interaction between the Lewis acidic silyl triflate and the aldehyde being rapid compared to the rate-determining cyclization.

1. E.W. Colvin. Silicon in organic synthesis. Butterworths, London. 1981; W.P. Weber. Silicon reagents for organic synthesis. Springer, Berlin. 1983; I. Fleming. *In* Comprehensive organic chemistry. Vol. 3. *Edited by* D.N. Jones. Pergamon, Oxford. 1979. Chap. 13.
2. P. Brownbridge. Synthesis, 1 (1983).
3. H. Emde, D. Domsch, H. Feger, U. Frick, A. Goetz, H.H. Hergott, K. Hofmann, W. Kober, K. Kraegeloh, G. Simchen, et al. Synthesis, 1 (1982).
4. M. Suzuki and R. Noyori. Yuki Gosei Kagaku Kyokaishi, **40**, 534 (1982).
5. Jahangir, M.A. Brook, D.B. MacLean, and H.L. Holland. Tetrahedron, **43**, 5761 (1987); Jahangir, M.A. Brook, D.B. MacLean, and H.L. Holland. Can. J. Chem. **65**, 2362 (1987); Jahangir, D.B. MacLean, M.A. Brook, and H.L. Holland. J. Chem. Soc. Chem. Commun. 1608 (1986).
6. S. Murata, M. Suzuki, and R. Noyori. Tetrahedron, **44**, 4259 (1988).

Can. J. Chem. Downloaded from www.nrcresearchpress.com by 203.198.23.82 on 09/08/12
For personal use only.

7. I. Fleming, J. Dunoguès, and R. Smithers. Org. React. **37**, 57 (1989).
8. G. Hagen and H. Mayr. J. Am. Chem. Soc. **113**, 4954 (1991).
9. M.D.E. Forbes, J.T. Patton, T.L. Myers, H.D. Maynard, D.W. Smith, Jr., G.R. Schulz, and K.B. Wagener. J. Am. Chem. Soc. **114**, 10978 (1992).
10. R.A. Benkeser and M.H. Yeh. J. Organomet. Chem. **264**, 239 (1984); V.M. Kopylov, I.S. Shragin, T.I. Rybkina, and A.I. Chernyshev. Zh. Obshch. Khim. **54**, 359 (1984); H. Schmoelzer and E. Hengge. J. Organomet. Chem. **260**, 31 (1984); R.H. Baney, J.H. Gaul, Jr., and T.K. Hilty. Organometallics, **2**, 859 (1983).
11. (*a*) D. Young and W. Kitching. Tetrahedron Lett. **24**, 5789 (1983); (*b*) H. Wetter, P. Scherer, and W.B. Schweizer. Helv. Chim. Acta, **62**, 1985 (1979); T. Hayashi, Y. Matsumoto, and Y. Ito. Organometallics, **6**, 884 (1987).
12. J.B. Lambert, G.-T. Wang, and D.H. Teramura. J. Org. Chem. **53**, 5422 (1988); J.B. Lambert and G.-T. Wang. Tetrahedron Lett. **29**, 2551 (1988); J.B. Lambert, G.-T. Wang, R.B. Finzel, and D.H. Teramura. J. Am. Chem. Soc. **109**, 7838 (1987); J.B. Lambert and E.C. Chelius. J. Am. Chem. Soc. **112**, 8120 (1990); A.J. Kresge and J.B. Tobin. J. Phys. Org. Chem. **4**, 587 (1991).
13. R.B. Walkup, R.R. Kane, and N.U. Obeyesekere. Tetrahedron Lett. **31**, 1531 (1990); M. Koreeda and L.G. Hamann. J. Am. Chem. Soc. **112**, 8175 (1990).
14. K. Krohn, K. Khanbabaee, and H. Rieger. Chem. Ber. **123**, 1357 (1990).
15. M. Wada, H. Ohki, and K. Akiba. Bull. Chem. Soc. Jpn. **63**, 1738 (1990).

Can. J. Chem. Downloaded from www.nrcresearchpress.com by 203.198.23.82 on 09/08/12
For personal use only.

Separation of metal-cyanide complexes by reversed-phase ion-interaction high-performance liquid chromatography

LOUIS GIROUX[1] AND DWIGHT J. BARKLEY[2]

Core Technologies and Services Laboratory, Mineral Sciences Laboratories, Canada Centre for Mineral and Energy Technology, Energy, Mines and Resources Canada, 555 Booth Street, Ottawa, ON K1A 0G1, Canada

Received January 5, 1993[3]

LOUIS GIROUX and DWIGHT J. BARKLEY. Can. J. Chem. **72,** 269 (1994).

Reversed-phase ion-interaction chromatography has been used to study the separation of Cu(I), Ag(I), Ni(II), Au(I), Co(III), Fe(III), and Fe(II) cyano complexes on silica and carbon-based reversed-phases with UV detection at 215 nm. Separation of the metal-cyanide complexes was affected by a number of experimental factors including the nature and concentration of the organic modifier, nature and concentration of the ion-pairing reagent, pH, and ionic strength of the mobile phase. Differences between the elution order of metallo-cyanides observed in the present work and in other investigations under similar experimental conditions are explained by a difference in the ionic strength of the mobile phase. Finally, this technique is used to analyze metal-cyanide complexes in a gold mill solution.

LOUIS GIROUX et DWIGHT J. BARKLEY. Can. J. Chem. **72,** 269 (1994).

La chromatographie d'appariement d'ions a été utilisée afin d'étudier la séparation de métallo-cyanures de Cu(I), Ag(I), Ni(II), Au(I), Co(III), Fe(III) et Fe(II) sur des colonnes à polarité de phases inversées de silice et de carbone avec détection UV à 215 nm. La séparation de ces complexes est influencée par de nombreux paramètres tels le type et la concentration du solvant organique, le type et la concentration de l'ion compensateur ainsi que par le pH et la force ionique de la phase mobile. Les différences entre l'ordre d'élution des métallo-cyanures observés dans la présente étude et au cours de travaux antérieurs sous des conditions expérimentales semblables sont expliquées en fonction de la variation de la force ionique de la phase mobile. Finalement, la technique est utilisée afin d'analyser la teneur en complexes métallo-cyanures d'une solution provenant d'un réservoir situé à proximité d'une mine d'or.

Introduction

In aqueous solution, cyanide can exist in different distinguishable forms. "Free cyanide" represents both CN^- ion and molecular HCN in a solution. They may come from alkali metal-cyanides or metallocyanide complexes that dissociate or decompose to varying extents. This kind of cyanide is the most toxic. On the other hand, "complexed cyanide" is coordinated to an element and is therefore bonded inside a complex. The most important cyano complexes involved in environmental issues are those of iron, copper, zinc, nickel, cobalt, and cadmium. Formation constants for these complexes are well established ranging from a low for $Cd(CN)_4^{2-}$ ($\log \beta = 18.9$) to a high for $Co(CN)_6^{3-}$ ($\log \beta = 64.0$) (1). The toxicity of this kind of cyanide is controlled by the acidity of the medium (toxicity increases as pH decreases) and to the amount of exposure to sunlight.

There are four ways to express cyanide levels in environmental samples: total cyanide, weak acid dissociable cyanide, cyanide amenable to chlorination, and free cyanide. Total cyanide is the amount determined by the acid reflux/distillation method; it includes weak acid dissociable cyanide and cyanides contained in all metallo-cyanide complexes except those of gold, cobalt, and platinum which do not release cyanide under any usual analytical conditions. Weak acid dissociable cyanide includes the cyanide ion, hydrogen cyanide, and cyano complexes of cadmium, copper, nickel, silver, and zinc but not those of iron (ferro and ferricyanides). Cyanide amenable to chlorination is the difference between the total amount of cyanide before and after chlorination; it is a measure of the ionisable cyanide species present in a sample (non-ionisable cyanide species are not oxidized by chlorine). In the gold processing industry, cyano complexes of cadmium, zinc, etc. (i.e. complexes with formation constants of $\log \beta < 20$) are also considered free cyanides.

The above procedures only lead to a partial differentiation of the various categories of cyanides in a solution. These methods can be subject to interference from components that are usually present along with the cyanide in samples from gold mill operations: sulphides, reduced sulphur compounds, and thiocyanates produced in the ore treatment process or with oxidizing agents such as chlorine (2). Furthermore, it is documented that different metallo-cyanides can exhibit varying degrees of environmental persistence and toxicology. For example, labile complexes such as $Cd(CN)_4^{2-}$ and $Zn(CN)_4^{2-}$ are less persistent and more toxic to fish than the more stable $Cu(CN)_3^{2-}$ and $Ni(CN)_4^{2-}$. On the other hand, strong metallo-cyanides, $Fe(CN)_6^{4-}$ and $Fe(CN)_6^{3-}$, by virtue of their high formation constants, could tentatively be expected to show limited toxicity. However, they are also known to photodecompose into free cyanides upon exposure to light (3). All these factors clearly indicate the need for more complete speciation studies, particularly in view of the widespread use of cyanide in gold extraction.

In reversed-phase ion-interaction chromatography, both stationary and mobile phases are the same as in regular reversed-phase techniques. A pairing-ion, usually hydrophobic, is also added to the mobile phase. Samples from this mode of separation are ionisable and can form an ion-pair with the pairing-ion. In the case of separation of metal-cyanide anions ($M(CN)_n^{z-ny}$, where $ny > z$), the pairing-ion present in the mobile phase is a cation, and is typically a quaternary ammonium ion.

Back in 1985, Pohlandt (4) was the first to use ion-interaction

[1]Present address: Combustion and Carbonization Research Laboratory, Energy Research Laboratories, Canada Centre for Mineral and Energy Technology, Energy, Mines and Resources Canada, Bells Corners Complex, Building 2, Ottawa, ON K1A 0G1, Canada. Author to whom correspondence may be addressed.

[2]Present address: 59 Ridgefield Crescent, Nepean, ON K2H 6S6, Canada.

[3]Revision received September 20, 1993.

Can. J. Chem. Downloaded from www.nrcresearchpress.com by 195.246.54.202 on 09/08/12
For personal use only.

Can. J. Chem. Downloaded from www.nrcresearchpress.com by 195.246.54.202 on 09/08/12
For personal use only.

chromatography to separate and quantify metal-cyanide complexes in gold processing solutions. Since then, several groups from Australia (5, 8) and South Africa (6, 7) have used the same method to separate metallo-cyanides. They have successfully applied the principle of ion-interaction chromatography to analyze precious metals in gold processing solutions and metallurgical and plant samples.

The main objective of this paper is to comment on the significant differences in the elution order of cyanometallate complexes of Cu(I), Ag(I), Ni(II), Au(I), Co(III), Fe(III), and Fe(II) on C_{18} and on the carbon-based reversed phases observed in our study and those of other scientists (5, 6, 8). This paper also discusses the effect of changing variables as (*i*) the nature and concentration of the organic modifier, (*ii*) the nature and concentration of the ion-pairing reagent, (*iii*) pH, and (*iv*) ionic strength of the mobile phase on the chromatographic separation of anionic cyano complexes at 215 nm. Finally, we have applied the reversed-phase ion-interaction chromatographic technique to determine the amount of metallo-cyanide in a leach liquor originating from a reservoir located near a Canadian gold mine.

Experimental

HPLC system

The HPLC system consisted of a Spectra Physics precision isocratic pump (Model 8810, Spectra Physics, San Jose, CA), a Spectra Physics SP 8810 autosampler with a Valco sample valve and a 50 μL sample loop, and a variable wavelength detector (Linear UVIS-200, Reno, NV) operating at 215 nm. The signal from the detector was monitored with a Spectra Physics SP-4270 computing integrator.

Three silica-based C_{18} reversed-phase columns (150 × 4.6 mm) were used in this study: (*i*) Supelcosil LC-18-DB (5 μm particle size), (ii) Millipore-Waters Nova-Pak C_{18} (4 μm particle size), and (*iii*) Du Pont – Zorbax R_x-C_{18} (5 μm particle size). These columns are restricted to mobile phases in the pH range 2–8. A crosslinked organic polymer (styrene–divinylbenzene) column, Interaction/ACT-1 (150 × 4.6 mm, 10 μm particle size), and a porous graphite column, Shandon-Hypercarb (100 × 4.6 mm, 7 μm particle size), were also used in this study. The last two columns are reported to be stable from pH 0–14.

Atomic absorption instrument

Atomic absorption spectroscopic analysis of the metals in a gold mill solution was performed with a GBC Model 908 AAS instrument (Dandenong, Australia).

Reagents and procedures

Mobile phases

Mobile phases were prepared using water purified with a Millipore (Bedford, MA) Milli-Q water treatment system, Burdick and Jackson of Canada LC-grade organic solvents (acetonitrile, methanol, ethanol, acetone, or tetrahydrofuran forming binary mixtures with water), an appropriate ion-interaction reagent and an inorganic modifier, NaH_2PO_4 (J.T. Baker Inc., Canada).

The ion-interaction reagents used were the tetraalkylammonium hydroxide series, $R_4N^+OH^-$ where R = C_1–C_4 (Sigma Chemical Co., St. Louis, MO) and the alkyltriethylammonium phosphate series, $R(C_2H_5)_3N^+H_2PO_4^-$ where R = C_5–C_8 and C_{12} (Regis Chemicals, Morton Grove, IL).

The mobile phases were filtered immediately prior to use through 0.45 μm Millipore-type membrane filters and degassed before use. An adjustment to the ionic strength of the mobile phases was made by adding NaH_2PO_4. The ionic strength values quoted in this paper are calculated using *solely* the concentration of the phosphate salt, taking into account the pH dependency of phosphate species ($H_2PO_4^-$ and HPO_4^{2-}), and do *not* include the concentrations of the pairing-ion reagent salts. The pH of the mobile phases were measured with a Corning Model 250 pH meter equipped with a glass–calomel electrode.

Metal-cyanide complexes

Standard solutions of the cyanide complexes of Zn(II), Au(I), Co(III), Fe(II) (Aldrich Chemical Co., Milwaukee, WI), Cd(II), Ni(II) (Alpha Inorganics, Beverly, MA), and Fe(III) (Allied Chemicals, New York, NY) were prepared by dissolving weighed amounts of the respective potassium salts in 0.1 M NaOH (BDH Inc., Canada). Solutions containing Cu(I) and Ag(I) complexes were prepared by the dissolution of CuCN (BDH Inc., USA) and AgCN (Fisher Scientific Ltd., Canada) with stoichiometric amounts of KCN (J.T. Baker Inc., Canada) in 0.1 M NaOH. Standard solutions containing mixtures of the metal-cyanide complexes were prepared from the individual standard solutions. Standard solutions were kept at an alkaline pH and stored in darkness to minimize degradation (3).

Most of the results reported in this investigation were obtained at a mobile phase pH of approximately 8. At this pH, individual complexes and mixtures of the various complexes are found to be appreciably more stable than at pH less than 8. When the pH of the eluent is lowered from 8 to 6, we observe (*i*) an increase in retention times for the cyanometallates and (*ii*) increasingly broader and unsymmetrical peaks caused by a greater dissociation of the complexes.

Gold mill sample

The metal-cyanide complexes were from a leach liquor sample from a Canadian gold mine.

Chromatographic separations

All separations were carried out at room temperature using a mobile-phase flow-rate of 1.0 mL min^{-1}. Each time we used a new column, or each time we studied the characteristics of a new mobile phase mixture, we allowed the analytical column to equilibrate with eluent for 1 h. Metallo-cyanides were identified by retention times. Under our chromatographic conditions, we were able to get absorption peaks for all complexes except Cd(II) and Zn(II) cyanides. These complexes were very weakly absorbing at 215 nm and at the same time decompose in the mobile phase, hence they were not studied further. Our method yielded reasonable results only when special care was taken to prepare the eluent because small variations in the concentrations of the mobile phase components had a marked effect on the retention times of the complexes.

Results and discussion

As mentioned in the Introduction, the focus of this paper is to explain the significant differences between our elution sequence of metal-cyanide complexes and those from other studies under apparently similar experimental conditions. Let us first make a few general comments on the effect of certain experimental parameters on the separation of anionic cyano complexes using reversed-phase ion-interaction chromatography.

Nature and concentration of the organic modifier

When using ion-interaction techniques to separate solutes, retention times and selectivities are markedly dependant on the mobile-phase composition and, in particular, on its organic solvent (9–11). By increasing the concentration of the organic modifier, acetonitrile or methanol, in the mobile phase, there is a decrease in retention times of the complexes on C_{18} columns, as has been observed (5, 6). We picked acetonitrile over methanol as the organic modifier since it provided a better resolution of the eluted complexes. When the concentration of the organic modifier in the mobile phase remains constant (32–40% v/v of acetonitrile), the complex retention times are longer on the carbon-based column because of its hydrophobic character (12).

Nature and concentration of the ion-interaction reagent

In reversed-phase ion-interaction systems, the anionic reten-

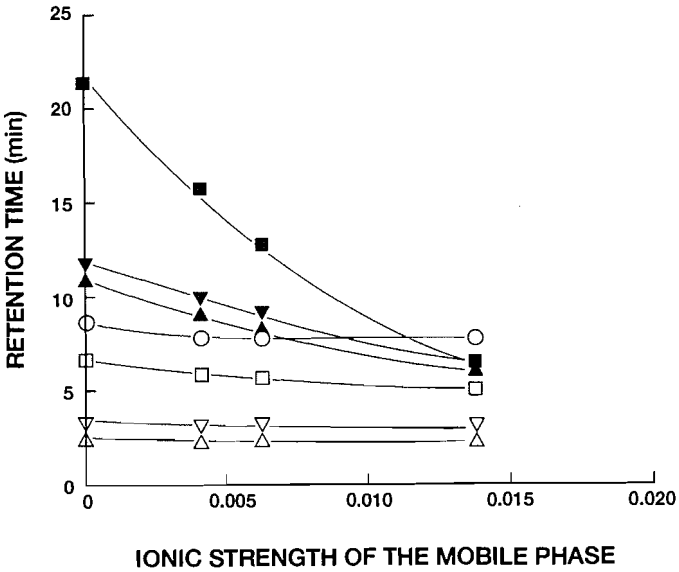

FIG. 1. Effect of ionic strength of the mobile phase on retention times of metal-cyanide complexes. As described in the text, the ionic strength values given in this figure are based exclusively on the concentrations of the phosphate species (Na_2HPO_4 and NaH_2PO_4) and *not* on the concentrations of the tetrabutylammonium ion; e.g. an ionic strength of zero, $I = 0$, refers to eluents prepared *without* the presence of phosphate ions. Experimental conditions: *column*, Waters Nova-Pak C_{18}; *mobile phase*, 4 mM tetrabutylammonium ion $(C_4H_9)_4N^+$, 32% v/v of acetonitrile, NaH_2PO_4 for ionic strength adjustment and pH = 8; *flow rate*, 1 mL min^{-1}; *detector*, UV at 215 nm; *sample volume*, 50 μL. Symbols for the cyanide complexes are as follows: △: Cu(I), ▽: Ag(I), □: Ni(II), ○: Au(I), ▲: Co(III), ▼: Fe(III), ■: Fe(II).

tion times increase with increasing pairing-ion (cation) concentration (9). Furthermore, increased pairing-ion concentration (e.g. tetrabutylammonium) leads to an increased retention of the metallo-cyanide complexes on the C_{18} columns. This observation, as reported by other workers (4, 6, 8), is attributed to an increase in the effective ion exchange capacity of the column.

The retention times of solutes also change with the type of pairing-ion. We have used the tetraalkylammonium series, where alkyl = C_1–C_4, and the alkyltriethylammonium series, where alkyl = C_5–C_8 and C_{12} straight chain groups in our studies while maintaining a constant pairing-ion concentration of 5 mM. Our results show that the tetrabutylammonium pairing-ion is more effective in separating the various metallo-cyanate complexes (4).

pH of the mobile phase

The mobile phase pH can be a useful parameter for achieving and optimising selectivity in reversed-phase liquid chromatography (13). When the pH of the mobile phase was lowered from 8 to 6, retention times increased for most complexes. A change in pH, however, had no effect on the retention time of the silver complex and led to a decrease in retention time for the copper complex. A possible explanation for an increased retention time of the five complexes at pH = 6 is that there is a greater ratio of di-to-monohydrogen phosphate ions $[H_2PO_4^-] = 14.3[HPO_4^{2-}]$, as calculated from the ionisation constant $K_2 = 7 \times 10^{-8}$.

Ionic strength

When the ionic strength of the mobile phase increases, the formation of ion-pairs generally decreases since the secondary ions compete to form ion-pairs with the pairing-ions (14). A plot of the ionic strength of the mobile phase on the retention time of the metal-cyanide complexes is shown in Fig. 1. Most complexes show shorter retention times. The greatest change is found in Fe(II) cyanide. At zero-ionic strength (based *exclusively* on the concentration of the phosphate species in the eluent, see Experimental), Fe(II) and Fe(III) cyanides are well separated; however, they were coeluted at an ionic strength of about 14×10^{-3}. At pH 8, adding phosphate ions (HPO_4^{2-} and $H_2PO_4^-$) to the mobile phase seems to reduce the electrostatic interaction between the most negatively charged Fe(II) complex (−4) and the pairing-ion more so than other complexes. Low negatively charged complexes such as Cu(I) (−2), Ag(I) (−1), and Au(I) (−1) show no change in their retention times.

By varying the ionic strength in the mobile phase there are changes in retention times and the elution order of metal-cyanide complexes. We shall elaborate on the second point in the following paragraph.

Elution order of metal-cyanide complexes

In this study, the cyano complexes elution order is identical to that reported by one group (7) but quite different from that reported by other groups (5, 6, 8).

In our study, when the mobile phase (i.e. organic solvent (acetonitrile), ion-interaction reagent (tetrabutylammonium hydroxide), and inorganic modifier (NaH_2PO_4)) were identical, all three silica-based C_{18} columns (Supelcosil, Waters, and Du Pont) gave essentially the same elution order for the complexes. The only difference between the Supelcosil column and the Waters and Du Pont columns was for Co(III) and Au(I) complexes; Co(III) is eluted earlier on the Supelcosil column and retained longer on both the Waters and Du Pont columns at relatively low ionic strengths ($<7 \times 10^{-3}$, again based *only* on the concentration of the phosphate species, see Experimental section) in the mobile phase. Pohlandt-Watson and Hemmings (7) used a similar Supelcosil column under similar mobile phase conditions and obtained essentially the same results (Cu(I), Ag(I), Ni(II), Co(III), Au(I), Fe(III), and Fe(II)). Our elution order was Cu(I), Ag(I), Ni(II), Au(I), Co(III), Fe(III), and Fe(II). Grigorova et al. (6) and Haddad and co-workers (5, 8), using a Waters Nova-Pak C_{18} column, observed the order Cu(I), Ag(I), Fe(II), Co(III), Ni(II), Fe(III), and Au(I). Here Grigorova et al. used a mobile phase of 2.5 mM tetrabutylammonium hydrogen sulphate – methanol (70:30 v/v), and Haddad and co-workers used a mobile phase of 5 mM tetrabutylammonium hydroxide – acetonitrile (77:23 v/v) (5) or 5 mM tetrabutylammonium chloride and/or bromide–acetonitrile (76:24 v/v) (8). In our work, while we have used a number of mobile phases consisting of various concentrations of ion-interaction reagents (e.g. tetraalkylammonium hydroxide or alkyltriethylammonium phosphate series), inorganic modifier (NaH_2PO_4), and organic solvents (acetonitrile, methanol, ethanol, acetone, or tetrahydrofuran), our best separation was achieved by using 4 mM tetrabutylammonium hydroxide – acetonitrile (68:32 v/v) for the mobile phase adjusted to a pH of about 8 with NaH_2PO_4.

The following are the major differences in mobile phases used in our work and those of Grigorova (6) and Haddad (5, 8): (*i*) counter-anion: HPO_4^{2-} and $H_2PO_4^-$ (major) and OH^- (minor) in our work HSO_4^-, Cl^-, Br^-, and OH^- in references 5, 6, and 8 bound to the cationic ion-pairing reagents containing a

Can. J. Chem. Downloaded from www.nrcresearchpress.com by 195.246.54.202 on 09/08/12
For personal use only.

Can. J. Chem. Downloaded from www.nrcresearchpress.com by 195.246.54.202 on 09/08/12
For personal use only.

complex	mg L^{-1}
$Cu(CN)_3^{2-}$	0.7
$Ag(CN)_2^-$	7.3
$Ni(CN)_4^{2-}$	4.0
$Au(CN)_2^-$	5.1
$Co(CN)_6^{3-}$	4.5
$Fe(CN)_6^{3-}$	3.7
$Fe(CN)_6^{4-}$	3.0

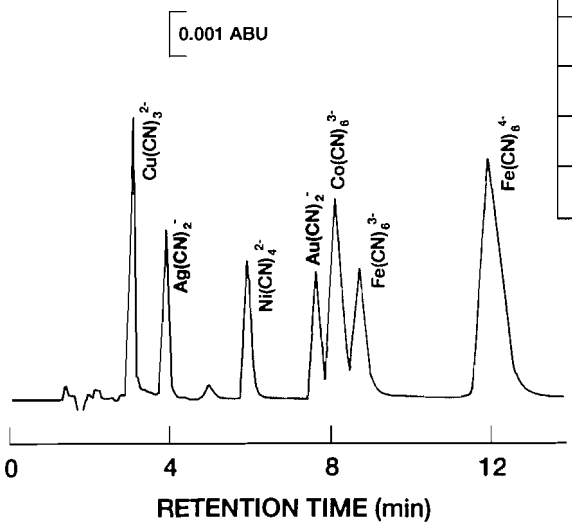

FIG. 2. Chromatogram of a synthetic mixture. Experimental conditions: *column*, Du Pont-Zorbax R_x-C_{18}; *mobile phase*, 4 mM tetrabutylammonium ion $(C_4H_9)_4N^+$, 35% v/v of acetonitrile, 1.25 mM NaH_2PO_4 and pH = 8; *flow rate*, 1 mL min^{-1}; *detector*, UV at 215 nm; *sample volume*, 50 μL.

quaternary nitrogen atom (R_4N^+, where R = C_4H_9 for most separations) and (*ii*) the presence of an inorganic modifier (NaH_2PO_4) in our work and none in references 5, 6, and 8. Haddad and Kalambaheti (8) and this group agreed that counter-anions only change the retention times of complexes (longer retention times for HPO_4^{2-}, $H_2PO_4^-$, and OH^- ions than Cl^- and Br^- ions) and *not* on their elution order. However, Pohlandt has shown that by adding inorganic modifiers (borates, carbonates, hydroxide, and phosphates) to the mobile phase the relative positions of the iron cyanide complexes, Fe(II) and Fe(III), in the chromatograms are affected (4). Furthermore, depending on the nature and concentration of the salt, the elution order for iron and gold complexes may be changed while the order of the other metallo-cyanides remains unchanged. For example, when the concentration of carbonate – hydrogen carbonate mixture added is less than 0.5 mM, the iron cyanide complexes were eluted after the gold complex but when the concentration is greater than 1.02 mM, iron cyanide complexes were eluted before the gold complex. Figure 1 illustrates the change in elution order of the complexes upon increasing the ionic strength of the mobile phase. At ionic strengths less than 6.5×10^{-3} (based exclusively on the concentration of phosphate species), an elution order of Cu(I), Ag(I), Ni(II), Au(I), Co(III), Fe(III), and Fe(II) is obtained on the Waters column, an order identical to that observed by Pohlandt-Watson and Hemmings (7) on a Supelcosil column. At ionic strengths between 7 and 9×10^{-3}, the elution orders for the Au(I) and Co(III) complexes are reversed. Furthermore, Au(I) complex is eluted before Fe(III) and Fe(II) complexes at ionic strengths of 9 and 11.5×10^{-3}, respectively. At an ionic strength of about 14×10^{-3}, the elution order takes the form Cu(I), Ag(I), Ni(II), Co(III), Fe(II) and Fe(III) co-eluted, and Au(I). A simple extrapolation of the ionic strength from 14×10^{-3} to approximately 20×10^{-3} (based on the concentration of phosphate ions only, as before) tentatively yields an identical elution order (Cu(I), Ag(I), Fe(II), Ni(II), Co(III), Fe(III), and Au(I)), as that found by Grigorova et al. (6) and Haddad and co-workers (5, 8), both of whose studies must have been carried out at ionic strengths somewhat higher than ours. To conclude, the ionic strength of the mobile phase is important to the elution order of metallo-cyanide complexes on silica-based columns. Different elution orders were observed depending on the ionic strength of the mobile phase and the presence of inorganic modifiers such as NaH_2PO_4. This work uses a Waters Nova-Pak C_{18} column and moderately low ionic strengths ($< 6 \times 10^{-3}$) whereas other workers used somewhat higher ($> 15 \times 10^{-3}$) ionic strengths (5, 6, 8).

Analysis of metal-cyanide complexes in a gold mill solution

Before analyzing a gold mill sample, we first analyzed complexes mixtures. Their calibration curves were linear over the concentration range 0.2 to 10 mg L^{-1}. A typical chromatogram is shown in Fig. 2. Figure 3 shows the gold mill complexes and their concentrations. The amount of metal deduced from concentrations of cyano complexes from liquid chromatographic (LC) method and atomic absorption spectrometry (AAS) showed good agreement except for copper, which was approximately 2.5 times higher by the LC determination (Table 1).

The higher Cu concentration might be attributed to a positive interference by UV-absorbing anions present in the sample and appear as interfering peaks in the final chromatogram (8) (such as Br^-, NO_2^-, NO_3^-, and SCN^-; SCN^- being the most likely present in gold mill effluents (2)). Although the gold mill sample was not analyzed for thiocyanate (SCN^-) in aqueous solution (16), this ion has a strong absorption band maximum in the far ultraviolet spectrum ($\epsilon \sim 3 \times 10^3$ M^{-1} cm^{-1}) at approximately 46 000 cm^{-1} (217 nm) which is near our detection wavelength (215 nm). Fagan and Haddad, using similar condi-

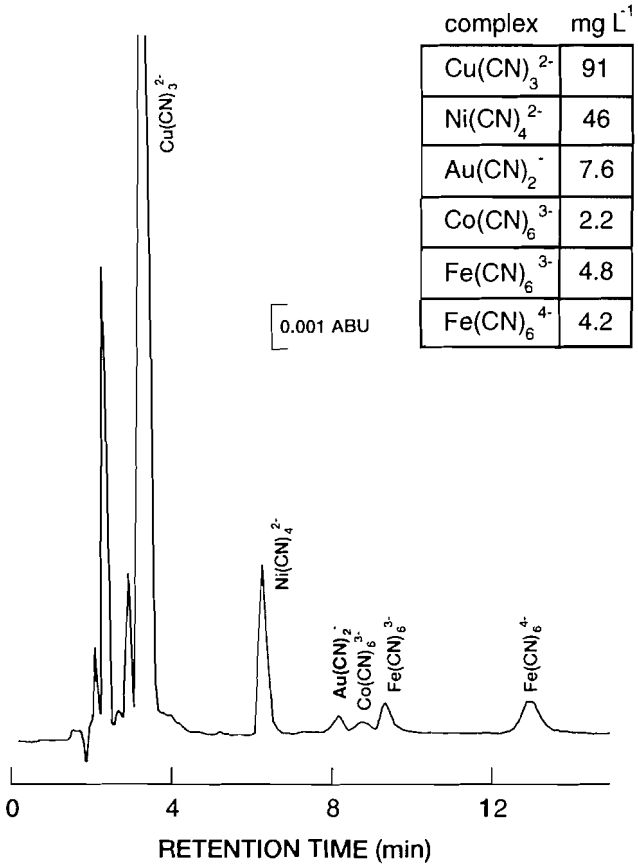

FIG. 3. Chromatogram of a gold mill solution from a Canadian mine. Experimental conditions: same as in Fig. 2.

tions, showed the thiocyanate ion to elute immediately before the copper(I) cyanide complex (17).

Conclusions

Reversed-phase ion-interaction chromatography can separate Cu(I), Ag(I), Ni(II), Au(I), Co(III), Fe(III), and Fe(II) cyanide complexes on silica-based C_{18} reversed-phase columns. These columns exhibited greater efficiency, selectivity, and stability than organic polymer and porous graphite columns which were used in the preliminary stages of our study. The difference between the elution orders of metallo-cyanides we observed and those in other studies was due to the difference in ionic strength of the mobile phase. Our procedure was simple and fast and usually took less than 15 min. The lower detection limit for cyanometallate complexes was about 0.1 mg L^{-1}. Our method can also be used to analyze gold mill samples, thus enabling the Canadian gold mining industry to better monitor metal-cyanide levels.

Acknowledgments

Financial support for this project and the permission to publish this paper was granted by the Department of Energy, Mines and Resources Canada. The authors wish to extend sincere thanks to L. McCullogh for his assistance in the AAS measurements, to S. Duguay, C. Glasgow, and E. Hinchberger for their help in the preparation of figures, and to P. Carrière, G. Laflamme, V. McNamara, Dr. G. Deschênes, and Dr. P. Riveros for useful discussions.

TABLE 1. Composition of a gold mill solution (metals) from a Canadian mine

Metal	Concentration (mg L^{-1}) LC[a]	AAS[b]
Zn	[c]	0.01
Cu	41	17
Cd	[d]	0.01
Ag	0	0.3
Ni	17	16
Au	6	5.8
Co	0.6	0.7
Fe	2.4	2.9

[a]LC (liquid chromatogrphic analysis); experimental conditions as in Fig. 2 caption.

[b]AAS (atomic absorption spectroscopic analysis).

[c](Not detected); zinc cyanide complex, $Zn(CN)_4^{2-}$, is very weakly absorbing at 215 nm ($\varepsilon < 1$ M^{-1} cm^{-1} 15)) and undergoes decomposition in the mobile phase.

[d](Not detected); cadmium cyanide complex, $Cd(CN)_4^{2-}$, is coeluted with the Cu(I) cyanide complex. It is also very weakly absorbing at 215 nm ($\varepsilon < 1$ M^{-1} cm^{-1} (15)) and undergoes decomposition in the mobile phase.

1. M.T. Beck. Pure Appl. Chem. **59**, 1703 (1987).
2. J. Ingles and J.S. Scott. State-of-the-art of processes for the treatment of gold mill effluents. An unpublished report of the Environmental Protection Service, Environment Canada, Ottawa. 1987.
3. C. Pohlandt. Report No. M128. Council for Mineral Technology, Randburg, Republic of South Africa. 1984.
4. C. Pohlandt. S. Afr. J. Chem. **38**, 110 (1985).
5. D.F. Hilton and P.R. Haddad. J. Chromatogr. **361**, 141 (1986).
6. B. Grigorova, S.A. Wright, and M. Josephson. J. Chromatogr. **410**, 419 (1987).
7. C. Pohlandt-Watson and M.-J. Hemmings. S. Afr. J. Chem. **41**, 136 (1988).
8. P.R. Haddad and C. Kalambaheti. Anal. Chim. Acta **250**, 21 (1991).
9. L.R. Snyder and J.J. Kirkland. Introduction to modern liquid chromatography. 2nd ed. Wiley, New York, NY. 1979.
10. P.R. Haddad and P.E. Jackson. Ion chromatography: principles and applications. Journal of Chromatography Library. Vol. 46. Elsevier, Amsterdam. 1990.
11. H. Colin, G. Guiochon, Z. Yun, J.C. Diez-Masa, and J. Jandera. J. Chromatogr. Sci. **21**, 179 (1983).
12. J.H. Knox and B. Kaur. *In* High performance liquid chromatography. *Edited by* P.R. Brown and H.A. Hartwick. Chemical analysis. Vol. 98. Wiley, New York, NY. 1989. pp. 189–222.
13. P.J. Schoenmakers, S. van Molle, C.M.G. Hayes, and L.G.M. Uunk. Anal. Chim. Acta, **250**, 1 (1991).
14. S.C. Su, A.V. Hartkopf, and B.L. Karger. J. Chromatogr. **199**, 523 (1976).
15. J. Brigando. Bull. Soc. Chim. Fr. **4**, 503 (1957).
16. E. Gusarsky and A. Treinin. J. Phys. Chem. **69**, 3176 (1965).
17. P.A. Fagan and P.R. Haddad. J. Chromatogr. **550**, 559 (1991).

Can. J. Chem. Downloaded from www.nrcresearchpress.com by 195.246.54.202 on 09/08/12
For personal use only.

Analysis of alkyl ketene dimer (AKD) by potentiometric titration

S. NYARKU[1] AND B. BRUCE SITHOLÉ[2]

Process Chemistry Division, Pulp and Paper Research Institute of Canada, 570 St. John's Boulevard, Point Claire, QC H9R 3J9, Canada

Received August 13, 1993

S. NYARKU and B. BRUCE SITHOLÉ. Can. J. Chem. **72,** 274 (1994).

A simple and precise potentiometric titration method has been developed for the determination of milligram quantities of alkyl ketene dimer (AKD) in non-aqueous solvents. It involves the addition of chloroform solutions of AKD to an excess of an organic base followed by the titration of excess base with perchloric acid in glacial acetic acid. The method was used to determine non-reacted AKD extracted from hand-sheets: our results agreed with those obtained by capillary gas chromatography. The method was also used to monitor the stability of AKD formulations. Wood resin components and stearone, a hydrolysis product of AKD, do not interfere.

S. NYARKU et B. BRUCE SITHOLÉ. Can. J. Chem. **72,** 274 (1994).

Un titrage potentiométrique simple et précis nous permet de déterminer la concentration de dimère d'alcanes cétèniques (AKD), de l'ordre du milligramme, dans des solvants non-aqueux. Une solution d'AKD dans du chloroforme est ajoutée à une base organique de concentration excessive et la base résiduelle est par la suite titrée avec de l'acide perchlorique préparée dans de l'acide acétique glaciale. Cette méthode a été utilisée pour la détermination de la quantité d'AKD non-réagi, extraite de formettes, et les résultats correspondent à ceux obtenus par chromatographie capillaire en phase vapeur. La méthode a également servi à vérifier la stabilité des formulations d'AKD. Les composés de la résine du bois ainsi que la stéarone, un produit de l'hydrolyse de l'AKD, n'interfèrent pas.

Can. J. Chem. Downloaded from www.nrcresearchpress.com by 195.246.54.202 on 09/08/12
For personal use only.

Introduction

Alkyl ketene dimer (AKD) is a sizing agent commonly used in neutral and alkaline papermaking. It belongs to a class of reactive sizes which react with cellulosic fibres to render the surface hydrophobic (1, 2). Sizing efficiency depends on several factors including retention, particle distribution on the fibre surfaces, spreading, and the extent of chemical reaction of the size. Several forms of AKD exist in alkaline papermaking systems. First, there is some evidence (3, 4) that it can bond chemically to hydroxyl groups of cellulosic fibres to form β-keto esters producing the required sizing effects and properties. This form is commonly called reacted or bound AKD. At best, only about 50% of the AKD reacts to affect the sizing of the paper (5, 6). It is therefore important to know the fate of the non-reacting AKD. Second, AKD can be physically adsorbed on the surface of paper fibres without chemical bonding; this form is called non-reacted or unbound AKD. Non-reacted AKD also contributes to sizing. However, reacted AKD is about three times more efficient (4). Third, AKD may be hydrolyzed to form keto-acids and ketones. Finally, when AKD does not interact with paper fibres and is not retained in the paper, it can be found in process waters in both unchanged and hydrolyzed forms. Therefore, in alkaline papermaking it is important to determine the proportion of the AKD added that is retained in the paper and the proportion of AKD added that exists in other forms, in order to properly understand the sizing process.

A number of methods have been used to analyze AKD. The more widely used methods involve the hydrolysis of AKD to yield a ketone (stearone), or the methylation of AKD to form keto-esters, followed by the analysis of stearone or keto-esters using chromatographic techniques, notably HPLC and GC (1, 6–8). GC mass spectrometry and pyrolysis GC have been used recently (9, 10). Radioactive tracer studies with ^{14}C have also been used to determine the proportion of reacted and unreacted AKD on paper fibres (5) while solid state NMR studies have been conducted with ^{13}C-labelled AKD (11). Ultrasonic attenuation of paper in water has been correlated with the amount of AKD in paper (12). The unique absorption band of AKD by its four-membered lactone ring at 1860 cm^{-1} in the infrared spectrum has been used both to identify and to quantify the dimer (13). Spectrophotometric techniques have been investigated, and used to investigate the effect of ageing on sizing (14).

This paper reports a new titration procedure developed to analyze AKD. The procedure, based on titrimetry, offers some advantages over chromatographic techniques.

Theory

Ketones and diketenes are known to react with organic bases (15). This reaction can be used to measure concentrations of AKD by first reacting AKD with an excess base, and then measuring the excess base by titrimetry. In this report morpholine was selected as the base mainly because, as a secondary amine, it is less susceptible to interferences than other bases bearing primary amino groups. The reaction of AKD with morpholine may be represented by

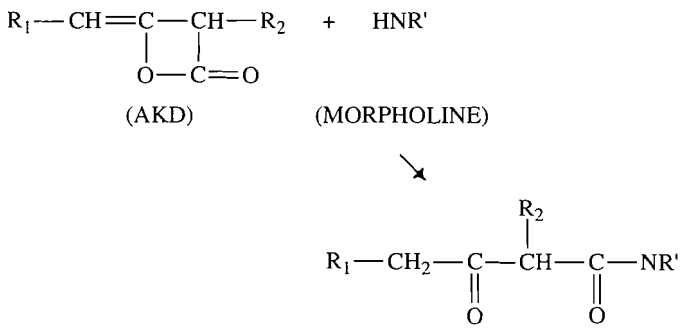

The developed procedure involves the addition of excess morpholine to AKD, followed by potentiometric back-titration of the excess morpholine with perchloric acid in acetic acid.

[1]Visiting Scientist, Chemistry Department, Brandon University, Brandon, MB, Canada R7A 6A9.

[2]To whom correspondence should be addressed.

Can. J. Chem. Downloaded from www.nrcresearchpress.com by 195.246.54.202 on 09/08/12
For personal use only.

Experimental

1. Materials

An AKD sample and an AKD emulsion (as used in alkaline papermaking mills) were obtained from a supplier in the paper industry. ACS reagent quality morpholine and perchloric acid were used as purchased without further purification. HPLC grade solvents were used in all investigations. A Metrohm 655 Dosimat automatic titrator connected to a Corning pH meter (Model 130) with a combination electrode was used for potentiometric titrations. Measurements were taken on the relative potential scale. The system was interfaced to a simple Apple computer system with a software program which gave a screen display of the progress of the titration and also allowed for determination of the titration end-point. As the titrations were done under non-aqueous conditions, all glassware and apparatus were dried carefully in an oven to ensure that the titrations would work properly.

2. Preparation of perchloric acid solution in acetic acid

An approximately 0.10 M perchloric acid solution was prepared by adding 4.3 mL 69–72% perchloric acid in 100 mL glacial acetic acid, followed by 15 mL acetic anhydride. The resulting mixture was allowed to cool for about 30 min before diluting to 500 mL with glacial acetic acid. This solution was then standardized with potassium hydrogen phthalate (KHP).

3. Standardization of perchloric acid solution with KHP

The perchloric acid solution was standardized by potentiometric titration with KHP. KHP (0.1064 g) was added to 25 mL glacial acetic acid and the mixture was heated gently to assist the dissolution of the solid. After cooling, the resulting solution was potentiometrically titrated with the perchloric acid, using the system described above. Three drops of a visual indicator, crystal violet, were added to display a purple-to-green colour change at the end-point. This change was sharp enough to be used as a visual indicator. However, in this work all end-point volumes were determined by a second derivative titration plot.

4. Preparation of morpholine solution in chloroform

Morpholine has a molar mass of 87.12 g/mol and a density of 0.996 g/mL. The approximately 0.10 M stock solution used in the experiments was prepared by diluting 0.90 mL morpholine with chloroform to 100.0 mL in a volumetric flask.

5. Standardization of morpholine solution with perchloric acid

Morpholine solution (5.00 mL) was transferred to a 100 mL titration beaker, followed by 20 mL chloroform. The mixture was titrated potentiometrically with standardized perchloric acid.

6. Titration of morpholine after the addition of AKD

Morpholine solution (5.00 mL) was added to 10.00 mL of 10 000 ppm AKD solution, followed by 10 mL chloroform. The mixture was allowed to stand for 15 min before potentiometric titration with the perchloric acid solution. The titration was repeated with larger volumes of the AKD solution and a calibration curve prepared from the results.

7. Precision

Precision of the titration procedure was determined by titration of 5 replicate samples of the same AKD solutions.

8. Interferences

The interferences of wood resin and stearone on the titration procedure was investigated by titration in the presence of 5.00 mL of 1000 ppm solutions of resin acids, fatty acids, tall oil, or stearone. The results were compared to the values obtained in the absence of the compounds.

9. Reaction kinetics

These were determined by titration of replicate samples which had been allowed to equilibrate for 15, 30, 60, 130, 250, 360, 400, and 500 min. The data points were analyzed to determine the reaction rate.

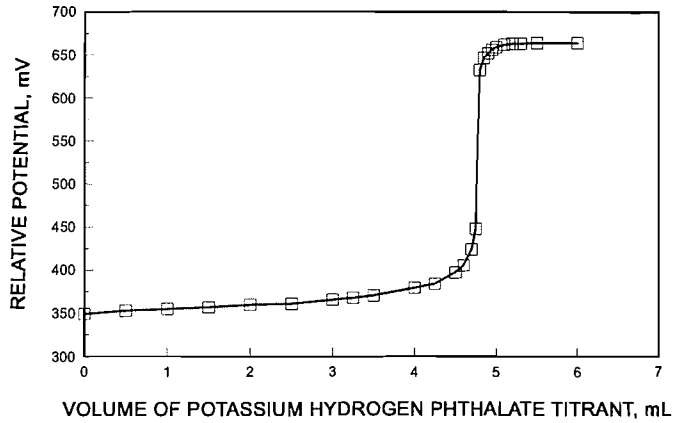

FIG. 1. Standardization of perchloric acid by potentiometric titration with potassium hydrogen phthalate.

10. Effect of the addition of various solvents

Due to the formation of a precipitate during the titration process, various solvents were used to determine their effect on the titration curves and the formation of the precipitate. The solvents investigated were acetone, acetonitrile, and toluene; these were chosen because of their polarity indices and their ability to dissolve AKD.

11. Stability of AKD mill emulsions

AKD emulsions can hydrolyze to yield stearone which is not effective in sizing and causes sticky deposition problems in pulp and papermaking (5). Conditions which induce hydrolysis include high temperature and change in pH of the AKD formulation (5). For example, recommended shelf lives of commercial emulsions are 2 weeks, 4 weeks, and 1 year at storage temperatures of 32°C, 24°C, and 4°C, respectively. It would be useful to have an easy method that could be used to monitor the stability of emulsions. A sample of an AKD emulsion was made to hydrolyze rapidly by adjusting its pH from 2.5 to 6 and equilibrating overnight. The original and hydrolyzed samples were then analyzed by the titrimetric procedure on 1 mL portions of the emulsions.

12. Unreacted AKD in paper

Handsheets sized with AKD were prepared in the laboratory using a Mark V Dynamic Handsheet Mold.[3] The handsheets were pressed at 420 kPa, dried on a cylinder speed dryer at 105°C, and cured for 10 min in an oven at 110°C. The unreacted AKD in the paper was extracted with chloroform (10) and the chloroform extracts were evaporated to known small volumes before analysis for AKD content by the potentiometric titration procedure. The results were confirmed by analysis of the same extracts by capillary gas chromatography (4).

Results and discussion

Figure 1 shows a typical titration curve for the standardizations of perchloric acid where the endpoint is clearly defined. Figure 2 shows a typical titration curve for the standardization of morpholine. During titration a precipitate was observed at a titre reading of about 2.00 mL, accompanied by a drop in the relative potential reading, as indicated by a bend in the initial rise of the titration curve. Second derivatives of titration plots were used to determine the end-points in all titration experiments. Titrations of the morpholine solution in the presence of

[3]B.B. Sitholé et al. In preparation.

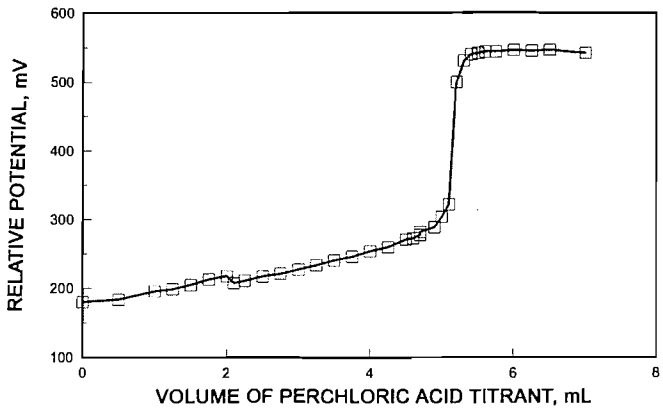

FIG. 2. Potentiometric titration of morpholine with perchloric acid.

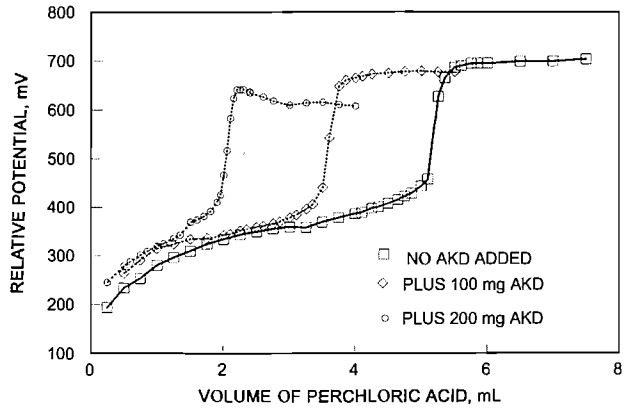

FIG. 3. Potentiometric titration of morpholine with and without AKD present.

AKD are shown in Fig. 3. From these titrations a linear calibration curve was prepared (Fig. 4) which was used to determine concentrations of unknown AKD solutions in the 1% range such as AKD formulations used in alkaline paper mills.

For lower concentrations of AKD more dilute solutions are required to prepare a calibration curve. Such a calibration curve, prepared by titrations with 0.0010 M stock solutions (100-fold dilutions of the solutions used in Fig. 4), could easily be described by the equation:

$$Y = -1.00 \times 10^{-3}X + V$$

where Y is the concentration of added AKD in ppm; X is the volume, in mL, of perchloric acid used to titrate the excess morpholine; V is the volume, in mL, of perchloric acid used to titrate the blank; and 0.001 is the slope of the straight line. This calibration curve was suitable for determining small amounts of AKD retained in paper.

The results of the precision studies, shown in Table 1, indicate good reproducibility of the technique, and the relative standard deviation was 1%. Although the formation of precipitates did not affect the titration end-points it was decided to investigate solvents which did not produce precipitates. No precipitates formed in the presence of polar solvents like acetone and acetonitrile; toluene, a non-polar solvent, caused the precipitate to occur earlier than in the case of chloroform alone. From these results it was decided to add acetone to the samples prior to titration to eliminate the formation of precipitate. Thus, subsequent experiments were performed in the presence of 5.0 mL of acetone.

Wood resin components and stearone did not interfere with the titration procedure, indicating that the procedure can be used to evaluate the stability of AKD emulsions and to determine the concentration of AKD in chloroform extracts of paper.

Kinetic studies

The reaction of AKD and morpholine may be represented by

	AKD + morpholine	⟶	AKD – morpholine
at time zero	a		
at time t	$a-x$		

a is the initial concentration of AKD, $a - x$ is the concentration of AKD remaining at time t, and x is the concentration of AKD – morphine generated, then for a first order reaction, the reaction rate is

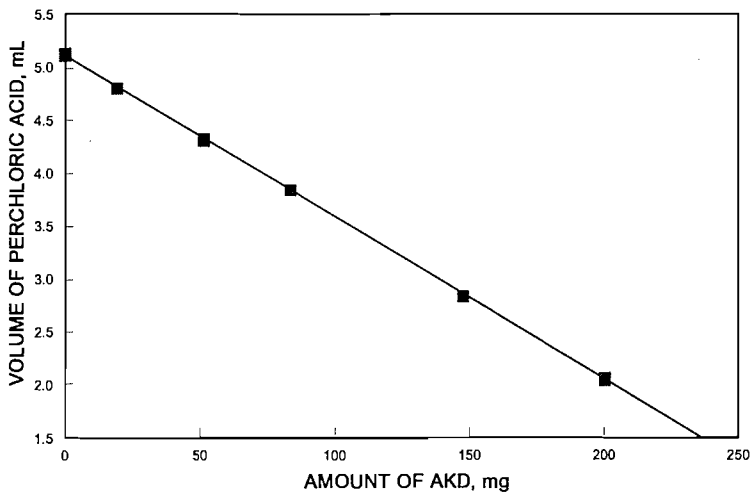

FIG. 4. Calibration curve for potentiometric titration of AKD with morpholine after equilibration for 15 min (200 mg AKD is equivalent to 20 mL of 10 000 ppm AKD solution).

Can. J. Chem. Downloaded from www.nrcresearchpress.com by 195.246.54.202 on 09/08/12
For personal use only.

TABLE 1. Reproducibility of the titration procedure – titration of 1.00 mL 5000 ppm AKD solution in 10 mL of 0.001 M morpholine

Sample	End-point, mL
1	5.480
2	5.393
3	5.416
4	5.348
5	5.320
Average	5.391±0.062

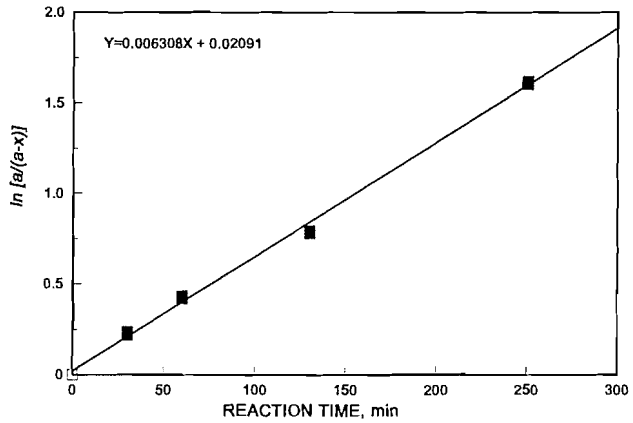

FIG. 5. Kinetics of the reaction between AKD and morpholine — a first order reaction.

$$\frac{dx}{dt} = k(a - x)$$

and the integrated equation is

$$\ln \frac{a}{a - x} = kt$$

When $\ln a(a - x)$ is plotted against time t, a straight line passing through the origin is obtained. The kinetic data indicate a first order reaction of AKD with morpholine (Table 2 and Fig. 5). It takes 6 h to complete a reaction between AKD and morpholine. However, it is not necessary to wait for all the AKD to be consumed before analysis; reproducible results were obtained if the samples were equilibrated for equal times, e.g., 15 min when about a fifth of the AKD will have been consumed. The kinetics are such that the concentration of AKD does not change much during the titration period.

Using the titration method to determine the amount of AKD extracted from paper

Titration was used to determine the amount of non-reacted AKD in laboratory-made papers sized with 2000 and 5000 ppm AKD. The amount of unreacted AKD in the chloroform extracts of the papers was determined first by titration and then by capillary GC. Table 3 (triplicate determinations) shows the good agreement between the two methods. Hence titration can be used in studies pertaining to AKD retention in alkaline papermaking.

Using titration to monitor the stability of AKD emulsions

Analysis of AKD emulsions showed there was 93.06 and 81.06% AKD in the original and hydrolyzed samples, respectively; thus hydrolysis caused a 13% loss of AKD in the hydrolyzed sample. Studies have shown that about 15% of the reactive diketene groups in commercial formulations are lost after 5 weeks storage at room temperature (16). The potentiometric titration result indicates the potentiometric procedure can be used to monitor the stability of AKD emulsions at mills as the equipment used is easily available. The method is much less cumbersome than analysis by gas chromatography which would entail drying aliquots of the emulsions, dissolution in chloroform, filtration, and derivatization of the AKD in the extracts before analysis.

TABLE 2. Kinetic data for the reaction of AKD with morpholine at room temperature

Reaction time t, min	Concentration of AKD found, ppm	$\ln a/(a - x)$
0	0	0
30	1222	0.239
60	1992	0.4269
130	3123	0.7869
250	4594	1.616
360	5733	—
400	5733	—
500	5733	—

TABLE 3. Comparison of the amounts of AKD in chloroform extracts by titration and GC analysis

	Concentration of unreacted AKD, ppm	
	Titration method	GC method
Sample 1: 2000 ppm AKD added	250, 247, 252	249, 248, 250
Sample 2: 5000 ppm AKD added	750, 753, 748	766, 768, 779

Conclusions

A new potentiometric method for the analysis of AKD has been developed and used to determine AKD amounts in sized paper samples and to monitor stability of AKD emulsions. Wood resin components and AKD hydrolysis products do not interfere in the analysis. Linear calibration curves were obtained for ppm samples and for samples in the percent range. This method is much faster and less cumbersome than chromatographic techniques.

Acknowledgement

We appreciate T. Tran's skilful technical assistance.

1. J.C. Roberts and D.N. Garner. Tappi J. **68**, 118 (1985).
2. D.B. Evans. *In* The sizing of paper. 2nd ed. *Edited by* W.F. Reynolds. Tappi Press. 1989. Chap. 2.
3. S.H. Nahm. J. Wood Chem. Technol. **6**, 89 (1986).
4. L. Odberg, T. Lindstrom, B. Liedberg, and J. Gustavson. Tappi J. **70**, 135 (1987).
5. F. Girardi. Proceedings of the TAPPI Papermakers Conference, Tappi Press, Atlanta. 1989. pp. 205–209.
6. T. Lindstrom and G. Soderberg. Nordic Pulp Pap. Res. J. **1**, 26 (1986).
7. B.L. Browning. Analysis of paper. 2nd ed. Marcel Dekker, New York. 1977.

Can. J. Chem. Downloaded from www.nrcresearchpress.com by 195.246.54.202 on 09/08/12
For personal use only.

8. W. Kamutzki and T. Krause. Das Papier. **7**, 311 (1982).
9. T. Yano, H. Ohtani, S. Tsuge, and T. Obokata. Analyst, **117**, 849 (1992).
10. J.D. Dart and D.V. McCalley. Analyst, **155**, 13 (1990).
11. K.J. Bottorff and M.J. Sullivan. Nordic Pulp Pap. Res. J. **1**, 86 (1993).
12. Y.I. Pan, S. Kuga, M. Usuda, and T. Kadoya. Tappi J. **68**, 98 (1985).
13. W.R. McCarthy and R.A. Stratton. Tappi J. **70**, 117 (1987).
14. J.C. Roberts and Y.J. Zhou. Proceedings, 1990 Pira Symposium on Neutral Papermaking, Stratford, England, Paper # 8, Jan. 1990.
15. C.F.H. Allen and A.H. Blatt. Organic chemistry – An advanced treatise. *Edited by* H. Gilman. 2nd. ed., Vol. 1, John Wiley, New York, 1953, pp. 663–665.
16. J. Marton. Tappi J. **73**, 139 (1990).

Can. J. Chem. Downloaded from www.nrcresearchpress.com by 195.246.54.202 on 09/08/12
For personal use only.

Stereochemistry and chiroptical properties of 1,3-dialkylaziridinones (α-lactams). Chiral rules for the nonplanar amide chromophore

G.V. SHUSTOV,[1] A.V. KACHANOV, I.I. CHERVIN, AND R.G. KOSTYANOVSKY
Institute of Chemical Physics, Russian Academy of Sciences, 117977, Moscow, Russia

AND

A. RAUK[1]
Department of Chemistry, University of Calgary, Calgary, AB T2N 1N4, Canada

Received May 14, 1993

G.V. SHUSTOV, A.V. KACHANOV, I.I. CHERVIN, R.G. KOSTYANOVSKY, and A. RAUK. Can. J. Chem. **72,** 279 (1994).

Structural features, configurational stability, and chiroptical properties of the nonplanar amide group in α-lactams were investigated by means of ab initio (6-31+G*) molecular orbital calculations on (1*R*)-aziridinone **1**, (1*R*)-1-methylaziridinone **2**, (1*R*,3*R*)-3-methylaziridinone **3**, (1*R*,3*R*)-1,3-dimethylaziridinone **4***a*, its *cis* diastereomer (1*S*,3*R*)-1,3-dimethylaziridinone **4***b*, and (1*R*,3*R*)-3-*tert*-butyl-1-methylaziridinone **5**, and by experimental CD spectra of 1-*tert*-butyl- and 1-(1′-adamantyl)-substituted 3(*R*)-3-*tert*-butylaziridinones **6** and **7**. The nitrogen inversion barriers of **4***a* and **4***b* are 2.8 and 1.6 kcal mol^{-1}, respectively. The lowest excited singlet state of all of the aziridinones is a valence state (the n_O–π_{CO}* transition); the second is a Rydberg state (the n_N–3*s* transition). The signs of the first and second Cotton effects in the CD spectra of the compounds **6** and **7** coincide with the calculated ones for **1** and **2** and the *trans* isomers **3**, **4***a*, and **5**. According to the calculated and experimental data for aziridinones **1–7** as well as to the well-known data for other nonplanar amides, the sign of the first Cotton effects is determined by the intrinsic chirality of the nonplanar amide chromophore and obeys a spiral rule. For cases where the chromophore has the conformation around the N—C(O) bond, which is close to the antiperiplanar, a reverse octant rule is proposed.

G.V. SHUSTOV, A.V. KACHANOV, I.I. CHERVIN, R.G. KOSTYANOVSKY et A. RAUK. Can. J. Chem. **72,** 279 (1994).

On a étudié les caractéristiques structurales, la stabilité configurationelle et les propriétés chiroptiques du groupe amide non planaire des α-lactames en faisant appel à des calculs d'orbitales moléculaires ab initio au niveau (6-31+G*) sur la (1*R*)-aziridinone **1**, la (1*R*)-1-méthylaziridinone **2**, la (1*R*,3*R*)-3-méthylaziridinone **3**, la (1*R*,3*R*)-1,3-diméthylaziridinone **4***a* ainsi que son diastéréoisomère *cis*, la (1*S*,3*R*)-1,3-diméthylaziridinone **4***b* et la (1*R*,3*R*)-3-*tert*-butylazirinidone **5** et à des expériences de dichroïsme circulaire (DC) sur 1-*tert*-butyl- et 1-(1′-adamantyl)-(3*R*)-3-*tert*butylaziridinones **6** et **7**. Les barrières à l'inversion de l'azote pour les composés **4***a* et **4***b* sont respectivement de 2,8 et 1,6 kcal mol^{-1}. L'état singulet excité le plus bas pour toutes les aziridinones est un état de valence (la transition n_O–π_{CO}*) et le deuxième est un état de Rydberg (la transition n_N–3*s*). Les signes des premier et deuxième effets Cotton (EC) observés dans les spectres de DC des composés **6** et **7** coïncident avec ceux calculés pour **1** et **2** et les isomères *trans* **3**, **4***a* et **5**. Sur la base des données expérimentales et calculées pour les aziridinones **1–7** ainsi que les données bien connues pour d'autres amides non planaires, le signe du premier EC est déterminé par la chiralité intrinsèque du chromophore de l'amide non planaire et il obéit à la règle de la spirale. Dans les cas où la conformation autour de la liaison N—C(O) du chromophore est pratiquement anti-périplanaire, on propose une inversion de la règle de l'octant.

[Traduit par la rédaction]

Introduction

A nonplanar amide group is contained in β-lactam antibiotics (1) and found in peptides (2). Unusual chemical and spectroscopic properties associated with the group, as well as the potential pharmacological activity of nonplanar amides, have attracted a great deal of attention (3). Most recently, these compounds were used for modelling the action of proteolitic fermenting reagents (4*a*), with respect to the problem of the origin of rotation barriers (4*b*), and as effective chiral reagents (4*c*). Hence there is great importance to recognition of the presence of the nonplanar amide group and to the determination of the absolute stereochemistry of compounds containing it. Both problems can be solved simultaneously by means of CD spectroscopy on the basis of the wavelength of the first (long wavelength) Cotton effect (CE) (3*a*) and using chiral rules connecting the sign of the CE with the stereochemistry of a molecule (3*a*, 5). It goes without saying that for the confident application of these rules and for the establishment of their limits, it is necessary to study the chiroptical properties of as a wide a range of nonplanar amides as possible. From this standpoint, 1,3-dialkylaziridinones (α-lactams), obtained earlier (6) in optical active form, are of special interest. The pyramidal configuration of the nitrogen atom and, therefore, the nonplanarity of the amide group in the ground state of α-lactams are established by X-ray diffraction (7) and confirmed by quantum chemical calculations (3*c*, 8). Weakening of the amide conjugation follows from the data of IR (3*a*, 3*c*, 9*a*), UV (9*b*), and PE spectra (9*a*, 9*c*).

A peculiarity of α-lactams, in comparison with other nonplanar amides, is incorporation of the N—C(O) amide bond into the strained three-membered ring. In the present work, an attempt to elucidate an influence of this peculiarity on the stereochemistry and the chiroptical properties of the amide chromophore was undertaken. For this purpose, ab initio quantum chemical calculations have been carried out on a series of aziridinones, including the parent molecule **1**, *N*-methylaziridinone **2**, (3*R*)-3-methylaziridinone **3**, the *cis* and *trans* isomers of (3*R*)-1,3-dimethylaziridinone **4***a* and **4***b*, and (3*R*)-1-methyl-3-*tert*-butylaziridinone **5**. The structure of the transition state to nitrogen inversion in **4**, **4-TS**, was also determined. For all compounds, the theoretical chiroptical properties were calculated. Experimentally, the CD spectra of two (3*R*)-1,3-dialkylaziridinones, **6**, and **7**, have been studied. The compounds **6** and **7**

[1]Authors to whom correspondence may be addressed.

Can. J. Chem. Downloaded from www.nrcresearchpress.com by 195.246.54.202 on 09/08/12
For personal use only.

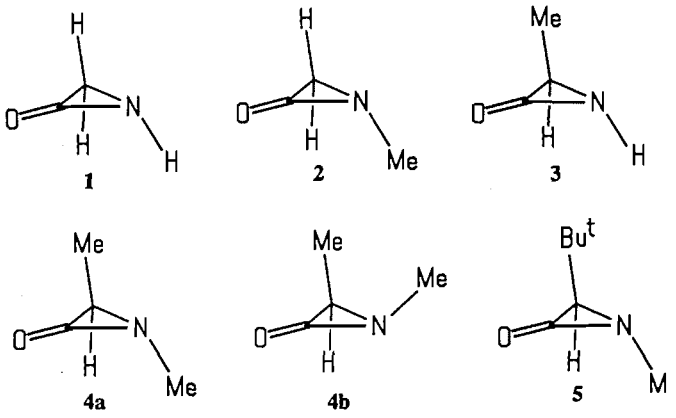

were obtained by cyclization of the corresponding amides of (*S*)-α- bromo-3,3-dimethylbutyric acid (Scheme 1). The (*R*)-absolute configuration at the C3 atom of aziridinones **6** and **7** follows from the stereochemistry of the cyclization.

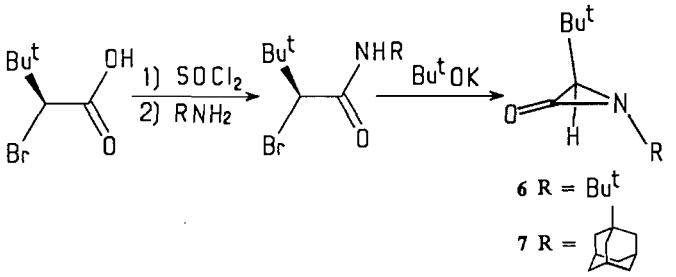

SCHEME 1

The possibilityof the application of a spiral rule (3*a*, 5) and a reverse octant rule (5*b*) to different instances of the nonplanar amide chromophore have been analyzed on the basis of the present aziridinone study, as well as by existing data on the chiroptical properties of other relatively rigid nonplanar amides, i.e., (1*S*,4*R*)-1-azabicyclo[3.2.0]heptan-7-one **8** (10*a*) (1*R*,5*R*)-1-azabicyclo[3.3.1]nonan-2-one **9** (10*b*), and (1*R*,4*S*)-6,6-dimethyl-1-azabicyclo[2.2.2]octan-2-one **10** (footnote 2).

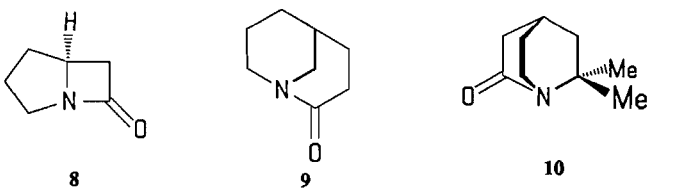

Results and discussion

Ab initio calculations were carried out earlier (3*c*, 8*b*) only for the parent aziridinone **1**, and only for its stationary states. We have carried out calculations on the parent, as well as on a number of alkylsubstituted aziridinones (Fig. 1). In particular, (3*R*)-1,3-dimethylaziridinone **4** and (3*R*)-1-methyl-3-*tert*-butylaziridinone **5** are more realistic models of the obtained α-lactams, which are stable only with N and C3 substituents (6, 11). Owing to constraints imposed by the small ring, the nitrogen atom has a pyramidal configuration in the ground state of aziridinones and, together with the carbonyl, forms the intrinsically chiral nonplanar amide group (Fig. 1). The out-of-plane angle (β, Fig. 1) is 51° for the two N—H aziridinones **1** and **3**, and 43°, 43°, and 44° for the *N*-methyl and *trans*-dialkylaziridinones **2**, **4***a*, and **5**, respectively. The nitrogen pyramid in the *cis*-dimethylaziridinone **4***b* is more flattened (β = 39°) owing to steric repulsion of the methyl groups. Even the modest flattening of the nitrogen pyramid in the *cis* isomer **4***b* leads to strengthening of the n_N–π_{CO}^* amide conjugation that is expressed in some shortening of the N—C(O) bond (−0.008 Å). Only a slight lengthening of the C=O bond (+0.002 Å) is calculated. The largest change of the bond lengths along this line is observed at reaching the nitrogen inversion transition state **4-TS**, which has the maximum amide conjugation. Nevertheless, even in the transition state **4-TS**, the nitrogen arrangement is not exactly planar (β = 2°), a consequence of the nonsymmetrical substitution at the C3 atom. The methyl group at the nitrogen atom has the *cis* orientation with respect to the methyl group at C3. Thus, the transition state **4-TS** is closer to the *cis* isomer **4***b* than to *trans*-**4***a* on the inversion coordinate.

It is of interest to note the nonplanarity of the carbonyl C2 atom in all of the computed structures, the distortion from planarity being always to the same side of the ring as the

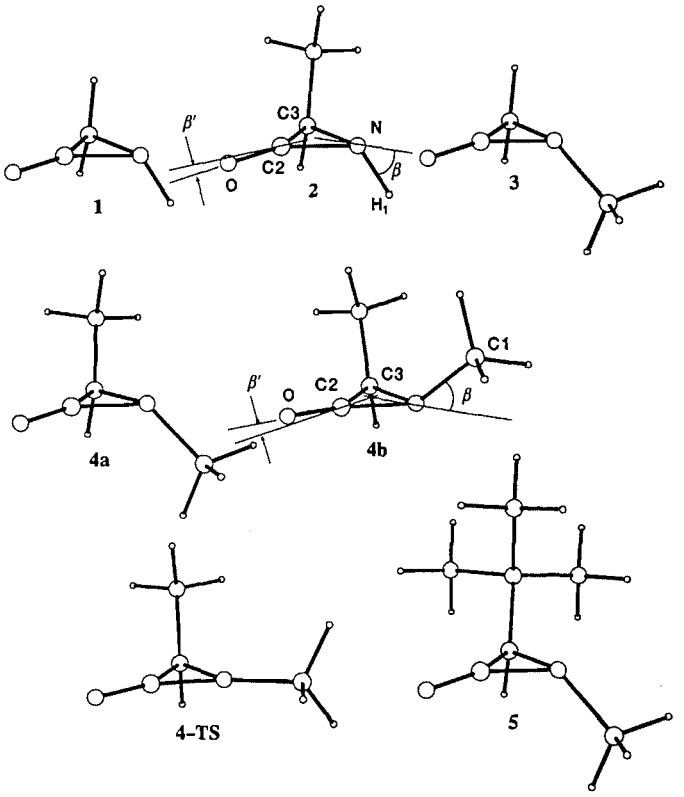

FIG. 1. Structures optimized at the 6-31 + G* level. Selected structural parameters (bond lengths in Å, bond angles in degrees) in the order **1**, **2**, **3**, **4***b*, **4-TS**, **5**, respectively: O—C2, 1.179, 1.181, 1.183, 1.184, 1.186, 1.190, 1.185; N—C2, 1.346, 1.349, 1.331, 1.334, 1.326, 1.297, 1.335; C2—C3, 1.456, 1.456, 1.462, 1.461, 1.465, 1.487, 1.460; N—C3, 1.497, 1.500, 1.485, 1.488, 1.491, 1.462, 1.488; ∠OC3N, 143.8, 143.3, 144.2, 143.6, 144.0, 145.9, 143.4; ∠OC2C3, 151.4, 151.8, 151.2, 151.6, 150.9, 151.1, 151.9; β, 51.0, 43.3, 50.9, 43.3, 38.6, 44.0; β′, 3.5, 4.5, 3.2, 4.4, 5.1, 0.7, 4.6. Relative energies (kcal mol^{-1}): **4***a*, 0.0; **4***b*, 1.2; **4-TS**, 2.8.

[2]P. Malon, private communication.

Can. J. Chem. Downloaded from www.nrcresearchpress.com by 195.246.54.202 on 09/08/12
For personal use only.

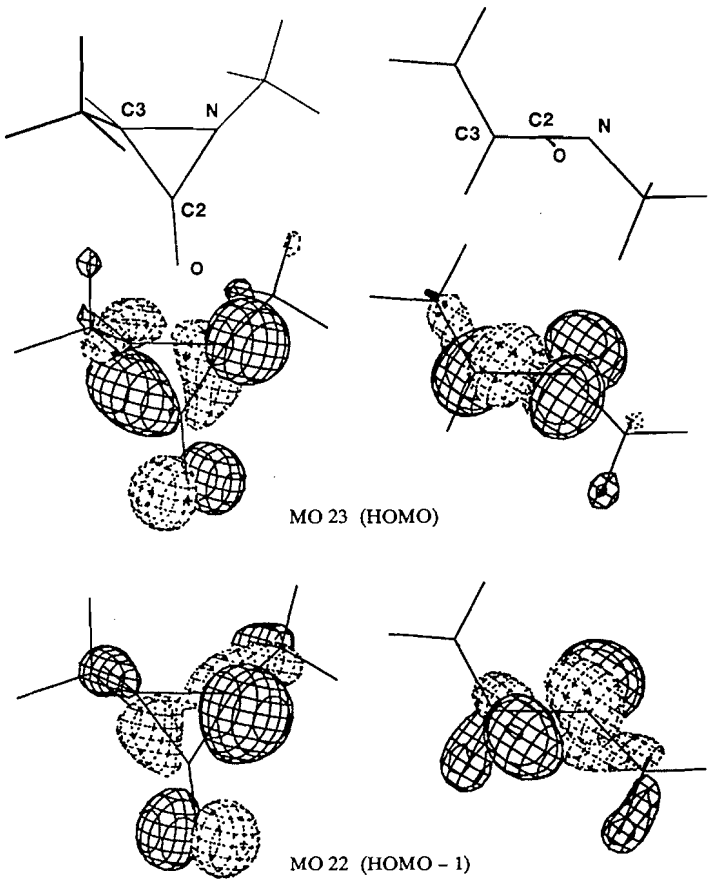

FIG. 2. The two upper occupied MOs involved in the electronic transitions of aziridinone **4***a*. Contour values, 0.075.

N-substituent or *anti* to the orientation of the N lone pair. It can be supposed that the nonplanarity of the C2 atom is connected with the asymmetrical environment on the side of the nitrogen atom or rather with the sp^n hybridization of the nitrogen lone electron pair, but not with the effect of the C2 atom insertion into the three-membered ring, because the transition to **4-TS** with almost planar nitrogen arrangement and with almost pure *p*-character of the nitrogen lone pair leads to the virtually complete flattening of C2 atom ($\beta' = 0.7°$ in **4-TS**). It is well known that in three-membered rings an overlapping of *cis*-oriented vicinal sp^n orbitals (the dihedral angle between the orbital axes is 0°) is more than the overlap of *trans*-oriented orbitals (12) (the dihedral angle is about 110°). Therefore, the *cis* orientation of the carbonyl with respect to the *N*-methyl group in compounds **1–5** is as expected for maximum n_N–π_{CO}* overlap.

The inequality of the outer valence angles at the carbonyl C2 atom, which is more pronounced than observed for other lactams (13), is a general structural feature of aziridinones. Evidently, as also observed elsewhere (13), the positive difference $\angle$C3C2O − $\angle$NC2O = 7.8 ± 0.9° in the valence angles (Fig. 1) is caused by the interaction of the nonbonding n_O orbital of the carbonyl oxygen with the Walsh orbitals of the aziridinone ring: a destabilizing interaction with the occupied orbital of the C2—C3 bond and a stabilizinginteraction with the antibonding orbital of the C2—N bond. An admixture of the Walsh orbitals with the n_O orbital in MO 23 (HOMO) and MO 22 (HOMO-1) may be seen on Fig. 2.

The nitrogen inversion barriers were determined for the *trans* and *cis* isomers of 1,3-dimethylaziridinone (**4***a* and **4***b*). The barriers, 2.8 kcal mol^{-1} and 1.6 kcal mol^{-1}, which should be typical for 1,3-dialkylaziridinones, in general, are less than that calculated for *N*-formylaziridine (≈6 kcal mol^{-1}) (5*a*). Undoubtedly in both the cases (aziridinone **4** and *N*-formylaziridine), the stabilization of the inversion transition state by the n_N–π_{CO}* amide conjugation is the main reason of the low pyramidal stability of the nitrogen atom, as is the case with unstrained amides. A characteristic feature of the electronic structure of the *N*-acylaziridine moiety, namely a stabilizing interaction between the π_{CO}* orbital and an occupied Walsh orbital of the ring, may be responsible for the higher barrier to inversion in *N*-acylaziridines. This interaction is not available in any conformation of aziridinones or in the (nearly) planar transition state to inversion in the *N*-acyl compounds.

Thus, the nonplanar amide group in α-lactams is more configurationally labile than in *N*-acylaziridines. However, unlike the latter, the inversion of the intrinsic chirality of this group is carried out only by the nitrogen inversion path and can be effectively controlled by the steric interaction of substituents at the N and C3 atoms. Indeed, assuming $\Delta S^0 = 0$, the calculated difference in energies of the *trans* and *cis* isomers **4***a* and **4***b* (Fig. 1) gives their ratio 88.7:11.3. Although we did not pursue the point with **5** because of its size, it is reasonable to expect that in the case of more bulky *tert*-alkyl N and C substituents in aziridinones **6** and **7**, the equilibrium is shifted completely towards the *trans* isomer.

An intense negative band of the dichroic absorption is observed in the 250-nm region of the CD spectra of (3*R*)-aziridinones **6** and **7** (Table 1, Figs. 3 and 4). The band sign coincides with the calculated sign for the CE of the first (lowest energy) electronic transition of each of the aziridinones investigated theoretically, with the exception of the *cis* diastereomer **4b** (Table 2). Aziridinones **1** and **2** do not possess an asymmetric carbon atom, but the sense of twist of the α-lactam chromophore is the same as in **3**, **4***a*, and **5**, and opposite to that found in **4***b*. The (3*R*)-*cis* isomer **4***b* has the rotational strength of the first transition with opposite sign. Therefore, the first CE sign in the CD spectra of aziridinones is determined only by the nitrogen configuration. The latter determines the chirality of the whole amide group. Right-spiral chirality (positive torsion O=C—N—C1 angle) corresponds to the (*S*)-absolute configuration of the nitrogen atom in aziridinones **1–3**, **4***a*, and **5**, and vice versa (**4***b*).

At first glance, there appears to be a discrepancy between the calculation and experiment in respect of the second CE of (3*R*)-*trans*-aziridinones. Thus, according to the calculation, the second CE of **4***a* and **5** has the same sign (negative) as the first CE (Table 2), while the short-wavelength part (at 200 nm) of the experimental CD spectra of aziridinones **6**, and **7** is characterized by a positive dichroic absorption (Table 1, Fig. 3). However, the moderate asymmetry of the 250-nm CD absorption band of both **6** (Fig. 3) and **7** (Fig. 4) suggests the possibility of a second negative component to the short-wavelength side of the first. Decomposition of the observed band at 250 nm in the CD and UV spectra of aziridinones **6** and **7** into their Gaussian components permits an additional CE near 230 nm, coinciding in sign with the first CE (Table 1, Fig. 4). Nevertheless, the experimental ratio of both the rotational and oscillator strengths of the first and second Gaussian components (Table 1) is significantly different from the ratio that is predicted theoretically (Table 2) for both **4***a* and **5**. It is of interest to note that the coincidence in sign between the first and second transitions is pre-

Can. J. Chem. Downloaded from www.nrcresearchpress.com by 195.246.54.202 on 09/08/12
For personal use only.

TABLE 1. Chiroptical properties[a] of aziridinones **6** and **7**

			CD and UV maxima					
			Observed		Gaussian components			
Compound	Solvent	Method	λ, nm	Δε or ε	λ, nm	Δλ, nm[b]	Δε or ε	$[R]^c$ or f^c
6	*n*-Heptane	CD	255	−8.946	254.9	19.1	−8.828	−31.39
					234.1	13.4	−1.558	−3.95
			205p[d]					
		UV	250	213	255	19.6	185	0.0042
					231.6	15.7	129	0.0029
	Gaseous phase	CD	251	−6.9[e]				
			195p					
	MeOH	CD	243	−6.363				
			202p					
7	*n*-Heptane	CD	254	−9.581	255.1	19.6	−9.374	−31.44
					232.8	13.3	−2.045	−5.11
		UV	251	194	254.9	20.3	181.5	0.0043
					232.9	13.1	102.5	0.0019
	MeOH	CD	243	−8.787				
			205p					

[a]Values of Δε and $[R]$ are not corrected to 100% enantiomeric purity.
[b]Half-width of a Gaussian band at $(1/e) \times \Delta\varepsilon$ or $(1/e) \times \varepsilon$.
[c]$[R] \approx 1.08 \times 10^{40} \times R$ in CGSE; f in CGSE.
[d]p, positive CD but without a maximum.
[e]ΔD, in cm, was measured in a 1-cm cell (sensitivity, 0.002 deg/cm) at 17°C.

Can. J. Chem. Downloaded from www.nrcresearchpress.com by 195.246.54.202 on 09/08/12
For personal use only.

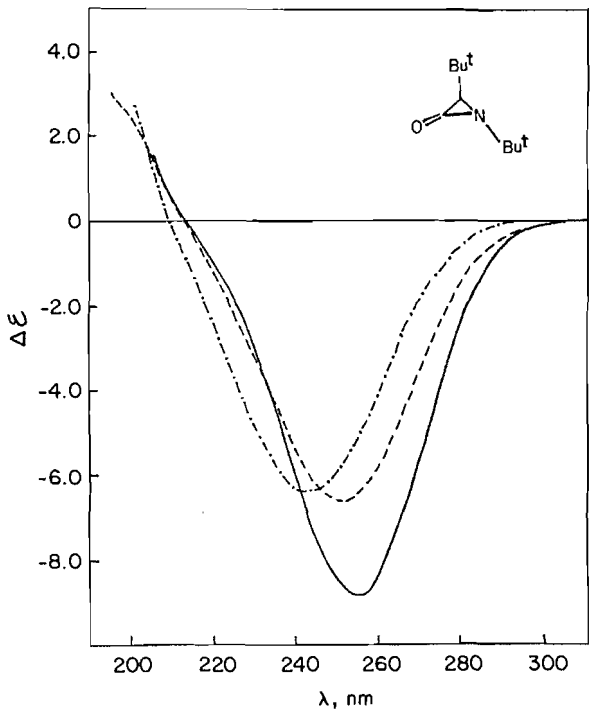

FIG. 3. The CD spectra of aziridinone **6** in heptane (—), gaseous phase (---) (see footnote *d* in Table 1), and MeOH (-·-).

dicted for the three *N*-alkylated aziridinones **2**, **4***a*, and **5**. In the case of the N—H aziridinones **1** and **3**, a strong CE of opposite sign is predicted for the second transition.

According to the calculations, only the first excited singlet state of aziridinones is a valence state. The next higher excited states have been determined as Rydberg states (Table 2). The first electronic transition is to the antibonding π_{CO}^* orbital and the second one is to a diffuse orbital which may be loosely described as a molecular 3*s* orbital (Fig. 5).Unlike the Rydberg transition, the first transition is not pure in the sense that it originates from a single canonical MO. One may deduce the initial orbital of the first electronic transition (i.e., the lower singly occupied MO), by examining the configurational mixing (5*b*) which comprises the lowest excited singlet state. The state description is dominated by two sets of configurations, one with MO 23 as the initial orbital and the other with MO 22 (Fig. 2). Both sets terminate in the same MO, the π_{CO}^* orbital (Fig. 5). As a result of such treatment, for example for *trans*-aziridinone **4***a* (Scheme 2), the initial orbital of the first transition is found

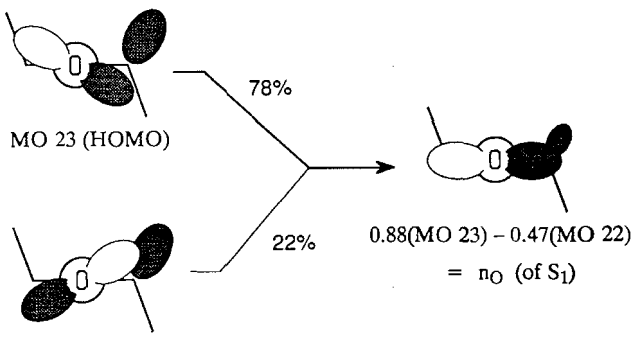

SCHEME 2

as almost pure 2*p* orbital of the carbonyl oxygen, lying in the ring plane and containing a minimum contribution of the nitrogen orbitals. Therefore, the first electronic transition of aziridinones can be described as the $n_O \rightarrow \pi_{CO}^*$ transition. The low values for the computed and experimental oscillator strengths (Tables 1 and 2) are consistent with such an assignment. Thus

Can. J. Chem. Downloaded from www.nrcresearchpress.com by 195.246.54.202 on 09/08/12
For personal use only.

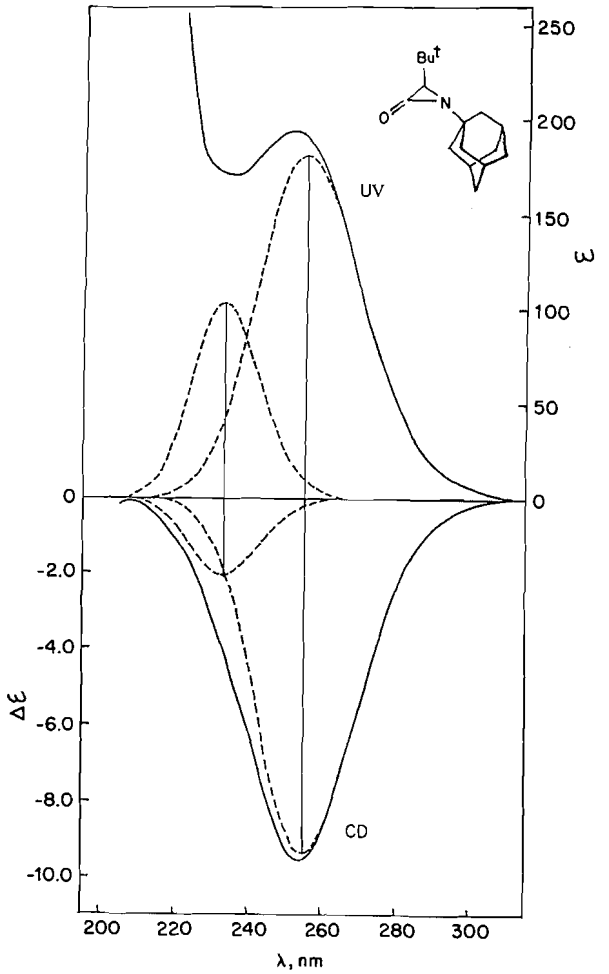

FIG. 4. The CD and UV spectra of aziridinone **7** in heptane and their Gaussian components (---).

the evident bathochromic shift (20–30 nm) of the first CE of aziridinones in comparison with usual planar amides as in the case of *N*-acylaziridines (5*a*) is caused mainly by lowering of the π_{CO}^* orbital energy, owing to a weakening of the amide conjugation.

Unlike the first excited state, the second one is formed almost exclusively by electron transition from MO 23 (HOMO) which has a considerable contribution of the nitrogen lone electron pair (Fig. 2). As a whole, this orbital is similar to the n_N orbital of *N*-formylaziridine (5*a*), from which the second electronic transition is to the 3*s* orbital in this compound. The evident hypsochromic shift of the observed dichroic absorption band in the CD spectra of aziridinones **6** and **7** in MeOH in comparison with the spectra in *n*-heptane and gaseous phase (Table 1, Fig. 3) is consistent both with the participation of the heteroatom lone electron pairs in the first and second electronic transition, and with the Rydberg nature of the second. Thus, a complete analogy in the orbital origin of the lower electronic transitions is observed between 1,3-*trans*-aziridinones and *N*-acylaziridines. The same conclusion is obtained for *cis*-aziridinones **4***b*.

The quasi-symmetry of aziridinones, i.e., quasi-C_s of the *cis* isomer **4***b* and quasi-C_2 of *trans*-aziridinones **1–3**, **4***a*, and **5–7**, makes them suitable models for testing the chiral rules. It is the spiral rule (3*a*, 5) and reverse octant rule (ROR) (5*b*), which connect the first CE sign with the stereochemistry of a molecule containing the nonplanar amide chromophore. According to the first rule, the positive CE corresponds to the negative torsion O=C—N—C angle and vice versa; on the second rule, the CE sign can be predicted as in the case of the usual carbonyl chromophore (14), but with the reverse octant signs (5*b*). It is necessary to note the same $n_O \rightarrow \pi_{CO}^*$ orbital origin of the nonplanar amide and carbonyl chromophores. The interchangeability of the rules follows from the examination of the stereochemistry and chiroptical properties of *N*-acyl- and *N*-nitrosoaziridines, and cyclopropylketones (5*b*).

At first glance one can come to the same conclusion in the cases of (3*R*)-*trans*-aziridinones **3**, **4***a*, and **5–7**, azetidinone **8**, and azabicylooctanone **9** (in the boat–chair conformation) as shown in Scheme 3. However, an attempt to apply the ROR to

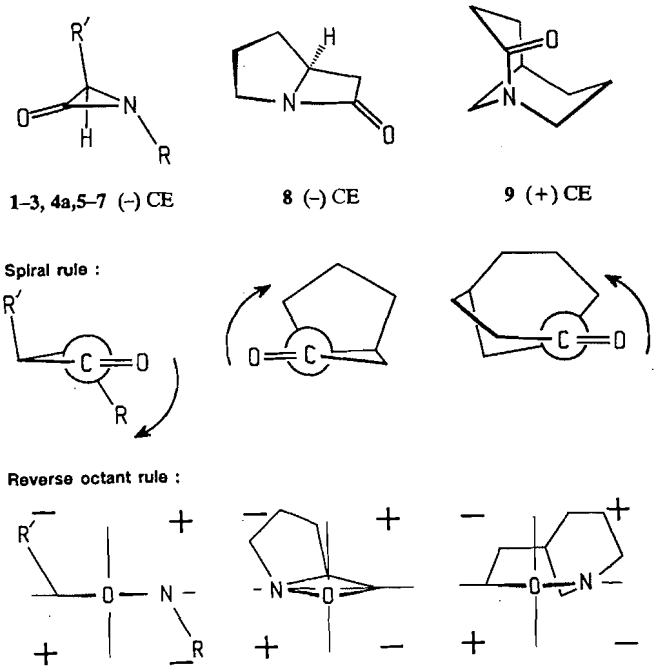

SCHEME 3

(3*R*)-*cis*-aziridinone **4***b* evidently indicates a limitation of the rule, because the methyl groups at the N and C3 atoms are found in oppositely signed octants and perturbations of the groups should compensate each other, resulting in a reduced rotational strength. Nevertheless according to the calculation, the value of the rotational strength of the $n_O \rightarrow \pi_{CO}^*$ transition of (3*R*)-*cis*-aziridinone **4***b* is even larger in absolute magnitude than that calculated for the (3*R*)-*trans*-isomer **4***a* (Table 2). In contrast to the ROR, the spiral rule correctly connects the first CE sign with the intrinsic chirality of the chromophore in (3*R*)-*cis*-aziridinone **4***b* (Scheme 4). On the other hand, the ROR well works in the cases of azabicyclooctanone **9** (in the chair–chair conformation) and quinuclidone **10** (Scheme 5).

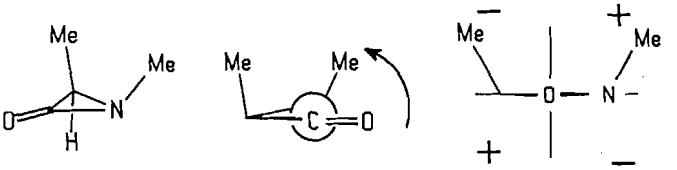

SCHEME 4

TABLE 2. Calculated properties of aziridinones **1–5**[a]

Property	1	2	3	4*a*	4*b*	5
E_{SCF}, hartree	−206.732 327	−245.765 652	−245.773 873	−284.806 762	−284.804 902	−401.912 249
MO energies (IP[b]), eV						
HOMO[c]	−11.1(10.0)	−10.7(9.6)	−10.8(9.73)	−10.5(9.4)	−10.4(9.4)	−10.4(9.7)
HOMO-1[c]	−12.6(11.6)	−12.0(10.8)	−12.4(11.4)	−11.8(10.7)	−11.6(10.5)	−11.7(11.1)
μ, debye	3.77	3.99	3.89	4.05	4.23	3.96
$S_0 \rightarrow S_1$ ($n_O \rightarrow \pi_{CO}^*$)						
ΔE, eV	6.02	6.25	6.02	6.15	6.31	6.48
$[R]^r$	−30.9	−35.0	−22.2	−22.3	37.0	−38.2
$[R]^v$	−11.1	−12.8	−2.5	−4.1	14.8	−21.4
f	0.0010	0.0024	0.0004	0.0011	0.0043	0.0041
$S_0 \rightarrow S_2$ ($n_N \rightarrow 3s$)						
ΔE, eV	7.89	7.98	7.87	7.97	7.82	8.12
$[R]^r$	41.0	−31.5	15.1	−24.83	−3.9	−42.6
$[R]^v$	29.9	−21.2	9.8	−16.7	−2.5	−29.2
f	0.0235	0.0220	0.0127	0.0061	0.0203	0.0200
$S_0 \rightarrow S_3$ ($n_N \rightarrow 3p$)						
ΔE, eV	8.59	8.56	8.57	8.68	8.63	8.75
$[R]^r$	−11.0	−6.7	6.6	−2.87	−24.0	3.1
$[R]^v$	−11.3	−4.6	2.0	−1.8	−13.3	2.1
f	0.0036	0.0086	0.0069	0.0122	0.0045	0.0148

[a]Geometries are optimized with 6-31+G* basis set (see Fig. 1).
[b]By the method of Ref. 19.
[c]See Fig. 2.

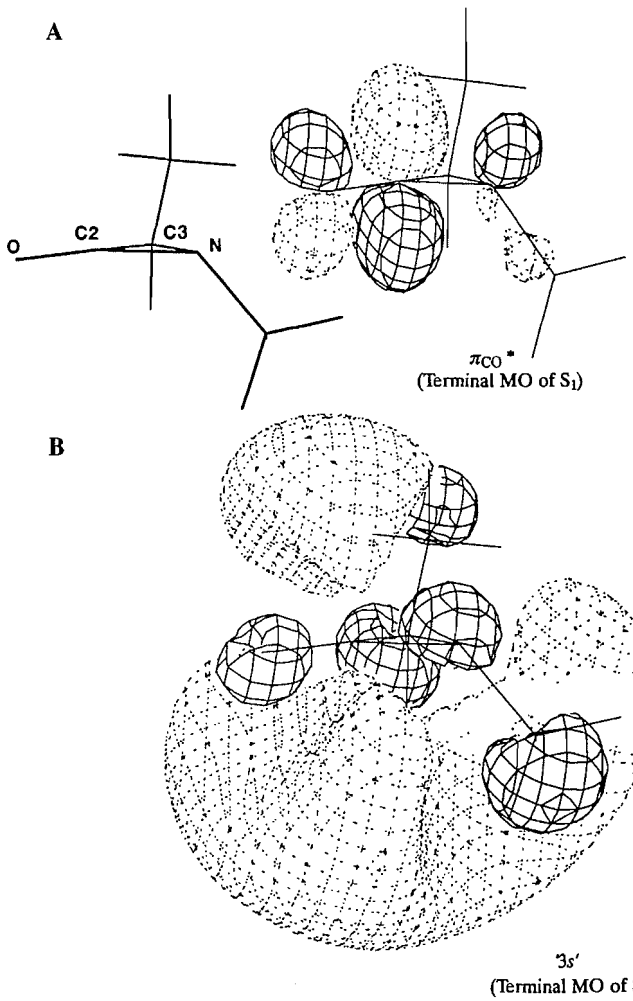

FIG. 5. The terminal orbitals of the lowest excited singlet states of aziridinone **4***a*. (A) First excited singlet state, contour value 0.075; (B) Rydberg orbital of next singlet state, contour value 0.025.

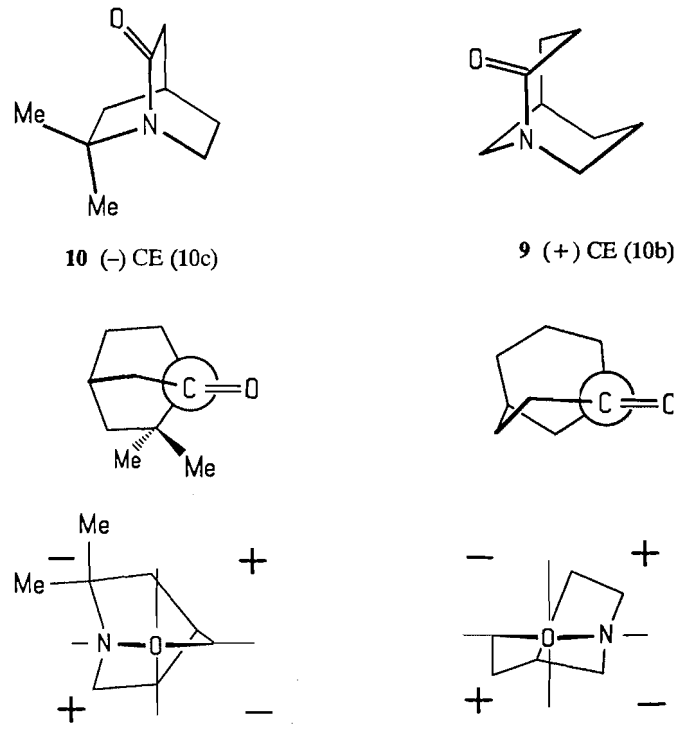

SCHEME 5

These compounds have a conformation around the N—C(O) bond, which is close to symmetrical antiperiplanar, and it is difficult to determine the sign of the torsion O=C—N—C angle for them.

Conclusions

1,3-Dialkylaziridinones (α-lactams), as do earlier investigated *N*-acylaziridines (5*a*), possess the stereochemically labile intrinsically chiral amide group. Inversion of the configuration of this group is carried out by pyramidal inversion of the nitrogen under the control of a carbon chiral centre. The chiroptical

Can. J. Chem. Downloaded from www.nrcresearchpress.com by 195.246.54.202 on 09/08/12
For personal use only.

properties of the nonplanar amide chromophore connected with the first electronic transition are independent from whatever influence causes the chromophore to become nonplanar. 1,3-Dialkylaziridinones and *N*-acylaziridines, for which nonplanarity of the amide chromophore is caused by insertion of the nitrogen atom into a strained three-membered ring, have the same features of the CD spectra as bicyclic amides (3*a*). All the compounds are different from virtually planar amides by the position of the long-wavelength absorption and high intensity of the first CE, the sign of which is determined only by the intrinsic chirality of the chromophore. In fact, the chromophore chirality is determined by the carbon chiral centres (thermodynamic control of the isomers populations) or by the chirality of a bicyclic molecule. Thus, there is the possibility of determination of the absolute stereochemistry of nonplanar amides on the basis of the first CE sign.

Both the chiral rules discussed above, which aim to connect the first CE sign with the absolute stereochemistry of the nonplanar amide, are empirical in character. Nevertheless, the spiral rule more correctly reflects the spiral nature of the nonplanar amide chromophore and may be used for all occurrences. In practice, this rule is preferred for compounds with a pronounced helicity of the chromophore, i.e., with the *syn*-clinal conformation (A, Scheme 6) around the N—C(O) bond. On the other hand, the ROR rule is more reliable for amides with a configuration that is close to antiperiplanar (B, Scheme 6):

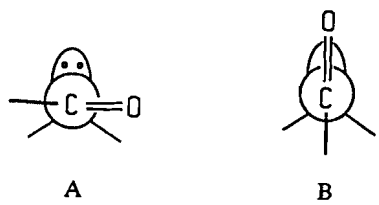

A B

SCHEME 6

Methods

Experimental

The CD spectra were measured on a JASCO J-500A spectropolarimeter with DP-500N dataprocessor, the UV spectra were measured on a Specord UV VIS spectrophotometer, the NMR spectra were measured on a Bruker WM-400 spectrometer (^{1}H, 400.13 MHz; ^{13}C, 100.62 MHz, in $CDCl_3$ from TMS), and optical rotation angles were determined on Autopol III and Polamat A polarimeters.

Amides of (S)-2-bromo-3,3-dimethylbutyric acid

A solution of (*S*)-2-bromo-3,3-dimethylbutyric acid (3.12 g, 16 mmol) (was prepared from L-*tert*-leucine according to ref. 15) and $SOCl_2$ (3.81 g, 32 mmol) in CH_2Cl_2 (15 mL) was refluxed for 7 h. After removal of the solvent in vacuo, the residual clear liquid (3.1 g) was dissolved in CH_2Cl_2 (20 mL) and added to a solution of *tert*-alkylamine (32 mmol) in CH_2Cl_2 (50 mL) with cooling (0°C) and stirring. After 2 h at 20°C, the reaction mixture was washed with 10% aqueous HCl (2 × 30 mL), water, and saturated aqueous $NaHCO_3$ (2 × 30 mL), and then dried ($CaCl_2$). After removal of the solvent, the residue was recrystallized from *n*-hexane–CH_2Cl_2.

(S)-N-tert-Butyl-2-bromo-3,3-dimethylbutyramide: yield 82%; mp 164–165°C (lit. (11*a*) mp 156–157°C racemate); $[\alpha]_D^{20}$ −36.6° (*c* 2.5, $CHCl_3$). ^{1}H NMR δ: 1.14 (9H, Bu^{t}C), 1.37 (9H, Bu^{t}N), 4.00 (1H, CH), 5.86 (1H, br s, NH).

(S)-N-(1′-Adamantyl)-2-bromo-3,3-dimethylbutyramide: yield 86%; mp 196–197°C (lit. (11*b*) mp 173–174°C racemate); $[\alpha]_D^{20}$ −32.1° (*c* 3.2, $CHCl_3$). ^{1}H NMR δ (*J*, Hz): 1.14 (9H, Bu^{t}C), 1.68 (6H, t, Ad, δ-CH_2, ^3J = 3.0), 2.01 (6H, d, Ad, β-CH_2, ^3J = 2.9), 2.06 (3H, br m, Ad, γ-CH), 3.97 (1H, CH), 6.22 (1H, br s, NH).

Aziridinones 6 and 7

Potassium *tert*-butoxide (0.74 g, 6.6 mmol) was added to a solution of (*S*)-amide (6 mmol) in absolute ether (100 mL) with cooling (−20°C) and stirring. After 15 min at 20°C, the precipitate was filtered off and the filtrate was evaporated in vacuo. The product was extracted from the residue with pentane. After removal of pentane, the residue was twice distilled in vacuo (aziridinone **6**) or twice recrystallized from *n*-hexane at −3°C (aziridinone **7**). Optical purities of the aziridinones, ≈86% for **6** and ≈88% for **7**, were determined according to Ref. 6*d* from the ^{1}H NMR spectra in $CDCl_3$–CCl_4 (1:4) in the presence of two equivalents of (*R*)-1-(9-anthryl)-2,2,2-trifluoroethanol by integration of the methine proton signals.

(3R)-1,3-Di-tert-butylaziridinone **6**: yield 43%; bp 29–32°C (0.2 Torr; 1 Torr = 133.3 Pa); $[\alpha]_D^{20}$ −253.8° (*c* 0.9, heptane) (lit. (6*c*)) bp 60°C (0.5 Torr), $[\alpha]_D^{20}$ −267.3° (*c* 1.25, hexane)). ^{1}H NMR δ: 0.99 (9H, Bu^{t}C), 1.29 (9H, Bu^{t}N), 2.74 (1H, CH). ^{13}C NMR δ (*J*, Hz): 26.95 (qm, $(CH_3)_3CC$, ^1J = 125.5, ^3J = 4.9, 2.8), 27.58 (qm, $(CH_3)_3CN$, ^1J = 126.2, ^3J = 4.2), 31.14 (m, Me_3CC, ^2J = 4.2), 54.09 (dm, CH, ^1J = 195.5, ^3J = 5.6), 55.98 (m, Me_3CN, ^2J = 4.2), 160.99 (d, CO, ^2J = 3.2).

(3R)-1-(1′-Adamantyl)-3-tert-butylaziridinone **7**: yield 58%; mp 75–76°C (lit. (11*b*) mp 79°C racemate); $[\alpha]_D^{20}$ −206.9 (*c* 1.0, heptane). ^{1}H NMR δ: 0.99 (9H, Bu^{t}C), 1.68 (6H, br t, Ad, δ-CH_2), 1.85 (6H, br q, Ad, β-CH_2), 2.14 (3H, br m, Ad, γ-CH), 2.83 (CH). ^{13}C NMR δ (*J*, Hz): 27.05 (q, $(CH_3)_3C$, ^1J = 126.2), 29.16 (d, Ad, γ-CH, ^1J = 133.2), 31.15 (Me_3C), 35.81 (t, Ad, δ-CH_2, ^1J = 127.6), 40.91 (t, Ad, β-CH_2, ^1J = 127.6), 53.30 (dm, CH, ^1J = 160.9, ^3J = 5.6), 56.29 (Ad, α-C), 160.88 (d, CO, ^2J = 3.1).

Theoretical

The geometries of (1*S*)-aziridinone **1**, (1*S*)-1-methylaziridinone **2**, (1*S*,3*R*)-3-methylaziridinone **3**, (1*S*,3*R*)-1,3-dimethylaziridinone **4***a*, its *cis*-diastereomer (1*R*,3*R*)-1,3-dimethylaziridinone **4***b*, and (1*S*,3*R*)-3-*tert*-butyl-1-methylaziridinone **5** were fully optimized by Hartree–Fock SCF calculations at the 6-31+G* level (16) by using the GAUSSIAN 90 (17) or 92 (18) system of programs. In the case of the (3*R*)-1,3-dimethylaziridinones **4***a* and **4***b*, the transition structure for pyramidal inversion at N, **4-TS**, was also located. The transition properties were determined with the same basis set. The diffuse *s* and *p* functions in this basis set permit a better description of the lowest few valence states and the identification of Rydberg states. Ionization potentials are calculated using a many body perturbation theory correction to Koopmans' theorem based on the work of Pickup and Goscinski (19). The frontier orbitals are displayed as modified Jorgensen–Salem plots (20).

The method used to calculate oscillator and optical rotatory strengths is the same as was used previously (5, 21, 22) and has been described in detail elsewhere (23). Partially correlated wave functions for the ground and excited states are determined to first order in Rayleigh–Schrödinger perturbation theory,

$$[1] \quad \Psi_n = \Psi_n^0 - \Sigma_j a_{nj} \Phi_j^0$$

where

$$[2] \quad a_{nj} = \langle \Psi_n^0 | H | \Phi_j^0 \rangle / (\langle \Phi_j^0 | H | \Phi_j^0 \rangle - \langle \Psi_n^0 | H | \Psi_n^0 \rangle)$$

H is the exact Hamiltonian, Φ_j^0 is a singlet singly or more highly excited configuration derived from the Hartree–Fock determinant, Φ_{HF}, and Ψ_n^0 is a linear combination of strongly interacting Φ_l^0 ($l \neq j$) selected from at most singly excited configurations. Thus, for the ground state, $\Psi_0^0 = \Phi_{HF}$. All configurations for which the interaction coefficient a_{nj} (eq. [2]) was greater than 0.05 were included in the zero-order part of the CI wave function. For reasons of expediency, the CI calculation was restricted to a window of 14 occupied orbitals and 48 unoccupied orbitals for each system.

Electric dipole transition moments in the length $\langle r \rangle_{0n}$ and velocity $\langle v \rangle_{0n}$ formalism and magnetic dipole transition moments $\langle m \rangle_{0n}$ are explicitly evaluated from

Can. J. Chem. Downloaded from www.nrcresearchpress.com by 195.246.54.202 on 09/08/12
For personal use only.

[3] $\langle r\rangle_{0n} = \Psi_0|\mu|\Psi_n\rangle$

[4] $\langle v\rangle_{0n} = \langle\Psi_0|\nabla|\Psi_n\rangle/(E_n - E_0)$

[5] $\langle m\rangle_{n0} = -i\langle\Psi_n|m|\Psi_0\rangle$

where the dipole, gradient, and magnetic moment operators, μ, ∇, and m, have their usual definitions and

[6] $E_n = \langle\Psi_n|H|\Psi_n\rangle$

Oscillator strengths f_{0n} are calculated by the mixed formalism

[7] $f_{0n} = \frac{2}{3}\langle\Psi_0|v|\Psi_n\rangle \cdot \langle r\rangle_{n0}$

Optical rotatory strengths are evaluated as

[8] $[R_{0n}]^r = \langle r\rangle_{0n} \cdot \langle m\rangle_{n0}$

and in the origin independent form

[9] $[R_{0n}]^v = \langle v\rangle_{0n} \cdot \langle m\rangle_{n0}$

The extent of agreement between eqs. [8] and [9] serves as a measure of the quality of the wave function and the reliability of the calculated rotational strengths for the particular states.

Acknowledgement

The authors thank the Natural Sciences and Engineering Research Council of Canada for financial support of part of this work.

1. (*a*) H.R. Pfaendler, J. Gosteli, R.B. Woodward, and G. Rihs. J. Am. Chem. Soc. **103**, 4526 (1981); (*b*) K.A. Durkin, M.J. Sherrod, and D. Liotta. J. Org. Chem. **54**, 5839 (1989).
2. (*a*) G.N. Ramachandran and A.S. Kolaskar. Biochim. Biophys. Acta, **303**, 385 (1973); (*b*) R.W. Woody. Biopolymers, **22**, 189 (1983).
3. (*a*) K. Blaha and P. Malon. Acta Univ. Palacki. Olomuc. **93**, 81 (1980); (*b*) H.K. Hall and A. El-Shekeil. Chem. Rev. **83**, 549 (1983); (*c*) A. Greenberg. *In* Structure and reactivity. *Edited by* J.F. Liebman and A. Greenberg. VCH Publishers, Inc., New York. 1988. Chap. 4, pp. 138–179.
4. (*a*) Q. Wang, A.J. Bennet, R.S. Brown, and B.D. Santarsiero. Can. J. Chem. **68**, 1732 (1990); (*b*) A.J. Bennet, V. Somayaji, R.S. Brown, and B.D. Santarsiero. J. Am. Chem. Soc. **113**, 7563 (1991); (*c*) D. Tanner and C. Birgersson. Tetrahedron Lett. **32**, 2533, 2536 (1991).
5. (*a*) G.V. Shustov, G.K. Kadorkina, S.V. Varlamov, A.V. Kachanov, R.G. Kostyanovsky, and A. Rauk. J. Am. Chem. Soc. **114**, 1616 (1992); (*b*) G.V. Shustov, A.V. Kachanov, G.K. Kadorkina, R.G. Kostyanovsky, and A. Rauk. J. Am. Chem. Soc. **114**, 8257 (1992).
6. (*a*) H.E. Baumgarten, J.F. Fuerholzer, R.D. Clark, and R.D. Thompson. J. Am. Chem. Soc. **85**, 3303 (1963). (*b*) S. Sarel, B.A. Wiessman, and Y. Stein. Tetrahedron Lett. 373 (1971); (*c*) H. Quast and H. Leybach, Chem. Ber. **124**, 849 (1991); (*d*) H. Quast and H. Leybach. Chem. Ber. **124**, 2015 (1991).
7. A.H.-J. Wang, I.C. Paul, E.R. Talaty, and A.E. Dupuy, Jr. J. Chem. Soc. Chem. Commun. 43 (1972).
8. (*a*) L. Treschanke and P. Rademacher. J. Mol. Struct. (THEOCHEM) **122**, 35 (1985); (*b*) A. Greenberg, Y. Y. Chiu, J.L. Johnson, and J.F. Liebman. Struct. Chem. **2**, 117 (1991).
9. (*a*) L. Treschanke and P. Rademacher. J. Mol. Struct. (THEOCHEM) **122**, 47 (1985); (*b*) E.R. Talaty, A. E. Dupuy, Jr., and T.H. Golson. J. Chem. Soc. Chem. Commun. 49 (1969); (*c*) A. Greenberg, T.D. Thomas, C.R. Bevilacqua, M. Corville, D. Ji, J.-C. Tsai, and G. Wu. J. Org. Chem. **57**, 7093 (1992).
10. (*a*) R. Busson and H. Vanderhaeghe. J. Org. Chem. **43**, 4438 (1978); (*b*) R. Brehm, D. Ohnhauser, and H. Gerlach. Helv. Chim. Acta, **70**, 1981 (1987).
11. (*a*) J.C. Sheehan and J.H. Beeson. J. Am. Chem. Soc. **89**, 362 (1967). (*b*) I. Lenguel and D.B. Uliss. J. Chem. Soc. Chem. Commun. 1621 (1968).
12. G.V. Shustov, S.N. Denisenko, N.L. Asfandiarov, L.R. Khusnutdinova, and R.G. Kostyanovsky. Izv. Akad. Nauk SSSR Ser. Khim. 1824 (1986).
13. L. Norskov-Lauritsen, H.-B. Burgi, P. Hofmann, and H.R. Schmidt. Helv. Chim. Acta, **68**, 76 (1985).
14. M. Legrand and M.J. Rougier. *In* Stereochemistry. Fundamentals and methods. *Edited by* H.B. Kagan. Georg Thieme Publishers; Stuttgart. 1977; Vol. 2, pp. 33–183.
15. W.G. Galetto and W. Gaffield. J. Chem. Soc. (C), 2437 (1969).
16. W.J. Hehre, L. Radom, P.v.R. Schleyer, and J.A. Pople. Ab initio molecular orbital theory. John Wiley & Sons, New York. 1986.
17. M.J. Frisch, M. Head-Gordon, G.W. Trucks, J.B. Foresman, H.B. Schlegel, K. Raghavachari, M.A. Robb, J.S. Binkley, C. Gonzalez, D.J. Defrees, D.J. Fox, R.A. Whiteside, R. Seeger, C.F. Melius, J. Baker, R.L. Martin, L.R. Kahn, J.J.P. Stewart, S. Topiol, and J.A. Pople. Gaussian 90. Gaussian, Inc., Pittsburgh. 1990.
18. M.J. Frisch, G.W. Trucks, M. Head-Gordon, P.M.W. Gill, M.W. Wong, J.B. Foresman, B.G. Johnson, H.B. Schlegel, M.A. Robb, E.S. Replogle, R. Gomperts, J.L. Andres, K. Raghavachari, J.S. Binkley, C. Gonzales, R.L. Martin, D.J. Fox, D.J. Defrees, J. Baker, J.J.P. Stewart, and J.A. Pople. Gaussian 92, Revision A. Gaussian, Inc., Pittsburgh. 1992.
19. B.T. Pickup and O. Goscinski. Mol. Phys. **26**, 1013 (1973).
20. W.L. Jorgensen and L. Salem. The organic chemists' book of orbitals. Academic Press, New York. 1973.
21. G.V. Shustov, S.V. Varlamov, I.I. Chervin, A.E. Aliev, R.G. Kostyanovsky, D. Kim, and A. Rauk. J. Am. Chem. Soc. **111**, 4210 (1989).
22. G.V. Shustov, S.V. Varlamov, A. Rauk, and R.G. Kostyanovsky. J. Am. Chem. Soc. **112**, 3403 (1990).
23. A. Rauk and J.M. Barriel. Chem. Phys. **25**, 409 (1977).

Can. J. Chem. Downloaded from www.nrcresearchpress.com by 195.246.54.202 on 09/08/12
For personal use only.

Parvifloracin and parviflorin: cytotoxic bistetrahydrofuran acetogenins with 35 carbons from *Asimina parviflora* (Annonaceae)

SUNIL RATNAYAKE, ZHE-MING GU, LAURA R. MIESBAUER, AND DAVID L. SMITH

Department of Medicinal Chemistry and Pharmacognosy, School of Pharmacy and Pharmacal Sciences, Purdue University, West Lafayette, IN 47907, U.S.A.

KARL V. WOOD

Department of Chemistry, School of Sciences, Purdue University, West Lafayette, IN 47907, U.S.A.

DEAN R. EVERT

Department of Horticulture, Georgia Agricultural Experimental Station, The University of Georgia, Tifton, GA 31793, U.S.A.

AND

JERRY L. MCLAUGHLIN[1]

Department of Medicinal Chemistry and Pharmacognosy, School of Pharmacy and Pharmacal Sciences, Purdue University, West Lafayette, IN 47907, U.S.A.

Received June 15, 1993

SUNIL RATNAYAKE, ZHE-MING GU, LAURA R. MIESBAUER, DAVID L. SMITH, KARL V. WOOD, DEAN R. EVERT, and JERRY L. MCLAUGHLIN. Can. J. Chem. **72**, 287 (1994).

Using lethality to brine shrimp, activity-directed fractionation of extracts of *Asimina parviflora* (Michx.) Dunal. (Annonaceae) has led to the isolation of two new and four known acetogenins (**1–6**). Compound **1**, parvifloracin, is the first nonadjacent bistetrahydrofuran acetogenin with 35 carbons. Compound **2**, parviflorin, is an unusual adjacent bistetrahydrofuran acetogenin with 35 carbons. Bullatacin (**3**), molvizarin (**4**), annonacin (**5**), and goniothalamicin (**6**) are also reported for the first time from this plant. Brine shrimp lethality test data and comparative cytotoxicities of **1–6** against three human solid tumor cell lines are presented.

SUNIL RATNAYAKE, ZHE-MING GU, LAURA R. MIESBAUER, DAVID L. SMITH, KARL V. WOOD, DEAN R. EVERT et JERRY L. MCLAUGHLIN. Can. J. Chem. **72**, 287 (1994).

Utilisant la létalité pour la crevette d'eau salée comme activité permettant l'orientation du fractionnement des extraits du *Asimina parviflora* (Michx.) Dunal (Annonaceae), on a isolé deux nouvelles acétogénines et quatre autres qui étaient déjà connues (**1–6**). Le composé **1**, la parvifloracine, est la première acétogénine à 35 carbones à contenir deux tétrahydrofuranes non adjacents. Le composé **2**, la parviflorine, est une acétogénine inhabituelle à 35 carbones avec deux tétrahydrofuranes adjacents. C'est aussi la première fois que l'on rapporte l'extraction de la bullatacine (**3**), de la molvizarine (**4**), de l'annonacine (**5**) et de la goniothalamicine (**6**) de cette plante. On présente les données du test de létalité pour la crevette d'eau salée ainsi que les cytotoxicités comparatives des composés **1–6** contre trois lignes de cellules tumorales solides des humains.

[Traduit par la rédaction]

Introduction

Asimina parviflora (Michx.) Dunal., dwarf paw paw, is a small shrub native to the southeastern United States (1). In our search for new potential anticancer and pesticidal constituents from the Annonaceae, we investigated the twigs for bioactive compounds. The brine shrimp lethality test (2, 3) (BST) detected bioactivity and was used to direct the fractionation. In a previous paper (4), we reported the isolation, identification, and cytotoxic activities of two new (asimicilone and 6-*cis*-decosenamide) and three known (asimicin, (+)-syringaresinol, and β-sitosterol β-D-glucopyranoside) natural compounds from the twigs. Further fractionation of the aqueous methanol soluble residue of the 95% ethanol extract has now led to the isolation of two new (**1**, **2**) and four known (**3–6**) annonaceous acetogenins. Parvifloracin (**1**) is the first nonadjacent bis-THF (tetrahydrofuran) ring acetogenin having 35 carbons and is the first nonadjacent bis-THF ring acetogenin reported in the genus *Asimina*. Parviflorin (**2**) is an adjacent bis-THF ring acetogenin with 35 carbons. Only three acetogenins with 35 carbons have been reported previously in the adjacent bis-THF ring class (neoannonin (5), molvizarin (6), and itrabin (7)). Bullatacin (**3**), molvizarin (**4**), annonacin (**5**), and goniothalamicin (**6**) are previously known acetogenins and are reported for the first time from this plant. These compounds were identified by using chemical and spectroscopic analyses. In this paper we discuss their isolation, identification, and cytotoxic activities.

Results and discussion

Parvifloracin (**1**) was obtained as a whitish wax with $[\alpha]_D^{22}$ +18.75 (*c* 0.08, EtOH). ^{1}H NMR, ^{13}C NMR, and mass spectral data of **1** and its acetate, trimethylsilyl (TMS), and perdeuterotrimethylsilyl (d-TMS) derivatives suggested that **1** belongs to the relatively rare class of bioactive nonadjacent bis-THF acetogenins (8–11). The high resolution FAB mass spectrum of **1** showed *m/z* at 611.4512 for MH^+ (calculated 611.4523) corresponding to the molecular formula $C_{35}H_{62}O_8$. The prominent absorption peak at 3466 cm^{-1} in the IR spectrum and the four successive losses of H_2O (*m/z* 18) from the molecular ion in the CIMS (*m/z* values at 592, 574, 556, 538) indicated the presence of four hydroxyl groups. These were further confirmed by preparation of a tetraacetyl derivative (**1***a*). The ^{1}H NMR spectrum of **1***a* showed four, three-proton singlets at δ 2.03, 2.07, 2.08, and 2.09 and two multiple proton resonances at δ 4.83 (3H) and

[1]Author to whom correspondence may be addressed.

Can. J. Chem. Downloaded from www.nrcresearchpress.com by 195.246.54.202 on 09/08/12
For personal use only.

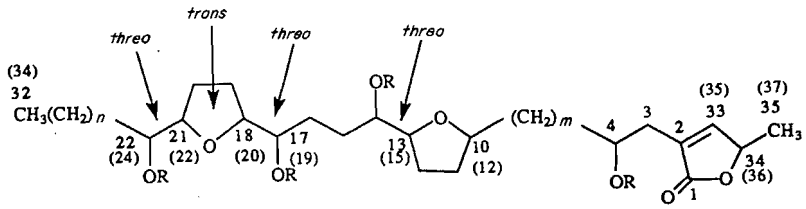

Compound	1	1*a*	7	7*a*	8
R	H	Ac	H	Ac	H
n	9	9	9	9	11
m	5	5	7	7	5

5.10 (1H) corresponding to downfield shifts on secondary hydroxyl-bearing carbons as compared with **1**. The CIMS of **1*a*** also showed successive losses of four AcOH units (*m/z* 60) from the MH^+ of the tetraacetate (*m/z* 719, 659, 599, 539). The tetra-TMS derivative (**1*b***) of **1** confirmed the presence of four hydroxyl groups by successive losses of TMSOH (*m/z* 90) from the derivatized molecule (*m/z* 808, 718, 628, 538).

The presence of an α,β-unsaturated γ-lactone subunit with an hydroxyl group at position 4 was suggested by the following characteristic features (8–11): a strong IR absorption peak (carbonyl) at 1745 cm^{-1} and a UV maximum at 223 nm; six proton resonances at δ 7.19 (1H, q, H-33), 5.06 (1H, qq, H-34), 3.87 (H, m, H-4), 2.53 (1H, dddd, H-3a), 2.40 (1H, dddd, H-3b), and 1.43 (3H, d, H-35); and six carbon resonances at δ 174.63 (C-1), 151.86 (C-33), 130.09 (C-2), 77.97 (C-34), 69.87 (C-4), and 19.06 (C-35).

The existence of two, nonadjacent tetrahydrofuran rings was suggested by proton resonances at δ 3.80 (H-13, -18, -21) and 3.87 (H-10) in **1** and 3.85 (H-10) and 3.96 (H-13, -18, -21) in **1*a*** and carbon resonances at δ 79.24 (C-10) and δ 81.96, 82.66, 82.68, (C-13, -18, -21) (8–11). The protons (δ 3.41, H-14, 17, and -22) attached to secondary hydroxylated carbons (δ 74.07, 74.25, 74.37 for C-12, -17, and -22) could be easily distinguished from those of the THF-flanking protons and carbons, as they resonated upfield compared with the latter. Two of these hydroxyl groups were assigned as adjacent to one THF ring, and one was assigned as adjacent to the other ring. The upfield shift of C-10 to δ 79.24 indicated that there was no hydroxyl group adjacent to one side of one of the THF rings. These conclusions were further supported by proton resonances of **1*a*** at δ 3.85 (H-10), 3.97 (H-13, -18, -21) and 4.83 (H-14, -17, -22). These NMR data are very similar to those of bullatanocin (**7**) and gigantecin (**8**), which are presented in Tables 1 and 2 for comparative purposes, as well as other nonadjacent bis-THF ring acetogenins (8–10).

The EIMS data of **1**, together with its tetraacetate (**1*a***), tetra-TMS (**1*b***), and d-TMS (**1*c***) derivatives, clearly resolved the carbon skeleton and the placement of the THF rings (Table 3). EIMS fragmentation patterns indicated that the two THF rings were located at C-10 and C-18 along the hydrocarbon chain and also supported the placement of the four hydroxyl groups at C-4, C-14, C-17, and C-22, as originally indicated by the NMR data.

The relative stereochemistries within the carbon centers C-13/C-14, C-17/C-18, and C-21/C-22 were determined by comparing the ^{13}C NMR signals of **1** for the hydroxylated carbons C-14, C-17, and C-22 at δ 74.07, 74.25, and 74.37 respec-

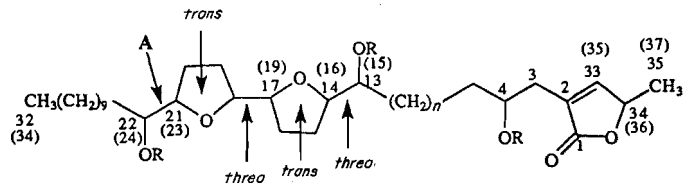

Compound	2	2*a*	3	4	9	9*a*
R	H	Ac	H	H	H	Ac
n	7	7	9	7	9	9
A	threo	threo	erythro	erythro	threo	threo

tively, as well as the ^1H NMR signals of **1** at δ 3.41 (H-13, -17, -22) and 3.80 (H-13/15, -17/19, -21/23/14), with those of model compounds of known relative stereochemistry (12–15). The comparison clearly indicated that the relative configurations between the above couples of adjacent chiral carbons were *threo*. Comparing with a group of diacetyl dibutylated bis-THF rings of known relative stereochemistry (13–15), the ^1H NMR signals of **1*a*** at δ 3.97 (H-13, -18, -21) and 4.83 (H-14, -17, -22) further supported these *threo* assignments, and the ^1H NMR signals of **1*a*** at δ 3.97 for H-18 and H-21 indicated the *trans* configuration of the substitution pattern of the C-18 to C-21 THF ring. Thus, the structure of compound **1** was determined as illustrated and named parvifloracin. Parvifloracin is the first nonadjacent bis-THF ring acetogenin with only 35 carbons, and this is the first report of the presence of a nonadjacent bis-THF ring acetogenin in the genus *Asimina*.

The second compound, parviflorin (**2**), was also isolated as a whitish wax with $[\alpha]_D^{22}$ +18.33 (*c* 0.06, EtOH). The high resolution CI mass spectrum of **2** showed *m/z* at 595.4573 for MH^+ (calculated 595.4574), corresponding to the molecular formula $C_{35}H_{62}O_7$. The prominent absorption peak at 3452 cm^{-1} in the IR spectrum and three successive losses of H_2O (*m/z* 18) from the molecular ion in the CIMS (*m/z* 577, 559, 541) indicated the presence of three hydroxyl groups. These were further confirmed by preparation of an acetyl derivative (**2*a***). The ^1H NMR spectrum of **2a** showed two singlets at δ 2.03 and 2.08 (three and six protons, respectively) and two multiple proton resonances at δ 4.83 (2H) and 5.01 (1H) corresponding to the downfield shifts on secondary hydroxyl-bearing carbons as compared with **2**. The CIMS of **2*a*** and EIMS of **2*b*** also showed successive losses of three AcOH units (*m/z* 60) from the triace-

Can. J. Chem. Downloaded from www.nrcresearchpress.com by 195.246.54.202 on 09/08/12
For personal use only.

TABLE 1. Comparison of ^{1}H NMR data of parvifloracin (**1**), parvifloracin tetraacetate (**1***a*), bullatanocin (**7**), bullatanocin tetraacetate (**7***a*), and gigantecin (**8**)

	Chemical shift,[a] multiplicity (J^b)				
Proton	**1**	**1***a*	**7**	**7***a*	**8**
3a	2.53,dddd (15.1,4.0,1.5)	2.57,dddd (16.7,4.4,3.0,1.2)	2.53,dddd (15.1,4.0,1.6,1.5)	2.57,dddd (18.4,3.4,2.9,1.2)	2.38,dddd
3b	2.40,dddd (15.1,8.5,1.5,1.2)	2.51,dddd (16.7,7.6,1.3)	2.40,dddd (15.1,1.5,1.3)	2.51,dddd (18.5,7.8,1.3,1.2)	2.51,dddd
4	3.87,m	5.10,dddd (10.2,8.0,4.4,3.5)	3.87,m	5.10,dddd (10.1,7.8,4.0,3.3)	3.87,m
5–9/(5–11)	1.23–1.74,m	1.23–1.64,m	1.71–1.21,m	1.63–1.21,m	
10/(12)	3.87,m	3.85,m	3.87,m	3.85,m	3.78,m
11,12/(13,14)	1.96–2.4,m	1.92–2.0,m	1.99–1.37,m	1.99–1.21,m	
13/(15)	3.80,m	3.97,m	3.80,m	3.96,m	3.87,m
14/(16)	3.41,m	4.83,m	3.41,m	4.83,m	3.40,m
15,16/(17,18)	1.23–1.74,m	1.23–1.64,m	1.71–1.21,m	1.63–1.21,m	
17/(19)	3.41,m	4.83,m	3.41,m	4.83,m	3.40,m
18/(20)	3.80,m	3.97,m	3.80,m	3.96,m	3.87,m
19,20(21,22)	1.96–2.4,m	1.92–2.0,m	1.99–1.37,m	1.99–1.21,m	
21/(23)	3.80,m	3.97,m	3.80,m	3.96,m	3.87,m
22/(24)	3.41,m	4.83,m	3.41,m	4.83,m	3.40,m
23–31/(25–33)	1.23–1.74,m	1.23–1.64,m	1.71–1.21,m	1.63–1.21,m	
32/(34)	0.87,t(7.0)	0.88,t(7.0)	0.89,t(7.0)	0.89,t(7.0)	
33/(35)	7.19,q(1.5)	7.08,q(1.5)	7.19,q(1.5)	7.08,q(1.5)	7.17,d
34/(36)	5.06,qq(7.0,1.5)	5.01,qq(7.0,1.5)	5.06,qq(6.9,1.5)	5.01,qq(7.0,1.5)	5.06,dq
35/(37)	1.43,d(7.0)	1.40,d(7.0)	1.42,d(6.9)	1.40,d(7.0)	1.41,d
4-OAc		2.026,s		2.03,s	
14/(16)-OAc		2.073,s		2.07,s	
17/(19)-OAc		2.075,s		2.07,s	
22/(24)-OAc		2.091,s		2.09,s	

[a]In ppm.
[b]In hertz.

Can. J. Chem. Downloaded from www.nrcresearchpress.com by 195.246.54.202 on 09/08/12
For personal use only.

tate **2***a* (*m/z* 661, 601, 541) as well as three TMSOH units (*m/z* 90) from the tri-TMS derivative **2***b* (*m/z* 721, 631, 541), respectively.

The presence of an α,β-unsaturated γ-lactone subunit with an hydroxyl group at the C-4 position (8–11) was suggested by a strong IR absorption peak (carbonyl) at 1753 cm^{-1} and UV maximum at 221 nm; six proton resonances at δ 7.17 (1H, q, H-33), 5.04 (1H, qq, H-34), 3.87 (1H, m, H-4), 2.53 (1H, dddd, H3a), 2.40 (1H, dddd, H-3b), and 1.43 (3H, d, H-35); and six carbon resonances at δ 174.52 (C-1), 151.71 (C33), 131.13 (C-2), 77.97 (C-34), 69.98 (C-4), and 19.16 (C-35).

The existence of two adjacent THF rings was demonstrated by proton resonances at δ 3.84 (H-14, 17, -18, -21) in **2** and 3.96 (H-14, -17, -18, -21) in **2***a*, and carbon resonances at δ 81.77, 81.79, 83.12, 83.15 (C-14, -17, -18, -21) (4, 8, 11, 16). The protons (δ 3.39, H-13 and -22) attached to secondary hydroxylated carbons (δ 74.05 and 74.07 for C-13 and -22) could be easily distinguished from those of the THF-flanking protons and carbons, as they resonated upfield compared with the latter. These assignments were further supported by proton resonances of **2***a* at δ 3.96 (H-14, -17, -18, -21) and δ 4.86 (H-13 and -22). These data are very similar to those of asimicin, which are presented in Tables 4 and 5 for comparative purposes, as well as other adjacent bis-THF ring acetogenins (4, 8, 11, 16, 17).

The EIMS and CIMS data of **2**, together with those of its triacetate (**2***a*), tri-TMS (**2***b*), and tri-dTMS (**2***c*) derivatives, resolved the carbon skeleton and placement of the THF rings (Table 6). Though the NMR data are very similar to those of asimicin (4, 8, 16, 17), the mass spectral data indicated that this

TABLE 2. Comparison of ^{13}C NMR data of parvifloracin (**1**), bullatanocin (**7**), and gigantecin (**8**)

	Chemical shift (ppm)		
Carbon	**1**	**7**	**8**
1	174.63	174.44	174.6
2	131.09	130.95	131.1
3	25.46–37.25	37.31–25.5	
4	69.87	69.74	69.9
5–9/(5–11)	25.46–37.25	37.31–25.5	
10/(12)	79.24	79.21	
11,12/(13,14)	25.46–37.25	37.31–25.5	
13/(15)	81.96[a]	81.97[b]	
14/(16)	74.07[c]	74.33[d]	74.1
15,16/(17,18)	25.46–37.25	37.31–25.5	
17/(19)	74.25[c]	74.21[d]	74.3
18/(20)	82.66[a]	82.67[c]	
19,20/(21,22)	25.46–37.25	37.31–25.5	
21/(23)	82.68[a]	82.65[b]	
22/(24)	74.37[c]	74.00[d]	74.4
23–30/(25–32)	25.46–37.25	37.31–25.5	
31/(33)	22.63	22.64	
32/(34)	14.07	14.10	
33/(35)	151.86	151.68	151.2
34/(36)	77.97	77.88	77.9
35/(37)	19.06	19.07	19.1

NOTE: *a–d* indicate that the assignments may be interchangeable within each group.

TABLE 3. Diagnostic EIMS fragmentation pattern of parvifloracin **1**, **1**-tetra-TMS (**1***b*), and **1**-tetra-d-TMS (**1***c*).

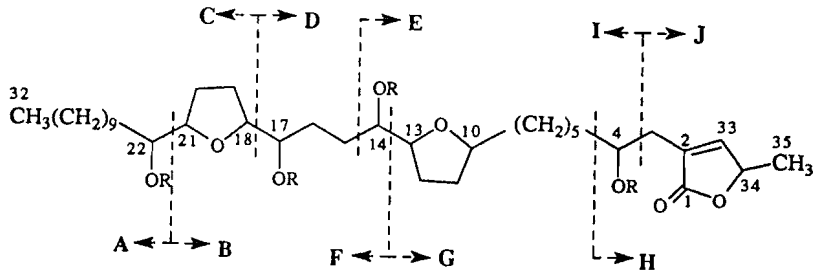

	m/z		
Fragment	**1**, R = H	**1***b*, R = TMS	**1***c*, R = d-TMS
A	171	243	252
B	439,[a]421[b]	655,565,[c]475[c]	682,583,[d]484[d]
C	241	313	322
D	369,[a]351,[b]333[b]	585,495,[c]405[c]	612,513,[d]414[d]
E	311,293[b]	455	473
F	329,[a]311[b]	545,455,[c]365[c]	572,473,[d]374[d]
G	281,263[b]	353	362
H	141,123[b]	213	222
I	499	787,697,[c]607[c]	823,724,[d]625[d]
J	111		

[a]Peaks were not seen.
[b]Loss of H_2O (*m/z* 18).
[c]Loss of TMSOH (*m/z* 90).
[d]Loss of d-TMSOH (*m/z* 99).

TABLE 4. Comparison of ^1H NMR data of parviflorin (**2**), parviflorin triacetate (**2***a*), asimicin (**9**), and asimicin triacetate (**9***a*)

	Chemical shift,[a] multiplicity (J^b)			
Proton	**2**	**2***a*	**9**	**9***a*
3a	2.53,dddd (15.0,3.5,1.6,1.5)	2.56,dddd (16.3,4.0,2.7,1.5)	2.54,dddd (15.0,3.5,1,7,1.5)	2.53,dddd (16.8,3.8,2.3,1.5)
3b	2.40,dddd (15.0,8.3,1.5,1.2)	2.50,dddd (16.3,7.8,1.3,1.2)	2.39,dddd (15.0,8.0,1.6,1.5)	2.48,dddd (16.8,7.4,1.3,1.2)
4	3.87,m	5.10,dddd (10.1,7.8,4.2,3.6)	3.84,m	5.09,dddd (10.3,8.0,5.2,3.2)
5–12/(5–14)	1.24–1.74,m	1.21–1.87,m	1.26–1.48,m	1.20–1.88,m
13/(15)	3.39,m	4.86,m	3.38,m	4.85,m
14/(16)	3.84,m	3.96,m	3.84,m	3.94,m
15,16/(17,18)	1.66–1.98,m	1.70–2.03,m	1.60–2.02,m	1.48–1.195,m
17,18/(19,20)	3.84,m	3.96,m	3.84,m	3.94,m
19,20(21,22)	1.66–1.98,m	1.70–2.03,m	1.60–2.02,m	1.48–1.195,m
21/(23)	3.84,m	3.96,m	3.84,m	3.94,m
22/(24)	3.39,m	4.86,m	3.38,m	4.85
23–31/(25–33)	1.24–1.74,m	1.21–1.87,m	1.26–1.48,m	1.20–1.88,m
32/(34)	0.87,t(7.0)	0.88,t(7.0)	0.87,t(7.0)	0.87,t(7.0)
33/(35)	7.18,q(1.5)	7.09,q(1.5)	7.18,q(1.5)	7.06,q(1.5)
34/(36)	5.06,qq(6.9,1.5)	5.02,qq(6.9,1.5)	5.06,qq(6.8,1.2)	5.01,qq(6.8,1.3)
35/(37)	1.43,d(6.9)	1.40,d(6.9)	1.42,d(6.8)	1.41,d(6.8)
4-OAc		2.03		2.01
13/15-OAc		2.08		2.06
22/24-OAc		2.08		2.06

[a]In ppm.
[b]In hertz.

Can. J. Chem. Downloaded from www.nrcresearchpress.com by 195.246.54.202 on 09/08/12
For personal use only.

TABLE 5. Comparison of ^{13}C NMR data of parviflorin (**2**) and asimicin (**9**)

Carbon	Chemical shift (ppm)	
	2	**9**
1	174.52	174.51
2	131.13	130.94
3	33.47[a]	33.29[b]
4	69.99	69.80
6–11/(6–13)	25.58–31.94	25.54–31.85
12/(14)	33.47[a]	33.17[b]
13/(15)	74.08[c]	73.91[d]
14/(16)	83.15[e]	83.08
15,16/(17,18)	25.58–31.94	25.54–31.85
17/(19)	81.79[f]	81.73
18/(20)	81.77[f]	81.73
19,20/(21,22)	25.58–31.94	25.54–31.85
21/(23)	83.12[e]	83.08
22/(24)	74.05[c]	73.93[d]
23/(25)	33.38[a]	33.17
24–30/(26–32)	25.58–31.94	25.54–31.85
31/(33)	22.73	22.64
32/(34)	14.17	14.09
33/(35)	151.72	151.74
34/(36)	77.97	77.92
35/(37)	19.17	19.05

NOTE: *a–f* indicate that the assignments may be interchangeable within each group.

compound is lacking two carbons in the hydrocarbon chain bearing the lactone ring. This conclusion was suggested by the *m/z* 283 (base peak) in the EIMS of **2**, together with *m/z* 427 (EIMS, 100%) in **2***b* and *m/z* 445 (EIMS, 100%) in **2***c*. These data confirmed that the positions of the THF rings are from C-14 to C-21. Other major mass fragments of **2**, e.g., at *m/z* 353/241 and 171/423, demonstrated that the second THF ring is attached to C-18, and this conclusion was supported by the mass spectral data of **2***b* and **2***c*. As usual, flanking OH groups are on each side of the adjacent bis-THF rings; this is true with all adjacent bis-THF ring acetogenins isolated so far, and both the NMR and mass spectral data substantiate this observation (8, 11).

The relative stereochemistries within the carbon centers C-13/C-14, C-17/C-18, and C-21/C-22 were determined by comparing the ^{13}C NMR signals of **2** for the hydroxylated carbons C-13 and C-22 at δ 74.05 and 74.07, as well as the ^{1}H NMR signals of **2** at δ 3.39 (H-13 and -22) and 3.84 (H-14, -17, -18 and -21), with those of model compounds of known relative stereochemistry (12–15). The comparison clearly showed that the relative configuration between the above pairs of adjacent chiral carbons were all of the *threo* type. By comparing with those of a group of diacetyl dibutylated bis-THF rings of known relative stereochemistry (13–15), the ^{1}H NMR signals of **2***a* at δ 3.85 (H-14, -17, -18, -21) and 4.83 (H-13, -22) further supported these *threo* assignments, and the ^{1}H NMR signals of **2***a* at δ 3.96 for H-14 and -17, and H-18 and -21, indicated the *trans* configuration of the substitution pattern of the C-14 to C-17 and C-18 to C-21 THF rings. The configuration of the chiral centers at C-4 and C-34 may be suggested to be 4*R*, 34*S*, since, as previously discussed, so far with the C-37 compounds, all are 4*R*, 36*S*. Thus, the structure of compound **2** was determined as illustrated and named parviflorin. This C-35 skeleton is relatively rare, since only three similar compounds (neoannonin (5), molvizarin (6) and itrabin (7)) have been reported to date.

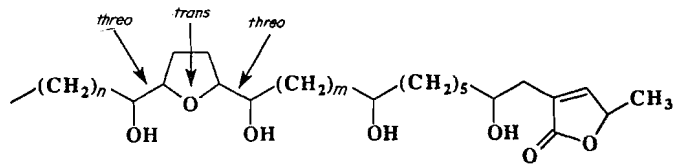

Annonacin (**5**) $n = 11$ $m = 4$

Goniothalamicin (**6**) $n = 13$ $m = 2$

Compounds **3** and **4** were also isolated as whitish waxes. ^{1}H NMR data were very similar in both cases, but mass spectral data showed different fragmentation patterns. The EIMS and CIMS of **3** and the EIMS of the TMS derivative of **3** showed identical fragments with bullatacin, an adjacent bis-THF ring acetogenin, previously isolated from *Annona bullata* (18), *Annona squamosa* (11), *Annona reticulata* (11), and *Asimina triloba* (17). TLC of **3** and bullatacin together gave the same R_f values. The EIMS and CIMS of **4** and the EIMS of the TMS derivative of **4** gave identical data with those of molvizarin, recently reported from *Annona cherimolia* (6). Therefore, **3** and **4** were identified as bullatacin and molvizarin, respectively.

Compounds **5** and **6** were also isolated as whitish waxes. ^{1}H NMR, EIMS, and CIMS of **5** and **6** and EIMS of their TMS derivatives clearly showed that these compounds were annonacin (previously isolated from several *Annona* species (11)) and goniothalamicin (previously isolated from *Goniothalamus giganteus* (19) and *Annona muricata* (20)), respectively; both are mono-THF ring acetogenins which are relatively rare in the *Asimina* genus. TLC with standard compounds available in our laboratory also confirmed the identity of these compounds.

Table 7 shows certain biological activities of all these compounds. As expected, both parvifloracin (**1**) and parviflorin (**2**) showed significant cytotoxicity to the three human solid tumor cell lines. Compound **1** showed very high toxicity against both lung and breast carcinoma cell lines. Compound **2** showed high toxicity against lung carcinoma with moderate toxicity against the colon cancer cell line. Both bullatacin (**3**) and molvizarin (**4**) showed high toxicity against all tumor cell lines; and bullatacin, thus far, is the most bioactive compound isolated from this plant. The mono-THF ring acetogenins, **5** and **6**, showed lesser activities than the bis-THF compounds, but they were still comparably as active as adriamycin. The mechanism of action of several acetogenins has been recently established; they are powerful inhibitors of NADH:ubiquinone oxidoreductase (complex I) in mitochondrial electron transport systems (25–27).

Experimental

Instrumentation

Optical rotations were measured on a Perkin Elmer 241 polarimeter. IR spectra were obtained on a Perkin Elmer 1420 IR spectrometer. UV spectra were obtained on a Beckman DU-7 UV spectrometer. ^{1}H and ^{13}C NMR spectra were obtained on a Varian VXR-500S spectrometer. Low resolutions EIMS and CIMS data were collected on a Finnigan 4000 spectrometer. Low resolution EIMS data of TMS derivatives were taken on a Kratos MS50. Exact masses for MS measurements were obtained on a Kratos MS50 spectrometer through peak matching. HPLC was performed with a Rainin HPLC using a Dynamax software system and a silica gel column (250 × 21 mm) equipped with a Rainin UV-1 detector set at 220 nm. Analytical TLC was made on silica gel

Can. J. Chem. Downloaded from www.nrcresearchpress.com by 195.246.54.202 on 09/08/12
For personal use only.

TABLE 6. Diagnostic EIMS fragmentation pattern of parviflorin **2**, **2**-tri-TMS (**2***b*), and **2**-tri-d-TMS (**2***c*).

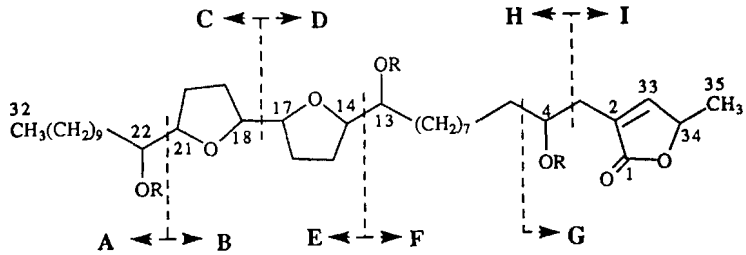

	m/z		
Fragment	**2**, R = H	**2***b*, R = TMS	**2***c*, R = d-TMS
A	171	243,153[a]	252
B	423[b]	567	585,486,[c]387[c]
C	241	313	322
D	353[b]	497,407[a]	515,416[c]
E	311	383,293[a]	392,293[c]
F	283,265[d]	427,337[a]	445,346[c]
G	141	213	222,123[c]
H	483	699,609,[a]519[b]	726,627,[c]528[c]
I	111		

[a]Loss of TMSOH (*m/z* 90).
[b]Peaks were not seen.
[c]Loss of d-TMSOH (*m/z* 99).
[d]Loss of H_2O (*m/z* 18).

TABLE 7. Biological activities[a] of compounds **1–6**

Compound	BST LC_{50} (μg/mL)	A-549 ED_{50} (μg/mL)	MCF-7 ED_{50} (μg/mL)	HT-29 ED_{50} (μg/mL)
1	2.01×10^{-2}	2.83×10^{-11}	$<10^{-12}$	2.15
2	8.8×10^{-2}	$<10^{-12}$	1.72	5.49×10^{-1}
3[b]	1.59×10^{-3}	$<10^{-12}$	$<10^{-12}$	10^{-12}
4	5.26×10^{-2}	$<10^{-12}$	2.77×10^{-9}	1.67×10^{-6}
5[c]	3.0×10^{-1}	$<10^{-3}$	1.0×10^{-2}	$<10^{-3}$
6[c]	24	8.0×10^{-3}	5.7×10^{-2}	1.1×10^{-3}
Adriamycin	8.0×10^{-2}[d]	1.49×10^{-4}	1.29×10^{-2}	4.85×10^{-3}

[a]BST = brine shrimp toxicity bioassay (2,3); A-549 lung carcinoma cell line (21); MCF-7 breast carcinoma cell line (22); HT-29 colon adenocarcinoma cell line (23).
[b]Data adapted from Hui et al. (18).
[c]Data adapted from Rieser et al. (20).
[d]Data from Anderson et al. (24).

plates (0.25 mm) developed with $CHCl_3$–MeOH (9:1 and 9.5:0.5) and hexane–acetone (3:2) and visualized using 5% phosphomolybdic acid in EtOH (8).

Plant material

Twigs of *A. parviflora* were collected and identified by one of us (D.R.E.) near Tifton, Ga., during August 1990. A voucher specimen is preserved in the herbarium of the Department of Medicinal Chemistry and Pharmacognosy, Purdue University.

Bioassays

The extracts, fractions, and pure compounds were routinely tested for lethality to brine shrimp larvae. In vitro cytotoxicity tests (7 days) to determine ED_{50} values against human tumor cell lines, were carried out at the Purdue Cancer Center, Cell Culture Laboratory, using standard protocols for A-549 (human lung carcinoma (24)), MCF-7 (human breast carcinoma (25)), and HT-29 (human colon adenocarcinoma (26)) with adriamycin as a positive control; ED_{50} values <4 μg/mL for pure compounds are considered significant.

Extraction and isolation

The twigs (<1 cm diameter, 3.5 kg) were extracted and partitioned, and the bioactive fraction (F005) was subjected to vacuum liquid column chromatography as described in a previous paper (4). Fraction 4 from the above column was further chromatographed using a gravity column and chromatotron plates to give three active fractions (fractions 4-5-2-2 (BST LC_{50} 5.56), 4-5-3-2 (BST LC_{50} 0.198), and 4-5-3-3 (BST LC_{50} 0.498)). A portion of fraction 4-5-3-2 (50 mg) was chromatographed on HPLC using hexane–THF–MeOH (90:1:9) to yield 31 mg asimicin, 12 mg parviflorin (**2**), 18 mg bullatacin (**3**), and 8 mg molvizarin (**4**). A portion of fraction 4-5-3-3 (43 mg) was chromatographed on HPLC in similar manner to yield 22 mg parvifloracin (**1**). Similarly, fraction 4-5-2-2 (34 mg) gave 15 mg annonacin (**5**) and 8 mg goniothalamicin (**6**) on HPLC separation.

Parvifloracin (1)

Whitish wax (22 mg); R_f value on silica gel TLC in $CHCl_3$–MeOH (9:1), 0.43; $[\alpha]_D^{22}$ +18.75° (*c* 0.08, EtOH); UV (EtOH) λ_{max}: 221 nm (ϵ = 8967); IR (film) cm^{-1}: 3466, 1745, 1722, 1645. CIMS (isobutane)

Can. J. Chem. Downloaded from www.nrcresearchpress.com by 195.246.54.202 on 09/08/12
For personal use only.

m/z (%): $[MH]^+$ 611 (100), $[MH - H_2O]^+$ 593 (12), $[MH - 2H_2O]^+$ 575 (42), $[MH - 3H_2O]^+$ 557 (11), $[MH - 4H_2O]^+$ 539 (2), 351 (22), 333 (3), 281 (9). EIMS data are given in Fig. 1. ^1H and ^{13}C NMR spectral data are given in Tables 1 and 2, respectively.

Acetylation of ***1***

Four milligrams of **1** was mixed with anhydrous pyridine – acetic anhydride (1:1) at room temperature overnight to give 3 mg of tetraacetate (**1***a*). CIMS (isobutane) *m/z* (%): 779 (5), 719 (100), 669 (29), 599 (6), 539 (20); EIMS *m/z* (%): 625 (2), 565 (20), 505 (2), 323 (100), 283 (36), 263 (30), 223 (10), 183 (4), 123 (16).

TMS and d-TMS derivatization of ***1***

A small quantity of **1** (<1 mg) was treated with 20 μL of *N,O*-bis(trimethylsilyl)acetamide (BSA) or d_{18}-bis(trimethylsilyl)trifloroacetamide (BSTFA) and 2 μL of pyridine (10:1) and heated at 70°C for 30 min to yield tetra-TMS derivative (**1***b*) or tetra-d-TMS derivative (**1***c*). EIMS data of both **1***b* and **1c** are given in Fig. 1.

*Parviflorin (****2****)*

Whitish wax (12 mg); R_f value on silica gel TLC in $CHCl_3$–MeOH (9.5:0.5), 0.37; $[\alpha]D^{22}$ +18.33° (*c* 0.06, EtOH); UV (EtOH) λ_{max} 223 nm (ϵ = 8405); IR (film) cm^{-1}: 3452, 1753, 1648. CIMS (isobutane) *m/z* (%): $[MH]^+$ 595 (72, $[MH - H_2O]^+$ 577 (100), $[MH - 2H_2O]^+$ 559 (17), $[MH - 3H_2O]^+$ 541 (1), 283 (46). EIMS data are given in Fig. 2; ^1H and ^{13}C NMR spectral data are given in Tables 3 and 4, respectively.

Acetylation of ***2***

Four milligrams of **2** was mixed with anhydrous pyridine – acetic anhydride (1:1) at room temperature overnight to give 3 mg of triacetate (**2***a*). CIMS (isobutane) *m/z* (%): 721 (8), 661 (100), 601 (95), 541 (16); EIMS *m/z* (%): 609 (1), 507 (9), 489 (10), 447 (11), 437 (51), 387 (7), 377 (27), 353 (9), 293 (26), 265 (11), 183 (3), 153 (5), 123 (26), 95 (100).

TMS and d-TMS derivatization of ***2***

A small quantity of **2** (<1 mg) was treated with 20 μL or BSA of BSTFA and 2 μL of pyridine (10:1) and heated at 70°C for 30 min to yield tetra-TMS derivative (**2***b*) or tetra-d-TMS derivative (**2***c*). EIMS data of both **2***b* and **2***c* are given in Fig. 2.

Acknowledgments

This research was supported by grant No. CA 30909 from the National Cancer Institute, National Institutes of Health. We thank the Cell Culture Laboratory, Purdue Cancer Center, for cytotoxicity testing.

1. M.B. Callaway. *In* The paw paw, *Asimina triloba*. Kentucky State University, Pub. No. CRS-Hort 1-901T, Frankfort, 1990. pp. 6, 7, and 16.
2. B.N. Meyer, N.R. Ferrigni, J.E. Putnam, L.B. Jacobsen, D.E. Nichols, and J.L. McLaughlin. Planta Med. **45**, 31 (1982).
3. J.L. McLaughlin. *In* Methods in plant biochemistry. Vol. 6. *Edited by* K. Hostettmann. Academic Press, London. 1991. p. 1.
4. S. Ratnayake, X.-P. Fang, J.E. Anderson, D.R. Evert, and J.L. McLaughlin. J. Nat. Prod. **55**, 1462 (1992).
5. K. Kawazu, J.P. Alcantara, and A. Kobayashi. Agric. Biol. Chem. **31**, 861 (1989).
6. D. Cortes, S.H. Myint, and R. Hocquemiller. Tetrahedron, **47**, 8195 (1991).
7. D. Cortes, S.H. Myint, M. Leboeuf, and A. Cave. Tetrahedron Lett. **32**, 6133 (1991).
8. J.K. Rupprecht, Y.-H. Hui, and J.L. McLaughlin, J. Nat. Prod. **53**, 237 (1990).
9. A. Alkofahi, J.K. Rupprecht, Y.-M. Liu, C.-J. Chang, D.L. Smith, and J.L. McLaughlin. Experientia, **46**, 539 (1990).
10. Z.-M. Gu, X.-P. Fang, M.J. Rieser, Y.-H. Hui, L.R. Miesbauer, D.L. Smith, K.V. Wood, and J.L. McLaughlin, Tetrahedron, **49**, 747 (1993).
11. X.-P. Fang, M.J. Rieser, Z.-M. Gu, G.-X. Zhao, and J.L. McLaughlin. Phytochem. Anal. **4**, 27 (1993).
12. L. Born, F. Lieb, J.P. Lorentzen, H. Moescher, M. Nonfon, R. Sollner, and D. Wendisch. Planta Med. **56**, 312 (1990).
13. T.R. Hoye and J.C. Suhadolnik. J. Am. Chem. Soc. **109**, 4402 (1987).
14. T.R. Hoye and Z.-P. Zhuang. J. Org. Chem. **53**, 5578 (1988).
15. M.J. Rieser, Y.-H. Hui, J.K. Rupprecht, J.F. Kozlowski, K.V. Wood, J.L. McLaughlin, P.A. Hanson, Z.-P. Zhuang, and T.R. Hoye. J. Am. Chem. Soc. **114**, 10 203 (1992).
16. J.K. Rupprecht, C.-J Chang, J.M. Cassady, J.L. McLaughlin, K.L. Mikolajczak, and D. Weisleder. Heterocycles, **24**, 1197 (1986).
17. G.-X. Zhao, Y.-H. Hui, J.K. Rupprecht, J.L. McLaughlin, and K.V. Wood. J. Nat. Prod. **35**, 347 (1992).
18. Y.-H. Hui, J.K. Rupprecht, Y.-M. Liu, J.E. Anderson, D.L. Smith, C.-J. Chang, and J.L. McLaughlin. J. Nat. Prod. **52**, 463 (1989).
19. A. Alkofahi, J.K. Rupprecht, D.L. Smith, C.-J. Chang, and J.L. McLaughlin. Experientia, **44**, 83 (1988).
20. M.J. Rieser, X.-P. Fang, J.K. Rupprecht, Y.-H. Hui, D.L. Smith, and J.L. McLaughlin. Planta Med. **59**, 91 (1993).
21. D.J. Giard, S.A. Aaronson, G.J. Todaro, P. Arnstein, J.H. Kersey, H. Dosik, and W.P. Parks. J. Natl. Cancer Inst. **51**, 1417 (1973).
22. H.D. Soule, J. Vazquez, A. Long, S. Albert, and M. Bennan. J. Natl. Cancer Inst. **51**, 1409 (1973).
23. J. Fogh (*Editor*). *In* Human tumor cells, in vitro. Plenum Press, New York. 1975. pp. 115–159.
24. J.E. Anderson, W. Ma, D.L. Smith, C.-J. Chang, and J.L. McLaughlin. J. Nat. Prod. **55**, 71 (1992).
25. M. Londershausen, W. Leicht, F. Lieb, and H. Moeschler. Pestic. Sci. **33**, 427 (1991).
26. M.A. Lewis, J.T. Arnason, B.J.R. Philogene, J.K. Rupprecht, and J.L. McLaughlin. Pestic. Biochem. Physiol. **45**, 15 (1993).
27. K.I. Ahammadsahib, R.M. Hollingworth, Y.-H. Hui, and J.L. McLaughlin. Life Sci. **14**, 1113 (1993).

Can. J. Chem. Downloaded from www.nrcresearchpress.com by 195.246.54.202 on 09/08/12
For personal use only.

Rotamers of dimethyl(acetyl)(η^5-cyclopentadienyl)platinum(IV) in the gas phase

M.C. JENNINGS AND R.J. PUDDEPHATT

Department of Chemistry, University of Western Ontario, London, ON N6A 5B7, Canada

Received August 6, 1993

M.C. JENNINGS and R.J. PUDDEPHATT. Can. J. Chem. **72**, 294 (1994).

The platinum(IV) complex, $[CpPt(CH_3)_2(COCH_3)]$, was examimed by IR spectroscopy in the gas phase and found to exist as an equilibrium mixture of two rotational conformers. The equilibrium was examined as a function of temperature by using gas phase IR and the energy difference between the rotamers was determined. Molecular modelling studies were also carried out and are consistent with a model in which the conformers correspond to different rotational positions of the acetyl group.

M.C. JENNINGS et R.J. PUDDEPHATT. Can. J. Chem. **72**, 294 (1994).

On a examiné le spectre infrarouge du complexe de platine(IV), $[CpPt(CH_3)_2(COCH_3)]$ en phase gazeuse et on a trouvé qu'il existe sous la forme d'un équilibre entre deux conformères rotationnels. On a déterminé la position de l'équilibre en fonction de la température à l'aide de l'ir en phase gazeuse et on a déterminé la différence d'énergie entre les rotamères. On a aussi réalisé des études des modèles moléculaires et elles sont en accord avec un modèle dans lequel les conformères correspondent à des positions rotationnelles différentes du groupe acétyle.

[Traduit par la rédaction]

Introduction

Infrared spectroscopy is well known as a useful tool for the study of isomerization reactions. For example, solution IR has been used to monitor both *cis*-to-*trans* and *fac*-to-*mer* isomerizations for organometallic complexes of the group 6 metals (1). Recently, the technique has been used for monitoring the equilibria between rotamers of organometallic complexes of the group 7 and 8 metals in solution (2–5). In particular, the η-cyclopentadienyl (Cp) derivatives $[CpFeL_2R]$ (L = CO, PR_3, R = alkyl, acyl, silyls) have been examined in great detail. Infrared spectroscopy provided evidence for the rotamers and allowed the thermodynamic properties to be determined experimentally (3*c*, 3*e*, 4), with the interpretations aided by theoretical studies using Extended Hückel, *ab initio*, and molecular modelling calculations (4–6). There has been some controversy about the precise interpretation (4, 5), but it is currently thought that the more stable rotamers are **A** and **B**, with **C** at higher energy.

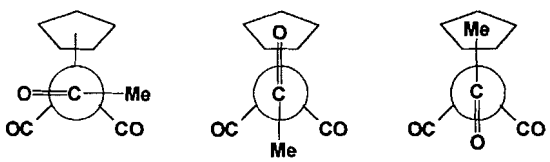

The complexes $[CpPtMe_3]$ and $[(\eta\text{-}C_5H_4Me)PtMe_3]$ are known to be excellent precursors for the chemical vapor deposition of platinum films (7). While extending this work to include platinum(IV) complexes of the general type [CpPtRR′R″] (R,R′,R″ = alkyl, acyl) as CVD precursors, it was noted that the IR spectrum of the known complex $[CpPtMe_2(COCH_3)]$, **1** (8), in the gas phase contained two bands due to ν(C═O), suggesting, by analogy to the case of $[CpFe(CO)_2(COMe)]$, the presence of two rotamers. Before the recent burst of interest in iron complexes, Shaver had already reported that **1** gave two carbonyl bands in the IR spectrum in both the solid state and in solution in hexane or carbon tetrachloride and had correctly interpreted this in terms of conformational isomers (8). At least two out of the three rotamers **D–F** were hypothesized to be present (8).

Since no study of this type of rotamers in the gas phase has been made (3–5, 8), a more detailed investigation of the gas phase equilibrium was carried out and is reported below. It should also be noted that, since the time of Shaver's study (8), molecular mechanics calculations have become routine and have led to conformational analysis of these molecules in terms of pseudooctahedral rather than pseudotetrahedral stereochemistry at the central metal (4, 5) and this naturally modifies the interpretation.

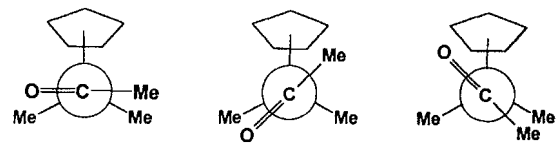

Results and discussion

The infrared spectrum of **1** in the gas phase at 70°C contained bands due to the cyclopentadienyl and methyl groups (9) and two extra, overlapping bands due to ν(C═O) at 1693 and 1667 cm^{-1} (Fig. 1*a*). Curvefitting allowed the ratio of absorbances $A(1667)/A(1693) = 0.92$ to be determined. Subsequent study showed that the IR spectrum of **1** in CH_2Cl_2 at 20°C also contained two bands due to ν(CO) at 1692 and 1668 cm^{-1} with $A(1668)/A(1692) = 0.99$ (Fig. 1*b*). The IR spectrum of a microcrystalline, sublimed sample of **1** as a Nujol mull was less well resolved but two ν(C═O) bands were observed at 1657 and 1694 cm^{-1} with $A(1657)/A(1694) = 3.2$ (Fig. 1*c*). Shaver reported ν(C═O) for **1** = 1693 (s) and 1663 (m) cm^{-1} in CCl_4 solution (8). If the two bands are assigned to two rotamers, then clearly both rotamers are present in both solution and gas phases; even in the solid state there is evidence for two rotamers (8). It should be noted that the ^1H NMR spectrum of **1** contained single resonances due to the C_5H_5, MePt, and MeCO protons even at low temperature (−80°C) and in agreement with the literature (8) and so, if rotamers are present, they must interconvert rapidly in solution to give a time-averaged NMR spectrum.

The relative absorbances of the two peaks due to ν(C═O) of **1** in the gas phase changed as a function of temperature, indicating a temperature dependence of the relative populations of the rotamers. By making the assumptions that there are only two rotamers and that the extinction coefficients for ν(C═O) are the

Can. J. Chem. Downloaded from www.nrcresearchpress.com by 195.246.54.202 on 09/08/12
For personal use only.

Can. J. Chem. Downloaded from www.nrcresearchpress.com by 195.246.54.202 on 09/08/12
For personal use only.

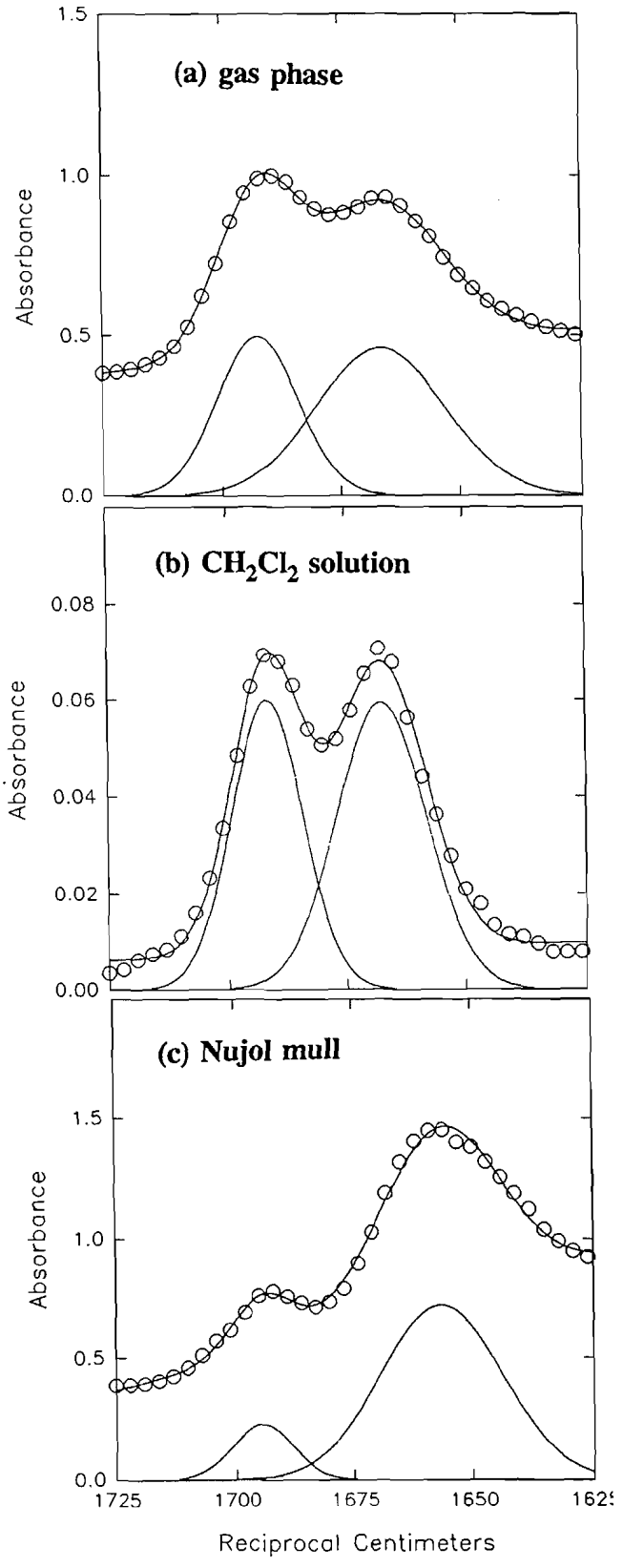

FIG. 1. Expanded IR spectrum with the fitted curve and the two individual curves of [$CpPtMe_2(COMe)$]: (*a*) in the gas phase at 70°C; (*b*) in CH_2Cl_2 solution at 20°C; (*c*) as a Nujol mull.

TABLE 1. Equilibrium constants, K, for rotameters as a function of temperature

Temperature (°C)	K
70	0.92
100	0.83
130	0.81
200	0.69

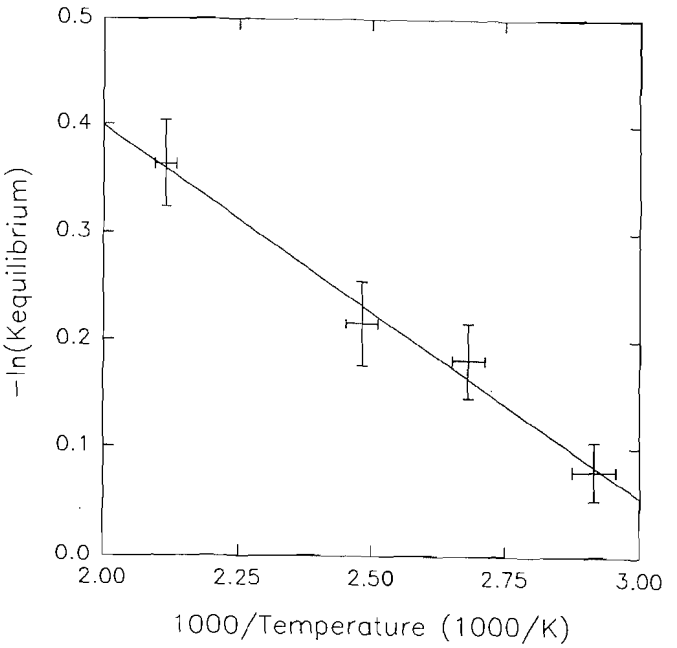

FIG. 2. Plot of ln K vs. $1/T$ (K) for [$CpPtMe_2(COMe)$] in the gas phase. The correlation coefficient for the graph, $R = 0.993$.

same for each rotamer, the equilibrium constant at each temperature can be estimated. In particular, the ratio of the absorbances due to ν(C═O) (Table 1) can be equated to the equilibrium constant, K, at each temperature. Similar assumptions have been made for the iron complexes discussed earlier (*3f*, 4). A plot of ln K vs. $1/T$ was linear (Fig. 2). From this plot, the enthalpy and entropy for the equilibrium were determined as $\Delta H_0 = -0.69 \pm 0.06$ kcal mol^{-1} and $\Delta S_0 = -2.17 \pm 0.04$ cal K^{-1} mol^{-1}. It should be noted that the enthalpy effect favours the rotamer with ν(C═O) = 1667 cm^{-1} and the entropy effect favours that with ν(C═O) = 1693 cm^{-1}. The enthalpy difference between rotamers for **1** is similar to those for similar complexes such as [$CpFe(CO)_2(SiCl_2Me)$] ($\Delta H_0 = 0.8$ kcal mol^{-1}) and [$CpFe(CO)_2(CH_2Ph)$] ($\Delta H_0 = 1.1 \pm 0.3$ kcal mol^{-1}) (*3e*, 4).

While the IR spectra of **1** indicate the presence of two rotamers, the precise structures cannot be determined by this method. Hence molecular modelling studies were carried out on **1** using an MMX package (10). The global minima are shown schematically as **1***a* and **1***b* in Fig. 3, with the minimum energy conformations viewed approximately down the acylplatinum bond shown below. The enthalpy difference between the most stable conformation **1***a* and conformation **1***b* is calculated to be 0.8 kcal mol^{-1}, in good agreement with the observed value of 0.69 ± 0.06 kcal mol^{-1}. No global minimum was identified for

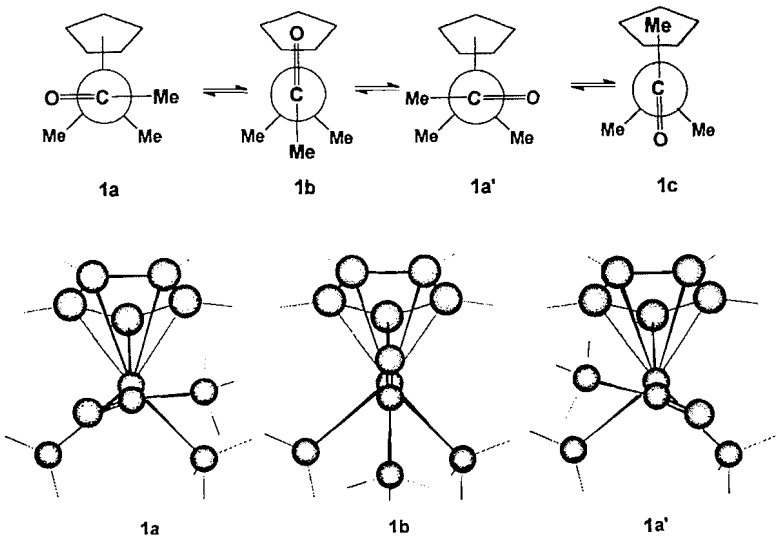

FIG. 3. The probable rotamers of $[CpPtMe_2(COMe)]$ and, below, the minimized structures for **1***a* and **1***b*.

the third possible rotamer **1***c*. The enthalpy of activation to rotation between the equivalent conformations **1***a* and **1***a'* via **1***b* was calculated to be 1.1 kcal mol^{-1} and via **1***c* it was 1.6 kcal mol^{-1}. Of course these barriers are much too low to allow observation of different rotamers by NMR spectroscopy. Mechanical spectroscopic studies have been carried out for **1** in a polymer matrix and indicated a barrier to rotation of the cyclopentadienyl ligand of 5.5 ± 0.6 kcal mol^{-1}, but this barrier is thought to arise from interactions between the Cp ligand and the matrix (11). The MMX calculations suggest a very low barrier to Cp ligand rotation in **1**. The optimized bond angles between the η^1 ligands (Me and MeCO) were in the range 90 ± 10° for all conformers, indicating that the complexes should be considered pseudooctahedral with the Cp ligand occupying three coordination sites, rather than pseudotetrahedral.

It should be noted that the calculated energy differences between rotamers and the activation energies to rotation are small and should therefore be treated with caution. If the calculated relative energies are correct, then the gas phase IR bands at 1667 and 1693 cm^{-1} can be assigned to rotamers **1***a* and **1***b*, respectively. There are two reasons to doubt this assignment. Firstly, in $[CpFe(CO)_2R]$, π-backbonding to R is thought to be stronger in the upright rotamer corresponding to **1***b*, although this is partly due to the presence of the π-acceptor carbonyl ligands and might be different in **1** in which the methyl ligands are σ-bonding only (6). The MMX-based assignment indicates that **1***b* has a *higher* ν(C═O) stretching frequency than **1***a*, indicating weaker backbonding to the acetyl group in **1***b*. Secondly, there are two equivalent rotamers of **1***a* but only one of **1***b*, and so the entropy effects might be expected to favour **1***a*. The MMX-based assignment indicates that the entropy effect favours **1***b*.

In conclusion, it has been shown that the equilibrium between rotamers in organotransition metal complexes can be studied by FTIR in the gas phase as well as in solution, provided the complexes have sufficient volatility. Molecular mechanics calculations can aid the assignment of structure to the rotamers (4, 5) but, since the calculated energy differences are small and since, as explained above, there are other reasons to doubt the assignments in the present case (6), our conclusions should be considered tentative until more sophisticated models than the MMX package used in this work are developed.

Experimental

Complex **1** was prepared according to the literature procedure (8) and was purified by sublimation under vacuum. ^{1}H-NMR($CDCl_3$): 1.14 (s, 6H, CH_3, ^2J(PtH) = 84.8 Hz), 2.46 (s, 3H, $C(O)CH_3$, ^3J(PtH) = 7.1Hz), 5.82 ppm (s, 5H, C_5H_5, ^2J(PtH) = 5.7 Hz). MS: found: *m/z* = 333; calcd. for $[CpPtMe_2(COMe)]^+$: *m/z* = 333. MP = 65°C.

Infrared spectroscopy

Gas phase IR spectra were recorded by using a Perkin-Elmer system 2000 FT-IR supported by the Infra Red Data Manager. The gas phase IR cell used was a glass cell (pathlength 10 cm, volume 78.2 mL) with two Teflon stopcocks and a cold finger attachment. The cell was equipped with NaCl windows and the entire cell was wrapped with heating tape and thermally controlled using a Eurotherm 808 controller coupled to a J-type thermocouple. In a typical experiment, the IR cell was charged with 25 mg of **1**, then evacuated at room temperature and then heated to the desired temperature before recording the IR spectrum. Spectra were recorded over the temperature range 70–200°C, limited at the low end by the volatility of **1** and at the high end by its stability limit.

The absorbance data from 1725–1625 cm^{-1} was loaded into a curve-fitting program and the spectrum was fitted with two Gaussian curves. Figure 1*a* shows the raw data points, the fitted curve and the two individual curves that sum to give the fitted curve. Excellent fits were obtained, from which the absorbance of the individual peaks as a function of temperature were determined.

The atoms of **1** were entered into the program PCMODEL-386, with the cyclopentadienyl ring as an aromatic substructure. The hydrogen atoms were placed in idealized positions. The Pt—C distances of the two methyl groups were initially fixed at 2.1 Å and the Pt—C distances of the Cp ring were all fixed at 2.3 Å, based on X-ray data on related complexes (7, 12). The initial structure also had the acetyl group staggered with respect to the Cp ring. From this starting point, the structure was allowed to minimize, giving one of the global minimum configurations. Barriers to rotation were then estimated by varying a dihedral angle defined as $\mathbf{CH_3C(O)PtCH_3}$ over the range 0–360° in 5° increments, with full minimization at each angle (4). The lowest energies occurred at torsion angles of 148 and 303°, corresponding to structures **1***a* and **1***a'*, while a much shallower minimum occurred at a dihedral angle of 50° corresponding to structure **1***b* (Fig. 3).

Can. J. Chem. Downloaded from www.nrcresearchpress.com by 195.246.54.202 on 09/08/12
For personal use only.

Acknowledgment

We thank the Natural Sciences and Engineering Research Council (Canada) for financial support.

1. (*a*) E.O. Fischer, H. Fischer, and H. Werner. Angew. Chem. **11**, 644 (1972); (*b*) B.D. Dombek and R.J. Angelici. J. Am. Chem. Soc. **98**, 4110 (1976); (*c*) D.J. Darensbourg. Inorg. Chem. **18**, 14 (1979); (*d*) A.M. Bond, S.W. Carr, and R. Colton. Organometallics, **3**, 541 (1984); (*e*) A.A. Ismail, F. Sauriol, and I.S. Butler. Inorg. Chem. **28**, 1007 (1989).
2. (*a*) I.S. Butler and T. Sawai. Inorg. Chem. **12**, 1994 (1973); (*b*) F. Calderazzo, K. Noack, and U. Schaerer. J. Organomet. Chem. **6**, 265 (1966).
3. (*a*) I. Pope, P. Sommerville, M. Laing, K.J. Hindson, and J.R. Moss. J. Organomet. Chem. **112**, 309 (1976); (*b*) R.D. Fischer, A. Vogler, and K. Noack. J. Organomet. Chem. **7**, 135 (1967); (*c*) K. Noack. J. Organomet. Chem. **7**, 151 (1967); (*d*) W. Jetz and W.A.G. Graham. J. Am. Chem. Soc. **89**, 2773 (1967); (*e*) J. Dalton. Inorg. Chem. **11**, 915 (1972).
4. S.C. Mackie, Y. Park, H.F. Shurvell, and M.C. Baird. Organometallics, **10**, 2993 (1991).
5. (*a*) J.I. Seeman and S.G. Davies. J. Am. Chem. Soc. **107**, 6522 (1985); (*b*) S.G. Davies, J.I. Seeman, and I.H. Williams. Tetrahedron Lett. **27**, 619 (1986).
6. B.E.R. Schilling, R. Hoffman, and D.L. Lichtenberger. J. Am. Chem. Soc. **101**, 585 (1979).
7. Z.L. Xue, H. Thridandam, H.D. Kaesz, and R.F. Hicks. Chem. Mater. **4**, 162 (1992).
8. A. Shaver. Can. J. Chem. **56**, 2281 (1978).
9. S.D. Robinson and B.L. Shaw. J. Chem. Soc. 1529 (1965).
10. J.J. Gajewski, K.E. Gilbert, and J. Mckelvey. PCMODEL-386, Serena Software, Bloomington, IN. Advanced molecular modelling. *Edited by* D. Liotta. JAI Press, Greenwich, CT. 1990.
11. A. Eisenberg, A. Shaver, and T. Tsutsui. J. Am. Chem. Soc. **102**, 1416 (1980).
12. G.W. Adamson, J.C.J. Bart, and J.J. Daly. J. Chem. Soc. A, 2616 (1971).

Can. J. Chem. Downloaded from www.nrcresearchpress.com by 195.246.54.202 on 09/08/12
For personal use only.

On the structure of S_4^{2+} and its formation from $2S_2^+$. *Ab initio* SCF and CASSCF studies

MOUSUMI SANNIGRAHI AND FRIEDRICH GREIN

Department of Chemistry, University of New Brunswick, Fredericton, NB E3B 6E2, Canada

Received June 22, 1993

MOUSUMI SANNIGRAHI and FRIEDRICH GREIN. Can. J. Chem. **72,** 298 (1994).

Ab initio studies up to the MP2/6-31G* level were performed on the geometry and energy of S_4^{2+}. Eleven different structures were considered. In the RHF/6-31G* method, the square structure is the most stable, followed by the *trans*-planar C_{2h} structure. S_4^{2+} (square) is 105.9 kcal/mol less stable than $2S_2^{2+}$. Minimum energy paths were calculated for the reaction $2S_2^+ \rightarrow S_4^{2+}$, both in C_{2v} and D_{2h} symmetry. Using RHF/6-31G*, the transition state lies about 50 kcal/mol above the energy of square planar S_4^{2+}. Using CASSCF or MP2 methods this energy can be significantly lowered (to about 33 kcal/mol in MP2/6-31G*). Calculated vibrational frequencies for the square structure are also given and compared with experimental values.

MOUSUMI SANNIGRAHI et FRIEDRICH GREIN. Can. J. Chem. **72,** 298 (1994).

On a effectué des études *ab initio* jusqu'au niveau MP2/6-31G* sur la géométrie et l'énergie de l'ion S_4^{2+}. On a considéré onze structures différentes. Dans la méthode RHF/6-31G*, la structure carrée est la plus stable, suivie par la structure *trans*-planaire, C_{2h}. L'ion S_4^{2+} (carré) est 105,9 kcal/mol moins stable que $2S_2^{2+}$. On a calculé les voies d'énergie minimale pour la réaction $2S_2^{2+} \rightarrow S_4^{2+}$ alors que les deux sont dans la symétrie C_{2v} et D_{2h}. Lorsqu'on utilise la méthode RHF/6-31G*, l'état de transition se trouve à environ 50 kcal/mol au-dessus de l'énergie du S_4^{2+} plan carré. En utilisant les méthodes CASSCF ou MP2, on peut diminuer considérablement cette énergie (jusqu'à environ 33 kcal/mol avec la méthode RHF/6-31G*). On rapporte aussi les fréquences vibrationnelles calculées pour la structure carrée et on les compare avec les valeurs expérimentales.

[Traduit par la rédaction]

Introduction

The first experimental identification that S_4^{2+} was square planar was made by Stevens (1) using magnetic circular dichroism. Gillespie et al. (2, 3), Clark et al. (4), and Minkwitz et al. (5) have carried out vibrational studies. Based on Gillespie's work (2), the bond distance of square planar S_4^{2+} was evaluated to be 2.00 Å (6). Passmore and co-workers (7–9) determined the structure of S_4^{2+} by X-ray crystallography. The most recent crystal structure determination of $S_4(AsF_6)_2 \cdot AsF_3$ leads to an average S—S bond distance of 1.999(6) Å for square planar S_4^{2+}. In addition to the dication, S_4^+ and S_4 have also been subjected to experimental investigation. The first evidence for the existence of S_4 and S_4^+ came from mass spectrometry experiments conducted on sulfur vapors by Berkowitz and co-workers (10, 11).

In most previous theoretical studies on S_4^{2+} (12–16), the cation has been assumed to possess a square (D_{4h}) structure based on the experimental results for S_4^{2+} and for the analogous cations Se_4^{2+} and Te_4^{2+} (17–20). While the planar D_{4h} structure is expected to have 6π-electron stabilization (21), the open chain form has the advantage of being less strained than the cyclic form. Theoretical studies on the D_{4h} isomer of S_4^{2+} were performed by Kao (14) who also included the rectangle (D_{2h}), the *cis*-planar (C_{2v}), *trans*-planar (C_{2h}), and the *gauche* (C_2) structure, using RHF methods with an STO-3G and a 44-31G basis set. It should be noted that none of the basis sets included polarization functions which are considered to be essential for calculations on sulfur compounds. The *trans*-planar form with a S—S short bond of 2.055 Å and a long bond of 2.383 Å at an angle of 104.9° was found to be the most stable, contrary to experimental results. The possibility of the existence of other isomers like the puckered ring (D_{2d}), tetrahedron (T_d), trigonal pyramid (C_{3v}), and trigonal planar structure (D_{3h}) was not explored. The structure and bonding of square planar S_4^{2+} have also been studied by Saethre and Gropen (12) using an ECP model and a Huzinaga basis set appended with *d*-functions. The S—S bond distance was found to be 1.999 Å.

In this paper we have undertaken an extensive *ab initio* study on the geometry of S_4^{2+}, taking eleven different structures into consideration and using a high level of basis set. In addition, we have also traced the reaction path for the dissociation of S_4^{2+} into two units of S_2^+.

Computational methods

Ab initio calculations were performed at various levels of theory using the GAUSSIAN suite of programs (22, 23). The geometries of eleven isomers, square planar (D_{4h}), rectangular (D_{2h}), rhombus (D_{2h}), *cis*-planar (C_{2v}), *cis*-nonplanar (C_2), *trans*-planar (C_{2h}), *trans*-nonplanar (C_2), trigonal planar (D_{3h}), trigonal pyramidal (C_{3v}), puckered ring (D_{2d}), and tetrahedral (T_d), were completely optimized, the overall symmetry being the only constraint, at the closed-shell restricted Hartree–Fock (RHF) level of theory with 3-21G* and 6-31G* basis sets. These basis sets include polarization functions which are known to be a requisite for studies on sulfur compounds if accurate results are desired (24, 25). Electron correlation has been taken into account by performing MP2/6-31G* geometry optimizations on the four most stable isomers. The potential energy curve for the dissociation of S_4^{2+} to two units of S_2^+ was traced in D_{2h} and C_{2v} symmetry, taking the distance between the mid-points of the S—S bonds as the reaction co-ordinate. To calculate the energy of the open-shell system S_2^+ the ROHF option of HONDO (26) was employed.

Results

Optimized geometries

The optimized equilibrium geometries for the different isomers of S_4^{2+} are given in Table 1.

At the 3-21G* level, the *cis*-planar isomer was found to be the most stable, followed closely by the rectangular and the *trans*- and *square*-planar forms. The rhombic isomer optimized to a square and the *cis*- and *trans*-nonplanar isomers became planar *cis* and *trans*, respectively. The *cis*-planar isomer was more stable than the rectangular form by 0.44 kcal/mol and dif-

Can. J. Chem. Downloaded from www.nrcresearchpress.com by 195.246.54.202 on 09/08/12
For personal use only.

TABLE 1. Optimized geometries and relative energies of various structures of S_4^{2+} (distances in Å, energies in kcal/mol)

Structure of S_4^{2+}	3-21G*			6-31G*		
	R	r	ΔE	R	r	ΔE
Square planar D_{4h}	1.985	1.985	1.36	1.990	1.990	0.00
Rectangular D_{2h}	2.962	1.779	0.44	2.963	1.778	10.00
cis-Planar C_{2v}	2.620	1.793	0.0[a]	2.404	1.840	7.04[e]
trans-Planar C_{2h}	2.375	1.821	0.59[b]	2.274	1.840	5.59[f]
Trigonal planar D_{3h}	—	1.840	108.22	—	1.855	110.00
Trigonal pyramidal C_{3v}	—	2.069	110.40[c]	—	2.082	113.80[g]
Puckered ring D_{2d}	—	2.118	95.11[d]	—	2.105	92.59[h]
Tetrahedral T_d	—	2.242	148.77	—	2.213	145.51

[a] $\theta = 102.3°$. [e] $\theta = 109.1°$.
[b] $\theta = 107.3°$. [f] $\theta = 107.1°$.
[c] $\theta = 135.9°$. [g] $\theta = 137.0°$.
[d] $\theta = 49.7°$. [h] $\theta = 49.6°$.

fered from the *trans* and square forms by 0.59 and 1.36 kcal/mol, respectively.

At the 6-31G* level the square planar isomer was found to be the most stable, 5.59 kcal/mol more stable than the *trans*-planar, 7.04 kcal/mol more than the *cis*-planar and 10.00 kcal/mol more than the rectangular isomer.

At the MP2/6-31G* level only the D_{4h}, D_{2h}, C_{2v}, and C_{2h} structures were studied. Here, the rectangular D_{2h} isomer was found to be the most stable, with $R = 3.063$ and $r = 1.889$ Å, followed by the square isomer at $\Delta E = 11.4$ kcal/mol and $R = 2.057$ Å. The *trans*-planar structure dissociated, whereas the *cis*-planar optimized to the rectangle.

According to Table 1 the optimized structures can be divided into two categories: regular-bonded and long-bonded. Among the regular-bonded ones are the square (1.98–2.06 Å), the tetrahedron (2.21–2.24 Å), the trigonal planar structure (1.84–1.85 Å), the puckered ring (2.10–2.12 Å), and the trigonal pyramidal structure (2.07–2.08 Å) (with optimized S—S distances given in parentheses). In all cases, the geometries were severely restricted, and all bond distances were forced to be the same. The most important long-bonded structure is the rectangle, with R = 2.96–3.06 Å, consisting of two S_2^+ units (r = 1.78–1.89 Å) loosely bound together. The *cis*-planar (R = 2.40–2.62 Å) and *trans*-planar (R = 2.27–2.37 Å) forms may also be included in this category, since in each case the two S_2^+ units (1.79–1.84 Å for *cis*-planar, and 1.82–1.84 Å for *trans*-planar) are weakly coupled. The ranges given for the bond distances arise from the differences in basis set and are seen to be quite small. Obviously, the deviations for long bonds are larger than for regular bonds.

Ignoring the structures which have (predictably) high energies, namely the tetrahedron, trigonal planar, puckered ring, and trigonal pyramidal, the structures competing for the lowest energy are the square structure with regular bonds, and the rectangular structure and the *trans*-planar and *cis*-planar structures with long bonds. Unfortunately, the methods and basis sets used do not allow for a clear decision on the most stable structure (in gas phase). It so happens that the square structure has an energy very similar to those of the long-bonded structures. The 6-31G* basis set predicts the square structure to be the most stable, in agreement with the measured crystal structure. The optimized R of 1.990 Å is very close to the experimental value of 2.0 Å. As will be discussed later, the square isomer represents a 6π electron system, whereas the rectangle corresponds to a π^*–π^* complex.

The optimized bond distances of S_2^+ are 1.781 Å in ROHF/3-21G* and 1.787 Å in ROHF/6-31G*. In 3-21G*, two S_2^+ units are more stable than the *cis*-planar structure of S_4^{2+} (the most stable one in this basis set) by 124.0 kcal/mol (and 125.4 kcal/mol relative to the square structure). In the 6-31G* basis set, two S_2^+ units are more stable than the square structure by 105.9 kcal/mol. The bond distance in an isolated S_2^+, 1.78–1.79 Å, is very similar to the (short) S—S distance in the long-bonded structures (1.78 Å).

Reaction paths for $2S_2^+ \rightarrow S_4^{2+}$

According to the optimized geometries given above, the reaction path $2S_2^+ \rightarrow S_4^{2+}$ will have two minima, one at a large distance (R = 2.3–3.0 Å) corresponding to the π^*–π^* complex, and the other at $R \cong 1.9$ Å, corresponding to a π-stabilized square. Therefore, two transition structures are expected, TS1 between the product and the π^* complex, and TS2 between the π^* complex and the reactants. The approach of the two S_2^+ radicals can be carried out in C_{2v} symmetry, which will go via the *cis*-planar complex and lead to a square-planar product, or in D_{2h} symmetry, in which case one gets the rectangle as an intermediate and again the square as a product. D_{2h} is a more restricted version of C_{2v}.

At large distances, one may also consider a nonplanar D_{2d} approach where the two S_2^+ units are perpendicular to each other. Enforcing D_{2d} symmetry would, however, lead to a tetrahedral product, which is shown to be highly unstable with respect to the square structure. A C_{2h} approach might also be considered, since it would allow in the 6-31G* basis set a *trans*-planar structure (lower in energy than *cis*-planar) as intermediate. However, a rotation about the central S—S bond would have to be performed in order to arrive at a square-planar product.

Overall, it was found best to study the C_{2v} pathway as well as the more restricted D_{2h} pathway. The reaction intermediates will be a *cis*-planar structure in C_{2v} and a rectangular structure in D_{2h}.

Woodward–Hoffmann analysis shows that the ground-state reaction leading from a square-planar structure to the reactants is symmetry forbidden, and requires a change in electron configuration. Figure 1 presents the Woodward–Hoffmann diagrams. The orbital labels S (symmetric) and A (antisymmetric) follow the general convention. Two planes of symmetry are preserved, indicated by I and II. For the reactants, the AS MO

Can. J. Chem. Downloaded from www.nrcresearchpress.com by 195.246.54.202 on 09/08/12
For personal use only.

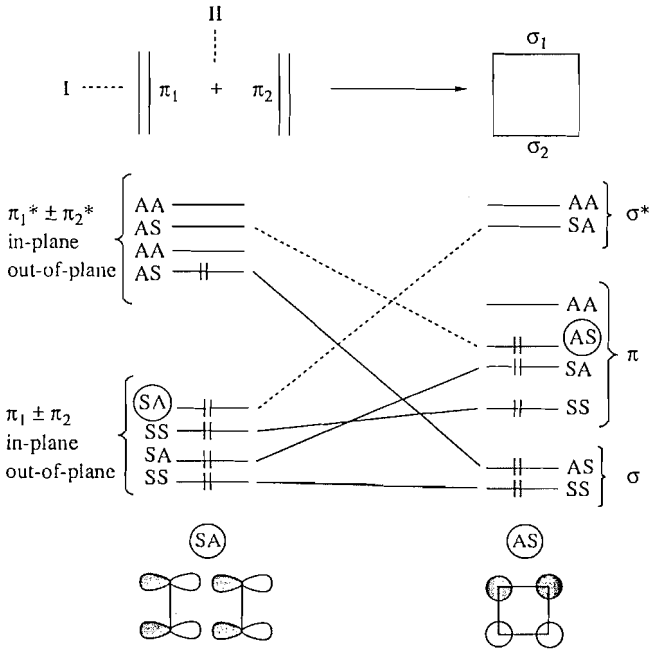

FIG. 1. Woodward-Hoffmann diagram for reaction $2S_2^+ \rightarrow S_4^{2+}$ (square).

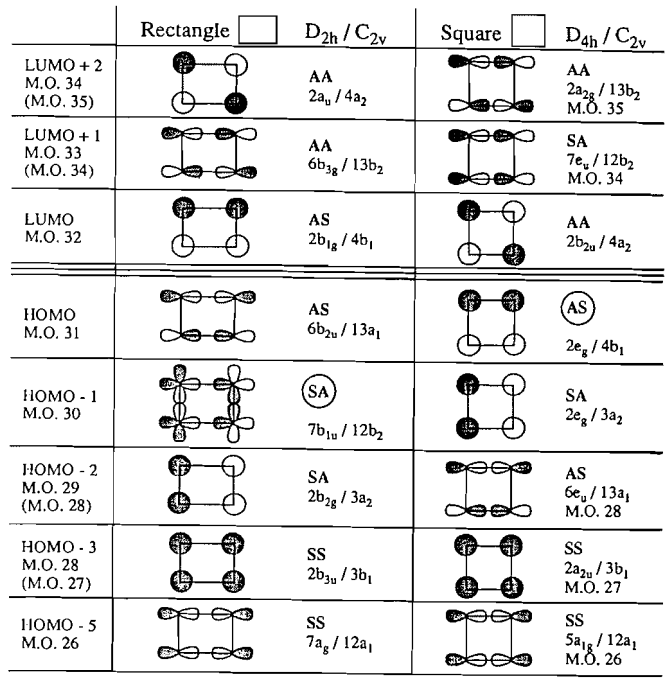

FIG. 2. MO diagrams for rectangular and square-planar S_4^{2+}, corresponding to MO's used in Fig. 1.

AS MO arising from in-plane and in-phase π_1^* and π_2^* interactions has been doubly occupied,since on approach this MO is more stable than the corresponding out-of-phase combination AA. Since the reaction intermediate is a π^*–π^* complex (with π_1^* and π_2^* in phase), the intermediate then has the same orbital occupation as the reactants.

It is seen that the occupied second SA orbital of the reactants (circled) crosses into an unoccupied SA MO of the product, and that in turn the occupied AS orbital of the product (circled) crosses into an unoccupied AS orbital of the reactants. The form of the occupied SA and AS orbitals involved in the crossing is shown at the bottom of Fig. 1. In C_{2v} (D_{2h}) symmetry, the crossing SA orbital of the reactants is a b_2 (b_{1u}) species, and the AS counterpart of the product is b_1 (b_{1g}). In D_{4h} symmetry, this last orbital is e_g.

In Fig. 2, the MO's of the rectangular complex and the square-planar product corresponding to those of the WH analysis are shown schematically together with the calculated ordering. It is seen that $7b_{1u}$ ($12b_2$ in C_{2v}) is occupied in the rectangle, and $2e_g$ ($4b_1$ in C_{2v}, $2b_{1g}$ in D_{2h}) in the product. Therefore, the SCF configuration of the rectangle (in D_{2h}/C_{2v} notation) is $...7b_{1u}^2 2b_{1g}^0/...12b_2^2 4b_1^0$, whereas of the product it is $...7b_{1u}^0 2b_{1g}^2/...12b_2^0 4b_1^2$. The reaction of $2S_2^+$ to the S_4^{2+} intermediate complex is symmetry allowed, since S_4^{2+} consists of two S_2^+ units loosely bound via favorable π^* interactions.

Single configuration methods like SCF do not allow for a smooth transition between two different configurations. The best one can do with SCF methods is to follow the individual configuration, and note their crossing point. In multireference methods an avoided crossing is encountered, at an energy somewhat lower than the energy of the configuration crossing point. The configurations now change smoothly into each other, resulting in a rounded-off potential maximum at the transition state.

For this purpose, the CASSCF option (27, 28) contained in GAUSSIAN90 was employed. Only two electrons, and two configurations ($..7b_{1u}^2 2b_{1g}^0 + ...7b_{1u}^0 2b_{1g}^2$ in D_{2h} symmetry) were correlated. For the lack of sufficient computer time, only the region around the transition state TS1 was investigated and the basis was restricted to 3-21G*.

In Figs. 3 and 4, minimum energy paths are given for the C_{2v} reaction in the 3-21G* and 6-31G* basis sets, respectively. Figures 5 and 6 show the corresponding minimum energy paths for D_{2h} symmetry. Figure 7 gives the D_{2h} path in the MP2/6-31G* optimization. In D_{2h} symmetry, the reaction coordinate is R, the same as that used before. However, in C_{2v} symmetry, R_{MM}, the distance between the midpoints of two S_2^+ units is chosen; it is defined in Fig. 3. In D_{2h} symmetry, R is of course identical to R_{MM}. In these figures, energy differences are given relative to the lowest-energy structure, which is the square structure in most but not all cases.

In both C_{2v} and D_{2h} pathways, TS1 is much higher in energy than TS2, as is expected from the Woodward–Hoffmann arguments given earlier. On the other hand, the TS2 energy is still quite high, about 25 kcal/mol above the π^* complex. Whereas TS1 is represented by a sharp peak, TS2 is very shallow, and occurs at high R values (about 5–6 Å).

The optimized values of R, R_{MM}, r, θ, and ΔE are summarized in Table 2. TS1, obtained from the crossing of the two SCF configurations, occurs at an energy (3-21G*/6-31G*) of 43.4/48.0 kcal/mol for the C_{2v} path, and 46.6/51.3 kcal/mol for the D_{2h} path (all relative to the square structure). CASSCF calculations performed in 3-21G* reduce the C_{2v} value from 43.4 to 36.0 kcal/mol, and the D_{2h} value from 46.6 to 39.0 kcal/mol. Only partial mixing of the two configurations could be accomplished. The transition state moved from R = 2.33 Å to R = 2.37–2.38 Å.

The second transition state TS2 has R_{MM} = 6.1 Å in C_{2v} with an energy 27.6/26.4 kcal/mol higher than the π^* complex, and R = 5.25 Å in D_{2h}, lying 28.2/25.4 kcal/mol above the π^* complex.

In the D_{2h} pathway calculated by MP2/6-31G*, TS1 has R =

Can. J. Chem. Downloaded from www.nrcresearchpress.com by 195.246.54.202 on 09/08/12
For personal use only.

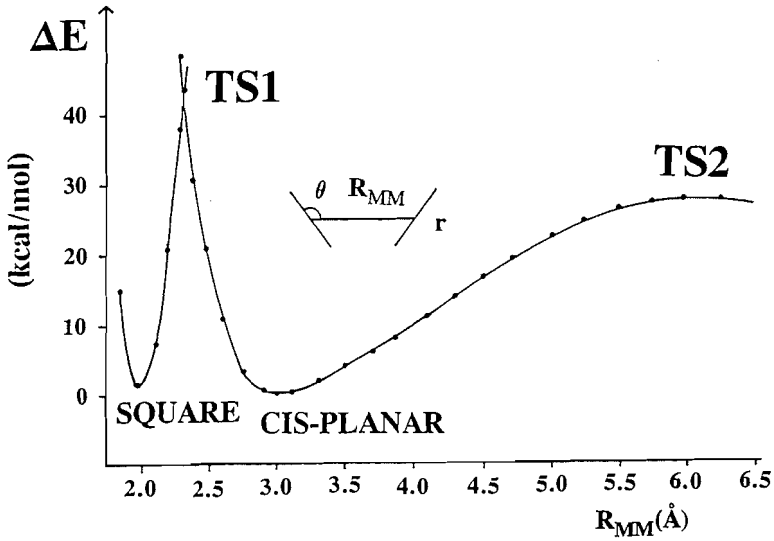

FIG. 3. Minimum energy path (RHF/3-21G*) for reaction $2S_2^+ \rightarrow S_4^{2+}$ in C_{2v} symmetry. Due to a change in electron configuration, TS1 is not well described in this method.

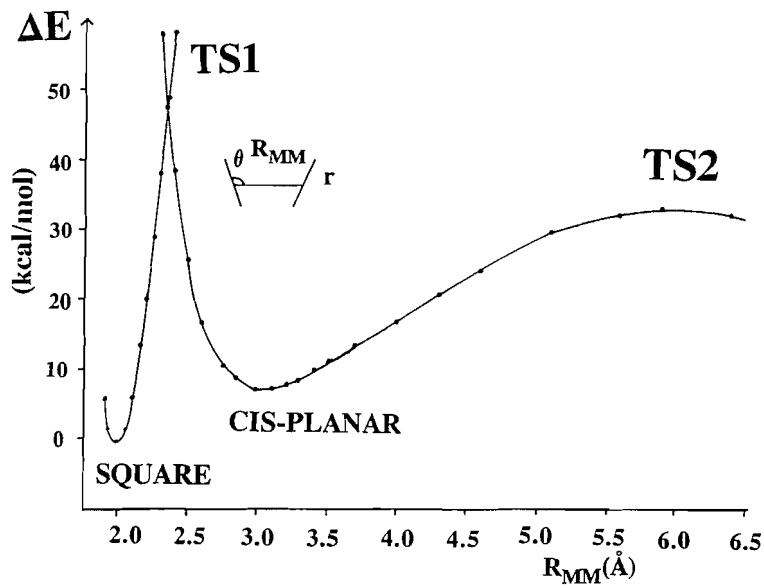

FIG. 4. Minimum energy path (RHF/6-31G*) for reaction $2S_2^+ \rightarrow S_4^{2+}$ in C_{2v} symmetry.

2.42 Å, and lies 21.7 kcal/mol above the square-planar form, whereas TS2 has a much shorter R (3.78 Å), lying only 3.2 kcal/mol above the rectangular structure (here it is the most stable). In this method, the energies of both transition states are significantly lower and the separation of the two S_2^+ units in TS2 has also decreased.

Vibrational frequencies

The vibrational frequencies of S_4^{2+} in its square form have been determined experimentally (2–5). The results considered to be the best (3) are shown in Table 3. Theoretical results, obtained with 3-21G* and 6-31G* basis sets, at the respective optimized square geometries, are also given in Table 3. Since the calculated frequencies are usually too large, it is customary to multiply them by a factor of 0.9. Such has been done here.

In the 6-31G* basis set, the largest disagreement between (scaled) theoretical and observed frequencies is 38 cm^{-1} for the B_{2g} vibration. The lowest energy vibration, B_{2u}, is both infrared- and Raman-forbidden, and has not been observed. B_{2u} is an out-of-plane vibration.

Conclusion

In crystal form, the structure of S_4^{2+} has been clearly established to be D_{4h}. *Ab initio* calculations show that because of a strong repulsion between two positive charges, the π-bonded D_{4h} structure competes with a loosely bonded S_2^+ dimer (C_{2v} or C_{2h}) in stability. The dimer results from π*–π* interaction. The Woodward–Hoffmann forbidden formation of S_4^{2+} (square) from $2S_2^+$ has an activation barrier of about 50 kcal/mol relative to the square structure (in RHF/6-31G*), the energy of

Can. J. Chem. Downloaded from www.nrcresearchpress.com by 195.246.54.202 on 09/08/12
For personal use only.

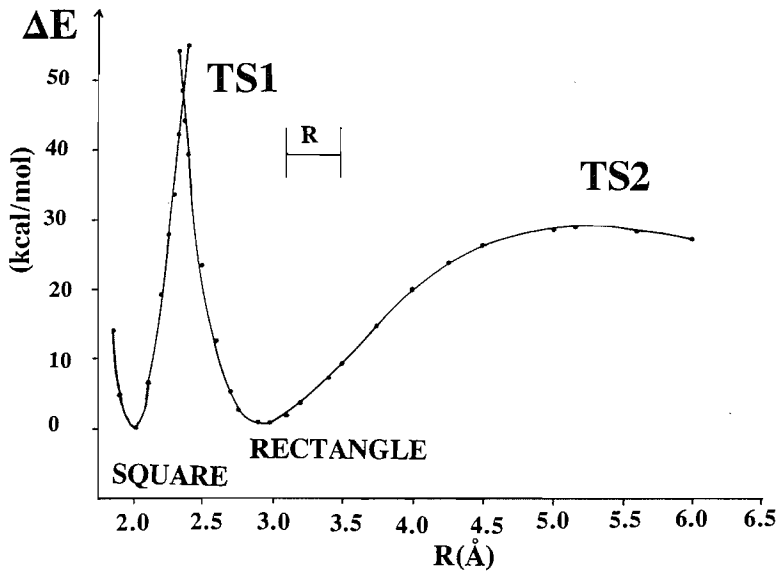

FIG. 5. Minimum energy path (RHF/6-31G*) for reaction $2S_2^+ \rightarrow S_4^{2+}$ in D_{2h} symmetry.

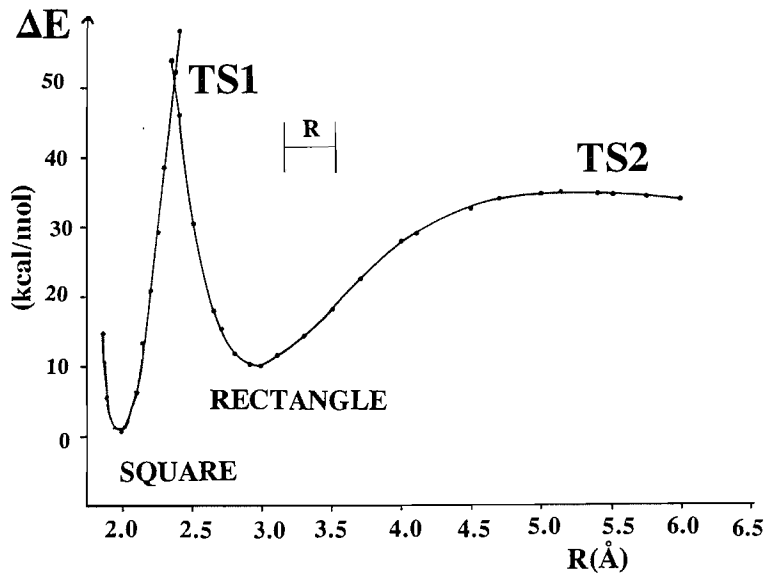

FIG. 6. Minimum energy path (RHF/6-31G*) for reaction $2S_2^+ \rightarrow S_4^{2+}$ in D_{2h} symmetry.

which can be lowered by configuration mixing (CASSCF) or by Möller–Plesset methods. Calculated vibrational frequencies compare well with experimental values.

Much higher levels of correlation methods (e.g. extensive MCSCF, or multireference CI) appear to be necessary to firmly establish the most stable structure of the intermediate, and thereby its energetic relation to the square structure. The same comment applies to a reliable estimate of the activation barrier. Nonconcerted mechanisms for the formation of S_4^{2+} are of interest and will be studied in future work.

Acknowledgements

Support of this research by NSERC and the University of New Brunswick is gratefully acknowledged. We thank Dr. J. Passmore for suggesting this topic and for his continuous encouragement. We also thank Scott Brownridge for preparing some of the figures.

1. P.J. Stevens. Chem. Commun. 1496 (1969).
2. R.J. Gillespie, J. Passmore, P.K. Ummat, and O.C. Vaidya. Inorg. Chem. **10**, 1327 (1971).
3. R.C. Burns and R.J. Gillespie. Inorg. Chem. **21**, 3877 (1982).
4. R.J.H. Clark, J.D. Trevore, and T.H.F. Lindsay. J. Chem. Soc. Dalton Trans. 2237 (1982).
5. R. Minkwitz, J. Nowicki, W. Sawodny, and K. Hartner. Spectrochim. Acta, Part A, **47A**, 151 (1991).
6. R. Steudel. Z. Naturforsch. Teil B. **30**, 281 (1975).
7. J. Passmore, G.W. Sutherland, and P.S. White. J. Chem. Soc. Chem. Commun. 330 (1980).
8. J. Passmore, G.W. Sutherland, and P.S. White. Inorg. Chem. **21**, 2717 (1982).
9. (*a*) J. Passmore, G.W. Sutherland, T.K. Whidden, P.S. White, and C.H. Wong. Can. J. Chem. **63**, 1209 (1985); (*b*) I. Dionne. M.Sc. Thesis. University of New Brunswick. 1993.
10. J. Berkowitz and J.R. Marquart. J. Chem. Phys. **39**, 275 (1963).
11. J. Berkowitz and C. Lifshitz. J. Chem. Phys. **48**, 4346 (1968).

Can. J. Chem. Downloaded from www.nrcresearchpress.com by 195.246.54.202 on 09/08/12
For personal use only.

TABLE 2. Optimized geometries and relative energies of transition structures TS1 and TS2 for the reaction $S_4^{2+} \rightarrow 2S_2^+$ (for comparison, corresponding data for the minima are also given; distances in Å, energies in kcal/mol)

	C_{2v}				D_{2h}		
Geometry	R_{MM}	r	θ	ΔE	R	r	ΔE
*3-21G**							
Square planar	1.985	1.985	90.0°	1.36	1.985	1.985	0.0
TS1 (SCF)	~2.33	~2.002	~90.0°	~43.4	~2.33	~2.003	~46.6
		~1.818	~100.3	~43.4		~1.772	~46.6
(CAS SCF)	~2.365	~1.9[a]	~95.0[a]	~36.0	~2.38	~1.9[a]	~39.0
cis-planar/rectangular	3.000	1.793	102.3°	0.00	2.962	1.779	0.92
TS2 (SCF)	6.105	1.783	128.5°	27.64	5.245	1.783	29.13
*6-31G**							
Square-planar	1.990	1.990	90.0°	0.0	1.990	1.990	0.0
TS1 (SCF)		~2.004	~90.0°	~48.0	~2.37	~2.009	~51.3
		1.826	~100.3°	~48.0		~1.777	~51.3
cis-planar/rectangular	2.998	1.819	109.1°	7.04	2.963	1.778	10.00
TS2 (SCF)	6.100	1.789	128.6°	33.47	5.250	1.778	35.38
*MP2/6-31G**							
Square planar					2.056	2.056	11.42
TS1 (MP2)					~2.42	~1.883	~33.10
Rectangular					3.063	1.889	0.0
TS2 (MP2)					3.775	1.889	3.18

[a]Estimated values.

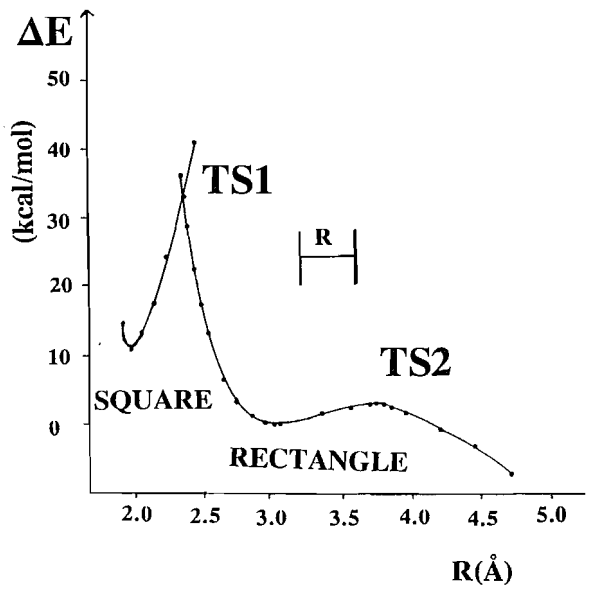

FIG. 7. Minimum energy path (MP2/6-31G*) for reaction $2S_2^+ \rightarrow S_4^{2+}$ in D_{2h} symmetry.

TABLE 3. Observed and calculated (×0.9) vibrational frequencies (in cm^{-1}) of S_4^{2+} in D_{4h} symmetry

Vibration	Observed ref. 3	3-21G*	6-31G*
B_{2u}	—	230	222
B_{1g}	383	415	405
E_u	542	497	515
A_{1g}	587	583	596
B_{2g}	603	626	641

12. L.J. Saethre and O. Gropen. Can. J. Chem. **70**, 348 (1992).
13. K. Tanaka, T. Yamabe, H. Terama, and K. Fukui. Inorg. Chem. **18**, 3591 (1979).
14. J. Kao. J. Mol. Struct. **63**, 293 (1980).
15. T.H. Tang, R.F.W. Bader, and P.J. McDougall. Inorg. Chem. **24**, 2047 (1985).
16. (*a*) F.L. Skrezenek, R.D. Harcourt. Theoret. Chim. Acta, **67**, 271 (1985); (*b*) G.V. Iandwijk, R.A.J. Janssen, and H.M. Buck. J. Am. Chem. Soc. **112**, 4155 (1990).
17. R.J. Gillespie and G.P. Pez. Inorg. Chem. **8**, 1229 (1969).
18. L.D. Brown, D.B. Crump, and R.J. Gillespie. Inorg. Chem. **10**, 2319 (1971).
19. P. Boldrini, I.D. Brown, M.J. Collins, R.J. Gillespie, E. Maharajh, D.R. Slim, and J.F. Sawyer. Inorg. Chem. **24**, 4302 (1985).
20. G. Cardinal, R.J. Gillespie, J.F. Sawyer, and G.J. Schrobilgen. Inorg. Chem. **25**, 2053 (1986).
21. (*a*) R. Steudel. Angew. Chem. Int. Ed. Engl. **14**, 655 (1975); (*b*) M. Schmidt. Angew. Chem. Int. Ed. Engl. **12**, 445 (1973).
22. M.J. Frisch, J.S. Binkley, K. Raghavachari, C.F. Melius, L. Martin, J.P.P. Stewart, F.W. Bobrowicz, C.M. Rohlfing, L.R. Kahn, D.F. Defrees, R. Seeger, R.A. Whiteside, D.J. Fox, E.M. Fleuder, and J.A. Pople. GAUSSIAN 86. Carnegie-Mellon Quantum Chemistry Publishing Unit, Pittsburgh, PA. 1984.
23. M.J. Frisch, M. Head-Gordon, G.W. Trucks, J.B. Foresman, H.B. Schlegel, K. Raghavachari, M. Robb, J.S. Binkley, C. Gonzalez, D.J. Defrees, D.J. Fox, R.A. Whiteside, R. Seeger, C.F. Melius, J. Baker, R.L. Martin, L.R. Kahn, J.J.P. Stewart, S. Topiol and J.A. Pople. GAUSSIAN 90, Revision. Gaussian, Inc., Pittsburgh, PA. 1990.
24. C.J. Marsden and B.J. Smith. J. Mol. Struct. **105**, 385 (1983).
25. (*a*) J.B. Collins, P.v.R. Schleyer, J.S. Binkley, and J.A. Pople. J. Chem. Phys. **64**, 5142 (1976); (*b*) P.A. Mezey and A. Haas. J. Chem. Phys. **77**, 80 (1977).
26. M. Dupuis, A. Farazdel, S.P. Karna, S.A. Maleundes, P. Mougenot, C. Daniel, R. Lindh, K. Dyall, B. Liu, J.D. Watts, H.O. Villar, G.J.B. Hurst, M. Schmidt, M.S. Gordon, S. Elbert, W. Stevens, H. Basch, J. Rys, H.F. King, M. Guest, T. Takada, D. Spangler, J.J. Wendoloski, B. Brooks, W. Ladaig, and P. Saxe. HONDO 8.1.
27. D. Hegarty and M.A. Robb. Mol. Phys. **38**, 1795 (1979).
28. R.H.E. Eade and M.A. Robb. Chem. Phys. Lett. **83**, 362 (1981).

Can. J. Chem. Downloaded from www.nrcresearchpress.com by 195.246.54.202 on 09/08/12
For personal use only.

Measurements and analysis of the excess enthalpies of some dichloroalkane + 2-ketone systems using UNIFAC group-contribution model

CONSOLACIÓN P. MENAUT,[1] JOSÉ M. PICO,[1] JOSEFA FERNÁNDEZ,[2] JOSÉ L. LEGIDO,[3] AND M. INMACULADA PAZ ANDRADE

Departamento de Física Aplicada, Campus Universitario, Universidad de Santiago, E-15706 Santiago de Compostela, Spain

Received June 3, 1993

CONSOLACIÓN P. MENAUT, JOSÉ M. PICO, JOSEFA FERNÁNDEZ, JOSÉ L. LEGIDO, and M. INMACULADA PAZ ANDRADE. Can. J. Chem. **72,** 304 (1994).

Experimental excess molar enthalpies h^E at 298.15 K and normal atmospheric pressure were obtained for the binary mixtures 1,2-dichloropropane + (2-propanone, 2-butanone, or 2-pentanone), 1,3-dichloropropane + (2-butanone or 2-pentanone), 1,4-dichlorobutane + (2-butanone or 2-pentanone) using a Calvet microcalorimeter. The h^E values for all the mixtures were negative. The experimental results used to test the capability of the interaction parameters of two versions of the UNIFAC group-contribution model to predict the proximity effect in these kind of mixtures.

CONSOLACIÓN P. MENAUT, JOSÉ M. PICO, JOSEFA FERNÁNDEZ, JOSÉ L. LEGIDO et M. INMACULADA PAZ ANDRADE. Can. J. Chem. **72,** 304 (1994).

Utilisant un microcalorimètre Calvet, on a mesuré les enthalpies molaires mieux expérimentales, h^E, à 298,15 K et à la pression normale des mélanges binaires 1,2-dichloropropane + (2-propanone, 2-butanone ou 2-pentanone), 1,3-dichloropropane + (2-butanone ou 2-pentanone) et 1,4-dichlorobutane + (2-butanone ou 2-pentanone). Les valeurs de h^E sont négatives pour tous les mélanges. On a utilisé les données expérimentales pour vérifier l'utilité des paramètres d'interaction de deux versions du modèle de contribution de groupe UNIFAC pour prédire l'effet de proximité dans ce type de mélange.

[Traduit par la rédaction]

Introduction

Group-contribution methods are powerful tools for estimating the thermophysical and thermodynamic properties of pure compounds and mixtures from experimental data on related substances. One of the problems with the current group-contribution models is the difficulty in predicting the thermodynamic properties of mixtures using a fixed set of parameters for the two main groups in the same molecule because the behaviour of the mixture varies with the proximity of the main groups.

The Cl—Cl proximity effect for dichloroalkane + alkane and dichloroalkane + polychloroalkane was analyzed by Kehiaian *et al.* (1–3) using the DISQUAC model. We have yet to find studies of this effect for dichloroalkane + 2-ketone binary mixtures.

Experimental excess enthalpies h^E of dichloroalkane + 2-ketone are very scarce in the literature. Heats of mixing of 2-propanone + dichloromethane have been measured at various temperatures (4–6), h^E of 1,2-dichloropropane + 2-propanone have been measured by Bougard and Jadot (7) and recently Kechavarz *et al.* (8) presented h^E data of 1,2-dichloroethane with several ketones. This lack of information and our interest in the proximity effect prompted us to investigate on thermodynamic properties of dichloroalkane + 2-ketone mixtures.

The present paper reports excess molar enthalpies at 298.15 K of the binary mixtures of 1,2-dichloropropane + (2-propanone, 2-butanone, or 2-pentanone), 1,3-dichloropropane + (2-butanone or 2-pentanone), 1,4-dichlorobutane + (2-butanone or 2-pentanone).

Experimental

2-Propanone (Aldrich >0.999), 1,3-dichloropropane and 1,4-dichlorobutane (Aldrich >0.99), 1,2-dichloropropane and 2-pentanone (Fluka >0.99), and 2-butanone (Fluka >0.995) were subjected to no further purification other than drying with Union Carbide 0.4 nm molecular sieves. Their densities measured with an Anton Paar 60/602 densimeter agree well with the literature values (9–11).

Binary mixtures were prepared by using a Mettler H51 balance (precision of 10^{-5} g) and air-tight stoppered bottles. Possible error in the mole fractions is estimated to be less 10^{-4}. All molar quantities are based on the IUPAC (12) relative atomic mass table.

Excess molar enthalpies, h^E, were measured with a standard Calvet microcalorimeter linked to a microcomputer through an analog digital card. The microcalorimeter was calibrated electrically using a stabilized current source (E.J.P. 30, Setaram). The performance of the apparatus was checked by determining excess enthalpies of *n*-hexane + cyclohexane at 298.15 K; our results differ by less than 1% from those of McGlashan and Stoeckli (13).

Results

Experimental results for the excess molar enthalpies at 298.15 K are listed in Table 1. To each set of h^E values a Redlich-Kister function

$$[1] \quad h^E/(\mathrm{J}\cdot\mathrm{mol}^{-1}) = x(1-x)\cdot\sum_{p=0}^{q} A_p\cdot(2x-1)^p$$

was fitted, where x is the molar fraction of dichloroalkane. The coefficients A_p and the standard deviation s given in Table 2 were calculated by unweighted least-squares method. The number of coefficients was determined using an F-test (14). Figure 1 shows the measured values of h^E plotted against x together with the curve fitted. The excess molar enthalpies for the system 1,2-dichloropropane + 2-propanone have been previously measured by Bougard and Jadot (7) at 302.92 K. Their equimolar excess enthalpies are 1% lower than our values at 298.15 K, both $h^E(x)$ curves have the same shape.

Discussion

In all mixtures studied the molar excess enthalpies are negative over the whole range of composition. In Fig. 2 the equimolar excess molar enthalpies $h^E(0.5)$ are plotted together with

[1]Present address: Departamento de Física, Universidad de La Coruña, 15006 La Coruña, Spain.

[2]To whom correspondence should be addressed.

[3]Present address: Departamento de Física Aplicada, Facultad de Ciencias, Universidad de Vigo, 36200 Vigo, Spain.

Can. J. Chem. Downloaded from www.nrcresearchpress.com by 195.246.54.202 on 09/08/12
For personal use only.

TABLE 1. Expermental excess molar enthalpies h^E at 298.15 K

x	h^E / J·mol^{-1}	x	h^E / J·mol^{-1}	x	h^E / J·mol^{-1}	x	h^{mL} / J·mol^{-1}
			(x) 1,2-dichloropropane + (1 − x) 2-propanone				
0.0746	−62.0	0.3457	−232.2	0.5269	−246.9	0.8729	−111.0
0.1585	−128.9	0.3881	−241.6	0.6061	−235.4	0.9379	−57.1
0.2490	−187.7	0.4272	−247.9	0.6794	−208.1		
0.2934	−211.6	0.4877	−252.1	0.7079	−198.1		
			(x) 1,2-dichloropropane + (1 − x) 2-butanone				
0.0920	−131.2	0.3812	−376.6	0.5921	−376.0	0.7847	−253.7
0.1862	−244.4	0.4254	−388.5	0.6348	−359.2	0.8353	−204.8
0.2416	−293.1	0.4766	−396.5	0.6775	−329.0	0.8959	−130.8
0.3201	−350.2	0.5203	−396.2	0.7433	−286.2		
			(x) 1,3-dichloropropane + (1 − x) 2-butanone				
0.0942	−83.4	0.3217	−203.5	0.5825	−201.9	0.8899	−69.9
0.1321	−113.3	0.3876	−212.2	0.6452	−187.2	0.9492	−35.2
0.1940	−151.5	0.4256	−219.5	0.6920	−170.6		
0.2368	−171.6	0.4980	−216.8	0.7842	−123.3		
0.2954	−196.6	0.5502	−208.0	0.8485	−91.5		
			(x) 1,4-dichlorobutane + (1 − x) 2-butanone				
0.0931	−83.3	0.3518	−191.6	0.5519	−169.7	0.7785	−103.8
0.1622	−125.4	0.3899	−189.9	0.6202	−152.4	0.8302	−80.9
0.2555	−168.3	0.4369	−190.3	0.6667	−137.4	0.8746	−62.4
0.3061	−182.4	0.5025	−179.2	0.7198	−122.8		
			(x) 1,2-dichloropropane + (1 − x) 2-pentanone				
0.0907	−118.5	0.3117	−334.3	0.5196	−387.6	0.7521	−263.6
0.1574	−194.4	0.3534	−359.0	0.5614	−377.6	0.8209	−195.3
0.2074	−247.2	0.4077	−372.0	0.6115	−359.5	0.9068	−104.0
0.2631	−297.4	0.4607	−382.5	0.6820	−316.3		
			(x) 1,3-dichloropropane + (1 − x) 2-pentanone				
0.0630	−64.8	0.3204	−216.6	0.5196	−219.8	0.7288	−149.1
0.1109	−110.7	0.3621	−223.0	0.5635	−209.2	0.8209	−108.0
0.2081	−172.8	0.4188	−225.8	0.5846	−204.5	0.9037	−63.0
0.2848	−204.1	0.4768	−222.0	0.6310	−186.7		
			(x) 1,4-dichlorobutane + (1 − x) 2-pentanone				
0.0654	−66.7	0.2997	−192.8	0.4979	−192.5	0.7288	−124.9
0.0968	−90.9	0.3496	−195.3	0.5531	−177.1	0.7530	−115.6
0.1963	−155.8	0.3872	−197.1	0.6244	−159.2	0.8033	−95.2
0.2507	−178.9	0.4313	−198.6	0.6949	−135.7	0.9166	−45.6

TABLE 2. Coefficients A_P for eq. [1] and standard deviations s

System	A_0	A_1	A_2	A_3	s
1,2-Dichloropropane +					
2-propanone	−1001.5	112.1	7.1	−246.5	1.5
2-butanone	−1581.3	103.4	110.9		2.5
2-pentanone	−1549.2	118.8	328.0		2.4
1,3-Dichloropropane +					
2-butanone	−865.5	185.4	32.4		1.9
2-pentanone	−882.6	293.3	−40.8	77.1	1.7
1,4-Dichlorobutane +					
2-butanone	−723.9	342.6	−77.6	−168.4	1.7
2-pentanone	−754.4	349.4	−105.3	−96.1	1.0

those of López *et al.* (15) for the binary mixtures containing the same dichloroalkanes and certain ketones. With the ketones the excess molar enthalpies are more negative for 1,2-dichloropropane (α,β positions of the chloro atoms) than for the α,ω-dichloroalkanes, being $h^E(0.5)$ slightly greater for the systems containing 1,4-dichlorobutane. The variation of h^E with ketone length is very similar for the three dichloroalkanes: first $h^E(0.5)$ diminishes rapidly from 2-propanone to 2-butanone, varying slowly from 2-butanone to 2-heptanone. It is interesting to note that the general behaviour of these mixtures is very similar to that observed in ester + dichloroalkane (16) but is completely different to that of 1-chloroalkane + 2-ketone, which presents positive excess enthalpies and a linear variation of h^E with the 1-chloroalkane length (17, 18).

Among the group-contribution models able to predict excess

Can. J. Chem. Downloaded from www.nrcresearchpress.com by 195.246.54.202 on 09/08/12
For personal use only.

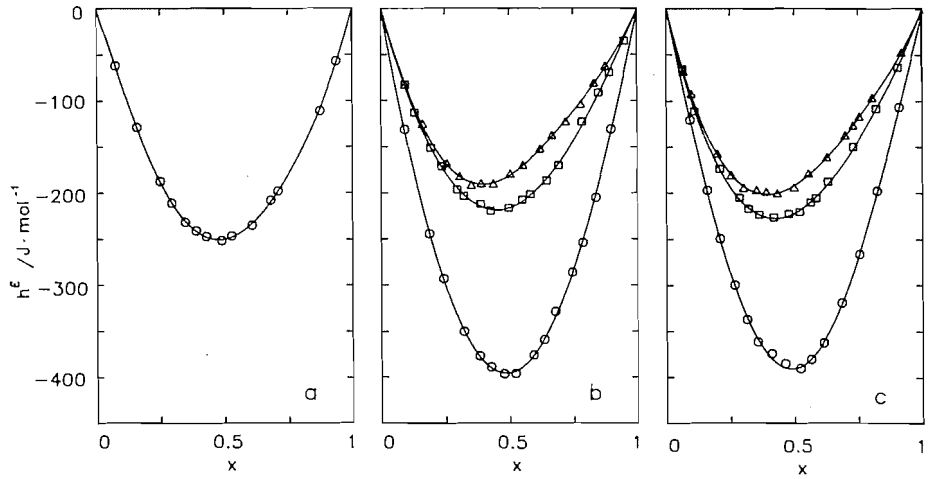

FIG. 1. Experimental excess molar enthalpies h^E at 298.15 K of (*a*) (*x*) dichloroalkane + (1 − *x*) 2-propanone, (*b*) (*x*) dichloroalkane + (1 − *x*) 2-butanone and (*c*) (*x*) dichloroalkane + (1 − *x*) 2-pentanone. Experimental points: ○, 1,2-dichloropropane; □, 1,3-dichloropropane; △, 1,4-dichlorobutane.

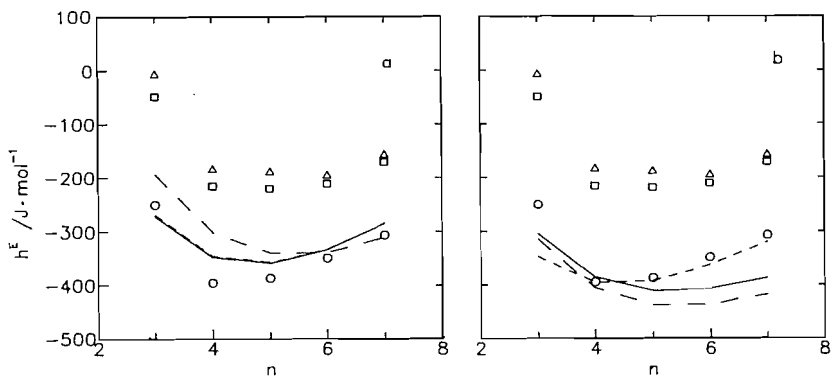

FIG. 2. Plot of h^E at 298.15 K of (0.5) dichloroalkane + (0.5) 2-ketone against *n*, the number of carbon atoms in 2-ketone. Experimental values (present paper and ref. 15): ○, 1,2-dichloropropane; □, 1,3-dichloropropane; △, 1,4-dichlorobutane. Theoretical predictions with UNIFAC model (*a*) Dang and Tassios, (*b*) Larsen *et al.*: (—) 1,2-dichloropropane; (----) 1,3-dichloropropane; (– – –) 1,4-dichlorobutane.

TABLE 3. Values of h^E (x = 0.5)/J·mol^{-1}) as obtained experimentally and using two group-contribution models

System	Expt.	Dang and Tassios (23)	Larsen *et al.* (20)
1,2-Dichloropropane +			
2-propanone	−250.5	−272.3	−304.4
2-butanone	−395.3	−347.7	−386.0
2-pentanone	−387.3	−359.3	−411.2
1,3-Dichloropropane +			
2-butanone	−216.4	−345.8	−395.8
2-pentanone	−220.7	−358.0	−392.3
1,4-Dichlorobutane +			
2-butanone	−180.9	−301.3	−406.3
2-pentanone	−189.4	−340.5	−437.6

enthalpies only the Larsen *et al.* (19, 20) and Dang and Tassios (21–23) versions of the UNIFAC model provide interaction parameters corresponding to the alkanone + chloroalkane systems. The predictions of the two versions are listed in Table 3 and plotted in Fig. 2 together with the experimental values for h^E(0.5). The mean deviation for the system containing 1,2-dichloropropane is about 9% for the Dang and Tassios version and 10% for the Larsen *et al.* version. For other mixtures the mean deviation is higher and in some cases its magnitude is of the same order as the experimental values. This is because the interaction parameters for both versions are calculated using the experimental values of 1,2-dichloroalkane + 2-propanone at 302.92 K as h^E database (19, 22).

Our analysis again shows that group-contribution models have great difficulties in predicting the variation of h^E with the distance between the two main groups (proximity effect). Two solutions have been proposed to solve this problem: (*a*) Define new functional groups whose atoms have the same electrical

Can. J. Chem. Downloaded from www.nrcresearchpress.com by 195.246.54.202 on 09/08/12
For personal use only.

charge in all molecules containing that functional group. The group should be approximately electroneutral (see Wu and Sandler, refs. 24, 25). However, the dichloroalkanes considered here have not yet been studied, (*b*) Keep the group definition the same and as simple as possible for any given class of compounds, but allow the interaction parameters to vary with the structure as in the DISQUAC model (1–3).

More experimental g^E and v^E data are needed to determine the parameters of DISQUAC and Nitta-Chao Models (26). Measurements of these quantities would be of interest to complete the theoretical studies of these mixtures.

1. H.V. Kehiaian and B. Marongiu. Fluid Phase Equilib. **40**, 23 (1988).
2. H.V. Kehiaian and B. Marongiu. Fluid Phase Equilib. **42**, 141 (1988).
3. J. Muñoz Embid, C. Berro, S. Otín, H.V. Kehiaian, and B. Marongiu. J. Chem. Eng. Data, **35**, 266 (1990).
4. D.R. Winterhalter and H.C. Van Ness. J. Chem. Eng. Data, **11**, 89 (1966).
5. T.J.V. Findlay and P.J. Kavanagh. J. Chem. Thermodyn. **6**, 367 (1974).
6. H.C. Van Ness and N.M. Abbot. Int. DATA Ser. Sel. Data Mixtures, Ser. A, 89 (1974).
7. J. Bougard and R. Jadot. J. Chem. Thermodyn. **9**, 491 (1977).
8. R. Kechavarz, J.P. Dubes, and H. Tachoire. Int. DATA Ser. Sel. Data Mixtures, Ser. A, 120(1990).
9. J.A. Riddick, W.B. Bunger, and T.K. Sakano. Organic solvents. Techniques of chemistry. 4th ed. Vol. 2. Wiley-Interscience, New York. 1986.
10. S.A. Munford and J.W.C. Philipps. J. Chem. Soc. 950 (1950).
11. T.E. Daubert and R.P. Danner. Data compilation tables of properties of pure compounds. AIChE, New York. 1985.
12. IUPAC. Pure Appl. Chem. **47**, 75 (1976).
13. M.L. McGlashan and H.F. Stoeckli. J. Chem. Thermodyn. **1**, 589 (1969).
14. P. Bevington. Data reduction and error analysis for the physical sciences. McGraw-Hill, New York. 1969.
15. E.R. López, J. García, J. Fernández, and M.I. Paz Andrade. J. Chem. Thermodyn. **25**, 1127 (1993).
16. G. Avedis, A.H. Roux, and J.-P.E. Grolier. Int. DATA Ser. Sel. Data Mixtures, Ser. A, 1 (1990).
17. J.M. Pico, C.P. Menaut, J. Fernández. J.L. Legido, M.I. Paz Andrade. J. Solution Chem. **20**, 115 (1991).
18. I. García, J.C. Cobos, J.A. González, and C. Casanova. Thermochim. Acta, **128**, 209 (1988).
19. B.L. Larsen. Thesis. Institut for Kemiteknik, Lynby, Denmark. 1986.
20. B.L. Larsen, P. Rasmussen, and A. Fredeslund. Ind. Eng. Chem. Res. **66**, 2274 (1987).
21. W. Rupp, S. Hetzel, I. Ojini, and D. Tassios. Ind. Eng. Chem. Process Des. Dev. **23**, 391 (1984).
22. D. Dang. Thesis. New Jersey Institute of Technology, Newark, NJ. 1984.
23. D. Dang and D.P. Tassios. Ind. Eng. Chem. Proc. Des. Dev. **25**, 22 (1986).
24. H.S. Wu and S.I. Sandler. Ind. Eng. Chem. Res. **30**, 881 (1991).
25. H.S. Wu and S.I. Sandler. Ind. Eng. Chem. Res. **30**, 889 (1991).
26. T. Nitta, E.A. Turek, R.A. Greenkorn, and K.C. Chao. AIChE J. **23**, 144 (1977).

Can. J. Chem. Downloaded from www.nrcresearchpress.com by 195.246.54.202 on 09/08/12
For personal use only.

On the role of hexafluoroisopropanol in Diels–Alder reactions of acid-sensitive reagents

CARLOS CATIVIELA, JOSÉ I. GARCÍA, JOSÉ A. MAYORAL,[1] AND LUIS SALVATELLA

Departamento de Química Orgánica y Química Física, Instituto de Ciencia de Materiales de Aragón, Universidad de Zaragoza-Consejo Superior de Investigaciones Científicas, 50009 Zaragoza, Spain

Received July 16, 1993

CARLOS CATIVIELA, JOSÉ I. GARCÍA, JOSÉ A. MAYORAL,[1] and LUIS SALVATELLA. Can. J. Chem. **72**, 308 (1994).

1,1,1,3,3,3-Hexafluoro-2-propanol (HFIP) is described as an excellent solvent for those Diels–Alder reactions in which Lewis-acid-sensitive reagents are used, leading to high yields with good regio- and *endo/exo* selectivities under very mild conditions.

CARLOS CATIVIELA, JOSÉ I. GARCÍA, JOSÉ A. MAYORAL[1] et LUIS SALVATELLA. Can. J. Chem. **72,** 308 (1994).

On met en évidence que le 1,1,1,3,3,3-hexafluoropropan-2-ol (HFIP) est un excellent solvant pour les réactions de Diels–Alder dans lesquelles on utilise des réactifs sensibles aux acides de Lewis; il en résulte d'excellents rendements avec de bonnes régio- et *exo/endo*-sélectivités, dans des conditions très douces.

[Traduit par la rédaction]

Introduction

In the last few years several works dealing with the effect of solvent on intermolecular Diels–Alder reactions have been published (1). Recently, we studied (2) how the solvent modifies the rate, *endo/exo*, and diastereofacial selectivities of the Diels–Alder reaction between (−)-menthyl acrylate and cyclopentadiene. In particular, solvents with a high hydrogen-bond-donating (HBD) ability, namely fluorinated alcohols, lead to selectivities that are comparable to those obtained when Lewis acids are used as catalysts. Therefore they behave as mild Lewis acids. These results prompted us to study the effect of this kind of solvents on the rate and *endo/exo* selectivity of the reaction between methyl acrylate and cyclopentadiene (Scheme 1).

To the best of our knowledge, there is no systematic work on the effect of the solvent on the regioselectivity of these reactions, so we have also studied the effect of fluorinated alcohols on the rate and regioselectivity of the reaction between isoprene and acrolein (Scheme 1).

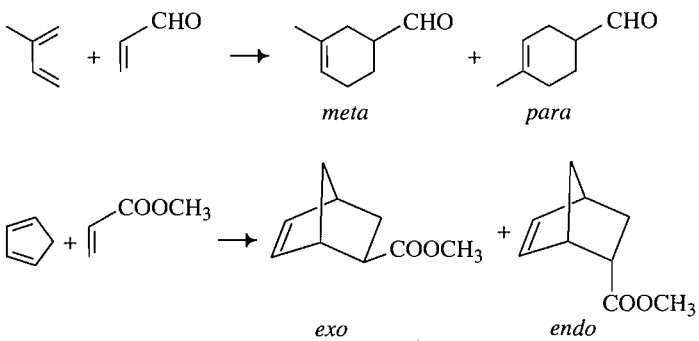

SCHEME 1

Results and discussion

Table 1 gathers the rate constants of the previously mentioned reactions carried out in several reaction media. The variation of the measured kinetic constants of the reaction between methyl acrylate and cyclopentadiene is plotted against the concentration of 1,1,1,3,3,3-hexafluoro-2-propanol (HFIP) in Fig. 1. As can be seen, the rate constant increases until 30% HFIP is present in the reaction medium, and then it remains constant.

To explain this behaviour, a specific interaction between the HBD solvent and the dienophile can be proposed. In fact, the dienophile IR carbonyl band moves from 1731 to 1709 cm^{-1} when passing from toluene to toluene/HFIP 70:30, spectra at intermediate HFIP concentrations showing the simultaneous presence of both carbonyl bands. It can thus be concluded that HFIP behaves as a mild Lewis acid.

However, when pure HFIP is used as a solvent, a further increase in the rate constant is experimentally observed. Two possible explanations could account for this abnormal behaviour. On the one hand, the change of the bulk properties of the reaction medium may modify the value of the rate constant through a nonspecific solvation mechanism. Alternatively, it is well known that HFIP is a relatively strong Brønsted acid ($pK_a = 9.3$), so that very reactive protonated dienophile species can be envisaged.

In the case of the acrolein IR carbonyl band, the simultaneous presence of both free (1699 cm^{-1}) and solvent-associated (1687 cm^{-1}) bands is observed until toluene/HFIP 90:10, which agrees with the noticeable increase in the rate constant observed when passing from 0% to 10% HFIP (Table 1 and Fig. 1). From this proportion of HFIP a further increase in the rate constant was not to be expected on the basis of a specifically solvated dienophile as reactive intermediate. However, a steady increase in the rate constant with the concentration of HFIP is observed. This increase is more marked when passing from 70 to 100% HFIP. The above mentioned hypotheses may again account for this behaviour. To choose between the hypotheses, the reaction was carried out in the presence of a small amount of a stronger Brønsted acid, namely trifluoroacetic acid (TFA, $pK_a = 0.52$), whose Lewis acidity (as defined by the Kamlet–Taft empirical solvent parameter α) was not expected to be very different from that of HFIP. The results obtained show that this reaction medium gives rise to a further acceleration of the reaction rate (Table 1). The noticeable increase in reaction rate is in agreement with a catalysis through proton transfer.

It might be thought that the behaviour of the HFIP is due to the presence of traces of hydrogen fluoride. To rule out this possibility, the reaction in pure HFIP was repeated in the presence of triethylamine. The reactions with and without NEt_3 led to almost identical results. A slight difference in rate was observed, which can be attributed to a base-catalyzed addition of HFIP to the dienophile, detected by GC–MS. However, the regioselectivity remained unchanged, which enables us to rule out the existence of a hydrogen fluoride-catalyzed reaction.

[1]Author to whom correspondence may be addressed. Telephone: (34-76)350475; FAX: (3476)567920; e-mail: CATIVIELA@CC.UNIZAR.ES.

Can. J. Chem. Downloaded from www.nrcresearchpress.com by 195.246.54.202 on 09/08/12
For personal use only.

TABLE 1. Rate constants of the Diels–Alder reaction of isoprene (6 mmol) with acrolein (2 mmol) (reaction A), and cyclopentadiene (6 mmol) with methyl acrylate (2 mmol) (reaction B) in 4 mL of several reaction media at 30°C

		Reaction A		Reaction B	
Solvent	[HFIP[a]] (mol L^{-1})	%Conversion[b] (24 h)	$k \times 10^6$ (L mol^{-1} s^{-1})	%Conversion[b] (24 h)	$k \times 10^4$ (L mol^{-1} s^{-1})
Water[c]	—	28.0	—	—	—
Methanol/water[d]	—	33.5	4.067(±0.300)	42.0	2.543(±0.350)
Toluene	—	2.0	0.260(±0.010)	2.5	0.238(±0.020)
Toluene/HFIP 97.5:2.5	0.25	30.0	3.112(±0.220)	6.0	0.578(±0.050)
Toluene/HFIP 95:5	0.5	37.0	7.683(±0.520)	20.0	1.052(±0.174)
Toluene/HFIP 90:10	1.0	52.0	14.690(±0.490)	35.0	1.242(±0.122)
Toluene/HFIP 70:30	3.0	90.0	47.440(±6.930)	83.0	1.978(±0.440)
Toluene/HFIP 50:50	5.0	100.0	71.930(±6.320)	100.0	1.886(±0.060)
Toluene/HFIP 30:70	7.0	100.0	119.000(±9.300)	100.0	1.874(±0.290)
HFIP	10.0	100.0	293.400(±13.780)	100.0	4.865(±0.850)
Toluene/HFIP 90:10 + TFA[e] 0.13 M	1.0	—	50.640(±1.430)	—	—
HFIP + NEt_3 0.05 M	10.0	—	237.300(±11.530)	—	—

[a]1,1,1,3,3,3-Hexafluoro-2-propanol.
[b]Determined by GC. Cycloadducts were charaterized by ^1H NMR and MS.
[c]Part of the reaction takes place in the organic phase, so kinetic measurements are not reliable.
[d]70:30 for the reaction of acrolein and 50:50 for the reaction of methyl acrylate.
[e]Trifluoroacetic acid.

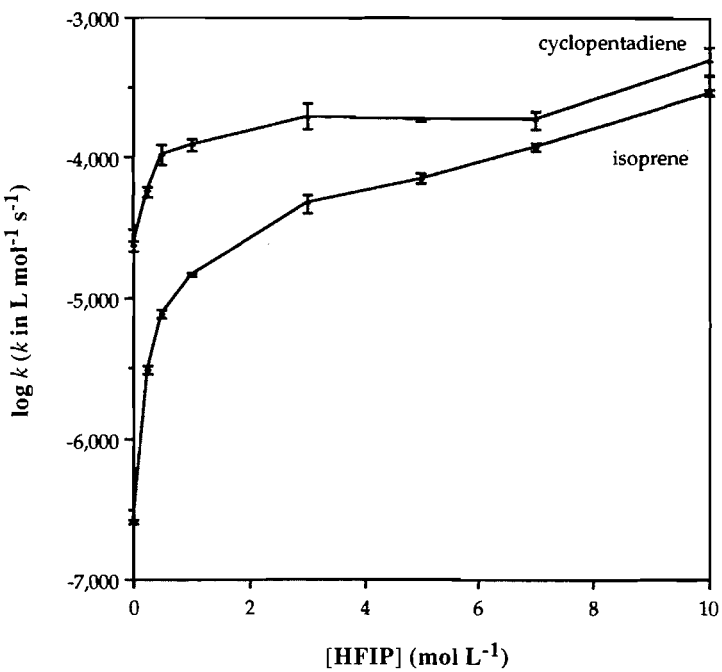

FIG. 1. The effect of concentration of HFIP on rates of the reactions of methyl acrylate with cyclopentadiene, and of isoprene with acrolein

The differences between both dienophiles deserve separate comment. The results obtained suggest that the ability of HFIP to transfer a proton to the dienophile increases with the possibility of solvation of the protonated intermediate by other molecules of HFIP, and with the basicity of the dienophile. Therefore, in pure HFIP, both dienophiles can be protonated, given the efficient solvation of the protonated species, but in reaction media with low proportions of HFIP, only the most basic dienophiles can lead to stable protonated intermediates.

Table 2 gathers the *para/meta* and *endo/exo* selectivities obtained in the reactions of isoprene with acrolein, and of cyclopentadiene with methyl acrylate, respectively (Scheme 1).

With regard to *para/meta* selectivities, the behaviour observed is parallel to that of the rate constants, the greatest increase being observed when passing from 0 to 5% HFIP. The influence of the abovementioned protonated intermediate on regioselectivity is corroborated by the reaction carried out in the presence of a small amount of TFA (Table 2).

endo/exo Selectivity also increases noticeably with the first addition of HFIP, and then remains almost constant. Unlike the rate constant, *endo/exo* selectivity does not significantly increase when the reaction is carried out in pure HFIP. To clarify this point, it would be useful to carry out some experiments in the presence of TFA. Unfortunately, in these conditions, a fast and

Can. J. Chem. Downloaded from www.nrcresearchpress.com by 195.246.54.202 on 09/08/12
For personal use only.

TABLE 2. Selectivities of the Diels–Alder reaction of acrolein (6 mmol) with isoprene (2 mmol) (*para/meta*) and cyclopentadiene (6 mmol) with methyl acrylate (2 mmol) (*endo/exo*) in 4 mL of several reaction media at 30°C

Solvent	[HFIP] (mol L^{-1})	*para/meta*	*endo/exo*
Methanol/water[a]	—	3.4	8.3
$LiClO_4$ (ether)[b]	—	9.0	7.3[c]
Toluene	—	2.3	2.7
Toluene/HFIP 97.5:2.5	0.25	3.5	4.7
Toluene/HFIP 95:5	0.5	3.7	5.7
Toluene/HFIP 90:10	1.0	4.2	6.1
Toluene/HFIP 70:30	3.0	5.3	7.0
Toluene/HFIP 50:50	5.0	7.1	7.0
Toluene/HFIP 30:70	7.0	8.2	7.4
HFIP	10.0	10.7	7.7
Toluene/HFIP 90:10 + TFA[d] 0.13 M	1.0	5.4	—

[a]70:30 for the reaction of acrolein and 50:50 for the reaction of methyl acrylate.
[b]5 M for the reaction of acrolein and 38.1% for the reaction of methyl acrylate (ref. 3).
[c]Reaction carried out at 20°C (ref. 4).
[d]Trifluoroacetic acid.

extensive oligomerization was experimentally observed. The diene oligomerization was also observed in reaction media with high concentrations of HFIP. The existence of this lateral reaction is in agreement with the role of the HFIP as a Brønsted acid.

It is well known that Diels–Alder reactions using acrolein as the dienophile often give undesirable results due to the fact that acrolein easily polymerizes. To overcome this problem, a variety of homogeneous (5) and heterogeneous (6) Lewis acids, high pressures (7), and acetals of acrolein (8) have been employed. Even under these conditions yields obtained with open-chain dienes are often less than 65%. Recently higher conversions (95%) were obtained by using uncommon organometallic compounds as catalysts (9). On the other hand, high percentages of conversion with high regioselectivities can be obtained in the reaction of acrolein and isoprene in solvent mixtures containing HFIP. When the reaction is carried out in a different fluorinated alcohol, namely, 2,2,2-trifluoroethanol (TFE, $pK_a = 12.9$), the conjugate addition of the solvent to the acrolein is observed, but this reaction does not take place with the more acidic and less nucleophilic HFIP.

It is noteworthy that the use of aqueous media in this reaction improves the results when compared with an "inert" solvent such as toluene. However, better results are obtained with HFIP, even in small proportions, which suggests that this solvent plays a catalytic role.

Recently, lithium perchlorate – diethyl ether was reported to be an excellent reaction medium for Diels–Alder reactions. Nevertheless, HFIP allows us to obtain a noticeably higher regioselectivity. Furthermore, HFIP has two additional advantages, namely, the higher solubility of reagents, and the easy recovery of most of the HFIP with a high degree of purity.

The reaction between methyl acrylate and cyclopentadiene in pure HFIP is fast and a high *endo/exo* value, slightly greater than that obtained with $LiClO_4$– ether, is observed. However, the best selectivity is achieved in methanol/water 70:30, with a reaction rate similar to that obtained in HFIP, and without extensive diene oligomerization. These results suggest that aqueous mixtures are more suitable for cyclopentadiene reactions.

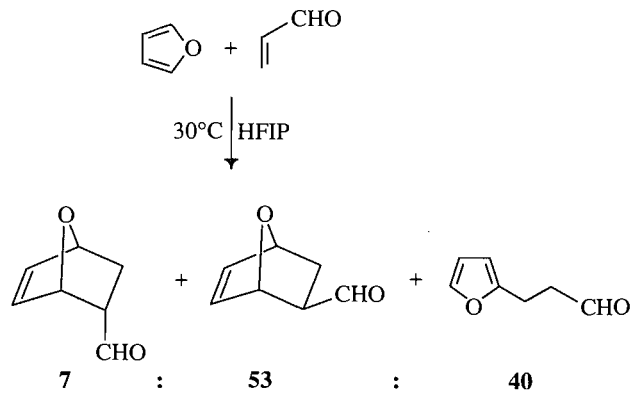

SCHEME 2

While HFIP is a suitable solvent for reactions of Lewis-acid-sensitive reagents, such as acrolein, it is not so good when they are sensitive to Brønsted acids, such as cyclopentadiene and 2,3-dimethylbutadiene. Thus, in the reaction between the latter and acrolein, cycloadducts are obtained in only 44% yield, and diene oligomerization is experimentally observed. Finally, we considered it was worth testing a cycloaddition where both diene and dienophile are acid-sensitive, namely the reaction between furan and acrolein (Scheme 2). In 48 h acrolein completely disappears, giving the corresponding oxanorbornene derivatives (*exo/endo* = 7.6) as major products. This is a very good result for a Diels–Alder reaction of furan (10). Together with the two Diels–Alder cycloadducts, 3-(2-furyl)-propanal is obtained. It has been reported (10) that oxanorbornene derivatives can lead thermally to this kind of product. However, all our treatments were carried out at room temperature, and the formation of the 3-(2-furyl)propanal was observed over short reaction times. Thus we propose that the use of a nucleophilic diene such as furan leads to a concurrence between the Diels–Alder and the conjugate addition, the former being the favoured reaction.

To sum up, HFIP is a suitable and recoverable solvent for Diels–Alder reactions, above all when the reagents are Lewis-acid-sensitive. The Friedel–Crafts addition observed when furan is used as diene indicates the possibility of using HFIP in a variety of acid-catalyzed organic reactions.

Experimental

HFIP, TFE, and TFA were purchased from Aldrich and used without further purification. Toluene, ether, and methanol were dried and purified according to standard procedures. ^1H NMR spectra were recorded in a Varian Unity 300 MHz apparatus. GC–MS experiments were performed using a VG Autospec trisector EBE spectrometer.

Reaction procedures

Isoprene + acrolein

A solution of isoprene (408 mg, 6 mmol) in the corresponding reaction medium (2 mL) was added to a thermostated (30 ± 0.1°C) solution of acrolein (112 mg, 2 mmol) in the same solvent or solvent mixture (2 mL). The solution was magnetically stirred and the reaction monitored by gas chromatography (FID from Hewlett–Packard 5890 II; cross-linked methyl silicone column, 23 mm × 0.2 mm × 0.33 μm; helium as carrier gas, 17 psi (1 psi = 6.9 kPa); injector temperature 230°C, detector temperature 250°C, oven temperature program: 50°C (3 min) – 25°C/min – 75°C (12 min); retention times: acrolein 1.9 min, toluene 4.8 min, *meta* cycloadduct 14.4 min, *para* cycloadduct 14.7 min).

In the reaction carried out in pure HFIP the stirring was maintained for 3 h, the solvent recovered by distillation under reduced pressure

Can. J. Chem. Downloaded from www.nrcresearchpress.com by 195.246.54.202 on 09/08/12
For personal use only.

(3.4 mL, 85% with a purity ≥ 98% determined by GC), and the mixture obtained dissolved in methylene chloride (5 mL) and treated with $Na_2CO_3 \cdot 10H_2O$. The solution was separated by filtration and the solvent eliminated under reduced pressure to afford 196 mg (79%) of a 11:1 mixture of *para* and *meta* cycloadducts. The ^1H NMR of the mixture did not indicate great differences between both adducts. The structural assignment of the cycloadducts was made on the basis of the experimental results previously described (5*a*, 9*a*, 11). Recently, a new method based on mass spectrometry coupled with theoretical calculations was reported for the structural assignment of Diels–Alder regioisomers (12). The results obtained through this methodology are in complete agreement with those previously described. ^1H NMR ($CDCl_3$), δ ppm: 9.674 (CHO *meta*), 9.665 (CHO *para*, d, J = 0.978 Hz), 5.37–5.38 (bs, 1H), 2.41–2.43 (m, 1H), 1.92–1.97 (m, 2H), 1.65–1.70 (m, 1H), 1.624 (d, J = 0.486 Hz). MS spectra: *para* cycloadduct, m/z = 124 ($M^{\cdot+}$, 70%), 67(100%); *meta* cycloadduct, m/z = 124 ($M^{\cdot+}$, 44%), 95(100%).

Cyclopentadiene + methyl acrylate

A solution of freshly distilled cyclopentadiene (396 mg, 6 mmol) in the corresponding reaction medium (2 mL) was added to a thermostated (30 ± 0.1°C) solution of methyl acrylate (172 mg, 2 mmol) in the same solvent or solvent mixture (2 mL). The solution was magnetically stirred and the reaction monitored by gas chromatography (FID from Hewlett-Packard 5890 II; cross-linked methyl silicone column, 23 mm × 0.2 mm × 0.33 μm; helium as carrier gas, 17 psi; injector temperature 230°C, detector temperature 250°C. oven temperature program: 50°C (3 min) – 25°C/min – 100°C (9 min); retention times: methyl acrylate 2.7 min, *exo* cycloadduct 12.7 min, *endo* cycloadduct 12.9 min). The structural assignment of the cycloadducts was made on the basis of their ^1H NMR spectra (13).

Furan + acrolein

A solution of furan (408 mg, 6 mmol) in HFIP (2 mL) was added to a thermostated (30 ± 0.1°C) solution of acrolein (112 mg, 2 mmol) in HFIP (2 mL). The solution was magnetically stirred for 48 h and the reaction monitored by TLC. The HFIP and the excess of furan were eliminated under reduced pressure and the mixture obtained was dissolved in methylene chloride (5 mL) and treated with $Na_2CO_3 \cdot 10H_2O$. The solution was separated by filtration and the solvent eliminated under reduced pressure. The resulting mixture was analysed by ^1H NMR in $CDCl_3$, its composition being determined by integration of the CHO signals: 9.790 ppm (t, J = 1.5 Hz, Friedel–Crafts adduct), 9.608 (d, J = 3.9 Hz, *exo* cycloadduct), 9.376 (d, J = 3.0 Hz, *endo* cycloadduct). The structural assignment of the cycloadducts was made taking into account the differences in the respective ^1H NMR spectra. Thus, the chemical shift of the formyl proton should be greater in the *exo* adduct because of the anisotropic effect of the double bond. This behaviour was previously described for other 2-substituted-7-oxabicyclo[2.2.1]hept-5-enes, carrying a carboxylic acid or ester substituent (14).

Acknowledgements

This work was made possible by the generous financial support of the Comisión Interministerial de Ciencia y Tecnología (Project MAT90-0778-C02-01). L. Salvatella would like to express his gratitude to the Diputación General de Aragón for a grant.

1. (*a*) H.-J. Schneider and N.K. Sangwan. J. Chem. Soc. Chem. Commun. 1787 (1986); (*b*) Angew. Chem. Int. Ed. Engl. **26**, 896 (1987); (*c*) N.K. Sangwan and H.-J. Schneider. J. Chem. Soc. Perkin Trans. 2, 1223 (1989); (*d*) G. Desimoni, G. Faita, P. Righetti, N. Tornaletti, and M. Visigalli. J. Chem. Soc. Perkin Trans. 2, 437 (1989); (*e*) G. Desimoni, G. Faita, and P. Righetti. Tetrahedron, **47**, 5857 (1991); (*f*) C. Cativiela, J.A. Mayoral, A. Avenoza, J.M. Peregrina, and M.A. Roy. J. Phys. Org. Chem. **3**, 414 (1990); (*g*) C. Cativiela, J.I. García, J.A. Mayoral, A. Avenoza, J.M. Peregrina, and M.A. Roy. J. Phys. Org. Chem. **4**, 48 (1991).
2. C. Cativiela, J.I. Carcía, J.A. Mayoral, A.J. Royo, L. Salvatella, X. Assfeld, and M.F. Ruiz-López. J. Phys. Org. Chem. **5**, 230 (1992).
3. R.A. Silva. Chem. Eng. News, **70**, 2 (1992).
4. R. Braun and J. Sauer. Chem. Ber. **119**, 1269 (1986).
5. (*a*) E.F. Lutz and G.M. Bailey. J. Am. Chem. Soc. **86**, 3899 (1964); (*b*) S. Danishefsky and M. Bednarski. Tetrahedron Lett. **26**, 2507 (1985).
6. (*a*) J. Ipaktschi. Z. Naturforsch. B: Anorg. Chem. Org. Chem. **41**, 496 (1986); (*b*) V.V. Veselovsky, A.S. Gybin, A.V. Lozanova, A.M. Moiseenkov, W.A. Smit, and R.A. Caple. Tetrahedron Lett. **29**, 175 (1988).
7. W.G. Dauben and H.O. Krabbenhoft. J. Org. Chem. **42**, 282 (1977).
8. (*a*) H.M.R. Hoffmann and H. Vathke-Ernst. Chem. Ber. **114**, 2208 (1981); (*b*) P.G. Gassman, P.A. Singleton, J.J. Wilwerding, and S.P. Chavan. J. Am. Chem. Soc. **109**, 2182 (1987); (*c*) P.G. Gassman and S.P. Chavan. J. Org. Chem. **53**, 2392 (1988); (*d*) T. Inokuchi, S.-I. Tanigawa, and S. Torii. J. Org. Chem. **55**, 3958 (1990).
9. (*a*) P.V. Bonnensen, C.L. Pucket, R.V. Honeychuck, and W.H. Hersch. J. Am. Chem. Soc. **111**, 6070 (1989); (*b*) A.S. Olson, W.J. Seitz, and M. Mahmun Hossain. Tetrahedron Lett. **32**, 5299 (1991); (*c*) W. Odenkirk, A.L. Reingold, and B. Bosnich. J. Am. Chem. Soc. **114**, 6392 (1992); (*d*) T.K. Hollis, N.P. Robinson, and B. Bosnich. Organometallics, **11**, 2745 (1992).
10. J.A. Moore and E.M. Partain III. J. Org. Chem. **48**, 1105 (1983), and references cited therein.
11. (*a*) K. Nakagawa, M. Sawai, Y. Ishii, and M. Ogawa. Bull. Chem. Soc. Jpn. **50**, 2487 (1977).
12. C. Cativiela, J.I. García, J. Garín, J.A. Mayoral, J. Orduna, and L. Salvatella. Org. Mass. Spectrom. **28**, 752 (1993).
13. J.C. Davis, Jr. and T.V. Van Auken. J. Am. Chem. Soc. **87**, 3900 (1965).
14. W.L. Nelson and D.R. Allen. J. Heterocycl. Chem. **9**, 562 (1972).

Can. J. Chem. Downloaded from www.nrcresearchpress.com by 195.246.54.202 on 09/08/12
For personal use only.

On the conformational preferences of the dehydrochlorination of α-chlorosulfoxides[1]

ADRIAN L. SCHWAN,[2] MICHAEL R. ROCHE, JOHN F. GALLAGHER, AND GEORGE FERGUSON

Guelph–Waterloo Centre for Graduate Work in Chemistry, Guelph Campus, Department of Chemistry and Biochemistry, University of Guelph, Guelph, ON N1G 2W1, Canada

Received April 7, 1993

ADRIAN L. SCHWAN, MICHAEL R. ROCHE, JOHN F. GALLAGHER, and GEORGE FERGUSON. Can. J. Chem. **72**, 312 (1994).

Several acyclic α-chlorosulfoxides have been shown to undergo a γ-dehydrochlorination upon treatment with LDA. The proposed immediate products of γ-dehydrochlorination, thiirane-*S*-oxides, are unstable under the basic conditions and react further with the LDA; the isolated products are usually *E*-alkenes and (or) *E*-vinyl sulfoxides. Some of the proposed intermediate thiirane-*S*-oxides, compounds **6**, **7**, **8**, and **18**, were synthesized independently and treated with one equivalent of LDA in order to mimic the second step of the overall dehydrochlorination/ring opening sequence. The products obtained from the reactions of compounds **6** and **18** compared favourably with those products which were believed to arise from certain conformations of α-chlorosulfoxides **1kB** and **1e**, respectively. The addition of one equivalent of LDA to **1kA** afforded a mixture containing thiirane-*S*-oxide **8**, which is proposed as the immediate product of γ-dehydrochlorination of **1kA**. The configurations of **1kB** and **1hA** were both shown to be *threo* by X-ray crystallographic studies. Those conformations which are preferred for the dehydrochlorination possess a geometry where the sulfinyl oxygen is *anti* to any of the substituents of the ring carbons.

ADRIAN L. SCHWAN, MICHAEL R. ROCHE, JOHN F. GALLAGHER et GEORGE FERGUSON. Can. J. Chem. **72**, 312 (1994).

On démontre que, par traitement avec du LDA, plusieurs α-chlorosulfoxydes subissent une γ-déshydrochloration. Les produits immédiats proposés pour cette réaction, les *S*-oxydes de thiirane, sont instables dans les conditions basiques de la réaction et réagissent à nouveau avec le LDA; les produits isolés sont habituellement des (*E*)-alcènes et (ou) des (*E*)-vinylsulfoxydes. On a synthétisé par des voies indépendantes quelques-uns des intermédiaires *S*-oxydes de thiirane proposés, les composés **6**, **7**, **8** et **18**, et, dans le but d'évaluer leur comportement dans la deuxième étape de la séquence globale de déshydrochloration/ouverture de cycle, on les a soumis à l'action d'un équivalent de LDA. Les produits obtenus lors des réactions des composés **6** et **18** se comparent favorablement avec les produits qui devraient être obtenus respectivement à partir de certaines conformations des α-chlorosulfoxydes **1kB** et **1e**. L'addition d'un équivalent de LDA sur le composé **1kA** conduit à un mélange contenant l'oxyde de thiirane **8** que l'on propose comme intermédiaire lors de la γ-déshydrochloration du produit **1kA**. Faisant appel à des études cristallographiques par diffraction des rayons X, on a déterminé que les configurations **1kB** et **1hA** sont *thréo*. Les conformations privilégiées pour la déshydrochloration possèdent une géométrie dans la quelle l'oxygène du sulfinyle est *anti* par rapport à tous les substituants carbonés du cycle.

[Traduit par la rédaction]

Introduction

The Ramberg–Bäcklund (α-halosulfone) rearrangement has been a popular synthetic tool for the synthesis of alkenes for several decades (1, 2). While related reactions have not met with the consistent acceptance of the α-halosulfone approach (3, 4), some variations have nevertheless been shown to be efficient routes to alkenes (4). Vogel, Weinges et al. (4) have shown that certain cyclic α-chloro*sulfoxides* undergo γ-dehydrochlorination to furnish the corresponding cycloalkene in high yield. Since the sulfoxide group possesses a chiral sulfur, it occured to us that the deprotonation/dehydrochlorination step in the γ-dehydrochlorination of α-chlorosulfoxides may proceed with some selectivity for either of the diastereotopic hydrogens that are the target of the base. Unfortunately, the obtention of alkene products in the previous work (4) affords no such stereochemical information.

The expected immediate products of γ-dehydrohalogenation of α-chlorosulfoxides are thiirane-*S*-oxides. Bonini et al. (5) have shown that some thiirane-*S*-oxides are attacked at sulfur by lithium amides and lithium alkyls to create alkene and at hydrogen (deprotonation) to induce ring opening and formation of lithium ethenesulfenate ions. The sulfenates could be captured at sulfur with methyl iodide to afford vinyl sulfoxides. The different ratio of alkene to vinyl sulfoxide was found to be dependent on the stereochemistry of the starting thiirane-*S*-oxides. Moreover, the *E*:*Z* ratio of the alkenes and of the vinyl sulfoxides was also found to be dependent on the stereochemistry of the starting thiirane-*S*-oxides (5). In a preliminary communication (6), we reported the γ-dehydrohalogenation of a series of acyclic α- chlorosulfoxides and one example that indicated the existence of stereochemical forces governing the course of the reaction.

It seemed to us that the stereochemical dependence on the mode of the deprotonation/ring opening of the thiirane-*S*-oxides and its efficiency could provide a handle for the evaluation of the γ-dehydrohalogenation of α-halosulfoxides. In this paper we demonstrate that the stereochemcial attributes of the reaction seem to be general and we report on chemistry aimed at determining the origin of the stereochemical constraints.

Results and discussion

Several α-chlorosulfoxides were prepared, including some diastereomeric mixtures and some separable pairs of diastereomers that were initially identified as the more polar and less polar isomers.[3] Each diastereomer was exposed to two equivalents of LDA at −78°C or 0°C and the mixtures were quenched with MeI or $PhCH_2Br$. Under these conditions, vinyl sulfoxides and alkenes were obtained in variable yields. In general those chlorosulfoxides with a phenyl attached to the α-carbon (to the sulfinyl) were consumed at −78°C; most of the other systems

[1]Presented in part at the 3rd International Conference on Heteroatom Chemistry, Riccione, Italy, June, 1992.

[2]Correspondence may be addressed to this author. FAX: 519-766-1499; e-mail address: SCHWAN@chembio.uoguelph.ca.

[3]This designation arises from the chromatographic behaviour of the pairs of isomers. The "**A**" compound is the less polar; the "**B**" compound is the more polar.

Can. J. Chem. Downloaded from www.nrcresearchpress.com by 195.246.54.202 on 09/08/12
For personal use only.

TABLE 1. Reactions of α-chlorosulfoxides **1** with LDA[a]

No.	1	Conditions	Products (% yield)[b]
1	**a**	A	**2a**(38)
2	**b**	B	**2b**(60); **3b**(8)
3	**c**	B	**2c**(50); **3c**(24)
4	**d**	C	**2d**(32)
5	**e**	A	**2e**(50)[c]; **4**(14)[c]
6	**f**	C	**2d**(49); **2f**(31)
7	**g**	D	**3g**(ca. 90)
8	**hA**	B	**2e**(48); **2h**(29)
9	**hB**	B	**2e**(4); **2h**(61)
10	**iA**	C	**2i**(22); **2m**(7); **3i**(6)
11	**iB**	C	**2i**(54); **2m**(17)
12	**jA**	C	**2j**(10); **2n**(9)[d]
13	**jB**	C	**2j**(56); **5**(10)
14	**kA**	A	**2k**(44); **2o**(27)[e]; **3k**(21)
15	**kB**	A	**2k**(18); **2p**(59)[e]
16	**lA**	C	**2l**(24); **2q**(10)[d,f]
17	**lB**	C	**2l**(42); **2q**(11)[d,f]

[a]See experimental section for full practical details.
[b]Yields are of chromatographed material where possible. See Experimental for the quantitation method of volatile alkenes.
[c]Yields based on consumed **1***e*.
[d]These isomeric products could not be separated.
[e]Material is 96% pure; it is contaminated with its opposite geometric isomer.
[f]The relative assignment of these isomers is not secure. The major product was deemed to be the *E* isomer.

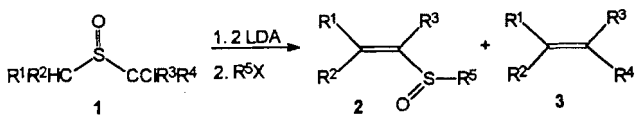

All R's=H unless otherwise noted

1a	R^1=H	**b**	R^1=Ph
c	R^1=R^3=Ph (3:2 mixture)		
d	R^1=$C_{11}H_{23}$	**e**	R^1=Ph$(CH_2)_2$
f	R^3=$C_{11}H_{23}$ (5.5:1 mixture)		
g	R^1=R^2=R^3=R^4=Me		
hA	R^3=Ph$(CH_2)_2$ (*threo*)		
hB	R^3=Ph$(CH_2)_2$ (*erythro*)		
iA	R^1=Ph; R^2=Me (less polar)		
iB	R^1=Ph; R^2=Me (more polar)		
jA	R^1= R^3=PhCH_2 (less polar)		
jB	R^1= R^3=PhCH_2 (more polar)		
kA	R^1=Ph; R^3=*n*Pr (less polar, *erythro*)		
kB	R^1=Ph; R^3=*n*Pr (more polar, *threo*)		
lA	R^1= R^3=Me (less polar)		
lB	R^1= R^3=Me(less polar)		

2a-l	R's as for **1** and
m	R^1=Me; R^2=Ph
n	R^2= R^3=PhCH_2
o	R^2=*n*Pr; R^3=Ph
p	R^1=*n*Pr; R^3=Ph
q	R^2=R^3=Me
2a, l, p	R^5=PhCH_2
	All others: R^5=Me
3	R's as for **1**

SCHEME 1

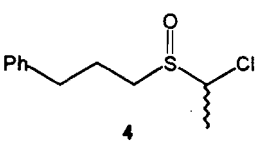

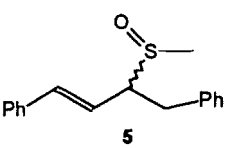

were warmed to 0°C to complete the reaction. The yields of vinyl sulfoxide and of alkene are listed in Table 1 (Scheme 1). Many systems failed to yield any alkene, while chlorosulfoxide **1g** afforded only tetramethyl ethylene. Vinyl sulfoxide geometry was established using the H-C=C-H ^{1}H NMR coupling constants where possible. Three particularly important cases (vide infra) could not be assigned on this basis, so the usefulness of lanthanide shift reagents was explored. It is known that the

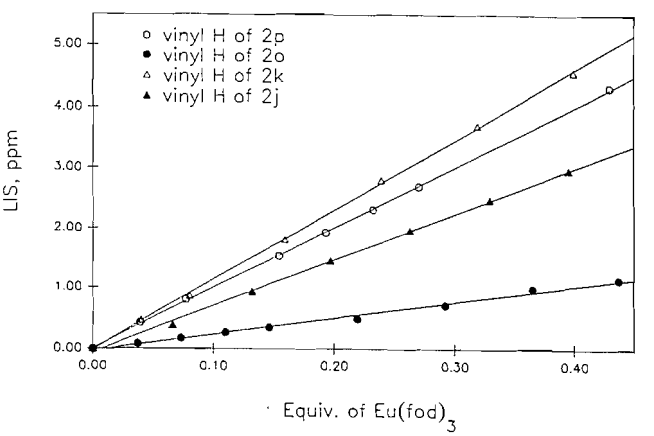

FIG. 1. Dependence of vinyl hydrogen ^{1}H NMR chemical shift on Eu(fod)$_3$ concentration.

sulfinyl functionality binds such reagents strongly (5, 7), and that vinyl hydrogens *cis* to the sulfinyl moiety in a vinyl sulfoxide are shifted noticeably downfield (5). Hence, isomers **2k**, **2o**, and **2p** as well as **2h** were mixed with increasing amounts of Eu(fod)$_3$ (see Experimental) in an NMR tube. The change in chemical shift of the vinyl hydrogen of each of the substrates was compared to the relative amount of shift reagent present and the data are presented in Fig. 1. It is clear that the vinyl hydrogens *cis* to a methylsulfinyl group (as in **2h**, **2k**, and **2p**) are most affected by the presence of the shift reagent; this is manifested by a conspicuous downfield movement. On the other hand, with **2o** the change in chemical shift of the vinyl hydrogen is much less significant, as expected for a hydrogen *trans* to the sulfoxide.

We suggest that the chemistry taking place is consistent with previous work (4, 5) and that our obtaining of vinyl sulfoxides

Can. J. Chem. Downloaded from www.nrcresearchpress.com by 195.246.54.202 on 09/08/12
For personal use only.

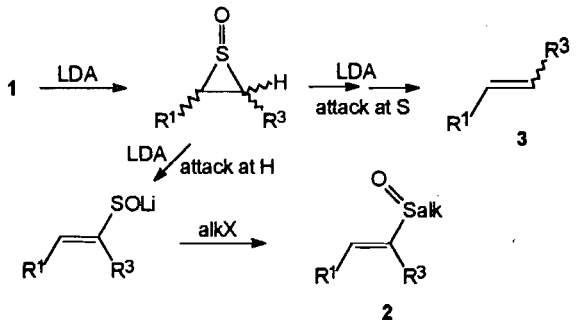

SCHEME 2

and alkenes is best explained by the following mechanism. The LDA induces a γ-dehydrochlorination reaction to form a short-lived thiirane-*S*-oxide, which is then attacked by a second equivalent of LDA at either sulfur or hydrogen (Scheme 2). Ring closure of **1g** yields tetramethyl ethylenesulfide-*S*-oxide, a compound that bears no ring hydrogens; further attack is only at sulfur in this instance. Each pair of diastereomers affords somewhat similar products although the less polar diastereomers among the sets tended to undergo the γ-dehydrochlorination less efficiently. The reactions of compounds **1h** and **1k** are shown in Schemes 3 and 5. In those reactions, the yields or identity of the products were notably different. Chlorosulfoxide **1hA** provided **2e** and **2h** in a ratio 1.66:1, whereas with **1hB** the ratio reverses to 1:15. The different reactivities of **1kA** and **1kB** are also striking. The γ-dehydrochlorination and subsequent reactions of **1kA** yielded alkene **3k** and vinyl sulfoxides **2k** and **2o**, but its corresponding diastereomer **1kB** afforded **2k** and, as a major product, **2p**, the vinyl sulfoxide possessing *cis-trans* geometry opposite to **2o**.

Due to the measurable differences in their chemistry, compounds **1hA/B** and **1kA/B** were viewed as suitable examples for a more detailed analysis of the conformations required for γ-dehydrochlorination and perhaps the origin of the stereochemical requirements of the ring closure. To begin, the relative stereochemistry of the chlorine and the sulfinyl oxygen in one of the starting isomers had to be determined. This was accomplished by single crystal X-ray analysis for two compounds, chlorosulfoxides **1kB** and **1hA**. Suitable crystals of **1kB** and **1hA** were obtained by recrystallization from 60–80 petroleum ether. The crystal structure analyses proceeded smoothly; the molecular dimensions are entirely in accord with accepted values and serve to establish the structures and relative stereochemistry unequivocally. Views of **1kB** and **1hA** showing the configuration and the conformation adopted in the solid state are in Fig. 2; from these diagrams it is clear that both **1kB** and **1hA** have the *threo* configuration. In both **1kB** and **1hA** in the solid state, the conformation adopted has the side chain maximally extended with the O—S—C—Cl torsion angle −57.9(3)° in **1kB** and 47.9(5)° in **1hA**.

The approach described herein entails the independent synthesis of transient thiirane-*S*-oxides of known stereochemistry and their treatment with *one* equivalent of LDA. Analysis of the products may allow some conclusions about the mode of ring closure to the thiirane-*S*-oxides. The mechanistic dissection requires two assumptions. The first is that the γ-dehydrochlorination proceeds via a double inversion mechanism from a conformation where the H—C, C—S, S—C, and C—Cl bonds form a "W" as in Fig. 3. Such a conformation seems to be the

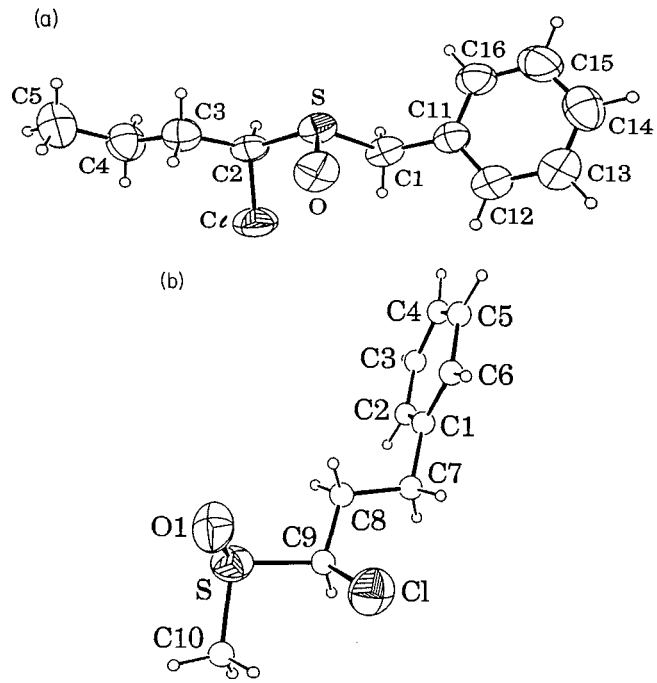

FIG. 2. AN ORTEP view of (*a*) molecule **1kB** and (*b*) **1hA** showing the *threo* configuration and the crystallographic numbering schemes. Thermal ellipsoids are drawn at the 50% level for non-H atoms; H atoms are shown as spheres of a small size.

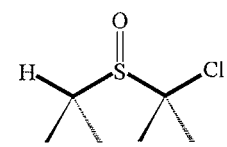

FIG. 3. Assumed "W" conformation for the γ-dehydrochlorination of α-chlorosulfoxides.

preferred geometry of dehydrohalogenation of α-halosulfones (1) and it is the only geometry available for the cyclic compounds of Vogel and Weinges (4). Those compounds undergo the γ-dehydrochlorination very efficiently (85–90%). Furthermore, the anion stabilizing effects of n–σ^* hyperconjugation (9) with the S—CClR′R″ bond are maximized when deprotonation occurs when the H—C, C—S, and S—C bonds are aligned as in the W conformation. The second assumption requires that the ring closure step is totally independent of the ensuing deprotonation step. This second assumption may not be valid due to the Lewis basic properties of the sulfinyl oxygen and the Lewis acidic nature of the lithium cations present. Some sort of coordination of the oxygen to a lithium cation may be present in the dehydrochlorination/ring opening mixture that cannot be matched by the use of thiirane-*S*-oxides alone.

Based on the first assumption, the possible conformations for ring closure of **1kA** and of **1kB** (two each) are shown in Scheme 3. From these drawings it can be seen that the conformation of **1kB** bearing *syn* phenyl and propyl groups (**C1**) should close to thiirane-*S*-oxide **6**. If the phenyl and propyl groups are *anti* (**C2**) during the dehydrochlorination, the product should be **7**. Similarly, for the *erythro* isomer **1kA**, closure of one conformation (**C3**) leads to **8** while reaction of the other (**C4**) affords **9**.

Can. J. Chem. Downloaded from www.nrcresearchpress.com by 195.246.54.202 on 09/08/12
For personal use only.

Can. J. Chem. Downloaded from www.nrcresearchpress.com by 195.246.54.202 on 09/08/12
For personal use only.

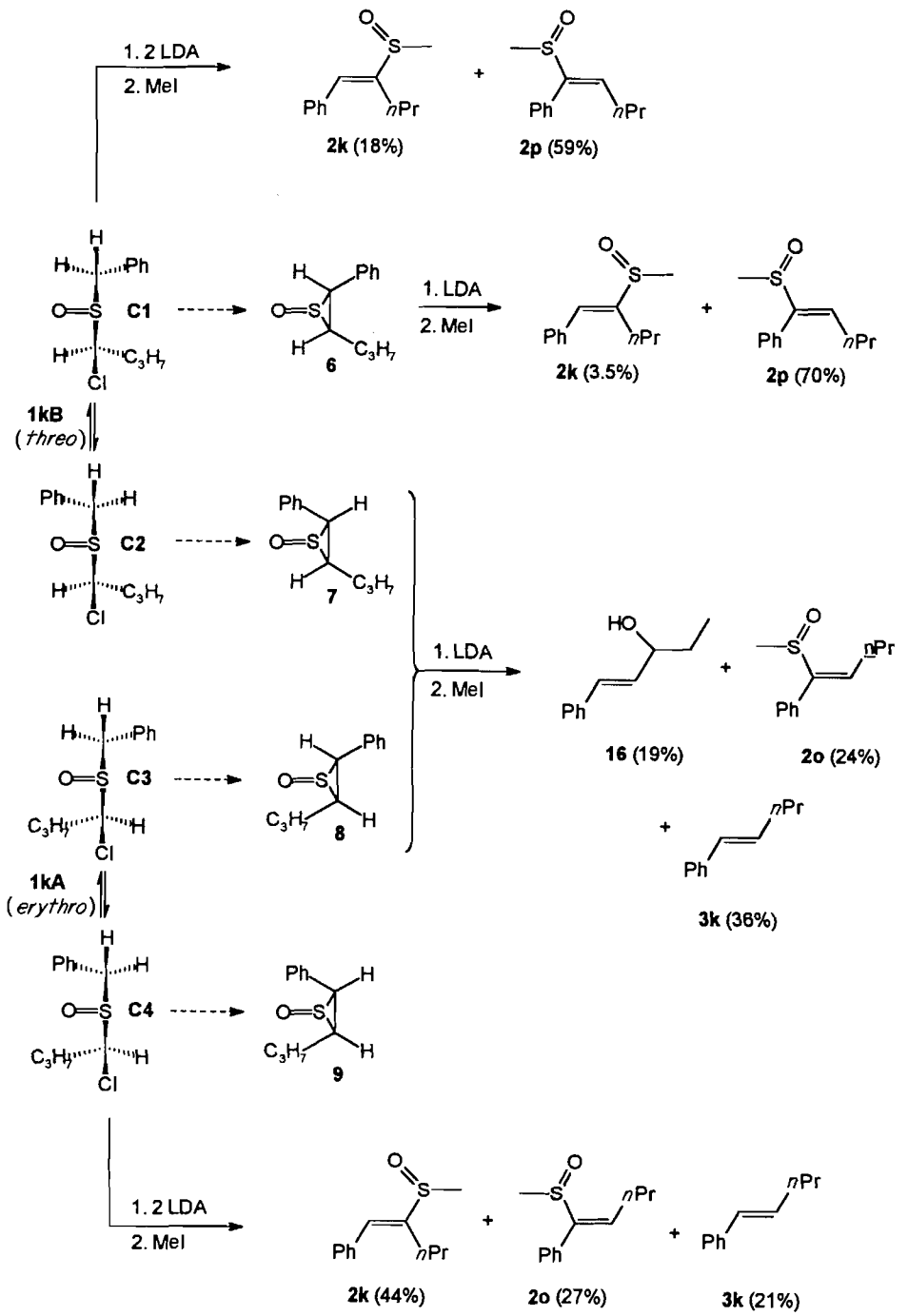

SCHEME 3

Using an oxidation step it was believed that **7** and (or) **8** would be accessible from thiirane **14**. Thiirane-*S*-oxide **6** should be readily available from thiirane **15** by oxidation. Thiirane-*S*-oxide **9** would probably be inaccessible via oxidation of **15** since oxidation of *cis*-stilbenesulfide affords only the isomer where the sulfinyl oxygen is *anti* to the phenyl groups (10). The requisite thiiranes were prepared from 1-phenylpentyne (**10**) as indicated in Scheme 4. Not surprisingly, oxidation of **15** afforded only one product; it was assigned the structure of thiirane-*S*-oxide **6** (10). Compound **6** is a thermally sensitive species and all handling of it was done at temperatures lower than 0°C. The reaction of **6** with LDA afforded predominantly vinyl sulfoxide **2p** (70%, 98% geometrically pure) and **2k** (3.5%) (Scheme 3). This result is in keeping with ring closure via conformation **C1**, since the products from γ-dehydrochlorination of **1kB** were **2p** (59%) and **2k** (18%) (Scheme 3). The yields are not exact matches with one another. The difference may be due to partial breakdown of our second assumption regarding the dependence of the two steps of the α-chlorosulfoxide to sulfenate reaction. It is also possible that the γ-dehydrochlorination does not proceed exclusively via **C1**, but that conformation **C2** is also important. Hence closure of **1kB** via **C2** to **7** may be responsible for the eventual formation of **2k**. Also worth noting at this stage is that the substituent

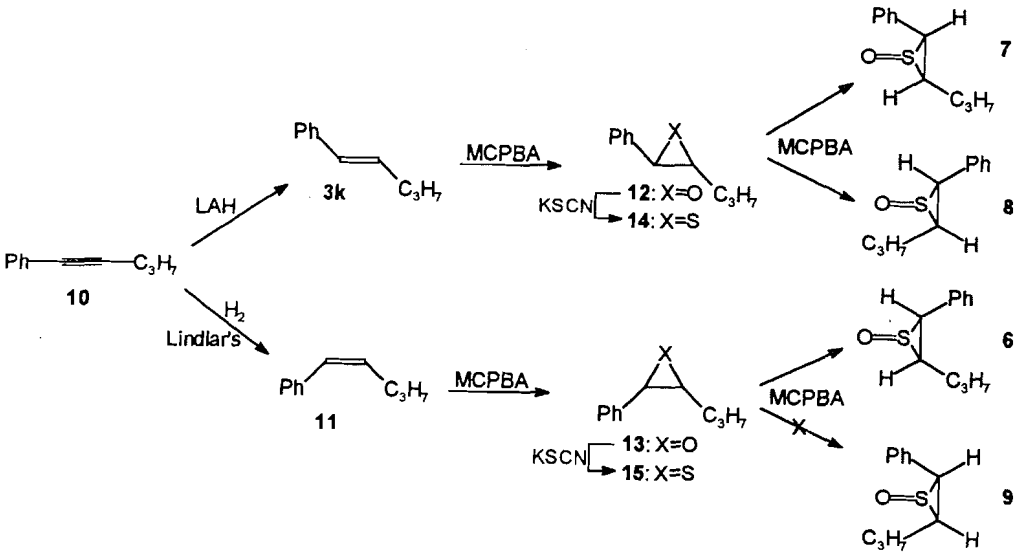

SCHEME 4

geometry of **6** is maintained during the conversion of **6** to **2p**. Bonini et al. observed similar retention of stereochemistry during the reaction of LDA with *cis*-stilbenesulfide-*S*-oxide (5).

The oxidation of thiirane **14** afforded a thermally sensitive mixture of thiirane-*S*-oxides **7** and **8**. The major isomer was judged to be compound **8** based on the relative ^{1}H NMR chemical shifts of the ring hydrogens of **7** and **8** (10). Separation of these isomers was impossible owing to their instability. Even removal of the chlorobenzoic acid oxidation by-product and dichloromethane solvent led to some decomposition of the components of the mixture. Therefore the mixture was treated as soon as possible with one equivalent of LDA. The products obtained were **2o** (24%, 95% geometric purity), *E*-1-phenylpentene (**3k**, 36%), and *E*-1-phenyl-1-penten-3-ol (**16**, 19%) (Scheme 3). Vinyl sulfoxide **2k** was not among the products of the reaction. The isolation of **16** is quite unexpected. The possibility existed that **16** originated from the decomposition products of either **7** or **8** and was not a product from the direct reaction of **7** or **8** with LDA.[4] To test this theory, a mixture of **7** and **8** was allowed to thermally decompose and alcohol **16** was indeed a significant component of the resulting mixture. Moreover, **16** was shown to survive the LDA treatment, as it was isolated (21%) from the LDA mediated reaction of the decomposed **7/8** mixture. It follows then that **16** is not a product of the reaction of **7** or **8** with LDA, but arises from partial decomposition of the substrates *before* the base reaction.

The other two products are compatible with the proposed ring closure mechanism. Conformation **C3** probably closes to **8**, which in turn affords **2o** since **2o** was obtained from both **1kA** (Scheme 3) and **8** directly. Similarly, alkene **3k** is a product common to both reactions. Therefore it can be concluded with some confidence that a significant share of **1kA** reacts by way of conformation **C3**.

The most telling evidence in support of the intermediacy of **8** in the ring closure of **1kA** is the observation of **8** in the reaction mixture. Thus the addition of *one* equivalent to LDA to a cold solution of **1kA** afforded a mixture that after work-up was

[1] 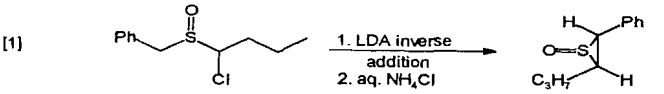

1kA (*erythro*) **8** (10-20%)

shown by ^{1}H NMR to contain **8** (eq. [1]). The mixture also included starting material and unidentified alkenes. The substituents on each face of **8** probably provide a steric barrier that retards the deprotonation, a reaction that was observed to be rapid for other substrates. The relatively slow reactivity of **8** allowed for its observation, and its detection provides clear evidence that **C3** is at least one of the conformations involved in the γ-dehydrochlorination of **1kA**.

The absence of **2k** is inexplicable. It is tempting to parallel the inability to analyze **9** with the absence of significant amounts of **2k** in the reaction mixtures of **6**, **7**, and **8** and state that **9** must be the main source of **2k**. However, it seems unlikely that γ-dehydrochlorination via **C4** would be very competitive. The alignment of all three substituents on one face of thiirane-*S*-oxide **9** during its formation would certainly lead to large nonbonded interactions. The possibility also exists that the preliminary assumptions surrounding this study have imperfections. At this time we cannot offer a sound explanation for the lack of **2k** in the reactions of the thiirane-*S*-oxides with LDA.

The second set of compounds that we scrutinized were the family of α-chlorosulfoxides containing **1e**, **1hA**, and **1hB**. Using the same assumptions as earlier, Scheme 5 depicts the only conformation available for the γ-dehydrochlorination of each of **1hA** and **1hB**. Due to a rapid sigmatropic rearrangement, thiirane-*S*-oxide **17** is unattainable (10). However, *anti*-4-phenyl-1,2-epithiobutane-*S*-oxide (**18**) could be synthesized by a pathway similar to that portrayed in Scheme 4. Its reaction with one equivalent of LDA at −78°C afforded **2e** (58%) and **2h** (12%) (Scheme 5). The reaction of **1hB** with two equivalents of LDA at −78°C provided a radically different result (Scheme 5) and the first conclusion to be made is that **1hB** does not close to **18**. Since **18** and **17** are the only two possible ring closure products, it follows then that **1hB** must close to **17** as Scheme 5 suggests. More importantly, although **17** cannot be

[4]Reasonable mechanisms can be proposed for the formation of **16** by way of LDA reacting with **7** or **8** and subsequent rearrangements or by a thermal reaction of **8** using LDA at a later stage.

Can. J. Chem. Downloaded from www.nrcresearchpress.com by 195.246.54.202 on 09/08/12
For personal use only.

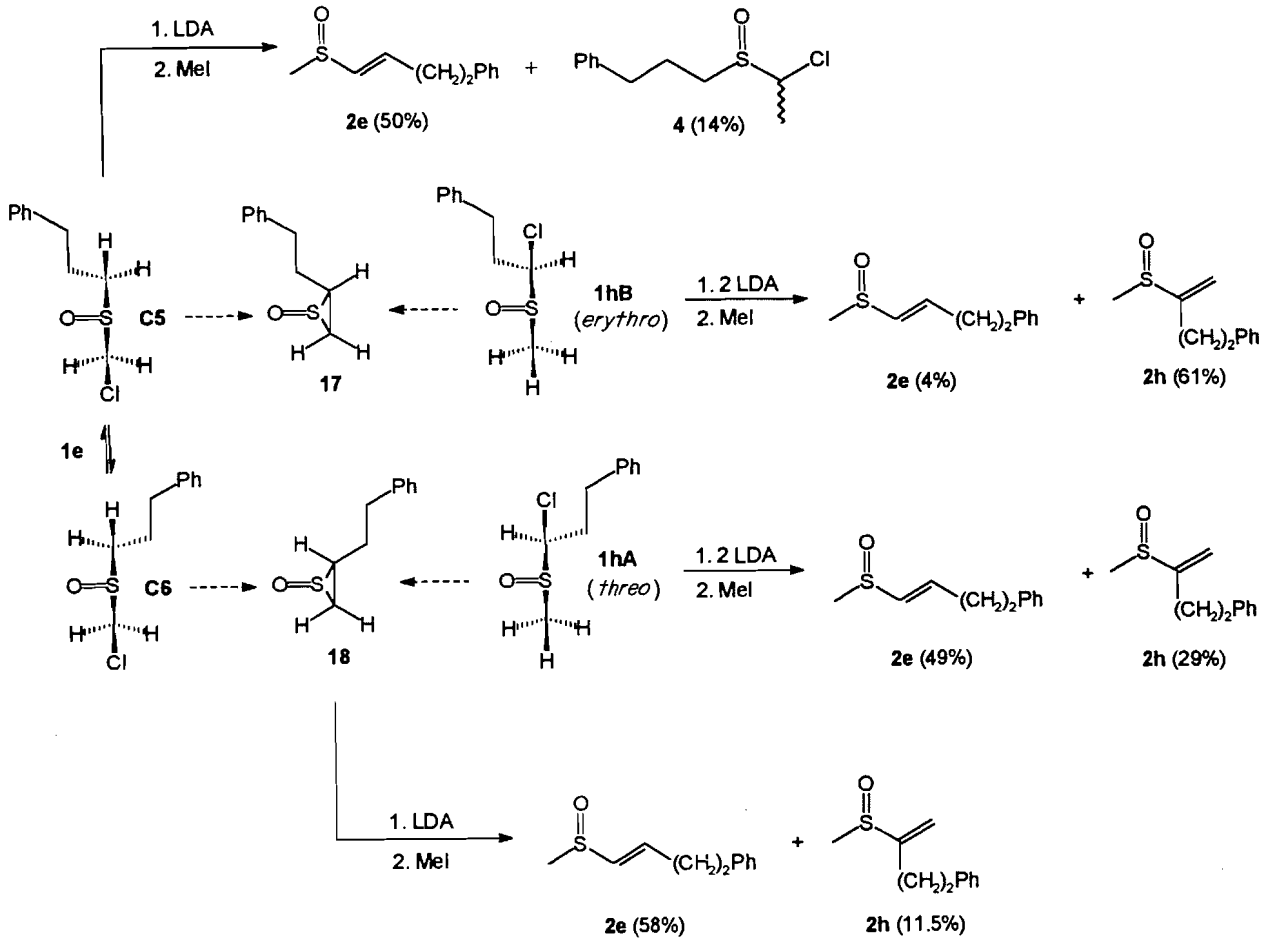

SCHEME 5

directly synthesized, *the 2-step reaction of 1kB serves as a reliable assessment of the deprotonation/ring opening behaviour of 17*. Consequently, we have essentially determined the ring opening products of **17** and **18**. The reaction of **1hA** with two equivalents of LDA and the reaction of **18** gave a parallel set of products (Scheme 5). The product ratio is not exact, but there remains enough evidence to suggest that **18** is a important intermediate on the pathway from **1kA** to **2e** and **2h**.

The γ-dehydrochlorination of **1e** may proceed through **C5** and (or) **C6** to afford transient thiirane-*S*-oxides **17** and (or) **18**, respectively, as shown in Scheme 5. Since the LDA chemistry of **17** and **18** is now established, determination of the preferred conformation of γ-dehydrochlorination of **1e** is relatively effortless. The only dehydrochlorination product arising from **1e** is vinyl sulfoxide **2e** (Table 1, entry no. 5; Scheme 5). Therefore **C6** is the preferred conformation for ring closure to thiirane-*S*-oxide **18**, since **18** and LDA yield predominately **2e**. The recovery of some **2h** from the reaction of **18**, but not from the **1e** mixture, is the lone inconsistency here.

Since the product manifold from the reaction of **18** does not exactly match that from **1e**, additional experiments were performed on **18** in order to better mimic the reaction conditions of **1e**. One experiment involved the addition of **18** to a cold equilibrated THF solution of LDA, LiCl, and di(isopropyl)amine. In a second experiment, LDA was added to a cold equilibrated THF solution of **18**, LiCl, and di(isopropyl)amine. However, in both cases, **2h** was a component of the reaction mixture and the **2h**:**2e** ratio was equal to that indicated in Scheme 5. The presence of **1h** in the reaction mixture of **18** is probably due to partial collapse of the initial assumptions made for this analysis.

The chemistry presented herein is evidence that acyclic, rotationally unconstrained α-chlorosulfoxides can undergo the γ-dehydrochlorination reaction with variable efficiency. The use of LDA, however, does not allow for the routine isolation of the proposed thiirane-*S*-oxide intermediates. Rather, the thiirane-*S*-oxides are attacked at sulfur or at hydrogen to afford ring-opened products. The LDA reaction of certain thiirane-*S*-oxides has provided a chemical means to obtain the geometrical requirements for the γ-dehydrochlorination of α-chlorosulfoxides such as **1kB**, **1e**, **1hB**, and **1hA**. The technique allows one to conclude that, upon ring closure, compounds represented by **1kB** and **1e** prefer the conformation where the sulfinyl oxygen is *anti* to the substituents of the ring carbons. We have also learned that the ring deprotonation step is apparently not completely independent on the preceding γ-dehydrochlorination reaction. Finally, the foregoing analysis offers strong evidence supporting the proposed mechanism presented in Scheme 2.

Experimental

General

Melting points were obtained on a Gallencamp capillary melting point apparatus and are uncorrected. All ^{1}H NMR spectra were run in $CDCl_3$ solution on a Varian Gemini 200 MHz NMR instrument or a Varian Unity 400 MHz NMR spectrometer using TMS or residual pro-

Can. J. Chem. Downloaded from www.nrcresearchpress.com by 195.246.54.202 on 09/08/12
For personal use only.

Can. J. Chem. Downloaded from www.nrcresearchpress.com by 195.246.54.202 on 09/08/12
For personal use only.

tium in $CDCl_3$ as internal standard. ^{13}C NMR spectra were obtained on the same instruments and were calibrated to the 77.0 ppm peak of $CDCl_3$. Infrared spectra were recorded as neat samples on a Bomem MB 100 IR spectrometer. Mass spectra were obtained using a Kratos MS890 double focusing mass spectrometer. Unless otherwise indicated, chromatographic separations were done either by flash chromatography on Merck silica gel or by centrifugal chromatography on a Chromatotron T instrument equipped with a 4 mm Merck Kieselgel 60 P_{254} silica gel plate. Solvents were distilled prior to use on the Chromatotron. THF was freshly distilled from benzophenone ketyl before use. Elemental analyses were performed by Guelph Chemical Laboratories.

Preparation of α-chlorosulfoxides **1**

α-Chlorosulfoxides **1a**, **1b**, **1c**, and **1d** have been synthesized previously (11). The other chlorosulfoxides were prepared by one of the following four methods.

Method A

The corresponding sulfide was stirred in dry CCl_4 at ice-water temperature. Solid, finely divided NCS (1.2 equiv.) was added in small portions. The mixture was allowed to stir for 4 h while the temperature warmed. The solution was filtered to remove the succinimide and was diluted with two volumes of CH_2Cl_2. This solution was cooled to −78°C (Dry Ice – acetone) and stirred with an efficient magnetic stirrer. A dry solution of MCPBA (0.90 equiv.) in CH_2Cl_2 was added dropwise over 15 min. The mixture was allowed to stir and warm over 6 h. It was recooled in ice water and filtered with suction through Celite. The filtrate was washed with 10% Na_2CO_3 solution (2 × 40 mL), with brine (30 mL), dried over $MgSO_4$, filtered, and concentrated.

Method B

A three-neck flask was equipped with a stir bar, a gas inlet, a low-temperature thermometer, and a gas outlet connected to a KOH/H_2O trap. The flask was charged with thiol, aldehyde, and CH_2Cl_2 (ca. 35 mL) and was cooled to −35°C (Dry Ice/ethanol–water). HCl was bubbled through the solution at a rate so that the temperature of the solution did not rise above −15°C. Reactions usually were 1.5 h in duration and were teminated when ^1H NMR or GC indicated a complete reaction. At this time solid $CaCl_2$ (3.5 equiv.) was added in small portions (**CAUTION**! vigorous effervescence). After all the $CaCl_2$ was added, the flask was attached to a rotary evaporatory with a water aspirator running at intermediate strength. The cold bath was maintained as the remaining HCl was removed. After about 45 min the solution was diluted with dry CH_2Cl_2 and was oxidized as in Method A above.

Method C

A flask charged with CH_2Cl_2, sulfoxide, and dry CaO was cooled to −78°C (Dry Ice – acetone). SO_2Cl_2 (1.2 equiv.) was added dropwise via syringe. The reaction stirred for 30 min and was quenched with an equal volume of water. The layers were separated and the aqueous layer was extracted with CH_2Cl_2 (1 × 40 mL). The combined organic layers were washed with brine, dried over $MgSO_4$, filtered, and concentrated.

Method D

The corresponding sulfoxide was stirred in dry CCl_4 at ice-water temperature. Solid, finely divided NCS (1.2 equiv.) was added in small portions. The mixture was allowed to stir for 4 h while the temperature warmed. An equal volume of ether was added to the mixture and it was filtered and concentrated.

*3-(Chloromethylsulfinyl)propyl benzene (**1e**)*

(Method B) From 7.07 g (47.0 mmol) of 3-phenylpropanethiol and 1.76 g (58.8 mmol) of paraformaldehyde was obtained 4.76 g (47%) of **1e** via recrystallization of the concentrated oxidation mixture; mp 58.5–60°C (60–80 petroleum). Spectral data for **1e**: IR (neat), cm^{-1}: 3005, 2935, 2866, 1603, 1498, 1457, 1398, 1145, 1076, 1045(s), 1007, 915, 862, 747; ^1H NMR (200 MHz), δ: 7.35–7.16 (m, 5H), 4.35 (abq centered at 4.35, J = 11.0 Hz, 2H), 2.82 (m, 4H), 2.15 (pentet, 7.7 Hz, 2H); ^{13}C NMR (50.3 MHz), δ: 139.93, 128.48, 128.30, 126.28, 55.90, 49.00, 34.43, 23.50; MS (ei), *m/z*(%): 218(0.4), 216(0.9), 119(28), 118(100), 115(24), 105(20), 103(12), 92(22), 91(99), 89(10), 78(10), 77(18), 63(25), 62(10); MS (ei, high resolution), *m/z*, calcd. for $C_{10}H_{13}{}^{35}ClOS$: 216.0373; found: 216.0369. Anal. calcd. for $C_{10}H_{13}ClOS$: C 55.42, H 6.05. found: C 55.36, H 5.93.

*1-Chloro-1-(methylsulfinyl)dodecane (**1f**)*

(Method C) From 3.20 g of dodecyl methyl sulfoxide was obtained 1.43 g (39%) of **1f** after chromatography. A recrystallized sample gave a 5.5:1 mixture of diastereomers; mp 64–65°C (30–60 petroleum). Spectral data for **1f**: IR (neat), cm^{-1}: 2947, 2908, 2849, 1464, 1291, 1043(s), 948, 727; ^1H NMR (200 MHz) (major isomer), δ: 4.48 (dd, J = 4.4 and 9.7 Hz, 1H), 2.62 (s, 3H), 2.30 (m, 1H), 1.96 (m, 1H), 1.72–1.48 (m, 2H), 1.28 (s (br), 16H), 0.90 (t, 3H); ^{13}C NMR (50.3 MHz) (major isomer), δ: 73.46, 34.05, 31.74, 30.80, 29.41 (2 C's), 29.30, 29.16, 29.12, 28.69, 26.14, 22.50, 13.91; MS (ei), *m/z*(%): 269(0.2), 267(0.9), 251(8), 249(20), 97(23), 85(31), 83(30), 71(47), 69(54), 64(100), 57(85), 55(53); MS (ei, high resolution), *m/z*, calcd. for $C_{13}H_{26}{}^{35}ClS$ ($[M - OH]^+$) 249.1464; found; 249.1448; calcd. for $C_{13}H_{26}{}^{37}ClS$ ($[M - OH]^+$): 251.1434; found: 251.1416; MS (ci, (methane)), *m/z*(%): 269(2.9), 267(8.1), 215(13), 87(7.5), 43(100). Anal. calcd. for $C_{13}H_{27}ClOS$: C 58.51, H 10.20; found: C 58.16, H 10.56.

*2-(1-Chloro-1-methylethylsulfinyl)propane (**1g**)*

(Method A) From 4.30 g (28.8 mmol) of isopropyl sulfide was obtained 1.07 g (22%) of **1g** after chromatography. Spectral data for **1g**: IR (neat), cm^{-1}: 2974, 2931, 1456, 1374, 1158, 1113, 1052(s); ^1H NMR (200 MHz), δ: 3.24 (septet, J = 7.0 Hz, 1H), 1.85 (s, 3H), 1.80 (s, 3H), 1.42 (d, J = 7.0 Hz, 3H), 1.28 (d, J = 7.0 Hz, 3H); ^{13}C NMR (50.3 MHz), δ: 79.40, 46.59, 28.47, 24.12, 20.13, 14.66; MS (ei), *m/z*(%): 170(0.5), 168(1.5), 126(8), 124(15), 93(5), 92(100), 91(36), 90(17), 88(6), 86(37), 84(57), 79(22), 77(73), 76(7), 75(11), 74(6), 59(15); MS (ei, high resolution), *m/z*, calcd. for $C_6H_{13}{}^{35}ClOS$: 168.0373; found: 168.0361;

*3-Chloro-3-(methylsulfinyl)propyl benzene (**1hA**)*

(Method D) From 1.16 g of 3-phenylpropyl methyl sulfoxide was obtained, after chromatography and recrystallization, 604 mg (44%) of **1hA**; mp 58–58.5°C (60–80 petroleum). Spectral data for **1hA**: IR (neat), cm^{-1}: 3059, 3031, 2941, 1602, 1497, 1453, 1425, 1404, 1052(s), 1028, 986, 945, 746; ^1H NMR (200 MHz), δ: 7.35–7.20 (m, 5H), 4.39 (dd, J = 4.0 and 10.2 Hz, 1H), 3.03 (m, 1H), 2.86 (m, 1H), 2.68–2.50 (m, 1H), 2.56 (s, 3H), 2.32 (m, 1H); ^{13}C NMR (50.3 MHz), δ: 139.08, 128.59, 128.40, 126.47, 72.44, 34.33, 32.71, 31.83; MS (ei), *m/z*(%): 218(1.2), 216(3.0), 155(9), 154(12), 153(29), 152(23), 118(11), 117(82), 116(10), 115(34), 92(24), 91(100), 89(10), 77(9), 65(34), 64(18), 63(18); MS (ei, high resolution), *m/z*, calcd. for $C_{10}H_{13}{}^{35}ClOS$: 216.0373; found: 216.0364; calcd. for $C_{10}H_{13}{}^{13}ClOS$: 218.0343; found: 218.0335. Anal. calcd. for $C_{10}H_{13}ClOS$: C 55.42, H, 6.05; found: C 55.59, H 6.05.

*3-Chloro-3-(methylsulfinyl)propyl benzene (**1hB**)*

(Method A) From 2.10 g (13.8 mmol) of sulfide was obtained a mixture of **1hB** and **1e**. Flash chromatography achieved partial separation. The impure **1hB** was dissolved in hot 60–80 petroleum and was allowed to cool on the bench. The remainder of the impurity (**1e**) crystallized out. The mother liquor was placed in the freezer (−22°C) to afford 583 mg of **1hB** (19%); mp 118.5–119°C. Spectral data for **1hB**: IR (neat), cm^{-1}: 3062, 3027, 2932, 2859, 1603, 1497, 1453, 1419, 1057(s), 946, 751; ^1H NMR (200 MHz), δ: 7.37–7.20 (m, 5H), 4.38 (dd, J = 2.9 and 10.2 Hz, 1H), 3.06 (ddd, J = 13.8, 9.0, and 4.7 Hz, 1H), 2.85 (dt, J = 13.8 and 8.0 Hz, 1H) 2.71 (s, 3H), 2.63 (m, 1H), 2.21 (m, 1H); ^{13}C NMR (50.3 MHz), δ: 139.17, 128.67, 128.56, 126.55, 74.19, 36.57, 33.38, 31.40; MS (ei), *m/z*(%): 218(2.7), 216(6.8), 155(16),

Can. J. Chem. Downloaded from www.nrcresearchpress.com by 195.246.54.202 on 09/08/12
For personal use only.

154(18), 153(46), 152(38), 118(24), 117(86), 116(16), 115(48), 92(38), 91(100), 89(16), 77(14), 75(12), 65(51), 64(29), 62(11); MS (ei, high resolution), *m/z*, calcd. for $C_{10}H_{13}{}^{35}ClOS$: 216.0373; found: 216.0354. Anal. calcd. for $C_{10}H_{13}ClOS$: C 55.42, H 6.05; found: C 55.21, H 6.21.

*1-(Chloromethylsulfinyl)ethyl benzenes (**1iA** and **1iB**)*

(Method B) The compounds were obtained from 1-phenylethanethiol (2.91 g, 21.09 mmol) and paraformaldehyde (0.76 g, 25.3 mmol). Chromatography yielded two fractions. The less polar fraction was composed of 640 mg (15%) of **1iA**. Spectral data for **1iA**: IR (neat), cm^{-1}: 3060, 3008, 2934, 2873, 1601, 1493, 1454, 1386, 1052(s), 970, 856, 769; ^1H NMR (200 MHz), δ: 7.42–7.30 (m, 5H), 4.05 (d, J = 11.2 Hz, 1H), 4.06 (q, J = 7.4 Hz, 1H), 3.62 (d, J = 11.2 Hz, 1H), 1.77 (d, J = 7.4 Hz, 3H); ^{13}C NMR (50.3 MHz), δ: 132.92, 128.89, 128.82, 128.63, 56.19, 52.12, 15.62; MS (ei), *m/z*(%): 178(12), 135(13), 106(30), 105(100), 104(35), 103(43), 92(10), 91(25), 79(49), 78(23), 77(52); MS (ci, methane), *m/z*(%): 205($(M + 1)^+$ for ^{37}Cl, 10), 203($(M + 1)^+$ for ^{35}Cl, 30), 106(45), 105(100), 104(61), 103(34), 91(18), 79(34), 78(21), 77(31), 63(46), 62(20). Further elution afforded 1.72 g (40%) of **1iB**. Spectral data for **1iB**: IR (neat), cm^{-1}: 3006, 2936, 1493, 1453, 1380, 1057(vs), 775; ^1H NMR (200 MHz), δ: 7.38–7.26 (m, 5H), 4.34 (d, J = 11.7 Hz, 1H), 4.22 (q, J = 7.2 Hz, 1H), 3.93 (d, J = 11.7 Hz, 1H), 1.74 (d, J = 7.2 Hz, 3H); ^{13}C NMR (50.3 MHz), δ: 135.19, 129.36, 128.88, 127.98, 59.13, 55.03, 15.14; MS (ei), *m/z*(%): 106(15), 105(100), 104(17), 103(20), 79(27), 78(12). MS (ci, methane), *m/z*(%): 205(16), 203(42), 151(28), 106(52), 105(100), 104(38), 103(28), 79(35), 78(15), 77(31).

*2-Chloro-2-(2-phenylethylsulfinyl)ethyl benzene (**1jA**)*

(Method A) From 2.48 g (10.2 mmol) of 2-phenylethyl sulfide was obtained a crude mixture containing **1jA**. The mixture was chromatographed once and recrystallized three times from 60–80 petroleum to afford 597 mg (20%) of **1jA**; mp 82.5–84°C. Spectral data for **1jA**: IR (neat), cm^{-1}: 3062, 3029, 2933, 1603, 1496, 1454, 1263, 1047(vs), 934, 747; ^1H NMR (200 MHz), δ: 7.38–7.17 (m, 10H), 4.60 (dd, J = 3.0 and 9.0 Hz, 1H), 3.69 (dd, J = 3.0 and 14.5 Hz, 1H), 3.33 (m, 1H), 3.19–3.01 (m, 4H); ^{13}C NMR (50.3 MHz), δ:138.40, 134.63, 129.76, 128.78, 128.54 (2 C's), 127.43, 126.82, 73.13, 51.21, 38.78, 28.16; MS (ei), *m/z*(%): 292(1.8). 154(32), 141(37), 140(13), 139(88), 138(11), 105(100), 104(50), 103(86), 92(23), 91(47), 79(18), 78(14), 77(44); MS (ei, high resolution), *m/z*, calcd. for $C_{16}H_{17}{}^{35}ClOS$: 292.0685; found: 292.0664; calcd. for $C_{10}H_{17}{}^{37}ClOS$: 294.0655; found: 294.0645. Anal. calcd. for $C_{16}H_{17}ClOS$: C 65.63, H 5.85; found: C 65.68, H 5.83.

*2-Chloro-2-(2-phenylethylsulfinyl)ethyl benzene (**1jB**)*

(Method D) From 5.65 g (21.9 mmol) of 2-phenylethyl sulfoxide was obtained, after chromatography and recrystallization, 4.21 g (65%) of **1jB**; mp 70–71°C (60–80 petroleum ether/EtOAc). Spectral data for **1jB**: IR (neat), cm^{-1}: 3062, 3029, 2934, 1602, 1495, 1454, 1267, 1051(s), 943, 743; ^1H NMR (400 MHz), δ: 7.38–7.22 (m, 10H), 4.59 (dd, J = 5.7 and 9.0 Hz, 1H), 3.62 (dd, J = 5.7 and 14.2 Hz, 1H), 3.25–3.10 (m, 3H), 3.01 (m, 2H); ^{13}C NMR (125 MHz), δ: 138.31, 135.18, 129.52, 128.85 (2 C's), 128.52, 127.59, 126.97, 73.84, 50.68, 38.42, 29.13; MS (ei), *m/z*(%): 292(1.9), 240(8), 154(28), 141(27), 140(12), 139(84), 138(18), 105(100), 104(34), 103(56), 91(36); MS (ei, high resolution), *m/z*, calcd. for $C_{16}H_{17}{}^{35}ClOS$: 292.0685; found: 292.0680; calcd. for $C_{10}H_{17}{}^{37}ClOS$: 294.0655; found: 294.0662. Anal. calcd. for $C_{16}H_{17}ClOS$: C 65.63, H 5.85; found: C 65.63, H 5.64

*(1-Chlorobutylsulfinyl)methyl benzenes (**1kA** and **1kB**)*

(Method B) The compounds were prepared from 4.84 g (39.0 mmol) of α-toluenethiol and 2.75 g (39.3 mmol) of butyraldehyde. Chromatography yielded two fractions. The less polar fraction was composed of 1.94 g (22%) of **1kA**; mp 29.5–31°C (30–60 petroleum). Spectral data for **1kA**: IR (neat), cm^{-1}: 3062, 3032, 2949, 2874, 1496, 1458, 1057, 760, 699; ^1H NMR (200 MHz), δ: 7.34 (s, 5H), 4.25–4.19 (m, 2H), 3.98 (d, J = 13.5 Hz, 1H), 2.15 (m, 1H), 1.87 (m, 1H), 1.68 (m, 1H), 1.42 (m, 1H), 0.90 (t, J = 7.3 Hz, 3H); ^{13}C NMR (50.3 MHz), δ: 130.22, 128.42, 128.21, (4th aryl C not evident), 69.92, 53.85, 32.47, 18.06, 12.68; MS (ei), *m/z*(%): 232(0.7), 230(1.8), 92(62), 91(100), 90(8), 89(14), 65(54), 63(10), 55(28), 53(5), 51(6), 45(6); MS (ei, high resolution), *m/z*, calcd. for $C_{11}H_{15}{}^{35}ClOS$: 230.0529; found: 230.0512. Further elution afforded 2.43 g (27%) of **1kB**; mp: 58–59°C (60–80 petroleum). Spectral data for **1kB**: IR (neat), cm^{-1}: 2950, 1494, 1454, 1041 (vs), 760, 697; ^1H NMR (200 MHz), δ: 7.37 (s, 5H), 4.34 (dd, J = 5.8 and 8.8 Hz, 1H), 4.18 (abq centered at 4.18, J = 12.5 Hz, 2H), 2.09 (m, 2H), 1.55 (m, 2H), 0.91 (t, J = 7.1 Hz, 3H); ^{13}C NMR (50.3 MHz), δ: 129.95, 129.34, 129.14, 128.74, 71.47, 55.56, 34.72, 19.51, 12.93; MS (ei), *m/z*(%): 232(1.0), 230(2.3), 121(6), 93(6), 92(71), 91(100), 90(15), 89(27), 77(8), 66(6), 65(65), 64(6), 63(19), 55(42), 53(7), 51(9), 45(6); MS (ei, high resolution), *m/z*, calcd. for $C_{11}H_{15}{}^{35}ClOS$: 230.0529; found: 230.0532. Anal. calcd. for $C_{11}H_{15}ClOS$: C 57.33, H 6.55; found: C 57.26, H 6.55.

*1-Chloro-1-(ethylsulfinyl)ethanes (**1lA** and **1lB**)*

(Method C) The compounds were prepared from 1.80 g (17.0 mmol) of ethyl sulfoxide. Chromatography yielded two fractions. The less polar fraction was distilled to afford 740 mg (31%) of **1lA**; bp 41°C/0.3 Torr (1 Torr = 133.3 Pa). Spectral data for **1lA**: IR (neat), cm^{-1}: 2962, 2879, 1451, 1377, 1058, 1022, 973, 778; ^1H NMR (200 MHz), δ: 4.53 (q, J = 6.7 Hz, 1H), 3.07 (dq, J = 6.5 and 13.4 Hz, 1H), 2.80 (dq, J = 6.7 and 13.4 Hz, 1H), 1.70 (d, J = 6.7 Hz, 3H), 1.41 (t, J = 6.5 Hz, 3H); ^{13}C NMR (50.3 MHz), δ: 66.54, 43.07, 19.21, 6.11; MS (ei), *m/z*(%): 142(2.8), 140(8.7), 78(100), 77(15), 65(16), 63(82), 61(18); MS (ei, high resolution), *m/z*, calcd. for $C_4H_9{}^{37}ClOS$: 142.0031; found: 142.0031; calcd. for $C_4H_9{}^{35}ClOS$: 140.0061; found: 140.0062. The more polar fraction was distilled to afford 651 mg (27%) of **1lB**; bp 40–41°C/0.1 Torr. Spectral data for **1lB**: IR (neat), cm^{-1}: 2974, 2938, 2878, 1451, 1377, 1067, 1050, 1022, 973, 780; ^1H NMR (200 MHz), δ: 4.68 (q, J = 6.9 Hz, 1H), 2.84 (m, 2H), 1.87 (d, J = 6.9 Hz, 3H), 1.35 (t, J = 6.5 Hz, 3H); ^{13}C NMR (50.3 MHz), δ: 67.37, 42.45, 18.46, 7.21; MS (ei), *m/z*(%): 142(2.3), 140(6.6), 78(100), 77(17), 65(18), 63(92), 61(19), 59(12); MS (ei, high resolution), *m/z*, calcd. for $C_4H_9{}^{37}ClOS$: 142.0031; found: 142.0030; calcd. for $C_4H_9{}^{35}ClOS$: 140.0061; found: 140.0062.

*Reactions of chlorosulfoxides **1** with LDA*

General procedure

To a three-neck round-bottom flask containing a stir bar was attached a serum cap, a three-way stopcock, and a stopper. The flask was flame-dried under vacuum and allowed to cool under dry N_2. It was charged with THF (10–20 mL), diisopropyl amine (2.3 equiv.), and cooled to −78°C. *n*-BuLi (2.15 equiv.) was added dropwise. The mixture was allowed to stir at 0°C for 30 min and was cooled to −78°C. The substrate (ca. 0.7–3.7 mmol) in THF (8–20 mL) was added dropwise and the mixture was stirred as indicated below. The mixtures were then quenched at −78°C with excess MeI in THF (4 mL). In some instances $PhCH_2Br$ (1 equiv. in THF (8 mL)) was employed as the electrophile; those are noted below. The mixture was then stirred for 12 h at which time saturated aqueous NH_4Cl (20 mL) was added. The layers were separated and the aqueous layer was extracted with EtOAc (2 × 10 mL). The combined organics were washed with brine and dried over $MgSO_4$. After filtration and concentration, the mixtures were subjected to centrifugal chromatography using EtOAc–hexanes mixtures as the mobile phase.

The different experimental conditions come about from the duration of chlorosulfoxide exposure to the base. Conditions A: chlorosulfoxide is stirred at −78°C for 1 h; Conditions B: chlorosulfoxide is stirred at −78°C for 20 min; Conditions C: chlorosulfoxide is stirred at 0°C for 1 h. The base treatment of chlorosulfoxide **1g** is an exception to this general procedure. That treatment is referred to as Conditions D in Table 1 and was as follows: An LDA in THF solution (3.15 equiv., prepared as above) was added to chlorosulfoxide **1g** in THF at −78°C. The cold bath was removed and the mixture was allowed to warm to room temperature. Tetramethylethene was identified as a component of the mixture by co-injection with an authentic sample on different

Can. J. Chem. Downloaded from www.nrcresearchpress.com by 195.246.54.202 on 09/08/12
For personal use only.

capillary GC columns. It was quantitated against an added internal standard of toluene. The yield of tetramethylethene was found to be ca. 90%.

*Reaction of **1a***

(Cond. A) From 247 mg (2.20 mmol) of **1a** was obtained 139 mg (38%) of **2a** using $PhCH_2Br$ as the electrophile; mp 48–49.5°C (60–80 petroleum) (lit. (12) mp 34–35°C).[5] Spectral data for **2a**: IR (neat), cm^{-1}: 3064, 3031, 1601, 1495, 1454, 1371, 1042, 986; ^1H NMR (200 MHz), δ: 7.36–7.23 (m, 5H), 6.58 (dd, J = 16.6 and 9.8 Hz, 1H), 5.96 (d, J = 16.6 Hz, 1H), 5.88 (d, J = 9.8 Hz, 1H), 3.98 (s, 2H); ^{13}C NMR (50.3 MHz), δ: 139.85, 130.04, 129.20, 128.51, 128.11, 122.09, 59.74; MS (ci, methane), *m/z*(%): 167(11), 149(6), 117(11), 115(8), 92(40), 91(100), 89(8), 65(33). Anal. calcd. for $C_9H_{10}OS$: C 65.03, H 6.06; found: C 65.03, H 5.89.

*Reaction of **1b***

(Cond. B) From 371 mg (1.97 mmol) of **1b** was obtained styrene (**3b**) (8%) and 196 mg (60%) of **2b**; mp: 60–61°C; (lit. (13) mp 61–62°C). The styrene was quantitated by determining the relative amounts of the two products in the crude mixture by ^1H NMR and extrapolating back once **2b** was isolated and quantitated.

*Reaction of **1c***

(Cond. B) From 244 mg (0.92 mmol) of a 3:2 mixture of diastereomers of **1c** and 2.4 equivalents of LDA was obtained by chromatography 40.5 mg (24%) of *trans*-stilbene (**3c**) and 112 mg (50%) of **2c** (5).

*Reaction of **1d***

(Cond. C) From 988 mg (3.71 mmol) of **1d** was obtained 286 mg (32%) of **2d**; mp 45–46°C (30–60 petroleum). Spectral data for **2d**: IR (neat), cm^{-1}: 3029, 2999, 2951, 2919(s), 2849(s), 1471, 1462, 1045(s), 974; ^1H NMR (200 MHz), δ: 6.54 (dt, J = 6.7 and 15.3 Hz, 1H), 6.32 (d, J = 15.3 Hz, 1H), 2.66 (s, 3H), 2.27 (m, 2H), 1.49 (m, 2H), 1.30 (s (br) 16H), 0.91 (t, J = 6.5 Hz); ^{13}C NMR (50.3 MHz), δ: 141.45, 133.71, 40.36, 31.75, 31.66, 29.36 (2 C's), 29.29, 29.09 (2 C's), 28.80, 27.83, 22.41, 13.83; MS (ei), *m/z*(%): 244(6), 229(210, 228(26), 227(100), 213(11), 123(7), 111(12), 110(21), 109(17), 97(27), 96(14), 95(34), 87(88), 83(34), 82(16), 81(36), 69(40), 68(16), 67(32), 61(18), 57(32), 55(55); MS (ei, high resolution), *m/z*, calcd. for $C_{14}H_{28}OS$: 244.1854; found: 244.1846. Anal. calcd. for $C_{14}H_{28}OS$: C 68.79, H 11.55; found: C 68.64, H 11.80.

*Reaction of **1e***

(Cond. A) From 397 mg (1.84 mmol) of **1e** was obtained 52 mg (14%) of **4**, 14 mg of **1e**, and 170 mg (50%) of **2e**. (Yields based on consumed **1e**.) Spectral data for **2e**: IR (neat), cm^{-1}: 3026, 3023, 2956, 1632(w), 1602, 1496, 1453, 1419, 1044(vs), 959, 748; ^1H NMR (200 MHz), δ: 7.33–7.15 (m, 5H), 6.50 (dt, J = 6.6 and 15.5 Hz, 1H), 6.24 (d, J = 15.5 Hz, 1H), 2.79 (t, J = 7.5, 2H), 2.55 (q, J = ca. 7 Hz, 2H), 2.53 (s, 3H); ^{13}C NMR (50.3 MHz), δ: 140.32, 138.91, 134.64, 128.33, 128.27, 126.09, 40.55, 34.28, 33.42; MS (ei), *m/z*(%): 195(M + 1, 13), 194(14), 177(10), 131(42), 130(22), 129(25), 128(13), 115(11), 103(19), 92(67), 91(100), 89(12), 88(19), 87(63), 86(75), 84(88), 77(12), 65(31), 63(14); MS (ei, high resolution), *m/z*, calcd. for $C_{11}H_{14}OS$: 194.0762; found: 194.0762. Spectral data for **4**: IR (neat), cm^{-1}: 3027, 2936, 2862, 1603, 1496, 1450, 1373, 1051(vs), 747; ^1H NMR (200 MHz), δ: 7.33–7.17 (m, 5H), 4.48 (q, J = 6.7 Hz, 1H), 2.99 (m, 1H), 2.84–2.65 (m, 3H), 2.17 (m, 2H), 1.83, (d, J = 6.7 Hz, 3H); ^{13}C NMR (50.3 MHz), δ: 140.18, 128.50, 128.39, 126.28, 67.60, 49.06, 34.53, 23.76, 19.14; MS (ei), *m/z*(%): 231(M + 1, 19), 230(7), 168(10), 119(19), 118(100), 117(49), 115(11), 105(13), 92(11), 91(86), 77(11), 65(13), 63(12); MS (ei, high resolution), *m/z*, calcd. for $C_{11}H_{15}{}^{35}ClOS$: 230.0532; found: 230.0515.

[5]The melting point discrepancy cannot be accounted for.

*Reaction of **1f***

(Cond. C) From 193 mg (0.724 mmol) of **1f** was obtained 56 mg (31%) of **2f** and 87 mg (49%) of **2d**. Spectral data for **2f**: IR (neat), cm^{-1}: 2924, 2854, 1629(w), 1461, 1061(s), 920; ^1H NMR (200 MHz), δ: 5.87 (s, 1H), 5.58 (s, 1H), 2.58 (s, 3H), 2.44–2.10 (m, 2H), 1.59 (m, 2H), 1.27 (s (br), 16H), 0.88 (t, J = 7.4 Hz, 3H); ^{13}C NMR (50.3 MHz), δ: 154.83, 114.98, 39.16, 31.69, 29.38 (2 C's), 29.29, 29.10 (2 C's), 28.91, 27.83, 27.72, 22.44, 13.85; MS (ei), *m/z*(%): 245(1.5), 244(0.1), 229(13), 228(17), 227(100), 97(17), 95(15), 83(28), 81(16), 69(38), 67(16), 64(18), 57(21), 55(55); MS (ci(methane)), *m/z*(%): 245 ([M + 1]$^+$, 54), 230 (16), 229(100), 227(16), 213(15), 88(42); MS (ei, high resolution), *m/z*, calcd. for $C_{14}H_{27}S$ ([M − OH]$^+$) 227.1827; found: 227.1839.

*Reaction of **1hA***

(Cond. B) From 216 mg (0.998 mmol) of **1hA** was obtained 56 mg (29%) of **2h** and 94 mg (48%) of **2e**. Spectral data for **2h**: IR (neat), cm^{-1}: 3061, 3027, 2924, 2858, 1630(w), 1603, 1496, 1454, 1419, 1051(vs), 934, 749; ^1H NMR (200 MHz), δ: 7.34–7.19 (m, 5H), 5.91 (s, 1H), 5.62 (s, 1H), 2.92 (t, J = 7.7 Hz, 2H), 2.62–2.45 (m, 2H), 2.54 (s, 3H); ^{13}C NMR (50.3 MHz), δ: 153.64, 140.17, 128.51, 128.31, 126.39, 115.83, 39.17, 34.15, 29.68; MS (ei), *m/z*(%): 194(40), 177(19), 131(37), 130(41), 116(18), 115(28), 92(61), 91(100), 89(10), 77(16), 73(20), 65(47), 64(14), 63(21). MS (ei, high resolution), *m/z*, calcd. for $C_{11}H_{14}OS$: 194.0762; found: 194.0751.

*Reaction of **1hB***

(Cond. B) From 160 mg (0.739 mmol) of **1hB** was obtained 87 mg (61%) of **2h** and 6 mg (4%) of **2e**.

*Reaction of **1iA***

(Cond. C) From 329 mg (1.62 mmol) of **1iA** was obtained α-methylstyrene (**3i**) (6%), 64 mg (22%) of **2i** (14), and 20 mg (7%) of **2m** (14). The α-methylstyrene was quantitated by determining the relative amounts of it and **2i** in the crude mixture by ^1H NMR and extrapolating back once **2i** was isolated and quantitated.

*Reaction of **1iB***

(Cond. C) From 329 mg (1.62 mmol) of **1iB** was obtained 137 mg (54%) of **2i** and 44 mg (17%) of **2m**.

*Reaction of **1jA***

(Cond. C) From 425 mg (1.45 mmol) of **1jA** was obtained an inseparable mixture of **2j** (40 mg, 10%) and **2n** (35 mg, 9%). Partial spectral data for **2n**: ^1H NMR (200 MHz), δ: 7.35–7.06 (m, 10H), 5.82 (qt, J = 1.5 and ca. 7.5 Hz, 1H), 2.50 (s, 3H). The remainder of the peaks were obscured by those for **2j**. ^{13}C NMR (50.3 MHz), δ: 145.00, 138.45, 137.94, 134.88, 129.47, 128.73, 128.67, 128.18, 126.67, 126.57, 38.46, 33.89, 31.42; IR (neat) (mixture of **2j** and **2n**), cm^{-1}: 3060, 3028, 2918, 1601, 1494, 1453, 1045(s), 948, 741; MS (ei), (mixture of **2j** and **2n**) *m/z*(%): 270(3), 253(23), 206(33), 205(31), 129(25), 128(21), 115(29), 103(13), 91(100), 77(16), 65(18).

*Reaction of **1jB***

(Cond. C) From 575 mg (1.97 mmol) of **1jB** was obtained 296 mg (56%) of **2j** and 57 mg (11%) of **5** as a 3:2 mixture of diastereomers. Spectral data for **2j**: mp 52–54°C (60–80 petroleum); IR (neat), cm^{-1}: 3060, 3026, 2913, 1601, 1495, 1453, 1045(s), 950, 744; ^1H NMR (200 MHz), δ: 7.37–7.21 (m, 8H), 7.10 (m, 2H), 6.62 (t, J = 7.4 Hz, 1H), 3.81 (abq, J = 16.4 Hz, 2H), 3.57 (d, J = 7.4 Hz, 2H), 2.41 (s, 3H); ^{13}C NMR (50.3 MHz), δ: 143.12, 138.19, 137.13, 133.57, 128.79, 128.65, 128.35, 128.27, 126.82, 126.54, 39.71, 34.38, 30.27; MS (ei), *m/z*(%): 270(4.6), 207(13), 206(56), 205(14), 129(31), 128(16), 115(19), 103(10), 91(100). Anal. calcd. for $C_{17}H_{18}OS$: C 75.52, H 6.71; found: C 75.45, H, 6.85. Spectral data for **5**: ^1H NMR (400 MHz) (diastereomer 1), δ: 7.41–7.23 (m, 10H), 6.50 (d, J = 15.8 Hz, 1H), 6.25 (dd, J = 9.3 and 15.8 Hz, 1H), 3.42 (m, 2H), 3.12 (dd, J = 13.3 and 8.3 Hz, 1H), 2.48 (s, 3H); ^1H NMR (400 MHz) (diastereomer 2), δ: 7.33 (m, 10H), 6.51 (d, J = 15.8 Hz, 1H), 5.99 (dd, J = 15.8 and

Can. J. Chem. Downloaded from www.nrcresearchpress.com by 195.246.54.202 on 09/08/12
For personal use only.

9.7 Hz, 1H), 3.63 (dt, J = 3.6 and ca. 9.9 Hz, 1H), 4.36 (dd, J = 3.6 and 13.6 Hz), 3.07 (dd, J = 10.1 and 13.6 Hz, 1H), 2.61 (s, 3H); ^{13}C NMR (100.6 MHz) (diastereomer 1), δ: 137.41, 135.69, 129.28, 128.61, 128.58, 128.49, 128.29, 126.77, 126.58, 120.52, 65.85, 35.04, 34.54; ^{13}C NMR (100.6 MHz) (diastereomer 2), δ: 137.16, 135.73, 129.48, 128.68 (2 C's), 128.53, 128.44, 126.73, 126,53, 121.44, 69.88, 35.85, 35.22; IR (neat) (mixture of isomers), cm^{-1}: 3059, 3027, 2921, 2854, 1601, 1495, 1452, 1413, 1260, 1039(s), 971, 748; MS (ei), (mixture of isomers) *m/z*(%): 270(0.3), 207(28), 206(54), 205(22), 191(13), 129(31), 128(25), 117(27), 115(24), 105(23), 103(10), 91(100), 77(14); MS (ci, methane) *m/z*(%): 271(0.5), 269(4.5), 207(32), 206(96), 205(23), 191(12), 133(20), 131(17), 129(21), 128(24), 127(13), 117(19), 115(17), 105(23), 103(15), 100(25), 92(18), 91(100), 89(17), 83(20), 81(14), 79(13), 78(13), 77(21), 75(17), 73(33).

Reaction of ***1kA***

(Cond. A) From 260 mg (1.13 mmol) of **1kA** was obtained *E*-1-phenyl-1-pentene (**3k**) (21%), 64 mg (27%, 96% pure, inseparable from 4% of **2p**) of **2o**, and 104 mg (44%) of **2k**. Alkene **3k** was quantitated by determining the relative amounts of it and **2k** in the crude mixture by ^{1}H NMR and extrapolating back once **2k** was isolated and quantitated. Spectral data for **2k**: IR (neat), cm^{-1}: 2961, 2930, 2872, 1492, 1454, 1416, 1057(s), 755, 697; ^{1}H NMR (200 MHz), δ: 7.41–7.28 (m, 5H), 7.16 (s, 1H), 2.75 (m, 1H), 2.65 (s, 3H), 2.25 (m, 1H), 1.63 (sextet, J = 7.0 Hz, 2H), 0.98 (t, J = 7.0 Hz, 3H); ^{13}C NMR (50.3 MHz), δ: 146.33, 134.91, 129.27, 128.97, 128.74, 128.27, 39.75, 28.31, 21.64, 13.86; MS (ei), *m/z*(%): 208(11), 192(13), 191(56), 145(63), 144(31), 143(22), 137(19), 130(27), 129(60), 128(31), 117(48), 116(26), 115(81), 105(19), 103(14), 92(29), 91(100), 89(11), 77(13), 67(10), 65(12), 63(10); MS (ei, high resolution), *m/z*, calcd. for $C_{12}H_{16}OS$: 208.0918; found: 208.0924. Spectral data for **2o**: IR (neat), cm^{-1}: 3056, 2959, 2931, 2870, 1645(w), 1492, 1460, 1443, 1414, 1063(vs), 762, 703; ^{1}H NMR (200 MHz), δ: 7.44–7.21 (m, 5H), 6.44 (t, J = 7.6 Hz, 1H), 2.36, (s, 3H), 2.20 (q, J = 7.6 Hz, 2H), 1.50 (sextet, J = 7.4 Hz, 2H), 0.90 (t, J = 7.3 Hz, 3H); ^{13}C NMR (50.3 MHz), δ: 144.81, 133.84, 132.05, 129.19, 128.96, 128.75, 36.85, 30.27, 22.10, 13.47; MS (ei), *m/z*(%): 208(1.6), 146(12), 145(100), 130(20), 129(15), 128(17), 117(42), 116(13), 115(42), 105(17), 103(17), 102(11), 91(87), 77(13), 67(13); MS (ei, high resolution), *m/z*, calcd. for $C_{12}H_{16}OS$: 208.0918; found: 208.0928.

Reaction of ***1kB***

(Cond. A) From 219 mg (0.95 mmol) of **1kB** was obtained 116 mg (59%, 96% pure, inseparable from 4% of **2o**) of **2p** and 36 mg (18%) of **2k**. Spectral data for **2p**: IR (neat), cm^{-1}: 2959, 2929, 2869, 1491, 1450, 1049(s), 761, 700; ^{1}H NMR (200 MHz), δ: 7.40 (m, 5H), 6.18 (t, J = 7.8 Hz, 1H), 2.54 (m, 2H), 2.14 (s, 3H), 1.54 (m, 2H), 1.00 (t, J = 7.1 Hz); ^{13}C NMR (50.3 MHz), δ: 143.90, 141.47, 134.40, 129.20, 128.58, 128.34, 37.43, 29.93, 22.42, 13.44; MS (ei), *m/z*(%): 208(8), 191(42), 145(77), 143(16), 130(20), 129(19), 128(25), 117(44), 116(14), 115(50), 105(19), 103(14), 102(10), 92(26), 91(100), 77(13), 67(9); MS (ei, high resolution), *m/z*, calcd. for $C_{12}H_{16}OS$: 208.0918; found: 208.0933. Anal. calcd. for $C_{12}H_{16}OS$: C 69.19, H 7.74; found: C 68.88, H 8.00.

Reaction of ***11A***

(Cond. C) From 255 mg (1.81 mmol) of **11A** was obtained 120 mg (34%) of an inseparable mixture of **2l** and **2q** (**2l**:**2q** = 2.4:1) using $PhCH_2Br$ as the electrophile. Spectral data for **2l** and **2q**: IR (neat) (mixture of isomers), cm^{-1}: 3062, 3030, 2921, 2857, 1644, 1602, 1495, 1450, 1035(vs) 769; ^{1}H NMR (400 MHz) (major isomer), δ: 7.33–7.17 (m, 5H), 5.89 (m, 1H), 3.89 (s, 2H), 1.87 (s, 3H), 1.67 (d, J = 6.9 Hz, 3H); ^{1}H NMR (200 MHz) (minor isomer), δ: 7.33–7.17 (m, 5H), 5.89 (m, 1H), 4.10 (d, J = 12.3 Hz, 1H), 3.89 (d, J = 12.3 Hz, 1H), 1.97 (s, 3H), 1.32 (d, J = 7.1 Hz, 3H); ^{13}C NMR (50.3 MHz) (mixture of isomers), δ: 137.55, 137.39, 132.90, 130.60, 130.14, 129.91, 129.83, 129.67, 128.48, 128.36, 127.96, 127.89, 57.86, 57.04, 13.60, 13.45, 12.46, 8.43; MS (ei), (mixture of isomers) *m/z*(%): 194(1.1), 145(6), 92(24), 91(100), 65(20). MS (ci, methane (mixture of isomers)), *m/z*(%): 195(7.4), 145(7.6), 92(14), 91(100), 65(11).

Reaction of ***11B***

(Cond. C) From 127 mg (0.90 mmol) of **11A** was obtained 93 mg (53%) of an inseparable mixture of **2l** and **2q** (**2l**:**2q** = 3.5:1) using $PhCH_2Br$ as the electrophile.

Synthesis of E-*2-phenyl-3-propyloxirane (**12**)*

To an ice-cooled mixture of 1-phenyl-1-pentyne (**10**) (Aldrich) (13.1 g, 90.8 mmol) in THF (200 mL) was added solid $LiAlH_4$ (8.62 g, 227 mmol) in small portions. The ice bath was removed and the mixture was refluxed for 20 h after which time the flask was cooled in ice and the mixture was quenched by the dropwise addition of water (10 mL). The mixture was filtered with suction through Celite. More water (200 mL) was added and the solution was extracted into pentane (3 × 50 mL). After drying ($MgSO_4$), filtration, and concentration (aspirator), GC indicated that product **3k** was 94% pure. To the crude **3k** was added CH_2Cl_2 (150 mL). The mixture was stirred while MCPBA (21.5 g (73% active), 90.8 mmol) in CH_2Cl_2 (250 mL) was added dropwise from an addition funnel. Stirring continued at room temperature for 14 h. The mixture was then filtered with suction through Celite, washed with saturated aqueous Na_2CO_3 (2 × 40 mL) and with brine, and dried over $MgSO_4$. After filtration and concentration (aspirator), the oxide was distilled to afford 10.1 g (68%, 94% pure by GC) of **12** (15); bp 62–63°C/0.4 Torr.

Synthesis of E-*1-phenyl-1,2-epithiopentane (**14**)*

A mixture containing **12** (2.83 g, 17.5 mmol), KSCN (2.54 g, 26.2 mmol), MeOH (20 mL), and H_2O (10 mL) was refluxed for 50 h. After cooling, H_2O (25 mL) was added to the mixture and it was extracted with 30–60 petroleum ether (3 × 20 mL). The organic extracts were combined, washed with H_2O (2 × 10 mL) and brine, and were dried over $MgSO_4$. After filtration and concentration (aspirator), the crude **14** was subjected to column chromatography on Al_2O_3(I) with hexanes as eluent. The elution afforded **3k**, **12**, and then **14** (739 mg, 24%). Spectral data for **14**: IR (neat), cm^{-1}: 3059, 3026, 2959, 2929, 2870, 1600, 1492, 1452, 1378, 1074, 1031, 759, 741; ^{1}H NMR (200 MHz), δ: 7.28 (s, 5H), 3.61 (d, J = 5.4 Hz, 1H), 3.04 (dt, J = 5.4 and 6.8 Hz, 1H), 1.91 (m, 1H), 1.69–1.51 (m, 3H), 0.99 (t, J = 6.9 Hz, 3H); ^{13}C NMR (50.3 MHz), δ: 139.35, 128.45, 127.42, 126.83, 44.78, 44.04, 38.51, 22.26, 13.71; MS (ei), *m/z*(%): 178(52), 149(16), 146(30), 136(27), 135(55), 122(15), 121(18), 118(28), 117(100), 116(21), 115(52), 104(27), 92(18), 91(75), 87(16), 77(13), 65(12); MS (ei, high resolution), *m/z*, calcd. for $C_{11}H_{14}S$: 178.0813; found: 178.0820.

Synthesis of E-*1-phenyl-1,2-epithiopentane-1-oxides (**7** and **8**)*

To a mixture of thiirane **14** (384 mg, 2.16 mmol) in dry CH_2Cl_2 (20 mL) cooled to −78°C was added dropwise a dry solution of MCPBA (511 mg (73% active), 2.16 mmol) in CH_2Cl_2 (20 mL). After 25 min the mixture was filtered with suction. The MCBA was precipitated from the cold solution as described by Kondo and Negishi (10). Usually four filtrations were required. The solvent was removed under reduced pressure while maintaining a cold bath and the result was a crude mixture of **7** and **8** (348 mg, 3.5:1 ratio, 83%). Partial spectral data for **7** and **8**: ^{1}H NMR (200 MHz), δ (major isomer): 3.52 (d, J = 10.5 Hz, 1H), 2.78 (dt, J = 10.5 and ca. 6.8 Hz, 1H); δ (minor isomer): 3.28 (d, J = 10.1 Hz, 1H), 3.20 (dt, 1H): ^{13}C NMR (50.3 MHz), δ (probable peaks for major isomer): 133.59, 128.89, 128.51, 126.63, 59.27, 51.51, 25.95, 21.78, 13.37.

Reaction of ***7*** *and* ***8*** *with LDA*

To a mixture of LDA (1.26 mmol) and THF (10 mL) stirred at −78°C was added thiirane-*S*-oxides **7** and **8** (228 mg, 1.17 mmol) in THF (10 mL). After stirring for 20 min at −78°C, excess MeI in LDA was added. The mixture was stirred for 12 h as the temperature warmed and work-up was as described for the α-chlorosulfoxides. The reaction afforded **3k** (36%), 36 mg (19%) of alcohol **16**, and 59 mg

Can. J. Chem. Downloaded from www.nrcresearchpress.com by 195.246.54.202 on 09/08/12
For personal use only.

(24%, contaminated with 5% of **2p**) of **2o**. The latter two products were obtained by chromatography. Alkene **3k** was quantitated by determining the relative amounts of it and **16** in the crude mixture by ^{1}H NMR and extrapolating back once **16** was isolated and quantitated.

Synthesis of Z-*2-phenyl-3-propyloxirane (**13**)*

A mixture of 1-phenyl-1-pentyne (4.71 g, 32.7 mmol), Lindlar's catalyst (Aldrich) (0.88 g), and quinoline (120 mg) were stirred in 60–80 petroleum ether (75 mL). A hydrogen containing balloon was attached to the apparatus and the H_2 was exposed to the mixture. The balloon was refilled 5 times over the course of 4 days at which time the mixture was filtered. The mixture was shown by GC to be 89% alkene **11**. The solution of **11** was stirred while MCPBA (7.74 g (73% active), 32.8 mmol) in CH_2Cl_2 (120 mL) was added dropwise from an addition funnel. Stirred continued at room temperature for 14 h. The mixture was then handled as for **12** above to afford 3.06 g (57%, 96% pure by GC) of **13** (15); bp 47–48°C/0.05 Torr.

Synthesis of Z-*1-phenyl-1,2-epithiopentane (**15**)*

A mixture containing **13** (1.77 g, 1.0 mmol), KSCN (1.47 g, 15.1 mmol), MeOH (20 mL), and H_2O (7 mL) was refluxed for 38 h. More KSCN (0.91 g) was added to the solution and it was refluxed for 4 h longer. Work-up as above for **14** afforded crude **15**, which was subjected to column chromatography on Al_2O_3(I) with hexanes as eluent. The elution afforded **11**, **13**, and then **15** (735 mg, 38%). Spectral data for **15**: IR (neat), cm^{-1}: 3059, 3026, 2959, 2929, 2870, 1600, 1492, 1452, 1378, 1074, 1031, 759, 741; ^{1}H NMR (400 MHz), δ: 7.42–7.25 (m, 5H), 4.15 (d, J = 6.9 Hz, 1H), 3.18 (m, 1H), 1.55–1.38 (m, 3H), 1.16 (m, 1H), 0.85 (t, J = 7.2 Hz, 3H); ^{13}C NMR (100.6 MHz), δ: 135.82, 129.16, 127.90, 127.24, 42.91, 42.54, 32.87, 22.56, 13.69; MS (ei), *m/z*(%): 178(80), 177(12) 149(31), 146(25), 136(35), 135(89), 122(27), 121(35), 118(28), 117(82), 116(26), 115(61), 104(25), 92(26), 91(100), 87(25), 78(12), 77(19), 65(15); MS (ei, high resolution), *m/z*, calcd. for $C_{11}H_{14}S$: 178.0813; found: 178.0808.

Synthesis of Z-*1-phenyl-1,2-epithiopentane-1-oxide (**6**)*

To a mixture of thiirane **15** (354 mg, 1.99 mmol) in dry CH_2Cl_2 (20 mL) cooled to −50°C was added dropwise a dry solution of MCPBA (464 mg (73% active), 1.96 mmol) in CH_2Cl_2 (15 mL). After 15 min the mixture was filtered with suction. The remaining MCBA was precipitated from the cold solution as described by Kondo and Nagishi (10). Usually three filtrations were required. The solvent was removed under reduced pressure while maintaining a cold bath and the result was fairly pure **6** (334 mg, 87%). Spectral data for **6**: IR (neat), cm^{-1}: 3059, 3029, 2960, 2931, 2871, 1601, 1495, 1454, 1381, 1062(vs), 978, 758; ^{1}H NMR (200 MHz), δ: 7.30 (m, 3H), 7.15 (m, 2H), 4.16 (d, J = 11.1 Hz, 1H), 3.37 (ddd, J = 5.7, 11.1, and 16.8 Hz, 1H), 1.58 (m, 2H), 1.41 (m, 1H), 1.17 (m, 1H), 0.95 (t, J = 7.2 Hz, 3H): ^{13}C NMR (50.3 MHz), δ: 131.41, 128.61, 128.41, 127.95, 58.95, 58.75, 26.96, 21.78, 13.57.

*Reaction of **6** with LDA*

To a mixture of LDA (0.96 mmol) and THF (10 mL) stirred at −78°C was added thiirane-*S*-oxide **6** (162.5 mg, 0.84 mmol) in THF (5 mL). After stirring for 15 min at −78°C, excess MeI in LDA was added. The mixture was stirred for 5 h as the temperature warmed and work-up was as described for the α-chlorosulfoxides. Chromatography afforded 204 mg (70%) of **2p** and 6 mg (3.5%) of **2k**.

*Search for **8** from **1kA***

A solution of **1kA** (161 mg, 0.70 mmol) in THF (10 mL) was stirred at −78°C. LDA (1.0 molar equiv., 1.4 M in cyclohexane, Aldrich) was added all at once. After 10 min, aqueous NH_4Cl (10 mL) was added and the cold solution was filtered with suction. The filtrate was concentrated while the temperature was kept below 0°C. Analysis of the mixture by ^{1}H NMR indicated the ring hydrogen peaks for **8** as well as peaks corresponding to **1kA** and several alkene containing species. The chemical yield of **8** was judged to be 10–20% from this NMR.

Synthesis of anti-*4-phenyl-1,2-epithiobutane*-S-*oxide (**18**)*

4-Phenylbutene (10.96 g, 83.0 mmol) was oxidized using MCPBA as described for **2k** and **11** above. The crude 2-(phenylethyl)oxirane (16) was stirred with KSCN (13.0 g, 134 mmol), MeOH (150 mL), and H_2O (50 mL) for 20 h. Work-up as above for **14** and **15** gave crude 4-phenyl-1,2-epithiobutane. Distillation of the mixture afforded 6.51 g (48% from alkene) of 4-phenyl-1,2-epithiobutane, 99.3% pure by GC; bp 79–81°C/0.45 Torr. Spectral data for 4-phenyl-1,2-epithiobutane: IR (neat), cm^{-1}: 3061, 3025, 2987, 2529, 2856, 1603, 1495, 1450, 1070, 747; ^{1}H NMR (400 MHz), δ: 7.28 (m, 2H), 7.21 (m, 3H), 2.91–2.76 (m, 3H), 2.49 (dd, J = 1.0 and 6.3 Hz, 1H), 2.22–2.12 (m, 1H), 2.15 (dd, J = 1.0 and 5.6 Hz, 1H), 1.73 (m, 1H); ^{13}C NMR (100.6 MHz), δ: 141.17, 128.47, 128.42, 126.04, 38.33, 35.64, 35.38, 25.95; MS (ei), *m/z*(%): 164(20), 131(20), 123(67), 117(37), 115(11), 104(10), 91(100), 65(21); MS (ei, high resolution), *m/z*, calcd. for $C_{10}H_{12}S$: 164.0657; found: 164.0674. To a stirred solution of 4-phenyl-1,2-epithiobutane (1.03 g, 6.28 mmol) in dry CH_2Cl_2 (20 mL) cooled to −78°C was added dropwise a dry solution of MCPBA (1.48 g (73%), 6.26 mmol) in CH_2Cl_2 (15 mL). The cold mixture was stirred for 45 min and was filtered with suction. The remainder of the work-up was as described for **6** above. Flash chromatography on silica gel in a jacketed, water-cooled column using ether as the eluent provided fractions of pure **18**. Low-temperature concentration of the combined fractions afforded 594 mg (53%) of **18**. Spectral data for **18**: IR (neat), cm^{-1}: 3066, 3025, 2923, 2855, 1603, 1496, 1454, 1065(vs), 748; ^{1}H NMR (200 MHz), δ: 7.37–7.18 (m, 5H), 3.02–2.82 (m, 1H), 2.86 (t, J = 7.4, 2H), 2.67 (dd, J = 6.7 and 10.3 Hz, 1H), 1.98 (dd, 6.7 and 9.6 Hz), 1.80–1.52 (m, 2H); ^{13}C NMR (50.3 MHz), δ: 139.86, 128.59, 128.47, 126.42, 49.53, 41.48, 33.87, 31.23.

*Reaction of **18** with LDA*

To a mixture of LDA (0.91 mmol) and THF (10 mL) stirred at −78°C was added thiirane-*S*-oxide **18** (153 mg, 0.85 mmol) in THF (5 mL). After stirring for 20 min at −78°C, excess MeI in LDA was added. The mixture was stirred overnight as the temperature warmed and work-up was as described for the α-chlorosulfoxides. Chromatography afforded 19 mg (11.5%) of **2h** and 96.5 mg (58%) of **2e**.

Lanthanide shift reagent experiments

The substrate (11–17 mg of compounds **2h**, **2k**, **2o**, **2p**) was placed in a 5-mm NMR tube along with 0.4 mL of $CDCl_3$. The ^{1}H NMR spectrum was recorded on the 400 MHz instrument. Small increments (2.94 mg or factors thereof) of Eu(fod)$_3$ (Resolve-Al EuFOD (Aldrich)) in $CDCl_3$ were added and the ^{1}H NMR was recorded after each addition. Specific attention was given to the downfield movement of the vinyl hydrogen of each substrate. The change in vinyl hydrogen chemical shift was compared to the amount of shift reagent added and the data are presented in Fig. 1.

*Crystal structure analyses of **1kB** and of **1hA***

Details of crystal data, data acquisition, structure solution, and refinement for both **1kB** and **1hA** are concisely summarized in Table 2. In each case the data crystal decayed somewhat over the course of the data collection; this was allowed for by appropriate scaling. The full crystallographic data (fractional coordinates, thermal parameters, molecular dimensions and structure factor listing) have been deposited.[6]

Acknowledgements

We thank the Natural Sciences and Engineering Research

[6]These data can be purchased from: The Depository of Unpublished Data, Document Delivery, CISTI, National Research Council Canada, Ottawa, ON K1A 0S2, Canada.

The tables of atomic coordinates and of bond lengths and angles have also been deposited with the Cambridge Crystallographic Data Centre, and can be obtained on request from The Director, Cambridge Crystallographic Data Centre, University Chemical Laboratory, 12 Union Road, Cambridge, CB2 1EZ, U.K.

TABLE 2. Summary of data collection, structure solution, and refinement details for α-chlorosulfoxides **1kB** and **1hA**

	1kB	**1hA**
(*a*) **Crystal Data**		
Empirical formula	$C_{11}H_{15}OSCl$	$C_{10}H_{13}OSCl$
fw	230.75	216.72
Color, habit	Colorless, block	Colorless, block
Crystal size, mm	0.25 × 0.25 × 0.45	0.10 × 0.15 × 0.25
Crystal system	Monoclinic	Monoclinic
a, Å	5.8152(3)	8.696(1)
b, Å	24.5045(23)	5.251(1)
c, Å	8.6124(5)	24.041(2)
α, °	90	90
β, °	95.035(4)	91.157(8)
γ, °	90	90
V, Å^3	1222.5(2)	1097.6(3)
Space group	$P2_1/n$	$P2_1/c$
Z	4	4
Molecular symmetry	None	None
F(000)	488	456
d_{calc}, g cm^{-3}	1.25	1.31
μ, mm^{-1}	0.44	0.49
(*b*) **Data acquisition**[a]		
Temp, °C	21	21
Unit-cell reflections (2θ range°)	25 (17–40)	25 (16–24)
Max. 2θ (°) for reflections	54	48
hkl range of reflections	−7 7, 0 31, 0 10	−9 9, 0 6, 0 27
Variation in 3 standard reflections	35% decay	30% decay
Reflections measured	2908	1746
Unique reflections	2661	1708
R_{int}	0.005	0.04
Reflections with $I > n\sigma(I)$, *n*	1477, 3.0	542, 2.0
(*c*) **Structure solution and refinement**[b]		
Solution method	Direct methods	Direct methods
H-atom treatment	Riding, C—H 0.95 Å	Riding, C—H 0.95 Å
No. of variables in LS	128	118
k in $w = 1/(\sigma^2F_o + kF_o^2)$	0.0012	0.0005
R, R_w, gof	0.037, 0.056, 1.22	0.083, 0.071, 1.56
Density range in final Δ-map, e Å^{-3}	−0.18, 0.19	−0.45, 0.39
Final shift/error ratio	<0.001	<0.01

[a]Data collection on an Enraf Nonius CAD4 diffractometer with graphite monochromatized Mo-Kα_1 radiation (λ 0.70926 Å).

[b]All calculations were done on a Silicon Graphics 4D-35TG computer system with the NRCVAX system of programs (ref. 8).

Council of Canada and the University of Guelph for supporting this research. We also wish to thank H. Stewart McKinnon for obtaining the mass spectra and two referees for helpful comments.

1. (*a*) L.A. Paquette. Org. React. **25**, 1 (1977); (*b*) E. Block, D. Putman, and A. Schwan. NATO ASI Ser. A: **197**, 257 (1990).
2. (*a*) R.K. Boeckman, Jr., S.K. Yoon, and D.K. Heckendorn. J. Am. Chem. Soc. **113**, 9682 (1991); (*b*) T. Fujisawa, B.I. Mobele, and M. Shimizu. Tetrahedron Lett. **32**, 7055 (1991); (*c*) D. Scarpetti and P.L. Fuchs. J. Am. Chem. Soc. **112**, 8084 (1990); (*d*) E. Block and D. Putman. J. Am. Chem. Soc. **112**, 4072 (1990); (*e*) K.C. Nicolaou, Y. Ogawa, G. Zuccarello, and H. Kataoka. J. Am. Chem. Soc. **110**, 7247 (1988).
3. (*a*) C.R. Johnson and H.G. Corkins. J. Org. Chem. **43**, 4140 (1978); (*b*) M. Heuschmann and H. Quast. Chem. Ber. **115**, 3384 (1982); (*c*) H. Quast and M. Heuschmann. Angew. Chem. Int. Ed. Engl. **17**, 867 (1978); (*d*) P. Burns, G. Capozzi, and P. Haake. Tetrahedron Lett. 925 (1972).
4. (*a*) E. Vogel, H. Wieland, L. Schmalstieg, and J. Lex. Angew. Chem. Int. Ed. Engl. **23**, 717 (1984); (*b*) K. Weinges, W. Kasel, J. Klein, G. Hubertus, H. Irngartinger, U. Huber-Patz, and H. Rodewald. Chem. Ber. **117**, 966 (1984); (*c*) K. Weinges, W. Kasel, U. Huber-Patz, H. Rodewald, and H. Irngartinger. Chem. Ber. **117**, 1868 (1984); (*d*) K. Weinges, W. Sipos, J. Klein, J. Deuter, and H. Irngartinger. Chem. Ber. **120**, 5 (1987).
5. (*a*) B.F. Bonini, G. Maccagnani, G. Mazzanti, and P. Zani. Gazz. Chim. Ital. **120**, 115 (1990); (*b*) B.F. Bonini, G. Maccagnani, G. Mazzanti, and P. Piccinelli. Tetrahedron Lett. 3987 (1979).
6. A.L. Schwan and D.A. Wilson. Tetrahedron Lett. **33**, 5897 (1992).
7. (*a*) F.A. Davis, R.T. Reddy, W. Han, and P.J. Carroll. J. Am. Chem. Soc. **114**, 1428 (1992); (*b*) H.B. Kagan and F. Rebiere. Synlett, **1**, 643 (1990); (*c*) G. Mazzanti, R. Ruinaard, L.A. Van Vliet, P. Zani, B.F. Bonini, and B. Zwanenburg. Tetrahedron Lett. **33**, 6383 (1992).

Can. J. Chem. Downloaded from www.nrcresearchpress.com by 195.246.54.202 on 09/08/12
For personal use only.

8. E.J. Gabe, Y. Le Page, J.-P. Charland, F.L. Lee, and P.S. White. J. Appl. Crystallogr. **22**, 384 (1989).
9. J.M. Lehn and G. Wipff. J. Am. Chem. Soc. **98**, 7498 (1976).
10. K. Kondo and A. Negishi. Tetrahedron, **27**, 4821 (1971).
11. (*a*) C.G. Venier, H.-H. Hsieh, and H.J. Barager III. J. Org. Chem. **38**, 17 (1973); (*b*) R.N.Loeppky and D.C.K. Chang. Tetrahedron Lett. 5415 (1968); (*c*) Y.H. Kim, S.C. Lim, H.R. Kim, and D.C. Yoon. Chem. Lett. 79 (1990); (*d*) F.E. Hardy, P.R.H. Speakman, and P. Robson. J. Chem. Soc. C, 2334 (1969).
12. R. Annunziata and M. Cinquini. J. Chem. Soc. Perkin Trans. 1, 1684 (1979).
13. G.A. Russell, E. Sabourin, and G.J. Mikol. J. Org. Chem. **31**, 2854 (1966).
14. M. Mikolajczyk, S. Grzejszczak, and A. Zatorski. J. Org. Chem. **40**, 1979 (1975).
15. Y. Tamura, S.M. Bayomi, K. Sumoto, and M. Ikeda. Synthesis, 693 (1977).
16. A.J. Davidson and R.O.C. Norman. J. Chem. Soc. 5404 (1964).

Can. J. Chem. Downloaded from www.nrcresearchpress.com by 195.246.54.202 on 09/08/12
For personal use only.

Synthesis, reactions, and interconversions of some 2-(trimethylsilyl)ethyl substituted sulfur compounds

ADRIAN L. SCHWAN,[1] DENIS BRILLON,[2] AND ROBERT DUFAULT

Guelph–Waterloo Centre for Graduate Work in Chemistry, Guelph Campus, Department of Chemistry and Biochemistry, University of Guelph, Guelph, ON N1G 2W1, Canada

Received July 19, 1993

ADRIAN L. SCHWAN, DENIS BRILLON, and ROBERT DUFAULT. Can. J. Chem. **72**, 325 (1994).

In an effort to probe the compatibility of the 2-(trimethylsilyl)ethyl sulfur moiety with standard organosulfur transformations, several 2-(trimethylsilyl)ethanethiol derivatives have been prepared in excellent yield. Thus 2-(trimethylsilyl)ethanethiol (**1**) and 2-(trimethylsilyl)ethyl disulfide (**4**) and its corresponding thiosulfinate **9** and thiosulfonate **10** have been synthesized. One method of formation of **4** involves the breakdown of a 1-(trimethylsilyl)ethyl unit while the 2-(trimethylsilyl)ethyl fragment survives. Oxidation of **4** or **9** to **10** did not proceed efficiently with common reagents, but proceeded well with an iodine/water system. 2-(Trimethylsilyl)ethyl sulfide (**11***a*) and its oxides (**13**, **14**) were also prepared in good yield. Sulfoxide **13** and 2-(trimethylsilyl)ethyl *tert*-butyl sulfoxide **15** were shown to be good precursors to 2-(trimethylsilyl)ethanesulfinyl chloride (**16**). (Trimethylsilyl)methyl sulfine reacted with **16** in an inefficient manner to give thiosulfonates **10**, **19**, and **20**. 2-(Trimethylsilyl)ethanesulfenyl chloride could be generated and captured by addition across cyclohexene. The reaction of thiosulfinate **9** with several thiosilanes is an excellent method for the synthesis of 2-(trimethylsilyl)ethyl containing mixed disulfides.

ADRIAN L. SCHWAN, DENIS BRILLON et ROBERT DUFAULT. Can. J. Chem. **72**, 325 (1994).

Afin de pouvoir étudier la compatibilité de la portion 2-(triméthylsilyl)éthyle sulfurée avec les transformations standard des composés organosulfurés, on a préparé plusieurs dérivés du 2-(triméthylsilyl)éthanethiol avec d'excellents rendements. On a ainsi synthétisé le 2-(triméthylsilyl)éthanethiol (**1**), le disulfure de 2-(triméthylsilyl)éthyle (**4**) ainsi que les thiosulfinate (**9**) et thiosulfonate (**10**) correspondants. Une méthode de préparation du composé **4** implique la désintégration d'une unité 1-(triméthylsilyl)éthyle alors que le fragment 2-(triméthylsilyl)éthyle survit. Sous l'influence des réactifs ordinaires, l'oxydation des composés **4** ou **9** en **10** ne se produit pas d'une façon efficace; toutefois, elle se produit bien dans un système iode/eau. On a aussi préparé le sulfure de 2-(triméthylsilyl)éthyle (**11***a*) et ses oxydes (**13** et **14**) avec de bons rendements. On a montré que le sulfoxyde **13** et 2-(triméthylsilyl)éthyl *tert*-butyl sulfoxyde sont de bons précurseurs du chlorure de 2-(triméthylsilyl)éthanesulfinyle (**16**). La (triméthylsilyl)méthyl sulfine réagit inefficacement avec le composé **16** pour conduire aux thiosulfonates **10**, **19** et **20**. Le chlorure de 2-(triméthylsilyl)éthanesulfényle peut être généré et capturé par addition sur du cyclohexène. La réaction du thiosulfinate **9** avec plusieurs thiosilanes est une excellent méthode de synthèse des disulfures mixtes contenant des unités 2-(triméthylsilyl)éthyles.

[Traduit par la rédaction]

Introduction

Combining organosulfur and organosilicon chemistry into one molecule offers a new array of synthetic methods (1). A subclass of this field is the chemistry of 2-(trimethylsilyl)ethyl sulfur compounds. Fuchs and co-workers (2) have shown that sulfur atoms can be introduced as a 2-(trimethylsilyl)ethyl unit using either nucleophilic or electrophilic chemistry, with subsequent removal of the 2-(trimethylsilyl)ethyl moiety. Schwan and Dufault have shown that the 2-(trimethylsilyl)ethyl group can be removed from alkyl and aryl 2-(trimethylsilyl)ethyl sulfoxides under Pummerer-like conditions (3). This fragmentation reaction serves as a useful preparation of sulfinyl chlorides. 2-(Trimethylsilyl)ethanesulfonyl chloride has been shown to be an excellent reagent for the functionalization and hence protection of amines (4). Deprotection with fluoride supplies the free amine as well as trimethylsilyl fluoride, sulfur dioxide, and ethylene. Similarly a 2-(trimethylsilyl)ethanesulfonyl-protected carbamate is a suitable reagent for Mitsunobu reactions (5).

The presence of a trimethylsilyl group β to a sulfoxide can also enhance the reactivity of the hydrogens α to the silicon during thermal sulfenic acid formation via [2,3] elimination reactions (6, 7). Furthermore, in some instances the silicon group itself is eliminated (6).

This field has tremendous potential for the generation of several types of sulfur-containing species via fragmentation chemistry and for strategic placement of sulfur atoms in organic molecules, as the Fuchs work indicates. Hence it is important to: (*i*) establish reliable routes to several 2-(trimethylsilyl)-ethanethiol and 2-(trimethylsilyl)ethane sulfur acid derivatives and (*ii*) determine the sorts of organosulfur transformations for which the 2-(trimethylsilyl)ethyl group is tolerant.

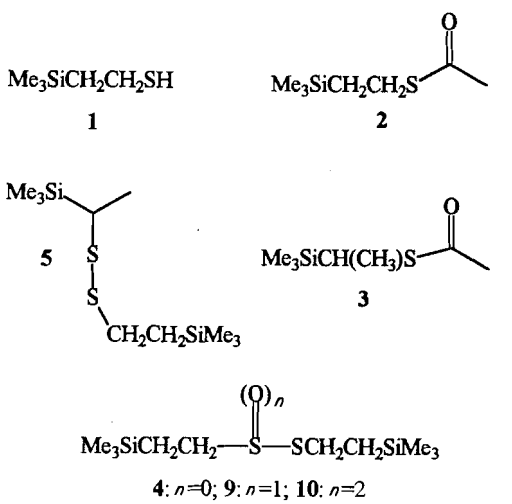

Results and discussion

The logical starting point in this exercise is the thiol. 2-(Trimethylsilyl)ethanethiol or β-ethyl silyl thiol (BEST, **1**) has been prepared previously. The synthesis is achieved by

[1]Author to whom correspondence may be addressed. FAX: 1-(519)-766-1499; e-Mail: SCHWAN@CHEMBIO.UOGUELPH.CA.

[2]Holder of an NSERC Postdoctorate Fellowship, 1992–1993.

Can. J. Chem. Downloaded from www.nrcresearchpress.com by 195.246.54.202 on 09/08/12
For personal use only.

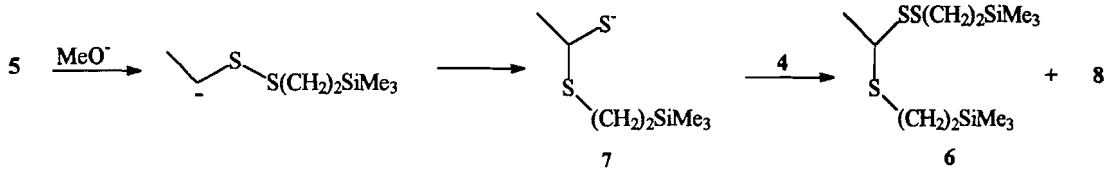

SCHEME 1

reduction (2) or hydrolysis (8) of 2-(trimethylsilyl)ethyl thiolacetate (**2**). Thiolester **2** is prepared by radical addition of thiolacetic acid to vinyltrimethylsilane (8). This yields two regioisomers (**2** and **3**) in a 90:10 ratio and distillation on a spinning band column is an excellent method for the removal of **3**. Pure **2** is then converted to thiol **1** by hydrolysis with potassium carbonate in a methanol–water solution. Under these hydrolysis conditions the thiol is obtained essentially quantitatively, with 98.5% purity (GC analysis). Distillation affords **1** in 95% yield, which represents an improvement over other methods (2, 8).

[1] $$2 \xrightarrow[N_2]{K_2CO_3} \underset{\mathbf{8}}{Me_3SiCH_2CH_2S^-} \xrightarrow{I_2} 4$$

Disulfide **4** can be obtained if the thiolacetate hydrolysis mixture is treated with I_2 (reaction [1], 99.7%). An interesting reaction was observed when we attempted to convert the contaminated **2** to **4** all in one pot. This was accomplished by treating the crude **2/3** mixture with methanolic KOH and allowing the mixture to stir for several days in a vessel open to air. Under the KOH/MeOH/air conditions, a sample of 90% pure **2** gave pure disulfide **4** in 57% yield. This corresponds to an 64% yield based on the amount of **2** actually present. The hydrolysis–oxidation sequence is a particularly robust approach that allows one to start with **2** that may be contaminated by α-silylthiolacetate **3**. A compound giving a retention time expected for isomeric disulfide **5** was observed by GC in the early stages of the reaction,[3] but decomposed under extended exposure to the methanolic KOH mixture. The disappearance of the unwanted isomer means one can prepare disulfide **4** without distilling the original thiolacetate mixture.

The loss of **5** could be followed by GC and was accompanied by an increase in intensity of a newer peak that had significantly longer retention time; when the reaction was stopped, only the new compound and **4** were evident. During the isolation of **4**, the new compound was also recovered and was assigned the structure **6**. This assignment was based primarily on NMR and MS data. In the ^{1}H NMR, there are two different sets of multiplets for the two $-CH_2CH_2-$ groups as well as the doublet and quartet expected for a 1,1-disubstituted ethyl unit. The MS provided major peaks corresponding to $[TMSCH_2CH_2S]^+$ (m/z = 133) and $[TMSCH_2CH_2SCHCH_3]^+$ (m/z = 161) fragments. The reaction conditions likely cause desilylation of the α-silyl species **5**. The short-lived anion probably rearranges via a precedented mechanism (9) to thiolate **7** (Scheme 1). Since this occurs after the formation of **4** is mostly complete, **7** probably then attacks a molecule of **4** to afford **6**. If the hydrolysis of **2** is complete, but the air oxidation of **8** to **4** is sluggish, then **7** can simply combine with **8** to yield **6**. Although this method of formation of **4** sacrifices two 2-(trimethylsilyl)ethyl units for every one unwanted 1-(trimethylsilyl)ethyl isomer, it is a simple synthetic alternative.

The oxidation of disulfide **4** to *S*-2-(trimethylsilyl)ethyl 2-(trimethylsilyl)ethanesulfinothioates[4] (**9**) with MCPBA is a facile operation with **9** being obtained in 95% yield. Thiosulfinate **9** was also obtained by reacting **1** with 2-(trimethylsilyl)-ethanesulfinyl chloride (vide infra). Some chemistry of **9** is demonstrated in a later section of this paper. The conversion of **9** to thiosulfonate **10** and the direct oxidation of **4** to **10** were not trivial tasks. Common oxidizing agents such as MCPBA, MMPP, and peracetic acid solution were not very successful (Table 1). The best yield for the conversion from **9** to **10** was 43% using MMPP while the transformation of **4** to **10** could only be achieved in 32% yield using MCPBA. The general belief is that thiosulfinates are oxidized by electrophilic reagents such as MCPBA and peracetic acid to afford a transient *vic*-disulfoxide (10). That *vic*-disulfoxide then fragments or rearranges to eventually yield the final product, a thiosulfonate. This pathway is not particularly effective for the oxidation of **9**, perhaps because the 2-(trimethylsilyl)ethyl groups are not compatible with the intermediates involved in the rearrangement to thiosulfonate. On the assumption that I_2 in an aqueous medium (11) may circumvent the *vic*-disulfoxide route by direct interaction with the sulfinyl group of **9**, we attempted oxidations with that reagent system. The I_2/H_2O combination proved satisfactory for the oxidation of **4** to **10** and was excellent for the conversion of **9** to **10** (Table 1). Although we found good success with the I_2/H_2O system, we are not in a position at this stage to confirm our initial assumptions regarding its mode of action.[5]

An uncommon, low yielding, but more direct approach to the thiosulfonate **10** was performed by oxidizing **2** with MCPBA. One equivalent of MCPBA yielded a mixture of **2** and **9**. Optimization of the oxidation conditions to 1.5 to 2 equivalents of MCPBA effected complete consumption of thiolacetate **2** and recovery of **10** in up to 28% yield. It is known that the oxidation of alkyl thiolesters with electrophilic agents first creates α-ketosulfoxides, which may break down under the reaction conditions to afford dialkyl disulfides (12). Under our conditions, it is probably disulfide **4** that is formed first and then is oxidized to **10**.

The symmetrically substituted 2-(trimethylsilyl)ethyl sulfide (**11***a*) was prepared by radical addition of **1** to vinyltrimethylsilane. Radical addition to the terminal carbon occurred 92% of the time; the desired isomer (**11***a*) was obtained pure by chromatography. The sulfide is readily oxidized to the sulfoxide (**13**) with $NaIO_4$ (3) (Scheme 2). The sulfoxide was also ob-

[3]Thiolacetates **2** and **3** are consumed in ca. 3 h under these conditions.

[4]The proper nomenclature is as listed for **9** and is *S*-2-(trimethylsilyl)ethyl 2-(trimethylsilyl)ethanesulfonothioates for **10**. We will use the trivial names of thiosulfinate for **9** and thiosulfonate for **10**.

[5]As part of a separate investigation, we are studying the scope and mechanism of the oxidation of other disulfides and thiosulfinates with the I_2/H_2O system.

Can. J. Chem. Downloaded from www.nrcresearchpress.com by 195.246.54.202 on 09/08/12
For personal use only.

TABLE 1. Syntheses of thiosulfonate **10**[a]

Starting material	Reagent	Temperature (°C)	Yield of **10** (%)
4	CH_3CO_3H (3.2 equiv., CH_2Cl_2)	−78 to +20	13
4	MCPBA (3.2 equiv., THF)	−78 to +20	32
4	MMPP (2.25 equiv., THF)	0	28[b]
4	I_2, $NaHCO_3$, H_2O; then $AgNO_3$	10 to 20	67
4	I_2, Ag_2CO_3, $NaHCO_3$, H_2O/dioxane	20[c]	72[d]
9	CH_3CO_3H (1.15 equiv., CH_2Cl_2)	−30 to +20	38
9	MCPBA (0.8 equiv., CH_2Cl_2)	−40 to +20	23
9	MMPP (1.75 equiv., THF)	17	43
9	I_2, H_2O/dioxane	0	90–95
2	MCPBA (1.5–2 equiv., CH_2Cl_2)	−78 to +20	<28[e]

[a]See experimental section for details.
[b]This mixture also contained **9** (18%).
[c]This mixture was stirred for 120 h.
[d]8% of **4** was also recovered.
[e]Yields were variable.

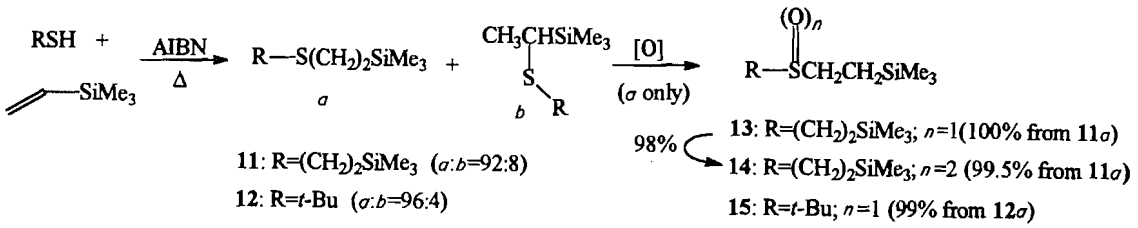

SCHEME 2

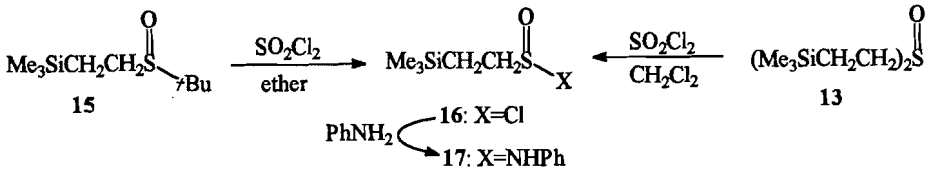

SCHEME 3

tained from the reaction of $LiCH_2S(O)CH_2Li$ and $TMSCH_2Cl$. This approach is not recommended: the yield was low and proper purification was extremely difficult. Sulfone (**14**) was obtained by oxidation of both sulfide **11***a* and sulfoxide **13** using peracetic acid solution. Our syntheses of **11***a* and **14** represent improvements over previously reported procedures (13).

As previously reported, the reaction of **13** with sulfuryl chloride affords 2-(trimethylsilyl)ethanesulfinyl chloride (**16**) in 67% isolated yield (Scheme 3) (3). 2-(Trimethylsilyl)ethyl chloride was a coproduct in this reaction (ca. 20%). Sulfinyl chloride **16** is also accessible via a shorter overall pathway, as shown in Scheme 3. The reaction of *tert*-butyl 2-(trimethylsilyl)ethyl sulfoxide (**15**) with sulfuryl chloride in ether[6] cleanly afforded **16**, probably via a fragmentation pathway. The structure of sulfinyl chloride **16** was confirmed by spectroscopic means while mass spectrometry was obtained on its *N*-phenyl sulfinamide derivative (**17**). The reaction of **16** with thiol **1** in the presence of base provides an alternative route to thiosulfinate **9** (57%).

Attempts were made to generate and capture trimethylsilylmethyl sulfine (**18**). Reaction of sulfinyl chloride (**16**) with of 0.65 equivalent of Et_3N usually affords sulfine, which can then be captured by the remaining sulfinyl chloride (14). The products isolated were vinyl 2-trimethylsilylethanethiosulfonate (**19**) and 2-(trimethylsilyl)ethenyl 2-trimethylsilylethanethiosulfonate (**20**) along with some thiosulfonate **10** (reaction [2]). We believe the oxygens on thiosulfonates **19** and **20** are on the sulfur opposite the vinyl group. The ^{13}C NMR chemical shift of the CH_2 group adjacent to the SO_2 in **10** is at 59.45 ppm while the CH_2 group next to the divalent sulfur resonates at 32.79 ppm. The ^{13}C NMR spectra of **19** and **20** show peaks at 58.58 and 58.22 ppm, respectively, with no peaks in the 15–50 ppm range. The absence of any peaks around 32 ppm for **19**

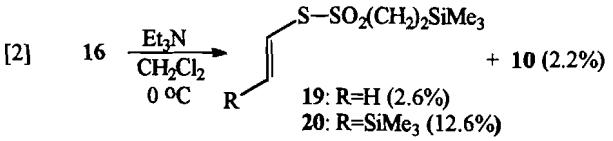

[6]In methylene chloride, the reaction mixture has many contaminants including 2-(trimethylsilyl)ethyl chloride and *tert*-butanesulfinyl chloride.

Can. J. Chem. Downloaded from www.nrcresearchpress.com by 195.246.54.202 on 09/08/12
For personal use only.

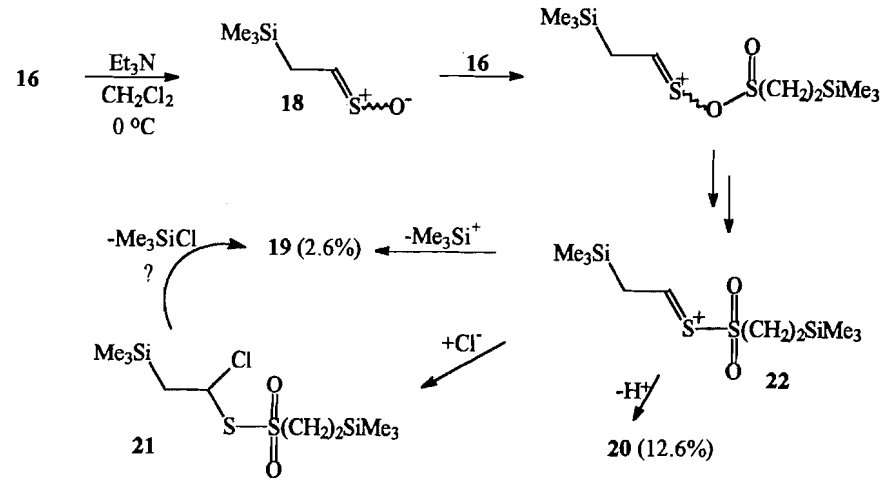

SCHEME 4

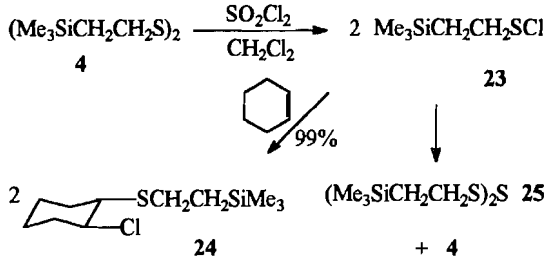

SCHEME 5

and **20** and the appearance of resonances close to 59 ppm provide evidence that the sulfonyl portion of **19** and **20** bears the 2-(trimethylsilyl)ethyl unit

Thiosulfonates **19** and **20** can be accounted for by branching off of the normal scheme leading to chlorinated thiosulfonate **21** (14) (Scheme 4). Rather than chloride capture of ion **22** at carbon, chloride attacks **22** at silicon to form the vinyl group. Chloride or amine base may also remove a hydrogen to yield **20**. The silicon atom has been shown to activate protons α to it (6). It is also possible that chloride does add to **22** to give **21**, which then loses TMSCl. The total yield of **19** and **20** could only be idealized to 15%. Obviously silylated sulfine **19** does not behave well under this treatment. Unchlorinated thiosulfonate (**10** in this case) is a recognized by-product and its formation has been accounted for previously (9*a*, 14*c*). Thiosulfonate **10** is the lone reaction product when ether or hexanes are employed as the reaction solvent.

The reaction of disulfide **4** with sulfuryl chloride was viewed as a method for the generation of 2-trimethylsilylethanesulfenyl chloride (**23**). The reaction was carried out at −78°C in CH_2Cl_2. Five minutes after the addition of sulfuryl chloride, cyclohexene was added to capture any sulfenyl chloride that had formed. β-Chlorosulfide **24** was formed in 99% yield (Scheme 5). The clean cleavage of the sulfur-sulfur bond without interference of the silicon group is quite different behaviour from 2-(trimethylsilyl)ethyl sulfoxides. In those instances, the 2-(trimethylsilyl)ethyl moiety is smoothly removed when the sulfoxides are treated with sulfuryl chloride (3). If nothing is added to capture **23**, two products result; one is disulfide **4**, which can simply arise from the reaction of two of **23** coming together (15). The second product that is formed is symmetric trisulfide **25**; Scheme 6 depicts one possible mechanism for its formation.[7] The total yield of the two products was variable (ca. 30–60%). In the mixtures containing **25**, GC chromatograms also showed the presence of 2-(trimethylsilyl)ethyl chloride, the expected by-product (Scheme 6). Under the sulfuryl chloride conditions, the yield of **25** can be optimized to 50%. The structure of **25** was confirmed by independent synthesis using the chemistry introduced by Capozzi et al. (16) for the preparation of symmetric trisulfides. Thus **25** was synthesized from bis(trimethylsilyl) sulfide and thiosulfinate **9** in 63% yield (reaction [3]).

[3] **9** + $Me_3Si—S—SiMe_3$ ⟶ **25** (63%) + **4** (16%)

The work of Capozzi et al. (16) also provided us with a method to generate mixed disulfides containing the 2-(trimethylsilyl)ethyl unit. The reaction involves the treatment of thiosulfinates with alkyl trimethylsilyl thioethers (reaction [4]).

[4] **9** + $RSSiMe_3$ (**27**) ⟶ $Me_3Si(CH_2)_2S—SR$ (**26**)

Several of the required trimethylsilyl thioethers are known compounds and were prepared according to established procedures (17). New silylated thioethers were prepared using the same methods. One unique starting material, trimethylsilyl thioacetate (**27***f*) was prepared as in reaction [5]. Due to the

[5] 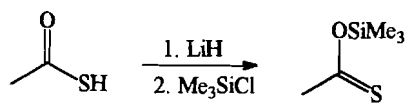

nearby carbonyl oxygen we were concerned that the silicon group may actually prefer an attachment to the oxygen. A previous reaction of thiolacetic acid and hexamethyldisilazane afforded the silylated product (**27***f*) with the silicon attached to the oxygen (18). An infrared spectrum of our material as a neat

[7]Other mechanistic possibilities exist and may be concurrent, since the union of two of **23** is actually a redox process that affords Cl_2 as a co-product. The low yield of **25** and low variable yields of (**4** + **25**) suggest that Cl_2 may be breaking down the molecules to small, unisolable fragments.

Can. J. Chem. Downloaded from www.nrcresearchpress.com by 195.246.54.202 on 09/08/12
For personal use only.

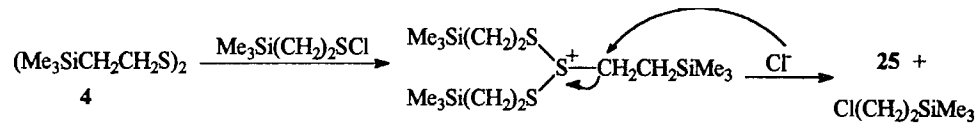

SCHEME 6

TABLE 2. Syntheses of mixed disulfides $RSSCH_2CH_2TMS$ (**26**) from trimethylsilyl thioethers **27** and thiosulfinate **9** (reaction [4])

Disulfide	R	Temperature (°C)	Yield (%)[a]
26*a*	CH_3	20–45	24
26*b*	$c\text{-}C_6H_{11}$	20–45	99
26*c*	$PhCH_2$	20–45	94
26*d*	$p\text{-}ClC_6H_4$	0–20	92
26*e*	$EtOC(O)CH_2$	0–45	88
26*f*	$CH_3C(O)$	0–20	87

[a]Isolated yields after chromatography.

liquid confirmed this structural assignment, since the spectrum contained a very weak carbonyl stretch (1715 cm^{-1}).[8] Even though the silylated thiolacetic acid was primarily a thiocarbonyl compound, the species performed as desired under the usual conditions. All of the mixed disulfides were synthesized in good yield with the exception of **26***a*. (Table 2) The trimethylsilyl thioether (**27***a*) required for the synthesis of **26***a* was a commercial product of unknown purity[9] and is also a volatile compound. Either of these reasons may be responsible for the low yield of **26***a*. *p*-Chlorophenylthiosilane was the most reactive thiosilane in our collection. The increased reactivity of arylthiosilanes over alkylthiosilanes has been recently noted (19). The 2-(trimethylsilyl)ethyl sulfur unit survives very well under the Capozzi reaction conditions. With the isolation of disulfide **26***f* in high yield we provide evidence that the Capozzi method is also satisfactory for the preparation of alkyl acyl disulfides, regardless of the atom attachment of the trimethylsilyl group in the starting silylated ester/thioester.

Experimental

General

Melting points were obtained on a Gallencamp capillary melting point apparatus and are uncorrected. All ^1H NMR spectra were obtained in $CDCl_3$ on a Varian Gemini 200 MHz instrument or a Varian Unity 400 MHz NMR spectrometer. Peaks were calibrated to the residual protium in $CDCl_3$ (7.26 ppm) or to internal tetramethylsilane. ^{13}C NMR spectra were obtained on the same instruments and were calibrated to the $CDCl_3$ (77.00 ppm). Infrared spectra were recorded as neat samples on a Bomem MB 100 IR spectrometer. Mass spectra were obtained using a Kratos MS890 double focussing mass spectrometer. Elemental analyses were performed by Guelph Chemical Laboratories. Gas chromatography was performed on a Varian 3400 capillary gas chromatograph equipped with a low-temperature SPI injection port. The chromatograph was equipped with a 15 m J&W DB-5 capillary GC column. Carrier gas (helium) flow was set to provide a constant column head pressure of 8 psi (1 psi = 6.9 kPa). Analytical TLC was performed using 0.25 mm Merck Kieselgel 60 F_{254} precoated silica gel plates. Visualization was accomplished with UV light, iodine and (or) anisaldehyde – sulfuric acid solution. Unless otherwise indicated, preparative chromatographic separations were done by flash chromatography on Merck silica gel (230–400 mesh). Dry ether was distilled from benzophenone ketyl directly prior to use. Dry CH_2Cl_2 was distilled from CaH_2 directly before use. Vinyltrimethylsilane was obtained from Hüls America (formerly Petrarch) and was used directly.

*Preparation of 2-(trimethylsilyl)ethanethiol (**1**)*

A 250-mL one-necked round-bottom flask, equipped with a reflux condenser and septum/balloon, was charged with vinyltrimethylsilane (63 g, 0.63 mol), thiolacetic acid (42.6 g, 0.561 mol), and AIBN (1.2 g). The mixture was brought to gentle reflux (oil bath 60–63°C) for 3.5 h. The mixture was then distilled on a spinning band distillation set-up using a water vacuum-line. The compound **3** (mixed with **2**) was collected at 82–84°C (14–18 Torr; 1 Torr = 133.3 Pa) (lit. (8) bp of pure **3** 81–82°C (22 Torr)) until GC analysis indicated a purity of >98% for distilled compound **2**; a total of 16.4 g of **2** and **3** were distilled from the mixture. The remaining distillate was cooled to 20°C and then distilled (83°C, 15 Torr) through a short-path distillation apparatus to give **2** (79.4 g, 80%; 99.7% pure by GC). In the following procedure all solvents were deoxygenated at 14 Torr for 0.5 h prior to use; except for diethyl ether. Potassium carbonate (4.42 g, 32 mmol) was added in one portion to a stirred solution of pure thiolacetate **2** (5.0 g, 28.4 mmol) in methanol (30 mL), water (15 mL), and ether (15 mL) under nitrogen at 20°C. The flask was equipped with a rubber septum and an N_2 balloon. The solution was stirred for 3.5 h at 20°C, and citric acid nonahydrate (6.7 g, 32 mmol) was added without a stopper on the flask. Diethyl ether was added (150 mL) and the organic layer was washed with a 1% aqueous citric acid solution (5 × 15 mL). The organic layer was dried on Na_2SO_4 and the solvent was removed in vacuo while maintaining a water bath temperature of 20°C to afford crude thiol **1** (3.79 g, 99.7%, 98.5% purity by GC). The compound was distilled under vacuum (56–57°C (26 Torr) (lit. (20) bp 52–54°C (25 Torr)) to afford pure **1** (3.63 g, 95%; 100% GC purity).

*Synthesis of disulfide **4***

To a mixture of **2** (62.1 g, 0.353 mmol), MeOH (900 mL), and H_2O (500 mL) was added solid K_2CO_3 (56 g). This mixture was stirred at room temperature for 4 h and solid I_2 (44.8 g, 0.176 mmol) was added in small portions. Then saturated aqueous $Na_2S_2O_3$ solution (100 mL) was added and the mixture was extracted with 30–60 petroleum ether (3 × 150 mL). The combined organic extracts were dried over Na_2SO_4 and concentrated (aspirator) to afford pure **4** (46.8 g, 99.7%; 100% pure by GC). Spectral data for **4**: IR (cm^{-1}): 2953, 1417, 1251, 1157, 1013; ^1H NMR (400 MHz) δ: 0.03 (s, 9H), 0.94 (m, 2H), 2.74 (m, 2H); ^{13}C NMR (100.6 MHz) δ: −1.77, 17.17, 34.80; MS (EI), *m/z*(%): 266(1), 238(16), 210(40), 195(17), 101(23), 74(26), 73(100). Anal. calcd. for $C_{10}H_{26}S_2Si_2$: C 45.05, H 9.83; found: C 45.19, H 9.64.

*One-pot synthesis of disulfide **4***

Crude thiolacetate **2** was prepared as above from vinyl trimethylsilane (14.2 g, 0.142 mol), thiolacetic acid (9.58 g, 0.126 mol), and AIBN (280 mg). To the crude mixture was added MeOH (200 mL) and KOH (13.2 g (85%), 0.200 mol). The mixture was stirred for 5 days without a stopper. Water (400 mL) was added and the mixture was extracted with pentane (3 × 60 mL). The combined organic extracts were dried over Na_2SO_4 and were filtered and concentrated (aspirator). Fractional distillation afforded **4** (9.64 g, 57%, bp 84–85°C (0.35 Torr)) followed by **6** (1.07 g) bp 123–124°C (0.4 Torr). Chromatogra-

[8]Our IR spectrum and our ^1H NMR data compared favourably to the data in the literature (18) for the *O*-silylated isomer.

[9]Methyl trimethylsilyl thioether (**23***a*) was purchased from Aldrich and was used without purification.

Can. J. Chem. Downloaded from www.nrcresearchpress.com by 195.246.54.202 on 09/08/12
For personal use only.

Can. J. Chem. Downloaded from www.nrcresearchpress.com by 195.246.54.202 on 09/08/12
For personal use only.

phy of the fraction containing **6** using 30–60 petroleum ether afforded pure **6**. Spectral data for trisulfide **6**: IR (cm^{-1}): 2954, 1442, 1416, 1251, 1158, 958, 939; ^1H NMR (400 MHz) δ: 0.02 (s, 9H), 0.03 (s, 9H), 0.78–1.00 (m, 4H), 1.63 (d, J = 6.8 Hz, 3H), 2.66–2.83 (m, 4H), 3.94 (q, J = 6.8 Hz, 1H); ^{13}C NMR (100.6 MHz) δ: −1.75 (2 C's), 17.07, 17.31, 22.29, 27.59, 35.79, 51.45; MS (EI), *m/z*(%): 165(22), 161(70), 133(75), 101(71), 74(32), 73(100); MS (CI, methane), *m/z*(%): 399($(M + TMS)^+$, 8), 327($(M + H)^+$, 5), 193(36), 165(72), 163(44), 162(58), 161(100), 135(16), 134(21), 133(86), 101(74), 91(22), 75(15), 74(23), 73(95). Anal. calcd. for $C_{12}H_{30}S_3Si_2$: C 44.16, H 9.68; found: C 44.57, H 9.27.

*Synthesis of 2-(trimethylsilyl)ethyl 2-(trimethylsilyl)ethanethiosulfinate (**9**)*

A solution of MCPBA (283 mg (73%), 1.2 mmol) in CH_2Cl_2 (10 mL) was added slowly to a solution of disulfide **4** (320 mg, 1.20 mmol) in CH_2Cl_2 (25 mL) at −40°C (Dry Ice – MeCN). The solution was stirred for 1 h and dry NH_3 was impinged on the surface of the solution to precipitate ammonium chlorobenzoate. The mixture was filtered with suction through Celite and was concentrated (aspirator). The crude material was purified by chromatography (EtOAc:30–60 petroleum ether; 1:19) to give thiosulfinate **9** (325 mg, 96%). Recrystallization from 30–60 petroleum ether gave mp 36–38°C and the following spectral data for **9**: IR (cm^{-1}): 2953, 2900, 1415, 1255(s), 1161, 1082(s), 1014; ^1H NMR (400 MHz) δ: 0.03 (s, 9H), 0.05 (s, 9H), 1.06 (m, 4H), 3.04 (m, 2H), 3.17 (m, 2H); ^{13}C NMR (100.6 MHz) δ: −1.87, −1.80, 10.40, 19.02, 28.99, 52.24; MS (EI), *m/z*(%): 256(10), 91(14), 73(100), 64(62); MS (CI, methane), *m/z*(%): 283($(M + H)^+$, 2.6), 205(26), 149(20), 148(23), 147(61), 134(22), 133(26), 132(32), 117(49), 106(24), 101(63), 91(35), 90(15), 85(36), 75(75), 74(59), 73(100), 59(38). Anal. calcd. for $C_{10}H_{26}OS_2Si_2$: C 42.50, H 9.27; found: C 42.61, H 9.65.

*Formation of thiosulfonate **10** by oxidation of **4***

Using MCPBA

A solution of MCPBA (276 mg (73%), 1.20 mmol) was added to a solution of disulfide **4** (100 mg, 0.376 mmol) in THF (8 mL) at −78°C. The solution was stirred while it warmed to 20°C over 6.5 h. Aqueous $NaHCO_3$ (10 mL) and 30–60 petroleum ether (10 mL) were added to the mixture; the layers were separated and the organic layer was dried over Na_2SO_4 and concentrated (aspirator). Chromatography (EtOAc:30–60 pet. ether 1:11) gave thiosulfonate **10** (36 mg, 32%). Spectral data for **10**: mp 29–30°C (30–60 petroleum ether); IR (neat) cm^{-1}: 2951, 1416, 1319, 1249, 1162, 1123; ^1H NMR (400 MHz) δ: 0.06 (s, 9H), 0.08 (s, 9H), 0.97 (m, 2H), 1.13 (m, 2H), 3.19 (m, 4H); ^{13}C NMR (100.6 MHz) δ: −1.96, −1.90, 10.61, 17.57, 32.79, 59.45; MS (EI), *m/z*(%): 178(14), 163(43), 147(46), 101(57), 90(24), 75(29), 74(20), 73(100), 59(21), 58(24); MS (CI, methane), *m/z*(%): 371($(M + TMS)^+$, 3), 343($(M + 45)^+$, 11), 315($(M + OH)^+$, 36), 299($(M + H)^+$, 0.3), 163(30), 153(15), 147(32), 101(58), 75(15), 74(28), 73(100). Anal. calcd. for $C_{10}H_{26}O_2Si_2S_2$: C 40.22, H 8.78; found: C 39.85, H 8.86.

Using MMPP

MMPP (720 mg, 80% pure) was added to a solution of disulfide **4** (100 mg, 0.376 mmol) and sodium bicarbonate (200 mg) in THF (7.5 mL) at 0°C. The solution was stirred for 8.5 h at 0°C. Water (10 mL) and 30–60 petroleum ether (20 mL) were added. The organic layer was dried over Na_2SO_4, filtered, and concentrated (aspirator). Chromatography gave the thiosulfonate **10** (31 mg, 28%) and the thiosulfinate **4** (19 mg, 18%).

Using peracetic acid

Peracetic acid solution (530 mg (35% active), 2.01 mmol) was added to a solution of **4** (100 mg, 0.376 mmol) in CH_2Cl_2 (10 mL) stirred at −78°C. The cold bath was removed and the mixture was stirred at 20°C for 6.5 h. Aqueous $NaHCO_3$ (10 mL) and 30–60 petroleum ether (10 mL) were added to the mixture; the layers were separated and the organic layer was dried over Na_2SO_4 and concentrated (aspirator). Chromatography gave thiosulfonate **10** (14 mg, 13%).

Using I_2 and Ag_2CO_3

Silver carbonate (170 mg, 0.616 mmol) was added to a mixture of disulfide **4** (101 mg, 0.376 mmol), sodium bicarbonate (250 mg, 0.298 mmol), and iodine (500 mg, 1.97 mmol) in dioxane (3 mL) and water (1 mL) at 20°C. The mixture was stirred with a gas outlet for 5 days at 20°C and was filtered and rinsed with water (5 mL) and 30–60 petroleum ether:ether (1:1) (20 mL). The aqueous layer was washed once with 30–60 petroleum ether (10 mL) and the combined organic layers were washed with a 5% aqueous sodium dithionite solution until the iodine coloration disappeared. The organic layer was dried over Na_2SO_4, filtered, and concentrated (aspirator). The crude material was purified by chromatography to give thiosulfonate **10** (82 mg, 72%) and some recovered disulfide **4** (8 mg, 8%). The yield of **10** based on consumed **4** was 79%.

Using I_2 and $AgNO_3$

A solution of silver nitrate (54 mg, 0.320 mmol) in water (2 mL) was added slowly (5 min) at 10°C to a solution of disulfide **4** (80 mg, 0.301 mmol), sodium bicarbonate (170 mg, 2.0 mmol), and iodine (170 mg, 0.66 mmol) in dioxane (3 mL). Some more iodine (220 mg) and $NaHCO_3$ (150 mg) were added after 4 h at 20°C. The mixture was stirred for a total of 50 h at 20°C. Work-up and chromatography as for **10** above afforded only thiosulfonate **10** (60 mg, 67%).

*Formation of thiosulfonate **10** by oxidation of **9***

Using MCPBA

A solution of MCPBA (34 mg (73%), 0.20 mmol) was added to a solution of **9** (50 mg, 0.177 mmol) in THF (8 mL) at −40°C. The solution was stirred for 40 min at −40°C and then at 20°C for 4 h. Chromatography (EtOAc:30–60 petroleum ether 1:11) of the mixture gave thiosulfonate **10** (12 mg, 23%).

Using MMPP

MMPP (210 mg, (80% pure), 0.341 mmol) was added to a solution of **9** (54 mg, 0.195 mmol) and sodium bicarbonate (200 mg) in THF (7.5 mL) at 17°C. The solution was stirred for 25 min at 17°C. Water (10 mL) and 30–60 petroleum ether (10 mL) were added. The organic layer was dried over Na_2SO_4, filtered, and concentrated (aspirator). Chromatography gave thiosulfonate **10** (23 mg, 43%).

Using peracetic acid

Peracetic acid solution (152 mg (35% active), 0.578 mmol) was added to a solution of **9** (50 mg, 0.177 mmol) and CH_2Cl_2 (2 mL) stirred at −30°C. The cold bath was removed and the mixture was stirred at 20°C for 3 h. Aqueous $NaHCO_3$ (10 mL) and 30–60 petroleum ether (10 mL) were added to the mixture; the layers were separated and the organic layer was dried over Na_2SO_4 was concentrated (aspirator). Chromatography gave thiosulfonate **10** (20 mg, 38%).

Using I_2

Thiosulfinate **9** (60 mg, 0.213 mmol) was added to a solution of iodine (60 mg, 0.236 mmol) in dioxane (2 mL) and water (1 mL) under nitrogen at 0°C. The solution was stirred for 1.5 h at 0°C, 30–60 petroleum ether:ether (1:1) (30 mL) was added. Work-up and chromatography as above afforded pure thiosulfonate **10** (60.5 mg, 95%) as a solid.

Formation of thiosulfonate **10** by oxidation of thiolacetate **2**

A solution of MCPBA (390 mg, 2.27 mmol) in CH_2Cl_2 (10 mL) was added over 10 min to a solution of the thiolacetate **2** (200 mg, 1.14 mmol) in CH_2Cl_2 (25 mL) at −78°C. The solution was stirred and warmed to room temperature over 14 h. The solvent was removed (aspirator) and the crude mixture was chromatographed to give thiosulfonate **10** (48 mg, 28%) as an oil.

*Synthesis of 2-(trimethylsilyl)ethyl sulfide (**11**a)*

A 25-mL flask was charged with thiol **1** (1.64 g, 12.2 mmol), vinyltrimethylsilane (1.90 g, 19.0 mmol), and AIBN (34 mg). The flask was heated under nitrogen at 50°C, then was sealed with a rubber septum.

Can. J. Chem. Downloaded from www.nrcresearchpress.com by 195.246.54.202 on 09/08/12
For personal use only.

The mixture was stirred at 73°C for 4 h. The crude mixture was concentrated and chromatographed twice using 30–60 petroleum ether as the eluting solvent to afford pure sulfide **11***a* (2.52 g, 88%) as an oil (GC purity: >99%). Spectral data for **11***a*: IR (neat) cm^{-1}: 2934, 1419, 1253, 1162, 1098, 1008; ^1H NMR (400 MHz) δ: 0.02 (s, 9H), 0.85 (m, 2H), 2.55 (m, 2H); ^{13}C NMR (100.6 MHz) δ: −1.77, 17.21, 27.26; MS (EI), *m/z*(%): 234(11), 163(55), 73(100). Anal. calcd. for $C_{10}H_{26}SSi_2$: C 51.21, H 11.17; found: C 51.43, H 11.43.

*Synthesis of 2-(trimethylsilyl)ethyl sulfoxide (**13**)*

To a stirred flask cooled to 0°C containing sulfide **11***a* (2.70 g, 11.5 mmol), MeOH (90 mL), and water (40 mL) was added solid $NaIO_4$ (2.47 g, 11.5 mmol). After 20 min of stirring, the ice bath was removed and the contents were stirred for 3.5 h longer. At that time, the solid was removed by suction filtration and the solid was washed with small portions of CH_2Cl_2. The liquid residue was diluted with an equal volume of water and was extracted with CH_2Cl_2 (3 × 30 mL). The combined organic layers were washed with brine, dried over $MgSO_4$, filtered, and concentrated (aspirator) to afford **13** (2.82 g, 98%) as a white crystalline solid; mp 51–52°C (30–60 petroleum ether). Spectral data for **13**: IR (neat) cm^{-1}: 2952, 1414, 1248, 1166, 1038; ^1H NMR (400 MHz) δ: 0.06 (s, 18H), 0.79 (dt, J = 4.7 and 13.7 Hz, 2H), 0.98 (dt, J = 4.7 and 13.7 Hz, 2H), 2.61 (m, 4H); ^{13}C NMR (100.6 MHz) δ: −1.89, 8.69, 46.47; MS (EI), *m/z*(%): 251($(M + H)^+$, 0.5), 222(19), 194(26), 163(16), 147(26), 133(20), 101(27), 75(29), 74(31), 73(100), 59(16); MS (CI, methane), *m/z*(%): 251($(M + H)^+$, 14), 235(38), 180(18), 179(18), 91(16), 90(51), 74(19), 73(44). Anal. calcd. for $C_{10}H_{26}OSSi_2$: C 47.98, H 10.48; found: C 48.02, H 10.86.

*Synthesis of **14** by oxidation of **13***

Peracetic acid solution (854 mg, (35%) 3.2 mmol) was added all at once to a solution of the sulfoxide **13** (500 mg, 2.0 mmol) in dichloromethane (10 mL) at 0°C. The solution was stirred for 1.5 h at 0°C, and K_2CO_3 (100 mg) and $MgSO_4$ (500 mg) were added. The mixture was diluted with petroleum ether (10 mL), decanted, concentrated, and purified by chromatography (EtOAc:hexanes 1:5) to give sulfone **14** (519 mg, 98%); mp 120.5–121.5°C (30–60 petroleum ether) (lit. (13) mp 122–123°C). Spectral data for **14**: IR (neat) cm^{-1}: 2955, 1417, 1313, 1255, 1172, 1130, 1105; ^1H NMR (400 MHz) δ: 0.06 (s, 9H), 1.01 (m, 2H), 2.87 (m, 2H); ^{13}C NMR (100.6 MHz) δ: −2.03, 8.28, 47.79; MS (EI), *m/z*(%): 223(30), 210(44), 147(59), 101(38), 75(16), 74(31), 73(100), 58(17); MS (CI, methane), *m/z*(%): 339($(M + TMS)^+$, 3.5), 311($(M + 45)^+$, 12), 267($M + H)^+$, 0.3), 223(57), 210(31), 147(49), 101(51), 75(19), 74(33), 73(100). Anal. calcd. for $C_{10}H_{26}O_2SSi_2$: C 45.09, H 9.85; found: C 45.00, H 10.22.

*Synthesis of **14** by oxidation of **11**a*

An aqueous solution of peracetic acid (35%) (800 mg, 3.82 mmol) was added all at once to a solution of sulfide **11***a* (251 mg, 1.07 mmol) in dichloromethane (8 mL) at 0°C. Treatment as indicated above gave sulfone **14** (284 mg, 99.5%).

Synthesis of tert*-butyl 2-(trimethylsilyl)ethyl sulfide (**12**a)*

Sulfide **12***a* was prepared in a manner similar to the synthesis of **11***a* using *tert*-butanethiol (5.28 g, 58.7 mmol), vinyltrimethylsilane (6.22 g, 62.2 mmol), and AIBN (137 mg). GC of the crude material showed the **12***a*:**12***b* ratio to be 96:4. Distillation of the reaction mixture afforded sulfide **12***a* (10.2 g, 86%) as a liquid (GC purity: 97.3%); bp 39–40°C (1.1 Torr). Spectral data for **12***a*: IR (neat) cm^{-1}: 2921, 1459, 1363, 1255, 1163, 855; ^1H NMR (400 MHz) δ: 0.01 (s, 9H), 0.79 (m, 2H). 1.30 (s, 9H), 2.53 (m, 2H); ^{13}C NMR (50.3 MHz) δ: −1.73, 16.81, 23.38, 30.87, 41.84; MS (EI), *m/z*(%): 190(5.6), 107(14), 91(54), 75(19), 73(100), 59(16), 57(79); MS (EI, high resolution), *m/z*(%) calcd. for $C_9H_{22}SSi$: 190.1212; found: 190.1218.

Synthesis of tert*-butyl 2-(trimethylsilyl)ethyl sulfoxide (**15**)*

Sulfide **12***a* was oxidized in a manner similar to **11***a* using sulfide **12***a* (6.31 g, 33.1 mmol), MeOH (55 mL), water (25 mL), and $NaIO_4$ (7.89 g, 33.1 mmol). Treatment and work-up as described above for **13** afforded quite pure **15** (6.56 g, 96%). A recrystallized sample gave mp 28–30°C and the following spectral data: IR (neat) cm^{-1}: 2933, 1467, 1363, 1252, 1159, 1034, 859; ^1H NMR (400 MHz) δ: 0.04 (s, 9H), 0.77 (dt, J = 4.7 and 13.7 Hz, 1H), 1.19 (dt, J = 4.6 and 13.7 Hz, 1H), 1.20 (s, 9H), 2.40 (m, 2H); ^{13}C NMR (100.6 MHz) δ: −1.83, 10.38, 22.98, 40.84, 52.81; MS (CI, methane), *m/z*(%): 207($(M + H)^+$, 95), 91(28), 90(100), 89(36), 74(370, 73(88), 57(22). Anal. calcd. for $C_9H_{22}OSSi$: C 52.37, H 10.74; found: C 52.36, H 10.70.

*Synthesis of sulfinyl chloride **16** by fragmentation of sulfoxide **13***

To a dry solution of CH_2Cl_2 (35 mL) and sulfoxide **13** (4.01 g, 16.0 mmol) stirred at −78°C was added SO_2Cl_2 (2.66 g, 19.7 mmol). The mixture was stirred for 20 min at −78°C and was allowed to warm to room temperature over 2 h. The volatile components were removed under vacuum. ^1H NMR of the mixture showed **16** to be the major product, with 2-(trimethylsilyl)ethyl chloride as a minor product (ca. 20%). The crude mixture was distilled under vacuum to afford 1.99 g (67%, some decomposition occurred) of pure **16**, bp 59–60°C (0.25 Torr). **CAUTION:** Although we have not encountered any problems, there is always a danger of explosion when distilling sulfinyl chlorides (21). Spectral data for **16**: IR (neat) cm^{-1}: 2942, 1412, 1370, 1252, 1153, 846; ^1H NMR (400 MHz) δ: 0.08 (s, 9H), 1.07 (m, 2H), 3.31 (m, 2H); ^{13}C NMR (100.6 MHz) δ: −1.96, 8.73, 60.85.

*Synthesis of sulfinyl chloride **16** by fragmentation of sulfoxide **15***

The synthesis of **16** above was repeated using **15** (6.16 g, 29.9 mmol) and SO_2Cl_2 (2.69 mL, 32.9 mmol) in ether at −78°C for 2 h before slowly warming to room temperature. The volatile components were removed under vacuum to afford **16** (5.58 g (>95% pure), >96% yield).

*Derivatization of **16***

Aniline (1.04 mL, 11.38 mmol) was added over 2 min to a solution of **16** (1.03 g, 5.55 mmol) in ether (25 mL) at 0°C. The solution was stirred 30 min at 20°C followed by filtration with suction through a frit. Removal of the solvents in vacuo afforded the crude sulfinanilide **17**. The mixture was dissolved in warm 30–60 petroleum ether (8 mL) and a minimum of CH_2Cl_2 and was stored −20°C overnight. The crystals were collected by filtration and the mother liquor was concentrated to yield a second batch of crystals. The recovered solid was washed quickly with cold petroleum ether and dried under vacuum to afford a total of 1.34 g (94%) of **17**. A second recrystallization gave crystals with mp 81–83°C (30–60 petroleum ether/CH_2Cl_2). Spectral data for **17**: IR (neat) cm^{-1}: 3157, 2955, 1601, 1496, 1245, 1052, 857; ^1H NMR (400 MHz) δ: 0.08 (s, 9H), 0.99 (m, 2H), 3.05 (m, 2H), 7.02–7.32 (m, 5H); ^{13}C NMR (100.6 MHz) δ: −1.96, 9.59, 51.55, 118.22, 122.90, 129.39, 141.49; MS (CI, methane), *m/z*(%): 314($(M + TMS)^+$, 12), 242($(M + H)^+$, 4), 213(44), 165(43), 150(19), 124(36), 123(16), 101(28), 93(50), 75(28), 74(23), 73(100).

*Reaction of sulfinyl chloride **16** with thiol **1** to form thiosulfinate **9***

A solution of thiol **1** (220 mg, 2.18 mmol) in CH_2Cl_2 (5 mL) was added slowly to a solution of sulfinyl chloride **16** (400 mg, 2.16 mmol) and K_2CO_3 (1 g) in CH_2Cl_2 (10 mL) at 0°C. The solution was stirred for 1 h and ether (10 mL) was added. The mixture was filtered and concentrated (aspirator). Purification as above gave thiosulfinate **9** (345 mg, 57%).

*Generation and capture of trimethylsilylmethyl sulfine (**18**)*

Triethyl amine (700 μL, 5.03 mmol) was added over a period of 5 min to a solution of sulfinyl chloride **16** (1.42 g, 7.70 mmol) in CH_2Cl_2 (40 mL) at 0°C. The solution was allowed to warm to room temperature and was stirred for 8 h. After concentration (aspirator), the mixture was chromatographed (EtOAc:petroleum ether 1:14 to 1:10 to 1:8) to afford 2-(trimethylsilyl)ethenyl 2-(trimethylsilyl)ethanethiosulfonate **20** (288 mg, 12.6%) followed by **10** (58 mg, 2.2%) and then ethenyl 2-(trimethylsilyl)ethanethiosulfonate **19** (46 mg, 2.6%). Spectral data for **20**: IR (neat) cm^{-1}: 2956, 2900, 1549, 1372, 1331, 1254,

Can. J. Chem. Downloaded from www.nrcresearchpress.com by 195.246.54.202 on 09/08/12
For personal use only.

1168, 1131, 849; ^{1}H NMR (400 MHz) δ: 0.06 (s, 9H), 0.13 (s, 9H), 1.13 (m, 2H), 3.22 (m, 2H), 6.38 (d, J = 17.9 Hz, 1H), 6.72 (d, J = 17.9 Hz, 1H); ^{13}C NMR (100.6 MHz) δ: −2.02, −1.65, 10.80, 58.58, 130.71, 142.15; MS (CI, methane), *m/z*(%): 369((M + TMS)$^+$, 9), 345((M + 45)$^+$, 22), 297((M + H)$^+$, 0.7), 210(23), 204(23), 189(32), 163(52), 147(46), 137(16), 101(70), 93(34), 92(63), 91(92), 75(40), 74(53), 73(100), 59(19), 58(16). Spectral data for **19**: IR (neat) cm^{-1}: 2942, 1413, 1318, 1252, 1173, 1129, 844; ^{1}H NMR (400 MHz) δ: 0.06 (s, 9H), 1.15 (m, 2H), 3.24 (m, 2H), 5.75 (s, J = 16.6 Hz, 1H), 5.80 (d, J = 9.1 Hz, 1H), 6.56 (dd, J = 9.1 and 16.6 Hz, 1H); ^{13}C NMR (100.6 MHz) δ: −2.00, 10.67, 58.21, 125.95, 126.12; MS (EI), *m/z*(%): 297((M + TMS)$^+$, 3), 269((M + 45)$^+$, 14), 225((M + H)$^+$, 1), 210(18), 149(19), 147(27), 137(59), 117(42), 101(82), 75(46), 74(50), 73(100), 59(35), 58(24).

*Capture of 2-(trimethylsilyl)ethanesulfenyl chloride (**23**) with cyclohexene*

Neat SO_2Cl_2 (223 mg, 1.65 mmol) was added to a solution of disulfide **4** (400 mg, 1.50 mmol) in dry CH_2Cl_2 (18 mL) at −78°C. After 5 min cyclohexene (1 mL) was quickly added. The mixture was allowed to stir for 30 min at −78°C and then for 1 h at room temperature. Concentration of the mixture (aspirator) afforded rather pure β-chlorosulfide **24** (744 mg, 99%). Spectral data for **24**: IR (neat) cm^{-1}: 2940, 2859, 1443, 1251, 848; ^{1}H NMR (400 MHz) δ: −0.03 (s, 9H), 0.82 (m, 2H), 1.35–1.71 (m, 6H), 2.14–2.25 (m, 2H), 2.61 (t, J = 8.6 Hz, 2H), 2.83 (m, 1H), 4.03 (m, 1H); ^{13}C NMR (50.3 MHz) δ: −1.85, 17.28, 22.80, 23.41, 27.85, 30.32, 33.48, 49.90, 63.76; MS (EI), *m/z*(%): 252(7.1), 250(17), 209(9), 207(23), 114(29), 101(27), 93(31), 91(19), 81(83), 80(42), 75(29), 74(26), 73(100). Anal. calcd. for $C_{11}H_{23}ClSS$: C 52.87, H 8.87; found: C 52.61, H 8.84.

*Synthesis of trisulfide **25** from disulfide **4***

A solution of SO_2Cl_2 (1.0 M in CH_2Cl_2, 0.94 mL, 0.94 mmol) was added to a solution of disulfide **4** (250 mg, 0.94 mmol) in dry CH_2Cl_2 (12 mL) at −78°C. The solution was then stirred for 7 h at 20°C. Concentration (aspirator) and chromatography (30–60 petroleum ether) afforded trisulfide **25** (93 mg, 50%) as an oil. Spectral data for **25**: IR (neat) cm^{-1}: 2953, 1416, 1252, 1158, 1013, 849; ^{1}H NMR (400 MHz) δ: 0.04 (s, 9H), 0.05 (s, 9H), 1.01 (m, 4H), 2.93 (m, 2H), 3.02 (m, 2H); ^{13}C NMR (100.6 MHz(δ: −1.74, 16.86, 17.13, 34.88, 35.37; MS (CI, methane), *m/z*(%): 371((M + TMS)$^+$, 15), 343((M + 45)$^+$, 14), 315((M + CH_4 + H)$^+$, 56), 299((M + H)$^+$, 1), 298(M, 2), 255(46), 242(61), 163(27), 101(69), 74(29), 73(100). Anal. calcd. for $C_{10}H_{26}S_3Si_2$: C 40.21, H 8.77; found: C 40.05, H 8.69.

*Synthesis of trisulfide **25** from bis(trimethylsilyl) sulfide and thiosulfinate **9***

Bis(trimethylsilyl) sulfide (22) (480 mg, 2.75 mmol) was added to a solution of thiosulfinate **9** (727 mg, 2.58 mmol) in distilled anhydrous $CHCl_3$ (4 mL) at 20°C. The solution was stirred for 24 h at 45°C and then was concentrated (aspirator). Chromatography (30–60 petroleum ether) afforded trisulfide **25** (481 mg, 63%) and disulfide **4** (108 mg, 16%).

*Preparation of trimethylsilyl thioethers **27***

Thiosilane **27***a* was purchased from Aldrich. Thiosilanes **27***b*, **27***c*, and **27***d* were prepared according to established procedures (17).

*Carboethoxyethyl trimethylsilyl sulfide **27**e*

Following the method of Glass (17*b*), a mixture of ethyl 2-mercaptoacetate (7.00 g, 58.2 mmol), hexamethyldisilazane (16.8 g, 104 mmol), and imidazole (129 mg, 1.93 mmol) was heated at 130°C 18 h under nitrogen. After cooling, thiosilane **27***e* (10.43 g, 93%) was collected by distillation (bp 97–98°C (14 Torr)) of the crude mixture. Spectral data for **27***e*: IR (neat) cm^{-1}: 2967, 2352, 1737, 1416, 1367, 1273, 1147, 1035; ^{1}H NMR (400 MHz) δ: 0.29 (s, 9H), 1.23 (t, J = 7.2 Hz, 3H), 3.14 (s, 2H), 4.13 (q, J = 7.2 Hz, 2H); ^{13}C NMR (100.6 MHz) δ: 0.50, 13.95, 27.87, 61.21, 170.98.

*Trimethylsilyl thioacetate **27**f*

Note: this flask must be equipped with a gas outlet, and the reaction must be performed under the fumehood. Lithium hydride (555 mg, 6.98 mmol) was added under nitrogen in portions of 50 mg to a solution of thiolacetic acid (4.83 g, 63.4 mmol) in dry dichloromethane (30 mL) at 0°C. The mixture was stirred for 10 min at 0°C. Neat trimethylchlorosilane (10 mL, 79.3 mmol) was then rapidly added. The reaction mixture was stirred for 20 min at 0°C, then for 2 h at 20°C. The mixture was filtered under nitrogen through a frit (dried and purged with nitrogen). The filtrate was distilled at 760 Torr, then under reduced pressure (14 Torr) using the water line equipped with a calcium chloride trap. A first fraction of yellow liquid was collected at 80–84°C (1.5 g), and a second fraction of an orange liquid identified as **27***f* (6.5 g, 66%) was collected at 82–84°C (18 Torr) (lit. (18) bp 84–85°C (18 Torr). Spectral data for **27***f*: IR (neat) cm^{-1}: 2960, 1715 (weak), 1285 (s), 1253, 1217, 1016, 851 (s); ^{1}H NMR (400 MHz) δ: 0.38 (s, 9H), 2.53 (s, 3H); ^{13}C NMR (100.6 MHz) δ: −0.01, 37.20, 161.13.

*General synthesis of 2-(trimethylsilyl)ethyl containing disulfides **26***

Thiosilane **27** was added under nitrogen to a solution of thiosulfinate **9** (0.5 equiv.; ca. 0.5 M in solvent) in dried and distilled chloroform at 0 or 20°C (Table 2). The temperature was raised and the mixture was stirred until reaction was complete (GC). The solvent was removed in vacuo (aspirator), and the crude product was purified by chromatography to afford disulfide **26**.

*2-(Trimethylsilyl)ethyl methyl disulfide (**26**a)*

A mixture of **9** (300 mg, 1.06 mmol) and **27***a* (300 μL) in chloroform (2 mL), heated at 45°C for 36 h, afforded after chromatography (petroleum ether 30–60) disulfide **26***a* (94 mg, 24%) as an oil. GC analysis: 99+% pure. Spectral data for **26***a*: IR (neat) cm^{-1}: 2953, 2916, 1420, 1252, 1157, 1095, 1014, 952; ^{1}H NMR (400 MHz) δ: 0.04 (s, 9H), 0.94 (m, 2H), 2.41 (s, 3H), 2.75 (m, 2H); ^{13}C NMR (100.6 MHz) δ: −1.75, 17.01, 23.24, 33.96; MS (EI), *m/z*(%): 152(39), 137(32), 101(22), 74(16), 73(100); MS (CI, methane), *m/z*(%): 253((M + TMS)$^+$, 19), 225((M + 45)$^+$, 70), 181((M + H)$^+$, 12), 165(26), 153(22), 149(36), 148(53), 147(100), 75(47), 73(66).

*2-(Trimethylsilyl)ethyl cyclohexyl disulfide (**26**b)*

A mixture of **9** (300 mg, 1.06 mmol) and **27***b* (550 μL) in chloroform (3 mL) heated at 45°C for 8 h, afforded after chromatography (30–60 petroleum ether – 2% EtOAc) disulfide **26***b* (520 mg, 99%). GC analysis: 100% pure. Spectral data for **26***b*: IR (neat) cm^{-1}: 2932, 2853, 1447, 1338, 1252, 1199, 1156, 1095, 1006; ^{1}H NMR (400 MHz) δ: 0.02 (s, 9H), 0.90 (m, 2H), 1.32 (m, 5H), 1.61 (m, 1H), 1.80 (m, 2H), 2.01 (m, 2H), 2.73 (m, 3H); ^{13}C NMR (100.6 MHz) δ: −1.74, 17.08, 25.65, 26.11, 32.96, 36.05, 49.54; MS (EI), *m/z*(%): 248(6.3), 222(15), 221(21), 220(85), 138(77), 123(31), 101(18), 83(28), 74(22), 73(100), 55(20). Anal. calcd. for $C_{11}H_{24}S_2Si$: C 53.20, H 9.75; found: C 53.11, H 10.05.

*2-(Trimethylsilyl)ethyl benzyl disulfide (**26**c)*

A mixture of **9** (500 mg, 1.77 mmol) and **27***c* (963 mg, 4.91 mmol) in chloroform (3 mL) heated at 45°C for 16 h afforded after chromatography (petroleum ether – 5% EtOAc) disulfide **26***c* (853 mg, 94%). GC analysis: 100% pure. Spectral data for **26***c*: IR (neat) cm^{-1}: 3062, 3029, 2952, 1601, 1494, 1454, 1415, 1252, 1199, 1157, 1096, 1070, 1016; ^{1}H NMR (400 MHz) δ: −0.05 (s, 9H), 0.77 (m, 2H), 2.35 (m, 2H), 3.90 (s, 2H), 7.34 (m, 5H); ^{13}C NMR (100.6 MHz) δ: −1.83, 16.94, 34.52, 43.67, 127.35, 128.45, 129.27, 137.90; MS (EI), *m/z*(%): 256(1.4), 229(16), 228(73), 101(27), 92(39), 91(100), 74(28), 73(98), 65(21). Anal. calcd. for $C_{12}H_{20}S_2Si$: C 56.23, H 7.87; found: C 56.02, H 7.89.

*2-(Trimethylsilyl)ethyl p-chlorophenyl disulfide (**26**d)*

Thioether **27***d* (190 μL, 0.798 mmol) was added at 0°C to a solution of **9** (90 mg, 0.319 mmol) in chloroform (1 mL). After 15 h at 20°C, chromatography (30–60 petroleum ether) afforded **26***d* (162 mg,

92%). GC analysis: 98% pure. Spectral data for **26***d*: IR (neat) cm^{-1}: 2953, 1571, 1473, 1415, 1388, 1252, 1158, 1091, 1011; ^1H NMR (400 MHz) δ: 0.01 (s, 9H), 0.93 (m, 2H), 2.77 (m, 2H), 7.30 (d, J = 8.7 Hz, 2H), 7.45 (d, J = 8.7 Hz, 2H); ^{13}C NMR (100.6 MHz) δ: −1.91, 16.79, 34.80, 128.67, 129.03, 132.54, 136.30; MS (EI), *m/z*(%): 278(0.8), 276(1.9), 250(14), 248(31), 145(10), 143(27), 108(22), 101(30), 92(85), 91(89), 90(17), 75(18), 74(30), 73(100), 65(22), 63(18). Anal. calcd. for $C_{11}H_{17}ClS_2Si$: C 47.82, H 6.21; found: C 47.61, H 5.88.

*2-(Trimethylsilyl)ethyl ethoxycarbonylmethyl disulfide (**26**e)*

Thioether **27***e* (643 mg, 3.35 mmol) was added at 0°C to a solution of **9** (450 mg, 1.54 mmol) in chloroform (3 mL). After 9 h at 45°C, chromatography (30–60 petroleum ether – EtOAc 20:1 to 10:1) afforded **26***e* (705 mg, 88%). GC analysis: 100% pure. Spectral data for **26***e*: IR (neat) cm^{-1}: 2957, 1736, 1407, 1265, 1138, 1029; ^1H NMR (400 MHz) δ: 0.03 (s, 9H), 0.92 (m, 2H), 1.30 (t, J = 7.2 Hz, 3H), 2.80 (m, 2H), 3.45 (s, 2H), 4.21 (q, J = 7.2 Hz, 2H); ^{13}C NMR (100.6 MHz) δ: −1.80, 14.14, 16.90, 34.67, 41.62, 61.64, 169.73; MS (EI), *m/z*(%): 224(36), 160(16), 117(26), 101(15), 91(15), 75(21), 74(15), 73(100); MS (CI, methane), *m/z*(%): 325($(M + TMS)^+$, 17), 297($(M + 45)^+$, 9), 253($(M + H)^+$, 1), 225(38), 224(54), 160(44), 119(34), 117(48), 92(25), 91(41), 75(39), 74(29), 73(100). Anal. calcd. for $C_9H_{20}O_2S_2Si$: C 42.82, H 7.98; found: C 42.96, H 8.11.

*2-(Trimethylsilyl)ethyl acetyl disulfide (**26**f)*

Thioester **27***f* (163 mg, 1.10 mmol) was added at 0°C to a solution of **9** (137 mg, 0.486 mmol) in chloroform (2 mL). After 15 h at 20°C, chromatography (30–60 petroleum ether – EtOAc 8:1) afforded **26***f* (176 mg, 87%). Spectral data for **26***f*: IR (neat) cm^{-1}: 2954, 1722, 1418, 1351, 1252, 1159, 1112, 1013; ^1H NMR (400 MHz) δ: 0.01 (s, 9H), 0.91 (m, 2H), 2.45 (s, 3H), 2.76 (m, 2H); ^{13}C NMR (100.6 MHz) δ: −1.87, 16.93, 28.86, 34.98, 195.12; MS (EI), *m/z*(%): 180(5.1), 133(18), 101(17), 91(15), 74(15), 73(100); MS (CI, methane), *m/z*(%): 281($(M + TMS)^+$, 15), 253($(M + 45)^+$, 43), 209($(M + H)^+$, 4), 181(51), 180(42), 151(30), 138(48), 123(24), 101(63), 91(21), 75(21), 74(44), 73(100), 59(17). Anal. calcd. for $C_7H_{16}OS_2Si$: C 39.62, H 7.60; found: C 39.71, H 7.84.

Acknowledgements

We are grateful to the Natural Sciences and Engineering Research Council of Canada for a research grant to A.L.S. and a post-doctoral fellowship to D.B. We thank Sandra L. Edmondson and Jason M. Fischer for technical assistance and H. Stewart MacKinnon for acquiring the mass spectra.

1. E. Block and M. Aslam. Tetrahedron, **44**, 281 (1988).
2. M.B. Anderson, M.G. Ranasinghe, J.T. Palmer, and P.L. Fuchs. J. Org. Chem. **53**, 3125 (1988).
3. A.L. Schwan and R. Dufault. Tetrahedron Lett. **33**, 3973 (1992).
4. S.M. Weinreb, D.M. Demko, T.A. Lessen, and J.P. Demers. Tetrahedron Lett. **27**, 2099 (1986).
5. J.A. Campbell and D.J. Hart. J. Org. Chem. **58**, 2900 (1993).
6. (*a*) M. Ochiai, S. Tada, K. Sumi, and E. Fujita. J. Chem. Soc. Chem. Commun. 281 (1982); (*b*) I. Fleming, J. Goldhill, and D.A. Perry. J. Chem. Soc. Perkin Trans 1, 1563 (1982).
7. (*a*) C.-N. Hsiao and H. Schechter. Tetrahedron Lett. **24**, 2371 (1983); (*b*) M. Ochiai. Yakugaku Kenkyu no Shinpo, **2**, 185 (1986); Chem. Abstr. **109**: 54866z (1988).
8. G.A. Gornowicz, J.W. Ryan, and J.L. Speier. J. Org. Chem. **33**, 2918 (1968).
9. (*a*) E. Block, A. Schwan, and D.A. Dixon. J. Am. Chem. Soc. **114**, 3492 (1992); (*b*) J.P. Danehy. Int. J. Sulfur Chem. Part B: **6**, 103 (1971); (*c*) A. Bulpin and S. Masson. J. Org. Chem. **57**, 4507 (1992).
10. P.L. Folkins and D.N. Harpp. J. Am. Chem. Soc. **115**, 3066 (1993), and references therein.
11. W.K. Musker and J. Takahashi Doi. *In* Reviews on heteroatom chemistry. Vol. 1. *Edited by* S. Oae. MYU, Tokyo. 1988. pp. 120–137.
12. H.J. Chaves das Neves and M.F. Machete. Tetrahedron Lett. 187 (1977).
13. W. Stamm. J. Org. Chem. **28**, 3264 (1963).
14. (*a*) F. Freeman. Chem. Rev. **84**, 117 (1984); (*b*) E. Block and A.A. Bazzi. Tetrahedron Lett. **23**, 4569 (1982); (*c*) F. Freeman and M.C. Keindl. J. Chem. Soc. Chem. Commun. 138 (1984).
15. M. Bogey, C. Demuynck, J.-L. Destombes, A. Gaumont, J.-M. Denis, Y. Vallée, and J.-L. Ripoli. J. Am. Chem. Soc. **111**, 7399 (1989).
16. G. Capozzi, A. Capperucci, A. Degl'Innocenti, R. Del Duce, and S. Menichetti. Gazz. Chim. Ital. **120**, 421 (1990).
17. (*a*) D.N. Harpp, B.T. Friedlander, C. Larsen, K. Steliou, and A. Stockton. J. Org. Chem. **43**, 3481 (1978); (*b*) R.S. Glass. J. Organomet. Chem. **61**, 83 (1973); (*c*) A.R. Bassindale and D.R.M. Walton. J. Organomet. Chem. **25**, 389 (1970).
18. G.A. Gornowicz and J.W. Ryan. J. Org. Chem. **31**, 3439 (1966).
19. G. Capozzi, S. Menichetti, and A. Rosi. J. Chem. Soc. Perkin Trans 2, 2247 (1992).
20. T.I. Ito and W.P. Weber. J. Org. Chem. **39**, 1694 (1974).
21. M.-L. Kee and I.B. Douglas. Org. Prep. Proced. **2**, 235 (1970).
22. J.-H. So and P. Boudjouk. Synthesis, 306 (1989).

Can. J. Chem. Downloaded from www.nrcresearchpress.com by 195.246.54.202 on 09/08/12
For personal use only.

Synthesis, conformational analysis, and molecular structure of 5-ethyl-5,6-dihydro-11*H*-dibenzo[*b,e*]azepine-6-thione

J. IRURRE[1] AND F. MARQUILLAS

Departament de Química Orgànica, CETS Institut Químic de Sarrià, 08017-Barcelona, Spain

AND

A. ALVAREZ-LARENA AND J.F. PINIELLA

Unitat de Cristallografia, Universitat Autònoma de Barcelona, 08193-Bellaterra, Spain

Received June 30, 1993

J. IRURRE, F. MARQUILLAS, A. ALVAREZ-LARENA, and J.F. PINIELLA. Can. J. Chem. **72**, 334 (1994).

5-Ethyl-5,6-dihydro-11*H*-dibenzo[*b,e*]azepine-6-thione has been synthesized and studied in the solid state and in solution by X-ray diffraction and ^{1}H DNMR, respectively. The crystals are monoclinic, $P2_1/n$, $a = 9.642(1)$, $b = 13.757(2)$, $c = 9.889((2)$ Å, $\beta = 98.57(1)°$, $Z = 4$. The structure has been solved by direct methods and refined to an R value of 0.040 for 1771 reflections with $I > 2.5\sigma(I)$. The seven-membered ring has a slightly deformed boat conformation. The activation barrier associated with the inversion ring has been determined, being $\Delta G^{\ddagger} = 21.6$ kcal/mol.

J. IRURRE, F. MARQUILLAS, A. ALVAREZ-LARENA et J.F. PINIELLA. Can. J. Chem. **72,** 334 (1994).

On a préparé et étudié la 5-éthyl-5,6-dihydro-11*H*-dibenzo[*b,e*]azépine-6-thione, dans son état solide par diffraction des rayons-X, et en dissolution par la ^{1}H RMND. Les cristaux sont monocliniques, $P2_1/n$, $a = 9{,}642(1)$, $b = 13{,}757(2)$, $c = 9{,}889(2)$ Å, $\beta = 98{,}57(1)°$, $Z = 4$. La structure a été résolue au moyen de méthodes directes et raffinée à une valeur de $R = 0{,}040$ par 1771 réflexions avec $I > 2{,}5\sigma(I)$. Le cycle heptagonal a une conformation bateau légèrement déformée. La barrière d'activation associée avec l'inversion du cycle a été determinée, étant $\Delta G^{\ddagger} = 21{,}6$ kcal/mol.

Introduction

11*H*-Dibenzo[*b,e*]azepine derivatives are a class of interesting compounds in consequence of their pharmacological properties, among them antidepressant and neuroleptic effects (1, 2). In these compounds the seven-membered ring usually assumes a boat conformation and an interconversion of one boat (I) to another (II) is observed (Fig. 1).

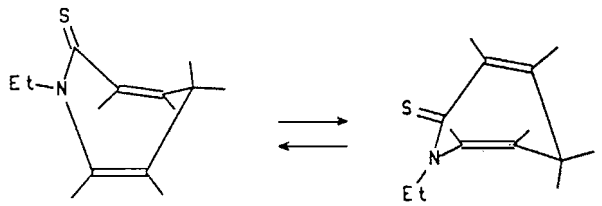

FIG. 1.

Some of us have synthesized and studied 11*H*-dibenzo[*b,e*]-azepines having an interconversion energy high enough to allow the separation of atropisomers (3). The atropisomers obtained are nonsuperimposable mirror images and therefore they are enantiomers. Their energy barriers were measured by racemization kinetics.

Now, we present the synthesis and conformational study of 11*H*-dibenzo[*b,e*]azepines **3** and **4** having a lower interconversion energy barrier than the above cited compounds. In this work the study has been carried out by dynamic nuclear magnetic resonance. We have also determined the conformation of **4** in the solid state by X-ray diffraction. The compounds **3** and **4** have been obtained according to Scheme 1. The lactam **2**, previously described (4), has been synthesized in the present work by a new method (reducing **1** with HI/AcOH). The alkylation of lactam **2** with iodoethane affords the *N*-ethyl derivative **3**. The thiolactam **4** is obtained from **3** by treatment with phosphorus pentasulphide in boiling pyridine.

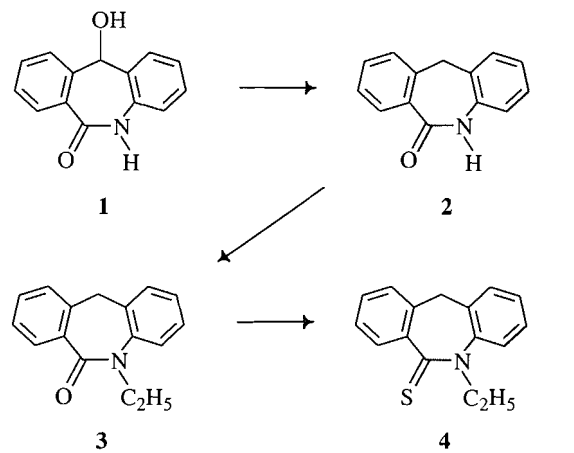

SCHEME 1

Experimental

General

The melting points were measured but not corrected. The IR spectra were taken on a Bomen–Michelson 100 apparatus. ^{1}H NMR spectra were recorded with TMS as internal standard on a Bruker AC80 (80 MHz) at 308 K; for the ^{1}H DNMR measurements this instrument is provided with a variable temperature unit calibrated with an ethylene glycol standard. The mass spectra were obtained using a Hewlett–Packard 5995 AGC/MS system at 70 eV. The UV spectra were recorded in a Hewlett–Packard 8450A instrument. CHN microanalyses were carried out on a Carlo–Erba EA1108 instrument.

Synthesis of 6-dihydro-11H-dibenzo[b,e]azepine-6-one (2)

A mixture of 5.0 g (22 mmol) of the alcohol **1**, 100 mL of acetic acid, and 30 mL of hydroiodic acid 57% was heated to reflux for 5 h. The reaction mixture was poured on water, decolourized with a $NaHSO_3$ solution, and the solid **2** that separated was filtered and dried. Yield 3.9 g (85%), mp 200°C (lit. (4) mp 202–204°C); IR (KBr) ν/cm^{-1}; 3180, 3100 (NH), 3040, 2970, 2920, 1655 (C=O), 1590, 1580,

[1]Author to whom correspondence may be addressed. Telephone: 34-3-2038900; FAX: 34-3-2056266.

Can. J. Chem. Downloaded from www.nrcresearchpress.com by 195.246.54.202 on 09/08/12
For personal use only.

TABLE 1. Crystal data and measurement parameters

$C_{16}H_{15}NS$	M_r = 253.36
a = 9.642(1) Å	Space group $P2_1/n$
b = 13.757(2) Å	Z = 4
c = 9.889(2) Å	D_x = 1.297 Mg m^{-3}
β = 98.57(1)°	μ = 0.22 mm^{-1}
V_c = 1297.1(3) Å^3	$F(000)$ = 536
Radiation	Mo Kα (λ = 0.71069 Å)
No. of collected reflections	2273
No. of unique reflections	2221
No. of observed reflections	1771 $I > 2.5\sigma(I)$
Data collection range (θ)	1°–25°
Scan method	ω/2θ
Range of *hkl*	−11/11; 0/16; 0/11

1500, 1460, 1440, 1380; ^{1}H RMN (DMSO-d_6) δ: 10.43 (br, 1H, NH), 7.90–6.90 (m, 8H, ArH), 3.91 (s, 2H, CH_2).

Synthesis of 5-ethyl-5,6-dihydro-11H-dibenzo[b,e]azepine-6-one (3)

A 60% dispersion of 0.6 g NaH in mineral oil (15 mmol) was washed with petroleum ether. The resulting NaH was added to a solution of 3.0 g (14 mmol) of the lactam **2** in 20 mL of dioxane. The mixture was stirred for 15 min and 2.3 g (15 mmol) of iodoethane were added. The solution was heated to reflux for 2 h. After evaporation of the solvent, the residue was distributed between a water–chloroform system. The organic layer was dried ($MgSO_4$). After evaporation of the solvent the residue was chromatographed through silica gel using chloroform as eluent. The compound **3** obtained was crystallized from ethanol. Yield 2.8 g (81%), mp 90°C; IR (film) ν/cm^{-1}: 3075, 3040, 2980, 2940, 1640 (C=O), 1600, 1580, 1495, 1460, 1380; UV (CH_3CN) λ/nm (log ε): 221 (4.28), 237 (3.99), 277 (3.52); ^{1}H NMR ($CDCl_3$) δ: 7.90–7.00 (m, 8H, ArH), 4.61 and 3.83 (2m, 2H, NCH_2), 4.25, 4.09, 3.59, 3.42 (q, J = 13.1, 2H, $ArCH_2Ar$), 1.31 (t, 3H, CH_3); MS *m/e*: 237 (98%), 222 (20), 209 (100), 208 (27), 180 (22), 165 (27), 152 (15). Anal. calcd. for $C_{16}H_{15}NO$: C 80.98, H 6.37, N 5.90; found: C 81.05, H 6.47, N 5.73.

Synthesis of 5-ethyl-5,6-dihydro-11H-dibenzo[b,e]azepine-6-thione (4)

A mixture of 1.6 g (6.7 mmol) of the lactam **3**, 50 mL of pyridine, and 4.5 g (20 mmol) of phosphorus pentasulphide was heated to reflux for 20 h. After evaporation of the solvent, the residue was distributed between a water–chloroform system. The organic layer was dried ($MgSO_4$). After evaporation of the solvent the residue was chromatographed through silica gel using chloroform as eluent. The compound **4** obtained was crystallized from ethanol. Yield 1.1 g (63%), mp 103°C; IR(film) ν/cm^{-1}: 3070, 2980, 2940, 1600, 1570, 1490, 1470, 1395, 1350, 1120 (C=S); UV (CH_3CN) λ/nm (log ε): 219 (4.31), 313 (4.16), 404 (2.73); ^{1}H NMR (DMSO-d_6) δ: 8.00–7.00 (m, 8H, ArH), 5.40 and 4.30 (2m, 2H, NCH_2), 3.97, 3.81, 3.74, 3.58 (q, J = 12.9, 2H, $ArCH_2Ar$), 1.26 (t, 3H, CH_3); MS *m/e*: 253 (100%), 252 (33), 225 (61), 224 (8), 193 (21), 192 (46), 178 (20), 165 (19). Anal. calcd. for $C_{16}H_{15}NS$: C 75.85, H 5.97, N 5.53, S 12.65; found: C 75.48, H 6.20, N 5.52, S 12.54.

X-ray structure determination and refinement

A suitable monocrystal (0.58 × 0.47 × 0.25 mm) was mounted on an Enraf–Nonius CAD4 automatic diffractometer using graphite-monochromated Mo Kα radiation. The cell parameters were obtained by a least-squares fit of 25 well-centred reflections in the range of 20° < 2θ < 28°. Intensity data were collected using the ω/2θ scan mode in the range 2° < 2θ < 50°. Crystal data and measurement conditions are given in Table 1. One intense reflection monitored every hour did not show any significant change in intensity during data collection. Intensities were corrected for Lorentz and polarization effects but not for absorption. The structure was solved by direct methods using the SHELXS program (5). All non-H atoms were found in this step. The refinement was performed by full-matrix least-squares methods (6). The positions of H-atoms were calculated and an overall isotropic thermal parameter was refined. The last anisotropic refinement cycle converged to R = 0.040, Rw = 0.051 with $Rw = \Sigma\Delta F w^{1/2}/\Sigma F_o w^{1/2}$ where $w = 1/(\sigma^2(F_o) + 0.00235F_o^2)$

Maximum and minimum heights in the final difference Fourier were 0.19 and −0.21 e Å^{-3}. The final atomic coordinates and equivalent isotropic temperature factors are given in Table 2. The scattering factors were taken from the International Tables for X-ray Crystallography (1974).

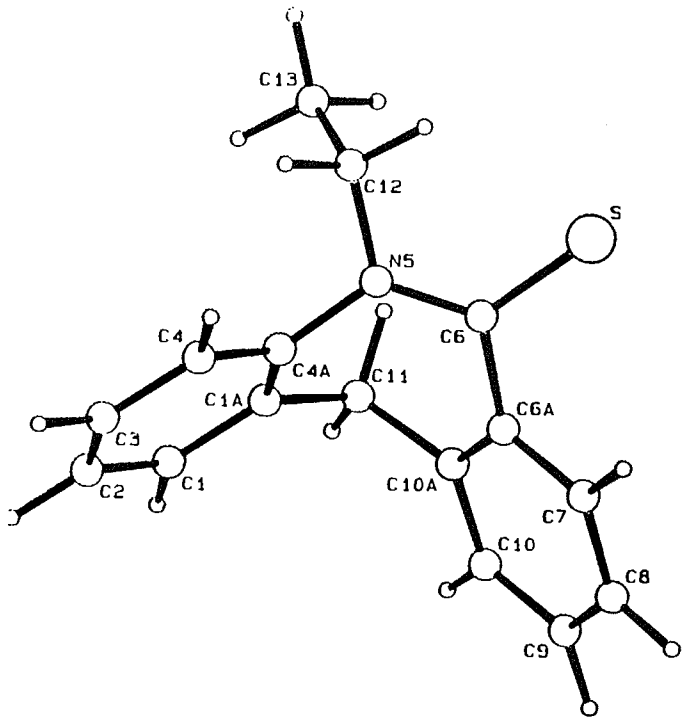

FIG. 2. Perspective view of the molecule.

Results and discussion

A view of the molecule is presented in Fig. 2. Bond distances, bond angles, and torsion angles are given in Tables 3, 4, and 5.[2]

The bond lengths and angles conform to standard values. The nitrogen is trigonal planar: the summation of the three bond angles around the nitrogen is 360.0°, and the C4A, N5, C12, and C6 deviations from their mean plane are small: 0.006(2), −0.014(2), 0.008(3), and 0.006(2) Å, respectively. Table 6 contains relevant conformational information about the title compound and all the 11*H*-dibenzo[*b,e*]azepines whose structures have been reported in the Cambridge Structure Database (7).In compound **4**, the seven-membered ring exhibits a boat conformation. The deviation from a pure boat is small, as pointed out by the asymmetry index ΔC_s[11]. This conformation is usual in this kind of compounds, although there are structures closer to a

[2]A full set of atomic coordinates, bond lengths and angles, and structure factor tables can be purchased from: The Depository of Unpublished Data, Document Delivery, CISTI, National Research Council Canada, Ottawa, ON K1A 0S2, Canada.

Tables of atomic coordinates and bond lengths and angles have also been deposited with the Cambridge Crystallographic Data Centre, and can be obtained on request from The Director, Cambridge Crystallographic Data Centre, University Chemical Laboratory, 12 Union Road, Cambridge, CB2 1EZ, U.K.

Can. J. Chem. Downloaded from www.nrcresearchpress.com by 195.246.54.202 on 09/08/12
For personal use only.

Can. J. Chem. Downloaded from www.nrcresearchpress.com by 195.246.54.202 on 09/08/12
For personal use only.

TABLE 2. Atomic coordinates ($\times 10^4$) and equivalent isotropic thermal parameters (Å^2) for nonhydrogen atoms with esd's in parentheses

	x/a	*y/b*	*z/c*	B_{eq}[a]
C1A	−3083(2)	4529(1)	6132(2)	3.09(6)
C1	−4281(2)	3977(2)	5747(2)	3.62(5)
C2	−5303(2)	3896(2)	6593(3)	4.37(7)
C3	−5121(3)	4354(2)	7831(3)	5.27(8)
C4	−3919(3)	4894(2)	8252(3)	5.03(8)
C4A	−2904(2)	4980(2)	7407(2)	3.44(5)
N5	−1702(2)	5590(1)	7822(2)	3.81(5)
C6	−360(2)	5300(2)	7876(2)	3.71(6)
C6A	−68(2)	4316(2)	7337(2)	3.50(5)
C7	952(2)	3743(2)	8084(3)	4.51(7)
C8	1335(3)	2862(2)	7566(3)	5.28(8)
C9	733(3)	2560(2)	6275(3)	5.11(8)
C10	−290(2)	3132(2)	5525(3)	4.06(7)
C10A	−711(2)	4001(2)	6051(2)	3.23(5)
C11	−1912(2)	4582(2)	5287(2)	3.37(5)
S	1013(1)	5994(1)	8487(1)	5.74(3)
C12	−2042(3)	6610(2)	8132(3)	4.82(7)
C13	−2529(3)	7166(2)	6859(3)	5.15(8)

[a] $B_{eq} = 8/3\pi^2 \Sigma_i \Sigma_j \boldsymbol{u}_{ij} a^*_i a^*_j \boldsymbol{a}_i \boldsymbol{a}_j$.

TABLE 3. Bond distances (Å) with esd's in parentheses

Bond	Distance
C6—S	1.671(2)
C6A—C10A	1.398(3)
C11—C10A	1.513(3)
C10—C10A	1.389(3)
C2—C1	1.389(3)
C1A—C1	1.386(3)
C4A—N5	1.441(2)
C6—N5	1.347(3)
C12—N5	1.483(3)
C6—C6A	1.496(3)
C7—C6A	1.385(3)
C1A—C4A	1.393(3)
C4—C4A	1.384(3)
C1A—C11	1.503(3)
C3—C2	1.365(4)
C9—C10	1.387(3)
C3—C4	1.387(3)
C8—C9	1.385(4)
C13—C12	1.488(4)
C8—C7	1.387(4)

TABLE 4. Bond angles (deg) with esd's in parentheses

Bonds	Angle
C11—C10A—C6A	119.6(2)
C10—C10A—C6A	119.5(2)
C10—C10A—C11	120.8(2)
C1A—C1—C2	121.0(2)
C6—N5—C4A	124.5(2)
C12—N5—C4A	114.6(2)
C12—N5—C6	120.9(2)
C6—C6A—C10A	121.5(2)
C7—C6A—C10A	119.5(2)
C7—C6A—C6	118.8(2)
C1A—C4A—N5	120.2(2)
C4—C4A—N5	119.3(2)
C4—C4A—C1A	120.3(2)
C1A—C11—C10A	106.2(2)
C3—C2—C1	119.7(2)
C4A—C1A—C1	118.6(2)
C11—C1A—C1	122.6(2)
C11—C1A—C4A	118.6(2)
C9—C10—C10A	120.8(2)
N5—C6—S	123.3(2)
C6A—C6—S	117.7(2)
C6A—C6—N5	119.0(2)
C3—C4—C4A	119.9(2)
C8—C9—C10	119.3(2)
C13—C12—N5	111.2(2)
C4—C3—C2	120.4(2)
C8—C7—C6A	120.5(2)
C7—C8—C9	120.3(2)

sofa conformation: BUCVAW (ΔC_s^{6a} = 13.1°), DENYUQ (ΔC_s^{4a} = 18.7°), and MIANSB (ΔC_s^{6a} = 17.5°). In these three molecules the bow, stern, and Ar–Ar′ interplanar angles are greater than in the case of 11*H*-dibenzo[*b*,*e*]azepines with a small ΔC_s[11]. The title compound, **4**, shows high values for these angles, in spite of its small asymmetry index ΔC_s[11]. In compound **4**, both aromatic rings form similar angles (38.8(1)° and 37.0(1)°) with the seven-membered ring mean plane. Both atropisomers are present in the unit cell (the space group does not below to an enantiomorph crystal class).

In solution, the ring inversion has been studied using ^{1}H DNMR for compound **4** and its antecedent **3**. The free energy for the conformational interconversion has been evaluated according to the coalescence temperature "lineshape" method (8).

The kinetic constant $K_c = \pi/\sqrt{2}\sqrt{\Delta\nu^2 + 6J^2}$ (9, 10). The analyzed signals belong to the two diastereotopic protons of the C11 methylene group. Table 7 shows the results obtained in the present work and those previously reported for compound **2** (11). From these results one remarks the increase of conformational rigidity when the hydrogen atom on N5 is substituted by an ethyl group (6.5 kcal/mol) as well as when the oxygen atom on the lactam is replaced by sulphur in the thiolactam function-

TABLE 5. Torsion angles (deg) with esd's in parentheses

Bonds	Angle	Bonds	Angle
C11—C10A—C10—C9	−174.7(2)	C6A—C10A—C10—C9	1.8(3)
C6A—C10A—C11—C1A	−64.5(2)	C11—C10A—C6A—C7	174.7(2)
C11—C10A—C6A—C6	−10.8(3)	C10—C10A—C6A—C7	−1.8(3)
C10—C10A—C6A—C6	172.6(2)	C10—C10A—C11—C1A	112.0(2)
C2—C1—C1A—C4A	1.8(3)	C2—C1—C1A—C11	176.0(2)
C1A—C1—C2—C3	−0.9(4)	C4A—N5—C6—S	−174.6(2)
C12—N5—C6—S	8.4(3)	C6—N5—C12—C13	103.1(3)
C4A—N5—C12—C13	−74.1(3)	C12—N5—C6—C6A	−170.1(2)
C4A—N5—C6—C6A	6.9(3)	C6—N5—C4A—C4	127.2(2)
C6—N5—C4A—C1A	−56.6(3)	C12—N5—C4A—C4	−55.7(3)
C12—N5—C4A—C1A	120.5(2)	C10A—C6A—C6—N5	48.8(3)
C10A—C6A—C6—S	−129.8(2)	C10A—C6A—C7—C8	−0.0(4)
C7—C6A—C6—N5	−136.7(2)	C7—C6A—C6—S	44.7(3)
C6—C6A—C7—C8	−174.6(2)	N5—C4A—C1A—C1	−177.5(2)
N5—C4A—C4—C3	176.3(2)	N5—C4A—C1A—C11	8.1(3)
C4—C4A—C1A—C1	−1.4(3)	C1A—C4A—C4—C3	0.2(4)
C4—C4A—C1A—C11	−175.8(2)	C10A—C11—C1A—C4A	66.8(2)
C10A—C11—C1A—C1	−107.4(2)	C1—C2—C3—C4	−0.3(4)
C10A—C10—C9—C8	0.2(4)	C4A—C4—C3—C2	0.7(4)
C10—C9—C8—C7	−2.1(4)	C6A—C7—C8—C9	2.0(4)

TABLE 6. Asymmetry parameter (12), ΔC_s^{11} (deg), bow and stern angles (13) (deg), and Ar–Ar′ interplanar angle (deg) for 11*H*-dibenzo[*b*,*e*]azepines

Refcode[a] (7)	ΔC_s^{11}	Bow	Stern	Ar–Ar′	Reference
4	5.5	54.0	43.8	75.6	This work
BUCVAW	33.8	52.6	39.6	69.1	2
MIANSB	27.5	51.1	43.2	73.8	14
DENYUQ	29.7	56.2	46.8	78.3	15
DUNXEP	2.3	47.2	37.0	63.9	1
DUNXIT(I)[b]	3.4	46.4	38.4	63.2	1
DUNXIT(II)	3.2	46.2	37.3	63.8	
DUNXOZ	1.6	45.2	35.9	61.0	1
SAPKOJ(I)[b]	10.2	54.4	37.8	68.4	16
SAPKOJ(II)	3.8	54.9	35.3	62.8	

[a]

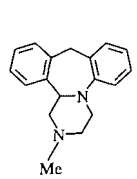

BUCVAW
MIANSB (HBr)

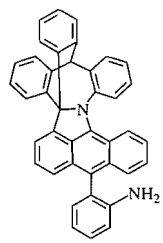

DENYUQ

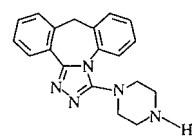

SAPKOJ

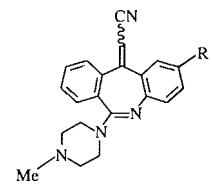

DUNXEP: R = H, (*E*)
DUNXIT: R = H, (*Z*)
DUNXOZ: R = Me, (*Z*)

[b]Two molecules in the asymmetric unit.

TABLE 7. Data and results from ^{1}H DNMR

Compound	Solvent[a]	Δν(Hz)	*J*(Hz)	T_c(K)	K_c(s^{-1})	$\Delta G^{\ddagger}$(kcal/mol)
2	Py/Cl_2CH_2	28.6	13.2	224	95.9	10.9
3	BrC_6D_5	54.1	13.1	355	139.7	17.4
4	DMSO-d_6	12.5	12.9	427	75.6	21.6

[a]The variation of $\Delta G^{\ddagger}$ due to the solvent is assumed negligible (11).

Can. J. Chem. Downloaded from www.nrcresearchpress.com by 195.246.54.202 on 09/08/12
For personal use only.

ality (4.2 kcal/mol). Both are steric effects that increase the instability of the intermediate conformations between the two boats. These steric effects are independent but additive to the strong angular strain from the C=N double bond character of the lactam or the thiolactam. This strain increases the population of the unstable planar intermediate conformation at the expense of the more flexible conformations of the seven-membered ring, where the C—N bond has a bond order near one, and thus the interconversion barrier is increased.

Acknowledgements

J.I. and F.M. thank the Fondo Nacional para el Desarrollo de la Investigación Científica y Técnica (Ministerio de Educación y Ciencia) for financial support (SEUI-PB87-0388).

1. G. Steiner, A. Franke, E. Hädicke, D. Lenke, H.J. Teschendorf, H.P. Hofmann, H. Kreiskott, and W.J. Worstmann. J. Med. Chem. **29**, 1877 (1986).
2. M. Van Meerssche and J.P. Declercq. Bull. Soc. Chim. Belg. **92**, 307 (1983).
3. J. Irurre, F. Marquillas, E. Narbón, C. Puig, and X. Gomis. An. Quim. **88**, 601 (1992).
4. J. Schmutz, F. Künzle, F. Hunziker, and A. Bürki. Helv. Chim. Acta, **48**, 336 (1965).
5. G.M. Sheldrick. SHELXS 86. Crystallogr. Comput.: Data Collect. Struct. Determ. Proteins Databases, Pap. Int. Summer Sch. 9th. *Edited by* G.M. Sheldrick, C. Krüger, and R. Goddard. Oxford University Press, Oxford. 1985. pp. 175–189.
6. G.M. Sheldrick. SHELXS 76. A computer program for crystal structure determination. University of Cambridge, England. 1976.
7. F.H. Allen, O. Kennard, and R. Taylor. Acc. Chem. Res. **16**, 146 (1983).
8. G. Binsch. Top. Stereochem. **3**, 97 (1968).
9. M. Ōki, H. Iwamura, and N. Hayakawa. Bull. Chem. Soc. Jpn. **37**, 1865 (1964).
10. R.J. Kurland, M.B. Rubin, and W.B. Wise. J. Phys. Chem. **74**, 961 (1970).
11. A. Linquist and J. Sandström. Chem. Scr. **5**, 52 (1974).
12. W.L. Duax, C.M. Weeks, and D.C. Rohrer. Top. Stereochem. **9**, 271 (1976).
13. V. Bertolasi, V. Ferretti, G. Gilli, and P.A. Borea. Cryst. Struct. Commun. **11**, 1481 (1982).
14. C. Van Rij and D. Feil. Tetrahedron, **29**, 1891 (1973).
15. H. Quast, P. Eckert, B. Seiferling, E.M. Peters, K. Peters, and H.G. von Schnering. Chem. Ber. **118**, 3058 (1985).
16. T. Boulanger, D.P. Vercauteren, G. Evrard, and F. Durant. J. Chem. Soc. Perkin Trans. 2, 217 (1989).

Can. J. Chem. Downloaded from www.nrcresearchpress.com by 195.246.54.202 on 09/08/12
For personal use only.

Electrolytic dissociation of sodium tetraphenylborate in 2-methoxyethanol/water binary solvent mixtures

FULVIO CORRADINI, ANDREA MARCHETTI, MARA TAGLIAZUCCHI, LORENZO TASSI,[1] AND GIUSEPPE TOSI
University of Modena, Department of Chemistry, via G.Campi, 183 41100 Modena, Italy

Received January 28, 1993

FULVIO CORRADINI, ANDREA MARCHETTI, MARA TAGLIAZUCCHI, LORENZO TASSI, and GIUSEPPE TOSI. Can. J. Chem. **72,** 339 (1994).

Thermodynamic properties from conductance data are reported for the $NaBPh_4$ electrolytic solutions in 2-methoxyethanol (component 1)/water (component 2) binary solvent mixtures, working at 19 temperatures ranging from −10 to +80°C and for 6 mixtures covering the $0.1865 \leq x_1 \leq 1$ composition range. Experimental conductivity data were analysed using the Fuoss–Hsia equation, and the chosen salt was found to associate to a certain extent in these solvent mixtures. The resulting dissociation constants (K) of the ion-pair have been used to test some empirical equations $K = K(T)$, $K = K(x_1)$, and $K = K(T, x_1)$. Furthermore, the present findings have been compared with our previously reported results from working with picric acid in the same mixtures and experimental conditions.

FULVIO CORRADINI, ANDREA MARCHETTI, MARA TAGLIAZUCCHI, LORENZO TASSI et GIUSEPPE TOSI. Can. J. Chem. **72,** 339 (1994).

On a déterminé les propriétés thermodynamiques de solutions électrolytiques de $NaBPh_4$ dans des mélanges binaires de solvants formés 2-méthoxyéthanol (composé 1)/eau (composé 2) à partir de données de conductance obtenues à 19 températures allant de −10 à +80°C et pour 6 mélanges de solvant couvrant les compositions $0{,}1865 \leq x_1 \leq 1$. On a analysé les données expérimentales de conductivité à l'aide de l'équation de Fuoss-Hsia et on a trouvé que le sel choisi est toujours partiellement associé dans ces mélanges de solvant. On a utilisé les constantes de dissociation (K) obtenues pour la paire d'ions de cet électrolyte pour évaluer quelques équations empiriques représentant les fonctions $K = K(T)$, $K = K(x_1)$ et $K = K(T, x_1)$. De plus, on a comparé les données obtenues avec les résultats que nous avons rapportés antérieurement en travaillant avec de l'acide picrique dans les mêmes mélanges et dans les mêmes conditions expérimentales.

[Traduit par la rédaction]

Introduction

In some recent investigations (1–4), we have studied the solvent effects on ionization and dissociation reactions that take place in binary nonaqueous and water (W) mixed media.

Initially, we chose picric acid (HPi) as the weak electrolyte and 1,2-ethanediol (ED) and 2-methoxyethanol (ME) as the nonaqueous solvents. Furthermore, we applied the conductometric method at 19 temperatures between $-10 \leq t/°C \leq +80$ and we worked with binaries covering the whole miscibility field expressed by the mole fraction of one component ($0 \leq x_i \leq 1$) in the mixed solvent systems. However, we encountered a number of difficulties in the computer analysis of experimental conductivity data in pure water and in the water-rich regions (1, 3), hence we have limited our investigations only to the region that is rich in organic solvent. Similar studies might have become more common in recent years, but a careful examination of the literature shows that very few papers report on the thermodynamic behavior and dissociation of reference electrolytes (5, 6).

Electrolytes in pure and mixed organic solvents are used in theoretical chemistry and chemical technology; it is therefore desirable to know their thermodynamic and transport properties in these media. Since these chemicals are important, it would be useful to generalize their electrolytic behavior in pure organic solvents and in water-mixed media either empirically or theoretically.

A wide variety of thermodynamic assumptions have been proposed in the literature, usually followed by interpretations of the values obtained. To expand on our knowledge, we have planned a series of studies on $NaBPh_4$ in ME/W mixtures, with an eye to learn the thermodynamic and thermomechanical behavior of the species in the mixed solvents. To investigate the physico-chemical aspects of solvent–cosolvent interactions, we have compared our findings with those previously obtained (7, 8).

Experimental

Materials

2-Methoxyethanol (containing <0.05% of water by mass according to Karl-Fischer titrations) was Carlo Erba (Milan) high purity grade. It was stored over 3 Å molecular sieves for many days before use, and the final purity was checked by gas chromatography (99.7% by mass), which confirmed the absence of other significant organic components. Water for making up the binaries was twice distilled over $KMnO_4$ in a quartz apparatus, and had specific conductance $< 7 \times 10^{-7}$ S cm^{-1} at 25°C. Sodium tetraphenylborate (STB), supplied by Fluka, was purified by recrystallization from hot acetone (spectrograde quality) and desiccated at 80°C.

Apparatus

The apparatus and procedures for measuring density (7), viscosity (8), and dielectric constant (ϵ) (3) have been described. Experimental ϵ values are summarized in Table I and is available as supplementary material.[2] Conductances of the solutions were measured with a Wayne Kerr 6425 Precision Component Analyzer, operating in the 2.5×10^{-9} to 10 S scale-end range, with a sensitivity of $\pm 0.01 \times 10^{-9}$ S and a field frequency of 1 kHz. This instrument is equipped with platinum electrodes (cell constants 10.538 cm and 1.040 cm) for measurements in the lower and upper specific conductivity (χ) limit, respectively. The thermostated measuring cell was embedded in a polyurethane protective jacket, and the temperature was controlled by a Lauda K2R thermostatic bath maintained to ±0.02°C over the entire temperature range. The thermal control was checked by a thermoresistance Pt 100 (Tersid, Milan) inserted into the measuring cell, collecting the resistance values by using the above mentioned WK 6425 PCA. Karl Fischer titrations were performed with an automatic titration system

[1]Author to whom correspondence may be addressed.

[2]Tables I to IX may be purchased from: the Depository of Unpublished Data, Document Delivery, CISTI, National Research Council Canada, Ottawa, Canada K1A 0S2.

Can. J. Chem. Downloaded from www.nrcresearchpress.com by 195.246.54.202 on 09/08/12
For personal use only.

TABLE 1. Binary composition of 2-methoxyethanol (ME, 1)/water (W, 2) solvent system

System	x_1	V_1/V_2 %	Molarity at 25°C ME	Molarity at 25°C W
A	1.0000	100/0	12.6318	—
B	0.6756	90/10	11.5283	5.5363
C	0.4792	80/20	10.3350	11.2336
D	0.3494	70/30	9.1028	16.9489
E	0.2564	60/40	7.8185	22.6785
F	0.1865	50/50	6.4974	28.4006

(Crison model KF431) equipped with a digital burette (Crison model KF738).

Procedure

The mixtures were prepared by weight just before use, by means of a Mettler PM 4800 Δ-range balance. The estimated error in the 2-methoxyethanol mole fraction, x_1, is $\leq 1.5 \times 10^{-4}$.

Different concentrations of $NaBPh_4$ solutions were obtained by successive dilution of the stock solution which was freshly prepared by weight. Concentrations in volume were then calculated from weight concentrations and densities.

Conductance readings were recorded when they become invariant with time and at regular interval of 15 min for each measurement. Solvent conductance corrections were applied to all data at different temperatures.

Results and discussion

The composition of the six solvent mixtures are denoted by the letters A to F, and the mole fraction and molarity of ME and W are shown in Table 1.

To determine the dissociation constants K ($K = K_A^{-1}$) for $NaBPh_4$ (STB) in the selected binary solvent system, conductance measurements were performed at 19 temperatures in the −10 to +80°C range, at 5°C intervals, for at least six different electrolytic concentrations and for each solvent mixture. The experimental data, reporting the equivalent conductances of STB in pure ME and in five binary ME/W mixtures, are tabulated in Tables II–VII.[2] The conductance data have been analysed with a more general conductivity equation proposed by Fuoss–Hsia (9), using a computer program that we modified to take into account the variation of the solution concentration with density. The following equation (10)

Equation 1

was used where the symbols have their usual meaning (3) and an iterative calculation procedure gives the association constant K_A, the limiting ionic conductivity Λ_0, and the interionic distance parameter $\mathring{a}$. To start the procedure an initial Λ_0 is necessary, and this quantity is estimated from an Onsager Λ vs. $C^{1/2}$ plot. In general, only a few iterations are necessary to provide convergence on K_A, Λ_0, and $\mathring{a}$.

The dissociation constant

Table 2 summarizes the dissociation constants of STB in ME/W mixtures obtained using eq. [1]. Unfortunately, there is poor agreement between our K value in the pure solvent ME and those reported in the literature at 25°C ($K = 4.14 \times 10^{-2}$) obtained by other authors (11). Figure 1 shows the plots K vs. t/°C for each binary mixture. These curves are obtained by fitting each set of experimental data using an equation of the type

$$[2] \quad \ln K = a_0 + a_1 T + a_2/T + a_3 \ln T$$

which represents the most commonly used integrated Van't Hoff equation for the dependence $K = K(T)$. The a_i coefficients in eq. [2], obtained by a multilinear regression program TSP (12), are listed in Table VIII (supplementary material), along with the standard deviation $\sigma(\ln K)$ for each binary mixture.

A brief examination of Fig. 1 shows the following features. (*i*) The curves change progressively in shape from convex with a temperature coefficient $d \ln K/dT < 0$ (A, B) up to mixture C, then turn into concave with a temperature coefficient $d \ln K/dT > 0$ (mixtures D, E, F). In particular, starting from pure ME (mixture A) the dissociation constant increases as the mole fraction of water in the mixture increases until curve C ($V_1/V_2 = 80/20$), and then decreases (inverting slope with respect to mixtures A and B) for mixtures D and E. It should be noted that in mixture E we get the lowest K for this electrolyte in the solvent system at the low temperatures. From this composition ratio, the K values further increase rapidly. (*ii*) Curve C shows a maximum around the middle temperature in the range investigated. (*iii*) Taking into account the progressive and regular variation of the $K = K(T)$ curves on passing from mixtures A to F and that the composition of binary solvent varies continuously in the range $0.1865 \leq x_1 \leq 1$, we can assume the K value also varies continuously between that in ME (solvent A) and that for mixture F at each temperature investigated.

Now, starting from the best-fitting equation [2], it is possible to evaluate the thermodynamic parameters for the ion-pair dissociation reaction in ME/W binaries by applying the standard thermodynamic relations of the form:

$$[3] \quad \Delta H^0 = R(a_1 T^2 - a_2 + a_3 T)$$

$$[4] \quad \Delta S^0 = R[a_0 + 2a_1 T + a_3(1 + \ln T)]$$

which provide the values for ΔH^0 and ΔS^0, respectively. Associated with these calculations are uncertainties originating from experimental errors in K and the choice of the function to represent the integrated Van't Hoff equation $K = K(T)$.

Figure 2 shows the variation of ΔH^0 and ΔS^0 with temperature. Useful information that can be derived from these curves include information on solute species, solute–solvent and solvent–cosolvent interactions.

It should first be noted that the signs and trends of ΔH^0 and ΔS^0 are different for different electrolytes. In particular, when considering the dissociation enthalpy, we are concerned with enthalpy changes due to differences between solvated ion pairs in solution and solvated free ions, and with changes in enthalpy due to differences in solute–solvent–cosolvent interactions.

We therefore divide the solvent systems into two distinct regions (13), M_I and M_{II}. Obviously, the thermodynamic properties to be described are sensitive to solute–solvents and solvent–cosolvent interactions.

(*i*) Region M_I, of composition $1 \geq x_1 \simeq 0.4792$

In this composition range, the thermodynamic properties of the solute exhibit a sharp solvent–cosolvent concentration dependence, reflecting an evident disruption of the heterocooperative fluctuations in the solvating sphere. Furthermore, except for pure ME (system A) for which the temperature coef-

Can. J. Chem. Downloaded from www.nrcresearchpress.com by 195.246.54.202 on 09/08/12
For personal use only.

TABLE 2. Dissociation constants (10^3 K/mol dm^{-3}) for $NaBPh_4$ in the 2-methoxyethanol/water solvent system at different temperatures

	System					
t/°C	A	B	C	D	E	F
−10	10.6 ± 0.1	42.2 ± 0.3	97.7 ± 0.8	9.91 ± 0.08	4.63 ± 0.02	14.7 ± 0.1
−5	10.3 ± 0.1	41.8 ± 0.2	99.0 ± 0.8	10.4 ± 0.1	5.02 ± 0.02	16.1 ± 0.1
0	9.96 ± 0.02	41.2 ± 0.2	100.2 ± 1.2	10.9 ± 0.1	5.26 ± 0.03	17.2 ± 0.2
5	9.28 ± 0.02	40.5 ± 0.3	101.3 ± 0.5	11.6 ± 0.1	5.48 ± 0.03	18.4 ± 0.2
10	8.85 ± 0.02	39.6 ± 0.2	101.9 ± 0.5	12.4 ± 0.1	5.68 ± 0.03	20.3 ± 0.2
15	8.42 ± 0.02	39.2 ± 0.4	104.2 ± 0.1	13.1 ± 0.1	5.96 ± 0.05	22.0 ± 0.2
20	7.97 ± 0.02	39.1 ± 0.2	103.6 ± 0.5	13.7 ± 0.1	6.72 ± 0.03	24.2 ± 0.3
25	7.64 ± 0.02	37.2 ± 0.4	105.1 ± 1.1	14.6 ± 0.1	7.03 ± 0.05	25.8 ± 0.4
30	7.52 ± 0.02	36.1 ± 0.4	104.8 ± 0.1	15.0 ± 0.1	7.53 ± 0.06	28.4 ± 0.5
35	7.40 ± 0.02	35.2 ± 0.4	105.1 ± 0.3	15.3 ± 0.2	7.92 ± 0.08	30.7 ± 0.4
40	7.30 ± 0.02	33.5 ± 0.4	104.1 ± 1.3	16.4 ± 0.1	8.17 ± 0.08	32.7 ± 0.5
45	7.29 ± 0.02	32.3 ± 0.4	103.7 ± 1.3	16.9 ± 0.1	8.64 ± 0.08	35.8 ± 0.5
50	7.27 ± 0.03	31.0 ± 0.4	102.6 ± 0.5	17.7 ± 0.2	8.82 ± 0.06	37.7 ± 0.4
55	7.27 ± 0.03	29.8 ± 0.5	102.8 ± 0.3	18.7 ± 0.2	9.37 ± 0.08	41.2 ± 0.5
60	7.12 ± 0.04	28.0 ± 0.4	100.9 ± 0.5	20.8 ± 0.2	9.57 ± 0.04	44.3 ± 0.4
65	6.89 ± 0.04	26.7 ± 0.3	99.0 ± 0.3	23.4 ± 0.2	10.5 ± 0.1	48.6 ± 0.5
70	6.48 ± 0.04	25.5 ± 0.4	98.1 ± 0.4	27.6 ± 0.2	11.5 ± 0.1	56.8 ± 0.6
75	5.82 ± 0.03	23.8 ± 0.4	94.8 ± 0.1	32.1 ± 0.3	13.2 ± 0.1	69.2 ± 0.7
80	4.99 ± 0.05	22.5 ± 0.4	92.4 ± 0.8	38.1 ± 0.3	14.8 ± 0.2	80.0 ± 1.0

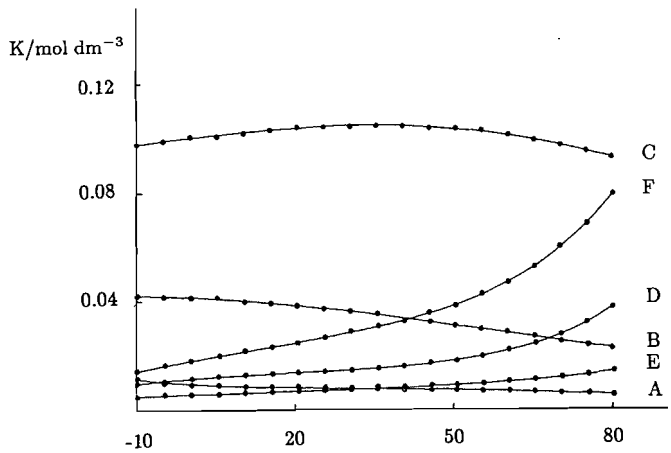

FIG. 1. Experimental dissociation constants of $NaBPh_4$ in 2-methoxyethanol/water at different temperatures and best fitting curves calculated by eq. [2].

ficient $d\Delta Y/dT < 0$ (with $Y = H^0, S^0$), the trend of the curves B, C in Fig. 2 seems to be strongly influenced by the hydrophobic character of ME and tetraphenylborate ion. In fact, the counterion Na^+ could probably be solvated through dipole- and dipole-induced interactions either by ME or W. On the other hand, BPh_4^- ion could be solvated only by ME via weaker interactions provided by short-contact distances between the phenyl groups and the alkyl chains —CH_2—CH_2— in the solvent molecules. A further description in terms of structural models could be made, taking into account that the lower boundary of M_I would correspond to a cosolvent concentration beyond which mixed solvated ions exist, since $d\Delta Y/dT < 0$ in this region, the slope decreases with increasing temperature, and is different for different composition. Thus we assume that the binary mixture having zero temperature coefficient ($d\Delta Y/dT = 0$) is a limiting composition. Within this region mixed solvated solute species can exist, at least to the first solvation sphere.

(*ii*) Region M_{II}, of composition $0.4792 \simeq x_1 > 0.1865$

In this region, dissociation is always endothermic. The variation in thermodynamic properties could reflect a situation in which mixed hydrogen bonding in the solvation sphere is replaced by coordination of the major component in the mixed solvent. In other words, in this region ME molecules should play a co-solute role towards the water molecules rather than a cosolvent role towards STB.

As for entropy, curves B, C and in part curve A, suggest that at a certain temperature an ordered structure is achieved around the solute and it may appear in the form of an ion pair or a free ion, even though this observation is not in agreement with thermokinetic effects. A more reliable explanation takes into account that an increase in temperature brings a decrease in the dielectric constant. Consequently, the charged species could act as structure maker in solution, their electrical field being strong enough to correctly orient the surrounding solvent molecules that form the solvation shell even as the temperature increases. Furthermore, this assumption agrees with the observation that electrostriction between adjacent species is reduced at higher temperatures, when the solvent dielectric constant is reduced compared with that at lower temperature.

In general, positive ΔS^0 values (or very small negative values in restricted temperature range) are obtained in the M_{II} region, confirming that solute dissociation acts as structure-breaker in these mixtures. This observation is in perfect agreement with thermokinetic effects.

We now perform an empirical study of the trend of K vs. binary composition to identify the dissociation behavior of STB in these mixed solvents. We have therefore plotted K vs. x_2 at certain temperatures as shown in Fig. 3.

At any temperature, the curve K vs. x_2 reaches a relative

Can. J. Chem. Downloaded from www.nrcresearchpress.com by 195.246.54.202 on 09/08/12
For personal use only.

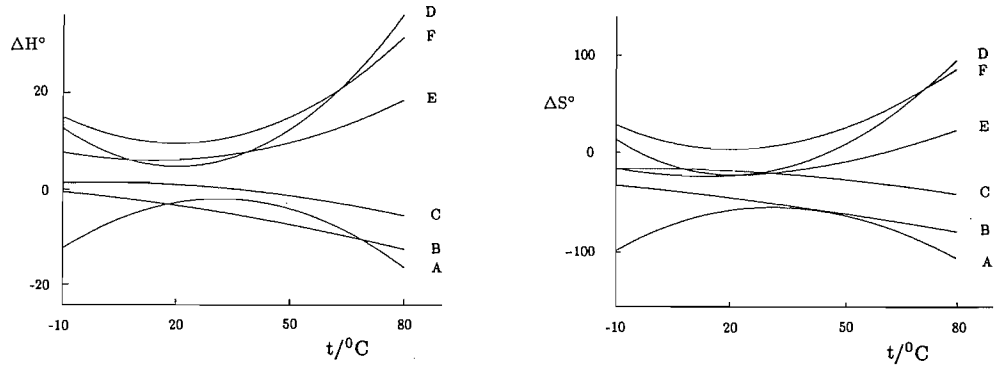

FIG. 2. Dependence on the temperature of ΔH^0 (kJ mol^{-1}), left, and ΔS^0 (J mol^{-1} K^{-1}), right, for the dissociation of $NaBPh_4$ in 2-methoxyethanol/water solvent system.

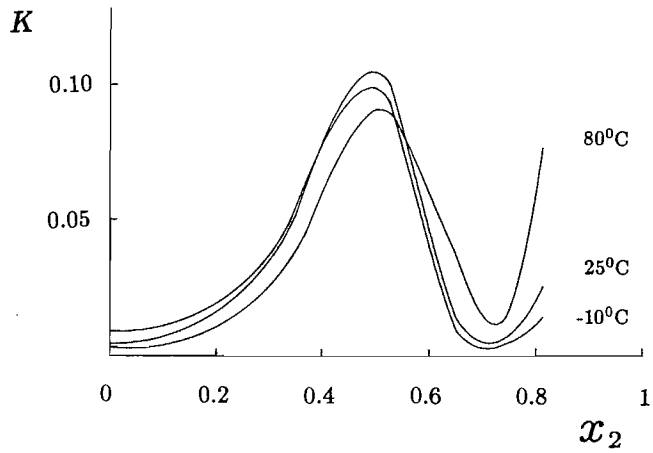

FIG. 3. Dissociation constants (K/mol dm^{-3}) of $NaBPh_4$ in 2-methoxyethanol/water solvent system as a function of binary composition at some selected temperatures.

maximum at $x_2 = 0.5$ (ME:W = 1:1) and then a relative minimum at $x_2 \simeq 0.65$ (ME:W = 1:2). A stable solvent–cosolvent complex ME·2W has been suggested in a previous work (7). According to our observation, this adduct shows the smallest interactions and solvabilities towards the constituting ions of the chosen solute. Consequently the ion-pair in this structure is stabilized and this is manifested as a minimum in the dissociation constant.

Nonlinear relationships like those shown in Fig. 3 suggest that correlation functions could be used to establish the dependence of K on binary composition. Because no model equation $K = K(x_1)$ is available in the literature, and our investigation is restricted to the $100/0 \geq V_1/V_2\% \geq 50/50$ composition range, the simplest attempt of correlation is represented by a polynominal expansion of the general form

$$[5] \quad \ln K = \sum_{j=0}^{n} b_j x_1^j$$

in which coefficients b_j for $n = 4$ are given in Table IX[2] along with the corresponding standard deviation $\sigma(\ln K)$ at each temperature studied.

Now, two empirical relationships are available: $K = K(T)$ and $K = K(x_1)$. To shorten the interpolation procedure, we have derived a single function $K = K(T, x_1)$ combining eqs. [2] and [5]

TABLE 3. c_i coefficients of eq. [6] for $NaBPh_4$ in the 2-methoxyethanol/water solvent system

Variable quantity	Coefficient	Value
	c_0	232.94
x_1	c_1	16851
x_1^2	c_2	−40897
x_1^3	c_3	19104
x_1^4	c_4	2159.3
T	c_5	−0.12428
Tx_1	c_6	7.1155
Tx_1^2	c_7	−19.142
Tx_1^3	c_8	14.402
Tx_1^4	c_9	−2.9818
T^{-1}	c_{10}	−17987
$T^{-1}x_1$	c_{11}	−323026
$T^{-1}x_1^2$	c_{12}	693599
$T^{-1}x_1^3$	c_{13}	−38752
$T^{-1}x_1^4$	c_{14}	−245827
ln T	c_{15}	−20.470
ln $(T)x_1$	c_{16}	−3180.8
ln $(T)x_1^2$	c_{17}	7908.6
ln $(T)x_1^3$	c_{18}	−4262.3

$\sigma(\ln K) = 7.9 \times 10^{-2}$

Equation [6] allows us to calculate the dissociation constant of

$$[6] \quad \ln K(T, x_1) = \ln K(T) \cdot \ln K(x_1)$$
$$= c_0 + c_1 x_1 + c_2 x_1^2 + c_3 x_1^3 + c_4 x_1^4 + c_5 T + c_6 T x_1 + c_7 T x_1^2 + c_8 T x_1^3 + c_9 T x_1^4 + \frac{c_{10}}{T} + c_{11}\frac{x_1}{T} + c_{12}\frac{x_1^2}{T} + c_{13}\frac{x_1^3}{T} + c_{14}\frac{x_1^4}{T} + c_{15} \ln (T) + c_{16} \ln (T) x_1 + c_{17} \ln (T) x_1^2 + c_{18} \ln (T) x_1^3 + c_{19} \ln (T) x_1^4$$

$Na^+BPh_4^-$ in the binaries for any combination of T and x_1. We now simplify eq. [6] by assuming c_{16} has no statistical weight ($\ll 1$) (12). This fitting equation, in which the c_k's are reported in Table 3, provides a set of calculated values that match very well the experimental values, and the average relative uncer-

Can. J. Chem. Downloaded from www.nrcresearchpress.com by 195.246.54.202 on 09/08/12
For personal use only.

TABLE 4. Interionic distances centre-to-centre (*å*/Å) for $NaBPh_4$ in 2-methoxyethanol / water solvent system at different temperatures

	System					
t/°C	A	B	C	D	E	F
−10	13.9	10.2	7.43	1.55	1.06	1.06
−5	13.8	10.5	7.66	1.59	1.08	1.09
0	13.8	10.7	7.89	1.63	1.10	1.12
5	13.4	11.0	8.13	1.68	1.12	1.15
10	13.2	11.2	8.35	1.73	1.15	1.19
15	13.0	11.5	8.65	1.79	1.17	1.24
20	12.7	11.9	8.84	1.84	1.21	1.28
25	12.7	12.0	9.11	1.91	1.24	1.33
30	12.8	12.2	9.34	1.96	1.27	1.39
35	13.0	12.5	9.58	2.01	1.30	1.44
40	13.2	12.7	9.78	2.10	1.34	1.50
45	13.5	12.9	10.0	2.17	1.37	1.58
50	13.8	13.1	10.3	2.25	1.40	1.65
55	14.2	13.3	10.5	2.36	1.44	1.74
60	14.4	13.5	10.7	2.52	1.48	1.84
65	14.4	13.7	10.9	2.74	1.54	1.97
70	14.3	13.9	11.2	3.09	1.55	2.19
75	13.6	14.0	11.3	3.51	1.69	2.55
80	12.5	14.2	11.5	4.11	1.70	2.92

tainty $\overline{\Delta K}$, evaluated by

$$[7] \quad \overline{\Delta K} = \frac{1}{N} \sum_{N} \frac{|K_{\text{exptl}} - K_{\text{calcd}}|}{K_{\text{exptl}}}$$

equals ±0.04 over all the 114 experimental K values in Table 2.

The interionic distance parameter

Table 4 summarizes the ion size-fitting parameter, *å*, obtained for $NaBPh_4$ in ME/W mixtures. Literature (14, 15) states that this fitting parameter is dependent on the conductivity equation [1] chosen and it appears to be related strictly to the association constant. This point introduces uncertainties in the determination of *å* and K_a, and the interpretation of the data obtained is ambiguous because of their mutual adjustment.

Nevertheless, being keeping the suggestions in literature in mind (14, 15), we can still get some information on the fitting parameter *å*. Even though we are not sure how *å* varies with temperature, as shown in Table 4, we can suggest trend. We can classify the mixtures into two groups, A, B, C and D, E, F (Table 4).

The first group is characterized by a very large *å* value, ranging from 7.43 to 14.4 Å, which is an indication of the presence of solvent-separated ion-pairs. It should be noted that the bulk solution in this composition range is probably formed by clusterized ME·2W units immersed in a matrix of additional ME molecules (7). Therefore, any solvation process should be performed first by free ME molecules and, eventually, by the voluminous ME·2W clusters. Consequently solvated ions could only interact at very long distances as shown in Table 4.

The second group of curves (D, E, F) seems to show a very different behavior. In fact, the value of *å* ranges from 1.06 to 4.11 Å, and only at temperatures higher than 70°C does the fitting parameter become significantly greater than 3 Å. Therefore in this composition range one suggests that the ion pairs are slightly separated by solvent molecules, the bulk of the solution comprises ME·2W complex adduct and water molecules.

A significant feature in the electrolytic behaviour of STB in ME/W mixture is that the bolaform tetraphenyl ion remains unsolvated in mixtures with $x_1 \leq 0.3494$ (mixture D), although the cut-off concentration might change.

Conclusions

Certain conclusions may be drawn from our results, when our previous work on the same mixtures are taken into consideration. Changes in the thermodynamic properties of a dissociating electrolyte, induced by changing solvent composition, often provide useful insights into the structural character of the binary systems. In fact, from the thermodynamic behaviour of the reference electrolyte we have witnessed the formation of a termolecular stable solvent–cosolvent aggregate ME·2W. The intrinsic characteristics and low dipole moments of ME·2W indicate poor solvability towards free ions since the solutes have low K values.

The present findings reinforce our previous observations and confirm the existence of a "limiting mixture" in the ME/W solvent system. In an earlier paper (3), a determination of the experimental dissociation constant of HPi in the same solvent system at various temperatures has been reported, and a sharp change in the trend in $K = K(T)$ curves allowed us to propose the existence of a singular binary composition that was called "limiting mixture". This particular solvent mixture was identified by an unambiguous inversion of the trend from concave to convex and its composition corresponded to two well-defined regions, separated by $x_1 \simeq 0.65$ (ME:W = 2:1).

Now, a comparison between our results and those in ref. 7 shows that the "limiting mixture" for the binary solvent system is not that detected using HPi, but the ME·2W termolecular adduct that was also observed by studying volumic properties of the mixed solvents (7). However, it should be noted that the behaviour of the electrolytes (HPi and STB) in ME/W mixtures should probably be attributed to the very different molecular structures of the selected species, in particular those of anions.

The apparent disagreement in these findings is an incentive to study other solutes in the same binary systems and to study other solvents so that we might understand the specific interactions between the different molecules.

Acknowledgments

The authors gratefully thank Professor C. Preti for helpful suggestions and encouragement and to the Consiglio Nazionale delle Ricerche (C.N.R.) of Italy for financial support.

1. G.C. Franchini, A. Marchetti, L. Tassi, and G. Tosi. J. Chem. Soc. Faraday Trans. 1, **84**, 4427 (1988).
2. G.C. Franchini, A. Marchetti, C. Preti, L. Tassi, and G. Tosi. J. Chem. Soc. Faraday Trans. 1, **85**, 1697 (1989).
3. A. Marchetti, E. Picchioni, L. Tassi, and G. Tosi. Anal. Chem. **61**, 1971 (1989).
4. G.C. Franchini, A. Marchetti, L. Tassi, and G. Tosi. Anal. Chem. **62**, 1004 (1990).
5. M. Spiro. *In* Physical chemistry of organic solvent systems. *Edited by* A.K. Covington and T. Dickinson. Plenum Press, London. 1973.
6. Y. Marcus. Rev. Anal. Chem. **5**, 53 (1980).
7. F. Corradini, G.C. Franchini, L. Marcheselli, L. Tassi, and G. Tosi. Aust. J. Chem. **45**, 1109 (1992).
8. F. Corradini, A. Marchetti, M. Tagliazucchi, L. Tassi, and G. Tosi. Aust. J. Chem. **46**, 1711 (1993).
9. R.M. Fuoss and K.L. Hsia. J. Am. Chem. Soc. **90**, 3055 (1968).
10. G. Roland, M.K. Chantooni, Jr., and I.M. Kolthoff. J. Chem. Eng. Data, **28**, 162 (1983).

Can. J. Chem. Downloaded from www.nrcresearchpress.com by 195.246.54.202 on 09/08/12
For personal use only.

11. D. Nandi, and D.K. Hazra. J. Chem. Soc. Faraday Trans. 1, **85**, 4427 (1989).
12. H. Hall (*Editor*). Time Series Processor – TSP – User's Guide. TSP International, Stanford, CA 94305. 1987.
13. R. Lumry, E. Battistel, and C. Jolicoeur. Faraday Symp. Chem. Soc. **17**, 93 (1982).
14. J.F. Skinner and R.M. Fuoss. J. Phys. Chem. **68**, 1882 (1964).
15. A.K. Covington and M.J. Tait. Electrochim. Acta, **12**, 113 (1967).

Can. J. Chem. Downloaded from www.nrcresearchpress.com by 195.246.54.202 on 09/08/12
For personal use only.

Optimization of pyrolysis–desorption chemical ionization mass spectrometry and tandem mass spectrometry of polysaccharides[1]

R.J. HELLEUR

Department of Chemistry, Memorial University of Newfoundland, St. John's, NF A1B 3X7, Canada

AND

PIERRE THIBAULT

Institute for Marine Biosciences, National Research Council of Canada, 1411 Oxford St., Halifax, NS B3H 3Z1, Canada

Received September 4, 1992[2]

R.J. HELLEUR and PIERRE THIBAULT. Can. J. Chem. **72**, 345 (1994).

The operating conditions for pyrolysis–desorption ammonia chemical ionization mass spectrometry and tandem mass spectrometry have been optimized and the technique evaluated for the production and analysis of structurally-informative pyrolytic fragmentation ions corresponding to intact anhydrohexose oligosaccharides, using amylose as the model polysaccharide. Among the various parameters examined it was found that the nature of the solvent used to adhere the sample to the emitter coil and the configuration of the emitter and the rate at which it is heated all play important roles in determining the efficiency of the pyrolytic process and the production of high mass fragment ions. Adjustment of reagent gas pressure together with source temperature also influence the chemical integrity of high mass oligomeric pyrolysis products. Under optimal operating conditions using ammonia reagent gas, the analyses of cellulose, laminarin, agars, and chitin gave relatively abundant ions corresponding to ammonium (or protonated) adducts of up to anhydrohexose tetrasaccharide. More importantly, the generation of such higher mass fragment ions provided a sustained ionic current of sufficient duration to perform tandem mass spectrometric analyses.

R.J. HELLEUR et PIERRE THIBAULT. Can. J. Chem. **72**, 345 (1994).

On a optimisé le mode opératoire de la pyrolyse/spectrométrie de masse par ionisation chimique par désorption d'ammoniac et de la spectrométrie de masse en tandem et on a évalué la technique pour le production et l'analyse d'ions de fragmentation pyrolytique pouvant fournir de l'information sur la structure d'oligosaccharides d'anhydrohexoses intacts, en utilisant l'amylose comme polysaccaride modèle. Parmi les divers paramètres examinés, on a trouvé que la nature du solvant utilisé pour faire adhérer l'échantillon sur la bobine émettrice et la configuration de l'émetteur ainsi que la vitesse à laquelle il est chauffé jouent tous des rôles importants dans la détermination de l'efficacité du processus pyrolytique et dans la productions des ions fragmentés de masse élevée. Un ajustement de la pression gazeuse du réactif avec la température de la source influence aussi l'intégrité chimique des produits de pyrolyse oligomérique de masse élevée. Dans des conditions d'opération optimales utilisant de l'ammoniac comme gaz réactif, les analyses de cellulose, de laminarine, d'agars et de chitine donnent toutes des ions relativement abondants correspondant aux adduits ammonium (ou protonés) de composés allant jusqu'au tétrasaccharide d'anhydrohexose. Ce qui est encore plus important est que la génération d'ions fragments d'une masse aussi élevée fournit un courant ionique pendant une période telle qu'elle permet de réaliser des analyses par spectrométrie de masse en tandem.

[Traduit par la rédaction]

Introduction

Pyrolysis – mass spectrometry (Py–MS) has a great potential for the rapid investigation of complex biopolymers such as polysaccharides, where structural information can be obtained from the fragment ions produced directly from solid samples. Several types of Py–MS techniques have been employed on carbohydrates including laser Py–MS (1, 2), Curie-point Py–MS (3, 4), and in-source, or, pyrolysis–desorption chemical ionization mass spectrometry (Py–DCI-MS) (5–8). Laser pyrolysis, often loosely referred to as laser desorption, is very well suited for the structural analysis of polysaccharides where intact "parent-molecular ions" and thermal fragmentation ions are generated following sample desorption using intense laser radiation. However, practical problems such as controlling the amount of energy deposited per unit sample volume and the technically complex instrumentation required still prevent laser Py–MS from becoming a routine analytical technique. Curie-point pyrolysis involves sample pyrolysis by inductive heating of a ferromagnetic filament using a high frequency coil. Although this method allows for very rapid heating rates and reproducible discrete pyrolysis temperatures, Curie-point Py–MS investigations are normally limited to the analysis of low mass pyrolysis products. Mass fragments higher than 250 dalton are usually not detected due to low transmission of these fragments to the ion source.

The in-source pyrolysis/ionization technique, Py–DCI–MS, where the sample is deposited on a platinum coil and then inserted inside a chemical ionization source by means of an extended probe, is a very simple procedure readily compatible with commercial MS instruments. A number of Py–DCI–MS investigations have been carried out to rapidly characterize polysaccharides using both positive-ion (5–8) and negative-ion (7, 8) chemical ionization. The most useful conditions for the analysis of carbohydrates involve ammonia positive-ion chemical ionization. Under in-source pyrolysis, polysaccharides fragment into a series of ions corresponding to intact, desorbed oligosaccharides with a terminal anhydro-sugar unit or with attached sugar ring-cleavage fragments (9). The ions generated are dependent on the position of the polymeric linkage and monomeric structure, and the resulting mass spectra of a range of polysaccharides thus reveal significant information on the structure of the original polymer. Further information on both carbohydrate linkage and sequencing may be obtained from tandem mass spectrometry (MS/MS) of the intact oligosaccharide fragments (5, 8, 10), although these experiments are difficult to reproduce for high mass fragment ions due to their short signal duration.

[1]NRCC No. 34894

[2]Revision received October 5, 1993.

Can. J. Chem. Downloaded from www.nrcresearchpress.com by 195.246.54.202 on 09/08/12
For personal use only.

Can. J. Chem. Downloaded from www.nrcresearchpress.com by 195.246.54.202 on 09/08/12
For personal use only.

Recently, Py–DCI–MS was applied to the characterization of a native polysaccharide isolated from *Yersinia ruckeri* (10). Under appropriate pyrolysis and ionization conditions this polysaccharide yielded anhydrohexosamine fragments which facilitated identification of the trimeric repeating unit of the polymer. MS/MS analyses of the trimeric fragments provided additional evidence of the proposed structure. Subsequently, off-line pyrolytic experiments of the bacterial polysaccharide revealed similar fragmentation characteristics, confirming that anhydro-oligosaccharides are the primary products of Py–DCI–MS.

Many of the previous Py–DCI–MS studies have not involved optimization of pyrolytic and ionization steps. In this paper we report optimization of the operating conditions of Py–DCI–MS in order to raise its analytical potential in characterizing a wider range of polysaccharide structures. As might be expected, various parameters such as heating rate and chamber temperature and pressure have important implications concerning the observation of "intact fragments" and useful mass spectral characteristics. The results of a systematic study of these and other parameters for Py–DCI–MS (and Py–DCI–MS/MS) analysis, such as proper sample adhesion and shape of the emitter coil are presented. The objectives of this study were to achieve (*i*) maximum generation and duration of medium-sized oligosaccharide fragments, and (*ii*) reproducible and structurally-informative mass spectra from a range of structurally different polysaccharides.

Experimental

Materials

Cellulose, amylose, chitin, laminarin, methanol, heptanol, ethane diol, glycerol, and tetraethylene glycol dimethyl ether (TGDE) were purchased from Sigma Chemicals. DCI platinum filaments were either purchased from VG Analytical, Manchester, UK, or fabricated. Agar samples, **V** and **VI**, were obtained from Dr. J.S. Craigie, NRC, Halifax.

Sample application

If necessary, polysaccharides were ground down to fine particles (100–250 μm). The samples (approximately 50 μg) were applied to the platinum filament as shown in Fig. 1. This technique allows for reasonably accurate sample weight measurements and reproducible sample size. The suspension on the filament was allowed to evaporate down in the vacuum lock before the DCI probe was inserted into the ion source. This pre-evaporation resulted in a satisfactory removal of much of the solvent, and was noted to distribute the sample evenly around on the filament surface.

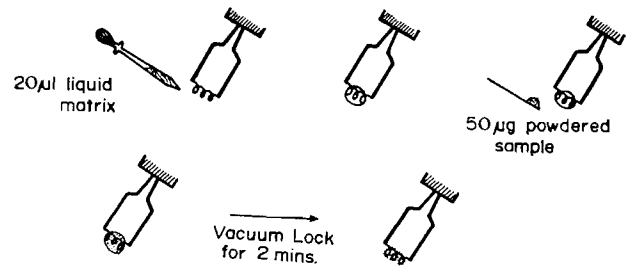

FIG. 1. Method of sample application onto the DCI filament.

Py–DCI–MS (MS/MS) analysis

Py–DCI mass spectra were obtained using a VG Analytical ZAB-EQ hybrid tandem mass spectrometer (VG Analytical, Manchester, UK) equipped with a VG 11-250J data system. For optimum analysis a combined electron impact – CI source was maintained at 150°C, and operated at an accelerating voltage of 8 kV, using an electron energy of 100 eV. For optimum experiments, the ammonia reagent gas was admitted into the source until the pressure at the ion gauge reached 3.0×10^{-4} mbar and the DCI filament was then heated through a linear ramp of 14 mA/s of about 30 s duration. Conventional mass spectra were obtained by scanning the mass spectrometer from *m/z* 140 to 700 at a rate of 2 s per scan cycle. In tandem MS the precursor ion beam was mass selected at a single focus point by adjusting the magnet and collisional activation was effected in the collision cell preceding the electrostatic sector. Helium was used as the collision gas at pressures such that the precursor ion intensity is attenuated by 90%. The fragments formed in the collision were analyzed by scanning the electrostatic sector. Tandem mass spectra were acquired in the multichannel analysis mode, each spectrum representing an accumulation of five to ten scans.

Results and discussion

In previous off-line pyrolysis experiments, it was discovered that considerable amounts of oligosaccharide material are produced from cellulose, **II** (6, 11, 12) as well as from other polysaccharides (11). The condensates from these pyrolyses contain anhydro-oligosaccharides of type **VII**. The main depolymerization process of polyhexoses is considered to take place via cleavage of the glycosidic bonds by an intramolecular trans-

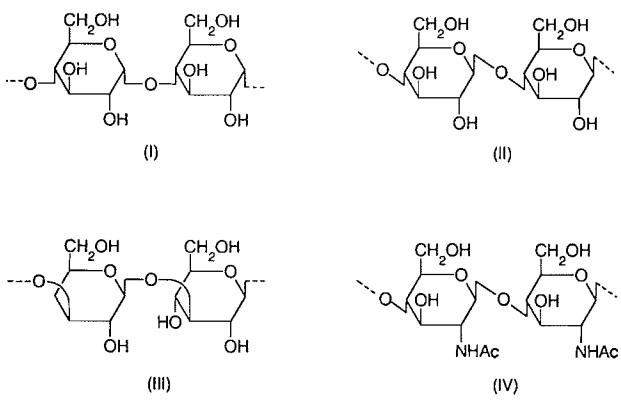

(V) R = H
(VI) R = H (25%), CH_3 (60%), 4- 0- Me- galactose (15%)

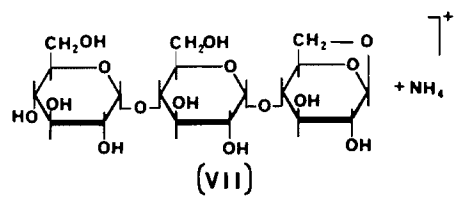

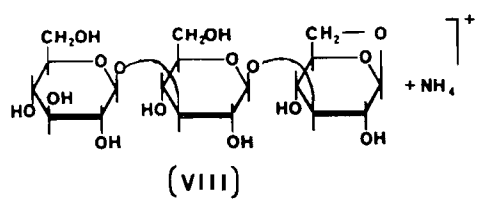

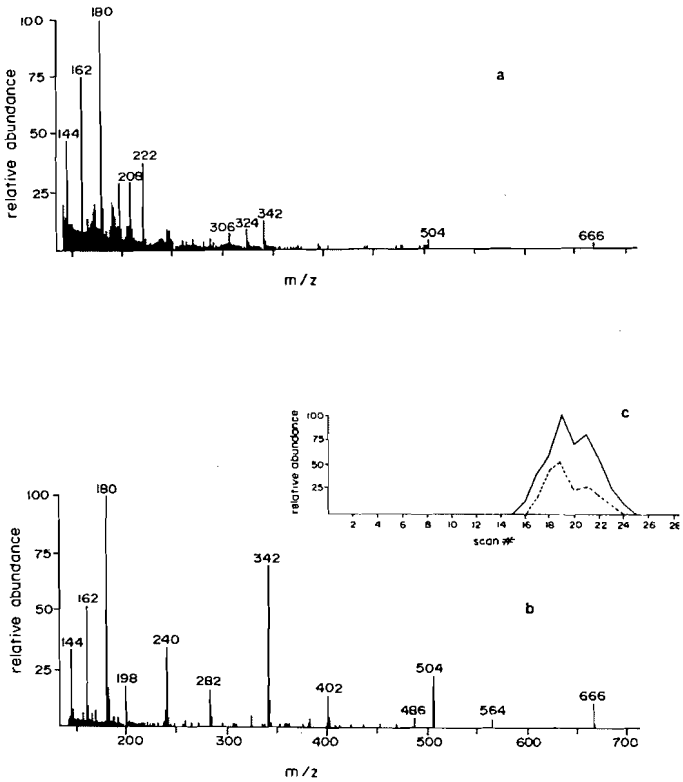

FIG. 2. Py–DCI mass spectra of (*a*) amylose previously suspended in water, (*b*) amylose previously suspended in TGDE solvent (scan 19), and (*c*) reconstructed mass chromatograms of *m/z* 504 and 666 (dashed line) from the analysis of amylose suspended in TGDE.

glycosylation mechanism (13), yielding a stable 1,6-anhydro sugar. In the present Py–DCI–MS study, amylose, **I**, was chosen as a model polysaccharide and ammonia was used as reagent gas. The Py–DCI spectra of amylose, Fig. *2b*, showed mass fragments *m/z* 180, 342, 504, and 666, assigned to ammonia adducts of intact 1,6-anhydro-(oligo)saccharides from the polysaccharide. These ions occurred in a series separated by 162 dalton, the general composition being described as $[(162)_n + NH_4]^+$. Values for *n*, which correspond to the number of hexose rings in the saccharide chain, have been observed to be much greater in Py–DCI–MS studies by Boon *et al*, where oligomers ranging from disaccharides up to undecasaccharides were observed (7). The range of oligomers observed in any one Py–DCI experiment is probably dependent on factors such as the thermal description regime, the design of the CI chamber, and the optical properties of the mass spectrometer used. Adjustable parameters of Py–DCI such as coil design are also important.

The Py–DCI mass spectrum of amylose (Fig. *2b*) shows, besides intact anhydro-oligomeric fragment ion series, another common series of ions (*m/z* 240, 402, 564) containing an intact oligomer attached to a ring-cleavage fragment (i.e., *m/z* = M + 60, where M is the intact oligosaccharide). It is believed that for most glucans, this type of ring-cleavage fragment series is the result of a reverse-aldolization type of pyrolysis mechanism and that the intensity of this ion series is dependent on the type of glycosidic linkage involved (7).

Sample adhesion

Normally, in classical DCI experiments, the solvent is important only in that it is used to transfer a soluble sample onto the DCI emitter coil from which it is subsequently desorbed and chemically ionized. In contrast, Py–DCI experiments of non-volatile polysaccharides involve a thermal fragmentation process leading to the desorption of intact molecules and ionization to parent-molecular ions. The pyrolysis/desorption step is usually optimized by rapid heating of the substrate, where there may be an explosive expulsion process of the large fragments into the CI plasma. Usually the lifetime of the fragment ions is short, a serious drawback to tandem MS experiments.

The choice of solvent for Py–DCI was investigated from the viewpoint of properly adhering a wide range of polysaccharide samples to the DCI coil probe as well as possibly assisting the pyrolysis/desorption process. In the latter case, the choice of solvent may be a fundamental step to successful Py–DCI–MS, similar to the supporting matrix requirements of Fast Atom Bombardment (FAB)–MS. In contrast to FAB–MS, however, solubility of the sample is not a requirement in Py–DCI. Ideally, the polymer sample should be in a fine powdered form and suspended in the solvent. A number of liquids, i.e., water, methanol, heptanol, ethane diol, glycerol, and TGDE were tried. Samples were deposited on the DCI coil containing a small drop of liquid as illustrated in Fig. 1. Methanol, water, and heptanol showed poor adhesive properties for cellulose and other samples, and glycerol, although showing good adhesion, gave strong interfering solvent ion clusters. It was finally discovered that ethane diol was very suitable for water-insoluble polysaccharides (e.g., cellulose) while the less polar solvent, TGDE, was suitable for water soluble samples (e.g., amylose). A comparison of Py–DCI–MS spectra of amylose suspended in water and TGDE is shown in Fig. *2a* and *b*. The case of TGDE resulted in both increased abundance of high mass fragment ions, and decreased levels of background ions. As well, re-constructed ion chromatograms of *m/z* 504 and 666 (Fig. *2c*) show reasonable lifetime and intensity of structurally-important high mass fragments such as tri- and tetra-oligomers.

Source temperature and pressure and coil heating rate

In normal DCI experiments the higher the ion source temperature the greater the fragmentation of the parent molecular ion. For Py–DCI measurements the problem of pyrolyzate condensation and source contamination must be addressed. Moreover, a high enough reagent gas pressure, in this case ammonia, is required to provide a situation where a large portion of the desorbed fragments, many as neutral species, are ionized through soft chemical ionization. An experiment was carried out whereby amylose was analyzed using different source temperatures and reagent gas pressures. The abundances of the pyrolysis fragment ions at 342, 504, and 666 were measured in a set of Py–DCI experiments where source temperatures and pressures were varied (Table 1). It was found that a reagent gas pressure (measured indirectly above the diffusion pump) of approximately 3×10^{-4} mbar and an ion source temperature of 150°C are about optimal conditions for observing a suitable abundance of high mass fragment ions. Under lower (120°C) or higher (180°C) source temperatures and low reagent gas pressures, abundances of high mass fragment ions were observed to decrease. The ammonia ion clusters *m/z* 18:35:52 under these conditions were in the ratio 1.4:0.8:0.3.

It has been suggested that rapid sample heating rate is a very important approach to enhancement of high mass fragment ions in Py–DCI studies. The effect of heating rate on molecular ion

Can. J. Chem. Downloaded from www.nrcresearchpress.com by 195.246.54.202 on 09/08/12
For personal use only.

TABLE 1. The effect of source temperature and reagent gas pressure on the relative abundances of ions *m/z* 504 and 666, ammonium adduct ions of anhydro-oligosaccharides generated from Py–DCI of amylose[a]

Source temperature/°C	Reagent gas pressure[c]/10^{-4} m bar	Sum of *m/z* 504 and 666 ion abundances[b]
120	1.5	0.43
	3.0	0.53
	4.5	0.74
150	1.5	0.76
	3.0	1.00
	4.5	0.92
180	1.5	0.73
	3.0	0.81
	4.5	0.78

[a]Experimental conditions; 50 μg amylose suspended in TGDE, filament heated through a linear ramp of 14 mA/s.
[b]Relative to sum of abundances at $T = 150°C$ and $P_{reagent} = 3.0 \times 10^{-4}$ mbar.
[c]Measured at the ion gauge.

TABLE 2. Absolute abundances of fragment ions *m/z* 342 and 504 generated from Py–DCI of amylose under various filament current ramps[a]

Filament current ramp. mA/s	Absolute abundance ($\times 10^6$)	
	m/z 342	*m/z* 504
70	3.4	0.7
28	5.6	1.8
14	9.2	2.2
7	7.6	1.9

[a]Experimental conditions; 50 μg of amylose suspended in TGDE, source temperature 150°C, and reagent gas pressure 3.0×10^{-4} mbar.

production can be estimated by varying the filament ramp and observing the time-resolved mass profile of key fragment ions. Amylose was thus subjected to Py–DCI at various filament current ramps ranging from 7 to 70 mA/s and the absolute intensities of ions at *m/z* 342 and 504 measured. The results are shown in Table 2. It was found that a filament current ramp of 14 mA/s was best for the satisfactory production of intact oligomeric fragment ions over a reasonable duration (Fig. 2*c*).

Shape of DCI filament

There are three basic configurations for DCI filaments; a single loop filament, or coil filaments positioned either above or between the two terminal posts as illustrated in Fig. 3. Each filament type was used for the Py–DCI analysis of amylose using the optimum operating conditions described above. The resulting Py–DCI mass spectra and the ion current profiles using absolute intensities (Fig. 3) showed that a coiled filament positioned above the terminal posts of the DCI probe is optimal for generating an abundance of intact higher mass fragment ions. This mass spectra was also relatively low in secondary fragmentation products, i.e., dehydration products (e.g., *m/z* 342 – H_2O) as compared to the Py–DCI experiment using the coil between the terminal posts.

Analysis of various glucans

The Py–DCI mass spectra for cellulose (**II**) and laminarin (**III**) glucans with (β-1,4) and (β-1,3) respectively, are shown in Figs. 4 and 5. These spectra, like the comparable spectra of **I**, an α-1,4 linked glucan (Fig. 2) gave strong ions of the anhydro-oligosaccharide series, although the relative efficiencies of their production varied. Each spectrum also contained additional and sometimes unique ions, still with the saccharide repeat unit. It is thought that these spectral differences among the glucans is the result of differences in linkage type and anomeric configuration. An extension of Py–DCI–MS is the potential application of tandem MS studies to differentiate linkage types (see below).

Analysis of heteropolysaccharides

Py–DCI–MS of heteropolysaccharides may provide very valuable structural information in that the polysaccharide polymer is characterized by its unique saccharide components and sequence. By way of illustration, two different types agar have been analyzed. One agar (**V**) has a simple polymeric backbone, a linear chain of alternating β1-3 linked d-galactopyranose, (**A**), and, α1-4 linked 3,6-anhydro-l-galactopyranose, (**B**), residues. The second agar structure (**VI**) is masked in the d-galactose units by methoxy and by 4-O-methyl-galactose residues at position C-6; the detailed structure of this agar has been reported elsewhere (14). The Py–DCI mass spectrum of the simple repeating agar **V** (Fig. 6) clearly shows the repeating saccharide sequence, i.e., *m/z* 324, 486, and 630. It is interesting to note that the mass spectrum also reveals monomeric fragment ions at *m/z* 180 (unit **A**) and 162 (unit **B**) of somewhat equal intensity. Other fragment ions, *m/z* 144, 270, 288, 306, and 468 are identified as dehydration products.

The more complex agar, **VI**, gave a mass spectra (Fig. 7) showing a series of oligomeric fragment ions that reveal the presence of methoxy groups on the d-galactose residue as indicated by the following ions (tentative structural assignments) at *m/z* 338 (methylated **A—B**), 500 (methylated **A—B—A**), 514 (methylated **A—B** – methylated **A**), 644 (methylated **A—B—A—B**), and 658 (methylated **A—B** – methylated **A—B**) where **A** and **B** refer to the two agar units. Some non-methoxy containing disaccharides fragments was observed at *m/z* 324. The limitation of the technique to identify and assign fragment ions of the 4-O-Me-galactose residues of the agar must be noted.

Analysis of amino sugar-containing polysaccharides

The applicability of optimized Py–DCI–MS to the analysis of amino sugar-containing polysaccharides was also evaluated. Chitin (**IV**) was chosen because of its linear and homogeneous structure. The Py–DCI–MS of chitin (Fig. 8) shows the expected series of ions associated with intact anhydro- oligosaccharide fragments at *m/z* 204, 407, and 610. These are not the usual ammoniated adduct ions. Instead, because of the strong proton affinity of the amino functional group, the amino sugar fragments are now protonated species. The remaining protonated ions are derived by dehydration.

Finally, it should be mentioned that the results of our concurrent study of the analysis of bacterial polysaccharides by Py–DCI–MS and Py–DCI–MS/MS (10) showed the versatility of the technique in characterizing *N*-containing heteropolysaccharides.

Tandem MS

In a previous study, tandem MS analysis of the anhydro- tri-

Can. J. Chem. Downloaded from www.nrcresearchpress.com by 195.246.54.202 on 09/08/12
For personal use only.

Can. J. Chem. Downloaded from www.nrcresearchpress.com by 195.246.54.202 on 09/08/12
For personal use only.

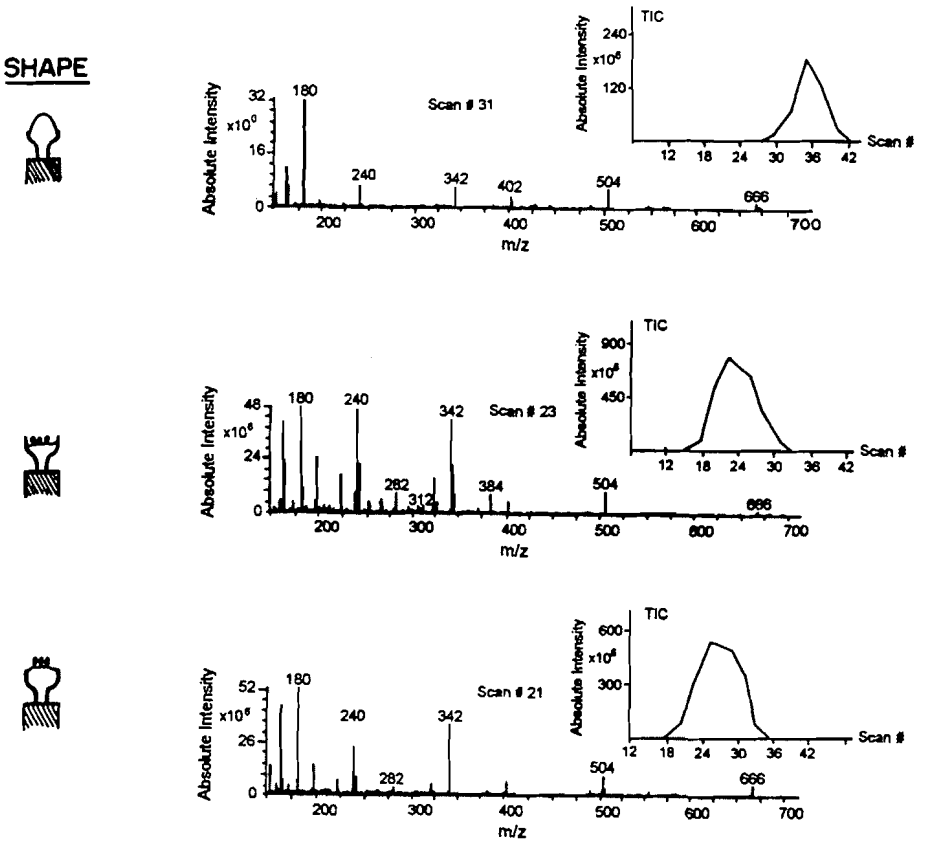

FIG. 3. Py–DCI mass spectra and total ion current profiles of amylose previously suspended in TGDE using various filament shapes.

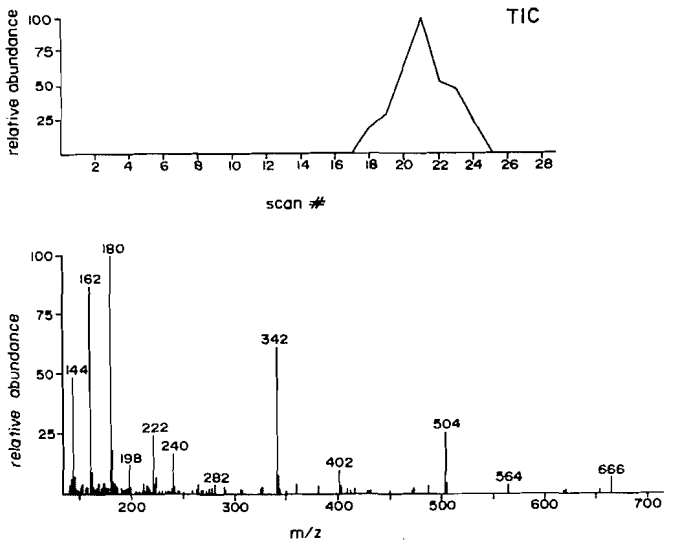

FIG. 4. Py–DCI mass spectra and total ion current profile of cellulose.

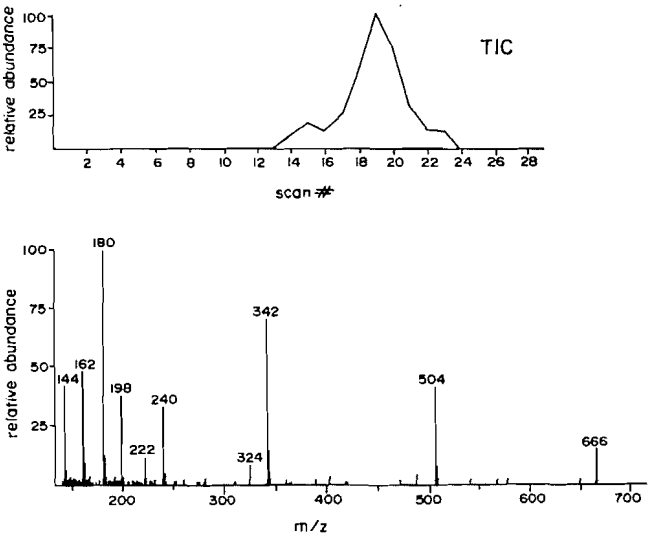

FIG. 5. Py–DCI mass spectra and total ion current profile of laminaran.

meric repeating unit fragment provided additional evidence for the proposed structure of an *N*-containing heteropolysaccharide and permitted rationalization of the observed fragment ions is the original Py–DCI–mass spectra (10).

To illustrate the potential of Py–DCI–MS/MS analysis in differing in linkage types of homosaccharides, two MS analyses and their product ion spectra (MIKES) under collisional activation are given. Figure 9 shows the product ion spectra of the intact anhydro-trisaccharide fragment ions from Py–DCI analysis of laminarin (β-1,3 linked) (Fig. 9*a*) and amylose (α-1,4 linked) (Fig. 9*b*). The two glucans can be readily differentiated by the unique presence of product ion *m/z* 288 in the amylose-derived spectrum. There is also a marked difference in the intensities of the other product ions between the two MIKES spectra. Reasons for these spectral differences have not been deduced.

Further applications of Py–DCI tandem MS will be described

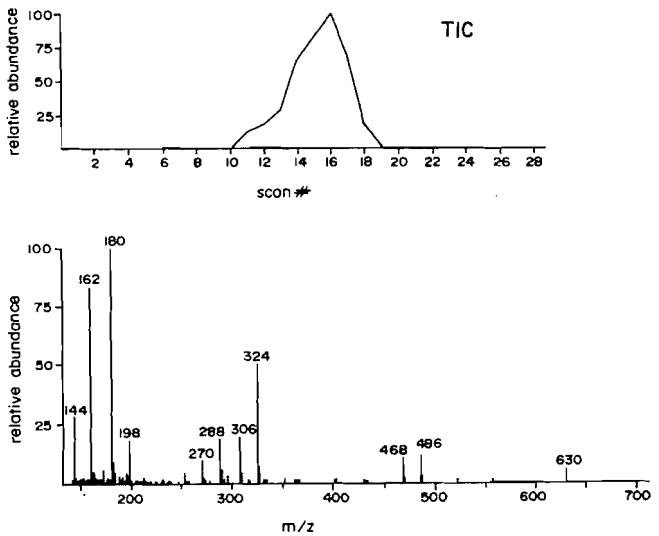

FIG. 6. Py–DCI mass spectra and total ion current of a purified agar.

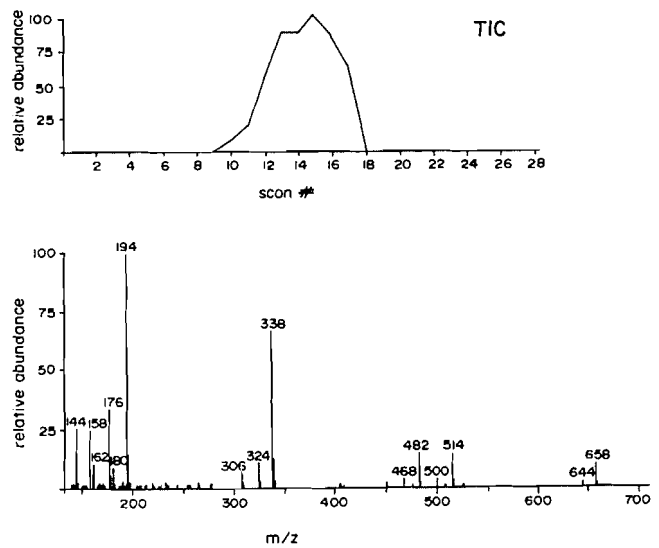

FIG. 7. Py–DCI mass spectra and total ion current of a highly substituted native agar.

in future papers. Our novel approach to structural analysis of these complex biomolecules is promising for applications such as polysaccharide screening and taxonomic studies of bacterial cell walls.

Conclusion

The optimized pyrolytic and desorption chemical ionization conditions under which these Py–DCI–MS experiments were conducted yield structurally useful mass spectra characteristic of the composition of a range of homo- and hetero-polysaccharides. In this study it was found that, in addition to the expected parameters such as source temperature, reagent gas pressure, and filament current ramp, proper adhesion of the sample with selected solvents and choice of filament configuration are important features in obtaining optimized conditions for Py–DCI analysis of carbohydrates. An important result of our work is the attainment of a long-lasting generation of intense fragment ions characteristic of intact anhydro-oligosaccharides. As a result of this the application of tandem MS techniques involving Py–DCI–MS of polysaccharides has become more feasible.

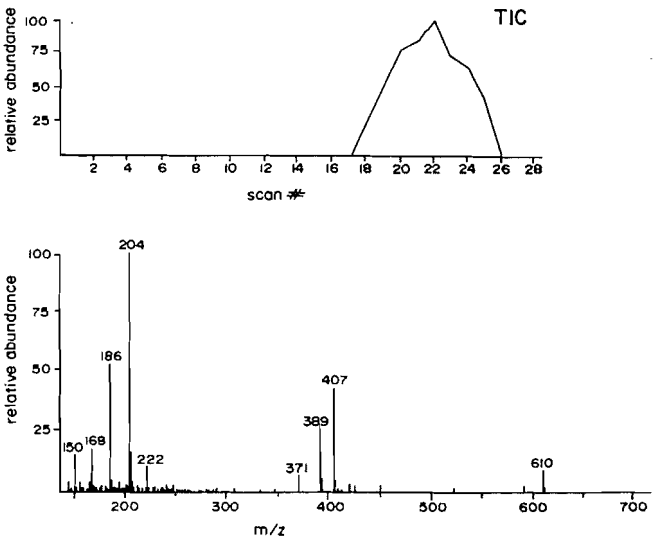

FIG. 8. Py–DCI mass spectra and total ion current of chitin.

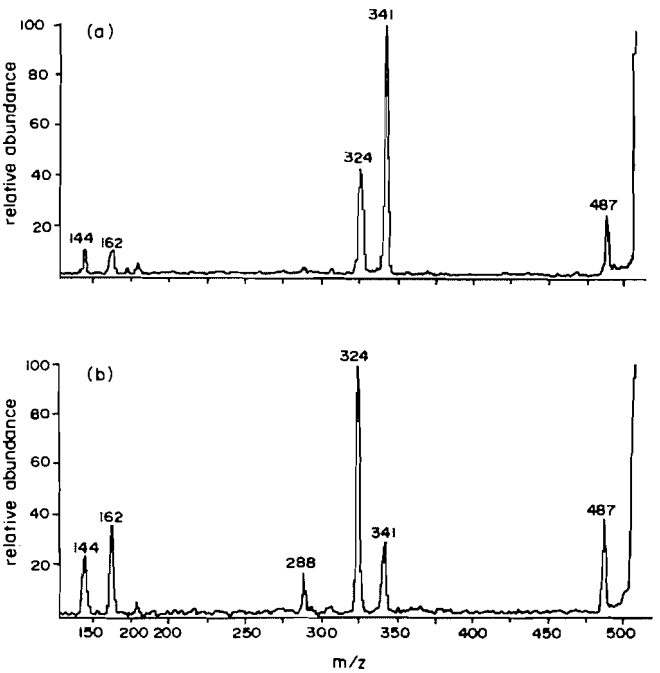

FIG. 9. Product ion spectra (MIKES) of the anhydro- trisaccharide ions of *m/z* 504 from (*a*) laminaran and (*b*) amylose obtained under collisional activation.

Acknowledgement

The work was funded in part (support to R.J.H.) by the Natural Sciences and Engineering Research Council of Canada.

1. M.L. Coates and C.L. Wilkins. Anal. Chem. **59**, 197 (1987).
2. Z. Lam, M.B. Comisarow, and G.G.S. Dutton. Rapid Commun. Mass Spectrom. **1**, 83 (1987).
3. A. van der Kaaden, J.J. Boon, J.W. de Leeuw, F de Lange, P.J.W. Schuyl, H.-R. Schulten, and U. Bahr. Anal. Chem. **56**, 2160 (1982).
4. A. van der Kaaden, J. Haverkamp, J.J. Boon, and J.W. de Leeuw. J. Anal. Appl. Pyrol. **5**, 199 (1983).
5. R.J. Helleur and R. Guevremont. J. Anal. Appl. Pyrol. **15**, 85 (1989).

Can. J. Chem. Downloaded from www.nrcresearchpress.com by 195.246.54.202 on 09/08/12
For personal use only.

6. A.D. Pouwels, G.B. Eijkel, P.W. Arisz, and J.J. Boon. J. Anal. Appl. Pyrol. **15**, 71 (1989).
7. J.A. Lomax, J.J. Boon, and R.A. Hoffmann. Carbohydr. Res. **221**, 219 (1991).
8. A.C. Tas, A. Kerkenaar, G.F. LaVos, and J. van der Greef. J. Anal. Appl. Pyrol. **15**, 55 (1989).
9. P.W. Arisz, J.A. Lomax, and J.J. Boon. Anal. Chem. **62**, 1519 (1990).
10. R.J. Helleur, P. Thibault, J.H. Banoub, and D.H. Shaw. Org. Mass Spectrom. **27**, 167 (1992).
11. R.J. Helleur and P. Jackman. Can. J. Chem. **68**, 1038 (1990).
12. D. St. A.G. Radlein, A. Grinshpun, J. Piskorz, and D.S. Scott. J. Anal. Appl. Pyrol. **12**, 39 (1987).
13. F. Shafizadeh and Y.L. Fu. Carbohydr. Res. **29**, 113 (1973).
14. J.S. Craigie, Z.C. Wen, and J.P. van der Meer. Bot. Mar. **27**, 55 (1984).

Can. J. Chem. Downloaded from www.nrcresearchpress.com by 195.246.54.202 on 09/08/12
For personal use only.

Synthesis and structure of 1,1,3,3,-tetramethyl-2-phenyl-2-(2′,6′-diphenyl-4′-pyrylio)-guanidinium diperchlorate

WLODZIMIERZ GALEZOWSKI,[1] PRADIP K. BAKSHI, KENNETH T. LEFFEK, AND T. STANLEY CAMERON

Department of Chemistry, Dalhousie University, Halifax, NS B3H 4J3 Canada

Received May 27, 1993

WLODZIMIERZ GALEZOWSKI,[1] PRADIP K. BAKSHI, KENNETH T. LEFFEK, and T. STANLEY CAMERON. Can. J. Chem. **72**, 352 (1994).

The reaction of 2-*N*-phenyl-1,1,3,3-tetramethylguanidine with 2,6-diphenylpyran-4-one in the presence of phosphorus oxychloride, followed by treatment with perchloric acid, yields 1,1,3,3-tetramethyl-2-phenyl-2-(2′,6′-diphenyl-4′-pyrylio)guanidinium diperchlorate. Crystals of this material are monoclinic, space group $P2_1/n$, $a = 14.535(3)$, $b = 13.685(3)$, $c = 23.579(7)$ Å, $\beta = 140.38(2)°$, $R = 0.0633$ based on 1691 observed reflections. The substitution of the positively charged pyrylio group on one of the three nitrogen atoms of the guanidinium cation disrupts the symmetry of the distribution of the positive charge on the nitrogen atoms. The two C—N bonds of the central carbon atom of the guanidinium ion to the two methylated nitrogen atoms show more double-bond character than that to the nitrogen carrying the pyrylio group.

WLODZIMIERZ GALEZOWSKI,[1] PRADIP K. BAKSHI, KENNETH T. LEFFEK et T. STANLEY CAMERON. Can. J. Chem. **72**, 352 (1994).

La réaction de la 2-*N*-phényl-1,1,3,3-tétramethylguanidine avec la 2,6-diphénylpyran-4-one, en présence d'oxychlorure de phosphore, suivie d'un traitement par de l'acide perchlorique fournit le diperchlorate de 1,1,3,3-tétraméthyl-2-phényl-2-(2′,6′-diphényl-4′-pyrylio)guanidinium. Les cristaux de ce composé sont monocliniques, groupe d'espace $P2_1/n$ avec $a = 14,535(3)$, $b = 13,685(3)$ et $c = 23,579(7)$ Å, $\beta = 140,38(2)°$ et $R = 0,0633$ pour 1691 réflexions observées. La substitution d'un groupe pyrylio chargé positivement d'un des trois atomes d'azote du cation guanidinium détruit la symétrie de la distribution de la charge positive sur les atomes d'azote. Les deux liaisons C—N de l'atome de carbone central de l'ion guanidinium avec les deux atomes d'azote méthylés présente plus de caractère double que celui vers l'azote portant le groupe pyrylio.

[Traduit par la rédaction]

Introduction

Primary and some secondary anilines, such as *N*-methylaniline, react with 2,6-diphenyl-4*H*-pyran-4-one **1** in the presence of $POCl_3$, to yield 4-aminosubstituted pyrylium salts, such as **2** (1, 2). In sterically hindered reactions, however, secondary aromatic amines can react as carbon nucleophiles (2). Attack as a carbon nucleophile also takes place with the tertiary base dimethylaniline, and Wizinger et al. (3) obtained 4-dimethylaminophenyl-2,6-diphenylpyrylium perchlorate **3** by its reaction with 2,6-diphenyl-4*H*-pyran-4-one **1** in the presence of $POCl_3$, a result subsequently confirmed by Reynolds and Van Allan (4). Other tertiary aromatic amines have been shown (2, 5) to react as carbon nucleophiles with the pyrone **1** in the presence of $POCl_3$.

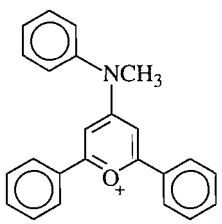

2

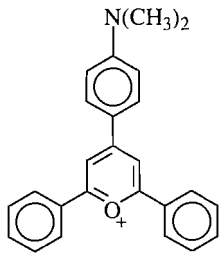

3

As part of our study (6, 7) of the reactions of substituted 2-*N*-phenyl-1,1,3,3-tetramethylguanidine bases (TMG) and the structure of the guanidinium ion (8), we investigated the reaction of 2-*N*-phenylTMG **4** with 2,6-diphenyl-4*H*-pyran-4-one **1** in the presence of $POCl_3$. Since the imino nitrogen atom in 2-*N*-phenylTMG should react as a tertiary centre, this molecule might be expected to react as a carbon nucleophile to yield the salt of the structure **6**, shown in Scheme 1. If the imino nitrogen of the *N*-phenylTMG were a sufficiently strong nucleophile, attack by this centre would give the salt **5**. However, there is no record of any reaction in which a tertiary amidine or a tertiary amine attacks the pyrone carbonyl group as an *N*-nucleophile.

Results and discussion

The product of the reaction was obtained as yellow needles, which gave a ^{13}C nmr spectrum in DMSO-d_6 consisting of 25 peaks. There should be 28 peaks if all the carbon atoms are non-equivalent. However, the two dimethylamino groups each give one peak, since there are only two peaks in that region at 41.3 and 42.2 ppm, reducing the total to 26. It is presumed that the carbon atom bonded to three nitrogen atoms would give a very weak signal, resulting in the 25 observed peaks. The ^1H nmr spectrum showed two methyl signals that did not coalesce in the temperature range 22–95°C. Since the salt **6** gave a single proton resonance for the 12 methyl hydrogens (9), this indicated that the product was probably **5**. This was confirmed by an X-ray structure determination. This finding that the tertiary amidine *N*-phenylTMG attacks the pyrone carbonyl group as an *N*-nucleophile is unique.

The structure of 5

Crystals were prepared for X-ray analysis by dissolving the product (0.2 g) in DMSO (1.5 cm^3), diluting this solution with acetone (10 cm^3), then adding glacial acetic acid (15 cm^3) dropwise with stirring. The solution was allowed to stand overnight and, as the acetone evaporated, the yellow needles formed. The X-ray analysis gave the bond lengths that are listed in Table 1, the bond angles listed in Table 2, and the torsional angles listed in Table 3. A view of the dication is shown in Fig. 1. The three bonds between the central carbon (C1) of the guanidinium group and the three nitrogen atoms are not of equal length in this dication, contrary to the finding in our previous structure determination of a protonated biphenylTMG compound (8). The C(1)—N(2) bond in the dication **5** is 1.391(12) Å, considerably longer, and therefore with much less double-bond character,

[1]Postdoctorate Fellow 1990.

Can. J. Chem. Downloaded from www.nrcresearchpress.com by 195.246.54.202 on 09/08/12
For personal use only.

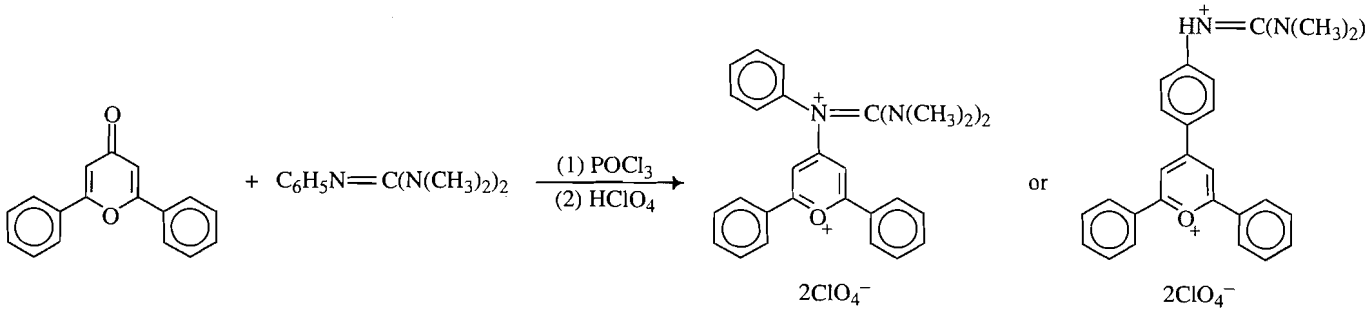

1 **4** **5** **6**

SCHEME 1

TABLE 1. Selected interatomic distances for $C_{28}H_{29}Cl_2N_3O_9$

Bond		Length (Å)
C(11)	—C(12)	1.417(13)
C(11)	—C(15)	1.382(13)
C(11)	—N(2)	1.391(12)
C(12)	—C(13)	1.356(13)
C(13)	—O(1)	1.355(11)
C(13)	—C(31)	1.467(11)
C(14)	—C(15)	1.374(13)
C(14)	—O(1)	1.376(11)
C(14)	—C(41)	1.439(11)
N(2)	—C(1)	1.391(12)
N(2)	—C(21)	1.451(10)
C(1)	—N(1)	1.324(12)
C(1)	—N(3)	1.319(13)
N(1)	—C(2)	1.476(13)
N(1)	—C(3)	1.465(14)
N(3)	—C(4)	1.470(14)
N(3)	—C(5)	1.459(15)
C(21)	—C(22)	1.368(9)
C(21)	—C(26)	1.361(9)
C(22)	—C(23)	1.387(9)
C(23)	—C(24)	1.349(9)
C(24)	—C(25)	1.372(9)
C(25)	—C(26)	1.385(9)
C(31)	—C(32)	1.404(9)
C(31)	—C(36)	1.370(9)
C(32)	—C(33)	1.379(9)
C(33)	—C(34)	1.364(9)
C(34)	—C(35)	1.380(9)
C(35)	—C(36)	1.381(9)
C(41)	—C(42)	1.378(8)
C(41)	—C(46)	1.379(8)
C(42)	—C(43)	1.374(8)
C(43)	—C(44)	1.349(8)
C(44)	—C(45)	1.368(8)
C(45)	—C(46)	1.379(8)

than the C(1)—N(1) and the C(1)—N(3) bonds at 1.324(12) and 1.319(13) Å, respectively. The C(1)—N(2) bond distance in an unprotonated tetramethylguanidino group attached to a phenyl ring has been determined[2] as 1.282(8) Å. The C(1)—N(1) and C(1)—N(3) bond lengths in the dication are roughly the same as those found previously in guanidinium ions (8). The N(2) atom

[2]P. Pruszynski, K.T. Leffek, B. Borecka, and T.S. Cameron. Unpublished work.

TABLE 2. Selected interbond angles $C_{28}H_{29}Cl_2N_3O_9$

Bond			Angle (deg)
C(12)	—C(11)	—C(15)	119.7 (8)
C(12)	—C(11)	—N(1)	119.8 (8)
C(15)	—C(11)	—N(1)	120.4 (8)
C(11)	—C(12)	—C(13)	118.4 (8)
C(12)	—C(13)	—O(1)	121.0 (8)
C(12)	—C(13)	—C(31)	127.7 (8)
O(1)	—C(13)	—C(31)	111.3 (7)
C(15)	—C(14)	—O(1)	118.4 (8)
C(15)	—C(14)	—C(41)	129.6 (8)
O(1)	—C(14)	—C(41)	111.9 (7)
C(11)	—C(15)	—C(14)	120.5 (9)
C(13)	—O(1)	—C(14)	121.9 (7)
C(11)	—N(2)	—C(1)	120.8 (8)
C(11)	—N(2)	—C(21)	121.6 (7)
C(1)	—N(2)	—C(21)	117.5 (7)
N(2)	—C(1)	—N(1)	118.2 (8)
N(2)	—C(1)	—N(3)	119.2 (9)
N(1)	—C(1)	—N(3)	122.6 (9)
C(1)	—N(1)	—C(2)	121.6 (8)
C(1)	—N(1)	—C(3)	123.9 (8)
C(2)	—N(1)	—C(3)	114.5 (8)
C(1)	—N(3)	—C(4)	120.2 (9)
C(1)	—N(3)	—C(5)	123.2 (9)
C(4)	—N(3)	—C(5)	116.6 (9)
N(2)	—C(21)	—C(22)	119.4 (6)
N(2)	—C(21)	—C(26)	117.1 (6)
C(22)	—C(21)	—C(26)	123.4 (6)
C(21)	—C(22)	—C(23)	118.2 (6)
C(22)	—C(23)	—C(24)	119.7 (6)
C(23)	—C(24)	—C(25)	121.0 (6)
C(24)	—C(25)	—C(26)	120.7 (6)
C(21)	—C(26)	—C(25)	116.9 (6)
C(13)	—C(31)	—C(32)	119.7 (6)
C(13)	—C(31)	—C(36)	121.0 (6)
C(32)	—C(31)	—C(36)	119.3 (6)
C(31)	—C(32)	—C(33)	119.3 (6)
C(32)	—C(33)	—C(34)	121.2 (6)
C(33)	—C(34)	—C(35)	119.4 (6)
C(34)	—C(35)	—C(36)	120.5 (6)
C(31)	—C(36)	—C(35)	120.3 (6)
C(14)	—C(41)	—C(42)	118.9 (6)
C(14)	—C(41)	—C(46)	122.3 (6)
C(42)	—C(41)	—C(46)	118.8 (5)
C(41)	—C(42)	—C(43)	119.4 (5)
C(42)	—C(43)	—C(44)	122.1 (6)
C(43)	—C(44)	—C(45)	118.7 (5)
C(44)	—C(45)	—C(46)	120.6 (5)
C(41)	—C(46)	—C(45)	120.3 (5)

Can. J. Chem. Downloaded from www.nrcresearchpress.com by 195.246.54.202 on 09/08/12
For personal use only.

Can. J. Chem. Downloaded from www.nrcresearchpress.com by 195.246.54.202 on 09/08/12
For personal use only.

TABLE 3. Selected torsional angles for $C_{28}H_{29}Cl_2N_3O_9$

Bonds				Angle (deg)
C(12)	—C(11)	—C(15)	—C(14)	−0.1 (12)
C(15)	—C(11)	—C(12)	—C(13)	1.3 (11)
C(12)	—C(11)	—N(2)	—C(1)	−159.5 (7)
C(12)	—C(11)	—N(2)	—C(21)	16.8 (10)
N(2)	—C(11)	—C(12)	—C(13)	−175.5 (7)
C(15)	—C(11)	—N(2)	—C(1)	23.6 (10)
C(15)	—C(11)	—N(2)	—C(21)	−160.0 (7)
N(2)	—C(11)	—C(15)	—C(14)	176.7 (7)
C(11)	—C(12)	—C(13)	—O(1)	−2.3 (11)
C(11)	—C(12)	—C(13)	—C(31)	177.4 (8)
C(12)	—C(13)	—O(1)	—C(14)	2.0 (10)
C(12)	—C(13)	—C(31)	—C(32)	4.8 (9)
C(12)	—C(13)	—C(31)	—C(36)	−174.2 (6)
O(1)	—C(13)	—C(31)	—C(32)	−175.5 (5)
O(1)	—C(13)	—C(31)	—C(36)	5.5 (9)
C(31)	—C(13)	—O(1)	—C(14)	−177.7 (6)
C(15)	—C(14)	—O(1)	—C(13)	−0.8 (10)
O(1)	—C(14)	—C(15)	—C(11)	−0.2 (11)
C(15)	—C(14)	—C(41)	—C(42)	6.4 (9)
C(15)	—C(14)	—C(41)	—C(46)	−174.2 (6)
C(41)	—C(14)	—C(15)	—C(11)	−179.2 (6)
O(1)	—C(14)	—C(41)	—C(42)	−172.6 (5)
O(1)	—C(14)	—C(41)	—C(46)	6.7 (8)
C(41)	—C(14)	—O(1)	—C(13)	178.4 (6)
C(11)	—N(2)	—C(1)	—N(1)	52.0 (11)
C(11)	—N(2)	—C(1)	—N(3)	−129.6 (9)
C(11)	—N(2)	—C(21)	—C(22)	51.7 (8)
C(11)	—N(2)	—C(21)	—C(26)	−127.6 (6)
C(1)	—N(2)	—C(21)	—C(22)	−131.9 (7)
C(1)	—N(2)	—C(21)	—C(26)	48.0 (8)
C(21)	—N(2)	—C(1)	—N(1)	−124.6 (8)
C(21)	—N(2)	—C(1)	—N(3)	53.9 (10)
N(2)	—C(1)	—N(1)	—C(2)	25.9 (10)
N(2)	—C(1)	—N(1)	—C(3)	−152.1 (8)
N(2)	—C(1)	—N(3)	—C(4)	26.1 (11)
N(2)	—C(1)	—N(3)	—C(5)	−149.8 (8)
N(1)	—C(1)	—N(3)	—C(4)	−155.5 (8)
N(1)	—C(1)	—N(3)	—C(5)	28.5 (12)
N(3)	—C(1)	—N(1)	—C(2)	−152.5 (8)
N(3)	—C(1)	—N(1)	—C(3)	29.5 (12)
N(2)	—C(21)	—C(22)	—C(23)	−178.3 (5)
N(2)	—C(21)	—C(26)	—C(25)	179.2 (5)
C(22)	—C(21)	—C(26)	—C(25)	0.0 (8)
C(26)	—C(21)	—C(22)	—C(23)	0.9 (8)
C(21)	—C(22)	—C(23)	—C(24)	−0.6 (8)
C(22)	—C(23)	—C(24)	—C(25)	−0.6 (8)
C(23)	—C(24)	—C(25)	—C(26)	1.5 (8)
C(24)	—C(25)	—C(26)	—C(21)	−1.2 (8)
C(13)	—C(31)	—C(32)	—C(33)	−178.5 (6)
C(13)	—C(31)	—C(36)	—C(35)	178.7 (6)
C(32)	—C(31)	—C(36)	—C(35)	−0.3 (8)
C(36)	—C(31)	—C(32)	—C(33)	0.4 (8)
C(31)	—C(32)	—C(33)	—C(34)	−0.1 (8)
C(32)	—C(33)	—C(34)	—C(35)	−0.3 (8)
C(33)	—C(34)	—C(35)	—C(36)	0.5 (8)
C(34)	—C(35)	—C(36)	—C(31)	−0.2 (8)
C(14)	—C(41)	—C(42)	—C(43)	−177.9 (6)
C(14)	—C(41)	—C(46)	—C(45)	178.3 (6)
C(42)	—C(41)	—C(46)	—C(45)	−2.3 (7)
C(46)	—C(41)	—C(42)	—C(43)	2.7 (7)
C(41)	—C(42)	—C(43)	—C(44)	−1.6 (8)
C(42)	—C(43)	—C(44)	—C(45)	−0.1 (7)
C(43)	—C(44)	—C(45)	—C(46)	0.6 (7)
C(44)	—C(45)	—C(46)	—C(41)	0.7 (7)

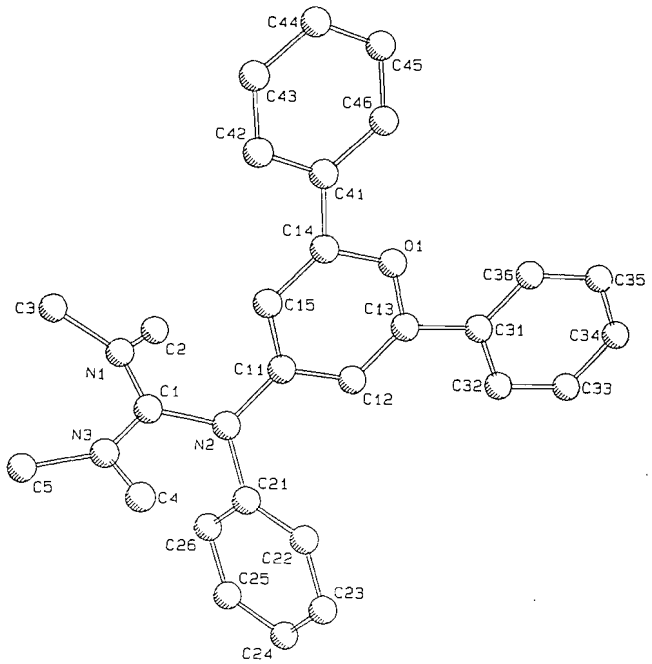

FIG. 1. The 1,1,3,3-tetramethyl-2-phenyl-2-(2′,6′-diphenyl-4′-pyrylio)-guanidinium dication.

has part of its bonding electrons donated towards the pyrylium ring, since the N(2)—C(11) bond is 1.391(12) Å, the same length as the C(1)—N(2) bond, giving both of these bonds some double-bond character. The bond to the phenyl ring N(2)—C(21) is a normal C—N single bond, 1.451(10) Å. Thus, the positive charge of the guanidinium group is predominantly delocalized on the N atoms of the two dimethylamino groups. Structure **5**, therefore, is a minor contributing structure to the resonance hybrid and structure **7** represents one of the two major contributing structures.

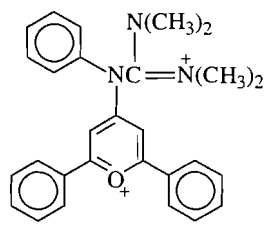

$2ClO_4^-$

7

This is the first guanidinium ion structure found in which the positive charge is largely located on the 1 and 3 nitrogen atoms. This is probably due simply to the presence of the second positive charge, on the pyrylium ring.

The 2,6-diphenylpyrylium and the *N*-phenyl groups are almost planar but the guanidinium group is not. Although the angles between the bonds to the C(1) and N(2) atoms are all close to 120°, the torsional angles are quite large. The bonds from N(2) to the two rings are at an angle of about 50–55° to those from C(1) to the two methylated nitrogens, which is larger than the angle of 32–33° found in a phenyltetramethylguanidinium ion (8). Rotation of the phenyltetramethylguanidinium group must be hindered, in solution, as indicated by the non-

Can. J. Chem. Downloaded from www.nrcresearchpress.com by 195.246.54.202 on 09/08/12
For personal use only.

equivalence of the methyl groups in the ^{1}H nmr spectrum; the general lack of symmetry in the molecule is confirmed by the 25 resonance signals observed in the ^{13}C nmr spectrum.

The UV–visible absorption spectrum of **7** in DMSO, in the presence of $HClO_4$, has a broad band at 380 nm.

Since the tetramethylguanidine group donates electrons to the phenyl ring ($\sigma_p = -0.86$) (9) more strongly than the dimethylamino group ($\sigma_p = -0.83$) (10), it is clear that the product **7** results from another factor, which overrides the increased carbon nucleophilicity of the phenyl ring, causing the phenyltetramethylguanidine to react as the nitrogen nucleophile. This is presumably the same factor that gives guanidines a much greater basicity than anilines, that is, the observed powerful nucleophilicity of the imino nitrogen in this reaction comes from the thermodynamic stability of the product **7** resulting from the delocalization of the positive charge onto the two dimethylamino groups.

Reaction of 7 with water

Although **7** is insoluble in water, fine white crystals were obtained when it was boiled in suspension for 1 h. Elemental analysis and the nmr spectrum indicated that the product was the salt **8**.

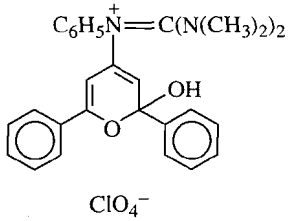

8

Experimental

1,1,3,3-Tetramethyl-2-phenyl-2-(2′,6′-diphenyl-4′-pyrylio)-guanidinium diperchlorate

Preparation

The reaction was carried out by heating a mixture of 2,6-diphenyl-4-pyrone (0.67 g, 0.0027 mol) (11), 2-*N*-phenyltetramethylguanidine (1.3 g, 0.0068 mol) (12), and $POCl_3$ (1.4 cm^3, 0.016 mol) at 100°C on a water bath for 40 min. The reaction mixture was protected from atmospheric moisture with a drying tube filled with silica gel. The thick red-brown product was dissolved in 6 cm^3 of glacial acetic acid and treated with 1.2 cm^3 of 60% $HClO_4$, dropwise. After cooling to room temperature, a yellow crystalline product (1.02 g) was separated by vacuum filtration. Recrystallization from glacial acetic acid gave a yellow product, mp 312–315°C with decomposition, yield 0.95 g, 57% based on the amount of the pyrone used. The product was recrystallized by solution in DMSO, followed by addition of acetone and glacial acetic acid. Yellow needles crystallized overnight, which, after washing several times with glacial acetic acid and drying under vacuum, gave mp 315–316°C, with decomposition; ^{1}H nmr δ (DMSO-d_6): 2.98 (6H, s), 3.37 (6H, s), 7.64–7.89 (11H, m), 8.07 (1H), 8.24 (2H, d), 8.35 (1H, d), 8.42 (2H, d); ^{13}C nmr δ (DMSO-d_6): 41.3, 42.2, 108.2, 108.5, 125.0, 125.3, 127.9, 128.3, 128.4, 128.6, 128.8, 129.0, 129.6, 129.7, 129.9, 130.1, 130.3, 131.0, 133.3, 133.7, 135.2, 136.3, 137.0, 137.9, 163.0. Anal. calcd. for $C_{28}H_{29}Cl_2N_3O_9$: C 54.03, H 4.69, Cl 11.39, N 6.75%; found: C 53.2, H 4.7, Cl 12.5, N 6.5%.

The major by-product of the reaction is the perchlorate salt of the original pyrone.

Reaction with water

7 (0.1 g) was boiled in water (80 cm^3) for 1 h. The hot reaction mixture was filtered and the filtrate gave fine white crystals (0.06 g), mp 175–180°C; ^{1}H nmr δ (DMSO-d_6): 2.84 (6H, s), 3.12 (6H, s), 4.4 (1H, br s), 7.38–7.76 (15H, m), 8.06–8.09 (2H, m). Anal. calcd. for $C_{28}H_{30}ClN_3O_6$: C 62.28, H 5.59, Cl 6.56, N 7.78%; found: C 62.0, H 5.6, Cl 7.4, N 7.5%.

Structure determination

Data collection

A light yellow needle-shaped crystal of $C_{28}H_{29}Cl_2N_3O_9$ having approximate dimensions of 0.100 × 0.150 × 0.350 mm was mounted on a glass fibre. All measurements were made on a CAD4 diffractometer with graphite-monochromated Mo Kα radiation.

Cell constants and an orientation matrix for data collection, obtained from a least-squares refinement using the setting angles of 25 carefully centred reflections in the range $20.0° < 2\theta < 26.0°$, corresponded to a monoclinic cell with dimensions a = 14.535 (3) Å, b = 13.685 (3) Å, c = 23.579 (7) Å, V = 2991 (3) Å^3, β = 140.38 (2)°.

For Z = 4 and F.W. = 622.46, the calculated density is 1.382 g/cm^3. Based on the systematic absences of ($n0l$: $h + l \neq 2n$) and ($0k0$: $k \neq 2n$), packing considerations, a statistical analysis of intensity distribution, and the successful solution and refinement of the structure, the space group was determined to be $P2_1/n$ (no. 14).

The data were collected at a temperature of 18 ± 1°C using the ω–2θ scan technique to a maximum 2θ value of 46.0°.

Data reduction

Of the 3016 reflections that were collected, 2930 were unique (R_{int} = 0.034). The intensities of three representative reflections, which were measured after every 200 reflections, remained constant throughout data collection, indicating crystal and electronic stability (no decay correction was applied).

The linear absorption coefficient for Mo Kα is 2.697 cm^{-1}. An empirical absorption correction using the program DIFABS (13) was applied, and resulted in transmission factors ranging from 0.903 to 1.089. The data were corrected for Lorentz and polarization effects.

Structure solution and refinement

The structure was solved by a direct method (14). The non-hydrogen atoms were refined anisotropically. The hydrogen atoms were placed in their geometrically calculated positions with a C—H distance of 1.08 Å; their positions and isotropic temperature factor were refined initially by riding on the attached C atoms. However, in the final refinement, the phenyl rings and the methyl groups were treated as a rigid body and the positions and temperature factors of the remaining hydrogen atoms were also kept fixed to improve the reflection–parameter ratio. Thus the final 7-block-matrix least-squares refinement (the function minimized was $\Sigma w(|F_o| - |F_c|)^2$ where $w = 1.7980/[\sigma(F) + 0.000886(F^2)]$) was based on 1691 observed reflections ($I > 2.00\sigma(I)$) and 426 variable parameters and converged (largest parameter shift was 0.654 times its esd)

with unweighted and weighted agreement factors of:

$$R = \Sigma||F_o| - |F_c|| / \Sigma|F_o| = 0.0633$$

$$R_w = [(\Sigma w(|F_o| - |F_c|)^2 / \Sigma w F_o^2)]^{1/2} = 0.0670$$

These atomic parameters give an R of 5.90 for the 1546 reflections with ($I > 3.00\sigma(I)$).

The SHELX weighting scheme, with w as stated above, was used during the refinement. The maximum and minimum peaks on the final difference Fourier map corresponded to 0.278 and -0.377 e$^-$/Å^3, respectively. Neutral atom scattering factors were taken from Cromer and Waber (15). Anomalous dispersion effects were included in F_{calc} (16); the values for $\Delta f'$ and $\Delta f''$ were those of Cromer (17). All calculations were performed using the SHELX 76 program (18). All diagrams were drawn by using the programs PLUTO (19) and ORTEP (20).[3]

Acknowledgement

The authors are grateful for financial support by the Natural Sciences and Engineering Research Council of Canada.

1. J.A. Van Allan and S. Chie Chang. J. Heterocycl. Chem. **11**, 1065 (1974).
2. J.A. Van Allan and G.A. Reynolds. J. Heterocycl. Chem. **13**, 73 (1976).
3. R. Wizinger, A. Grune, and E. Jacobi. Helv. Chim. Acta, **39**, 1 (1956).
4. G.A. Reynolds and J.A. Van Allan. J. Heterocycl. Chem. **11**, 405 (1974).
5. G.A. Reynolds and J.A. Van Allan. J. Heterocycl. Chem. **12**, 367 (1975).
6. K.T. Leffek, P. Pruszynski, and K. Thanapaalasingham. Can. J. Chem. **67**, 590 (1989).
7. P. Pruszynski and K.T. Leffek. Can. J. Chem. **69**, 205 (1991).
8. P. Pruszynski, K.T. Leffek, B. Borecka, and T.S. Cameron. Acta Crystallogr. Sect. C: Cryst. Struct. Commun. **C48**, 1638 (1992).
9. W. Galezowski, K.T. Leffek, and P. Pruszynski. Can. J. Chem. **70**, 2390 (1992).
10. D.D. Perrin, B. Dempsey, and E.P. Serjeant. *In* pK_a prediction for organic acids and bases. Chapman and Hall, London. 1981. App. A. 1.
11. D. Vörlander and G.A. Meyer. Chem. Ber. **45**, 3355 (1912).
12. H. Bredereck and K. Bredereck. Chem. Ber. **94**, 2278 (1961).
13. N. Walker and D. Stuart. Acta Crystallogr. Sect. A: Found. Crystallogr. **A39**, 158 (1983).
14. G.M. Sheldrick. SHELXS86. *In* Crystallography Computing 3. *Edited by* G.M. Sheldrick, C. Kruger, and R. Goddard. Oxford University Press, Oxford, U.K. 1985. p. 175.
15. D.T. Cromer and J.T. Waber. International tables for X-ray Crystallography. Vol. IV. Kynoch Press, Birmingham, U.K. 1974. Table 2.2 A.
16. J.A. Ibers and W.C Hamilton. Acta Crystallogr. **17**, 781 (1964).
17. D.T. Cromer. International tables for X-ray crystallography. Vol. IV. Kynoch Press, Birmingham, U.K. 1974. Table 2.3.1.
18. G.M. Sheldrick. SHELX76. Program for crystal structure determination. Univ. of Cambridge, Cambridge, U.K. 1976.
19. S. Motherwell and W. Clegg. PLUTO: program for plotting molecular and crystal structures. Univ. of Cambridge, Cambridge, U.K. 1978.
20. C.K. Johnson. ORTEP II: Report ORNL-5138. Oak Ridge National Laboratory, Oak Ridge, Tenn. 1976.

[3]A complete set of data for X-ray structure determination can be purchased from: The Depository of Unpublished Data, Document Delivery, CISTI, National Research Council Canada, Ottawa, ON K1A 0S2,Canada.

Experimental details and tables of atomic positional parameters, interatomic distances, and interatomic angles have also been deposited with the Cambridge Crystallographic Data Centre, and can be obtained on request from The Director, Cambridge Crystallographic Data Centre, University Chemical Laboratory, 12 Union Road, Cambridge, CB2 1EZ, U.K.

Can. J. Chem. Downloaded from www.nrcresearchpress.com by 195.246.54.202 on 09/08/12
For personal use only.

Application of electrogenerated triphenylmethyl anion as a base for alkylation of arylacetic esters and arylacetonitriles and isomerization of allylbenzenes

SHOHEI SUZUKI, MITSUKO KATO, AND SHOICHI NAKAJIMA[1]

Faculty of Pharmaceutical Sciences, Hoshi University, Ebara 2-4-41, Shinagawa-ku, Tokyo, Japan 142

Received March 3, 1993[2]

SHOHEI SUZUKI, MITSUKO KATO, and SHOICHI NAKAJIMA. Can. J. Chem. **72**, 357 (1994).

Phenylacetic esters and phenylacetonitriles were alkylated with alkyl halides, at the position α to an ester or nitrile, either at room temperature (20°C) or at −78°C, by making use of electrogenerated triphenylmethyl anion (trityl anion). Double-bond isomerization of allylbenzenes was also effectively accomplished by use of this electrogenerated base (EGB).

SHOHEI SUZUKI, MITSUKO KATO et SHOICHI NAKAJIMA. Can. J. Chem. **72**, 357 (1994).

Soumis à l'action d'halogénures d'alkyles, soit à la température ambiante (20°C) soit à −78°C, en utilisant des anions triphénylméthyles (anions trityles) électrogénérés, les esters phénylacétiques et les phénylacétonitriles sont alkylés en position α. On a aussi réalisé l'isomérisation de la double liaison d'allylbenzènes en utilisant cette base électrogénérée (BEG).

[Traduit par la rédaction]

Introduction

The principal advantage of electrochemical reactions lies in the fact that they do not require thermal energy to overcome activation barriers, and hence are applicable to thermally sensitive compounds (1). *N,N*-Dimethylformamide (DMF) and tetraalkylammonium salt are frequently used as solvent and supporting electrolyte, respectively, in cathodic reactions, and both favor S_N2 nucleophilic substitutions. This is because DMF is a polar aprotic solvent, in which nucleophiles are only very slightly solvated and are consequently highly active. The latter electrolyte is a phase-transfer catalyst in which the ammonium cation of the supporting electrolyte binds very weakly with the cathodically generated anionic species, thus favoring nucleophilic reactions.

Further, electrochemically generated anionic species sometimes show a higher reactivity than the same species non-electrochemically produced,[3] possibly because anionic species near the electrode are, so to speak, "naked" and so very reactive, as a result of binding of the counter cation to the electrode (2).

In 1969, Iversen and Lund (3) first demonstrated the synthetic utility of anionic species electrogenerated from azobenzene (3). Baizer et al. named such anionic species and their precursors "electrogenerated bases (EGB's)" and "pro-bases", respectively (4). Some onium salts (5), carbon tetrachloride (6), 2-pyrrolidone (7), azo compounds (8), activated alkenes (9), and oxygen (10) were subsequently found to be effective pro-bases. Thus the cathodic generation of EGB's is attracting increasing interest in the field of synthetic organic chemistry (11).

Recently triphenylmethane, which has a pK_a value of 30, was found to be a pro-base yielding trityl anion, a highly basic anion able to abstract a proton even from rather mildly acidic compounds such as cyclohexanones (12). The trityl anion was suggested to be generated by one-electron reduction of triphenylmethane, with evolution of hydrogen (12).

In the present paper, we would like to report two applications of the electrochemically generated trityl anion, i.e., for the alkylation (Scheme 1) of phenylacetic esters **1** and phenylacetonitriles **3** to give **2** and **4**, respectively, at room temperature (20°C) or at −78°C, and for the double-bond isomerization (Scheme 2) of allylbenzenes **5** to **6** and 1,4-dihydronaphthalene **8** to 1,2-dihydronaphthalene **9** at room temperature (20°C).

TABLE 1. Electrochemical alkylation of esters and nitriles[a]

Product	Method	Yield (recovered) (%)[b]
2*a*	A	36 (31)
2*b*[1]	A	47 (40)
2*b*[1]	A′	36 (40)
2*b*[1]	C	40 (29)
2*b*[2]	A	36 (31)
2*c*[1]	C	42 (24)
2*c*[2]	A	47 (30)
4*a*	A	0
4*a*	B	14 (70)
4*a*	C	73 (27)
4*b*$_1$	A	0
4*b*$_1$, **4***b*$_2$	C	72, 24 (0)

[a]Electrolyses were carried out by passing 2 F/mol of triphenylmethane (constant current, 50 mA) into DMF solution (30 mL) containing triphenylmethane (2 mmol) and TEATs (4 mmol). A: Substrate added before electrolysis (−78°C). A′: Substrate added before electrolysis (−20°C). B: Substrate added after electrolysis (−78°C). C: Substrate added after electrolysis (−78°C). The amount of substrate was one-fourth of that used in experiment B.

[b]Yields determined by HPLC.

Results and discussion

Alkylation of phenylacetic esters and phenylacetonitriles

When a DMF solution of an alkyl phenylacetate **1***a–c*, tetraethylammonium *p*-toluenesulfonate (TEATs), and methyl iodide (or ethyl bromide) was heated at 100°C for 3 h, no alkylation product **2***a–c* was obtained. However, this alkylation did occur at room temperature (20°C), or at −78°C, when the solution was placed in a cathodic compartment and an electric current (constant current, 50 mA) was passed through the solution, provided that triphenylmethane was added to the catholyte before the start of electrolysis. Thus it appears that triphenylmethane acts as a pro-base affording an EGB by cathodic reduction. The nitriles **3***a–b* were electrochemically alkylated in a similar way to give **4***a–b* (Scheme 1 and Table 1).

[1]Author to whom correspondence may be addressed. Telephone: 03-3786-1011; FAX: 03-3787-0036.

[2]Revision received October 5, 1993.

[3]For example, the alcoholate anion generated electrochemically was demonstrated to have higher reactivity than the same anion non-electrochemically produced. See footnote 6 of ref. 1.

Can. J. Chem. Downloaded from www.nrcresearchpress.com by 195.246.54.202 on 09/08/12
For personal use only.

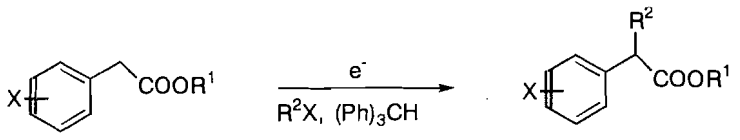

1 *a*, X = H, R^1 = Et
b, X = 4-MeO, R^1 = Et
c, X = 3,4-dimethoxy, R^1 = Me

2 *a* , X = H, R^1 = Et, R^2 = Me
b_1, X = 4-MeO, R^1 = Et, R^2 = Me
b_2, X = 4-MeO, R^1 = Et, R^2 = Et
c_1, X = 3,4-dimethoxy, R^1 = Me, R^2 = Me
c_2, X = 3,4-dimethoxy, R^1 = Me, R^2 = Et

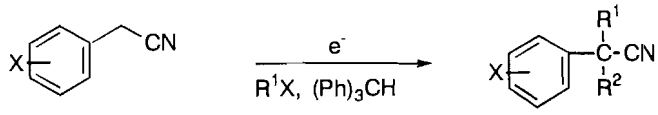

3 *a*, X = H
b, X = 4-MeO

4 *a* , X = H, R^1 = Me, R^2 = H
b_1, X = 4-MeO, R^1 = Me, R^2 = H
b_2, X = 4-MeO, R^1 = Me, R^2 = Me

SCHEME 1

In all these reactions, alkylating agents were added, not before, but after electrolysis, in order to avoid their cathodic degradation.[4] In the alkylation of esters, the products could be obtained equally well by adding esters before (methods A and A′ in Table 1) and after (method C in Table 1) electrolysis. However, in the case of nitriles, products were obtainable only when the nitriles were added after electrolysis (compare 14% yield of run **4***a*B with 0% yield of runs **4***a*A and **4***b*$_1$A). It is possible that the nitriles underwent reductive cleavage at the C—CN bond in runs **4***a*A and **4***b*$_1$A.[5] In the case of nitriles, the pro-base should preferably be used in a fourfold excess, since the resulting trityl anion is apparently consumed in side reactions during and after electrolysis, e.g., for deprotonation of the supporting electrolyte (as suggested in the literature (13)) (compare 73% yield of **4***a*C with 14% yield of **4***a*B).[6]

Arylacetic esters and nitriles have been alkylated under a wide variety of conditions (14) including the use of phase-transfer catalysts (15) such as tetraalkylammonium salts (16). In the present method, the trityl anion generated electrochemically couples with tetraalkylammonium cation in situ, and works effectively as a base for C-H acid, thus making the reaction possible under relatively mild conditions.

Isomerization of allylbenzenes

Isomerization of safrole **5***a* to isosafrole **6***a* is an important step in the industrial synthesis of heliotropin (3,4-methylenedioxybenzaldehyde). This double-bond isomerization has long been accomplished on an industrial scale by heating with alkali at high temperature, e.g., 180–200°C (17), 243–245°C (18), or 380–400°C (19). This isomerization has also been accomplished at room temperature by an electrochemical method (20). In the latter case, however, the authors focused on the hydrodimerization reaction which occurred in DMF solution, but not on the isomerization reaction that took place in acetonitrile.

We have examined the isomerization, and determined the yields of *cis* and *trans* isomers produced by the electrochemical double-bond isomerizations of safrole **5***a* to isosafrole **6***a*, estragole **5***c* to anethole **6***c*, allylbenzene **5***b* to 1-propenylbenzene **6***b*, 1-allyl-3,4-dimethoxybenzene **5***d* to 1,2-dimethoxy-4-(1-propenyl)- benzene **6***d*, and 1,4-dihydronaphthalene **8** to 1,2-dihydronaphthalene **9**, as shown in Scheme 2 and Table 2.

Electrolyses were performed at a constant current of 50 mA in acetonitrile solution containing a substrate allylbenzene and tetraethylammonium tetrafluoroborate ($TEABF_4$), in the presence or absence of triphenylmethane; water cooling was used to maintain the temperature at 20°C.

As shown in Table 2, the *trans*/*cis* ratio of the products ranged from 7.6 to 12.3. The use of triphenylmethane as a pro-base increased the yield of **6** and decreased that of **7**. No hydrodimerization products were obtained.

We also conducted the electrolysis, at various constant reduction potentials, of **5***a* to **6***a* and **7***a* in order to investigate the relationship between the potential and the composition of the products (Fig. 1).

Considering the E_p value of −1.7 V *vs.* SCE of triphenylmethane on a Pt electrode,[7] the results shown in Fig. 1 seem to indicate that the isomerization was promoted by the trityl anion when triphenylmethane was present, but was caused by another anionic species when it was not, possibly by the anion radical (21) afforded as an intermediate of the reduction of **5** to **7**.

[4]Methyl iodide and ethyl bromide, particularly the former, are easily degraded into alkyl radical and halogeno anion by one-electron reduction, ref. 22.

[5]The C═CN bond is cleaved in neutral medium, affording alkane and cyanide anion, ref. 23.

[6]If triphenylmethane were used in an equimolar amount to the nitrile, the substrate anion produced might react not only with alkyl halide but also with the starting nitrile (Thorpe type reaction, ref. 24).

[7]The E_p value of triphenylmethane was determined by the present authors by cyclic voltammetry on the Pt electrode: substrate, 1 mM; 0.4 M $NaClO_4$/acetonitrile; scan rate, 50 mV/s.

Can. J. Chem. Downloaded from www.nrcresearchpress.com by 195.246.54.202 on 09/08/12
For personal use only.

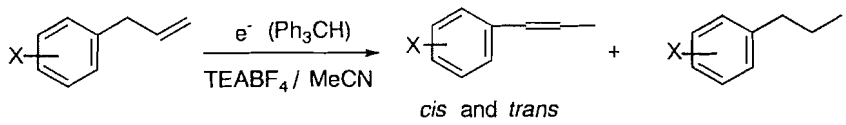

5*a*, X = 3,4-Methylenedioxy
b, X = H
c, X = 4-MeO
d, X = 3,4-Dimethoxy

6*a*, X = 3,4-Methylenedioxy
b, X = H
c, X = 4-MeO
d, X = 3,4-Dimethoxy

7*a*, X = 3,4-Methylenedioxy
b, X = H
c, X = 4-MeO
d, X = 3,4-Dimethoxy

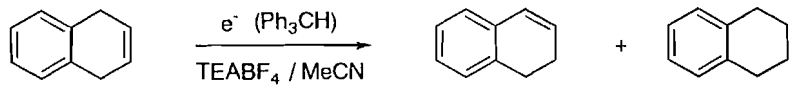

8 **9** **10**

SCHEME 2

TABLE 2. Electrochemical isomerization of allylbenzenes[a]

Ph$_3$CH		Isomerized product yield (%)[b] *cis*-**6**	*trans*-**6**		Reduction product (**7** or **10**) yield (%)[b]	Recovered (**5** or **8**) (%)[b]
Yes	**6***a*	4.9	70.2	**7***a*	3.6	7.3
No		4.8	57.2		6.5	10.4
Yes	**6***b*	5.0	67.6	**7***b*	6.9	17.3
No		3.4	44.0		25.6	22.7
Yes	**6***c*	10.5	49.2	**7***c*	0	35.8
No		4.6	37.3		8.5	46.6
Yes	**6***d*	4.9	67.7	**7***d*	0.3	18.7
No		3.9	58.7		14.4	12.4
Yes	**9**	48.2	—	**10**	25.4	22.6
No		30.2	—		38.8	20.6

[a]Electrolyses were carried out by passing 2 F/mol of substrate (constant current, 50 mA) into an acetonitrile solution (30 mL) containing triphenylmethane (2 mmol) and TEABF$_4$ (4 mmol).
[b]Yields determined by GLC.

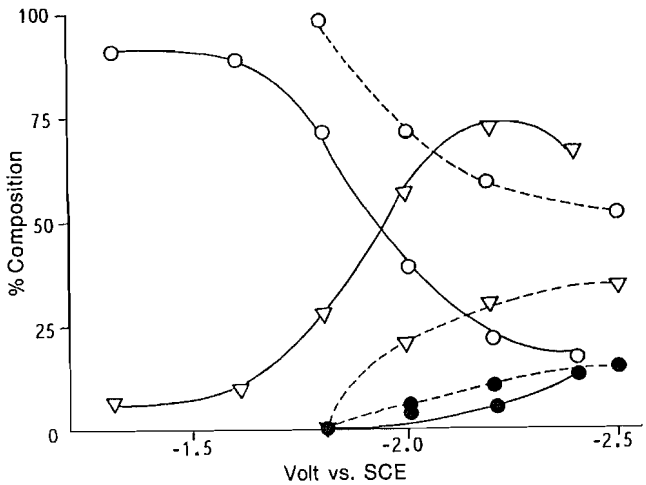

FIG. 1. Isomerization of **5***a* to **6***a* by cathodic reduction in the presence (———) or absence (– – – –) of triphenylmethane; ○, **5***a*; ▽, **6***a*; ●, **7***a*.

Experimental

^{1}H NMR spectra were obtained with a JEOL JNM FX-100 spectrometer at 100 MHz (with TMS as an internal standard). Infrared (IR) spectra were recorded with a Hitachi model 215 grating spectrophotometer and mass spectra (MS) were obtained with a JEOL JMS D-300 spectrometer. Gas–liquid chromatography (GLC) was performed on a Shimadzu GC-4CM PF instrument. Thin-layer chromatography (TLC) was conducted on precoated Silica gel 60 F_{254} plates (Art. 5715, Merck) and spots were detected under ultraviolet light (254 nm). High-performance liquid chromatography (HPLC) was conducted with a JASCO 880-PU apparatus equipped with a gradient elution module and a variable-wavelength detector (Soma S-310 A model 2) set at 275 nm. A Senshu Pak.ODS-1251-S (No. 3331, 4.6 × 250 mm) column was used. Low-pressure liquid chromatography (LPLC) was performed with a Chemco Low-Prep pump (81-M-2) and a glass column (20 × 1.5 cm) packed with silica gel SI-25-120 (25-44, Nihon Seimitsu Kagaku Co., Ltd.).

Electrolysis apparatus

Electrolyses were performed, unless otherwise noted, at a constant current of 50 mA in the cathodic compartment of a two-compartment H-type cell equipped with a glass-frit (No. 3G) diaphragm and Pt plate (4 cm^2) electrodes under stirring with a magnetic stirrer. A Hokuto

Can. J. Chem. Downloaded from www.nrcresearchpress.com by 195.246.54.202 on 09/08/12
For personal use only.

Can. J. Chem. Downloaded from www.nrcresearchpress.com by 195.246.54.202 on 09/08/12
For personal use only.

Denko HA-105 potentio-galvanostat connected with a Hokuto Denko HF-201 current integrator was used.

Electrochemical alkylation

The alkylations according to methods A and A′ in Table 1 were performed in DMF (Aldrich, less than 0.005% H_2O content) solution (30 mL) containing ethyl phenylacetate (**1***a*), ethyl 4-methoxyphenylacetate (**1***b*), methyl 3,4-dimethoxyphenylacetate (**1***c*), phenylacetonitrile (**3***a*) or 4-methoxyphenylacetonitrile (**3***b*) (2 mmol), together with triphenylmethane (2 mmol) and TEATs (4 mmol). After 2 F/mol (on the basis of triphenylmethane) of current had passed (constant current, 50 mA) at −78°C (runs A) or at 20°C (run A′), an alkylating agent, MeI (runs **2***a*, **2***b*$_1$, **4***a*, and **4***b*$_1$) or EtBr (runs **2***b*$_2$ and **2***c*$_2$) (4 mmol), was added, and the solution was stirred for 1 h at the same temperature, then for 12 h at 20°C to complete the reaction, as determined by HPLC.

The reaction according to method B in Table 1 was conducted in a similar way except that phenylacetonitrile was added after the electrolysis of triphenylmethane. The reactions according to method C in Table 1 were conducted similarly, except that the amount of the substrate used was one fourth of that of method B.

After the reaction, catholyte and anolyte were combined. The residue, after evaporation of the solvent, was dissolved in ether (250 mL), washed twice with saturated aqueous NaCl (200 mL), dried over Na_2SO_4, and evaporated. Then the alkylated products, except the commercially available **2***a* and **4***a*, were purified by column chromatography (CC) on silica gel. The solvent used for CC was hexane–acetone (5:1) (for **2***a*), hexane–CCl_4 (gradient, for **2***b*$_1$ and **2***b*$_2$), CCl_4–acetone (20:1) (for **2***c*$_1$), or hexane–acetone (40:1) (for **2***c*$_2$ and **4***b*$_1$). When further purification was necessary, LPLC was conducted with hexane–acetone (20:1) (for **2***c*$_1$ and **2***c*$_2$). The pure products thus obtained were identified by MS, IR, and ^{1}H NMR spectral analyses, and used as standard samples for the HPLC determinations. For HPLC, ethyl benzoate (for **2***a*), phenylacetonitrile (for **4***b*$_1$), and 4-methoxyphenylacetonitrile (for all other products) were used as internal standards.

*Ethyl 2-(4-methoxyphenyl)propanoate (2*b$_1$*)*

Colorless liquid. IR (CCl_4, cm^{-1}): 2840 (CH_3O), 1732 (C=O), 1380 (CH_3-C-C). ^{1}H NMR ($CDCl_3$, δ): 1.13 (3H, t, J = 5 Hz, CH_3-C-O), 1.47 (3H, d, J = 7 Hz, CH_3-C-C), 3.65 (1H, q, J = 7 Hz, CH), 3.79 (3H, s, CH_3O), 4.11 (2H, q, J = 7 Hz, CH_2O), 6.85 (2H, d, J = 9 Hz, Ar), 7.22 (2H, d, J = 9 Hz, Ar). High resolution electron impact mass spectrum (Hreims) *m/z*, calcd. for $C_{12}H_{16}O_3$: 208.1099 (M^+); found: 208.1094.

*Ethyl 2-(4-methoxyphenyl)butanoate (2*b$_2$*)*

Colorless liquid. IR (CCl_4, cm^{-1}): 2840 (CH_3O), 1735 (C=O). ^{1}H NMR ($CDCl_3$, δ): 0.88 (3H, t, J = 7 Hz, CH_3-C-C), 1.20 (3H, t, J = 5 Hz, CH_3-C-O), 1.90 (2H, dq, CH_2), 3.38 (1H, t, J = 5 Hz, CH), 3.78 (3H, s, CH_3O), 4.10 (2H, q, J = 6 Hz, CH_2-O), 6.84 (2H, d, J = 9 Hz, Ar), 7.22 (2H, d, J = 9 Hz, Ar). Hreims *m/z*, calcd. for $C_{13}H_{18}O_3$: 222.1250 (M^+); found: 222.1245.

*Methyl 2-(3,4-dimethoxyphenyl)propanoate (2*c$_1$*)*

Colorless liquid. IR (CCl_4, cm^{-1}): 2835 (CH_3O), 1740 (C=O), 1380 (CH_3). ^{1}H NMR ($CDCl_3$, δ): 1.48 (3H, d, J = 7 Hz, CH_3-C-C), 3.66 (1H, q, J = 7 Hz, CH), 3.66 (3H, s, $COOCH_3$), 3.86 (3H, s, CH_3O), 3.88 (3H, s, CH_3O), 6.80 (3H, s, Ar). Hreims *m/z*, calcd. for $C_{12}H_{16}O_4$: 224.1050 (M^+); found: 224.1051.

*Methyl 2-(3,4-dimethoxyphenyl)butanoate (2*c$_2$*)*

Colorless liquid. IR (CCl_4, cm^{-1}): 2840 (CH_3O), 1740 (C=O), 1380 (CH_3). ^{1}H NMR ($CDCl_3$, δ): 0.94(3H, t, J = 7 Hz, CH_3-C-C), 1.92 (2H, m, CH_2), 3.40 (1H, t, J = 8 Hz, CH), 3.68 (3H, s, $COOCH_3$), 3.84 (3H, CH_3O), 3.86 (3H, CH_3O), 6.81 (3H, s, Ar). Hreims *m/z*, calcd. for $C_{13}H_{18}O_4$: 238.1207 (M^+); found: 238.1208.

*2-(4-Methoxyphenyl)propanenitrile (4*b$_1$*)*

Colorless liquid. IR (CCl_4, cm^{-1}): 2245 (CH_3O). ^{1}H NMR ($CDCl_3$, δ): 1.62 (3H, d, J = 7 Hz, CH_3), 3.83 (1H, q, J = 7 Hz, CH), 3.81 (3H, s, CH_3O), 7.01 (2H, d, J = 8 Hz, Ar), 7.30 (2H, d, J = 8 Hz, Ar). Hreims *m/z*, calcd. for $C_{10}H_{11}NO$: 161.0839 (M^+); found: 161.0839.

*2-(4-Methoxyphenyl)-2-methylpropanenitrile (4*b$_2$*)*

Colorless liquid. IR (CCl_4, cm^{-1}): 2245 (CH_3O). ^{1}H NMR ($CDCl_3$, δ): 1.73 (6H, s, 2 × CH_3), 3.83 (3H, s, CH_3O), 6.90 (2H, d, J = 8 Hz, Ar), 7.40 (2H, d, J = 8 Hz, Ar). Hreims *m/z*, calcd. for $C_{11}H_{13}NO$: 175.0997 (M^+); found: 175.0997.

Electrochemical isomerization of allylbenzenes

Electrochemical isomerizations (Table 2) were performed in acetonitrile (Aldrich, less than 0.005% H_2O content) solution (30 mL) containing a substrate (2 mmol) and $TEABF_4$ (4 mmol), in the presence or absence of triphenylmethane (2 mmol), until 2.0 F/mol of substrate had been consumed (constant current, 50 mA) at 20°C (cooling was done with water). Products were separated by evaporation of the solvent, dissolution of the residue in $CHCl_3$, washing of the solution with saturated aqeous NaCl, drying on Na_2SO_4, and removal of the solvent. The crude products thus obtained were purified by CC followed by LPLC on silica gel, and identified by MS, IR, and ^{1}H NMR spectral analyses. The yields of the reaction products were determined by GLC: column (3.2 × 2,000 mm), 10% polyethyleneglycol 20 M on Chromosorb W AWDMCS; column temperature, 190°C; injection temperature, 240°C; flow rate, 60 mL/min.

Isomerization of safrole **5***a* at a constant potential of −1.3, −1.6, −1.8, −2.0, −2.2, −2.4, or −2.5 V vs. SCE (Fig. 1) was conducted in a similar way but on a smaller (one fourth) scale.

1. K. Arai, S. Tamura, T. Masumizu, K. Kawai, S. Nakajima, and A. Ueda. Can. J. Chem. **68**, 903 (1990).
2. S. Nakajima, T. Masumizu, K. Arai, C. Shaw, K. Nozawa, and K. Kawai. *In* Recent advances in electroorganic synthesis. *Edited by* S. Torii. Elsevier, Amsterdam. 1987. p. 265.
3. P.E. Iversen and H. Lund. Tetrahedron Lett. 3523 (1969).
4. (*a*) M.M. Baizer, J.L. Chruma, and D.A. White. Tetrahedron Lett. 5209 (1973); (*b*) M.M. Baizer. Tetrahedron, **40**, 935 (1984).
5. P.E. Iverson. Tetrahedron Lett. 55 (1971).
6. S.T. Nugent, M.M. Baizer, and R.D. Little. Tetrahedron Lett. **23**, 1339 (1982).
7. (*a*) T. Shono, S. Kashimura, and H. Nogusa. J. Org. Chem. **49**, 2043 (1984); (*b*) T. Shono, O. Ishige, H. Uyama, and S. Kashimura. J. Org. Chem. **51**, 546 (1986); (*c*) T. Shono, S. Kashimura, K. Ishizaki, and O. Ishige. Chem. Lett. 1311 (1983); (*d*) T. Komori, T. Nonaka, and T. Fuchigami. Chem. Lett. 11 (1986); (*e*) T. Shono, S. Kashimura, and H. Nogusa. Chem. Lett. 425 (1986).
8. (*a*) P.E. Iversen and H. Lund. Tetrahedron Lett. **20**, 33 (1969); (*b*) L. Kistenbrugger, P. Mischke, J. Voss, and G. Wiegand. Justus Liebigs Ann. Chem. 461 (1980); (*c*) P.J. Kinlen, R.D. Goodin, and F.D. Woodard. J. Electroanal. Chem. **190**, 185 (1985).
9. (*a*) M. Minato, T. Nonaka, and T. Fuchigami. Chem. Lett. 1071 (1986); (*b*) R.R. Mehta, V.L. Pardini, and J.H.P. Utley. J. Chem. Soc. Perkin Trans. 1, 2981 (1982).
10. (*a*) P.M. Allen, U. Hess, and C.S. Foote. Synth. Commun. **12**, 123 (1982); (*b*) M. Sugahara and M.M. Baizer. Tetrahedron Lett. **24**, 2223 (1983); (*c*) M. Sugahara and M.M. Baizer. J. Org. Chem. **48**, 4931 (1983); (*d*) W.T. Monte, M.M. Baizer, and R.D. Little. J. Org. Chem. **48**, 803 (1983).
11. J.H.P. Utley. Top. Curr. Chem. **142**, 1310 (1987).
12. T. Fuchigami, K. Suzuki, and T. Nonaka. Electrochem. Acta, **35**, 239 (1990).
13. T. Fuchigami. Denki Kagaku, **60**, 5 (1992).
14. (*a*) A.C. Cope, H.L. Holmes, and H.O. Hause. Org. React. **9**, 107 (1957); (*b*) J. Dockx. Synthesis, 441 (1973); (*c*) E.V. Dehmlow, Angew. Chem. Int. Ed. Engl. **13**, 170 (1974).
15. (*a*) M.M. Makosza and M. Ludwikow. Angew. Chem. Int. Ed. Engl. **13**, 665 (1974); (*b*) D. Landini and F. Montanari. J. Chem. Soc. Chem. Commun. 879 (1974); (*c*) M. Cinquini and F. Montanari. J. Chem. Soc. Chem. Commun. 393 (1975); (*d*) M. Mikolajczyk, S. Grzejszczak, and A. Zatorski. Tetrahedron Lett. 3757 (1975).

16. (*a*) M. Mikolajczyk, S. Grzejszczak, M. Midura, and A. Zatorski. Synthesis, 278 (1975); (*b*) Tetrahedron Lett. 183 (1977); (*c*) M. Makosza and A. Jonczyk. Org. Synth. **55**, 91 (1975).
17. (*a*) R. Horiuchi. J. Chem. Soc. Jpn. **45**, 209 (1925); (*b*) S. Nagai. J. Chem. Ind. Tokyo, **23**, 56 (1920).
18. Y. Ogata. Japan 5,331 (1951); Chem. Abstr. **47**, 9360c (1953).
19. T. Nagase, G. Suzukamo, and M. Fukano. Japan Appl. 70,104,647 (1970); Chem. Abstr. **77**, 61540n (1972).
20. M. Kimura, N. Moritani and Y. Sawaki. *In* Electroorganic Syntheses (M.M. Baizer Memorial Symposium). *Edited by* R.D. Little and N.L. Weinberg. Marcel Dekker, New York. 1991. p. 61.
21. M.R. Rifi and F.H. Covitz. *In* Introduction to organic electrochemistry. Marcel Dekker, New York. 1974. p. 228.
22. M.R. Rifi. *In* Techniques of chemistry. Vol. 5. Part 2. Technique of electroorganic synthesis. *Edited by* N.L. Weinberg. John Wiley, New York. 1975. p. 171.
23. M.M. Baizer and H. Lund. *In* Organic electrochemistry. 2nd ed. Marcel Dekker, New York. 1983. p. 387.
24. H. Barton, F.G.P. Remfry, and J.F. Thorpe. J. Chem. Soc. **85**, 1726 (1904).

Can. J. Chem. Downloaded from www.nrcresearchpress.com by 195.246.54.202 on 09/08/12
For personal use only.

Apparent molar heat capacities and volumes of some aqueous solutions of aliphatic amino acids at 288.15, 298.15, 313.15, and 328.15 K

ANDREW W. HAKIN,[1] MICHELLE M. DUKE, SHERI A. KLASSEN, ROBERT M. MCKAY, AND KATHRYN E. PREUSS
Department of Chemistry, University of Lethbridge, 4401 University Drive, Lethbridge, AB T1K 3M4, Canada
Received July 15, 1993

ANDREW W. HAKIN, MICHELLE M. DUKE, SHERI A. KLASSEN, ROBERT M. MCKAY, and KATHRYN E. PREUSS. Can. J. Chem. **72**, 362 (1994).

The thermodynamics of amino acid systems are key to the understanding of protein chemistry. We have found that many previous studies of the apparent molar volumes and heat capacities of aqueous solutions of amino acids were conducted at the standard temperature of 298.15 K. This does not allow for the fact that most biological processes occur at temperatures removed from this standard condition.

In an attempt to address this imbalance we have measured densities and heat capacities for aqueous solutions of glycine, L-alanine, L-serine, and L-threonine at 288.15, 298.15, 313.15, and 328.15 K using a Picker flow microcalorimeter. Apparent molar volumes and heat capacities, and the associated standard state partial molar properties have been calculated. Constant pressure variations of revised Helgeson, Kirkham, and Flowers equations have been fitted to calculated standard state volumes and heat capacities over the temperature range 288.15 to 328.15 K. These equations may be used to estimate standard state volumes and heat capacities, and hence equilibrium constants, for aqueous amino acid systems at higher temperatures.

ANDREW W. HAKIN, MICHELLE M. DUKE, SHERI A. KLASSEN, ROBERT M. MCKAY et KATHRYN E. PREUSS. Can. J. Chem. **72**, 362 (1994).

Les caractéristiques thermodynamiques des systèmes d'acides aminés sont la clé de la compréhension de la chimie des protéines. On a trouvé que plusieurs études antérieures sur les volumes molaires apparents et sur les capacités calorifiques de solutions aqueuses d'acides aminés ont été conduites à la température standard de 298,15 K. Ces résultats ne tiennent pas compte du fait que les processus biologiques se produisent à des températures différentes de cette condition standard.

Dans le but de corriger cette situation, on a measuré les densités et les capacités calorifiques de solutions aqueuses de glycine, de L-alanine, de L-sérique et de L-thréonine à 288,15, à 298,15, à 313,15 et à 328,15 K en faisant appel à un microcalorimètre à écoulement de Picker. On a calculé les volumes molaires apparents et les capacités calorifiques ainsi que les propriétés molaires partielles associées dans l'état standard. On a ajusté les variations à pression constante des équations révisées de Helgeson, Kirkham et Flowers avec les volumes et les capacités calorifiques calculés de l'état standard sur la plage de température allant de 288,15 à 328,15 K. On peut utiliser ces équations pour évaluer les volumes et les capacités calorifiques de l'état standard et, donc, les constantes d'équilibre des systèmes d'acides aminés aqueux à des températures plus élevées.

[Traduit par la rédaction]

Introduction

A review of volumetric and thermochemical data for aqueous amino acid systems reveals that the majority of previous studies were conducted at the standard temperature of 298.15 K (1–11). This is surprising when one considers that many living systems, which contain proteins, polypeptides, and hence amino acids, operate at temperatures removed from the standard.

Studies have indicated that there are classes of organisms which exist in submarine hot springs at temperatures in excess of 383.15 K (12). In addition, experimental studies on peptide hydrolysis rates have found that these compounds can exist at high temperatures for long periods of time (13). Also, several authors (14, 15) have discussed the role of organisms in the biodegradation of oil deposits. The geology of oil deposits dictates that any indigenous organisms must endure a wide spectrum of temperature and pressure conditions.

To assess the validity of high temperature and pressure life forms it is necessary to investigate the thermodynamic properties of the organic molecules, namely amino acids, which constitute peptides and proteins.

In an attempt to probe the high temperature regime of aqueous amino acid systems, we have commenced a volumetric and thermochemical investigation of their behavior as a function of temperature.

Attempts have been made to model the high temperature and pressure thermodynamic behaviour of amino acids using revised Helgeson, Kirkham, and Flowers (HKF) continuum models (16, 17). These models are constructed from experimental thermodynamic data collected at 298.15 K and ambient pressure. Realizing the importance of such modelling procedures, we have fitted constant pressure variations of the revised HKF equations for neutral organic species to calculated standard state heat capacities and volumes for aqueous solutions of glycine, L-alanine, L-serine, and L-threonine. These data can be used to calculate the temperature dependencies of equilibrium constants, or Gibbs energies, of the aqueous amino acid systems over the experimental temperature range. In addition, these models allow for the extrapolation of thermodynamic data to higher temperatures.

Experimental

Glycine (99+%), L-alanine (99+%), L-serine (99+%), and L-threonine (99+%) were obtained from Sigma Chemicals Limited. The acids were purified by repeated recrystallization from water and were dried and stored over phosphorus pentoxide in a vacuum oven set at 50°C. The NMR spectra of the amino acids were obtained on a Brüker 250 MHz instrument using D_2O as an internal standard. The recorded spectra were in excellent agreement with reference spectra (18).

All solutions were prepared by weight on the molality concentration scale using bi-distilled, degassed water. Solutions were stored in sealable 125 mL Nalgene bottles.

Densities were measured relative to water with a vibrating tube

[1]Author to whom correspondence should be addressed.

Can. J. Chem. Downloaded from www.nrcresearchpress.com by 195.246.54.202 on 09/08/12
For personal use only.

Can. J. Chem. Downloaded from www.nrcresearchpress.com by 195.246.54.202 on 09/08/12
For personal use only.

flow densimeter (19) (Sodev O2D). The densimeter is connected to a programmable circulating thermostat and has a working temperature range of 0–75°C with a thermal stability of ±0.001°C. This experimental apparatus routinely measures densities with part per million precision.

Calibration constants for the densimeter at 288.15, 298.15, 313.15, and 328.15 K were calculated from the measured time periods of vibration and the densities of dry nitrogen gas and water (20). Calibration constants were determined prior to and following each series of experiments.

Volumetric heat capacities were measured relative to water using a Picker flow microcalorimeter (21). Automated data collection is achieved by interfacing one component of the system, a Hewlett-Packard HP-3456A digital voltmeter, via an IOtech Personal 488 PC/IEEE 488 controller, to a 386SX-16 MHz IBM clone computer. A BASIC program controls data collection and storage. It directs data to a commercial visualization package for interpretation and the calculation of volumetric heat capacities.

An inherent problem of Picker flow microcalorimeters is that they generally suffer from small heat leaks (22). These heat leaks are greatly reduced by evacuating the chamber that houses the calorimetric cells to a vacuum of approximately 1.5×10^{-6} mbar (1 bar = 100 000 Pa). A one inch stainless steel vacuum line incorporating a Leybold D4A backing pump and an Edwards EO 50/60 air cooled diffusion pump was constructed for this purpose. The calorimeter is connected to the vacuum line with a Cajon O-ring fitting. Small residual heat leaks are easily corrected for by a heat loss correction factor (23). This factor is determined periodically by measuring the specific heat capacities of aqueous sodium chloride solutions at the temperature of interest.

Results and discussion

Apparent molar volumes, $V_{2,\phi}$, were calculated from measured density data using the equation:

$$[1] \qquad V_{2,\phi} = \left[\frac{M}{\rho}\right] - \left[\frac{\rho - \rho_1^0}{m\rho\rho_1^0}\right]$$

where m is the molality of the solution, M is the molecular weight of the solute, ρ_1^0 is the density of pure water, and ρ is the density of the solution under study.

The apparent molar heat capacities, $C_{p,2,\phi}$, of our solutions were calculated using eq. [2]:

$$[2] \qquad C_{p,2,\phi} = Mc_p + \frac{(c_p - c_{p,1}^0)}{m}$$

where c_p is the specific heat capacity of the solution, and $c_{p,1}^0$ is the specific heat capacity of pure water.

Estimated uncertainties in apparent molar volumes, $\delta V_{2,\phi}$, were calculated using the equation reported by Hedwig (24):

$$[3] \qquad \delta V_{2,\phi} = -\left[M + \frac{1000}{m}\right]\frac{\delta\rho}{\rho^2}$$

The uncertainty in solution density, $\delta\rho$, was estimated to be 5×10^{-6} g cm^{-3}. In using eq. [3], we note that contributions to $\delta V_{2,\phi}$ arising from uncertainties in solution concentrations are assumed to be negligible.

Estimated uncertainties in our apparent molar heat capacities, $\delta C_{p,2,\phi}$, arise primarily from two sources (25); errors in experimental molalities, and errors associated with the measurement of the displacements of the heat capacity curves. In using Hedwig's expression, eq. [4], for the uncertainty in apparent molar heat capacity, $\delta C_{p,2,\phi}$, we once again assume that errors arising from solution concentrations are negligible.

$$[4] \qquad \delta C_{p,2,\phi} = \left(M + \frac{1000}{m}\right)\delta c_p$$

The uncertainty in specific heat capacity, δc_p, was estimated to be 7×10^{-5} J K^{-1} g^{-1} (26).

Densities, apparent molar volumes, and apparent molar heat capacities are reported as a function of concentration for glycine, L-alanine, L-serine, and L-threonine in Tables 1, 2, 3, and 4, respectively. Calculated uncertainties in apparent molar heat volumes and heat capacities have been included in parentheses in each table.

The apparent molar properties of the investigated aqueous amino acid systems were found to be well represented by the linear equation:

$$[5] \qquad Y_{2,\phi} = Y_{2,\phi}^0 + S_Y m$$

where Y represents the extensive thermodynamic property of interest, $Y_{2,\phi}^0$ is the value of $Y_{2,\phi}$ at infinite dilution, m is the molality of the solution, and S_Y is the experimental slope. The appropriate form of eq. [5] was fitted to our calculated $V_{2,\phi}$, and $C_{p,2,\phi}$ data using weighted linear least squares regression analyses. Weights used in these analyses were calculated as the reciprocals of the square in the uncertainties in apparent molar volumes and heat capacities i.e., $1/(\delta V_{2,\phi})^2$ and $1/(\delta C_{p,2,\phi})^2$.

Partial molar properties of solutes, $\bar{Y}_2$, can be calculated from apparent molar properties, $Y_{2,\phi}$, using the equation:

$$[6] \qquad \bar{Y}_2 = Y_{2,\phi} + n_2\left(\frac{\partial Y_{2,\phi}}{n_2}\right)_{T,p,n_1}$$

By definition, in the limit $n_2 \rightarrow 0$, the standard state property, $\bar{Y}_2^0$, is equal to the apparent molar property at infinite dilution, $Y_{2,\phi}^0$.

Table 5 compares calculated standard state volumes and heat capacities to available literature data (1–9, 29) at each investigated temperature. A review of this table indicates that the majority of literature data refer to 298.15 K. The volumetric study by Kharakoz (6) was the only one that we could find that reports standard state volume data over the same experimental temperature range as that selected in this investigation. However, we were unable to locate standard state volume data for aqueous L-threonine solutions above 298.15 K. The excellent agreement shown between our standard state data and available literature data affords us a high degree of confidence in our experimental procedures and equipment.

There are far less standard state heat capacity data reported in the literature than standard state volume data. A comparison of our calculated standard state heat capacity data to those available in the literature indicates very good agreement. Nevertheless, there is a noticeable discrepancy between Jolicoeur's (2) corrected value of $\bar{C}_{p,2}^0 = 45.5$ J K^{-1} mol^{-1} for glycine at 298.15 K, reported by Hedwig, Reading, and Lilley (11), and our value of 37.6 J K^{-1} mol^{-1}. However, we note that our value is in good agreement with the only other standard state heat capacity value (3), derived from flow calorimetric data, that we could find in the literature.

Standard state heat capacity data at temperatures removed from 298.15 K are scarce. A comparison of our reported value of $\bar{C}_{p,2}^0 = 57.8$ J K^{-1} mol^{-1} for glycine in water at 313.15 K

Can. J. Chem. Downloaded from www.nrcresearchpress.com by 195.246.54.202 on 09/08/12
For personal use only.

TABLE 1. Densities, ρ, apparent molar volumes, $V_{2,\phi}$, and apparent molar heat capacities, $C_{p,2,\phi}$, of aqueous solutions of glycine at 288.15, 298.15, 313.15, and 328.15 K[a]

m (mol kg^{-1})	ρ (g cm^{-3})	$V_{2,\phi}$ (cm^3 mol^{-1})	$C_{p,2,\phi}$ (J K^{-1} mol^{-1})
		288.15 K	
0.0112	0.999471	42.16 (0.45)	—
0.0483	1.000671	42.47 (0.10)	16.8 (1.5)
0.0893	1.002000	42.75 (0.06)	17.5 (0.8)
0.1426	1.003705	42.60 (0.04)	18.1 (0.5)
0.1916	1.005259	42.66 (0.03)	20.4 (0.4)
0.2391	1.006760	42.72 (0.02)	21.2 (0.3)
0.2820	1.008102	42.76 (0.02)	21.6 (0.3)
0.3376	1.009830	42.83 (0.01)	23.9 (0.2)
0.3970	1.011668	42.89 (0.01)	24.4 (0.2)
0.4666	1.013783	42.96 (0.01)	26.8 (0.2)
		298.15 K	
0.0112	0.997445	39.64 (0.45)	29.9 (6.2)
0.0483	0.998596	42.92 (0.10)	36.0 (1.5)
0.0893	0.999892	43.37 (0.06)	41.4 (0.8)
0.1426	1.001541	43.40 (0.04)	40.2 (0.5)
0.1916	1.003072	43.38 (0.03)	39.2 (0.4)
0.2391	1.004518	43.54 (0.02)	41.1 (0.3)
0.2820	1.005821	43.60 (0.02)	42.5 (0.3)
0.3376	1.007541	43.56 (0.01)	42.4 (0.2)
0.3970	1.009323	43.65 (0.01)	43.6 (0.2)
0.4666	1.011395	43.70 (0.01)	44.6 (0.2)
		313.15 K	
0.0112	0.992572	43.74 (0.45)	70.1 (6.2)
0.0483	0.993718	44.05 (0.10)	59.4 (1.5)
0.0893	0.994992	43.98 (0.06)	61.6 (0.8)
0.1426	0.996629	44.05 (0.04)	60.4 (0.5)
0.1916	0.998098	44.23 (0.03)	58.7 (0.4)
0.2391	0.999528	44.28 (0.02)	64.0 (0.3)
0.2820	1.000812	44.32 (0.02)	60.6 (0.3)
0.3376	1.002461	44.38 (0.01)	62.2 (0.2)
0.3970	1.004219	44.42 (0.01)	64.2 (0.2)
0.4666	1.006253	44.48 (0.01)	64.8 (0.2)
		328.15 K	
0.0112	0.986048	43.86 (0.46)	—
0.0483	0.986179	44.44 (0.11)	—
0.0893	0.988437	44.43 (0.06)	75.9 (0.8)
0.1426	0.990042	44.58 (0.04)	77.2 (0.5)
0.1916	0.991513	44.64 (0.03)	75.8 (0.4)
0.2391	0.992934	44.67 (0.02)	79.1 (0.3)
0.2820	0.994202	44.72 (0.02)	77.4 (0.3)
0.3376	0.995842	44.76 (0.02)	79.2 (0.2)
0.3970	0.997584	44.80 (0.01)	76.8 (0.2)
0.4666	0.999599	44.86 (0.01)	77.6 (0.2)
0.0483	0.987184	44.32 (0.11)	—
0.0893	0.988425	44.57 (0.06)	79.5 (0.8)
0.1426	0.990034	44.65 (0.04)	73.4 (0.5)
0.1916	0.991511	44.65 (0.03)	76.1 (0.4)
0.2391	0.992924	44.71 (0.02)	78.2 (0.3)
0.2820	0.994184	44.79 (0.02)	76.0 (0.3)
0.3376	0.995821	44.83 (0.02)	77.0 (0.2)
0.3970	0.997584	44.80 (0.01)	78.1 (0.2)
0.4666	0.999588	44.88 (0.01)	77.9 (0.2)

[a]Estimated uncertainties for $V_{2,\phi}$ and $C_{p,2,\phi}$ in parentheses.

TABLE 2. Densities, ρ, apparent molar volumes, $V_{2,\phi}$, and apparent molar heat capacities, $C_{p,2,\phi}$, of aqueous solutions of L-alanine at 288.15, 298.15, 313.15, and 328.15 K[a]

m (mol kg^{-1})	ρ (g cm^{-3})	$V_{2,\phi}$ (cm^3 mol^{-1})	$C_{p,2,\phi}$ (J K^{-1} mol^{-1})
		288.15 K	
0.0233	0.999787	59.65 (0.22)	133.1 (3.0)
0.0380	1.000209	59.89 (0.13)	131.6 (1.8)
0.0599	1.000844	59.90 (0.08)	130.3 (1.2)
0.0852	1.001614	59.47 (0.06)	127.0 (0.8)
0.1103	1.002288	60.03 (0.05)	125.7 (0.6)
0.1427	1.003232	59.92 (0.04)	127.5 (0.5)
0.2238	1.005509	60.10 (0.02)	129.1 (0.3)
0.2484	1.006194	60.14 (0.02)	129.3 (0.3)
0.2794	1.007077	60.09 (0.02)	127.7 (0.3)
0.0233	0.999790	59.52 (0.22)	120.4 (3.0)
0.0380	1.000218	59.65 (0.13)	124.0 (1.8)
0.0599	1.000887	59.18 (0.08)	121.3 (1.2)
0.0852	1.001587	59.78 (0.06)	127.0 (0.8)
0.1103	1.002306	59.87 (0.05)	125.7 (0.6)
0.1427	1.003235	59.90 (0.04)	127.5 (0.5)
0.2794	1.007082	60.07 (0.02)	127.7 (0.3)
		298.15 K	
0.0233	0.997717	60.43 (0.22)	139.4 (3.0)
0.0380	0.998137	60.47 (0.13)	141.3 (1.8)
0.0599	0.998756	60.55 (0.08)	141.4 (1.2)
0.0852	0.999474	60.56 (0.06)	142.2 (0.8)
0.1103	1.000182	60.58 (0.05)	142.8 (0.6)
0.1427	1.001095	60.58 (0.04)	143.0 (0.5)
0.2238	1.003339	60.69 (0.02)	142.9 (0.3)
0.2484	1.004014	60.72 (0.02)	143.4 (0.3)
0.2794	1.004867	60.73 (0.02)	144.3 (0.3)
		313.15 K	
0.0233	0.992874	61.20 (0.22)	159.2 (3.0)
0.0380	0.993292	61.05 (0.13)	153.9 (1.8)
0.0599	0.993887	61.38 (0.08)	156.3 (1.2)
0.0852	0.994602	61.22 (0.06)	155.9 (0.8)
0.1103	0.995298	61.24 (0.05)	153.7 (0.6)
0.1427	0.996196	61.23 (0.04)	156.6 (0.5)
0.2238	0.998389	61.40 (0.02)	157.5 (0.3)
0.2484	0.999059	61.40 (0.02)	158.5 (0.3)
0.2794	0.999890	61.43 (0.02)	158.4 (0.3)
		328.15 K	
0.0233	0.986356	61.12 (0.22)	180.9 (3.0)
0.0380	0.986758	61.51 (0.13)	176.0 (1.8)
0.0599	0.987363	61.59 (0.08)	173.9 (1.2)
0.0852	0.988057	61.69 (0.06)	163.5 (0.8)
0.1103	0.988757	61.62 (0.05)	169.4 (0.6)
0.1427	0.989641	61.67 (0.04)	167.9 (0.5)
0.2238	0.991812	61.87 (0.02)	168.7 (0.3)
0.2484	0.992481	61.84 (0.02)	169.1 (0.3)
0.2794	0.993315	61.83 (0.02)	172.0 (0.3)

[a]Estimated uncertainties for $V_{2,\phi}$ and $C_{p,2,\phi}$ in parentheses.

indicates very good agreement with the value of 57.5 J K^{-1} mol^{-1} reported by Gucker, Ford, and Moser (9).

Recent papers have indicated that biologically derived amino acids and peptides can exist at substantially elevated temperatures and pressures (12–15). In trying to understand this phenomenon, there have been several attempts to investigate the

Can. J. Chem. Downloaded from www.nrcresearchpress.com by 195.246.54.202 on 09/08/12
For personal use only.

TABLE 3. Densities, ρ, apparent molar volumes, $V_{2,\phi}$, and apparent molar heat capacities, $C_{p,2,\phi}$, of aqueous solutions of L-serine at 288.15, 298.15, 313.15, and 328.15 K[a]

m (mol kg^{-1})	ρ (g cm^{-3})	$V_{2,\phi}$ (cm^3 mol^{-1})	$C_{p,2,\phi}$ (J K^{-1} mol^{-1})
		288.15 K	
0.0194	0.999991	59.17 (0.26)	78.1 (3.6)
0.0388	1.008630	59.62 (0.13)	91.6 (1.8)
0.0744	1.002455	59.80 (0.07)	92.9 (0.9)
0.1023	1.003702	59.86 (0.05)	92.1 (0.7)
0.1385	1.005312	59.89 (0.04)	93.7 (0.5)
0.2059	1.008265	60.05 (0.02)	96.5 (0.3)
0.2394	1.008732	60.06 (0.02)	96.8 (0.3)
0.2812	1.011531	60.15 (0.02)	97.1 (0.3)
0.3114	1.012829	60.19 (0.02)	100.2 (0.2)
0.0194	0.999947	61.44 (0.26)	—
0.0388	1.000859	59.73 (0.13)	—
0.0744	1.002458	59.77 (0.07)	—
0.1023	1.003705	59.82 (0.05)	—
0.1385	1.005311	59.89 (0.04)	—
0.2059	1.008271	60.02 (0.02)	—
0.2394	1.009733	60.06 (0.02)	—
0.2812	1.011548	60.09 (0.02)	—
0.3114	1.012844	60.14 (0.02)	—
		298.15 K	
0.0194	0.997911	60.22 (0.26)	108.3 (3.6)
0.0388	0.998766	60.80 (0.13)	111.8 (1.8)
0.0744	1.000337	60.72 (0.07)	114.0 (0.9)
0.1023	1.001553	60.83 (0.05)	116.6 (0.7)
0.1385	1.003137	60.81 (0.04)	117.1 (0.5)
0.2059	1.006036	60.95 (0.02)	119.4 (0.3)
0.2394	1.007470	60.97 (0.02)	118.7 (0.3)
0.2812	1.009236	61.05 (0.02)	120.7 (0.3)
0.3114	1.010512	61.08 (0.02)	121.2 (0.2)
0.0194	0.997908	60.74 (0.26)	112.5 (3.6)
0.0388	0.998771	60.67 (0.13)	116.5 (1.8)
0.0744	1.000335	60.75 (0.07)	115.1 (0.9)
0.1023	1.001558	60.77 (0.05)	117.9 (0.7)
0.1385	1.003132	60.84 (0.04)	117.0 (0.5)
0.2059	1.006037	60.93 (0.02)	117.3 (0.3)
0.2394	1.007480	60.93 (0.02)	119.7 (0.3)
0.2812	1.009219	61.12 (0.02)	121.5 (0.3)
0.3114	1.010532	61.02 (0.02)	119.6 (0.2)
0.1023	1.001554	60.81 (0.05)	—
0.0744	1.000333	60.77 (0.07)	—
		313.15 K	
0.0194	0.993060	61.83 (0.26)	138.5 (3.6)
0.0388	0.993867	61.60 (0.13)	136.6 (1.8)
0.0744	0.995441	61.71 (0.07)	138.0 (0.9)
0.1023	0.996639	61.75 (0.05)	141.3 (0.7)
0.1385	0.998186	61.78 (0.04)	141.7 (0.5)
0.2059	1.001032	61.89 (0.02)	141.0 (0.3)
0.2394	1.002438	61.92 (0.02)	143.1 (0.3)
0.2812	1.004172	61.98 (0.02)	142.7 (0.3)
0.3114	1.005430	62.00 (0.02)	141.5 (0.2)
		328.15 K	
0.0194	0.986526	62.49 (0.26)	152.1 (3.6)
0.0388	0.987361	62.34 (0.13)	157.7 (1.8)
0.0744	0.988886	62.26 (0.07)	160.7 (0.9)
0.1023	0.990069	62.33 (0.05)	159.9 (0.7)
0.1385	0.991597	62.38 (0.04)	158.9 (0.5)
0.2059	0.994414	62.48 (0.02)	160.9 (0.3)
0.2394	0.995810	62.49 (0.02)	161.9 (0.3)
0.2812	0.997535	62.53 (0.02)	159.3 (0.3)
0.3114	0.998765	62.59 (0.02)	163.2 (0.2)

[a]Estimated uncertainties for $V_{2,\phi}$ and $C_{p,2,\phi}$ in parentheses.

thermodynamics of these systems at elevated temperatures and pressures (16, 17). Thermodynamic data are very difficult to obtain experimentally under these conditions, and so there has been considerable interest in estimating data using continuum models that are based on measured thermodynamic data at 298.15 K and atmospheric pressure. In this regard, the revised HKF equations of state for aqueous species have found widespread popularity. Two recent papers (16, 17) have applied this model to neutral organic species in water to obtain estimates for thermodynamic properties at 5 kbar and 1000°C.

The revised HKF equations of state for standard state volumes and heat capacities are defined by the expressions:

$$[7] \qquad \bar{V}^0 = a_1 + \frac{a_2}{\Psi + P} + \left(a_3 + \frac{a_4}{\Psi + P}\right)\left(\frac{1}{T - \theta}\right) - \omega_e Q$$

$$[8] \qquad \bar{C}_p^0 = c_1 + \frac{c_2}{(T-\theta)^2} - \left[\frac{2T}{(T-\theta)^3}\right] \times \left[a_3(P - P_r) + a_4 \ln\left(\frac{\Psi + P}{\Psi + P_r}\right)\right] + \omega_e T X$$

where a_1, a_2, a_3, a_4, c_1, and c_2 are species dependent parameters; θ and Ψ represent solvent dependent parameters. T, P, and P_r represent the temperature and pressure of interest and the reference pressure (1 bar), respectively. ω_e defines the effective Born coefficient for the neutral organic aqueous species of interest and is assumed to be independent of temperature and pressure. Hence the solvation contributions to the standard state properties in eqs. [7] and [8] are represented by $-\omega_e Q$ and $\omega_e TX$, respectively. Q and X are defined using the temperature and pressure dependencies of the dielectric constant of water, as in eqs. [9] and [10].

$$[9] \qquad Q = \frac{1}{\epsilon}\left(\frac{\partial \ln \epsilon}{\partial P}\right)_T$$

$$[10] \qquad X = \frac{1}{\epsilon}\left[\left(\frac{\partial^2 \ln \epsilon}{\partial T^2}\right)_P - \left(\frac{\partial \ln \epsilon}{\partial T}\right)_P^2\right]$$

At constant pressure, eq. [7] may be reduced to:

$$[11] \qquad \bar{V}^0 = \sigma + \frac{\xi}{T - \theta} - \omega_e Q$$

where σ and ξ are defined by the expressions:

$$[12] \qquad \sigma = a_1 + \frac{a_2}{\Psi + P}$$

$$[13] \qquad \xi = a_3 + \frac{a_4}{\Psi + P}$$

In a similar manner eq. [8] may be reduced under the constant

Can. J. Chem. Downloaded from www.nrcresearchpress.com by 195.246.54.202 on 09/08/12
For personal use only.

TABLE 4. Densities, ρ, apparent molar volumes, $V_{2,\phi}$, and apparent molar heat capacities, $C_{p,2,\phi}$, of aqueous solutions of L-threonine at 288.15, 298.15, 313.15, and 328.15 K[a]

m (mol kg^{-1})	ρ (g cm^{-3})	$V_{2,\phi}$ (cm^3 mol^{-1})	$C_{p,2,\phi}$ (J K^{-1} mol^{-1})
		288.15 K	
0.0087	0.999485	75.19 (0.57)	173.6 (8.0)
0.0144	0.999754	73.63 (0.35)	181.2 (4.9)
0.0294	1.000363	76.10 (0.17)	188.3 (2.4)
0.0435	1.000951	76.50 (0.12)	194.2 (1.6)
0.0640	1.001837	76.16 (0.08)	193.2 (1.1)
0.0911	1.002991	76.12 (0.06)	194.8 (0.8)
0.1069	1.003657	76.15 (0.05)	190.3 (0.7)
0.1236	1.004367	76.13 (0.04)	190.1 (0.6)
0.1597	1.005905	76.01 (0.03)	189.9 (0.4)
0.1685	1.006252	76.15 (0.03)	190.9 (0.4)
0.1597	1.005904	76.01 (0.03)	189.9 (0.4)
0.0640	1.001837	76.16 (0.08)	189.6 (1.1)
0.1597	1.005904	76.01 (0.03)	—
		298.15 K	
0.0087	0.997424	76.19 (0.57)	213.6 (8.0)
0.0144	0.997657	76.75 (0.35)	202.8 (4.9)
0.0294	0.998297	76.61 (0.17)	202.4 (2.4)
0.0435	0.998883	76.91 (0.12)	207.5 (1.6)
0.0640	0.999741	76.90 (0.08)	207.5 (1.1)
0.0911	1.000871	76.93 (0.06)	206.3 (0.8)
0.1069	1.001527	76.94 (0.05)	208.5 (0.7)
0.1236	1.002221	76.96 (0.04)	208.4 (0.6)
0.1597	1.003719	76.92 (0.03)	208.2 (0.4)
0.1685	1.004074	76.94 (0.03)	208.4 (0.4)
0.0087	0.997427	75.70 (0.57)	215.1 (8.0)
0.0144	0.997652	77.10 (0.35)	215.1 (4.9)
0.0294	0.998289	76.85 (0.17)	—
0.0435	0.998883	76.89 (0.12)	209.3 (1.6)
0.0640	0.999737	76.96 (0.08)	207.4 (1.1)
0.0911	1.000868	76.95 (0.06)	208.7 (0.8)
0.1069	1.001530	76.92 (0.05)	209.5 (0.7)
0.1236	1.002218	76.98 (0.04)	209.9 (0.6)
0.1597	1.003719	76.92 (0.03)	210.1 (0.4)
0.1685	1.004076	76.95 (0.03)	210.6 (0.4)
		313.15 K	
0.0087	0.992598	75.97 (0.57)	216.0 (8.0)
0.0144	0.992816	77.73 (0.35)	231.0 (4.9)
0.0294	0.993442	77.67 (0.17)	232.2 (2.4)
0.0435	0.994018	77.91 (0.12)	230.3 (1.6)
0.0640	0.994856	77.97 (0.08)	226.6 (1.1)
0.0911	0.995967	77.94 (0.06)	231.5 (0.8)
0.1069	0.996611	77.94 (0.05)	230.1 (0.7)
0.1236	0.997289	77.98 (0.04)	230.4 (0.6)
0.1597	0.998765	77.88 (0.03)	231.7 (0.4)
0.1685	0.999114	77.93 (0.03)	231.0 (0.4)
		328.15 K	
0.0144	0.986284	78.58 (0.35)	270.2 (4.9)
0.0294	0.986889	78.93 (0.17)	247.7 (2.4)
0.0435	0.987480	78.49 (0.12)	246.6 (1.6)
0.0640	0.988302	78.68 (0.08)	246.6 (1.1)
0.0911	0.989407	78.58 (0.06)	244.5 (0.8)
0.1069	0.990051	78.52 (0.05)	241.9 (0.7)
0.1236	0.990716	78.62 (0.04)	241.9 (0.6)
0.1597	0.992170	78.58 (0.03)	246.5 (0.4)
0.1685	0.992499	78.73 (0.03)	249.7 (0.4)

[a]Estimated uncertainties for $V_{2,\phi}$ and $C_{p,2,\phi}$ in parentheses.

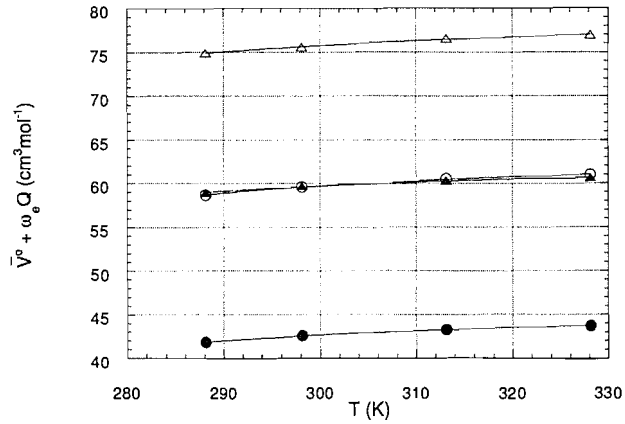

FIG. 1. Standard state volumes plus Born term versus temperature (15 to 55°C) for ● glycine, ▲ L-alanine, ○ L-serine, △ L-threonine. Solid curves denote the fits of the revised HKF constant pressure equations, eq. [11], to standard state volume data.

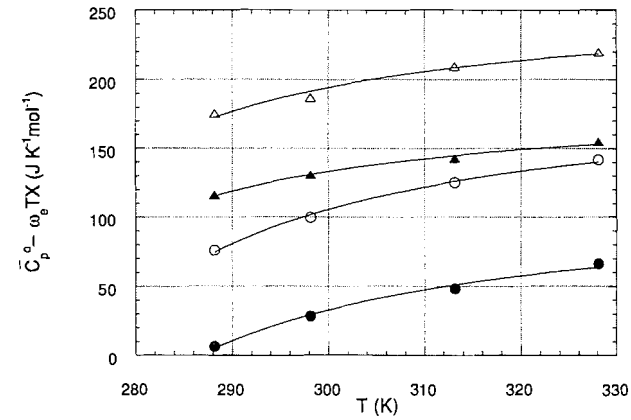

FIG. 2. Standard state heat capacities Born term versus temperature (15 to 55°C) for ● glycine, ▲ L-alanine, ○ L-serine, △ L-threonine. Solid curves denote the fits of the revised HKF constant pressure equations, eq. [14], to standard state heat capacity data.

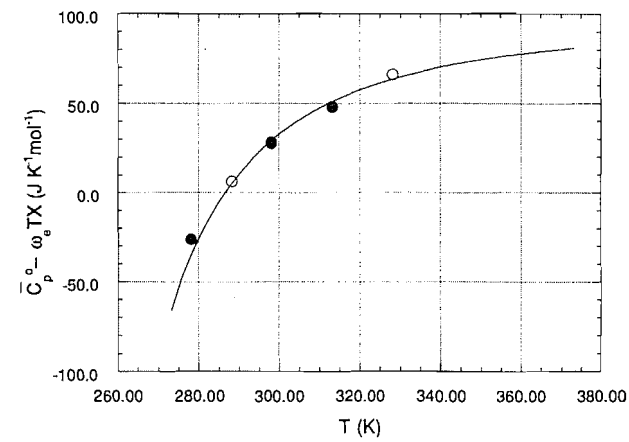

FIG. 3. Standard state heat capacities minus Born term versus temperature for aqueous solutions of glycine. The solid curve represents the fit of the revised HKF constant pressure equation, eq. [14], to calculated standard state heat capacity data. ○ standard state heat capacity data obtained in this investigation, ● standard state heat capacity data from ref. 9.

Can. J. Chem. Downloaded from www.nrcresearchpress.com by 195.246.54.202 on 09/08/12
For personal use only.

TABLE 5. Comparison of calculated $\bar{V}_2^0$ and $\bar{C}_{p,2}^0$ data with literature data

T (K)	$\bar{V}_2^0$ (cm^3 mol^{-1})	$\bar{C}_{p,2}^0$ (J K^{-1} mol^{-1})
	Glycine	
288.15	42.48 (42.35,[e] 42.4[f])	15.2
298.15	43.26 (43.19,[a] 43.25,[b] 43.39,[c] 43.26,[e] 43.3,[f] 43.19,[g] 43.33[h])	37.6 (39.2,[b] 36.7,[c] 45.5[j])
313.15	44.01 (43.9[f])	57.8 (57.5[i])
328.15	44.51 (44.3[f])	76.4
	L-Alanine	
288.15	59.67 (59.9[f])	126.3
298.15	60.47 (60.42,[a] 60.45,[b] 60.62,[c] 60.4,[f] 60.47[g])	141.2 (141.4,[b] 145.6,[c] 142.5[k])
313.15	61.14 (61.2[f])	153.7
328.15	61.53 (61.6[f])	166.5
	L-Serine	
288.15	59.70 (59.8[f])	89.0
298.15	60.66 (60.62,[a] 60.62,[b] 60.8[f])	114.1 (117.4[b])
313.15	61.63 (61.7[f])	140.0
328.15	62.22 (62.2[f])	157.9
	L-Threonine	
288.15	76.18 (76.03[e])	192.8
298.15	76.90 (76.83,[a] 76.86,[d] 76.59,[e] 78.00[h])	205.3 (210[d])
313.15	77.93	228.5
328.15	78.52	240.2

[a]Reference 1.
[b]Reference 2.
[c]Reference 3.
[d]Reference 4.
[e]Reference 5.
[f]Reference 6.
[g]Reference 7.
[h]Reference 8.
[i]Reference 9.
[j]Reference 11 (value calculated from data in ref. 2).
[k]Reference 29.

TABLE 6. Calculated parameters to eqs. [11] and [14]

Amino acid	σ (cm^3 mol^{-1})	ξ (cm^3 K mol^{-1})	$\omega_e \times 10^{-5}$[a] (J mol^{-1})
Glycine	46.63	−285.59	−0.97487
L-Alanine	63.30	−257.30	−1.11210
L-Serine	64.58	−350.22	−1.52381
L-Threonine	80.20	−319.49	−1.94849

Amino acid	c_1 (J K^{-1} mol^{-1})	c_2 (J K mol^{-1})	$\omega_e \times 10^{-5}$[a] (J mol^{-1})
Glycine	96.73	-3.3124×10^5	−0.97487
L-Alanine	174.33	-2.1274×10^5	−1.11210
L-Serine	177.50	-3.7226×10^5	−1.52381
L-Threonine	244.67	-2.6094×10^5	−1.94849

[a]Data obtained from ref. 16.

pressure condition of $P = P_r$ to give:

$$[14] \qquad \tilde{C}_p^0 = c_1 + \frac{c_2}{(T-\theta)^2} + \omega_e T X$$

Regression analyses have been used to fit eqs. [11] and [14] to calculated standard state volumes and heat capacities for each amino acid system. Values for Q and X at the reference pressure, P_r, were calculated using a program that was constructed using the procedures outlined in refs. 27 and 28. This program utilised the equations reported by Johnson and Norton (30) for the calculation of the temperature and pressure dependencies of the dielectric constant of water. Values for ω_e for each amino acid were obtained from the compilations reported by Shock and Helgeson (16). In an attempt to remain consistent with the Shock and Helgeson analyses, the solvent parameter θ was given a value of 228 K in all of our fitting procedures. Calculated values for σ, ξ, c_1, and c_2 are reported in Table 6. These values are in fair agreement with those calculated from the compilations reported by Shock and Helgeson (16). Uncertainties in the standard state volume and heat capacity data at 298.15 K and 1 bar, used in the Shock and Helgeson analyses, were reported to be $\sim \pm 2$ cm^3 mol^{-1} and $\sim \pm 8.368$ J K^{-1} mol^{-1}, respectively. These uncertainties are reflected in the uncertainties of the a_1, a_2, a_3, a_4, c_1, and c_2 parameters of eqs. [7] and [8]. Uncertainties in our standard state volumes and heat capacities are estimated to be less than 0.5 cm^3 mol^{-1} and 2 J K^{-1} mol^{-1}, respectively. This difference in uncertainties necessarily results in different estimates of the values for the a_i (i = 1 to 4) and c_i (i = 1 to 2) parameters.

Figures 1 and 2 compare calculated standard state volumes and heat capacities to those estimated using the revised HKF constant pressure equations (solid curves) as a function of temperature.

The equations reported in Table 6 can be used to estimate standard state volumes and heat capacities at temperatures outside the limited range investigated in this study. Figure 3 shows the calculated dependence of the standard state heat capacities of aqueous solutions of glycine over the temperature range 273.15 to 373.15 K. These data were calculated using the HKF constant pressure equation, eq. [14], and show very good agreement with the experimental $\bar{C}^0_{p,2}$ data of Gucker, Ford, and Moser (9).

There is clearly a need for high temperature and pressure data for aqueous amino acid systems. Such data are very difficult to obtain experimentally. The revised HKF equations for neutral organic species provide a method of estimating high temperature and pressure thermodynamic behaviour.

In continuation of this theme, we have commenced a study of the temperature dependence of the thermochemical and volumetric properties of other aliphatic and aromatic amino acids. These data will be presented in future papers. Our eventual aim is to establish a group additivity scheme for amino acids and peptides that can be applied to biological systems in the high temperature regime.

Acknowledgements

The authors are grateful to the Natural Sciences and Engineering Research Council of Canada (NSERC) for operating support and to the University of Lethbridge for equipment funding. K.E.P. is grateful to NSERC for the award of an Undergraduate Student Research Award and S.A.K. is grateful to NSERC for the award of an Undergraduate Student Research Award Targeted for Women Students.

1. A.K. Mishra and J.C. Ahluwalia. J. Phys. Chem. **88**, 86 (1984).
2. C. Jolicoeur and J. Boileau. Can. J. Chem. **56**, 2707 (1978).
3. G. DiPaola and B. Belleau. Can. J. Chem. **56**, 1827 (1978).
4. C. Jolicoeur, B. Riedl, D. Desrochers, L.L. Lemelin, R. Zamojska, and O. Enea. J. Solution Chem. **15**, 109 (1986).
5. R.K. Wadi and R.K. Goyal. J. Solution Chem. **21**, 163 (1992).
6. D.P. Kharakoz. Biophys. Chem. **34**, 115 (1989).
7. F.J. Millero, A. Lo Surdo, and C. Shin. J. Phys. Chem. **82**, 784 (1974).
8. S. Cabani, G. Conti, E. Matteoli, and M.R. Tiné. J. Chem. Soc. Farada Trans. 1, **77**, 2385 (1981).
9. F.T. Gucker, W.L. Ford, and C.E. Moser. J. Phys. Chem. **43**, 153 (1939).
10. G.R. Hedwig. J. Chem. Thermodyn. **23**, 123 (1991).
11. G.R. Hedwig, J.F. Reading, and T.H. Lilley. J. Chem. Soc. Faraday Trans. **87**, 1751 (1991).
12. H. Zhao, A.G. Wood, F. Widdel, and M.P. Bryant. J. Bacterio. **172**, 3959 (1990).
13. M.H. Engel, Y. Quian, S.A. Macko, and J. Deming. GSA Abstr. Prog. **23**, A25 (1991).
14. L.R. Brown. Chem. Eng. Prog. **83**, 35 (1987).
15. I. Rubinstein, C. Spyckerelle, and D.W.S. Westlake. Geochim. Cosmochim. Acta, **41**, 1341 (1977).
16. E.L. Shock and H.C. Helgeson, Geochim. Cosmochim. Acta, **54**, 915 (1990).
17. E.L. Shock. Geochim. Cosmochim. Acta, **56**, 3481 (1992).
18. C.J. Pouchert and J.R. Campbell. The Aldrich Library of NMR Spectra. Vol. III. Aldrich Chemical Co. Inc., Wisconsin. 1974.
19. P. Picker, E. Tremblay, and C. Jolicoeur. J. Solution Chem. **3**, 377 (1974).
20. G.S. Kell. J. Chem. Eng. Data, **12**, 66 (1967).
21. P. Picker, P.-A. Leduc, P.R. Philip, and J.E. Desnoyers. J. Chem. Thermodyn. **3**, 631 (1971).
22. J.K. Hovey. Ph.D. Thesis, University of Alberta, Edmonton, Alta. 1988.
23. J.E. Desnoyers, C. DeVisser, G. Perron, and P. Picker. J. Solution Chem. **5**, 605 (1976).
24. G.R. Hedwig. J. Solution Chem. **17**, 383 (1988).
25. P.P. Saluja, R.J. Lemire, and J.C. LeBlanc. J. Chem. Thermodyn. **24**, 181 (1992).
26. P.R. Philip, J.E. Desnoyers, and A. Hade. Can. J. Chem. **51**, 187 (1973).
27. H.C. Helgeson and D.H. Kirkham. Am. J. Sci. **274**, 1089 (1974).
28. H.C. Helgeson and D.H. Kirkham. Am. J. Sci. **276**, 97 (1976).
29. J.C. Ahluwalia, C. Ostiguy, G. Perron, and J.E. Desnoyers. Can. J. Chem. **55**, 3364 (1977).
30. J.W. Johnson, and D. Norton. Am. J. Sci. **291**, 541 (1991).

Can. J. Chem. Downloaded from www.nrcresearchpress.com by 195.246.54.202 on 09/08/12
For personal use only.

Thermodynamic properties of the Na–Bi–Pb system

PETER J. TUMIDAJSKI
Materials Laboratory, Institute for Research in Construction, National Research Council of Canada
Ottawa, ON, Canada K1A 0R6
Received April 28, 1993

PETER J. TUMIDAJSKI. Can. J. Chem. **72**, 369 (1994).

Thermodynamic properties of Na in an equimolar Bi–Pb alloy were determined at 723 K for compositions of $0.0075 \leq X_{Na} \leq 0.1000$ from electromotive force measurements on Na metal concentration cells with a solid Na–β-Al_2O_3 electrolyte. A coulometric titration technique was used to electrochemically generate the Na metal in the Bi–Pb alloy. The results indicate that, as Na is added to Bi–Pb, the liquid becomes more associated and suggests complex species formation with an ionic character intermediate between those observed for the constituent binaries.

PETER J. TUMIDAJSKI. Can. J. Chem. **72**, 369 (1994).

Utilisant des mesures de la forme électromotrice de cellules de la concentration du sodium métallique avec un électrolyte solide Na–β-Al_2O_3, on a déterminé les propriétés thermodynamiques du sodium dans un alliage équimoléculaire de Bi–Pb, à 723 K, à des concentrations de $0{,}0075 \leq X_{Na} \leq 0{,}1000$. On a utilisé une technique de titrage coulométrique pour générer le sodium métallique dans l'alliage Bi–Pb d'une façon électrochimique. Les résultats indiquent que, lorsqu'on ajoute du Na au Bi–Pb, le liquide devient plus associé et suggère qu'il y a formation d'espèces complexes possédant un caractère ionique intermédiaire entre celui observé pour les constituants binaires.

[Traduit par la rédaction]

Introduction

There is an interesting type of liquid alloy that exhibits a tendency toward a metal to non-metal transition (MNM) at certain compositions. Associated with the MNM transition are changes in the thermodynamic, transport, magnetic, and optical properties, which indicates a fundamental change in the structure and energetics of the alloy. An explanation of the behavior of these alloys has proved challenging. One alloy system with the MNM transition are the Na-based alloys with Bi or Pb. The thermodynamic properties of the Na–Bi and Na–Pb binary alloys have recently been studied (1–6). The ternary Na–Bi–Pb alloy for the eutectic solvent composition ($X_{Bi} = 0.43$) has also been studied (7), but the measurements were performed using a Na conducting glass electrolyte which is prone to degradation and uncertain measurements. In this paper, we report on the Na activity coefficients in the equimolar Bi–Pb alloy using a solid Na–β-Al_2O_3 electrolyte. The technique has been proven to yield highly reliable thermodynamic properties, and is a further contribution from this author on the alkali-based alloys (8–12). The results are useful for the understanding of the thermodynamic behavior of the ternary systems, and how they compare to the constituent binaries. In addition, there is an increased understanding of the influence of multicomponent solvents on the atomic interactions involving the alkali metals.

Experimental

The experimental apparatus and procedure have been described elsewhere (8–13). Consequently, only a brief outline is given here. The electrochemical cell consisted of two half cells, the reference electrode (RE) and a working electrode (WE), and an associated counter electrode (CE). The cell can be described schematically as

$$Na_{(RE)}//Na\text{–}\beta\text{-}Al_2O_3// \; Na\text{–}Bi_{(CE)}//Na\text{–}Bi\text{–}Pb_{(WE)}$$

The RE consisted of pure Na hermetically sealed in a Na–β-Al_2O_3 closed end tube. The WE consisted of an Na–Bi–Pb alloy sealed in a similar tube. A schematic diagram of a typical half-cell arrangement is given in Fig. 1. The composition of the WE was accurately varied by coulometric titration. Both half-cells were immersed to the same depth in a stirred Na–(95%)Bi alloy bath contained in a molybdenum crucible. Its function was to provide electrical contact, and to serve as a source and sink of alkali metal during coulometric titration.

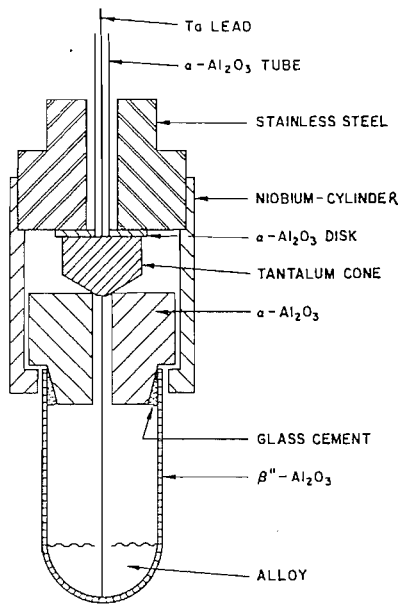

FIG 1. Typical half-cell arrangement.

Cells were loaded inside a high purity argon glove box. Accurately weighed amounts of high purity Bi and Pb were loaded into the cell in small pieces; the Na metal was generated by coulometric titration that involved the application of a potential across the electrolyte between the WE and the CE. At the temperatures of the experiments, there is negligible electronic transport through the solid electrolyte. Consequently, exactly one mole of the Na metal will be transported for each Faraday of charge. Compositional changes can be controlled down to the ppm range. Additionally, the introduction of oxides or impurity ions is avoided.

High purity Na (99.99%), Bi (99.999%), and Pb (99.999%) were used. The fabrication and the sealing procedures for the β-Al_2O_3 were described elsewhere (8–13). Temperatures were measured with a calibrated (Pt–Pt 10% Rh) thermocouple directly immersed in the CE.

Can. J. Chem. Downloaded from www.nrcresearchpress.com by 195.246.54.202 on 09/08/12
For personal use only.

Can. J. Chem. Downloaded from www.nrcresearchpress.com by 195.246.54.202 on 09/08/12
For personal use only.

TABLE 1. Values of cell voltage (with respect to pure liquid Na) and activity coefficients for the Na–Bi–Pb system

X_{Na}	T (K)	E_{cell} (mV)	ln γ_{Na}
0.0075	722.5	−842.9	−8.6449
0.0153	722.6	−785.2	−8.4298
0.0228	722.7	−755.1	−8.3439
0.0271	722.7	−742.8	−8.3192
0.0272	723.2	−742.1	−8.3035
0.0366	723.2	−721.0	−8.2618
0.0489	723.0	−699.0	−8.2019
0.0557	721.7	−686.4	−8.1497
0.0586	720.8	−681.8	−8.1391
0.0705	721.1	−667.8	−8.0941
0.0796	722.3	−657.8	−8.0383
0.0893	721.4	−651.3	−8.0608
0.1000	720.4	−638.3	−7.9798

Results and discussion

The cell reaction for the alkali metal concentration cell is

[1] $$Na_{(pure,\ liquid)} \Leftrightarrow Na_{(Na\text{–}Bi\text{–}Pb\ alloy,\ liquid)}$$

The cell voltage can be expressed with the corresponding Nernst equation in the form

[2] $$E = -\frac{R \times T}{F} \ln \gamma_{Na} - \frac{R \times T}{F} \ln X_{Na}$$

where F is the Faraday constant, R is the universal gas constant, T is the absolute temperature, and X_{Na} and γ_{Na} represent, respectively, the Na metal mole fraction and activity coefficient. The reference state corresponds to pure liquid Na metal at 723 K. Table 1 records the values of measured cell voltage at 723 K. The cell voltage data were collected for both directions of the current in the coulometric titration (i.e. $i > 0$ and $i < 0$). The cell voltages did not drift, and they were stable and reproducible for several days after each titration. This confirmed reversibility.

The Na activity coefficients were calculated with eq. [2]. Figure 2 is the compositional plot of the activity coefficients at 723 K for this study and for the previous work on the constituent binaries (1–2). It can be seen that Na activity coefficients are very small, and there is a marked deviation from ideality. The Na metal activity coefficients increase in the order (Na–Bi) → (Na–Bi–Pb) → (Na–Pb). The activity coefficients for all systems have been fitted to polynomial equations summarized in Table 2. Also included in Table 2 are the Henrian activity coefficients, γ^h_{Na}, and the partial excess free energy of mixing for Na at 723 K defined as

[3] $$\Delta\bar{G}^{xs}_{Na} = R \times T \ln \gamma^h_{Na}$$

The compositional dependence of the logarithm of the activity coefficients relates information on the solution correlation functions. Saboungi and Corbin (1), based on the work of Kirkwood-Buff (14), defined the limiting slope as

[4] $$\epsilon = \left(\frac{\partial \ln \gamma_{Na}}{\partial X_{Na}}\right)_{X_{Na} \to 0}$$

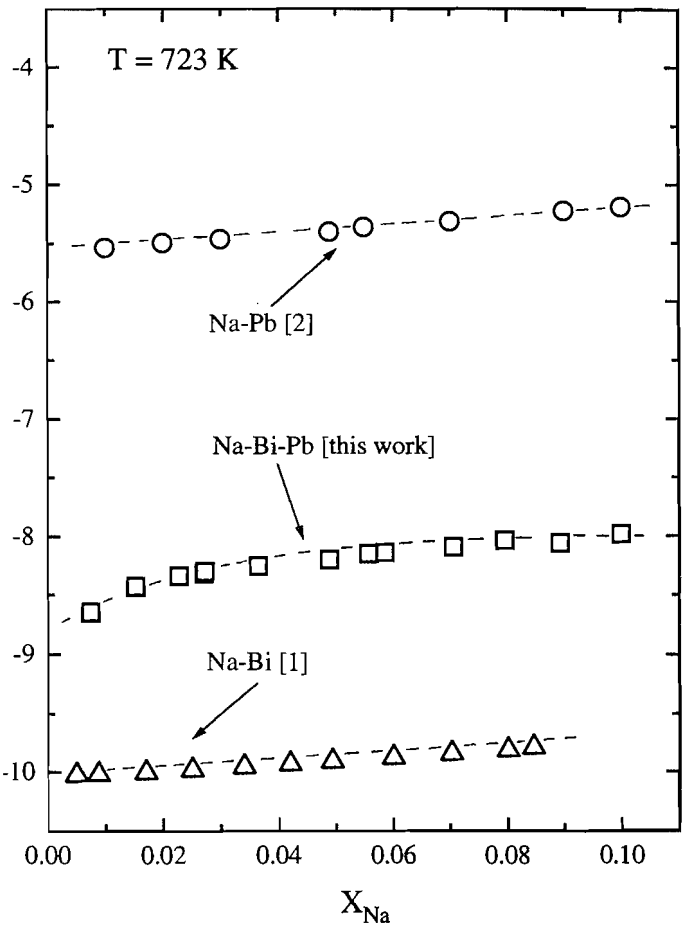

FIG. 2. Isothermal compositional variation of ln γ_{Na} for the Na–Bi–Pb system at 723 K.

This limiting slope is related to the solution correlation functions through

[5] $$\epsilon = -G^0_{22}/v_1$$

where G^0_{22} is the limit of the integral of the radial pair distribution function of the solute Na, and v_1 is the molar volume of the solvent at infinite dilution of the solute. The limiting slope is related to the kind and degree of ordering within solutions. A positive value for ϵ indicates attraction between the Na atoms and the solvent atoms (either Bi or Pb), and a high probability of preferred co-ordination (i.e. complex formation) in the liquid state. A zero value for ϵ means that there is a random distribution for the atoms. A negative value for ϵ represents the situation where there are attractive forces between like atoms and repulsive forces between unlike atoms. Such a situation may be represented by the formation of Na_2. However, the thermodynamic data must be supplemented by direct structural experiments like X-ray and neutron diffraction studies. The limiting slopes have been calculated and are tabulated in Table 2. The limiting slope for the Na–Bi–Pb alloy was calculated based on the linear portion of the curve as indicated in Fig. 2. It can be seen that the limiting slopes for all cases reported in Table 2 are positive, suggesting a repulsion between the Na atoms. There is probably some form of charge transfer and a local ordering. The theoretical limit of the magnitude of ϵ is the co-ordination number of an ideal ionic system (i.e., 4

TABLE 2. Thermodynamic values for the Na–Bi–Pb systems at 723 K

		$\ln \gamma_{Na} = A + BX^2 + CX^3 + DX^4$						
System	Reference	A	B	C	D	$\ln \gamma^h_{Na}$	$\Delta\bar{G}^{xs}_{Na}$ (kJ mol^{-1})	ϵ
Na–Bi	Ref. 1	−10.050	2.850	—	—	−10.050	−60.41	2.850
Na–Bi–Pb	This work	−8.7913	26.311	−372.63	1908.2	−8.7913	−52.85	3.360[a]
Na–Bi–Pb[b]	Ref. 7	—	—	—	—	−8.5443	−51.36	—
Na–Pb	Ref. 2	−5.5708	3.120	10.61	−45.05	−5.5708	−33.49	3.120

[a]Calculated from the linear portion of curve.
[b]Eutectic solvent composition $X_{Bi} = 0.43$.

→ 6). Since the value for ϵ in this study is slightly less than the lower theoretical limit, either long range electronic interactions or a screening effect which decreases the effective range of the coulombic repulsions between the charged Na atoms may be present. Values for ϵ increase in the solvent order (Bi) → (Bi–Pb) → (Pb) which is in consonance with the ionic radii and the activity coefficient data.

1. M.L. Saboungi and T.P. Corbin. J. Phys. F: Met. Phys. **14**, 13 (1984).
2. M.L. Saboungi, S.J. Herron, and R. Kumar. Ber. Bunsenges. Phys. Chem. **89**, 375 (1980).
3. H.P. Pfeiffer, R.J. Heus, and J.J. Egan. Chemical metallurgy – A tribute to Carl Wagner. *Edited by* N.A. Gokcen. The Metallurgical Society, Warrendale, PA. (1981). pp. 327–338.
4. S. Matsunaga, T. Ishiguro, and S. Tamaki. J. Phys. F: Met. Phys. **13**, 587 (1983).
5. M. Iwase, S. Sugino, E. Ischise, and Y. Waseda. High-Temp. Mater. Proc. **6**, 143 (1984).
6. P. Hubberstey and A.W. Castleman. J. Elect. Soc. **119**, 963 (1972).
7. O.I. Vorob'eva, A.G. Morachevskii, and E.A. Maiorova. Elektrokhimiya, **4**, 1424 (1982).
8. P.J. Tumidajski, A. Petric, A.D. Pelton, T. Takenaka, and M.L. Saboungi. J. Phys. C: Condensed Matter, **2**, 209 (1990).
9. P.J. Tumidajski and M.L. Saboungi. Calphad, **14**, 89 (1990).
10. P.J. Tumidajski and J. Keuhler. Can. J. Chem. **68**, 247 (1990).
11. P.J. Tumidajski. Can. J. Chem. **69**, 458 (1991).
12. P.J. Tumidajski and J.M. Toguri. Can. Met. Quart. **30**, 169 (1991).
13. M.L. Saboungi, S.R. Leonard, and J. Ellefson. J. Chem. Phys. **85**, 6072 (1986).
14. J.G. Kirkwood and F.P. Buff. J. Chem. Phys. **19**, 774 (1958).

Can. J. Chem. Downloaded from www.nrcresearchpress.com by 195.246.54.202 on 09/08/12
For personal use only.

The role of catalyst activation in the enantioselective hydrogenation of methyl acetoacetate over silica-supported nickel catalysts

MARK A. KEANE[1]

Chemistry Department, University of Glasgow, Glasgow G12 8QQ, Scotland

Received August 18, 1993

MARK A. KEANE. Can. J. Chem. **72**, 372 (1994).

A range of Ni–SiO_2 catalysts have been prepared by homogeneous precipitation–deposition and impregnation techniques and modified with aqueous solutions of *R*-(+)-tartaric acid (TA) to induce enantioselectivity in the asymmetric hydrogenation of a prochiral β-ketoester (methyl acetoacetate) to a β-hydroxyester ((*R*)-(−)-methyl 3-hydroxybutyrate). The effects of catalyst precursor preparation, nickel loading, and precalcination on the reduction of the precursor were examined and the nature of the resultant nickel particle size distribution is described. The influence of metal–support interactions on the uptake of TA was investigated and data on the corrosive metal leaching and the consequent changes in metal dispersion are presented. Modification of the catalysts with TA not only induced enantioselectivity, but also increased the turnover frequency by up to 15 times that observed for the unmodified surface. The amount of TA adsorbed and the fractional surface coverage by TA is related to the degree of enantiodifferentiation. The effects of variations in supported nickel metal particle sizes (in the overall range of 1.4–13.6 nm) on the reaction rate and enantioselectivity were examined; while the selectivity was independent of metal particle size, the rate of hydrogenation was found to be structure sensitive and a correlation between reaction rate sensitivity and particle size is presented.

MARK A. KEANE. Can. J. Chem. **72**, 372 (1994).

On a préparé une série de catalyseurs Ni–SiO_2 par des techniques de précipitation–dépôt et d'imprégnation homogènes et on les a modifiés avec des solutions aqueuses d'acide *R*-(+)-tartrique (AT) dans le but d'induire de l'énantiosélectivité dans l'hydrogénation asymétrique d'un ester β-cétonique prochiral (acétoacétate de méthyle) en ester β-hydroxylé, (*R*)-(−)-3-hydroxybutyrate de méthyle. On a évalué les effets de la préparation des précurseurs des catalyseurs, de la quantité de nickel et de la précalcination sur la réduction du précurseur et on décrit la nature de la distribution des grosseurs des particules de nickel qui en résulte. On a étudié l'influence des interactions métal–support sur la quantité d'AT adsorbé et on présente des données concernant le lixiviation par des métaux corrosifs et sur les changements qui en résultent sur la dispersion du métal. La modification des catalyseurs par l'AT n'induit pas seulement de l'énantiosélectivité, le fréquence d'échange est 15 fois plus rapide que sur une surface non modifiée. La quantité d'AT adsorbée et la fraction de la surface qui est couverte sont reliées au degré d'énantiodifférentiation. On a examiné les effets des variations dans les grosseurs des particules du nickel supporté (grosseurs allant de 1,4 à 13,6 nm) sur la vitesse de réaction et sur l'énantiosélectivié; alors que l'on a trouvé que la sélectivité est indépendante de la grosseur des particules métalliques, la vitesse d'hydrogénation est sensible à la structure et on présente une corrélation entre la sensibilité de la vitesse réactionnelle et la grosseur des particules.

[Traduit par la rédaction]

Introduction

It is now well established (1 and 2, and references therein) that the heterogeneous hydrogenation of methyl acetoacetate (MAA) on nickel catalysts yields methyl 3-hydroxybutyrate (MHB) as the hydrogenated product. While the bare nickel metal generates a racemic product (3–5), modification of the nickel surface by treatment with an optically pure isomer of an amino or hydroxy acid results in the preferential formation of one of the possible enantiomeric forms of MHB (1–4, 6–38). Modification of the activated catalyst is generally achieved in an aqueous solution of the optically active modification reagent. The modified catalyst is then recovered, washed, and immersed in an organic liquid phase containing the reactant. The reaction has been carried out over a variety of supported (3, 4, 18–20, 28, 30, 31, 37, 38) and unsupported (1–3, 11, 28, 29, 32, 36) nickel systems, principally in the liquid phase (3, 4, 11, 19, 20, 27–32, 34, 35, 37, 38), but gas phase transformations have also been reported (23, 26, 30, 36). In attempting to define the nature of the surface sites that promote enantiodifferentiation, the effects of varying the modification conditions have been considered (1, 3, 4, 18, 24, 25, 27, 28, 32, 33) and the reaction variables have also been altered to optimize the enantioselectivity process (1, 4, 10, 12, 14, 17, 34). Regardless, there is still no consensus of opinion regarding the actual source of the enantiocontrol and, to date, the efforts made to relate optical yield to the coverage of the catalyst surface by the modifier have been largely unsuccessful (20, 27, 33, 35, 36). The system is further complicated by the corrosive nature of tartaric acid (TA) adsorption on the surface nickel metal, which can result in the dissolution of over half the initial metal content (3, 4, 25, 28). There is, however, general agreement (1, 3, 4, 20, 25, 31) that the overall values of enantiomeric excess reflect the relative contributions of the TA-modified selective and the bare nickel nonselective metal sites.

From the data presented previously (3, 4, 25), it has become apparent that to obtain maximum enhancement of enantioselectivity it is necessary to pay strict attention to the control of each of the steps involved in the genesis of the enantiodifferentiating sites. Although the modification and reaction steps have received considerable attention, the role of catalyst precursor preparation and activation has largely been ignored. The dependence (20, 21, 37, 38) or independence (30) of enantioselectivity on metal particle dimensions remains open to question. With regard to the published reports of MAA hydrogenation on nickel catalysts, reaction rates have either been omitted or included as addenda to the enantioselectivity data. It has, however, been concluded in a number of instances (7, 12, 17) that the adsorbed modifier lowers the hydrogenation rate by occlud-

[1]Present address: Department of Chemistry and Biochemistry, University of Guelph, Guelph, ON N1G 2W1, Canada. telephone: 519-824-4120, ext. 8110; FAX: 519-766-1499.

Can. J. Chem. Downloaded from www.nrcresearchpress.com by 195.246.54.202 on 09/08/12
For personal use only.

ing part of the active metal surface. In addition, several workers have noted a difficulty in obtaining reproducible product compositions (10, 12, 18, 23, 24, 31). In this paper, accurate MAA hydrogenation rates and enantioselectivities are reported for a range of well characterized Ni–SiO_2 catalysts prepared by impregnation and homogeneous precipitation–deposition and modified with optically pure TA. The effect of systematically varying the metal crystallite size on the modification process and ultimately on the rate of MAA conversion and the degree of enantioselectivity is examined.

Experimental

Catalyst activation, modification, and characterization

A range of nickel-loaded (1.5–20.3% w/w Ni) catalysts were prepared by the homogeneous precipitation–deposition of nickel onto a nonporous microspheroidal Cab-O-Sil 5M silica as described in detail elsewhere (4). In addition, an 11.6% w/w Ni–Cab-O-Sil 5M silica catalyst was prepared by impregnation to incipient wetness (39). The water content of the precursors prepared by the deposition–precipitation technique was less than 5% w/w, while the impregnated precursor contained 8% w/w water. The hydrated supported precursors (sieved in the mesh range of 150–125 μm) were normally activated by heating in a 150 cm^3 min^{-1} stream of deoxygenated and predried hydrogen at a fixed rate of 5 K min^{-1} to a final temperature in the range of 673–1073 ± 3 K which was maintained for 18 h. For comparative purposes, certain samples were precalcined (at 5 K min^{-1}) at 723 ± 2 K for 16 h in a purified stream (150 cm^3 min^{-1}) of air, cooled to room temperature, and subjected to the hydrogen treatment described above. Temperature-programmed reduction experiments were performed separately; in each case, 200 mg of the hydrated precursor was heated (with or without in situ precalcination) at 5 K min^{-1} in a 150 cm^3 min^{-1} flow of 6% v/v H_2 in N_2 to temperatures in the range of 673–1073 ± 3 K and the hydrogen consumption was measured using a thermal conductivity cell. The reduction step was also monitored by thermogravimetry using a Pye Unicam thermobalance; both the weight loss (TG) and the rate of weight loss (DTG) were recorded.

The reduced catalysts were flushed in a purified stream (200 cm^3 min^{-1}) of nitrogen, cooled to room temperature, and contacted with 100 cm^3 of 0.01 mol dm^{-3} aqueous solutions of TA. The pH of the modifying solution was preadjusted to the isoelectric point (5.1) for TA using 1 and 0.01 mol dm^{-3} aqueous NaOH solutions for rough and fine adjustments, respectively. The modification was performed in air with constant agitation (600 rpm) for 2 h at 343 ± 2 K. TA was of AnalaR grade and the prepared solutions were found to be better than 99% pure by HPLC; the concentrations of the TA solutions used in the modifications were reproducible to within ±1%. After modification, the catalyst was decanted and washed with distilled water (1 × 25 cm^3), methanol (2 × 25 cm^3), and *n*-butanol (2 × 25 cm^3) before being stored in the latter prior to use. In accordance with the work of Smith and Musoiu (10), the total washing time was kept to within 40–50 min. All the solvents and modifying solutions used in this study were thoroughly degassed by purging with purified helium and heating under vacuum. The nickel content of the postmodifier solution, resulting from an acid leaching of the catalyst, was determined by AA spectrophotometry as described elsewhere (4). Nickel metal dispersions, before and after modification, were determined by carbon monoxide chemisorption (4). The supported metal phase was also characterized by transmission electron microscopy (JEOL JEM-1200EX); the samples were passivated in a 120 cm^3 min^{-1} flow of 1% v/v O_2 in N_2 at 298 ± 1 K for 1 h, before being dispersed on standard copper grids. Micrographs of the pure support were obtained for comparative purposes. The nickel metal particles were taken as being spherically shaped and the particle diameters were accordingly measured from the micrographs.

The amount of TA adsorbed on selected samples was determined by analyzing the pre- and postmodification solutions by HPLC (Spectra Physics). A Spherisorb 5μ C8 packed column (Alltech Association, 250 × 4.6 mm) was used with 0.2 mol dm^{-3} phosphoric acid (Aldrich, >99%) as the mobile phase and detection was by UV (λ = 187 nm). As nickel tartrate (NiTA) has been tentatively identified as the steroselective active site formed by the corrosive adsorption of TA on nickel (18, 30), a correction for the presence of NiTA in the postmodifier was made by preparing a range of aqueous TA–NiTA solutions (of varying NiTA concentration), which were then used to construct a 30-point calibration curve. To enhance sensitivity and accuracy (which was within ±3%), the signal from the integrator was digitized and stored on disc for subsequent analysis using a WINner LABNET routine. The amount of TA adsorbed was calculated as the difference between the values obtained for the solutions before and after modification. NiTA was prepared according to the method of Hoek and Sachtler (18).

Catalytic procedure

The liquid phase hydrogenation of MAA (10 cm^3), using *n*-butanol as a solvent (40 cm^3), was carried out at 343 ± 2 K in a 250-cm^3 glass vessel fitted with a condenser, hydrogen inlet, and thermocouple well. A 60 cm^3 min^{-1} stream of purified hydrogen was bubbled through the suspension that was kept under constant agitation at 600 rpm. Details of the catalytic apparatus are available elsewhere (4). The extent of hydrogenation was determined by HPLC using a Pirkle type 1A 5μ reversible column (250 × 4.6 mm) with a 10% isopropyl alcohol (IPA) – 90% hexane mixture as the mobile phase. The overall degree of hydrogenation was converted to mol% MHB using a 21-point calibration plot; a quadratic equation was used to fit these data to better than ±1%. Optical yields (O.Y.) were determined from measurements of optical rotation (AA-10 Automatic Digital Polarimeter) using the equation

$$\text{O.Y.} = \frac{[\alpha]_D^T}{[\alpha]_0^T} = \frac{100\,\alpha}{[\alpha]_0^T\, lc}$$

where $[\alpha]_D^T$ is the specific rotation of the product solution measured at the sodium D-line and temperature T (293 ± 3 K), $[\alpha]_0^T$ is the specific rotation of the pure enantiomer under the same conditions (−22.95° for *R*-(−)-MHB), α is the measured optical rotation, l is the path length (20 cm) of the cell, and c is the solute concentration. Optical rotation versus *R*-(−)-MHB concentration (in MAA–butanol) data were fitted to a quadratic equation to better than ±2%, which was then used to determine the optical yield of the product; optical yields were reproducible to ±4%. In this paper, optical selectivity is expressed in terms of enantiomeric excess (e.e.), which is defined as

$$\%\text{e.e.} = 100\,\frac{[R\text{-}(-)\text{MHB}] - [S\text{-}(+)\text{-MHB}]}{[R\text{-}(-)\text{MHB}] + [S\text{-}(+)\text{-MHB}]}$$

Results and discussion

Modification of the Ni–SiO_2, prepared by homogeneous precipitation–deposition (HPD) or impregnation (IMP), with *R*-(+)-TA yielded *R*-(−)-MHB as the preferred hydrogenation product. With regard to the published studies (20, 21, 37, 38) which have ascribed structure sensitivity to the asymmetric conversion of MAA, the quoted enantioselectivities were related, in each case, to the dimensions of the metal particles supported on the premodified catalyst. As shown in an earlier report (4), the composition of the modified catalyst differs considerably from the freshly reduced catalyst. To positively attribute a metal particle size effect to the reaction, it is imperative that the catalytic data are related to the conditions prevailing at the active surface during catalysis.

In this study the catalysts were activated, with or without a precalcination step, by temperature programmed reduction (TPR) where the ultimate metal dispersion was reproducible to within ±3%. Representative TPR profiles are presented in Fig. 1 and the pertinent reduction parameters are listed in Table 1.

Can. J. Chem. Downloaded from www.nrcresearchpress.com by 195.246.54.202 on 09/08/12
For personal use only.

Can. J. Chem. Downloaded from www.nrcresearchpress.com by 195.246.54.202 on 09/08/12
For personal use only.

The profiles generated during the direct reduction of the HPD catalysts (Fig. 1*a*) all exhibit the same basic shape, consisting of a major broad peak with a maximum intensity in the temperature range of 810–850 K and a minor peak that attains a maximum at ca. 580 K. These two distinct peaks suggest the presence of two nickel species that differ in the degree of interaction with the support and hence in the ease of reduction. The low temperature peak arises at a slightly higher temperature than that recorded for unsupported NiO (565 K) and can be attributed to the reduction of a precipitated hydroxide species, which interacts weakly with the support. The bulk of the hydrogen consumption occurs at much higher temperatures and can be interpreted as resulting from a reduction of nickel hydroxysilicate, which has been shown to form on catalysts prepared by precipitation–deposition (40, 41). It may be noted that the total hydrogen consumption exceeds, in most cases, the theoretical value for a complete reduction of the nickel content; the excess hydrogen may be due to a spillover from the nickel metal and is held on the support. From a consideration of peak areas, the higher loaded HPD catalysts exhibit a greater proportion of the readily reduced hydroxide species, i.e., 8% of the total nickel content in the case of Ni–SiO_2-20.3 compared with 2% in the case of Ni–SiO_2-1.5. In addition, the high temperature peak associated with the nickel-rich sample, while being broader, attains a maximum at a lower temperature than the nickel dilute samples (Table 1). It can, therefore, be inferred that nickel–support interactions are stronger at lower metal loadings with the result that a higher reduction temperature is required to attain a maximum in the reduction rate. The TPR profiles of the precalcined samples (representative profile shown in Fig. 1*b*) are characterized by a single broad peak that emerged over a higher temperature range (T_{max} = 850–875 K) than the main hydrogen consumption peak recorded for the uncalcined samples (Table 1). The calcination step, in effect, removed the low temperature peak and stabilized the unreduced surface nickel, possibly by eliminating some of the structural water of the hydrosilicate species and making it more difficult to reduce. In contrast to the HPD technique, catalyst preparation by impregnation has received considerable attention (41–44). The TPR profiles generated during the direct reduction and precalcination–reduction of the impregnated catalyst are shown in Fig. 1*c*. Four peaks were identified (Table 1) for the former case: a small ill-defined peak at T_{max} = 528 K, which has been ascribed (45) to an endothemic phase transition from rhombohedral to cubic NiO which occurs simultaneously with reduction; a minor (573 K) and a major (610 K) peak, which can be attributed to the process

$$H_2 + NiO \rightarrow H_2O + Ni$$

where the minor peak (with a T_{max} similar to that for bulk NiO) is associated with the reduction of very weakly interacting NiO and the higher temperature peak represents the reduction of NiO which interacts to a greater extent with the carrier; and a broad peak with T_{max} = 693 K, which may be due to the more difficult reduction of a surface nickel silicate species. The reduction of the precalcined sample generated a small peak at T_{max} = 503 K, which is thought to be due to the reduction of traces of Ni(III) oxide (43), and a broad peak at T_{max} = 658 K with a shoulder, which can be considered to represent the reduction of both surface NiO and nickel silicate. As with the HPD catalysts, the introduction of the calcination step shifted the T_{max} of the principal peak to a higher value. Taking an overview of the TPR data, it can be concluded that the activation of the HPD catalysts requires higher reduction temperatures owing to the stronger interaction of unreduced nickel with the support, and this interaction is further strengthened by the incorporation of a precalcination step.

The implications of different precursor–carrier interaction strengths due to the preparation and activation procedures on the dispersion of the surface active nickel metal phase are given in Tables 2 and 3. The nickel metal dispersion data were obtained from CO chemisorption and the metal dispersion is expressed as $(Ni_{surface}/Ni_{total}) \times 100\%$. The percentage of nickel dispersion was observed to decrease with increasing nickel loading and reduction temperature. However, under the same reduction conditions the metal phase generated from the HPD precursor was better dispersed than that supported on the activated IMP catalyst. The stronger interaction between nickel and the silica support must persist in the reduced state, with the result that the nickel metal particles are more strongly anchored to the HPD surface. In the case of the nickel-rich samples, there is an increased probability of metal atoms being in close proximity to facilitate agglomeration, a process that is further promoted at higher temperatures and results in a decrease in the exposed nickel area. In contrast to the impregnated samples, precalcination of the HPD catalysts had little effect on metallic dispersion (Table 3). As proposed elsewhere (41, 44), the precalcination of an impregnated precursor can result in the growth of the weakly interacting unreduced nickel species (presumably NiO), which in the reduced state generates a poorly dispersed supported metallic phase. The extent of the nickel–support interaction in the HPD precursors mitigates against such a sintering effect and, as shown in Fig. 1*b*, precalcination increased the stability of the catalyst precursor with an accompanying slight improvement in dispersion (Table 3). As with direct reduction, the percentage of nickel dispersion was lowered on raising the reduction temperature of the precalcined samples.

The supported nickel metal particle size was determined from the dispersion measurements according to the relationship (46) $d = 101/D$ where D is the dispersion or percentage of exposed metal atoms and d is the surface weighted average crystallite diameter, assuming (spherical) particles $\leq$1 nm to be 100% dispersed. In this study, reduction of the range of nickel-loaded HPD samples listed in Table 2 generated nickel particles with average diameters in the range of 1.4–3.7 and 1.7–5.9 nm for reduction temperatures of 723 and 1073 K, respectively. In contrast, the average diameter of nickel particles supported on the impregnated carrier was considerably greater (Table 3) as a direct consequence of the lower nickel–support interaction and higher mobility of the reduced metal leading to the formation of metal aggregates. The nature of the distribution of metal particle sizes, as determined by transmission electron microscopy, is illustrated in Fig. 2 for representative catalysts. Histograms were constructed based on counts of at least 500 particles and a smooth line was drawn through the midpoint of each bar maximum to facilitate the inclusion of a number of particle size distribution (PSD) plots in one figure. It can be seen that the range of sizes of the particles supported on the HPD catalyst is narrow (0.5–6 nm) and is broadened slightly (0.5–8 nm) upon elevating the reduction temperature. The impregnated sample, on the other hand, with a similar nickel content is characterized by a much broader PSD with supported particles of up to 20 nm detected. It should be noted that the average particle diameter computed from electron

TABLE 1. TPR characteristics of Ni–SiO_2 catalyst prepared by HPD and IMP

Catalyst precursor	Uncalcined T_{max}[a] (K)	Uncalcined H_2 consumption[b] (10^{-2}L g^{-1})	Precalcined T_{max}[a] (K)	Precalcined H_2 consumption[b] (10^{-2}L g^{-1})
Ni–SiO_2-1.5[c]	850[d]	0.7	875	0.6
Ni–SiO_2-6.2	580, 842	3.7	870	3.3
Ni–SiO_2-11.9	580, 828	5.8	863	5.0
Ni–SiO_2-15.2	580, 815	8.1	855	6.8
Ni–SiO_2-20.3	580, 810	10.5	850	8.4
Ni–SiO_2-11.6[e]	528, 573, 610, 693	5.7	503, 658	5.3

[a]Temperature corresponding to maximum in hydrogen consumption.
[b]Reproducible to better than ±5%.
[c]% w/w Ni, prepared by HPD.
[d]Ill-defined peak at ca. 580 K.
[e]% w/w Ni, prepared by IMP.

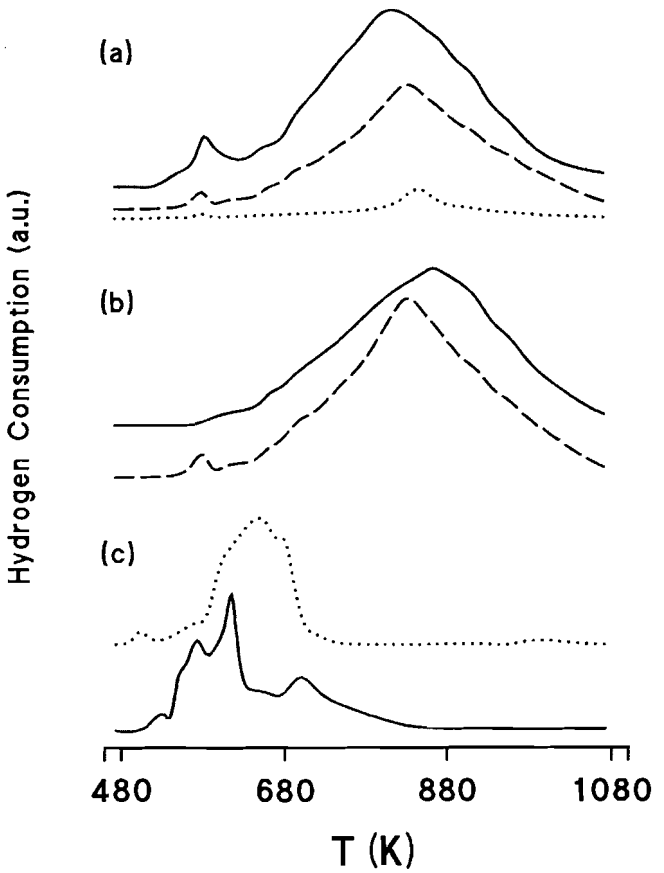

FIG. 1. (*a*) TPR profiles of Ni–SiO_2-1.5(···), Ni–SiO_2-11.9 (- - -), and Ni–SiO_2-20.3 (–) prepared by HPD and reduced without a precalcination step. (*b*) TPR profiles generated during the direct reduction (- - -) and during the reduction of precalcined (–) Ni–SiO_2-11.9 prepared by HPD. (*c*) TPR profiles generated during the direct reduction (–) and during the reduction of precalcined (···) Ni–SiO_2-11.6 prepared by IMP.

microscopy data was up to 10% lower than that inferred from the CO chemisorption measurements.

It is now well established (3, 4, 25, 28) that the generation of the enantioselective site is a corrosive process and results in the extraction of nickel atoms from the metal lattice. There is strong spectroscopic evidence (1) to suggest that TA is adsorbed on the metal surface as a carboxylate. In accordance with the work of Sachtler and colleagues (18, 30), we can assume that TA interacts with the surface nickel to form a NiTA complex which can either remain on the silica carrier to form a supported selective site or diffuse into solution. As shown in Table 2, the concentration of nickel in the postmodifier increased with increasing nickel loading. Under identical modification conditions, a greater proportion of nickel was lost from the impregnated surface (Table 3). The stronger metal–support interactions observed for the HPD catalysts must enhance nickel stability and render the supported metal phase less susceptible to leaching during TA treatment. Precalcination, which has been shown to further enhance metal stability, was also observed to lower the concentration of leached nickel (Table 3). The effect of TA treatment on the particle size distribution is illustrated in Fig. 2. It is clearly evident that the TA treatment removes the smaller nickel particles and shifts the average crystallite diameter to a higher value (Table 3). The smaller nickel particles, which have a higher surface free energy (47), are therefore preferentially leached from the catalyst and nickel particles smaller than 2 nm are particularly susceptible to the corrosive effects of TA. It follows then that a high temperature sintering of the active metal inhibits nickel leaching, as shown in Table 3. The percentage of the initial nickel content leached as a function of reduction temperature is shown in Fig. 3*a* for three representative catalysts. The fraction of the initial nickel content remaining on the surface after modification was greater for the higher loaded samples and increased in each case as particle growth (via increased reduction temperature) was promoted. This effect is most pronounced for the nickel dilute sample where an elevation of the reduction temperature of Ni–SiO_2-1.5 from 673 to 1073 K resulted in over 1.5 times the concentration of nickel remaining on the support.

The number of TA molecules adsorbed was found to increase with increasing metal loading (Table 2). Under the stated modification conditions TA adsorption reached equilibrium after ca. 1 h. It has been demonstrated elsewhere (4) that the amount of TA adsorbed is both time and temperature dependent. On subjecting the calcined (unreduced) samples to the same TA treatment, the residual nickel in solution was less than 10 ppm, while the adsorbed TA phase was less than 6×10^{17} molecules per gram of catalyst. The site for TA adsorption is therefore the supported nickel metal, and TA interaction with the silica support and unreduced nickel is slight. At a particular nickel loading, decreased dispersion due to sintering lowered the concentration of adsorbed TA (Tables 2 and 3). The surface

Can. J. Chem. Downloaded from www.nrcresearchpress.com by 195.246.54.202 on 09/08/12
For personal use only.

TABLE 2. The effect of reduction temperature on the extent of nickel leaching. TA uptake, and the dispersion of nickel supported on a range of nickel loaded pre- and post-modified HPD catalysts

Catalyst sample	Reduced at 723 K				Reduced at 1073 K			
			%D[c]				%D[c]	
	10^{-19} N^a	ppm Ni[b]	*b*	*a*	10^{-19} N^a	ppm Ni[b]	*b*	*a*
Ni–SiO_2-1.5	0.6	45	73	37	0.5	31	60	32
Ni–SiO_2-6.1	1.5	118	54	31	1.4	82	38	26
Ni–SiO_2-11.9	2.8	161	40	28	2.7	111	25	19
Ni–SiO_2-15.2	3.4	188	33	26	3.1	147	20	18
Ni–SiO_2-20.3	4.0	217	27	23	3.5	184	17	16

[a]Number of TA molecules retained by the catalyst.
[b]Concentration of leached nickel in the postmodifier.
[c]Nickel metal dispersion before (*b*) and after (*a*) modification.

TABLE 3. The effect of reduction temperature and the incorporation of a precalcination step on the extent of nickel leaching, TA uptake, nickel dispersion, crystallite size, and the ultimate surface coverage by TA in the modification of a HPD and IMP catalyst of similar nickel loading

Catalyst activation	10^{-19} N^a	ppm Ni[b]	%D^c		d^d (nm)		θ_{TA}
			b	*a*	*b*	*a*	
Direct reduction							
11.9 (HPD)[e]							
723 K[f]	2.8	161	40	28	2.5	3.6	0.23
1073 K	2.7	111	25	19	4.0	5.3	0.32
11.6 (IMP)[g]							
723 K	1.3	198	17	12	5.9	8.4	0.32
1073 K	1.2	148	9	7	11.2	13.8	0.41
Precalcination							
11.9 (HPD)							
723 K	2.5	145	43	32	2.4	3.2	0.17
1073 K	2.4	100	26	21	3.9	4.8	0.23
11.6 (IMP)							
723 K	1.1	162	11	9	9.1	10.9	0.27
1073 K	1.1	114	7	6	13.6	15.7	0.37

[a]Number of TA molecules retained by the catalyst.
[b]Concentration of leached nickel in the postmodifier.
[c]Nickel metal dispersion before (*b*) and after (*a*) modification.
[d]Average nickel particle diameter before (*b*) and after (*a*) modification.
[e]Prepared by HPD.
[f]Reduction temperature.
[g]Prepared by IMP.

coverage by TA (θ_{TA}) as a function of reduction temperature is shown in Fig. 3*b*. As TA is adsorbed from solution, there is an accompanying removal of nickel from the solid into the liquid phase, which in effect dilutes the concentration of surface adsorption sites. The fractional coverage by TA is governed by the interplay between the uptake of TA from solution, the number of available adsorption sites, and the extent to which the adsorption sites are removed in the corrosive adsorption step. In the case of the higher nickel-loaded samples, the values of θ_{TA} increased with increasing reduction temperature, although the concentration of surface TA was lower (Table 2) owing to the overwhelming effect of sintering which reduced the number of potential adsorption sites; i.e., the end result is a decrease in the number of adsorbed TA molecules (Table 2), but an increase in the fractional coverage of the more poorly dispersed adsorption sites. The nickel-dilute sample, on the other hand, exhibited a marked decrease in the degree of coverage by TA with an increase in the temperature of activation. In this case, while the elevation of reduction temperature was again accompanied by a decrease in the concentration of the adsorbed modifier, the enhanced stability of the surface nickel metal resulted in a greater number of adsorption sites surviving the corrosive TA treatment, all of which translates into a lower concentration of TA adsorbed on a surface bearing a greater number of adsorption sites.

The apparent reaction rate (expressed here as the number of moles of MAA reacted per hour) was obtained by treating the variation of hydrogenation activity with time (at $t > 1$ h, where

Can. J. Chem. Downloaded from www.nrcresearchpress.com by 195.246.54.202 on 09/08/12
For personal use only.

Can. J. Chem. Downloaded from www.nrcresearchpress.com by 195.246.54.202 on 09/08/12
For personal use only.

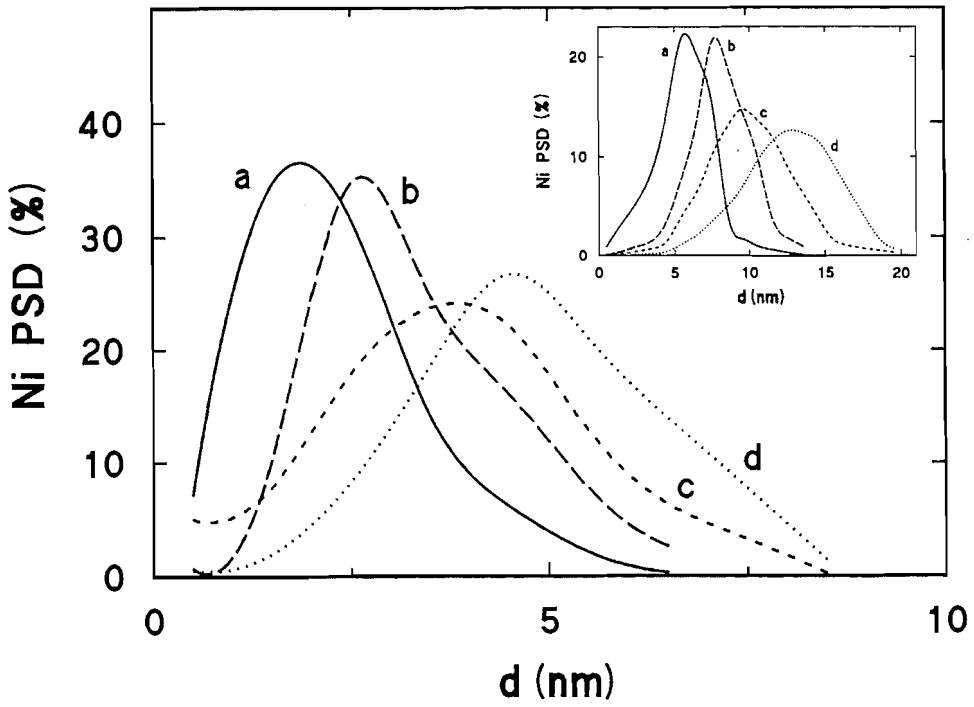

FIG. 2. Particle size distribution (PSD) of nickel supported on Ni–SiO_2-11.9 (HPD) reduced without precalcination at 723 K in the premodified (*a*) and postmodified (*b*) states and at 1073 K in the premodified (*c*) and postmodified (*d*) states. Inset: PSD of Ni–SiO_2-11.6 (IMP); *a–d*, as above.

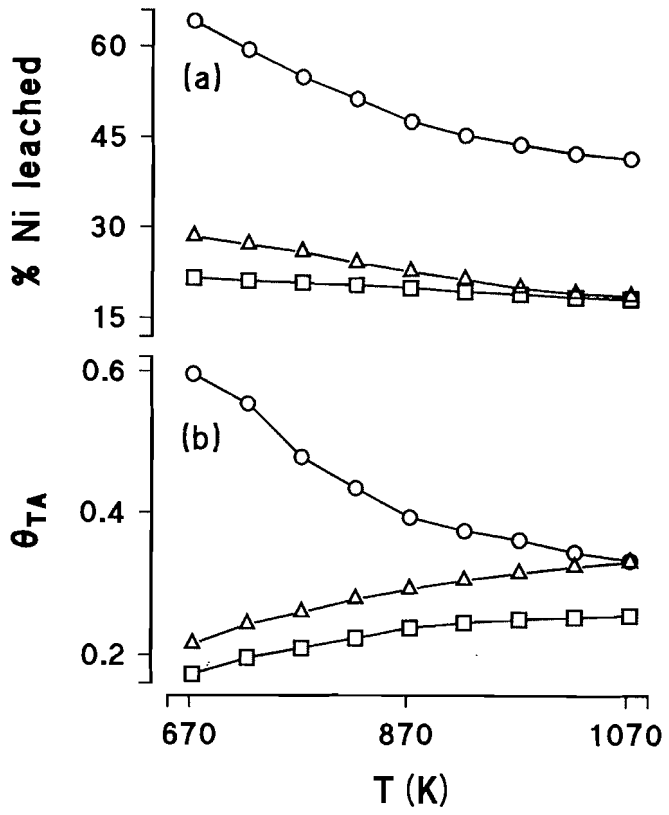

FIG. 3. The effect of reduction temperature (without precalcination) on (*a*) the percentage initial metal content leached and (*b*) the fractional surface coverage by TA. (○) Ni–SiO_2-1.5 (HPD); (△) Ni–SiO_2-11.9 (HPD); (□) Ni–SiO_2-20.3 (HPD).

the contribution of reactant diffusion and reactant–surface interactions is negligible (5)) as a linear relationship and determining the slope of the reaction profile. The effect of particle size (in the range of 1.3–6.9 nm) for the pre- and post-modified catalysts on the apparent rate is presented in Fig. 4, where the changes in particle diameter due to the TA treatment has been taken into account. The range of metal particle sizes were generated by variations in nickel loading and (or) reduction temperature. The graphical relationships presented in Fig. 4 show unambiguously that MAA hydrogenation to MHB is a structure-sensitive reaction and, over the range of particle sizes considered, activity decreased with increasing particle size. The variation in rate with the average nickel diameter for both the modified and unmodified systems has been fitted in Fig. 4 to an expression of the form $R/d = A\exp(-kd)$, to give

$$\text{Unmodified system: } R/d = 4.61(\pm 0.11)\exp[-0.454(\pm 0.012)d]$$

$$\text{Modified system: } R/d = 3.84(\pm 0.13)\exp[-0.249(\pm 0.009)d]$$

where A is a constant and k can be considered to reflect the dependency of the apparent rate on d. Deviations from the fit can be accounted for by a combination of experimental error and the assumptions used to estimate particle sizes. The apparent rates, over the range of particle sizes, were considerably higher for the modified samples. This observation is in direct conflict with earlier reports (7, 12, 17) where the adsorption of TA was observed to inhibit hydrogenation activity by blocking the active surface metal. However, Wells and co-workers (48) and Blaiser and co-workers (49) studying the enantioselective hydrogenation of α-ketoesters over platinum catalysts have also observed an increase in the hydrogenation rate due to the presence of the adsorbed cinchona alkaloid modifier. This

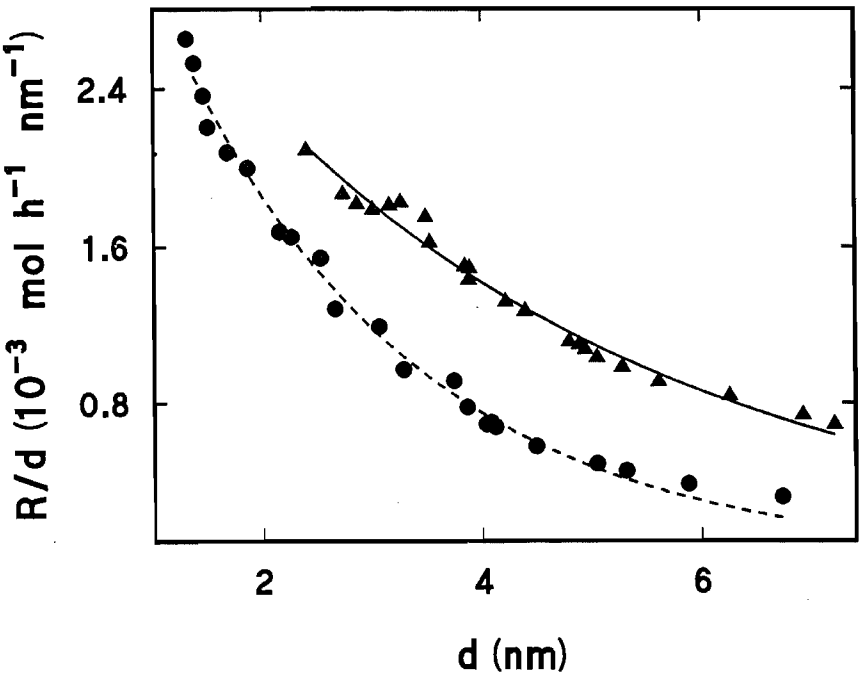

FIG. 4. The relationship between the reaction rate (expressed per nanometre of nickel metal) and the average diameter of the nickel crystallites (d) supported on a range of HPD catalysts reduced in the range of 673–1073 K in the premodified (●) and postmodified (■) states. The dashed line represents the relationship $R/d = 4.61(\pm0.11)\exp[-0.454(\pm0.012)d]$ and the solid line represents the relationship $R/d = 3.84(\pm0.13)\exp[-0.249(\pm0.009)d]$.

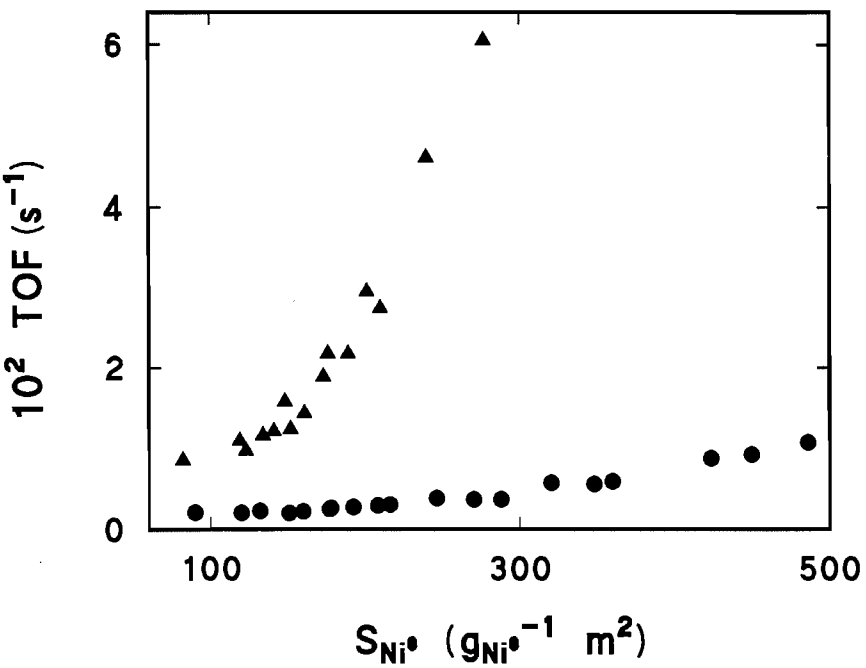

FIG. 5. The relationship between the turnover frequency (TOF) and the nickel metal surface area (per gram of supported nickel metal) for a range of premodified (●) and postmodified (▲) HPD catalysts.

enhancement of activity may be attributable to an increased concentration of surface-adsorbed hydrogen; while the adsorbed TA phase restricts the access of the MAA molecules to the surface metal atoms, the hydrogen can readily adsorb on these sites. Consequently, there is a greater reservoir of dissociated hydrogen on the modified surface, whereas the transport of hydrogen to the unmodified surface is achieved via multilayers of adsorbed MAA (5, 50). The contribution of the more active smaller (<2 nm) nickel metal particles to the overall rate is lower in the case of the modified samples because (*i*) these particles are preferentially leached from the surface into solution during modification and (*ii*) the increase in surface active hydrogen due to the presence of adsorbed TA may promote MAA hydrogenation to a greater extent than the combined action of the surviving small nickel particles. Consequently, the modified catalysts exhibit a lower dependency (lower k values)

Can. J. Chem. Downloaded from www.nrcresearchpress.com by 195.246.54.202 on 09/08/12
For personal use only.

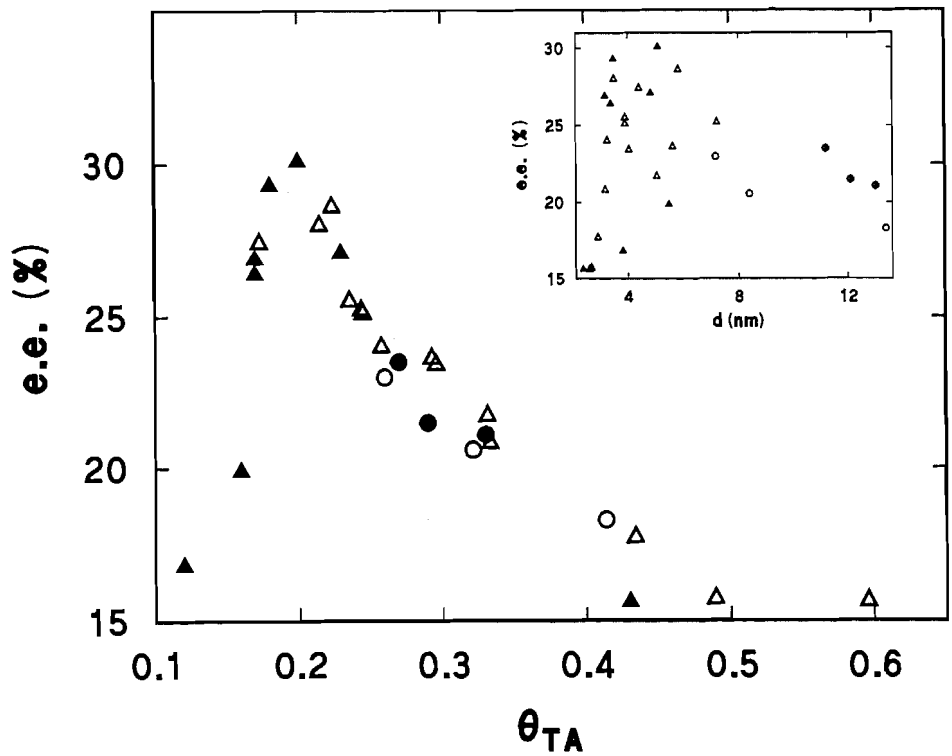

FIG. 6. The relationship between enantiomeric excess (e.e.) and surface coverage by TA (θ_{TA}) for a range of HPD catalysts reduced with (▲) or without (△) precalcination and the 11.6% w/w Ni-impregnated catalyst reduced with (●) or without (○) precalcination in the temperature range of 673–1073 K. Inset: relationship between enantiomeric excess and the average nickel crystallite diameter (d); symbols as above.

of apparent rate on crystallite size than is the case for the unmodified systems. The promoting effect of surface TA on the hydrogenation activity is better illustrated in Fig. 5 where the turnover frequency (TOF) or the number of MAA molecules converted per metal site per second is plotted against the surface metal area (expressed per gram of supported nickel metal), taking account of the changes in the nature of the surface metal as a result of modification. Both the modified and (to a lesser extent) the unmodified catalyst system exhibit an increase in turnover number with increasing metal area. Depending on the catalyst metal loading and pretreatment conditions, the TOF values were up to 15 times greater for the modified surface. Modification by TA, therefore, not only induces enantioselectivity, but also substantially promotes the rate of hydrogenation of MAA.

Nitta et al. (20, 21, 37, 38) have attributed observed differences in enantioselectivities to variations in the morphology of the supported nickel metal and to differences in the strength of nickel–support interactions. They concluded that optical yield was enhanced by surfaces where weak precursor–carrier interactions generated larger (more selective) nickel crystallites. In view of the high degree of structure sensitivity which they observed, Nitta et al. (37) have even suggested that the asymmetric hydrogenation of MAA may be used as a probe for the crystallite size distribution of nickel metal supported on a heterogeneous catalyst. However, as shown in the inset of Fig. 6, in the case of the HPD and IMP catalysts considered in this study there is no direct relationship between the average nickel particle diameter and the enantiomeric excess. Under the stated modification conditions, nickel particles of similar dimensions generated quite dissimilar e.e. values. The scatter of the selectivity data over the range of particle diameters is such that there is no discernible general trend in the e.e. versus d plot. Sachtler and colleagues (30) likewise observed no systematic change in enantioselectivity over the nickel particle size range of 4–11 nm. It must be stressed that the investigations carried out by Nitta et al. did not address the corrosive effects of TA adsorption and the optical yield in each instance was related to the nature of the metal phase in the premodified catalyst. The divergence in the data generated in this study with that reported by Nitta and co-workers (20, 21, 37, 38) highlights the difficulty in attempting to compare different enantioselective systems where the possible permutations of experimental variables involved in the catalyst preparation, activation, modification, and reaction steps mitigates against anything but a tentative qualitative comparison.

While there was no distinct relation between e.e. and d, enantioselectivity was observed to pass through a maximum at θ_{TA} = ca. 0.2 as illustrated in Fig. 6 where asymmetric data for 28 separate catalyst systems are related to surface coverage by modifier. The existence of a maximum in enantioselectivity at a low surface modifier coverage has been attributed to a sandwich effect (3, 4, 25) where both TA and MAA are coadsorbed on the catalyst surface. In the posited model, at θ_{TA} > ca. 0.2 there is a crowding effect, where the adsorbed MAA species is sandwiched between two TA molecules causing a destructive chemical interference, which results in the predominant formation of racemic MHB. Conversely, at θ_{TA} < ca. 0.2 only a fraction of the adsorbed MAA is sterically influenced, while the majority of MAA again undergoes racemic hydrogenation. Accordingly, the optimum TA treatment is one in which the distance between adsorbed TA molecules is large enough to ensure that an adsorbed MAA molecule interacts with only one modifier molecule, but small enough to minimize the number of racemic sites. The structural requirements of the nickel surface under the TA

Can. J. Chem. Downloaded from www.nrcresearchpress.com by 195.246.54.202 on 09/08/12
For personal use only.

overlayer are therefore facile in that there was no observable dependence of enantioselectivity on the regime of particle sizes which survive corrosion by TA. Rather, the fractional coverage of the surface by TA appears to be the critical factor in determining the ultimate enantiomeric excess. However, the modification step can perhaps be viewed as a structure-sensitive process in that the larger (>2 nm) supported nickel particles are more effective in anchoring the modifier to the support, whereas the smaller nickel particles are leached into solution.

Conclusions

1. Ni–SiO_2 precursors prepared by HPD exhibit stronger nickel–support interactions than do IMP precursors and consequently require higher temperatures (T_{max}) to attain maxima in hydrogen consumption during temperature-programmed reduction. The metallic phase supported on the HPD carrier is in the form of much smaller nickel crystallites, which are characterized by a narrow size distribution. Precalcination (in the case of the IMP precursor) and increased reduction temperatures (for both IMP and HPD precursors) generated larger metal particles.

2. Modification by TA is a corrosive process that preferentially leaches smaller nickel particles (<2 nm) from the surface, thereby shifting the average metal crystallite diameter to higher values. The metallic phase is more strongly held on the HPD surface and the percentage of the initial metal content leached from the surface decreases with increasing nickel loading. The fractional surface coverage by TA is governed by the extent of TA uptake from the liquid phase and the number of adsorption sites that survive the corrosive leaching by TA.

3. The dependency of the rate on the average crystallite diameter can be represented by (*i*) $R/d = 4.61(\pm 0.11)\exp[-0.454(\pm 0.012)d]$ for the unmodified catalyst system and (*ii*) $R/d = 3.84(\pm 0.13)\exp[-0.249(\pm 0.009)d]$ for the modified catalyst system. In both cases the apparent rate decreases with increasing metal particle size. The modified samples exhibit up to 15 times the turnover rate of the bare nickel metal owing to a higher surface coverage of active hydrogen on the modifier surface.

4. The ultimate degree of enantioselectivity is independent of the regime of particle sizes present after modification; i.e., enantioselectivity is a facile process, whereas the rate of hydrogenation is structure sensitive. Enantiomeric excess is, however, strongly influenced by modifier coverage and an optimum value of $\theta_{TA} = 0.2$ is identified as providing the surface conditions for optimum enantioselectivity, regardless of the average nickel particle diameter.

Acknowledgement

The author is grateful to G. Webb (Chemistry Department, Glasgow University) for the use of some experimental facilities.

1. Y. Izumi. Adv. Catal. **12**, 215 (1983).
2. H.U. Blaser. Tetrahedron; Asymmetry, **2**, 843 (1991).
3. A. Bennett, S. Christie, M.A. Keane, R.D. Peacock, and G. Webb. Catal. Today, **10**, 363 (1991).
4. M.A. Keane and G. Webb. J. Catal. **136**, 1 (1992).
5. M.A. Keane. Zeolites, **13**, 14 (1993); **13**, 22 (1993); **13**, 330 (1993).
6. T. Harada, M. Yamamoto, S. Onaka, M. Imaida, H. Ozaki, A. Tai, and Y. Izumi. Bull. Chem. Soc. Jpn. **54**, 2323 (1981).
7. D.O. Hubbell and P. Rys. Chimia, **24**, 442 (1970).
8. N.D. Zubareva, V.V. Chernysheva, Y.A. Grigorev, and E.I. Klabunovskii. Bull. Acad. Sci. USSR Div. Chem. Sci. 476 (1987).
9. V.V. Chernysheva, I.P. Murina, and E.I. Klabunovskii. Bull. Acad. Sci. USSR Div. Chem. Sci. 689 (1983).
10. G.V. Smith and M. Musoiu. J. Catal. **60**, 184 (1979).
11. H. Brunner, M. Muschiol, T. Wishert, and J. Wiehl. Tetrahedron: Asymmetry, **1**, 159 (1990).
12. T. Harada, Y. Haraki, Y. Izumi, J. Muraoka, H. Ozaki, and A. Tai. *In* Proceedings of the 6th International Congress on Catalysis, London, 1976. *Edited by* G.C. Bond, P.B. Wells, and F.C. Tompkins. The Chemical Society, London. 1977. p. 1024.
13. Y. Nitta, T. Imanaka, and S. Teranishi. J. Catal. **80**, 31 (1983).
14. E.I. Klabunovskii. Russ. J. Phys. Chem. **47**, 765 (1973).
15. E.N. Lipgart, Y.I. Petrov, and E.I. Klabunovskii. Kinet. Katal. **12**, 1491 (1971).
16. L.H. Gross and P. Rys. J. Org. Chem. **39**, 2429 (1974).
17. H. Ozaki, A. Tai, S. Kobatake, H. Watanabe, and Y. Izumi. Bull. Chem. Soc. Jpn. **51**, 3559 (1978).
18. A. Hoek and W.M.H. Sachtler. J. Catal. **58**, 276 (1979).
19. Y. Nitta, F. Sekine, J. Sasaki, T. Imanaka, and S. Teranishi. J. Catal. **79**, 211 (1983).
20. Y. Nitta, T. Utsumi, T. Imanaka, and S. Teranishi. J. Catal. **101**, 376 (1986).
21. Y. Nitta, M. Kawabe, and T. Imanaka. Appl. Catal. **30**, 141 (1987).
22. T. Osawa, T. Harada, and A. Tai. J. Catal. **121**, 7 (1990).
23. A. Hoek, H.M. Woerde, and W.M.H. Sachtler. *In* Proceedings of the 7th International Congress on Catalysis, Tokyo, 1980. *Edited by* K. Tanabe and T. Sieyama. Kodansha/Elsevier, Tokyo/Amsterdam. 1981. p. 376.
24. G. Wittmann, G.B. Bartok, M. Bartok, and G.V. Smith. J. Mol. Catal. **60**, 1 (1990).
25. M.A. Keane and G. Webb. J. Mol. Catal. **73**, 91 (1992).
26. I. Yasumori, M. Yozeki, and Y. Inoue. Faraday Discuss. Chem. Soc. **71**, 385 (1981).
27. D.R. Richards, H.H. Kung, and W.M.H. Sachtler. J. Mol. Catal. **36**, 329 (1986).
28. M.A. Keane and G. Webb. J. Chem. Soc. Chem. Commun. 1619 (1991).
29. H. Brunner, K. Amberger, and J. Wiehl. Bull. Soc. Chim. Belg. **100**, 571 (1991).
30. L. Fu, H.H. Kung, and W.M.H. Sachtler. J. Mol. Catal. **42**, 29 (1987).
31. L.J. Bostelaar and W.M.H. Sachtler. J. Mol. Catal. **27**, 387 (1984).
32. S. Tatsumi. Bull. Chem. Soc. Jpn. **41**, 408 (1970).
33. M.J. Fish and D.F. Ollis. J. Catal. **50**, 353 (1977).
34. T. Tanabe. Bull. Chem. Soc. Jpn. **46**, 1482 (1973).
35. T. Harada, A. Tai, M. Yamamoto, H. Ozaki, and Y. Izumi. *In* Proceedings of the 7th International Congress on Catalysis, Tokyo, 1980. *Edited by* K. Tanabe and T. Sieyama. Kodansha/Elsevier, Tokyo/Amsterdam. 1981. p. 364.
36. I. Yasumori, Y. Inoue, and K. Okabe, K. *In* Proceedings of the International Symposium on the Relations between Heterogeneous and Homogeneous Phenomena, Brussels, 1974. Elsevier, Amsterdam. 1975. p. 41.
37. Y. Nitta, T. Imanaka, and S. Teranishi. J. Catal. **96**, 429 (1985).
38. Y. Nitta, T. Utsumi, T. Imanaka, and S. Teranishi. Catal. Lett. 1339 (1984).
39. B. Coughlan and M.A. Keane. Zeolites, **11**, 2 (1991).
40. J.W.E. Coenen. Appl. Catal. **54**, 65 (1989).
41. M. Montes, C. Pennemann de Bosscheyde, B.K. Hodnett, F. Delannay, P. Grange, and B. Delmon. Appl. Catal. **12**, 309 (1984).
42. M. Houalla, F. Delannay, I. Matsuura, and B. Delmon. J. Chem. Soc. Faraday Trans. 1, **76**, 2128 (1980).
43. B. Mile, D. Stirling, M.A. Zammitt, A. Lovell, and M. Webb. J. Catal. **114**, 217 (1988).
44. G.A. Martin, C. Mirodatos, and H. Praliaud. Appl. Catal. **1**, 367 (1981).
45. A. Jones and B.P. MacNicol. *In* Temperature programmed reduction for solid materials. Marcel Dekker, New York. 1986.
46. J.S. Smith, P.A. Thrower, and M.A. Vannice. J. Catal. **68**, 270 (1981).

Can. J. Chem. Downloaded from www.nrcresearchpress.com by 195.246.54.202 on 09/08/12
For personal use only.

47. W.M.H. Sachtler, C.R. Kiliszek, and B.E. Nieuwenhuys. Thin Solid Films, **2**, 43 (1968).
48. I.M. Sutherland, A. Ibbotson, and P.B. Wells. J. Catal. **125**, 77 (1990); P.A. Meheux, A. Ibbotson, and P.B. Wells. J. Catal. **128**, 387 (1991).
49. J.T. Wehrli, A. Baiker, D.M. Monti, and H.U. Blaser. J. Mol. Catal. **61**, 207 (1990).
50. M.A. Keane and G. Webb. J. Catal. In press.

Can. J. Chem. Downloaded from www.nrcresearchpress.com by 195.246.54.202 on 09/08/12
For personal use only.

Studies of nonsteroidal anti-inflammatory drugs: azapropazone

THERESA FAUCONNIER, COLIN J.L. LOCK,[1] RUSSELL A. BELL, AND JAMES F. BRITTEN

Laboratories for Inorganic Medicine, Departments of Chemistry and Pathology, McMaster University, ABB266A, Hamilton, ON L8S 4M1, Canada

AND

K.D. RAINSFORD

Division of Biomedical Sciences, Sheffield Hallam University, Sheffield, S1 1WB, England

Received August 16, 1993

THERESA FAUCONNIER, COLIN J.L. LOCK, RUSSELL A. BELL, JAMES F. BRITTEN, and K.D. RAINSFORD. Can. J. Chem. **72,** 382 (1994).

The structure of azapropazone, 5-(dimethylamino)-9-methyl-2-propyl-1*H*-pyrazolo[1,2-*a*][1,2,4]benzotriazine-1,3(2*H*)-dione, was determined by single crystal X-ray diffraction. Crystals were orthorhombic ($P2_12_12_1$), with a = 5.570(1) Å, b = 14.593(3) Å, c = 19.270(4) Å, and Z = 4. Intensities were measured on a Rigaku AFC6-R diffractometer with Cu-Kα radiation and 2316 reflections were used to determine the structure. Contrary to previous postulates, the tricyclic portion of the molecule is not planar. Azapropazone is a zwitterion with the negative charge delocalized over the β-keto-enol system and with the proton on N(6) of the triazine ring. The nonplanarity of the molecule is caused by steric interaction of a methyl group on the exocyclic dimethylamino group with O(3) of the keto-enol system. Bond lengths and angles are normal. NMR studies showed that at room temperature rapid inversion occurs between the two enantiomers, but this inversion slows at low temperatures with $\Delta G^{\ddagger}$ = 44.9(2) kJ mol^{-1}. The product derived from opening of the pyrazolidine ring of azapropazone by formic acid is not as previously formulated. The compound is 3-dimethylamino-7-methyl-1-valeryl-1,4-dihydro-1,2,4-benzotriazine. Its structure was determined by single crystal X-ray diffraction. Crystals were monoclinic ($P2_1/n$), with a = 10.240(2) Å, b = 12.608(3) Å, c = 13.176(3) Å, β = 108.46(3)°, and Z = 4. Intensities were measured on a Rigaku AFC6-R diffractometer with Cu-Kα radiation and 2209 reflections were used to determine the structure. The conformation of the benzotriazine ring system was very similar to that observed in azapropazone and bond lengths and angles were normal.

THERESA FAUCONNIER, COLIN J.L. LOCK, RUSSELL A. BELL, JAMES F. BRITTEN et K.D. RAINSFORD. Can. J. Chem. **72,** 382 (1994).

On a déterminé la structure de l'azapropazone, la 5-(diméthylamino)-9-méthyl-2-propyl-1*H*-pyrazolo[1,2*a*]benzotriazine-1,3-(2*H*)-dione, par diffraction des rayons X. Les cristaux sont orthorhombiques ($P2_12_12_1$), avec a = 5,570(1) Å, b = 14,593(3) Å, c = 19,270(4) Å et Z = 4. On a mesuré les intensités à l'aide d'un diffractomètre Rigaku AFC6-R, avec le rayonnement Kα du Cu et on a utilisé 2316 réflexions pour déterminer la structure. Contrairement aux postulats antérieurs, la portion tricyclique de la molécule n'est pas plane. L'azapropazone est un zwitterion avec une charge négative délocalisée sur le système β-céto-énolique et avec le proton sur le N(6) du noyau triazine. Le caractère non-planaire de la molécule est provoqué par une interaction stérique du groupe méthyle porté par le groupe diméthylamino exocyclique avec le O(3) du système céto-énolique. Les longueurs des liaisons et les angles sont normaux. Les études de RMN ont montré que, à la température ambiante, il se produit une interconversion rapide entre les deux énantiomères, mais que l'inversion est ralentie à basse température avec un $\Delta G^{\ddagger}$ = 44,9(2) kJ mol^{-1}. Le produit obtenu par ouverture du noyau pyrazolidine de l'azapropazone par l'acide formique ne correspond pas à celui qui avait été formulé antérieurement. Le composé est le 3-diméthylamino-7-méthyl-1-valéryl-1,4-dihydro-1,2,4-benzotriazine. On a déterminé la structure par diffraction des rayons X par un cristal unique. Les cristaux sont monocliniques ($P2_1/n$), avec a = 10,240(2) Å, b = 12,608(3) Å, c = 13,176(3) Å, β = 108,46(3)° et Z = 4. On a mesuré les intensités à l'aide d'un diffractomètre Rigaku AFC6-R, avec le rayonnement Kα du Cu et on a utilisé 2209 réflexions pour déterminer la structure. La conformation du système du noyau benzotriazine est très semblable à celle observée dans l'azapropazone et les longueurs des liaisons et les angles sont normaux.

[Traduit par la rédaction]

Introduction

Nonsteroidal anti-inflammatory drugs (NSAIDs) are oral agents that inhibit prostanoid synthesis by blocking the production of cyclooxygenase (1). There are many useful NSAIDs, occurring in seven different chemical classes (2). Azapropazone was originally classified as a pyrazolone because of its structural similarities to another NSAID, phenylbutazone, but additional chemical studies suggest that it should be reclassified as a benzotriazine (3). The drug is used to treat various forms of arthritis and has found some success in European centres, although it is still not widely used in North America. The structure of azapropazone or 5-(dimethylamino)-9-methyl-2-propyl-1*H*-pyrazolo[1,2-*a*][1,2,4]benzotriazine-1,3(2*H*)-dione(**1**) as found in the Merck Index (4) is shown as **A**.

By use of NMR evidence, Fenner and Mixich determined that, in solution, there is no hydrogen atom at C(2) of the pyrazolone ring and suggested, therefore, that azapropazone is a zwitterion with the negative charge delocalized between the two ketone groups and with the proton on N(6) of the benzotriazine group, (shown as structure **B**) (5). Because the proton that is absent from the C(2) position cannot be located directly, since there is rapid exchange, there has been some debate in the literature as to its exact location. Despite references to the work by Fenner and Mixich, Dean interpreted the NMR results as giving evidence of a keto-enol structure with strong hydrogen bonding between the hydroxy proton and the exocyclic dimethylamino group, as seen in structure **C** (6). Such an interpretation seems most unlikely since, in our experience, exocyclic amine groups adjacent to ring double bonds tend to show considerable conjugation between the amine and the double bond, with consequent removal of the "lone pair" electron density and shortening of the

[1]Author to whom all correspondence should be addressed.

Can. J. Chem. Downloaded from www.nrcresearchpress.com by 195.246.54.202 on 09/08/12
For personal use only.

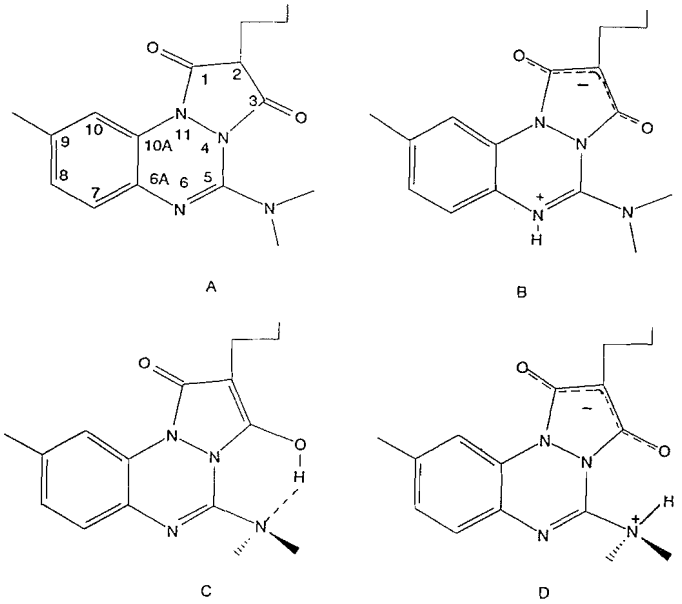

C(ring)–N distance. In addition, the amine group is then usually nearly coplanar with the double bond system. Despite Dean's argument that there will be a repulsive steric interaction between the methyl group on the amine and the hydroxy group, we did not think this would be sufficient to completely overcome the conjugation and thus Dean's postulated structure seems doubtful. Another postulated structure is that shown as structure **D**, where the hydrogen atom is directly bonded to the nitrogen atom of the dimethylamino group (6). For reasons already given, this structure also seems unlikely. The NMR spectra show that the peak from the aromatic proton at C(10) is pushed downfield about 1 ppm from the other aromatic protons because of interaction of the proton with the deshielding cone of the carbonyl group at C(1). For this reason, and because of the delocalization in the molecule, Fenner and Mixich stated that the three rings of azapropazone form a "vollständig planaren trizyklischen System" (completely planar tricyclic system) (5). We were not convinced by this because, while there is considerable delocalization in the benzotriazine system and the pyrazolidine ring, it does not extend to the N–N region and thus there seems to be no absolute reason for the tricyclic system to be planar. Further, Walker assumed that, despite the solution results, the solid compound existed in the diketone form, although no rationale was given (7). Because of these conflicting views, we have determined the structure of azapropazone.

Experimental

The ^{1}H NMR spectra for azapropazone (**1**) and the product (**2**) derived from opening the pyrazolidine ring of **1** by formic acid were recorded with use of a Bruker AC-200 spectrometer operating at a frequency of 200.1300 MHz, equipped with a 4.70-T cryomagnet and an Aspect 3000 computer. The instrument zero was locked to deuterium of the solvent. The ^{1}H NMR spectra for both samples were obtained using CD_3OD solutions in 32 scans at a spectral width of 2.4 kHz (16K, 0.293 Hz/data point).

The low-temperature NMR data were obtained with use of a Bruker AC-300 spectrometer operating at a frequency of 300.1300 MHz, equipped with a 7.0463-T cryomagnet and an Aspect 3000 computer. The solvent was CD_3OD which provided the deuterium lock signal. Data were acquired in 8 scans at a spectral width of 2.994 kHz (16K, 0.3655 Hz/data point). The spectra were recorded every 5° from −85 to −65°C and −50 to −40°C and every 1° from −65 to −50°C (s, singlet; d, doublet; t, triplet; qt quartet of triplets; tt, triplet of triplets).

X-ray structure determination

Crystals were selected after examination for sharp extinctions with a polarizing microscope and mounted on glass fibres with epoxy glue. Unit cells were obtained by least-squares refinements of the angular coordinates of 24 reflections with θ from 25.0° to 37.4° for **1** and 21.2° to 39.7° for **2**. The details of data acquisition and treatment are given in Table 1. Hydrogen atoms adjacent to atoms in the tricylic ring system were found from the difference maps, but were not refined. Hydrogen atoms in the exocyclic alkyl groups were placed in calculated positions and rode on the atoms to which they were attached. Atomic coordinates and isotropic temperature factors are given in Tables 2 (**1**) and 3 (**2**). Both compounds presented difficulties in the refinement of atoms C(22) and C(23), which were clearly disordered. Many different refinements were tried, with partial occupancies of multiple sites or restraints on bond lengths, but none were satisfactory or better than the results presented here.[2]

Azapropazone, 1

Azapropazone was kindly provided by Siegfried Pahrma AG, Zotingen, Switzerland, as a yellow powder and recrystallized from methanol to give colourless needles, mp 244–247°C (lit. (4) mp 247–248°C). ^{1}H NMR (200 MHz in CD_3OD at 25°C) δ: 0.91 (3H, t, $J_{23,22}$ = 7.3 Hz, $-CH_2CH_2CH_3$), 1.49 (2H, qt, $J_{22,23}$ =7.3 Hz, $J_{22,21}$ = 7.4 Hz, $-CH_2CH_2CH_3$), 2.14 (2H, t, $J_{21,22}$ = 7.4 Hz, $-CH_2CH_2CH_3$), 2.29 (3H, s, CH_3 aromatic), 3.19 (6H, s, $-N(CH_3)_2$), 6.89 (1H, d, $J_{8,7}$ = 8.3 Hz, aromatic); 7.00 (1H, d, $J_{7,8}$ = 8.3 Hz, aromatic), 8.04 (1H, s, aromatic). ^{1}H NMR (300 MHz in CD_3OD) δ: at −40°C, 3.17 (6H, s, $-N(CH_3)$); at −85°C, 3.08 (3H, s, $N(CH_3)$), 3.21, (3H, s, $-N(CH_3)$).

3-Dimethylamino-7-methyl-1-valeryl-1,4-dihydro-1,2,4-benzotriazine, 2

Azapropazone (1 g) was refluxed with formic acid (10 mL) for 1 h. Volatile solvent was removed by rotoevaporation at 70°C under vacuum (1 Torr; 1 Torr = 133.3 Pa) to give a pale yellow oil. The oil was dissolved in 2-butanone and the solution was allowed to evaporate in air, whereupon pale orange crystals were separated. Yield, 0.544 g, 60%; mp 159–163°C (lit. (8) mp 161–162°C). ^{1}H NMR (200 MHz in CD_3OD at 25°C) δ: 0.95 (3H, t, $J_{23,22}$ = 7.2 Hz, $-COCH_2CH_2CH_2CH_3$), 1.41 (2H, qt, $J_{22,23}$ = 7.3 Hz, $J_{22,21}$ = 7.3 Hz, $COCH_2CH_2CH_2CH_3$), 1.63 (2H, tt, $J_{21,22}$ = 7.3 Hz, $J_{21,2}$ = 3.9 Hz, $-COCH_2CH_2CH_2CH_3$), 2.26 (2H, s, CH_3 aromatic), 2.69 (2H, t, $J_{2,21}$ = 3.9 Hz, $-COCH_2CH_2CH_2CH_3$), 2.95 (6H, s, $N(CH_3)_2$), 6.79 (1H, d, $J_{8,7}$ = 8.1 Hz, aromatic), 6.89 (1H, d, $J_{7,8}$ = 8.1 Hz, aromatic), 7.49 (1H, s, aromatic).

Results and discussion

The molecule of azapropazone is shown in Fig. 1 and bond lengths and angles are given in Table 4. The molecule is a zwitterion and, as postulated by Fenner and Mixich, the proton from C(2) appears at the N(6) position. As can be seen from Fig. 1B, the tricyclic part of the molecule is *not* planar. The nonplanarity of the tricyclic system is best exemplified by the dihedral angles between the best planes through each of the rings. These values are as follows: rings 1–2 (see below), 11.7(7)°; rings 2–3, 32.9(7)°; rings 1–3, 44.5(7)°. The nonplanarity at N(11) is

[2]Tables of anisotropic displacement coefficients, hydrogen atom coordinates, best planes, dihedral and torsional angles, and observed and calculated structure factors for **1** and **2** can be purchased from: The Depository of Unpublished Data, Document Delivery, CISTI, National Research Council Canada, Ottawa, ON K1A 0S2, Canada.

Tables of hydrogen atom coordinates, best planes, and angles have also been deposited with the Cambridge Crystallographic Data Centre, and can be obtained on request from The Director, Cambridge Crystallographic Data Centre, University Chemical Laboratory, 12 Union Road, Cambridge, CB2 1EZ, U.K.

Can. J. Chem. Downloaded from www.nrcresearchpress.com by 195.246.54.202 on 09/08/12
For personal use only.

TABLE 1. Structure determination summary for **1** and **2**

	1	**2**
	Crystal data	
Formula	$C_{16}H_{20}N_4O_2$	$C_{15}H_{22}N_4O$
Colour, habit	Colourless needle	Orange hexagonal plate
Crystal size (mm)	0.2 × 0.2 × 1.0	1.0 × 1.0 × 0.3
Crystal system	Orthorhombic	Monoclinic
Space group	$P2_12_12_1$	$P2_1/n$
a (Å)	5.570(1)	10.240(2)
b (Å)	14.593(3)	12.608(3)
c (Å)	19.270(4)	13.176(3)
β (deg)	—	108.46(3)
Volume (Å^3)	1566.3(5)	1613.6(8)
Z	4	4
Formula weight	300.4	274.4
Density (calc.) (Mg/m^3)	1.274	1.129
Absorption coefficient (mm^{-1})	0.703	0.585
F(000)	640	592
	Data collection[a]	
Index ranges	$-6 \le h \le 6$	$-4 \le h \le 10$
	$0 \le k \le 16$	$-13 \le k \le 14$
	$0 \le l \le 21$	$-14 \le l \le 14$
Reflections collected	2689	2358
Independent reflections	2316 (R_{int} = 0.0161)	2209 (R_{int} = 0.0537)
Reflections used	2316	2209
Absolute corrected T_{min}	0.681	0.717
T_{max}	1.635	1.202
	Solution and refinement[b]	
No. of parameters refined	201	171
Final R indices		
R	0.0950	0.1671
wR	0.0563	0.0703
Goodness-of-fit, S	2.68	1.63
Largest Δ/σ	0.210	0.001
Mean Δ/σ	0.053	0.000
Data:parameter ratio	11.5:1	12.9:1
Largest difference peak (e Å^{-3})	0.75	0.58
Largest difference hole (e Å^{-3})	−0.89	−0.45

[a]Diffractometer used, Rigaku AFC6-R; radiation, Cu-Kα (λ = 1.54178 Å); temperature, 298 K; monochromator, highly oriented graphite crystal; 2θ range, 5.0–120.0°; scan type, 2θ–θ; scan speed, variable; 2.00–29.30°/min in ω; scan range (ω), 2.00° plus Kα-separation; background measurement, stationary crystal and stationary counter at beginning and end of scan, each for 25.0% of total scan time; standard reflections, 3 measured every 100 reflections; absorption correction, DIFABS (14).

[b]System used, Siemens SHELXTL PLUS (PC version); solution, direct methods; refinement method, full-matrix least squares; quantity minimized, $\Sigma w(|F_o| - |F_c|)^2$; absolute structure, not determined; extinction correction, not applied; hydrogen atoms, riding model, fixed isotropic U; weighting scheme, $w^{-1} = \sigma^2(F)$.

almost certainly caused by the repulsive interaction of the methyl groups on the exocyclic amine with O(3). The effects of this repulsion, which is illustrated by the nonzero dihedral angle between the atoms of the amine group (C(51)N(5)C(52)) and N(4)C(5)N(6), 24.1(8)°), are transmitted through the rigid parts of the molecule where there is significant π bonding. Normally in systems such as this N(11) would be nearly coplanar with the three atoms attached to it, but N(11) is 0.395 Å out of the C(10A)C(1)N(4) plane. The nonplanarity is further reflected in two of the bond angles of 112.0(3)° for C(10A)N(11)N(4) and 104.8(3)° for C(1)N(11)N(4), which are substantially reduced from the normal 120°.

The benzene ring (ring 1) is nearly planar (maximum deviation, C(10), 0.014 Å), although there is some suggestion of a bend in the ring about the C(7)C(10) axis. The two halves are then planar (maximum deviation, C(8), C(9), 0.006 Å) and the dihedral angle between the two halves is 1.9(7)°. Bond lengths and angles within the ring are not significantly different and agree well with those recorded for other aromatic systems (9).

The triazine ring (ring 2) is nonplanar, adopting a skewed boat conformation. Thus N(11)C(10A)C(6A)N(6) is planar (maximum deviation, C(10A), C(6A), 0.006 Å) and at 1.3(7)° to C(7)C(6a)C(10A)C(10)), whereas C(5) is 0.433 Å and N(4) is 0.708 Å out of the former plane. Bond lengths within the ring show that N(11)—N(4) is a single bond and that there is relatively little conjugation in C(10A)—N(11) or C(6A)—N(6), where the lengths are close to single bond values (10). There is considerable conjugation in the N(6)C(5)N(4)N(5) system, although there is more conjugation of the N(6)—C(5) double bond (1.313(6) Å) with C(5)—N(5) than with C(5)—N(4) (1.313(7) versus 1.366(6) Å). This is also reflected in the size of the angles: 123.2(4) for N(6)C(5)N(5) >

Can. J. Chem. Downloaded from www.nrcresearchpress.com by 195.246.54.202 on 09/08/12
For personal use only.

TABLE 2. Atomic coordinates ($\times 10^4$) and equivalent isotropic displacement coefficients ($Å^2 \times 10^3$) for **1**

	x	*y*	*z*	*U*(eq)[a]
C(1)	418(9)	5071(3)	3143(3)	45(2)
C(2)	−66(9)	5098(3)	3854(2)	43(2)
C(3)	−556(9)	4243(3)	4112(2)	45(2)
N(4)	−603(7)	3640(2)	3503(2)	40(1)
C(5)	−1047(10)	2725(3)	3426(2)	45(2)
N(6)	152(9)	2305(3)	2930(2)	52(2)
C(6A)	2033(10)	2748(3)	2556(2)	45(2)
C(7)	3779(11)	2254(4)	2209(3)	62(2)
C(8)	5503(11)	2731(4)	1836(3)	67(2)
C(9)	5561(10)	3664(4)	1807(2)	54(2)
C(10)	3839(10)	4155(3)	2182(2)	50(2)
C(10A)	2061(9)	3707(3)	2549(2)	39(2)
N(11)	162(7)	4149(2)	2906(2)	40(1)
O(1)	988(7)	5680(2)	2722(2)	59(1)
C(21)	202(11)	5937(3)	4293(3)	61(2)
C(22)	2909(28)	5868(7)	4649(6)	196(8)
C(23)	3114(30)	6607(8)	4976(6)	287(11)
O(3)	−978(7)	3940(2)	4695(2)	58(1)
N(5)	−2537(9)	2301(3)	3845(2)	56(2)
C(51)	−4606(11)	2754(4)	4175(3)	69(2)
C(52)	−2436(15)	1293(4)	3904(3)	97(3)
C(91)	7408(11)	4179(5)	1389(3)	76(3)

[a]Equivalent isotropic *U* defined as one third of the trace of the orthogonalized $\mathbf{U}_{ij}$ tensor.

TABLE 3. Atomic coordinates ($\times 10^4$) and equivalent isotropic displacement coefficients ($Å^2 \times 10^3$) for **2**

	x	*y*	*z*	*U*(eq)[a]
C(1)	2756(6)	5431(4)	4227(4)	54(2)
C(2)	2710(6)	5156(4)	5317(4)	65(3)
N(4)	40374(5)	3818(3)	4393(3)	51(2)
C(5)	3868(5)	2965(5)	3807(4)	49(2)
N(6)	3337(4)	2961(3)	2714(4)	56(2)
C(6A)	3462(5)	3896(4)	2186(4)	49(2)
C(7)	3517(5)	3910(5)	1150(4)	56(2)
C(8)	3710(5)	4856(5)	699(5)	62(3)
C(9)	3927(5)	5795(4)	1282(4)	57(3)
C(10)	3852(5)	5777(4)	2309(4)	54(3)
C(10A)	3571(5)	4834(4)	2740(4)	46(2)
N(11)	3396(4)	4721(3)	3769(3)	48(2)
O(1)	2247(4)	62487(3)	37543(3)	675(2)
N(5)	4250(5)	2011(4)	4313(4)	64(2)
C(51)	4806(6)	1172(4)	3825(5)	88(3)
C(52)	4645(6)	1993(4)	5474(5)	87(3)
C(21)	2148(9)	6024(6)	5828(6)	159(6)
C(22)	2383(11)	5923(8)	7154(8)	193(5)
C(23)	1618(12)	5143(9)	7090(10)	260(7)
C(91)	4219(7)	6828(5)	794(5)	88(3)

[a]Equivalent isotropic *U* defined as one third of the trace of the orthogonalized $\mathbf{U}_{ij}$ tensor.

120.6(4) for N(5)C(5)N(4) > 116.2(4)° for N(4)C(5)N(6). As expected, because of the steric interaction of the C(51) methyl group and O(3), the dimethylamino group is twisted from the plane of the triazine ring by an average 24.3. However, the torsional angles on either side of the dimethylamino group are unequal (N(4)C(5)N(5)C(51), 30.1(7)°; N(4)C(5)N(5)C(52), −160.9(5)°; N(6)C(5)N(5)C(51), −152.1(5)°; N(6)C(5)N(5)-C(52), 16.9(8)°). This suggests that the conjugation has been decreased and thus there is a small tendency to nonplanarity at the amino nitrogen atom (N(5)). N(5) is out of the plane of its surrounding carbon atoms by 0.076 Å, which is unusual in such a system.

The pyrazolidine ring (ring 3) is also roughly planar (maximum deviation, N(4), 0.038 Å), with O(1) and O(3) also close to this plane (0.009 and 0.097 Å). The planarity is caused by the delocalization of the negative charge around the diketone system, although this is not symmetric. Thus, C(1)—C(2) is longer than C(2)—C(3) (1.398(7) Å, 1.369(6) Å, 3.15σ, $\sigma = (\sigma_1^2 + \sigma_2^2)^{1/2}$) and C(1)—O(1) is longer than C(3)—O(3) (1.244(6) Å, 1.231(6) Å, 1.86σ), although this difference is hardly signif-

Can. J. Chem. Downloaded from www.nrcresearchpress.com by 195.246.54.202 on 09/08/12
For personal use only.

Can. J. Chem. Downloaded from www.nrcresearchpress.com by 195.246.54.202 on 09/08/12
For personal use only.

TABLE 4. Bond lengths (Å) and angles (deg) for **1** and **2**

	1	2
	Lengths	
C(1)—C(2)	1.398(7)	1.492(8)
C(3)—N(4)	1.467(6)	
C(5)—N(6)	1.317(6)	1.368(6)
C(6A)—C(7)	1.383(8)	1.383(8)
C(8)—C(9)	1.363(8)	1.390(8)
C(10)—C(10A)	1.382(7)	1.387(7)
N(11)—C(1)	1.428(6)	1.359(7)
C(6A)—C(10A)	1.400(7)	1.375(7)
C(2)—C(21)	1.496(7)	1.492(10)
C(22)—C(23)	1.254(16)	1.243(16)
C(5)—N(5)	1.313(7)	1.370(7)
N(5)—C(52)	1.476(7)	1.454(7)
C(2)—C(3)	1.369(6)	
N(4)—C(5)	1.366(6)	1.304(7)
N(6)—C(6A)	1.426(7)	1.395(7)
C(7)—C(8)	1.386(8)	1.374(8)
C(9)—C(10)	1.398(7)	1.380(8)
C(10A)—N(11)	1.418(6)	1.430(7)
N(4)—N(11)	1.435(5)	1.436(5)
C(1)—O(1)	1.244(6)	1.232(6)
C(21)—C(22)	1.660(16)	1.691(13)
C(3)—O(3)	1.231(6)	
N(5)—C(51)	1.472(8)	1.445(8)
C(9)—C(91)	1.508(8)	1.523(8)
	Angles	
N(11)C(1)C(2)	108.7(4)	116.2(4)
C(2)C(3)N(4)	105.1(4)	
N(4)C(5)N(6)	116.2(4)	124.1(5)
N(6)C(6A)C(7)	121.7(4)	122.9(5)
C(10A)C(6A)C(7)	120.5(5)	119.4(5)
C(7)C(8)C(9)	121.9(6)	121.3(6)
C(9)C(10)C(10A)	120.8(5)	119.9(5)
C(10)C(10A)C(6A)	119.2(4)	120.9(5)
C(10A)N(11)C(1)	120.7(4)	125.4(4)
N(4)N(11)C(1)	105.1(3)	117.7(4)
O(1)C(1)C(2)	132.0(4)	123.0(5)
C(21)C(2)C(3)	124.1(4)	
C(1)C(2)C(3)	111.6(4)	
N(11)N(4)C(5)	118.3(3)	111.3(4)
C(5)N(6)C(6A)	121.9(4)	117.0(4)
N(6)C(6A)C(10A)	117.8(4)	117.8(5)
C(6A)C(7)C(8)	118.7(5)	119.6(5)
C(8)C(9)C(10)	118.5(5)	118.6(5)
C(10)C(10A)N(11)	124.6(4)	125.3(5)
C(6A)C(10A)N(11)	116.2(4)	113.9(4)
C(10A)N(11)N(4)	112.0(3)	116.8(4)
N(11)C(1)O(1)	119.3(4)	120.8(5)
C(1)C(2)C(21)	123.9(4)	113.5(5)
C(2)C(21)C(22)	105.9(5)	117.5(6)
C(21)C(22)C(23)	103.8(11)	96.3(9)
O(3)C(3)N(4)	120.8(4)	
N(5)C(5)N(6)	123.2(4)	117.8(5)
C(5)N(5)C(52)	119.5(5)	117.9(4)
C(8)C(9)C(91)	122.4(5)	120.9(5)
C(2)C(3)O(3)	134.1(5)	
N(4)C(5)N(5)	120.6(4)	118.2(4)
C(5)N(5)C(51)	123.3(4)	121.2(5)
C(51)N(5)C(52)	116.3(5)	116.0(4)
C(91)C(9)C(10)	119.2(5)	120.5(5)

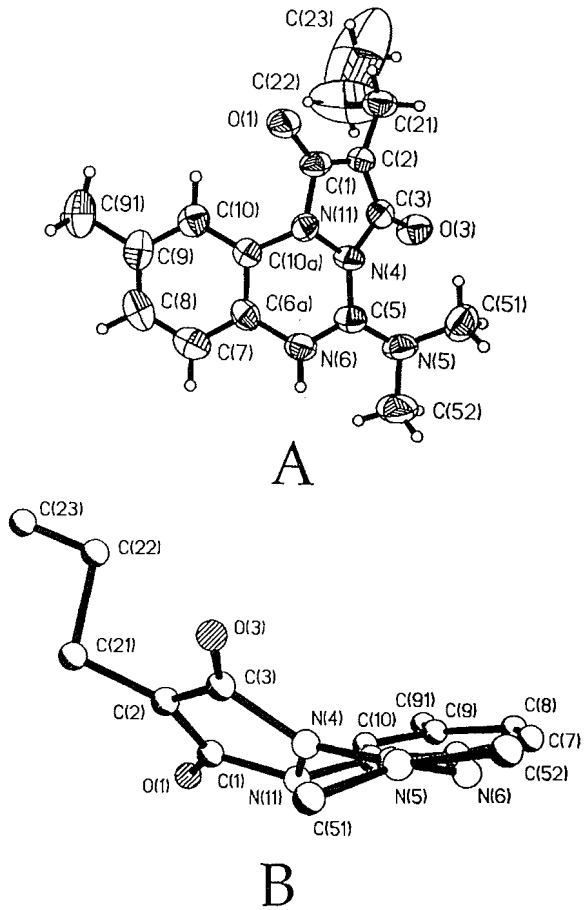

FIG. 1. (A) The molecule of azapropazone showing the atom numbering. (B) The nonhydrogen atoms in azapropazone viewed along N(5)C(5) and showing the nonplanarity of the tricyclic system.

icant. There is little conjugation of this system to N(11)—C(1) or C(3)—N(4) where the lengths are close to single bond values (10).

A legitimate question is whether the solid state structure is relevant to solution conditions, since the NMR spectra show that the methyl groups are equivalent, whereas the structure shows that this should not be so. In addition, one cannot locate the proton in solution because of exchange, so there may be some doubt as to whether it is still attached to N(6). The packing of the unit cell (Fig. 2) addresses the second question. The proton attached to N(6) (which was located from the difference map) forms a quite strong hydrogen bond to O(1) of an adjacent molecule (N(6)...O(1), 2.759(6) Å) (see Fig. 2). Thus, the proton could easily transfer to the oxygen atom if this was energetically preferable and the proton is not kept at N(6) because of steric hindrance. The crystal packing consists of spiral chains of molecules in the *b* direction, each molecule bound to the next by the N(6)—H(6)...O(1) hydrogen bond. In the *a* direction translationally equivalent molecules are adjacent and stacked so that there may be some weak π–π interactions,[3] but in the *c* direction the interactions are van der Waals.

[3]D.P. Santry has calculated (personal communication) that interactions between the π systems of aryl rings will be 6–9 kcal mol^{-1} if there is complete overlap of the rings and they are 3.4 Å apart. The variation in the values is caused by varying orientation of the rings. Such energies are reduced as the overlap is reduced.

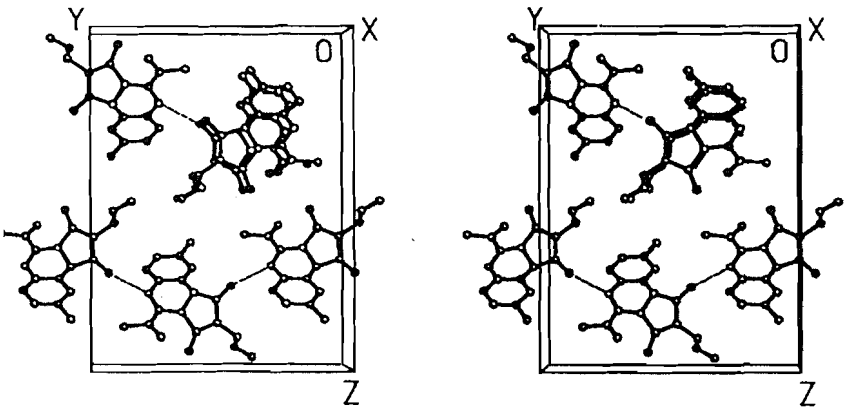

FIG. 2. The packing of azapropazone in the unit cell. Hydrogen bonds are given by broken lines.

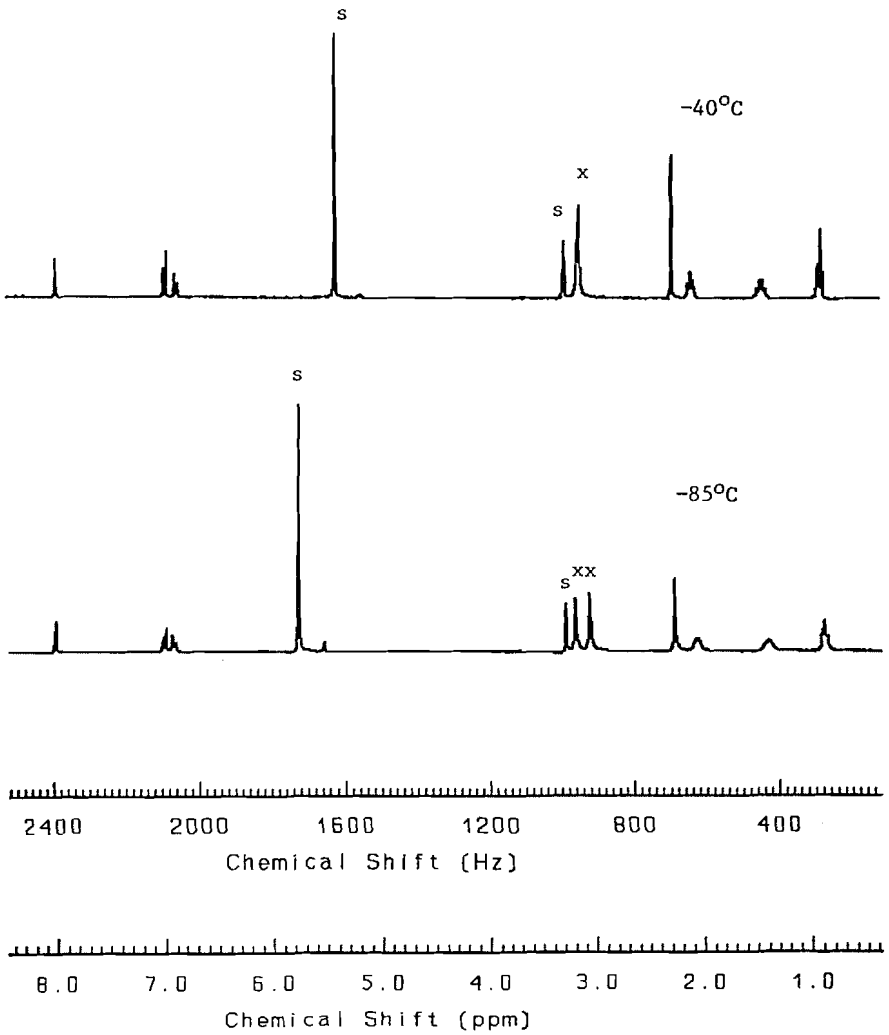

FIG. 3. The proton NMR spectra of azapropazone (**1**) at −40°C and −85°C, which show the resolution of the peak caused by the methyl groups on the exocyclic amine group (*x*) into two peaks at the lower temperature. The solvent peaks are indicated by *s*.

The equivalence of the methyl protons in the NMR spectrum could be because the ring system is rigidly planar with the dimethylamino group at right angles to this plane or the structure shown is the limiting structure in solution and the equivalence is caused by a rapid inversion of the molecule to the other enantiomer, with a consequent rotation of the dimethylamino group about C(5)N(5) by 310° when C(51) will be swapped with C(52).

We have tested this latter model by measuring the NMR spectra at various temperatures and found that it is correct. As can be seen in Fig. 3, the peak caused by the dimethylamino group is still a singlet at −40°C, but by −85°C it has been resolved into two peaks, corresponding to the two inequivalent methyl groups seen in the crystal structure. The variable temperature studies showed that the coalescence temperature for the two peaks was −54 ± 1°C and calculation showed that this

Can. J. Chem. Downloaded from www.nrcresearchpress.com by 195.246.54.202 on 09/08/12
For personal use only.

Can. J. Chem. Downloaded from www.nrcresearchpress.com by 195.246.54.202 on 09/08/12
For personal use only.

corresponded to $\Delta G^{\ddagger} = 44.9 \pm 0.2$ kJ mol^{-1} for the exchange of the dimethylamino methyl groups. The downfield shift of the aromatic proton at C(10) relative to the other aromatic protons, mentioned above, does not present a problem. The solid state structure shows that the proton is still close enough to the deshielding cone of the carbonyl group C(1)O(1) to allow for the downfield shift effect observed in the NMR spectra, and the relative positions of these two atoms do not shift significantly as inversion takes place.

As noted, the molecule found in the solid state is chiral and we have previously described problems that can be caused by the use of racemic mixtures of enantiomers in the treatment of patients (11–13). This is unlikely to be a problem with azapropazone because of the rapid inversion between the two enantiomers. Nevertheless, it is likely that one enantiomer of azapropazone is preferred for binding to the biological site of action.

To see whether the effects that we observed were peculiar to azapropazone itself, we decided to look at other derivatives. In particular, we tried to prepare the hydrochloride salt of azapropazone and one of the compounds where the pyrazolidine ring had been opened, 3-dimethylamino-7-methyl-2-valeryl-1,2-dihydro-1,2,4-benzotriazine, **2** (8). The former compound was of interest because it should have the distortions observed in azapropazone itself, and because Dean has argued that the protonation site will be N(6), whereas we know that this site is already protonated in the neutral compound. Unfortunately, we were unable to prepare crystals of the desired compound. Solutions of azapropazone acidified with hydrochloric acid decomposed very rapidly, becoming brown after 10 min, even when stored in the dark. The latter compound was of interest because with the opening of the pyrazolidine ring some of the strain caused by the interaction of the methyl group on the exocyclic amine with the ketone group will have been removed. The compound became of greater interest when examination of the proton NMR spectrum showed that the peak assigned to the hydrogen atom attached to C(10) showed a similar downfield shift to that observed in azapropazone.

The procedure used to make this molecule was that of Mixich, and involved refluxing azapropazone with formic acid for 1 h and then recrystallizing the product from 2-butanone (8). On the basis of NMR results Mixich suggested that the pyrazolidine opened at N(11). The NMR spectrum of the product seems to be consistent with the proposed structure but, as noted above, the aromatic proton at C(10) is downfield about 0.5 ppm from the other aromatic protons, which should not be the case if the carbonyl group is no longer proximate.

The determination of the crystal structure explained the NMR spectrum. The molecule (which is numbered incorrectly, but in the same way as azapropazone to facilitate comparisons) is shown in Fig. 4 and bond lengths and angles are given in Table 4. The structure shows that the pyrazolidine ring opened not at N(11) but at N(4). It is possible that the strain on the ring caused by the closeness of the methyl group of the dimethylamino group and O(3) in azapropazone caused the ring to open at N(4). As a result the carbonyl group is still close enough to the aromatic proton to cause a downfield shift. Based on the structure determined, **2** should be named 3-dimethylamino-7-methyl-1-valeryl-1,4-dihydro-1,2,4-benzotriazine.

Many of the structural features are similar to azapropazone, although there are significant differences.The benzene ring (ring 1) is nearly planar (maximum deviation, C(10A), 0.013

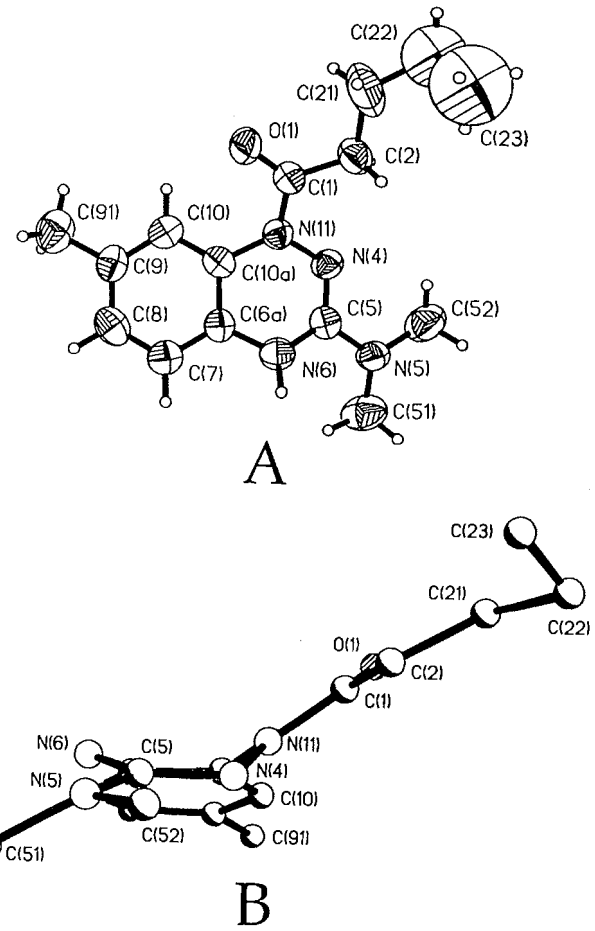

FIG. 4. (A) The molecule of **2** showing the atom numbering. (B) The nonhydrogen atoms in **2** viewed along C(5)...C(6A) and showing the nonplanarity of the tricyclic system.

Å), although again there is some evidence of a fold in the ring, but this time it is about C(8)C(10A) when the two halves are planar (maximum deviation C(7), C(6a), 0.006 Å) and the dihedral angle between the two planes is 4.5(9)°. Bond lengths and angles are normal (8).

The triazine ring (ring 2) shows some significant differences from ring 2 in **1**. The C=N double bond is now between N(4) and C(5), which leaves the protonated N(6) position uncharged. The ring adopts a boat conformation, but in this case it is much more symmetric (plane C(6A)N(6)C(10A)N(11), 4.7(8)° to the benzene ring; maximum deviation, C(6A), 0.028 Å; C(5), 0.629 Å; N(4), 0.754 Å out of plane). With the removal of the restrictions of the pyrazolidine ring N(11) is only 0.031 Å out of the plane C(10A)C(21)N(4). The delocalization around the dimethylamino portion of the ring is less than in **1**, as shown by the bond lengths (N(4)—C(5), 1.304(7) Å; N(6)—C(5), 1.368(6) Å; N(5)—C(5), 1.370(7) Å) and these changes are reflected in small changes in the other bond lengths in the ring. Again the dimethyl amino group is not coplanar with N(4)C(5)N(6) and in this case the average angle is 29.3°, but the differences in the torsional angles are greater (N(4)C(5)N(5)C(51), −146.1(5)°; N(4)C(5)N(5)C(52), 8.2(8)°; N(6)C(5)N(5)C(51), 33.6(7)°; N(6)C(5)N(5)C(52), −172.1(5)°). The smaller conjugation to the dimethylamino group leads to greater nonplanarity at N(5), which lies 0.183 Å out of the C(5)C(51)C(52) plane. The NMR spectrum (see Experimental) showed that the two methyl

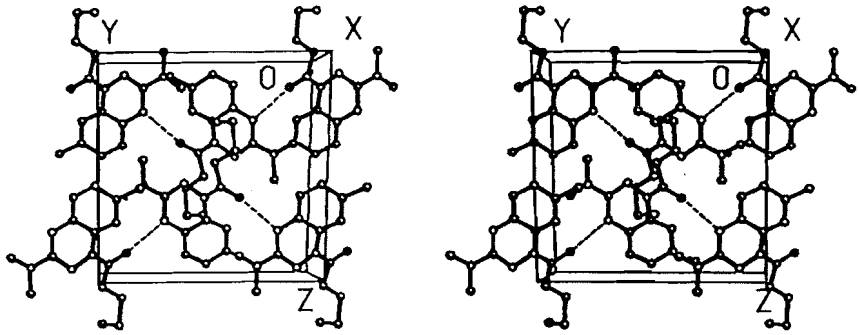

FIG. 5. The packing of **2** in the unit cell. Hydrogen bonds are given by broken lines.

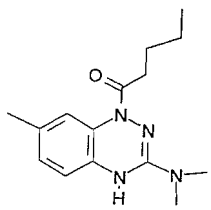

2

groups were equivalent, but this time they did not become inequivalent at low temperature (−85°C). This could be for two reasons. The separation of the individual methyl signals will be smaller and the barrier to rotation may be smaller because the conjugation of the dimethylamino group to the double bond in the ring is smaller, as noted above.

The crystal packing of **2** (Fig. 5) shows similarity to that of **1**. Spiral chains of molecules in the *b* direction are formed by each molecule forming an N(6)—H(6)...O(1) hydrogen bond to the next molecule (N(6)...O(1), 2.834(7) Å). However, the chains are related by a 2_1 axis, so that molecules do not lie adjacent to a translationally equivalent one, as in **1**; therefore interactions between chains in both the *a* and *c* directions are van der Waals.

In conclusion, we have shown by single crystal X-ray crystallography and NMR spectroscopy that the postulated structures for azapropazone and the open-ring derivative are wrong. These results suggest that the products of other reactions of azapropazone might bear reexamination.

1. A.J. Bollet. Textbook of rheumatology. 2nd ed. *Edited by* W.N. Kelley, E.D. Harris, S. Ruddy, and C.B. Sledge. W.B. Saunders Co., Philadelphia. 1985. pp. 752–773.
2. P.M. Conn and G.F. Gebhart. Essentials of pharmacology. F.A. Davis Co., Philadelphia. 1989. p. 313.
3. F.S. Walker. Side effects of anti-inflammatory drugs. *Edited by* K.D. Rainsford and G.P. Velo. MTP Press, Lancaster, England. 1987. pp. 431–438.
4. M. Windholz (*Editor*). The Merck Index. 10th ed. Merck & Co. Inc., Rahway, N.J. 1983. p. 106.
5. H. Fenner and G. Mixich. Arzneim. Forsch. **23**, 667 (1973).
6. F.M. Dean. Azapropazone: over two decades of clinical use. *Edited by* K.D. Rainsford. Kluwer Academic Publishers, Dordrecht, Holland. 1991. pp. 9–19.
7. F.S. Walker. Anti-inflammatory and anti-rheumatic drugs. Vol. II. CRC Press, Boca Raton, Fla. 1985. pp. 1–32.
8. G. Mixich. Helv. Chim. Acta, **51**, 532 (1968).
9. L.E. Sutton (*Editor*). Tables of interatomic distances and configuration of molecules and ions. The Chemical Society, London, England. 1965.
10. L. Pauling. Nature of the chemical bond. Cornell University Press, Ithaca, N.Y. 1960.
11. W.F. Kean, C.J.L. Lock, and H.E. Howard-Lock. Lancet, **338**, 1565 (1991).
12. H.E. Howard-Lock, C.J.L. Lock, and W.F. Kean. J. Rheumatol. **13**, 1000 (1986).
13. H.E. Howard-Lock and C.J.L. Lock. Can. Chem. News, **39**, 7 (1987).
14. N. Walker and D. Stewart. Acta Crystallogr. Sect. A: Found. Crystallogr. **39**, 158 (1983).

Can. J. Chem. Downloaded from www.nrcresearchpress.com by 195.246.54.202 on 09/08/12
For personal use only.

Characterization of the molecular weight distribution of polypropylene and polyethylene by turbidity at the lower critical solution temperature

TAKOUHI BOHOSSIAN AND GENEVIÈVE DELMAS
Département de chimie, Université du Québec à Montréal, Case postale 8888, Succursale A, Montréal, QC H3C 3P8, Canada
AND
HENRI BENOÎT
Institut Charles Sadron, 6 rue Boussingault, Strasbourg, Cédex 67083, France
Received July 12, 1993

TAKOUHI BOHOSSIAN, GENEVIÈVE DELMAS, and HENRI BENOÎT. Can. J. Chem. **72**, 390 (1994).

The characterization in butane of noncrystalline atactic polypropylene (ncPP) (**1**) with a narrow molecular weight distribution (MWD) is presented. It uses a new technique based on a thermogram, consisting of turbidity peaks developed in a solution at a Lower Critical Solution Temperature (LCST) during a step-by-step temperature increase. Several refinements concerning the analysis of data have been added to the expressions used in earlier work on polyethylene. The relation between the volume of the concentrated phase and the attenuation of light has been developed from an expression of the scattered light by a biphasic system. The thermograms gave a good agreement in M_w and M_w/M_n for four well-characterized ncPP samples. Wide MWD isotactic PP samples (**2**) were also analyzed in a mixture of butane and 2-methylbutane. Solution behavior at the LCST of **1** and **2** was compared.

TAKOUHI BOHOSSIAN, GENEVIÈVE DELMAS et HENRI BENOÎT. Can. J. Chem. **72**, 390 (1994).

Nous présentons la caractérisation dans le butane de polypropylene atactique ayant une distribution de poids moléculaire (DPM) étroite. Nous utilisons une nouvelle technique basée sur l'analyse d'un thermogramme. Celui-ci consiste de pics de turbidité développés dans une solution à une température critique de démixion inférieure lors d'une augmentation par palier de la température. L'analyse des données a été raffinée par rapport à un précédent travail sur le polyéthylène. À partir d'une expression de lumière diffusée par un système biphasique, nous avons developpé une relation entre le volume de la phase concentrée et l'atténuation de lumière. Les thermogrammes donnent un bon accord avec M_w et M_w/M_n pour quatre échantillons bien caractérisés de PP atactique. Des échantillons de PP isotactique ayant une large DPM sont aussi analysés dans un mélange de butane et 2-méthylbutane et leur comportement en solution comparé à celui du PP atactique.

Can. J. Chem. Downloaded from www.nrcresearchpress.com by 195.246.54.202 on 09/08/12
For personal use only.

Introduction

Before introduction of size exclusion chromatography (SEC), the molecular weight distribution (MWD) of polymers was determined through the preparation and analysis of fractions, the values of their different average molecular weights being obtained from light scattering (M_w) and osmotic pressure (M_n). The existence of a molecular weight dependent liquid–liquid phase separation, with an upper critical solution temperature (UCST) in appropriate solvents situated at low temperature for the amorphous polymers and usually at high temperature for crystalline samples, permits the separation of fractions of different average molecular weights (MW). At a lower critical solution temperature (LCST) situated usually above the solvent boiling point, fractionation can also be used for characterization purposes (1), with the fractions of lower and lower MW being prepared by a succession of temperature increases instead of temperature decreases (or addition of nonsolvent) used at a UCST. The method has not been widely applied because of the difficulties of separating phases under pressure. Modification of the LCST method to make it simpler would meet a need for an alternative to the SEC characterization, which is costly and whose operation is complex at high temperature.

The special feature of the present technique is avoiding the extraction of the concentrated phase, which is normally required for analysis of the amount of polymer and its MW. These two parameters are evaluated instead for each fraction from the attenuation of transmitted light and the temperature of phase separation.

The resolution of the technique is determined by the number of temperature increments that one chooses to make between T_1, the temperature of the onset of turbidity in the solution, and T_f, the temperature at which a temperature increment does not induce any further turbidity in the solution. Since the turbidity response to a phase separation is high, even for small values of the refractive index increment dn/dc, minute amounts of concentrated phase generated by small temperature increments above T_1 are measurable, which leads to a good resolution in the high MW tail of the distribution. The accuracy of the MWD will depend on many parameters, but in particular on the relations used to transform the temperature into average MW (eq. [4] below) and the attenuation of transmitted light into amount of polymer (eq. [5] below). Early work on turbidity at a UCST reported the possibility of quantitative analysis (2, 3) of MWD. In more recent investigations (4–8) on characterization of MWD at a LCST, two empirical equations have been shown to give satisfactory results for the characterization of polyethylene (PE) (4), linear low-density polyethylene (5), and polyisoprene (6). Analysis of polypropylene (PP) by the LCST technique met with difficulties since, in the solvent used for PE, the phase separation of PP occurs at high temperature (65 K higher than for PE) leading to poor resolution in MWD.

The aim of the present paper is to report results in volatile solvents that give good resolution in MWD. Well-characterized high M_w atactic PP (ncPP) samples with a narrow MWD are used to define the optimal forms for eqs. [1] and [2]. Analysis of wide MWD isotactic PP (iPP) samples in the same solvents is reported.

Experimental

Chemicals

Polymers

PP: The noncrystalline PP samples were given to us graciously by Dr. H.J. Barth (now at the Research Center of Du Pont in Wilm-

Can. J. Chem. Downloaded from www.nrcresearchpress.com by 195.246.54.202 on 09/08/12
For personal use only.

ington). Their preparation and characterization have been reported recently (9, 10). Osmometry, light scattering, and intrinsic viscosity were measured to characterize the samples and establish a standard SEC curve for PP at different temperatures. They will be referred to in the following text as SEC-characterized samples. To make clear that these samples, which are hydrogenated poly(1,3-dimethyl-1-butenylene), are not the soluble PP produced commercially, the abbreviation ncPP will be used. The samples of iPP (B1, B2) were from Himont (Varennes, Que.). They were characterized by SEC, but the uncertainty in M_w and M_w/M_n was large.

PE: The narrow MWD samples (C1–C4), from the National Institute of Standards and Technology (NIST), have been analyzed previously (4).

Solvents

Pentane, 2-methylbutane, and 2,4-dimethylpentane were of the highest grade (>99%) from Aldrich and used without purification. Butane and the mixture of butane and 2-methylbutane (2:1 w/w) were from the Mathieson Company (Calgary). ncPP was analyzed in the volatile solvents and the mixture, iPP was analyzed in the mixture, and PE was analyzed in 2,4-dimethylpentane.

Antioxidant

Irganox B-215 is a Ciba-Geigy (1:2) mixture of Irganox 1010, a sterically hindered phenolic antioxidant, and of Irgafos 168, an organophosphite synergist. The antioxidant was used only for PP.

Method and apparatus

A step-by-step T increase in a solution at a LCST forms a succession of equilibria with concentrated phases richer and richer in lower molecular weights. Below T_1, the transmitted light is stable and is not changed by a temperature increment. At T_1 and above, a temperature increment produces a phase-separation induced turbidity. The apparatus consists of a small cylindrical oven that heats a sealed glass tube containing the solution to be analyzed. The oven is controlled by a temperature programmer (Eurotherm) that assures a temperature stability of the oven of 0.1 K. Absolute values of T are measured. A beam of coherent light (Reichert, Cambridge Instruments) passes radially through the glass tube and is received on a silicon photocell (Silonex NLS6161) situated at 15 cm from the oven.

I_0 and I are the intensities received on the sensitive surface s, from the clear and the turbid solutions, respectively. I decreases sharply after the temperature jump since the light goes across a two-phase medium, but increases again back to I_0 when the concentrated phase sediments. The only parameter used in the calculation is h_i, the maximum attenuation of light (i.e., $h_i = (I_0 - I)/I_0$), called later simply turbidity. With the turbidity peaks being numbered between 1 and f (the sum of the turbidity), the total thermogram is $\sum_{i=1}^{i=f} h_i$. This sum is used to obtain the fraction h_i^* of turbidity corresponding to each peak:

$$[1] \qquad \text{Sum of turbidity} = \sum_{i=1}^{i=f} h_i = S$$

$$[2] \qquad \text{Fraction of turbidity} = h_i^* = h_i S^{-1}$$

$$[3] \qquad \text{Cumulative turbidity} = \sum_{i=1}^{i} h_i^*$$

The cumulative turbidity, which varied between 0 and 1, was multiplied by 100 in Figs. 1 and 3. The value of I_0 does not come into the calculation, because if the relative maximum attenuation was calculated, I_0 would enter in the numerator and denominator of eq. [2].

The specific sum of turbidity (S/c) is needed for comparison of the thermograms made at different concentration c. The value of I_0 must be the same in each thermogram. The value of S/c, which does not depend on c in a small range of c, constitutes a good check of an adequate dissolution before the start of the thermogram.

$T_{1/2}$ is the temperature at which the cumulative turbidity is 0.5. To avoid interference with the kinetics of formation of the concentrated phase by lack of homogeneity in the solution (dust, bubbles), the first temperature increase leading to phase separation was initiated only after the solution had been left below T_1 for 2 h. For the same reason, the time interval between temperature increments was kept larger than the time necessary to recover I_0. The temperature increments, (ΔT_i) were chosen to obtain the best resolution in MWD, i.e., to have a large number of fractions particularly in the high MW range. For broad MWD samples, the first few fractions typically constitute a few percent of the total polymer, while for narrow MWD samples the first few T jumps separate a larger fraction (see Appendix). No fraction should be too large ($h_i < I_0/5$), because due to backscattering and other effects, eq. [2] would then be no longer valid. A temperature increment produces in the solution still another effect than the formation of the next fraction. It changes the temperature-dependent equilibrium between the phases that have already been separated; the concentrated phase loses some solvent since the equilibrium polymer volume fraction of the concentrated phase increased with T. Owing to the small temperature increments and the size of each fraction, this effect is small and was neglected.

Preparation of solution

For the homogeneous narrow MWD samples, T_1 was very consistent from one run to another. For wide MWD samples that were not received as fine powder but as pellets or films, the risk of scattered data due to sampling was not negligible. Since there was some difficulty in the preparation of a stock quantity of sample from solution (increased crystallinity, degradation), the present data came from "as received" samples on which several measurements were done. Samples with the same T_1 and somewhat different h_1 were used for computation. If T_1 was different, the measure was disregarded. The value of M_w was mainly sensitive to the magnitude of the turbidity peaks obtained at low T; i.e., h_1, h_2, and h_3 evolved usually at T_1, $T_1 + 1$, and $T_1 + 2$ K.

Choice of the solvent

The more volatile the solvent, the better, since it gave lower LCST and a better resolution, particularly in the high MW region as illustrated by the relation between T_i and M_i shown in Fig. 2. Curves *a*, *b*, and *c* correspond to the $T_i(M_i)$ relationship for butane, the mixture of butane and 2-methylbutane, and pentane, respectively. For crystalline and semicrystalline samples, it was necessary to compromise and use less volatile solvents to avoid the risk of stable crystalline aggregates.

Dissolution

Whatever the technique, the prerequisites for an adequate characterization in solution are to prepare a molecularly dissolved polymer and to avoid shear and thermal or oxidative degradation during the time of analysis. Polymer (2–8 mg), solvent, and antioxidant (2–8 mg) were introduced into a glass tube; N_2 was bubbled through the mixture, cooled by Dry Ice, for 2 h, after which the glass tube was sealed. Solutions whose final concentration c varied between 0.1 and 0.8% for PP and 0.6 and 2% for PE were obtained by rotating the tube gently. In the volatile solvents employed, dissolution was faster (3 h at 130°C) for iPP than in trichlorobenzene (12, 13) where a molecularly homogenous solution was obtained only after 30 h at 165°C. For ncPP, a residence time at 60°C of a few hours was sufficient to dissolve the aggregates. The addition of Irganox was not found necessary for the PE solutions.

Analysis of heterogeneity and conditions for homogenization

The quality of the dissolution was investigated by turbidity and calorimetry at the LCST itself as reported elsewhere (8). The value of T_1 and the shape of the turbidity peak gave an immediate assessment of the quality of the dissolution. A large first turbidity peak due to aggregates signalled incomplete homogenization. A finer quantitative measurement of homogenization was given by the cumulative turbidity which, in well-homogenized solutions, was found (4) to be constant when normalized by c. Homogenization was improved by dilution or, for crystalline samples, by slow crystallization in a temperature gradient and redissolution prior to the LCST analysis. As reported elsewhere (8), the migration of the concentrated phase towards the bottom of the tube could be followed in a sensitive C80 calorimeter programmed with a continuous temperature ramp. The

Can. J. Chem. Downloaded from www.nrcresearchpress.com by 195.246.54.202 on 09/08/12
For personal use only.

trace revealed the presence of aggregates and also the slow dissolution of microcrystals at high T. Conditions necessary for a homogeneous solution could be determined from the calorimetric trace at the LCST.

For each fraction, phase separation took place in a short time, i.e., during the beginning and the maximum of the turbidity peak (about 20 min). The fraction contained a distribution of molecular weights in equilibrium with the dilute solution from which it separated. The fact that the cumulative curves for well-dissolved solutions of different concentrations overlapped was an indication that the fraction that separated had the equilibrium distribution of molecular weights.

Prevention and analysis of degradation

Degradation in solution was limited owing to the absence of oxygen, the relatively low temperature, and the gentle stirring. These precautions were not sufficient for ncPP and iPP solutions that were protected by the addition of Irganox.

Degradation involving chain scission was detected by a decrease in the size of the first turbidity peak or (and) its shift to higher temperature. It was used to see the possible degradation occurring during the dissolution time or taking the thermogram itself. The fact that, in the actual conditions of the analysis, T_1 was unchanged and h_1 diminished by less than 10% after taking a complete thermogram attested to the reliability of the high temperature peaks of the first thermogram. The time for the total analysis (including dissolution), with temperature increments separated by 100 min, was between 15 and 28 h depending on the polydispersity. At the end of the first thermogram, the content of carbonyl groups measured by IR in the polymer was not higher than in the original sample.

Quantitative analysis of the data

Basic assumptions

A quantitative measurement of the MWD rests on the following assumptions (4).

1. A relationship between the temperature of phase separation (T_i) and the average MW (M_i) of the polymer phase separating at that temperature. The following equation is a reasonable relation verified in a similar form at the UCST.

$$[4] \qquad T_i = T_\infty + BM_i^{-1/2}$$

where T_∞ is the temperature of phase separation for an infinite MW and B is a constant that increases with solvent volatility.

2. A relationship between the turbidity (h_i) and weight fraction (m_i) of polymer phase separating. The attenuation of light is used as a balance for analyzing the fraction. The simple relation below is used, where k is a temperature-independent constant and n is a number to be determined in the following section. The value $n = 1$ has been used in previous work.

$$[5] \qquad m_i = kh_i^n$$

The differential and integral weight distributions and the average molecular weights M_w and M_n were only a function of the set of (h_i, T_i) and of T_∞ and B. With $n = 1$ in eq. [5] one obtains

$$[6] \qquad M_n = \frac{[\sum(h_i^*/M_i)]^{-1}}{M_w = \sum(h_i^* M_i)}$$

A distribution curve in semilogarithmic coordinates is obtained by differentiating the cumulative curve with respect to ln M.

Refinements in the analysis

Light attenuation and amount of the concentrated phase

Calculation of the amount of polymer undergoing a phase separation from turbidity data is difficult, since the size distribution of the droplets of the concentrated phase is unknown and changes with time. A justification of the empirical equation [5] (with an adequate value of n) would be desirable. An approximate expression is developed in the following paragraphs.

In the turbid systems analyzed at the LCST, the scattered light comes from the diphasic medium of different refractive index. The integral of Porod developed by Guinier (14) is a simple form for the scattered light. Since in nonpolar systems density and refractive index vary similarly, the scattered light is a function of ρ_1 and ρ_2, the density of the two phases:

$$[7] \qquad I(r)r^2\,dr = K(\rho_1 - \rho_2)^2\phi(1-\phi)$$

where I is the scattered light at the distance r from the axes of the beam, ϕ and $1-\phi$ are the volume fractions of the concentrated and dilute phases, and K is a constant. $I(r)$ becomes zero as soon as the solid angle of observation is larger than a few degrees. In the thermogram, the change of signal h_i on the photocell due to scattering of light can be written as

$$[8] \qquad \int I(r)2r\,dr \simeq \int I(r)r\,dr$$

To find a numerical relation between the integrals in eqs. [7] and [8], $I(r)$ is assumed to follow a Gaussian law:

$$I(r) = \bar{e}^{-(r^2/\alpha^2)}$$

where α is a constant. With $r/\alpha = u$, eq. [7] becomes

$$[9] \qquad \int I(r)r^2\,dr = \alpha^3 \int e^{-u^2}u^2\,du = \alpha^3 K'$$

with the same assumption, eq. [8] is written as

$$[10] \qquad \int I(r)r\,dr = \alpha^2 \int e^{-u^2}u\,du = \alpha^2 K''$$

with

$$K' = \int e^{-u^2}u^2\,du$$

and

$$K'' = \int e^{-u^2}u\,du$$

Numerical evaluation of eqs. [9] and [10] shows that for small values of u (or r) they are correlated with a good approximation by eq. [11] below.

$$[11] \qquad \left[\int I(r)r^2\,dr\right]^{1/3} = \left[\int I(r)r\,dr\right]^{1/2} \text{ or } \left[\int I(r)r^2\,dr\right] = \left[\int I(r)r\,dr\right]^{3/2}$$

The integral on the right is the quantity measured by the photocell $h_i^{3/2}$; the integral on the left is the quantity given by eq. [7].

After some rearrangement, the attenuation of light is found to be related to the volume fraction of the concentrated phase

formed at each T_i by the relation

[12] $h_i^{3/2} = \text{constant}(\rho_1 - \rho_2)^2\phi(1-\phi)$

which, in dilute solution, becomes

$$h_i^{3/2} = \text{constant}(\rho_1 - \rho_2)^2 m_i$$

Equation [5] will be then replaced by

[13] $m_i = kh_i^{3/2}$

The effect on M_w and M_n of using either eq. [13] or [5] will be given in Table 2.

Measurement of the incremental volume changes of the concentrated phase with the T steps was tried but did not lead to the establishment of a distribution curve, as explained in the Appendix.

Temperature of phase separation T_i *and the average molecular weight* M_i

The relationship between T_i and M_i in eq. [4] is a very convenient way to relate molecular size and phase-separation temperature. It has been justified by many experimental data on cloud-point curves (CPC) at the UCST and LCST. In the literature (15–17) the value of T^{-1} rather than T is related to $M^{-1/2}$. The present form reflects the increase of solubility of the low MW with T. If T^{-1} were used in the ordinate of Fig. 3, the slopes of the lines would change sign, but not magnitude. As indicated in the Appendix the interaction parameter χ increases with T at the LCST, while it decreases at a UCST. Since phase separation occurs over a large T interval (12–20 K for the narrow MWD standards), an average T_i, namely $T_{1/2}$, has to be used rather than T_i to obtain T_∞ and B from the thermograms of the standards. For a sample with a wide MWD, the interval of phase separation can vary between 20 and 90 K, the lower MW phase separating near the liquid–vapor critical temperature T_c of the solvent. Over this range of T, eq. [4] with a constant value of B is inadequate. Instead of making an empirical correction, an equation of state for the solvent is used that describes the variation of the volume V with temperature up to T_c. The relationship between the equation of state parameters and the LCST is given in the Appendix.

Free volume theory of polymer solutions

The free volume theories of polymer solutions (11, 15–17) predict the existence of LCSTs and their trend with MW. The relationship

[14] $T_i = f(M_i)$

can be calculated with different curvatures (such as the traces of Fig. 2) by changing the parameters related to the difference of free volume or chemical nature between polymer and solvent. For ncPP, the parameters are chosen to fit M_w and M_w/M_n but there is not a unique choice of parameters to attain this result. A linear relationship as in eq. [4] is quite satisfactory for the three samples with similar MW (A1–A3), but gives too high a M_w for sample A4. Details of the calculations are given in the Appendix.

Calculation of MW averages

The averages are calculated from smoothed cumulative curves with a small interval (0.10) of the abscissa, which is ln M. For samples whose MWD is not far from ln-normal, there are several advantages in using the ln-normal representation of Fig. 3. Smoothing is unambiguous over the main part of the cumulative curve, since the experimental points are on a straight line and also the departure from a ln-normal distribution at the high or low MW tails (of the distribution) is more apparent on a ln-normal scale than on a linear scale. The ln-normal distribution depends on two parameters, namely M_0, characterizing the molecular weight of the maximum of the distribution curve, and σ, characterizing its width (18). Due to the analytical expression of the distribution (see Appendix), M_0 and σ can be read directly from the cumulative curve and M_w and M_n can be calculated. If the experimental points do not all lead to a straight line but rather to a curve at the extremities, the averages must be calculated point by point as was done here.

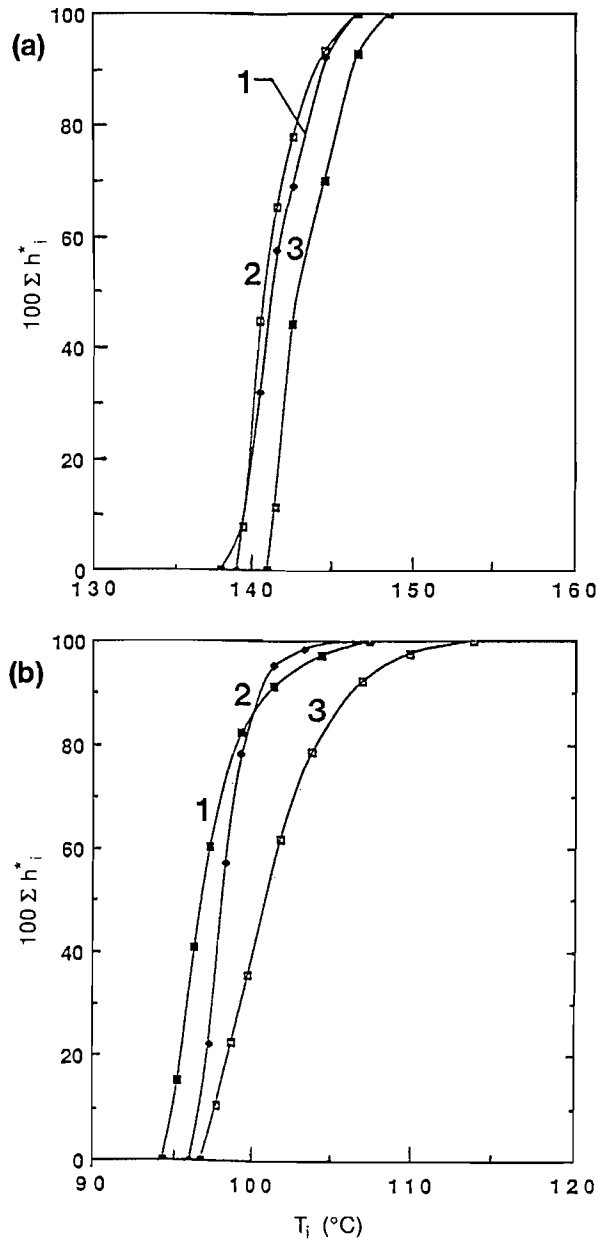

FIG. 1. Cumulative curves ($\sum h_i^*, T_i$) for three high MW and narrow MWD ncPP samples (A1–A3) in (*a*) 2-methylbutane and (*b*) butane. (1 = A1, 2 = A2, 3 = A3.) The curves $\sum h_i^{*3/2}$ not drawn here would be slightly steeper.

Can. J. Chem. Downloaded from www.nrcresearchpress.com by 195.246.54.202 on 09/08/12
For personal use only.

TABLE 1. Characterization of noncrystalline polypropylene (ncPP) with a narrow MWD by SEC and turbidity at a LCST in butane

			LCST[a]							
	SEC		$h^{3/2}$ (eq. [10])			h (eq. [5])			Thermogram	
ncPP sample[b]	$M_w \times 10^{-3}$	M_w/M_n	$M_w \times 10^{-3}$	M_w/M_n	$M_0 \times 10^{-3}$	$M_w \times 10^{-3}$	M_w/M_n	$M_0 \times 10^{-3}$	T_1 (°C)	$T_{1/2}$ (°C)
A1	340	1.3	365	1.24	350	340	1.44	337	95.25	96.5
A2	268	1.08	253	1.10	240	251	1.19	231	97.25	98
A3	202	1.2	167	1.28	147	150	1.48	123	97.75	101
A4	11	1.3	13.4	1.1	13.1	—	—	—	116.5	124

[a]Using the correlation drawn in Fig. 2. The ln-normal cumulative curves for A1–A4 in Fig. 3.
[b]Cumulative curves in Fig. 1*b* (A1–A3).

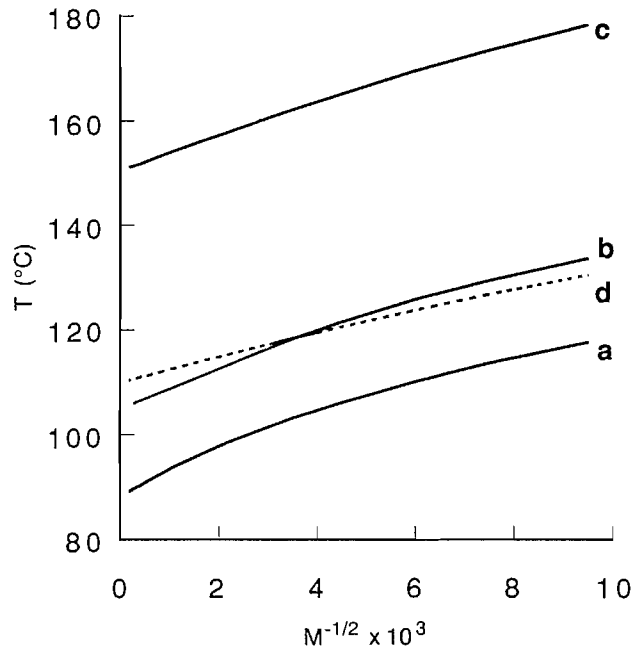

FIG. 2. Correlation between the temperature of phase separation T_i and the average MW in (*a*) butane, (*b*) the mixture of butane and 2-methylbutane, and (*c*) pentane. The equation of state parameters are fitted to the thermogram characteristics of the narrow MWD ncPP samples to obtain the SEC values of M_w and M_n. Dotted line, correlation used for wide MWD iPP.

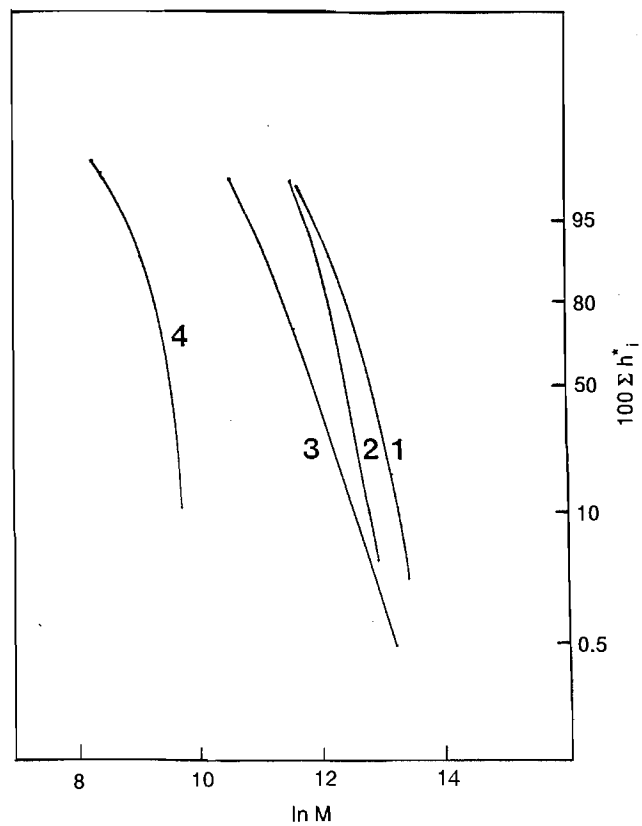

FIG. 3. The ln-normal cumulative curves for the four narrow MWD samples of ncPP in butane. The M_w and M_n are obtained by integrating the curves with $\Delta \ln M = 0.1$. The MW, M_0 of the maximum of the distribution curve M_0, corresponds to the abscissa with 0.5 as ordinate, on the cumulative curve. Curves 1–4 are for A1–A4.

Results and discussion

The MWD of the samples with not very different MWs were measured in four solvents (*n*-pentane, 2-methylbutane, butane, and the butane–2-methylbutane mixture) in order to determine the volatility needed for sufficient resolution. Figures 1*a* and 1*b* clearly give the answer: the resolution is satisfactory in butane (Fig. 1*b*), but just at the limit in 2-methylbutane (Fig. 1*a*). The spacing of the $T_{1/2}$ between the three samples whose M_w are 340 000, 268 000, and 202 000 is 6.5 K in butane and 2.5 K in 2-methylbutane.

The parameters of the equation of state have been calculated to fit the LCST results in these solvents. Numerical values for the relation $T_i = f(M_i)$ (eq. [14]) have been plotted in Fig. 2 for three solvent media: butane, the butane–methylbutane mixture, and *n*-pentane. The smaller slope of curve *c* for pentane, particularly in the high MW region, reflects the fact that this alkane (and obviously higher alkanes such as 2,4-dimethylbutane used for characterizing PE) cannot give a refined MWD for high MW samples.

The results for A1, A3, and A4 in the mixture of butane and 2-methylbutane are comparable to those in butane. The same constants except one (T^*) have been used for the butane and the mixture. T^* is higher in the mixture in order to raise the T_i by 16 K.

The cumulative curves with the ln-normal coordinates are given in Fig. 3 for A1–A4. One sees at a glance the lower polydispersity of A2 (curve 2) with a higher slope than curves 1, 3, and 4. The results are quite satisfactory, the M_w and polydispersity for the three samples being in the same order

Can. J. Chem. Downloaded from www.nrcresearchpress.com by 195.246.54.202 on 09/08/12
For personal use only.

TABLE 2. Comparison of two equations for the relationship between attenuation of light and amount of polymer phase separating. Test on narrow and broad MWD PP and PE samples

	SEC			LCST					
				$h^{3/2}$ (eq. [10])			h (eq. [5])		
Sample	$M_w \times 10^{-3}$	M_w/M_n	Solvent	$M_w \times 10^{-3}$	M_w/M_n	$M_0 \times 10^{-3}$	$M_w \times 10^{-3}$	M_w/M_n	$M_0 \times 10^{-3}$
ncPP									
A1	340	1.3	Mixture[a]	359	1.28	338	340	1.48	332
A3	202	1.2	Mixture	131	1.14	128	125	1.21	125
A4	11	1.3	Mixture	11.1	1.1	10.7	11.6	1.1	11.1
iPP									
B1	150	2.5–3.5	Mixture	145	2.59	123	135.4	3.28	109.1
B2	870–950	5.4	Mixture	1000	5.37	628	1050	10.50	609.2
PE									
C1	119	1.20	2,4-DMC_5[a]	120	1.12	114	122	1.25	112
C2	32	1.10	2,4-DMC_5	27.5	1.04	27.0	27.0	1.05	26.4
C3	11.6	1.15	2,4-DMC_5	12.4	1.17	11.4	12.2	1.22	11.1
C4	6.75	<1.1	2,4-DMC_5	6.6	1.03	6.5	6.4	1.06	6.2

[a]Butane + 2-methylbutane.
[b]2,4-Dimethylpentane.

as those obtained by SEC. The reason for A3 having too low a MW in butane and in the mixture is not clear. Values of M_w and M_w/M_n nearer that obtained by SEC could be obtained by changing slightly curve a of Fig. 2.

Comparison of eqs. [5] and [13]

Changing n from 1 to 1.5 (eqs. [5] and [13]) corresponds to giving more weight to the large peaks, i.e., to reducing the polydispersity of the sample. Tables 1 and 2 give the results of M_w and M_w/M_n for the two equations. For the narrow MWD samples, ncPP (A1–A4) in butane or the mixture and PE (C1–C4) in 2,4-dimethyl pentane, the value $n = 1.5$ gives lower polydispersity by 0.1–0.2. In samples with a higher polydispersity (B1–B2), the effect is larger. Consequently, eq. [13] should be used for M_w and MWD calculations.

Since ultimately, the calibration developed for ncPP samples will be used to analyze isotactic industrial samples, the thermograms of two samples B1 and B2 of Table 2 have been analyzed in the mixture of solvents. B1 is more highly stereoregular than B2. It was found that to obtain the polydispersity value given by SEC, the calibration curve has to be changed as indicated by the dotted line in Fig. 2. Several explanations for this effect are presented. The LCSTs of ncPP and iPP have been found (19) to differ by about 1 K in solvents with a low volatility (LCST near 200°C): (*i*) the effect of tacticity. In systems like the present one with a low LCST, the effect will be probably larger: (*ii*) the effect of polydispersity on solubility. The T_i of narrow and broad MWD samples could be predicted to cross as is seen in Fig. 2 by a simple qualitative argument: (*iii*) the inherent difficulty of comparing techniques without a close control of conditions. Furthermore, using the SEC polydispersity values to test the LCST technique is not recommended, since many factors change the value of M_w/M_n. The value of M_w/M_n for wide MWD samples depends so much on the tails of the distribution that a more reliable way to compare different samples using the same SEC apparatus has been developed (13). It consists of the comparison of M_0 and of the distribution curve over a range of ln M on both sides of M_0. This test could be achieved easily using the SEC and LCST cumulative curves obtained on the same samples: (*iv*) the sensitivity of iPP to degradation in solution. The conditions used to dissolve and analyze iPP (high T residence, shear) are more severe for the SEC than for the LCST technique. The concentration of low M_w may have been increased by the SEC analysis itself, making comparison of the results inappropriate. Another unknown in the analysis of semicrystalline polymers is the concentration of aggregates. It has been shown by calorimetry (20) and intrinsic viscosity measurements (21) on PE and on iPP (unpublished) that the lifetime of strained crystals may be very long and is solvent dependent. Aggregates and small crystals are difficult to detect in solutions except by light scattering. However, since the light scattered by a solution at a LCST is about 10 000 times larger than that of the same solution far from a LCST, the method could be used to detect aggregates in complex polymer mixture. A definite analysis of the solution properties of narrow MWD samples and of wide MWD samples of ncPP and iPP should be made with as much control as possible of the effects mentioned above.

Conclusion

The method of characterizing the MWD by turbidity at a LCST has been reanalyzed in terms of the equations for the treatment of data. It is found that the relation $m = kh_i^n$ should be used with $n = 1.5$. The mixture of solvents (butane and 2-methylbutane) constitutes a suitable compromise to dissolve and characterize with good resolution highly stereoregular high MW PP samples. The small shift necessary to calibrate iPP from the calibration curve of ncPP may have several origins, such as different solubility (due to tacticity or polydispersity) or different state of the solutions in the SEC and LCST techniques.

Acknowledgements

The characterized ncPP fractions have made this work possible and we thank Dr. H.G. Barth for his gift of narrow MWD

Can. J. Chem. Downloaded from www.nrcresearchpress.com by 195.246.54.202 on 09/08/12
For personal use only.

ncPP fractions. The support of the Natural Sciences and Engineering Research Council of Canada is gratefully acknowledged.

1. G. Allen and C.H. Baker. Polymer, **6**, 181 (1965).
2. J.R. Urwin. *In* Light scattering from polymer solution. *Edited by* M.B. Hughlin. Academic Press Ltd., London. p. 789.
3. W.H. Beattie and H. Jung. J. Colloid Interface Sci. **27**, 581 (1968).
4. A. Barbalata, T. Bohossian, K. Prochazka, and G. Delmas. Macromolecules, **21**, 3286 (1988).
5. A. Barbalata, T. Bohossian, and G. Delmas. J. Appl. Polym. Sci. **46**, 411 (1992).
6. T. Bohossian and G. Delmas. Polymer, **30**, 1965 (1989).
7. M. Besombes, J.F. Menguel, and G. Delmas. J. Polym. Sci., Part B: Polym. Phys. **26**, 1111 (1988).
8. T. Bohossian and G. Delmas. J. Polym. Sci. **30**, 993 (1992).
9. J.W. Mays and L.J. Fetters. Macromolecules, **22**, 921 (1989).
10. J.W. Mays, S.S. Huang, M.J. Washall, and H.J. Barth. Water Associates Symp. Gas (1987).
11. G. Charlet and G. Delmas. Polymer, **22**, 1181 (1981).
12. V. Grinshpun and A. Rubin., J. Appl. Polym. Sci. **30**, 2413 (1985).
13. R. Lew, D. Suwanda and S.T. Balke. J. Appl. Polym. Sci. **4**, 1019, 1033, 1049, 1065 (1988).
14. A. Guinier. Diffr. Imaging Tech. Mater. Sci. 2nd Ed. (1978).
15. D. Patterson. J. Polym. Sci. **16**, 3379 (1968).
16. J.M.G. Cowie and I.J. McEven. Macromolecules, **7**, 29 (1974).
17. G. Delmas and D. Patterson. J. Polym. Sci. **C30**, 1 (1970).
18. L.H. Peebles. Molecular weight distribution in polymers. Wiley-Interscience, New York (1971).
19. J.M.G. Cowie and I.J. McEven. J. Polym. Sci., Part B: Polym. Phys. **72**, 1675 (1976).
20. H. Phuong-Nguyen and G. Delmas. Macromolecules, **25**, 414 (1992).
21. H. Phuong-Nguyen. Ph.D. thesis, McGill University, Montréal (1991).
22. S. Varennes, G. Charlet and G. Delmas. Polym. Eng. Sci. **24**, 98 (1984).

Can. J. Chem. Downloaded from www.nrcresearchpress.com by 195.246.54.202 on 09/08/12
For personal use only.

Appendix

Justification of the hypothesis

The validity of the equations used in this paper is discussed in detail in ref. 4. We report here the three tests developed to ensure the suitability of eq. [5]. The first consists of analyzing the cumulative turbidities for 11 solutions of narrow MWD samples with ϕ_2 values such as $0.018 < \phi_2 < 0.04$. $\sum h_i$ is found to be a linear function of ϕ_2 that extrapolates to the origin. In the second test, a cumulative curve is made using solutions of different concentrations. When $(\sum h_i)/\phi_2$ is plotted against T_i, a single cumulative curve is obtained. The third test is a correlation of gravimetric and turbidimetric analysis. Several solutions at the same concentration are prepared and analyzed by their thermograms taken from T_1 to a temperature T_i which is different for each tube. The concentrated phase of each solution is characterized by $\sum_{i=1}^{i} h_i^*$, its cumulative turbidity between T_1 and T_i. After equilibrium at T_i the polymer concentrated phase is then separated and its weight w_i is determined gravimetrically for each solution. For seven solutions measured over the interval of phase separation, a good correlation is obtained between $\sum_{i=1}^{i} h_i^*$ or $\sum_{i=1}^{i} h_i^{*3/2}$ and w_i.

The ln-normal distribution

The ln(normal) distribution function is expressed (18) as

$$W(\ln M) = (\text{constant})(\sigma^{-1}) \times \exp[-(\ln M - \ln M_0)^2 0.5\sigma^{-2}]$$

[A1]
$$\sigma = (\sigma^+\sigma^-)^{1/2}$$
$$\sigma^+ = \ln M_A - \ln M_0$$
$$\sigma^- = \ln M_0 - \ln M_B$$

M_A and M_B are the abscissas of the points whose ordinates on the cumulative curve (Fig. 3) are 0.16 and 0.84, respectively, and

$$M_w = M_0 e^{0.5\sigma^2}$$
$$M_n = M_0 e^{-0.5\sigma^2}$$

Equation of state calculations

Parameters for the solvents and the polymer

The reduced volumes and temperatures can be calculated from the expansion coefficients α:

$$\tilde{v}^{1/3} = \frac{(4/3)\alpha T + 1}{\alpha T + 1}$$

and

$$\tilde{T} = \tilde{v}^{-1}(1 - \tilde{v}^{-1/3})$$
$$\tilde{T} = T/T^*$$

in the van der Waals model used by several authors (11, 15, 17, 19).

The T^*s are calculated to be equal to 3990 for butane, 4460 for 2,4-dimethylpentane, 6363 for PE, and 5962 for PP. c_1 $(= P^*V^*/T^*)$ is calculated equal to 1.1 for the solvents used. P^*, V^*, and T^* are the reducing parameters for P, V, and T. For instance, knowing $\tilde{v}$ from α and the above equation and $V/\tilde{v}$, the molar volume from the density $V^* = V/\tilde{v}$.

Parameters for the $T_i = f(M_i)$ *curve*

The critical χ parameter is equal to

$$\chi = c_1 v^2 f(\tilde{v}) + c_1 \tau^2 f'(\tilde{v})$$
$$= 0.5(1 + r^{-1/2})^2$$
$$\approx 0.5 + r^{-1/2}$$

with r being V (polymer)/V (solvent). The terms $c_1 v^2$ and $c_1 \tau^2$, the chemical and free volume differences between polymer and solvent, are independent of T.

The two functions $f(\tilde{v}) = (1 - v^{-1/3})^{-1}$, which diminishes when T increases, and $2f'(\tilde{v}) = [(4/3)\tilde{v}^{-1/3} - 1]^{-1}$, which increases with T, give an expression of the temperature variation of the two contributions to the χ parameter when the temperature increases. Approaching the LCST, the first term becomes negligible compared with the second one. Consequently, the reduced LCST (LCST/T_c) is, for several polymers in many solvents, almost exclusively a function of $c_1\tau^2$:

$$\tau^2 = [1 - (T^*_{\text{solvent}}/T^*_{\text{polymer}})]^2$$

with $c_1 v^2 = 0$. The calculated values of $c_1\tau^2$ are 0.115 for the system PE–2,4-DMC$_5$ and 0.095 for the PP–solvent mixture.

The values of T_1 are 155 and 130°C, respectively (instead of 130 and 110°C). Because of the inadequacy of the simple van der Waals model for the solvent near T_c, the range of the $T_i(M_i)$ curve is much lower than the experimental one.

The parameters have to be changed to fit the experimental temperatures. There is not a unique way to find the $T_i = f(M_i)$ curve that fits the experimental data. Parameters used are as follows: for ncPP in mixture, $T^* = 4400$, $c_1\tau^2 = 0.1083(1 + 1.1r^{-1/2})$, and $c_1\nu^2 = 0.023$; for ncPP in butane, same parameters except $T^* = 4235$; for iPP in mixture, $T^* = 4459$, $c_1\tau^2 = 0.159(1 + 0.3r^{-1/2})$, and $c_1\nu^2 = 0$.

No correction was made to the data to take into account the increase of pressure P between T_1 ($\approx$ 4 atm; 1 atm = 101.3 kPa) and T_f ($\approx P_c$).

Examples of thermograms

The peaks of the thermogram used to draw the cumulative curves are listed below for sample A1 ($c = 0.2\%$ in butane).

Temperature (°C)	$\frac{h_i}{\sum h_i}$	$\frac{h_i^{3/2}}{\sum h_i^{3/2}}$	$10^{-3}M_w$[a]
92.25	0.15	0.14	545
96.25	0.26	0.30	400
97.25	0.19	0.20	300
99.25	0.22	0.25	184
101.25	0.09	0.06	121
104.25	0.06	0.03	70
107.25	0.03	0.01	43.5

[a]From eq. [14].

In arbitrary units, $\sum h_i = 171$, $\sum h_i^{3/2} = 950$, and $J_0 = 230$.

Variation of the volume of the concentrated phase during the course of the thermogram

The concentrated phase accumulates at the bottom of the tube during the T steps. The increase of the volume of the concentrated phases, V(concentrated phase), or of the ratio V(concentrated phase)/V(dilute phase) versus T permits building a cumulative curve similar to that obtained by the turbidity measurements. However, it has been found that at higher T (i.e., above $T_{1/2}$) the ratio levels off and even diminishes. Several parameters (concentration, polydispersity, reequilibration of the phases at high T) influence the ratio of the two phases that has been calculated for an upper critical solution temperature in the case of monodiperse sample. At the LCST, besides the reequilibration of the phases at high T, another factor is important, namely the higher compressibility of the dilute phase than of the concentrated phase near T_c. Consequently, the measurements of volumes of phases cannot be used as a quantitative analysis of the MWD.

Thermograms obtained in a temperature ramp

When the turbidity of the solution is monitored in a temperature ramp (0.5 K/min for instance), it goes through a maximum and falls again to 0 due to sedimentation of the concentrated phases. The technique has been used for differentiating complex mixtures of homopolymers and copolymers whose LCST are situated at different temperatures (PE, PP, and EP copolymers) (7, 22). After the main peak, smaller turbidity peaks, similar to harmonics of the main peak, appear at high T over a period of 30–80 min at the end of the phase separation. They have been attributed to the displacement of the solvent towards the top of the tube during the reequilibration of the phases.

Can. J. Chem. Downloaded from www.nrcresearchpress.com by 195.246.54.202 on 09/08/12
For personal use only.

Oxidation of D-gluconic acid by chromium(VI) in perchloric acid[1]

SANDRA R. SIGNORELLA, MABEL I. SANTORO, MIRTA N. MULERO, AND LUIS F. SALA[2]

Departamento de Química-Fisica, Facultad de Ciencias Bioquímicas y Farmacéuticas, Universidad Nacional de Rosario, Suipacha 531, (2000) Rosario, Argentina

Received April 21, 1993

SANDRA R. SIGNORELLA, MABEL I. SANTORO, MIRTA N. MULERO, and LUIS F. SALA. Can. J. Chem. **72**, 398 (1994).

The oxidation of gluconic acid by chromium(VI) in perchloric acid has been found to follow the rate law: $-d[Cr^{VI}]/dt = (k'_1 + k'_2[GA])[H^+]^2[Cr^{VI}]$, where $k'_1 = (7.1 \pm 0.2) \times 10^{-4}$ M^{-2} s^{-1} and $k'_2 = (9.4 \pm 0.2) \times 10^{-2}$ M^{-3} s^{-1}. This rate law corresponds to the reaction leading to the formation of 2-ketogluconic acid by C—H cleavage when a 20-fold or higher excess of acid over chromium(VI) is employed. Buildup and decay of chromium(V) intermediates accompany the decay of chromium(VI). Chromium(V) rates of decay are similar or slower than those of chromium(VI), as observed by electron paramagnetic resonance (epr) and visible spectrophotometry.

SANDRA R. SIGNORELLA, MABEL I. SANTORO, MIRTA N. MULERO et LUIS F. SALA. Can. J. Chem. **72**, 398 (1994).

On a trouvé que l'oxydation de l'acide gluconique par le chrome(VI) dans l'acide perchlorique suit la loi de vitesse : $-d[Cr^{VI}]/dt = (k'_1 + k'_2[GA])[H^+]^2[Cr^{VI}]$ dans laquelle $k'_1 = (7{,}1 \pm 0{,}2) \times 10^{-4}$ M^{-2} s^{-1} et $k'_2 = (9{,}4 \pm 0{,}2) \times 10^{-2}$ M^{-3} s^{-1}. Cette loi de vitesse correspond à la réaction conduisant à la formation de l'acide 2-cétogluconique par le clivage de C—H lorsqu'on utilise une quantité d'acide qui est au moins 20 fois plus grande que celle du chrome(VI). Une accumulation et une décomposition des intermédiaires du chrome(V) accompagne la décomposition du chrome(VI). La résonance paramagnétique éléctronique (rpe) et la spectrophotométrie visible permettent d'observer que les vitesses de décomposition du chrome(V) sont semblables ou plus lentes que celles du chrome(VI).

[Traduit par la rédaction]

Introduction

It is well known that chromium(VI) compounds are carcinogenic (1) and mutagenic (2), and this deleterious behavior of chromium(VI) has been attributed to stable Cr(V) intermediates generated within the cells (3). Ligands that possess two oxygen atoms able to form five-membered rings about the metal atom, such as 1,2-diols and α-hydroxyacids, are reported to stabilize chromium(V) intermediates (4–6) after further interaction with biological reductants (7).

Chromic acid oxidation of α-hydroxyacids has been extensively studied (8–13). These oxidations may yield products coming from either C—C (8–13) or C—H cleavage (9, 10, 14), depending on the particular molecular characteristics, through mechanisms involving either two-electron or three-electron initial oxidation of substrate by chromium(VI). In any case, chromium(V) intermediates have been observed.

Since there are no general patterns for the oxidation of α-hydroxyacids by chromium(VI), we report here the first kinetic study on the chromic oxidation of a polyhydroxyacid (D-gluconic acid).

Experimental

Materials

D-Gluconic acid sodium salt (Sigma grade), potassium dichromate (Cecarelly c.a.), perchloric acid (G.R., E. Merck), acrylonitrile (Aldrich grade), and sodium perchlorate (Fluka grade) were used without further purifications.

Spectrophotometric measurements

Kinetics measurements were made at 350 nm by monitoring the absorbance changes on a Guilford Response II spectrophotometer with fully thermostated cell compartments. Rate constants deduced from multiple determinations were within ±5% of each other. In most experiments the concentration of chromium(VI) was kept constant at 7×10^{-4} M while the gluconic acid concentration was varied from 0.014 M to 0.091 M. In one set of experiments, [GA], $[H^+]$, and T were kept constant whereas $[Cr(VI)]_0$ was varied from 3×10^{-3} to 2×10^{-2} M. Mixtures of sodium perchlorate and perchloric acid were used to maintain a constant ionic strength of 1.50 M. Disappearance of Cr(VI) was followed until at least 80% conversion. Reactant solutions were previously thermostated, and were transferred into a cell of 1 cm path length immediately after mixing. Experiments were performed at 30°C, unless otherwise mentioned.

Cr(V) was monitored spectrophotometrically by following the absorbance growth and decay at 750 nm of mixtures of Cr(VI) (7×10^{-3} M) and gluconic acid (0.14–0.56 M) in 0.50 M $HClO_4$, $I = 1.50$ M, at 30°C, with a path length of 1 cm.

Electron paramagnetic resonance measurements

The epr spectra were recorded with a Bruker spectrometer model ER-200, and g values were measured by reference to diphenylpicrylhydracyl (DPPH, $g = 2.0036$). Spectra were acquired at a frequency of ca. 9.8 Hz with a centered field of 3557 G, a sweep width of 100 G, and a variable modulation amplitude. The sample tube and cavity were kept at 25°C.

Product analysis

Under conditions used in the kinetic measurements (ratios of gluconic acid (GA):Cr(VI) from 20 to 130), qualitative identification of 2-ketogluconic acid (KGA) as the reaction product was carried out by paper chromatography. KGA was identified against an authentic sample using *n*-butanol – acetic acid – water (4:1:5) as eluent. Paper chromatograms were visualized by two kinds of development reagents: a three-stage dip of silver nitrate, sodium hydroxide, and sodium thiosulfate (15) and *p*-anisidine reagent (16). Under these conditions, carbon dioxide was never detected.

To identify the Cr(III) complexes present in solution after reaction completion, uv–vis spectra of these solutions were registered and compared with spectra obtained from a Cr(III) solution and mixtures of gluconic acid or KGA and Cr(III) in 0.50 M $HClO_4$. Under these experimental conditions, KGA did not complex Cr(III), as revealed by a spectrum identical to that of the Cr(III) solution. On the other hand, GA–Cr(III) mixtures showed shifted Cr(III) bands with higher extinction coefficients, compared to those of the free ion, as previously reported for a similar system (17). Given the close agreement (vide infra) of both visible and uv spectral maxima and the intensities between the observed species in the reaction solution and that of the

[1]Presented at the 24 Reunión Bienal Real Sociedad Española de Química. September 21–24, 1992, Málaga, Torremolinos, Spain.

[2]Author to whom correspondence may be addressed.

Can. J. Chem. Downloaded from www.nrcresearchpress.com by 195.246.54.202 on 09/08/12
For personal use only.

TABLE 1. Concentration of gluconolactone and gluconic acid in the starting solutions[a]

$[HClO_4]$/M	C_T[b] 10^2/M	R[c]	[GL] 10^3/M	[GA] 10^2/M	$[G^-]$ 10^5/M
0.25	5.03	+0.133	1.23	4.91	3.54
0.75	5.28	+0.171	2.76	5.00	1.24
1.00	4.81	+0.192	4.21	4.39	8.47

[a]Values used in calculations: molar rotations: +23.5° (GL), +2.12° (GA), +5.25° (G^-); $K = [H^+][G^-]/[GL] + [GA] = 1.76 \times 10^{-4}$ (19).
[b]C_T = [GA] + [GL] + $[G^-]$, where GL and G^- refer to gluconolactone and gluconate, respectively.
[c]Optical rotation.

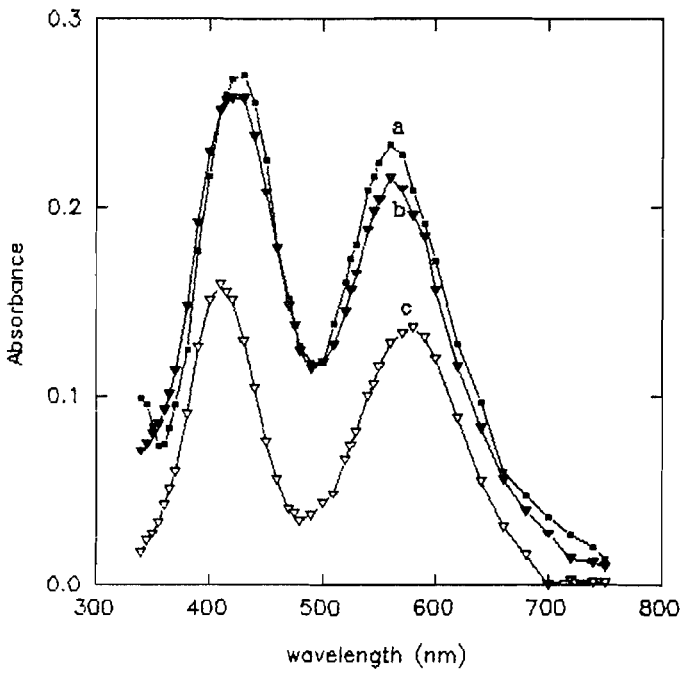

FIG. 1. Absorption spectra of (*a*) A reaction mixture after completion ($[Cr(VI)]_0 = 0.01$ M, [GA] = 0.50 M); (*b*) $[Cr(III)]_0 = 0.01$ M, [GA] = 0.50 M; (*c*) $[Cr(III)]_0 = 0.01$ M. In every case $[H^+] = 0.50$ M, $T = 30°C$, and $I = 1.50$ M.

GA–Cr(III) mixture prepared independently, the binary complex present in the solution may correspond to the complex GA–Cr(III) (428 nm, $\epsilon = 27\ M^{-1}\ cm^{-1}$; 560 nm, $\epsilon = 22\ M^{-1}\ cm^{-1}$) (Fig. 1).

Test for free radicals

A solution of $K_2Cr_2O_7$ (7×10^{-4} M, 2 mL) in 0.50 M $HClO_4$ was added to a mixture of 1.00 M (2 mL) gluconic acid in 0.50 M $HClO_4$ and 0.50 mL of 1.50 M acrylonitrile at 30°C. After 30 min a white precipitate of a polymer appeared slowly. Blank experiments in the absence of gluconic acid or $K_2Cr_2O_7$ did not show formation of any such precipitate.

Results and discussion

Gluconic acid lactonization is acid catalyzed and equilibrium mixtures are reached rapidly in highly acid solutions (18). The acid:lactone proportion in the starting solution may be calculated by optical rotation measurements at given hydrogen ion concentrations (19). Table 1 shows the composition of the substrate solution at three different perchloric acid concentrations. Given the high GA proportion in the starting solution, GA is considered the reactive species in the kinetic discussion below and [GA] is referred to as the total substrate concentration. Nevertheless a possible lactone cooxidation might not be disregarded.

Rate studies

We observed deviations from first-order decay of absorbance at 350 nm over short time periods. This behavior has frequently been attributed to strongly absorbing Cr(V) intermediates formed in the course of the reaction (20). Considering Cr(V) absorbance superimposition, absorbance data at 350 nm vs. time curves were fitted to eq. [1]:

$$[1]\quad Abs^{350} = Abs^{VI} + Abs^{V} = Abs_0 \exp(-2k_6t) + k_6[Cr(VI)]_0\epsilon^{V}(\exp(-k_5t) - \exp(-2k_6t))/(2k_6 - k_5)$$

where ϵ^V refers to the molar absorption due to Cr(V) at 350 nm and was assumed to be 1200 $M^{-1}\ cm^{-1}$ (21) and k_6 and k_5 refer to the rate of disappearance of Cr(VI) and Cr(V), respectively. In this equation, k_6 appears in the numerator of the preexponential term and $2k_6$ appears in the denominator and in the exponential terms because only half of the Cr(VI) reaches Cr(III) through a Cr(V) intermediate, according to the following reaction scheme:

$$[2]\quad Cr(VI) \xrightarrow[k_6]{GA} \text{+ KGA}$$

$$Cr(IV) \xrightarrow{GA} \underset{(fast)}{\xrightarrow{Cr(VI)}} Cr(V) + Cr(III) + KGA$$

$$Cr(V) \xrightarrow[k_5]{GA} Cr(III) + KGA$$

Figure 2 shows a typical curve for one run at 350 nm that fits experimental data well.

From eq. [1], values of k_{obs} ($2k_6$) and k_5 may be obtained and they are tabulated in Table 2. If Cr(V) decays faster than Cr(VI) oxidation, pseudo-first-order rate constants might be calculated from the linear part of ln Abs vs. time curves. However, values obtained from this approach differ from those calculated by eq. [1] at any hydrogen ion concentration. Observed rate constants were also calculated at various [Cr(VI)] ($(3–20) \times 10^{-3}$ M) but at constant T (30°C), [GA] (0.042 M), $[H^+]$ (0.5 M), and I = 1.5 M.

The rate constant was found to be constant with increasing amounts of Cr(VI), which affirms the assumption of a first-order dependence of the rate upon [Cr(VI)].

Values of k_5 and k_6 may be also calculated by eq. [3], which fits the experimentally observed Cr(V) intermediate growth and decay curve at 750 nm well (Fig. 2):

$$[3]\quad Abs^{750} = k_6[Cr(VI)]_0\epsilon^{V}(\exp(-k_5t) - \exp(-2k_6t))/(2k_6 - k_5)$$

Can. J. Chem. Downloaded from www.nrcresearchpress.com by 195.246.54.202 on 09/08/12
For personal use only.

TABLE 2. Observed pseudo-first-order rate constants (*a*) $2k_6$ and (*b*) k_5 for Cr(VI) reduction for different $HClO_4$ and gluconic acid concentrations. $T = 30°C$; $[Cr(VI)]_0 = 7 \times 10^{-4}$ M; $I = 1.50$ M

(a)

	$10^4 k_{obs}{}^a$ (s^{-1}) for $[HClO_4]$/M of					
10^2[GA]/M	0.25	0.38	0.50	0.75	1.00	1.50
1.4	1.46	3.30	3.77	12.0	22.8	41.0
2.8	—	—	—	—	—	79.5
4.2	3.80	6.20	9.75	24.1	47.1	106
5.6	4.44	7.26	11.6	35.6	58.6	131
7.0	5.26	9.30	13.0	41.8	80.0	164
8.4	—	—	—	—	—	191
9.1	7.94	12.6	18.4	50.8	—	—

(b)

	$10^4 k_5{}^a$ (s^{-1}) for $[HClO_4]$/M of					
10^2[GA]/M	0.25	0.38	0.50	0.75	1.00	1.50
1.4	2.90	2.36	10.6	6.88	8.66	22.8
2.8	—	—	—	—	—	36.0
4.2	11.8	14.0	22.6	26.9	28.4	53.0
5.6	10.5	16.8	26.6	30.1	33.0	69.7
7.0	12.3	19.7	30.5	34.6	38.0	62.3
8.4	—	—	—	—	—	57.3
9.1	7.32	9.92	17.4	21.5	—	—

[a]Rate constants obtained from multiple determinations (normally four).

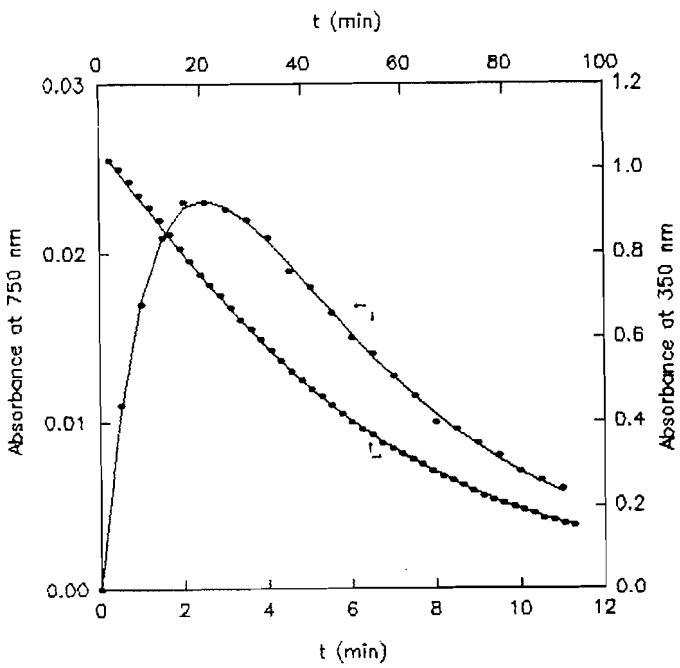

FIG. 2. Absorbance vs. time curves for Cr(VI) and chromium(V) oxidation of gluconic acid at 350 nm: $[Cr(VI)] = 7 \times 10^{-4}$ M, [GA] = 0.014 M, $[HClO_4] = 0.50$ M, $I = 1.50$ M, $T = 30°C$; and at 750 nm: $[Cr(VI)] = 7 \times 10^{-3}$ M, [GA] = 0.14 M, $[HClO_4] = 0.50$ M, $I = 1.50$ M, $T = 30°C$. $T_{max} = 2.5$ min.

where ϵ^V refers here to Cr(V) molar absorption at 750 nm. The best fit of data is obtained when $\epsilon^V = 38$ M^{-1} cm^{-1} (12). By using this ϵ^V, derived rate constants are coincident with those calculated by eq. [1]. Higher values of ϵ^V give rate constants increasingly different from those obtained by eq. [1] and simulated curves fit experimental data points more poorly. Since a 10-cm path length cell was not accessible when these studies were made, tenfold higher initial Cr(VI) and gluconic acid concentrations were necessary to follow absorbance changes at 750 nm. In this way, $k_5/10$ and $2k_6/10$ values calculated by eq. [3] were coincident with those obtained from eq. [1], when the same gluconic/Cr(VI) ratio and $[HClO_4]$ were employed.

The maximum Cr(V) concentration calculated at T_{max} represents up to 22% of the total chromium concentration. The growth and decay of Cr(V) were also followed by epr measurements. The epr spectrum is dominated by a sharp band at $g = 1.976$, with the four peaks ^{53}Cr (9.55% abundance, $I = 3/2$) and hyperfine bands at 18.1 spacing, typical of five-coordinate oxochromate(V) complexes (22). Figure 3 shows a typical curve for peak-to-peak heights of Cr(V) epr signals vs. t obtained on a reacting solution. T_{max} values observed by this technique are rather coincident with those expected by applying $(\ln(2k_6/k_5))/(2k_6 - k_5)$ derived from eq. [3]. T_{max} may be calculated by using k_5 or k_6 values obtained from either eq. [1] or eq. [3] (in the second case values of $k_5/10$ and $2k_6/10$ are used since tenfold higher initial reactant concentrations are needed to detect Cr(V) complexes at 750 nm). In this way, T_{max} observed by epr are within 5–10% of expected values; i.e., for conditions in Fig. 3, the expected T_{max} is 12.6 min ($2k_6 = 0.0498$ min^{-1} and $k_5 = 0.118$ min^{-1}) instead of the experimentally observed 13.5 min. This difference may be accounted for, in part, by the 5°C lower temperature for the epr measurements. Larger differences at higher chromium concentration are due to Cr(III) epr signal overlapping.

At six different acidities, plots of k_{obs} vs. GA concentration gave good straight lines with a positive intercept from which values of k_1 and k_2 were determined (Table 3). Plots of k_1 and k_2

Can. J. Chem. Downloaded from www.nrcresearchpress.com by 195.246.54.202 on 09/08/12
For personal use only.

TABLE 3. Values for k_1 and k_2 for different $[HClO_4]$

$[HClO_4]$/M	0.25	0.38	0.50	0.75	1.00	1.50
$10^4 k_1$ (s^{-1})	0.22	1.25	1.41	4.44	7.22	15.9
$10^3 k_2$ (M^{-1} s^{-1})	7.98	11.9	18.1	52.0	98.7	210

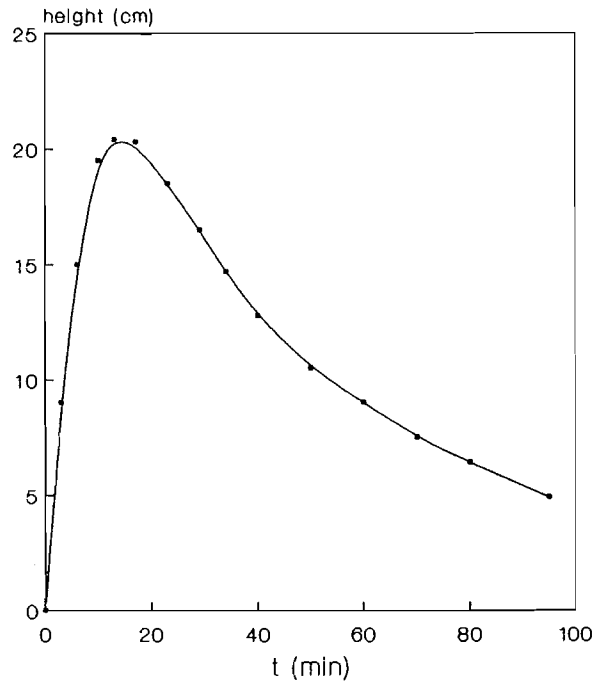

FIG. 3. Peak-to-peak heights of Cr(V) epr signals vs. time: [GA] = 0.035 M, $[Cr^{VI}]_0 = 7 \times 10^{-4}$ M, $[HClO_4] = 0.50$ M, $T = 25°C$. T_{max} = 13.5 min.

vs. $[H^+]^2$ gave straight lines, showing that the complete rate law is given by:

$$[4] \quad -d[Cr(VI)]/dt = k_{obs}[Cr^{VI}] = (k_1' + k_2'[GA])[H^+]^2[Cr^{VI}]_0$$

where $k_1' = (7.1 \pm 0.2) \times 10^{-4}$ M^{-2} s^{-1} and $k_2' = (9.4 \pm 0.2) \times 10^{-2}$ M^{-3} s^{-1}, and $[Cr^{VI}]_0$ represents the total Cr(VI) concentration.

Values of k_5 (Table 2) were not employed to determine the kinetic law for Cr(V) oxidation of GA because of the complex k_5 dependence on [GA] and $[H^+]$. Work is in progress to obtain more data points necessary for this study.

Mechanism

A mechanism consistent with experimental data, is given in the following scheme:

$$[5] \quad Cr(VI) + GA \underset{}{\overset{K_1}{\rightleftharpoons}} [Cr(VI) \cdot GA]^- \quad (A^-)$$

$$[6] \quad A^- + H^+ \overset{K_2}{\rightleftharpoons} AH$$

$$[7] \quad AH + H^+ \overset{K_3}{\rightleftharpoons} AH_2^+$$

$$[8] \quad AH_2^+ \xrightarrow{k_I} KGA + Cr(IV)$$

$$[9] \quad GA + AH_2^+ \xrightarrow{k_{II}} KGA + Cr(IV)$$

In the pH range studied here, Cr(VI) exists mainly as $Cr_2O_7^{2-}$ (23). Thus the first step of the proposed mechanism may be interpreted as the formation of a monochelate with GA acting as a bidentate ligand bound to Cr(VI) through the 2-hydroxylic and carboxylic groups, as shown in eqs. [10] or [11]:

[10] $Cr_2O_7^{2-} + GA \rightleftharpoons$

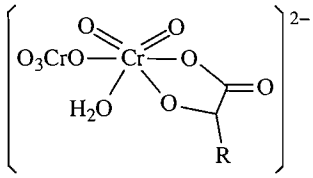

or

[11] $Cr_2O_7^{2-} + GA \rightleftharpoons$

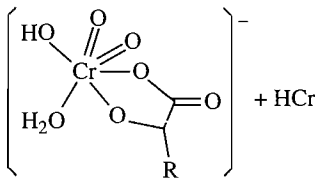

$+ HCrO_4^-$

(A^-)

However, since the observed rate constants are independent of the initial concentration of Cr(VI), it is possible that the reactive species is the bis(chelate) and that all the Cr(VI) is converted to the monochelate in the first step:

$$[12] \quad [Cr_2O_7(GA)_2]^{2-} \rightleftharpoons 2A^-$$

In these equations a six-coordinate structure is proposed for A^-, even though a five-coordinate one might also be considered. This anionic intermediate may be doubly protonated (eqs. [6] and [7]) to form AH_2^+, which may decompose directly to Cr(IV) and KGA (eq. [8]) or in the presence of another GA molecule (eq. [9]) through two competitive two-electron pathways.

According to the proposed mechanism, the full rate law for the oxidation of GA by Cr(VI), under conditions studied in the kinetic measurements, can be written:

$$[13] \quad -d[Cr(VI)]/dt = (k_I + k_{II}[GA])K_1K_2K_3[GA][H^+]^2[Cr(VI)]_T$$

Since:

$$[14] \quad [Cr(VI)]_T = [Cr(VI)](1 + K_1[GA] + K_1K_2[GA][H^+] + K_1K_2K_3[GA][H^+]^2)$$

Replacing Cr(VI) in eq. [13]:

$$[15] \quad -d[Cr(VI)]/dt = \frac{(k_I + k_{II}[GA])K_1K_2K_3[GA][H^+]^2[Cr(VI)]_T}{1 + K_1[GA] + K_1K_2[GA][H^+] + K_1K_2K_3[GA][H+]^2}$$

Can. J. Chem. Downloaded from www.nrcresearchpress.com by 195.246.54.202 on 09/08/12
For personal use only.

Thus, if K_1[GA] is the largest term in the denominator, eq. [15] will be simplified to the experimentally observed form.

After the slow steps, reactions [16], [17], and [18] may take place:

$$[16]\quad GA + Cr(IV) \xrightarrow{\text{fast}} GA^{\bullet} + Cr(III)$$

$$[17]\quad GA^{\bullet} + Cr(VI) \xrightarrow{\text{fast}} KGA + Cr(V)$$

$$[18]\quad GA + Cr(V) \xrightarrow{k_{III}} KGA + Cr(III)$$

Cr(IV) formed in the slow steps yields the final Cr(III) and the GA· radical by a later fast step. GA· radical formation is supported by the observer polymerization after addition of acrylonitrile. These radicals may react with Cr(VI) to yield the oxidation product and Cr(V), which reacts with GA to produce KGA and Cr(III) in a two-electron step. The proposed mechanism is in agreement with the initial assumption that only half of Cr(VI) reaches Cr(III) through a Cr(V) intermediate.

Spectrophotometric analysis of the Cr(III) products showed that GA–Cr(III) is the binary complex present at the end of the reaction. Some authors (24) have concluded that initial one-electron reduction of the Cr(VI) leads to Cr(III) entrapment of oxidized substrate, whereas initial two-electron reduction leads to the Cr(III) entrapment of excess substrate. If this generalization were accepted, observation of the Cr(III)–GA complex as product implies an initial two-electron reduction of Cr(VI) by gluconic acid, such as proposed in the mechanism.

Conclusions

The above results show that reduction of Cr(V) occurs at a similar rate and concurrently with Cr(VI) and that the steady-state chromium(V) concentration may be up to 22% of the total chromium present in solution. Consequently, Cr(V) and Cr(VI) absorbances at 350 nm are always superimposed, and an equation taking this situation into account has to be employed. We have observed no effect of the substrate on the absorbance of Cr(VI) at 350 nm such as occurred in other systems in which Cr(VI) esters are observed (25). For example, cyclic aldohexoses, where hydroxyl groups seem to be better disposed to bind Cr(VI) or Cr(V) (6), yield detectable esters even in highly acid conditions. That KGA was the only detected reaction product clearly shows that C—H scission at the α-carbon is preferred to C—C scission for the oxidation of GA by Cr(VI). Oxidation of GA by Cr(VI) resembles that of lactic acid (10) more than that of sugars, though it plainly differs, either in mechanism or oxidation products, from other α-hydroxyacids studied (8).

Acknowledgements

We thank the National Research Council of Argentina, The Third World Academy of Science, and the National University of Rosario for financial support.

1. A. Standeven and K. Wetterhahn. J. Am. Coll. Toxicol. **8**, 1275 (1989).
2. J. Aiyar, H. Berkovits, and K. Wetterhahn. Chem. Res. Toxicol., **3**, 595 (1990).
3. S. Brauer and K. Wetterhahn. J. Am. Chem. Soc. **113**, 3001 (1991).
4. M. Krumpolc, B.G. De Boer, and J. RoCek. J. Am. Chem. Soc. **100**, 145 (1978).
5. H. Nishino and K. Kochi. Inorg. Chim. Acta, **174**, 93 (1990).
6. L. Sala, S. Signorella, M. Rizzotto, M. Frascaroli, and M. Gandolfo. Can. J. Chem. **70**, 2046 (1992).
7. M. Branca, A. Dessi, H. Kozlowstai, G. Micera, and J. Swiatek. J. Inorg. Biochem. **39**, 217 (1990).
8. M. Mitewa and P. Bontchev. Coord. Chem. Rev. **61**, 241 (1985).
9. S. Signorella, S. Garcia, and L. Sala. Polyhedron, **11**, 1391 (1992).
10. G. Haight, G. Jwisich, M. Kelso, and P. Merrill. Inorg. Chem. **24**, 2740 (1985).
11. D. Ip and J. RoCek. J. Am. Chem. Soc. **101**, 6311 (1979).
12. M. Krumpolc and J. RoCek. J. Am. Chem. Soc. **99**, 137 (1977).
13. S. Ramesh, S. Mahapatro, J. Lui, and J. RoCek. J. Am. Chem. Soc. **103**, 5772 (1981).
14. K. Srinivasa and J. RoCek. J. Am. Chem. Soc. **100**, 2789 (1978).
15. W. Travelyan, D. Proctor, and J. Harrison. Nature, **166**, 444 (1950).
16. L. Haugh, J. Jones, and N. Wadman. J. Chem. Soc. 1702 (1950).
17. M. Branca and G. Micera. Inorg. Chim. Acta, **153**, 61 (1988).
18. Y. Pocker and E. Green. J. Am. Chem. Soc. **95**, 113 (1973).
19. D. Sawyer and J. Bagger. J. Am. Chem. Soc. **81**, 5302 (1959).
20. V. Srinivasan and J. RoCek. J. Am. Chem. Soc. **96**, 127 (1974).
21. M. Krumpolc and J. RoCek. Inorg. Synth. **20**, 63 (1980).
22. R. Bramley, J. Ji, R. Judd, and P. Lay. Inorg. Chem. **29**, 3089 (1990).
23. M. CieSlak-Golonka. Coord. Chem. Rev. **109**, 223 (1991).
24. D. Kwong and D. Pennington. Inorg. Chem. **23**, 2528 (1984).
25. F. Hasan and J. RoCek. J. Am. Chem. Soc. **94**, 9073 (1972).

Can. J. Chem. Downloaded from www.nrcresearchpress.com by 195.246.54.202 on 09/08/12
For personal use only.

The photochemical nucleophile–olefin combination, aromatic substitution (photo-NOCAS) reaction. Part 5: methanol–monoterpenes (α- and β-pinene, tricyclene, and nopol), 1,4-dicyanobenzene[1]

DONALD R. ARNOLD[2] AND XINYAO DU
Department of Chemistry, Dalhousie University, Halifax, NS B3H 4J3, Canada

Received April 30, 1993

DONALD R. ARNOLD and XINYAO DU. Can. J. Chem. **72**, 403 (1994).

The reactivity of the radical cations of α- and β-pinene (**8** and **9**), tricyclene (**18**), and nopol (**23**) has been studied. The radical ions were generated, in acetonitrile–methanol (3:1), by single electron transfer (set) to the singlet excited state of 1,4-dicyanobenzene (**1**). Biphenyl (**3**) was used as a codonor. The cyclobutane rings of the initially formed radical cations of α- and β-pinene ($\mathbf{8}^{+\cdot}$ and $\mathbf{9}^{+\cdot}$) cleave to distonic radical cations that react as tertiary alkyl cations and allylic radicals. The results of *ab initio* molecular orbital calculations (STO-3G) are consistent with the observation that the positive charge is largely associated with the tertiary alkyl moiety while the spin density is largely distributed over the allylic radical. There was no evidence, experimental or theoretical, indicative of a bonding interaction between the cationic and allylic moieties of these distonic radical cations. The cyclobutane ring cleavage is irreversible. The radical cation of tricyclene (**18**) also gives 1:1:1 (nucleophile:cyclopropyl:aromatic) adducts. The regio- and stereochemistry of the adducts, and the nucleophile selectivity, are all indicative of nucleophile-assisted cleavage of the radical cation ($\mathbf{18}^{+\cdot}$). The radical cation of nopol ($\mathbf{23}^{+\cdot}$) also cleaves to the distonic radical cation. The cyclobutane ring cleavage must be rapid; intramolecular 1,5-*endo* cyclization of the hydroxyl group cannot compete.

DONALD R. ARNOLD et XINYAO DU. Can. J. Chem. **72**, 403 (1994).

On a étudié la réactivité des cations radicalaires des α- et β-pinènes (**8** et **9**), du tricyclène (**18**) et du nopol (**23**). On a générés les ions radicalaires dans un mélange acétonitrile–méthanol (3 : 1) par un transfert d'un seul électron (set) à l'état excité singulet du 1,4-dicyanobenzène (**1**). On a utilisé le biphényle (**3**) comme codonneur. Les noyaux cyclobutane des cations radicalaires qui se forment initialement à partir des α- et β-pinènes ($\mathbf{8}^{+\cdot}$ et $\mathbf{9}^{+\cdot}$) se clivent en cations radicalaires distoniques qui réagissent comme cations alkyles tertiaires et radicaux allyliques. Les résultats de calculs d'orbitales moléculaires *ab initio* (STO-3G) sont en accord avec l'observation que la charge positive est associée largement avec la portion alkyle tertiaire alors que la densité de spin est largement distribuée sur le radical allylique. Il n'y a pas d'indications, soit expérimentale ou théorique, pour suggérer l'existence d'une interaction de liaison entre les portions cationiques et allyliques de ces cations radicalaires distoniques. Le clivage du noyau cyclobutane est irréversible. Le cation radicalaire du tricyclène (**18**) donne aussi des adduits 1 : 1 : 1 (nucléophile : cyclopropyle : aromatique). La régio- et la stéréochimie des adduits et la sélectivité du nucléophile indiquent toutes que le clivage du cation radicalaire ($\mathbf{18}^{+\cdot}$) est assisté par le nucléophile. Le cation radicalaire du nopol ($\mathbf{23}^{+\cdot}$) se clive aussi en cation radicalaire distonique. Le clivage du noyau cyclobutane doit être rapide car la cyclisation intramoléculaire 1,5-*endo* du groupe hydroxyle ne peut lui faire compétition.

[Traduit par la rédaction]

Can. J. Chem. Downloaded from www.nrcresearchpress.com by 195.246.54.202 on 09/08/12
For personal use only.

Introduction

In a typical photo-NOCAS reaction, irradiation of an acetonitrile–methanol (3:1) solution of 1-methylcyclohexene (**2**), 1,4-dicyanobenzene (**1**) and biphenyl (**3**) yields the photo-NOCAS adducts **4–7** (reaction [1]) (3). The *anti*-Markovnikov adducts **4** and **5** are the major products; minor products include the Markovnikov adducts **6** and **7**. Reaction occurs when the solution is irradiated in the absence of added biphenyl (**3**); however, the yield of products and the efficiency of the reaction are improved when this codonor is included in the irradiated solution. The proposed mechanism is summarized in Scheme 1 (4).

Reaction [1]

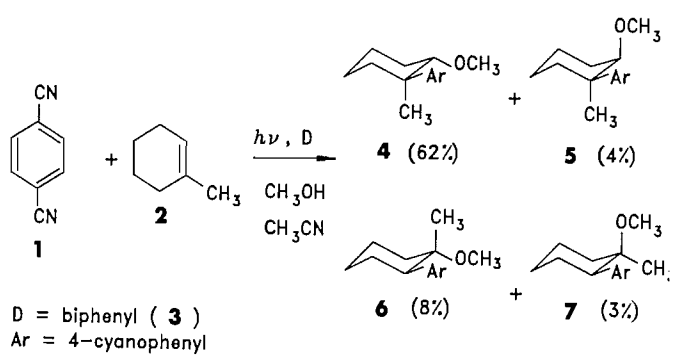

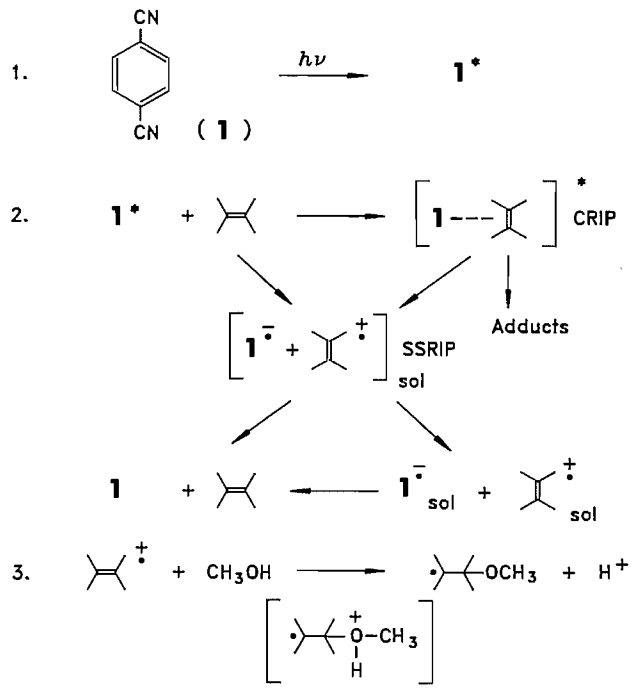

[1]This is also Part 31 of the series Radical Ions in Photochemistry; see refs. 1 and 2 for preceding parts of these series. A preliminary account of some of this work has been published (1*b*).

[2]Author to whom correspondence may be addressed.

Can. J. Chem. Downloaded from www.nrcresearchpress.com by 195.246.54.202 on 09/08/12
For personal use only.

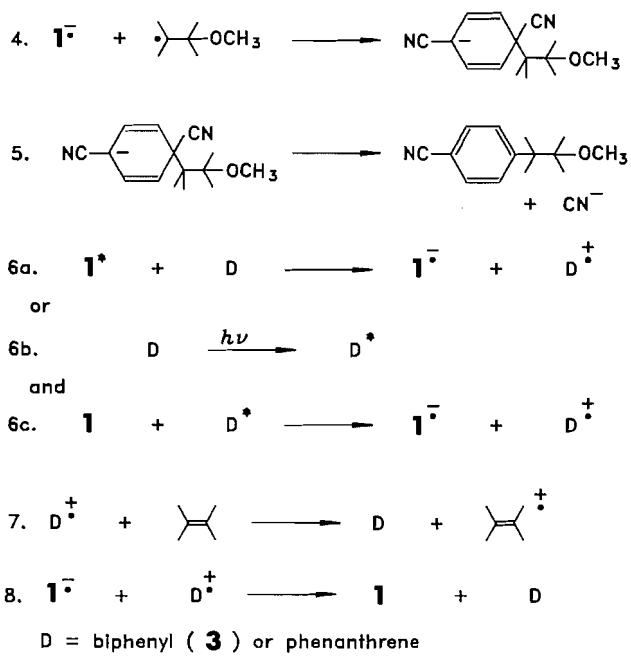

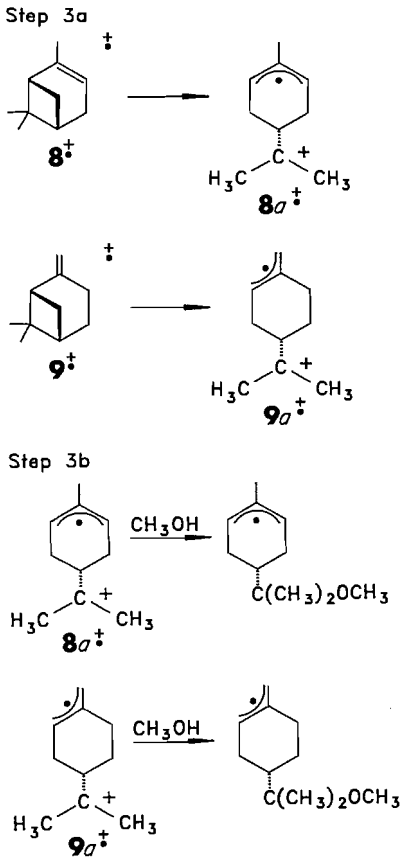

SCHEME 1

There were three initial objectives for this work: (*i*) to provide additional examples illustrating the scope and synthetic utility of the photo-NOCAS reaction; (*ii*) to add support for the proposed mechanism; and (*iii*) to learn more about the reactivity of the unusual intermediates involved.

This reaction is potentially useful for synthesis. A nucleophile, an olefin, and an aromatic compound are combined in one simple step. Two new bonds are made during the process. The products are often difficult to prepare by more traditional methods. Nevertheless, this procedure will not be considered generally in retrosynthetic analysis unless/until the scope and limitations of the reaction are well defined. Such an understanding is usually based upon knowledge of the reaction mechanism. In comparison to reactions involving the more common intermediates (carbocations, carbanions, and radicals), relatively little is known about the reactivity of radical ions. In the context of the present study, the reactivity of the intermediate carbocation and radical, formed as a result of electrophilic or radical addition to α- and β-pinene (**8** and **9**), has been determined (5, 6) and, in fact, could now be predicted. The cyclobutylcarbinyl cation and radical have been studied; both undergo rapid cyclobutane ring cleavage (7, 8). The reactivity of the radical cations of α- and β-pinene ($\mathbf{8}^{+\cdot}$ and $\mathbf{9}^{+\cdot}$) is less well understood (9). Will the cyclic-alkene radical cation remain intact or will the cyclobutane ring cleave? If the cyclobutane ring cleaves, what will be the charge and spin density distribution on the resulting distonic radical cation? If the cyclobutane ring cleaves, will cleavage be reversible, and will there be any bonding interaction between the radical and cationic centres of the distonic radical cation?

Results

Under the usual reaction conditions (1, 3), solutions of 1,4-dicyanobenzene (**1**) (0.05 M), biphenyl (**3**) (0.015 M), and α-pinene (**8**) or β-pinene (**9**) (0.1 M) in acetonitrile–methanol (3:1) were irradiated through a Pyrex filter with a medium-pressure mercury vapour lamp. Progress of the reaction was followed by capillary column gas chromatography using a mass selective detector (gc/ms). After more than 95% of **1** was consumed, the products were isolated by medium-pressure liquid chromatography on silica gel (mplc). The results are shown in reactions [2] and [3]. Yields are based upon 1,4-dicyanobenzene (**1**) as the limiting reagent.

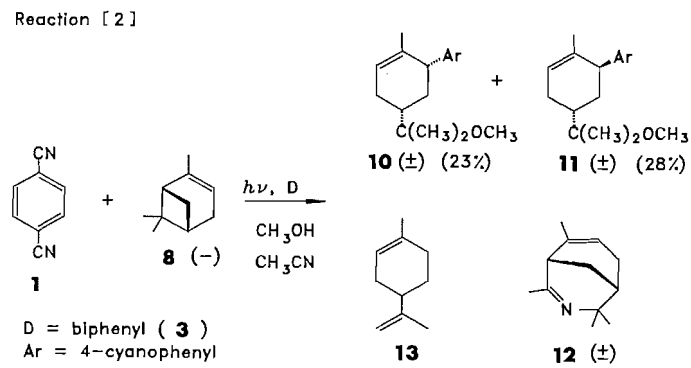

The photo-NOCAS products obtained from α-pinene (**8**), **10** and **11**, indicate that the cyclobutane ring has cleaved before the addition of methanol (reaction [2]). An additional product, imine **12**, is also formed from a ring-cleaved intermediate. Solutions of **10**, **11**, and **12** are optically inactive; these products are formed as racemic mixtures. A sample of α-pinene (**8**), recovered from the photolysate, showed no decrease in optical activity. Limonene (**13**) was identified (gc/ms, retention time, and fragmentation pattern) but was not isolated from the chromatographic column (mplc).

Three photo-NOCAS adducts (**14–16**) and the cyclic imine (**17**) are formed from β-pinene (**9**) under these conditions (reaction [3]). All of these products are optically active; presumable, with retention of configuration at C-5, that is, *S* from the laevorotatory enantiomer of β-pinene (**9**) (10). A sample of β-

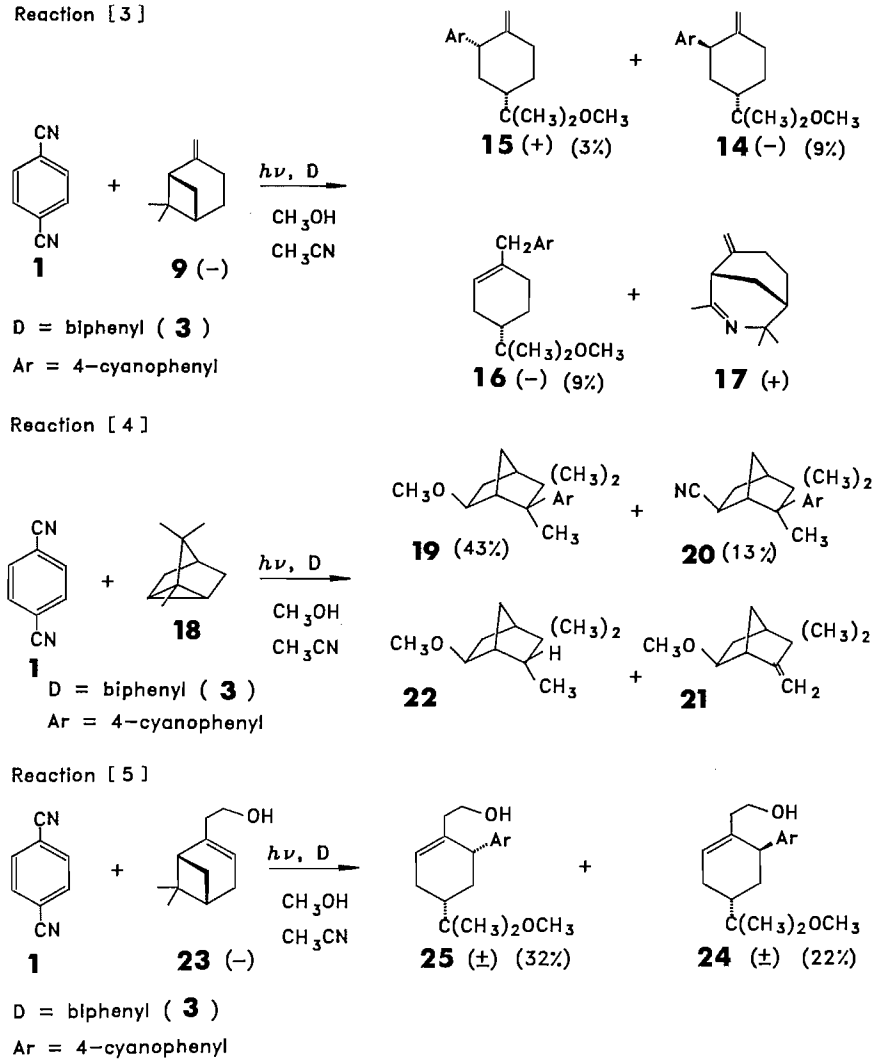

pinene (**9**) recovered from the crude photolysate had the same specific rotation as starting material.

Reactions [2] and [3] occur upon irradiation in the absence of added biphenyl (**3**); the ratio of the photo-NOCAS adducts and cyclic imine is unaffected. However, the yield of these products and the efficiency of reaction are increased upon the addition of this codonor. The polarity of the solvent also has an affect; the photo-NOCAS products were obtained, in the same ratio, from reaction [2] carried out in benzene–methanol (3:1), but the yield and efficiency were lower than when acetonitrile–methanol (3:1) was used as solvent.

Irradiation of a solution of 1,4-dicyanobenzene (**1**) (0.08 M), biphenyl (**3**) (0.08 M), and tricyclene (**18**) (0.1 M) in acetonitrile–methanol (3:1) gave two 1:1:1 adducts (**19** and **20**) as well as ethers (**21** and **22**) (reaction [4]). These products were not detected (gc/ms) in reaction [2]; nor were the photo-NOCAS adducts **14–16**, formed from α-pinene (**8**) in reaction [2], detected in this reaction. Little reaction occurred when a similar solution of **1** and **18**, without the codonor **3**, was irradiated.

When this irradiation was carried out under conditions identical to those described above (reaction [4]) except using acetonitrile–perdeuteriomethanol (3:1) as the solvent, the same four products were obtained; the mass spectra of **19**, **21**, and **22** reflect deuterium incorporation. For **19**, the base peak at 186 (*m/z*) due to $C_{12}H_{12}NO$ and the molecular ion peak at 269 due to $C_{18}H_{23}NO$ move to 189 and 272, consistent with the incorporation of three deuterium atoms on the methoxy methyl group. Also, for **21** the molecular ion ($C_{11}H_{18}O$) at 166 (*m/z*) is replaced by a peak at 169, indicative of three deuteria on the methoxy methyl group. In the mass spectrum of **22** the molecular ion ($C_{11}H_{20}O$) peak at 168 (*m/z*) and the second largest peak in the spectrum at 85 *m/z* (65%) due to C_5H_9O are replaced by peaks at 171 and 88, again indicative of incorporation of three (only) deuterium atoms. These observations provide evidence that the ethers **21** and **22** form by disproportionation of the intermediate radical; we will return to this point later. A solution of 1,4-dicyanobenzene (**1**) (0.06 M), biphenyl (**3**) (0.05 M), and (−) nopol (**23**) (0.1 M) in acetonitrile–methanol (3:1) was irradiated through a Pyrex filter with a medium pressure mercury vapour lamp (reaction [5]). The photo-NOCAS adducts **24** and **25** were isolated by dry-column flash chromatography (dcfc) on silica gel. Starting with laevorotatory nopol (**23**), neither **24** nor **25** showed any optical rotation; both are formed as the racemic mixture. There was no evidence for products resulting from intramolecular cyclization. Small amounts of an imine and of isomerization products, analogous to the imine **12** and limonene (**13**) formed in reaction [2], were detected (gc/ms) but were not isolated. When this irradiation was carried out in pure acetonitrile as solvent (no methanol), no volatile adducts (**1** + **23**) were detected (gc/ms).

Oxidation potentials, necessary for the discussion of the mechanism, were measured by cyclic voltammetry (Table 1).

Can. J. Chem. Downloaded from www.nrcresearchpress.com by 195.246.54.202 on 09/08/12
For personal use only.

Can. J. Chem. Downloaded from www.nrcresearchpress.com by 195.246.54.202 on 09/08/12
For personal use only.

TABLE 1. The oxidation potentials of some prospective donors and the calculated free energy change (ΔG) for the electron transfer process to the excited singlet excited state of 1,4-dicyanobenzene (**1**) as the acceptor

Donor	$E^{ox}_{1/2}$ (V)[a]	ΔG (kJ/mol)[b]
Biphenyl (**3**)	1.85	−75.1
α-Pinene (**8**)	1.75	−84.8
β-Pinene (**9**)	2.20	−41.4
Tricyclene (**18**)	2.31	−30.8
Nopol (**23**)	1.74	−85.8
Limonene (**13**)	2.15	—
1-Methylcyclohexene	1.93[c]	—
Methylenecyclohexane	>2.80	—

[a]Oxidation potentials, estimated as 0.028 V before the peak potential measured at a platinum electrode, relative to the saturated calomel electrode (sce) using tetraethylammonium perchlorate (0.1 M TEAP) as the electrolyte in acetonitrile (ref. 11).

[b]Based on the Weller equation (ref. 12); $E_{0,0}$ (**1**) = 408.4 kJ mol^{-1}, $E^{ox}_{1/2}$ (**1**) = −1.66 V. The Coulombic attraction term was taken to be 5.40 kJ mol^{-1} (ref. 4).

[c]Reference 3.

Structure determination

The mass spectra of the photo-NOCAS adducts (**10**, **11**, and **14–16**) from α-pinene (**8**) and β-pinene (**9**) (reactions [2] and [3]) all have base peaks at 73 *m/z* [-$C(CH_3)_2OCH_3$], evidence that the original four-membered ring has cleaved and the methoxy group is bonded to the isopropyl side chain, rather than to the ring. The ^{1}H and ^{13}C nmr spectra for the photo-NOCAS adducts **10** and **11** from α-pinene (**8**) have similar features. The stereochemical assignments were based on differences in the observed vicinal ^{1}H coupling constants. Adduct **10** was established as the *cis* isomer, having the benzylic hydrogen in the axial position, because of the large coupling constant observed (3.36 ppm, $J_{axial-axial}$ 9.3 Hz) compared to that of the *trans* isomer **11** in which the benzylic hydrogen shows up as a broad singlet (3.41 ppm).

The stereochemical assignments of **14** and **15** from β-pinene (**9**) were based on the same type of evidence. In the ^{1}H nmr spectrum of the product assigned as the *cis* isomer **15**, a large coupling constant (3.29 ppm, $J_{axial-axial}$ 11.3 Hz) was observed. In contrast, in the ^{1}H nmr spectrum of the *trans* isomer, a broad singlet was observed (3.77 ppm). In the ^{1}H nmr spectrum of **16**, a two-hydrogen singlet in the benzylic proton region (3.30 ppm) and evidence for only one vinyl hydrogen (5.49 ppm) are indicative of the assigned structure.

The structure assigned for the two 1:1:1 adducts, **19** and **20**, from reaction [4], were also based largely on an analysis of the ^{1}H nmr spectra. The bicyclo[2.2.1]heptane carbon skeleton was easily established. Stereochemical assignments were based largely upon observed nuclear Overhauser effects (nOe). For **19**, irradiation of the bridge hydrogens on C-7 (1.80 ppm) causes a significant increase in the intensity of the signal assigned to the *exo*-methyl group on C-5. The signal due to the methyl group on C-6 (1.24 ppm) was unaffected; therefore, this methyl group must be *endo*. Irradiation of the methyl group on C-6 causes an increase in the signal assigned to the hydrogen on C-2, which must therefore be *endo*, and in the aromatic region. Additional support for the C-2 hydrogen being in the *endo* position comes from the observed coupling pattern; the proton on C-2 (3.81 ppm) is not measurably coupled to the proton on C-1 and the small coupling constants (6.6, 2.0 Hz) observed between this proton and the protons on C-3 are typical of $J_{endo-endo}$ and $J_{endo-exo}$.

Similar reasoning was used for the stereochemical assignment of **20**. Irradiation of the methyl on C-6 (1.28 ppm) causes a definite nuclear Overhauser enhancement of the C-2 proton signal at 3.30 ppm: therefore, both the C-6 methyl and the C-2 proton must be *endo*. In support of this assignment, the signal due to the proton on C-2 is only weakly coupled (9.0, 4.2 Hz) to the vicinal protons on C-3.

The structures assigned to the ethers **21** and **22** were confirmed by alternative synthesis (Scheme 2) and by comparison of spectra (^{1}H nmr, ir) with those reported for the analogous alcohol (13). A study of the effect, on the ^{1}H nmr spectrum, of adding the shift reagent Eu(fod)$_3$ was useful for assigning the stereochemistry of **22**. This reagent is known to complex with the oxygen of the methoxy group and to shift signals of nearby hydrogens downfield (14). The observed order of the magnitude of this downfield shift was *exo* H-3 > H-1 > H on the carbon of the methoxy group > H-2; the effect on the other signals was relatively small.

The ^{1}H nmr spectra of the photo-NOCAS adducts **24** and **25**, obtained from (−) nopol (**23**) (reaction [5]) were similar to those of **10** and **11** from α-pinene (**8**) (reaction [2]) described above. Solutions of **24** and **25** were optically inactive. Both **24** and **25** are oils; they were converted into crystalline 3,5-dinitrobenzoate derivatives, **26** (*trans*) and **27** (*cis*), by a standard procedure (15). The structural assignments of **26** and **27**, based initially upon ^{1}H nmr spectra, were firmly established by X-ray crystallography on single crystals.[3]

Computational details

Ab initio molecular orbital calculations were carried out with the GAUSSIAN 86 (16) or GAUSSIAN 90 (17) series of programmes. Open-shell species were treated in the unrestricted Hartree–Fock (UHF) formalism. The charge and spin distributions were calculated by Mulliken population analysis (18). The limitations of this method have been discussed (19). The calculated (STO-3G) total energies are summarized in Table 2.

The calculations on α-pinene (**8**) and on the radical cation of α-pinene (**8**$^{+\cdot}$) were carried out at the STO-3G level with full

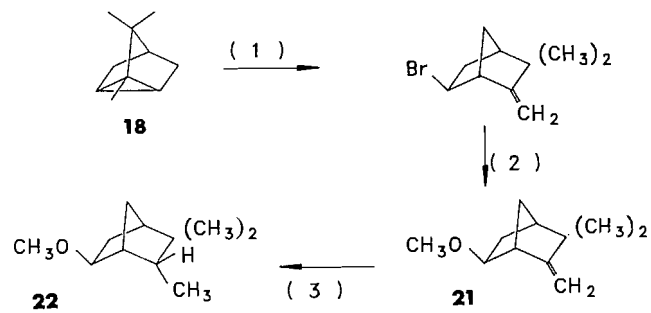

SCHEME 2

[3]These data may be purchased from: The Depository of Unpublished Data, Document Delivery, CISTI, National Research Council Canada, Ottawa, Canada K1A 0S2.

Details of data collection, structural analysis and refinement, and tables of interatomic distances and bond angles have also been deposited with the Cambridge Crystallographic Data Centre and can be obtained on request from the Director, Cambridge Crystallographic Data Centre, University Chemical Laboratory, 12 Union Road, Cambridge, CB2 1EZ, U.K.

TABLE 2. The calculated (STO-3G) total energies (au) for α-pinene (**8**), tricyclene (**18**), and related radical cations

	Total energy (au)
α-Pinene (**8**)	−383.38502
α-Pinene radical cation ($\mathbf{8}^{+\bullet}$) (ring-closed)	−383.18284
α-Pinene radical cation ($\mathbf{8}a^{+\bullet}$) (distonic)	−383.16633
α-Pinene radical cation ($\mathbf{8}b^{+\bullet}$) (distonic)	−383.16531
Tricyclene (**18**)	−383.42385
Tricyclene ($\mathbf{18}^{+\bullet}$)	−383.20017

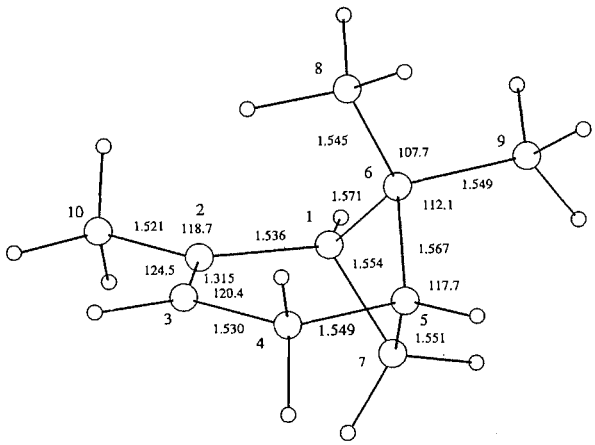

FIG. 1. The fully optimized (STO-3G) structure of α-pinene (**8**).

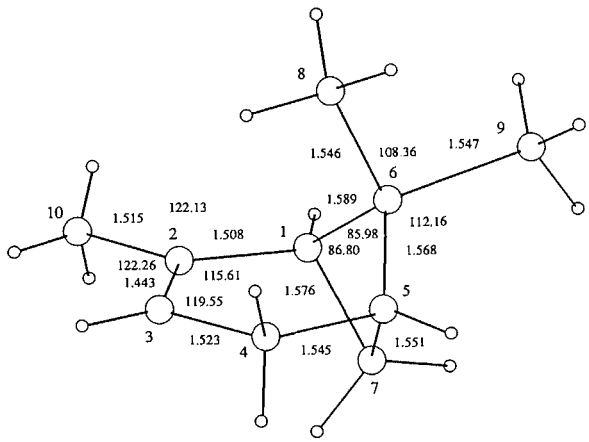

FIG. 2. The fully optimized (STO-3G) structure of the initial, ring-closed, radical cation of α-pinene ($\mathbf{8}^{+\cdot}$).

optimization of geometry. The optimized structures (Figs. 1 and 2) were confirmed to be minima by frequency calculation. The charge and spin distribution on $\mathbf{8}^{+\cdot}$ are listed in Table 3.

The ring-cleaved structure, the distonic radical cation of α-pinene ($\mathbf{8}^{+\cdot}$), could exist in at least three conformations: $\mathbf{8}a^{+\cdot}$, $\mathbf{8}b^{+\cdot}$, and $\mathbf{8}c^{+\cdot}$ (Fig. 3). Calculations on conformers $\mathbf{8}a^{+\cdot}$ and $\mathbf{8}b^{+\cdot}$ started with a C_s symmetry constraint; the alkyl moiety and the allylic moiety were perpendicular. A stationary point was identified which was then fully optimized. Figures 4 and 5 are of the fully optimized structures for conformers $\mathbf{8}a^{+\cdot}$ and $\mathbf{8}b^{+\cdot}$, and Tables 4 and 5 list the distribution of spin and charge. The fully optimized structure of conformer $\mathbf{8}a^{+\cdot}$ maintains C_s symmetry. In the optimized structure for conformer $\mathbf{8}b^{+\cdot}$, the plane of the alkyl moiety defined by C-8, C-9, and C-10 is not perpendicular to the plane of the allylic moiety C-1, C-2, and C3; the dihedral angle between C-5, C-7, C-8, and C-9 is ca. 30°.

TABLE 3. The charge and spin distribution calculated (STO-3G) for the radical cation of α-pinene ($\mathbf{8}^{+\bullet}$) (Fig. 2)

			Spin			
No.[a]	Group	Atomic charge	Carbon	Hydrogen(s)		
1	CH	0.027	−0.037	0.001		
2	C	0.207	0.302			
3	CH	0.201	0.777			
4	CH_2	0.110	−0.092	0.026	0.028	
5	CH	0.061	0.001			
6	C	0.058	0.031			
7	CH_2	0.074	0.029	0.002	0.003	
8	CH_3	0.025	0.006	0.000	0.000	−0.003
9	CH_3	0.056	−0.002	0.000	0.000	0.002
10	CH_3	0.181	−0.039	0.015	0.002	0.016

[a]Numbering of carbon atoms in Fig. 2.

TABLE 4. The charge and spin distribution calculated (STO-3G) for the distonic radical cation formed upon ring cleavage of the radical cation of α-pinene ($\mathbf{8}^{+\bullet}$) (Fig. 4)

			Spin			
No.[a]	Group	Atomic charge	Carbon	Hydrogen(s)		
1	C	0.008	−0.850			
2	CH	0.039	1.033	−0.078		
3	CH	0.039	1.032	−0.078		
4	CH_3	0.048	0.097	−0.028	−0.013	−0.012
5	CH_2	0.055	−0.123	0.017	0.036	
6	CH_2	0.055	−0.123	0.017	0.036	
7	CH	0.043	0.035	−0.003		
8	C	0.302	−0.005			
9	CH_3	0.205	−0.001	0.000	0.000	0.000
10	CH_3	0.206	0.000	0.000	0.000	0.000

[a]Numbering of carbon atoms in Fig. 4.

TABLE 5. The charge and spin distribution calculated (STO-3G) for the distonic radical cation formed upon ring cleavage of the radical cation of α-pinene ($\mathbf{8}b^{+\bullet}$) (Fig. 5)

			Spin			
No.[a]	Group	Atomic charge	Carbon	Hydrogen(s)		
1	C	0.000	−0.845			
2	CH	0.024	1.032	−0.078		
3	CH	0.022	1.022	−0.077		
4	CH_3	0.048	0.097	−0.028	−0.014	−0.011
5	CH_2	0.064	−0.124	0.019	0.038	
6	CH_2	0.080	−0.122	0.016	0.036	
7	CH	0.052	0.032	−0.004		
8	C	0.299	0.011			
9	CH_3	0.207	0.001	−0.001	0.000	0.001
10	CH_3	0.203	−0.001	0.001	0.000	0.000

[a]Numbering of carbon atoms in Fig. 5.

A convenient starting point for the calculation of conformer $\mathbf{8}c^{+\cdot}$ is the fully optimized structure for conformer $\mathbf{8}b^{+\cdot}$, revised by rotating the C-7, C-8 bond until the alkyl moiety and the allyl moiety were parallel. The fully optimized structure reverted to conformer $\mathbf{8}b^{+\cdot}$.

The *ab initio* calculations on tricyclene (**18**) and on the radical cation of tricyclene ($\mathbf{18}^{+\cdot}$) were also carried out with the STO-3G basis set; the open-shell, spin-unrestricted (UHF) pro-

Can. J. Chem. Downloaded from www.nrcresearchpress.com by 195.246.54.202 on 09/08/12
For personal use only.

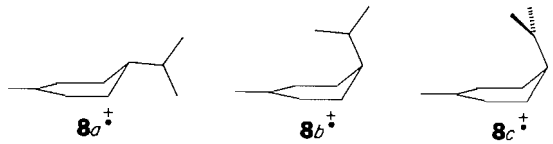

FIG. 3. The ring-cleaved distonic radical cation of α-pinene ($8^{+\cdot}$) can exist in three (at least) conformations $8a^{+\cdot}$, $8b^{+\cdot}$, and $8c^{+\cdot}$.

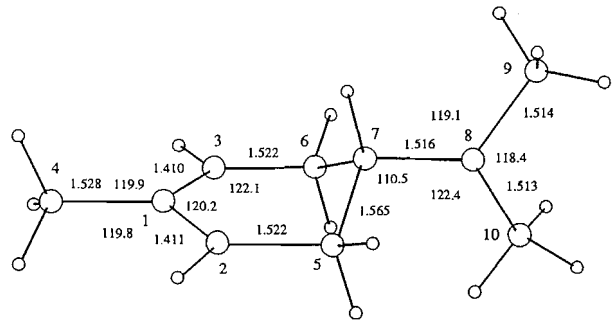

FIG. 4. The fully optimized (STO-3G) structure of the distonic radical cation of α-pinene ($8a^{+\cdot}$).

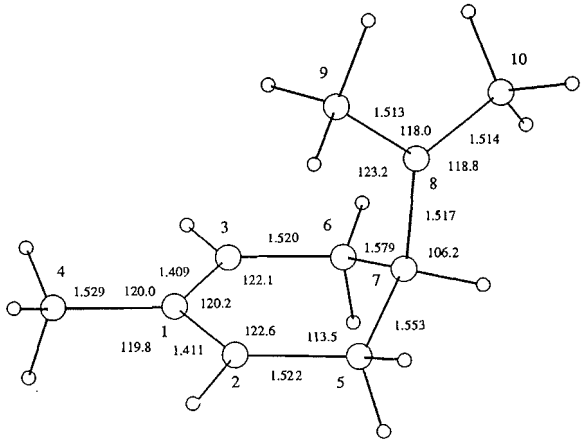

FIG. 5. The fully optimized (STO-3G) structure of the distonic radical cation of α-pinene ($8b^{+\cdot}$).

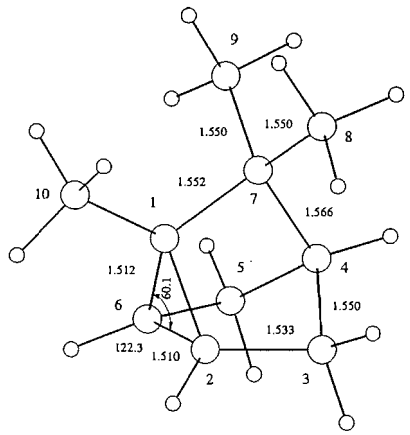

FIG. 6. The fully optimized (STO-3G) structure of tricyclene (**18**).

cedure was used for $18^{+\cdot}$. The fully optimized structure for **18**, shown in Fig. 6, has C_s symmetry. For the radical cation $18^{+\cdot}$, the structure was first optimized with a C_s symmetry constraint. Further calculation found there was one imaginary frequency; therefore, this symmetric stationary point is a transition state, not an energy minimum. The total energy of this structure was

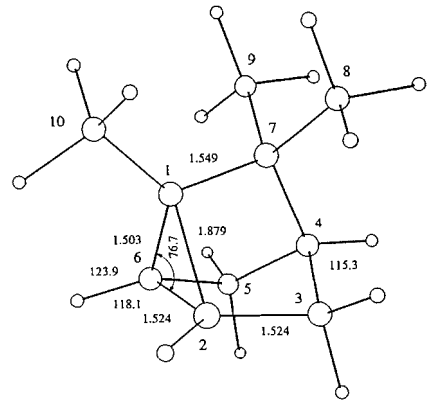

FIG. 7. The fully optimized (STO-3G) structure of the radical cation of tricyclene ($18^{+\cdot}$).

TABLE 6. The calculated (STO-3G) charge and spin distribution for the radical cation of tricyclene ($18^{+\cdot}$) (Fig. 7)

No.[a]	Group	Atomic charge	Spin			
			Carbon	Hydrogen(s)		
1	C	0.139	0.474			
2	CH	0.173	0.750	−0.055		
3	CH_2	0.103	−0.085	0.015	0.031	
4	CH	0.071	0.011	−0.002		
5	CH_2	0.100	0.039	−0.003	−0.002	
6	CH	0.094	−0.167	0.027		
7	C	0.038	−0.050			
8	CH_3	0.072	0.026	−0.002	0.002	−0.002
9	CH_3	0.058	0.012	−0.001	−0.001	−0.001
10	CH_3	0.151	−0.059	0.017	0.003	0.024

[a]Numbering of carbon atoms in Fig. 7.

found to be −383.19049 (au) and the distances between C-2, C-6 and C-1, C-2 (or C-1, C-6) are 1.439 Å and 1.692 Å, respectively.

We were unable to find a minimum for a ring-cleaved structure for $18^{+\cdot}$. Beginning with an initial structure without a three-membered ring, one where the distance between C-1 and C-2 was 2.5 Å and that between C-2 (or C-1) and C-6 was 1.5 Å, the calculation converged to an optimized structure that does have a three-membered ring ($18^{+\cdot}$); however, the C-1, C-2 bond length is quite long (1.879 Å) (Fig. 7). Further calculation on this structure for $18^{+\cdot}$ showed that it is a minimum. The energy for this fully optimized structure is lower than that for the structure with a symmetry plane by 25.2 kJ mol^{-1}). As expected for $18^{+\cdot}$, the positive charge is delocalized over the whole radical cation, and the spin is mainly localized across the lengthened C-1, C-2 bond; the less heavily substituted carbon (C2) has the greater spin density (Table 6).

Discussion

Reactions of α- and β-pinene (8 and 9) (reactions [2] and [3])

The salient features of the proposed mechanism (Scheme 1) remain intact. Initial excitation (step 1) involves the ^1L_b transition of 1,4-dicyanobenzene (**1**). The prospective donors, **8** and **9**, are transparent in the ultraviolet at wavelengths transmitted through Pyrex; the ^1L_b absorption band of **1** extends out to ca. 290 nm.

Electron transfer from **8** and **9** to the singlet excited state of **1**

Can. J. Chem. Downloaded from www.nrcresearchpress.com by 195.246.54.202 on 09/08/12
For personal use only.

Can. J. Chem. Downloaded from www.nrcresearchpress.com by 195.246.54.202 on 09/08/12
For personal use only.

is spontaneous (step 2). When the ΔG for electron transfer, calculated by the Weller equation (equation [6]), is exergonic by –20 kJ mol^{-1} or more, quenching of the excited singlet state by the electron transfer process is diffusion controlled (12). In this polar solvent, acetonitrile–methanol (3:1), electron transfer leads directly to the solvent-separated radical ion pair (SSRIP). Further solvation/separation is competitive with back electron transfer.

[6] (ref. 12) $\Delta G_{et} = F[E^{ox}_{1/2}(D) - E^{red}_{1/2}(A) - e/\epsilon\alpha] - E_{0,0}(A)$

The efficiency of the reaction and the yield of products are increased upon addition of the codonor biphenyl (**3**). The radical cation of biphenyl ($\mathbf{3}^{+\cdot}$) can accept an electron from **8** or **9** (step 7). The overall increase in efficiency of the reaction is attributed to a slower rate of back electron transfer within the SSRIP ($\mathbf{1}^{-\cdot}$ and $\mathbf{3}^{+\cdot}$), the result of a smaller reorganizational energy, which leads to a greater proportion of freely solvated radical ions (1, 20).

The next step in the proposed mechanism, addition of the nucleophile (methanol) to the radical cation $\mathbf{8}^{+\cdot}$ or $\mathbf{9}^{+\cdot}$ (step 3), must be slower than cleavage of the cyclobutane ring. The rate constant for the addition of methanol to the radical cation of alkyl-substituted alkenes is not known; however, the addition of methanol to the radical cation of aryl-substituted alkenes has been measured (21). Methanol adds to the radical cation of 1,1diphenylethylene with a rate constant 1.6×10^9 M^{-1} s^{-1}; more stable or more sterically hindered radical cations react more slowly (21*a*). There was no evidence of products expected from addition of methanol to the original double bond of $\mathbf{8}^{+\cdot}$ or to the terminal methylene carbon of $\mathbf{9}^{+\cdot}$.

The observed cyclobutane ring cleavage of $\mathbf{8}^{+\cdot}$ and $\mathbf{9}^{+\cdot}$ (step 3a) raises the question — are these cyclic radical cations minima? The *ab initio* calculations carried out on $\mathbf{8}^{+\cdot}$ indicate the initially formed radical cation is indeed a minimum (Table 2); in fact, the initially formed cyclic radical cation $\mathbf{8}^{+\cdot}$ is 0.01651 au (43 kJ mol^{-1}) more stable than the ring-cleaved distonic radical cation $\mathbf{8}a^{+\cdot}$. This order of stability, pertinent to the gas phase, may be reversed in polar solvent. Solvation of the more localized cationic centre of the distonic radical cation will play a major role in stabilizing $\mathbf{8}a^{+\cdot}$ and $\mathbf{9}a^{+\cdot}$. While the initial radical cations $\mathbf{8}^{+\cdot}$ and $\mathbf{9}^{+\cdot}$ may be shallow minima, cyclobutane ring cleavage (step 3a) must be rapid.

The oxidation potentials of α- and β-pinene (**8** and **9**), listed in Table 1, are significantly lower that those of the model compounds 1-methylcyclohexene and methylenecyclohexane. These anodic processes are not reversible. The oxidation potentials listed have been estimated from the peak potentials observed on the cyclic voltammograms with a 100 or 200 mV s^{-1} sweep rate (11). Therefore, these values do not have thermodynamic significance; in fact, the peak potentials for **8** and **9** may be significantly shifted as a result of rapid/concerted cyclobutane ring cleavage during the anodic process. Further study is required.

Reactions [2] and [3] are regioselective; cleavage of the cyclobutane ring (step 3a) affords a distonic radical cation, which reacts as a radical at the allylic moiety and as a carbocation at the tertiary alkyl moiety (step 3b). These observations are consistent with the general rule: cleavage of radical cations occurs selectively to give the carbocation of that fragment with the lower radical oxidation potential (3, 22). The oxidation potentials of the relevant allylic radicals are not known; nevertheless, there is good reason to believe that the oxidation of the tertiary alkyl radical is the lower. The oxidation potential of the *tert*-butyl radical is 0.09 V (sce) and the oxidation potential of the benzylic radical is 0.73 V (23). Even the cumyl radical has an oxidation potential of 0.16 V, which is still greater than that of the *tert*-butyl radical (23). The observed regioselectivity is also in agreement with the calculations of spin and charge densities on the distonic radical cation $\mathbf{8}a^{+\cdot}$ (Fig. 4 and Table 4). The spin density is largely delocalized over the allylic moiety and the positive charge is largely on the tertiary alkyl moiety.

The specific rotation of α-pinene (**8**) recovered after 95% conversion of **1** (reaction [2]) is essentially the same as before irradiation. Under these reaction conditions, cleavage of the radical cation $\mathbf{8}^{+\cdot}$ to $\mathbf{8}b^{+\cdot}$ (step 3a) must be irreversible; reaction of the distonic radical cation with methanol must be rapid. Furthermore, there is no evidence for any bonding interaction between the radical and cation centres in the distonic radical cation $\mathbf{8}b^{+\cdot}$ that might maintain chirality; the photo-NOCAS adducts **10** and **11** are racemic. The *ab initio* calculations also show that there is no interaction between the allylic radical and cationic moieties. The distances between C-8 and C-1 (3.551 Å) and between C-8 and C-1 and C-3 (3.295 and 3.171 Å) are too great for appreciable interaction (Fig. 5). These observations contrast with the results obtained upon γ-radiation of α-pinene (**8**) where racemization was observed (9*e*).

The reduction potentials of the intermediate allylic radicals must be more negative than that of **1** (-1.66 V); otherwise, electron transfer would occur and the allylic radical would thus be reduced to the allylic anion. The reduction potentials of these radicals are not known, but the results seem reasonable. The unsubstituted allyl radical is reduced at −1.63 V (sce) and alkyl substitution at the terminal position will make the reduction potential more negative by ca. 0.2 V (24).

Coupling of the allylic radicals with the radical anion of 1,4-dicyanobenzene ($\mathbf{1}^{-\cdot}$), at the *ipso* position, shows little stereo- or regioselectivity; **10** and **11** are formed in almost equal amounts and **14** and **16** are only slightly favoured over **15**. The preference for formation of the *trans* adducts **11** and **14** indicates that coupling from the *pseudo*-axial position is slightly favoured.

In addition to the photo-NOCAS adducts, two interesting products incorporating acetonitrile, imines **12** and **17**, are formed in reactions [2] and [3]. These products also derive from the distonic radical cations $\mathbf{8}a^{+\cdot}$ and $\mathbf{9}a^{+\cdot}$. The regiochemistry of **12** and **17** is consistent with initial attack of the cationic centres of the distonic radical cations on the nitrogen of the cyano group. These products have been observed upon electrochemical oxidation of the pinenes (**8** and **9**) (9*b*,*c*,*d*).

The mechanism for formation of the rearrangement product limonene (**13**) from α-pinene (**8**) in reaction [2] is also of interest. The triplet excited state of α-pinene (**8**), generated by triplet energy transfer using acetophenone as a photosensitizer (triplet energy transfer), gives *cis*- and *trans*-ocimene (**28**) as the major rearrangement products; limonene (**13**) was a minor product (reaction [7]) (25*a*). Limonene (**13**) is also a minor product

Reaction [7]

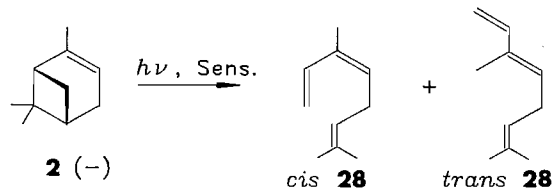

Sens. = acetophenone

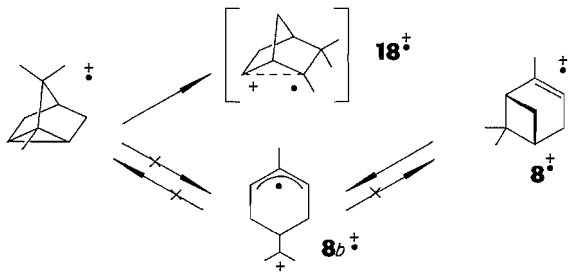

FIG. 8. The radical cations of α-pinene ($\mathbf{8}^{+\cdot}$) and tricyclene ($\mathbf{18}^{+\cdot}$) are related.

from the direct irradiation of α-pinene (**8**) (25*b*). We believe formation of **13** in reaction [2] also involves the radical cation $\mathbf{8}b^{+\cdot}$. A likely mechanism for formation of **13** entails a proton shift from one of the methyl groups of the tertiary cation to the allylic radical. The *ab initio* calculations indicate that one of the methyl hydrogens is close to the allylic radical; the C-3, H distance is only 2.5 Å in $\mathbf{8}^{+\cdot}$ and the C-2, H distance is only 2.7 Å in $\mathbf{8}b^{+\cdot}$ (Figs. 2 and 5).

Formation of this rearrangement product (**13**) in reaction [2] originally (before the structures of the adducts were firmly established) raised the possibility that the photo-NOCAS adducts **10** and **11** actually derive from secondary reaction of **13**. Irradiation of acetonitrile–methanol solutions of **1**, **3**, and **13** under these conditions does indeed lead to formation of photo-NOCAS adducts; however, these adducts are different from those obtained in reaction [2].[4]

Reaction of tricyclene (18) (reaction [4])

The radical cations of α-pinene ($\mathbf{8}^{+\cdot}$) and tricyclene ($\mathbf{18}^{+\cdot}$) are related (Fig. 8). A strong bonding interaction between the cation and the central carbon of the allylic radical in the distonic radical cation $\mathbf{8}b^{+\cdot}$ could lead to ring closure and formation of $\mathbf{18}^{+\cdot}$. Indeed, the calculations indicate that $\mathbf{18}^{+\cdot}$ is more stable (88.9 kJ mol^{-1}) than the distonic radical cation $\mathbf{8}b^{+\cdot}$, even more stable than $\mathbf{8}^{+\cdot}$ (45.5 kJ mol^{-1}) (Table 2). Nevertheless, the products from reaction [2] indicate that there is no interconversion of these radical cations.

The fact that only the *exo* isomers, **19–22**, are formed in reaction [4] suggests cyclopropyl ring opening is assisted by nucleophilic attack. The observed regiochemistry is also consistent with this mechanism; nucleophilic attack occurs at the less hindered centre (C-2, Fig. 7). Formation of the nitrile **20** as a major product, even though the only cyanide ion present is that generated during the rearomatization step (step 5), is also consistent with involvement of nucleophile during the cleavage step. Cyanide ion is significantly more nucleophilic than methanol; the rate of addition of methanol to $\mathbf{18}^{+\cdot}$ must be several orders of magnitude slower that addition of cyanide ion (21*b*, 26).

The calculations are in accord with these observations. The radical cation $\mathbf{18}^{+\cdot}$ has the three-membered ring still intact; the long C-1, C-2 bond (1.88 Å) bears a major portion of the spin and charge densities, with the positive charge largely on C-2 where nucleophilic attack occurs.

The ethers **21** and **22** result from disproportionation of the tertiary alkyl radical intermediate. An alternative mechanism for the formation of **22**, reduction of the intermediate tertiary radical by electron transfer from the 1,4-dicyanobenzene radical anion ($\mathbf{1}^{-\cdot}$), followed by protonation of the resulting anion, is inconsistent with the incorporation of only three deuterium atoms upon irradiation in acetonitrile–perdeuteriomethanol (27). The reduction potential of the tertiary alkyl radical is more negative that the reduction potential of **1** (−1.66 V).

Reaction with (−) nopol (23) (reaction [5])

The radical cation of α-pinene ($\mathbf{8}^{+\cdot}$) apparently undergoes rapid cleavage of the cyclobutane ring giving the distonic radical cation $\mathbf{8}b^{+\cdot}$. Yet, the *ab initio* calculations show that the initial radical cation $\mathbf{8}^{+\cdot}$ is significantly (43.4 kJ mol^{-1}) more stable than the distonic radical cation $\mathbf{8}b^{+\cdot}$. This dichotomy has been explained on the basis of a solvent effect; the localized cationic centre of the distonic radical cation will be stabilized by solvent interaction. Nevertheless, a rapid reaction with nucleophile might trap the initially formed radical cation before the cyclobutane ring cleaves. It was with this possibility in mind that the reactivity of nopol (**23**) was investigated. Intramolecular 1,5-*endo* cyclization of the hydroxyl group with the radical cation $\mathbf{23}^{+\cdot}$ might be rapid enough to compete with ring cleavage.[5]

When the irradiation was carried out in the usual mixed solvent system, acetonitrile–methanol (3:1), the products **24** and **25** expected from the ring-cleaved distonic radical cation were obtained (reaction [5]). Both **24** and **25** are formed as the racemic mixtures; the distonic radical cation $\mathbf{23}^{+\cdot}$ is achiral. Irradiation in pure acetonitrile did not give cyclized products. Clearly, ring opening of the initially formed radical cation is more rapid that 1,5-*endo* cyclization.

Experimental

General methods

The ^{1}H and ^{13}C nmr spectra were recorded on either a Nicolet 360 NB (361.1 or 90.8 MHz) or a Bruker AC 250 (250.1 or 62.9 MHz) nmr spectrometer, and are reported in parts per million (ppm) to higher frequency from tetramethylsilane. Infrared spectra (ir) were recorded on either an air-purged Perkin–Elmer 180 or on a Nicolet 205 infrared spectrometer and are reported in wavenumbers (ν) relative to the 1602 cm^{-1} absorption of polystyrene film. Optical activity was determined with a Perkin–Elmer model 141 polarimeter using ca. 1% solutions in $CHCl_3$. Exact mass determinations were carried out using a ZAB-E spectrometer. Elemental analyses were performed by Canadian Microanalytical Services Inc., Delta, B.C., and agreed to within ±0.3 of the calculated values. Melting points were determined using a Cybron Corporation Thermolyne melting point apparatus linked to a digital thermocouple, and were corrected.

The photo-NOCAS products were isolated by medium-pressure liquid chromatography (mplc) using a 2.5 cm × 1 m column packed with thin-layer chromatography (tlc) grade silica gel (Merck) at 15 psi helium (1 psi = 6.9 kPa). The chromatograms were usually developed either with a hexane – methylene chloride or hexane – 50% diethyl ether in hexane linear solvent gradient. The eluent was monitored and collected by a uv spectrometer – fraction collector. Dry column flash chromatography (dcfc) was performed using tlc grade silica gel

[4]Limonene (**13**) can be viewed as a 1,5-diene; the radical cation of 2,5-dimethyl-1,5-hexadiene forms photo-NOCAS adducts indicative of 1,6-*endo*, *endo* cyclization. Limonene (**13**) forms photo-NOCAS adducts with methanol and 1,4-dicyanobenzene (**1**) analogous to those formed from 1-methylcyclohexene (**2**) (reaction [1]); we found no evidence for cyclization of the diene radical cation ($\mathbf{13}^{+\cdot}$) (D.R. Arnold and D. Connor, unpublished results).

[5]Cyclization, 1,5-*endo*, does compete favourably with intermolecular reaction with methanol with the radical cation of 2-(1-cyclohexen-1-yl)ethanol (X. Du and D.R. Arnold, unpublished results).

Can. J. Chem. Downloaded from www.nrcresearchpress.com by 195.246.54.202 on 09/08/12
For personal use only.

Can. J. Chem. Downloaded from www.nrcresearchpress.com by 195.246.54.202 on 09/08/12
For personal use only.

(Merck) (28). Preparative gas chromatography (prep-gc) was carried out on a Wilkens Aerograph A-700 instrument using a 3/8 in. × 10 ft aluminum column packed with 40% SE-30 on Chromosorb W 60/80 NAW.

Materials

(1*S*)-(−)-α-Pinene (**8**), $[\alpha]_D^{20°C}$ −50.7 (neat), (1*S*)-(−)-β-pinene (**9**), $[\alpha]_D^{20°C}$ −21 (neat), (*R*)-(+)-limonene (**13**), $[\alpha]_D^{20°C}$ + 123 (neat), tricyclene (**18**) (99%), and (1*R*)-(−)-nopol (**23**) (98%) were obtained from Aldrich. These compounds were used as received except samples used for the oxidation potential measurements were purified by prep-gc. The shift reagent, tris(6,6,7,7,8,8,8,)heptafluoro-2,2-dimethyl-3,5-octanedionato)europium ($Eu(fod)_3$), was obtained from Norell Chemical Co., Inc.

Cyclic voltammetric measurements

Oxidation potentials were measured by cyclic voltammetry using an apparatus similar to that previously described (29). Since the anodic wave was irreversible, the half-wave potential was taken as 0.028 V before the anodic peak potential (11).

Irradiations

Irradiations were generally carried out using a CGE 1-kW medium-pressure mercury vapour lamp contained in a water-cooled quartz immersion well. The temperature was maintained at 10°C. The solvent generally was acetonitrile–methanol (3:1 by volume) at a typical concentration of 1,4-dicyanobenzene (**1**) 0.05 M and olefin of 0.1 M. The concentration of biphenyl (**3**) varied over the range 0.02–0.1 M. Solutions were placed in 2 cm i.d. Pyrex tubes or 5 mm Pyrex nmr tubes, degassed by ebullition with dry nitrogen and sealed.

Formation of photo-NOCAS adducts from methanol, α-pinene (8), and 1,4-dicyanobenzene (1) (reaction [2])

A solution of α-pinene (**8**) 3.05 g (22.4 mmol), 1,4-dicyanobenzene (**1**) 1.44 g (11.2 mmol), and biphenyl (**3**) 0.52 g (3.4 mmol) in 160 mL acetonitrile–methanol (3:1) was degassed by nitrogen ebullition for 5 min and irradiated through Pyrex for 72 h. The volatile components of the photolysate, removed by distillation, included **8** and isomerization products (gc/ms). The major isomerization product has a retention time (gc/fid) and mass spectrum (gc/ms) identical with those of an authentic sample of limonene (**13**). The specific rotation of the starting material **8** was $[\alpha]_D^{20°C}$ −56.7 ($CHCl_3$); a sample of **8** isolated (prep-gc) from the reaction mixture, after 95% consumption of **1**, had $[\alpha]_D^{20°C}$ −54.4 ($CHCl_3$). The nonvolatile residue was separated by mplc using the hexanes – methylene chloride solvent gradient. The photo-NOCAS products were eluted, as oils, in the order **10**, then **11**. In addition to the photo-NOCAS products and limonene (**13**), another major product (**12**) was eluted from the column with ethyl acetate or with a methylene chloride – methanol solvent gradient. The crude yield of **12** ranges between 20 and 35% (based on the initial amount of **8**). A pure sample of **12** was obtained by prep-gc.

cis-6-(4-Cyanophenyl)-4-(1-methoxy-1-methylethyl)-1-methylcyclohexene (**10**, 23%); ir (liq. film, NaCl, P.-E.) ν: 3033 (w), 2970 (s), 2933 (s), 2827 (m), 2228 (s), 1607 (s), 1503 (s), 1453 (m), 1381 (s), 1365 (s), 1150 (s), 1076 (s), 840 (s); ^{1}H nmr ($CDCl_3$, 360NB) δ: 7.58 (d, 2H, *J* = 8.2 Hz, arom), 7.27 (d, 2H, *J* = 8.2 Hz, arom), 5.69 (d, 1H *J* = 4.32 Hz, =CH), 3.36 (m, 1H, *J* = 9.3 Hz, benzylic proton), 3.18 (s, 3H, OCH_3), 2.10–1.84 (m, 3H), 1.38 (s, 3H, $=CCH_3$), 1.31–1.20 (m, 2H), 1.11 (s, 3H), 1.09 (s, 3H); ^{13}C nmr ($CDCl_3$, 360NB) δ: 151.69 (s, 1C, arom), 133.77 (q, 1C, *J* = 5.2 Hz, =C), 132.20 (dd, 2C, *J* = 5.7 Hz, 164.2 Hz, arom), 128.89 (dd, 2C, *J* = 4.5 Hz, 164.8 Hz, arom), 125.35 (dd, *J* = 4 Hz, 154.1 Hz, =CH), 119.01 (d, *J* = 4.7 Hz, CN), 109.82 (t, *J* = 8.8 Hz, 1C, arom), 76.14 (s, 1C), 48.81 (q, *J* = 139.9 Hz, OCH_3), 48.81 (d, *J* = 130.3 Hz, CH), 42.45 (d, *J* = 126.4 Hz, CH), 35.41 (t, *J* = 128.5 Hz, CH_2), 27.15 (t, *J* = 127.5 Hz, CH_2), 22.28 (q, *J* = 125.3 Hz, CH_3), 21.52 (q, *J* = 127.9 Hz, CH_3), 21.48 (q, *J* = 125.5 Hz, CH_3); ms *m/z*: 269 (0.10), 254 (0.17), 237 (3.4), 194 (5.4), 154 (3.8), 116 (4.1), 93 (3.9), 77 (4.1), 74 (3.8), 73 (100). Anal. calcd. for $C_{18}H_{23}NO$: C 80.25, H 8.61, N 5.20; found: C 79.94; H 8.38, N 5.38.

trans-6-(4-Cyanophenyl)-4-(1-methoxy-1-methylethyl)-1-methylcyclohexene (**11**, 28%); ir (KBr disk, P.-E.) ν: 3034 (w), 2972 (s), 2933 (s), 2827 (m), 2228 (s), 1607 (s), 1502 (s), 1452 (m), 1382 (s), 1364 (s), 1154 (s), 1074 (s), 900 (m), 840 (s) 806 (m); ^{1}H nmr ($CDCl_3$, 360NB) δ: 7.59 (d, 8.2 Hz, 2H, arom), 7.31 (d, 8.4 Hz, 2H, arom), 5.78–5.77 (m, 1H, =CH), 3.41 (s, 1H, ArCH), 2.83 (s, 3H, OCH_3), 2.11–1.61 (m, 5H), 1.59 (d, 1.05 Hz, 3H, $=CCH_3$), 1.01 (s, 3H, CH_3), 0.97 (s, 3H, CH_3); ^{13}C nmr ($CDCl_3$, 360NB) δ: 150.43 (s, arom), 132.52 (m, small coupling, arom), 131.93 (dd, 5.5, 163.9 Hz, arom), 129.28 (d, 159.7 Hz, arom), 125.55 (dd, 4.2 Hz, 153.5 Hz, =CH), 119.08 (s, CN), 109.74 (t, 8.8 Hz, arom), 75.95 (s, tertiary carbon), 48.29 (q, 140.4 Hz, OCH_3), 45.91 (d, 128.0 Hz, CH), 34.45 (d, 124.0 Hz, CH), 32.17 (t, 131 Hz, CH_2), 27.08 (t, 126.0 Hz, CH_2), 22.43 (q, 128.0 Hz, CH_3), 22.12 (q, 125.5 Hz, CH_3), 22.05 (q, 129.0 Hz, CH_3); ms *m/z*: 237 (3.9), 194 (10.02), 154 (3.7), 116 (3.9), 91 (3.0), 77 (3.9), 74 (3.9), 73 (100).

A sample of **11** was further purified by additional chromatography (mplc) and then bulb-to-bulb distillation. A colourless crystalline sample was obtained, mp 57.5°C. Anal. calcd. for $C_{18}H_{23}NO$: C 80.25, H 8.61, N 5.20, found; C 80.38, H 8.32, N 5.34.

Imine **12** is a known compound (9*b*,*c*): ir (liq. film, NaCl, P.-E.) ν: 3035(w), 2964 (s), 2935 (s), 2915 (s), 2870 (m), 2838 (m), 1667 (s), 1455 (s), 1382 (m), 1330 (m), 1295 (m), 867 (s), 782 (m); ^{1}H nmr ($CDCl_3$, 360NB) δ: 5.35 (m, 1H, *w1/2* = 9.3 Hz, =CH), 2.51 (s, 1H, br $w_{1/2}$ = 7.4 Hz), 2.23 (m, 1H, 19.1 Hz, AB pattern), 2.17 (m, 1H, 19.1 Hz, AB pattern), 2.05 (s, 3H), 1.86 (m, 1H), 1.84 (m, 1H, 11.1 Hz), 1.82 (d, 3H, 1.58 Hz), 1.56 (m, 1H, 11.1 Hz), 1.21 (s, 3H), 1.15 (s, 3H); ^{13}C nmr ($CDCl_3$, 360NB) δ: 167.15, 134.48, 122.23, 58.50, 40.30, 33.35, 31.72, 28.81, 28.22, 27.92, 25.46, 23.90. These spectra (ir, ^{1}H nmr, ^{13}C nmr) were identical to spectra provided by B. Delpech (9*b*,*c*). ms *m/z*: 177 (2), 136 (11), 121 (5), 94 (13), 93 (100), 92 (42), 91 (33), 80 (11), 79 (19), 77 (32), 65 (15).

Formation of photo-NOCAS adducts from methanol, β-pinene (9), and 1,4-dicyanobenzene (1) (reaction [3])

The procedure used was similar to that described above for the preparation of adducts from α-pinene (**8**). The specific rotation of the starting material **9** was $[\alpha]_D^{20°C}$ −15.5 ($CHCl_3$); a sample of **9** isolated (prep-gc) from the reaction mixture after ca. 90% of **1** was consumed had $[\alpha]_D^{20°C}$ −15.9 ($CHCl_3$). In this case, only traces of isomerization products of **9** were detected (gc/ms). The crude photolysate was partly separated by mplc eluting with the hexanes – dichloromethane solvent gradient. Fractions containing mixtures of photo-NOCAS products were combined and rechromatographed (mplc) with the hexane – 50% diethyl ether, hexane solvent gradient. Three photo-NOCAS adducts were eluted in the order **14**, **16**, and **15**, obtained as colourless oils. Further elution of the column with ethyl acetate gave imine **17** in 30% yield (based upon β-pinene (**9**)). The imine was further purified by prep-gc.

cis-2-(4-Cyanophenyl)-4-(1-methoxy-1-methylethyl)-1-methylenecyclohexane (**15**, 3%); $[\alpha]_D^{20°C}$ −51.9 ($CHCl_3$); ^{1}H nmr ($CDCl_3$, 360NB) δ: 7.60 (d, 8.2 Hz, 2H, arom), 7.23 (d, 8.2 Hz, 2H, arom), 4.72 (d, 1.5 Hz, 1H, vinyl proton), 3.88 (d, 1.5 Hz, 1H, vinyl proton), 3.29 (m, 1.7 Hz, 11.3 Hz, 1H, ArCH), 3.19 (s, 3H, OCH_3), 2.54 (m, 1H, 13.3 Hz), 2.20 (m, 1H), 2.03–1.92 (m, 2H), 1.86–1.78 (m, 1H), 1.50 (ddd, 1H, 12.3, 12.3, 12.2), 1.26 (dddd, 1H, 12.9, 12.9, 12.9, 4.0), 1.15 (s, 3H, CH_3), 1.12 (s, 3H, CH_3); ^{13}C nmr ($CDCl_3$, 360NB) δ: 151.50 (d, 4.0 Hz, arom), 148.99 (d, 6.9 Hz, =C), 131.97 (dd, 4.7 Hz, 159.4 Hz, arom), 129.52 (d, 160.4 Hz, arom), 119.06 (s, CN), 110.11 (d, 2.8 Hz, arom), 108.57 (t, 145.8 Hz, $=CH_2$), 76.37 (s, tertiary carbon),50.05 (q, 140.4 Hz, OCH_3), 48.79 (d, 125.1 Hz, ArCH), 46.31 (d, 127.2 Hz, CH), 36.21 (t, 126.7 Hz, CH_2), 34.59 (t, 131.1 Hz, CH_2), 28.21 (t, 125.3 Hz, CH_2), 22.43 (q, 125.5 Hz, CH_3), 21.95 (q, 124.6 Hz, CH_3). ms *m/z*: 237 (1.8), 194 (3.5), 140 (3.1) 127 (2.1) 116 (3.1), 74 (3.9), 73 (100). Anal. calcd. for $C_{18}H_{23}NO$: C 80.25, H 8.61, N 5.20; found: C 80.10, H 8.61, N 5.53.

trans-2-(4-Cyanophenyl)-4-(1-methoxy-1-methylethyl)-1-methylenecyclohexane (**14**, 9%): $[\alpha]_D^{20°C}$ +6.7 ($CHCl_3$); ir (liq. film, NaCl, Nicolet) ν: 3040 (w), 2973 (s), 2936 (s), 2899 (s), 2830 (m), 2228 (s),

Can. J. Chem. Downloaded from www.nrcresearchpress.com by 195.246.54.202 on 09/08/12
For personal use only.

1607 (m), 1505 (m), 1466 (w), 1382 (m), 1365 (m), 1144 (m), 1078 (s), 823 (w); ^{1}H nmr ($CDCl_3$, 360 NB) δ: 7.61 (d, 8.4 Hz, 2H, arom), 7.45 (d, 8.1 Hz, 2H, arom), 5.00 (dd, 2.0 Hz, 1H, =CH), 4.90 (dd, 1.0, 2.0 Hz, 1H, =CH), 3.77 (br s, 1H, Arch), 3.12 (s, 3H, OCH_3), 2.52 (m, 1H, =CCH), 2.35 (m, 1H, =CCH), 2.02 (m, 1H, O-CCH), 1.76 (m, 1H, CH), 1.68–1.57 (m, 2H, CH_2), 1.15 (m, 1H, CH), 1.10 (s, 3H, CH_3), 1.05 (s, 3H, CH_3); ^{13}C nmr ($CDCl_3$, 360NB) δ: 148.67 (s, arom), 148.33 (s, =C), 132.08 (dd, 5.4 Hz, 162.7 Hz, arom), 128.14 (d, 161.3 Hz, arom), 119.08 (s, CN), 111.98 (t, 153.1 Hz, =C), 109.52 (s, arom), 76.37 (s, tertiary carbon), 48.79 (q, 140.1 Hz, OCH_3), 46.70 (d, 132.1 Hz, ArCH), 39.93 (d, 124.1 Hz, CH), 31.96 (t, 133.2 Hz, CH_2), 31.34 (t, 130.4 Hz, CH_2), 29.07 (t, 130.4 Hz, CH_2), 22.32 (q, 124.7 Hz, CH_3), 21.83 (q, 125.5 Hz, CH_3). ms *m/z*: 254 (0.4), 237 (2.4), 194 (6.1), 116 (3.1), 74 (5.0), 73 (100). Anal. calcd. for $C_{18}H_{23}NO$: C 80.25, H 8.61, N 5.20; found: C 80.34, H 8.70, N 5.36.

1-(4-Cyanophenylmethyl)-4-(1-methoxy-1-methylethyl)cyclohexene (**16**, 9%); $[\alpha]_D^{20°C}$ −138.6 ($CHCl_3$); ir (liq. film, NaCl, Nicolet) ν: 3041 (w), 2973 (s), 2936 (s), 2899 (s), 2830 (m), 2228 (s), 1607 (m), 1503 (m), 1467 (w), 1381 (m), 1364 (m), 1143 (m), 1079 (s), 822 (w); ^{1}H nmr ($CDCl_3$, 360NB) δ: 7.56 (d, 8.2 Hz, 2H, arom), 7.27 (d, 8.2 Hz, 2H, arom), 5.49 (d, 5.1 Hz, 1H, =CH), 3.30 (s, 2H, $ArCH_2$), 3.17 (s, 3H, OCH_3), 2.10–1.60 (m, 6H), 1.21 (m, 1H), 1.09 (s, 6H, $2CH_3$); ^{13}C nmr ($CDCl_3$, 360NB), δ: 146.08 (s, arom), 135.77 (d, 6.4 Hz, =C), 132.03 (dd, 4.7 Hz, 159.3 Hz, arom), 129.56 (dd, 4.7 Hz, 158.8 Hz, arom), 124.09 (d, 155.2 Hz, =CH), 119.09 (s, CN), 109.75 (s, arom), 76.46 (s, tertiary carbon), 48.76 (q, 140.2 Hz, OCH_3), 44.16 (t, 125.5 Hz, $ArCH_2$), 41.70 (d, 121.9 Hz, CH), 29.07 (t, 124.2 Hz, CH_2), 26.87 (t, 125.6 Hz, CH_2), 23.78 (t, 126.9 Hz, CH_2), 22.19 (q, 126.0 Hz, CH_3), 21.83 (q, 124.9 Hz, CH_3). ms *m/z*: 254 (1.0), 237 (24.5), 121 (16.9), 116 (17.3), 79 (7.0), 73 (100). Anal. calcd. for $C_{18}H_{23}NO$: C 80.25, H 8.61, N 5.20; found: C 80.13, H 8.45, N 5.33.

Imine **17** is a known compound (*9b,c*): $[\alpha]_D^{20°C}$ +769.4 ($CHCl_3$); ir (liq. film, P.-E.) ν: 3067 (w), 2972 (s), 2934 (s), 2863 (m), 1668 (m), 1649 (s), 1455 (m), 1361 (m), 1286 (m), 1242 (m), 869 (m); ^{1}H nmr ($CDCl_3$, 360NB) δ: 4.76 (s. 1H, br $w_{1/2}$ = 3.8 Hz, =CH), 4.12 (s, 1H, br $w_{1/2}$ = 4.7 Hz, =CH), 2.82 (m, $w_{1/2}$ = 7.4 Hz, 1H, 3.0 Hz), 2.06 (dddd, 1H, 12.5, 2.6, 2.7, 3.5 Hz), 2.08–2.04 (2H), 2.00 (m, 1H, 15.0 Hz), 1.88 (s, 3H), 1.71 (m, 1H, $w_{1/2}$ = 11.8, 3.3 Hz), 1.58 (ddd, 1H, 12.5, 3.3, 3.0), 1.51 (m, 1H), 1.31 (s, 3H), 1.20 (s, 3H); ^{13}C nmr ($CDCl_3$, 360 NB) δ: 166.13, 148.17, 108.54, 57.54, 46.07, 35.16, 31.37, 29.91, 29.46, 28.98, 27.23, 25.84. The spectra (ir, ^{1}H nmr, ^{13}C nmr) were identical to spectra provided by B. Delpech (*9b,c*). ms *m/z*: 177 (1.6) 136 (26.8), 121 (7), 94 (14), 93 (100), 91 (19), 80 (14), 79 (25), 77 (21), 69 (18).

*Formation of 1:1:1 adducts and ethers from methanol, tricyclene (**18**), and 1,4-dicyanobenzene (**1**) (reaction [4])*

A solution of tricyclene (**18**) 445 mg (3.3 mmol), biphenyl (**3**) 450 mg (2.9 mmol), and 1,4-dicyanobenzene (**1**) 340 mg (2.7 mmol) in 35 mL acetonitrile–methanol (3:1) was degassed by nitrogen ebullition for 5 min and irradiated through Pyrex for 7 days. The volatile components of the photolysate, **18** and some of the ethers **21** and **22**, were removed by distillation. The nonvolatile residue was separated by repetitive dcfc; hexane–dichloromethane was used as eluent for the first column. Biphenyl (**3**) (98%) and unchanged **1** were partially recovered. The two 1:1:1 adducts (**19** and **20**) were partly separated. The ethers (**21** and **22**) were eluted as a mixture and were further separated by prep-gc (20% SE-30 150°C). Fractions containing **19** and **20** were rechromatographed (dcfc) using hexane – ethyl acetate as the solvent gradient. The methanol:**18**:**1** adduct (**19**) was isolated in 43% and the cyanide:**18**:**1** adduct (**20**) was obtained in 14% yield. Further purification of **19** and **20** was achieved by crystallization from methanol.

exo-*6-(4-Cyanophenyl)-5,5-dimethyl*-exo-*2-methoxy-endo-6-methylnorbornane* (**19**): mp 74.2-75.2°C; ir (KBr disk, Nicolet) ν: 3040 (w), 2966 (s), 2937 (s), 2877 (m), 2227 (s), 1607 (s), 1506 (s), 1467 (s), 1453 (s), 1373 (m), 1214 (s), 1091 (s), 1069 (s), 1018 (s), 841 (s); ^{1}H nmr ($CDCl_3$, 360NB) δ: 7.56 (d, 8.6 Hz, 2H, arom), 7.42 (d, 8.6 Hz, 2H, arom), 3.81 (dd, 6.6 Hz, 2.0 Hz, 1H, H2), 3.31 (s, 3H, methoxy), 2.70 (br s, 1H, H1), 2.16 (ddd, 14.5 Hz, 6.6 Hz, 2.6 Hz, 1H, *endo*-H3), 1.82 (s, br, 1H, H4), 1.80 (dm, 8.9 Hz, 1H, H7s), 1.65 (d, 8.9 Hz, 1H, H7a), 1.34 (ddd, 14.5 Hz, 4.0 Hz, 2.0 Hz, 1H, *exo*-H3), 1.24 (s, 3H, methyl), 1.07 (s, 3H, methyl), 0.53 (s, 3H, exo-5-methyl); ^{13}C nmr ($CDCl_3$, 360NB) δ: 154.45 (s), 131.21 (d), 128.13 (d), 119.07 (s), 108.90 (s), 79.70 (d), 55.89 (q), 51.29 (d), 50.33 (d), 48.32 (s), 42.39 (s), 33.32 (q), 32.22 (t), 31.52 (t), 23.86 (q), 23.12 (q); ms, *m/z*: 269 (0.3), 237 (11), 211 (21), 196 (17.3), 186 (100), 168 (26), 154 (18), 116 (13). Anal. calcd. for $C_{18}H_{23}NO$: C 80.25, H 8.61, N 5.20; found: C 80.25, H 8.55, N 5.25.

exo-*2-Cyano-5,5-dimethyl*-exo-*6-(4-cyanophenyl)*-endo-*6-methylnorbornane* (***20***): mp 148.1–148.7°C; ir (KBr disk, P.-E.) ν: 2970 (s), 2900 (m), 2800 (w), 2230 (s), 1610 (m), 1520 (m), 1470 (m), 820 (m), ^{1}H nmr ($CDCl_3$, 360NB) δ: 7.54 (d, 8.5 Hz, 2H, arom.), 7.40 (d, 8.5 Hz, 2H, arom.), 3.30 (ddd, 9.0 Hz, 4.2 Hz, 1.9 Hz, 1H, H2), 2.97 (s, br 1H, H1), 2.25 (ddd, 13.5 Hz, 9.0 Hz, 2.5 Hz, 1H, *endo*-H3), 2.11 (ddd, 11.1 Hz, 2.5 Hz, 1.9 Hz, 1H, H7s), 1.99 (dd, 3.8 Hz, 1.2 Hz, 1H, H4), 1.80 (m, 11.1 Hz, 1H, H7a), 1.79 (m, 13.5 Hz, 1H, *exo*-H3), 1.28 (s, 3H, methyl), 1.11 (s, 3H, methyl), 0.56 (s, 3H, methyl); ^{13}C nmr ($CDCl_3$, 360NB) δ: 152.57 (s), 131.43 (d), 127.92 (d), 123.90 (s), 118.75 (s), 109.55 (s), 51.92 (d), 50.76 (d), 49.39 (s), 42.74 (s), 34.60 (t), 31.43 (q), 29.84 (t), 26.92 (d), 24.29 (q), 22.73 (q); ms, *m/z*: 264 (48), 249 (13), 221 (21), 181 (41), 154 (39), 131 (45.8), 116 (24), 83 (82), 55 (100). Anal. calcd. for $C_{18}H_{20}N_2$: C 81.78, H 7.63, N 10.60; found: C 81.66, H 7.46, N 10.64.

Preparation of exo-*6-methoxycamphene (**21**) and 5,5-dimethyl*-exo-*2-methoxy*-endo-*6-methyl-norbornane (**22**) (Scheme 2)*

A solution of tricyclene (**18**) (1.55 g) and *N*-bromosuccinimide (2.13 g) in $CHCl_3$ (15 mL) was refluxed for 2.5 h. The solvent was evaporated and a solution of Li_2CO_3 (1.0 g) in methanol–dioxane (1:1) (15 mL) was added; the resulting solution was refluxed for 15 h. The reaction mixture was filtered, the solution was concentrated on a rotary evaporator, and the resulting mixture was chromatographed (dcfc) using hexane–dichloromethane as eluent. A pure sample of **21** was obtained by prep-gc (40% SE-30). Catalytic hydrogenation of **21** (H_2, 1 atmosphere/Pd, 9 h) (1 atm = 101.3 kPa) gave **22**.

exo-*6-Methoxycamphene* (***21***): ^{1}H nmr ($CDCl_3$, 360NB) δ: 4.88 (dd, 1.5 Hz, 0.8 Hz, 1H), 4.66 (s, 1H), 3.31 (ddd, 6.9 Hz, 3.0 Hz, 3.0 Hz, 1H, H6), 3.30 (s, 3H, methoxy), 2.83 (br, s, 1H, H1), 2.12 (ddd, 13.5 Hz, 6.9 Hz, 2.8 Hz, 1H, *endo*-H5), 1.91 (ddd, 4.2 Hz, 1.3 Hz, 1.5 Hz, 1H, H4), 1.67 (dddd, 10.0 Hz, 3.0 Hz, 2.8 Hz, 1.5 Hz, 1H, H7s), 1.51 (ddd, 10.0 Hz, 1.3 Hz, 1.3 Hz, 1H, H7a), 1.23 (dddd, 13.5 Hz, 4.2 Hz, 3.0 Hz, 0.8 Hz, 1H, *exo*-H5), 1.05 (s, 3H, methyl), 0.99 (s, 3H, methyl); ^{13}C nmr ($CDCl_3$, AC250) δ: 161.45 (s), 102.90 (t), 83.13 (d), 56.33 (q), 51.30 (d), 47.25 (d), 41.40 (s), 34.11 (t), 33.75 (t), 29.28 (q), 25.45 (q). ms, *m/z*: 166 (0.9), 134 (52), 119 (100), 93 (47), 91 (43), 79 (20), 77 (22).

5,5-Dimethyl-exo-*2-methoxy*-endo-*6-methylnorbornane* (***22***): ^{1}H nmr ($CDCl_3$, 360NB) δ: 3.52 (ddd, 6.9 Hz, 4.2 Hz, 0.7 Hz, 1H, H2), 3.24 (s, 3H, methoxy), 2.12 (dd, 3.7 Hz, 0.8 Hz, 1H, H1), 2.05 (ddd, 13.5 Hz, 6.9 Hz, 3.0 Hz, 1H, *endo*-H3), 1.76 (dd, 4.4 Hz, 0.8 Hz, 1H, H4), 1.58 (dd, 7.5 Hz, 3.7 Hz, 1H, H6), 1.52 (m, 9.8 Hz, 3.0 Hz, 1.5 Hz, 1H, H7s), 1.39 (ddd, 9.8 Hz, 1.6 Hz, 1.5 Hz, 1H, H7a), 1.14 (ddd, 13.5 Hz, 4.4 Hz, 4.2 Hz, 1H, *exo*-H3), 0.95 (s, 3H, methyl), 0.83 (d, 3H, 7.5 Hz, methyl), 0.74 (s, 3H, methyl); ^{13}C nmr ($CDCl_3$, AC250) δ: 77.35 (d), 55.86 (q), 48.38 (d), 48.34 (d), 42.80 (d), 36.23 (s), 34.80 (t), 33.90 (t), 31.82 (q), 21.22 (q), 11.07 (q). ms, *m/z*: 168 (1.6), 136 (26), 121 (40), 95 (100), 85 (65), 67 (40), 55 (40).

*The photosensitized (electron transfer) irradiation of tricyclene (**18**) in acetonitrile–perdeuteriomethanol (CD_3OD)*

When the irradiation of **18** was carried out as described above but in acetonitrile–methanol-d_4 (3:1) solution, the four products (**19–22**) were formed (gc/ms); however, the mass spectra indicate that incorporation of the deuterated methoxy group (CD_3) occurs in **19**, **21**, and **22**. The base peak and the molecular ion peak in the mass spectrum of **19**

Can. J. Chem. Downloaded from www.nrcresearchpress.com by 195.246.54.202 on 09/08/12
For personal use only.

become 189 *m/z* ($C_{12}H_9D_3NO$) and 272, instead of 186 and 269. The only notable change in the mass spectrum of **21** is that the molecular ion peak becomes *m/z* 169. In the mass spectrum of **22** the molecular ion peak at 168 *m/z* and the peak at 85 are substituted by 171 and 88.

*Formation of photo-NOCAS adducts (**24** and **25**) from nopol (**23**) (reaction [5])*

A solution of (−)-nopol (**23**) 2.68 g (16.1 mmol), biphenyl (**3**) 1.14 g (7.4 mmol), and 1,4-dicyanobenzene (**1**) 1.33 g (10.4 mmol) in 160 mL acetonitrile–methanol (3:1) was degassed by nitrogen ebullition for 5 min and irradiated through Pyrex for 10 days. The volatile components of the photolysate were removed by distillation. The nonvolatile residue was chromatographed (dcfc) eluting with an ethyl acetate – hexane solvent gradient. The photo-NOCAS adducts (**24** and **25**) were partially separated; **24** was eluted before **25**. Fractions containing mixtures of the two were rechromatographed (dcfc). Optical rotation measurements show both **24** and **25** were optically inactive.

trans-*6-(4-Cyanophenyl)-1-(2-hydroxyethyl)-4-(1-methoxy-1-methylethyl)-1-cyclohexene (**24**)*: ir (liq. film, P.-E.) *ν*: 3410 (s), 3030 (w), 2970 (s), 2925 (s), 2227 (s), 1604 (s), 1500 (m), 1465 (m), 1380 (m), 1067 (s), 890 (s), 832 (s), 735 (s); ^{1}H nmr ($CDCl_3$, 360NB) δ: 7.59 (d, 2H, J = 8.1 Hz), 7.33 (d, 2H, J = 8.1 Hz), 5.88 (m, 1H, with small coupling constants), 3.61 (t, 2H, 6.54 Hz), 3.57 (s, br. 1H, $w_{1/2}$ = 14 Hz), 2.83 (s, 3H), 2.26–1.90 (5H), 1.80–1.57 (3H), 1.02 (s, 3H), 0.97 (s, 3H); ^{13}C nmr ($CDCl_3$, 360NB) δ: 150.11 (s), 133.15 (s), 131.80 (d), 129.18 (d), 127.11 (d), 118.83 (s), 109.62 (s), 75.84 (s), 60.41 (t), 48.13 (q), 43.73 (d), 38.50 (t), 34.34 (d), 31.92 (t), 26.84 (t), 21.97 (q), 21.87 (q); ms *m/z*: 267 (1.8), 206 (10), 116 (6), 91 (6), 77 (6), 73 (100), 55 (6).

cis-*6-(4-Cyanophenyl)-1-(2-hydroxyethyl)-4-(1-methoxy-1-methylethyl)-1-cyclohexene (**25**)*: ir (liq. film, P.-E.) *ν*: 3420 (s), 3035 (w), 2970 (s), 2925 (s), 2225 (s), 1604 (s), 1500 (m), 1465 (m), 1380 (m), 1067 (s), 890 (s), 830 (s), 730 (s); ^{1}H nmr ($CDCl_3$, 360NB) δ: 7.58 (d, 2H, J = 7.9 Hz), 7.28 (d, 2H, J = 7.9 Hz), 5.81 (m, 1H, J = 5.2 Hz), 3.46–3.55 (3H), 3.17 (s, 3H), 2.13–1.71 (7H), 1.26 (ddd, 1H, coupled to one of the protons at 3.46–3.55 ppm), 1.10 (s, 3H), 1.08 (s, 3H); ^{13}C nmr ($CDCl_3$, 360NB) δ: 151.17 (s), 134.36 (d), 132.14 (d), 128.76 (d), 126.97 (d), 118.75 (s) 109.70 (s), 75.96 (s), 60.24 (t), 48.64 (q), 46.88 (d), 42.11 (d), 37.77 (t), 35.32 (t), 27.00 (t), 21.99 (q), 21.30 (q); ms *m/z*: 267 (1.5), 206 (7), 116 (4), 91 (5), 77 (5), 73 (100), 55 (6).

Both photo-NOCAS adducts (**24** and **25**) were converted into 3,5-dinitrobenzoate esters by the standard procedure (15). In a typical preparation, 3,5-dinitrobenzoyl chloride 0.165 g (0.72 mmol) and **24**, 0.210 g (0.72 mmol) were dissolved in 1.5 mL pyridine. The solution was stirred at room temperature for 2 h. The derivative was isolated by dcfc using dichloromethane–hexane solvent gradient as eluent, followed by recrystallization using ethanol–acetone as solvent. Analytical samples were recrystallized from dichloromethane–hexane solution to give light yellow crystals.

*The 3,5-dinitrobenzoate derivative of **24** (*trans *26*)*: mp 149.2–150.5°C; ^{1}H nmr ($CDCl_3$, AC250) δ: 9.23 (m, 1H), 9.11 (m, 2H), 7.62 (d, 2H, 7.9 Hz), 7.36 (d, 2H, 7.9 Hz), 5.96 (m, 1H), 4.48 (m, 2H), 3.64 (m, $w_{1/2}$ = 11.0 Hz), 2.84 (s, 3H), 2.50 (ddd, 1H, 15.3, 7.4, 7.2 Hz), 2.33–2.10 (2H), 1.98–1.69 (3H), 1.62 (m, 1H), 1.01 (s, 3H), 0.97 (s, 3H); ^{13}C nmr ($CDCl_3$, AC250) δ: 162.36 (C), 149.79 (C), 148.68 (C), 133.90 (C), 132.24 (CH), 132.15 (C), 129.37 (CH), 129.32 (CH), 128.35 (CH), 122.45 (CH), 118.94 (CN), 110.28 (C), 75.86 (C), 64.98 (CH_2), 48.45 (CH_3O), 44.17 (CH), 34.69 (CH), 34.65 (CH_2), 32.16 (CH_2), 27.10 (CH_2), 22.07 ($2CH_3$). For the X-ray crystal structure, see footnote 3.

*The 3,5-dinitrobenzoate derivative of **25** (*cis *27*)*: mp 154.7–155.0°C; ^{1}H nmr ($CDCl_3$, AC250) δ: 9.19 (1H, m), 9.07 (2H, m), 7.60 (2H, d, 7.8 Hz), 7.30 (2H, d, 7.8 Hz), 5.83 (1H, m), 4.33 (2H, dd, 6.1, 7.9 Hz), 3.54 (1H, m, $w_{1/2}$ = 24 Hz), 3.14 (s, 3H), 2.35 (dt, 1H, 14.6, 7.9 Hz), 2.18–1.92 (4H), 1.81 (m, 1H), 1.26 (ddd, 1H, 12.2, 11.9, 11.8, coupled to the proton at 3.54 ppm), 1.08 (s, 3H), 1.06 (s, 3H); ^{13}C nmr ($CDCl_3$, AC250) δ: 162.34, 150.809, 148.67, 133.89, 133.43, 132.65, 129.37, 129.90, 129.29, 122.41, 118.90, 110.43, 76.03, 64.78, 48.92, 47.13, 42.64, 35.54, 33.90, 27.25, 22.17, 21.36. For X-ray crystal structure, see footnote 3.

Acknowledgements

This work was supported by a grant from the Natural Sciences and Engineering Research Council of Canada. We thank Dr. D.L. Hooper at the Atlantic Regional Magnetic Resonance Centre at Dalhousie University for the high-field NMR spectra and for help in the preparation of the manuscript. Exact mass measurements were carried out by Mr. D. Embree at the Institute for Marine Biosciences, Halifax. We also thank Dr. T.S. Cameron at Dalhousie for the X-ray analyses of **26** and **27**.

1. (*a*) K. McMahon and D.R. Arnold. Can. J. Chem. **71**, 450 (1993); (*b*) D.R. Arnold and X. Du. J. Am. Chem. Soc. **111**, 7666 (1989).
2. A.L. Perrott and D.R. Arnold. Can. J. Chem. **70**, 272 (1992).
3. D.R. Arnold and M.S. Snow. Can. J. Chem. **66**, 3012 (1988).
4. R.M. Borg, D.R. Arnold, and T.S. Cameron. Can. J. Chem. **62**, 1785 (1984).
5. (*a*) O. Wallach. Justus Liebigs Ann. Chem. **227**, 283 (1884); (*b*) Justus Liebigs Ann. Chem. **239**, 34 (1887); (*c*) F.M. Flavitsky. Ber. Dtsch. Chem. Ges. **20**, 1957 (1887); (*d*) M.S. Kharasch and W.B. Reynolds. J. Org. Chem. **9**, 148 (1944).
6. (*a*) J.-M. Fang, M.-Y. Chen, M.-C. Cheng, G.-H. Lee, Y. Wang, and S.-M. Peng. J. Chem. Research (S), 272 (1989); (*b*) J.A. Claisse, D.I. Davies, and L.T. Parfitt. J. Chem. Soc. (C), 258 (1970); (*c*) J. Iyoda and I. Shiihara. J. Org. Chem. **35**, 4267 (1970).
7. T.S. Sorensen, I.J. Miller, and K. Ranganayakulu. Aust. J. Chem. **26**, 311 (1973).
8. (*a*) M. Castaing, M. Pereyre, M. Ratier, P.M. Blum, and A.G. Davies. J. Chem. Soc. Perkin Trans. 2, 287 (1979); (*b*) A.L.J. Beckwith and G. Moad. J. Chem. Soc. Perkin Trans. 2, 1083 (1980); (*c*) L. Kaplan. J. Org. Chem. **33**, 2531 (1968); (*d*) J.W. Wilt, L.L. Maravetz, and J.F. Zawadzki. J. Org. Chem. **31**, 3018 (1966).
9. (*a*) B.-W. Zhang, Y.-F. Ming, and Y. Cao. Photochem. Photobiol. **40**, 581 (1984); (*b*) B. Delpech and Q. Khuong-Huu. J. Org. Chem. **43**, 4898 (1978); (*c*) A. Pancrazi, I. Kabore, B. Delpech, and Q. Khuong-Huu. Tetrahedron Lett. 3729 (1979); (*d*) C. Mirand, G. Massiot, and L. Levy. J. Org. Chem. **47**, 4169 (1982); (*e*) T.H. Bates, J.V.F. Best, and T.F. Williams. J. Chem. Soc. 1521 (1962); (*f*) T.H. Bates, J.V.F. Best, and T.F. Williams. J. Chem. Soc. 1531 (1962).
10. W. Klyne and J. Buckingham (*Editors*). Atlas of stereochemistry. Absolute configuration of organic molecules. Vol. 1. 2nd ed. Chapman and Hall, London. 1978. p. 82.
11. (*a*) R.S. Nicholson and I. Shain. Anal. Chem. **36**, 706 (1964); (*b*) Anal. Chem. **37**, 178 (1965).
12. D. Rehm and A. Weller. Isr. J. Chem. **8**, 259 (1970).
13. D.G. Patil, J.S. Yadav, H.P.S. Chawla, and S. Dev. Indian J. Chem. **22B**, 189 (1983).
14. K.A. Kime and R.E. Sievers. Aldrichimica Acta, **10**, 54 (1977).
15. R.L. Shriner, R.C. Fuson, and D.Y. Curtin. Systematic identification of organic compounds. 4th ed. J. Wiley and Sons, New York. 1948.
16. M.J. Frisch, J.S. Binkley, H.B. Schlegel, K. Raghavachari, C.F. Melius, R.L. Martin, J.J.P. Stewart, F.W. Bobrowicz, C.M. Rohlfing, L.R. Kahn, D.J. DeFrees, R. Seeger, R.A. Whiteside, D.J. Fox, E.M. Fleuder, and J.A. Pople. GAUSSIAN 86, Release H, Carnegie Mellon University, Pittsburgh, Pa. 1984.
17. M.J. Frisch, M. H.-Gordon, G.W. Trucks, J.B. Foresman, H.B. Schlegel, K. Raghavachari, M. Robb, J.S. Binkley, C. Gonzalez, D.J. DeFrees, D.J. Fox, R.A. Whiteside, R. Seeger, C.F. Melius, J. Baker, R.L. Martin, L.R. Kahn, J.J.P. Stewart, S. Topiol, and J.A. Pople. GAUSSIAN 90, revision H, Gaussian, Inc., Pittsburgh, Pa. 1990.
18. R.S. Mulliken. J. Chem. Phys. **23**, 1833 (1955).
19. W.J. Hehre, L. Radom, P.v.R. Schleyer, and J.A. Pople. *Ab initio* molecular orbital theory. Wiley, New York. 1986.
20. (*a*) A.P. Schaap, L. Lopez, and S.D. Gagnon. J. Am. Chem. Soc.

105, 663 (1983); (*b*) T. Majima, C. Pac, A. Nakasone, and H. Sakurai. J. Am. Chem. Soc. **103**, 4499 (1981); (*c*) S. Mattes and S. Farid. Org. Photochem. **6**, 233 (1983).
21. (*a*) S.L. Mattes and S. Farid. J. Am. Chem. Soc. **104**, 1454 (1982); (*b*) J. Am. Chem. Soc. **108**, 7356 (1986); (*c*) L.J. Johnston and N.P. Schepp. J. Am. Chem. Soc. **115**, 6564 (1993).
22. R. Popielarz and D.R. Arnold. J. Am. Chem. Soc. **112**, 3068 (1990).
23. D.D.M. Wayner, D.J. McPhee, and D. Griller. J. Am. Chem. Soc. **110**, 132 (1988).
24. (*a*) B. Jaun, J. Schwarz, and R. Breslow. J. Am. Chem. Soc. **102**, 5741 (1980); (*b*) D.D.M. Wayner and D. Griller. *In* From atoms to polymers: isoelectronic analogies. *Edited by* J.F. Liebman and A. Greenberg. VCH Publishers, Inc., New York. 1989.
25. (*a*) G. Frank. J. Chem. Soc. (B), 130 (1968); (*b*) R. Mayer, K. Bochov, and W. Zieger. Z. Chem. **4**, 384 (1964).
26. (*a*) V.R. Rao and S.S. Hixson. J. Am. Chem. Soc. **101**, 6458 (1979); (*b*) K. Mizuno, J. Ogawa, H. Kagano, and Y. Otsuji. Chem. Lett. 437 (1981); (*c*) P.H. Mazzocchi and C. Somich. Tetrahedron Lett. **29**, 513 (1988); (*d*) J.P. Dinnocenzo, W.P. Todd, T.R. Simpson, and I.R. Gould. J. Am Chem. Soc. **112**, 2462 (1990).
27. (*a*) P.G. Gassman and K.D. Olson. J. Am. Chem. Soc. **104**, 3740 (1982); (*b*) P.G. Gassman and G.T. Carroll. Tetrahedron, **42**, 6201 (1986).
28. L.M. Harwood. Aldrichimica Acta, **18**, 25 (1985).
29. A. Okamoto, M.S. Snow, and D.R. Arnold. Tetrahedron, **42**, 6175 (1986).

Can. J. Chem. Downloaded from www.nrcresearchpress.com by 195.246.54.202 on 09/08/12
For personal use only.

Photochemical nucleophile–olefin combination, aromatic substitution (photo-NOCAS) reaction. Part 6: methanol, nonconjugated dienes, and 1,4-dicyanobenzene[1]

DONALD R. ARNOLD,[2] KIMBERLY A. MCMANUS, AND XINYAO DU
Department of Chemistry, Dalhousie University, Halifax, NS B3H 4J3, Canada

Received March 1, 1993[3]

DONALD R. ARNOLD, KIMBERLY A. MCMANUS, and XINYAO DU. Can. J. Chem. **72**, 415 (1994).

Irradiation, through Pyrex, of an acetonitrile–methanol (3:1) solution of 1,4-dicyanobenzene (**1**) and 1,5-hexadiene (**9**) leads to formation of *ortho* and *meta* cyclic adducts (**13–16**) arising from the intermediate exciplex. There was no evidence for interaction between the two double bonds of this nonconjugated diene. The oxidation potential of **9** is high enough (>3 V vs. sce) to preclude single electron transfer (SET); no photo-NOCAS products are formed. Similar irradiation of acetonitrile–methanol solutions of **1** and 2-methyl-1,5-hexadiene (**10**) does yield a photo-NOCAS product (**17**); reaction occurs only on the more heavily substituted double bond. The additional substitution on the double bond lowers the oxidation potential (2.70 V vs. sce) of this diene to the point where SET from **10** to the excited singlet state of **1** can occur. In this case, no cycloaddition products are formed; the exciplex is quenched by electron transfer. There was no evidence for interaction between the two double bonds of the initially formed radical cation $\mathbf{10}^{+\cdot}$, or between the terminal double bond and the β-alkoxyalkyl radical of the intermediate leading to the photo-NOCAS product. The photo-NOCAS product (**19**) was also formed when 2,5-dimethyl-1,5-hexadiene (**11**) was subjected to these reaction conditions. In this case, when biphenyl (**4**) was added as a codonor, in addition to the photo-NOCAS product, products (**21** *cis* and *trans*) resulting from cyclization of the initially formed acyclic radical cation $\mathbf{11}^{+\cdot}$ to give the 1,4-dimethylcyclohexane-1,4-diyl radical cation were also observed. This 1,6-*endo*, *endo* cyclization of $\mathbf{11}^{+\cdot}$ must be rapid enough to compete with reaction with methanol. There was no evidence for cyclization (neither 1,4-*exo* nor 1,5-*endo*) of the intermediate β-alkoxyalkyl radical. When the radical cation of 2,5-dimethyl-1,4-hexadiene ($\mathbf{12}^{+\cdot}$) is generated under these reaction conditions, photo-NOCAS products **22** and **23** are formed at the more heavily substituted double bond, along with the conjugated tautomer 2,5-dimethyl-2,4-hexadiene (**24**). The mechanisms for these transformations are discussed.

DONALD R. ARNOLD, KIMBERLY A. MCMANUS et XINYAO DU. Can. J. Chem. **72**, 415 (1994).

L'irradiation, dans un tube de Pyrex, d'une solution acétonitrile–méthanol (3 : 1) de 1,4-dicyanobenzène (**1**) et de hexa-1,5-diène (**9**) conduit à la formation d'adduits cycliques *ortho* et *méta* (**13–16**) qui dérivent de l'exciplexe intermédiaire. On n'a aucune donnée suggérant l'existence d'une interaction entre les deux doubles liaisons de ce diène non conjugué. Le potentiel d'oxydation du composé **9** est suffisamment élevé (>3 V vs. sce) pour empêcher un transfert d'un seul électron (SET); il ne se forme aucun produit de photo-NOCAS. Une irradiation semblable de solutions acétonitrile–méthanol du composé **1** en présence de 2-méthylhexa-1,5-diène (**10**) conduit à la formation d'un produit photo-NOCAS, **17**; la réaction ne se produit que sur la portion la plus substituée de la double liaison. La substitution plus grande sur la double liaison abaisse le potentiel d'oxydation (2,70 V vs. sce) de ce diène au point où une réaction de transfert d'un seul électron du produit **10** vers l'état singulet excité du produit **1** peut se produire. Dans ce cas, il ne se forme pas de produits de photoaddition; l'exciplexe est désactivé par le transfert d'électron. Il n'y a pas de données suggérant la présence d'interactions entre les deux doubles liaisons du cation radicalaire $\mathbf{10}^{+\cdot}$ qui se forme initialement ou entre la double liaison terminale et le radical β-alcoxyalkyle de l'intermédiaire qui conduirait au produit photo-NOCAS. Le produit photo-NOCAS (**19**) se forme aussi lorsqu'on soumet le 2,5-diméthylhexa-1,5-diène à ces conditions réactionnelles. Dans ce cas, lorsqu'on ajoute du biphényle (**4**) comme codonneur, on observe, en plus du produit photo-NOCAS, la formation de produits (**21** *cis* et *trans*) qui résultent de la cyclisation du cation radicalaire acyclique $\mathbf{11}^{+\cdot}$ (qui se forme originalement) pour donner le cation radicalaire 1,4-diméthylcyclohexane-1,4-diyle. Cette cyclisation 1,6-*endo*, *endo* de $\mathbf{11}^{+\cdot}$ doit être assez rapide pour se faire de préférence à la réaction avec le méthanol. Il n'y a aucune donnée permettant de suggérer une cyclisation (soit 1,4-*exo* ou 1,5-*endo*) du radical intermédiaire β-alcoxyalkyle. Quand le cation radicalaire du 2,5-diméthylhexa-1,4-diène ($\mathbf{12}^{+\cdot}$) est généré dans ces conditions réactionnelles, les produits photo-NOCAS **22** et **23** se forment au niveau de la double liaison le plus substituée aux côtés du tautomère conjugué, 2,5-diméthylhexa-2,4-diène (**24**). On discute des mécanismes de ces transformations.

[Traduit par la rédaction]

Introduction

The photochemical nucleophile–olefin combination, aromatic substitution (photo-NOCAS) reaction is a useful synthetic procedure. A nucleophile, an olefin, and an aromatic molecule can be combined to yield a more complex difunctional molecule in one simple step. Archetypical examples of this reaction are the combination of methanol and 2,3-dimethyl-2-butene (**2**), substituting on 1,4-dicyanobenzene (**1**) (reaction [1]); and the combination of methanol and 2-methylpropene (**6**), substituting on 1,4-dicyanobenzene (**1**) (reaction [2]) (3). The proposed mechanism is shown in Scheme 1 (3). This work is part of our continuing effort to define the scope and synthetic utility of the photo-NOCAS reaction. We have subjected 1,4- and 1,5-dienes to the photo-NOCAS reaction conditions, exploring the possibility that cyclized products might be obtained. A further objective of this project was to gain additional insight into the mechanism of the reaction and into the nature of the unusual intermediates involved.

Reaction occurs when acetonitrile–methanol (3:1) solutions of an olefin and an aromatic compound are irradiated through Pyrex (Scheme 1, steps 1–5). However, the efficiency of the reaction and the yield of photo-NOCAS products may be increased by the addition of a codonor, e.g., biphenyl (**4**) (steps 1, 6a, and 7), or by the addition of a photosensitizer (electron transfer), e.g., phenanthrene (**5**) (steps 6b, 6c, and 7). The actual

[1]This is also Part 32 of the series Radical Ions in Photochemistry; see refs. 1 and 2 for preceding parts of these series.

[2]Author to whom correspondence may be addressed.

[3]Revision received October 12, 1993.

Can. J. Chem. Downloaded from www.nrcresearchpress.com by 195.246.54.202 on 09/08/12
For personal use only.

Can. J. Chem. Downloaded from www.nrcresearchpress.com by 195.246.54.202 on 09/08/12
For personal use only.

Reaction [1] (3)

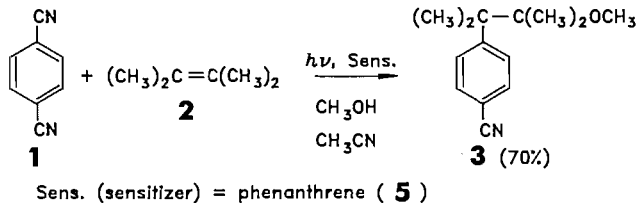

Sens. (sensitizer) = phenanthrene (**5**)

Reaction [2] (3)

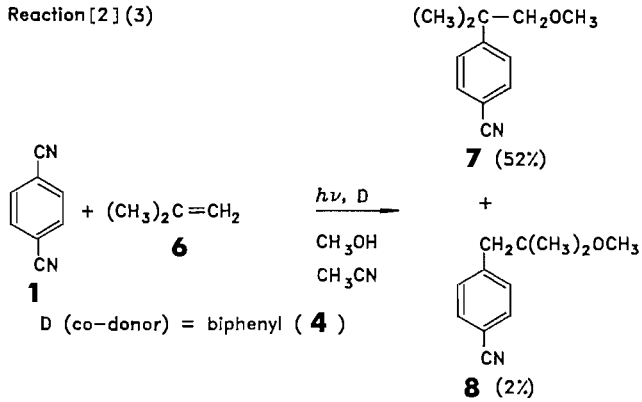

D (co-donor) = biphenyl (**4**)

function of the codonor in increasing the efficiency of the reaction is not fully understood. The explanation we favour is that escape to fully solvated radical ions from the solvent-separated radical ion pair (SSRIP) formed between the aromatic electron acceptor and the codonor may be more efficient. The relative efficiency of formation of solvated radical ions is a function of differences in reorganization energy, influencing the rate of the competing back electron transfer process within the alternative SSRIPs (steps 2 and 8) (4). It has also been proposed that the codonor, or sensitizer, radical cation and the olefin may form a complex radical cation and that this may modify the reactivity of the alkene radical cation (*3b*, 5). The characterization of a benzene–ethylene radical cation complex adds credence to this suggestion (*5c*).

There are two steps in the proposed mechanism during which cyclization of an intermediate from a nonconjugated diene may occur: the radical cation of the diene may cyclize prior to reaction with nucleophile, that is, between steps 2 and 3 or between steps 7 and 3 (Scheme 1). For example, the initially formed radical cation of a 1,5-diene might cyclize 1,6-*endo*, *endo* to a cyclohexane-1,4-diyl radical cation in competition with reaction with methanol. Complex formation between the codonor or sensitizer radical cation and the diene (step 7) may influence the rates of these competing processes. Alternatively, the intermediate β-alkoxyalkyl radical may cyclize before substitution on the radical anion of the electron acceptor (between steps 3 and 4). These cyclization modes should be distinguishable based upon the structure of the product(s).

Rules for predicting rates and regiochemistry of cyclization of common intermediates, i.e., carbocations, carbanions, and radicals, have developed rapidly over the past few years, to the point where a cyclization step can be included in retrosynthetic analysis (6). Analogous rules for the cyclization of radical ions have not yet been defined.

Results

The nonconjugated dienes chosen for study were: 1,5-hexadiene (**9**), 2-methyl-1,5-hexadiene (**10**), 2,5-dimethyl-1,5-hexadiene (**11**), and 2,5-dimethyl-1,4-hexadiene (**12**); **9**, **10**, and **11** were available commercially. 2,5-Dimethyl-1,4- hexadiene (**12**) was prepared by a two-step procedure involving photochemically induced tautomerization of 5-methyl-3-hexen-2-one to the nonconjugated isomer 5-methyl-4-hexen-2-one followed by a Wittig reaction with triphenylphosphine methylene ylide (Scheme 2) (7).

The irradiations were generally carried out on acetonitrile–methanol (3:1) solutions of 1,4-dicyanobenzene (**1**) and the diene, with and without added biphenyl (**4**) or phenanthrene (**5**). Progress of the reaction was followed by capillary column gas

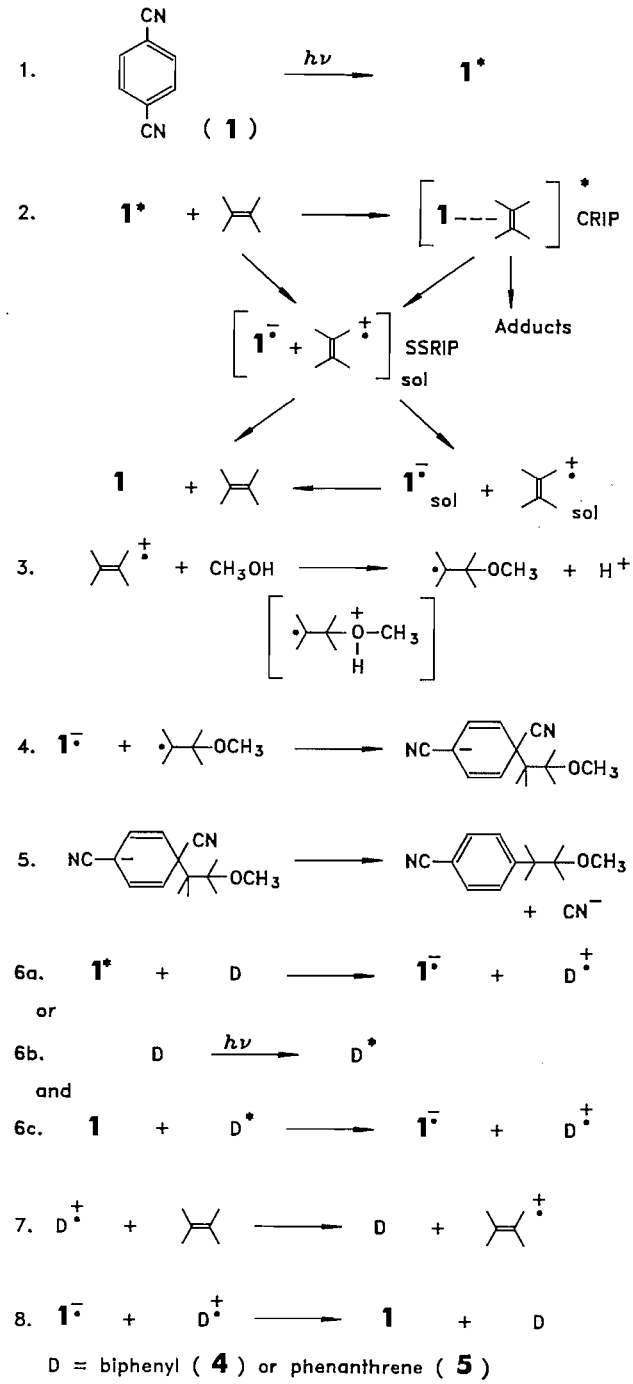

D = biphenyl (**4**) or phenanthrene (**5**)

SCHEME 1

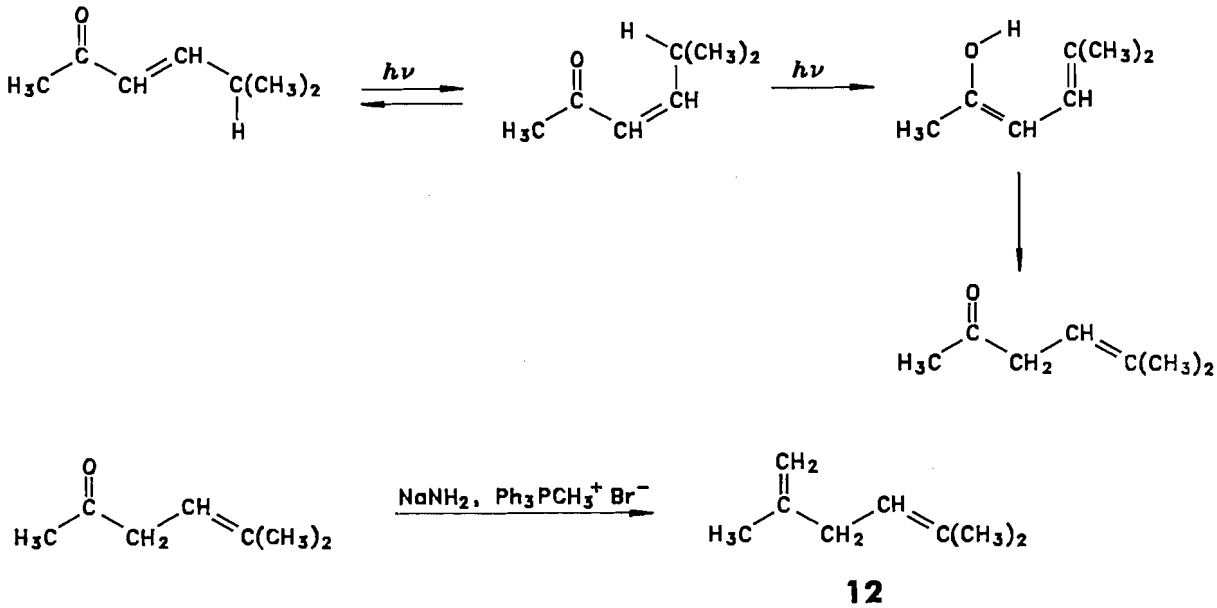

SCHEME 2 (ref. 7)

chromatography with a mass selective detector (gc/ms). Product ratios and yields were based upon isolated pure compounds, generally separated by medium-pressure liquid chromatography (mplc), or upon gas chromatography using a calibrated flame ionization detector (gc/fid). Yields were based upon the amount of 1,4-dicyanobenzene (**1**) consumed; the diene was generally present in excess.

Irradiation of a solution of 1,4-dicyanobenzene (**1**) and 1,5-hexadiene (**9**) gave cycloaddition products **13–16** (combined yield 54%) (reaction [3]). The major products are *meta*

Reaction [3]

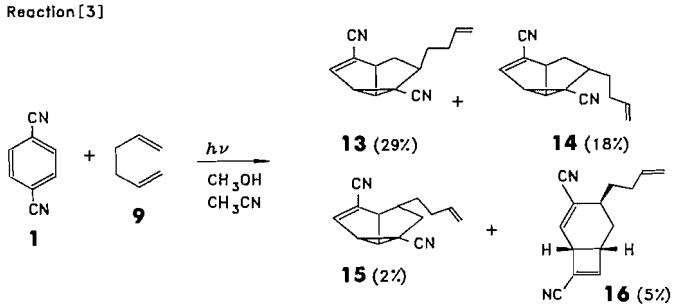

adducts **13**, **14**, and **15**. A minor product **16** is the result of *ortho*-cyclization followed by thermal or photochemical rearrangement (reaction [4]); there is precedence for this cyclization and rearrangement (8, 9). There was no evidence for any interaction between the two double bonds of the diene. No photo-NOCAS products were detected (gc/ms). The addition of biphenyl (**4**) to this reaction mixture caused a decrease in the efficiency of the reaction; still, no photo-NOCAS products were observed. The addition of phenanthrene (**5**) completely quenched the reaction.

Reaction [4]

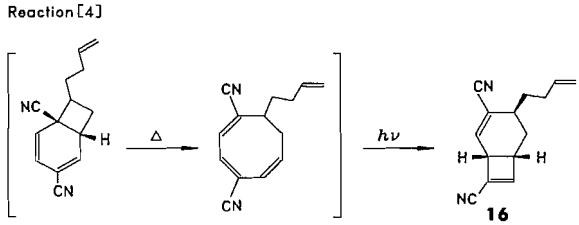

Irradiation of an acetonitrile–methanol solution of 1,4- dicyanobenzene (**1**) and 2-methyl-1,5-hexadiene (**10**) gave the *anti*-Markovnikov photo-NOCAS adduct **17** in low yield (4%) (reaction [5]). Also isolated from this reaction was the

Reaction [5]

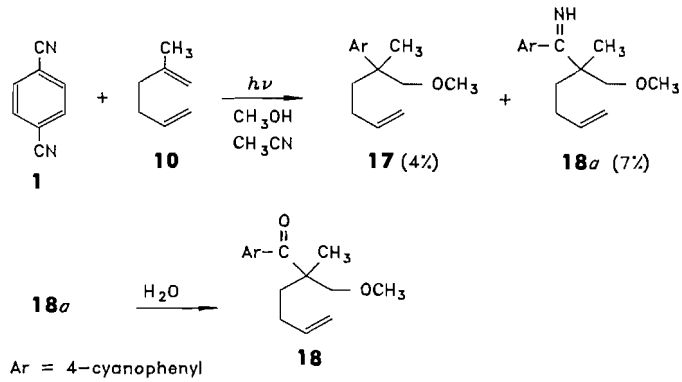

4-cyanophenyl ketone **18** (7%). This ketone was not present in the initial photolysate (gc/ms); imine **18***a* is the primary product. Hydrolysis of the imine to the ketone occurs during the isolation procedure.

The addition of the codonor, biphenyl (**4**), increased the efficiency and yield of formation of the photo-NOCAS product (**17**, 31%). There was no imine or ketone detected in this reaction. Phenanthrene (**5**) was less effective than biphenyl (**4**) in increasing the efficiency of this reaction.

In these reactions of **10**, there was no evidence for formation of products resulting from cycloaddition to the aromatic ring, reaction occurs only at the more heavily substituted double bond, and there was no indication of interaction between the two double bonds.

Irradiation of an acetonitrile–methanol solution of 1,4-dicyanobenzene (**1**) and 2,5-dimethyl-1,5-hexadiene (**11**) also gave

Can. J. Chem. Downloaded from www.nrcresearchpress.com by 195.246.54.202 on 09/08/12
For personal use only.

the photo-NOCAS adduct (**19**) in low yield (8%). Again, in this case, imine **20***a* was detected in the photolysate and ketone **20** (3%) was isolated following mplc (reaction [6]). **The addition**

Reaction [6]

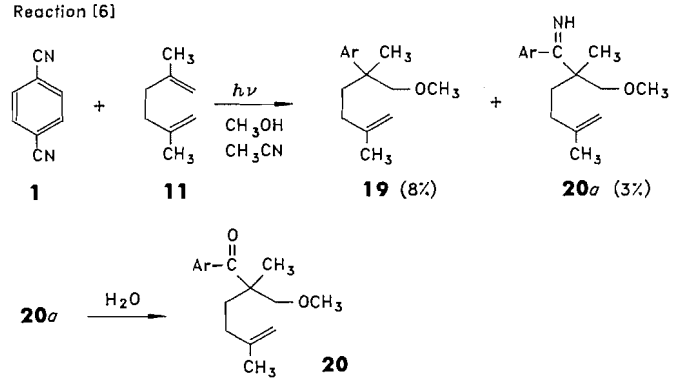

of biphenyl (4) has a profound influence on this reaction. The yield of photo-NOCAS adduct **19** increases (to 16%); and, the *cis*- and *trans*-cyclized products (**21** *cis* and *trans*) are also formed (combined yield 13%). Imine **20***a* was not a product under these conditions (reaction [7]).

Reaction [7]

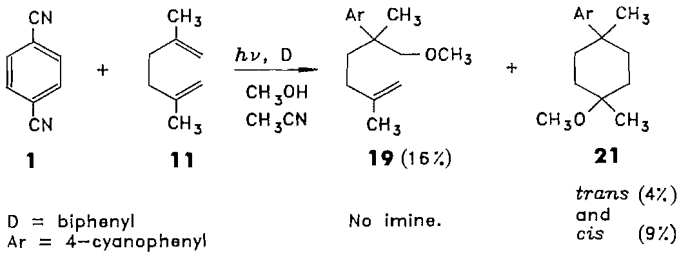

The ratio of cyclic to acyclic products (**21** *cis* and *trans*/**19**) depends upon the concentration of both biphenyl (**4**) and methanol. Increasing the concentration of biphenyl (**4**) increases the relative yield of cyclized products (Fig. 1). Increasing the concentration of methanol, between 0.2 and 2.0 M, leads to a decrease in the relative yield of cyclized products (Fig. 2). Further increase in methanol concentration has little effect (**21** *cis* and **21** *trans*/**19** = 0.35 at [CH_3OH] 7 M).

Irradiation of an acetonitrile–methanol solution of 1,4-dicyanobenzene (**1**), biphenyl (**4**), and 2,5-dimethyl-1,4-hexadiene (**12**) gave photo-NOCAS products (reaction [8]). Both the *anti*-Markovnikov (**22**, 16%) and Markovnikov (**23**, 9%)

Reaction [8]

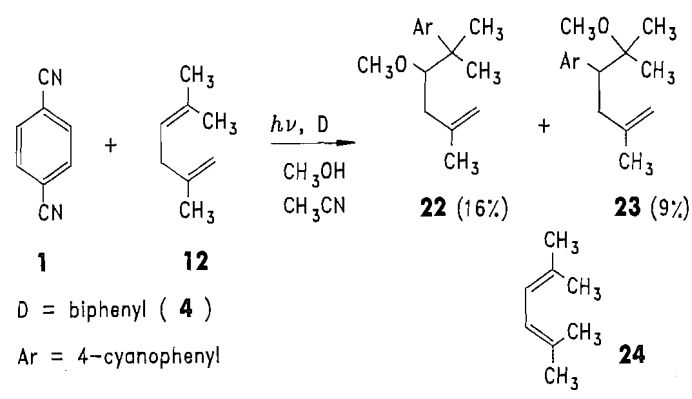

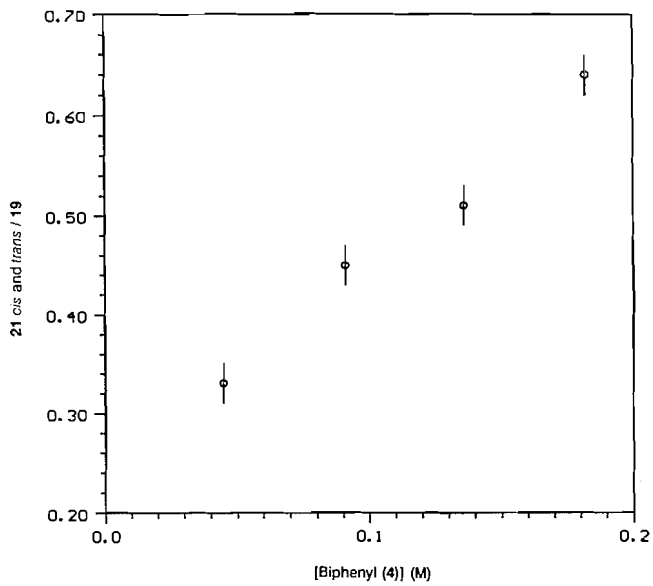

FIG. 1. In reaction [7], the ratio of cyclized products to acyclic product (**21** *cis* and *trans*/**19**) increases with increasing biphenyl (**4**) concentration.

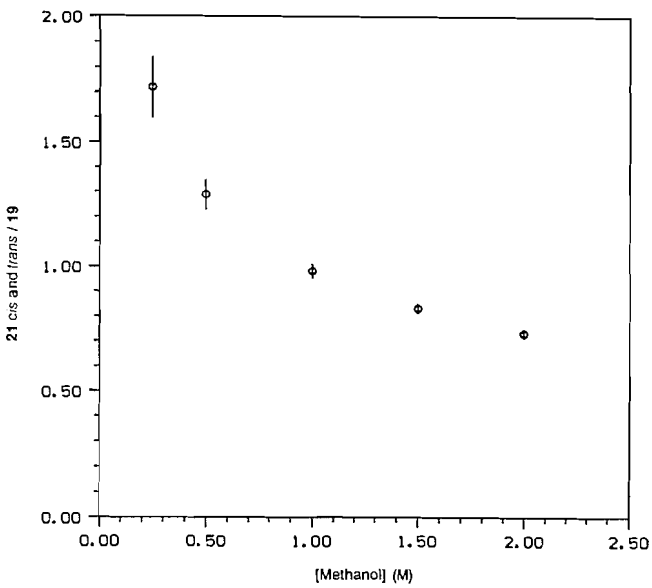

FIG. 2. In reaction [7], the ratio of cyclized products to acyclic product (**21** *cis* and *trans*/**19**) decreases with increasing methanol concentration.

adducts were obtained. Photo-NOCAS reaction occurs only at the more heavily substituted double bond. Another product of this reaction was the conjugated tautomer of **12**, 2,5-dimethyl-2,4-hexadiene (**24**).[4] There was no evidence for interaction between the two double bonds of **12**.

Generally, in those reactions carried out with added codonor (**4**) or photosensitizer (**5**), the codonor or photosensitizer was largely recovered. However, characterization of products formed in trace amounts found 2-cyanobiphenyl (**25**), 4-cyano-

[4]This conjugated diene (**24**) forms the photo-NOCAS adduct, *trans*-2-(4-cyanophenyl)-5-methoxy-2,5-dimethyl-3-hexene, in excellent yield (82%) under these conditions (K.A. McManus and D.R. Arnold, unpublished results).

Can. J. Chem. Downloaded from www.nrcresearchpress.com by 195.246.54.202 on 09/08/12
For personal use only.

Can. J. Chem. Downloaded from www.nrcresearchpress.com by 195.246.54.202 on 09/08/12
For personal use only.

TABLE 1. Oxidation potentials of the dienes and the calculated free energy change (ΔG_{et}) for the electron transfer process involving the singlet excited state of 1,4-dicyanobenzene (**1**) as the electron acceptor and the diene as electron donor

Diene	$E^{ox}_{1/2}$ (V)[a]	ΔG_{et} (kJ/mol)[b]
1,5-Hexadiene (**9**)	>3.00	>35.7
2-Methyl-1,5-hexadiene (**10**)	2.70	6.81
2,5-Dimethyl-1,5-hexadiene (**11**)	2.60	−2.84
2,5-Dimethyl-1,4-hexadiene (**12**)	2.28	−33.7

[a]Oxidation potentials were measured by cyclic voltammetry at a platinum electrode relative to the saturated calomel electrode (SCE) using tetraethylammonium perchlorate (0.1 M TEAP) as the electrolyte in acetonitrile. The anodic wave was irreversible, so the half-wave was estimated to be 0.028 V before the peak potential (10).

[b]Based upon the Weller equation (11): $E_{0,0}$ (**1**) 408.4 kJ/mol, $E^{red}_{1/2}$ (**1**) −1.66 V, the Coulombic attraction term was taken to be 5.4 kJ/mol (3*b*).

biphenyl (**26**), and 3,5-dimethoxy-4-phenylcyclohexanecarbonitrile (**27**) when **4** was used; and 9-methoxy-9,10-dihydrophenanthrene (**28**) and 9-cyano-9,10-dihydrophenanthrene (**29**) from irradiations containing **5**.

Oxidation potentials of the dienes (**9–12**), necessary for an understanding of the mechanism, were measured by cyclic voltammetry (Table 1).

Structural assignments

The structural assignments for new compounds were based primarily upon ^{1}H and ^{13}C nmr spectra. Mass spectra (including exact mass determination), infrared spectra, and elemental analyses were also helpful. In one case (**27**), the structure was determined by an X-ray analysis of a single crystal.

The cycloaddition products **13–16** obtained from 1,5-hexadiene (**9**) (reaction [3]) provided the greatest challenge. Assignments were based upon analysis of ^{1}H nmr spectra, aided by comparison with reported spectra for similar compounds (8, 9), by computer simulation, and by molecular mechanics calculations of the structure. Consider first the *meta* adducts **13–15**. Other possible structures, i.e., *ortho* or *para* cycloadducts or azetines, were easily ruled out; signals in the vinyl region of the ^{1}H nmr spectra of **13–15** are indicative of four olefinic protons. The 3-butenyl side chain was readily identified in all of these structures. There are 12 possible regio- and stereoisomers for the *meta* adducts.

The ^{1}H nmr spectrum of the major product 7-*endo*-(3-butenyl)-4,8-dicyanotricyclo[3.3.0.0^{2,8}]oct-3-ene (**13**) shows a distinctive doublet of doublets, due to one proton, in the aliphatic region (1.80 ppm). This signal, assigned to the *endo* proton on C-6, is strongly coupled to the geminal *exo* proton (2.69 ppm, 13.2 Hz). Decoupling experiments show that this *exo* proton is also strongly coupled to the proton (3.5 ppm, 5.5 Hz) assigned to the methine group (C-5), and to the *exo* proton on C-7 (2.94 ppm, 11.4 Hz). The *endo* proton on C-6 is not significantly coupled to the proton on C-5 and is only weakly coupled to the *exo* proton on C-7 (0.9 Hz). The proton on C-5 is coupled (1.2 Hz) to the *exo* proton on C-7. This long-range W-coupling establishes the regiochemistry of the alkenyl side chain as *endo*. The proton on C-5 is also coupled to the vicinal proton on C-1 (3.45 ppm, 5.8 Hz). The proton on C-1 is coupled to another vicinal proton on C-2 (2.62 ppm, 6.6 Hz). And the proton on C-2 is coupled to the vinyl proton on C-3 (6.54 ppm, 2.5 Hz).

The other major *meta* adduct has been assigned structure 7-*exo*-(3-butenyl)-4,8-dicyanotricyclo[3.3.0.0^{2,8}]oct-3-ene (**14**). The spectrum of **14** is similar to that of **13**, the distinguishing features are in the coupling of the signals assigned to the protons on C-5, C-6, and C-7. The proton on C-5 is coupled (5.08 Hz) with the vicinal proton *exo* on C-6. This proton is strongly coupled (13.4 Hz) to a proton which must be geminal, *endo* on C-6, thus establishing the regiochemistry; the side chain must be attached at C-7. For **13**, long-range W-coupling between the proton on C-7 and the proton on C-5 is significant (1.2 Hz), indicative of an *exo* proton on C-7. For **14**, these protons are only weakly coupled (0.5 Hz), which is consistent with an *endo* proton on C-7; therefore, the alkenyl side chain is *exo*.

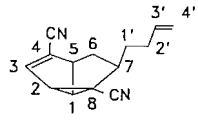

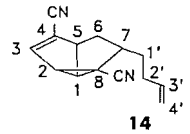

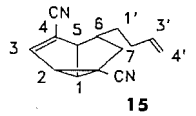

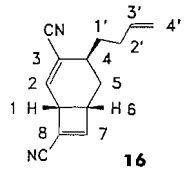

The minor *meta* cycloaddition product from reaction [3] has been assigned structure 6-*exo*-(3-butenyl)-4,8-dicyanotricyclo-[3.3.0.0^{2,8}]oct-3-ene (**15**). The absence of a distinctive doublet of doublets in the aliphatic region of the ^{1}H nmr spectrum of this isomer, characteristic of an *endo* proton on C-6, with strong geminal coupling to another proton on C-6, is an indication that this isomer has the alkenyl side chain in the *exo* position on C-6. The *endo* proton on C-6 shows up as a complex multiplet (2.20–2.30 ppm) coupled (6.8 Hz) to the nonequivalent protons on the adjacent methylene of the alkenyl side chain, and to the *endo* proton on C-7 (4.6 Hz). The protons on C-7 (1.92–2.02 ppm) show geminal coupling (5.7 Hz). The spectrum shows one proton (3.27 ppm) assigned to the proton at the bridgehead (C-5), coupled strongly to only one proton (3.29 ppm, 5.8 Hz) assigned to the proton at the apex of the three bridgeheads (C-1). The proton on C-5 shows no further coupling to adjacent proton(s); the four-carbon chain must be in the *exo* position on C-6. The proton on C-1 is coupled, not only to the proton on C-5, but also to the allylic proton on C-2 (2.74 ppm, 5.7 Hz). The proton at C-2 is also coupled to the vinyl proton on C-3, which shows up as a sharp doublet (6.46 ppm, 2.5 Hz).

The fourth compound from reaction [3] has been assigned structure *trans*-4-(3-butenyl)-*cis*-3,8-dicyanobicyclo[4.2.0]-octa-2,7-diene (**16**). Literature precedents for the complex thermal and photochemical rearrangements involved during reaction [4], and comparison of the ^{1}H nmr spectra of **16** with those reported for similar compounds were helpful in arriving at this conclusion (8, 9).

The protons associated with the four-carbon chain were readily identified by comparison with the spectra of **13–15**. One of the vinyl protons in the bicyclic system shows up as a doublet of doublets (C-2, 6.79 ppm), coupled to the allylic proton on C-4 (2.20 ppm, 2.5 Hz), and to the bridgehead proton on C-1 (3.74 ppm, 5.5 Hz). The other vinyl proton, on C-7, is a doublet (6.89 ppm, 1.2 Hz) coupled to the proton on the other bridgehead (C-6, 3.34 ppm). The proton on C-6 is a multiplet (couplings: 1.2, 3.3, 4.1, and 5.9 Hz). The proton on C-1 is a multiplet, coupled to the proton on C-5 (W-coupling, 1.5 Hz),

Can. J. Chem. Downloaded from www.nrcresearchpress.com by 195.246.54.202 on 09/08/12
For personal use only.

to the proton on C-6 (4.1 Hz), and to the proton on C-2 (5.5 Hz). The proton on C-4 is a complex multiplet; the coupling constants for the protons on the adjacent methylene, C-5 (1.35 and 2.08 ppm), are 10.3 and 4.9 Hz, respectively. This large coupling is indicative of the four-carbon chain being *trans* to the cyclobutene ring. The remaining assignments are listed in the experimental section; they are all consistent with the structure, and are in good agreement with those reported for similar structures (8).

The photo-NOCAS product from reaction [5] was assigned the structure 5-(4-cyanophenyl)-6-methoxy-5-methyl-1-hexene (**17**). The aliphatic region of the ^{1}H nmr spectrum exhibits resonances corresponding to two adjacent methylene groups (C-3 and C-4) and a singlet corresponding to a methyl group bonded to a quaternary centre. A sharp singlet at 3.29 ppm represents a methoxy methyl group. A distinctive AB-type coupling pattern at 3.37 and 3.49 ppm supports a methoxy-substituted methylene group adjacent to a chiral centre; two sharp doublets are observed with a coupling constant of 9.1 Hz. There is evidence for three vinyl protons, indicative of the terminal alkene. The aromatic region of the ^{1}H nmr spectrum shows a distinctive AA′XX′ coupling pattern, which is consistent with the *para*-substituted ring.

The imine **18***a* was not isolated; hydrolysis of the imine to the ketone **18** occurs during the chromatographic separation of the crude photolysate. The gc/ms of the initial mixture indicates that the ketone is not present; however, there is a peak with a retention time similar to that of the ketone and with a similar ms fragmentation pattern that we attribute to the imine. The ^{1}H nmr spectrum of the ketone, 1-(4-cyanophenyl)-2-methoxymethyl-2-methyl-5-hexen-1-one (**18**), is similar to that of the photo-NOCAS product **17**. Proof for the aryl-conjugated carbonyl group was found in the infrared spectrum, a strong carbonyl stretch at 1687 cm^{-1}. The ^{13}C nmr spectrum also exhibits a singlet at 208.10 ppm, characteristic of a carbonyl carbon bonded to a tertiary centre.

The adducts formed from 2,5-dimethyl-1,5-hexadiene (reaction [6]) were assigned structures 5-(4-cyanophenyl)-6-methoxy-2,5-dimethyl-1-hexene (**19**) and 1-(4-cyanophenyl)-2-methoxymethyl-2,5-dimethyl-5-hexen-1-one (**20**). The ^{1}H nmr spectrum of **19** is similar to that of **17**; a sharp singlet at 3.29 ppm represents a methoxy methyl group and a distinctive AB-type coupling pattern at 3.38 and 3.49 ppm supports a methoxy-substituted methylene group adjacent to a chiral centre. Two sharp doublets with a coupling constant 9.1 Hz are observed. The ^{1}H nmr spectrum of **19** shows only two slightly broadened singlets in the vinyl-proton region, indicative of the terminal methylene group. The spectra from **20** were similar to those of **19**.

The gross structure of the cyclized photo-NOCAS adducts, *cis*- and *trans*-1-(4-cyanophenyl)-4-methoxy-1,4-dimethylcyclohexane (*cis* and *trans* **21**) from reaction [7] was easily established from the ABCD-type coupling pattern in the aliphatic region of the ^{1}H nmr spectra and two types of methylene groups in the ^{13}C nmr spectra. For *cis*-**21**, there are two singlets in the aliphatic region of the ^{1}H nmr spectrum, corresponding to the two methyl groups. A shift reagent (europium (III) tris-1,1,1,2,2,3,3-heptafluoro-7,7-dimethyl-4,5-octanedione) was used to determine which methyl group was attached to the quaternary carbon bearing the methoxy group. This shift reagent is known to complex with the oxygen of the methoxy group and, thus, selectively shift the geminal methyl group (12). The signal (1.00 ppm) due to the methyl group next to the methoxy group and the signal (1.14 ppm) due to the methyl group bound to the same carbon as the 4-cyanophenyl group were thus distinguished. The *cis* configuration of this compound was then established on the basis of a nuclear Overhauser experiment (NOE). When the high-frequency (1.14 ppm) signal due to the methyl group next to the 4-cyanophenyl group was irradiated, an increase in the signal due to the cyclohexane protons was observed. Therefore, this methyl group must be in the axial position, close to the axial protons on the cyclohexane ring. No change was observed when the low-frequency (1.00 ppm) methyl signal was similarly irradiated.

The ^{1}H nmr spectrum of the *trans* isomer was similar to that of the *cis* isomer just described. In this case, the signal due to the methyl group next to the methoxy group occurs at 1.18 ppm and that due to the methyl on the carbon bearing the 4-cyanophenyl group is at 1.24 ppm. Nuclear Overhauser enhancement experiments on this isomer show no enhancement of the signal due to the cyclohexane protons upon irradiation of either methyl group; thus, both methyl groups are in the equatorial position.

These configuration/conformation assignments are supported by molecular mechanics calculations.[5] Consider first the model systems: 1-methoxy-1-methylcyclohexane and 1-methyl-1-(4-cyanophenyl)cyclohexane. Molecular mechanics calculations indicate that both the methoxy and the 4-cyanophenyl groups prefer the axial position; the methyl group is equatorial in the global minimum for both compounds. For 1-methoxy-1-methylcyclohexane the difference in energy for the two conformations (methoxy equatorial − methoxy axial) is 5.4 kJ mol^{-1}, and for 1-methyl-1-(4-cyanophenyl)cyclohexane the 4-cyanophenyl axial conformer is 2.5 kJ mol^{-1} more stable than the conformer with the 4-cyanophenyl group equatorial. The evidence from the ^{1}H nmr study suggests that in the global minimum for *trans*-1-(4-cyanophenyl)-4-methoxy-1,4-dimethylcyclohexane (**21** *trans*), both of the methyl groups are in the equatorial position. This is consistent with the molecular mechanics calculations, which show this conformer to be 7.7 kJ mol^{-1} more stable than the conformer having both of the methyl groups in the axial position. For *cis*-1-(4-cyanophenyl)-4-methoxy-1,4-dimethylcyclohexane (**21** *cis*), the ^{1}H nmr evidence shows that the methyl group next to the 4-cyanophenyl group is in the axial position; the molecular mechanics calculations show that this conformer is 5.2 kJ mol^{-1} more stable than the conformer that places the methyl group next to the methoxy group in the axial position.

The ^{1}H nmr spectra of the photo-NOCAS products **22** and **23** (reaction [8]) both show four sharp singlets for the four methyl groups, two slightly broadened singlets in the vinyl-proton region, and a coupled pattern for the three protons associated with the methylene and methine groups. The distinction between the two isomers was made on the basis of chemical shift for the protons and carbon adjacent to the 4-cyanophenyl and methoxy groups. For **22**, the methylene and methine protons show up as an AA′X pattern. The proton on the carbon bearing the methoxy group shows up as an apparent triplet at relatively low field (3.32 ppm, 5.9 Hz) coupled to the adjacent

[5]The molecular mechanics programme used for these calculations was PCMODEL, a product of Serena Software, Bloomington, Ind. Similar results have been reported for 1-methyl-1-phenylcyclohexane and for 1-methoxy-1-methylcyclohexane (13).

Can. J. Chem. Downloaded from www.nrcresearchpress.com by 195.246.54.202 on 09/08/12
For personal use only.

methylene hydrogens (1.91 ppm). This regiochemistry is supported by the ^{13}C nmr spectrum; the methine carbon bearing the methoxy group is a doublet at 87.98 ppm. A singlet at 43.74 ppm provides evidence that the aryl group is bonded to the quaternary carbon. For **23**, the methylene protons at 2.50 and 2.64 ppm and the methine proton at 2.95 ppm are coupled in a typical ABX pattern. The chemical shift of the methine proton is typical for a benzylic proton. The ^{13}C nmr spectrum of this isomer shows a singlet at low field (76.44 ppm), which is consistent with a methoxy-substituted quaternary carbon, and a doublet (53.38 ppm) for the carbon bearing the aryl group.

Generally the codonor and photosensitizer (electron transfer) were largely recovered; however, small amounts of 2-cyanobiphenyl (**25**), 4-cyanobiphenyl (**26**), and 3,5-dimethoxy-4-phenylcyclohexanecarbonitrile (**27**) were detected when biphenyl (**4**) was used as a codonor. Characterization of **25** and **26** was achieved by direct comparison (gc/ms, retention time, and fragmentation pattern) with authentic samples. The structure assigned to **27** rests firmly on an X-ray diffraction analysis of a single crystal, isolated from reaction [7] (see Appendix, Depository of Unpublished Data).[6] Molecular mechanics calculations on **27** are consistent; the conformer having the methoxy groups in the axial position is more stable than the alternative chair conformer by 7.2 kJ mol^{-1}. Minor products, 9-methoxy-9,10-dihydrophenanthrene (**28**) and 9-cyano-9,10-dihydrophenanthrene (**29**), obtained when phenanthrene (**5**) was used as a photosensitizer, were characterized by direct comparison (gc/ms, retention time and fragmentation pattern, ^1H nmr) with authentic samples.

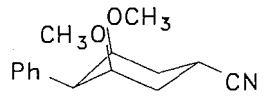

27

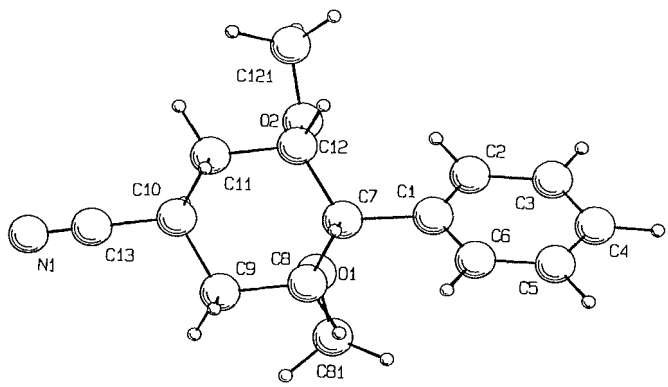

27

Discussion

The proposed mechanism for the photo-NOCAS reaction, shown in Scheme 1, has been described in detail in previous publications in this series (1, 3); all of the results reported here are consistent with the general features of this mechanism. In the absence of added photosensitizer, the initial excitation involves absorption into the ^1L_b band of 1,4-dicyanobenzene (**1**) (step 1). These nonconjugated dienes, **9–12**, are transparent at wavelengths transmitted through Pyrex (>280 nm).

Step 2 in the proposed mechanism involves single electron transfer (SET) from the diene to the singlet excited state of 1,4-dicyanobenzene (**1**). The rate of this process can be predicted from the singlet energy and reduction potential of the electron acceptor (**1**), and the oxidation potential of the electron donor, i.e., the diene, on the basis of the Weller equation (eq. [9]) (11). These values are given in Table 1. Electron transfer occurs at the diffusion-controlled rate when the free energy for electron transfer (ΔG_{et}, eq. [9]) is exergonic by -20 kJ mol^{-1} or more (11). The free energy of electron transfer to the excited singlet state of **1** from 1,5-hexadiene (**9**) is highly endergonic (>35.7 kJ mol^{-1}). Electron transfer should not occur in this case and the observations (reaction [3]) are in accord with this prediction

$$[9] \quad \Delta G_{et} = F[E^{ox}_{1/2}\ (D) - E^{red}_{1/2}\ (A) - e/\epsilon\alpha] - E_{0,0}(A) \qquad \text{(ref. 11)}$$

The products obtained from reaction [3] are consistent with involvement of an intermediate polar exciplex (8, 9, 14). The mode of cycloaddition, *ortho* or *meta*, can be predicted on the basis of the polarity of the exciplex assessed by the ΔG_{et} for complete electron transfer. With benzonitrile, for example, *ortho* adducts form if ΔG_{et} is less than 164 kJ mol^{-1} while *meta* adducts result if ΔG_{et} is greater than 164 kJ mol^{-1} (14*b*). We have been unable to measure the oxidation potential of **9**; only a minimum value, >3 V (vs. sce), could be determined. This is consistent with literature values for other terminal alkenes, some of which have oxidation potentials greater than 3.5 V (vs. sce) (15). If the correlation observed with benzonitrile also pertains to **1**, the predominant formation of *meta* adducts from **1** and **9** requires the oxidation potential of **9** to be ca. 4 V. There is no evidence for interaction between the two double bonds of **9**, which would lower the oxidation potential below that expected for a normal terminal mono-alkene.

The major products from reaction [3], *meta* adducts **13**, **14**, and **15**, are the result of addition of **9** across the 1,3-position of the 1,4-dicyanobenzene ring. This regiochemistry is consistent with the detailed mechanism for *meta*-adduct formation, beginning with the initially formed polar exciplex (9*a*). Minor product **16** is the result of *ortho* addition of **9** across the 1,2-position of 1,4-dicyanobenzene. Subsequent thermal or photochemical ring opening followed by photochemical cyclization, illustrated in reaction [4], can account for formation of **16**. This sequence has adequate precedent (8).

The addition of the potential codonor, biphenyl (**4**), to the irradiation mixture quenches the formation of these cycloadducts. Biphenyl (**4**), of course, quenches the excited singlet state of 1,4-dicyanobenzene (**1**) by the electron transfer mechanism. This quenching leads to formation of the radical ions $\mathbf{4}^{+\cdot}$ and $\mathbf{1}^{-\cdot}$ (Scheme 1, step 6a). Still, no photo-NOCAS products are formed. Clearly, the oxidation potential of **9** is sufficiently greater than that of biphenyl (**4**) that the radical cation $\mathbf{4}^{+\cdot}$ cannot serve as a codonor with it; electron transfer from **9** to $\mathbf{4}^{+\cdot}$ (step 7) is endergonic by >115 kJ mol^{-1}. Phenanthrene (**5**)

[6]These data may be purchased from: The Depository of Unpublished Data, Document Delivery, CISTI, National Research Council Canada, Ottawa, Canada K1A 0S2.

Details of data collection, structural analysis and refinement, and tables of interatomic distances and bond angles have also been deposited with the Cambridge Crystallographic Data Centre and may be obtained on request from the Director, Cambridge Crystallographic Data Centre, University Chemical Laboratory, 12 Union Road, Cambridge, CB2 1EZ, U.K.

Reaction [10] (1)

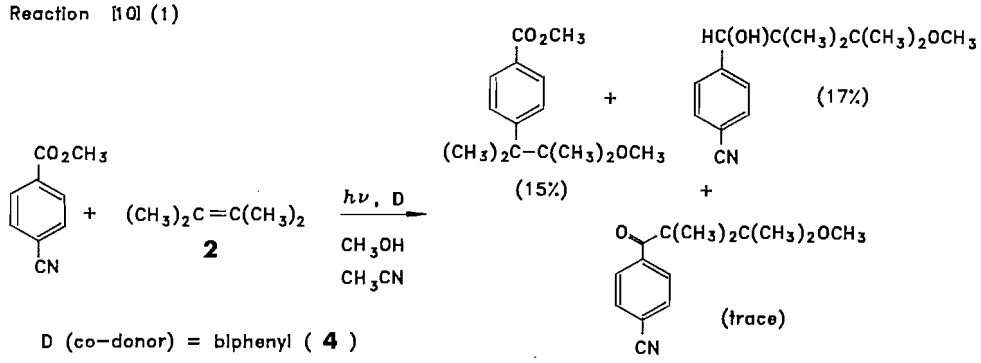

quenches the reaction simply by competitive light absorption. In this case also, radical ions $\mathbf{5}^{+\cdot}$ and $\mathbf{1}^{-\cdot}$ will form (steps 6b and c), but electron transfer from **9** to $\mathbf{5}^{+\cdot}$ is unfavourable. Back electron transfer (step 8) completes the quenching mechanism.

Electron transfer does occur from 2-methyl-1,5-hexadiene (**10**) to the excited singlet state of 1,4-dicyanobenzene (**1**) (step 2). Even though electron transfer is endergonic (6.8 kJ mol^{-1}), radical ions form and the photo-NOCAS product is obtained (reaction [5]). Radical ion formation involving electron transfer from 2-methylpropene (**6**) to the excited singlet state of **1**, in reaction [2], involves a similar endergonic process (3). As expected, the photo-NOCAS product **17** is the *anti*-Markovnikov adduct. The radical cation $\mathbf{10}^{+\cdot}$ reacts with methanol at the terminal carbon of the more heavily substituted double bond to give the β-alkoxy-*tert*-alkyl radical (step 3), this radical attacks the *ipso* position of the radical anion $\mathbf{1}^{-\cdot}$ (step 4), and the intermediate cyclohexadienyl anion rearomatizes, with loss of cyanide ion (step 5), to give the photo-NOCAS product. No products resulting from cycloaddition of diene **10** to the aromatic ring were detected (gc/ms) in this case; either the exciplex does not form or it is rapidly deactivated by electron transfer.

Another product of this reaction was imine **18***a*, isolated as ketone **18** following chromatography of the photolysate. One explanation for imine formation would involve radical – radical anion coupling at the carbon of the cyano group; however, the spin density (calculated, STO-3G) at the cyano carbon in the radical anion is relatively small, only ca. 0.1 that at the *ipso* position (1). An alternative explanation: the radical anion, $\mathbf{1}^{-\cdot}$, may reduce the β-alkoxyalkyl radical to the anion, then further reaction can be viewed as a nucleophilic attack of the anion on the cyano group of neutral 1,4-dicyanobenzene (**1**). The reduction potential of the tertiary radical may be less negative than the reduction potential of **1** (16). While reduction of the radical to the anion may be favourable, the rate of this electron transfer may be slow due to the large reorganization energy involved in this process (16, 17). We have never observed attack on the cyano group of 1,4-dicyanobenzene (**1**) before; however, we have used this mechanism to explain the analogous formation of products resulting from attack on the carboxyl carbonyl during the photo-NOCAS reaction of methyl *para*-cyanobenzoate (reaction [10]) (1).

The addition of biphenyl (**4**) increases the efficiency of formation and the yield of photo-NOCAS product **17**. No imine (or ketone) was formed under these conditions. Biphenyl (**4**) functions as a codonor (step 6a), followed by complex formation between $\mathbf{4}^{+\cdot}$ and **10**. Electron transfer from **10** to $\mathbf{4}^{+\cdot}$ (step 7) is endergonic (85 kJ mol^{-1}); reaction with methanol may involve the small equilibrium concentration of $\mathbf{10}^{+\cdot}$ or attack of methanol may occur on the complex. The increased efficiency of the reaction is thought to be due to slower back electron transfer between $\mathbf{1}^{-\cdot}$ and $\mathbf{4}^{+\cdot}$ within the SSRIP, the result of a smaller reorganization energy for $\mathbf{4}^{+\cdot}$ returning to **4**.

No cyclic products were observed from reaction [5]. The radical cation $\mathbf{10}^{+\cdot}$ apparently does not cyclize. Reaction occurs only at the more heavily substituted double bond. The rate of attack of methanol on the initially formed acyclic radical cation ($\mathbf{10}^{+\cdot}$) must be rapid enough to prevent cyclization. We will return to this point later.

The intermediate β-alkoxyalkyl radical also does not cyclize. A 1,4-*exo* radical cyclization is thermodynamically unfavourable and the alternative 1,5-*endo* radical cyclization is slow for steric reasons; as a result, reaction of the β-alkoxyalkyl radical with the 1,4-dicyanobenzene radical anion ($\mathbf{1}^{-\cdot}$) is rapid enough to compete with cyclization (6*i*,*j*).

Results from the irradiation of an acetonitrile–methanol (3:1) solution of 1,4-dicyanobenzene (**1**) and 2,5-dimethyl-1,5-hexadiene (**11**) were similar to those observed with the monomethyl analog **10**. The oxidation potential of **11** is low enough that electron transfer to the excited singlet state of **1** is exergonic (−2.8 kJ mol^{-1}); both the photo-NOCAS adduct (**19**) and the imine (**20***a*) were obtained (reaction [6]). There was no evidence for cyclization of the initially formed radical cation $\mathbf{11}^{+\cdot}$ or of the intermediate β-alkoxyalkyl radical under these conditions.

However, cyclized products, *cis*- and *trans*-4-(4-cyanophenyl)-1-methoxy-1,4-dimethylcyclohexane (**21** *cis* and *trans*), were obtained when biphenyl (**4**) was added to the irradiation mixture (reaction [7]). The ratio of cyclic to acyclic products is a function of biphenyl (**4**) and methanol concentration (Figs. 1 and 2). The observation that the ratio of cyclic to acyclic product (**21** *cis* and *trans*/**19**) decreases with increasing methanol concentration, between 0.2 and 2.0 M, is good evidence that it is the acyclic radical cation ($\mathbf{11}^{+\cdot}$) that cyclizes — not the β-alkoxyalkyl radical. Furthermore, the regiochemistry of the cyclized products is inconsistent with prior formation of a β-alkoxyalkyl radical that involves preferential attack of methanol on the terminal carbon. The effect of biphenyl (**4**) can be explained if the reaction of the complex (**4** with **11**)$^{+\cdot}$ with methanol is slower than that of uncomplexed $\mathbf{11}^{+\cdot}$.

Scheme 1 must be modified to include a cyclization step between steps 7 and 3 to allow formation of the 1,4-dimethylcyclohexane-1,4-diyl radical cation (step 3a). Reaction of the cyclized radical cation with methanol leads to formation of the 4-methoxy-1,4-dimethylcyclohexyl radical (step 3b); addition of this radical to the 1,4-dicyanobenzene radical anion ($\mathbf{1}^{-\cdot}$) continues the mechanistic sequence. On the reasonable assump-

Can. J. Chem. Downloaded from www.nrcresearchpress.com by 195.246.54.202 on 09/08/12
For personal use only.

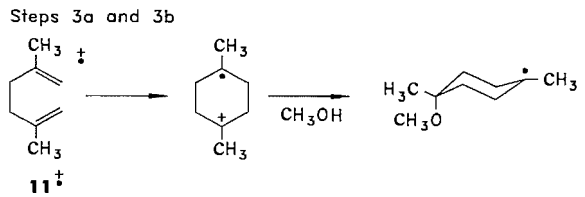

tion that there is little interaction between the radical centre and the remote methoxy group, the preferred conformation of this cyclohexyl radical will be *pseudo*-chair with the methoxy group in the axial position. The dominant (70%) formation of the diastereomer bearing the methoxy and 4-cyanophenyl groups *cis* (**21** *cis*) is consistent with the favoured transition state for addition of this radical to the 1,4-dicyanobenzene radical anion ($\mathbf{1}^{-\cdot}$) involving equatorial attack (18).

The observation that cyclic products are obtained from radical cation $\mathbf{11}^{+\cdot}$, while no cyclic products were observed from $\mathbf{10}^{+\cdot}$, is tentatively explained on thermodynamic grounds. The calculated (MINDO/3) activation energy for cyclization of the parent radical cation of 1,5-hexadiene (**9**) to the cyclohexane-1,4-diyl radical cation is <8 kJ mol^{-1} (19*a*). These calculations also indicate that the cyclohexane-1,4-diyl radical cation is 140 kJ mol^{-1} **more** stable than the acyclic diene radical cation $\mathbf{9}^{+\cdot}$. In marked contrast, recent thermochemical calculations suggest that the 1,4-dimethylcyclohexane-1,4-diyl radical cation is 10 kJ mol^{-1} **less** stable than the acyclic diene radical cation $\mathbf{11}^{+\cdot}$ (19*b*). Therefore, cyclization of the *syn, syn-gauche* conformation of $\mathbf{11}^{+\cdot}$ to 1,4-dimethylcyclohexane-1,4-diyl radical cation may be reversible. A rapid equilibration between the acyclic and cyclic radical cations may explain why the ratio of cyclic to acyclic products (**21** *cis* and *trans*/**19**) levels off at higher methanol concentration (>2 M).

It seems likely that 1-methylcyclohexane-1,4-diyl radical cation is even less stable relative to the acyclic radical cation $\mathbf{10}^{+\cdot}$. The lack of cyclic products from reaction [5] may be the result of an unfavourable equilibrium for the 1-methylcyclohexane-1,4-diyl radical cation.

Molecular mechanics calculations of **10** and **11** identify several low-lying conformations, differing little in energy; furthermore, the rotational barriers between conformers must be small, <15 kJ mol^{-1}.[7] Cyclization through a *pseudo*-chair transition state requires the *syn, syn-gauche* conformation of the diene (Figs. 3*b* and 4*b*). This reactive conformer of **11** has nine conformers of lower energy and is only 7.7 kJ mol^{-1} above the global minimum (Fig. 4*a*). In marked contrast, the reactive *syn, syn-gauche* conformer of **10** has 21 conformers of lower energy and is 9.5 kJ mol^{-1} above the global minimum (Fig. 3*a*). Clearly the conformation required for cyclization is statistically and energetically favoured in the case of **11** relative to **10**.

The rate constant for addition of methanol to aryl-substituted alkene radical cations is in the range 10^7–10^9 M^{-1} s^{-1} (20). The rate of reaction of alkyl-substituted alkene radical cations is not known but reaction is probably even more rapid. It therefore seems likely that the initial rate of 1,6-*endo*, *endo* cyclization is determined by the rate of conformational change to the *syn, syn-gauche* conformer. This can account for the dependence of the product ratio (**21** *cis* and *trans*/**19**) on methanol concentration.

[7]The molecular mechanics programme used for these calculations was MM3(92). Chiral conformers were counted as two individual conformers.

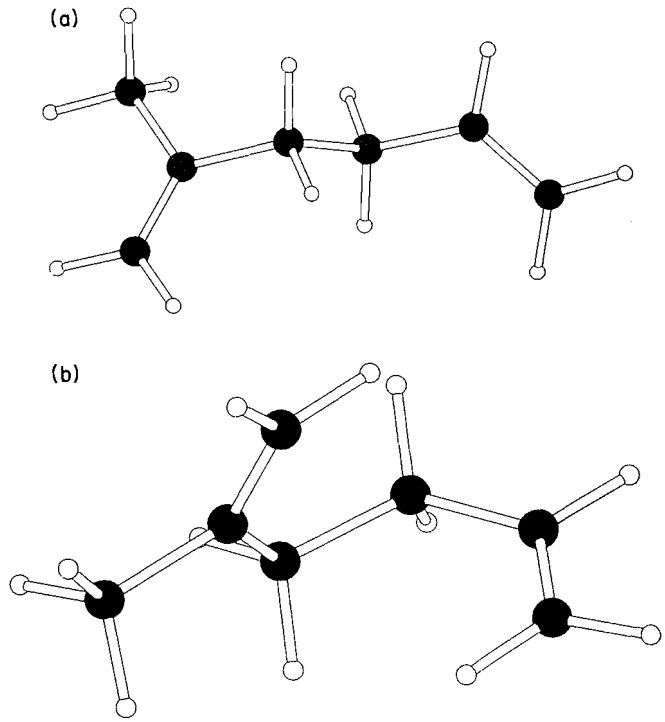

FIG. 3. (*a*) The global minimum (MM3) conformer of 2-methyl-1,5-hexadiene (**10**). (*b*) The *syn, syn-gauche* conformer of 2-methyl-1,5-hexadiene (**10**).

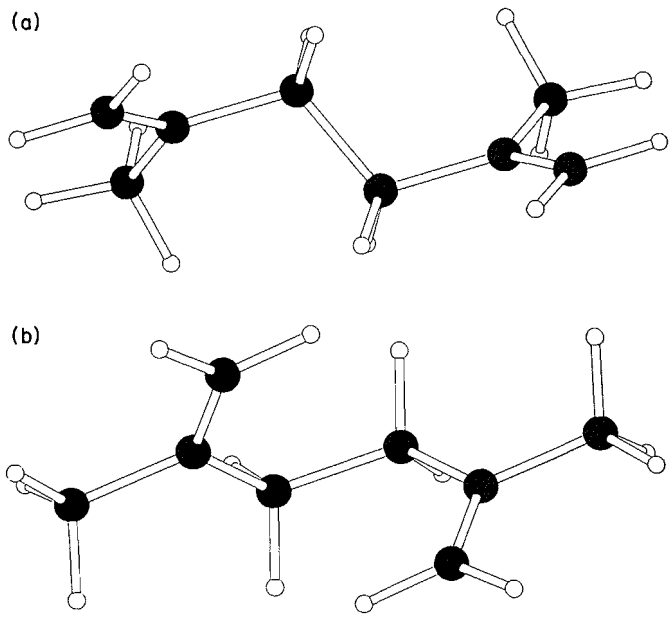

FIG. 4. (*a*) The global minimum (MM3) conformer of 2,5-dimethyl-1,5-hexadiene (**11**). (*b*) The *syn, syn-gauche* conformer of 2,5-dimethyl-1,5-hexadiene (**11**).

When a Freon (CF_3CCl_3) matrix of 1,5-hexadiene was subjected to radiolytic oxidation (irradiated with γ-rays) at 77 K, there was no evidence for the acyclic diene radical cation $\mathbf{9}^{+\cdot}$. The observed spectra were attributed to the cyclohexane-1,4-diyl radical cation (21). When the matrix was annealed or photobleached the signal from the cyclohexane-1,4-diyl radical cation decreased with a corresponding growth of the signal for the cyclohexene radical cation. When

Can. J. Chem. Downloaded from www.nrcresearchpress.com by 195.246.54.202 on 09/08/12
For personal use only.

Can. J. Chem. Downloaded from www.nrcresearchpress.com by 195.246.54.202 on 09/08/12
For personal use only.

2,5-dimethyl-1,5-hexadiene (**11**) was studied under somewhat different conditions, neither the acyclic radical cation $\mathbf{11}^{+\cdot}$ nor the 1,4-dimethylcyclohexane-1,4-diyl radical cation were detected; the observed spectrum was attributed to the *trans*-3,6-dimethylcyclohexene radical cation (22). Apparently, cyclization and rearrangement occurred rapidly under these conditions. In view of these reports of facile rearrangement of cyclohexane-1,4-diyl radical cations, it is significant that we found no evidence for the rearrangement of the 1,4-dimethylcyclohexane-1,4-diyl radical cation $\mathbf{11}^{+\cdot}$ during reaction [7].

Previous studies have shown that the cyclohexane-1,4-diyl radical cation is an intermediate in the SET-induced Cope rearrangement (19, 23). In the special case of 2,5-diphenyl-1,5-hexadiene, the radical cation produced by SET to the excited singlet state of 9,10-dicyanoanthracene cyclizes to the bis-benzylic, resonance-stabilized, 1,4-diphenylcyclohexane- 1,4-diyl radical cation, which could be trapped by oxygen to give the bicyclic peroxide (23*b*).

The products obtained from 2,5-dimethyl-1,4-hexadiene (reaction [8]) are consistent with the proposed mechanism (1, 3). The major photo-NOCAS product is the *anti*-Markovnikov adduct **22**. Formation of a small amount of Markovnikov adduct **23** is expected from this, a trisubstituted alkene (3). In this case also, reaction occurs only at the more heavily substituted double bond, i.e., the site of lower oxidation potential. Deprotonation of the radical cation $\mathbf{12}^{+\cdot}$, to give the allylic radical, reduction of this radical by $\mathbf{1}^{-\cdot}$, and reprotonation of the resulting ambident anion, gives the conjugated tautomer **24**. There was no evidence for cyclization of the acyclic radical cation or of the intermediate β-alkoxyalkyl radical.

The minor products, 2-cyanobiphenyl (**25**), 4-cyanobiphenyl (**26**), and 3,5-dimethoxy-4-phenylcyclohexanecarbonitrile (**27**), detected in reactions using biphenyl (**4**) as codonor, and isolated from reaction [7], are consistent with the involvement of $\mathbf{4}^{+\cdot}$. Similarly, 9-methoxy-9,10-dihydrophenanthrene (**28**) and 9-cyano-9,10-dihydrophenanthrene (**29**) are expected products following nucleophilic addition to the phenanthrene radical cation ($\mathbf{5}^{+\cdot}$), formed when phenanthrene is added as a photosensitizer. The mechanism for formation of **27** must involve several steps. Addition of cyanide ion, generated during the rearromatization step (step 5), to the *para* position of radical cation $\mathbf{4}^{+\cdot}$, followed by hydrogen abstraction by the resulting radical, will give a dihydro-4-cyanobiphenyl. Subsequent addition of two moles of methanol to the radical cation of the phenylcyclohexadiene and phenylcyclohexene can account for this product.

Experimental

General information

^{1}H and ^{13}C nmr spectra were obtained from a Bruker 300 MSL spectrometer or a Nicolet 360 NB spectrometer. Spectra are reported in parts per million (ppm) relative to tetramethylsilane. Infrared spectra (ir) were recorded on an air-purged Perkin–Elmer 180 grating spectrometer and are reported in wavenumbers (cm^{-1}) relative to the 1601.4 cm^{-1} absorption band of polystyrene film. Elemental analyses were performed by Canadian Microanalytical Service Ltd., B.C. Exact mass determinations were obtained on a ZAB-E mass spectrometer. Melting points were determined using a Cybron Corporation Thermolyne apparatus with a digital thermocouple and are corrected. Product yields were determined using a Hewlett–Packard (HP) 5890 gas chromatograph with a DB-1701 fused silica WCOT column (30 m × 0.25 mm, 0.25-μm film thickness) and a calibrated flame ionization detector (gc/fid) and are based upon 1,4-dicyanobenzene (**1**) as the limiting reagent. An HP 3392A integrator was interfaced with the gc/fid to obtain peak areas. An HP 5890 gas chromatograph with a 5% phenyl methyl silicone fused silica WCOT column (25 m × 0.20 mm, 0.33-μm film thickness) interfaced with an HP 5970 mass selective detector (gc/ms) was also used for product analyses. Mass spectra are reported as *m/z* (relative intensity). Separation of product mixtures was generally carried out using preparative medium-pressure liquid chromatography (mplc) (3*b*). The mplc unit consists of a 2.5 cm × 1 m column packed with thin-layer chromatography (tlc) grade silica gel (without binder) (cat. no. 7747 Merck) at a pressure of 15 psi using helium (1 psi = 6.9 kPa). Connected to the mplc was a uv spectrophotometer – fraction collector that collects ca. 10-mL fractions. Another method used for product separation was flash chromatography (fc) on a 35 mm × 160 mm column (Column A) or a 30 mm × 180 mm column (Column B) (24*a*). The columns were packed with silica gel that was 230–400 mesh, 60 Å (Aldrich), under 3 psi of nitrogen. Dry column flash chromatography (dc/fc) was also used (24*b*). The column was packed with thin-layer chromatography grade silica gel (without binder) (cat. no. 7747 Merck). Fraction sizes were ca. 5 mL. Preparative-GC (prep/gc) was carried out using a Varian Aerograph A700 or 920, fitted with either 10% FFAP on Chromasorb W 60/80 or 40% SE-30 Chromasorb W 60/80 columns.

Materials

Acetonitrile (Fisher ACS grade) was distilled twice, first from sodium hydride and then from phosphorus pentoxide. It was then passed through a column of basic alumina, refluxed over calcium hydride for 24 h (under a nitrogen atmosphere), fractionally distilled (under nitrogen), and stored over molecular sieves (3 Å) (25). Methanol was distilled and then stored over molecular sieves (4 Å). 1,4-Dicyanobenzene (**1**) (Aldrich) was purified by treatment with Norite in methylene chloride, followed by recrystallization from 95% ethanol. Tetraethylammonium perchlorate (TEAP) (Aldrich) was recrystallized three times from water and then dried in a vacuum oven for 15 h, 70°C, 0.25 Torr (1 Torr = 133.3 Pa). 1,5-Hexadiene (**9**) 98%, 2-methyl-1,5-hexadiene (**10**) 99%, 2,5-dimethyl-1,5-hexadiene (**11**) 90% and 99%, and 5-methyl-3-hexen-2-one 80% were obtained from Aldrich Chemical Co.

Irradiations

Irradiations were generally carried out on solutions of acetonitrile–methanol (3:1) with 1,4-dicyanobenzene (**1**), the diene, and with or without a codonor/photosensitizer. Solutions were irradiated in either 2 cm i.d. Pyrex tubes or 5 mm Pyrex nmr tubes, which were degassed by nitrogen ebullition. These samples were irradiated at 10°C using a CGE 1-kW or an Hanovia 450-W medium-pressure mercury vapour lamp contained in a water-cooled quartz immersion well.

Cyclic voltammetric measurements

Cyclic voltammetry was used to obtain the oxidation potential of the dienes. The apparatus has been described (26). The working electrode was a platinum sphere (1 mm diameter) and the counter electrode was a platinum wire. The reference electrode was a saturated calomel electrode (sce), which was connected to the solution (TEAP 0.1 M, acetonitrile) through a Luggin capillary. The dienes were purified by prep/gc using a 0.95 cm × 350 cm aluminum column packed with 40% SE-30 on Chromosorb W 60/80 NAW. The diene concentration was ca. 0.005 M. Since the anodic wave was irreversible, the half-wave potential was taken as 0.028 V before the anodic peak potential (10).

*Formation of 1,5-hexadiene (**9**) – 1,4-dicyanobenzene (**1**) cyclic adducts **13–16**: reaction [3]*

A solution of 1,5-hexadiene (**9**) (6.4 g, 0.078 mol) and 1,4-dicyanobenzene (**1**) (2.5 g, 0.020 mol) in acetonitrile–methanol (3:1, 270 mL) was degassed by nitrogen ebullition for 15 min and irradiated for 67 h. The solvent was removed by rotary evaporation to yield a dark brown photolysate (5.0 g). Methylene chloride was added to this mixture to precipitate unreacted **1**, which was then removed by suction filtration. Aliquots (0.3–0.5 g) of this mixture were chromatographed (mplc) using a linear solvent gradient (hexanes – 75% diethyl ether, 25% hexanes). The products eluted in the order **13**, **15**, **14**, and **16**.

Can. J. Chem. Downloaded from www.nrcresearchpress.com by 195.246.54.202 on 09/08/12
For personal use only.

Fractions containing mixtures were combined and rechromatographed. The yields were determined by calibrated gc/fid; the total yield was 54%.

7-endo-*(3-Butenyl)-4,8-dicyanotricyclo[3.3.0.0^{2,8}]oct-3-ene* (**13**)

The yield of **13** was 29%: ^{1}H nmr (361.08 MHz, $CDCl_3$) δ_{TMS}: 1.61–1.71 (m, 2H, $^2J_{1'a-1'b}$ = 7.8 Hz, $^3J_{1'a-7}$ = 7.7 Hz, $^3J_{1'b-7}$ = 7.7 Hz, $^3J_{1'a-2'}$ = 7.5 Hz, $^3J_{1'b-2'}$ 7.5 Hz, CH_2 adjacent to allylic methylene group on the side chain (1′a-H, 1′b-H)), 1.80 (dd, 1H, $^2J_{6endo-6exo}$ = 13.2 Hz, $^3J_{6endo-7exo}$ = 0.9 Hz, small coupling to 5-H (6*endo*-H)), 2.15–2.22 (m, 2H, $^3J_{1'a-2'}$ = 7.5 Hz, $^3J_{1'b-2'}$ = 7.5 Hz, $^3J_{2'-3'}$ = 7.0 Hz, $^4J_{2'-4'cis}$ = 1.2 Hz, $^4J_{2'-4'trans}$ = 1.6 Hz, allylic CH_2 group (2′-H)), 2.62 (dd, 1H, $^3J_{2-1}$ = 6.6 Hz, $^3J_{2-3}$ = 2.5 Hz, allylic H (2-H)), 2.69 (m, 1H, $^2J_{6exo-6endo}$ = 13.2 Hz, $^3J_{6exo-7exo}$ = 11.4 Hz, $^3J_{6exo-5}$ = 5.5 Hz, *exo*-H at C6 (6*exo*-H)), 2.94 (m, 1H, $^3J_{7exo-6exo}$ = 11.4 Hz, $^3J_{1'a-7}$ = 7.7 Hz, $^3J_{1'b-7}$ = 7.7 Hz, $^3J_{7exo-6endo}$ = 0.9 Hz, $^4J_{7exo-5}$ = 1.2 Hz, (7*exo*-H)), 3.45 (m, 1H, $^3J_{1-2}$ = 6.6 Hz, $^3J_{1-5}$ = 5.8 Hz (1-H)), 3.50 (m, 1H, $^3J_{5-1}$ = 5.8 Hz, $^3J_{5-6exo}$ = 5.5 Hz, $^4J_{5-7exo}$ = 1.2 Hz, small coupling to 6*endo*-H (5-H), 5.03 (m, 1H, $^3J_{4'cis-3'}$ = 10.2 Hz, $^2J_{4'cis-4'trans}$ = 1.6 Hz, $^4J_{4'cis-2'}$ = 1.2 Hz, terminal vinyl H (4′*cis*-H)). 5.08 (m, 1H, $^3J_{4'trans-3'}$ = 17.1 Hz, $^2J_{4'trans-4'cis}$ = 1.6 Hz, $^4J_{4'trans-2'}$ = 1.6 Hz, terminal vinyl hydrogen (4′*trans*-H)), 5.77 (m, 1H, $^3J_{3'-4'trans}$ = 17.1 Hz, $^3J_{3'-4'cis}$ = 10.2 Hz, $^3J_{3'-2'}$ = 7.0 Hz, vinyl H (not on ring) (3′-H)), 6.54 (d, 1H, $^3J_{3-2}$ = 2.5 Hz, vinyl H on ring (3-H)); ^{13}C nmr (90.80 MHz, $CDCl_3$) δ: 29.69 (s, 8-C), 33.03 (t, 126.5 Hz), 34.12 (t, 127.7 Hz), 41.05 (d, 173.2 Hz), 44.39 (t, 131.0 Hz), 44.54 (d, 130.8 Hz), 46.59 (d, 183.8 Hz), 52.82 (d, 145.1 Hz), 114.83 (s), 115.84 (t, 156.3 Hz, terminal vinyl CH_2), 120.91 (s, CN), 122.86 (s, CN), 137.16 (d, 150.7 Hz), 143.67 (d, 173.8 Hz); ms *m/z*: 55(100), 64(15), 77(34), 91(23), 104(42), 115(21), 120(20), 128(34), 141(26), 142(26), 155(21), 168(42), 195(26), 209(42), 210 ($M^{+\cdot}$, 10). Anal. calcd. for $C_{14}H_{14}N_2$: C 79.96, H 6.71, N 13.32; found (using a mixture of 13% **14** and 87% **13**): C 79.70, H 6.77, N 13.28.

6-exo-*(3-Butenyl)-4,8-dicyanotricyclo[3.3.0.0^{2,8}]oct-3-ene* (**15**)

The yield of **15** was 2%: infrared (PE-180) *ν*: 3079 (m), 2929 (s), 2859 (m), 2234 (s), 2229 (s), 1643 (m), 1600 (w), 1454 (m), 1309 (w), 1009 (m), 997 (m), 979 (m), 899 (m), 844 (m), 829 (w); ms *m/z*: 55 (100), 77 (18), 115 (23), 128 (32), 141 (56), 142 (25), 168 (92), 182 (33), 209 (24), 210 ($M^{+\cdot}$, 7). ^{1}H nmr (361.08 MHz, $CDCl_3$) δ_{TMS}: 1.59 (m, 2H, $^3J_{1'a-2'}$ = 7.1 Hz, $^3J_{1'b-2'}$ = 7.1 Hz, $^3J_{1'a-6}$ = 6.8 Hz, $^3J_{1'b-6}$ = 6.8 Hz, $^3J_{1'a-1'b}$ = 5.5 Hz, CH_2 adjacent to allylic methylene (1′a-H, 1′b-H)), 1.92–2.02 (m, 2H, $^2J_{7exo-7endo}$ = 5.7 Hz, $^3J_{6-7endo}$ = 4.6 Hz, CH_2 on ring (7*exo*-H, 7*endo*-H)), 2.07–2.18 (m, 2H, $^3J_{1'a-2'}$ = 7.1 Hz, $^3J_{1'b-2'}$ = 7.1 Hz, $^3J_{2'-3'}$ = 6.6 Hz, $^4J_{2'-4'cis}$ = 1.1 Hz, $^4J_{2'-4'trans}$ = 1.5 Hz, allylic CH_2 (2′-H)), 2.20–2.30 (m, 1H, $^3J_{1'a-6}$ = 6.8 Hz, $^3J_{1'b-6}$ = 6.8 Hz, $^3J_{6-7endo}$ = 4.6 Hz, H on alkyl substituted carbon (6-H)), 2.74 (m, 1H, $^3J_{1-2}$ = 5.7 Hz, $^3J_{2-3}$ = 2.5 Hz, H at bridgehead adjacent to alkene (2-H)), 3.27 (d, 1H, $^3J_{1-5}$ = 5.8 Hz, H at bridgehead (5-H)), 3.29 (dd, 1H, $^3J_{1-5}$ = 5.8 Hz, $^3J_{1-2}$ = 5.7 Hz, H at apex of three bridge-heads (1-H)), 5.02 (m, 1H, $^3J_{3'-4'cis}$ = 10.3 Hz, $^2J_{4'cis-4'trans}$ = 1.6 Hz, $^4J_{2'-4'cis}$ = 1.1 Hz, terminal vinyl H (4′*cis*-H)), 5.06 (m, 1H, $^3J_{3'-4'trans}$ = 17.1 Hz, $^2J_{4'cis-4'trans}$ = 1.6 Hz, $^4J_{2'-4'trans}$ = 1.5 Hz, terminal vinyl H (4′*trans*-H)), 5.78 (m, 1H, $^3J_{3'-4'trans}$ = 17.1 Hz $^3J_{3'-4'cis}$ = 10.3 Hz, $^3J_{2'-3'}$ = 6.6 Hz, vinyl H (3′-H)), 6.46 (d, 1H, $^3J_{2-3}$ = 2.5 Hz, vinyl H on ring (3-H)); ^{13}C nmr (90.80 MHz, $CDCl_3$) δ: 24.02 (s, C-8), 31.01 (t, 134.4 Hz), 31.56 (t, 135.02 Hz), 32.57 (t, 134.4 Hz), 42.38 (d, 133.8 Hz), 43.92 (d, 145.9 Hz), 52.96 (d, 133.6 Hz), 56.92 (d, 145.1 Hz), 114.72 (s), 115.77 (t, 154.4 Hz, terminal vinyl CH_2), 119.64 (s, CN), 120.91 (s, CN), 137.16 (d, 151.0 Hz), 141.39 (d, 174.1 Hz); Exact Mass *m/z* calcd. for $C_{14}H_{14}N_2$: 210.1138; found: 210.1133.

7-exo-*(3-Butenyl)-4,8-dicyanotricyclo[3.3.0.0^{2,8}]oct-3-ene* (**14**)

The yield of **14** was 18%: ^{1}H nmr (361.08 MHz, $CDCl_3$) δ_{TMS}: 1.57–1.70 (m, 2H, CH_2 adjacent to allylic methylene group on the side chain (1′a-H, 1′b-H)), 1.95 (ddd, 1H, $^2J_{6exo-6endo}$ = 13.4 Hz, $^3J_{6exo-5}$ = 5.1 Hz, $^3J_{6exo-7endo}$ = 1.3 Hz, (6*exo*-H)), 1.98–2.25 (m, 4H, allylic CH_2 group (2′-H), (7*endo*-H, 6*endo*-H)), 2.70 (ddd, 1H, $^3J_{2-1}$ = 6.7 Hz, $^3J_{2-3}$ = 2.6 Hz, $^4J_{2-7endo}$ = 0.8 Hz, (2-H)), 3.32 (dd, 1H, $^3J_{1-2}$ = 6.7 Hz, $^3J_{1-5}$ = 5.7 Hz, (1-H)), 3.49 (ddd, 1H, $^3J_{5-1}$ = 5.7 Hz, $^3J_{5-6exo}$ = 5.1 Hz, $^3J_{5-6endo}$ = 0.5 Hz, (5-H)), 5.02 (m, 1H, $^3J_{4'cis-3}$ = 10.2 Hz, $^2J_{4'cis-4'trans}$ = 1.6 Hz, $^4J_{4'cis-2'}$ = 1.2 Hz, (4′*cis*-H)), 5.06 (m, 1H, $^3J_{4'trans-3'}$ = 17.1 Hz, $^2J_{4'trans-4'cis}$ = 1.6 Hz, $^4J_{4'-2'}$ = 1.6 Hz (4′*trans*-H)), 5.77 (m, 1H, $^3J_{3'-4'trans}$ = 17.1 Hz, $^3J_{3'-4'cis}$ = 10.2 Hz, $^3J_{3'-2'}$ = 7.0 Hz, vinyl H (not on ring) (3′-H)), 6.48 (d, 1H, $^{P3}J_{2-3}$ = 2.6 Hz, vinyl H on ring (3-H)); ^{13}C nmr (75.47 MHz, DEPT, $CDCl_3$) δ: 28.77 (s, C-8), 31.77 (t), 32.21 (t), 36.21 (d), 42.07 (d), 45.62 (d), 46.77 (t), 51.46 (d), 114.64 (s), 115.70 (t, terminal vinyl CH_2), 119.40 (s, CN), 120.00 (s, CN), 137.25 (d), 141.53 (d); ms *m/z* 55 (59), 63 (48), 64 (29), 77 (59), 91 (28), 104 (39), 115 (100), 120 (20), 128 (48), 141 (58), 142 (90), 168 (90), 182 (45), 195 (48), 209 (76), 210 ($M^{+\cdot}$, 38). Anal. calcd. for $C_{14}H_{14}N_2$: C 79.96, H 6.71, N 13.32; found (using a mixture of **14** (13%) and **13** (87%)): C 79.70, H 6.77, N 13.28.

trans-*4-(3-Butenyl)-3,8-dicyano*-cis-*bicyclo[4.2.0]octa-2,7-diene* (**16**)

The yield of **16** was 5%: infrared (PE-180) *ν*: 3081 (w), 2941 (s), 2871 (m), 2231 (s), 1641 (m), 1616 (w), 1586 (w), 1456 (m), 1376 (w), 1156 (w), 981 (m), 906 (s), 871 (m), 856 (m), 786 (w); ^{1}H nmr (361.08 MHz, $CDCl_3$) δ_{TMS}: 1.35 (m, 1H, $^2J_{5a-5b}$ = 13.5 Hz, $^3J_{4-5a}$ = 10.3 Hz, $^3J_{5a-6}$ = 5.9 Hz, H on methylene group adjacent to bridgehead (5*endo*-H)), 1.58 (m, 1H, $^2J_{1'a-1'b}$ = 13.7 Hz, $^3J_{1'a-2'}$ = 8.8 Hz, $^3J_{1'a-4}$ = 5.1 Hz, H on methylene group adjacent to allylic methylene group (1′a-H)), 1.64 (m, 1H, $^2J_{1'a-1'b}$ = 13.7 Hz, $^3J_{1'b-2'}$ = 8.8 Hz, $^3J_{1'b-4'}$ = 5.1 Hz, H on methylene group adjacent to allylic methylene group (1′b-H)), 2.08 (m, 1H, $^2J_{5a-5b}$ = 13.5 Hz, $^3J_{4-5b}$ = 4.9 Hz, $^3J_{5b-6}$ = 3.3 Hz, $^4J_{1-5b}$ = 1.5 Hz, H on methylene group adjacent to bridgehead (5*exo*-H)), 2.13 (m, 2H, $^3J_{1'a-2'}$ = 8.8 Hz, $^3J_{1'b-2'}$ = 8.8 Hz, $^3J_{2'-3'}$ = 6.8 Hz, $^4J_{2'-4'trans}$ = 1.6 Hz, $^4J_{2'-4'cis}$ = 1.3 Hz, allylic methylene group on the side chain (2′-H)), 2.20 (m, 1H, $^3J_{4-5a}$ = 10.3 Hz, $^3J_{1'a-4}$ = 5.1 Hz, $^3J_{1'b-4}$ = 5.1 Hz, $^3J_{4-5b}$ = 4.9 Hz, $^4J_{2-4}$ = 2.5 Hz, allylic H adjacent to cyano-substituted alkene (4-H)), 3.34 (m, 1H, $^3J_{5a-6}$ = 5.9 Hz, $^3J_{1-6}$ = 4.1 Hz, $^3J_{5b-6}$ = 3.3 Hz, $^3J_{6-7}$ = 1.2 Hz, H on bridgehead (6-H)), 3.74 (m, 1H, $^3J_{1-2}$ = 5.5 Hz, $^3J_{1-6}$ = 4.1 Hz, $^4J_{1-5b}$ = 1.5 Hz, H on bridgehead (1-H)), 5.02 (m, 1H, $^3J_{3'-4'cis}$ = 10.2 Hz, $^2J_{4'cis-4'trans}$ = 1.6 Hz, $^4J_{2'-4'cis}$ = 1.3 Hz, terminal vinyl H (4′*cis*-H)), 5.07 (m, 1H, $^3J_{3'-4'trans}$ = 16.9 Hz, $^2J_{4'trans-4'cis}$ = 1.6 Hz, $^4J_{2'-4'trans}$ = 1.6 Hz, terminal vinyl hydrogen (4′*trans*-H)), 5.80 (m, 1H, $^3J_{3'-4'trans}$ = 16.9 Hz, $^3J_{3'-4'cis}$ = 10.2 Hz, $^3J_{2'-3'}$ = 6.8 Hz, vinyl H (not on ring) (3′-H)), 6.79 (dd, 1H, $^3J_{1-2}$ = 5.5 Hz, $^4J_{2-4}$ = 2.5 Hz, vinyl H on six-membered ring (2-H)) 6.89 (d, 1H, $^3J_{6-7}$ = 1.2 Hz, vinyl H on four-membered ring (7-H)); ^{13}C nmr (90.80 MHz, $CDCl_3$) δ: 29.72 (t, 130.2 Hz), 30.65 (t, 123.5 Hz), 32.06 (d, 140.8 Hz), 32.06 (t, 126.8 Hz), 41.16 (d, 145.6 Hz), 42.99 (d, 160.5 Hz), 112.34 (s), 115.70 (t, 154.2 Hz, terminal vinyl methylene), 116.35 (s), 117.55 (s), 121.42 (s), 137.18 (d, 150.6 Hz), 141.41 (d, 165.0 Hz), 154.48 (d, 179.5 Hz); ms *m/z*: 51 (19), 55 (6), 67 (40), 77 (10), 89 (22), 116 (100), 128 (23), 129 (16), 141 (6), 156 (33), 157 (23), 168 (8), 183 (2), 209 (5), 210 ($M^{+\cdot}$, 1). Exact Mass calcd. for $C_{14}H_{14}N_2$: 210.1112; found: 210.1115.

The effect of added biphenyl on reaction [3]

A solution of 1,5-hexadiene (**9**) (0.4 g, 0.005 mol), 1,4-dicyanobenzene (**1**) (1.2 g, 0.010 mol), and biphenyl (**4**) (1.5 g, 0.0097 mol) in 160 mL of acetonitrile–methanol (3:1) was degassed by nitrogen ebullition for 15 min and irradiated for 123 h. The solvent was removed by rotary evaporation; 3.1 g (9% yield) of a mixture of **13–16** was obtained. Products were identified by comparison of retention times (gc/fid) with the products isolated from reaction [3]. No additional products were detected (gc/ms).

*Formation of the methanol, 2-methyl-1,5-hexadiene (**10**), 1,4-dicyanobenzene (**1**) photo-NOCAS adducts **17** and **18**: reaction [5]*

A solution of 2-methyl-1,5-hexadiene (**10**) (0.4 g, 0.004 mol) and 1,4-dicyanobenzene (**1**) (0.2 g, 0.001 mol) in acetonitrile–methanol (3:1, 40 ml) was degassed by nitrogen ebullition for 15 min and irradiated for 119 h. The solvent was removed by rotary evaporation to yield 0.4 g of a crude photolysate, which was separated by mplc using a linear solvent gradient (hexanes – 50% diethyl ether, 50% hexanes).

Can. J. Chem. Downloaded from www.nrcresearchpress.com by 195.246.54.202 on 09/08/12
For personal use only.

Products were eluted in the order **17** (9 mg), then **18** (17 mg), followed by unreacted **1** (36 mg). Fractions rich in **18** were combined and rechromatographed (fc, column B) eluting with dichloromethane.

5-(4-Cyanophenyl)-6-methoxy-5-methyl-1-hexene (17)

The yield of **17** was 4%: the mass spectrum, fragmentation pattern, and retention time were identical to those for the compound obtained in greater yield when biphenyl (**4**) was present during the irradiation (see below).

1-(4-Cyanophenyl)-2-methoxymethyl-2-methyl-5-hexen-1-one (18)

The yield of **18** was 7%: infrared (PE-180) ν: 3084 (m), 2987 (s), 2932 (s), 2245 (s), 1687 (s), 1642 (m), 1606 (w), 1557 (w), 1477 (m), 1452 (m), 1417 (w), 1397 (m), 1386 (m), 1367 (w), 1277 (w), 1227 (m), 1202 (m), 1107 (w), 977 (m), 937 (m), 902 (m), 832 (m), 762 (w), 722 (w); ^{1}H nmr (361.08 MHz, $CDCl_3$) δ_{TMS}: 1.29 (s, 3H, CH_3), 1.60 (m, 1H, H on methylene group), 1.95 (m, 3H, 3H of CH_2-CH_2), 3.29 (s, 3H, OCH_3), 3.37 (d, 1H, $^2J_{7a-7b}$ = 9.0 Hz, H on methoxy-substituted carbon (7a-H)), 3.55 (d, 1H, $^2J_{7a-7b}$ = 9.0 Hz, H on methoxy-substituted carbon (7b-H)), 4.96 (m, 1H, $^3J_{5-6cis}$ = 10.4 Hz, $^2J_{6cis-6trans}$ < 2.0 Hz, $^4J_{4-6cis}$ < 2.0 Hz, terminal vinyl H (6*cis*-H)), 5.00 (m, 1H, $^3J_{5-6trans}$ = 17.0 Hz, $^2J_{6cis-6trans}$ < 2.0 Hz, $^4J_{4-6trans}$ < 2.0 Hz, terminal vinyl H (6*trans*-H)), 5.73 (m, 1H, $^3J_{5-6trans}$ = 17.0 Hz, $^3J_{5-6cis}$ = 10.4 Hz, $^3J_{4-5}$ = 6.3 Hz, vinyl H (5-H)), 7.61 (d, 2H, $^3J_{2'-3'}$ = 8.2 Hz, $^3J_{5'-6'}$ = 8.2 Hz, H's adjacent to carbonyl-substituted aryl carbon (2′-H, 6′-H)), 7.69 (d, 2H, $^3J_{2'-3'}$ = 8.2 Hz, $^3J_{5'-6'}$ = 8.2 Hz, H's adjacent to cyano-substituted aryl carbon (3′-H, 5′-H)); ^{13}C nmr (90.80 MHz, $CDCl_3$) δ: 20.19 (q, 128.0 Hz, CH_3), 28.43 (t, 124.1 Hz, CH_2 adjacent to allylic methylene), 35.00 (t, 126.0 Hz, allylic CH_2), 52.55 (s, quaternary carbon, methyl and aryl substituted), 59.14 (q, 141.2 Hz, OCH_3), 78.69 (t, 141.9 Hz, OCH_2), 113.79 (s, quaternary aryl carbon cyano substituted), 115.06 (t, 155.2 Hz, terminal vinyl CH_2), 118.15 (s, CN), 127.24 (dd, 166.4 Hz, 4.3 Hz, aromatic CH adjacent to carbonyl-substituted aryl carbon), 131.87 (d, 165.8 Hz, aromatic CH adjacent to cyano-substituted aryl carbon), 137.71 (d, 152.5 Hz, vinyl CH), 144.15 (s, quaternary aryl carbon carbonyl substituted), 208.10 (s, C=O); ms *m/z*: 55 (51), 67 (34), 68 (20), 81 (100), 85 (24), 95 (48), 102 (50), 130 (52), 171 (19), 203 (17), 229 (1) 257 (1). Anal. calcd. for $C_{16}H_{19}NO_2$: C 74.68, H 7.44, N 5.44; found: C 74.35, H 7.40, N 5.42.

The effect of added biphenyl on reaction [5]

A solution of 2-methyl-1,5-hexadiene (**10**) (0.4 g, 0.004 mol), 1,4-dicyanobenzene (**1**) (0.5 g, 0.004 mol), and biphenyl (**4**) (0.3 g, 0.002 mol) in acetonitrile–methanol (3:1, 40 mL) was degassed by nitrogen ebullition for 15 min and irradiated for 119 h. The solvent was removed by rotary evaporation yielding 1.3 g of photolysate, which was separated by mplc using a linear solvent gradient (hexanes – 50% diethyl ether, 50% hexanes).

5-(4-Cyanophenyl)-6-methoxy-5-methyl-1-hexene (17)

The isolated yield of **17** was 31%: infrared (PE-180) ν: 3080 (w), 2980 (s) 2932 (s), 2880 (s), 2836 (m), 2825 (m), 2246 (s), 1641 (m), 1610 (m), 1509 (m), 1458 (m), 1409 (w), 1390 (w), 1370 (w), 1194 (w), 1101 (s), 1018 (w), 985 (w), 905 (m), 830 (m), 730 (w); ^{1}H nmr (361.08 MHz, $CDCl_3$) δ_{TMS}: 1.36 (s, 3H, CH_3), 1.65–1.95 (m, 4H, CH_2-CH_2 (CH_2 (3-H), CH_2 (4-H))), 3.29 (s, 3H, OCH_3), 3.37 (d, 1H, $^2J_{6a-6b}$ = 9.1 Hz, H on methoxy-substituted carbon (6a-H)), 3.49 (d, 1H, $^2J_{6a-6b}$ = 9.1 Hz, H on methoxy-substituted carbon (6b-H)), 4.90 (dd, 1H, $^3J_{1cis-2}$ = 10.6 Hz, $^2J_{1cis-1trans}$ < 2.0 Hz, $^4J_{1cis-3}$ < 2.0 Hz, terminal vinyl H (1*cis*-H)), 4.94 (dd, 1H, $^3J_{1trans-2}$ = 16.8 Hz, $^2J_{1cis-1trans}$ < 2.0 Hz, $^4J_{1trans-3}$ < 2.0 Hz, terminal vinyl H (1*trans*-H)), 5.72 (m, 1H, $^3J_{1trans-2}$ = 16.8 Hz, $^3J_{1cis-2}$ = 10.6 Hz, $^3J_{2-3}$ = 6.2 Hz, vinyl H (2-H)), 7.44 (d, 2H, $^3J_{2'-3'}$ = 8.5 Hz, $^3J_{5'-6'}$ = 8.5 Hz, H's adjacent to alkyl-substituted aryl carbon (2′-H, 6′-H)), 7.61 (d, 2H, $^3J_{2'-3'}$ = 8.5 Hz, $^3J_{5'-6'}$ = 8.5 Hz, H's adjacent to cyano-substituted aryl carbon (3′-H, 5′-H)); ^{13}C nmr (90.80 MHz, $CDCl_3$) δ: 22.51 (q, 127.7 Hz, CH_3), 28.22 (t, 127.2 Hz, CH_2), 38.19 (t, 129.2 Hz, CH_2), 42.76 (s, quaternary carbon, methyl and aryl substituted), 59.34 (q, 140.7 Hz, OCH_3), 81.10 (t, 140.6 Hz, OCH_2), 109.72 (s, quaternary aryl carbon cyano substituted), 114.41 (t, 155.4 Hz, terminal vinyl CH_2), 119.04 (s, CN), 127.35 (dd, 160.7 Hz, 6.0 Hz, aromatic CH adjacent to alkyl-substituted aryl carbon), 131.88 (dd, 165.4 Hz, 5.8 Hz, aromatic CH adjacent to cyano-substituted aryl carbon), 138.35 (d, 151.0 Hz, vinyl CH), 151.61 (s, quaternary aryl carbon alkyl substituted); ms *m/z*: 55 (31), 103 (16), 116 (56), 127 (6), 130 (100), 142 (31), 158 (27), 184 (5), 188 (16), 229 (2). Anal. calcd. for $C_{15}H_{19}NO$: C 78.56, H 8.35, N 6.11; found: C 78.71, H 8.39, N 6.22.

Formation of the methanol, 2,5-dimethyl-1,5-hexadiene (11): 1,4-dicyanobenzene (1) photo-NOCAS adducts 19 and 20, reaction [6]

A solution of 2,5-dimethyl-1,5-hexadiene (**11**) (0.8 g, 0.009 mol) and 1,4-dicyanobenzene (**1**) (0.5 g, 0.004 mol) in acetonitrile–methanol (3:1, 80 mL) was degassed by nitrogen ebullition for 15 min and irradiated for 115 h. The solvent was removed by rotary evaporation to yield 1.3 g of a photolysate that was separated by chromatography (mplc) using a linear solvent gradient (hexanes – 50% diethyl ether, 50% hexanes). Products were eluted in the order **19** and **20** followed by unreacted 1,4-dicyanobenzene (**1**).

5-(4-Cyanophenyl)-6-methoxy-2,5-dimethyl-1-hexane (19)

The yield of **19** was 8%: infrared (PE-180) ν: 3073 (w), 2973 (s), 2933 (s), 2883 (s), 2841 (m), 2241 (s), 1648 (m), 1608 (m), 1507 (m), 1451 (m), 1405 (w), 1386 (w), 1373 (m), 1305 (s), 1195 (m), 1173 (w), 1018 (w), 963 (w), 948 (w), 878 (m), 828 (m), 728 (w); ^{1}H nmr (361.08 MHz, $CDCl_3$) δ_{TMS}: 1.37 (s, 3H, CH_3), 1.66 (s, 3H, CH_3), 1.62–1.89 (m, 4H, CH_2-CH_2), 3.29 (s, 3H, OCH_3), 3.38 (d, 1H, $^2J_{6a-6b}$ = 9.1 Hz, H on methoxy- substituted carbon (6a-H)), 3.49 (d, 1H, $^2J_{6a-6b}$ = 9.1 Hz, H on methoxy-substituted carbon (6b-H)), 4.60 (s, 1H, terminal vinyl H), 4.66 (s, 1H, terminal vinyl H), 7.44 (d, 2H, $^3J_{2'-3'}$ = 8.4 Hz, $^3J_{5'-6'}$ = 8.4 Hz, H's adjacent to alkyl-substituted aryl carbon (2′-H, 6′-H)), 7.61 (d, 2H, $^3J_{2'-3'}$ = 8.4 Hz, $^3J_{5'-6'}$ = 8.4 Hz, H's adjacent to cyano-substituted aryl carbon (3′-H, 5′-H)); ^{13}C nmr (90.80 MHz, $CDCl_3$) δ: 22.49 (q, 126.2 Hz, CH_3), 22.60 (q, 126.2 Hz, CH_3), 31.97 (t, 123.3 Hz, CH_2), 37.14 (t, 127.1 Hz, CH_2), 42.76 (s, quaternary carbon, methyl and aryl substituted), 59.34 (q, 140.6 Hz, OCH_3), 81.23 (t, 141.2 Hz, OCH_2), 109.62 (t, 153.2 Hz, terminal vinyl CH_2), 109.72 (s, quaternary aryl carbon cyano substituted), 119.03 (s, CN), 127.37 (dd, 160.9 Hz, 5.4 Hz, aromatic CH adjacent to alkyl-substituted aryl carbon), 131.89 (dd, 165.3 Hz, 5.4 Hz, aromatic CH adjacent to cyano-substituted aryl carbon), 145.70 (s, vinyl quaternary carbon), 151.67 (s, quaternary aryl carbon alkyl substituted); ms *m/z*: 55 (66), 69 (100), 102 (7), 116 (49), 129 (12), 130 (88), 142 (42), 143 (40), 174 (12), 175 (65), 188 (16), 198 (12), 243 (2). Anal. calcd. for $C_{16}H_{21}NO$: C 78.97, H 8.70, N 5.76; found: C 78.99, H 8.55, N 5.84.

1-(4-Cyanophenyl)-2-methoxymethyl-2,5-dimethyl-5-hexen-1-one (20)

The yield of **20** was 3%: infrared (PE-180) ν: 3075 (w), 2926 (s), 2235 (s), 1726 (m), 1688 (s), 1651 (m), 1606 (w), 1454 (m), 1398 (m), 1386 (m), 1376 (m), 1278 (m), 1236 (m), 1196 (m), 1176 (m), 1106 (s), 1018 (w), 976 (w), 941 (m), 876 (w), 836 (m), 761 (w); ^{1}H nmr (361.08 MHz, $CDCl_3$) δ_{TMS}: 1.30 (s, 3H, CH_3), 1.68 (s, 3H, CH_3), 1.80–2.10 (m, 4H, CH_2-CH_2), 3.29 (s, 3H, OCH_3), 3.37 (d, 1H, $^2J_{7a-7b}$ = 9.0 Hz, H on methoxy-substituted carbon (7a-H)), 3.56 (d, 1H, $^2J_{7a-7b}$ = 9.0 Hz, H on methoxy-substituted carbon (7b-H)), 4.63 (s, 1H, terminal vinyl H), 4.70 (s, 1H, terminal vinyl H), 7.62 (d, 2H, $^3J_{2'-3'}$ = 8.2 Hz, $^3J_{5'-6'}$ = 8.2 Hz, H's adjacent to carbonyl-substituted aryl carbon (2′-H, 6′-H)), 7.69 (d, 2H, $^3J_{2'-3'}$ = 8.2 Hz, $^3J_{5'-6'}$ = 8.2 Hz, H's adjacent to cyano-substituted aryl carbon (3′-H, 5′-H)); ^{13}C nmr (90.80 MHz, $CDCl_3$) δ: 20.21 (q, 127.7 Hz, CH_3), 22.48 (q, 127.3 Hz, CH_3), 32.16 (t, 123.5 Hz, CH_2), 34.02 (t, 127.5 Hz, CH_2), 52.59 (s, quaternary carbon, methyl and aryl substituted), 59.15 (q, 141.2 Hz, OCH_3), 78.74 (t, 138.5 Hz, OCH_2), 110.28 (t, 152.7 Hz, terminal vinyl CH_2), 113.82 (s, quaternary aryl carbon cyano substituted), 118.16 (s, CN), 127.27 (dd, 165.6 Hz, 5.2 Hz, aromatic CH adjacent to carbonyl-substituted aryl carbon), 131.90 (dd, 166.4 Hz, 4.4 Hz, aromatic CH adjacent to cyano-substituted aryl carbon), 144.16 (s, quaternary carbon), 145.02 (s, quaternary carbon), 208.54 (s, C=O); ms *m/z*: 55 (93), 67 (84), 68

Can. J. Chem. Downloaded from www.nrcresearchpress.com by 195.246.54.202 on 09/08/12
For personal use only.

(75), 69 (24), 81 (35), 85 (47), 95 (75), 102 (87), 109 (57), 130 (99), 171 (100), 203 (97), 271 (1). Anal. calcd. for $C_{17}H_{21}NO_2$: C 75.24, H 7.80, N 5.16; found: C 74.80, H 7.92, N 4.98. Exact Mass calcd. for $C_{17}H_{21}NO_2$: 271.1573; found: 271.1572.

*The effect of added biphenyl (**4**) on reaction [7]*

A solution of 2,5-dimethyl-1,5-hexadiene (**11**) (1.8 g, 0.016 mol), 1,4-dicyanobenzene (**1**) (1.8 g, 0.014 mol), and biphenyl (**4**) (1.1 g, 0.0071 mol) in acetonitrile–methanol (3:1, 160 mL) was degassed by nitrogen ebullition for 15 min and irradiated for 88 h. The solvent was removed by rotary evaporation to yield 4.5 g of a photolysate that was separated by chromatography (mplc) using a linear solvent gradient (hexanes – 50% diethyl ether, 50% hexanes). Products were eluted in the order **26**, **25**, **19**, **21** *trans*, **21** *cis*, **27**, followed by unreacted **1**. Fractions rich in **21** *trans* were combined and rechromatographed (fc, column B) using dichloromethane as eluent. Fractions rich in **27** were combined and rechromatographed (fc, column A) using 40% diethyl ether – 60% hexanes as eluent.

*5-(4-Cyanophenyl)-6-methoxy-2,5-dimethyl-1-hexene (**19**)*

The yield of **19** was 13%: the mass spectrum and ^{1}H nmr spectrum were identical to the spectra of the compound described above (reaction [6]).

cis-*1-(4-Cyanophenyl)-4-methoxy-1,4-dimethylcyclohexane (**21** cis)*

The yield of **21** *cis* was 6%: ^{1}H nmr (361.08 MHz, $CDCl_3$) δ_{TMS}: 1.00 (s, 3H, equatorial CH_3 attached to a methoxy-substituted quaternary carbon), 1.14 (s, 3H, axial CH_3 attached to an aryl-substituted quaternary carbon), 1.70 (bd, 2H, $^2J_{3eq-3ax} = {}^2J_{5eq-5ax} = 13.7$ Hz, equatorial H's adjacent to CH_3, OCH_3-substituted carbon (3eq-H, 5eq-H)), 1.70–1.84 (m, 4H, axial H's adjacent to CH_3, OCH_3-substituted carbon and axial H's adjacent to CH_3, aryl-substituted carbon (2ax-H, 3ax-H, 5ax-H, 6ax-H)), 2.01 (bd, 2H, $^2J_{2eq-2ax} = {}^2J_{6eq-6ax} = 14.2$ Hz, equatorial H's adjacent to CH_3, aryl-substituted carbon (2eq-H, 6eq-H)), 3.20 (s, 3H, axial OCH_3 attached to methyl-substituted carbon), 7.48 (d, 2H, $^3J_{2'-3'} = 8.5$ Hz, $^3J_{5'-6'} = 8.5$ Hz, H's adjacent to alkyl-substituted aryl carbon (2′-H, 6′-H)), 7.62 (d, 2H, $^3J_{2'-3'} = 8.5$ Hz, $^3J_{5'-6'} = 8.5$ Hz, H's adjacent to cyano-substituted aryl carbon (3′-H, 5′-H)).

*NOE experiment on **21** cis*

The high-frequency methyl signal (1.14 ppm) was irradiated and an increase in peak intensity of ca. 6% occurred in the cyclohexane hydrogen region, indicating an axial methyl group. The low-frequency methyl signal (1.00 ppm) was irradiated and no change was observed in the intensity of the peaks within the cyclohexane hydrogen region, indicating an equatorial methyl group.

*Shift reagent study used to assign chemical shifts to methyl groups of **21** cis*

Europium(III) tris-1,1,1,2,2,3,3-heptafluoro-7,7-dimethyl-4,5-octanedione ($Eu(fod)_3$) was used as the shift reagent. To 5 mg of *cis*-4-(4-cyanophenyl)-1-methoxy-1,4-dimethylcyclohexane (**21** *cis*) was added 4.5×10^{-6} mol of $Eu(fod)_3$ in five increments. With each addition a ^{1}H nmr spectrum was taken and the shift of each methyl group signal measured. A graph of the chemical shift of each methyl group as a function of $Eu(fod)_3$ concentration yielded slopes for the low (1.00 ppm) and high (1.14 ppm) frequency signals for the methyl groups in the ratio 1.6. The low-frequency signal was thus assigned to the methyl group attached to the methoxy-substituted carbon and the high-frequency signal to the methyl group on the aryl-substituted carbon.

Infrared (PE-180) ν: 3054 (w), 2939 (s), 2874 (m), 2826 (m), 2234 (s), 1604 (m), 1504 (m), 1462 (m), 1451 (m), 1394 (w), 1374 (m), 1304 (w), 1274 (m), 1197 (w), 1139 (m), 1114 (m), 1076 (s), 1039 (w), 1014 (w), 934 (m), 859 (m), 824 (m), 726 (w); ^{13}C nmr (90.80 MHz, $CDCl_3$) δ: 24.05 (q, 125.6 Hz, CH_3), 24.05 (q, 125.6 Hz, CH_3), 32.24 (t, 125.8 Hz, two CH_2 groups), 32.32 (t, 125.8 Hz, two CH_2 groups), 38.60 (s, quaternary carbon, aryl methyl substituted), 48.54 (q, 141.3 Hz, OCH_3), 72.53 (s, methoxy, methyl-substituted quaternary carbon), 109.25 (s, quaternary carbon cyano substituted), 119.08 (s, CN), 127.00 (d, 165.0 Hz, aromatic CH adjacent to alkyl-substituted aryl carbon), 132.20 (d, 171.0 Hz, aromatic CH adjacent to cyano-substituted aryl carbon), 153.54 (s, quaternary aryl carbon alkyl substituted); ms *m/z*: 55 (75), 72 (75), 77 (12), 85 (100), 86 (24), 115 (16), 116 (40), 128 (12), 130 (12), 142 (12), 143 (19), 196 (13), 212 (2), 228 (21), 243 (1). Anal. calcd. for $C_{16}H_{21}NO$: C 78.97, H 8.70, N 5.76; found: C 79.37, H 8.82, N 5.85.

trans-*1-(4-Cyanophenyl)-4-methoxy-1,4-dimethylcyclohexane (**21** trans)*

The yield of **21** *trans* was 3%: ^{1}H nmr (361.08 MHz, $CDCl_3$) δ_{TMS}: 1.18 (s, 3H, equatorial CH_3 attached to a methoxy-substituted quaternary carbon), 1.24 (s, 3H, equatorial CH_3 attached to an aryl-substituted quaternary carbon), 1.50–1.60 (m, 4H, axial and equatorial H's adjacent to CH_3, OCH_3-substituted carbon (3eq-H, 3ax-H, 5eq-H, 5ax-H)), 1.72 (bd, 2H, equatorial H's adjacent to CH_3, aryl-substituted carbon (2eq-H, 6eq-H)), 1.99 (m, 2H, axial H's adjacent to CH_3, aryl-substituted carbon (2ax-H, 6ax-H)), 3.15 (s, 3H, axial OCH_3 attached to methyl-substituted carbon), 7.49 (d, 2H, $^3J_{2'-3'} = 8.3$ Hz, $^3J_{5'-6'} = 8.3$ Hz, H's adjacent to alkyl-substituted aryl carbon (2′-H, 6′-H)), 7.60 (d, 2H, $^3J_{2'-3'} = 8.3$ Hz, $^3J_{5'-6'} = 8.3$ Hz, H's adjacent to cyano-substituted aryl carbon (3′-H, 5′-H)).

*NOE experiments on **21** trans*

Both methyl group signals were individually irradiated and no increase of peak intensity was observed in the cyclohexane hydrogen region. This was taken as evidence that both methyl groups are equatorial.

Infrared (PE-180) ν: 2973 (s), 2943 (s), 2833 (m), 2241 (s), 1605 (m), 1504 (m), 1465 (m), 1433 (w), 1403 (w), 1373 (m), 1271 (m), 1218 (w), 1188 (w), 1128 (m), 1078 (s), 1013 (m), 953 (w), 843 (m), 828 (s); ^{13}C nmr (90.80 MHz, $CDCl_3$) δ: 23.87 (q, 123.7 Hz, CH_3), 25.89 (q, 128.3 Hz, CH_3), 31.92 (t, 125.9 Hz, two CH_2 groups), 32.83 (t, 126.6 Hz, two CH_2 groups), 37.22 (s, quaternary carbon, aryl methyl substituted), 48.45 (q, 140.5 Hz, OCH_3), 72.41 (s, quaternary carbon, methoxy methyl substituted), 109.26 (s, quaternary carbon cyano substituted), 119.12 (s, CN), 126.30 (d, 159.6 Hz, aromatic CH adjacent to alkyl-substituted aryl carbon), 131.99 (d, 159.5 Hz, aromatic CH adjacent to cyano-substituted aryl carbon), 156.62 (s, quaternary aryl carbon alkyl substituted); ms *m/z*: 55 (16), 72 (17), 77 (3), 85 (100), 86 (5), 115 (4), 116 (10), 128 (3), 130 (4), 142 (4), 143 (5), 196 (5), 212 (1), 228 (6), 243 (1). Anal. calcd. for $C_{16}H_{21}NO$: C 78.97, H 8.70, N 5.76; found: C 78.98, H 8.70, N 5.76.

*3,5-Dimethoxy-4-phenylcyclohexanecarbonitrile (**27**)*

The melting point of **27** was 125.6–125.9°C: infrared (PE-180) ν: 2987 (m), 2957 (s), 2930 (s), 2884 (s), 2832 (m), 2242 (s), 1606 (w), 1497 (m), 1454 (m), 1442 (m), 1384 (w), 1372 (m), 1310 (w), 1192 (m), 1107 (s), 1077 (s), 1037 (m), 958 (w), 852 (w), 767 (m), 727 (w), 697 (s); ^{1}H nmr (361.08 MHz, $CDCl_3$) δ_{TMS}: 1.75 (ddd, 2H, $^2J_{2ax-2eq} = 13.9$ Hz, $^3J_{1-2ax} = 12.7$ Hz, $^3J_{2ax-3} = 2.5$ Hz, axial H's on methylene groups (2ax-H)), 2.49 (ddd, 2H, $^2J_{2ax-2eq} = 13.9$ Hz, $^3J_{1-2eq} = 3.1$ Hz, $^3J_{2eq-3} = 2.0$ Hz, equatorial H's on methylene groups (2eq-H)), 2.68 (t, 1H, $^3J_{3-4} = 3.2$ Hz, benzyl H (4-H)), 3.25 (m, 1H, $^3J_{1-2ax} = 12.7$ Hz, $^3J_{1-2eq} = 3.1$ Hz, H on cyano-substituted methylene (1-H)), 3.26 (s, 6H, OCH_3), 3.67 (ddd, 2H, $^3J_{3-4} = 3.2$ Hz, $^3J_{2ax-3} = 2.5$ Hz, $^3J_{2eq-3} = 2.0$ Hz, H's on methoxy substituted methylene (3-H)), 7.23–7.51 (m, 5H, aryl H's); ^{13}C nmr (90.80 MHz, $CDCl_3$) δ: 18.52 (d, 140.8 Hz, CH), 32.37 (t, 129.7 Hz, two CH_2 groups), 49.28 (d, 118.2 Hz, CH), 58.18 (q, 140.9 Hz, OCH_3), 77.99 (d, OCH), 122.96 (s, CN), 126.72 (d, 159.8 Hz, aryl CH), 128.03 (d, 159.7 Hz, aryl CH), 129.27 (d, 158.9 Hz, aryl CH), 140.42 (s, quaternary aryl carbon); ms *m/z*: 51 (3), 55 (3), 58 (6), 65 (5), 75 (3), 77 (4), 88 (3), 91 (19), 96 (21), 101 (3), 115 (22), 116 (3), 117 (21), 127 (3), 128 (5), 155 (100), 156 (11), 177 (7), 213 (7), 245 (3), 246 (1). X-Ray data: Appendix.[6]

*2,5-Dimethyl-1,4-hexadiene (**12**)*

5-Methyl-4-hexen-2-one was prepared by the photochemically

induced tautomerization of 5-methyl-3-hexen-2-one (*7a*). The Wittig reaction was carried out using the standard procedure (*7b*). Sodium (0.8 g, 0.04 mol) was placed in a three- necked round-bottom flask equipped with a Dry Ice condenser protected with a calcium chloride drying tube. A gas inlet tube was connected to an ammonia tank and ammonia was introduced, as a gas, until ca. 100 mL was condensed. A small portion of ferric nitrate was added. The mixture was stirred and after 15 min the colour turned from blue to dark gray. Methyltriphenylphosphonium bromide (10 g, 0.028 mol) was then added using a powder addition funnel and the reaction was stirred for 30 min. 5-Methyl-4-hexen-2-one (3.1 g, 0.028 mol) was added in decahydronaphthalene (100 mL, distilled under reduced pressure and stored over molecular sieves (4 Å)). The ammonia was allowed to evaporate and the Dry Ice condenser was replaced by a water-cooled condenser and a drying tube. The reaction mixture was allowed to stir overnight and was then washed with water until the aqueous layer was no longer basic. The organic layer was distilled under atmospheric pressure; fractions boiling between 142 and 189°C contained the desired diene. Pure 2,5-dimethyl-1,4-hexadiene was obtained by prep/gc (40% SE-30). The ^{1}H nmr spectrum was identical to that reported (*7c*). ^{1}H nmr (361.08 MHz, $CDCl_3$) δ_{TMS}: 1.62 (s, 3H, CH_3), 1.71 (s, 3H, CH_3), 1.73 (s, 3H, CH_3), 2.68 (d, 2H, $^3J_{3-4}$ = 7.6 Hz, CH_2 (3-H)), 4.68 (br s, 2H, $^2J_{1-1'}$ = 1.1 Hz, terminal vinyl methylene (1-H, 1′-H)), 5.18 (m, 1H, $^3J_{3-4}$ = 7.6 Hz, vinyl CH (4-H)); ^{13}C nmr (90.80 MHz, $CDCl_3$) δ: 17.62 (q, 133.9 Hz, CH_3), 22.55 (q, 125.0 Hz, CH_3), 25.77 (q, 126.2 Hz, CH_3), 36.53 (t, 126.8 Hz, CH_2), 109.62 (t, 154.8 Hz, terminal vinyl CH_2), 121.84 (d, 153.0 Hz, vinyl CH), 132.88 (s, quaternary carbon bearing two methyl groups), 145.44 (s, quaternary carbon monomethylated); ms *m/z*: 53 (24), 55 (43), 67 (92), 95 (100), 110 (30), 111 (3).

*Formation of the methanol, 2,5-dimethyl-1,4-hexadiene (**12**), 1,4-dicyanobenzene (**1**) photo-NOCAS adducts **22** and **23**: reaction [8]*

A solution of 2,5-dimethyl-1,4-hexadiene (**12**) (0.5 g, 0.004 mol), 1,4-dicyanobenzene (**1**) (0.6 g, 0.005 mol), and biphenyl (**4**) (1.5 g, 0.010 mol) in acetonitrile–methanol (3:1, 80 mL) was degassed by nitrogen ebullition for 15 min and irradiated for 26 h. The solvent was removed, on a rotary evaporator, and the crude photolysate was separated by chromatography (mplc) using a linear solvent gradient (hexanes – 50% diethyl ether, 50% hexanes). Products were eluted in the order **22**, then **23**, followed by unreacted **1**. Fractions rich in **23** were combined and rechromatographed (dc/fc) eluting with dichloromethane.

*5-(4-Cyanophenyl)-4-methoxy-2,5-dimethyl-1-hexene (**22**)*

The yield of **22** was 16%: the melting point was 42.1–42.8°C; infrared (PE-180) ν: 3072 (w), 2970 (s), 2930 (s), 2825 (m), 2128 (s), 1644 (w), 1602 (m), 1500 (m), 1440 (m), 1400 (m), 1380 (m), 1360 (m), 1171 (m), 1090 (s), 1050 (m), 1010 (m), 971 (m), 820 (m); ^{1}H nmr (361.08 MHz, $CDCl_3$) δ_{TMS}: 1.34 (s, 3H, CH_3), 1.36 (s, 3H, CH_3), 1.71 (s, 3H, CH_3), 1.91 (d, 2H, $^3J_{3-4}$ = 5.9 Hz, CH_2 (3-H)), 3.27 (s, 3H, OCH_3), 3.32 (t, 1H, $^3J_{3-4}$ = 5.9 Hz, CH (4-H)), 4.71 (br s, 1H, terminal vinyl H), 4.74 (br s, 1H, terminal vinyl H), 7.52 (d, 2H, $^3J_{2'-3'}$ = 8.6 Hz, $^3J_{5'-6'}$ = 8.6 Hz, H's adjacent to alkyl-substituted aryl carbon (2′-H, 6′-H)), 7.60 (d, 2H, $^3J_{2'-3'}$ = 8.6 Hz, $^3J_{5'-6'}$ = 8.6 Hz, H's adjacent to cyano-substituted aryl carbon (3′-H, 5′-H)); ^{13}C nmr (90.80 MHz, $CDCl_3$) δ: 22.67 (q, 122.1 Hz, CH_3), 23.89 (q, 120.0 Hz, CH_3), 25.16 (q, 122.3 Hz, CH_3), 40.11 (t, 125.7 Hz, CH_2), 43.74 (s, quaternary carbon aryl substituted), 61.14 (q, 141.1 Hz, OCH_3), 87.98 (d, 139.9 Hz, OCH), 109.60 (s, quaternary aryl carbon, cyano substituted), 112.78 (t, 154.1 Hz, terminal vinyl CH_2), 119.05 (s, CN), 127.47 (d, 160.2 Hz, aromatic CH adjacent to alkyl-substituted aryl carbon), 131.66 (d, 165.3 Hz, aromatic CH adjacent to cyano-substituted aryl carbon), 143.19 (s, quaternary aryl carbon, alkyl substituted), 153.26 (s, vinyl quaternary carbon); ms *m/z*: 55 (6), 57 (4), 67 (25), 69 (16), 71 (6), 99 (100), 100 (6), 116 (16), 129 (8), 130 (7), 156 (13), 188 (24), 243 (1). Anal. calcd. for $C_{16}H_{21}NO$: C 78.97, H 8.70, N 5.76; found: C 78.90, H 8.84, N 5.72.

*4-(4-Cyanophenyl)-5-methoxy-2,5-dimethyl-1-hexene (**23**)*

The yield of **23** was 9%: the melting point was 62.9–63.9°C; infrared (PE-180) ν: 3181 (w), 3081 (m), 3036 (m), 2829 (m), 2229 (s), 1831 (w), 1801 (w), 1646 (m), 1606 (s), 1506 (s), 1461 (s), 1418 (s), 1382 (s), 1374 (s), 1365 (s), 1306 (w), 1276 (m), 1236 (s), 1181 (s), 1140 (s), 1066 (s), 1019 (m), 939 (w), 884 (s), 854 (s), 826 (s), 787 (m), 753 (m), 716 (w); ^{1}H nmr (361.08 MHz, $CDCl_3$) δ_{TMS}: 1.05 (s, 3H, CH_3), 1.12 (s, 3H, CH_3), 1.56 (s, 3H, CH_3), 2.50 (dd, 1H, $^3J_{3a-3b}$ = 14.5 Hz, $^3J_{3a-4}$ = 12.0 Hz, H on methylene group (3a-H)), 2.64 (br d, 1H, $^3J_{3a-3b}$ = 14.5 Hz, $^3J_{3b-4}$ = 3.2 Hz, H on methylene group (3b-H)), 2.95 (dd, 1H, $^3J_{3a-4}$ = 12.0 Hz, $^3J_{3b-4}$ = 3.2 Hz, H on aryl-substituted carbon (4-H)), 3.22 (s, 3H, OCH_3), 4.44 (br s, 1H, terminal vinyl H), 4.55 (br s, 1H, terminal vinyl H), 7.33 (d, 2H, $^3J_{2'-3'}$ = 8.3 Hz, $^3J_{5'-6'}$ = 8.3 Hz, H's adjacent to alkyl substituted aryl carbon (2′-H, 6′-H)), 7.54, (d, 2H, $^3J_{2'-3'}$ = 8.3 Hz, $^3J_{5'-6'}$ = 8.3 Hz, H's adjacent to cyano-substituted aryl carbon (3′-H, 5′-H)); ^{13}C nmr (90.80 MHz, $CDCl_3$) δ: 22.37 (q, 123.9 Hz, CH_3), 22.83 (q, 126.5 Hz, CH_3), 23.52 (q, 125.5 Hz, CH_3), 37.30 (t, 126.6 Hz, CH_2), 49.22 (q, 140.5 Hz, OCH_3), 53.38 (d, 125.5 Hz, CH, aryl substituted), 76.44 (s, quaternary carbon, methoxy substituted), 109.99 (s, quaternary aryl carbon, cyano substituted), 112.43 (t, 153.7 Hz, terminal vinyl CH_2), 119.13 (s, CN), 130.56 (d, 162.8 Hz, aromatic CH adjacent to alkyl-substituted aryl carbon), 131.35 (d, 160.8 Hz, aromatic CH adjacent to cyano-substituted aryl carbon), 143.29 (s, quaternary aryl carbon, alkyl substituted), 147.51 (s, vinyl quaternary carbon); ^{13}C nmr (90.80 MHz, $(CD_3)_2CO$) δ: 22.24 (q), 22.94 (q), 23.51 (q), 37.75 (t), 49.11 (q, OCH_3), 53.65 (d), 76.96 (s, quaternary carbon, methoxy substituted), 110.58 (s, quaternary aryl carbon, cyano substituted), 112.47 (t, terminal vinyl CH_2), 119.50 (s, CN), 131.72 (d, aromatic CH adjacent to alkyl-substituted aryl carbon), 131.76 (d, aromatic CH adjacent to cyano-substituted aryl carbon), 144.49 (s, quaternary aryl carbon, alkyl substituted), 148.74 (s, vinyl quaternary carbon); ms *m/z*: 53 (5), 55 (12), 73 (100), 74 (16), 89 (6), 103 (10), 115 (12), 116 (23), 127 (10), 128 (12), 129 (12), 130 (16), 140 (12), 154 (12), 156 (19), 196 (12), 211 (1), 243 (1). Anal. calcd. for $C_{16}H_{21}NO$: C 78.97, H 8.70, N 5.76; found: C 78.68, H 8.32, N 5.72.

Acknowledgements

This work was supported by a grant from the Natural Sciences and Engineering Research Council of Canada. We thank Dr. D.L. Hooper at the Atlantic Regional Magnetic Resonance Centre at Dalhousie University for the high-field NMR spectra and for help in the preparation of the manuscript. Exact mass measurements were carried out by Mr. D. Embree at the Institute for Marine Biosciences, Halifax. We are grateful to Dr. T.S. Cameron at Dalhousie for the X-ray analysis of **27**. We also wish to acknowledge very helpful comments from a referee.

1 (*a*) D.R. Arnold and X. Du. Can. J. Chem. **71**, 403 (1993); (*b*) K. McMahon and D.R. Arnold. Can. J. Chem. **71**, 450 (1993).
2. A.L. Perrott and D.R. Arnold. Can. J. Chem. **70**, 272 (1992).
3. (*a*) R.M. Borg, D.R. Arnold, and T.S. Cameron. Can. J. Chem. **62**, 1785 (1984); (*b*) D.R. Arnold and M.S. Snow. Can. J. Chem. **66**, 3012 (1988).
4. (*a*) I.R. Gould, D. Ege, J.E. Moser, and S. Farid. J. Am. Chem. Soc. **112**, 4290 (1990); (*b*) P. Suppan. Top. Curr. Chem. **163**, 95 (1992).
5. (*a*) T. Majima, C. Pac, and H. Sakurai. Chem. Lett. 1133 (1979); (*b*) A. Terahara, H. Ohya-Nishiguchi, N. Hirota, and A. Oku. J. Phys. Chem. **90**, 1564 (1986); (*c*) T. Bally, K. Roth, and R. Straub. J. Am. Chem. Soc. **110**, 1639 (1988).
6. (*a*) J.E. Baldwin. J. Chem. Soc., Chem. Commun. 734 (1976); (*b*) A.L.J. Beckwith and C.H. Schiesser. Tetrahedron, **41**, 3925 (1985); (*c*) A.L.J. Beckwith, G. Phillipou, and A.K. Serelis. Tetrahedron Lett. **22**, 2811 (1981); (*d*) A.L.J. Beckwith. Tetrahedron, **37**, 3073 (1981); (*e*) A.L.J. Beckwith and T. Lawrence. J. Chem. Soc. Perkin Trans. 2, 1535 (1979); (*f*) A.L.J. Beckwith, I.A. Blair,

Can. J. Chem. Downloaded from www.nrcresearchpress.com by 195.246.54.202 on 09/08/12
For personal use only.

and G. Phillipou. Tetrahedron Lett. **26**, 2251 (1974); (*g*) R. Srinivasan and K.H. Carlough. J. Am. Chem. Soc. **89**, 4932 (1967); (*h*) E. Fischer and R. Gleiter. Angew. Chem. Int. Ed. Engl. **28**, 925 (1989); (*i*) C. Walling and M.S. Pearson. J. Am. Chem. Soc. **86**, 2262 (1964); (*j*) M.A.M. Bradney, A.D. Forbes, and J. Wood. J. Chem. Soc. Perkin Trans. 2, 1655 (1973); (*k*) J.W. Wilt, L.L. Maravetz, and J.F. Zawadzki. J. Org. Chem. **31**, 3018 (1966).

7. (*a*) N.C. Yang and M.J. Jorgenson. Tetrahedron Lett. **19**, 1203 (1964); (*b*) H.J. Bestmann. Angew. Chem. Int. Ed. Engl. **4**, 583 (1965); (*c*) R.S. Bly and R.T. Swindell. J. Org. Chem. **30**, 10 (1965).
8. (*a*) P.J. Wagner and K. Nahm. J. Am. Chem. Soc. **109**, 6528 (1987); (*b*) J. Am. Chem. Soc. **109**, 4404 (1987); (*c*) K.B. Cosstick, M.G.B. Drew, and A. Gilbert. J. Chem. Soc. Chem. Commun. 1867 (1987).
9. (*a*) E.M. Osselton, E.S. Krijnen, E.L.M. Lempers, and J. Cornelisse. Recl. Trav. Chim. Pays-Bas, **105**, 375 (1986); (*b*) M.G.B. Drew, A. Gilbert, P. Heath, A.J. Mitchell, and P.W. Rodwell. J. Chem. Soc. Chem. Commun. 750 (1983).
10. (*a*) R.S. Nicholson and I. Shain. Anal. Chem. **36**, 706 (1964); (*b*) Anal. Chem. **37**, 178 (1965).
11. (*a*) D. Rehm and A. Weller. Isr. J. Chem. **8**, 259 (1970); (*b*) Ber. Bunsen-ges. Phys. Chem. **73**, 834 (1969).
12. T. Okutani, A. Morimoto, T. Kaneko, and K. Masuda. Tetrahedron Lett. **16**, 1115 (1971).
13. (*a*) N.L. Allinger and M.T. Tribble. Tetrahedron Lett. **35**, 3259 (1971); (*b*) J.J. Uebel, E.L. Nickoloff, W.T. Cole, and C.B. Grant. Tetrahedron Lett. **28**, 2637 (1971).
14. (*a*) J. Mattay. Tetrahedron, **41**, 2393 (1985); (*b*) Tetrahedron, **41**, 2405 (1985); (*c*) W. Ferree, Jr., J.B. Grutzner, and H. Morrison. J. Am. Chem. Soc. **93**, 5502 (1971); (*d*) J. Cornelisse, V.Y. Merritt, and R. Srinivasan. J. Am. Chem. Soc. **95**, 6197 (1973); (*e*) V.Y. Merritt, J. Cornelisse, and R. Srinivasan. J. Am. Chem. Soc. **95**, 8250 (1973); (*f*) J. Cornelisse and R. Srinivasan. Chem. Phys. Lett. **20**, 278 (1973); (*g*) R. Srinivasan and J.A. Ors. Chem. Phys. Lett. **42**, 506 (1976); (*h*) J. Mattay, H.D. Scharf, and H. Leismann. Mol. Photochem. **9**, 119 (1979); (*i*) H. Leismann and J. Mattay. Tetrahedron Lett. **44**, 4265 (1978); (*j*) J. Cornelisse. Chem. Rev. **93**, 615 (1993).
15. (*a*) M. Fleischmann and D. Pletcher. Tetrahedron Lett. **60**, 6255 (1968); (*b*) K.K. Barnes and C.K. Mann. J. Org. Chem. **32**, 1474 (1967).
16. C.P. Andrieux, I. Gallardo, and J.-M. Saveant. J. Am. Chem. Soc. **111**, 1620 (1989).
17. (*a*) R. Fuhlendorff, A. Occhialini, S.U. Pedersen, and H. Lund. Acta Chem. Scand. **43**, 803 (1989); (*b*) G.D. Sargent and G.A. Lux. J. Am. Chem. Soc. **90**, 7160 (1968).
18. W. Damm, B. Giese, J. Hartung, T. Hasskerl, K.N. Houk, O. Huter, and H. Zipse. J. Am. Chem. Soc. **114**, 4067 (1992).
19. (*a*) N.L. Bauld, D.J. Bellville, R. Pabon, R. Chelsky, and G. Green. J. Am. Chem. Soc. **105**, 2378 (1983); (*b*) T. Tsuji, T. Miura, K. Sugiura, Y. Matsumoto, and S. Nishida. J. Am. Chem. Soc. **115**, 482 (1993).
20. (*a*) S.L. Mattes and S. Farid. J. Am. Chem. Soc. **108**, 7356 (1986); (*b*) L.J. Johnston and N.P. Schepp. J. Am. Chem. Soc. **115**, 6564 (1993).
21. (*a*) Q.-X. Guo, X.-Z. Qin, J.T. Wang, and F. Williams. J. Am. Chem. Soc. **110**, 1974 (1988); (*b*) F. Williams, Q.-X. Guo, D.C. Bebout, and B.K. Carpenter. J. Am. Chem. Soc. **111**, 4133 (1989).
22. L.S. Prasad, R. Ding, E.G. Bradford, L.D. Kispert, and H. Wang. Isr. J. Chem. **29**, 33 (1989).
23. (*a*) K. Lorenz and N.L. Bauld. J. Catal. **95**, 613 (1985); (*b*) T. Miyashi, A. Konno, and Y. Takahashi. J. Am. Chem. Soc. **110**, 3676 (1988); (*c*) H.D. Roth and H. Weng. In press.
24. (*a*) W.C. Still, M. Kahn, and A. Mitra. J. Org. Chem. **43**, 2923 (1978); (*b*) L.M. Harwood. Aldrichimica Acta, **18**, 25 (1985).
25. A. Okamoto, M.S. Snow, and D.R. Arnold. Tetrahedron, **42**, 6175 (1986).
26. D.R. Arnold and D.D.M. Wayner. Can. J. Chem. **64**, 100 (1986).

Can. J. Chem. Downloaded from www.nrcresearchpress.com by 195.246.54.202 on 09/08/12
For personal use only.

Chemistry of the shellfish toxin domoic acid: characterization of related compounds[1]

JOHN A. WALTER, MICHAEL FALK, AND JEFFREY L.C. WRIGHT[2]

Institute for Marine Biosciences, National Research Council of Canada, 1411 Oxford Street, Halifax, NS B3H 3Z1 Canada

Received September 28, 1993

JOHN A. WALTER, MICHAEL FALK, and JEFFREY L.C. WRIGHT. Can. J. Chem. **72**, 430 (1994).

Five new compounds related to the neurotoxin domoic acid have been characterized by spectroscopic methods. They include a diastereoisomer that occurs naturally with domoic acid in mussels and four hydrogenation products. The stereochemistry of the two epimeric tetrahydro derivatives could not be assigned on the basis of the NMR data alone because of high conformational flexibility. However, a clear-cut assignment was possible by molecular modelling in combination with the NMR data.

JOHN A. WALTER, MICHAEL FALK et JEFFREY L.C. WRIGHT. Can. J. Chem. **72**, 430 (1994).

Faisant appel à des méthodes spectroscopiques, on a caractérisé cinq nouveaux composés reliés à l'acide domoïque, une neurotoxine. Ils comprennent un diastéréoisomère que l'on retrouve naturellement avec l'acide domoïque présent dans les moules ainsi que quatre produits d'hydrogénation. À cause de la grande flexibilité conformationnelle, on n'a pas pu attribuer la stéréochimie des deux dérivés tétrahydrogénés épimères en faisant uniquement appel aux des données de la RMN. Toutefois, il a été possible de faire une attribution sans ambiguïté en faisant appel aux modèles moléculaires en combinaison avec les données de la RMN.

[Traduit par la rédaction]

Can. J. Chem. Downloaded from www.nrcresearchpress.com by 195.246.54.202 on 09/08/12
For personal use only.

Introduction

The discovery of domoic acid **1** as a new shellfish toxin (1) has stimulated studies of its pharmacology and toxicology (2–9). It is the most potent member of a group of amino acid analogues called excitotoxins, which bind to specific membrane-bound kainate receptors and α-amino-3-hydroxy-5-methyl-4-isoxazolepropionic acid (AMPA) receptors found in certain neuronal cells of the brain (8). Recently we reported a study of the binding of nine compounds (**1–9**) related to domoic acid, to kainate receptors, and to AMPA receptors in rat forebrain membranes (8). Four of these compounds, domoic acid **1** and its three geometrical isomers **2–4**, which were isolated from contaminated shellfish tissue and from the producing microalga *Nitzschia pungens* forma *multiseries*, have been characterized previously (1, 10). We now provide details of the preparation and characterization of the remaining five compounds used in the binding study, including a naturally occurring C5′ diastereoisomer **5** of domoic acid isolated from mussel tissue.

The assignment of the stereochemistry of the two tetrahydro derivatives **8** and **9** required molecular modelling. Modelling indicated that each epimer occurs in several stable conformations, which differ as to ring pucker and orientation of side chains. Nevertheless, a clear-cut distinction between the two epimers was possible upon comparing the conformationally averaged interproton distances, derived from molecular modelling, with the difference–NOE results. The distinction was further confirmed by a comparison of experimental and calculated interproton coupling constants. We report our modelling procedure in detail, because of its general applicability to conformationally flexible molecules.

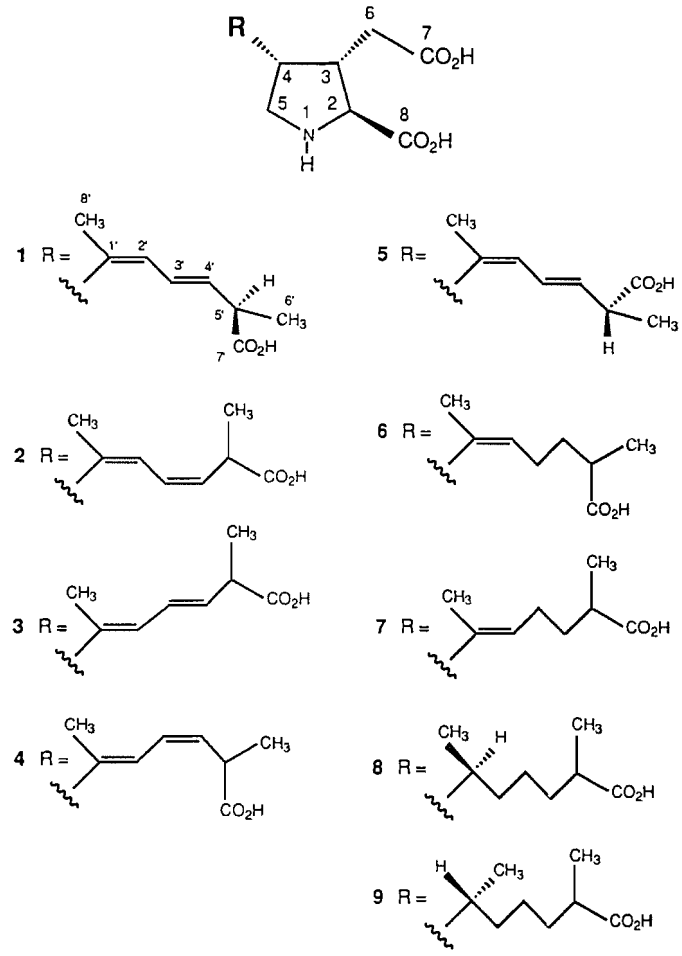

Results and discussion

C5′ epimer of domoic acid

HPLC–DAD analysis of toxic mussel extracts containing domoic acid indicated the presence of other compounds having similar UV spectra. The most abundant of these were isolated and identified as the geometrical isomers **2–4**, which are more readily obtained by UV irradiation of domoic acid (10). Repeated HPLC yielded another related compound with a retention time very close to domoic acid (relative retention time (rrt) 1.07), identical UV and IR spectra, and virtually identical ^1H and ^{13}C spectra (Tables 1 and 2), but a different optical rotation ($[\alpha]_D^{25}$ −48.8). Our identification of this compound as the C5′ epimer **5** was aided by obtaining ^1H and ^{13}C spectra of a ca. 3:2 mixture (at pH 3.4) of **1** and **5**, respectively, which permitted

[1]NRCC No. 34900.

[2]Author to whom correspondence may be addressed. Telephone: 902-426-8275, FAX: 902-426-9413.

TABLE 1. ^{1}H and ^{13}C chemical shifts (ppm)[a] for domoic acid **1** and compounds **5–9**

Compound (pH)	2	3	4	5α	5β	6a	6b	7	8
				δ(H) and multiplicity					
1 (3.4)	3.98 d	3.05 dddd	3.84 ddd	3.49 dd	3.71 dd	2.76 dd	2.50 dd		
5 (3.4)	3.98 d	3.05 dddd	3.84 ddd	3.49 dd	3.71 dd	2.76 dd	2.50 dd		
6 (2.1)	4.09 d	3.02 dddd	3.66 ddd	3.44 dd	3.63 dd	2.73 dd	2.54 dd		
7 (2.4)	4.18 d	3.14 dddd	3.07 ddd	3.49 dd	3.63 dd	2.51 bd[b]	2.51 bd[b]		
8 (4.5)	4.08 d	3.00 dddd	2.05 dddd	3.12 dd	3.64 dd	2.48 dd	2.08 dd		
9 (3.3)	4.16 d	3.03 dddd	2.08 dddd	3.10 dd	3.68 dd	2.69 dd	2.24 dd		
				δ(C)					
1 (3.4)	67.1	44.6	42.7	49.1		35.4		177.5	174.9
5 (3.4)	67.1	44.6	42.7	49.1		35.4		177.5	174.9
6 (1.6)	66.1	43.8	42.4	49.6		35.2		177.8	173.8
7 (2.4)	67.6	43.2	49.4	48.7		35.5		179.0	175.1
8 (4.5)	69.2	44.1	48.5	50.3		37.9		182.8	176.6
9 (3.3)	68.7	43.5	48.5	50.1		34.8		179.2	176.1

Compound	1′	2′a	2′b	3′a	3′b	4′a	4′b	5′	6′	7′	8′
					δ(H) and multiplicity						
1		6.13 d		6.35 dd		5.78 dd		3.30 dq	1.27 d		1.81 s
5		6.13 d		6.35 dd		5.80 dd		3.30 dq	1.27 d		1.81 s
6		5.45 ddq		2.05 dddd	1.94 dddd	1.62 dddd	1.52 dddd	2.46 ddq	1.12 d		1.70 d
7		5.25 ddq		2.14 bddd[b]	2.14 bddd[b]	1.74 dddd	1.59 dddd	2.55 ddq	1.19 d		1.68 d
8	1.53 m	1.48 m	1.16 m	1.38 m	1.23 m	1.57 m	1.36 m	2.34 ddq	1.18 d		0.89 d
9	1.53 m	1.35 m	1.16 m	1.43 m	1.27 m	1.59 m	1.47 m	2.52 ddq	1.15 d		0.95 d
					δ(C)						
1	133.8	132.8		128.6		135.2		44.9	18.6	181.9	23.5
5	133.8	132.8		128.5		135.1		44.8	18.5	181.9	23.5
6	131.7	134.4		27.6		35.2		41.5	19.9	184.4	23.6
7	132.4	130.2		27.4		35.0		41.3	19.2	184.6	19.9
8	33.5	36.7		26.4		36.8		45.2	20.4	189.1	19.4
9	33.6	37.0		25.8		36.0		42.2	19.1	185.3	19.5

[a]Solvent, D_2O; reference TSP in concentric tube; temperature = 20°C; s, singlet; d, doublet; q, quartet; m, multiplet; b, broad. Data previously reported (1, 5) for domoic acid are included for comparison. Most spectra were obtained with a Bruker MSL-300 spectrometer at 300.13 MHz (^{1}H) and 75.5 MHz (^{13}C). HMQC and HMBC spectra used for assignment of ^{13}C spectra of **6–9** were recorded with a Bruker AMX-500 spectrometer at 500.13 MHz.

[b]Overlapping resonances, geminal coupling not measureable.

chemical shift differences between the two compounds to be measured with high precision. All ^{1}H chemical shifts and coupling constants of **5** and **1** agreed within error (ca. 0.3 Hz at 300 MHz), except for δ(H) of H4′ which in **5** was shifted to lower field by 0.017 ppm. Similarly, all ^{13}C chemical shifts were identical within <0.01 ppm except for very slight upfield shifts of the C2′ (0.02 ppm), C3′ (0.10 ppm), C4′ (0.08 ppm), C5′ (0.14 ppm), and C6′ (0.09 ppm) resonances of **5**. The ^{1}H NOEs (Table 3) of **5** were larger than those previously obtained for **1**, and some additional small NOEs were attributed to improvements in sample preparation and better elimination of paramagnetic impurities. The NOEs observed (Table 3) were all compatible with structures **1** and **5**, but would not have been consistent with changes in stereochemistry at any position other than C5′. The combined evidence, in particular the small chemical shift deviations that are greatest in the vicinity of the 5′ position, is only consistent with **5** being the 5′ epimer of **1**. This compound is present in trace amounts in mussel tissue, but was more conveniently obtained from domoic acid by epimerization following treatment with sodium methoxide. It is noteworthy that similar treatment of the geometrical isomer **4** yielded a compound presumed to be the corresponding C5′ diastereoisomer (HPLC resolved a component with very similar retention time to that of **4**).

Dihydro derivatives of domoic acid

Partial reduction of domoic acid with hydrogen in the presence of 10% Pd–charcoal yielded two major reduction products separable by reversed-phase chromatography. The FABMS data indicated that these compounds were both dihydro derivatives, and they were readily shown by ^{1}H NMR spectroscopy (Tables 1 and 2) to be the 1′,2′ *Z* (rrt 1.57) and 1′,2′ *E* (rrt 1.20) compounds **6** and **7**, respectively. Spin–spin coupling connectivity throughout each structure was analyzed from COSY spectra, leading to the ^{1}H assignments in Table 1. Coupling constants (Table 2) indicated negligible changes in average ring conformation. In each case, the position of the double bond in the major side chain was established by the observation of a small coupling between an olefinic methyl group and a single olefinic proton. The NOE results (Table 3) confirmed the double bond position and verified the double bond configuration in each derivative. In addition, the NOE data revealed the signifi-

Can. J. Chem. Downloaded from www.nrcresearchpress.com by 195.246.54.202 on 09/08/12
For personal use only.

TABLE 2. Scalar coupling constants J(H,H) (Hz)[a] for domoic acid and compounds **5–9**

Compound	Coupled pair 2,3	3,4	3,6a	3,6b	4,5α	4,5β	4,1′	5α,5β	6a,6b	1′,8′	2′,8′
1	8.1	8.4	5.8	9.1	7.3	7.9		−12.2	−16.7		
5	8.3	8.1 ± 0.5	5.7	8.9	7.5	7.9		−12.2	−16.9		
6	8.0	8.0	6.4	8.5	9.4	7.6		−12 ± 1	−16.8		1.0
7	4.1	7.4	7.4	7.0	10.5	7.5		−11.9	—[b]		0.7
8	1.3	6.0	4.6	10.9	12.1	8.0	10.5	−11.8	−16.0	6.5	
9	1.1	5.8	4.0	11.7	12.2	7.9	10.5	−11.8	−16.4	6.5	

Compound	Coupled pair 2′,3′a	2′,3′b	3′a,3′b	3′a,4′a	3′a,4′b	3′b,4′a	3′b,4′b	4′a,4′b	4′a,5′	4′b,5′	5′,6′
1	11.1			14.9					7.8		7.1
5	11.0			14.9					7.7		7.0
6	7.0	8.0	−15.0	5.7	6.0 ± 0.5	6.0 ± 0.5	5.0 ± 0.5	−14.0	7.0 ± 0.5	8.0 ± 0.5	7.0
7	6.9	6.9	—[b]	7.3 ± 0.5	7.3 ± 0.5	7.3 ± 0.5	7.3 ± 0.5	−13.8	8.5 ± 0.5	8.5 ± 0.5	7.0
8	←				Coupling not analyzed					→	7.0
9	←				Coupling not analyzed					→	7.0

[a]Error is ca. ±0.3 Hz unless stated. pH was as for ^{1}H data in Table 1. Coupling connectivity was confirmed by ^{1}H COSY spectra. Some couplings were determined by simulation using Bruker PANIC program. Geminal couplings were assumed negative; signs of other couplings were not determined and are given as magnitudes only.

[b]Overlapping resonances, geminal coupling not measureable.

cant effect of the geometry of the side-chain double bond on the preferred conformations of **6** and **7**. For example, the H_38' protons of the *Z* isomer **6** show NOE to H5α and H6b, suggesting a preferred orientation of the large side chain in which the H_38' methyl group tends to lie between these protons, with less tendency to rotate to the vicinity of H3, H4, or H5β. This observation is further supported by the occurrence of NOEs between H4 and H_23', and between H3 and H3′a. Interestingly, a similar pattern of NOEs involving H_38' is observed in **1** and **2** (10), which also possess a 1′,2′ *Z* configuration. By contrast, the corresponding pattern of NOEs to H_38' in the *E* isomer **7** to H2, H4, H6a, and H6b is indicative of a different preferred orientation in which the H_38' group tends to lie in the vicinity of H4, resembling **3** and **4** (10). The NOE between H2′ and H5α is also consistent with this orientation.

These results suggest that the preferred orientation of the larger side chain is strongly influenced by the configuration of the double bond. Furthermore, the orientation of the side chain also has a profound effect on the biological activity: the *Z* isomer **6**, in which the preferred conformers most strongly resemble those of the parent compound domoic acid **1**, has essentially equivalent potency compared with the natural toxin (8). In contrast, the binding efficiency of the *E* isomer **7** is diminished by three orders of magnitude (8).

Tetrahydro derivatives of domoic acid

Reduction of domoic acid with hydrogen in the presence of PtO_2 has been reported to yield a tetrahydro derivative (11), although details were incomplete and no reference was made to either of the possible C1′ diastereoisomers **8** and **9**. We were able to separate two products following PtO_2 reduction, the UV spectrum (end-absorbance only) and FAB mass spectrum (*m/z*: MH^+ 316), indicating complete reduction in each case. Later, both compounds were obtained also by Pd–charcoal reduction. Once again, confirmation of the structures **8** and **9** was based on NMR spectroscopy. The ^{1}H and ^{13}C NMR spectra (Tables 1 and 2) of these compounds were very similar and devoid of olefinic resonances. The differences in the spectral data for these compounds compared with **1** were readily accounted for by reduction only of the two side-chain double bonds without epimerization at the chiral centres in the ring. The difference in the J(2,3) coupling constant compared with **1** (Table 2) suggests a twisting of the ring so that the average H2C2C3H3 angle approaches 90°. NOE results (Table 3) indicated that the compounds differed in their C1′ stereochemistry; **8** showed NOEs between H5β and H_38' and between H4 and H_38', whereas **9** showed NOEs between H_38' and H3, H4, and H6a. Because of the high conformational flexibility of these molecules, the assignment of the C1′ stereochemistry was not possible on the basis of the NMR data alone. Molecular modelling using SYBYL and comparison with the NOE and spin–spin coupling results was necessary in order to assign **8** and **9**, respectively, to the 1′ *S* and 1′ *R* isomers of tetrahydrodomoic acid, as well as for the derivation of their preferred conformations, as follows.

Conformational search (see Experimental) yielded four conformers of **R** and five conformers of **S** with energies within 3 kcal/mol of that of the lowest-energy conformer. These low-energy conformers are listed in Table 4; the lowest energy conformers are shown in Fig. 1. In deriving the average distances and angles, we assumed that the fractional populations of conformers are determined by their Boltzmann factors, which neglects entropy differences.

The pyrrolidine ring in the low-energy conformers of **R** and **S** is in the 3-*exo* and 5-*exo* envelope forms (Table 4). (The number in the designation of these forms refers to the out-of-plane atom; *endo* and *exo* refer to that atom being on the same side as the C-2 carboxylate, or on the other side.) Our results indicate that about 90% of **R** and **S** molecules in solution has the 3-*exo* ring pucker. In this behaviour, **R** and **S** both differ from domoic acid, which according to our recent work appears to be largely in the 5-*exo* form. This explains the major differences in the measured values of the coupling constants for ring protons, notably J(2,3) and J(3,4) (Table 2).

The low-energy conformers of **R** and **S** include all three pos-

Can. J. Chem. Downloaded from www.nrcresearchpress.com by 195.246.54.202 on 09/08/12
For personal use only.

TABLE 3. ^{1}H nuclear Overhauser enhancements (%)[a] for compounds **5–9**

Compound	pH	NOE (%) 2	3	4	5α	5β	6a	6b
5	2.3	H3 3.0 H8′ 1.0	H4 4.1 H6a 1.0 H6b 1.2	H3 9.5 H3′ 15.5	H5β 15.5 H6a 3.1 H6b 3.1 H8′ 2.7	H5α 19.7	H3 3.6 H6b 23.0	H3 3.0 H6a 20.9 H8′ 1.5
6	2.1	H3 1.7 H6a 1.4 H6b 0.8 H8′ 1.2	H4 8.7 H2 1.9 H6a 0.9 H6b 0.7	Overlaps H5β H3 12.0 H5α 12.5[b] H3a′ 5.0 H3b′ 4.0	H4 and (or) H5β 21.8 H8′ 1.4	Overlaps H4 H5α 12.5[b]	H2 2.4 H3 3.6 H6b and (or) H5′ 2.9	Overlaps H5′ H6a 23.3 H3 4.5 H8′ 0.7
7	2.4	H3 2.8 H6ab 2.3 H8′ 0.5	Overlaps H4 H2 5.2 H6ab 2.3	Overlaps H3 H5β 6.2 H2′ 6.6 H8′ 1.9	H5β 20.5 H2′ 11.1 H6ab 1.9	H5α 12.2 H4 9.3	Overlaps H6b and H5′ H2 13.1 H5α 1.8 H3 9.2 H8′ 1.1	Overlaps H6a and H5′ H2 13.1 H5α 1.8 H3 9.2 H8′ 1.1
8	3.5	H3 1.7 H6b 2.3	H2 5.5 H6a 1.3 H4 6.5 H1′–H4′ 2.8[c]	H5β 5.2 H3 4.3 H8′ 1.6	H5β 23.4 H6b 2.7 H2′–H4′ 3.8[c]	H5α 23.0 H4 5.2 H8′ 1.6	H3 3.2 H6b 16.4 H2′–H4′ 12.1[c]	H2 3.3 H3 1.5 H6a 14.9
9	2.3	H3 2.3	H2 2.6 H6a 25.7 H4 5.1 H8′ 0.8	H5β 1.8 H5α and H3 6.3[c] H8′ 1.0	H4 3.9 H5β 16.9 H6b 4.2 H1′–H4′ 13[c]	H4 5.9 H5α 22.0	H3 2.0 H6b 22.0 H1′–H4′ 4.2[c]	H2 3.6 H4 22.3 H6a 14.1

Compound	NOE (%) 1′	2′	3′a	3′b	4′a	4′b	5′	6′	8′
5		H8′ 2.9 H4′ 11.3	H4 14.5 H5′ 9.0 H6′ 0.8		H2′ 11.9 H5′ 3.2 H6′ 0.4		H3′ 4.9 H4′ 4.4 H6′ 1.8	H3′ 1.9 H4′ 4.6 H5′ 10.0	H2 4.5 H5α 5.0 H6b 4.0 H2′ 11.0
6		H8′ 2.4 H3′a 1.1 H3′b 2.5 H4′a 2.3 H4′b 0.9 H5′ 1.8	H2′ 4.2 H4 8.1 H3 1.3 H5′ 2.8	H2′ 6.4 H4 3.1 H5′ 2.0	H2′ 4.2 H5′ 5.4 H3′a 1.2 H3′b 2.6	H2′ 5.9 H5′ 5.0	Overlaps H6b H6′ 2.4	H5′ 6.7 H4′a 7.2 H4′b 6.2	H2′ 14.3 H2 7.0 H5α 5.8 H6b 3.1
7		H5α 7.2 H4 and (or) H3 3.7 H3′ 5.3	Overlaps H3b [b]→ H8′ 3.6 H2′ 5.3 H5′ 10.3	Overlaps H3a ←[b] H4′a 1.5 H4′b 4.0 H6′ 0.4	H4′b 11.3 H5′ 2.7 H3′ab 2.3	H4′a 12.4 H5′ 8.6 H3′ab 2.1	Overlaps H6ab H4′a 2.7 H4′b 4.4 H6′ 3.8 H8′ 1.1	H5′ 10.0 H4′a 2.4 H4′b 1.9	Part overlaps H4′a H4 9.4 H6ab 3.5 H3′ab 3.6 H2 1.8
8	←		Not irradiated			→	H1′–H4′ 4.1[c] H6′ 1.8	H5′ 7.2 H4 3.1 H1′–H4′ 20.5[c]	H5β 2.8 H4 4.0 H1′ 5.4
9	←		Not irradiated			→	H1′–H4′ 6.6[c] H6′ 2.5	H4 2.5 H1′–H4′ 24.0[c] H5′ 9.5	H3 and H5α 7.1[c] H4 2.2 H6a 2.1 H1′ 5.8

[a]Enhancement measurements were taken when H at the head of the column was irradiated. Solvent D_2O; temperature, 20°C; pH meter readings uncorrected for use in D_2O; error, ca. ± 0.5% for single protons and ca. ± 0.3% for methyl protons.
[b]May also be due to irradiation of overlapping resonance.
[c]Total NOE for all overlapping resonances.

sible staggered states with respect to rotation about the C3—C6 bond (corresponding to the torsional angle t_{36} = C2C3C6C7 taking the values of about −60, +60, and 180°). There are also three possible staggered states with respect to rotation about the C4—C1′ bond (corresponding to the torsional angle $t_{41'}$ = C3C4C1′C2′ taking the values of about −60, +60, and 180°), but in the low-energy conformers only $t_{41'} \approx -60°$ occurs for **R** and only $t_{41'} \approx 180°$ occurs for **S**. This constitutes a major dif-

Can. J. Chem. Downloaded from www.nrcresearchpress.com by 195.246.54.202 on 09/08/12
For personal use only.

TABLE 4. SYBYL energies and geometries of low-energy conformers of **R** and **S**

	Conformer				
	1	2	3	4	5
			Molecule S		
Energy (kcal)	12.8897	13.5471	13.8363	14.7723	15.7515
Boltzmann population	0.6326	0.2083	0.1278	0.0263	0.0050
Ring conformation	3-*exo*	3-*exo*	3-*exo*	5-*exo*	5-*exo*
Torsion $t_{41'}$	−59.4	−58.4	−63.0	−66.8	−68.9
Torsion t_{36}	−61.6	+57.9	−167.0	−62.0	−166.5
			Molecule R		
Energy (kcal)	13.5981	14.1247	14.6610	15.0517	
Boltzmann population	0.6015	0.2471	0.0998	0.0516	
Ring conformation	3-*exo*	3-*exo*	5-*exo*	3-*exo*	
Torsion $t_{41'}$	173.7	177.0	171.4	171.4	
Torsion t_{36}	−61.5	+56.5	−59.8	−164.9	

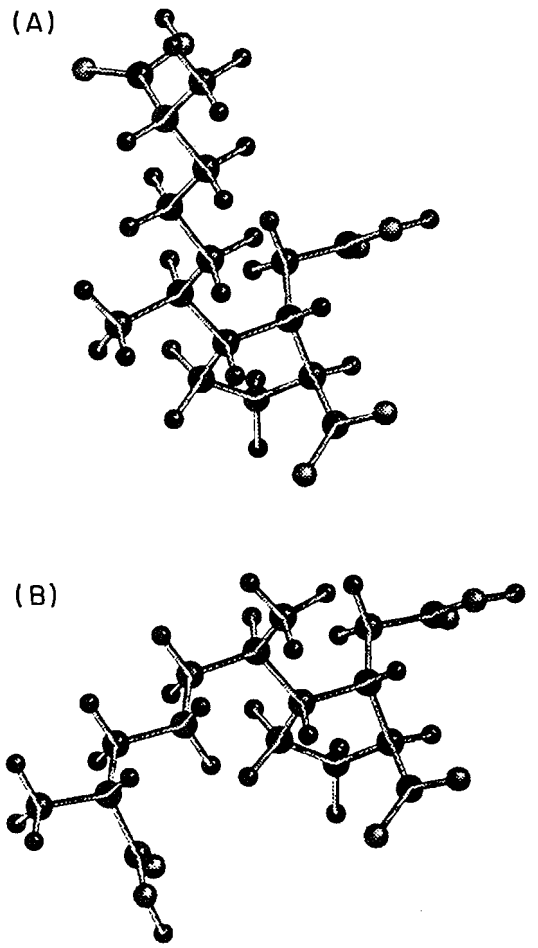

FIG. 1. The dominant conformers of tetrahydro domoic acid epimers **S** and **R** from SYBYL modelling. (A): **S** = **8**, conformer 1, energy = 12.8897 kcal/mol, population 63.23%. (B): **R** = **9**, conformer 1, energy = 13.5981 kcal/mol, population 60.15%.

ference in the conformational behaviour of these two epimers, permitting an unequivocal distinction on the basis of NMR spectral data.

Comparison of calculated H–H distances with NOE data

The interproton distances were determined for each conformer and the mean distance was obtained as a population-weighted average over all conformers, weighting the distances by inverse sixth power (12). The distances involving the three methyl hydrogens required further averaging in the same fashion. Table 5 compares the interproton distance obtained from modelling with NOE data adapted from Table 3. For each proton pair, the presence of an NOE in one epimer and not in the other was taken to indicate a shorter H–H distance. Under this condition, the comparison implies that **8** must be **S** and **9** must be **R**.

Comparison of experimental and calculated H,H couplings

Each HCCH dihedral angle, χ_i, involving vicinal ring protons was determined for every conformer i. From each of these dihedrals, the vicinal coupling constant J_i (Hz) was calculated by the Karplus-type equation $J_i = 8.5 \cos^2\chi_i + 1.4$ (for $0 \leq \chi_i \leq 90$) or $J_i = 10.5 \cos^2\chi_i + 1.4$ (for $90 \leq \chi_i \leq 180$), as recommended by Pogliani et al. (13). The mean coupling constant was obtained as the population-weighted average. The calculated coupling constants are compared with the experimental values in Table 6. The absolute values are not expected to fit well, considering the uncertainty of the numerical parameters in the Karplus equation. However, the relative values show clear trends consistent with the conclusions from NOEs. Any small modification of the constants in the Karplus equation would not affect these trends. Therefore, relative magnitudes of the experimental and calculated coupling constants confirm that **8** is **S** and **9** is **R**.

Conclusion

The potency of the few naturally occurring kainate (or domoate) neurotoxins has been investigated (14, 15). These neurotoxins are all characterized by a structural moiety that resembles glutamic acid and they can be considered as conformationally restricted forms of this amino acid. Furthermore, it has been shown that neurological activity in the kainoids requires that the stereochemistry of the C2 and C3 positions, bearing respectively carboxyl and carboxymethyl groups, be *S* (14, 15). Our binding studies (8) with the domoic acid derivatives discussed in this report have demonstrated the important influence of the major side chain, and specifically the essential requirement of a 1′,2′ double bond in the *Z* configuration, for strong binding to kainate and AMPA receptors.

The study of neurological processes using chemical probes

Can. J. Chem. Downloaded from www.nrcresearchpress.com by 195.246.54.202 on 09/08/12
For personal use only.

TABLE 5. Comparison of structurally important H–H distances derived from molecular modelling for **S** and **R** with experimentally observed NOEs for **8** and **9**

Experimental NOE			H–H distances (Å) from modelling			
Proton pair	**8**	**9**	Proton pair	**S** isomer	**R** isomer	Conclusions
H4,H5α	No	?	H4,H5(pro-*R*)	3.04	3.05	H5β is pro-*S*
H4,H5β	Yes	Yes	H4,H5(pro-*S*)	2.36	2.38	
H3,H8′	No	Yes	H3,H8′	4.88	2.85	**8** is **S**
H4,H8′	Yes	Yes	H4,H8′	2.94	2.90	
H5α,H8′	No	No	H5(pro-*R*),H8′	2.98	4.70	**8** is **S**
H5β,H8′	Yes	No	H5(pro-*S*),H8′	2.84	4.84	
H6a,H8′	No	Yes	H6(pro-*R*),H8′	4.98	3.05	H6a is pro-*R*; **8** is **S**
H6b,H8′	No	No	H6(pro-*S*),H8′	4.96	4.50	
H3,(H1′–H4′)	Yes	No	H3,H1′	3.48	3.45	**8** is **S**
			H3,H2′	2.49	4.81	

TABLE 6. Comparison of scalar coupling constants *J*(H,H) involving the ring protons derived from molecular modelling for **S** and **R** with experimentally observed values for **8** and **9**

Experimental values			Calculated values			
	J(H,H)			*J*(H,H)		
Coupled pair	**8**	**9**	Coupled pair	**S**	**R**	Conclusions
H2,H3	1.3	1.1	H2,H3	1.86	1.97	Not clear
H3,H4	6.0	5.8	H3,H4	6.62	5.87	Not clear
H3,H6a	4.6	4.0	H3,H6(pro-*R*)	4.81	4.31	H6a is pro-*R*; **8** is **S**
H3,H6b	10.9	11.7	H3,H6(pro-*S*)	8.96	9.34	H6b is pro-*S*; **8** is **S**
H4,H5α	12.1	12.2	H4,H5(pro-*R*)	9.84	10.16	H5α is pro-*R*
H4,H5β	8.0	7.9	H4,H5(pro-*S*)	7.07	6.73	H5β is pro-*S*

requires careful stereochemical and conformational definition of these probes. This study and our previous work (10) defines the stereochemical parameters for all the probes used in a recent study of binding efficacy to kainate and AMPA receptors present in certain neuronal cells. In addition, the modelling studies not only define the stereochemistry of the two C1′ epimers, but also reveal major differences in their solution conformation. These data will be valuable in future ligand–receptor binding studies with the purified receptor protein.

Experimental

All solvents were HPLC grade from Anachemia. Distilled water was further purified by passage through a Millipore water-purification system (Milli-QR) equipped with ion-exchange and carbon filters. Melting points are uncorrected and were observed with a Kofler-type hot-stage apparatus. Optical rotations and all IR, UV, NMR, and MS were, unless otherwise stated in the text or tables, recorded with instruments and conditions described previously (1). In HPLC experiments, the retention times of products were measured relative to domoic acid. NMR spectra were assigned and spin–spin coupling constants were measured with the aid of 2D COSY and $^{13}C,^{1}H$ heterocorrelation spectra and simulations using the Bruker PANIC program. ^{1}H and ^{13}C data for compounds **1** and **5–9** are reported in Table 1, with some previously reported data being included for convenience.

Isolation of domoic acid C5′ epimer

Large-scale purification of domoic acid from frozen, cooked mussel tissue (5 kg), following procedures already described (1, 5), yielded a fraction that, by HPLC–DAD analysis, contained mainly domoic acid **1** (>85%), three geometrical isomers **2–4**, and another compound **5** subsequently identified as the C5′ epimer of **1**. The latter had a fractionally longer retention time (rrt 1.07) than domoic acid. The epimer was collected from repeated small-scale semipreparative reversed-phase HPLC runs (Vydac 201 TP1010, 10 μm, isocratic elution 5% acetonitrile–water containing 0.1% TFA, flow rate 2.8 mL/min); $[\alpha]_D^{24}$ −48.8 (*c* 0.18, H_2O); $\lambda_{max}(H_2O)$: 242 nm.

Conversion of domoic acid to C5′ epimer

Domoic acid (31 mg) was dissolved in dry methanol (40 mL) containing sodium methoxide (0.77 g) and the mixture was warmed (68°C) under nitrogen for 75 h. The mixture was neutralized with HCl (1 N) and evaporated to dryness. Analysis of the mixture at this stage showed approximately equimolar amounts of domoic acid and **5**. The diastereoisomer was purified by gradient reversed-phase vacuum chromatography using acetonitrile–water with 0.1% acetic acid, followed by semipreparative HPLC (Vydac 201 TP1010, 5% acetonitrile – water with 0.05% TFA), and was identical (rrt, UV, IR, NMR, and MS) with the material isolated from toxic mussel tissue.

Preparation of Z- and E-dihydrodomoic acids

Domoic acid (50 mg) was dissolved in water–MeOH (1:1, 30 mL) containing 10% Pd–charcoal (20 mg, Matheson Coleman and Bell, Canada) and stirred (40–60 min) in an atmosphere of hydrogen. HPLC analysis (Vydac 201 TP1010) of the mixture revealed almost complete consumption of the starting material and the appearance of two new

Can. J. Chem. Downloaded from www.nrcresearchpress.com by 195.246.54.202 on 09/08/12
For personal use only.

major compounds shown later to be *Z*- and *E*-dihydrodomoic acids **6** and **7** (rrt 1.57 and 1.20, respectively). The catalyst was removed by filtration, the solvent was concentrated to dryness, and the products were isolated by semipreparative HPLC (conditions as above, 15% acetonitrile as eluant). Following many repeated HPLC runs, the faster-eluting product (12.7 mg) was obtained as a white powder and identified as **7**: $[\alpha]_D^{24}$ −19.8; FABMS *m/z*: MH^+ 314; IR (KBr): 2980 (br), 1713, 1676, 1200, 840, 800 cm^{-1}; ^1H and ^{13}C NMR, see Table 1. The slower-eluting product (4.16 mg) was obtained as a white solid and identified as **6**: $[\alpha]_D^{24}$ −71.6; FABMS *m/z*: MH^+ 314; IR (KBr): 2984 (br), 1712 (br), 1217, 825 (br) cm^{-1}; ^1H and ^{13}C NMR, see Table 1. Traces of the tetrahydro derivatives and some other minor products were observed, but no attempt was made to isolate them in this experiment.

Preparation of the C1′ diastereoisomers of tetrahydrodomoic acid

Domoic acid (30 mg) was dissolved in water (5 mL) containing PtO_2 (hydrate, 4.3 mg, Aldrich, U.S.A.) and stirred in an atmosphere of hydrogen. HPLC analysis of the reaction after 1 h indicated a less complex mixture than that obtained in the dihydro preparation, with complete reduction of domoic acid to compounds subsequently determined to be the tetrahydro C1′ diastereoisomers **8** and **9**. Removal of the catalyst and concentration to dryness gave a white solid from which the diastereomers were separated by semipreparative HPLC. The faster-eluting product (rrt 1.63, 9.6 mg) was obtained as a white solid and identified as **8**, the 1′ *S* tetrahydro derivative: FABMS *m/z*: MH^+ 316; IR (KBr): 2970 (br), 1708, 1414, 1224 cm^{-1}; ^1H and ^{13}C NMR, see Table 1. The slower-eluting product (rrt 2.35, 18.6 mg) was also obtained as a white solid and identified as **9**, the 1′ *R* tetrahydro derivative: FABMS *m/z*: MH^+ 316; IR (KBr): 2938 (br), 1718, 1415, 1224 cm^{-1}; ^1H and ^{13}C NMR, see Table 1.

Molecular modelling

Molecular modelling was carried out on a Personal Iris 4D/35 TurboGraphic workstation (Silicon Graphics, Inc., Mountain View, Calif.) using SYBYL molecular modelling software (Version 6.0, Tripos Associates, St. Louis, Mo.). SYBYL representations of the two tetrahydro isomers were derived from the crystallographic structure of domoic acid (16) by changing the two carbon–carbon double bonds to single bonds, adding four hydrogens, and minimization. The two isomeric structures thus generated, named **R** and **S** (corresponding to the chirality at C1′), were verified to have the following chirality:

	C2	C3	C4	C1′	C5′
R	*S*	*S*	*R*	*R*	*R*
S	*S*	*S*	*R*	*S*	*R*

It may be noted that the chirality at C4 is *S* for both domoic acid (16) and kainic acid (17), but it formally changes to *R* in the tetrahydrodomoic acids, because reduction of the C1′=C2′ bond switches the priorities of carbons C1′ and C3. The two structures were modelled as zwitterions, with a positively charged N atom, a negatively charged C8 carboxylate, and uncharged C7 and C7′ carboxyls. This state of zero net charge is appropriate to domoic acid and its analogues at pH ≈ 3, near their isoelectric point (18), at which the NMR data were collected. The minimizations and molecular dynamics simulations reported here were carried out with the TRIPOS force field (19), but analogous results were obtained under the MM2 force field (20). The electrostatic term was computed with atomic partial charges calculated according to the method of Gasteiger and Marsili (21, 22). The influence of aqueous environment was modelled by a dielectric continuum with the dielectric constant set at $\epsilon = 80$ (23).

Conformational search

Conformation space of **R** and **S** was searched by means of a molecular dynamics simulation with step size of 1 fs (23). Each epimer was subjected to a total sojourn of 50 000 fs at the effective temperature of 1500 K, this temperature–time combination having been found sufficient to ensure rapid and thorough exploration of the available conformation space. The instantaneous molecular geometry was recorded every 2000 fs until 250 geometries were collected. To save computer time, no annealing was attempted. The 250 molecular geometries were minimized and all distinct conformations with energies within 3 kcal/mol of the minimum were retained. The threshold of distinctness was 0.1 Å RMS deviation of nonhydrogen-atom distances, the lowest-energy representative of each conformation being retained.

Acknowledgements

We thank Cheryl Craft, Pat LeBlanc, and Don Leek for their technical assistance, Don Embree for mass spectrometry, and Peter Arseneau for developing several programs in SYBYL programming language.

1. J.L.C. Wright, R.K. Boyd, A.S.W. deFreitas, M. Falk, R.A. Foxall, W.D. Jamieson, M.V. Laycock, A.W. McCulloch, A.G. McInnes, P. Odense, V.P. Pathak, M.A. Quilliam, M.A. Ragan, P.G. Sim, P. Thibault, J.A. Walter, M. Gilgan, D.J.A. Richard, and D. Dewar. Can. J. Chem. **67**, 481 (1989).
2. J.E. Bruni, R. Bose, C. Pinsky, and G. Glavin. Brain Res. Bull. **26**, 419 (1991).
3. E. Preston and I. Hynie. Can. J. Neurol. Sci. **18**, 39 (1991).
4. G.R. Stewart, C.F. Zorumski, M.T. Price, and J.W. Olney. Exp. Neurol. **110**, 127 (1990).
5. R.J. Sutherland, J.M. Hoesing, and I.Q. Whishaw. Neurosci. Lett. **120**, 221 (1990).
6. R.A.R. Tasker, B.J. Connell, and S.M. Strain. Can. J. Physiol. Pharmacol. **69**, 378 (1991).
7. L. Tryphonas, J. Truelove, and F. Iverson. Toxicol. Pathol. **18**, 297 (1990).
8. D.R. Hampson, X. Huang, J.W. Wells, J.A. Walter, and J.L.C. Wright. Eur. J. Pharmacol. **218**, 1 (1992).
9. A. Novelli, M.T. Fernandez-Sanchez, J. Kispert, A. Torreblanca, S. Gascon, and V. Zitko. Amino Acids, **2**, 233 (1992).
10. J.L.C. Wright, M. Falk, A.G. McInnes, and J.A. Walter. Can. J. Chem. **68**, 22 (1990).
11. T. Takemoto and K. Daigo. Chem. Pharm. Bull. **6**, 578 (1958).
12. C. Hervé du Penhoat, A. Imberty, N. Roques, V. Michon, J. Mentech, G. Descotes, and S. Pérez. J. Am. Chem. Soc. **113**, 3720 (1991).
13. L. Pogliani, M. Ellenberger, and J. Valat. Org. Magn. Reson. **7**, 61 (1975).
14. J.T. Slevin, J.F. Collins, and J.T. Coyle. Brain Res. **265**, 169 (1983).
15. J.C. Watkins, P. Krogsgaard-Larsen, and T. Honore. Trends Pharmacol. Sci. **11**, 25 (1990).
16. K. Nomoto, T. Takemoto, M. Maeda, Y. In, M. Doi, M. Inoue, and T. Ishida. Biochem. Biophys. Res. Commun. **187**, 325 (1992).
17. P. Narula, H.C. Patel, A. Srinivasan, and T.P. Singh. Indian J. Phys. **62A**, 439 (1988).
18. J.A. Walter, D.M. Leek, and M. Falk. Can. J. Chem. **70**, 1156 (1992).
19. M. Clark, R.D. Cramer III, and N. Van Opdenbosch. J. Comput. Chem. **10**, 982 (1989).
20. N.L. Allinger. J. Am. Chem. Soc. **99**, 8127 (1977).
21. J. Gasteiger and M. Marsili. Tetrahedron, **36**, 3219-28 (1980).
22. J. Gasteiger and M. Marsili. Org. Magn. Reson. **15**, 353 (1981).
23. S.D. O'Connor, P.E. Smith, F. Al-Obeidi, and B.M. Pettitt. J. Med. Chem. **35**, 2870 (1992).

Can. J. Chem. Downloaded from www.nrcresearchpress.com by 195.246.54.202 on 09/08/12
For personal use only.

Solvent and crown ether/cryptand effects on the oximate-promoted 1,2-elimination from β-phenylmercaptoethyl *p*-nitrophenolate. Formation and reactivity of a crown ether-complexed potassium oximate ion pair

ERWIN BUNCEL,[1] ANURAG KUMAR, HAI-QI XIE, AND ROBERT Y. MOIR
Department of Chemistry, Queen's University, Kingston, ON K7L 3N6 Canada

AND

J. GARFIELD PURDON
Defence Research Establishment Suffield, Ralston, AB T1A 8K6, Canada

Received March 26, 1993

Can. J. Chem. Downloaded from www.nrcresearchpress.com by 195.246.54.202 on 09/08/12
For personal use only.

ERWIN BUNCEL, ANURAG KUMAR, HAI-QI XIE, ROBERT Y. MOIR, and J. GARFIELD PURDON. Can. J. Chem. **72**, 437 (1994).

The reactions of β-phenylmercaptoethyl *p*-nitrophenolate (**1**) with three potassium oximates, viz. potassium 2,3-butanedione monoximate (BDOK), acetophenone oximate (APOK), and acetone oximate (AOK) have been investigated in two nonhydroxylic dipolar aprotic solvents, tetraglyme and dimethyl sulfoxide (DMSO). The reaction products, as determined by ^{1}H NMR spectroscopy, were *p*-nitrophenoxide ion and phenyl vinyl sulfide, in accord with an elimination process. A kinetic spectrophotometric study showed that in tetraglyme, the addition of oxime and water in small amounts drastically decreased the rate of reaction of **1** with APOK as a result of hydrogen-bonding interactions with the oximate anion. In tetraglyme as solvent the addition of 2.2.2 cryptand greatly enhanced the reactivity of the oximates but the macrocyclic crown ether DC-18-C6 had much smaller effect on rate. The results are consistent with formation of a crown ether-complexed potassium oximate ion pair, which is much less reactive than the free anion formed in the presence of 2.2.2 cryptand but more reactive than the potassium oximate ion pair. The kinetic data were analyzed to obtain specific rate coefficients for reaction of APOK as the dissociated anion, the ion-paired species, and as the crown ether-complexed oximate; equilibrium constants for potassium oximate ion pair formation and for the crown ether-complexed ion pair were obtained. In DMSO as solvent the rate of reaction remained unaffected on addition of the metal ion complexing agents, indicating that ion pairing is not important in this solvent. The reactivity of the free oximate anions in both solvents increased in the order BDOK < APOK < AOK, which parallels the pK_a's of the corresponding oximes in DMSO. The unusually high reactivity of oximates in the low polarity tetraglyme compared to polar DMSO could be explained on the basis of stabilization of the transition state in tetraglyme. Trends in k^{TG}/k^{DMSO} for the oximates follow reactivity–selectivity considerations.

ERWIN BUNCEL, ANURAG KUMAR, HAI-QI XIE, ROBERT Y. MOIR et J. GARFIELD PURDON. Can. J. Chem. **72**, 437 (1994).

On a étudié les réactions du *p*-nitrophénolate de β-phénylmercaptoéthyle (**1**) avec trois oximates de potassium, les sels de potassium du monooximate de la 2,3-butanedione (BDOK), de l'oximate de l'acétophénone (APOK) et de l'oximate de l'acétone (AOK), dans deux solvants dipolaires non hydroxyliques, le tétraglyme et le diméthylsulfoxyde (DMSO). Les produits réactionnels, tels que déterminés par la RMN du ^{1}H, sont l'ion *p*-nitrophénolate et le sulfure de phényle et de vinyle; ceci est en accord avec un processus d'élimination. Une étude cinétique réalisée par spectrophotométrie montre que, dans le diglyme, l'addition de l'oxime et de l'eau en faibles quantités réduit d'une façon drastique la vitesse de réaction du composé **1** avec l'APOK, à cause d'interactions par liaison hydrogène avec l'anion oximate. Dans le tétraglyme comme solvant, l'addition du cryptand 2.2.2 augmente d'une façon appréciable la réactivité des oximates, mais l'éther couronne macrocyclique, DC-18-C6, provoque un effet beaucoup plus faible sur la vitesse. Les résultats sont en accord avec la formation d'une paire d'ions oximate de potassium complexée par l'éther couronne qui est beaucoup moins réactive que l'anion libre qui se forme en présence du cryptand 2.2.2, mais plus réactive que la paire d'ions oximate de potassium. On a analysé les données cinétiques afin d'obtenir les coefficients de vitesse spécifique pour la réaction de l'APOK sous la forme d'anion dissocié, de paire d'ions et d'oximate complexé par l'éther couronne; on a obtenu les constantes d'équilibre pour la formation de la paire d'ions oximate de potassium et pour la paire d'ions complexée par l'éther couronne. Dans le DMSO comme solvant, la vitesse de la réaction n'est pas affectée par l'addition d'agents pouvant complexer les ions métalliques; ceci indique que la formation de paires d'ions n'est pas importante dans ce solvant. La réactivité des anions oximates libres dans les deux solvants augmente dans l'ordre BDOK < APOK < AOK; cet ordre est parallèle aux pK_a des oximes correspondantes dans le DMSO. On peut expliquer la réactivité inhabituellement élevée des oximates dans le tétraglyme de faible polarité par comparaison avec celle observée dans le DMSO par une stabilisation de l'état de transition dans le diglyme. Les tendances dans le rapport k^{TO}/k^{DMSO} des oximates suivent les considérations de réactivité–sélectivité.

[Traduit par la rédaction]

Introduction

Ever since mustard gas was used as a chemical warfare agent, its destruction has been a challenging problem to chemists. During the last several decades a number of reports have appeared in the literature on the nucleophilic reactions of 2-chloroethyl sulfide derivatives, as models of sulfur mustard, 2,2′-dichlorodiethyl sulfide (1–9).

The nature of the reaction medium plays an important role in determining the reaction pathways of ethyl sulfide derivatives. For reactions of 2-chloroethyl *p*-tolyl sulfide with ethoxide in ethanol, Oae and Yano (3) observed 47% elimination and 53% substitution, whereas in 80% aqueous ethanol (w/w) Bird and Stirling (5) found 100% substitution. The most widely accepted mechanism for substitution reactions of ethyl sulfide derivatives in hydroxylic solvents involves intramolecular displacement of chloride ion by sulfur yielding an episulfonium ion, followed by attack of nucleophile resulting in substitution,

[1]Author to whom correspondence may be addressed.

Can. J. Chem. Downloaded from www.nrcresearchpress.com by 195.246.54.202 on 09/08/12
For personal use only.

an S_N intramolecular process (4–8). There appear to be only two reports of a direct S_N2 displacement, for the reactions of ethyl sulfide derivatives with thiophenolate ions in DMSO (10, 11).

To the best of our knowledge, no reports are available concerning nucleophilic reactions of ethyl sulfide derivatives under homogeneous conditions in nonhydroxylic solvents of low polarity where these compounds are expected to be fairly soluble in contrast to their low solubility in aqueous media. It was of interest, therefore, to examine how a change of reaction medium from hydroxylic to nonhydroxylic would affect the reactivity and reaction pathways of ethyl sulfide derivatives.

In this work, the nucleophilic reactions of β-phenylmercaptoethyl *p*-nitrophenolate (**1**) with three potassium oximates, namely, potassium 2,3-butanedione monoximate (BDOK), acetophenone oximate (APOK), and acetone oximate (AOK) were investigated. These so-called α-nucleophiles are known to be highly reactive due to the presence of an unshared electron pair on the atom adjacent to the reacting site (12–16). Two nonhydroxylic solvents of different polarity were examined, namely, tetraglyme and DMSO. Tetraglyme was chosen as the solvent of low polarity because of its potential advantages in nucleophilic displacement reactions (17). The effect of added metal ion complexing agents was examined in both solvents. The importance of hydrogen-bonding interactions on reactivity in tetraglyme was also examined.

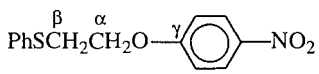

1

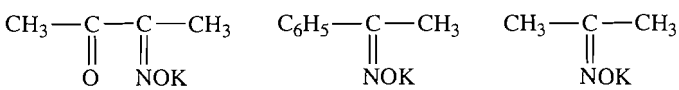

BDOK APOK AOK

Results

Reaction product identification

There are four possible pathways for the reaction of **1** with an oximate anion (Ox^-): (1) nucleophilic substitution at the aliphatic carbon centre attached to the oxygen, yielding β-phenylmercaptoethyl oximate and *p*-nitrophenoxide ion; (2) nucleophilic substitution at the aromatic carbon centre attached to oxygen, yielding β-phenylmercaptoethoxide ion and *O*-(4-nitrophenyl)oxime; (3) elimination, yielding phenyl vinyl sulfide (PVS) and *p*-nitrophenoxide ion; and (4) nucleophilic substitution at the aliphatic carbon centre attached to the sulfur atom, yielding thiophenoxide ion and *p*-nitrophenylethyl oximate. Reactions (1)–(3) are shown in Scheme 1; reaction (4) is not shown since this is not expected to occur in the present case with *p*-nitrophenoxide as leaving group, though it remains a possibility with other phenolates.

Product analysis of the reactions of **1** with the oximates in tetraglyme and DMSO was carried out by ^{1}H NMR spectroscopy. The only process occurring in the reaction system examined in tetraglyme as well as DMSO was elimination. The formation of PVS was confirmed by the appearance of two doublets at δ 5.34 (H_c, J_{ac} = 16.6) and 5.43 (H_b, J_{ab} = 9.59), a double doublet at δ 6.72(H_a, J_{ac} = 16.6, J_{ab} = 9.59), and a multiplet at δ 7.33 for the PhS moiety. Two "doublets" at δ 5.90 (*ortho* 2H, J = 9.56) and 7.72 (*meta* 2H, J = 9.57) were assigned to *p*-nitrophenoxide ion, while a multiplet at δ 7.64 was due to the phenyl moiety of

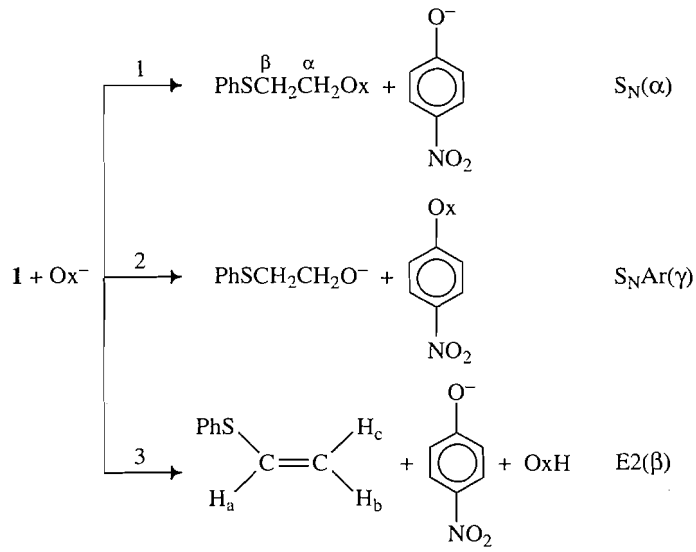

SCHEME 1

acetophenone oximate anion/oxime. The ^{1}H NMR spectra of authentic samples of PVS and *p*-nitrophenoxide ion were used to confirm the formation of the elimination products.

Kinetic studies in tetraglyme

The kinetics of the reaction of **1** with oximates BDOK, APOK, and AOK in tetraglyme have been studied by standard or stopped-flow UV–VIS spectrophotometric methods in the absence and presence of metal ion complexing agents. The reactions were monitored under pseudo-first-order conditions with the oximate in large excess by following the changes in absorbance at λ_{max} of *p*-nitrophenoxide ion (424–435 nm). Pseudo-first-order rate constants (k_{obs}) were calculated from the linear plots of $\ln (A_\infty - A_t)$ versus time t by a least-squares linear regression method, Table 1.

The plot for the variation of k_{obs} with the oximate concentration in the reaction of **1** with APOK in the absence of metal ion complexing agents exhibits downwards curvature (Fig. 1). Addition of 2.2.2 ([2.2.2]/[APOK] = 1.23) to the reaction mixture drastically increased the rate of reaction and the plot of k_{obs} vs. [APOK] was linear (Fig. 1). The second-order rate constant for reactions of the free oximate anion, $k_2 = k_{Ox^-}$, calculated from the slope of the plot for the reaction containing 2.2.2 is 9.22 M^{-1} s^{-1} (Table 2). Addition of DC-18-C6, with [DC18-C6]/[APOK] = 14.9, was found to increase the rate to a much smaller extent and the plot of k_{obs} vs. [APOK] appears to be linear (Fig. 1).

The other two oximates, BDOK and AOK, were found to be insoluble in tetraglyme in the absence and presence of DC-18-C6, but both became soluble in the presence of 2.2.2. Rate data for the reaction of **1** with BDOK and AOK in the presence of 2.2.2 are given in Table 1. The plots of k_{obs} vs. [OxK] were linear (Fig. 2) and yield k_2 from the slope (Table 2).

The effect of varying the concentration of complexing agents at constant APOK is shown in Fig. 3 and results are given in Table 3. Increasing [2.2.2] at constant [APOK] led to a marked increase in rate until a maximum value (130-fold increase) was reached with [2.2.2]/[APOK] = 1.0, following which addition of more 2.2.2 had no effect on the rate. In contrast, added DC-18-C6 had a much smaller effect on the rate of reaction. A 3.5-fold increase in rate was observed with [DC18C6]/

Can. J. Chem. Downloaded from www.nrcresearchpress.com by 195.246.54.202 on 09/08/12
For personal use only.

TABLE 1. Pseudo-first-order rate constants for the reaction of **1** with oximates (BDOK, APOK, and AOK) in tetraglyme in the absence and presence of DC-18-C6 and 2.2.2 cryptand complexing agents

OxK	Complexing agent	10^3 [OxK] (M)	[Complexing agent]/[OxK]	Temperature (°C)	$10^3 k_{obs}$ (s^{-1})
BDOK	2.2.2	2.51	1.66	60	0.0198
		5.02	1.66		0.0407
		7.52	1.66		0.0665
		11.3	1.66		0.0655
		15.0	1.66		0.111
		18.8	1.66		0.129
APOK	None	1.93		25	0.116
		3.39			0.175
		4.84			0.234
		6.29			0.264
		7.74			0.320
		9.19			0.330
	DC-18-C6	2.02	14.9	25	0.322
		3.53	14.9		0.510
		5.04	14.9		0.747
		6.55	14.9		0.974
		8.06	14.9		1.25
		9.57	14.9		1.42
	2.2.2	1.07	1.23	25	9.40
		1.43	1.23		13.1
		1.78	1.23		15.6
		2.14	1.23		19.8
		2.49	1.23		23.7
AOK	2.2.2	1.87	1.16	25	322
		2.62	1.16		504
		3.37	1.16		586
		4.11	1.16		707
		4.80	1.16		905

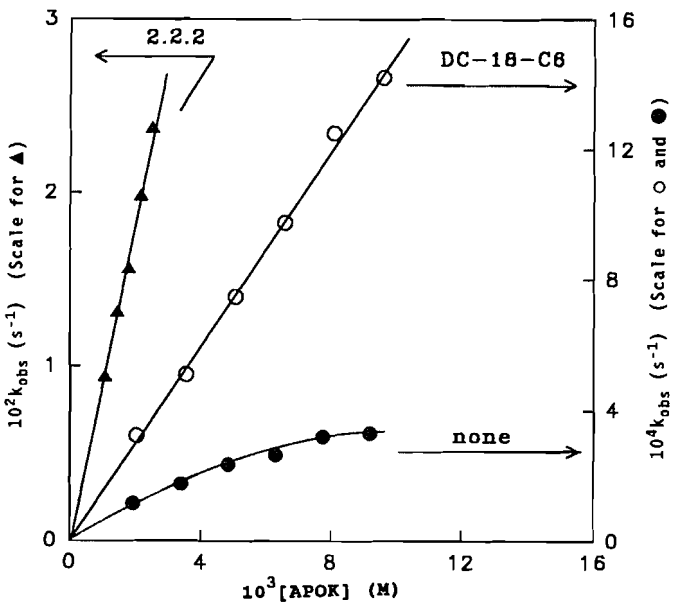

FIG. 1. Plots of k_{obs} vs. [APOK] for the reaction of **1** ((4.29–5.31) × 10^{-5} M) with APOK in tetraglyme in the absence (●) and presence (○, DC-18-C6 and ▲, 2.2.2) of metal ion complexing agents at 25°C.

[APOK] = 4.8, following which addition of more DC-18-C6 had almost no effect on the rate of reaction.

Our earlier investigations have shown the powerful role of hydrogen-bonding interactions in tetraglyme (17).[2] Therefore, it was thought worthwhile to examine the effect of added oxime and water on the rate of reaction of oximate with **1**. It was found that both acetophenone oxime (APOH) and water show a marked rate-retarding effect on the reaction of **1** with APOK in tetraglyme, see Figs. 4 and 5, and Tables 4 and 5.[3,4]

Kinetic studies in DMSO

Kinetic data for reaction of **1** with APOK and AOK were determined at 25°C (Table 6) but the reaction of **1** with BDOK in DMSO was found to be very slow at 25°C and rate constants were obtained at 60°C. The plots of log k_{obs} *vs* log[OxK] for the reactions of APOK and AOK are shown in Fig. 6. The effect of added DC-18-C6 and 2.2.2 cryptand was examined for the reac-

[2]E. Buncel, Ng. van Truong, and H.-Q. Xie, unpublished results.

[3]A referee has suggested that addition of H_2O to the oximate system could lead to generation of OH^-. This possibility cannot be rigorously excluded; pK_a values of oximes in tetraglyme containing H_2O are not known (in water, the pK_a of acetophenone oxime is 12.4).

[4]The possibility that addition of water could change the reaction pathway to some extent, from elimination to substitution, has also been suggested. For example, it has been observed by S.P. McManus and R.M. Karaman (unpublished work) that in the reaction system $PhSCH_2CH_2Cl$ + PhOK in *N*-methylpyrrolidone/water, substitution product can be observed in trace quantities by GC–MS with 12% water present. Since in the present study the percent water was ≤1%, the advent of substitution seems unlikely. We thank Prof. S.P. McManus for provision of these results prior to publication.

TABLE 2. Second-order rate constants for the reaction of **1** with oximates in tetraglyme and DMSO

Solvent	OxK	Complexing agent	Temperature (°C)	k_2 ($M^{-1}s^{-1}$)
Tetraglyme	BDOK	2.2.2	60	7.06×10^{-3}
	APOK	2.2.2	25	9.22
	AOK	2.2.2	25	182
DMSO	BDOK	—	60	4.18×10^{-5}
	APOK	—	25	6.82×10^{-2}
	AOK	—	25	17.6

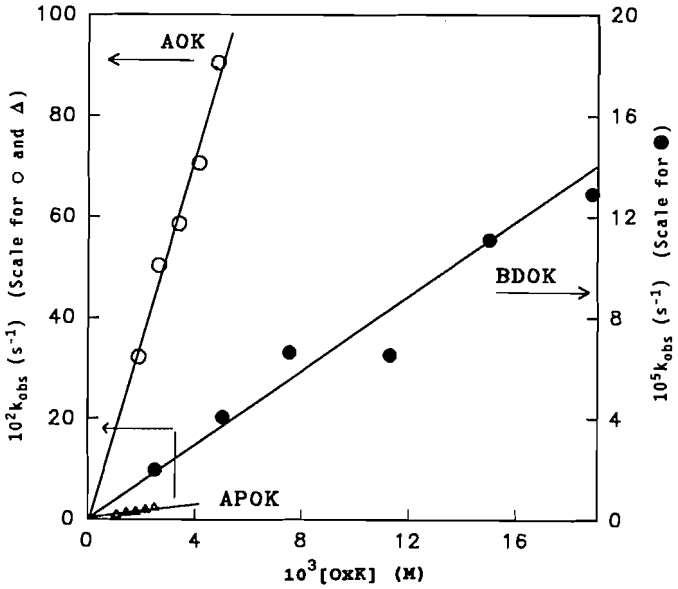

FIG. 2. Plots of k_{obs} vs. [OxK] for the reaction of **1** ((4.63–5.33) × 10^{-5} M) with BDOK at 60°C (●), APOK (△) and AOK (○) at 25°C, in tetraglyme in the presence of 2.2.2 cryptand.

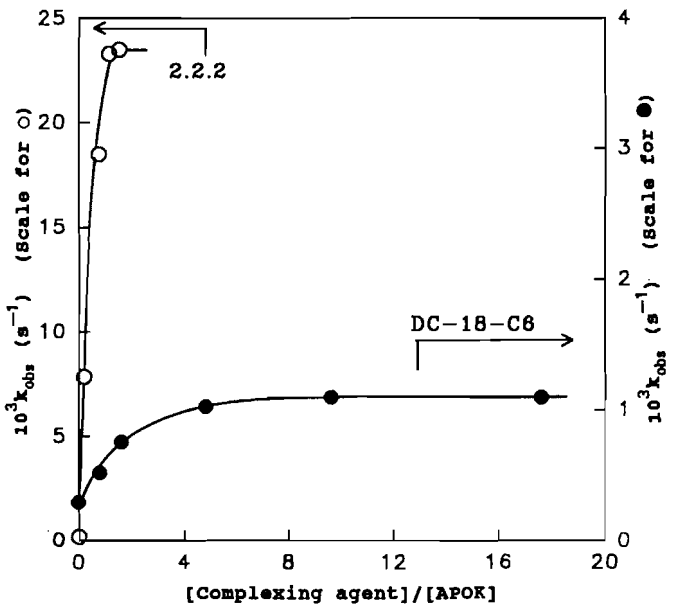

FIG. 3. Plot showing the effect of added DC-18-C6 (●) and 2.2.2 cryptand (○) on the reaction of **1** with APOK in tetraglyme at 25°C.

TABLE 3. Kinetic data on the effect of added crown ether (DC-18-C6) and 2.2.2 cryptand complexing agents on the reaction of **1** with APOK in tetraglyme at 25°C

10^3 [APOK] (M)	10^3 [Complexing agent] (M)	[Complexing agent]/[APOK]	$10^3 k_{obs}$ (s^{-1})
(*a*) Added DC-18-C6			
7.40	0.00	0.000	0.296
7.40	5.93	0.801	0.526
7.40	11.9	1.60	0.759
7.40	35.6	4.80	1.03
7.40	71.1	9.61	1.10
7.40	130	17.6	1.10
(*b*) Added 2.2.2			
3.14	0.000	0.000	0.178
3.14	0.592	0.188	7.83
3.14	2.37	0.755	18.5
3.14	3.55	1.13	23.3
3.14	4.73	1.51	23.5

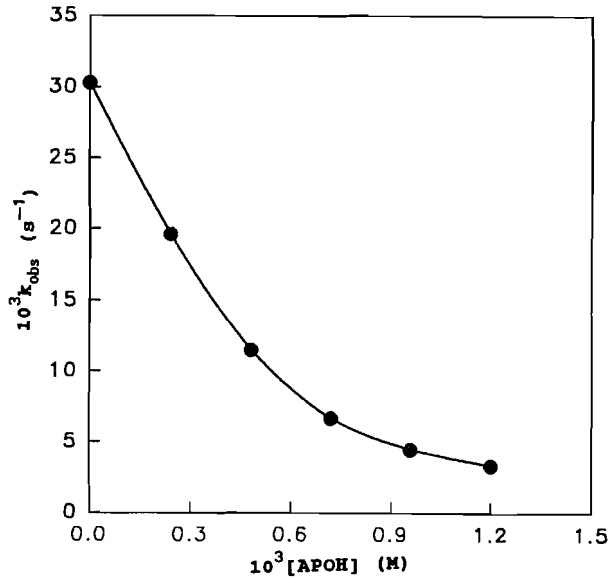

FIG. 4. Plot showing rate-retarding effect of added acetophenone oxime (APOH) on the reaction of **1** (4.73×10^{-5} M) with APOK in tetraglyme in the presence of 2.2.2 at 25°C.

tion of **1** with APOK in DMSO but both additives had no effect on rate (Table 7).

Discussion

Reaction mechanism

The results of the ^{1}H NMR product analyses of the reaction

Can. J. Chem. Downloaded from www.nrcresearchpress.com by 195.246.54.202 on 09/08/12
For personal use only.

TABLE 4. Effect of added acetophenone oxime (APOH) on the observed rate constants for the reaction of **1** with APOK in tetraglyme in the presence of 2.2.2 cryptand at 25°C

10^3 [APOK] (M)	10^3 [2.2.2] (M)	[2.2.2]/[APOK]	10^3 [APOH] (M)	$10^3 k_{obs}$ (s^{-1})
3.53	8.96	2.53	0.00	30.3
3.53	8.96	2.53	0.24	19.6
3.53	8.96	2.53	0.48	11.5
3.53	8.96	2.53	0.72	6.63
3.53	8.96	2.53	0.96	4.46
3.53	8.96	2.53	1.20	3.33

TABLE 5. Effect of added water on the observed rate constants for the reaction of **1** with APOK in tetraglyme in the presence of 2.2.2 cryptand at 25°C

10^3 [APOK] (M)	10^3 [2.2.2] (M)	[2.2.2]/[APOK]	% H_2O (v/v)	$10^3 k_{obs}$ (s^{-1})
2.73	5.84	2.13	0.00	25.3
2.73	5.84	2.13	0.04	5.70
2.73	5.84	2.13	0.10	1.56
2.73	5.84	2.13	0.20	0.53
2.73	5.84	2.13	0.40	0.11
2.73	5.84	2.13	1.00	0.03

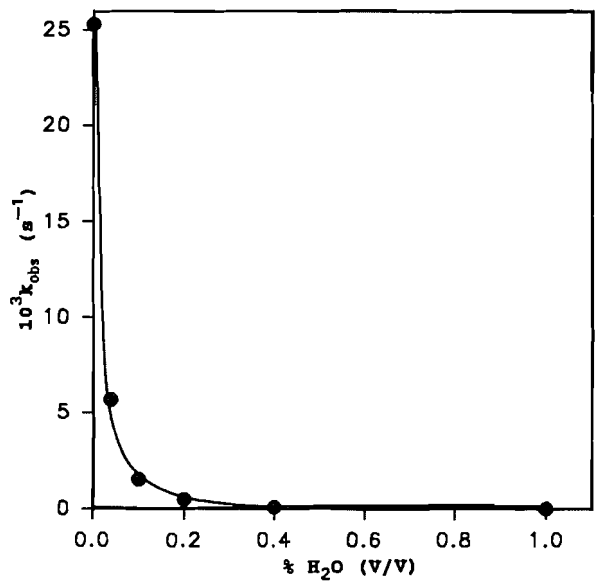

FIG. 5. Plot showing rate-retarding effect of added water on the reaction of **1** (4.73×10^{-5} M) with APOK in tetraglyme in the presence of 2.2.2 at 25°C.

TABLE 6. Pseudo-first-order rate constants for the reaction of **1** with oximates in DMSO

OxK	10^3 [OxK] (M)	Temperature (°C)	k_{obs} (s^{-1})
BDOK	89.3	60	3.56×10^{-6}
	119		5.22×10^{-6}
	149		6.54×10^{-6}
	179		7.27×10^{-6}
	208		8.77×10^{-6}
	223		9.35×10^{-6}
APOK	3.94	25	2.79×10^{-4}
	5.90		4.06×10^{-4}
	7.87		5.26×10^{-4}
	9.84		6.56×10^{-4}
	11.8		8.06×10^{-4}
	13.8		8.94×10^{-4}
AOK	0.86	25	1.44×10^{-2}
	1.28		2.21×10^{-2}
	1.68		3.14×10^{-2}
	2.09		3.81×10^{-2}
	2.87		4.68×10^{-2}

of **1** with oximates in tetraglyme and DMSO ruled out the possibility of nucleophilic substitution at any of the carbon centres. The only process observed was elimination, which could occur by an E1cb or E2 mechanism (18, 19). In another study from this laboratory (20), no H/D exchange was observed for reaction of **1** with EtOD–DMSO-d_6 containing EtO^-, excluding an E1cb mechanism. Since oximates are less basic than ethoxide, the concerted E2 mechanism is highly probable for the reaction of **1** in the present study. The competing pathways, substitution and elimination, for the present system are shown in Scheme 2.

It is noteworthy that, in the majority of the cases reported hitherto, nucleophilic reactions of 2-chloroethyl sulfide derivatives in hydroxylic solvents proceed largely by substitution at the carbon centre attached to chlorine (2, 5–7). However, in the present investigations of the reaction of **1** with oximates in non-hydroxylic solvents, base-promoted 1,2-elimination was found to be the only process occurring. It appears that the nature of the substituent on sulfur, the leaving group nucleofugality, base strength, and the reaction medium, all play important roles in determining the course of these reactions.

Oae and Yano (3) have reported the reaction of a number of 2-chloroethyl phenyl sulfide derivatives with EtONa in EtOH. They found that when *p*-methoxyphenyl on sulfur was replaced by the *p*-chlorophenyl moiety, the course of reaction changed from 50–50% elimination–substitution to 100% elimination. This suggests that an electron-withdrawing substituent on sulfur favours elimination, which is in accord with the present study, in that the electron-withdrawing phenyl group facilitates elimination over substitution.

Can. J. Chem. Downloaded from www.nrcresearchpress.com by 195.246.54.202 on 09/08/12
For personal use only.

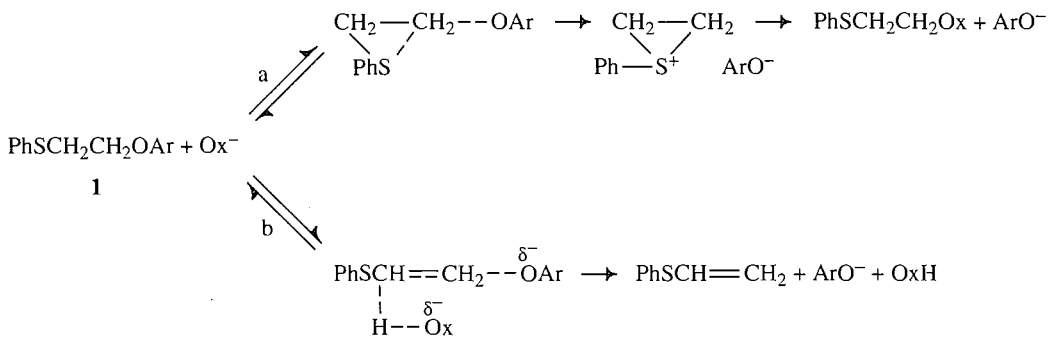

SCHEME 2

TABLE 7. Kinetic data on the effect of added complexing agents on the reaction of **1** with APOK in DMSO at 25°C

10^3 [APOK] (M)	10^3 [Complexing agent] (M)	[Complexing agent]/[APOK]	$10^4 k_{obs}$ (s^{-1})
(*a*) Added DC-18-C6			
5.75	0.00	0.000	3.62
5.75	2.11	0.367	3.71
5.75	4.22	0.734	3.71
5.75	6.33	1.10	3.78
5.75	8.44	1.47	3.72
5.75	10.5	1.82	3.75
(*b*) Added 2.2.2			
8.25	0.00	0.000	5.79
8.25	2.18	0.264	5.81
8.25	4.37	0.529	5.88
8.25	6.56	0.795	5.86
8.25	10.9	1.32	5.71

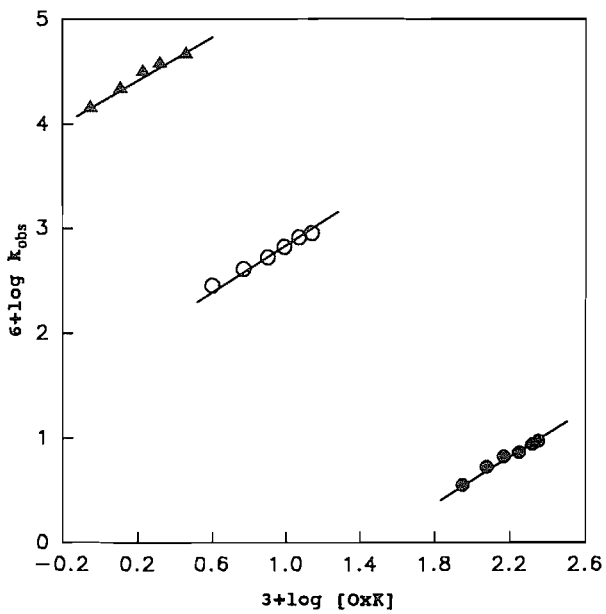

FIG. 6. Plots of log k_{obs} vs. log [OxK] for the reaction of **1** ((3.31–4.35) × 10^{-5} M) with BDOK (●) at 60°C, APOK (○), and AOK (▲) at 25°C, in DMSO.

It is also apparent that unimolecular formation of the episulfonium ion intermediate, leading to substitution (path a in Scheme 2) would be favoured by a better leaving group, which would explain why substitution predominates with chlorine as leaving group and not with *p*-nitrophenoxy in the present study. However, the change in solvent from protic to aprotic would also favour elimination over substitution. Finally, the base-enhancing properties of DMSO towards nucleophiles is another factor which would tend to favour the elimination pathway b in Scheme 2, relative to the substitution pathway a.

Reactivity in tetraglyme

(a) Free oximate anions and ion pairs

As seen in Fig. 1 for the reaction of **1** with APOK in tetraglyme (data in Table 1), in the absence of metal ion complexing agents the plot of k_{obs} vs. [APOK] exhibits downward curvature. Addition of excess of DC-18-C6 ([DC18C6]/[APOK] = 14.9) increases the rate by a relatively small extent and in approximately linear manner. However, 2.2.2 cryptand ([2.2.2]/[APOK] = 1.23) greatly increases the rate of reaction and the plot of k_{obs} vs. [APOK] is linear (Fig. 1).

The downward curvature observed in the plot of k_{obs} vs. [APOK] in the absence of complexing agents (Fig. 1), as well as the very large increase in rate with added 2.2.2 (Figs. 1 and 3), are indicative of a mechanism in which the ion-paired nucleophile is much less reactive than the free ion. Considering that in the present system both free and ion-paired oximate could be reactive species, product formation will be according to Scheme 3 where S refers to the substrate.

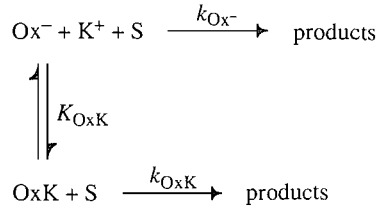

SCHEME 3

The overall pseudo-first-order rate equation will be as in eq. [1]. The ion-paired and free anion species are interrelated by the equilibrium constant K_{OxK} (eq. [2]).

$$[1] \quad k_{obs} = k_{Ox^-}[Ox^-] + k_{OxK}[OxK]$$

$$[2] \quad K_{OxK} = \frac{[OxK]}{[Ox^-][K^+]}$$

Can. J. Chem. Downloaded from www.nrcresearchpress.com by 195.246.54.202 on 09/08/12
For personal use only.

TABLE 8. Comparison of observed and (DLS) calculated k_{obs} values for the reaction of **1** with APOK in tetraglyme and contribution of dissociated and ion-paired species at 25°C[a]

10^3 [APOK] (M)	10^4 k_{obs} ($^{-1}$)		% Contribution to rate	
	Obsd.	Calcd.	APO^-	APOK
1.93	1.16	1.25	78.4	21.6
3.39	1.75	1.78	73.3	26.7
4.84	2.34	2.24	69.6	30.4
6.29	2.64	2.66	66.8	33.2
7.74	3.20	3.06	64.4	35.6
9.19	3.30	3.44	62.5	37.5

[a] k_{Ox^-} = 9.22 M^{-1} s^{-1}, k_{OxK} = 0.0141 M^{-1} s^{-1}, K_{OxK} = 1.69 × 10^7 M^{-1}.

Scheme 3 contains two rate constants and one equilibrium constant: k_{Ox^-}, the rate constant for the reaction of free acetophenone oximate anion; k_{OxK}, the rate constant for the reaction of the acetophenone oximate ion pair; and K_{OxK}, the association constant of the acetophenone oximate ion pair. Since at equilibrium, $[K^+] = [Ox^-]$, then $[OxK] = K_{OxK}[Ox^-]^2$ and substitution for [OxK] in eq. [1] yields eq. [3].

$$[3] \quad k_{obs} = k_{Ox^-}[Ox^-] + k_{OxK}K_{OxK}[Ox^-]^2$$

The rate constant for the acetophenone oximate (Ox^-) free anion was obtained from the slope of the linear plot in Fig. 1 in the presence of 2.2.2 by linear regression analysis, as $k_{APO^-} = k_{Ox^-}$ = 9.22 M^{-1} s^{-1}. The nonlinear differential least-squares (DLS) curve fitting of the experimental data to eq. [3] yielded the values $k_{APOK} = k_{OxK}$ = 1.41 × 10^{-2} M^{-1} s^{-1} and K_{OxK} = 1.69 × 10^7 M^{-1}.

Thus dissection of k_{obs} into contributions by free and ion-paired acetophenone oximate by the DLS treatment yields $k_{APO^-}/k_{APOK} = k_{Ox^-}/k_{OxK}$ = 9.22/1.41 × 10^{-2} = 654, which is consistent with the qualitative observations in Fig. 1 that follow from free APO^- being much more reactive than ion-paired APOK.

Having obtained values for k_{Ox^-}, k_{OxK} (i.e., k_{APO^-} and k_{APOK}) and K_{OxK}, it is now possible to calculate the relative contribution of each species, i.e., free ions and ion pairs, to the overall rate (Table 8). It is seen from Table 8 that at the lowest concentration studied ([APOK] = 1.93 × 10^{-3} M) the contributions of APO^- and APOK to the overall rate are 78.4 and 21.6%, respectively, whereas at the highest concentration studied ([APOK] = 9.19 × 10^{-3} M) the contributions of APO^- and APOK change to 62.5 and 37.5%, respectively. This change, coupled with the fact that APOK is much less reactive than APO^-, leads to the downward curvature observed in Fig. 1 with increasing APOK concentration.

(b) Crown ether-complexed potassium oximate

It is interesting to contrast the kinetic behaviour in the reaction of **1** with APOK in tetraglyme in the presence of added 2.2.2 and DC-18-C6 (Figs. 1 and 3). It follows from Fig. 3 that addition of 1 equivalent of 2.2.2 leads to complete formation of cryptated K^+, i.e., $K^+ \subset$ 2.2.2, and the free anion. This results in the plateau in Fig. 3 corresponding to reaction of free APO^-, and the linear plot in Fig. 1 from which k_{APO^-} can be calculated. Qualitatively, the much smaller increase in rate and sensitivity to crown ether, which is apparent in Fig. 3 on increasing the ratio [DC18C6]/[APOK], would indicate that complexation by DC-18-C6 is much less effective and the linearity of the plot in Fig. 1 for data in the presence of DC-18-C6 would appear to be coincidental. This could be explained in light of the known complexing abilities towards K^+ of the solvent tetraglyme (21), which competes effectively with DC-18-C6 present in the system in relatively small concentrations.

Quantitatively, one can analyze the kinetic results for the reaction of **1** with APOK in tetraglyme in the presence of DC-18-C6 on the basis of formation of a crown ether-complexed potassium oximate ion pair, $APO^-K^+ \subset$ DC-18-C6. The expression for k_{obs} according to such a scenario would be as in eq. [4], where OxKCr refers to the crown ether-complexed ion pair for which the equilibrium constant of formation is given in eq. [5].

$$[4] \quad k_{obs} = k_{Ox^-}[Ox^-] + k_{OxK}[OxK] + k_{OxKCr}[OxKCr]$$

$$[5] \quad K_{OxKCr} = \frac{[OxKCr]}{[OxK][Cr]}$$

Equation [4] can be solved by DLS treatment assuming the k_{Ox^-}, k_{OxK}, and K_{OxK} values obtained previously from experiments in the presence and absence of 2.2.2 cryptand, respectively, apply equally to this situation.

Using the data in Table 1 at constant [Crown]/[OxK] ratio and varying [OxK], one obtains from DLS treatment the values k_{OxKCr} = 0.151 M^{-1} s^{-1} and K_{OxKCr} = 211 M^{-1} (Table 9). Data in Table 3 with a variable [Crown]/[OxK] ratio and constant [OxK] similarly yield k_{OxKCr} = 0.155 M^{-1} s^{-1} and K_{OxKCr} = 112. Using the combined set of "constant" and "variable" experimental data (Tables 1 and 3) in the DLS treatment yields k_{OxKCr} = 0.154 M^{-1} s^{-1} and K_{OxKCr} = 116 M^{-1}, however, with much better limits in the standard deviation and *p*-parameters (Table 9). Calculated k_{obs} values using these derived values of k_{OxKCr} and K_{OxKCr} agree very well with experimental values, no systematic deviations being apparent, which gives confidence to the validity of the DLS treatment and the model used.

The relative contributions of the different terms in the crown ether containing experiments can be calculated using the above values of k_{OxKCr} and K_{OxKCr} as well as the previously derived k_{Ox^-}, k_{OxK}, and K_{OxK} values. The results (Tables 10, 11) show that the crown ether-complexed ion pair is the predominant species present in concentration as well as the major contributor to the rate. The next major species is the ion pair but its contribution to the rate is less than that of the free anion even though the latter is the least abundant species present. There are also interesting trends in the relative abundance and the contributions of the various species as the overall oximate concentration is varied (Tables 10, 11).

Finally, one can comment on the relative magnitudes of the rate coefficients in these systems. That the free anion is by far the most reactive species (k_{Ox^-}/k_{OxK} = 654), is to be expected. It is interesting, however, that the crown-complexed potassium oximate ion pair is more reactive than the uncomplexed ion pair (k_{OxKCr}/k_{OxK} = 11). This order of reactivity is in agreement with a presumably looser binding of anion in the crown complex than in the ion pair itself. Alternatively, one can envisage a greater negative charge density on the oxygen centre of the oximate anion in the complexed species, and hence a greater reactivity.

Can. J. Chem. Downloaded from www.nrcresearchpress.com by 195.246.54.202 on 09/08/12
For personal use only.

TABLE 9. Determination of rate and equilibrium constants for crown-complexed potassium oximate (k_{OxKCr} and K_{OxKCr}) in the reaction of **1** with APOK in tetraglyme in the presence of DC-18-C6

[DC-18-C6]/[APOK]	k_{OxKCr} (M^{-1} s^{-1})	K_{OxKCr} (M^{-1})	S.D.	*p*-Parameter[e] (k_{OxKCr})	*p*-Parameter[e] (K_{OxKCr})
"Constant"[a,b]	0.151	211	0.0000263	198	1.15×10^7
"Variable"[c]	0.155	112	0.0000376	132	6.08×10^5
"Combined"[d]	0.154	116	0.0000285	78	5.50×10^5

[a]Constant ratio of [DC-18-C6]/[APOK] = 14.9, varying [APOK] (Table 1).
[b]A second solution in the DLS treatment for the constant [crown]/[OxK] data yielded $K_{OxKCr} = 8.0 \times 10^6$ but this high *p*-parameter (7.27×10^{13}) solution was discarded since it was not found for the solution of the "variable" or the "combined" data, as well as being chemically unreasonable because of competition between solvent tretraglyme and the crown for complexation of K^+ (see text).
[c]Variable ratio of [DC-18-C6]/[APOK], constant [APOK] = 7.4×10^{-3} M (Table 3).
[d]Combined "constant" and "variable" sets; the preferred set.
[e]The *p*-parameter offers a choice in the calculation of the standard deviations of the adjustable parameters. Commonly, the *p*-parameter is multiplied by the standard deviation from the calculated curve (e.g., 0.0000285), obtaining, e.g., standard deviations of 0.0022 (for k_{OxKCr}) and 15.7 (for K_{OxKCr}) in the last line of the table. However, for difficulties in this procedure, see for example ref. 30.

TABLE 10. Relative concentrations of contributing species (as percentage of total reagent concentration) for the reaction of **1** with APOK in tetraglyme in the presence of DC-18-C6 at 25°C[a]

10^3 [APOK] (M)	[DC-18-C6]/[APOK]	% as APO^- free anion	% as APOK ion pair	% as APOK–crown complex
Set 1[b]				
2.02	14.9	0.261	23.19	76.55
3.53	14.9	0.158	14.82	85.02
5.04	14.9	0.113	10.90	88.99
6.55	14.9	0.0882	8.62	91.29
8.06	14.9	0.0723	7.13	92.80
9.57	14.9	0.0613	6.08	93.86
Set 2[c]				
7.40	0.801	0.236	69.80	29.96
7.40	1.60	0.202	50.96	48.83
7.40	4.80	0.134	22.42	77.44
7.40	9.61	0.0971	11.80	88.10
7.40	17.6	0.0724	6.56	93.37

[a]$k_{Ox^-} = 9.22$ M^{-1} s^{-1}, $k_{OxK} = 0.0141$ M^{-1} s^{-1}, $K_{OxK} = 1.69 \times 10^7$ M^{-1}, $k_{OxKCr} = 0.154$ M^{-1} s^{-1}, $K_{OxKCr} = 116$ M^{-1}.
[b]Data from Table 1.
[c]Data from Table 3.

(c) Relative reactivities of three oximates

The reactions of BDOK and AOK with **1** in tetraglyme could be studied in the presence of 2.2.2 only, because both oximates were found to be insoluble in tetraglyme in the absence and presence of DC-18-C6. It is interesting that when small quantities of the corresponding oximes are present, the oximate salts become soluble in tetraglyme in the presence of DC-18-C6, probably through hydrogen bonding. The inability of DC-18-C6 to solubilize BDOK and AOK in tetraglyme further demonstrates the relative ineffectiveness of DC-18-C6 to compete with tetraglyme solvent in complexation of K^+ and corroborates the above discussion on the relatively small effect of DC-18-C6 in enhancing the rate of the APOK reaction in tetraglyme.

The reaction of **1** with AOK in tetraglyme in the presence of 2.2.2 was found to be faster than with APOK and required study by stopped-flow spectrophotometry. The relative order of reactivity of oximates towards **1** in tetraglyme in the presence of 2.2.2 was BDOK < APOK < AOK, i.e., in order of their pK_a's (vide infra) with k_2 values of 0.00706, 9.22, and 182 M^{-1} s^{-1}, respectively, for the three oximates.

(d) Hydrogen-bonding effect on oximate reactivity

The effect of added acetophenone oxime (APOH) and water on the rate of reaction of **1** with 2.2.2-complexed APOK in tetraglyme was examined. Figures 4 and 5 show a marked rate-retarding effect of added APOH and water. The presence of only 0.04% H_2O causes a 5-fold decrease in the rate of reaction. It is apparent that hydrogen-bonding interactions with the acetophenone oximate anion (APO^-) result in decreased reactivity. Previously, for the reaction of *p*-nitrophenyl diphenylphosphinate with phenoxide ion in tetraglyme, added phenol was similarly found to greatly reduce reactivity (17).

3. Reactivity in DMSO

Whereas the reaction of **1** with APOK and AOK in DMSO could be studied conveniently at 25°C, BDOK was found to react very slowly and rate constants were obtained at 60°C. The plots of k_{obs} vs. [OxK] for the reaction of **1** with BDOK, APOK, and AOK in DMSO are linear with zero intercept, showing that reaction due to solvent alone is not significant. The relative order of reactivities of the oximates, shown in Fig. 6 as log–

Can. J. Chem. Downloaded from www.nrcresearchpress.com by 195.246.54.202 on 09/08/12
For personal use only.

TABLE 11. Rate share between contributing species for the reaction of **1** with APOK in tetraglyme in the presence of DC-18-C6, i.e., free APO^- anion, ion-paired APOK, and crown-complexed APOK at 25°C[a]

10^3 [APOK] (M)	[DC-18-C6]/[APOK]	% Contribution to rate: APO^- free anion	APOK ion pair	APOK–crown complex
Set 1[b]				
2.02	14.9	16.52	2.24	81.24
3.53	14.9	9.83	1.41	88.76
5.04	14.9	6.98	1.03	91.99
6.55	14.9	5.41	0.81	93.78
8.06	14.9	4.42	0.66	94.92
9.57	14.9	3.73	0.57	95.70
Set 2[c]				
7.40	0.801	27.97	12.62	59.40
7.40	1.60	18.40	7.09	74.51
7.40	4.80	9.14	2.34	88.52
7.40	9.61	6.11	1.13	92.76
7.40	17.6	4.40	0.61	94.99

[a]k_{Ox^-} = 9.22 M^{-1} s^{-1}, k_{OxK} = 0.0141 M^{-1} s^{-1}, K_{OxK} = 1.69 × 10^7 M^{-1}, k_{OxKCr} = 0.154 M^{-1} s^{-1}, K_{OxKCr} = 116 M^{-1}.
[b]Data from Table 1.
[c]Data from Table 3.

log plots, parallel the pK_a's of the corresponding oximes in DMSO:

	AOK	APOK	BDOK
k_2, M^{-1} s^{-1}	17.6	6.82×10^{-2}	4.18×10^{-5}
Temperature (°C)	25	25	60
pK_a (DMSO) of oxime (22, 23)	26.0	21.5	16.9

For the reaction of **1** with APOK in DMSO the negligible effect of added DC-18-C6 and 2.2.2 on the rate (Table 7) suggests that ion-pairing phenomena are not important in DMSO, in contrast to the situation in tetraglyme. As a strongly ionizing solvent with a high dielectric constant (ϵ = 45), ion-pair phenomena are rarely observed in DMSO (24).

Solvent effects on reactivity: ground state versus transition state interactions

It is interesting that the overall reactivity in tetraglyme is greater than in DMSO. On the assumption that the potassium oximate + 2.2.2 system reflects the reactivity of free oximate anion in tetraglyme (TG) and that potassium oximate alone correspondingly represents free oximate anion reactivity in DMSO (since ion-pair phenomena are not important in DMSO), one obtains:

Oximate	BDOK	APOK	AOK
k^{TG}/k^{DMSO}	169	135	10

Medium effects on the rate of a chemical reaction are usually interpreted in terms of the relative stabilization/destabilization of the transition state compared to the ground state (reactants) (25). Thus, any factors stabilizing the transition state for elimination would accelerate reaction; conversely, stabilization of the ground state would lead to rate retardation, and combination of the two effects is also possible.We suggest that the higher reactivity in tetraglyme compared to DMSO in the present system may be explained on the basis of polarizability principles. The transition state involved in base promoted 1,2-elimination reactions (Scheme 2) has considerably delocalized charge density, and since the polarizability (α) of tetraglyme is higher than of DMSO ($\alpha_{TG} = 22.7 \times 10^{-24}$ cm^3 and $\alpha_{DMSO} = 7.98 \times 10^{-24}$ cm^3),[5] tetraglyme would tend to stabilize the transition state to a greater extent than DMSO. At the same time, one would expect that the reactants would have similar energy in DMSO and tetraglyme. We are considering here the cryptated potassium ion, $K^+ \subset 2.2.2$, the oximate anion, and **1**; these relatively large ionic species and the neutral substrate are not expected to be subject to large differential solvation in the two media. Thus, the overall effect is one of stabilization of the transition state in tetraglyme, which will tend to rate acceleration compared to DMSO as solvent.

Noteworthy above is that the ratio k^{TG}/k^{DMSO} decreases with increasing Ox^- reactivity, and parallels the increasing pK_a's of the oximates. This trend follows the reactivity–selectivity argument (27), i.e., the less reactive nucleophile is more selective. This behaviour may be explained by considering trends in the transition states involved in tetraglyme and DMSO. If the location of the transition states were the same in both solvents then a constant value for this ratio would be expected. The fact that k^{TG}/k^{DMSO} is greater in the direction of the weaker base is an indication that the transition state is earlier in tetraglyme than in DMSO, which is also in accord with Hammond's postulate (28).

Conclusions

The present study of the reaction of β-phenylmercaptoethyl *p*-nitrophenolate (**1**) with three potassium oximates, AOK, APOK, and BDOK, in DMSO and tetraglyme solvents has allowed us to draw a number of conclusions:

1. The reactions proceed via E2 elimination processes in these solvents.

[5]Polarizability (α) was calculated by using the equation (26): $\alpha = [(n^2 - 1)/(n^2 + 2)](M/d)(3/4\pi N)$.

Can. J. Chem. Downloaded from www.nrcresearchpress.com by 195.246.54.202 on 09/08/12
For personal use only.

Can. J. Chem. Downloaded from www.nrcresearchpress.com by 195.246.54.202 on 09/08/12
For personal use only.

2. In tetraglyme the small reactivity of oximates coupled with the large accelerating effect of 2.2.2 cryptand on rate points to formation of less reactive ion pairs in the absence of metal ion complexing agent. Added DC-18-C6 leads to a much smaller increase in rate since complexation of K^+ by the solvent tetraglyme competes with DC-18-C6. The kinetic data are analyzed in terms of parallel reactions of free oximate, ion-paired potassium oximate, and crown ether-complexed potassium oximate. Rate constants and equilibrium constants for these species are derived ($k_{Ox^-} \gg k_{OxKCr} > k_{OxK}$).

3. The relative order of reactivity of the three oximates in tetraglyme and DMSO, i.e., AOK > APOK > BDOK, was found to parallel the pK_a values of the corresponding oximes in DMSO.

4. The unusually high reactivity in tetraglyme compared to DMSO is explained on the basis of stabilization of the transition state in tetraglyme as a result of its higher polarizability.

5. Added oxime and water had a marked rate-retarding effect on rates in tetraglyme, indicating the powerful role of hydrogen-bonding interactions between oximate anion and oxime or water.

Experimental

Materials

β-Phenyl mercaptoethyl *p*-nitrophenolate (**1**) was synthesized by reaction of 2-chloroethyl phenyl sulfide with *p*-nitrophenol in aqueous ethanol (water:ethanol = 1:3 v/v) containing KOH and recrystallized from hexane, mp 79°C. (A representative procedure is given in the accompanying paper (20).) The resulting product was characterized by ^{1}H NMR, IR, and elemental analysis (Anal. calcd.: C 61.09, H 4.73, N 5.09; found: C 61.51, H 5.13, N 5.14). Phenyl vinyl sulfide (PVS) was prepared by a previously published procedure, bp 66°C/ 3 Torr (lit. (3) bp 83°C/14 Torr) (1 Torr = 133.3 Pa).

Dimethyl sulfoxide (DMSO) was refluxed over calcium hydride for 3 h, then fractionally distilled at low pressure, bp 35°C/2 Torr (20). Tetraglyme was refluxed over sodium metal for 3 h, then fractionally distilled (bp 110°C/2 Torr). Prior to use it was freshly redistilled from sodium (29). The purified solvents were stored under a nitrogen atmosphere and solvent was transferred by syringe while passing nitrogen. The 2.2.2-cryptand (Merck) and DC-18-C6 (Aldrich) were recrystallized from hexane and acetonitrile, respectively, and stored in a glove box.

The oximate samples, BDOK, APOK, and AOK, were procured from Raylo Chemicals and found to contain significant amounts of the corresponding oxime as impurity. The oximates were purified by two methods: (*i*) heating at 110°C under vacuum for 24 h; (*ii*) Soxhlet extraction with THF (for BDOK) and diethyl ether (for APOK and AOK). The purified oximates were stored under an argon atmosphere in a glove box. Their purity was examined spectrophotometrically by recording the spectra of the oximate solution, first in DMSO alone as reference, and then in the presence of EtOK/EtOH (for BDOK: [BDOK] = 2×10^{-2} M, [EtOK] = 1×10^{-2} M, 10-mm cell; for APOK: [APOK] = 6.58×10^{-2} M, [EtOK] = 8×10^{-3} M, 1-mm cell; final percentage of EtOH in DMSO was ca. 0.3% (v/v)). Any free oxime present is converted to oximate on addition of EtOK/EtOH, and the mol% of oxime could be estimated from the increase in absorbance in the spectra recorded in the absence and presence of EtOK. The samples of BDOK and APOK showed two absorption peaks in DMSO: BDOK (300 nm, $\epsilon = 22\,700$ M^{-1} cm^{-1} and 465 nm, $\epsilon = 67.5$ M^{-1} cm^{-1}); APOK (326 nm, $\epsilon = 14\,000$ M^{-1} cm^{-1} and 400 nm, $\epsilon = 133$ M^{-1} cm^{-1}). The analysis was carried out at the higher wavelength, less intense peak, which allowed analysis of higher oximate concentrations. The purified BDOK and APOK samples were found to be free of oxime. However, AOK could not be analyzed by this method as it does not show absorbance in the UV–visible region.

Kinetic procedures

Kinetics of the reaction of **1** with APOK and BDOK were studied spectrophotometrically under pseudo-first-order conditions by following the changes in absorbance at λ_{max} of *p*-nitrophenoxide ion (425–435 nm) on a Perkin Elmer Lambda-5 spectrophotometer equipped with thermostatted multiple cell transport system. Pseudo-first-order rate constants were calculated by a least-squares linear regression method using a Zenith computer. Experimental infinity absorbance values (closely similar to the theoretical values) were used in the linear plot of ln ($A_\infty - A_t$) vs. time, which gave k_{obs} from the slope. For the very slow reaction of **1** with BDOK in DMSO ($k_{obs} < 10^{-5}$ s^{-1}), theoretical infinity absorbance values were used to obtain pseudo-first-order rate constants. From replicate runs the error in any particular measured rate constant is estimated not greater than ca. ±3%.

The rate of the much faster reaction of **1** with AOK in tetraglyme in the presence of 2.2.2 was followed at λ_{max} of *p*-nitrophenoxide ion (432 nm) on a Hi-Tech stopped-flow spectrophotometer equipped with a thermostatable water bath coupled to a McPherson monochromator and Can-Tech transient recorder. The spectral traces were displayed on a B&K precision oscilloscope and the data were treated directly by a Zenith computer. The reproducibility of k_{obs} was found to be within ±1%.

Product analysis

The nature of the reaction products in tetraglyme and DMSO was determined by ^{1}H NMR spectroscopy using a Bruker 200 or 400 MHz instrument. In tetraglyme the reaction of **1** with the potassium oximates was carried out in the presence of 2.2.2 cryptand ([**1**] = 0.01 M, [OxK] = 0.02 M, and [2.2.2] = 0.03 M). The reaction mixtures were kept at room temperature for 12 h, after which ^{1}H NMR spectra were recorded. The spectra showed complete conversion into products as indicated by the absence of peaks due to **1**. The NMR data in tetraglyme were referenced with respect to CD_3SOCD_2H/CD_3SOCD_3 contained in a capillary tube inserted in the NMR tube, while for reactions in DMSO the solvent served as the reference.

Acknowledgement

This research was supported by the Department of Supply and Services Canada. Discussions with Professor J. Hirst are acknowledged.

1. C.G. Swain. J. Am. Chem. Soc. **66**, 1966 (1944).
2. P.D. Bartlett and C.G. Swain. J. Am. Chem. Soc. **71**, 1406 (1949).
3. S. Oae and Y. Yano. Tetrahedron, **24**, 5721 (1968).
4. M.J. Blandamer, H.S. Golkin, and R.E. Robertson. J. Am. Chem. Soc. **91**, 2678 (1969).
5. R. Bird and C.J.M. Stirling. J. Chem. Soc. Perkin Trans. 2, 1221 (1973).
6. (*a*) Y.-C. Yang, J.R. Ward, R.B. Wilson, W. Burrow, and J.S. Winterle. Thermochim. Acta, **114**, 313 (1987); (*b*) Y.-C. Yang, J.A. Baker, and J.R. Ward. Chem. Rev. **92**, 1729 (1992).
7. (*a*) S.P. McManus, N. Neamati-Mazraeh, M.S. Paley, B.A.Hovanes, and J.M. Harris. Tetrahedron Lett. **26**, 4571 (1985); (*b*) S.P. McManus, N. Neamati-Mazraeh, B.A. Hovanes, M.S. Paley, and J.M. Harris. J. Am. Chem. Soc. **107**, 3393 (1985); (*c*) S.P. McManus, M.R. Sedaghat-Herati, and J.M. Harris. Tetrahedron Lett. **28**, 5299 (1987); (*d*) S.P. McManus, R.M. Karman, M.R. Sedaghat-Herati, N. Neamati-Mazraeh, B.A. Hovanes, M.S. Paley, and J.M. Harris. J. Org. Chem. **52**, 2518 (1987); (*e*) S.P. McManus, M.R. Sedaghat-Herati, R.M. Karman, N. Neamati-Mazraeh, S.M. Cowell, and J.M. Harris. J. Org. Chem. **54**, 1911 (1989); (*f*) M.R. Sedaghat-Herati, J.M. Harris, and S.P. McManus. Tetrahedron, **44**, 7479 (1988).
8. Y.-C. Yang, J.R. Ward, and T. Luteran. J. Org. Chem. **51**, 2756 (1986).
9. J.M. Harris, M.S. Paley, M.R. Sedaghat-Herati, and S.P. McManus. J. Org. Chem. **50**, 5230 (1985).
10. M.R. Sedaghat-Herati, S.P. McManus, and J.M. Harris. J. Org. Chem. **53**, 2539 (1988).

11. J.M. Harris, M.R. Sedaghat-Herati, and S.P. McManus. J. Org. Chem. **53**, 3893 (1988).
12. E. Buncel and I.H. Um. J. Chem. Soc. Chem. Commun. 595 (1986).
13. (*a*) S. Hoz and E. Buncel. Tetrahedron, **45**, 3663 (1989); (*b*) Isr. J. Chem. **26**, 313 (1985).
14. J.L. Wolk, M.R. Hajnal, S. Hoz, R.M. Tarkka, and E. Buncel. Can. J. Chem. **68**, 1182 (1990).
15. F. Terrier, F. Degorre, D. Kiffer, and M. Laloi. Bull. Soc. Chim. Fr. 415 (1988).
16. F. Terrier, P. MacCormack, E. Kizilian, J.C. Halle, P. Demerseman, F. Guir, and C. Lion. J. Chem. Soc. Perkin Trans. 2, 153 (1991).
17. E. Buncel, E.J. Dunn, Ng. van Truong, R.A.B. Bannard, and J.G. Purdon. Tetrahedron Lett. 31(45), 6513 (1990).
18. W.H. Saunders, Jr. and A.F. Cockerill. Mechanisms of elimination reactions. John Wiley & Sons, New York. 1973.
19. M.J. Pregel and E. Buncel. J. Chem. Soc. Perkin Trans. 2, 307 (1991).
20. H.-Q. Xie, Ng. van Truong, E. Buncel, and J.G. Purdon. Can. J. Chem. **71**, 448 (1994).
21. (*a*) E. Buncel, H.S. Shin, Ng. van Truong, R.A.B. Bannard, and J.G. Purdon. J. Phys. Chem. **92**, 4176 (1988); (*b*) Ng. van Truong, A.R. Norris, H.S. Shin, E. Buncel, R.A.B. Bannard, and J.G. Purdon. Inorg. Chim. Acta, **184**, 59 (1991).
22. F.G. Bordwell and G.Z. Ji. J. Org. Chem. **57**, 3019 (1992).
23. I.H. Um. Ph.D. Thesis, Queen's University (1987).
24. E. Buncel and H. Wilson. Adv. Phys. Org. Chem. **14**, 133 (1977).
25. (*a*) E. Buncel and H. Wilson. Acc. Chem. Res. **12**, 42 (1979); (*b*) J. Chem. Educ. **57**, 629 (1980).
26. A.J. Parker. Chem. Rev. **69**, 1 (1968).
27. E. Buncel and H. Wilson. J. Chem. Educ. **64**, 475 (1987).
28. G.S. Hammond. J. Am. Chem. Soc. **77**, 334 (1955).
29. D.D. Perrin and W.L.F. Armarego. Purification of laboratory chemicals. 3rd ed. Pergamon Press, New York. 1988.
30. W.H. Press, B.P. Flannery, S.A. Teukolsky, and W.T. Vetterling. Numerical recipes in C. Cambridge University Press, New York. 1988. p. 522.

Can. J. Chem. Downloaded from www.nrcresearchpress.com by 195.246.54.202 on 09/08/12
For personal use only.

Basicity, nucleophilicity, and nucleofugality in the elimination–substitution reactions of β-phenylmercaptoethyl phenolates in DMSO–ethanol media

HAI-QI XIE, NGUYEN TRUONG, AND ERWIN BUNCEL[1]
Department of Chemistry, Queen's University, Kingston, ON K7L 3N6, Canada

AND

J. GARFIELD PURDON
Defence Research Establishment Suffield, Ralston, AB T1A 8K6, Canada

Received March 26, 1993

HAI-QI XIE, NGUYEN TRUONG, ERWIN BUNCEL, and J. GARFIELD PURDON. Can. J. Chem. **72**, 448 (1994).

Kinetic studies have been performed on the base-promoted 1,2-elimination reactions of a series of β-phenylmercaptoethyl phenolates with potassium ethoxide in EtOH–DMSO media, yielding phenyl vinyl sulfide. The E2 mechanism was indicated by the absence of H/D exchange in the substrate when the reaction in EtOD–DMSO-d_6 containing EtO^- was carried to partial completion. The Brønsted coefficient values (β_{LG}, effect of nucleofugality on reaction rate) of ca. 0.30 and ca. 0.98 were estimated for the reaction in pure DMSO and ethanol, respectively. Comparison of the results with reported reactions of substrates of similar structure revealed the important role of the phenyl group on sulfur, the leaving-group nucleofugality, and the medium basicity, in controlling the reaction pathways (elimination versus substitution).

HAI-QI XIE, NGUYEN TRUONG, ERWIN BUNCEL et J. GARFIELD PURDON. Can. J. Chem. **72**, 448 (1994).

On a réalisé des études cinétiques sur les réactions d'élimination-1,2 effectuées sur une série de phénolates de β-phénylmercaptoéthyle sous l'influence de bases comme l'éthylate de potassium dans un milieu EtOH–DMSO qui conduisent au sulfure de phényle et de vinyle. L'absence d'échange H/D dans le substrat lorsque la réaction, effectuée dans du EtOH–DMSO-d_6 contenant du EtO^-, n'est complétée que d'une façon partielle indique que le mécanisme est E2. Les valeurs du coefficient de Brønsted (β_{LG}, effet du caractère nucléofuge sur la vitesse de réaction) sont d'environ 0,30 et 0,98 et elles correspondent aux évaluations qui ont été faites pour les réactions dans le DMSO pur et dans l'éthanol pur respectivement. Une comparaison des résultats avec ceux rapportés pour les réactions de substrats de structure semblable révèlent le rôle important du groupe phényle sur le soufre, du caractère nucléofuge du groupe partant et de la basicité du milieu sur les voies réactionnelles (élimination vs. substitution).
[Traduit par la rédaction]

Introduction

Considerable information has accumulated in the past several decades on the reactions of β-chloroethyl sulfide derivatives, R-S-CH_2CH_2-Cl (**1**), with nucleophiles in various aqueous and nonaqueous media (1–9). However, there is controversy as to the mechanisms of these reactions as well as the prediction of reaction pathways, elimination versus substitution, under given conditions.

It is generally accepted that the mechanism of nucleophilic substitution of β-chloroethyl sulfide derivatives involves an anchimerically assisted intramolecular displacement of chloride ion by sulfur, which is accompanied by the formation of an episulfonium ion intermediate of some degree of stability (2–7, 10):

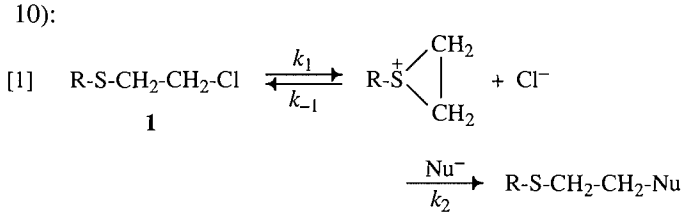

Stirling and co-workers (6) obtained strong evidence for rate-determining formation of the cyclic sulfonium ion intermediate in eq. [1] and reported the spectroscopic observation of cyclic sulfonium ions in several cases. However, Robertson and co-workers (8) questioned the existence of this species as a discrete intermediate since this should result in the formation of ethylene sulfide as well as the substitution product R-S-CH_2CH_2-Nu, whereas the latter is the only product detected.

In most investigations of the reactions of β-chloroethyl sulfide derivatives, nucleophilic substitution was the only reaction mode detected (1–8); only in one case were both base-promoted 1,2-elimination and nucleophilic substitution simultaneously observed (6*b*, 9). Thus it was reported in one study that β-chloroethyl *p*-tolyl sulfide undergoes 47% elimination – 53% substitution with EtONa in EtOH at 40–65°C (9), while in another study 100% substitution was observed in 80% aqueous EtOH (w/w) at 45°C for the same substrate (6*b*).

The present study is concerned with the title substrates **2**, in which substituted phenolates (X-PhO) are the leaving groups while the sulfur carries a phenyl group, and with the effect of varying the reaction medium on the rate. We report here the results of kinetic studies on the reactions of the family of β-phenylmercaptoethyl phenolates (**2**) with potassium ethoxide in ethanol – dimethyl sulfoxide (EtOH – DMSO) media.

Results

Product identification

There are several possible pathways for the reaction of **2** with potassium ethoxide in EtOH–DMSO mixtures (Scheme 1). Pathway (a) corresponds to nucleophilic substitution at C(α) with phenolate as the leaving group, while in path (b) substitution at C(β) would result in thiophenolate leaving. Path (c) corresponds to nucleophilic attack at aromatic carbon in an S_NAr process. Pathways (d) and (e) are elimination processes at C(α) and C(β), respectively, with thiophenolate and phenolate as leaving groups.

^1H NMR analysis of the reaction product for substrate **2***h*, a typical compound in this series, with EtOK in 20% EtOD – 80% DMSO-d_6 (v/v), showed that 1,2-elimination by pathway (e) was the only reaction occurring. The formation of PVS was

[1]Author to whom correspondence may be addressed.

Can. J. Chem. Downloaded from www.nrcresearchpress.com by 195.246.54.202 on 09/08/12
For personal use only.

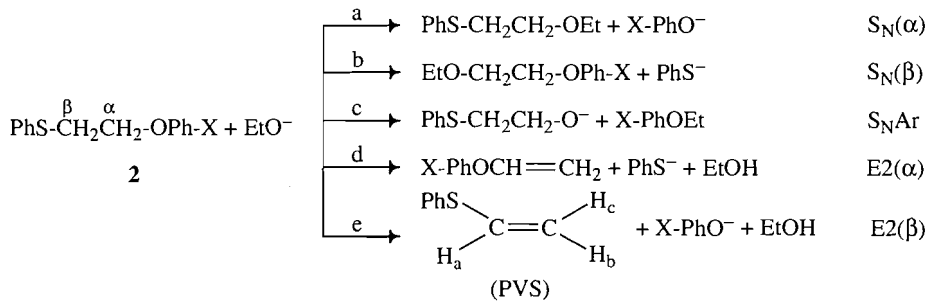

X = H (**2***a*); *p*-Me (**2***b*); *p*-Cl (**2***c*); *p*-CHO (**2***d*); *p*-$COCH_3$ (**2***e*); *p*-CN (**2***f*); *m*-NO_2 (**2***g*); *p*-NO_2 (**2***h*)

SCHEME 1

characterized by the appearance of multiplets at δ 7.1–7.4 for the PhS ring protons, a double doublet at δ 6.72 for H_a, and two doublets at δ 5.43 and 5.33 for H_b and H_c, respectively. The generation of potassium *p*-nitrophenoxide was shown by two doublets at δ 7.75 and 5.98, corresponding to the *meta* and *ortho* protons respectively. ^{1}H NMR spectra of the authentic compounds confirmed the formation of PVS and potassium *p*-nitrophenoxide in the reaction mixtures.

Hydrogen/deuterium exchange

Base-promoted 1,2-elimination may occur via an E1cb-reversible mechanism which would result in the observation of H/D exchange on C(β) of the substrate (11). To test whether such an exchange occurred, less than one equivalent of EtOK in EtOD was added to the solution of substrate **2***h* in DMSO-d_6 ([EtOK]/[**2***h*] = 1/2, 5% EtOD – 95% DMSO-d_6 v/v). The proton NMR spectrum of the solution was recorded after the reaction was allowed to take place overnight. By comparing the integrations of the signals corresponding to the ring protons and the β protons, it was found that no H/D exchange occurred on C(β) of the unreacted substrate, within experimental error of the measurement.

Kinetic studies with potassium ethoxide in EtOH–DMSO mixtures

Kinetic studies for the reactions of substrates **2** with EtOK were performed in various EtOH–DMSO mixtures. It was observed that at high ethoxide concentrations, the plots of k_{obs} vs. [EtOK] were curved upward. Figure 1 shows a typical curved plot of k_{obs} vs. [EtOK] for the reaction of **2***h* in 5% EtOH – 95% DMSO (v/v) at 25.0°C.

In most kinetic experiments, relatively low EtOK concentrations (≤0.1 M) were used and linear k_{obs} vs. [EtOK] plots were obtained. The second-order rate constants k_2 could therefore be calculated from the slopes of these plots. All the k_{obs} vs. [EtOK] plots showed negligible intercept at [EtOK] = 0, indicating the absence of significant contribution from solvent to the observed reaction rates.

A kinetic experiment was also performed on the reaction of **2***h* with ethoxide in the presence of the K^+-complexing agent, dicyclohexyl-18-crown-6-ether (DC18C6). The experiments conducted with **2***h* at [EtOK] = 0.02 M in 20% EtOH – 80% DMSO (v/v) at 25.0°C (Supplementary Table 1) showed that, within experimental error, added DC18C6 had no effect on the observed reaction rate (k_{obs} = 2.72 (±0.08) × 10^{-4} s^{-1}, [DC18C6]/[EtOK] = 0–4).

Two series of kinetic experiments were performed with potassium ethoxide as base in EtOH–DMSO mixtures. In the first set, the reaction of **2***h* with EtOK was studied at 25.0°C in EtOH–DMSO mixtures of DMSO content ranging from 50 to 95% DMSO (v/v) (45.6–94.1% DMSO (mol/mol)). The k_{obs} values are recorded in Supplementary Tables 2–9 while the k_2 values obtained are presented in Table 1. In the second set, kinetic experiments for the reactions of various substituted β-phenylmercaptoethyl phenolates, **2***a*–**2***h*, with EtOK were conducted at 45.0°C in three EtOH-DMSO mixtures, containing 65, 80, and 90% DMSO (v/v). The k_{obs} values are listed in Supplementary Tables 10–33 while k_2 values are listed in Table 2.[2]

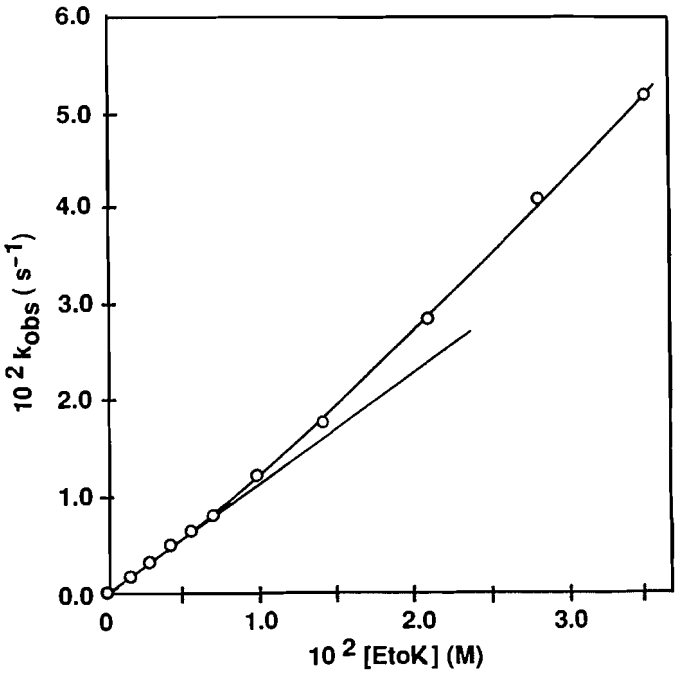

FIG. 1. Plot of k_{obs} vs. [EtOK] for reaction of **2***h* with EtOK in 5% EtOH – 95% DMSO (v/v) at 25.0°C.

Discussion

Reaction pathway

We have shown that the reaction of β-phenylmercaptoethyl

[2]Supplementary material mentioned in the text can be purchased from: The Depository of Unpublished Data, Document Delivery, CISTI, National Research Council Canada, Ottawa, ON K1A 0S2, Canada.

Can. J. Chem. Downloaded from www.nrcresearchpress.com by 195.246.54.202 on 09/08/12
For personal use only.

Can. J. Chem. Downloaded from www.nrcresearchpress.com by 195.246.54.202 on 09/08/12
For personal use only.

TABLE 1. Second-order rate constants for reaction of β-phenylmercaptoethyl *p*-nitrophenolate (**2*h***) with EtOK in EtOH–DMSO mixtures at 25.0°C

EtOH:DMSO (v/v)	Mole fraction DMSO	H_-[a]	k_2 (mol^{-1} L s^{-1})
5:95	0.941	20.40	1.13
10:90	0.883	19.50	1.77×10^{-1}
15:85	0.826	19.11	4.28×10^{-2}
20:80	0.769	18.80	1.25×10^{-2}
25:75	0.716	18.50	4.97×10^{-3}
30:70	0.661	18.20	2.73×10^{-3}
40:60	0.555	17.42	5.67×10^{-4}
50:50	0.456	16.65	1.47×10^{-4}

[a]Data from ref. 12(*a*).

TABLE 2. Second-order rate constants for reactions of β-phenylmercaptoethyl phenolates (**2*a*–2*h***) with EtOK in EtOH–DMSO mixtures at 45.0°C

	Substituent X	k_2 (mol^{-1} L s^{-1}) 65% DMSO v/v	80% DMSO v/v	90% DMSO v/v
2*a*	H	6.22×10^{-5}	8.26×10^{-4}	1.21×10^{-2}
2*b*	*p*-Me	2.83×10^{-5}	5.04×10^{-4}	7.10×10^{-3}
2*c*	*p*-Cl	2.34×10^{-4}	4.30×10^{-3}	4.89×10^{-2}
2*d*	*p*-CHO	3.31×10^{-3}	3.39×10^{-2}	3.56×10^{-1}
2*e*	*p*-MeCO	1.23×10^{-3}	1.68×10^{-2}	1.91×10^{-1}
2*f*	*p*-CN	2.90×10^{-3}	3.65×10^{-2}	3.97×10^{-1}
2*g*	*m*-NO_2	2.26×10^{-3}	2.92×10^{-2}	3.16×10^{-1}
2*h*	*p*-NO_2	1.06×10^{-2}	1.07×10^{-1}	1.06

p-nitrophenolate **2*h*** with EtOK in EtOH–DMSO proceeds by 1,2-elimination to give phenyl vinyl sulfide and *p*-nitrophenoxide. The absence of hydrogen/deuterium exchange in the substrate when the reaction is carried out in EtOD–DMSO-d_6 to partial completion allows one to rule out the possibility of an $(E1cb)_r$ type-mechanism. The $(E1cb)_{ir}$ mechanism can also be ruled out by the observation of a significant leaving group effect (β_{LG}) and the requirement of σ^- values for the best fit in Hammett plots (vide infra). An E1 mechanism can readily be ruled out by the base concentration dependence of the rate. Hence an E2 mechanism for the reaction is established.

Reactivity of potassium ethoxide in EtOH–DMSO mixtures

The upward curvature that is apparent in the plots of k_{obs} vs. [EtOK] for **2*h*** in EtOH–DMSO mixtures at relatively high base concentrations, as illustrated in Fig. 1, could conceivably be the result of reactive ion-pair species (12, 13) such as $[(EtO)_2K]^-$, etc. and (or) excess basicity (14) of the media at high EtOK concentrations.

If ion pairing of EtOK in EtOH–DMSO mixtures in fact contributes to the upward curvature of the k_{obs} vs. [EtOK] plots, then addition of DC18C6 to the reaction mixtures should reduce the reaction rate compared to the rate at the same EtOK concentration but in the absence of complexing agent. The kinetic experiments conducted in the presence of DC18C6 unambiguously showed the absence of ion pairing of EtOK in the EtOH–DMSO mixtures, since the reaction rate was not affected by the addition of DC18C6. This conclusion is in accord with the commonly observed finding that DMSO, with a high dielectric constant ($\epsilon = 45$), is a strong ionizing solvent in which ion pairing is generally not significant. Although in ethanol ion pairing can often be important (12, 13), the solvent mixtures used in this study were in the region of high DMSO composition ((45.1–94.1% DMSO (mol/mol)), which would tend to diminish the ion pairing of EtOK.

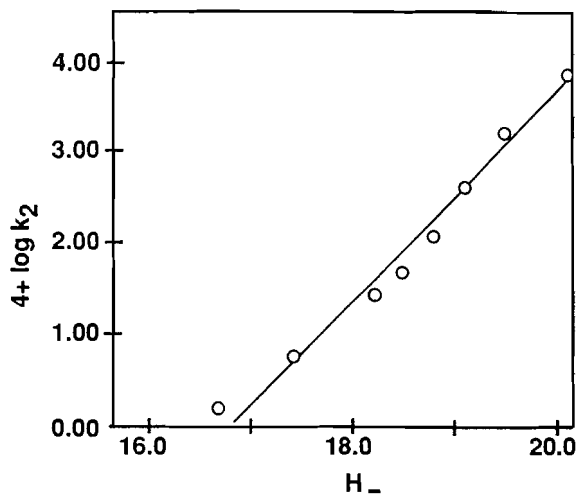

FIG. 2. Plot of log k_2 vs. H_- for reaction of **2*h*** with EtOK in various EtOH–DMSO mixtures at 25.0°C.

The upward curvature in the plot of k_{obs} vs. [EtOK] (Fig. 1) can hence be ascribed to excess basicity of EtOK in EtOH-DMSO mixtures (14). Base strength is known to be a major factor in determining reaction rates in elimination processes (15). At low base concentrations, both ion pairing and excess basicity are generally believed not to be significant and in the present study a linear dependence of k_{obs} upon [EtOK] was observed. Therefore, k_2 values were determined at low EtOK concentrations.

Table 1 shows that the second-order rate constants for reaction of **2*h*** with EtOK at low base concentrations are greatly enhanced on increasing the DMSO content, from 1.47×10^{-4} M^{-1} s^{-1} in 50% EtOH – 50% DMSO (v/v) to 1.13 M^{-1} s^{-1} in 5% EtOH – 95% DMSO (v/v). This observation is in complete accord with the well-known increased basicity of EtOK resulting on addition of DMSO to ethanol (14). Although H_- values for the EtOK–EtOH–DMSO system are not available, one can correlate the k_2 values with the H_- acidity function determined with Na^+ as the counterion at 20°C (14*a*). A plot of log k_2 versus H_- for EtONa–EtOH–DMSO is shown in Fig. 2. While the points may be represented by a linear graph as shown, with slope of 1.08 ± 0.06, they could also be joined in the form of a curved plot, which could be indicative of a mechanistic change.[3] It would be desirable to test other base-promoted elimination processes by changing the EtOH–DMSO composition, via the rate–H_- correlation, in order to obtain further insight into this mechanistic criterion.

Nucleofugality in reactions with potassium ethoxide

The kinetic data obtained on varying the substituent on the phenolate moiety (Table 2) show that the more electron withdrawing the substituent, the higher the reactivity of substrate **2** with potassium ethoxide in a given DMSO–EtOH medium. A

[3]We thank a referee for this suggestion.

TABLE 3. Hammett ρ and correlation coefficient values (R^2) for reactions of substituted β-phenylmercaptoethyl phenolates **2** with EtOK in EtOH–DMSO mixtures at 45.0°C as a function of mole fraction DMSO

	% DMSO (v/v)		
	65	80	90
f_{DMSO}	0.602	0.766	0.880
ρ (R^2)[a]	2.53 (0.93)	2.34 (0.94)	2.20 (0.95)
ρ^0 (R^2)[a]	2.57 (0.93)	2.38 (0.94)	2.24 (0.95)
ρ^- (R^2)[a]	1.74 (0.97)	1.58 (0.95)	1.49 (0.96)

[a]ρ, ρ^0, and ρ^- were obtained using the corresponding σ, σ^0, and σ^-, respectively (16).

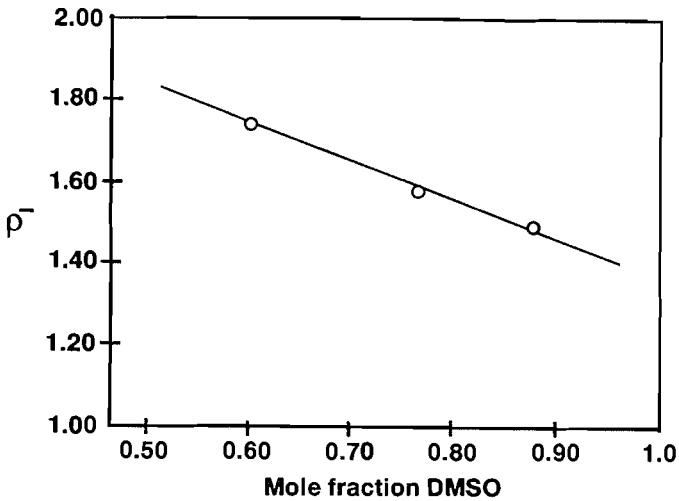

FIG. 3. Plot showing ρ^- as function of mole fraction DMSO for reactions of **2** with EtO^- in EtOH–DMSO media at 45.0°C.

Hammett-type treatment of the data in Table 2 showed that the fit of the various log k_2 – σ plots is dependent on the type of σ values chosen for the substituents (16). The results are summarized in Table 3 in the form of ρ values and correlation coefficients (R^2) resulting from use of different types of σ values in the log k_2 vs. σ plots. It is seen that use of σ^- leads to the best fit, indicating that substituents on the leaving aryloxy moiety interact with the oxygen center according to their resonance capability. This in turn is consistent with a substantial negative charge being developed on the aryloxy oxygen in the rate-determining transition state, i.e., a high degree of E2 character.

A plot of ρ^- values at the different DMSO–EtOH solvent compositions shows good linearity (Fig. 3) and can be extrapolated to 100% DMSO, yielding $\rho^- = 1.38$. The observed decreasing ρ^- values with increasing DMSO content, i.e., decreasing sensitivity of the reaction rate to substituents with increasing reactivity, are of interest since they apparently represent an example of adherence to the reactivity–selectivity principle (RSP) (17).

Poh has estimated the Hammett constant for the ionization of substituted phenols in pure DMSO, as $\rho^-(K_a) = 4.33$ (18). The ratio of $\rho^-(k_2)$ as estimated above to $\rho^-(K_a)$, i.e., β_{LG}, gives a measure of the effect of the leaving group on reactivity. This β_{LG} value is generally interpreted as being a measure of the extent of bond cleavage between the phenolate oxygen and the α-carbon in the transition state for elimination (19). Thus we obtain, for pure DMSO, $\beta_{LG} = \rho^-(k_2)/\rho^-(K_a) = 1.38/4.33 = 0.32$.

The high-quality linear regression in Fig. 3 (correlation constant = 0.9995) suggests that extrapolation to pure ethanol can be made, yielding $\rho^-(k_2) = 2.27$ in EtOH, although the extent of the required extrapolation brings some doubt to the procedure. Assuming that the resulting $\rho^-(k_2)$ value is valid, when combined with the ρ value (+2.23) for the ionization of phenol in EtOH (20*a*) this yields a β_{LG} value of 1.02. The greater value of β_{LG} in ethanol compared to that in DMSO is in accord with the Hammond postulate, noting that the reaction rate in ethanol is estimated to be ca. 10^8-fold slower than in DMSO, which will lead to a later transition state in ethanol medium.

Another approach was also used to estimate the β_{LG} values for reactions of **2** with potassium ethoxide in pure DMSO. First, plots of log k_2 vs. mole fraction of DMSO (f_{DMSO}) were constructed; these showed good linearity with correlation coefficients $R > 0.99$ for all substrates, **2***a*–**2***h*. The second-order rate constants k_2 for each substrate were then extrapolated to pure DMSO. Secondly, pK_a values of substituted phenols in pure DMSO were estimated graphically by interpolation on a plot of pK_a(DMSO) vs. $pK_a(H_2O)$. Then, a Brønsted plot of log k_2 versus pK_a in DMSO was constructed and yielded $\beta_{LG} = 0.28$ with a correlation coefficient of 0.96.

A similar procedure was applied for the estimation of β_{LG} in EtOH. The pK_a values in 95% EtOH – 5% H_2O were used as an approximation of pK_a values in pure EtOH. The plot of log k_2 vs. pK_a gave $\beta_{LG} = 0.94$ with a correlation coefficient $R = 0.98$. It is noteworthy that the β_{LG} values obtained with the second approach are identical, within experimental error, to those estimated by the method previously described. This encourages confidence in the validity of the estimated β_{LG} values.

It is interesting that the β_{LG} value determined in this study (ca. 0.98 EtOH) is higher than the values reported by Stirling and co-workers (20) in an investigation of the nucleofugality of the same leaving groups in E1cb processes induced by sulfone, sulfoxide, and cyano groups in ethanol medium (β_{LG} = 0.67, 0.54, and 0.79, respectively).

Elimination versus substitution

As stated in the Introduction, the majority of the investigations with substrates **1** have reported nucleophilic substitution (pathway a in Scheme 1) even in the absence of strong nucleophiles, e.g., hydrolysis in neutral aqueous solution (2, 8). However, in the present reaction systems no substitution products could be detected and the reactions are found to be completely 1,2-elimination processes.

The competition between elimination and substitution in the reaction of R-S-CH_2CH_2-L (**3**) with a base/nucleophile (B/Nu) can be analyzed by means of Scheme 2. Nucleophilic substitu-

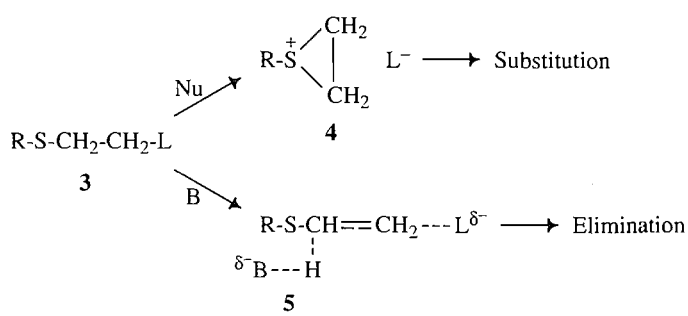

SCHEME 2

Can. J. Chem. Downloaded from www.nrcresearchpress.com by 195.246.54.202 on 09/08/12
For personal use only.

Can. J. Chem. Downloaded from www.nrcresearchpress.com by 195.246.54.202 on 09/08/12
For personal use only.

tion in **3** can in principle occur either via the cyclic sulfonium intermediate mechanism or by a concerted direct S_N2 displacement process, but for simplicity we show only the episulfonium intermediate since omission of the S_N2 process will not affect the conclusions of our discussion.

Clearly, factors stabilizing **4** and the transition state leading up to it will promote substitution over elimination, while factors favoring **5** will increase alkene over substitution products. The most important factors controlling the reaction pathway are the nature of the substituent, R, the leaving group, L, the base/nucleophile, B/Nu, and the solvent. These will now be considered in turn.

Substituent R on sulfur

Oae and Yano (9) studied the reaction of a series of substituted β-chloroethyl aryl sulfides with EtONa in EtOH (eq. [2]) and obtained the following results on variation of X for the yield of alkene: CH_3O, 42.5%; CH_3, 47.9%; H, 76.0%; Cl, 100%; NO_2, 100%.

[2] $p\text{-X-C}_6\text{H}_4\text{-S-CH}_2\text{CH}_2\text{-Cl} +$

$$\text{EtONa} \xrightarrow[\text{EtOH}]{60^\circ} \begin{cases} \text{X-C}_6\text{H}_4\text{-S-CH=CH}_2 \\ \text{X-C}_6\text{H}_4\text{-S-CH}_2\text{-CH}_2\text{-OEt} \end{cases}$$

It is apparent that the stronger the electron-withdrawing nature of substituent X, the higher the olefin yield and vice versa. For example, replacement of the *p*-methoxyphenyl group on sulfur by *p*-chlorophenyl changes the reaction from ca. 58% substitution to 100% elimination. The unsubstituted phenyl residue favors elimination.

It is interesting that in a recent study Yang and co-workers (21) found that the series of substrates $\text{R-S-CH}_2\text{CH}_2\text{Cl}$ undergo hydrolysis concurrently with decomposition to dithioether when R = Me, Et, PhCH_2, ClCH_2CH_2, and HOCH_2CH_2, but when R = Ph no hydrolysis is observed. This suggests that the phenyl substituent on sulfur has an influence on susceptibility of the substrates to nucleophilic substitution.

The electron pair on sulfur can be delocalized on the phenyl ring, i.e.,

$$\underset{\mathbf{6}}{\text{Ar-S-CH}_2\text{-CH}_2\text{-OAr}} \longleftrightarrow \underset{\mathbf{6a}}{{}^-\text{Ar=S}^+\text{-CH}_2\text{-CH}_2\text{-OAr}}$$

Charge density on sulfur is reduced through structures such as **6***a* and the intramolecular substitution or anchimeric assistance pathway resulting in cyclic sulfonium **4** becomes inhibited. As well, the partial positive charge on sulfur enhances the acidity of the β-protons and stabilizes the elimination transition state **5**, with the result that elimination is favored.

Leaving group

A better leaving group should favor the formation of **4** relative to **5** and hence favor substitution. Since phenolates are poorer leaving groups than chloride, elimination in **2** and **6** will be favored relative to the β-chloroethyl sulfide derivatives **1**.

Base and solvent

It is well known that stronger bases favor elimination over substitution (15). DMSO is known to greatly increase the basicity of ethoxide compared to protic media by desolvating the ethoxide anion (22). However, a strongly solvating medium such as water would stabilize the charge-separated species **4** more effectively than **5** and hence favor substitution. A change of reaction medium from ethanolic to aqueous should hence lead to substitution rather than elimination. Accordingly, the reaction of β-chloroethyl *p*-tolyl sulfide with EtONa in EtOH at 60°C gives 47% elimination and 53% substitution (9). However, the same reaction conducted in 80% aqueous EtOH (w/w) at 40–65°C was reported to proceed entirely by substitution (8). Recent work by McManus and co-workers (23) on solvolysis of 2-chloroethyl methyl sulfide in methanol–water mixtures indicates that there is both transition state stabilization and ground state destabilization of alkyl β-chloroethyl sulfides by water molecules. Thus increased solvation promoting substitution over elimination is supported by the available evidence.

Conclusions

β-Phenylmercaptoethyl phenolates, **2**, react with potassium ethoxide in EtOH–DMSO mixtures exclusively by a base-promoted 1,2-elimination pathway. The reaction occurs by a concerted E2 mechanism in which negative charge is significantly delocalized onto the phenolate ring and partially stabilized by the β-phenyl sulfenyl group in the transition state. The preference for elimination rather than substitution in the present reaction system is believed to be due mainly to: (*a*) the electron-withdrawing phenyl group on sulfur; (*b*) relatively poor leaving-group ability of the phenolates; (*c*) enhanced basicity of potassium ethoxide in DMSO.

Experimental

Solvents and reagents

Ethanol and dimethyl sulfoxide (DMSO) were purified by standard literature methods (24). The mixed solvents were prepared by the following procedure. The desired volume of distilled EtOH was transferred to a septum-sealed 10-mL volumetric flask with a gas-tight syringe and DMSO was added up to the mark. The molar composition of the EtOH–DMSO mixtures was determined from the measured weights of ethanol and DMSO.

Potassium ethoxide solutions in EtOH or EtOD were prepared by allowing potassium metal (Aldrich Analytical Grade) cut under petroleum ether to react with freshly distilled ethanol under a nitrogen atmosphere. The EtOK solution was titrated against potassium hydrogen phthalate and stored in a freezer. Dicyclohexyl-18-crown-6-ether (DC-18-C-6, Aldrich) was recrystallized from acetonitrile and stored in a dry-box.

Synthesis of substrates 2

β-Phenylmercaptoethyl phenolates (**2**) were synthesized by the reaction of β-chloroethyl phenyl sulfide with a mixture of potassium hydroxide and the corresponding phenol in aqueous ethanol (water: ethanol = 1:2–1:3 v/v). A typical procedure is described below.

A mixture of potassium hydroxide (60.0 mmol) and the substituted phenol (79.5 mmol) in 100 mL aqueous ethanol (1:1 v/v) was added slowly with magnetic stirring to 60.9 mmol of β-chloroethyl phenyl sulfide in 100 mL ethanol contained in a 3-necked round-bottom flask. The resulting solution was refluxed overnight, then cooled to room temperature, and the precipitated product was filtered and washed with distilled water. The collected solid was recrystallized from hexane, petroleum ether – hexane, or acetone – hexane mixtures.

In the case of β-phenylmercaptoethyl *m*-nitrophenolate this procedure yielded an oily material that was separated from the ethanolic layer by means of a separatory funnel. Distillation yielded a pale yellow oil, bp 190–195°C/0.8–1 Torr(1 Torr = 133.3 Pa). This was dis-

solved in hot hexane and allowed to cool slowly, yielding the product as a crystalline material.

The purified products were characterized by NMR, IR, elementary analysis, and melting point. The physical constants as well as the NMR and IR parameters of compounds **2***a*–**2***h* are given in Supplementary Tables 34 and 35.[2]

Kinetic measurements

Reactions of potassium ethoxide with substrates **2** in EtOH–DMSO mixtures were studied spectrophotometrically by following the appearance of the absorption due to the generated aryloxide ions. The reactions were performed under pseudo-first-order conditions with base concentrations at least 50-fold in excess over the substrate. The observed rate constants (k_{obs}) were calculated from linear plots of $\ln(A_\infty - A_t)$ versus time. Generally, about four reaction half-lives were used in the calculation of k_{obs}. Kinetic studies were performed on a Perkin–Elmer Lambda 5 UV–visible spectrophotometer equipped with a temperature-controlled cell compartment (±0.1°C).

Hydrogen/deuterium exchange

A 25-μL aliquot of 1 M EtOK/EtOD was added to 0.5 mL CD_3SOCD_3 solution containing 14 mg **2***h* (0.051 mmol). The solution was allowed to stand overnight at room temperature, resulting in ca. 50% conversion to products, and the ^{1}H NMR spectrum of the reaction mixture was recorded.

NMR studies

NMR spectra were recorded on a Bruker 400 MHz NMR instrument with tetramethylsilane (TMS) or DMSO-d_6 as internal references.

Acknowledgement

We thank the Department of National Defence, Supply and Services Canada, and the Natural Sciences and Engineering Research Council of Canada for financial support of this research, and Professor S.P. McManus for helpful comments.

1. B. Cohen. *In* Kinetics of reactions of sulfur and nitrogen mustard. Summary Tech. Rep. Div. 9, NDRC. 1946.
2. C.G. Swain. J. Am. Chem. Soc. **66**, 1966 (1944).
3. P.D. Bartlett and C.G. Swain. J. Am. Chem. Soc. **71**, 1406 (1949).
4. (*a*) Y.-C. Yang, J.A. Baker, and J.R. Ward. Chem. Rev. **92**, 1729 (1992); (*b*) Y.-C. Yang, J.R. Ward, R.B. Wilson, W. Burrow, and J.S. Winterle. Thermochim. Acta, **114**, 313 (1987); (*c*) Y.-C. Yang, J.R. Ward, and T. Luteran. J. Org. Chem. **51**, 2756 (1986).
5. E.J. Dunn and R.K. Miller. DREO TN 90-9, January 1990.
6. (*a*) A.C. Knipe and C.J.M. Stirling. J. Chem. Soc. (B), 1218 (1968); (*b*) R. Bird and C.J.M. Stirling. J. Chem. Soc. Perkin Trans. 2, 1221 (1973).
7. (*a*) S.P. McManus, N. Neamati-Mazraeh, M.S. Paley, B.A. Hovanes, and J.M. Harris. Tetrahedron Lett. **26**, 4571 (1985); (*b*) S.P. McManus, N. Neamati-Mazraeh, B.A. Hovanes, M.S. Paley, and J.M. Harris. J. Am. Chem. Soc. **107**, 3393 (1985); (*c*) S.P. McManus, M.R. Sedaghat-Herati, and J.M. Harris. Tetrahedron Lett. **28**, 5299 (1987); (*d*) S.P. McManus, R.M. Karaman, R. Sedaghat-Herati, N. Neamati-Mazraeh, B.A. Hovanes, M.S. Paley, and J.M. Harris. J. Org. Chem. **52**, 2518 (1987); (*e*) Y.-C. Yang, L.L. Szafraniec, W.T. Beaudry, and J.R. Ward. J. Org. Chem. **52**, 1637 (1987); (*f*) M.R. Sedaghat-Herati, S.P. McManus, and J.M. Harris. J. Org. Chem. **53**, 2539 (1988); (*g*) J.M. Harris, M.R. Sedaghat-Herati, and S.P. McManus. J. Org. Chem. **53**, 3893 (1988); (*h*) S.P. McManus, M.R. Sedaghat-Herati, R.M. Karaman, N. Neamati-Mazraeh, S.M. Cowell, and J.M. Harris. J. Org. Chem. **54**, 1911 (1989).
8. M.J. Blandamer, H.S. Golinkin, and R.E. Robertson. J. Am. Chem. Soc. **91**, 2678 (1969).
9. S. Oae and Y. Yano. Tetrahedron, **24**, 5721 (1968).
10. A. Streitwieser, Jr. *In* Solvolytic displacement reactions. McGraw–Hill, New York. 1962.
11. M.J. Pregel and E. Buncel. J. Chem. Soc. Perkin Trans. 2, 307 (1991).
12. (*a*) M. Szwarc. *In* Ion and ion pairs in organic reactions. Wiley–Interscience, New York. 1972; (*b*) J.G. Pritchard and A.A. Bothner-By. J. Phys. Chem. **64**, 1271 (1960); (*c*) E. Buncel and B.C. Menon. J. Phys. Chem. **91**, 3879 (1987).
13. (*a*) E. Buncel and M.J. Pregel. J. Chem. Soc. Chem. Commun. 1566 (1989); (*b*) E.J. Dunn, R.Y. Moir, E. Buncel, J.G. Purdon, and R.A.B. Bannard. Can. J. Chem. **68**, 1837 (1990); (*c*) M. J. Pregel, E. J. Dunn, and E. Buncel. Can. J. Chem. **68**, 1846 (1990); (*d*) M.J. Pregel, E.J. Dunn, and E. Buncel. J. Am. Chem. Soc. **113**, 3545 (1991).
14. (*a*) C.H. Rochester. *In* Acidity functions. Academic Press, New York. 1979; (*b*) F.G. Bordwell. Acc. Chem. Res. **21**, 456 (1988); (*c*) A. Bagno, G. Scorrano, and F. Terrier. J. Chem. Soc. Perkin Trans. 2, 1017 (1990).
15. W.H. Saunders, Jr. and A.F. Cockerill. *In* Mechanisms of eliminations. Wiley–Interscience, New York. 1973.
16. O. Exner. *In* Correlation analysis in chemistry. *Edited by* N.B. Chapman and J. Shorter. Plenum Press, New York. 1978.
17. E. Buncel and H. Wilson. J. Chem. Educ. **64**, 475 (1987).
18. B.-L. Poh. Aust. J. Chem. **33**, 1175 (1980).
19. T.H. Lowry and K.S. Richardson. Mechanism and theory in organic chemistry. 3rd ed. Harper and Row, New York. 1987. Chap. 7.
20. (*a*) J. Crosby and C.J.M. Stirling. J. Chem. Soc. B, 679 (1970); (*b*) P.J. Thomas and C.J.M. Stirling. J. Chem. Soc. Perkin Trans. 2, 1130 (1978); (*b*) C.J.M. Stirling. Acc. Chem. Res. **12**, 198 (1979).
21. D.K. Rohrbaugh, Y.-C. Yang, and J.R. Ward. CRDEC TR-88140 (1988).
22. (*a*) T.B. McMahon and P. Kebarle. J. Am. Chem. Soc. **99**, 2222 (1977); (*b*) H. Achassi-Sorkhabi, J.C. Hallé, and F. Terrier. J. Chem. Res. (S), 196 (1978); (M), 2545 (1978); (*c*) E. Buncel and H. Wilson. Adv. Phys. Org. Chem. **14**, 133 (1977).
23. M.R. Sedaghat-Herati, J.M. Harris, and S.P. McManus. Tetrahedron, **44**, 7479 (1988).
24. D.D. Perrin. Purification of laboratory chemicals. 2nd ed. Pergamon Press, New York. 1980.

Can. J. Chem. Downloaded from www.nrcresearchpress.com by 195.246.54.202 on 09/08/12
For personal use only.

Temperature dependence of the volumetric properties of binary mixtures containing oxaalkane + *c*-hexane

JOSÉ PELETEIRO, CLARA A. TOVAR, AND ENRIQUE CARBALLO
Departamento de Física Aplicada, Facultad de Ciencias, Campus de Orense, Universidad de Vigo, 32004 Orense, Spain
JOSÉ L. LEGIDO
Departamento de Física Aplicada, Facultad de Ciencias, Apdo 874, Universidad de Vigo, 36200 Vigo, Spain
AND
LUIS ROMANÍ[1]
Departamento de Física Aplicada, Facultad de Ciencias, Campus de Orense, Universidad de Vigo, 32004 Orense, Spain
Received May 10, 1993

JOSÉ PELETEIRO, CLARA A. TOVAR, ENRIQUE CARBALLO, JOSÉ L. LEGIDO, and LUIS ROMANÍ. Can. J. Chem. **72**, 454 (1994).

Excess molar volumes of mixtures of 2,5-dioxahexane + *c*-hexane, 2,5,8-trioxanonane + *c*-hexane, 2,5,8,11-tetraoxadodecane + *c*-hexane, and 2,5,8,11,14-pentaoxapentadecane + *c*-hexane were determined from density measurements at 283.15, 288.15, 298.15, and 308.15 K. These results allowed the following mixing quantities to be reported in the range of concentration: α, $(\delta V^E/\delta T)_P$, and $(\delta H^E/\delta P)_T$, at 298.15 K. The values obtained were then compared with the values calculated by using the Flory theory and the Nitta–Chao theory of liquid mixtures.

JOSÉ PELETEIRO, CLARA A. TOVAR, ENRIQUE CARBALLO, JOSÉ L. LEGIDO et LUIS ROMANÍ. Can. J. Chem. **72**, 454 (1994).

Utilisant des mesures de densités effectuées à 283,15, 288,15, 298,15 et 308,15 K, on a déterminé les volumes molaires en excès pour les mélanges de 2,5-dioxahexane + *c*-hexane, 2,5,8-trioxanonane + *c*-hexane, 2,5,8,11-tétraoxadodécane + *c*-hexane et 2,5,8,11,14-pentaoxapentadécane + *c*-hexane. Ces résultats ont permis de rapporter les quantités de mélange suivantes, pour les plages de concentration mentionnées: α, $(\delta V^E/\delta T)_P$ et $(\delta H^E/\delta P)_T$, á 298,15 K. On a alors comparé les valeurs obtenues avec les valeurs calculées en utilisant la théorie de Flory et la théorie de Nitta–Chao des mélanges liquides.
[Traduit par la rédaction]

Introduction

The behaviour of the polioxyethylenglycol dimethylethers, also called glymes and having the general formula (CH_3—O—(—CH_2—CH_2—O—)$_n$—CH_3), has been studied in different mixtures (1–3). The similarities of their chains with the *n*-alkane chains have been emphasized; nevertheless, there are significant structural differences with those. First of all, the glyme molecules are polar, with their dipolar momentum increasing as does the length of the chain (4, 5), whereas the *n*-alkanes are apolar. Secondly, glymes have less conformational flexibility than *n*-alkanes, due to the weak *anomeric effect* present in the groupings of atoms (—O—CH_2—CH_2—O—) (6). This effect is much more noticeable in acetals, which contain the group (—O—CH_2—O—).

Bhattacharyya and Patterson (7) have measured the densities and excess volume at several temperatures for cyclohexane + *n*-alkane mixtures. Starting from these, they have calculated the values of $(\delta V^E/\delta T)_P$ and $(\delta^2 V^E/\delta T^2)_P$ analyzing the results in terms of Flory theory.

The aim of present work is to study the differential behaviour of glyme + cyclohexane mixtures in relation to *n*-alkane + cyclohexane mixtures. As a first step, we have determined the densities of mixtures of *c*-hexane with monoglyme (2,5-dioxahexane, DOHX), diglyme (2,5,8-trioxanonane, TON), triglyme (2,5,8,11-tetraoxadodecane, TODD), and tetraglyme (2,5,8,11,14-pentaoxapentadecane, POPD) at different temperatures; starting from these experimental facts, the values of V^E, α, $(\delta V^E/\delta T)_P$ and $(\delta H^E/\delta P)_T$ have been calculated. By using the theories of Flory and Nitta–Chao, those same values are calculated and the capacity of both theories for the prediction of parameters of order in glyme–cyclohexane mixtures is then studied.

[1]To whom the correspondence should be addressed.

Experimental

Cyclohexane and monoglyme were obtained from Aldrich (HPLC grade, better than 99.9%); diglyme and triglyme were supplied from Fluka. Diglyme: puriss. p. a. >99.5%; triglyme: purum >98%), and tetraglyme from Merck (zur synthese, >98%). The chemicals were all partially degassed, dried over Fluka type 4Å molecular sieves, and otherwise used as supplied.

Densities of the pure liquids and mixtures were measured with a Kyoto Electronics densimeter. Using a Hetoterm PF-CBIIe thermostat, the vibrating-tube temperature was kept at better than ±0.005 K. The experimental technique has been previously described (8, 9). Through weighing, mole fractions were determined. The densities of the pure liquids agree closely with the literature values as shown in Table 1. The precision of the densities was ±0.00001 g cm^{-3} and mole fraction ±0.00005.

Experimental results

Experimental densities, ρ, of binary mixtures (Tables 2–5) were fitted as a function of the mole fraction and the temperature to a polynomial of the type:

$$[1] \qquad \rho/(\text{g cm}^{-3}) = \sum_{i=1}^{3}\sum_{j=1}^{3} A_{ij} x^{i-1}(T - T_0)^{j-1}$$

where x is the mole fraction of oxaalkane, T is the temperature, and T_0 is the temperature of 278.15 K.

The experimental excess molar volumes, V^E (also in Tables 2–5), were determined from the densities of the pure liquids and their mixtures. They were fitted as a function of the mole fraction and temperature, to a polynomial of the form:

$$[2] \qquad V^E/(\text{cm}^3\ \text{mol}^{-1}) = x(1-x)\sum_{i=1}^{3}\sum_{j=1}^{3} B_{ij}(2x-1)^{i-1}(T - T_0)^{j-1}$$

Can. J. Chem. Downloaded from www.nrcresearchpress.com by 195.246.54.202 on 09/08/12
For personal use only.

Can. J. Chem. Downloaded from www.nrcresearchpress.com by 195.246.54.202 on 09/08/12
For personal use only.

where x is the mole fraction of oxaalkane, T is the temperature, and T_0 is the temperature of 278.15 K.

The coefficients A_{ij} and B_{ij} and standard deviation given in Tables 6 and 7 were obtained by an optimization process which employed a Marquardt's algorithm (10). Figures 1–4 show the experimental excess molar volumes and the fitted curves $V^E(x,T)$.

Berti et al. (11) have measured the excess molar volumes of mixtures of monoglyme and diglyme with cyclohexane at 298.15 K. Their values, 1.27 $cm^3\ mol^{-1}$ at $x = 0.5$ for both mixtures, are similar to ours. The curve of mixtures cyclohexane + monoglyme is almost symmetrical whereas for the diglyme + cyclohexane is shifted towards greater concentration of cyclohexane. The excess molar volumes increase with temperature, the growth being more marked for the glymes of short chain.

The values of cubic expansion coefficient (α) for the liquids and their mixtures (Fig. 5) were computed by analytic derivation of eq. [1] for each mixture at 298.15 K.

We have obtained the following values of α for pure liquids: $\alpha_{DOHX} = 1.268 \times 10^{-3}\ K^{-1}$, $\alpha_{TON} = 1.060 \times 10^{-3}\ K^{-1}$, $\alpha_{TODD} = 0.965 \times 10^{-3}\ K^{-1}$, $\alpha_{POPD} = 0.921 \times 10^{-3}\ K^{-1}$, $\alpha_{c\text{-HEX}} = 1.212 \times 10^{-3}\ K^{-1}$. The bibliography values are $\alpha_{DOHX} = 1.274 \times 10^{-3}\ K^{-1}$ (12), $\alpha_{TON} = 1.0602 \times 10^{-3}\ K^{-1}$ (12), $\alpha_{TODD} = 0.9771 \times 10^{-3}\ K^{-1}$ (12) or $0.929 \times 10^{-3}\ K^{-1}$ (21), $\alpha_{c\text{-HEX}} = 1.215 \times 10^{-3}\ K^{-1}$ (13) or $1.217 \times 10^{-3}\ K^{-1}$ or $1.220 \times 10^{-3}\ K^{-1}$ (14). They agree closely.

$(\delta V^E/\delta T)_P$ and $(\delta H^E/\delta P)_T = V^E - (T)(\delta V^E/\delta T)_P$ values (Figs. 6 and 7) were computed by analytical derivation of eq. [2] at 298.15 K for each mixture.

Theoretical models

(a) Flory model

The Flory model (15, 16) permits a prediction of the molar volume of the mixture and the excess molar volume starting from the equation of the state as a function of the reduced variables:

$$[3] \qquad \tilde{p}\tilde{v}/\tilde{T} = [\tilde{v}^{1/3}/(\tilde{v}^{1/3} - 1)] - 1/(\tilde{v}\tilde{T})$$

where

$$[4] \qquad \tilde{v} = V/V^* = [(1 + (4/3)\alpha T)/(1 + \alpha T)]^3$$

$$[5] \qquad \tilde{p} = p/p^* = p/(\alpha T\tilde{v}^2/\kappa_T)$$

$$[6] \qquad \tilde{T} = T/T^* = (\tilde{v}^{1/3} - 1)/\tilde{v}^{4/3}$$

The excess molar volume can be determined from the expression:

$$[7] \qquad V^E = \left(\sum_{i=1}^{2} x_i V_i^*\right)\left(\tilde{v} - \sum_{i=1}^{2} \phi_i \tilde{v}_i\right)$$

where

$$\phi_i = x_i V_i^* / \sum_{j=1}^{2} x_j V_j^*$$

The parameter dV^E/dT (8) is calculated from the following expression:

TABLE 1. Densities of the pure liquids

Substance	T^a	ρ^b Experimental	ρ^b Literature	
DOHX	283.15	0.87808		
	288.15	0.87270		
	298.15	0.86183	0.8616 (12)	0.86370 (14)
			0.86208 (2)	0.85387 (11)
	308.15	0.85082		
TON	283.15	0.95350		
	288.15	0.94866		
	298.15	0.93872	0.9384 (14)	0.93882 (20)
			0.93967 (21)	0.93892 (11)
	308.15	0.92870		
TODD	283.15	0.99498		
	288.15	0.99028		
	298.15	0.98079	0.9811 (12)	0.98000 (21)
	308.15	0.97127		
POPD	283.15	1.01948		
	288.15	1.01502		
	298.15	1.00569	1.0066 (21)	
	308.15	0.99642		
C_6H_{12}	283.15	0.78778		
	288.15	0.78317	0.78318 (13)	
	298.15	0.77380	0.77382 (13)	0.77388 (11)
	308.15	0.76438	0.76461 (13)	

[a] In K.
[b] In g cm^{-3}.

$$[8] \qquad dV^E/dT = \left[\left(\sum_{i=1}^{2} x_i V_i^*\right) \cdot (\tilde{T} \cdot (d\tilde{v}/d\tilde{T})) - \left(\sum_{i=1}^{2} x_i V_i^* \cdot (\tilde{T} \cdot (d\tilde{v}/d\tilde{T}))_i\right)\right] \cdot T^{-1}$$

where

$$[9] \qquad \tilde{T} = (\phi_1 p_1^* \tilde{T}_1 + \phi_2 p_2^* \tilde{T}_2)/[\phi_1 p_1^* + \phi_2 p_2^* - \phi_1\phi_2 X_{12}/(\phi_2 + (S_1/S_2)\phi_1)]$$

The parameter X_{12} was obtained by employing a Marquardt's algorithm (10) in an optimization process, using all experimental data at 298.15 K. The relationship of the molecular surface areas of contact was estimated from the characteristic volumes of the components, using the assumption that the molecules are approximately spherical (16).

Table 8 shows the data used in the application of the Flory model.

(b) Nitta–Chao model

The Nitta–Chao model (Nitta et al. (17)) is based on the cell theory, with the function of molecular cell partition being obtained by using the hard sphere state equation (Carnahan and Starling (18)). The equation of state expressed completely in reducing variables:

$$[10] \qquad \tilde{p}\tilde{v}/\tilde{T} = 1 + \tilde{v}(4\tilde{v} - 2)/(\tilde{v} - 1)^3 - (1 + \kappa\tilde{v})\exp(\kappa/\tilde{v})/(\tilde{v}\tilde{T})$$

Can. J. Chem. Downloaded from www.nrcresearchpress.com by 195.246.54.202 on 09/08/12
For personal use only.

TABLE 2. Densities and excess molar volumes for (x) 2,5-dioxahexane + ($1 - x$) c-hexane[a]

	283.15 K		288.15 K		298.15 K		308.15 K	
x	ρ	V^E	ρ	V^E	ρ	V^E	ρ	V^E
0.01499	0.78839	0.09365	0.78378	0.09328	0.77440	0.09393	0.76497	0.09453
0.01876	0.78852	0.12030	0.78392	0.11850	0.77457	0.11479	0.76507	0.12519
0.05308	0.79016	0.30152	0.78553	0.30261	0.77609	0.30908	0.76657	0.31990
0.08199	0.79156	0.45146	0.78688	0.45832	0.77748	0.45715	0.76791	0.47270
0.10306	0.79274	0.53920	0.78808	0.54229	0.77853	0.55990	0.76892	0.57927
0.15632	0.79576	0.75583	0.79105	0.76306	0.78147	0.78086	0.77182	0.79870
0.20539	0.79896	0.89969	0.79422	0.90786	0.78453	0.93452	0.77478	0.96143
0.27255	0.80373	1.04547	0.79890	1.06086	0.78910	1.09279	0.77924	1.12488
0.30043	0.80579	1.09583	0.80095	1.11039	0.79109	1.14609	0.78118	1.18059
0.35470	0.81002	1.16599	0.80516	1.17866	0.79522	1.21588	0.78520	1.25590
0.41074	0.81466	1.20470	0.80972	1.22286	0.79972	1.25920	0.78958	1.30354
0.46143	0.81904	1.21781	0.81408	1.23370	0.80400	1.27070	0.79379	1.31405
0.51254	0.82361	1.21346	0.81858	1.23332	0.80848	1.26253	0.79823	1.30149
0.55533	0.82770	1.17808	0.82266	1.19452	0.81246	1.22731	0.80210	1.27111
0.61564	0.83356	1.11957	0.82849	1.13314	0.81820	1.16392	0.80776	1.20385
0.66174	0.83830	1.04515	0.83321	1.05579	0.82279	1.09216	0.81229	1.12831
0.70562	0.84292	0.96353	0.83779	0.97388	0.82737	1.00050	0.81676	1.03810
0.76420	0.84933	0.82945	0.84414	0.83985	0.83367	0.85760	0.82301	0.88546
0.79803	0.85317	0.73772	0.84796	0.74612	0.83740	0.76610	0.82670	0.78954
0.85640	0.86006	0.55235	0.85480	0.55886	0.84415	0.57360	0.83336	0.59120
0.90080	0.86535	0.41006	0.86009	0.41045	0.84941	0.41747	0.83850	0.43686
0.94661	0.87117	0.22468	0.86587	0.22315	0.85505	0.23346	0.84416	0.23578
0.97990	0.87542	0.09057	0.87008	0.08891	0.85928	0.08667	0.84827	0.09319

[a]Units: ρ = g cm^{-3}; V^E = cm^3 mol^{-1}.

TABLE 3. Densities and excess molar volumes for (x) 2,5,8-trioxanonane + ($1 - x$) c-hexane[a]

	283.15 K		288.15 K		298.15 K		308.15 K	
x	ρ	V^E	ρ	V^E	ρ	V^E	ρ	V^E
0.01669	0.79048	0.12570	0.78589	0.12331	0.77652	0.12394	0.76707	0.12902
0.02627	0.79199	0.20096	0.78740	0.19880	0.77805	0.19711	0.76858	0.20413
0.05873	0.79733	0.41444	0.79272	0.41543	0.78337	0.41451	0.77395	0.41528
0.08858	0.80244	0.56796	0.79781	0.57164	0.78837	0.58191	0.77887	0.59459
0.10986	0.80610	0.66600	0.80146	0.67093	0.79202	0.68086	0.78247	0.70061
0.16367	0.81533	0.88340	0.81068	0.89052	0.80119	0.90627	0.79162	0.92658
0.21250	0.82391	1.01369	0.81923	1.02388	0.80967	1.04730	0.80003	1.07443
0.25677	0.83162	1.10940	0.82692	1.12126	0.81732	1.14656	0.80766	1.17442
0.30988	0.84087	1.18581	0.83613	1.20170	0.82650	1.22788	0.81686	1.24800
0.34624	0.84717	1.21901	0.84242	1.23508	0.83278	1.26003	0.82303	1.29253
0.41699	0.85944	1.22904	0.85468	1.24373	0.84493	1.27730	0.83514	1.31023
0.46451	0.86746	1.22907	0.86269	1.24340	0.85289	1.28050	0.84310	1.30833
0.53077	0.87863	1.18064	0.87383	1.19646	0.86402	1.23054	0.85420	1.25555
0.61167	0.89185	1.10860	0.88703	1.12402	0.87725	1.14513	0.86742	1.16463
0.65700	0.89937	1.01773	0.89456	1.02943	0.88472	1.05463	0.87483	1.07717
0.71023	0.90797	0.91396	0.90316	0.92317	0.89332	0.94305	0.88341	0.96188
0.75979	0.91597	0.78972	0.91113	0.80084	0.90125	0.81998	0.89131	0.83838
0.82210	0.92589	0.61402	0.92104	0.62490	0.91115	0.63882	0.90119	0.65216
0.87163	0.93348	0.48943	0.92865	0.49509	0.91881	0.49656	0.90882	0.50805
0.90800	0.93935	0.33838	0.93450	0.34479	0.92464	0.34464	0.91463	0.35470
0.96044	0.94739	0.15939	0.94251	0.16756	0.93257	0.17239	0.92260	0.17094
0.98464	0.95098	0.08548	0.94614	0.08658	0.93619	0.09042	0.92618	0.09120

[a]Units: ρ = g cm^{-3}; V^E = cm^3 mol^{-1}.

Can. J. Chem. Downloaded from www.nrcresearchpress.com by 195.246.54.202 on 09/08/12
For personal use only.

TABLE 4. Densities and excess molar volumes for (x) 2,5,8,11-tetraoxadodecane + ($1-x$) c-hexane[a]

	283.15 K		288.15 K		298.15 K		308.15 K	
x	ρ	V^E	ρ	V^E	ρ	V^E	ρ	V^E
0.02712	0.79530	0.23674	0.79069	0.23752	0.78128	0.24512	0.77181	0.25464
0.05712	0.80367	0.44369	0.79904	0.44762	0.78966	0.45211	0.78021	0.45998
0.08749	0.81207	0.61366	0.80472	0.62050	0.79799	0.63276	0.78846	0.65340
0.10810	0.81762	0.72269	0.81299	0.72675	0.80351	0.74661	0.79402	0.76191
0.15915	0.83133	0.90676	0.82668	0.91313	0.81714	0.94152	0.80760	0.96440
0.20875	0.84416	1.03550	0.83947	1.04703	0.82995	1.07179	0.82041	1.09411
0.25617	0.85591	1.13108	0.85122	1.14196	0.84167	1.17051	0.83213	1.19233
0.30427	0.86736	1.20018	0.86261	1.21945	0.85308	1.24583	0.84350	1.27190
0.37515	0.88347	1.25168	0.87876	1.26379	0.86927	1.28225	0.85969	1.30693
0.41022	0.89117	1.24994	0.88646	1.26139	0.87690	1.29000	0.86733	1.31252
0.47912	0.90569	1.21644	0.90100	1.22501	0.89147	1.24527	0.88191	1.26605
0.51159	0.91217	1.20357	0.90746	1.21487	0.89791	1.23791	0.88834	1.26014
0.56876	0.92355	1.10660	0.91885	1.11491	0.90933	1.13075	0.89981	1.14246
0.60998	0.93121	1.06406	0.92652	1.07014	0.91704	1.08015	0.90753	1.08776
0.66943	0.94208	0.94845	0.93737	0.95664	0.92794	0.95628	0.91847	0.95522
0.70779	0.94893	0.85034	0.94422	0.85764	0.93475	0.86261	0.92523	0.86915
0.75218	0.95644	0.76116	0.95175	0.76264	0.94223	0.77520	0.93268	0.78643
0.80698	0.96556	0.60811	0.96087	0.61011	0.95136	0.61743	0.94184	0.62358
0.86199	0.97430	0.45508	0.96961	0.45603	0.96011	0.46186	0.95060	0.46321
0.90012	0.98014	0.34742	0.97542	0.35303	0.96593	0.35624	0.95648	0.34590
0.94570	0.98703	0.19362	0.98234	0.19294	0.97281	0.20192	0.96330	0.20152
0.97079	0.99064	0.12284	0.98594	0.12361	0.97644	0.12670	0.96693	0.12594

[a]Units: ρ = g cm^{-3}; V^E = cm^3 mol^{-1}.

TABLE 5. Densities and excess molar volumes for (x) 2,5,8,11,14-pentaoxapentadecane + ($1-x$) c-hexane[a]

	283.15 K			288.15 K		298.15 K		308.15 K	
x	ρ	V^E	x	ρ	V^E	ρ	V^E	ρ	V^E
0.02435	0.79721	0.24735	0.02419	0.79273	0.22132	0.78331	0.22972	0.77386	0.23633
0.05603	0.80941	0.47517	0.05228	0.80341	0.45005	0.79397	0.46272	0.78455	0.46722
0.07701	0.81726	0.59722	0.07729	0.81292	0.57968	0.80352	0.58640	0.79403	0.60184
0.10933	0.82898	0.74852	0.11749	0.82724	0.78779	0.81783	0.79798	0.80833	0.81541
0.11774	0.83203	0.77012	0.15610	0.84042	0.92399	0.83104	0.92941	0.82156	0.94474
0.15918	0.84603	0.93017	0.20824	0.85723	1.04347	0.84775	1.06227	0.83824	1.08543
0.21073	0.86253	1.05352	0.23821	0.86634	1.09399	0.85689	1.10787	0.84741	1.12521
0.26186	0.87771	1.14274	0.29660	0.88288	1.18400	0.87343	1.19982	0.86399	1.21268
0.31469	0.89240	1.18784	0.37748	0.90388	1.23030	0.89453	1.22951	0.88514	1.23610
0.36278	0.90477	1.22606	0.42621	0.91555	1.22531	0.90618	1.22798	0.89682	1.22912
0.42464	0.91975	1.21955	0.46084	0.92341	1.21313	0.91409	1.20711	0.90474	1.20743
0.46344	0.92854	1.20618	0.51512	0.93528	1.14414	0.92596	1.13760	0.91658	1.14470
0.52880	0.94257	1.14029	0.54832	0.94210	1.10520	0.93278	1.10050	0.92340	1.10881
0.61439	0.95938	1.02244	0.62234	0.95640	1.00239	0.94715	0.98478	0.93785	0.97835
0.66049	0.96783	0.93856	0.65830	0.96297	0.93615	0.95376	0.90884	0.94445	0.90727
0.70403	0.97545	0.84635	0.70600	0.97142	0.81692	0.96214	0.80271	0.95284	0.80060
0.75834	0.98469	0.67979	0.76704	0.98149	0.68071	0.97223	0.66267	0.96293	0.66270
0.76117	0.98512	0.67816	0.80603	0.98762	0.58294	0.97837	0.56291	0.96908	0.56223
0.80844	0.99265	0.54099	0.85198	0.99454	0.46068	0.98529	0.44282	0.97601	0.43962
0.84391	0.99793	0.46215	0.92234	1.00457	0.26143	0.99534	0.23959	0.98603	0.24543
0.91180	1.00770	0.26776	0.94444	1.00760	0.19291	0.99835	0.17540	0.98904	0.18215
0.96138	1.01443	0.12167	0.97952	1.01221	0.09737	1.00300	0.07155	0.99374	0.06869
0.96809	1.01533	0.09886							

[a]Units: ρ = g cm^{-3}; V^E = cm^3 mol^{-1}.

Can. J. Chem. Downloaded from www.nrcresearchpress.com by 195.246.54.202 on 09/08/12
For personal use only.

TABLE 6. Coefficients A_{ij} of eq. [1] and standard deviations (s)

System	DOHX + c- hexane		
A_{ij}	$j = 1$	$j = 2$	$j = 3$
$i = 1$	7.92014E-1	−9.14955E-4	−5.71703E-7
$i = 2$	4.98960E-2	−1.55694E-4	−3.19701E-7
$i = 3$	4.15711E-2	1.26139E-5	1.46542E-8
		s = 1.6E-4	
System	TON + c-hexane		
A_{ij}	$j = 1$	$j = 2$	$j = 3$
$i = 1$	7.91631E-1	−9.12183E-4	−6.32415E-7
$i = 2$	1.78643E-1	−1.22370E-4	4.76762E-7
$i = 3$	−1.17419E-2	6.91865E-5	−5.93426E-7
		s = 3.1E-4	
System	TODD + c-hexane		
A_{ij}	$j = 1$	$j = 2$	$j = 3$
$i = 1$	7.92829E-1	−9.49425E-4	4.63311E-7
$i = 2$	2.81088E-1	2.12190E-5	−2.37148E-6
$i = 3$	−7.50818E-2	−1.22269E-5	1.77210E-6
		s = 5.0E-4	
System	POPD + c-hexane		
A_{ij}	$j = 1$	$j = 2$	$j = 3$
$i = 1$	7.92070E-1	−9.02170E-4	−8.86482E-7
$i = 2$	4.09519E-1	−1.63304E-4	1.65805E-6
$i = 3$	−2.79218E-1	6.18219E-4	−6.09713E-6
$i = 4$	1.16592E-1	−6.53806E-4	7.74308E-6
$i = 5$	−1.49235E-2	1.89482E-4	−2.78600E-6
		s = 8.5E-5	

TABLE 7. Coefficients B_{ij} of eq. [2] and standard deviations (s)

System	DOHX + c-hexane		
B_{ij}	$j = 1$	$j = 2$	$j = 3$
$i = 1$	4.78499	1.17942E-2	1.01249E-4
$i = 2$	−7.56536E-1	−4.47750E-3	6.76925E-5
$i = 3$	6.18706E-1	−1.17559E-2	2.26494E-4
		s = 5.3E-3	
System	TON + c-hexane		
B_{ij}	$j = 1$	$j = 2$	$j = 3$
$i = 1$	4.75977	1.45010E-2	−6.69267E-5
$i = 2$	−1.54047	6.64919E-4	−1.15137E-4
$i = 3$	1.24441	−1.40094E-2	2.95358E-4
		s = 1.2E-2	
System	TODD + c-hexane		
B_{ij}	$j = 1$	$j = 2$	$j = 3$
$i = 1$	4.73229	8.40717E-3	−2.91420E-5
$i = 2$	−2.02568	−6.88580E-3	−1.00758E-4
$i = 3$	1.25490	5.89800E-3	−3.84688E-5
		s = 1.8E-2	
System	POPD + c-hexane		
B_{ij}	$j = 1$	$j = 2$	$j = 3$
$i = 1$	4.77244	−9.62085E-3	2.13445E-4
$i = 2$	−1.60411	−3.04331E-2	4.49781E-4
$i = 3$	−0.10934	4.84266E-2	−8.50795E-4
$i = 4$	−2.05140	9.16523E-2	−2.22928E-3
$i = 5$	2.20916	−2.87322E-2	5.03232E-4
		s = 9.2E-3	

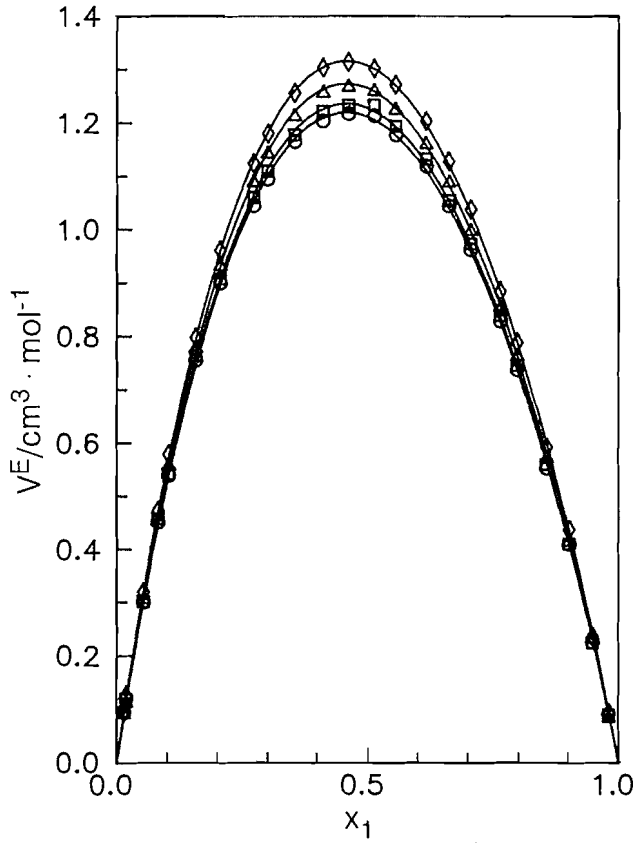

FIG. 1. Experimental excess molar volumes V^E, (x_1) monoglyme + ($1 - x_1$) c-hexane at (○), 283.15 K; (□), 288.15 K; (△), 298.15 K; (◇), 308.15 K.

where κ a constant whose value is 0.7, the reduced variables are defined by

$$[11] \qquad \tilde{p} = pV^*/cNkT^*$$

$$[12] \qquad \tilde{T} = 2ckT/n\tilde{Q}_e$$

where c is the number of external degrees and

$$[13] \qquad \tilde{Q}_e = \sum\sum N_{ij}E_{ij}$$

For N_{ij}, the number of contacts, the quasi-chemical approximation is used.

The energy of the interaction is expressed by

$$[14] \qquad E_{ij} = -(\epsilon_{ij}/\tilde{v}) \exp(\kappa/\tilde{v}) = \sigma_{ij}$$

where ϵ_{ij} is the dispersive interaction energy parameter.

The chemical association energy σ_{ij} is temperature dependent and is given by

$$[15] \qquad \frac{\sigma_{ij}}{T} = \frac{\sigma_{ij}^0}{T_0} + \sigma'_{ij}\left(\frac{1}{T} - \frac{1}{T_0}\right)$$

where σ_{ij}^0 and σ'_{ij} are characteristic parameters of this model.

The temperature dependence of the hard core volume of group i, V_i^*, is given by the empirical expression

$$[16] \qquad V_i^* = V_{i0}^* \exp\left[a_i\left(\frac{1}{T} - \frac{1}{T_0}\right)\right]$$

Can. J. Chem. Downloaded from www.nrcresearchpress.com by 195.246.54.202 on 09/08/12
For personal use only.

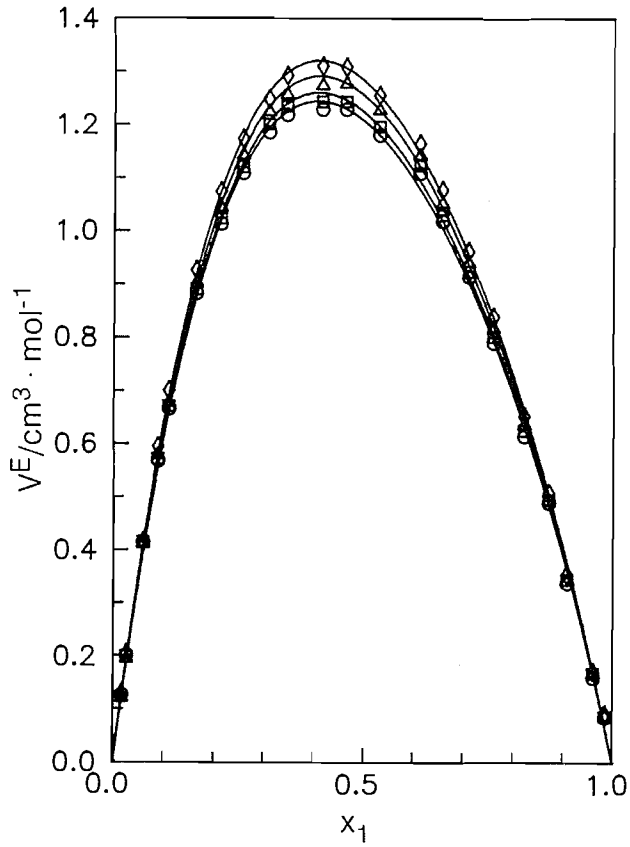

FIG. 2. Experimental excess molar volumes V^E, (x_1) diglyme + ($1-x_1$) *c*-hexane at (○), 283.15 K; (□), 288.15 K; (△), 298.15 K; (◇), 308.15 K.

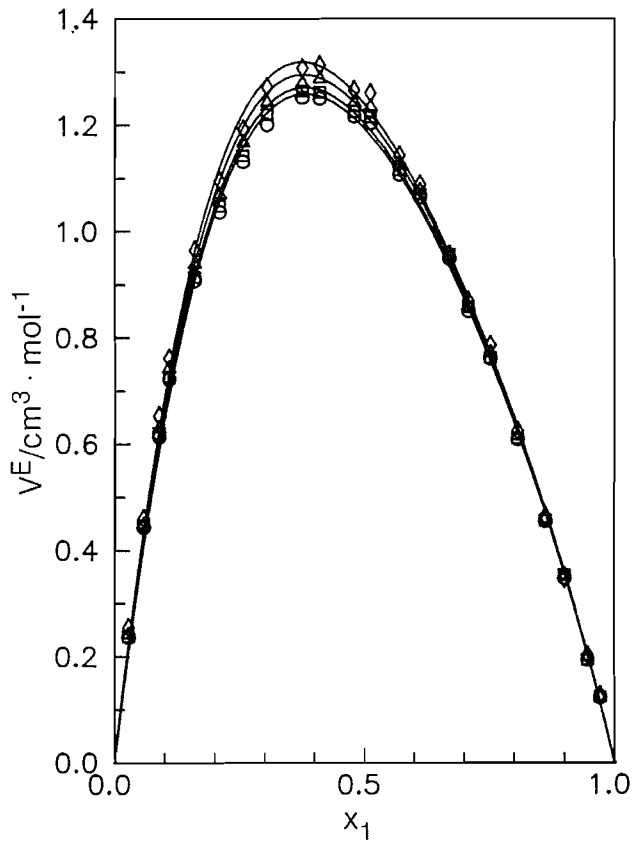

FIG. 3. Experimental excess molar volumes V^E, (x_1) triglyme + ($1-x_1$) *c*-hexane at (○), 283.15 K; (□), 288.15 K; (△), 298.15 K; (◇), 308.15 K.

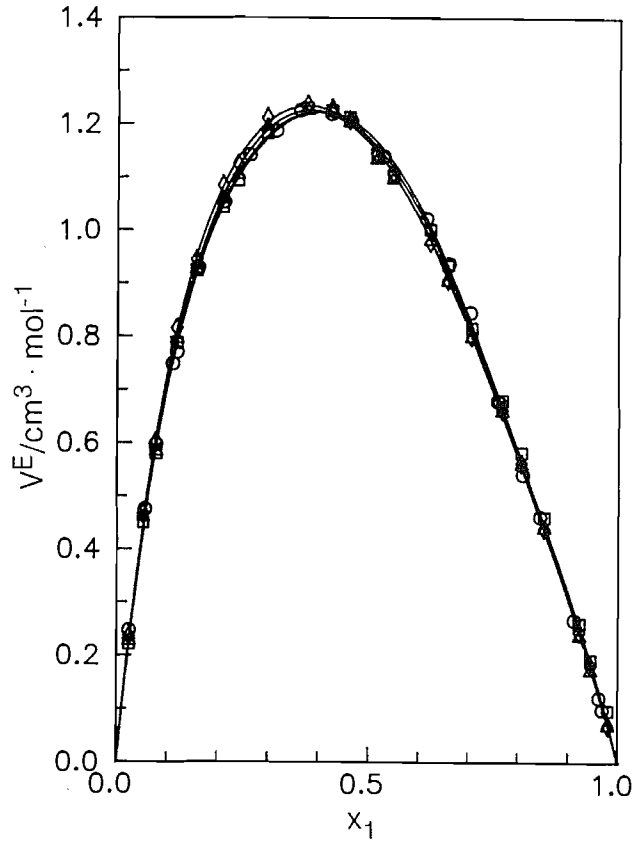

FIG. 4. Experimental excess molar volumes V^E, (x_1) tetraglyme + ($1-x_1$) *c*-hexane at (○), 283.15 K; (□), 288.15 K; (△), 298.15 K; (◇), 308.15 K.

where V^*_{i0} is the hard core volume at temperature T_0 (normally 298.15 K).

Both a_i and V^*_{i0} are characteristic parameters that are determined by fitting the theoretical equations to experimental data.

The configurational energy is given by

$$[17] \quad U_{conf}/NkT = -\sum\sum_{i\geq j} N_{ij}/NkT[(\epsilon_{ij}/\tilde{v}) + \exp(0.7/\tilde{v}) + \sigma'_{ij}] - (\delta \ln V^*/\delta \ln T)/(pV/NkT)$$

The molar heat of mixing for low pressure liquids is

$$[18] \quad H^E = U_{conf} - \sum x_A U_{A0,conf}$$

The expressions for the thermodynamic properties of both pure liquids and mixtures are derived by the standard methods of statistical thermodynamics.

Table 9 shows the characteristic parameters used.

Results and discussion

The V^E to mole fraction 0.5 as studied is represented in Fig. 8 as a function of the temperature, using eq. [2] and the coefficients B_{ij} in Table 7. An almost linear increase of the excess volume with the temperature can be observed. The lower the linear increase, the larger the glyme chain.

The calculated values for $(\delta V^E/\delta T)_P$, (shown in Fig. 6) are positive for the three systems, being negative for mixture with TODD at concentrations greater than 0.5. The values for $(\delta H^E/\delta P)_T$ (Fig. 7) are positive in the range of concentration

TABLE 8. Experimental data and characteristic parameters used in the Flory theory at 298.15 K

Component	$10^{-3} \times \alpha^a$	$\kappa_T{}^b$	V^c	V^{*d}	p^{*e}	T^{*f}
DOHX	1.268	1.1145 [12]	104.57	80.43	573.4	4626.7
TON	1.060	0.8216 [12]	142.93	113.45	610.6	5068.2
TODD	0.965	0.7071 [12]	181.72	146.49	626.1	5335.8
POPD	0.921	0.5896 [21]	221.02	179.51	706.1	5479.1
C_6H_{12}	1.212	1.1360 [16]	108.76	84.34	529.0	4730.1

System	S_1/S_2	$X_{12}{}^g$	H^E_{exp} $(x = 0.5)^h$	H^E_{cal} $(x = 0.5)^h$
DOHX + C_6H_{12}	1.0160	69.57	1355 [22]	1497
TON + C_6H_{12}	0.9059	73.32	1658 [22]	1957
TODD + C_6H_{12}	0.8319	75.76	1755 [22]	2349
POPD + C_6H_{12}	0.7774	87.06		3036

[a] In K^{-1}.
[b] In GPa^{-1}.
[c] In $cm^3\ mol^{-1}$.
[d] In $cm^3\ mol^{-1}$.
[e] In MPa.
[f] In K.
[g] In $J\ cm^{-3}$.
[h] In $J\ mol^{-1}$.

Can. J. Chem. Downloaded from www.nrcresearchpress.com by 195.246.54.202 on 09/08/12
For personal use only.

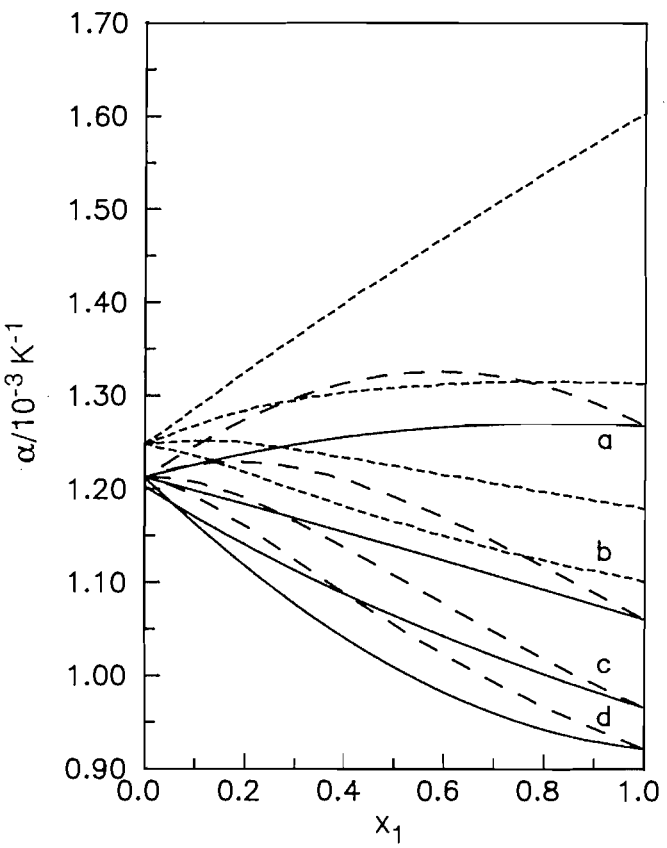

FIG. 5. Cubic expansion coefficients α at 298.15 K: (*a*), (x_1) monoglyme + ($1 - x_1$) *c*-hexane; (*b*), (x_1) diglyme + ($1 - x_1$) *c*-hexane; (*c*), (x_1) triglyme + ($1 - x_1$) *c*-hexane; (*d*), (x_1) tetraglyme + ($1 - x_1$) *c*-hexane; (—), derivation eq. [1]; (- - -), Nitta–Chao model; (– – –), Flory model.

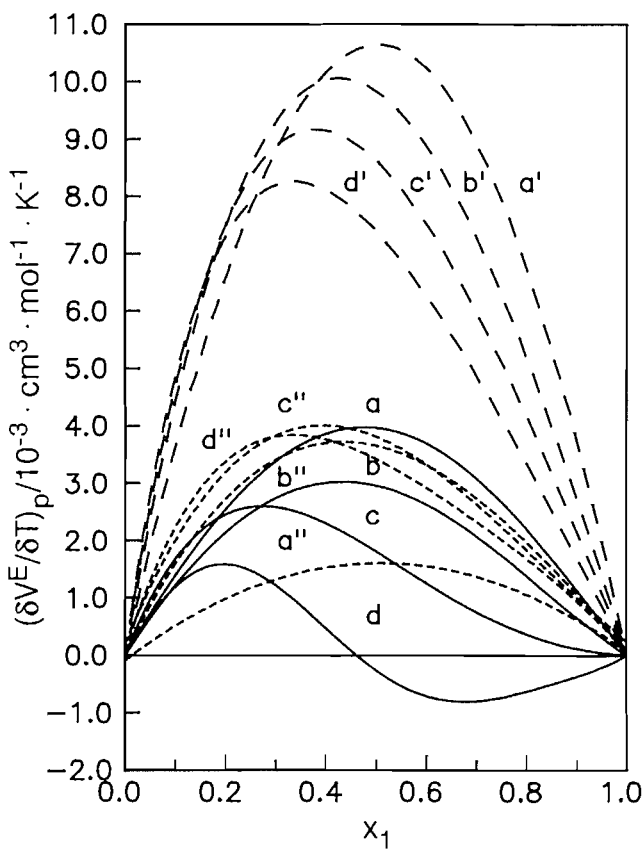

FIG. 6. $(\partial V^E/\partial T)_P$: (*a*), ($x_1$) monoglyme + ($1 - x_1$) *c*-hexane; (*b*), ($x_1$) diglyme + ($1 - x_1$) *c*-hexane; (*c*), ($x_1$) triglyme + ($1 - x_1$) *c*-hexane; (*d*), ($x_1$) tetraglyme + ($1 - x_1$) *c*-hexane at 298.15 K. (—), derivation eq. [2]; (- - -), Nitta–Chao model; (– – –), Flory model.

TABLE 9. Characteristic parameters for Nitta et al. model calculated by Nitta et al. (17) and Eckart et al. (19).

Group	V_{i0}^{*b}	$a_i{}^a$	c_i	Q_i	$\epsilon_{ii}{}^c$	
—CH_3	13.46	23.7	0.338	6.71	2515	
—CH_2	10.25	23.7	0.093	4.27	2515	
—CH_2—r	9.76	21.2	0.165	4.84	2674	
—O—	4.10	55.1	0.128	1.90	6532	
$\epsilon_{ij}(CH_n, O)^c$	$\epsilon_{ij}(CH_2$—r, $O)^c$	$\epsilon_{ij}(CH_2$—r, $CH_n)^c$	$\sigma^0(O, O)^c$	$\sigma'(O, O)^c$	
3500	3738	2572	6540	8763	

[a] In K.
[b] In $cm^3\ mol^{-1}$.
[c] In J mol^{-1}.

Can. J. Chem. Downloaded from www.nrcresearchpress.com by 195.246.54.202 on 09/08/12
For personal use only.

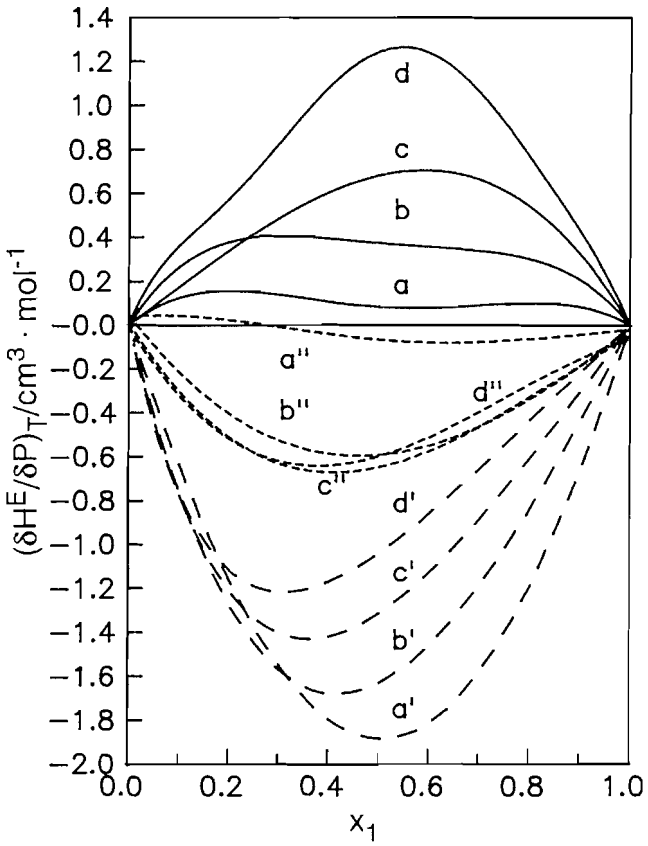

FIG. 7. $(\partial H^E/\partial P)_T$: (*a*), ($x_1$) monoglyme + ($1 - x_1$) *c*-hexane; (*b*), ($x_1$) diglyme + ($1 - x_1$) *c*-hexane; (*c*), ($x_1$) triglyme + ($1 - x_1$) *c*-hexane; (*d*), ($x_1$) tetraglyme + ($1 - x_1$) *c*-hexane at 298.15 K. (—), from eq. [2]; (- - -), Nitta–Chao model; (– – –), Flory model.

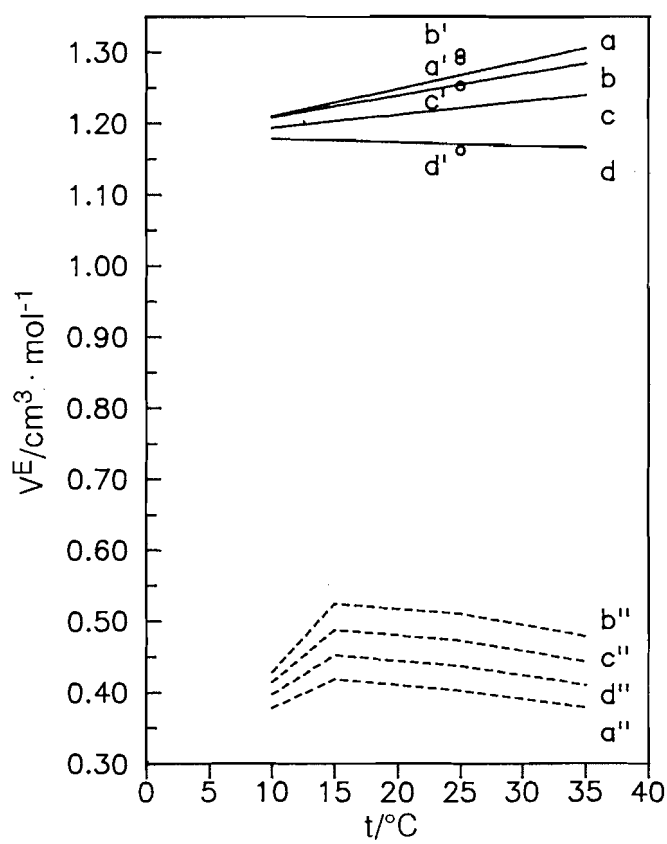

FIG. 8. Plot V^E ($x_1 = 0.5$) (*a*), monoglyme + *c*-hexane; (*b*), diglyme + *c*-hexane; (*c*), triglyme + *c*-hexane; (*d*), tetraglyme + *c*-hexane against *t*. (—), values from eq. [2]; (- - -), Nitta–Chao model; (○), Flory model.

and inverted in relation to $(\delta V^E/\delta T)_P$ values increasing with the ether chains length.

Calculations from the Flory's theory showed that values for α, $(\delta V^E/\delta T)_P$, and $(\delta H^E/\delta P)_T$, are very different from the experimental ones. The theoretical values of $(\delta V^E/\delta T)_T$ parameter is three or five times bigger than the experimental value, although it reproduces both the decrease and the deviation of the maximum as a function of glyme chain. Theoretical values of $(\delta H^E/\delta P)_T$ are negative, while the experimental ones are positive. The V^E values at $x = 0.5$ (Fig. 8) are in the same order as the experimental ones except for DOHX + *c*-hexane. In view of this we conclude that the Flory's theory can not explain the behaviour of the glyme–cyclohexane mixture, just the opposite that of the alkane–cyclohexane mixture (7).

A possible explanation of this is to take into account the polarity of the glyme molecules, which produces dipole–dipole and dipole – induced dipole associations that are not considered in the Flory's model.

The Nitta–Chao theory was applied using the parameters for both alkane–alkane and alkane–ether interactions shown in Table 7. The latter have been calculated by Eckart et al. (19), beginning with experimental data on monoether-alkane

mixtures. The results obtained do not reproduce the experimental tendencies of V^E. For the parameters $(\delta V^E/\delta T)_P$ and $(\delta H^E/\delta P)_T$ the calculated values are closer to the experimental results than those of the Flory theory. These results suggest that the ether groups in glymes behave differently from the ether groups in monoethers. This is probably associated with the appearance of the anomeric effect in those molecules which have two atoms of oxygen separated by one or two methylene groups. This effect causes the glyme chains or acetal chains to have a more rigid structure than those of the monoethers or hydrocarbons of similar size.

Acknowledgements

This work is part of Research Project XUGA 39901B90. The authors are indebted to the Dirección Xeral de Ordenación Universitaria e Política Científica (Xunta de Galicia) for financial support.

1. H.V. Kehiaian, M.R. Tine, L. Lepori, E. Matteoli, and B. Maronguiu. Fluid Phase Equilib. **46**, 131 (1989).
2. L.M. Trejo, M. Costas, and D. Patterson. J. Chem. Soc. Faraday Trans. **87**, 3001 (1991).
3. L. Andreoli-Ball, S.J. Sum, L.M. Trejo, M. Costas, and D. Patterson. Pure Appl. Chem. **62**, 2097 (1990).
4. K. Kimura and R. Fujishiro. Bull. Chem. Soc. Jpn. **39**, 608 (1966).
5. H.D. Purohit and R.J. Sengwa. Bull. Chem. Soc. Jpn. **64**, 2030 (1991).
6. L.N. Lauritsen and N.L. Allinguer. J. Comput. Chem. **5**, 326 (1984).
7. S.N. Bhattacharyya and D.J. Patterson. Chem. Soc. Faraday Trans. 1, **81**, 375 (1985).
8. T.P. Iglesias, J.L. Legido, L. Romaní, and M.I. Paz Andrade. Phys. Chem. Liq. **25**, 135 (1993).
9. M.T. Lorenzana, J.L. Legido, E. Jiménez, J. Fernández, L. Pías, J. Ortega, and M.I. Paz Andrade. J. Chem. Thermodyn. **21**, 1017 (1989).
10. D.W. Marquardt. J. Soc. Ind. Appl. Math. **11**, 431 (1963).
11. F. Berti, L. Lepori, and E. Mateoli. Fluid Phase Equilib. **44**, 285 (1989).
12. T. Treszczanowicz. Thermochim. Acta, **160**, 253 (1990).
13. M.B. Ewing and K.K. March. J. Chem. Thermodyn. **9**, 357 (1977).
14. J.A. Riddick, W.B. Bunger, and T.K. Sakano. Organic solvents. Techniques of chemistry. Vol. 2. 4rd ed. Wiley–Interscience, New York. 1986.
15. P.J. Flory. J. Am. Chem. Soc. **87**, 1833 (1965).
16. A. Abe and P.J. Flory. J. Am. Chem. Soc. **87**, 1838 (1965).
17. T. Nitta, E. Turek, R.A. Greenkorn, and K.C. Chao. A.I.Ch.E. J. **23**, 144 (1977).
18. N.F. Carnahan and K.E. Starling. J. Chem. Phys. **51**, 635 (1969).
19. D.E. Eckart, D.W. Arnold, R.A. Greenkorn, and K.C. Chao. A.I.Ch.E. J. **32**, 307 (1986).
20. H. Nakai, H. Soejima, R. Tamura, H. Ogawa, S. Murakami, and Y. Toshiyasu. Thermochim. Acta, **185**, 15 (1991).
21. T. Treszczanowicz, G.C. Benson, and B.C. Y.-Lu. Thermochim. Acta, **168**, 95 (1990).

Can. J. Chem. Downloaded from www.nrcresearchpress.com by 195.246.54.202 on 09/08/12
For personal use only.

Molecular recognition XIV.[1] Monte Carlo simulation of the hydration of the combining site of a Lectin[2]

H. BEIERBECK,[3] L.T.J. DELBAERE,[4] M. VANDONSELAAR,[4] AND R.U. LEMIEUX[5]

Department of Chemistry, University of Alberta, Edmonton, AB T6G 2G2, Canada

Received February 3, 1993[6]

H. BEIERBECK, L.T.J. DELBAERE, M. VANDONSELAAR, and R.U. LEMIEUX. Can. J. Chem. **72**, 463 (1994).

Monte Carlo simulations of the hydration of the combining sites of the divalent lectin IV of *Griffonia simplicifolia* were carried out using the X-ray structure of the native lectin at 2.15 Å resolution. The regions of the combining sites are identical shallow polyamphiphilic cavities with a surface area of approximately 240 Å^2 and an average depth of only about 2.2 Å. To reduce the CPU time requirements for Monte Carlo simulations of the hydration of the combining site of the native lectin, a fragment of the protein structure was examined that contained only 62 of the 243 amino acid residues and was present in both of the two subunits of the protein. This portion of the lectin, which encompassed the combining site and its immediate surroundings, was examined, employing 250 water molecules to near symmetrically cover an area of about 370 Å^2 over and about the combining site with a density of 1 at 300 K. As was previously found in similar studies of the hydration of the Lewis b tetrasaccharide, the nonpolar regions are much less densely hydrated than the adjacent polar regions. This situation is considered to arise because of the hydrogen-bonding requirement for water molecules to bridge over nonpolar regions of varying dimensions. It is expected, therefore, that the association of complementary hydrophilic surfaces in aqueous solution must involve, in addition to the establishment of the usual intermolecular forces of attraction, a collapse of water structure over "flickering cavities" for return to bulk. This collapse can be expected to contribute to the driving force for association both through a decrease in enthalpy (higher density) and through an increase in entropy (greater disorder). This property of hydrated polyamphiphilic surfaces may contribute importantly to the driving force of all associations in aqueous solution since virtually all organic molecules are polyamphiphilic in character.

H. BEIERBECK, L.T.J. DELBAERE, M. VANDONSELAAR et R.U. LEMIEUX. Can. J. Chem. **72**, 463 (1994).

On a effectué des simulations de Monte Carlo sur l'hydratation de sites de combinaison de la lectine bivalente IV du *Griffonia simplicifolia* en utilisant la structure cristalline déterminée à une résolution de 2,15 Å par diffraction des rayons X de la lectine naturelle. Les régions des sites de combinaison sont des cavités polyamphiphiles identiques peu profondes d'une superficie d'environ 240 Å^2 et d'une profondeur moyenne d'environ 2,2 Å. Dans le but de réduire le temps d'ordinateur requis pour les simulations de Monte Carlo de l'hydratation du site de combinaison de la lectine naturelle, on a examiné un fragment de la structure de la protéine qui ne contenait que 62 des 243 résidus d'acides aminés mais qui est présent dans les deux sous-unités de la protéine. On a examiné cette portion de la lectine, qui comprend le site de combinaison et ses environs immédiats, en employant 250 molécules d'eau conduisant à une couverture pratiquement symétrique d'une surface d'environ 370 Å^2 au-dessus et autour du site de combinaison, avec une densité de 1 à 300 K. Comme on l'a observé dans des études similaires antérieures sur l'hydratation du tétrasaccharide b de Lewis, les régions non polaires sont moins hydratées que les régions polaires adjacentes. On considère que la situation découle des nécessités des liaisons hydrogènes des molécules d'eau qui doivent créer des ponts de dimensions diverses au-dessus des régions non polaires. On suppose donc que, dans une solution aqueuse, l'association de surfaces hydrophiles complémentaires doit impliquer, en plus de la création des forces intermoléculaires d'attraction, une désintégration de la structure de l'eau au-dessus « des cavités vacillantes P» et son retour vers l'ensemble de la solution. On peut s'attendre à ce que cette désintégration contribue à la force motrice aidant à l'association par le biais d'une diminution de l'enthalpie (plus grande densité) et d'une augmentation de l'entropie (plus grand désordre). Il est possible que cette propriété des surfaces polyamphiphiles hydratées contribue d'une façon importante à la force motrice de toutes les associations en solutions aqueuses puisque pratiquement toutes les molécules organiques possèdent un caractère polyamphiphile.

[Traduit par la rédaction]

Introduction

In the course of our studies of the recognition of oligosaccharides by antibodies and lectins (1), we became convinced that hydration effects should not be neglected in attempts to understand why molecular associations occur in aqueous media. Of course, the importance of changes in the interaction energies between water molecules in causing the association of nonpolar surfaces has long been appreciated. However, the classical hydrophobic effect (2) cannot be invoked to account for the noncovalent binding of highly hydrophilic surfaces in aqueous solution, as we have now established for the association of several oligosaccharides by proteins (3–6).

The polar interactions established between complementary, polyamphiphilic surfaces (4) provided by an oligosaccharide and the combining site of a protein are attractive and surely contribute importantly to the specificity of the recognition (1). However, these attractive polar forces are not necessarily of prime importance to the stability of the complex. This can arise should the difference between the energy of interaction of the two complementary surfaces with water (in large excess) prior to complexation be greater than the interaction between these surfaces once the complex has formed. To our knowledge, this possibility has not previously received quantitative analysis in the context of a model that represents a real situation. This is why we undertook computer simulations of hydration by Monte Carlo methods of a structually well-defined oligosaccharide, a lectin with a specific affinity for the oligosaccharide and the oligosaccharide–lectin complex that is formed.

[1]For Part XIII, see ref. 31.

[2]Presented in part at the 202nd National Meeting of the American Chemical Society, New York, N.Y., August 25–30, 1991.

[3]Research Associate, 1985–present.

[4]Department of Biochemistry, University of Saskatchewan, Saskatoon, SK S7N 0W0, Canada.

[5]Author to whom correspondence may be addressed. Telephone: 403-492-3599. FAX: 403-492-8231.

[6]Revision received October 7, 1993.

Can. J. Chem. Downloaded from www.nrcresearchpress.com by 195.246.54.202 on 09/08/12
For personal use only.

Can. J. Chem. Downloaded from www.nrcresearchpress.com by 195.246.54.202 on 09/08/12
For personal use only.

The system used as a model is the association of the lectin, termed GS-IV, which is readily isolated (7) from the plant *Griffonia simplicifolia*, and a tetrasaccharide, termed Le^b-OMe, which corresponds in structure to the Lewis b human blood group determinant (8). The calculations reported in this communication were achieved using the X-ray structures for the native lectin at 2.15 Å resolution. Although the structures are now known at 2.0 Å resolution (9), the calculations were not repeated since the very small differences do not influence the conclusions reached in this initial study. A detailed description of Monte Carlo methods used to examine the hydration of Le^b-OMe has already been reported (10). As in the present study, the energies of interaction between the receptor and water and between water molecules were evaluated with Clementi's potentials (11–13).

The lectin GS-IV is a metalloglycoprotein that consists of two largely homologous subunits, each of which binds one molecule of Le^b-OMe in identical combining sites (14). A correspondence of the crystal structure of the complex with that in solution emerged from a comparison of the binding potencies of Le^b-OMe and selectively deoxygenated and *O*-methylated derivatives (15). Furthermore, the structure of Le^b-OMe in the crystalline complex (9, 15) is in close agreement with the solution conformational preference predicted by HSEA calculations and confirmed by ^1H nmr spectroscopy (16, 17). We were further encouraged to embark on the Monte Carlo simulations by the observation that the X-ray structures of the amino acid residues that form the combining site in the native GS-IV are virtually superimposable on their positions in the complex (see Fig. 2C) (9).

As mentioned above, we have reported the results of Monte Carlo simulations of the hydration of Le^b-OMe (10). There were significant differences in the interactions of the hydrophilic and hydrophobic surface areas with water. The hydrophilic groups were found to be tightly solvated and the water dipoles strongly aligned around polar substituents. In contrast, the hydrophobic surfaces were much more weakly solvated. The inner water shell was on average about 1 Å farther away from the ligand, and there was no correlation whatever between the orientation of the water dipoles and solute surface features. This picture supported earlier expectations (1) that the filling of voids present in a layer of perturbed water molecules at the surface of polyamphiphilic surfaces provides an important driving force for association.

That such changes in water structure can play an important role in the overall driving force for association is well demonstrated by the results we obtained on probing the combining site of Le^b-OMe with monodeoxy derivatives of the ligand (3, 15). The effect on binding could only be measured when, in the complex, the affected hydroxyl group was at or near the periphery of the combining site. In all cases the differential change in entropy was small because of enthalpy–entropy compensation. However, differential changes in enthalpy as high as 6 kcal/mol result from differences in the hydration shells over the small areas affected by the deoxygenation (3). In the case of an association involving the large surfaces from which water must be expelled to bulk, much larger changes involving water must occur that favor complex formation. The main purpose of this communication is to document in detail the molecular association that was chosen for study and to describe how the Monte Carlo method was used to simulate the hydration of the protein surface that provides the combining site. The preliminary results are seen to provide qualitative support for the expectation responsible for the project: namely, that the association of hydrophilic species is driven in part by a decrease in the exposure to water of polyamphiphilic surfaces.

TABLE 1. The 62 amino acid residues about and including the combining sites of the $(Le^b\text{-OMe})^2$-GS-IV complex used in the present calculations[a]

Positions from the *N*-terminus	Amino acids
27	D
38–39	KP
46–52	PV***RS***SAG
84–91	GAPTA***D***GL
102–118	VK*DYGGF*LGLFR*H*ETAA
129	E
131–142	DT*WINKDW*NDPP
144–145	PH
153–154	IV
167	Y
218–226	SAGV*GY*DEV

[a]Those residues in italics are in van der Waals contact with the ligand. Those in bold italics are hydrogen bonded to Le^b-OMe.

Methods

The Monte Carlo method published by Metropolis et al. (18) was applied as previously reported for the hydration of Le^b-OMe (10). For the Monte Carlo simulation of GS-IV, the lectin was represented by a model comprised of 62 of the 243 amino acid residues of one subunit. These residues, listed in Table 1, were chosen on the basis of their distances from Le^b-OMe in the crystal structure of the complex and are not necessarily contiguous. This model for the protein is small enough to permit simulations at acceptable CPU times and large enough to accommodate at least three layers of water around the combining site, which is at the centre of the model and herein referred to as the receptor. N-terminal residues were converted to amines and C-terminal residues to amides, in order to minimize the structural changes resulting from cutting the peptide chain. All Asp, Glu, Lys, and Arg side chains were assumed to be electrically charged. The X-ray coordinates for the native GS-IV lectin (Fig. 2B) and its complex with Le^b-OMe (Fig. 2A) at 2.15 Å resolution were used throughout the calculations.

It was necessary to establish an enclosure for 250 water molecules on top and around the combining site with the dimensions along the x and y axes of sufficient length to provide at least three water molecules beyond the periphery of the site. The first step was to set the vector from the center of mass of the protein fragment in the complex to the center of mass of the ligand as the z-axis of a Cartesian coordinate system. The complex was then replaced by the native lectin by least-squares superposition (Fig. 2C). The water enclosure was then built on and above the orientation thus achieved for the combining site of the native lectin.

The cross section of the box on the lectin fragment is 21.0×17.6 Å. The final dimension of the box was established in two steps. The top of the box was first set arbitrarily and the volume of the box, so defined, determined. The surface of the protein inside the box was defined, following Connolly (19), by rolling a sphere of 1.5 Å radius over the lectin fragment so that distances from the top of the box could be determined. The top of the box was then divided into a grid of equal areas that were about 0.1×0.1 Å. The distances of the centers of these grid

TABLE 2. Class assignments for the atoms in the residues listed in Table 1, for the evaluation of the receptor–water interaction energies[a]

Class designation	Substitution pattern
H01	Methyl group hydrogens
H12	α-Hydrogens
H13	Hydrogens on secondary and tertiary sp^3 carbons
H14	Hydrogens on sp^2 carbons
H18	Hydroxyl group hydrogens
H21	H_2-N hydrogens on N-terminal residues
H22	H_2N hydrogens of C-terminal residues and side chain amides
H23	H-N hydrogens of peptide bonds
H24	H-N(sp^2) hydrogens in *His, Trp*
H28[b]	H-N hydrogens of charged *Arg* and *Lys* side chains
C01	Methyl group carbons
C13	Secondary and tertiary sp^3 carbons
C14	NH_3^+-bearing carbon of *Lys*
C15	Alcoholic sp^2 and sp^3 carbons
C16	Carbon in C-terminal and side chain amides and C_ζ of *Arg*
C17	α-Carbons of peptide bonds
C18	Hydrogen-bearing sp^2 carbons
C19	C_γ, $C_{\delta 2}$, and $C_{\varepsilon 1}$ in *His*, C_γ and $C_{\delta 1}$ in *Trp*
C22	C_γ in *Phe* and *Tyr*, $C_{\delta 2}$ in *Trp*
C24	$C_{\varepsilon 2}$ in *Trp*
C28	Amide carbons in peptide bonds
C34[b]	Carboxylate carbons
N01	Nitrogen in C-terminal amides
N02	Nitrogen in N-terminal amino acids
N04	Nitrogen in peptide bonds
N05	$N_{\delta 1}$ in *His*
N06	$N_{\varepsilon 2}$ in *His*, $N_{\varepsilon 1}$ in *Trp*
N10[b]	*Arg* side chain nitrogen
N11[b]	*Lys* side chain nitrogen
O03	Oxygen in hydroxyl groups
O07	Oxygen in side chain amides
O08	Oxygen of peptide bonds and C-terminal amides
O17[b]	Carboxylate oxygen

[a]Class definitions and enery parameters taken from ref. 11, unless indicated otherwise (see footnote *b*).
[b]Class definitions and energy parameters taken from ref. 12.

squares from the surface of the protein were then summed up and multiplied by the area of the grid square to provide the volume of the box. The height of the box was then adjusted to provide the volume that would be occupied by 250 water molecules at a density of one.

Following the procedure developed by Metropolis et al. (18), in order to avoid the water interfacing with void, the box was surrounded in the *x*, *y* plane by eight boxes of identical dimensions and water contents. This 3×3 array was then topped by inverting the water coordinates in the bottom layer through the center of the top face of the original box. The internuclear distances used in the energy calculations were the distances from the water molecules in the original box to the receptor atoms in the same box and to the closest of the 18 images of each of the other water molecules in the original box.

The energies of interaction between the receptor and water and between water molecules were evaluated with Clementi's potentials (11–13), as previously described for the hydration of Le^b-OMe (10). The class assignments are shown in Table 2.

All simulations were carried out on a model consisting of one receptor and 250 water molecules at 300 K and unit water density. Each simulation consisted of 1000 equilibration and 5000 sampling cycles, starting from randomly positioned and oriented water molecules. In each cycle every water molecule was tentatively moved once, in a different random sequence and in random translational and rotational steps of maximally 0.1 Å and 0.1 radians along and around the three coordinate axes. The water coordinates after every tenth sampling cycle were stored in a file for later analysis. The convergence toward equilibrium of calculated energies of interaction is plotted in Fig. 3.

The energy and density plots of Figs. 4 and 5 were established by moving a 4 Å thick cross section of the water-accessible space above the combining site down through the box in 0.5 Å steps. The cuts through the hydration shell were either straight and parallel to the box top or followed the contours of the receptor surface, which was again defined by a probe sphere of 1.5 Å radius. The weight used in the density evaluations (Fig. 5) was the sum of the masses of all nuclei falling into any given volume slice.

The calculations were carried out on a Cray X-MP computer at the Ontario Center for Large Scale Computing and on Convex 210 and IBM RS/6000 model 560 computers at the University of Alberta.[7]

[7]A copy of the computer programs may be purchased from: The Depository of Unpublished Data. Document Delivery, CISTI, National Research Council Canada, Ottawa, Canada K1A 0S2.

Can. J. Chem. Downloaded from www.nrcresearchpress.com by 195.246.54.202 on 09/08/12
For personal use only.

Can. J. Chem. Downloaded from www.nrcresearchpress.com by 195.246.54.202 on 09/08/12
For personal use only.

Discussion and results

Water is a unique liquid of crucial importance to life. Accordingly, hydration phenomena have received enormous attention. A series of comprehensive treatises of the more physical and chemical aspects of the subject, edited by Franks (20), review the developments up to 1981. These monumental efforts together with the publication (21) of the proceedings of a conference on the biophysics of water, held in 1981, remain highly pertinent. The subject is still under intensive investigation as evidenced by the search for a realistic view of the hydrophobic effect presented by Muller (22) in 1990 and the simple two-structure model for liquid water published by Benson and Siebert (23) in 1992. Nevertheless, the results of our investigations of the recognition of oligosaccharides by proteins are not well accommodated by prevailing notions on the subject, which largely focus on entropy barriers (24, 25) and the energies of interaction between groups at the complementary surfaces that interact to form the complex.

Franks (26) has suggested, "... if a sugar molecule is introduced into water, the ease of forming sugar–water hydrogen bonds will depend to a large extent on the spacings and orientations of the polar groups relative to the -OH geometry in water." Such considerations have led to an emphasis on how water may affect the molecular conformation of the presumed conformationally highly flexible reactants — either the protein (24) or the oligosaccharide (25). On the other hand, a great deal of evidence based on nuclear magnetic resonance has accumulated that the naturally abundant sugars and their glycosides show marked conformational preferences in aqueous solution. This characteristic is particularly evident for branched oligosaccharide structures (6, 27). Recently, Galema and Høiland (28) reported partial molar compressibilities for a variety of mono- and disaccharides. The results appear to indicate a dependence on how well the carbohydrate fits the presumed three-dimensional hydrogen-bonded structure of water. However, as recently reiterated by Benson and Siebert (23), water is a "structural" liquid because the molecules are held together by strong oriented polar forces, usually hydrogen bonds. Random network models are normally envisaged that lead, as suggested in 1957 by Frank and Wen (29), to highly transient well-defined clusters of water molecules of lower entropy than average for the system but with stronger than average hydrogen bonds. These structural fluctuations (flickering clusters) (29) do not allow water molecules to fill space well and voids are expected. For similar reasons, it was thought that water must have difficulty in filling the space over polyamphiphilic surfaces (3, 6) and this expectation found support in Monte Carlo simulations of the water structure at 300 K over the surface of the tetrasaccharide displayed in Fig. 1 (10). These calculations infer a random connectivity in that all the possible hydrogen bonds exist between structurally rigid molecules with some so stretched and bent as to be essentially broken. The potential functions used in the Monte Carlo calculations, to be discussed below, encompass all the forces often invoked in discussions of this type such as dispersion (van der Waals) forces, polar interactions, and hydrogen bonds. Thus, in view of the great complexity in a system employing 250 water molecules interacting over 62 amino acid residues, a number of simplifying assumptions had to be made. Nevertheless, the picture that evolved is expected to be of real significance to the appreciation of the role of water in biological associations and, thereby, of major heuristic value.

The X-ray crystal structure of a portion of the GS-IV (Le^b-OMe)$_2$ complex at 2.15 Å resolution involving 62 amino acid residues is displayed in Fig. 2A where the five hydroxyl groups that remain in contact with water are identified (see Fig. 1) (15). The corresponding 2.15 Å X-ray crystal structure of the native GS-IV is presented in Fig. 2B where five of the amino acid residues that form hydrogen bonds with Le^b-OMe (see Fig. 1) are identified. The region of the combining site is seen to be a shallow polyamphiphilic cavity with a surface area of approximately 240 Å^2 and average depth of about 2.2 Å. In Fig. 2C, the Le^b-OMe was removed from the complex (Fig. 2A) to leave the 62 amino acid residues in and about the combining site. Selected atoms at the periphery are displayed in yellow. These atoms are superimposed on top of the corresponding atoms of the native lectin (Fig. 2B), which are displayed in red. The purpose of this figure is to demonstrate that there occur only slight adjustments of the protein structure in the course of complex formation. Likely, little energy separates these two conformers and the range of fluctuation is small. Therefore, it is expected that the results obtained in the Monte Carlo simulation of the hydration of the native lectin will be well representative of the hydration clusters about all conformers at thermal equilibrium (300 K).

Figures 2D, 2E, and 2F display the water structure that was randomly built at 300 K over the receptor portion of the native lectin, which contains the combining site (Fig. 2B), and that

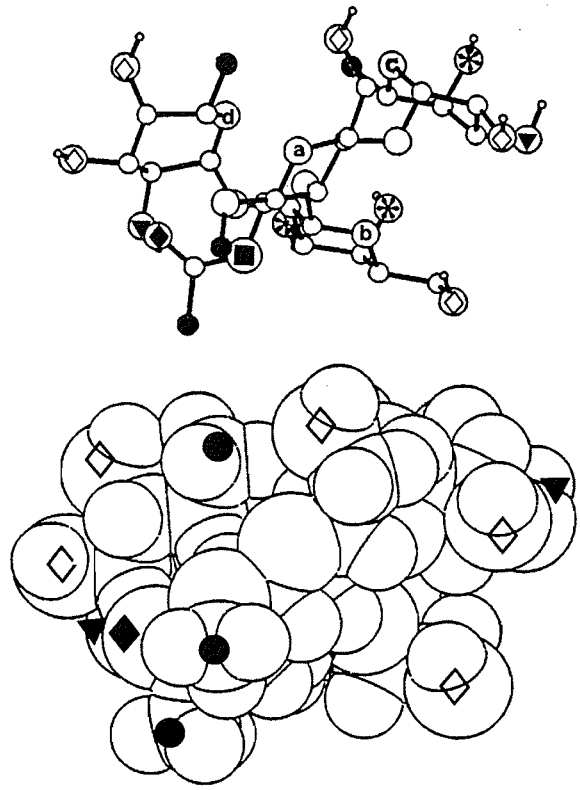

FIG. 1. Stick and CPK models of the Le^b-OMe tetrasaccharide, α-L-Fuc(1d → 2b)-β-D-Gal(1b → 3a)-[α-L-Fuc(1c → 4a)]-β-D-GlcNAc-OMe, as viewed in Fig. 2A in the complex with the lectin GS-IV. The ring oxygen atoms of the four sugar units are identified with the letters a, b, c, and d, ★ identifies the three key hydroxyl groups, ▼ identifies the two hydroxyl groups that are hydrogen bonded to the protein near the periphery of the combining site, ◇ identifies the five hydroxyl groups that remain in contact with the water, ◆ identifies the carbonyl oxygen of the acetamide group, and ● refers to methyl groups.

Can. J. Chem. Downloaded from www.nrcresearchpress.com by 195.246.54.202 on 09/08/12
For personal use only.

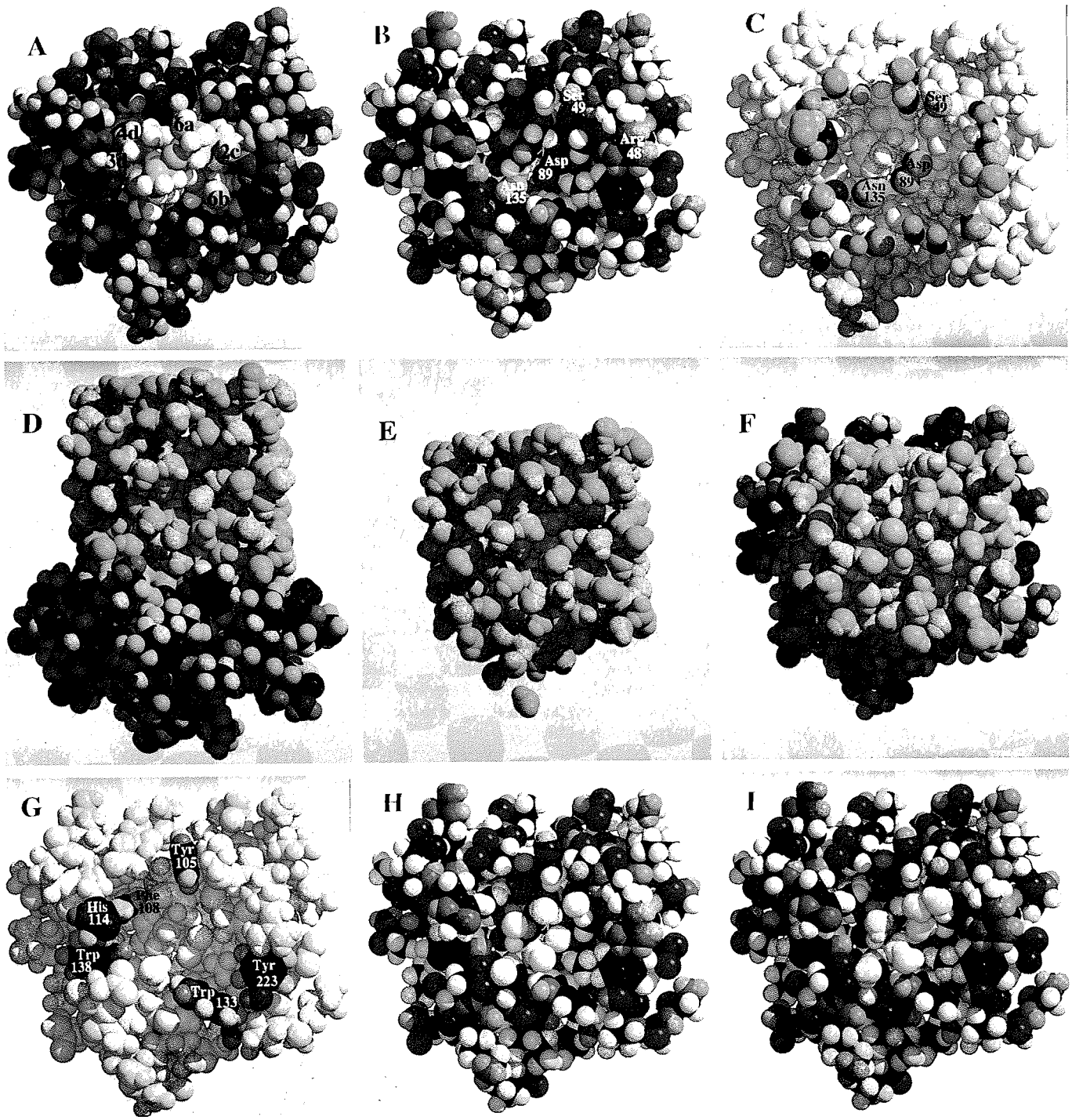

FIG. 2. CPK representations of the models used in the Monte Carlo simulations of the hydration of the combining site of the fourth lectin of *Griffonia simplicifolia* (GS-IV). A. X-ray structure at 2.15 Å resolution of the complex between GS-IV (dark colours) and Le^b-OMe (light colours). The five labelled hydroxyl groups of Le^b-OMe remain in contact with water. The combining site is represented in the simulations by 62 of the 243 residues of one of the two GS-IV subunits. B. X-ray structure at 2.15 Å of the same 62 residues in native GS-IV, shown in the same orientation as the complex in Fig. 2A. The labelled GS-IV residues are hydrogen bonded to hydroxyl groups 3b, 4b, and 4c of Le^b-OMe. All Monte Carlo simulations were carried out with this fragment. C. Structure of native GS-IV, as shown in Fig. 2B. Atoms that are hydrogen bonded to Le^b-OMe and atoms on the periphery of the combining site, i.e., in contact with both Le^b-OMe and water, are highlighted in red. The corresponding atoms in the GS-IV complex are superimposed in yellow. D. Side view of the 62 residues of GS-IV shown in Fig. 2B, covered by a block of 250 water molecules at the end of a typical Monte Carlo run at unit density and 300 K. The block of water in this figure and in Figs. 2E and 2F has a cross section of about 21.0 × 17.6 Å and an average height of 20.2 Å. E. The block of water shown in Fig. 2D, without the GS-IV residues. F. Top view of the hydration cluster shown in Fig. 2D. G. The GS-IV residues shown in Fig. 2B with the aromatic residues encircling the combining site highlighted. H. The GS-IV residues shown in Fig. 2B, with the seven oxygen atoms of water molecules (light blue) in the combining site found by X-ray crystallography. I. Native GS-IV with those seven water molecules (light blue) in the cluster in Figs. 2D–2F that most closely reproduce the X-ray water oxygen coordinates in Fig. 2H. The standard deviation between the water oxygen coordinates in Figs. 2H and 2I was about 1.2 Å.

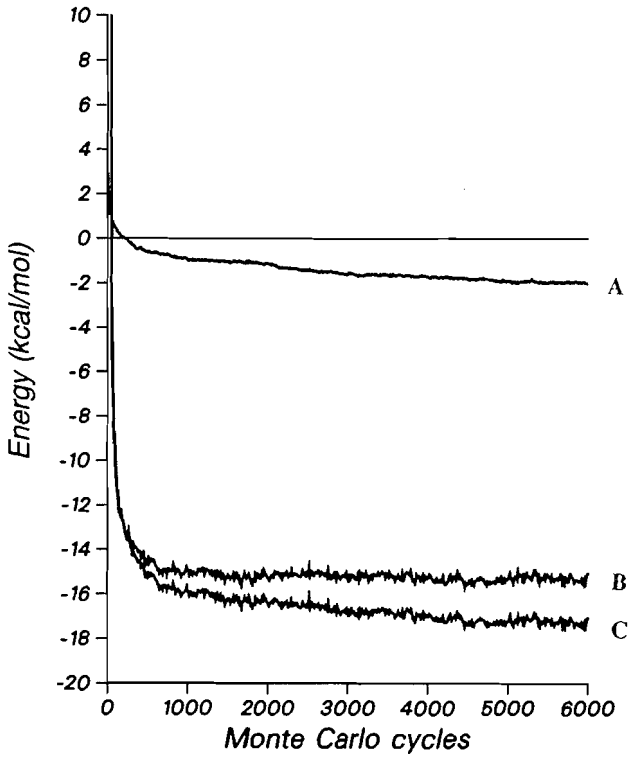

FIG. 3. The convergence toward equilibrium of calculated energies of interaction on extending the number of Monte Carlo cycles. A. The average energy of interaction between any one of the 250 molecules in the ensemble (Fig. 2D) and the amino acid residues (Fig. 2B). B. The average energy of interaction of a water molecule with the other water molecules in the system (Fig. 2E). C. The average energy of interaction between a water molecule and the other molecules in the ensemble (the sum of plots A and B).

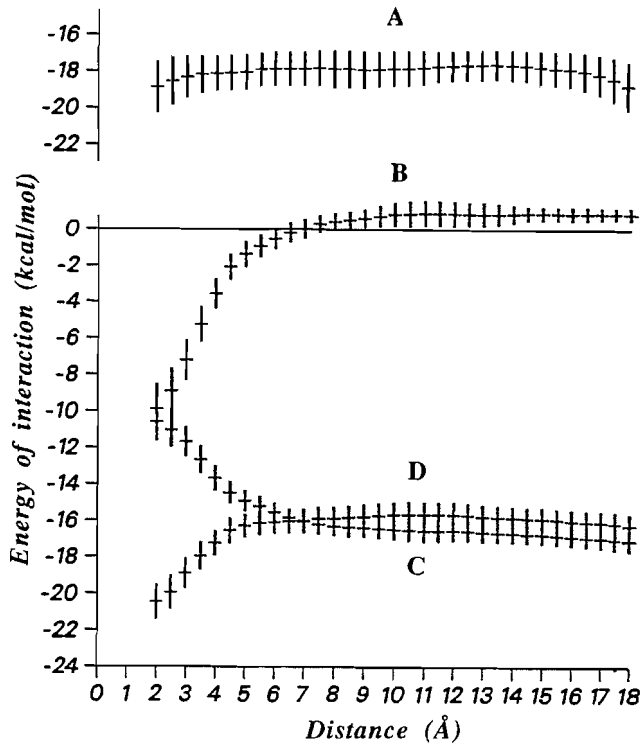

FIG. 4. Changes in energies of interaction with distance. A. Energies of interaction for a 21.0 × 17.6 × 20.2 Å rectangular block of 250 water molecules with initial density set at 1.0. B. Changes in water–receptor interaction energies with distance from the receptor surface. C. Changes in water–water interaction energies with distance from the receptor surface. D. Sum of curves B and C.

was brought to simulated thermal equilibrium by 6000 Monte Carlo cycles. The course of this equilibrium study is presented in Fig. 3. Plot B of this figure indicates that the energy of interaction between water molecules reaches a steady state after 1000 cycles. This is not quite the case for the energy of interaction with the protein, as seen in Fig. 3A. Nevertheless, the foregoing discussions are based on samplings in the range of 1000–6000 Monte Carlo cycles since to do so was compatible with the available CPU times. In view of the necessarily overall semiquantitative nature of this study, the drift in energy of interaction of only about 1 kcal/mol over the 1000–6000 Monte Carlo cycles is considered insignificant especially since, as we shall see, this represents only a small fraction of the actual energies of interaction that come into play.

That the Monte Carlo calculations simulate well the hydration of the protein is supported by the following observations. First of all, the simulation of bulk water provided results that are acceptable in terms of certain known physical properties of water. Calculation of the hydrogen bond strength for the interaction of two water molecules for which the nuclei of the oxygen and a hydrogen of one are colinear with the nucleus of the other provides a bond strength of 5.8 kcal/mol (13), in good agreement with the about 5.7 kcal/mol value that is commonly accepted (23). The water–water interaction energies plotted in Fig. 4 are average energies of interaction between any one of the water molecules and all the others. The average calculated energy gained on condensation (or required for vaporization) is half the estimated value (−18 kcal/mol), since the sum of the average water–water interaction energies counts every pairwise interaction twice. This −9 kcal/mol value is in fair agreement with the experimental heat of vaporization, 10.5 kcal/mol (23). The calculations find further support in the close resemblance of Figs. 2H and 2I. A number of strongly held water molecules were located in the crystal structure of the native GS-IV (Fig. 2B). Those present in the cavity of the combining site are displayed in Fig. 2H. It is seen that a very similar array of seven water molecules was produced by the Monte Carlo simulation and, as seen from plot B of Fig. 4, must be strongly held in place near the surface of the receptor. We conclude, therefore, that the Monte Carlo simulations likely provide a realistic semiquantitative appraisal of the interaction energies between the molecules in the ensemble.

As seen in Fig. 3, the hydration of the protein fragment reached thermal equilibrium after 1000 Monte Carlo cycles. It is seen (plot B) that the equilibrium energy of interaction between the water molecules reached a steady state near −15 kcal/mol. The interactions of the water molecules with the protein fragments nearly reached equilibrium after 1000 cycles with an interaction energy of approximately −1.0 kcal/mol. However, in this case, the energy of interaction, as indicated above, changed slowly to about −2 kcal/mol after 6000 cycles. This small increase in the strength of the interaction with increasing Monte Carlo cycles likely resulted from water molecules slowly penetrating the protein structure. The occurrence of this phenomenon, however, has no bearing on the goal for the investigation, which was to demonstrate the presence of a strongly perturbed layer of water at the surface of the combining site. That this is in fact the case is readily appreciated from

Can. J. Chem. Downloaded from www.nrcresearchpress.com by 195.246.54.202 on 09/08/12
For personal use only.

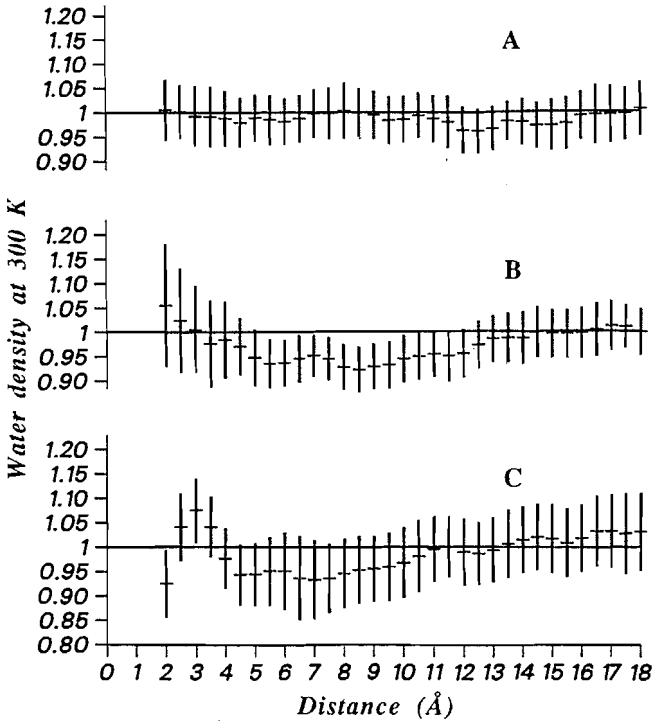

FIG. 5. Changes in density with distance for 4 Å cross sections of water structures averaged over 10 separate Monte Carlo runs taking samples every 50 cycles up to 5000 cycles in each run. A. Densities for a 21.0 × 17.6 × 20.2 Å rectangular block of 250 water molecules with initial density set at 1.0. B. Densities of the water structure displayed in Fig. 2D calculated in terms of straight cross sections. C. Same as in B except that the cross sections followed the contour of the combining site.

the slope of plot C in Fig. 4. It is seen that the energy of interaction between water molecules increases from about −10 kcal/mol to near −17 kcal/mol as the distance of the water molecules increases from 2 to 8 Å.

The plot in Fig. 4A indicates that our Monte Carlo simulation method assigns a value of close to −18 kcal/mol for the energy of interaction of water molecules in bulk. The averaging of the energies of interaction between water molecules near the protein surface with those approaching bulk conditions is responsible for the average interaction in Fig. 3B not reaching that for bulk water in the model used.

The structural changes revealed by the energy gradients (Fig. 4) are also reflected in density variations (Fig. 5). Near the receptor the density of the hydration shell is at a maximum. At intermediate distances the density goes through a minimum and at larger distances it approaches the density of bulk water. It is also noteworthy at this time that the strongly held water molecules of the first layer can be expected to be of lower entropy content than those in bulk water. Thus, their release on complex formation should counteract the increase in enthalpy required for dehydration of the receptor site. Furthermore, in a manner similar to the increases in entropy that arise from the release to bulk of the "flickering clusters" (29) of the hydrophobic effect, it can be expected that "flickering cavities" in the structure of water over polyamphiphilic surfaces also provide a favorable change in entropy. The next stage of this investigation will be Monte Carlo simulations of the actual association between Le^b-OMe and GS-IV.

We wish to emphasize that the interaction energies calculated are for only one energetically favorable conformer for each of the water, tetrasaccharide, and lectin molecules. The hydration of other conformers will surely not produce the same numerical values. However, we do not expect that our general conclusion will be radically changed. We consider, therefore, that the condensation of perturbed water molecules from polyamphiphilic surfaces will prove of broad involvement in the course of biological associations. This opinion appears supported by the thermodynamic data for polyphenol interactions with water recently reported by Dangles and Brouillard (30).

Acknowledgements

This research was supported by an operational grant to R.U.L. by the Natural Sciences and Engineering Research Council of Canada (A170). We thank the Supercomputer Allocation Committee of the University of Alberta for access to its computing facilities.

1. R.U. Lemieux. Chem. Soc. Rev. **18**, 347 (1989).
2. C. Tanford. The hydrophobic effect: formation of micelles and biological membranes. 2nd ed. John Wiley & Sons, Inc., New York. 1980.
3. R.U. Lemieux, L.T.J. Delbaere, H. Beierbeck, and U. Spohr. Ciba Found. Symp. **158**, 231 (1991).
4. U. Spohr, E. Paszkiewicz-Hnatiw, N. Morishima, and R.U. Lemieux. Can. J. Chem. **70**, 254 (1992).
5. R. Cromer, U. Spohr, D.P. Khare, J. LePendu, and R.U. Lemieux. Can. J. Chem. **70**, 1511 (1992).
6. R.U. Lemieux. ACS Symp. Ser. **519** (1993).
7. S. Shibata, I.J. Goldstein, and D.A. Baker. J. Biol. Chem. **257**, 9324 (1982).
8. U. Spohr, O. Hindsgaul, and R.U. Lemieux. Can. J. Chem. **63**, 2644 (1985).
9. L.T.J. Delbaere, M. Vandonselaar, L. Prasad, J.W. Quail, K.S. Wilson, and Z. Dauter. J. Mol. Biol. **230**, 950 (1993).
10. H. Beierbeck and R.U. Lemieux. Can. J. Chem. **68**, 820 (1990).
11. G. Corongiu and E. Clementi. Gazz. Chim. Ital. **108**, 273 (1978).
12. G. Ranghino, E. Clementi, and S. Romano. Biopolymers, **22**, 1449 (1983).
13. O. Matsuoka, E. Clementi, and M. Yoshimine. J. Chem. Phys. **64**, 1351 (1976).
14. L.T.J. Delbaere, M. Vandonselaar, L. Prasad, J.W. Quail, J.R. Pearlstone, M.R. Carpenter, L.B. Smillie, P.V. Nikrad, U. Spohr, and R.U. Lemieux. Can. J. Chem. **68**, 1116 (1990).
15. P.V. Nikrad, H. Beierbeck, and R.U. Lemieux. Can. J. Chem. **70**, 241 (1992).
16. H. Thøgersen, R.U. Lemieux, K. Bock, and B. Meyer. Can. J. Chem. **60**, 44 (1982).
17. R.U. Lemieux and K. Bock. Arch. Biochem. Biophys. **221**, 125 (1983).
18. N. Metropolis, A.W. Rosenbluth, M.N. Rosenbluth, A.H. Teller, and E. Teller. J. Chem. Phys. **21**, 1087 (1953).
19. M.L. Connolly. J. Appl. Crystallogr. **16** 548 (1983).
20. F. Franks (*Editor*). Water. A comprehensive treatise. Recent advances. Vol. 7. Plenum Press, New York. 1982.
21. F. Franks and S.F. Mathias (*Editors*). Biophysics of water. John Wiley & Sons, New York. 1982.
22. N. Muller. Acc. Chem. Res. **23**, 23 (1990).
23. S.W. Benson and E.D. Siebert. J. Am. Chem. Soc. **114**, 4269 (1992).
24. M.R. Eftink, A.C. Anusiem, and R.L. Biltonen. Biochemistry, **22**, 3884 (1983).
25. J.P. Carver, S.W. Micknick, A. Imberty, and D.A. Cumming. Ciba Found. Symp. **145**, 6 (1989).
26. F. Franks. Water. Royal Society of Chemistry, Burlington House, London. 1984. p. 56.
27. R.U. Lemieux. Explorations with sugars. How sweet it was. Pro-

Can. J. Chem. Downloaded from www.nrcresearchpress.com by 195.246.54.202 on 09/08/12
For personal use only.

files, pathways and dreams. Autobiographies of eminent chemists. Jeffrey I. Seeman, Series Editor. American Chemical Society, Washington, D.C. 1990. p. 99.
28. S.A. Galema and H. Høiland. J. Phys. Chem. **95**, 5321(1991).
29. H.S. Frank and W.-Y. Wen. Discuss. Faraday Soc. **24**, 133 (1957).
30. O. Dangles and R. Brouillard. Can. J. Chem. **70**, 2174 (1992).
31. R.U. Lemieux, M.-H. Du, U. Spohr, S. Acharya, and A. Surolia. Can. J. Chem. **72**, 158 (1994).

Can. J. Chem. Downloaded from www.nrcresearchpress.com by 195.246.54.202 on 09/08/12
For personal use only.

Gas and solution phase thermochemistry and transition energies of $NH_2^\bullet$ and $NH_3^{\bullet+}$, and their aquo complexes: an *ab initio* study

DAKE YU, ARVI RAUK,[1] AND DAVID A. ARMSTRONG[1]

Department of Chemistry, The University of Calgary, Calgary, AB T2N 1N4, Canada

Received May 5, 1993

This paper is dedicated to Professor John C. Polanyi on the occasion of his 65th birthday

DAKE YU, ARVI RAUK and DAVID A. ARMSTRONG. Can. J. Chem. **72**, 471 (1994).

Ab initio calculations were performed on several aquo complexes of $NH_2^\bullet$, and $NH_3^{\bullet+}$, and on monomeric parent species. The geometries were optimized at the HF/6-31+G* level and the vibrational frequencies were calculated. The total energies and the binding energies of complexes were evaluated at the MP2/6-31+G* + ZPE level of theory. Gas and aqueous solution phase thermodynamic properites of $NH_2^\bullet$ and $NH_3^{\bullet+}$ and several other species were calculated. The examination of solution phase properties of the radicals was facilitated by study of the structures and transition energies of aquo complexes. H-bonding interaction energies decreased in the order OH···N > OH···O > NH···O, but were generally stronger than σ–σ* interactions involving the unpaired electron. From calculations with the CIS method, the weak absorption observed at 520 nm for aqueous $NH_2^\bullet$ is confirmed as a $^2B_1 \rightarrow {}^2A_1$ transition, while the stronger $NH_2^\bullet$ absorption occurring below 250 nm and the absorption of $NH_3^{\bullet+}$, which rises monotonically below 370 nm, are attributed to solvent-to-solute charge transfer bands. The solution free energies and related E^0 values for $NH_2^\bullet$ and $NH_3^{\bullet+}$ are in agreement with those of Stanbury. The *ab initio* structure studies show that water protons are bound to N, and proton transfer from solvent in reaction [18], $NH_2^\bullet + e^- + H_2O \rightarrow NH_3 + OH^-$, is likely to be the dominant redox reaction of $NH_2^\bullet$ in alkaline solution. The free energy of solution of $NH_3^{\bullet+}$ is shown to be larger than that of NH_4^+.

DAKE YU, ARVI RAUK, et DAVID A. ARMSTRONG. Can. J. Chem. **72**, 471 (1994).

On a effectué des calculs *ab initio* sur plusieurs complexes aqueux du $NH_2^\bullet$ et $NH_3^{\bullet+}$ et sur les espèces monomères parentes. On a optimisé les géométries au niveau HF/6-31+G* et on a calculé les fréquences vibrationnelles. On a évalué les énergies totales et les énergies de liaison des complexes au niveau MP2/6-31+G*+ZPE de la théorie. On a calculé les propriétés thermodynamiques du $NH_2^\bullet$ et $NH_3^{\bullet+}$ et des plusieurs autres espèces en phase gazeuse et en solution. L'examen des propriétés des radicaux en solution a été rendu plus facile par l'étude des structures et des énergies de transition des complexes aqueux. Les énergies d'interaction des liaisons hydrogènes diminuent dans l'ordre OH···N > OH···O > NH···O; toutefois, elles sont généralement plus fortes que les interactions σ–σ* impliquant l'électron non apparié. Sur la base de calculs faisant appel à la méthode CIS, on peut confirmer que la faible absorption observée à 520 nm pour le $NH_2^\bullet$ aqueux est due à une transition $^2B_1 \rightarrow {}^2A_1$ alors que l'absorption plus forte du $NH_2^\bullet$ apparaissant en-dessous de 250 nm et celle du $NH_3^{\bullet+}$, qui augmente d'une façon monotone en-dessous de 370 nm, sont attribuées à des bandes de transfert de charge du soluté. Les énergies libres en solution et les valeurs de E^0 apparentées pour le $NH_2^\bullet$ et le $NH_3^{\bullet+}$ sont en accord avec celles de Stanbury. Les études de structures *ab initio* montrent que les protons de l'eau sont liés à l'azote et que le transfert de proton du solvant dans la réaction [18], $NH_2^\bullet + e^- + H_2O \rightarrow NH_3 + OH^-$, est probablement la réaction rédox la plus important du $NH_2^\bullet$ en solution alcaline. On montre que l'énergie libre de solution du $NH_3^{\bullet+}$ est plus importante que celle du NH_4^+.

[Traduit par la rédaction]

1. Introduction

The $NH_2^\bullet$ and $NH_3^{\bullet+}$ radicals, which can be formed by H atom or electron abstraction from ammonia, are of considerable importance in inorganic redox chemistry (1–3). They are also prototypes of the nitrogen-centered organic amino radicals that occur in numerous organic and biochemical systems (4, 5), and their reactions are of interest in corrosion chemistry (6). In aqueous solution, $NH_2^\bullet$ radicals can be made in reaction [1]

[1] $$Ti^{III} + NH_2OH \rightarrow Ti^{IV} + NH_2^\bullet + OH^-$$

or in pulse radiolysis by abstraction of H atoms from NH_3 with $OH^\bullet$ (7, 8)

[2] $$OH^\bullet + NH_3 \rightarrow H_2O + NH_2^\bullet$$

$NH_3^{\bullet+}$ cations can be made by photolysis of NH_3 complex ions (1, 9), e.g.,

[3] $$Co^{III}(NH_3)_6^{3+} + h\nu \rightarrow Co^{II}(NH_3)_5(NH_3^\bullet)^{3+}$$

I

[4] $$\mathbf{I} \rightarrow Co^{II}(NH_3)_5^{2+} + NH_3^{\bullet+}$$

[1]Authors to whom correspondence may be addressed.

Radicals produced by those methods have been examined by polarography (10, 11) and ESR (12, 13), and the kinetics of some of their reactions have been investigated by fast-reaction techniques (6–9, 13). Extensive gas phase investigations on the species have been conducted (14–16) and theoretical calculations on their energies and structures have been made at relatively high level (17).

Because of the very great interest in the reactions and properties of nitrogen-centered radicals in aqueous systems, we decided to examine the existing data on the gas phase structures and thermochemical properties of $NH^{\bullet-}$, $NH_2^\bullet$, and $NH_3^{\bullet+}$ and the related species shown in Scheme 1, in which the experimental and calculated (G2, in parentheses) values of enthalpy changes (14, 17) are given in kJ mol^{-1}.

We also used *ab initio* methods to investigate the aquo complexes of $NH_2^\bullet$ and $NH_3^{\bullet+}$. Here the objectives were to obtain an understanding of the interactions between the radicals and the H_2O solvent molecules, and to determine how the structures and energy levels of the nitrogen centers might be affected in these complexes. Three types of interaction have been considered: (a) H bonds of H_2O to the N lone pairs of the radicals, (b) H bonds of the $NH_x^\bullet$ radicals to lone pairs of H_2O, and (c) σ–σ* lone pair to unpaired electron interactions, as illustrated in Scheme 2.

Can. J. Chem. Downloaded from www.nrcresearchpress.com by 195.246.54.202 on 09/08/12
For personal use only.

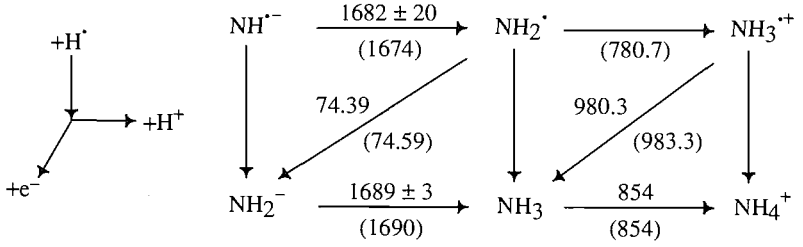

SCHEME 1

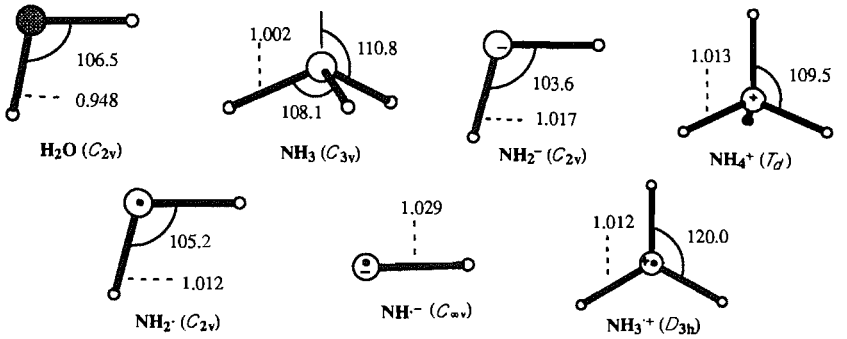

FIG. 1. HF/6-31+G* optimized structures of monomeric species. The filled balls stand for oxygen atoms, the open ones for nitrogen (large) and hydrogen (small). Bond lengths in Å and angles in degrees.

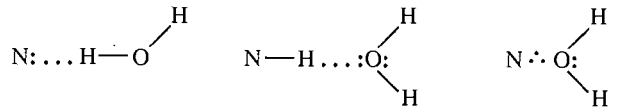

SCHEME 2

To the extent that it is important, the last type of interaction in particular would be expected to have a strong effect on the redox properties and absorption spectra of the radicals. Because of the possibility of radical–solute interactions in more concentrated ammonia solutions, we also examined the corresponding interactions between the radicals and NH_3 molecules.

The computational details are described in Sect. 2. The results of these computations are presented and discussed in Sect. 3. In Sect. 4, the results are used in a critical examination of the thermodynamic and redox properties, and the UV–visible absorption spectra of $NH_2^{\cdot}$ and $NH_3^{\cdot+}$ in aqueous solution. General conclusions are summarized in Sect. 5.

2. Computation details

Ab initio *calculations*

All *ab initio* calculations presented here were performed with the GAUSSIAN 90 molecular orbital packages (18). The geometries of the molecules were optimized at the HF level with the 6-31+G* basis set, which includes diffuse functions important for species with nonbonded electrons. Convergence of the geometry was to the limit imposed internally in GAUSSIAN 90. No symmetry was assumed at the beginning of each geometry optimization, but if the optimization ended with a nearly symmetric structure, the molecule's symmetry was verified. Vibrational frequencies were calculated to verify the character of all the structures as minima on the potential energy surfaces. The vibrational frequencies calculated at the HF/6-31+G* level were scaled by a factor of 0.89 (19) in considering the zero-point energy (ZPE) corrections and in the calculation of thermodynamic properties. Correlation corrections to the total energies were estimated by single-point calculations with the same basis set at the level of second-order Møller–Plesset perturbation theory (MP2). The energies and oscillator strengths of the lower electronically excited states were calculated using the all singles configuration interaction (CIS), as implemented in GAUSSIAN 90, with the same basis set. The CIS model is not expected to yield accurate excitation energies, but should correctly characterize the lower electronically excited states. For the complexes, the binding energies were defined as $E_b = E(\text{complex}) - \Sigma E(\text{fragment})$, where the E's are total electronic energies plus ZPE values of the species at the HF/6-31+G* optimized geometries. These binding energies were calculated using both the HF/6-31+G* and the MP2/6-31+G* energies. Overestimation of the binding energy because of basis set superposition effects is expected to be small (less than 3 kJ mol^{-1} on the basis of a previous study (20) on similar systems), and was not explicitly taken into account.

Thermodynamic properties

Ideal gas thermodynamic functions C_P^0, S^0, and $H^0 - H_0^0$ in the temperature range 0–298.15 K and at 1 bar (= 100 kPa) were calculated by standard statistical thermodynamic methods based on the rigid rotor – harmonic oscillator model. The lowest vibrational modes were treated as internal rotations. The barriers for the internal rotations around the hydrogen bonds are usually very low; therefore, the calculations were carried out using the free rotor model for such rotations. The values of S^0 and $H^0 - H_0^0$ for the reference elements are taken from ref. 21. The calculation of $\Delta_f H^0$ and $\Delta_f G^0$ values reliable to ±10 kJ mol^{-1} requires either the knowledge of $\Delta_f H_0^0$ from calculations at the G2 level (17) or an experimental value of $\Delta_f H^0$ of comparable or better reliability at at least one temperature. Values of $\Delta_f H^0$ were calculated for species where such results were available. The most reliable values of $\Delta_f H^0$ are used in conjunction with the entropy data to obtain $\Delta_f G^0$.

3. Computational results and discussion

The optimized geometries of the monomeric species and the complexes are plotted in Figs. 1 and 2, respectively. Ex-

Can. J. Chem. Downloaded from www.nrcresearchpress.com by 195.246.54.202 on 09/08/12
For personal use only.

Can. J. Chem. Downloaded from www.nrcresearchpress.com by 195.246.54.202 on 09/08/12
For personal use only.

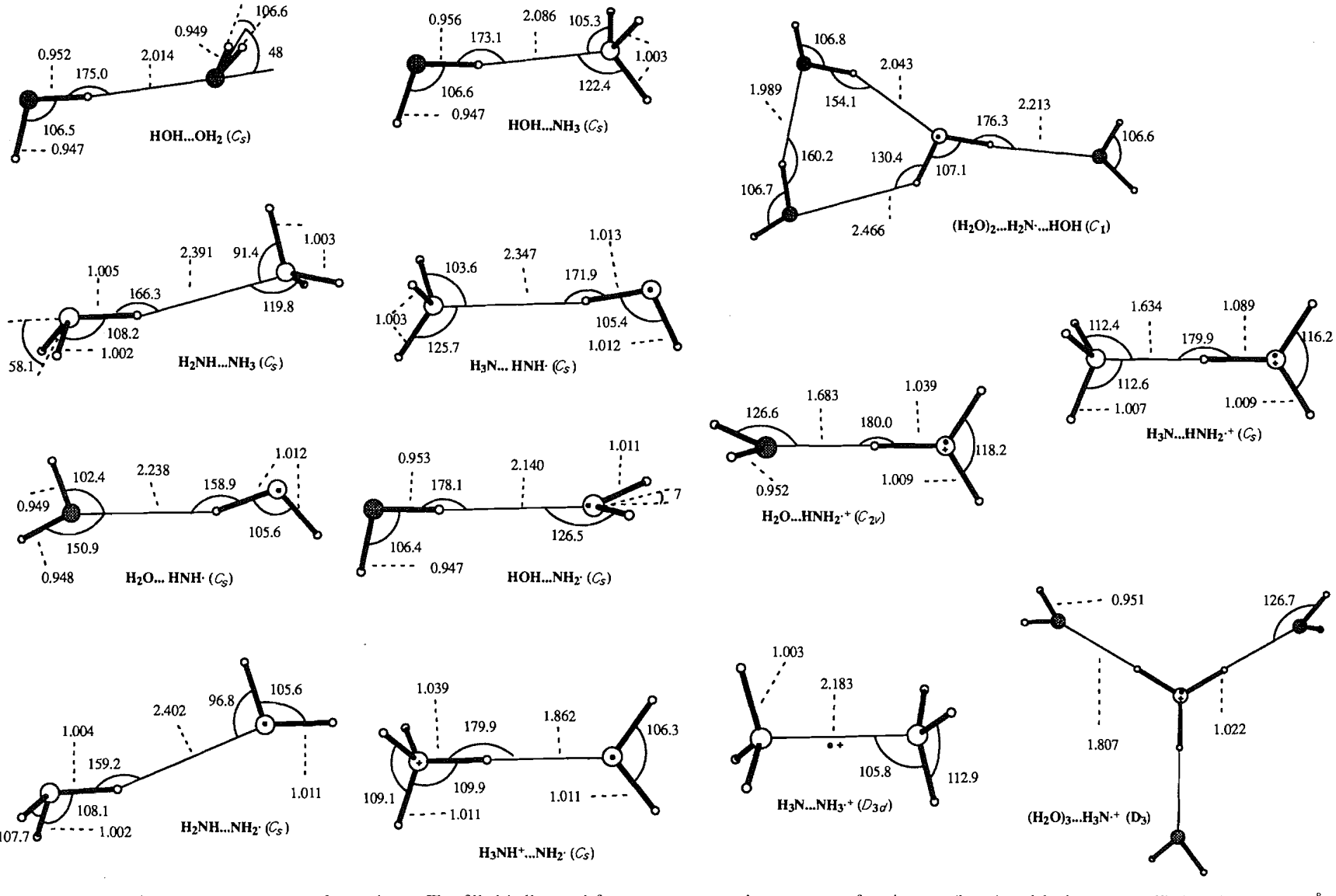

FIG. 2. HF/6-31+G* optimized structures of complexes. The filled balls stand for oxygen atoms, the open ones for nitrogen (large) and hydrogen (small). Bond lengths in Å and angles in degrees.

TABLE 1. Total electronic energy E and vibrational energy ZPE

	E(HF/6-31+G*)[a] (hartree)	ZPE[a] (kJ mol^{-1})	E(MP2/6-31+G*)[a] (hartree)	E(G2)[b] (hartree)
H_2O	−76.017743	60.2	−76.208740	−76.33205
NH_3	−56.189499	97.1	−56.362653	−56.45865
NH_2^-	−55.518083	52.0	−55.708053	−55.81743
NH_4^+	−56.531277	139.9	−56.700411	−56.78140
$NH_2^\bullet$	−55.560851	54.0	−55.696238	−55.78902
$NH^{\bullet -}$	−54.904372	20.1	−55.054080	−55.15319
$NH_3^{\bullet +}$	−55.873340	91.7	−56.004027	−56.08410
$HOH\cdots OH_2$	−152.044059	130.0	−152.428468	
$HOH\cdots NH_3$	−132.217299	167.2	−132.584513	
$H_2NH\cdots NH_3$	−112.383395	200.4	−112.731781	
$H_2O\cdots HNH^\bullet$	−131.583559	120.6	−131.911555	
$H_3N\cdots HNH^\bullet$	−111.756069	158.4	−112.066549	
$HOH\cdots NH_2^\bullet$	−131.587033	123.7	−131.915883	
$H_2NH\cdots NH_2^\bullet$	−111.754353	157.7	−112.064543	
$H_3NH^+\cdots NH_2^\bullet$	−112.125829	204.3	−112.434180	
$(H_2O)_2\cdots H_2N^\bullet\cdots HOH$	−283.641206	261.9	−284.357973	
$H_2O\cdots HNH_2^{\bullet +}$	−131.927847	161.6	−132.253253	−132.450892[c]
$H_3N\cdots HNH_2^{\bullet +}$	−112.107966	198.0	−112.418642	
$(H_2O)_3\cdots H_3N^{\bullet +}$	−284.021081	298.2	−284.733983	
H_3N–$NH_3^{\bullet +}$	−112.098287	205.8	−112.425527	

[a]Evaluated at HF/6-31+G* optimized geometries.
[b]From ref. 17 unless otherwise stated.
[c]From ref. 20.

Can. J. Chem. Downloaded from www.nrcresearchpress.com by 195.246.54.202 on 09/08/12
For personal use only.

cept for a few hydrogen atoms in $(H_2O)_2\cdots H_2N^\bullet\cdots HOH$ and $(H_2O)_3\cdots \boldsymbol{H}_3N^{\bullet +}$, the full geometries of the molecules can be determined from the listed characteristic parameters and the symmetry types. The formulae, total electronic energies, and ZPE values of the aquo complexes, which were found to be minima on the potential energy surfaces, and of the monomeric species are listed in Table 1, along with G2 energies for some of the species from other studies (17, 20). The vibrational frequencies are reported in Table 2. Gas phase thermodynamic data for the monomeric species and the complexes at 0–298.15 K have been given in Tables 3 and 4, according to whether the calculations of $\Delta_f H^0$ and $\Delta_f G^0$ were performed. The binding energies of the complexes are collected in Table 5.

Throughout the paper, three dots (···) have been used to separate complexed partners and proximity denotes the nature of the interaction. Thus $HOH\cdots NH_3$ denotes a complex between water and ammonia with an OH···N bond. The "isomeric" complex with an O···HN bond would be denoted as $H_2O\cdots HNH_2$. Where necessary for clarity, the hydrogen-bonded H atom is distinguished by bold italic font $\boldsymbol{H}$.

Monomeric species

The equilibrium structures of H_2O and NH_3 are well established and will not be discussed. However, it may be noted that the optimized geometries at the HF/6-31+G* level are reasonable compared with those of experiments (H_2O: expt. (21) HO = 0.9584 Å, < HOH = 104.45° and calcd. HO = 0.948 Å, < HOH = 106.5°; NH_3: expt. (21) HN = 1.0124 Å, < HNH = 106.67° and calcd. HN = 1.002 Å, < HNH = 108.1°).

The experimental geometries for NH_4^+ and $NH_2^\bullet$ are also available. For NH_4^+, calculated HN bond lengths are 0.01 Å shorter than the experimental value (expt. HN = 1.026 (22), 1.021±0.003 Å (23); calcd. 1.013 Å). For $NH_2^\bullet$ the calculated HN bonds are 0.01 Å shorter, while the HNH angle is larger by 2° than the experimental values (expt. (21) HN = 1.024 Å, < HNH = 103°, calcd. HN = 1.012 Å, < HNH = 105.2°). The optimized $NH_3^{\bullet +}$ has D_{3h} symmetry, with HN bond lengths identical to those in $NH_2^\bullet$.

The scaled (by a factor of 0.89) HF/6-31+G* vibrational frequencies obtained here for H_2O, 1599, 3623, and 3730 cm^{-1}, agree well with experimental values, 1595, 3657, and 3756 cm^{-1} (21). This was also true for NH_3 frequencies; calculated: 1039, 1644, 3292, and 3414 cm^{-1}; experimental (21): 950, 1627, 3336, and 3444 cm^{-1}, respectively. For NH_4^+, only the degenerate NH stretch frequencies have been measured (24), being 3343 cm^{-1} (calculated 3305 cm^{-1}). The calculated frequencies of $NH_2^\bullet$ (1502, 3220, and 3311 cm^{-1}) also show good agreement with the measured (21) ones (1499, 3173, and 3220 cm^{-1}).

The ideal gas thermodynamic properties at 298.15 K can be compared with the available experimental results, which are given in Table 3. For the values of C_p^0, S^0, and $H_0 - H_0^0$, which are used in the calculations of $\Delta_f H^0$ and $\Delta_f G^0$ at different temperatures in columns six, seven, and eight, the agreement is excellent. The agreement between the values of $\Delta_f H^0$ derived from G2 energies (column six) and the most reliable experimental values (column seven, bold font) is also good. Given that the values of NH_3 and $NH_2^\bullet$ are the best known (16), the experimental values of $\Delta_f H^0$ for the other species in column seven of Table 3 were checked from the enthalpy of reaction for the processes in Scheme 1. It may be noted that in most instances this confirmed the values reported in ref. 14 as being the most reliable.

Enthalpies of ionization and proton affinities at 298.15 K were calculated from the G2 energies of ref. 17, using the $H^0 - H_0^0$ data in Table 3. These are presented in Scheme 1, along with available experimental data, which were also corrected to 298.15 K where necessary. As previously observed

Can. J. Chem. Downloaded from www.nrcresearchpress.com by 195.246.54.202 on 09/08/12
For personal use only.

TABLE 2. HF/6-31+G* vibrational frequencies (cm^{-1})

H_2O	1797	4071	4191						
NH_3	1168	1847	1847	3699	3836	3836			
NH_2^-	1663	3481	3555						
NH_4^+	1634	1634	1634	1883	1883	3576	3713	3713	3713
$NH_2^\bullet$	1688	3619	3720						
$NH^{\bullet -}$	3365								
$NH_3^{\bullet +}$	892	1667	1667	3571	3770	3770			
$HOH\cdots OH_2$	145	146	166	187	362	649	1806	1826	4028
	4068	4165	4181						
$HOH\cdots NH_3$	34	165	192	1944	437	707	1239	1839	1842
	1845	3696	3827	3892	3958	4154			
$N_2NH\cdots NH_3$	13	100	112	128	247	392	1205	1214	1841
	1847	1850	1876	3681	3696	3815	3825	3828	3830
$H_2O\cdots HNH^\bullet$	55	70	125	141	316	330	1708	1803	3626
	3731	4068	4184						
$H_3N\cdots HNH^\bullet$	25	111	142	154	318	437	1220	1717	1845
	1846	3607	3695	3710	3826	3828			
$HOH\cdots NH_2^\bullet$	29	147	168	218	429	603	1694	1829	3641
	3743	4013	4162						
$H_2NH\cdots NH_2^\bullet$	54	95	124	128	292	347	1204	1693	1846
	1869	3628	3691	3730	3828	3828			
$H_3NH^+\cdots NH_2^\bullet$	2	273	297	323	451	600	1597	1680	1686
	1710	1902	1907	3185	3641	3659	3745	3745	3755
$(H_2O)_2\cdots H_2N^\bullet\cdots HOH$	27	31	37	77	111	115	131	168	185
	201	231	273	338	367	413	516	688	812
	1719	1802	1831	1846	3645	3751	3924	3985	4069
	4152	4159	4184						
$H_2O\cdots HNH_2^{\bullet +}$	89	283	306	333	361	558	1079	1658	1697
	1821	3180	3689	3804	4031	4128			
$H_3N\cdots HNH_2^{\bullet +}$	2	288	375	431	613	640	1266	1431	1600
	1761	1838	1842	2285	3669	3681	3783	3783	3803
$(H_2O)_3\cdots H_3N^{\bullet +}$	43	43	52	52	72	72	195	280	280
	286	308	308	344	344	368	500	603	603
	1148	1718	1718	1820	1820	1820	3400	3542	3542
	4046	4046	4047	4047	4147	4147			
$H_3N\cdots NH_3^{\bullet +}$	82	431	448	559	560	602	602	1204	1765
	1765	1781	1782	3679	3698	3861	3861	3862	3862

(25, 26), agreement is good to within a few kJ mol^{-1} in all cases where comparison is possible. For NH_2^- the experimental proton affinity leads to $\Delta_f H^0 = 114.6$ kJ mol^{-1} at 298 K, while the more recent and precise (±0.5 kJ mol^{-1} (15)) electron attachment enthalpy of $NH_2^\bullet$ yields 112.8 kJ mol^{-1}. The value adopted is 113.0 kJ mol^{-1}, the same as that previously listed in ref. 14. There is no experimental proton affinity for $NH_2^\bullet$. However, the G2 proton affinity of this species and the ionization enthalpy of NH_3 give $\Delta_f H^0$ of $NH_3^{\bullet +}$ 938 and 937 kJ mol^{-1}, respectively. Both are in acceptable agreement with 934 kJ mol^{-1} in Table 3, column seven, which can be calculated from the experimental IP of NH_3 as in ref. 14. The consistency of the data obtained by the two routes for both NH_2^- and $NH_3^{\bullet +}$ also confirms the reliability of $\Delta_f H^0_{298} = 189$ kJ mol^{-1} for $NH_2^\bullet$.

Scheme 1 gives only one route to each of the species NH_4^+ and $NH^{\bullet -}$. For the former the experimental and G2 proton affinities are effectively identical and the value of $\Delta_f H^0_{298}$ (630 kJ mol^{-1}) used here is the same as in ref. 14. For the latter, the G2 result in Table 3 is preferred, since it is more reliable than the current experimental result. The values of $\Delta_f G^0$ listed in the last column of Table 3 were calculated from the most reliable values of $\Delta_f H^0$ and the entropies in Table 3. They are used in Sect. 4 in the evaluation of solution properties.

Complexes

The structures of the complexes plotted in Fig. 2 are minima on the potential energy surfaces as verified by the fact that all their vibrational frequencies are real. However, in some cases, as indicated by the low vibrational frequencies in Table 2, the minima are so shallow that the relative orientations of the fragments can change substantially without significant change in energies. In other words, for some complexes more than one conformer with similar total energy might exist.

For binary complexes, there are six more vibrational modes than the sum in the fragments and the total ZPE correction is significant even for the weakly hydrogen-bonded complexes. With the frequencies of normal modes involving the hydrogen bond having fewer than a few hundred wave numbers, the ZPE corrections ranged from 6 to 9 kJ mol^{-1}. In the strongly bonded H_3N–$NH_3^{\bullet +}$ species, the six extra vibrational modes reduce the binding energy by 20 kJ mol^{-1} from the vibrationless binding energy. In $(H_2O)_2\cdots H_2N^\bullet\cdots HOH$, there are 4 hydrogen bonds and 18 extra vibrational modes. The ZPE correction is 24 kJ mol^{-1}. It is clear that ZPE corrections should be included in considering the binding energies in forming complexes.

As stated above, total energies of individual species at the G2 level are generally accurate to ±10 kJ mol^{-1}, and, because

TABLE 3. Ideal gas thermodynamic properties of isolated species and $H_2O\cdots HNH_2^{\bullet+}$

	T (K)	C_p^0 (J K^{-1} mol^{-1})	S^0 (J K^{-1} mol^{-1})	$H^0 - H_0^0$ (kJ mol^{-1})	$\Delta_f H^0$ (G2) (kJ mol^{-1})	$\Delta_f H^0$ (expt.) (kJ mol^{-1})	$\Delta_f G^{0\,a}$ (kJ mol^{-1})
H_2O	0	0.0	0.0	0.0	−240.4	−238.9	−238.9
	100	33.3	151.9	3.3	−241.7	−240.2	−236.5
	200	33.3	174.9	6.7	−242.4	−240.9	−232.6
	298.15	33.5(33.58)[b]	188.2(188.82)[b]	9.9(9.90)[b]	−243.3	**−241.8**[b]	−228.4
NH_3	0	0.0	0.0	0.0	−33.6	−39.1	−39.1
	100	33.3	155.3	3.3	−36.5	−42.0	−34.2
	200	33.5	178.4	6.7	−38.4	−43.9	−25.8
	298.15	35.0(35.06)[b]	192.1(192.45)[b]	10.0(9.99)[b]	−40.6	**−46.1**[b]	−16.4
NH_2^-	0	0.0	0.0	0.0	118.8	115.9	115.9
	100	33.3	152.2	3.3	117.5	114.6	117.5
	200	33.3	175.2	6.7	116.8	113.9	120.7
	298.15	33.6	188.6	9.9	115.9	**113 ± 4**[c]	124.3
NH_4^+	0	0.0	0.0	0.0	650.1	641.3	641.3
	100	33.3	149.0	3.3	645.7	636.8	650.3
	200	33.4	172.1	6.7	642.5	633.6	665.0
	298.15	34.7	185.6	10.0	638.8	**630**[c]	681.1
$NH_2^{\bullet}$	0	0.0	0.0	0.0	193.4	191.9	191.9
	100	33.3	157.8	3.3	192.1	190.6	193.0
	200	33.3	180.8	6.7	191.4	189.9	195.6
	298.15	33.6(33.85)[a]	194.1(195.00)[a]	9.9(9.94)[a]	190.5	**189**[c]	198.6
$NH^{\bullet-}$	0	0.0	0.0	0.0	**331.6**		331.6
	100	29.1	145.6	2.9	331.5		330.0
	200	29.1	165.8	5.8	331.7		328.4
	298.15	29.1	177.4	8.7	331.7	340 ± 21[c]	326.8
$NH_3^{\bullet+}$	0	0.0	0.0	0.0	949.8	940.9	940.9
	100	33.3	155.5	3.3	946.9	938.0	945.7
	200	34.2	178.7	6.7	945.0	936.1	954.2
	298.15	36.7	192.8	10.2	942.9	**934.0**[c]	963.5
$H_2O\cdots HNH_2^{\bullet+}$	0	0.0	0.0	0.0	**618.1**		618.1
	100	47.8	215.7	4.0	611.2		631.8
	200	64.7	254.6	9.7	607.7		653.8
	298.15	73.7	282.2	16.5	604.8		677.1

[a]Calculated based on S^0 of column 4 of this table, S^0 of reference elements from ref. 34, and $\Delta_f H^0$ of column 5 or 6 of this table in bold font.
[b]Experimental values taken from ref. 34.
[c]Experimental values taken from ref. 14.

Can. J. Chem. Downloaded from www.nrcresearchpress.com by 195.246.54.202 on 09/08/12
For personal use only.

of some cancellation of residual errors, the actual errors in the binding energies of complexes from calculations based on G2 energies should be similar. Another study (20) indicated that the magnitude of binding energies of hydrogen-bonded complexes evaluated from energies obtained at the HF/6-31+G* level were a few kJ mol^{-1} lower than those derived with G2 level energies, while MP2/6-31+G* level energies gave binding energies that were higher by a similar amount. The data for $H_2O\cdots HNH_2^{\bullet+}$ shown in Table 5 illustrate this point. The correct binding energies are therefore likely to lie somewhere between the HF/6-31+G* and MP2/6-31+G* values in Table 5. The relative magnitudes of either the HF or the MP2 values indicate clearly which types of interaction are significant and likely to affect the properties of the $NH_2^{\bullet}$ and $NH_3^{\bullet+}$ in an aqueous environment.

Complexes of $NH_2^{\bullet}$: implications for solution

The H-bond energies involving the neutral $NH_2^{\bullet}$ radical are similar to those for NH_3 (see Table 5). The higher basicity of the nitrogen lone pair and lower acidity of the NH bond are reflected in the fact that the binding energies of $HO\boldsymbol{H}\cdots NH_x$ species are larger than those of $H_2O\cdots HNH_x$. In fact $H_2O\cdots HNH_2$ did not converge to a stable geometry. With a C_s constraint, geometry optimization for $H_2O\cdots HNH_2$ results in a saddle point at an O$\cdots$H distance of 2.336 Å. The binding energies are then found to be 4.5 and 8.7 kJ mol^{-1} at the HF and MP2 levels, respectively. The higher amine lone pair basicity is also borne out from a comparison of the data for $HO\boldsymbol{H}\cdots NH_3$ in Table 5 (17.5 and 25.6 kJ mol^{-1} at the HF and MP levels, respectively) with results for $HO\boldsymbol{H}\cdots OH_2$, for which we found binding energies of 13.9 and 20.3 kJ mol^{-1} at the HF and MP2 levels, respectively. The water dimer has been studied at high levels of *ab initio* calculations by Frisch et al. (26). They found the binding energy of $HO\boldsymbol{H}\cdots OH_2$ to be 22.3 kJ mol^{-1} at the MP4/6-311++G(3df,3dp)//MP2/6-311++G(2d,2p) level before inclusion of ZPE. The ZPE-corrected binding energy (8.6 kJ mol^{-1} at the HF/6-31+G* level) is comparable to the present HF result.

In contrast to previous studies (27–29), we found that the H atoms from H_2O and NH_3 groups have an "eclipsed" arrangement in $HO\boldsymbol{H}\cdots NH_3$ as indicated in Fig. 2. The "staggered" conformer has similar electronic energy (differing by less than 1 kJ mol^{-1}), but has one imaginary frequency (34i cm^{-1}). This is also true for $H_3N\cdots \boldsymbol{H}NH^{\bullet}$ and $H_2N\boldsymbol{H}\cdots NH_3$. These results suggest that the bifurcated H–N to lone pair interactions are favored or the bifurcated H–H repulsions are disfavored.

Can. J. Chem. Downloaded from www.nrcresearchpress.com by 195.246.54.202 on 09/08/12
For personal use only.

TABLE 4. Ideal gas thermodynamic properties of complexes

	T (K)	C_p^0 (J K^{-1} mol^{-1})	S^0 (J K^{-1} mol^{-1})	$H^0 - H_0^0$ (kJ mol^{-1})
$HOH\cdots OH_2$	100	57.4	223.4	4.5
	200	67.9	266.8	10.8
	298.15	73.1	295.0	17.8
$HOH\cdots NH_3$	100	55.0	223.8	4.4
	200	66.3	265.8	10.5
	298.15	73.2	293.6	17.4
$H_2NH\cdots NH_3$	100	63.6	240.7	5.0
	200	73.6	288.4	12.0
	298.15	79.3	318.9	19.5
$H_2O\cdots HNH^{\bullet}$	100	64.0	237.9	5.0
	200	73.1	285.6	11.9
	298.15	76.6	315.5	19.3
$H_3N\cdots HNH^{\bullet}$	100	60.6	237.1	4.8
	200	71.5	283.0	11.4
	298.15	76.9	312.7	18.7
$HOH\cdots NH_2^{\bullet}$	100	56.0	227.5	4.4
	200	67.2	270.2	10.6
	298.15	72.9	298.2	17.5
$H_2NH\cdots NH_2^{\bullet}$	100	63.3	240.5	5.0
	200	73.4	288.1	11.9
	298.15	78.0	318.3	19.3
$H_3NH^+\cdots NH_2^{\bullet}$	100	47.0	224.9	4.0
	200	63.2	263.0	9.6
	298.15	71.9	290.0	16.2
$(H_2O)_2\cdots H_2N^{\bullet}\cdots HOH$	100	111.1	329.0	7.5
	200	144.3	417.9	20.6
	298.15	159.6	478.7	35.6
$H_3N\cdots HNH_2^{\bullet+}$	100	43.4	222.9	3.9
	200	58.9	257.9	9.0
	298.15	70.0	283.6	15.4
$(H_2O)_3\cdots H_3N^{\bullet+}$	100	95.5	306.8	6.9
	200	135.1	386.9	18.7
	298.15	153.7	444.6	32.9
$H_3N\cdots NH_3^{\bullet+}$	100	40.4	206.7	3.8
	200	58.4	240.1	8.7
	298.15	72.4	266.2	15.2

Attempts were also made to study σ–σ^* (three electron – two orbital) interactions between H_2O and H_3N lone pair electrons and the unpaired electron of $NH_2^{\bullet}$. Although attractive, these did not converge to stable minima and showed no evidence for the formation of stable structures in the gas phase. In fact structures with such configurations reverted to the hydrogen-bonded conformations discussed above. However, to estimate the extent of σ–σ^* attraction that must be present in solution, we optimized the $O\cdots N$ distance by constraining the H_2O and H_2N planes parallel to each other and with the hydrogens having a staggered arrangement. This arrangement maximizes the HOMO–SOMO interaction. Without including the vibrational energy correction, the maximum binding energy was found to be 4.5 kJ mol^{-1} at the HF/6-31+G* level, at an $O\cdots N$ separation of 3.2 Å. Inclusion of the ZPE correction would make the binding energy negative. In similar calculations, the $H_2N^{\bullet}$ and NH_3 interaction was repulsive at all $N\cdots N$ distances, the repulsion increasing monotonically to 6 kJ mol^{-1} at the N–N van der Waals sparation of 3 Å. We conclude, therefore, that these σ–σ^* interactions are of minimal importance for the solvation of $NH_2^{\bullet}$.

From Table 5 it is evident that there are no cases where the binding of $NH_2^{\bullet}$ to NH_3 is significantly stronger than to H_2O.[2] Thus in aqueous systems with less than molar NH_3, $NH_2^{\bullet}$ will effectively be surrounded by H_2O molecules. In that regard the $(H_2O)_2\cdots \boldsymbol{H}_2N^{\bullet}\cdots \boldsymbol{H}OH$ complex (Fig. 2) is particularly interesting in that it reflects $H_2O\cdots H_2O$ bonding as well as $H_2O\cdots NH_2^{\bullet}$ bonding. It is therefore closer than the dimeric clusters to the type of structure likely to be encountered in aqueous solution. The four heavy atoms are coplanar. There are two $O\cdots \boldsymbol{H}N^{\bullet}$, one $O\boldsymbol{H}\cdots N^{\bullet}$, and one $O\boldsymbol{H}\cdots O$ bonds, with one of the $O\cdots \boldsymbol{H}N^{\bullet}$ bonds significantly nonlinear. The total binding energies at the HF and MP2 levels are 47 and 69 kJ mol^{-1}, respectively, in both cases just 5 kJ mol^{-1} higher than the sum of the energies of the individual hydrogen bonds as measured in appropriate binary complexes in Table 5.

The importance of bonds between the $(H_2O)_x\cdots \boldsymbol{H}_2N^{\bullet}$

[2]Note that ΔG^0 values for binding, which can be obtained from the thermodynamic data in Tables 3 and 4, and the binding energies in Table 5, lead to the same conclusions.

TABLE 5. Binding energies (kJ mol^{-1}) of aquo complexes

Interaction type	Species involved: $H_3N^{\bullet+}$	$NH_2^{\bullet}$	Filled shell analogues
H bonds			
Lone pair of O to H of H_2O			$H_2O\cdots HOH$
HF/6-31+G*//HF/6-31+G* + ZPE			13.9
MP2/6-31+G*//HF/6-31+G* + ZPE			20.3
Lone pair of O to H of NH_x	$H_2O\cdots HNH_2^{\bullet+}$	$H_2O\cdots HNH^{\bullet}$	$H_2O\cdots HNH_2$
HF/6-31+G*//HF/6-31+G* + ZPE	87.7	7.4	(4.5)[a]
MP2/6-31+G*//HF/6-31+G* + ZPE	97.7	11.6	(8.7)[a]
G2	91.2		
Lone pair of N to H of NH_x	$H_3N\cdots HNH_2^{\bullet+}$	$H_3N\cdots HNH^{\bullet}$	$H_3N\cdots HNH_2$
HF/6-31+G*//HF/6-31+G* + ZPE	110.4	8.5	6.0
MP2/6-31+G*//HF/6-31+G* + ZPE	128.3	13.6	11.5
		$H_3NH^+\cdots NH_2^{\bullet}$	
HF/6-31+G*//HF/6-31+G* + ZPE		79.2	
MP2/6-31+G*//HF/6-31+G* + ZPE		89.2	
OH to lone pair of N		$HOH\cdots NH_2^{\bullet}$	$HOH\cdots NH_3$
HF/6-31+G*//HF/6-31+G* + ZPE		13.7	17.5
MP2/6-31+G*//HF/6-31+G* + ZPE		20.2	25.6
NH to lone pair of N		$H_2NH\cdots NH_2^{\bullet}$	
HF/6-31+G*//HF/6-31+G* + ZPE		4.7	
MP2/6-31+G*//HF/6-31+G* + ZPE		9.0	
σ–σ^* lone pair to N unpaired			
H_2O lone pair	$H_2O\therefore NH_3^+$	$H_2O\therefore NH_2$	
HF/6-31+G*//HF/6-31+G*	(~ 18)[b]	(~ 5)[b]	
H_3N lone pair	$H_3N\therefore NH_3^+$	$H_3N\therefore NH_2$	
HF/6-31+G*//HF/6-31+G* + ZPE	78.0	(—)[c]	
MP2/6-31+G*//HF/6-31+G* + ZPE	139.4		

[a]HF/6-31+G* geometry has one imaginary frequency ($\nu_1 = 88i$ cm^{-1}), see text.
[b]Binding energies estimated with certain constraints on the geometries, see text.
[c]Monotonically repulsive with decreasing of the N–N distance.

Can. J. Chem. Downloaded from www.nrcresearchpress.com by 195.246.54.202 on 09/08/12
For personal use only.

complexes and the H_2O network can be emphasized by comparing the relative stabilities of the above discussed $(H_2O)_2\cdots \boldsymbol{H}_2N^{\bullet}\cdots \boldsymbol{H}OH$ structure and that of the isomer $H_2O\cdots \boldsymbol{H}HN^{\bullet}\cdots \boldsymbol{H}O\boldsymbol{H}\cdots OH_2$, which can be formed by replacing an $O\cdots \boldsymbol{H}N^{\bullet}$ hydrogen bond with an $O\boldsymbol{H}\cdots O$ hydrogen bond. If the binding energy of $HO\boldsymbol{H}\cdots OH_2$ species is larger than that of $H_2O\cdots \boldsymbol{H}HN^{\bullet}$ as shown in Table 5 and above, $H_2O\cdots \boldsymbol{H}HN^{\bullet}\cdots \boldsymbol{H}O\boldsymbol{H}\cdots OH_2$ should be more stable than $(H_2O)_2\cdots \boldsymbol{H}_2N^{\bullet}\cdots \boldsymbol{H}OH$. Indeed, we found that the former is favored by 6.8 kJ mol^{-1} at the MP2/6-31+G* + ZPE level (5.2 kJ mol^{-1} at the HF/6-31+G* + ZPE level). Again, the binding energies of individual hydrogen bonds are fairly additive, with the total bonding energy only 3 kJ mol^{-1} higher than the sum of individual binding energies.

In $(H_2O)_2\cdots \boldsymbol{H}_2N^{\bullet}\cdots \boldsymbol{H}OH$ (Fig. 2), the HN$\boldsymbol{H}$ angle is increased from 105.2° in free $NH_2^{\bullet}$ to 107.1° to accommodate the cyclic $N\boldsymbol{H}\cdots O\boldsymbol{H}\cdots O\boldsymbol{H}\cdots N$ structure. However, the N$\boldsymbol{H}$ distances do not alter significantly, only one of them changing from 1.012 Å in free $NH_2^{\bullet}$ to 1.011 Å. The tendency for maintenance of the $NH_2^{\bullet}$ structure is also clear in $HO\boldsymbol{H}\cdots NH_2^{\bullet}$ and $H_2O\cdots \boldsymbol{H}NH^{\bullet}$, where the NH distances remain the same as in free $NH_2^{\bullet}$ and the HNH angles of both are 105.6°, only slightly altered from 105.2° in free $NH_2^{\bullet}$.

Complexes of $NH_3^{\bullet+}$

As indicated by the results in Table 5, the presence of the charge on the $NH_3^{\bullet+}$ cation radical causes the binding energies to increase by an order of magnitude, and the interactions become dipole oriented with linear H bonds. The structures of $H_2O\cdots \boldsymbol{H}NH_2^{\bullet+}$ and $(H_2O)_3\cdots \boldsymbol{H}_3N^{\bullet+}$ have been reported elsewhere (20) and we will only summarize their main features here. The optimized $H_2O\cdots \boldsymbol{H}NH_2^{\bullet+}$ structure has C_{2v} symmetry with the radical center $N^{\bullet+}$ being planar. The hydrogen atoms of the water molecule lie in a plane perpendicular to it, without significant change of structure from the isolated H_2O. In $(H_2O)_3\cdots \boldsymbol{H}_3N^{\bullet+}$, the planes defined by the water molecules form angles of 67.3° with the $NH_3^{\bullet+}$ plane and give this complex a D_3 structure. The hydrogen bonds in $(H_2O)_3\cdots \boldsymbol{H}_3N^{\bullet+}$ are 0.124 Å longer, and the average binding energy is 13 kJ mol^{-1} less than that of $H_2O\cdots \boldsymbol{H}NH_2^{\bullet+}$. For $H_2O\cdots \boldsymbol{H}NH_2^{\bullet+}$, the interaction energy, −91.2 kJ mol^{-1}, has been previously evaluated (20) at the G2 level, which is 3 kJ mol^{-1} more negative than the HF value and 6 kJ mol^{-1} less negative than the MP2 value. The $H_3N\cdots \boldsymbol{H}NH_2^{\bullet+}$ bond is about 30 kJ mol^{-1} stronger than the $H_2O\cdots \boldsymbol{H}NH_2^{\bullet+}$ bond. Thus if $NH_3^{\bullet+}$ were present in a solution where the NH_3 concentration was significant, there would

Can. J. Chem. Downloaded from www.nrcresearchpress.com by 195.246.54.202 on 09/08/12
For personal use only.

be preferential complexation by this species. However, at pHs where $NH_3^{\cdot+}$ exists in water (see Sect. 4), NH_3 will be protonated and this interaction will not be significant. Since the isomeric interaction $H_3NH^+\cdots NH_2^{\cdot}$ is slightly weaker than that for $H_2O\cdots HNH_2^{\cdot+}$, it can also be neglected.

The optimized structures of $H_3N\cdots HNH_2^{\cdot+}$ and its "isomer" $H_3NH^+\cdots NH_2^{\cdot}$ are both dipole orientated ($< NHN \approx 180°$) with C_s symmetry. $H_3NH^+\cdots NH_2^{\cdot}$ is 34 kJ mol^{-1} more stable than $H_3N\cdots HNH_2^{\cdot+}$ at the MP2/6-31+G* + ZPE level. However, the binding energy is 39 kJ mol^{-1} less than that of $H_3N\cdots HNH_2^{\cdot+}$. In forming the hydrogen bond in $H_3N\cdots HNH_2^{\cdot+}$, the NH distance is lengthened by 0.08 Å and < HNH is narrowed by 4° from those of $H_3N^{\cdot+}$, while changes in NH_3 local structure are minor. The hydrogen bond length is 1.634 Å, shorter by 1.066 Å from the van der Waals separation.[3] In $H_3NH^+\cdots NH_2^{\cdot}$, the structures of the fragments are little altered.

The planar (D_3) structure of $(H_2O)_3\cdots H_3N^{\cdot+}$ means that in aqueous solution H_2O molecules will be free to approach the $N^{\cdot+}$ center from above and below the plane of the N—H bonds along the axis of symmetry. There will be a strong ion–dipole interaction, which will orient the dipole moment of the H_2O molecules toward the $N^{\cdot+}$ center. Calculations on $H_2O\cdot\cdot NH_3^+$ started with this orientation indicated that the binding energy was 34 kJ mol^{-1} (HF/6-31+G* + estimated ZPE). As well as the ion–dipole interaction, this includes a component due to σ–σ^* interaction, i.e., an interaction between the singly occupied MO (SOMO) and one of the lone pairs of H_2O. Attempts were made to establish whether the σ–σ^* part of the interaction is significant. However, as in the case of $NH_2^{\cdot}$, these structures did not correspond to stable minima in the gas phase. Calculations were performed for $H_2O\cdots NH_3^{\cdot+}$ constrained to adopt a geometry in which the ion–dipole interaction is minimized while maximizing the σ–σ^* interaction (SOMO–HOMO): with the O···N bond perpendicular to H_2O plane and with a staggered arrangement between the H atoms of the two fragments. The optimized (with the constraints) O···N distance is found to be 2.703 Å and the radical centre is within 1° of planarity. The binding energy at the HF/6-31+G* level is 25.6 kJ mol^{-1}. After correction by the estimated ZPE contribution (about 8 kJ mol^{-1}), the σ–σ^* attraction is about 18 kJ mol^{-1}. This represents a maximum value for the σ–σ^* interaction since it still includes a minor contribution from the ion–dipole interaction.

The optimized structure of $H_3N\cdots NH_3^{\cdot+}$ has staggered conformation with D_{3d} symmetry (Fig. 2). This structure was reported earlier by Gill and Radom (30), and our present results agree with theirs. As shown in Table 5, the σ–σ^* interaction for $H_3N\cdots NH_3^{\cdot+}$ does exhibit strong bonding. This difference from H_2O can be attributed to the match in the orbital energies when identical atoms are involved (31). Again, because free NH_3 is unimportant at pHs where $NH_3^{\cdot+}$ exists, the role of $H_3N\cdots NH_3^{\cdot+}$ should be minimal in aqueous systems. It could, however, be of importance in liquid ammonia. In the present study, H_3N–$NH_3^{\cdot+}$ is the only species in which the interactions between the fragments are dominated by the σ–σ^* interaction of heavy atoms.

[3]The van der Waals radii are 1.2, 1.4, and 1.5 Å for H, O, and N atoms, respectively, as given in the Handbook of Chemistry and Physics.

4. Solution properties

Absorption spectra

The results of the CIS/6-31+G* calculations of vertical excitation properties of $NH_2^{\cdot}$ and $NH_3^{\cdot+}$ are listed in Table 6.

$NH_2^{\cdot}$

For $NH_2^{\cdot}$ in the gas phase, only one transition is predicted to fall below 8 eV. The vertical transition from the $^2B_1$ ground state to the $^2A_1$ state is predicted to occur at 2.43 eV (511 nm), with oscillator strength $f = 0.0040$. The lowest excited $^2A_1$ state is linear and the transition in the gas phase displays pronounced nonvertical characteristics: a broad absorption band extending from 450 to 740 nm, with band maxima at 516, 571, and 630 nm (32). The computed vertical excitation wavelength agrees well with the first band maximum in the gas phase. The transition corresponds to the excitation of an electron from the doubly occupied nonbonding "*sp*^{n}" hybrid orbital ($3a_1$) to the higher singly occupied nonbonding orbital ($1b_1$), which is in essence the 2*p* orbital on nitrogen. In aqueous solution, as discussed above, the $NH_2^{\cdot}$ species experiences three types of interaction with the neighboring water molecules. The effects of these on the wavelength of the $^2B_1 \rightarrow {}^2A_1$ transition may be deduced from the data in Table 6. In complexes with water or ammonia of the type, X:···HNH$^{\cdot}$, this transition is largely unperturbed, being slightly red shifted. In complexes where the $3a_1$ orbital is involved in hydrogen bonding (of type, X–H···:$NH_2^{\cdot}$, the transition is blue shifted by an amount characteristic of the acidity of the X–H bond: X–H = H_2N–H, −15 nm; X–H = HO–H, −40 nm; X–H = H_3N–H^+, −110 nm. The blue shift is expected on the basis that the hydrogen-bonding interaction lowers the energy of the "*sp*^{n}" ($3a_1$) orbital relative to the 2*p* orbital (SOMO). It is also seen in $(H_2O)_2\cdots H_2N^{\cdot}\cdots HOH$ where both types of H bond are present. As mentioned above, no small complexes arising from "σ"-type interactions between the SOMO and nonbonded electrons of water or ammonia are stable. Nevertheless, such configurations must exist in solution. The three-electron two-orbital interactions effectively raise the energy of the singly occupied MO ($1b_1$) without affecting the energy of the $3a_1$ orbital, thereby causing a blue shift of the longest wavelength transition. We have assessed the effect of such a σ-type interaction on the wavelength (λ) and oscillator strength (f) of the $^2B_1 \rightarrow {}^2A_1$ transition by constraining the planes of a single $NH_2^{\cdot}$–H_2O pair to be parallel at several fixed separations, r: r = 2.5 Å, λ = 431 nm, f = 0.006; r = 3.0 Å, λ = 475 nm, f = 0.005; r = 3.5 Å, λ = 494 nm, f = 0.004. At the van der Waals distance (3Å), a modest blue shift is predicted with little gain in oscillator strength. In pulse-irradiated ammonia solutions at high pH, there is observed a broad (width ≈ 200 nm) but weak absorption band peaking near 520 nm, and this has been attributed to $NH_2^{\cdot}$ (7). Given the highly nonvertical nature of the transition, the theoretical data are satisfactorily compatible with the observed solution phase spectra. Also, as expected, the absorption intensity is very weak (ϵ = 80 M^{-1} cm^{-1} (7)).

The second absorption for gaseous $NH_2^{\cdot}$, $^2B_1 \rightarrow {}^2B_1$ ($3a_1 \rightarrow 4a_1$), is predicted by CIS/6-31+G* to occur at 145 nm with oscillator strength f = 0.0240. Inclusion of additional diffuse and polarization functions to the basis set (CIS/6-311++G**) alters the predicted properties of this absorption only slightly (154 nm, f = 0.0277), indicating that the lowest excited $^2B_1$ state is a valence state, as is the lowest $^2A_1$ state. In complexes

Can. J. Chem. Downloaded from www.nrcresearchpress.com by 195.246.54.202 on 09/08/12
For personal use only.

TABLE 6. UV properties of the radicals calculated at HF/6-31+G*

		Excitation energy		Oscillator strength	
		Energy (eV)	λ (nm)	f	Description
$NH_2^{\bullet}$ $^2B_1$	1 $^2A_1$	2.42	511	0.0040	$3a_1 \rightarrow 1b_1$
	2 $^2B_1$	8.55	145	0.0240	$3a_1 \rightarrow 4a_1$
$H_2O\cdots HNH^{\bullet}$ $^2A''(^2B_1)$	1 A''	2.41	515	0.0039	
	2 A''	7.57	164	0.0	$n_O \rightarrow n_N$(CT)
$H_3N\cdots HNH^{\bullet}$ $A''(^2B_1)$	1 A''	2.37	523	0.0039	$3a_1 \rightarrow 1b_1$
	2 A'	7.42	167	0.0	$n_{NH_3} \rightarrow n_{NH_2}$(CT)
$HOH\cdots NH_2^{\bullet}$ $A'(^2B_1)$	1 A'	2.63	471	0.0037	$3a_1 \rightarrow 1b_1$
	2 A''	7.68	161	0.0	$n_O \rightarrow n_N$(CT)
$H_2NH\cdots NH_2^{\bullet}$ $A''(^2B_1)$	1 A''	2.50	495	0.0037	$3a_1 \rightarrow 1b_1$
	2 A'	7.23	171	0.0	$n_{NH_3} \rightarrow n_{NH_2}$(CT)
$H_3NH^+\cdots NH_2^{\bullet}$ $A''(^2B_1)$	1 A''	3.09	401	0.0038	$3a_1 \rightarrow 1b_1$
	2 A''	7.52	165	0.0	
$(H_2O)_2\cdots H_2N^{\bullet}\cdots HOH$ $(^2B_1)$	1	2.62	472	0.0034	$3a_1 \rightarrow 1b_1$
	2	7.41	167	0.0	$n_O \rightarrow n_N$(CT)
$NH_3^{\bullet+}$ $^2A_2''$	1 E''	8.01	155	0.0	$e' \rightarrow a_2''$
$H_2O\cdots HNH_2^{\bullet+}$ B_1 $(^2A_2'')$	1 B_1	6.80	182	0.0	$n_O \rightarrow n_N$(CT)
	2 A_2	7.98	155	0.0	$\sigma_{NH} \rightarrow n_N(e' \rightarrow a_2'')$
$H_3N\cdots HNH_2^{\bullet+}$ $A''(^2A_1'')$	1 A''	4.95	250	0.0001	$n_{NH_3} \rightarrow n_{NH_3^+}$(CT)
	2 A''	7.95	156	0.0	$\sigma_{NH} \rightarrow n_N(e' \rightarrow a_2'')$
$(H_2O)_3\cdots H_3N^{\bullet+}$ $(^2A_2')$	1 ^2E	6.92	179	0.0	$n_O \rightarrow n_N$(CT)
H_3N–$NH_3^{\bullet+}$ $(^2A_{2u})$	1 $^2A_{1g}$	4.39	282	0.3795	$3a_{1g} \rightarrow 3a_{2u}(\sigma_{NN} \rightarrow \sigma^*_{NN})$
	2 ^2E_g	8.65	143	0.0	$1e_g \rightarrow 3a_{2u}(\sigma_{NN} \rightarrow \sigma^*_{NN})$

with one or three water molecules, however, the nature of the second lowest energy transition changes radically, to a charge transfer from water to $NH_2^{\bullet}$, near 165 nm, with $f = 0.0000$. The wavelength of the corresponding charge transfer band in solution will be poorly modelled by the data in Table 6, since the effect of a polarizable medium of high dielectric constant will be to stabilize the charge transfer state and lead to a substantial red shift of the absorption wavelength. According to the procedure of Treinin and Hayon (33), assuming a "radius" of 1.75 Å for $NH_2^{\bullet}$, one can predict the position of the charge transfer band to be near 200 nm. Experimentally, $NH_2^{\bullet}$ in liquid water has a second absorption beginning below 250 nm (7) that was attributed by Pagsberg to a charge transfer transition (7). The present analysis supports this assignment.

$NH_3^{\bullet+}$

The results of the CIS/6-31+G* calculations of the vertical excitation properties of $NH_3^{\bullet+}$ and several complexes with water and ammonia are listed in Table 6. In the gas phase, the lowest electronic absorption, $^2A_2'' \rightarrow {}^2E''$ ($1e' \rightarrow 1a_2''$) is predicted to occur at 155 nm with zero oscillator strength. In complexes with water, this transition is unperturbed, but a charge transfer transition is predicted to occur at longer wavelength, near 180 nm, also with almost zero oscillator strength. With the better donor, ammonia, the hydrogen-bonded complex, $H_3N\cdots HNH_2^{\bullet+}$, has a charge transfer transition at 250 nm. Ammonia also forms a three-electron σ-bonded complex with $NH_3^{\bullet+}$, H_3N–$NH_3^{\bullet+}$, symmetry D_{3h}, of stability comparable to the hydrogen-bonded complex. The lowest energy transition, $^2A_{2u} \rightarrow {}^2A_{1g}$ ($3a_{1g} \rightarrow 3a_{2u}$, $\sigma_{NN} \rightarrow \sigma_{NN}^*$), is predicted to occur at 282 nm and is strongly electric dipole allowed, $f = 0.3795$. As mentioned above, no water complexes with three-electron bonding comparable to H_3N–$NH_3^{\bullet+}$ are stable. As with $NH_2^{\bullet}$, however, such transient configurations must exist in solution and provide an opportunity for $\sigma_{ON} \rightarrow \sigma_{ON}^*$ transitions. Because of the polarization of the σ_{ON} and σ_{ON}^* orbitals, such transitions are, in fact, charge transfer transitions and may have appreciable oscillator strength. We have examined the qualitative functional dependence upon separation (r) of the absorption wavelength (λ) and oscillator strength (f) of charge transfer transitions by constraining the planes of water and $NH_3^{\bullet+}$ to be parallel at several fixed separations (r), the orientation of which maximizes the effects of σ–σ* interaction: $r = 2.5$ Å, $\lambda = 194$ nm, $f = 0.136$; $r = 3.0$ Å, $\lambda = 190$ nm, $f = 0.061$; $r = 3.5$ Å, $\lambda = 187$ nm, $f = 0.029$. Thus, at the van der Waals separation (3 Å), a transition near 190 nm with moderately strong oscillator strength is predicted in the gas phase. Experimentally, the UV spectrum of $NH_3^{\bullet+}$ exhibits a monotonic absorption beginning at 370 nm and increasing to the limit of measurement, 290 nm (9). Using an adaptation of the method of Treinin and Hayon (7), for the process

$$[5] \qquad h\nu + H_2O\cdots NH_3^{\bullet+} \rightarrow H_2O^{\bullet+}\cdots NH_3$$

one can predict that the charge transfer transition should occur near 250 nm.[4] The computations therefore support the charge transfer character of the transition observed in the low pH region of aqueous $NH_3^{\bullet+}$ (9).

[4]The transition energy is principally governed by the difference in the ionization potential of water, $I(H_2O)$, and the electron affinity of amminium, $E(NH_3^{\bullet+})$, modified by the solvation energy of $NH_3^{\bullet+}$ (Table 7), and the instantaneous solvent response to the development of charge on H_2O (32).

Can. J. Chem. Downloaded from www.nrcresearchpress.com by 195.246.54.202 on 09/08/12
For personal use only.

TABLE 7. Solution thermodynamic data at 298.15 K

	$\Delta_f G^0_{(g)}$[a] (kJ mol^{-1})	$\Delta G^{0b}_{(s)}$ (kJ mol^{-1})	$\Delta_f G^0_{(aq)}$ (kJ mol^{-1})	pK_a
NH_4^+	681	757[c]	-79.3 ± 0.5[d]	9.3[d]
$NH_3^{\cdot+}$	963	732[c]	178 ± 7[e]	2.3[f]
NH_3	−16.4	−10.1[d]	-26.5 ± 0.5[d]	36[g]
$NH_2^{\cdot}$	199	−8.0[h]	191 ± 4[h]	—
NH_2^-	124	−1463[c]	180 ± 25[h]	—

[a]From Table 3.
[b]The values for ions are conventional free energies of solution, see text.
[c]Calculated from present $\Delta_f G^0_{(g)}$ and $\Delta_f G^0_{(aq)}$ and using eqs. [6]–[13].
[d]Experimental values from ref. 34.
[e]Calculated from ΔG^0 of reaction [14] based on pK_R of $NH_3^{\cdot+}$ = 2.3.
[f]From ref. 9.
[g]Average of 34 and 38 from ref. 37 and 40, respectively.
[h]Calculated as described in text.

Thermodynamic data

Solution thermodynamic data for NH_4^+, NH_2^-, and the radical species $NH_3^{\cdot+}$ and $NH_2^{\cdot}$ at 298.15 K are given in Table 7, along with the values of $\Delta_f G^0_{(g)}$ from Table 3. The values of $\Delta_f G^0_{(aq)}$ for NH_3 and NH_4, the pK_a of NH_4^+, and the free energy of solution of NH_3 have been taken from ref. 34. Other data have been derived as indicated in the footnotes and explained below. Here it is worth recalling that for negative B^- ions the free energy of formation in aqueous solution, $\Delta_f G^0_{(aq)}$ is given by the free energy change in reaction [6] (34),

$$[6] \qquad \text{ESSB} + \frac{1}{2} H_{2(g)} \rightarrow B^- + H^+$$

where ESSB means the stoichiometric quantities of Elements in their Standard States at one Bar needed to form B^-. For other species the subscript (g) indicates gas phase reactant, standard state 1 bar, while the absence of any notation indicates aqueous solution, standard state 1 molar. The free energy changes in reactions [7] and [8]

$$[7] \qquad \text{ESSB} + \frac{1}{2} H_{2(g)} \rightarrow BH_{(g)}$$

$$[8] \qquad BH_{(g)} \rightarrow B^-_{(g)} + H^+_{(g)}$$

respectively define $\Delta_f G^0_{(g)}$ of $BH_{(g)}$ and the gas phase acidity, $\Delta G^0_{(acid)}$ of $B^-_{(g)}$. The *conventional* free energy of solution of B^-, ΔG^0_s (con. of B^-), is equal to the sum of the absolute free energies of solution of B^- and H^+ ($\Delta G^0_s(B^-) + \Delta G^0_s(H^+)$), and is given by the free energy change of reaction [9] (34)

$$[9] \qquad B^-_{(g)} + H^+_{(g)} \rightarrow B^- + H^+$$

For present purposes it is equivalent to $\{\Delta_f G^0_{(aq)}(B^-) - \Delta_f G^0_{(g)}(BH) - \Delta G^0_{(acid)}(B^-_{(g)})\}$. These equations are needed for the calculation of the properties in Table 5. The analogous equations for positive ions are:

$$[10] \qquad \text{ESSB} + H^+ \rightarrow A^+ + \frac{1}{2} H_{2(g)}$$

$$[11] \qquad \text{ESSB} \rightarrow A^+_{(g)} + e^-$$

$$[12] \qquad e^- + H^+_{(g)} \rightarrow \frac{1}{2} H_{2(g)}$$

$$[13] \qquad H^+ + A^+_{(g)} \rightarrow H^+_{(g)} + A^+$$

and ΔG^0_s (con. of A^+), defined by the free energy change for reaction [13], is given by $\{\Delta_f G^0_{(aq)}(A^+) - \Delta_f G^0_{(g)}(A^+) + \Delta_f G^0_{(g)}(H^+)\}$. The gaseous free energy of formation of the proton, $\Delta_f G^0_{(g)}(H^+)$, calculated on the basis of the ion convention (14) used here, is 1517 kJ mol^{-1}.

For the $NH_2^{\cdot}$ radical, previous studies (3) have assumed that the energy of the σ–σ^* interaction between the N unpaired electron and the H_2O lone pairs would be too small to influence the solution free energy. The discussion in Sect. 3 confirms this. Also from Table 5 the strongest interaction with H_2O is the OH to N lone pair H bond, and this is slightly weaker for $NH_2^{\cdot}$ than for NH_3. That feature and the fact that there are only two H atoms for NH—O bonds in $NH_2^{\cdot}$, as opposed to three in NH_3, argues in favour of a slightly smaller magnitude of $-\Delta G^0_s$ for $NH_2^{\cdot}$ than for NH_3, for which $-\Delta G^0_s$ is 10 kJ mol^{-1}. The value of 8 kJ mol^{-1} used by Stanbury (3) on the basis of comparisons with model systems therefore seems entirely justified. $\Delta_f G^0_{(aq)}$ for $NH_2^{\cdot}$ in Table 5 was calculated from $\Delta_f G^0_{(g)}$ on the basis of this value. Errors in $\Delta G^0_{(s)}$ would not exceed 2 kJ mol^{-1} and, combined with the ±2 kJ mol^{-1} error uncertainty in $\Delta_f G^0_{(g)}$, lead to a ±4 kJ mol^{-1} error in $\Delta_f G^0_{(aq)}$ ($NH_2^{\cdot}$).

As in ref. 3, $\Delta_f G^0_{(aq)}$ for $NH_3^{\cdot+}$ was calculated from the free energy change in reaction [14]

$$[14] \qquad NH_3^{\cdot+} \rightarrow NH_2^{\cdot} + H^+$$

The pK_a of $NH_3^{\cdot+}$, pK_R, was first reported to be 3.65 (35) and then subsequently 6.7 (8). However, neither is valid because these studies did not recognize the correct mechanism of the reaction of protonated hydroxylamine with the solvated electron, which was later clarified in ref. 13. The only reliable value of pK_R, which is 2.3, is that of Hoffman and Olson (9), and gives $\Delta G^0_{[14]}$ = 13.1 kJ mol^{-1}. With this result and $\Delta_f G^0_{(aq)}$ for $NH_2^{\cdot}$ from Table 5, one finds $\Delta_f G^0_{(aq)}$ of $NH_3^{\cdot+}$ = 178 kJ mol^{-1}.

From that and $\Delta_f G^0_{(g)}$ of $NH_3^{\cdot+}$ (= 963 kJ mol^{-1}), ΔG^0_s (con.) for $NH_3^{\cdot+}$ is found to be 732 kJ mol^{-1}. Reference to Table 7 shows that this is 25 kJ mol^{-1} more negative than ΔG^0_s for NH_4^+. The difference is of the same magnitude as that found between ΔG^0_s for $(CH_3)_3N^{\cdot+}$ and $(CH_3)_3NH^+$ in our earlier publication (36). It therefore supports the conclusion that the planar amminium ions are more strongly solvated than the tetrahedral ammonium species. This conclusion was first arrived at by Pearson (37) for $NH_3^{\cdot+}$, but largely on the basis of the value pK_R = 6.7, now known to be incorrect. A value ΔG^0_s of $NH_3^{\cdot+}$, which is more negative than that of NH_4^+, is also strongly supported by the calculations of free energies of hydration of NH_4^+ and $NH_3^{\cdot+}$ in ref. 20.

The authors are unaware of any experimental data from which $\Delta_f G^0_{(aq)}$ or ΔG^0_s (con.) of $NH^{\cdot-}$ can be obtained. However, based on the Born model of ion solvation and a consideration of relative atomic dimensions, the magnitude of ΔG^0_s (con.) of $NH^{\cdot-}$ cannot be more than that of OH^-, which from current data in refs. 14 and 34 is −1535 kJ mol^{-1}. That value would yield $\Delta_f G^0_{(aq)}$ ($NH^{\cdot-}$) = 320 kJ mol^{-1} and a minimum pK_a of 22 for $NH_2^{\cdot}$ in reaction [15]:

$$[15] \qquad NH_2^{\cdot} \rightarrow NH^{\cdot-} + H^+$$

Thus ionization of $NH_2^{\cdot}$ would be unimportant in aqueous systems and $NH^{\cdot-}$ has not been considered further here.

The values of $\Delta_f G^0_{(aq)}$ and ΔG^0_s (con.) of NH_2^- in Table 7 are subject to a considerable uncertainty (±25 kJ mol^{-1}),

Can. J. Chem. Downloaded from www.nrcresearchpress.com by 195.246.54.202 on 09/08/12
For personal use only.

because they were obtained from estimates of the pK_a of NH_3 and these involved extrapolations from nonaqueous systems (37). Based on the relative size of the ions one would expect ΔG^0_s (con.) of NH_2^- to lie in between those for OH^- and Cl^-, which from current data in refs. 14 and 34 are -1535 and -1408 kJ mol^{-1}, respectively. The value of -1463 kJ mol^{-1} in Table 7 is therefore in the expected range.

Redox chemistry

The standard reduction potential for the fundamental half-reaction [16], $E^0(NH_2^{\bullet}/NH_2^-)$,

[16] $\quad NH_2^{\bullet} + e^- \rightarrow NH_2^-$

is given by $-\{\Delta_f G^0_{(aq)}(NH_2^-) - \Delta_f G^0_{(aq)}(NH_2^{\bullet})\}/F$, where F is the Faraday constant. The values of $\Delta_f G^0_{(aq)}$ in Table 7 yield $E^0(NH_2^{\bullet}/NH_2^-) = 0.11 \pm 0.30$ V, and the large uncertainty makes meaningless any attempt to predict the redox properties of $NH_2^{\bullet}$ on the basis of reaction [16]. However, given the very high pK_a of NH_3, there is an enormous driving force for protonation. Thus reaction [17]

[17] $\quad NH_2^{\bullet} + e^- + H^+ \rightarrow NH_3$

is likely to be the more relevant half-reaction. In any case this is certainly the appropriate half-reaction when protonation equilibria are ensured and the pH is above 9.3 (i.e., both NH_4^+ and $NH_3^{\bullet+}$ deprotonated). From the structure of $(H_2O)_2 \cdots H_2N^{\bullet} \cdots HOH$ in Fig. 2, one can see that proton transfer from the solvent as represented in reaction [18]

[18] $\quad NH_2^{\bullet} + e^- + H_2O \rightarrow NH_3 + OH^-$

should be facile, and this path could be dominant at high pHs.[5]

Because of the relatively minor uncertainties in the $\Delta_f G^0_{(aq)}$ data for $NH_2^{\bullet}$ and NH_3 in Table 5, the standard reduction potential for half-reaction [17] ($E^0(NH_2^{\bullet}, H^+/NH_3) = 2.25 \pm 0.10$ V) can be obtained with much greater precision than $E^0(NH_2^{\bullet}/NH_2^-)$. More useful is an equation for the pH dependence of the redox potential of the radical/ammonia system with protonation equilibrium. Using the conventions in ref. 38, one can write:

$$[19] \quad E_{h(\text{radical/ammonia})} = E^0(NH_2^{\bullet}, H^+/NH_3) - \frac{RT}{F} \ln \frac{N_T}{N_R} - \frac{RT}{F} \ln \left(1 + \frac{a_{H^+}}{\gamma_{R^+} K_R}\right) \left[a_{H^+} \left(1 + \frac{a_{H^+}}{\gamma_{N^+} K_A}\right)\right]^{-1}$$

Here N_T and N_R are the total concentrations $\{[NH_3] + [NH_4^+]\}$ and $\{[NH_2^{\bullet}] + [NH_3^{\bullet+}]\}$, respectively, a_{H^+} is the hydrogen ion activity, γ_{N^+} and γ_{R^+} are the activity coefficients and K_A and K_R the ionization constants of NH_4^+ and $NH_3^{\bullet+}$, respectively. The activity coefficients of neutral species have been taken as unity. For $N_T = N_R$, $E_{h(\text{radical/ammonia})}$ is 1.48 V at pH 13 and it increases to 1.60 V at pH 11. Thus it is evident that $NH_2^{\bullet}$ is likely to be a much stronger oxidant in alkaline media than implied by even the highest estimate of $E^0(NH_2^{\bullet}/NH_2^-)$. Confirmation of that comes from the observation in ref. 13 of the oxidation of a series of substituted phenolate ions ($XC_6H_4O^-$) having $E^0(XC_6H_4O^{\bullet}/XC_6H_4O^-)$ values as high as 0.8 V. The fact that the rates tend to be slow ($\sim 10^7$ dm^3 mol^{-1} s^{-1}) is an indication of the substantial rearrangement needed for protonation to accompany electron transfer in reaction [18]. The situation may be similar to that reported for the tryptophan radical (39), and studies of the activation energy of these $NH_2^{\bullet}$ oxidations of phenolates would be well worthwhile.

Between pH 9.3 and 2.3 reaction [20]

[20] $\quad NH_2^{\bullet} + e^- + 2H^+ \rightarrow NH_4^+$

will replace [17] as the dominant equilibrium process, and $E_{h(\text{radical/ammonia})}$ reaches values of 1.85, 2.09, and 2.45 at pHs of 8, 6, and 3, respectively. From a kinetic point of view of course the acquisition of two protons is more difficult than one, and rates of oxidation by $NH_2^{\bullet}$ in this pH region will probably not reflect these large potentials. On the other hand the inherent stability of NH_4^+ toward oxidation can be appreciated. For example, taking $\Delta_f G^0_{(aq)}$ of $OH^{\bullet}$ equal to 26 kJ mol^{-1} (3) and using the data in Table 7, one finds values of 6 and -47 kJ mol^{-1}, respectively, for $\Delta G^0_{[21]}$ and $\Delta G^0_{[22]}$

[21] $\quad OH^{\bullet} + NH_4^+ \rightarrow H_2O + H^+ + NH_2^{\bullet}$

[22] $\quad OH^{\bullet} + NH_3 \rightarrow H_2O + NH_2^{\bullet}$

From the corresponding equilibrium constants, for reaction [21] with $[NH_4^+] = [H^+] \approx 10^{-2}$ M, the ratio of radicals, $[NH_2^{\bullet}]/[OH^{\bullet}]$, at equilibrium would be ≈ 0.1, while for reaction [22] above the pK_a of NH_4^+ the ratio would be $\approx 10^8 \times [NH_3]$. The well-recognized (7, 8, 13) difference in reactivity of NH_4^+ and NH_3 toward $OH^{\bullet}$ can therefore be understood.

Below pK_R the radicals are protonated and [23]

[23] $\quad NH_3^{\bullet+} + e^- + H^+ \rightarrow NH_4^+$

is the important equilibrium reaction. Here the H_2O molecules in the solvation shell of $NH_3^{\bullet+}$ have their protons directed away from the $N^{\bullet+}$ center, and proton transfer from solvent is not likely to be as facile as for $NH_2^{\bullet}$ in alkaline solution. From a kinetic point of view reaction [23] may therefore be a two-step process:

[24] $\quad NH_3^{\bullet+} + e^- \rightarrow NH_3$

[25] $\quad NH_3 + H^+ \rightarrow NH_4^+$

Based on the $\Delta_f G^0_{(aq)}$ data in Table 5, $E^0(NH_3^{\bullet+}/NH_3)$ is 2.12 V. This is in agreement with Stanbury's estimate (3), which was also based on $pK_r = 2.3$. Thus $NH_3^{\bullet+}$ is a very strong oxidant.

5. Summary and conclusions

The G2 results for isolated species have been shown to be in excellent agreement with available gas phase experimental data. This agreement and the consistency between different reaction paths has confirmed the reliability to ± 2 kJ mol^{-1} of the values of $\Delta_f H^0_{(g)}$ for $NH_2^{\bullet}$, NH_2^-, and $NH_3^{\bullet+}$. Gas phase thermodynamic functions, with $\Delta_f G^0_{(g)}$ based on the most reliable values of $\Delta_f H^0_{(g)}$, have been calculated for $NH_2^{\bullet}$, NH_2^-, $NH^{\bullet-}$, $NH_3^{\bullet+}$, and NH_4^+.

Ab initio calculations, which established the structures, binding energies, and transition energies of aquo complexes, have been used as an aid in evaluating the solution structure and free energies and interpreting the absorption spectra of $NH_2^{\bullet}$ and $NH_3^{\bullet+}$ in solution. The weak absorption observed experi-

[5] Note that $E_{[17]}$ and $E_{[18]}$ are identical at the same pH.

Can. J. Chem. Downloaded from www.nrcresearchpress.com by 195.246.54.202 on 09/08/12
For personal use only.

mentally at 520 nm for the former is confirmed as a $^2B_1 \rightarrow {}^2A_1$ transition, probably slightly blue shifted due to interaction with H_2O. The stronger $NH_2^\bullet$ absorption occurring below 250 nm has been identified as a solvent-to-solute charge transfer band. The absorption of $NH_3^{\bullet+}$, which arises monotonically below 370 nm, is also attributed to a solvent-to-solute charge transfer band.

Based on the energetics of H-bonding interactions, Stanbury's value of $\Delta G^0_{(s)}$ of $NH_2^\bullet = -8.0$ kJ mol^{-1} is justified. The present study also confirms the reliability of his values of $E^0(NH_2^\bullet, H^+/NH_3)$, $E^0(NH_3^{\bullet+}/NH_3)$, and $\Delta_f G^0_{(aq)}$ for $NH_2^\bullet$ and $NH_3^{\bullet+}$. Also the free energy of solution of $NH_3^{\bullet+}$ is shown to be larger[6] than that of NH_4^+. Examination of the redox chemistry of $NH_2^\bullet$ in the light of the structures of the aquo complexes suggests that reaction [18],

$$[18] \qquad NH_2^\bullet + e^- + H_2O \rightarrow NH_3 + OH^-$$

which involves proton transfer from solvent, is likely to be the major half-reaction in alkaline solution. The present thermochemical data also explain the reason for the stability of NH_4^+ toward attack by $OH^\bullet$ radicals.

6. Acknowledgement

The financial support of the Natural Sciences and Engineering Research Council of Canada is gratefully acknowledged.

1. J.F. Endicott. *In* Concepts of inorganic photochemistry. *Edited by* A.W. Adamson and P.D. Fleischauer. Wiley, New York. 1975. p. 81.
2. A.M. Newton and T.W. Swaddle. Can. J. Chem. **52**, 2751 (1974).
3. D.M. Stanbury. Adv. Inorg. Chem. **33**, 69, (1989).
4. Y.L. Chow, W.C. Danen, S.F. Nelsen, and D.H. Rosenblatt. Chem. Rev. **78**, 243 (1978).
5. T.P. Singer, R.W. Van Korff, and D.L. Murphy (*Editors*). Monoamine oxidase: structure, function, and altered functions. Academic Press, New York. 1979; and references cited therein.
6. B. Hickel and K. Sehested. Radiat. Phys. Chem. **39**, 355 (1992).
7. P.B. Pagsberg. Riso Report No. 256, Danish atomic energy commission, Riso, Denmark. 1972.
8. M. Simic and E. Hayon. J. Am. Chem. Soc. **93**, 5982 (1971).
9. M.Z. Hoffman and K.R. Olson. J. Phys. Chem. **82**, 2631 (1978).
10. G. Farnia, R. Tomat, and E. Vianello. J. Chem. Soc. Perkin Trans. 2, 763 (1975).
11. R. Tomat and A. Rigo. J. Electroanal. Chem. **63**, 329 (1975).
12. B.C. Gilbert and P.R. Marriott. J. Chem. Soc. Perkin Trans. 2, 987 (1977), and references therein.
13. P. Neta, P. Maruthamuthu, P.M. Carton, and R.W. Fessenden. J. Phys. Chem. **82**, 1875 (1978).
14. S.G. Lias, J.E. Bartmess, J.F. Liebman, J.L. Holmes, R.D. Levin, and W.G. Mallard. J. Phys. Chem. Ref. Data, **17**, Suppl. No. 1 (1988).
15. C.T. Wickham-Jones, K.M. Ervin, G.B. Ellison, and W.C. Lineberger. J. Chem. Phys. **91**, 2762 (1989).
16. W.R. Anderson. J. Phys. Chem. **93**, 530 (1989).
17. L.A. Curtiss, K. Raghavachari, G.W. Trucks, and J.A. Pople. J. Chem. Phys. **94**, 7221 (1991).
18. M.J. Frisch, M. Head-Gordon, G.W. Trucks, J.B. Foresman, H.B. Schlegel, K. Raghavachari, M.A. Robb, J.S. Binkley, C. Gonzalez, D.J. Defrees, D.J. Fox, R.A. Whiteside, R. Seeger, C.F. Melius, J. Baker, R.L. Martin, L.R. Kahn, J.J.P. Stewart, S. Topiol, and J.A. Pople. Gaussian, Inc., Pittsburgh, Pa. 1990.
19. J.A. Pople, H.B. Schlegel, R. Krishnan, D.J. Defrees, J.S. Binkley, M.J. Frisch, R.A. Whiteside, R.F. Hout, and W.J. Hether. Int. J. Quantum Chem. Symp. **15**, 269 (1981).
20. D.A. Armstrong, A. Rauk, and D. Yu. Can. J. Chem. **71**, 1368 (1993).
21. JANAF thermochemical tables. 2nd ed. Natl. Stand. Ref. Data Ser. NSRDS–NBS 31. U.S. Government Printing Office, Washington, D.C. 1971, and update in ref. 34.
22. W. Meyer. J. Chem. Phys. **58**, 1017 (1973).
23. T. Nakanaga and T. Amano. Can. J. Phys. **64**, 1356 (1986).
24. M.E. Jacox. J. Phys. Chem. Ref. Data, **13**, 945 (1984).
25. B.J. Smith and L. Radom. J. Phys. Chem. **95**, 10549 (1991).
26. M.J. Frisch, J.E. Del Bene, J.S. Binkley, and H.F. Schaefer III. J. Chem. Phys. **84**, 2279 (1986).
27. J.E. Del Bene. J. Comput. Chem. **10**, 603 (1989).
28. J.A. Pople. Faraday Discuss. Chem. Soc. **73**, 7 (1982).
29. Z. Latajka and S. Scheiner. J. Comput. Chem. **8**, 674 (1987).
30. P.M.W. Gill and L. Radom. J. Am. Chem. Soc. **110**, 4931 (1988).
31. T. Clark. J. Am. Chem. Soc. **110**, 1672 (1988).
32. G. Herzberg and D.A. Ramsay. Faraday Discuss. Chem. Soc. **14**, 11 (1953); S.C. Ross, F.W. Birss, M. Vervloet, and D.A. Ramsay. J. Mol. Spectrosc. **129**, 436 (1988).
33. A. Treinin and E. Hayon. J. Am. Chem. Soc. **97**, 1716 (1975).
34. D.D. Wagman, W.H. Evans, V.B. Parker, R.H. Schumm, I. Halow, S.M. Bailey, K.L. Churney, and R.L. Nuttall. J. Phys. Chem. Ref. Data, **11**, Suppl. No. 2 (1982).
35. X. Tarrago. Ann. Chim. (Paris), **5**, 5 (1960).
36. D.A. Armstrong, A. Rauk, and D. Yu. J. Am. Chem. Soc. **115**, 666 (1993).
37. R.G. Pearson. J. Am. Chem. Soc. **108**, 6109 (1986).
38. P. Wardman. J. Phys. Chem. Ref. Data, **18**, 1637 (1989).
39. S.V. Jovanovic, S. Steenken, and M.G. Simic. J. Phys. Chem. **95**, 684 (1991).
40. J. March. Advanced organic chemistry, reactions, mechanism and structure. 3rd ed. J. Wiley & Sons, New York. 1985.
41. M. Meot-Ner and L.W. Sieck. J. Am. Chem. Soc. **113**, 4448 (1991); J. E. Szulejko and T.B. McMahon. Int. J. Mass Spectrom. Ion. Processes, **109**, 279 (1991).
42. J.E. Szulejko and T.B. McMahon. J. Am. Chem. Soc. **115**, 7839 (1993).

[6]Experimental results in 1991 (41) indicated that an increase of 14 kJ mol^{-1} in the proton affinity of NH_3 might be needed. Since the values of $\Delta_f H^0_{(298)}$ and $\Delta_f G^0_{(298)}$ for $NH_{4(g)}^+$ in Table 3 are calculated from this proton affinity, $\Delta G^0_{(s)}$ of NH_4^+ would be altered and the difference between $\Delta G^0_{(s)}$ of $NH_3^{\bullet+}$ and NH_4^+ would increase by 14 kJ mol^{-1}. The proton affinity of 854 kJ mol^{-1} used here is supported by more recent experimental results (42), which contradict the increase in proton affinity, and by higher level *ab initio* calculations reviewed in ref. 42. Thus the difference in $\Delta G^0_{(s)}$ of $NH_3^{\bullet+}$ and NH_4^+ remains near 25 kJ mol^{-1}.

Effect of multiple encounters on vibrational to translational energy transfer

NEIL SNIDER
Department of Chemistry, Queen's University, Kingston, ON K7L 3N6, Canada
Received June 4, 1993
This paper is dedicated to Professor John C. Polanyi on the occasion of his 65th birthday

NEIL SNIDER. Can. J. Chem. **72**, 484 (1994).

Vibrational to translational energy transfer was studied computationally and analytically for collinear, impulsive collisions with square well oscillators, harmonic oscillators, and Morse oscillators. At a fixed temperature T the average number of encounters is between one and two if the vibrational energy E_v is large compared to kT and (or) if the relative mass of the collider is small. If these conditions are met, $\langle \Delta E \rangle$, the average energy transferred per collision, varies nearly linearly with E_v over a wide range. If the average number of encounters is greater than two, $\langle \Delta E \rangle$ as a function of E_v has a more complicated form. The average final energy, $\langle \Delta E \rangle + E_v$ is less than what is predicted by the single encounter impulsive collision (SEI) model. Other things being equal, the ratio of the actual average final energy to the SEI average final energy is roughly the same for all of the above mentioned oscillators.

NEIL SNIDER. Can. J. Chem. **72**, 484 (1994).

Faisant appel à des méthodes de calculs et analytiques, on a étudié le transfert d'énergie de vibration en énergie de translation de collisions colinéaires et impulsives avec des oscillateurs à puits carré, des oscillateurs harmoniques et des oscillateurs de Morse. À une température donnée, T, la moyenne des rencontres se situe entre un et deux si l'énergie de vibration, E_v, est importante par rapport à kT et (ou) si la masse relative de l'entité que entre en collision est faible. Lorsque ces conditions sont remplies, $\langle \Delta E \rangle$, l'énergie moyenne transférée par collision, varie d'une façon pratiquement linéaire avec E_v pour un grand ensemble de valeurs. Si le nombre moyen des rencontres est plus grand que deux, la variation de $\langle \Delta E \rangle$ en fonction de E_v prend une forme beaucoup plus compliquée. L'énergie finale moyenne, $\langle \Delta E \rangle + E_v$, est plus faible que la valeur prédite par le modèle de la collision impulsive à rencontre unique (SEI). Tous les autres facteurs étant égaux, le rapport de l'énergie finale moyenne réelle par rapport à celle calculée par le modèle de la collision impulsive à rencontre unique est approximativement la même pour tous les oscillateurs mentionnés plus haut.

[Traduit par la rédaction]

Introduction

Vibrational excitation and deexcitation are known to be important in a number of chemical reactions. For example, in gas phase recombination of diatomic molecules the molecule is initially formed with a large amount of vibrational energy. The rate constant for such a reaction decreases with increasing temperature. Professor Polanyi (1) was one of the first to note that slow vibrational deactivation of the nascent diatomic is one factor that brings about this atypical temperature dependence of the rate constant. Also, in unimolecular reactions the importance of energy transfer is well known. Methods have been devised whereby one may decouple the energy transfer steps from the reaction steps and thereby extract energy transfer information from rate data for unimolecular reactions (2). More recently, experimental methods for obtaining energy transfer information by more direct means have been developed (3, 4). These developments have increased the interest in theoretical interpretation of vibrational energy transfer.

Given the power of present day computers, one may simulate by classical trajectories the energy transfer in systems with several degrees of freedom. These calculations have provided ample information concerning the factors that affect energy transfer. On the other hand, the amount of detail in a model with several degrees of freedom is so large as to limit one's understanding of the collision dynamics. Hence, there is a need to investigate simple models where the factors that influence energy transfer are in better focus. The simplest of such models even provide analytic formulas.

One factor that influences not only energy transfer but also energy disposal in chemical reactions is the occurrence of multiple encounters in the course of a collision. Professor Polanyi's group was the first to note the effect of multiple encounters on energy disposal in reactive collisions (5). Strictly speaking, multiple encounters only occur if the interaction potential is of the form of a hard wall. If the interaction potential is of finite range, then secondary, tertiary, etc. encounters are defined only in a rough sense. The earliest theoretical investigations (6–10) of the effects of multiple encounters on energy transfer were carried out on collinear, impulsive models of atom–diatom collisions,

$$AB(E_v) + C \longrightarrow AB(E_v') + C$$

where E_v and E_v' are the vibrational energies of AB before and after the collision. The present paper may be regarded as a sequel to these early works.

At its most detailed level, energy transfer is characterized by a probability distribution function $\rho(\Delta E)$ where ΔE is given by

$$\Delta E = E_v' - E_v$$

A more coarse-grained description of the energy transfer is obtained from the lower moments of ρ. Of these, the first moment $\langle \Delta E \rangle$ is the most easily accessible experimentally. If the A–B interaction is a square well, i.e., if AB is a "string oscillator" (6), then analytic formulas exist for $\rho(\Delta E)$ and for $\langle \Delta E \rangle$ (6, 9, 10). Thus it is of interest to establish the extent to which the string oscillator's $\rho(\Delta E)$ and $\langle \Delta E \rangle$ are good approximations to $\rho(\Delta E)$ and $\langle \Delta E \rangle$ for more realistic oscillators, i.e., the harmonic oscillator and the Morse oscillator.

The dependence of $\langle \Delta E \rangle$ on E_v is of some interest. In many studies, both experimental (11–14) and theoretical (15–17), $\langle \Delta E \rangle$ has been found to vary linearly with E_v in some intermediate range of E_v. At high E_v, $-\langle \Delta E \rangle$ has been found to level off or, at the least, to have a decreasing first derivative (11, 15). A classical trajectory study of AB + C with AB mod-

Can. J. Chem. Downloaded from www.nrcresearchpress.com by 195.246.54.202 on 09/08/12
For personal use only.

Can. J. Chem. Downloaded from www.nrcresearchpress.com by 195.246.54.202 on 09/08/12
For personal use only.

eled as a Morse oscillator showed that a leveling off and an eventual downturn of $-\langle\Delta E\rangle$ are consequences of increasing anharmonicity (18). At low E_v, $\langle\Delta E\rangle$ has been found to vary as E_v^p where p is around two or larger (14, 17). This behavior has been ascribed to a number of factors, one of which is multiple encounters (17). It is therefore of interest to investigate the form of $\langle\Delta E\rangle$ as a function of E_v for simple models wherein collisions consist of one or more impulsive encounters.

It has been argued that multiple encounters play an important role in collisions of a monatomic molecule with a large polyatomic molecule and that a simple model, namely the biased random walk model, makes accurate predictions for such collisions (19, 20). One of the notable predictions of the biased random walk model is that $\rho(\Delta E)$ is a Gaussian. It is therefore of interest to determine the form of $\rho(\Delta E)$ for collinear, impulsive models at mass ratios such that the average number of encounters per collision is large. The investigation here reported addresses this matter and those mentioned before it.

Equations of motion

The model here considered is one of a structureless particle of mass m_C colliding collinearly with a particle of mass m_B, which is bound to a third particle of mass m_A. The interaction potential between B and C is a hard wall. Thus a collision consists of N impulsive encounters. Three different potentials were assumed: the square well, the harmonic, and the Morse.

The equations of motion for such a model have been amply discussed in the literature (7–10). What follows is a summary of those basic relations which are necessary to indicate the way in which the results here reported were calculated.

If coordinates and time are suitably scaled, the B–C distance z may be expressed as

$$[1] \qquad z = \pm b_0 g_n^{1/2}\theta - \sigma(\theta)$$

where g_n is the ratio of the relative kinetic energy to the vibrational energy following the nth encounter, θ is a dimensionless variable proportional to time, and b_0 is related to the masses of A, B, and C,

$$[2] \qquad b_0 = \tan\psi = \left[\frac{m_B(m_A + m_B + m_C)}{m_A m_C}\right]^{1/2}$$

The angle ψ is the skew angle in the potential energy surface. The function $\sigma(\theta)$ depends on the nature of the A–B potential. For the string oscillator σ is given by

$$\sigma(\theta) = -\theta \qquad \text{for } \theta < \theta_n$$
$$= \theta - \theta_n \qquad \text{for } \theta > \theta_n$$

where θ_n is directly proportional to the time that the oscillator would have required to reach the point of the nth encounter if at time zero it had been at the origin of the oscillator coordinate. For the string oscillator the origin is here taken to be the inner turning point. For the harmonic oscillator with the origin at the outer turning point σ is given by

$$\sigma(\theta) = \cos(\theta + \theta_n) - \cos\theta_n$$

The Morse oscillator may be bound or unbound after the nth encounter, and the form of σ depends on this factor. In addition, σ depends not only on the parameter θ_n but also on a parameter α_n defined by

$$\alpha_n = \cos^{-1}\left[\left(\frac{E_{vn}}{d_e}\right)^{1/2}\right] \qquad \text{for } E_{vn} < d_e$$
$$= \cosh^{-1}\left[\left(\frac{E_{vn}}{d_e}\right)^{1/2}\right] \qquad \text{for } E_{vn} > d_e$$

where E_{vn} is the vibrational energy of the oscillator following the nth encounter and d_e is the dissociation energy. The Morse oscillator σ is given by

$$\sigma = \tan\alpha_n \ln\left[\frac{\cos\alpha_n\cos(\theta+\theta_n)+1}{\cos\alpha_n\cos\theta_n+1}\right] \text{ for } E_{vn} < d_e$$
$$= \tanh\alpha_n \ln\left[\frac{\cosh\alpha_n\cosh(\theta+\theta_n)-1}{\cosh\alpha_n\cosh\theta_n-1}\right]$$
$$\text{for } E_{vn} > d_e$$

One sees that the first of the above formulas for σ reduces to the harmonic oscillator formula in the limit of vanishingly small E_{vn}. For all three oscillators, the pertinent parameters have been absorbed into the dimensionless dynamical variables.

For θ positive but close to zero, z is positive. The necessary and sufficient condition for an $(n+1)$th encounter is that z go negative at some positive value of θ, call it θ'_{n+1}. For the string oscillator θ'_{n+1} may be found in closed form. For the other oscillators the appropriate zero of $z(\theta)$ must be determined numerically. Newton's method is a convenient computational method for this determination, but one must take care to choose the initial value of θ such that the iteration converges properly. In the investigation here reported the iteration was started at the first inflection point in $z(\theta)$. It should be noted that for the harmonic and the Morse oscillators θ_{n+1} generally differs from θ'_{n+1} because the location of the turning points depends on g_{n+1}. The relation between θ'_{n+1} and θ_{n+1} is established by the condition that the oscillator displacement relative to the potential minimum is unchanged in an impulsive encounter.

From θ'_{n+1} one may determine g_{n+1} from the law of conservation of energy and the fact that z-momentum only changes sign in an impulsive collision. One thereby obtains

$$[3] \qquad \pm g_{n+1}^{1/2} = (\pm g_n^{1/2}\cos 2\psi + u_n \sin 2\psi)$$
$$\times [1 + (g_n - u_n^2)\sin^2 2\psi \mp 2g_n^{1/2}u_n \sin 2\psi \cos 2\psi]^{-1/2}$$

where the upper sign refers to motion of C away from AB, ψ is given by eq. [2], and u_n is given by

$$u_n = \frac{d\sigma}{d\theta}\Big)_{\theta=\theta'_{n+1}}$$

If there is no subsequent encounter then, by conservation of energy, ΔE is given by

$$[4] \qquad \frac{\Delta E}{E_v} = (g - g_N)(1 + g_N)^{-1}$$

where N is defined above and g is the ratio of the initial relative kinetic energy E_r to the initial vibrational energy E_v.

Can. J. Chem. Downloaded from www.nrcresearchpress.com by 195.246.54.202 on 09/08/12
For personal use only.

It is well known (7–10) that for the string oscillator and for the harmonic oscillator, g_N depends not on E_r and E_v separately but only on their ratio g. For the Morse oscillator, on the other hand, g_N does depend on E_r and E_v separately.

To obtain $\langle\Delta E\rangle$, one must average over an appropriate ensemble of θ_0's. For the string oscillator a uniform ensemble of θ_0's is the appropriate one. More generally, it is the ensemble derived from a uniform ensemble of z's. Thus the desired ensemble of θ_0's is obtained by solving eq. [1], taking for the left hand side values of z that are equally spaced. Such calculations are also done conveniently using Newton's method. Let the average of ΔE over this ensemble be denoted $\langle\Delta E\rangle_g$. The thermal average of $\langle\Delta E\rangle$ is found from $\langle\Delta E\rangle_g$ via Boltzmann averaging,

$$\frac{\langle\Delta E\rangle}{E_v} = \beta_v \int_0^\infty \frac{\langle\Delta E\rangle_g}{E_v} \exp(-\beta_v g)\, dg$$

with β_v equal to E_v/kT. In what follows the subscript g will be dropped if it is obvious that an average at fixed relative kinetic energy is being considered.

Results

Dependence of $\langle\Delta E\rangle$ *on initial vibrational energy*

Figure 1 shows plots of $-\langle\Delta E\rangle/kT$ vs. E_v/kT for the harmonic oscillator at b_0 values of 0.414, 1.000, and 2.414. These b_0 values represent ψ values of 22.5°, 45°, and 67.5°. The curve for $b_0 = 2.414$ is nearly a straight line, although careful inspection shows it to be slightly downward concave. The curve for $b_0 = 1.000$ has a minimum at E_v equal to a few tenths of kT. To a good approximation, both plots are straight lines over a considerable range of E_v. For E_v less than kT the curve for $b_0 = 0.414$ is rather similar to that for $b_0 = 1.000$. The most striking feature of the $b_0 = 0.414$ curve is the nearly level portion which extends from 5 kT to 10 kT. As will be shown below, this leveling of the curve is due to multiple encounters. Calculations at small g and $b_0 = 0.414$ indicate that $-\langle\Delta E\rangle$ increases linearly with E_v for this value of b_0 at E_v beyond the range covered by Fig. 1.

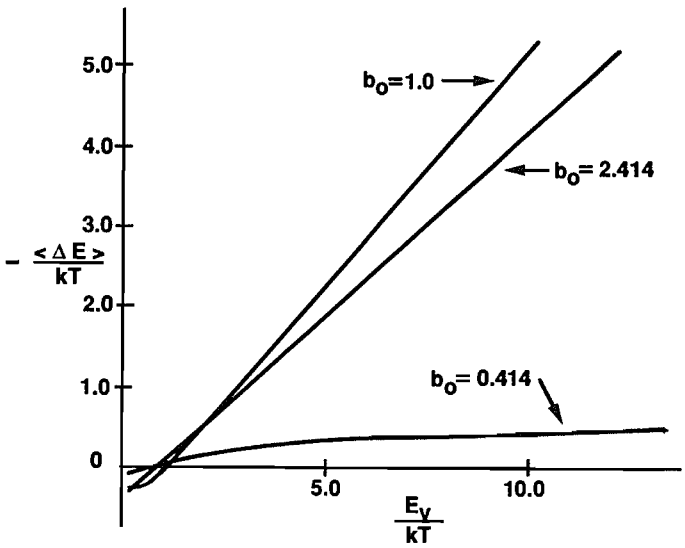

FIG. 1. Average energy transferred per collision as a function of initial vibrational energy for a harmonic oscillator in collinear, impulsive collisions at different mass ratios.

Energy transfer probability distributions

The function $\rho(\Delta E)$ for the string oscillator is obtainable in closed form. In general, the formula is quite complicated, but for small b_0 and moderate to large β_v it is not so complicated as to be uninstructive. In previous treatments of the string oscillator (6, 9) the distribution over final momenta was derived. Even though ΔE is related in a simple way to the squares of the initial and the final momenta, a derivation of $\rho(\Delta E)$ for the string oscillator seems appropriate here by way of reinforcing the connection between this work and what has gone before. This derivation is presented in Appendix A.

The final result is expressed more succinctly in terms of h, the ratio of the final vibrational energy to the initial,

$$h = 1 + \Delta E/E_v$$

For β_v sufficiently large that the condition

$$\exp(-\beta_v b_0^{-2}) \approx 0$$

is met one has for the string oscillator

$$[5]\quad \rho(h) \approx \beta_v \sum_{N>n_-(h)}^{\mathcal{N}-1} D_N^{-1}\{\cos[(N-1)\psi] - h^{-1/2}\cos[(N+1)\psi]\} \exp[-\beta_v \csc^2 2N\psi(h^{1/2} - \cos 2N\psi)^2] \quad \text{for } h < 1$$

$$\approx \beta_v \sum_{N>n_+(h)}^{\mathcal{N}-1} D_N^{-1}\{h^{-1/2}\cos[(N-1)\psi] - \cos[(N+1)\psi]\} \exp[-\beta_v \cos^2 2N\psi(h^{1/2} - \cos 2N\psi)^2] \quad \text{for } h > 1$$

where $\mathcal{N}$ is the largest integer such that $2\mathcal{N}\psi$ is less than π, $n_\pm(h)$ is given by

$$n_\pm(h) = \psi^{-1}\tan^{-1}\left(b_0 \frac{\pm h^{1/2} \mp 1}{h^{1/2}+1}\right)$$

and D_N is given by

$$D_N = (\cos 2N\psi + 1)\{\cos[(N-1)\psi] - \cos[(N+1)\psi]\}$$

The interested reader may consult Appendix A for the derivation of eq. [5]. Inspection of eq. [5] gives the impression that $\rho(h)$ is not far different from the exponential function

$$[6]\quad \rho(h) \sim \exp[\alpha(h-1)] \quad \text{for } h < 1$$

$$\sim \exp[\gamma(1-h)] \quad \text{for } h > 1$$

which has been used frequently to model the energy transfer distributions (2).

Can. J. Chem. Downloaded from www.nrcresearchpress.com by 195.246.54.202 on 09/08/12
For personal use only.

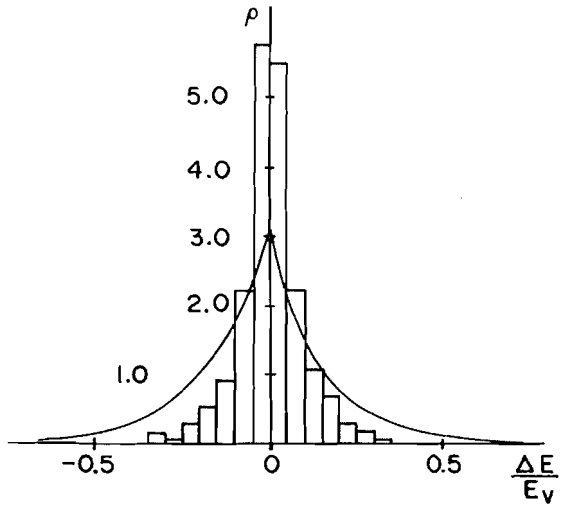

FIG. 2. Energy transfer probability distributions for collinear impulsive collisions at $kT = E_v$ and $b_0 = 0.132$. Histogram: harmonic oscillator. Solid line: string oscillator.

Figure 2 shows a plot of $\rho(\Delta E)$ derived from eq. [5] along with one computed for the harmonic oscillator, both for $b_0 = 0.132$ ($\psi = 7.5°$) and E_v equal to kT. The $\rho(\Delta E)$ for the harmonic oscillator is narrower, but both curves are closely approximated by eq. [6]. The average number of encounters for both of the ensembles to which these plots pertain is about six.

SEI model

In the SEI model the outcome of the collision is assumed to be that of the first encounter. The SEI model gives the following formula for $\langle \Delta E \rangle$ for all the oscillators considered when g is greater than b_0^2,

$$\langle \Delta E \rangle_{SEI}/E_v = [g - (2 - b_0^{-2})\langle E_k \rangle/E_v] \sin^2 2\psi$$

where $\langle E_k \rangle$ is the average kinetic energy of the oscillator. For the string oscillator $\langle \Delta E \rangle_{SEI}$ is also known analytically for g less than b_0^2,

$$\langle \Delta E \rangle_{SEI}/E_v = (g - 1) \sin^2 2\psi + g^{1/2} \sin 4\psi$$

These equations may be obtained easily from eqs. [3] and [4] by setting N equal to one and taking the lower sign on the right of eq. [3]. For the harmonic oscillator and the Morse oscillator one can show that for g approaching zero, $\langle \Delta E \rangle_{SEI}$ has the asymptotic form

$$[7] \qquad \langle \Delta E \rangle_{SEI}/E_v = -2\pi \tan\frac{\alpha}{2} \sin^2 2\psi b_0 g^{1/2}$$

where α is given by $\alpha = \cos^{-1}[(E_v/d_e)^{1/2}]$. The harmonic oscillator formula is obtained by setting α equal to $\pi/2$. A derivation of eq. [7] is provided in Appendix B.

For the string oscillator there are values of g for which the SEI model is exact, i.e., for which no multiple encounters occur. Figure 3 shows the regions of the ψ–χ_0 plane in which the SEI model is and is not exact for the string oscillator. The angle χ_0, which is defined by

$$[8] \qquad \chi_0 = \tan^{-1}(g^{-1/2})$$

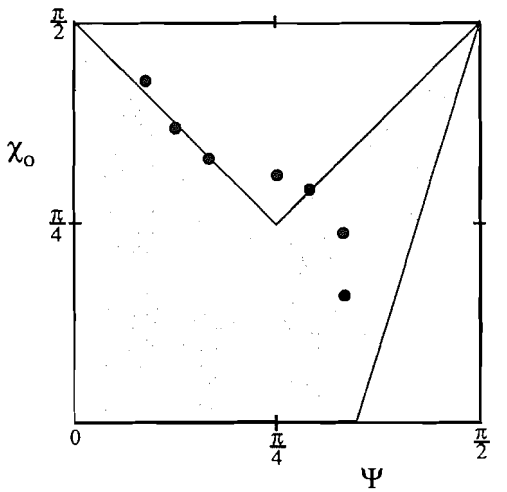

FIG. 3. Multiple encounter regions in the ψ–χ_0 plane for collinear impulsive collisions. Shaded region is the multiple encounter region for the string oscillator. Filled circles indicate the boundary of the region wherein the multiple encounters correction for the hamonic oscillator is less than 0.9.

is used in place of g in order to provide a neater representation. For all of the other oscillators the SEI model becomes exact asymptotically as g goes to zero, i.e., as χ_0 goes to $\pi/2$. Figure 3 also indicates the boundary of the region of the ψ–χ_0 plane wherein the average of h for the harmonic oscillator is less than 0.9 of the SEI average of h. Because it does yield simple formulas and because its underlying assumptions are correct in certain limits, the SEI model has merit as a standard of comparison.

It may be proven generally that $\langle \Delta E \rangle_{SEI}$ is greater than or equal to the actual $\langle \Delta E \rangle$ for the string oscillator at a given g.[1] The computations carried out in the course of this investigation suggest that this result is a general one for all oscillators. It implies that the ratio of the actual average final vibrational energy to the SEI final energy always lies between zero and one,

$$0 < \langle h \rangle/\langle h \rangle_{SEI} \leq 1$$

In Table 1 are shown values of $\langle h \rangle/\langle h \rangle_{SEI}$ for the different oscillators at the same values of b_0 and g. One sees that they are all less than one. What is also noteworthy is that they do not differ greatly for the different oscillators.

Discussion

It is apparent from the aforementioned results that multiple encounters have considerable effect on the energy transfer only if b_0 is less than one. For b_0 greater than one the average number of encounters is between one and two, and $\langle \Delta E \rangle$ differs appreciably, if at all, from $\langle \Delta E \rangle_{SEI}$ only in limited ranges of g. This point is illustrated in Fig. 3. It is to be noted in Fig. 3 that at sufficiently large ψ there is a lower boundary to the region in which multiple encounters take place. This boundary intersects the ψ axis at the minimum value of ψ for which multiple encounters do not take place in impulsive collisions for which the oscillator is initially moving outward. It has been known for some time that for the harmonic oscillator this value

[1]N. Snider, unpublished results.

Can. J. Chem. Downloaded from www.nrcresearchpress.com by 195.246.54.202 on 09/08/12
For personal use only.

TABLE 1. Ratio of actual final vibrational energy to SEI final vibrational energy as a function of initial relative kinetic energy at $b_0 = 0.414$

	$\langle h\rangle/\langle h\rangle_{SEI}$			
			Morse oscillator	
g	String oscillator	Harmonic oscillator	$\cos\alpha = 0.816$	$\cos\alpha = 0.949$
0.105	1.000	0.979	0.894	0.906
0.301	0.687	0.675	0.758	0.791
0.616	0.506	0.551	0.656	0.677
1.079	0.486	0.535	0.568	0.566
1.715	0.391	0.481	0.371	0.476
2.813	0.288	0.247	0.315	0.380
3.912	0.229	0.238	0.305	0.330

TABLE 2. Final vibrational energy and SEI final vibrational energy as a function of initial vibrational energy for the harmonic oscillator

	$E_v\langle h\rangle_{SEI}/kT$		$\langle h\rangle/\langle h\rangle_{SEI}$	
E_v/kT	$b_0 = 0.414$	$b_0 = 2.414$	$b_0 = 0.414$	$b_0 = 2.414$
0.250	0.918	0.631	0.378	0.992
0.500	1.257	0.767	0.431	0.978
1.000	1.831	1.038	0.536	0.954
2.000	2.835	1.582	0.672	0.936
3.000	3.783	2.129	0.746	0.938
4.000	4.713	2.676	0.798	0.944
5.000	5.636	3.226	0.839	0.951
8.000	8.393	4.898	0.914	0.966
10.000	10.230	6.025	0.941	0.973
15.000	14.840	8.902	0.973	0.982

of ψ is about 50° (8). It is equal to 60° for the string oscillator (9).

When multiple encounters do occur, they tend to lower the final vibrational energy, i.e., they enhance the deactivation of the oscillator. This effect may be roughly understood as follows: coming into the final encounter, the oscillator usually has a large amount of vibrational kinetic energy as a result of previous encounters. The oscillator is readily deactivated if its vibrational energy is in the form of kinetic energy rather than potential energy (18). Thus the final encounter results in considerable loss of vibrational energy from the oscillator. As seen from Tables 1 and 2, the final vibrational energy in a multiple encounter collision may be only a few tenths of what is predicted on the assumption of a single encounter.

As mentioned above, a linear dependence of $\langle\Delta E\rangle$ on E_v has been noted in several studies, both experimental and theoretical. Figure 1 shows that for the harmonic oscillator model considered here, $\langle\Delta E\rangle$ varies nearly linearly with E_v over a wide range of E_v. If b_0 is greater than or approximately equal to one, this range of linearity begins at E_v roughly equal to kT. Rather more complex behaviour of $\langle\Delta E\rangle$ as a function of E_v occurs at small values of b_0. This behaviour is analyzed in Table 2. It is shown there that the SEI final vibrational energy varies almost linearly with E_v when b_0 is equal to 2.414, and also when b_0 is equal to 0.414, provided that E_v is greater than 5 kT. For $b_0 = 2.414$ the multiple encounter correction factor is never less than 0.93. For $b_0 = 0.414$ this correction factor is considerably less than one at small E_v, and it approaches one as E_v increases. Since a more positive rate of change of the final energy results in a less positive rate of change of $-\langle\Delta E\rangle$, the increase of the multiple encounters correction factor arrests the increase of $-\langle\Delta E\rangle$. This effect is most pronounced for E_v between 5 kT and 10 kT where both the correction factor and its derivative are fairly large. At E_v above 10 kT the derivative of the multiple encounters correction factor is small enough that $-\langle\Delta E\rangle$ as a function of E_v is first concave upward and then linear.

For the Morse oscillator it has been known for some time that $-\langle\Delta E\rangle$ as a function of E_v goes through a maximum and eventually goes negative (18). It is well understood that this behaviour is due to anharmonicity. As seen from Table 1, the multiple encounter corrections for the Morse oscillator tend to be somewhat lower than those for the harmonic oscillator when g is small and somewhat higher when g is large. At low g, anharmonicity increases the likelihood of multiple encounters, both because the initial encounter may take place further from the outer turning point and because it is more probable that the first encounter will be with the oscillator when it is moving inward, a situation that may preclude reversal of the direction of motion of the collider. At high values of g these differences between the harmonic oscillator and the Morse oscillator are less important, and the deciding factor is the tendency for ΔE in a given encounter to be higher if the oscillator is anharmonic. In none of the cases here considered do the multiple encounters corrections differ greatly for the Morse oscillators as compared to the harmonic oscillator. This finding is not in agreement with results of a previous study of the effects of anharmonicity on energy transfer (21). This previous study was, however, limited to the case of zero initial vibrational energy and thus pertains to a different energy range.

As seen from Fig. 1, $\langle\Delta E\rangle$ for the harmonic oscillator varies linearly with E_v if E_v is somewhat larger than kT and if b_0 is greater than or about equal to one. For smaller b_0, linear behaviour also occurs but at higher values of E_v. At very large E_v, $\langle\Delta E\rangle$ varies as $E_v^{1/2}$, as is shown in Appendix B. The linear dependence may be explained as a consequence of there being more energy for the oscillator to transfer if E_v is large. For E_v sufficiently large this linear increase is offset by the restriction of collisions to single encounters with the oscillator near its outer turning point. When the oscillator is so positioned, most of its energy is in the form of potential energy, which is not transferable in an impulsive encounter. The computations here reported indicate that the resulting $E_v^{1/2}$ dependence of $\langle\Delta E\rangle$ does not set in until E_v is well above 10 kT.

In a qualitative sense the dependence of $\langle\Delta E\rangle$ on E_v found in the present study is similar to what has been found in other studies. The utility of collinear studies is limited, however, because quantitative comparisons are ambiguous: it is not clear what to take for E_v in the case of a molecule with many vibrational degrees of freedom. It has been proposed that one should take E_v to be the total vibrational energy divided by the total number of vibrational modes (20). A more reasonable course might be to divide the total vibrational energy by the number of active modes. How the active modes are to be determined is an open question.

It has been found that $\rho(\Delta E)$ may be a rather complicated function for collinear models (22). In particular, ρ often has secondary peaks, and these peaks may occur at large, negative, values of ΔE. Peaks at large, negative, ΔE are indicative of

so-called supercollisions, which have recently attracted some interest, both experimental (23) and theoretical (24). It is to be noted that such peaks are almost nonexistent in the $\rho(\Delta E)$'s calculated in this investigation, which focussed on cases in which the number of encounters is large. As seen from Fig. 2, $\rho(\Delta E)$ in such cases is very nearly exponential. The exponential behaviour arises because the range of possible ΔE's increases with the number of encounters. In turn, the number of encounters increases with increasing g. Thus, the exponential behavior is related to the Boltzmann factor $\exp(-\beta_v g)$, which weights the thermal average over g. In no case here considered was $\rho(\Delta E)$ well approximated by a Gaussian, as predicted by the biased random walk model. Apparently, the vibrational mode that interacts with the collider must interact with other modes as well if the biased random walk model is to be an appropriate model for the collision.

Conclusion

Early work on collinear models (6–10) provided a sketch of the role of multiple encounters in energy transfer. Multiple encounters have a major effect on energy transfer only for ψ less than 45°. Thus, impulsive collisions for which mass combinations are such that ψ is appreciably greater than 45° are, to a good approximation, single encounter events. It has been proposed here that the effect of multiple encounters be quantified in terms of a factor that corrects the final vibrational energy predicted by the SEI model. For ψ less than 45° this factor is small at low E_v, and it increases at a decreasing rate with increasing E_v. When combined with the more or less linearly varying SEI final energy, the result is a curve with a broad inflection. Other things being equal, and provided that E_r is not extremely large, this correction for multiple encounters is nearly the same for the string oscillator, the harmonic oscillator, and the Morse oscillator. This finding has an added appeal in that the correction factor can be expressed analytically in the case of the string oscillator.

The effect of multiple encounters on $\rho(\Delta E)$ is to make it more nearly like the ρ for the exponential model. This result suggests that the Gaussian form of $\rho(\Delta E)$ predicted by the biased random walk model requires not only multiple encounters between the collider and the vibrational modes of the molecule but also concurrent interactions among these modes. An investigation of this combination of interactions in a relatively simple model is presently under consideration.

Acknowledgements

This work was supported by a grant from the Natural Sciences and Engineering Research Council of Canada. Much of it was carried out while the author was on sabbatical leave at Northwestern University. The hospitality of Northwestern's Chemistry Department is gratefully acknowledged. The work owes much to helpful discussions with Professor George Schatz.

1. J.C. Polanyi. J. Chem. Phys. **31**, 1338 (1959).
2. D.C. Tardy and B.S. Rabinovitch. Chem. Rev. **77**, 369 (1977).
3. I. Oref and D.C. Tardy. Chem. Rev. **90**, 1407 (1990).
4. X. Yang and A. Wodtke. Int. Rev. Phys. Chem. **12**, 123 (1993).
5. P.J. Kuntz, E.M. Nemeth, J.C. Polanyi, S.D. Rosner, and C.E. Young. J. Chem. Phys. **44**, 1168 (1966).
6. B. Widom. J. Chem. Phys. **28**, 918 (1958).
7. S.W. Benson, G.C. Berend, and J.C. Wu. J. Chem. Phys. **38**, 25 (1963).
8. D. Secrest. J. Chem. Phys. **51**, 421 (1969).
9. R.J. Rubin. J. Chem. Phys. **40**, 1069 (1964); M.P. Hanson and M. Blomme. J. Chem. Phys. **50**, 4324 (1969); M.P. Hanson and L.G. Werbelow. J. Chem. Phys. **58**, 3669 (1973).
10. H.K. Shin. Vibrational energy transfer. *In* Modern theoretical chemistry. Vol. 2A. *Edited by* W.H. Miller. Plenum Press, New York. 1976.
11. H. Hippler, L. Lindemann, and J. Troe. J. Chem. Phys. **83**, 3906 (1985); M. Heymann, H. Hippler, D. Nahr, H.J. Plach, and J. Troe. J. Phys. Chem. **92**, 5507 (1988); J. Shi and J.R. Barker. J. Chem. Phys. **88**, 6219 (1988); H. Hippler, B. Otto, and J. Troe. Ber. Bunsen-ges. Phys. Chem. **93**, 428 (1989); B.M. Toselli, J.D. Brenner, M.L. Yerram, W.E. Chin, K.D. King, and J.R. Barker. J. Chem. Phys. **95**, 176 (1991).
12. J.E. Dove, H. Hippler, and J. Troe. J. Chem. Phys. **82**, 1907 (1985).
13. K.M. Beck and R.J. Gordon. J. Chem. Phys. **87**, 5681 (1987); **92**, 6011 (1990).
14. M. Heymann, H. Hippler, and J. Troe. J. Chem. Phys. **87**, 3867 (1987); B. Abel, B. Herzog, H. Hippler, and J. Troe. J. Chem. Phys. **91**, 900 (1989).
15. H. Hippler, H.W. Schranz, and J. Troe. J. Phys. Chem. **90**, 6158 (1986).
16. M. Bruehl and G.C. Schatz. J. Phys. Chem. **92**, 7223 (1988).
17. G. Lendvay and G.C. Schatz. J. Phys. Chem. **95**, 8748 (1991); J. Chem. Phys. **98**, 1034 (1993).
18. D.J. Nesbitt and J.T. Hynes. J. Chem. Phys. **76**, 6002 (1982).
19. R.G. Gilbert. J. Chem. Phys. **80**, 5501 (1984); R.G. Gilbert and I. Oref. J. Phys. Chem. **95**, 5007 (1991).
20. D.L. Clarke, I. Oref, R.G. Gilbert, and K.F. Lim. J. Chem. Phys. **96**, 5983 (1992).
21. T. Ree and H.K. Shin. J. Chem. Phys. **84**, 5545 (1986).
22. N. Snider. Chem. Phys. **159**, 339 (1992).
23. J.M. Morgulis, S.S. Sapers, C. Steel, and I. Oref. J. Chem. Phys. **90**, 923 (1989).
24. G. Lendvay and G.C. Schatz. J. Phys. Chem. **94**, 8864 (1990); D.L. Clarke, K.C. Thompson, and R.G. Gilbert. Chem. Phys. Lett. **182**, 357 (1991).

Appendix A. Derivation of the energy transfer Probability distribution function for the string oscillator

Let h_N be the ratio of final vibrational energy to initial vibrational energy in an N-encounter collision. One sees from ref. 10 that for the string oscillator h_N is given by

$$[A1] \qquad h_N = \frac{\sin^2(\chi_0 + 2N\psi)}{\sin^2 \chi_0}$$

where χ_0 is given by eq. [8]. In terms of h, the final vibrational energy divided by the initial vibrational energy, the energy transfer distribution function is given by

Can. J. Chem. Downloaded from www.nrcresearchpress.com by 195.246.54.202 on 09/08/12
For personal use only.

Can. J. Chem. Downloaded from www.nrcresearchpress.com by 195.246.54.202 on 09/08/12
For personal use only.

$$[A2] \qquad \rho(h) = \beta_v \int_0^\infty \sum_N f_N \delta(h - h_N) \exp(-\beta_v g)\, dg$$

$$= \beta_v \sum F_N(h) \exp[-\beta_v g_N(h)]$$

where β_v is E_v/kT, $f_N(g)$ is the probability of an N-encounter collision, and $F_N(h)$ is given by

$$[A3] \qquad F_N(h) = f_N \left(\frac{dg}{dh}\right)_{g=g_N(h)}$$

where $g_N(h)$ is the value of g for which an N-encounter collision results in a final to initial vibrational energy ratio equal to h. From eqs. [A1] and [8] one obtains

$$[A4] \qquad g_N(h) = \frac{h^{1/2} - \cos 2N\psi}{\sin 2N\psi}$$

The formula for f_N may be found in the literature (10). For χ_0 greater than ψ one has

$$f_N = -\frac{\sin N\psi \cos[\chi_0 + (N+1)\psi]}{\sin \psi} \qquad \text{for } \frac{\pi}{2} - (N+1)\psi < \chi_0 < \frac{\pi}{2} - N\psi$$

$$= 1 + \frac{\sin[(N-1)\psi] \cos[\chi_0 + N\psi]}{\sin \psi} \qquad \text{for } \frac{\pi}{2} - N\psi < \chi_0 < \frac{\pi}{2} - (N-1)\psi$$

Using eq. [8] to eliminate χ_0 in favor of g and then using eqs. [A3] and [A4], one obtains

$$[A5] \qquad F_N(h) = \{\cos[(N-1)\psi] - h^{-1/2} \cos[(N+1)\psi]\} D_N^{-1} \qquad \text{for } h < 1$$

$$= \{h^{-1/2} \cos[(N-1)\psi] - \cos[(N+1)\psi]\} D_N^{-1} \qquad \text{for } h > 1$$

where D_N is given by

$$D_N = \cos(2N\psi + 1)\{\cos[(N-1)\psi] - \cos[(N+1)\psi]\}$$

Thus for β_v sufficiently large that the condition

$$\exp(-\beta_v b_0^{-2}) \approx 0$$

is met, one has from eqs. [A2]–[A5]

$$[A6] \qquad \rho(h) \approx \beta_v \sum_{N > n_-(h)}^{\mathcal{N}-1} D_N^{-1} \{\cos[(N-1)\psi] - h^{-1/2} \cos[(N+1)\psi]\} \exp[-\beta_v \csc^2 2N\psi (h^{1/2} - \cos 2N\psi)^2]$$

for $h < 1$

$$\approx \beta_v \sum_{N > n_+(h)}^{\mathcal{N}-1} D_N^{-1} \{h^{-1/2} \cos[(N-1)\psi] - \cos[(N+1)\psi]\} \exp[-\beta_v \csc^2 2N\psi (h^{1/2} - \cos 2N\psi)^2]$$

for $h > 1$

where $\mathcal{N}$ is the largest integer such that $2\mathcal{N}\psi$ is less than π and the $n_\pm(h)$ are given by

$$n_\pm(h) = \psi^{-1} \tan^{-1}\left(b_0 \frac{\pm h^{1/2} \mp 1}{h^{1/2} + 1}\right)$$

Equation [A6] is the same as eq. [5] of the main text.

Appendix B. Derivation of large E_v asymptotic formula for $\langle \Delta E \rangle$ for collinear, impulsive collisions

If E_v is large compared to E_r, then encounters take place when the oscillator is near its outer turning point. If the force on the oscillator is continuous there, then eq. [1] may be approximated near the turning point by a quadratic equation,

[B1] $$z = -b_0 g^{1/2}\xi - 1/2C\xi^2 \text{ for } \xi < 0$$
$$= b_0 g^{1/2}(1-\xi) - 1/2C\xi^2 \text{ for } \xi > 0$$

where ξ is related to the θ of eq. [1] by a linear transformation and C is related to the restoring force on the oscillator at its outer turning point x_+ as in eq. [B2],

[B2] $$C = \frac{\tau}{(2\mu E_v)^{1/2}} \left(\frac{dV}{dx}\right)_{x=x_+}$$

The denominator $(2\mu E_v)^{1/2}$ in eq. [B2] is the maximum momentum of the oscillator. The other factor is the absolute value of the momentum that the oscillator would have if it were subjected for one period τ of its oscillation to a constant force equal to the force at the outer turning point. For the harmonic oscillator this ratio of momenta is equal to 2π. For anharmonic oscillators such as the Morse oscillator it is smaller than 2π, as will be discussed below.

To obtain $\langle \Delta E \rangle$, one averages over a uniform ensemble of z's. If g is small, ξ is limited to values from ξ_- to ξ_+ where ξ_- is the negative value of ξ at which the derivative of z changes sign. For ξ_+ one has

$$z(\xi_+) = z(\xi_-)$$

[B3] $$b_0 g^{1/2}(1-\xi_+) - 1/2C\xi_+^2 = \frac{b_0^2 g}{2C}$$

For small g one may solve for ξ_+, retaining only terms of order $g^{1/2}$. This gives

[B4] $$\xi_+ = \left(\frac{2b_0}{C}\right)^{1/2} g^{1/4}$$

The distribution function over ξ is proportional to minus the derivative of z,

[B5] $$\rho(\xi) \sim b_0 g^{1/2} + C\xi$$

The proportionality constant is of order $g^{-1/2}$ for small g. Since positive ξ may be of order $g^{1/4}$, one may neglect the first term in eq. [B5] for positive ξ and both terms for negative ξ,

[B6] $$\rho(\xi) \approx \frac{2\xi}{\xi_+^2} \qquad 0 \le \xi \le \xi_+$$

Equation [B6] is correct for sufficiently small g.

At small g, single encounters dominate. Thus the SEI formula is appropriate. This formula is found from eqs. [3] and [4] by setting N equal to one, taking the lower sign on the right of eq. [3], and setting u equal to $C\xi$. To lowest order in g, this gives

$$\frac{\Delta E}{E_v} = -C^2\xi^2 \sin^2 2\psi + O(g^{3/4})$$

Averaging over ξ using the distribution function of eq. [B6] and eliminating ξ_+ using eq. [B4] one obtains

[B7] $$\frac{\langle \Delta E \rangle}{E_v} = -Cb_0 g^{1/2} \sin^2 2\psi$$

For the Morse oscillator one may readily show that the force at the outer turning point and the period are given by

[B8] $$-F(x_+) = \left(\frac{dV}{dx}\right)_{x=x_+} = (2kE_v)^{1/2}(1-\cos\alpha)$$

$$\tau = 2\pi(\mu/k)^{1/2} \csc\alpha$$

where k is the harmonic force constant and α is defined in the main text following eq. [7]. Equations [B2], [B7], and [B8] give eq. [7] of the main text.

It is to be noted that for a Morse oscillator near its dissociation limit α goes to zero. Thus as this limit is approached, the period of the oscillator diverges as α^{-1}. This divergence is offset in eq. [B2] by the α^2 dependence of the force at the outer turning point, the result being that C approaches zero as α approaches zero.

Can. J. Chem. Downloaded from www.nrcresearchpress.com by 195.246.54.202 on 09/08/12
For personal use only.

Studies of femtosecond relaxation dynamics and fast ion–molecule reactions with low-energy electrons

L. SANCHE,[1] M. MICHAUD, AND L. PARENTEAU

Groupe du Conseil de recherches médicales du Canada, Faculté de médecine et Centre d'excellence en Dynamique moléculaire et interfaciale, Université de Sherbrooke, Sherbrooke, QC J1H 5N4, Canada

Received June 16, 1993

This paper is dedicated to Professor John C. Polanyi on the occasion of his 65th birthday

L. SANCHE, M. MICHAUD, and L. PARENTEAU. Can. J. Chem. **72**, 492 (1994).

Electron localization in solids and liquids is caused by time-dependent perturbations of the media surrounding the charge. The perturbations active on the femtosecond time scale include electronic polarization, as well as intra and intermolecular vibrational excitations, which contribute to the formation of a potential well around the charge. It is shown that information on these perturbations as well as on femtosecond reactions can be obtained by studying the formation of transient anions in dielectric solids and at their surfaces using high-resolution electron beam techniques at low energies (0–20 eV). The results obtained with Ar, N_2, O_2, and organic thin solid films condensed on a Pt substrate are described.

L. SANCHE, M. MICHAUD et L. PARENTEAU. Can. J. Chem. **72**, 492 (1994).

La localisation des électrons dans des solides et dans des liquides est provoquée par des perturbations du milieu entourant la charge qui sont dépendantes du temps. Les perturbations qui sont actives au niveau de la femtoseconde comprennent la polarisation électronique ainsi que les excitations vibrationnelles intra- et intermoléculaires qui contribuent à la formation d'un puits de potentiel autour de la charge. On démontre que l'on peut obtenir de l'information relative à ces perturbations ainsi qu'à celles des réactions d'une durée de l'ordre de la femtoseconde en étudiant la formation d'anions transitoires dans les diélectriques solides ainsi qu'à leurs surfaces en faisant appel à des techniques de faisceaux d'électrons à haute résolution à basses énergies (0–20 eV). On décrit les résultats obtenus avec les gaz Ar, N_2 et O_2 et des films organiques solides minces sur un substrat de Pt.

[Traduit par la rédaction]

1. Introduction

The dynamics of solvation of charged species in liquids and solids as well as their effects on the mechanisms of fast reactions are topics of interest in many areas of chemistry and chemical physics (1). With the advent of femtosecond laser techniques, it is now possible to probe such dynamical processes at much shorter times and thus extend our comprehension of ultrafast reactions and of the mechanisms of solvation involved during the early stages of the charge localization (2). As the field is progressing, ultrafast reactions and charge-transfer dynamics are beginning to be probed at fluid interfaces (4, 5), but such measurements are technically extremely difficult mainly due to the small signal intensities and problems in delineating between interface and bulk signals. As a result, our present understanding of solvation dynamics at interfaces is limited to theoretical phenomenological models (6, 7) and simulations (8–10).

The purpose of the present article is to show that femtosecond studies are not necessarily limited to those performed with ultrashort laser pulses but that complementary information on processes occurring within the femtosecond time scale can be obtained from high-resolution low-energy electron beam experiments performed on molecular and dielectric thin films.[2] What appears as the most interesting aspect of the low-energy electron experiments is their ability to investigate ultrafast solvation processes and reactions at the surface and interfaces of solids as well as within very thin dielectric films, an experimental domain that is practically unexplored by present femtosecond pump-probe methods. Although many electron scattering and attachment experiments have been performed to date (3), the possibility of obtaining femtosecond information from some of them has, to our knowledge, never been explained and exploited. In this article we explain under what conditions such information can be obtained and for what sort of systems. We describe in the following sections three types of low-energy electron experiments and show the relationship between the results obtained from them and specific processes occurring on a femtosecond time scale. Depending on the experiment, different information can be obtained on ultrafast dynamical processes occurring in thin films and at the surfaces of dielectric solids. This is exemplified by the results obtained from the different types of experiments.

In Sect. 2, it is shown how high-resolution electron energy loss (HREEL) spectroscopy can provide information on the electronic polarization as well as intra- and intermolecular vibrational excitations that contribute to the solvation of an anion in a molecular solid at times of 1–100 fs. In Sect. 3, the electron-stimulated desorption (ESD) method for the detection of anions produced by slow electron impact is explained. It is shown that this method makes it possible to detect anion–molecule reactions occurring over a time scale of 10–100 fs. Finally, a technique capable of identifying ultrafast mechanisms, which eventually cause electron localization at the surface of a dielectric, is described in Sect. 4.

2. Femtosecond anion solvation dynamics

A. Principle of the method and experiment

The basic idea behind this experiment is to fabricate during a short time (1–100 fs) an anion within a molecular solid film or at its surface and study the effects of this transitory localization of an electron on a molecule. Such measurements can be performed with a high-resolution electron energy loss (HREEL) spectrometer of the type described (11) in Fig. 1. It consists essentially of two concentric hemispherical deflectors, a monochromator and an analyzer with appropriate electron optics and a closed-cycle refrigerated cryostat. Electrons leaving the monochromator are focused on a dielectric film that is condensed on a metal

[1]Author to whom correspondence may be addressed.

[2]For a review of low-energy electron experiments with thin dielectric solid films, see ref. 3.

Can. J. Chem. Downloaded from www.nrcresearchpress.com by EESC ESCOLA DE ENGENHARIA on 09/08/12
For personal use only.

Can. J. Chem. Downloaded from www.nrcresearchpress.com by EESC ESCOLA DE ENGENHARIA on 09/08/12
For personal use only.

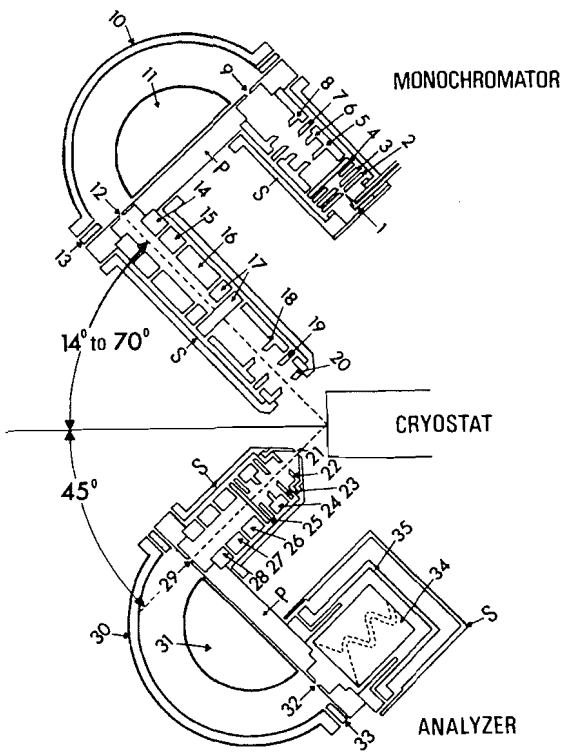

FIG. 1. Schematic diagram of hemispherical electron energy loss spectrometer. Electrons emitted from filament (1) are focused at the entrance (9) of the deflector region (10 and 11) by the zoom lens (6, 7, and 8). Energy dispersion is produced by applying a potential of about 1V between two concentric hemispheres (10, 11, 30, and 31). Imaging and energy control of the electron beam is achieved by means of electrostatic zoom lenses with cylindrical (14–16, 26–28) and aperture (6 to 8, 23 to 25) electrodes. Electrons are detected with a channeltron (34).

substrate. This latter is electrically isolated by a ceramic plate and secured by a press fit to the cold end of the cryostat. The angle of incidence θ_0 can be varied from 14° to 70° from the film's normal. Depending on the instrument, the target film can be rotated and may be cooled down to 15 K. Electrons reflected at $\theta_d = 45°$ from the film are measured by the analyzer. All components of the apparatus are housed in a UHV system reaching pressures below 10^{-10} Torr (1 Torr = 133.3 Pa). The current I_t (E) arriving at the metal substrate can be measured as a function of incident electron energy. In these experiments, I_t is in order of a nÅ and the absolute electron energy scale is calibrated within ±0.15 eV with respect to the vacuum level by measuring the onset of electron transmission through the films. The metal substrate consists of a polycrystalline metal sheet that can be cleaned by resistive heating. The condensed film is grown using a gas-volume expansion dosing procedure (12) and its thickness calibrated by monitoring the quantum size effect (QSE) features observed for ultrathin films (13). With this calibration, the film thicknesses (10–500 Å) can usually be estimated with an accuracy equal to or better than 30%, assuming a layer-by-layer growth.

Energy-loss spectra are recorded by fixing the energy of one deflector while sweeping the energy of the other one. The energy dependence of the magnitude of a given energy-loss event (i.e., the excitation function) is obtained by sweeping the energy of both deflectors with a potential difference between them corresponding to the probed energy loss. HREEL spectra are usually recorded with overall resolutions ranging from 8 to 20 meV FWHM.

As shown schematically in Fig. 2, electrons entering the dielectric film scatter elastically and inelastically with the atoms and (or) molecules forming the film. A large portion of those that exit the film have

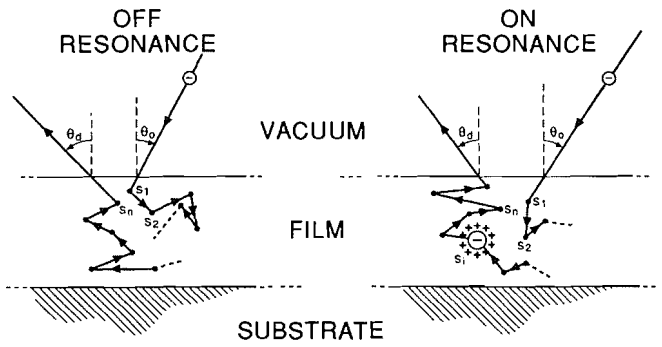

FIG. 2. Schematic diagram representing multiple scattering of an electron from sites s_1–s_n in a dielectric film. The incoming electron is incident at angle θ_0 and exists at angle θ_d with respect to the film normal. At site s_i on the right, the electron is temporarily captured by an atom or molecule of the film. This localization polarizes temporarily (1–100 fs) the lattice in the vicinity of site s_i.

lower energies because of energy losses after scattering on sites s_1–s_n. The exact relative amounts of energy imparted to the various inter- and intramolecular excitation modes in the solid can be known by measuring the energy distribution of these backscattered electrons (i.e., by recording HREEL spectra). Such HREEL spectra can be recorded at one particular emission angle θ_d, for different incident energies. At a specific well-defined incident electron energy, corresponding to that of an electron resonance at a site s_i (Fig. 2), the scattering electron can be trapped for a short time (10^{-15}–10^{-14} s) by an atom or a molecule of the solid and subsequently be released (3). Thus, at the resonance energy, the HREEL spectrum contains two types of information: that arising from multiple scattering plus that from the temporary formation of a negative ion at a molecular site s_i within the dielectric. The difference between the "on" and "off" resonance spectra provides information on energy transfer to inter- and intramolecular excitation modes of the solid during the lifetime of the transitory anion (on the solvation dynamics occurring at times of 1–100 fs). In other words, this technique measures the effect on the lattice of creating an anion for a short time, and the information obtained corresponds to changes initiated during its lifetime. The lifetime of condensed phase anions can be modified by changing their distance from a metal surface (14) or their environment (14, 15). The polarization energy of the anion in a given medium is another parameter that can be extracted from electron beam experiments (14). It simply arises from the energy difference between that of a given anion in vacuum and that recorded in a given material. If similar information is needed for an anion created at the surface of a dielectric, then a submonolayer consisting of molecules different from those of the multilayer dielectric film is deposited on it. Tuning the incident electron energy to that required to form a transient anion of the adsorbate molecule causes additional inter- and intramolecular vibrational excitation arising from the charge being temporarily trapped by the surface molecule. In this manner, the relaxation of the surface can be measured during the lifetime of the resonance.

B. Results and discussion

The early dynamics involved in the formation of an anion in a thin solid film can easily be demonstrated from electron-scattering experiments on rare gas solid (RGS) films. In RGS, an electron resonance occurs slightly below the energy threshold for creating the lowest bulk exciton (16). In solid Ar, for example, the lowest transient anion state of Ar^- occurs at 11.8 eV and has an estimated lifetime of 2.2×10^{-14} s (16). This Ar^- state is a core-excited resonance (i.e., a one-hole, two-electron state composed of a 4s electron bound to the electronic excited state formed from the atomic orbitals (...$3s^2$, $3p^5$, 4s)). It has the isolated (i.e., gas phase) configuration (...$3s^2$, $3p^5$, $4s^2$) $^2P_{3/2}$ $^2P_{1/2}$.

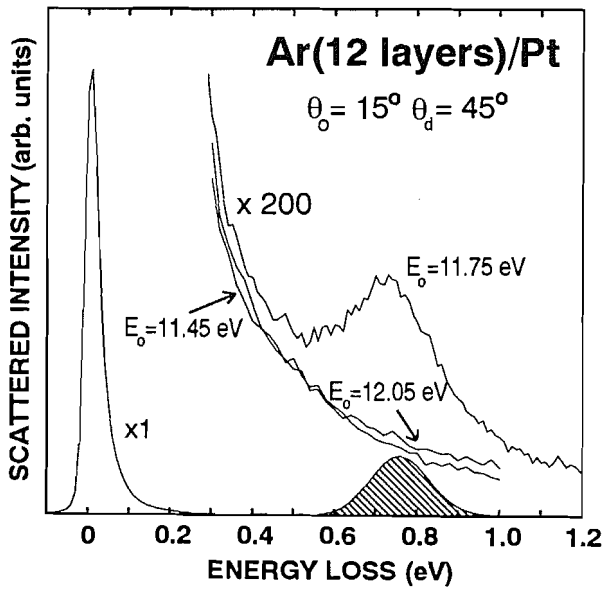

FIG. 3. Electron energy loss spectra of a 12-layer film of Ar recorded for three different incident energies E_0. The incident angle θ_0 is fixed at 15° and that of analysis θ_d at 45°. At incident energy E_0 = 11.75 eV an Ar^- state is formed in the solid causing the addition of a peak in the phonon energy loss tail recorded at E_0 = 11.45 and 12.05 eV. The hatched curve results from the calculation of the interaction between a time-dependent charge located on a lattice site and the acoustical phonons.

In the condensed phase, this resonance is 0.25 eV below the n = 1 bulk exciton; it is formed by the binding of an electron to the $n = 1,1'$ (the prime denoting the $j = \frac{1}{2}$ spin-orbit partner) excitons in the bulk. Since the anion state involves the coupling of an electron with an exciton, which occurs in condensed matter, it is more properly termed an *electron–exciton complex* (17).

Figure 3 shows HREEL spectra recorded with the spectrometer described in Fig. 1 (16). These spectra were obtained with a 12-layer film of Ar at θ_0 = 15° and θ_d = 45°, for incident energies slightly below the $n = 1,1'$ bulk-exciton energies, which are located at 12.06 and 12.24 eV, (18) respectively. The hatched curve results from the calculation of the energy-loss distribution, to be discussed later. The peak near 0 eV corresponds to electrons scattered quasielastically from the film whereas the tail arises from multiple energy losses to phonon modes of the crystal. At incident energies E_0 = 11.45 and 12.05 eV, the phonon tail is characteristic of "off-resonance" conditions and similar to other data recorded at energies where no resonances exist. However, "on resonance" (i.e., at E_0 = 11.75), the Ar^- state is formed and a phonon peak is superimposed on the phonon energy-loss tail attributed to multiple scattering within the solid. Subtracting the off-resonance data from the HREEL data recorded at E_0 = 11.75 eV provides the contribution to phonon excitation in the Ar lattice due to formation of an anion state during 2.2×10^{-14} s in solid Ar.

The effect of a transient anion state on the surrounding Ar matrix can be described by considering the interaction between a time-dependent charge located on a lattice site and the acoustical phonons treated by a quantum-mechanical description. Such a problem has been addressed in detail recently by Mills (19) in connection with the suppression of the resonant elastic peak (20) in electron scattering from a van der Waals solid. The results of the analysis leads, among other things, to an expression for the multiphonon loss feature whose intensity and mean energy loss depend mainly on the electron residence time τ_R and the polarizability of the surrounding atoms or molecules (i.e., dielectric constant ϵ of the medium). More specifically, it can be shown for a charge e, whose time dependency varies according to $e(t) = e \exp(-|t|/2\tau_R)$ on a lattice site, that the total probability to excite 1,2,..., m,... phonons with an energy loss between Ω and $(\Omega + d\Omega)$ is given by

$$[1a] \quad \frac{dP^{(tot)}}{d\Omega} = \sum_{m=1}^{\infty} \frac{\gamma^m \exp(-\gamma)}{m!} \frac{\exp\,[-(\Omega - m\bar{\omega})^2/2m(\Delta\omega)^2]}{(2\pi m)^{1/2}\,\Delta\omega}$$

In this expression $m\bar{\omega}$ and $m^{1/2}\Delta\omega$ correspond to the mean frequency and the frequency width of the m phonon-loss process, respectively (19). In the spirit of the Debye model for the longitudinal acoustic phonon at zero temperature, we have the prescription that $\bar{\omega} = 4\omega_D/5$ and $\Delta\omega = \omega_D\sqrt{2/75}$ with ω_D the Debye frequency (19). In eq. [1*a*], the term γ is referred to as a pseudo-Debye–Waller factor because it depends on the transient character of the scattering event, whereas the usual Debye–Waller factor involves only the overall momentum transfer (19). It is given explicitly by

$$[1b] \quad \gamma = \frac{2}{3} \frac{e^4(\epsilon - 1)^2\omega_D\tau_R}{\hbar M a_0^2 c_l^2[1 + (\omega_D\tau_R)^2]^2}$$

where M is the mass of the atom, a_0 the nearest-neighbor distance, c_l the longitudinal sound velocity, and ϵ the dielectric constant appropriate to the frequency range τ_R^{-1}.

Calculations were performed with eqs. [1] using only τ_R as an adjustable parameter and considering that solid Ar has a nearest-neighbor distance of 3.75 Å at 20 K, a dielectric constant of 1.66, a Debye energy of 8 meV, and a longitudinal velocity of sound of 1.64×10^{10} cm/s (18). The result of the calculation (16) with $\tau_R = 2.2 \times 10^{-14}$ s is displayed as the hatched curve in Fig. 3. It should be noted that the energy of the maximum was quite sensitive to τ_R; a variation of τ_R by 10% resulted in a 15% change for the energy of the maximum.

When similar short-lived anion states are formed in a molecular solid, they can also induce, besides phonon excitations, intramolecular vibrational excitation during their lifetime. When the scattering electron is temporarily captured at a molecular site ("on-resonance" condition, Fig. 2), the molecular orbitals at and near this site are strongly perturbed and the nuclei of the transient anion move to a new equilibrium position, thus initiating considerable nuclear motion (i.e., intramolecular vibrational excitation). This interaction is so effective in producing vibrationally excited molecules that it often dominates all other inelastic processes around the resonance energy. To illustrate this phenomena we have chosen the example of N_2^- formation in solid N_2. The energy-loss spectra for electrons of 2.9, 19.8, and 10.8 eV incident at θ_0 = 14° on a 25-layer solid film of N_2 are shown in Fig. 4 (21). The vertical gain for each curve or portion of a curve is referenced to the elastic peak of the top tracing. In the energy-loss range 0–2.5 eV, the top curve is composed of two overlapping series of vibrational levels (i.e, a weak and a strong progression). For low vibrational quantum numbers (v = 1–4) the two progressions cannot be separated, but at higher values (v = 5–8) sharp peaks belonging to the weak progression become visible on the low-energy side of much broader and more intense energy-loss

Can. J. Chem. Downloaded from www.nrcresearchpress.com by EESC ESCOLA DE ENGENHARIA on 09/08/12
For personal use only.

Can. J. Chem. Downloaded from www.nrcresearchpress.com by EESC ESCOLA DE ENGENHARIA on 09/08/12
For personal use only.

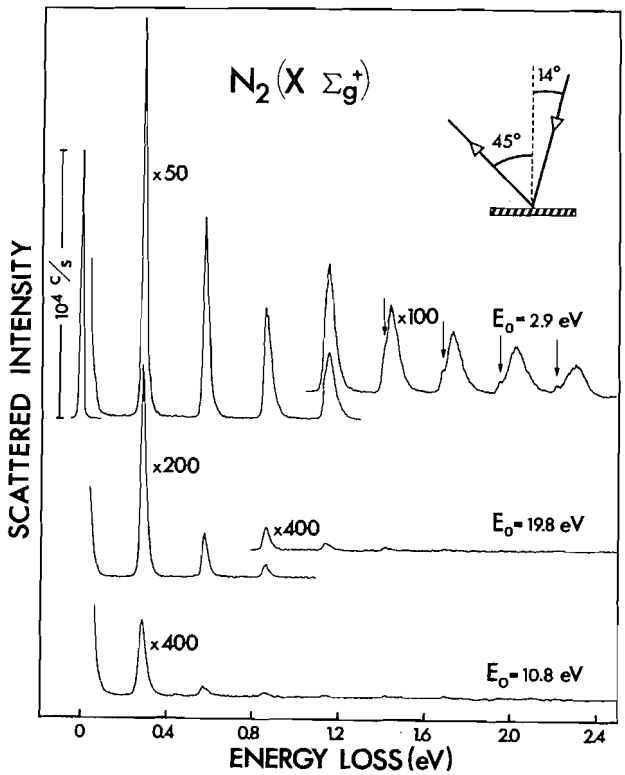

FIG. 4. Electron energy loss spectra of a multilayer disordered 25-layer film of N_2 recorded at primary energies of 2.9, 19.8, and 10.8 eV. The intensity of the elastic peak is indicated in counts/second (c/s). The enhancement in vibrational excitation of ground-state N_2 at 2.9 and 19.8 eV results from the formation of temporary negatively charged N_2^- states in the solid.

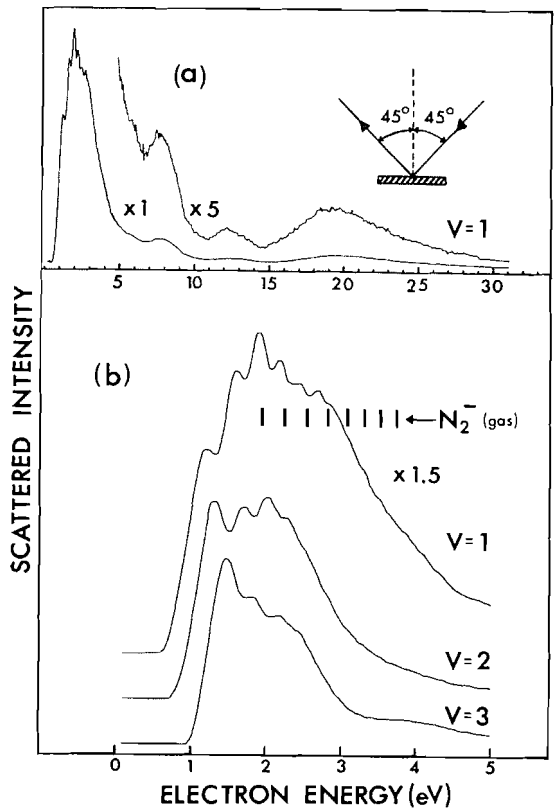

FIG. 5. (*a*) Energy dependence of the excitation of the first intramolecular vibrational level of a 12-layer film of N_2. The four maxima are interpreted as due to the formation of temporary N_2^- states. (*b*) Excitation functions from 0 to 5 eV for the first three intramolecular vibrational levels of a 12-layer film of N_2. The oscillatory structure is due to nuclear motion within the temporary N_2^- state.

peaks forming the strong progression. The latter exhibits a small anharmonicity (anharmonic constant = 0.22 ∓ 0.15 meV), whereas, for the former, the anharmonic constant is estimated to be 1.80 ∓ 0.15 meV from the last four vibrational levels. The anharmonicity of the weak progression is typical of vibrational excitation of ground-state molecular nitrogen (1.79 meV) in the gas phase (22). Both progressions result from vibrational excitation of ground-state $N_2(X^1\Sigma_g^+)$ in the solid; the weak series corresponds to single scattering events whereas the strong one results from multiple excitation of vibrational modes of N_2 convoluted with multiple intermolecular phonon modes (11). These multiple scatterings increase the energy and broaden the energy width of each peak. They indicate that *electrons scatter within the solid* since these effects are much weaker on single layer deposits and practically unobservable at submonolayer coverages.

The three energy-loss curves in Fig. 4 clearly indicate that the vibrational intensities are strongly dependent on the primary beam energy. The 10.8 eV spectrum correspond to a nonresonant condition whereas with incident electrons of 2.9 and 19.8 eV the $^2\Pi_g$ and $^2\Sigma_u$ states of the N_2^- state are formed, respectively. The lifetime of the $^2\Pi_g$ anion state has been estimated at a value of 3×10^{-15} s (23) and that of the $^2\Sigma_u$ state is of the order of 10^{-15} s. The effect of anion formation for such a short time is quite obvious from the results of Fig. 4. Compared to the values measured off resonance at an incident energy E_0 = 10.8 eV, the intensities of overtones of the fundamental frequency of N_2 are *enhanced by* approximately an order of magnitude at E_0 = 19.8 eV and by *two orders of magnitude* at E_0 = 2.9 eV. The increase in the magnitude of a given intramolecular vibrational mode at the resonance energies can be measured by monitoring the dependence on incident electron energy of the energy loss to that mode. Such an excitation function for the $v = 1$ vibrational level of ground state N_2 between 0 and 30 eV, recorded with a 12-layer film of N_2 film (23), is shown in Fig. 5(*a*). The four maxima can be ascribed to transient anion formation (24). The symmetries of the 2, 12, and 19 eV anions are $^2\Pi_g$, $^2\Delta_g$, and $^2\Sigma_g^+$, respectively, but the configuration of the 8 eV state is still undetermined in both the gas and solid phase. The lowest energy feature in Fig. 5(*a*) is displayed on an extended scale in the upper portion of Fig. 5(*b*) along with the excitation functions of the $v = 2$ and $v = 3$ vibrational levels. The oscillatory structure, which modulates the broad peak in each excitation function, results from vibrational motion of the $^2\Pi_g$ transient N_2^- state (23). The vertical bars in Fig. 5(*b*) represent the energies of the first eight "quasi-vibrational peaks" of that state as recorded in the $v = 1$ decay channel in gaseous N_2 (24). The average spacing for the first six peaks is 0.27 eV as compared to the corresponding value of 0.29 eV in the solid (23). From the shift of the first vibrational peak in the upper curve of Fig. 5(*b*) in going from 1.93 eV in the gas to 1.23 eV in the film, the value of 0.7 eV for the relaxation energy of N_2^- in N_2 is obtained. *This lowering of the energy of the $^2\Pi_g$ anion is due to electronic polarization of the surrounding N_2 molecules by the temporarily localized charge.*

Can. J. Chem. Downloaded from www.nrcresearchpress.com by EESC ESCOLA DE ENGENHARIA on 09/08/12
For personal use only.

3. Femtosecond ion–molecule surface reactions

A. Principle of the method and experiment

When molecular transient anion states are dissociative, they may produce fragments if the lifetime of the resonance is of the order of, or longer than, a vibrational period (3). Since at least one of the fragments usually has a positive electron affinity, dissociation of the anion state can produce a stable anion and a neutral molecule, atom, or radical (3). In the simplest case of a diatomic molecule AB, this process, named dissociative electron attachment (DEA), may be represented as $e + AB \rightarrow (AB^-)^* \rightarrow A + B^-$ or $A^* + B^-$. When this reaction occurs near the surface of a dielectric, the fragment anion B^- can escape into the vacuum only if it possesses sufficient kinetic energy to escape the polarization potential that it induces at the surface of the solid. For molecular solids, the kinetic energies required for the escape of the fragment anion in the direction normal to the surface are of the order of 0.5–1.0 eV. The steepness of the potential energy curve of the intermediate state AB^- is usually such that the B^- ion is propelled with sufficient energy to escape into the vacuum, if its velocity vector is properly oriented with respect to the surface. Of course, the B^- anion does not necessarily escape into the vacuum and may undergo reactive scattering with neighboring molecules. Assuming that the AB molecule is deposited at the surface of a molecular solid film composed of molecules CD, dissociative electron attachment to AB produces B^- ions that can react with electron volts of energies with CD. In this case, reactions of the type

$$[2] \quad B^- + CD \rightarrow BCD^- \rightarrow BC + D^-$$

are possible; i.e., there is the formation of a new intermediate anion BCD^- that can decay by dissociation into new products if, again, the lifetime of BCD^- is longer than, or of the order of, its vibrational period and one of the possible new fragments has a positive electron affinity. In the example of eq. [2], the D^- fragment must also have sufficient kinetic energy to be observed in vacuum. Thus, the observation of such D^- ions in vacuum necessarily implies that they were produced as the result of a dissociating state BCD^- (i.e., that both dissociation limits $B^- + CD$ and $BC + D^-$ lie below the BCD^- state) (25). Reactions of the type represented by eq. [1] therefore occur in times of the order of the vibrational periods of the intermediate anion BCD^- (i.e., 10^{-14}–10^{-13} s). Such ultrafast reactions can be detected by measuring the anion products (e.g., D^-) that escape to vacuum in electron-stimulated desorption (ESD) experiments. Anions desorbing from a multilayer film can be measured by replacing the analyzer shown in lower portion of Fig. 1 by a mass spectrometer. A portion of the negative ions, which are desorbed by electrons impinging on the film from the monochromator, is focused by the ion lenses at the entrance of the mass spectrometer. This latter measures, at a given mass, the yield of anions as a function of incident electron energy.

B. Results and discussion

Examples of anion production by DEA are illustrated by the two upper curves (*a*) and (*b*) in Fig. 6. The former represents the energy dependence of the O^- current produced by electron impact on a multilayer film of O_2 whereas the latter was recorded by discriminating anions having energies less than 1.8 eV with a retardation potential V_R. The broad peaks located around 8 and 13 eV in curves (*a*) and (*b*) have been ascribed to the dissociative attachment reaction (26).

$$[3] \quad e^- + O_2(^3\Sigma_g^-) \rightarrow O_2^-(^2\Pi_u, {}^2\Sigma_{g,u}^+) \rightarrow O^-(^2P) + O(^3P, {}^1D)$$

The 8 eV peak contains contributions from the decay of the $^2\Pi_u$ and $^2\Sigma_g^+$ transitory states of O_2^- whereas the 13 eV peak arises mainly from a higher- energy symmetry-forbidden $^2\Sigma_u^+$ O_2^- state. The O^- ions produced by the Σ states are, on the average, more energetic and therefore less affected by the retardation potential V_R. The remaining curves (i.e., (*c*)–(*g*) in Fig. 6) illustrate the energy dependence of the OH^- yields produced by electron impact on a 3-layer film of oxygen covered by a monolayer of C_nH_{2n+2} molecules (n = 1, 2, 4, 5, and 6). At submonolayer coverages, these OH^- yield functions exhibit the same characteristics but the signal is lower. In fact, in the submonolayer regime the magnitude of the OH^- signal is found to be directly proportional to the number of condensed hydrocarbon molecules. Since no compound at the film surface contains both hydrogen and oxygen. OH^- ions cannot be produced by direct electron impact. However, they can result from reactions between molecules (i.e., O_2 and C_nH_{2n+2}) in their ground states and anions produced directly by the electron beam (i.e., O^-, H^-, and CH_n^-, n = 1–3). A priori, OH^- can be formed via the reactions (25),

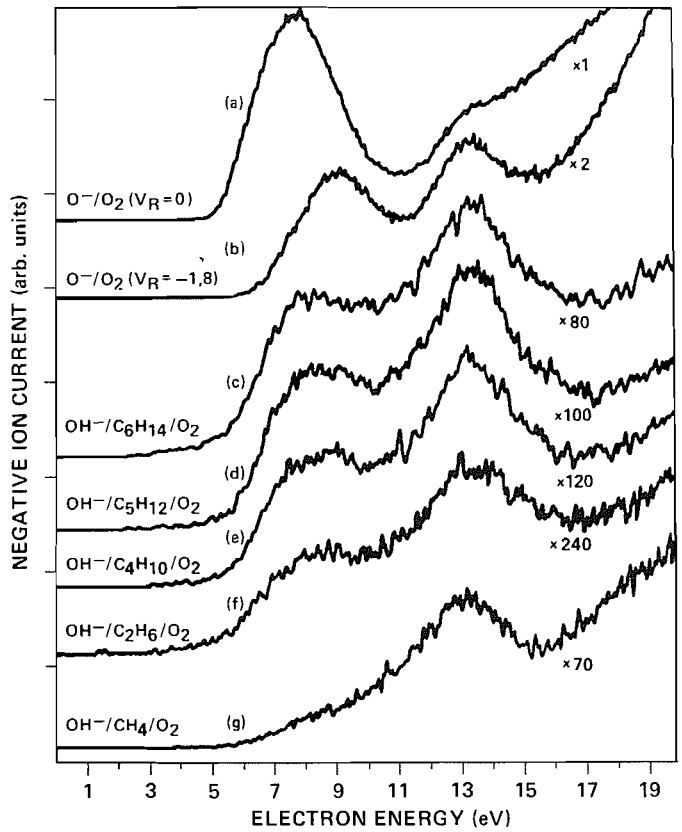

FIG. 6. Energy dependence of electron-stimulated desorption of negative ions in the range 1–20 eV. Curves (*a*) and (*b*), O^- desorption from a 3-layer O_2 film. V_R is a potential retarding the negative ions at the entrance of the mass spectrometer. Curves (*c*)–(*g*), OH^- desorption form a 3-layer O_2 film covered with a single layer of C_nH_{2n+2} (n = 1, 2, 4, 5, and 6) molecules. Curves (*c*)–(*g*) were recorded with V_R = 0.

$$[4] \quad O^- + C_nH_{2n+2} \rightarrow C_nH_{2n+2}O^- \rightarrow OH^- + C_nH_{2n+1}$$

or the reactions

$$[5a] \quad H^- + O_2 \rightarrow OH^- + O$$

and

$$[5b] \quad CH_n^- + O_2 \rightarrow OH^- + CH_{n-1}O$$

Any OH^- formed by reactions [5] would bear the "signature"

Can. J. Chem. Downloaded from www.nrcresearchpress.com by EESC ESCOLA DE ENGENHARIA on 09/08/12
For personal use only.

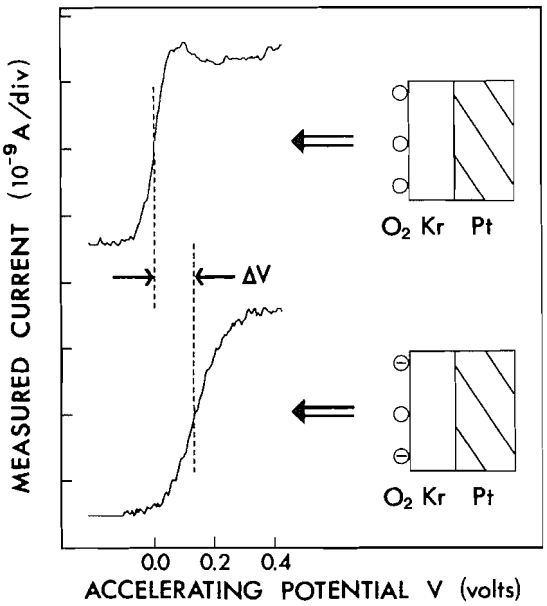

FIG. 7. Current transmitted through an uncharged (top) and a charged (bottom) 20-layer Kr film covered with 0.1 layer of O_2 as a function of the accelerating potential V of the incident electron beam.

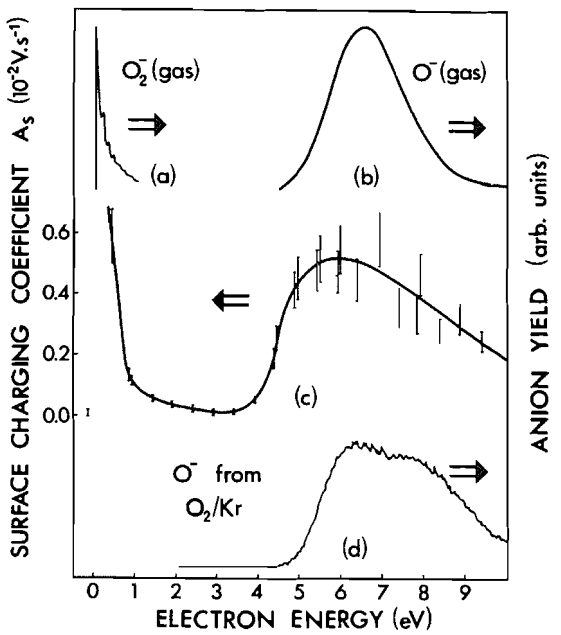

FIG. 8. Anion yields produced by 0–10 eV electron impact on (*a*) and (*b*) gaseous O_2 and on (*d*) a 0.1 layer of O_2 deposited on a 20-layer film of Kr. (*c*) Electron energy dependence of the surface-charging coefficient A_s for a 0.1 layer of O_2 deposited on a 20-layer film of Kr.

of the yield functions for H^- or CH_n^-. However, these are much different than that for O^- production (27) and the OH^- product can therefore only be ascribed to reaction [4] where the energetic O^- ions are generated by the DEA reaction described in eq. [3]. In other words, the features in the curves (*a*) and (*b*), which represent the electron energy dependence of the O^- yield, are reflected into the electron energy dependence of the OH^- yield and thus serve as a signature to detect and identify reaction [4]. As explained in the previous subsection, this reaction takes place during times of the order of the vibrational period of the C_nH_{2n+2}–O^- stretching bond.

4. Mechanism of electron trapping

A. Method and experiment

In this section it is shown that, from our knowledge of elementary excitations and transient anion formation in both gas and condensed phases, it is possible to identify the initial mechanism, *operative on a time scale of 10–1000 fs*, that is responsible for electron trapping near the surface of a dielectric. The initial mechanism can be inferred by measuring the incident electron energy dependence of the trapping cross section. This latter cross section is obtained from the measure of the charges that accumulate on a dielectric film after bombardment with a low-energy electron beam during a given time at a specific energy. The energy dependence of the electron-trapping cross section is obtained by repeating this measurement for different incident electron energies.

This new method of charge measurement (28) is derived from low-energy electron transmission (LEET) spectroscopy (12). In a LEET experiment, a monoenergetic electron beam impinges on a multilayer solid film grown on a metal substrate (12). Referring to the apparatus in Fig. 1, a LEET spectrum is recorded by measuring on the metal substrate the electron current, which traverses the film, as a function of a potential V applied between the substrate and the electron source (12). When electrons have just enough energy to enter into the film from vacuum, a sharp rise, termed the injection curve (IC), is seen in LEET spectra (28). The IC for an uncharged film is represented by the upper curve of Fig. 7. When the same film is charged at the surface by the electron beam, the IC is shifted by ΔV to a higher accelerating potential, as shown by the lower curve in Fig. 7, since the incoming electrons must possess additional kinetic energy to overcome the negative potential barrier. The IC is also broadened as a result of the spatial current-density distribution (28).

Treating the dielectric film as a charged capacitor, the potential barrier ΔV is related to the surface charge density $\sigma(t)$, which has accumulated after bombardment time t, by the relation (28)

$$[7] \quad \Delta V(t) = \sigma(t)h/\epsilon$$

where $\sigma(t) = \sigma_0(1 - e^{-\beta t})$ and $\beta = \mu J_0/e$; ϵ is the dielectric constant of the film, h is the film thickness, σ_0 is the initial ($t = 0$) trap density, μ is the trapping cross section, J_0 is the incident current density, and e is the unit charge. *In the limit* $t \rightarrow 0$ *we can define a charging coefficient* $A_s = d\Delta V/dt$ *that is directly proportional to the trapping cross section* (i.e., $d\Delta V/d|_{t=0} = (h\sigma_0 J_0/\epsilon e)\mu = A_s$). In the experiment, the IC of the uncharged film is first recorded before bombarding the film at a given energy. The IC is again rapidly recorded and the shift ΔV determined by comparison with the initial IC. Such a cycle can be repeated many times on the same film with the same potential V to obtain the time dependence of the process. Otherwise, to measure the thickness and the energy dependence, a new film has to be deposited for each data point. As an example, the shift ΔV= 130 meV in Fig. 7 was obtained after a bombardment at 7.3 eV of 20-layer film of Kr covered with 0.1 layer of O_2 (29). Here, the Kr solid does not charge significantly during the time of bombardment in the absence of the O_2 adsorbate, so that charging can be attributed to electron trapping near or at the position of O_2 molecules. By repeating such measurements for small bombardment times (i.e., in the limit $t \rightarrow 0$) at different energies, the incident electron energy dependence of the charging coefficient of trapping cross section can be obtained.

B. Results and discussion

The surface charging coefficient A_s for 0.1 layer of O_2 condensed onto a 20-layer film of Kr (29) is represented by the middle curve (*c*) in Fig. 8, as a function of the energy of the electron beam that causes charging. The result in Fig. 8 is comparable to the energy dependence of the anion yields derived from the gas-phase attachment rate coefficient for stable O_2^- production (30) (Fig. 8(*a*)) and the gas-phase DEA cross sec-

tion (31) (Fig. 5(*b*)). Curve (*d*) represents the ESD signal from a 20-layer film of Kr covered with 0.1 layer of O_2.

From the correspondence between the curves of Fig. 8, electron trapping at the surface of the Kr film above 4 eV can be ascribed to dissociation of the $^2\Pi_u$ state of O_2^- into the limit $O(^3P) + O^-(^2P)$. Although the desorbing $O^-(^2P)$ ions could also arise from the $^2\Sigma_g^+$ state of O_2^- as seen in Fig. 6, only a small fraction of the signal is thought to arise from that state since it must be formed near another O_2 molecule in order to violate the $\Sigma^- \leftrightarrow \Sigma^+$ selection rule (32). The maximum in the charging coefficient A_s is found about 0.6 eV below the maximum in the gas-phase O^- yield due to the lowering of the $^2\Pi_u$ resonance by the polarization potential of the Kr surface. Thus, the DEA maximum in the ESD yield arises from the same O_2^- surface state as that in the charging signal. However, the DEA maximum lies at a higher energy since, in order to overcome the polarization force of the Kr film, desorbing O^- ions must arise, on the average, from a higher energy portion in the Franck–Condon region of the O_2^- $^2\Pi_u$ potential energy curve.

In the 0–1.2 eV range, temporary electron attachment to gaseous O_2 leads to formation of the $^2\Pi_g$ resonance state of O_2^- that occurs in vibrational levels $v \geq 4$, since the $v < 4$ levels lie below the ground state of O_2 (30). However, if vibrational energy is transferred to another particle during the lifetime of the $^2\Pi_g$ anion, the $v < 4$ levels can be reached and the electron becomes permanently attached to the molecule. A similar stabilization process is responsible for surface charge accumulation in the range 0–2 eV. The electron can either lose energy to vibrationally excite O_2 via the $^2\Pi_g$ O_2^- state and afterwards stabilize at a trapping site, or the $^2\Pi_g$ state may itself stabilize by energy transfer to phonons. The estimated lifetime of the $^2\Pi_g$ O_2^- state within O_2 clusters is of the order of 10^{-12} s (33), which is comparable to the phonon vibrational period of the Kr lattice (5×10^{-13} s) (34). Hence, assuming a similar lifetime on Kr, the additional electron resides a sufficiently long time at an O_2 site to polarize the phonon modes of the Kr lattice. In conclusion, the initial mechanism of electron localization at the O_2 site in the 0–2 eV range is due to electron stabilization via the $^2\Pi_g$ resonance, whereas in the 4–10 eV region it is due to $O^-(^2P)$ formed by dissociation of the intermediate $^2\Pi_u$ state of O_2^-.

Acknowledgements

This research is sponsored by the Medical Research Council of Canada and by the Canadian Centers of Excellence in Molecular and Interfacial Dynamics.

1. G.R. Fleming. Chemical applications of ultrafast spectroscopy. Oxford University Press, New York. 1986.
2. P.F. Barbara and W. Jarzeba. Adv. Photochem. **15**, 1 (1990).
3. L. Sanche. *In* Excess electrons in dielectric media. *Edited by* C. Ferradini and J.-P. Jay-Gerin. CRC Press, Boca Raton, Fla. 1991. Chap. 1.
4. E.V. Sitzmann and K.B Eisenthal. J. Chem. Phys. **90**, 2831 (1989).
5. S.R. Meech and K. Yoshihara. Chem. Phys. Lett. **174**, 423 (1990).
6. G. van der Zwan and R.M. Mazo. J. Chem. Phys. **82**, 3344 (1985).
7. M. Urbakh and J. Klafter. J. Phys. Chem. **96**, 3480 (1992).
8. I. Benjamin. J. Chem. Phys. **95**, 3698 (1991).
9. D.A. Rose and I. Benjamin. J. Chem. Phys. **95**, 6856 (1991).
10. D.A. Rose and I. Benjamin. J. Phys. Chem. **96**, 9561 (1992).
11. L. Sanche and M. Michaud. Phys. Rev. B, **30**, 6078 (1984).
12. L. Sanche. J. Chem. Phys. **71**, 4860 (1979).
13. G. Perluzzo, L. Sanche, C. Gaubert, and R. Bauding. Phys. Rev. B, **30**, 4292 (1984).
14. M. Michaud and L. Sanche. J. Electron Spectrosc. Relat. Phenom. **51**, 237 (1990).
15. M. Huels, L. Parenteau, and L. Sanche. XVIII International Conference on the Physics of Electronic and Atomic Collisions, Denmark. 1993.
16. M. Michaud, P. Cloutier, and L. Sanche. Phys. Rev. B, **47**, 4131 (1993); **48**, 11336 (1993).
17. G. Bader and L.G. Caron. J. Chem. Phys. **77**, 3166 (1982), and references cited therein.
18. G. Zimmerer. *In* Excited-state spectroscopy in solids. *Edited by* U.M. Grassono and N. Terzi. North-Holland, Amsterdam. 1987. p. 37.
19. D.L. Mills. Phys. Rev. B, **45**, 36 (1992).
20. U. Fano, J.A. Stephens, and M. Inokuti. J. Chem. Phys. **85**, 6239 (1986).
21. L. Sanche and M. Michaud. Chem. Phys. Lett. **84**, 497 (1981).
22. G. Herzberg. Spectra of diatomic molecules. van Nostrand, Princeton. 1966. p. 553.
23. L. Sanche and M. Michaud. Phys. Rev. B, **27**, 3856 (1983).
24. H. Ehrhardt and K. Willmann. Z. Phys. **204**, 462 (1967).
25. L. Sanche and L. Parenteau. Phys. Rev. Lett. **59**, 136 (1987).
26. L. Sanche, L. Parenteau, and P. Cloutier. J. Chem. Phys. **91**, 2664 (1989).
27. P. Rowntree, L. Parenteau, and L. Sanche. J. Phys. Chem. **95**, 4902 (1991).
28. R.M. Marsolais, M. Deschênes, and L. Sanche. Rev. Sci. Instrum. **60**, 2724 (1989).
29. L. Sanche and M. Deschênes. Phys. Rev. Lett. **61**, 2096 (1988).
30. D. Spence and G.J. Schulz. Phys. Rev. A, **5**, 724 (1972).
31. D. Rapp and D.D. Briglia. J. Chem. Phys. **43**, 1480 (1965).
32. H. Sambe and D.E. Ramaker. Chem. Phys. Lett. **139**, 386 (1987).
33. Y. Hatano. *In* Electronic and atomic collisions. *Edited by* D.C. Lorentz Elsevier, New York. 1986.
34. K. Kern, P. Zeppenfield, R. David, and G. Comsa. Phys. Rev. B, **35**, 886 (1987).

Can. J. Chem. Downloaded from www.nrcresearchpress.com by EESC ESCOLA DE ENGENHARIA on 09/08/12
For personal use only.

The vibrational dependence of the dipole moment of hydrogen fluoride

J.A. BARNES, T.E. GOUGH,[1] AND M. STOER
Department of Chemistry, University of Victoria, Victoria, BC V8W 3P6, Canada
Received June 24, 1993
This paper is dedicated to Professor John C. Polanyi on the occasion of his 65th birthday

J.A. BARNES, T.E. GOUGH, and M. STOER. Can. J. Chem. **72**, 499 (1994).

Molecular beam laser Stark spectroscopy has been used to measure the $v = 3$ vibrational state dipole moment of hydrogen fluoride as 1.9614 ± 0.0021 debye. This measurement allows μ_v to be expressed as a power series expansion in $(v + \frac{1}{2})$ without the use of infrared intensity data. A detailed comparison is made with similar series based mainly on infrared intensity data and more recent *ab initio* calculations.

J.A. BARNES, T.E. GOUGH et M. STOER. Can. J. Chem. **72**, 499 (1994).

On a utilisé la spectroscopie au laser à faisceau moléculaire de Stark pour déterminer que le moment dipolaire de l'état vibrationnel $v = 3$ du fluorure d'hydrogène est égal à 1,9614 ± 0,0021 debye. Cette mesure permet d'exprimer μ_v comme une expansion d'une série de puissance en $(v + \frac{1}{2})$ sans être obligé d'utiliser des données d'intensité en infrarouge. On fait une comparaison détaillée de séries semblables obtenues principalement à l'aide d'intensités en infrarouge et avec des calculs *ab initio* plus récents.

[Traduit par la rédaction]

Can. J. Chem. Downloaded from www.nrcresearchpress.com by 195.246.54.202 on 09/08/12
For personal use only.

1. Introduction

The dipole moment function of hydrogen fluoride continues to be a topic of interest, partly because the molecule is sufficiently small to be amenable to high-quality theoretical treatment and partly because of the availability of significant amounts of relevant experimental data. In addition, the central role of emission from vibrationally excited hydrogen fluoride in chemical lasers (1–3) and as a probe of reaction dynamics provides an incentive for as quantitative an understanding of the dipole moment of hydrogen fluoride as is possible.

The dipole moment function obtained by Werner and Rosmus using highly correlated Self-Consistent Electron Pairs/Coupled Electron Pair Approximation (SCEP/CEPA) wave functions long provided the best agreement between *ab initio* and experimental functions up to the $v = 9$ level (4). More recently, Zemke et al. have taken a potential energy function of hydrogen fluoride based on spectroscopic measurements (5) and imposed upon it the proper long-range behaviour by including both dispersion and exchange effects (6). This potential was then combined with a new *ab initio* dipole moment function, complete for all internuclear distances, to calculate line intensities and dipole moments (7). The results were in excellent agreement with experimental data, particularly that of Sileo and Cool (8). For high levels of vibrational excitation, the results of Zemke et al. represent a marked improvement over those of Werner and Rosmus. That this improvement is largely due to the more realistic potential energy function used can be inferred from the fact that the dissociation limit determined by this function ($D_e = 49362 \pm 5$ cm^{-1}) differs markedly from that obtained from the full CI, "benchmark" calculations of Bauschlicher et al. (48960 cm^{-1}) (9).

A calculation using density functional techniques (10), which are computationally more efficient, was found to improve upon the results obtained from self-consistent field methods that neglect electron correlation. However, the calculations were confined to the equilibrium geometry and seem less accurate than those performed using the SCEP/CEPA method.

Sileo and Cool performed an extensive series of measurements of overtone emission intensities for hydrogen fluoride (8) and these have been the main source of experimental data to which theoretical results have been compared. Many of the systematic errors inherent in measuring emission intensities are less important in Sileo and Cool's analysis, which only uses ratios of such intensities. However, one experimentally determined dipole moment is necessary to establish absolute values of dipole moments from Sileo and Cool's data (8). Measurements of the dipole moments of the $v = 0$ and $v = 1$ states of hydrogen fluoride provide a second source of experimental information that, although more limited, is both more precise and more accurate than that of emission intensities (11, 12). In addition, the intensity of the fundamental vibrational absorption of hydrogen fluoride has been carefully remeasured, once again providing precise but limited information (13). Comparison between experiment and theory is most conveniently done by converting the combined body of experimentally measured quantities, appropriately weighted, into an experimental dipole moment function. This is normally expressed as a power series in the internuclear distance, preferably augmented by some expression to enable extrapolation outside of the range of internuclear distances covered by the experiment. Ogilvie has published the coefficients of such a power series up to sixth order and also carefully analysed standard errors for these coefficients using a Monte Carlo method (14).

Zemke et al. (7) claim that their calculated dipole moments are numerically significant to 10^{-4} debye. This precision exceeds that of infrared intensity measurements, which are also subject to systematic errors on the order of a few percent. Therefore, it is of interest to measure the dipole moments of hydrogen fluoride in higher vibrational states than the $v = 0$ and $v = 1$ states so far reported. Below, the measurement of the dipole moment of hydrogen fluoride in $v = 3$ using Stark splitting of the 3←0 overtone is reported. Such measurements have a systematic error of 0.01% and a precision of 10^{-3} debye.

2. Experimental

The laser molecular beam spectrometer used in the present study is depicted in Fig. 1. The current apparatus is similar to that used previously (15); however, the laser system has been replaced by a Coherent 899 Ti–sapphire laser pumped by a Coherent Innova 200 Ar ion laser. The Ti–sapphire laser provides tunable near-infrared radiation (11 300–13 000 cm^{-1}), with a peak power of 2 W single frequency and a line width of ≈4 MHz. The line width was determined by mea-

[1]Authors to whom all correspondence should be addressed.

Can. J. Chem. Downloaded from www.nrcresearchpress.com by 195.246.54.202 on 09/08/12
For personal use only.

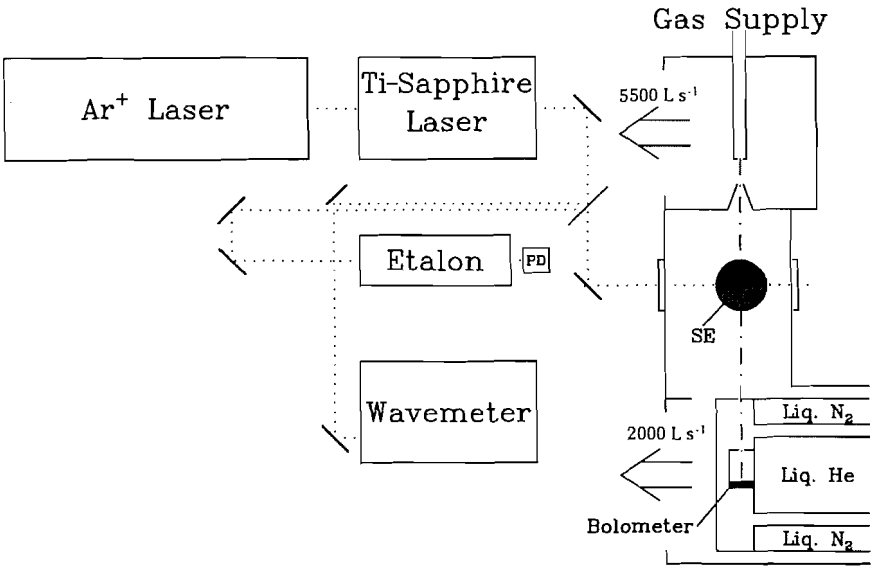

FIG. 1. Schematic of the apparatus used for the optothermal molecular beam Stark spectroscopy. SE, Stark electrodes; PD, photodiode; Liq., liquid.

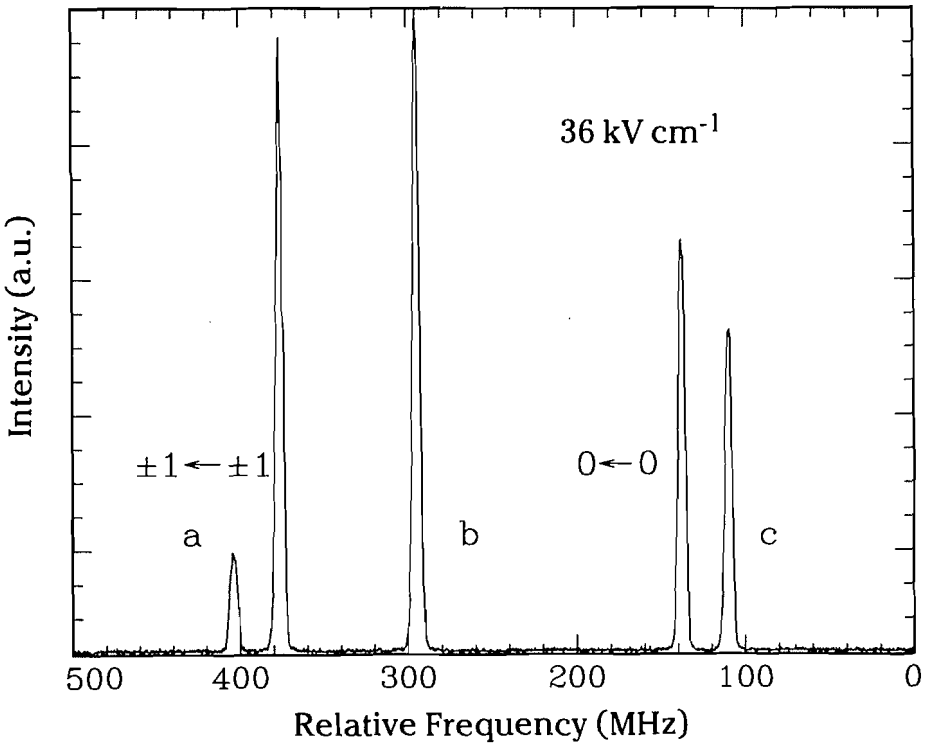

FIG. 2. Experimental Stark split spectrum of the $R(1)$ transition of the $v = 3 \leftarrow 0$ band of hydrogen fluoride, induced by an applied field of 36 kV cm^{-1}.

suring a rotational vibrational molecular beam transition. The output polarization of the laser was rotated 45° with respect to the Stark electric field, to allow observation of transitions obeying $\Delta M = 0, \pm 1$ selection rules. Although the Ti–sapphire laser is frequency stabilized, an etalon was used to verify the linearity of the laser scan. The free spectral range of the etalon was 300 MHz; however, it was slightly misaligned to provide stable transverse etalon modes with a frequency spacing of 100 MHz.

The 5% hydrogen fluoride in helium gas mixture was expanded through a 100-μm diameter nozzle, with a stagnation pressure optimized at 0.5 atm (1 atm = 101.3 kPa). A 500-μm skimmer was used to further collimate the molecular beam. Rather than using a gas cell, the HF rotational line positions for the $v = 3 \leftarrow 0$ vibrational transition were located using results from Fishburne and Rao (*16*) and a Burleigh wavemeter. The J=2←1 rotational transition at 11 441.41 cm^{-1} was split with Stark fields of ≈40 kV cm^{-1}. A typical spectrum is shown in Fig. 2 with the transitions labelled according to Fig. 3. Absolute frequencies were not needed and the Stark electrode spacing did not need to be known exactly because, as is shown later, only the ratio of the line splittings $(b - c)/(a - b)$ was of interest.

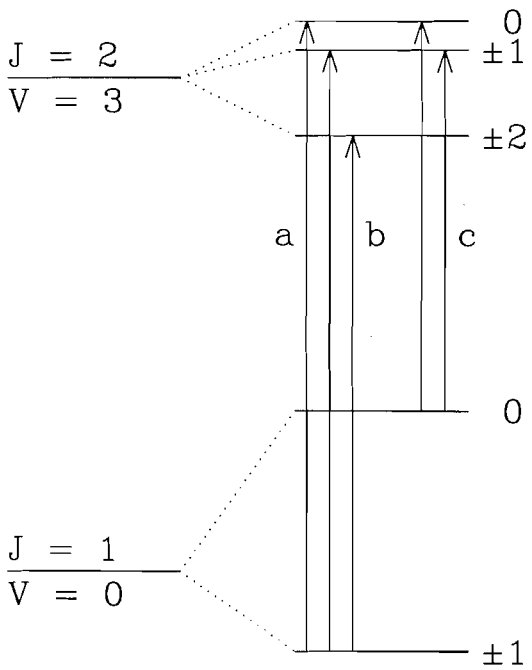

FIG. 3. Energy levels and transitions corresponding to the spectrum depicted in Fig. 2.

This ratio was found to be 1.679 ± 0.005 experimentally, gathered from the analysis of 40 separate scans. The principle source of error may be attributed to drifts in the frequency of the laser.

3. Analysis of data

For a diatomic molecule in an electric field, the electrical energies of the J and M levels will be given by

$$[1] \qquad \epsilon_{v,J,M} = \epsilon^{(2)}_{v,J,M} + \epsilon^{(P)}_{v,J,M} + \epsilon^{(4)}_{v,J,M}$$

where the dominant term is the second-order dipole – applied electric field interaction (17):

$$[2] \qquad \epsilon^{(2)}_{v,J,M} = \frac{\mu_v^2 E^2}{2hB_v} \frac{J(J+1) - 3M^2}{J(J+1)(2J-1)(2J+3)}$$

The dipole moment (μ_v) and the rotational constant (B_v) are for the specified vibrational state v, and the appropriate selection rules for the present experiment are given in Fig. 3. The effects due to the polarizability anisotropy ($\epsilon^{(P)}_{v,J,M}$) and the fourth-order dipole – applied electric field interaction $\epsilon^{(4)}_{v,J,M}$ are less than 0.5% for applied electric fields in the order of 40 kV cm^{-1}. It is therefore not necessary to know the exact electric field for the fourth-order correction. The electric field was estimated from the second-order term, after calculating the upper state dipole moment based on second-order perturbations alone.

The effects of the anisotropy of the polarizability are compensated for by applying the following correction (18):

$$[3] \qquad \epsilon^{(P)}_{J,M} = -\frac{(\alpha_\parallel - \alpha_\perp)E^2}{2} \frac{2J^2 + 2J - 1 - 2M^2}{(2J+3)(2J-1)}$$

where $(\alpha_\parallel - \alpha_\perp)$ or $\Delta\alpha$ is the anisotropy of the polarizability of the molecule. The vibrational dependence of $\Delta\alpha$ has been ignored, since $\epsilon^{(P)}_{J,M}$ is much less than $\epsilon^{(2)}_{v,J,M}$. Observing that both $\epsilon^{(2)}_{v,J,M}$ and $\epsilon^{(P)}_{J,M}$) are a function of E^2, one can express the excited state dipole moment in terms of the ratio $(b-c)/(a-b)$ for the $(v = 3, J = 2 \leftarrow v = 0, J = 1)$ transition, the ground state dipole moment, and the appropriate rotational constants:

$$[4] \qquad \mu_3^2 = \frac{B_3}{C_S}\left[\frac{63\mu_0^2}{20B_0} C_S + \Delta\alpha C_P \left(4\frac{(b-c)}{(a-b)} - \frac{42}{35}\right)\right] \times \left[\frac{(b-c)}{(a-b)} + \frac{3}{4}\right]^{-1}$$

where C_S and C_P are the second-order Stark and polarizability constants, respectively.

Once the second-order corrections had been evaluated, the electric field was estimated by comparison of the measured splitting $(a-c)$ with the splitting calculated from the second-order determination of the dipole. The fourth-order correction was then calculated using eq. [5] (18),

$$[5] \qquad \epsilon^{(4)}_{v,J,M} = \frac{\mu_v^4 E^4}{8h^3 B_v^3}\left\{\frac{[(J+1)^2 - M^2][(J+2)^2 - M^2]}{(2J+1)(2J+5)(J+1)^2(2J+1)^3} + \frac{[(J-1)^2 - M^2](J^2 - M^2)}{(2J-3)(2J+1)J^2(2J-1)^3} + \frac{(J^2 - M^2)[(J+1)^2 - M^2]}{(2J-1)(2J+3)(2J+1)^2J^2(J+1)^2} + \frac{[(J+1)^2 - M^2]^2}{(2J+3)^2(2J+1)^2(J+1)^3} - \frac{[J^2 - M^2]^2}{(2J+1)^2(2J-1)^2J^3}\right\}$$

Table 1 lists the required variables and the results of all of the calculations.

4. Discussion

Figure 4 provides a convenient format for assessing the information available concerning the dependence upon vibrational quantum number of the dipole moment of hydrogen fluoride. In this figure, the theoretical results of Zemke et al. (7) have been subtracted from the corresponding experimental values. The circles denote measurements made using Stark splitting of spectra using various molecular beam techniques and the diamonds are dipole moments as reported by Sileo and Cool. The discrepancy between the two sets of data arises because of the incorrect value of μ_e used in their analysis. It is perfectly valid to adjust the diamonds upwards a constant amount so that the two sets of data overlap at $v = -\frac{1}{2}$; it is essential to make such an adjustment before attempting comparisons with theoretical predictions of the quality claimed by Zemke et al. After the adjustment is made, the two sets of experimental data are in excellent agreement and it seems clear that the theory underestimates μ_e by 0.004 debye and overestimates the rate at which μ_v increases with v at least for $v < 4$. Nevertheless, the agreement over the full range of available data of better than ± 0.005 debye is most impressive.

The triangle in Fig. 4 represents the value for μ_2 calculated by Bass et al. (12) from an experimental dipole moment function based on molecular beam electric resonance measure-

Can. J. Chem. Downloaded from www.nrcresearchpress.com by 195.246.54.202 on 09/08/12
For personal use only.

Can. J. Chem. Downloaded from www.nrcresearchpress.com by 195.246.54.202 on 09/08/12
For personal use only.

TABLE 1. Experimentally measured dipole moment for hydrogen fluoride

Variable	Value	Reference
B_0	20.559 7299 cm^{-1}	21
B_3	18.269 30 cm^{-1}	Calculated from 21
μ_0	1.826 567 debye	12
$\alpha_{\parallel} - \alpha_{\perp}$	0.220 ± 0.020 A^3	22
C_S	$0.253\,415$ MHz $D^{-2} \left(\frac{V}{cm}\right)^{-2}$	
C_P	$1.679\,17 \times 10^{15}$ MHz $cm^{-3} \left(\frac{V}{cm}\right)^{-2}$	
E	36 kV cm^{-1}	
μ_3	1.961 2 debye	From eq. [4]
μ_3	1.9614 ± 0.0021 debye	Corrected for eq. [5]

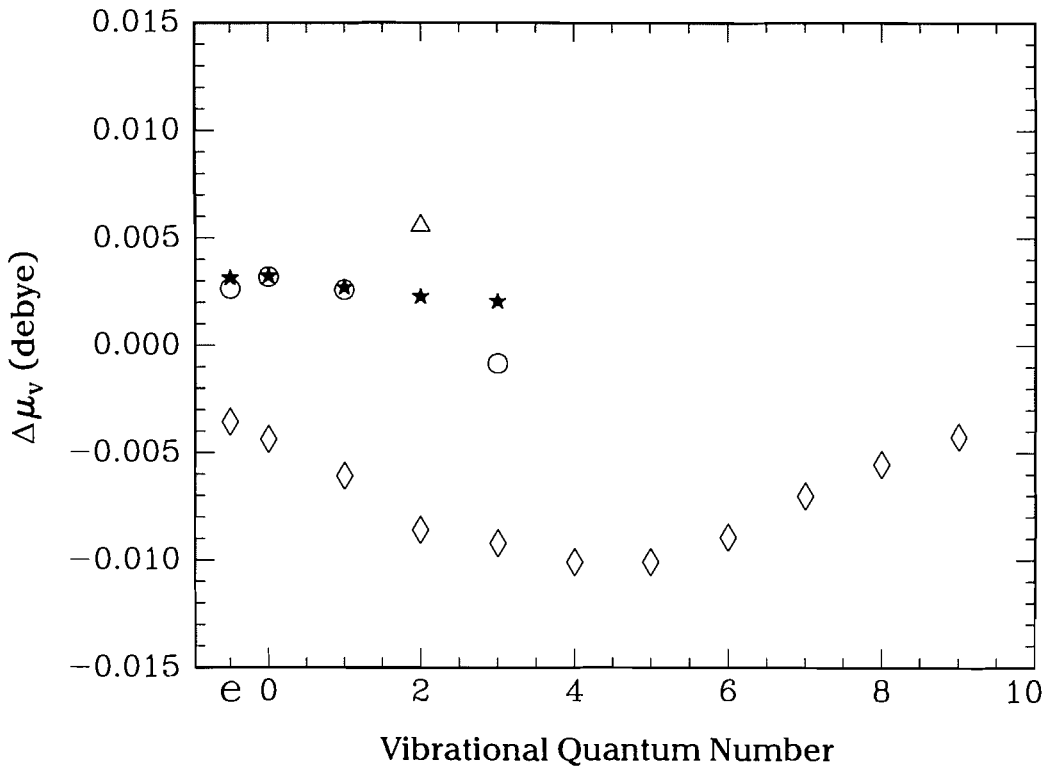

FIG. 4. Plot of the difference between the experimentally determined dipole moments and the *ab initio* dipole moment data taken from Zemke et al. (7) for hydrogen fluoride (see Table 2). ◇, data from Sileo and Cool (8); ○, data from Bass et al. (12) and the present work; △, calculated by Bass et al. (12) based on existing experimental data at the time; ★, calculated using the Herman and Short theory (19) together with values for the M_j and a_j taken from Ogilvie (14).

ments of μ_0 and μ_1 and the transition dipole moments $\langle 0|\mu|1\rangle$ and $\langle 0|\mu|3\rangle$. It seems clear that this value of 1.9232 debye for μ_2 is in error; in fact, the *ab initio* value of 1.9176 is five times closer to the interpolated value of 1.9185 debye established by the present measurement of μ_3. The problems encountered in establishing dipole moment functions have been discussed by Bass et al. (12). What follows examines the accuracy with which dipole moments may be extracted from these functions.

Experimental values for the dipole moment, observed for several vibrational states, are most conveniently expressed as a power series in $(v + \frac{1}{2})$ where v is the vibrational quantum number.

$$[6] \qquad \mu_v = \sum P_j \left(v + \frac{1}{2}\right)^j$$

The dipole moment function, on the other hand, is normally expressed as a Taylor series in the reduced internuclear displacement from equilibrium.

$$[7] \qquad M(x) = \sum M_j x^j; \qquad x = \frac{(R - R_e)}{R_e}$$

With this choice of dipole moment function, expressions for dipole moments and transition dipole moments can be written as a series of linear equations and thus experimental values of these quantities can be used to determine a set of values of M_j. The maximum value of j in either approach is determined by the quantity and quality of the available experimental data. Because the number of measurements of transition intensities greatly exceeds the number of measurements of vibrationally

TABLE 2. Experimental and theoretical dipole moments for hydrogen fluoride

Variable (debye)	Theory		Experiment		
	Zemke et al. (7)	Ogilvie (14)	Sileo and Cool (8)	Bass et al. (12)	This work
μ_e	1.7996	1.8027	1.796	1.80309	1.8022
μ_0	1.8234	1.8265	1.819	1.826567	
μ_1	1.8711	1.8738	1.865	1.873693	
μ_2	1.9176	1.9199	1.909	1.9232	1.9185
μ_3	1.9622	1.9643	1.953		1.9614

TABLE 3. Numerical expressions for P_j as a function of M_j

P_0 $M_0 + (4.405 \times 10^{-5})M_1 + (4.687 \times 10^{-5})M_2 + (1.685 \times 10^{-5})M_3 + (1.602 \times 10^{-6})M_4$

P_1 $(3.423 \times 10^{-2})M_1 + (5.068 \times 10^{-3})M_2 + (2.985 \times 10^{-6})M_3 + (9.442 \times 10^{-7})M_4 + (1.158 \times 10^{-7})M_5 + (4.507 \times 10^{-9})M_6$

P_2 $(4.689 \times 10^{-4})M_1 + (7.074 \times 10^{-4})M_2 + (1.446 \times 10^{-4})M_3 + (6.519 \times 10^{-6})M_4 + (2.793 \times 10^{-8})M_5 + (3.537 \times 10^{-9})M_6$

P_3 $(9.440 \times 10^{-6})M_1 + (1.880 \times 10^{-5})M_2 + (1.220 \times 10^{-5})M_3 + (2.449 \times 10^{-6})M_4 + (1.706 \times 10^{-7})M_5 + (3.606 \times 10^{-9})M_6$

P_4 $-(5.000 \times 10^{-6})M_1 + (2.034 \times 10^{-7})M_2 + (4.383 \times 10^{-7})M_3 + (1.790 \times 10^{-7})M_4 + (3.230 \times 10^{-8})M_5 + (2.622 \times 10^{-9})M_6$

Can. J. Chem. Downloaded from www.nrcresearchpress.com by 195.246.54.202 on 09/08/12
For personal use only.

state-specific dipole moments, the power series (eq. [7]) is the most commonly used. Indeed, for hydrogen fluoride the present measurement allows, for the first time, the determination of P_2 (Table 2), whereas values for M_j up to $j = 6$ are available in the literature. A third form of expansion, the wave function approximation, has been shown to be equivalent to the power series (eq. [7]) (14).

Interconversion between the coefficients of the two expansions is possible following the paper of Herman and Short (19) who showed that P_j may be expressed in terms M_j, B_e/w_e, and a_j, the potential energy coefficients in the Dunham function (20). Previous work seems to have overestimated the rate of convergence of this approach, partly perhaps in deference to the tedious algebra involved. Programs capable of implementing symbolic computation have removed this latter obstacle: accordingly, a Maple™ program was written to rederive the expressions given by Herman and Short, but including terms up to $(B_e/w_e)^4$ and Dunham potential energy coefficients up to a_6. These limits were established by the nonavailability of expressions for the Dunham coefficients higher than Y_{40}. Analytical expressions for P_j ($j = 0$ through 4) are given in the Appendix and Table 3 provides the numerical expressions for P_j as functions of M_j obtained by substituting the values of a_i given by Ogilvie (14) for hydrogen fluoride. As a test of these expressions, the dipole moment function of Zemke et al. (7) was fit to a power series and the resultant values of M_j were substituted into the expressions in Table 3 to obtain values of P_j. These were then used to calculate values of μ_v ($v = 0$ through 3), which agreed to within 10^{-3} debye of the corresponding values calculated by Zemke et al. (7), indicating that both the values of a_j and expressions for P_j are satisfactory for the present purpose. In Table 4 a comparison is made between the P_j values based on Ogilvie's M_j (14) and the expressions in Table 3, and the values obtained directly from eq. [6] and experimentally determined dipole moments.

TABLE 4. Comparison of the literature and present values for P_j

P_j	Ogilvie (14)	This work
P_0	1.8027	1.8022
P_1	0.04774	0.04931
P_2	-1.209×10^{-4}	−0.001091
P_3	-8.958×10^{-5}	
P_4	-1.677×10^{-6}	

The values of M_j obtained by Ogilvie from a careful analysis of dipole moments and infrared intensities for hydrogen fluoride were then used, in a similar manner, to calculate values of μ_v for $v = -\frac{1}{2}$ and 0 through 3. These results have been inserted into Fig. 4 as solid stars. It can be seen that the M_j values suggested by Ogilvie provide better agreement with the trend established by the present measurement than that obtained by Muenter and co-workers (12). Even so, the agreement seems to be deteriorating with increasing v.

Experimental determination of the dipole moments of higher vibrational states seems advisable. The most obvious experiment is to use a dye laser working on R6G to interrogate $v = 4$. However, intracavity doubling of the Ti–sapphire laser will provide radiation of suitable energy to reach $v = 7$. With an efficient multipass system, the present apparatus should provide satisfactory signal to noise for the successful implementation of such an experiment.

Acknowledgements

The authors wish to thank the Natural Sciences and Engineering Research Council of Canada for their financial support.

1. J.C. Polanyi. J. Chem. Phys. **34**, 347 (1961).
2. J.C. Polanyi. Appl. Opt. Chem. Lasers Suppl. 2, 109 (1965).

3. J.C. Polanyi. Appl. Opt. **10**, 1717 (1971).
4. H.-J. Werner and P. Rosmus. J. Chem. Phys. **73**, 2319 (1980).
5. J.A. Coxon and P.G. Hajigeorgiou. J. Mol. Spectrosc. **142**, 254 (1990).
6. W.T. Zemke, W.C. Stwalley, J.A. Coxon, and P.G. Hajigeorgiou. Chem. Phys. Lett. **177**, 412 (1991).
7. W.T. Zemke, W.C. Stwalley, S.R. Langhoff, G.L. Valderrama, and M.J. Berry. J. Chem. Phys. **95**, 7846 (1991).
8. R.N. Sileo and T.A. Cool. J. Chem. Phys. **65**, 117 (1976).
9. C.W. Bauschlicher, Jr., S.R. Langhoff, S.P. Walch, P.R. Taylor, and R.L. Raffe. J. Chem. Phys. **88**, 1743 (1988).
10. F. Sim, D.R. Salahub, and S. Chin. Int. J. Quantum Chem. **43**, 463 (1992).
11. J.S. Muenter and W. Klemperer. J. Chem. Phys. **52**, 6033 (1970).
12. J.M. Bass, R.L. DeLeon, and J.S. Muenter. J. Chem. Phys. **86**, 4305 (1987).
13. A.S. Pine, A. Fried, and J.W. Elkins. J. Mol. Spectrosc. **109**, 30 (1985).
14. J.F. Ogilvie. J. Phys. B: At. Mol. Opt. Phys. **21**, 1663 (1988).
15. T.E. Gough, R.E. Miller, and G. Scoles. Faraday Discuss. Chem. Soc. **71**, 77 (1981).
16. E.S. Fishburne and K.N. Rao. J. Mol. Spectrosc. **19**, 290 (1966).
17. C.H. Townes and A.L. Schawlow. Microwave spectroscopy. Dover, New York. 1975.
18. L.H. Scharpen, J.S. Muenter, and V.W. Laurie. J. Chem. Phys. **46**, 2431 (1967).
19. R.M. Herman and S. Short. J. Chem. Phys. **48**, 1266 (1968).
20. J.L. Dunham. Phys. Rev. **41**, 721 (1932).
21. H.G. Hedderich, K. Walker, and P.F. Bernath. J. Mol. Spectrosc. **149**, 314 (1991).
22. J.S. Muenter. J. Chem. Phys. **56**, 5409 (1972).

Can. J. Chem. Downloaded from www.nrcresearchpress.com by 195.246.54.202 on 09/08/12
For personal use only.

Appendix

[A1] $$P_0 = M_0 + \left[\left(-\frac{21a_1^3}{8} + \frac{23a_1a_2}{4} - \frac{15a_3}{4}\right)M_1 + \left(\frac{7a_1^2}{4} - \frac{3a_2}{2}\right)M_2 - \frac{7}{4}a_1M_3 + \frac{3}{2}M_4\right]\frac{B_e^2}{w_e^2}$$

[A2] $$P_1 = (-3a_1M_1 + 2M_2)\frac{B_e}{w_e} + \left[\left(-\frac{31\,185a_1^5}{256} + \frac{14\,259a_1^3a_2}{32} - \frac{5145a_1^2a_3}{16} + \frac{715a_2a_3}{4} + \frac{795a_1a_4}{4} - \frac{4677a_1a_2^2}{16} - \frac{175a_5}{2}\right)M_1 + \left(\frac{10\,395a_1^4}{128} + \frac{335a_2^2}{8} + \frac{475a_1a_3}{4} - \frac{75a_4}{2} - \frac{3213a_1^2a_2}{16}\right)M_2 + \left(-\frac{95a_3}{2} + \frac{459a_1a_2}{4} - \frac{1155a_1^3}{16}\right)M_3 + \left(-\frac{67a_2}{2} + \frac{459a_1^2}{8}\right)M_4 - \frac{95}{2}a_1M_5 + 25M_6\right]\frac{B_e^3}{w_e^3}$$

[A3] $$P_2 = \left[\left(39a_1a_2 - 15a_3 - \frac{45a_1^3}{2}\right)M_1 + (15a_1^2 - 6a_2)M_2 - 15a_1M_3 + 6M_4\right]\frac{B_e^2}{w_e^2} + \left[\left(\frac{1393\,515a_2a_1^5}{64} - \frac{1890\,135a_2^2a_1^3}{64} - \frac{4390\,155a_1^7}{1024} + \frac{948\,525a_1^2a_3a_2}{32} + \frac{174\,015a_4a_1^3}{16} + \frac{72\,255a_2^3a_1}{8} - 11\,760a_4a_1a_2 - 5805a_1a_3^2 - \frac{108\,885a_5a_1^2}{16} - \frac{84\,285a_2^2a_3}{16} + \frac{11\,655a_5a_2}{4} + \frac{10\,935a_4a_3}{4} + 3465a_1a_6 - \frac{4063\,725a_1^4a_3}{256} - \frac{2205a_7}{2}\right)M_1 + \left(\frac{1463\,385a_1^6}{512} - \frac{719\,955a_1^4a_2}{64} + \frac{310\,065a_1^2a_2^2}{32} - \frac{1707a_2^3}{2} - 7335a_1a_2a_3 - \frac{8535a_1^2a_4}{2} + \frac{2655a_2a_4}{2} + \frac{3255a_3^2}{4} + \frac{4095a_1a_5}{2} + \frac{119\,325a_1^3a_3}{16} - 490a_6\right)M_2 + \left(-\frac{1365a_5}{2} + \frac{8535a_1a_4}{4} + \frac{7335a_2a_3}{4} - \frac{71\,595a_1^2a_3}{16} - \frac{62\,013a_1a_2^2}{16} + \frac{239\,985a_1^3a_2}{32} - \frac{627\,165a_1^5}{256}\right)M_3 + \left(-\frac{885a_4}{2} + \frac{5121a_2^2}{8} + \frac{7335a_1a_3}{4} - \frac{62\,013a_1^2a_2}{16} + \frac{239\,985a_1^4}{128}\right)M_4 + \left(-\frac{1085a_3}{2} + \frac{7335a_1a_2}{4} - \frac{23\,865a_1^3}{16}\right)M_5 + \left(-\frac{885a_2}{2} + \frac{8535a_1^2}{8}\right)M_6\right]\frac{B_e^4}{w_e^4}$$

[A4] $$P_3 = \left[\left(-\frac{19\,035a_1^5}{64} + \frac{7545a_1^3a_2}{8} - \frac{2055a_1a_2^2}{4} - \frac{2175a_1^2a_3}{4} + 225a_2a_3 + 255a_1a_4 - 70a_5\right)M_1 + \left(\frac{6345a_1^4}{32} - \frac{1575a_1^2a_2}{4} + \frac{85a_2^2}{2} + 175a_1a_3 - 30a_4\right)M_2 + \left(-\frac{705a_1^3}{4} + 225a_1a_2 - 70a_3\right)M_3 + \left(\frac{225a_1^2}{2} - 34a_2\right)M_4 - 70a_1M_5 + 20M_6\right]\frac{B_e^3}{w_e^3}$$

[A5] $$P_4 = \left[\left(-\frac{2430\,855a_1^7}{512} + \frac{697\,095a_2a_1^5}{32} - \frac{839\,475a_2^2a_1^3}{32} - \frac{1753\,425a_1^4a_3}{128} + \frac{27\,195a_2^3a_1}{4} + \frac{357\,825a_1^2a_3a_2}{16} \right.\right.$$
$$\left. + \frac{61\,875a_4a_1^3}{8} - \frac{24\,945a_2^2a_3}{8} - 7080a_4a_1a_2 - \frac{7455a_1a_3^2}{2} - \frac{30\,345a_5a_1^2}{8} + \frac{2415a_5a_2}{2} + \frac{2715a_4a_3}{2} + 1470a_1a_6 - 315a_7\right)M_1$$
$$+ \left(\frac{810\,285a_1^6}{256} - \frac{348\,975a_1^4a_2}{32} + \frac{124\,725a_1^2a_2^2}{16} + \frac{48\,825a_1^3a_3}{8} - 375a_2^3 - 4830a_1a_2a_3 - 2715a_1^2a_4 + 495a_2a_4\right.$$
$$\left. + \frac{945a_3^2}{2} + 945a_1a_5 - 140a_6\right)M_2 + \left(-\frac{347\,265a_1^5}{128} + \frac{116\,325a_1^3a_2}{16} - \frac{24\,945a_1a_2^2}{8} - \frac{29\,295a_1^2a_3}{8}\right.$$
$$\left. + \frac{2415a_2a_3}{2} + \frac{2715a_1a_4}{2} - 315a_3\right)M_3 + \left(\frac{116\,325a_1^4}{64} - \frac{24\,945a_1^2a_2}{8} + \frac{1125a_2^2}{4} + \frac{2415a_1a_3}{2} - 165a_4\right)M_4$$
$$\left. + \left(-\frac{9765a_1^3}{8} + \frac{2415a_1a_2}{2} - 315a_3\right)M_5 + \left(\frac{2715a_1^2}{4} - 165a_2\right)M_6\right]\frac{B_e^4}{w_e^4}$$

Can. J. Chem. Downloaded from www.nrcresearchpress.com by 195.246.54.202 on 09/08/12
For personal use only.

The vibrational circular dichroism spectra of 2-methylaziridine: dominance of the asymmetric centre at nitrogen

ARVI RAUK,[1] THOMAS EGGIMANN, HELMUT WIESER, GENNADII V. SHUSTOV, AND DANYA YANG
Department of Chemistry, The University of Calgary, Calgary, AB, T2N 1N4, Canada
Received March 17, 1993
This paper is dedicated to Professor John C. Polanyi on the occasion of his 65th birthday

ARVI RAUK, THOMAS EGGIMANN, HELMUT WIESER, GENNADII V. SHUSTOV, and DANYA YANG. Can. J. Chem. **72**, 506 (1994).

The experimental VCD spectrum of (2*R*)-2-methylaziridine has been measured in the region 800–1500 cm^{-1}. The *ab initio* implementation of the Vibronic Coupling Theory (VCT) of Nafie and Freedman, using the 6-31G$^{*(0.3)}$ basis set, in the common origin and distributed origin gauges and with uniformly and optimally scaled quantum mechanical force fields, is used to investigate the chiroptical properties. VCD spectra are computed for both *cis* and *trans* invertomers. The predicted VCD spectrum of 2-methylaziridine (the equilibrium mixture) is dominated by that of the *trans* diastereomer, not simply because of its greater abundance but because the rotatory strengths of many absorptions in the mid-IR are oppositely signed and of similar magnitude in the two invertomers which differ in absolute configuration at nitrogen. The VCD spectrum of 2-methylaziridine is compared in detail to that of 2-methyloxirane. In the region of the methyl group deformations and CH_2 scissor, the theoretical (*R*)-2-methyloxirane VCD spectrum displays a much closer similarity to the *cis*-(2*R*)-2-methylaziridine than to the *trans* diastereomer.

ARVI RAUK, THOMAS EGGIMANN, HELMUT WIESER, GENNADII V. SHUSTOV et DANYA YANG. Can. J. Chem. **72**, 506 (1994).

On a mesuré le spectre VCD expérimental de la (2*R*)-2-méthylaziridine dans la région de 800 à 1500 cm^{-1}. Pour l'étude des propriétés chiroptiques, on a fait appel à l'implantation *ab initio* de la théorie de couplage vibronique (TCV) de Nafie et Freedman, utilisant une base 6-31G$^{*(0.3)}$, dans des calibrations d'origines commune et dispersée avec des champs de force de mécanique quantique à graduations uniforme et optimale. On a calculé les spectres VCD pour les invertomères *cis* ainsi que *trans*. Le spectre VCD calculé pour la 2-méthylaziridine (mélange à l'équilibre) est dominé par celui du diastéréoisomère *trans*, non seulement á cause de sa plus grande abondance, mais parce que les forces rotatoires de plusieurs absorptions de l'IR moyen sont de signes opposés et d'amplitudes semblables dans les deux invertomères qui diffèrent par leur configuration au niveau de l'azote. On a effectué une comparaison détaillée du spectre VCD de la 2-méthylaziridine avec celui du 2-méthyloxirane. Dans la région des déformations du groupe méthyle et des vibrations de cisaillement du CH_2, le spectre VCD théorique du (*R*)-2-méthyloxirane présente une similarité beaucoup plus grande avec celle de la *cis*-(2*R*)-2-méthylaziridine qu'avec celle du diastéréoisomère *trans*.

[Traduit par la rédaction]

Introduction

The explicit connection between the infrared (IR) spectrum of a substance and its molecular structure has begun to be elucidated in the last decade with the increasing availability of reliable *ab initio* force fields and atomic polar tensors (APT) for intensity calculations. The coincident introduction of chiroptical techniques in the form of vibrational circular dichroism (VCD) spectroscopy and the Raman equivalent (ROA) has promised further insights. Extraction of the inherent information from the latter techniques (and to some extent the former) has been hampered by theoretical difficulties which have largely been overcome with the introduction of practical nonempirical formalisms by Nafie and Freedman (1), Stephens (2), and Buckingham, Fowler, and Galwas (3) and their computer implementations by Stephens and coworkers (4), Morokuma and Sugeta (5), and Dutler (6), Yang (7, 8), and Rauk (6–8). An *ab initio* approximate model, LMO-VCD (9), implemented by Polavarapu (10) has also proved to be effective. The structural rigidity and relatively small size of three-membered ring compounds makes them ideal platforms for assessment of both experimental and theoretical procedures. The parent achiral compounds can be rendered optically active by isotopic substitution. Investigations have been reported on 1,2-dideuterio- (4) and 1,2-dicyanocyclopropane (11), the deuterated oxiranes (6, 12, 13) and their (deuterated) methyl (7, 14, 15) and dimethyl (7, 16) derivatives, and on (deuterated) methyl- (17) and dimethylthiiranes (18). The analogous nitrogen heterocycle has escaped attention, perhaps since it lacks the conformational rigidity of the carbon, oxygen and sulfur analogues. 2-Methylaziridine exists as an equilibrium mixture of *trans* and *cis* diastereoisomeric forms whose composition has been determined by nmr (19) and IR (20) measurements. Following an earlier partial assignment on the basis of an empirical force field (21), a complete assignment of the IR spectrum has been carried out on the basis of scaled *ab initio* force fields (22).

The *ab initio* Vibronic Coupling Theory (VCT) formalism for IR and VCD intensities developed by Nafie and Freedman (1) has been used to investigate the complete IR and VCD spectra of (*S*,*S*)-2,3-dideuterooxirane and the other deuterated isotopomers (13), of ethanol and α-deuterioethanol (23), of a series of small model molecules, including isotopically chiral ammonia, hydrazine (24), hydrogen peroxide (24), oxaziridine (8), and of the methyl- (7) and dimethyl-oxiranes (7, 16) and thiiranes (18). Applications to substituted oxiranes (7, 13, 16) and thiiranes (18), where direct comparison with experimental VCD spectra was possible suggest that the basis set designated as 6-31G$^{*(0.3)}$ (obtained by reducing the exponent of 3*d* orbitals of C, N, and O from 0.8 to 0.3) provides reliable IR and VCD intensities.

We report herein an extension of the VCT/6-31G$^{*(0.3)}$ methodology to an investigation of the 2-methylaziridine system and compare the results with the investigation of 2-methyloxirane.

[1]Author to whom correspondence may be addressed.

Can. J. Chem. Downloaded from www.nrcresearchpress.com by 195.246.54.202 on 09/08/12
For personal use only.

Can. J. Chem. Downloaded from www.nrcresearchpress.com by 195.246.54.202 on 09/08/12
For personal use only.

Theory

The vibronic coupling theory of Nafie and Freedman (1) as implemented at the *ab initio* level by Dutler, Yang, and Rauk (6–8) yields values for the dipole strength, D_j, and rotatory strength, R_j, of the jth normal mode:

$$[1] \qquad D_j = \mu^{VC}_{(00,01),j} \cdot \mu^{VC}_{(01,00),j}$$

$$[2] \qquad R_j = \mathrm{Im}\,(\mu^{VC}_{(00,01),j} \cdot m^{VC}_{(01,00),j})$$

where

$$[3.1] \qquad \mu^{VC}_{(00,01),j} = \left(\frac{\hbar}{2\omega_j}\right)^{1/2}\left[\sum_{n=1}^{n_{atoms}} \xi_n s_n^j - 2\sum_{n=1}^{n_{atoms}}\sum_{i=1}^{n_{electrons}}\sum_{e=1}^{n_{ex}} \langle\Psi_0^a|r_i|\Psi_e^a\rangle\langle\Psi_e^a\left|\frac{\partial}{\partial R_n}\right|\Psi_0^a\rangle s_n^j\right]$$

$$[3.2] \qquad = \left(\frac{\hbar}{2\omega_j}\right)^{1/2}\left[\sum_{n=1}^{n_{atoms}} \xi_n s_n^j - 2\sum_{n=1}^{n_{atoms}}\sum_{i=1}^{n_{electrons}} \langle\Psi_0^a\left|r_i\frac{\partial}{\partial R_n}\right|\Psi_0^a\rangle s_n^j\right]$$

and

$$[4] \qquad m^{VC}_{(00,01),j} = \frac{1}{2c}\left(\frac{\hbar\omega_j}{2}\right)^{1/2}\left[-i\sum_{n=1}^{n_{atoms}} \xi_n(R_n \times s_n^j) - \frac{2\hbar}{m_e}\sum_{n=1}^{n_{atoms}}\sum_{i=1}^{n_{electrons}}\sum_{e=1}^{n_{ex}} \langle\Psi_0^a|r_i \times p_i|\Psi_e^a\rangle\langle\Psi_e^a\left|\frac{\partial}{\partial R_n}\right|\Psi_0^a\rangle s_n^j \frac{1}{E_e^0 - E_0^0}\right]$$

The superscript VC denotes that these expressions describe a vibronic coupling mechanism for IR and VCD intensities. The subscript (00,01) (or (01,00)) signifies that the transition is between the $v = 0$ and $v = 1$ vibrational levels of the ground electronic state of the molecule. The reader is referred to references 6–8 for further explanation of the notation. Electric dipole strengths derived from eq. [3] are formally equivalent to the Atomic Polar Tensor (APT) theory. Stephens circumvents the summation over excited states in eq. [4] by invoking the magnetic field dependence of the wavefunction, a procedure which requires solution of the perturbed Hartree–Fock equations in the presence of a magnetic field (2). In VCT, the sum over excited states which appears in the second term of eq. [4] must be explicitly evaluated. In a normal implementation all transition moments are evaluated at a common origin, the molecular centre of mass (VCT-CO). The VCT has also been implemented in the distributed origin (with origins at nuclei) gauge of Stephens (25), VCT-DO (8).

Computational Details

The geometries of *trans*- and *cis*-2-methylaziridine, determined by complete optimization at the restricted Hartree–Fock level of theory using the 6-31G* and 6-31G*$^{(0.3)}$ basis sets, have been reported previously (22). Bond lengths are calculated to be a little longer by the 6-31G*$^{(0.3)}$ basis set than the usual 6-31G* basis set, an effect also observed with optimization at the MP2 level of theory. The computed energy separation of the two invertomers, 2.17 kJ mol^{-1}, assuming $\Delta S \approx 0$, implies a *trans/cis* mixture of 0.706:0.294 at 298 K. IR and VCD intensities were accomplished by the program system VCT90,[2] which implements the vibronic coupling theory (VCT) of Nafie and Freedman (1) at the *ab initio* level. Both uniformly scaled and optimally scaled force fields (22) were used, and the transition moments were evaluated with the 6-31G*$^{(0.3)}$ basis set in the common origin (molecular centre of mass — VCT-CO) and distributed origin (at nuclear centres — VCT-DO) gauges. Simulated IR and VCD spectra were obtained assuming a Lorentzian lineshape of width at half height of 10 cm^{-1}.

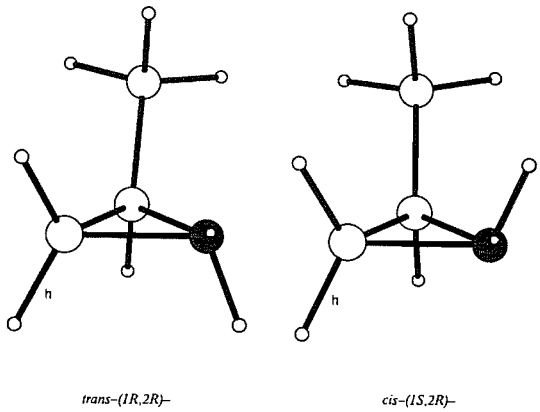

FIG. 1. The RHF//6-31G*$^{(0.3)}$ geometries of (1*R*,2*R*)-2-methylaziridine (*trans*) and (1*S*,2*R*)-2-methylaziridine (*cis*).

Experimental Details

(2*R*)-(+)-2-Methylaziridine, bp 65–66°, $[\alpha]_D^{20}$ +12.4° (c 1.7, 95% EtOH) (lit. 27, bp 66–67°, $[\alpha]_D^{25}$ + 12.4 (c 2.6, EtOH)) was prepared from (2*R*)-(−)-2-amino-1-propanol ($[\alpha]_D^{19}$ − 18° (neat), Aldrich) according to ref. 27 was purified additionally by distilling over Na (metal). An optical purity for the sample was not determined specifically. However, it is well established (28) that the conversion of 2-amino-1-propanol to aminopropyl hydrogen sulphate and further cyclization of the latter are carried out without affecting the chiral centre, and the optical purity of 2-methylaziridine will not be less than the optical purity of the starting material, i.e. 2-amino-1-propanol.

The absorption spectrum was measured with a Nicolet 8000 FT-IR spectrometer, and for VCD, a linear polarizer, a ZnSe photoelastic modulator (Hinds International), a *f*/1 ZnSe focusing lens, and the necessary electronic equipment were added to the instrument as described elsewhere (23). A narrow band MCT detector cooled with liquid nitrogen was used for all experiments. The interferometer was operated at an effective resolution of 4 cm^{-1}, coadding 50 scans and 20 000 scans for the absorption and VCD spectra, respectively.

Solutions of (2*R*)-2-methylaziridine in carbon tetrachloride were prepared to record absorption and VCD spectra. Neat CCl_4 was utilized to subtract the VCD background. In order to detect absorption dependent VCD artifacts as well as to positively identify genuine VCD bands, three spectra were recorded with solutions of different concentration in different cells. The bands reported in Tables 1 and 2 were reproduced in all experiments, except for the negative feature at 1265 cm^{-1}, which may be a spurious signal. The absorption and VCD spectra reported here (Figs 2 and 3) were measured with solutions of concentrations of 0.27 M (KBr cell, 0.5 mm) and 1.1 M (KBr cell, 0.1 mm), respectively. The poor signal-to-noise in the VCD spectrum is attributed firstly to the small signal size (caused by partial cancella-

[2]VCT90: based on FREQ85 (6) to which is added the VCT-DO implementations (8) and which has been modified to be compatible with GAUSSIAN 90 (26).

Can. J. Chem. Downloaded from www.nrcresearchpress.com by 195.246.54.202 on 09/08/12
For personal use only.

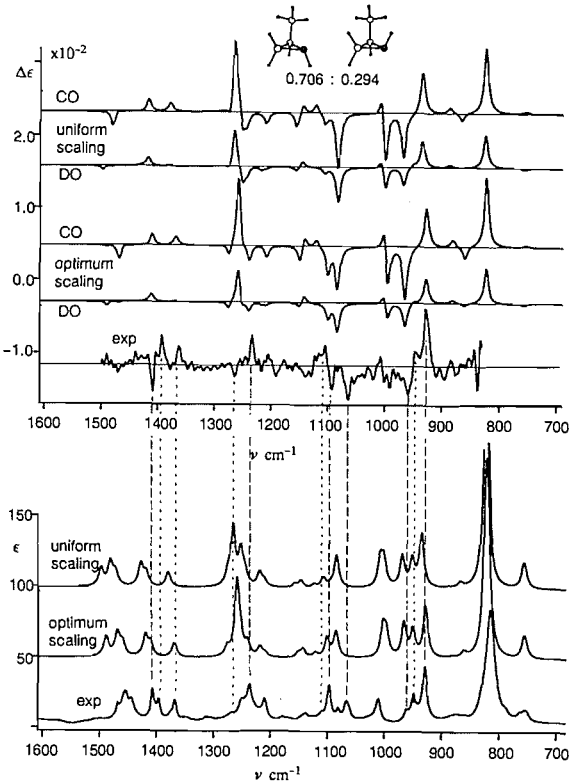

FIG. 2. Theoretically simulated (VCT/6-31G*(0.3); 0.706 *trans*: 0.294 *cis*) and experimental VCD and IR absorption spectra of (2*R*)-2-methylaziridine in the region 700–1600 cm^{-1}. Correlation of VCD and absorption features: *trans* – – – –; *cis* - - - - - -.

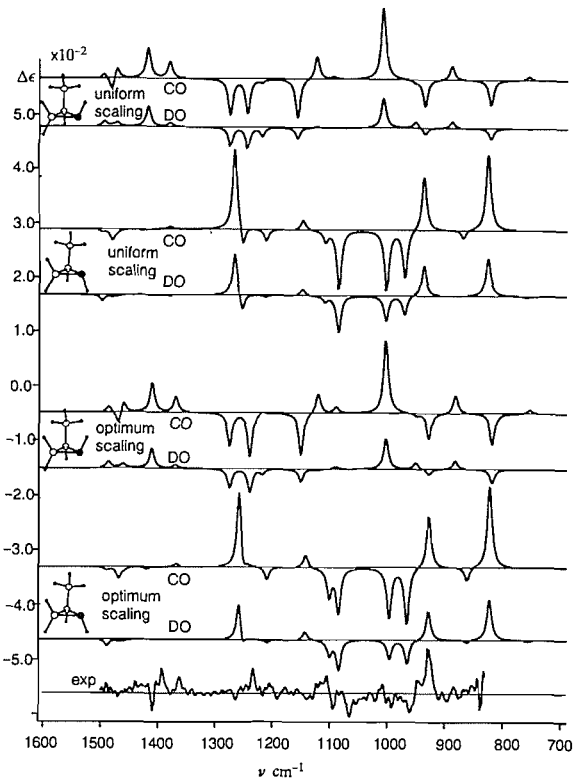

FIG. 3. Theoretically simulated (6-31G*(0.3) basis set) and experimental VCD spectra of *cis*- and *trans*-(2*R*)-2-methylaziridine in the region 700–1600 cm^{-1}.

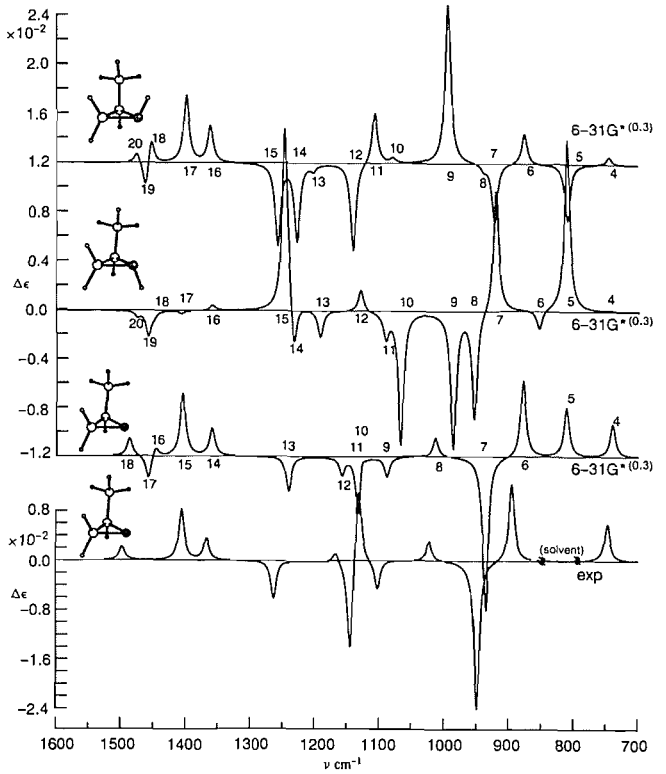

FIG. 4. Simulated VCD spectra VCT-CO/6-31G*(0.3) theory in the region 700–1600 cm^{-1} for the individual invertomers of (2*R*)-2-methylaziridine (top two spectra), and of the VCT-CO/6-31G*(0.3) (third spectrum) and experimental (bottom) VCD spectra of (2*R*)-2-methyloxirane. The experimental spectrum of the oxirane is simulated on the basis of published frequencies and intensities (ref. 15). The numbering refers to modes displayed in Figs 5 and 6, and (for the aziridine) listed in Tables 1 and 2.

tion of VCD bands of opposite sign arising from the two invertomers) and secondly to a deterioration of the interferometer optics.[3]

Results and discussion

The structures of *cis*- and *trans*-(2*R*)-2-methylaziridine are shown in Fig. 1. Geometric details, relative energies, and complete vibrational assignments of the two inversional diastereomers of 2-methylaziridine have been reported (22). Only details required for the discussion of the VCD spectra are repeated here (Tables 1 and 2). Some substantial differences are predicted in the frequencies of equivalent vibrational modes of the two isomers. Normal modes, ν_6 and ν_{11}, primarily rocking and wagging motions of the CH_2 group, occur 20 and 18 cm^{-1} to lower frequency in *trans*-2-methylaziridine (Table 1) than in the *cis* diastereomer (Table 2). On the other hand, ν_8, a mixed mode consisting of C—CH_3 stretch and ring distortion, is at higher frequency by 12 cm^{-1} for the *trans* isomer. Lesser perturbations to lower (ν_1, ν_9, ν_{10}, ν_{12}, ν_{13}, ν_{15}, and ν_{25}) and higher (ν_{14}, ν_{17}, ν_{23}, and ν_{27}) frequencies in the *trans* compared to the *cis* conformer are resolved in the experimental IR spectrum (22) and therefore may be significant for the in-

[3]Over the period of the last year, the alignment of the beamsplitter and mirrors of the Michaelson interferometer has been worsening, resulting in a loss of energy at the polarization optics. Furthermore, the optimal VCD signal is not located in the optical axis anymore, causing additional energy loss, and a deterioration of the appearance of the recorded VCD spectrum.

TABLE 1. VCT/6-31G*(0.3) vibrational properties of (1*R*,2*R*)-2-methylaziridine (*trans*)

Mode	Freq. cm^{-1} calc[b]	Freq. cm^{-1} calc[c]	Freq. cm^{-1} exp[e]	$D^{a,b}$	$D^{a,c}$	$R^{b,d}$ CO	$R^{b,d}$ DO	$R^{c,d}$ CO	$R^{c,d}$ DO	R exp	Assignments
ν_1	199	198	200[f]	4.0	4.4	0.2	0.6	0.0	0.6		CH_3 torsion
ν_2	345	371	387[f]	52.7	53.8	0.5	2.8	0.7	3.1		$\perp CH_3$
ν_3	378	408	401	86.8	82.5	−3.2	−5.4	−3.0	−5.3		$\parallel CH_3$
ν_4	757	757	764	33.9	28.9	0.3	−1.5	−0.1	−1.4		asym ring def
ν_5	824	823	818	283.9	288.1	61.0	30.1	65.3	32.1		asym ring def
ν_6	867	861	871	7.6	8.8	−6.6	−0.3	−10.5	−2.3		CH_2 rock, $\perp$CH
ν_7	935	928	929	62.0	61.4	38.5	21.6	37.0	20.4	(+)	CH_2 rock, $\perp$NH
ν_8	969	966	961	44.6	50.3	−32.4	−13.3	−38.1	−16.5	(−)	C-CH_3 str, ring def
ν_9	1001	996	1005	36.0	32.2	−39.4	−16.6	−32.5	−12.5		$\parallel$NH, $\perp$CH
ν_{10}	1084	1084	1069	42.6	32.5	−35.7	−22.5	−27.1	−18.0	(−)	CH_3 rock, $\perp$h,[g] $\perp$CH
ν_{11}	1107	1100	1096	12.4	25.0	−6.3	−3.3	−16.4	−9.1	(−)	CH_2 wag
ν_{12}	1146	1142	1137	8.7	10.5	5.7	3.7	7.3	4.8		$\perp$CH, CH_2 twist
ν_{13}	1211	1209	1210	6.6	4.3	−6.4	−1.0	−6.7	−1.6		$\parallel$CH, $\perp$NH
ν_{14}	1252	1253	1243	38.0	17.6	−11.8	−9.8	−12.7	−8.6	(+)	$\perp$NH, CH_2 rock
ν_{15}	1266	1258	1250	66.2	82.1	43.2	22.3	44.6	21.9		$\parallel$NH, CH_2 rock
ν_{16}	1379	1369	1371	7.0	7.1	1.1	−0.4	1.5	−0.2		CH_3 umb
ν_{17}	1428	1420	1412	21.8	20.5	−0.6	0.3	−0.8	0.2	(−)	CH_2 scis, CH_3 umb
ν_{18}	1473	1460	1444	9.2	9.2	−0.9	−0.5	−0.9	−0.5		asym CH_3 def
ν_{19}	1481	1469	1457	14.0	14.1	−4.8	−0.6	−4.8	−0.7		asym CH_3 def
ν_{20}	1498	1489	1496	14.9	16.9	−1.0	−2.6	−1.2	−2.8		CH_2 scis
ν_{21}	2860	2880	2882	40.1	39.8	0.7	1.9	0.7	1.9		CH_3 sym str
ν_{22}	2929	2950	2939	42.9	42.7	0.0	−0.2	0.1	−0.2		CH_3 asym str
ν_{23}	2943	2964		2.3	2.2	7.9	8.8	7.8	8.6		CH_3 asym str, CH str
ν_{24}	2951	2972		49.2	48.8	−12.0	−16.7	−11.8	−16.5		CH_2 sym str
ν_{25}	2968	2989	2981	52.8	52.7	11.2	13.6	11.1	13.5		CH str
ν_{26}	3043	3065	3065	26.9	26.7	−2.3	−4.0	−2.3	−4.0		CH_2 asym str
ν_{27}	3369	3338	3343	3.9	3.9	−0.8	−0.5	−0.8	−0.5		NH str

[a] In unit of 10^{-40} esu^2 cm^2.
[b] Uniformly scaled by 0.912.
[c] Optimally scaled force field (ref. 22).
[d] In unit of 10^{-44} esu^2 cm^2.
[e] Reference 22.
[f] Reference 29.
[g] Bond *h* (see Fig. 1).

terpretation of the VCD spectrum of the equilibrium mixture discussed below. The nature of the vibrations are particularly complex in the range 800–1400 cm^{-1}. In the assignments listed in Tables 1 and 2, only the major group motions are identified, in decreasing order of their apparent involvement. The modes are discussed further in their connection to VCD spectra and in comparisons with 2-methyloxirane.

The VCD spectrum of (2R)-2-methylaziridine

VCT/6-31G*(0.3) optical rotatory strengths, *R*, calculated in the CO and DO gauges using uniformly and optimally scaled force fields, are listed in Tables 1 and 2. The close correspondence between optimum scaling and uniform scaling of 6-31G*(0.3) force fields has been noted (22), and is apparent in the similarities in the dipole and rotary strengths calculated from the two force fields (Tables 1 and 2). Previous experience with VCT/6-31G*(0.3) (7, 8, 16, 18) suggests that most calculated rotatory strengths in the mid-IR region will have the correct sign and will be within a factor of 2 in absolute magnitude of experiment and of the most accurate results achievable with the present level of theory. Comparison of the CO and DO columns of the two tables shows that the dominant effect of change of gauge is to reduce the intensities of the strongest transitions by approximately a factor of 2 in the mid-IR region. Several of the rotatory strengths of the weaker transitions change sign (Table 1, ν_{16}, ν_{17}, ν_{22}; Table 2, ν_4, ν_8, ν_{19}, ν_{23}) as a consequence of the change of gauge.

The experimental VCD spectrum of (2*R*)-2-methylaziridine is shown in Fig. 2 together with the observed IR spectrum. The VCD spectrum is very weak. Direct correlation (dashed lines, Fig. 2) of the VCD features with bands in the IR spectrum, as well as examination of the VCD spectra obtained at three different concentrations, assist to distinguish real features from the high background noise level. A quantitative analysis of the spectrum is not possible. However, the dominant feature, a positive Cotton Effect (CE) at 928 (929)[4] cm^{-1} (ν_7), as well as the negative CE at 960 (961) cm^{-1} (ν_8) coincide with the peak attributed to the *trans* isomer (Table 1), as do the two negative features at 1065 (1069) cm^{-1} (ν_{10}) and 1094 (1096) cm^{-1} (ν_{11}), the positive feature at 1235 (1243) cm^{-1} (ν_{14}) and the sharp negative feature at 1411 (1412) cm^{-1} (ν_{17}). Five features may be tentatively attributed to the *cis* isomer: 947 (949) cm^{-1} (ν_8), 1107 (1114) cm^{-1} (ν_{11}), 1265 (1268 cm^{-1}) (ν_{15}), 1364 (1373) cm^{-1} (ν_{16}), 1394 (1400) cm^{-1} (ν_{17}) (Table 2). Simulated VCD spectra of the equilibrium mixture at room

[4] In this section the number cited for wave length corresponds to that observed in CCl_4 solution. The value in parentheses is the corresponding position in the gas phase spectrum and coincides with the values listed in Tables 1 and 2.

Can. J. Chem. Downloaded from www.nrcresearchpress.com by 195.246.54.202 on 09/08/12
For personal use only.

TABLE 2. VCT/6-31G*(0.3) vibrational properties of (1*S*,2*R*)-2-methylaziridine (*cis*)

Mode	Freq. cm^{-1} calc[b]	Freq. cm^{-1} calc[c]	Freq. cm^{-1} exp[e]	$D^{a,b}$	$D^{a,c}$	$R^{b,d}$ CO	$R^{b,d}$ DO	$R^{c,d}$ CO	$R^{c,d}$ DO	R exp	Assignments
ν_1	212	210	213[f]	4.8	4.9	1.9	1.4	1.6	1.3		CH_3 torsion
ν_2	347	374		17.9	15.8	−3.2	−4.2	−2.8	−3.9		$\perp CH_3$
ν_3	379	408	401	26.5	23.8	1.1	0.6	1.4	0.6		$\parallel CH_3$
ν_4	754	754	756	44.2	42.8	3.1	−0.5	3.3	−0.2		asym ring def
ν_5	821	818	818	281.5	286.6	−20.4	−8.7	−24.8	−10.8		asym ring def
ν_6	888	882	891	2.4	3.9	10.4	4.8	13.8	6.2		CH_2 rock, $\perp$CH
ν_7	934	927	926	43.7	44.2	−18.8	−4.7	−17.9	−4.1		CH_2 rock, $\perp$NH
ν_8	951	950	949	94.3	92.8	−1.8	4.2	−1.7	4.4	(+)	C-CH_3 str, ring def
ν_9	1007	1002	1007	95.1	101.5	46.9	19.2	47.7	19.4		$\parallel$NH, $\perp$CH
ν_{10}	1094	1090	1080	7.0	7.1	1.2	0.0	3.5	1.2		CH_2 wag, h[g] wag
ν_{11}	1123	1121	1114	9.4	13.4	13.6	0.7	11.8	−0.6	(+)	$\perp$h[g] wag
ν_{12}	1157	1151	1146	12.1	13.8	−22.3	−6.2	−24.2	−7.2		$\perp$CH
ν_{13}	1219	1218	1218	39.7	27.3	−1.5	−4.7	1.6	−2.6		$\parallel$CH, $\perp$CH
ν_{14}	1245	1240	1237	33.5	34.5	−18.0	−10.8	−22.7	−12.0		$\perp$NH, CH_2 rock
ν_{15}	1275	1276	1268	24.1	22.7	−18.6	−9.5	−16.7	−9.6	(−)	$\parallel$NH, CH_2 rock
ν_{16}	1381	1370	1373	20.0	19.0	7.8	1.9	7.4	1.6	(+)	CH_3 umb, $\parallel$CH
ν_{17}	1419	1412	1400	30.9	31.4	14.0	9.4	13.6	9.0	(+)	CH_2 scis, CH_3 umb
ν_{18}	1473	1461	1464	8.8	8.9	5.2	1.7	5.2	1.7		asym CH_3 def
ν_{19}	1483	1471	1475	20.9	21.0	−5.7	0.5	−5.6	0.4		asym CH_3 def
ν_{20}	1496	1487	1481	4.4	5.7	2.1	2.2	2.7	2.8		CH_2 scis
ν_{21}	2855	2875	2878	35.5	35.3	0.4	1.0	0.4	1.0		CH_3 sym str
ν_{22}	2926	2947		26.9	26.7	5.1	6.0	5.0	5.9		CH_3 asym str
ν_{23}	2930	2951		36.6	36.3	0.5	−0.7	0.5	−0.7		CH_3 asym str, CH str
ν_{24}	2952	2973		42.5	42.1	−7.3	−10.3	−7.3	−10.2		CH_2 sym str
ν_{25}	2982	3003	3007	40.9	40.8	6.7	8.3	6.7	8.3		CH str
ν_{26}	3044	3066	3066	28.7	28.6	−2.0	−0.7	−1.9	−0.7		CH_2 asym str
ν_{27}	3356	3324	3320	3.1	3.1	−0.3	−0.7	−0.3	−0.6		NH str

[a] In unit of 10^{-40} esu^2 cm^2.
[b] Uniformly scaled by 0.912.
[c] Optimally scaled force field (ref. 22).
[d] In unit of 10^{-44} esu^2 cm^2.
[e] Reference 22.
[f] Reference 29.
[g] Bond *h* (see Fig. 1).

temperature (298 K), in the range 700–1600 cm^{-1}, calculated in the CO and DO gauges and using uniformly and optimally scaled force fields, are also shown in Fig. 2. All spectra show the same gross characteristics. Nine of the eleven features identified in the experimental VCD spectrum and assigned to either the *trans* or *cis* aziridine, are reproduced in the simulated spectra. The dominant positive CE at 928 (929) cm^{-1} and the negative CE at 960 (961) cm^{-1} correspond closely to similar features in the simulated spectra and originate from the *trans* isomer. The predicted VCD spectrum of the *cis* isomer is completely different in this region (Fig. 3). The two negative features, 1065 (1069) cm^{-1} and 1094 (1096) cm^{-1}, also unambiguously assignable to the *trans* isomer, are more accurately reflected in the optimally scaled than the uniformly scaled spectra. However, the positive feature observed at 1235 (1243) cm^{-1} (ν_{14}, Table 1) must originate from the strong positive rotatory strength calculated for ν_{15} of the *trans* isomer, and may reflect a misassignment of this band. There is no calculated origin for the negative CE which coincides with the observed position of ν_{17} (1411 (1412) cm^{-1}) of the *trans* isomer. However, we believe this 'feature' to be real since it appears in VCD spectra measured at three different concentrations. The weak positive shoulder at 947 (949) cm^{-1}, attributed to ν_8 of the *cis* isomer, is reproduced correctly in the VCT-DO calculations but not by VCT-CO. On the other hand, the positive CE at 1107 (1114) cm^{-1}, assigned to ν_{11} of the *cis* isomer, is reproduced well by VCT-CO but all but vanishes with VCT-DO. All other features attributed to the *cis* isomer have plausible counterparts in the predicted spectra of the *cis* isomer, and are present in the simulated spectrum of the equilibrium mixture. Additional intriguing similarities between the observed and simulated spectra may be perceived upon examination of the spectra of Fig. 1, but only those experimental features which are also discernible in the VCD spectra of more dilute solutions than that shown herein have been discussed.

The equilibrium mixture consists of two species which have the same absolute configuration at C but opposite sterochemistry at N. The simulated VCD spectra of *trans*-(1*R*,2*R*)- and *cis*-(1*S*,2*R*)-2-methylaziridine are shown separately in Fig. 3. Examination of the VCD spectra of the individual diastereomers may be expected to reveal some features which are constant, reflecting the local configurational similarity at C, and some features which change sign in accordance with the different absolute configurations at N. A perusal of the data in Tables 1 and 2 reveals that of the 20 bands below 1500 cm^{-1}, 13 are predicted to be of opposite sign in the two diastereomers, suggesting a disproportionate influence of the absolute configuration at N. A number of the modes of the *cis* isomer have counterparts of oppositely signed Cotton effects at very nearly the same frequency in the more abundant *trans* iso-

Can. J. Chem. Downloaded from www.nrcresearchpress.com by 195.246.54.202 on 09/08/12
For personal use only.

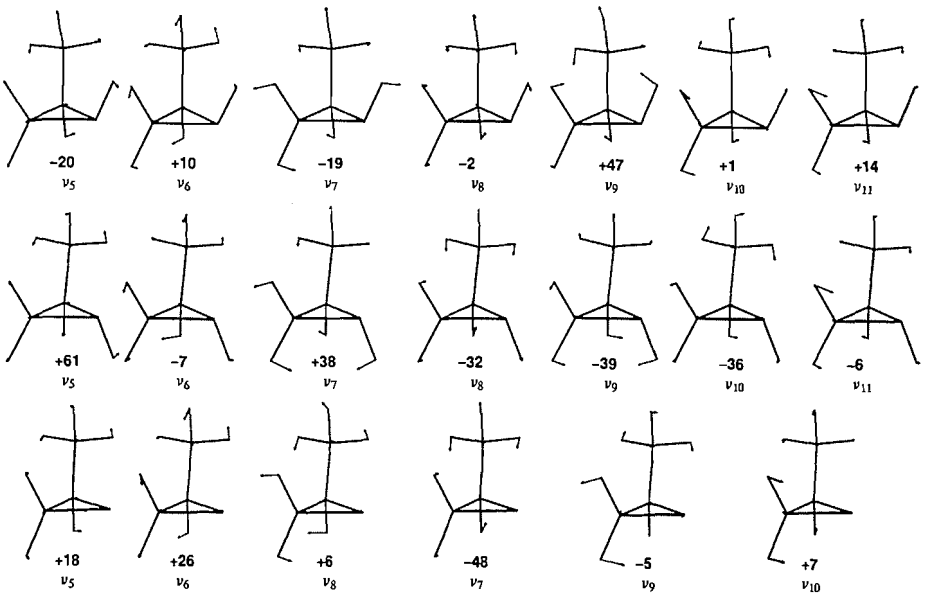

FIG. 5. Cartesian displacement vector representation of some of the normal modes between 800 and 1100 cm^{-1} of *cis*- and *trans*-(2*R*)-2-methylaziridine and (*R*)-2-methyloxirane (top, middle and bottom rows respectively). The bold-face numbers are the calculated rotational strengths in units of $esu^2\ cm^2$ ($\times 10^{44}$). The numbering is consistent with Fig. 4 and Tables 1 and 2.

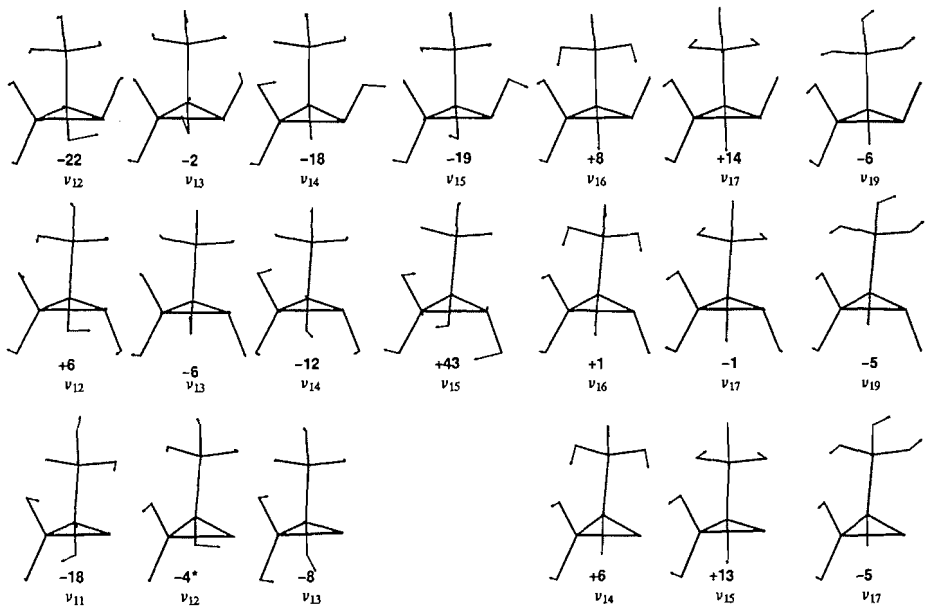

FIG. 6. Cartesian displacement vector representation of some of the normal modes between 1100 and 1500 cm^{-1} of *cis*- and *trans*-(2*R*)-2-methylaziridine and (*R*)-2-methyloxirane (top, middle and bottom rows, respectively). The bold-face numbers are the calculated rotational strengths in units of $esu^2\ cm^2$ ($\times 10^{44}$). The numbering is consistent with Fig. 4 and Tables 1 and 2.

mer and therefore do not show up in the VCD spectrum of the mixture. Thus complete occultation of the *cis* VCD spectrum occurs at ν_5, ν_7, and ν_9, and only a weak CD couplet survives at ν_{15}. Relatively strong CEs are predicted for these modes. Indeed, the only VCD signals which may be attributed to the *cis* conformer with some confidence, are five bands at 947 (949), 1107 (1114), 1265 (1268), 1364 (1373), and 1394 (1400) cm^{-1} ν_8, ν_{11}, ν_{15}, ν_{16}, and ν_{17}, respectively.

Although not observable with the present instrumentation, the data for the CH and NH stretching region are presented in Tables 1 and 2 for completeness. It is curious that all of the stretching vibrations, *including the NH stretch*, are calculated to have the same sign of CE in the two diastereomers.

Comparison with (R)*-2-methyloxirane*

The calculated VCD spectra (VCT-CO/6-31G$^{*(0.3)}$) of (1*S*,2*R*- and (1*R*,2*R*)-2-methylaziridine (*cis* and *trans*, respectively) are compared to the theoretical and experimental VCD spectrum of (*R*)-2-methyloxirane in Fig. 4. Most of the normal modes of all three species in the region 700–1600 cm^{-1} are displayed in displacement vector representation in Figs 5 and 6. In an earlier study of 2-methyl- and 2,3-dimethyloxirane (7),

Can. J. Chem. Downloaded from www.nrcresearchpress.com by 195.246.54.202 on 09/08/12
For personal use only.

Can. J. Chem. Downloaded from www.nrcresearchpress.com by 195.246.54.202 on 09/08/12
For personal use only.

it was noted that most of the absorptions in the 800–1600 cm^{-1} range were characteristic of the absolute configuration in the two closely related compounds, i.e. might serve as configurational markers. As the structures of the two aziridines and the oxirane shown in Fig. 4 have the same absolute configuration at the asymmetric carbon atom, it is of interest to analyze those features of the VCD spectrum which remain constant and are consistent with the oxirane spectrum. A visual inspection of the structures of the three compounds reveals gross similarities between the skeletal distortions of the oxirane and the *trans* aziridine, but there is little similarity between the VCD spectra. Indeed, the VCD spectrum of 2-methyloxirane bears a stronger similarity to that of the *cis*-aziridine, particularly in the region above 1300 cm^{-1} which is dominated by the methyl umbrella motions and deformations and has a component of CH_2 scissoring motion. It has already been noted above that much of the VCD of the aziridines is dominated by the configuration at N. The normal modes above 1300 cm^{-1}, ν_{16}–ν_{20}, have little participation from the N—H group. Three of these are displayed in Fig. 6 together with the equivalent modes of 2-methyloxirane. One of the methyl umbrella–CH_2 scissor combinations ν_{16} (ν_{14} in the oxirane), has the same signed CE in all three species, as does one of the asymmetric methyl distortions, ν_{19} (ν_{17} in the oxirane). However, the second methyl umbrella – CH_2 scissor combination, ν_{17} (ν_{15} in the oxirane), while visually almost identical in the three compounds, has almost a zero CE in the *trans* aziridine and a moderately strong positive CE in the other two structures. Likewise, the second asymmetric methyl distortion ν_{18} ((ν_{16} in the oxirane), not shown in Fig. 6, is visually identical in all three substances but has the same signed CE in the oxirane and *cis*-aziridine (positive), but a weak negatively signed CE in the *trans* isomer. A significant difference between the *cis* and *trans* isomers is the orientation of the non-bonded electron pair of the nitrogen (n_N) relative to the C—CH_3 bond (σ_{CC}) (Scheme 1).[5] In the *cis* isomer, the alignment of the n_N and σ_{CC} orbitals favour maximum interaction between them whereas the overlap appears less favourable in the *trans* isomer. Interaction of the non-bonded electron pair of oxygen with the adjacent groups is always present. It is of interest to speculate that the similarity between the predicted *vibrational* CD spectra of (2*R*)-2-methyloxirane and *cis*-(2*R*)-2-methylaziridine in the region has an *electronic* origin.

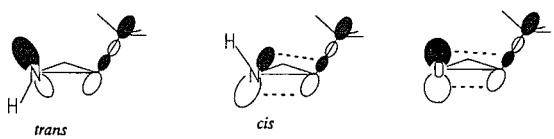

SCHEME 1

In 2-methyloxirane, the in- and out-of-phase methyl rock – CH_2 rock combinations, ν_8 and ν_9, respectively (Fig. 5) have oppositely signed and almost equal CEs. The in-phase combination most closely resembles ν_7 in each aziridine, which additionally has a strong contribution from the perpendicular NH motion. The CE is determined by the NH motion, being strongly positive (as for ν_8 of the oxirane) in the *trans* isomer and moderately negative in the *cis*. There is no single mode in the aziridines which corresponds closely to the out-of-phase combination. Mode ν_9, which has a similar involvement of the NH bend has strong and oppositely signed CE in the two invertomers.

[5]Scheme 1 is intended only to demonstrate that the *cis* isomer bears an electronic similarity to 2-methyloxirane not shared by the *trans* invertomer. At present it cannot be determined whether the similarity in the predicted VCD spectra can be attributed to a n–σ^* interaction as shown, or to a n–σ interaction, or both.

Summary

The experimental VCD spectrum of (2*R*)-2-methylaziridine has been measured in the region, 800–1500 cm^{-1}. The *ab initio* implementation of the Vibronic Coupling Theory (VCT) of Nafie and Freedman, using the 6-31G$^{*(0.3)}$ basis set, in the CO and DO gauges, and with uniformly and optimally scaled *ab initio* force fields, is used to investigate the chiroptical properties. VCD spectra are computed for both *cis* and *trans* invertomers. The predicted VCD spectrum of 2-methylaziridine (the equilibrium mixture) is dominated by that of the *trans* diastereomer, due to its greater abundance and extensive cancellation of the rotatory strengths of many absorptions in the mid-IR which are oppositely signed and of similar magnitude in the two invertomers. Although weak, a number of the features of the experimental spectrum may be identified as originating from either the *trans* or the *cis* aziridine. The VCD spectrum of 2-methylaziridine is compared in detail to that of 2-methyloxirane. In the region of the methyl deformation and CH_2 scissor, the predicted VCD spectrum of (*R*)-2-methyloxirane displays a much closer similarity to the predicted VCD spectrum of *cis*-(2*R*)-2-methylaziridine than to that of the *trans* diastereomer, a phenomenon attributed to the possible interactions of the heteroatom lone pairs with the neighboring alkyl group.

Acknowledgement

The financial support of the Natural Sciences and Engineering Research Council of Canada is gratefully acknowledged.

1. L.A. Nafie and T.B. Freedman. J. Chem. Phys. **78**, 7108 (1983).
2. P.J. Stephens. J. Phys. Chem. **89**, 748 (1985).
3. A.D. Buckingham, P.W. Fowler, and P.A. Galwas. Chem. Phys. **112**, 1 (1987).
4. M.A. Lowe, G.A. Segal, and P.J. Stephens. J. Am. Chem. Soc. **108**, 248 (1986).
5. K. Morokuma and H. Sugeta. Chem. Phys. Lett. **134**, 23 (1987).
6. R. Dutler. Ph.D. Dissertation, The University of Calgary, Calgary, AB. 1988.
7. A. Rauk and D. Yang. J. Phys. Chem. **96**, 437 (1992).
8. D. Yang and A. Rauk. J. Chem. Phys. **97**, 6517 (1992).
9. (*a*) T.W. Walnut and L.A. Nafie. J. Chem. Phys. **67**, 1501 (1977); (*b*) L.A. Nafie and T.W. Walnut. Chem. Phys. Lett **49**, 441 (1977).
10. L.A. Nafie and P.L. Polavarapu. J. Chem. Phys. **75**, 2935 (1981).
11. K.J. Jalkanen, P.J. Stephens, R.D. Amos, and N.C. Handy. J. Am. Chem. Soc. **109**, 7193 (1987).
12. (*a*) K.J. Jalkanen, P.J. Stephens, R.D. Amos, and N.C. Handy. J. Am. Chem. Soc. **110**, 2012 (1988); (*b*) K.J. Jalkanen, P.J. Stephens, R.D. Amos, and N.C. Handy. J. Am. Chem. Soc. **110**, 5598 (1988).
13. R. Dutler, and A. Rauk. J. Am. Chem. Soc. **111**, 6957 (1989).
14. M.A. Lowe, P.J. Stephens, and G.A. Segal. Chem. Phys. Lett. **123**, 108 (1986).
15. R.W. Kawiecki, F. Devlin, P.J. Stephens, R.D. Amos, and N.C. Handy. Chem. Phys. Lett. **145**, 411 (1988).
16. S.T. Pickard, H.E. Smith, P.L. Polavarapu, T.M. Black, A. Rauk, and D. Yang. J. Am. Chem. Soc. **114**, 6850 (1992).
17. H. Dothe, M.A. Lowe, and J.S. Alper. J. Phys. Chem. **92**, 6246 (1988).
18. P.L. Polavarapu, S.T. Pickard, H.E. Smith, T.M. Black, A. Rauk, and D. Yang. J. Am. Chem. Soc. **113**, 9747 (1991).

19. A. Lopez, M.M. Gauthier, R. Martino, and A. Lattes. Org. Magn. Reson. **12**, 418 (1979).
20. R. Martino, A. Lattes, F. Imberlin, and R. Mathis. C.R. Acad. Sci. Ser. C, **274**, 156 (1972).
21. E.R. Razumova and R.G. Kostyanovskii. Izv. Akad. Nauk SSSR Ser, Khim. **9**, 2003 (1974).
22. A. Rauk, T. Eggimann, H. Wieser, and D. Yang. Can. J. Chem. **70**, 464 (1992).
23. R.A. Shaw, H. Wieser, R. Dutler, and A. Rauk. J. Am. Chem. Soc. **112**, 5401 (1990).
24. A. Rauk, R. Dutler, and D. Yang. Can. J. Chem. **68**, 258 (1990).
25. P.J. Stephens. J. Phys. Chem. **91**, 1712 (1987).
26. M.J. Frisch, M. Head-Gordon, G.W. Trucks, J.B. Foresman, H.B. Schlegel, K. Raghavachari, M.A. Robb, J.S. Binkley, C. Gonzalez, D.J. DeFrees, D.J. Fox, R.A. Whiteside, R. Seeger, C.F. Melius, J. Baker, R.L. Martin, L.R. Kahn, J.J. Stewart, S. Topiol, and J.A. Pople. GAUSSIAN 90. Gaussian, Inc. Pittsburgh, PA. 1990.
27. Y. Minoura and M. Takebayashi. J. Am. Chem. Soc. **81**, 4689 (1959).
28. O.C. Dermer and G.E. Ham. Ethylenimine and other aziridines. Academic Press, N.Y., London. 1969. p. 591.
29. J.R. Durig, S.F. Bush, and W.C. Harris. J. Chem. Phys. **50**, 2851 (1969).

Can. J. Chem. Downloaded from www.nrcresearchpress.com by 195.246.54.202 on 09/08/12
For personal use only.

^{13}C NMR spectroscopic studies of C-nitroso compounds. The orientation of the nitroso group in substituted nitrosobenzenes

BRIAN G. GOWENLOCK,[1] MAILER CAMERON, ALAN S.F. BOYD, BAHEEJA M. AL-TAHOU, AND PAUL MCKENNA
Department of Chemistry, Heriot-Watt University, Ricarton, Edinburgh, EH14 4AS, Scotland

Received June 24, 1993

This paper is dedicated to Professor John C. Polanyi on the occasion of his 65th birthday

BRIAN G. GOWENLOCK, MAILER CAMERON, ALAN S.F. BOYD, BAHEEJA M. AL-TAHOU, and PAUL MCKENNA. Can. J. Chem. **72**, 514 (1994).

The carbon-13 chemical shifts of several substituted nitrosobenzenes are reported. It is shown that the NO group can be orientated to lie in the plane of the ring when constrained either by a bulky *ortho* substituent or in the solid state. In the presence of 2,6-di-*tert*-butyl substituents the NO group is twisted into orthogonality with the ring. The changes in the ^{13}C chemical shifts are larger for the NO group than for other functional groups. It is suggested that these effects are a consequence of the electronic character of the NO group and that the nitrogen lone pair of electrons is of fundamental importance in producing these unique effects. The dimeric nitroso functional group does not display these properties.

BRIAN G. GOWENLOCK, MAILER CAMERON, ALAN S.F. BOYD, BAHEEJA M. AL-TAHOU et PAUL MCKENNA. Can. J. Chem. **72**, 514 (1994).

On a mesuré les déplacements chimiques en RMN du ^{13}C de plusieurs nitrosobenzènes substitués. On montre que, sous l'influence d'un substituant *ortho* volumineux ou à l'état solide, le groupe NO peut être orienté de façon à se trouver dans le plan du noyau. En présence de substituants 2,6-di-*tert*-butyles, le groupe NO est déplacé et il est alors orthogonal au noyau. Les changements dans les déplacements chimiques du ^{13}C sont plus importants avec le groupe NO qu'avec d'autres groupes fonctionnels. On suggère que ces effets sont une conséquence du caractère électronique du groupe NO et que la paire libre d'électrons de l'azote est d'une importance fondamentale dans la production de ces effets uniques. Le groupe fonctionnel nitroso dimère ne présente pas ces propriétés.

[Traduit par la rédaction]

Introduction

Over 20 years ago, Okazaki and Inamoto (1) studied the ^{1}H nmr spectra of *ortho*-substituted nitrosobenzenes. Their studies demonstrated that the chemical shifts of aromatic, methyl, methoxyl, and *tert*-butyl protons at the *ortho* positions are abnormal. They suggested that most of the unsymmetrically substituted nitrosobenzenes exist as a conformer where the oxygen atom of the nitroso group is on the opposite side (*anti*) to the substituent, and hence protons in the same side (*syn*) to the nitroso oxygen show unusually high chemical shifts and those *anti* to the nitroso oxygen exhibit unusually low chemical shifts. They showed that in 2,5-di-*tert*-butylnitrosobenzene the molecule existed almost entirely as conformer **1** whereas for other *ortho*-substituted nitrosobenzenes there was an equilibrium between the forms **2***a* and **2***b* (R = Me, MeO, Cl, Br) with the

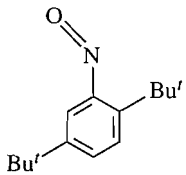

1

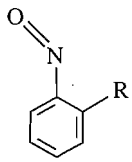

2*a*

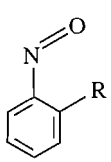

2*b*

form **2***a* predominating, particularly at low temperature. A similar conclusion had been reached by Sundberg (2) for R = Me, *n*Pr, *n*Bu. Okazaki and Inamoto extended their studies to the case of 2,4,6-tri-*tert*-butylnitrosobenzene (TBNB) where the chemical shifts of the *ortho tert*-butyl protons were interpreted in terms of the NO group being considered to be almost perpendicular to the plane of the benzene ring. This orthogonality of the NO group has also been invoked by Barclay in photochemical and other studies of TBNB (3, 4).

Because of our interest in the ^{13}C nmr spectra of substituted nitrosobenzenes (5), and the information available in the literature for the ^{13}C nmr effects of freezing out of the rotation of the NO group in nitrosobenzene (6) and of substituted *p*-nitrosoanilines (7, 8) at low temperatures, we embarked on the studies reported here. Subsequently we extended our studies to the coordination chemistry of C-nitrosoarenes (9, 10). A publication on the solid state ^{13}C CP/MAS nmr spectrum of *p*-nitrosodimethylaniline (11) has complemented our study.

In our earlier study (5) we noted the unique effect of the NO group in that its powerful π-electron-accepting property enabled it to dominate other electron-accepting groups in the *para* position of the ring and produce in them electron-donating properties. The monomeric nitroso group has long been realised (12) to be very different in character from the *cis* and *trans* dimeric $-N_2O_2$ functions. These differences are reflected in the very different substituent chemical shifts exhibited by nitrosobenzene and the two dimeric forms (13, 14).

Throughout this paper we shall refer to all aromatic nitroso compounds as derivatives of nitrosobenzene and hence adopt the numbering system based upon **3**. The steric effects of the

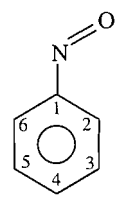

3

[1]Author to whom correspondence may be addressed at Department of Chemistry, University of Exeter, Exeter, EX4 4QD, United Kingdom.

Can. J. Chem. Downloaded from www.nrcresearchpress.com by 195.246.54.202 on 09/08/12
For personal use only.

TABLE 1. Carbon-13 chemical shifts for ring carbons in substituted nitrosobenzenes (20°C, $CDCl_3$ solvent unless otherwise stated)

Substituent(s)	State	C-1	C-2	C-3	C-4	C-5	C-6
2-Iodo	Solution	162.1	109.2	141.4	136.6	128.2	109.0
2-Methyl	Solution	164.9	142.1	132.9	136.1	125.6	107.3
2-Methoxy	Solution	162.0	158.8	115.3	138.8	119.6	108.8
2-*tert*-Butyl	Solution	165.7	152.2	125.8	135.4	127.7	106.5
2-Methyl-6-*tert*-butyl	Solution	167.5	118.0	125.4	130.7	133.4	153.6
2,5-Di-*tert*-butyl	Solution	165.9	148.9	127.6	132.3	149.7	103.3
2,6-Di-*tert*-butyl	Solution	176.3	142.4	125.7	129.9	125.7	142.4
2,4,6-Tri-*tert*-butyl	Solid state	174.5	141.9	122.1	151.2	122.1	141.9
	Solution	173.5	142.8	122.7	153.4	122.7	142.8
	Solution[a] (20°C)	174.5	143.5	123.5	154.2	123.5	145.5
	Solution[a] (0°C)	174.3	143.3	123.4	154.2	123.4	145.3
	Solution[a] (−20°C)	174.0	143.1	123.2	154.0	123.2	143.1
	Solution[a] (−40°C)	173.7	142.9	123.0	153.9	123.0	142.9
	Solution[a] (−60°C)	173.4	142.6	122.8	153.6	122.8	142.6
	Solution[a] (−80°C)	173.4	142.6	122.9	153.7	122.9	142.6
4-Methylamino	Solid state	163.3	109.5	114.6	158.1	114.6	143.1

[a]CD_2Cl_2 solvent.

substituent groups arise therefore from substitution in the 2 and 6 positions.

Experimental

Nitroso compounds

2,4,6-Tri-*tert*-butylnitrosobenzene and *trans*-dimeric 2-methyl nitrosobenzene were commercially available, *trans*-dimeric 2-iodo and 2-methoxynitroso benzene were donated by Professor W. Lüttke, having been prepared by the literature methods (15, 16). 2,5-Di-*tert*-butylnitrosobenzene (17) was prepared by mild oxidation of the corresponding aniline using *m*-chloroperbenzoic acid. 2-*tert*-Butylnitrosobenzene (18) was similarly prepared. 2,6-Di-*tert*-butylnitrosobenzene was prepared in a similar manner to the literature syntheses for other sterically hindered nitrosobenzenes (17). 2,6-Di-*tert*-butylaniline (0.5 g, 2.4 mmol) in dichloromethane (5 cm^3) was cooled in an ice–salt bath while perbenzoic acid (0.6 g, 4.8 mmol) in dichloromethane (5 cm^3) was added dropwise. The reaction mixture was kept overnight at −20°C and a brown colour developed. Column chromatography (silica, petroleum ether 40–60) gave 2,6-di-*tert*-butylnitrosobenzene (0.25 g, 45%) as a blue oil, λ_{max} ($CHCl_3$) 761 nm, ϵ 50.5 $dm^3\ mol^{-1}\ cm^{-1}$; δ_H (200 MHz, $CDCl_3$) 7.25 (3H, m, 3,4,5-H), 1.15 (18H, s, 2,6-di-*t*Bu); *m/z* 219 (M^+ 31%), 57 (*t*Bu, 100%). 2-Methyl-6-*tert*-butylnitrosobenzene was similarly prepared. 2-Methyl-6-*tert*-butyl aniline (1 g, 5.65 mmol) in dichloromethane (10 cm^3) was cooled in an ice–salt bath while perbenzoic acid (1.55 g, 11.0 mmol) in dichloromethane (10 cm^3) was added dropwise. The reaction mixture was kept overnight at −20°C, then neutralised with $NaHCO_3$ solution. Removal of the solvent using a rotary film evaporator at room temperature left a green oil that was purified by column chromatography as above, giving 2-methyl-6-*tert*-butylnitrosobenzene as a blue oil, λ_{max} ($CHCl_3$) 789 nm, ϵ 43 $dm^3\ mol^{-1}\ cm^{-1}$; δ_H (200 MHz, $CDCl_3$) 7.6 (1H, dd, 3-H), 7.35 (1H, t, 4H), 6.95 (1H, dq, 5-H), 1.85 (3H, s, CH_3), 1.65 (9H, s, *t*Bu). *trans*-Dimeric 2,6-dimethyl-, 2,6-diethyl-, and 2,6-diisopropylnitrosobenzene were prepared by controlled oxidation of the corresponding amines (18, 19). *p-N*-methylamino nitrosobenzene was donated by Professor F. Bell.

Instrumental

Natural abundance, broad band proton-decoupled ^{13}C nmr spectra were measured using a Bruker WP 200 spectrometer operating at 50.32 MHz, the solvent being either $CDCl_3$ or CD_2Cl_2. The ^{13}C nmr spectra of solid samples were measured by the SERC service at the Industrial Research Laboratories, University of Durham, at 75.431 MHz using cross polarization (CP) magic angle spinning (MAS) and high-power decoupling and also at the University of East Anglia at 50.3 MHz with CPMAS and high-power decoupling.

Results and discussion

The chemical shifts for the ring carbons of substituted monomeric nitrosobenzenes are listed in Table 1 and are considered under two major headings. The first group comprises those molecules with substituents in the 2 position and no substituent at C-6, together with the 2-methyl-6-*tert*-butyl substituents and solid 4-methylaminonitrosobenzene. The second group is restricted to the two examples where both the C2 and C6 positions carry *tert*-butyl groups. These two separate classes are expected to conform to those originally established by Okazaki and Inamoto (1). In the first group the NO is expected to lie in plane with the ring and displaced away from the 2-substituent (I, Me, MeO, *t*-Bu, 2,5-di-*t*-Bu), away from the larger substituent (2-Me-6-*t*-Bu), or in plane with the ring in a solid monomeric compound as noted by Penner and Wasylishen (11) and ourselves (10). The common feature of these spectra is that the C atom to which the NO group lies *syn* has a chemical shift much lower than would be predicted by use of substituent chemical shifts as given by Ewing (20) in combination with those for the NO group (5, 13, 14). This difference between calculated and observed shifts is 12–14 ppm and can best be appreciated by comparison with the calculated values for C-6 in 2-methyl-1-X-benzene, **4** (X = F, Cl, Br, I, NO_2, CHO, CN, OH, COOH, OMe, NH_2, NHEt, Me, Et, *cis*-N_2O_2, *trans*-N_2O_2)

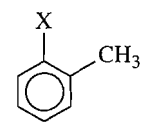

4

where the difference varies between 4 ppm lower and 2 ppm higher. It is apparent that the effect of the NO group is unique, as suggested by Lunazzi et al. (6). A further example of the effect can be seen from comparison of the predicted and observed chemical shifts for the molecules **5** (21), **6** (22) and **7** (23). The observed C-6 chemical shifts are 110.5, 121.8, and 129.9 respectively.

Comparison of **5** with **6** implies that in the latter the steric restraints are such that the NO group can rotate freely at room temperature whereas in the former the NO group adopts the

Can. J. Chem. Downloaded from www.nrcresearchpress.com by 195.246.54.202 on 09/08/12
For personal use only.

TABLE 2. A comparison of substituent chemical shifts in compounds **8** and **9** (all values in ppm)

X	SCS(X) in **8**[a]	SCS(X) in **9**[b]	Difference	Reference
COOH	10.8	2.1	8.7	24
COCl	14.1	5.0	9.1	24
CO_2Me	9.0	2.0	7.0	24
CONHPh	13.1	6.5	6.6	24
$CONMe_2$	10.7	8.1	2.6	24
COEt	17.7	8.8	8.9	24
CHO	17.8	8.4	9.4	25
COMe	18.1	8.9	9.2	26
CN	−13.1	−15.7	2.6	27
OMe	38.0	31.4	6.6	28
Br	2.3	−5.8	8.1	26
NNPh	32.0	24.0	8.0	29
$NNC_6H_2(Bu^t)_3$	35.3	25.1	10.2	29
NH_2	21.7	18.2	3.5	[d]
NMe_2	31.9	22.5	7.4	30
NO_2	27.6	19.9	7.7	26
$N{=}CH_2$	31.3	24.7(±2)[c]	6.6(±2)	30
NO	54.1[e]	37.6	16.5	5[e]

[a]Based upon *C*H chemical shift in 1,3,5-tri-*tert*-butylbenzene 119.4 ppm (24).
[b]Based upon *C*H chemical shift in benzene 128.5 ppm (24) and compilation (20).
[c]Assumed on basis of N=CHPh.
[d]B.G. Gowenlock and A.S.F. Boyd. Unpublished observations.
[e]This work.

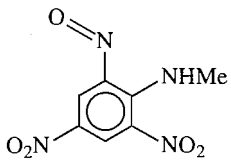

5

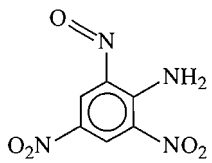

6

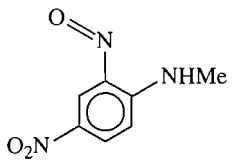

7

equilibrium position *anti* to the NHMe substituent. Comparison of **5** with **7** suggests that the absence of NO_2 *ortho* to the NHMe removes the steric constraints and allows the NO to rotate freely at room temperature. It should be noted that comparison with *o*-substituted benzaldehyde establishes that this effect on the ^{13}C nmr spectra is absent for the isoelectronic CHO group. A referee has suggested that hydrogen bond formation may take place between the NH and NO groups in compounds **5**, **6**, and **7** assisted by the "acidifying" of the NH by the presence of the nitro group at C5. Such a contribution would, however, orientate the NO group away from C6 and towards C2 because of the

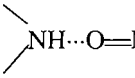

structural unit. We therefore prefer the explanation of a steric constraint that operates effectively for 5 but is absent for 6 and 7. It is necessary to have further study of related compounds to confirm our preference.

We now turn to the two examples where the bulky *tert*-butyl substituents are placed in both the 2 and 6 positions. The effect on the C-1 chemical shift is considerable and there is no difference between the C-2 and C-6 shifts. As free rotation is ruled out on steric grounds it therefore seems that the orthogonality of the NO group, as proposed originally by Okazaki and Inamoto, is the most probable cause of these effects. To substantiate such considerations it is necessary to compare the substituent chemical shifts for C-X in the molecules **8** and **9** to see whether the variation of X for a wide range of functional groups indicate any

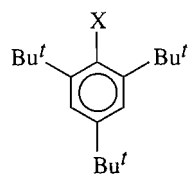

8

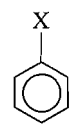

9

features of note compared with X-NO. Such considerations were employed by Relles (24) for six different examples of X and in Table 2 we present a considerably expanded series of values.

Inspection of Table 2 shows that the effect on the substituent chemical shifts for X-NO is much greater (16.5 ppm) than for 17 other functional groups (average value 7.2 ppm). The isoelectronic groups CHO and $N{=}CH_2$ together with NNPh are different from NO in that the substituent chemical shift effect is much lower (9.4–6.6 ppm). The effect of 2,4,6-trisubstitution by the *tert*-butyl groups is expected to cause a pronounced twisting of many functional groups out of coplanarity with the ring (Br and CN are obvious exceptions). It should be noted that the inability of TBNB to self-dimerise is due to steric considerations. Cross dimerisation with other C-nitroso compounds has been established (4, 31) and therefore the electronic rearrangements necessary (12, 32) for formation of the $-N_2O_2-$ functions are unaffected by the presumed orthogonality of the NO group in TBNB. This may therefore imply that the unusual effect on the C-1 substituent chemical shift in TBNB arises from the changing interaction of the lone pair of electrons, located primarily on the N atoms, with the π-electrons of the ring.

Can. J. Chem. Downloaded from www.nrcresearchpress.com by 195.246.54.202 on 09/08/12
For personal use only.

Can. J. Chem. Downloaded from www.nrcresearchpress.com by 195.246.54.202 on 09/08/12
For personal use only.

We note therefore that ^{13}C nmr spectroscopy has revealed three features of unique interest for nitrosobenzene and derivatives thereof, namely, the *syn* effect of in-plane NO, and the orthogonal effect due to steric hindrance, in addition to the dominating effect of the π-electron-attracting NO over other π-electron-attracting groups in the *para* position (5). So far as the last of these effects is concerned, neither CNDO/2 nor STO-3G calculations have been successful in accounting for the difference between the NO group and all other functional groups (33). Theoretical studies for the *syn* effect are limited to the approximate magnetic anisotropy calculations for the nitroso group (1).

There is an STO-3G study of the conformation and charge distributions of a large number of monosubstituted benzenes (34) that is relevant to our study of the orthogonal NO group in TBNB. Hehre, Radom, and Pople point out that whereas the substituent withdraws π-electrons from the ring in planar nitrosobenzene there is π-charge donation from the nitrogen lone pair in the orthogonal form, and the charge alternation is reversed. The authors suggest that this may have interesting consequences in the properties of those nitrosobenzenes constrained to be orthogonal and note the absence of this effect in the orthogonal form of nitrobenzene. In addition to these theoretical calculations Batich and Donald (35) have demonstrated an unusual affect on the N(1*s*) peak in the XPS spectrum of TBNB and, in attempting to correlate this with the orthogonality of the NO group, have shown by CNDO/2 calculations that the charge on the N approximately doubles on going from an in-plane to an orthogonal conformation, while the charge on the O remains the same. These electronic effects may be mirrored by the distinctive difference for NO in the substituent chemical shifts summarised in Table 2.

It is also of interest to note that the orthogonal orientation of the NO group in TBNB implies that in the, yet to be synthesised, analogous molecule 1,3-di-nitroso-2,4,6-tri-*tert*-butylbenzene, atropisomeric forms will exist. These will be (*a*) the two nitroso groups having their O atoms on the same side of the ring and (*b*) the two nitroso groups having their O atoms above and below the plane of the ring.

In principle it would be appropriate to study the ^{13}C nmr spectra of the series of 2,4,6-trialkylnitrosobenzene monomers (alkyl = Me, Et, iPr, *t*Bu) to obtain information on the increasing steric constraints on the NO group. The triisopropylnitrosobenzene has yet to be synthesised and consequently we decided to limit our study to the series of 2,6-dialkylnitrosobenzenes. The first three members of the series form crystalline *trans* dimers and in solution at room temperature there is only a small amount of dissociation to the monomer for the 2,6-dimethyl compound. Heating the sample produces more monomer but decomposition reactions predominate for the ethyl (19) and isopropyl compounds. Consequently it is not possible to achieve the above objective. The ^{13}C nmr spectral data of the dimers are shown in Table 3. These are closely similar to the values predicted from substituent chemical shifts (14, 20).

In conclusion, it may be noted that the dimeric nitroso group does not possess a lone pair of electrons and that, as a consequence of the increase in both the CNO angle and the NO bond length as compared with the monomer, the distance between the O atom and the C-2 atom in the benzene ring will be slightly increased. These considerations encouraged us to study the CPMAS ^{13}C nmr spectrum of solid dimeric 4-bromonitrosobenzene in order to observe whether the splitting of the C-2 and C-6 chemical shifts, characteristic of the *syn* effect in monomeric nitrosobenzenes, would occur. As was to be expected, the compound displayed only four chemical shifts: 140.0 (C-1), 125.1 (C-2), 127.7 (C-3), and 126.4 (C-4) ppm. It is known that in the solid state the benzene rings are tilted only slightly from coplanarity with the $C_2N_2O_2$ central unit (36) and we therefore conclude that the *syn* effect is not a property of the dimeric nitroso functional group. Our studies point therefore to the importance of the nitrogen lone pair in producing the characteristic structural properties of the NO group. More advanced molecular orbital calculations than STO-3G would appear to be necessary to resolve this problem. The experimental techniques of ^{1}H and ^{13}C nmr spectroscopy produce complementary evidence for the *syn* and orthogonal effects of sterically constrained NO groups.

TABLE 3. ^{13}C Chemical shifts for dimeric 2,6-dialkylnitrosobenzenes in $CDCl_3$ solution at 19°C (values in ppm relative to Me_4Si)

Alkyl	C-1	C-2,6	C-3,5	C-4
Me	141.4	132.7	128.9	130.3
Et	140.6	138.3	126.9	130.6
iPr	139.3	143.2	124.6	130.8

Acknowledgements

We wish to thank the Science and Engineering Research Council (SERC) for the use of the solid state NMR facility at the University of Durham, and Professor R.K. Harris and Dr. D.C. Apperley for the spectra obtained. B.G.G. thanks the Leverhulme Trust for the award of an Emeritus Fellowship. M.C. thanks the SERC for a research studentship. B.M.A-T. thanks the Kuwaiti Government for the provision of a maintenance grant. We also thank Professor W. Lüttke for the gift of some nitroso compounds and record our indebtedness to the late Professor B.M. Wepster for the gift of 2-methyl-6-*tert*-butylaniline, and the late Professor F. Bell for the gift of 4-methylaminonitrosobenzene.

1. R. Okazaki and N. Inamoto. J. Chem. Soc. B, 1583 (1970).
2. R.J. Sundberg. Tetrahedron, **23**, 1583 (1967).
3. L.R.C. Barclay, P.G. Khazanie, K.A.H. Adams, and E. Reid. Can. J. Chem. **55**, 3273 (1977).
4. L.R.C. Barclay, D.L. Carson, J.A. Gray, M. Grossman, P.G. Khazanie, J.R. Milton, and C.E. Scott. Can. J. Chem. **56**, 2665 (1978).
5. B.M. Al-Tahou and B.G. Gowenlock. Recl. Trav. Chim.Pays-Bas, **105**, 353 (1986).
6. L. Lunazzi, D. Macciantelli, and G. Placucci. Tetrahedron Lett. **21**, 975, (1980).
7. Y.K. Grishin, N.M. Seryeyev, O.A. Subbotin, and Y.A. Ustynyuk. Mol. Phys. **25**, 297 (1973).
8. V.V. Negrebetskii, A.U. Bokanov, and B.I. Stepanov. Zh. Strukt. Khim. **22**, 88 (1981).
9. M. Cameron, B.G. Gowenlock, and G. Vasapollo. Chem. Soc. Rev. **19**, 355 (1990).
10. M. Cameron, B.G. Gowenlock, R.V. Parish, and G. Vasapollo. J. Organomet. Chem. In press.
11. G.H. Penner and R.E. Wasylishen. Can. J. Chem. **67**, 525 (1989).
12. B.G. Gowenlock and W. Lüttke. Q. Rev. (London), **12**, 321 (1958).
13. R.H. Cox and M. Hamada. Org. Magn. Reson. **12**, 322 (1979).
14. K.G. Orrell, V. Sik, and D. Stephenson. Magn. Reson. Chem. **25**, 1007 (1987).

15. E. Bamberger. Ber. Dtsch. Chem. Ges. **28**, 249 (1895).
16. A. Rising. Ber. Dtsch. Chem. Ges. **35**, 3036 (1902).
17. R. Okazaki, T. Hosagai, E. Iwadare, M. Hashimoto, and N. Inamoto. Bull. Chem. Soc. Jpn. **42**, 3611 (1969).
18. K. Hirota and H.A. Itano. J. Biol. Chem. **253**, 3477 (1978).
19. S.J. Wratten, H. Fujiwara, and R.T. Solsten. J. Agric. Food Chem. **35**, 484 (1987).
20. D.F. Ewing. Org. Magn. Reson. **12**, 499 (1979).
21. J. Kavalek, V. Machacek, V. Sterba, and A. Lycka. Collect. Czech. Chem. Commun. **53**, 1033 (1988).
22. V. Machacek, M.M.M. Hassanien, V. Sterba, and A. Lycka. J. Chem. Soc. Perkin Trans. 2, 867 (1987).
23. V. Machacek, C. Sterba, I. Kolb, and A. Lycka. Collect. Czech. Commun. **53**, 1044 (1988).
24. H.M. Relles. J. Magn. Reson. **39**, 481 (1980).
25. H. Lumbroso, J. Cure, R. Okazaki, A. Ishii, and N. Inamoto. Z. Naturforsch. **40A**, 1157 (1985).
26. J. Koudelka, D. Saman, and O. Exner. Collect. Czech. Chem. Commun. **50**, 208 (1985).
27. E.T.K. Haupt and D. Leibfritz. Spectrochim. Acta A, **45**, 119 (1989).
28. K.S. Dhami and J.B. Stothers. Can. J. Chem. **44**, 2855 (1966).
29. L.R.C. Barclay, J.M. Dust, S. Brownstein, and E.J. Gabe. Org. Magn. Reson. **17**, 175 (1981).
30. G.A. Harff, A. Sinnema, and B.M. Wepster. Recl. Trav. Chim. Pays-Bas, **98**, 71 (1979).
31. K.G. Orrell, D. Stephenson, and J.H. Verlaque. J. Chem. Soc. Perkin Trans. 2, 1297 (1990).
32. T. Minato, S. Yamabe, and H. Oda. Can. J. Chem. **60**, 2740 (1982).
33. G. Butt, R.D. Topsom, B.G. Gowenlock, and J.A. Hunter. Theochem, **164**, 399 (1988).
34. W.J. Hehre, L. Radom, and J.A. Pople. J. Am. Chem. Soc. **94**, 1496 (1972).
35. C.D. Batich and D.S. Donald. J. Am. Chem. Soc. **106**, 2758 (1984).
36. C. Darwin and D.C. Hodgkin. Nature, **166**, 827 (1950).

Can. J. Chem. Downloaded from www.nrcresearchpress.com by 195.246.54.202 on 09/08/12
For personal use only.

A theoretical study on the interaction of dinitrogen with rhodium

T.H. FANG, M.L. MCKEE,[1] AND S. D. WORLEY[1]

Department of Chemistry, Auburn University, Auburn, AL 36849, U.S.A.

Received March 31, 1993

This paper is dedicated to Professor John C. Polanyi on the occasion of his 65th birthday

T.H. FANG, M.L. MCKEE, and S.D. WORLEY. Can. J. Chem. **72**, 519 (1994).

Ab initio theoretical computations have been performed for RhN_2, Rh^+N_2, $Rh(N_2)_2$, and $Rh^+(N_2)_2$ species. The computed vibrational frequencies and binding-energy trends are in qualitative accord with prior FTIR studies of N_2 interacting with supported Rh films. Computations of the type described herein should be useful in aiding the assignment of observed infrared bands to specific surface species in future work.

T.H. FANG, M.L. MCKEE et S.D. WORLEY. Can. J. Chem. **72**, 519 (1994).

On a effectué des calculs théoriques *ab initio* sur les espèces RhN_2, Rh^+N_2, $Rh(N_2)_2$ et $Rh^+(N_2)_2$. Les fréquences de vibrations calculées ainsi que les tendances observées dans les énergies de liaison sont en accord qualitatif avec des études de FTIR antérieures sur le N_2 en interaction avec des films supportés de Rh. Des calculs du type décrit dans ce travail devraient dans le future s'avérer utiles pour aider à attribuer des bandes, observées dans l'infrarouge, à des espèces de surface spécifiques.

[Traduit par la rédaction]

Introduction

Work has been progressing in these laboratories during the past decade pertaining to the study on the processes of interaction of small molecules with supported transition metals. The primary approach in these investigations has been to utilize Fourier transform infrared spectroscopy in identifying reactive surface species on supported catalyst films (see, for example, ref. 1). Recently, a novel high-pressure–infrared-cell reactor has been constructed for the purpose of identifying reactive surface species on supported transition-metal films upon exposure to gases at high pressures such as might be encountered in industrial chemical reactors. The first experiments employing the high-pressure-cell reactor involved the interaction of dinitrogen with supported rhodium at ambient temperature and pressures up to 8000 torr (2–4). Several interesting dinitrogen surface species were detected at ambient temperature using FTIR which had only previously been observed at low pressures (≤218 torr) and temperatures below 240 K (5). Employing the integrated areas of the N—N stretching mode band for $N_2/Rh/TiO_2$ as a measure of surface coverage, adsorption equilibrium constants as a function of temperature were obtained and used to predict the heat of adsorption for $N_2/Rh/TiO_2$ to be -10.2 kcal mol^{-1} extrapolated to zero coverage (4).

The purpose of the present study was to use *ab initio* theoretical computations to further our understanding of the interaction process for N_2/Rh. Of course, the computations necessarily refer to the gas-phase species, rather than to N_2 interacting with solid state supported Rh, and such calculations are difficult and tentative because of *d*-orbital participation, modeling the inner core, and the necessary use of unrestricted Hartree–Fock methods. Nevertheless, prior studies in these laboratories using similar computations have significantly aided our interpretation of the experimental observations for the interaction of CO (6) and H_2/CO (7) with supported Rh, so we feel justified in using the same theoretical approach for N_2/Rh.

There have been several elegant theoretical studies reported pertaining to the interaction of N_2 with Pd(8); Ti, Cr, Fe, Co, and Ni (9); Ni (10); and Cr^+ and Co^+ (11). However, in the case of Rh, as far as we are aware, only a semi empirical study of the electronic structure of RhN_2 (12) and an *ab initio* investigation of $RhCl(PH_3)_2N_2$ (13) have been reported, although several other interesting theoretical studies of rhodium carbonyl, oxide, and hydride species have recently appeared (14–16). There have been no reported computations of RhN_2 binding energies and vibrational frequencies; this work will address these important parameters.

Theoretical

For the *ab initio* computations in this study, the 36 core electrons of Rh were replaced by a relativistic effective core potential (RECP) as generated by Hay and Wadt (17). The outer valence orbitals (5*s*, 4*d*, and 5*p*) were represented by a (3*s*3*p*4*d*) primitive Gaussian basis contracted to (2*s*2*p*2*d*) to form a basis set denoted as BAS2 which has been employed earlier in these laboratories for Rh computations (6, 7). The valence double-ζ basis set of Dunning and Huzinaga (18) was used for nitrogen. Closed-shell systems were computed by using restricted Hartree–Fock formulism, while open-shell systems employed unrestricted Hartree–Fock formulism (19). All geometric variables were optimized (20) at the BAS2 level within an assumed symmetry point group. The most difficult aspect of this study was to ensure that the dominant configuration was correctly chosen. In order to ensure that the best choice was made, many optimizations were performed with alternate occupation of the starting molecular orbitals. The best choice for a particular electronic state was determined by the lowest PMP4/ECP D-ζ energy.

For the case of linear Rh^0N_2, symmetry breaking and spin contamination in the wave function required the use of the method described by the Herzberg (21) in computing the N—N vibrational stretching frequency.

Results and discussions

The various species for which computations were performed in this work are shown in Fig. 1. The optimized geometries for the various species are also indicated in Fig. 1. The computed absolute energies and $\langle S^2 \rangle$ values for the species are shown in Table 1. All levels of theory predicted that the ^4F state of Rh was lower in energy than the ^2D state. The computed excitation energy for the $Rh(^4F) \leftarrow Rh(^2D)$ was 0.0276 hartree units which was in reasonable accord with the experimental value (22) of 0.015 hartrees. The computed ionization energy for $Rh(^4F)$ was 0.247 hartrees, in good agreement with the experimental value (22) of 0.274 hartrees. The computed bond length

[1]Authors to whom correspondence may be addressed.

Can. J. Chem. Downloaded from www.nrcresearchpress.com by 195.246.54.202 on 09/08/12
For personal use only.

TABLE 1. Computed absolute energies (hartrees)[a] and $\langle S^2 \rangle$ values

Species	Symmetry	Computed absolute energy UHF	PMP2	PMP4	$\langle S \rangle^2$ Calculated	Expected
N_2	$D_{\infty h}$	−108.87816	−109.10718	−109.10575	0.00	0.00
$Rh(^4F)^b$	K	−22.13678	−22.17092	−22.18820	3.75	3.75
$Rh(^2D)^b$	K	−22.07396	−22.14947	−22.16060	1.46	0.75
$Rh^+(^3F)^b$	K	−21.90216	−21.95331	−21.94091	2.00	2.00
RhN_2						
(End-on)	$C_{\infty v}$	−130.98102	−131.32190	−131.34666	0.85	0.75
(Side-on)	C_{2v}	[c]	[c]	[c]	[c]	[c]
Rh^+N_2						
(End-on)	$C_{\infty v}$	−130.80971	−131.08121	−131.08899	2.01	2.00
(Side-on)	C_{2v}	−130.78215	−131.04980	−131.05485	2.00	2.00
$Rh(N_2)_2$						
(Linear)	$D_{\infty h}$	−239.88357	−240.47672	−240.50052	0.76	0.75
(Bent, 90°)	C_{2v}	−239.86830	−240.45274	−240.48152	1.00	0.75
$Rh^+(N_2)_2$						
(Linear)	$D_{\infty h}$	−239.71985	−240.23594	−240.24574	2.02	2.00
(Bent, 90°)	C_{2v}	−239.71279	−240.22091	−240.22929	2.02	2.00

[a]1 hartree = 627.5 kcal mol^{-1}.
[b]The Rh populations for the optimized states were ^4F ($4d^{8.0}5s^{1.0}$), ^2D ($4d^{8.5}5s^{0.5}$), and ^3F ($4d^{8.0}$).
[c]No bonding interaction predicted.

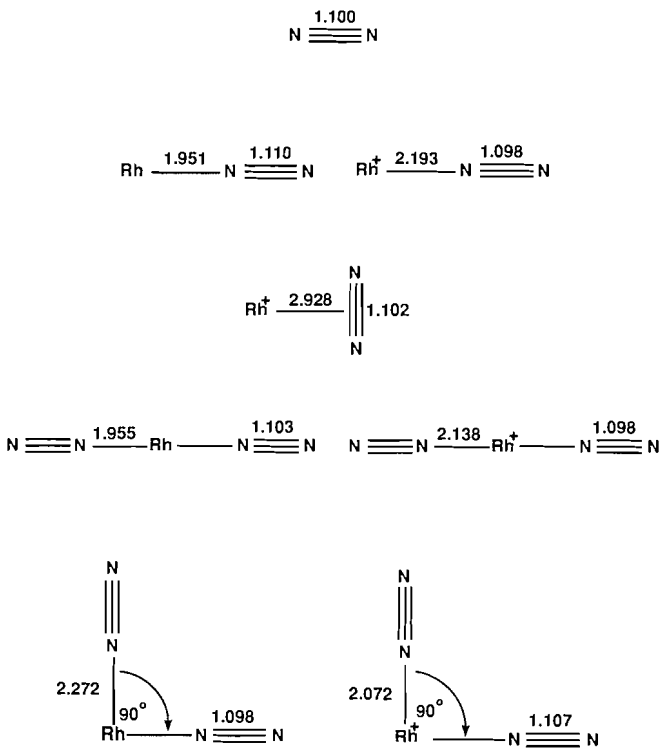

FIG. 1. Computed optimized geometries for the species considered in this work.

for dinitrogen (1.100 Å) was in excellent accord with experimental data (1.094 Å) (23), as was the computed vibrational stretching frequency (2331.5 cm^{-1} after correction by the standard factor of 0.9) as compared to 2331 cm^{-1} obtained from the Raman spectrum (5).

For the Rh^0N_2 species the *ab initio* computations predicted that N_2 should be bonded "end-on" to Rh. All attempts to compute a "side-on" Rh^0N_2 species were not successful, as the optimized geometry produced Rh and N_2 separated beyond reasonable bonding distance (>4 Å). On the other hand, for Rh^+N_2 both end-on and side-on species could be computed, but the calculations clearly predicted that end-on bonding represented the lower energy geometry by 0.034 hartrees (21.3 kcal mol^{-1}).

For the Rh^0 and Rh^+ gem dinitrogen species the computations in both cases predicted the optimum geometry to be linear for the gas-phase species. However, for supported Rh a linear geometry is rather unlikely for steric reasons. Hence calculations were carried out for the two species in which the NRhN bond angle was constrained to be 90°, the value reported for the Rh gem-dicarbonyl species for Rh/Al_2O_3 (24). These computations indicated that the energies of the bent gem dinitrogen Rh^0 and Rh^+ species lie above those of the corresponding linear species by 11.9 and 10.0 kcal mol^{-1}, respectively. Thus, the *ab initio* computations predict that the gas-phase gem-dinitrogen species should be linear, but a 10–12 kcal mol^{-1} decrease in energy for the bent species might clearly occur for a surface due to metal–support interactions and steric constraints.

The computations performed in this study which were most relevant to recent experimental work in these laboratories were the binding energies and N—N vibrational stretching frequencies for the various species given in Table 2. The end-on RhN_2 species at the PMP4 level of theory was predicted to have a binding energy of 33.1 kcal mol^{-1}, a value substantially greater than that measured from infrared data for $N_2/Rh/TiO_2$ (10.2 kcal mol^{-1}). The discrepancy can be attributed to the fact that supported Rh would be expected to bind N_2 to a different extent than gas-phase Rh because of the electronic and steric interaction of Rh with the support material. The *ab initio* computations reported here must be considered only as a qualitative aid in interpreting the experimental data. Nevertheless, the *ab initio* trends are informative. For example, the calculations predict that the end-on Rh^0N_2 species should be bound to a greater extent by 6.5 kcal mol^{-1} than is the Rh^+N_2 species and that the

Can. J. Chem. Downloaded from www.nrcresearchpress.com by 195.246.54.202 on 09/08/12
For personal use only.

TABLE 2. Metal population, binding energies (kcal mol^{-1}), and N—N stretching frequencies (cm^{-1})[a]

Species	Rh_{pop}	Binding energies UHF	PMP2	PMP4	ν_{N-N}
RhN_2					
(End-on)	$4d^{8.6}5s^{0.3}5p^{0.1}$	21.3	22.4	33.1	2239[b]
(Side-on)	$4d^{8.0}5s^{1.0}$	[c]	[c]	[c]	[c]
Rh^+N_2					
(End-on)	$4d^{8.0}$	18.4	24.3	26.6[d]	2266
(Side-on)	$4d^{8.0}$	1.1	4.6	5.1[d]	2313
$Rh(N_2)_2$					
(Linear)	$4d^{8.6}5s^{0.4}$	7.6[e]	26.2[e]	31.6[e]	[b]
(Bent, 90°)	$4d^{8.7}5s^{0.2}5p^{0.1}$	7.8[e]	18.6[e]	25.7[e]	1897, 1899
$Rh^+(N_2)_2$					
(Linear)	$4d^{8.0}$	19.2[e]	27.0[e]	29.3[e]	2293, 2298
(Bent, 90°)	$4d^{8.0}$	19.2[e]	22.4[e]	24.1[e]	2268.5, 2268.8

[a]Calculated values have been corrected by the standard factor of 0.9.
[b]Symmetry breaking in the wave function; the 2239 cm^{-1} value was calculated by Herzberg's method (21).
[c]No bonding interaction predicted.
[d]Values of 21.5 and 5.7 kcal mol^{-1} were computed in ref. 13 for the complexes $RhCl(PH_3)_2$ (η^1–N_2) and $RhCl(PH_3)_2$ (η^2–N_2), respectively.
[e]Values are averages for the two N_2 moieties. In general the binding energy for the second N_2 moiety was slightly larger than for the first.

N—N stretching vibrational frequency should be lower for Rh^0N_2 (2239 cm^{-1}) than for Rh^+N_2 (2266 cm^{-1}). The experimental infrared spectrum for high-pressure N_2 interacting with Rh/Al_2O_3 contained bands at 2256, 2276, 2301 and 2330 cm^{-1} which were assigned tentatively to end-on Rh^0N_2, a $Rh^{\delta+}N_2$ species, a second $Rh^{\delta+}N_2$ species, and physisorbed N_2 on Al_2O_3 (2). Prior work performed at low temperatures and pressures had identified the same infrared bands and suggested similar band assignments (5). A matrix isolation study of RhN_2 species (25) exhibited an N—N stretching frequency of 2154 cm^{-1}, which was 100 cm^{-1} lower than the value for supported Rh; the calculated value falls between the two measured values. The 2256 cm^{-1} band was considerably more intense than the 2276 or 2301 cm^{-1} bands for a prereduced Rh/Al_2O_3 surface; whereas the converse was true for a preoxidized surface. Thus the computed frequencies and binding energies for Rh^0N_2 and Rh^+N_2 are qualitatively consistent with these observations. The computations suggest that the 2256 cm^{-1} band should indeed be assigned to an end-on Rh^0N_2 species (computed, 2239 cm^{-1}) while the 2276 cm^{-1} band could be assigned to an end-on Rh^+N_2 species (computed, 2266 cm^{-1}). The infrared band at 2301 cm^{-1} could then be assigned to a $Rh^+(N_2)_2$ species (computed, 2293/2298 cm^{-1}, linear; 2268.5/2268.8 cm^{-1}, 90° bent). Closely spaced bands corresponding to the gem disubstituted Rh^+ as predicted by the *ab initio* calculations would not have been resolved in the experiment, and the frequency might be expected to lie between the value for linear and 90° bent in that the NRhN bond angle would likely lie between the 90° and 180° extremes.

Thus, the experimental and theoretical data are consistent, at least in a qualitative sense. We believe that *ab initio* computations of the type used in this work, which employ relativistic core potentials for transition metals, can be useful in investigations of the structures and bonding of surface species. Upon refinement, these types of *ab initio* computations may become a primary means of assignment of infrared frequencies to specific surface species.

Acknowledgement

On the occasion of his 65th birthday, the authors wish to acknowledge the numerous outstanding contributions to chemical physics made by Professor John C. Polanyi.

1. C.A. Rice, S.D. Worley, C.W. Curtis, J.A. Guin, and A.R. Tarrer. J. Chem. Phys. **74**, 6487 (1981); M.A. Henderson and S.D. Worley, J. Phys. Chem. **89**, 1417 (1985); D.K. Paul, M.L. McKee, S.D. Worley, N.W. Hoffman, D.H. Ash, and J. Gautney. J. Phys. Chem, **93**, 4598 (1989).
2. J.P. Wey, H.D. Burkett, W.C. Neely, and S.D. Worley. J. Am. Chem. Soc. **113**, 2919 (1991).
3. J.P. Wey, W.C. Neely, and S.D. Worley. J. Phys. Chem. **95**, 8879 (1991).
4. J.P. Wey, C.G. Worley, W.C. Neely, and S.D. Worley. J. Phys. Chem. **96**, 7088 (1992).
5. H.P. Wang and J.T. Yates. J. Phys. Chem. **88**, 852 (1984).
6. M.L. McKee, C.H. Dai, and S.D. Worley. J. Phys. Chem. **92**, 1056 (1988).
7. M.L. McKee and S.D. Worley. J. Phys. Chem. **92**, 3699(1988).
8. M.R.A. Blomberg and Per E.M. Siegbahn. Chem. Phys. Lett. **179**, 524 (1991).
9. Per E.M. Siegbahn. J. Chem. Phys. **95**, 364 (1991).
10. G. Ciullo, M. Rosi, A. Sgamellotti, and C. Floriani. Chem. Phys. Lett. **185**, 522 (1991).
11. C.W. Bauschlicher, H. Partridge, and S.R. Langhoff. J. Phys. Chem. **96**, 2475 (1992).
12. S.M. Vinogradova and Yu. G. Borod'ko. Russ. J. Phys. Chem. **47**, 449 (1973).
13. S. Sakaki, K. Morokuma, and K. Ohkubo. J. Am. Chem. Soc. **107**, 2686 (1985).
14. I. Papai, A. Goursot, A. St-Amant, and D.R. Salahub. Theor. Chim. Acta. **84**, 217 (1992).
15. G.J. Mains and J.M. White. J. Phys. Chem. **95**, 112 (1991).
16. J. Koutecky, G. Pacchioni, and P. Fantucci. Chem. Phys. **99**, 87 (1985).
17. P.J. Hay and W.R. Wadt. J. Chem. Phys. **82**, 270, 299 (1984).
18. T.H. Dunning and P.J. Hay. *Modern theoretical chemistry.* Plenum, New York. 1976. pp. 1–28.

Can. J. Chem. Downloaded from www.nrcresearchpress.com by 195.246.54.202 on 09/08/12
For personal use only.

19. W.J. Hehre, L. Radom, P.v.R. Schleyer, and J.A. Pople. *Ab initio* molecular orbital theory. John Wiley and Sons, New York. 1986.
20 GAUSSIAN 86: M.J. Frisch, et al. Carnegie-Mellon Quantum Chemistry Publishing Unit, Carnegie-Mellon University: Pittsburgh, PA. The ECP code was obtained from the Theoretical Division, Los Alamos National Laboratory, Los Alamos, NM.
21. G. Herzberg. Molecular spectra and molecular structure II. Infrared and Raman spectra of polyatomic molecules. D. Van Nostrand, New York. 1945. p. 173.
22. C.E. Moore. Atomic energy levels. U.S. Natl. Bur. Stand. Circ. 467, US GPO, Washington, DC. 1949.
23. G. Herzberg. Molecular spectra and molecular structure I. Spectra of diatomic molecules. D. Van Nostrand, New York. 1950. p. 552.
24. J.T. Yates, T.M. Duncan, S.D. Worley, and R.W. Vaughan. J. Chem. Phys. **70**, 1219 (1979).
25. G.A. Ozin and A.V. Voet. Can. J. Chem. **51**, 3332 (1973).

Can. J. Chem. Downloaded from www.nrcresearchpress.com by 195.246.54.202 on 09/08/12
For personal use only.

Transition state dynamics of F + Br_2 reactive scattering

ZHEN ZHENG ZHU, RICHARD W.P. WHITE, DAVID J. SMITH, AND ROGER GRICE
Chemistry Department, University of Manchester, Manchester, M13 9PL, England

Received January 15, 1993

This paper is dedicated to Professor John C. Polanyi on the occasion of his 65th birthday

ZHEN ZHENG ZHU, RICHARD W.P. WHITE, DAVID J. SMITH, and ROGER GRICE. Can. J. Chem. **72**, 523 (1994).

Reactive scattering of F atoms with Br_2 molecules has been studied at an initial translational energy $E \sim 16$ kJ mol^{-1} using a supersonic beam of F atoms seeded in Ne buffer gas. Laboratory angular and velocity distributions of BrF product have been measured. They show sharp peaking in the forward direction with almost isotropic wide angle scattering of relative intensity ~0.2. Approximately half the total available energy is disposed into product translation for scattering in the forward and backward directions with slightly lower translational energy for the sideways scattering. The combination of sharp forward scattering and high product translational energy is attributed to early migratory trajectories in large impact parameter collisions whereby the F atom reacts with the more distant Br atom of the Br_2 molecule lying in the forward hemisphere. The isotropic wide angle scattering arises from direct trajectories in which the F atom reacts with the nearer Br atom of the Br_2 molecule. Migratory dynamics are promoted by charge transfer interaction of the form $Br_2^+F^-$ which stabilises the potential energy surface in elongated isosceles triangular FBr_2 configurations as well as in slightly bent FBrBr configurations. Comparison is made with the dynamics of the F + Cl_2, I_2, and CCl_3Br reactions.

ZHEN ZHENG ZHU, RICHARD W.P. WHITE, DAVID J. SMITH et ROGER GRICE. Can. J. Chem. **72**, 523 (1994).

Utilisant un rayon supersonique d'atomes de fluor placés dans un gaz tampon de Ne et opérant à une énergie initiale de translation d'environ 16 kJ mol^{-1}, on a étudié la diffusion réactive des atomes de fluor par des molécules de brome. On a mesuré les distributions des vitesses et des angles du produit BrF; la vitesse présente un important maximum dans la direction avant avec un grand angle de dispersion pratiquement isotrope d'intensité relative d'environ 0,2. Environ la moitié de l'énergie totale disponible est utilisée pour provoquer une translation du produit dans les directions avant et arrière alors qu'une quantité légèrement inférieure d'énergie de translation est utilisée pour une diffusion latérale. On attibue la combinaison d'une diffusion importante vers l'avant et d'une énergie de translation élevée du produit à des trajectoires de migration précoces dans des collisions avec des paramètres d'impact importants alors que l'atome de fluor réagit avec l'atome de brome de la molécule de Br_2 se trouvant dans l'hémisphère avant. Le grand angle de dispersion isotrope découle de trajectoires directes dans lesquelles l'atome de fluor réagit avec l'atome de brome le plus près dans la molécule de Br_2. Les dynamiques migratoires sont amplifiées par l'interaction de transfert de charge de la forme $Br_2^+F^-$ qui stabilise la surface d'énergie potentielle dans les configurations élongées de forme triangle isocèle du FBr_2 ainsi que dans les configurations légèrement déformées du FBrBr. On a fait une comparaison des dynamiques des réactions des atomes de fluor avec respectivement le Cl_2, le I_2 et le CCl_3Br.

[Traduit par la rédaction]

Can. J. Chem. Downloaded from www.nrcresearchpress.com by 195.246.54.202 on 09/08/12
For personal use only.

Stripping dynamics with the angular distribution of product scattering peaking sharply in the forward direction have been observed frequently in reactive scattering experiments since the earliest studies of the reactions of alkali atoms with halogen molecules (1). Classical trajectory studies (2) of these reactions which proceed via an electron jump mechanism (1) show sharply peaked scattering in the forward direction only when charge migration is allowed between the halogen atoms of the halogen anion formed by the electron jump with a consequent shift in the Coulomb attraction to the alkali cation. When charge migration is inhibited, then sharp scattering is observed only in the spectator stripping limit (1) when there is no repulsion between the halogen atoms of the halogen anion. Sharp forward peaking is also observed in the case of a short-lived collision complex (3) where the translational energy of the forward and the less intense backward scattering is determined by the centrifugal barrier (4) in the exit valley of the potential energy surface. The reaction of F atoms with ICl molecules (5, 6) shows short-lived collision complex behaviour while the reactive scattering of F atoms with I_2 molecules shows evidence (7–9) of migratory dynamics. The reaction of F atoms with Cl_2 molecules (10) was interpreted in terms of a very short-lived collision complex while the reaction of F atoms with Br_2 molecules (11) appears to follow a stripping mechanism with sharp forward peaking but also with disposal of almost half the total available energy into product translation. However, the F + Br_2 reaction has been studied only at an initial translational energy $E \sim 33$ kJ mol^{-1} which is more than half the reaction exoergicity. Consequently it is difficult to decide whether the high product translational energy arises primarily frpm the initial translational energy or from the repulsive energy released in the exit valley of the potential energy surface. The measurements reported here are carried out a lower initial translational energy of $E \sim 16$ kJ mol^{-1} to allow the role of repulsion between products in a stripping reaction to be examined in greater detail.

[1] $F + Br_2 \rightarrow BrF + Br$

This also provides a basis for comparison with recent scattering measurements on the F + Cl_2 reaction (12) at an initial translational energy of $E \sim 16$ kJ mol^{-1}.

Experimental

The apparatus was the same as that previously employed in the study of the F + ICl reaction (6) using a high pressure microwave discharge source (13) with an alumina discharge tube to produce a supersonic beam of F atoms seeded in Ne buffer gas. The velocity distribution of the F atoms peaked at $v_{pk} \sim 1310$ m s^{-1} with a full width at half maximum intensity of $v_{wd} \sim 485$ m s^{-1}, corresponding to a Mach number of $M \sim 4.5$. The Br_2 beam issued from a glass nozzle of diameter ~0.2 mm using a stagnation pressure ~ 30 Torr maintained by a reservoir at −12°C. The velocity distribution of the Br_2 beam measured by a rotatable mass spectrometer detector using a pseudo-random cross-correlation time-of-flight analysis (14), peaks at $v_{pk} \sim 445$ m s^{-1} with a full width at half maximum intensity of $v_{wd} \sim 147$ m s^{-1}, corresponding to a Mach number of M ~ 6.

Can. J. Chem. Downloaded from www.nrcresearchpress.com by 195.246.54.202 on 09/08/12
For personal use only.

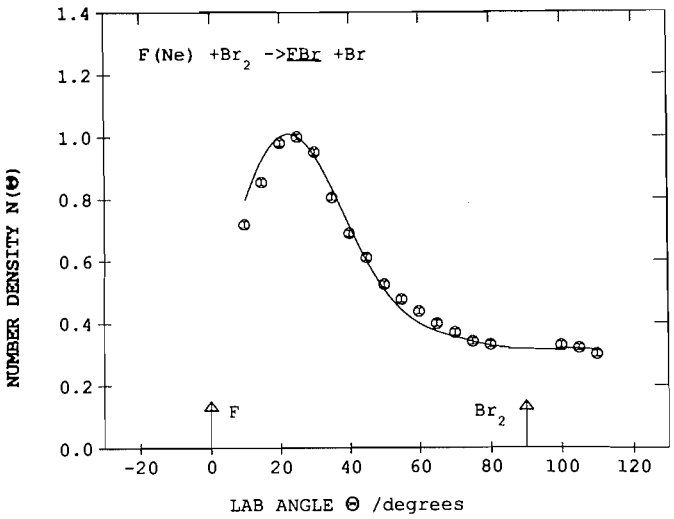

FIG. 1. Laboratory angular distribution (number density) for BrF reactive scattering from F + Br_2 at an initial translational energy of E = 16 kJ mol^{-1}. Solid line shows the fit of the Entemann kinematic analysis.

Results

Angular distribution measurements of BrF reactive scattering yield ~30 counts s^{-1} against a background of ~9 counts s^{-1}. The laboratory angular distribution of BrF number density shown in Fig. 1 peaks close to the F atom beam. The laboratory velocity distributions of BrF flux shown in Fig. 2 were measured using integration times of ~2500 *s* to gain signal-to-noise ratios of ~20 at the peaks of the distribution. Transformation of these laboratory data to centre-of-mass coordinates has been performed using the numerical inversion procedure of Siska (15) and yielded a contour map of the differential reaction cross section as showing in Fig. 3. Figure 3 shows a sharp peak in the forward direction at a centre-of-mass scattering angle of θ = 0° with a lower relative intensity ~0.20 at wider scattering angles. These features are very similar to those previously determined for F atoms seeded in He buffer gas (11).

For a more quantitative comparison, the kinematic analysis has also been carried out using the stochastic method of Entemann and Herschbach (16). Here the differential cross section is expressed as a product of an angular function $T(\theta)$ and a velocity distribution $U(u, \theta)$ which is parametrically dependent on scattering angle θ. The Halpern Strutinski formula (17) multiplied by an exponential decay (3) and with an additional constant term was employed for the angular function

$$[2]\quad T(\theta) = (1 - c)\exp(-\sin^2\theta/4\langle\cos^2\alpha'\rangle)I_0(\sin^2\theta/4\langle\cos^2\alpha'\rangle) \times \exp(-\theta/\theta^*) + c$$

where I_0 denotes the zeroth order modified Bessel function (18), α' the helicity angle between the initial orbital angular momentum **L** and the final relative velocity v' and θ^* the decay parameter. The velocity function was of the same form as that previously employed (11) at a higher initial translational energy. The resulting angular function with the parameters $\langle\cos^2\alpha'\rangle^{1/2} = 0.35$, $\theta^* = 70°$, and $c = 0.16$ and the product translational energy distributions shown in Fig. 4 confirm the results of the Siska transformation. The angular distribution is similar to that previously estimated at a higher initial translational energy (11) but with a somewhat broader forward peak of width ~30° at half maximum intensity compared with ~20° at higher initial translational energy. The product translational energy distributions, which are the same to within experimental uncertainty as those obtained at higher initial translational energy (11), show higher product translational energy for scattering in the forward and backward directions than for sideways scattering. The backfits of the Entemann transformation are shown as solid curves in Figs. 1 and 2. The peak E'_{pk} and average E'_{av} product translational energies are listed in Table 1, together with the initial translational energy E and reaction exoergicity ΔD_0 calculated from the BrF and Br_2 bond energies of Huber

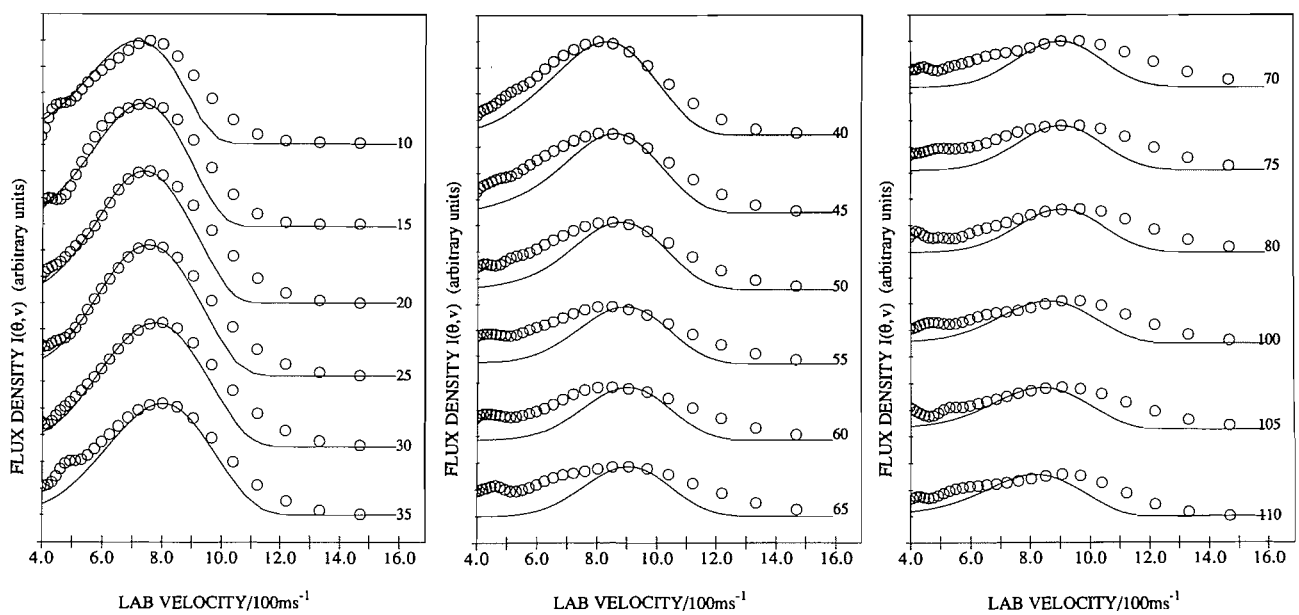

FIG. 2. Laboratory velocity distributions (flux density) of reactively scattered BrF from F + Br_2 at an initial translational energy of E = 16 kJ mol^{-1}. Solid lines show the fit of the Entemann kinematic analysis.

TABLE 1. Reaction energetics: reactant translation energy E, peak product translational energy E'_{pk} average product translational energy E'_{av} reaction exoergicity ΔD_0

	E'_{pk}/kJ mol^{-1}		E'_{av}/kJ mol^{-1}		
E/kJ mol^{-1}	θ = 0°, 180°	θ = 90°	θ = 0°, 180°	θ = 90°	ΔD_0/kJ mol^{-1}
16	35	25	41	29	56

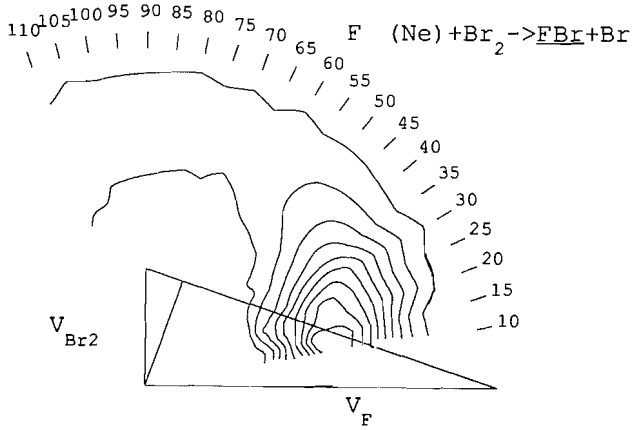

FIG. 3. Polar contour map of BrF flux from F + Br_2 as a function of centre-of-mass scattering angle θ and velocity u obtained by the Siska method. Incident F atom direction is denoted by θ = 0°, incident Br_2 direction θ = 180°.

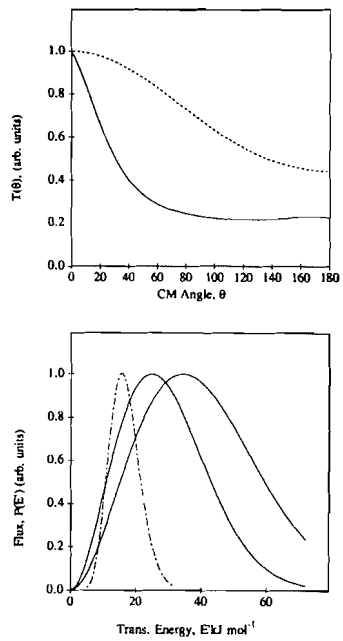

FIG. 4. Angular function $T(\theta)$ and translational energy distributions $P(E')$ for F + Br_2 at an initial translational energy E = 16 kJ mol^{-1}. Left-most product translational energy distribution corresponds to θ = 90°, right-most distribution to θ = 0°, 180°. Dashed curve shows the distribution of initial translational energy. Dotted curve shows the angular distribution predicted by the DIPR model with the parameters n = 0 and q = 4.0.

and Herzberg (19). Approximately half the total available energy $E + \Delta D_0$ is disposed into product translation for the forward and backward scattering $f_{pk}' \sim 0.49$ and $f_{av}' \sim 0.57$, while a significant though lower fraction $f_{pk}' \sim 0.35$ and $f_{av}' \sim 0.40$ is disposed into translation for the sideways scattering. These fractions are all slightly higher than those previously determined at a higher initial translational energy (11). The rate constant for the F + Br_2 reaction $k = 1.9 \times 10^{11}$ dm^3 mol^{-1} s^{-1}, determined at 298 K in a discharge flow experiment (20), corresponds to a total reaction cross section $Q_r \sim 60$ Å^2 at an initial translational energy $E \sim 2.5$ kJ mol^{-1}.

Discussion

The present results confirm the confluence of stripping dynamics with a relatively high product translational energy for the F + Br_2 reaction which was indicated by previous reactive scattering measurements (11) at a higher initial translational energy. The trajectory calculations by Kuntz, Mok, and Polanyi (2) suggest that this arises on a potential energy surface for an exoergic reaction with both attraction between the reactants and repulsion between the products, only when early migratory trajectories involve a transfer of the bonding of the reactant atom between the two atoms of the reactant diatomic molecule. Indeed more extensive migratory dynamics have been proposed (21) for the strongly exoergic F + I_2 reaction, yielding mainly vibrational and rotational excitation of the product IF molecules. In the case of a potential energy surface with a significant potential energy well, sharp forward peaking may also arise from shortlived collision complex dynamics (3) as is observed for the F + ICI reaction (5, 6). However, the peak product translational energy for scattering in the forward and backward directions is then governed by the maximum centrifugal barrier in the exit valley of the potential energy surface (4) where

$$[3] \quad B_m' \cong \mu E/\mu'$$

where μ, μ' denote the reactant and product reduced masses. Since eq. [3] predicts a value of only $B_m' \cong 6$ kJ mol^{-1} which lies far below the peak product translational energy $E_{pk}' = 35$ kJ mol^{-1} determined in these experiments, it may be concluded that the F +Br_2 reaction involves stripping dynamics over a surface with both attraction between the reactants and repulsion between the products rather than a short-lived collision complex on a surface with a deep potential energy well. The observed angular and product translational energy distributions are therefore determined by the reactant transition state located in the entrance valley of the potential energy surface.

As illustrated in Fig. 5 for reactant transition states lying in the plane of collision, the reactant F atom may interact initially either with the Br atom of the Br_2 molecule lying in the forward hemisphere (Fig. 5*a*) with respect to the initial relative velocity or with the Br atom lying in the backward hemisphere for collisions near the maximum impact parameter $b_m \sim 4.5$ Å. However, for collisions at smaller impact parameters $b < 3$ Å the F

Can. J. Chem. Downloaded from www.nrcresearchpress.com by 195.246.54.202 on 09/08/12
For personal use only.

TABLE 2. Estimated structure for the reactant transition state: interbond angle β, bond lengths, r_{BrF}, r_{BrBr}, and principal moments of inertia I_a, I_b, I_c

β/deg	r_{BrF}/Å	r_{BrBr}/Å	$I_a/10^{-46}$ kg m^2	$I_b/10^{-46}$ kg m^2	$I_c/10^{-46}$ kg m^2
135	3.0	2.3	6.2	72.3	78.5

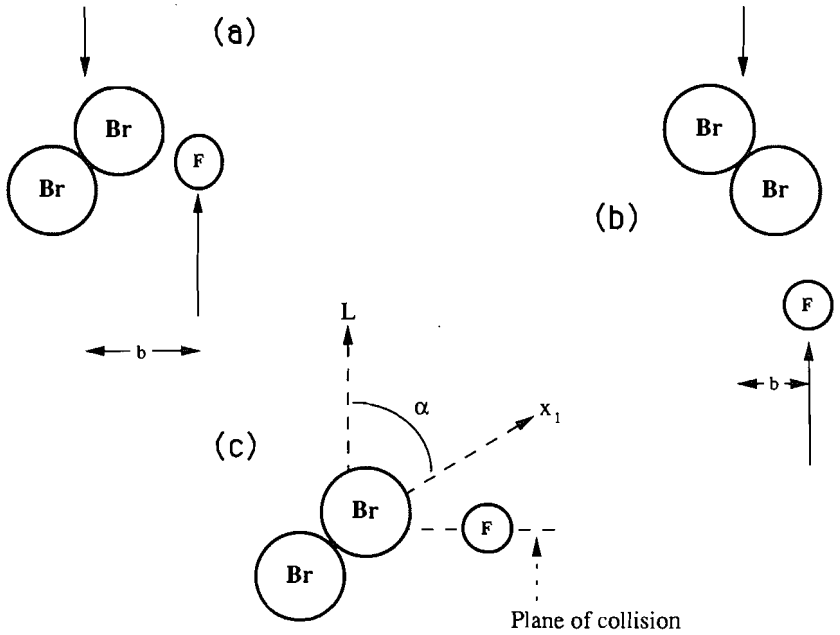

FIG. 5. Reactant transition state for the F + Br_2 reaction; *a*, *b* lying in the plane of collision, *c* lying out of the plane of collision. The principal axis of lowest moment of inertia is denoted by x_1. The initial orbital angular momentum $\boldsymbol{L}$ is perpendicular to the plane of collision.

atom can interact only with the Br atom of the Br_2 molecule lying in the backward hemisphere (Fig. 5*b*). For collisions with the Br atom located in the backward hemisphere, the initial momentum of the F atom will be directed toward the Br atom resulting in direct reaction dynamics. Since the F atom is lighter than the Br atoms by a factor 4, the bond direction of the Br_2 molecule is likely to be largely maintained as the transition state dissociates to reaction products. This is the basic assumption of the DIPR model (2, 22, 23), which predicts roughly isotropic wide angle scattering when the impulse imparted to the product Br atom is large compared with its initial momentum as a reactant. This momentum ratio may be estimated approximately (22) from the peak product translational energy for scattering in the sideways direction

$$[4] \quad q = [m_{FBr} m_{Br_2} E'_{pk}/(m_F m_{Br} E)]^{1/2}$$

which yields q ~ 4 using the values of E and E'_{pk} for the sideways scattering in Table 1. However, the experimental angular distribution is more sharply forward peaked than the DIPR angular distribution calculated from eq. [5] for an unbiased orientation dependence shown in Fig. 4.

$$[5] \quad I(\theta) = (2/q)\cos\theta + [(q + q^{-1}\cos 2\theta)/(q^2 - \sin^2\theta)^{1/2}]$$

For collisions with the Br atom located in the forward hemisphere, the contraction of the FBr bond is likely to be forestalled as the initial momentum of the F atom counteracts the attraction toward the Br atom. In these circumstances the precessional motion of the reactant transition state will become established before dissociation of the Br_2 bond occurs and the direction of product scattering then reflects both the initial orientation of the Br_2 molecule and the range of precessional motion of the transition state. Typical reactant transition states with the Br_2 bond length close to the equilibrium value ~2.3 Å, an extended BrF bond length ~3 Å, and an interbond angle ~135° provide an excellent approximation to a prolate symmetric top as shown by the moments of inertia listed in Table 2. Consequently, the Halpern Strutinski term in eq. [2] may be associated with the precession of such transition states while the isotropic term may be associated with more direct reaction dynamics. Figure 5*c* shows the reactant transition state with the axis of the Br_2 molecule inclined at a maximum angle to the plane of collision, such that the x_1 axis of the transition state lies at a helicity angle α to the initial orbital angular momentum $\boldsymbol{L}$ which is equal to the total angular momentum to a good approximation for large impact parameter collisions. Both the total angular momentum and its projection on the symmetry axis will be conserved as the prolate symmetric top transition state dissociates to products. Hence the value of $\langle\cos^2\alpha'\rangle^{1/2} = 0.35$ estimated for the Halpern Strutinski function of eq. [2] corresponds to reactant transition states with a helicity angle α ~ 70° and hence to Br_2 molecules initially inclined at an angle ~20° to the plane of collision. The decay parameter θ = 70° estimated from eq. [2] corresponds to the precession of reactant transition states persisting for ~$\frac{1}{5}$ of a rotational period in the plane of collision before dissociation in large impact parameter collisions. Integration of eq. [2] over the scattering angle θ

$$[6] \quad Q_r \propto \int_0^{\pi} T(\theta)\sin\theta d\theta$$

shows that the Halpern Strutinski function contributes some

Can. J. Chem. Downloaded from www.nrcresearchpress.com by 195.246.54.202 on 09/08/12
For personal use only.

Can. J. Chem. Downloaded from www.nrcresearchpress.com by 195.246.54.202 on 09/08/12
For personal use only.

44% to the total reaction cross section and the isotropic term 56%. If the Halpern Strutinski term were attributed entirely to collisions at large impact parameters, this would correspond to a range 3.5 Å $\leq b \leq$ 4.5 Å with the isotropic scattering being attributed to smaller impact parameters $b <$ 3.5 Å. The angular distribution measured previously for F + Br_2 (11) at a higher initial translational energy of $E \sim$ 33 kJ mol^{-1} shows similar behaviour though with a sharper forward peak corresponding to transition states precessing closer to the plane of collision and persisting for a smaller fraction of the rotational period.

The lifetime of the exponential decay in eq. [2] refers to the forward scattered peak at $\theta = 0°$ as the time origin, which in turn relates to the reaction of F atoms at large impact parameters in Fig. 5 with the Br_2 molecule axis lying almost parallel to the initial relative velocity vector. Forward scattering in this case requires migratory trajectories whereby the F atom interacts initially with the nearer Br atom, before passing through an elongated isosceles triangular FBr_2 configuration and finally interacting with the further Br atom as the Br_2 molecule dissociates to form BrF products scattering in the forward direction. Clearly, migratory trajectories of this kind require that the potential energy surface remain attractive in the elongated triangular FBr_2 configuration as well as in the slightly bent FBrBr configuration of the transition state shown in Fig. 5. Diatomics-in-molecules calculations on the F + F_2 (24) and Cl + Cl_2 (25) potential energy surfaces show that broadside approach is inhibited by conical intersections between $^2A_1$ and $^2B_2$ potential energy surfaces. However, the $^2B_2$ potential energy surface will be stabilised in the elongated isosceles triangular configuration by F^- + $Br_2^+(^2\Pi_g)$ ion pair states, arising from charge transfer interaction (26) in the F + Br_2 system. Indeed *ab-initio* calculations (27) show the strongly bent configuration of the FIH radical to be more stable than the slightly bent configuration. Hence early migratory trajectories are likely to be promoted by the charge distribution of the Br_2^+ cation which extends over both Br atoms in the F + Br_2 reaction.

The extent of charge transfer interaction in the reactions of F atoms with halogen and interhalogen molecules (26) depends upon the ionisation potential of the molecule. Nominal crossing radii (28) between the ionic F^+ + XY^- potential energy surface and the covalent F + XY surface may be calculated from the formula

$$[7] \quad r_c = e^2/4\pi\epsilon_0[I(XY) - A(F)]$$

where I(XY) denotes the ionisation potential of the halogen molecule (19, 29) and A(F) the electron affinity of the F atom (30). The values of the crossing radii listed in Table 3 only slightly exceed the equilibrium bond lengths of the halogen fluoride product molecules (19), which indicates that only partial charge transfer will occur in both the reaction intermediate and the halogen fluoride product molecule. This may be estimated crudely by taking the ratio of the dipole moment of the halogen fluoride molecule (31) to that of the corresponding alkali fluoride molecule (32) which yields fractional charge transfers of ~0.24 for IF, ~0.16 for BrF, and ~0.10 for ClF. The same trend of decreasing charge transfer is expected along the sequence of reactions F + I_2, Br_2, and Cl_2.

The most extensive charge transfer occurs in the F + I_2 reaction where trajectory calculations (21) suggest that the attractiveness of the potential energy surface gives rise to both early (2) and late (33–35) migratory dynamics. The diatomic halogen

TABLE 3. Nominal crossing radii r_c between ionic F^- + XY^+ and covalent F + XY potential energy surfaces compared with equilibrium bond lengths r_e of the product XF molecule

XY	r_c/Å	r_e/Å
Cl_2	1.8	1.63
Br_2	2.0	1.76
I_2	2.5	1.91
ICl	2.1	1.91
$BrCCl_3$	1.9	1.76
ICH_3	2.4	1.91

cations $XY^+(^2\Pi)$ are more strongly bound and have shorter bond lengths (19, 36) than the corresponding halogen molecules. Consequently, charge transfer interaction will reduce repulsion in the exit valley of the potential energy surface to a greater extent for F + I_2 than for F + Br_2, though the entrance valleys are attractive on both potential energy surfaces. In the F + Cl_2 reaction where there is more limited charge transfer interaction than for F + Br_2, the reactant transition state (12) is formed at the top of a low potential energy barrier in the entrance valley of the potential energy surface. As described previously (37), the dynamics of the F + CCl_3Br reaction show close agreement with the DIPR model and are consistent with the predominance of direct trajectories. This contrasts with the F + Br_2 reaction dynamics where migratory trajectories foster more sharply peaked forward scattering. The difference may be attributed to the more localised charge distribution of the CCl_3Br^+ cation which is located predominantly on the Br atom in the F + CCl_3Br reaction.

Acknowledgements

This paper is dedicated to Professor John C. Polanyi, who first identified the role of migration in chemical reaction dynamics, on the occasion of his 65th birthday.

Support of this work by SERC and the European Commission is gratefully acknowledged.

1. D.R. Herschbach. Adv. Chem. Phys. **10**, 319 (1966).
2. P.J. Kuntz, E.M. Nemeth, and J.C. Polanyi. J. Chem. Phys. **50**, 4607 (1969); P.J. Kuntz, M.H. Mok, and J.C. Polanyi. J. Chem. Phys. **50**, 4623 (1969).
3. G.A. Fisk, J.D. McDonald, and D.R. Herschbach. Discuss. Faraday Soc. **44**, 228 (1967).
4. S.A. Safron, N.D. Weinstein, D.R. Herschbach, and J.C. Tully. Chem. Phys. Lett. **12**, 564 (1972).
5. N.C. Firth, D.J. Smith, and R. Grice. Mol. Phys. **61**, 859 (1987).
6. R.D. Jarvis, R.W.P. White, Z.Z. Zhu, D.J. Smith, and R. Grice. Mol. Phys. **75**, 587 (1992).
7. N.C. Firth, N.W. Keane, D.J. Smith, and R. Grice, Faraday Discuss. Chem. Soc. **84**, 53 (1987).
8. N.C. Firth, N.W. Keane, D.J. Smith, and R. Grice. Mol. Phys. **66**, 1223 (1989).
9. B. Girard, N. Billy, G. Gouedard, and J. Vigué. J. Chem. Phys. **88**, 2342 (1988); Europhys. Lett. **14**, 13 (1991).
10. N.C. Firth and R. Grice. Mol. Phys. **60**, 1261 (1987).
11. N.C. Firth and R. Grice. Mol. Phys. **60**, 1273 (1987).
12. Z.Z. Zhu, D.J. Smith, and R. Grice. J. Chem. Soc. Faraday Trans. **89**, 1487 (1993).
13. P.A. Gorry and R. Grice. J. Phys. E: Sci. Instrum. **12**, 857 (1979).
14. C.V. Nowikow and R. Grice. J. Phys. E: Sci. Instrm. **12**, 515 (1979).
15. P.E. Siska. J. Chem. Phys. **59**, 6052 (1973).

16. E.A. Entemann and D.R. Herschbach. Discuss Faraday Soc. **44**, 289 (1967).
17. I. Halpern and V.M. Strutinski, Proc. 2nd Int. Conf. Peaceful Uses of Atomic Energy, Geneva, 1958. p. 408.
18. M. Abramowitz and I.A. Stegun. Handbook of mathematical functions. Dover, New York. 1965. p. 416.
19. K.P. Huber and G. Herzberg. Constants for diatomic molecules. Van Nostrand Reinhold, New York. 1979.
20. E.H. Appleman and M.A.A. Clyne. J. Chem. Soc. Faraday Trans. 1, **71**, 2072 (1975).
21. N.W. Keane, J.C. Whitehead, and R. Grice. J. Chem. Soc. Faraday Trans. 2, **85**, 1081 (1989).
22. M.T. Marron. J. Chem. Phys. **58**, 153 (1973).
23. P.J. Kuntz. Trans. Faraday Soc. **66**, 2980 (1970).
24. J.J. Duggan and R. Grice. J. Chem. Soc. Faraday Trans. **80**, 795 (1984).
25. J.J. Duggan and R. Grice. J. Chem. Soc. Faraday Trans. **80**, 809 (1984).
26. L.M. Loewenstein and J.G. Anderson. J. Phys. Chem. **91**, 2993 (1987).
27. S.A. Kucharski and R.J. Bartlett. J. Chem. Phys. **95**, 433 (1991).
28. R. Grice and D.R. Herschbach. Mol. Phys. **27**, 159 (1974).
29. D.C. Driscoll, J.A. Bishop, B.J. Sturm, P.A. Dowben, and G.C. Olsen. J. Vac. Sci. Technol. **A4**, 823 (1986).
30. R.S. Berry and C.W. Reimann. J. Chem. Phys. **38**, 1540 (1963).
31. S.A. Kucharski, J. Noga, and R.J. Bartlett. J. Chem. Phys. **88**, 1035 (1988).
32. A.L. McClellan. Tables of experimental dipole moments. Freeman, San Francisco. 1963.
33. J.C. Polanyi, J.L. Schreiber, and W.J. Skrlac. Faraday Discuss. Chem. Soc. **67**, 66 (1979).
34. J.C. Polanyi and W.J. Skrlac. Chem. Phys. **23**, 167 (1977).
35. D. Brandt and J.C. Polanyi. Chem. Phys. **35**, 23 (1978); **45**, 65 (1980).
36. A. Benz and H. Morgner. Mol. Phys. **58**, 223 (1986).
37. R.D. Jarvis, N.C. Firth, D.J. Smith, and R. Grice. Mol. Phys. **79**, 323 (1993).

Can. J. Chem. Downloaded from www.nrcresearchpress.com by 195.246.54.202 on 09/08/12
For personal use only.

Valence shell absolute photoabsorption oscillator strengths, constrained dipole oscillator strength distributions, and dipole properties for CH_3NH_2, $(CH_3)_2NH$, and $(CH_3)_3N$

GORDON R. BURTON, WING FAT CHAN, GLYN COOPER, AND C.E. BRION
Department of Chemistry, The University of British Columbia, Vancouver, BC V6T 1Z1, Canada
AND
ASHOK KUMAR[1,2] AND WILLIAM J. MEATH[2]
Department of Chemistry, The University of Western Ontario, London, ON N6A 5B7, Canada
Received April 6, 1993
This paper is dedicated to Professor John C. Polanyi on the occasion of his 65th birthday

GORDON R. BURTON, WING FAT CHAN, GLYN COOPER, C.E. BRION, ASHOK KUMAR, and WILLIAM J. MEATH. Can. J. Chem. **72**, 529 (1994).

Dipole (e,e) spectroscopy has been used to measure the absolute photoabsorption oscillator strengths (cross sections) for the valence shells of CH_3NH_2, $(CH_3)_2NH$, and $(CH_3)_3N$ from the photoabsorption threshold to 250 eV at low resolution (~1 eV fwhm) and to 31 eV at high resolution (0.048 eV fwhm). The observed peaks in the photoabsorption spectra of the methylamines have been assigned to transitions to Rydberg orbital upper states. Our measured photoabsorption data, augmented by mixture rule estimates for high photon energies, have been used in conjunction with Thomas–Reiche–Kuhn sum rule and molar refractivity constraints, to construct constrained dipole oscillator strength distributions for each of the methylamines. From these constrained dipole oscillator strength distributions a wide range of related dipole properties have been calculated for each of the methylamines, and in most cases the results so obtained represent the first (reliable) determination of these properties.

GORDON R. BURTON, WING FAT CHAN, GLYN COOPER, C.E. BRION, ASHOK KUMAR et WILLIAM J. MEATH. Can. J. Chem. **72**, 529 (1994).

On fait appel à la spectroscopie dipolaire (e,e) pour mesurer la photoabsorption absolue, les intensités de l'oscillateur (section droite) des électrons de valence du CH_3NH_2, $(CH_3)_2NH$ et du $(CH_3)_3N$ à partir du seuil de photoabsorption de 250 eV à basse résolution (environ 1 eV fwhm) et à 31 eV à haute résolution (0,048 eV fwhm). On a attribué les pics observés dans les spectres de photoabsorption des méthylamines à des transitions de Rydberg des orbitales des états supérieurs. Nous avons utilisé nos données de photoabsorption mesurées et des évaluations par la règle de mélanges pour les photons de haute énergie, de concert avec la règle de la somme de Thomas-Reiche-Khulm et avec les contraintes de réfractivité molaire, pour construire la distribution des intensités de l'oscillateur du dipôle contraint de chaque méthylamine. A partir des distributions des intensités de l'oscillateur du dipôle contraint, on a calculé un très grand nombre de propriétés des dipôles apparentés pour chaque méthylamine et les résultats ainsi obtenus représentent dans la plupart des cas la première détermination (fiable) de ces propriétés.

[Traduit par la rédaction]

1. Introduction

The absolute photoabsorption spectra of the methylamines are of interest and importance in many areas of science and technology. For example, monomethylamine has been observed in the interstellar medium (1), in the atmosphere of Halley's comet (2, 3), has been included in models of the atmospheres of Uranus and Saturn (4, 5), and is known from photochemistry to be a low-energy source of NH_2 and NH radicals (6). The use of trimethylamine as an additive ("seed" compound) to improve the performance of UV pre-ionized lasers has been explored (7). Therefore, absolute photoabsorption oscillator strength (cross section) data for the methylamines, and the associated dipole properties, are of importance in astrophysics, laser physics, photochemistry, or in any other application where the interaction of high-energy radiation or particles with these molecules is to be understood. Such measurements and properties should also provide a test-bed for *ab initio* calculations of absolute oscillator strengths and dipole properties. However, few such calculations have been reported for the methylamines. The study of photoabsorption oscillator strength data and dipole properties for series of related molecules also yields useful information about functional group additivity trends and their effects on the absorption of highly energetic electromagnetic radiation. A systematic study of such trends can be used to predict the oscillator strength distributions and dipole properties of larger, more complex molecules for which no data exist, or for which direct measurement may be difficult (8–11).

There is very little absolute photoabsorption oscillator strength data available in the literature for the methylamines which is in striking contrast to the wealth of quantitative information available for the parent member of this series, NH_3 (for a recent review see refs. 12, 13). Absolute photoabsorption spectra for the methylamines and ammonia have been reported by Tannenbaum et al. (14) in the limited energy region 4.8–7.8 eV. In other work, Bertrand et al. (15) have measured differential photoabsorption oscillator strengths for CH_3NH_2 and $(CH_3)_2NH$ at 10.03 eV, and Grosjean and Bletzinger (7) have measured the absolute photoabsorption spectrum of $(CH_3)_3N$ from 8.0–10.8 eV.

In our experimental study of the methylamines CH_3NH_2 (monomethylamine, methanamine), $(CH_3)_2NH$ (dimethyl-

[1]Permanent address: Department of Physics, Meerut University, Meerut 250004, India.

[2]Associated with the Centre for Interdisciplinary Studies in Chemical Physics, University of Western Ontario, London, ON N6A 5B7, Canada.

Can. J. Chem. Downloaded from www.nrcresearchpress.com by EESC ESCOLA DE ENGENHARIA on 09/08/12
For personal use only.

Can. J. Chem. Downloaded from www.nrcresearchpress.com by EESC ESCOLA DE ENGENHARIA on 09/08/12
For personal use only.

amine, *N*-methylmethanamine), and $(CH_3)_3N$ (trimethylamine, *N*,*N*-dimethylmethanamine), detailed and wide-ranging absolute oscillator strength data are obtained for these molecules in the energy region from the first excitation threshold to 250 eV. In our associated theoretical work these measured oscillator strengths are used along with mixture rule data, and molar refractivity and Thomas–Reiche–Kuhn (TRK) sum rule constraints, to determine constrained dipole oscillator strength distributions (DOSDs) for these molecules. The DOSDs are, in turn, used to determine reliable values for many of the important dipole properties for the methylamines. Section 2 outlines the experimental techniques and methods used in the present work to determine the absolute high- and low-resolution oscillator strength data for the methylamines using dipole (e,e) spectroscopy. These data are presented in section 3 along with a detailed discussion of the measured spectra and the spectral assignments. The general method used for the construction of the DOSDs and for the evaluation of the dipole properties of the methylamines is outlined in section 4, and the results are given in section 5 along with an analysis of the uncertainty limits placed on the results for the dipole properties. Recently, these same procedures have been used to evaluate the DOSD and many of the dipole properties for NH_3 (12).

2. Experimental methods

The dipole (e,e) spectrometers and procedures used in the present work to determine the absolute low-resolution (~1 eV fwhm) (16–20) and high-resolution (0.048 eV fwhm) (21–23) oscillator strengths for the methylamines using dipole (e,e) spectroscopy have been described in detail previously. This technique involves high energy electron scattering at negligible momentum transfer and has been shown to provide data which are entirely equivalent to those obtained using conventional optical methods (24). In the dipole (e,e) method the continuously tuneable energy loss of the scattered electrons is entirely equivalent to a photon energy. Thus, it is possible to measure a photoabsorption spectrum from a few to a few hundred eV, spanning the UV, VUV, and soft X-ray regions of the electromagnetic spectrum, using a single apparatus. This type of measurement would not be possible with a single optical spectrometer since several monochromators would be necessary to span the same energy region.

The low-resolution (LR) measurements for the methylamines (~1 eV fwhm) were made using an incident electron beam of 8000 eV, and the scattered electrons were energy analyzed and detected at a mean scattering angle of zero degrees (acceptance angle of 1.4×10^{-4} sr) (16). The scattering conditions of high incident electron beam energy, small acceptance angles about a mean scattering angle of zero degrees, and small energy losses relative to the incident beam energy, ensure that the momentum transfer is small and that predominantly dipole-allowed transitions are excited. The absolute photoabsorption oscillator strengths were determined by Bethe–Born conversion and partial TRK sum-rule normalization of the measured background-subtracted electron energy-loss spectrum as follows. The relative oscillator strength spectra were measured for each of the methylamines from the electronic excitation threshold to an equivalent photon energy of 250 eV. These data were placed on an absolute scale by first fitting a curve of the form

$$[1] \qquad \frac{df}{dE} = AE^{-1.5} + BE^{-2.5} + CE^{-3.5}$$

to the high-energy portion of the valence-shell relative oscillator strength tail from 90 to 250 eV. In eq. [1], df/dE is the differential oscillator strength, E is the energy loss (or equivalent photon energy), and A, B, and C are best-fit parameters to the data. The values of the parameters were found to be 7.326 $eV^{0.5}$, 108.3 $eV^{1.5}$, and 4.980×10^4 $eV^{2.5}$, respectively, for monomethylamine, 9.932 $eV^{0.5}$, 151.6 $eV^{1.5}$, and 6.071×10^4 $eV^{2.5}$, for dimethylamine, and 14.53 $eV^{0.5}$, −200.6 $eV^{1.5}$, and 1.008×10^5 $eV^{2.5}$, for trimethylamine. In earlier work, curves having this empirical functional form have been found to provide much more satisfactory fits to the measured high-energy (typically 100–250 eV) of the valence-shell oscillator strength distributions of polyatomic molecules than the predicted Born dipole asymptotic $E^{-3.5}$ dependence which is only expected to be valid at extremely high photon energies (see section 4 below). For example, in the cases of C_2H_2 (25), C_2H_4 (26), and CH_3OH (27) these procedures have led to satisfactory absolute oscillator strength scales. This curve was then integrated from 250 eV to infinite energy for each spectrum in order to provide an estimate of the valence-shell oscillator strength contribution above the last measured differential oscillator strength data point at 250 eV. Using these procedures ~7% of the total valence-shell oscillator strength distribution is predicted to be above 250 eV for each of the three methylamines. The total area under the valence-shell spectrum (i.e., the contribution from the measured oscillator strengths plus that under the extrapolated curve) was normalized to 14.54 for monomethylamine, 20.75 for dimethylamine, and 26.96 for trimethylamine. These integrated values correspond to the total number of valence-shell electrons in these molecules plus a small contribution (~5%) to account for the Pauli-excluded transitions from the inner-shells (the nitrogen and carbon K shells) to the already-occupied valence-shell orbitals. The Pauli-excluded transition contribution was estimated for each molecule from sums of atomic corrections based on Hartree–Slater calculations (28, 29). The absolute oscillator strength data thus obtained are estimated to be accurate to ±5%. The small random errors associated with the photoabsorption measurements are indicated by the small scatter in the data points.

The high-resolution (HR) measurements (0.048 eV fwhm) of the methylamines were made using a 3000 eV monochromated incident electron beam (21). An empirical Bethe–Born conversion factor has recently been determined for this spectrometer (22) which permits the conversion of the measured background-subtracted energy-loss spectrum to a relative oscillator strength spectrum. The high-resolution relative oscillator strength spectrum thus obtained for each of the methylamines was placed on an absolute scale by single point normalization in the smooth continuum region to the corresponding low-resolution photoabsorption oscillator strength data obtained in the present work. The high accuracy of this method for determining high-resolution oscillator strengths has been verified by the excellent agreement (22, 30) between recently measured photoabsorption data for atomic helium, and molecular hydrogen, and high-level *ab initio* calculations.

The high-purity gas samples used in the present study, monomethylamine (98.0%), dimethylamine (99.0%), and trimethylamine (99.0%), were obtained from Matheson Gas Company lecture bottles and were used without further purification. No impurity peaks were detected in the high-resolution electron energy-loss spectra.

3. Results and discussion

3.1. Electronic structure of the methylamines

The symmetry groups of highest symmetry that CH_3NH_2, $(CH_3)_2NH$, $(CH_3)_3N$, belong to are C_s, C_s, and C_{3v}, respectively. The molecular orbital configurations of the ground states of these molecules in the independent particle model are as follows:

CH_3NH_2:

$$\underbrace{(1a')^2}_{N1s}\ \underbrace{(2a')^2}_{C1s}\ \underbrace{(3a')^2(4a')^2(1a'')^2(5a')^2(6a')^2(2a'')^2(7a')^2}_{\text{Valence shell}}$$

$(CH_3)_2NH$:

$$\underbrace{(1a')^2}_{N1s}\ \underbrace{(1a'')^2(2a')^2}_{C1s}\ \underbrace{(3a')^2(2a'')^2(4a')^2(5a')^2(6a')^2(3a'')^2(4a'')^2(5a'')^2(7a')^2(8a')^2}_{\text{Valence shell}}$$

TABLE 1. Vertical ionization potentials for the electronic states of the methylamines obtained from photoelectron spectroscopic measurements (31–37)

Monomethylamine		Dimethylamine		Trimethylamine	
Electronic state	VIP (eV)	Electronic state	VIP (eV)	Electronic state	VIP (eV)
$7a'$	9.64[a]	$8a'$	8.97[e]	$6a_1$	8.44[e]
$2a''$	13.22[a]	$7a'$	12.70[e]	$5e$	(12.3, 12.74)[e]
$6a'$	14.42[a]	$5a''$	13.09[e]	$1a_2$	13.1[e]
$5a'$	15.45[a]	$4a''$	13.9[e]	$4e$	13.67[e]
$1a''$	16.85[a]	$3a''$	15.19[e]	$3e$	15.68[e]
$4a'$	21.9[b]	$6a'$	15.5[e]	$5a_1$	16.0[e]
$3a'$	27.5[b]	$5a'$	16.69[e]	$4a_1$	19.46[e]
		$4a'$	20.6[b]	$2e$	22.5[b]
		$2a''$	22.4[b]	$3a_1$	28.3[b]
		$3a'$	28.0[b]		
$2a'$	291.60[c]	$2a'$	291.43[f]	$1e$	291.26[g]
		$1a''$		$2a_1$	
$1a'$	405.17[d]	$1a'$	404.93[d]	$1a_1$	404.82[d]

[a]Reference 32.
[b]Reference 31.
[c]Reference 35.
[d]References 34, 37.
[e]Reference 33.
[f]Quoted by Sodhi and Brion (46) as the average of the carbon K-shell VIPs for monomethylamine and trimethylamine.
[g]Reference 36 as corrected in ref. 75.

$(CH_3)_3N$:

$$\underbrace{(1a_1)^2}_{N1s}\ \underbrace{(2a_1)^2(1e)^4}_{C1s}\ \underbrace{(3a_1)^2(2e)^4(4a_1)^2(5a_1)^2(3e)^4(4e)^4(1a_2)^2(5e)^4(6a_1)^2}_{\text{Valence shell}}$$

The vertical ionization potentials (VIPs) of the valence-shell states of the methylamines have been determined using high-resolution HeI and HeII photoelectron spectroscopy (31–33), while the inner shell states have been measured using X-ray photoelectron spectroscopy (34–37). The electronic configurations and vertical ionization potentials for the methylamines are summarized in Table 1.

3.2. *Low resolution measurements for the methylamines*

The low-resolution (~1 eV fwhm) valence-shell absolute photoabsorption oscillator strengths for monomethylamine, dimethylamine, and trimethylamine measured in the present work from the first excitation threshold to 250 eV using dipole (e,e) spectroscopy are shown in Figs. 1, 2, and 3, and are given numerically in Tables 2, 3, and 4, respectively. Panel (*a*) of Figs. 1–3 shows the full measured spectra from the photoabsorption threshold to 250 eV, panel (*b*) shows the spectra from 30–100 eV, and panel (*c*) shows the 86–250 eV energy region. The absolute photoabsorption data below 30 eV are shown, and described, in greater detail in conjunction with the high-resolution results (see section 3.3 below). It is interesting to note from Figs. 1–3 that our measured low-resolution oscillator strength spectra each exhibit essentially the same trend with the sums of calculated (38) and experimental (39) atomic oscillator strengths for the constituent atoms. In particular, the summed atomic oscillator strength data agree quite well with the measured molecular photoabsorption oscillator strength data for the methylamines from 70 eV to the limit of the measured data at 250 eV. However, below 70 eV the summed atomic oscillator strength data (38, 39) are increasingly lower than the present data for all three molecules. Above 170 eV the atomic sums are slightly lower than the measured results.

It has often been assumed (see, for example, ref. 40), that the sums of atomic oscillator strengths are equal to molecular oscillator strengths sufficiently far (≥30 eV) above an atomic *inner-shell* ionization edge. At such photoelectron energies it is assumed that molecular effects, such as shape resonances, have died out and that the ejected electron "sees" mainly an atomic core as it is ionized. However, in the 70–250 eV energy region of the valence-shell photoabsorption spectra of the methylamines the electron is not ejected from an atomic-like (core) orbital, so it is interesting to note that there is generally quite good agreement between the sums of atomic data, and our reported molecular oscillator strengths in this energy region. The fact that the curves cross at ~170 eV, that is, that the atomic oscillator strength sums for each methylamine are higher than the corresponding measured oscillator strengths from 90 to 170 eV, but are slightly lower from 170 to 250 eV, is not surprising since both sets of data should be subject to the same *total* integrated oscillator strength over the entire energy range (from zero to infinity) according to the TRK sum rule. The small differences between the theoretical (38) and experimental (39) summed atomic oscillator strength data from 100 to 240 eV, as seen in panel *c* of Figs. 1–3, are due, at least in part, to errors involved in the digitization of the logarithmic plots reported for the theoretical data (38). The digitization error will compound as the number of carbon atoms increases.

3.3. *High resolution measurements for the methylamines*

The high-resolution (0.048 eV fwhm) absolute photoabsorption spectra of monomethylamine, dimethylamine, and trimethylamine from 4–31 eV are shown on Figs. 4, 5, and 6, respectively. Also shown on the figures are the low-resolution oscillator strength data obtained in the present work (see section 3.2 above). It can be seen that our high- and low-resolution oscillator strength data are in good agreement with each other

Can. J. Chem. Downloaded from www.nrcresearchpress.com by EESC ESCOLA DE ENGENHARIA on 09/08/12
For personal use only.

Can. J. Chem. Downloaded from www.nrcresearchpress.com by EESC ESCOLA DE ENGENHARIA on 09/08/12
For personal use only.

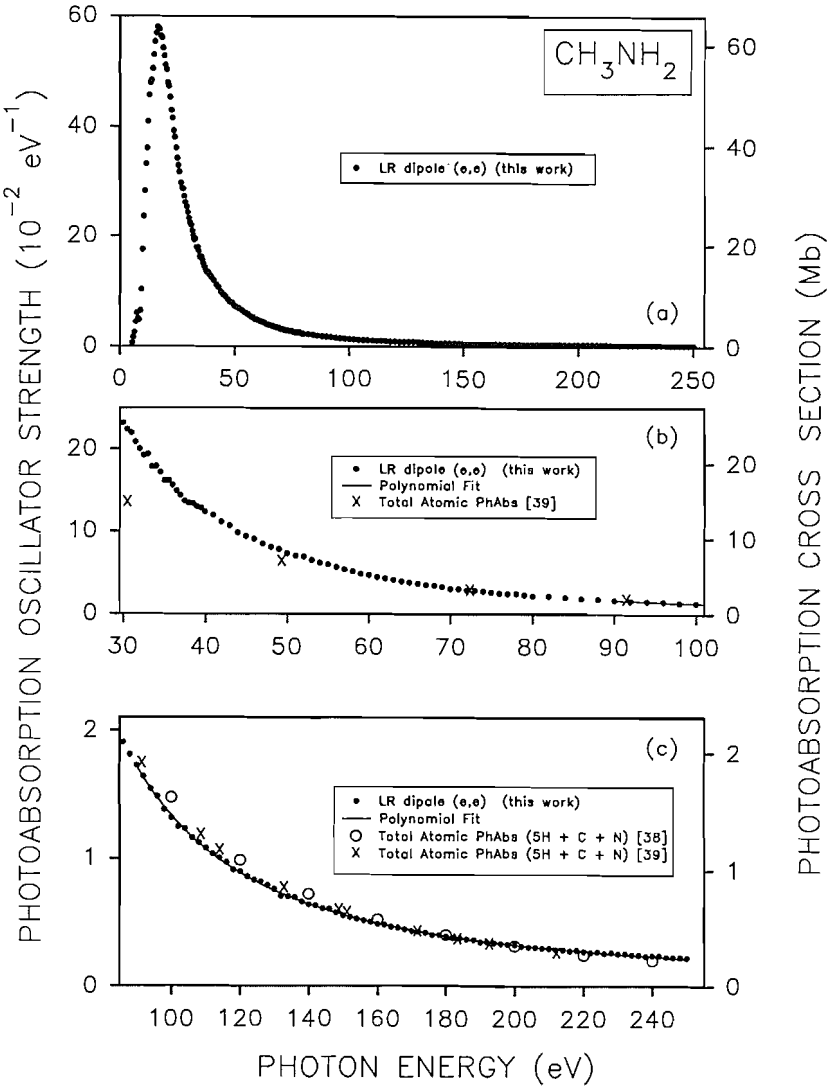

FIG. 1. Absolute oscillator strengths for the photoabsorption of CH_3NH_2 obtained at a resolution of ~1 eV fwhm: (*a*) the entire measured spectrum from 5.5–250 eV; (*b*) 30–100 eV; (*c*) the high-energy valence-shell tail from 86–250 eV. Also shown on (*b*) and (*c*) are the valence-shell polynomial fit (solid line), and the theoretical (38) and experimental (39) summed atomic oscillator strengths for the constituent atoms of CH_3NH_2 (open circles and crosses, respectively).

over the entire range of measurement (4–31 eV). This is an important consistency check on our measurements since the high- and low-resolution dipole (e,e) spectrometers have different Bethe–Born factors owing to their different scattering kinematics and geometries.

Since no *ab initio* calculations of transition energies and oscillator strengths have been reported for the methylamines, definite assignments of the spectra cannot be made. Therefore, in the present work, the transferability of Rydberg term values (41–43) has been used to make tentative assignments for the more prominent features observed in Figs. 4–6. It might be expected that the electronic spectra of the methylamines will be dominated by transitions to Rydberg orbitals from the occupied valence orbitals since this behaviour appears to be the situation for the related molecules CH_4 (44, 45) and NH_3 (44, 46). Transitions which have Rydberg upper states can be characterized by the fact that the observed term values, T, fit into a mathematical progression of the form:

$$[2] \qquad T = \mathrm{VIP} - E = \frac{R}{(n - \delta_l)^2}$$

where E is the measured absorption energy, VIP is the vertical ionization potential of the initial state, R is the Rydberg constant (13.606 eV), n is the principal quantum number, and δ_l is the quantum defect. Electron momentum spectroscopy has demonstrated that the highest occupied molecular orbitals (HOMOs) of the methylamines have a mixed s and p character with the s content increasing with successive methylation (47, 48). Therefore transitions are expected from the HOMO to s, p, and d Rydberg manifolds since atomic selection rule arguments have been found (41–43) to be a helpful guide for interpretation of molecular spectra. On this basis, we have assigned the lowest energy peaks in the spectra as transitions from the respective HOMO orbitals to the $3s$ and $3p$ Rydberg orbitals for each of the methylamines. From these HOMO assignments the energies of the corresponding $3s$ and $3p$ transitions from

Can. J. Chem. Downloaded from www.nrcresearchpress.com by EESC ESCOLA DE ENGENHARIA on 09/08/12
For personal use only.

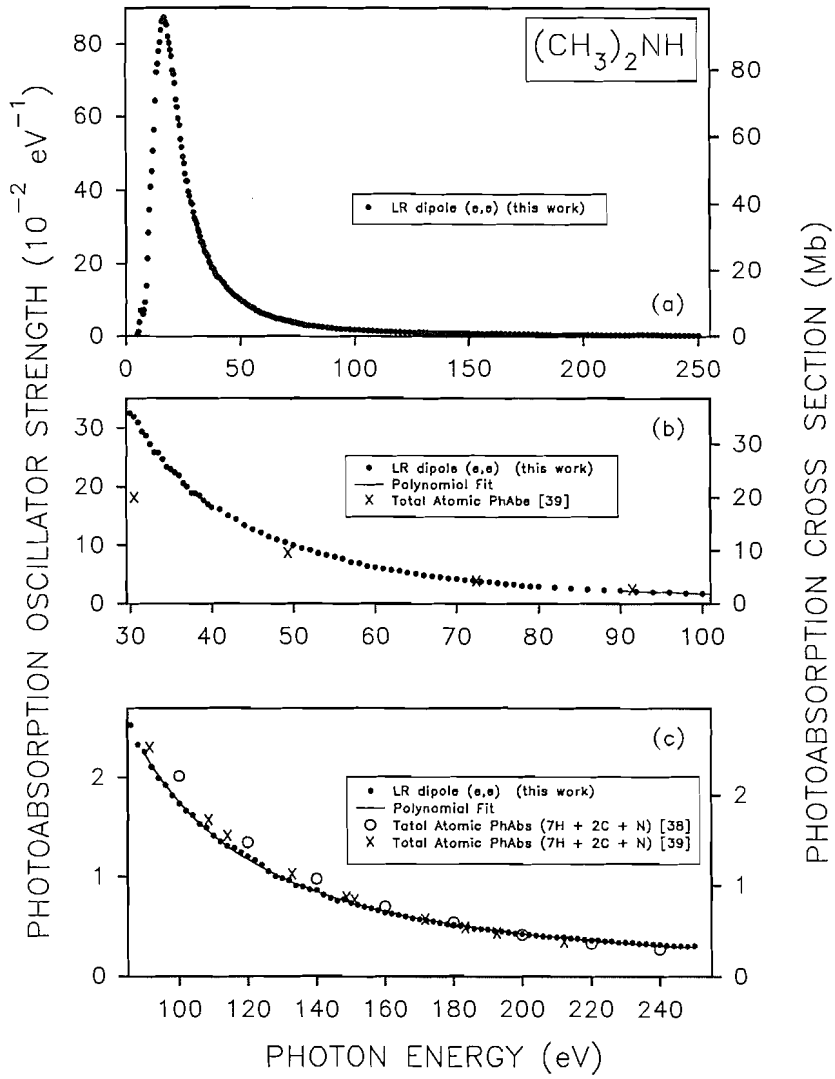

FIG. 2. Absolute oscillator strengths for the photoabsorption of $(CH_3)_2NH$ obtained at a resolution of ~1 eV fwhm: (*a*) the entire measured spectrum from 5.0–250 eV; (*b*) 30–100 eV; (*c*) the high-energy valence-shell tail from 86–250 eV. Also shown on (*b*) and (*c*) are the valence-shell polynomial fit (solid line), and the theoretical (38) and experimental (39) summed atomic oscillator strengths for the constituent atoms of $(CH_3)_2NH$ (open circles and crosses, respectively).

the other occupied molecular orbitals have been calculated assuming transferability of term values, and the resulting manifolds are shown in Figs. 4–6. The VIPs on the manifolds are from photoelectron spectroscopy measurements (31–33). The positions of the 3*d* and 4*s* Rydberg orbitals are degenerate and are each predicted from eq. [2] to have to term value of 1.51 eV, which assumes quantum defects of 1 and 0 for the *s* and *d* Rydberg orbitals, respectively (49). It can be seen from Figs. 4–6 that the excitation spectra of the methylamines correspond quite closely to a superposition of peaks due to the predicted transitions to Rydberg orbitals. The assignments suggested by the transferability of Rydberg term values, as shown in Figs. 4–6, are summarized in Tables 5, 6, and 7, for monomethylamine, dimethylamine, and trimethylamine, respectively. For each observed transition the term value (Tables 5–7) was calculated from the measured peak energy and the ionization potential of the initial state. Then, as a consistency check on each assignment, the denominator of the right-hand side of eq. [2] was evaluated for each term value and the predicted principal quantum number, and the predicted character of the final Rydberg state were considered to be confirmed if the quantum defect was in the range $0.8 \leq \delta_l \leq 1.3$ for *s* Rydberg orbitals, $0.4 \leq \delta_l \leq 0.8$ for *p* Rydberg orbitals, and $0.0 \leq \delta_l \leq 0.2$ for *d* Rydberg orbitals (49). As a result of this analysis and with the above assumptions, it is found that all of the major observed spectral features in the valence-shell photoabsorption spectra of the methylamines can be assigned using this Rydberg orbital scheme. The resulting Rydberg term values show good agreement with those for the corresponding transitions in the carbon and nitrogen K-shell inner-shell electron energy-loss (ISEELS) spectra of the methylamines reported earlier from this laboratory by Wight and Brion (44), and by Sodhi and Brion (46). Such transferability between inner shell and valence shell spectra is to be expected for Rydberg transitions (41–43).

The low energy portions of the valence-shell spectra of the

Can. J. Chem. Downloaded from www.nrcresearchpress.com by EESC ESCOLA DE ENGENHARIA on 09/08/12
For personal use only.

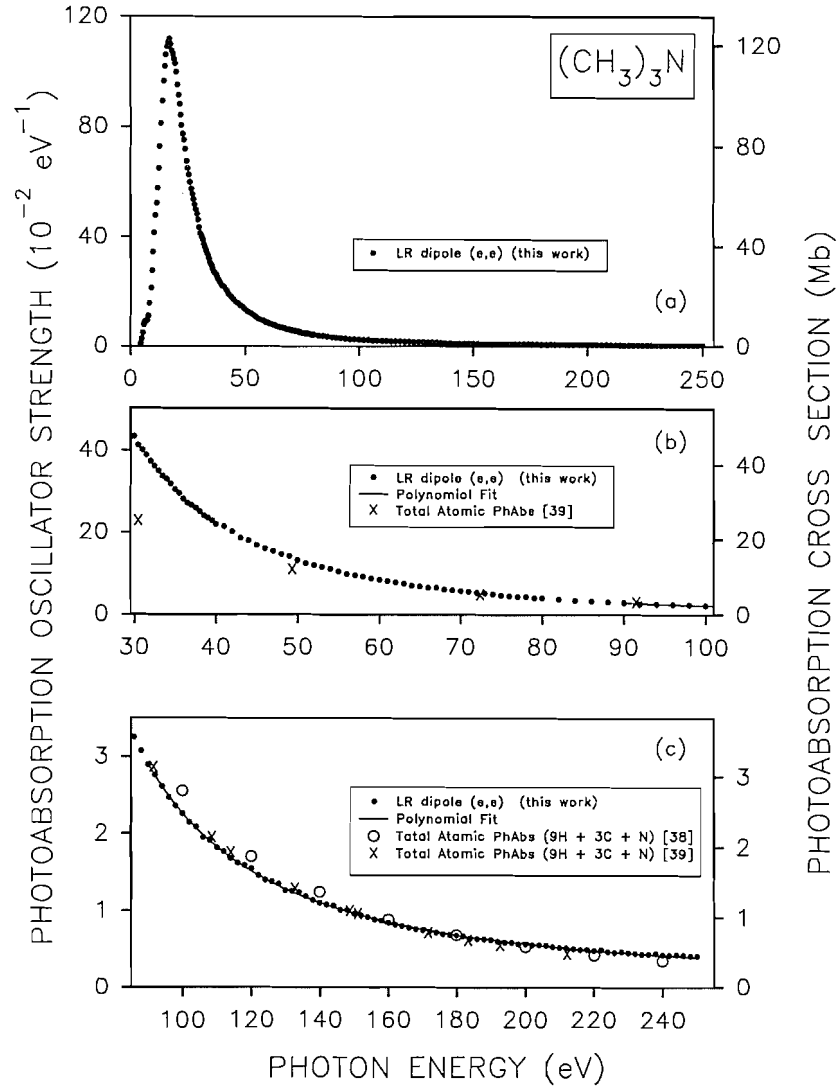

FIG. 3. Absolute oscillator strengths for the photoabsorption of $(CH_3)_3N$ obtained at a resolution of ~1 eV fwhm: (*a*) the entire measured spectrum from 4.5–250 eV; (*b*) 30–100 eV; (*c*) the high-energy valence-shell tail from 86–250 eV. Also shown on (*b*) and (*c*) are the valence-shell polynomial fit (solid line), and the theoretical (38) and experimental (39) summed atomic oscillator strengths for the constituent atoms of $(CH_3)_2N$ (open circles and crosses, respectively).

methylamines from 4–10 eV are shown in Fig. 7. In addition to the 3*s*, 3*p*, and the degenerate 3*d*, 4*s* assignments discussed above, the predicted positions of the 4*p* and 5*p* Rydberg orbitals are also shown. It can be seen that there is good correspondence between all the predicted Rydberg transition energies and the various structures in the oscillator strength data. Also shown are the previously reported and limited range photoabsorption data of Grosjean and Bletzinger (7), Tannenbaum et al. (14), and Bertrand et al. (15). It can be seen from the figure that the data reported by Tannenbaum et al. (14) are marginally higher, and have a slightly different shape than the present work for all three of the methylamines. The photoabsorption oscillator strength values reported by Bertrand et al. (15) at 123.6 nm (10.03 eV) are ~10% and ~20% higher than the present work for monomethylamine and dimethylamine, respectively. The data reported by Grosjean and Bletzinger (7) for trimethylamine agree well with the present results from 8.1–9.0 eV, but are lower above 9.0 eV to the limit of their data at 10.4 eV. In higher resolution optical work Tannenbaum et al. (14) observed vibrational progressions in the $3s \leftarrow 7a'$ and $3p \leftarrow 7a'$ transitions in monomethylamine, and in the $3p \leftarrow 8a'$ transition in dimethylamine. Evidence for these vibrational progressions in the $3p \leftarrow 7a'$ transition of monomethylamine and in the $3p \leftarrow 8a'$ transition of dimethylamine can be seen in the presently reported, somewhat lower resolution, spectra.

4. Computational methods for dipole oscillator strength distributions and related properties

The dipole oscillator strength distribution (DOSD) for a molecule is given by the molecular differential dipole oscillator strength, (df/dE), as a function of photon energy E, from the electronic photoabsorption threshold, E_0, to very high energy. Many important molecular dipole properties (50–52) can be evaluated if the DOSD for the given molecule is available. Those of particular interest for this paper include the dipole oscillator strength sums S_k, the analogous logarithmic dipole sums L_k, and the related mean excitation energies I_k, defined

TABLE 2. Oscillator strengths for the total photoabsorption of monomethylamine from 5.5 to 250.0 eV

Energy (eV)	Oscillator strength[a] 10^{-2} (eV^{-1})	Energy (eV)	Oscillator strength[a] 10^{-2} (eV^{-1})	Energy (eV)	Oscillator strength[a] 10^{-2} (eV^{-1})	Energy (eV)	Oscillator strength[a] 10^{-2} (eV^{-1})
5.5	0.57	23.5	39.20	52.0	6.85	120.0	0.90
6.0	1.57	24.0	38.01	53.0	6.49	125.0	0.82
6.5	2.51	24.5	36.04	54.0	6.17	130.0	0.76
7.0	4.47	25.0	34.20	55.0	5.95	135.0	0.70
7.5	5.96	25.5	32.86	56.0	5.67	140.0	0.64
8.0	4.95	26.0	31.70	57.0	5.36	145.0	0.60
8.5	4.79	26.5	29.67	58.0	5.15	150.0	0.55
9.0	6.45	27.0	28.76	59.0	4.85	160.0	0.48
9.5	10.26	27.5	28.56	60.0	4.73	170.0	0.43
10.0	17.53	28.0	27.18	61.0	4.52	180.0	0.39
10.5	23.61	28.5	26.10	62.0	4.37	190.0	0.35
11.0	28.25	29.0	25.35	63.0	4.18	200.0	0.32
11.5	33.26	29.5	24.31	64.0	3.98	210.0	0.30
12.0	36.10	30.0	23.22	65.0	3.85	220.0	0.27
12.5	40.91	30.5	22.40	66.0	3.73	230.0	0.25
13.0	45.66	31.0	21.97	67.0	3.54	240.0	0.24
13.5	47.88	32.0	19.98	68.0	3.45	250.0	0.22
14.0	48.33	33.0	19.35	69.0	3.33		
14.5	50.54	34.0	17.87	70.0	3.09		
15.0	53.00	35.0	16.13	71.0	3.08		
15.5	55.34	36.0	15.59	72.0	2.89		
16.0	56.88	37.0	14.35	73.0	2.87		
16.5	58.01	38.0	13.40	74.0	2.76		
17.0	57.72	39.0	13.00	75.0	2.64		
17.5	57.61	40.0	12.34	76.0	2.51		
18.0	56.35	41.0	11.93	77.0	2.47		
18.5	56.07	42.0	11.12	78.0	2.47		
19.0	54.18	43.0	10.65	79.0	2.31		
19.5	52.78	44.0	9.82	80.0	2.22		
20.0	51.10	45.0	9.37	85.0	1.97		
20.5	50.27	46.0	9.05	90.0	1.72		
21.0	47.83	47.0	8.48	95.0	1.51		
21.5	47.19	48.0	8.04	100.0	1.32		
22.0	45.23	49.0	7.81	105.0	1.20		
22.5	42.85	50.0	7.28	110.0	1.08		
23.0	41.48	51.0	6.99	115.0	0.99		

[a] $\sigma(\text{Mb}) = 1.0975 \times 10^2\ df/dE\ (\text{eV}^{-1})$.

by

$$[3] \qquad S_k = \int_{E_0}^{\infty} \left(\frac{E}{E_H}\right)^k \left(\frac{df}{dE}\right) dE$$

$$[4] \qquad L_k = \int_{E_0}^{\infty} \left(\frac{E}{E_H}\right)^k \left(\frac{df}{dE}\right) \ln(E/E_H) dE$$

$$[5] \qquad I_k = E_H \exp[L_k/S_k]$$

where E_H is the Hartree unit of energy. The index k can take many different values (e.g. $k = 5/2, 2, 1, 0, -1/2, -1, -3/2, -2, -3, -4, \ldots$) and each choice corresponds to a different molecular property with respect to eqs. [3]–[5]. These properties are important in a variety of areas (9–11, 50–54). For example: the straggling (I_1, S_1), the stopping (I_0), and the total (I_{-1}, S_{-1}) inelastic scattering cross sections of fast charged particles in matter, charge densities at nuclei (S_2), Lamb shifts (I_2), moments of the DOSD ($S_{-2}, S_{-4}, S_{-6}, \ldots$) occur in the Cauchy expansion of the molar refractivity of molecules, $S_{-1}, S_{-3}, S_{-3/2}, S_{-2}$, and L_{-2} can be used to obtain estimates for the dipole–dipole dispersion energies between molecules, and accurate values for the dipole properties are of importance in testing *ab initio*, non-empirical, or other methods for evaluating the properties (53, 55–61). Another important property related to molecular DOSDs is the molar refractivity, R_λ, of a dilute molecular gas. R_λ is related to the refractive index, $n(\lambda)$, and the dynamic dipole polarizability, $\alpha(\lambda)$, of the gas at wavelength λ by

$$[6] \qquad R_\lambda = \frac{1}{\rho}\left[\frac{n^2(\lambda)-1}{n^2(\lambda)+2}\right] = \frac{4\pi}{3} N(E_H)^2 a_0^3 \int_{E_0}^{\infty} \frac{(df/dE)}{E^2 - (hc/\lambda)^2} dE = \frac{4\pi}{3} N\alpha(\lambda)$$

where a_0 is the Bohr radius, ρ is the molar density of the gas, h is Planck's constant, N is Avogadro's number, and c is

Can. J. Chem. Downloaded from www.nrcresearchpress.com by EESC ESCOLA DE ENGENHARIA on 09/08/12
For personal use only.

Can. J. Chem. Downloaded from www.nrcresearchpress.com by EESC ESCOLA DE ENGENHARIA on 09/08/12
For personal use only.

TABLE 3. Oscillator strengths for the total photoabsorption of dimethylamine from 5.0 to 250.0 eV

Energy (eV)	Oscillator strength[a] 10^{-2} (eV^{-1})	Energy (eV)	Oscillator strength[a] 10^{-2} (eV^{-1})	Energy (eV)	Oscillator strength[a] 10^{-2} (eV^{-1})	Energy (eV)	Oscillator strength[a] 10^{-2} (eV^{-1})
5.0	0.45	23.0	59.42	52.0	9.22	120.0	1.20
5.5	1.10	23.5	57.60	53.0	8.71	125.0	1.09
6.0	3.82	24.0	53.73	54.0	8.30	130.0	0.99
6.5	7.02	24.5	51.70	55.0	7.97	135.0	0.91
7.0	6.90	25.0	48.89	56.0	7.70	140.0	0.87
7.5	6.00	25.5	47.30	57.0	7.05	145.0	0.78
8.0	7.18	26.0	44.41	58.0	6.89	150.0	0.74
8.5	9.41	26.5	42.44	59.0	6.46	160.0	0.64
9.0	13.99	27.0	42.47	60.0	6.25	170.0	0.57
9.5	21.53	27.5	39.62	61.0	6.05	180.0	0.52
10.0	28.47	28.0	38.42	62.0	5.80	190.0	0.47
10.5	34.64	28.5	36.75	63.0	5.62	200.0	0.43
11.0	40.92	29.0	36.23	64.0	5.31	210.0	0.39
11.5	45.21	29.5	34.09	65.0	5.10	220.0	0.37
12.0	50.68	30.0	32.52	66.0	4.89	230.0	0.34
12.5	56.39	31.0	30.92	67.0	4.74	240.0	0.32
13.0	64.23	32.0	28.72	68.0	4.59	250.0	0.31
13.5	72.26	33.0	25.93	69.0	4.37		
14.0	74.58	34.0	24.79	70.0	4.17		
14.5	77.99	35.0	23.02	71.0	4.05		
15.0	80.45	36.0	22.02	72.0	3.96		
15.5	83.82	37.0	20.08	73.0	3.77		
16.0	86.18	38.0	18.89	74.0	3.68		
16.5	86.71	39.0	17.73	75.0	3.52		
17.0	87.31	40.0	16.49	76.0	3.34		
17.5	86.15	41.0	16.17	77.0	3.33		
18.0	85.24	42.0	15.16	78.0	3.04		
18.5	82.01	43.0	14.50	79.0	2.99		
19.0	80.30	44.0	13.44	80.0	2.93		
19.5	78.40	45.0	12.76	85.0	2.60		
20.0	76.60	46.0	12.26	90.0	2.26		
20.5	72.71	47.0	11.45	95.0	1.96		
21.0	71.54	48.0	10.94	100.0	1.74		
21.5	69.09	49.0	10.58	105.0	1.57		
22.0	64.55	50.0	10.03	110.0	1.41		
22.5	62.58	51.0	9.52	115.0	1.30		

[a]$\sigma(\text{Mb}) = 1.0975 \times 10^2\ df/dE\ (\text{eV}^{-1})$.

the speed of light. The electronic static dipole polarizability is given by $\alpha_d = \alpha(\lambda = \infty) = a_0^3 S_{-2}$.

The constrained least-squares procedure employed to construct the DOSD for a given molecule, from a given initial data base of (df/dE) versus E values, has been discussed in some detail previously (50) and has been applied to a wide variety of atoms and molecules (62). In summary, the excitation energies for the molecule are divided into N_0 energy regions from threshold to very large values of E. The initial differential dipole oscillator strength data for the ith spectral region is modified according to

$$[7] \qquad (df/dE)^i_{\text{mod}} = (1 + a_i)(df/dE)^i_{\text{initial}},\ i = 1, 2, \ldots, N_0$$

such that the total modified DOSD satisfies constraints through the choice of the $\{a_i\}$. The constraints of choice are the molar refractivity, R_λ, for two well-spaced (63–65) λ values, and the TRK sum rule, $S_0 = N$, where N is the number of electrons in the molecule. A DOSD can be constructed for each initial data base for a given molecule. The amount of modification of the initial (df/dE) versus E data that is required to satisfy the constraints can be represented by the standard deviation (STD) defined by

$$[8] \qquad (\text{STD}) = \left[\sum_{i=1}^{N_0} (a_i - \bar{a})^2 / N_0\right]^{\frac{1}{2}}$$

where $\bar{a}$ is the mean of the a_i values.

Each adopted DOSD is represented by a set of data points, E_l and $(df/dE)_l$, for $l = 1, 2, \ldots, N_p \gg N_0$, and a set of interpolating functions to connect the points. For very high photon energies, i.e. $E \geq 10^9$ eV, the (df/dE) are represented by the Born dipole formula (66), $AE^{-3.5}$. The dipole properties represented in eqs. [3]–[6] are readily evaluated using this representation of the DOSDs (50).

5. Dipole oscillator strength distributions and properties for the methylamines

5.1. General considerations

The experimental dipole oscillator strengths used to construct the DOSDs for the methylamines are our low- and high-

TABLE 4. Oscillator strengths for the total photoabsorption of trimethylamine from 4.5 to 250.0 eV

Energy (eV)	Oscillator strength[a] 10^{-2} (eV^{-1})	Energy (eV)	Oscillator strength[a] 10^{-2} (eV^{-1})	Energy (eV)	Oscillator strength[a] 10^{-2} (eV^{-1})	Energy (eV)	Oscillator strength[a] 10^{-2} (eV^{-1})
4.5	1.08	22.5	80.50	51.0	12.42	115.0	1.65
5.0	2.70	23.0	77.31	52.0	11.95	120.0	1.54
5.5	4.82	23.5	75.11	53.0	11.46	125.0	1.39
6.0	7.72	24.0	71.85	54.0	11.03	130.0	1.26
6.5	8.96	24.5	67.46	55.0	10.35	135.0	1.21
7.0	9.00	25.0	64.94	56.0	9.79	140.0	1.10
7.5	9.40	25.5	62.70	57.0	9.49	145.0	1.03
8.0	10.90	26.0	59.99	58.0	9.10	150.0	0.95
8.5	15.48	26.5	57.57	59.0	8.70	160.0	0.84
9.0	21.22	27.0	55.64	60.0	8.36	170.0	0.75
9.5	27.51	27.5	53.67	61.0	8.13	180.0	0.68
10.0	34.47	28.0	51.82	62.0	7.75	190.0	0.62
10.5	41.53	28.5	50.02	63.0	7.51	200.0	0.57
11.0	47.80	29.0	48.35	64.0	7.10	210.0	0.52
11.5	52.34	29.5	46.17	65.0	6.85	220.0	0.48
12.0	57.74	30.0	43.32	66.6	6.61	230.0	0.45
12.5	64.95	31.0	40.06	67.0	6.48	240.0	0.42
13.0	72.85	32.0	37.28	68.0	6.10	250.0	0.41
13.5	80.98	33.0	34.87	69.0	5.91		
14.0	89.14	34.0	32.87	70.0	5.78		
14.5	96.27	35.0	30.27	71.0	5.62		
15.0	101.81	36.0	28.05	72.0	5.34		
15.5	106.03	37.0	26.46	73.0	5.17		
16.0	108.80	38.0	24.93	74.0	4.94		
16.5	110.49	39.0	23.40	75.0	4.60		
17.0	111.61	40.0	21.79	76.0	4.54		
17.5	109.68	41.0	21.29	77.0	4.45		
18.0	107.29	42.0	20.07	78.0	4.35		
18.5	106.20	43.0	18.61	79.0	4.11		
19.0	104.36	44.0	17.77	80.0	4.04		
19.5	102.67	45.0	16.85	85.0	3.39		
20.0	99.60	46.0	15.96	90.0	2.90		
20.5	95.05	47.0	15.30	95.0	2.54		
21.0	91.39	48.0	14.55	100.0	2.26		
21.5	88.04	49.0	14.05	105.0	2.02		
22.0	84.09	50.0	13.10	110.0	1.82		

[a] $\sigma(\text{Mb}) = 1.0975 \times 10^2\ df/dE\ (\text{eV}^{-1})$.

resolution data reported in sections 3.2 and 3.3, respectively. Previous DOS data (see section 1), which are sparse as a function of E and limited to $E < 10.8$ eV, are not considered in the constrained DOSD analysis that follows. The input data are augmented, particularly for $E \geq 250$ eV, by the mixture rules

$$[9] \quad \frac{df}{dE}((CH_3)_nNH_{3-n} = \frac{df}{dE}(NH_3) + \frac{df}{dE}(C_{n+1}H_{2n+4}) - \frac{df}{dE}(CH_4),\ n = 1, 2, 3$$

$$[10] \quad \frac{df}{dE}((CH_3)_nNH_{3-n}) = \frac{df}{dE}(NH_3) + \frac{df}{dE}(CH_4) - \frac{df}{dE}(H_2),\ n = 1$$

$$= \frac{df}{dE}(CH_3NH_2) + (n-1)\left[\frac{df}{dE}(CH_4) - \frac{df}{dE}(H_2)\right],\ n = 2, 3$$

The input for these mixture rules are the recommended DOSD for NH_3 obtained from Burton et al. (12) and the recommended DOSDs for $C_{n+1}H_{2n+4}$, $n = 1, 2, 3$, CH_4, and H_2 developed by Jhanwar et al. (63), Thomas and Meath (67), and Zeiss et al. (50), respectively.

DOSDs for each methylamine have been constructed by considering the following combinations of DOS data:

DOSD1: E_0–E_f^{HR} (high-resolution data); E_f^{HR}–250.0 eV (low-resolution data); >250 eV (mixture rule [9]). The electronic absorption thresholds (E_0) and the upper energy limit of the high-resolution measurements (E_f^{HR}) are E_0 = 5.083, 4.962, and 4.711 eV and E_f^{HR} = 30.15, 31.26, and 30.96 eV for CH_3NH_2, $(CH_3)_2NH$, and $(CH_3)_3N$, respectively.
DOSD2: As in DOSD1 except the high-resolution data is replaced by the low-resolution data from $E_0 - E_f^{HR}$.
DOSD3: As in DOSD1 except mixture rule [9] is replaced by mixture rule [10].
DOSD4: As in DOSD2 except mixture rule [9] is replaced by mixture rule [10].

The photon energies in each case were divided into N_0 = 24

Can. J. Chem. Downloaded from www.nrcresearchpress.com by EESC ESCOLA DE ENGENHARIA on 09/08/12
For personal use only.

Can. J. Chem. Downloaded from www.nrcresearchpress.com by EESC ESCOLA DE ENGENHARIA on 09/08/12
For personal use only.

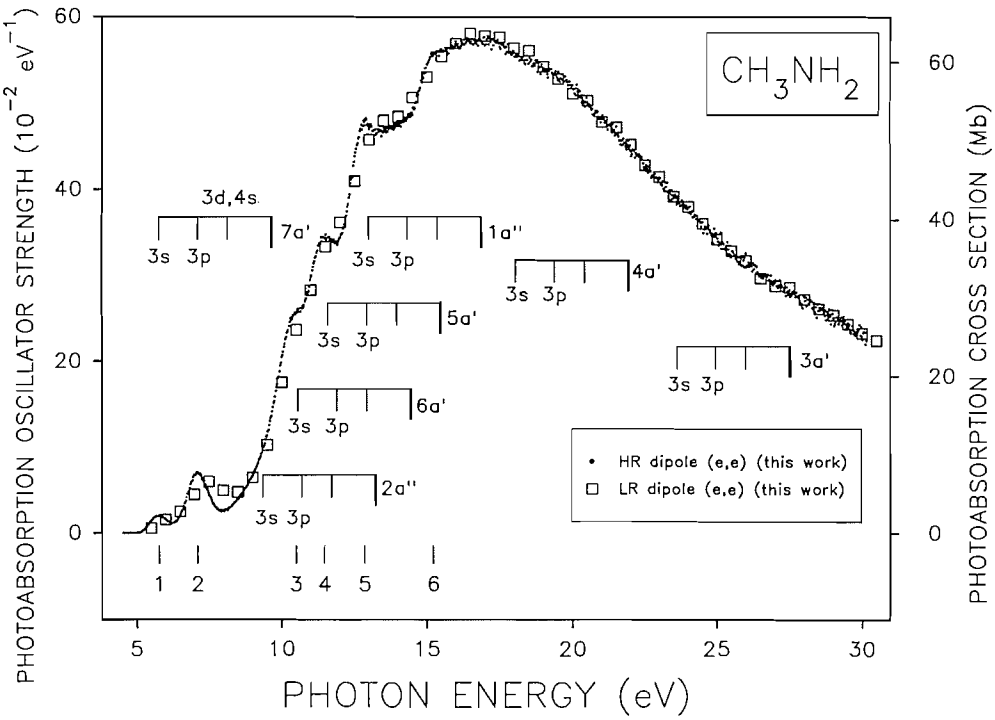

FIG. 4. Comparison of the experimental high- and low-resolution (0.048 eV fwhm and ~1 eV fwhm, respectively) absolute oscillator strength spectra for the photoabsorption of CH_3NH_2. The numbered vertical lines indicate the positions of the observed spectral features—see Table 5. For each ion state the vertical ionization potential (heavy solid vertical line) is shown along with the positions (vertical lines) of the 3*s* and 3*p* Rydberg transitions as predicted using the same term values as for the lowest energy transitions (labelled 1 and 2) in the spectrum. The positions of the 3*d*,4*s* Rydberg transitions have been predicted using eq. [2]. The manifolds assume transferability of Rydberg term values (see text for details).

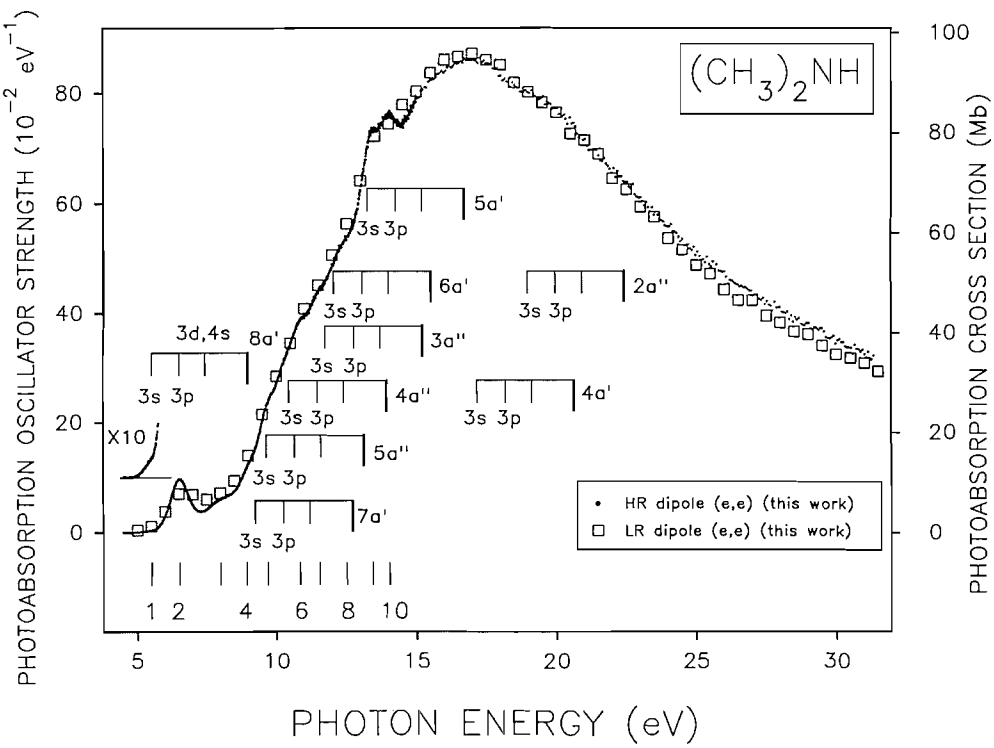

FIG. 5. Comparison of the experimental high- and low-resolution (0.048 eV fwhm and ~1 eV fwhm, respectively) absolute oscillator strength spectra for the photoabsorption of $(CH_3)_2NH$. The numbered vertical lines indicate the positions of the observed spectral features—see Table 6. For each ion state the vertical ionization potential (heavy solid vertical line) is shown along with the positions (vertical lines) of the 3*s* and 3*p* Rydberg transitions as predicted using the same term values as for the lowest energy transitions (labelled 1 and 2) in the spectrum. The positions of the 3*d*,4*s* Rydberg transitions have been predicted using eq. [2]. The manifolds assume transferability of Rydberg term values (see text for details).

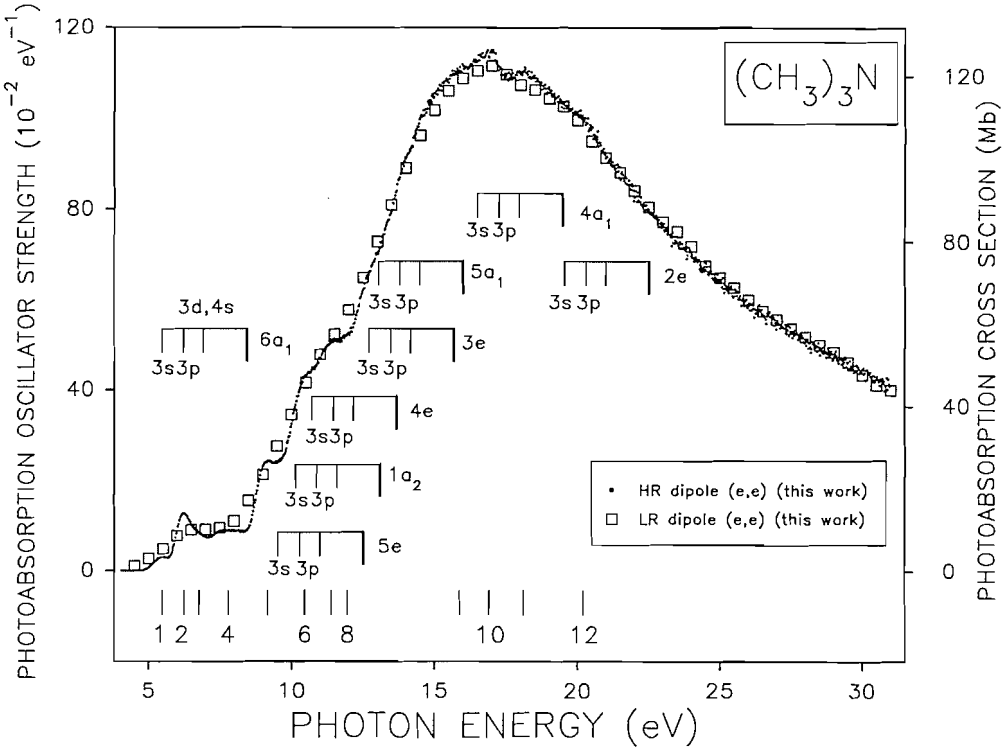

FIG. 6. Comparison of the experimental high- and low-resolution (0.048 eV fwhm and ~1 eV fwhm, respectively) absolute oscillator strength spectra for the photoabsorption of $(CH_3)_3N$. The numbered vertical lines indicate the positions of the observed spectral features—see Table 7. For each ion state the vertical ionization potential (heavy solid vertical line) is shown along with the positions (vertical lines) of the 3*s* and 3*p* Rydberg transitions as predicted using the same term values as for the lowest energy transitions (labelled 1 and 2) in the spectrum. The positions of the 3*d*,4*s* Rydberg transitions have been predicted using eq. [2]. The manifolds assume transferability of Rydberg term values (see text for details).

TABLE 5. Energies, term values, and proposed spectral assignments for the observed photoabsorption peaks in the high-resolution spectrum of monomethylamine

Peak	Photon energy (eV)	Term value (eV)					Proposed assignment final orbital				
		7*a*′	2*a*″	6*a*′	5*a*′	1*a*″	7*a*′	2*a*″	6*a*′	5*a*′	1*a*″
1	5.77	3.87	—	—	—	—	3*s*	—	—	—	—
2	7.10	2.54	—	—	—	—	3*p*	—	—	—	—
3	10.50	—	2.72	3.92	—	—	—	3*p*	3*s*	—	—
4	11.48	—	—	2.94	3.97	—	—	—	3*p*	3*s*	—
5	12.86	—	—	1.56	2.59	3.99	—	—	3*d*, 4*s*	3*p*	3*s*
6	15.2	—	—	—	—	1.6	—	—	—	—	3*d*, 4*s*
VIP (eV)[a]		9.64	13.22	14.22	15.45	16.85					

[a]From the PES measurements of Potts et al. (31) and Katsumata et al. (32).

energy intervals as suggested by the structure in the input DOS data. The four initial DOSDs were each modified, for each molecule, using the constrained least squares approach outlined in section 4, to satisfy $S_0 = N$ and molar refractivity constraints which depend on the particular molecule considered (see what follows).

5.2. Monomethylamine

The molar refractivity constraints used are the values of R_λ for λ = 6440.24 Å and 4359.56 Å, obtained from the refractive index measurements of Ramaswamy (68). The STDs for the four resulting DOSD*i*s are 2.17, 2.59, 2.18, and 2.57 for $i = 1, 2, 3$, and 4, respectively. These results indicate that there is little to choose between the two mixture rules and that the high-resolution DOS data is more reliable for low E than the low-resolution data, as expected.

The integrated oscillator strengths for the constrained DOSD1, together with those corresponding to the initial DOS data for DOSD1, are given in Table 8. Generally the integrated oscillator strengths obtained from the initial high- and low-resolution measurements agree with each other, and with the constrained results, to within the estimated experimental errors of about ±5%. All exceptions are marginal except in the case of the low-resolution result for 10–11.8 eV which disagrees with the constrained integrated oscillator strength by ~12%. It should be pointed out that the integrated oscillator strengths obtained from the initial high- and low-resolution DOS data may be expected to differ in the discrete excitation

Can. J. Chem. Downloaded from www.nrcresearchpress.com by EESC ESCOLA DE ENGENHARIA on 09/08/12
For personal use only.

TABLE 6. Energies, term values, and proposed spectral assignments for the observed photoabsorption peaks in the high-resolution spectrum of dimethylamine

Peak	Photon energy (eV)	Term value (eV)							Proposed assignment final orbital						
		8a′	7a′	5a″	4a″	3a″	6a′	5a′	8a′	7a′	5a″	4a″	3a″	6a′	5a′
1	5.52	3.45	—	—	—	—	—	—	3*s*	—	—	—	—	—	—
2	6.52	2.45	—	—	—	—	—	—	3*p*	—	—	—	—	—	—
3	8.0	1.0	—	—	—	—	—	—	4*p*, 5*p*	—	—	—	—	—	—
4	9.0	—	3.7	—	—	—	—	—	—	3*s*	—	—	—	—	—
5	9.7	—	3.0	3.4	—	—	—	—	—	3*p*	3*s*	—	—	—	—
6	10.9	—	—	2.2	3.0	—	—	—	—	—	3*p*	3*s*	—	—	—
7	11.5	—	—	1.6	2.4	3.7	—	—	—	—	3*d*, 4*s*	3*p*	3*s*	—	—
8	12.5	—	—	—	—	2.7	3.0	—	—	—	—	—	3*p*	3*s*	—
9	13.41	—	—	—	—	—	2.1	3.28	—	—	—	—	—	3*p*	3*s*
10	14.02	—	—	—	—	—	1.5	2.67	—	—	—	—	—	3*d*, 4*s*	3*p*
VIP (eV)[a]		8.97	12.70	13.09	13.9	15.19	15.5	16.69							

[a]From the PES measurements of Potts *et al.* (31) and Kimura and Osafune (33).

TABLE 7. Energies, term values, and proposed spectral assignments for the observed photoabsorption peaks in the high-resolution spectrum of trimethylamine

Peak	Photon energy (eV)	Term value (eV)						Proposed assignment final orbital					
		$6a_1$	5*e*	$1a_2$	4*e*	$4a_1$	2*e*	$6a_1$	5*e*	$1a_2$	4*e*	$4a_1$	2*e*
1	5.48	2.96	—	—	—	—	—	3*s*	—	—	—	—	—
2	6.23	2.21	—	—	—	—	—	3*p*	—	—	—	—	—
3	6.8	1.6	—	—	—	—	—	3*d*, 4*s*	—	—	—	—	—
4	7.8	0.6	—	—	—	—	—	4*p*, 5*p*	—	—	—	—	—
5	9.18	—	3.32	—	—	—	—	—	3*s*	—	—	—	—
6	10.46	—	2.00	2.6	3.21	—	—	—	3*p*	3*p*	3*s*	—	—
7	11.39	—	—	1.7	2.28	—	—	—	—	3*d*, 4*s*	3*p*	—	—
8	12.0	—	—	1.1	1.7	—	—	—	—	4*p*	3*d*, 4*s*	—	—
9	15.9	—	—	—	—	3.6	—	—	—	—	—	3*s*	—
10	16.90	—	—	—	—	2.56	—	—	—	—	—	3*p*	—
11	18.10	—	—	—	—	1.36	—	—	—	—	—	3*d*, 4*s*	—
12	20.2	—	—	—	—	—	2.3	—	—	—	—	—	3*p*
VIP (eV)[a]		8.44	12.5[b]	13.1	13.67	19.46	22.5						

[a]From the PES measurements of Pots et al. (31) and Kimura and Osafune (33).
[b]Average of the energies of the two components of the 5*e* state (33).

energy region since the fine structure in the DOSs is less well resolved in the low-resolution measurements (12).

The dipole properties evaluated using constrained DOSD*i*, $i = 1$–4, differ little from each other, particularly for DOSD1 and DOSD3. Nominally the results obtained from constrained DOSD1 are chosen as recommended values since they are derived using spectroscopically more reliable input data (DOSD1 also has, marginally with respect to DOSD3, the smallest STD of the four constrained DOSDs for monomethylamine). The recommended dipole properties S_k, L_k, and I_k for CH_3NH_2 are given in Table 9. Results for the molar refractivities of CH_3NH_2, evaluated using the constrained DOSD1, are listed in Table 10 which also contains the available experimental data for R_λ. The agreement with experiment is precise for the three values of R_λ not used as constraints; for most values of λ the results of Table 10 augment the (sparse) experimental data for R_λ as a function of λ.

It is interesting to note that our value of $S_{-2} = 26.50$ (Table 9) is ~0.15% higher than the value obtained by Ramaswamy (68) by fitting the relation $(n(\lambda) - 1) = A/(B - \lambda^{-2})$ to his refractive index data. The value of $(n(\lambda)-1)$ at $\lambda = 6440.24$ Å generated by this relation is ~0.1% lower than the measured value and therefore the extrapolated value for $\lambda = \infty$ (which yields S_{-2}) is also expected to be low in support of our recommended result for S_{-2}. The value of $S_{-2} = 26.75$ due to Wolf (69), obtained from dielectric constant measurements, is ~0.9% higher than our recommended value.

Table 9 also contains the values of the dipole properties S_k, L_k, and I_k obtained from the initial DOSD1 that lead to our constrained DOSD1 for methylamine. The results for the dipole and logarithmic dipole sums obtained from the initial DOSD are smaller in magnitude than the recommended values for all k (for example S_0 and S_{-2} are ~3% and ~4.5% lower). This is in agreement with the generally low, relative to the constrained integrated DOSs, initial DOS values used to construct the constrained DOSD.

There are apparently no *ab initio* calculations for the properties of CH_3NH_2. Metzger and Rhee (70), using a complete neglect of differential overlap/finite perturbation plus polarization approach, obtained $S_{-2} = 26.93$ which is ~1.6% higher than our recommended result. A value of $S_{-2} = 25.10$, about 5.6% lower than our value, has been calculated by Kaur et al.

Can. J. Chem. Downloaded from www.nrcresearchpress.com by EESC ESCOLA DE ENGENHARIA on 09/08/12
For personal use only.

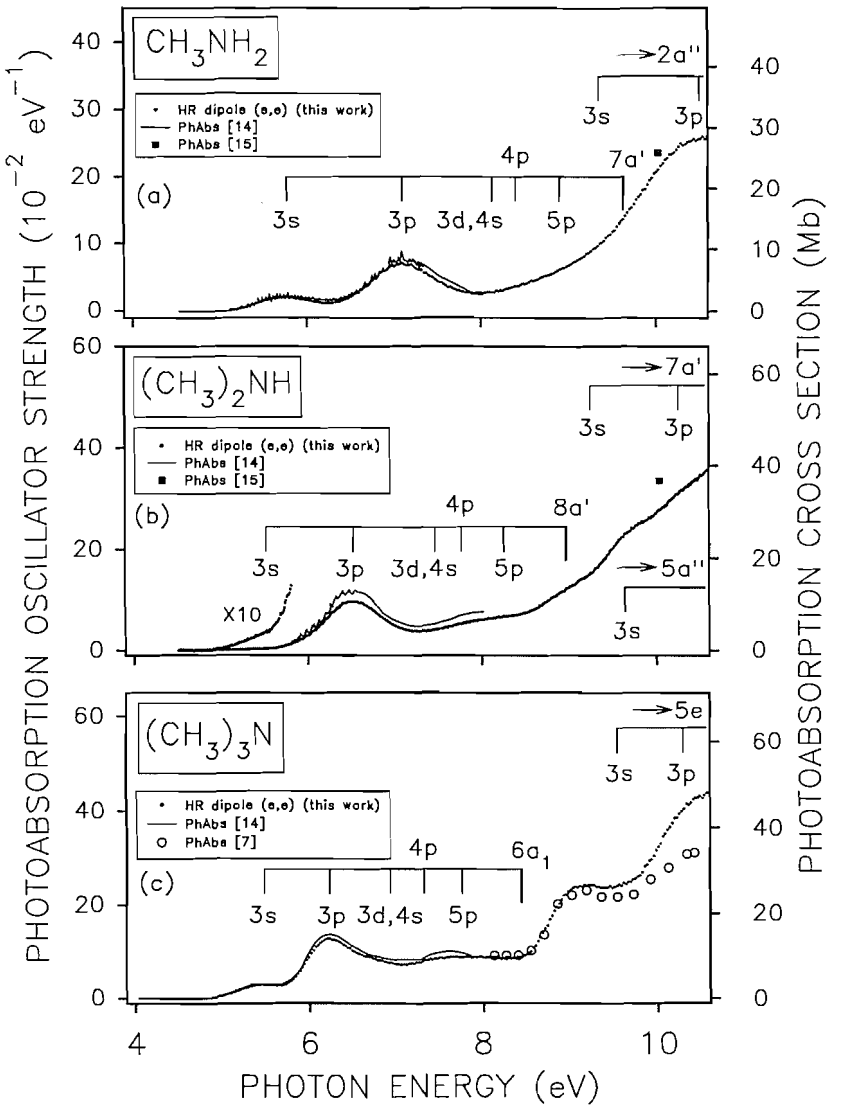

FIG. 7. High-resolution (0.048 eV fwhm) absolute oscillator strengths for photoabsorption of the methylamines in the low-energy valence-shell region from 4–10 eV: (*a*) monomethylamine; (*b*) dimethylamine; (*c*) trimethylamine. Also shown on the figures are previously reported absolute photoabsorption oscillator strength measurements (14, 15, 7). The Rydberg manifolds are as in Figs. 4–6 and Tables 5–7 with the addition of the predicted positions of the 4*p* and 5*p* Rydberg transitions (see text for details).

(71) using a double perturbation theory approach, developed by Amos and Yoffe (72), and a non-local pseudo-potential floating spherical gaussian model.

5.3. Dimethylamine and trimethylamine

There are no refractive index measurements for these molecules. Wolf (69) obtained a value of $S_{-2} = 39.06$ for $(CH_3)_2NH$ from dielectric constant measurements. For NH_3 and CH_3NH_2 his results for S_{-2} are ~1% higher than the recommended values evaluated from the constrained DOSDs for these molecules ((12) and section 5.2). Therefore, Wolf's S_{-2} value is not used as a constraint for constructing the DOSD for $(CH_3)_2NH$; there is no analogous result for $(CH_3)_3N$. For dimethylamine and trimethylamine the refractivity constraints are developed as outlined below.

The unmodified DOSD1 for CH_3NH_2 yields $R_{\lambda_1} = 9.6713$ and $R_{\lambda_2} = 9.9389$ cm^3 mol^{-1} for the values of λ, $\lambda_1 = 6440.24$ and $\lambda_2 = 4359.56$ Å, associated with the accurate values of R_λ, 10.1216 and 10.4032 cm^3 mol^{-1}, used as constraints in the construction of constrained DOSD1 for monomethylamine. These results yield ratios

$$[11] \quad \begin{cases} r_{\lambda_1} = R_{\lambda_1}(\text{accurate})/R_{\lambda_1}(\text{unmodified DOSD1}) \\ \qquad = 1.0466 \\ r_{\lambda_2} = R_{\lambda_2}(\text{accurate})/R_{\lambda_2}(\text{unmodified DOSD1}) \\ \qquad = 1.0467 \end{cases}$$

The experimental oscillator strengths for all three amines are measured using the same techniques and the refractivity constraints are completely dominated by the DOS data for $E \leq 150$ eV. Assuming that the experimental errors in the three sets of input data used to construct the DOSDs for the three molecules are essentially the same as a function of E, we assume that the ratios [11] apply to $(CH_3)_2NH$ and $(CH_3)_3N$ as well as CH_3NH_2. The molar refractivity constraints for dimethylamine and trimethylamine are therefore chosen to be the values evaluated using unmodified DOSD1 and λ_1 and λ_2 scaled by the ratios given by [11], namely $R_{\lambda_1} = 14.7845$ and

Can. J. Chem. Downloaded from www.nrcresearchpress.com by EESC ESCOLA DE ENGENHARIA on 09/08/12
For personal use only.

Can. J. Chem. Downloaded from www.nrcresearchpress.com by EESC ESCOLA DE ENGENHARIA on 09/08/12
For personal use only.

TABLE 8. Integrated dipole oscillator strengths for CH_3NH_2[a]

Energy region (eV)	Constrained values: DOSD1	High-resolution data	Low-resolution data	Mixture rule	
				Equation [9]	Equation [10]
5.083–6.261	1.560(−2)	1.513(−2)	1.460(−2)		
6.261–8.059	7.829(−2)	7.406(−2)	7.918(−2)		
8.059–10.00	1.708(−1)	1.640(−1)	1.608(−1)		
10.00–11.80	5.563(−1)	5.204(−1)	4.887(−1)		
11.80–14.00	1.029(0)	9.617(−1)	9.544(−1)		
14.00–16.00	1.109(0)	1.059(0)	1.057(0)		
16.00–18.00	1.178(0)	1.136(0)	1.150(0)		
18.00–20.00	1.106(0)	1.077(0)	1.084(0)		
20.00–25.00	2.230(0)	2.143(0)	2.154(0)		
25.00–30.15	1.477(0)	1.445(0)	1.451(0)		
30.15–40.00	1.690(0)		1.654(0)	1.686(0)	1.909(0)
40.00–50.00	9.721(−1)		9.608(−1)	9.823(−1)	9.817(−1)
50.00–70.00	9.947(−1)		9.832(−1)	1.013(0)	1.011(0)
70.00–100.0	6.201(−1)		6.157(−1)	6.579(−1)	6.557(−1)
100.0–150.0	4.319(−1)		4.298(−1)	4.579(−1)	4.293(−1)
150.0–200.0	2.099(−1)		2.094(−1)	2.110(−1)	2.097(−1)
200.0–250.0	1.328(−1)		1.326(−1)	1.098(−1)	1.102(−1)
250.0–283.8	4.816(−2)			4.808(−2)	4.874(−2)
283.8–400.0	7.892(−1)			7.687(−1)	8.306(−1)
400.0–425.0	3.694(−1)			3.663(−1)	3.609(−1)
425.0–1000.0	2.191(0)			2.090(0)	2.007(0)
1000.0–10^4	5.955(−1)			5.915(−1)	5.779(−1)
10^4–10^6	5.216(−3)			5.216(−3)	4.894(−3)
10^6–∞	8.555(−8)			8.555(−8)	8.556(−8)

[a]This table contains the integrated oscillator strengths resulting from constrained DOSD1 and from the unmodified experimental or mixture rule data considered in this work.

TABLE 9. The dipole sums S_k, logarithmic dipole sums L_k, and mean excitation energies I_k, for various values of k, for CH_3NH_2 calculated using the initial and constrained DOSD1; the values obtained from the constrained DOSD are recommended

Property	Initial DOSD1	Constrained DOSD1	Property	Initial DOSD1	Constrained DOSD1
S_2	9.583(3)	9.668(3)	S_{-12}	3.120(6)	3.243(6)
S_1	1.240(2)	1.272(2)			
S_0	1.745(1)	1.800(1)			
$S_{-1/2}$	1.508(1)	1.562(1)	L_2	5.864(4)	5.895(4)
S_{-1}	1.641(1)	1.706(1)	L_1	3.960(2)	4.052(2)
$S_{-3/2}$	1.977(1)	2.063(1)	L_0	1.208(1)	1.233(1)
S_{-2}	2.532(1)	2.650(1)	L_{-1}	−4.807(0)	−5.127(0)
$S_{-5/2}$	3.403(1)	3.569(1)	L_{-2}	−1.382(1)	−1.459(1)
S_{-3}	4.772(1)	5.014(1)			
S_{-4}	1.057(2)	1.113(2)	I_2 (eV)	1.236(4)	1.210(4)
S_{-5}	2.721(2)	2.865(2)	I_1 (eV)	6.628(2)	6.571(2)
S_{-6}	8.056(2)	8.468(2)	I_0 (eV)	5.437(1)	5.397(1)
S_{-8}	9.898(3)	1.036(4)	I_{-1} (eV)	2.030(1)	2.015(1)
S_{-10}	1.628(5)	1.697(5)	I_{-2} (eV)	1.577(1)	1.569(1)

$R_{\lambda_2} = 15.1965$ cm^3 mol^{-1} for $(CH_3)_2NH$ and $R_{\lambda_1} = 19.0998$ and $R_{\lambda_2} = 19.6938$ cm^3 mol^{-1} for $(CH_3)_3N$. The value of $S_{-2} = 38.70$ obtained by using the refractivity constraints for $(CH_3)_2NH$ is ~0.9% lower than the result of Wolf (69) referred to earlier which is consistent with the analogous results for NH_3 and $(CH_3)_2NH$ also discussed previously (ref. 12, and section 5.2).

For dimethylamine and trimethylamine the STDs for the four constrained DOSDs, DOSDi with i = 1–4, are STD = 2.19, 3.96, 2.20, and 3.93, and STD = 2.42, 6.43, 2.39, and 6.42, respectively. The dipole properties for each molecule evaluated using constrained DOSDi, i = 1–4, are very similar, especially for DOSD1 and DOSD3 which are based on the most spectroscopically reliable DOS data. The results obtained from DOSD1 and DOSD3 are, nominally, recommended for $(CH_3)_2NH$ and $(CH_3)_3N$, respectively (they correspond, marginally, to the lowest STDs for the constrained DOSDs of the respective molecules).

The integrated oscillator strengths and the dipole properties S_k, L_k, and I_k corresponding to both the initial and constrained DOSD1 and DOSD3 for $(CH_3)_2NH$ and $(CH_3)_3N$, respectively, are given in Tables 11–14; the molar refractivi-

TABLE 10. Values of the molar refractivity, in $cm^3\ mol^{-1}$, of CH_3NH_2 (ideal gas, STP) evaluated using the constrained DOSD1 and a comparison with the available experimental data (68)

	Molar refractivity			
λ (Å)	Constrained DOSD1	Experiment (68)	λ (Å)	Molar refractivity constrained DOSD1
6709.0	10.10		4047.0	10.49
6440.24	10.12[a]	10.12	3861.0	10.56
6328.0	10.13		3342.0	10.82
6104.0	10.15		2968.0	11.15
5893.0	10.17		2894.0	11.24
5462.25	10.21	10.21	2753.0	11.44
5087.23	10.26	10.26	2577.0	11.82
4801.25	10.31	10.31	2346.0	12.90
4359.56	10.40[a]	10.40		

[a]Used as constraints in constructing the DOSD.

TABLE 11. Integrated dipole oscillator strengths for $(CH_3)_2NH$[a]

Energy region (eV)	Constrained values: DOSD1	High-resolution data	Low-resolution data	Mixture rule	
				Equation [9]	Equation [10]
4.962–5.703	1.939(−3)	1.933(−3)	7.377(−3)		
5.703–7.256	9.370(−2)	8.806(−2)	8.795(−2)		
7.256–9.000	1.211(−1)	1.175(−1)	1.481(−1)		
9.000–11.00	5.753(−1)	5.424(−1)	5.605(−1)		
11.00–13.00	1.038(0)	9.819(−1)	1.024(0)		
13.00–15.00	1.558(0)	1.481(0)	1.486(0)		
15.00–18.00	2.671(0)	2.528(0)	2.565(0)		
18.00–20.00	1.644(0)	1.602(0)	1.608(0)		
20.00–25.00	3.312(0)	3.185(0)	3.128(0)		
25.00–31.26	2.610(0)	2.545(0)	2.410(0)		
31.26–40.00	1.997(0)		1.963(0)	2.355(0)	2.149(0)
40.00–50.00	1.320(0)		1.305(0)	1.358(0)	1.329(0)
50.00–70.00	1.331(0)		1.316(0)	1.400(0)	1.366(0)
70.00–100.0	8.140(−1)		8.086(−1)	9.021(−1)	8.634(−1)
100.0–150.0	5.696(−1)		5.669(−1)	6.166(−1)	5.769(−1)
150.0–200.0	2.794(−1)		2.787(−1)	2.796(−1)	2.780(−1)
200.0–250.0	1.794(−1)		1.791(−1)	1.467(−1)	1.694(−1)
250.0–283.8	6.439(−2)			6.429(−2)	6.478(−2)
283.8–400.0	1.560(0)			1.504(0)	1.557(0)
400.0–425.0	4.710(−1)			4.674(−1)	4.681(−1)
425.0–1000.0	2.981(0)			2.848(0)	2.908(0)
1000.0–10^4	8.010(−1)			7.958(−1)	7.932(−1)
10^4–10^6	6.982(−3)			6.982(−3)	6.822(−3)
10^6–∞	1.128(−7)			1.127(−7)	1.128(−7)

[a]This table contains the integrated oscillator strengths resulting from constrained DOSD1 and from the unmodified experimental or mixture rule data considered in this work.

ties evaluated from the constrained DOSDs are contained in Table 15 for 6709 Å $\geq \lambda \geq$ 2346 Å. For both molecules the integrated oscillator strengths obtained from the initial high- and low-resolution measurements, and from the constrained DOSDs, generally agree with each other to within the estimated experimental errors of $\sim \pm 5\%$. All the exceptions are marginal except for the low-resolution data for both molecules below $E \leq 9$ eV; as pointed out in section 5.2, see also ref. 12, the integrated oscillator strengths, in the discrete energy region, evaluated with low-resolution data need not be realistic.

A comparison of the dipole properties evaluated using the initial versus the constrained DOSD1 and DOSD3 for $(CH_3)_2NH$ and $(CH_3)_3N$, respectively, can be used to discuss the effects of the constrained DOSD method for these molecules. Analogous to monomethylamine, the values for the dipole and logarithmic dipole sums evaluated using the initial DOSDs for dimethylamine and trimethylamine are smaller in magnitude than the recommended values for all k. The effects are similar for all three molecules, particularly for the properties dominated by the photoabsorption spectra for $E \leq 250$ eV. For these properties, e.g., the S_k, $k \leq -1.5$, the effects of the constraint procedure are ~4–5% and are within the errors ($\pm 5\%$) associated with the high- and low-resolution experimental data used to construct the constrained DOSD for each molecule for $E \leq 250$ eV. A detailed discussion of the photon

Can. J. Chem. Downloaded from www.nrcresearchpress.com by EESC ESCOLA DE ENGENHARIA on 09/08/12
For personal use only.

TABLE 12. Integrated dipole oscillator strengths for $(CH_3)_3N$[a]

Energy region (eV)	Constrained values: DOSD1	High-resolution data	Low-resolution data	Mixture rule	
				Equation [9]	Equation [10]
4.711–5.641	1.547(−2)	1.516(−2)	3.183(−2)		
5.641–7.005	1.260(−1)	1.179(−1)	1.128(−1)		
7.005–9.480	3.388(−1)	3.214(−1)	3.656(−1)		
9.480–11.35	7.668(−1)	7.295(−1)	7.502(−1)		
11.35–13.36	1.270(0)	1.213(0)	1.271(0)		
13.36–15.50	2.169(0)	2.062(0)	2.015(0)		
15.50–17.68	2.555(0)	2.444(0)	2.405(0)		
17.68–20.00	2.552(0)	2.462(0)	2.425(0)		
20.00–25.00	4.247(0)	4.042(0)	4.064(0)		
25.00–30.96	3.171(0)	3.067(0)	3.096(0)		
30.96–40.00	2.786(0)		2.709(0)	2.729(0)	2.994(0)
40.00–50.00	1.747(0)		1.717(0)	1.816(0)	1.687(0)
50.00–70.00	1.777(0)		1.746(0)	1.783(0)	1.737(0)
70.00–100.0	1.089(0)		1.078(0)	1.149(0)	1.107(0)
100.0–150.0	7.369(−1)		7.314(−1)	7.793(−1)	7.219(−1)
150.0–200.0	3.642(−1)		3.629(−1)	3.498(−1)	3.460(−1)
200.0–250.0	2.372(−1)		2.366(−1)	1.844(−1)	2.065(−1)
250.0–283.8	8.155(−2)			8.089(−2)	8.135(−2)
283.8–400.0	2.492(0)			2.277(0)	2.326(0)
400.0–425.0	5.733(−1)			5.739(−1)	5.667(−1)
425.0–1000.0	3.895(0)			3.634(0)	3.626(0)
1000.0–10^4	1.001(0)			1.003(0)	9.909(−1)
10^4–10^6	8.428(−3)			8.748(−3)	8.427(−3)
10^6–∞	1.400(−7)			1.400(−7)	1.400(−7)

[a]This table contains the integrated oscillator strengths resulting from constrained DOSD3 and from the unmodified experimental or mixture rule data considered in this work.

TABLE 13. The dipole sums S_k, logarithmic dipole sums L_k, and mean excitation energies I_k, for various values of k, for $(CH_3)_2NH$ calculated using the initial and constrained DOSD1; the values obtained from the constrained DOSD are recommended

Property	Initial DOSD1	Constrained DOSD1	Property	Initial DOSD1	Constrained DOSD1
S_2	1.288(4)	1.299(4)	S_{-12}	3.713(6)	3.913(6)
S_1	1.737(2)	1.783(2)			
S_0	2.518(1)	2.600(1)			
$S_{-1/2}$	2.188(1)	2.269(1)	L_2	7.830(4)	7.871(4)
S_{-1}	2.390(1)	2.487(1)	L_1	5.474(2)	5.603(2)
$S_{-3/2}$	2.885(1)	3.011(1)	L_0	1.704(1)	1.741(1)
S_{-2}	3.699(1)	3.870(1)	L_{-1}	−7.131(0)	−7.590(0)
$S_{-5/2}$	4.973(1)	5.214(1)	L_{-2}	−2.023(1)	−2.134(1)
S_{-3}	6.977(1)	7.327(1)			
S_{-4}	1.548(2)	1.629(2)	I_2 (eV)	1.189(4)	1.163(4)
S_{-5}	3.989(2)	4.204(2)	I_1 (eV)	6.357(2)	6.297(2)
S_{-6}	1.177(3)	1.241(3)	I_0 (eV)	5.355(1)	5.316(1)
S_{-8}	1.395(4)	1.472(4)	I_{-1} (eV)	2.019(1)	2.005(1)
S_{-10}	2.134(5)	2.251(5)	I_{-2} (eV)	1.575(1)	1.568(1)

energy dependence of the dipole properties can be found in the literature (8, 63–65, 73).

The recommended dipole properties for $(CH_3)_2NH$ and $(CH_3)_3N$, evaluated using the constrained DOSD1 and DOSD3, respectively, given in Tables 13 and 14 are apparently the only (reliable) values for these properties available in the literature to date.

5.4. The reliability of the calculated dipole properties

The uncertainties in our recommended values of the dipole properties of the methylamines can be estimated by comparing the recommended results with those derived from alternative constrained DOSDs satisfying the same constraints (12, 50, 62). The uncertainty estimates obtained in this way are less reliable for those properties that do not depend significantly on portions of the DOSD which dominate the constraints, for example properties corresponding to $k = 2$, to a lesser extent to $k = 1$, and for $k < -4$.

Using the results for the properties evaluated using various alternate constrained DOSDs for the methylamines, we estimate the uncertainties in the recommended results for the dipole properties of these molecules to be $\leq$2–3% for S_2, L_2,

Can. J. Chem. Downloaded from www.nrcresearchpress.com by EESC ESCOLA DE ENGENHARIA on 09/08/12
For personal use only.

TABLE 14. The dipole sums S_k, logarithmic dipole sums L_k, and mean excitation energies I_k, for various values of k, for $(CH_3)_3N$ calculated using the initial and constrained DOSD3; the values obtained from the constrained DOSD are recommended

Property	Initial DOSD3	Constrained DOSD3	Property	Initial DOSD3	Constrained DOSD3
S_2	1.606(4)	1.630(4)	S_{-12}	1.117(7)	1.168(7)
S_1	2.244(2)	2.341(2)			
S_0	3.265(1)	3.400(1)			
$S_{-1/2}$	2.813(1)	2.928(1)	L_2	9.726(4)	9.810(4)
S_{-1}	3.061(1)	3.192(1)	L_1	7.000(2)	7.247(2)
$S_{-3/2}$	3.699(1)	3.865(1)	L_0	2.274(1)	2.382(1)
S_{-2}	4.769(1)	4.990(1)	L_{-1}	−9.063(0)	−9.574(0)
$S_{-5/2}$	6.479(1)	6.790(1)	L_{-2}	−2.682(1)	−2.822(1)
S_{-3}	9.243(1)	9.698(1)			
S_{-4}	2.165(2)	2.277(2)	I_2 (eV)	1.161(4)	1.119(4)
S_{-5}	6.056(2)	6.377(2)	I_1 (eV)	6.156(2)	6.084(2)
S_{-6}	1.973(3)	2.080(3)	I_0 (eV)	5.461(1)	5.484(1)
S_{-8}	2.885(4)	3.038(4)	I_{-1} (eV)	2.023(1)	2.016(1)
S_{-10}	5.353(5)	5.619(5)	I_{-2} (eV)	1.550(1)	1.546(1)

TABLE 15. Values of the molar refractivity, in $cm^3\ mol^{-1}$, of $(CH_3)_2NH$ and $(CH_3)_3N$ (ideal gas, STP) evaluated using the constrained DOSD1, and DOSD3, respectively

	Molar refractivity			Molar refractivity	
λ (Å)	$(CH_3)_2NH$	$(CH_3)_3N$	λ (Å)	$(CH_3)_2NH$	$(CH_3)_3N$
6709.0	14.76	19.06	4047.0	15.33	19.89
6440.24	14.78	19.10	3861.0	15.42	20.03
6328.0	14.80	19.12	3342.0	15.81	20.62
6104.0	14.82	19.15	2968.0	16.28	21.37
5893.0	14.85	19.19	2894.0	16.40	21.59
5462.25	14.92	19.29	2753.0	16.69	22.12
5087.23	14.99	19.39	2577.0	17.19	23.25
4801.25	15.06	19.49	2346.0	18.30	24.84
4359.56	15.20	19.69			

I_2, S_1, L_1, $\leq 1\%$ for S_k, $-5 \leq k \leq 0$, R_λ for all λ, and for L_{-1}, L_{-2}, I_1, I_{-1}, I_{-2}, ≤ 2–3% for L_0 and I_0. For $k \leq -6$ the errors in the S_k are estimated to be ≤ 1–2% for S_{-6}, increasing to $\leq 8\%$ for S_{-12}. The estimation of the uncertainties in the recommended results for the dipole properties for the methylamines is based on the assumption that the molar refractivities used as constraints in the construction of the DOSDs have errors of the magnitude associated with accurate experimental measurements (a few tenths of a percent). While this is a valid assumption for monomethylamine, it becomes less probable for dimethylamine and trimethylamine due to the method, outlined in section 5.3, used to obtain the R_λ constraints for the two larger methylamines. The effects on the calculated properties S_k, L_k, and I_k of varying the R_λ constraints has been discussed previously and, as expected from the structure of integrals [3] and [4], it is largest for $k \leq -2$ and increases as k decreases from $k = -2$ (64, 74).

6. Acknowledgements

This collaborative research project received financial support from the Canadian National Networks of Centres of Excellence (Centres of Excellence in Molecular and Interfacial Dynamics) and from the Natural Sciences and Engineering Research Council (NSERC) of Canada. A Graduate Fellowship from the University of British Columbia (W.F.C.) and a NSERC Postgraduate Scholarship (G.R.B.) are gratefully acknowledged.

1. T.W. Harquist (*Editor*). Molecular astrophysics - a volume honouring Alexander Dalgarno. Cambridge Press, Cambridge. 1990.
2. S. Leach. 4th Eur. Workshop on Molecular Spectroscopy and Photon Induced Dynamics. Oxford. 1987.
3. M. Feston. 4th Eur. Workshop on Molecular Spectroscopy and Photon Induced Dynamics. Oxford. 1987.
4. B. Fegley, Jr. and R.G. Prinn. Nature, **318** 48 (1985); Astrophys. J. **299**, 1067 (1985).
5. C.M. Leung, E. Herbst, and W.F. Huebner. Astrophys. J. **56**, 231 (1984).
6. M.-J. Hubin-Franskin, J. Delwiche, F. Tollet, M. Furlan, and J.E. Collin. J. Phys. B: At. Mol. **21**, 189 (1988).
7. D.F. Grosjean and P. Bletzinger. IEEE J. Quant. Elec., **QE13**, 898 (1977).
8. G.D. Zeiss, W.J. Meath, J.C.F. MacDonald, and D.J. Dawson. Mol. Phys. **39**, 1055 (1980).
9. G.D. Zeiss, W.J. Meath, J.C.F. MacDonald, and D.J. Dawson. Radiat. Res. **70**, 284 (1977).
10. B.L. Jhanwar, W.J. Meath, and J.C.F. MacDonald. Radiat. Res. **96**, 20 (1983).
11. B.L. Jhanwar, W.J. Meath, and J.C.F. MacDonald. Radiat. Res. **106**, 288 (1986).
12. G.R. Burton, W.F. Chan, G. Cooper, C.E. Brion, A. Kumar, and W.J. Meath. Can. J. Chem. **71**, 341 (1993).

Can. J. Chem. Downloaded from www.nrcresearchpress.com by EESC ESCOLA DE ENGENHARIA on 09/08/12
For personal use only.

13. G.R. Burton, W.F. Chan, G. Cooper, and C.E. Brion. Chem. Phys. **177**, 217 (1993).
14. E. Tannenbaum, E.M. Coffin, and A.J. Harrison. J. Chem. Phys. **21**, 311 (1953).
15. C. Bertrand, G. Collin, and H. Gagnon. J. Chim. Phys. **72**, 719 (1975).
16. C. Backx, R.R. Tol, G.R. Wight, and M.J. Van der Wiel. J. Phys. B; At. Mol. **8**, 2050 (1975).
17. C. Backx and M.J. Van der Wiel. J. Phys. B; At. Mol. **8**, 3020 (1975).
18. F. Carnovale and C.E. Brion. Chem. Phys. **74**, 253 (1983).
19. Y. Iida, F. Carnovale, S. Daviel, and C.E. Brion. Chem. Phys. **105**, 211 (1986) and references therein.
20. X. Guo, G. Cooper, W.F. Chan, G.R. Burton, and C.E. Brion. Chem. Phys. **161**, 453 (1992).
21. S. Daviel, C.E. Brion, and A.P. Hitchcock. Rev. Sci. Instrum. **55**, 182 (1984).
22. W.F. Chan, G. Cooper, and C.E. Brion. Phys. Rev. A; Gen. Phys. **44**, 186 (1991).
23. W.F. Chan, G. Cooper, X. Guo, and C.E. Brion. Phys. Rev. A; Gen. Phys. **45**, 1420 (1992).
24. J.W. Gallagher, C.E. Brion, J.A.R. Samson, and P.W. Langhoff. J. Phys. Chem. Ref. Data, **17**, 9 (1988).
25. G. Cooper, T. Ibuki, Y. Iida, and C.E. Brion. Chem. Phys. **125**, 307 (1988).
26. T. Ibuki, G. Cooper, and C.E. Brion. Chem. Phys. **129**, 295 (1989).
27. G.R. Burton, W.F. Chan, G. Cooper, and C.E. Brion. Chem. Phys. **167**, 349 (1992).
28. J.A. Wheeler and J.A. Bearden. Phys. Rev. **46**, 755 (1934).
29. M. Inokuti. Private communication.
30. W.F. Chan, G. Cooper, and C.E. Brion. Chem. Phys. **168**, 375 (1992).
31. A.W. Potts, T.A. Williams, and W.C. Price. J. Chem. Soc. Faraday Trans. **54**, 104 (1972).
32. S. Katsumata, T. Iwai, and K. Kimura. Bull. Chem. Soc. Jpn. **46**, 3391 (1973).
33. K. Kimura and K. Osafune. Mol. Phys. **29**, 1073 (1975).
34. P. Finn, R.K. Pearson, J.M. Hollander, and W.L. Jolly. Inorg. Chem. **10**, 378 (1971).
35. J.S. Jen and T.D. Thomas. J. Electron Spectrosc. Relat. Phenom. **4**, 43 (1974).
36. W.P. Perry, T.F. Schaar, and W.L. Jolly. J. Am. Chem. Soc. **97**, 4899 (1975).
37. B.E. Mills, R.L. Martin, and D.A. Shirley. J. Am. Chem. Soc. **98**, 2380 (1976).
38. J.J. Yeh and I. Lindau. At. Data Nucl. Data Tables, **32**, 1 (1985).
39. B.L. Henke, P. Lee, J.J. Tanaka, R.L. Shimabukuro, and B.K. Fujikawa. At. Data Nucl. Data Tables, **27**, 1 (1982).
40. R. McClaren, S.A.C. Clark, I. Ishii, and A.P. Hitchcock. Phys. Rev. A: At. Mol. **36**, 1683 (1987).
41. R.N.S. Sodhi and C.E. Brion. J. Electron Spectrosc. Relat. Phenom. **37**, 97 (1985).
42. R.N.S. Sodhi and C.E. Brion. J. Electron Spectrosc. Relat. Phenom. **37**, 125 (1985).
43. R.N.S. Sodhi and C.E. Brion. J. Electron Spectrosc. Relat. Phenom. **37**, 145 (1985).
44. G. Wight and C.E. Brion. J. Electron Spectrosc. Relat. Phenom. **4**, 25 (1974).
45. J.W. Au, G. Cooper, G.R. Burton, T.N. Olney, and C.E. Brion. Chem. Phys. **173**, 209 (1993).
46. R.N.S. Sodhi and C.E. Brion. J. Electron Spectrosc. Relat. Phenom. **36**, 187 (1985).
47. A.O. Bawagan and C.E. Brion. Chem. Phys. Lett. **137**, 573 (1987).
48. A.O. Bawagan and C.E. Brion. Chem. Phys. **123**, 51 (1988).
49. M. Robin. Higher excited states of polyatomic molecules - Vol. 1. Academic Press, New York. 1974.
50. G.D. Zeiss, W.J. Meath, J.C.F. MacDonald, and D.J. Dawson. Can. J. Phys. **55**, 2080 (1977).
51. J.O. Hirschfelder, W. Byers Brown, and S.T. Epstein. Adv. Quant. Chem. **1**, 255 (1964).
52. U. Fano and J.W. Cooper. Rev. Mod. Phys. **40** 441 (1968); **41**, 724 (1969).
53. G.D. Zeiss and W.J. Meath. Mol. Phys. **33**, 1155 (1977) and references therein.
54. D.J. Margoliash and W.J. Meath. J. Chem. Phys. **68**, 1426 (1978).
55. F. Mulder, G.F. Thomas, and W.J. Meath. Mol. Phys. **41**, 249 (1980).
56. F. Mulder and W.J. Meath. Mol. Phys. **42**, 629 (1981).
57. B.L. Jhanwar and W.J. Meath. Chem. Phys. **67**, 185 (1982).
58. W.J. Meath and A. Kumar. Int. J. Quant. Chem. **24**, 501 (1990).
59. A. Kumar and W.J. Meath. Theor. Chim. Acta, **82**, 131 (1992).
60. G.H.F. Diercksen, J. Oddershede, I. Paidarova, and J. Sabin. Int. J. Quant. Chem. **39**, 755 (1991).
61. A.J. Thakkar, H. Hettema, and P.E.S. Wormer. J. Chem. Phys. **97**, 3252 (1992).
62. A. Kumar, G.R.G. Fairley, and W.J. Meath. J. Chem. Phys. **83**, 70 (1985), and some of the references therein. See also references (58, 59) and some of the references therein.
63. B.L. Jhanwar, W.J. Meath, and J.C.F. MacDonald. Can. J. Phys. **59**, 185 (1981); **61**, 1027 (1983).
64. A. Kumar and W.J. Meath. Can. J. Phys. **63**, 417 (1985).
65. A. Kumar and W.J. Meath. Can. J. Chem. **63**, 1616 (1985).
66. H.A. Bethe and E.E. Salpeter. Quantum mechanics of one- and two-electron atoms. Springer-Verlag, Berlin. 1957.
67. G.F. Thomas and W.J. Meath. Mol. Phys. **34**, 113 (1977).
68. K.L. Ramaswamy. Proc. Indian Acad. Sci. **A4**, 675 (1936).
69. F.U. Wolf. Hand-und-Jahrbuch der Chemischen Physik, Band. 6, Abschn. I, Leipzig, Germany. 1935. s262.
70. R.M. Metzger and C.H. Rhee. Mol. Cryst. Liq. Cryst. **85**, 81 (1982).
71. S. Kaur, V. Saxena, R.C. Rastogi, and N.K. Ray. Indian J. Chem. **27A**, 1013 (1988).
72. A.T. Amos and J.A. Yoffe. J. Chem. Phys. **63**, 4723 (1975).
73. W.J. Meath, D.J. Margoliash, B.L. Jhanwar, A. Koide, and G.D. Zeiss. *In* Intermolecular forces. *Edited by* B. Pullman. Reidel, Dordrecht. 1981. p 101.
74. B.L. Jhanwar and W.J. Meath. Can. J. Chem. **62**, 373 (1984).
75. A.A. Bakke, H.-W. Chen, and W.L. Jolly. J. Electron Spectrosc. Relat. Phenom. **20**, 333 (1980).

Can. J. Chem. Downloaded from www.nrcresearchpress.com by EESC ESCOLA DE ENGENHARIA on 09/08/12
For personal use only.

New dihydrogen complexes: the synthesis and spectroscopic properties of iron(II), ruthenium(II), and osmium(II) complexes containing the *meso*-tetraphos-1 ligand

MARIA TERESA BAUTISTA, KELLY ANNE EARL, PATRICIA ANNE MALTBY, ROBERT HAROLD MORRIS,[1] AND CAROLINE THERESIA SCHWEITZER

Department of Chemistry and the Scarborough Campus, University of Toronto, Toronto, ON M5S 1A1, Canada

Received July 19, 1993

This paper is dedicated to Professor John C. Polanyi on the occasion of his 65th birthday

MARIA TERESA BAUTISTA, KELLY ANNE EARL, PATRICIA ANNE MALTBY, ROBERT HAROLD MORRIS, and CAROLINE THERESIA SCHWEITZER. Can. J. Chem. **72**, 547 (1994).

The synthesis and properties of dihydrogen complexes *trans*-$[MH(H_2)L]^+$, M = Fe, Ru, Os, which contain the ligand *meso*-tetraphos-1, *S,R*-$Ph_2PCH_2CH_2P(Ph)CH_2CH_2P(Ph)CH_2CH_2PPh_2$ (L) are described. There are interesting possibilities of isomerism in such *trans* complexes because the axial binding sites at the metal are different, one being surrounded by four phenyl groups and the other by two phenyl groups. The osmium complex is prepared in an unusual reaction of *cis*-β-$Os(Cl)_2L$ with H_2 (1 atm) and $NaBPh_4$ (1 mol) in THF or by the reaction of *trans*-OsH(Cl)L with $NaBPh_4$ and H_2. The iron and ruthenium complexes were made by a reaction of HBF_4 with complexes *trans*-$M(H)_2L$ that have inequivalent *trans* hydrides. The ruthenium complex was also prepared starting from isomers of *trans*-RuH(Cl)L. The H—H distance in the rapidly spinning dihydrogen ligand has been calculated from T_1(min) data to be 0.88, 0.89, and 0.99 Å for the complexes of Fe, Ru, Os, respectively. The presence of the H—D bond in the isotopomers *trans*-$[MH(HD)L]^+$ and *trans*-$[MD(HD)L]^+$ is also confirmed by the observation of $^1J_{HD}$ coupling constants of 32, 33.5, and 26.4 Hz for Fe, Ru, and Os, respectively. There is no rapid intramolecular H atom exchange in these complexes in contrast to those with di-*tert*-phosphine ligands like $[MH(H_2)(dppe)_2]^+$ or to the trihydride $Re(H)_3L$. Described also are the properties of the precursor complexes including *cis*-β- and *trans*-$Ru(Cl)_2L$ and derivatives of the dihydrogen complexes *trans*-$[MH(L')L]^+$, L' = CH_3CN (on Ru and Os), PMe_2Ph (on Ru), and CO (on Os). Trends in the NMR properties of isostructural complexes are reported.

MARIA TERESA BAUTISTA, KELLY ANNE EARL, PATRICIA ANNE MALTBY, ROBERT HAROLD MORRIS et CAROLINE THERESIA SCHWEITZER. Can. J. Chem. **72**, 547 (1994).

On décrit la synthèse et les propriétés des complexes dihydrogénés *trans*-$[MH(H_2)L]^+$ (M = Fe, Ru et Os) qui contiennent le ligand *méso*-tétraphos-1, *S,R*-$Ph_2PCH_2CH_2P(Ph)CH_2CH_2P(Ph)CH_2CH_2PPh_2$ (L). Dans de tels composés, il existe des possibilités intéressantes d'isomérie parce que les sites de liaisons axiales sur le métal sont différents; en effet, l'un est entouré de quatre groupes phényles alors que l'autre est entouré par deux. On a préparé le complexe d'isomium par une réaction inhabituelle du *cis*-β-$Os(Cl_2)L$ avec du H_2 (1 atm) et du $NaBPh_4$ (1 mol) dans le THF ou par la réaction du *trans*-OsH(Cl)L avec du $NaBPh_4$ et du H_2. On a préparé les complexes du fer et du ruthénium par réaction du HBF_4 avec les complexes $M(H)_2L$ qui comportent deux hydrures inéquivalents. On a aussi préparé le complexe de ruthénium à partir des isomères du *trans*-RuH(Cl)L. En se basant sur des données de T_1(min), on a calculé que la distance H—H dans le ligand dihydrogéné avec un spin rapide sont respectivement 0,89, 0,89 et 0,99 Å pour les complexes du Fe, du Ru et du Os. On a aussi confirmé l'existence de la liaison H—D dans les isotopomères *trans*-$(MH(HD)L]^+$ et *trans*-$[MD(HD)L]^+$ par l'observation de constantes de couplages $^1J_{HD}$ de 32, 33,5 et 26,4 Hz respectivement pour les complexes du Fe, du Ru et du Os. Il n'existe pas d'échange rapide intramoléculaire d'atome de H dans ces complexes; ce comportement est en opposition avec ce qui a été observé avec les ligands di-*tert*-phosphines comme $[MH(H_2)(dppe)_2]^+$ ou le trihydrure $Re(H)_3L$. On décrit aussi les propriétés des complexes précurseurs, y compris celles des *cis*-β- et *trans*-$Ru(Cl)_2L$ et des dérivés des complexes dihydrogénés *trans*-$[MH(L')L]^+$ dans lesquels L' = CH_3CN (sur le Ru et le Os), PMe_2Ph (sur le Ru) et CO (sur le Os). On rapporte les tendances dans les propriétés RMN des complexes isostructuraux.
[Traduit par la rédaction]

Introduction

The reactions of complexes that contain an intact dihydrogen molecule (1) have represented a rapidly expanding field of study since the report of the first molecular hydrogen complex in 1984 (2). A common reaction of the complexes *trans*-$[M(H_2)(H)L_2]^+$, M = Fe, Ru, Os and L = $PEt_2CH_2CH_2PEt_2$ (depe) and $PPh_2CH_2CH_2PEPh_2$ (dppe), is the intramolecular exchange of H atoms between the hydride and H_2 sites (3–6). To better understand this intramolecular hydrogen atom exchange, we have prepared new dihydrogen complexes of the tetradentate phosphine $Ph_2PCH_2CH_2P(Ph)CH_2CH_2P(Ph)CH_2CH_2PPh_2$ (tet-1). This ligand exists as a mixture of two diastereomers, the *meso* (*S,R*) and *rac* (*S,S*; *R,R*) forms (7). The topologies that these diastereomers adopt when coordinated in an octahedral complex are denoted by the *cis*-α, *cis*-β, and *trans* nomenclature (8) (Fig. 1). All three configurations may be attained by *rac*-tet-1 (structure *cis*-α-III contains the *rac*-tet ligand), but the *cis*-α geometry is not physically possible for the *meso* ligand. Therefore octahedral *meso*-tet-1 complexes adopt either structure *trans*-I or *cis*-β-II.

This isomerism was not fully appreciated in early studies of its coordination chemistry (9–12) until the work of Brown and Canning (13). Taqui Khan and Mohiuddin partially characterized a complex [RuCl(tet-1)]Cl, which was a one to one electrolyte in nitromethane (9). This complex reacted with dihydrogen gas directly to give a partially characterized complex RuH(Cl)(tet-1). Unfortunately they did not determine if it was the *meso* or *rac* ligand that was involved and could not determine the stereochemistry of these complexes.

The preliminary report of our work (14) described how the complexes *trans*-$[M(H_2)(H)L]^+$, M = Fe, Os, L = *meso*-tet-1, held the H_2 and H ligands *trans* to each other so that no H-atom exchange occurred, while for the complex *cis*-α-$[OsH_3$(*rac*-tet-1)$]^+$ there was rapid exchange of the H atoms. The present work describes in full detail the properties of the Fe and Os

[1]Author to whom correspondence may be addressed.

Can. J. Chem. Downloaded from www.nrcresearchpress.com by 195.246.54.202 on 09/08/12
For personal use only.

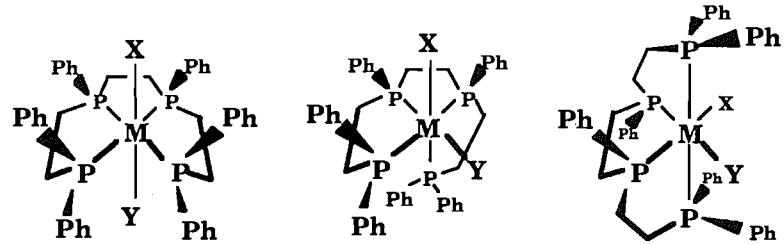

FIG. 1. Three geometric isomers observed for the tet-1 ligands.

Can. J. Chem. Downloaded from www.nrcresearchpress.com by 195.246.54.202 on 09/08/12
For personal use only.

complexes as well as new Ru complexes containing the *meso*-tet-1 ligand (abbreviated below as L). A future paper will describe the *rac*-tet-1 chemistry (15).

An interesting feature of the *trans* structure I is that the axial sites are inequivalent due to the arrangement of the phenyl groups; site X is "surrounded" by four phenyl groups whereas site Y has only two phenyl groups near it. The crystal structures of *trans*-$[FeH(N_2)L]Br$ (11) and *trans*-$RuCl_2L$ (12) clearly demonstrate this feature. The dinitrogen ligand is located in the four-phenyl binding site in the former complex. Such complexes offer the interesting possibility of recognition of ligands on the basis of molecular size. The X-ray crystal structures of the square-planar complex $[PtL]BPh_4$ (16) and some dimolybdenum complexes Mo_2Br_4L (17) have also been reported.

Experimental

General

Oxygen and water were excluded at all times by the use of a glove box supplied with purified nitrogen or vacuum lines supplied with purified nitrogen or argon where necessary. Benzene, tetrahydrofuran (THF), diethyl ether, and hexanes were dried over and distilled from sodium-benzophenone ketyl. Methanol was dried over magnesium methoxide, and ethanol over magnesium ethoxide. Acetone was dried over potassium carbonate. Dichloromethane and 1,2-dichloroethane were distilled from calcium hydride. Deuterated solvents were dried over Linde type 4 Å molecular sieves and degassed prior to use. Reagents were obtained from commercial sources and used without further purification. The phosphine ligands were used as purchased from Strem Chemicals or Digital Specialty Chemicals Ltd. with the exception of tetraphos-1 which had to be separated into its *meso* and *racemic* forms (see below). Ruthenium(III) trichloride trihydrate, ammonium hexachloroosmate(IV), and sodium hexachloroosmate(IV) were received as a loan from Johnson-Matthey Co. Tri-μ-chloro-hexakis(ethyldiphenylphosphine)diosmium(II) chloride dihydrate, $[Os_2Cl_3(PEtPh_2)_6]Cl\cdot 2H_2O$, was prepared by the method described by Chatt and Hayter (18). The compounds *cis*-$RuCl_2(DMSO)_4$ (19–21) and $PPh_2CH_2CH_2Cl$ (22) were prepared by literature methods.

Infrared spectra were recorded on a Nicolet 5DX FTIR spectrometer as Nujol mulls. NMR spectra were recorded on Varian XL-400 (400 MHz for ^1H, 162 MHz for ^{31}P), Varian XL-200 (200 MHz for ^1H, 81 MHz for ^{31}P), Varian Gemini 200 (200 MHz for ^1H), or Varian Gemini 300 (300 MHz for ^1H, 120.5 MHz for ^{31}P) spectrometers. Attempted 2D NMR experiments and an NOEDIFF experiment were performed on a Bruker AM-500 (500 MHz for ^1H, 202.5 MHz for ^{31}P) at McMaster University by Dr. D. Hughes. VT T_1 measurements were obtained on the XL-400 spectrometer using the inversion–recovery method. ^{31}P chemical shifts were measured, either internally or externally, relative to 1% $P(OMe)_3$ in C_6D_6 sealed in coaxial capillaries, but are reported in parts per million (ppm) from 85% H_3PO_4 ($\delta P(OMe)_3 = 140.4$ ppm) (see Tables 1 and 2). ^1H chemical shifts were measured relative to partially deuterated solvent peaks, but are reported relative to tetramethylsilane (see Table 2 for the high-field data). First-order NMR spectra were simulated using the "First order NMR" program (23) and second-order spectra were simulated using the LAOCN 5 program (24). In the abbreviated NMR data listed below "p" refers to a pentet to distinguish it from "q", a quartet.

Microanalyses were performed on a sample handled under an inert atmosphere by Canadian Microanalytical Services, Delta, B.C. Several samples did not give acceptable analysis despite repeated attempts and despite the fact that they appeared pure by ^1H and ^{31}P NMR. Fast atom bombardment mass spectrometry (FAB MS) spectra were obtained with a VG 70-250S mass spectrometer using a 3-nitrobenzyl alcohol (NBA) or 2-nitrophenyloctylether (NPOE) matrix. A PAR model 273 potentiostat was used for cyclic voltammetry studies. The electrochemical cell contained a Pt working electrode, W secondary electrode, and Ag wire reference electrode in a Luggin capillary. The cyclic voltammograms were collected in THF containing 0.2 M n-Bu_4NPF_6 as the supporting electrolyte. Reported potentials are referenced to ferrocene, which was added to these solutions.

Synthesis of $Ph(Li)PCH_2CH_2P(Li)Ph\cdot 4THF$ (Lippe·4THF) (25)

Under 1 atm Ar (101.3 kPa), finely chopped lithium metal (2.3 g, 0.33 mol) was added to 60 mL THF. After cooling this mixture to 0°C, a solution of dppe (13.5 g, 0.0339 mol) in 80 mL THF was added dropwise, with stirring, over a period of 1 h during which time the mixture became orange-yellow. This mixture was then refluxed for 45 min resulting in a dark red solution. The warm solution was filtered through Celite to remove the excess lithium. The volume of the filtrate was reduced to 20 mL and cooled to −78°C. The yellow precipitate was then filtered and washed twice with 5 mL of cold diethyl ether. A bright yellow powder (12.6 g, 68%) was obtained. ^1H NMR (THF-d_8, 200 MHz) δ: 7.0–6.1 (m, PC_6H_5), 2.3 (m, PCH_2CH_2P), 3.6, 1.7 (m, THF). ^{31}P NMR (THF, 200 MHz) δ: 200.9 (s).

Synthesis of $Ph_2PCH_2CH_2P(Ph)CH_2CH_2P(Ph)CH_2CH_2PPh_2$ (tet-1) (7, 26)

Under 1 atm Ar, $Ph_2CH_2CH_2Cl$ (22) (8.0 g, 0.032 mol) in 100 mL THF was added dropwise over 1 h to an ice-cooled solution of Lippe·4THF (8.8 g, 0.016 mol) in 100 mL THF. During this time the solution discoloured from bright yellow to nearly colourless. This solution was refluxed for 0.75 h and then allowed to cool. 30 mL of saturated NH_4Cl (aq) solution was added with vigorous stirring. The THF layer was decanted and the aqueous layer was washed with 20 mL THF. The THF layers were combined and dried over $MgSO_4$. The $MgSO_4$ was then filtered from the THF and the volume was reduced to 30 mL. EtOH (90 mL) was added and the mixture was cooled overnight and filtered the next day. The white solid (8.2 g, 76%) obtained was a mixture of the *meso* and *racemic* isomers. The isomers were separated by adding 5 g of tet-1 to 100 mL of CH_2Cl_2 and 25 mL of EtOH. This suspension was heated for 1 h. Upon cooling, the insoluble portion was filtered off and washed with EtOH; the process of dissolving the insoluble portion and heating was repeated two more times, yielding 3.5 g of the *meso* isomer. All the filtrate portions were combined and the volume reduced to 25 mL. The *rac*-tet-1 isomer precipitated

Can. J. Chem. Downloaded from www.nrcresearchpress.com by 195.246.54.202 on 09/08/12
For personal use only.

out and was filtered off. The yield of *rac*-tet-1 was 1.25 g. ^{1}H NMR (CD_2Cl_2, 200 MHz, both isomers) δ: 7.3 (m, PC_6H_5), 2.0–1.5 (at least 3 m, PCH_2CH_2P).

Properties of the *meso* isomer: mp 189°C, $^{31}P\{^1H\}$, δ (toluene, 81 MHz, 290 K): −13.2 ppm (P_A), −16.9 ppm (P_X, AA′XX′, $J_{AX} = J_{A'X'} = 27.4$ Hz, $J_{XX'} = 23.0$ Hz, $J_{AX'} = J_{A'X} = 0.3$ Hz, $J_{AA'} = 0$).

Properties of the *rac* isomer: mp 118°C, $^{31}P\{^1H\}$, δ (toluene, 81 MHz, 290 K): −13.2 ppm (P_A), −17.1 (P_X, AA′XX′, same couplings as the *meso* isomer).

Preparation of cis-α-*$OsCl_2$(rac-tet-1) and* cis-β-*$OsCl_2$L, L* = meso-*tet-1*

$[Os_2Cl_3(PEtPh_2)_6]Cl{\cdot}2H_2O$ (2.45 g, 1.33 mmol) and tet-1 (1.85 g, 2.76 mmol) were heated together with stirring. A brown liquid formed at 160°C and turned yellow at 185°C. The temperature was increased to 204°C and the viscous yellow solution allowed to cool. Free $PEtPh_2$ was washed from the lemon yellow mass with hexane (3 × 20 mL). The solid was stirred in THF (2 × 20 mL) and the *cis*-α-$OsCl_2$(*rac*-tet-1) isomer was filtered off, washed (3 × 5 mL THF), and dried in vacuo (0.8 g, 32%). The properties of the *rac*-tet-1 osmium complexes will be described elsewhere (15). *cis*-β-$OsCl_2$L was precipitated from the yellow filtrate, after volume reduction to 5 mL, by addition of hexane (15 mL). THF–hexane recrystallization yielded 1.63 g (66.5%) of the pale yellow solid. Anal. calcd. for $C_{42}H_{42}Cl_2OsP_4$:C 54.14, H 4.54; found: C 54.14, H 4.62. FAB MS calcd. for $C_{42}H_{42}{}^{35}Cl_2{}^{195}OsP_4$: 932.0; obsd.: 932 ($M^+$), 897 ($M^+ - Cl$).

Preparation of trans-*OsHClL*

Method A

A slurry of $LiAlH_4$ (0.036 g, 0.95 mmol) in THF (5 mL) was added to a stirred solution of *cis*-β-$OsCl_2$L (0.269 g, 0.289 mmol) in THF (10 mL). After refluxing for 10 min, and cooling, EtOH (5 mL) was added to the pale orange mixture. Solvent was removed under vacuum and the beige residue was treated with THF (15 mL) and filtered through Celite. The volume of the dirty yellow filtrate was reduced to dryness, NaCl (0.038 g, 0.65 mmol) and acetone (20 mL) were added, and the slurry refluxed for 2 h. After solvent removal and filtration of the THF soluble portion, the yellow filtrate was concentrated to 2 mL and the pale yellow product precipitated by addition of hexane (10 mL); 0.166 g (64%) was obtained. IR (Nujol): 1943 (w, br, Os-H cm^{-1}). FAB MS calcd.for $C_{42}H_{43}{}^{35}Cl{}^{192}OsP_4$: 898.1; obsd.: 898 ($M^+$), 861 ($M^+ - ClH_2$). $E_{1/2}(Os^{3+}/Os^{2+})$ is −0.31 V in THF, versus Fc^+/Fc; 0.2 M NBu_4BF_4. In some preparations a minor isomer is also obtained (see Table 2).

Method B

cis-β-$OsCl_2$L (0.085 mmol) and $NaBPh_4$ (0.096 mmol) were stirred for 20 min in 5 mL THF under 1 atm dihydrogen. Then NEt_3 (0.086 mmol) was added and the mixture was stirred for 15 min. The solvent was evaporated and the residue was dissolved in acetone-d_6. The only hydride resonances were due to major *trans*-OsH(Cl)L at −22.6 ppm (J_{PH} = 17.5 Hz) and an unknown compound in small amount at −10.6 ppm (br).

Synthesis of trans-*$RuCl_2$L (27)*

meso-tet-1 (1.00 g, 1.49 mmol) in 60 mL toluene was added dropwise to *cis*-$RuCl_2(DMSO)_4$ (0.722 g, 1.49 mmol) in 80 mL refluxing toluene. This yellow solution was refluxed for 1.5 h, after which time the solvent was removed under reduced pressure. The yellow residue was washed with hexanes (2 × 30 mL) affording 1.19 g (94%) of product.

Synthesis of trans-*RuHClL*

trans-$RuCl_2$L (4.50 g, 5.34 mmol) was dissolved in 80 mL THF and then, with stirring, $LiAlH_4$ (2.00 g, 52.7 mmol) was added. The mixture was refluxed for 24 h, cooled, and then 7 mL EtOH was added. After solvent evaporation, 100 mL of benzene was added to the residue and the mixture stirred overnight. The next day the lithium salts were removed by filtration through Celite. The filtrate was reduced to dryness and the tan residue was washed with hexanes and dried (2.00 g, 46%). IR (Nujol): 1989 (Ru-H) cm^{-1}. ^{1}H NMR (C_6D_6, 200 MHz) δ: 8.4–6.7 (m, PC_6H_5), 3.1–0.9 (at least 9 m, PCH_2CH_2P), −17.6 (p, Ru*H* of minor isomer, $^2J_{PH}$ = 17.6 Hz); −20.9 (p, Ru*H* of major isomer, $^2J_{PH}$ = 20.8 Hz). T_1 (measured at 400 MHz, THF-d_8) for hydride of minor isomer versus that of major isomer, respectively, at the indicated temperature: 819 vs. 717 ms at 294 K, 503 vs. 481 at 251 K, 422 vs. 417 ms at 230 K, 377 vs. 374 ms at 207 K, 298 vs. 287 ms at 187 K. Anal. calcd. for $C_{42}H_{43}ClP_4Ru{\cdot}C_6H_6$: C 65.0, H 5.6, Cl 4.0; found: C 65.3, H 6.2, Cl 3.9. FAB MS calcd. for $C_{42}H_{43}{}^{35}ClP_4{}^{102}Ru$: 808; obsd.: 771 ($M^+ - 2H - Cl$).

Observation of cis-β-*$Os(H)_2$L*

This was prepared from *cis*-β-$OsCl_2$L (0.059 g, 0.063 mmol), dihydrogen gas, $NaBPh_4$ (0.034 g, 0.093 mmol), NaO^{t}Bu (0.019 g, 0.20 mmol), and 10 mL of a THF–^{t}BuOH solvent mixture with 15 h of stirring. ^{31}P NMR indicated the presence of *cis*-β-OsH_2L. The mixture was allowed to stir for a further 19 h; the ^{31}P NMR spectrum did not change. A pale yellow residue, which proved difficult to crystallize, resulted from the benzene-soluble portion.

Synthesis of trans-*$Ru(H)_2$L*

Under 1 atm Ar, *trans*-RuHClL (0.090 g, 0.11 mmol) was dissolved in 4.5 mL THF and 1.5 mL EtOH. NaOEt (0.030 g, 0.44 mmol) was added and the solution was stirred overnight. The next morning, the pale yellow solution was evaporated to dryness and the residue was redissolved in benzene. The NaCl formed was filtered off through Celite and the volume of the filtrate was reduced to 1 mL. Addition of hexanes caused precipitation of a pale yellow solid (0.042 g, 49%). IR (Nujol): 1966 (w, Ru-H) cm^{-1}. ^{1}H NMR (C_6D_6, 200 MHz) δ: 8.6–6.7 (m, PC_6H_5), 2.7–0.9 (6 m, PCH_2CH_2P), −7.9 (m, Ru*H*, $^2J_{HP}$ = 15.0 Hz, 20.0 Hz, $^2J_{HH}$ = 14.0 Hz), −10.2 (dp, Ru*H*, $^2J_{HP}$ = 18.0 Hz, 19.0 Hz, $^2J_{HH}$ = 14.0 Hz). $E_{1/2}(Ru^{3+}/Ru^{2+})$ is –0.40 V in THF versus Fc^+/Fc. T_1 (measured at 400 MHz, THF-d_8) for hydride at −7.9 ppm versus that at −10.2 ppm, respectively, at the indicated temperature: 695 vs. 880 ms at 295 K, 463 vs. 580 at 249 K, 394 vs. 500 ms at 227 K, 315 vs. 415 ms at 207 K, 183 vs. 280 ms at 185 K. FAB MS calcd. for $C_{42}H_{44}{}^{102}RuP_4$: 774; obsd.: 773 ($M^+ - H$), 772 ($M^+ - 2H$), 771 ($M^+ - 3H$).

Synthesis of trans-*$Fe(H)_2$L*

$FeCl_2$ (0.10 g, 0.79 mmol) was added to the *meso*-tet-1 (0.54 g, 0.80 mmol) in 50 mL THF and stirred for 5 min to give a green solution. $NaBH_4$ (0.1 g, 2.64 mmol) in 5 mL ethanol was added and this mixture stirred for 6 h. After filtering off the borate salts, the volume of the yellow filtrate was reduced to 5 mL and the FeH_2L precipitated out by repeatedly adding 5 mL diethyl ether and reducing the volume to 5 mL until the precipitate formed. The bright yellow solid was filtered off and washed with diethyl ether (80% yield). IR (Nujol): 1724 (Fe-H) cm^{-1}; δ (^{1}H, C_6D_6, 400 MHz): −12.76 (dtt, 1H, J_{HP} = 41.1, 33.6, J_{HH} = 18.2 Hz, T_1 = 0.58 s), −14.68 (dp, 1H, J_{HP} = 38.2, J_{HH} = 18.2 Hz, T_1 = 0.63 s). FAB MS calcd. for $C_{42}H_{44}{}^{56}FeP_4$: 728.3; obsd.: 726 ($M^+ - 2H$).

Synthesis of trans-*$[OsH(H_2)L]BPh_4$*

Method A

cis-β-$OsCl_2$L (0.094 g, 0.10 mmol) and $NaBPh_4$ (0.038 g, 0.11 mmol) were placed under a H_2 atmosphere and 10 mL THF were added. The solid immediately reddened. The solution was degassed and the red-orange colour quickly faded to pale yellow with the production of a fine white precipitate (NaCl). The mixture was stirred under H_2 for 21 h, filtered through Celite under an argon atmosphere, and the solvent removed under vacuum to yield a a pale yellow mass. The solid proved unstable to recrystallization attempts and thus spectral solutions were prepared from the crude product under an argon atmosphere. Solutions exposed to air readily decompose to a green

Can. J. Chem. Downloaded from www.nrcresearchpress.com by 195.246.54.202 on 09/08/12
For personal use only.

solution. δ (^{1}H, CD_2Cl_2, 213 K, 400 MHz): −6.58 (s, 2H, T_1(min) = 31 ± 1 ms), −11.38 (p, 1H, J_{HP} = 18.9 Hz, T_1(min) = 143 ± 2 ms). FAB MS calcd. for $C_{42}H_{45}{}^{192}OsP_4$: 865.1; obsd.: 861 ($M^+$ − 4H).

Method B

This synthesis is analogous to that above with the exceptions that *trans*-OsHClL and not *cis*-β-$OsCl_2L$ is the precursor complex, and the only visual evidence of reaction is NaCl formation; shorter reaction times are generally employed.

Observation of Os(HD)H, Os(HD)D, and Os(D_2)H isotopomers of [OsH(H_2)L]BPh_4

Acetone-d_6 solutions of *trans*-[OsH(H_2)L]BPh_4 show changes in the high-field ^{1}H NMR spectrum (200 MHz) over time, owing to intermolecular H^+/D^+ exchange with acetone-d_6. Several ^{1}H NMR spectra of samples with varying degrees of deuterium incorporation were analyzed. Two 1:1:1 triplets grow in at −6.36 (J_{HD} = 26.4 Hz) and −6.28 ppm (J_{HD} = 26.4 Hz) due, respectively, to the Os(HD)H and Os(HD)D isotopomers. Concomitant change in the terminal hydride resonance is observed. Pentets (J_{PH} ~ 18.5 Hz) emanating from the Os(HD)H and Os(D_2)H isotopomers emerge at −11.29 and −11.37 ppm, respectively. The $[OsH(HD)L]^+$ isotopomer appears first.

J_{HD} values were confirmed at 400 MHz by using an inversion–recovery pulse sequence to null the H_2 signal (from Os(H_2)X, X = H, D, isotopomers) which has a shorter T_1 time than the HD signals.

Synthesis of trans-*[RuH(H_2)L]$^+X^-$, X^- = BPh_4^-, PF_6^-, BF_4^-*

Method A

trans-RuHClL (0.26 g, 0.32 mmol) was dissolved in 5 mL THF. Under 1 atm H_2, $NaBPh_4$ (0.165 g, 0.482 mmol) was added ($NaPF_6$ can be used in place of $NaBPh_4$) and the mixture was allowed to stir for 4.5 h. The yellow solution was then evaporated to dryness and the residue was redissolved in CH_2Cl_2. The mixture was then filtered through Celite and the volume of the filtrate reduced to 2 mL. Addition of MeOH caused precipitation of a tan solid (0.23 g, 66%). IR (Nujol): 1964 (Ru-H) cm^{-1}. ^{1}H NMR (CD_2Cl_2, 200 MHz) δ: 8.6–6.7 (m, PC_6H_5), 3.0–0.9 (6 m, PCH_2CH_2P), −5.1 (br s, Ru(H_2)), −12.7 (p, Ru*H*, $^2J_{HP}$ = 18.9 Hz). FAB MS calcd. for $C_{42}H_{45}P_4{}^{102}Ru$: 775; obsd.: 772 ($M^+$ − 3H).

Method B

trans-Ru(H_2)L (0.10 g, 0.12 mmol) was suspended in 3 mL diethyl ether. Under 1 atm H_2, 1 drop of $HBF_4{\cdot}Et_2O$ was added with stirring. A white solid immediately precipitated. This white solid was allowed to settle and the ether supernatant was syringed out. The solid (0.83 g) was then washed with diethyl ether (2 × 2 mL) to remove the excess acid.

Reaction of trans-*[RuH(H_2)L]BPh_4 with excess lithium chloride*

Under 1 atm Ar, *trans*-[RuH(H_2)L]BPh_4 (0.030 g, 0.027 mmol) was dissolved in 5 mL THF and LiCl (0.023 g, 0.54 mmol) was added. This mixture was stirred overnight, after which time the solvent was removed and the residue was redissolved in benzene. This was then filtered through Celite and the volume of the filtrate was reduced to 1 mL. Addition of hexanes produced a tan-yellow precipitate (0.015 g, 68%), which was identified as the major isomer of *trans*-RuH(Cl)L (see above).

Reaction of trans-*[RuH(H_2)L]BPh_4 with D_2*

trans-[RuH(H_2)L]BPh_4 (0.020 g, 0.18 mmol) was dissolved in 0.7 mL CD_2Cl_2 in a 5 mm NMR tube. Deuterium was gently bubbled through the solution for 1 min. A ^{1}H NMR spectrum (200 MHz) was collected immediately and again after 30 h, to observe any changes in the shape and (or) intensity of the hydride signal. Sets of 1:1:1 triplets were observed over time due to the Ru(HD)(H) and Ru(HD)(D) isotopomers (see below). The $^1J_{HD}$ values were confirmed by performing an inversion–recovery pulse sequence on the sample to null out the H_2 signal.

Synthesis of trans-*[FeH(H_2)L]BF_4*

Fe(H_2)L (0.5 g, mmol) was partially dissolved in 50 mL of diethyl ether to produce a yellow suspension. Under 1 atm of Ar or H_2, 0.5 mL of $HBF_4{\cdot}Et_2O$ (excess) was added dropwise over a period of 1 min with stirring. Immediately a yellow, powdery solid precipitated out, causing the solution to turn almost colourless. The solid was filtered off and washed several times with diethyl ether (80% yield). FAB MS calcd. for $C_{42}H_{45}{}^{56}FeP_4$: 729.3; obsd.: 729 (M^+).

Synthesis of [FeH(HD)L]BF_4

To prepare a solution of DBF_4, D_2O was added dropwise to 1 mL of $HBF_4{\cdot}Et_2O$ until the effervescence ceased. Addition of 0.1 mL of this mixture to a suspension of Fe(H_2)L (0.03 g, 0.041 mmol) in ether proceeded as described above. δ (^{1}H, CD_2Cl_2, 293 K): −9.80 (1:1:1 t, $^1J_{HD}$ = 32.3 Hz). δ (^{2}H{^{1}H}, CH_2Cl_2, 293 K): −9.81 (s).

Preparation of trans-*[OsH(CH_3CN)L]BPh_4*

trans-[OsH(H_2)L]BPh_4 (0.204 mmol) was prepared as a pale yellow residue as described previously. Under an Ar atmosphere, 2 mL THF and 2 mL CH_3CN were added to the pale yellow residue and the resulting solution refluxed for 2.5 h. After cooling, the solvent was removed and replaced with 2 mL acetone and 5 mL CH_2Cl_2. Addition of 5 mL MeOH followed by solvent reduction to ~6 mL and cooling yielded the cream-coloured product, which was washed with Et_2O and dried in vacuo (0.134 g, 52%). IR (Nujol): 2258 (w, C-N), 1952 (mw, Os-H) cm^{-1}. FAB MS calcd. for $C_{44}H_{46}N^{192}OsP_4$: 904.1; obsd.: 904 (M^+), 861 (M^+ − CH_3CN − H_2), and very weak peaks at 925 and 1077 due to Os species.

Preparation of trans-*[OsH(CO)L]BPh_4*

THF (10 mL) was added to a yellow residue of *trans*-[OsH(H_2)L]BPh_4 (0.10 mmol) and the pale yellow solution was refluxed under CO atmosphere for ~4 h. After cooling, the solution volume was reduced to ~0.5 mL and 1 mL acetone was added. Addition of 5 mL MeOH to the slurry followed by cooling yielded the cream-coloured product, which was washed with Et_2O and dried in vacuo (0.055 g, 45%). IR (Nujol): 1989 (m, C-O),1900 (w, Os-H) cm^{-1}. FAB MS calcd. for $C_{43}H_{43}O^{192}OsP_4$: 891.1; obsd.: 891 (M^+), 861 (M^+ − CO − H_2), and very weak peaks at 925 and 1077 due to Os species.

Synthesis of trans-*[RuH(PMe_2Ph)L]PF_6*

trans-RuHClL (0.10 g, 0.12 mmol) was dissolved in 5 mL THF. PMe_2Ph (0.017 g, 0.12 mmol) and $NaPF_6$ (0.021 g, 0.12 mmol) were added with stirring. This pale yellow mixture was stirred for 24 h, after which time the solvent was removed under reduced pressure. The residue was redissolved in CH_2Cl_2 and the solution was filtered through Celite. The volume of the filtrate was reduced to 2 mL and addition of diethyl ether afforded a pale yellow solid (0.073 g, 56%). ^{1}H NMR (THF-d_8, 200 MHz) δ: 8.3–6.5 (m, PC_6H_5), 2.8–1.0 (6 m, PCH_2-CH_2P), 0.8 (d, PCH_3), −13.7 (dp, RuH, *cis*-$^2J_{HP}$ = 20.6 Hz, *trans*-$^2J_{HP}$ = 59.3 Hz). FAB MS calcd. for $C_{50}H_{54}P_5{}^{102}Ru$: 912, obsd.: 912 ($M^+$), 772 ($M^+$ − H − PMe_2Ph).

Synthesis of trans-*[RuH(CH_3CN)L]PF_6*

trans-RuHClL (0.12 g, 0.15 mmol) was dissolved in 3 mL CH_3CN – 2 mL THF. $NaBF_4$ (0.024 g, 0.22 mmol) was added and the solution was stirred for 24 h. The solvent was then removed under reduced pressure and the pale yellow residue was redissolved in CH_2Cl_2. After filtering through Celite, the volume of the filtrate was reduced to 2 mL and addition of diethyl ether produced a pale yellow solid (0.072 g, 54%). IR (Nujol): 1991 (Ru-H) cm^{-1}. ^{1}H NMR (CD_2Cl_2, 200 MHz) δ: 8.0–6.8 (m, PC_6H_5), 2.8–1.0 (6 m, PCH_2CH_2P), 1.9 (s, CH_3CN), −18.3 (p, Ru*H*, $^2J_{HP}$ = 19.7 Hz). FAB MS calcd. for $C_{44}H_{46}NP_4{}^{102}Ru$: 814; obsd.: 771 ($M^+$ − 2H − CH_3CN).

Results and discussion

Synthesis of the tet-1 ligand

A new route was discovered for the preparation of tet-1 (eq.

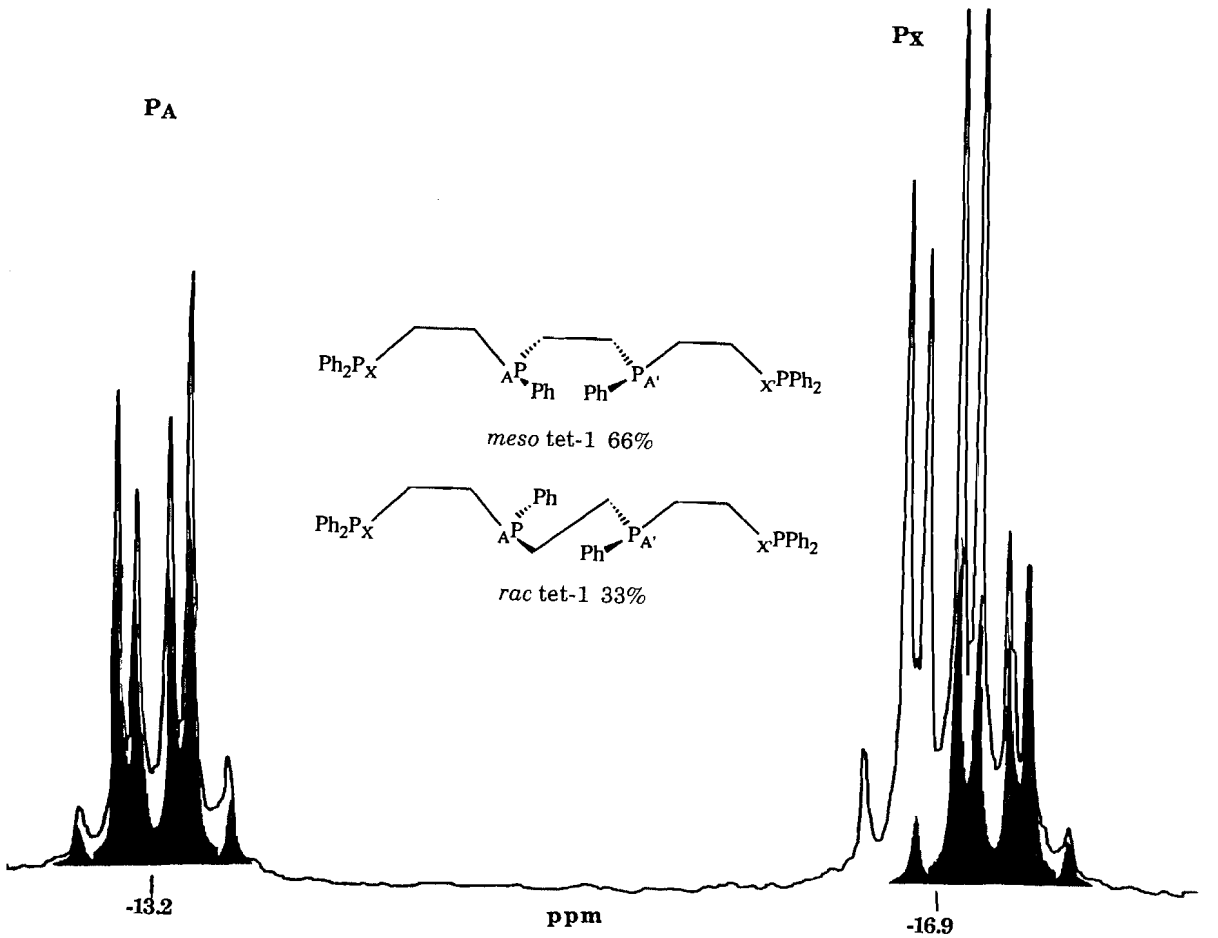

FIG. 2. $^{31}P\{^{1}H\}$ NMR spectrum of tet-1 in THF. Shaded resonances are due to the *rac* form of the ligand.

[1]) in higher yield than the published method (26). This involved the reaction of the dilithium diphosphide, Lippe·4THF, with 2 equiv. of $Ph_2CH_2CH_2Cl$ (eq. [1]) to give the tet-1 ligand as a ratio of about 70% *meso*/30% *rac* according to ^{31}P NMR.

[1] $Ph(Li)PCH_2CH_2P(Li)Ph \cdot 4THF + 2\ Ph_2CH_2CH_2Cl \rightarrow$

$Ph_2PCH_2CH_2P(Ph)CH_2CH_2P(Ph)CH_2CH_2PPh_2 + 2\ LiCl + 4\ THF$

The *rac* and *meso* forms are separated by fractional crystallization. The ^{31}P NMR spectrum of each isomer in THF is an AA'XX' pattern with the high-field XX' part displaying a slightly different chemical shift for each isomer (see Fig. 2). The X phosphorus nuclei are thought to be the terminal ^{31}P nuclei of the chain. As indicated in the introduction, this paper will describe the chemistry of the *meso*-tet-1 ligand, abbreviated L.

Synthesis of the precursor complexes

A mixture of the dichlorides *cis*-β-$OsCl_2L$ and *cis*-α-$OsCl_2$(*rac*-tet-1) (15) was prepared from $[Os_2Cl_3(PPh_2Et)_6]Cl \cdot 2H_2O$ and the commercially available *meso/rac* tet-1 mixture in the absence of solvent at 200°C (reaction [2]) by a method similar to that of Chatt and Hayter (18).

[2] $[Os_2Cl_3(PPh_2Et)_6]Cl + meso/rac\text{-tet-1} \rightarrow 1.4\ cis\text{-}\beta\text{-}OsCl_2L$

$+ 0.6\ cis\text{-}\alpha\text{-}OsCl_2(rac\text{-tet-1}) + 6\ PPh_2Et$

Under the reaction conditions employed, the phosphorus centres of the free ligand racemize to give the thermodynamic ratio of 66% *meso*, 33% *rac* (13) so that complexes containing both forms of the ligand are obtained. The osmium dichlorides are easily separated since the *rac*-tet-1 complex (33% of the mixture) is much less soluble in THF than *cis*-β-$OsCl_2L$. *cis*-β-$OsCl_2L$, as a light yellow powder, was characterized by elemental analysis, FAB MS, and ^{31}P NMR, for which the ANQY spin pattern is very distinctive (Table 1 and see below).

A mixture of isomers, *trans*-OsH(Cl)L, is produced in reaction [3], which is analogous to the one used to prepare *trans*-$OsHCl(depe)_2$ (28, 29).

[3] *cis*-β-$OsCl_2L + LiAlH_4$

$\xrightarrow[\text{2. EtOH}]{\text{1. reflux in THF}} \xrightarrow{\text{3. NaCl acetone}}$

major-*trans*-OsH(Cl)L + minor-*trans*-OsCl(H)L

The "major" isomer is the one produced in larger amount (≥70%) and sometimes exclusively. The light yellow mixture was characterized by FAB MS, IR, and ^{1}H and ^{31}P NMR (Table 2 and see below). Since the two axial sites of these *trans*-MXYL complexes are different, the two isomers differ in the placement of hydride and chloride ligands relative to the four-phenyl binding site. NMR methods establish that the com-

Can. J. Chem. Downloaded from www.nrcresearchpress.com by 195.246.54.202 on 09/08/12
For personal use only.

TABLE 1. $^{31}P\{^1H\}$ NMR spectral data of some *cis*-β-MXYL complexes (refer to Fig. 3 for the numbering scheme)

Complex	δP_1 (ppm)	δP_2 (ppm)	δP_3 (ppm)	δP_4 (ppm)	J_{12} (Hz)	J_{13} (Hz)	J_{14} (Hz)	J_{23} (Hz)	J_{24} (Hz)	J_{34} (Hz)
$OsCl_2L$[a]	5.9	68.3	44.4	11.0	5.5	327.0	16.4	2.4	5.5	2.4
$RuCl_2L$[a]	28.4	109.9	73.7	57.4	14.3	356.3	29.3	18.3	27.5	9.6
$Os(H)_2L$[a]	41.0	97.3	72.1	45.3	0	252.7	17.5	11	11	10
$[RhO_2L]^+$[b]	42.1	111.0	67.3	58.1	3	416	22	10	11	11

[a]In THF.
[b]In CH_2Cl_2, from ref. 13.

TABLE 2. ^1H (hydride region) and $^{31}P\{^1H\}$ (AA'QQ') NMR spectral data for complexes *trans*-MX(Y)L

	^1H NMR			^{31}P NMR			
Complex	Solvent	δH[a] (ppm)	$^2J_{PH}$ (Hz)	Solvent	δP_Q[b] (ppm)	δP_A[b] (ppm)	*trans*-$^2J_{AQ}$ (Hz)
$RuCl_2L$				Toluene	41.4	98.4	290
Major OsH(Cl)L	C_6D_6	−22.2 p	17.5	THF	26.6	61.8	248
Minor OsH(Cl)L	C_6D_6	−19.6 p	13.5	THF	31.9	89.5	248
Major RuH(Cl)L	C_6D_6	−20.9 p	20.8	THF	55.7	93.8	248
Minor RuH(Cl)L	C_6D_6	−17.6 p	17.6	THF	58.1	117.1	243
$Ru(H)_2L$	C_6D_6	−7.9 dtt[c]	15, 20	THF	76.4	120.4	227
		−10.2 dp[c]	18, 19				
$Fe(H)_2L$	C_6D_6	−12.8 dtt[d]	34, 41	THF	101.6	143.5	n.r.[e]
		−14.7 dp[d]	38, 38				
$[OsH(H_2)L]^+$	CD_2Cl_2	−6.6 s	0	THF	32.5	78.0	185
		−11.4 p	19				
$[RuH(H_2)L]^+$	CD_2Cl_2	−5.1 s	0	THF	63.4	107.4	193
		−12.7 p	19				
$[FeH(H_2)L]^+$	CD_2Cl_2	−9.8 s	0	THF	89.6	130.3	58
		−16.7 p	44				
$ReH(H)_2L$[f]	C_6D_6	−6.9 tt	5, 17	THF	56.0	100.6	n.r.[e]
$[OsH(CH_3CN)L]^+$	ac-d_6	−18.7 p	17.9	ac	31.2	70.8	221
$[RuH(CH_3CN)L]^+$	CD_2Cl_2	−18.3 p	19.7	CH_3CN	60.4	101.3	220
$[OsH(CO)L]^+$	ac-d_6	−10.6 p	20.7	THF	28.0	70.6	183
$[RuH(PMe_2Ph)L]^+$	THF-d_8	−13.7 dp[g]	20.6	THF	58.7[h]	98.7[h]	201[h]

[a]p = pentet, ac = acetone.
[b]P_A are the internal phosphorus atoms while P_Q are the terminal phosphorus atoms of the tetraphos chain.
[c]J_{HH} = 14 Hz.
[d]J_{HH} = 18 Hz.
[e]Not resolved.
[f]Reference 44.
[g]*trans*-$^2J_{PH}$ = 59.3 Hz.
[h]δ(PMe_2Ph) = −14.3 p, *cis*-$^2J_{PP}$ = 20.0 Hz.

plexes are *trans* but do not allow the unambiguous assignment of the structure of the isomers. Crystals suitable for an X-ray study were not available. On the basis of steric repulsion arguments, it can be postulated that the major isomer has the smaller hydride ligand in the four-phenyl binding site.

We find that all three steps of reaction [3] are necessary. The reaction of lithium aluminum hydride with *cis*-dichlorobis(diphosphine)osmium(II) compounds is known to produce the corresponding dihydrido and *trans*-hydridochloro complexes (28, 30). However, addition of ethanol following the reaction often does not completely cleave aluminum species associated with the osmium centre. Treatment with sodium chloride in boiling acetone circumvents this problem (step 3 in reaction [3]) (29).

A alternative route to the major isomer of OsH(Cl)L is outlined in reaction [4].

[4] *cis*-β-$OsCl_2L$ + $NaBPh_4$ $\xrightarrow{\text{1. stir in THF, } H_2}$ $\xrightarrow{\text{2. } NEt_3}$ major-*trans*-OsH(Cl)L

In the first step, the complex $[OsH(H_2)L]BPh_4$ is generated along with HCl (see below). The second step produces $[NEt_3H]Cl$, which reacts with the dihydrogen complex to give the product, H_2, and $[NEt_3H]BPh_4$.

When *cis*-β-$OsCl_2L$ was reacted with $NaBPh_4$ and three equivalents of NaO^{t}Bu in THF under H_2, the complex *cis*-β-$Os(H)_2L$ was produced. This was characterized only by NMR (Table 1 and see below).

The starting material for the ruthenium chemistry, *trans*-$RuCl_2L$, is prepared in about 90% yield by the reaction of the pure *meso* isomer of L with the *cis*-$RuCl_2(DMSO)_4$ complex as in eq. [5].

[5] *cis*-$RuCl_2(DMSO)_4$ + L $\xrightarrow{\text{reflux in toluene}}$ *trans*-$RuCl_2L$ + *cis*-β-$RuCl_2L$

The yellow *trans* isomer has already been identified (27). A

Can. J. Chem. Downloaded from www.nrcresearchpress.com by 195.246.54.202 on 09/08/12
For personal use only.

Can. J. Chem. Downloaded from www.nrcresearchpress.com by 195.246.54.202 on 09/08/12
For personal use only.

small amount of the *cis*-β isomer is also identified in the reaction mixture by use of ^{31}P NMR (Table 1, see below).

Hydrido ruthenium complexes are prepared from the relatively inert complex *trans*-$RuCl_2L$ according to reaction [6].

[6] *trans*-$RuCl_2L$ + excess $LiAlH_4$ $\xrightarrow{\text{1. reflux in THF}}$ impure-*trans*-$Ru(H)_2L_2$ $\xrightarrow{\text{2. } Cl^-, EtOH}$ major-*trans*-RuH(Cl)L + minor-*trans*-RuCl(H)L

In the first step, the new complex *trans*-$Ru(H)_2L$ is produced along with aluminum salts that are difficult to remove; the dihydride is identified in the reaction mixture by ^{31}P NMR. An inseparable mixture of isomers of *trans*-RuH(Cl)L is produced in the second step. The minor isomer makes up about 15% of the mixture. The tan-coloured mixture was characterized by elemental analysis, FAB MS, and NMR as described below. The properties are analogous to those of the *trans*-OsH(Cl)L isomers. The mixture as a Nujol mull has a very weak hydride stretch at 1989 cm^{-1}. $^1H/^{31}P$ hetercorrelation and nOe difference NMR spectroscopy did not allow unambiguous assignment of the stereochemistry of these isomers (31). Two attempts were made at obtaining a crystal structure of needles of *trans*-RuHClL, both of which failed due to crystal degradation.

The second step of reaction [6] probably proceeds via protonation of RuH_2L by ethanol to give *trans*-$[RuH(H_2)L]^+$, which then reacts with chloride to give the RuH(Cl)L products. The reactions of alcohols with dihydrides to give dihydrogen complexes is well established (6, 32–34). The reaction of *trans*-$[RuH(H_2)L]^+$ with chloride to give *trans*-RuH(Cl)L is described below.

The pale-yellow dihydride *trans*-$Ru(H)_2L$ is prepared in 50% yield by reacting the mixture of RuH(Cl)L isomers with sodium ethoxide (eq. [7]).

[7] *trans*-RuH(Cl)L + NaOEt $\xrightarrow{\text{THF}}$ *trans*-$Ru(H)_2L$ + unidentified products

The FAB MS of the dihydride had peaks in the correct isotopic distribution for $[RuHL]^+$. The loss of dihydrogen from $[RuH(H_2)L]^+$ (see below), the product of the protonation of RuH_2L by the nitrobenzylalcohol matrix, would explain this observation. The ^1H and ^{31}P NMR spectra are fully consistent with the *trans*-dihydride formulation (Table 2 and see below). A weak absorption in the IR at 1966 cm^{-1} may be the Ru–H stretch. Attempts at making RuH_2L directly by reacting $RuCl_2L$ and NaOEt were only partially successful because some starting material remained after several days of reaction at reflux in THF.

trans-$Fe(H)_2L$ was prepared in 80% yield according to eq. [8] in a similar fashion to $FeH_2(dppe)_2$ (35).

[8] $FeCl_2$ + L + $NaBH_4$ $\xrightarrow{\text{THF/EtOH}}$ *trans*-$Fe(H)_2L$ + unidentified products

The bright yellow powder has a low-frequency H–Fe–H stretch at 1724 cm^{-1} characteristic of *trans* hydrides. The complex was also characterized by elemental analysis, FAB MS, and NMR (see Table 2). The major ion according to the mass spectrum was FeL^+; the loss of hydride ligands under these conditions is not uncommon (34).

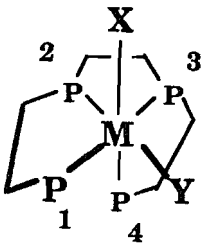

FIG. 3. Numbering scheme.

NMR spectra of the precursor complexes with a cis-β *geometry*

Table 1 lists the parameters that define the ANQY first-order spin systems of these complexes. The numbering of the nuclei are shown in Fig. 3 and follow the example of Brown and Canning (13).

The nuclei P_2 and P_3 are characterized in each case by the largest downfield shifts produced because they are part of two five-member rings (36). Nuclei P_1 and P_3 are uniquely defined by a large *trans*-$^2J_{13}$ coupling constant. This ranges from 253 Hz for *cis*-β-$Os(H)_2L$, to 327 Hz for *cis*-β-$OsCl_2L$, and to 416 Hz for the only complex of this type in the literature, *cis*-β-$[RhO_2L]^+$ (13). There is a marked similarity between the last complex and $Os(H)_2L$ in terms of chemical shifts and *cis* coupling constants. For all the complexes the following relation applies:

$$\delta P_2 > \delta P_3 > \delta P_4 > \delta P_1$$

By inspection of Fig. 3, one notes that the complex *cis*-β-$Os(H)_2L$ will have inequivalent hydrides. Indeed there are two resonances in the ^1H NMR spectrum, one at −7.7 ppm as a doublet of quartets of doublets (dqd) with coupling constants *trans*-$^2J_{PH}$ of 56, *cis*-$^2J_{PH}$ of 15, and *cis*-$^2J_{HH}$ of 4 Hz and the other at −10.21 ppm as a dqd pattern with *trans*-$^2J_{PH}$ of 64, *cis*-$^2J_{PH}$ of 15, and *cis*-$^2J_{HH}$ of 4 Hz.

NMR spectra of the precursor complexes trans-*MX(Y)L*

The $^{31}P\{^1H\}$ NMR spectra of the Ru and Os complexes are distinctive AA′QQ′ patterns with a large *trans*-$^2J_{AQ}$ coupling (Fig. 4). The *cis* couplings $^2J_{AA'}$, $^2J_{QQ'}$, and $^2J_{AQ'} = {}^2J_{A'Q}$ are not resolved at 81 MHz. The downfield resonance is always assigned to P_A, the central P atoms of the tet-1 chain, which are in two five-member rings. Table 2 lists the chemical shifts and *trans*-$^2J_{AQ}$ coupling constant. The Fe complexes have a smaller coupling *trans*-$^2J_{AQ}$, which is difficult to resolve (Fig. 5).

There is the usual trend (6) in chemical shifts for isostructural complexes MHClL, MH_2L, and $[MH(H_2)L]^+$ (see belowalso):

$$\delta(PFe) > \delta(PRu) > \delta(POs)$$

An additional trend is the downfield shift of $\delta(^{31}P)$ on substitution of chloride by hydride:

$$\delta(LRuH_2) > \delta(LRuHCl) > \delta(LRuCl_2)$$

There is a surprisingly large difference between the major and minor isomers of *trans*-MH(Cl)L, both for Ru and Os, in terms of the chemical shift of the P_A nuclei in the middle of the tet-1 chain. A simple interchange of *trans* H and Cl ligands

Can. J. Chem. Downloaded from www.nrcresearchpress.com by 195.246.54.202 on 09/08/12
For personal use only.

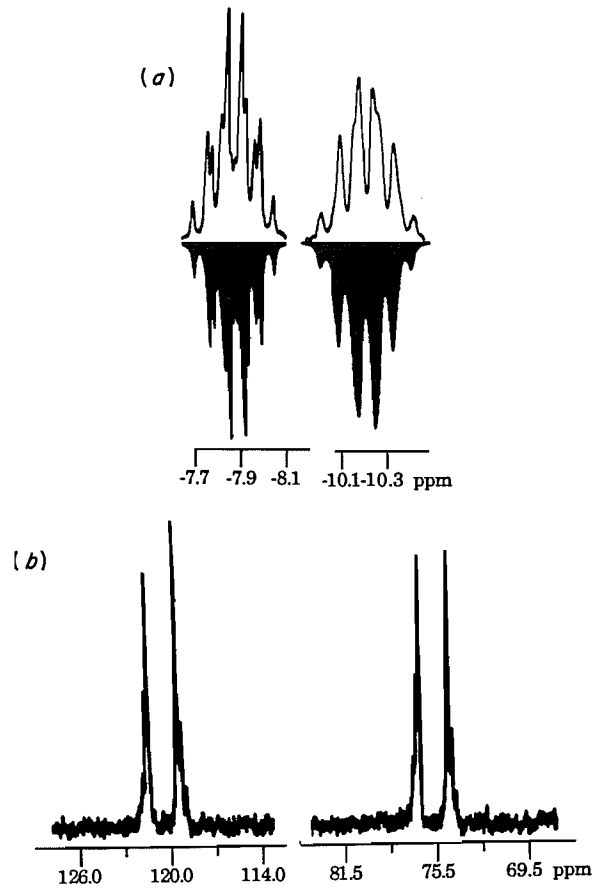

FIG. 4. (*a*) The observed ^1H NMR spectrum (200 MHz) and simulated (inverted spectrum) in the high-field region of *trans*-$Ru(H)_2L$ in C_6D_6. (*b*) The $^{31}P\{^1H\}$ NMR spectrum (120.5 MHz) of *trans*-$Ru(H)_2L$ in THF.

between the four-phenyl and two-phenyl binding sites greatly perturbs the chemical shift tensor of P_A.

In the high-field ^1H NMR spectra, resonances due to terminal hydrides in the *trans*-MH(X)L complexes should have different couplings *cis*-$^2J_{PH}$, between hydride and atoms P_A and P_Q. In most cases these constants are very similar and so pentets (or doublets of pentets for X = H) are observed.

The spectra of complexes *trans*-$M(H)_2L$ have distinct hydride resonances for the two inequivalent hydrides, one in the four-phenyl site and the other in the two-phenyl site. There is a rarely observed *trans*-$^2J_{HH}$ coupling because of this inequivalence. The magnitudes of these couplings for Ru and Fe are surprisingly small — 14 and 18 Hz, respectively — when compared to *trans*-$^2J_{PP}$ coupling constants (Table 2) and the *trans*-$^2J_{PH}$ coupling of 59.3 Hz for *trans*-$[RuH(PMe_2Ph)L]PF_6$ (see below). The other report of such a *trans*-$^2J_{HH}$ coupling is the 5.0 Hz coupling in *mer*-$IrH_3\{N(SiMe_2CH_2PPh_2)_2\}$ (37). We note that the following relationship might exist between *trans*-$^2J_{PH}$, *trans*-$^2J_{PP}$, and *trans*-$^2J_{HH}$ constants:

$$|trans\text{-}^2J_{PH}| \approx (trans\text{-}^2J_{PP})^{1/2}(trans\text{-}^2J_{HH})^{1/2}$$

For the Ru complexes of this work the absolute values are ≈60, ≈260, and 14, respectively. For Fe complexes the few values known are less than 20 Hz for each of these *trans* couplings (38–41).

If one assumes that the ring currents of the neighbouring phenyl groups diamagnetically shield the hydride, then one can assign the higher field resonance to the hydride in the four-phenyl site. On this basis the hydride with the resonance at −10.2 ppm for Ru and −14.7 for Fe is in the four-phenyl site in the complexes *trans*-$M(H)_2L$. One might also assume that the hydride in the four-phenyl site would have a shorter spin lattice relaxation time, T_1, because there are eight *ortho* protons on the phenyls near this site to relax the hydride nucleus while there are only four *ortho* protons potentially near to the other site. By this criterion the hydride with the other resonance (at −7.9 ppm for RuH_2L) is in the four-phenyl site because it has the shorter T_1, at all temperatures between 294 and 180 K, than the other hydride with δ −10.2 (see experimental section). Similarly, the downfield hydride resonance of FeH_2L also has a shorter T_1 at 293 K. Therefore these NMR arguments contradict each other and do not give an unambiguous assignment. The problem with these ideas is that the preferred orientation of the phenyl groups is not known.

These arguments do appear to be consistent when assigning the hydrides of the major and minor isomers of *trans*- RuH(Cl)L. The major isomer has the hydride with more negative chemical shift of −20.9 ppm versus −17.6 ppm for the minor isomer (Table 2). The T_1 values for the hydride of the major isomer are smaller at all temperatures between 294 and 180 K relative to those of the minor isomer (see experimental section). This assignment is also consistent with steric arguments where the major isomer will have the chloride at the two-phenyl site. Similarly, the major isomer of OsH(Cl)L has the higher field hydride resonance and probably also has the chloride at the two-phenyl site.

Preparation of the dihydrogen complexes $[MH(H_2)L]^+$

The white dihydrogen complexes *trans*-$[MH(H_2)L]^+$, M = Os, Ru, of which only one isomer is ever obtained, are made by the reaction of both isomers of *trans*-RuHClL or the pure major isomer of *trans*-OsHClL with a slight excess of $NaBPh_4$ under one atmosphere of hydrogen (eq. [9]).

[9] *trans*-MHClL + 1.5 $NaBPh_4$ + H_2 (g) → *trans*-$[MH(H_2)L]BPh_4$ + NaCl

It is therefore likely that rearrangement of the ligand framework occurs for one of the *trans*-RuHClL isomers prior to dihydrogen coordination to the vacant axial site. The complexes are unstable and difficult to precipitate. They have been characterized by ^1H and ^{31}P NMR (see below) and FAB MS. The Ru complex has a weak IR absorption at 1964 cm^{-1}, which might be assigned to the Ru—H stretch. There was no evidence for an absorption due to the H—H stretch. *trans*-$[RuH(H_2)L]BPh_4$ does not lose dihydrogen in solution or the solid state when under argon or vacuum as readily as does *trans*-$[RuH(H_2)(dppe)_2]BPh_4$ (6). A sample of *trans*-FeHClL failed to give the Fe dihydrogen complex under the conditions of reaction [9]. Similarly the five-coordinate complex [FeHL]Br (10) failed to react with 1 atm H_2 even though it reacted with N_2 to give $[FeH(N_2)L]Br$ (11).

trans-$[OsH(H_2)L]BPh_4$ is more readily prepared, in less than 24 h, directly from the dichloride precursor in THF at 293 K in the unusual reaction [10].

[10] *cis*-β-$OsCl_2L$ + $NaBPh_4$ + 2 H_2 → *trans*-$[OsH(H_2)L]BPh_4$ + NaCl + HCl

Can. J. Chem. Downloaded from www.nrcresearchpress.com by 195.246.54.202 on 09/08/12
For personal use only.

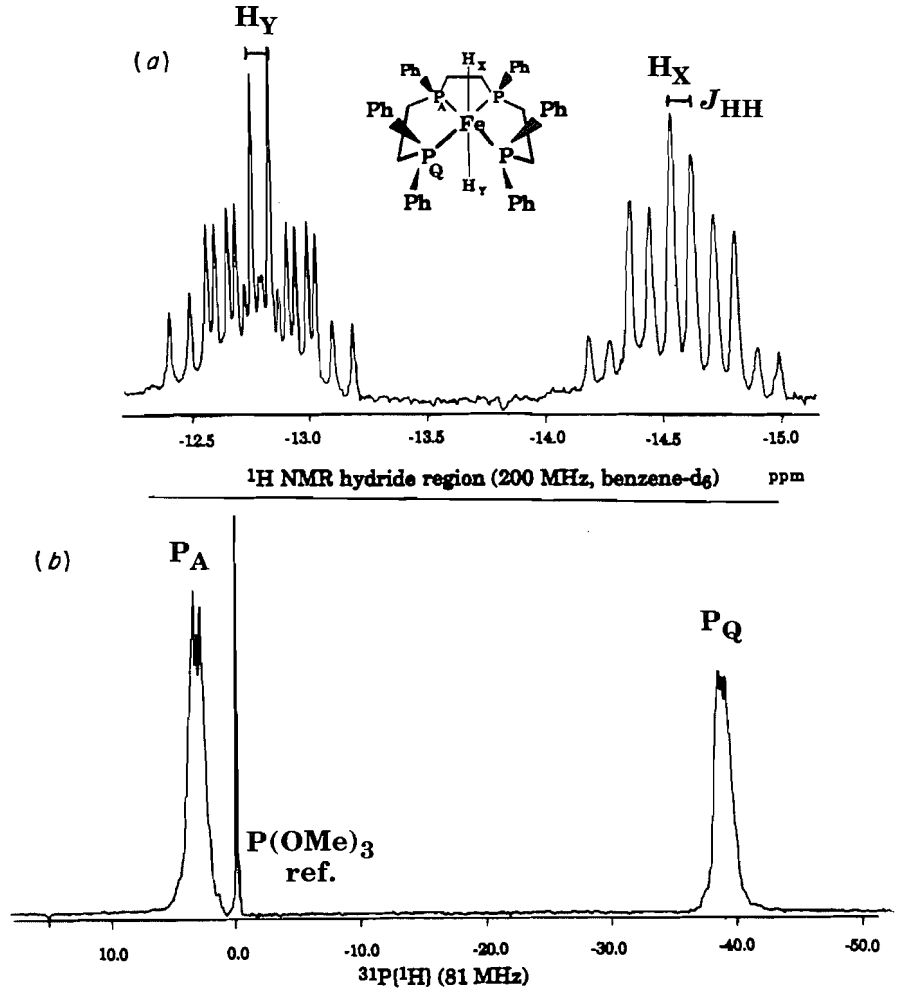

FIG. 5. The (*a*) ^{1}H NMR and (*b*) ^{31}P{^{1}H} NMR spectra of *trans*-Fe(H)$_2$L referenced to P(OMe)$_3$ (δ(P(OMe)$_3$) = 140.4 versus H_3PO_4).

The HCl was indirectly detected by ^{1}H NMR at the end of the reaction by adding NEt_3 and observing $HNEt_3^+$ and the OsH(Cl)L produced as in reaction [4]. The isomer of the dihydrogen complex is the same one as produced in reaction [9]. Reaction [10] probably proceeds via an, as yet undetected, intermediate complex $[OsCl(H_2)L]^+$, which readily loses HCl (42). The complexes *trans*$[MCl(H_2)(diphosphine)_2]^+$, M = Os, Ru, have been recently reported (31, 42, 43).[2]

Protonation of *trans*-M(H)$_2$L, M = Fe, Ru, in ether yielded H_2 complexes (reaction [11]).

[11] *trans*-M(H)$_2$L + HBF_4 → *trans*-[MH(H$_2$)L]BF_4

The Ru complex in solution produced by reaction [11] has identical properties to the one made via reaction [9]. The iron complex is an air-sensitive pale-yellow solid that was characterized by FAB MS and NMR (see below).

NMR properties of the dihydrogen complexes trans-*[MH(H$_2$)L]$^+$*

The ^{31}P NMR spectra (Table 2) of these complexes are AA′QQ′ patterns characteristic of the *trans* geometry of these complexes. The ^{1}H NMR spectra (Table 2) are all similar to that of the Fe complex shown in Fig. 6 (bottom). The dihydrogen peak is broad with a short T_1 value while the terminal hydride resonance is a sharp pentet with fortuitously equivalent *cis*-$^2J_{PH}$ coupling constants and with a long T_1 value (Table 3). The lack of a resolved *cis*-$^2J_{PH}$ coupling in the H_2 resonance is a common feature of dihydrogen complexes (6).

The sharp pentet resonance of the terminal hydride of the Fe and Os complexes contrasts with the broad resonances observed for the corresponding complexes $[MH(H_2)(dppe)_2]^+$ (see, for example, Fig. 6). The dppe complexes are fluxional because of H-atom exchange between the H and H_2 ligands and this causes line broadening at room temperature. This is clearly prevented in the tet-1 complexes because there is no line broadening or averaging of T_1 values of the H and H_2 ligands. The seven-coordinate trihydride complex $Re(H)_3L$ has rapid intramolecular H-atom exchange (44). Therefore the role of the tet-1 ligand in the cationic dihydrogen complexes is to favor six-coordination over seven-coordination.

Variable temperature measurements of the T_1 values of the hydrogen ligands (Table 3) were used to positively identify the presence of an H—H bond in these new dihydrogen complexes. Calculated curves were fitted to the observed T_1 values for the dihydrogen and hydride ligands to obtain an accurate minimum T_1 time, T_1(min), and a dihydrogen bond length, d_{HH}, with the assumption of rapid H_2 spinning as described previously (45). This assumption is valid because the deuterated isotopomers of these complexes have large J(H, D) couplings (see below). The

[2]Also P.A. Maltby. Ph.D. thesis, University of Toronto, 1993.

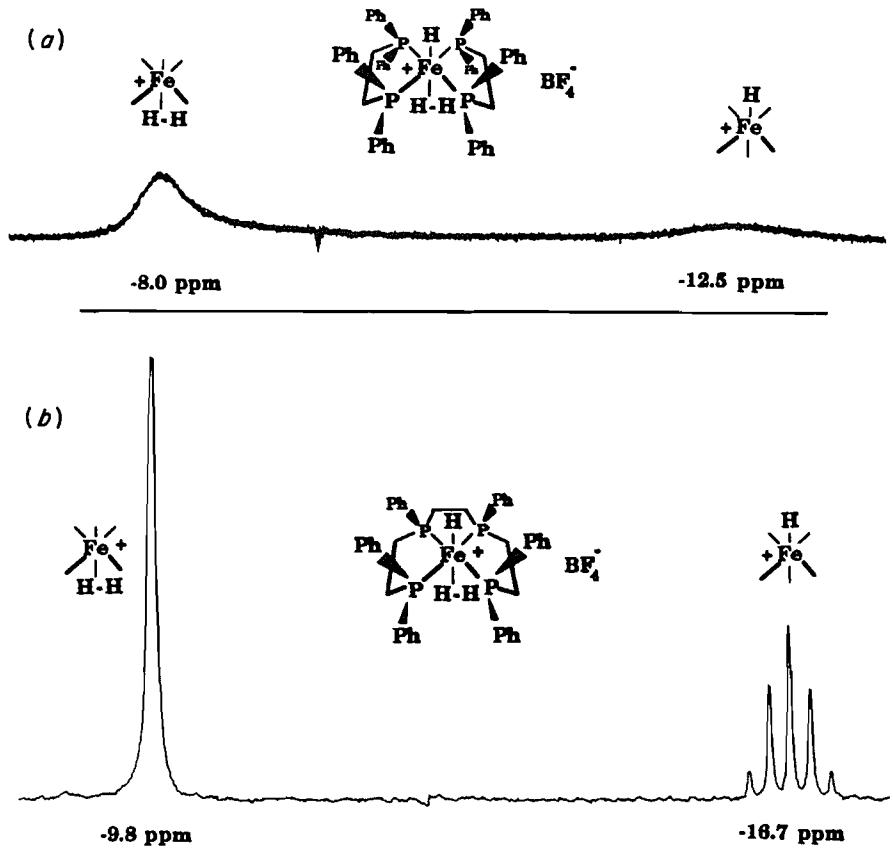

FIG. 6. (*a*) ^{1}H NMR spectrum (high-field region) at 200 MHz of $[FeH(H_2)(dppe)_2]BF_4$ in acetone-d_6 at 20°C. (*b*) Corresponding spectrum of the complex $[FeH(H_2)L]BF_4$ in CD_2Cl_2 at 20°C.

TABLE 3. Observed (and calculated[a]) T_1 values of the dihydrogen and hydride ligands in the complexes $[MH(H_2)L]^+$

			$[FeH(H_2)L]BF_4$[b]			
T, K	293	271	254	233		
T_1 of $Fe(H_2)$, ms	35(30)	22(23)	19(19)	18(18)		
T_1 of FeH, ms	700(592)	425(458)	380(393)	360(360)		
			$[RuH(H_2)L]BF_4$[b]			
T, K	295	272	252	230	208	187
T_1 of $Ru(H_2)$, ms	30(35)	25(27)	22(22)	20(20)	23(24)	33(40)
T_1 of RuH, ms	829(761)	643(585)	528(483)	457(451)	445(530)	444(875)
			$[OsH(H_2)L]BPh_4$[b]			
T, K		279	263	248	213	193
T_1 of $Os(H_2)$, ms		42(42)	39(36)	36(32)	32(34)	33(49)
T_1 of OsH, ms		189(197)	168(167)	156(147)	143(156)	

[a]See Table 4 for parameters used in calculating T_1 values.
[b]In CD_2Cl_2 at 400 MHz.

minimum T_1 and temperature data obtained are listed in Table 4. As anticipated, the observed T_1 values for hydrides are much higher than those for dihydrogen ligands. The T_1 value for the terminal hydride on osmium seems anomalously short; we have no explanation for this. Intramolecular exchange cannot explain this result because there is no temperature where the (H_2) and hydride T_1 values are completely averaged (fast exchange) or where they are near to those of the Fe and Ru complexes (the possible no exchange situation).

A correction of d_{HH} to account for relaxation of the H_2 nuclei by neighboring phenyl protons yields d_{HH}(corr.); this was done by subtracting the relaxation rate of the terminal hydride from the relaxation rate of the dihydrogen ligand by use of eq. [4] of ref. 6. The d_{HH}(corr.) distances are similar for the Fe and Ru complexes (0.88, 0.89 Å, respectively) while the Os complex has a somewhat elongated H—H bond (0.99 Å). These values are typical of dihydrogen complexes of the type *trans*-$[MH(H_2)(diphosphine)_2]^+$ (6, 34). For example, the corresponding distances for the series $[MH(H_2)(dppe)_2]^+$ are 0.87 for Fe, 0.90 for Ru, and 1.02 Å for Os.

Can. J. Chem. Downloaded from www.nrcresearchpress.com by 195.246.54.202 on 09/08/12
For personal use only.

TABLE 4. Observed T_1(min) values for H_2 and terminal hydride ligands and calculated H—H distances

Complex	$T_1^{min}(H_2)$ (ms)	T (K)	$T_1(H)$ (ms)	d_{HH} (Å)	d_{HH}(corr.) (Å)
$[FeH(H_2)L]^+$	18 ± 1[a]	230	360 ± 10[a]	0.87[b]	0.88 ± 0.02
$[RuH(H_2)L]^+$	20 ± 1[a]	230	450 ± 15[a]	0.88[c]	0.89 ± 0.02
$[OsH(H_2)L]^+$	32 ± 1[a]	230	150 ± 5[a]	0.95[d]	0.99 ± 0.01

[a]400 MHz.
[b]τ_0 = 1.2 ps, E_a = 2.6 kcal mol^{-1}.
[c]τ_0 = 0.9 ps, E_a = 2.6 kcal mol^{-1}.
[d]τ_0 = 0.9 ps, E_a = 2.6 kcal mol^{-1}.

TABLE 5. ^{1}H NMR data for the HD complexes

Complex	δ(HD)	^1J(H, D) (Hz)	T (K)	ν (MHz)
$[FeH(HD)L]^+$	−9.80	32 ± 1	293	200
$[RuH(HD)L]^+$	−5.35	33.5 ± 0.5[a]	293	400
$[RuD(HD)L]^+$	−5.28	33.5 ± 0.5	293	400
$[OsH(HD)L]^+$	−6.36	26.4 ± 0.4	293	400
$[OsD(HD)L]^+$	−6.28	26.4 ± 0.4	293	400

[a]*trans*-$^2J_{HH}$ of 4.5 Hz also resolved.

A number of NMR experiments were conducted to try to determine which axial site was occupied by the dihydrogen ligand of *trans*-$[RuH(H_2)L]^+$. An NOEDIFF experiment in which the terminal hydride was saturated resulted in an enhancement of a multiplet centred near 6.86 ppm corresponding probably to an *ortho* proton on a phenyl. Unfortunately a 2D ^{1}H–^{31}P COSY experiment and a selective phosphorus decoupling experiment failed to indicate to which phosphorus this phenyl group was attached.

NMR properties of isotopomers of the dihydrogen complexes $[MH(H_2)L]^+$

The osmium dihydrogen complex, when dissolved in acetone-d_6, slowly exchanges its hydrogen ligands for deuterium by an, as yet, unexplained mechanism. The reaction is observed by means of ^{1}H NMR where resonances ascribed to the following isotopomers grow and then diminish with the extent of reaction: $[OsH(HD)L]^+$ and $[OsD(H_2)L]^+$, then $[OsD(HD)L]^+$ and $[OsH(D_2)L]^+$. The complexes containing the HD ligand give spectra with 1:1:1 triplets with $^1J_{HD}$ coupling constants of 26.4 Hz, characteristic of an intact H—D bond (Table 5).

Isotopomers of the ruthenium complex were prepared by reaction of *trans*-$[RuH(H_2)L]^+$ with 1 atm D_2 in CD_2Cl_2. The $^1J_{HD}$ values were confirmed at 400 MHz by using an inversion–recovery pulse sequence (Fig. 7) to null the H_2 signals (from $Ru(H_2)X$, X = H, D) as they have a shorter T_1 time than the HD signals. Figure 7 shows three 1:1:1 triplets with $^1J_{HD}$ values of 33.5 ± 0.4 Hz. If only one isomer of *trans*-$[Ru(H_2)(H)L]^+$ exists, then one would expect two 1:1:1 triplets (due to the (HD)(H) and (HD)(D) isotopomers) and not three. The observed spectrum is explained as: the low-field 1:1:1 triplet (labelled as *) is due to the (HD)(D) isotopomer and the other two triplets (labelled as ◆ and ◇) are due to the (HD)(H) isotopomer, which has additional coupling between (*H*D)(*H*) ($^2J_{HH}$ = 4.5 Hz). The (HD)(H) isotopomer also has additional couplings in the HD resonance probably due to $^2J_{HP}$. The terminal hydride signal at −12.7 ppm appears as a broad pentet.

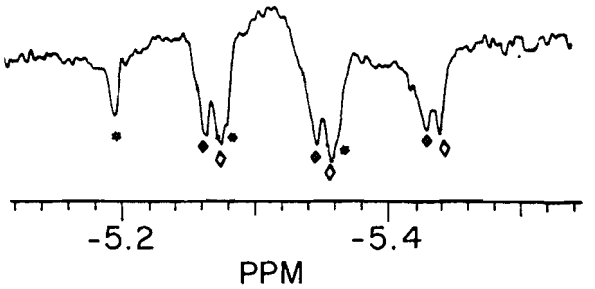

FIG. 7. ^{1}H NMR (400 MHz) of *trans*-$[Ru(H_2)(H)L]BPh_4$ isosopomers in CD_2Cl_2 at −5.3 ppm with H_2 signals nulled by the inversion–recovery method. The three 1:1:1 triplets are labelled as *, ◆, and ◇.

The complex $[FeH(HD)L]BF_4$ precipitated from ether when $Fe(H)_2L$ was reacted with an HBF_4–D_2O mixture. A ^{1}H NMR spectrum of this sample dissolved in CD_2Cl_2 has a 1:1:1 triplet with $^1J_{HD}$ = 32 Hz at −9.8 ppm corresponding to the HD ligand.

The formation of all possible isotopomers in the reactions of the Ru and Os dihydrogen complexes suggests that there may be very slow intramolecular exchange to equilibrate isotopomers $[MH(HD)L]^+$ with $[MD(H_2)L]^+$ and $[MD(HD)L]^+$ with $[MH(D_2)L]^+$. This equilibration might also proceed via intermolecular H^+/D^+ transfer reactions.

Comparison to the complexes $[MH(H_2)(dppe)_2]^+$

Table 6 summarizes some physical properties of the tetraphos complexes and related dppe complexes. The H—H bond lengths of the H_2 ligand determined from T_1(min) data decrease as Os > Ru ≈ Fe for both sets of complexes. The $^1J_{HD}$ couplings, however, suggest that the H—H bond order in the iron compounds is lower than in the ruthenium complexes. This contradiction has not yet been resolved. The possible reason for the elongation of the H—H bond in the osmium complexes has been discussed (5).

The slight H—H shortening of the tetraphos complexes relative to the dppe ones is probably because they are constrained to a less distorted octahedral geometry than the dppe complexes. In an extreme reversal of this effect, the large PPh_3 ligands in the trihydride complex $[Os(H)_3(PPh_3)_4]^+$ prevent the attainment of an octahedral geometry and therefore the formation of a dihydrogen ligand (46). The shortening cannot be attributed to a decrease in backbonding to the H_2 caused by lower energy *d* electrons in the tetraphos complexes because, in every case examined, the tetraphos complex is more reducing than the corresponding dppe complex (Table 6). The irreversible oxidation of *trans*-$[FeH(H_2)L]^+$ occurs at a more negative potential than that of the *trans*-$[FeH(H_2)(dppe)_2]^+$ complex. All of the

Can. J. Chem. Downloaded from www.nrcresearchpress.com by 195.246.54.202 on 09/08/12
For personal use only.

TABLE 6. Comparison of physical properties of dihydrogen complexes $[MH(H_2)L]^+$ and $[MH(H_2)L'_2]^+$, M = Fe, Ru, Os, L′ = dppe

M	d_{HH}(corr.) (Å)	J_{HD} (Hz)	$E_{1/2}(M^{3+}/M^{2+})^a$ V vs. Fc^+/Fc	$E_{1/2}(M^{3+}/M^{2+})^a$ V vs. Fc^+/Fc	ν(CO)^b (cm^{-1})
	$[MH(H_2)L]^+$	$[MH(HD)L]^+$	$[MH(H_2)L]^+$	MHClL	$[MH(CO)L]^+$
Fe	0.88	32	0.7^c	−0.76	
Ru	0.89	33.5		−0.28	
Os	0.99	26.4		−0.31	1989
	$[MH(H_2)L'_2]^+$	$[MH(HD)L'_2]^+$	$[MH(H_2)L'_2]^+$	$MHClL'_2$	$[MH(CO)L'_2]^+$
Fe	0.89	30	0.8^c	−0.71	1950
Ru	0.90	32	>1^c	−0.12	1987
Os	1.02	25.5	1.15^c	−0.14	2003

^{a}THF, 0.2 M n-Bu_4NPF_6 electrolyte, 250 mV s^{-1}.
^{b}Nujol mull.
^{c}Peak potential for the oxidation wave.

MH(Cl)L electrochemical potentials are more negative than corresponding dppe complexes. Even the ν(CO) of *trans*-$[OsH(CO)L]^+$ is lower than that of *trans*-$[OsH(CO)(dppe)_2]^+$.

Reactions that probe the stereochemistry of the complexes

When *trans*-$[RuH(H_2)L]BPh_4$ was reacted with an excess of LiCl, major-*trans*-RuHClL was exclusively formed, implying that the Cl^- ligand in this isomer occupies the same axial site as the H_2 ligand in *trans*-$[RuH(H_2)L]BPh_4$:

[12] *trans*-$[MH(H_2)L]^+ + Cl^- \rightarrow$ major-*trans*-MH(Cl)L

Similarly reaction [4] implies that the osmium dihydrogen complex also reacts stereoselectively with chloride to give the major isomer as indicated in reaction [12].

The coordinated dihydrogen in *trans*-$[OsH(H_2)L]^+$ when dissolved in THF is readily displaced by carbon monoxide or excess acetonitrile at reflux conditions or, allowing for longer reaction times, at room temperature.

[13] *trans*-$[OsH(H_2)L]BPh_4 + L' \rightarrow$ *trans*-$[OsH(L')L]BPh_4 + H_2$

(L′ = CO, $NCCH_3$)

Infrared (ν_{CO} = 1989; ν_{CN} = 2258 cm^{-1}), ^1H NMR (high-field pentet), and ^{31}P NMR (AA′QQ′, see Table 2) data advise an octahedral geometry for the products with L′ *trans* to the terminal hydride. For both products only one isomer is isolated, suggesting a stereoselective reaction where L′ assumes only one axial site, presumably that formerly occupied by the H_2 ligand.

The Cl^- ligand in *trans*-RuHClL is substituted for a CH_3CN or PMe_2Ph ligand in the presence of $NaBF_4$ or $NaPF_6$ in THF solvent (reaction [14]).

[14] *trans*-RuH(Cl)L + L′ + NaY → *trans*-[RuH(L′)L]Y + NaCl

(L′ = $NCCH_3$, PMe_2Ph, Y = BF_4 or PF_6)

The mixture of isomers of RuH(Cl)L produce the new pale-yellow complexes *trans*-[Ru(H)(L′)L]Y as only one isomer. As in the case of the preparation of *trans*-$[RuH(H_2)L]BPh_4$ (reaction [9]), this implies that some rearrangement of the ligand framework has occurred in one of the *trans*-RuHClL isomers prior to coordination of incoming ligand. It is very likely that the large PMe_2Ph ligand occupies the 2-phenyl binding site.

The high-field region of the ^1H NMR spectra of *trans*-$[Ru(H)(CH_3CN)L]^+$ consists of a pentet, again confirming the *trans* geometry. For *trans*-$[Ru(H)(PMe_2Ph)L]PF_6$, the hydride region in the ^1H NMR contains a doublet of pentets. The ^{31}P NMR resonances are also consistent with the *trans* geometry.

Conclusions

High-yielding routes to starting materials containing the ligand *meso*-tetraphos-1 have been developed. The topology of the ligand is either *cis*-β in the complexes $OsCl_2L$, $Os(H)_2L$, and $RuCl_2L$ or *trans* in the complexes $RuCl_2L$, MH(Cl)L, M = Os, Ru, and $M(H)_2L$, M = Ru, Fe. The *trans* complexes have axial binding sites with different steric requirements; the favored isomer is thought to be the one with the hydride in the four-phenyl binding site and the other larger ligand (e.g., Cl^-) in the two-phenyl site. The different sites make the *trans* hydrides in the complexes $M(H)_2L$ inequivalent and allow the observation of the coupling constant *trans*-$^2J_{HH}$ in the ^1H NMR spectrum.

Scheme 1 outlines the interconversions of the complexes and summarizes their relative stereochemistries with respect to the inequivalent axial sites. Until a single crystal X-ray diffraction study of one of the complexes in the chain is done, the assignments must be regarded as tentative. Scheme 1 starts with the dihydride complexes *trans*-$M(H)_2L$, which are prepared from the dichlorides $M(Cl)_2L$. The dihydrides *trans*-$M(H)_2L$ are isolated as pure solids or are observed as intermediates between the dichlorides and the hydridochloro complexes MH(Cl)L before treatment with EtOH in the presence of aluminum salts and then NaCl–acetone. The new dihydrogen complexes *trans*-$[MH(H_2)L]^+$ are prepared by one of two methods: (1) chloride abstraction from *cis*-β-MCl_2L or MH(Cl)L in the presence of hydrogen gas or (2) protonation of *trans*-$M(H)_2L$. Only one isomer of the dihydrogen complexes is obtained, probably the one with H_2 ligand in the two-phenyl site, and this is independent of the synthetic route. However, we speculate that if *trans*-$[FeH(H_2)L]Br$ could be prepared from [FeHL]Br in a similar fashion to *trans*-$[FeH(N_2)L]Br$ (11), which has the N_2 ligand in the four-phenyl site, then a different isomer should be produced than the one prepared by protonation of $Fe(H)_2L$. Only one isomer, major-*trans*-MH(Cl)L, is observed when the dihydrogen complexes are substituted with Cl^- (Scheme 1). Both isomers of *trans*-MHClL appear to be completely converted to the compounds *trans*-$[MH(L')L]^+$, L′ = H_2,

Can. J. Chem. Downloaded from www.nrcresearchpress.com by 195.246.54.202 on 09/08/12
For personal use only.

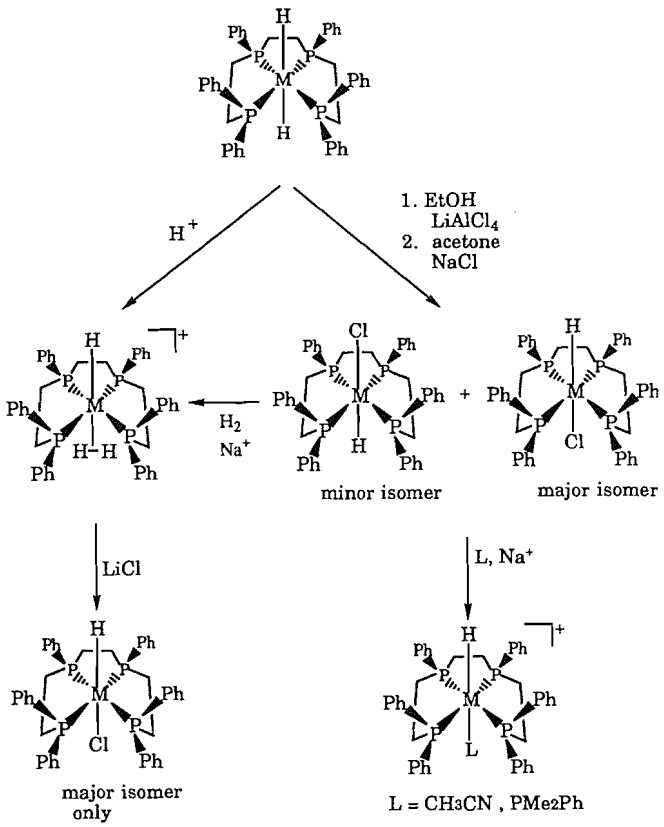

SCHEME 1

CH_3CN, PMe_2Ph, of which only one isomer is obtained. The mechanism that allows the conversion of both isomers into one product is not yet known. For steric reasons, it is argued that the L′ ligand occupies the less sterically crowded two-phenyl site.

The dihydrogen ligand is thought to be rapidly spinning in the complexes *trans*-$[MH(H_2)L]^+$. The Fe and Ru complexes have similar bond lengths (0.88, 0.89 Å, respectively) while the Os complex has a somewhat elongated H—H bond of 0.99 Å. These dimensions are very similar to those of the complexes *trans*-$[MH(H_2)(dppe)_2]^+$. The complexes *trans*-$[MH(H_2)L]^+$ hold the dihydrogen and hydride ligands rigidly *trans* to each other. Unlike the complexes *trans*-$[MH(H_2)(dppe)_2]^+$ (M = Fe, Os) which exhibit rapid intramolecular exchange of H atoms between the hydride and H_2 sites at room temperature, the *meso*-tet-1 complexes do not. This tetraphos ligand is thought to disfavour the formation of the seven-coordinate trihydride $[M(H)_3L]^+$, which is responsible for the H-atom exchange. The seven-coordinate complex $Re(H)_3L$ does undergo rapid intramolecular H-atom exchange (44).

Acknowledgements

This research was supported by grants to R.H.M. from the Natural Sciences and Engineering Research Council of Canada and from the donors of the Petroleum Research Fund administered by the American Chemical Society, and by a loan of ruthenium and osmium salts from Johnson Matthey Co. We thank Dr. Alex Young for measuring the FAB mass spectra and Nick Plavac for running some NMR spectra.

1. P.G. Jessop and R.H. Morris. Coord. Chem. Rev. **121**, 155 (1992).
2. G.J. Kubas, R.R. Ryan, B.I. Swanson, P.J. Vergamini, and H.J. Wasserman. J. Am. Chem. Soc. **106**, 451 (1984).
3. R.H. Morris, J.F. Sawyer, M. Shiralian, and J.D. Zubkowski. J. Am. Chem. Soc. **107**, 5581 (1985).
4. J.S. Ricci, T.F. Koetzle, M.T. Bautista, T.M. Hofstede, R.H. Morris, and J.F. Sawyer. J. Am. Chem. Soc. **111**, 8823 (1989).
5. K.A. Earl, G. Jia, P.A. Maltby, and R.H. Morris. J. Am. Chem. Soc. **113**, 3027 (1991).
6. M.T. Bautista, E.P. Cappellani, S.D. Drouin, R.H. Morris, C.T. Schweitzer, A. Sella, and J. Zubkowski. J. Am. Chem. Soc. **113**, 4876 (1991).
7. R.B. King, P.R. Heckley, and J.C. Cloyd. Z. Naturforsch. **29B**, 574 (1974).
8. B. Bosnich, W.G. Jackson, and S.B. Wild. J. Am. Chem. Soc. **95**, 8269 (1973).
9. M.M. Taqui Khan and R. Mohiduddin. J. Coord. Chem. **6**, 171 (1977).
10. M. Bacci and C.A. Ghilardi. Inorg. Chem. **13**, 2398 (1974).
11. C.A. Ghilardi, S. Midollini, L. Sacconi, and P. Stoppioni. J. Organomet. Chem. **205**, 193 (1981).
12. V. Rivera, E.R. De Gil, and B. Fontal. Inorg. Chim. Acta, **98**, 153 (1985).
13. J.M. Brown and L.R. Canning. J. Organomet. Chem. **267**, 179 (1984).
14. M.T. Bautista, K.A. Earl, P.A. Maltby, and R.H. Morris. J. Am. Chem. Soc. **110**, 4056 (1988).
15. M.T. Bautista, P.A. Maltby, R.H. Morris, and C.T. Schweitzer. In preparation.
16. P. Bruggeller, H. Nar, and A. Messerschmidt. Acta Crystallogr. Sect. C: Cryst. Struct. Commun. **C48**, 817 (1992).
17. J.-D. Chen, F.A. Cotton, and B. Hong. Inorg. Chem. **32**, 2343 (1993).
18. J. Chatt and R.G. Hayter. J. Chem. Soc. 896 (1961).
19. C.T. Schweitzer. M.Sc. Thesis, University of Toronto (1989).
20. I.P. Evans, A. Spencer, and G. Wilkinson. J. Chem. Soc. Dalton Trans. 204 (1973).
21. E. Alessio, G. Mestroni, G. Nardin, W.M. Attia, M. Calligaris, G. Sava, and S. Zorzet. Inorg. Chem. **27**, 4099 (1988).
22. S. Grim and R. Barth. J. Organomet. Chem. **94**, 327 (1975).
23. T. Burrow. First order simulation program, written in Microsoft Quick Basic (1990).
24. L. Cassidei and O. Sciacovelli. Quantum Chemistry Progam Exchange No. 458, LAOCN 5.
25. P. Brooks, D.C. Craig, M.J. Gallagher, A.D. Rae, and A. Sarroff. J. Organomet. Chem. **323**, C1 (1987).
26. R.B. King and P.N. Kapoor. J. Am. Chem. Soc. **93**, 4158 (1971).
27. B. Fontal. Acta Cient. Venez. **33**, 202 (1982).
28. J. Chatt and R.G. Hayter. J. Chem. Soc. 2605 (1961).
29. K.A. Earl. M.Sc. Thesis, University of Toronto (1987).
30. S.D. Ibekwe and U.A. Raebur. J. Organomet. Chem. **19**, 447 (1969).
31. C.T. Schweitzer. Ph.D. Thesis, University of Toronto (1993).
32. N. Bampos and L.D. Field. Inorg. Chem. **29**, 587 (1990).
33. M.V. Baker, L.D. Field, and D.J. Young. J. Chem. Soc. Chem. Commun. 546 (1988).
34. E.P. Cappellani, S.D. Drouin, G. Jia, P.A. Maltby, R.H. Morris, and C.T. Schweitzer. J. Am. Chem. Soc. In press.
35. W.G. Peet and D.H. Gerlach. Inorg. Synth. **15**, 38 (1974).
36. P. Garrou. Chem. Rev. **81**, 229 (1981).
37. M.D. Fryzuk and P.A. MacNeil. Organometallics, **2**, 682 (1983).
38. P. Meakin, E.L. Muetterties, and J.P. Jesson. J. Am. Chem. Soc. **95**, 75 (1973).
39. C.A. Tolman, S.D. Ittel, A.D. English, and J.P. Jesson. J. Am. Chem. Soc. **100**, 4080 (1978).
40. S.D. Ittel, C.A. Tolman, A.D. English, and J.P. Jesson. J. Am. Chem. Soc. **100**, 7577 (1978).
41. C. Bianchini, M. Peruzzini, and F. Zanobini. J. Organomet. Chem. **354**, C19 (1988).
42. E.P. Cappellani, P.A. Maltby, R.H. Morris, C.T. Schweitzer, and M.R. Steele. Inorg. Chem. **28**, 4437 (1989).

Can. J. Chem. Downloaded from www.nrcresearchpress.com by 195.246.54.202 on 09/08/12
For personal use only.

43. A. Mezzetti, A. Del Zotto, P. Rigo, and E. Farnetti. J. Chem. Soc. Dalton Trans. 1525 (1991).
44. G. Jia, A.J. Lough, and R.H. Morris. J. Organomet. Chem. **461**, 147 (1993).
45. M.T. Bautista, K.A. Earl, P.A. Maltby, R.H. Morris, C.T. Schweitzer, and A. Sella. J. Am. Chem. Soc. **110**, 7031 (1988).
46. A.R. Siedle, R.A. Newmark, and L.H. Pignolet. Inorg. Chem. **25**, 3412 (1986).

Can. J. Chem. Downloaded from www.nrcresearchpress.com by 195.246.54.202 on 09/08/12
For personal use only.

An *ab initio* study of the structures, barriers for internal rotation, vibrational frequencies, and thermodynamic functions of the hydrochlorofluorocarbon CH_3CF_2Cl and the corresponding radical CH_2CF_2Cl

S.J. Paddison, Yonghua Chen, and E. Tschuikow-Roux[1]

Department of Chemistry, University of Calgary, Calgary, AB T2N 1N4, Canada

Received June 24, 1993

This paper is dedicated to Professor John C. Polanyi on the occasion of his 65th birthday

S.J. Paddison, Yonghua Chen, and E. Tschuikow-Roux. Can. J. Chem. **72**, 561 (1994).

Ab initio molecular orbital calculations were performed using the GAUSSIAN 90 system of programs at the HF/6-31G* level of theory, on the hydrochlorofluorocarbon (HCFC) 1-chloro-1,1-difluoroethane and the 1-chloro-1,1-difluoroethyl radical. Equilibrium geometries, barriers for internal rotation, and harmonic vibrational frequencies were thus calculated. A single conformational minimum in the potential energy surface was located for both the radical and the parent molecule. The radical center in CH_2CF_2Cl was found to be nonplanar. Transition structures for internal rotation about the C—C bond were located for both the molecule and the radical using analytical methods. The rotation barriers, evaluated at the fourth-order Møller–Plesset perturbation theory ((U)MP4/6-311G**/6-31G*), were calculated after inclusion of zero-point vibrational energy differences to be 1.11 and 4.12 kcal/mol for the radical and the parent molecule, respectively. Computed thermodynamic properties including heat capacity, entropy, enthalpy, and free energy functions are reported as a function of temperature. Using an experimentally measured heat of formation of CH_3CF_2Cl at 298 K, the heat of formation of CH_2CF_2Cl was calculated to be -74.3 ± 1.7 kcal/mol. Tabulations of $\Delta H^0_{f,T}$, $\Delta G^0_{f,T}$, and $\log_{10} K_{f,T}$ over the temperature range of 0–1500 K are also reported for both species.

S.J. Paddison, Yonghua Chen et E. Tschuikow-Roux. Can. J. Chem. **72**, 561 (1994).

Utilisant des programmes du système GAUSSIAN 90 au niveau HF/6-31G* de la théorie, on a effectué des calculs *ab initio* d'orbitales moléculaires sur l'hydrocarbure fluoré et chloré (HCFC), 1-chloro-1,1-difluoroéthane, et sur le radical 1-chloro-1,1-difluoroéthyle. On a ainsi calculé les géométries à équilibre, les barrières à la rotation interne et les fréquences vibrationnelles harmoniques. Tant pour le radical que pour la structure fondamentale, on n'a localisé qu'une seule surface d'énergie potentielle. On a trouvé que, pour le CH_2CF_2Cl, le centre radicalaire n'est pas plan. Faisant appel à des méthodes analytiques, on a localisé les structures de transition pour la rotation interne autour de la liaison C—C tant de la molécule que du radical. On a évalué les barrières à la rotation par la théorie perturbationnelle de Møller–Plesset du quatrième ordre ((U)MP4/6-311G**/6-31G*) après inclusion des différences d'énergie vibrationnelle au point zéro et on a trouvé qu'elles sont respectivement de 1,11 et de 4,12 kcal/mol pour le radical et pour la structure fondamentale. On rapporte les propriétés thermodynamiques calculées, y compris la capacité calorifique, l'entropie, l'enthalpie et les fonctions d'énergie libre, en fonction de la température. Utilisant une valeur expérimentale pour la chaleur de formation du CH_3CF_2Cl, à 298 K, on a calculé que la chaleur de formation du CH_2CF_2Cl est égale à $-74,3 \pm 1,7$ kcal/mol. Pour chacune des deux espèces, on rapporte aussi des tableaux des valeurs des $\Delta H^0_{f,T}$, $\Delta G^0_{f,T}$ et du $\log_{10} K_{f,T}$ pour les températures allant de 0 à 1500 K.

[Traduit par la rédaction]

Introduction

Because of the influence of the fully halogenated chlorofluorocarbons (CFC's) on the equilibrium concentration of stratospheric ozone (1), and the fact that the presence of these CFC's in the stratosphere has largely been the result of their use as aerosol propellants and in the refrigeration and air conditioning industry, investigations continue to be made into determining environmentally acceptable substitutes. One such acceptable and promising refrigerant is the hydrochlorofluorocarbon, 1-chloro-1,1-difluoroethane (CH_3CF_2Cl) (2), commonly referred to in industry as HCFC-142b or simply R142b. Evaluation of the performance of a potential refrigerant requires knowledge and understanding of its thermophysical and thermodynamic properties. It has therefore been the purpose, in part, of this study to further the existing knowledge of the fundamental thermodynamic properties of CH_3CF_2Cl.

1-Chloro-1,1-difluoroethane is a promising alternate to the ozone-depleting CFC's because it offers the capability of hydrogen abstraction by tropospheric hydroxyl radicals, thus effectively limiting the amount of bound chlorine that reaches the stratosphere (3). This reaction is represented by the chemical equation:

$$CH_3CF_2Cl + OH \rightarrow CH_2CF_2Cl + H_2O$$

The resulting radical (CH_2CF_2Cl) is then converted into compounds that are less harmful with respect to atmospheric ozone depletion. Therefore, an understanding of this upper atmosphere chemistry requires knowledge of both kinetic and thermochemical data of the conjugate chloro-fluoro ethyl radical.

In this paper we report *ab initio* calculations on the CH_2CF_2Cl radical and the parent molecule, CH_3CF_2Cl. Equilibrium geometries and rotational transition structures were fully optimized at the Hartree–Fock level with the 6-31G* basis set. Fourth-order Møller–Plesset perturbation theory was then used to estimate electron correlation. These total energies were combined with the calculated harmonic vibrational frequencies and moments of inertia to facilitate a tabulation of standard thermodynamic functions: enthalpy, free energy, entropy, and heat capacity as a function of temperature for both the molecule and the radical. The calculated harmonic vibrational spectra and rotational barriers for CH_3CF_2Cl are compared with the corresponding experimentally determined data. Very recently, the vibrational frequencies for the equilibrium structure of CH_3CF_2Cl were calculated by *ab initio* methods: the GAUSSIAN 82 suite of programs being utilized with both the 3-21G** and 6-31G** basis sets (4). However, no *ab initio* calculations have been reported for the transition structure of the molecule.

[1]Author to whom correspondence may be addressed.

Can. J. Chem. Downloaded from www.nrcresearchpress.com by 195.246.54.202 on 09/08/12
For personal use only.

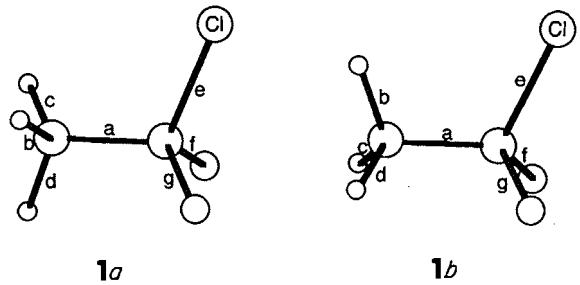

FIG. 1. Definition of the RHF/6-31G* optimized structural parameters for CH_3CF_2Cl (refer to Table 1): equilibrium geometry, **1***a*; transition structure, **1***b*.

From a homodesmic reaction involving the ethyl radical and a calorimetrically measured heat of formation of CH_3CF_2Cl (5), the heat of formation of the CH_2CF_2Cl radical has been evaluated. No experimental or theoretical studies have been reported in the literature for CH_2CF_2Cl and therefore this paper presents structural, spectroscopic, and thermodynamic information that has been heretofore unavailable.

Method

The GAUSSIAN 90 system of programs (6) was implemented for all calculations. The internal 6-31G* basis set (7) along with analytical gradients was used to completely optimize the geometry of the molecule CH_3CF_2Cl at the restricted Hartree–Fock (RHF) level of theory, and the geometry of the radical CH_2CF_2Cl at the unrestricted Hartree–Fock (UHF) level of theory. The minimum energy structures for both species were located using the Schlegel algorithm for gradient minimization (8). Minor spin contamination is suggested in the optimization of the geometry for the radical with the expectation value of $\hat{S}^2$ being approximately 0.76. Electron correlation changes on the relative energies of the stationary points were estimated by single-point calculations at the MP4/6-311G**//HF/6-31G* level (9, 10). Zero-point vibrational energy (ZPVE) corrections were obtained by way of a harmonic frequency analysis using analytical second derivatives at the HF/6-31G*//6-31G* level. The harmonic frequency analysis also provided the frequencies for the derivation of thermodynamic functions and, with calculated intensities, a prediction of the IR spectra. For each purpose, the harmonic frequencies were uniformly scaled by a factor of 0.9 to compensate for systematic overestimation of the values at the HF-SCF level (11). Rather than including the frequency of the "harmonic" torsional mode in ZPVE corrections to rotational barriers and thermodynamic calculations, the mode was treated as a hindered rotation (12).

Results and discussion

1. Geometries of equilibrium and transition structures

1-Chloro-1,1-difluoroethane, CH_3CF_2Cl (1)

Geometry optimization on the RHF/6-31G* potential energy surface for the CH_3CF_2Cl molecule confirms the expected single equilibrium conformation, **1***a*, and single transition structure, **1***b*, both of C_s symmetry. Figure 1 diagrams the two structures with definition of the parameters. The computed numerical values for these structural parameters and the total energies for the geometries are tabulated in Tables 1 and 2, respectively. Examination of the calculated bond distances and bond angles reveals an equilibrium structure that is intuitively expected and reasonable: the sp^3 hybridization of the methyl group is practically preserved and its position is staggered relative to the CF_2Cl group so as to minimize steric effects.

The calculated geometry for the equilibrium conformation is in quite good agreement with the microwave spectroscopic analysis of Graner and Thomas (13) (Table 1). The only significant difference is in the carbon–chlorine bond distance. Graner and Thomas assigned a value of 1.736 Å, based on a graphical correlation of C—C and C—F bond distances with C—Cl bond distances observed in chlorofluoromethanes, which is 0.039 Å shorter than the present value. It may be noted here that the structural parameters calculated at the higher MP2/6-31G* level of theory differ very little from the HF/6-31G* geometry as shown in an earlier study (14).

TABLE 1. Structural parameters for CH_3CF_2Cl at RHF/6-31G*

Parameter[a]	**1***a*; C_s	**1***b*; C_s
a	1.504 (1.490)[c]	1.522
b	1.081 (1.090)[d]	1.081
c	1.081 (1.090)[d]	1.081
d	1.082 (1.090)[d]	1.081
e	1.775 (1.736)[c]	1.777
f	1.328 (1,328)[c]	1.329
g	1.328 (1.328)[c]	1.329
ab	110.0	111.9
ac	110.0	108.8
ad	107.9	108.8
ae	112.6	113.5
af	110.6	110.9
bc	109.7	109.0
bd	109.5 (108.1)[d]	109.0
cd	109.5 (108.1)[d]	109.2
ef	107.9	107.4
eg	107.9	107.4
fg	107.0	106.0
bae	−60.5	0.0
bac	−121.0	−120.6
bad	119.5	120.6
eaf	120.8	120.9
eag	−120.8	−120.9

[a]Refer to Fig. 1 for definition of parameters: e.g., a = bond length (Å), ab = bond angle (°), abc = dihedral angle (°). Numbers in parentheses refer to the microwave study of ref. 13 and include some assumptions.
[b]Geometry; symmetry.
[c]Calculated in ref. 13 based on assumed methyl-group structure and graphical interpolation.
[d]Assumed.

The only *ab initio* MO calculation on CH_3CF_2Cl reported in the literature is the very recent work of Sakka et al. (4). Not surprisingly, their calculations using the 6-31G** basis set generated an equilibrium structure that is virtually identical to ours. They did not report any calculations for the transition structure.

The transition structure is also an anticipated structure with the two groups eclipsed relative to one another. Comparison with the equilibrium structure indicates that this higher energy structure is both elongated and flattened: the C—C, C—Cl, and C—F bond distances are all slightly longer and the carbon–carbon–chlorine bond angle is slightly larger (Table 1). This alteration in structure is obviously the result of steric repulsion between the halogen atoms and the hydrogen atoms.

Rotation about the C—C bond in the CH_3CF_2Cl molecule is hindered by the transition structure, **1***b* (Fig. 1). With the zero-point vibrational energy difference Δ(ZPVE) included, conformation **1***b* is higher in energy than **1***a* by 3.94 and 4.12 kcal/mol at the RHF/6-31G* and MP4/6-311G**//6-31G* levels, respectively. Comparison with the experimentally determined rota-

Can. J. Chem. Downloaded from www.nrcresearchpress.com by 195.246.54.202 on 09/08/12
For personal use only.

TABLE 2. Calculated energies (hartree) of CH_2CF_2Cl, CH_3CF_2Cl, CH_2CH_3, and CH_3CH_3

Conformer	Basis set		
	HF6-31G*//6-31G*	(U)MP4/6-311G**//6-31G*	ZPVE[a]
CH_3CF_2Cl			
1*a* (equilibrium)	−735.843879	−736.839696	34.45
1*b* (rotation TS1)	−735.837190	−736.832712	34.16
Rot. barrier (**1***b* − **1***a*)[b]	4.20(3.94)	4.38(4.12)	
CH_2CF_2Cl			
2*a* (equilibrium)	−735.207864	−736.164667	24.46
2*b* (rotation TS1)	−735.205679	−736.162213	23.98
Rot barrier (**2***b* − **2***a*)[b]	1.37(0.95)	1.54(1.11)	
CH_2CH_3	−78.597149	−78.944269	39.75
CH_3CH_3	−79.228755	−79.614127	50.05

[a]Unscaled zero point vibrational energy, in kcal/mol.
[b]Energy difference in kcal/mol, data in parentheses are values including the term Δ(ZPVE) × 0.9 with torsional frequencies excluded.

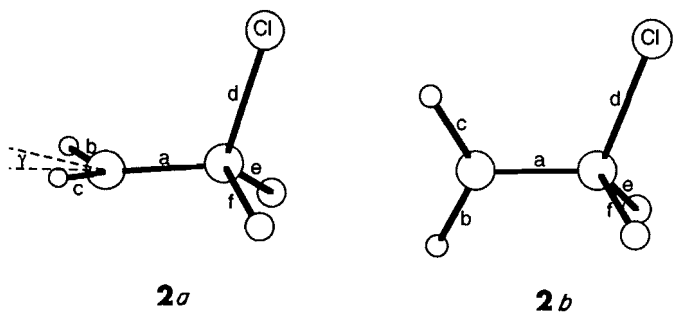

FIG. 2. Definition of the UHF/6-31G* optimized structural parameters for CH_2CF_2Cl (refer to Table 3): equilibrium geometry, **2***a*; transition structure, **2***b*.

tional barriers of ethane (2.96 kcal/mol (15)), 1,1difluoroethane (3.215 kcal/mol (16)), and chloroethane (3.691 kcal/mol (17)) substantiates the observed increase in rotational barrier with halogen substitution. The experimentally determined values from far-infrared and microwave studies range from 3.7 (16) to 4.40 ± 0.10 (13) kcal/mol and thus the calculated values fall well within this range.

1-Chloro-1,1-difluoroethyl radical, CH_2CF_2Cl (2)

The CH_2CF_2Cl radical possesses C_s symmetry and exists as one equilibrium conformation, **2***a*, and one transition structure, **2***b*. Both structures are shown in Fig. 2. Structural parameters are listed in Table 3 and the total energies are given in Table 2. Conformation **2***a* has a nonplanar radical center, with an out-of-plane angle γ = 15.6° (γ is defined by the C—C axis and the plane formed by the radical site group). The pyramidalization of the radical center in CH_2CF_2Cl is very similar to that in CH_2CH_2Cl (γ = 15.0° (14)) and fairly similar to that in CH_2CF_2H (γ ≈ 12.8° (19)). The equilibrium conformations of CH_2CF_2Cl and CH_2CH_2Cl are nearly identical, with the pertinent feature being that the C—Cl bond is eclipsed with the singly occupied molecular orbital (SOMO) at the radical site. However, the CH_2CF_2H radical has two conformations, one in which the β hydrogen nearly eclipses with the SOMO and the other in which one of the fluorine atoms is in the plane of the SOMO. The strong geometrical preference observed in both the CH_2CF_2Cl and CH_2CH_2Cl radicals is a result of the strong two-center one-electron hyperconjugative interaction between

TABLE 3. Structural parameters for CH_2CF_2Cl radical UHF/6-31G*

Parameter[a]	**2***a*; C_1[b]	**2***b*; C_s
a	1.479	1.486
b	1.071	1.073
c	1.071	1.069
d	1.787	1.770
e	1.326	1.331
f	1.326	1.331
ab	118.3	117.0
ac	118.3	121.5
ad	111.8	112.5
ae	111.2	110.9
af	111.2	110.8
bc	120.9	121.5
de	107.4	108.0
df	107.4	108.0
bad	−81.3	180.0
cad	81.3	0.0
dae	120.0	121.2
daf	−120.0	−121.0
bae	−38.7	58.8
caf	38.7	121.2
cae	158.6	−121.2
γ	15.6	0.0

[a]Refer to Fig. 2 for definition of parameters: e.g., a = bond length (Å), ab = bond angle (°), abc = dihedral angle (°), γ = out-of-plane angle (°).
[b]Geometry; symmetry.

the SOMO and the σ^*_{CCl} antibonding orbital (20). Comparison of the equilibrium structures reveals that the C—Cl bond distance in the CH_2CF_2Cl radicals is 0.039 Å shorter than in the CH_2CH_2Cl radical, and that the C—F bond distance in CH_2CF_2Cl is approximately 0.02 Å shorter than in CH_2CF_2H. The shortening of these bonds is anticipated as a result of both electrostatic effects and negative hyperconjugation that accompanies halogen substitution at the β carbon atom (21).

The transition structure, **2***b*, hinders rotation about the C—C bond. Conformation **2***b* actually corresponds to both the rotation of the CF_2Cl group and the inversion of the CH_2 radical center, and thus may be referred to as a rotation/inversion transition structure. As recorded in Table 2, the transition structure

Can. J. Chem. Downloaded from www.nrcresearchpress.com by 195.246.54.202 on 09/08/12
For personal use only.

TABLE 4. Moments of inertia,[a] symmetry (σ), and vibrational frequencies of the CH_3CF_2Cl molecule

	1*a*	**1***b*
I_a	1.5680(1.6027)	
I_b	2.5619(2.5885)	
I_c	2.6383(2.6607)	
I_r	0.05117	
σ	3	

Freq[b]					
Expt.[e]	Calcd.	IR Int[c]	Symmetry	Assignment[d]	Freq[d]
3035	2999	7.8	A″	CH_3 asym str	3004
3035	2997	9.7	A′	CH_3 asym str	3002
2965	2920	3.8	A′	CH_3 sym str	2928
1447	1462	0.7	A″	CH_3 def	1469
1447	1462	0.3	A′	CH_3 def	1462
1395	1424	33.0	A′	CH_3 umb	1421
1202	1244	200.8	A″	CF_2 asym str	1240
1230	1241	165.8	A′	CF_2 str + C–C str	1233
1134	1133	203.2	A′	CH_3 rock + C–Cl str	1132
967	992	44.0	A″	CH_3 rock	980
904	909	131.2	A′	CF_2 str + CH_3 rock + C–Cl str	910
683	665	61.9	A′	C–Cl str	669
543	525	20.6	A′	CF_2 wag	537
438	425	0.6	A′	C–Cl str + CF_2 wag	437
426	417	0.1	A″	CF_2 rock	428
334	329	0.7	A″	CF_2 twist	338
305	295	1.0	A′	C–Cl bend	315
272	246	0.01	A″	Torsion	239i

[a]Units: 10^{-38} g cm^2. Values in parentheses from microwave study, ref. 13.
[b]Frequencies (in cm^{-1}) are calculated at UHF/6-31G*//6-31G* and scaled by 0.9.
[c]Intensity is calculated by the atomic polar method as implemented in GAUSSIAN 90, in km/mol. Only the relative magnitude of calculated intensities is considered significant.
[d]Combination bands are listed in decreasing order of apparent importance based on observation of animated normal modes: str = stretch; umb = umbrella; scis = scissor; def = deformation; (a)sym = (a)symmetric.
[e]Reference 24.

Can. J. Chem. Downloaded from www.nrcresearchpress.com by 195.246.54.202 on 09/08/12
For personal use only.

has a rotational barrier of 0.95 and 1.11 kcal/mol at the UHF/6-31G* and UMP4/6-311G** levels, respectively, which are approximately 0.4 kcal/mol lower than similarly calculated values for CH_2CH_2Cl (1.58 kcal/mol (14)) and approximately 1 kcal/mol higher than in CH_2CF_2H (0.02 kcal/mol (19)). In comparison with the CH_2CF_2H radical, the substantial increase in the rotational barrier of β-chlorine-substituted ethyl radicals (CH_2CH_2Cl, CH_2CF_2Cl) is mainly due to the fact that the transition structures of the chlorinated ethyl radicals are energetically not favored as a result of loss of strong negative hyperconjugation between the SOMO and the σ^*_{CCl} orbital, although there is a weak compensating hyperconjugation between π_{CH2} and σ^*_{CCl} (14). In CH_2CF_2H, the hyperconjugation between the SOMO and σ^*_{CF} orbital in the equilibrium geometry is relatively weak and comparable to the hyperconjugation between the π_{CH2} and σ^*_{CF} orbitals in the transition structure. The observation of a slightly lower rotational barrier in the CH_2CF_2Cl radical as compared to the CH_2CH_2Cl radical may be attributed to the slightly weak interaction between the SOMO and the σ^*_{CF} in the transition structure of CH_2CF_2Cl, which stabilizes the transition structure and thus reduces the rotational barrier of the CH_2CF_2Cl radical.

2. Vibrational frequencies, moments of inertia, and thermodynamic properties

The infrared (IR) and Raman spectra of 1-chloro-1,1-difluoroethane was first experimentally measured by Nielsen and co-workers (18). Far-infrared studies were later conducted by Sage (22) and Brown et al. (23). Durig et al. (24) measured the complete spectra of the molecule in both the solid and gas states and were able to complete and refine the normal mode assignments of earlier work. Their assignments are adopted for purposes of comparison and thermodynamic calculations, and are listed in Table 4. Sakka et al. (4) calculated the harmonic frequencies for the equilibrium conformation of CH_3CF_2Cl (**1***a* in our notation) at the 3-21G, 3-21G**, and 6-13G** levels of theory and then scaled the force field using a method originally developed by Shimanouchi (25) and later revised by Hirakawa and Hamada (26). Sakka et al. obtained good agreement with the experimentally measured frequencies. In the present paper we have carried out frequency calculations for both the equilibrium conformation (**1***a*) and the transition structure (**1***b*) at the UHF/6-31G*//6-31G* level of theory. The results, scaled by 0.9 (11), together with computed IR intensities for the equilibrium structure are listed in Table 4. Assignments based on inspection of animations of the normal modes of the equilibrium conformation are also provided. Comparison of our scaled frequencies with the experimentally measured spectra (24) is quite satisfactory. Also listed in Table 4 are the calculated moments of inertia, which are in good agreement with the microwave study of Graner and Thomas (13).

No experimental IR and Raman spectroscopic data for the 1-chloro-1,1-difluoroethyl radical are available in the literature. Table 5 lists the results of the frequency calculations for the

TABLE 5. Moments of inertia,[a] symmetry number (σ), and vibrational frequencies of the CH_2CF_2Cl radical

	2*a*			**2***b*
I_a	1.5305			
I_b	2.5150			
I_c	2.5419			
I_r	0.02927			
σ	1			
Freq[b]	IR. Int[c]	Symmetry	Assignment[d]	Freq[b]
3135	0.3	A″	CH_2 asym str	3140
3024	0.5	A′	CH_2sym str	3021
1426	23.0	A′	CH_2 scis	1427
1255	171.5	A′	C–C str + C–F str	1237
1249	192.5	A″	CF_2 asym str + CH_2 rock	1161
956	358.6	A′	C–F str + C–Cl str	1121
946	40.3	A″	CH_2 rock	906
710	111.1	A′	C–F str + C–C str + C–Cl str	666
538	13.2	A′	CH_2 wag	538
521	12.6	A′	Umb + CF_2 scis	494
418	0.4	A″	CF_2 rock	426
416	6.1	A′	Umb + C–Cl str	352
336	0.2	A″	CF_2 twist	310
278	7.3	A′	Umb + C–C–Cl bend	297
189	2.0	A″	Torsion	165i

[a]Units: 10^{-38} g cm^2.
[b]Frequencies (in cm^{-1}) are calculated at UHF/6-31G*//6-31G* and scaled by 0.9.
[c]Intensity is calculated by the atomic polar method as implemented in GAUSSIAN 90, in km/mol. Only the relative magnitude of calculated intensities is considered significant.
[d]Combination bands are listed in decreasing order of apparent importance based on observation of animated normal modes: str = stretch; scis = scissor; (a)asym = (a)symmetric; umb = umbrella.

equilibrium and transition structures of the radical (**2***a* and **2***b*, respectively) performed at a similar level of theory as the parent molecule. However, unlike the parent molecule, the assignments of the normal modes of the radical were somewhat more difficult because many of the local modes are coupled. The most intense vibrational modes are seen in the C—C, C—F, and C—Cl bond stretches. These normal modes along with the CH_2 rock are the modes likely to be identified when the experimental IR spectra is measured.

The transition structures, **1***b* and **2***b*, each possess a single imaginary frequency (239i and 165i cm^{-1}, respectively) corresponding to the torsional mode.

Ideal gas thermodynamic functions C_p^0, S^0, $H^0 - H_0^0$, and $-(G^0 - H_0^0)/T$ in the temperature range 0–1500 K and 1 atm of pressure (101.3 kPa) were calculated by standard methods of statistical thermodynamics based on the rigid rotor — harmonic oscillator model. The results are listed in Tables 6 and 7. The reduced moments of inertia, I_r, for internal rotation of unsymmetrical groups were calculated on the basis of the formulation of Pitzer (27), using a Fortran computer program as employed by us previously (19, 28, 29).

With exception of the torsional modes, experimentally observed frequencies were used in the statistical thermodynamic calculations for CH_3CF_2Cl, and computed vibrational frequencies of the equilibrium conformation (scaled × 0.9 (11)) were used for CH_2CF_2Cl. To further assess the effect of residual frequency differences between observed and computed frequencies on thermodynamic properties of CH_3CF_2Cl, the heat capacity and entropy were also calculated based on computed (×0.9) frequencies for structure **1***a* (Table 6). The contributions of the torsional mode to the thermodynamic properties of both the parent molecule and the radical were calculated as a simple hindered rotation (12) based on (U)MP4/6-311G**//6-31G* evaluated barriers.

The calculation of the temperature dependence of $\Delta H^0_{f,T}$, $\Delta G^0_{f,T}$, and $K_{f,T}$ for either species requires knowledge of their enthalpy of formation at a reference temperature. Papina and Kolesov (5) determined the heat of formation of the parent molecule, CH_3CF_2Cl, to be -126.6 ± 1.2 kcal/mol at 298.15 K from a measurement of the enthalpy of combustion of gaseous CH_3CF_2Cl in a rotating bomb calorimeter. However, the literature does not contain any experimentally measured or theoretically estimated heat of formation of the radical CH_2CF_2Cl.

In previous publications (19, 28–30) we demonstrated the calculation and the reliability of "theoretical" radical heats of formation by coupling *ab initio* calculated energy changes for homodesmic reactions with the known heats of formation of other reaction components. For the purpose of determining the heat of formation of the CH_2CF_2Cl radical, the following homodesmic reaction was chosen:

$$CH_3CF_2Cl + CH_3CH_2 \rightarrow CH_2CF_2Cl + CH_3CH_3$$

The criteria for the choice of components in atom transfer reactions have been discussed previously (19, 29). It suffices to note here that the number of each type of bond must be conserved, and, furthermore, it is desirable to have maximum similarity in hybridization at the radical center (as measured by the out-of-plane angle, γ) between reactant and product radicals. This ensures that errors due to basis set and partial neglect of electron correlation will nearly cancel. We chose the CH_3CH_2 radical as the hydrogen-abstracting radical in the above homodesmic reaction because CH_3CH_2 has a similar nonplanarity (γ = 13.6° (28)) to that of the CH_2CF_2Cl radical (γ =

Can. J. Chem. Downloaded from www.nrcresearchpress.com by 195.246.54.202 on 09/08/12
For personal use only.

TABLE 6. Ideal gas thermodynamic properties for CF_2ClCH_3

T (K)	$C_p^{0a,b}$ (cal K^{-1} mol^{-1})	S^{0b} (cal K^{-1} mol^{-1})	$-(G^0 - H_0^0)/T$ (cal K^{-1} mol^{-1})	$H^0 - H_0^0$ (kcal mol^{-1})	ΔH_f^0 (kcal mol^{-1})	ΔG_f^0 (kcal mol^{-1})	log K_f
0	0.0	0.0	0.0	0.0	−123.72	−123.72	∞
100	9.98(10.06)[10.06]	57.77(57.80)[57.81]	49.37	0.84	−125.09	−120.84	264.09
200	15.43(15.56)[15.46]	66.38(66.50)[66.50]	55.80	2.12	−125.93	−116.25	127.03
298.15	19.92(19.96)[19.71]	73.40(73.55)[73.49]	60.47	3.86	−126.60[c]	−111.34	81.62
300	20.00(20.04)[19.79]	73.52(73.67)[73.61]	60.55	3.89	−126.61	−111.25	81.05
400	23.85(23.81)[23.48]	79.83(79.97)[79.82]	64.60	6.09	−127.13	−106.05	57.94
500	26.92(26.85)[26.55]	85.49(85.63)[85.40]	68.22	8.64	−127.50	−100.73	44.03
600	29.31(29.23)[29.03]	90.62(90.74)[90.47]	71.53	11.45	−127.76	−95.35	34.73
700	31.19(31.13)[31.04]	95.28(95.39)[95.10]	74.59	14.48	−127.93	−89.93	28.08
800	32.70(32.66)[32.70]	99.55(99.65)[99.36]	77.45	17.68	−128.02	−84.50	23.08
900	33.95(33.92)[34.09]	103.48(103.57)[103.29]	80.13	21.01	−128.06	−79.06	19.20
1000	35.00(34.99)[35.25]	107.11(107.20)[106.94]	82.65	24.46	−128.03	−73.61	16.09
1100	35.89(35.88)[36.24]	110.49(110.58)[110.35]	85.03	28.00	−127.97	−68.18	13.55
1200	36.65(36.65)[37.08]	113.64(113.74)[113.54]	87.29	31.63	−127.87	−62.74	11.43
1300	37.30(37.30)[37.80]	116.61(116.70)[116.54]	89.43	35.33	−127.73	−57.32	9.64
1400	37.86(37.87)[38.41]	119.39(119.49)[119.36]	91.47	39.10	−127.59	−51.91	8.10
1500	38.34(38.37)[38.95]	122.02(122.11)[122.03]	93.42	42.90	−127.43	−46.51	6.78

[a]Between 300 and 1000 K, C_p^0 fits the polynomial $C_p^0 = a_0 + a_1T + a_2T^2 + a_3T^3 + a_4T^4$ with $a_0 = 1.650727$, $a_1 = 3.279704 \times 10^{-2}$, $a_2 = -2.308279 \times 10^{-5}$, $a_3 = 4.536686 \times 10^{-9}$, $a_4 = 1.36412 \times 10^{-12}$.

[b]Based on experimental frequencies, Table 4. Numbers in parentheses are based on theoretical scaled frequencies (Table 4) with torsional mode treated as hindered rotation. Numbers in square brackets are based on theoretical scaled frequencies with the torsional mode treated as a harmonic vibration.

[c]Experimental value from ref. 5.

TABLE 7. Ideal gas thermodynamic properties for CH_2CF_3Cl radical

T (K)	C_p^{0a} (cal K^{-1} mol^{-1})	S^0 (cal K^{-1} mol^{-1})	$-(G^0 - H_0^0)/T$ (cal K^{-1} mol^{-1})	$H^0 - H_0^0$ (kcal mol^{-1})	ΔH_f^0 (kcal mol^{-1})	ΔG_f^0 (kcal mol^{-1})	log K_f
0	0.0	0.0	0.0	0.0	−72.67	−72.67	∞
100	11.30	60.23	51.08	0.915	−73.58	−70.80	154.73
200	16.40	69.69	58.14	2.31	−74.01	−67.83	74.12
298.15	20.20	76.98	63.18	4.11	−74.29[b]	−64.74	47.45
300	20.26	77.10	63.27	4.15	−74.30	−64.68	47.12
400	23.23	83.36	67.53	6.33	−74.49	−61.44	33.57
500	25.47	88.79	71.25	8.77	−74.62	−58.17	25.42
600	27.18	93.60	74.58	11.41	−74.70	−54.87	19.99
700	28.51	97.89	77.61	14.20	−74.75	−51.55	16.10
800	29.59	101.77	80.39	17.11	−74.78	−48.24	13.18
900	30.48	105.31	82.96	20.11	−74.78	−44.92	10.91
1000	31.22	108.56	85.36	23.20	−74.76	−41.60	9.09
1100	31.86	111.57	87.61	26.35	−74.71	−38.29	7.61
1200	32.39	114.36	89.72	29.57	−74.65	−34.98	6.37
1300	32.86	116.97	91.72	32.83	−74.58	−31.68	5.33
1400	33.25	119.42	93.61	36.14	−74.50	−28.38	4.43
1500	33.60	121.73	95.41	39.48	−74.42	−25.08	3.65

[a]Between 300 and 1000 K, C_p^0 fits the polynomial $C_p^0 = a_0 + a_1T + a_2T^2 + a_3T^3 + a_4T^4$ with $a_0 = 2.7711845$, $a_1 = 3.443512 \times 10^{-2}$, $a_2 = -3.80818 \times 10^{-5}$, $a_3 = 2.094214 \times 10^{-8}$, $a_4 = -4.347977 \times 10^{-12}$.

[b]Assigned, based on homodesmic reaction (see text).

15.6°). In addition, both the heat of formation of ethane ($\Delta H^0_{f,298} = -20.24 \pm 0.12$ (31)) and of the ethyl radical $\Delta H^0_{f,298} = 28.36 \pm 0.4$ (32)) are well established.

Table 2 lists the (U)MP4/6-311G**//6-31G* total energies and the calculated zero-point vibrational energies (ZPVE) for all relevant species in the above homodesmic reaction. The computed endothermicity after corrections for ZPVE and temperature is 3.69 kcal/mol, and the corresponding "theoretical" heat of formation of the radical is $\Delta H^0_{f,298}(CH_2CF_2Cl) = -74.3 \pm 1.7$ kcal/mol, where the error limit represents cumulative uncertainties in the ΔH^0_f values of the other compounds in the reaction.

Acknowledgement

The financial support of the Natural Sciences and Engineering Research Council of Canada is gratefully acknowledged. We are indebted to Dr. R.A. Kydd of this department for providing Fortran programs for the calculation of the reduced moments of inertia and rotational energy levels and to Dr. A. Rauk for helpful consultation. We also thank Academic Computing Services of the University of Calgary for a generous grant of computer time.

Can. J. Chem. Downloaded from www.nrcresearchpress.com by 195.246.54.202 on 09/08/12
For personal use only.

1. M.J. Molina and F.S. Rowland. Nature, **249**, 810 (1974).
2. M.O. McLinden. Int. J. Refrig. **13**, 149 (1990).
3. WMO, Atmospheric Ozone, Scientific Assessment of Stratospheric Ozone, World Meteorological Organization, Global Ozone Research and Monitoring Project Report No. 20, Volume II, Appendix; AFEAS Report, Geneva, Switzerland. 1989.
4. T. Sakka, Y. Ogata, and M. Iwasaki. J. Phys. Chem. **96**, 10697 (1992).
5. T.S. Papina and V.P. Kolesov. Vestn. Mosk. Univ. Ser. 2: Khim. **19**, 500 (1978).
6. M.J. Frisch, M. Head-Gordon, G.W. Trucks, J.B. Foresman, H.B. Schlegel, K. Raghavachari, M. Robb, J.S. Binkley, C. Gonzalez, D.J. Defrees, J. Fox, R.A. Whiteside, R. Seeger, C.F. Melius, J. Baker, R.L. Martin, L.R. Kahn, J.J.P. Stewart, S. Topial, and J.A. Pople. GAUSSIAN 90, Revision F. Gaussian, Inc., Pittsburgh, Pa. 1990.
7. (*a*) W.J. Hehre, R. Ditchfield, and J.A. Pople. J. Chem. Phys. **56**, 2257 (1972); (*b*) M.M. Frankl, W.J. Pietro, W.J. Hehre, J.S. Binkley, M.S. Gordon, D.J. DeFrees, and J.A. Pople. J. Chem. Phys. **77**, 3654 (1982).
8. H.B. Schlegel. J. Comput. Chem. **3**, 214 (1982).
9. (*a*) C. Moller and M.S. Plesset. Phys. Rev. **46**, 618 (1934); (*b*) J.A. Pople, R. Krishnan, H.B. Schlegel, and J.S. Binkley. Int. J. Quantum Chem. **14**, 545 (1978); (*c*) R. Krishnan, M.J. Frisch, and J.A. Pople. J. Chem. Phys. **72**, 4244 (1980); (*d*) R. Krishnan, J.S. Binkley, R. Seeger, and J.A. Pople. J. Chem. Phys. **72**, 650 (1980).
10. (*a*) R. Krishnan and J.A. Pople. Int. J. Quantum Chem. **14**, 91 (1978); (*b*) R. Krishnan, M.J. Frisch, and J.A. Pople. J. Chem. Phys. **72**, 4244 (1980).
11. J.A. Pople, H.B. Schlegel, R. Krishnan, D.J. DeFrees, J.S. Binkley. M.J. Frisch, R.A. Whiteside, R.F. Hout, and W.J. Hehre. Int. J. Quantum Chem. Symp. **15**, 269 (1981).
12. G.N. Lewis and M. Randall. Thermodynamics. 2nd ed. McGraw–Hill, New York. 1961.
13. G. Graner and C. Thomas. J. Chem. Phys. **49**, 4160 (1968).
14. Y. Chen and E. Tschuikow-Roux. J. Phys. Chem. **96**, 7266 (1992).
15. J.R. Durig, S.M. Craven, and J. Bragin. J. Chem. Phys. **53**, 38 (1970).
16. S.S. Chen, A.S. Rodgers, J. Chao, R.C. Wilhoit, and B.J. Zwolinski. J. Phys. Chem. Ref. Data, **4**, 441 (1975).
17. T. Shimanouchi. Natl. Stand. Ref. Data Ser. (U.S. Natl. Bur. Stand.), **39** (1972).
18. D.C. Smith, G.M. Brown, J.R. Nielsen, R.M. Smith, and C.Y. Liang. J. Chem. Phys. **20**, 473 (1952).
19. Y. Chen, A. Rauk, and E. Tschuikow-Roux. J. Chem. Phys. **93**, 6620 (1990).
20. F. Bernardi, A. Bottoni, J. Fossey, and J. Sorba. Tetrahedron, **42**, 5567 (1986).
21. E.W. Ignacio and H.B. Schlegel. J. Phys. Chem. **96**, 5830 (1992).
22. G.W. Sage. Ph.D. Thesis, Harvard University, 1962.
23. F. Brown, A.D.H. Clague, N.D. Heithanys, D.F. Koster, and A. Danti. J. Mol. Spectrosc. **24**, 163 (1967).
24. J.R. Durig, S.M. Craven, C.W. Hawley, and J. Bragin. J. Chem. Phys. **57**, 131 (1972).
25. T. Shimanouchi. Normal vibration of molecules. Computer Centre, The University of Tokyo, Tokyo. 1968.
26. A. Hirakawa and Y. Hamada. Normal vibrational analysis of molecules. Computer Centre, The University of Tokyo, Tokyo. 1990.
27. K.S. Pitzer. J. Chem. Phys. **14**, 239 (1946).
28. Y. Chen, A. Rauk, and E. Tschuikow-Roux. J. Chem. Phys. **93**, 1187 (1990).
29. Y. Chen, A. Rauk, and E. Tschuikow-Roux. J. Chem. Phys. **94**, 7299 (1991).
30. Y. Chen, A. Rauk, and E. Tschuikow-Roux. J. Chem. Phys. **95**, 2774 (1991).
31. J. Chao, R.C. Wilhoit, and B.J. Zwolinski. J. Phys. Chem. Ref. Data, **2**, 427 (1973).
32. M. Brouard, P.D. Lightfoot, and M.J. Pilling. J. Phys. Chem. **90**, 445 (1986).

Can. J. Chem. Downloaded from www.nrcresearchpress.com by 195.246.54.202 on 09/08/12
For personal use only.

Infrared chemiluminescence studies of the reactions of H atoms with CCl_3, CF_2Cl, and CH_2CH_2Cl radicals at 300 and 475 K: recombination–elimination vs. abstraction mechanisms

E. ARUNAN,[1] R. RENGARAJAN, AND D.W. SETSER[2]

Department of Chemistry, Kansas State University, Manhattan, KS 66506, U.S.A.

Received June 9, 1993

This paper is dedicated to Professor John C. Polanyi on the occasion of his 65th birthday

E. ARUNAN, R. RENGARAJAN, and D.W. SETSER. Can. J. Chem. **72**, 568 (1994).

The reactions of H atoms with CCl_3, CF_2Cl, and CH_2CH_2Cl radicals have been studied in a flow reactor at 300 and 475 K by observation of the infrared emission from the HCl and HF products. These reactions were observed as secondary reactions from the H + CCl_3Br, CF_2ClBr, and CH_2Cl–CH_2I chemical systems. The conditions in the flow reactor were controlled so that the nascent vibrational distributions of HCl and HF were recorded. The pattern of vibrational energy disposal to HCl was used to differentiate between Cl atom abstraction and recombination–elimination mechanisms. The H atom reactions with CCl_3 and CF_2Cl radicals occur only via a recombination–elimination mechanism and give HCl(v) or HF(v) in a unimolecular step. Thus, the Cl atom abstraction reactions must have $\geq$3.0 kcal mol^{-1} higher activation energy than the recombination reaction. From observation of the ratio of the HCl and HF products from CHF_2Cl*, the difference in threshold energies for HF and HCl elimination was determined to be ~13 kcal mol^{-1}. On the other hand, Cl atom abstraction does compete with recombination–elimination in the H + CH_2CH_2Cl reaction, the branching fraction is ~0.3 at 300 K and ~0.6 at 475 K.

E. ARUNAN, R. RENGARAJAN et D.W. SETSER. Can. J. Chem. **72**, 568 (1994).

Opérant dans un réacteur à écoulement, à 300 et 475 K, et faisant appel à l'observation de l'émission en infrarouge du HCl et du HF produits, on a étudié les réactions des atomes de H avec les radicaux CCl_3, CF_2Cl et CH_2CH_2Cl. On a observé ces réactions sous la forme de réactions secondaires des systèmes chimiques H + CCl_3Br, CF_2ClBr et CH_2Cl–CH_2I. Les conditions présentes dans le réacteur à écoulement sont contrôlées d'une façon telle que les distributions vibrationnelles naissantes du HCl et du HF puissent être enregistrées. On a utilisé les patrons de distribution de l'énergie vibrationnelle du HCl pour différencier entre les mécanismes d'enlèvement d'atome de Cl et d'élimination–recombinaison. Les réactions des atomes de H avec les radicaux CCl_3 et CF_2Cl ne se produisent que par un mécanisme d'élimination–recombinaison et elles conduisent à du HCl(v) et du HF(v) dans une étape unimoléculaire. Les réactions d'enlèvement d'atome de Cl doivent donc avoir une énergie d'activation qui est $\geq$3,0 kcal mol^{-1} plus élevée que celle de la réaction de recombinaison. En se basant sur le rapport de HCl et HF produits à partir du CHF_2Cl*, on a déterminé que la différence entre les énergies seuils pour l'élimination de HF et de HCl doit être −13 kcal mol^{-1}. Par ailleurs, l'enlèvement de l'atome de Cl est en compétition avec la réaction de recombinaison–élimination dans la réaction de H + CH_2CH_2Cl; la fraction de bifurcation est d'environ 0,3 à 300 K et d'environ 0,6 à 475 K.

[Traduit par la rédaction]

I. Introduction

The reactions of H atoms with CCl_3, CF_2Cl, and CH_2CH_2Cl radicals at 300 and 475 K have been studied by observation of the HCl and (or) HF product from the infrared chemiluminescence in a fast flow reactor (1–3). The objective was to employ the characteristic vibrational energy disposal patterns to differentiate between the unimolecular HCl or HF elimination reactions from fluorochloromethanes and ethanes (4–7) formed by H-atom recombination vs. the direct, bimolecular Cl-atom abstraction reactions by H atoms (3, 4, 8), even though the two pathways give the same chemical products. The pathway that we identify as Cl-atom abstraction frequently is called a disproportionation reaction in the free radical literature. The current experiments are a logical extension of our earlier report on the room temperature reactions of H with CF_3, CH_2CH_2F, CH_2CF_3, and other fluorine-containing organic radicals (5). These systems exclusively react by the H-atom recombination, HF-elimination pathway because abstraction of F atoms has a high activation energy, and these reactions can serve to define the typical energy disposal pattern for three- and four-centered HF-elimination reactions. Other studies in the literature (6), especially from multiphoton infrared excitation (9) and classical chemical activation (10), show that the dynamics for unimolecular HCl and HF elimination should be similar. The fundamental thesis of the present analysis is that direct abstraction can be identified by examination of the HCl(v) distributions, since the mean fraction of the vibrational energy released to HCl for direct Cl-atom abstraction will be 0.35–0.50 with an inverted distribution (3, 8), whereas the distribution for HCl elimination is expected to be non-inverted with $\langle f_V \rangle \sim 0.15$ (5–7).

The three reaction systems that were studied in the present work are summarized below with the ΔH_0^0 in kcal mol^{-1} given in parentheses. Reactions [1a], [2a], and [3a] represent the recombination plus unimolecular elimination mechanism. Reactions [1b], [2b], and [3b] represent direct abstraction on the singlet or triplet potentials.

$$[1a]\quad H + CCl_3 \rightarrow CHCl_3^* \rightarrow CCl_2(\tilde{X}^1A_1) + HCl \qquad (-41)$$

$$[1b]\quad \rightarrow CCl_2(\tilde{X}^1A_1 \text{ or } \tilde{a}^3B_1) + HCl \qquad (-41 \text{ or } -29)$$

$$[2a]\quad H + CF_2Cl \rightarrow CHF_2Cl^* \rightarrow CF_2(\tilde{X}^1A_1) + HCl \qquad (-54)$$

$$[2b]\quad \rightarrow CF_2(\tilde{X}^1A_1 \text{ or } \tilde{a}^3B_1) + HCl \qquad (-54 \text{ or } 4)$$

$$[2c]\quad \rightarrow CHF_2Cl^* \rightarrow CFCl(\tilde{X}^1A') + HF \qquad (-46)$$

$$[3a]\quad H + CH_2CH_2Cl \rightarrow CH_3CH_2Cl^* \rightarrow HCl + C_2H_4 \qquad (-84)$$

$$[3b]\quad \rightarrow HCl + C_2H_4 \qquad (-84)$$

[1]Present address: Department of Chemistry, University of Illinois at Urbana-Champaign, Urbana, IL 61801, U.S.A.

[2]Author to whom correspondence may be addressed.

Can. J. Chem. Downloaded from www.nrcresearchpress.com by EESC ESCOLA DE ENGENHARIA on 09/08/12
For personal use only.

TABLE 1. Thermochemistry[a] for the addition–elimination unimolecular reactions

Molecule	$\langle E\rangle^b$	ΔH_0^{0c}	$E_0^{\ddagger d}$	$\langle E\rangle - \Delta H_0^{0e}$	E_p^f	E_x^g
$CH_3CH_2Cl^*(-HCl)$	105.0 ± 2.0	17.0 ± 0.2	55.0 ± 2.0	88.0 ± 2.0	38.0 ± 2.0	50.0 ± 2.0
$CHF_2Cl^*(-HCl)$	102.0 ± 2.0	48.2 ± 2.0	57.0 ± 3.8	53.8 ± 2.0	8.8 ± 3.8	45.0 ± 3.8
$CHF_2Cl^*(-HF)$	102.0 ± 2.0	53.5 ± 4.0	70 ± 4	48.5 ± 4.0	16.5 ± 4.0	32.0 ± 4.0
$CHCl_3^*(-HCl)$	95.5 ± 2.0	55.0 ± 2.0	≈60[h]	40.5 ± 4.0	≈5.0	≈35.0

[a]All entries are in kcal mol^{-1} for reaction on the singlet potential surface.
[b]The total available energy released to the molecule from reactions [1*a*], [2*a*], and [3*a*] for 450 K experiments. The energy for CH_3CH_2Cl is reduced to 103.6 kcal mol^{-1} at 300 K.
[c]The enthalpy change for elimination of HCl (or HF) from the molecule.
[d]The threshold energy for HCl (or HF) elimination; see text for references. The $E_0^{\ddagger}$(HF) for CHF_2Cl was assigned in this work, see text.
[e]Total energy available to the products for the elimination pathway is $\langle E\rangle - \Delta H_0^0$; the available energy for abstraction could be slightly higher if there is an activation energy.
[f]Potential energy released during the reaction, $E_0^{\ddagger} - \Delta H_0^0$.
[g]Excess energy, $\langle E\rangle - E_0^{\ddagger}$, released during the reaction.
[h]The $E_0^{\ddagger}$ from ref. 12 is lower than the currently accepted ΔH_0^0. The reverse reaction is also likely to have a barrier, and $E_0^{\ddagger}$ was set at 60 kcal mol^{-1}.

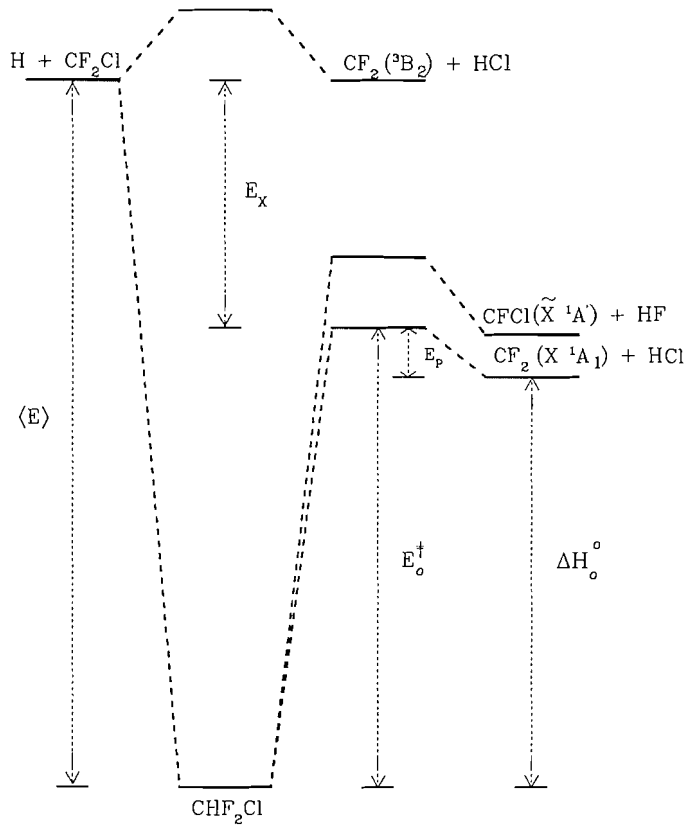

FIG. 1. Schematic representation of the reaction profile for the three-centered elimination reactions of H + CF_2Cl. The diagram is similar for four-centered elimination, but E_p is larger. The values for the energy quantities are given in Table 1.

Direct abstraction of F from CF_2Cl would have a larger activation energy than Cl abstraction, so that reaction is not listed for reaction [2]. The ground states of CCl_2, CF_2, and CFCl are the singlet states; thus, the potential surfaces that correlate to the triplet carbene states lie above the singlet potential surfaces. The recombination–elimination pathways are expected to involve only the singlet potentials. In principle, the Cl-atom abstraction reactions can proceed on either surface, but the singlet potentials probably have lower activation energy.

The HCl channel from CHF_2Cl^* previously was observed (5) using the F + CHFCl reaction to generate CHF_2Cl^*. The HF channel could not be observed in that work because of the strong HF emission from the primary reaction. The thermochemistry for the unimolecular reactions corresponding to [1*a*], [2*a*], and [3*a*] is summarized in Table 1 for 450 K and the symbols are defined in Fig. 1. The average energies of the molecules are given by $\langle E\rangle = D_0(\mathrm{H-R}) + E_a(\mathrm{H+R}) + nRT$ where E_a is the activation energy and nRT is the thermal energy of the H atom and radical reactants; the energies are $\gtrsim$100 kcal mol^{-1}. The activation energies were taken as zero. The C—H bond energies, D_0, for reactions [1]–[3] were obtained from ref. 11. The threshold energies, $E_0^{\ddagger}$, for HCl elimination from CH_3CH_2Cl (10*a*) and CHF_2Cl (12) were obtained from the literature. The E_a given in ref. 12 for the $CHCl_2$ reaction is smaller than the currently favored ΔH^0 for the reaction, which cannot be true. Also, the reverse reaction, CCl_2 + HCl, is likely to have a small barrier. Allowing for a 5 kcal mol^{-1} barrier for the reverse reaction, $E_0^{\ddagger}$ was set at 60 kcal mol^{-1} for reaction [1*a*]. The $E_0^{\ddagger}$ for HF elimination from CHF_2Cl was assigned from the ratio of rate constants for HF and HCl elimination and $E_0^{\ddagger}$(HCl) (12). The $\Delta H_{f0}^0(CF_2) = -42.6$ kcal mol^{-1} was taken from ref. 13*c* and $\Delta H_{f0}^0(CCl_2) = -52.1$ kcal mol^{-1} was taken from recent experimental work (13*a*, *b*). The thermochemistry for CFCl is not firmly established. We prefer the theoretical estimates of Francisco et al. (14*a*) ($\Delta H_{f0}^0 \approx 7$ kcal mol^{-1}) and Rodriquez and Hopkinson (14*b*) ($\Delta H_{f0}^0 = 3.3$ kcal mol^{-1}) over the experimental estimate of Lias et al. (15) ($\Delta H_{f0}^0 = -2 \pm 7$ kcal mol^{-1}), and we used 5 kcal mol^{-1}. The energy that would be available to the products from abstraction on the singlet surfaces would be larger than the value given in column 5 of Table 1 by the difference in E_a values for abstraction vs. recombination. The least certain values in Table 1 are the threshold energies for the three-centered elimination reactions. This affects the E_p values, which also are the threshold energies for addition of the carbenes to HCl or HF.

Reactions [1]–[3] were observed as secondary steps in a flow reactor containing excess H atoms with the precursor molecules CCl_3Br, CF_2ClBr, CH_2Cl-CH_2I (and also CH_2Cl-CH_2Br), respectively. Previously, we had used only iodine containing precursor molecules for generating the radicals (5). However, the primary reactions with some bromine-containing molecules are sufficiently fast, especially at 475 K, that they can augment the supply of useful precursor molecules for studies of H atom + radical reactions in our flow reactor. The HBr(v) chemilumines-

Can. J. Chem. Downloaded from www.nrcresearchpress.com by EESC ESCOLA DE ENGENHARIA on 09/08/12
For personal use only.

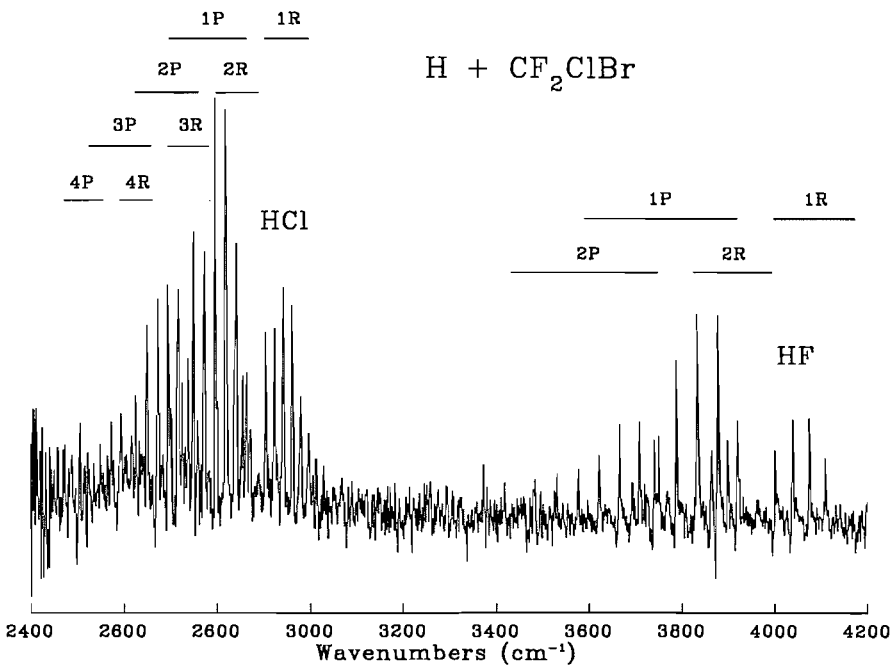

FIG. 2. Infrared emission spectrum from the H + CF_2ClBr system; the concentrations are 3.0×10^{13} and 2.0×10^{13} for [H] and [CF_2ClBr], respectively, and the reaction time is 0.5 ms.

cence from the primary steps could be observed, but the data are not very interesting because only HBr ($v = 0$ and 1) are generated. The H + CF_3 (generated from H + CF_3I) reaction also was studied at 475 K as a reference reaction, and the energy disposal pattern to HF was the same as in our previous room temperature study (5).

The vibrationally excited chloromethane and chloroethane molecules can be collisionally stabilized at high pressure (10), so the abstraction and addition–elimination mechanisms actually become identifiable in terms of the chemical products at high pressure. Dobis and Benson (16) recently emphasized that chlorination of hydrocarbons is an especially effective means to crack hydrocarbons because the recombination steps and direct abstraction (disproportionation) give olefins + HCl. The present work also has relevance to recent work for H + vinyl chloride kinetics (17). Typical values of disproportionation to recombination ratios of alkyl radicals range from 0.1 to 0.5 (18, 19). The question of direct abstraction vs. atom recombination at the radical site followed by unimolecular decomposition is of general importance for the interactions of open-shell atoms and polyatomic radicals. The infrared chemiluminescence technique may be one way to search for these abstraction reactions in atom plus radical encounters.

II. Experimental methods

The experimental method employed the reaction of excess H atoms with precursor molecules in a linear flow reactor. The H atoms were generated by a microwave discharge in H_2–Ar mixtures, and they were introduced at the front of the reactor. Additional Ar carrier gas was added separately at the entrance of the reactor to achieve a total pressure of 0.5–1.0 Torr (1 Torr = 133.3 Pa). The CF_3I, CCl_3Br, CF_2ClBr, and CH_2Cl–CH_2I (or CH_2Cl–CH_2Br) reagents were added via a ring injector 40 cm downstream from the H-atom inlet as a 5–10% mixture in Ar just before the observation window (a 4 cm diameter NaCl flat). Typical concentrations of H and the organic reagent were $(1–3) \times 10^{13}$ and $(0.5–5.0) \times 10^{13}$ molecules cm^{-3}, respectively. The H-atom concentration was assigned from measurement of 50% dissociation of the H_2. For some experiments the CH_2ClCH_2I (or CCl_3Br) was added by flowing Ar over the liquid sample at 300 K. Variable temperature experiments were done by heating the portion of the flow reactor extending from the H_2 and Ar inlets to the observation window (40 cm). The temperature of the reactor was regulated by the voltage supplied to the heating tapes. The temperature of the gas at the downstream edge of the NaCl window was measured with a thermocouple. This temperature was always the same as the temperature of the Boltzmann rotational distribution for HX(v) that was assigned from the emission spectra.

The highest possible flow velocity was ≈ 120 m s^{-1}, corresponding to a reaction time of ~0.2 ms for a reaction zone of 2.5 cm. The Ar pressure could be varied from 0.3 to 1.0 Torr without loss of pumping speed. The HF(v) and HCl(v) vibrational relaxation was fully arrested for these conditions and the rotational relaxation of HF was partly arrested (5, 20). Increasing the reaction time to ≈0.5 ms was required to observe some of the secondary reactions. For these conditions the vibrational distributions from the secondary reaction are hardly affected by relaxation, and the observed distributions are close to the nascent ones. Since HX emission could be observed from H + CF_3 and H + CH_2CH_2Cl (from CH_2ClCH_2I) for the fastest flow speed, we used these reactions for monitoring the degree of vibrational relaxation for other operating conditions.

The emission spectra were recorded at 1–2 cm^{-1} resolution with a Biorad (FTS-60) spectrometer; the individual rotational lines are easily observed, as shown in Fig. 2. A quartz filter with a cutoff at ≈ 2200 cm^{-1} was used to reduce the blackbody radiation for experiments at elevated temperature. The gain on the InSb detector also was reduced to avoid saturation. The rotational population in individual levels was obtained from the peak height of each vibrational–rotational line after division by the instrumental response function and the Einstein coefficient for the particular transition. Improved Einstein coefficients are available for HF and HCl, and their reliability should be better than 5% (21). The HBr coefficients (22) probably are less reliable, but only qualitative observations were made for HBr(v). The HCl and HBr rotational distributions were always Boltzmann at the temperature of the reactor. For some reactions, e.g., H + CF_3, the HF($v = 1$) distribution has a small component for $J \geq 8$ in addition to the Boltzmann component. But this was not the case for the H + CF_2Cl reaction.

Commercial tank grade Ar was purified by passage through molec-

Can. J. Chem. Downloaded from www.nrcresearchpress.com by EESC ESCOLA DE ENGENHARIA on 09/08/12
For personal use only.

TABLE 2. HX(v) distributions from the halomethane elimination reactions[a]

Reaction	P_0	P_1	P_2	P_3	P_4	λ_V	$\langle f_V \rangle_{HX}$[c]
$H + CF_3 \rightarrow HF(v)$[b]		58.0	30.0	10.0	2.0	-5.1 ± 0.7	0.16
	50.0	29.0	15.0	5.0	1.0		(0.06)
$H + CF_2Cl \rightarrow HCl(v)$		58.0	26.5	10.5	5.0	-3.0 ± 0.6	0.13
	45.2	31.7	14.5	5.8	2.7		(0.08)
$\rightarrow HF(v)$		70	27	3	—	-3.0 ± 0.6	(0.12)
	60.4	27.7	10.7	1.2	—		(0.05)
$F + CHFCl \rightarrow HCl(v)$[d]		51.4	26.5	15.1	7.0	-2.2 ± 0.3	0.12
	43.5	28.9	14.9	8.5	3.9		(0.09)
$H + CCl_3 \rightarrow HCl(v)$		73	22	5	—	-2.7 ± 0.4	0.11
	59.8	29.3	8.8	2.0	—		(0.06)

[a]The P_0 values were assigned from linear vibrational surprisal plots. The vibrational distributions did not change significantly for experiments at 300 and 475 K.
[b]Example of a typical three-centered elimination distribution; the $\langle E \rangle - \Delta H_0^0$ is 52 kcal mol^{-1} and the data are from ref. 5.
[c]The number in parentheses is the mean fraction of vibrational energy for the prior distribution.
[d]Data from ref. 5 at 300 K from the F + CH_2FCl reaction system.

ular sieve traps cooled to liquid N_2 temperature. Tank grade H_2 was used without further purification. All reagents were purified by several freeze–pump–thaw cycles before loading. The CF_3I and CH_2ClCH_2I were purchased from PCR Inc. The CCl_3Br, CF_2ClBr, and CH_2Cl–CH_2Br were obtained from Columbia Organic Chemicals Co.

III. Results

A. *General observations*

The HBr emissions from the primary reaction with CCl_3Br, CF_2ClBr, and CH_2ClCH_2Br were not analyzed in detail, as our interest was in the atom + radical secondary reactions. The H + CH_2ClCH_2I reaction could be studied with maximum pumping speed (120 m s^{-1}) at 300 K and the observed HCl(v) distribution should be nascent, as judged from other extensive studies in this flow reactor. Even if the pumping speed was reduced by a factor of 2, the HCl(v) distribution was unchanged. If the pumping speed was reduced to ~70 m s^{-1}, HCl emission could be observed from the H + CCl_3Br and CF_2ClBr systems. By analogy to the H + CH_2ClCH_2I reaction, these HCl(v) (and HF(v)) distributions should be nascent. For all three systems the distributions were invariant to changes in [H] and [reagent] for the shortest times that could be used. The HF(v) and HCl(v) emission spectrum from H + CF_2ClBr is shown in Fig. 2. The CH_2ClCH_2Br reaction did not give emission at 300 K unless the pumping speed was greatly reduced. The activation energy for Br abstraction from CH_2ClCH_2Br is evidently higher than for CCl_3Br and CF_2ClBr, presumably because of a higher bond energy. With heating to 475 K, HCl emission could be observed from all four reactions. However, even at 475 K, the HCl emission from CH_2ClCH_2Br was observable only for relatively long reaction times, and the HCl(v) distribution was relaxed compared to the data from the CH_2ClCH_2I system. Table 2 gives a summary of the HX(v) distributions observed for the H + CCl_3Br and CF_2ClBr systems. Table 3 summarizes the experimental results from the H + CH_2ClCH_2I system.

The HCl emission arises only from secondary reaction, since Cl abstraction from the parent compounds has a large activation barrier compared to Br or I atom abstraction. As a test of this thesis, an experiment was done with the H + $CHCl_3$ reaction at 475 K, but no HCl emission was observed for our experimental conditions.

We made no effort to extract information from the temperature dependence of the total emission intensities. For the system with small E_a for the primary step, e.g., CF_3I and CH_2ClCH_2I, the HF and HCl emission intensities actually were slightly smaller at 475 K than at 300 K, because the concentrations and reaction time decrease with temperature, providing that the total pressure is constant and the gas flows delivered to the reactor are constant. The HBr emission intensity from CCl_3Br increased with temperature, but the HCl emission intensity was slightly reduced for the higher temperature. One difficulty with trying to interpret the dependence of the total emission intensity on temperature is that the [H] may not be constant because of the change in the rate of H atom recombination on the wall with temperature. Since the secondary reactions have a second-order dependence on [H], any loss of [H] severely affects the H + radical reaction rate. Direct measurement of the [H], at the observation window, is needed before the temperature dependence of the total emission intensities can be interpreted.

TABLE 3. Summary of HCl(v) distributions for H + CH_2ClCH_2I experiments[a]

No.	$[H_2]$[b]	T (K)	P_1	P_2	P_3	P_4	P_5[c]
1	4.1	300	16.7	27.6	30.3	16.2	9.2
2	6.8	300	15.8	27.2	30.5	17.2	9.2
3	10.0	300	18.3	29.0	28.5	15.8	8.3
4	24.0	300	20.8	29.3	27.7	15.0	7.3
5	24.0	300	19.0	28.2	28.0	17.0	7.7
6	10.9	413	13.9	21.3	28.1	22.5	14.2
7	24.0	475	16.4	23.3	24.8	21.5	13.9
8	24.0	475	15.5	22.7	26.0	22.5	13.2

[a]All experiments were carried out at 0.5 Torr Ar for a reaction time of 0.25 ms.
[b]$[H_2]$ in 10^{12} molecules cm^{-3}; the $[CH_2ClCH_2I]$ was fixed at 2.0×10^{13} molecule cm^{-3}.
[c]P_6 could be estimated as 1/2 P_5. For runs 6–8, trace amounts of $v = 7$ were also observed.

B. *H + CCl_3*

The HCl distribution from this reaction at 300 K was P_1–P_3 = 74:21:5; the distribution observed at 475 K, 72:23:5, was unchanged. These distributions were recorded for a reaction time of 0.4 ms and they were invariant to change in $[CCl_3Br]$ and $[H_2]$. Since the distribution does not change with temperature, HCl(v) seems to arise only from the recombination–elimination mechanism. The available energy is 40 kcal mol^{-1},

Can. J. Chem. Downloaded from www.nrcresearchpress.com by EESC ESCOLA DE ENGENHARIA on 09/08/12
For personal use only.

TABLE 4. HCl(v) distributions[a] from the H + CH_2CH_2Cl reaction

Condition	P_0	P_1	P_2	P_3	P_4	P_5	P_6	λ_V	f_V
300 K	—	17.4	27.0	28.0	15.6	8.2	3.8	−11.8 ± 0.8	0.20
(exper.)	20.8	13.8	21.4	22.2	12.3	6.5	3.0		
475 K	—	12.9	19.9	26.2	20.9	13.2	6.9	−14.2 ± 0.3	0.25
(exper.)	12.1	13.4	19.6	23.3	19.3	12.3			
Cl + CH_2CH_2	—	39.0	29.0	22.0	10.0			−10.1 ± 0.3	0.18
(elimin.)[b]	29.9	27.3	20.3	15.4	7.1				(0.04)[c]
H + CH_2CH_2Cl	28.8	24.2	18.6	13.0	8.3	4.7	2.4	[c]	0.155
(elimin.)[c]									(0.04)
H + CH_2CH_2Cl	0	0	17.9	32.1	25.0	14.3	10.7	—	0.33
(abstract.)[d]									

[a]The second line for the first three entries includes the P_0 obtained from the linear surprisal plot; the distribution is then renormalized.
[b]From ref. 26. The available energy is 64 kcal mol^{-1}.
[c]Pure elimination distribution calculated using $\lambda_V = -10.1$ and $\langle E \rangle - \Delta H_0^0 = 88$ kcal mol^{-1}. The elimination distribution is slightly different for the two temperatures due to the change in $\langle E \rangle$, but the difference is not significant. The $\langle f_V \rangle$ for the prior distribution is 0.04.
[d]Abstraction distribution obtained by deconvolution of the experimental distribution from the pure elimination distribution. The distribution from abstraction was forced to be the same for both temperatures.

which could give HCl(v = 5); however, the highest observed level was HCl(v = 3). The P_0 was estimated using a linear surprisal analysis, and the overall distribution after renormalizing is P_0–P_3 = 60:29:9:2. The full statistical model was used to calculate the vibrational prior. The λ_V for this reaction was −2.7 and the $\langle f_V \rangle$ was 0.11. To the best of our knowledge, there are no other theoretical or experimental HCl(v) distributions from the unimolecular decomposition of $CHCl_3$* available for comparison. This HCl(v) distribution is characteristic of three-centered elimination reactions with a small E_p (5, 6).

C. $H + CF_2Cl$

The HCl(v) distribution obtained from this reaction was P_1–P_4 = 57.8:27.4:9.4:5.4 at 300 K and 58.0:25.8:11.1:5.1 at 475 K. As demonstrated in Fig. 2, HF(v) emission also was observed. The HF(v) distribution was P_1–P_3 = 70.5:27.0:2.5 and 70.0:27.0:3.0 at 300 and 475 K, respectively. The HCl(v) and HF(v) distributions did not change with temperature and neither did the ratio of HF(v) to HCl(v). These distributions suggest that the HF and HCl are formed solely by unimolecular elimination from CHF_2Cl*. Linear surprisal plots were used to estimate the P_0 values, and the full distributions are given in Table 2. The HCl(v) distribution from CHF_2Cl* previously observed from the F + CHFCl reaction system is also given in Table 2 for comparison. The small difference in the two HCl distributions is a consequence of the larger $\langle E \rangle$ for F + CHFCl, and the $\langle f_V \rangle$ for the two reactions are almost the same: 0.13 and 0.12. The HF(v) distribution from CHF_2Cl is somewhat less extended than the HF(v) distribution from CHF_3 because the available energy is larger for the latter.

The HF and HCl intensities were corrected for the respective Einstein coefficients and instrumental response function to find the HF($v \geq 1$)/HCl($v \geq 1$) ratio, which was 0.17. Including the P_0 values from the surprisal calculations for HCl and HF distributions increases the ratio to 0.24. The CF_2 + HCl channel was observed to be the more important channel in the IRMPD studies of CHF_2Cl* (9*b*, 23). Martinez and Herron (23*a*) did observe CFCl, but they estimated that the CF_2 + HCl channel accounted for 99% of the reaction. The IRMPD experiments have a much lower $\langle E \rangle$ than the chemical activation experiments, and the HF/HCl ratio would be smaller. Our HF/HCl ratio suggests that the $E_0^{\ddagger}$ for the HF channel is ~13 kcal mol^{-1} higher than that of the HCl channel; this estimate was obtained by comparing the sums of states for the HF and HCl elimination transition states, vide infra.

D. $H + CH_2CH_2Cl$

A summary of the experimental results of various [H_2] and temperatures are given in Table 3. The HCl(v) emission intensity was strong and the results were always consistent. The emission was observed after a reaction time of 0.2 ms, and we believe that the HCl(v) distributions are the nascent vibrational distributions. A special search was necessary for HCl(v = 6) emission, since the HCl(6–5) band falls into the region where CO_2 background absorption occurs. Experiments with extensive flushing of the FTIR spectrometer and long time signal averaging gave a spectrum that could be analyzed and the P_5 to P_6 ratio was 2:1. Trace emission from v = 7 also could be seen. The average HCl(v) distribution observed from this reaction at 300 K was P_1–P_6 = 17:27:28:16:8:4. The available energy of 88 kcal mol^{-1} could give up to HCl(v = 11), and the highest observed HCl(v) level does not extend to the thermochemical limit. The HCl(v) distribution at 475 K was even more highly inverted: HCl(v) P_1–P_6 = 13:20:26:21:13:7. These HCl(v) distributions were highly reproducible at these two temperatures and they were invariant to changes of [H] and [CH_2ClCH_2I]. These slightly inverted distributions are very different from the HF(v) vibrational distributions observed from the HF elimination reactions of CH_3CH_2F and CH_3CF_3 (3).

Leone and co-workers (24) have studied the Cl + CH_3CH_2 reaction, which proceeds by the recombination–elimination mechanism to produce HCl(v). Their HCl(v) distribution, which is shown in Table 4, could be fitted with a linear surprisal plot, and the λ_V (−10.1) is very similar to the slope of the linear surprisal plot for HF elimination (5) from CH_3CH_2F and CH_3CF_3. Scaling a λ_V = −10.1 distribution to the energy for reaction [3] gives a "pure" HCl(v) elimination distribution suitable for comparison to our results. The comparison, see Table 4, clearly indicates that the HCl(v) from the H + CH_2CH_2Cl reaction must be the result of more than just the recombination–elimination reaction. We suggest that the observed HCl(v) distribution from H + CH_2CH_2Cl is the sum of recombination–elimination and abstraction components, with abstraction becoming more pronounced as the temperature is increased. Our

Can. J. Chem. Downloaded from www.nrcresearchpress.com by EESC ESCOLA DE ENGENHARIA on 09/08/12
For personal use only.

Can. J. Chem. Downloaded from www.nrcresearchpress.com by EESC ESCOLA DE ENGENHARIA on 09/08/12
For personal use only.

attempt to deconvolute the experimental distribution into the components representing the abstraction and elimination pathways is described in Sect. IV.3.

IV. Discussion

A. *Summary of energy disposal for addition–elimination vs. recombination reactions*

Although the chemical identity of the products is the same from recombination–elimination and from direct abstraction, the vibrational energy disposal patterns to the HCl (or HF) products from the two channels should be much different. The chemically activated halomethane and haloethane molecules with $\sim$100 kcal mol^{-1} of energy have unimolecular lifetimes (statistical limit) that range from picosecond (halomethanes) to nanosecond (haloethanes). The unimolecular elimination reactions yield HX(v) distributions that monotonically decline with increasing f_V and the $\langle f_V(HX)\rangle$ values are typically $\approx$0.15 with vibrational surprisal plots that are linear with slightly negative slopes (5–7). The transition state configurations and the dynamics of the HX elimination reactions are reasonably well understood (25–27). Since the excess energy for $CHCl_3$* and CHF_2Cl* is large, and since the formation steps are not state selective, the mode specific reaction pathways (27) found for photoexcited HFCO are not expected to be important. Stated another way, the relaxation of the energy released primarily in the H—C bond is expected to attain a microcanonical distribution before HX elimination occurs (28). In contrast, the characteristic HX(v) distributions from direct Cl or F abstraction by H atoms over repulsive potentials are sharply inverted and rather narrow with $\langle f_V(HX)\rangle = 0.4$; the vibrational surprisals are not linear and the distributions do not extend to the thermochemical limit (3, 4, 8). The rotational energy disposal from elimination and abstraction reactions are both rather modest (4–6), so the rotational energy disposal pattern is not very useful in distinguishing between the two reaction pathways. The energy disposal for Cl atom abstraction from polyatomic molecules by H atoms is representative of the class of reactions in which the dynamics are limited by kinematic constraints associated with the motion of the light H atom over a repulsive surface (3, 4, 8, 22). This pattern of energy disposal was characterized by Polanyi in a classic series of papers dealing with the reactions of H atoms with the diatomic halogen molecules (29).

Recombination reactions of methyl-type radicals with H atoms generally are considered to have nearly zero activation energies with rate constants of (1–2) $\times$ 10^{-10} cm^3 s^{-1} (30), whereas the abstraction pathways could have small positive activation energies. The halogen–carbon bond energies are large, D(Cl—CCl_2) = 62 kcal mol^{-1} and D(F—CF_2) = 87 kcal mol^{-1}, and Cl- or F-atom abstraction to give singlet carbenes is not expected to compete with recombination. Our method of observation would not be sensitive to direct abstraction on the triplet surface for H + CCl_3 and CF_2Cl giving triplet state carbenes because the available energy is rather low; see reactions [1b] and [2b]. The only case where H-atom abstraction might be expected at modest temperatures is H + CH_2CH_2Cl.

B. *HX elimination reactions from halomethanes*

The energy disposals to HX(v) from $CHCl_3$* and CHF_3*, respectively, are similar; but, the HF(v) distribution from CHF_3* does have a slightly larger negative λ_V and a larger $\langle f_V\rangle$. The HF(v) and HCl(v) distributions from CHF_2Cl* are more similar to the $CHCl_3$* reaction. The larger $\langle f_V(HF)\rangle$ from CHF_3* probably arises from the larger potential energy that is released in the exit channel. In our previous work (5), the energy released to the products from unimolecular processes with statistical lifetimes was treated as the sum of the statistical fraction of the excess energy (6), and the fraction of the potential released to HX, e.g., eq. [4].

$$[4]\quad \langle E_V(HX)\rangle = a\langle E_X\rangle + b\langle E_P\rangle$$

For the halomethanes the a value was $\approx$0.1 and the b value was $\approx$0.35. Using these a and b values with the thermochemistry in Table 1 gives good agreement with the experimental $\langle f_V\rangle$ values for $CHCl_3$* and CHF_2Cl*. For example, the $\langle f_V(HCl)\rangle$ for $CHCl_3$* and CHF_2Cl* are calculated to be 0.13 and 0.14 compared to the observed values of 0.11 and 0.13. The E_p is small for these reactions and the energy release is dominated by the excess energy, which is statistically distributed among the modes at the transition state geometry. As already noted, the mode-specific unimolecular rates (27) found for photoexcitation of HFCO at energies near $E_0^{\ddagger}$ are not expected for the highly energized $CHCl_3$* and CHF_2Cl* molecules.

The recombination rate constants (300 K) for H atoms with methyl-type radicals are large, near the orbiting limits (30), and little or no steric requirement exists. If we assume that a 5% contribution to HCl (high v) from abstraction could have been observed, then the activation energy for abstraction must be 3 kcal mol^{-1} (for similar pre-exponential factors for [1a] vs. [1b]). The H-atom reactions with NF_2 (31a), SF_5 (22), and CF_3O (31b) also proceed by addition–elimination mechanisms; however, these bimolecular rate constants are somewhat smaller than for H + methyl-type radicals. Comparison with the ClO (32a)[3] and NFCl (32b) reactions is worthwhile. The unpaired electron in these radicals is in a delocalized π orbital and the H atom seems to add to more than one site. For this reason and also because of the very short HOCl lifetime and a surface crossing in the exit channel, the energy disposal to HCl + O(^3P) differs from the normal HX elimination pattern.

The branching ratio for HF vs. HCl formation from CHF_2Cl* was 0.24 at $\langle E\rangle$ = 102 kcal mol^{-1}. This ratio is equal to the ratio of RRKM rate constants, which reduces to the ratio of sums of states of the two transition states. We assigned frequencies of 1275(1), 1050(2), 800(1), 670(2), 600(2) and 1160(1), 950(2), 780(3), 500(2) to obtain pre-exponential factors of $\sim 1.5 \times 10^{13}$ per reaction path for the thermal rate constants at 800 K for HCl and HF elimination, respectively. For these transition states a $\Delta E_0^{\ddagger}$ difference of 13 $\pm$ 1 kcal mol^{-1} was required to get a branching ratio of 0.12 for a reaction path degeneracy of 1 for each channel.

C. *H + CH_2CH_2Cl reaction*

The HCl(v) distribution and the $\langle f_V(HCl)\rangle$ from this reaction differ from the typical pattern found from the four-centered elimination reactions of CH_3CH_2Cl*, CH_3CH_2F*, and CH_3CF_3*. The recent work of Leone and co-workers (24) in which CH_3CH_2Cl* was formed by the Cl + CH_3CH_2 recombination reaction represents an important benchmark, because the HCl(v) distribution was as expected from a four-centered HX elimination process. Therefore, we infer that the Cl + CH_3CH_2 reaction proceeds entirely by atom–radical recombination fol-

[3]The broken line shown in Fig. 5 of ref. 32a should be ignored; the surprisal plot is not linear.

Can. J. Chem. Downloaded from www.nrcresearchpress.com by EESC ESCOLA DE ENGENHARIA on 09/08/12
For personal use only.

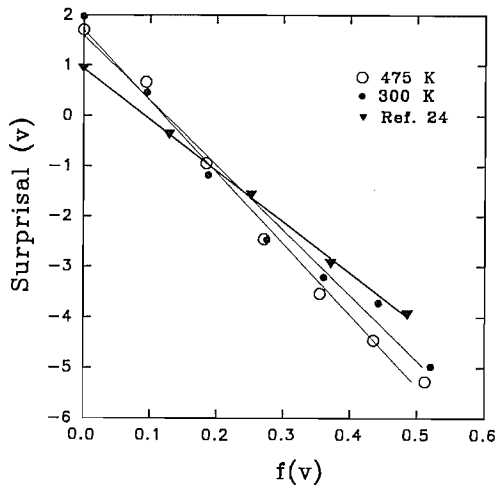

FIG. 3. Surprisal plots for the HCl(v) distributions from H + CH_2CH_2Cl at 300 K (filled circles) and 475 K (open circles) and the Cl + CH_3CH_2 reaction (filled triangles) from ref. 24. Note the smaller slope of the plot from the Cl + CH_3CH_2 reaction.

lowed by subsequent HCl elimination. Since the observed HCl(v) distribution from H + CH_2CH_2Cl differs from the distribution given by Cl + CH_3CH_2, we believe that the former is the sum of a direct abstraction pathway plus a recombination-elimination pathway. Our experiment cannot give the ground state vibrational population, P_0, but some estimate is needed before deconvolution of the experimental distribution can be made into abstraction and elimination components. Since the overall experimental distribution did fit (fortuitously) a linear surprisal plot, extrapolations were used to estimate the experimental P_0 values at both temperatures; see Table 4. The full statistical model for the HCl + CH_2CH_2 products was used to calculate the prior HCl(v) distribution. Figure 3 shows the surprisal plots for our data, and the corresponding plot from the HCl(v) distribution associated with the pure elimination reaction as provided by the Cl + CH_3CH_2 reaction. In some instances, surprisal analysis can distinguish two-component product distributions. However, direct abstraction pathways (by H atoms) do not give linear surprisals, and two linear portions of the surprisal plot for H + CH_2ClCH_2 would not be expected. It is fortuitous, but convenient, that the raw experimental distributions can be represented by a linear surprisal, but with a larger $-\lambda_V$ than for the "pure" elimination distribution.

The CH_3CH_2Cl* formation pathways of H(Cl) + CH_2CH_2-Cl(CH_3CH_2) seem unlikely to be sufficiently state selective to cause nonstatistical unimolecular lifetimes. The main difference in the formation process would be the considerably higher rotational energy carried into CH_3CH_2Cl* by the Cl + CH_3CH_2 recombination reaction. The vibrational energy disposal to HCl from unimolecular reaction of the chemically activated CH_3CH_2Cl* formed by the two recombination reactions should be similar. We used $\lambda_V = -10.1$ with $\langle E \rangle = 105$ kcal mol^{-1} to estimate the "pure" HCl(v) elimination distribution associated with our H + CH_2CH_2Cl reaction. The calculated "pure" HCl(v) distribution is presented in Table 4. There is a very definite difference between this "pure" HCl(v) elimination distribution and our experimental distributions.

Two assumptions are necessary in order to estimate a branching fraction and the HCl(v) distribution for the Cl atom abstraction reaction. We focused attention on the HCl($v = 0$) population

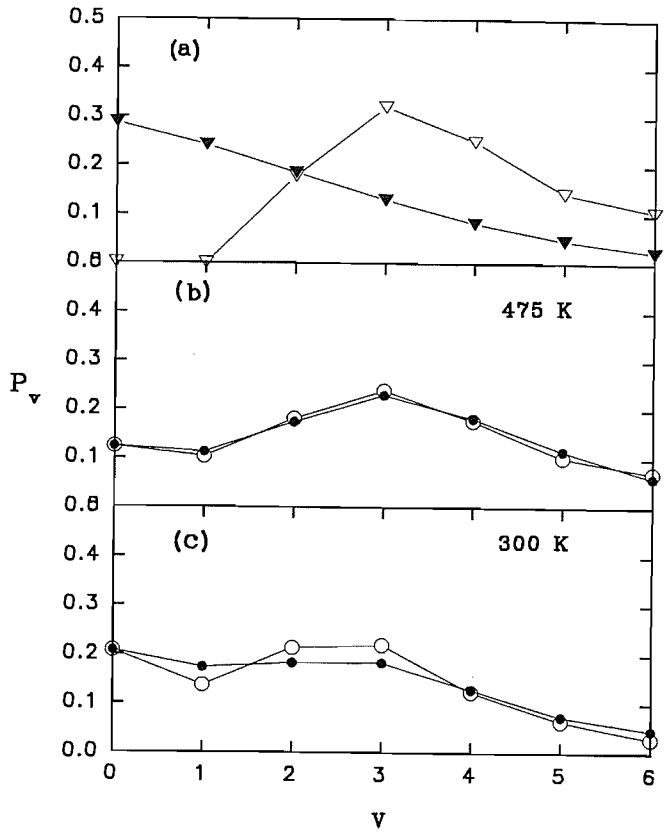

FIG. 4. (*a*) Comparison of the pure elimination (▼) and the abstraction (▽) HCl vibrational distributions from the H + CH_2CH_2Cl reaction. The abstraction distribution is the average distribution that best fits all the experimental distributions. (*b*) The 475 K experimentl distributions are compared to the sum of the two components with weights of 0.57 and 0.43 for abstraction and elimination, respectively. (●)-P_v observed and (○)-P_v calculated. (*c*) Same as Fig. 4*b* except at 300 K with weights of 0.28 and 0.72 for abstraction and elimination, respectively.

and assumed that HCl($v = 0$) arises only from the elimination reaction. This assumption together with using a linear surprisal distribution with $\lambda_V = -10.1$ for the elimination distribution directly leads to the fraction of the reaction going through the abstraction channel, f_a. Thus, f_a was determined to be 0.28 at 300 K and 0.57 at 475 K. To obtain an overall average distribution for abstraction, we assumed that the vibrational distribution from the abstraction channel does not change with temperature and adopted a single distribution for the abstraction process. The deconvolution method is not sufficiently sensitive to extract temperature-dependent distributions for the abstraction reaction. In any event, the change in thermal energy of CH_2ClCH_2 will not affect the HCl(v) distribution for abstraction, which depends on the release of repulsive energy by the potential. The best vibrational distribution for the abstraction channel was selected so that when combined with the "pure" elimination distribution, the experimental distributions were reproduced. Figure 4 shows the two separate components, and the synthetic overall distributions are compared with the experimental ones at 300 and 475 K. The agreement between the synthetic distribution and the experimental ones is satisfactory. The vibrational distribution that was assigned to the abstraction channel is given in the last line of Table 4. The $\langle f_V \rangle$ for this inverted distribution is 0.33, which is similar to the majority of other Cl-atom abstraction reactions from polyatomic inorganic

Can. J. Chem. Downloaded from www.nrcresearchpress.com by ESC ESCOLA DE ENGENHARIA on 09/08/12
For personal use only.

molecules such as Cl_2O, NO_2Cl, and $NFCl_2$ (32*b*). The derived distribution for the abstraction reaction has a negligible P_1 value. Although the true value may not be zero, a small P_1 is consistent with direct abstraction.

The structure of the chloroethyl radical must closely resemble that for ethyl radical with sp^2 bonding at the localized radical center. The $D_0(Cl—CH_2CH_2)$ is only ~18.5 kcal mol^{-1}, which is lower than for the other Cl-containing polyatomic molecules, such as NO_2Cl, Cl_2O, and $NFCl_2$, that have been studied to obtain HCl(v) distribution. These inorganic molecules have rate constants (3, 31) in the 2×10^{-11} cm^3 molecule^{-1} s^{-1} range at 300 K. Assuming an enhancement in the abstraction rate constant with reduced bond energy, a competition between Cl-atom abstraction and recombination for CH_2CH_2Cl is reasonable. Based on the present knowledge, an abstraction channel from a radical may be expected for radicals with especially weak bond energies at a β-position to the radical center and for radicals with delocalized orbitals containing the unpaired electron (32). The question of abstraction vs. recombination for F + SiH_n (n = 1–3) reactions has been discussed (33). Abstraction seemed to be favored for SiH_2, but the singlet recombination pathways were favored over the triplet abstraction pathways for SiH_3 and SiH.

V. Conclusions

The H + CCl_3 and H + CF_2Cl reactions proceed by recombination, giving $CHCl_3$* and CHF_2Cl* molecules, which subsequently eliminate HCl (or HF) to give monotonically declining HCl(v) vibrational distributions with $\langle f_V \rangle$ equal to ~0.12. The H + CF_2Cl reaction also gives HF(v) + CFCl, and the HF/HCl ratio was assigned as 0.24. This ratio was combined with RRKM calculations and the experimental $E_0^{\ddagger}$(HCl) to estimate $E_0^{\ddagger}$(HF) as 70 kcal mol^{-1}. The small ratio of the HF to HCl strongly suggests that $\Delta H_f^0(HCl) + \Delta H_f^0(CF_2) < \Delta H_f^0(HF) + \Delta H_f^0(CFCl)$. Based upon comparison to the vibrational energy disposal to HCl from the Cl + CH_3CH_2 reaction, both direct Cl abstraction and recombination–elimination reaction pathways were assigned to the H + CH_2CH_2Cl reaction. Separating the two reaction pathways, based on an assumed "pure" HCl(v) elimination distribution, suggests that the branching fraction for abstraction is ~0.3 at 300 K. A weak temperature dependence enhances the abstraction pathway at higher temperature.

Acknowledgments

This work was supported by the National Science Foundation under grant CHE-9120489. We are extremely grateful for permission from Dr. Leone to use the data from ref. 24 prior to publication. We are pleased to contribute this paper in honor of the 65th birthday of Professor Polanyi. The development of the infrared chemiluminescence laboratory at Kansas State University was stimulated by the remarkably successful work of Professor Polanyi in this field.

1. B.S. Agrawalla and D.W. Setser. J. Phys. Chem. **90**, 2450 (1986).
2. S. Wategaonkar and D.W. Setser. J. Chem. Phys. **86**, 4477 (1987).
3. S.J. Wategaonkar and D.W. Setser. J. Chem. Phys. **90**, 251 (1989).
4. (*a*) B.E. Holmes and D.W. Setser. *In* Physical chemistry of fast reactions. Vol. 2. *Edited by* I.W.M. Smith. Planum, New York. 1980; (*b*) B.S. Agrawalla and D.W. Setser. *In* Gas phase chemiluminescence and chemi-ionization. *Edited by* A. Fontijn. Elsevier, Amsterdam. 1985.
5. E. Arunan, S.J. Wategaonkar, and D.W. Setser. J. Phys. Chem. **95**, 1539 (1991).
6. E. Zamir and R.D. Levine. Chem. Phys. **52**, 253 (1980).
7. J.J. Sloan. J. Phys. Chem. **92**, 18 (1988).
8. M.A. Wickramaaratchi, D.W. Setser, B. Hildebrandt, B. Korbitzer, and H. Heydtmann. Chem. Phys. **84**, 105 (1984).
9. (*a*) C.R. Quick, Jr., and C. Wittig. J. Chem. Phys. **72**, 1694 (1980); (*b*) A.S. Sudbo, P.A. Schultz, Y.R. Shen, and Y.T. Lee. J. Chem. Phys. **69**, 2312 (1978).
10. (*a*) K. Dees and D.W. Setser. J. Chem. Phys. **49**, 1193 (1968); (*b*) D.W. Setser, T-S. Lee, and W.C. Danen. J. Phys. Chem. **89**, 5799 (1988); (*c*) D.J. Rakestraw and B.E. Holmes. J. Phys. Chem. **95**, 3968 (1991).
11. (*a*) D.E. McMillen and D.M. Golden. Annu. Rev. Phys. Chem. **33**, 493 (1982); (*b*) K. Miyokawa and E. Tschuikow-Roux. J. Phys. Chem. **96**, 7328 (1992); (*c*) Y. Chen and E. Tschuikow-Roux. J. Phys. Chem. **96**, 7266 (1992).
12. K.P. Schug, H.Gg. Wagner and F. Zabel. Ber. Bunsen-ges. Phys. Chem. **83**, 167 (1979).
13. (*a*) J.A. Paulino and R.R. Squires. J. Am. Chem. Soc. **113**, 5573 (1991); (*b*) D.W. Kohn, E.S.J. Robles, C.F. Logan, and P. Chen. J. Phys. Chem. **97**, 4936 (1993); (*c*) M.W. Chase, Jr., C.A. Davies, J.R. Downey, Jr., D.J. Frurip, R.A. McDonald, and A.N. Syverud. J. Phys. Chem. Ref. Data, **14**, Suppl. No. 1 (1985).
14. (*a*) J.S. Francisco, A.N. Goldstein, Z. Li, Y. Zhao, and I.H. Williams. J. Phys. Chem. **94**, 4791 (1990); (*b*) C.F. Rodriquez and A.C. Hopkinson. J. Phys. Chem. **97**, 849 (1993).
15. S.G. Lias, Z. Karpas and J.F. Liebman. J. Am. Chem. Soc. **107**, 6089 (1985).
16. (*a*) O. Dobis and S.W. Benson. J. Am. Chem. Soc. **112**, 1023 (1990); (*b*) J. Am. Chem. Soc. **113**, 6377 (1991).
17. R.B. Barat and J.W. Bozzelli. J. Phys.Chem. **96**, 2454 (1992).
18. M.J. Lexon, R.M. Marshall, and H. Purnell. J. Chem. Soc. Faraday Trans. **88**, 663 (1992).
19. G.O. Pritchard, S.H. Abbas, J.M. Kennedy, S.J. Paquette, D.B. Hudson, M.A. Meleason, and D.D. Shoemaker. Int. J. Chem. Kinet. **22**, 1051 (1990).
20. E. Arunan, D. Raybone, and D.W. Setser. J. Chem. Phys. **97**, 6348 (1992).
21. E. Arunan, D.W. Setser, and J.F. Ogilvie. J. Chem. Phys. **97**, 1734 (1992).
22. R.J. Malins and D.W. Setser. J. Chem. Phys. **73**, 5666 (1980).
23. (*a*) R.I. Martinez and J.T. Herron. Chem. Phys. Lett. **84**, 180 (1981); (*b*) J.C. Stephenson and D.S. King. J. Chem. Phys. **78**, 1867 (1983).
24. P.W. Seakins, E.L. Woodbridge, and S.R. Leone. J. Phys. Chem. **97**, 5633 (1993).
25. (*a*) S. Kato and K. Morokuma. J. Chem. Phys. **73**, 3900 (1980); (*b*) R.M. Benito and J. Santamaria. J. Phys. Chem. **92**, 5028 (1988); (*c*) L.M. Raff and R.W. Graham. J. Phys. Chem. **92**, 5111 (1988).
26. (*a*) J.D. Goddard and H.F. Schaefer III. J. Chem. Phys. **93**, 4907 (1990); (*b*) J.S. Francisco and Y. Zhao. J. Chem. Phys. **96**, 7586 (1992).
27. (*a*) Y.S. Choi and C.B. Moore. J. Chem. Phys. **97**, 1010 (1992); (*b*) W.H. Green, Jr., C.B. Moore, and W.F. Polik. Annu. Rev. Phys. Chem. **43**, 591 (1992).
28. (*a*) A.B. Trenwith, and B.S. Rabinovitch. J. Phys. Chem. **86**, 3447 (1982); (*b*) W.L. Hase. J. Phys. Chem. **90**, 365 (1986); (*c*) C.R. Park, and J.R. Wiesenfeld. J. Chem. Phys. **95**, 8160 (1991).
29. (*a*) J.C. Polanyi, J.F. Sloan, and J. Wanner. J. Chem. Phys. **13**, 1 (1976); (*b*) J.C. Polanyi, J.L. Schreiber, and J. Sloan. J. Chem. Phys. **9**, 403 (1975); (*c*) K.G. Anlauf, D.S. Horne, R.G. Macdonald, J.C. Polanyi, and K.B. Woodall. J. Chem. Phys. **57**, 1561 (1972); (*d*) J.C. Polanyi. Acc. Chem. Res. **5**, 161(1972).
30. (*a*) R.J. Duchovic and W.L. Hase. J. Chem. Phys. **82**, 3599 (1988); (*b*) K.P. Lim, and J.V. Michael. J. Chem. Phys. **98**, 3919 (1993); (*c*) K.J. Hughes, A.R. Pereira, and M.J. Pilling. Ber. Bunsenges. Phys. Chem. **96**, 1352 (1993).
31. (*a*) R.J. Malins and D.W. Setser. J. Phys. Chem. **85**, 1342 (1981); (*b*) R. Rengarajan and D.W. Setser. J. Phys. Chem. Submitted (1994).

32. (*a*) S.J. Wategaonkar and D.W. Setser. J. Chem. Phys. **90**, 6223 (1989); (*b*) E. Arunan, C.P. Liu, D.W. Setser, J.V. Gilbert, and A.D. Coombe. J. Phys. Chem. In press.

33. K. Sato, H. Yamada, and S. Iwabuchi. J. Chem. Phys. **98**, 2844 (1993).

Can. J. Chem. Downloaded from www.nrcresearchpress.com by EESC ESCOLA DE ENGENHARIA on 09/08/12
For personal use only.

Gas-phase association reactions of fullerene cations: modelling the influence of charge state and other molecular parameters on association efficiency

SIMON PETRIE AND DIETHARD K. BOHME[1]

Department of Chemistry and Centre for Research in Earth and Space Science, York University, North York, ON M3J 1P3, Canada

Received July 2, 1993

This paper is dedicated to Professor John C. Polanyi on the occasion of his 65th birthday

SIMON PETRIE and DIETHARD K. BOHME. Can. J. Chem. **72**, 577 (1994).

The efficiency of association reactions of fullerene cations observed in helium at pressures of 0.35–0.4 Torr sustained in a Selected-Ion Flow Tube (SIFT) at room temperature has been examined with a view to the influence of the charge state and the size of the fullerene ion and the size, structure, and degree of unsaturation of the neutral. The association efficiency is found to be strongly dependent on these molecular parameters. The calculated lifetime of the intermediate collision complex provides insight into the well depth associated with the formation of this complex and the effectiveness of vibrational and (or) rotational degrees of freedom of the reactants in the dispersal of the energy of complex formation. The results are considered in terms of single-well and double-well models for the potential energy surface leading to association and are best accommodated by the double-well model involving the formation of an initial electrostatic collision complex that must overcome a barrier to proceed to the formation of a chemically bonded adduct. The observed competition between association and charge transfer can also be accommodated with a double-well model, which provides a lower limit for the depth of the electrostatic well for those systems that exhibit such competition.

SIMON PETRIE et DIETHARD K. BOHME. Can. J. Chem. **72**, 577 (1994).

Dans le but de déterminer l'influence de l'état de la charge, de la grosseur de l'ion fullerène et la grosseur, la structure et le degré d'insaturation de l'espèce neutre, on a étudié l'efficacité des réactions d'association des cations de fullerène observées dans l'hélium, à des pressons de 0,35–0,4 Torr, et qui se produisent dans un tube à écoulement d'ion choisi (SIFT), à la température ambiante. On a trouvé que l'efficacité de l'association varie beaucoup avec ces paramètres moléculaires. Le temps de vie calculé du complexe de collision intermédiaire fournit des données sur la profondeur du puits associé à la formation de ce complexe et sur l'efficacité des degrés de liberté vibrationnels et (ou) rotationnels des réactifs dans la dispersion de l'énergie de formation du complexe. On considère les résultats en fonction des modèles à un et à deux puits pour la surface d'énergie potentielle conduisant à l'association et ils s'accommodent mieux avec le modèle à double puits impliquant la formation d'un complexe de collision électrostatique initial qui doit vaincre une barrière avant de procéder à la formation d'un adduit chimiquement lié. La compétition observée entre l'association et le transfert de charge peut aussi être accommodée avec un modèle à double puits qui fournit une limite inférieure pour la profondeur du puits électrostatique des systèmes qui présentent une telle compétition.

[Traduit par la rédaction]

Can. J. Chem. Downloaded from www.nrcresearchpress.com by 195.246.54.202 on 09/08/12
For personal use only.

Introduction

The occurrence of bond formation is a central feature of chemistry. The process of association

[1] $$A + B \rightarrow AB$$

is the most direct means of chemical bond formation, and a study of the kinetics of association therefore offers insight into the factors affecting the efficiency of bond formation.

The laboratory study of the kinetics of association reactions in the gas phase has been dominated by the investigation of ion–molecule association processes

[2] $$A^+ + B \rightarrow AB^+$$

for two reasons. Firstly, ion–molecule reactions are easily studied by a variety of mass-spectrometric techniques (1). Secondly, owing to the attractive ion–dipole and ion – induced dipole interaction (2), ion–molecule reactions are generally of higher efficiency than neutral–neutral reactions (which are often inhibited by activation energy barriers).

Reactions of type [2] are also possible with multiply charged species A^{n+}, and indeed some examples of association reactions of simple (atomic and diatomic) gas-phase dications have been reported (3–5). However, ions bearing multiple charges are often prone to Coulomb explosion and, because of their relatively high appearance energies, their association with molecules must often compete with other processes: charge transfer or dissociative charge transfer in the case of multiply charged atomic and diatomic ions and proton transfer in the case of hydrogenated polyatomic ions. For these reasons, it has not been possible to examine the kinetics of association for multiply charged ions in any detail. Indeed, there appear to have been no previous measurements of reactions of type [2] involving trications A^{3+} or ions of higher charge state.

This situation has changed with the availability of Buckminsterfullerene, C_{60} (6). It is now relatively easy to produce the stable cations $C_{60}^{\cdot+}$, C_{60}^{2+}, $C_{60}^{\cdot 3+}$, C_{60}^{4+}, and $C_{60}^{\cdot 5+}$ in the laboratory for experimental study (7–9), so that a unique opportunity has arisen to explore the physicochemical aspects of association as a function of the reactant ion charge state. To this end, we previously reported the first quantitative measurements of the kinetics of association reactions involving the ions $C_{60}^{\cdot+}$, C_{60}^{2+}, and $C_{60}^{\cdot 3+}$ (10–18). For example, we characterized primary and higher order association leading to the formation of single-, double-, and triple-handled adducts as typified by structures **I** (10), **II** (13), and **III** (15).

Here we shall focus on selected-ion flow tube (SIFT) measurements on ion–molecule reactivity previously performed in our laboratory upon the fullerene ions $C_{60}^{\cdot+}$, C_{60}^{2+}, $C_{60}^{\cdot 3+}$, C_{56}^{n+}, C_{58}^{n+}, and C_{70}^{n+} ($n = 1, 2$) (10–18). We shall use the

[1]Author to whom correspondence may be addressed.

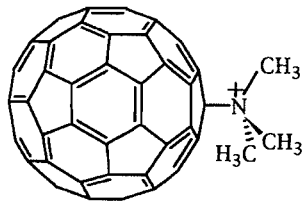

I

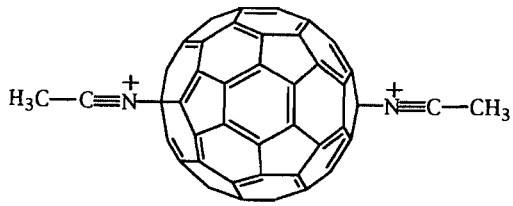

II

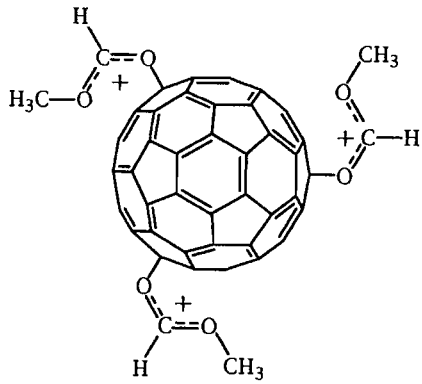

III

results of these studies to investigate the dependence of association efficiency upon the physical parameters of the reactants (ion size and charge state; neutral size, structure, and degree of unsaturation), and hence to infer the nature of the potential energy surface leading to association. Furthermore, a number of systems are considered in which competing bimolecular channels have been observed. Our primary objective is to obtain an overall perspective for a range of novel association reactions involving fullerene ions and various neutral molecules.

Discussion

We previously reported a large number of reactions of the fullerene cations C_{60}^{n+} (n = 1, 2, 3) (10–18). Some of these results are presented in Tables 1–5. These tables are arranged to illuminate the general features of the efficiency of bond formation with fullerene ions: the influence of charge state, ion size, neutral size, degree of unsaturation of the neutral, and its structure. As is customary, we have defined the efficiency as the ratio of the measured effective bimolecular reaction rate coefficient to the calculated collision rate coefficient, $k(2)_{obs}/k_c$.

The pressure dependence of the efficiency of association has not been investigated systematically. However, results observed for the reaction of $C_{60}^{\cdot+}$ with ethylamine (10) and the reaction of C_{60}^{2+} with allene (11) have indicated that, for these systems, collisional stabilization, eq. [3]:

$$[3] \quad C_{60}^{n+} + X + M \rightarrow C_{60}.X^{n+} + M^*$$

dominates over radiative stabilization, eq. [4]:

$$[4] \quad C_{60}^{n+} + X \rightarrow C_{60} \cdot X^{n+} + h\nu$$

at the pressures of our SIFT experiments.

A few association reactions with multiply charged fullerene cations have been observed with other experimental techniques but these observations have been entirely qualitative. McElvany et al. (7, 21) used the FT–ICR technique to observe the occurrence of the association reactions

$$[5] \quad C_{56}^{\cdot 3+} + C_2H_2 \rightarrow C_{56} \cdot C_2H_2^{\cdot 3+}$$

$$[6] \quad C_{60}^{\cdot 3+} + C_2H_2 \rightarrow C_{60} \cdot C_2H_2^{\cdot 3+}$$

Garvey and co-workers (22) inferred the occurrence of the association reaction

$$[7] \quad C_{60}^{2+} + NH_3 \rightarrow C_{60} \cdot NH_3^{2+}$$

in a triple quadrupole MS/MS/MS apparatus, although the dicationic adduct $C_{60} \cdot NH_3^{2+}$ was not directly observable in their experiments. We have observed reaction [7] directly (9). Also, our observation of repeated association of 1,3-butadiene (16)

$$[8] \quad C_{60} \cdot (C_4H_6)_n^{2+} + C_4H_6 \rightarrow C_{60} \cdot (C_4H_6)_{n+1}^{2+}$$

for n = 0–5 was recently duplicated by Schwarz and coworkers[2] for n = 0–2 in an FT–ICR cell. The observation of the addition reactions [5], [6], and [8] under FT–ICR conditions ($P \sim 10^{-7}$–10^{-3} Torr; 1 Torr = 133.3 Pa) suggests that these reactions may be occurring in a bimolecular fashion by radiative association as in eq. [4].

A. Empirical correlations

Charge state of the fullerene ion

The efficiency of association increases dramatically with increasing charge, as shown in the values reported in Table 1. An increase in association efficiency of ~3 orders of magnitude operates for an increase in charge state from +1 to +2 for the reactions with NH_3 and n-C_3H_7CN, or from +2 to +3 for the reactions with HCN and C_2H_2. This enhancement in reaction efficiency with charge state is larger than (although within experimental uncertainty of) the factor of 100–500 found for the enhancement in association efficiency for reactions of M^{n+} (M = Mg, Ca, Ba; n = 1, 2) with H_2O, N_2, CO, CO_2, N_2O, and O_2 (3). For those reactions of C_{60}^{2+} that exhibit association with near unit efficiency, an enhancement in efficiency with increasing charge state from +2 to +3 is not observable. Similarly, an enhancement in efficiency is not experimentally observable when two successive charge states are both seen to be unreactive as is the case for the reactions of $C_{60}^{\cdot+}$ and C_{60}^{2+} with HCN and C_2H_2.

Size of the fullerene ion

The efficiency of association with various neutrals is noted in Table 2 for the species C_{56}^{n+}, C_{58}^{n+}, C_{60}^{n+}, and C_{70}^{n+}. Association is seen to be much more efficient for C_{56}^{n+} and C_{58}^{n+} than for the slightly larger ion C_{60}^{n+}, which in turn undergoes association with somewhat higher efficiency than C_{70}^{n+}.

[2]H. Schwarz, personal communication.

Can. J. Chem. Downloaded from www.nrcresearchpress.com by 195.246.54.202 on 09/08/12
For personal use only.

TABLE 1. Effect of ion charge state upon fullerene ion–molecule association reaction efficiency

Reaction[a]	k_c[a]	$k(2)_{obs}$[c]	$k(3)_{obs}$[d]	$k(2)/k_c$[e]	$\tau(\beta = 0.03)$[f]	$\tau(\beta = 1.0)$[f]
$C_{60}^{\cdot+}$ + HCN	2.12	<0.001[g]	<0.009[h]	<0.0005	<0.003	<0.00008
C_{60}^{2+} + HCN	4.23	<0.001[g]	<0.009[h]	<0.0003	<0.0007	<0.00002
$C_{60}^{\cdot 3+}$ + HCN	6.35	2.5[g]	22	0.39	0.76	0.023
$C_{60}^{\cdot+}$ + C_2H_2	0.89	<0.001[i]	<0.008[h]	<0.0011	<0.005	<0.0002
C_{60}^{2+} + C_2H_2	1.78	<0.001[i]	<0.008[j]	<0.0006	<0.0013	<0.00004
$C_{60}^{\cdot 3+}$ + C_2H_2	2.67	0.15[k]	1.3	0.056	0.10	0.0031
$C_{60}^{\cdot+}$ + NH_3	1.69	<0.001[l]	<0.009[j]	<0.0006	<0.004	<0.0001
C_{60}^{2+} + NH_3	3.37	1.2[l]	10	0.36	0.93	0.028
$C_{60}^{\cdot 3+}$ + NH_3	5.04	3.9[l]	>34[m]	0.77	>1	>0.04
$C_{60}^{\cdot+}$ + n-C_3H_7CN	2.08	<0.001[g]	<0.009[h]	<0.0005	<0.003	<0.00008
C_{60}^{2+} + n-C_3H_7CN	4.15	3.9[g]	>34[m]	0.94	>2	>0.07
$C_{60}^{\cdot 3+}$ + n-C_3H_7CN	6.23	6.3[g]	>55[m]	1.0	>1	>0.05

[a]Addition reaction, studied using the SIFT technique at a temperature of 294 ± 2 K and at a helium buffer gas pressure of 0.35 ± 0.01 Torr unless otherwise specificed.

[b]ADO collision rate coefficient in units of 10^{-9} cm^3 molecule^{-1} s^{-1}, calculated according to the method of Su and Bowers (19).

[c]Observed effective bimolecular rate coefficient for addition, in units of 10^{-9} cm^3 molecule^{-1} s^{-1}.

[d]Termolecular rate coefficient, in units of 10^{-26} cm^6 molecule^{-2} s^{-1}, calculated from $k(2)_{obs}$. A lower limit to $k(3)_{obs}$ has been assigned to those reactions for which association accounts for ≥50% of collisions, since these reactions are presumed to be saturated at the experimental buffer gas pressure used.

[e]Association efficiency, as defined in the text.

[f]Collision complex lifetime in units of 10^{-6} s, calculated from the termolecular rate coefficient $k(3)_{obs}$ for the factor β as shown for the efficiency of collisional stabilization by helium.

[g]Rate coefficients previously reported in ref. 13.

[h]Upper limit assigned to termolecular rate coefficient, association efficiency, and collision complex lifetime; no association was observed.

[i]Rate coefficients previously reported in ref. 11.

[j]Upper limit assigned to termolecular rate coefficient, association efficiency, and collision complex lifetime; association was observed to occur.

[k]Rate coefficients previously reported in ref. 20.

[l]Rate coefficients previously reported in ref. 10.

[m]Lower limit assigned to termolecular rate coefficient, association efficiency, and collision complex lifetime; association is presumed to be saturated at the operating pressure of these experiments.

TABLE 2. Effect of fullerene ion size upon ion–molecule association reaction efficiency

Reaction[a]	k_c[a]	$k(2)_{obs}$[a]	$k(3)_{obs}$[a]	$k(2)/k_c$[a]	$\tau(\beta = 0.03)$[a]	$\tau(\beta = 1.0)$[a]
C_{56}^{2+} + C_2H_4	1.86	0.021[b]	0.18	0.011	0.031	0.00092
C_{58}^{2+} + C_2H_4	1.86	0.019[b]	0.17	0.010	0.028	0.00084
C_{60}^{2+} + C_2H_4	1.86	<0.001[c]	<0.008[d]	<0.0006	<0.001	<0.00004
$C_{56}^{\cdot+}$ + NH_3	1.69	0.0096[b]	0.084	0.0057	0.031	0.00093
$C_{58}^{\cdot+}$ + NH_3	1.69	0.034[b]	0.30	0.020	0.11	0.0033
$C_{60}^{\cdot+}$ + NH_3	1.69	<0.001[e]	<0.009[d]	<0.0006	<0.004	<0.0001
C_{56}^{2+} + CH_3CN	4.70	4.3[b]	>37[f]	0.91	>2	>0.07
C_{58}^{2+} + CH_3CN	4.69	4.2[b]	>37[f]	0.90	>2	>0.07
C_{60}^{2+} + CH_3CN	4.68	0.080[g]	0.70	0.017	0.047	0.0014
C_{70}^{2+} + CH_3CN	4.66	0.029[g]	0.25	0.0062	0.017	0.00051
C_{60}^{2+} + CH_2CCH_2	1.85	0.080[c]	0.61	0.043	0.10	0.0031
C_{70}^{2+} + CH_2CCH_2	1.85	0.009[c]	0.069	0.005	0.012	0.00034

[a]See footnotes *a–f* for Table 1.

[b]Rate coefficients previously reported in ref. 18.

[c]Rate coefficients previously reported in ref. 11.

[d]Upper limit assigned to termolecular rate coefficient, association efficiency, and collision complex lifetime; asociation was observed to occur.

[e]Rate coefficients previously reported in ref. 10.

[f]Lower limit assigned to termolecular rate coefficient, association efficiency, and collision complex lifetime; association is presumed to be saturated at the operating pressure of these experiments.

[g]Rate coefficients previously reported in ref. 13.

Can. J. Chem. Downloaded from www.nrcresearchpress.com by 195.246.54.202 on 09/08/12
For personal use only.

TABLE 3. Effect of neutral reactant size upon fullerene ion–molecule association reaction efficiency

Reaction[a]	k_c[a]	$k(2)_{obs}$[a]	$k(3)_{obs}$[a]	$k(2)/k_c$[a]	$\tau(\beta = 0.03)$[a]	$\tau(\beta = 1.0)$[a]
$C_{60}^{\cdot+} + NH_3$	1.69	<0.001[b]	<0.009[c]	<0.0006	<0.004	<0.0001
$C_{60}^{\cdot+} + CH_3NH_2$	1.44	0.015[b]	0.13	0.010	0.060	0.0018
$C_{60}^{\cdot+} + C_2H_5NH_2$	1.34	0.050[b]	0.43	0.037	0.21	0.0064
$C_{60}^{\cdot+} + (CH_3)_2NH$	1.22	0.85[b]	>7.4[d]	0.70	>4	>0.1
$C_{60}^{\cdot+} + (CH_3)_3N$	1.05	1.0[b]	>8.7[d]	0.95	>5	>0.15
$C_{60}^{2+} + HCN$	4.23	<0.001[e]	<0.009[f]	<0.0003	<0.0007	<0.00002
$C_{60}^{2+} + CH_3CN$	4.68	0.080[e]	0.70	0.017	0.047	0.0014
$C_{60}^{2+} + CH_3CH_2CN$	4.41	2.5[e]	0.57	>22[d]	>1.5	>0.04
$C_{60}^{2+} + n\text{-}C_3H_7CN$	4.15	3.9[e]	>34[d]	0.94	>2	>0.07
$C_{60}^{2+} + i\text{-}C_3H_7CN$	3.93	4.3[e]	>37[d]	1.1	>3	>0.09
$C_{60}^{2+} + C_2H_4$	1.86	<0.001[g]	<0.008[c]	<0.0006	<0.001	<0.00004
$C_{60}^{2+} + C_3H_6$	1.98	1.3[g]	>10[d]	0.66	>1	>0.04
$C_{60}^{2+} + 1\text{-}C_4H_8$	1.94	2.2[g]	>17[d]	1.1	>2	>0.08

[a]See footnotes *a–f* for Table 1.
[b]Rate coefficients previously reported in ref. 10.
[c]Upper limit assigned to termolecular rate coefficient, association efficiency, and collision complex lifetime; association was observed to occur.
[d]Lower limit assigned to termolecular rate coefficient, association efficiency, and collision complex lifetime; association is presumed to be saturated at the operating pressure of these experiments.
[e]Rate coefficients previously reported in ref. 13.
[f]Upper limit assigned to termolecular rate coefficient, association efficiency, and collision complex lifetime; no association was observed.
[g]Rate coefficients previously reported in ref. 11.

TABLE 4. Effect of unsaturation of neutral reactant upon fullerene ion–molecule association reaction efficiency

Reaction[a]	k_c[a]	$k(2)_{obs}$[a]	$k(3)_{obs}$[a]	$k(2)/k_c$[a]	$\tau(\beta = 0.03)$[a]	$\tau(\beta = 1.0)$[a]
$C_{60}^{2+} + CH_3CH_2CN$	4.41	2.5[b]	>22[c]	0.57	>1.5	>0.04
$C_{60}^{2+} + CH_2CHCN$	4.51	0.070[b]	0.61	0.016	0.042	0.0013
$C_{60}^{2+} + CH_3COC_2H_5$	3.06	1.2[d]	10	0.39	1.1	0.032
$C_{60}^{2+} + CH_3COCCH$	2.89	0.13[d]	1.1	0.045	0.12	0.0037
$C_{60}^{2+} + C_3H_8$	1.90	<0.001[e]	<0.008[f]	<0.0006	<0.001	<0.00004
$C_{60}^{2+} + C_3H_6$	1.98	1.3[e]	>10[c]	0.66	>1.5	>0.04
$C_{60}^{2+} + CH_3CCH$	2.27	0.5[e]	3.8	0.22	0.53	0.016
$C_{60}^{2+} + CH_2CCH_2$	1.85	0.08[e]	0.61	0.043	0.10	0.0031

[a]See footnotes *a–f* for Table 1.
[b]Rate coefficients previously reported in ref. 13.
[c]Lower limit assigned to termolecular rate coefficient, association efficiency, and collision complex lifetime; association is presumed to be saturated at the operating pressure of these experiments.
[d]Rate coefficients previously reported in ref. 15.
[e]Rate coefficients previously reported in ref. 11.
[f]Upper limit assigned to termolecular rate coefficient, association efficiency, and collision complex lifetime; association was observed to occur.

Size of the neutral reactant

Association efficiency increases, sometimes dramatically, with increasing molecular size for molecules featuring the same functional groups, as shown in Table 3.

Degree of unsaturation of the neutral reactant

Two different trends are evident in the values reported in Table 4. For hydrocarbons, association efficiency is apparently highest when the hydrocarbon contains one C=C double bond; for functionalized organic molecules such as nitriles and ketones, however, efficiency is highest when the alkyl chain of the molecule is saturated.

Structure of the neutral reactant

Results reported in Table 5 indicate that the efficiency of association of C_{60}^{n+} with different isomers can differ by more than one order of magnitude.

B. Single-well model

We begin with a consideration of the simplest potential energy surface that may be used to describe the association of C_{60}^{n+} with a molecule X: the single-well model shown in Fig. 1. The kinetic and energetic parameters associated with such a model are straightforward and may be used to provide a first-order appreciation of the factors that affect association efficiency. At pressures at which the observed association reaction has not become saturated (i.e., above which collisional stabilization can still increase the efficiency of association), the association efficiency, $k(2)_{obs}/k_c$, is directly related to the lifetime of the collision complex, τ_d, since $k(2)_{obs} = k(3)_{obs}[He]$ and $k(3)_{obs} = k_c k_s \tau_d$. Here $k(3)_{obs}$ is the experimental termolecular rate coefficient for adduct formation, k_c is the theoretical rate coefficient for collision complex formation, and k_s is the theoretical rate coefficient for collisional stabilization.

Can. J. Chem. Downloaded from www.nrcresearchpress.com by 195.246.54.202 on 09/08/12
For personal use only.

TABLE 5. Effect of neutral reactant structure upon fullerene ion–molecule association reaction efficiency

Reaction[a]	k_c[a]	$k(2)_{obs}$[a]	$k(3)_{obs}$[a]	$k(2)/k_c$[a]	$\tau(\beta = 0.03)$[a]	$\tau(\beta = 1.0)$[a]
$C_{60}^{\cdot+} + C_2H_5NH_2$	1.34	0.050[b]	0.43	0.037	0.21	0.0064
$C_{60}^{\cdot+} + (CH_3)_2NH$	1.22	0.85[b]	>7.4[c]	0.70	>4	>0.12
$C_{60}^{2+} + C_2H_5OH$	2.77	0.033[d,e]	0.26	0.012	0.030	0.00091
$C_{60}^{2+} + (CH_3)_2O$	2.46	0.003[d]	0.024	0.0012	0.0031	0.000093
$C_{60}^{2+} + CH_3COOH$	2.42	0.40[f]	3.2	0.17	0.42	0.013
$C_{60}^{2+} + HCOOCH_3$	2.43	0.011[f]	0.089	0.0045	0.012	0.00035
$C_{60}^{2+} + CH_3CCH$	2.27	0.50[g]	3.8	0.22	0.53	0.016
$C_{60}^{2+} + CH_2CCH_2$	1.85	0.080[g]	0.61	0.043	0.10	0.0031

[a]See footnotes *a–f* for Table 1.
[b]Rate coefficients previously reported in ref. 10.
[c]Lower limit assigned to termolecular rate coefficient, association efficiency, and collision complex lifetime; association is presumed to be saturated at the operating pressure of these experiments.
[d]Rate coefficients previously reported in ref. 14.
[e]Rate coefficient ascribed to adduct formation; a minor channel (10%) leading to hydroxide abstraction was noted also.
[f]Rate coefficients previously reported in ref. 15.
[g]Rate coefficients previously reported in ref. 11.

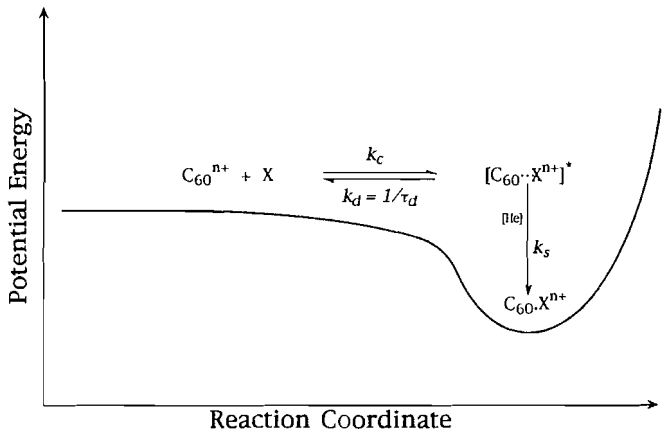

FIG. 1. Schematic diagram of the potential energy surface leading to association, for a single-well model. While such a model may not accurately represent the potential energy surface, consideration of the kinetic parameters involved is straightforward and provides an insight into the factors affecting association efficiency in the reactions of fullerene cations.

The mean lifetime, τ_d, of the collision complex can be determined with the expression

$$[9] \qquad \tau_d = k(3)_{obs}/k_c k_s$$

The usual value assumed for k_c is the ADO collision rate coefficient for this reaction, while k_s is assigned a value $k_s = \beta k_{s(c)}$ where β denotes the efficiency of the collisional stabilization process and $k_{s(c)}$ is the Langevin rate coefficient for collision with helium. In Tables 1–5, which list computed lifetimes, we have used values of $\beta = 0.03$ and 1.0 for the probability of stabilization per collision at 294 K, in the expectation that this range of values encompasses the true probability of collision complex stabilization. The upper limit of $\beta = 1$ is almost certainly unrealistic, since it is unlikely that every collision of a helium atom with the fullerene surface serves to stabilize the chemical bond between the adduct moiety X and one C atom of the fullerene lattice. Ion cyclotron resonance (ICR) studies on a number of association reactions (23, 24) have indicated values of $\beta \leq 0.3$ for helium buffer gas. In any event, we anticipate that β will remain essentially invariant for a series of reactions of fullerene ions C_{60}^{n+} with similar compounds X (for example, the series of nitriles $C_nH_{2n+1}CN$) and so any consistent trend in the calculated complex lifetimes in such a series is expected to be meaningful.

The collision complex lifetime τ_d is generally considered to depend strongly upon the number of degrees of freedom available for energy dispersal, and upon the depth of the potential well for collision complex formation. The expression (25):

$$[10] \qquad \tau_d = \tau_0 \left(\frac{D + 3RT}{3RT}\right)^{s-1}$$

indicates the nature of the expected dependence upon the well depth D and upon the number of degrees of freedom s. Although eq. [10] is overly simplistic in the light of current theoretical investigations of association reactions, we consider that this equation has sufficient qualitative validity to be useful in a consideration of collision complex lifetimes.

What do the computed lifetimes in Tables 1–5 tell us about the features of the single-well potential energy surfaces?

1. The very high apparent dependence of the collision complex lifetime upon charge state, showing a large increase in lifetime with increasing charge state in reactions featuring the same neutral and presumably possessing the same number of degrees of freedom, suggests that the depth of the potential well corresponding to collision complex formation increases substantially with increasing charge state.

2. The substantial enhancement in inferred collision-complex lifetimes for association reactions of C_{56}^{n+} and C_{58}^{n+} (over those apparent for C_{60}^{n+}) can be accounted for, as we have discussed previously (18), by a consideration of the degree of pyramidalization of the carbon atom sites upon the fullerene ion surface. Three types of carbon atom sites can be distinguished for fullerenes, on the basis of the geometry of the surrounding ring system. In Buckminsterfullerene, C_{60}, each C atom forms the apex of one pentagonal and two hexagonal faces (a [C_5, C_6, C_6] site). Other fullerenes also feature such sites, but small fullerenes (C_n, $n < 60$) also contain some

Can. J. Chem. Downloaded from www.nrcresearchpress.com by 195.246.54.202 on 09/08/12
For personal use only.

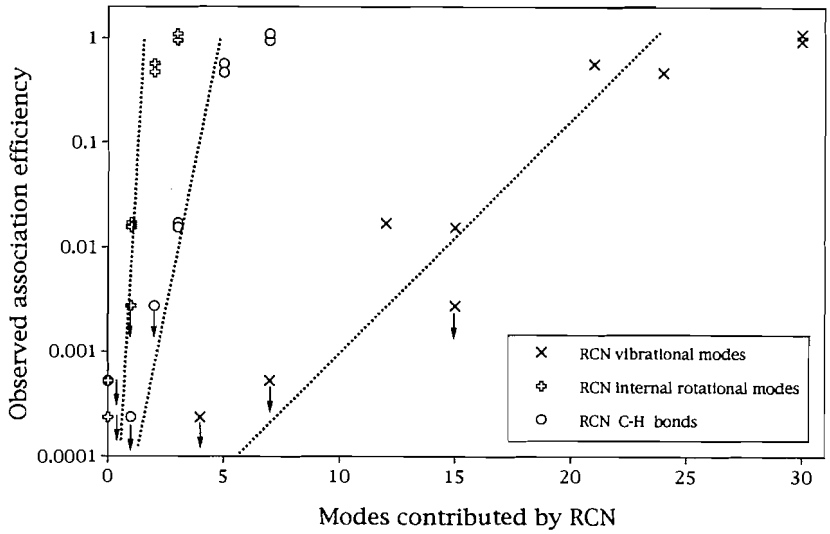

FIG. 2. Graph showing the observed efficiency of the association reaction C_{60}^{2+} + RCN for a variety of nitriles, plotted as a function of the total number of vibrational modes, the number of internal rotational modes, or the number of carbon–hydrogen bonds in the reactant nitrile RCN. Upper limits to the association reactions with HCN, with C_2N_2, and with $CH_2(CN)_2$ are denoted by downward-pointing arrows beside the appropriate symbol. Dotted lines are intended as an aid to visualizing the trends in the data rather than as a quantitative best-fit to the data. The general trend for association efficiency to increase with increasing reactant size is apparent. The kinetic data, which were presented previously in ref. 13, were obtained at 294 ± 2 K at a helium buffer gas pressure of 0.35 ± 0.01 Torr.

Can. J. Chem. Downloaded from www.nrcresearchpress.com by 195.246.54.202 on 09/08/12
For personal use only.

[C_5, C_5, C_6] sites, and larger fullerenes ($C_n, n > 60$) feature ($n - 60$) sites of type [C_6, C_6, C_6]. The degree of pyramidalization at the carbon atom in question increases with an increasing proportion of pentagonal C_5 rings. The experimental values reported in Table 2 suggest strongly that the more highly pyramidal [C_5, C_5, C_6] sites found in C_{56}^{n+} and C_{58}^{n+} are substantially more reactive than the [C_5, C_6, C_6] sites of C_{60}^{n+}; there is some indication, also, that the [C_6, C_6, C_6] sites (which have the lowest degree of pyramidalization) are the least reactive, since C_{70}^{n+} is seen to form adducts with a lower efficiency than is C_{60}^{n+}. The depth of the potential well involved in collision complex formation thus appears to be greatest for [C_5, C_5, C_6] sites and smallest for [C_6, C_6, C_6] sites, in keeping with expectations of the amount of distortion necessary at each site to attain tetrahedral coordination of the carbon atom concerned.

3. The trend evident in Table 2 also suggests that the fullerene ion contributes few degrees of freedom to the collison complex. C_{70}^{n+} has 105 C—C bonds whereas C_{60}^{n+} has 90 such bonds; C_{60}^{n+}, despite having fewer vibrational degrees of freedom than C_{70}^{n+}, is seen to associate more efficiently and therefore presumably has a longer-lived collision complex. This observation indicates that the increase in the number of degrees of freedom for C_{70}^{n+} over C_{60}^{n+} is not sufficient to overcome the effect of an apparently shallower potential well.

4. Table 3 indicates that the increasing alkyl substitution of the reactant noticeably increases the collision complex lifetime, presumably by increasing the number of degrees of freedom of the collision complex. Another effect of increasing alkyl substitution is perhaps that of charge stabilization by inductive donation of electrons to the charge site in question (that is, increasing the depth of the potential well). This inductive effect may play a role in the efficiencies seen for $C_{60}^{\cdot+}$ with the series of amines $(CH_3)_nNH_{3-n}$ (n = 0–3) and in the very large change in association efficiency of C_{60}^{2+} with ethylene and with propylene, but inductive charge stabilization cannot account for the trend seen in the nitriles (for example, an increase in the collision complex lifetime by a factor of at least 30 is apparent in the progression from CH_3CN to C_2H_5CN).

The data for the nitriles is also shown in Fig. 2, which plots the observed association efficiency against several molecular parameters for the reactions of C_{60}^{2+} with RCN given in Table 3, as well as for the reactions with the dinitriles C_2N_2 and $CH_2(CN)_2$ and with the unsaturated nitriles CH_2CHCN and CH_2CHCH_2CN. It is apparent from Fig. 2 that, although the general trend is for association efficiency to increase with the total number of substituent vibrational modes, the relation is not monotonic. A better fit is obtained in this instance for the dependence of association efficiency upon the number of C—H bonds within the nitrile, although too few of the reactants RCN exhibit association reactions within the range of efficiences $k(2)/k_c \sim 0.001$–0.3 (that is, above the limit for detection of a reaction by the SIFT technique, and below the expected onset of saturation of the association channel) for the fit to be compelling. These reactions, for which association is the sole observable product channel in all instances studied to date, should occur at lower efficiency at a substantially reduced buffer gas pressure. Therefore, the association reactions of C_{60}^{2+} with the larger nitriles (which occur with high efficiency under SIFT conditions) would seem to be a promising system for further study of association efficiency, using a lower pressure technique such as ICR, which has already been shown capable of detecting fullerene-ion addition products (7, 21, and footnote 2).

5. Association reactions do not occur with saturated hydrocarbons, but are observed with unsaturated hydrocarbons and with functionalized organic molecules (Table 4). This suggests that association involves bond formation without concomitant bond breaking, as we previously discussed elsewhere (11, 12). Also, where a functional group (C=C, or an atom such as O or N featuring a lone pair) is present within the molecule, further unsaturation serves to reduce the apparent collision complex

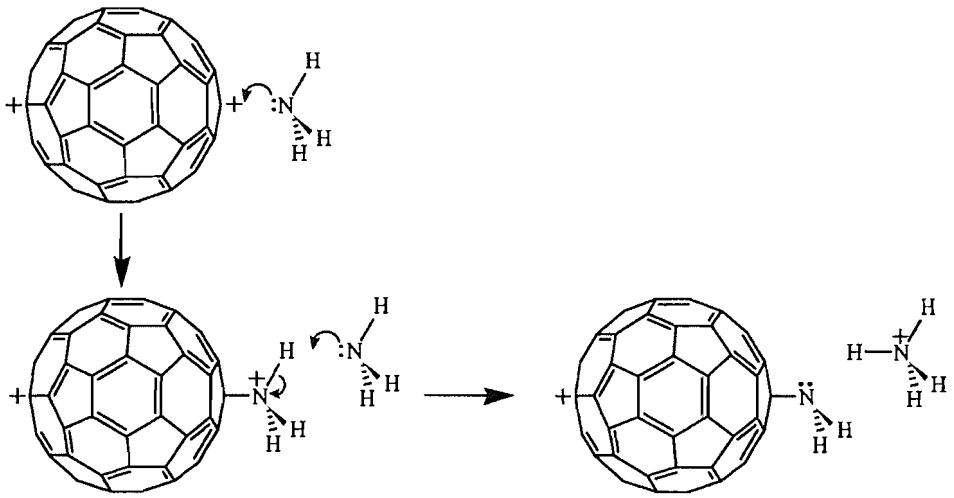

SCHEME 1

lifetime, most probably as a consequence of reduction in the number of available vibrational or internal rotational modes for excess energy dispersal.

6. Substantially different lifetimes are apparent for isomers of organic compounds (Table 5). A number of differing factors may affect the lifetime in such cases: inductive stabilization of charge by a differing number of alkyl groups, steric effects favouring bond formation with one isomer over another, and a difference in the number of effective degrees of freedom (for example, for rotation of alkyl groups in hindered and unhindered complexes). These effects may often occur in competition with each other and are, therefore, best considered on a case-by-case basis since they are not easily accommodated by a simple and general potential energy model for collision complex formation and stabilization.

C. Double-well model

The dependence of association efficiency upon ion charge state, evident in the data shown in Table 1, suggests that the electrostatic interaction between the reactant ion and the neutral is a major component of the collision complex potential well. However, the subsequent reactivity of fullerene adduct ions in several instances, often by proton transfer, (10, 13, 26):

[11] $C_{60} \cdot NH_3^{2+} + NH_3 \rightarrow C_{60} \cdot NH_2^{+} + NH_4^{+}$

[12] $C_{60} \cdot HCN^{\cdot 3+} + HCN \rightarrow C_{60} \cdot CN^{\cdot 2+} + HCNH^{+}$

but exhibiting also methyl cation transfer in some cases:

[13] $C_{60} \cdot HCOOCH_3^{\cdot 3+} + HCOOCH_3 \rightarrow C_{60} \cdot COOH^{\cdot 2+} + HC(OCH_3)_2^{+}$

is more consistent with the expected reactivity of chemically bonded adducts formed as shown in Scheme 1 than with the likely reactivity of electrostatically bound complexes. The greater facility for complex formation observed with the adjacent-pentagon fullerene ions C_{56}^{n+} and C_{58}^{n+} than with the isolated-pentagon ions C_{60}^{n+} and C_{70}^{n+} is suggestive of tetrahedral coordination at the site of addition and therefore also supports covalent bond formation. It thus appears likely that the potential energy surface may involve two minima rather than a single potential well. A double-well surface of this type is shown in Fig. 3. Nevertheless, we stress that the evidence favouring a double-well potential surface over a single-well model is rather circumstantial.

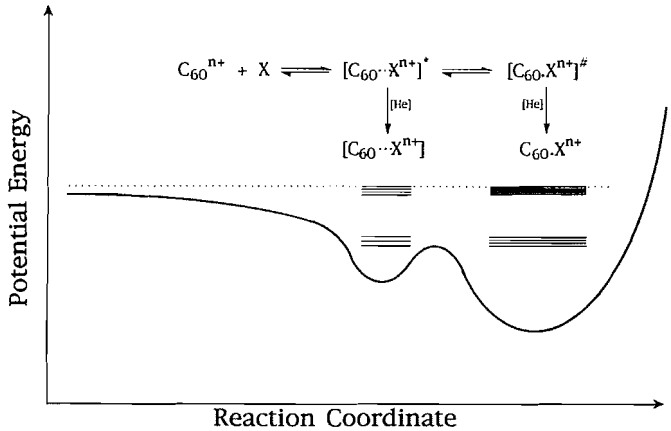

FIG. 3. Schematic diagram of the potential energy surface leading to association, for a double-well model. The barrier between the electrostatically bound complex, $[C_{60}\cdots X^{n+}]$, which is expected to correspond to the initial structure of the collision complex, and the covalently bonded adduct, $[C_{60}\cdot X^{n+}]$, is considered to arise from the energetic requirement to distort the fullerene surface in order to achieve sp^3 hybridization at the carbon atom involved in bond formation. The dotted line shows the total thermal and potential energy of reactants; also shown schematically are the relative densities of states for the electrostatically bound complex and the covalently bonded adduct at the total energy of reactants and at the height of the submerged barrier. The density of states ratio is expected to consistently favour covalent bond formation, since this potential well is expected to have greater depth.

A possible rationalization for the existence of a barrier between the electrostatically bound collision complex and the covalently bonded adduct is the necessity to distort the fullerene carbon framework at the site of the fullerene-substituent bond formation, so as to achieve sp^3 hybridization at this site on the fullerene surface. Such a barrier would presumably be more easily traversed for the adjacent-pentagon [C_5, C_5, C_6] charge sites in C_{56}^{n+} and C_{58}^{n+} (which, on geometric grounds, are expected to have a comparatively high degree of pyramidalization, and of sp^3 character, prior to interaction with the re-

Can. J. Chem. Downloaded from www.nrcresearchpress.com by 195.246.54.202 on 09/08/12
For personal use only.

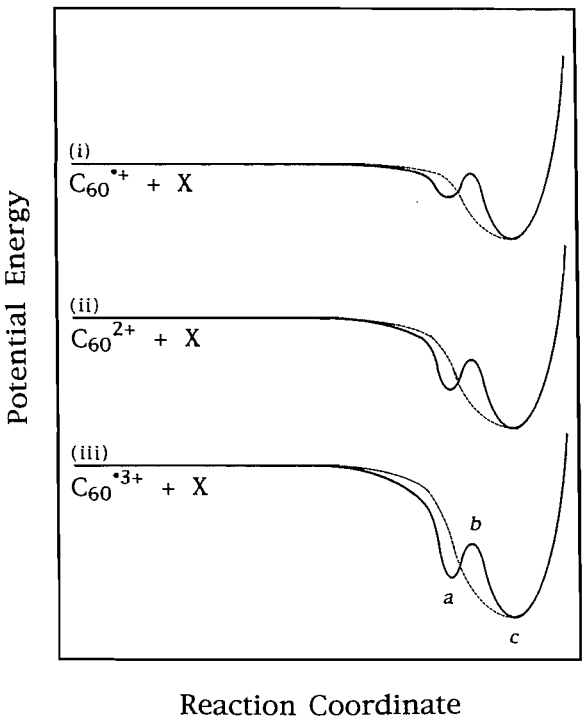

FIG. 4. Schematic diagram illustrating the increasing depth of the potential well(s) leading to adduct formation, and of the barrier to covalent bond formation in the double-well model, with increasing charge state.

actant neutral) than for the charge sites in C_{60}^{n+} and larger fullerenes: this can account for the observed trend (Table 2) for fullerene ion sizes. Traversal of the barrier should also be more facile for collision complexes having a higher charge state, since the barrier height (relative to the electrostatic well depth) should be essentially independent of charge state while the electrostatic well depth will increase with charge state. We have illustrated this point schematically in Fig. 4.

The double-well model provides for the collisional stabilization of the electrostatically bound collision complex as well as of the chemically bonded adduct, and thus two isomeric structures of the association product are possible. We have not yet observed any evidence (upon the basis of subsequent reactivity) that supports this possibility: however, if the well depth for chemical bond formation is substantially greater than the depth of the electrostatic well as we have suggested, then the density of states in the energy window above the barrier to interconversion is expected to consistently favour chemical bond formation and so the chemically bonded adduct should be the major product of the association reaction provided that the collision complex is sufficiently long-lived to allow an equilibrium to be attained between the two minima.

Several other examples can be found in the literature, of reaction processes in positive ion – molecule chemistry involving discrete potential wells for electrostatically and covalently bound complexes. The negative temperature dependence observed for the methyl cation transfer reaction

[14] $(CH_3)_2Cl^+ + C_6H_5CH_3 \rightarrow C_6H_5(CH_3)_2^+ + CH_3Cl$

suggests that this exothermic reaction occurs on a surface involving at least two minima (27), and studies of other alkyl cation transfer reactions of dialkylchloronium ions (28–31) also indicate that a barrier exists between electrostatic complex formation and the transition to a covalently bonded adduct.

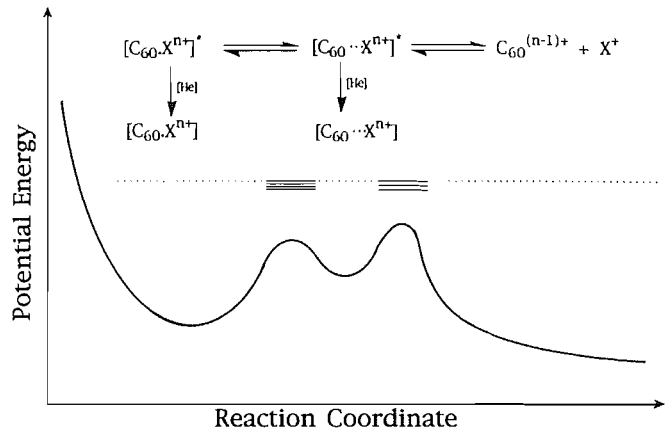

FIG. 5. Schematic diagram illustrating the potential energy surface involved in the competition between covalently bonded adduct formation and accessible charge transfer in the reaction of a polycation C_{60}^{n+} and a neutral X. For simplicity, the channel leading back from the (electrostatically bound) collision complex $[C_{60}\cdots X^{n+}]^*$ to reactants has not been included. Covalent bond formation can only compete effectively with charge transfer if the density of states above the (submerged) barrier to bond formation exceeds that above the (submerged) Coulombic barrier to charge transfer from a polycation: the occurrence of such competition in a reaction thus provides a lower limit to the depth of the potential well in the reaction concerned.

Similar potential energy surfaces have been proposed to explain the observed reactivity of gas-phase electrophilic aromatic substitution reactions (32, 33). The kinetics of ferrocene protonation (34):

[15] $BH^+ + Fe(C_5H_5)_2 \rightarrow Fe(C_5H_5)_2H^+ + B$

are similarly indicative of a barrier between electrostatically bound and covalently bonded adduct structures: this barrier is interpreted as arising from a change in geometry upon protonation. These examples demonstrate that the existence of barriers to bond formation in ion–molecule reactions may be rather common, especially when bond formation necessitates substantial distortion or deformation of the reactants.

D. Competition with charge transfer

The occurrence of association becomes a more complex issue in the presence of a competing exothermic bimolecular product channel such as charge transfer. This is especially true for reactions of the multiply charged ions C_{60}^{2+} and $C_{60}^{\bullet 3+}$, since charge separation reactions of such ions are inhibited by a substantial reverse activation energy barrier δ arising from the Coulombic repulsion between the product ions, which are initially formed in close mutual proximity (20, 35, 36). We have presented elsewhere a model for the potential energy surface involved in charge separation reactions of fullerene ions (37), which indicates a barrier height of $\delta = 1.80 \pm 0.16$ eV for reactions of the type

[16] $C_{60}^{2+} + X \rightarrow C_{60}^{\bullet +} + X^{\bullet +}$

and $\delta = 4.5 \pm 0.4$ eV for the reactions

[17] $C_{60}^{\bullet 3+} + X \rightarrow C_{60}^{2+} + X^{\bullet +}$

We have observed association reactions in competition with accessible charge transfer. Several reactions of this type are listed in Table 6. If our proposal of a double-well model is correct, then such reactions provide some indication of the relative barrier heights (in the forward direction) for chemical

Can. J. Chem. Downloaded from www.nrcresearchpress.com by 195.246.54.202 on 09/08/12
For personal use only.

TABLE 6. Reactions exhibiting competition between association and charge transfer

Reaction	IE(X)[a]	$-(\Delta H^0 + \delta)$[b]	B.R.$_{assn}$[c]	B.R.$_{ct}$[c]	$k(2)_{obs}$[d]	k_c[e]
$C_{60}^{2+} + (C_2H_5)_2O$[f]	9.51 ± 0.01	0.08	0.1	0.9	0.91	2.30
$C_{60}^{2+} + c\text{-}C_4H_8O$[f]	9.41 ± 0.02	0.18	0.6	0.4	1.9	2.50
$C_{60}^{2+} + CH_3COC_3H_7$[g]	9.38 ± 0.01	0.21	0.9	0.1	1.8	2.99
$C_{60}^{2+} + (C_2H_5)_2CO$[g]	9.31 ± 0.01	0.28	0.75	0.25	1.9	2.99
$C_{60}^{2+} + c\text{-}C_5H_8O$[g]	9.25 ± 0.01	0.34	0.3	0.7	2.8	3.31
$C_{60}^{2+} + (CH_3)_2CCH_2$[h]	9.239 ± 0.003	0.35	0.9	0.1	2.4	2.03
$C_{60}^{2+} + (Z)\text{-}2\text{-}C_4H_8$[h]	9.108 ± 0.008	0.48	0.2	0.8	3.4	1.96
$C_{60}^{2+} + C_4H_6$[h]	9.07[i]	0.52	0.8	0.2	1.0	1.94
$C_{60}^{2+} + CH_3NH_2$[j]	8.97 ± 0.02	0.62	0.9	0.1	2.6	2.68
$C_{60}^{2+} + C_2H_5NH_2$[j]	8.86 ± 0.02	0.73	0.7	0.3	2.6	2.68
$C_{60}^{2+} + (CH_3)_2NH$[j]	8.23 ± 0.08	1.36	0.1	0.9	2.9	2.44
$C_{60}^{\cdot 3+} + CH_2CHCN$[k]	10.91 ± 0.01	0.18	0.9	0.1	4.0	6.77
$C_{60}^{\cdot 3+} + CH_3OH$[f]	10.85 ± 0.01	0.24	0.2	0.8	2.5	4.38
$C_{60}^{\cdot 3+} + HCOOCH_3$[g]	10.815 ± 0.005	0.28	1.0	0	2.9	3.65
$C_{60}^{\cdot 3+} + CH_3COOH$[g]	10.66 ± 0.02	0.43	1.0	0	4.2	3.63
$C_{60}^{\cdot 3+} + CH_3COOCH_3$[g]	10.27 ± 0.02	0.82	0.9	0.1	3.4	3.50
$C_{60}^{\cdot 3+} + CH_2CHCH_2CN$[k]	10.20 ± 0.05	0.89	0.6	0.4	6.6	5.81
$C_{60}^{\cdot 3+} + CH_3COCCH$[g]	10.17 ± 0.02	0.92	0.2	0.8	4.5	4.33
$C_{60}^{\cdot 3+} + NH_3$[j]	10.16 ± 0.01	0.93	1.0	0	1.2	3.37
$C_{60}^{\cdot 3+} + C_2H_5CHO$[g]	9.953 ± 0.05	1.14	0.25	0.75	4.2	4.72

[a]Ionization energy (in eV) of the reactant neutral, obtained from the tabulation of Lias et al. (38) unless otherwise indicated.
[b]Calculated depth of the submerged barrier to charge transfer, obtained as the difference between the observed threshold to charge transfer (IE = 9.59 ± 0.11 eV for C_{60}^{2+}, IE = 11.09 ± 0.09 eV for $C_{60}^{\cdot 3+}$) 20, 36, 37, and IE(X).
[c]Experimentally obtained branching ratios (±30%) for association and for charge transfer, respectively.
[d]Observed effective bimolecular rate coefficient for addition, in units of 10^{-9} cm^3 molecule^{-1} s^{-1}.
[e]ADO collision rate coefficient in units of 10^{-9} cm^3 molecule^{-1} s^{-1}, calculated according to the method of Su and Bowers (19).
[f]Results previously reported in ref. 14.
[g]Results previously reported in ref. 15.
[h]Results previously reported in ref. 11.
[i]Reported in ref. 39.
[j]Results previously reported in ref. 10.
[k]Results previously reported in ref. 13.

bond formation and for charge transfer as we have illustrated in Fig. 5. The experimental results obtained to date show that association is able to compete to some extent with charge transfer reactions whose exothermicity exceeds the threshold value δ by up to ~0.6 eV for reactions of C_{60}^{2+}, and up to ~1.0 eV for $C_{60}^{\cdot 3+}$. At first glance there appears little evidence of a clear trend between exothermicity of charge transfer and the observed branching ratio for charge transfer, but this is understandable given the wide range in addition efficiencies that could be expected for these compounds in the absence of a competing charge transfer channel. For example, our studies of amine, nitrile, alcohol, and ketone addition reactions with C_{60}^{n+} indicate that nitrogen-containing nucleophiles (especially amines) are substantially more efficient at forming adducts than are the oxygen-containing nucleophiles (especially ethers). If these intrinsic differences in addition efficiency are taken into consideration, it is possible to discern a tendency (in any given class of compounds) for charge transfer to become dominant as it becomes sufficiently exothermic, as would be expected.

The results listed in Table 6 suggest that the barrier to bond formation for these reactions is submerged by at least 0.6 eV and 1.0 eV for doubly and triply charged ions, respectively. This places, also, a lower limit on the collision complex well depth in these examples (since this depth must exceed that of the submerged barrier to bond formation, if the double-well model is correct). If the collision complex well depth arises solely from the electrostatic and ion–dipole attractions between a (point-charge) fullerene ion and the neutral reactant in question, these lower limits indicate a separation of the reactants in the collision complex of no greater than 4.8 Å for C_{60}^{2+}+CH_3NH_2 and 4.5 Å for $C_{60}^{\cdot 3+}$ + NH_3. This distance restriction does not appear unreasonably restrictive — such a separation does not necessitate bond formation between the reactants. However, it is not clear how well the fullerene polycations conform to such a point-charge model: certainly the magnitude of the reverse activation energy barrier to charge transfer is better accommodated (in the case of charge transfer from C_{60}^{2+} and, we anticipate, from $C_{60}^{\cdot 3+}$) by assuming that the charges upon the fullerene polycation are initially as widely separated as is possible on the surface of a 7.0 Å spheroid. If the fullerene ion is not treated as a point charge, the required separation between the ion and the neutral (to produce an electrostatic well of greater depth than the submerged barrier to charge transfer) will be substantially less than the maximum separation permitted by a point-charge model.

Conclusions

The efficiency of association reactions of fullerene cations observed to occur in helium at the comparatively high pressures (0.35–0.4 Torr) sustained in a SIFT apparatus at room temperature has been scrutinized in terms of the influence of the charge state and the size of the fullerene ion and the size, structure, and degree of unsaturation of the neutral. The association efficiency is found to be strongly dependent on these molecular parameters. The magnitude of the efficiency, when translated into the lifetime of an intermediate collision complex, provides insight into the well depth associated with the formation of this complex and the effectiveness of vibrational and (or) rotational degrees of freedom in the fullerene cation

Can. J. Chem. Downloaded from www.nrcresearchpress.com by 195.246.54.202 on 09/08/12
For personal use only.

Can. J. Chem. Downloaded from www.nrcresearchpress.com by 195.246.54.202 on 09/08/12
For personal use only.

and the added neutral molecule in the dispersal of the excess energy of the complex.

The observed results are considered in the light of a single-well and a double-well model for the potential energy surface leading to association, but they are best accommodated by the double-well model involving the formation of an initial electrostatic collision complex, which must overcome a barrier (corresponding to the energetic requirement for localized surface deformation) to proceed to the formation of a chemically bonded adduct. The observation of competition of association with charge transfer can also be accommodated with a double-well model, which provides a lower limit for the depth of the electrostatic well for those systems that exhibit such competition. More insight into the nature of the potential energy surface would be provided by more detailed investigations of the pressure dependence (including the very low pressure regime) and of the influence of temperature upon association efficiency. Investigation of the chemistry of higher charge states such as C_{60}^{4+} and $C_{56}^{\cdot 5+}$ may also yield further information on the factors governing association reactions of fullerene ions.

The discussion of the models for the potential energy surfaces associated with fullerene-adduct formation is necessarily rather qualitative in nature. Several theoretical models do exist that treat, in a quantitative or semi-uantitative fashion, features of the potential energy surfaces for radiatively and collisionally stabilized association reactions (40). However, these models generally require a reasonably detailed knowledge of the exothermicity of adduct formation and the vibrational frequencies of the collision complex. In the present context, the thermochemistry of derivatized ionized fullerenes is as yet virtually unknown, and the ab initio calculation of vibrational spacings for a derivatized fullerene ion $C_{60}{\cdot}X^{n+}$ requires a major investment in computing time: at present, no such calculations have been reported. It is, therefore, not yet possible to model theoretically the efficiency of fullerene ion addition reactions, although such an aim is certainly desirable to augment or critically assess the models for the potential energy surface for association that we have presented here.

Acknowledgements

D.K.B. thanks the Natural Sciences and Engineering Research Council of Canada for the financial support of this research and the Canada Council for a Killam Research Fellowship.

1. J.M. Farrar and W.H. Saunders, Jr. (*Editors*). Techniques for the study of ion–molecule reactions. Techniques of Chemistry. Vol. XX. Wiley–Interscience, New York. 1988.
2. D.K. Bohme. *In* Structure/reactivity and thermochemistry of ions. *Edited by* P. Ausloos and S.G. Lias. Reidel, Dordrecht, The Netherlands. 1987. p. 219.
3. K.G. Spears and F.C. Fehsenfeld. J. Chem. Phys. **56**, 5698 (1972).
4. L.M. Roth and B.S. Freiser. Mass Spectrom. Rev. **10**, 303 (1991).
5. R. Tonkyn and J.C. Weisshaar. J. Am. Chem. Soc. **108**, 7128 (1986).
6. W. Krätschmer, L.D. Lamb, K. Fostiropoulos, and D.R. Huffman. Nature, **347**, 354 (1990).
7. S.W. McElvany and S.B.H. Bach. 39th Conf. Mass Spectrom. Allied Topics, Nashville, Tenn. 1991. p. 422.
8. S.W. McElvany, M.M. Ross, and J.H. Callahan. Acc. Chem. Res. **25**, 162 (1992).
9. H. Schwarz, T. Weiske, D.K. Bohme, and J. Hrusak. *In* Buckminsterfullerenes. *Edited by* W.E. Billups and M.A. Ciufolini. VCH, New York. 1993. p. 257.
10. (*a*) G. Javahery, S. Petrie, A. Ketvirtis, J. Wang, and D.K. Bohme. Int. J. Mass Spectrom. Ion Processes, **116**, R7 (1992); (*b*) G. Javahery, S. Petrie, H. Wincel, J. Wang, and D.K. Bohme. J. Am. Chem. Soc. **115**, 5716 (1993).
11. S. Petrie, G. Javahery, J. Wang, and D.K. Bohme. J. Am. Chem. Soc. **114**, 9177 (1992).
12. S. Petrie, G. Javahery, and D.K. Bohme. J. Am. Chem. Soc. **115**, 1445 (1993).
13. G. Javahery, S. Petrie, J. Wang, H. Wincel, and D.K. Bohme. J. Am. Chem. Soc. **115**, 9701 (1993).
14. G. Javahery, S. Petrie, H. Wincel, J. Wang and D.K. Bohme. J. Am. Chem. Soc. **115**, 6295 (1993).
15. S. Petrie, G. Javahery, H. Wincel, J. Wang and D.K. Bohme. Int. J. Mass Spectrom. Ion Processes. In press.
16. J. Wang, G. Javahery, S. Petrie, and D.K. Bohme. J. Am. Chem. Soc. **114**, 9665 (1992).
17. H. Becker, G. Javahery, S. Petrie, P.-C. Cheng, H. Schwarz, L.T. Scott, and D.K. Bohme. J. Am. Chem. Soc. **115**, 11636 (1993).
18. S. Petrie and D.K. Bohme. Nature, **365**, 426 (1993).
19. T. Su and M.T. Bowers. Int. J. Mass Spectrom. Ion Phys. **12**, 347 (1973).
20. G. Javahery, H. Wincel, S. Petrie, and D.K. Bohme. Chem. Phys. Lett. **204**, 467 (1993).
21. S.W. McElvany, M.M. Ross, and J.H. Callahan. Mater. Res. Soc. Symp. Proc. **206**, 697 (1991).
22. J.J. Stry, M.T. Coolbaugh, E. Turos, and J.F. Garvey. J. Am. Chem. Soc. **114**, 7914 (1992).
23. P.R. Kemper, L.M. Bass, and M.T. Bowers. J. Phys. Chem. **89**, 1105 (1985).
24. M.J. McEwan, A.B. Denison, V.G. Anicich, and W.T. Huntress. Int. J. Mass Spectrom. Ion Processes, **81**, 247 (1987).
25. A. Good. Trans. Faraday Soc. **67**, 3495 (1971).
26. S. Petrie, G. Javahery, and D.K. Bohme. Int. J. Mass Spectrom. Ion Processes, **124**, 145 (1993).
27. D.K. Sen Sharma and P. Kebarle. J. Am. Chem. Soc. **104**, 19 (1982).
28. T.F. Magnera and P. Kebarle. *In* Ionic processes in the gas phase. *Edited by* M.A. Almoster Ferreira. Reidel, Dordrecht, The Netherlands. 1982. p. 135.
29. P.J. Mathews and J.A. Stone. Can. J. Chem. **66**, 1239 (1988).
30. M. Speranza and G. Laguzzi. J. Am. Chem. Soc. **110**, 30 (1988).
31. M. Attina, F. Cacace, and A. Ricci. Angew. Chem. Int. Ed. Engl. **30**, 1457 (1991).
32. F. Cacace, M.E. Crestoni, A. Dimarzio, and S. Fornarini. J. Phys. Chem. **95**, 8731 (1991).
33. M. Attina and F. Cacace. Gazz. Chim. Ital. **118**, 241 (1988).
34. M.G. Ikonomou, P. Kebarle, and J. Sunner. J. Phys. Chem. **92**, 6308 (1988).
35. L.M. Roth and B.S. Freiser. Mass Spectrom. Rev. **10**, 303 (1991).
36. S. Petrie, G. Javahery, J. Wang, and D.K. Bohme. J. Phys. Chem. **96**, 6121 (1992).
37. S. Petrie, J. Wang, and D.K. Bohme. Chem. Phys. Lett. **204**, 473 (1993).
38. S.G. Lias, J.E. Bartmess, J.F. Liebman, J.L. Holmes, R.D. Levin, and W.G. Mallard. J. Phys. Chem. Ref. Data, **17**, Suppl. no. 1 (1988).
39. R.C. Weast (Editor). CRC handbook of chemistry and physics CRC Press, Boca Raton, Fla. 1986.
40. (*a*) D.R. Bates and E. Herbst. *In* Rate coefficients in astrochemistry. *Edited by* T.J. Millar and D.A. Williams. Kluwer, Dordrecht, The Netherlands. 1988. p. 17; (*b*) R.C. Dunbar. Int. J. Mass Spectrom. Ion Processes, **100**, 423 (1990); (*c*) E. Herbst and R.C. Dunbar. Mon. Not. R. Aston. Soc. **253**, 341 (1991); (*d*) S.C. Smith, M.J. McEwan, and R.G. Gilbert. J. Chem. Phys. **90**, 1630 (1989).

Experimental and theoretical study of monoligand complexes of nickel atoms with simple alkynes[1]

S.A. MITCHELL,[2] M.A. BLITZ, AND R. FOURNIER

Steacie Institute for Molecular Sciences, National Research Council of Canada, 100 Sussex Dr., Ottawa, ON K1A 0R6, Canada

Received July 20, 1993

This paper is dedicated to Professor John C. Polanyi on the occasion of his 65th birthday

S.A. MITCHELL, M.A. BLITZ, and R. FOURNIER. Can. J. Chem. **72**, 587 (1994).

Monoligand complexes of nickel atoms with simple alkynes have been investigated by kinetic studies of association reactions of nickel atoms with ethyne, propyne, and 2-butyne in the gas phase near room temperature, and by quantum chemical calculations on the Ni[C_2H_2] complex using a Linear Combination of Gaussian-Type Orbitals – Density Functional (LCGTO–DF) method. Experimental estimates of binding energies of the monoligand complexes have been made by using RRKM unimolecular reaction theory to model the pressure dependence of second-order rate coefficients for the association reactions: $\Delta E_0^0 = 46 \pm 6$, 37 ± 5, and 29 ± 5 kcal mol^{-1}, for Ni[C_2H_2], Ni[propyne], and Ni[2-butyne], respectively. The trend in binding energy with methyl substitution on ethyne is discussed and compared with similar data for monoligand complexes of alkynes with copper atoms. The harmonic vibrational frequencies and binding energy for the $^1A_1$ ground state of Ni[C_2H_2] have been calculated using the LCGTO–DF method, and the results are compared with experimental data on the infrared spectrum of matrix-isolated Ni[C_2H_2] and with the estimate of the binding energy of Ni[C_2H_2] from the present experimental study. There is excellent agreement between the experimental and theoretical results. The calculations indicate that at least one triplet state of Ni[C_2H_2] is bound relative to ground state Ni + C_2H_2 reactants. This is consistent with indications from the kinetic results that the association reaction occurs on more than one potential energy surface.

S.A. MITCHELL, M.A. BLITZ et R. FOURNIER. Can. J. Chem. **72**, 587 (1994).

On a étudié les complexes monocoordinés d'atomes de nickel avec des alcynes simples en réalisant des études cinétiques par réactions d'association d'atomes de nickel avec de l'éthyne, du propyne et du but-2-yne, en phase gazeuse, à la température ambiante et par des calculs chimiques quantiques sur le complexe Ni[C_2H_2] par une méthode de combinaison linénaire d'orbitales de type gaussien – densité fonctionnelle (LCGTO–DF). On a évalué les énergies de liaison expérimentales des complexes monocoordinés en utilisant la théorie de réaction unimoléculaire RRKM pour créer un modèle de la relation entre la pression et les coefficients de vitesse pour les réactions d'association du deuxième ordre : $\Delta E_0^0 = 46 \pm 6$, 37 ± 5 et 29 ± 5 kcal mol^{-1} respectivement pour Ni[C_2H_2], Ni[propyne] et Ni[but-2-yne]. On discute de l'évolution dans l'énergie de liaison avec des substitutions successives par des groupes méthyles et on la compare avec des données semblables obtenues avec des complexes monocoordinés de cuivre par des alcynes. Faisant appel à la méthode LCGTO–DF, on a calculé les fréquences vibrationnelles harmoniques et l'énergie de liaison de l'état fondamental $^1A_1$ du Ni[C_2H_2] et on a comparé les résultats avec les données expérimentales du spectre infrarouge du Ni[C_2H_2] isolé dans une matrice et avec les évaluations de l'énergie de liaison du Ni[C_2H_2] obtenus dans la présente étude expérimentale. Il existe un excellent accord entre les résultats expérimentaux et théoriques. Les calculs indiquent que, par rapport à l'état fondamental des réactifs Ni + [C_2H_2], au moins un état triplet du Ni[C_2H_2] est lié. Ceci est en accord avec les indications obtenues à partir des résultats cinétiques selon lesquels une réaction d'association se produit sur plus d'une surface d'énergie potentielle.

[Traduit par la rédaction]

1. Introduction

Interactions of unsaturated hydrocarbons with nickel atomic centres are important in several areas of chemistry including homogeneous and heterogeneous catalysis. This has led to extensive studies of the nature of bonding of alkenes and alkynes on single-crystal nickel surfaces and small nickel particles (1), and in nickel coordination complexes (2). Monoligand complexes of nickel atoms with ethene and ethyne are interesting model systems that may provide useful insights into the nature of bonding in more complex metal centres. Because of their relative simplicity, these model systems are well suited for detailed studies using quantum chemical theoretical methods. These methods, in turn, are important for interpreting experimental results. It is therefore of great interest to compare experimental and theoretical results for these 1:1 complexes. This paper describes such a comparison for monoligand complexes of nickel atoms with simple alkynes.

Infrared spectra have been reported for Ni[C_2H_2]$_n$ (n = 1 and 2) (3, 4) and Ni[C_2H_4]$_n$ (n = 1–3) (5, 6) complexes isolated in low-temperature inert gas matrices. An important step in the understanding of these systems was made with the ab initio calculations of Widmark et al. (7), which showed that the monoligand complexes Ni[C_2H_2] and Ni[C_2H_4] have ground states of singlet spin-multiplicity, similar to Ni[CO]. This is in contrast to the triplet ground state of atomic nickel. Recently, the complex Ni[C_2H_4] was investigated by gas phase kinetic studies of the association reaction of nickel atoms with ethene (8, 9), and by quantum chemical calculations using density functional methods (10). From the kinetic studies, the binding energy of Ni[C_2H_4] was estimated as 35.2 ± 4.2 kcal mol^{-1}. This estimate was made by modeling kinetic data using unimolecular reaction theory and by using in these model calculations the molecular structure and harmonic vibrational frequencies of the complex from density functional calculations (10). These calculated frequencies were in good agreement with experimental infrared spectra (6). Furthermore, the experimental estimate of the binding energy of the complex from the kinetic studies was in good agreement with the theoretical value from the density functional calculations. These studies show that Ni[C_2H_4] is a rather strongly bound π complex with a singlet ground state, and with at least one excited

[1]NRCC No. 35270.

[2]Author to whom correspondence may be addressed.

Can. J. Chem. Downloaded from www.nrcresearchpress.com by 195.246.54.202 on 09/08/12
For personal use only.

Can. J. Chem. Downloaded from www.nrcresearchpress.com by 195.246.54.202 on 09/08/12
For personal use only.

state of triplet spin-multiplicity that is relatively weakly bound with respect to ground state nickel and ethene.

In the present study of complexes of nickel atoms with alkynes, a similar approach involving the combination of gas phase kinetic studies and density functional calculations has been used. Also similar to the study of $Ni[C_2H_4]$, the results of matrix-isolation infrared spectroscopic studies of $Ni[C_2H_2]$ (3, 4) proved very useful for comparison with predicted harmonic vibrational frequencies.

2. Experimental section

Details of the experimental method for kinetic studies of Ni atoms near room temperature have been described previously (8, 11). Nickel atoms were produced by pulsed laser photolysis of nickelocene vapour in a static pressure reaction cell, using an excimer laser pumped dye laser operating at 650 nm. Photolysis pulses were 0.75 mJ/pulse, and were focused using a 30 cm focal length lens. Detection of Ni atoms was by saturated resonance fluorescence excitation, using a second excimer laser pumped dye laser operating at 341.477 nm. Photolysis and probe laser beams were in a collinear and counterpropagating arrangement. Kinetic traces showing the time decay of the relative population of Ni atoms due to reaction with the precursor nickelocene or with added alkyne reactant were obtained by scanning the photolysis–probe interpulse delay in preset increments and averaging the fluorescence signal over 40–100 laser shots at each increment of delay. Kinetic traces typically consisted of 200 points, and were acquired over a period of several minutes using a laser repetition rate of 20 Hz. The traces were recorded by repetitively scanning the full range of interpulse delay, so that the stability of the signal could be monitored during the data acquisition period. Kinetic traces were fitted to single-exponential decays, allowing sufficient time at the beginning of the trace for complete relaxation of metastable states of Ni atoms (12). Exponential decays were fitted over at least three half-lives, and showed no systematic deviations from single-exponential decay behavior.

The Pyrex reaction cell was temperature stabilized by use of circulating ethylene glycol. Temperature measurement was by a Chromel–Alumel thermocouple probe that was situated near the reaction zone. Pressure measurement was by Baratron capacitance manometers. Ethyne was obtained from Matheson of Canada, propyne (96%) from Wiley Organics, and 2-butyne (99%) from Aldrich. All reactants were extensively degassed before use. The purity of the ethyne sample with respect to contamination by acetone was checked by FT-IR spectroscopy, and only a trace of acetone was observed.

3. Computational method

We performed all-electron Kohn–Sham calculations using the program deMon (13) in which the orbitals, charge density, and exchange-correlation potential are expanded in terms of Gaussian functions. A description of the Linear Combination of Gaussian-Type Orbitals – Density Functional (LCGTO–DF) formalism can be found in ref. 14. We did three sets of calculations: (1) with a local spin density (LSD) potential and energy functional (15); (2) with the LSD potential and adding gradient corrections of Becke (16) and Perdew (17) perturbatively to the exchange-correlation energy (BP/LSD); and (3) adding gradient corrections to the exchange-correlation potential and energy self-consistently (BP). In general, adding gradient corrections dramatically improves the binding energies; it often improves geometries but it usually does not give more accurate vibrational frequencies (18–20). Therefore the BP results should be regarded as more reliable and our discussion will be centred mainly around BP results.

The orbital basis sets we used have the contraction patterns (63321/5211/41) for the nickel atom, (6311/311/1) for carbon, and (311/1) for hydrogen. The auxiliary basis sets used for fitting the charge density and those for fitting the exchange-correlation potential had the same form. On nickel, the auxiliary bases had the form (10, 5, 5) (10 *s*, 5 *p*, and 5 *d* uncontracted functions), on carbon it had the form (8, 4, 4), and for hydrogen the bases were of the type (6, 2, 2). Further details are given in Appendix A. The basis set superposition error (BSSE) was estimated by the counterpoise method at the LSD level. It was found to be 4.6 kcal mol^{-1} at the equilibrium geometries of both the singlet and triplet states of the complex. This is somewhat larger than the counterpoise correction found in a similar study of the nickel–ethene complex, 3.6 kcal mol^{-1} (10). This is expected on account of the shorter nickel–carbon distances in $Ni[C_2H_2]$. Geometry optimization was carried out with a standard gradient method and harmonic vibrational analysis was performed through finite differences of analytical gradients. The $Ni[C_2H_2]$ binding energies that we report here were corrected for BSSE (−4.6 kcal mol^{-1} for both singlet and triplet) and include the change in zero-point energy (−1.0 kcal mol^{-1} for singlet, +0.1 kcal mol^{-1} for triplet).

The binding energies were calculated with respect to a nonspherical (integer occupation numbers) triplet $3d^9 4s^1$ nickel atom, which is the calculated ground state. In Kohn–Sham calculations, different occupations of the *d* orbitals for the same configuration give slightly different total energies (see, for instance, ref. 21). For both singlet and triplet $3d^9 4s^1$ configurations, the different *d* occupations gave energies that differed by at most 1.2 kcal mol^{-1}. For each of these configurations, we used the average of the largest and smallest calculated energies. When spherical symmetry is imposed, the energy of the triplet $3d^9 4s^1$ configuration is 9 kcal mol^{-1} larger than in the nonspherical treatment. The $3d^{n-1}4s^1$–$3d^{n-2}4s^2$ energy separation (*sd* splitting) is poorly described by most theoretical methods and, in particular, by DF calculations. When the ground state of a metal–ligand complex correlates to an excited $3d^{n-1}4s^1$ configuration of the atom in the dissociation limit, it is common to apply an empirical correction based on known atomic energy levels to the calculated dissociation energy (22, 23). For nickel, both the DF calculation and the multiplet-averaged experimental ground state configurations are triplet $3d^9 4s^1$ and no correction for the *sd* splitting is needed. The ground state $Ni[C_2H_2]$ complex dissociates to a ground state C_2H_2 molecule and a singlet $3d^9 4s^1$ nickel atom. Therefore, the $3d^9 4s^1$ singlet – triplet splitting of the nickel atom is relevant. The experimental value for this splitting is 7.7 kcal mol^{-1} (24) while the BP/LSD value for a nonspherical Ni atom is 9.6 kcal mol^{-1}. The agreement is good and we chose not to apply any correction for this atomic splitting. The calculated energy for the $3d^{10}$ configuration relative to the triplet ground state is 42.7 kcal mol^{-1}, which also compares well to experiment, 40.0 kcal mol^{-1}. Other configurations of the nickel atom are not expected to be important for a description of the complex: the $3d^8 4s^2$ configuration of nickel leads to a repulsive interaction with the ligand and the $3d^8 4s4p$ configuration has a very high energy and contributes very little to the bonding.

4. Results and discussion

4.A. Kinetic results

Kinetic traces were recorded for reactions of Ni atoms with ethyne, propyne, and 2-butyne in CO_2 buffer gas at 295 and 325 K. In the absence of added reactant, Ni was removed by reaction with the precursor nickelocene, which was present at a pressure of ≈3 mTorr (1 Torr = 133.3 Pa). A "background" removal rate was therefore present in all kinetic traces. This

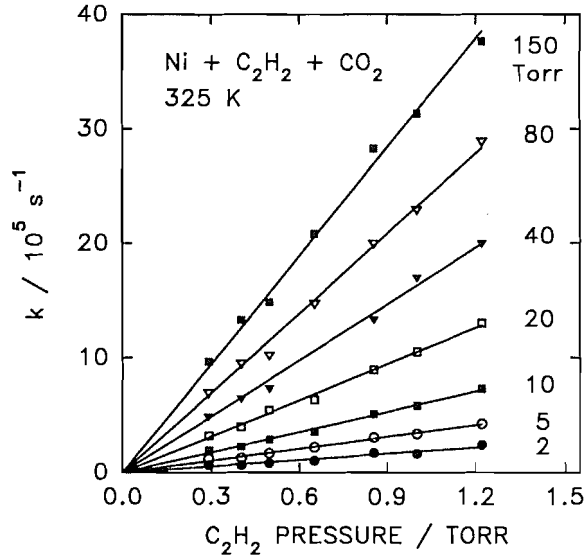

FIG. 1. Pseudo-first-order rate coefficients for reaction of nickel atoms with ethyne in carbon dioxide buffer gas at 325 K, versus ethyne pressure at various total pressures.

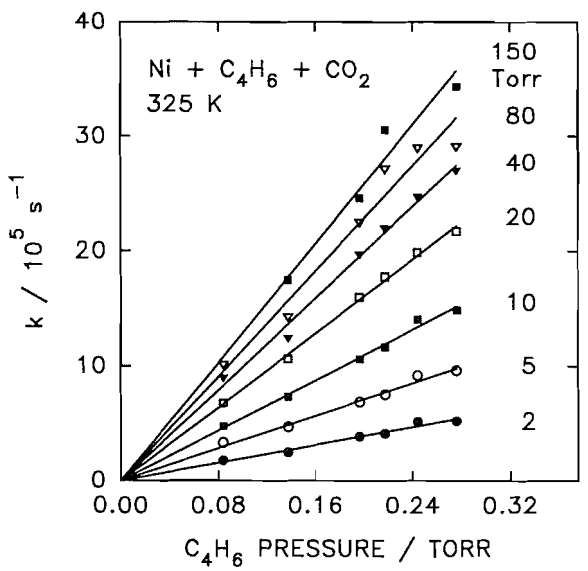

FIG. 2. Pseudo-first-order rate coefficients for reaction of nickel atoms with 2-butyne in carbon dioxide buffer gas at 325 K, versus 2-butyne pressure at various total pressures.

background rate was measured for each new nickelocene sample, before addition of reactant, and was subtracted from the rate measured with reactant present. The background rate was approximately 0.4×10^5 s^{-1}, and the corrected reaction rates were in the range $(0.8–38) \times 10^5$ s^{-1}. For each pressure of added reactant, the total pressure was made up to 2, 5, 10, 20, 40, 80, and 150 Torr, using CO_2 buffer gas. In Figs. 1 and 2 are shown pseudo-first-order removal rates of Ni atoms due to reaction with ethyne and 2-butyne, respectively, as a function of reactant pressure at the various total pressures at 325 K. These rates were corrected for the contribution due to reaction with precursor. The slopes of these plots constrained through the origin are second-order rate coefficients for the association reactions. All second-order rate coefficients are summarized in Tables 1 and 2, and are plotted against total pressure in Figs. 3, 4, and 5, for ethyne, propyne, and 2-butyne, respectively. The

TABLE 1. Second-order rate coefficients for association reactions of Ni atoms with ethyne, propyne, and 2-butyne in CO_2 buffer gas at 295 K

Reactant	Pressure range (Torr)[a]	Total pressure (Torr)	k_r (10^{-11} cm^3 s^{-1})
Ethyne	0.29–1.0	2	0.751 ± 0.023
		5	1.47 ± 0.07
		10	2.54 ± 0.09
		20	4.17 ± 0.12
		40	6.41 ± 0.18
		80	9.27 ± 0.29
		150	11.8 ± 1.4
Propyne	0.17–0.50	2	13.1 ± 0.36
		5	18.2 ± 0.54
		10	23.9 ± 0.69
		20	28.8 ± 0.98
		40	34.3 ± 0.64
		80	37.6 ± 1.6
		150	39.9 ± 2.8
2-Butyne	0.08–0.28	2	7.90 ± 0.41
		5	14.1 ± 0.46
		10	20.7 ± 0.62
		20	29.8 ± 1.1
		40	34.4 ± 1.5
		80	39.5 ± 2.5

[a]Pressure range of reactant.

uncertainties in Tables 1 and 2 are for 95% confidence limits and include only random errors. The lines drawn through the data points in Figs. 3–5 show fits to the data obtained by using RRKM calculations. From these calculations, the binding energies of the monoligand Ni–alkyne complexes were estimated. The method used to obtain these estimates is described in the following section.

4.B. Analysis of kinetic data

The rate coefficients in Tables 1 and 2 are for association reactions of the type shown in reaction [1]

[1] $$Ni + C_2H_2 + CO_2 \rightarrow Ni[C_2H_2] + CO_2$$

The bath gas, composed mainly of CO_2, serves to stabilize $Ni[C_2H_2]^*$ collision complexes, and this gives rise to a dependence of the second-order rate coefficient k_r on total pressure [M] that has the form shown in eq. [2].

[2] $$k_r = \frac{k_{r0}[M]}{1 + \frac{k_{r0}[M]}{k_{r\infty}}} \times F([M])$$

Here k_{r0} is the limiting low-pressure, third-order rate constant, $k_{r\infty}$ is the limiting high-pressure, second-order rate constant, and $F([M])$ is a function that approaches unity at both very low ($k_{r0}[M]/k_{r\infty} \ll 1$) and very high ($k_{r0}[M]/k_{r\infty} \gg 1$) pressure (25). There is thus a linear dependence of k_r on [M] at low pressure, with slope k_{r0}, and at high pressure k_r approaches a limiting value given by $k_{r\infty}$.

At very low pressure an equilibrium is established between Ni + C_2H_2 reactants and $Ni[C_2H_2]^*$ collision complexes. The low-pressure rate constant k_{r0} is proportional to the equilibrium constant for formation of $Ni[C_2H_2]^*$. Since this equilibrium constant is proportional to the volume of phase space associated with the collision complex, there is a correlation between

Can. J. Chem. Downloaded from www.nrcresearchpress.com by 195.246.54.202 on 09/08/12
For personal use only.

TABLE 2. Second-order rate coefficients for association reactions of Ni atoms with ethyne, propyne, and 2-butyne in CO_2 buffer gas at 325 K

Reactant	Pressure range (Torr)[a]	Total pressure (Torr)	k_r (10^{-11} cm^3 s^{-1})
Ethyne	0.29–1.22	2	0.620 ± 0.068
		5	1.17 ± 0.048
		10	1.99 ± 0.068
		20	3.54 ± 0.11
		40	5.50 ± 0.23
		80	7.81 ± 0.25
		150	10.6 ± 0.34
Propyne	0.18–0.54	2	10.6 ± 0.39
		5	15.5 ± 0.77
		10	20.3 ± 0.82
		20	25.5 ± 1.1
		40	30.5 ± 0.43
		80	35.2 ± 1.5
		150	42.0 ± 5.5
2-Butyne	0.08–0.28	2	6.59 ± 0.41
		5	12.0 ± 0.56
		10	18.5 ± 0.64
		20	27.1 ± 0.59
		40	33.5 ± 1.2
		80	38.5 ± 3.0
		150	43.5 ± 4.3

[a]Pressure range of reactant.

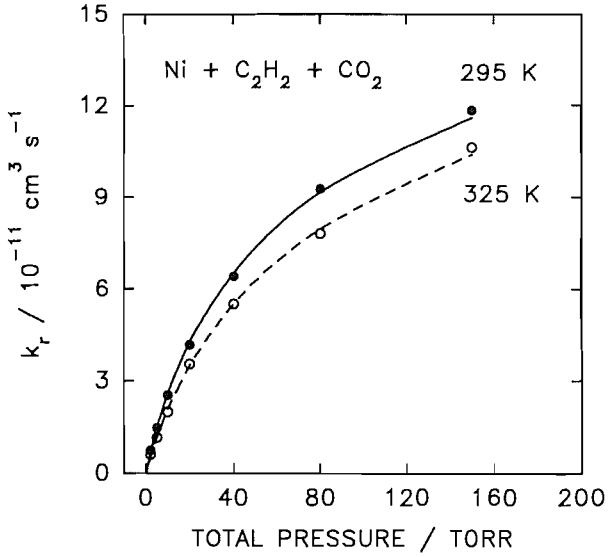

FIG. 3. Second-order rate coefficients for reaction of nickel atoms with ethyne in carbon dioxide buffer gas at 295 and 325 K, versus total pressure. The lines drawn through the data points show fitted rate coefficients from RRKM calculations.

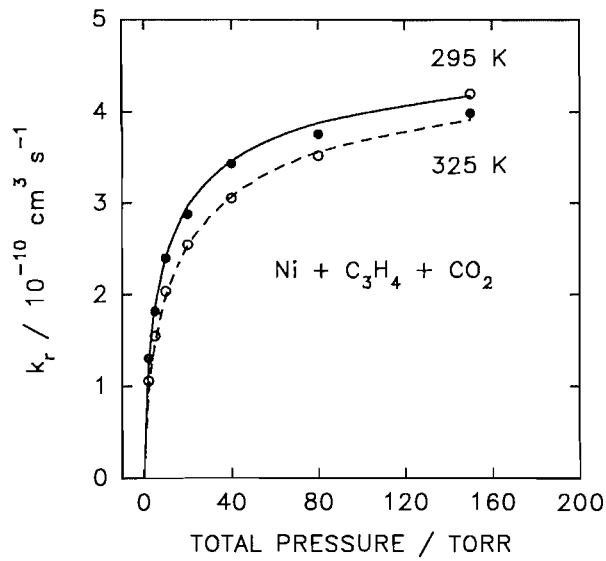

FIG. 4. Second-order rate coefficients for reaction of nickel atoms with propyne in carbon dioxide buffer gas at 295 and 325 K, versus total pressure. The lines drawn through the data points show fitted rate coefficients from RRKM calculations.

the magnitude of the low-pressure rate constant and the binding energy of the complex. This is the basis for the estimation of binding energies from kinetic data for association reactions (11). In practice, k_{r0} is calculated in terms of k_{u0}, the low pressure rate constant for the unimolecular dissociation reaction of the complex, i.e., the reverse of reaction [1]. k_{r0} and k_{u0} are related by the equilibrium constant K_{eq} for the association reaction, $k_{r0} = k_{u0}K_{eq}$. By using unimolecular reaction theory, k_{u0} may be calculated for an assumed threshold dissociation energy, if the structure and vibrational frequencies of the complex are known. If the molecular parameters of the dissociation products are also known, then this is sufficient to specify the equilibrium constant K_{eq}, and hence k_{r0}. This assumes that the threshold dissociation energy of the complex is equal to the thermochemical dissociation energy, i.e., there is no activation energy for the association reaction. In this case the vibrational frequencies and moments of inertia of the Ni + alkyne fragments and the Ni[alkyne] complex are sufficient to calculate k_{r0} for an assumed binding energy. The binding energy may therefore be estimated by systematically varying this parameter until agreement is found between calculated and observed low-pressure association rate constants. In practice there are additional details of the reaction that need to be specified, but these are of secondary importance. These details are given for the Ni + alkyne reactions in Sect. 4.C below.

The kinetic data for Ni + alkyne association reactions shown in Figs. 3–5 are in the falloff region of eq. [2], between limiting high- and low-pressure behavior. It is the low-pressure rate constant that is important for estimating the binding energy of the complex, but the falloff region is strongly influenced by the low-pressure rate constant, and therefore carries information on the binding energy. To model the falloff behavior it is necessary to explicitly consider the limiting high-pressure rate constant $k_{r\infty}$. RRKM theory provides a means of modeling the pressure dependence of the unimolecular dissociation rate constant k_u, and, by use of the equilibrium constant, that of the association (or recombination) rate constant k_r (26). In previous work on association reactions of Ni atoms with ethene and propene, we estimated binding energies of the monoligand complexes by modeling kinetic data in the falloff region, using RRKM calculations (8, 9).

An important feature of the Ni + alkene association reactions is that reaction occurs on more than one potential energy surface, and this is the case for the Ni+alkyne reactions as well. This is shown by the observation of rate coefficients near the high-pressure limit that are too large to be consistent with reaction only on the ground state surface of singlet

Can. J. Chem. Downloaded from www.nrcresearchpress.com by 195.246.54.202 on 09/08/12
For personal use only.

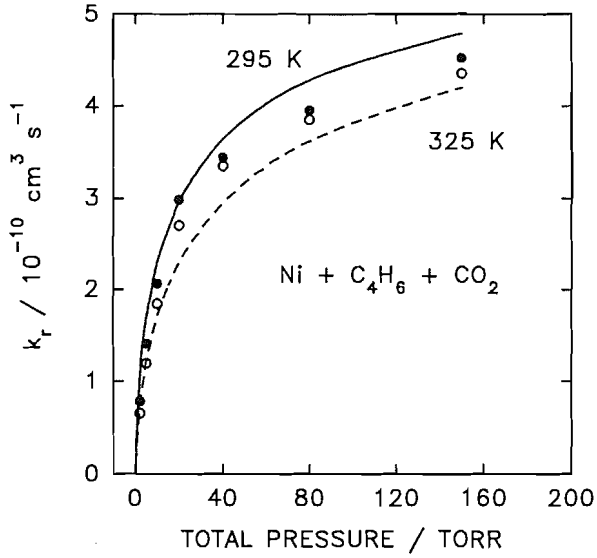

FIG. 5. Second-order rate coefficients for reaction of nickel atoms with 2-butyne in carbon dioxide buffer gas at 295 and 325 K, versus total pressure. The lines drawn through the data points show fitted rate coefficients from RRKM calculations.

spin-multiplicity. As described in Sect. 4.E, the ground state of the Ni[C_2H_2] complex is a singlet, and there is at least one triplet state that is bound relative to ground state Ni(^3F) + C_2H_2. There is a restriction on the maximum value of the high-pressure rate constant for reaction on a singlet potential surface, due to the low value of the ratio of electronic partition functions of the product and the reactants in this case. The maximum value is given by a rate constant for capture, determined by the long-range part of the atom–molecule interaction potential, multiplied by the ratio of electronic partition functions $Q_{el}(\text{Ni}[C_2H_2])/Q_{el}(\text{Ni}) = 1/11.66$ (at 295 K) (9). Estimates of rate constants for capture for Ni + alkynes, described in Sect. 4.C, are near 7×10^{-10} cm^3 s^{-1}, so the maximum value of $k_{r\infty}$ for reaction on the ground state potential surface is near 6×10^{-11} cm^3 s^{-1} in all cases. As shown in Figs. 3–5, the observed rate coefficients extend to significantly higher values than this maximum. This can be explained by considering that reaction may occur on excited state potential surfaces as well as on the ground state surface. As noted above, the theoretical results in Sect. 4.E indicate that one or more triplet states of Ni[C_2H_2] are bound relative to Ni + C_2H_2 reactants. These states are in all likelihood responsible for the large apparent values of $k_{r\infty}$.

A simple rate equations model for recombination on two potential energy surfaces has been described (9). In this model collision complexes are formed in, and may be collisionally stabilized in, both electronic states, and transitions may occur between the electronic states in the isolated collision complex. It was shown that, if the excited electronic state is significantly less strongly bound than the ground state, then for moderate total pressure the form of the pressure dependence of the association rate coefficient is the same as that shown in eq. [2], i.e., the same as that for reaction on one potential energy surface. In this case the occurrence of reaction in the excited electronic state is reflected in the apparent value of the limiting high-pressure rate constant. This apparent value is larger than the maximum value consistent with reaction only in the ground electronic state, to an extent governed by the relative rates of dissociation and electronic relaxation of the collision complex in the excited electronic state (9). The data for Ni + alkyne reactions can be understood in these terms. It is important to note that in the limiting case considered, the low-pressure association rate constant is not significantly affected by the excited state reaction, even though the high-pressure rate constant may be strongly affected. This has implications for the use of unimolecular reaction theory for the estimation of binding energies from kinetic data. In particular, it is justifiable to model kinetic data in the falloff region, and to obtain an estimate of the binding energy of the complex, by proceeding in the same manner as for the case where reaction occurs only in the ground electronic state. The only difference is that in this case it is necessary to treat the limiting high-pressure rate constant as an apparent value, with magnitude between k_∞ and $k_\infty + k'_\infty$, where k_∞ is the (hypothetical) high-pressure rate constant for reaction only in the ground state, and k'_∞ is that for reaction only in the excited state (9). In the RRKM calculations, discussed in the following section, this is described by considering that reaction occurs only in the ground electronic state, but allowing the electronic degeneracy of the transition state (denoted $g^{\ddagger}$) to be effectively greater than that of the ground electronic state (9).

In a previous study of Ni + alkene reactions (9), k_∞ and k'_∞ were estimated by assuming that the transition states for the association reactions were loose transition states, in the phase space limit of RRKM theory (26). In this limit the high-pressure rate constants are at their maximum values, given by the rate constant for capture multiplied by the ratio of electronic partition functions, as noted above. The same approach was used in the present study of Ni + alkyne reactions. Details of the estimation of capture rates are given in the following section.

The model for the association reaction thus involves recombination on both the ground state, singlet potential surface of the complex and on one or more excited state, triplet potential surfaces. Collision complexes in the relatively weakly bound excited electronic states undergo electronic relaxation to the ground state in competition with collisional relaxation and dissociation on the excited state potential surfaces. The occurrence of reaction on singlet and triplet potential surfaces implies that the triplet surfaces that correlate with ground state Ni(^3F) + alkyne reactants are crossed by a singlet surface, and spin changing transitions occur readily in the crossing region due to spin-orbit coupling. On the basis of comparisons with potential curves for the complex Ni[CO] (11), and considering a simple model for the magnitude of the spin-orbit coupling interaction in the complex, it has been argued that this is a plausible model for Ni + alkene reactions (9). The same arguments can be used for Ni + alkyne reactions. The important singlet surface correlates the ($^1A_1$) ground state of Ni[C_2H_2] with Ni(d^9s^1 ^1D) + C_2H_2 reactants, for which the excitation energy is ≈ 8 kcal mol^{-1} relative to ground state reactants.

4.C. RRKM calculations

RRKM calculations were performed using the UNIMOL suite of FORTRAN programs (26). The general approach was to select a model for the Ni–alkyne complex, including vibrational frequencies and moments of inertia, and then fit calculated to observed Ni + alkyne recombination rate coefficients by varying two parameters in the calculations: the binding energy of the complex (dissociation energy at 0 K), ΔE_0^0; and the electronic degeneracy of the transition state, $g^{\ddagger}$. Examples of fitted

Can. J. Chem. Downloaded from www.nrcresearchpress.com by 195.246.54.202 on 09/08/12
For personal use only.

TABLE 3. Parameters obtained by fitting calculated to observed rate coefficients for association reactions of Ni atoms with ethyne, propyne, and 2-butyne in CO_2 buffer gas, using RRKM calculations

Reactant	Model	T(K)	k_{r0} (10^{-28} cm^6 s^{-1})	$k_{r\infty}$ (10^{-10} cm^3 s^{-1})	$g^{\ddagger}$	ΔE_0^0 (kcal mol^{-1})
C_2H_2	—	295	1.1	2.0	3.5	46.1
		325	0.93	2.0		
Propyne	I	295	48	4.6	7.7	34.5
		325	35	4.7		
Propyne	II	295	50	4.6	7.7	40.0
		325	37	4.7		
2-Butyne	I	295	56	6.0	10	25.5
		325	35	6.0		
2-Butyne	II	295	61	6.1	10	31.5
		325	39	6.1		

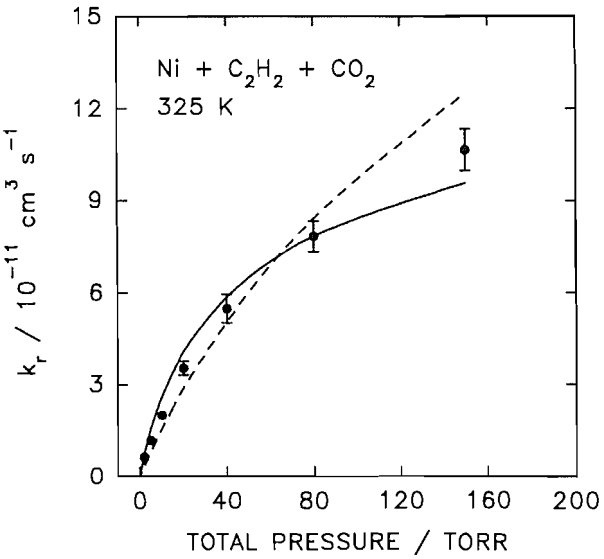

FIG. 6. Second-order rate coefficients for reaction of nickel atoms with ethyne in carbon dioxide buffer gas at 325 K, versus total pressure. Solid and broken lines show fitted rate coefficients from RRKM calculations, obtained by varying the parameter $g^{\ddagger}$ with the binding energy constrained as 49 and 43 kcal mol^{-1}, respectively.

rate coefficients at 295 and 325 K are shown in Figs. 3–5. The parameter ΔE_0^0 controls the slope of the pressure dependence at low pressure (rate constant k_{r0}), and $g^{\ddagger}$ controls the asymptotic limit of the rate coefficient at high pressure (rate constant $k_{r\infty}$). Note that since $g^{\ddagger}$ describes the extent of the participation of excited electronic states of the complex in the association reaction, it has a minimum value of 1.0, corresponding to reaction only in the ground state of singlet spin-multiplicity (electronic degeneracy = 1.0), and a maximum value given by the magnitude of the electronic partition function of atomic Ni (11.7 at 295 K and 11.9 at 325 K). This maximum value corresponds with the case where every collision of Ni with alkyne leads to motion on the ground state potential surface of the complex. In this case the apparent high-pressure rate constant is given by the rate constant for capture (see below).

In the fits to the data the parameters $g^{\ddagger}$ and ΔE_0^0 are to some extent correlated, but the effect of the correlation on the parameter ΔE_0^0 is rather small. This is because the dependence of k_{r0} on ΔE_0^0 is very strong, increasing with the complexity of the ligand molecule. Thus, the exponent n in the relationship $k_{r0} \sim (\Delta E_0^0)^n$ was found to be n = 7.1, 11, and 13, for the complex with ethyne, propyne, and 2-butyne, respectively. The correlation between the parameters ΔE_0^0 and $g^{\ddagger}$ for the C_2H_2 reaction at 325 K is illustrated by the fits shown in Fig. 6. The solid and dashed lines show fitted rate coefficients obtained by optimizing $g^{\ddagger}$ with ΔE_0^0 constrained to be 3 kcal mol^{-1} greater and smaller, respectively, than the value obtained when both parameters were optimized, 46 kcal mol^{-1}. The corresponding values of $g^{\ddagger}$ are 2.5, 7.7, and 3.5, for the solid and broken lines in Fig. 6 and for the case where both parameters were optimized, respectively. This shows that the binding energy is much better determined by these data than is $g^{\ddagger}$. The values of ΔE_0^0 and $g^{\ddagger}$ obtained by optimizing both parameters for each alkyne, using the same parameters to describe the 295 and 325 K data, are summarized in Table 3. Also given in Table 3 are the fitted values of k_{r0} and $k_{r\infty}$. The fits to the data are shown in Figs. 3–5.

In the calculations for the Ni + C_2H_2 reaction, the vibrational frequencies and structural parameters for Ni[C_2H_2] were taken from the results of density functional calculations described in Sect. 4.E. The vibrational frequencies and moment of inertia of C_2H_2, needed for the calculation of the equilibrium constant, were taken from the JANAF thermochemical tables (27). A different approach was required for the reactions involving propyne and 2-butyne, because explicit calculations of vibrational frequencies and equilibrium structures are not available for these Ni–alkyne complexes. In these cases two models were considered for each complex, models I and II. These were chosen to represent opposite extremes in their effects on the parameter ΔE_0^0, and descriptively represent relatively loose (model I) and tight (model II) vibrational frequencies for the complex. For simplicity, in both models the vibrational frequencies of the free ligand molecules (28) were assumed to be unperturbed in the complex, and the vibrations of the nickel atom relative to the ligand were described by a single, doubly degenerate frequency, designated $\bar{\omega}$. In both Ni[propyne] and Ni[2-butyne] the number of methyl torsional modes exceeds by one the number present in the respective free ligand molecule (0 in propyne and 1 in 2-butyne). Models I and II differed in the treatment of these torsional modes and in the assumed value of the frequency $\bar{\omega}$. In model I the torsions were treated as free rotors and $\bar{\omega}$ was assigned the relatively low value 300 cm^{-1}, and in model II the torsions were treated as vibrations, with frequency corresponding to 300 cm^{-1}, and $\bar{\omega}$ was assigned the relatively high value 500 cm^{-1}. In all cases

Can. J. Chem. Downloaded from www.nrcresearchpress.com by 195.246.54.202 on 09/08/12
For personal use only.

Can. J. Chem. Downloaded from www.nrcresearchpress.com by 195.246.54.202 on 09/08/12
For personal use only.

the geometry of the complex was chosen to resemble as closely as possible the calculated equilibrium geometry of Ni[C_2H_2] (Sect. 4.E). The vibrational frequencies and moments of inertia used in the RRKM calculations are given in Appendix B. In Table 3, the parameters $g^{\ddagger}$ and ΔE_0^0 are given for calculations using models I and II for the propyne and 2-butyne reactions. The fits to the data shown in Figs. 4 and 5 were obtained using model II in both cases.

The relationship between the parameter $g^{\ddagger}$ and the apparent value of the high-pressure rate constant, $k_{r\infty}$ in Table 3, is as follows: $k_{r\infty} = g^{\ddagger} \times k_{\infty}$, where k_{∞} is the high-pressure rate constant for reaction only on the ground state potential surface. As noted in the previous section, k_{∞} was calculated assuming a loose transition state, and is therefore given approximately by a capture rate multiplied by the ratio of electronic partition functions of the complex and separated reactants. The capture rate may be estimated in a straightforward manner form the polarizabilities of Ni and the alkyne reactant (9). In the RRKM calculations, this capture rate was approximately reproduced as the variationally minimized rate constant (26) for the specified long-range potential. Details are given in Appendix B.

4.D. Binding energies

There are several sources of uncertainty in the binding energies of the Ni[alkyne] complexes obtained by modeling the kinetic data using RRKM calculations. In the first place there are uncertainties in the details of the molecular models, including particularly the vibrational frequencies. This is illustrated by the differing binding energies obtained by using models I and II for the propyne and 2-butyne reactions, as shown in Table 3. The model I and model II results are seen to differ by $\approx$6 kcal mol^{-1} in both cases. From these results it is estimated that there is an error of at least $\pm$3 kcal mol^{-1} in the binding energies of these complexes due to uncertainty in the molecular models. The situation is different for the Ni[C_2H_2] complex, because in this case there are available theoretical predictions of vibrational frequencies, and, as discussed in Sect. 4.E, the predicted frequencies are in excellent agreement with experimental data from matrix-isolation studies. An estimate of the associated uncertainty in the binding energy may nevertheless be made by allowing for a systematic error of $\pm$5% in all calculated frequencies. This would lead to an error of $\pm$2 kcal mol^{-1} in the binding energy for Ni[C_2H_2].

Even in the case where structural parameters and vibrational frequencies of the Ni[alkyne] complexes are accurately known, the RRKM calculations may lead to incorrect binding energies because of insufficient knowledge or limitations of the method of calculation of other factors, including particularly collisional energy transfer parameters. We assume that the fundamental assumptions of RRKM theory are valid for the reactions considered. Evidence in support of this assumption for the case of the Ni + C_2H_4 association reaction has been described elsewhere (9). The most significant limitation of the method of calculation is thought to be associated with the collision efficiency factor β_c. This is because the low-pressure rate constant k_{r0} is directly proportional to β_c, and there are no well-established methods for the calculation of this quantity (26). It may be noted, however, that the calculated collision efficiency factors for CO_2 buffer gas, $\beta_c \approx 0.4$ (see Appendix B), appear reasonable in comparison with many studies of unimolecular reactions (26). For the purpose of error estimation, we have assumed that the methods used are capable of calculating k_{r0} to within a factor of 2 (26). This corresponds to contributions to the uncertainties in the estimated binding energies of approximately $\pm$5, $\pm$3, and $\pm$2 kcal mol^{-1}, for the complexes with ethyne, propyne, and 2-butyne, respectively.

As noted in the previous section, the parameters ΔE_0^0 and $g^{\ddagger}$ obtained from the fits to the data are to some extent correlated. In addition, there are uncertainties and scatter in the data, and both of these effects contribute to the uncertainty in the binding energies. By performing fits to the data of the type illustrated in Fig. 6, these contributions have been estimated as $\pm$1, $\pm$3, and $\pm$3 kcal mol^{-1}, for the complexes with ethyne, propyne, and 2-butyne, respectively. An additional source of uncertainty is due to the involvement of excited electronic states of the complexes in the association reactions, and their possible contributions to the low-pressure rate constants. It was noted in Sect. 4.B that, if the excited states are much less strongly bound than the ground state, then these contributions are expected to be negligible, even though the effect on the *high*-pressure rate constant may be large. The theoretical results in Sect. 4.E indicate that the assumption of relatively weakly bound excited states is justified. RRKM calculations were performed using simple models for the triplet states of the complexes, based on the theoretical results in Sect. 4.E. For triplet state binding energies as high as 16 kcal mol^{-1}, the contributions to the observed low-pressure rate constants were found to be negligible. It therefore appears reasonable to disregard this source of uncertainty in the binding energies. If this were not justified, then the estimated binding energies would tend to be too high. By propagating the above-mentioned estimates of relative uncertainties, and considering the results in Table 3, the following estimates of binding energies were obtained: $\Delta E_0^0 = 46 \pm 6$, 37 ± 5, and 29 ± 5 kcal mol^{-1}, for Ni[C_2H_2], Ni[propyne], and Ni[2-butyne], respectively.

Our results therefore show a distinct trend to lower binding energy of the Ni[alkyne] complex with methyl substitution on ethyne. This trend can be understood in terms of the inductive effect of the methyl group in the free ligand molecule. In propyne and 2-butyne the methyl groups are electropositive (29), and cause a buildup of electronic charge on the unsaturated carbon atoms, relative to the charges for ethyne. This results in a destabilization of the highest occupied (π-bonding) molecular orbital and a pronounced drop in the ionization potential (eV) (30): ethyne (11.41), propyne (10.36), and 2-butyne (9.56). A similar destabilization is thought to occur for the π^*-antibonding molecular orbitals, and accounts for the near constancy of the experimentally observed $\pi \rightarrow \pi^*$ valence state transition energies among the simple alkynes (31). According to the description of the bonding mechanism of Ni[C_2H_2] discussed in the following section, an important component of the bond arises from a transfer of charge from a *d*-orbital on nickel to the π^*-orbital of ethyne. Such a transfer of charge should be relatively disfavored for propyne, and more so for 2-butyne, because of the polarization of electronic charge in the alkyne due to the inductive effect of the methyl group.

It is interesting to note that the trend in the binding energies of the Ni–alkyne complexes is opposite to the trend found for the corresponding Cu–alkyne complexes (32). Thus, the binding energies of the copper complexes increase with methyl substitution on ethyne. Note, however, that the copper complexes are much less strongly bound ($\approx$8 kcal mol^{-1}) (32). The weaker binding correlates with a reduced importance

Can. J. Chem. Downloaded from www.nrcresearchpress.com by 195.246.54.202 on 09/08/12
For personal use only.

TABLE 4. Total energy (hartrees) and equilibrium geometry of ethyne and of the lowest singlet and triplet states of the nickel–ethyne complex (bond lengths in Å, angles in degrees)

	Ethyne[a]	
	LSD	BP
R(CC)	1.212	1.216
R(CH)	1.080	1.075
Energy[b]	−76.59923	−77.33397
	Singlet Ni[C_2H_2]	
	LSD	BP
R(NiC)	1.790	1.823
R(CC)	1.289	1.293
R(CH)	1.094	1.091
∠CCH	151.8	151.0
Energy	−1582.07531	−1585.67248
	Triplet Ni[C_2H_2]	
	LSD	BP
R(NiC_1)	1.768	1.804
R(NiC_2)	1.897	1.962
R(CC)	1.315	1.313
R(CH_1)	1.100	1.096
R(CH_2)	1.102	1.097
∠$C_1C_2H_2$	137.5	138.9
∠$C_2C_1H_1$	146.6	147.4
Energy	−1582.01289	−1585.62034

[a]The experimental bond distances are R(CC) = 1.203 Å and R(CH) = 1.060 Å, see ref. 36.
[b]The calculated energies for the nickel atom in its triplet $3d^9 4s$ ground state are −1505.35327 (LSD) and −1508.25429 (BP).

of metal→ligand backdonation of electronic charge compared to the nickel complexes. This is shown by the trend in binding energies with methyl substitution, and also by the shifts of the CC stretching frequencies (cm^{-1}) in the infrared spectra of matrix-isolated Ni[C_2H_2] ($\Delta\omega \approx -330$) and Cu[$C_2H_2$] ($\Delta\omega \approx -100$) complexes (4), relative to the frequency for the free ethyne ligand.

4.E. Calculated properties of Ni[C_2H_2]

The ground state of Ni[C_2H_2] is a singlet ($^1A_1$) with C_{2v} geometry. The calculated binding energies for this singlet are 71 kcal mol^{-1} (LSD), 46 kcal mol^{-1} (BP/LSD), and 46 kcal mol^{-1} (BP). It is not easy to make an empirical estimate of the true binding energy on the basis of BP/LSD calculations. The BP/LSD scheme overestimates the true binding energies of Cr[CO], Ni[CO], and Cu[CO] by about 12 kcal mol^{-1}. On the other hand, BP/LSD bond energies for Cu_2 (33), $(CO)_5Cr$–CO and $(CO)_3Ni$–CO (19), and for many organic molecules (34) are within 4 kcal mol^{-1} of the experimental values. We think that comparisons of BP/LSD calculations with experiments for metal–ligand complexes are too few to establish a clear trend in the accuracy of BP/LSD bond energies for these systems. Empirical evidence from previous BP/LSD calculations only suggests that BP/LSD dissociation energies of metal–ligand complexes can either overestimate the true value (by up to 15 kcal mol^{-1}) or be very close to it, but that it probably does not underestimate it.

TABLE 5. Harmonic frequencies for five isotopomers of C_2H_2 obtained from density functional (BP) calculations and from analysis of experimental data. The numbers in parentheses are the calculated infrared intensities (km/mol)

Frequencies (cm^{-1})		Isotopic shifts (cm^{-1})	
Calcd.	Expt.[a]	Calcd.	Expt.
	HCCH		
540 (0)[b]	624		
730 (108)	747		
2016 (0)	2011		
3360 (90)	3415		
3456 (0)	3497		
	HCCD		
467 (6)	528	73	96
663 (78)	693	67	54
1882 (2)	1884	134	127
2625 (29)	2656	735	759
3414 (38)	3460	42	37
	DCCD		
449 (0)	520	91	104
536 (59)	548	194	199
1786 (0)	1790	230	221
2467 (48)	2508	893	907
2758 (0)	2779	698	718
	$H^{13}C^{13}CH$		
536 (0)	619	4	5
730 (108)	746	0	1
1983 (0)	1978	33	33
3354 (89)	3410	6	5
3444 (1)	3485	12	12
	$H^{13}C^{13}CH$		
532 (0)	615	8	9
729 (108)	744	1	3
1950 (0)	1945	66	66
3350 (89)	3405	10	10
3430 (0)	3472	26	25

[a]See ref. 35.
[b]The harmonic frequencies calculated by the LSD method for HCCH are 561, 718, 2032, 3337, and 3438 cm^{-1}.

The geometry of the ethyne ligand relaxes upon bonding to nickel (see Table 4). As expected, the CC bond length increases (by 0.08 Å), the CH bond length remains almost unchanged, and the CH bonds move out of the CC axis and away from the nickel atom (by 29°). A LCGTO–DF–(BP/LSD) calculation shows that this distortion on the isolated ethyne molecule increases its energy by 16 kcal mol^{-1}.

The lowest triplet state ($^3A''$) is bound but is much less stable, the binding energies being 33 kcal mol^{-1} (LSD), 14 kcal mol^{-1} (BP/LSD), and 14 kcal mol^{-1} (BP). The equilibrium geometry of this triplet is planar but only has C_s symmetry, one of the nickel–carbon interatomic distances being about 0.15 Å larger than the other.[3] The Kohn–Sham orbital energies suggest that there may be two other triplet states stable relative to

[3]In their study of triplet nickel–ethene, Pápai et al. (ref. 10) found that the equilibrium geometry is sensitive to the accuracy of the integration grid. Our present optimized geometry for the triplet state of nickel–ethyne may not be very precise, but there is little doubt that it has C_s symmetry.

TABLE 6. Harmonic frequencies (cm^{-1}) and infrared intensities (km/mol, in parentheses) calculated with gradient corrections (BP) for five isotopomers of NiC_2H_2 in the singlet ground state; assigned observed fundamentals are shown in brackets below the corresponding calculated values

Mode[a]	NiC_2H_2	$NiC^{13}CH_2$	$Ni^{13}C_2H_2$	NiC_2DH[b]	NiC_2D_2
NiC asy s + CH ip b	541 (13) [545][c]	534 (12) [536]	527 (11) [530]	479 (17)	462 (20)
NiC sym s + CH op b	585 (1)	582 (1)	577 (1)	496 (15)	478 (11)
NiC sym s	596 (2)	590 (2)	585 (2)	575 (3)	505 (2)
CH op b	661 (81) [657]	658 (81) [655]	657 (80) [653]	618 (49)	500 (39) [506]
CH sym ip b	801 (0)	797 (2)	795 (0)	687 (8)	670 (1)
CH asy ip b	825 (81) [844]	820 (79) [838]	813 (82) [833]	816 (52) [829]	709 (36) [717]
CC s	1655 (14) [1640]	1626 (14) 1692.4][d] [1590.7]	1597 (13) [1563]	1592 (13) [1576]	1538 (11) [1534]
CH asy s	3168 (4)	3162 (4)	3159 (4)	2396 (3)	2324 (3)
CH sym s	3217 (1)	3210 (1)	3201 (0)	3197 (3)	2466 (3)
C_2H_2: CH b	731 (108) [730.9]	730 (108) [729.5]	729 (108) [728.5]	664 (78) [675.9]	537 (59) [548.4] [542.9]

[a]Abbreviations used: asy = asymmetric, sym = symmetric, s = stretch, b = bend, ip = in-plane, op = out-of-plane. The description of the modes refers to NiC_2H_2 but also applies fairly well to the other four isotopomers. When a mode has important contributions from two internal coordinates, the most important contributor is given first.

[b]For NiC_2DH the description of some normal modes differs from that in the four other cases. The descriptions are as follows:

479 cm^{-1}: NiC_D stretch, where C_D is the carbon atom bonded to deuterium.
496 cm^{-1}: NiC asymmetric stretch with some CD out-of-plane bend.
575 cm^{-1}: NiC_H stretch, where C_H is the carbon atom bonded to hydrogen.
618 cm^{-1}: CH out-of-plane bend.
687 cm^{-1}: CD in-plane bend.
816 cm^{-1}: CH in-plane bend.
1592, 2396, 3197: similar to the other isotopomers with H changed to D where appropriate.

[c]Experimental frequencies are taken from ref. 4.

[d]In agreement with Kline et al., we think that this band and the one at 1590.7 cm^{-1} arise from the combination of the fundamental of the CC stretch and first overtone of the CH asymmetric in-plane bend.

dissociation and having approximate BP binding energies of 11 and 2 kcal mol^{-1}.

Since vibrational frequencies are key quantities in the RRKM modeling, it is important to assess the reliability of the frequencies we calculated. A detailed comparison of frequencies calculated by the LCGTO–DF method with experiment has been done for the nickel–ethene complex (10). It showed that the LCGTO–DF frequencies of $Ni[C_2H_4]$ are within a few percent of experimental values and that IR intensities, while in error by typically 40%, are accurate enough to help assign IR spectra.

In Table 5 we show our calculated harmonic frequencies for five isotopomers of ethyne and a set of harmonic frequencies deduced from experimental data (35). The calculated frequencies and intensities for HCCH are qualitatively correct. The average percent error on the calculated frequencies is only 3.8% and most of this error comes from the lowest CCH bending mode. The isotopic shifts are also qualitatively correct but the error for the two lowest frequency modes of HCCD is about 25%. The CC stretch frequency and all its isotopic shifts are remarkably well reproduced by the calculations. The CH stretches and isotopic shifts are very good. Not unexpectedly, the largest errors occur for the two relatively low-frequency bending modes. If we compare our calculated frequencies with the experimental fundamentals (36) instead, the overall agreement for HCCH is just as good while the agreement for the isotopic shifts deteriorates slightly.

Now we compare our calculated frequencies for the nickel–ethyne complex to the infrared bands observed by Kline et al. in a matrix isolation study (4). Note that Kline et al. observed groups of closely spaced lines instead of sharp lines, possibly due to interaction with the matrix. In our table we show only the average value of the close-lying lines seen in the experiment. In Table 6 we list the calculated harmonic frequencies and IR intensities (in parentheses); the positions of the bands observed by Kline et al. are shown in square brackets underneath the calculated ones. There are two differences between our assignment and the one given in ref. 4. First, we assign the 657 cm^{-1} band in $Ni[C_2H_2]$ (and related bands in the other isotopomers) to a CH symmetric out-of-plane bend, not to a CH in-plane bend. Second, we do not find a mode in $Ni[C_2H_2]$ with wavenumber near 730 cm^{-1} and appreciable intensity (the CH symmetric in-plane bend has near-zero intensity) and therefore we tentatively assign this band (and the related ones in other isotopomers) to the intense CH bend of unreacted ethyne. With the exception of the calculated 618 cm^{-1} band of NiC_2HD, we find observed bands corresponding to each of the modes with calculated frequency larger than 500 cm^{-1} and intensity larger than 10 km mol^{-1}. Conversely, we can relate almost every group of observed bands to calculated fre-

Can. J. Chem. Downloaded from www.nrcresearchpress.com by 195.246.54.202 on 09/08/12
For personal use only.

Can. J. Chem. Downloaded from www.nrcresearchpress.com by 195.246.54.202 on 09/08/12
For personal use only.

quencies with appreciable intensity. Overall, the agreement between calculated and observed wavenumbers is excellent, but one should bear in mind that the harmonic approximation may partly cancel other sources of error. The important point, however, is that calculated frequencies are qualitatively correct and within a few percent of the observed values. Moreover, if the assignments are correct, the frequency shifts with isotopic substitutions are typically within 10 or 20% of those observed.

In Table 7 we list the set of frequencies and infrared intensities for the singlet and triplet states calculated with the LSD and BP methods. Similar to what was found for nickel–ethene (10), the bands are generally more intense in the triplet state than in the singlet ground state. Adding gradient corrections to the exchange-correlation has a modest effect on the harmonic frequencies although the lower frequencies usually decrease by a few percent. If we ignore the low-intensity modes, for which the calculated values are not very reliable, the effect of gradient corrections on intensities in the singlet state is small. In the triplet state, the effect of gradient corrections on the intensity of the two nickel–carbon stretches is large. Although the LSD and BP equilibrium geometries differ significantly, the BP/LSD and BP binding energies are within 1 kcal mol^{-1} of each other.

The bonding in singlet $Ni[C_2H_2]$ is mostly due to a donation–backdonation mechanism involving the bonding and antibonding π orbitals of ethyne in the plane of the complex and a nickel d orbital. The number of electrons donated to the metal (n_D) and backdonated to the ligand (n_B) are essentially identical to those found for the nickel–ethene complex: $n_D \approx 0.28$ and $n_B \approx 0.56$. The orbital energy differences between the predominantly CC π bonding orbital with nickel d admixture and the predominantly nickel d orbital with CC π^*-antibonding admixture are also very similar: 1.69 eV for the nickel–ethyne complex and 1.78 eV for nickel–ethene. It is not easy to rationalize the somewhat larger binding energy of nickel–ethyne compared to nickel–ethene (the calculated values are 46 and 40 kcal mol^{-1}, respectively, see ref. 10) on the basis of the calculations. The bonding mechanism and extent of donation and backdonation are similar in the two complexes. One factor does clearly favor a sightly larger binding energy in nickel–ethyne: the mixing of the nickel $4p_y$ orbital into the out-of-plane ethyne π bonding orbital. The Mulliken population of the nickel $4p_y$ orbital is 0.08 in $Ni[C_2H_2]$ whereas it is zero in $Ni[C_2H_4]$ since it cannot mix effectively with any orbital of ethene.

The bond order for each of the nickel–carbon bonds is 0.90 while the CC bond order is decreased from its value of 2.96 in ethyne to 1.76. The decrease in CC bond strength is mostly due to π backdonation from the d_{xz} orbital of nickel into the in-plane $C(2p_z)$—$C(2p_z)$ π^*-antibonding orbital of ethyne.

The three lowest energy valence orbitals of the complex are essentially unperturbed orbitals of ethyne, the CC $2s$ σ-bonding orbital and two CH bond orbitals. The next two lowest are the bonding π orbitals of ethyne with roughly 15% admixtures of nickel s and d_{zz} orbitals (for the in-plane, orbital energy $\epsilon = -8.3$ eV) and nickel d_{yz} and $4p_y$ (for the out-of-plane, $\epsilon = -7.8$ eV). These two orbitals are less CC bonding than in ethyne and are bonding between the nickel and carbon atoms. The next orbital ($\epsilon = -6.6$ eV) has 70% nickel d_{xz} character and 25% CC in-plane antibonding π character. It contributes to the nickel–carbon bond and weakens the carbon–carbon bond. The next three orbitals, with energies −5.0, −4.7, and −4.4 eV, are essentially nonbonding nickel d orbitals with some nickel $4s$ character. The next orbital, which is the HOMO, has energy −4.2 eV and is roughly 80% nickel d_{yz} with a 20% contribution from the ethyne out-of-plane π-bonding orbital: it is antibonding between nickel and carbon. The LUMO has an energy of −2.7 eV and is an *spd* hybrid centered almost entirely on the nickel atom.

TABLE 7. Harmonic frequencies (cm^{-1}) and infrared intensities (km/mol, in parentheses) calculated for the lowest singlet and triplet states of the nickel–ethyne complex

	Singlet	
Mode	LSD	BP
NiC asy s[a]	564 (16)	541 (13)
CH op b	595 (1)	585 (1)
NiC sym s	628 (4)	596 (2)
CH op b	656 (86)	661 (81)
CH sym ip b	804 (1)	801 (0)
CH asy ip b	834 (75)	825 (81)
CC s	1678 (10)	1655 (14)
CH s	3166 (13)	3168 (4)
CH s	3217 (4)	3217 (1)
	Triplet	
Mode	LSD	BP
NiC_2 s[b] + C_2H ip b	382 (303)	342 (150)
CH asy op b	513 (92)	525 (93)
CH sym ip b	564 (592)	508 (644)
NiC_1 s	643 (16)	623 (73)
CH sym op b	807 (2)	773 (3)
CH asy ip b	898 (118)	871 (137)
CC s	1462 (664)	1468 (591)
CH s	3065 (12)	3087 (10)
CH s	3111 (5)	3129 (12)

[a]See footnote to Table 6 for the meaning of the abbreviations.

[b]C_2 is the carbon atom furthest from the nickel atom, C_1 is the nearest.

The bonding in the triplet state differs from the above description. Although the triplet is much less stable than the singlet, the sum of the two nickel–carbon bond orders is 1.89, compared to 1.80 for the singlet state. The nickel $4p$ population is 0.27 (it is 0.11 in the singlet) most of which is in the majority spin HOMO orbital, an *spd* hybrid on nickel with some ethyne π^* character. This hybrid orbital is centred mostly on nickel and points away from the carbon atom furthest from it. This polarization of the nickel atom offsets the partial atomic charges and, as a result, the dipole moment in the triplet has its positive end pointing toward the carbon atom furthest from nickel. This is contrary to the singlet state in which the dipole moment is "normal" (the positive end is on the nickel atom). These characteristics show that the smaller binding energy of the triplet can be attributed to a larger repulsion of the nickel $4s$ orbital with the in-plane π orbital of ethyne. In the singlet state, hybridization of the nickel s and d orbitals reduces this repulsive interaction. This mechanism is not possible in the triplet state and, instead, the $4s$ orbital of nickel is hybridized with the $4p$ orbital. This is reminiscent of the situation in NiCO (37) and, more generally, in high-spin transition metal

monocarbonyls (22). The C_{2v} to C_s distortion in going from the singlet to the triplet state of nickel–ethyne can also be put in parallel with the linear and bent geometries of low-spin and high-spin transition metal monocarbonyls (22). It is tempting to invoke the same explanation, namely, the decrease in σ repulsion upon "bending". Finally, the energy differences between the singlet and triplet states of nickel–ethyne and nickel–carbonyl complexes are also similar: 32 and 36 kcal mol^{-1}, respectively.

5. Conclusion

Nickel atoms form strongly bound π complexes with simple alkynes. Kinetic studies show that there is no activation energy for bond formation, and indicate that both the ground state and one or more excited electronic states of the complex take part in the association reaction. The binding energies of Ni[C_2H_2], Ni[propyne], and Ni[2-butyne] have been estimated by using unimolecular reaction theory to model kinetic data for the association reactions. There is a distinct trend to lower binding energy with methyl substitution on ethyne. This trend is opposite to the one found in previous work on copper–alkyne complexes, and has been explained by considering the influence of the inductive effect of the methyl group on the extent of metal→ligand backdonation in the complex. Quantum chemical calculations using a LCGTO–DF method indicate that the electronic structure of Ni[C_2H_2] is very similar to that of Ni[CO] and Ni[C_2H_4]. This is consistent with experimental results that show these complexes have similar binding energies. Harmonic vibrational frequencies calculated using the LCGTO–DF method for the $^1A_1$ ground state of Ni[C_2H_2] in several isotopic variants are in good agreement with fundamental frequencies observed in the infrared spectra of matrix-isolated Ni[C_2H_2]. When the calculated equilibrium structure and vibrational frequencies of Ni[C_2H_2] are used in the unimolecular reaction theory calculations to estimate the binding energy of Ni[C_2H_2] from kinetic data, there is excellent agreement between the experimental estimate and the theoretically predicted binding energy.

1. M.P. Lapinski and J.G. Ekerdt. J. Phys. Chem. **94**, 4599 (1990), and references cited therein.
2. P.W. Jolly and G. Wilke. The organic chemistry of nickel. Vol. 1. Academic Press, New York. 1974.
3. G.A. Ozin, D.F. McIntosh, W.J. Power, and R.P. Messmer. Inorg. Chem. **20**, 1782 (1981).
4. E.S. Kline, Z.H. Kafafi, R.H. Hauge, and J.L. Margrave. J. Am. Chem. Soc. **109**, 2402 (1987).
5. H. Huber, G.A. Ozin, and W.J. Power. J. Am. Chem. Soc. **98**, 6508 (1976).
6. T. Merle-Mejean, C. Cosse-Mertens, S. Bouchareb, F. Galan, J. Mascetti, and M. Tranquille. J. Phys. Chem. **96**, 9148 (1992).
7. (*a*) P.-O. Widmark, B.O. Roos, and P.E.M. Siegbahn. J. Phys. Chem. **89**, 2180 (1985); (*b*) P.-O. Widmark, G.J. Sexton, and B.O. Roos, J. Mol. Struct. **135**, 235 (1986).
8. C.E. Brown, S.A. Mitchell, and P.A. Hackett. Chem. Phys. Lett. **191**, 175 (1992).
9. S.A. Mitchell. Int. J. Chem. Kinet. **26**, 97 (1994).
10. I. Pápai, J. Mink, R. Fournier, and D.R. Salahub. J. Phys. Chem. **97**, 9986 (1993).
11. S.A. Mitchell. *In* Gas-phase metal reactions. *Edited by* A. Fontijn. Elsevier, Amsterdam. 1992. pp. 227–252.
12. C.E. Brown, M.A. Blitz, S.A. Decker, and S.A. Mitchell. ACS Symp. Ser. **530**, 177 (1993).
13. A. St-Amant and D.R. Salahub. Chem. Phys. Lett. **169**, 387 (1990); A. St-Amant. Thèse de doctorat, Université de Montréal, 1992.
14. D.R. Salahub, R. Fournier, P. Mlynarski, I. Pápai, A. St-Amant, and J. Ushio. *In* Proceedings of the Ohio Supercomputer Center Workshop on the theory and applications of density functional theory to chemistry, Columbus, Ohio. May 7–9, 1990. *Edited by* J. Labanowsky and J. Andzelm. Springer Verlag, New York. 1991.
15. S.H. Vosko, L. Wilk, and M. Nusair. Can. J. Phys. **58**, 1200 (1980).
16. A.D. Becke. Phys. Rev. A, **38**, 3098 (1988).
17. J.P. Perdew. Phys. Rev. B, **33**, 8822 (1986).
18. J.P. Perdew, J.A. Chevary, S.H. Vosko, K.A. Jackson, M.R. Pederson, D.J. Singh, and C. Fiolhais. Phys. Rev. B, **46**, 6671 (1992).
19. L. Fan and T. Ziegler. J. Phys. Chem. **96**, 6937 (1992).
20. A.D. Becke. J. Chem. Phys. **97**, 9173 (1992).
21. F.W. Kutzler and G.S. Painter. Phys. Rev. B, **43**, 6865 (1991).
22. R. Fournier. J. Chem. Phys. **99**, 1801 (1993).
23. L.A. Barnes, M. Rosi, and C.W. Bauschlicher, Jr. J. Chem. Phys. **94**, 2031 (1991).
24. J. Sugar and C. Corliss. J. Phys. Chem. Ref. Data, **14**, Suppl. No. 2 (1985).
25. J. Troe. Ber. Bunsen-Ges. Phys. Chem. **87**, 161 (1983).
26. R.G. Gilbert and S.C. Smith. Theory of unimolecular and recombination reactions. Blackwell, Oxford. 1990.
27. JANAF Thermochemical Tables. 3rd ed. Dow Chemical Company, Midland, Mich. J. Phys. Chem. Ref. Data, **14**, Suppl. No. 1 (1985).
28. J.L. Duncan. Spectrochim. Acta, **20**, 1197 (1964).
29. A.F. Marchington, S.C.R. Moore, and W.G. Richards. J. Am. Chem. Soc. **101**, 5529 (1979).
30. R.S. Stradling, M.A. Baldwin, A.G. Loudon, and A. Maccoll. J. Chem. Soc. Faraday Trans. 2, **72**, 871 (1976).
31. W.M. Flicker, O.A. Mosher, and A. Kuppermann. J. Chem. Phys. **69**, 3311 (1978).
32. M.A. Blitz, S.A. Mitchell, and P.A. Hackett. J. Phys. Chem. **97**, 5298 (1993).
33. A.D. Becke. ACS Symp. Ser. **394**, (1989).
34. J. Andzelm and E. Wimmer. J. Chem. Phys. **96**, 1280 (1992).
35. G. Strey and I.M. Mills. J. Mol. Spectrosc. **59**, 103 (1976).
36. G. Herzberg. Molecular spectra and molecular structure II: infrared and Raman spectra of polyatomic molecules. Krieger, Malabar, Fla. 1991.
37. M.R.A. Blomberg, U.B. Brandemark, P.E.M. Siegbahn, K.B. Mathisen, and G. Karlström. J. Phys. Chem. **89**, 2171 (1985).
38. K.-H. Hellwege (*Editor*). Landolt-Börnstein, Group II, Vol. 7. Structure data of free polyatomic molecules. Springer-Verlag, Berlin. 1976.
39. R. Cambi, D. Cappelletti, G. Liuti, and F. Pirani. J. Chem. Phys. **95**, 1852 (1991).
40. M.R.A. Blomberg, U.B. Brandemark, and P.E.M. Siegbahn. Chem. Phys. Lett. **126**, 317 (1986).
41. R.C. Weast (*Editor*). CRC Handbook of Chemistry and Physics. 69th ed. CRC Press, Boca Raton, Fla. 1988. p. E-73.
42. N. Godbout, D.R. Salahub, J. Andzelm, and E. Wimmer. Can. J. Chem. **70**, 560 (1992).
43. W.J. Hehre, L. Radom, P.v.R. Schleyer, and J.A. Pople. Ab initio molecular orbital theory. Wiley, New York. 1986.

Appendix A: Basis sets

The orbital basis set used for nickel was devised by Godbout et al. (42) and those for carbon and hydrogen are essentially those given in ref. 43. The exponents and coefficients for orbital basis sets are given below in the format: ("exponent 1 of function 1": "coefficient 1 of function 1"; "exponent 2 of function 1"...), ("exponent 1

Can. J. Chem. Downloaded from www.nrcresearchpress.com by 195.246.54.202 on 09/08/12
For personal use only.

of function 2": "coefficient 1 of function 2"; ...) etc ... Auxiliary basis sets are uncontracted, only the exponents are listed below.

Orbital basis sets

Nickel (63321/5211/311)

s: (72509.04: 0.00172075; 10879.18: 0.01316375; 2471.646: 0.06565671; 695.826: 0.2259027; 225.375: 0.4689157; 77.24016: 0.3672841), (150.3641: 0.1061215; 17.33109: −0.6228997; 7.048855: −0.4512631), (13.0064: −0.219559; 2.068282: 0.711174; 0.7963434: 0.4199687), (1.140761: 0.1345042; 0.1364956: −0.579118), (0.04864015: 1.0) *p*: (925.3782: 0.0089808; 218.3792: 0.06725683; 69.0759: 0.2587199; 24.79419: 0.506708; 9.117727: 0.3412531), (4.886556: 0.3302654; 1.852057: 0.5465753), (0.6748905: 1.0), (0.1351: 1.0) *d*: (29.22966: 0.06539529; 7.878914: 0.286013; 2.386116: 0.4971564), (0.6282437: 1.0), (0.104: 1.0)

Carbon (6311/311/1)

s: (3047.525: 0.001834737; 457.3695: 0.01403732; 103.9487: 0.06884262; 29.1016: 0.2321844; 9.286663: 0.4679413; 3.163927: 0.362312), (8.1830029: −0.1193324; 1.9565406: −0.1608542; 0.5660193: 1.143456) (0.1622254: 1.0), (0.0438: 1.0) *p*: (8.1830029: 0.06899907; 1.9565406: 0.316424; 0.5660193: 0.7443083), (0.1622254: 1.0), (0.0438: 1.0) *d*: (0.8: 1.0)

Hydrogen (311/1)

s: (14.95889: 0.034946; 2.2563909: 0.234727; 0.5112084: 0.8137573), (0.1219492: 1.0), (0.036: 1.0) *p*: (1.1: 1.0)

Charge density fit basis sets

Nickel

s: 62500.0; 12500.0; 3100.0; 780.0; 195.0

s, *p*, and *d*: 61.0; 12.2; 3.04; 0.76; 0.19

Carbon

s: 1500.0; 330.0; 94.3; 27.0

s, *p*, and *d*: 9.92; 2.2; 0.63; 0.18

Hydrogen

s: 70.0; 10.0; 2.0; 0.2

s, *p*, and *d*: 0.7; 0.04

Exchange-correlation potential fit basis sets

Nickel

s: 20800.0; 4170.0; 1033.0; 260.0; 65.0

s, *p*, and *d*: 20.3; 4.07; 1.01; 0.253; 0.063

Carbon

s: 500.0; 110.0; 31.4; 9.0

s, *p*, and *d*: 3.3; 0.73; 0.21; 0.06

Hydrogen

s: 25.0; 3.0; 0.7; 0.07

s, *p*, and *d*: 0.2; 0.015

Appendix B: Details of RRKM calculations

Program and options

All calculations were performed using the UNIMOL suite of FORTRAN programs (26). The calculations included angular momentum conservation in the falloff region. The intermolecular potential for the buffer gas CO_2 and Ni[alkyne] complex was specified by Lennard–Jones parameters σ and ϵ. These were estimated by using the methods described by Gilbert and Smith (26), taking 16.3 Å^3 as the additive volume increment associated with Ni, and taking the ϵ associated with Ni[alkyne] to be the same as the value estimated for the alkyne by using the boiling point of the alkyne. This led to σ/Å = 4.50, 4.75, and 4.97, and ϵ/K = 177, 213, and 233, for the reactions with C_2H_2, propyne, and 2-butyne, respectively. Weak collision effects were included by running the MASTER segment of the program, using the exponential-down form of the energy transfer distribution function, and taking 500 cm^{-1} as the average downward energy transfer. This led to calculated values of the collision efficiency $\beta_c \cong 0.49$, 0.40, and 0.37, for the reactions with C_2H_2, propyne, and 2-butyne, respectively.

Vibrational frequencies (cm^{-1}) and moments of inertia (amu Å^2)

Degeneracies are shown in parentheses. *C_2H_2* (cm^{-1}) (ref. 27): 3374, 1974, 3282, 612 (2), 729 (2); *C_2H_2* (amu Å^2) (27): 14.32, $\sigma = 2$; *Ni[C_2H_2]* (cm^{-1}) (Table 7): 3217, 3168, 1655, 825, 801, 596, 661, 585, 541; *Ni[C_2H_2]* (amu Å^2) (from data in Table 4): 70.73, 55.50, 15.22, $\sigma = 2$; *propyne* (cm^{-1}) (28): 3334, 2920, 2142, 1382, 931, 3008 (2), 1452 (2), 1053 (2), 633 (2), 328 (2); *propyne* (amu Å^2) (ref. 38): 59.21, 59.21, 3.281,

Can. J. Chem. Downloaded from www.nrcresearchpress.com by 195.246.54.202 on 09/08/12
For personal use only.

$\sigma = 3$; *Ni[propyne], model I* (cm^{-1}): propyne frequencies + 300 (2) + free rotor with $B = 6.49$ cm^{-1} and $\sigma = 3$; *Ni[propyne], model II* (cm^{-1}): propyne frequencies + 500 (2) + 300; *Ni[propyne]* (amu Å^2): 168.1, 136.3, 35.09, $\sigma = 1$; *2-butyne* (cm^{-1}) (ref. 28): 2916, 2240, 1380, 725, 2915, 1382, 1152, 2973(2), 1456(2), 1054(2), 213(2), 2966(2), 1448(2), 1029(2), 371(2) + free rotor with $B = 10.23$ cm^{-1} and $\sigma = 3$; *2-butyne* (amu Å^2) (ref. 38): 152.3, 152.3, 6.591, $\sigma = 6$; *Ni[2-butyne], model I* (cm^{-1}): 2-butyne frequencies + 300 (2) + two free rotors with $B = 5.68$ cm^{-1} and $\sigma = 3$; *Ni[2-butyne], model II* (cm^{-1}): 2-butyne frequencies + 500 (2) + 300 (2); *Ni[2-butyne]* (amu Å^2): 271.5, 141.1, 136.9, $\sigma = 2$.

High-pressure rate constants

The transition states for the association reactions were taken to be in the phase space limit, with unperturbed ligand molecules undergoing free rotation at a distance of ≈6 Å from the nickel atom. The parameter used to describe the Morse potential for the metal–ligand interaction was adjusted in such a way that the variationally minimized high-pressure rate constant for the association reaction (not including electronic degeneracy factors) was in approximate agreement with a capture rate estimated from the C_6 parameter for the Ni–alkyne interaction. C_6 parameters were estimated (39) from the polarizabilities (Å^3) of Ni (7.9) (40), C_2H_2 (3.4) (39), propyne (5.6) (39), and 2-butyne (7.4) (41). These values led to capture rate constants of $\approx 7 \times 10^{-10}$ cm^3 s^{-1} for all reactions.

Can. J. Chem. Downloaded from www.nrcresearchpress.com by 195.246.54.202 on 09/08/12
For personal use only.

Electron spin resonance study of the reaction of hydrogen atoms with methane

PAUL-MARIE MARQUAIRE,[1] ASHOK GHOSE DASTIDAR, KIM C. MANTHORNE, AND PHILIP D. PACEY[2]

Department of Chemistry, Dalhousie University, Halifax, NS B3H 4J3, Canada

Received July 12, 1993

This paper is dedicated to Professor John C. Polanyi on the occasion of his 65th birthday

PAUL-MARIE MARQUAIRE, ASHOK GHOSE DASTIDAR, KIM C. MANTHORNE, and PHILIP D. PACEY. Can. J. Chem. **72**, 600 (1994).

The reaction: $H + CH_4 \rightarrow CH_3 + H_2$ has been investigated in a flow system between 348 and 421 K. Hydrogen atoms were generated in a microwave discharge, introduced to the reactor through a movable injector, and monitored by electron spin resonance. After an initial decay attributed to reaction with impurity, the hydrogen atom concentration decayed in a pseudo-first-order manner. Ethane was detected by gas chromatography, consistent with its formation by the following reaction: $2CH_3 \rightarrow C_2H_6$. The amount of ethane formed at 421 K was only 0.015 times the amount of hydrogen atoms reacting. Most methyl radicals were assumed to have been removed by the process: $H + CH_3 + M \rightarrow CH_4 + M$. Because of this process, two hydrogen atoms were removed each time the title reaction occurred. Applying this stoichiometric factor, the rate constant for the elementary reaction was calculated to be 2.5×10^3 L mol^{-1} s^{-1} at 348 K, increasing to 2.0×10^4 L mol^{-1} s^{-1} at 421 K. Most of the previous discrepancy between kinetics and thermochemistry has been eliminated; the exothermicity at 0 K was reduced to 0.8 ± 0.4 kJ mol^{-1}, which corresponds to a standard heat of formation of the methyl radical of 145 kJ mol^{-1}. Properties of the activation barrier have been inferred from the experimental data with the aid of transition state theory. The fitted barrier height was 63 ± 1 kJ mol^{-1}, the average of five low-frequency vibrational term values was 640 ± 30 cm^{-1}, and the characteristic tunnelling temperature was 500 ± 30 K.

PAUL-MARIE MARQUAIRE, ASHOK GHOSE DASTIDAR, KIM C. MANTHORNE et PHILIP D. PACEY. Can. J. Chem. **72**, 600 (1994).

Opérant dans un système à écoulement, à des températures allant de 348 à 421 K, on a étudié la réaction : $H + CH_4 \rightarrow CH_3 + H_2$. On a généré les atomes d'hydrogène par une décharge microonde, introduite dans le réacteur par une injecteur mobile et on les a suivis par résonance paramagnétique électronique. Après une décroissance initiale attribuée à une réaction avec une impureté, la concentration des atomes d'hydrogène diminue en suivant un pseudo-ordre un. La chromatographie gazeuse nous a permis de détecter la présence d'éthane qui se formerait par la réaction : $2CH_3 \rightarrow C_2H_6$. La quantité d'éthane qui se forme à 421 K ne correspond qu'à 0,015 fois la quantité d'atomes d'hydrogène qui réagit. On fait l'hypothèse que la plupart des radicaux méthyles sont éliminés par le processus : $H + CH_3 + M \rightarrow CH_4 + M$. Par ce processus, deux atomes d'hydrogène sont enlevés chaque fois que la première réaction se produit. En appliquant ce facteur stoechiométrique, on a pu calculer que la constante de vitesse pour la réaction élémentaire est égale à $2,5 \times 10^3$ L mol^{-1} s^{-1}, à 348 K, et qu'elle augmente jusqu'à $2,0 \times 10^4$ L mol^{-1} s^{-1}, à 421 K. On a ainsi éliminé les anciennes divergences entre la cinétique et la thermochimie; l'exothermicité à 0 K est réduite à $0,8 \pm 0,4$ kJ mol^{-1}, ce qui correspond à une chaleur de formation standard du radical méthyle de 145 kJ mol^{-1}. On a déduit les propriétés de la barrière d'activation à partir des données expérimentales et en faisant appel à la théorie de l'état de transition. La hauteur ajustée de la barrière est de 63 ± 1 kJ mol^{-1}, la moyenne de cinq valeurs pour des termes vibrationnels de basse fréquénce est de 640 ± 30 cm^{-1} et la température caractéristique de l'effet tunnel est de 500 ± 30 K.

[Traduit par la rédaction]

Introduction

The reaction

$$[1, -1] \quad H + CH_4 \rightleftarrows H_2 + CH_3$$

is important in combustion and is reasonably simple to treat theoretically. However, the reaction is controversial because the ratio of forward and reverse rate constants disagrees with the equilibrium constant calculated from accepted thermodynamic parameters (1–6). The discrepancy is a factor of six in the rate constant ratio at 372 K, or 5 kJ mol^{-1} in the enthalpy of reaction. Both the forward and reverse reactions have been studied repeatedly with no resolution to this problem. Most studies of the forward reaction at low temperature, where the disagreement with thermochemistry is clearest, have employed the flow discharge technique (7–12). Some results are presented in Table 1. However, there has been disagreement regarding the stoichiometry of the system. Some authors (8–10) assumed that hydrogen atoms were removed only by reaction [1]. Others (7) assumed reaction [1] was always followed by reaction [2]:

TABLE 1. Rate constants from the literature in the present experimental temperature range

Source	T (K)	$k_1 \times 10^{-4}$ (L mol^{-1} s^{-1})
Berlie and LeRoy (7)	372	2.4
Berlie and LeRoy (7)	412	4.4
Kurylo, Hollinden, and Timmons (10)	424	13–20
Kurylo and Timmons (9)	426	4–8

$$[2] \quad H + CH_3 + M \rightarrow CH_4 + M$$

In this article we report results of a new flow discharge study in which we attempt to address the issues above. To study the stoichiometry, we have determined absolute hydrogen atom concentrations by electron spin resonance spectrometry (ESR) and have measured the rate of ethane formation by gas chromatography. We have simulated the system by computer using recent values (13–15) of the rate constant for reaction [2] and for other secondary reactions.

Experimental

The apparatus and experimental procedure were similar to those used for an earlier study of the reaction of H with D_2(16). Methane (Linde,

[1]Permanent address: Département de chimie physique des réactions, URA 328 du CNRS, ENSIC, BP 451, 54001 Nancy, France.

[2]Author to whom correspondence may be addressed.

Can. J. Chem. Downloaded from www.nrcresearchpress.com by 195.246.54.202 on 09/08/12
For personal use only.

TABLE 2. Summary of experimental conditions and fitted rate constants

P (Torr)	v (cm s^{-1})	$[CH_4] \times 10^4$ (mol L^{-1})	$[H] \times 10^8$ (mol L^{-1})	k_3 (s^{-1})	$k_1 \times 10^{-4a}$ (L mol^{-1} s^{-1})
		421 K			
5	78	0.86	6	0.1	3.2, 2.2
6	85	0.65	15	0.8	2.1, 1.9
6	84	0.66	9	0.2	2.5, 2.0
					Avg. 2.0
		390 K			
20	112	4.9	1	2.8	0.76, 0.76
20	156	3.6	6	1.9	0.95, 1.06
					Avg. 0.91
		373 K			
25	100	5.9	6	1.1	0.58, 0.58
		363 K			
25	115	5.8	2		0.46, 0.47
		348 K			
25	98	6.1	1	0.6	0.25, 0.25
25	100	6.2	2	0.5	0.25, 0.26
30	68	9.1	1	2.3	0.24, 0.25
					Avg. 0.25

[a]The first entry in this column was obtained by the method of ref. 18; the second by a fit to eq. [5].

UHP, 99.9%, or Matheson Research, 99.99%), helium (Atlantic Oxygen Ltd., 99.996%), and hydrogen (Atlantic Oxygen Ltd., 99.99%) flowed through traps packed with molecular sieve (5 Å, 80–100 mesh) to ballast bulbs of known volumes and then to needle valves or MKS 1159B mass flow controllers. The flow rates could be determined by cutting off the flow to a bulb and observing the rate of pressure decrease with a Bell and Howell (model CEC1000) pressure transducer. The helium and hydrogen then passed through the cavity of a microwave generator (Microtron 200, Electro-Medical Supplies) and along a 7 mm o.d., cylindrical quartz injector into the reactor. The interiors of the injector and the reactor had been coated with Teflon liquid (Dupont 856-200). Above 390 K the surface rate constant on Teflon was found to increase and phosphoric acid was used in the hot part of the reactor and Teflon in the ESR cavity. The injector could be moved along the axis of the 22-mm i.d., cylindrical Pyrex reactor by passing through an o-ring seal. A 70 cm length of the reactor was surrounded by an insulated jacket connected to an external thermostatted circulating bath (Lauda, RCS-6). Two Cu–constantan thermocouples were located in wells in the jacket for temperature measurements. For experiments at 421 K the insulated jacket was replaced by an 80 cm long, 3 cm o.d. copper pipe, wrapped with mullite paper and with nichrome heating ribbon. Methane or the blank gas, He, was introduced at the upstream end of the reactor. At the downstream end was an E-235 large-access, cylindrical cavity, part of a Varian E-1096, X-band spectrometer, followed by a connection for withdrawing samples for gas chromatographic analysis, an MKS (Baratron 122AA) pressure transducer, and an MKS (model 248A) exhaust control valve, controlled by an Omega (CN-2000) pressure controller.

The experimental procedure involved setting the CH_4 and blank gas flow rates to equal values and setting the pressure controller to the desired reactor pressure. The H atom peak at 2921 G was traced with the injector at the upstream end of the jacket, first with the blank gas flowing and then with CH_4 flowing. The injector was moved successively along the reactor and sets of peaks were recorded.

The ESR spectrometer and cavity were calibrated by tracing the F and G peaks in the spectrum of O_2 with instrument settings like those in a kinetic experiment but with a measured pressure of air in the cavity. Provided the air pressure was below 3 Torr (1 Torr = 133.3 Pa), the O_2 peaks were well resolved and gave consistent calibrations. The procedure of Westenberg (17) was then used to translate measured first moments of hydrogen atom peaks to absolute concentrations of hydrogen atoms. Both O_2 and H peaks were traced at a number of instrument settings to check that the response was linear. Hydrogen atom peak widths were independent of concentration, enabling peak heights to be used for routine kinetic analysis.

Gas chromatographic analysis was performed using a 1.7 m silica gel column at 25°C with flame ionization detection.

Results

Experimental conditions are listed in Table 2. The upper limit on the pressure was set by the need to maintain low pressures and fast flow in the discharge to provide measurable hydrogen atom concentrations. The lower limit was set by the need to keep the gas phase reaction substantially greater than the wall reaction. In all cases the wall rate constant, k_3, was found from a plot of $\ln[H]_0$ against time (18). Calculation of k_1 will be described in the Discussion.

$$[3] \quad H \rightarrow \tfrac{1}{2}H_2$$

Figure 1 shows the results of two experiments at 421 K. Plotted horizontally are the residence times of the atoms in contact with methane in the hot zone of the reactor, calculated as the distance from the tip of the injector to the downstream end of the jacket or furnace, divided by the flow velocity, v. Plotted vertically is the natural logarithm of the hydrogen atom concentration observed in the ESR cavity. The points on the left-hand axis (at $t = 0$) correspond to replacement of the reactant, methane, by helium. It can be seen that at times less than about 0.2 s, the hydrogen atom concentration dropped sharply with increasing time. After about 0.2 s, the peaks fell more gradually with increasing residence time. The slopes depended on the concentration of methane in the system. At lower temperatures, there

Can. J. Chem. Downloaded from www.nrcresearchpress.com by 195.246.54.202 on 09/08/12
For personal use only.

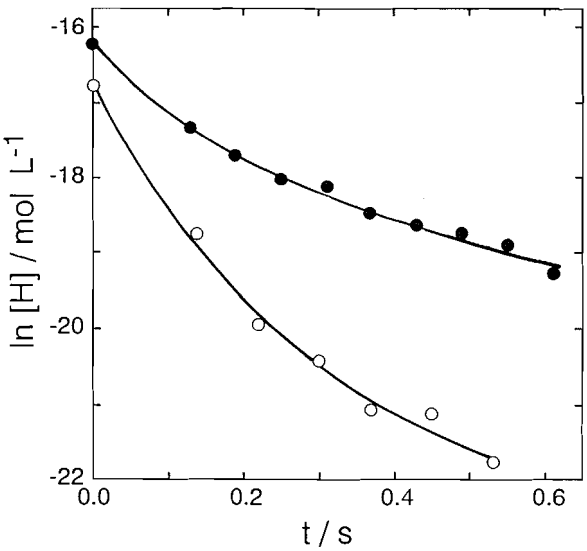

FIG. 1. Concentration of hydrogen atoms as a function of their residence time in contact with CH_4 at 421 K in two experiments: ●, $[CH_4] = 0.66 \times 10^{-4}$ mol^{-1} L^{-1}; ○, $[CH_4] = 0.86 \times 10^{-4}$ mol^{-1} L^{-1}; —, nonlinear least-squares fits of eq. [5] to the data.

TABLE 3. Comparison of electron spin resonance and gas chromatographic analyses at 421 K and 1.7 Torr of CH_4 and 4.4 Torr of He

t (s)	[H] (ppm)	$[C_2H_6]$ (ppm)	$[C_2H_6]/([H]_0 - [H])$
0	422	0	
0.13	137	4.5	0.016
0.37	42	5.7	0.015
0.49	32	5.9	0.015
0	685	0	
0.59	13	8.4	0.013

was again a sharp drop between the point on the left-hand axis in plots like Fig. 1 and subsequent points, but there was usually no detectable curvature among the latter points.

Table 3 gives a comparison of the decline in hydrogen atom concentration with the increase in ethane concentration as the residence time increased in two experiments at 421 K. The initial hydrogen atom concentration, $[H]_0$, was about 60% greater in the second experiment. The ethane yields were much smaller than the decreases in hydrogen atom concentrations. The average ratio was 0.015. At lower temperatures the amounts of ethane produced were so small they could not be detected.

The ESR spectrum (17) of the oxygen atom was detected at 4262 G when no methane was flowing in the system. The peak corresponded to a concentration of oxygen atoms one-tenth the concentration of hydrogen atoms.

Discussion

There are two experimental observations that require explanations before we may interpret the results.

Stoichiometry

The first observation is the measurement of ethane yields only 0.015 times as great as the loss of hydrogen atoms. Each ethane molecule formed resulted from the removal of two radicals:

[4] $2CH_3 \rightarrow C_2H_6$

Thus, from the experimental data in Table 3 it may be concluded that reaction [4] removed methyl radicals 0.03 times as often as hydrogen atoms were removed by all processes. In three earlier studies (8–10) it was assumed that methyl radicals formed in reaction [1] would always recombine by reaction [4]. If this were true, ethane yields would be half the loss of hydrogen atoms, 30 times greater than we observed. Except for possible surface reactions, these studies equated the rate of removal of H with the rate of reaction [1]. In other words, the stoichiometric factor was assumed to be unity. In ref. 7, on the other hand, it was assumed that ethane formation by reaction [4] did not occur and that reaction [1] was always followed by reaction [2]. In this case the rate of removal of H would be twice the rate of reaction [1] and the stoichiometric coefficient would be two. At temperatures below 400 K we were unable to detect ethane peaks, in agreement with this assumption. From our experiments at 421 K in Table 3, with an ethane yield 0.03 times as great as expected under the first assumption, the stoichiometric coefficient is calculated to be 1.97. Sepehrad et al. (11) found final ethane yields at 640–818 K that were between 0.003 and 0.32 times their decreases in hydrogen atom concentrations.

Initial decay

The second observation requiring explanation is the curvature of plots, like those in Fig. 1, of logarithm of concentration vs. time. The experiments were designed to have three orders of magnitude more CH_4 than H, so that [H] was expected to decline in a pseudo-first-order fashion, giving a linear plot of ln[H] versus time.

A possible explanation would be parallel removal of hydrogen atoms by two different reactants, one of which was depleted before the other. One such reactant would be methane, and another could be an impurity in the methane. The olefins are the only group of known impurities that could react rapidly enough to affect the kinetics (19). However, the stated impurity content of the research grade methane was less than 1 ppm of C_2H_4 and less than 2 ppm of C_3H_6; these amounts would be insufficient to account for the observed initial decrease in H atom concentration. We have confirmed by gas chromatographic analysis that these impurities were undetectable at the 1 ppm level in both grades of methane used. However, Kurylo et al. (9, 10) used only 99.5% pure methane (20), so olefin impurities may have affected their results.

Another possible source of impurity is the gases flowing in the injector tube. The oxygen atoms observed may have resulted from oxygen or water in the helium. These atoms react with methane an order of magnitude faster than hydrogen atoms (4, 21), by the mechanism in Table 4. The methyl and formyl radicals and formaldehyde formed by attack of O atoms and OH radicals would act as apparent impurities in the methane, removing hydrogen atoms by several rapid reactions. The mechanism in Table 4 was simulated on a VAX 8800 computer by numerical integration of the differential equations for the rates of formation and removal of all the species listed. Results of integrations by the Euler, Runge–Kutta, and Gear methods (22) agreed with each other within 1%, provided suitable convergence limits were used. Rate constants were taken from recent compilations (4, 21) or from a fit to experimental data (14). For reaction [2], CH_4 was assumed to be an equally effective third body as C_2H_6. The limiting high-pressure rate con-

Can. J. Chem. Downloaded from www.nrcresearchpress.com by 195.246.54.202 on 09/08/12
For personal use only.

TABLE 4. Rates of elementary processes from simulation of an experiment at 421 K with 1.7 Torr of CH_4, 4.4 Torr of He, and $[H]_0$ and $[O]_0$ equal to 400 and 120 ppm, respectively

Reaction	Ref. for k	Rate × 10^8 at 0.13 s (mol L^{-1} s^{-1})	Rate × 10^8 at 0.49 s (mol L^{-1} s^{-1})
$H + CH_4 \rightarrow H_2 + CH_3$	This work	4.63	1.19
$H + CH_3 + M \rightarrow CH_4 + M$	14	4.36	0.96
$2CH_3 \rightarrow C_2H_6$	21	0.17	0.12
$O + CH_4 \rightarrow OH + CH_3$	21	0.03	0.00
$O + CH_3 \rightarrow CH_2O + H$	21	0.03	0.00
$O + CH_2O \rightarrow OH + CHO$	21	0.00	0.00
$H + CH_2O \rightarrow H_2 + CHO$	21	2.31	0.13
$H + CHO \rightarrow H_2 + CO$	21	2.32	0.13
$OH + CH_4 \rightarrow H_2O + CH_3$	21	0.04	0.00
$OH + CH_3 \rightarrow CH_3OH$	21	0.00	0.00
$O + OH \rightarrow H + O_2$	21	0.00	0.00
$O + CHO \rightarrow OH + CO$	21	0.00	0.00
$O + CHO \rightarrow H + CO_2$	21	0.00	0.00
$H + O_2 + M \rightarrow HO_2 + M$	21	0.01	0.00
$O + HO_2 \rightarrow OH + O_2$	21	0.00	0.00
$H + HO_2 \rightarrow 2OH$	21	0.01	0.00
$H + CH_2O \rightarrow CH_3O$	4	2.57	0.14
$H + CH_3O \rightarrow CH_2O + H_2$	4	2.60	0.14
$OH + CH_2O \rightarrow H_2O + CHO$	21	0.00	0.00
$-d[H]/dt$		18.78	2.69
$(-d[H]/dt)/R_1$		4.06	2.26
[H] (ppm)		152	39
$[C_2H_6]$ (ppm)		1.6	3.8
$[C_2H_6]/([H]_0 - [H])$		0.007	0.011

stant was used for reaction [4] because compilations indicate there is little pressure dependence in the present conditions (6). The concentrations and temperature employed in the calculations for Table 4 corresponded to the second and fourth lines of Table 3 and to the second and eighth points in the upper curve in Fig. 1. The initial oxygen atom concentration was adjusted to roughly fit the figure. The O atom concentration was predicted to fall by three orders of magnitude between the first and second points on the curve and continue to decline in a first-order manner. In addition to reactions [1] and [2], hydrogen atoms were calculated to be removed significantly by four reactions with CH_2O, CHO, and CH_3O. The reaction of H with C_2H_6 was not included because its rate was only about 1% of the rate of reaction [4]. At the shorter residence time, the stoichiometric coefficient, $(-d[H]/dt)/R_1$, was 4.06, explaining the steep slope observed at this point in Fig. 1. By 0.49 s the stoichiometric factor was calculated to be only 2.26, close to the value of 1.97 estimated from ethane yields in the first part of the Discussion. The quotient, $[C_2H_6]/([H]_0 - [H])$ was estimated to have values of 0.007 and 0.011, somewhat less than the experimental values of 0.016 and 0.015. This is reasonable agreement, considering that k_2 is uncertain by a factor of two and that other rate constants have similar uncertainties.

There is a possibility that radical–radical reactions could occur in the cool zone between the end of the heated reactor and the ESR cavity or sample bulb. Based on the simulation described above, we estimate that such reactions should only affect measured concentrations by about 1%.

We have employed two methods to extract the rate constant for reaction [1] from data like those in Fig. 1.

The simplest method involved dropping the point on the vertical axis, obtained from experiments with blank gas flowing, as well as the next point, if this point were clearly above the line formed by the remaining points. The slope of this line was then taken, k_3 was subtracted, and the resulting apparent first-order rate constant was divided by $[CH_4]$ and by the stoichiometric coefficient of two. This method was based on that recommended by Westenberg and de Haas (18) and involves the assumption that k_3 is not affected when He is replaced by CH_4/He mixtures. The results are the first entries in the final column of Table 2.

We have also fitted a biexponential decay equation to the experimental data by nonlinear least squares (23).

$$[5] \quad [H] = A \exp(-at) + B \exp(-bt)$$

The slower decay constant, a, was reduced by k_3, and was then divided by two and by $[CH_4]$ and equated to the rate constant, k_1. The results are the second entries in the final column of Table 2. The faster decay constant, b, corresponded to the rapid initial drop in [H]. The sum, $A + B$, was equated to the initial concentration, $[H]_0$, but the ratio, B/A, was treated as a third variable parameter. Two results of these fits are shown as the smooth curves in Fig. 1.

In most cases values obtained by the two techniques in Table 2 were in good agreement. The cases where the first value exceeded the second involved the two curved plots in Fig. 1. The values obtained at identical temperatures but otherwise differing conditions also agreed well, as seen in Table 2. The biexponential decay expression was considered to allow for the initial decay in a more consistent and objective manner, so values obtained in this way were used to obtain the averages quoted.

The present results at 421 K are a factor of eight slower than

Can. J. Chem. Downloaded from www.nrcresearchpress.com by 195.246.54.202 on 09/08/12
For personal use only.

Can. J. Chem. Downloaded from www.nrcresearchpress.com by 195.246.54.202 on 09/08/12
For personal use only.

TABLE 5. Parameters of the transition state from fits to experimental data and from theoretical calculations

Source	$E_f - E_r$ (kJ mol^{-1})	E_f (kJ mol^{-1})	ω_B (cm^{-1})	T^* (K)
Old expt. (5)	−5.5 ± 0.5	55.5 ± 1.5	772 ± 37	460 ± 41
New expt.	−1.0 ± 0.4	62.7 ± 1.2	638 ± 28	504 ± 26
JANAF (25)	−0.1			
PolCl (32)	9.3	65.1	855	(223)

the results reported in ref. 10 at 424 K. The difference is due partly to the stoichiometric factor of two. There was also a clear trend in the results in ref. 10 toward lower rate constants at longer residence times, similar to the trend noted in Fig. 1. In two experiments at slow flows Kurylo et al. (9) obtained a rate constant of 4×10^4 L mol^{-1} s^{-1}, which, when divided by the stoichiometric coefficient, would agree with the present result.

Thermochemical and kinetic parameters

The present, slower rate constants can be expected to agree better with the accepted thermochemistry and the rate constant of the reverse reaction. To test this we have fitted a transition-state theory model by nonlinear least squares to the data of the present work and literature data for the reverse reaction. The model was described in detail in ref. 5. One change was made by including an extra $\frac{1}{3}$ in the classical partition function (24) for rotation of H_2 in the reverse reaction:

$$[6] \quad Q_r = \frac{8\pi^2 I k_B T}{\sigma h^2} + \frac{1}{3}$$

The extra term adjusted the partition function for quantum effects. Moments of inertia and vibrational frequencies of the reactants were taken from the JANAF Thermochemical Tables (25). The products of moments of inertia of the transition state were taken from a bond energy, bond order calculation (26). This is the most uncertain part of the input, but we have shown elsewhere that it does not significantly affect the output (5). The latter consists of the effective barrier height in the forward direction, E_f; the characteristic tunnelling temperature, T^*; the geometric mean of five low-frequency, transition-state bending term values, ω_B; and the difference between forward and reverse barrier heights, $E_f - E_r$.

The results of these fits are shown in Table 5. In the second column are listed values of $E_f - E_r$, which is equal to ΔH_0^0, the enthalpy of reaction at 0 K. Zero point vibrational energies are included in the barrier heights. In the first line are our results from three years ago (5), incorporating data available until that time. The reaction was found to be 5.5 kJ mol^{-1} exothermic, in contrast to the 0.1 kJ mol^{-1} exothermicity from the JANAF tables (25) in the third line. In the second line are the results obtained by discarding the old data for the forward reaction and including only the results of the present work and the recently published shock tube study by Rabinowitz et al. (27). The exothermicity is now found to be 1.0 ± 0.4 kJ mol^{-1}. The quoted uncertainty is one standard deviation. Considering the possibility of systematic errors in either the forward or reverse kinetic studies, we feel these results are essentially in agreement with the JANAF value. If the shock tube data were not included, the exothermicity would be 0.8 ± 0.4 kJ mol^{-1}. Alternatively, equilibrium constants can be calculated from the present results at 373–421 K and individual rate constants for the reverse reaction from the literature (28–31). With the partition functions calculated as above, but without the use of transition state theory, the exothermicity was calculated to be 0.9 ± 0.7 kJ mol^{-1}. In the fourth line of the table is given the result of an ab initio calculation (32), which predicts the reaction to be endothermic.

One can turn the present result around and use it to find the heat of formation of the methyl radical. Using JANAF results (25) for the other species and the value of $E_f - E_r$ from the new experiments, one finds $\Delta_f H^0 298(CH_3) = 34.6$ kcal mol^{-1} or 145 kJ mol^{-1}. This may be compared to 34.8 kcal mol^{-1} from JANAF (25) and 35.1 kcal mol^{-1} from forward and reverse kinetics on the Cl atom analogue (33) of reaction [1]. There is room for further refinement, but clearly the thermochemistry of reaction [1] has now rejoined the mainstream.

The remaining three columns in Table 5 give the fitted properties of the transition state. First is E_f, the height of the activation barrier including zero point energy. This is 7 kJ mol^{-1} higher with the new experimental data than it had appeared to be with the old. It is now in better agreement with the ab initio results (32) in the table and with a new ab initio value of 60 kJ mol^{-1}.[3] Comparisons with other surfaces are available in ref. 5. The mean of the transitional bending frequencies has moved lower, away from the ab initio result. It has been pointed out elsewhere (34) that these frequencies change quickly near the barrier top and the reaction bottleneck does not coincide with the top of the potential energy barrier. The characteristic tunnelling temperature is a measure of the curvature across the top of the barrier and of the importance of quantum mechanical tunnelling through the barrier. This parameter is unchanged within experimental uncertainty with the new experimental results. Tunnelling dominates this reaction even at a temperature of 500 K. The value of T^* from the ab initio calculations is not directly comparable, as it refers to curvature of the potential energy barrier without vibrational zero point energy.

It is interesting to note that Polanyi (35) calculated a classical barrier height of 56 kJ mol^{-1} many years ago.

The experimental data and the fitted curves are illustrated in Fig. 2. The curves were obtained using the transition-state theory model of ref. 5, adjusted by the inclusion of eq. [6], with the parameters in the second line of Table 5. The two fitted curves are closely parallel, indicating that the equilibrium constant is almost independent of temperature. The experiments at low temperatures on the reverse reaction, all obtained by static photolysis (28–31), are consistent with each other. For the forward reaction we have not shown the earlier flow discharge results (7–11), as they may have been affected by impurities or effects of reaction [2].We have also omitted some combustion studies (1, 3, 4, 6), where the temperature often changed rapidly during the reaction. To prevent crowding, we have only been able to show a quarter of the plentiful points of Rabinowitz et al. (27).

We have recently learned of new shock tube experiments on reaction [1] and its reverse. Wintergerst and Frank (WF)(40) obtained rates for reaction [1] about twice as fast as those of Rabinowitz et al. (27). For the reverse reaction they found rate constants twice as fast as unpublished results of Klemm.[4] Clearly, more work is needed at high temperatures. However, WF said their forward and reverse rate constants, on their own, agree with the established thermochemistry, and that the

[3]P. Marshall, private communication, August 1993.

[4]R.B. Klemm, private communication cited in ref. 40.

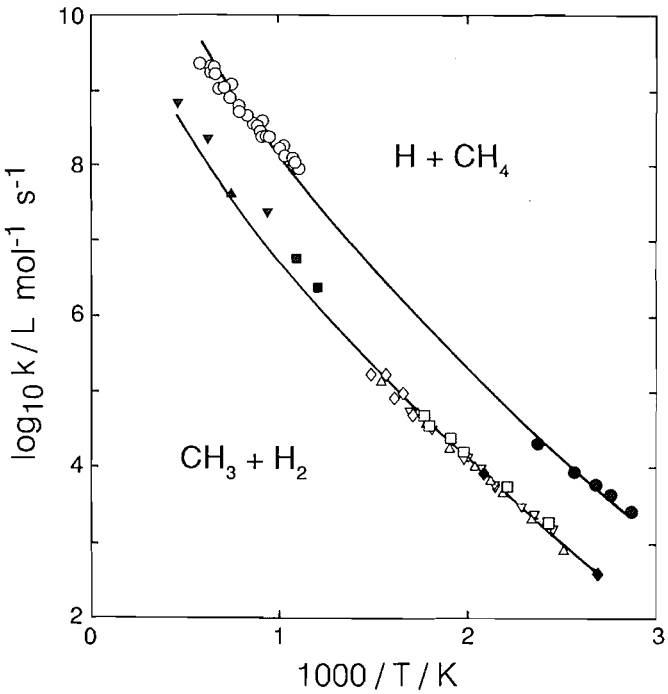

FIG. 2. Arrhenius plot of selected results for reaction [1] and [−1]: experiment, reaction [1]: ●, this work; ○, ref. 27; experiment, reaction [−1]: □, ref. 28; △, ref. 29; ▽, ref. 30; ◇, ref. 31; ▼, ref. 36; ▲, ref. 37; ■, ref. 38; ◆, ref. 39; —, nonlinear least-squares fits of transition state theory model to the experimental data.

Brookhaven results of Rabinowitz et al. and Klemm, on their own, are also consistent with the established thermochemistry.

The central conclusions of this work are that in measurements of the rate constant for reaction [1] careful attention must be paid to stoichiometric factors and impurity effects, that the rate constants for reaction [1] at 348–421 K are much slower than previously thought, and that the thermochemistry for reaction [1] from kinetic studies is now in reasonable agreement with results of other techniques. More generally, "direct" studies, like most studies (7, 9, 10) of reaction [1], are not necessarily more reliable than indirect studies involving a composite mechanism, like the photochemical studies (28–31) of reaction [−1]. We can now see that some studies of the forward reaction involved an unsuspected composite mechanism. The accuracy of the indirect photochemical studies is confirmed by the present work.

Acknowledgements

The authors thank the Natural Sciences and Engineering Research Council of Canada for financial support; D.R. Arnold, J.A. Coxon, W.E. Jones, and O. Knop for lending equipment; R.B. Klemm and J. Troe for sending preprints; S.W. Benson and O. Dobis for advice regarding Teflon coating; and I.S. Jayaweera and H. Furue for experimental assistance. P.-M.M. thanks the Cooperation Franco-Canadienne and the DCPR-URA n° 328, CNRS, Nancy, France, for financial support.

1. R.W. Walker. J. Chem. Soc. A, 2391 (1968).
2. J.A. Kerr and M.J. Parsonage. Evaluated kinetic data on gas phase hydrogen transfer reactions of methyl radicals. Butterworths, London. 1976.
3. R.W. Shaw. J. Phys. Chem. Ref. Data, **7**, 1179 (1978).
4. W. Tsang and R.F. Hampson. J. Phys. Chem. Ref. Data, **15**, 1087 (1986).
5. H. Furue and P.D. Pacey. J. Phys. Chem. **94**, 1419 (1990).
6. D.L. Baulch, C.J. Cobos, R.A. Cox, C. Esser, P. Frank, T. Just, J.A. Kerr, M.J. Pilling, J. Troe, R.W. Walker, and J. Warnatz. J. Phys. Chem. Ref. Data, **21**, 411 (1992).
7. M.R. Berlie and D.J. LeRoy. Can. J. Chem. **32**, 650 (1954).
8. J.W.S. Jamieson and G.R. Brown. Can. J. Chem. **42**, 1638 (1964).
9. M.J. Kurylo and R.B. Timmons. J. Chem. Phys. **50**, 5076 (1969).
10. M.J. Kurylo, G.A. Hollinden, and R.B. Timmons. J. Chem. Phys. **52**, 1773 (1970).
11. A. Sepehrad, R.M. Marshall, and H. Purnell. J. Chem. Soc. Faraday Trans. 1, **75**, 835 (1979).
12. W.E. Jones and J.L. Ma. Can. J. Chem. **64**, 2192 (1986).
13. M. Brouard, M.T. MacPherson, and M.J. Pilling. J. Phys. Chem. **93**, 4047 (1989).
14. C.J. Cobos and J. Troe. Z. Phys. Chem. NF, **167**, 129 (1990).
15. I. R. Slagle, D. Gutman, J.W. Davies, and M.J. Pilling. J. Phys. Chem. **92**, 2455 (1988).
16. I.S. Jayaweera and P.D. Pacey. J. Phys. Chem. **94**, 3614 (1990).
17. A.A. Westenberg. Prog. React. Kinet. **7**, 23 (1973).
18. A.A. Westenberg and N. de Haas. J. Chem. Phys. **46**, 490 (1967).
19. W.E. Jones, S.D. MacKnight and L. Teng. Chem. Rev. **73**, 407 (1973).
20. M.J. Kurylo. Thesis, Catholic University of America, Washington, 1969.
21. N. Cohen. Int. J. Chem. Kinet. **18**, 59 (1986).
22. W.H. Press, S.A. Teukolsky, W.T. Vetterling, and B.P. Flannery. Numerical recipes in Fortran. 2nd ed. Cambridge University Press, Cambridge. 1992. pp. 701–744.
23. M. Ralston. *In* BMDP statistical software. *Edited by* W.J. Dixon. University of California, Berkeley, Calif. 1983. p. 305.
24. G. Herzberg. Molecular spectra and molecular structure. II. Infrared and Raman spectra of polyatomic molecules. Van Nostrand, Princeton. 1945. p. 505.
25. M.W. Chase, Jr., C.A. Davies, J.R. Downey, Sr., D.J. Frurip, R.A. McDonald, and A.N. Syverud. JANAF thermochemical tables. 3rd ed. U.S. Department of Commerce, Washington, D.C. 1986.
26. A.A. Zavitsas and A.A. Melikian. J. Am. Chem. Soc. **97**, 2757 (1975).
27. M.J. Rabinowitz, J.W. Sutherland, P.M. Patterson, and R.B. Klemm. J. Phys. Chem. **95**, 674 (1991).
28. T.G. Majury and E.W.R. Steacie. Can. J. Chem. **30**, 800 (1952).
29. J.S. Shapiro and R.E. Weston. J. Phys. Chem. **76**, 1669 (1972).
30. S. Davison and M. Burton. J. Am. Chem. Soc. **74**, 2307 (1952).
31. H. Gesser and E.W.R. Steacie. Can. J. Chem. **34**, 113 (1956).
32. S.P. Walch. J. Chem. Phys. **72**, 4932 (1980).
33. O. Dobis and S.W. Benson. Int. J. Chem. Kinet. **19**, 691 (1987).
34. R. Steckler, K.J. Dykema, F.B. Brown, G.C. Hancock, D.G. Truhlar, and T. Valencich. J. Chem. Phys. **87**, 7024 (1987).
35. J.C. Polanyi. J. Chem. Phys. **23**, 1505 (1955).
36. W. Moller, E. Mozzhukhin, and H.G. Wagner. Ber. Bunsen-Ges. Phys. Chem. **90**, 854 (1986).
37. T.C. Clark, and J.E. Dove. Can. J. Chem. **51**, 2155 (1973).
38. P.C. Kobrinsky and P.D. Pacey. Can. J. Chem. **52**, 3665 (1974).
39. R.M. Marshall and G. Shahkar. J. Chem. Soc. Faraday Trans. 1, **77**, 2271 (1981).
40. U. Wintergest and P. Frank. Abstracts, 12th Int. Symp. on Gas Kinetics, Reading, England. 1992.

Can. J. Chem. Downloaded from www.nrcresearchpress.com by 195.246.54.202 on 09/08/12
For personal use only.

Infrared–ultraviolet double resonance measurements on the temperature dependence of rotational and vibrational self-relaxation of NO($X^2\Pi$, $v = 2, j$)

MICHAEL J. FROST,[1] MEEZANUL ISLAM, AND IAN W.M. SMITH[2]

School of Chemistry, The University of Birmingham, Edgbaston, Birmingham B15 2TT, U.K.

Received August 5, 1993

This paper is dedicated to Professor John C. Polanyi on the occasion of his 65th birthday

MICHAEL J. FROST, MEEZANUL ISLAM, and IAN W.M. SMITH. Can. J. Chem. **72**, 606 (1994).

Infrared–ultraviolet double resonance experiments have been performed to measure the rates of rotational and vibrational self-relaxation in NO at three temperatures: 295 K, 200 K, and 77 K. Pulses of tunable infrared radiation from an optical parameteric oscillator have been used to excite molecules into selected rotational levels (j = 0.5, 6.5, or 15.5) in the $|v = 2; \Omega = 1/2\rangle$ vibronic component of the $X^2\Pi$ electronic ground state of NO. Loss of population from the initially excited level was observed by making time-resolved laser-induced fluorescence measurements on appropriate lines in the $A^2\Sigma^+ - X^2\Pi(2,2)$ band. The rate constants for removal of population from specific rovibronic levels are essentially independent of j and at 295 K agree well with previous direct measurements on a range of v, j levels. The rotationally thermalized population in $v = 2$ relaxes by vibration–vibration (V–V) energy exchange, NO($v = 2$) + NO($v = 0$) → 2 NO($v = 1$), at a rate which is almost independent of temperature and which seems to be uninfluenced by the presence of spin-orbit degeneracy in, and attractive forces between, the NO collision partners.

MICHAEL J. FROST, MEEZANUL ISLAM et IAN W.M. SMITH. Can. J. Chem. **72**, 606 (1994).

Dans le but de mesurer les vitesses d'autorelaxation rotationnelle et vibrationnelle du NO, on a réalisé des expériences de double résonance infrarouge–ultraviolet à trois températures, 295 K, 200 K et 77 K. On a utilisé des pulsations d'une radiation infrarouge ajustable, obtenues à l'aide d'un oscillateur optique paramétrique, pour exciter les molécules vers des niveaux rotationnels choisis (j = 0,5, 6,5 ou 15,5) du $|v = 2; \Omega = 1/2\rangle$ composante vibronique de l'état électronique fondamental $X^2\Pi$ du NO. On a observé la perte de population de l'état excité initial en effectuant, sur les raies appropriées de la bande $A^2\Sigma^+ - X^2\Pi(2,2)$, des mesures de fluorescence induites au laser et résolues dans le temps. Les constantes de vitesse pour les pertes de population à partir de niveaux rovibroniques donnés sont essentiellement indépendantes de j et, à 295 K, elles sont en bon accord avec les mesures directes effectuées antérieurement sur un ensemble de niveaux v, j. La relaxation de la population thermalisée par rotation dans $v = 2$ se fait par un échange d'énergie vibration–vibration (V–V), NO($v = 2$) + NO($v = 0$) →2NO($v = 1$), à une vitesse qui est pratiquement indépendante de la température et qui ne semble pas être influencé par la présence d'une dégénérescence spin-orbite dans ou par les forces d'attraction entre les partenaires de collision du NO.

[Traduit par la rédaction]

1. Introduction

The capacity of double resonance techniques to reveal the state-resolved details of energy transfer processes has been appreciated for some time. In experiments of this kind, the Boltzmann distribution of molecules over rovibronic levels is perturbed by pumping a particular spectroscopic transition using a powerful monochromatic source, usually a laser, and then the rates and pathways of the relaxation processes which reestablish equilibrium are examined using spectroscopic techniques. When the pump and probe sources are both pulsed tunable lasers, two types of measurement can be performed. In the first, the frequency of the probe laser is fixed to correspond to the frequency of a discrete transition in the molecule under investigation, and the time delay between excitation and probe lasers is scanned to yield kinetic information about how the population in the selected level evolves in time. Alternatively, the time delay between the two laser pulses is fixed and the frequency of the probe laser is scanned. The spectrum that is obtained contains information about the relative populations in different molecular states at the instant the second laser is fired. If the chosen delay is much shorter than the average time between collisions in the gas sample, then the populations in levels other than that directly accessed in the pump process directly reflect the state-to-state rate coefficients for transfer from the initially populated level into neighbouring levels.

Experiments in which laser-induced fluorescence is used to probe the kinetic behaviour of populations in excited rovibrational levels of electronic ground states have been pioneered by Orr and co-workers, in a series of elegant experiments, initially on D_2CO and HDCO (1) and more recently on C_2H_2 and C_2D_2 (2). In addition, Crim and co-workers (3), Zacharias and co-workers (4), and Frost and Smith (5) have all performed recent double resonance experiments on different states of C_2H_2. Earlier in our laboratory, Smith and Warr (6) had performed preliminary measurements on the vibrational relaxation pathways in HCN using the double resonance technique. In the present work, as in the experiments of Frost and Smith (5) and Smith and Warr (6), a $LiNbO_3$ based optical parametric oscillator (OPO) is used as the "pump" source to prepare an initial population in a selected rovibronic level of the molecule under investigation.

The present paper reports infrared–ultraviolet double resonance measurements on the temperature dependence of collisional energy transfer processes in NO. Radiation from the OPO has been used to prepare molecules in either the j = 0.5, 6.5, or 15.5 rotational level in the $\Omega = 1/2$ lower spin-orbit component of the $X^2\Pi$, $v = 2$ vibronic level. In this paper, we report rate coefficients for *total* removal of population (i.e.,to all final states) with NO itself as the collision partner for several initial rotational states, as well as rate coefficients for vibrational self-relaxation from $v = 2$. The temperature dependences of these processes have been investigated by carrying out experiments at 295 K, 200 K, and 77 K.

The rates of collisional rotational and vibrational energy

[1]Present address: JILA, University of Colorado, Boulder, CO 80309-0440, U.S.A.

[2]Author to whom correspondence may be addressed.

Can. J. Chem. Downloaded from www.nrcresearchpress.com by EESC ESCOLA DE ENGENHARIA on 09/08/12
For personal use only.

Can. J. Chem. Downloaded from www.nrcresearchpress.com by EESC ESCOLA DE ENGENHARIA on 09/08/12
For personal use only.

transfer provide a probe of the intermolecular potential acting between the collision partners. In this respect, double resonance experiments on NO are especially interesting, as well as being relatively easy to perform, because the electronic ground state of NO is $^2\Pi$. NO is known to form a dimer with a dissociation energy (D_0) equivalent to ca. 800 cm^{-1} (7) and to undergo unusually rapid vibrational–translational (V–T) relaxation (8), probably as a result of an electronically non-adiabatic mechanism (9). In this context, it is particularly interesting to examine relaxation processes at low temperature, where the dissociation energy of $(NO)_2$ becomes appreciably greater than kT.

Our experiments and the results that we have obtained on rotational energy transfer are closely related to those of Sudbo and Loy (10), reported in 1982. They excited specific (j,Ω) levels in NO($v = 2$) using the output from a pulsed F-centre laser pumped by a Nd:YAG laser. Populations in specific ($v = 2$, j, Ω) levels were then detected using a tunable ultraviolet laser to ionize molecules via levels in the $A^2\Sigma^+(v = 2)$ vibronic level in a (1 + 1) resonance-enhanced multiphoton ionization process. As well as obtaining total relaxation rates out of particular (j,Ω) levels, they obtained state-to-state rate coefficients by fixing the frequency of the probe laser and scanning that of the excitation laser with the delay between the two laser pulses set at a fraction of the average time between NO–NO collisions. However, their measurements were all performed at room temperature and they could only derive an upper limit to the rate constant for vibrational relaxation of NO($v = 2$).

More recently, Wodtke and co-workers obtained rotational (11, 12) and vibrational (11, 13) relaxation rates within and for high vibrational levels of NO ($8 \leq v \leq 24$). Theirs might be described as a *triple* resonance method. Levels in the $X^2\Pi$ ground state are populated by stimulated emission pumping (SEP), two tunable dye lasers being deployed to "*pump-and-dump*" molecules into selected rovibronic levels with high v. A third tunable laser is then used to observe how the excited population that has been created evolves as collisions cause relaxation.

2. Experimental

The apparatus and experimental procedures used in the present work were very similar to those described previously by Frost and Smith (5), so only essential details of the experiments, and ways in which they differ from the earlier ones, are described here. A schematic diagram of the experimental arrangement is given as Fig. 1 in the paper by Frost (5*b*).

In the present experiments, NO was excited to single selected rovibronic levels using pulses of tunable radiation at ca. 2.7 μm from a $LiNbO_3$ OPO that was pumped by the fundamental output from a Nd:YAG laser. The pulse energy in the idler beam of the OPO at the required wavelength was in the range 0.1–1.0 mJ, its fluence at the observation region was 0.5–5.0 mJ cm^{-2}, and its bandwidth was ca. 0.3 cm^{-1}. This output was tuned into resonance with lines in the P-branch of the ($v = 2 \leftarrow 0$; $\Omega = 1/2 \leftarrow 1/2$) sub-band using a monochromator and a spectrophone containing 20 Torr of NO and 20 Torr of argon (1 Torr = 133.3 Pa).

The probe radiation was provided by a dye laser (Lambda Physik, FL2000) pumped by an excimer laser (Lumonics, series 400) operating on XeCl. The fundamental output from the dye laser was frequency-doubled in a BBO crystal to provide radiation at 222 nm, in order to excite NO in the (2,2) band of the $A^2\Sigma^+$–$X^2\Pi$ band system. The probe radiation contained <10 μJ per pulse, had a bandwidth of ca. 0.2 cm^{-1}, and irradiated a region ca. 2 mm in diameter in the centre of the cylindrical volume illuminated by the output from the OPO. To discriminate against scattered radiation from the probe laser, the fluorescence was observed, using a photomultiplier tube (EMI, model 9781B), through a UG11 broad-band filter, which effectively cuts out radiation below ca. 250 nm. In some experiments (see below), NO in $v = 1$ was observed. In these the probe radiation was tuned to lines in the (1,1) band; the arrangements for observing fluorescence remained the same.

The cell used for the present experiments was different from that employed by Frost and Smith (5). However, it was very similar to that used recently (14) in experiments to determine the rate constants for reactions of OH radicals at low temperatures. It is constructed from three concentric Pyrex tubes, so that the inner tube, in which the gas sample of pure NO or NO diluted in argon is placed, is surrounded by a double jacket. The outer jacket is permanently evacuated and refrigerant is placed in, or circulated through, the inner jacket, which is 30 cm long. To achieve low temperatures in the present experiments, either liquid N_2 was placed in the inner jacket or methanol that had been cooled in Dry Ice was flowed slowly through it. The vapour pressure of NO at 77 K is only 81 mTorr (= 1.02×10^{16} molecule cm^{-3}), but this was quite adequate for all the experiments that were carried out in the present series. Statistical mechanical calculations based on the spectroscopic properties of the $(NO)_2$ dimer (7, 15) show that the mole fraction of $(NO)_2$ under these conditions is less than 10^{-4}. We assume here that the static gas in the observation region is at the temperature of the walls. This is consistent with spectroscopic observations made on NO that had rotationally been completely relaxed. We also note that the rates of the processes under investigation in the present work show very little dependence on temperature.

CaF_2 windows were mounted at each end of the central tube in which NO was placed. The two laser beams counterpropagated along the central axis of this cell. To view the LIF from electronically excited NO, the cell had to be fitted with quartz windows. One window is attached to a short sidearm, which is joined to the central tube at its midpoint and passes through the inner jacket. The second window is mounted on the outer wall of the evacuated jacket. The photomultiplier tube, the filter, and a collecting lens are mounted in a housing that is clamped to the jacketed cell so that fluorescence, which passes through the quartz windows, is collected and directed onto the photomultiplier tube. Pressures in the cell are measured directly, using a 0–10 Torr capacitance manometer (MKS Baratron, model 222BA).

The equipment for controlling the firing of the two lasers and for recording, accumulating, and analysing the LIF signals has been described by Frost and Smith (5) and the description is not repeated here.

NO (Electrochem Ltd., 99.99%) was admitted to the vacuum line via a liquid N_2 trap and was purified by trap-to-trap distillations until it condensed in liquid N_2 as a pure white solid. Ar (BOC, zero grade, 99.998%) was used without further purification.

3. Results and discussion

In the present experiments the fraction of NO excited by the OPO laser pulse in the region probed by the ultraviolet laser was estimated. This was done by using the intensities of lines in the (1,1) band of the $A^2\Sigma^+$–$X^2\Pi$ system excited in a room temperature sample for calibration. The intensities of these lines could then be compared either with those excited in the (2,2) band, making due allowance for differences in Franck–Condon factors and dye laser intensities, or by comparing the (1,1) spectrum from a thermal sample with that recorded following the excitation of NO to $v = 2$, with a delay time chosen to be sufficiently long to allow complete rotational relaxation and for the vibration-to-vibration (V–V) energy exchange process:

$$[1] \quad NO(v = 2) + NO(v = 0) = 2\,NO(v = 1); \quad \Delta E/hc = 28\ cm^{-1}$$

to have gone to completion, but short enough for insignificant V–T relaxation to have occurred. These comparisons indicated that, for excitation to $v = 2$, $j = 6.5$ at room temperature, the concentration of NO excited by the pulse from the OPO was ca. 10^{-3} times the *total* concentration of NO present.

Can. J. Chem. Downloaded from www.nrcresearchpress.com by EESC ESCOLA DE ENGENHARIA on 09/08/12
For personal use only.

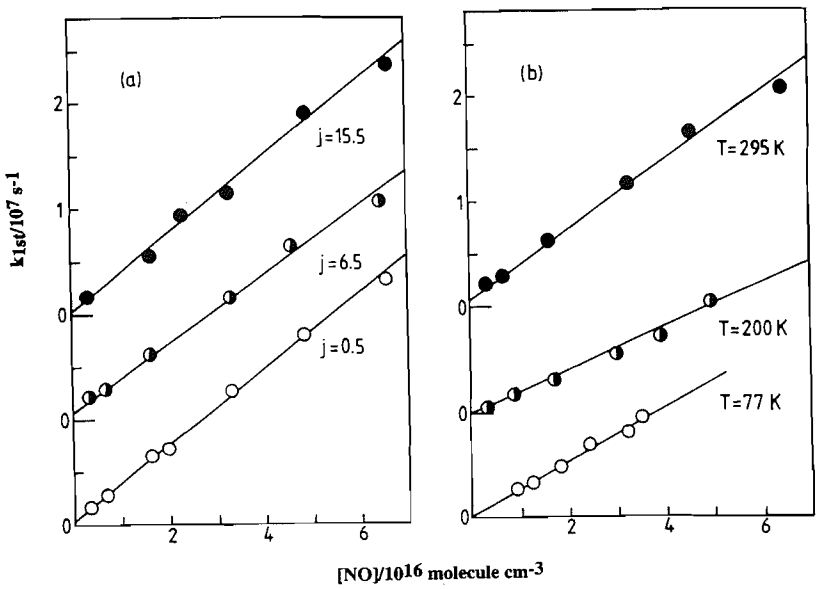

FIG. 1. First-order rate constants for the decay of LIF signals from initially populated rovibronic state $|v = 2, j, \Omega = 1/2\rangle$ plotted against concentration of NO: (*a*) for $j = 0.5$ (○), 6.5 (◑), and 15.5 (●) at 295 K: (*b*) for $j = 6.5$ at 295 K (●), 200 K (◑), and 77 K (○). The values of k_{1st} and [NO] for the data at 77 K are both one third for the values indicated on the axes, and the plots are displaced vertically for clarity.

(a) Rotational self-relaxation of NO (v = 2; j = 0.5, 6.5, 15.5; Ω = 1/2)

Experiments on rotational self-relaxation were carried out on samples of undiluted NO. Measurements were performed using NO concentrations in the range $(0.3 - 6.0) \times 10^{16}$ molecule cm^{-3}. The intensities of the LIF signals, which were recorded at different delay times, always accurately fitted a single exponential decay yielding a first-order rate constant (k_{1st}) for relaxation of population in the initially excited level for the chosen temperature and concentration of NO. For the range of NO concentrations used, mean relaxation lifetimes varied between ca. 1 μs and 50 ns.

The values of k_{1st} determined in a given series of experiments and at a particular temperature were then plotted against the corresponding concentrations, [NO], yielding a second-order rate constant for self-relaxation of the initially excited $|v, j, \Omega\rangle$ state in NO–NO collisions at that particular temperature. This rate constant corresponds to that for overall relaxation from the initial rovibronic level. It may contain contributions from transfers to j levels in both Ω components. Several plots of k_{1st} versus [NO] are showing in Fig. 1. Panel (*a*) compares data for relaxation from different rotational levels at room temperature, 295 K. Panel (*b*) shows results for relaxation from the state, $|v = 2, j = 6.5, \Omega = 1/2\rangle$, at the three temperatures of our experiments: 295 K, 200 K, and 77 K. The second-order rate constants for rotational self-relaxation resulting from all our experiments are summarized in Table 1. Each value quoted is the average of at least two series of experiments on a particular rovibronic level and at a given temperature. It can be seen that, at room temperature, the overall rotational relaxation rates are independent of j, in the range of j, Ω covered in our experiments.

The rate constants derived in the way just described are clearly not obtained under single collision conditions, and they characterize the rate at which the initial population ($N_{i,0}$) in the selected state i relaxes to the population ($N_{i,e}$) in the same state once complete rotational (and spin-orbit) relaxation has occurred. The equation describing the rate of change of population $N_{i,t}$ is

TABLE 1. Rate constants ($k/10^{-10}$ cm^3 molecule^{-1} s^{-1}) for relaxation and for total transfer from specific rovibronic levels, $|v = 2, j, \Omega = 1/2\rangle$, together with collisional probabilities for total transfer, in collisions with NO at different temperatures

T/K	$j = 0.5$	$j = 6.5$	$j = 15.5$
295	3.60 ± 0.24	3.08 ± 0.16	3.50 ± 0.12
	3.56	2.93	3.43
	1.22	1.00	1.16
200	1.85 ± 0.10	2.08 ± 0.18	1.76 ± 0.28
	1.82	1.95	1.74
	0.66	0.75	0.63
77	1.80 ± 0.16	2.43 ± 0.16	2.67 ± 0.23
	1.70	2.22	2.67
	0.63	0.83	1.00

[a]Obtained by dividing the observed rate constant by Z^0_{LJ}, the second-order rate constant for all collisions assuming a Lennard–Jones potential between the NO collision partners.

$$dN_{i,t}/dt = -\Sigma k_{i\to j}[NO]N_{i,t} + \Sigma k_{i\leftarrow j}[NO]N_{j,t}$$

where $k_{i\to j}$ and $k_{i\leftarrow j}$ are state-to-state rate constants for transfer from and to the observed state, $N_{j,t}$ are populations in all other rotational and spin-orbit states in $v = 2$ at time t, and both summations are over j. The first term on the right-hand side of this rate equation can clearly be written as $-k_{i\to}[NO]\ N_t^*$, where $k_{i\to} = \Sigma k_{i\to j}$ is the rate constant for *total* removal of population from the prepared state i.

To estimate values of $k_{i\to}$, we assume that the second term on the right-hand side of the rate equation can be written as $k_{i\leftarrow}[NO]\Sigma N_{j,t}$. Within this approximation, the observed relaxation rate constant is equal to $(k_{i\to} + k_{i\leftarrow})$ and, since at long times $dNi/d_t = 0$, the ratio of the rate constants is given by $k_{i\leftarrow}/k_{i\to} = N_{j,t=\infty}/\Sigma N_{j,t=\infty}$ and can be calculated using statistical mechanics. The rate coefficients $k_{i\to}$ for *total* removal of population from specific rovibronic levels are listed as the second entry in each element of Table 1. The values decrease slightly as

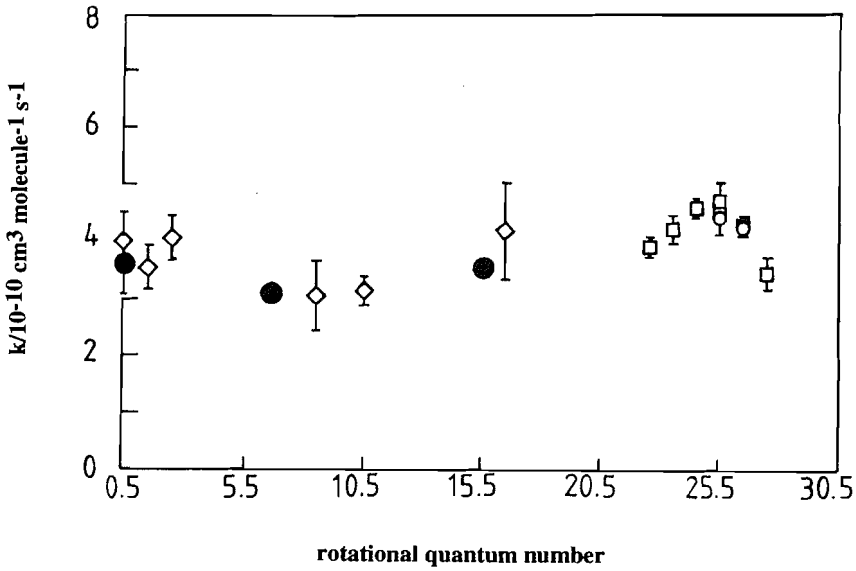

FIG. 2. Second-order rate constants for removal from specific rotational levels $j = 0.5$, 6.5, and 15.5 in $|v = 2, \Omega = 1/2\rangle$ (●) compared with similar data for levels in $v = 2$ (◇) (10) and in $v = 8$ (○) and 19 (□) (13).

the temperature is lowered and this effect appears to be greatest for the lowest rotational state investigated.

Table 1 also lists the collisional probabilities for removal from specific levels. These numbers are derived by dividing the observed second-order rate constants for *total* removal by the rate constants calculated for all collisions assuming that a Lennard–Jones potential acts between two NO molecules. The collisional probabilities are all within a factor of two of unity, confirming again the efficiency of rotational energy transfer. The reduced collision rate goes some way to explaining the reduction in relaxation rate coefficients that is observed below room temperature, but the probabilities do seem somewhat reduced at lower temperatures. This could reflect a reduction in the endothermic state-to-state rate coefficients (e.g., those for transfer to levels in the higher Ω component) as the temperature is lowered.

Our results at room temperature can be compared most directly with those of Sudbo and Loy (10) and of Yang and Wodtke (12). To facilitate these comparisons, Fig. 2 displays the rate constant for total decay from selected rovibronic levels obtained for different v, j levels in these three sets of measurements. It can be seen that the rate coefficients are essentially independent of both rotational and vibrational level over quite wide ranges of v and j, within the accuracy of the experimental results. A similar conclusion has been reached for rotational energy transfer in C_2H_2, as a result of a number of recent measurements (2–5).

Rate constants for total removal of population from a given rovibronic level can also be compared with line-broadening data for spectroscopic transitions terminating on the same state. For states in the electronic ground states of N_2 (16) and C_2H_2 (5*a*), for example, it appears that rate constants derived from the two kinds of measurements correlate well, indicating that energy transfer, rather than elastic m_j-changing collisions, are predominantly responsible for collision broadening in rovibrational transitions in these $^1\Sigma_g^+$ molecules. A large number of studies have been carried out on the pressure broadening of infrared transitions of NO. One of the most recent and thorough is that carried out by Pine et al. (17) on lines in the (2,0) first overtone band. The collision-broadening coefficients, which they determined at room temperature, are slightly higher for lines between $^2\Pi_{3/2}$ components than for lines in the $^2\Pi_{1/2} - {}^2\Pi_{1/2}$ sub-band. The self-broadening coefficients for the R(0.5), R(6.5), and R(15.5) lines in the latter sub-band translate into rate coefficients varying from 5.5×10^{-10} to 4.8×10^{-10} to 4.5×10^{-10} cm^3 molecule^{-1} s^{-1}, there being a slight decrease in the broadening coefficients as the rotational energy levels involved in the transition increase. These rate coefficients are about 50% higher than those observed in the direct studies of population transfer made by Sudbo and Loy (10), Yang and Wodtke (12), and ourselves.

The reason for this difference is not obvious. Sudbo and Loy's analysis indicates that, in the case of self-relaxation, the transfer of molecules between Ω components makes a significant contribution to population transfer, as well as j-changing transitions within the same Ω component, but that this is not true when the collision partner is other than NO. In any case, there seems to be no reason why this effect should destroy the correlation between rate coefficients derived from collision-broadening data and those determined directly in relaxation experiments. However, calculations by Orlikowski and Alexander (18) suggest that NO–NO collisions may be unusual in another respect: namely, in that the usual propensity for m_j-preserving collisions is relaxed in this case due to the $^2\Pi$ electronic nature of both collision partners. It therefore seems possible that m_j-changing collisions make some contribution to pressure broadening in pure NO. It will be interesting to check whether the difference between rotational energy transfer rates for NO measured directly and inferred from line-broadening measurements extends to collision partners other than NO itself.

(b) Vibrational self-relaxation of NO (v = 2)

Experiments on vibrational self-relaxation of NO($v = 2$) were carried out on samples of NO diluted to 10 Torr in argon. The argon diluent helps to cause rapid equilibration of the excited population over rotational levels, and decreases the rate at which the excited state population diffuses out of the region

Can. J. Chem. Downloaded from www.nrcresearchpress.com by EESC ESCOLA DE ENGENHARIA on 09/08/12
For personal use only.

Can. J. Chem. Downloaded from www.nrcresearchpress.com by EESC ESCOLA DE ENGENHARIA on 09/08/12
For personal use only.

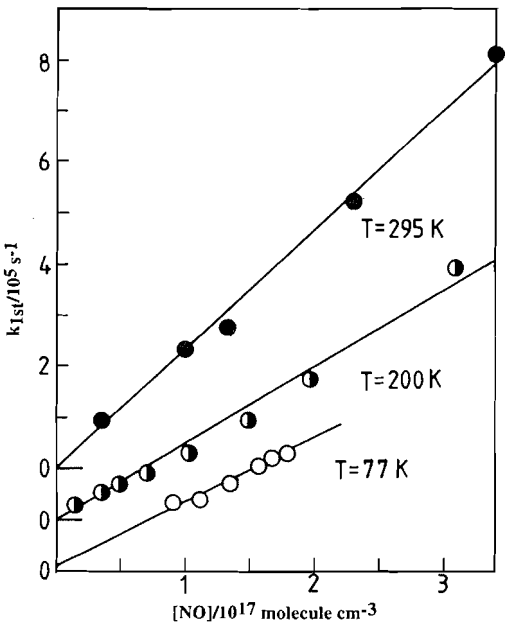

FIG. 3. First-order rate constants for the decay of LIF signals from NO(v = 2), in which the rotational and spin-orbit populations have become thermalised, plotted against concentration of NO. The values of k_{1st} and [NO] for the data at 77 K are one fifth and one tenth respectively, of the values indicated on the axes, and the plots are displaced vertically for clarity.

illuminated by the probe laser. Its effect on the rate of vibrational relaxation was negligible (8). Vibrational relaxation of NO(v = 2) is approximately two orders of magnitude slower than rotational relaxation. Therefore, in these measurements, the concentrations of NO used were in the range $(3 - 30) \times 10^{16}$ molecule cm^{-3}. As before the LIF signals always accurately fitted single exponential decays yielding first-order rate constants for transfer of population from $|v = 2\rangle$ with a thermal distribution of molecules over the rotational levels of both spin-orbit components.

Examples of the plots of k_{1st} against [NO] are shown in Fig. 3. The gradients of the lines yield the second-order constants ($k_{e'}$) for vibrational relaxation from NO(v = 2), which undoubtedly occurs by the slightly endothermic V–V exchange process represented by eq. [1]. These rate constants, those (k_e) for the reverse exothermic process calculated by applying the principle of detailed balance, and collisional probabilities for both processes are listed in Table 2.

The rate constants and probabilities for V–V energy transfer obtained in the present experiments at 295 K are compared with previous values for the same process determined at room temperature. Neither the measurements of Macdonald and Sopchyshyn (19) nor those of Horiguchi and Tsuchiya (20) can be described as direct, since in neither case was the mode of vibrational excitation state-specific. Stephenson's measurements (8) were made by exciting NO(v = 1) with a frequency-doubled CO_2 laser and observing the time-dependent behaviour of the (2,1) band emission as the vibrational level populations came into equilibrium, using a cold gas filter to discriminate against (1,0) emission. Our result at 295 K is in reasonable agreement with that of Stephenson (8).

Yang, Kim, and Wodtke (13) measured room temperature rate constants for the deactivation of NO($v \geq 8$) by NO. Their conclusion is that up to ca v = 8 the removal of NO molecules

TABLE 2. Rate constants (10^{-12} cm^3 molecule^{-1} s^{-1}) and collisional probabilities for V–V energy exchange in the endothermic ($k_{e'}$) and exothermic (k_e) directions in NO–NO and CO–CO collisions

T/K	$k_{e'}$ (NO–NO)[a]	k_e (NO–NO)[b]	k_e (CO–CO)[c]
295	2.44 ± 0.3	2.80 ± 0.3 0.0096	—
		3.8 ± 0.9 (8a)	3.46 ± 0.1 (24)
		2.3 ± 0.2 (19)	—
		1.6 ± 1.1 (18)	—
200	1.60 ± 0.3	2.0 ± 0.4 0.0072	4.25 (24)[d]
77	2.10 ± 0.2	3.5 ± 0.3 0.0130	—

[a]Rate constant for NO(v = 2) + NO(v = 0) → 2NO(v = 1).
[b]Rate constant for 2NO(v = 1) → NO(v = 2) + NO(v = 0).
[c]Rate constant for 2CO(v = 1) → CO(v = 2) + CO(v = 0).
[d]Interpolated from Stephenson's results (24) obtained at temperatures between 105 K and 300 K.

from excited vibrational levels in collisions with unexcited NO is dominated by V–V energy exchange. At higher levels of excitation, other mechanisms involving chemical forces appear to come into play. Using their data, one can compare the value of k_e/v for NO(v − 1) + NO(v = 1) → NO(v) + NO (v = 0) and v = 8, with our value of the same quantity for v = 2. The resultant "reduced rate constants" are 2.25×10^{-13} and 1.3×10^{-12} cm^3 molecule^{-1} s^{-1}, respectively. The decrease in the reduced rate constant that is observed with the increase in energy discrepancy from $\Delta E/hc$ = 28 cm^{-1} to 223.5 cm^{-1} is in sensible agreement with both theoretical expectation (13, 21, 22) and from extensive work on vibrational relaxation in CO (23).

We are unaware of any measurements of V–V energy exchange in NO–NO collisions at temperatures below room temperature. However, Stephenson and Mosburg (24) studied this process in CO at temperatures between 100 K and 300 K. Values of k_e for 2 CO(v = 1) → CO(v = 2) + CO(v = 0) are given for comparison in Table 2. A comparison of both the absolute values of the rate constants for V–V exchange and their variation with temperature suggests that the $^2\Pi$ electronic character of the ground state of NO exerts no significant influence on the rate of V–V energy exchange in contrast to its role in facilitating V–T energy transfer (8, 9). The similarity of the rate constants for V–V energy exchange in NO–NO and CO–CO collisions and their insensitivity to temperature suggest that, in both cases, energy transfer occurs under the influence of long-range attractive forces, arising from the electrostatic charge distributions in the molecules and their modulation by the molecular vibrations, in accord with the long-established theory of Sharma and Brau (25).

4. Summary and conclusions

A double resonance method, using tunable laser sources of infrared and ultraviolet radiation, has been employed to determine rate constants for rotational energy transfer in collisions between NO(v = 2, j, Ω = 1/2) and other NO molecules, for three different j levels and at three different temperatures. The rate constants are insensitive to the initial rotational level but decrease slightly as the temperature is lowered. The reasons for this change will be explored in future measurements of state-to-state rate coefficients and their dependence on temper-

ature, and the generality of this finding will be examined by investigating the effect of collision partners other than NO.

By performing similar experiments on NO samples diluted in argon and over longer pulse–probe time-scales, rate constants have also been measured for the self-relaxation of NO($v = 2$) by V–V energy transfer. The rate constants and their relative insensitivity to temperature indicate that in NO, at least for low vibrational levels, as for CO, V–V energy exchange occurs under the influence of long-range, attractive forces and the existence of spin-orbit degeneracy in NO is unimportant.

Acknowledgements

We are grateful to the Science and Engineering Research Council (SERC) for support of this work. We should also like to thank a referee who pointed out that transfer of molecules back into the initially populated level might be significant in our experiments.

1.(*a*) J.G. Haub and B.J. Orr. Chem. Phys. Lett. **107**, 162 (1984); (*b*) J. Chem Phys. **86**, 3380 (1987); (*c*) C.P. Bewick and B.J. Orr. J. Chem. Phys. **93**, 8634 (1990).
2.(*b*) B.L. Chadwick and B.J. Orr. J. Chem. Phys. **95**, 5476 (1991); (*b*) J. Chem. Phys. **97**, 3007 (1992).
3.(*a*) E. Carrasquillo, A.L. Utz, and F.F. Crim. J. Chem. Phys. **88**, 5976 (1988); (*b*) A.L. Utz, J.D. Tobiason, E. Carrasquillo, M.D. Fritz, and F.F. Crim. J. Chem. Phys. **97**, 389 (1992); (*c*) J.D. Tobiason, A.L. Utz and F.F. Crim. J. Chem. Phys. **97**, 7437 (1992).
4. (*a*) R. Dopheide, W.B. Gao, and H. Zacharias. Chem. Phys. Lett. **182**, 21 (1991); (*b*) R. Dopheide and H. Zacharias. J. Chem. Phys. **99**, 4864 (1993).
5. (*a*) M.J. Frost and I.W.M. Smith. Chem. Phys. Lett. **191**, 574 (1992); (*b*) M.J. Frost. J. Chem. Phys. **98**, 8572 (1993).
6. I.W.M. Smith and J.F. Warr. J. Chem. Soc. Faraday Trans. **87**, 205 (1991).
7. M.P. Casassa, J.C. Stephenson, and D.S. King. J. Chem. Phys. **89**, 1966 (1988).
8. (*a*) J.C. Stephenson. J. Chem. Phys. **59**, 1523 (1973); (*b*) J. Chem. Phys. **60**, 4289 (1974).
9. (*a*) E.E. Nikitin. Opt. Spectrosc. **9**, 8 (1960); E.E. Nikitin and S. Ya. Umanski. Faraday Discuss. Chem. Soc. **53**, 1 (1972).
10. (*a*) Aa.S. Sudbo and M.M.T. Loy. Chem. Phys. Lett. **82**, 135 (1981); (*b*) J. Chem. Phys. **76**, 3646 (1982).
11. X. Yang, J.M. Price, J.A. Mack, C.G. Morgan, C.A. Rogaski, D. McGuire, E.H. Kim, and A.M. Wodtke, J. Phys. Chem. **97**, 3944 (1993).
12. X. Yang and A.M. Wodtke. J. Chem. Phys. **96**, 5123 (1992).
13. (*a*) X. Yang, E.H. Kim, and A.M. Wodtke. J. Chem. Phys. **93**, 4483 (1990); (*b*) J. Chem. Phys. **96**, 5111 (1992).
14. P. Sharkey and I.W.M. Smith. J. Chem. Soc. Faraday Trans. **89**, 631 (1993).
15. C.M. Western, P.R.R. Langridge-Smith, and B.J. Howard. Mol. Phys. **44**, 145 (1981).
16. G.O. Sitz and R.L. Farrow. J. Chem. Phys. **93**, 7883 (1990).
17. A.S. Pine, A.G. Maki, and N.-Y. Chou. J. Mol. Spectrosc. **114**, 132 (1985).
18. T. Orlikowski and M.H. Alexander. J. Chem. Phys. **80**, 4133 (1984).
19. R.G. MacDonald and F.C. Sopchyshyn. Chem. Phys. **94**, 455 (1985).
20. H. Horiguchi and S. Tsuchuja. Jpn. J. Appl. Phys. **18**, 1207 (1979).
21. (*a*) R.N. Schwartz, Z.I. Slawsky, and K.F. Herzfeld. J. Chem. Phys. **20**, 591 (1952); (*b*) R.N. Schwartz and K.F. Herzfeld. J. Chem. Phys. **22**, 767 (1954).
22. (*a*) D. Rapp and P. Englander-Golden. J. Chem. Phys. **40**, 573 (1964); J. Chem. Phys. **43**, 316 (1965).
23. G. Hancock and I.W.M. Smith. Appl. Opt. **10**, 1827 (1971).
24. J.C. Stephenson and E.R. Mosburg, Jr. J. Chem. Phys. **60**, 3562 (1974).
25. (*a*) R.D. Sharma and C.A. Brau. J. Chem. Phys. **50**, 924 (1969); (*b*) R.D. Sharma. Phys. Rev. **177**, 102 (1969).

Can. J. Chem. Downloaded from www.nrcresearchpress.com by EESC ESCOLA DE ENGENHARIA on 09/08/12
For personal use only.

Dynamics of the reaction of nascent ethynyl with hydrogen

SHINTARO TASAKI, SUNITA SATYAPAL, AND RICHARD BERSOHN
Department of Chemistry, Columbia University, New York, NY 10027, U.S.A.

Received May 6, 1993

This paper is dedicated to Professor John C. Polanyi on the occasion of his 65th birthday

SHINTARO TASAKI, SUNITA SATYAPAL, and RICHARD BERSOHN. Can. J. Chem. **72**, 612 (1994).

At room temperature ethynyl radicals, C_2H, react only slowly with hydrogen molecules in spite of the fact that the reaction $C_2H + H_2 \rightarrow C_2H_2 + H$ is exothermic by 26 kcal/mol. Nascent C_2H (C_2D) radicals produced by photodissociation of C_2H_2 (C_2D_2) at 193 nm are shown to be as reactive with D_2 (H_2) as fluorine atoms with rate constants of $(2.3 \pm 0.4) \times 10^{-11}$ and $(3.2 \pm 0.5) \times 10^{-11}$ cm^3 molecule^{-1} s^{-1} respectively. The H and D atoms have average kinetic energies of 7.6 ± 0.7 and 7.8 ± 1.0 kcal/mol, respectively. About 70% of the available energy is therefore released as internal energy. The enhanced reactivity of the nascent ethynyl is ascribed to partial mixing of the vibrationally excited *X* state with the *A* state. This reactivity is rapidly lost in collisions with N_2. Overall the reaction of excited C_2H with H_2 is shown to be remarkably similar to the reaction of F atoms with H_2.

SHINTARO TASAKI, SUNITA SATYAPAL et RICHARD BERSOHN. Can. J. Chem. **72**, 612 (1994).

Même si la réaction $C_2H + H_2 \rightarrow C_2H_2 + H$ est exothermique (26 kcal/mol), les radicaux éthynyles, C_2H, ne réagissent que lentement avec l'hydrogène moléculaire à la température ambiante. On a montré que, vis-à-vis du D_2 (H_2), les radicaux C_2H (C_2D) naissants, obtenus par photodissociation du C_2H_2 (C_2D_2) à 193 nm, sont aussi réactifs les atomes de fluor; les constantes de vitesse sont respectivement de $2,3 \pm 0,4 \times 10^{-11}$ et $3,2 \pm 0,5 \times 10^{-11}$ cm^3 molecule^{-1} s^{-1}. Les énergies cinétiques des atomes de H et de D sont respectivement de 7,6 ± 0,7 et 7,8 ± 1,0 kcal/mol. Environ 70% de l'énergie disponible est donc émise sous forme d'énergie interne. On attribue la plus grande réactivité des radicaux éthynyles naissants à un mélange partiel de l'état *X* vibrationnellement excité avec l'état *A*. Cette réactivité est rapidement perdue lors de collisions avec N_2. On démontre que, dans l'ensemble, la réaction du C_2H excité avec le H_2 est très semblable à la réaction des atomes de F avec le H_2.
[Traduit par la rédaction]

One of the most extensively studied reactions in chemical dynamics is $F + H_2$. Its attractiveness stems from the facts that (*a*) H_2 has only two electrons and therefore *ab initio* calculations of the potential surface are conceivable and (*b*) H_2 and the HF product have a sparse set of widely spaced internal states. There is a set of three closely related reactions which have the essential similarity that they are highly exothermic reactions with H_2. These are

[1] $F + H_2 \rightarrow HF + H$ $\quad \Delta H = -35$ kcal/mol

[2] $CN + H_2 \rightarrow HCN + H$ $\quad \Delta H = -16$ kcal/mol

[3] $C_2H + H_2 \rightarrow HCCH + H$ $\quad \Delta H = -27$ kcal/mol

There are chemical connections. CN, being a pseudohalogen, has some chemical properties similar to those of a fluorine atom. C_2H is isoelectronic with CN and therefore might be expected to react similarly. All three reactants, F, CN, and C_2H have high electron affinities, 3.62, 3.82 (ref. 1), and 2.94 (ref. 2) eV, respectively. The extreme exoergicity of the $F + H_2$ reaction results in an early barrier which in turn leads to strong vibrational excitation of the HF product. The activation energy in each case is relatively small, being 1.0 ± 0.5, 5.6 ± 0.6, and 2.9 kcal/mol for reactions [1], [2], and [3], respectively (3). The barrier for the $F + H_2$ reaction is known to be least in the collinear geometry and at low energies the reaction is an abstraction with the HF recoiling backward in the center-of-mass system. Here we report a study of the dynamics of the reaction of C_2H with H_2 to see how similar it is to the reaction of F with H_2.

The rate constant for reaction [3] has been studied by a number of groups with generally concordant results (3–5). Table 1 lists the rate constants at room temperature measured in different ways. In the earliest measurement C_2H was generated by a discharge in a mixture of C_2HBr and excess H_2 (2). C_2H concentrations were measured as a function of time and H_2 pressure by mass spectroscopy (4). In other experiments C_2H was generated by a shock wave in a mixture of C_2H_2 and H_2 and the concentration of C_4H_2 was measured as a function of time and H_2 pressure (4). A competition was set up between the reaction of C_2H with C_2H_2 and with H_2 allowing both rate constants to be measured. In still another experiment a C_2H_2 and H_2 mixture in an excess of He was photolyzed and C_4H_2 was measured as a function of time and H_2 pressure (5).

There was excellent agreement between the results of six different groups (4–8) that the rate constant for reaction [3] at room temperature is in the range 1.5 to 7×10^{-13} cm^3 molecule^{-1} s^{-1}. Shock wave experiments showed that the rate constant increases by a factor of 50 between 300 and 2800 K from which an activation energy of 2.9 kcal/mol can be inferred.

Renlund et al. generated C_2H by 193 nm dissociation of C_2H_2, C_2HBr, and HC_2CHO (9). They monitored the CH(*A*–*X*) emission resulting from the reaction:

[4] $C_2H(X^2\Sigma) + O_2(^3\Sigma_g) \rightarrow CH(A^2\Delta) + CO_2(^1\Sigma)$

as a function of time and H_2 pressure. From these data they found a value for the rate constant of reaction [3] at room temperature of $(1.2 \pm 0.3) \times 10^{-11}$. Later this same group found a value of 2.7×10^{-11} by monitoring the decay of the C_2H $A \rightarrow X$ emission (10). Total pressures in their experiments never exceeded 0.8 Torr and were carried out at observation times of 2–10 μs. In contrast, Laufer and Bass (5) used pressures of 20–700 Torr of He at observation times of 5–20 μs without seeing any pressure effect. Lange and Wagner (4) used 4.2 Torr in a 300–900 μs observation time. Typical pressures and times in the shock wave experiments were 5 Torr and 100 μs.

The results of Wittig's group (9, 10) differ from those of all other workers. Our explanation is that they were generating

Can. J. Chem. Downloaded from www.nrcresearchpress.com by 195.246.54.202 on 09/08/12
For personal use only.

TABLE 1. Rate constants for $C_2H + H_2 \rightarrow HCCH + H$

k (cm^3 $molecule^{-1}$ s^{-1})	T (K)	Reference	Method
1.7×10^{-13}	320	4	(C_2H) (t)
$(1.52 \pm 0.11) \times 10^{-13}$	298	5	(C_4H_2) (t)
1.47×10^{-13}	298	6	(C_4H_2) (t)
$(4.8 \pm 0.3) \times 10^{-13}$	300	7	(C_2H) (t)
$(7.1 \pm 1.1) \times 10^{-13}$	300	8	(H) (t)
$(1.2 \pm 0.3) \times 10^{-11}$	300	9	$C_2H + O_2 \rightarrow CH(A) + CO_2$ CH(*A*) (t)
$(2.7 \pm 0.5) \times 10^{-11}$	300	10	(C_2H) (t)

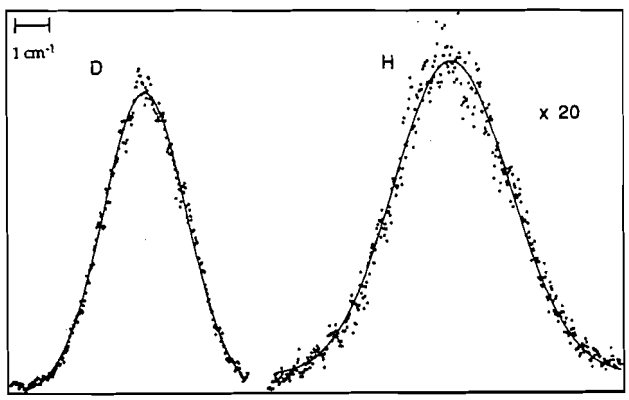

FIG. 1. Fluorescence excitation curves for reactant D atoms generated by photodissociation of C_2D_2 mixed with H_2 at 193.3 nm and product H atoms.

C_2H species with excess internal energy from all the molecules which they photodissociated whereas the other workers' measurements were made with thermalized C_2H radicals. A rough measure of the degree of relaxation of the C_2H radicals is furnished by the product in Torr–μs of the total pressure and the time over which the reaction is observed. For the Wittig experiments this product was 1.6 but it was 100 in the work of Laufer and Bass and 1260 in the experiments of Lange and Wagner. The experiments to be described here were carried out at pressures ≤ 0.1 Torr and times of 200 ns yielding a product of 0.02 Torr–μs.

Experimental

The techniques of hydrogen atom detection have been described previously (11). Briefly, a 193.3 nm ArF laser is used to dissociate C_2H_2 and at a later time, typically 200 ns later a probe laser at 121.6 nm is used to excite H atoms or D atoms in the system (Fig. 1). No H atom signal was seen in the absence of 193.3 nm light. To minimize two photon effects which would dissociate the C_2H ArF laser fluences were kept below 25 mJ/cm^2 (12, 13). Typical pressures were 20 millitorr of acetylene and 50 millitorr of hydrogen. The gases were premixed with different ratios with no change in the measured rate constants. H/D ratios were measured at various time delays and gave consistent rate constants. The vuv light was generated by two photon resonant frequency difference mixing in Kr and by frequency tripling in Kr with the same results in each case. Errors in the rate constants and average kinetic energies are the standard deviations of 5–6 runs. The kinetic energies are subject to an additional error due to difficulty in establishing the baseline.

Results

Because it was necessary to distinguish between hydrogen atoms formed by photodissociation of acetylene and those formed by reaction of ethynyl with hydrogen molecules, reaction [3] could not be directly studied. Instead two isotopic versions were used.

TABLE 2. Rate coefficients and energy disposal

Reaction	k (cm^3 $molecule^{-1}$ s^{-1})	$\langle E_T \rangle$ (kcal/mol)	$\langle b_T \rangle$
$HCC + D_2$	$(2.3 \pm 0.4) \times 10^{-11}$	7.8 ± 1.0	0.29
$DCC + H_2$	$(3.2 \pm 0.5) \times 10^{-11}$	7.6 ± 0.7	0.28
$F + H_2$	2.6×10^{-11}[a]	12.9 ± 1.9[b]	0.37

[a]Reference 20.
[b]S. Tasaki. Unpublished work.

[5] $C_2D + H_2 \rightarrow C_2DH + H$

[6] $C_2H + D_2 \rightarrow C_2HD + D$

The ethynyl radicals were generated by dissociating acetylene or deuteroacetylene. The great advantage in this choice is that for every $C_2H(D)$ generated by photodissociation an H(D) is simultaneously formed. Therefore the ethynyl radical in all its complex distribution over internal states does not have to be detected; only the two isotopic hydrogen atoms need be detected. The product H(D) can then be measured simultaneously with the reactant $C_2H(C_2D)$. The simple kinetic equation for the H atom concentration:

[7] $d(H)/dt = k(C_2D)(H_2)$

can be solved at short times, t for the rate coefficient k with the result that

[8] $1/k = (C_2D)/(H)(H_2)t = (D)/(H)(H_2)t$

The ratio of the atomic concentrations is given simply by the ratio of the areas under the fluorescence excitation curves. The results for the rate coefficients k, the average translational energy of the products and the fraction of the available energy released as translational energy $\langle f_T \rangle$ are given in Table 2. The ratio of the rate coefficient for the reaction of H_2 to that of the reaction with D_2 is roughly the square root of two, the ratio of the relative reactant velocities of the two reactions. Also the rate coefficient for this almost totally unrelaxed or nascent ethynyl radical is within experimental error the same as the result of Wittig (6) which was also obtained using unrelaxed ethynyl radicals. The agreement between these rate coefficients obtained by rather different experiments is satisfying.

One should distinguish between rate constants and rate coefficients. Rate constants can be defined as the constants extracted from kinetic equations describing the reactions of

Can. J. Chem. Downloaded from www.nrcresearchpress.com by 195.246.54.202 on 09/08/12
For personal use only.

Can. J. Chem. Downloaded from www.nrcresearchpress.com by 195.246.54.202 on 09/08/12
For personal use only.

reactants at thermal equilibrium. Rate coefficients have the same dimensions as rate constants but apply to reactants which are not in thermal equilibrium.

Discussion

In the foregoing it has been tacitly assumed that when acetylene is photodissociated at 193.3 nm three energetic species are formed directly: ethynyl radicals, hydrogen atoms, and triplet vinylidene. In principle, any of them could react with hydrogen molecules to form hydrogen atoms. Reactive collisions between D(H) and $H_2(D_2)$ can be ruled out by the following arguments. The hydrogen atoms produced by the photodissociation of acetylene have an average kinetic energy of 8.0 ± 1.4 (D) and 9.5 ± 1.5 (H) kcal/mol in the lab frame. However, in the center of mass frame, the average relative kinetic energy is only about 4 kcal/mol for the D + H_2 pair and about 5 kcal/mol for the H + D_2 pair. Because the barrier for the H + H_2 reaction is 8 kcal/mol most of the hydrogen atoms do not have enough kinetic energy to react. Moreover, the reaction cross section just above the threshold is very small (11, 14). Finally, addition of 2 torr of He to the reaction mixture of C_2D_2 and H_2 substantially slows down the hydrogen atoms (15) but had no effect on the product yield.

The other possible reactant with hydrogen is the still mysterious triplet vinylidene which is the principal product of absorption of a 193 nm photon by acetylene. Fahr and Laufer (16) found that when C_2D_3Cl is dissociated at wavelengths >155 nm that the resulting D_2CC ($^3B_2$) was quenched by H_2 without any reaction. In other words, during the collision the molecule passed from the triplet surface to a singlet surface on which it rapidly isomerized to DCCD. The rate constant for quenching was $(3.38 \pm 0.61) \times 10^{-14}$ cm^3 molecule^{-1} s^{-1}, three to four orders of magnitude smaller than a gas kinetic rate constant. This rate, characteristic of a forbidden process, is much slower than any of the rates of reaction listed in Table 1. Indeed the quenching rate constant for N_2 molecules is $(8.5 \pm 0.2) \times 10^{-15}$ cm^{3}molecule^{-1} s^{-1}. On the other hand, the rate coefficient for quenching by N_2 of the reaction of C_2D with H_2 inferred from a 50% quenching by 200 mtorrr is 1.5×10^{-12} in the same units. The easy quenching of the reaction by N_2 implies an easy V–V energy transfer in which the N_2 molecule can accept about 2300 cm^{-1} from the nascent C_2D.

Thus by a process of elimination we conclude that the reactant with the hydrogen molecules is ethynyl. The rate coefficient which we obtain is very close to that obtained by Wittig (9, 10) which in turn was much larger than the thermal rate constant measured by others. However, this difference is presumed to be the result of a great difference in reactivity between unrelaxed nascent ethynyl (this work and Wittig (10)) and thermally equilibrated ethynyl.

The origin of the enhanced reactivity of the nascent ethynyl is not immediately obvious. The average internal energy of ethynyls generated by 193.3 nm photodissociation of room temperature acetylene is 8–9 kcal/mol or 2800–3150 cm^{-1}. Thus the average ethynyl can have at most one or two quanta in the vibrational modes which stretch bonds which will not be broken during the reaction. It is also not clear how excitation of the HCC bend would affect a reaction barrier. However, the $A^2\pi$ state lies only 3600 cm^{-1} above the $X^2\Sigma$ ground state. Consequently there will be extensive mixing of the vibrationally excited ground state with the electronically excited state. A rough description of the *A* state is that an electron in a π bonding state has been promoted to a Σ state (17). The potential surface *vis-a-vis* an incoming H_2 molecule should be quite different from that of the ground state and the small barrier to reaction may be removed. Table 2 shows that the only isotope effect on the ethynyl–hydrogen reaction is that the H_2 molecules have an average speed $(2)^{1/2}$ times that of the D_2 molecule. This is again consistent with a negligible barrier to reaction for these excited ethynyl radicals.

In conclusion we have demonstrated that nascent ethynyls generated by photodissociation of acetylene are far more reactive with H_2 than room temperature ethynyls. In this reaction about 70% of the available energy is released as internal energy, presumably mainly as vibration. This reaction of nascent C_2H has much in common with the paradigm F + H_2 reaction in exothermicity, rate constant and high vibrational energy release. In fact Harding et al. did an *ab initio* calculation of the potential surface for ground state C_2H and H_2 (18). They found that the saddle point was collinear and located in the reagent region of configuration space with the H_2 bond distance elongated by only 6% and the bond distances in C_2H unchanged. The theoretical prediction is that the reaction $C_2H + H_2$ like the reaction F + H_2 is a collinear abstraction with an early barrier (19).

Acknowledgment

This research was supported by the U.S. Department of Energy.

1. R. Klein, R.P. McGinnis, and S.R. Leone. Chem. Phys. Lett. **100**, 475 (1983).
2. B.K. Janousek, J.I. Brauman, and J. Simons. J. Chem.Phys. **71**, 2057 (1979).
3. NIST chemical kinetics Database. *Distributed by* Office of Standard Reference Data, NIST, Gaithersburg, MD 20899.
4. W. Lange and H.G. Wagner. Ber. Bunsenges. Phys. Chem. **79**, 165 (1985).
5. A.H. Laufer and A.M. Bass. J. Phys. Chem. **83**, 310 (1979).
6. W. Gardiner, T. Tanzawa, T. Koike, and K. Morinaga. Bull. Chem. Soc. Jpn. **58**, 1851 (1985).
7. J.W. Stephen, J.L. Hall, H. Solka, W.B. Han, R.F. Curl, and G.F. Glass. J. Phys. Chem. **91**, 5740 (1987).
8. M. Koshi, N. Nishida, and H. Matsui. J. Phys. Chem. **96**, 5875 (1992).
9. A.M. Renlund, F. Shokoohi, H. Reisler, and C. Wittig. Chem. Phys. Lett. **84**, 293 (1981).
10. F. Shokoohi, T.A. Watson, H. Reisler, F. Kong, A.M. Renlund, and C. Wittig. J. Phys. Chem. **90**, 5695 (1986).
11. G.W. Johnston, B. Katz, K. Tsukiyama, and R. Bersohn. J. Phys. Chem. **91**, 5445 (1987).
12. B.A. Balko, J. Zhang, and Y.T. Lee. J. Chem. Phys. **94**, 7958 (1990).
13. S. Satyapal and R. Bersohn. J. Phys. Chem. **95**, 8004 (1991).
14. I. Schechter and R.D. Levine. Int. J. Chem. Kinet. **18**, 1023 (1986).
15. J. Park, N. Shafer, and R. Bersohn. J. Chem. Phys. **91**, 7861 (1989).
16. A. Fahr and A.H. Laufer. J. Phys. Chem. **90**, 5064 (1986).
17. S. Shih, S.D. Peyerimhoff, and R.J. Buenker. J. Mol. Spectr. **61**, 167 (1977).
18. L.B. Harding, G.C. Schatz, and R.A. Chiles. J. Chem. Phys. **76**, 5172 (1982).
19. J.C. Polanyi and W.H. Wong. J. Chem. Phys. **51**, 1439 (1968).
20. W.B. DeMore et al. Jet Propulsion Laboratory Report 87–41. 1987.

Reaction dynamics studies of a simple tetraatomic system: AA + BA ↔ A + ABA

STEFAN KOPPE, THOMAS LAURENT, PRAKASH D. NAIK,[1] HANS-ROBERT VOLPP,[2] AND JÜRGEN WOLFRUM

Physikalisch-Chemisches Institut der Universität Heidelberg, Im Neuenheimer Feld 253, 69120 Heidelberg, Federal Republic of Germany

Received August 13, 1993

This paper is dedicated to Professor John C. Polanyi on the occasion of his 65th birthday

STEFAN KOPPE, THOMAS LAURENT, PRAKASH D. NAIK, HANS-ROBERT VOLPP, and JÜRGEN WOLFRUM. Can. J. Chem. **72**, 615 (1994).

We have studied the reaction of translationally excited hydroxyl radicals with molecular hydrogen at different center-of-mass energies. H/D atoms produced in the reaction have been detected under single collision conditions by means of vacuum ultraviolet laser-induced fluorescence at the Lyman-α transition. By calibrating the H/D signals from the reaction against H atom signals from the H_2S and HCl photolysis, respectively, the following absolute reactive cross sections were determined: $OH + H_2 \rightarrow H + H_2O$: $\sigma_R(0.17\ eV) = (0.08 \pm 0.03)$ Å^2, $\sigma_R(0.22\ eV) = (0.60 \pm 0.30)$ Å^2; $OH + D_2 \rightarrow D + HOD$: $\sigma_R(0.28\ eV) = (0.22 \pm 0.05)$ Å^2, $\sigma_R(0.37\ eV) = (0.43 \pm 0.09)$ Å^2. With translationally excited H atoms, we have also studied the reverse reaction system, $H + D_2O$. In this case the OD product radicals were detected under single collision conditions with quantum state resolution by means of laser-induced fluorescence. By calibrating the OD signals from the reaction against OH signals from the H_2O_2 photolysis, absolute reaction cross sections were measured for $H + D_2O \rightarrow OD + HD$: $\sigma_R(1.5\ eV) = (0.07 \pm 0.04)$ Å^2, $\sigma_R(1.8\ eV) = (0.10 \pm 0.03)$ Å^2, and $\sigma_R(2.2\ eV) = (0.11 \pm 0.03)$ Å^2. At different center-of-mass collision energies nascent population distributions of the OD product fine-structure components were determined. It has been found that at all collision energies OD radicals are produced exclusively in their vibrational ground state, with only a small amount of the total available energy appearing in the rotational degree of freedom. A comparison of the dependence of the reaction cross section on the translational energy shows that relative reagent translation is more effective to promote reactivity in the reaction $OH + H_2$ and $OH + D_2$ than in the reaction $H + D_2O$. This, together with a preferential population of the symmetric $^2\Pi(A')$ Λ-doublet state (with the unpaired π orbital lying in the plane of rotation) at high OD rotational quantum numbers, suggests that the reaction $H + D_2O \rightarrow OD + HD$ proceeds through a planar transition state via a direct mechanism, where the OD moiety acts as a spectator, and where the reaction barrier is located at a "later" position of the reaction coordinate.

STEFAN KOPPE, THOMAS LAURENT, PRAKASH D. NAIK, HANS-ROBERT VOLPP et JÜRGEN WOLFRUM. Can. J. Chem. **72**, 615 (1994).

On a étudié la réaction de radicaux hydroxyles excités d'un point de vue translationnel avec de l'hydrogène moléculaire, à diverses énergies du centre de masse. On a détecté les atomes H/D produits dans la réaction dans des conditions de collision unique, en faisant appel à la fluorescence induite par un laser dans l'ultraviolet lointain au niveau de la transition Lyman-α. En calibrant les signaux de H/D de la réaction à l'aide des signaux d'atomes H provenant de la photolyse du H_2S et du HCl respectivement, on a déterminé les sections droites réactives absolues suivantes : $OH + H_2 \rightarrow H + H_2O$: $\sigma_R(0,17\ eV) = (0,08 \pm 0,03)$ Å^2, $\sigma_R(0,22\ eV) = (0,60 \pm 0,30)$ Å^2; $OH + D_2 \rightarrow D + DOH$: $\sigma_R(0,28\ eV) = (0,22 \pm 0,05)$ Å^2, $\sigma_R(0,37\ eV) = (0,43 \pm 0,09)$ Å^2. Utilisant des atomes d'H excités d'une façon translationnelle, on a aussi étudié le système réactionnel inverse, $H + D_2O$. Dans ce cas, pour détecter les radicaux OD produits dans des conditions de collision unique, avec une résolution de l'état quantique, on a fait appel à la fluorescence induite au laser. En calibrant les signaux OD de la réaction à l'aide de signaux OH obtenus par photolyse de H_2O_2, on a mesuré les sections droites absolues de la réaction $H + D_2O \rightarrow OD + HD$: $\sigma_R(1,5\ eV) = (0,07 \pm 0,04)$ Å^2, $\sigma_R(1,8\ eV) = (0,10 \pm 0,03)$ Å^2 et $\sigma_R(2,2\ eV) = (0,11 \pm 0,03)$ Å^2. On a déterminé, à diverses énergies de collision du centre de masse, les distributions de population naissante de composantes de la structure fine du produit OD. On a trouvé que, pour toutes les énergies de collision, les radicaux OD ne sont produits que dans leur état vibrationnel fondamental; seule une faible partie de l'énergie totale disponible apparaît dans le degré de liberté rotationnel. Une comparaison de la dépendance de la section droite de la réaction sur l'énergie de translation montre que la translation relative du réactif est plus efficace pour promouvoir la réactivité dans les réactions $OH + H_2$ et $OH + D_2$ que dans la réaction $H + D_2O$. Ce résultat, pris avec le fait que la population de l'état doublet symétrique-Λ, $^2\Pi(A')$ (comportant une orbitale π non appariée se trouvant dans le plan de rotation), est préférée pour les nombres quantiques élevés de OD, suggère que la réaction $H + D_2O \rightarrow OH + HD$ se produit par un mécanisme direct impliquant un état de transition plan alors que la portion OD agit comme spectateur et que la barrière à la réaction se trouve dans la « dernière » partie des coordonnées de la réaction.

[Traduit par la rédaction]

1. Introduction

Since the first pioneering infrared chemiluminescence studies of Cashion and Polanyi (1), observation and interpretation of vibrational product state distributions as well as the investigation of the influence of selective reagent vibrational (2, 3) and (or) translational excitations on the rate of reaction have remained central in the field of bimolecular reaction dynamics (4–6). A reaction that has been the subject for a large number of dynamical, both experimental and theoretical, studies, is the reaction $F + H_2 \rightarrow HF + H$ (which is isoelectronic to the four-atom $OH + H_2$ reactive system, investigated in this paper) and its deuterated counterparts. This reaction, as one of the simplest examples of an exothermic chemical reaction, has become a benchmark system (besides the thermoneutral hydrogen exchange reaction $H + H_2 \rightarrow H_2 + H$ (7)) for comparison between experimental and theoretical studies of atom + diatomic molecule systems. For this reaction detailed information about the product energy distribution has been determined

[1]On sabbatical leave from Chemistry Division, Bhabha Atomic Research Center, Bombay, India.

[2]Author to whom correspondence may be addressed. Telephone: 6221-564248. Telefax: 6221-564255. E-Mail: AW2@VM.URZ.UNI-HEIDELBERG.DE or AW2@DHDURZ1.

Can. J. Chem. Downloaded from www.nrcresearchpress.com by 195.246.54.202 on 09/08/12
For personal use only.

Can. J. Chem. Downloaded from www.nrcresearchpress.com by 195.246.54.202 on 09/08/12
For personal use only.

by infrared chemiluminescence experiments (8), chemical laser experiments (9), and from crossed molecular beam experiments (10). Thermal rate constants have also been measured over a wide temperature range (11, 12). Extensive theoretical studies of this reaction system have been carried out by Muckerman (13) and Polanyi and Schreiber (14) using the quasi-classical trajectory (QCT) method, developed in the 1960s by Bunker, Karplus, Polanyi, and their co-workers. Especially in Polanyi's studies, emphasis was given to studying the fundamental relationships between features of the underlying PES (potential energy surface) and the related dynamical aspects of the reactive collision of A + BC → AB + C systems. Based on the results of a series of extensive QCT studies (15) on different model semi-empirical, LEPS (London–Eyring–Polanyi–Sato) (16), and BEBO (bond-energy bond-order) (17) potential energy surfaces it was possible to derive several general principles (18). Although it emerged mainly from investigations of atom–diatom systems, as we will see later in this article, Polanyi's general description still holds in a variety of reactions, even those involving polyatomic reagents. In trajectory calculations of A + BCD → AB + CD systems Raff (19) and Smith (20) found that, compared to the newly formed bond AB, the "old" CD bond is only moderately excited. The influence of special mass combinations (e.g., where A is light compared to BCD) and geometries (bent transition states) on the efficiency of channelling energy into vibration of the "old" CD bond has been discussed in ref. 21.

Among bimolecular four-atom systems, the reaction

[1] $H + H_2O \rightarrow OH + H_2 \qquad \Delta H_0^0 = 62$ kJ/mol

and its reverse reaction

[2] $OH + H_2 \rightarrow H + H_2O$

have become prototypes for comparison between quantum state resolved experiments and bimolecular collision theory of reactions involving four atoms. LEPS and BEBO potential energy surfaces were constructed by Zellner and Smith in 1973 (22). The fact that three of the atoms involved in the reaction are hydrogen atoms furthermore favoured the development of a global *ab initio* potential energy surface. Already in the year 1980 an *ab initio* PES of the HHOH(A') gound state, the so called WD/SE (Walch–Dunning/Schatz–Elgersma) potential energy surface (23, 24), was constructed. The H-H-O-H transition state of reaction [1] was found to be bent and planar, with the H—O—H angle being very close to that in the free H_2O molecule, and with an O—H—H angle of 15° (25). The WD/SE-PES has a classical barrier of 0.923 eV for reaction [1], which is very close to the vibrationally adiabatic barrier of 0.94 eV, reported in ref. 26, and has an overall endoergicity of 0.659 eV. New *ab initio* surfaces were derived only recently by Isaacson (27) and Dunning et al. (28).

The first pioneering QCT studies of reaction [1] were carried out by Schatz et al. (29). They examined the influence of reagent translational excitation as well as normal-mode and local-mode excitation on the reactivity and the product state energy partitioning in reaction [1]. Additional quasi-classical (30–32) and quantum-classical (33) studies were carried out for reactions [1] and [2]. Quantum scattering studies on the dynamics of reaction [1] carried out by Clary in 1991 (34) represent the first quantum mechanical calculations for a four-atom reaction with realistic nonlinear geometry. Further quantum calculations of mode specificity in reaction [1] were reported also by Bowman and Wang (35), and by Clary (36). Most recently, quantum mechanical calculations on the dynamics of reaction [1], applying negative imaginary potentials (37), have been reported by Baer and co-workers (38).

The first experiments on the influence of translational excitation and isotopic substitution on the dynamics and on the absolute reaction cross section of reaction [2] were carried out by Wolfrum and co-workers (39, 40). Dynamics studies of reaction [2] have also been carried out by Kessler and Kleinermanns (41) and Honda et al. (42). Different experiments on the influence of selective vibrational excitation of H_2O on the reaction dynamics of reaction [1] and its isotopically substituted counterparts have been carried out. The first example of mode-selective chemistry of highly vibrationally excited H_2O with room temperature H atoms was reported by Crim and coworkers (43). The first experiments on the reaction of translationally excited H atoms with HOD/D_2O molecules, which are prepared only with low levels of vibrational excitation, were reported by Zare and co-workers (44). Measurements in which the HD product molecules from the reaction H + D_2O were detected with quantum state resolution were also reported recently from Zare's laboratory (45). Also recently, in Leone's group (46), the first measurements were carried out in which the rotational and vibrational excitation of water molecules by translationally excited H atoms has been investigated.

Due to the great importance of reaction [2] in combustion and atmospheric chemistry, the thermal rate constant was measured over an extended temperature range (47, 48). Additionally, in several experiments on the state specific kinetics of reaction [2], it was found that H_2 vibrational excitation promotes reactivity more than does vibrational excitation of OH (49). Only recently experimental results of a reaction dynamics study of the reaction OH + D_2 were reported in a communication by Casavecchia and co-workers (50), who measured the HOD product angular distribution using a crossed molecular beams setup.

In this article we report the first results of reaction dynamics studies of reaction [2] with translationally excited reactants. To study the influence of isotopic substitution on the dynamics we also investigated the reaction of OH with molecular deuterium, for which the two following reaction pathways

[3*a*] $OH + D_2 \rightarrow HOD + D$

[3*b*] $OH + D_2 \rightarrow D_2O + H$

are possible. In addition we studied the influence of reagent translation on the dynamics and the absolute reactive cross sections of reaction [1] by investigating the reaction H + D_2O.

[4*a*] $H + D_2O \rightarrow OD + HD$

$\rightarrow OH + D_2$

For all reactions [2], [3], and [4] we measured absolute reactive cross sections and branching ratios at different collision energies.

2. Experimental

The experiments we report here were performed using two separate experimental setups, which are depicted schematically in Figs. 1 and 2. In all experiments we used the laser photolysis/laser-induced fluorescence (LP/LIF) "pump–probe" technique. It is essentially the same

Can. J. Chem. Downloaded from www.nrcresearchpress.com by 195.246.54.202 on 09/08/12
For personal use only.

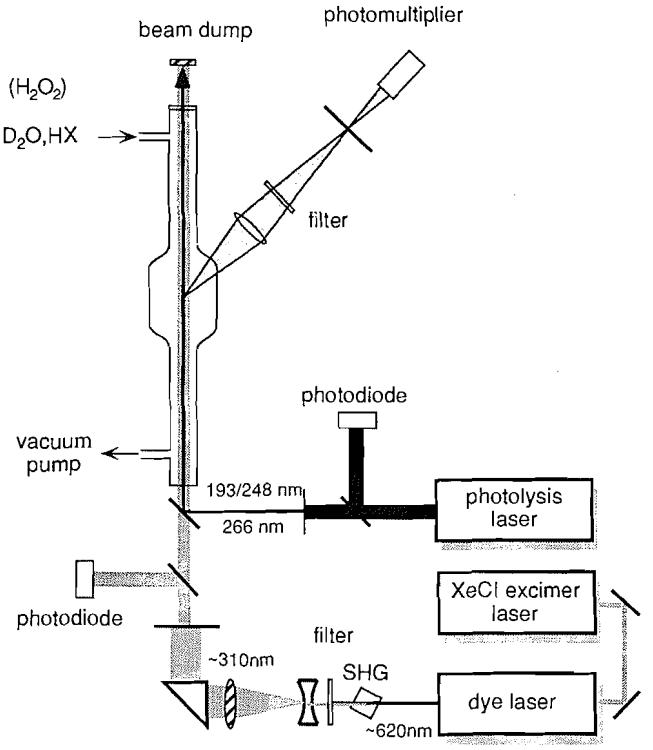

FIG. 1. Schematic diagram of the experimental setup that was used to study the reaction H + D_2O.

method already used to measure reaction cross sections and OH quantum state distributions for the reactions H + NO (51*a*), H + O_2 (51*b*), and H + CO_2 (51*c*).

Reaction [4] was studied in a Teflon-coated quartz reactor (depicted in Fig. 1) equipped with long sidearms acting as a baffle system to keep scattered light out of the fluorescence-collecting optics. The experiments were carried out in flowing mixtures of HX (with HX being either H_2S UCAR, electronic grade, or HI UCAR, 98%) and room temperature D_2O (Merck 99.8%) with a ratio of 1:10 at a total pressure of typically 50–70 mTorr (measured by a MKS Baratron) (1 Torr = 133.3 Pa). H_2S was used without further purification; HI was pumped through a cooling trap to remove I_2 impurities before entering the reaction cell. Translationally excited H atoms were generated by photodissociation of the HX precursor using an excimer laser (Lambda LPX 205) with unstable resonator optics. The laser was operated at 20 Hz with an ArF mixture (emission wavelength 193 nm) to photodissociate H_2S and with a KrF mixture (emission wavelength 248 nm) to photodissociate H_2S and HI. A circular diaphragm with an aperture of 3 mm was used to skim off a homogeneous irradiated part of the unfocused rectangular excimer profile to provide the photolysis beam. In addition we used the fourth harmonic of a Nd:YAG laser (Spectra Physics GCR 11, operated at 10 Hz) to photodissociate HI at 266 nm. Energies of 5 mJ/pulse at 193 nm (at this pulse energy no OD background from the direct D_2O photolysis was detectable), 10 mJ/pulse at 248 nm, and 5 mJ/pulse at 266 nm (measured with an energy detector Gentec ED 200) were used in the experiment. With these pulse energies both the OD signals from the reaction as well as the OH signals from the H_2O_2 photodissociation showed a linear dependence on the photolysis laser intensity. We therefore conclude that with the above-mentioned pulse energies no nonlinear effects in either the HX or the H_2O_2 photodissociation were present. For the calibration measurements H_2O_2 was pumped through the cell at a total pressure of typically 10 mTorr. Prior to use, the H_2O_2 (85% PEROXID Chemie) was pumped through the cell for at least 3 days until it reached a final concentration >99.8% (determined by titration).

Typically, 60–150 ns after the photolysis laser pulse, the nascent OD/OH product radicals were probed by a second copropagating laser beam via laser-induced fluorescence of the $A^2\Sigma^+ \leftarrow X^2\Pi$ system. The UV probe beam (bandwidth 0.2 cm^{-1}) in the wavelength region of 305–320 nm was provided by a frequency-doubled dye laser (Lambda FL 2002 EC) working with Rhodamine B, pumped by a XeCl excimer laser (Lambda EMG 201 MSC). To ensure a linear dependence of the OH/OD fluorescence on the probe laser intensity the probe beam was attenuated and expanded with a telescope to a diameter of 12 mm and aligned to overlap the 3 mm diameter photolysis beam in the focus of observation. The emitted OH fluorescence was collected by a lens ($f = D = 50$ mm) and projected through a 1 × 5 mm slit aperture and a UV filter (Schott UG 11, 1 mm) upon the cathode of a photomultiplier (EMI 9781 B, voltage 620 V). The OH/OD LIF signal as well as the photolysis and probe intensities (both measured with photodiodes) were recorded with a 3-channel boxcar system (SRS 250) and transferred to a microcomputer (HP series 9000, model 320) via an analog-to-digital converter (SRS 235). The OH/OD fluorescence signals were normalized to both photolysis and probe laser intensity. OH/OD LIF spectra were recorded between 306.5 and 324 nm, where most of the OH/OD($A^2\Sigma^+$, $v' = 0, 1 \leftarrow X^2\Pi$, $v'' = 0, 1$) transitions are located. Line positions of the OH/OD(A–X) transitions were taken from refs. 52 and 53.

The experiments in which H/D atoms from reactions [2] and [3] were detected were carried out in a flow reactor with a slightly modified design. Due to the need to directly connect the VUV generation cell to the reactor, we had to switch to a crossed laser beam setup, schematically shown in Fig. 2. These experiments were carried out in a flowing mixture of H_2O_2 and room temperature H_2 (>99.999%) or D_2 (>99.7%) with a ratio of 1:10 at a total pressure of 60–120 mTorr, using the 248 nm (193 nm) laser photolysis of H_2O_2 to produce translationally excited OH radicals. For the calibration measurements H_2S (UCAR electronic grade), HCl (>99.999%) was pumped through the cell at a total pressure of 5 mTorr. The H,D product atoms were probed by a VUV laser beam, via laser-induced fluorescence at the corresponding Lyman-α transition, 80–150 ns after the photolysis laser pulse. The VUV probe laser beam was carefully aligned to overlap the photolysis beam at right angles in the viewing region of the detector. The LIF signal was measured by a solar blind photomultiplier (Hamamatsu model R1259, denoted as PM 1 in Fig. 2) at right angles to both the pump and probe laser beam, through a band pass filter (ARC, model 122-VN-ID, $\lambda_c = 122$ nm, FWHM = 20 nm). The VUV probe beam intensity was monitored before and after passing through the reaction cell with two additional solar blind photomultipliers (denoted PM 2 and PM 3 in Fig. 2).

The VUV probe laser light (bandwidth 0.4 cm^{-1}) for H (121.567 nm) and D (121.534 nm) atom detection was generated by resonant third-order sum-difference frequency conversion ($\omega_{VUV} = 2\omega_R - \omega_T$) in a phase-matched Kr–Ar mixture (54). The frequency ω_R ($\lambda_R = 212.55$ nm) is in resonance with the 4*p*-5*p* (1/2, 0) two-photon transition in Kr and ω_T is the tuning frequency ($\lambda_T = 844$–848 nm). The fundamental laser radiation was obtained from two tunable dye lasers (Lamda FL 2002 EC), simultaneously pumped by a XeCl excimer laser (Lambda 201 MSC), one of which (ω_R) was frequency doubled with a BBO II crystal. The generated Lyman-α light was separated from the fundamental lasers by a monochromator lens (denoted as ML in Fig. 2). The Lyman-α probe beam via photolysis of the precursor molecule H_2O_2 produces a significant amount of additional H atoms. To distinguish these H atoms from the H atoms produced in the reaction, a shutter was inserted in the photolysis beam path. At each step of the scan, the signal was first averaged with the shutter opened and again averaged with the shutter closed. A point-by-point subtraction procedure was adopted, to obtain a signal free from the background H atoms described above. All photomultiplier signals (from PM 1, PM 2, PM 3), as well as the photolysis and probe laser intensity signals were recorded with a 4-channel boxcar system (SRS 250) and transferred to the laboratory computer, via an analog-to-digital converter (SRS 235), where the H/D atom LIF signal was normalized to both photolysis and probe laser intensities. To obtain a satisfactory S/N ratio each point in the recorded spectra was averaged over at least 30 laser shots. In all the experiments we carefully checked

Can. J. Chem. Downloaded from www.nrcresearchpress.com by 195.246.54.202 on 09/08/12
For personal use only.

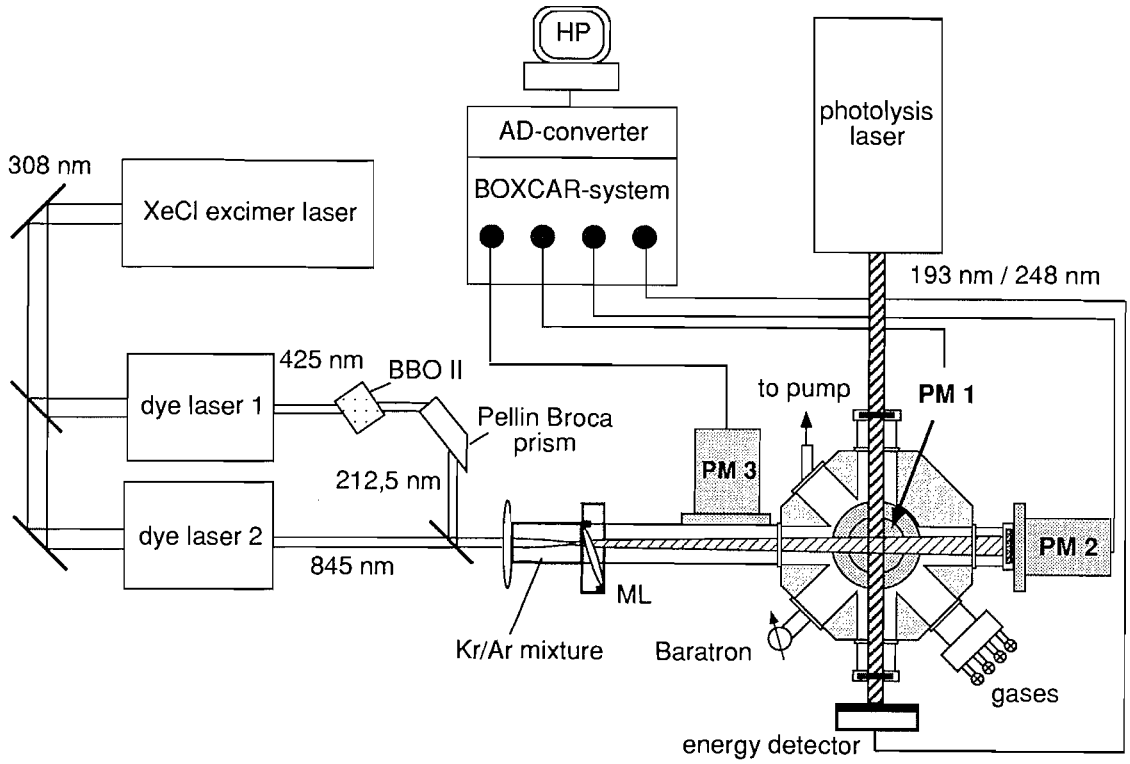

FIG. 2. Schematic diagram of the experimental setup that was used to study the reactions OH + H_2/D_2 (ML = monochromator lens; PM = photomultiplier).

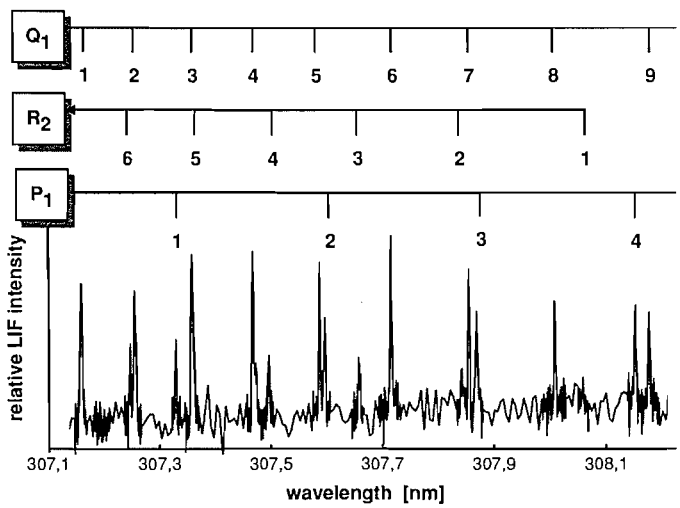

FIG. 3. Part of the OD($A^2\Sigma^+$, $v' = 0 \leftarrow X^2\Pi$, $v'' = 0$) LIF spectrum from the reaction H + D_2O at $E_{c.m.}$ = 2.2 eV

that the flow rate in the reaction cell was high enough to ensure total gas renewal in the volume sampled between two successive laser shots.

3. Experimental results

In Fig. 3 a typical LIF spectrum of OD radicals produced in reaction [4*a*] is shown, where the "hot" H atoms with an average center-of-mass energy of $E_{c.m.}$ = 2.2 eV were generated by 193 nm photolysis of H_2S. Each point in the recorded spectrum was averaged over 40 laser shots. To determine the relative number densities n_i of OD and OH radicals in the absorbing rotational level i we used the following linear relationship

$$[5] \quad I_{meas,ik} = Cn_iB_{ik}\nu_{ik}I_{probe}I_{photo}$$

where B_{ik} is the Einstein coefficient of absorption (taken from (refs. 55 and 56) and ν_{ik} is the wavenumber for the transition $i \rightarrow k$. I_{probe} is the probe laser intensity and I_{photo} the intensity of the photodissociation laser. C is a factor that describes the effects of the detector system such as quantum efficiency, geometrical collection efficiency, etc. on the measured LIF intensity. $I_{meas,ik}$ is determined by numerical integration of the corresponding spectral line profile $i \rightarrow k$ in the digitized LIF spectrum. Overlapping lines were deconvoluted by fitting separate Gaussian functions to the digitized LIF spectrum using a numerical least-squares fitting procedure. For overlapping satellite and main lines the sum was determined and separated into components by the known ratio of their Einstein coefficients.

Typical Lyman-α H atom and D atom spectral lines are shown in Fig. 4. The H atoms were generated from the 248-nm photodissociation of H_2S. The D atoms were produced in the reaction OH + D_2. From the spectral line, relative H and D atom number densities were determined by numerical integration of the corresponding spectral line profiles using a linear relationship similar to eq. [5].

3.A. $H + D_2O$

The electronic ground state of the OH/OD radical is a $^2\Pi$ state. Therefore there is an unpaired π orbital lying perpendicular to the internuclear axis. Due to the interaction between the spin of the electron and the electronic angular momentum, every rotational state is split into two spin-orbit states, $\Pi_{1/2}$ and $\Pi_{3/2}$. In the rotating molecule the interaction between the electronic angular momentum and the rotational angular momentum splits every spin-orbit state into two Λ components (57), denoted as $\Pi(A')$ and $\Pi(A'')$ according to ref. 58. In the high J limit, where Hund's case (*b*) description is appropriate, the electronic wave function in both spin-orbit states has a definite

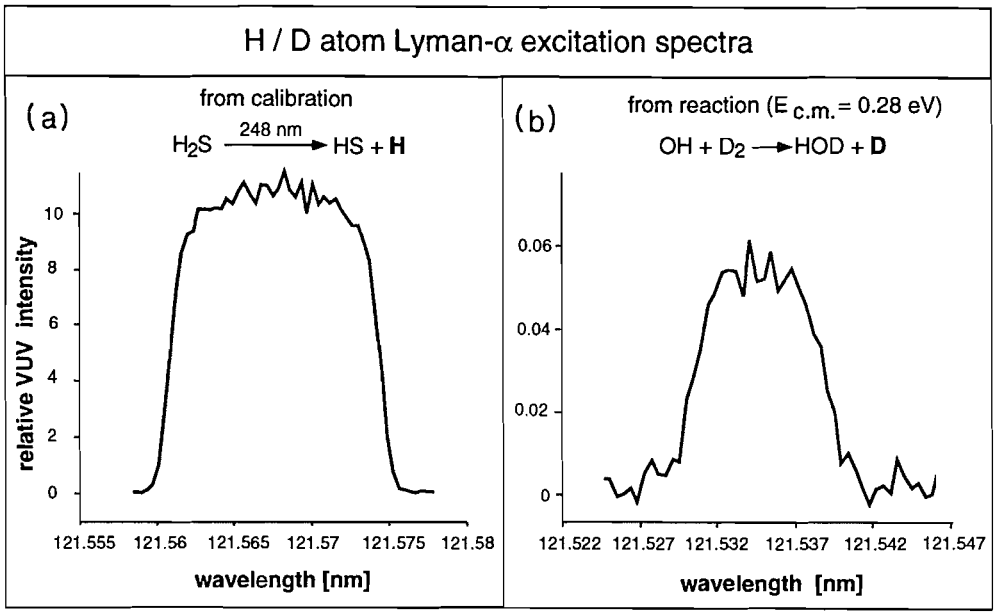

FIG. 4. H/D atom spectral lines. (*a*) H atoms from the 248 nm photolysis of H_2S. (*b*) D atoms from the reaction OH + D_2 → HOD + D at $E_{c.m.}$ = 0.28 eV.

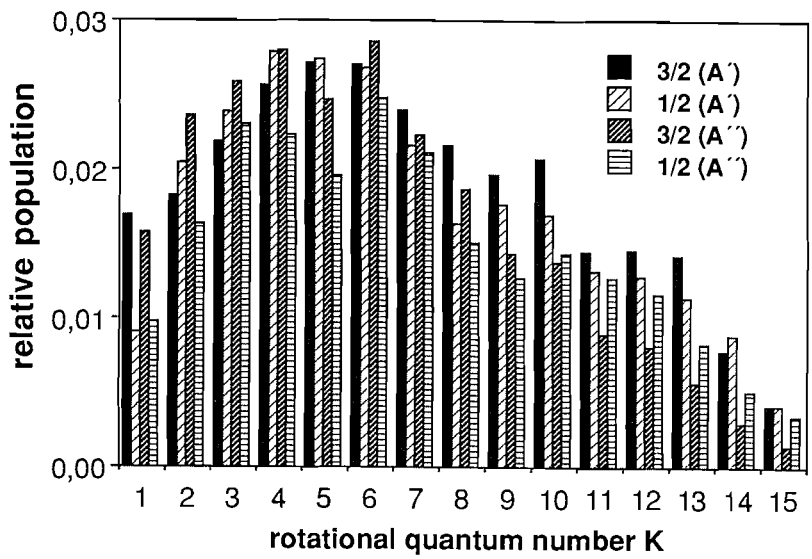

FIG. 5. Population distribution of the rotational fine structure states of the OD($v = 0$) products from reaction [4*a*] at $E_{c.m.}$ = 2.2 eV. The distribution has been normalized to have a total population of unity.

reflection symmetry with respect to the plane of rotation. In this case the $\Pi(A')$ Λ-doublet states can be characterized by the π molecular orbital lobes being located in the plane of rotation, while in case of the $\Pi(A'')$ Λ-doublet states the π molecular orbital lobes are oriented perpendicular to the plane of rotation.

In Fig. 5 the OD($v = 0$) product rotational fine-structure distribution from reaction [4*a*] at $E_{c.m.}$ = 2.2 eV is shown. From the relative population of the fine-structure energy levels we calculate the average OD rotational energy to be $\langle E_{Rot} \rangle$ = 0.06 eV. This means that only about 4% of the excess energy in the reaction appears in the rotational degree of freedom of the OD radicals. At the other collision energies we found a similar behaviour. At 1.5 eV, 7%, and at 1.8 eV, 5% of the total available energy appears as rotational energy of the OD products. At none of the collision energies used in our investigation could any OD($v = 1$) products be observed. From our S/N ratio we determined the upper limit for the OD $v = 1/v = 0$ ratio to be 0.05 ± 0.01.

From the fine-structure distribution we determined the population ratio of the two spin-orbit components. The $\Pi_{3/2}/\Pi_{1/2}$ ratio (weighted by $K/(K + 1)$ to account for the different degeneracy of the two spin-orbit states) is almost unity for all rotational quantum numbers K. On the other hand a markedly preferential population for the $\Pi(A')$ states at high rotational quantum numbers was found, when we calculated the Λ-doublet ratio $\Pi(A')/\Pi(A'')$, shown in Fig. 6.

Absolute reactive cross sections were measured applying the method introduced by Kleinermanns and Wolfrum (59). Using pulsed laser systems (typical pulse duration 8–10 ns), this method allows measurements of absolute product radical num-

Can. J. Chem. Downloaded from www.nrcresearchpress.com by 195.246.54.202 on 09/08/12
For personal use only.

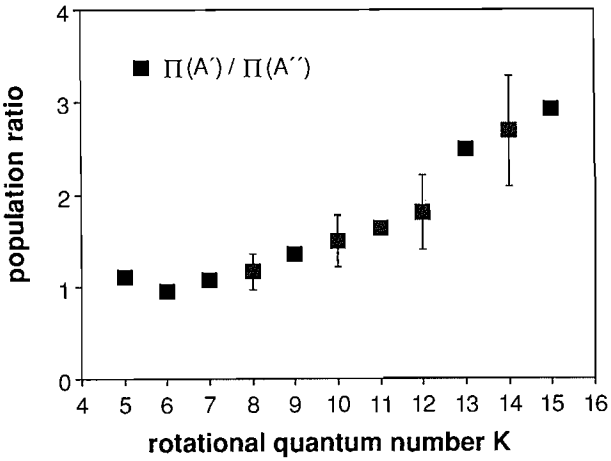

FIG. 6. Population ratio $\Pi(A')/\Pi(A'')$ of the OD(v = 0) Λ-components at high rotational numbers.

ber densities with a time resolution high enough to determine absolute reaction cross sections under single collision conditions. This method utilizes a well-defined radical source to calibrate the LIF signal from unknown number densities obtained in the reaction. In this work we used the well-characterized photodissociation of H_2O_2 (60) to generate well-defined OH number densities. The final equation [6], to calculate the absolute reaction cross section given in ref. 40, consists of several directly measurable parameters.

$$[6]\quad \sigma = (n_{R,i} f_{C,n} \phi^{OH} \sigma^{H_2O_2}[H_2O_2])/(n_{C,i} f_{R,n} \sigma^{HX}[HX][D_2O] t v_{rel})$$

Here [A] denote the concentrations of species involved (usually given in cm^{-3}), which are calculated directly from the corresponding partial pressures. Values for the H_2O_2 absorption cross sections $\sigma^{H_2O_2}$ and the corresponding quantum yields ϕ^{OH} were taken from ref. 61. σ^{HX} denotes the absorption cross section of the H atom precursor molecule HX. Absorption cross sections for HI at 248 and 266 nm were taken from ref. 62. In the case where the 248 and 266 nm HI photolysis was used to generate H atoms, the absorption cross sections given in ref. 62 were multiplied with the $I(^2P_{3/2})/I(^2P_{1/2})$ branching ratios given in ref. 62. This was necessary to account for the fact that at both photodissociation wavelengths only the "fast" H atoms from the $H + I(^2P_{3/2})$ dissociation channel have enough energy to overcome the reaction barrier. v_{rel} is the relative velocity of the reactants, calculated from energy and momentum conservation of the HX photodissociation at the given photolysis wavelength of the experiment using the formulas given in ref. 63. In the case of the 193-nm H_2S photodissociation (where X = HS) the average relative velocity was determined by weighted averaging over the measured H atom distribution reported in ref. 64. $n_{R,i}$ denotes the relative number density (calculated using eq. [3]) of OD radicals from the reaction in the fine-structure state i, $n_{C,i}$ is the relative number density of OH radicals in the same fine-structure state i from the H_2O_2 photolysis. $f_{R,i}$ and $f_{C,i}$ refer to the corresponding relative population of the fine-structure state i. The delay time t was determined directly by measuring the time difference between the pump and probe stray light pulses on a fast oscilloscope (Tektronik model 485, 350 MHz).

As one can see from eq. [6], prior to the measurement of the absolute reaction cross section, the complete OD/OH vibrational and rotational distribution for the reaction and the H_2O_2 photolysis had to be determined. After this, a single spectral OD line starting from one fine-structure level i was recorded in the reaction. After flushing the cell with N_2 (for at least 30 min), H_2O_2 was flowed through the reactor (again for at least 20 min, to ensure complete wall passivation of the reaction cell) and the corresponding OH spectral line was recorded in the H_2O_2 photodissociation. With this procedure, which was repeated several times for different nonoverlapping Q and P branch spectral lines, we determined the following absolute reactive cross sections for reaction [4a]:

$$\sigma_R(1.5\text{ eV}) = (0.07 \pm 0.04)\ \text{Å}^2$$

$$\sigma_R(1.8\text{ eV}) = (0.10 \pm 0.03)\ \text{Å}^2$$

$$\sigma_R(2.2\text{ eV}) = (0.11 \pm 0.03)\ \text{Å}^2$$

Each of the following values represents the mean value calculated from at least eight independent calibration measurements using the method described above. The experimental error was calculated from the errors of the entries of eq. [6] on the basis of simple error propagation. Errors of the absorption cross sections and quantum yields were taken from the corresponding references. The absolute error in the measurement of the delay time t between photolysis and probe laser pulse (which is due to the intrinsic time jitter of both lasers) was estimated to be ±5 ns.

In several of the OD spectra we recorded, we found weak but clearly detectable OH(v = 0, K = 1–8) signals. In contrast to this, within our detection limit, no OH(v = 1) were found. Several test runs at a photolysis wavelength of 193 nm were carried out, where only D_2O was pumped through the cell. In this case no OH signals were detectable. So we conclude that the OH signals are not due to the direct photolysis of H_2O/HOD impurities of our D_2O sample. In all the measurements we found that OH signals were only present when HX/D_2O mixtures were pumped through the reactor. Even though the HX and D_2O were mixed just before entering the reaction cell we cannot rule out the possibility of fast heterogenous isotope exchange reactions in the short part of the line where both compounds are present. This could lead to H_2O/HOD and later in the reactor, via H + H_2O/HOD, to OH formation. Therefore we suggest that our values R^* represent upper limits for the ratio $R = \sigma[4b]/\sigma[4a]$ of the reaction cross sections. By comparing the relative number densities of the observed OH rotational levels (which have been corrected to account for the OH contribution arising from the reaction of H atoms with the small amount of H_2O/HOD impurities (0.2%) specified by the D_2O manufacturer, using the cross sections reported in refs. 39a and 44b) with those of the corresponding OD rotational levels, we determined the following values:

$$R^*(1.5\text{ eV}) = (4.1 \pm 0.5) \times 10^{-3}$$

$$R^*(1.8\text{ eV}) = (4.2 \pm 0.5) \times 10^{-3}$$

$$R^*(2.2\text{ eV}) = (4.9 \pm 0.4) \times 10^{-3}$$

These values are consistent with the qualitative observation made in ref. 42 and the ratio of the thermal rate constants $k[4b]/k[4a]$ reported in ref. 65.

Can. J. Chem. Downloaded from www.nrcresearchpress.com by 195.246.54.202 on 09/08/12
For personal use only.

Can. J. Chem. Downloaded from www.nrcresearchpress.com by 195.246.54.202 on 09/08/12
For personal use only.

3.B. OH + H_2/D_2

The method used to determine absolute reaction cross sections for these reactions is in principle the same as already described above. The differences are that here H_2O_2 was used as a precursor for translationally excited OH radicals and that H/D atoms were detected on the product side. The H/D atom signals from the reaction of OH with molecular hydrogen and deuterium were calibrated against H atom signals from the HX (X = Cl, HS) photolysis.

As already discussed in ref. 60, H_2O_2 photodissociation at 248 and 193 nm is a convenient source of translationally almost monoenergetic OH($v = 0$) radicals. At 193 nm only 2% OH($v = 1$) frequents have been detected, and at 248 nm the OH radicals are produced exclusively in the vibrational ground state. At both wavelengths the population of the OH rotational states can be described by a sharply peaked Gaussian-like distribution. At 193 nm the maximum of the rotational state distribution is located at $K = 12$, with a FWHM of $\Delta K \approx 3$, and at 248 nm the maximum of the distribution is located at $K = 6$, with a FWHM of $\Delta K \approx 4$.

To calculate the absolute reaction cross sections we used an equation similar to eq. [6]. The absolute reaction cross section for reaction [3*a*], for example, was determined using the following expression:

$$[7] \quad \sigma = (n_R \sigma^{HX}[HX])/(n_C \phi^{OH} \sigma^{H_2O_2}[H_2O_2][D_2] t v_{rel})$$

In this case n_R denotes the relative number density of the D atoms produced in the reaction and n_C is the relative number density of H atoms produced in the HX photolysis. The mean relative velocity v_{rel} in the center-of-mass frame was calculated from the average laboratory velocities (4.0 km/s at 248 nm and 4.6 km/s at 193 nm) given in refs. 66 and 51*c*, using the formulas from ref. 63. In the special case of reactions [2] and [3*b*], the direct photolysis of H_2O_2 at 193 nm already generates an H-atom background signal. So, n_R in eq. [7] has to be taken as the difference between the relative number densities of H atoms produced in the reaction and the H atom background generated by direct 193 nm photolysis of H_2O_2. In the case of H_2O_2 photolysis at 248 nm, no H atoms were observed from the direct photolysis, within our detection limit. So in this case it was not necessary to apply the above-mentioned subtraction method.

Repeating the calibration procedure several times at different reactant pressures and delay times, the following absolute reactive cross sections for the reactions [2] and [3*a*] were determined:

$$\sigma_{R,[2]}(0.17 \text{ eV}) = (0.08 \pm 0.03) \text{ Å}^2$$

$$\sigma_{R,[2]}(0.22 \text{ eV}) = (0.60 \pm 0.30) \text{ Å}^2$$

$$\sigma_{R,[3a]}(0.28 \text{ eV}) = 0.22 \pm 0.05) \text{ Å}^2$$

$$\sigma_{R,[3a]}(0.37 \text{ eV}) = 0.43 \pm 0.09) \text{ Å}^2$$

The subtraction procedure to eliminate the H atom background originating from the 193 nm photolysis of H_2O_2 magnifies significantly the experimental error involved in the cross section measurement. As a consequence, for reactions [2] and [3*b*] it was not possible to measure reaction cross sections with an accuracy better than 0.1 Å^2 in the case of photolysis at 193 nm. Nevertheless, we could not detect any H atom signals that could clearly be assigned to reaction [3*b*]. Therefore, we determined an upper limit of the reaction cross section to be 0.1 Å^2 for $E_{c.m.} = 0.37$ eV (photolysis wavelength 193 nm) taking into account the above-mentioned errors, and 0.001 Å^2 for $E_{c.m.} = 0.28$ eV (photolysis wavelength 248 nm). Thus we report the following K^* values, being upper limits for the ratio $K = \sigma[3b]/\sigma[3a]$ of the reaction cross sections.

$$K^*(0.28 \text{ eV}) = 4.5 \times 10^{-3}$$

$$K^*(0.37 \text{ eV}) = 2.3 \times 10^{-1}$$

It should be noted that, due to the special mass combination of the reactants, the width (FWHM) in the collision energy distribution arising from the thermal motion of the reactants is substantially large (0.095 and 0.11 eV at $E_{c.m.} = 0.17$ eV and $E_{c.m.} = 0.22$ eV, for reaction [2]; 0.12 and 0.15 eV at $E_{c.m.} = 0.28$ eV and $E_{c.m.} = 0.37$ eV, for reaction [3]). This large inherent spread in $E_{c.m.}$ limits the resolution for closer investigation of the variation of the cross section with energy, so that additional measurements of cross sections near threshold with this method will hardly provide more detailed information regarding the excitation function.

4. Discussion

The rather small branching ratios R^* and K^* that we determined in our study clearly indicate that reactions [1] and [2] proceed almost exclusively with a direct mechanism rather than with an indirect mechanism via an H_3O intermediate.

The low rotational excitation and the absence of vibrational excitation of the OD product radicals from reaction [4*a*] (identical results were found in previous studies of reaction [1]) furthermore support the conclusion that the reaction proceeds by a direct abstraction mechanism without forming a long-lived complex (which would lead to a statistical distribution of the available energy over the product degrees of freedom). As already discussed in refs 44 and 42, the low degree of vibrational excitation of the OD products can be attributed to special features of the transition-state geometry (24). A comparison of the OD bond length of the nonreacting OD bond at the transition state with the equilibrium values in the D_2O and OD molecules shows that the OD bond length is almost unchanged in going from reagents through the transition state to the products. This condemns the OD moiety to play the role of a spectator during the reactive collision.

Different explanations have been given to account for the generally low rotational excitation of OH radicals produced via reaction [1]. In ref. 39*a* an impulsive model was presented, in which OH rotation is excited by impulsive forces between the O atom and the departing H_2 molecule. In this model the degree of OH rotational excitation is limited by the small mass of the H_2 fragment and the small "lever arm" (which is defined as the distance between the center of mass of the OH molecule and the O atom) on which the impulsive force can exert torque during the breakup of the transition state. Owing to the fact that in the case of OD the lever arm is about twice as long as it is in OH, one would expect in general a higher degree of rotational excitation for OD products from reaction [4*a*] than for the OH products from reaction [1].

In refs. 29 and 40 a simple stripping model was discussed. In this picture the OH rotational excitation is produced by simply mapping reagent (H_2O) bend excitation onto the OH rotation.

Can. J. Chem. Downloaded from www.nrcresearchpress.com by 195.246.54.202 on 09/08/12
For personal use only.

The final average rotational energy of the OH/OD products from reaction [1]/[4*a*] should therefore be proportional to the energy in the H_2O/D_2O zero-point bending motion, which becomes a free OH/OD rotational motion after the reaction. Thus the average rotational energy of OH products from reaction [1] should always be about 1.4 times the average rotational energy of OD products from reaction [4*a*].

The results of several experimental and theoretical studies have shown that it is not possible to explain all the experimental results within the framework of simply one of the above-mentioned models (43, 44). At $E_{c.m.}$ = 1.5, 1.8, and 2.2 eV we and other workers (44*c*) found more rotational excitation in OD from reaction [4*a*] than in OH from reaction [1], while at a higher energy of 2.5 eV (39*b*, 40) the opposite behaviour was found. This led us to conclude that the mechanism responsible for the hydroxyl product rotational excitation changes from an impulsive mechanism at lower collision energies to a stripping mechanism at higher energies. In QCT studies of reaction [4*a*] it was found that, in qualitative agreement with our experimental results, the OD product rotational excitation indeed decreases with increasing collision energy (32*c*).

In Fig. 6 the population ratio $\prod(A')/\prod(A'')$ of the OD Λ-doublet components is plotted against the rotational quantum number K. At $E_{c.m.}$ = 2.2 eV we found that the $\prod(A')/\prod(A'')$ ratio of the OD radicals from reaction [4*a*] increases monotonically with increasing rotational quantum number, reaching a value of about 3 at the highest K probed. The same behaviour was found at $E_{c.m.}$ = 1.5 eV (44) and 1.8 eV. Preferential population of the symmetric OH $\prod(A')$ Λ-doublet component has also been reported for the OH fine-structure distributions from reaction [1] (39, 42, 44*b*, 44*c*). Integration of the observed $\prod(A')/\prod(A'')$ ratio over the rotational quantum states populated in the reaction furthermore shows that the total cross section for producing OD in the $\prod(A')$ state in reaction [4*a*] is significantly larger than the total cross section for producing OD in the $\prod(A'')$ state. This may be understood on the basis of a simple classical model: An analysis of the normal mode eigenvector of the imaginary frequency in the transition state of reaction [1] shows that this mode is mainly an OH stretch (35*c*). So, the preferential population observed for the OD A' states in reaction [4*a*] simply reflects that a perpendicular collision of H with D_2O (which would lead to OD in the A'' state) has less chance to couple with the O—D stretching in the transition state, which would move the system along the reaction coordinate. On the other hand, a planar approach has more chance to couple with the O—D stretching, leading to the higher cross section for OD formation with the unpaired π orbital lobes left in the plane of reagent approach.

In Fig. 7 we have compared our experimental absolute reactive cross sections of reaction [4*a*] with the results of recent QCT calculations (32*c*). For comparison, QCT results for reaction [1] are also included, together with experimental values reported in refs. 39*a*, 40, and 41. As one can see, the reaction cross sections are generally small, showing a pronounced isotope effect, which is very well reproduced by the QCT calculation. For reaction [4*a*] the reaction cross section increases only about 30% when the collision energy is increased from 1.5 to 2.5 eV. This has to be compared to the increase of reactivity when energy is added as D_2O reagent vibration. In ref. 44*c* it was demonstrated that an increase of 0.35 eV in the asymmetric stretch vibration (0, 0, 1) of D_2O increases the cross section by at least 400%. Similar enhancement in the reactivity has been

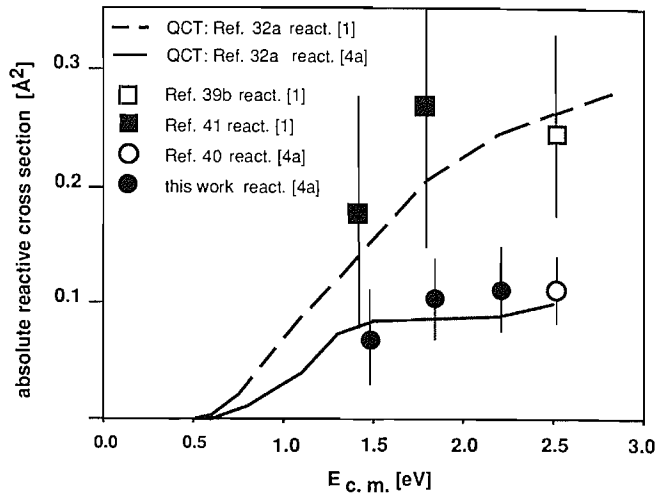

FIG. 7. Absolute reactive cross section for $H + D_2O \rightarrow OD + HD$ (reaction [4*a*]). For comparison, both experimental and theoretical results obtained for $H + H_2O \rightarrow OH + H_2$ (reaction [1]) have also been included.

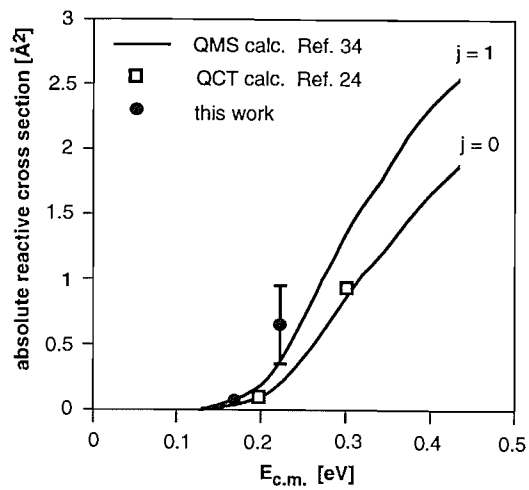

FIG. 8. Absolute reactive cross section of the reaction $OH + H_2 \rightarrow H_2O + H$.

observed in the studies of Crim and co-workers (43), where the influence of H_2O vibrational overtone excitation on the reactivity of reaction [1] was investigated. This behaviour is consistent with the general principle for the effects of translational versus vibrational energy on the reaction cross section of endothermic reactions with a "late" barrier (15*b*). In several *ab initio* studies it has been found that the reactions [1] and [4*a*] have a "late" barrier (23) and thus the behaviour described above is as expected.

In Fig. 8 we have compared our experimental absolute reaction cross sections of reaction [2] with results from recent QMS (quantum mechanical scattering) calculations (34) and previous QCT studies (24) of reaction [2]. In the case of reaction [2] we found that translational excitation is more efficient in promoting reactivity than it is for the reverse reaction [1]. This is in good agreement with the above-mentioned principle, because the reaction barrier is now located at an "early" stage of the reaction coordinate.

At this point it should be mentioned that the experimental conditions are somewhat different from the assumptions made

Can. J. Chem. Downloaded from www.nrcresearchpress.com by 195.246.54.202 on 09/08/12
For personal use only.

in the dynamical calculations. In the experiments the OH radicals are highly rotationally excited, while, for example, the QCT cross sections (depicted in Fig. 8) were calculated for nonrotating OH (24). The influence of OH rotation on the reactivity was investigated in a separate study on the original WD/SE PES (which has some well-known nonphysical features in the OH + H_2 channel) by the same workers (29*d*), where they found that the cross section decreases with increasing rotational number. The QMS cross sections (depicted in Fig. 8) were calculated for nonrotating OH and for OH with one quantum of rotation using a slightly modified version of the WD/SE potential (in which a damping function was added to remove the above-mentioned defects of the original PES).

Harrison and Mayne (31) carried out a detailed QCT study on the influence of reagent rotation on the reactivity of reaction [2], using the original WD/SE PES and the RB (Rashed–Brown) modification (30*b*) of the WD/SE PES. They found that the way OH rotation influences the reactivity is very sensitive to details (and therefore also to the defects) of the potential. Their results suggest that most of the previous results (29*d*, 30*b*) were affected by the presence of artificial wells (hills, in case of the RB modification) in the OH + H_2 entrance channel.

For comparison with our experimental results, additional studies (both quantum mechanical and quasi-classical) of the influence of OH rotation (up to at least 20 quanta) and isotopic substitution on the reactive cross section of [2] on new PES are clearly needed. This would allow us to average the theoretical OH rotational state specific cross sections over the OH reagent rotational state distributions and the collision energy distribution used in the experiments, a procedure that is clearly necessary for a detailed comparison.

Acknowledgments

The financial support of the Deutsche Forschungsgemeinschaft is gratefully acknowledged. The authors would like to thank D.C. Clary, G. Nyman, and G.C. Schatz for stimulating discussions. P.D.N. thanks the KFA Jülich for a fellowship under the Indo-German bilateral agreement.

1. J.K. Cashion and J.C. Polanyi. J. Chem. Phys. **30**, 317 (1959); Proc. R. Soc. London, A: **258**, 529 (1960); J. Chem. Phys. **35**, 600 (1961).
2. M. Kneba and J. Wolfrum. Annu. Rev. Phys. Chem. **31**, 47 (1980).
3. I.W.M. Smith. *In* Advances in gas-phase photochemistry and kinetics. Vol. 2. *Edited by* M.N.R. Ashfold and J.E. Baggot. The Royal Society of Chemistry, London. 1989. pp. 53–104.
4. R.D. Levine and R.B. Bernstein. *In* Molecular reaction dynamics and chemical reactivity. Oxford University Press, Oxford. 1987.
5. G.W. Flynn and R.E. Weston, Jr. Annu. Rev. Phys. Chem. **37**, 551 (1986).
6. N.F. Scherer, L.R. Khundkar, R.B. Bernstein, and A.H. Zewail. J. Chem. Phys. **87**, 1451 (1987).
7. H. Buchenau, J.P. Toennies, J. Arnold, and J. Wolfrum. Ber. Bunsen-Ges. Phys. Chem. **94**, 1231 (1990).
8. J.C. Polanyi and D.C. Tardy. J. Chem. Phys. **51**, 5717 (1969); N. Jonathan, C.M. Melliar-Smith, and D.H. Slater. Mol. Phys. **20**, 93 (1971); J.C. Polanyi and K.B. Woodall. J. Chem. Phys. **57**, 1574 (1972).
9. J.H. Parker and G.C. Pimentel. J. Chem. Phys. **51**, 91 (1969).
10. T.P. Schafer, P.E. Siska, J.M. Parson, F.P. Tully, Y.C. Wong, and Y.T. Lee. J. Chem. Phys. **53**, 3385 (1970); D.M. Neumark, A.M. Wodtke, G.N. Robinson, C.C. Hayden, and Y.T. Lee. J. Chem. Phys. **82**, 3045 (1985); D.M. Neumark, A.M. Wodtke, G.N. Robinson, C.C. Hayden, K. Shobatake, R. Sparks, T.P. Schafer, and Y.T. Lee. J. Chem. Phys. **82**, 3067 (1985).
11. K.H. Homann, W.C. Solomon, J. Warnatz, H. Gg. Wagner, and C. Zetsch. Ber. Bunsen-Ges. Phys. Chem. **74**, 585 (1970); K.L. Kompa and J. Wanner. Chem. Phys. Lett. **12**, 568 (1972).
12. E. Wurzberg and P.L. Houston. J. Chem. Phys. **72**, 4811 (1980); R.F. Heidner III, J.F. Bott, C.E. Gardner, and J.E. Melzer. J. Chem. Phys. **72**, 4815 (1980).
13. J.T. Muckerman. J. Chem. Phys. **54**, 1155 (1971); J. Chem. Phys. **56**, 2947 (1972).
14. J.C. Polanyi and J.L. Schreiber. Discuss. Faraday Soc. **62**, 267 (1977).
15. (*a*) J.C. Polanyi and W.H. Wong. J. Chem. Phys. **51**, 1439 (1969); (*b*) M.H. Mok and J.C. Polanyi. J. Chem. Phys. **51**, 1451 (1969); (*c*) J. Chem. Phys. **53**, 4588 (1970).
16. F. London. Z. Elektrochem. **35**, 552 (1929); H. Eyring and M. Polanyi. Z. Phys. Chem. Abt. B: **12**, 279 (1931); S. Sato. J. Chem. Phys. **23**, 592, 2465 (1955).
17. H.S. Johnston. Adv. Chem. Phys. **3**, 131 (1960).
18. J.C. Polanyi. Acc. Chem. Res. **5**, 161 (1972).
19. L.M. Raff. J. Chem. Phys. **44**, 1202 (1966).
20. I.W.M. Smith. Discuss. Faraday Soc. **44**, 194 (1967).
21. J.C. Polanyi and J.L. Schreiber. *In* Physical chemistry — an advanced treatise. Vol. VI A. *Edited by* H. Eyring, D. Henderson, and W. Jost. Academic Press, New York. 1974. pp. 383–487.
22. R. Zellner and I.W.M. Smith. J. Chem. Soc. Faraday Trans. 2, **69**, 1617 (1973).
23. S.P. Walch and T.H. Dunning. J. Chem. Phys. **72**, 1303 (1980).
24. G.C. Schatz and H. Elgersma. Chem. Phys. Lett. **73**, 21 (1980).
25. G.C. Schatz and H. Elgersma. *In* Potential energy surfaces and dynamics calculations. *Edited by* D. Truhlar. Plenum, New York. 1981.
26. D.G. Truhlar and A.D. Isaacson. J. Chem. Phys. **77**, 3516 (1982).
27. A.D. Isaacson. J. Phys. Chem. **96**, 531 (1992).
28. T.H. Dunning, L.B. Harding, and E. Kraka. *In* Supercomputer algorithms for reactivity, dynamics, and kinetics of small molecules. *Edited by* A. Lagaña. Kluwer, Dordrecht, The Netherlands. 1989. pp. 57–71.
29. G.C. Schatz, J.L. Colton, and M.C. Grant. J. Phys. Chem. **88**, 2971 (1984); H. Elgersma and G.C. Schatz. Int. J. Quantum. Chem. Symp. **15**, 611 (1981); G.C. Schatz. J. Chem. Phys. **74**, 1133 (1981); G.C. Schatz and S.P. Walch. J. Chem. Phys. **72**, 776 (1980).
30. (*a*) N.J. Brown and O. Rashed. J. Chem. Phys. **85**, 4348 (1986); (*b*) J. Chem. Phys. **82**, 5506 (1985).
31. J.A. Harrison and M. Mayne. J. Chem. Phys. **88**, 7424 (1988).
32. (*a*) K. Kudla and G.C. Schatz. J. Chem. Phys. **95**, 8267 (1991); (*b*) Chem. Phys. Lett. **193**, 507 (1992); (*c*) J. Chem. Phys. **98**, 4645 (1993).
33. G.D. Billing. Chem. Phys. **146**, 63 (1990).
34. D.C. Clary. J. Chem. Phys. **95**, 7298 (1991).
35. (*a*) D. Wang and J.M. Bowman. J. Chem. Phys. **96**, 8906 (1992); (*b*) J.M. Bowman and D. Wang. J. Chem. Phys. **96**, 7852 (1992); (*c*) D. Wang and J.M. Bowman. J. Chem. Phys. **98**, 6235 (1993).
36. D.C. Clary. J. Chem. Phys. **96**, 3656 (1992); Chem. Phys. Lett. **192**, 34 (1992).
37. (*a*) D. Neuhauser and M. Baer. J. Phys. Chem. **94**, 185 (1990); (*b*) M. Baer and D. Neuhauser. J. Chem. Soc. Faraday Trans. **86**, 1721 (1990); (*c*) M.S. Child. Mol. Phys. **72**, 89 (1991); (*d*) T. Seideman and W.H. Miller. J. Chem. Phys. **96**, 4412 (1992).
38. H. Szichman, I. Last, A. Baram, and M. Baer. J. Phys. Chem. **97**, 6436 (1993).
39. (*a*) K. Kleinermanns and J. Wolfrum. Appl. Phys. B: **B34**, 5 (1984); (*b*) A. Jacobs, H.R. Volpp, and J. Wolfrum. 24th Int. Symp. on Combustion. The Combustion Institute, Pittsburgh, Pa. 1992. p. 605.
40. A. Jacobs, H.R. Volpp, and J. Wolfrum. Chem. Phys. Lett. **196**, 249 (1992).
41. K. Kessler and K. Kleinermanns. Chem. Phys. Lett. **190**, 145 (1992).
42. K. Honda, M. Takayanagi, T. Nishiya, H. Ohoyama, and I. Hanazaki. Chem. Phys. Lett. **180**, 321 (1991).

43. A. Sinha, M.C. Hsiao, and F.F. Crim. J. Chem. Phys. **92**, 6333 (1990); A. Sinha. J. Phys. Chem. **94**, 4391 (1990); F.F. Crim, M.C. Hsiao, J.L. Scott, A. Sinha, and R.L van der Wal. Philos. Trans. R. Soc. London, A: **332**, 259 (1990); A. Sinha, M.C. Hsiao, and F.F. Crim. J. Phys. Chem. **95**, 8263 (1991).
44. (*a*) M.J. Bronikowski, W.R. Simpson, B. Girad, and R.N. Zare. J. Chem. Phys. **95**, 8647 (1991); (*b*) M.J. Bronikowski, W.R. Simpson, and R.N. Zare. J. Phys. Chem. **97**, 2194 (1993); (*c*) J. Phys. Chem. **97**, 2204 (1993).
45. D.E. Adelman, S.V. Filset, and R.N. Zare. J. Chem. Phys. **98**, 4636 (1993).
46. C.M. Lovejoy, L. Goldfarb, and S.R. Leone. J. Chem. Phys. **96**, 7180 (1992).
47. R.C. Oldenborg, G.W. Loge, D.M. Harradine, and K.R. Winn. J. Phys. Chem. **96**, 8425 (1992); P. Frank and Th. Just. Ber. Bunsen-Ges. Phys. Chem. **89**, 198 (1985); A.R. Ravishankara, J.M. Nicovich, R.L. Thompson, and F.P. Tully. J. Phys. Chem. **85**, 2498 (1981); F.P. Tully and A.R. Ravishankara. J. Phys. Chem. **80**, 3126 (1980).
48. R.C. Oldenborg, G.W. Loge, D.M. Harradine, and K.R. Winn. J. Phys. Chem. **96**, 8425, (1992).
49. (*a*) J.E. Spencer, H. Endo, and G.P. Glass. 16th Symp. Int. on Combustion. The Combustion Institute, Pittsburgh, Pa. 1976. p. 829; (*b*) G.C. Light and J.H. Matsumo. Chem. Phys. Lett. **58**, 578 (1978); (*c*) R. Zellner and W. Steinert. Chem. Phys. Lett. **81**, 568 (1981).
50. M. Alagia, N. Balucani, P. Casavecchia, D. Stranges, and G.G. Volpi. J. Chem. Phys. **98**, 2459 (1993); P. Casavecchia, N. Balucani, and G.G. Volpi. *In* Research in chemical kinetics. Vol. 1. *Edited by* R.G. Compton and G. Hancock. Elsevier, Amsterdam. 1993.
51. (*a*) A. Jacobs, F.M. Schuler, H.R. Volpp, M. Wahl, and J. Wolfrum. Ber. Bunsen-Ges. Phys. Chem. **94**, 1390 (1990); (*b*) A. Jacobs, H.R. Volpp, and J. Wolfrum. Chem. Phys. Lett. **177**, 200 (1991); (*c*) A. Jacobs, M. Wahl, R. Weller, and J. Wolfrum. Chem. Phys. Lett. **158**, 161 (1989).
52. G.H. Dieke and H.M. Crosswhite. J. Quant. Spectrosc. Radiat. Transfer, **2**, 97 (1962).
53. M.A.A. Clyne, J.A. Coxon, and A.R. Woon Fat. J. Mol. Spectrosc. **46**, 146 (1973).
54. (*a*) G. Hilber, A. Lago, and R. Wallenstein. J. Opt. Soc. Am. B: Opt. Phys. **4**, 1753 (1987); (*b*) J.P. Marangos, N. Shen, H. Ma, M.H.R. Hutchison, and J.P. Connerade. J. Opt. Soc. Am. **B7**, 1254 (1990).
55. I.L. Chidsey and D.R. Crosley. J. Quant. Spectrosc. Radiat. Transfer, **23**, 187 (1980).
56. W.L. Dimpfl and J.L. Kinsey. J. Quantum Spectrosc. Radiat. Transfer, **21**, 233 (1979).
57. R.N. Zare. Angular momentum. Wiley, New York. 1988.
58. M.H. Alexander, P. Andresen, R. Bacis, R. Berson, F.J. Comes, P.J. Dagdigijan, R.N. Dixon, R.W. Field, G.W. Flynn, K.-H. Gericke, E.R. Grant, B.J. Howard, J.R. Huber, D.S. King, J.L. Kinsey, K. Kleinermanns, K. Kuchitsu, A.C. Luntz, A.J. McCaffery, B. Pouilly, H. Reisler, S. Rosenwaks, E.W. Rothe, M. Shapiro, J.P. Simons, R. Vasedev, J.R. Wiesenfeld, C. Wittig, and R.N. Zare. J. Chem. Phys. **89**, 1749 (1988).
59. K. Kleinermanns and J. Wolfrum. J. Chem. Phys. **80**, 1446 (1984).
60. A. Jacobs, M. Wahl, R. Weller, and J. Wolfrum. Appl. Phys. B: **B42**, 173 (1987).
61. G.L. Vaghjiani and A.R. Ravishankara. J. Chem. Phys. **92**, 996 (1990); G.L. Vaghjiani, A.A. Turnipseed, R.F. Warren, and A.R. Ravishankara. J. Chem. Phys. **96**, 5878 (1992).
62. G.N.A. van Veen, K.A. Mohamed, T. Baller, and A.E. de Vries. Chem. Phys. **74**, 261 (1983).
63. W.J. van der Zande, R. Zhang, R.N. Zare, K.G. McKendrick, and J.J. Valentini. J. Phys. Chem. **95**, 8205 (1991).
64. R.E. Contineti, B.A. Balko, and Y. Lee. Chem. Phys. Lett. **182**, 400 (1991).
65. N.E. Bibler and R.F. Firestone. J. Chem. Phys. **76**, 621 (1972).
66. M.P. Docker, A. Hodgson, and J.P. Simons. *In* Advances in gas-phase photochemistry and kinetics. Vol. 1. *Edited by* M.N.R. Ashfold and J.E. Baggot. The Royal Society of Chemistry, London. 1989. pp. 115–137.

Can. J. Chem. Downloaded from www.nrcresearchpress.com by 195.246.54.202 on 09/08/12
For personal use only.

Vibrational specificity for charge transfer versus deactivation in $N_2^+(v = 0, 1, 2)$ + Ar and O_2 reactions

SHUJI KATO, MICHAEL J. FROST,[1] VERONICA M. BIERBAUM, AND STEPHEN R. LEONE[2]

Joint Institute for Laboratory Astrophysics, National Institute of Standards and Technology and University of Colorado, Department of Chemistry and Biochemistry, University of Colorado, Boulder, CO 80309-0440, U.S.A.

Received June 30, 1993

This paper is dedicated to Professor John C. Polanyi on the occasion of his 65th birthday

SHUJI KATO, MICHAEL J. FROST, VERONICA M. BIERBAUM, and STEPHEN R. LEONE. Can. J. Chem. **72**, 625 (1994).

Rate constants for charge transfer and vibrational deactivation in the $N_2^+(X^2\Sigma_g^+, v = 0, 1, 2)$ + Ar and O_2 reactions are directly measured by a state-resolved optical detection method. The novel, selected-ion flow tube, laser-induced fluorescence (SIFT–LIF) technique is used to study the vibrationally specific reactions at near-thermal collision energy. The total rate constant for $N_2^+(v = 1, 2)$ + Ar increases by more than a factor of 40 relative to $N_2^+(v = 0)$. This enhancement is due exclusively to an increase in the charge transfer channel. The charge transfer rate constants for the $N_2^+(v)$ + Ar reaction are found to be almost identical for $v = 1$ and $v = 2$; this differs slightly from previous results at higher collision energies. The vibrational deactivation rate constant for the $N_2^+(v = 1)$ + Ar reaction is measured for the first time; the upper limit for the branching fraction is ≈3%, confirming that this reaction is a useful monitor for $N_2^+(v > 0)$. The total rate constant for $N_2^+(v = 1, 2) + O_2$ increases by factors of 2.6 and 3.3, respectively, relative to $N_2^+(v = 0)$. In contrast to the N_2^+ + Ar reaction, this enhancement is largely due to the occurrence of vibrational deactivation, which is found to be slightly faster for $v = 2$ than for $v = 1$. For $N_2^+(v = 2) + O_2$, the $v = 2 \rightarrow 1$ and $v = 2 \rightarrow 0$ vibrational deactivation channels are found to occur with comparable rates. The lack of substantial enhancement in the charge transfer channel in the $N_2^+(v) + O_2$ reaction by vibrational excitation (up to $v = 2$) is in contrast to the observed translational enhancement, which opens a higher lying, endothermic $O_2^+(a^4\Pi_u)$ product channel. These results are consistent with a short-range, curve-crossing mechanism that efficiently channels energy into the $O_2^+(a^4\Pi_u)$ state.

SHUJI KATO, MICHAEL J. FROST, VERONICA M. BIERBAUM et STEPHEN R. LEONE. Can. J. Chem. **72**, 625 (1994).

Faisant appel à une méthode de détection optique résolue par état, on a mesuré directement les constantes de vitesse du transfert de charge et de la désactivation vibrationnelle dans les réactions $N_2^+(X^2\Sigma_g^+, v = 0, 1$ et $2)$ + Ar et O_2. On utilise la nouvelle technique de fluorescence induite au laser avec tube à écoulement pour ion choisi (SIFT–LIF) pour étudier les réactions vibrationnellement spécifiques à une énergie de collision pratiquement thermale. La constante de vitesse totale pour la réaction $N_2^+(v = 1$ et $2)$ + Ar augmente 40 fois plus rapidement que celle pour $N_2^+(v = 0)$. Cette différence est presqu'exclusivement due à une augmentation dans le canal du transfert de charge. On a trouvé que les constantes de vitesse de transfert de charge pour la réaction $N_2^+(v)$ + Ar sont pratiquement identiques pour $v = 1$ et $v = 2$; ces observations diffèrent légèrement des résultats antérieurs obtenus à des énergies de collision plus élevées. On a mesuré pour la première fois la constante de vitesse de la désactivation vibrationnelle de la réaction $N_2^+(v = 1)$ + Ar; la limite supérieure pour la fraction de bifurcation est d'environ 3%, confirmant que cette réaction est une façon utile de suivre le $N_2^+(v > 0)$. La constante de vitesse globale pour la réaction $N_2^+(v = 1$ et $2) + O_2$ augmentent respectivement par des facteur de 2,6 et 3,3 par rapport à la réaction de $N_2^+(v = 0)$. Par opposition à ce qui est observé pour la réaction N_2^+ + Ar, cette augmentation est principalement due à l'existence d'une désactivation vibrationnelle qui est légèrement plus rapide pour $v = 2$ que pour $v = 1$. Pour la réaction $N_2^+(v = 2) + O_2$, on a trouvé que les vitesses des canaux de désactivation vibrationnelle $v = 2 \rightarrow 1$ et $v = 2 \rightarrow 0$ sont comparables. Le manque d'augmentation substantielle dans le canal de transfert de charge de la réaction de $N_2^+(v) + O_2$ par l'excitation vibrationnelle (jusqu'à $v = 2$) est en opposition avec l'augmentation translationnelle observée pour cette réaction qui ouvre une voie vers un produit endothermique $O_2^+(a^4\Pi_u)$, de niveau plus élevé. Ces résultats sont en accord avec un mécanisme à courte distance, avec croisement de courbe, qui oriente efficacement l'énergie dans l'état $O_2^+(a^4\Pi_u)$.

[Traduit par la rédaction]

Introduction

The effect of vibrational excitation on ion–molecule reactions is one of the most fundamental issues of interest in state-selective and state-to-state chemistry (1–3), as well as in the chemistry of the upper atmosphere (see, for example, ref. 4). We recently developed a selected-ion flow tube, laser-induced fluorescence (SIFT–LIF) instrument to study vibrationally state-specific, thermal energy ion–molecule reactions (5). Here, N_2^+ ions in a mixture of vibrational states are mass selected and injected into a relatively high-pressure He buffer gas. The translational and rotational temperatures of the N_2^+ ions are rapidly thermalized by collisions with He, while the vibrational temperature can be high (5). The vibrational states of the reactant and product ions are monitored with sensitive LIF detection using a high repetition rate dye laser. Under low-energy conditions where translation-to-vibration (T–V) energy transfer is negligible, we recently demonstrated an efficient vibration-to-vibration (V–V) energy transfer during the resonant charge exchange between $^{15}N_2^+(v = 2)$ and $^{14}N_2$ (6).

Direct optical detection of ion vibrational states with the SIFT–LIF instrument allows us to explore new aspects of ion–molecule reactions, e.g., vibrational specificity for charge transfer (CT) versus deactivation (q) at thermal energies,

$$[1] \qquad N_2^+(v) + M \xrightarrow{k_{CT}} N_2 + M^+$$

$$[2] \qquad \xrightarrow{k_q} N_2^+(v' < v) + M$$

[1] NATO/SERC (U.K.) Research Fellow.

[2] Author to whom correspondence may be addressed. Staff member, Quantum Physics Division, National Institute of Standards and Technology. Telephone: (303) 492-5128; FAX: (303) 492-5504; e-mail: SRL@JILA. Colorado. edu.

Can. J. Chem. Downloaded from www.nrcresearchpress.com by 195.246.54.202 on 09/08/12
For personal use only.

Can. J. Chem. Downloaded from www.nrcresearchpress.com by 195.246.54.202 on 09/08/12
For personal use only.

which occur with rate constants k_{CT} and k_q, respectively. Although there have been a number of SIFT measurements of k_{CT} and k_q using monitor reactions that are specific to the ion vibrational states (7), this approach is limited by the availability of appropriate monitor reactions. Photoelectron–photoion coincidence (PEPICO) techniques can examine the reactions of vibrationally selected reactants, but are blind to the change in the vibrational states of the ions (1, 2). Measuring both k_{CT} and k_q by direct state selection in a flow tube will give detailed insight into the dynamics of ion–molecule reactions under low-energy conditions where there have been relatively few studies. In the present paper, we study the vibrational specificity for the reactions $N_2^+(v = 0, 1, 2)$ with Ar and O_2.

For the $N_2^+(v)$ + Ar reaction, we investigate the charge transfer rate constants at lower collision energies than in previous studies. The N_2^+ + Ar reaction is nearly thermoneutral and has been extensively studied both experimentally and theoretically (1*a*, 2, 8). Detailed information on the potential energy surfaces for the reverse process, $Ar^+ + N_2$, has also been obtained. Recently, Ng and co-workers (9) studied the charge transfer cross sections for $N_2^+(v = 0, 1, 2)$ with Ar in the range of center-of-mass collision energies (E_{cm}) from ≈1 eV to 320 eV. The classical path theory of Parlant and Gislason (10) reproduced these results quite well. What is most striking in the experimental and theoretical results is that the Franck–Condon mechanism, which has usually been considered valid for a wide range of E_{cm}, is applicable only above ≈200 eV for this reaction. In the lower E_{cm} region, energy resonance becomes more important. Between 1 and 10 eV, a mechanism involving curve crossing on adiabatic vibronic potential energy surfaces reproduces the experimental results well (10). However, the charge transfer reaction at collision energies below 1 eV is less well explored both experimentally and theoretically. In this region, curve crossing might be inefficient due to the reduced collision energy, and alternatively an intermediate complex might play a significant role. In the SIFT–LIF instrument, k_{CT} can be studied as a function of the vibrational excitation in N_2^+ at these lower values of E_{cm}.

The vibrational deactivation of $N_2^+(v)$ by Ar can also be investigated. This process cannot be studied with a conventional monitor reaction, because Ar is the only monitor species available to distinguish between $N_2^+(v = 0)$ and $N_2^+(v > 0)$. It has long been assumed that collisional deactivation by Ar is negligible, and this is a prerequisite for using Ar as a monitor of $N_2^+(v)$ (7). However, this assumption has never been tested. The N_2^+ + Ar reaction also has practical importance, because it is an excellent reference reaction for other studies with the SIFT–LIF instrument; direct measurement of absolute rate constants is difficult with this technique because of the complicated flow characteristics, and hence a reference reaction is required (5).

In contrast to the $N_2^+(v)$ + Ar reaction, the $N_2^+(v) + O_2$ charge transfer reaction is highly exothermic (3.509 eV for $N_2^+(v = 0)$) and electronically excited product states are energetically accessible. Koyano et al. used the PEPICO technique to study this reaction at relatively high E_{cm} and concluded that *vibrational* excitation of N_2^+ did not result in the formation of electronically excited O_2^+ products (11). On the other hand, Schultz and Armentrout recently reported experimental evidence that reactant *translational* energy can couple to an electronically excited product state (12). Using the SIFT–LIF technique, we investigate the vibrational enhancement of the charge transfer channel at thermal energies, where translational enhancement is negligible.

The reaction of $N_2^+(v) + O_2$ is also an ideal system for studying level-specific vibrational deactivation, since for this reaction the relatively efficient vibrational deactivation can compete with the charge transfer channel, which occurs with a moderate rate. Vibrational deactivation in ion–molecule collisions is known to be much more efficient than that in neutral–neutral collisions (7). This efficient deactivation has been explained by the formation of an intermediate complex due to the charge-induced dipole interaction. However, little is known about the level-specific vibrational deactivation in ion–molecule systems, in contrast to neutral–neutral systems where direct V–T, V–V, and vibrational predissociation mechanisms are known to play a major role. Finally, the reaction of $N_2^+(v) + O_2$ is important in the chemistry of the E and F regions of the earth's atmosphere (13).

Experimental

The SIFT–LIF instrument is described in ref. 5. The apparatus (Fig. 1) consists of an electron-impact ion source, a SIFT mass filter to select ions, an ion injector, and a reaction flow tube. The flow tube section is equipped with neutral reactant inlets, an LIF detection port with a photomultiplier assembly, and a downstream mass filter for final product analysis. An excimer laser-pumped dye laser is used for the LIF probing of ion internal states using time-gated photon-counting detection.

Ion production, injection, and reaction

Vibrationally excited N_2^+ ions are generated in an electron-impact ion source. The source unit has a rhenium filament, a grid, and an electron repeller. The grid potential is set at 47 V relative to experiment ground, and the bias between the grid and the filament is fixed at −80 V in order to produce 80 V electron impact on ≈2.7 Pa (20 mTorr) N_2 in the ion source. The N_2^+ ions are quickly extracted from the ion source region into the SIFT chamber, before vibrational deactivation or reaction occurs by collisions with N_2 precursors. The SIFT chamber (3×10^{-3} Pa under operation) contains a differentially pumped quadrupole mass filter (1×10^{-3} Pa under operation). After passing through a series of focusing elements (ring electrodes and an Einzel lens), the ions enter the mass filter, which selects only N_2^+ ions from other undesired ions produced in the ion source, such as N^+. The selected N_2^+ ions pass through another Einzel lens, and are focused onto the ion injection orifice (2 mm in diameter) at the exit of the SIFT chamber. The ions are efficiently injected into a stream of He buffer gas, which is at a pressure of 80 Pa (0.6 Torr), with the aid of a venturi inlet that minimizes the backstreaming of He into the SIFT chamber (5). The injection orifice is set at a potential of 0 V, and the potential difference between the grid and the injection orifice determines the nominal injection potential of the ions (47 eV for singly charged ions). The flow tube section downstream of the SIFT injector is at a common potential of 0 V, so that there is no potential gradient in the region where the ion–molecule reactions take place. A radial reactant inlet, located 4.4 cm downstream of the injection orifice, introduces the reactant gases (argon (99.996% pure) and oxygen (99.997% pure)). The inlet has 18 pinholes (0.37 mm in diameter) equally spaced around the perimeter to provide rapid and uniform mixing of the reactant gas and the N_2^+ ions that are entrained in the He buffer gas.

LIF detection

The LIF detection of N_2^+ is performed 11 cm downstream of the injection orifice with an excimer laser-pumped dye laser operating at typically 100 Hz. The $B^2\Sigma_u^+ \leftarrow X^2\Sigma_g^+$ electronic transition is used to monitor the rotational and vibrational states of N_2^+ ions. In all cases the pump transition is saturated. The (1,0) band at 358 nm is used for excitation followed by (1,2) emission at 424 nm for the LIF detection of $N_2^+(v = 0)$; excitation of (0,1) at 428 nm and (0,2) at 471 nm, both followed by (0,0) emission at 391 nm, is used for detection of $N_2^+(v = 1)$ and $N_2^+(v = 2)$, respectively. The intense (0,0) fluorescence, due to a favorable Franck–Condon factor, facilitates good LIF

Can. J. Chem. Downloaded from www.nrcresearchpress.com by 195.246.54.202 on 09/08/12
For personal use only.

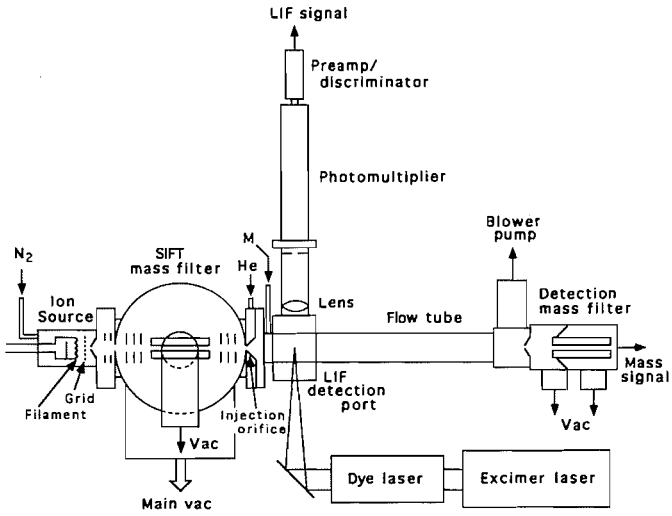

FIG. 1. SIFT–LIF instrument.

detection of the $v = 1$ and $v = 2$ states even with relatively small populations compared to $v = 0$. For a measurement of the vibrational population ratio between $v = 1$ and $v = 2$ using a single laser scan, excitation of (1,2) at 424 nm followed by emission of (1,1) at 388 nm is used for $v = 2$ detection, and this is combined with the above measurement for $v = 1$. The output signal is acquired with gated photon-counting detection after a short delay (≈10 ns) following the laser pulse and a sufficiently long collection time (≥200 ns). The gating time is at least three times the radiative lifetime of N_2^+ (B) (≈60 ns), and the fraction of molecules that radiate during the gating time is greater than 95%. The total $N_2^+(v)$ ion density at the LIF detection region is estimated to be $\approx 1 \times 10^5$ cm^{-3} (5). Signals are collected for a given flow rate of a neutral reactant, and then more than 10 data points are taken to construct a full kinetic plot in one run. Usually at least two complete runs are carried out to check the experimental reproducibility and construct a final kinetic plot.

Analytical procedures

Figure 2 summarizes the kinetic scheme for the reaction of $N_2^+(v = 0, 1, 2)$ with Ar and O_2. The fraction of $N_2^+(v = 3)$ was previously shown to be negligible (6). The $N_2^+(v > 0)$ states decay via charge transfer (eq. [1]) and vibrational deactivation (eq. [2]) with rate constants, $k_{CT,v}$ and $k_{q,vv'}$, respectively ($v > v'$). The loss of N_2^+ vibrationally excited states by collision with He buffer or by radiative decay is completely negligible during the short reaction time (5). Charge transfer is the only channel for $N_2^+(v = 0)$ decay. The sum of $k_{CT,v}$ and $k_{q,vv'}$ gives the total rate of removal ($k_{total,v}$) for each vibrational level, v. The population of each vibrational state is described by

$$[3]\quad d[N_2^+(v=2)]/dt = -(k_{CT,2} + k_{q,21} + k_{q,20})[N_2^+(v=2)][M]$$

$$[4]\quad d[N_2^+(v=1)]/dt = k_{q,21}[N_2^+(v=2)][M] - (k_{CT,1} + k_{q,10})[N_2^+(v=1)][M]$$

$$[5]\quad d[N_2^+(v=0)]/dt = k_{q,10}[N_2^+(v=1)][M] + k_{q,20}[N_2^+(v=2)][M] - k_{CT,0}[N_2^+(v=0)][M]$$

where M represents the neutral reactant (M = Ar or O_2). We transform the variables in eqs. [3]–[5] as:

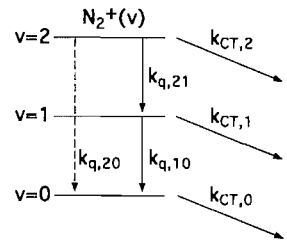

FIG. 2. Kinetics scheme for the $N_2^+(v = 0, 1, 2)$ + M reaction. The $k_{CT,v}$ and $k_{q,vv'}$ ($v > v'$) are the rate constants for charge transfer and vibrational deactivation, respectively, of $N_2^+(v)$ with M (=Ar, O_2).

$$[6]\quad [M]dt = d([M]t) \equiv dX$$

$$[7]\quad Y_i \equiv [N_2^+(v=i)]/[N_2^+(v=i)]_0 \qquad (i = 0, 1, 2)$$

where Y_i is the population for $N_2^+(v = i)$ at a certain [M], normalized to that at [M] = 0. The solutions to eqs. [3]–[5] are

$$[8]\quad Y_2 = \exp(-A_1X)$$

$$[9]\quad Y_1 = \exp(-A_3X) + \frac{A_2}{A_1 - A_3} \times (\exp(-A_3X) - \exp(-A_1X))$$

$$[10]\quad Y_0 = \exp(-A_5X) + \frac{A_4}{A_3 - A_5}(\exp(-A_5X) - \exp(-A_3X)) + \frac{A_6}{A_1 - A_5}(\exp(-A_5X) - \exp(-A_1X)) + \frac{A_2A_4}{(A_1 - A_3)(A_3 - A_5)(A_5 - A_1)}\{(A_3 - A_1) \times \exp(-A_5X) + (A_1 - A_5)\exp(-A_3X) + (A_5 - A_3)\exp(-A_1X)\}$$

where

$$[11]\quad A_1 \equiv k_{CT,2} + k_{q,21} + k_{q,20}$$

$$[12]\quad A_2 \equiv k_{q,21}R_{21}$$

$$[13]\quad A_3 \equiv k_{CT,1} + k_{q,10}$$

$$[14]\quad A_4 \equiv k_{q,10}R_{10}$$

$$[15]\quad A_5 \equiv k_{CT,0}$$

$$[16]\quad A_6 \equiv k_{q,20}R_{20}$$

and

$$[17]\quad R_{ij} \equiv [N_2^+(v=i)]_0/[N_2^+(v=j)]_0$$

The second term in Y_1 and the second and third terms in Y_0 (the double exponentials) correspond to the rise and decay due to relaxation from their upper levels, $v = 2 \rightarrow 1$, $v = 1 \rightarrow 0$, and $v = 2 \rightarrow 0$, respectively. The last triple-exponential component in Y_0 corresponds to the stepwise relaxation from

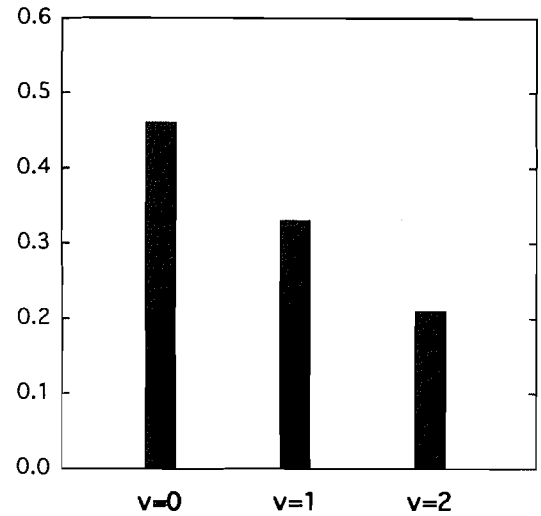

FIG. 3. Vibrational population distribution of N_2^+ observed at an injection potential of 47 eV.

$v = 2$ to $v = 1$ to $v = 0$. The equation for Y_2 is fit to a $v = 2$ kinetic plot to determine A_1. Using this value of A_1, Y_1 is fit to a $v = 1$ plot for A_2 and A_3. In a similar manner, Y_0 can be fit to the $v = 0$ data for A_4, A_5, and A_6. However, the simultaneous three-parameter best fit to Y_0 is not always unique. Thus, in the $N_2^+ + O_2$ reaction, we conducted an additional experiment using the downstream mass filter to reduce the number of parameters to be fit, as will be discussed later.

Results

Vibrational distribution of N_2^+

The rotational structure in an observed LIF spectrum confirms that the rotational temperature (T_{rot}) of N_2^+ at the LIF detection point is thermalized to ≈300 K (5), because of fast rotational equilibration of the $N_2^+(v)$ entrained in the relatively high buffer gas pressure (80 Pa). It is reasonable that the translational temperature (T_{trans}) of $N_2^+(v)$ is also ≈300 K at the point of LIF detection, since relaxation of translational energy should be even faster. Because of the high stagnation pressure behind the venturi inlet, the He flow just downstream of the inlet is an intense hypersonic flow where T_{rot} and T_{trans} must be extremely low. However, shock wave recovery across the Mach disk immediately results in the recovery of T_{rot} and T_{trans} to ≈300 K even before the neutral reactant addition (5). Therefore the He flow provides a bath for ion–molecule reactions at $T_{trans} \approx T_{rot} \approx 300$ K, although the laboratory-frame kinetic energy of N_2^+ (E_{lab}) can be high because of the initial velocity of the He flow after recovering from the Mach disk.

We previously showed (5) that the vibrational population of N_2^+ is dependent on the injection potential. The population ratio between $v = 2$ and $v = 1$ is measured directly by integrating specific rotational lines in the LIF spectrum, as discussed in ref. 5. This population ratio is combined with the fraction of $v = 0$, which is measured using the Ar-monitor reaction or the $N_2^+ + N_2$ resonant charge transfer reaction (5). The vibrational population distribution is determined to be (46 ± 1%) for $v = 0$, (33 ± 1%) for $v = 1$, and (21 ± 1%) for $v = 2$ at an injection potential of 47 eV (Fig. 3). Since vibrational levels up to $v = 2$ are appreciably populated, the effective vibrational temperature (T_{vib}) is estimated from the observed distribution as ≈8000 K. The population of $v = 3$, however, seems to deviate from a prediction (≈10%) based on the effective T_{vib}, and is rather small. Because of the relatively large populations of the higher vibrational levels ($v = 1$ and $v = 2$), the deactivation of a specific vibrational level can appear as an obvious rise in the kinetic plot for the corresponding lower level. This initial population distribution will be used in eqs. [12], [14], and [16] to determine $k_{q,21}$, $k_{q,10}$, and $k_{q,20}$.

$N_2^+(v) + Ar$ reaction

Kinetic plots for the $N_2^+(v) + Ar$ reactions are shown in Fig. 4(*a*)–(*c*). The reactions of $N_2^+(v = 2)$ and $N_2^+(v = 1)$ are almost equal in their decay rates, and are as fast as the $N_2^+(v = 2 \text{ and } 1) + N_2$ resonant charge transfer reactions (5). The $v = 2$ reactions should obey a single exponential decay since the population of the upper level ($v = 3$) is negligible, and indeed an exponential decay curve provides a good fit to the data shown in Fig. 4(*a*). The $v = 1$ reaction can be fit with a single exponential decay curve (Fig. 4(*b*)), or with the exact expression in eq. [9]. This indicates that the branching fraction for the $v = 2$ vibrational deactivation is extremely small compared to that for the $v = 2$ charge transfer; thus the minor contribution of the $v = 2$ to $v = 1$ deactivation cannot be detected as a superposition on the $v = 1$ kinetic plot, which decays very rapidly.

The situation is different for the $N_2^+(v = 0) + Ar$ reaction (Fig. 4(*c*)). The charge transfer reaction of $N_2^+(v = 0)$ with Ar is slightly endothermic, and is known to be very slow ($k_{CT,0} = 2 \times 10^{-13}$ cm^3 molecule^{-1} s^{-1}) at 300 K (14). Furthermore, the time constant for the appearance of a $v = 1 \rightarrow 0$ deactivation component is very short due to the large total rate of removal of $v = 1$ ($k_{total,1}$). Thus the extent of vibrational deactivation from $v = 1 \rightarrow 0$ can in principle be observed in the kinetic plot for $v = 0$. Each data point in Fig. 4(*c*) contains 5–10 measurements and the error bars represent one standard deviation of the mean. In the analysis here, the last term in eq. [10] for stepwise $v = 2 \rightarrow 1 \rightarrow 0$ relaxation is negligible compared to the second, double exponential term for $v = 1 \rightarrow 0$ relaxation, since the amount of $N_2^+(v = 1)$ arising from $v = 2$ is appreciably smaller than that originally in $v = 1$. The $v = 0$ plot is represented slightly better by the exact analytical formula (solid curve) than by a single exponential decay curve (long-dashed line) for which no vibrational deactivation is assumed (the ratio of the chi squared values, χ^2 (exact formula)/χ^2 (single exponential) = 0.83). The short-dashed line in Fig. 4(*c*) represents only the first term in eq. [10], giving $k_{CT,0}$, and the rise of the solid line above the short-dashed line corresponds to the best fit for vibrational deactivation from $v = 1 \rightarrow 0$ (≈3% of the total rate of removal of $N_2^+(v = 1)$).

$N_2^+(v) + O_2$ reaction

The kinetic plot for $N_2^+(v = 2) + O_2$ (Fig. 5(*a*)) shows that the total removal rate is smaller than that for $N_2^+(v = 2) + Ar$. The reaction obeys a simple exponential decay, which again is consistent with a negligible amount of $N_2^+(v = 3)$. The kinetic plot of $N_2^+(v = 1)$ (open circles in Fig. 5(*b*)) reveals a definite deviation from a single exponential decay, and fitting by the exact formula (eq. [9]) is shown by the solid curve. The single exponential component in eq. [9] is subtracted from the total kinetic plot, and the residual component, which corresponds to the vibrational deactivation from $v = 2$ to $v = 1$, is shown by the open triangles and the associated solid curve.

The kinetic plot for $N_2^+(v = 0) + O_2$ (Fig. 5(*c*)) more clearly reveals the vibrational deactivation from upper levels, with

Can. J. Chem. Downloaded from www.nrcresearchpress.com by 195.246.54.202 on 09/08/12
For personal use only.

Can. J. Chem. Downloaded from www.nrcresearchpress.com by 195.246.54.202 on 09/08/12
For personal use only.

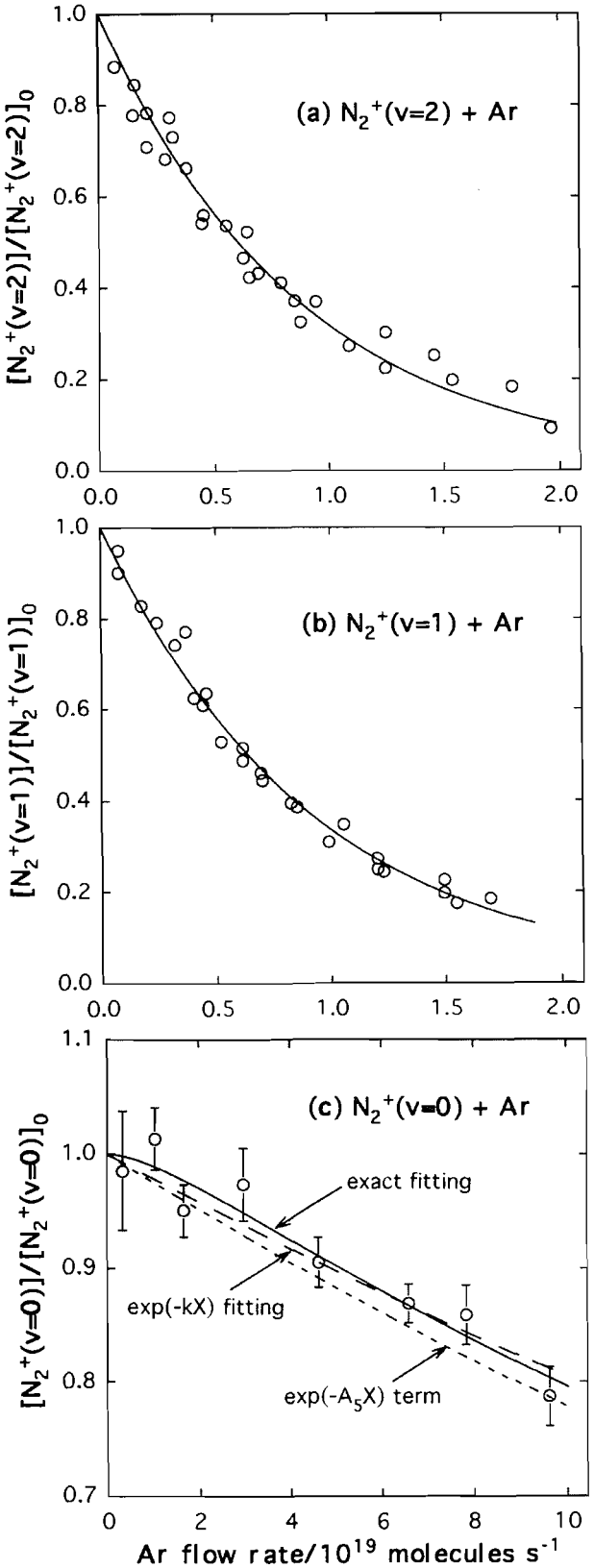

FIG. 4. Kinetic plots of (*a*) $N_2^+(v = 2)$ + Ar, (*b*) $N_2^+(v = 1)$ + Ar, and (*c*) $N_2^+(v = 0)$ + Ar reactions. In (*c*), the solid line represents the fitting with the exact analytical formula (eq. [10]), and the long-dashed line (– –) the fitting with a single exponential (e^{-kX}) for which no vibrational deactivation is assumed. The ratio of the chi squared values, χ^2 (exact formula)/χ^2 (single exponential) = 0.83. The short-dashed line (- - -) in (*c*) represents only the first term in eq. [10]. The rise of the solid line above the short-dashed line corresponds to the $v = 1 \rightarrow 0$ vibrational deactivation.

an obvious initial rise peaked at O_2 flow rates of (1–2) × 10^{19} molecules s^{-1} (open circles). Although it should be possible to separate the $v = 1 \rightarrow 0$ and $v = 2 \rightarrow 0$ processes by an analysis of the $N_2^+(v = 0) + O_2$ kinetic plots, it is difficult in practice, since the total rates of loss for $N_2^+(v = 2)$ and $N_2^+(v = 1)$ are unfortunately very close in magnitude. The $v = 2 \rightarrow 0$ component, if any, should thus appear in the $N_2^+(v = 0) + O_2$ kinetic plot with almost the same rise and decay time constants as those of the $v = 1 \rightarrow 0$ component and cannot be separated. Thus, in a separate experiment with the downstream mass filter, the N_2^+ ion counts are measured as a function of O_2 flow rate (Fig. 6). Although there is slight nonlinearity in Fig. 6, within experimental error, the N_2^+ counts are found to decrease exponentially. The absence of a significant faster decaying component superimposed on the single exponential decay indicates that the rate constants for charge transfer ($k_{CT,2}$, $k_{CT,1}$, and $k_{CT,0}$) have similar values. Thus the fitting parameters in eq. [10], A_4, A_5, and A_6, can be reduced to a single value ($k_{CT,0} \equiv A_5$). When Y_0 is fit to the $v = 0$ plot and the single exponential component in eq. [10] is subtracted from the total kinetic plot, the open triangles and the associated solid curve show the residual component due to the vibrational deactivation of higher levels. The residual is automatically fractioned into three components for vibrational relaxation, $v = 1 \rightarrow 0$ and $v = 2 \rightarrow 0$, which produce a faster decay, and $v = 2 \rightarrow 1 \rightarrow 0$, which produces a more gradual decay (dashed curves). We note that if the slight deviation from a single exponential decay in Fig. 6 is fit exactly, the best fit is obtained when $N_2^+(v = 2)$ (≈21% of the total $N_2^+(v)$ population) is assumed to transfer charge ≈50% faster than $N_2^+(v = 1)$ or $N_2^+(v = 0)$. Thus the present experimental data do not allow us to exclude a slight vibrational enhancement of the $N_2^+(v = 2)$ charge transfer channel. However, a dramatic effect, as observed in the translational enhancement of the $N_2^+ + O_2$ reactivity, is clearly ruled out.

Rate constants

Because of the close proximity of the neutral reactant inlet and the LIF detection port to the ion injector, the He flow in this region is not well developed and laminar. The flow characteristics near the SIFT injector were discussed in detail previously (5); this discussion included experimental observations of the $N_2^+(v)$ rotational temperature, effects of He flow rate on kinetic plots, dependence of the product yield in the Ar-monitor reaction on the reactant inlet position, and theoretical considerations of shock wave recovery. These considerations suggest that there is fast, turbulent flow in the reaction volume just downstream of the SIFT injector, consistent with previous studies (15, 16). Therefore absolute rate constants cannot be determined directly.

However, the $N_2^+(v = 2) + O_2$ and $N_2^+(v = 1$ or 2) + Ar plots demonstrate that the reactions exhibit first-order kinetics with respect to the amount of added reactant, when relaxation from upper levels is negligible. Therefore the mixing efficiency of the reactant and the He buffer gas is independent of the amount of the reactant added, even under the nonideal flow conditions near the SIFT injector. Thus a reference reaction can be used to infer relative rate constants, and kinetic plots can be analyzed using the expressions in eqs. [8]–[10]. We use the $N_2^+(v = 1) + Ar$ reaction as a reference because (*i*) it is a simple system where vibrational relaxation from upper levels is negligible, (*ii*) the reaction is relatively fast and hence is less affected by possible impurities, (*iii*) the rate constant

Can. J. Chem. Downloaded from www.nrcresearchpress.com by 195.246.54.202 on 09/08/12
For personal use only.

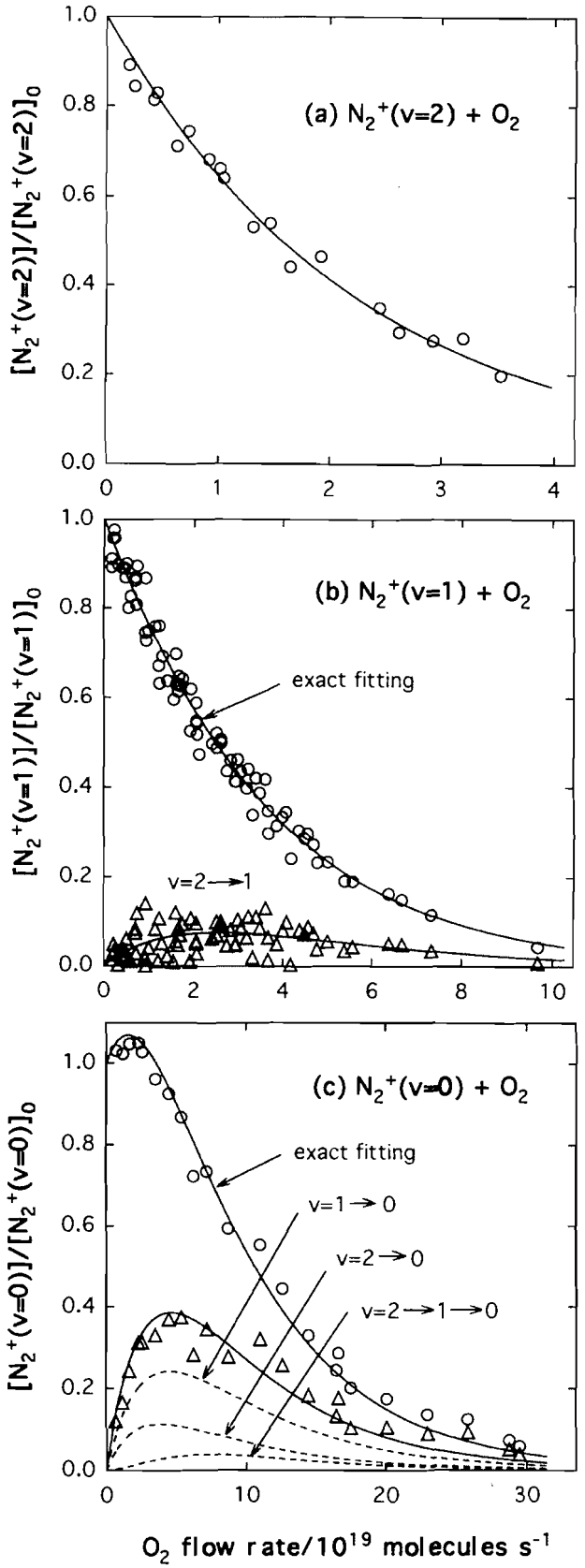

FIG. 5. Kinetic plots of (*a*) $N_2^+(v = 2) + O_2$, (*b*) $N_2^+(v = 1) + O_2$, and (*c*) $N_2^+(v = 0) + O_2$ reactions. In (*b*), the total kinetic plot (open circles) is fitted with the exact formula (eq. [9]). The single exponential component in eq. [9] is subtracted from the total plot, and the residual component for the $v = 2 \rightarrow 1$ deactivation is shown by the open triangles and the associated solid curve. In (*c*), the total kinetic plot (open circles) is fitted with the exact formula (eq. [10]). The single exponential component in eq. [10] is subtracted from the total plot, and the residual component for the vibrational deactivation of higher levels is shown by the open triangles and the associated solid curve. The residual is separated into three components for $v = 1 \rightarrow 0$, $v = 2 \rightarrow 0$, and $v = 2 \rightarrow 1 \rightarrow 0$ vibrational deactivation, as shown by the dashed curves.

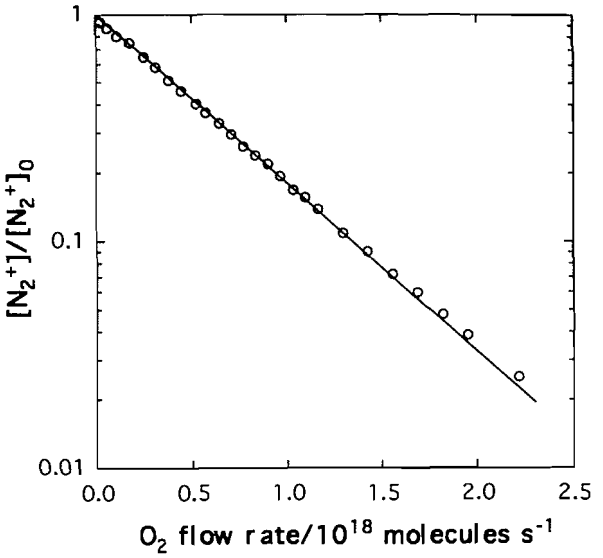

FIG. 6. The N_2^+ ion counts (open circles) detected with the downstream mass filter as a function of O_2 flow rate. The N_2^+ counts are normalized to that at zero O_2 flow ($\equiv [N_2^+]_0$). The solid line represents the single exponential decay.

for a mixture of vibrationally excited states ($v > 0$, i.e., a mixture of $v = 1$ and $v = 2$) has been reported (4×10^{-10} cm^3 molecule^{-1} s^{-1} (14)) and the vibrational energy dependence is very small as is evident from Fig. 4(*a*) and (*b*), and (*iv*) the kinetic energy dependence for $N_2^+(v > 0)$ + Ar is also known to be very minor (17).

Table 1 summarizes the rate constants for $N_2^+(v)$ + Ar and O_2, which are obtained by using the $N_2^+(v = 1)$ + Ar reaction as a reference. The errors should accumulate toward lower vibrational levels because of the sequential fitting procedure; however, only relative errors are included in Table 1 (1σ of the mean) in order to emphasize the reactivity difference between two adjacent vibrational levels. The results show there is a negligible difference between the reactivities of $N_2^+(v = 1)$ and $N_2^+(v = 2)$ with Ar. The extent of vibrational deactivation for $N_2^+(v = 1)$ is estimated to be $\approx$3% ($k_{q,10} = 1.2 \times 10^{-11}$ cm^3 molecule^{-1} s^{-1}). However, this value may be an upper limit, since the quality of the fit by the exact analytical formula in eq. [10] is only slightly better than that from a single exponential. Accordingly, the value of $k_{CT,1}$ (3.88×10^{-10} cm^3 molecule^{-1} s^{-1}) can be regarded as a lower limit. Note that the $N_2^+(v = 0)$ + Ar reaction is $\approx$45 times slower than $N_2^+(v > 0)$ + Ar, but at the same time this value is $\approx$45 times faster than the reported rate constant at 300 K (14). This enhanced reactivity of $N_2^+(v = 0)$ has been discussed in detail (5) and is attributed to a higher collision energy of $N_2^+(v = 0)$ in the vicinity of the SIFT injector, as will be discussed in the next section. For the $N_2^+(v = 2)$ + O_2 reaction, $k_{q,21}$ and $k_{q,20}$ each constitute about half of the overall quenching rate constant, $k_{q,2}$. Thus the $v = 2 \rightarrow 1$ and $v = 2 \rightarrow 0$ channels are comparable in the vibrational deactivation of $N_2^+(v = 2)$.

TABLE 1. Reaction rate constants for $N_2^+(v)$ + M reactions

M	k^a	$v = 0$	$v = 1$	$v = 2$
Ar	k_{total}	0.092 ± 0.013^b	4.00 ± 0.08^c	4.21 ± 0.14
	k_{CT}	0.092 ± 0.013^b	$\geq 3.88 \pm 0.09$	—[d]
	k_q	—	$\leq 0.12 \pm 0.04$	—[d]
O_2	k_{total}	0.49 ± 0.02	1.27 ± 0.10	1.62 ± 0.05
	k_{CT}	0.49 ± 0.02	0.49 ± 0.02	0.49 ± 0.02^e
	k_q	—	0.78 ± 0.08	1.13 ± 0.05^e

[a] k_{CT}, k_q, and k_{total} (= k_{CT} + k_q) are the rate constants for charge transfer, vibrational relaxation, and total decay, respectively, in units of 10^{-10} cm^3 molecule^{-1} s^{-1}. The errors respresent 1σ of the mean.

[b] Larger than 300 K values due to the higher collision energy (<0.23 eV).

[c] Reference reaction. The error in the rate constant of the reference reaction is not shown, and the error bar for k_{total} (±0.08) simply reflects the fitting error.

[d] Not measured.

[e] These values and their error bars result if the data in Fig. 6 are treated as a single exponential decay. If the slight curvature is fit exactly, k_{CT} increases by ≈50% and k_q decreases accordingly. Thus a slight vibrational enhancement of the $N_2^+(v = 2) + O_2$ charge transfer channel cannot be ruled out by the current experimental data.

TABLE 2. Rate constants for the $N_2^+(v) + O_2$ reaction at 300 K[a]

$k_{CT,0}$	$k_{CT,v>0}$	$k_{q,v>0}$	Method[b]	Reference
0.65			FA	18
0.50			FDT	19
0.43			FA	13
0.51			SIFT	20
0.47			SIFT	21
0.49	0.49		FDT	22
0.5	0.5	1.2	SIFT	23
0.5	0.5	1	SIFDT	24
		0.52	ICR	25
	0.45	1	SIFDT	26
0.98 (±0.60)			GIBMS	12
0.49	0.49 ($v = 1$)	0.78 ($v = 1$)	SIFT-LIF	This work
	0.49 ($v = 2$)[c]	1.13 ($v = 2$)[c]		

[a] In units of 10^{-10} cm^3 molecule^{-1} s^{-1}.

[b] FA = flowing afterglow, FDT = flow-drift tube, SIFT = selected-ion flow tube, SIFDT = selected-ion flow-drift tube, ICR = ion cyclotron resonance, GIBMS = guided-ion beam mass spectrometry, SIFT–LIF = selected-ion flow tube, laser induced fluorescence.

[c] Refer to footnote *e* in Table 1.

Table 2 compiles previous results for the $N_2^+(v) + O_2$ reaction (12, 13, 18–26). With $N_2^+(v = 1)$ + Ar as a reference reaction, our value of $k_{CT,0}$ for the $N_2^+(v = 0) + O_2$ reaction (Table 1) agrees well with these previous values. Also for the $N_2^+(v) + N_2$ reaction (27), k_{total} agrees with previous values by using $N_2^+(v = 1)$ + Ar as a reference reaction. Since the collision energy in the vicinity of the SIFT injector may be higher than thermal, however, the possible dependence of the rate constant on kinetic energy could be important for other systems. The rate constants for $N_2^+(v = 1)$ and $N_2^+(v = 2)$ with O_2, on average, agree with previous overall values for $N_2^+(v > 0)$ at 300 K.

Discussion

Charge transfer between N_2^+(v = 0) and Ar

The charge transfer reaction of $N_2^+(v = 0)$ with Ar (eq. [18]) is slightly endothermic (0.178 eV) and extremely slow at 300 K (2×10^{-13} cm^3 molecule^{-1} s^{-1}), while the charge transfer of $N_2^+(v = 1)$ (eq. [19]) is nearly resonant and very fast (4×10^{-10} cm^3 molecule^{-1} s^{-1}) (14).

[18] $N_2^+(v = 0) + Ar \rightarrow N_2(v = 0) + Ar^+(^2P_{3/2}) - 0.178$ eV

[19] $N_2^+(v = 1) + Ar \rightarrow N_2(v = 0) + Ar^+(^2P_{3/2}) + 0.092$ eV

Since the average collision energy at 300 K (0.039 eV) is smaller than the enthalpy required for the endothermic reaction [18], only those $N_2^+(v = 0)$ ions in the Boltzmann distribution with high translational (and possibly rotational) energies can participate in the charge transfer. Indeed, the charge transfer of $N_2^+(v = 0)$ is suppressed to an immeasurable level at 80 K (14). We also confirmed the 300 K rate constant for reaction [18] by measuring both the N_2^+ and Ar^+ ion counts using the downstream mass filter in the traditional way.

In contrast, the $N_2^+(v = 0)$ + Ar reaction near the LIF region proceeds at a much faster rate (Table 1), although it is still a very slow reaction. The enhanced reactivity is due to greater collision energies of $N_2^+(v = 0)$ immediately downstream of the ion injector, and the origin of the enhancement is discussed in this section. There has been some controversy concerning the kinetic energy dependence of the $N_2^+(v = 0)$ + Ar reaction (9, 17, 28–31): Lindinger et al. (17) first observed a strong kinetic energy dependence of reaction [18], while beam experiments reported only a moderate dependence (9, 28, 29). Later, Lindinger and co-workers (30) studied the vibrational

Can. J. Chem. Downloaded from www.nrcresearchpress.com by 195.246.54.202 on 09/08/12
For personal use only.

Can. J. Chem. Downloaded from www.nrcresearchpress.com by 195.246.54.202 on 09/08/12
For personal use only.

excitation of $N_2^+(v = 0)$ in collisions with He buffer gas using a drift tube at E_{cm} above 0.2 eV, and they observed that vibrational excitation was significant at higher collision energies. In ref. 30, they interpreted their previous results for the enhanced reactivity of the $N_2^+(v = 0)$ + Ar reaction (17) in terms of contributions from vibrationally excited N_2^+. Recently, Schultz and Armentrout conducted an important experiment (31) in which they measured the kinetic energy dependence of reaction [18] under single collision conditions at energies down to $E_{cm} \approx 0.1$ eV. Their study clearly revealed a pure kinetic energy dependence, which was as steep as the apparent E_{cm} dependence previously observed using a drift tube (17). Therefore, at kinetic energies where the E_{cm} does not significantly exceed the vibrational spacing of the N_2^+ ions (0.27 eV) and only $N_2^+(v = 0)$ ions are present, the $N_2^+(v = 0)$ + Ar reaction is enhanced by kinetic energy.

The approximate collision energy in the SIFT–LIF instrument can be inferred from previous observations. Unfortunately, there have been no drift tube data specifically for the $N_2^+(v = 0)$ + Ar reaction at kinetic energies appreciably below 1 eV. However, if the drift tube data by Lindinger et al. (17) are extrapolated to lower E_{cm}, our rate constant of 9.2×10^{-12} cm^3 molecule^{-1} s^{-1} (Table 1) would correspond to a collision energy of $\approx$0.3 eV. Other results suggest an upper limit for the collision energy in the SIFT–LIF experiment. Recently, Schultz and Armentrout (12) observed the onset of N_2O^+ formation from $N_2^+(v = 0)$ + O_2 at $E_{cm} < 1$ eV, which corresponds to the thermochemical threshold of 0.74 eV. We observe no N_2O^+ product from the $N_2^+(v)$ + O_2 reaction for $v \leq 2$. This energy would correspond to an E_{cm} of 0.23 eV in our experiment for N_2^+ + Ar. In summary, we believe that the average kinetic energy in collisions of N_2^+ with Ar in the SIFT–LIF instrument is significantly greater than thermal, but probably below 0.23 eV; this is also supported by a flow analysis of the He buffer gas (5). This slightly enhanced kinetic energy increases the rate coefficient of the $N_2^+(v = 0)$ + Ar reaction above that of its thermal energy value, in keeping with the results of Schultz and Armentrout.

Vibrational deactivation of N_2^+(v = 1) by Ar

The vibrational deactivation of $N_2^+(v = 1)$ in collisions with Ar is found to be very slow ($k_{q,10} \leq 1.2 \times 10^{-11}$ cm^3 molecules^{-1} s^{-1}), in keeping with previous SIFT results at 300 K for other rare gas atoms: 4.5×10^{-15} cm^3 molecule^{-1} s^{-1} for He (30*b*), 4.5×10^{-12} for Ne (23), and 5×10^{-12} for Kr (32). Kemper and Bowers measured the vibrational deactivation of $N_2^+(v > 0)$ with He, Ne, Kr, and Xe (25) using an ICR. They interpolated their results and estimated the Ar deactivation rate as $\approx 9 \times 10^{-12}$ cm^3 molecule^{-1} s^{-1} at collision energies of $\approx$0.3 eV. Our measured value for Ar is in good agreement with these expectations; Ar is not a special quencher for $N_2^+(v)$ compared to other rare gas atoms in spite of its rapid charge transfer probability. The inefficient vibrational deactivation ensures that Ar is a good monitor for detecting $N_2^+(v > 0)$ with negligible perturbation of the vibrational states.

The potential well depth for $N_2^+(v = 0)$ + Ar has been experimentally estimated as 0.91 eV (Teng and Conway (33) and Linn et al. (34)), in good agreement with a recent theoretical value (0.785 eV (35)); the electron exchange interaction between the reagents contributes to this well depth (36). The potential well for this system is also highly anisotropic (35). Although a deep well with large anisotropy usually results in high efficiencies for vibrational deactivation (7), this is not the case for $N_2^+(v = 1)$ + Ar where rapid charge transfer occurs. The diabatic potential energy surface for $N_2^+(v = 1)$ + Ar is pushed upward because of the avoided crossing with the charge transfer state $Ar^+(^2P_{3/2})$ + $N_2(v = 0)$, resulting in a rather shallow well (35). The potential energy surface is similar for $N_2^+(v = 2)$ + Ar (35), and the vibrational deactivation of $N_2^+(v = 2)$ with Ar, although not measured, is also expected to be very inefficient.

Charge transfer between N_2^+(v = 1 and 2) and Ar

There are two energetically accessible channels for the charge transfer between $N_2^+(v = 2)$ and Ar:

$$[20] \quad N_2^+(v = 2) + Ar \rightarrow N_2(v = 1) + Ar^+(^2P_{3/2}) + 0.069 \text{ eV}$$

$$[21] \quad N_2^+(v = 2) + Ar \rightarrow N_2(v = 0) + Ar^+(^2P_{1/2}) + 0.180 \text{ eV}$$

The first of these has an even smaller energy defect than does $N_2^+(v = 1)$ + Ar, eq. [19]. The charge transfer of $N_2^+(v = 1$ and 2) + Ar can be discussed in terms of total rates of removal (k_{total}) since vibrational deactivation is extremely inefficient. The total removal rate of $v = 2$ is slightly greater than that of $v = 1$, although the difference of 5% lies within experimental error. This result differs from those at higher E_{cm} where the cross section for $v = 2$ is significantly greater than that for $v = 1$ (Kato et al., $E_{cm} \geq 0.3$ eV (28), Govers et al., ≥ 8 eV (29), Ng and co-workers, ≥ 5.8 eV (9)). At the lowest energy of 1.2 eV, Ng and co-workers (9) observed a slight preference for the $N_2^+(v = 1)$ charge transfer over $N_2^+(v = 2)$, although the error bars are relatively large (9*b*); the most advanced theory of Parlant and Gislason (10*b*,*c*) agrees with the results of Ng and co-workers, including the reversal of the reactivities between $v = 2$ and $v = 1$ at 1.2 eV. At an estimated collision energy of 0.3–0.5 eV, Mahan et al. (37) detected no measurable vibrational dependence of the charge transfer for $N_2^+(v = 1)$ and $N_2^+(v = 2)$ with their rf quadrupole ion trap. Unfortunately, systematic data (experimental and theoretical) are lacking in this energy region. Nevertheless our observation that $k_{CT,1} \approx k_{CT,2}$ is in general agreement with other low-energy data and suggests that a different mechanism e.g., formation of an intermediate complex, may be operative, compared to that at high collision energies.

Charge transfer between N_2^+(v) and O_2

Figure 7 summarizes the results of k_{total}, $k_{CT,}$, and k_q for the $N_2^+(v)$ + O_2 reaction. The values of $k_{CT,}$ for $v = 0$, $v = 1$, and $v = 2$ are similar; we conclude that k_{CT} is insensitive to vibrational excitation of N_2^+. In addition, the total rates of removal of $N_2^+(v = 1)$ and $N_2^+(v = 2)$ are substantially larger than that of $N_2^+(v = 0)$, indicating that vibrational deactivation is efficient. However, we do not believe that charge transfer is suppressed by competition with vibrational deactivation since the total rate is still only about 20% of the collision rate.

At thermal energies, there have been several measurements of the $N_2^+(v > 0)$ + O_2 charge transfer rate constant (Table 2) using flow tube techniques coupled to mass spectrometry (22–24, 26). These measurements used the Ar-monitor reaction to probe $N_2^+(v > 0)$, and hence no distinction could be made between $v = 1$ and $v = 2$, although Ferguson et al. (26) suggested that the vibrational excitation of N_2^+ was predominantly $v = 1$. In their kinetic plots of N_2^+ (consisting of a mixture of $v = 0, 1, \ldots$) + O_2, they detected only a single decay component, which had the same slope as that of

Can. J. Chem. Downloaded from www.nrcresearchpress.com by 195.246.54.202 on 09/08/12
For personal use only.

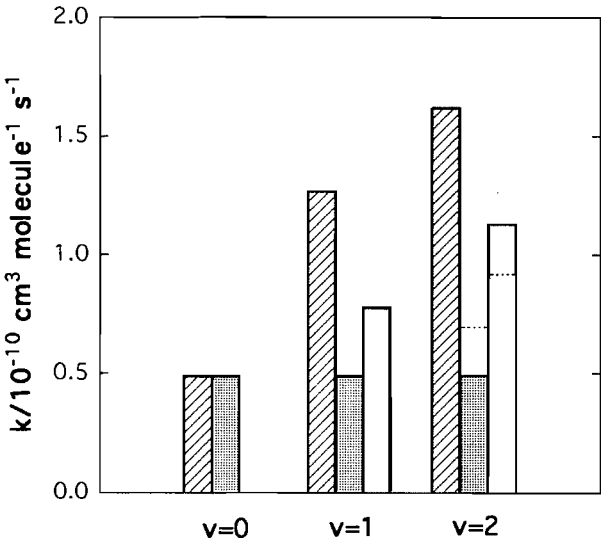

FIG. 7. Rate constants, k_{total} (striped bar), k_{CT} (shaded bar), and k_q (white bar), for $N_2^+(v) + O_2$ reaction (data from Table 1), assuming a single exponential decay in Fig. 6. For $N_2^+(v = 2)$, the dotted bars indicate the values of k_{CT} and k_q determined by fitting the slight curvature in Fig. 6 exactly. Refer to footnote *e* in Table 1.

the $N_2^+(v = 0) + O_2$ decay, and concluded that the charge transfer for $N_2^+(v > 0) + O_2$ has the same rate constant as $N_2^+(v = 0) + O_2$. Our results are consistent with these previous data, and demonstrate that the $N_2^+ + O_2$ charge transfer is not substantially enhanced by N_2^+ vibrational excitation up to $v = 2$.

Koyano et al. (11) were the first to study the $N_2^+(v) + O_2$ charge transfer reaction with selected vibrational states, although at a relatively high E_{cm}. Using the PEPICO technique, they reacted $N_2^+(X^2\Sigma_g^+, v = 0\text{–}3)$ and $N_2^+(A^2\Pi_u, v = 0\text{–}3)$ with O_2 at $E_{cm} = 2.1$ eV. They detected no change in the charge transfer cross sections for $N_2^+(X, v)$ as a function of vibrational quantum number up to $v = 3$, while the charge transfer was dramatically enhanced for $N_2^+(A)$. Figure 8 shows the energy level diagram for the set of state-to-state reactions,

$$[22] \quad N_2^+(X^2\Sigma_g^+, A^2\Pi_u; v) + O_2 \rightarrow N_2(X^1\Sigma_g^+, v') + O_2^+(X^2\Pi_g, a^4\Pi_u; v'').$$

The most recent compilation by Laher and Gilmore (38) is used to calculate the energy levels. The potential well depth of the $(N_2 \cdots O_2^+)$ complex with respect to the $N_2 + O_2^+(X)$ product state is experimentally estimated to be ≈0.23 eV (39–41). Based on the lack of vibrational enhancement of the $N_2^+(X, v) + O_2$ charge transfer reaction for higher v levels that are resonant with the $O_2^+(a, v'' = 0)$ product state (0.523 eV), Koyano et al. concluded that the products are $O_2^+(X)$, not $O_2^+(a)$. However, this seems to disagree with the high probability for the reverse reaction $O_2^+(a) + N_2 \rightarrow O_2 + N_2^+$ (42).

Schultz and Armentrout (12) recently reported a guided-ion beam mass spectrometry study of the $N_2^+(v = 0) + O_2$ reaction at E_{cm} from thermal (0.04 eV) to 20 eV. The charge transfer cross section monotonically decreases with E_{cm} up to ≈1 eV (more rapidly than the energy-dependent Langevin cross section decreases), and then suddenly increases above ≈1 eV. For the higher E_{cm} regime where a long-range direct mechanism might dominate the charge transfer process, their results and interpretation may be understood. According to the

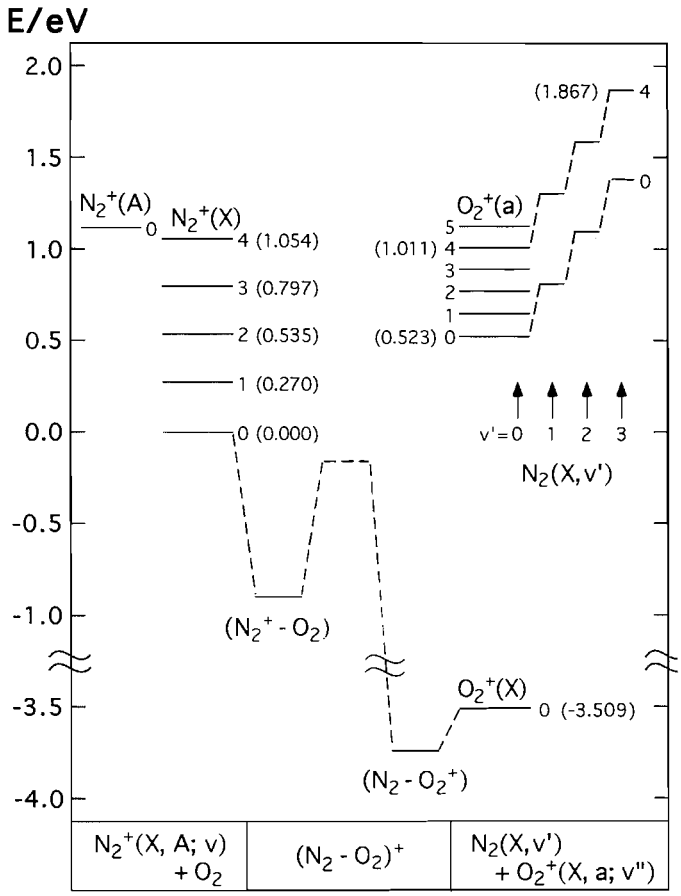

FIG. 8. Energy level diagram for the state-to-state reaction, $N_2^+(X^2\Sigma_g^+, A^2\Pi_u; v) + O_2 \rightarrow N_2(X^1\Sigma_g^+, v') + O_2^+(X^2\Pi_g, a^4\Pi_u; v'')$. The vibrational quantum number is designated by the arabic number attached to each level. Energy values relevant to the discussion are shown in parentheses (in eV).

Franck–Condon criteria for a long-range vertical transition, the product state is *not* $O_2^+(a, v'' = 0)$, which corresponds to the adiabatic ionization potential (I.P.) of O_2, but $O_2^+(a, v'' \approx 4)$ (43), where the vertical ionization is peaked at 1.011 eV (Fig. 8). The product state of $N_2(v')$ is most likely $v' = 0$, since the $N_2^+(X) \rightarrow N_2(X)$ transition is almost vertical and $v' \approx v$ will hold. Thus the charge transfer cross section for $N_2^+ + O_2$ increases above $E_{cm} \approx 1$ eV by opening of the $O_2^+(a)$ channel.

Therefore, it is not surprising that Koyano et al. did not observe a vibrational enhancement in the $N_2^+(v) + O_2$ charge transfer. At their E_{cm} of 2.1 eV, the charge transfer might be dominated by the long-range direct process. Two cases may be distinguished. If the translational energy is not effectively channelled into the $O_2^+(a)$ product state, then vibrational excitation of $N_2^+(v)$ even up to $v = 3$ (0.797 eV) is not sufficient to access $N_2(v' = 0) + O_2^+(a, v'' = 4)$ at 1.011 eV. Furthermore, Franck–Condon arguments would favor formation of $N_2(v' = 3) + O_2^+(a, v'' = 4)$ products from the $N_2^+(v = 3) + O_2$ reaction (Fig. 8), which lie at even higher energy. Alternatively, as Schultz and Armentrout pointed out (12), the $N_2^+(v = 0)$ state might already be coupled with the $O_2^+(a)$ product state if the 2.1 eV translational energy is effectively channelled into the reaction coordinate. Then, further vibrational excitation of the N_2^+ reactant is not as effective in enhancing the charge transfer. In their interpretation, however, it seems difficult to explain the significantly enhanced reactivity of $N_2^+(A)$ observed by Koyano et al. (11).

Can. J. Chem. Downloaded from www.nrcresearchpress.com by 195.246.54.202 on 09/08/12
For personal use only.

It is important to explore the effects of vibration on the $N_2^+ + O_2$ charge transfer reaction at low E_{cm}. Under our experimental conditions, collision energies are so low that a short-range charge transfer mechanism will be operative, as suggested for the $^{15}N_2^+(v = 2) + {}^{14}N_2$ reaction (6). The Franck–Condon mechanism will not apply and adiabatic ionization to $O_2^+(a, v'' = 0)$ becomes feasible via an ion–molecule intermediate complex. The $N_2^+(v = 2)$ state (0.535 eV) is almost exactly resonant with the final product state ($O_2^+(a, v'' = 0) = 0.523$ eV) (Fig. 8). The observed $k_{CT,2}$, however, does not show a noticeable increase relative to $k_{CT,0}$ or $k_{CT,1}$. This implies that the vibrational energy is isolated and cannot be effectively channeled into the reaction coordinate or necessary surface crossings to access the $O_2^+(a)$ state. Once coupled with the $O_2^+(X)$ product state, the reaction is very exothermic (3.509 eV for $N_2^+(v = 0)$) and additional vibrational excitation of the $N_2^+(v)$ reactant is not effective in promoting the reaction.

For the $Ar^+ + O_2$ reaction, which has nearly the same energetics as $N_2^+ + O_2$, channeling of translational energy into the $O_2^+(a)$ product state has recently been demonstrated by Scherbarth and Gerlich (44). They used laser-induced photofragmentation detection of $O_2^+(a)$ and directly observed its formation at collision energies above the thermochemical threshold (0.345 eV). It would not be surprising if this type of energy coupling also occurs for the $N_2^+ + O_2$ reaction, since there is a drastic change in the charge transfer cross section with E_{cm} (12). However, the long-range, Franck–Condon mechanism is probably not responsible for the energy coupling; this coupling requires that the translational energy be converted to compensate for the reaction endothermicity, whereas the direct Franck–Condon mechanism produces little momentum transfer.

Another mechanism that might be operative in the $N_2^+ + O_2$ charge transfer is a short-range interaction, i.e., curve crossing to the $O_2^+(a)$ product state at a repulsive part of the potential energy surface. This mechanism can account for the different effects of translational and vibrational energy in the $N_2^+ + O_2$ reaction. An alternative short-range mechanism is curve crossing to the $O_2^+(a)$ state at an attractive part of the potential (Landau–Zener or Demkov type), which is promoted only by the translational energy. With these mechanisms, the different reactivity of the $N_2^+(A)$ reactant (11) may be discussed in terms of a curve crossing on a different potential energy surface.

It is difficult, however, to consider further details because of the lack of information on the structure of the $(N_2^+ \cdots O_2)$ complex and its relevant potential energy surface: Molecular orbital considerations suggest that the equilibrium structure of the $(N_2^+ \cdots O_2)$ complex is either rectangular or T-shaped (with O_2 forming the top of the T) (26). On the other hand, based on a dissociation product distribution at higher collision energies ($E_{cm} \geq 1$ eV), Schultz and Armentrout recently suggested a linear or bent $(N–N \cdots O–O)^+$ structure for the intermediate complex leading to charge transfer or dissociation (12).

Vibrational deactivation of $N_2^+(v)$ by O_2

There have been several previous measurements of the $N_2^+(v) + O_2$ deactivation rate constants. Dobler et al. (23, 24) and Ferguson et al. (26) measured k_q at thermal energies using flow tube techniques, while Kemper and Bowers (25) used an ICR instrument at $E_{cm} \approx 0.3$ eV (Table 2). All previous studies employed the Ar-monitor reaction and hence did not resolve the N_2^+ vibrationally excited states. In contrast, our experiment measures k_q for individual vibrational levels of N_2^+. Apart from our recent work with $N_2^+(v)$, there have been only a few other studies of ion deactivation with vibrational state discrimination (3*a*, 45). The deactivation rate constant of $O_2^+(v = 2)$ has been found to be approximately twice that of $O_2^+(v = 1)$ for several collision partners, which was explained in terms of predissociation of van der Waals clusters (45). Level-specific vibrational deactivation of $NO^+(v)$ was studied for some alkyl halide collision partners (3*a*). No systematic trend was observed for the $NO^+(v)$ deactivation; however, in this system deactivation competes with charge transfer, i.e., the sum of k_{CT} and k_q equals the collision rate constant (3*a*).

For $N_2^+(v)$ deactivation with O_2, only a weak dependence upon vibrational level is found (Fig. 7). On average, the values $k_{q,2}$ and $k_{q,1}$ agree with the values of the overall $k_q(v > 0)$ of 1×10^{-10} cm^3 molecule^{-1} s^{-1} reported at thermal energies. The smaller $k_q(v > 0)$ obtained with the ICR technique (Table 2) might be due to a kinetic energy effect; Dobler et al. observed a slight decrease (≈25%) of $k_q(v > 0)$ at $E_{cm} \approx 0.5$ eV (24).

We believe that the vibrational deactivation of $N_2^+(v)$ with O_2 occurs via a short-range mechanism at the low E_{cm} of our study. Neither N_2^+ nor O_2 has a permanent dipole moment that would facilitate long-range V–V transfer, although ion-induced dipole forces can be large. Further, the energy defect between the vibrational levels of N_2^+ and O_2 is rather large (≈620 cm^{-1} exothermic). This large gap would also hamper direct V–V energy transfer from $N_2^+(v)$ to O_2 upon collision. Since the rate constant for the vibrational deactivation of $N_2^+(v)$ with O_2 has a negative kinetic energy dependence in the relatively low E_{cm} region (24), a direct V–T (Landau–Teller) mechanism for the vibrational energy transfer is unlikely at the E_{cm} of our study. Therefore, nibrational relaxation most likely occurs in the $(N_2^+ \cdots O_2)$ intermediate complex (Fig. 8). Since vibrational deactivation is even more efficient than charge transfer, the charge transfer leading to $O_2^+(X)$ most likely takes place in the short-range intermediate complex as well. If formation of $O_2^+(X)$ occurred at long distances, the resulting $(N_2 \cdots O_2^+(X))$ complex would immediately dissociate to $N_2 + O_2^+(X)$ products due to the large exothermicity (3.509 eV), and no vibrational deactivation of $N_2^+(v)$ could occur.

Apart from symmetric charge transfer systems such as $N_2^+ + N_2$ and $O_2^+ + O_2$, the $N_2^+(v) + O_2$ reaction exhibits anomalously efficient vibrational deactivation compared to other ion–molecule systems (26). Ferguson et al. interpreted this in terms of a short-range, electron exchange interaction between N_2^+ and O_2 that effectively deepens the attractive well of the $(N_2^+ \cdots O_2)$ intermediate complex and increases the complex lifetime (26), e.g.,

$$[23] \qquad N_2^+ + O_2 \rightarrow N_2 + O_2^+(a^4\Pi_u) - 0.523 \text{ eV}$$

Separation of the complex to the $O_2^+(a)$ product is endothermic and does not occur (36). Assuming a moderate exchange integral of 0.8 eV for the electronic coupling between the N_2^+–O_2 and N_2–$O_2^+(a)$ states, we estimate interaction energies of 0.6, 0.7, and 0.8 eV for the $N_2^+(v = 0)$, $N_2^+(v = 1)$, and $N_2^+(v = 2)$ reactants, respectively. These interaction energies are added to the electrostatic interaction energy between N_2^+ and O_2 (≈0.2 eV) to give the effective well depths. The value of $k_{q,2}$, which is slightly greater than $k_{q,1}$, can be accounted for by this short-range mechanism.

Can. J. Chem. Downloaded from www.nrcresearchpress.com by 195.246.54.202 on 09/08/12
For personal use only.

The idea of vibrational deactivation via an intermediate complex is consistent with the kinetic energy dependence of k_q. Dobler et al. (24) observed a gradual decrease of k_q with E_{cm} in the $N_2^+(v)$ + O_2 system for the E_{cm} region below 0.5 eV; an increased E_{cm} shortens the lifetime of the complex, resulting in a smaller k_q. Above 0.5 eV, on the other hand, they observed a gradual increase in k_q. This implies that a short-range, impulsive interaction becomes important in the higher E_{cm} region. This kinetic energy effect complies with the proposed mechanism for the channeling of translational energy into the $O_2^+(a)$ product state, i.e., a short-range interaction is operating above ≈1 eV. We also believe that the steeper decrease in the charge transfer cross section with E_{cm} in the region below ≈1 eV (12) can be explained by this intermediate complex mechanism, rather than by the long- range, Franck–Condon arguments of Schultz and Armentrout (12). The overlap between the lowest unoccupied molecular orbital of N_2^+ and the highest occupied molecular orbital of $O_2(\Pi_g^* 2p)$, which leads to the $O_2^+(X)$ product state, is poor (26). Thus charge transfer to the $O_2^+(X)$ state can be inefficient and depends critically on the lifetime of the complex.

Finally, it is noted that both $\Delta v = -1$ and $\Delta v = -2$ processes occur in the deactivation of $N_2^+(v = 2)$. The $\Delta v = -1$ loss mechanism is most likely for direct V–T and V–V processes, but $\Delta v = -2$ loss may be important for low-energy collisions involving an ion–molecule intermediate complex. Indeed, an efficient V–V transfer ($\Delta v = -2$) was recently observed in the $^{15}N_2^+(v = 2)$ + $^{14}N_2$ resonant charge transfer reaction (6). It is likely that vibrational deactivation during an ion–molecule interaction depends on multiple factors, e.g., collisional energy and trajectory, structure, vibrational frequency, and lifetime of the ion–molecule pair. More studies are needed to establish a comprehensive understanding of vibrational phenomena in ion–molecule collisions.

Conclusions

Vibrational specificity for charge transfer versus deactivation in the $N_2^+(X, v = 0, 1, 2)$ + Ar and O_2 reactions was studied at near-thermal collision energy with the SIFT–LIF technique. The $N_2^+(v = 1)$ + Ar reaction proves to be an excellent reference reaction for obtaining absolute rate constants for other ion–molecule reactions.

Some enhancement is observed for the reactivity of $N_2^+(v = 0)$ with Ar in the LIF region compared to that at 300 K, most likely because of a slightly higher collision energy (<0.23 eV). The charge transfer rate constants for $v = 1$ and $v = 2$ with Ar are nearly the same, contrary to the behavior observed previously at higher collision energies. The vibrational deactivation of $N_2^+(v = 1)$ with Ar is very inefficient (≤3% of the total reaction), similar to the $N_2^+(v)$ deactivation with other rare gas quenchers. This is rationalized by a rather shallow potential well for the $N_2^+(v = 1)\cdots$Ar system due to an avoided crossing of the potential energy curves.

The vibrational dependence of the $N_2^+(v)$ + O_2 charge transfer reaction was studied at near-thermal energy where the effect of translational energy is negligible; reaction enhancement by an energy coupling to the endothermic $O_2^+(a^4\Pi_u)$ product state was not observed for $N_2^+(v)$ + O_2 following vibrational excitation of up to $v = 2$, while translational energy has been reported to couple efficiently into the $O_2^+(a^4\Pi_u)$ product state. Since it is unlikely that a long-range, direct Franck–Condon mechanism with little momentum transfer is effective in converting relative translational energy into product internal excitation, the energy coupling to the $O_2^+(a^4\Pi_u)$ state must take place via another mechanism, i.e., crossing of potential energy curves at shorter distances. Highly efficient, slightly level-dependent vibrational deactivation of $N_2^+(v = 1, 2)$ with O_2 is explained by a deep potential well due to an electron exchange interaction within a short-range ion–molecule intermediate complex. The observed vibrational energy dependence of the $N_2^+(v)$ + O_2 rate constants (charge transfer and deactivation), along with a variety of previous results, is consistent with a mechanism involving short-range interactions.

Acknowledgement

The authors gratefully acknowledge the support of this research by the Air Force Office of Scientific Research. The National Science Foundation also provided some equipment for this research. They also thank Dr. W. Freysinger for helpful discussions.

1. (*a*) O. Dutuit. *In* Fundamentals of gas phase ion chemistry. *Edited by* K.R. Jennings. Kluwer Academic, Dordrecht. 1991. pp. 21–54; (*b*) S.L. Anderson. *In* Fundamentals of gas phase ion chemistry. *Edited by* K.R. Jennings. Kluwer Academic, Dordrecht. 1991. pp. 183–196.
2. M. Baer and C.-Y. Ng (*Editors*). State-selected and state-to- state ion–molecule reaction dynamics. Part 1: Experiment. Part 2: Theory. John Wiley and Sons, New York. 1992. *In* Adv. Chem. Phys. **82** (1992).
3. (*a*) T. Wyttenbach and M.T. Bowers. J. Phys. Chem. **96**, 8920 (1992); (*b*) A. Tachibana, T. Suzuki, and T. Yamabe. J. Chem. Phys. **97**, 4921 (1992), and references cited therein.
4. W.A. Abdou, D.G. Torr, P.G. Richards, and M.R. Torr. J. Geophys. Res. **87**, 6324 (1982). **89**, 9069 (1984).
5. S. Kato, M.J. Frost, V.M. Bierbaum, and S.R. Leone. Rev. Sci. Instrum. **64**, 2808 (1993).
6. M.J. Frost, S. Kato, V.M. Bierbaum, and S.R. Leone. J. Chem. Phys. **98**, 5993 (1993).
7. E.E. Ferguson. J. Phys. Chem. **90**, 731 (1986).
8. P.M. Guyon, T.R. Govers, and T. Baer. Z. Phys. D: At. Mol. Clusters, **4**, 89 (1986), and references cited therein.
9. (*a*) C.-L. Liao, R. Xu, and C.Y. Ng. J. Chem. Phys. **85**, 7136 (1986); (*b*) J.-D. Shao, Y.-G. Li, G.D. Flesch, and C.Y. Ng. J. Chem. Phys. **86**, 170 (1987).
10. (*a*) G. Parlant and E.A. Gislason. Chem. Phys. **101**, 227 (1986); (*b*) J. Chem. Phys. **91**, 5359 (1989); (*c*) E.A. Gislason, G. Parlant, and M. Sizun. *In* State-selected and state-to-state ion–molecule reaction dynamics. Part 2: Theory. *Edited by* M. Baer and C.-Y. Ng. John Wiley and Sons, New York. 1992. pp. 321–421. *In* Adv. Chem. Phys. **82** (1992).
11. I. Koyano, K. Tanaka, T. Kato, and S. Suzuki. Faraday Discuss. Chem. Soc. **84**, 265 (1987).
12. R.H. Schultz and P.B. Armentrout. J. Chem. Phys. **95**, 121 (1991).
13. W. Lindinger, F.C. Fehsenfeld, A.L. Schmeltekopf, and E.E. Ferguson. J. Geophys. Res. **79**, 4753 (1974).
14. D. Smith and N.G. Adams. Phys. Rev. A, **23**, 2327 (1981).
15. G. Dupeyrat, B.R. Rowe, D.W. Fahey, and D.L. Albritton. Int. J. Mass Spectrom. Ion Phys. **44**, 1 (1982).
16. T.M. Miller, R.E. Wetterskog, and J.F. Paulson. J. Chem. Phys. **80**, 4922 (1984).
17. W. Lindinger, F. Howorka, P. Lukac, S. Kuhn, H. Villinger, E. Alge, and H. Ramler. Phys. Rev. A, **23**, 2319 (1981).
18. A.L. Farragher. Trans. Faraday Soc. **66**, 1411 (1970).
19. M. McFarland, D.L. Albritton, F.C. Fehsenfeld, E.E. Ferguson, and A. L. Schmeltekopf. J. Chem. Phys. **59**, 6620 (1973).
20. D. Smith, N.G. Adams, and T.M. Miller. J. Chem. Phys. **69**, 308 (1978).
21. M. Tichy, A.B. Rakshit, D.G. Lister, N.D. Twiddy, N.G. Adams, and D. Smith. Int. J. Mass Spectrom. Ion Phys. **29**, 231 (1979).

22. E. Alge and W. Lindinger. J. Geophys. Res. **86**, 871 (1981).
23. W. Dobler, F. Howorka, and W. Lindinger. Plasma Chem. Plasma Process. **2**, 353 (1982).
24. W. Dobler, H. Villinger, F. Howorka, and W. Lindinger. Int. J. Mass Spectrom. Ion Phys. **47**, 171 (1983).
25. P.R. Kemper and M.T. Bowers. J. Chem. Phys. **81**, 2634 (1984).
26. E.E. Ferguson, R. Richter, and W. Lindinger. J. Chem. Phys. **89**, 1445 (1988).
27. M.J. Frost, S. Kato, V.M. Bierbaum, and S. R. Leone. J. Chem. Phys. In press.
28. T. Kato, K. Tanaka, and I. Koyano. J. Chem. Phys. **77**, 834 (1982).
29. T.R. Govers, P.M. Guyon, T. Baer, K. Cole, H. Fröhlich, and M. Lavollée. Chem. Phys. **87**, 373 (1984).
30. (*a*) W. Federer, H. Ramler, H. Villinger, and W. Lindinger. Phys. Rev. Lett. **54**, 540 (1985); (*b*) M. Kriegel, R. Richter, W. Lindinger, L. Barbier, and E.E. Ferguson. J. Chem. Phys. **88**, 213 (1988); **91** (E), 4426 (1989).
31. R.H. Schultz and P.B. Armentrout. Chem. Phys. Lett. **179**, 429 (1991).
32. W. Dobler, H. Ramler, H. Villinger, F. Howorka, and W. Lindinger. Chem. Phys. Lett. **97**, 553 (1983).
33. H.H. Teng and D.C. Conway. J. Chem. Phys. **59**, 2316 (1973).
34. S.H. Linn, Y. Ono, and C. Y. Ng. J. Chem. Phys. **74**, 3342 (1981).
35. G. Parlant, P. Archirel, and E.A. Gislason. J. Chem. Phys. **92**, 1211 (1990).
36. E.A. Gislason and E.E. Ferguson. J. Chem. Phys. **87**, 6474 (1987).
37. B.H. Mahan, C. Martner, and A. O'Keefe. J. Chem. Phys. **76**, 4433 (1982).
38. R.R. Laher and F.R. Gilmore. J. Phys. Chem. Ref. Data, **20**, 685 (1991).
39. G.S. Janik and D.C. Conway. J. Phys. Chem. **71**, 823 (1967).
40. C.V. Speller, M. Fitaire, and A.M. Pointu. J. Chem. Phys. **79**, 2190 (1983).
41. K. Hiraoka and G. Nakajima. J. Chem. Phys. **88**, 7709 (1988).
42. W. Lindinger, D.L. Albritton, M. McFarland, F.C. Fehsenfeld, A.L. Schmeltekopf, and E.E. Ferguson. J. Chem. Phys. **62**, 4101 (1975).
43. K. Kimura, S. Katsumata, Y. Achiba, T. Yamazaki, and S. Iwata. *In* Handbook of HeI photoelectron spectra of fundamental organic molecules. Halsted, New York. 1981.
44. S. Scherbarth and D. Gerlich. J. Chem. Phys. **90**, 1610 (1989).
45. H. Böhringer, M. Durup-Ferguson, D.W. Fahey, F.C. Fehsenfeld, and E.E. Ferguson. J. Chem. Phys. **79**, 4201 (1983).

Can. J. Chem. Downloaded from www.nrcresearchpress.com by 195.246.54.202 on 09/08/12
For personal use only.

$O(^3P_j)$ atom formation from photodissociation of ozone in the visible and ultraviolet region

SAYED MOHAMMED SHAMSUDDIN, YOUSUKE INAGAKI, YUTAKA MATSUMI, AND MASAHIRO KAWASAKI[1]

Institute for Electronic Science and Graduate School of Environmental Earth Science, Hokkaido University, Sapporo 060, Japan

Received May 10, 1993

This paper is dedicated to Professor John C. Polanyi on the occasion of his 65th birthday

SAYED MOHAMMED SHAMSUDDIN, YOUSUKE INAGAKI, YUTAKA MATSUMI, and MASAHIRO KAWASAKI. Can. J. Chem. **72**, 637 (1994).

The photodissociation of ozone at 266, 308, and 532 nm has been studied for $O_3 \rightarrow O_2(X^3\Sigma_g^-) + O(2p^3P_j)$, probing $O(^3P_j)$ atomic photofragments by a vacuum ultraviolet laser-induced fluorescence method. Angular distributions and average kinetic energies are determined by measuring Doppler profiles of the $O(^3P_j)$ photofragments. Anisotropy parameters β for the angular distributions are 0.81 ± 0.10 at 266 nm, 0.60 ± 0.10 at 308 nm, and −0.68 ± 0.09 at 532 nm. These values are consistent with the assignment of the photoexcited states, that is, $^1B_2$ in the ultraviolet and $^1B_1$ in the visible region. Average center-of-mass translational energies are 44, 38, and 21 kcal/mol for photodissociation at 266, 308, and 532 nm, respectively. The j-branching ratios of $O(^3P_j)$ produced from the photodissociation at 266 nm are $(j = 2)/(j = 1)/(j = 0) = (0.55 \pm 0.03)/(0.32 \pm 0.03)/(0.12 \pm 0.03)$, which are close to the state degeneracy $(2j + 1)$ ratios. At 308 and 532 nm the branching ratios are $(j = 2)/(j = 1)/(j = 0) = (0.66 \pm 0.03)/(0.27 \pm 0.03)/(0.09 \pm 0.01)$ and $(0.74 \pm 0.03)/(0.20 \pm 0.02)/(0.05 \pm 0.01)$, respectively. Population of the $j = 2$ level increases with decreasing photon energies. The ratios obtained are discussed in terms of the adiabaticity of the potential surfaces during bond breakup as a function of the relative speed of separation.

SAYED MOHAMMED SHAMSUDDIN, YOUSUKE INAGAKI, YUTAKA MATSUMI et MASAHIRO KAWASAKI. Can. J. Chem. **72**, 637 (1994).

Faisant appel à une méthode de fluorescence induite au laser dans l'ultraviolet lointain pour déterminer les photofragments atomiques $O(^3P_j)$, on a étudié la photodissociation de l'ozone à 266, à 308 et à 532 nm selon la réaction $O_3 \rightarrow O_2(X^3\Sigma_g^-) + O(2p^3P_j)$. On a déterminé les distributions angulaires et les énergies cinétiques moyennes en mesurant les profils de Doppler des photofragments $O(^3P_j)$. Les paramètres d'anisotropie β des distributions angulaires sont respectivement 0,81 ± 0,10 à 266 nm, 0,60 ± 0,10 à 308 nm et −0,68 ± 0,09 à 532 nm. Ces valeurs sont en accord avec l'attribution des états photoexcités qui sont respectivement $^1B_2$ dans l'ultraviolet et $^1B_1$ dans la région du visible. Les énergies de translation moyennes du centre de masse sont 44, 38 et 21 kcal/mol respectivement pour les dissociations à 266, 308 et 532 nm. Les rapports de bifurcations du $O(^3P_j)$ produit par dissociation à 266 nm sont $(j = 2)/(j = 1)/(j = 0) = (0{,}55 \pm 0{,}03)/(0{,}32 \pm 0{,}03)/(0{,}12 \pm 0{,}03)$; ces résultats sont très proches des rapports pour l'état dégénéré $(2j + 1)$. À 308 et à 532 nm, les rapports de bifurcations sont respectivement $(j = 2)/(j = 1)/(j = 0) = (0{,}66 \pm 0{,}03)/(0{,}27 \pm 0{,}03)/(0{,}09 \pm 0{,}01)$ et $(0{,}74 \pm 0{,}03)/(0{,}20 \pm 0.02)/(0{,}05 \pm 0.01)$. La population du niveau $j = 2$ augmente avec une diminution des énergies du photon. On discute des résultats obtenus en termes de l'adiabaticité des surfaces de potentiel durant le bris de la liaison en fonction de la vitesse relative de séparation.

[Traduit par la rédaction]

Introduction

The visible and ultraviolet absorption spectrum of ozone consists of three diffuse bands, known as the Hartley band $^1B_2 \leftarrow \tilde{X}^1A_1$, 200–300 nm, f = 2.3×10^{-1}; the Huggins band $^1B_2 \leftarrow \tilde{X}^1A_1$, 300–360 nm; and the Chappuis band $^1B_1 \leftarrow \tilde{X}^1A_1$, 450–850 nm (1–3). The Hartley band, which is essentially diffuse because of its dissociative nature, is the most intense of these bands. The Hartley band corresponds to transitions into the saddle-geometry region of the $^1B_2$ excited state surface corresponding to ground state equilibrium configurations with strong Franck–Condon overlap as shown in Fig. 1. To the red end of the Hartley band there is a much weaker bank system called the Huggins band. The Huggins system corresponds to transitions into the bound portions of the $^1B_2$ surface with weak Franck–Condon factors (1). The $2^1A_1 \leftarrow \tilde{X}^1A_1$ transition was calculated by Hay and Dunning (2) to appear at ~270 nm with $f = 2.0 \times 10^{-6}$. Hence this band is too weak to be observed in a one-photon excitation due to the overlap of the intense Hartley band.

There are two significant photodissociation paths for O_3 in the Hartley band:

[1] $O_3 \rightarrow O(^1D) + O_2(a^1\Delta_g)$, $\Delta H = 92$ kcal/mol

[2] $O_3 \rightarrow O(^3P) + O_2(X^3\Sigma_g^-)$, $\Delta H = 24$ kcal/mol

The following path is spin-forbidden from the photoprepared $^1B_2$ state and is expected to play a lesser role in the photochemistry:

[3] $O_3 \rightarrow O(^3P) + O_2(a^1\Delta_g)$, $\Delta H = 47$ kcal/mol

The dissociation channel [1], which has a quantum yield of 0.85–0.9 (4, 5), is referred to as a singlet channel and the quantum yield of the triplet channel [2] is 0.1–0.15 (4) in the Hartley band. Fairchild et al. (6) and Sparks et al. (7) reported the formation of both $O(^3P) + O_2(X^3\Sigma_g^-)$ and $O(^1D) + O_2(a^1\Delta_g)$. Kinugawa et al. (8) studied the photodissociation of O_3 by probing $O(^3P_j)$ atomic fragments with a resonance-enhanced multiphoton ionization method. They reported the angular and kinetic energy distributions determined by measuring time-of-flight spectra. Daniels and Wiesenfeld (9) probed the vibrationally excited $O_2(X^3\Sigma_g^-, v'' = 9, 12, \text{and } 15)$ produced from the 248-nm photodissociation of O_3. They estimated that the rovibrational energy is one half of the available energy (E_{avl}).

For the Chappuis band photodissociation of O_3, Valentini and co-workers (10, 11) reported the nascent vibrational and rotational distribution of O_2. They found that the O_2 photofragments are always formed in the ground O_2 $(X^3\Sigma_g^-)$ state, and there was no evidence for production of the excited $O_2(^1\Delta_g)$

[1]Author to whom correspondence may be addressed.

Can. J. Chem. Downloaded from www.nrcresearchpress.com by EESC ESCOLA DE ENGENHARIA on 09/08/12
For personal use only.

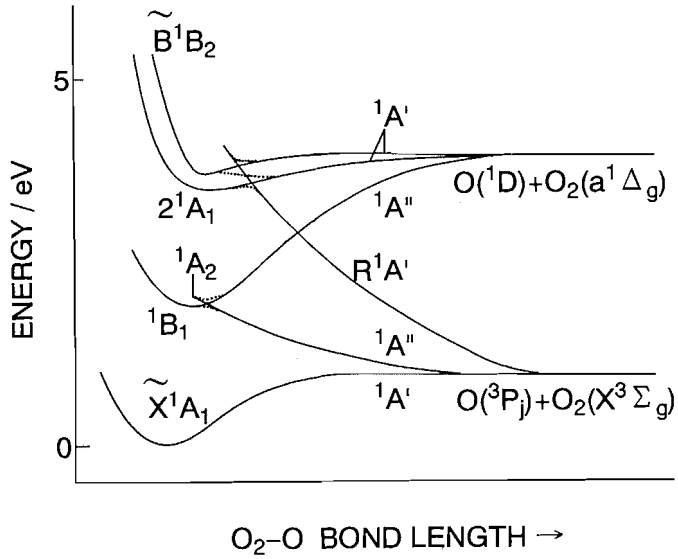

FIG. 1. Schematic section through the approximate low-lying singlet potential energy surfaces of O_3 along a dissociation coordinate $R(O_2—O)$ taken from Hay et al. (3), Daniels and Wiesenfeld (9), and Banichevich and Peyerimhoff (26). Broken lines represent avoided crossing. Symmetry representations are shown in C_{2v} near the equilibrium positions and in C_s at the asymptotic region. The curves for $^1B_1$ and $^1A_2$, which were estimated from the results calculated by Hay and Dunning (2), are added to the original figure of Hay et al. (3).

state, although both channels [2] and [3] are thermochemically allowed after Chappuis band excitation at $\lambda < 611$ nm.

To understand photodissociation dynamics, which involves the generation of atoms that possess nonvanishing electronic angular momentum, it is important to obtain branching ratios among fine-structure states of photofragment atoms. The $O(^3P_j)$ electronic states are split in energy due to spin-orbit interactions. The energy separations are $\Delta E(^3P_1–^3P_2) = 0.45$ kcal/mol and $\Delta E(^3P_0–^3P_1) = 0.19$ kcal/mol. These energy separations are very small compared with the available energy E_{avl} in the photodissociation of O_3 at 532 nm ($E_{avl} = 30$ kcal/mol), 308 nm (69 kcal/mol), and 266 nm (83 kcal/mol). The j-branching ratios of $O(^3P_j)$ atoms generated from the photodissociation of oxygen molecules have been reported at several wavelengths (12–14). Resulting j-branching ratios were interpreted by the nonadiabatic couplings of potential energy surfaces during bond breakup.

In this paper, we report the laser-induced fluorescence (LIF) detection of $O(^3P_j)$ from the photodissociation of O_3. We present the angular distributions, average kinetic energies, and j-branching ratios of $O(^3P_j)$ in the photodissociation of O_3 molecules to $O(^3P_j)$ + $O_2(^3\Sigma_g^-)$ fragments at the Hartley band (266 nm), the Huggins band (308 nm), and the Chappuis band (532 nm).

Experimental

Oxygen atoms were detected by a vacuum ultraviolet (VUV) laser-induced fluorescence method for $O(3s^3S^0 \leftarrow 2p^3P_j)$ at 130.22 nm for $j = 2$, 130.48 nm for $j = 1$, and 130.60 nm for $j = 0$. The VUV laser was generated by four-wave difference mixing ($2\omega_1–\omega_2$) with Kr gas (15), using two dye lasers (Lambda Physik FL 3002E) pumped by a XeCl excimer laser (Questek 2520vβ). The wavelength of ω_1 was 212.56 nm, which was two-photon resonant with Kr $5p[1/2]_0$, and the wavelength of ω_2 was around 578.1, 572.8, and 570.6 nm for $j = 2$, 1, and 0, respectively. The laser power was about 0.3 and 2 mJ/pulse for ω_1 and ω_2, respectively, at a pulse duration of 15 ns. The ω_1 and ω_2 light beams were focused into a Kr (25 Torr; 1 Torr = 133.3 Pa) cell with a lens ($f = 200$ mm). The generated VUV laser light was introduced into a photodissociation chamber through a LiF window. The VUV laser light reflected by a surface of a LiF window held in the chamber was led into a cell filled with nitric oxide gas (3.5 Torr). Thus, intensity of the VUV light was monitored by the photoionization current of the NO gas. At ~130 nm, near the ionization threshold of the NO molecules, the ionization efficiency varies as a function of the VUV laser wavelength. We calibrated this efficiency by observing relative populations of thermalized $O(^3P_j)$ atoms at 300 K. The laser line width of the probe VUV laser light was obtained experimentally by measurement of the line width for thermalized $O(^3P_2)$ atoms. The laser line width was 0.3 cm^{-1} as a full width at half maximum (FWHM). Under the conditions of O_3 (5 mTorr) + N_2 (1 Torr) and 10–20 μs delay between photolysis (266 nm) and probe laser pulses, Doppler widths and relative j-level intensities of $O(^3P_j)$ atoms did not change as a function of delay (10–20 μs) because the $O(^3P_j)$ atoms were translationally thermalized with the Boltzmann population among the j-levels at 300 K. We thus calibrated the j-branching ratios with the thermalized j-level intensities at 20 μs delay.

The resonant LIF signal of $O(^3P_j)$ from the photodissociation of O_3 (5–20 mTorr) was detected by a solar blind photomultiplier (Hamamatsu, R1259), a narrow band interference filter at 130 nm (Acton Research, 130-N-1D), and a gated integrator (Stanford Research Systems, SR250). The harmonics of a YAG laser system (Quanta-Ray, DCR-11) were used for 266 and 532 nm photodissociation, the polarization degree of which was more than 99%. An excimer laser (Lambda Physik, EMG 101 MSC) was also used as a dissociation light source, which was operated in the XeCl mode. A polarizer comprising 10 quartz plates was used to linearly polarize the 308-nm light. The degree of polarization of the output was 0.94. The dissociation laser light was focused with a cylindrical lens ($f = 500$ mm), which was introduced into the chamber through light baffles with a quartz window at right angles to the VUV laser and the fluorescence monitor direction. The intensity of the dissociation light was 1, 5, and 20 mJ/pulse at 266, 308, and 532 nm, respectively. The delay between the photolysis and probe laser pulses was 80 ns.

Ozone, freshly prepared from dry oxygen by using a commercial ozonizer, was trapped on silica gel at liquid N_2 temperature prior to storage at room temperature in a glass bulb at a pressure of 100 Torr. Ozone gas was introduced into the vacuum chamber through tubing and a needle valve which were made of poly(tetrafluoroethylene). LIF signals of oxygen atoms were detected without the dissociation laser light when the ω_1 probe laser intensity was high. Since this signal was due to photodissociation of ozone at 212.56 nm of the ω_1 laser light, we reduced this ω_1 intensity as much as possible for the photolysis experiment.

Results

A. Fine-structure branching ratios

Ozone molecules were photodissociated by linearly polarized laser light at 266, 308, and 532 nm. Figure 2 shows VUV LIF excitation spectra of the $O(^3P_j, j = 2, 1, 0)$ around 130 nm resulting from the photodissociation of O_3 at 532 nm. These atomic lines are broadened due to the Doppler effects. Figure 3 shows the linear dependence of the LIF signal of $O(^3P_2)$ on the vacuum ultraviolet probe laser intensity in the photodissociation at 266 nm. The LIF signal of $O(^3P_1)$ also had a linear dependence on the probe laser intensity. The j-branching ratios of $O(^3P_j)$ for O_3 photodissociation at 266, 308, and 532 nm were obtained from the excitation spectra and are listed in Table 1. To check the saturation effect we measured the j-branching ratios at two different dissociation laser intensities, namely, 0.3 and 1.0 mJ/pulse at 266 nm. Both results gave the same j-branching ratios. The j-branching ratios reach the state degeneration ratios (2j + 1) in the photodissociation at 266 nm while

Can. J. Chem. Downloaded from www.nrcresearchpress.com by EESC ESCOLA DE ENGENHARIA on 09/08/12
For personal use only.

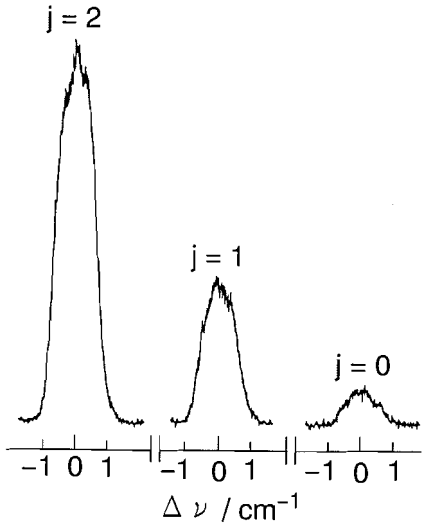

FIG. 2. Vacuum ultraviolet laser-induced fluorescence spectra of the $O(^3P_j)$ atoms at 130.2–130.6 nm from photodissociation of ozone (20 mTorr) at 532 nm.

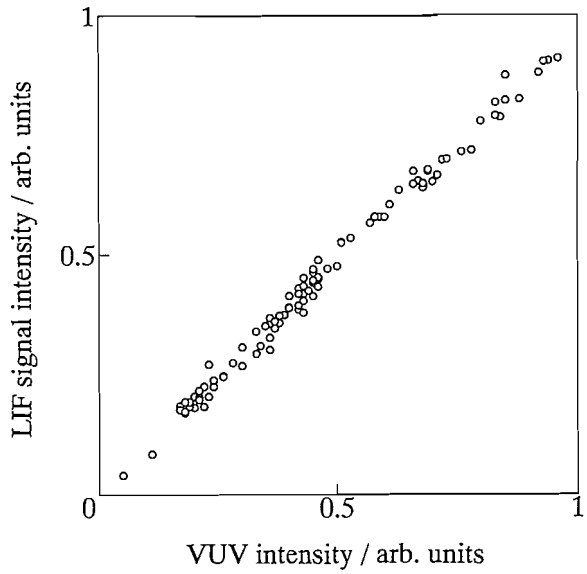

FIG. 3. Linear dependence of the laser-induced fluorescence signal intensity of $O(^3P_2)$ atoms with the probe vacuum ultraviolet laser intensity. $O(^3P_2)$ atoms are generated from O_3 photodissociation at 266 nm.

the population of the $j = 2$ level increases with decreasing photon energy at 308 and 532 nm.

B. Doppler profiles of the oxygen atom photofragments and kinetic energy release

Figure 4 shows the Doppler profiles for $O(^3P_2)$ from photodissociation of O_3 at 266, 308, and 532 nm by the VUV LIF technique. By scanning the laser wavelength around the resonance frequency of the oxygen atom at ~130 nm, the shapes of the fluorescence excitation curve were measured. Two Doppler profiles are shown for each excitation wavelength; these were taken under the $\Theta = 0°$ and 90° configurations. Θ is the angle between the electric vectors of the linearly polarized dissociation laser ($\boldsymbol{E}_d$) and the propagation direction of the probe laser ($\boldsymbol{k}_p$).

The following eq. [4] gives an average translational energy of

TABLE 1. Fine-structure branching ratios of the oxygen atom $O(2p^3P_j)$ from ozone photodissociation at 266, 308, and 532 nm

λ_{diss}[a] (nm)	Population[b] $j = 2$	$j = 1$	$j = 0$
266	0.55 ± 0.03	0.32 ± 0.03	0.12 ± 0.03
308	0.66 ± 0.03	0.27 ± 0.03	0.09 ± 0.01
532	0.74 ± 0.03	0.20 ± 0.02	0.05 ± 0.01
Statistical[c]	0.56	0.33	0.11
Adiabatic[d]	1	0	0

[a]Dissociation wavelength.
[b]Normalized populations. Errors are one standard deviations for 5–10 measurements.
[c]Degeneracy ratio, $2j + 1$.
[d]Adiabatic limit value (see text).

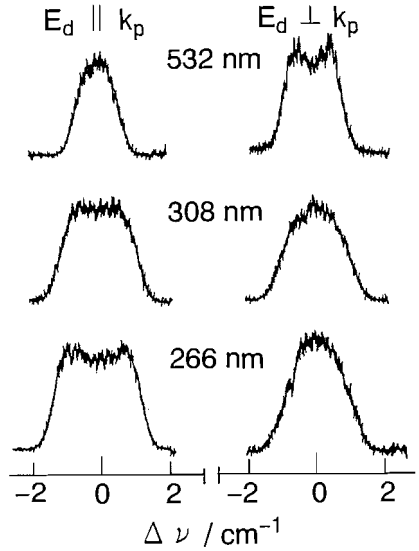

FIG. 4. Doppler profiles of $O(^3P_2)$, from photodissociation of ozone (5–20 mTorr) at 266, 308, and 532 nm, by vacuum ultraviolet laser-induced fluorescence at 130.22 nm. $\boldsymbol{E}_d//\boldsymbol{k}_p$ and $\boldsymbol{E}_d \perp \boldsymbol{k}_p$ imply that the directions of the electric vector of linearly polarized dissociation laser light are parallel with and perpendicular to the propagation directions of the probe laser beam, respectively.

oxygen atom fragments in the laboratory frame, $\langle E_t^{lab}(O)\rangle$, for photodissociation with linearly polarized light,

$$[4] \quad \langle E_t^{lab}(O)\rangle = (1/2)m(O)\{\langle v_\parallel{}^2\rangle + 2\langle v_\perp{}^2\rangle\}$$

where $m(O)$ is the molecular weight of an O atom and $\langle v_\parallel{}^2\rangle$ and $\langle v_\perp{}^2\rangle$ are the averages of the squared velocity projection parallel and perpendicular to the polarization vector of the photolysis laser, respectively (17). The values of $\langle v_\parallel{}^2\rangle$ and $\langle v_\perp{}^2\rangle$ can be derived from the second moments of the Doppler profiles. The kinetic energy release in the center-of-mass frame, $\langle E_t\rangle$, is calculated by

$$[5] \quad \langle E_t\rangle = [m(O_3)/m(O_2)][\langle E_t^{lab}(O)\rangle - (3/2)kTm(O)/m(O_3)]$$

where the $(3/2)kTm(O)/m(O_3)$ term in the right-hand side of eq. [5] is attributable to the thermal motion of O_3 parent molecules at 300 K and is negligibly small (~0.3 kcal/mol).

The Doppler widths of the $O(^3P_j)$ atom from the O_3 photodissociation at 266 and 308 nm are about six times larger than

Can. J. Chem. Downloaded from www.nrcresearchpress.com by EESC ESCOLA DE ENGENHARIA on 09/08/12
For personal use only.

TABLE 2. Average translational energies of $O(^3P_j)$ + $O_2(^3\Sigma_g^-)$ photofragments from ozone at 266, 308, and 532 nm

λ_{diss} (nm)	E_{avl}[a] (kcal/mol)	$\langle E_t \rangle$ (kcal/mol)			$\langle E_t \rangle$[b] (kcal/mol)	$\langle f_t \rangle$ (=$\langle E_t \rangle/E_{avl}$)	
		$j = 2$	$j = 1$	$j = 0$		This work	Others
266	83	43	45	46	44	0.53	0.50[c]
308	69	35	44	44	38	0.55	—
532	30	22	20	20	21	0.70	0.66[d]

[a]Available energy, $h\nu - D_0$; $h\nu$: photon energy; D_0: bond dissociation energy of O_3 to $O(^3P_j)$ + $O_2(^3\Sigma_g^-)$.
[b]Average center-of-mass translational energy weighted for the j-distribution.
[c]At 248 nm. The most probable value is taken from Fig. 14 of Daniels and Wiesenfeld (9).
[d]At 560–638 nm, Levene et al. (11).

TABLE 3. Anisotropy parameters β for angular distributions of fragment $O(^3P_j)$ atoms from photodissociation of ozone at 266, 308, and 532 nm

λ_{diss} (nm)	β_{eff}[a]				
	$j = 2$	$j = 1$	$j = 0$	$\langle \beta_{eff} \rangle$	β[b]
266	0.83 ± 0.10	0.75 ± 0.12	0.65 ± 0.08	0.79 ± 0.10	0.81 ± 0.10
308	0.63 ± 0.10	0.35 ± 0.09	0.44 ± 0.04	0.54 ± 0.09	0.60 ± 0.10
532	−0.70 ± 0.08	−0.42 ± 0.10	−0.63 ± 0.09	−0.64 ± 0.08	−0.68 ± 0.09

[a]Calculated from the second moments of the Doppler profiles by eq. [8]. Errors are one standard deviation for 5–19 measurements.
[b]$\beta = \beta_{eff}/f$ where f is the correction factor for molecular rotation in eq. [10] and β_{eff} is a weighted average value for $j = 2$, 1, and 0. β at 308 nm is corrected for imperfect polarization of the dissociation laser light.

the probe laser line width (FWHM = 0.3 cm^{-1}), and hence the contributions of this laser line width to the calculated values of the second moments are negligibly small (<3%). However, at 532 nm this line-width effect is not negligible. We simulated the Doppler profiles with the convolution of the laser line width and estimated the correction factors for the average kinetic energies due to the laser line width. Our simulation indicated the overestimation due to the line width is 13 and 9% at a kinetic energy of 20 and 24 kcal/mol, respectively. The values obtained for the average kinetic energy release in the center-of-mass frame, $\langle E_t \rangle$, at 266 and 308 nm, and the corrected values at 532 nm are listed in Table 2 for each j-level of the $O(^3P_j)$ atoms.

C. Angular distribution of the oxygen atom fragments

The general velocity distribution of atoms from the photodissociation of molecules with linearly polarized light is given by

$$[6] \quad f(v) \propto 1 + \beta P_2 (\varepsilon \cdot v)$$

where β is the anisotropy parameter, $P_2(x)$ is the second Legendre polynomial, and ε is the electric vector of incident photons. This leads to a spectral profile of photofragment atoms with a speed of $v = (2E_t^{lab}(O)/m(O))^{1/2}$ (16),

$$[7] \quad g(v) \propto \left[1 + b\beta P_2\left(\frac{v_z}{v}\right)\right]\Theta(v - |v_z|)$$

where v_z is $(v - v_0)c/v_0$, c the speed of light, and $\Theta(x)$ is the step function: $\Theta(x) = 1$ for $x \geqq 0$ and $\Theta(x) = 0$ for $x < 0$. The value of b is 1 for E_d perpendicular to k_p and $-1/2$ for E_d parallel to k_p.

The effective anisotropy parameter β_{eff} for the angular distributions of the photofragments is calculated (17) by

$$[8] \quad \beta_{eff} = 5\{\langle v_\parallel^2 \rangle - \langle v_\perp^2 \rangle\}/\{\langle v_\parallel^2 \rangle - \langle v_\perp^2 \rangle\}$$

The effective anisotropy parameters thus calculated are listed in Table 3 for 266, 308 and 532 nm. The β_{eff} values averaged for the j-populations are positive at 266 and 308 nm while that at 532 nm is negative.

When the dissociation lifetime of the photoexcited state is shorter than the rotational period of the parent molecule, the value of the anisotropy parameter β is given by

$$[9] \quad \beta = 3\cos^2\chi - 1$$

where χ is the angle between the directions of the electronic transition moment and the dissociation bond (18). However, parent molecular rotation reduces anisotropy by a factor f, which can be approximated for a small deflection of the original velocity vector (18):

$$[10] \quad f = 1 - 3RT/[(2)^{1/2}E_t]$$

Since E_t is 21 kcal/mol at 532 nm, f is ~0.94 and a small amount of distortion is produced in the value of β_{eff}. The corrected value for the anisotropy parameter is −0.68 ± 0.09, which is given by $\beta = \beta_{eff}/f$. A similar correction was made for the photodissociation at 266 and 308 nm. At 308 nm, our β value should be corrected due to the incomplete polarization of the excimer laser light according to Dzvonik et al. (19). The corrected values, β, are listed in Table 3. Fairchild et al. (6) presented a β value of −0.73 for the photodissociation at 600 nm to the $O(^3P_j)$ + $O_2(^3\Sigma_g^-)$ channel, which is in good agreement with our value of −0.68 ± 0.09 at 532 nm. For the $O(^3P_j)$ + O_2 $(^3\Sigma_g^-)$ channel, they also reported values of 0.52, 0.77, and 1.20 at 274, 277, and 281 nm, respectively. Kinugawa et al. (8)

Can. J. Chem. Downloaded from www.nrcresearchpress.com by EESC ESCOLA DE ENGENHARIA on 09/08/12
For personal use only.

Can. J. Chem. Downloaded from www.nrcresearchpress.com by EESC ESCOLA DE ENGENHARIA on 09/08/12
For personal use only.

reported $\beta = 0.7 \pm 0.1$ at 226 nm. Our value of 0.81 ± 0.10 at 266 nm agrees with their values.

Discussion

A. *Photoexcitation and dissociation processes*

A one-dimensional sketch of the diabatic potential curves along a dissociation coordinate, $R(O_2—O)$, is presented in Fig. 1. The ground state $O_3(\tilde{X}^1A_1)$ has a C_{2v} equilibrium geometry ($R = 1.2717$ Å, $\theta = 116.78°$) and correlates asymptotically with $O_2(^3\Sigma_g^-) + O(^3P_j)$. The $^1B_2$ state of O_3 has a C_{2v} saddle point at $R = 1.405$ Å and $\theta = 108.4°$ (2). An avoided crossing takes place between the $^1B_2$ and repulsive R^1A' states due to the same representation $^1A'$ in the C_s symmetry of the dissociation path. This repulsive R^1A' potential surface correlates to $O(^3P_j) + O_2(^3\Sigma_g^-)$. Another avoided crossing may occur between the R^1A' and 2^1A_1 states, since the symmetry of the 2^1A_1 states becomes $^1A'$ at the C_s symmetry. Consequently, the adiabatic dissociation path of O_3 molecules excited to the $^1B_2$ surface leads to $O(^1D) + O(^1\Delta_g)$ fragments (3). Upon UV band excitation, ozone molecules are excited to the $^1B_2(^1A')$ state and then predominantly dissociate to $O(^1D) + O_2(a^1\Delta_g)$ along the adiabatic surface. However, about 10% of the excited ozone molecules dissociate to $O(^3P_j) + O_2(^3\Sigma_g^-)$ along the R^1A' state due to non-adiabatic transitions (4).

The visible band (400–700 nm) is assigned to the $^1B_1$–$\tilde{X}^1A_1$ transition (2). The $^1B_1$ state has $R = 1.370$ Å and $\theta = 117.7°$, which becomes the $^1A''$ state in the C_s symmetry and correlates to $O(^1D) + O_2(^1\Delta_g)$ (2). The $^1A_2$ state that locates near the $^1B_1$ state at their equilibrium geometries is correlated with $O(^3P_j) + O_2(^3\Sigma_g^-)$. The avoided crossing takes place between these $^1B_1$ and $^1A_2$ states, since the symmetries of these two states become $^1A''$ at the asymptotic C_s region. At 532 nm, ozone molecules are excited to the $^1B_1(^1A'')$ state and then dissociate to $O(^3P_j) + O_2(^3\Sigma_g^-)$ through this repulsive $^1A_2(^1A'')$ state.

B. *Dissociation anisotropy*

Fairchild et al. (6) calculated an anisotropic parameter of the photofragment angular distribution of the $O(^1D) + O_2(^1\Delta_g)$ channel for the UV transition of $O_3(\tilde{B}^1B_2 \leftarrow \tilde{X}^1A_1)$. They obtained $\beta = 1.17$, assuming that (a) the transition moment lies perpendicular to the C_{2v} axis, (b) the dissociation lifetime τ is zero, and (c) the bond angle θ is the same as that of the ground state (116.7°). Their experimental results for the $O(^1D) + O_2(^1\Delta_g)$ channel indicate that the angular distribution is independent of photodissociation wavelengths over the range 274–300 nm and their β values (1.2 ± 0.2) are close to the calculated value of $\beta = 1.17$. For the predissociative formation of $O(^3P)$, our β value is 0.81 ± 0.10 at 266 nm. Since a β value is a function of both a lifetime τ and an angle χ of the dissociating state, the difference in the β values between the $O(^1D)$ and $O(^3P)$ channels would be due to different lifetimes and (or) structures of the dissociating O_3 parent molecules for the singlet and triplet channels. However, the lifetime of the photoprepared $^1B_2$ state must be the same for both the singlet and triplet channels. Since the β value for $O(^1D)$ is close to the calculated value, the lifetime should be very short. The difference in the β values between the singlet and triplet channels may be due to a structural change in the triplet channel. Daniels and Wiesenfeld (9) reported sharply peaked rotational distributions of $O_2(X^3\Sigma_g^-, v'' = 9, 12, 15)$ in the photodissociation of O_3 at 248 nm. They proposed an impulsive approximation, which reproduces their experimental peak positions and approximate widths of the distributions. If this impulsive model is an accurate depiction of the dissociation, the lifetime should be very short. The only way to obtain agreement between the peaks of their rotational and our angular distributions within the context of the impulsive model is to assume that the lifetime is very short and the bond angle $\theta = 102 \pm 4°$, which leads to $\beta = 0.81 \pm 0.10$. This bond angle θ is a little smaller than those of the equilibrium position between the ground $^1A_1$ and the excited $^1B_2$ states. That geometry might approximate a configuration for which coupling is strong between the photoprepared $O_3(^1B_2)$ and the interacting R^1A' states.

At 308 nm, the Huggins band is assigned to transition into $O_3(\tilde{B}^1B_2)$ with weak Franck–Condon factors (1). The quantum yield of $O(^1D)$ formation is ca. 0.9 at 266 nm, ca. 0.5 at 300 nm, and less at 308 nm (4, 20). In addition, the observed anisotropy parameter at 308 nm is 0.60 ± 0.10, which is smaller than 0.81 ± 0.10 at 266 nm. Because the formation of $O(^3P)$ atoms from $O_3(^1B_2)$ is predissociative, the dissociation dynamics would be sensitive to the available energy in the dissociation process as well as to the internuclear distance to which the O_3 molecule is excited. Hence, the photodissociation dynamics of O_3 at 308 nm would not be the same as that at 266 nm.

The first diffuse absorption band at 450–850 nm is assigned to a transition from the ground $\tilde{X}^1A_1$ state into the repulsive $^1B_1$ state. Since the transition moment for the $^1B_1$–$\tilde{X}^1A_1$ absorption lies perpendicular to the molecular plane of ozone, this transition corresponds to $\beta = -1$, based on eq. [9], if the dissociation lifetime is very short. The obtained value of -0.68 ± 0.09 is a little smaller than -1, which may be explained by the geometrical change after the photoexcitation or by the lifetime longer than the rotational period during curve crossing of this $^1B_1$ state to the repulsive $^1A''$ state.

C. *Kinetic energy release in the photodissociation*

A fraction of the available energy released into the translational energy, $\langle f_t \rangle = \langle E_t \rangle / E_{avl}$, is shown in Table 2. Since our Doppler measurement is not very sensitive to a translational energy distribution, only the average translational energy is obtained from eq. [4]. About one half of the available energy goes into the translational freedom in the photodissociation at the UV band, while 70% of the available energy is released into the translational freedom at the visible band. The results obtained are in good agreement with the values estimated from the vibronic distribution of the O_2 fragment for both the visible and ultraviolet bands (9, 10).

D. *The* j*-branching ratios in the* $O(^3P_j)$ *levels*

The j-branching ratios of $O(^3P_j)$ and $Cl(^2P_j)$ that are produced from the photodissociation of O_2 (12–14), HCl (21), Cl_2 (22), and chlorinated methanes (23) have been studied. The j-branching ratios in photodissociation processes should be determined by two factors: one is the adiabatic correlation between the dissociating molecular states and the atomic states. The other is non-adiabatic coupling during bond breakup. Two extreme cases can be considered, that is, adiabatic and diabatic or recoil limits (24). When the fragment separation is sufficiently fast, the electronic and spin angular vectors do not recouple according to the adiabatic state correlation, since there is not enough time for electrons to adjust themselves during bond breakup. In this diabatic or recoil limit, only the density of the product states is considered and hence the population of the specific j-level of $O(^3P_j)$ is proportional to the degeneracy $(2j + 1)$, that is, $(j = 2)/(j = 1)/(j = 0) = 0.56/0.33/0.11$.

Can. J. Chem. Downloaded from www.nrcresearchpress.com by EESC ESCOLA DE ENGENHARIA on 09/08/12
For personal use only.

On the other hand, when the fragments separate more slowly, the dissociation is expected to proceed according to the adiabatic state correlation between the molecular states and the separated fragments. For the photodissociation of diatomic molecules, the correlation diagram is constructed so that the projection (Ω value) of the total angular momentum along the nuclear axis is conserved between molecular states and atomic states. In the case of the O_3 photodissociation process, the molecule keeps C_s symmetry during bond breakup. The combination of the $O_2(^3\Sigma_g^-)$ + $O(^3P_j)$ product states generates, in total, 27 electronic levels of the O_3 molecular electronic states, which are two $^1A'$, two $^3A'$, two $^5A'$, one $^1A''$, one $^3A''$, and one $^5A''$. The adiabatic correlation diagram connects the lowest 15 molecular electronic levels of the 27 molecular levels with the $O(^3P_j, j = 2)$ + $O_2(^3\Sigma_g^-)$ product state, the next nine electronic states with $j = 1$, and the next three with $j = 0$. The R^1A' and $^1A''(^1A_2)$ surfaces, which are responsible for the dissociation of O_3 after the photoexcitation at ultraviolet and visible wavelengths, respectively, should be adiabatically correlated with the $O_2(^3\Sigma_g^-)$ + $O(^3P_j, j = 2)$ product states, taking into account the ab initio electronic states (2). If the dissociation takes place adiabatically on the R^1A' or $^1A_2(^1A'')$ surfaces, the formation of $O(^3P_2)$ is expected according to this adiabatic state correlation. The expectation values for the j-branching ratios in the adiabatic limit are $(j = 2)/(j = 1)/(j = 0) = 1/0/0$.

Our experimental results on the branching ratios at 266 nm are $(j = 2)/(j = 1)/(j = 0) = 0.55/0.32/0.12$, which are quite close to the diabatic limit values. Those at 308 and 532 nm are between the diabatic and adiabatic limit values as shown in Table 1. Non-adiabatic couplings during bond breakup with other electronic surfaces of the same symmetry are responsible for the formation of $j = 1$ and $j = 0$ levels of $O(^3P_j)$ due to the fast nuclear kinetic motion. Those non-adiabatic couplings may take place in the O_2—O long-distance region, since the potential surfaces become asymptotically degenerate in that region due to the small energy separations among the j-levels. The degree of adiabaticity is expressed by the following relation:

$$[8] \quad \xi = (R/v)/(\hbar/\Delta E)$$

where R is the length of the interaction region and v is the relative speed of the separating atoms (25). When the separation speed between the fragments is slow in the asymptotic interaction region, the adiabaticity parameter ξ is large. ΔE is the energy separation of the interacting states. The value of ξ is large for a large value of ΔE. The spin-orbit energy separations ΔE_{so} of each j state of the fragment atoms can be used for the value of ΔE in the long nuclear distance region, and hence, $\hbar/\Delta E$ or $\hbar/\Delta E_{so}$ is considered as a time for relevant electrons to precess during the breakup. When the dissociation wavelength is longer, that is, the speed is slower in the long nuclear distance region, the j-branching ratios become closer to the adiabatic limit. Thus, the dissociation wavelength dependence of the j-branching ratios listed in Table 1 is explained by the adiabaticity of the relevant potential curves.

Conclusion

We have measured the average kinetic energies, the anisotropy angular parameters, and the j-branching ratios of the $O(^3P_j)$ photofragments from photodissociation of O_3 in the Hartley (266 nm), the Huggins (308 nm), and the Chappuis (532 nm) bands. The obtained values of the anisotropic angular parameters are consistent with assignment of the optical transitions, $^1B_2$–$\tilde{X}^1A_1$ for the Hartley and the Huggins bands and $^1B_1$–$\tilde{X}^1A_1$ for the Chappuis band. The j-branching ratios of the $O(^3P_j)$ products depend solely on the separation speed of the photofragments.

Acknowledgments

A part of this work was supported by a Grant-in-Aid from the Ministry of Education, Science, and Culture of Japan (Monbusho), and the Sumitomo Foundation. S.M.S. thanks Monbusho for awarding a Scholarship for Foreign Students.

1. A. Shinha, D. Imre, J.H. Goble, Jr., and J.L. Kinsey. J. Chem. Phys. **84**, 6108 (1986).
2. P.J. Hay and T.H. Dunning. J. Chem. Phys. **67**, 2290 (1977).
3. P.J. Hay, R.T. Pack, R.B. Walker, and E.J. Heller. J. Phys. Chem. **86**, 862 (1982).
4. R.P. Wayne. Atmos. Environ. **21**, 1683 (1987).
5. W.B. DeMore, S.P. Sander, D.M. Golden, M.J. Molina, R.F. Hampson, M.J. Kurylo, C.J. Howard, and A.R. Ravishankara. JPL Publ. **90-1** (NASA Jet Propulsion Lab. Pasadena, Calif.). 1990.
6. C.E. Fairchild, E.J. Stone, and G.M. Lawrence. J. Chem. Phys. **69**, 3632 (1978).
7. R.K. Sparks, L.R. Carlson, K. Shobatake, M.L. Kowalczyk, and Y.T. Lee. J. Chem. Phys. **72**, 1401 (1980).
8. T. Kinugawa, T. Sato, T. Arikawa, Y. Matsumi, and M. Kawasaki. J. Chem. Phys. **93**, 3289 (1990).
9. M.J. Daniels and J.R. Wiesenfeld. J. Chem. Phys. **98**, 321 (1993).
10. D.S. Moore, D.S. Bomse, and J.J. Valentini. J. Chem. Phys. **79**, 1745 (1983).
11. H.B. Levene, J-C. Nieh, and J.J. Valentini. J. Chem. Phys. **87**, 2583 (1987).
12. Y. Matsumi and M. Kawasaki. J. Chem. Phys. **93**, 2481 (1990); J. Chem. Phys. **94**, 6338 (1991).
13. Y.-L. Huang and R.J. Gordon. J. Chem. Phys. **94**, 640 (1991).
14. K. Tonokura, N. Shafer, Y. Matsumi, and M. Kawasaki. J. Chem. Phys. **95**, 3394 (1991).
15. G. Hilber, A. Lago, and R. Wallenstein. J. Opt. Soc. Am. **B4**, 1753 (1987).
16. R.N. Zare and D.R. Herschbach. Proc. IEEE, **51**, 173 (1963).
17. H.L. Kim, S. Satyapal, P. Brewer, and R. Bersohn. J. Chem. Phys. **91**, 1047 (1989).
18. S-C. Yang and R. Bersohn. J. Chem. Phys. **61**, 4400 (1974).
19. M. Dzvonik, S-C. Yang, and R. Bersohn. J. Chem. Phys. **61**, 4408 (1974).
20. P.W. Fairchild and E.K.C. Lee. Chem. Phys. Lett. **60**, 36 (1978).
21. K. Tonokura, Y. Matsumi, M. Kawasaki, S. Tasaki, and R. Bersohn. J. Chem. Phys. **97**, 8210 (1992).
22. Y. Matsumi, K. Tonokura, and M. Kawasaki. J. Chem. Phys. **97**, 1065 (1992).
23. Y. Matsumi, K. Tonokura, M. Kawasaki, S. Satyapal, and R. Bersohn. J. Chem. Phys. **94**, 2669 (1991).
24. S.J. Singer, K.F. Freed, and Y.B. Band. Adv. Chem. Phys. **61**, 1 (1985).
25. R.D. Levine and R.B. Bernstein. Molecular reaction dynamics and chemical reactivities. Oxford University Press, New York. 1987. p. 315.
26. A. Banechevich and S.D. Peyerimhoff. Chem. Phys. **174**, 93 (1993).

Internal, translational, and angular momentum product state distributions of CuF molecules desorbing associatively from copper surfaces

A. Bracker,[1] P. Jakob,[2] U. Näher,[3] M. Rüdiger,[4] K. Sugawara,[5] and J. Wanner
Max-Planck-Institut für Quantenoptik, Hans-Kopfermann-Str. 1, 85748 Garching, Germany
Received July 7, 1993

This paper is dedicated to Professor John C. Polanyi on the occasion of his 65th birthday

A. Bracker, P. Jakob, U. Näher, M. Rüdiger, K. Sugawara, and J. Wanner. Can. J. Chem. **72**, 643 (1994).

The dry etching reaction of solid copper surfaces with fluorine atoms or molecules has been studied with laser-induced fluorescence spectroscopy. The reaction product, copper monofluoride, CuF, is produced in the $X^1\Sigma^+$ electronic ground state and desorbs into the gas phase at surface temperatures above approximately 750 K. Rotationally resolved LIF excitation spectra of the $C^1\Pi \leftarrow X^1\Sigma^+$ band system of CuF molecules desorbing from an isotopically purified ^{63}Cu polycrystalline sample are obtained under conditions of coherent saturation. From the product state analysis it is deduced that the rovibrational product populations are in thermal equilibrium with the surface. The same holds for the translational velocity distribution obtained by Doppler-shift measurements. A pronounced polarization effect, particularly strong for Q branch transitions, can be traced back to photoselection of single-parity levels in the Λ doublets of the $C^1\Pi$ state. A theoretical analysis for the distribution of J vectors, based on the formalism of Greene and Zare, shows that the measured degree of polarization is quantitatively in agreement with an isotropic distribution of rotational angular momentum vectors. The vibrational and translational product equilibration is not affected by changing the reactants from F_2 molecules to F atoms, which increases the exoergicity of the overall reaction. The results are interpreted in terms of the absence of a barrier for desorption and a long residence time of the chemisorbed CuF molecules at the copper surface. The lack of any translational and rotational cooling is discussed within the framework of a model.

A. Bracker, P. Jakob, U. Näher, M. Rüdiger, K. Sugawara et J. Wanner. Can. J. Chem. **72**, 643 (1994).

Faisant appel à la spectroscopie de fluorescence induite au laser, on a étudié la réaction de gravure à sec de surface solides de cuivre par des atomes ou des molécules de fluor. Le monofluorure de cuivre, CuF, produit par la réaction se forme dans l'état électronique fondamental $X^1\Sigma^+$ et il se désorbe vers la phase gazeuse à des températures de surface supérieures à environ 750 K. Les spectres d'excitation LIF, résolus en fonction de la rotation, du système de bandes $C^1\Pi \leftarrow X^1\Sigma^+$ des molécules de CuF qui se désorbent d'un échantillon polycristallin de ^{63}Cu isotopiquement purifié, ont été obtenus dans des conditions de saturation cohérente. En se basant sur une analyse de l'état du produit, on en déduit que les populations de produit rovibrationnel sont en équilibre thermique avec la surface. Il en est de même pour la distribution de la vitesse de translation obtenue par des mesures de déplacement Doppler. On peut attribuer un effet important de polarisation, particulièrement fort pour les transitions des branches Q, à une photosélection des niveaux de parité unique dans les doublets Λ de l'état $C^1\Pi$. Une analyse théorique de la distribution des niveaux J, basée sur le formalisme de Greene et Zare, montre que le degré de polarisation mesuré est en bon accord quantitatif avec une distribution isotrope des vecteurs des moments de rotation angulaire. L'équilibre vibrationnel et translationnel du produit n'est pas affecté par un changement de réactifs de molécules F_2 à atomes F qui augmente l'exoergicité de la réaction globale. On interprète les résultats en fonction de l'absence d'une barrière à la désorption et à un temps de résidence élevé des molécules de CuF chemisorbées à la surface du cuivre. On discute du manque de refroidissement translationnel et rotationnel à l'aide d'un modèle.

[Traduit par la rédaction]

1. Introduction

As in the field of gas-phase reaction dynamics, measurements of product state distributions by laser spectroscopy have proven essential in understanding the dynamics of reactive desorption (1, 2). Primarily, these measurements address the question of exoergicity sharing between the solid and the various degrees of freedom of the gaseous products. Contrary to a common assumption, both systems are not necessarily at equilibrium. This can be true for both direct and indirect gas–surface reactions. For a direct surface reaction, the product state distribution reflects the dynamics of the entire process from gaseous reactants to products. An example of this is the relatively rare Eley–Rideal mechanism for an exoergic reaction in which a gaseous atom reacts with an adsorbate. This mechanism has recently been invoked to explain the results of three independent studies of the recombination of H atoms at metal surfaces (3–5). The high vibrational product excitation has been modelled with quantum mechanical calculations by Kratzer and Brenig (6). The potential energy surface results in dynamics that in many respects resemble that seen for direct gas phase reactions (see, for example, the work of John C. Polanyi (7)). Most cases, however, involve an indirect mechanism, where the initial reactants are dissociatively adsorbed and then associatively desorbed (Langmuir–Hinshelwood mechanism). Even though the adsorbed reactants are fully equilibrated with the surface, a pronounced disequilibrium in the various degrees of freedom of the desorbing products may occur. The following nonequilibrium features have been observed in the desorption step of indirect surface reactions.

The most typical example for nonequilibrium in the vibrational degree of freedom is the recombinative desorption of hydrogen from Cu surfaces as shown first by Kubiak et al. (8). The experimental observation of "vibrational heating" has been interpreted by Brenig et al. in terms of an early barrier

[1]Present address: Dept. of Chemistry, University of California, Berkeley, CA 94720, U.S.A.

[2]Present address: Physikdepartment E 20, Technische Universität München, 85748 Garching, Germany.

[3]Present address: Max-Planck-Institut für Festkörperforschung, 70569 Stuttgart, Germany.

[4]Present address: Max-Planck-Institut für Biochemie, 82152 Martinsried, Germany.

[5]Present address: National Institute for Advanced Interdisciplinary Research, Tsukuba, Ibaraki, 305, Japan.

Can. J. Chem. Downloaded from www.nrcresearchpress.com by 195.246.54.202 on 09/08/12
For personal use only.

Can. J. Chem. Downloaded from www.nrcresearchpress.com by 195.246.54.202 on 09/08/12
For personal use only.

for desorption (9) in analogy with the Polanyi rules for gas phase reactions (7). Consequently for this system a significant "translational heating" was reported by Comsa and David (10). The barrier to adsorption was then probed by Rendulic et al. in experiments of vibrationally assisted sticking (11).

In studies of associative or recombinative desorption by the groups of Lin, Somorjai, Zacharias, and co-workers (OH(OD)/Pt(111) (12), NO/Pt(111) (13, 14), and H_2 (D_2)/Pd(100) (15)), rotational product analysis showed a "rotational cooling" effect, in which the desorbing diatomics take up on average less rotational energy per molecule than accommodation to the surface temperature would allow. This effect was small for OH and OD desorbing from Pt (12) but quite large for NO/Pt (13, 14) and H_2/Pd (15). Microscopic reversibility arguments by Brenig et al. (16) and Muhlhausen et al. (17) provide a plausible explanation of this effect: strongly rotating molecules have a lower sticking coefficient, which implies a lower desorption yield at high J.

In a detailed theoretical treatment of associative desorption, Yang and Rahman (18) predicted that rotational cooling should be associated with an alignment effect, where the rotational angular momentum is preferentially aligned parallel to the surface normal. From a mechanistic point of view their model assumes a strong coupling between rotational and translational degrees of freedom of the desorbing molecules. The same holds for calculations done by Muhlhausen et al. (17). Experimentally, no alignment effect was observed for the associative desorption of OH and OD from Pt(111) (12). However, in the trapping–desorption channel of NO scattered from a Pt(111) surface, the helicopter type of rotation was preferred while direct inelastic scattering was dominated by the cartwheel motion (19).

In this work we report a detailed product state analysis of copper monofluoride, which is the dominant product in the heterogeneous reaction of gaseous fluorine with solid copper at temperatures of about 900 K as applied in this experiment.[6] We report results on rotational, vibrational, and translational energy distributions of associatively desorbing CuF molecules as well as on their angular momentum distribution. To our knowledge this is the first complete state-specific investigation of an etching reaction. Rotationally resolved excitation spectra were obtained by applying laser-induced fluorescence (LIF) to the CuF $C^1\Pi$–$X^1\Sigma^+$ band system. This transition has the highest transition probability of a series of electronically excited states of CuF that are accessible to a LIF experiment in the visible spectral range. Besides the P and R branches, a Q branch can also be used for the rovibrational analysis.

In an earlier article reporting a preliminary vibrational product state analysis based on rotationally unresolved excitation spectra (20), we found that the distribution of the gaseous products seems to be largely determined by the surface temperature. This observation was independent of the copper crystal face. Also, the vibrational distributions were not affected when the fluorine reactant beam energy was increased, or when fluorine molecules were replaced by atoms, both of which increase the exoergicity in the entrance channel of the CuF formation reaction. We thus noted that a product state analysis only gives insight into the final step of the surface reaction, namely, the desorption of the products (20). This observation is in contrast to molecular beam scattering of molecules from surfaces for which the initial state of the reactants does influence the product state (21); the associative desorption process in our case may therefore be characterized as a half collision. In this paper we address the question of whether or not thermal equilibrium is maintained throughout the overall reaction, i.e., whether nonthermal effects influence the internal energy distribution of the desorbing CuF product.

This paper is organized as follows: After the experimental description in Sect. 2, we present in Sect. 3A the laser excitation spectra. In Sects. 3B and 3C the rotational and vibrational analyses are presented. In Sect. 3D we derive the translational product distribution from a Doppler-shift technique and in 3E we determine the distribution of J vectors from polarization measurements. In Sect. 4 we discuss our results within the framework of the present theoretical understanding of the dynamics of molecules desorbing from surfaces. The conclusions are summarized in Sect. 5.

2. Experiment

Figure 1 shows a diagram of the experimental setup. A molecular beam of fluorine impinges on a copper surface, which can be heated up to 1100 K. The cryobaffled vacuum chamber is pumped to a base pressure of 3×10^{-8} mbar (1 bar = 100 kPa), caused mostly by N_2 and O_2. The high sample temperature during the experiments (750–1100 K) and the fluorine exposure, however, effectively prevent accumulation of residual gas particles on the surface, as verified by Auger spectroscopy.[7] No time dependence of the measured fluorescence intensities is found after starting the experiment and we thus conclude that artifacts due to minor surface contaminants are below our detection limit. In initial experiments, polished Cu(111) and Cu(110) single crystals of 99.999% purity were used. Since the outcome of the reaction was found to be independent of the copper crystal face, a polycrystalline sample of purified ^{63}Cu (99.6% purity) was prepared to simplify the data analysis. A blind with a 1×5 mm slit above the copper sample was used to minimize thermal background radiation in the photomultiplier and to reduce the spot size of desorbing CuF.

The fluorine molecular beam (99.999% purity) expanded at a typical flow of 0.5 standard cubic centimeters/min (sccm) from a sapphire nozzle with an i.d. of 0.2 mm, which was mounted in a differentially pumped chamber. The fluorine beam entered the main chamber through a skimmer, and led to a pressure increase to the 10^{-7} mbar range. For some experiments referred to in the discussion, fluorine molecules were exchanged with F atoms as reactants. In this case the dissociation of F_2 was achieved by a microwave discharge, also indicated in Fig. 1.

Rotationally resolved excitation spectra of the $C^1\Pi \leftarrow X^1\Sigma^+$ band system of the desorbing CuF molecules were recorded with an actively stabilized ring dye laser with coumarin 102 dye pumped by a Kr^+ laser. In single-mode operation at several megahertz bandwidth, the tunable laser yielded a typical output power of 60 mW. The laser wavelength was measured by a homebuilt wavemeter of the Hall and Lee type with an accuracy of ± 0.02 cm^{-1} (22, 23). The laser beam was directed parallel to the copper surface at a distance of 13 mm. CaF_2 windows with an antireflection coating were mounted at the chamber ports perpendicular to the laser beam. Stray laser light is suppressed by a set of light baffles shown in Fig. 1. The detection system consisted of an imaging system, a cutoff filter to reduce background radiation from the surface for $\lambda \geq 550$ nm, a photomultiplier tube, and a photon counting system. The linewidth of the individual rotational transitions under these conditions is essentially determined by Doppler broadening. For additional experiments with increased spectral resolution, a slit of 1.0 mm width shown in Fig. 1 was placed in front of the detection system. For the determination of

[6]Besides CuF there are also higher polymers desorbing into the gas phase. These are the subject of another publication: K. Sugawara, Th. Wach, and J. Wanner, to be published.

[7]P. Jakob, Th. Wach, and J. Wanner, unpublished results.

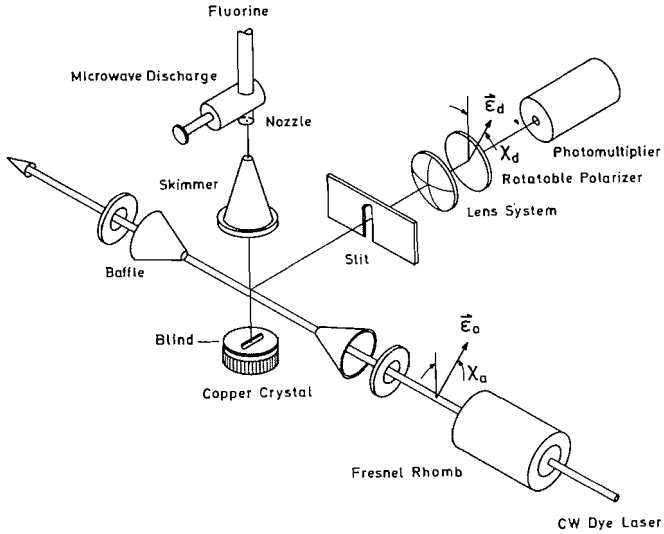

FIG. 1. Experimental arrangement for investigating the reaction of fluorine with solid copper.

translational velocities of the desorbing products, the blind with one slit was replaced by a double slit arrangement (see Sect. 3D).

A Fresnel rhomb was inserted in the laser beam to rotate the polarization plane. Care was taken that no other polarizing optical elements were in the beam path. For the rotational population measurements the plane of polarization was parallel to the copper surface. For the alignment measurements, a mutually orthogonal geometry was established between the laser beam and the axis of the detection system and the surface normal. For these experiments a rotatable polarization filter was placed in front of the photomultiplier tube.

3. Results

A. *Excitation spectrum of the* $C^1\Pi \leftarrow X^1\Sigma^+$ *transition*

Because of their low vibrational frequency (24) and the high temperature of the copper surface (in the range of 750–1100 K), the desorbing CuF molecules are observed in vibrational product levels $v'' = 0$ to $v'' = 4$ of the $X^1\Sigma^+$ ground state. In principle, a rotational analysis is possible in each of these levels. The spectroscopic constants of the various branches and vibrational levels have been published by Ahmed et al. from absorption measurements (25). With our experimental setup, considerably more accurate values of the rotational constants can be obtained (26). Rotational levels up to $J = 78$ have been studied, corresponding to a spectral range between 20 246 and 20 313 cm^{-1}.

Figure 2 shows a typical ring laser scan (approximately 35 GHz width) of the Q branch band head of the ($v' = 0, v'' = 0$) transition. Except for low J lines, the rotational structure is fully resolved. Figure 3 shows the Q band heads of the (0,0), (1,1), and (2,2) transitions with increased resolution using the setup of slits depicted in Fig. 1. As becomes evident, the rotational lines are subject to a hyperfine splitting due to the $I_{Cu} = 3/2$ and $I_F = 1/2$ nuclear spin of ^{63}Cu and ^{19}F, respectively. A comprehensive illustration and analysis of the hyperfine effects will be given elsewhere (27).

B. *Rotational population analysis*

Before describing our results we need to consider another topic of relevance to this particular system. In narrow-band fluorescence excitation spectra, saturation occurs readily, even at modest laser power. In a rotational product state analysis of the IF molecule (also using a ring dye laser), Billy et al.

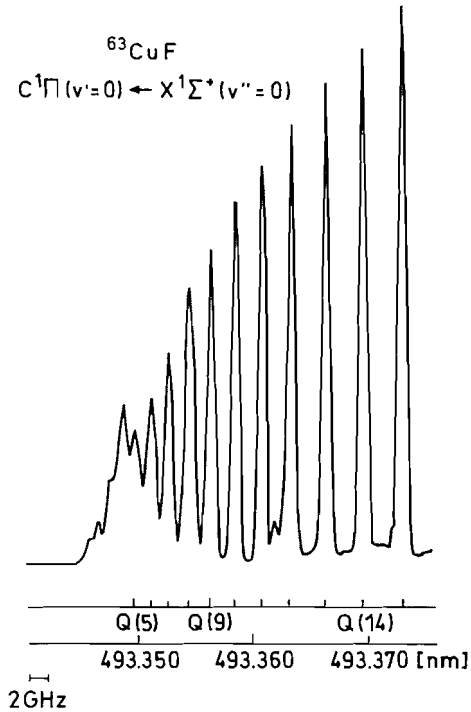

FIG. 2. Typical laser excitation spectrum of the Q branch head of the $C^1\Pi \leftarrow X^1\Sigma^+$ ($v' = 0, v'' = 0$) band of associatively desorbing CuF molecules. Due to the use of an isotopically pure polycrystalline copper sample, the rotational structure is well resolved.

observed, in agreement with coherent saturation theory, a linear dependence of single-line fluorescence intensity with the transition dipole moment and the laser field strength (28). The same result was found for the $C \leftarrow X$ transition of CuF (23, 29). This is depicted in Fig. 4 by plotting the intensity of an arbitrary rotational line vs. the laser intensity in a double logarithmic scale. The slope of the curve is 0.5 in the range of 0.5–20 mW typically used in the experiments. Earlier data in the range of 1–100 mW confirm this behavior (23). Below 0.5 mW, the saturation effect gradually diminishes and the slope of the curve becomes steeper. For our experiments this implies that the population of the individual rotational levels within one band can be derived from the measured integrated intensities by normalization using [laserpower × Hönl–London factors × Franck–Condon factors/$(2J'' + 1)$]$^{1/2}$. The complete formula for deriving rotational population number densities $N(v'', J'')$ in different vibrational levels used in this work is given by:

$$N(v'', J'') \propto \frac{I_{\text{fluores.}}\sqrt{(2J'' + 1)}}{v\sqrt{I_{\text{Laser}} q_{v'v''} S_{J'J''}}}$$

where v denotes the frequency of the transition and I_{Laser} the laser intensity. Franck–Condon factors $q_{v'v''}$ were taken from ref. 30. Hönl–London factors $S_{J'J''}$ for the C–X transition of CuF were adapted from Herzberg (31). In the data evaluation, fluorescence line intensities $I_{\text{fluores.}}$ are determined by integration of the individual peak areas. This procedure accounts for resolved or unresolved splitting due to hyperfine effects occurring for Q lines at low J and for P and R lines at low as well as high J. For unsplit lines, the fluorescence intensity can be approximated by the product of peak height and linewidth. With this type of analysis, as expected, a single distribution

Can. J. Chem. Downloaded from www.nrcresearchpress.com by 195.246.54.202 on 09/08/12
For personal use only.

Can. J. Chem. Downloaded from www.nrcresearchpress.com by 195.246.54.202 on 09/08/12
For personal use only.

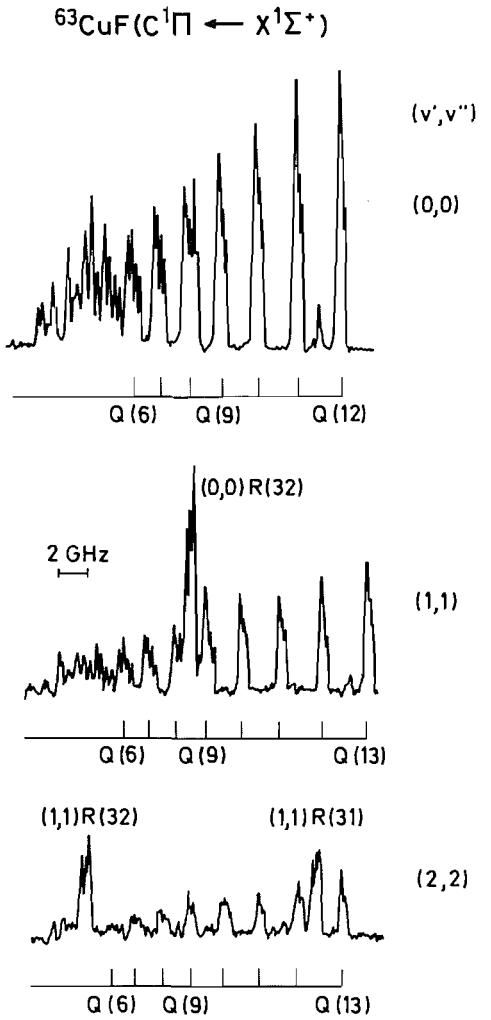

FIG. 3. Q branch heads of the (0,0), (1,1), and (2,2) bands. These spectra show that a rotational population analysis is possible in different vibrational levels. The resolution is improved by observing the fluorescence with a slit placed in front of the detection system as depicted in Fig. 1. Under these conditions of reduced Doppler width, the hyperfine splitting becomes apparent, particularly for low J levels.

measured in the P branch is identical with the Q branch distribution measured at the same surface temperature (not shown). Since the translational velocities belonging to individual v, J levels are found to be identical (see below), no flux–density correction needs to be considered, i.e., measured relative number densities and product flux are identical.

The experimentally determined populations of rotational levels J and vibrational manifolds v, in the following referred to as $N'(v,J)$, are displayed in Fig. 5 in a Boltzmann logarithmic plot for surface temperatures T_s = 890 K (*a*) and 935 K (*b*). This format is generally chosen since thermal equilibrium distributions will produce straight lines with the slope indicating the corresponding temperature. The rotational temperatures agree well with the surface temperatures and there is only a slight dependence on the vibrational level. The higher v manifolds seem to give somewhat lower values of the rotational temperature, which, however, still fall within the error limits. To test whether the measured distributions are affected by secondary collisions in the gas phase, additional argon was passed through the nozzle, which was kept at room temperature. The distributions did not change to any measurable extent. In our

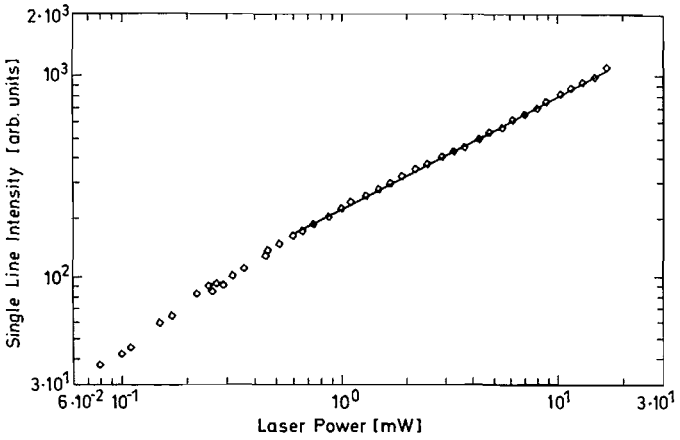

FIG. 4. Dependence of the fluorescence intensity of the Q(29) line on laser power, plotted on a double logarithmic scale. The straight line with a slope of 0.5 denotes the region where the fluorescence intensity is proportional to the square root of the laser power. According to coherent saturation theory, this implies a linear dependence of the laser power on the transition dipole moment.

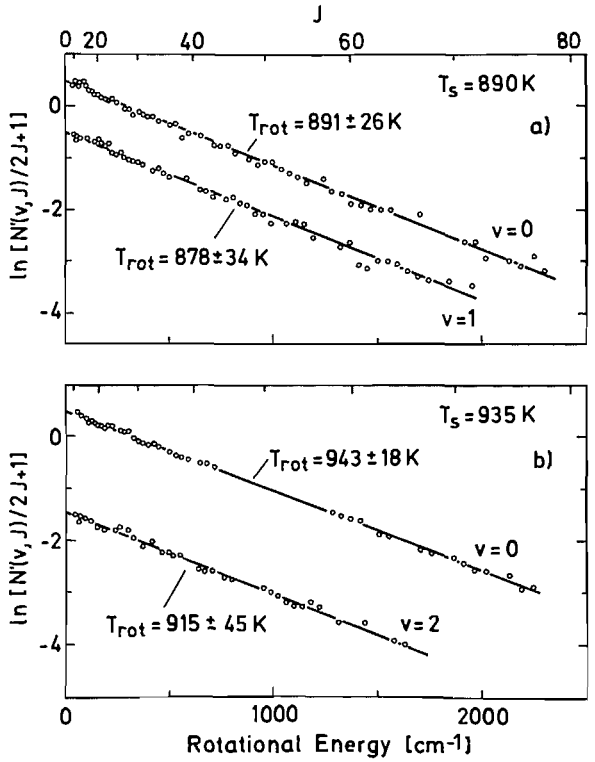

FIG. 5. Boltzmann plots of the rotational populations for different vibrational levels v = 0, 1, 2 and surface temperatures (a) 890 K; (b) 935 K. The slopes yield rotational temperatures that are equivalent to the surface temperatures, indicating complete rotational accommodation of the desorbing CuF molecules with the copper surface.

preliminary paper on the rotational analysis of v = 1, an incomplete treatment of saturation theory was used that resulted in a slight upward bending of the Boltzmann plot at low J values, leading to a lower rotational temperature for these levels (29). Hence at this stage it is important to note that the CuF molecules do not show any rotational cooling effect.

C. Vibrational population analysis

Generally, the vibrational population analysis is done by summing up the rotational populations in each vibrational

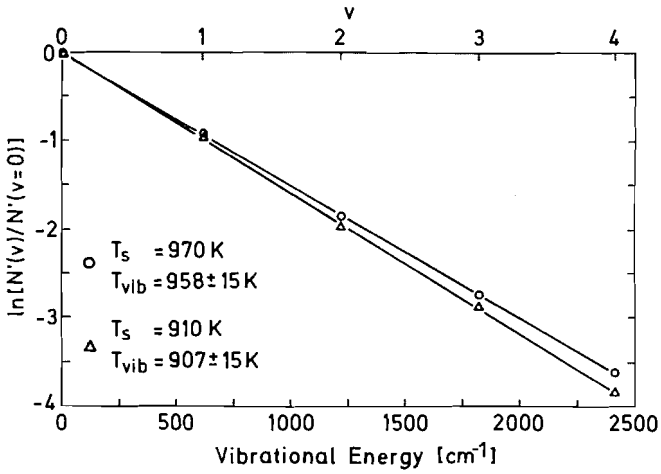

FIG. 6. Vibrational Boltzmann plots for product levels $v = 0$–4 and two surface temperatures. The open circles refer to $T_s = 970$ K; the triangles to $T_s = 910$ K. Both lines are normalized to N' ($v = 0$). The slopes indicate full equilibrium with the surface temperature.

level. In our case the analysis is simplified by the fact that the rotational distributions are of the Boltzmann type and that the rotational temperature is independent of the vibrational level. Hence it is possible to derive the vibrational population distribution from intensity measurements of one particular rotational line occurring in all vibrational bands under consideration. One such line, Q(29) occurs in the (0,0)–(4,4) bands without overlapping with other transitions. A correction for the rotational anharmonicity, i.e., the decrease of the rotational constant with the vibrational quantum level, was applied, leading to a small change only. For details of this type of analysis see ref. 32. The analysis was eased by the fact that the linewidth of this particular Q branch transition is essentially given by its Doppler width, which, as will be shown below, is independent of the vibrational level. Finally it was verified that the result of this analysis is independent of the rotational level J.

The result of the vibrational population analysis is displayed in a logarithmic Boltzmann plot in Fig. 6 for two different surface temperatures $T_s = 910$ K and 970 K. Again, in each case we obtain a straight line with the slope identical to the surface temperature within the error bars. If we compare this observation with earlier results deduced from rotationally unresolved excitation spectra, the Boltzmann behavior and the dependence of the vibrational population distribution on the surface temperature is confirmed. The previously noted slight vibrational heating (20), however, has vanished. This may be mainly due to overlapping bands in the analysis of rotationally unresolved excitation spectra.

D. Product translational analysis

To measure translational energies of the desorbing CuF molecules, we use the fact that the linewidth of the laser is considerably narrower than individual Doppler-broadened CuF rotational lines. Shifting the laser frequency by $\Delta\nu$ from the nominal resonance frequency ν of the CuF transition then selects a particular velocity component $v_\parallel$ of the molecules parallel to the laser beam according to:

$$\Delta\nu = \nu \frac{v_\parallel}{c}$$

For a well-defined source spot, $v_\parallel$ is related to the velocity v

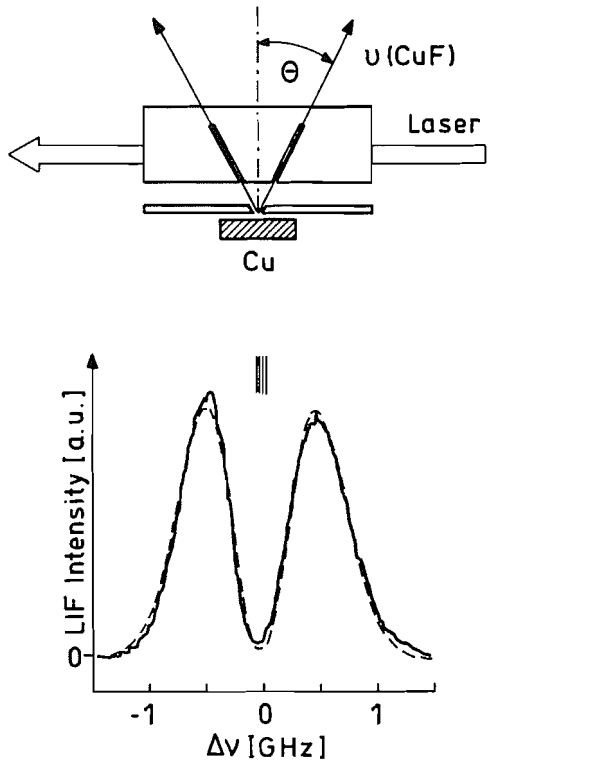

FIG. 7. The upper part of the figure shows an arrangement of slits placed in front of the detection system to measure the translational velocity. According to the position of the slits, the originally Doppler broadened line ($v' = 0, v'' = 0$) P(17) splits into two components shown in the lower part of this figure. The solid line refers to the experiment. Vertical bars denote the hyperfine splitting pattern of the P(17) line. The broken line represents a fit to the data (see text for the parameters of the velocity distribution).

of the CuF molecule via $v_\parallel = v \sin\theta$, with θ being the angle of desorption with respect to the surface normal. We therefore attached a blind with two slits at angles $\pm\theta$, as depicted in Fig. 7; the velocity distribution then is directly obtained via

$$v = c \frac{\Delta\nu}{\nu \sin\theta}$$

To correlate values of the velocity v obtained by this method to a particular product translational distribution at a temperature T_t, we need to understand our mode of detection in more detail. In the simplest case, for a cw laser in the limit of weak excitation and for short lifetimes of the excited states, number densities with a $v^2 f(v) = v^2 \exp(-mv^2/2kT_t)$ distribution are measured. However, variations from these conditions change this to $v^{2+\delta} f(v)$, with $-1 < \delta < 1$. An excellent description of this issue is given by Hefter and Bergmann (33). For a measured distribution $v^{2+\delta} f(v)$, the most likely velocity $\bar{v}$ is given by

$$\bar{v} = \left[(2+\delta)\frac{kT_t}{m}\right]^{1/2}$$

and the corresponding temperature of the distribution, T_t, can be calculated according to

$$T_t = \frac{m\bar{v}^2}{(2+\delta)k}$$

Can. J. Chem. Downloaded from www.nrcresearchpress.com by 195.246.54.202 on 09/08/12
For personal use only.

Can. J. Chem. Downloaded from www.nrcresearchpress.com by 195.246.54.202 on 09/08/12
For personal use only.

The lower part of Fig. 7 shows a typical spectrum of the (0–0) P(17) line obtained at T_s = 1025 K and θ = 31°. The four vertical bars indicate the hyperfine splitting of this line. To estimate δ and T_t, we fit this spectrum to a distribution $v^{2+\delta}f(v)$ for each hyperfine component by using a least-squares method. The dotted line in the figure shows the best fit. The fitted values of δ and T_t were 0.03 ± 0.09 and 1036 ± 41 K, respectively, indicating that in the present case we measure the density distribution and that the translational energy of CuF is at thermal equilibrium with the surface temperature.

Independent of the absolute value of $\bar{v}$, however, we can draw important conclusions just by comparing the measured splittings of lines belonging to various J and v levels. In our case we find that the splitting, and thus the corresponding velocity, is independent of the rotational and vibrational level. This indicates that the rovibrational and the translational degrees of freedom are decoupled.

E. Polarization measurements

LIF experiments offer the possibility of relatively uncomplicated determination of molecular alignment by varying the polarization direction of the laser. In the simplest case the spectrally unresolved fluorescence is detected without any polarizing elements, thus representing the sum over all polarizations. From such measurements, it is possible to determine the dominant parameter of the distribution function, i.e., the polarization anisotropy. This method is particularly straightforward if the molecular transition used for the investigation is a Q branch of a $\Sigma \rightarrow \Pi$ transition for which the electronic transition dipole moment is parallel to the J axis in the high-J limit (34). The treatment, however, is based on the assumption that the unresolved fluorescence represents an unweighted sum over P, Q, and R branches, which means it is isotropic (21, 35).

We used the Q branch of the $C^1\Pi$–$X^1\Sigma^+$ band of CuF for analysis. The result of such a polarization measurement (according to Fig. 1, with the polarizer in front of the detection system being removed) is shown in Fig. 8. Here the LIF intensity of the (0,0) Q (29) line is plotted as a function of the angle χ_a between the linear polarization vector of the laser and the surface normal. Clearly a polarization effect can be seen. Under the assumption of isotropic fluorescence this result would imply that on average a greater fraction of the desorbing molecules have their J axis aligned parallel to the surface normal, thereby representing a preference for helicopter motion (29).

However, the assumption of isotropic fluorescence due to superposition of P, Q, and R branches is not valid for the C–X transition of CuF: the $C^1\Pi$ state shows a strong Λ-doubling effect. The sublevels e and f of each rotational quantum state J have opposite parity. In the $X^1\Sigma^+$ state, on the other hand, there is no doubling, and the rotational quantum states have alternate parity with succeeding values of J. As transitions between two states must satisfy the selection rule $\pm \leftrightarrow \mp$ (31), there is a direct correlation: Q transitions $\leftrightarrow f$ levels and P/R transitions $\leftrightarrow e$ levels. Therefore excitation and fluorescence transitions are restricted to Q↑Q↓ and PR↑PR↓, respectively. Hence, the Q excitation leads by photoselection to an anisotropic distribution of J vectors that may be fully responsible for the measured polarization effect.

To distinguish between this photoselection effect and a possible dynamical effect, we carried out a test for the presence of

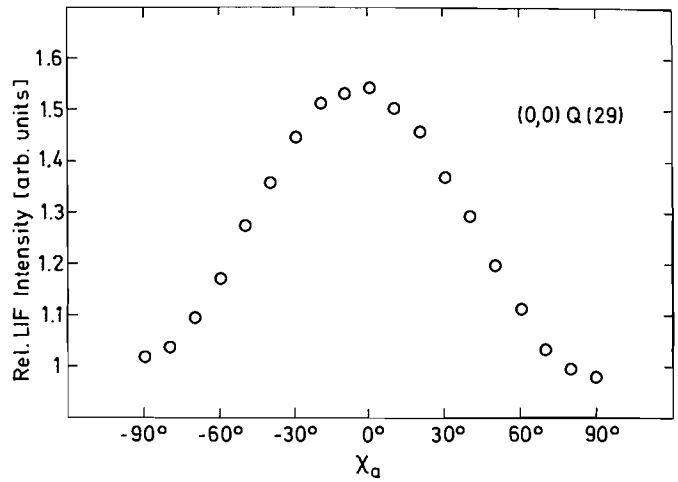

FIG. 8. Polarization effect of the LIF signal of desorbing CuF as a function of the angle χ_a between the laser electric field vector and the surface normal. The data for this figure are based on a measurement using the Q(29) line at a laser power of 1 mW. The fluorescence light is spectrally unresolved and recorded without a polarizer in front of the detection system.

alignment as described by Greene and Zare (36). This requires an experimental configuration with the excitation direction, detection direction, and the axis of cylindrical symmetry (i.e., the surface normal) being mutually orthogonal, and a polarization-sensitive detection of the fluorescence intensity (Fig. 1). The LIF intensity is now measured as a function of the settings of the polarization analyzer, χ_d, and the Fresnel rhomb, χ_a. Setting χ_d = 90° in our system, the LIF intensity of any rotational line of CuF turned out to be independent of χ_a. This finding, according to Greene and Zare (36), clearly indicates an isotropic distribution of the CuF molecules, i.e., no alignment of the desorbing molecules occurs.

To explain the observed polarization effect (Fig. 8) quantitatively, we adapted the expression for the LIF intensity in the high-J limit $I(\chi_a, \chi_d)$ given by Greene and Zare (eq. 21 of ref. 36) to a Q↑Q↓ transition:

$$I(0°, 0°) = \frac{9}{5} + \frac{18}{7}A_0^{(2)} + \frac{72}{35}A_0^{(4)}$$

$$I(90°, 0°) = \frac{3}{5} + \frac{3}{14}A_0^{(2)} - \frac{36}{35}A_0^{(4)}$$

$$I(0°, 90°) = \frac{3}{5} + \frac{3}{14}A_0^{(2)} - \frac{36}{35}A_0^{(4)}$$

$$I(90°, 90°) = \frac{3}{5} - \frac{3}{7}A_0^{(2)} + \frac{9}{35}A_0^{(4)}$$

For unpolarized detection one has to sum over the intensities for $\chi_d = 0°$ and $\chi_d = 90°$:

$$I(0°) = \frac{12}{5} + \frac{39}{14}A_0^{(2)} + \frac{36}{35}A_0^{(4)}$$

$$I(90°) = \frac{6}{5} - \frac{3}{14}A_0^{(2)} - \frac{27}{35}A_0^{(4)}$$

In our case of an isotropic distribution of product species, the molecular alignment parameters $A^{(k)}$ with $k > 0$ are identically zero. Then we obtain for the degree of polarization:

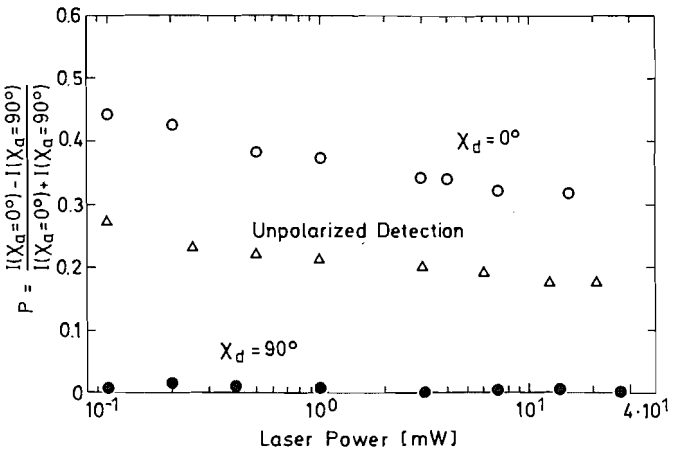

FIG. 9. Dependence of the polarization effect for the line Q(29) on the power of the exciting laser. The open circles denote the data points obtained using a polarizer in the detection system with $\chi_d = 0°$ (see Fig. 1). The full circles refer to $\chi_d = 90°$. For comparison with Fig. 8, the corresponding data with no polarizer in the detection system are marked by triangles.

$$P = \frac{I(\chi_a = 0°) - I(\chi_a = 90°)}{I(\chi_a = 0°) + I(\chi_a = 90°)}$$

$$P = \begin{cases} \frac{1}{2} & \text{for } \chi_d = 0° \\ 0 & \text{for } \chi_d = 90° \\ \frac{1}{3} & \text{without polarization analyzer} \end{cases}$$

The results of the measurements of P are depicted in Fig. 9. As the formalism of Greene and Zare does not take into account saturation effects, our measurements were extended to the lowest possible laser power. The theoretical values represented above for P in the limit of no saturation are in good agreement with the data. Also, the observed decrease of polarization with increasing laser power (Fig. 9) agrees qualitatively with the theoretical treatment of saturation effects on alignment measurements by Janssen et al. (37).

The polarization effect of P and R lines can be treated in the same manner: In the case of a PR↑PR↓ transition, an isotropic distribution of desorbing molecules and unpolarized detection, one obtains the value $P = 1/13$, in good agreement with our results for the (0,0) P(29) line of the C–X, as well as for the (0,0) P(30) line of the B–X, system of CuF (32).

4. Discussion

We include in the discussion two additional experimental observations not described in the main body of this paper. First, the validity of the CuF product state analysis under conditions of coherent saturation described in the present paper was confirmed in the following calibration experiment: An effusive CuF beam was produced by thermal dissociation of CuF_2 (38). This was done by heating a mixture of CuF_2 and copper powder in a copper oven with a 0.5 mm orifice. Temperatures between 850 and 1100 K were used. We assume that the CuF molecules are formed by the reaction $CuF_2 + Cu \rightarrow 2$ CuF and effuse at complete equilibrium with the oven temperature. Applying the analysis outlined above, this assumption was indeed confirmed for the vibrational, rotational, and translational degrees of freedom of the beam molecules. Also, an analogous polarization effect was found as reported in Sect. 3E.

In a second series of experiments, F_2 was replaced by F atoms as reactants in the etching of the copper surface. In this way the exoergicity of the system was significantly increased from about $\Delta H = -8$ kJ/mol to $\Delta H = -87$ kJ/mol, as can be calculated using values for bond dissociation energies given in ref. 24. No change was noticed regarding the internal product state distributions and the alignment measurements of the CuF molecules.

The invariance of product state distributions as the reactants are changed from F_2 molecules to F atoms provides clear evidence that the exoergicity of any intermediate step in the CuF formation reaction has no effect on the product state distribution of the desorbed molecules. In other words, CuF molecules have lost any memory of the initial formation reaction and the observations of this study refer to the last step in the sequence of elementary processes: adsorption, diffusion, reaction, and desorption. Further, the exoergicity of the reaction is dissipated to the surface until thermal equilibrium is reached. Hence the residence time of CuF at the surface must be significantly longer than the time needed for equilibration with the heat bath of the sample, which should be on the order of a few picoseconds. This estimate assumes that CuF is chemisorbed at the Cu surface before it thermally desorbs.

As mentioned in the introduction, even for thermally desorbing molecules, deviations of product state distributions from thermal equilibrium with the surface temperature T_s may occur. We therefore discuss why thermal equilibrium distributions were in fact observed in this system.

First, nonequilibrium product distributions may result from vibrational and translational heating. These are dynamic effects observed, for example, for the hydrogen/Cu system (8–11, 39). They are most likely to occur if the desorption process is correlated with a change in the bond length of the desorbing molecule and if there is a barrier in the reaction path for desorption. Our result of surface-equilibrated translational and vibrational product state distributions therefore implies the absence of a barrier in the desorption channel of CuF molecules leaving the Cu surface. This interpretation is in agreement with our experimental observation that the translational and vibrational degrees of freedom are decoupled to a high degree and that higher than thermal velocities have not been observed.

A second possibility for the occurrence of nonequilibrium effects has been termed "cooling," for example, of translational and rotational energies of thermally desorbing molecules. This effect has been attributed to the relative inefficiency of energy transfer between the surface and the molecule as it escapes. There is a consensus that the molecules gradually acquire the energy necessary for desorption while they vibrate in the binding well (hindered translation in z-direction) (40). In a model for translational cooling introduced by Tully (41) it is assumed that there is a limited amount of energy E_{ex} that can, on average, be exchanged per vibrational period between the substrate and the molecule. If $E_{ex} < kT_s$, the molecules that finally pass the binding well will, on average, have less excess energy than kT_s, which is seen as cooling. This relation may be conveniently deduced by applying microscopic reversibility arguments to the reverse process. For adsorption of molecules with a gas temperature T_g equal to T_s, sticking would be inhibited if the average energy E_{ex} transferred to the substrate per vibrational period is less than kT_g. In this case the sticking

Can. J. Chem. Downloaded from www.nrcresearchpress.com by 195.246.54.202 on 09/08/12
For personal use only.

Can. J. Chem. Downloaded from www.nrcresearchpress.com by 195.246.54.202 on 09/08/12
For personal use only.

coefficient would decrease with increasing normal component of the translational energy of the incoming molecules. In contrast, increasing E_{ex} would result in an increasing sticking coefficient, which finally approaches the value of 1 for $E_{ex} \gg kT_s$ (for simplicity any orientational effects are omitted in this discussion). On the basis of detailed balance this implies that the cooling effect vanishes completely for $E_{ex} \gg kT_s$.

Internal degrees of freedom, mainly rotation, that are correlated with the desorption process may be subject to a cooling effect as well. In the case of $E_{ex} \gg kT_s$ there is no rotational cooling effect expected, since the trans–rot coupling in general has a small influence on the sticking coefficient, which is dominated by E_{ex}. For $E_{ex} < kT_s$, the extent of cooling then varies according to the coupling strength of a particular molecular motion to the adsorbate liberation mode. In general the rotational cooling is accompanied by a small alignment effect, since the cartwheel mode is depleted (18, 19). This effect is expected to disappear for a high sticking coefficient.

In summary, the model of Tully rationalizes in a descriptive way that the translational and rotational energy distributions will be thermalized when $E_{ex} \gg kT_s$ or cooled for $E_{ex} < kT_s$. In the case of CuF, E_{ex} seems to be much higher than kT_s ($T_s = 1100$ K), since we found no deviations from equilibration with the surface temperature for any of our experimental conditions. This implies a large energy transfer rate between CuF and the copper surface. The experimental observations are quite different for the NO/Pt(111) system, where significant rotational cooling was found in trapping desorption molecular beam scattering (42, 43) as well as in associative desorption (13, 14) and TPD experiments (44) at values for $T_s > 350$ K.

5. Conclusions

We have shown that the CuF/Cu system is one of the few examples of a gas–surface reaction for which a complete product characterization can be obtained in a single experiment by means of laser spectroscopy. The main result of our investigation of the dynamics of associatively desorbing CuF molecules is that all internal degrees of freedom and the translational energies are fully equilibrated with the surface temperature. Also, the distribution of J vectors is isotropic and no alignment is found. The results of the product state analysis are interpreted in terms of the absence of a barrier for desorption and a long residence time of the chemisorbed CuF molecules at the copper surface after the formation reaction of Cu with adsorbed fluorine atoms. Applying microscopic reversibility arguments, our result of complete thermal equilibration of desorbing CuF molecules indicates a high sticking coefficient for CuF on copper surfaces that is largely independent of E_{kin} and the internal energy distributions of CuF.

Acknowledgements

We gratefully acknowledge the support of this work by the Sonderforschungsbereich SFB 338. We thank K.L. Kompa for continued support, X.R. Chen and K. Wagemann for their engagement in the early stage of this work, and C. Haug for valuable discussions. We thank Th. Wach for a careful reading of the manuscript and A. Steyer for technical assistance. K.S. is indebted to the Alexander von Humboldt-Stiftung for the award of a stipend.

1. H. Zacharias. Int. J. Mod. Phys. B, **4**, 45 (1990).
2. M. Asscher and G.A. Somorjai. *In* Atomic and molecular beam methods. Vol. 2. *Edited by* G. Scoles, D. Lainé, and U. Valbusa. Oxford University Press, New York, Oxford. 1992. p. 488.
3. R.I. Hall, I. Cadez, M. Landau, F. Pichou, and C. Schermann. Phys. Rev. Lett. **60**, 337 (1988).
4. P.J. Eenshuistra, J.H.M. Bonnie, J. Los, and H.J. Hopman. Phys. Rev. Lett. **60**, 341 (1988).
5. C.T. Rettner. Phys. Rev. Lett. **69**, 383 (1992).
6. P. Kratzer and W. Brenig. Surf. Sci. **254**, 275 (1991).
7. J.C. Polanyi. Chem. Scr. **27**, 229 (1987); Science, **236**, 680 (1987).
8. G.D. Kubiak, G.O. Sitz, and R.N. Zare. J. Chem. Phys. **83**, 2538 (1985).
9. W. Brenig, S. Küchenhoff, and H. Kasai. Appl. Phys. A: **51**, 115 (1990); S. Küchenhoff, W. Brenig, and Y. Chiba. Surf. Sci. **245**, 389 (1991).
10. G. Comsa and R. David. Surf. Sci. **117**, 77 (1982).
11. G. Anger, A. Winkler, and K.D. Rendulic. Surf. Sci. **220**, 1 (1989); H.F. Berger, M. Leisch, A. Winkler, and K.D. Rendulic. Chem. Phys. Lett. **175**, 425 (1990).
12. D.S.Y. Hsu, M.A. Hoffbauer, and M.C. Lin. Surf. Sci. **184**, 25 (1987); D.S.Y. Hsu and M.C. Lin. J. Chem. Phys. **88**, 432 (1988).
13. M. Asscher, W.L. Guthrie, T.-H. Lin, and G.A. Somorjai. J. Phys. Chem. **88**, 3233 (1984).
14. D.S.Y. Hsu, D.W. Squire, and M.C. Lin. J. Chem. Phys. **89**, 2861 (1988).
15. L. Schröter, R. David, and H. Zacharias. Surf. Sci. **258**, 259 (1991).
16. W. Brenig, H. Kasai, and H. Müller. Surf. Sci. **161**, 608 (1985); C. Haug and W. Brenig. Surf. Sci. **262**, 271 (1992).
17. C.W. Muhlhausen, L.R. Williams, and J.C. Tully. J. Chem. Phys. **83**, 2594 (1985).
18. K. Yang and T.S. Rahman. J. Chem. Phys. **93**, 6834 (1990).
19. D.C. Jacobs, K.W. Kolasinski, R.J. Madix, and R.N. Zare. J. Chem. Phys. **87**, 5038 (1987); D.C. Jacobs, K.W. Kolasinski, S.F. Shane, and R.N. Zare. J. Chem. Phys. **91**, 3182 (1989).
20. X.R. Chen, K. Wagemann, J. Wanner, W. Brenig, and S. Küchenhoff. Surf. Sci. **224**, 570, (1989); K. Wagemann, X.R. Chen, U. Näher, and J. Wanner. Vacuum, **41**, 733 (1990).
21. D.J. Auerbach. *In* Atomic and molecular beam methods. Vol. 2. *Edited by* G. Scoles, D. Lainé, and U. Valbusa. Oxford University Press, New York, Oxford. 1992. p. 444.
22. J.L. Hall and S.A. Lee. Appl. Phys. Lett. **29**, 367 (1976).
23. U. Näher. Diploma Thesis, Technische Universität München, 1990. MPQ Report 149 (1990).
24. G. Herzberg and K.P. Huber. Molecular spectra and molecular structure IV. Constants of diatomic molecules. van Nostrand Reinhold, New York. 1979. p. 202.
25. F. Ahmed, R.F. Barrow, A.H. Chojnicki, C. Dufour, and J. Schamps. J. Phys. B: At. Mol. Phys. **15**, 3801 (1982).
26. P. Jakob, K. Sugawara, and J. Wanner. J. Mol. Spectrosc. **160**, 596 (1993).
27. P. Jakob, K. Sugawara, J. Wanner, A. Bath, and E. Tiemann. Can. J. Phys. Submitted (G. Herzberg special issue).
28. N. Billy, B. Girard, G. Gouédard, and J. Vigué. Mol. Phys. **61**, 65 (1987).
29. U. Näher, A. Bracker, X.R. Chen, P. Jakob, and J. Wanner. J. Phys. Chem. **95**, 8376 (1991).
30. R.W. Schwenz and J.M. Parson. J. Chem. Phys. **73**, 259 (1980).
31. G. Herzberg. Molecular spectra and molecular structure I. Spectra of diatomic molecules. 2nd ed. van Nostrand Reinhold, New York. 1950. p. 252.
32. M. Rüdiger. Diploma Thesis, Ludwig-Maximilians-Universität München, 1991. MPQ Report 159 (1991).
33. U. Hefter and K. Bergmann. *In* Atomic and molecular beam methods. Vol. 1. *Edited by* G. Scoles, D. Bassi, U. Buck, and D. Lainé. Oxford University Press, New York, Oxford. 1988. p. 193.
34. R.N. Zare. Mol. Photochem. **4**, 1 (1972).

35. A.C. Luntz, A.W. Kleyn, and D.J. Auerbach. Phys. Rev. B, **25**, 4273 (1982).
36. C.H. Greene and R.N. Zare. J. Chem. Phys. **78**, 6741 (1983).
37. M.H.M. Janssen, D.H. Parker, and S. Stolte. Chem. Phys. **113**, 357 (1987); M.H.M. Janssen, M.A. Quesada, D.H. Parker, and S. Stolte. NATO ASI Ser. C: **245**, 311 (1988).
38. T.C. Ehlert and J.S. Wang. J. Phys. Chem. **81**, 2069 (1977).
39. H.A. Michelsen, C.T. Rettner, and D.J. Auerbach. J. Chem. Phys. **98**, 8294 (1993).
40. W. Brenig. Z. Phys. B: Condens. Matter, **48**, 127 (1982).
41. J.C. Tully. *In* Kinetics of interface reactions. *Edited by* M. Grunze and H.J. Kreuzer. Springer, Berlin. 1987. p. 37.
42. J. Segner, H. Robota, W. Vielhaber, G. Ertl, F. Frenkel, J. Häger, W. Krieger, and H. Walther. Surf. Sci. **131**, 273 (1983).
43. M. Asscher, W.L. Guthrie, T.-H. Lin, and G.A. Somorjai. J. Phys. Chem. **78**, 6992 (1983).
44. D.A. Mantell, R.R. Cavanagh, and D.S. King. J. Chem. Phys. **82**, 1046 (1985); J. Chem. Phys. **84**, 5131 (1986).

Can. J. Chem. Downloaded from www.nrcresearchpress.com by 195.246.54.202 on 09/08/12
For personal use only.

The role of molecular flexibility in accelerating intramolecular vibrational relaxation

G.A. BETHARDY, XIAOLIANG WANG, AND DAVID S. PERRY[1]
Department of Chemistry, University of Akron, Akron OH 44325-3601, U.S.A.
Received August 5, 1993
This paper is dedicated to Professor John C. Polanyi on the occasion of his 65th birthday

G.A. BETHARDY, XIAOLIANG WANG, and DAVID S. PERRY. Can. J. Chem. **72**, 652 (1994).

Evidence is presented to show that intramolecular vibrational relaxation (IVR) is faster in flexible molecules when the initially prepared vibration is close to the bond about which the large-amplitude motion occurs. In each of 1-pentyne, ethanol, and propargyl alcohol, IVR lifetimes are known for two different hydride stretches and in each molecule internal rotation connects *gauche* and *trans* conformers. In each case the vibration that is closer to the center of flexibility shows faster relaxation. This trend is supported by the available IVR lifetimes for other flexible molecules (hydrogen peroxide, 1-butene, *n*-butane, methyl formate, and propargyl amine) and for some "rigid" molecules (1-butyne, isobutane, propyne, *trans*-2-butene, and *tert*-butylacetylene). The lifetimes for the halogenated molecules, 2-fluoroethanol, 1,2-difluoroethane, *trans*-1-chloro-2-fluoroethane, and trifluoropropyne are all in the range expected for rigid molecules. An algorithm is presented for the consistent calculation of IVR lifetimes from discrete frequency-resolved spectra, which range from the sparse through intermediate coupling cases. Wherever possible, the reported lifetimes have been calculated (or recalculated) from the original line positions and intensities. The lifetimes may be compared directly to those deduced from homogeneously broadened spectral features with a Lorentzian contour.

G.A. BETHARDY, XIAOLIANG WANG et DAVID S. PERRY. Can. J. Chem. **72**, 652 (1994).

On présente des données pour démontrer que la relaxation vibrationnelle intramoléculaire (RVI) est plus rapide dans les molécules flexibles lorsque la vibration préparée initialement est proche de la liaison autour de laquelle le mouvement de grande amplitude se produit. Dans le pent-1-yne, l'éthanol et l'alcool propargylique, les temps de vie des RVI des deux modes différents d'élongation de l'hydrure sont connus et, pour chaque molécule, la rotation interne permet de joindre les conformères *gauche* et *trans*. Dans chaque cas, la vibration la plus proche du centre de flexibilité présente la relaxation la plus rapide. Cette tendance est supportée par les temps de vie RVI disponibles pour d'autres molécules flexibles (peroxyde d'hydrogène, but-1-ène, *n*-butane, formate de méthyle et amine propargylique) et pour quelques molécules « rigides » (but-1-yne, isobutane, propyne, *trans*-but-2-ène et *tert*-butylacétylène). Les temps de vies des molécules halogénées, 2-fluoroéthanol, 1,2-difluoroéthane, *trans*-1-chloro-2-fluoroéthane et trifluoropropyne sont tous de l'ordre de grandeur attendu pour des molécules rigides. On présente un algorithme qui permet de calculer d'une façon cohérente les temps de vie RVI à partir de spectres discrets résolus en fréquence qui couvrent les cas des couplages faibles à intermédiaires. Dans tous les cas possibles, les temps de vie rapportés ont été calculés (ou recalculés) à partir des positions et des intensités originales des bandes. On peut comparer les temps de vie directement à ceux déduits à partir de caractéristiques spectrales élargies d'une façon homogène avec un contour lorentzien.

[Traduit par la rédaction]

Introduction

McIlroy (1) found that the presence of a low-energy skeletal isomerization accelerated the intramolecular vibrational relaxation (IVR) of aliphatic C—H stretches in the series of small hydrocarbons that he studied. For example, 1-butyne, propane, isobutane, and *trans*-2-butene cannot isomerize easily and exhibited IVR lifetimes in the range from 130 ps up to several hundred ps. On the other hand, *n*-butane, 1-butene, and 1-pentyne can isomerize and appear to have IVR lifetimes for the aliphatic C—H fundamentals in the vicinity of 30 ps. The pertinent isomerization pathways involve conformational change of the carbon skeleton as the result of internal rotation about a carbon–carbon bond. Since all of the molecules with longer lifetimes contain aliphatic methyl groups, McIlroy did not conclude that IVR was accelerated by the internal rotation of a methyl group.

Chemical timing experiments (2) have shown that relaxation of the ring vibrations, 3^1 and 3^15^1, in the S_1 electronic state of *p*-fluorotoluene and d_3-*p*-fluorotoluene is much faster (τ = 1–15 ps) than for the corresponding vibrations in *p*-difluorobenzene ($\tau \geq 150$ ps). The acceleration of IVR in the former compounds was attributed to the methyl rotor, which increases the density of vibrations interacting with the prepared ring vibrations.

The loss of rotational structure in the C=O fundamental and overtone bands of a series of carbonyl compounds has been correlated with the number and proximity of the methyl rotors (3). The decrease in the rotational band structure in the series, methyl formate, acetaldehyde, methyl acetate, and acetone, was attributed to vibrational mode mixing but the authors did not attempt to deduce IVR lifetimes from the unresolved spectra.

In this paper, additional IVR lifetimes will be derived for molecules capable of large-amplitude motion. Facile internal rotation about certain chemical bonds gives rise to both flexibility and conformational change. We will refer to such bonds as *centers of flexibility*. It will be shown that the acceleration of IVR is correlated with the *proximity* of the prepared vibration to a center of flexibility. McIlroy's shorter lifetimes were obtained from estimates of the homogeneous widths in partially resolved spectra. Where possible, we will use discretely resolved and rotationally assigned spectra for the calculation of lifetimes. This approach ensures that the results are free of interferences from inhomogeneous structure.

Other factors that have been correlated with fast IVR are a high density of low-order resonances in the energy region of

[1]Author to whom correspondence may be addressed. Telephone: 216-972-6825. FAX: 216-972-6407. e-mail: perry@atlas.chemistry.uakron.edu.

Can. J. Chem. Downloaded from www.nrcresearchpress.com by 195.246.54.202 on 09/08/12
For personal use only.

Can. J. Chem. Downloaded from www.nrcresearchpress.com by 195.246.54.202 on 09/08/12
For personal use only.

the excited chromophore (4, 5) and excitation of extreme motion states, which concentrate the vibrational amplitude into a single internal coordinate (6). Extremely fast IVR can result from a strong low-order resonance. In the C—H overtones of benzene (7) and of some hydrocarbons with a single C—H bond (8), the 1:2 C—H stretch–bend resonance gives rise to interaction widths of about 100 cm^{-1} ($\tau \approx 50$ fs). To investigate the role of molecular flexibility, we concentrate on systems where such strong low-order resonances are not involved and where the other factors mentioned in this paragraph are thought to be approximately constant. IVR lifetimes for vibrations that are in the same molecule but at different distances from a center of flexibility will be compared.

Experimental lifetimes

The largest body of systematic data on IVR lifetimes comes from frequency-resolved infrared spectra. At low resolution, IVR results in broadened infrared spectral features. When the features are Lorentzian in shape and arguably free of interfering inhomogeneous structure, the IVR lifetime is given by

$$[1] \qquad \tau = \frac{1}{2\pi\Delta\nu}$$

where $\Delta\nu$ is the full-width-at-half-maximum (FWHM) of the broadened lineshape. Equation [1] assumes that only the upper state of the infrared transition relaxes. In the time domain, a Lorentzian lineshape corresponds to an exponential decay

$$[2] \qquad |\langle\Psi(t=0)|\Psi(t)\rangle|^2 = \exp\left(-\frac{t}{\tau}\right)$$

At high resolution for bound systems, each broadened lineshape is revealed as a clump of discrete transitions from the vibrational ground state to a set of molecular eigenstates. Excitation of a single eigenstate does not result in any time-dependent relaxation; it is simply the direct preparation of a mixed state. Each eigenstate is a mixture of the bright state, that is, the vibrational mode responsible for the infrared oscillator strength, and a number of dark states. However, a hypothetical coherent excitation of an entire clump of eigenstates by a very short pulse of light would result in the preparation at $t = 0$ of the zero-order bright state. This coherent superposition would then decay in time, resulting in the transfer of vibrational amplitude from the bright state to other vibrational degrees of freedom. The survival probability of the bright state is given by (9, 10)

$$[3] \qquad |\langle\Psi(t=0)|\Psi(t)\rangle|^2 = \frac{\sum_i \sum_j I_i I_j \cos\left[\frac{(E_i - E_j)t}{\hbar}\right]}{\left(\sum_j I_j\right)^2}$$

where the I_i are the intensities of the eigenstates in the clump and the E_i are their energies. Each summation in eq. [3] extends over all of the pure sequence lines in a clump of molecular eigenstates. Radiative decay, which would give a homogenous width to each eigenstate, has been neglected.

Both eqs. [2] and [3] dictate an initial decay of the bright state, but there are two important differences. First, eq. [2] decays to zero at long times but eq. [3] decays to the dilution factor, which is given by

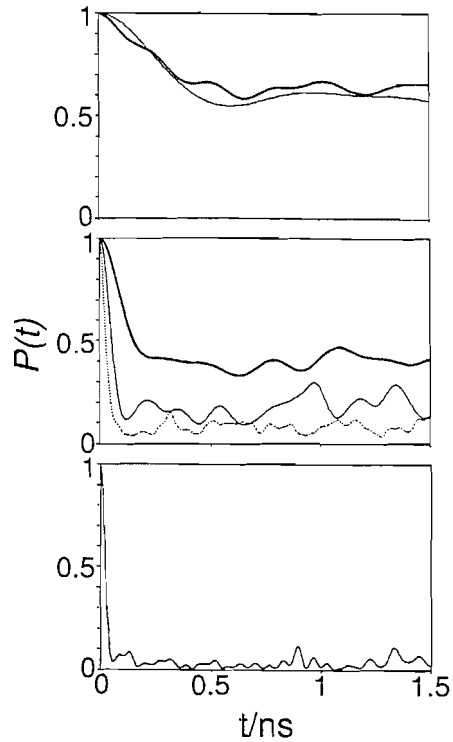

FIG. 1. Averaged decay curves for hydride stretches prepared with one quantum of excitation as calculated from discrete frequency-resolved spectra. Upper: 1-Butyne ν_{16} methyl C—H (thick line) and ν_1 acetylenic C—H (thin). Middle: Ethanol ν_{14} methyl C—H for $K_a = 0$ (thick), 1 (thin), and 2 (dotted). Lower: Ethanol ν_1 O—H.

$$[4] \qquad \phi_d = \frac{\sum_i I_i^2}{\left(\sum_i I_i\right)^2}$$

When there are only a few intense lines in a clump, the long time limit may be much greater than zero as shown in the top panel of Fig. 1. Second, the form of eq. [3] dictates that quantum beats, which are seen as oscillations around the long time limit, will follow the initial decay. Equation [3] approaches the form of eq. [2] in the statistical limit where there are a great many lines in the clump.

We wish to derive IVR lifetimes from decays of the type given by eq. [3] that may be compared directly with those obtained from eq. [1]. For this purpose, quantum beats are not relevant, therefore we average the decay curves for all of the available bright states within a certain group. The averaged survival probability is given by

$$[5] \qquad P(t) = \frac{1}{n}\sum_{k=1}^{n} |\langle\Psi_k(t=0)|\Psi_k(t)\rangle|^2$$

where k labels each of the n combinations of rotational and nuclear spin quantum numbers that contribute to the average. Figure 1 shows $P(t)$ for hydride stretches in 1-butyne and ethanol. The effect of averaging is to reduce the apparent amplitude of the quantum beats. Other types of averaging,

TABLE 1. Experimental IVR lifetimes

Molecule	Band	Reference	Frequency (cm^{-1})	K_a'	τ (eqs. [3]–[6]) (ps)	$\tau = 1/2\pi\langle\Delta\nu\rangle$ (ps)
1-Butyne	≡C-H	1, 9	3333	0, 1	269[a]	285[a]
	Methyl C—H[b]	10	2991	0–2	270	320
Ethanol	O—H	13	3678	0, 1	28[c]	20
	Methyl C—H	12	2990	0	116	123
				1	58	51
				2	32	27
1-Pentyne	≡C-H (*gauche*)	1	3333	All at 6 K	Unresolved	241[d]
	(*trans*)	1	3334			442[d]
	Methyl C—H	9	2980	All at 6 K	Unresolved	<40
Propargyl	O—H	14	3663	1, 3	110[e]	
alcohol	≡C-H	14	3331		500[e]	

[a]Recalculated by us from the original line positions and intensities.

[b]Lifetimes are given for the asymmetric methyl C—H stretch, ν_{16}. The lifetime for the symmetric C—H stretch, ν_3, is given on p. 253 of ref. 1 as 664 ps but line positions and frequencies were not published. If eqs. [3]–[6] were applied to the original data for ν_3, a somewhat shorter lifetime would be expected.

[c]This value reduces to 25 ps when an approximate correction for water absorption is applied.

[d]Conflicting values of the ≡C-H lifetimes are given by these authors; the lifetimes listed here are from p. 253 of ref. 1 and are consistent with Fig. 11 of ref. 9.

[e]Could not be recalculated using eqs. [3]–[6] because the detailed line positions and intensities are not yet published.

e.g., with Boltzmann weights, could be implemented where the data are sufficient in order to simulate specific kinds of time-domain experiments.

To account for the long time limit, $P(t) \rightarrow \phi_d$, $P(t)$ will be compared to the form

$$[6] \qquad P(t) = \phi_d + (1 - \phi_d) \exp\left(-\frac{t}{\tau}\right)$$

The relaxation time τ can then be estimated as the time required for $P(t)$ to decay to $\phi_d + (1/e)(1 - \phi_d)$. Use of $1/e$ as a reference point for the definition of τ when $\phi_d > 1/e$ is clearly inappropriate, and even when $\phi_d < 1/e$, it would give systematically longer lifetimes. For the purpose of calculating τ, ϕ_d is conveniently estimated as the time average of $P(t)$ for a period of several nanoseconds beginning after the initial decay.

The suitability of eq. [6] for defining τ is demonstrated by the agreement (Table 1) with eq. [1] where Δν is now the FWHM of the clump. The algorithm for evaluating Δν for clumps of eigenstates has been shown to be consistent with the Bixon–Jortner formula right down into the sparse limit (11).

The application of eq. [3] requires pure sequence spectra, that is, spectra that represent only a single set of good quantum numbers. In some cases, such as 1-butyne and ethanol, the vibrational ground state is actually a closely spaced doublet that results from tunnelling between equivalent positions of the methyl group. The eigenstate-resolved spectra of these molecules are the superposition of two pure sequences, which must be at least approximately separated for the purpose of determining lifetimes (1, 9, 10, 12). The effect of such approximate separations on the accuracy of the derived IVR lifetimes is discussed in the appendix.

Figure 1 shows decay curves for 1-butyne (1, 9, 10) and ethanol (12, 13). The IVR lifetimes taken from these curves and those for 1-pentyne (1, 9) and propargyl alcohol (14) are listed in Table 1. These four are the only molecules for which we have IVR lifetimes data for two different hydride stretch fundamentals.

Proximity to a center of flexibility

The IVR lifetimes of the methyl and acetylenic C—H stretching vibrations in 1-butyne are nearly identical at about 270 ps (10). Evidently, for the consideration of IVR, there is no intrinsic difference between these aliphatic and acetylenic C—H stretches. However, in 1-pentyne (1) the methyl C—H ($\tau \leq 40$ ps) relaxation rate is much faster than that of the acetylenic C—H ($\tau = 241$, 442 ps). 1-Pentyne contains the accelerating influence of a skeletal isomerization. Internal rotation about the C3—C4 bond gives rise to *gauche* and *trans* forms of pentyne. The faster relaxation rate of the methyl hydrogen (C5) could be because it is *closer* to the center of flexibility (the C3—C4 bond) than the acetylenic hydrogen (C1).

In ethanol, both the methyl C—H (12) and the O—H (13) relax rapidly, indicating that the internal rotation about the C—O bond may be accelerating the IVR. As in pentyne this internal rotation give rise to *gauche* and *trans* forms of the molecule. Accordingly, in ethanol the C—O bond is identified as the center of flexibility. The O—H chromophore, which is adjacent to the C—O bond, relaxes more rapidly than the methyl C—H, which is two bonds away. Note that internal rotation about the C—O bond only involves the movement of the hydroxyl proton and therefore cannot be called a skeletal isomerization. We attribute the acceleration of IVR in ethanol primarily to the internal rotation of the hydroxyl group because internal rotation of an aliphatic methyl group *by itself* has not been associated with greatly accelerated IVR. As noted in the introduction, the methyl C—H vibrations in 1-butyne, propane, isobutane, and *trans*-2-butene all have longer relaxation times than in the systems where *gauche–trans* isomerization is possible.

These trends are supported by recent data (14) on propargyl alcohol ($H\text{-}C{\equiv}C\text{-}CH_2OH$). As in ethanol, internal rotation about the C—O bond connects the *gauche* and *trans* geometries. Once again, the O—H, which is adjacent to the center of flexibility, relaxes much more rapidly than the acetylenic C—H, which is three bonds away.

The data are summarized in Fig. 2 where the lifetimes are

Can. J. Chem. Downloaded from www.nrcresearchpress.com by 195.246.54.202 on 09/08/12
For personal use only.

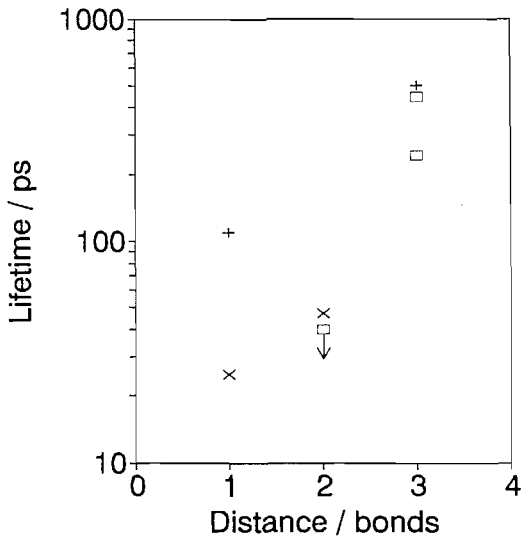

FIG. 2. IVR lifetimes are plotted against the distance of the chromophore from the isomerizing bond. For ethanol (×), there is the O—H stretch (n = 1) and the methyl C—H (n = 2). For pentyne (η), there is the methyl C—H (n = 2) and the *gauche* and *trans* forms for the acetylenic C—H (n = 3). For propargyl alcohol (+), there is the O—H (n = 1) and the acetylenic C—H (n = 3). The downward pointing arrow indicates that the plotted point is an upper bound.

plotted against the distance of the chromophore from the center of flexibility. We use the integer n to denote the distance in bonds between the chromophore and the center of flexibility. To address the role of molecular flexibility in enhancing IVR, we propose a model defined by the following points:

1. All hydride stretches are equivalent. Differences between relaxation rates will be attributed to the local environment of the hydride bond and not specifically to its chemical identity.

2. Proximity to a center of flexibility tends to accelerate the rate of IVR. Clearly, other systematic effects such as those mentioned in the introduction must be taken into account where they are relevant, and extremely strong low-order resonances will dominate the rate when they are present.

Discussion

Alternative point of view

An alternative point of view would be to focus on the chemical identity of the chromophore. For example, in Fig. 2, all of the points for which the chromophore is three bonds removed from the center of flexibility are acetylenic C—H stretches and they are all long lifetimes. All of the O—H stretches relax quickly. Then, only for the methyl C—H's would it be necessary to consider the role of molecular flexibility.

Although the alternative point of view may also be consistent with the data, the model proposed above offers the following advantages:

1. It offers a very general way of thinking about IVR. There are many molecules that have one or more internal rotations that allow conformational change. The concept of proximity to a center of flexibility provides for the scaling of IVR rates for very large molecules and for molecules embedded in a condensed phase. For subject molecules larger than a certain size, addition of more substituents remote from the chromophore should have a negligible effect on the IVR rate. From the available data, the typical length scale appears to be two or three chemical bonds. The proximity requirement is also apparent from condensed phase hydroxyl relaxation times (15, 16), which are found to depend strongly on the local environment of three or four atoms, but which vary only over a small range for a wide variety of condensed phase environments. These studies included surface-bound O—H, the solid state, and liquid solution. Indeed, the O—H lifetime for ethanol is only a little different in the isolated molecule (25 ps (13)) from that in CCl_4 solution (70 ps (16)).

2. The model makes a wide range of predictions based on points 1 and 2 above. Experiments can be designed that would test the equivalence of chemically distinct chromophores or that would test the prediction of accelerated IVR.

3. The model raises questions that point to further experiments. What kinds of molecular flexibility accelerate IVR? Which is most important, the barrier height or the symmetry of the potential? What role is played by ring puckering or other types of fluxional behavior? The lifetimes presented above are for the relaxation of hydride stretches. What is the role of molecular flexibility in the relaxation of other types of vibrations?

What kind of flexibility?

The existing data already give some indication about the types of large amplitude motion that accelerate IVR. The low-barrier cases for which we have data all exhibit fast IVR. These include ethanol (374 cm^{-1} for *trans*→*gauche*[2] (17)) and propargyl alcohol (68 cm^{-1} for *gauche*→*gauche* (18)). The low-barrier (30 cm^{-1}) 6-fold symmetric methyl internal rotation of S_1 *p*-fluorotoluene is associated with fast relaxation of the Franck–Condon active modes (2).

We have seen that methyl internal rotation is not very effective in enhancing the rate of IVR for cases (e.g., 1-butyne) where the barrier is high (≈1100 cm^{-1}) and 3-fold symmetric. On the other hand, the high barrier in 1-pentyne (1088 cm^{-1} for *gauche*→*gauche* (19)) is associated with fast relaxation of the methyl C—H. The relaxation in 1-pentyne might be faster because the three minima in the isomerization coordinate are inequivalent or because isomerization causes a significant reorientation of the rotational axes (20).

In Fig. 2, the O—H lifetime (n = 1) for propargyl alcohol is seen to be longer than for ethanol and even is longer than the methyl C—H lifetime (n = 2) of ethanol and 1-pentyne. The latter two molecules have a high-barrier methyl internal rotation in addition to the *gauche–trans* isomerization coordinate whereas propargyl alcohol does not. This comparison provides a hint that aliphatic methyl internal rotation, in combination with another large-amplitude coordinate, might play a role in enhancing IVR even if, by itself, it is generally less effective than some other types of molecular flexibility.

Comparison to other molecules

There are several other flexible molecules for which IVR lifetimes are known for a single chromophore (Table 2). For hydrogen peroxide (21–23) there are data for three bands but each of these represents predominantly O—H excitation. The trend of the data for these flexible molecules supports the proposed model. The longest lifetime in this group is for the

[2]The Fourier components of the potential, V_1 = 57, V_2 = −0.8, and V_3 = 360.7 cm^{-1}, were adjusted from those given in ref. 17 (57, +0.8, and 395 cm^{-1}, respectively) in order to obtain agreement with the observed torsional energy differences (listed in Table VIII of ref. 17) of O-H and O-D ethanol.

Can. J. Chem. Downloaded from www.nrcresearchpress.com by 195.246.54.202 on 09/08/12
For personal use only.

TABLE 2. Additional experimental IVR lifetimes

Molecule	Band[a]	Reference[b]	n^c	τ (ps)[d]
Other flexible molecules				
HOOH	4 O—H + O—H′	23	1	28[e]
	5 O—H + O—O	22	1	6[e]
	6 O—H	21	1	4[e]
1-Butene	Methyl C—H	1	2	31[e]
n-Butane	Methyl C—H	1	2	18[e]
Methyl formate	Methyl C—H	25	2	70
Propargyl amine	≡C-H	24	3	250, 400[f]
"Rigid" molecules				
Isobutane	Methyl C—H	1		<177[e]
Propyne	≡C-H + Methyl C-H	28		2650[g]
	2 ≡C-H	Footnote 3		800
	3 ≡C-H	Footnote 4		264
trans-2-Butene	Methyl C—H	1		132[e]
tert-Butylacetylene	≡C-H	4		200[e]
Halogenated molecules				
2-Fluoroethanol	Methyl C—H	29		565[h]
1,2-Difluoroethane	Methyl C—H	30		490[g,h]
trans-CH_2Cl-CH_2F	Methyl C—H	31		No decay
HC≡C-CF_3	1 ≡C-H	34		430
	2 ≡C-H	34		1360

[a]Numbers that indicate overtones of the indicated fundamentals and combination bands are designated with a "+"

[b]Source of the spectroscopic data.

[c]Number of bonds between the chromophore and the center of flexibility.

[d]The available data for rotational levels $K = 0$–2 and $J \leq 16$ were used in each case. Where discrete line positions and frequencies are available, τ was calculated by us using eqs. [3]–[6].

[e]Calculated from estimated homogenous widths as in the last column of Table 1.

[f]Could not be recalculated using eqs. [3]–[6] because the line positions and intensities have not yet been published.

[g]There are at most two observed features in each pure sequence clump. Even the averaged decays, $P(t)$, show very prominent quantum beats.

[h]The observed clumps are the superposition of A' and A'' (in C_s) pure sequence clumps. Reasonable but approximate separations into A' and A'' clumps were accomplished by the method described in ref. 10.

acetylenic C—H in propargyl amine (24), which is distant from the center of flexibility. In 1-butene (1), *n*-butane (1), and methyl formate (25), where the chromophores are closer to the center of flexibility, the lifetimes are shorter. The shortest lifetimes are for hydrogen peroxide where the excitation is adjacent to the O—O bond about which internal rotation can occur. The *trans* barrier is 386 cm^{-1} (26), which places it in the low-barrier group mentioned above. Note that hydrogen peroxide is above the dissociation limit in these bands but that the width of the wider features is dominated by IVR.

Molecules that do not have flexibility of the type that enhances IVR may be called "rigid" molecules. According to our model, rigid molecules ought to relax as slowly as in cases for which the chromophore is distant from a center of flexibility. Indeed, we find that the IVR lifetimes for all of the rigid molecules listed in Table 2 are greater than 100 ps.

Note that the acetylenic C—H fundamentals in $(CD_3)_3C$-C≡C-H and $(CF_3)_3C$-C≡C-H both relax faster (40 ps and 60 ps, respectively) than is the case for $(CH_3)_3C$-C≡C-H (200 ps) (4). In the d_9 compound, the enhanced relaxation rate is understood in terms of an increase in the number of low-order resonances (4, 5). Similarly, a decrease in the number of low-order resonances accounts for the exceptionally long lifetime (2 ns (27)) found for in $(CH_3)_3Si$-C≡C-H. The reasons for the fast relaxation in the f_9 compound are not known.

The role of extreme motion states in accelerating IVR (6) can also be seen in Table 2. Because of the nature of the dipole selection rules, infrared spectroscopy tends to prepare hydride stretches that are localized and therefore qualify as extreme motion states. With the advent of double resonance excitation schemes it has become possible to deliberately prepare initial states in which the energy is divided between widely separated hydrogens. Such delocalized combination vibrations should, by implication, relax more slowly than extreme motion states. In propyne, the acetylenic C—H plus methyl C—H combination band (28) does relax more slowly than either of the localized overtones of the acetylenic C—H.[3,4] For hydrogen peroxide, the relaxation times increase in the order: 6 O—H < 5 O—H + O—O < 4 O—H + O—H′, which is also consistent with an enhancement of the relaxation rate by extreme motion states.

It is evident from this discussion that these other systematic effects must be taken into account in addition to the distance of the chromophore from a center of flexibility.

The data in Table 2 provide further insight into the possible role of aliphatic methyl internal rotors. Among the flexible

[3]A. McIlroy, D.J. Nesbitt, E. Th. Kerstel, B.H. Pate, K.K. Lehmann, and G. Scoles. J. Chem. Phys. In press.

[4]J.E. Gambogi, E.R. Th. Kerstel, K.K. Lehmann, and G. Scoles. J. Chem. Phys. In press.

Can. J. Chem. Downloaded from www.nrcresearchpress.com by 195.246.54.202 on 09/08/12
For personal use only.

Can. J. Chem. Downloaded from www.nrcresearchpress.com by 195.246.54.202 on 09/08/12
For personal use only.

molecules in Table 2, only *n*-butane has two methyl internal rotors in addition to the *gauche–trans* isomerization coordinate and it has the shortest lifetime of those listed for $n = 2$. Among the rigid molecules, those with two or more methyl rotors (isobutane, *trans*-2-butene, and *tert*-butylacetylene) have shorter lifetimes than does propyne or 1-butyne. The shortest lifetimes in this group are for isobutane and *trans*-2-butene where the methyl C—H's are excited. However, in 1-butyne the single methyl rotor does not cause the methyl C—H to relax more quickly than the acetylenic C—H. The effects mentioned in this paragraph are rather small in comparison with the possible range of variation of IVR lifetimes, so that confident conclusions are not possible at this time. Let us only say that the data are consistent with a modest enhancement of IVR by aliphatic methyl rotors, particularly when there are two or more interacting internal rotors within the molecule.

The lifetimes for the halogenated molecules listed in Table 2 are all very long. 2-Fluoroethanol (29) has two internal rotors, which connect five distinct conformations, yet the lifetime of the methyl C—H is in the range of hundreds of picoseconds as would be expected for a rigid molecule. The most stable geometry is the *Gg'* conformer in which there are intramolecular interactions between the fluorine and the hydroxyl hydrogen. Conversion to the next most stable conformer (*Tt*) has a barrier of more than 1500 cm^{-1} and involves motion along both internal rotation coordinates. It seems that 2-fluoroethanol behaves as a more rigid molecule than ethanol. It is also possible that halogenation produces a decrease in the number of low-order resonances. In 1,2-difluoroethane (30) and 1-chloro-2-fluoroethane (31), the mass of the halogen atoms brings the density of states into the range (five and nine symmetry-allowed states per cm^{-1}, respectively (31)) where IVR is expected (32, 33) but the intramolecular interactions remain slight. The lifetimes for the four halogenated molecules, including trifluoropropyne (34), all fall in the range expected for rigid molecules even though three of them may undergo conformational change by movement of a halogen (X) atom. It appears that internal rotation of a CH_2X group does not provide molecular flexibility of the type that accelerates IVR.

Why does molecular flexibility accelerate IVR?

While the experimental results provide empirical evidence that molecular flexibility plays an important role in accelerating IVR, we would also like to know why this is so. A definitive answer to this question can only come from careful dynamical calculations on realistic potentials for a number of molecules. However, some insight can be obtained from an examination of the potential for the large-amplitude degrees of freedom.

Consider the torsional potential about the C—O bond of ethanol[2] as an example. In Fig. 3, this potential is compared to a harmonic potential with the same curvature at the minimum. Even at energies as low as the hydride fundamentals, it can be seen that these potentials are very different and that the energy level structures bear little resemblance. In general, we expect that the large-amplitude coordinates that are responsible for molecular flexibility will be the most anharmonic degrees of freedom in the molecule.

Of more relevance than the form of the potential for any single coordinate is the nature of the coupling between coordinates. For example, the barrier to methyl internal rotation of ethanol increases from 1158 cm^{-1} to 1331 cm^{-1} on conversion from the *trans* to the *gauche* form. This change of barrier height can be modelled by allowing the V_3 term of

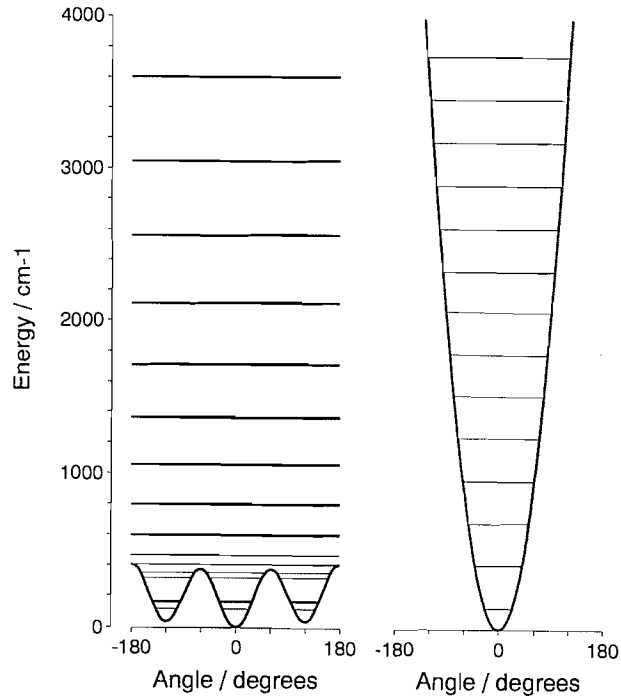

FIG. 3. Potential energy curves (see footnote 2) and energy levels for the C—O torsion of ethanol (left) and for a harmonic oscillator with the same curvature at the minimum (right). The *trans* minimum is at 0° and the *gauche* minima are at ±120°. The energy levels result from a diagonalization of the one-dimensional torsional problem using the kinetic energy coefficients given in ref. 17. Nondegenerate levels are shown as a thin line. Levels that are doubly degenerate within the resolution of the figure are represented with a thick line. The highest energy levels displayed are comparable to one quantum of the O—H stretch.

the methyl internal rotation potential to depend on the C—O torsion angle, α:

$$[7] \qquad V_3 \approx (1273 - 115\cos\alpha)\,cm^{-1}$$

If we use a product-free rotor basis

$$[8] \qquad \psi_m(\alpha)\psi_n(\beta) = \frac{1}{2\pi}\exp(im\alpha)\exp(in\beta) \quad \text{with } m,\ n = 0, \pm1, \pm2, \ldots$$

then the potential matrix elements coupling the two internal rotors are

$$[9] \qquad \langle\psi_{m'}\psi_{n'}|\frac{115}{2}\cos\alpha\cos3\beta|\psi_m\psi_n\rangle = \frac{115}{8}\delta_{m',m\pm1}\delta_{n',n\pm3}\,cm^{-1}$$

The angle β is the coordinate of the methyl internal rotation. Coupling matrix elements also arise from the kinetic energy operator (35). At first glance eq. [9] appears to be a coupling of relatively low order; however, this apparent simplicity exists only in the free rotor basis. The one-dimensional eigenfunctions, $\phi(\alpha)$ and $\phi(\beta)$, bear little resemblance to free rotor wavefunctions. To illustrate this point, the ground state eigenfunctions, $\phi_0(\alpha)$ and $\phi_0(\beta)$, are given in Table 3 in the free rotor basis.

Therefore matrix elements of eq. [9], when expressed in the product basis, $\phi(\alpha)\phi(\beta)$, will yield both low- and high-order couplings between the two internal rotors. Although we do not

TABLE 3. Ground state torsional eigenfunctions for ethanol in the free rotor basis

m or n	C—O Torsion[a]	C—C Torsion[b]
0	0.57	0.63
±1	0.44	0.00
±2	0.30	0.00
±3	0.20	0.49
±4	0.10	0.00
±5	0.04	0.00
±6	0.02	0.24
±7	0.01	0.00
±9	0.00	0.08
±12	0.00	0.02

[a]For the C—O torsion, the one-dimensional eigenfunctions are given as the coefficients of the expansion $\phi_0(\alpha) = \Sigma c_m \exp(im\alpha)$ and were obtained by diagonalization of the torsional Hamiltonian (see footnote 2).

[b]For the C—C torsion, the expansion is $\phi_0(\beta) = \Sigma c_n \exp(in\beta)$. The potential coefficient, $V_3 = 1158\ cm^{-1}$; and the kinetic coefficient, $\mu^{(0)} = 6.445\ cm^{-1}$ are from ref. 17.

have convenient analytical expressions for the matrix elements, we should not be surprised to find other instances of relatively strong high-order coupling between an internal rotor and vibrations having significant amplitude in its vicinity. One such example is the coupling of the methyl rotor to ring modes in *p*-fluorotoluene (36). Therefore, relatively strong couplings of both low and high order can result from the extreme anharmonicity of large-amplitude coordinates and may contribute to the importance of molecular flexibility in accelerating IVR.

Conclusion

Empirical evidence has been presented to show that the proximity of a prepared vibration to a center of flexibility is associated with accelerated IVR. It has been pointed out that molecular flexibility can give rise to substantial low- and high-order couplings that may enhance the rate of intramolecular relaxation.

It must be emphasized that the role of molecular flexibility is only a part of the story about IVR. Other systematic effects such as the density of low-order resonances and the properties of extreme motion states must also be taken into account. Specific strong low-order resonances can dominate the relaxation in the cases where they are active. The unique properties of individual molecules generate scatter in the measured lifetimes and some exceptions to generally valid trends should be expected.

Acknowledgements

The authors are grateful to K.K. Lehmann, G.T. Fraser, B.H. Pate, and L.A. Philips for providing experimental results from their laboratories in advance of publication. The assistance of George Rogers in the computation of decay curves and lifetimes is appreciated. Support for this work was provided by the Division of Chemical Sciences, Office of Basic Energy Sciences, Office of Energy Research, United States Department of Energy under grant DE-FG02-90ER14151. This support does not constitute endorsement by DOE of the views expressed in this article.

1. A. McIlroy. Ph.D. Thesis, University of Colorado, Boulder, Colorado (1991).
2. D.B. Moss and C.S. Parmenter. J. Chem. Phys. **98**, 6897 (1993).
3. V.A. Walters, S.D. Colson, D.L. Snavely, K.B. Wiberg, and B.M. Jamison. J. Phys. Chem. **89**, 3857 (1985).
4. J.E. Gambogi, R.P. L'Esperance, K.K. Lehmann, B.H. Pate, and G. Scoles. J. Chem. Phys. **98**, 1116 (1993); J.E. Gambogi, K.K. Lehmann, B.H. Pate, G. Scoles, and X. Yang. J. Chem. Phys. **98**, 1748 (1993).
5. A.A. Struchbrukhov and R.A. Marcus. J. Chem. Phys. **98**, 6044 (1993).
6. J.E. Gambogi, J.H. Timmermans, K.K. Lehmann, and G. Scoles. J. Chem. Phys. **99**, 8559 (1993).
7. E.L. Sibert, W.P. Reinhardt, and J.T. Hynes. J. Chem. Phys. **81**, 1115 (1984).
8. H.R. Dubal and M. Quack. J. Chem. Phys. **81**, 3779 (1984); J.E. Baggot, M.-C. Chuang, R.N. Zare, H.R. Dubal, and M. Quack. J. Chem. Phys. **82**, 1186 (1985); J. Segall, R.N. Zare, H.R. Dubal, M. Lewerenz, and M. Quack. J. Chem. Phys. **86**, 634 (1987); A. Amrein, H. Hollenstein, M. Quack, R. Zenobi, J. Segall, and R.N. Zare. J. Chem. Phys. **90**, 3944 (1989).
9. A. McIlroy and D.J. Nesbitt. J. Chem. Phys. **92**, 2229 (1990).
10. G.A. Bethardy and D.S. Perry. J. Chem. Phys. **98**, 6651 (1993).
11. D.S. Perry. J. Chem. Phys. **98**, 6665 (1993).
12. G.A. Bethardy and D.S. Perry. J. Chem. Phys. **99**, 9400 (1993).
13. G.T. Fraser, B.H. Pate, G.A. Bethardy, and D.S. Perry. Chem. Phys. **175**, 223 (1993).
14. G.T. Fraser, B.H. Pate, J. Gambogi, K.K. Lehmann, and G. Scoles. Paper FA02 presented at the OSU International Symposium on Molecular Spectroscopy, Columbus, Ohio, June 15–19, 1992.
15. E.J. Heilweil, M.P. Casassa, R.R. Cavanagh, and J.C. Stevenson. J. Chem. Phys. **82**, 5216 (1985); M.P. Casassa, E.J. Heilweil, J.C. Stevenson, and R.R. Cavanagh. J. Chem. Phys. **84**, 2361 (1986); E.J. Heilweil. Chem. Phys. Lett. **129**, 48 (1986).
16. E.J. Heilweil, M.P. Casassa, R.R. Cavanagh, and J.C. Stevenson. J. Chem. Phys. **85**, 5004 (1986).
17. R.K. Kakar and C.R. Quade. J. Chem. Phys. **72**, 4300 (1980).
18. E. Hirota. J. Mol. Spectrosc. **26**, 335 (1968).
19. F.J. Wodarczyk and E.B. Wilson. J. Chem. Phys. **56**, 166 (1972).
20. H. Li, G.S. Ezra, and L.A. Philips. J. Chem. Phys. **97**, 5956 (1992).
21. X. Luo and T.R. Rizzo. J. Chem. Phys. **93**, 8620 (1990).
22. X. Luo and T.R. Rizzo. J. Chem. Phys. **94**, 889 (1991).
23. X. Luo, P.R. Fleming, and T.R. Rizzo. J. Chem. Phys. **96**, 5659 (1992).
24. A.M. Andrews, G.T. Fraser, and B.H. Pate. Paper TuA4, OSA High Resolution Spectroscopy Meeting, Salt Lake City, Utah, January 1993; Paper RB03, OSU International Symposium on Molecular Spectroscopy, Columbus, Ohio, June 14–18, 1993.
25. G.M. Stewart and J.D. McDonald. J. Chem. Phys. **75**, 5949 (1981).
26. R.L. Hunt, R.A. Leacock, C.W. Peters, and K.T. Hecht. J. Chem. Phys. **42**, 1931 (1965).
27. E.R. Th. Kerstel, K.K. Lehmann, T.F. Mentel, B.H. Pate, and G. Scoles. J. Phys. Chem. **95**, 8282 (1991).
28. J. Go, T.J. Cronin, and D.S. Perry. Chem. Phys. **175**, 127 (1993).
29. C.L. Brummel, S.W. Mork, and L.A. Philips. J. Chem. Phys. **95**, 7041 (1991).
30. S.W. Mork, C.C. Miller, and L.A. Philips. J. Chem. Phys. **97**, 2971 (1992).
31. C.C. Miller, M. Shen, and L.A. Philips. J. Phys. Chem. **97**, 537 (1993).
32. D.J. Nesbitt, and S.R. Leone. Chem. Phys. Lett. **87**, 123 (1982).
33. G.M. Stewart and J.D. McDonald. J. Chem. Phys. **78**, 3907 (1983).
34. B.H. Pate, K.K. Lehmann, and G. Scoles. J. Chem. Phys. **95**, 3891 (1991).
35. J.V. Knopp and C.R. Quade. J. Chem. Phys. **53**, 1 (1970).
36. D.B. Moss, C.S. Parmenter, and G.E. Ewing. J. Chem. Phys. **86**, 51 (1987).

Can. J. Chem. Downloaded from www.nrcresearchpress.com by 195.246.54.202 on 09/08/12
For personal use only.

Appendix: Errors from the approximate separation of tunnelling states

The procedure for approximately separating the two pure sequences that are related by a tunnelling motion has been described previously (10). The separation relies on the fact that the tunnelling splitting of the zero-order bright state is negligible compared to the spectral resolution. Therefore, one has the requirement that the two pure sequence clumps share a common center of gravity. This, together with the known nuclear spin weights, allows an approximate separation of the observed spectra that should, in principle, yield reliable average IVR lifetimes.

However, in real spectra, some of the weaker lines will be missed. In this case, the centers of gravity of the pure sequence clumps may no longer coincide, giving systematic errors in the way the observed lines are separated into tunnelling species. Relative to a correct separation of the observed lines, the estimated homogeneous clump widths would be too large and therefore the estimated IVR lifetimes would be too short. On the other hand, most of the missed lines will be in the wings of the clump, which will tend to give an estimated width that is too low and a lifetime that is too long.

Some insight into the net result of these two opposing effects can be found in our existing random matrix calculations (11). These calculations simulate the experimental spectra as the superposition of two pure sequences under a range of signal-to-noise conditions. The average calculated clump widths for the 1-butyne ν_{16} band are found to be about 10% less at the signal-to-noise of the experiment than at infinite signal-to-noise. By implication, the estimated lifetimes would be about 10% too long. We conclude that, when the assumptions of the random matrix calculation are valid, the loss of weak lines in the wings of the clumps is a more important source of error than the misalignment of the centers of gravity of the pure sequence clumps. The crucial assumption that the dark states are strongly coupled to each other is thought to be at least approximately valid for 1-butyne (11) and ethanol (12).

However, when this assumption does not hold, the error in the lifetimes may be larger and in the opposite direction. For example, the bright state could couple with a large matrix element to a particular zero-order dark state that has a large tunnelling splitting. If the dark state is off resonance and borrows insufficient intensity to be detected in the spectrum, the pure sequence clumps would be shifted by different amounts or even in different directions. This may be the case for propargyl amine. Rigorous assignment of the tunnelling species by a double resonance technique showed that the misalignment between the pure sequence clumps was about one quarter of the clump width (24).

Can. J. Chem. Downloaded from www.nrcresearchpress.com by 195.246.54.202 on 09/08/12
For personal use only.

Crossed-beam studies of radical reaction dynamics: $CN + O_2 \rightarrow NCO\ (\tilde{X}^2\Pi) + O$

R. GLEN MACDONALD[1] AND KOPIN LIU[1,2]

Argonne National Laboratory, Chemistry Division, 9700 South Cass Ave., Argonne, IL 60439, U.S.A.

DAVID M. SONNENFROH

Physical Sciences, Inc., Andover, MA 01810, U.S.A.

AND

DI-JIA LIU

Allied Signal, Inc., 50 E. Algouquin Rd., Des Plaines, IL 600175014, U.S.A.

Received July 27, 1993

This paper is dedicated to Professor John C. Polanyi on the occasion of his 65th birthday

R. GLEN MACDONALD, KOPIN LIU, DAVID M. SONNENFROH, and DI-JIA LIU. Can. J. Chem. **72**, 660 (1994).

The title reaction has been studied in a crossed molecular beam apparatus. Both the product state distributions and the translational energy dependence of the reaction cross sections were measured under single collision conditions. Excellent agreement was found over a wide temperature range (26–3800 K) between rate constants deduced from the translational excitation function and recent thermal kinetic data. The rotational state distribution was found to be very cold compared to the reaction exothermicity, and could be described by a Boltzmann temperature of 110 K for all *K*-doublet levels. The vibronic state distribution was also found to be cold, with 70% of the products formed in the vibrational ground state. By comparing the molecular beam results for vibronic state distributions with those obtained from recent bulb experiments, it was conjectured that there appears to be a strong correlation between rotation in the reactants and bending excitation in the products.

R. GLEN MACDONALD, KOPIN LIU, DAVID M. SONNENFROH et DI-JIA LIU. Can. J. Chem. **72**, 660 (1994).

On a étudié la réaction mentionnée dans le titre à l'aide d'un appareil à faisceau moléculaire croisé. Utilisant des conditions de collision unique, on a étudié les distributions des états des produits ainsi que la relation entre l'énergie de translation et les sections droites de la réaction. Sur une large plage de températures (26–3800 K), on a observé un excellent accord entre les constantes de vitesse obtenues à partir de la fonction d'excitation translationnelle et des données récentes de cinétique thermique. On a trouvé que la distribution de l'état rotationnel est très froide si on la compare avec l'exothermicité de la réaction et qu'on peut la décrire par une température de Boltzmann de 110 K pour tous les niveaux *K*-doublets. On a aussi trouvé que la distribution de l'état vibronique est froide; en effet, 70% des produits se forment dans l'état vibrationnel fondamental. En comparant les résultats des faisceaux moléculaires pour les distributions de l'état vibronique avec ceux obtenus lors d'expériences récentes avec des bulbes, on peut imaginer qu'il existe une forte corrélation entre la rotation des réactifs et l'excitation de déformation des produits.
[Traduit par la rédaction]

1. Introduction

The reaction of the cyano radical (CN) with O_2 is an important step in NO_x formation and destruction in fuel-rich flames, and in other combustion processes such as the burning of coal. It is perhaps also becoming one of the most thoroughly studied radical–radical and four-atom reaction systems. The reaction has three exothermic product channels:

[1]	$CN + O_2 \rightarrow NCO + O$	$\Delta H_0 = -13.7$ kcal mol^{-1}
[2]	$\rightarrow CO + NO$	$\Delta H_0 = -110$ kcal mol^{-1}
[3]	$\rightarrow N + CO_2$	$\Delta H_0 = -93$ kcal mol^{-1}

A new, precise determination of the heat of formation of NCO by Cyr et al. (1) was used in calculating the exothermicity of reaction [1]. There are many indications that the reaction of $CN + O_2$ is dominated by channel [1], whereas channel [3] is generally believed to be unlikely. Schmatjko and Wolfrum (2) monitored CO formed in channel [2] and estimated it to account for 6% of the total $CN + O_2$ reaction rate at room temperature. However, more recently Cooper et al. (3) measured the temperature dependence of the yield of channel [2] and found it to be 23% at 300 K, decreasing to a few percent at 600 K. Such a high yield at low temperature and a negative temperature dependence are quite surprising in that the formation of CO + NO is expected to proceed through a four-center transition state, generally involving a sizable barrier to reaction. Consequently, a small yield at low temperatures increasing with temperature would seem more reasonable.

In terms of overall reaction rate, only quite recently has the kinetic behavior of this reaction been accurately determined over a wide temperature range, from 26 K to 4000 K (4–7). It was found that the thermal rate constant was relatively large and exhibited a pronounced negative temperature dependence, i.e., the rate constant decreased with increasing temperature. The exact origin of this negative temperature dependence is subject to some controversy. The large rate constant and negative temperature dependence suggest that the reaction proceeds through an intermediate complex on an attractive potential energy surface with no significant barrier to complex formation. On the other hand, a recently developed rotationally adiabatic capture theory (8) predicts that even a direct abstraction reaction, as opposed to a complex formation reaction, could also exhibit a negative temperature dependence. According to this approach, the reaction cross section decreases as internal rotation, j, of the reactants increases at a given temperature. As a result, the negative temperature dependence arises from the Boltzmann averaging over the initial rotational state distribution, which shifts the population towards the higher rotationally excited (less

[1]Authors to whom correspondence may be addressed. Phone: (708) 252-7742; Fax: (708) 252-4470 (at Argonne National Laboratory).

[2]Present address: Institute of Atomic and Molecular Sciences (IAMS), Academia Sinica, PO Box 23-166, Taipei, Taiwan 10764.

Can. J. Chem. Downloaded from www.nrcresearchpress.com by EESC ESCOLA DE ENGENHARIA on 09/08/12
For personal use only.

Can. J. Chem. Downloaded from www.nrcresearchpress.com by ESC ESCOLA DE ENGENHARIA on 09/08/12
For personal use only.

reactive) states, with increasing temperature. Thus, the observed negative temperature dependence of the thermal rate constants can be rationalized equally well by two opposite reaction mechanisms.

The theoretical characterization of the reaction between CN + O_2 is complicated by the very nature of radical–radical processes. Considering the most important channel [1], in planar geometry, there are two NCOO potential energy surfaces of $^2A''$ and $^4A''$ symmetries that correlate with both CN ($X^2\Sigma^+$) + O_2 ($^3\Sigma^-$) and NCO ($X^2\Pi$) + O (^3P). The doublet surface will have lower energy because of its lower spin multiplicity, and is believed to be the reactive one. As just alluded to in the previous paragraph, one of the outstanding questions concerning reaction [1] is whether or not the reaction involves a transient, bound NCOO complex. The $^2A''$ state arises from the bonding interactions between the unpaired electron on CN and one of the unpaired electrons on O_2. From a comparison of the known bond strengths in related compounds, such as X—NO (X:F, Cl), CN—NO, and X—O_2, it has been estimated (9) that the bond energy for a NC—OO complex would be about 15 kcal mol^{-1}. This estimate is very close to the new value of 13.7 kcal mol^{-1} for the exothermicity of reaction [1]. Based on these considerations, it is likely that there is at most a very shallow well on the NCOO surface, and reaction [1] would occur essentially via a direct O-atom abstraction path. On the other hand, a recent *ab initio* calculation (10) yielded a bond energy of about 45 kcal mol^{-1}, which is closer to Benson's estimate (10) of 35 kcal mol^{-1}. These values will lead to a considerably deeper well on the NCOO potential energy surface, ca. 20–30 kcal mol^{-1} more stable than the NCO + O products. A transient, bound NCOO intermediate would then be expected, which could play a significant role in the kinetics/dynamics of this reaction. Clearly, a more precise determination of the bond energy of the NC – OO intermediate is needed. Despite the current uncertainties in this quantity, it is likely that no substantial potential well (>20 kcal mol^{-1}) is involved. However, the observed pressure independence of thermal rate constants over a limited range does not necessarily rule out a complex formation reaction mechanism.

Reported here is a crossed-beam investigation of reaction [1]. A nearly complete characterization of the NCO ($\tilde{X}^2\Pi$) product state distributions under single collision conditions was attempted. This vast amount of information was then used to shed light on some of the controversies and unresolved issues posed above. During the course of this study, we became aware of two independent investigations, in Dagdigian's (11) and Smith's (9) groups, on the vibronic state distribution of the NCO product from reaction [1]. A comparison of the results from all three studies leads to an intriguing correlation between the bending excitation of NCO product and the rotational motion of the "spectator" CN reagent. Implications of this correlation for future study of polyatomic reaction dynamics are also outlined.

2. Experimental

The experiments were carried out in a crossed-beam machine described previously (12), so that only a brief description of the apparatus will be given here. It consists of two collimated, pulsed supersonic beam sources that are differentially pumped and independently rotatable through 2π radians. The CN ($X^2\Sigma^+$) radical was produced almost exclusively in $N = 0$ by photolyzing C_2N_2 directly in front of a pulsed molecular beam valve at 193 nm using an ArF laser. The C_2N_2 was diluted (~4%) in N_2 or mixtures of N_2 and H_2. The CN state distribution in the primary beam was monitored by laser-induced fluorescence (LIF) using the CN $B^2\Sigma^+ \leftrightarrow X^2\Sigma^+$ transition (13) and is shown in Fig. 1 for the case with N_2 as carrier gas. As is evident from the figure, the CN radical is rotationally relaxed because of the strong supersonic expansion (backing pressures of ~15 atm (1 atm = 101.3 kPa) and a nozzle diameter of 0.5 mm). Photolysis of C_2N_2 at 193 nm produces vibrationally excited CN (14), and about 6% of the CN radicals remained vibrationally excited even after this strong supersonic expansion. Various relaxation partners (CF_4, NO, and Xe) were added to the gas mixture to vibrationally relax CN radicals; however, only a modest reduction in the vibrational population of CN ($X^2\Sigma^+$) was found over that with N_2 as carrier gas. A similar CN ($X^2\Sigma^+$) internal state distribution to that shown in Fig. 1 was found when using a mixture of N_2 and H_2 as carrier gas.

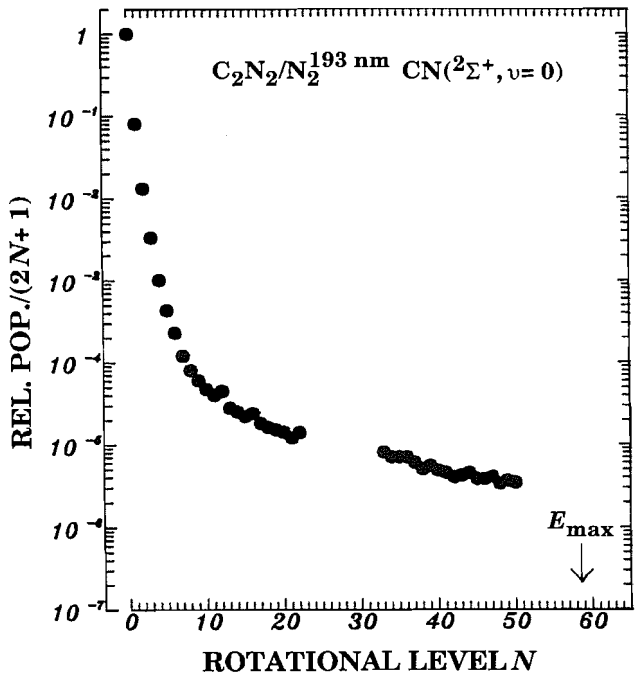

FIG. 1. Relative population of CN ($X^2\Sigma^+$) produced in 193 nm photolysis of C_2N_2 (~4%) dilute in N_2 carrier gas. The initial few rotational states are described by a Boltzmann rotational temperature of ~2 K while the tail is described by 70 K. The gap between $N = 22$ and 32 is due to bandhead formation.

A unique feature of this apparatus is the ability to select the initial translational energy by merely changing the intersection angle between the two beam sources without varying any other beam parameter. In this mode of operation it is possible to measure the excitation function for a selected product state by setting the dye laser at a wavelength that probes a selected product state and then varying the angle between the two beam sources. The product state distribution may also be determined for a fixed initial translational energy of the reactants by fixing the intersection angle of the beams and then scanning the dye laser to obtain a LIF excitation spectrum.

To facilitate data analysis and to improve spectral resolution by reducing power-broadening effects, the LIF spectra were taken in the linear power dependence regime, typically 2–4 μJ/pulse with a laser beam diameter of 5–6 mm, for the complete determination of the product rotational and fine-structure state distributions of the NCO vibrational ground state. A gated photon counting technique, using a Stanford Research model SR-400, was employed to enhance the S/N ratio. No other NCO $\tilde{X}^2\Pi$ vibrational level was sufficiently populated from reaction [1] to allow such detailed measurements. Instead, near-saturated LIF (~200 μJ/pulse, and boxcar averaging) scans around the bandheads were used to obtain the vibronic state distributions. Near-saturated LIF also reduces most of the Franck–Condon factor dependence of the observed signals.

Can. J. Chem. Downloaded from www.nrcresearchpress.com by EESC ESCOLA DE ENGENHARIA on 09/08/12
For personal use only.

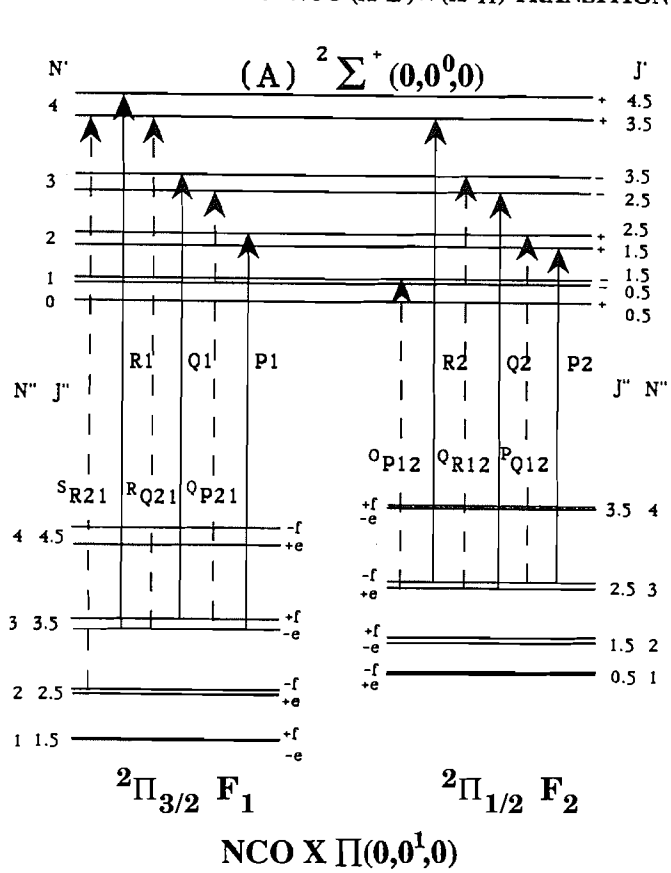

FIG. 2. A schematic representation of the NCO $\tilde{A}^2\Sigma^+(000) \leftrightarrow \tilde{X}^2\Pi(00^10)$ transition. The solid lines represent main branch transitions while the dotted lines represent satellite branches. The closely spaced levels labeled by alternating parity and *e/f* are the *K* doublets. Like OH, *A* is negative for NCO and the lower energetic spin-orbit state is $^2\Pi_{3/2}$.

The spectroscopy of the NCO $\tilde{A}^2\Sigma \leftrightarrow \tilde{X}^2\Pi$ transition has been well documented (15). For clarity, a schematic of the energy levels involved in probing the rotational states of the two spin-orbit manifolds of the ground vibrational level are shown in Fig. 2. Because of the large spin-orbit constant, *A*, and smallrotational constant, *B*, the NCO $\tilde{X}^2\Pi$ (00^10) state is a prototypical Hund's case (a) radical ($Y = A/B = -245$), and the spectroscopic labeling is similar to that for the analogous transition in the more familiar OH radical. The dye laser resolution (0.08 cm^{-1}) is not sufficient to separate some of the main branch transitions from their associated satellite branches (see Fig. 2) in either spin-orbit manifold. Thus, the nascent *K*-doublet population (the closely spaced *e/f* labeled states for a given rotational quantum number *J*, analogous to the λ-doublet of a diatomic radical) was determined by comparing the intensity of satellite transitions such as the $^sR_{21}$ branch probing 1*f* levels in the $^2\Pi_{3/2}$ manifold to the sum of the intensities of the main branch R_1 and associated satellite branch $^rQ_{21}$, probing 1*e* levels, of the same *J*. Similarly, in the $^2\Pi_{1/2}$ spin-orbit manifold the intensity of the main branch R_2 was used for probing 2*f*-labeled states, and the sum of the main branch Q_2 and its associated satellite branch $^qR_{12}$ probed 2*e*-labeled states. The branches, P_1 and $^OP_{12}$, also probing *e*-labeled levels, were used as a check on the populations obtained from the other branch probing the same *K*-doublet levels. The necessary rotational line strengths of the transitions were calculated according to the intermediate case formulae given in ref. 16. The unique levels of a Renner–Teller manifold, those designated by $K = |l + \Lambda|$, are characterized by bandhead formation in the $Q_1 + {}^qP_{21}$ branch in the lower spin-orbit component and the P_2 branch transitions in the upper spin-orbit component (15). These features were used to determine the vibronic state distribution as well as the excitation functions.

Generally, the LIF technique acts as a number density detector; however, in a scattering experiment the desired quantity is the cross section, which is proportional to particle flux. A number density-to-flux transformation is necessary to extract the cross-section information from measured LIF populations. A simple method has been developed in this laboratory to correct for this transformation without a prior knowledge of the product angular distribution (17). Briefly, this method relies on the fact that different kinematics should lead to the same cross section for production of the same product state at the same initial translational energy. With the present apparatus it is possible to vary the radical beam velocity by changing the effective mass of the carrier gas (mixtures of C_2N_2 and N_2 versus C_2N_2, N_2, and H_2) without changing any other characteristic of the molecular beams. The same cross-section measurement can therefore be made with very different kinematic arrangements. Indeed, it has been shown (17) that by applying this method to the present reaction even a qualitative picture of the product angular distribution can be inferred in a favorable kinematic situation.

3. Results

A. *Rotational state and K-doublet distribution*

A survey LIF excitation spectrum of the NCO $\tilde{X}\,^2\Pi_{3/2}$ (00^10) product from reaction [1] is shown in Fig. 3 for an initial translational energy of 0.7 kcal mol^{-1}. This spectrum was taken under partially saturated LIF (~100 μJ) conditions, and illustrates two important observations. An inspection of the $Q_1 + {}^qP_{21}$ bandhead, which occurs at $J \sim 13.5$, clearly reveals that the nascent NCO is formed with little rotational excitation. A cold rotational distribution is also evident from the appearance of the other branches shown in the figure. This is remarkable considering that the energy available to the reaction products is 14.4 kcal mol^{-1}, and rotational levels up to $J \sim 110$ in the vibrational ground state could be populated on energetic grounds alone. Also note that there appears to be an underlying unresolved feature on the blue side of the $Q_1 + {}^qP_{21}$ bandhead. From this scan alone, it is not clear whether this is due to overlapping of adjacent lines because of power broadening or to the presence of some other unresolved transition. Nevertheless, it is apparent that spectral congestion is a severe problem if the nascent population in *K*-doublet states is to be determined.

In Fig. 4 is shown a scan over the $R_1 + {}^rQ_{21}$ and $^sR_{21}$ branch region for a similar initial translational energy as that of Fig. 3, but under much reduced laser power (~3 μJ). It is obvious from Fig. 4 that many of the previously overlapped lines are now resolved, and a clearer picture of the final product state distribution of NCO emerges. Note that the peaks of low *J* for the $R_1 + {}^rQ_{21}$ branch still do not reach the baseline and that the unresolved feature, evident in Fig. 3, still persists though much less pronounced. In a preliminary account (18) of this study little work had been done on any state other than NCO $\tilde{X}^2\Pi_{3/2}$ (00^10), and spectra similar to that shown in Fig. 4 were analyzed under the assumption that the unresolved feature was due to spectral congestion. This analysis led to the conclusion that there was an unusual preference for production of *K*-doublet levels of *f*-type symmetry at *low J* quantum numbers. Since then a large amount of information has accumulated about the vibronic state distribution of NCO from reaction [1] and also about the spectroscopy of higher vibronic states. The exact frequency of the transitions involving low *J* quantum states for the NCO $\tilde{A}^2\Sigma$ $(010) \leftrightarrow \tilde{X}\kappa\Sigma^-(01^10)$ transition are still not known; however, they can be calculated to be in the low *J* region of the $R_1 + {}^rQ_{21}$ and $^sR_{21}$ branches. More convincingly, other work (19) on the inelastic scattering of NCO $\tilde{X}^2\Pi_{3/2}$ (00^10) by He carried out in this laboratory does not show the same behaviour as

Can. J. Chem. Downloaded from www.nrcresearchpress.com by EESC ESCOLA DE ENGENHARIA on 09/08/12
For personal use only.

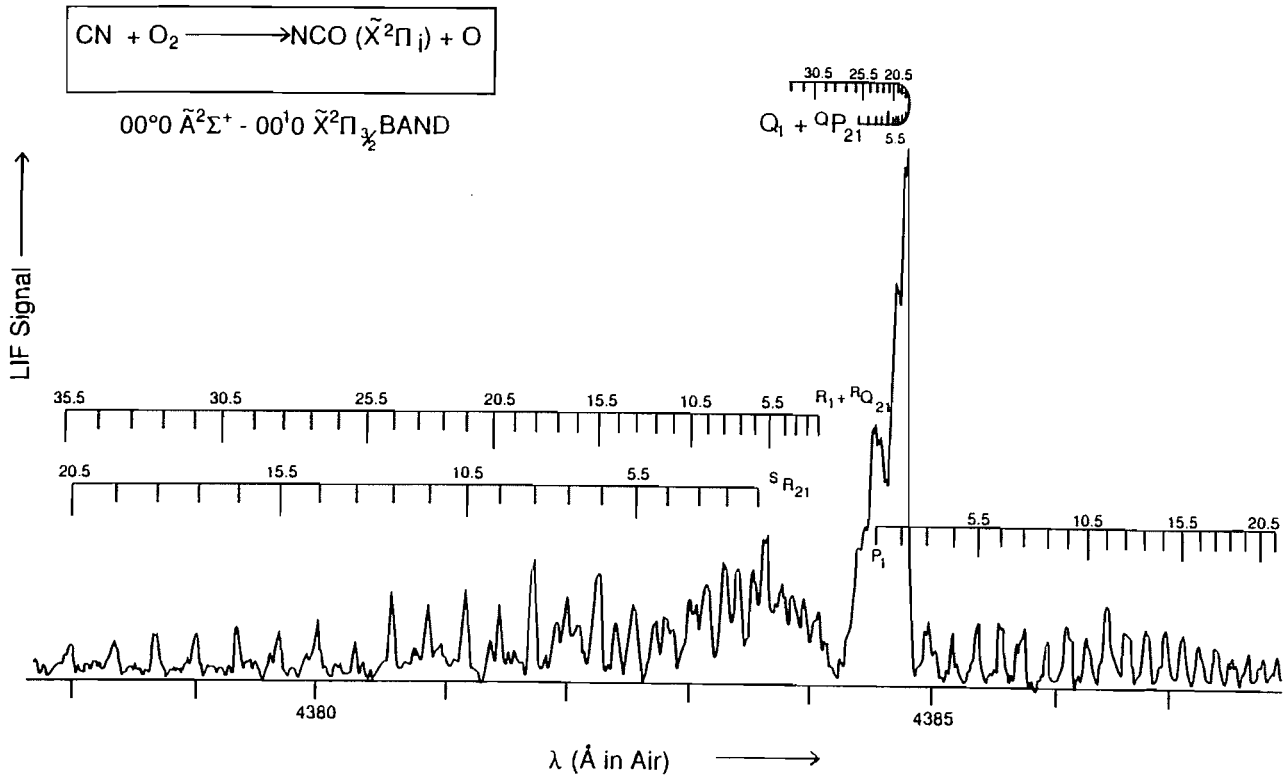

FIG. 3. A rapid survey scan over the $Q_1 + {}^qP_{21}$ bandhead region of NCO $\tilde{A}^2\Sigma^+ \leftrightarrow \tilde{X}^2\Pi$ indicating that the nascent rotational product state distribution from reaction [1] is cold. This LIF spectrum was obtained under partially saturated conditions and should be compared to the spectrum in Fig. 4. The collision energy was 0.7 kcal mol^{-1}.

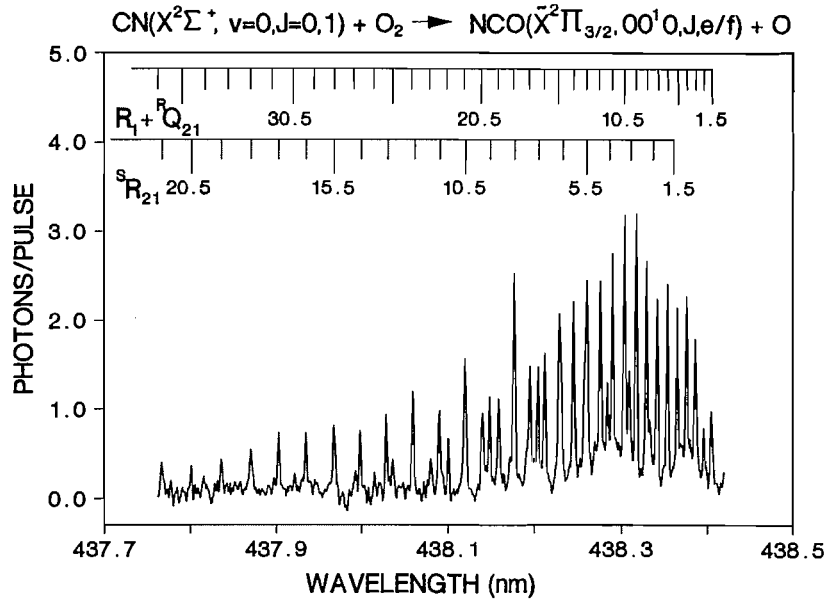

FIG. 4. An unsaturated LIF spectrum of the ${}^sR_{21}$ and $R_1 + {}^rQ_{21}$ branches of the NCO $\tilde{A}^2\Sigma^+(000) \leftrightarrow \tilde{X}^2\Pi_{3/2}(00^10)$ band recorded using single photon counting. Note that lines of low J do not terminate on the baseline (see text). This spectrum was recorded at an E_0 of 0.8 kcal mol^{-1}.

seen in Figs. 3 and 4. The peaks arising from the low J states of the $R_1 + {}^rQ_{21}$ and ${}^sR_{21}$ branches do indeed terminate on the baseline, even at higher laser power. It thus appears that the underlying feature in Figs. 3 and 4 is more likely due to transitions arising from the vibrationally excited $\tilde{X}\kappa\Sigma^-(01^00)$ state. A re-analysis of the low J data for the $R_1+{}^rQ_{21}$ and ${}^sR_{21}$ branches, assuming that the $\tilde{X}\kappa\Sigma^-(01^00)$ vibronic level contributed to the observed unresolved background, was carried out. The results of this new analysis are presented in Fig. 5. The uncongested $P_1(e)$ branch was also used to measure cross sections for the production of 1e-labeled K doublets. Generally, the agreement in cross sections for the different branches was better than $\pm 10\%$. The error bars in Fig. 5 reflect ± 2 standard deviations from the average of at least 5 spectra and the average of the branches for production of 1$e$labeled K doublets. The ratio of the populations in the two K doublets for different J states is

Can. J. Chem. Downloaded from www.nrcresearchpress.com by EESC ESCOLA DE ENGENHARIA on 09/08/12
For personal use only.

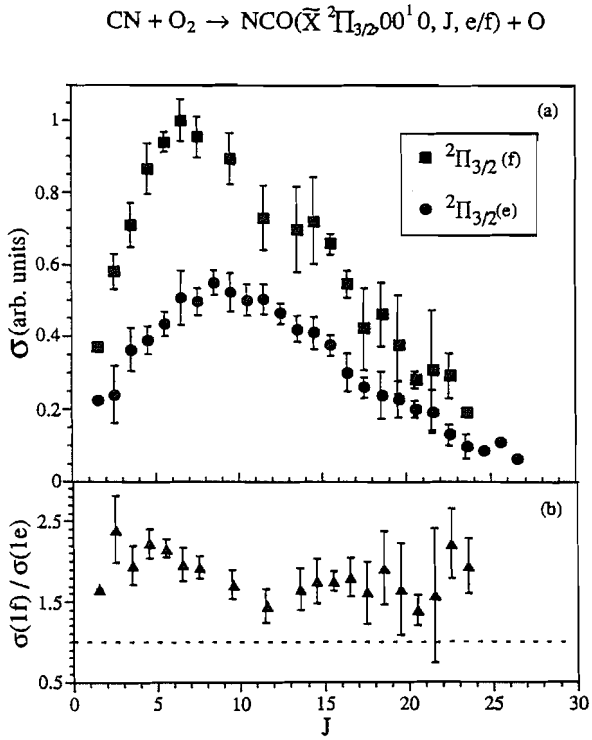

FIG. 5. (*a*) The nascent rotational and *K*-doublet population of NCO $\tilde{X}^2\Pi_{3/2}(00^10)$ from reaction [1] for an initial E_0 of 0.8 kcal mol^{-1}. NCO is formed with little rotational excitation. The error bars indicate the scatter in at least five independent measurements. Missing rotational states, especially in the *f*-labeled *K*-doublet manifold, are due to severely overlapped lines in the spectrum. Panel (*b*) is the ratio of *f*/*e*-labeled *K*-doubletstates vs. rotational quantum number showing a propensity of ~2 favoring *f* levels independent of *J*. A statistical distribution would give 1.

shown in panel (*b*) of Fig. 5. A comparison of this panel to the earlier work reveals that the propensity for production of 1*f*-labeled *K* doublet is approximately constant for all the observed *J* states, and the unusual increase in this propensity for low *J* states reported previously is *not* present. It should be noted that the peak in the rotational level distribution is indeed very low, peaking at $J \sim 6.5$ for 1*f* levels and at 8.5 for 1*e* levels.

Figure 6 is a typical LIF spectrum for the NCO $\tilde{A}^2\Sigma(000) \leftrightarrow \tilde{X}^2\Pi_{1/2}(00^10)$ band showing the $Q_2 + {}^qR_{12}$ (probing 2*e* levels) and R_2 (probing 2*f* levels) branches for the excited spin-orbit state of NCO produced in reaction [1]. The ${}^oP_{12}$ (*f*) branch was used as a check for cross sections derived from the R_2 branch. Again, the cross section appears to peak at low *J* values, just as for the lower spin-orbit state, NCO $^2\Pi_{3/2}$, shown in Fig 4. The gaps in the spectrum indicate that only the peak was scanned and the baseline in this region was not scanned. Shown in Fig. 7 are the *K*-doublet cross sections deduced from spectra such as shown in Fig. 6. Similar to the lower NCO $(00^10)^2\Pi_{3/2}$ spin-orbit component, the rotational state population appears to peak near $J \sim 9.5$ for both *K*-doublet components. In the lower panel of Fig. 7 the propensity for favoring the 2*f K* doublet is shown. As shown in Figs. 5 and 7, the *K*-doublet preference for the *f*-level is approximately independent of *J* by a factor of about 1.7 in both spin-orbit manifolds.

A closer inspection of Figs. 5 and 7 suggests a Boltzmann like behavior for the rotational level distributions. This is borne out in Fig. 8 where the complete rotational level distributions for the vibronic ground state manifold are plotted in a Boltzmann manner. In each *K*-doublet manifold, except for the lowest few *J* states, which appear to have a slight excess population over a Boltzmann prediction, the distributions are well characterized by a straight line with slope corresponding to a rotational temperature of 110 K. When summed over all *K*-doublet populations within each spin-orbit manifold, a propensity of $^2\Pi_{3/2}/^2\Pi_{1/2} \sim 2.3$ is found. This, in conjunction with the *K*-doublet preference of $1f/1e \sim 2f/2e \sim 1.7$, yields an approximate fine-structure propensity of $1f > 1e > 2f > 2e$ for all *J* at a translational energy, E_0, of 0.8 kcal mol^{-1}.

B. Vibronic state distribution

As already noted, the signal-to-noise ratio was not sufficient to obtain resolved single rotational state spectra for any vibronically excited state. However, it was possible to extract the total population in a given vibronic state by integrating over the bandhead regions under saturated LIF conditions. Typical spectra at $E_0 = 0.8$ kcal mol^{-1} are shown in Fig. 9 for the unique levels of the Renner–Teller vibronic manifold. In Fig. 9 the panels on the left probed the $Q_1 + {}^qP_{21}$(e) bandhead for the energetically lower spin-orbit component, while those on the right probed the P_2 (f) bandhead of the more energetic spin-orbit component. It is clear from Fig. 9 that the reaction does not populate excited vibronic states of NCO to any significant extent under crossed-beam conditions. This is in dramatic contrast to the vibronic state distribution obtained in other work under bulb conditions (9, 11). It should be pointed out that with high laser power the bandheads in the difference spectra are actually superimposed over a broad featureless background. The exact nature of this collision-induced background is not yet clear, and it was subtracted out in the data analysis.

A summary of the vibronic state distribution, as measured in this work, is shown in Fig. 10. The contribution from all the rotational states of a vibronic component were estimated by integrating over the bandhead region, and using the *J*-averaged rotational line strengths for saturated LIF detection (20). For the unique levels, only one *K*-doublet component of a spin-orbit pair forms a bandhead; thus, to account for the population in the other *K*-doublet component the population ratio measured for the two spin-orbit components of the $^2\Pi(00^10)$ manifold, Fig. 5 and Fig. 7, was used. The underlying unresolved feature near the blue side of the Q_1 bandhead, similar to that shown in Fig. 3, was tentatively assigned to the $\kappa\Sigma^-(01^00)$ state as discussed in the previous section. The exact locations of the bandheads of most of the excited vibronic states of NCO were previously measured by Dagdigian and co-workers (21), and by Sears and co-workers (22). Information about most of the Franck–Condon factors involved is also available from the dispersed fluorescence experiment (22).[3] Based on the relative magnitudes of the Franck–Condon factors, the dependence of observed signals on them is likely to be largely eliminated using the near-saturated LIF detection scheme. Many regions where vibronic transitions have previously been observed were scanned in the present experiments; however, only a few, as exemplified in Fig. 9, were detected with sufficient signal-to-noise to be analyzed. Populations in the other vibronic states are presumably so small that they are below our detection sensitivity. A complete summary of the vibronic levels and the

[3]Also, F.J. Northrup, private communication.

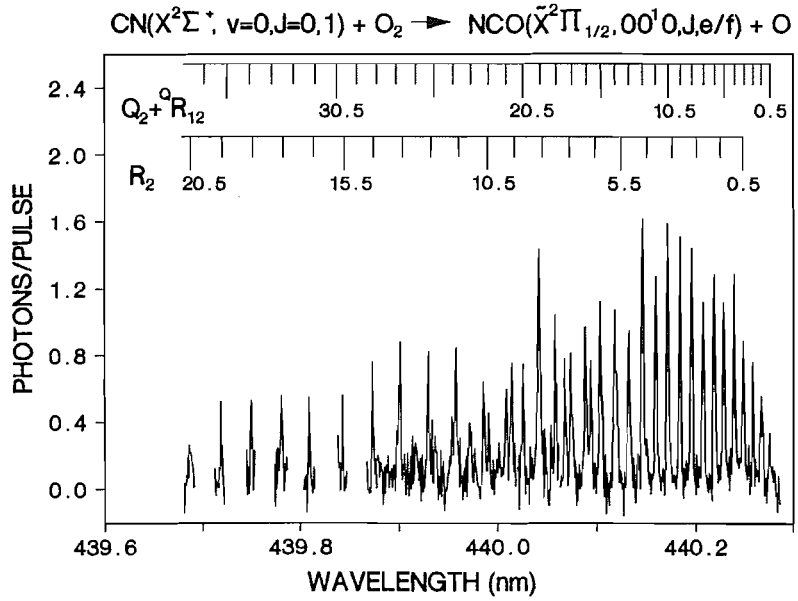

FIG. 6. An unsaturated LIF spectrum of the R_2 and $Q_2 + {}^qR_{12}$ branches of the NCO $\tilde{A}^2\Sigma^+(000) \leftrightarrow \tilde{X}^2\Pi_{1/2}(00^10)$ band recorded using single photon counting. This spectrum was recorded at an E_0 of 0.8 kcal mol^{-1}.

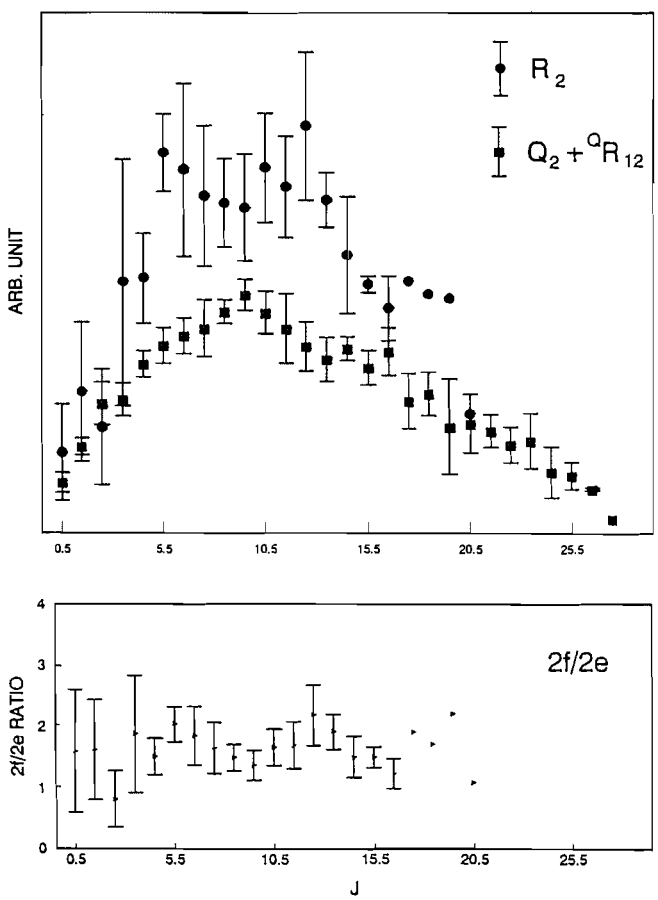

FIG. 7. (*a*) The nascent *K*-doublet level population of NCO $\tilde{X}^2\Pi_{1/2}(00^10)$ from reaction [1] for an E_0 of 0.8 kcal mol^{-1}. The error bars are $\pm 2\sigma$ in the data. Clearly the nascent NCO population peaks at low rotational excitation. The bottom panel is the ratio of $2f/2e$ as a function of rotational state showing $2f$ is favored by ~ 1.8 independent of J. A statistical distribution would give 1.

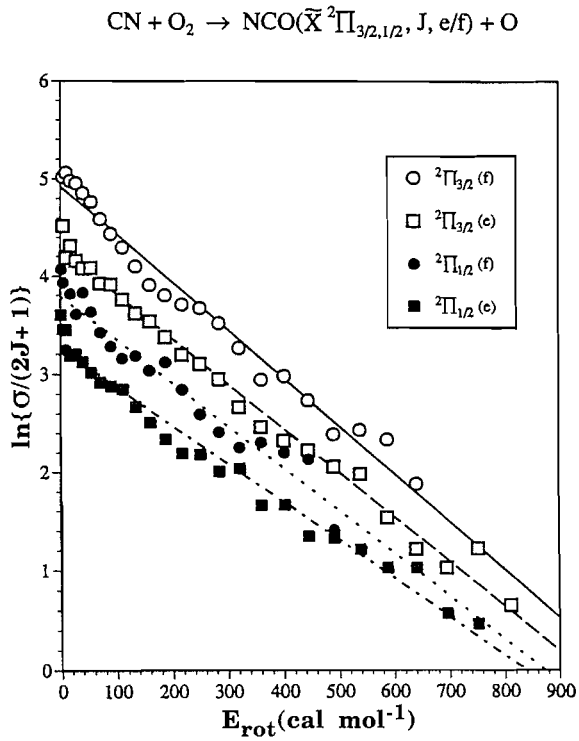

FIG. 8. A Boltzmann rotational temperature plot of the complete *K*-doublet level distribution of the vibronic ground state for NCO from reaction [1] at an E_0 of 0.8 kcal mol^{-1}. The distribution for each *K*-doublet manifold is well described by a rotational temperature of 110 K.

spectroscopic transitions scanned in this work is given in Table 1.

There are several notable features about this vibronic state distribution. First, the overall distribution is quite cold with almost half of the nascent NCO product formed in the lowest vibronic state, $^2\Pi_{3/2}(00^10)$. Second, a clear mode selectivity is

Can. J. Chem. Downloaded from www.nrcresearchpress.com by EESC ESCOLA DE ENGENHARIA on 09/08/12
For personal use only.

Can. J. Chem. Downloaded from www.nrcresearchpress.com by EESC ESCOLA DE ENGENHARIA on 09/08/12
For personal use only.

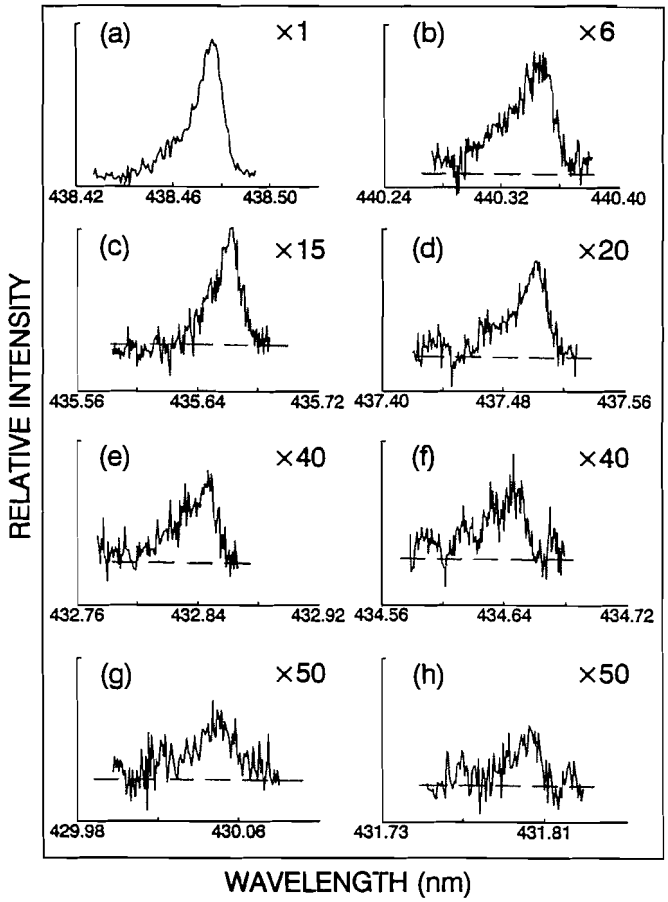

FIG. 9. Selected unique level vibronic bandhead spectra for the NCO product from reaction [1] for an E_0 of 0.8 kcal mol^{-1}. The left-hand panels ((*a*), (*c*), (*e*), and (*g*)) monitor the $Q_1 + {}^qP_{21}$ bandhead of the lower energy spin-orbit component while the right-hand panels ((*b*), (*d*), (*f*), and (*h*)) monitor the $P_2 + {}^pQ_{12}$ bandhead of the more energetic spin-orbit component. Note that the area of the bandhead region was used as a measure of the total population with the zero signal level indicated by the dashed line, *not* the *x*-axis. There is a broad collision-induced signal, which becomes more obvious for the more sensitive scales. Panels (*a*) and (*b*) probe $^2\Pi(00^10)$, (*c*) and (*d*) $^2\Delta(01^20)$, (*e*) and (*f*) $^2\Phi(02^30)$, and (*g*) and (*h*) $^2\Gamma(03^40)$.

revealed, with the order of selectivity: bend > anti-symmetric stretch > symmetric stretch. Third, the population in bending states decreases quite dramatically with increasing excitation. Fourth, within each bending excitation there is a strong propensity for the formation of the unique levels, and the only non-unique Renner–Teller components that have significant population to be detected are those with Σ vibronic symmetry.

In Fig. 11 is plotted the observed spin-orbit propensity for the unique levels. There is a clear preference for the lower spin-orbit component with this preference decreasing slightly as the internal vibronic energy increases. The energy difference between spin-orbit components is much smaller than the available reaction exothermicity, and if they were populated statistically in reaction [1], the ratio would be one. Note that the ratio of 2.45 for the $^2\Pi(00^10)$ ground vibronic state is in excellent agreement with that obtained from the rotational state distribution measurement. For the non-unique levels (i.e., Σ vibronic states), however, the more energetic spin-orbit component is favored by approximately a factor of two, as can be seen in Fig. 11.

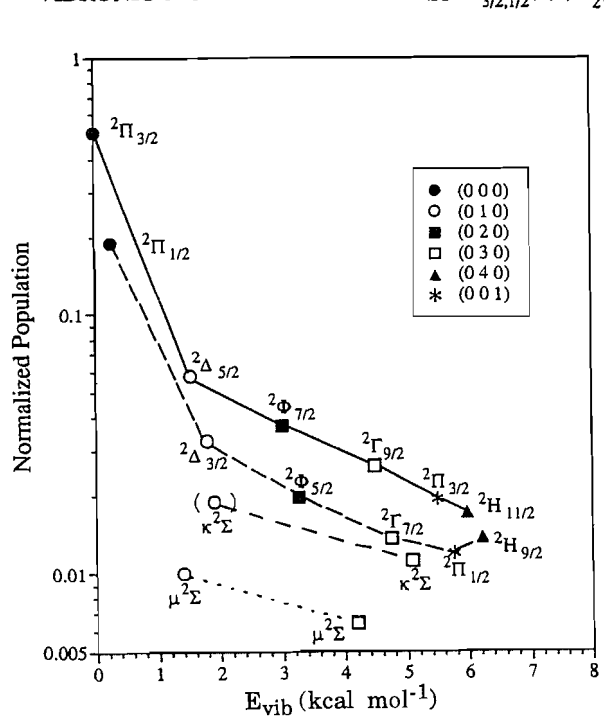

FIG. 10. The complete vibronic state distribution of those manifolds that were detected in this work measured at an E_0 of 0.8 kcal mol^{-1}. The parentheses indicate only a tentative estimate for $\kappa^2\Sigma$ population, see text. Note that the ground vibronic state accounts for 70% of the NCO reaction product from reaction [1].

C. *Excitation function*

In a previous publication (17) the excitation function for the ground vibronic state, $^2\Pi_{3/2}(00^10)$, was reported. That measurement was carried out by fixing the probe laser wavelength at the bandhead peak while the translational energy was varied. The monitored product states, thus, have *J* values ranging from approximately 10.5 to 16.5. Alternatively, one can do a short wavelength scan over the bandhead region at each energy to cover the complete *J* populations and to eliminate the possible change in bandhead shape as the energy changes. The results of these measurements are shown in Fig. 12(*a*) for both $^2\Pi_{3/2}(00^10)$ and $^2\Pi_{1/2}(00^10)$ states. The excitation function for the $^2\Pi_{3/2}(00^10)$ state is in good agreement with the previous peak-height determination, indicating no dramatic change in *J* distributions with an increase in translational energy. In the bottom panel of Fig. 12 is shown the translational energy dependence of the ratio of the cross sections of the spin-orbit states, $^2\Pi_{3/2}$ to $^2\Pi_{1/2}$. A nearly constant propensity was observed over the energy range from 0.7 to 7 kcal mol^{-1}. The average value of 2.4 is again consistent with the other two independent determinations, as alluded to earlier.

A similar determination could be made for the unique levels of the first excited bending manifold, $^2\Delta_{5/2,3/2}(01^20)$. To improve the statistical uncertainties this measurement was done using the peak-height approach, and the result is shown in Fig. 13(*a*). As can be seen, the cross section for producing $^2\Delta_{5/2,3/2}(01^20)$ has almost the identical translational dependence as that for the ground vibronic manifold. Shown in Fig. 13(*b*) is the translational energy dependence of the ratio of the cross sections $^2\Delta_{5/2}$ to $^2\Delta_{3/2}$. Similar to the ground vibronic level, Fig. 12(*b*), this ratio is nearly constant over this energy

TABLE 1. Summary of the NCO ($\tilde{X}^2\Pi$) product vibronic levels and bandhead transitions probed in this work

Lower level NCO ($X^2\Pi$)	Observed	Upper level NCO ($\tilde{A}^2\Sigma$) (branch)
$(00^10)\ ^2\Pi_{3/2,1/2}$	Yes	$(000)\ ^2\Sigma\ (Q_1, P_2)$
$(010)\ \mu^2\Sigma$	Yes	$(010)\ ^2\Pi\ (Q_1 + Q_2)$
$^2\Delta_{5/2,3/2}$	Yes	$(010)\ ^2\Pi\ (Q_1, P_2)$
$\kappa^2\Sigma$	OL[a]	$(010)\ ^2\Pi\ (Q_1 + Q_2)$
$(020)\ \mu^2\Pi$	No	$(100)\ ^2\Sigma$; $(020)\ ^2\Delta\ (Q_1, P_1)$; $(020)\ ^2\Sigma\ (Q_1, P_1)$
$^2\Phi_{7/2,5/2}$	Yes	$(020)\ ^2\Delta\ (Q_1, P_2)$
$\kappa^2\Pi$	No	$(100)\ ^2\Sigma$; $(020)\ ^2\Delta\ (Q_1, P_1)$; $(020)\ ^2\Sigma\ (Q_1, P_1)$
$(10^10)\ ^2\Pi_{3/2,1/2}$	No	$(100)\ ^2\Sigma\ (Q_1, P_2)$; $(000)\ ^2\Sigma\ (Q_1, P_2)$; $(020)\ ^2\Sigma\ (Q_1, P_2)$
$(030)\ \mu^2\Sigma$	Yes	$(030)\ ^2\Pi\ (Q_1 + Q_2)$
$\mu^2\Delta$	No	$(030)\ ^2\Phi\ (Q_1)$; $(030)\ ^2\Pi\ (Q_1)$
$^2\Gamma_{9/2,7/2}$	Yes	$(030)\ ^2\Phi\ (Q_1, P_2)$
$\kappa^2\Delta$	No	$(030)\ ^2\Phi\ (Q_1)$; $(030)\ ^2\Pi\ (Q_1)$
$\kappa^2\Sigma$	Yes	$(030)\ ^2\Pi\ (Q_1 + Q_2)$
$(11^20)\ ^2\Delta_{5/2}$	No	$(030)\ ^2\Pi\ (Q_1)$; $(010)\ ^2\Pi\ (Q_1)$
$(00^11)\ ^2\Pi_{3/2,1/2}$	Yes	$(001)\ ^2\Sigma\ (Q_1, P_2)$
$(040)\ \mu^2\Pi$	No	$(040)\ ^2\Delta\ (Q_1)$; $(040)\ ^2\Sigma\ (Q_1)$
$\mu^2\Phi$	No	$(040)\ ^2\Delta\ (Q_1)$; $(040)\ ^2\Gamma\ (Q_1)$
$^2H_{11/2,9/2}$	Yes	$(040)\ ^2\Gamma\ (Q_1, P_2)$
$\kappa^2\Phi$	No	$(040)\ ^2\Delta\ (Q_1)$
$\kappa^2\Pi$	No	$(040)\ ^2\Delta\ (Q_1)$; $(040)\ ^2\Sigma\ (Q_1)$
$(050)\ ^2I_{13/2,11/2}$	No	$(050)\ ^2H\ (Q_1, P_2)$

[a]Overlapped transition.

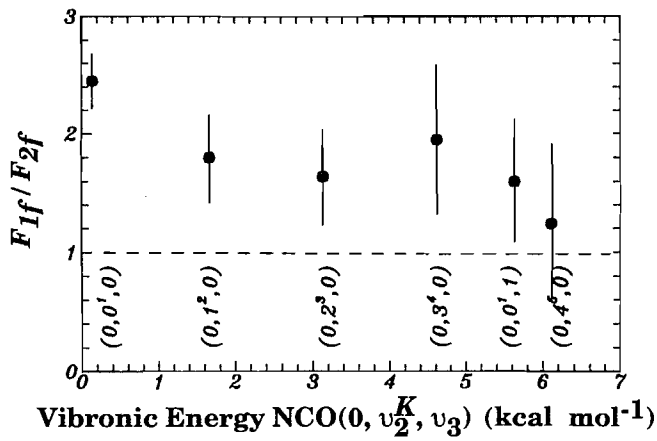

FIG. 11. Final product state distribution for spin-orbits states of NCO for an E_0 of 0.8 kcal mol^{-1} vs. internal energy. The vertical lines are the uncertainty in the data of $\pm 2\sigma$. Only the branches observed are plotted with the levels denoted by F_{1f} (the lower energetic state) and F_{2f} (the upper state), see Fig. 2. Note the apparent decrease in the preference for the lower energetic spin-orbit state as the product vibronic energy increases.

range, but the lower spin-orbit component is favored by a factor of 1.9, slightly smaller than that for the ground vibronic manifold. Again, this ratio is in good agreement with the independent measurement reported in Fig. 10.

4. Discussion

A. *Comparison with kinetic rate constants*

As mentioned in the Introduction, it has only been over the past few years that the thermal rate constants for reaction [1] have been measured reliably over a wide temperature range by several groups (4–7). The reported negative temperature dependence (though in a non-Arrhenius form) of the thermal rate constants was conjectured to be typical of radical–radical reactions possessing little or no barrier to reaction. Stoecklin et al. (23) recently applied a rotationally adiabatic capture theory, combined with various sudden approximations, to calculate rate constants and their temperature dependence for reaction [1]. In their approach, the reaction rate is determined by "capture" arising from the long-range interaction between the dipole moment of CN and the quadrupole moment of O_2. The calculated rotationally selected rate constants, $k_j(T)$, were found to increase with increasing temperature but decrease significantly with increasing j at a given temperature, T. As a result of this very strong sensitivity of $k_j(T)$ to j, the overall thermal rate constant exhibits a negative temperature dependence. When compared with the experimental results, however, the calculated values display a more gradual temperature dependence. For example, the calculated value at 26 K of $\sim 0.9 \times 10^{-10}$ cm^3 molec^{-1} s^{-1} is in excellent agreement with the experimental value of 1.08×10^{-10} cm^3 molec^{-1} s^{-1}. However, at room temperature the theoretical value is ~ 5 times greater than the experimental one. Stoecklin et al. (23) suggested that this discrepancy is likely due to the short-range chemical interactions or nonadiabatic electronic transitions involved in this reaction. Indeed, this suggestion has received considerable support from a more recent calculation (10) based on a "realistic" *ab initio* potential that fully incorporates the short-range interactions. By using a version of variational RRKM theory on this potential, Klippenstein and Kim (10) were able to decrease the discrepancy by a factor of approximately two. Although two different theories were employed to calculate the rate constant for reaction [1], both calculations dealt with only the rate of association between CN and O_2 so that they are only sensitive to the features of the potential energy surface in the entrance channel.

The observed negative temperature dependence of the ther-

Can. J. Chem. Downloaded from www.nrcresearchpress.com by EESC ESCOLA DE ENGENHARIA on 09/08/12
For personal use only.

Can. J. Chem. Downloaded from www.nrcresearchpress.com by EESC ESCOLA DE ENGENHARIA on 09/08/12
For personal use only.

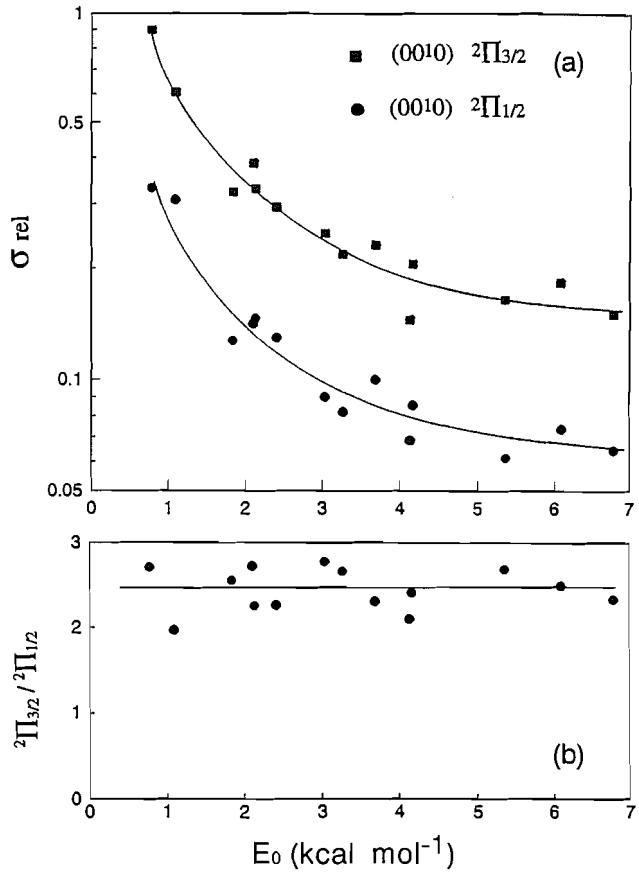

FIG. 12. (*a*) Excitation function for $^2\Pi_{3/2}(00^10)$, ■, and $^2\Pi_{1/2}(00^10)$, ●, manifold NCO produced in reaction [1]. Panel (*b*), ratio of the cross sections for the production of $^2\Pi_{3/2}$ and $^2\Pi_{1/2}$ of the ground vibronic state vs. E_0. The preference for the lower energetic spin-orbits state is independent of initial energy.

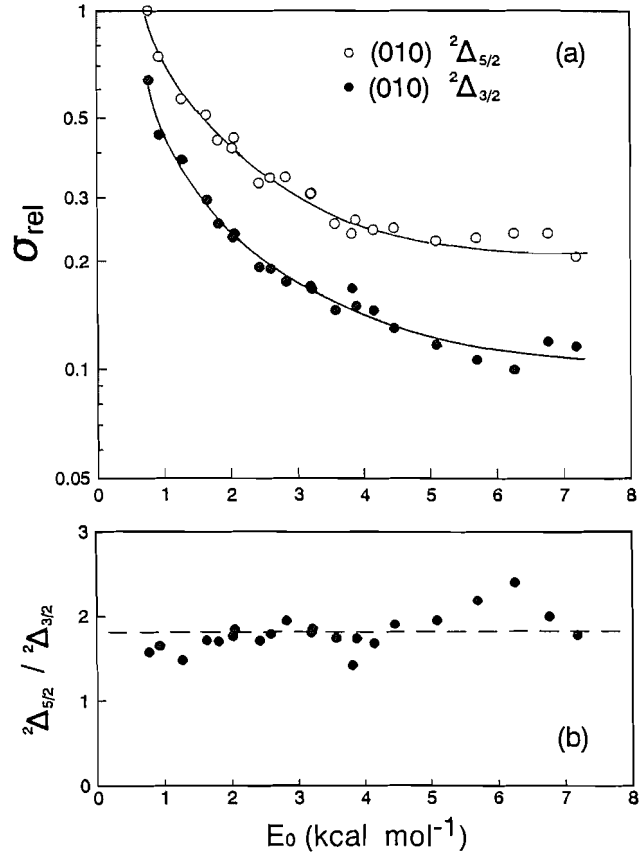

FIG. 13. (*a*) Excitation function for the unique Renner–Teller components, (○) $^2\Delta_{5/2}(01^20)$, and (●) $^2\Delta_{3/2}(01^20)$ for NCO produced in reaction [1]. Panel (*b*), same as Fig. 12, except ratio $^2\Delta_{5/2}$ and $^2\Delta_{3/2}$ of (01^20) is plotted. Note that the preference for the lower energetic spin-orbit manifold is slightly smaller upon bending excitation.

mal rate constant is in qualitative accord with the rapidly decreasing excitation functions found in this work, Figs. 12 and 13. More quantitative comparison can be made by noticing that the general shape of the excitation function shows no sign of a reaction barrier even at E_0 as low as 0.7 kcal mol^{-1}. Moreover, the vibronic-resolved cross sections shown in Figs. 12 and 13 exhibit the same dependence on translational energy, and these four states account for nearly 80% of the final NCO product state distribution. The cross sections, σ, shown in Figs. 12 and 13 have a functional dependence of E_0 of $\sigma \propto E_0^{-1}\exp(0.0323E_0)$, and it is anticipated that the total reaction cross section to produce all product states will behave in a similar fashion. Using this analytic expression and averaging it over a Boltzmann translational energy distribution, the temperature dependence of a molecular beam derived thermal rate constant was determined. These results and the available thermal rate constant data are summarized in Fig. 14. The molecular beam derived rate constant was arbitrarily normalized to the 298 K data of Durant and Tully (4). Considering that this comparison is made over such a wide range of the temperature, from 26 K to 3800 K, the overall agreement between the molecular beam data and the thermal rate constant data is quite gratifying and remarkable. Even at the low- and high-temperature ends, the deviations are no more than 50%. At the low-temperature end, the deviation could easily arise from an imprecise extrapolation of $\sigma(E_0)$ from the beam results. At the high-temperature end, the small difference may reflect an increasingly important role of channel [2] because the overall reaction rate constant for removal of reactants is measured in thermal experiments, whereas only the NCO + O product channel was monitored in the beam experiments.

The near-perfect agreement between thermal rate constant measurements and the beam-derived rate constant, shown in Fig. 14, provides compelling evidence not only that channel [1] dominates the overall reaction rate constant, but also that the negative temperature dependence for this reaction is entirely determined by the translational energy dependence of the reaction cross section for the lowest few reactant rotational states. It is instructive to examine this comparison more closely. Under molecular beam conditions the initial rotational state distribution of CN ($^2\Sigma^+$) was measured to have 90% of the CN radicals in the lowest two rotational states, Fig. 1. Similarly, the O_2 molecule is expected to be rotationally cold, although the rotational state distribution was not measured. This should be contrasted with the thermal situation where many rotational states of the reactants are populated and the distribution shifts dramatically towards higher values j with increasing temperature. Without losing generality let us consider the state-specific rate constant for a single rotor. The thermal rate constant, $k(T)$, can be expressed as a sum over the rotational state-specific rate constant, $k_j(T)$, weighted by the corresponding population factor, $P_j(T)$, i.e.,

$$[4] \quad k(T) = \sum_j P_j(T)k_j(T)$$

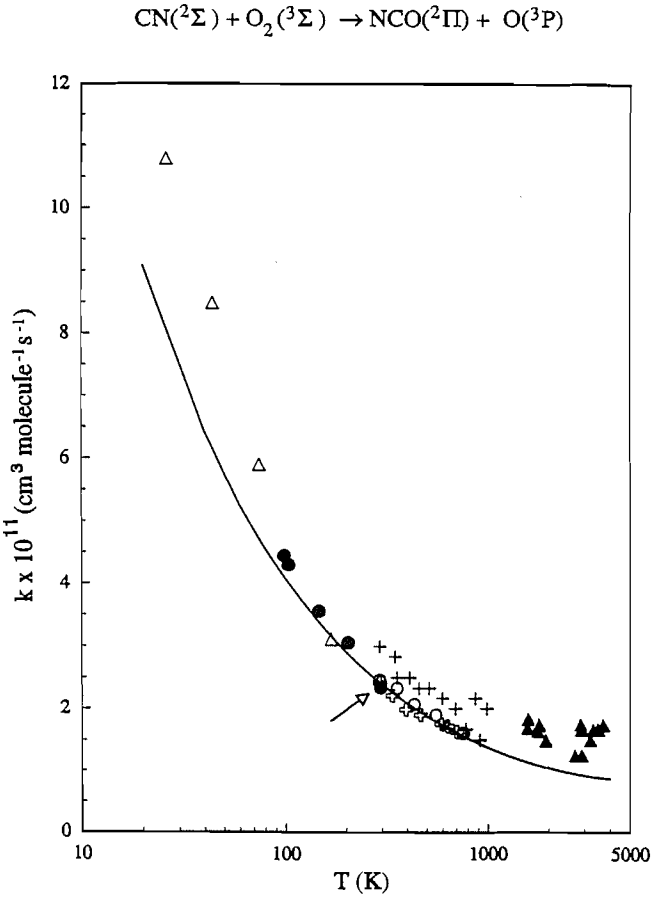

FIG. 14. A comparison of a Boltzmann averaged excitation function, Figs. 12(*a*) and 13(*a*), for essentially CN ($J = 0$) and O_2 ($J = 1$) reactants with available thermal rate constant data: (Δ) Sims et al. 5 (*c*); (●) Sims and Smith, 5(*b*); (⌖) Sims and Smith, 5(*a*); (○) Durant and Tully (4); (+) Atakan et al. (6); and (▲ Davidson et al. (7). Solid line thermal rate constant derived from fit to excitation function, this work (see text). The arrow indicates where the molecular beam derived rate constant was normalized to the kinetic data.

This may be rearranged to factor out the Boltzmann-averaged molecular beam derived rate constant, $k_{j=0}(T)$, as

$$[5] \quad k(T) = k_{j=0}(T) \sum_j P_j(T)(k_j(T)/k_{j=0}(T))$$

The excellent agreement in the temperature dependencies between $k(T)$ and $k_{j=0}(T)$, as shown in Fig. 14, implies that

$$[6] \quad \sum_j P_j(T)(k_j(T)/k_{j=0}(T)) \sim \text{constant}$$

Because $P_j(T)$ is simply the normalized Boltzmann factor for the rotational state j of the reactant, i.e., $\Sigma_j P_j(T) = 1$, it is very likely that $k_j(T)/k_{j=0}(T) \sim$ constant, or a near j-independence of rotational state-selected rate constant, $k_j(T)$, is implied. These implications are in sharp contrast to the above-mentioned predictions of the rotationally adiabatic capture theory. As will be argued later, the assumption of rotational adiabaticity may still be valid for this reaction. Hence, entirely consistent with previous theoretical suggestions (23), the failure of the adiabatic capture theory is likely caused by the dominance of short-range chemical interactions rather than long-range electrostatic forces in defining the transition-state region for this reaction.

B. Energy disposal and vibronic state distribution

A nearly complete characterization of the product state distributions was carried out in this study. Cold distributions were found for all internal degrees of freedom of the NCO product. Assuming a similar rotational state distribution for all vibronic states, as suggested by the LIF bandhead shape, the energy disposal into the NCO product is summarized as follows: $\langle f \rangle_{\text{elect.}} \sim 0.6\%$, $\langle f \rangle_{\text{rot.}} \sim 1.7\%$, $\langle f \rangle_{\text{bend}} \sim 5.5\%$, and $\langle f \rangle_{\text{asym.stretch}} \sim 1.3\%$. The remaining~91% of the available energy must then be channelled into O-atom internal states and (or) translational motion of the products. Energetically, only the ground electronic state, ^3P, of the O-atom is allowed. Even if all O-atoms from the reaction are produced in the highest spin-orbit state, $^3P_0$, there still remains ~85% of the available energy for the product translational degree of freedom. Such high specificity in energy disposal is very difficult to reconcile if the NCOO intermediate has a deep potential well with a small exit channel barrier. Under such circumstances, some degree of energy randomization would be expected.

In terms of vibronic state distribution, Fig. 10 reveals (as guided by the connecting lines) that, except for ground vibronic states, the population for a given spin-orbit or Renner–Teller component exhibits a near-exponential decline with the vibrational energy content of the NCO product. Furthermore, within a factor of two, the slopes of these exponential declines are roughly the same regardless of the nature of the final state components. The vibronic distribution for this reaction was also determined by two other groups using a pump-and-probe technique under bulb conditions. Sauder et al. (11) photolyzed C_2N_2 at 193 nm and probed the NCO product vibronic state distribution by LIF. Phillips et al. (9) used a very similar procedure, except that NCNO was photolyzed at 532 nm to generate the +CN radical. The latter technique prepares CN radicals with little internal excitation energy, while photolysis of C_2N_2 produces a rotationally and translationally hot CN reagent. In spite of the different methods of generating the CN radical, relaxation of rotational and translational degrees of freedom is assumed to occur more rapidly than CN reaction. The initial translational energy in the molecular beam experiments, $E_0 = 0.8$ kcal mol^{-1}, is very close to the mean kinetic energy available to 300 K reactants, so that all three studies, Sauder et al. (11) Phillips et al. (9), and this work should be comparable, at least as far as initial translational energy is concerned.

The results for the nascent unique level vibronic state distributions of the bending manifold are shown in Fig. 15 for all three studies. There is clearly a striking difference between the measurements from the beam and the bulb experiments. Substantially more excitation in the bending motion of NCO was found in the bulb experiments, even though there is only a qualitative agreement between their distributions. In the beam experiments it was found that bending excitation was the preferred mode and that the unique levels were always more populated. On the other hand, under bulb conditions, substantially more population was found in the non-unique levels of the bending excitations as well in the stretching modes. Thus, if the total vibronic state distribution (i.e., including all contributions for a given $(v_1 v^K 2 v_3)$ vibronic manifold) is examined, the difference between the beam and bulb results becomes even more dramatic. For example, nearly 70% of the NCO was found to be formed in the two spin-orbit states of the ground vibronic level in this work, while only ~3% was estimated under bulb conditions!

Can. J. Chem. Downloaded from www.nrcresearchpress.com by EESC ESCOLA DE ENGENHARIA on 09/08/12
For personal use only.

Can. J. Chem. Downloaded from www.nrcresearchpress.com by EESC ESCOLA DE ENGENHARIA on 09/08/12
For personal use only.

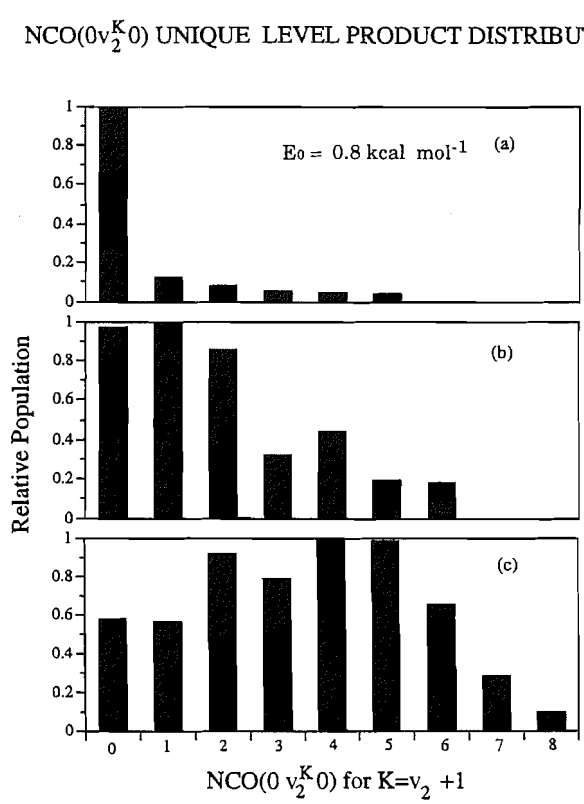

FIG. 15. A comparison of initial NCO unique level vibronic state distributions determined for reaction [1]. Top panel, this work; middle, Sauder et al. (11); and bottom, Phillips et al. (9). Note the dramatic difference in the molecular beam derived distribution for rotationally unexcited reactants and the bulbderived distribution for a "thermalized" rotational state distribution of both reactants.

Some of these discrepancies could arise from the different ways of extracting the population information from LIF spectra. Based on available spectroscopic data, Sauder et al. (11) calculated NCO $A \leftrightarrow X$ vibronic band strengths and used these results to deduce population distributions. On the other hand Phillips et al. (9) assumed that the bandhead intensities of the unique levels could be used to directly determine their populations. A similar assumption was made in this work; however, here the LIF spectra were taken under near-saturated conditions to ensure their validity. Judging from the reported vibronic band strength values and the data from dispersed fluorescence measurements,[3] only a minor deviation is anticipated between the two population-extraction approaches. This anticipation is also consistent with the appearance of the reported LIF spectra, Fig. 9 of this work, Fig. 3 of ref. 9, and Fig. 7 of ref. 11. A second problem concerns the extent of relaxation in the bulb experiments. Two kinds of vibronic relaxation can take place. First, there are collision-induced intermixing processes among the spin-orbit and Renner–Teller components in a given bending vibronic manifold. A recent study (24) of the inelastic scattering of NCO + He in this laboratory clearly demonstrated that these intermixing processes are highly selective and can be as efficient as rotational relaxation. Thus, these rapid processes could distort the vibronic component populations within a given vibrational manifold under bulb conditions. Second, there are collisional relaxation processes that change vibrational quantum numbers, i.e., the typical V–V and V–(R,T) processes similar to those for closed-shell molecules. These processes were examined in the bulb experiments by monitoring the temporal profiles of the LIF signals as a function of the time delay between the pump and probe lasers. The estimated relaxation rate constants, on the order of 10^{-13} cm^3 molec^{-1} s^{-1}, are consistent with those obtained for NCO + noble gases from an independent study (25). Thus, it appears that although the relative populations among the spin-orbit and Renner–Teller components could be partially equilibrated in the bulb experiments, the overall vibronic distribution should still largely reflect the nascent one. Yet, as shown in Fig. 15, the bulb experiments yielded much hotter distributions than the beam results.

The origin of these differences is quite intriguing. It can be reconciled if there is a strong dependence of the NCO vibrational distribution on the initial CN and (or) O_2 rotational states, as has been discussed in previous work (9, 11). Briefly, this strong dependence on reactant rotational states could arise from an adiabatic correlation between the bending excitation in the NCO product and the rotations of the reagents. Adiabaticity implies a retention of quantum state throughout a reactive collision. A low (high)-j reagent will then transform into a low (high) excitation in the bending motion of the product. A similar concept was also introduced in a recent theoretical calculation by Clary (26) on a diatom + diatom reaction system, H_2 + OH $\rightarrow$ H_2O + H. In these quantum scattering calculations it was found that there was a strong correlation between the spectator rotor, OH(j) in this case, and H_2O bending excitation. This observation was rationalized by a Franck–Condon projection of the bending motion of H_2O onto the rotational quantum states of the spectator diatom, OH. Clary noted that this correlation could be a unique feature, and quite general for many other diatom + diatom systems. It appears that the comparison of NCO vibronic distributions from the beam and the bulb studies provides an excellent experimental example of this prediction. From this view, the difference in vibronic bending excitation reported in the two bulb experiments may well arise from slight differences in the initial rotational state distribution of CN, the spectator rotor. Again, if the NCOO intermediate involves a long-lived complex, such strong adiabaticity would be lost due to strong couplings of the internal motions in the complex.

The above-mentioned adiabatic correlation is intimately related to the more familiar concept of vibrational adiabaticity often encountered in reaction dynamics (27). In the case of a simple A + BC system, there is the notion of a vibrationally adiabatic barrier to the reaction in interpreting the effect of reagent vibrational excitation on the reaction dynamics, as well as the use of vibrationally adiabatic transition-state theory analysis for rate constant calculations (28). In the case of AB + CD (or A + BCD) vibrational adiabaticity has also been invoked for describing the spectator bond (or mode specificity in the triatom). In these cases adiabaticity involves the "conserved" vibrational motion, which is only weakly coupled to the reaction coordinate and consequently exhibits little change in character, e.g., bond length and frequency, throughout the reaction process, or at least during the motion up to the transition state. One intriguing aspect of the present reagent-rotation to product-bend correlation is the large disparity in their energy content as rotational quantum states evolve through bending motions in the transition state and then finally transform into product-bending states. This situation bears some resemblance to the well-known correlation found in direct photofragment processes (29), in which the rotational distribution of the diatom fragment is often found to be strongly correlated with the

Can. J. Chem. Downloaded from www.nrcresearchpress.com by EESC ESCOLA DE ENGENHARIA on 09/08/12
For personal use only.

bending motion of the parent molecule. However, this half-collision correlation arises from the sudden nature of the Franck–Condon projection of the optical transition and the limit of negligible exit channel effects. In this spirit, one would perhaps expect that for a chemical reaction such adiabaticity between reagent rotation and product bend may not be strong enough to survive at all due to the forces involved in the chemical transformation and the smallness of rotational energy spacings. Evidence gathered thus far, however, points to the opposite finding, at least, for the spectator rotor. Clearly, weak anisotropies of the interaction potential with small barriers in both the entrance and exit channels will be the prerequisites for the existence of such a correlation. More importantly, this interpretation, if correct, will have significant implications for future studies of polyatomic reaction dynamics. It should at least send a cautious warning when one tries to infer the transition state geometry and (or) potential energy surface from product rovibrational state distributions for a polyatomic reaction system, a usual practice in the study of a typical A + BC reaction.

C. Spin-orbit and Renner–Teller propensities

Under beam conditions, within a given bending excitation the unique levels are always preferentially populated, as is evident from Fig. 10. The unique levels are so called because the electronic orbital angular momentum is largely unquenched (30) and still strongly coupled to the, now nonlinear, internuclear axis, even though the bending vibration is excited. As a consequence, electron spin can readily couple to Λ, the projection of electronic orbital angular momentum on the internuclear axis, and the spin-orbit interaction is retained. For all other Renner–Teller components Λ is no longer a good quantum number and the spin-orbit interaction is quenched. In other words, Renner–Teller and spin-orbit interactions are two competing forces. It is speculated that the observed propensity for unique levels may be the imprint of a linear geometry for the NC··O backbone in the transition state, because it is in this region that the electronic configuration for the NCO product is established. It is gratifying to note that this speculation is in accord with a recent *ab initio* calculation (10), as well as with a simple molecular orbital picture outlined in ref. 11. Due to the competing nature of spin-orbit and Renner–Teller interactions, at higher bending excitations the Renner–Teller interaction will prevail and the strength of the spin-orbit interaction will weaken. Thus, the spin-orbit propensity is anticipated to diminish with increasing bending excitation. This expectation is nicely borne out in Fig. 11, in which a statistical spin-orbit ratio is approached at higher bending excitations. The *ab initio* results (10) also predicted a C—O—O angle to be ~115°; however, a bent NCO··O structure is not inconsistent with the cold rotational and bending distributions observed in this study. The *ab initio* calculations (10) revealed that as the reaction proceeds the CO bond formation is accompanied by a gradual dissolution of the O_2 bond. As a result, only a small torque is expected to be exerted on the NCO product by a nonimpulsive departure of the O atom.

5. Conclusion

The reaction of $CN + O_2 \rightarrow NCO + O$ has been studied under crossed-beam conditions. A nearly complete characterization of energy disposal and excitation functions has been reported. Through extensive comparisons with previous kinetic and dynamic studies a clearer picture of this reaction has emerged. It is a barrierless radical–radical reaction. The attractive nature of the potential in the entrance channel results in a rapid decrease in reaction cross sections with increasing translational energy. This in turn leads to a negative temperature dependence of the thermal rate constant. The near j-independence of state-specific rate constants implies a weak anisotropy in the entrance channel. The association of CN and O_2 forms, at most, a weakly bound collision intermediate, which has little influence on the reaction dynamics. As a result, the reaction behaves more like a direct O-atom abstraction process. This is in sharp contrast to a typical radical–radical reaction, in which a deep potential well is usually involved, resulting in complex formation with the reaction proceeding via successive bond-forming, bond-breaking processes. A strong correlation between CN rotation ("spectator" rotor) and NCO bending excitation was conjectured. Weak anisotropies of the interaction potential with small or no barriers in both the entrance and exit channels are the necessary conditions for such an adiabatic correlation. This finding is believed to be generic and should have significant implications in our further understanding of polyatomic reaction dynamics in general. For example, will the concept of a rotationally adiabatic transition state be essential in our theoretical description of reaction kinetics/dynamics? Many of the fine-structure propensities observed in this work are not yet fully understood, e.g., the K-doublet propensity, the preferences for spin-orbit components and non-unique levels (i.e., $\Sigma >$ the others)? Further theoretical developments in this area will be needed.

Acknowledgments

We thank Dr. F.J. Northrup for providing the NCO dispersed fluorescence data prior to publication. This work was supported by the U.S. Department of Energy, Office of Basic Energy Science, Division of Chemical Sciences, under Contract W-31-109-ENG-38.

1. D.R. Cyr, R.E. Continetti, R.B. Metz, D.L. Osborn, and D.M. Neumark. J. Chem. Phys. **97**, 4937 (1992).
2. K.J. Schmatjko and J. Wolfrum. Ber. Bunsen-Ges. Phys. Chem. **82**, 419 (1978).
3. W.F. Cooper, J. Park, and J.F. Hershberger. J. Phys. Chem. **97**, 3283 (1993).
4. J.L. Durant, Jr. and F.P. Tully. Chem. Phys. Lett. **154**, 568 (1989).
5. (*a*) I.R. Sims and I.W.M. Smith. J. Chem. Soc. Faraday Trans. 2, **84**, 527 (1988); (*b*) Chem. Phys. Lett. **151**, 481 (1988); (*c*) I.R. Sims, J.L. Queffelec, A. Defrance, C. Rebrio-Rowe, D. Travers, B.R. Rowe, and I.W.M. Smith. J. Chem. Phys. **97**, 8798 (1992).
6. B. Atakan, A. Jacobs, M. Wahl, R. Weller and J. Wolfrum. Chem. Phys. Lett. **154**, 449 (1989).
7. D.F. Davidson, A.J. Dean, M.D. DiRosa, and R.K. Hanson. Int. J. Chem. Kinet. **23**, 1035 (1991).
8. (*a*) D.C. Clary. Mol. Phys. **53**, 1 (1984); (*b*) Commun. At. Mol. Phys. **24**, 145 (1990).
9. L.F. Phillips, I.W.M. Smith, R.P. Tuckett, and C.J. Whitham. Chem. Phys. Lett. **183**, 254 (1991).
10. S.J. Klippenstein and Y.W. Kim. J. Chem. Phys. **99**, 5790 (1993).
11. D.G. Sauder, D. Patel-Misra, and P.J. Dagdigian. J. Chem. Phys. **95**, 1696 (1991).
12. R.G. Macdonald and K. Liu. J. Chem. Phys. **91**, 821 (1989).
13. R. Engleman Jr. J. Mol. Spectrosc. **49**, 106 (1974).
14. R. Lu, J.B. Halpern, and W.M. Jackson. J. Phys. Chem. **88**, 3419 (1984).
15. (*a*) R.N. Dixon. Philos. Trans. R. Soc. London, Ser. A, **252**, 165 (1960); (*b*) P.S.H. Bolman, J.M. Brown, A. Carrington, I. Kopp, and P.A. Ramsey. Proc. R. Soc. London, Ser. A, **343**, 17 (1975).
16. I. Kovacs. Rotational structure in the spectra of diatomic molecules. Elsevier, New York. 1969.

cules. Elsevier, New York. 1969.
17. D.M. Sonnenfroh and K. Liu. Chem. Phys. Lett. **176**, 183 (1991).
18. D.M. Sonnenfroh, R.G. Macdonald, and K. Liu. J. Chem. Phys. **93**, 1478 (1990).
19. (*a*) R.G. Macdonald and K. Liu. J. Phys. Chem. **95**, 9630 (1991); (*b*) J. Chem. Phys. **97**, 978 (1992).
20. D.M. Sonnenfroh, R.G. Macdonald, and K. Liu. J. Chem. Phys. **94**, 6508 (1991).
21. D. Patel-Misa, D.G. Sauder, and P.J. Dagdigian. J. Chem. Phys. **93**, 5448 (1990).
22. (*a*) F.J. Northrup, M. Wu, and T.J. Sears. J. Chem. Phys. **96**, 7218 (1992); (*b*) M. Wu, F.J. Northrup, and T.J. Sears. J. Chem. Phys. **97**, 4583 (1992).
23. T. Stoecklin, C.E. Dateo, and D.C. Clary. J. Chem. Soc. Faraday Trans. **87**, 1667 (1991).
24. R.G. Macdonald and K. Liu. J. Chem. Phys. **98**, 3716 (1993).
25. C.J. Astbury, G. Hancock, and K.G. McKendrick. J. Chem. Soc. Faraday. Trans. **89**, 405 (1993).
26. D.C. Clary. J. Chem. Phys. **96**, 3656 (1992).
27. I.W.M. Smith. Kinetics and dynamics of elementary gas reactions. Butterworth, London. 1980.
28. D.G. Truhlar, A.D. Isaacson, and B.C. Garrett. Theory of chemical reaction dynamics. *Edited by* M.J. Baer. CRC Press, Boca Raton, Fla. 1985.
29. R. Schinke. Annu. Rev. Phys. Chem. **39**, 39 (1988).
30. Ch. Jungen and A.J. Merer. *In* Modern spectroscopy: modern research. Vol. II. *Edited by* K.N. Rao. Academic, New York. 1976. Chap. 2.

Can. J. Chem. Downloaded from www.nrcresearchpress.com by EESC ESCOLA DE ENGENHARIA on 09/08/12
For personal use only.

Molecules in strong laser fields: vibrational inversion and harmonic generation

ERIC E. AUBANEL AND ANDRÉ D. BANDRAUK[1]

Laboratoire de chimie théorique, Faculté des sciences, Université de Sherbrooke, Sherbrooke, QC J1K 2R1, Canada

Received July 2, 1993

This paper is dedicated to Professor John C. Polanyi on the occasion of his 65th birthday

ERIC E. AUBANEL and ANDRÉ D. BANDRAUK. Can. J. Chem. **72**, 673 (1994).

We examine two consequences of the unique behaviour of molecules in strong fields. First, by time gating of laser-induced avoided crossings with femtosecond laser pulses, one can obtain efficient vibrational inversion into a narrow distribution of vibrational levels of a molecular ion. We demonstrate this by numerical solution of the time-dependent Schrödinger equation for H_2^+. Second, we show results of numerical calculation with vibrationally excited H_2^+ of harmonic generation up to the 11th order of an intense 1064-nm laser. We predict that competition of photodissociation can be minimized by trapping the molecule in high-field-induced potential wells, thus enhancing the high-order harmonic generation process. Furthermore, the harmonic spectrum can serve as a measure of the structure of these laser-induced potentials.

ERIC E. AUBANEL et ANDRÉ D. BANDRAUK. Can. J. Chem. **72**, 673 (1994).

On examine deux conséquences du comportement particulier des molécules dans un champ fort. En premier lieu, la provocation, à l'aide de pulsations laser de femtoseconde, d'un déclenchement intermittent des croisements évités par une induction au laser permet d'obtenir une inversion vibrationnelle efficace dans une distribution étroite des niveaux vibrationnels d'un ion moléculaire. On démontre cette affirmation par une solution numérique de l'équation de Schrödinger en fonction du temps pour le H_2^+. En deuxième lieu, on présente les résultats de calculs numériques avec du H_2^+ vibrationnellement excité d'une génération harmonique jusqu'au 11^e ordre d'un laser intense à 1064 nm. On fait la prédiction qu'il est possible de minimiser la compétition de la dissociation en piégeant la molécule dans des puits de potentiel de champ élevé et que l'on peut ainsi améliorer le processus de génération harmonique d'ordre élevé. De plus, le spectre harmonique peut servir à la mesure de la structure de ces potentiels induits au laser.

[Traduit par la rédaction]

1. Introduction

The study of molecules in strong fields is establishing itself as an important part of chemical physics, particularly because of its role in the control of photodissociation dynamics (see, e.g., ref. 1). Strong laser fields induce high-order multiphoton absorption and emission that can lead to the creation of field induced potentials (2). In this paper we will show how one can exploit field-induced potentials to obtain efficient vibrational inversion, and multiphoton absorptions to generate high-order harmonics of a 1-μm laser.

High vibrational excitation in a molecule is desirable either as a means to achieve selective dissociation of chemical bonds or to prepare selectively excited reactants. Over 30 years ago, J.C. Polanyi proposed an infrared laser based on vibrational excitation achieved by chemical reaction in the gas phase (3). Other ways to achieve high vibrational excitation include the climbing of the vibrational ladder using a frequency-chirped infrared laser pulse (4) and excitation via an electronically excited state with visible–ultraviolet lasers (stimulated emission pumping, SEP) (5). In the case of infrared-inactive molecules, the SEP method is required. This method is complicated, however, if the lifetime of the excited state is shorter than the interaction time with the laser needed to achieve complete inversion. If the electronically excited state is bound, one can use the STIRAP (stimulated Raman adiabatic passage) or counterintuitive method (6), where the order of the pump and Stokes lasers is reversed from the usual intuitive order. If the excited electronic state is repulsive, a special high-field method is necessary, as was recently examined in detail by us (7), so that stimulated emission becomes more rapid than dissociation.

In this paper we will summarize our method, which we call vibrational inversion via time gating of laser-induced avoided crossings, and present new results of high harmonic generation from vibrationally excited H_2^+. The latter will show interesting features of vibrational trapping via the laser-induced avoided-crossing mechanism.

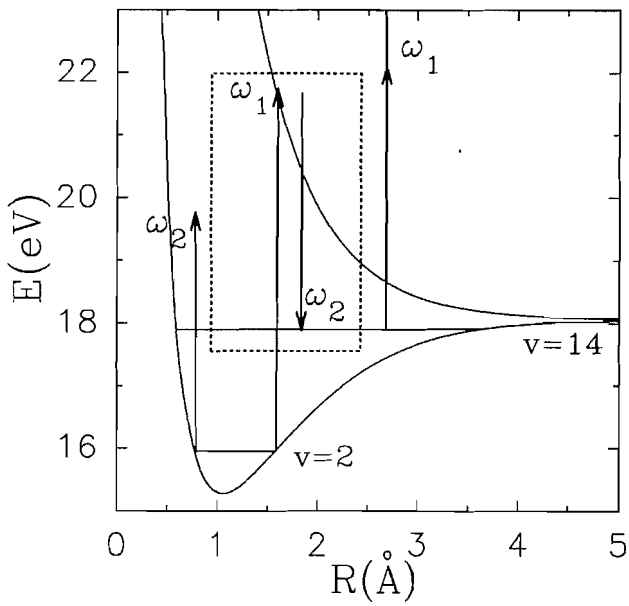

FIG. 1. Inversion scheme (inside dotted box) for H_2^+, starting from $v = 2$ and ending at $v = 14$, using two lasers of wavelengths $\lambda_1 = 213$ nm and $\lambda_2 = 320$ nm. Also shown are two one-photon nonresonant processes that can compete.

2. Vibrational inversion

Consider the problem of inverting the vibrational population of H_2^+ in its bound $^2\Sigma_g^+$ state. One must do so via the excited $^2\Sigma_u^+$ state. Figure 1 (inside dotted lines) illustrates the case for inver-

[1]Author to whom correspondence may be addressed.

Can. J. Chem. Downloaded from www.nrcresearchpress.com by EESC ESCOLA DE ENGENHARIA on 09/08/12
For personal use only.

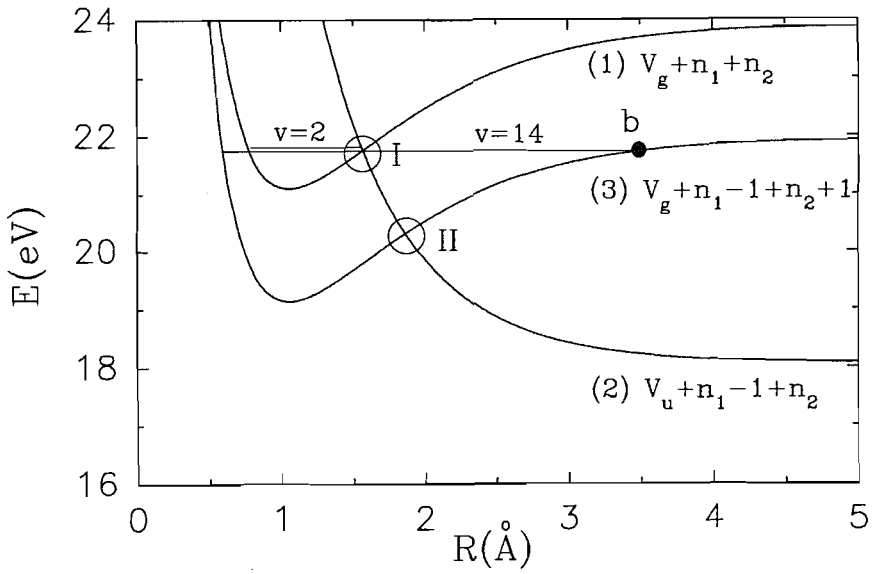

FIG. 2. Three-dressed-state representation of the excitation scheme of Fig. 1, showing crossing I due to laser 1 and crossing II due to laser 2.

sion from vibrational level $v = 2$ to $v = 14$ using lasers of frequencies $\lambda_1 = 213$ nm and $\lambda_2 = 320$ nm. If one simply applies laser 1 followed by laser 2, most of the excitation is lost as photodissociation. The same thing happens if one applies the lasers in the reverse order, unlike the situation in Na_2 (6) where the excited electronic state is bound, unless the laser intensities are high enough. The reason for this is evident when one considers the dressed states of the molecule–field system (Fig. 2) (1): (*i*) $V_g + n_1\hbar\omega_1 + n_2\hbar\omega_2$, where population initially resides; (*ii*) $V_u + (n_1 - 1)\hbar\omega_1 + n_2\hbar\omega_2$; and (*iii*) $V_g + (n_1 - 1)\hbar\omega_1 + (n_2 + 1)\hbar\omega_2$. The second state corresponds to absorption of one photon ω_1 and the third state to subsequent emission of one photon ω_2. Curve crossings I and II due to lasers 1 and 2, respectively, become avoided crossings as each laser is turned on, through the field–molecule coupling:

$$[1] \quad \hbar\Omega_i(\text{eV}) = 1.45 \times 10^{-7} \sqrt{I_i\,(\text{W/cm}^2)}\ \mu\ (\text{a.u.})$$

where Ω_i is the Rabi frequency of laser i ($i = 1, 2$), I is the laser intensity, and $\mu = eR/2$ is the electronic transition moment (8). Note that we do not take into account rotational excitation, so we place the molecule parallel to the laser polarization.

One can see from Fig. 2 how the counterintuitive method might work: first turn on laser 2 so that crossing II is adiabatic (1) (i.e., the crossing probability between the two field–molecule states is high), then turn on laser 1 to release the initial vibrational wave function through crossing I, and finally turn off both lasers before the wave packet returns to the initial state after hitting turning point *b*. This leaves H_2^+ in the ground state at $v = 14$. For crossing II to be adiabatic, laser 2 must be very intense ($>10^{13}$ W/cm^2). Laser 1 must be intense as well, to dissociate all of the initial wave function in a time shorter than the return time from turning point *b*.

The discussion in the previous paragraph has only taken into account resonant transitions (inside the dotted line, Fig. 1). At the high intensity required to make crossing II adiabatic, the initial $v = 2$ state can be nonresonantly photodissociated with laser 2. The solution that we propose to avoid this problem is to apply two simultaneous pulses. Competition with other multiphoton nonresonant processes leads to possible dissociative loss into two channels: a nonresonant low kinetic energy channel corresponding to net absorption of one photon of frequency ω_2 from $v = 2$, which dominates at high intensity, and a resonant high kinetic energy channel corresponding to net absorption of one photon of frequency ω_1 from $v = 2$, which dominates at low intensity. An optimum intensity can be found that minimizes dissociative loss in both channels (7). Figure 3 shows the final bound state population after application of two simultaneous pulses of wavelengths $\lambda_1 = 213$ nm and $\lambda_2 = 320$ nm, having a 10-fs rise to a 13-fs plateau at 2×10^{13} W/cm^2 followed by a 10-fs fall, to H_2^+ in $v = 2$, from numerical solution of the time-dependent Schrödinger equation assuming the molecule to be aligned with the field polarization and neglecting rotational excitation (7). Less than 20% dissociation and almost complete

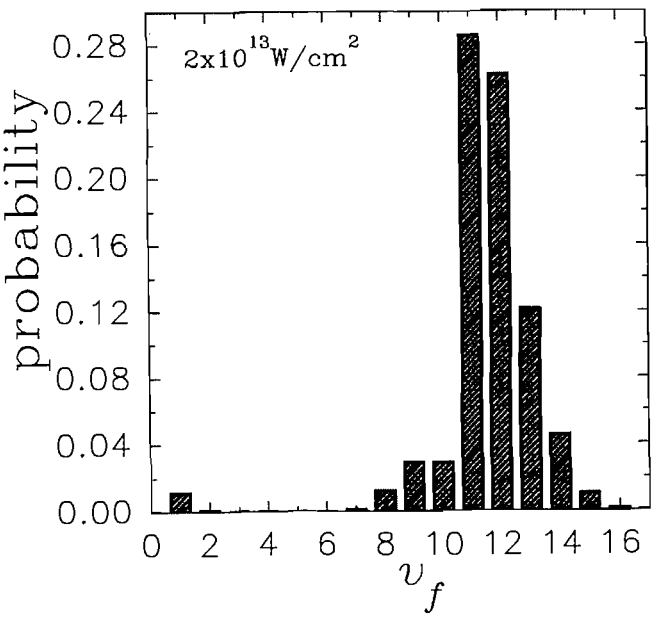

FIG. 3. Final vibrational populations of $^2\Sigma_g^+$ state from exact calculations of rotationless H_2^+ initially in $v = 2$, for two simultaneous pulses of wavelengths $\lambda_1 = 213$ nm and $\lambda_2 = 320$ nm, having a 10-fs rise to a 13-fs plateau at 2×10^{13} W/cm^2 followed by a 10-fs fall. The total final ground state population is 0.81.

Can. J. Chem. Downloaded from www.nrcresearchpress.com by EESC ESCOLA DE ENGENHARIA on 09/08/12
For personal use only.

Can. J. Chem. Downloaded from www.nrcresearchpress.com by EESC ESCOLA DE ENGENHARIA on 09/08/12
For personal use only.

inversion of the remaining bound population occurred into a distribution centered around $v = 11$. Inversion into $v = 14$ alone did not occur, owing to the large dynamic Stark shifts resulting from the high intensities used. We have also shown in ref. 7 that rotational excitation increases slightly the dissociative loss and broadens the distribution of excited vibrational levels.

Thus we have exploited the concept of laser-induced avoided crossings (Fig. 2), necessary to interpret high-field effects, to control population inversion. We expect that heavier diatomic molecular ions, with less steep repulsive potentials and slower nuclei, would allow even better control. The increased electronic complexity of heavier molecules would not pose a problem if resonant transitions were used, and if the two desired electronic potentials were linked by a particularly large transition moment, as is the case for charge-transfer transitions (9, 10).

3. Harmonic generation

One of the features of strong laser fields is their ability to induce a nonlinear response in atoms and molecules:

$$[2] \quad \mu^{ind}(t) = \alpha\, E(t) + \beta\, E(t)^2 + \gamma\, E(t)^3 + \ldots$$

where μ^{ind} is the induced dipole, $E(t)$ is the applied field, and α, β, and γ are the first-, second-, and third-order polarizabilities of the atom or molecule. For centrosymmetric systems such as H_2^+, one expects only odd-order polarizabilities ($\alpha,\gamma,\ldots$) to contribute. Even-order polarizabilities ($\beta,\ldots$) can only occur in symmetry broken systems (11). At laser intensities of the order 10^{13} W/cm^2 and higher, the response of the system becomes highly nonlinear, i.e., many terms in eq. [2] become large. For sinusoidal time-dependent fields, one can see that the second term in eq. [2] will produce oscillations of μ^{ind} at twice the laser frequency (second harmonic), the third term will produce oscillations at three times the laser frequency (third harmonic), and so on (11). The study of harmonic generation in atoms in intense fields has been actively studied in recent years (see, e.g., ref. 12), and now attention is being focused on molecules. Molecular ions in particular have been the focus of attention (9, 10) because of their charge resonance states, which couple very strongly to electromagnetic fields (transition moments proportional to $R/2$ (8); see eq. [1]).

The induced dipole in H_2^+ can be evaluated from a time series of the nuclear wave functions χ_g and χ_u obtained from numerical solution of the time-dependent Schrödinger equation. The induced dipole is obtained by evaluating the expectation value of the electronic coordinate along the laser polarization (z); here we use a double electronic state ($^2\Sigma_g^+$ and $^2\Sigma_u^+$) representation of H_2^+ and ignore rotation:

$$\begin{aligned}[3] \quad \mu_{H_2^+}^{ind}(t) &= \langle \chi_g(R,t)\, \phi_g(r,R) + \chi_u(R,t)\, \phi_u(r,R)\, |z|\, \phi_g(r,R) \\ &\quad \times \chi_g(R,t) + \phi_u(r,R)\, \chi_u(R,t) \rangle \\ &= 2\mathrm{Re}\langle \chi_g(R,t)\, \phi_g(r,R)\, |z|\, \phi_u(r,R)\, \chi_u(R,t) \rangle \\ &= \mathrm{Re}\langle \chi_g(R,t)\, |R|\, \chi_u(R,t) \rangle \end{aligned}$$

where r and R are the electronic and internuclear coordinates, respectively.

Before we proceed we should address three possible processes that could compete with harmonic generation in molecules: photoionization, photodissociation, and rotational excitation. The first is partly circumvented by the choice of molecular ions, which have higher ionization potentials than their parent neutral molecules. Calculations show that the ionization rate for H_2^+ exceeds 10^{13} s^{-1} for intensities greater than 10^{14} W/cm^2 (13). The competition between ionization, photodissociation, and harmonic generation is the subject of ongoing study by our group. We will address here only the competition of photodissociation with harmonic generation. The effect of rotation will be the subject of an upcoming publication (14).

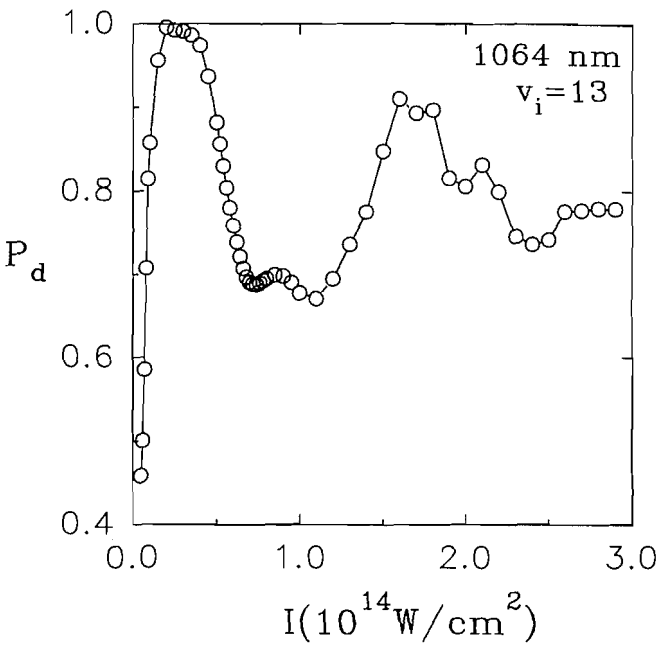

FIG. 4. Photodissociation probability from initial level $v = 13$, $\lambda = 1064$ nm, and 30-cycle pulse with 5-cycle linear ramp.

Numerical calculations have shown that molecular photodissociation can be stabilized in the presence of strong laser fields, owing to trapping in laser-induced bound states (1, 2, 15–18). An example of this is shown in Fig. 4, where the photodissociation probability P_d for H_2^+ starting in $v = 13$ and a laser wavelength of 1064 nm is shown as a function of peak intensity. The pulses used consisted of a 5-cycle linear ramp to a 25-cycle plateau (total time 106 fs). For details of the calculation, which employed a split-operator algorithm, refer to refs. 14–16. After a rise to complete dissociation, P_d goes through a series of minima, which can be attributed to trapping in laser-induced potential wells (14–16).

For our harmonic generation spectra we use a longer pulse of 200 cycles with the same 5-cycle linear ramp. The power spectra are calculated by Fourier transforming the dipole moment:

$$[4] \quad P(\omega_0 \nu) = \int_0^\infty \mu_{H_2^+}^{ind}(t)\, e^{i\omega_0 \nu t}\, \chi(t)\, dt$$

where ν is the harmonic order and ω_0 is the laser frequency; the function $\chi(t)$ is equal to one between 6 and 200 cycles, and zero otherwise; this reduces the noise in the spectra due to the turn-one of the pulse (10, 19). In Figs. 5 and 6 we show harmonic generation spectra at intensities of 7.4×10^{13} and 1.6×10^{14} W/cm^2, corresponding to a minimum and maximum in P_d (Fig. 4), respectively. In Fig. 5 one can see that split peaks at even and odd harmonics are produced up to 11th order. The even harmonics can be interpreted as odd harmonics that are split (Rabi splitting) by the strong laser field (9, 10). Alterna-

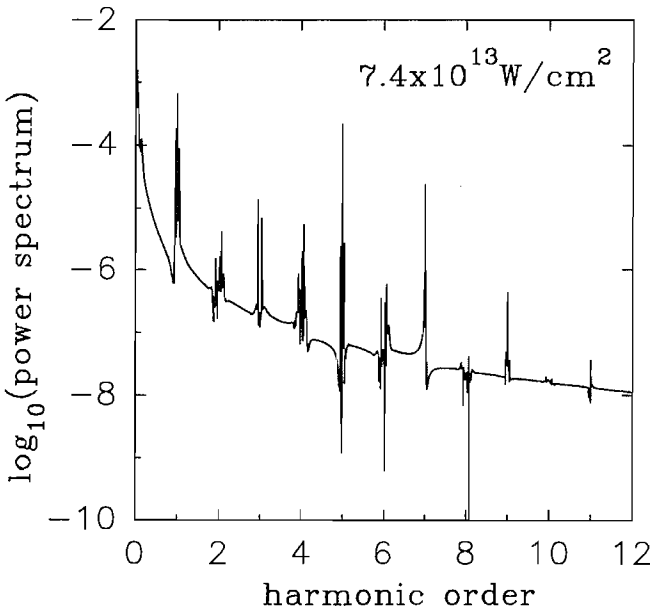

FIG. 5. Harmonic generation spectrum at 7.4×10^{13} W/cm^2, $v = 13$, and $\lambda = 1064$, and with 200-cycle pulse with a 5-cycle linear ramp, obtained from induced dipole moment (eq. [4]) from 6 cycles to end of pulse.

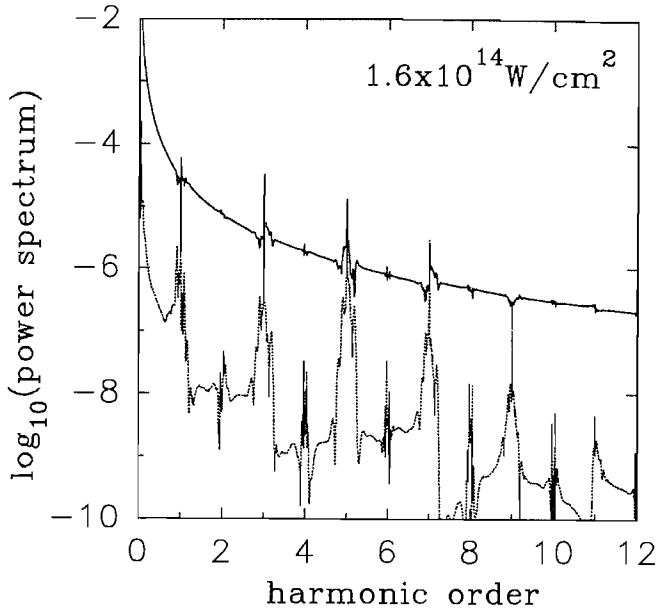

FIG. 6. Same as Fig. 5, except at 1.6×10^{14} W/cm^2 (solid line). Also shown is the result of subtracting the linear trend in the dipole moment before Fourier transforming to obtain the spectrum (dotted line).

tively, one can think of the field creating a symmetry-broken electronic state, $1\sigma_g + 1\sigma_u \propto 1s_{a(b)}$; i.e., the electron becomes localized on one atom on a femtosecond time scale; this will result in generation of even harmonics. This spectrum correlates very well with a simple two-level calculation with the internuclear distance fixed at 6 a.u. (the right turning point of $v = 13$) (10, 14); i.e., the relative efficiencies of the harmonics are well reproduced. Additional structure results from the nuclear motion that allows harmonic generation into several adiabatic vibrational levels, i.e., levels of the field- induced potential well (10, 14). From exact calculations (i.e., electronic motion treated exactly) on H_2^+ fixed at $R = 6$ au., it is observed that the molecular contribution, reproduced by the two-level model and the two-electronic state results shown here (minus structure due to vibrational motion), is separate from the atomic contribution that occurs at higher harmonic order (10).

The harmonic generation spectrum at 1.6×10^{14} W/cm^2 (Fig. 6, solid line) is nearly obscured by the background. The peaks that do appear are all less intense than those in Fig. 5. This contrasts with calculations based on H_2^+ with fixed nuclei, and with the two-level model, where higher order harmonic generation is obtained at higher intensity (10). The explanation lies in the competition between harmonic generation and photodissociation. We found that harmonic generation occurs only at short ($R < 5$ Å) internuclear distances, where the electronic states are nondegenerate. This is not surprising, since both from the point of view of perturbation theory, and from the high-field analytic solution of the two-level model, no harmonic generation can occur in a system of degenerate states (10). With this in mind, one can make the link between photodissociation and harmonic generation, namely, that more of the former means less of the latter. All that the photodissociating fragments contribute is a linear trend in $\mu_{H_2^+}^{ind}(t)$ that gives rise to the large background in the solid line in Fig. 6. The dotted line in the same figure shows the result of subtraction of this linear trend from the dipole moment before Fourier transforming to obtain the spectrum; the background is greatly reduced and a similar structure as in Fig. 5 is revealed, i.e., split peaks around even and odd harmonics, but much weaker in intensity. The interplay between photodissociation and harmonic generation should now be evident. At intensities where photodissociation is minimized, owing to trapping in laser-induced potentials, harmonic generation will be maximized and vice versa.

4. Conclusions

In this note we have shown that laser-induced avoided crossings, necessary to explain laser–molecule interactions in strong laser fields, can be exploited to achieve vibrational inversion into a narrow distribution of vibrational levels in diatomic molecules via a dissociative excited state. We then showed that vibrationally excited H_2^+ can generate harmonics up to 11th order of an intense, but less than 10^{14} W/cm^2, 1064-nm laser. Of course, harmonic generation could be produced from vibrationally relaxed H_2^+, but less efficiently, owing to a smaller transition moment ($\propto R/2$) and a larger number of photons needed to make the transition from the ground to the excited state. Harmonic generation from vibrationally relaxed H_2^+ with a higher frequency laser would be less efficient as well, since the intensity of a given harmonic depends inversely on the laser frequency (10), and competition from ionization would be more important. Finally, for harmonic generation to compete with photodissociation, laser-induced avoided crossings must be exploited to achieve stabilization of photodissociation. One sees that high-order (nonperturbative) harmonic generation can serve as an excellent diagnostic tool to probe intense field–molecule interactions and dynamics.

1. A.D. Bandrauk. Molecules in laser fields. Marcel Dekker, New York. 1993.
2. A.D. Bandrauk and M.L. Sink. Chem. Phys. Lett. **57**, 569 (1978); J. Chem. Phys. **74**, 1110 (1981); J. Yuan and T.F. George. J. Chem. Phys. **68**, 3040 (1978).

Can. J. Chem. Downloaded from www.nrcresearchpress.com by EESC ESCOLA DE ENGENHARIA on 09/08/12
For personal use only.

3. J.C. Polanyi. J. Chem. Phys. **34**, 347 (1961).
4. S. Chelkowski, A.D. Bandrauk, and P.B. Corkum. Phys. Rev. Lett. **65**, 2355 (1990); S. Chelkowski and A.D. Bandrauk. Chem. Phys. Lett. **186**, 264 (1991); J. Chem. Phys. **99**, 4279 (1933).
5. C. Kitrell, E. Abramson, J.L. Kinsey, S.A. McDonald, D.E. Reisner, R.W. Field, and D.H. Katayama. J. Chem. Phys. **75**, 2056 (1981); C.H. Hamilton, J.L. Kinsey, and R.W. Field. Annu. Rev. Phys. Chem. **37**, 493 (1986).
6. U. Gaubatz, P. Rudecki, S. Schiemann, and K. Bergmann. J. Chem. Phys. **92**, 5363 (1990).
7. E.E. Aubanel and A.D. Bandrauk. J. Phys. Chem. **97**, 12620 (1993).
8. R.S. Mulliken. J. Chem. Phys. **7**, 20 (1939).
9. M. Yu. Ivanov, P.B. Corkum, and P. Dietrich. Laser Phys. **3**, 375 (1993); M.Y. Ivanov and P.B. Corkum. Phys. Rev. A: Gen. Phys. **48**, 580 (1993).
10. T. Zuo, S. Chelkowski, and A.D. Bandrauk. Phys. Rev. A: Gen. Phys. **48**, 3837 (1993).
11. Y.R. Shen. The principles of nonlinear optics. John Wiley, New York. 1984.
12. A. L'Huillier, K.J. Schafer, and K.C. Kulander. J. Phys. B: At. Mol. Opt. Phys. **24**, 3315 (1991).
13. S. Chelkowski, T. Zuo, and A.D. Bandrauk. Phys. Rev. A: Gen. Phys. **46**, R5342 (1992).
14. E.E. Aubanel, T. Zuo, and A.D. Bandrauk. Phys. Rev. A: Gen. Phys. In press.
15. E.E. Aubanel, A.D. Bandrauk, and P. Rancourt. Chem. Phys. Lett. **197**, 419 (1992).
16. E.E. Aubanel, A.D. Bandrauk, and J.M. Gauthier. Phys. Rev. A: Gen. Phys. **48**, 2145 (1993).
17. A. Giusti-Suzor and F.H. Mies. Phys. Rev. Lett. **68**, 3869 (1992).
18. G. Yao and S.I. Chu. Chem. Phys. Lett. **197**, 413 (1992).
19. S. Chelkowski and A.D. Bandrauk. Phys. Rev. A: Gen. Phys. **44**, 788 (1991).

Can. J. Chem. Downloaded from www.nrcresearchpress.com by EESC ESCOLA DE ENGENHARIA on 09/08/12
For personal use only.

Optical properties of poly-HCN and their astronomical applications

BISHUN N. KHARE,[1] CARL SAGAN, AND W. REID THOMPSON
Laboratory for Planetary Studies, Cornell University, Ithaca, NY 14853, U.S.A.
AND
EDWARD T. ARAKAWA, CAROLINE MEISSE, AND PAGE S. TUMINELLO[2]
Health and Safety Research Division, Oak Ridge National Laboratory, Oak Ridge, TN 37831, U.S.A.
Received July 27, 1993
This paper is dedicated to Professor John C. Polanyi on the occasion of his 65th birthday

BISHUN N. KHARE, CARL SAGAN, W. REID THOMPSON, EDWARD T. ARAKAWA, CAROLINE MEISSE, and PAGE S. TUMINELLO. Can. J. Chem. **72**, 678 (1994).

Matthews (1992) has proposed that HCN "polymer" is ubiquitous in the solar system. We apply vacuum deposition and spectroscopic techniques previously used on synthetic organic heteropolymers (tholins), kerogens, and meteoritic organic residues to the measurement of the optical constants of poly-HCN in the wavelength range 0.05–40 μm. These measurements allow quantitative comparison with spectrophotometry of organic-rich bodies in the outer solar system. In a specific test of Matthews' hypothesis, poly-HCN fails to match the optical constants of the haze of the Saturnian moon, Titan, in the visible and near-infrared, derived from astronomical observations and standard models of the Titan atmosphere. In contrast, a tholin produced from a simulated Titan atmosphere matches within the probable errors. Poly-HCN is much more N-rich than Titan tholin.

BISHUN N. KHARE, CARL SAGAN, W. REID THOMPSON, EDWARD T. ARAKAWA, CAROLINE MEISSE et PAGE S. TUMINELLO. Can. J. Chem. **72**, 678 (1994).

Matthews (1992) a suggéré que le HCN à l'état de polymère est omniprésent dans le système solaire. Dans ce travail, on applique des techniques de déposition sous vide et spectroscopiques utilisées antérieurement sur des hétéropolymères organiques de synthèse (« tholines »), des kérogènes et des résidus organiques météoritiques pour mesurer les constantes optiques du poly-HCN aux longueurs d'onde allant de 0,05 à 40 μm. Ces mesures permettent d'établir une comparaison quantitative avec la spectrophotométrie de corps riches en produits organiques dans le système solaire externe. Dans le cas spécifique de la vérification de l'hypothèse de Matthews, le poly-HCN ne concorde pas avec les constantes optiques de la brume de la lune de Saturne, Titan, dans le visible et le proche infrarouge qui ont été obtenues à partir d'observations astronomiques et de modèles standard de l'atmosphère de Titan. Par ailleurs, une tholine produite dans un atmosphère de Titan simulé concorde aux erreurs probables. Le poly-HCN est beaucoup plus riche en N que la tholine de Titan.
[Traduit par la rédaction]

1. Introduction

In a long series of papers, Clifford Matthews has argued that "polymeric" HCN may be readily formed in the solar system and may account for the dark surface coatings seen on many objects in the outer solar system. Specifically, claims are made for the dark involatile surface of the nucleus of Comet Halley, D-class asteriods, the rings of Uranus, the dark hemisphere of Iapetus, the orange-brown clouds of Jupiter and Saturn, and the haze of Titan (1–3).

Laboratory experiments have demonstrated that complex organic solids are readily formed by the action of UV light and (or) charged particles on atmospheres and icy surfaces containing simple carbon-bearing molecules. These heteropolymers are often generated by the participation of many chemical species, and mechanisms by which gas-phase species participate in forming the chemical structure of the solid have been proposed. Under more limited conditions, polymers may form from nearly pure starting materials — for example, UV light catalyzes the formation of "polyacetylenes" (polyethyne) in planetary atmospheres (4), and UV acting on solid ethyne in outer planet condensation hazes also produces polymeric residues.

Another widely discussed candidate for polymerization is HCN. While HCN is more often just one of many participating species in polymer formation (e.g., in the radiation chemistry of N_2–CH_4 atmospheres), "pure" HCN polymers are possible in principle. Whatever its chemical origin, the -C≡N (nitrile) group is important in organic residues in several types of solar system bodies: the 2.2 μm C≡N overtone band has been tentatively identified in the dust of "new" comets, on D-type asteroids, in the Uranian rings, and on the dark side of Iapetus (5). Matthews (6) claims that the polymerization of hydrogen cyanide is a universal process; CH_4 and NH_3 are simple cosmically abundant molecules that easily produce (7) HCN on irradiation with charged particles or UV photons; also, HCN is known to polymerize (8) in the condensed state or when irradiated as a gas, to "poly-HCN". The argument for "poly-HCN" rests on its alleged ease of formation and its dark color. No measurements of its optical constants have been made heretofore; no detailed comparison of laboratory and astronomical spectra has shown a best fit for "poly-HCN"; and no radiative transfer models have been used to compare laboratory optical constants of "poly-HCN" with the spectra of solar system bodies.

Generally, organic heteropolymers produced in astronomical environments where N atoms are available contain some nitrile component. Khare and Sagan (9) produced a brown organic solid by long-wavelength ultraviolet irradiation of abundant gases in reducing planetary atmospheres; the solid exhibits a 4.5 μm C≡N nitrile or isocyanide fundamental band. We proposed (9) that a heteropolymer containing nitriles and polynitriles may be a common constituent of aerosols in the outer solar system, and later coined the name tholin (10) for such complex materials. The 4.5 μm band was also found in tholin

[1]Author to whom correspondence may be addressed.
[2]Also at University of Tennessee, Knoxville, TN 37996, U.S.A.

Can. J. Chem. Downloaded from www.nrcresearchpress.com by 195.246.54.202 on 09/08/12
For personal use only.

made from equimolar amounts of CH_4 and NH_3 with 2.5% water vapor (11), and in Titan tholin (12) made from 90% N_2 and 10% CH_4.

In the identification, by Cruikshank et al., (5) of the 2.2 μm first overtone band of the C≡N fundamental in reflection spectra of several bodies throughout the outer solar system, the fit to tholins was at least as good as the fit to "poly-HCN". The two are far from being the same materials. At the very least, we can say that the 2.2 μm feature is not diagnostic of "poly-HCN". However, while we believe the C≡N bond in these materials usually arises from heteropolymers in whose formation HCN played at most only a part, pure "poly-HCN" provides an interesting end member of this class of organic solids.

Poly-HCN (henceforth, we drop the quotation marks) can be categorized (13) into three major forms: (*a*) true polymeric $(HCN)_n$, the repetition of the same monomeric unit *n* times; (*b*) HCN heteropolymer or oligomer (not polymer), which has the same rough abundance of organic functional groups producing roughly the same IR spectrum, but is not repetitive, especially in its hydrocarbon and other side chains; and (*c*) HCN aqueous solution polymer or oligomer, which contains oxygenated side chains and other components. These three different forms of poly-HCN need not have the same IR spectrum; e.g., form *c* does not exhibit the 4.5 μm C≡N absorption, or its corresponding 2.2 μm overtone. While HCN is an important minor species in some astronomical environments, it is hard to imagine atmospheres or ices in the solar system or beyond made of pure HCN, free of other components, and producing pure poly-HCN.

Laboratory experiments, done at Cornell University (14–16) and elsewhere, show that the gas- and solid-phase product molecules are diverse even in simulation experiments starting with only a few major precursor gases. We have found that tholin synthesized from a crude simulation of Jupiter is not pure poly-HCN but is a heteropolymer with a variety of moieties (13). The same conclusion is also drawn from the pyrolytic GC–MS results on this tholin as well as on Titan tholin (14, 15, 17); hundreds of pyrolytic products were detected in both tholins. But a diagnostic test is the comparison of laboratory optical constants of poly-HCN with optical constants derived from astronomical and spacecraft observations.

We previously (18, 19) applied the technique of thermal evaporation and successfully determined the optical constants of kerogen, the organic residue obtained from the Murchison carbonaceous chondrite, and ice tholin (made from charged particle irradiation of $C_2H_6/H_2O \sim 1{:}6$ at 77 K). Here we present results of measurements of the optical constants of poly-HCN in the form of thermally evaporated thin films.

Lunin et al. (20) have studied the properties of thin films of polyparacyanogen that, like poly-HCN, contains C≡N in its structure. They prepared a thin film by electron-beam evaporation in vacuum, a technique sometimes substituted for thermal evaporation in vacuum. They found that the preparation of thin films is very dependent on the structure of the original polymer. On the basis of the preservation of elemental (C, H, N) ratios and agreement of IR spectra of the original polymers and films, they conclude that electron-beam spray coating in vacuum leads to splitting of the macromolecules into low-molecular-weight fragments that completely preserve the chemical structure of the original polymer. These fragments, on deposition on the substrate, recombine to form macromolecules. Our experience with the vacuum evaporation technique applied to other organic residues indicates a similar preservation of the chemical character of the original material (18, 19).

2. Production of poly-HCN

2.1. Synthesis of HCN and poly-HCN

Hydrogen cyanide is readily produced by the action of electric discharges, high temperatures, or ionizing radiation upon a variety of reducing or nonoxidizing atmospheres. The yields are particularly high if electric discharges are applied. The type of atmosphere used for the source of H, C, and N atoms to produce HCN seems relatively unimportant until higher oxidation states are reached. Miller (21) produced HCN along with CO, CO_2, and N_2 from a mixture of CH_4, NH_3, H_2O, and H_2 after coronal discharge. Sagan and Miller (22), in an experiment crudely simulating the deep atmosphere of Jupiter, found HCN, CH_3CN, C_2H_2, C_2H_4, and C_2H_6 in a coronal discharge through a gas mixture containing H_2, CH_4, and NH_3, with H_2 in excess. Many subsequent experiments in neutral to reducing C- and N-containing gas mixtures also found HCN to be a major product. Cyanogen is routinely found in sunspots and in the photospheres of cool stars.

One of the common methods for preparing anhydrous hydrogen cyanide in the laboratory is by the action of sulfuric acid on sodium cyanide, potassium cyanide, or potassium ferrocyanide (23); for example,

$$[1] \qquad NaCN + H_2SO_4 \rightarrow HCN + NaHSO_4$$

In the Andrussow process, the major commerical method (24) for producing HCN gas, the reaction takes place between NH_3, CH_4, and air over a platinum catalyst at 1100°C:

$$[2] \qquad CH_4 + NH_3 + 1.5O_2 \rightarrow HCN + 3H_2O$$

Poly-HCN employed in our study was obtained from E.I. du Pont de Nemours & Co., Inc. Its infrared spectrum indicates that it is probably composed of a mixture of all three types of poly-HCN (13). Its IR spectrum is nearly identical to that of poly-HCN prepared by Matthews (see ref. 5).

Poly-HCN formation normally occurs in aqueous solution. It can also occur in anhydrous solvents, but requires a compound capable of creating CN^- ions in the solvent. Polymerization occurs readily when both CN^- and HCN are major components in solution, specifically, when $4.0 < pH < 10.5$. The rate of polymerization and the form of the final polymer will depend on the interactions with other species in solution. HCN does not polymerize in the vapor phase.

We obtained poly-HCN samples from two places in the du Pont manufacturing system. One sample came from piping immediately after the HCN production reactors. The products in reaction [2] are cooled to very near the dew point to remove water produced in the reaction. There are places in the piping where the gases are cooled locally to below the dew point and these aqueous droplets absorb some HCN and unreacted NH_3, which brings the pH into the polymerization range.

Another sample came from the purification train. Here HCN polymerizes from HCN in water with no additional solutes. The solutions are normally stabilized to pH <2 with an acid, but if HCN condenses in a spot where there is no acid, it will begin to polymerize and seed further polymerization. We used this poly-HCN sample collected from the walls of the purification line for optical constants measurements.

Völker (25, 26) proposes that poly-HCN is formed via imi-

Can. J. Chem. Downloaded from www.nrcresearchpress.com by 195.246.54.202 on 09/08/12
For personal use only.

TABLE 1. Elemental composition (weight percent)

Elements	Poly-HCN synthesized in water (26)	Anhydrous poly-HCN made in organic solvent (26)	du Pont poly-HCN (<0.03% sulfur impurity) employed in making film (this work)	Tholin from plasma discharge through 9:1 N_2/CH_4 mixture at 0.2 mbar pressure (11, 12)	Tholin reactant composition (12)
C	41.4	45	30.7	47.7	4.48
H	4.0	4.0	4.1	6.4	1.50
N	43.2	51.3	46.7	29.3	94.02
O	11.4		18.5	16.6	

noacetonitrile, which is a dimer of hydrogen cyanide and is considered to be formed by reaction between HCN and CNH according to a scheme known for the addition of isonitriles to nitriles:

[3] $HCN + CNH \rightarrow H-C(=N-H)-C\equiv N$

A recent study of HCN dimers was made by Evans et al. (27, 28). Some controversy over the structure of dimeric HCN is summarized by Ferris and Hagan (29). A detailed study of the mechanism of HCN polymerization has been given by Sanchez et al. (30), Ferris et al. (31), Ferris and Edelson (32), and Ferris (33).

2.2. *Properties of HCN and poly-HCN*

While HCN is a colorless, poisonous, low-viscosity liquid said to have an odor characteristic of bitter almonds, poly-HCN is a brown-black solid having hardly any odor, although a freshly prepared poly-HCN has a slight odor of the monomer and, occasionally, of ammonia (26). Poly-HCN is not known to have any toxic effects. Details on the synthesis and structure of poly-HCN were given recently by Matthews and Ludicky (34) and earlier by Völker (26).

HCN has a melting point of −13.24°C, a boiling point of 25.70°C, and a density 0.7150 g cm^{-3} at 0°C. It can polymerize violently in the presence of heat, alkaline materials, or moisture. Once initiated, polymerization becomes uncontrollable since the reaction is autocatalytic, producing heat and alkalinity (NH_3). Confined polymerization can cause a violent explosion.[3] This is part of the appeal of the proposal that cometary outbursts are due to HCN polymerization (35).

The density of poly-HCN was measured by determining the weight and volume of a 13 mm pellet of poly-HCN prepared by compressing du Pont poly-HCN powder at 1700 atmospheres. A density of 1.49 g cm^{-3} was obtained; this is a lower limit due to residual void space inside the pellet. The density of our evaporated films, prepared subsequently, was measured using the float and sink method (employing a series of varying density solutions made from CCl_4 and CH_3OH). This method yielded a value of 1.54 ± 0.005 g cm^{-3}. The density of unpressed fluffy du Pont poly-HCN powder, determined by helium pycnometry, gave a value of 1.620 ± 0.004 g cm^{-3}. This technique avoids error caused by void volume and should be taken as the best value for the density of du Pont poly-HCN.

The average value of the atomic composition of du Pont poly-HCN determined by Schwarzkopf Microanalytical Laboratory and Galbraith Laboratories, Inc. (after correcting for oxygen and hydrogen due to exposure of poly-HCN to 0.034% SO_2 and 0.026% H_2SO_4 used as a stabilizer for HCN gas in the du Pont manufacturing plant) is given in Table 1. The balance of the remaining large amount of oxygen in this kind of sample probably occurs from the interaction of the poly-HCN with H_2O during formation from the product stream. No correction for oxygen or hydrogen due to exposure of poly-HCN to water (or subsequent exposure to air) is made.

The sulfur, oxygen, and incremental hydrogen impurities are due to exposure of poly-HCN to sulfur compounds and water in the plant and, perhaps, to the air during storage of the poly-HCN. These impurities do not affect the measurement of the optical constants, since infrared spectra of the evaporated and redeposited film of poly-HCN at 800 K agree with those of the anhydrous poly-HCN of Völker (26) and Cruikshank et al. (5).[4] Table 1 also includes; for comparison, the average elemental composition of Titan tholins determined by Schwarzkopf and Galbraith. It clearly shows that poly-HCN and Titan tholin have very different elemental compositions, as is also reflected in their optical constants (see below).

2.3. *Comparison of the infrared spectra of poly-HCN from several sources*

Völker (26) has shown that poly-HCN synthesized in water has elemental composition 41.4% C, 4.0% H, and 43.2% N. The remaining ~11% he attributes to O atoms without indicating any specific position for the oxygen atoms in the proposed structure of the poly-HCN (Fig. 1(*a*)). No IR band corresponding to the C≡N stretching vibration at 4.5 μm is found in the transmission spectrum. Anhydrous poly-HCN (Fig. 1(*b*)) made in organic solvents such as chloroform has elemental composition 45% C, 4.0% H, and 51.3% N and exhibits a strong C≡N band at 4.5 μm. The presence and absence of this feature results from different structures of the monomer units as shown in Figs. 1(*a*) and (*b*). Völker (26) finds that the oxygen does not react with the polymer, but the presence of water vapor in moist air causes oxygen to be incorporated into the polymer. Cruikshank et al. (5) report that anhydrous poly-HCN (Fig. 1(*b*)) shows a diminution of the 4.5 μm feature with time, on treating with water at room temperature until its complete disappearance after 6 months.

Figure 2 shows the transmission and reflectance spectra of poly-HCN from du Pont Co. thermally evaporated and redeposited in our laboratory, compared with poly-HCN from several sources. "Electropolymeric" HCN (36) prepared by

[3]du Pont Material Safety Data Sheet H-12264-1. du Pont Co., Chemicals and Pigments Department, Chestnut Run Plaza, P.O. Box 80709, Wilmington, Del. (1989).

[4]D.P. Cruikshank et al. Private communication (1993).

Can. J. Chem. Downloaded from www.nrcresearchpress.com by 195.246.54.202 on 09/08/12
For personal use only.

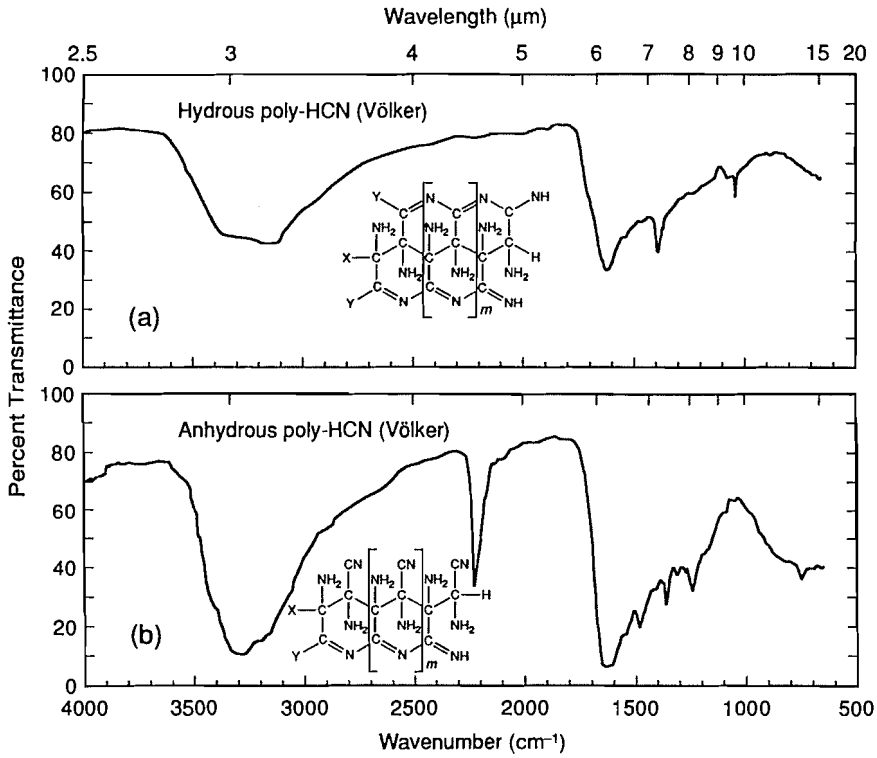

FIG. 1. Infrared spectra of poly-HCN (*a*) synthesized in water and (*b*) synthesized in organic solvents such as chloroform. Both spectra are taken from Völker (26). Note the similarity of (*b*) with Fig. 2(*b*) below, allowing for the lower resolution here.

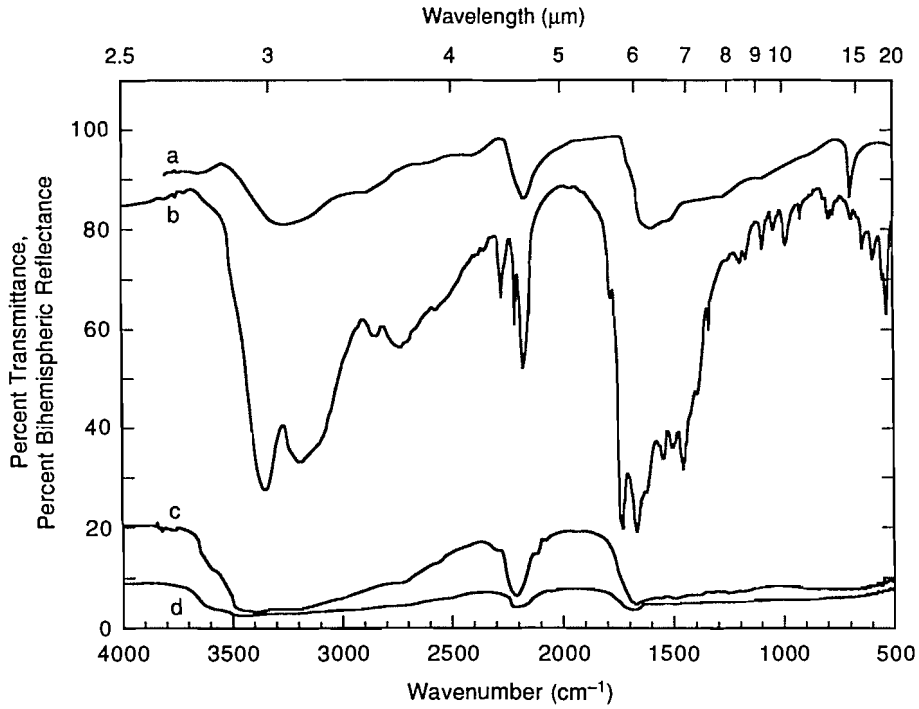

FIG. 2. Comparison of the infrared transmission spectra of (*a*) electropolymeric-HCN (arbitrary units) (36) with (*b*) thermally evaporated and redeposited poly-HCN from du Pont de Nemours under high vacuum in the present work, (*c*) bihemispheric reflectance spectrum of anhydrous poly-HCN (5, footnote 4), and (*d*) bihemispheric reflectance spectrum of hydrous poly-HCN (5, footnote 4).

0.5 mA arc discharge through HCN shows weak IR absorptions. The reflection spectrum of anhydrous poly-HCN is from a sample prepared by Matthews and Ludicky in which liquid HCN with a catalytic trace of triethylamine was allowed to stand at room temperature for 30 days. Ammonia can also be used in place of triethylamine as a catalyst (7, 8). The initially colorless liquid becomes a yellow-orange-brown sludge, ending as a dark brown, almost black, powder (5). The hydrated poly-HCN is obtained by stirring this powder in cold water for 3 days and drying to yield a black solid material. The

Can. J. Chem. Downloaded from www.nrcresearchpress.com by 195.246.54.202 on 09/08/12
For personal use only.

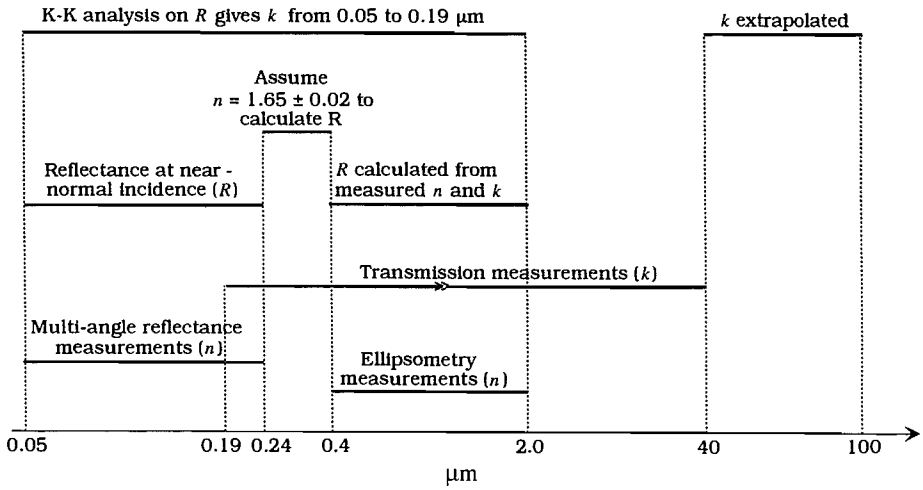

FIG. 3. Techniques employed in the measurement of the optical constants of a film prepared by thermal evaporation of poly-HCN and redeposition under high vacuum. The assumed value of n derives from ellipsometry.

reflection spectra of both anhydrous and hydrous poly-HCN obtained by Cruikshank et al.[4] are also reproduced here (Fig. 2). The comparison is only qualitative. Our vacuum-evaporated film exhibits all the major bands corresponding to functional groups present in the unheated poly-HCN from other sources, but the relative strength of the bands varies considerably. It is not expected that poly-HCN prepared under different conditions will produce identical infrared spectra (13).

3. Experimental

As discussed earlier (18, 19) in our continuing studies of the optical properties of organic residues, it is difficult to measure the imaginary part, k, of the complex refractive index by transmission measurements of solid materials that are in powdery form, since pulverized samples cause severe multiple scattering of the incident light. It is necessary instead to prepare optical quality films, particularly for the transmission measurements in the UV and visible where scattering is the greatest.

3.1. Thin film preparation

We prepared optical quality thin films of poly-HCN by thermal evaporation under high vacuum as described elsewhere (19). It was not possible to make suitable films thicker than $t = 1.5$ μm since thick films contained foggy areas. We therefore produced films of various thicknesses ranging from 0.05 to 1.5 μm. The exact thickness of the films is checked only after the spectral measurements are completed. A Sloan Angstrometer (model M-100) was used to measure the thickness of the thinner films. For $t \simeq 0.75$ μm, we measured the thickness from the interference pattern produced by light reflected from the front and back surfaces of the film in the wavelength range 0.4–2.5 μm, assuming an index of refraction $n = 1.65 \pm 0.02$ for this region. This value of n was determined previously by an independent ellipsometric measurement on a pressed pellet of poly-HCN.

Evaporation took place at a temperature of 800 ± 100 K at 10^{-5}–10^{-6} Torr (1 Torr = 133.3 Pa). The color of the molybdenum crucible at which the poly-HCN began to evaporate was used to determine the temperature. Evaporated poly-HCN was condensed onto optical quality CsI and CaF_2 substrates transparent from 0.3 to 50 μm and from 0.13 to 9 μm, respectively, and kept at room temperature. The thin films were colorless initially, turning yellowish with increasing thickness. By weighing the molybdenum crucible before and after evaporation, we determined that ~80% of the poly-HCN was evaporated.

3.2. Spectroscopic measurements

The infrared spectrum from 2.5 to 40 μm of unheated poly-HCN was obtained by measuring the transmission through a compressed pellet in a CsI matrix using a Mattson Galaxy 6020 FTIR spectrometer at 1 cm^{-1} resolution. The transmission spectrum from 2.5 to 40 μm of vacuum-evaporated films of poly-HCN on CsI substrates was obtained using a Perkin–Elmer model 983 spectrometer, also at 1 cm^{-1} resolution. Shimadzu UV250 and Cary 14 spectrophotometers were used in the ranges 0.19–0.9 μm and 0.4–2.5 μm, respectively. A Seya–Namioka monochromator was used from 0.13 to 0.4 μm for transmission measurements and from 0.13 to 0.24 μm for reflectance measurements. A McPherson model 247 grazing incidence monochromator enabled us to extend the reflectance measurements down to 0.05 μm.

Figure 3 summarizes the techniques used in the determination of the optical constants n and k, as discussed in detail elsewhere (12, 18, 19). Figure 4(*a*) shows the spectrum of unheated poly-HCN in a CsI matrix using a technique described by Khare and Sagan (37), and Fig. 4(*b*) shows the spectrum of a vacuum-evaporated and redeposited film of poly-HCN. We find that the du Pont poly-HCN (Fig. 4(*a*)) is not as hydrous as the hydrous poly-HCN of Völker (26) (Fig. 4(*d*)). The features in unheated du Pont poly-HCN better resemble those of the anhydrous poly-HCN (Fig. 4(*c*)) of Völker (26). This is reasonable since the du Pont poly-HCN is a mixture of both hydrous and anhydrous polymers. The infrared spectrum of our thermally evaporated film (Fig. 4(*b*)) is close to that of anhydrous poly-HCN (Figs. 1(*b*), 4(*c*)). The thermal evaporation technique has the advantage of removing adsorbed water and producing films exhibiting the strong band at 4.5 μm (2222 cm^{-1}) characteristic of C≡N as seen in the spectrum of anhydrous poly-HCN.

Films prepared by thermal evaporation under high vacuum (Fig. 4(*b*)) were used in the present investigation for the determination of the optical constants. These films are suspected to be more anhydrous than the anhydrous poly-HCN of Völker (26) as seen in the increase in the strength and multiplicity of the C≡N band at 4.5 μm if the decrease in the strength and multiplicity of the C≡N band is directly related to the degree of hydrolysis of poly-HCN. Table 2 lists all the bands found in our thermally evaporated films of poly-HCN. The infrared spectrum of a complex organic solid such as poly-HCN shows absorption bands that are due to well-known chemical functional groups. Possible assignments of some of the bands based on Bellamy (38), Szymanski (39), Pasto and Johnson (40), and Colthup (41) are presented in Table 2. These assignments are tentative and could change when the structure of this poly-HCN is better determined. The appearance of the C≡N spectral feature, as well as its strength and position, is known to vary from sample to sample. Our evaporated poly-HCN, being a mixture of all three types of poly-HCN and free from water, produces four distinct peaks, varying in intensity and wavelength, near 4.5 μm.

Can. J. Chem. Downloaded from www.nrcresearchpress.com by 195.246.54.202 on 09/08/12
For personal use only.

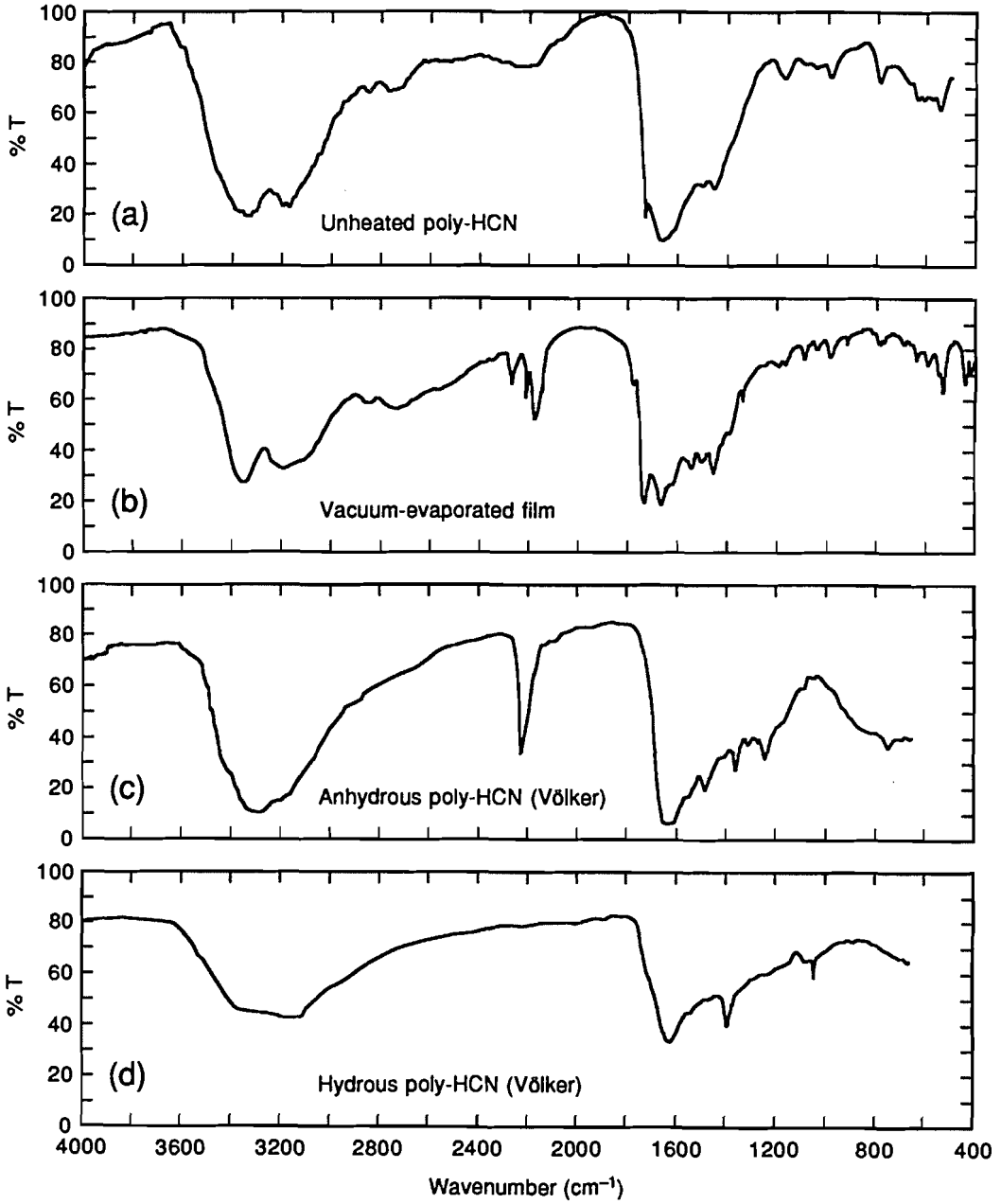

FIG. 4. Infrared spectra of poly-HCN (*a*) unheated in CsI matrix, (*b*) vacuum evaporated and redeposited at 800 ± 100 K on a CsI substrate, compared with (*c*) anhydrous poly-HCN made in organic solvents such as chloroform (26), and (*d*) hydrous poly-HCN made in water (26).

4. Optical constants

4.1. Direct measurements of the real part of the refractive index n

We measure n directly on films of evaporated poly-HCN using ellipsometry from 0.4 to 2 μm and multi-angle reflectance from 0.05 to 0.24 μm, as previously described (12). We also carried out ellipsometric measurements on solid pressed pellets made from unheated poly-HCN.

4.2. Direct measurement of the imaginary part of the refractive index k

The transmittance T of a thin film with thickness t on a thick substrate is given by Khare et al. (12) as

$$[4] \qquad T = T_s \frac{(1-R)}{(1-R_0)^2} \exp(-4\pi kt/\lambda)$$

where T_s = transmission of the bare substrate, R = normal-incidence reflectance of the film–substrate system, $R_0 = [(n_s - 1)/(n_s + 1)]^2$ is the normal-incidence reflectance at the substrate–air interface, and n_s is the real part of the refractive index of the substrate.

By considering R as independent of t, we determined k from the slope of the straight line drawn by plotting $\ln(T_s/T)$ against t. The advantage of this method is that we did not need to know n for either the substrate or the film. k was determined in this way from 0.19 to 40 μm.

4.3. Kramers–Krönig (K–K) analysis of k

For the wavelength range 0.05–0.19 μm, where it was not possible to measure k directly due to low film transmission and lack of suitable substrates, we determined k from reflectance measurements using the Kramers–Krönig relation given by dis-

Can. J. Chem. Downloaded from www.nrcresearchpress.com by 195.246.54.202 on 09/08/12
For personal use only.

Can. J. Chem. Downloaded from www.nrcresearchpress.com by 195.246.54.202 on 09/08/12
For personal use only.

TABLE 2. Assignment[a] of absorption features in the infrared spectra of anhydrous thermally evaporated poly-HCN under high vacuum

Frequency (ν) cm^{-1}	Wavelength (λ)(μm)	intensity[b]	Vibrational classification	Functional groups
3380	2.99	vs	Hydrogen bonded N—H stretching	Aromatic
3185	3.14	vs	C—H stretching or N—H stretching	Aromatic
2850	3.51	m	$—CH_2$	
2730	3.66	m	—[c]	
2565	3.90	m	—[c]	
2265	4.42	m	C≡N stretching	Aromatic
2208	4.53	m		
2170	4.61	m		
2150 sh	4.65 sh	m		
1778	5.62	m	Benzene ring overtone	
1730	5.78	vs	C=N stretching	
1665	6.01	vs	C=N stretching or NH_2 bending	
1618	6.18	s	NH_2 scissoring deformation	Amines RNH_2
1540	6.49	s	Side chain asymmetric CN stretching	
1500	6.49	s	Benzene ring	
1453	6.88	s	In-plane C—H bending	
1416	7.06	w	In-plane C—H bending	
1389	7.20	w	CH or NH bending	
1336	7.49	w	—[c]	
1195	8.37	w	NH_2 rocking	
1170	8.55	w		
1091	9.17	w	C—C stretching	
1043	9.59	w	—[c]	
985	10.15	m	$—CH=CH_2$	
918	10.89	w	—[c]	
788	12.69	w	C=N torsion	
767	13.04	w	C—H bending deformation	Aromatic C—H
686	14.58	vw	Substituted benzene	
637	15.70	w	HCNC bending	
593	16.86	w	HNCN bending	
549 sh	18.21 sh	m	—[c]	
529	18.90	m	—[c]	

[a]Analysis is based on Bellamy (38), Szymanski (39), Pasto and Johnson (40), and Colthup (41).
[b]Intensity code: s = strong, m = medium, w. = weak, sh = shoulder.
[c]Unclassified.

persion relation analysis. This relationship is given by

$$[5] \qquad k(\omega) = \frac{-2\sqrt{R_N(\omega)}\sin\phi(\omega)}{1 + R_N(\omega) - 2\sqrt{R_N(\omega)}\cos\phi(\omega)}$$

where $R_N(\omega)$ is the normal-incidence reflectance at energy $\hbar\omega$ and $\phi(\omega)$, the phase change upon reflection at photon energy $\hbar\omega$, is given by

$$[6] \qquad \phi(\omega) = \frac{\omega}{\pi} P \int_0^\infty \frac{\ln R_N(\omega')}{(\omega')^2 - \omega^2}\, d\omega'$$

where P stands for the Cauchy principle value (42).

Normal-incidence reflectance values from 0.05 to 0.24 μm, where the reflectance was too low to measure directly, were extrapolated from the reflectance measured at non-normal angles of incidence. R_N was calculated in the 0.4–2.0 μm region using Fresnel's equation

$$[7] \qquad R_N = \frac{(n-1)^2 + k^2}{(n+1)^2 + k^2}$$

with the n and k values determined from ellipsometric and transmission measurements, respectively. For the 0.24–0.4 μm region, we calculated R_N by assuming that the real part of the index of refraction n equals 1.65 ± 0.02 for the entire region. The k values were determined from transmission measurements. For $\lambda > 0.4$ μm, we assumed a constant reflectance equal to the value at 0.4 μm since the reflectance in this low-energy region will not influence the values of k calculated in the K–K analysis in the 0.05–0.24 μm region. For the high-energy extrapolation ($\lambda < 0.05$ μm), we used the exponential form $R(E) = a \exp(-b)$ where the constants a and b were determined by requiring that the k values obtained in the K–K analysis agree with those determined earlier from transmission measurements in the region 0.19–0.24 μm.

The values of k obtained from this analysis are plotted in Fig. 5 and tabulated in Table 3. The k values are estimated to be accurate to ±20%. A detailed plot of k that clearly shows the 2.2 μm overtone band is shown for the wavelength range 1.5–5 μm (Fig. 6).

4.4. *Kramers–Krönig analysis of* n

A program based on the Kramers–Krönig relation between n

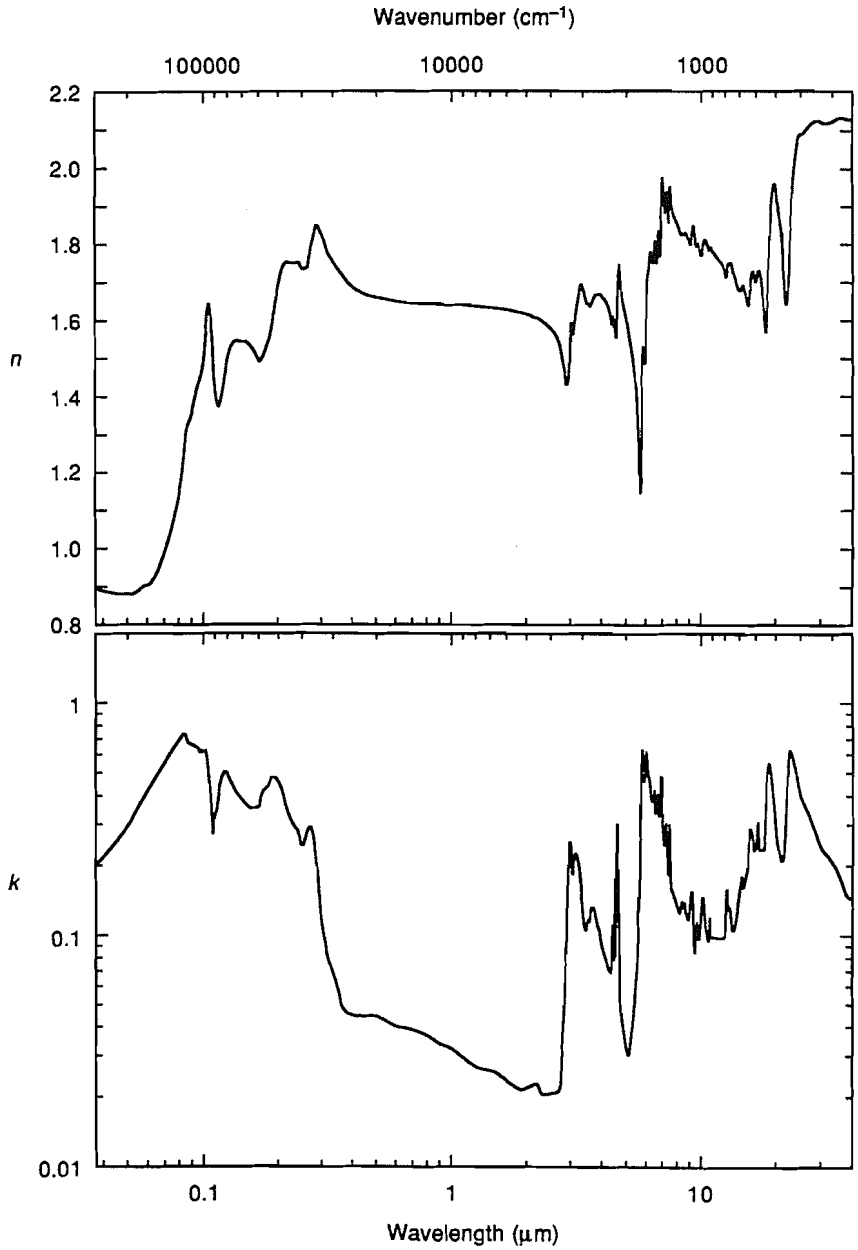

FIG. 5. Real (n) and imaginary (k) values of the complex refractive index as a function of wavelength of films prepared by thermal evaporation and redeposition under high vacuum of poly-HCN from du Pont Co.

and k (43) gave us n over the entire range of the measurements from the k values obtained above between 0.05 and 40 μm. The values of n were obtained from the following integral over the photon energy E

$$[8] \qquad n(E) - 1 = \frac{2}{\pi} P \int_0^\infty \frac{E'k(E')}{(E')^2 - E^2} \, dE'$$

The low-energy integration in eq. [8] was truncated at 100 μm, since the contribution to the integral from above 100 μm has no significant effect on the n values in the region of interest. A linear interpolation was chosen between $k = 0.144$ at $\lambda = 40$ μm and $k = 0.001$ at 100 μm. For the high-energy integration, the k values were extrapolated for $\lambda < 0.05$ μm using a power law $k = k(E_u)E^{-2}$, where $k(E_u)$ was the measured value of the imaginary part of the refractive index at 0.05 μm (24.8 eV), and E is in electron volts. The exponent −2 comes for the theoretical behavior of the imaginary part of the refractive index at high energies (42, 44). The high-energy cutoff for the integration was chosen to make the calculated values of n agree with the measured values in the 0.4–2.0 μm region. The values of n obtained from the Abeles (45) method from 0.4 to 0.625 μm agreed well with the values of n obtained using ellipsometry. The Abeles method is a variation of the Brewster angle method in which n is determined from scans of angular reflectance of thin films on thick substrates. The values of n from the K–K analysis agreed well with the values of n in the region from 0.05 to 0.24 μm determined by multi-angle reflectance measurements. The complete n spectrum from 0.05 to 40 μm is shown in Fig. 5. The n values

Can. J. Chem. Downloaded from www.nrcresearchpress.com by 195.246.54.202 on 09/08/12
For personal use only.

Can. J. Chem. Downloaded from www.nrcresearchpress.com by 195.246.54.202 on 09/08/12
For personal use only.

TABLE 3. Real (n) and imaginary (k) parts of the complex refractive index of thermally evaporated poly-HCN

λ (μm)	n	k	λ (μm)	n	k	λ (μm)	n	k
0.0373	0.896	0.200	0.194	1.634	0.477	2.233	1.605	0.0222
0.0401	0.890	0.218	0.205	1.718	0.432	2.251	1.604	0.0217
0.0432	0.885	0.239	0.216	1.752	0.352	2.276	1.602	0.0211
0.0475	0.882	0.273	0.227	1.751	0.307	2.300	1.600	0.0207
0.0494	0.883	0.289	0.240	1.752	0.280	2.349	1.595	0.0205
0.0502	0.884	0.296	0.248	1.740	0.245	2.398	1.591	0.0206
0.0506	0.883	0.300	0.250	1.735	0.244	2.448	1.586	0.0206
0.0510	0.882	0.304	0.252	1.733	0.245	2.500	1.579	0.0207
0.0514	0.881	0.309	0.253	1.733	0.244	2.541	1.574	0.0208
0.0523	0.882	0.319	0.258	1.735	0.264	2.583	1.567	0.0208
0.0560	0.894	0.367	0.260	1.737	0.272	2.623	1.560	0.0209
0.0576	0.900	0.387	0.262	1.738	0.278	2.656	1.552	0.0210
0.0593	0.905	0.408	0.264	1.742	0.286	2.685	1.544	0.0212
0.0602	0.905	0.420	0.266	1.754	0.286	2.703	1.538	0.0214
0.0610	0.906	0.430	0.268	1.769	0.292	2.715	1.534	0.0217
0.0616	0.908	0.438	0.270	1.782	0.291	2.730	1.528	0.0221
0.0629	0.916	0.454	0.272	1.795	0.292	2.740	1.522	0.0224
0.0677	0.959	0.517	0.274	1.804	0.282	2.778	1.502	0.0308
0.0750	1.054	0.616	0.276	1.813	0.273	2.831	1.475	0.0497
0.0805	1.145	0.690	0.278	1.821	0.263	2.857	1.452	0.0647
0.0827	1.198	0.720	0.280	1.829	0.247	2.897	1.433	0.113
0.0838	1.238	0.730	0.286	1.849	0.200	2.941	1.446	0.193
0.0849	1.279	0.725	0.290	1.846	0.165	2.963	1.477	0.242
0.0854	1.296	0.718	0.300	1.826	0.114	2.970	1.493	0.250
0.0866	1.322	0.683	0.305	1.814	0.102	2.985	1.528	0.251
0.0873	1.328	0.670	0.310	1.798	0.0925	2.995	1.548	0.250
0.0891	1.343	0.663	0.314	1.787	0.0847	3.008	1.575	0.242
0.0904	1.359	0.658	0.320	1.774	0.0775	3.030	1.593	0.202
0.0925	1.389	0.650	0.326	1.764	0.0733	3.040	1.589	0.190
0.0954	1.429	0.630	0.330	1.758	0.0701	3.050	1.582	0.186
0.0969	1.442	0.610	0.336	1.750	0.0662	3.060	1.574	0.185
0.0984	1.458	0.620	0.340	1.745	0.0639	3.068	1.567	0.185
0.100	1.483	0.610	0.344	1.740	0.0606	3.086	1.566	0.211
0.102	1.544	0.620	0.350	1.733	0.0569	3.100	1.579	0.217
0.103	1.581	0.600	0.356	1.726	0.0531	3.137	1.608	0.225
0.104	1.620	0.552	0.360	1.722	0.0498	3.160	1.625	0.221
0.105	1.635	0.501	0.366	1.716	0.0480	3.180	1.639	0.217
0.106	1.643	0.459	0.373	1.708	0.0468	3.200	1.651	0.212
0.108	1.607	0.349	0.380	1.702	0.0460	3.236	1.674	0.199
0.109	1.534	0.274	0.400	1.688	0.0450	3.297	1.693	0.154
0.111	1.443	0.327	0.500	1.659	0.0443	3.333	1.688	0.131
0.113	1.396	0.348	0.600	1.650	0.0402	3.400	1.669	0.110
0.115	1.377	0.406	0.700	1.645	0.0388	3.448	1.653	0.106
0.117	1.383	0.449	0.800	1.643	0.0366	3.483	1.645	0.113
0.119	1.404	0.480	0.900	1.642	0.0337	3.505	1.645	0.117
0.122	1.451	0.502	1.000	1.640	0.0322	3.522	1.645	0.117
0.124	1.483	0.500	1.100	1.639	0.0298	3.552	1.641	0.115
0.129	1.529	0.457	1.200	1.637	0.0278	3.571	1.638	0.118
0.133	1.543	0.428	1.300	1.635	0.0265	3.600	1.640	0.130
0.138	1.546	0.400	1.400	1.633	0.0261	3.664	1.652	0.132
0.149	1.543	0.362	1.500	1.632	0.0255	3.704	1.660	0.130
0.155	1.533	0.352	1.600	1.630	0.0243	3.780	1.668	0.119
0.163	1.511	0.352	1.700	1.627	0.0230	3.846	1.668	0.109
0.168	1.495	0.360	1.800	1.624	0.0221	3.899	1.669	0.105
0.170	1.493	0.390	1.900	1.620	0.0214	3.950	1.668	0.0950
0.175	1.508	0.421	2.000	1.617	0.0218	3.999	1.663	0.0892
0.182	1.539	0.437	2.100	1.612	0.0223	4.167	1.647	0.0763
0.188	1.578	0.477	2.200	1.606	0.0228	4.200	1.642	0.0740

TABLE 3. (*concluded*)

λ (μm)	*n*	*k*	λ (μm)	*n*	*k*	λ (μm)	*n*	*k*
4.300	1.622	0.0700	6.630	1.752	0.378	10.965	1.791	0.100
4.348	1.600	0.0694	6.650	1.766	0.399	11.169	1.780	0.0982
4.366	1.592	0.0827	6.667	1.783	0.405	11.500	1.769	0.0980
4.396	1.601	0.111	6.700	1.825	0.400	12.275	1.741	0.0978
4.428	1.613	0.0981	6.738	1.835	0.342	12.398	1.732	0.0984
4.468	1.584	0.0796	6.750	1.823	0.330	12.500	1.718	0.103
4.492	1.587	0.144	6.780	1.791	0.329	12.651	1.717	0.145
4.507	1.583	0.176	6.812	1.769	0.363	12.710	1.728	0.158
4.529	1.573	0.0862	6.850	1.788	0.438	12.781	1.741	0.150
4.558	1.555	0.185	6.887	1.870	0.480	12.903	1.748	0.131
4.589	1.637	0.288	6.965	1.975	0.340	13.072	1.748	0.132
4.598	1.655	0.154	6.993	1.968	0.301	13.189	1.751	0.122
4.651	1.720	0.191	7.042	1.937	0.262	13.333	1.740	0.108
4.696	1.746	0.0830	7.143	1.891	0.247	13.793	1.702	0.114
4.717	1.725	0.0487	7.160	1.885	0.252	14.388	1.678	0.161
4.762	1.682	0.0454	7.194	1.898	0.299	14.577	1.688	0.180
4.800	1.662	0.0430	7.250	1.937	0.259	14.706	1.691	0.164
5.000	1.603	0.0321	7.330	1.908	0.186	15.152	1.664	0.180
5.128	1.563	0.0305	7.353	1.886	0.185	15.385	1.642	0.200
5.263	1.516	0.0387	7.370	1.865	0.185	15.625	1.660	0.281
5.405	1.455	0.0511	7.380	1.857	0.191	16.000	1.723	0.270
5.556	1.344	0.0813	7.440	1.901	0.300	16.260	1.723	0.233
5.627	1.261	0.147	7.469	1.945	0.245	16.500	1.702	0.240
5.650	1.211	0.146	7.500	1.949	0.185	16.754	1.709	0.275
5.687	1.147	0.257	7.514	1.947	0.175	16.949	1.727	0.296
5.770	1.316	0.619	7.547	1.924	0.160	17.000	1.730	0.250
5.780	1.370	0.625	7.600	1.901	0.157	17.219	1.725	0.234
5.790	1.425	0.622	7.847	1.867	0.143	17.699	1.668	0.235
5.821	1.527	0.537	8.051	1.850	0.132	17.900	1.614	0.237
5.848	1.529	0.465	8.197	1.834	0.126	18.232	1.574	0.405
5.870	1.509	0.460	8.265	1.827	0.131	18.500	1.666	0.530
5.876	1.505	0.460	8.368	1.827	0.140	18.868	1.834	0.533
5.904	1.501	0.465	8.434	1.829	0.135	19.000	1.876	0.500
5.935	1.489	0.480	8.475	1.826	0.132	19.679	1.959	0.337
5.961	1.489	0.527	8.547	1.826	0.139	20.000	1.937	0.274
6.000	1.567	0.612	8.610	1.830	0.135	20.500	1.876	0.230
6.010	1.599	0.614	8.750	1.823	0.122	21.277	1.750	0.215
6.020	1.627	0.612	8.969	1.803	0.122	21.500	1.703	0.230
6.048	1.693	0.575	9.050	1.799	0.140	21.751	1.655	0.294
6.078	1.720	0.514	9.100	1.806	0.150	22.139	1.652	0.452
6.098	1.722	0.490	9.174	1.826	0.155	22.600	1.760	0.600
6.107	1.723	0.487	9.200	1.833	0.153	22.727	1.804	0.623
6.138	1.725	0.483	9.322	1.847	0.113	22.900	1.866	0.615
6.173	1.748	0.477	9.400	1.832	0.0900	24.310	2.075	0.460
6.199	1.765	0.462	9.434	1.821	0.0844	25.000	2.091	0.396
6.230	1.776	0.434	9.500	1.802	0.0900	26.000	2.098	0.360
6.262	1.779	0.406	9.537	1.795	0.0967	28.177	2.123	0.288
6.289	1.773	0.390	9.615	1.796	0.113	30.000	2.123	0.240
6.293	1.772	0.389	9.686	1.801	0.111	31.790	2.120	0.222
6.369	1.755	0.378	9.762	1.798	0.101	34.000	2.128	0.200
6.391	1.752	0.381	9.852	1.785	0.0968	35.423	2.133	0.183
6.424	1.757	0.395	9.998	1.771	0.121	38.000	2.131	0.150
6.457	1.779	0.414	10.080	1.776	0.138	40.000	2.132	0.144
6.485	1.804	0.409	10.152	1.789	0.146			
6.500	1.809	0.352	10.332	1.810	0.126			
6.525	1.806	0.339	10.526	1.804	0.104			
6.579	1.771	0.338	10.823	1.785	0.100			
6.600	1.759	0.340	10.893	1.788	0.120			

Can. J. Chem. Downloaded from www.nrcresearchpress.com by 195.246.54.202 on 09/08/12
For personal use only.

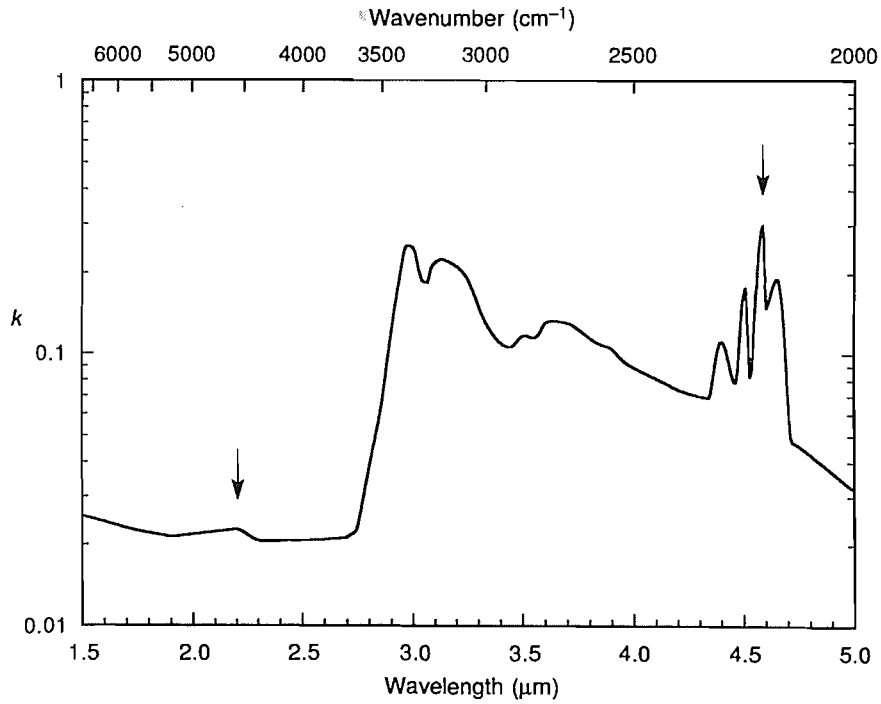

FIG. 6. The 2.2 μm overtone band of the C≡N stretching fundamental vibration at 4.5 μm in evaporated poly-HCN. Both features are marked by arrows.

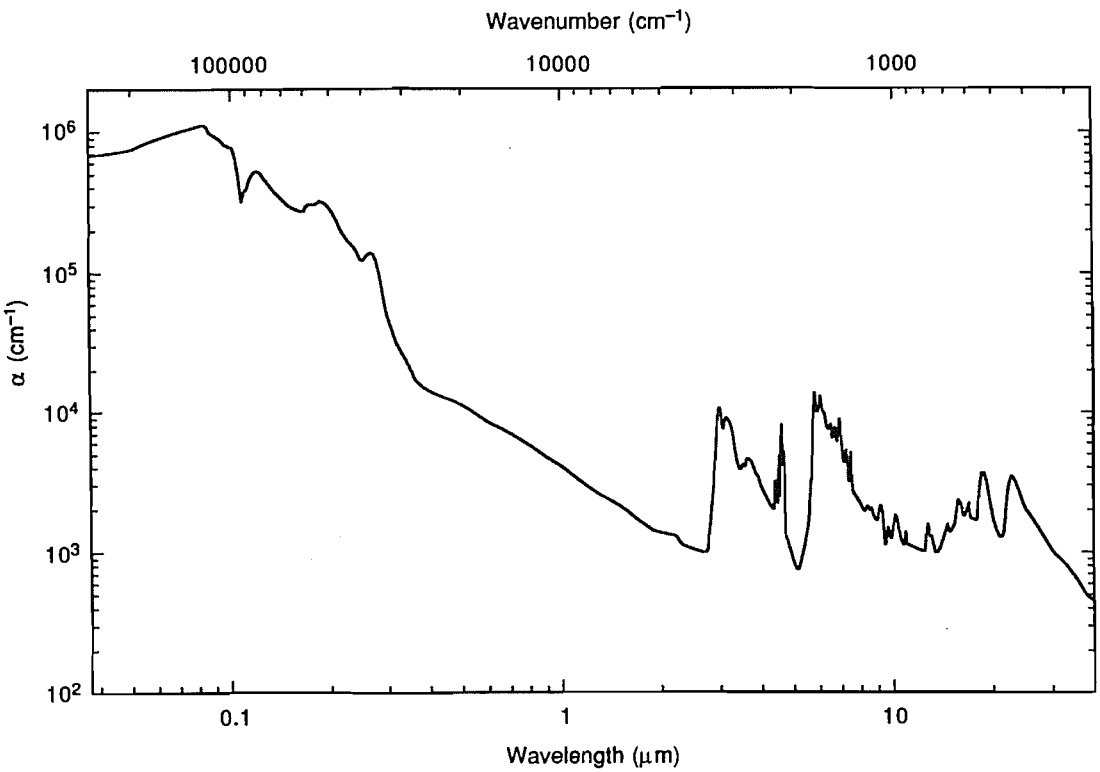

FIG. 7. Absorption coefficient (α) versus wavelength for evaporated and redeposited poly-HCN.

Can. J. Chem. Downloaded from www.nrcresearchpress.com by 195.246.54.202 on 09/08/12
For personal use only.

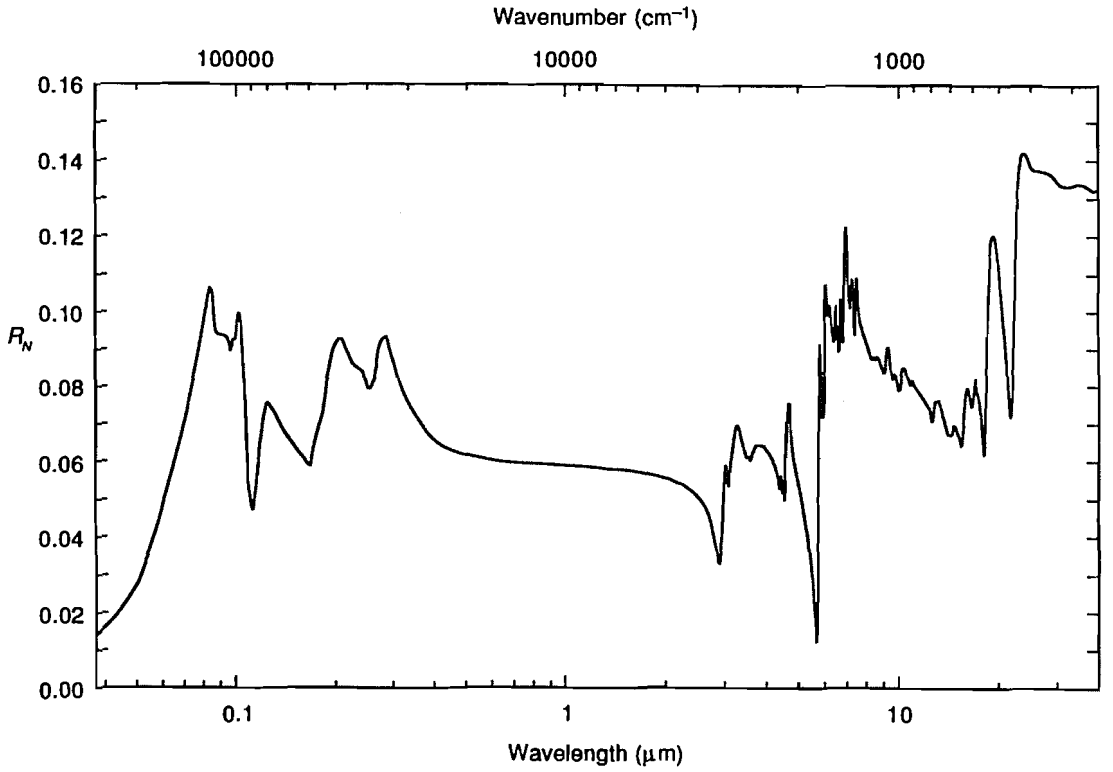

FIG. 8. Normal-incidence reflectance versus wavelength of evaporated and redeposited poly-HCN films.

are tabulated in Table 3 and are accurate to ±0.01 in absolute value and to ±0.002 on a relative scale.

4.5. Absorption coefficient, normal-incidence reflectance, dielectric function, and optical energy-loss function $Im(-1/\epsilon)$

The absorption coefficient α as a function of wavelength is shown in Figure 7. The normal-incidence reflectance R_N calculated from eq. [7] for a specular surface of poly-HCN is shown in Fig. 8. Dielectric constants $\epsilon_1 = n^2 - k^2$ and $\epsilon_2 = 2nk$ and the optical energy-loss function $\text{Im}(-1/\epsilon) = \epsilon_2/(\epsilon_1^2 + \epsilon_2^2)$ as a function of incident photon energy are shown in Fig. 9.

5. Comparison with the polymers of Bar-Nun et al. and Podolak et al.

Figure 10 shows the comparison of the imaginary part of the refractive index (k) of the evaporated and redeposited poly-HCN films determined in our investigation with the values calculated from the absorption coefficient ($-\log I/I_0$ per μm film thickness) of "poly-HCN" produced by Bar-Nun et al. (46) and Podolak et al. (47) from the photolysis of 5% HCN in CH_4 or argon. These authors identify their film as poly-HCN. Bar-Nun et al. (46) compare the absorption coefficients of their photochemically produced "poly-HCN" film with their photochemically produced polymers of C_2H_2 and C_2H_4, after correcting for the loss of light due to scattering. We assume that this correction also includes the loss of light due to reflection from the substrate and film. Thus, k is calculated for their photo-produced polymer (46) by substituting $-\log I/I_0$ values in the equation, $k = -0.183\lambda \log I/I_0\ \mu m^{-1}$, where λ is the wavelength in μm. We find poor agreement between our data and those of Bar-Nun et al. (46) and Podolak et al. (47), especially in the ultraviolet. For example, our k value at 0.21 μm is 3.96×10^{-1}, which is about an order of magnitude higher than the Bar-Nun et al. and Podolak et al. value of 2.5×10^{-2}. These authors have not displayed the infrared spectra of their putative poly-HCN so we cannot compare with the infrared spectra of other investigators.

Direct photolysis of HCN in the gas phase at 1850 Å yields $(CN)_2$, H_2, CH_4, NH_3, N_2H_4, C_2H_6, and CH_3NH_2 along with some undefined polymeric material (48). Becker and Hong (49) find similar products in their photolysis of HCN gas at 1850 Å except for H_2 and C_2H_6. They believe that H_2 is present but are unable to confirm this because of instrumental limitations. No "poly-HCN" is indicated by Mizutani et al. (48) or Becker and Hong (49) in their photolytic products. Mizutani et al. (48), in their study of the photochemical reaction of HCN and its polymeric products, refer to such polymers as "HCN polymers" only for convenience, since neither the composition nor the structures of the components of these materials are determined. Mizutani et al. caution that the degree of polymerization for some of the compounds may be sufficiently small that it may not be proper to call them polymers in the strict sense. Mizutani et al. (50) exhibit the infrared spectra of the brown polymer produced by the photochemical reaction of hydrogen cyanide in gas phase at 1849 Å; this may be what Bar-Nun et al. (46) would have obtained for their polymer. On comparing this spectrum with our unheated poly-HCN and vacuum-evaporated film of poly-HCN (Fig. 11), we find, as expected, spectral differences, although they are perhaps no more than the spectral differences among the several varieties of poly-HCN (Figs. 1, 2, 4). $(CN)_2$ is a major photolytic product of HCN and readily produces $(CN)_2$ ethanedinitrile homopolymers $(CN)_n$, also known as paracyanogen,

Can. J. Chem. Downloaded from www.nrcresearchpress.com by 195.246.54.202 on 09/08/12
For personal use only.

Can. J. Chem. Downloaded from www.nrcresearchpress.com by 195.246.54.202 on 09/08/12
For personal use only.

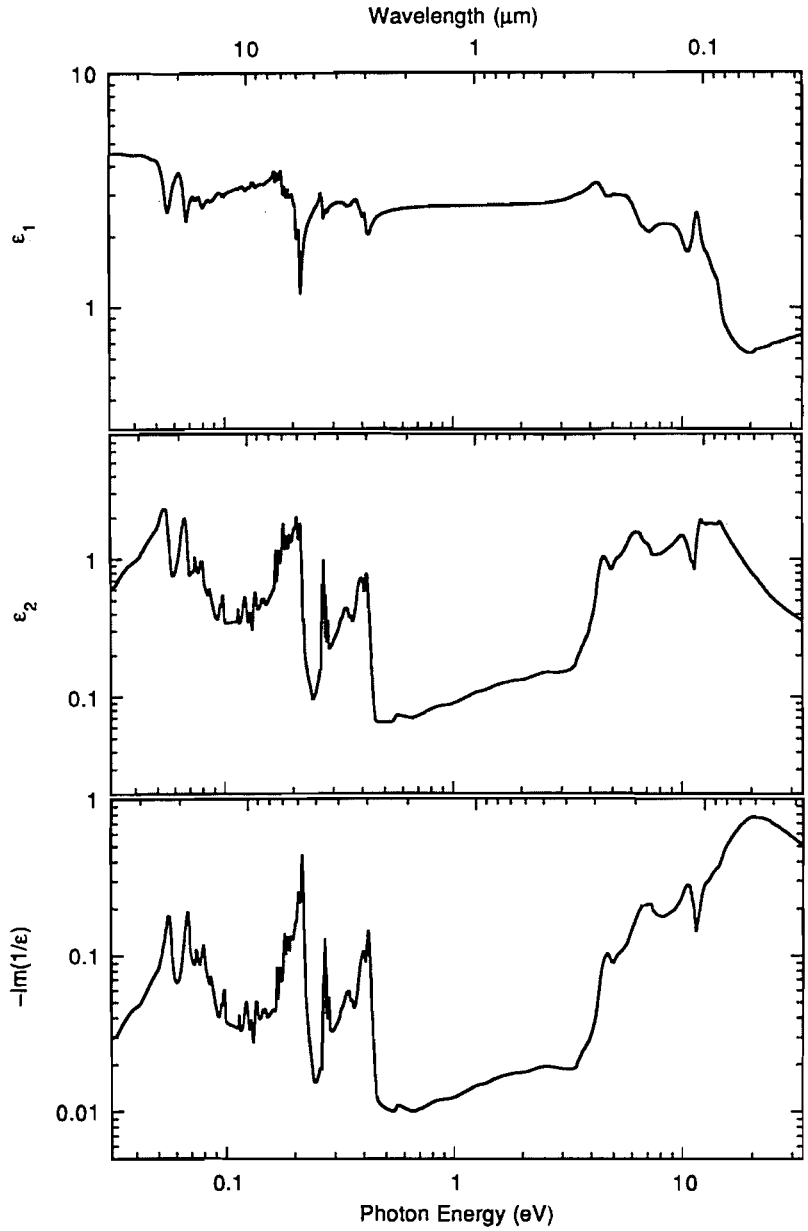

FIG. 9. Dielectric constants, ϵ_1 and ϵ_2, and energy loss function, $\mathrm{Im}(-1/\epsilon)$, of evaporated and redeposited poly-HCN as a function of photon energy.

on heating to above 400°C. It may be that Bar-Nun et al. and Podolak et al. have produced $(CN)_n$ polymer, possibly along with a Titan tholin-like material. This is further substantiated by the results of Hogness and Ts'ai (51) who found that C_2N_2 gas upon ultraviolet absorption between 2145 and 2240 Å dissociates either into two normal CN radicals or one normal and one excited CN radical, which combine with C_2N_2 producing $(CN)_3$. Thus the quantum efficiency for the photochemical reaction $(CN)_2 \rightarrow$ paracyanogen $[(CN)_n]$ is 3 moles per einstein.

Photons at 1847 Å employed by Bar-Nun et al. (46) and Podolak et al. (47) from a Hg-lamp photolysis of 5% HCN in CH_4 or argon have an energy of 6.7 eV. The approximate dissociation energy of the H—CN bond is 5.64 eV (52). Even if all the remaining 1.07 eV is partitioned to the H atom as kinetic energy, it is still insufficient to dissociate CH_4 (the bond dissociation energy for H—CH_3 is 4.42 eV.) However, it may be possible that the CN radical could attack CH_4, triggering reactions leading to Titan tholin-like material. A comparison with the imaginary part of the refractive index (k) of Titan tholin (12) is also shown in Fig. 10. The data of Bar-Nun et al. and Podolak et al., as expected, do not fit the optical constants data for Titan tholin either. Bar-Nun et al. and Podolak et al. also state that their $-\log I/I_0$ values are essentially the same whether the polymer is produced by photolyzing 5% HCN in CH_4 or Ar. This clearly indicates that CH_4 does not participate in the production of their polymer, eliminating the possibility of a Titan tholin-like material being produced.

Bar-Nun et al. and Podolak et al. did not measure the density of their polymer, but instead assumed a value of 1.18 g cm^{-3}, that of polyacrylonitrile (53). We measured the density of the du Pont poly-HCN employed in our measurement of the opti-

Can. J. Chem. Downloaded from www.nrcresearchpress.com by 195.246.54.202 on 09/08/12
For personal use only.

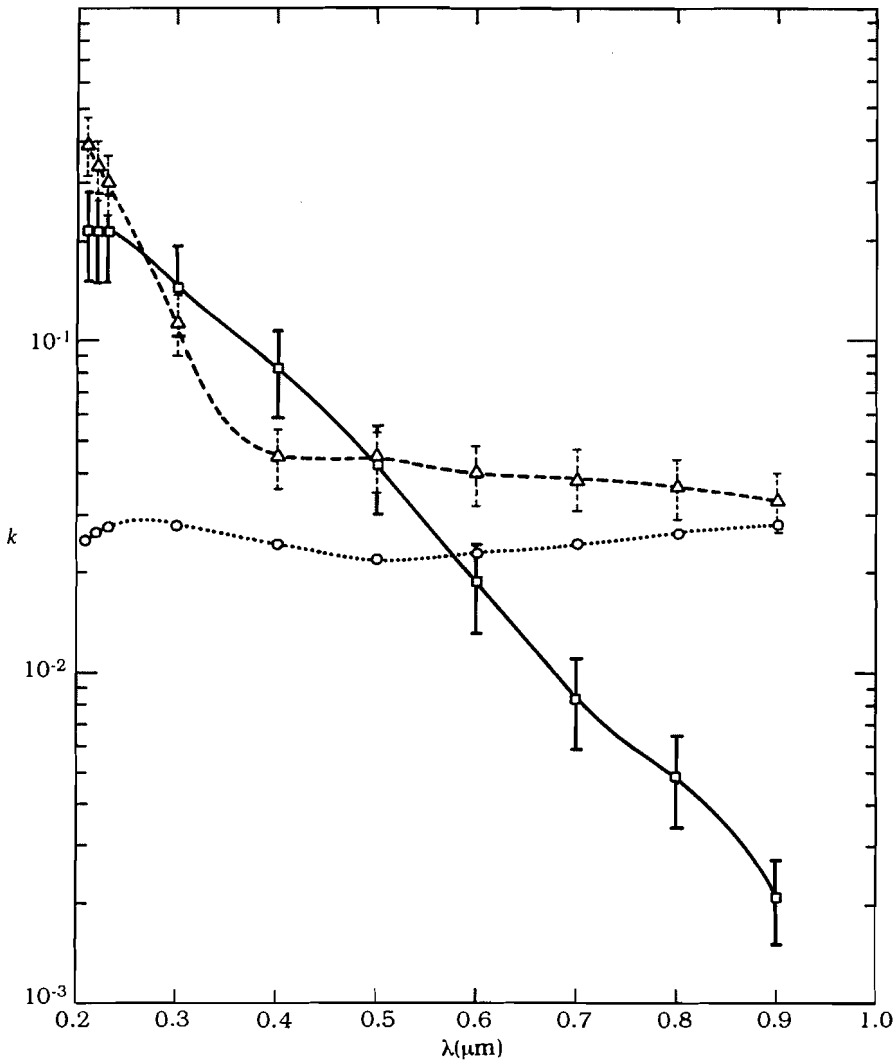

FIG. 10. Comparison of the imaginary part of the refractive index (k) of poly-HCN determined in this investigation (△) with the values calculated from the $-\log I/I_0$ per μm thick film of poly-HCN produced from the photolysis of 5% HCN in CH_4 or argon by Bar-Nun et al. (46); Podolak et al. (47) (○). Imaginary part of the refractive index (k) of Titan tholin (12) is also shown (□).

cal constants by helium pycnometry and found a value of 1.620 ± 0.004 g cm^{-3} for the du Pont poly-HCN. With this higher density, a thinner film thickness, which produces higher k values, is obtained. However, these new k values still do not help produce a match with the k values reported here. We conclude that the polymer produced by Bar-Nun et al. and Podolak et al. is not poly-HCN. It could be mainly paracyanogen with a Titan tholin-like material and a minor component of poly-HCN.

6. Comparison with other bodies in the solar system

The specular reflectance of smooth surfaces of poly-HCN in the visible part of the spectrum (Fig. 8) is about 6%. This is in the range of estimates for cometary nuclei and other dark surfaces in the outer solar system. But many other plausible organic materials have similar reflectances, for example, organic residues produced by irradiation of mixtures of hydrocarbon and water ices (19).

As an example of the application of these optical constant results to claims of abundant poly-HCN in the outer solar system, consider the haze of Saturn's large satellite Titan. Matthews (1, 54) proposes that this is due to poly-HCN and generated from HCN in the Titanian atmosphere. In Fig. 12, we plot in crosshatching the values of k from 0.3 to 0.9 μm for the Titan haze (55) deduced from groundbased data of the geometric albedo (56–58) and from 16.67 to 40 μm from Voyager spacecraft observations (59). The deduced values for $k(\lambda)$ are derived from standard models of atmospheric structure and aerosol distribution. The reduced data apply from the near ultraviolet to the middle infrared, with, unfortunately, no observations available between about 1.5 and about 10 μm, where possibly diagnostic chemical functional groups lie. If spectral features were detectable in the near- to middle-infrared, other diagnostic distinctions might be made (for example, note the difference in ratios of the 3 μm C—H absorption features and the 4.5 μm C≡N features in poly-HCN compared with Titan tholin.) Plotted in the same figure are the results of the present paper for poly-HCN and the optical constants obtained in the laboratory for Titan tholin, the organic solid produced by irradiating simulated Titanian atmospheres (12, 60). Estimated uncertainties in the model-dependent values of k for the Titan haze are about ±40% (61), while those for the laboratory observations are estimated to be about ±20% for poly-HCN and ±30% for Titan tholin. Titan tholin fits the Titan observations

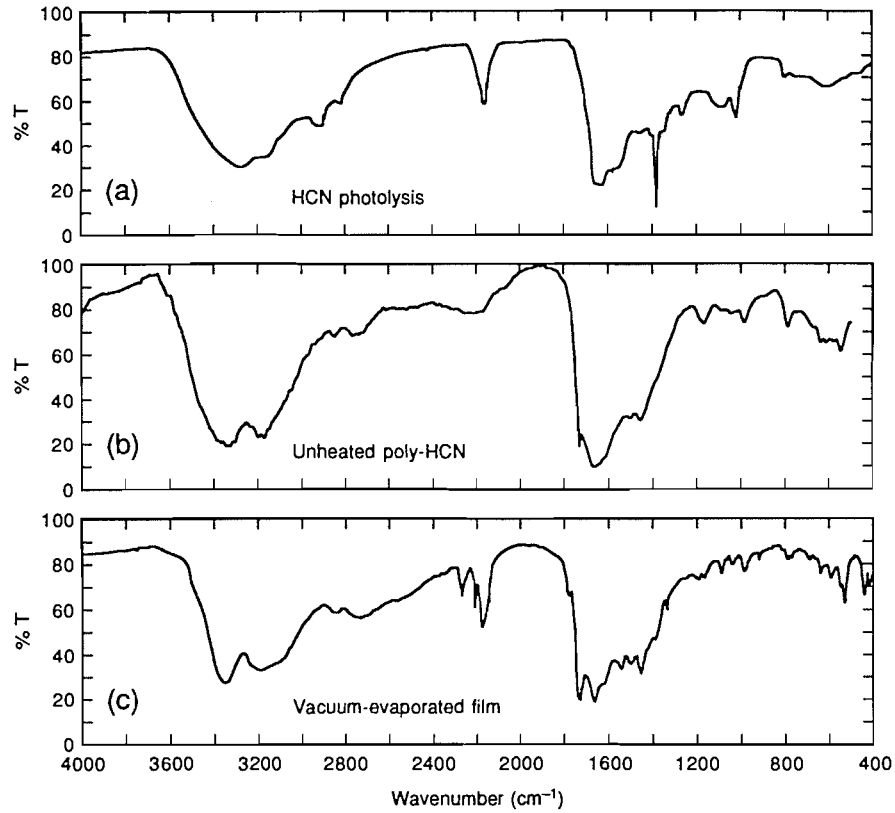

FIG. 11. The infrared spectra of (*a*) brown polymer produced by the photochemical reaction of hydrogen cyanide in gas phase at 1849 Å (50) is compared with (*b*) unheated poly-HCN and (*c*) vacuum evaporated film of poly-HCN.

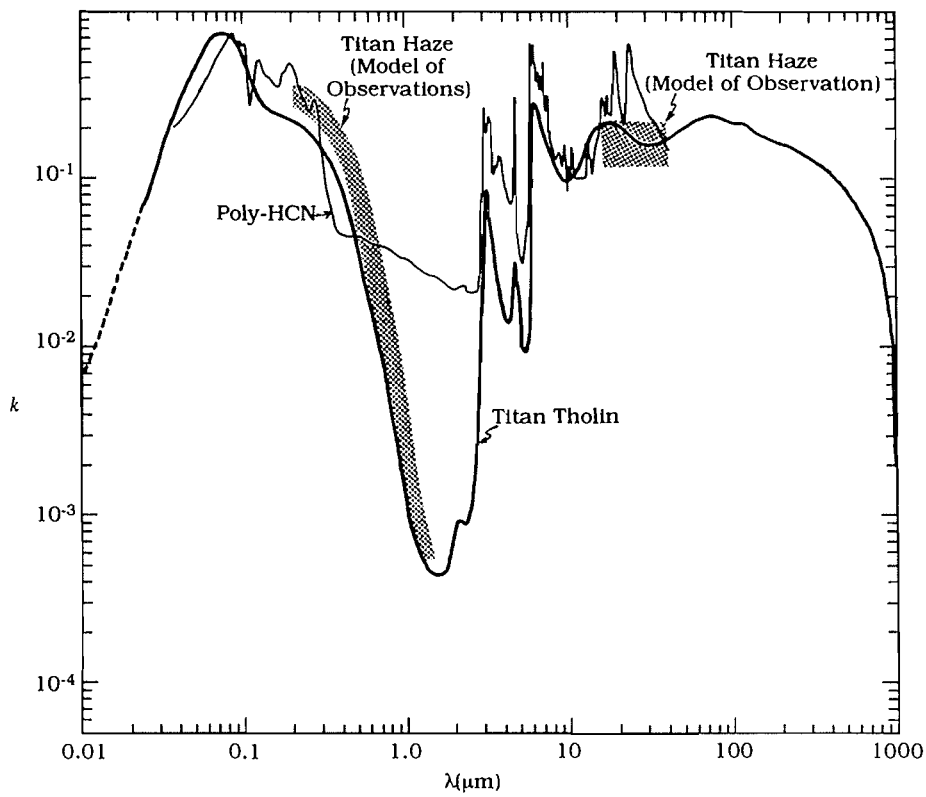

FIG. 12. Comparison of the imaginary part, *k*, of the complex refractive index from 0.3 to 0.9 μm of the organic haze of Titan (55), derived from groundbased data of the geometric albedo (56–58) and from 16.67 to 40 μm (59) after normalizing *k* at 40 μm, with *k* for poly-HCN (this paper), and for the organic residue (Titan tholin) obtained from plasma discharge through a 9:1 N_2/CH_4 mixture (60, 12). Probable errors of the groundbased data are shown by the stippling from 0.2 to 1.0 μm, *k* from 16.67 to 40 μm is normalized to Titan tholin at 40 μm. Probable errors for the laboratory measurements are about ±20% for poly-HCN and ±30% for Titan tholin.

Can. J. Chem. Downloaded from www.nrcresearchpress.com by 195.246.54.202 on 09/08/12
For personal use only.

Can. J. Chem. Downloaded from www.nrcresearchpress.com by 195.246.54.202 on 09/08/12
For personal use only.

within the probable errors (60), and no other proposed material does. It is apparent that, in the visible and near-infrared, the fit is far better for Titan tholin than for poly-HCN. Titan tholin is much redder in the visible than poly-HCN, and poly-HCN displays a sharp discontinuity (absorption edge) at about 0.35 μm, which neither the Titan haze nor Titan tholin display. In the long visible and near-infrared, poly-HCN exhibits one to two orders of magnitude larger values of k than does Titan or Titan tholin. Poly-HCN can therefore be at best a minor constituent of the Titan haze.

The volatile component of Titan tholin, when examined by sequential and nonsequential pyrolytic GC–MS, reveals over 100 products, including aliphatic hydrocarbons, nitriles, polycyclic aromatic hydrocarbons, amines, pyroles, pyrazines, pyridines, pyrimidines, and, perhaps, the purine adenine (15, 17). Independent evidence for the presence of PAHs has now been found (62). A number of these compounds are not present in poly-HCN and would not be expected to be released on volatilization of poly-HCN. In addition, of course, it makes intuitive sense that the organic solid generated by irradiation of simulated Titanian atmospheres, experiments that successfully and quantitatively reproduce the gas-phase organics in Titan's atmosphere (63), should be the best candidate for the organic haze of Titan (60).

Pesce-Rodriguez et al. (64) suggest that the similarity between "HCN polymers" and the Murchison meteorite is "striking", at least in the middle infrared. However, a comparison of the optical constants of poly-HCN, reported here, and those of an organic residue from the Murchison carbonaceous chondrite (18) reveals major discrepancies. Meteoritic organics are not poly-HCN.

As model optical constants of other hazes and surfaces in the outer solar system become available, they also can be compared with laboratory optical constants of poly-HCN, tholins, and other materials, as done here for Titan, and the claims for poly-HCN assessed on a case-by-case basis. Much simpler comparisons of laboratory with planetary spectra may also be useful, but may not be nearly as definitive. The exclusion of poly-HCN as the principal constituent of the Titan haze does not exclude its presence elsewhere. It might, for example, be that poly-HCN is too neutrally colored in the visible to explain reddish clouds and surfaces, but might be a useful model for much blacker surfaces. However, other, perhaps more likely, materials — such as some PAHs or elemental carbon (or tholins produced from CH_4) — may prove more successful. Because of its low albedo and explosive polymerization, poly-HCN is a reasonable candidate for the dark lag deposit of cometary nuclei. Our measured values of the optical constants may find use in modelling of the cometary dust.

We have recently used Hapke scattering theory and a linear superposition of the optical constants of a number of materials in an attempt to explain the observed spectrum of 5145 Pholus, a very red asteroid or comet on an eccentric orbit with aphelion beyond Uranus (65). All good fits seem to require ~10% poly-HCN, or some other material with similar strong absorption in the near-infrared.

7. Acknowledgements

This research was supported by NASA grant NAGW 3273, "Studies of Satellite and Planetary Atmospheres", NASA Planetology Grant NAGW 1870, the Kenneth T. and Eileen L. Norris Foundation, and by the U.S. Department of Energy contract DE-AC05-84OR 21400 with Martin Marietta Energy Systems, Inc. We thank C.N. Matthews for stimulating this study and for supplying poly-HCN for our preliminary spectral studies, R. Geyer and L. Pesce of du Pont for bulk samples of poly-HCN employed in the measurement of the optical constants, and Chris McKay for his interest and advice in this project.

1. C.N. Matthews. Origins Life, **21**, 421 (1992).
2. C.N. Matthews and R. Ludicky. Proc. ESLAB Symp. 20th, Exploration of Halley's Comet. Eur. Space Agency [Spec. Publ.] ESA SP-250, 273 (1986).
3. C.N. Matthews and R. Ludicky. Solid State NMR Polym. [Proc. Annu. Chem. Conf. North Am. Solid State NMR Polym.], 3rd, 1988. *Edited by* L.J. Mathais. Plenum, New York. 1991. p. 331.
4. M. Allen, J.P. Pinto, and Y.L. Yung. Astrophys. J. **242**, L125 (1980).
5. D.P. Cruikshank, L.J. Allamandola, W.K. Hartmann, D.J. Tholen, R.H. Brown, C.N. Matthews, and J.F. Bell. Icarus, **94**, 345 (1991).
6. C.N. Matthews. The search for extraterrestrial life: recent developments. *Edited by* M.D. Papagiannis. 1985. p. 151.
7. C.N. Matthews and R.E. Moser. Proc. Natl. Acad. Sci. U.S.A. **56**, 1087 (1966).
8. C.N. Matthews and R.E. Moser. Nature, **215**, 1230 (1967).
9. B.N. Khare and C. Sagan. Icarus, **20**, 311 (1973).
10. C. Sagan and B.N. Khare. Nature, **277**, 102 (1979).
11. C. Sagan, B.N. Khare, and J.S. Lewis. Saturn. *Edited by* T. Gehrels and M.S. Matthews. University of Arizona Press, Tucson. 1984. p. 788.
12. B.N. Khare, C. Sagan, E.T. Arakawa, F. Suits, T.A. Callcott, and M.W. Williams. Icarus, **60**, 127 (1984).
13. G.D. McDonald, B.N. Khare, W.R. Thompson, and C. Sagan. Icarus, **94**, 354 (1991).
14. B.N. Khare, C. Sagan, J.E. Zumberge, D.S. Sklarew, and B. Nagy. Icarus, **48**, 290 (1981).
15. B.N. Khare, C. Sagan, W.R. Thompson, E.T. Arakawa, F. Suits, T.A. Callcott, M.W. Williams, S. Shrader, H. Ogino, T.O. Willingham, and B. Nagy. Adv. Space Res. **4**, 59 (1985).
16. B.N. Khare, C. Sagan, H. Ogino, B. Nagy, C. Er, K.H. Schram, and E.T. Arakawa. Icarus, **68**, 176 (1986).
17. P. Ehrenfreund, J.J. Boon, J. Commandeur, C. Sagan, W.R. Thompson, and B.N. Khare. Adv. Space Res. In press.
18. B.N. Khare, W.R. Thompson, C. Sagan, E.T. Arakawa, C. Meisse, and I. Gilmour. Proc. Int. Conf. Lab. Res. Planetary Atmospheres, 1st, NASA CP-3077, 340 (1990).
19. B.N. Khare, W.R. Thompson, L. Cheng, C. Chyba, C. Sagan, E.T. Arakawa, C. Meisse, and P.S. Tuminello. Icarus, **103**, 290 (1993).
20. A.F. Lunin, L.A. Pakhomov, V.A. Vinokurov, V.F. Novikov, V.N. Barybin, V.R. Mkrtychan, and A.V. Burobin. Khim. Vys. Energ. **12**, 380 (1978).
21. S.L. Miller. J. Am. Chem. Soc. **77**, 2351 (1955).
22. C. Sagan and S.L. Miller. Astron. J. **65**, 499 (1960).
23. K. Ziegler. Hydrogen cyanide (anhydrous) organic synthesis. Vol. I. *Edited by* Henry Gilman. John Wiley & Sons, Inc., New York. 1932. p. 307.
24. W.R. Jenks. Kirk–Othmer concise encyclopedia of chemical technology. Wiley–Interscience Publications, New York. 1985. p. 334.
25. T. Völker. Angew. Chem. **69**, 728 (1957).
26. T. Völker. Angew. Chem. **72**, 379 (1960).
27. R.A. Evans, P. Lorenčak, T. Ha, and C. Wentrup. J. Am. Chem. Soc. **113** 7261 (1991).
28. R.A. Evans, S.M. Lacombe, M.J. Simon, G. Pfister-Guillouzo, and C. Wentrup. J. Phys. Chem. **96**, 4801 (1992).
29. J.P. Ferris and W.J. Hagan, Jr. Tetrahedron, **40**, 1093 (1984).

30. R.A. Sanchez, J.P. Ferris, and L.E. Orgel. J. Mol. Biol. **30**, 223 (1967).
31. J.P. Ferris, D.B. Donner, and W. Lotz. J. Am. Chem. Soc. **94**, 6968 (1972).
32. J.P. Ferris and E.H. Edelson. J. Org. Chem. **43**, 3989 (1978).
33. J.P. Ferris. Science, **203**, 1135 (1979).
34. C.N. Matthews and R. Ludicky. Adv. Space Res. **12**, 21 (1992).
35. T.W. Rettig, S.C. Tegler, D.J. Pasto, and M.J. Mumma. Astrophys. J. **398**, 293 (1992).
36. F. Woeller and C. Ponnamperuma. Icarus, **10**, 386 (1969).
37. B.N. Khare and C. Sagan. Science, **189**, 722 (1975).
38. L.J. Bellamy. The infrared spectra of complex molecules. John Wiley & Sons, New York. 1975.
39. H.A. Szymanski. Infrared band handbook. Plenum, New York. 1963.
40. D.J. Pasto and C.R. Johnson. Organic structure determination. Prentice-Hall, Inc., Englewood Cliffs, N.J. 1969.
41. N.B. Colthup. J. Opt. Soc. Am. **40**, 397 (1950).
42. M.W. Williams, E.T. Arakawa, and T. Inagaki. *In* Handbook on synchrotron radiation. Vol. 4. *Edited by* S. Ebashi, M. Koch, and E. Rubenstein. Elsevier Science Publishers, New York. 1991.
43. T. Inagaki, L.C. Emerson, E.T. Arakawa, and M.W. Williams. Phys. Rev. B, **13**, 2305 (1976).
44. M.W. Williams, R.N. Hamm, E.T. Arakawa, L.R. Painter, and R.D. Birkhoff. Int. J. Radiat. Phys. Chem. **7**, 95 (1975).
45. F. Abeles. J. Phys. Radium, **11**, 310 (1950).
46. A. Bar-Nun, I. Kleinfeld, and E. Ganor. J. Geophys. Res. **93**, 8383 (1988).
47. M. Podolak, N. Noy, and A. Bar-Nun. Icarus, **40**, 193 (1979).
48. H. Mizutani, H. Mikuni, M. Takahasi, and N. Noda. Origins Life, **6**, 513 (1975).
49. R.S. Becker and J.H. Hong. J. Phys. Chem. **87**, 163 (1983).
50. H. Mizutani, H. Mikuni, and M. Takahasi. Chem. Lett. 573 (1972).
51. T.R. Hogness and L. Ts'ai. J. Am. Chem. Soc. **54**, 123 (1932).
52. J.G. Calvert and J.N. Pitts, Jr. Photochemistry. John Wiley & Sons, Inc., New York. 1966. p. 826.
53. J. Brandrup and E.H. Immergut. Polymer handbook. Interscience, New York. 1966.
54. C.N. Matthews. Origins Life, **12**, 281 (1982).
55. C.P. McKay, J.B. Pollack, and R. Courtin. Icarus, **80**, 23 (1989).
56. J.S. Neff, D.C. Humm, J.T. Bergstrahl, A.L. Cochran, W.D. Cochran, E.S. Barker, and R.G. Tull. Icarus, **60**, 221 (1984).
57. J.S. Neff, T.A. Ellis, J. Apt, and J.T. Bergstrahl. Icarus, **62**, 425 (1985).
58. U. Fink and H.P. Larson. Astrophys. J. **233**, 1021 (1979).
59. R.E. Samuelson and L.A. Mayo. Icarus, **91**, 207 (1991).
60. C. Sagan, W.R. Thompson, and B.N. Khare. Acc. Chem. Res. **25**, 286 (1992).
61. C.P. McKay and O.B. Toon. Proc. Symp. Titan. Eur. Space Agency, [Spec. Publ.] ESA SP 338, 185 (1992).
62. C. Sagan, B.N. Khare, W.R. Thompson, G.D. McDonald, M.R. Wing, J.L. Bada, T. Vo-Dinh, and E.T. Arakawa. Astrophys. J. **414**, 399 (1993).
63. W.R. Thompson, T.J. Henry, J.M. Schwartz, B.N. Khare, and C. Sagan. Icarus, **90**, 57 (1991).
64. R.A. Pesce-Rodriguez, S.A. Liebman, and C.N. Matthews. Int. Conf. Origins Life, Barcelona, 10th, July 4–9, 1993.
65. P.D. Wilson, C. Sagan, and W.R. Thompson. Icarus. In press.

Can. J. Chem. Downloaded from www.nrcresearchpress.com by 195.246.54.202 on 09/08/12
For personal use only.

A density functional theory study of the free radicals NH_2, NF_2, NCl_2, PH_2, PF_2, and PCl_2

MAGGIE A. AUSTEN, LEIF A. ERIKSSON,[1] AND RUSSELL J. BOYD[2]

Department of Chemistry, Dalhousie University, Halifax, NS B3H 4J3, Canada

Received July 29, 1993

This paper is dedicated to Professor John C. Polanyi on the occasion of his 65th birthday

MAGGIE A. AUSTEN, LEIF A. ERIKSSON, and RUSSELL J. BOYD. Can. J. Chem. **72**, 695 (1994).

The linear combination of Gaussian-type orbitals – density functional theory (LCGTO–DFT) approach is used to study geometries and hyperfine structures of a set of neutral radicals. Each of the title molecules is investigated by means of local density approximation calculations, and using the Becke–Perdew and Perdew–Wang–Perdew corrections to the exchange and correlation functionals. The effects of local vs. non-local potentials and of various basis sets are investigated. Total densities and unpaired spin densities are compared. The isotropic couplings are found to be very dependent on the type of exchange functional used, whereas the anisotropic couplings are relatively insensitive to the choice of basis set and functional. In most cases, the Perdew–Wang exchange corrections provide isotropic couplings in satisfactory agreement with experiment.

MAGGIE A. AUSTEN, LEIF A. ERIKSSON et RUSSELL J. BOYD. Can. J. Chem. **72**, 695 (1994).

On a utilisé la combinaison linéaire d'orbitales de type gaussien avec la théorie de densité fonctionnelle (LCGTO-DFT) pour étudier les géométries et les structures hyperfines d'un ensemble de radicaux neutres. On a étudié chacune des molécules mentionnées dans le titre à l'aide de calculs d'approximation de la densité locale et en utilisant les corrections de Becke–Perdew et Perdew–Wang–Perdew pour les fonctions d'échange et de corrélation. On a examiné les effets des potentiels locaux et non locaux ainsi que de divers ensembles de base. On a comparé les densités totales et les densités de spin non pairés. On a trouvé que les couplages isotropes sont très dépendants sur le type de fonction d'échange utilisé alors que les couplages anisotropes sont relativement insensibles au choix de l'ensemble de base et de la fonction. Dans la plupart des cas, les corrections d'échange de Perdew–Wang fournissent des couplages isotropes qui sont en accord satisfaisant avec les données expérimentales.

[Traduit par la rédaction]

Can. J. Chem. Downloaded from www.nrcresearchpress.com by 195.246.54.202 on 09/08/12
For personal use only.

1. Introduction

The six molecules investigated — NH_2, NF_2, NCl_2, PH_2, PF_2, and PCl_2 — have previously been subject to detailed theoretical and experimental studies. Most theoretical work has, quite naturally, been devoted to the structure and properties of the smallest of the compounds, NH_2. In particular, the detailed work by Grein and co-workers (1, 2), using multireference configuration interaction theory (MRCI) and extended basis sets, has yielded geometries and hyperfine (hf) structures of very high accuracy. The coupled cluster (CC) calculations by Sekino and Bartlett (3) and the coupled electron pair approximation (CEPA) studies by Pöhlchen et al. (4) have also yielded very accurate determinations of the properties of NH_2.

The hyperfine structures of NH_2 and NF_2 have recently been investigated by means of CI including all single and double excitations from a single reference determinant (CISD) (5). In this study, the fairly small but highly successful basis sets by Chipman (6) were employed. Chipman previously pointed out the importance of very high exponents of the *s*-functions in the bases (6), and uses, as opposed to many other scientists in the field, only a very moderate expansion in terms of higher orbital quantum numbers.

In an *ab initio* study of the geometry of difluoroamidogen (NF_2), Cai et al. (7) have shown that both correlation effects and a basis set that includes polarization functions are important for an appropriate description of the ground state geometry. For NF_2 (8), and for PH_2 (9), multiconfiguration SCF (MCSCF) studies have yielded geometries and ground state properties in very good agreement with experiment.

On the other hand, UHF calculations by Hinchliffe and Bounds (10), on the entire series presently investigated, also yielded geometries in good agreement with experiment. The computed hyperfine (hf) coupling constants also reported in that study are, after annihilation of the spin contamination, in reasonable agreement with experiment in most cases.

The aim of the present study is to investigate how well density functional theory (DFT) can perform on this group of compounds, in terms of equilibrium geometries as well as their hyperfine structures. We have previously shown that DFT can yield highly accurate equilibrium geometries and isotropic hf couplings for hydrocarbon radical cations (11, 12) even at the local density level, whereas for heteroatoms a non-local description of the exchange and correlation functional is often required in order to reproduce experimental data (13).

The paper is organized as follows. We first outline the theoretical model used, although we refer to previous work (12, 13) for more detailed descriptions of the hf calculations. For two excellent reviews, see also ref. 14. In Sect. 3, the optimized geometries, isotropic and anisotropic hf structures, and the total and unpaired spin densities are presented. We conclude in Sect. 4 with a summary of the results.

2. Method

In this study, we use the linear combination of Gaussian-type orbitals – density functional theory (LCGTO–DFT) program deMon (15) for all geometry optimizations. The particular version employed was slightly modified (16) to allow for partial inclusion of symmetry in the calculations. The hyperfine calculation routine is by Malkin and co-workers (12, 13). The isotropic hf coupling on centre N is obtained from the equation

$$[1] \quad a^{(N)}_{\text{isotropic}} = \frac{8\pi}{3} g\beta g_N \beta_N \sum_{\mu,\nu} P^{\alpha-\beta}_{\mu,\nu} \langle \phi_\mu(0) | \phi_\nu(0) \rangle$$

and is a direct measure of the spin density at the corresponding nucleus. The elements of the anisotropic hf tensor are obtained as

[1] Present address: Department of Physics, University of Stockholm, Box 6730, 113 85 Stockholm, Sweden.

[2] Author to whom correspondence may be addressed.

Can. J. Chem. Downloaded from www.nrcresearchpress.com by 195.246.54.202 on 09/08/12
For personal use only.

$$[2] \quad T_{i,j} = g\beta g_N \beta_N \sum_{\mu,\nu} P^{\alpha-\beta}_{\mu,\nu} \langle \phi_\mu | r^{-5}(r^2\delta_{i,j} - 3r_i r_j) | \phi_\nu \rangle$$

and are indirectly related to the spatial distribution of the density. This arises as a result of interactions between the magnetic moments of the electron and the nuclei, and is also referred to as the dipolar hf coupling due to the integral expression. The local density approximation (LDA) of Vosko, Wilk, and Nusair (17) is used. In addition, a non-local correction to the correlation functional, by Perdew (18), is used in conjunction with two different non-local corrections to the exchange functional, one by Becke (19), and one by Perdew and Wang (20). These combinations of corrections to the exchange and correlation functionals will be referred to as BP and PWP, respectively. In all calculations, the auxiliary basis sets used are (5,1;5,1) for H, (5,2;5,2) for N and F, and (5,4;5,4) for P and Cl (21). The orbital basis sets used are all based on Huzinaga's $9s5p$ or $11s7p$ series ($5s$ or $6s$ for the hydrogens) (22), to which we add a set of one or two polarization functions. These are loosely contracted to form the (51111/2111/1) and (5111111/211111/11) bases, respectively (23). These basis sets have been employed with great success in *ab initio* and DFT calculations of nuclear magnetic resonance (NMR) parameters (23, 24), as well as in previous DFT studies of hyperfine structures (12, 13). The contracted basis sets will be referred to as IGLO-II and IGLO-III, respectively, from their original individual gauge of localized orbitals (IGLO) – NMR applications (23). The IGLO-III bases are also used in uncontracted form, and then are labelled IIIu-d_2 and IIIu-d_4 in the present study. In IIIu-d_2, the two d-type polarization functions are added to the $11s7p$ bases, whereas in IIIu-d_4, four polarization functions are added. IGLO-III is used for all atoms, IGLO-II is used for P and Cl, IIIu-d_2 and IIIu-d_4 are used for N, H, and F.

2.1 Geometry optimization and hyperfine structure calculations

In all calculations, the hf structures were computed at the same level of theory as in the corresponding geometry optimizations. For some of the systems, the hf calculations were also performed on the experimental geometries.

NH_2: The orbital basis sets are varied such that the same set is used for both atomic types in all calculations. Thus the molecule is studied using nine different theoretical models: LDA/IGLO-III, LDA/IIIu-d_2, LDA/IIIu-d_4, BP/IGLO-III, BP/IIIu-d_2, BP/IIIu-d_4, PWP/IGLO-III, PWP/IIIu-d_2, and PWP/IIIu-d_4.

NF_2: The same combinations of basis sets and potentials are used as in NH_2.

NCl_2: The IGLO-III basis set is used for N in all calculations. The IGLO-III and IGLO-II basis sets are used for Cl, giving a total of six theoretical models. No experimental geometries have been reported for this molecule.

PH_2: Only the IGLO-III orbital basis set is used for P together with the IGLO-III, IIIu-d_2, and IIIu-d_4 basis sets for H, giving nine sets of data.

PF_2: The same models are used as in the PH_2 study. No experimental geometries are found in the literature.

PCl_2: The orbital basis sets IGLO-II and IGLO-III are used. This gives six data sets. For this molecule also, there are no experimental geometries available for comparison.

Finally, the hyperfine structures are calculated for NH_2, NF_2, and PH_2, using the experimental geometries. Only the IGLO-III basis set is employed, but the effect of non-local corrections is examined. All anisotropic hf parameters are in the principal magnetic coordinate system.

2.2 Density study

The total and unpaired spin densities (ρ^{tot} and ρ^u, respectively), and the Laplacian of ρ^{tot} ($\nabla^2\rho^{tot}$) are plotted for NH_2, NF_2, and PH_2, at the experimental geometries. The calculations required for this study were done using the PROAIM package by Bader and co-workers (25). Only the IGLO-III basis set was used, and the Laplacians were analysed using the LDA only. For the densities, however, all three potential forms were used in each case, giving three plots per density analysed. For the final analysis, density differences between the three functionals were plotted. All plots are done in the molecular (yz) plane, the z axis being the C_2 axis of the system, with an increment in density of 0.100 au between each contour in the plots.

3. Results

3.1 Geometries

Optimized and experimental geometries are presented in Tables 1*a* and 1*b*, along with previous theoretical data. The DFT-optimized geometries show very little dependence on basis set, but are affected by the choice of functional form.

In amidogen (NH_2), all the optimized bond lengths are very similar, and all are somewhat overestimated. Bond angles are well reproduced, but slightly too small. The LDA gives the longest bond lengths and the largest angles.

In NF_2, the bond lengths are again somewhat too long. In this case, the LDA gives the shortest bond lengths, which are in excellent agreement with experiment. The bond angles are also very well reproduced, and all potentials give very similar results. The uncontracted IIIu-d_2 basis set, however, gives noticeably smaller angles than the other two.

In NCl_2, the LDA gives the smallest angles and, as in NF_2, the shortest bonds. Relative to previous UHF results (10), R_{NCl} is shorter and $\angle$ClNCl is larger at all DFT levels presently used. An examination of the nitrogen series shows that non-local corrections do affect the optimized geometries slightly, but that the potentials have different effects on different molecules.

In PH_2, the bond lengths are consistently too long relative to experiment, and the angles are underestimated by 0.9°–1.7°. In this case, the LDA gives the worst agreement with experiment, with some of the longest bonds and the smallest angles.

In the rest of the phosphorus series, the LDA gives the shortest bonds and the smallest angles.

Looking at both the phosphorus and the nitrogen compounds it can be seen that in the halide-containing molecules, the non-local corrections tend to lengthen the bonds, and open the angles, whereas in the hydrogen-containing molecules, the corrections tend to shorten the bond. All potentials overestimate the bond lengths and underestimate the bond angles in NH_2, NF_2, and PH_2, relative to experiment.

The success of the LDA to produce accurate ground state geometries is well known (11, 26, 27), and it has also been found, in the case of hydrogen-containing compounds, that non-local effects generally lead to shorter X—H bonds. Bonds between heteroatoms, on the other hand, generally become enlongated at the BP and PWP levels, relative to the LDA results (13, 28). The present results are in good agreement with the previous findings.

Comparing the changes in geometry down the nitrogen series with those down the phosphorus series, some interesting differ-

TABLE 1*a*. DFT-optimized geometries using the IGLO-III basis set. Bond lengths are in angstroms, bond angles are in degrees

Molecule		LDA	BP	PWP	Expt.[a]	UHF[b]	MCSCF[c,d]
NH_2	Bond length	1.038	1.036	1.036	1.024	1.009	
	Bond angle	103.1	102.7	102.9	103.3	104.2	
NF_2	Bond length	1.349	1.380	1.391	1.349	1.352	1.361
	Bond angle	103.4	103.6	103.5	103.3	104.7	103.2[c]
NCl_2	Bond length	1.689	1.725	1.718	—	1.731	
	Bond angle	110.8	111.2	111.3	—	109.8	
PH_2	Bond length	1.438	1.436	1.437	1.418	1.405	1.442
	Bond angle	90.0	90.7	90.6	91.7	92.3	92.9[d]
PF_2	Bond length	1.590	1.612	1.622	—	1.572	
	Bond angle	97.9	98.2	98.1	—	98.0	
PCl_2	Bond length	2.041	2.074	2.074	—	2.065	
	Bond angle	102.1	103.1	103.1	—	102.2	

[a]Reference 35.
[b]Reference 10.
[c]Reference 8.
[d]Reference 9.

TABLE 1*b*. Effects of basis set and potential on optimized geometries of NH_2 and NF_2. Bond lengths in angstroms, bond angles are in degrees

		NH_2		NF_2	
Funct.	Basis	Bond length	Bond angle	Bond length	Bond angle
LDA	IGLO-III	1.038	103.1	1.349	103.4
	IIIu-d_2	1.038	103.1	1.350	103.1
	IIIu-d_4	1.037	103.1	1.350	103.5
BP	IGLO-III	1.036	102.7	1.380	103.6
	IIIu-d_2	1.036	102.8	1.383	103.2
	IIIu-d_4	1.035	102.8	1.382	103.6
PWP	IGLO-III	1.036	102.9	1.391	103.5
	IIIu-d_2	1.036	103.1	1.395	103.0
	IIIu-d_4	1.035	103.0	1.395	103.5

ences are found. The experimental angles in NH_2 and NF_2 are identical, and the optimized values differ by only 0.5°. The angle in NCl_2 is calculated to be 8° larger. On the other hand, between PH_2 and PF_2, the calculated angles widen by 8°. Between PF_2 and PCl_2 the angle increases by just over 4°.

The smaller changes in angle are accompanied by larger changes in bond length, to compensate for the increased steric repulsion. The bond length increases by 30% (+0.35 Å) between NH_2 and NF_2, and by 20% (+0.35 Å) between NF_2 and NCl_2. Going down the phosphorus series, from PH_2 to PF_2 to PCl_2, the bond lengthens by 10% (+0.2 Å) and then by 30% (+0.5 Å).

As a whole, the geometries obtained in the present study agree well with experiment, where available, and are in qualitative agreement with previous theoretical data (cf. Table 1*a*). Interesting to note is that the non-local DFT calculations consistently predict more elongated bonds for the phosphorus compounds than does UHF, although the bond angles generally differ very little between various levels of theory.

3.2 Hyperfine structures

3.2.1 Isotropic couplings

Most hyperfine calculations are done directly following the corresponding LCGTO–DFT geometry optimization, using the same theoretical model (basis set and potential). Previous work has shown that isotropic coupling constants are highly geometry dependent (13, 29). However, by comparing the results computed at the experimental and DFT–optimized geometries, it can be seen that the geometry changes involved in this study are too small to make a significant difference. Furthermore, the changes are much larger when introducing non-local corrections than when the geometry and (or) basis sets are varied.

An examination of the isotropic coupling constants for ^{14}N in NH_2 (Table 2*a*) shows that the geometry is a much less significant factor than the basis set. Looking at the BP results we see that the optimized geometries from the three basis sets (cf. Table 1*b*) are virtually identical, although not in perfect agreement with the experimental geometry (cf. Table 1*a*). Nevertheless, the Fermi contact term calculated with the IGLO-III basis set at the experimental geometry is very similar to that obtained at the IGLO-III optimized geometry, but quite different from the IIIu-d_2 and IIIu-d_4 values. This trend continues through the rest of the molecules.

From these considerations it can be concluded that in this study geometry effects are of minor importance, particularly for the three smallest systems. The choice of basis set, however, does have a small effect on the isotropic coupling constant. Tables 2*a* and 2*b* also show that the largest factor affecting the Fermi contact term is the non-local correction used. Changing the potential can cause a doubling or tripling of the a_{iso} value. This was also observed in a detailed study of the hf structure of ^{17}O in the water cation (13), and is related to the corrections in the core and valence tails of the density, brought about by the non-local gradient corrections (cf. ref. 31). Consequently, the LDA and the BP corrections generally give numerically too small values.

The PWP level of theory gives excellent results for N in NH_2

Can. J. Chem. Downloaded from www.nrcresearchpress.com by 195.246.54.202 on 09/08/12
For personal use only.

Can. J. Chem. Downloaded from www.nrcresearchpress.com by 195.246.54.202 on 09/08/12
For personal use only.

TABLE 2(*a*). Effects of geometry, basis set, and potential on the hf parameters of ^{14}N in NH_2. All hf calculations at the experimental geometry are done using the IGLO-III basis set; other hf calculations are done at the same level of the theory as the corresponding geometry optimization. All couplings are in MHz

Calc.	Nucleus	a_{iso}	T_x	T_y	T_z
LDA/IGLO-III	N	5.7	−43.3	−43.2	86.5
	H	−53.2	−53.2	−9.2	62.4
LDA/IIIu-d_2	N	3.2	−43.3	−43.1	86.4
	H	−54.7	−53.1	−9.1	62.3
LDA/IIIu-d_4	N	3.6	−43.4	−43.3	86.7
	H	−54.6	−53.4	−9.1	62.5
LDA/IGLO-III	N	5.7	−43.3	−43.2	86.5
(exp.geo)	H	−52.3	−54.7	−8.6	63.3
BP/IGLO-III	N	12.6	−44.3	−43.4	87.7
	H	−61.3	−53.5	−8.4	61.9
BP/IIIu-d_2	N	9.3	−44.4	−43.3	87.7
	H	−63.6	−53.3	−8.3	61.6
BP/IIIu-d_4	N	9.7	−44.5	−43.6	88.1
	H	−63.7	−53.7	−8.3	62.0
BP/IGLO-III	N	12.7	−44.3	−43.4	87.7
(exp.geo)	H	−60.9	−54.8	−7.9	62.7
PWP/IGLO-III	N	27.4	−45.2	−44.0	89.1
	H	−50.7	−52.5	−7.7	60.3
PWP/IIIu-d_2	N	31.0	−45.2	−43.9	89.1
	H	−55.0	−52.6	−7.8	60.3
PWP/IIIu-d_4	N	31.2	−45.5	−44.1	89.7
	H	−55.4	−53.1	−7.9	60.9
PWP/IGLO-III	N	27.5	−45.1	−44.0	89.0
(exp.geo)	H	−50.6	−53.9	−7.2	61.1

and H in PH_2, and very good results for P in PF_2. BP gives the best agreement with experiment for H in NH_2. The Cl results are difficult to evaluate, as the coupling constants are very small. The absolute value of the calculated Fermi contact term is never greater than 6 MHz. Both in NCl_2 and PCl_2, the LDA and BP give negative results, and PW gives positive results. The experimental values are (−)9.7 and (+)15.4 MHz, respectively.

Experimentally, only absolute numbers can be obtained, and the assignment of signs is often based on discussions of direct vs. induced spin densities or with the aid of theoretical predictions. For NCl_2 the interpretation of ESR spectra has led to some disagreement regarding the size of $a_{iso}(^{14}N)$, and the signs of the $a_{iso}(^{35}Cl)$, $A_x(^{14}N)$, and $A_y(^{14}N)$ values (30, 32) ($A_q = T_q + a_{iso}$). The anisotropic $A(^{14}N)$ couplings have been reported as ±14, ±14, and 112 MHz for A_x, A_y, and A_z, respectively. Choosing the convention +14 MHz for A_x and A_y leads to an $a_{iso}(^{14}N)$ value of 47 MHz and the anisotropic T_x, T_y, T_z values −33, −33, +65 MHz, respectively. However, letting the experimentally observed A_x and A_y couplings assume the values $2 \times (-14)$ MHz, we instead obtain 28, −42, −42, and 84 MHz for a_{iso}, T_x, T_y, and T_z. These agree better with the calculated hf couplings.

Regarding the sign on the $a_{iso}(^{35}Cl)$ coupling in NCl_2, both the present PWP and previous UHF calculations (10) yield a positive number. We are therefore inclined to believe that an error has also occurred in the assignment of the experimental chlorine coupling.

TABLE 2(*b*). Effects of geometry, basis set, and potential on the hf parameters of ^{31}P in PH_2. All hf calculations at the experimental geometry are done using the IGLO-III basis set; other hf calculations are done at the same level of theory as the corresponding geometry optimizations. The IGLO-III basis set is used for P in all calculations. All couplings are in MHz

Calc.	Nucleus	a_{iso}	T_x	T_y	T_z
LDA/IGLO-III	P	30.0	−308.6	−295.6	604.2
	H	−35.2	−17.9	2.7	15.2
LDA/IIIu-d_2	P	32.3	−308.7	−295.7	604.3
	H	−36.7	17.9	2.7	15.2
LDA/IIIu-d_4	P	33.5	−306.3	−293.6	599.9
	H	−36.9	−17.8	2.9	14.9
LDA/IGLO-III	P	33.1	−308.5	−295.9	604.3
(exp.geo)	H	−34.4	−18.3	3.2	15.1
BP/IGLO-III	P	117.2	−300.1	−279.2	579.3
	H	−42.5	−18.3	2.6	15.7
BP/IIIu-d_2	P	129.4	−299.7	−279.3	−579.0
	H	−44.9	−18.3	2.6	15.7
BP/IIIu-d_4	P	119.1	−298.2	−277.8	576.0
	H	−46.2	−18.3	2.8	15.4
BP/IGLO-III	P	120.9	−299.9	−279.4	579.2
(exp.geo)	H	−41.7	−18.7	3.1	15.6
PWP/IGLO-III	P	290.2	−299.2	−279.2	578.4
	H	−48.4	−18.7	1.8	16.8
PWP/IIIu-d_2	P	281.4	−298.7	−278.9	577.6
	H	−47.5	−18.5	2.1	16.4
PWP/IIIu-d_4	P	297.2	−296.8	−277.6	574.5
	H	−51.8	−18.7	2.0	16.7
PWP/IGLO-III	P	295.0	−299.0	−279.4	578.3
(exp.geo)	H	−47.4	−19.1	2.4	16.7

As a whole, the isotropic hf couplings are in satisfactory agreement with experiment, when computed at the PWP level. The agreement is, however, not perfect for all cases studied; in particular the phosphorus and difluoroamidogen couplings deviate a fair amount. An explanation for this could be either that the basis sets employed are not sufficiently large for describing the atomic orbital integrals at the various nuclei, or that we lack diffuse functions in the bases, whereby we do not fully take into account the very diffuse electron clouds in the P atom and the halides. It should be noted that the basis sets employed, although being of "TZP" quality, have not been optimized with respect to producing highly accurate hf structures.

The differences in isotropic couplings in the nitrogen and phosphorus series show very clearly the influence of the 3*s* shell on the P atoms. The differences in spin angular momenta ($I(^{14}N) = 1$; $I(^{31}P) = 1/2$) and magnetic dipole moments (ratio $^{14}N/^{31}P \approx 0.36$), cf. eq. [1], only partially account for the difference of a factor of 5–10 in a_{iso} values of the two nuclei (cf. Tables 2*a* and 2*b*). The larger spin density at the P nuclei also affects the isotropic couplings of the substituents, where those bonded to phosphorus have numerically smaller couplings than those bonded to nitrogen.

3.2.2 Anisotropic results

Anisotropic hf couplings computed at the DFT level are generally highly insensitive to basis set and functional form (13).

TABLE 3. Theoretical and experimental[a] hyperfine structures. All couplings are in MHz. All calculations from the present study employ the IGLO-III basis set, and optimized geometries. The isotopes investigated are ^{1}H, ^{14}N, ^{19}P, and ^{35}Cl

Molecule	Potential	Nucleus	a_{iso}	T_x	T_y	T_z
NH_2	LDA	N	5.7	−43.3	−43.2	86.5
		H	−53.2	−53.2	−9.2	62.4
	BP	N	12.6	−44.3	−43.4	87.7
		H	−61.3	−53.5	−8.4	61.9
	PWP	N	27.4	−45.2	−44.0	89.1
		H	−50.7	−52.5	−7.7	60.3
	Expt.[b]	N	27.9	−44.6	−43.1	87.7
		H	−67.2	−55.4	−5.2	65.8
	UHFAA[c]	N	25.4			
		H	−49.7			
	ROHF-CI/ [5*s*2*p*1*d*/3*s*1*p*][d]	N	25.2			
		H	−65.8			
	MRDCI/ [8*s*5*p*2*d*/5*s*2*p*][e]	N	24.1	−42.9	−42.4	85.3
		H	−63.4	−54.3	−7.3	61.7
NF_2	LDA	N	9.4	−44.9	−44.5	89.4
		F	40.3	−302.9	−250.4	553.3
	BP	N	16.9	−47.3	−45.3	92.5
		F	86.3	−281.1	−236.0	517.1
	PWP	N	24.4	−47.9	−45.7	93.7
		F	110.1	−258.6	−245.5	504.0
	Expt.[f]	N	47.9	−45.1	−45.1	90.3
		F	167.1	−213.5	−213.4	427
	UHFAA[c]	N	49.8			
		F	144.8			
	ROHF-CI/ [5*s*2*p*1*d*/3*s*1*p*][d]	N	53.8			
		F	194.3			
NCl_2	LDA	N	2.5	−34.9	−34.3	69.2
		Cl	−5.3	−39.2	−27.5	66.7
	BP	N	5.7	−36.7	−36.3	73.0
		Cl	−1.3	−36.4	−23.4	59.8
	PWP	N	15.0	−38.0	−36.7	74.7
		Cl	6.0	−33.1	−25.5	58.5
	Expt.[g]	N	28	−42	−42	84
		Cl	(−)9.7	−38	−38	77
	UHFAA[c]	N	31.6			
		Cl	7.9			
PH_2	LDA	P	30.0	−308.6	−295.6	604.2
		H	−35.2	−17.9	2.7	15.2
	BP	P	117.2	−300.1	−279.2	579.3
		H	−42.5	−18.3	2.6	15.7
	PWP	P	290.2	−299.2	−279.2	578.4
		H	−48.4	−18.7	1.8	16.8
	Expt.[h]	P	217 – 244	−303	−318	621
		H	−48 – −51	−3	−3	5
	UHFAA[c]	P	175.8			
		H	−31.7			
PF_2	LDA	P	16.0	−312.4	−298.9	611.3
		F	5.3	−170.5	−154.8	325.3
	BP	P	102.6	−313.4	−285.7	599.1
		F	44.2	−165.1	−142.4	307.6
	PWP	P	245.7	−313.2	−288.2	601.4
		F	62.6	−176.5	−142.5	319.0
	Expt.[g,i]	P	237.1	−313.3	−313.3	626.5
		F	92.1	−129.9	−129.9	259.7

Can. J. Chem. Downloaded from www.nrcresearchpress.com by 195.246.54.202 on 09/08/12
For personal use only.

TABLE 3. (*concluded*)

Molecule	Potential	Nucleus	a_{iso}	T_x	T_y	T_z
PCl_2	LDA	P	−8.7	−279.2	−271.5	550.6
		Cl	−3.5	−24.7	−20.0	44.6
	BP	P	43.2	−281.9	−264.9	546.7
		Cl	−1.6	−23.1	−16.9	40.0
	PWP	P	158.6	−281.4	−266.7	548.1
		Cl	3.8	−23.6	−16.5	40.0
	Expt.[j]	P	190.4	−334.6	−287.0	621.6
		Cl	1.1	−23.0	−15.7	38.6
	Expt.[g]	P	211.3	−274.9	−274.9	549.7
		Cl	15.4	−15.4	−15.4	30.7
	UHFAA[c]	P	269.0			
		Cl	7.6			

[a]See also reference 14*b*, pp. 369, 370, and references therein.
[b]Reference 36.
[c]Reference 10.
[d]References 1, 2.
[e]Reference 5.
[f]Reference 37.
[g]References 30, 32.
[h]References 38, 32.
[i]Reference 39.
[j]Reference 34.

This is also observed in the present study. Most of the results are in very good agreement for N and P (especially using the LDA), and in fair agreement for F and Cl. The experimental values found for the anisotropic coupling constants of H in PH_2 are quite uncertain and are not well reproduced by the theory. All other calculated couplings have the correct sign and approximate magnitude. Most of the calculated coupling constants for N, F, and Cl (in PCl_2) are larger than the experimental absolute values, whereas the anisotropic ^{31}P and ^{35}Cl (in NCl_2) couplings generally are underestimated (cf. Tables 2*a* and 2*b*, and Table 3).

The anisotropic results vary much less than the isotropic ones. The non-local corrections still affect the results, but to a much smaller degree. BP and PWP generate very similar results. Geometry and basis set effects are about the same as for the isotropic couplings. PWP calculations done on PH_2 using the IGLO-II basis set for P, and the three different bases for H, show that the geometries and isotropic and anisotropic hf couplings were no more affected by changing the basis set for P than they were when only varying that of H.

The anisotropic ^{14}N couplings and ^{31}P couplings are quite similar in each series of compounds, irrespective of substituent. The substituents, on the other hand, show large variations in anisotropic values, depending on the central atom. The N-containing compounds always yield numerically much larger anisotropic couplings on the H, F, and Cl atoms. This is partially a reflection of the smaller angles observed in the P compounds, leading to larger modifications in the $T_{x,y,z}$ values. The lower substituent isotropic couplings in the P series, on the other hand, can be partially related to the longer bond distances observed in these systems, through the resulting decrease in overlap integrals.

3.3 Total and unpaired spin densities

We now turn to the analysis of the total and unpaired spin densities in an attempt to explain the observed differences in hf structures for the various compounds investigated. Analysis of

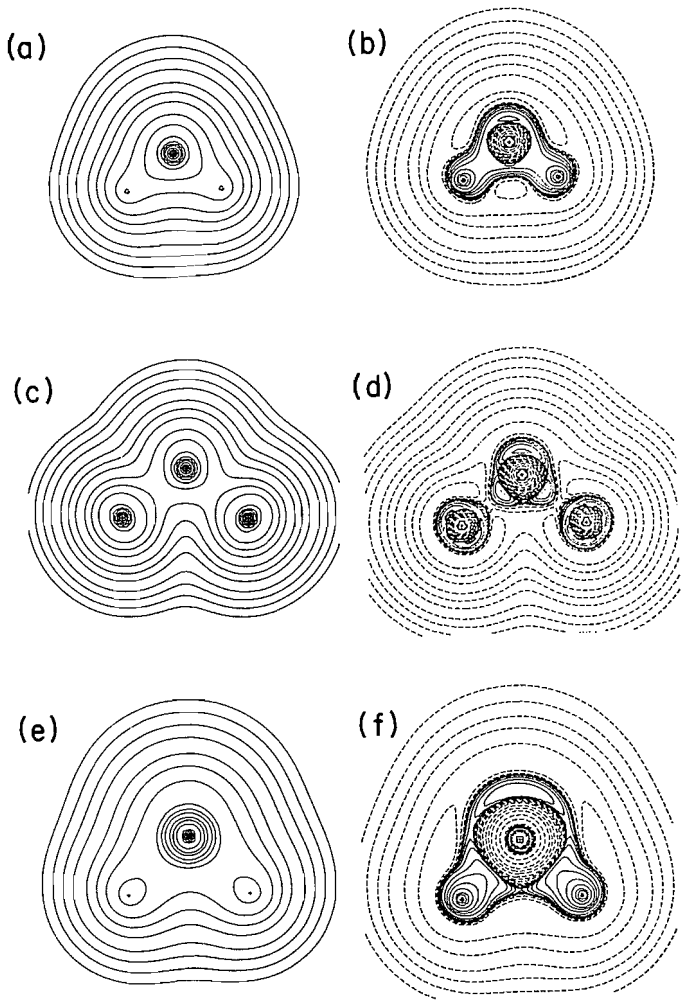

FIG. 1. Total charge densities (*a*), (*c*), and (*e*) and their Laplacians (*b*), (*d*), and (*f*) calculated at the LDA/IGLO-III level; (*a*), (*b*) NH_2; (*c*), (*d*) NF_2; (*e*), (*f*) PH_2.

Can. J. Chem. Downloaded from www.nrcresearchpress.com by 195.246.54.202 on 09/08/12
For personal use only.

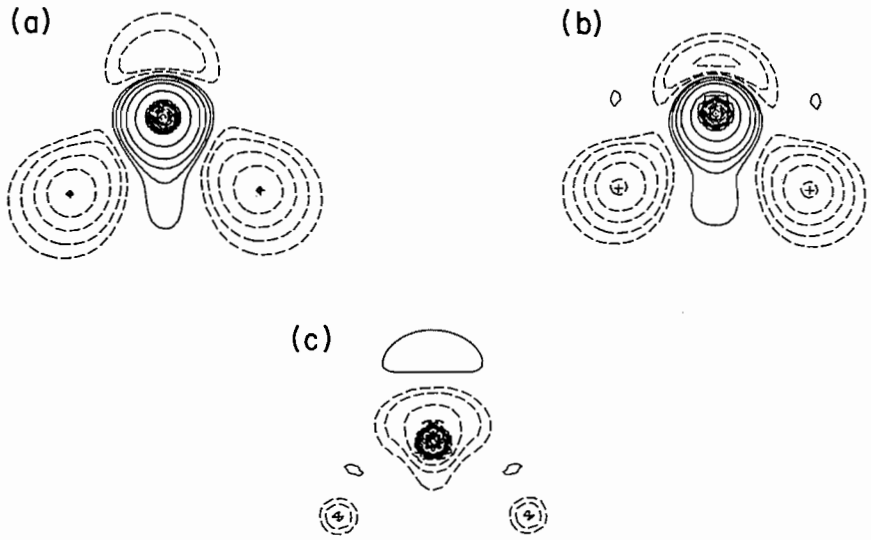

FIG. 2. Difference in ρ^{tot} of NH_2 between the (*a*) LDA/IGLO-III and BP/IGLO-III, (*b*) LDA/IGLO-III and PWP/IGLO-III, and (*c*) BP/IGLO-III and PWP/IGLO-III levels.

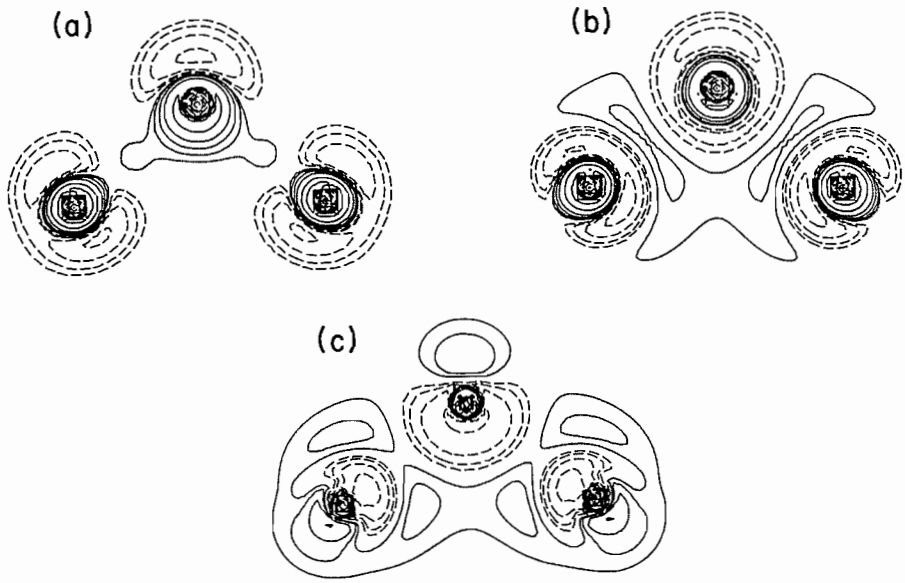

FIG. 3. Difference in ρ^{tot} of NF_2 between the (*a*) LDA/IGLO-III and BP/IGLO-III, (*b*) LDA/IGLO-III and PWP/IGLO-III, and (*c*) BP/IGLO-III and PWP/IGLO-III levels.

the differences in the spin densities obtained from the various DFT calculations, or from the LDA and different *ab initio* methods, has proven to be a very successful tool for understanding the fundamentally different results observed in the molecular calculations (13, 33). In the present study we will concentrate on the three systems NH_2, NF_2, and PH_2.

In Fig. 1, we show the total charge densities and their Laplacians, for the three systems as obtained from the LDA/IGLO-III calculations at the experimental geometries. The Laplacians of the LDA densities clearly indicate the shell structures of the N, F, and P atoms, as well as the buildup of electron density along the bonds. The latter effect is a reflection of the covalent character of the bonds. $\nabla^2\rho^{tot}$ (NF_2) differs markedly from the other two in that there is a very strong polarization of the valence shells, although there is also a region of electron depletion between the atoms. In Figs. 2–4 the corresponding differences in ρ^{tot} are displayed (*a* = LDA − BP; *b* = LDA − PWP; *c* = BP − PWP). When considering the differences in total densities, we note that plots *a* and *b* of each molecule have very similar features. For all three molecules, the LDA seems to favour the inner-valence shells of the heavy atoms (solid lines), whereas the BP and PWP non-local corrections lead to a larger density in the core and outer-valence regions of the molecules (broken lines). These methods also generate a much higher amount of total density at the hydrogen atoms. The differences in ρ^{tot} between the two non-local correction schemes (Figs. 2–4*c*) show that the BP method (solid lines) enhances these effects to a greater extent than does PWP at the heavy atoms, whereas the reverse is true at the hydrogens.

The LDA unpaired spin densities and the LDA – BP, LDA –

Can. J. Chem. Downloaded from www.nrcresearchpress.com by 195.246.54.202 on 09/08/12
For personal use only.

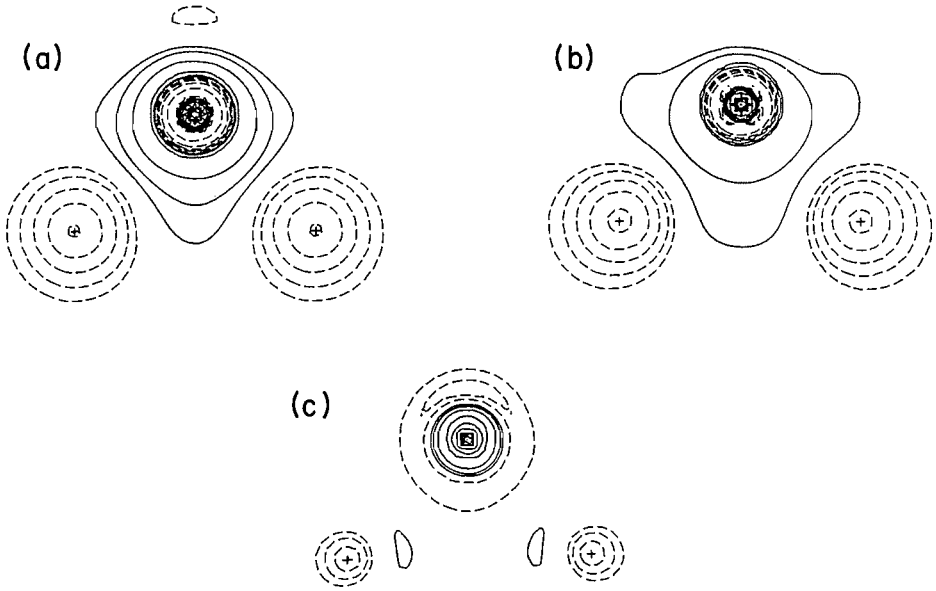

FIG. 4. Difference in ρ^{tot} of PH_2 between the (*a*) LDA/IGLO-III and BP/IGLO-III, (*b*) LDA/IGLO-III and PWP/IGLO-III, and (*c*) BP/IGLO-III and PWP/IGLO-III levels.

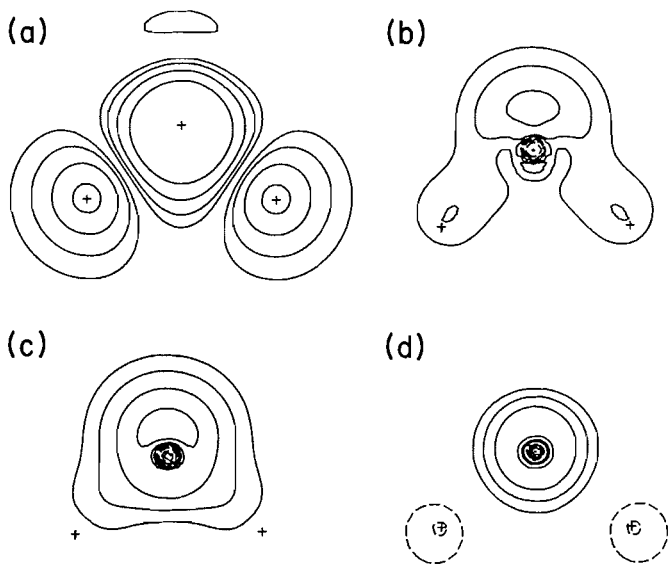

FIG. 5. (*a*) Unpaired spin density of NH_2. Differences in ρ^u of NH_2 between the (*b*) LDA/IGLO-III and BP/IGLO-III, (*c*) LDA/IGLO-III and PWP/IGLO-III, and (*d*) BP/IGLO-III and PWP/IGLO-III levels.

PWP, and BP – PWP differences in ρ^u are depicted in Figs. 5–7. The ^{14}N unpaired spin densities (Figs. 5*a* and 6*a*) are very similar, whereas for the phosphorus atom (Fig. 7*a*) ρ^u is more contracted to the core region. The fluorine densities differ considerably from the other ones, and clearly indicate the presence of the 2*p* shell. For the ρ^u difference plots of NH_2 and PH_2 (Figs. 5 and 7) the same observation is made as for $\Delta\rho^{tot}$, that electron density is transferred by the non-local corrections towards the core regions of the heavy atoms. The non-local corrections thus localize quite strongly the unpaired electron density at the nuclei of the central atoms. The differences between the BP and PWP methods are, as opposed to the observations made for $\Delta\rho^{tot}$, that PWP enhances the effect to a greater extent than does BP. This can be directly related to the magnitudes of the isotropic hf couplings, which increase significantly along the series LDA–BP–PWP.

Similar arguments also hold for the substituents. In the case of the fluorine atoms, Fig. 6 indicates a significant buildup in spin density along the same series, which is very nicely reflected in the $a_{iso}(^{19}F)$ couplings (Table 3). For hydrogen, on the other hand, there is little difference in spin density between the three potentials, and correspondingly little difference in the a_{iso} values.

4. Summary

The six neutral radicals NH_2, NF_2, NCl_2, PH_2, PF_2, and PCl_2 have been studied at the LCGTO–DFT level of theory. The ground state geometries were optimized at the local and non-local levels, and were found to agree well with experimental and previous theoretical results (Tables 1*a* and 1*b*). In particular, the bond angles are remarkably stable, whereas the non-local corrections lead to an elongation of the bonds between heteroatoms. The effects of contracting the basis set, as well as the number of polarization functions added, are negligible in terms of equilibrium geometries.

The isotropic hyperfine parameters, also computed in the present study, are far more sensitive to basis set contraction and, even more so, to functional form used. Overall, the PWP non-local correction gives the most satisfactory agreement with previous ESR and laser magnetic resonance (LMR) measurements. As has previously been observed (13), the fluorine atoms seem particularly difficult in this respect. The anisotropic hf couplings, on the other hand, are reproduced very well at all levels of theory, and for all systems, except the hydrogens in PH_2. A reinterpretation is suggested for the previously reported hf parameters of NCl_2, lowering the value of $a_{iso}(^{14}N)$ by 19 MHz. The remaining differences in hf structures can be explained in terms of insufficient basis sets or, to some extent, matrix effects in the ESR measurements that may cause changes in geometry and (or) electron distribution in the molecules. In particular, the spin densities for NF_2, PF_2, and PCl_2 have been

Can. J. Chem. Downloaded from www.nrcresearchpress.com by 195.246.54.202 on 09/08/12
For personal use only.

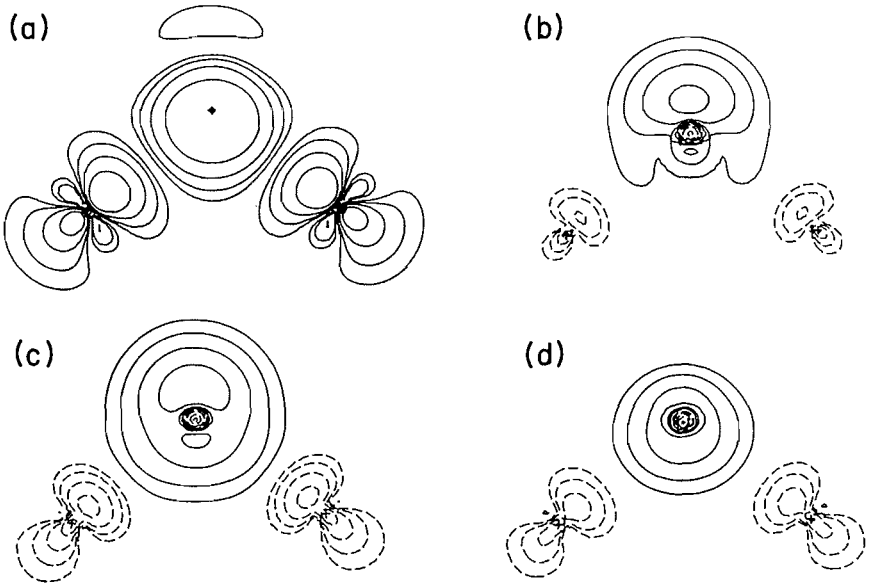

FIG. 6. (*a*) Unpaired spin density of NF_2. Differences in ρ^u of NF_2 between the (*b*) LDA/IGLO-III and BP/IGLO-III, (*c*) LDA/IGLO-III and PWP/IGLO-III, and (*d*) BP/IGLO-III and PWP/IGLO-III levels.

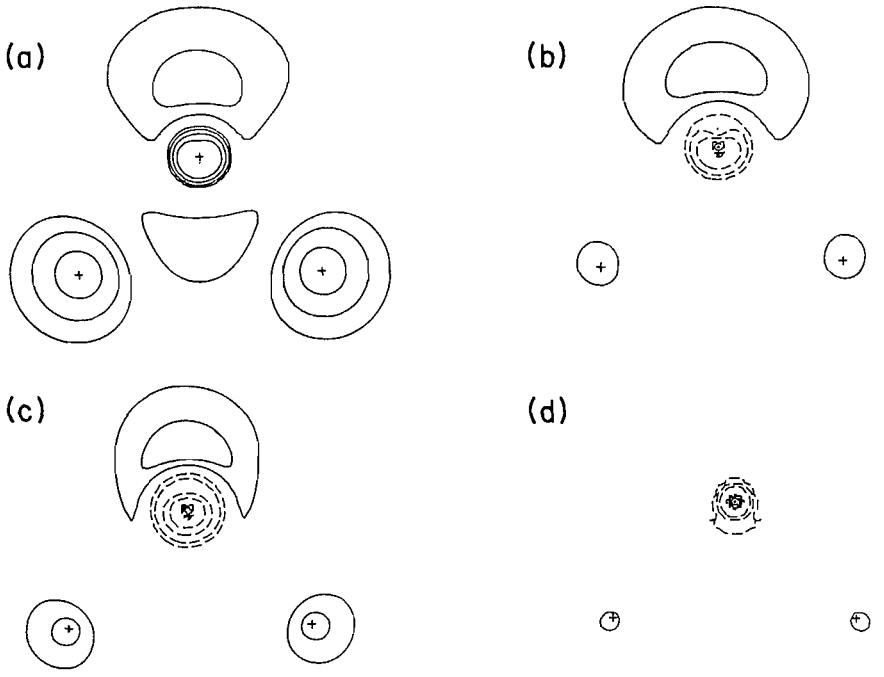

FIG. 7. (*a*) Unpaired spin density of PH_2. Differences in ρ^u of PH_2 between the (*b*) LDA/IGLO-III and BP/IGLO-III, (*c*) LDA/IGLO-III and PWP/IGLO-III, and (*d*) BP/IGLO-III and PWP/IGLO-III levels.

shown to be relatively uncertain (34) due to molecular motion in the matrices, even at temperatures as low as 4 K. In PCl_2, observed in a PCl_3 matrix at 25 and 77 K, raising the temperature was furthermore found to shift both the isotropic and anisotropic hf parameters towards the chlorine atoms.

The differences in isotropic hf couplings in NH_2, NF_2, and PH_2 are explained by analyzing the differences in unpaired spin densities, as obtained at the LDA, BP, and PWP levels of theory. Both the non-local corrections to the exchange and correlation functionals transfer unpaired spin from the inner-valence to the core and the outer-valence regions of the heavy atoms. The effect is stronger at the PWP level, and the differences in unpaired spin densities directly reflect the differences in a_{iso} values obtained with the different methods. The differences in densities between the BP and PWP methods show the effects of the functionals used for describing the electron exchange (19, 20), since both methods employ the same corrections to the correlation functionals (18).

Acknowledgements

The financial support of the Swedish Natural Sciences Research Council (NFR), the Killam Trust, and the Natural

Can. J. Chem. Downloaded from www.nrcresearchpress.com by 195.246.54.202 on 09/08/12
For personal use only.

Sciences and Engineering Research Council of Canada (NSERC) is gratefully acknowledged.

1. B. Engels, M Perié, W. Reuter, S.D. Peyerimhoff, and F. Grein. J. Chem. Phys. **96**, 4526 (1992).
2. K. Funken, B. Engels, S.D. Peyerimhoff, and F. Grein. Chem. Phys. Lett. **172**, 180 (1990).
3. H. Sekino and R. J. Bartlett. J. Chem. Phys. **82**, 4225 (1985).
4. M. Pöhlchen, V. Staemmler, and R. Jaquet. Konferenz für Theoretische Chemie, Ponteresina (1988).
5. T. Noanako, K. Morihashi, and O. Kikuchi. Bull. Chem. Soc. Jpn. **65**, 603 (1992).
6. D.M. Chipman. Theor. Chim. Acta, **76**, 73 (1989); J. Chem. Phys. **91**, 5455 (1989).
7. Z.L. Cai, G.H. Sha, and M.B. Huang. Chem. Phys. Lett. **178**, 273 (1991).
8. K.A. Peterson, R.C. Mayrhofer, and R.C. Woods. J. Chem. Phys. **93**, 5020 (1990).
9. S.A. Pope, I.H. Hillier, and M.F. Guest. Faraday Symp. Chem. Soc. **19**, 109 (1984).
10. A. Hinchcliffe and D.G. Bounds. J. Mol. Struct. **54**, 231 (1979).
11. L.A. Eriksson, R.J. Boyd, and S. Lunell. J. Am. Chem. Soc. **115**, 6896 (1993).
12. L.A. Eriksson, V.G. Malkin, O.L. Malkina, and D.R. Salahub. J. Chem. Phys. **99**, 9756 (1993).
13. L.A. Eriksson, O.L. Malkina, V.G. Malkin, and D.R. Salahub. J. Chem. Phys. In press.
14. (*a*) W. Meyer. J. Chem. Phys. **51**, 5149 (1969); (*b*) W. Weltner, Jr. Magnetic atoms and molecules. van Nostrand, New York. 1983.
15. A. St-Amant and D.R. Salahub. Chem. Phys. Lett. **169**, 387 (1990); A. St-Amant. Ph.D. Thesis, Université de Montréal, 1991; D.R. Salahub, R. Fournier, P. Mlynarski, I. Papai, A. St-Amant, and J. Ushio. *In* Density functional methods in chemistry. *Edited by* J. Labanowski and J. Andzelm. Springer-Verlag, New York. 1991.
16. C. Daul, A. Goursot, and D.R. Salahub. Proceedings from the NATO ARW on Grid Methods in Atomic and Molecular Quantum Calculations. *Edited by* C. Leforestier. In press.
17. S.H. Vosko, L. Wilk, and M. Nusair. Can. J. Phys. **58**, 1200 (1980).
18. J.P. Perdew. Phys. Rev. B, **33**, 8822 (1986); **34**, 7406 (1986).
19. A.D. Becke. Phys. Rev. A, **38**, 3098 (1988).
20. J.P. Perdew and Y. Wang. Phys. Rev. B, **33**, 8800 (1986).
21. F. Sim, D.R. Salahub, S. Chin, and M. Dupuis. J. Chem. Phys. **95**, 4317 (1991).
22. S. Huzinaga. J. Chem. Phys. **42**, 1293 (1965); S. Huzinaga and Y. Sakai. J. Chem. Phys. **50**, 1371 (1969).
23. W. Kutzelnigg, U. Fleischer, and M. Schindler. NMR: Basic Princ. Prog. **23**, 165 (1990).
24. V.G. Malkin, O.L. Malkina, and D.R. Salahub. Chem. Phys. Lett. **204**, 80 (1993); **204**, 87 (1993).
25. F.W. Biegler-König, R.F.W. Bader, and T. Tang. J. Comput. Chem. **3**, 317 (1982); R.J. Boyd and L.C. Wang. J. Comput. Chem. **10**, 367 (1989); R.W.F. Bader. Chem. Rev. **91**, 893 (1991).
26. J. Andzelm and E. Wimmer. J. Chem. Phys. **96**, 1280 (1992).
27. B.G. Johnson, P.M.W. Gill, and J.A. Pople. J. Chem. Phys. **98**, 5612 (1993).
28. L.A. Eriksson, J. Wang, R.J. Boyd, and S. Lunell. J. Phys. Chem. **98**, 792 (1994).
29. D. Feller. J. Chem. Phys. **93**, 579 (1990); S.P. Karna, F. Grein, B. Engels, and S.D. Peyerimhoff. Int. J. Quantum Chem. **36**, 255 (1989); Mol. Phys. **69**, 549 (1990).
30. M.S. Wei, J.H. Current, and J. Gendell. J. Chem. Phys. **57**, 2431 (1972).
31. V. Tschinke and T. Ziegler. Can. J. Chem. **67**, 460 (1988); L. Fan and T. Ziegler. J. Chem. Phys. **94**, 6057 (1991).
32. B.W. Fullam, S.P. Mishra, and M.C.R. Symons. J. Chem. Soc. Dalton Trans. 2145 (1974).
33. L.C. Wang and R.J. Boyd. J. Chem. Phys. **90**, 1083 (1989); R.F.W. Bader. Chem. Rev. **91**, 893 (1991); L.C. Wang, L.A. Eriksson, R.J. Boyd, Z. Shi, and B. Johnson. J. Phys. Chem. In press.
34. L. Bonanzolla, J.P. Michaut, and J. Roncin. J. Chem. Phys. **75**, 4829 (1981).
35. (*a*) K. Dressler and D.A. Ramsay. Phil. Trans. R. Soc. London, A: **251**, 553 (1959); (*b*) R.D. Brown, F.R. Burden, P.D. Godfrey, and J.R. Gillard. J. Mol. Spectrosc. **25**, 301 (1974); (*c*) R.N. Dixon, G. Duxbury, and D.A. Ramsay. Proc. R. Soc. London, A: **296**, 137 (1967); J.M. Berthou, B. Pascat, H. Guenebaut, and D.A. Ramsay. Can. J. Phys. **50**, 2265 (1972).
36. G.W. Hills and J.M. Cook. J. Mol. Spectrosc. **94**, 456 (1982); J.P. Michaut, J. Roncin, and R. Marx. Chem. Phys. Lett. **36**, 599 (1975).
37. C.A. McDowell, H. Nakajima, and P. Raghunathan. Can. J. Chem. **48**, 805 (1970); P.H. Kasai and E.B. Whipple. Mol. Phys. **9**, 497 (1965).
38. P.B. Davies, D.K. Russell, B.A. Thrush, and H.E. Redford. Chem. Phys. **44**, 421 (1979); R.L. Morehouse, J.J. Christiansen, and W. Gordy. J. Chem. Phys. **45**, 1747 (1966); G.S. Jackel and W. Gordy. Phys. Rev. **176**, 443 (1968).
39. M.S. Wei, J.H. Current, and J. Gendell. J. Chem. Phys. **52**, 1592 (1970).

Can. J. Chem. Downloaded from www.nrcresearchpress.com by 195.246.54.202 on 09/08/12
For personal use only.

The lowest energy excited states of the binuclear silver(I) halide complexes, $Ag_2(dmb)_2X_2$. Metal-centered or charge transfer states?

DANIEL PICHÉ[1] AND PIERRE D. HARVEY[2]

Département de chimie, Université de Sherbrooke, Sherbrooke, PQ J1K 2R1, Canada

Received May 21, 1993

This paper is dedicated to Professor John A. Polanyi on the occasion of his 65th birthday

DANIEL PICHÉ and PIERRE D. HARVEY. Can. J. Chem. **72**, 705 (1994).

The nature of the lowest energy excited states of the $Ag_2(dmb)_2X_2$ complexes (X = Cl, Br, I; dmb = 1,8-diisocyano-p-menthane) have been addressed both experimentally and theoretically. It is shown that the lowest energy excited states of the complexes are charge transfer states from the silver-halide frame to the isocyanide ligands (M/XLCT) based upon UV–visible spectra and emission polarization ratio measurements, and extended Hückel molecular orbital calculations (EHMO). The metal-centered $d\sigma^* \rightarrow p\sigma$ bands have been observed in the higher energy region of the spectra (232–242 nm). The complexes are luminescent ($440 \leq \lambda_e \leq 480$ nm) both in a glass and in the solid state at 77 K where the emission lifetimes, τ_e, range from 20 to 90 μs, which depend upon the nature of the halide (for the solid state data) and the media. No emission is observed at room temperature.

DANIEL PICHÉ et PIERRE D. HARVEY. Can. J. Chem. **72**, 705 (1994).

La nature des états excités de plus basse énergie des complexes $Ag_2(dmb)_2X_2$ (X = Cl, Br, I; dmb = 1,8-diisocyano-p-menthane) a été étudiée expérimentallement et théoriquement. Il est montré que ces états sont des états de transfert de charge des centres argent-halogènes aux ligands isocyanures (M/XLCT) tels que montrés par les spectres UVvisible et les mesures des rapports de polarisation, et des calculs d'orbitales moléculaires Hückle étendue (EHMO). Les bandes métal-centrée du type $d\sigma^* \rightarrow p\sigma$ ont été observées dans les régions de haute énergie des spectres (232–242 nm). Les complexes sont luminescents ($440 \leq \lambda_e \leq 480$ nm) pour l'état solide et les solutions rigides à 77 K, où les durées de vie d'émission, τ_e, se situent entre 20 et 90 μs, lesquels dépendent de la nature de l'halogène (pour les mesures de l'état solide) et le milieu. Aucune émission n'a été observée à la température ambiante.

Can. J. Chem. Downloaded from www.nrcresearchpress.com by 195.246.54.202 on 09/08/12
For personal use only.

Introduction

The investigation of the luminescence properties of the mono-, bi- and polynuclear d^{10} species (M = Ni^0, Pd^0, Pt^0 and Cu^+, Ag^+, Au^+) has become a subject of increasing interest (1–5). For the bi- and polynuclear complexes, the role of (ground and excited states) metal–metal interactions of these and related d^{10} species have attracted substantial attention among experimentalists (6, 7), have been the topic of research from a theoretical point of view (4*c*, 8), and have also been the subject of occasional reviews (4*d*, 7*f*, 9). There has been some discussion concerning the assignment of the lowest energy emission of tetranuclear cuprous halide clusters, $Cu_4X_4L_4$ (where X = Cl, Br, or I, and L = a nitrogen or phosphine organic base), where both halide-to-ligand charge transfer (XLCT) and ligand-to-copper charge transfer (XMCT) assignments have been proposed along with a metal-centered (MC) assignment (4*b–g*). In some occasions double emissions have been reported where both MC and XLCT states are found to be luminescent (4*g*). Such properties lead to the obvious difficulty in making the appropriate assignment. We have recently synthesized and characterized by X-ray diffraction, a series of new silver polynuclear complexes of the type $Ag_2(dmb)_2X_2$ (see Scheme I) and $Ag_n(dmb)_2I_n$ (where X = Cl, Br, I and n = 2–4) (6*a*, *b*). In particular, the binuclear series is of particular interest since it is a prototype example for weak metal–metal interactions. In comparison with the tetranuclear species, $Cu_4X_4L_4$, cited above where multiple Cu···Cu (and X···X) interactions occur within the cubane-like structure of the clusters, the d^{10}–d^{10} dimeric species $Ag_2(dmb)_2X_2$ (X = Cl, Br, I) represent ideal systems to study the true nature of the lowest energy excited state, and the effect of the halide atoms on these states.

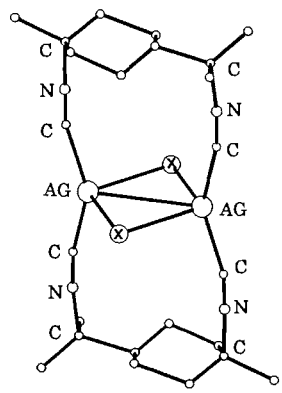

SCHEME I. Structure of the $Ag_2(dmb)_2X_2$ complexes.

Indeed, the $Ag_2(dmb)_2X_2$ (X = Cl, Br, I) complexes exhibit Ag···Ag separations ($r(Ag_2)$) ranging from 3.347 to 3.452 Å where the silver–silver stretching frequencies ($\nu(Ag_2)$) are found between 33 and 42 cm^{-1} (6*a*). We now wish to report our recent spectroscopic, photophysical, and Extended Hückel Molecular Orbital (EHMO) results on the binuclear silver-halide complexes. The lowest energy excited states are found to be silver-halide-to-isocyanide charge transfer excited states (M/XLCT), they exhibit luminescence properties at 77 K.

Experimental section

Materials

$Ag_2(dmb)_2X_2$ (X = Cl, Br, I) (6*a*), $[Ag_2(dmpm)_2)_2](PF_6)_2$ (10), and $Ag_2(dmpm)_2Br_2$ complexes (6*c*) were prepared according to literature procedures. Ethanol (Fisher), acetonitrile (Fisher), and butyronitrile (Aldrich Chemical Company) were purified according to standard pro-

[1]Undergraduate student.

[2]To whom correspondence may be addressed.

Can. J. Chem. Downloaded from www.nrcresearchpress.com by 195.246.54.202 on 09/08/12
For personal use only.

cedures (11). All spectroscopic measurements were performed immediately after Ar(g) bubbling degassing of the solutions, unless stated otherwise.

Apparatus

The absorption spectra were acquired on a Hewlett Packard 8452 A diode array spectrophotometer. The emission and excitation spectra were obtained using either a Spex Fluorolog II spectrometer or a PTI LS100 spectrometer. Part of the emission lifetime measurements were also performed on the PTI LS100 instrument. The second part of the measurements was made using the Spex Fluorolog II spectrometer equipped with the Spex 1934 D phosphorimeter set-up (for lifetimes > 20 ps).

Experimental procedures

The Φ_E values were measured using 9,10-diphenylantracene as the standard according to published procedures (12). The polarization ratios (N) were measured according to literature procedures (see, for examples, ref. 13).

The polarization ratio, N, is given by $(I_V/I_H)_V(I_H/I_V)_H$ where $(I_V/I_H)_V$ is the ratio of the intensities of vertically to horizontally polarized emissions when excited with vertically polarized light $(I_H/I_V)_H$ is the ratio of the intensities of horizontal and vertical emissions with horizontally polarized excitation. N is then related to the relative orientation of transition moments in absorption and emission.

Computational details

All MO calculations were of the extended Hückel type (EHMO) using a modified version of the Wolfsberg–Helmholz formula (14). The atomic parameters used for C and H are taken from ref. 15. The atomic parameters used for Ag (16*a*), Cl (16*b*), Br (16*c*), and I (16*d*) were also from literature. The Ag—C, C≡N, Ag—X (X = Cl, Br, I), and C—H bond lengths used for the computations are 2.14, 1.13, 2.70 (X = Cl), 2.80 (X = Br), 2.92 (X = I), and 1.05 Å as found crystallographically (6*a*). All angles were also taken from our previous X-ray studies. Because of limitations in the size of the molecules handled by the program, dmb was replaced by two methylisocyanide ligands. Pictorial representation of the orbitals was obtained using CACAO graphics package included in the software (17).

Results and discussion

Ultraviolet–visible spectra

The MO scheme for two linear L—M—L moieties interacting in a D_{2h} configuration has already been reported by Zietlow-Heinrich (18). For d^{10} species, the lowest energy electronic transition arises from a "d-to-p" type transition (3*a*). In our recent investigations on d^9–d^9 Pd_2 species (19), HOMO and LUMO are found to be $d\sigma$ and $d\sigma^*$ orbitals where both orbitals were composed of a combination of $d_{x^2y^2}$ and d_{z^2} metal atomic orbitals as major components, and some p_z, s, and ligand orbitals as minor components. The assignment of the $d\sigma \rightarrow d\sigma^*$ electronic transitions is based on the intensities of the electronic bands, the temperature dependence of the band-shapes (and of the absorption wavelength maxima). Typically an electronic band associated with a $d\sigma \rightarrow d\sigma^*$ transition undergoes a blue-shift along with an increase in intensity upon cooling of the sample (20). The behavior reflects the disappearance of "hot bands" for vibrationally-active Franck–Condon modes which are thermally populated. In the case of $d\sigma \rightarrow d\sigma^*$ transitions, the Franck–Condon active vibrational mode is $\nu(M_2)$ (100–180 cm^{-1}) (19, 20*a*). For systems related to this work, the d^{10} species $(L—M—L)_2$ will give rise to $d\sigma^* \rightarrow p\sigma$ electronic transitions (2). The electronic bands associated with the latter transitions also exhibit sensitive spectroscopic changes with temperature, notably for the band width. The d^{10}–d^{10}

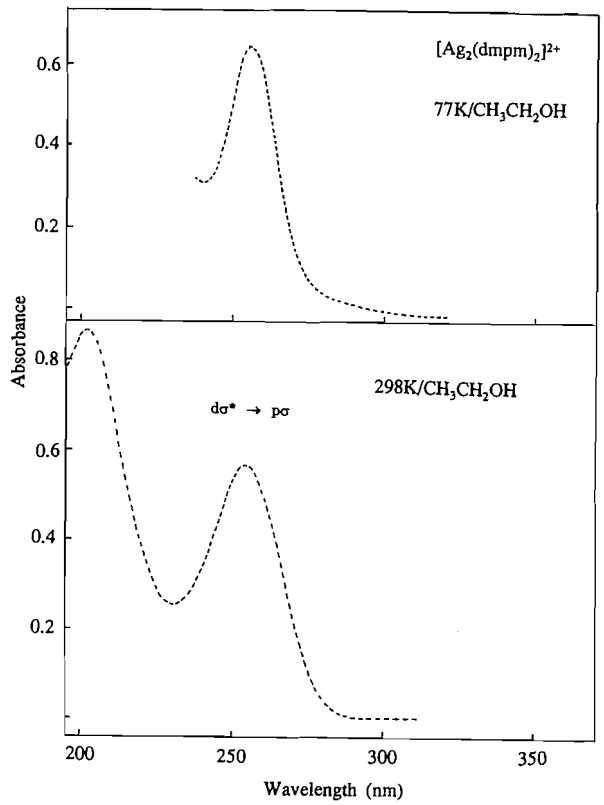

FIG. 1. Ultraviolet–visible spectra of $Ag_2(dmpm)_2^{2+}$ in ethanol at 77 and 298 K. The spectra were recorded using two different solution concentrations and cell set-ups.

$Ag_2(dmpm)_2^{2+}$ compound (dmpm = $((CH_3)_2P)_2CH_2$) was used as a reference point for the assignments. All attempts to make $Ag_2(dmb)_2^{2+}$ dimers failed. Using counter anions PF_6^-, BF_4^-, and NO_3^-, the only isolated and well-characterized products are found to be the relatively insoluble polymeric $\{[Ag(dmb)_2](Y)\}_n$ compounds (Y = PF_6^-, BF_4^-, NO_3^-) (1*a*). This $Ag_2(dmpm)_2^{2+}$ binuclear compound has been crystallographically characterized by others (as PF_6^- salt) (21); where a D_{2h} local symmetry is observed with $r(Ag_2)$ = 3.041 Å. The PF_6^- anion is not known to be a ligand capable of strong interactions with an unsaturated metal, and it is reasonably therefore assumed that no $Ag^+\cdots PF_6^-$ interaction occurs in solution. The spectrum for $Ag_2(dmpm)_2^{2+}$ is characteristic of a binuclear compound without other types of interaction (except for $Ag^+\cdots$solvent interaction). The uv-spectra for $Ag_2(dmpm)_2^{2+}$ in ethanol at 298 and 77 K (Fig. 1) exhibit the typical spectroscopic behavior of a $d\sigma^* \rightarrow p\sigma$ transition similar to those previously encountered for other related d^{10}–d^{10} complexes ($M_2(dppm)_3$: M = Pd, Pt; dppm = $((C_6H_5)_2P)_2CH_2$, $r(M_2)$ ~3 Å) (2*b*); and $Au_2(dppm)_2^{2+}$ (22)). The absorptivity of this band is typical, 18 200 ± 200 M^{-1} cm^{-1} (λ_{max} = 254 nm; ethanol at 298 K), and confirm the assignment. The small red shift (from 254 (298 K) to 258 nm (77 K)) is indicative of the expected increase in force constant of the Franck–Condon active mode (in this case a metal–metal force constant) (23). For d^{10}–d^{10} $M_2(dppm)_3$ complexes (M = Pd, Pt), time-resolved resonance Raman spectroscopy (TRS) confirmed that the $\nu(M_2)$ values increased from the ground to the lowest energy triplet excited state (120 to 152 cm^{-1} for Pd, 102.5 to 120 cm^{-1} for Pt) (24).

To obtain information on the effect of halides on the absorption spectra of Ag_2 systems, the $Ag_2(dmpm)_2Br_2$ spectrum,

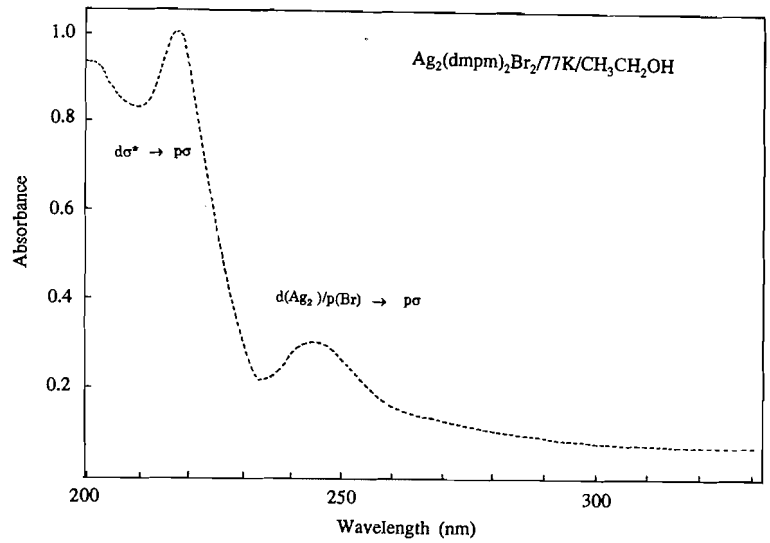

FIG. 2. Ultraviolet–visible spectrum of $Ag_2(dmpm)_2Br_2$ in ethanol at 77 K.

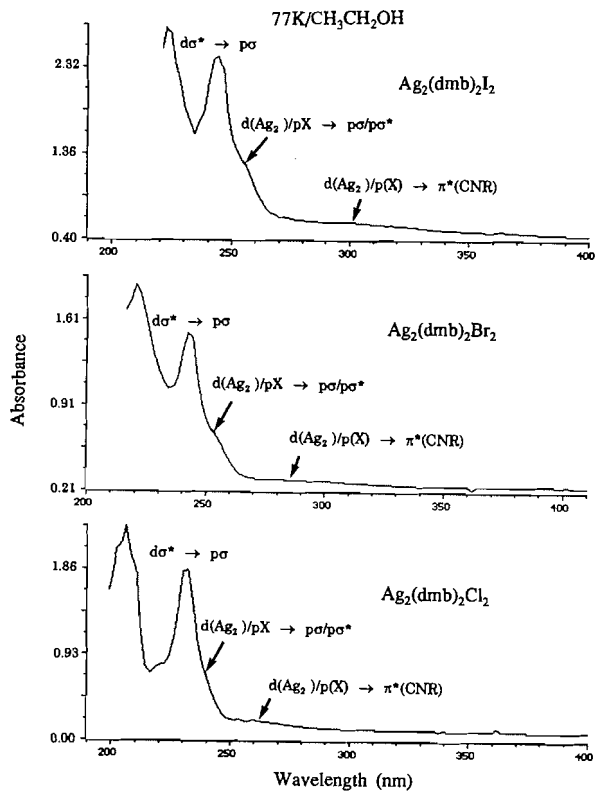

FIG. 3. Ultraviolet–visible spectra of the $Ag_2(dmb)_2X_2$ complexes (X = Cl, Br, I) in ethanol at 77 K.

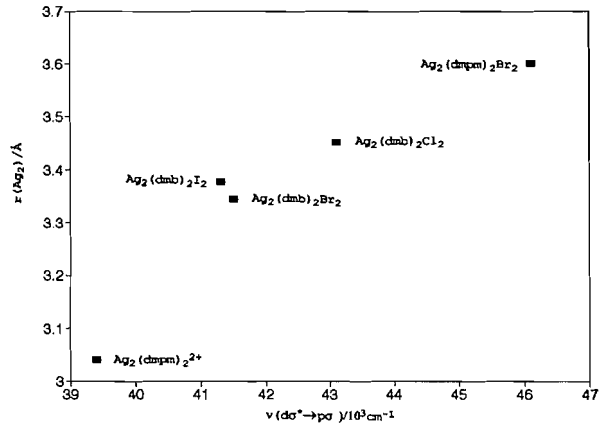

FIG. 4. Graph of $r(Ag_2)$ vs. λ ($d\sigma^*$–$p\sigma$).

recently characterized crystallographically by our group (6*c*), has been measured. The $r(Ag_2)$ value is 3.601 Å in this case, which should place the $d\sigma^* \rightarrow p\sigma$ transition well below 258 nm (λ_{max} found for $Ag_2(dmpm)_2^{2+}$). Indeed, a strong absorption is found at 217 nm for $Ag_2(dmpm)_2Br_2$ ($\epsilon \sim 19\,400 \pm 200$ M^{-1} cm^{-1}, ethanol, 298 K) associated with the $d\sigma^* \rightarrow p\sigma$ transition (Fig. 2). Moreover, a weaker broad band is observed at ~244 nm ($\epsilon = 4200$ M^{-1} cm^{-1}) with a long tail spreading to 300 nm. These features are undoubtedly due to the presence of the Br ion. This behavior is also systematically observed for $Ag_2(dmb)_2X_2$ complexes (X = Cl, Br, I) as shown in Fig. 3 (at 77 K). The $d\sigma^* \rightarrow p\sigma$ bands are well-resolved and are found at 232 (Cl), 241 (Br), and 242 nm (I). The absorptivity values ($d\sigma^* \rightarrow p\sigma$; in ethanol at 298 K) are as follows: 19 600 (Cl), 18 300 (Br), and 20 400 M^{-1} cm^{-1} (I) (experimental uncertainty is 10%). As expected, the $\lambda(d\sigma^* \rightarrow p\sigma)$ values correlate with $r(Ag_2)$ (Fig. 4) and further support the assignment. Similar to the $Ag_2(dmpm)_2Br_2$ spectra, weaker intensity features ($\epsilon \sim$ 5000–8000 M^{-1} cm^{-1}) appear as a shoulder in the $Ag_2(dmb)_2X_2$ spectra (X = Cl, Br, I) ~ 10–15 nm on the low energy side of the $d\sigma^* \rightarrow p\sigma$ band. Finally, weak and broad features ($\epsilon \sim$ 800–1500 M^{-1} cm^{-1}) are observed in the 250–350 nm range. It is possible that unresolved singlet-triplet absorptions also occur in this same region contributing to the broadening of the bands. The spectroscopic data for these five compounds are compared in Table 1. These results are now interpreted from a theoretical point of view.

Molecular orbital calculations

In this work, the Extended Hückel Molecular Orbital calculation methods (EHMO) were used for assignment purposes. They are known to be qualitative (25) but are also found to give the correct relative energy MO levels in most cases. Recently our research group (26) used EHMO to compute MO levels for polynuclear $M_3(dppm)_3CO^{2+}$ complexes (M = Pd, Pt), which

Can. J. Chem. Downloaded from www.nrcresearchpress.com by 195.246.54.202 on 09/08/12
For personal use only.

TABLE 1. Spectroscopic data for the Ag_2 species at 298 K[a]

Ag_2 species	r(Ag···Ag)/ Å	λ_{max}/ ±1 nm	ν_{max}/ ±200 cm^{-1}	$\varepsilon/M^{-1}\ cm^{-1}$ (±10%)	Assignments[b]
$Ag_2(dmpm)_2^{2+}$	3.041 (21)	254	39 400	18 000	$d\sigma^* \rightarrow p\sigma$
$Ag_2(dmpm)_2Br_2$	3.601 (6*c*)	217	46 100	19 400	$d\sigma^* \rightarrow p\sigma$
		244	41 000	4 700	$d(Ag_2)/p(X) \rightarrow p\sigma/p\sigma^*$
$Ag_2(dmb)_2Cl_2$	3.451 (6*a*)	232	43 100	19 600	$d\sigma^* \rightarrow p\sigma$
		240	41 700	7 100	$d(Ag_2)/p(X) \rightarrow p\sigma/p\sigma^*$
		~260	~38 500	1 430	$d(Ag_2)/p(X) \rightarrow \pi^*(CNR)$
$Ag_2(dmb)_2Br_2$	3.345 (6*a*)	241	41 500	18 300	$d\sigma^* \rightarrow p\sigma$
		253	39 500	5 600	$d(Ag_2)/p(X) \rightarrow p\sigma/p\sigma^*$
		~280	~35 100	780	$d(Ag_2)/p(X) \rightarrow \pi^*(CNR)$
$Ag_2(dmb)_2I_2$	3.378 (6*a*)	242	41 300	20 400	$d\sigma^* \rightarrow p\sigma$
		257	38 900	8 000	$d(Ag_2)/p(X) \rightarrow p\sigma/p\sigma^*$
		~295	~33 900	1 390	$d(Ag_2)/p(X) \rightarrow \pi^*(CNR)$

[a]In ethanol solutions.
[b]The assignments are based upon the comparison of the ν_{max} and ε values, and the EHMO findings (see text).

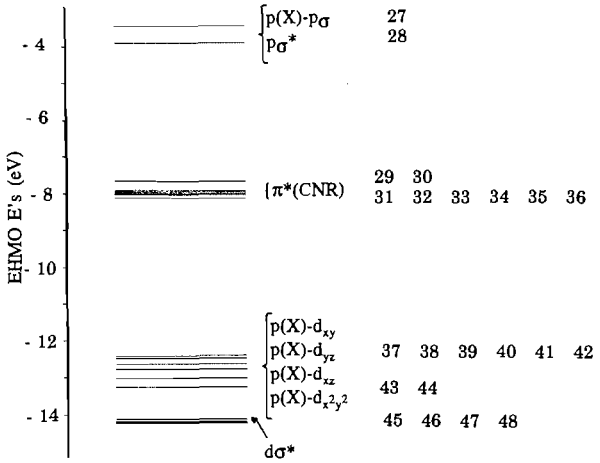

FIG. 5. General MO energy diagram for the model compounds $Ag_2(CNCH_3)_4X_2$ (X = Cl, Br, I). The numbers on the right are the numbers used in the text.

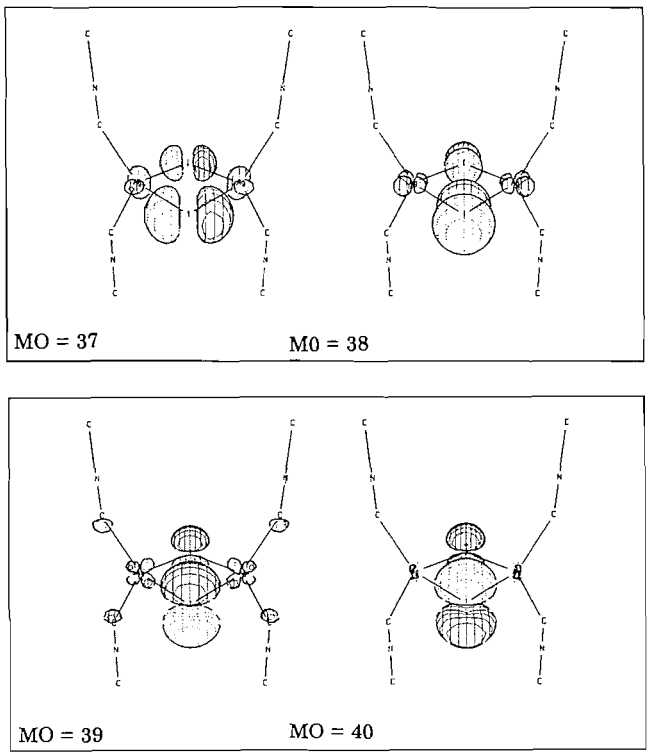

FIG. 6. Picture of the HOMO and HOMO-*n* (MO #37 to 40).

were eventually compared to the ones obtained by the more "accurate" approximate density function theoretical computations (27). The MO levels did not change in relative order between the two types of calculations (except for one level above LUMO). This comparison implies some degree of reliability for EHMO calculation in this case, despite the fact that there is almost a two-fold difference in transition energies between EHMO computations and experimental results. This phenomenom is not unusual with EHMO. The energy separation between the nd^{10} and $nd^9(n+1)s^1$ configurations of Ag^+ is ~39 000 cm^{-1} (4.83) eV (28).

The key features of the present calculations are (*1*) LUMO is a MO of the CNR π* system, (*2*) HOMO is very difficult to establish because of the proximity of many other MO levels, (*3*) HOMO is mixed in character where both silver and halide atomic orbitals are involved, and (*4*) above the set of eight MO π* (CNR) levels lie more MO levels associated with some interactions between metal and halide atomic orbitals. The latter MO's are also close to one another. A general MO scheme is presented in Fig. 5.

The computed EHMO HOMO–LUMO energy gap varies a little with the halide (~5.0, 4.7, and 4.5 eV for X = Cl, Br, I, respectively) and would correspond to an electronic transition taking place in the 250–275 nm range. We find that the nearly degenerate LUMO and LUMO + *n* (*n* = 1–7), orbitals #29 to #36, and the HOMO and HOMO-*n* (*N* = 1–5), orbitals #37 to #42, are essentially orthogonal (Figs. 6 and 7 show the MO picture for MO #37 to #42). An electronic transition between these LUMO (and LUMO + *n*), and the HOMO (and HOMO − *n*) would lead to uv–visible with very weak intensities. The broad bands located in the 250–350 nm range are in reasonable agreement with this description. It is not surprising that the set of π*(CNR) MO systems is found to be LUMO, since recently Ziegler *et al.* have shown that the LUMO in $Pt(CN)_4^{2-}$ was indeed one of the ligand π*(CN^-) orbitals using approximate density function theoretical calculations (29), which was eventually confirmed by Patterson *et al.* using relativistically modi-

Can. J. Chem. Downloaded from www.nrcresearchpress.com by 195.246.54.202 on 09/08/12
For personal use only.

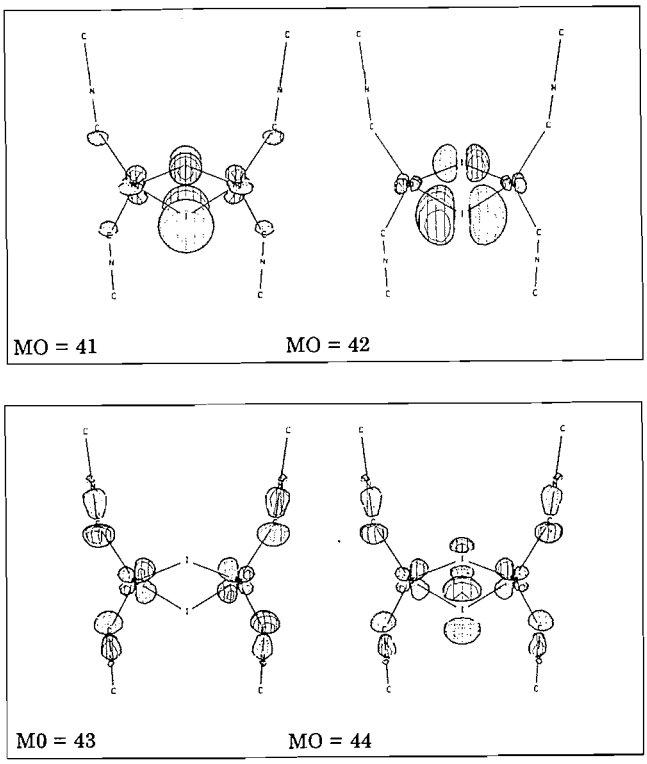

FIG. 7. Picture of MO's #41 to #44.

fied EHMO computations (7*b*). No other MO is found within ~4 eV of the LUMO. The nature of the LUMO appears to be well addressed. For the purpose of this work, it does not appear possible or relevant to identify which of the MO (#29 to #36) is the actual true LUMO. These MO's are practically identical in nature and are nearly degenerate.

The nature of the HOMO is more difficult to address since in all three cases (X = Cl, Br, I), the MO #37 to #42 are located within 1 eV, and the relative MO ordering for each individual MO differs slightly from one another. Many MO's between #37 and #44 arise essentially from interactions between the Ag_2 $d\pi$, $d\pi^*$, $d\delta$, and $d\delta^*$ MO's, and the halide p_x, p_y, and p_z orbitals. Due to the complexity of the MO's, it appears more reasonable to treat them as a whole. They will be referred to as $d(Ag_2)/p(X)$. A detailed list of the atomic orbital contributions to each individual MO's has been deposited.[3] The lowest energy electronic transition will also be referred to as $d(Ag_2)/p(X) \rightarrow \pi^*(CNR)$.

The presence of the shoulders located at ~240, 253, and 257 nm for X = Cl, Br, and I, respectively (Fig. 3) is now considered. The absorptivities of these features (6 000 – 8 000 M^{-1} cm^{-1}) appear to be too great to arise from an electronic transition between two orthogonally oriented orbitals ($d(Ag_2)/p(X)$ and $\pi((CNR))$. The upper MO's (#27 and #28) must be considered. These are $p\sigma$ and $p\sigma^*$ orbitals, and are mainly composed of $p_z(Ag)$ orbitals with some contribution of the *s* orbitals. The mixture of silver p_z and *s* orbitals is consistent with the previous theoretical calculations (SFC-Xα) reported by Cotton et al. (8*e*) on the $Ag_2(RN_3R)_2$ complex (R = C_6H_5). MO's #27 ($p\sigma$) and #28 ($p\sigma^*$) are shown in Fig. 8. Intuitively, one would have placed $p\sigma^*$ above $p\sigma$, but EHMO suggested otherwise. The reason is that $p\sigma^*$ (Ag_2) interacts very weakly with halide *p* orbitals (4–6%), while $p\sigma$ interacts more strongly with MO composed of 10%, 14%, and 18% of halide *p* orbitals for X = Cl, Br, and I, respectively. The latter interactions are found to be anti-bonding in nature, explaining why the $p\sigma$ orbital is unusually more destabilized. The energy gap between $p\sigma$ and $p\sigma^*$ is small, which is consistent with the long Ag···Ag separations (3.35 to 3.45 Å) and the low-frequency $\nu(Ag_2)$ (33 to 42 cm^{-1}) (6*a*). The shoulders (~240 nm, Cl; 253 nm, Br; 257 nm, I) are assigned to one (or more) $d(Ag_2)/p(X) \rightarrow p\sigma/p\sigma^*$ electronic transition(s).

For the $d\sigma^* \rightarrow p\sigma$ transition discussed in the previous section, both $d\sigma$ and $d\sigma^*$ MO's are found among MO #45 and #46 (depending on the halide), which lie about 1 to 1.8 eV below the $d(Ag_2)/p(X)$ orbitals. The $d\sigma^*$ orbital is also composed of some $\pi^*(CNR)$ orbitals, which is consistent with previous findings for d^7–d^7 system (see, for instance, $(M_2(CO)_{10}$, M = Mn, Re (30)), but does not include any halide component. Consequently, $d\sigma^* \rightarrow p\sigma$ electronic transition carries only some weak charge transfer character (as the $p\sigma$ is found to possess from 4 to 6% *p*(X) component).

Contrary to d^{10}–d^{10} $M_2(dppm)_3$ complexes (M = Pd, Pt), $Ag_2(dmb)_2X_2$ complexes (X = Cl, Br, I) do not exhibit $^{1,3}(d\sigma^*p\sigma)^*$ states as lowest energy excited states. This fact is due not only to the presence of halides, but also to the presence of isocyanide ligands. The complexes are found to be luminescent, and their emissive spectroscopic properties are as follows.

The observed absorptivities ($5000 < \epsilon < 8000$ M^{-1} cm^{-1}; Table 1) are in the appropriate range for transitions of the type $d\pi(M_2) \rightarrow d\sigma^*$ (20, 30). Typically, the latter ranges from 2 200 to 5 300 M^{-1} cm^{-1} for d^7–d^7 Mn_2 and Co_2 $d\pi(M_2) \rightarrow d\sigma^*$ bands (20, 30). The difference here is the contribution of the halide orbitals to the HOMO, and the possibility of more than one electronic transition occurring at nearly the same energy, which explains the slightly higher intensity in the Ag_2 complexes.

Emission spectra and lifetimes

Luminescence of $Ag_2(dmb)_2X_2$ complexes (X = Cl, Br, I) is readily observed at 77 K as shown in Figs. 9–11. The emission wavelength maxima (λ_{max}) appear at 440, 458, and 443 nm for X = Cl, Br, and I, respectively. The energy gap between the emission and the intense $d\sigma^* \rightarrow p\sigma$ bands are 20 400 cm^{-1}, 19 700 cm^{-1}, and 18 700 cm^{-1}, for X = Cl, Br, and I, respectively. Interestingly, the λ_{max} values in the solid state do not follow perfectly the halide trend ($\lambda_{max}(Cl) < \lambda_{max}(Br) < \lambda_{max}(I)$), but rather follow *r*(Ag···Ag): $\lambda_{max}(Cl) < \lambda_{max}(I) < \lambda_{max}(Br)$ (for *r*(Ag···Ag) = 3.451, 3.378, 3.345 Å, respectively). For comparative purposes the emission spectrum of $Ag_2(dmpm)_2^{2+}$ in ethanol at 77 K is obtained and exhibits a structureless band at λ_{max} = 371 nm (27 000 cm^{-1}), which is only 11 800 cm^{-1} away from the $d\sigma^* \rightarrow p\sigma$ absorption band in this case. This comparison confirms that the metal-centered $^{1,3}(d\sigma^*p\sigma)^*$ cannot be the lowest energy excited state in the $Ag_2(dmb)_2X_2$ complexes (X = Cl, Br, I).

Emission lifetimes range from 20 to 90 μs for samples in solid state and in glasses at 77 K (see Table 2 for details). By taking the λ_{max} values for the lowest energy absorption bands ($d(Ag_2)/p(X) \rightarrow \pi^*(CNR)$), the energy gap between the

[3]Tables of atomic orbital contributions of the MO's #27–#46 for the $Ag_2(dmb)_2X_2$ complexes (X = Cl, Br, I; 18 pages) have been deposited. This supplementary material may be purchased from: The Depository of Unpublished Data, Document Delivery, CISTI, National Research Council Canada, Ottawa, ON K1A 0S2, Canada.

Can. J. Chem. Downloaded from www.nrcresearchpress.com by 195.246.54.202 on 09/08/12
For personal use only.

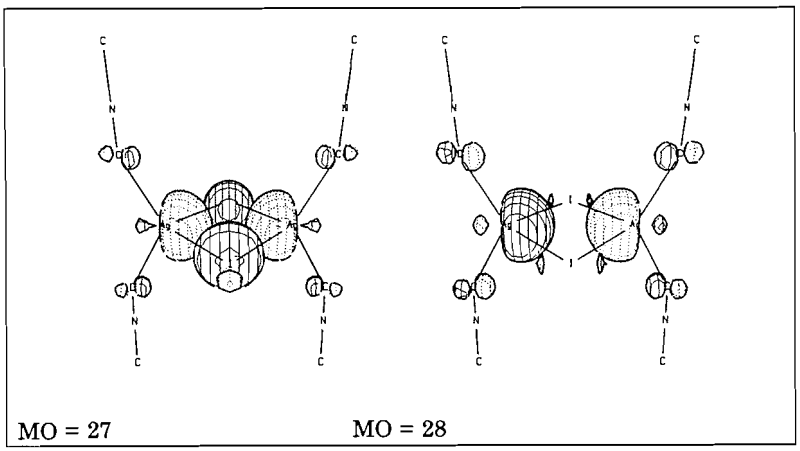

FIG. 8. Picture of the MO's #27 and #28.

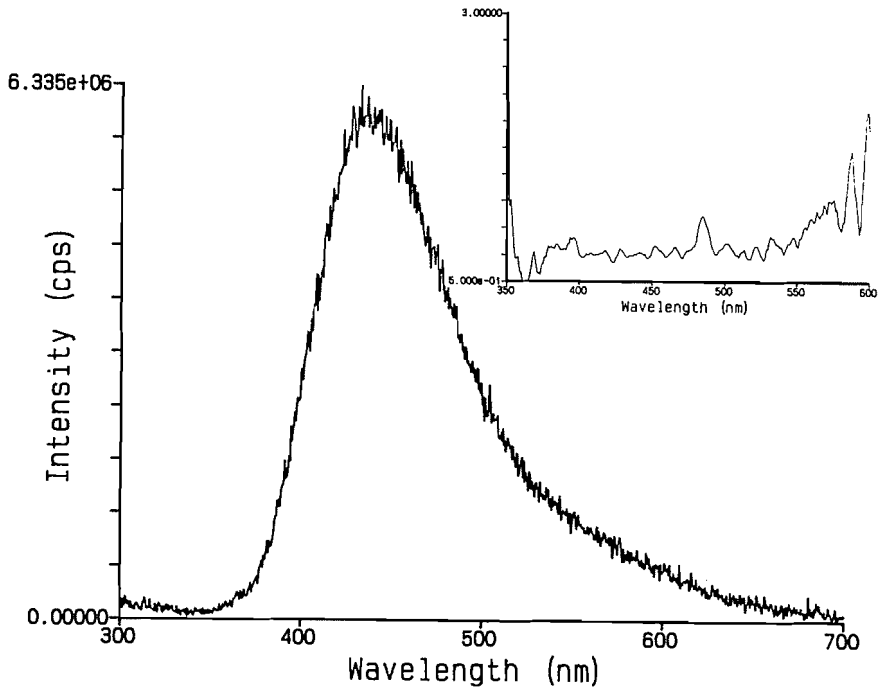

FIG. 9. Emission spectrum of $Ag_2(dmb)_2Cl_2$ in ethanol at 77 K (λ_{ex} = 235 nm). Inset: polarization ratio N vs. λ_{em} (λ_{ex} = 235 nm).

TABLE 2. Emission data and lifetimes at 77 K

	Ethanol		Butyronitrile		Solid state[a]	
X	λ_{max}	τ_e	λ_{max}	τ_e	λ_{max}	τ_e
Cl	450	27 ± 1	455	29 ± 1	440	88 ± 5
Br	460	24 ± 1	465	26.5 ± 1.0	458	54 ± 1
I	470	24 ± 1	480	28 ± 1	443	33 ± 1

[a]In NaCl matrix.

absorption and emission bands (Δ) is ~4000 cm^{-1}. This value compares favorably with those reported for related d^{10}–d^{10} $M_2(dba)_3$ complexes (M = Pd, Pt; $\Delta \sim 5000\ cm^{-1}$) for which MLCT excited states are found as the lowest excited states (*2b*). Hence, the long emission lifetimes and this separation between absorption and emission peaks indicate that the luminescence is phosphorescence.

The polarization ratio, N, as a function of emission wavelength has also been measured. Theoretically N varies from 0.5 to 3. A value of $N = 3$ indicates that the emission is polarized parallel to the dipole moment change involved in the absorption process, while when $N = 0.5$, the luminescence is polarized perpendicular to the absorption. Figures 9 and 10 show the N graph vs. λ (insets) at 77 K (ethanol glasses) for the emission spectra of the $Ag_2(dmb)_2X_2$ complexes (X = Cl, Br). The iodo compound was not investigated. The N values for both Cl and Br derivatives range between 0.75 and 0.80 across the spectrum, demonstrating clearly that the emission does rise from an absorbing state with a transition moment perpendicularly polarized to the emission. Two comments must be made. First, the fact that N does not reach the theoretical value of 0.5 could be due to depolarization induced by glass imperfection and solvent-induced depolarization. Second, N values higher than 0.5 could be due to the possibility that the excitation may be taking place into two differently polarized and undeconvoluted

Can. J. Chem. Downloaded from www.nrcresearchpress.com by 195.246.54.202 on 09/08/12
For personal use only.

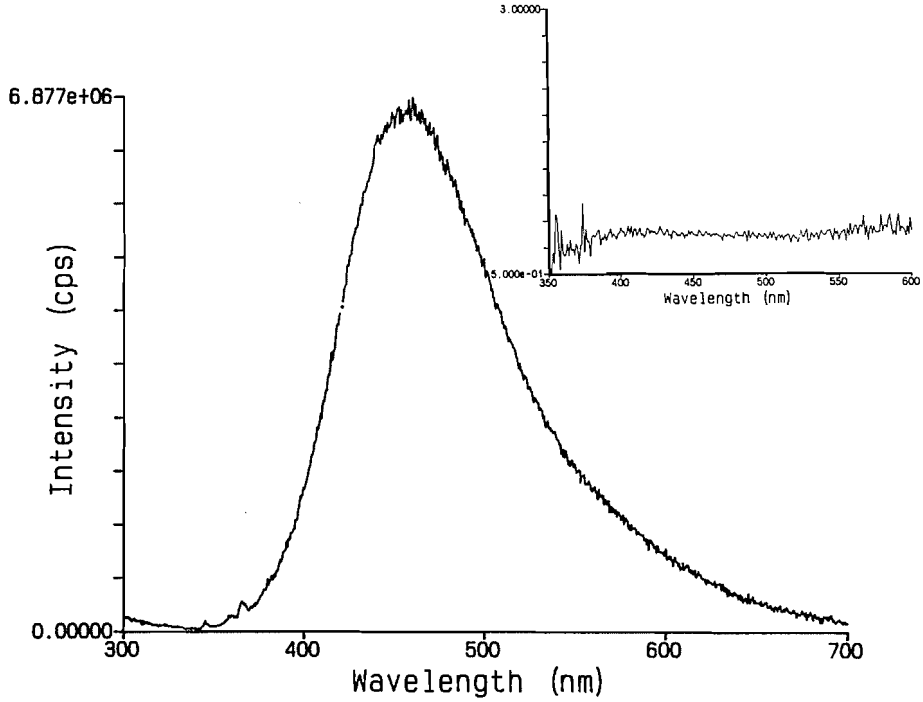

FIG. 10. Emission spectrum of $Ag_2(dmb)_2Br_2$ in ethanol at 77 K (λ_{ex} = 240 nm). Inset: Polarization ratio N vs. λ_{em} (λ_{ex} = 240 nm).

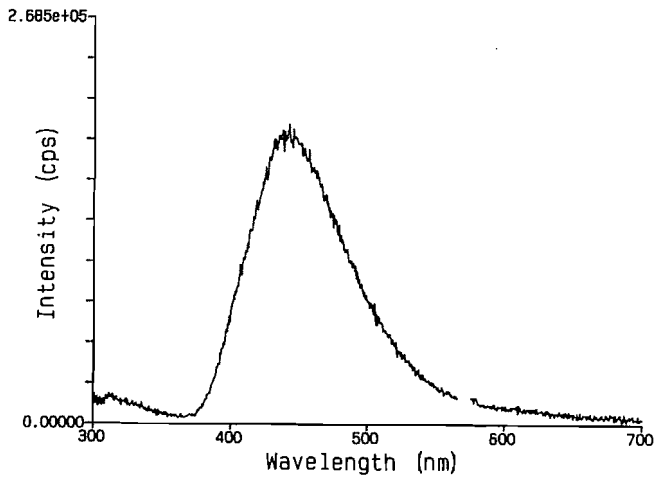

FIG. 11. Emission spectrum of $Ag_2(dmb)_2I_2$ in ethanol at 77 K (λ_{ex} = 270 nm). The weak feature located at 310 nm is due to a residual impurity.

bands. The $d\sigma^*p\sigma$ band where the excitation takes place is z-polarized. The emission (phosphorescence) of the $^3(d\sigma^*p\sigma)^*$ states is known to be z-polarized (31). The experimental results indicate that the emission must be either x- or y-polarized. This result shows that the $^3(d\sigma^*p\sigma)^*$ state is not the lowest. Unfortunately, this result does not *prove* that the emission arises from a charge transfer state as discussed in the previous section, but it is consistent with the assignment.

We have compared the emission lifetimes (τ_e) of the complexes in the solid state and in solution at 77 K (Table 1). In the solid state (all in NaCl pellets), the τ_e values behave in a typical fashion expected for internal heavy atom effect for X = Cl → X = I where τ_e decreases from 88, to 54, to 33 μs (X = Cl, Br, I, respectively). In solution τ_e decreases significantly (for Cl and Br) and appears to be only slightly dependent upon the nature of the solvent (ethanol vs. butyronitrile), and the nature of the halide (some halide-dependence of λ_{max} is also observed). For comparative purposes, τ_e for $Ag_2(dmpm)_2^{2+}$ (PF_6^- salt) in ethanol at 77 K has been measured; τ_e = 49.3 ± 0.9 μs in this case. This value appears in the appropriate range (of the investigated complexes) but is significantly larger under the same experimental conditions. If we consider that the dmb and dmpm ligands are similar in terms of excited state deactivation via the bridging ligands, then the overall lifetime results can be tentatively explained by the presence of some small degree of photo-induced lability of the halides (also involving the solvent molecules to keep the metal centers saturated). A careful study of both emission spectra and lifetimes vs. temperature is needed to address this behavior. This was not the purpose of this work. All emission decays were monoexponential and time-resolved emission spectra did not reveal the presence of a second emission, ruling out the possibility of an upper emissive state. No emission was observed at room temperature. Except for $Ag_2(dmpm)_2^{2+}$ (this work) and solid $[AgP(OCH_3)_3Cl]_4$ (32), a literature search confirms that the absence of luminescence at room temperature for d^{10} species is general, and could be due, in part, to the photochemical sensitivity of the Ag^+ compounds.

Concluding remarks

Lai and Zink (4*h*) used Franck–Condon analysis to assign the emission band of a titrameric Cu(I) complexes ($Cu_4X_4(dmpp)_4$; X = Cl, Br, I; dmpp = 1-phenyl-3,4-dimethylphosphole). The emission spectrum was assigned to a one-electron transition terminating on the phosphole ligand on the basis of the vibronic analysis. The MLCT (Cu → phosphole ligand) assignment was preferred over a halide ligand-to-ligand phosphate charge transfer (XLCT) because there was no significant shift in the energies of the emission bands of the complexes for X = Cl, Br, and I (4*h*). On the other hand, Ford *et al.* (4*g*) compared the spectro-

Can. J. Chem. Downloaded from www.nrcresearchpress.com by 195.246.54.202 on 09/08/12
For personal use only.

Can. J. Chem. Downloaded from www.nrcresearchpress.com by 195.246.54.202 on 09/08/12
For personal use only.

scopic properties of $Cu_4X_4L_4$ complexes (X = Cl, Br, I; L = pyridine (py) and 2-(diphenylmethyl) pyridine(dpmp)) and were able to demonstrate evidence for multiple emission arising from XMCT and MC triplet excited states, strongly arguing on the dependencies of the emission band energies with X and r(Cu···Cu) (4*g*). In this work there is a sensitive halide dependence on λ_{max} and τ_e, and some trend associated with r(Ag···Ag) for the solid state emission data (λ_{max}). This dual dependency strongly supports this assignment for the lowest energy transition ($d(Ag_2)/p(X) \rightarrow \pi^*(CNR)$. Overall, these experimental and theoretical investigations have allowed us to understand how the nature of the lowest energy excited states in the d^{10}–d^{10} species may vary with the nature of the ligands. Clearly, the presence of unsaturated ligands (such as isocyanide) place the π^*(CNR) MO's right at the LUMO position automatically inducing a CT state in the d^{10}–$d^{10}Ag_2$ MO frame. There should not be any surprise to induce charge transfer state in the d^{10} species (Cu^I, Ag^I, and Au^I) with unsaturated ligand (with relatively low π^* MO's) since the unoccupied silver/halide orbitals are relatively highly destabilized. It appears that if the synthesis of such complexes is possible, the nature of the LUMO can be changed (i.e. for instance via pyridine-like ligands (33)), where depending upon the substitution, the HOMO–LUMO gap and the excited state redox properties can be altered in a predictable way. We have also shown how the $d\sigma^* \rightarrow p\sigma$ transition energy varies with $r(Ag_2)$. For these complexes, the $r(Ag_2)$ values appear to be set by the presence of bridging halides rather than the bridging dmb ligands. It does not seem to be trivial to change $r(Ag_2)$ as a means of lowering the $^{1,3}(d\sigma^*p\sigma)$ state to the lowest energy excited state. Hence, the photochemical behavior of the $Ag_2(dmpm)_2^{2+}$ and $Ag_2(dmb)_2X_2$ complexes (X = Cl, Br, I) are strongly suspected to be different.

Acknowledgements

This research was funded by NSERC (Natural Sciences and Engineering Research Council) and FCAR (Fonds concertés pour l'avancement de la recherche). P.D.H. thanks Professor Tom Ziegler (University of Calgary) and André D. Bandrauk (Université de Sherbrooke) for fruitful discussion on the theoretical calculations.

1. (*a*) D. Perreault, M. Drouin, A. Michel, and P.D. Harvey. Inorg. Chem. **31**, 3688 (1992); (*b*) P.D. Harvey and L. Gan. Inorg. Chem. **30**, 3239 (1991); (*c*) D. Perreault, M. Drouin, A. Michel, and P.D. Harvey. Inorg. Chem. **30**, 2 (1991).
2. (*a*) P.D. Harvey and H.B. Gray. Polyhedron, **9**, 1949 (1990); (*b*) P.D. Harvey, F. Adar, and H.B. Gray. J. Am. Chem. Soc. **111**, 1312 (1989); (*c*) P.D. Harvey and H.B. Gray. J. Am. Chem. Soc. **110**, 2145 (1988); (*d*) P.D. Harvey, W.P. Schaefer, and H.B. Gray. Inorg. Chem. **27**, 1101 (1988).
3. (*a*) J.V. Caspar. J. Am. Chem. Soc. **107**, 6718 (1985); (*b*) M.N.I. Khan, J.P. Fackler, Jr., C. King, J.C. Wang, and S. Wang. Inorg. Chem. **27**, 1672 (1988); (*c*) C.M. Che, W.T. Wong, T.-F. Lai, and H.-L. Kwong. J. Chem. Soc., Chem. Commun. 243 (1989); (*e*) A.L. Balch, J.K. Nagle, D.E. Oram, and P.E. Reedy, Jr. J. Am. Chem. Soc. **110**, 454 (1988); (*f*) S. Wang, J.P. Fackler, Jr., C. King, and J.C. Wang. J. Am. Chem. Soc. **110**, 3308 (1988).
4. (*a*) M. Henary and J.I. Zink. J. Am. Chem. Soc. **111**, 7404 (1989); (*b*) C.K. Ryu, K.R. Kyle, and P.C. Ford. Inorg. Chem. **30**, 3982 (1991); (*c*) K.R. Kyle, C.K. Ryu, and P.C. Ford. J. Am. Chem. Soc. **113**, 2954 (1991); (*d*) K.R. Kyle, W.E. Palke, and P.C. Ford. Coord. Chem. Rev. **95**, 35 (1990); (*e*) K.R. Kyle and P.C. Ford. J. Chem. Soc. Chem. Commun. 714 (1989); (*g*) C.K. Ryu, M. Vitale, and P.C. Ford. Inorg. Chem. **32**, 869 (1993); (*h*) D.C. Lai and J.I. Zink. Inorg. Chem. **32**, 2594 (1993).
5. (*a*) N.P. Rath, E.M. Holt, and K. Tanimura. J. Chem. Soc. Dalton Trans. 2303 (1986); (*b*) N.P. Rath, E.M. Holt, and K. Tanimura. Inorg. Chem. **24**, 3934 (1985); (*c*) A. Vogler and H. Kunkely. J. Am. Chem. Soc. **108**, 7211 (1986); (*d*) E. Eitel, D. Oelkrug, W. Hiller, and J. Strähle. Z. Naturforsch. **35b**, 1247 (1980); (*e*) H.D. Hardt and H.-J. Stroll. Z. Anorg. Allg. Chem. **480**, 199 (1981); (*f*) H.D. Hart and H.-J. Stroll. Z. Anorg. Allg. Chem. **480**, 193 (1981).
6. (*a*) D. Perreault, M. Drouin, A. Michel, and P.D. Harvey. Inorg. Chem. **32**, 1903 (1993); (*b*) P.D. Harvey, M. Drouin, and D. Perreault. J. Chem. Soc. Dalton Trans. 1365 (1993); (*c*) D. Perreault, M. Drouin, A. Michel, V.M. Miskowski, W.P. Schaefer, and P.D. Harvey. Inorg. Chem. **31**, 695 (1992).
7. (*a*) T.M. McCleskey and H.B. Gray. Inorg. Chem. **31**, 1733 (1992); (*b*) Z. Assefa, F. Destefano, M.A. Garepapaghi, J.H. La Casce, Jr., S. Ouellete, M.R. Corson, J.K. Nagle, and H.H. Patterson. Inorg. Chem. **30**, 2862 (1991); (*c*) A.C. Balch, V.J. Catalano, and M.M. Olmstead. Inorg. Chem. **29**, 585 (1990); (*d*) C.-M. Che, H.-L. Kwon, V.W.-W. Yam, and K.-C. Cho. J. Chem. Soc. Chem. Commun. 885 (1989); (*e*) F. Sabin, C.K. Ryu, A. Volger, and P.C. Ford. Inorg. Chem. **31**, 1941 (1992); (*f*) C. Kutal. Coord. Chem. Rev. **99**, 213 (1990).
8. (*a*) K.M. Merz, Jr. and R. Hoffmann. Inorg. Chem. **27**, 2120 (1988); (*b*) Y. Jiang, S. Alvarez, and R. Hoffmann. Inorg. Chem. **24**, 749 (1985); P.D. Mehrotra and R. Hoffmann. Inorg. Chem. **17**, 2187 (1978); (*d*) A. Dedieu and R. Hoffmann. J. Am. Chem. Soc. **100**, 2074 (1978); (*e*) F.A. Cotton, X. Feng, M. Matusz, and R. Poli. J. Am. Chem. Soc. **110**, 7077 (1988); (*f*) C. King, J.-C. Wang, Md.N.I. Khan, and J.P. Fackler, Jr. Inorg. Chem. **28**, 2145 (1989).
9. M. Jansen. Angew. Chem. Int. Ed. Engl. **27**, 1098 (1987).
10. H.H. Karsh and U. Schubert. Z. Naturforsch. **B37**, 186 (1982).
11. (*a*) D.D. Perrin, W.L.F. Armarego, and D.R. Perrin. Purifications of laboratory chemical. Pergamon. Oxford. 1966; (*b*) A.J. Gordon and R.A. Ford. The chemist's companion: a handbook of practical data, techniques, and references. Wiley, New York. 1972. p. 436.
12. E.C. Lim, J.D. Laposa, and J.M.H. Yu. J. Mol. Spectrosc. **19**, 412 (1966), and references therein.
13. (*a*) B. Zelent, P.D. Harvey, and G. Durocher. Can. J. Spectrosc. **29**, 23 (1984); (*b*) Can. J. Spectrosc. **28**, 188 (1983); (*c*) P.D. Harvey, B. Zelent, and G. Durocher. Spectrosc. Int. J. **2**, 128 (1983).
14. J.H. Ammeter, H.B. Burgi, J.C. Thibeault, and R. Hoffmann. J. Am. Chem. Soc. **100**, 3686 (1978).
15. (*a*) R. Hoffmann and W.N. Lipscomb. J. Chem. Phys. **36**, 2179 (1962); (*b*) J. Chem. Phys. **37**, 2872 (1962); (*c*) R. Hoffmann. J. Chem. Phys. **39**, 1397 (1963).
16. (*a*) D.A. Jorgensen and R. Hoffmann. J. Phys. Chem. **94**, 3046 (1990); (*b*) R.H. Summerville and R. Hoffmann. J. Am. Chem. Soc. **98**, 7240 (1976); (*c*) S. Alvarez, F. Mota, and J. Novoa. J. Am. Chem. Soc. **109**, 6586 (1987); (*d*) E. Canadell and O. Eisenstein. Inorg. Chem. **22**, 2398 (1983).
17. C. Mealli and D. Proserpio. J. Chem. Educ. **67**, 399 (1990).
18. M. Zeitlow-Heinrich. Ph.D. Thesis. California Institute of Technology. 1988.
19. P.D. Harvey and Z. Murtaza. Inorg. Chem. In press.
20. (*a*) V.M. Miskowski, T.P. Smith, T.M. Loehr, and H.B. Gray. J. Am. Chem. Soc. **107**, 7925 (1985); (*b*) H.B. Abrahamson, C.C. Frazier, D.S. Ginley, H.B. Gray, J. Lilienthal, D.R. Tyler, and M.S. Wrighton. Inorg. Chem. **16**, 1554 (1977).
21. H.H. Karsh and U. Schubert. Z. Naturforsch. **B37**, 186 (1982).
22. C.-M. Che, H.-L. Kwong, C.-K. Poon, and V.W.-W. Yam. J. Chem. Soc. Dalton Trans. 3215 (1990).
23. C.J. Ballhausen. Molecular electronic structures of transitions metal complexes. McGraw-Hill, New York. 1979. pp. 132–135.
24. P.D. Harvey, R.F. Dallinger, W.H. Woodruff, and H.B. Gray. Inorg. Chem. **28**, 3057 (1989).
25. T.A. Albright, J.K. Burdett, and M.-H. Whangbo. Orbital interactions in chemistry. Wiley, New York. 1984.

26. R. Provencher and P.D. Harvey. Inorg. Chem. **32**, 61 (1993).
27. P.D. Harvey, Z. Murtaza, S.M. Hubig, and T. Ziegler. To be published.
28. L.E. Orge. J. Chem. Soc. 4186 (1958).
29. T. Ziegler, J.K. Nagle, J.G. Snijders, and E.J. Baerends. J. Am. Chem. Soc. **111**, 5632 (1989).
30. R.A. Levenson and H.B. Gray. J. Am. Chem. Soc. **97**, 6042 (1975).
31. J.G. Brummer and G.A. Crosby. Chem. Phys. Lett. **112**, 15 (1984).
32. A. Vogler and H. Kunkely. Chem. Phys. Lett. **158**, 74 (1989).
33. D. Li, C.-M. Che, W.-T. Wong, S.-J. Shich, and S.-M. Peng. J. Chem. Soc. Dalton Trans. 653 (1993).

Can. J. Chem. Downloaded from www.nrcresearchpress.com by 195.246.54.202 on 09/08/12
For personal use only.

Non-equilibrium kinetics of bimolecular reactions. Part 6. Transient rate coefficients

CHRIS CARRUTHERS AND HESHEL TEITELBAUM[1]
Department of Chemistry, University of Ottawa, Ottawa, ON K1N 6N5, Canada
Received June 30, 1993
This paper is dedicated to Professor John C. Polanyi on the occasion of his 65th birthday

CHRIS CARRUTHERS and HESHEL TEITELBAUM. Can. J. Chem. **72**, 714 (1994).

The master equation is solved numerically for the time dependence of the vibrational level populations of HCl (treated as a simple harmonic oscillator) during the bimolecular exchange reaction, Br + HCl → HBr + Cl, taking into account the competition between reaction and vibrational equilibration subject to Landau–Teller T–V excitation. Strong deviations from Boltzmann distributions are found. A wide range of reactant concentrations, diluent concentrations and temperatures were explored. It was found that no significant reaction occurs before the establishment of a steady vibrational population distribution, confirming that the rate coefficient for non-equilibrium bimolecular exchange reactions can be determined from a simple analytical steady state treatment (J. Chem. Soc. Faraday Trans. **87**, 229 (1991)). The rate of an isolated elementary bimolecular reaction, A + BC → AB + C, under non-equilibrium conditions can deviate seriously from the standard expression, k_{eq}[A][BC], and is better given by the law

$$d[BC]/dt = -k_{eq}[A]\,[BC]/\{1 + 1/(a + g[R]/[A])\}$$

where [R] is the concentration of the collisional equilibrator, R, and a and g are constants depending only on temperature. This generalized rate law describes not only the initial rate but also the rate all the way up to completion, in the absence of the reverse reaction.

CHRIS CARRUTHERS et HESHEL TEITELBAUM. Can. J. Chem. **72**, 714 (1994).

On a résolu l'équation maîtresse d'une façon numérique pour la corrélation avec le temps des populations des niveaux vibrationnels du HCl (traité comme un oscillateur harmonique simple) au cours de la réaction d'échange bimoléculaire, Br + HCl → HBr + Cl, en tenant compte de la compétition entre la réaction et l'équilibre vibrationnel sujet à l'excitation Landau–Teller T–V. On a trouvé d'importantes déviations par rapport aux distributions de Boltzmann. On a examiné une grande variété de concentrations de substances réactives, de concentrations des diluants et de températures. On a trouvé qu'il ne se produit aucune réaction significative avant qu'une distribution stationnaire de la population vibrationnelle ne s'établisse; ceci confirme que le coefficient de vitesse des réactions d'échange bimoléculaire non équilibrées peut être déterminé par un traitement analytique simple de l'état stationnaire (J. Chem. Soc. Faraday Trans. **87**, 229 (1991)). Il est possible que la vitesse d'une réaction bimoléculaire élémentaire isolée, A + BC → AB + C, soumise à des conditions non équilibrées puisse dévier d'une façon importante par rapport à l'expression standard, k_{eq}[A][BC], et elle est mieux exprimée par la loi

$$d[BC]/dt = -k_{eq}[A][BC]/\{1 + 1/(a + g[R]/[A])\}$$

dans laquelle [R] est la concentration de l'équilibreur collisionnel, R, et a et g sont des constantes qui ne dépendent que de la température. Cette loi de vitesse ne décrit pas seulement la vitesse initiale et, en l'absence de réaction inverse, elle décrit aussi la vitesse jusqu'à la fin de la réaction.

[Traduit par la rédaction]

Introduction

In chemical kinetics the rate of low pressure diatomic or polyatomic dissociation of the molecule AB in collision with itself or with an inert species, M,

[1] $$AB + M \rightarrow A + B + M$$

is given by the simple expression

[2] $$d[AB]/dt = -k_d[AB]\{[AB] + [M]\}$$

where k_d is termed the rate coefficient. It has been shown that k_d depends in a complicated way on the concentrations of AB and M, leading to the non-linear mixture rule (1, 2), but that k_d is otherwise constant, except through the implicit dependence of [AB] on time. This result is valid on condition that the molecular dissociation occurs isothermally and that a steady-state vibrational level population is established quickly. Before the steady state is established, i.e. during this "incubation period", reaction occurs with negligible rate. The properties of the incubation time have been discussed in the case of diatomic dissociation (3, 4), and in the case of polyatomic dissociation (5) from a theoretical point of view. The phenomenon is manifested as a delay in the onset of chemical reaction, and it has been observed at high temperatures for the thermal dissociation of diatomic molecules (6–9) and of polyatomic molecules (10). However, the phenomenon has never been evaluated in detail for bimolecular reactions, even though exactly the same principles are involved. The incubation time, the depressed value of the rate coefficient and activation energy, as well as the non-linear mixture rule are all caused by depleted vibrational (and rotational) energy level populations which are directly involved with the reaction in question. The competition between reaction and energy transfer processes establishes the degree of severity of the effect, and this competition is also present in the bimolecular reaction

[3] $$A + BC \rightarrow AB + C$$

[1]Lady Davis Visiting Professor, Hebrew University of Jerusalem, Jerusalem.

Can. J. Chem. Downloaded from www.nrcresearchpress.com by 195.246.54.202 on 09/08/12
For personal use only.

Can. J. Chem. Downloaded from www.nrcresearchpress.com by 195.246.54.202 on 09/08/12
For personal use only.

In the past few years we have embarked on a series of studies (11–15) designed to investigate the non-equilibrium kinetics of reaction [3]. One of the most interesting results was the discovery that, even though there are a large number of components to [3], one for each vibrational state of BC, and a correspondingly large number of energy transfer processes, it was still possible to express the rate of reaction simply and to still account for the non-equilibrium vibrational level populations. Thus, instead of the usual "equilibrium" rate for the forward reaction being given by

$$[4] \qquad \mathrm{d[A]/d}t = -k_{eq}[\mathrm{A}][\mathrm{BC}]$$

we have the improved version

$$[5] \qquad \mathrm{d[A]/d}t = -k_{eq}[\mathrm{A}][\mathrm{BC}]/\{1 + f(T)[\mathrm{A}]/[\mathrm{R}]\} = \mathrm{d[BC]/d}t$$

where $f(T)$ is a temperature-dependent constant involving the reactive rate constants and the energy transfer rate constants, while [R] is the concentration of the molecules, R, responsible for (de-)exciting BC (11).

If one writes the more exact rate expression, eq. [5], in the usual phenomenological form, eq. [4] (with k_{eq} replaced by k), one can see that the phenomenological rate coefficient, k, is related to k_{eq} by

$$k/k_{eq} = \{1 + f(T)[\mathrm{A}]/[\mathrm{R}]\}^{-1}$$

Equation [5] was derived by solving the master equation, which describes the rate of change with time of [BC(v)], the concentration of BC in the specific vibrational level, v. In order to obtain a closed form expression like [5] it was assumed that (*a*) the rotational distribution is equilibrated and therefore plays no special role; (*b*) reaction occurs for the most part from a single most important vibrational level; (*c*) BC is a truncated harmonic oscillator; (*d*) only a single species, R, is responsible for vibrationally relaxing BC; (*e*) only single-quantum T–V relaxation processes are significant; (*f*) a steady state vibrational distribution is established before the reagents react to a significant extent; or (*g*) before the reverse reaction begins to interfere. The philosophy of our approach is to examine each assumption separately. In this process we have found that use of eq. [5] is indeed not as restricted as implied by the above list. For example, even if reaction occurs from all possible levels, and even if all species, A, BC, and R participate in the vibrational relaxation of BC, eq. [5] is still valid (12). A more general version of [5] is nevertheless available (13). We also found that when anharmonicity, and multiple quantum-jumps, and non-Landau–Teller vibrational transitions are accounted for, the deviation from eq. [5] is of the order of 1% (14). Some aspects of the reverse reaction have been examined as well (15). As the deviations from eq. [4] predicted by eq. [5] can be very large (11) under some conditions, it is worthwhile examining all factors affecting the general usefulness of eq. [5]. Therefore in this study we examine one of the remaining assumptions: How good is the steady-state assumption?

The most sensitive test of eq. [5] can be carried out when its predictions are dramatic. Therefore we have chosen the test case

$$[6] \qquad \mathrm{Br} + \mathrm{HCl} \rightarrow \mathrm{HBr} + \mathrm{Cl}$$

for which k/k_{eq} can be as small as 0.03 (12). We present the results as predicted by the steady-state calculation whose method is described in ref. 12 and compare them with the results of a full solution of the master equation, including transient effects.

Procedure

Reaction [6] can be decomposed into the following elementary processes:

$$[7] \qquad \mathrm{Br} + \mathrm{HCl}(v) \rightarrow \mathrm{HBr} + \mathrm{Cl}$$

$$[8] \qquad \mathrm{R} + \mathrm{HCl}(v) \rightarrow \mathrm{R} + \mathrm{HCl}(v')$$

where R represents all relaxer species present (here Br, HCl, and an inert diluent, M = Ar or He). We have shown (14) that the single-quantum jump harmonic oscillator approximation is a very good one for the purposes of generalizing the reaction rate expression [5]. Therefore, we set $v' = v + 1$ or $v' = v - 1$, and use the Landau–Teller scaling relations

$$[9] \qquad k_{v,v-1} = vk_{1,0}$$

$$[10] \qquad k_{v,v+1} = (v+1)k_{0,1}$$

to relate transitions between higher vibrational levels and those between $v = 0$ and $v = 1$. If k_v and $k_{v,v'}$ are the rate constants for reactions [7] and [8], respectively, then the differential equation describing the rate of change of the population, N_v, of HCl in level v is given by

$$[11] \qquad -\mathrm{d}N_v/\mathrm{d}t = k_{v,v-1}N_vN_\mathrm{R} + k_{v,v+1}N_vN_\mathrm{R} - k_{v-1,v}N_{v-1}N_\mathrm{R} - k_{v+1,v}N_{v+1}N_\mathrm{R} + k_vN_\mathrm{Br}N_v$$

In eq. [11] each term containing N_R is actually a sum of terms

$$[12] \qquad k_{i,j}N_\mathrm{R} = k_{i,j}{}^{\mathrm{Br}}N_\mathrm{Br} + k_{i,j}{}^{\mathrm{HCl}}N_\mathrm{HCl} + k_{i,j}{}^{\mathrm{M}}N_\mathrm{M}$$

where terms of the form N_X represent the concentration of species X. In its present form eq. [11] ignores the reverse reaction which is exothermic and very fast. The implication is that the reverse reaction does not interfere with the establishment of a steady forward process. In other words, we are concentrating only on that early part of reaction [6] before products begin to form significantly. We have already shown that this is legitimate (11) when we are interested in merely determining the contribution of reaction [6] to the total rate.

Equation [11] can be solved analytically in the steady-state limit, by setting $\mathrm{d}(N_v/N_\mathrm{HCl})/\mathrm{d}t = 0$. The result is eq. [5]. We use that result in order to establish a baseline for comparison with the more complex case, where the steady-state assumption is not made. In both cases we use the same set of microscopic rate constants.

We integrated the set of stiff differential equations [11] using an implementation of the algorithm of Byrne and Hindmarsh (16) which is based on the work of Gear (17, 18). Both the initial integration step-size and the tolerance parameter space was explored to find sufficiently stringent values such that the end result for the phenomenological rate coefficient, k, was invariant to better than one part in 10^6. Additionally, we checked for chemical accuracy by comparing the results of $\sum_v N_v$ with the integral of $\mathrm{d}N_\mathrm{Br}/\mathrm{d}t = \sum_v k_vN_\mathrm{Br}N_v$. The two results were

Can. J. Chem. Downloaded from www.nrcresearchpress.com by 195.246.54.202 on 09/08/12
For personal use only.

identical within one part in 10^{10} by the end of the integration, indicating that round-off errors did not accumulate to serious levels. Two other checks were performed. First, the absolute values of the concentrations of the reagents were changed by 12 orders of magnitude (keeping the relative concentrations the same). The expectation (12) that there would be no change in the value obtained for k was indeed borne out. Second, the value of $k_{1,0}$ was artificially increased by orders of magnitude. As the relaxation rate gets larger and larger, there is less and less depletion of the vibrational levels caused by reaction from those levels, and therefore the value of k should approach k_{eq} at all times. This was indeed observed.

As initial conditions we chose five temperatures in the range 300–3000 K, and three mole fractions (i.e. [Br]/[M] = 0.01 to 1.0). The analytical solution (11, 12) assumed that either He or HCl was the collider but not both. In the case of the numerical solution, a finite amount of HCl must be present even if R = He, but the amount of HCl present must be such that it does not contribute significantly to relaxation in order that the present study be validly compared to the analytical study. Therefore, whatever value is chosen for [HCl], the ratio of [HCl]/[He] must be sufficiently small — at least as small as $k_{1,0}^{He}/k_{1,0}^{HCl}$ or 2.8×10^{-3}. We found that [HCl]/[He] = 10^{-6} represented the situation M = He accurately.

The values of the microscopic reactive and non-reactive rate constants used as input to the calculation are given in ref. 11. The output of the calculation is the set of N_v i.e. [HCl(v)] as a function of time. From this we could calculate the fractional level population, $y_v = N_v/\sum_v N_v$. The phenomenological rate coefficient is defined in exactly the same way that is done in an experiment, namely

$$[13] \qquad k = -\mathrm{d[HCl]}/\mathrm{d}t/([\mathrm{Br}][\mathrm{HCl}])$$

This can be rewritten in a more convenient form (12) as

$$[14] \qquad k = \sum_v y_v k_v$$

from which we can see how each level contributes to the observed rate coefficient. Depending on the choice of the initial population distribution, y_v and hence k vary with time. We started the integration with the population distribution equal to the Boltzmann population distribution at the temperature, T, in question. For comparison purposes we also evaluated the equilibrium value of k, i.e. k_{eq}, according to

$$[15] \qquad k_{eq} = \sum_v y_v^{eq} k_v$$

which is equivalent to the k_{eq} defined in eq. [4]. Here y_v^{eq} is the Boltzmann fractional level population at the temperature T. Having started out at $t = 0$ with the Boltzmann distribution, the value of k at $t = 0$, i.e. $k_{t=0}$, is the same as k_{eq}. Hence $k/k_{t=0}$ is simply k/k_{eq}.

Results

Figures 1 and 2 are plots of k normalized by its initial value, $k_{t=0}$, for the six sets of initial conditions at $T = 300$ K. Note that the abcissa is log ξ where ξ is the extent of reaction. Extent of reaction is here defined as $\xi = ([\mathrm{Br}]_0 - [\mathrm{Br}])/[\mathrm{Br}]_0$ if Br is the limiting reagent, or $\xi = ([\mathrm{HCl}]_0 - [\mathrm{HCl}])/[\mathrm{HCl}]_0$ if HCl is the limiting reagent, with $[\mathrm{Br}]_0$ and $[\mathrm{HCl}]_0$ being the

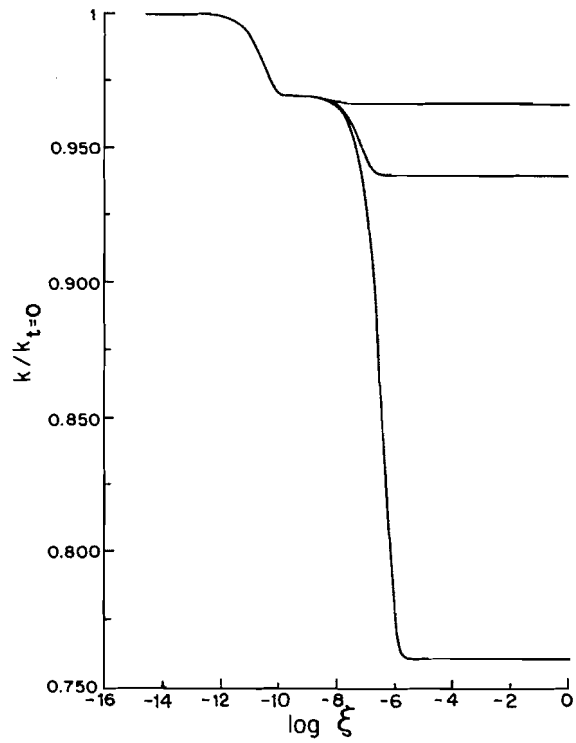

FIG. 1. The normalized phenomenological rate coefficient as a function of the reaction progress variable for R = He, $T = 300$ K. From top to bottom, [Br]/[R] = 0.01, 0.1, and 1, respectively.

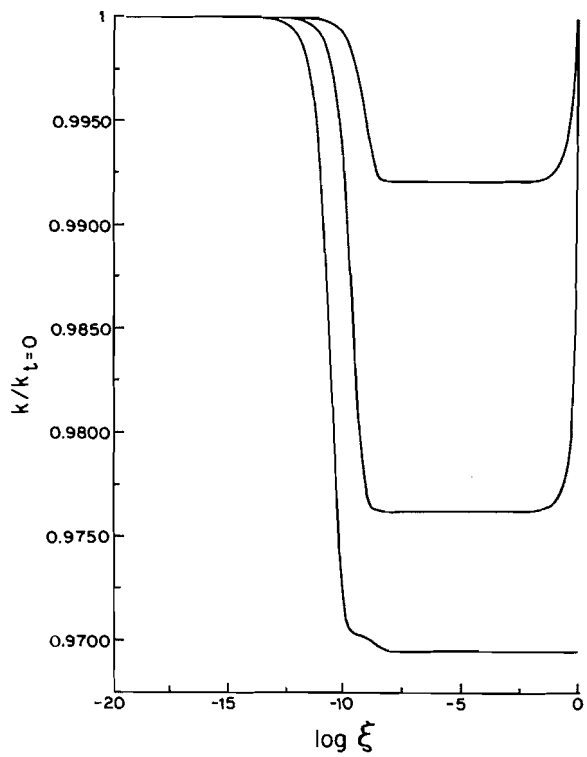

FIG. 2. The normalized phenomenological rate coefficient as a function of the reaction progress variable for R = HCl, $T = 300$ K. From top to bottom, [Br]/[R] = 0.01, 0.1, and 1, respectively.

Can. J. Chem. Downloaded from www.nrcresearchpress.com by 195.246.54.202 on 09/08/12
For personal use only.

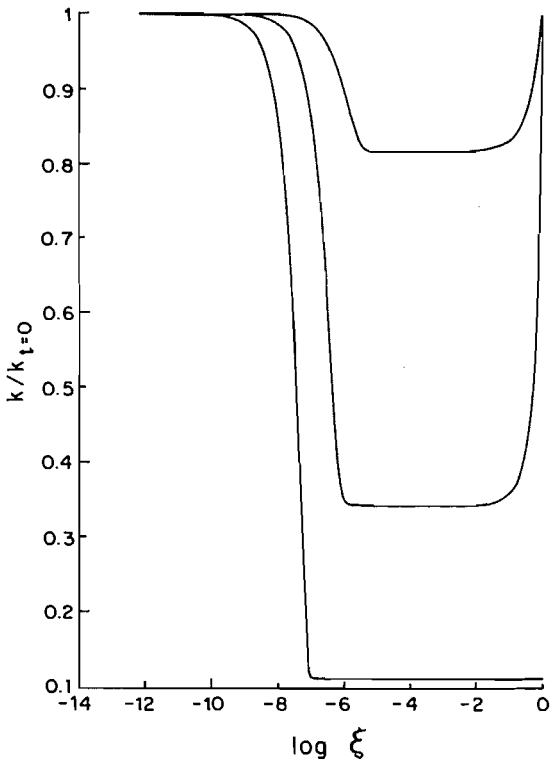

FIG. 3. The normalized phenomenological rate coefficient as a function of the reaction progress variable for R = HCl, T = 500 K. From top to bottom, [Br]/[R] = 0.01, 0.1, and 1, respectively.

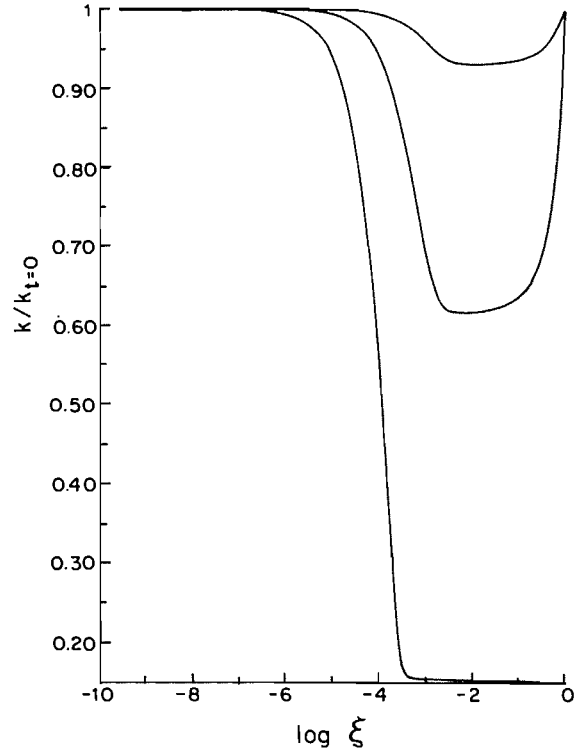

FIG. 4. The normalized phenomenological rate coefficient as a function of the reaction progress variable for R = HCl, T = 1000 K. From top to bottom, [Br]/[R] = 0.01, 0.1, and 1, respectively.

initial reagent concentrations. This choice of variables allows for the significant events over the whole course of the reaction to be displayed on a single graph and facilitates comparison of different sets of initial conditions. As can be seen in Figs. 1 and 2, $k/k_{t=0}$ starts out at unity and decreases monotonically to a smaller constant value; at later times, depending on the initial concentrations, $k/k_{t=0}$ either remains at that constant value (Fig. 1) or rises to its equilibrium value, $k_{eq}/k_{t=0} = k_{eq}/k_{eq} = 1$ (Fig. 2). The latter case prevails when Br, as the minor or limiting reagent, begins to disappear. Then the reaction perturbs the population distribution less and less until the y_v return to their original values, y_v^{eq}. The plateau which appears at log $\xi = -10$ to -8 will be discussed below. It is the intermediate values, during which the reagent concentrations are changing (log $\xi = -3$ to -1), which are most interesting. With some expected exceptions, the phenomenological rate coefficient is constant in this time regime and, it turns out, is equal in all cases to the value predicted by the analytical steady-state procedure of ref. 12 (see below).

Figures 3 to 6 are plots of the normalized rate coefficient at the other temperatures for R = HCl. The same general forms are evident as in Figs. 1 and 2, but with increasing temperature (and presumably increasing disturbance to the vibrational population distribution) the time regime where k is constant becomes shorter and shorter, until at 3000 K there are no vestiges of this constant regime, except when [Br]/[HCl] = 1. (That special case will be discussed below.) This could mean, in principle, that under some conditions, the reaction is so fast that a steady distribution is never established in time, i.e. the reaction proceeds during the transient phase. Note, however, that the distortion from constancy begins around log ξ

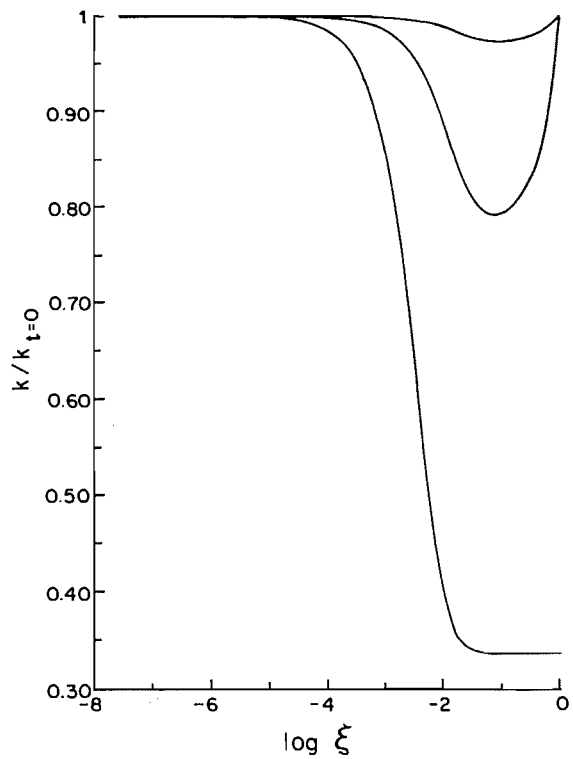

FIG. 5. The normalized phenomenological rate coefficient as a function of the reaction progress variable for R = HCl, T = 2000 K. From top to bottom, [Br]/[R] = 0.01, 0.1, and 1, respectively.

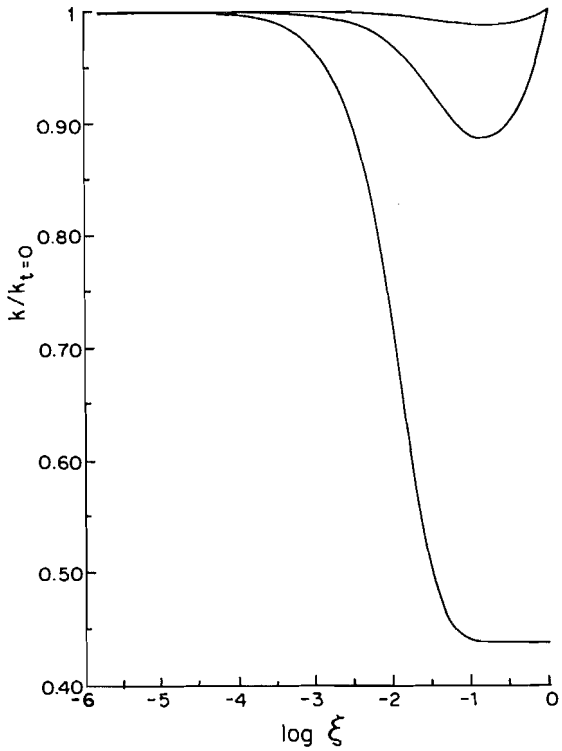

FIG. 6. The normalized phenomenological rate coefficient as a function of the reaction progress variable for R = HCl, T = 3000 K. From top to bottom, [Br]/[R] = 0.01, 0.1, and 1, respectively.

$= -1$, i.e. when approximately 10% of the reagents have already disappeared. When reagent disappearance is taken into account, as we shall see below, the distortion nevertheless fits exactly into the pattern predicted by eq. [5] because, as is well known, a steady state condition does not necessarily imply constant reagent concentrations or constant fractional level populations.

The dependence of $k/k_{t=0}$ on R was as expected (11), with the most dramatic effects for R = He, the least efficient relaxer. The temperature dependence also turned out as expected (12). It is around 500 K that the disparity between k and k_{eq} is the largest.

Discussion

Table 1 shows a comparison between the results of the minimum value of the exact numerical integration (the fourth column) and the prediction of the steady state analysis (the last column) for k/k_{eq}. The latter results are taken from ref. 12, where they obey a variant of eq. [5]. Using eqs. [5] and [13], we see that the steady state results can essentially be considered as equal to $\{1 + f(T)[A]/[R]\}^{-1}$. For the exact results we chose the constant plateau value or the minimum value for $k/k_{t=0}$. Note the excellent agreement between the analytical and the exact results. The cases where agreement was not better than 1 part in 10^5 were those where $k/k_{t=0}$ reached a minimum and immediately increased, i.e. where significant reagent loss was occurring. However, even under these extreme conditions agreement was still around 1 part in 100, indicating that significant reaction occurred only after a steady vibrational population distribution was established.

Equation [5] can be tested, as suggested in ref. 12, by plotting a graph of $k/(k_{eq}-k)$ vs. $k_{1,0}[R]/[Br]$. Such a graph should be linear. In this study $k_{1,0}[R]$ is $(k_{1,0}^{He}[He] + k_{1,0}^{HCl}[HCl])$. Figure 7*a* shows such a plot to be linear over 4 orders of magnitude of the abcissa at 500 K, whether M = He or M = HCl. We chose 500 K because it is at that temperature where k deviates most from k_{eq}. However, it is more instructive to examine the case of 3000 K, where deviations are relatively small, because the smaller the deviations the more stringent the test, and because it affords an opportunity to test eq. [5] not only when k/k_{eq} is constant but also when it is changing due to the disappearance of reagents. Again here the test plot (see Fig. 7*b*) is linear for the regime where k is constant. Therefore Fig. 7 shows that

$$[16] \qquad d[Br]/dt = \frac{-k_{eq}[Br][HCl]}{1 + \dfrac{1}{a + bk_{10}[R]/[Br]}}$$

where a and b are constants (slope and intercept in Fig. 7). Under conditions of extreme reactivity, eq. [16] is essentially the same as eq. [5].

The regime where k reapproaches k_{eq} coincides exactly with $\log \xi = -1.5$ or greater, i.e. where reagents begin to disappear significantly. Consequently, for this regime we must first evaluate [Br] as a function of time before determining the abcissa values. This can be done by integrating eq. [11] numerically, as in this study, or eq. [16] analytically. Before doing so, how-

TABLE 1. Comparison of numerical and analytical (steady state) results

R	T/K	[Br]/[R]	$k/k_{t=0}$	k/k_{eq} (ref. 12)
He	300	0.01	0.96672	0.96672
		0.1	0.93998	0.93998
		1	0.76083	0.76083
	500	0.01	0.16409	0.16409
		0.1	0.084968	0.084968
		1	0.073802	0.073802
	1000	0.01	0.72021	0.72021
		0.1	0.22937	0.22937
		1	0.030605	0.030605
	2000	0.01	0.90912	0.90912
		0.1	0.55283	0.55283
		1	0.15738	0.15738
	3000	0.01	0.95471	0.95472
		0.1	0.69078	0.69079
		1	0.22999	0.22999
HCl	300	0.01	0.99215	0.99215
		0.1	0.97628	0.97628
		1	0.96953	0.96953
	500	0.01	0.81716	0.81716
		0.1	0.34289	0.34289
		1	0.11164	0.11164
	1000	0.01	0.93196	0.93134
		0.1	0.61890	0.61747
		1	0.15334	0.15335
	2000	0.01	0.97308	0.97032
		0.1	0.79318	0.78081
		1	0.33730	0.33731
	3000	0.01	0.98748	0.98510
		0.1	0.88672	0.87085
		1	0.43926	0.43926

Can. J. Chem. Downloaded from www.nrcresearchpress.com by 195.246.54.202 on 09/08/12
For personal use only.

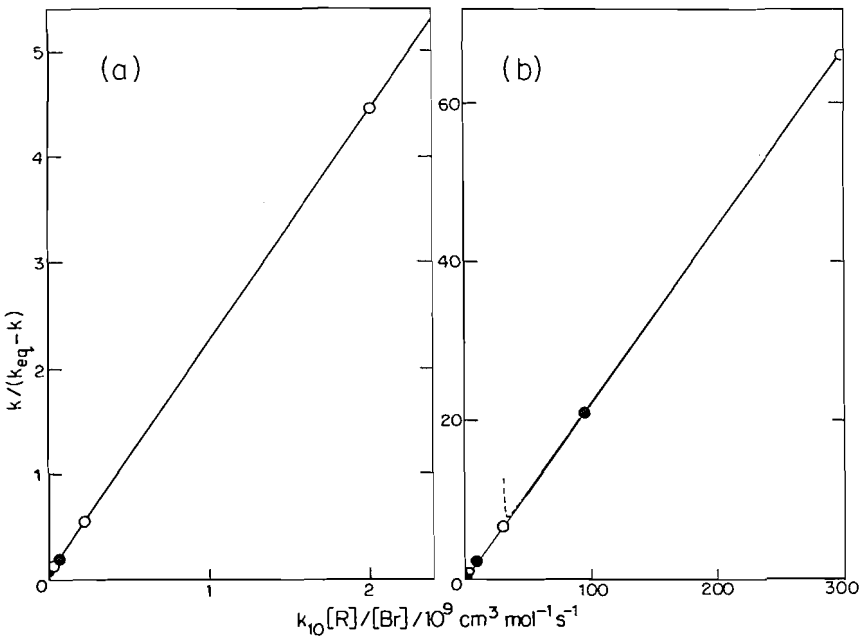

FIG. 7. Dependence of the relative depression of the nonequilibrium rate coefficient on the relative relaxability and reactivity of the bimolecular reagent. ○ R = HCl; ● R = He. (*a*) T = 500 K; abcissae of the points cover the range 5.3 × 10^5 to 2.0 × 10^9 cm^3 mol^{-1} s^{-1}; (*b*) T = 3000 K. The straight lines correspond to the steady state conditions. Superimposed on (*b*) is a dashed line corresponding to the transient regime, and a heavy line corresponding to conditions prevalent during the disappearance of the reagents.

ever, we note the special case of R = He. In this case, there is so little HCl that HCl is the limiting reagent. Hence [Br] is a quasi-constant, and the denominator in eq. [16] is time-invariant. Therefore it is not surprising to see in Fig. 1 that once the steady state regime commences, k remains constant. In the case of R = HCl, k returns to its equilibrium value except for the special case [Br]/[HCl] = 1. Because of the stoichiometry, if this ratio is initially unity, it will be unity at all times. Hence the denominator in eq. [16] is a pure constant again, and Figs. 2–6 can be understood. In all other cases, as the reaction proceeds and [Br] → 0, the denominator in eq. [16] approaches unity.

The abcissa for the test plot (when R = HCl and $[HCl]_0 \neq [Br]_0$) is simply $k_{1,0}^{HCl}[HCl]/[Br]$. Its evaluation, even when [HCl] and [Br] vary strongly with time, is facilitated by using ξ directly. Thus, using mass balance and the definition of ξ here, i.e. $\xi = ([Br]_0 - [Br])/[Br]_0$, we see that

$$[17] \quad k_{1,0}[R]/[Br] = k_{1,0}^{HCl}\{[HCl]_0 + [Br] - [Br]_0\}/[Br]$$
$$= k_{1,0}^{HCl}\{[HCl]_0/[Br]_0 - \xi\}/\{1 - \xi\}$$

It is now easy to analyze the regime, log ξ = −1.5 to 0, and add the continuous set of points to Fig. 7*b*. We chose the case $[Br]_0/[HCl]_0$ = 0.1 at 3000 K, corresponding to the middle curve in Fig. 6. The results fall on the same straight line as the steady-state results, confirming the validity of eq. [16] (and its high reactivity version, eq. [5]) over several orders of magnitude in $[Br]_0/[R]_0$ and over the portion of the reaction where reagents are changing dramatically. Also shown in Fig. 7*b* as a dashed line, for comparison, is the portion of the reaction occurring in the transient zone. Although, for this extreme case, 10% of the reagent Br has disappeared before a steady vibrational distribution is established, once the steady distribution is formed, eq. [16] is mathematically valid at all times thereafter. (Of course, once we account for the reverse

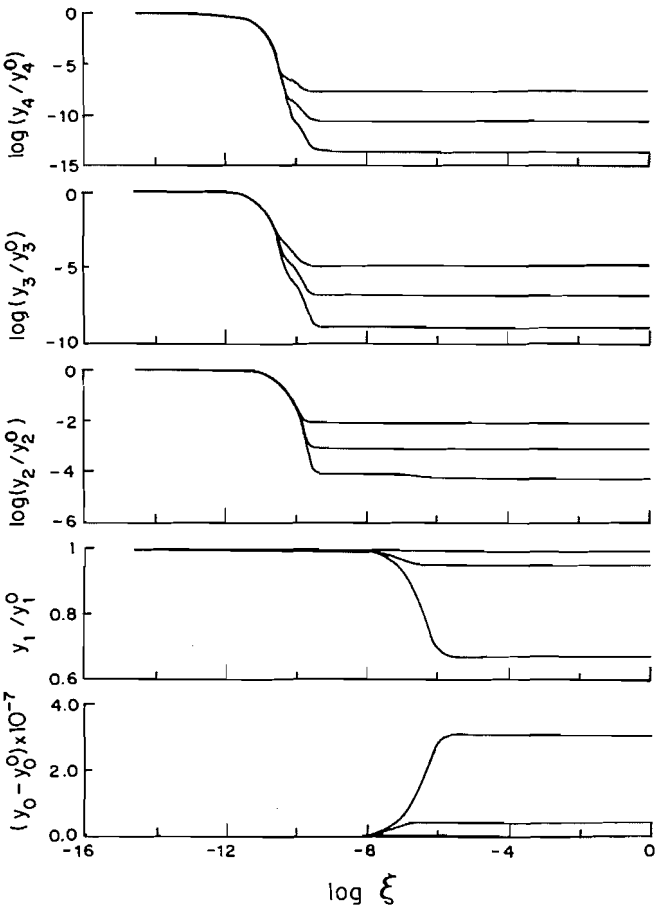

FIG. 8. Changes in the relative fractional level population as a function of the reaction progress variable for v = 0–4, R = He, T = 300 K, and various values of [Br]/[R] as in Fig. 1. From top to bottom in each plot [Br]/[R] = 0.01, 0.1, and 1, respectively. Superscripts refer to initial values of y_v.

Can. J. Chem. Downloaded from www.nrcresearchpress.com by 195.246.54.202 on 09/08/12
For personal use only.

process, the application of eq. [16] is limited in practice to those times before significant amounts of products are formed.)

Some of the transient behaviour visible in Figs. 1 and 2 is also of interest. Figure 1 shows a sudden drop in k at log $\xi = -11$ and another drop at log $\xi = -7$ when R = He at 300 K. The first feature is seen from Fig. 8 to be the effect of the depletion of y_2, the fractional level population of $v = 2$. Closer examination of the curves for y_2, y_3, and y_4 in Fig. 8 reveals that these levels are seriously depleted (by as much as a factor of 10^{15} in the case of y_4), and so all of these variables decrease at log $\xi = -11$ to the point where none of them makes any contribution to the phenomenological rate coefficient, k. k then remains constant until log $\xi = -7$, at which point y_1 becomes depleted, resulting in the second feature. Similar behaviour occurs in Fig. 2 for R = HCl at 300 K. A shoulder is visible at log $\xi = -9$, but is less pronounced than in Fig. 1 because of the higher reactivity of the lower vibrational levels and the consequently smaller spread in the magnitudes of the microscopic rate constants and their associated time scales. At higher temperatures all levels are depleted on the same time scale, and no plateaux are observed.

Conclusion

Except for very high temperatures no significant amount of reaction occurs before the establishment of a steady state vibrational level population distribution of the bimolecular reagent for the reaction Br + HCl $\longrightarrow$ HBr + Cl. Under all conditions the numerically exact phenomenological rate coefficient obeys the analytical rate law, eq. [16], from the end of the transient zone right up to the end of the reaction, $\xi = 1$ (in the absence of the reverse reaction).

Acknowledgements

H.T. is very grateful to the Natural Sciences and Engineering Research Council of Canada for the award of an International Collaborative Research Grant, to the Lady Davis Foundation for the award of a Visiting Professorship at the Hebrew University of Jerusalem, and to the Fritz Haber Center for Molecular Dynamics for financial support. H.T. is also very grateful to Professor Assa Lifshitz for the hospitality extended during his stay in Jerusalem.

1. C. Carruthers and H. Teitelbaum. Chem. Phys. **127**, 351 (1988).
2. J. Troe. Ber. Bunsenges. Phys. Chem. **84**, 829 (1980).
3. H. Teitelbaum. Can. J. Chem. **69**, 2927 (1982).
4. W. Forst and A.P. Penner. J. Chem. Phys. **72**, 1435 (1980).
5. J.E. Dove and J. Troe. Chem. Phys. **35**, 1 (1978).
6. M. Camac and A. Vaughan. J. Chem. Phys. **34**, 460 (1961).
7. K.L. Wray. *In* 10th Int. Symp. on Combustion. The Combustion Institute, Pittsburgh, PA. 1965. p. 523.
8. W.S. Watt and A.L. Myerson. J. Chem. Phys. **51**, 1638 (1969).
9. J.P. Appleton, M. Steinberg, and D.J. Liquornik. J. Chem. Phys. **48**, 599 (1968); **49**, 2468 (1968).
10. J.E. Dove, W.S. Nip, and H. Teitelbaum. *In* 15th Int. Symp. on Combustion, The Combustion Institute, Pittsburgh, PA. 1974. p. 903.
11. H. Teitelbaum. J. Chem. Soc. Faraday Trans. 2, **84**, 1889 (1988).
12. C. Bowes, N. Mina, and H. Teitelbaum. J. Chem. Soc. Faraday Trans. **87**, 229 (1991).
13. H. Teitelbaum. J. Phys. Chem. **94**, 3328 (1990).
14. H. Teitelbaum. Chem. Phys. Lett. **202**, 242 (1993).
15. H. Teitelbaum. Chem. Phys. **173**, 91 (1993).
16. G.D. Byrne and A.C. Hindmarsh. ACM Trans. on Math. Software, **1**, 71 (1975).
17. C.W. Gear. Numerical initial value problems in ordinary differential equations. Prentice-Hall, Englewood Cliffs, NJ. 1971.
18. C.W. Gear. Commun. ACM **14**, 176 (1971).

Can. J. Chem. Downloaded from www.nrcresearchpress.com by 195.246.54.202 on 09/08/12
For personal use only.

Fluorimetric measurement of the activity of surface-immobilized monolayers of enzyme using a dual emission probe

JOHN D. BRENNAN,[1] VANJA KUKAVICA, KRISHNA M.R. KALLURY, AND ULRICH J. KRULL[2]

Chemical Sensors Group, Department of Chemistry, Erindale Campus, University of Toronto, 3359 Mississauga Road North, Mississauga, ON L5L 1C6, Canada

Received June 25, 1993

This paper is dedicated to Professor John C. Polanyi on the occasion of his 65th birthday

JOHN D. BRENNAN, VANJA KUKAVICA, KRISHNA M.R. KALLURY, and ULRICH J. KRULL. Can. J. Chem. **72**, 721 (1994).

A sensitive assay for measurement of the activity of hydrolase enzymes that are immobilized onto quartz and silicon dioxide surfaces was developed. Measurements are based on the changes of the fluorescence properties of the probe carboxy-seminaptharhodafluor-X that are caused by pH variations associated with the reaction of urea with urease. The results indicated a loss of activity in 8 days, and a half-life of 3 days, when urease was immobilized onto quartz surfaces that were first derivatized with a 16-carbon spacer chain.

JOHN D. BRENNAN, VANJA KURKAVICA, KRISHNA M.R. KALLURY et ULRICH J. KRULL. Can. J. Chem. **72**, 721 (1994).

On a développé une méthode sensible pour mesurer l'activité des enzymes hydrolases immobilisées sur des surfaces de quartz ou de dioxyde de silicium. Les mesures sont basées sur les changements dans les propriétés de fluorescence de la sonde carboxy-seminaphtarhodafluor-X qui sont causées par des variations de pH associées à la réaction de l'urée avec l'uréase. Les résultats indiquent que, lorsque l'uréase est immobilisée sur des surfaces de quartz qui ont été antérieurement soumises à une dérivatisation à l'aide d'une chaîne d'espacement contenant 16 carbones, il y a perte d'activité en 8 jours et que la demi-vie est de 3 jours.

[Traduit par la rédaction]

Introduction

One of the major steps in the preparation of biosensors involves the immobilization of a selective biorecognition element onto the surface of a transducer (1). Selectivity is normally achieved through the use of antibodies or enzymes (2), and these proteins are generally immobilized (3–5) onto substrates such as metals (electrochemical sensors) or quartz (piezoelectric or optical sensors). The goal of the immobilization technique is to place the protein onto the surface at a high density and with a high biochemical activity. It is also desirable to maintain the activity of the protein over a long period of time to permit repetitive and continuous use of the sensor. To investigate the effects of the immobilization technique on the stability of the protein, an assay of the activity of the immobilized protein is required. Ultimately, knowledge of the initial activity and rate of denaturation of immobilized proteins may enable the determination of the optimum parameters for operation of the sensor in terms of its sensitivity and long-term stability.

Several techniques for measuring the activity of immobilized antibodies have been reported (6–8), but there has been much less progress in the measurement of the activity of immobilized enzymes. The general approach for determining the activity of immobilized enzymes is to use silica gel or control pore glass to maximize the surface area and thus the amount of enzyme that is immobilized (4). This allows a standard colourimetric assay to be done. The development of more sensitive methods designed to determine the activity of enzymes that are immobilized onto the surface of a small optically transparent device such as an optical fiber is only now being addressed, and requires new technology since the very small amount of enzyme present (typically on the order of 1–2 μg, of which only a portion is active) precludes the generation of a measurable signal over short time periods when using standard methods such as UV–visible absorption measurements (9). The sensitivity of fluorescence methods may permit an activity assay to be done for such small amounts of active enzyme in a volume on the order of microlitres.

A particularly useful pH-sensitive fluorophore is carboxy-seminaphtharhodafluor-X (SNARF-X), which has a single excitation wavelength that is insensitive to changes of pH, and two emission maxima that change in relative intensity as a function of pH (10). The ratio of the intensities at the two emission maxima can be used to remove instrumental drift and photobleaching problems. Since the amount of product formed in the enzyme–substrate reaction is small, only a small change in pH and fluorescence intensity will be observed. This would lead to limitations of signal-to-noise if detection was done at only a single wavelength. The ability to compute a ratio of two peaks within a single spectrum can reduce such difficulties since the absolute intensity of fluorescence becomes unimportant, and the ratio method avoids interference associated with long-term drift of the instrument and the concentration of the probe.

An enzyme that has been used extensively in the development of biosensors is urease (11), mainly owing to the chemical significance of urea, and the high turnover number and inherent stability of the protein (12). Urease catalyzes the hydrolysis of urea to produce ammonium and carbonate ions, and yields products that render a solution more basic as the reaction proceeds. This paper describes the use of SNARF-X as an indicator in the activity assay of urease that is immobilized onto quartz wafers. The results indicate that the new assay technique is capable of measuring activities as low as 1000 units g^{-1} from less than 2 μg of enzyme in a period of less than 1 h. Studies of the practical application of chemically modified surfaces have shown that the rate of denaturation of urease is reduced when the enzyme is immobilized on a quartz surface via a 16-carbon spacer chain.

[1]Present address: Institute for Biological Sciences, National Research Council of Canada, Ottawa, ON K1A 0R6, Canada.

[2]Author to whom correspondence may be addressed.

Can. J. Chem. Downloaded from www.nrcresearchpress.com by 195.246.54.202 on 09/08/12
For personal use only.

Can. J. Chem. Downloaded from www.nrcresearchpress.com by 195.246.54.202 on 09/08/12
For personal use only.

Experimental

Chemicals

Urease (EC 3.5.1.5) type 1V from jack bean, urea, and phenol red were purchased from Sigma Chemical Company (St. Louis, Mo.), and used without further purification. Two different lots of urease were used, one with an activity of 105 000 units g^{-1}, the other with an activity of 30 000 units g^{-1}, where 1 unit is equivalent to the hydrolysis of 1 μmol of urea per minute at pH 8.0. 16-Hydroxy hexadecanoic acid, dimethyldichlorosilane, and chloroplatinic acid were purchased from Aldrich Chemical Company (Milwaukee, Wis.), and were used as received.

The fluorescent probe carboxy-seminaphtharhodafluor-X (SNARF-X) was purchased from Molecular Probes (Eugene, Oreg.). All water was obtained from a Milli-Q 5-stage cartridge purification system (Millipore Corp., Mississauga, Ont., Canada) and had a specific resistance not less than 18 MΩ cm. All other chemicals were of reagent grade. The quartz wafers and silicon wafers (p-doped, naturally oxidized) were purchased from Heraeus-Amersil Inc. (Sayerville, N.J.) and International Wafer Service (Portola Valley, Calif.), respectively.

Equipment

For the development of the fluorescence assay, excitation and emission spectra were collected using an SLM 4800 spectrofluorimeter (SLM Instruments, Inc., Champaign, Ill.). The spectrofluorimeter used concave holographic monochromators of 2 nm mm^{-1} dispersion and spectra were collected digitally using an 8 nm bandwidth for both the excitation and emission monochromators. The output of the quartz halogen lamp was corrected for intensity drift by using the ratio of the emission for the sample and the emission of a reference cell containing a Rhodamine B quantum counter at a concentration of 3 g L^{-1} in ethanol (13). For the bulk assay, all samples were placed in a 1 cm^2 quartz cuvette and fluorescence was collected at an angle of 90° with respect to the excitation beam. For the assay of urease immobilized on a surface, the quartz or silicon wafer was placed in a 1 cm^2 cuvette with an internal volume of 500 μL. A model 9817A "Red Sensitive" PMT (Hamamatsu, Bridgewater, N.J.) was used for this work.

X-ray photoelectron spectroscopy (XPS) of covalently stabilized monolayers was done using a Leybold MAX-200 spectrometer (Leybold-Heraeus, Cologne, Germany) with excitation by unmonochromatized Mg K_α radiation and a spot size of 2×4 mm^2. An excitation voltage of 1253.6 eV, a detection voltage of 2.65 eV, and an emission current of 20 μA were utilized. Pass energies of 192 and 48 eV were used for broad and narrow region scans, respectively. A take-off angle of 90° was used for both broad region and narrow region scans. The reported intensities were corrected for Scofield factors and instrument transmission factors using software routines provided by Leybold. The shapes of the peaks indicated that no compensation for differential surface charging was necessary. Satellite peaks that resulted from the unmonochromatic Mg K_α radiation were subtracted from all spectra. The binding energy scale of the spectrometer was calibrated to the Ag($3d_{5/2}$) and Cu($2p_{3/2}$) peaks at 368.3 and 932.7 eV, respectively, and the binding energy scale was shifted to place the C(1*s*) peak at 285.0 eV.

Ellipsometry of silicon wafers that were coated with immobilized enzymes was done with a Rudolph Research AutoEL-II null reflection ellipsometer (Rudolph Research Corp., Flanders, N.J.) utilizing a wavelength of 632.8 nm and an incident angle of 70°. Measured values of Δ and Ψ were converted to thickness and refractive index information using software originally developed by McCracken (14).

Absorption spectra were recorded with a Hewlett Packard 8452A diode array spectrometer using a total integration time of 1 second per spectrum.

Procedures

Colourimetric assay of enzyme activity in bulk solution

The colourimetric measurement of the activity of urease in solution was based on the procedure of Stefanac et al. (9). A stock solution of phenol red was prepared by adding 2 g of phenol red to 28.4 mL of 0.1 M NaOH and diluting with water to 1 L. A standard solution of phenol red was prepared by diluting 10 mL of the stock phenol red solution to 1 L with 0.066 M phosphate buffer solution. A standard urea solution was prepared by dissolving 12 g of urea in 1 L of 0.066 M phosphate buffer to give a final concentration of 0.2 M urea. Standard solutions of urease in water were prepared with concentrations ranging from 0 to 1.0 mg mL^{-1}.

For measurement of urease activity, a volume of 0.1 mL of urease solution was added to a volume of 2.4 mL of the standard urea solution, and 2.5 mL of the standard phenol red solution was immediately added. The solution was mixed and 3 mL of the solution was added to a cuvette. Absorbance was measured from each solution at a wavelength of 560 nm. The activity was calculated by using a standard calibration curve, which was constructed by measuring the absorbance of ammonium carbonate solutions in 0.066 M phosphate buffer.

Fluorimetric assay of enzyme activity in bulk solution

A stock solution of 10^{-6} M SNARF-X was prepared in 0.066 M phosphate buffer at a pH of 7.4 immediately before use. Fresh solutions of 0.2 M urea were prepared in 0.066 M phosphate buffer at pH 7.4 immediately before use. Solutions of urease were prepared immediately before use at concentrations ranging from 0 to 1.0 mg mL^{-1} in distilled water. Volumes of 2.5 mL of the SNARF-X solution, 2.4 mL of the urea solution, and 0.1 mL of the urease solution were added to a solution vessel, mixed, and 3 mL of the solution was immediately transferred to a 1 cm^2 cuvette for fluorescence measurements. Fluorescence spectra were measured at 21°C at 10 min intervals over a period of 60 min. Excitation was at 337 or 488 nm, and emission was collected between 550 and 750 nm. A 340-nm long-pass filter was used in cases where the excitation was at 337 nm to remove the second harmonic radiation at 674 nm that was reflected from the sample. The activity was calculated by using a standard calibration curve, which was constructed by measuring the fluorescence from ammonium carbonate solutions (0–50 μM) in 0.066 M phosphate buffer that contained 1×10^{-6} M SNARF-X.

Analysis of emission spectra involved the smoothing of the spectra, determination of the position of the two peak maxima, integration of each peak over a 30 nm window that was centered on the peak maximum, and ratioing of the intensity of the two fluorescence peaks, which were centered at approximately 595 and 650 nm. The emission ratio stated in the results is 650 nm/595 nm for the pH titration curve of SNARF-X and urease assay results.

Preparation of immobilized enzymes

Quartz and silicon wafers were cleaned as described elsewhere (15). Adsorption of urease onto silicon wafers was done by incubating the wafers in a solution consisting of 1 mg mL^{-1} of urease in phosphate buffer (pH 7.4) for a period of 12 h. The extent of coverage was determined by ellipsometry assuming a refractive index of 1.50 for the coating (16). A minimum of five spots were measured to provide an average thickness value for each sample.

Covalent immobilization of urease onto C-16 spacer chains began with the preparation of covalently immobilized membranes with acyl chains consisting of 16 carbons and containing carboxylic acid headgroups. The multistep synthesis is described below and shown in Fig. 1.

16-Hydroxy hexadecanoic acid (1 mmol) was refluxed in a solution of 10 mL of methanol and 0.5 mL of concentrated hydrochloric acid for 5 h under anhydrous conditions. The reaction mixture was then poured into a 100 mL solution of 2% sodium bicarbonate at pH 8. An extraction with ether was carried out and the ether layer was washed thoroughly with water, dried over anhydrous magnesium sulfate, and concentrated in a rotary evaporator. The resulting methyl ester of 16-OH hexadecanoic acid was obtained in almost 100% yield. The purity of the methyl ester was checked using FTIR and ^1H NMR.

The methyl ester (1 mmol) was dissolved in 25 mL of a mixture of dry toluene containing 1.1 mmol of dimethyldichlorosilane and 10 mg of chloroplatinic acid catalyst. This mixture was refluxed for 16 h. The

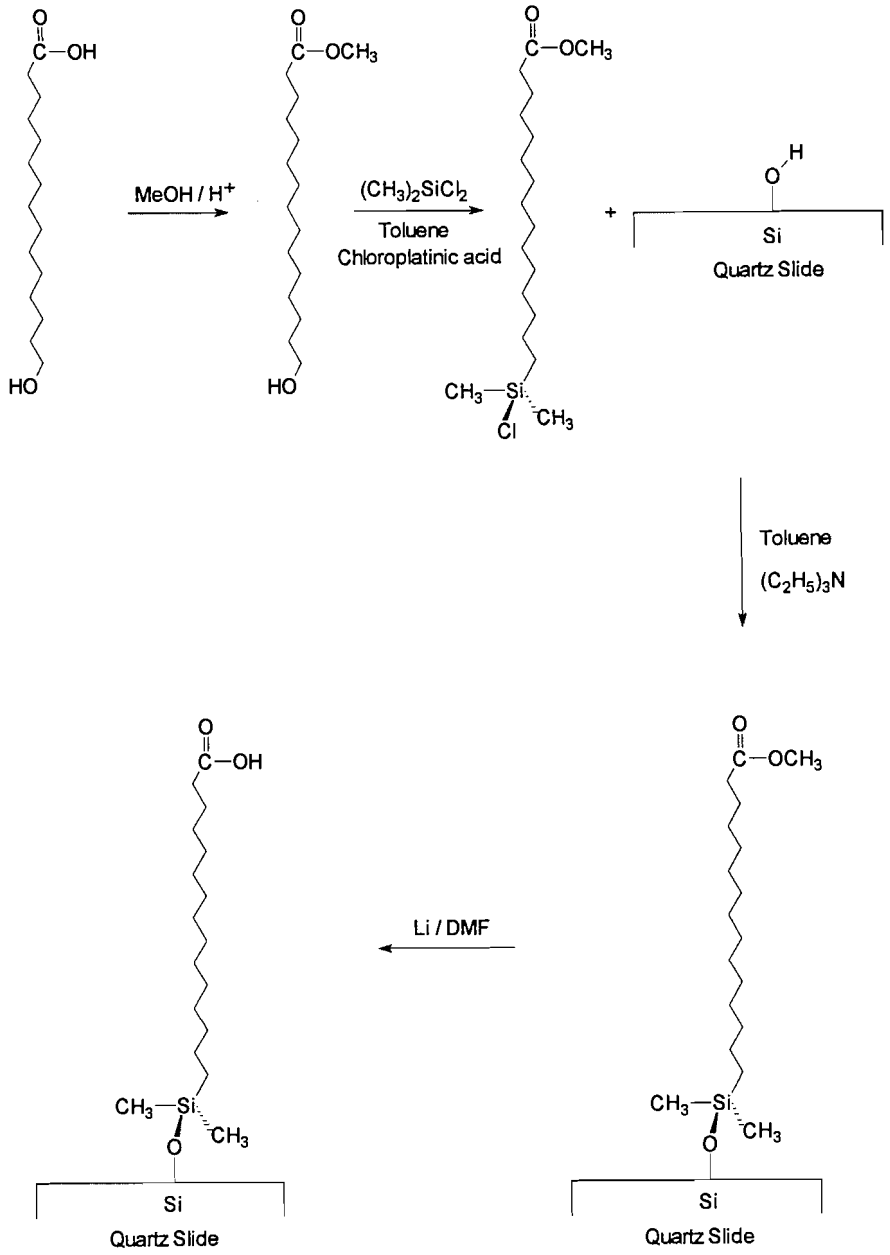

FIG. 1. An outline of the synthetic procedure used to covalently immobilize fatty acid membranes onto quartz wafers starting from 16-OH hexadecanoic acid.

solvent and unreacted silane were removed under vacuum. The mixture was then distilled under vacuum and the fraction boiling at 140–145°C at a pressure of 1 Torr (= 133.3 Pa.) was collected.

Quartz wafers were washed in hot detergent for 30 min, and were then sonicated for 30 min. The wafers were washed in distilled water, soaked in chromic acid for 10–15 min, and rinsed thoroughly with distilled water. The wafers were then dried, for at least 30 min, in an oven at 110°C. The clean wafers were suspended in 10 mL of a 1% solution of 16-(dimethylchlorosilyloxy) hexadecanoic acid methyl ester in toluene. A few drops of triethylamine catalyst was added and the mixture was allowed to stand under nitrogen at room temperature overnight. The wafers were removed, washed thoroughly with dichloromethane, and dried in a vacuum desiccator.

The quartz wafers were suspended in 10 mL of dimethyl formamide and 500 mg of lithium iodide was added. This mixture was refluxed under nitrogen for 16 h after which the wafers were washed with water, methanol, chloroform, and then acetone. The wafers were then dried in a vacuum desiccator.

Urease was immobilized onto the carboxylic acid membranes by activating the membrane with carbonyl diimidazole (CDI) prior to immobilization of urease. This reaction scheme is shown in Fig. 2. The substrate was suspended in THF (5 mL) and 20 mg of CDI was added. The substrate was allowed to stand at room temperature for 2 h and was then washed with THF. The substrate was suspended in water (1 mL) and urease (1 mg) was added. The mixture was allowed to stand for 12 h at 5°C. The substrate was washed with water and stored at −20°C until used.

Fluorimetric assay of activity of immobilized enzymes

The assay of immobilized urease was first done using enzyme that was adsorbed on silicon wafers. The enzyme-coated wafers (dimensions of 1.8 cm × 0.6 cm) were placed in a 500 μL cuvette containing 0.2 M urea and 10^{-6} M SNARF-X. A blank sample, consisting of a clean silicon wafer, was also prepared. Fluorescence spectra of both the enzyme-coated wafer and a blank wafer were collected every 10 min for a period of 1 h, and were compared to calibration curves to

Can. J. Chem. Downloaded from www.nrcresearchpress.com by 195.246.54.202 on 09/08/12
For personal use only.

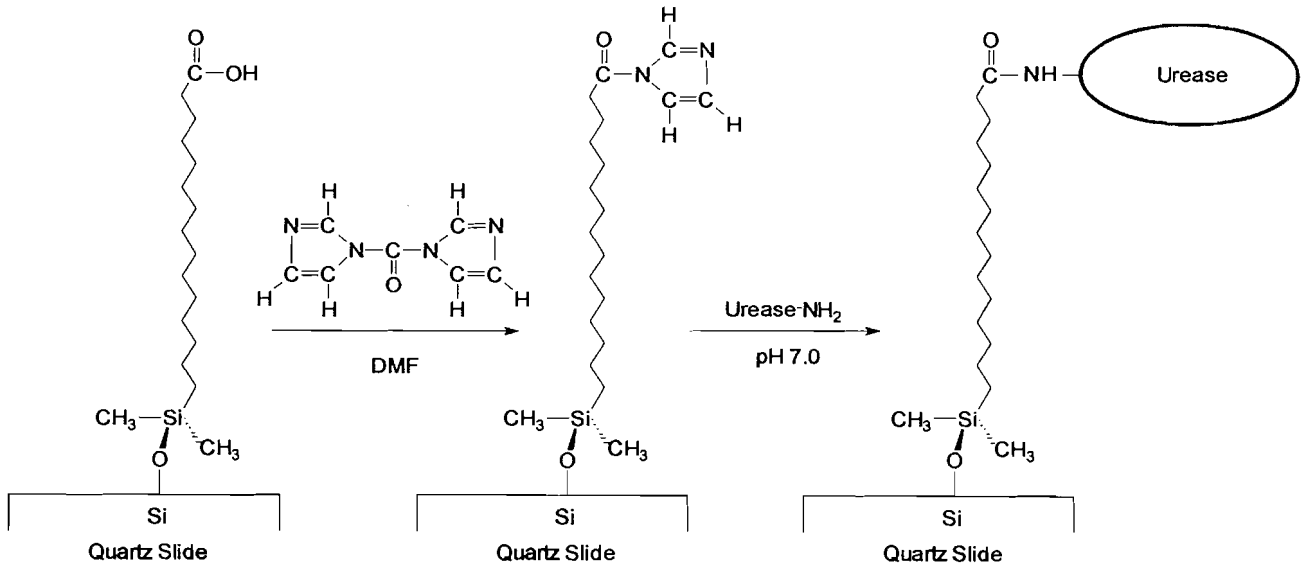

FIG. 2. An outline of the immobilization of urease onto carboxylic acid membranes by activation with carbonyldiimidazole (CDI).

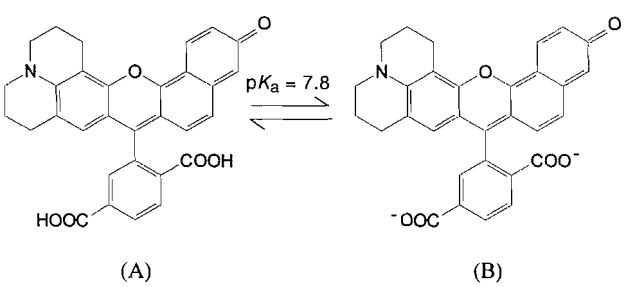

FIG. 3. Equilibrium between protonated and deprotonated forms of SNARF-X. (A) emits at 595 nm; (B) emits at 620 nm and 650 nm.

determine the activity of the immobilized enzyme. Following each assay the silicon wafers were again characterized by ellipsometry to determine the extent of desorption of the protein during the assay.

Results and discussion

Assay of activity of urease in bulk solution

The new fluorimetric assay of enzyme activity was based on changes in the emission spectrum of the fluorescent probe SNARF-X that occurred as a result of changes in the pH of solution as the catalytic reaction proceeded. The structure of the probe in the protonated and deprotonated forms is shown in Fig. 3. SNARF-X was chosen over other dual emission probes such as SNARF-1, because the pK_a of SNARF-X ($pK_a = 7.8$) (10) is closest to the pH range of interest in this work. The pK_a values of the other dual emission probes were in the region of 6.5–6.9 (10). SNARF-X was also chosen because it is possible to excite the probe over a broad range of wavelengths. In the work reported here, the probe was excited using radiation at a wavelength of either 337 or 488 nm, which correspond to the output of a nitrogen laser and an argon ion laser, respectively. The ability to excite fluorescence using a wide range of sources is a major advantage of this probe. Finally, the SNARF-X probe was chosen because the ability to monitor the ratio of two emission peaks eliminates problems that may arise from instrumental drift. This is especially important in cases where small amounts of fluorophore are present, such as assays of surface-immobilized enzymes, since the instrument is usually operating at the limits of performance.

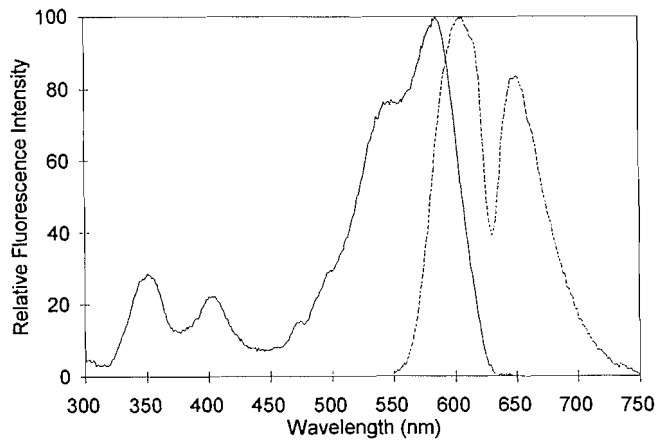

FIG. 4. Excitation and emission spectra of SNARF-X at pH 7.4. (—) Excitation spectrum, (---) emission spectrum.

The presence of two emission peaks in SNARF-X arises from the fact that the energy associated with the singlet state is different when the dye is in the protonated and deprotonated forms. SNARF-X has emission wavelengths of about 595 and 650 nm, which correspond to the protonated and deprotonated form of the probe, respectively. The presence of negative charges on the ring structure for the deprotonated form of the probe will result in a redistribution of electron density throughout the ring system. The new electronic structure will cause the energy of the excited state to decrease, and the energy of the ground state to increase slightly, owing to an increase in solvent dipolar reorientation around the probe (i.e., the charged probe has a larger dipole moment and thus the solvent red shift will occur to a larger extent) (17). The excitation and emission spectra for SNARF-X at pH 7.4 are shown in Fig. 4.

To determine the sensitivity of SNARF-X to changes in pH, solutions of the probe (concentrations of 10^{-6} M) were tested at pH values between 6.5 and 9.2. Figure 5*a* shows spectra of SNARF-X at various pH values. As the pH increases, the intensity of the peak that is centered at 650 nm increases accordingly.

Can. J. Chem. Downloaded from www.nrcresearchpress.com by 195.246.54.202 on 09/08/12
For personal use only.

Can. J. Chem. Downloaded from www.nrcresearchpress.com by 195.246.54.202 on 09/08/12
For personal use only.

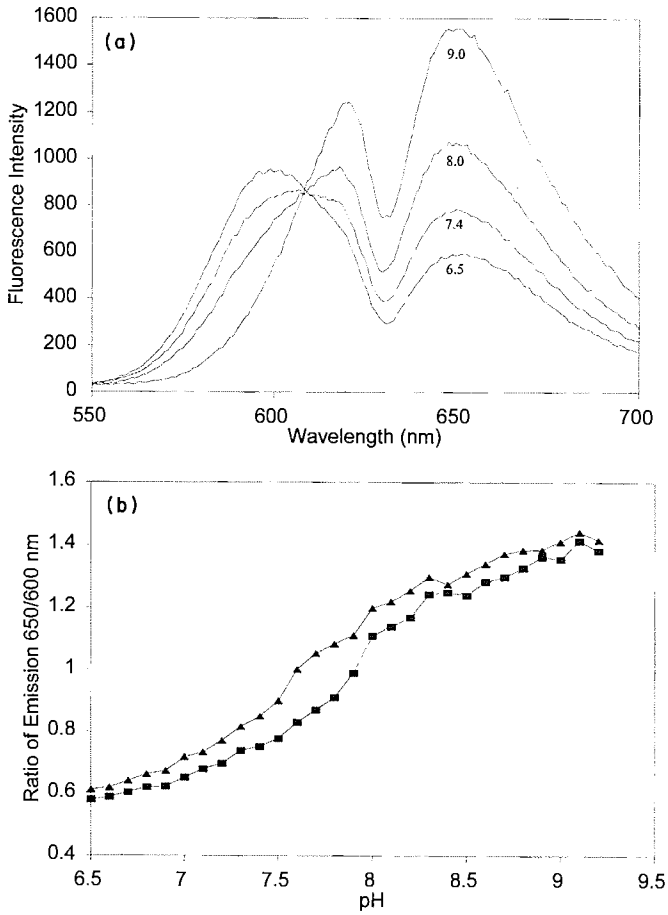

FIG. 5. Sensitivity of SNARF-X emission to pH. (A) Spectra of 10^{-6} M SNARF-X in 66 mM phosphate buffer at various values of pH; (B) Ratio of emission of SNARF-X (650 nm/595 nm) at various values of pH. (▲) Excitation at 337 nm, (■) Excitation at 488 nm.

At low values of pH, the protonated form of the probe has an emission peak centered at 595 nm. However, as the pH increases, this peak not only decreases in intensity but shifts to a maximum of 620 nm. It seems likely that the peak that is originally at a wavelength of 595 nm is due to the protonated form of the probe, and that the peaks at 620 and 650 nm are both due to the deprotonated form of the probe. The peaks at 620 and 650 nm correspond to the real emission peak and a Woods Anomaly peak, respectively (for the deprotonated form). The Woods Anomaly peak is used in this work to provide the largest signal-to-noise ratio, and to avoid spectral overlap with the peak at 595 nm. It is evident that even at pH 6.5 the peak at 595 nm has a shoulder at 620 nm, indicating that emission from the deprotonated form is still occurring.

The analysis of the SNARF-X emission was based on calculating the ratio of the two emission peaks. A variety of different methods could have been utilized to calculate the ratio. For example, it was possible to simply measure the intensity at wavelength values of 595 and 650 nm and compute the ratio of the values (18). However, this method is highly susceptible to problems with noise in the spectrum, since only two data points are being used to calculate the ratio. An alternative would be to calculate the average intensity within two different regions of the spectrum, which would reduce many of the problems associated with noise in the spectrum, and would provide more precise data. In this work, the averaging was done over the regions centered at 595 and 650 nm, and the ratio of the two intensity values was calculated (see Fig. 5*b*). Using this method, changes in the emission ratio of SNARF-X could be used to detect changes of pH as small as 0.02 units in the region between pH values of 7.0 and 8.5 with a precision of ±0.01 pH unit.

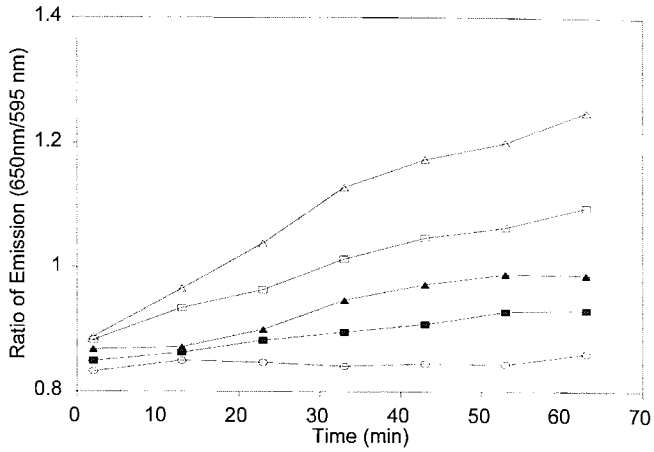

FIG. 6. Fluorimetric assay of the activity of urease in bulk solution. (○) 0 μg mL^{-1} urease, (■) 5 μg mL^{-1} urease, (▲) 10 μg mL^{-1} urease, (□) 15 μg mL^{-1} urease, (△) 20 μg mL^{-1} urease.

The activity of an enzyme depends on the kinetics associated with the enzyme–substrate reaction. The turnover number for urease in solution is 1.0×10^{-4} s^{-1} (12), and the Michaelis constant is 2.5×10^{-2} M (12). These constants may change when urease is immobilized on a surface because of limitations in mass transport of the urea to the surface. The assay of urease activity in solution and on surfaces utilized conditions in which the substrate (urea) was in large excess of the Michaelis constant for the enzyme (ca. 8 K_M), so that the rate of reaction was limited mainly by the rate of turnover of the urea to ammonium and carbonate ions, and was not dramatically affected by mass transport limitations for surface-based assays. All urease assays were done at an initial pH value of 7.4. The assay was done in a 66 mM phosphate buffer to eliminate problems with pH shifts that resulted from autohydrolysis of urea and absorption of CO_2 gas into solution. The presence of the buffer also allowed the sensitivity of the assay to be adjusted so that different concentrations of enzyme could be analyzed in a reasonable time without the pH rapidly shifting outside the useful range of the fluorescent probe.

Final enzyme concentrations between 0 and 20 μg mL^{-1} were used for all assays since higher concentrations of enzyme caused the pH to shift outside the useful range of the SNARF-X probe (i.e., above pH 9.2) in periods of minutes, making it difficult to determine the initial slope of the response curve. Assays were generally done over a period of 60 min. However, activities were calculated using the initial slope of the response curve since some of the curves showed asymptotic behaviour at longer times owing to the insensitivity of SNARF-X to changes of pH at values above 9.2.

Figure 6 shows a typical response curve for an assay of urease in bulk solution at concentrations of 0, 5, 10, 15, and 20 μg mL^{-1}. The activity of this lot was determined to be 32.0 ± 3.0 units mg^{-1}, which was in good agreement with the activity stated by the supplier (30 units mg^{-1}). There was some variation in the initial ratio of the two peaks for the various enzyme concentrations studied, which suggested that the initial pH val-

Can. J. Chem. Downloaded from www.nrcresearchpress.com by 195.246.54.202 on 09/08/12
For personal use only.

TABLE 1. Comparison of specific activity of urease in bulk solution and adsorbed onto silicon (1 unit is equivalent to the hydrolysis of 1 μmol of urea per minute at pH 8.0)

Protein	Stated activity[a] (units mg^{-1})	Colourimetric activity (units mg^{-1})	SNARF-X activity (units mg^{-1})
Urease in solution			
Sample no. 1	30.0	26.0 ± 1.0	32.0 ± 3.0
Sample no. 2	105.0	98.7 ± 2.2	101.6 ± 5.3
Urease adsorbed onto silicon	105.0	—	85.6 ± 7.5

[a]Quoted by supplier for urease in solution at pH 8.0.

TABLE 2. Ellipsometric and XPS data for samples studied. Thickness values calculated by ellipsometry assume an index of refraction of 1.50 for all films. All thickness values quoted are increases in relative thickness between bare silicon wafers and coated silicon wafers

Sample (see Figs. 1 and 2)	Thickness (nm) (ellipsometry)	Thickness (nm) (XPS)	Change in thickness (nm) by ellipsometry (compared to membrane alone)
Urease adsorbed onto silicon	12.3 ± 1.6	13.6 ± 0.9	—
C-16 carboxylic acid membrane	2.8 ± 0.1	5.3 ± 0.5	—
C-16 carboxylic acid membrane + urease immobilized by CDI (before assay)	8.5 ± 0.1	12.0 ± 1.1	5.7 ± 0.2

ues of the individual solutions were slightly different. Since it is the initial slopes that are of concern in this work, the initial pH is not very important provided that it is close to pH 7.4. Figure 6 indicates that significant autohydrolysis does not occur during the course of the assay. Nonetheless, the slope calculated for the blank was subtracted from the slopes obtained in the presence of urease to remove any contribution that could be attributed to autohydrolysis. The values of the specific activity as calculated by either the SNARF-X or phenol red assay for two different lots of urease are given in Table 1.

Assay of activity from immobilized enzymes

An oxidized silicon wafer was suspended into a solution containing 1 mg mL^{-1} of urease (activity of 105 units mg^{-1}) in 10 mM phosphate buffer, and was stirred over a period of 12 h at 4°C. The low temperature was employed to minimize denaturation of the enzyme. Ellipsometric measurements were used for determination of the amount of protein adsorbed onto the silicon dioxide layer at the surface of the wafer. The thickness of the urease layer that was immobilized onto the wafer was found to be 12.3 ± 1.6 nm. Thickness values (averaged over three samples) for all samples studied as measured by ellipsometry and XPS are given in Table 2. All thickness values obtained by ellipsometry assumed an organic film refractive index of 1.50 (16). The dimensions of urease are about 10.0 nm × 10.0 nm × 11.0 nm (19). The results of Table 2 show that the thickness values that were calculated by XPS or ellipsometry were accurate to within about 25% of the expected thickness value of 10.3 nm, and to within 15% of the thickness values calculated by ellipsometry. The excellent agreement between the thickness values obtained by either XPS, which requires that the sample be in ultra-high vacuum, or ellipsometry, which requires that the sample be in air, and the expected thickness values for a monolayer of urease suggests that dehydration of the protein was not a serious problem.

If a monolayer is assumed to have an average thickness of 10.3 nm, then there are approximately 1.19 ± 0.15 monolayers of urease adsorbed onto the surface (using the thickness values obtained by ellipsometry). The silicon wafer had dimensions of 1.8 cm × 0.6 cm, resulting in a surface area of 1.08 cm^2 per side. If the area per urease molecule is taken to be ca. 100 nm^2, then there will be $(1.08 \pm 0.14) \times 10^{12}$ molecules or $(1.79 \pm 0.23) \times 10^{-12}$ moles of urease per monolayer on the surface, or a total of $(2.13 \pm 0.28) \times 10^{-12}$ moles of urease. The molecular weight of urease is 478000 g mol^{-1}, which corresponds to a mass of 1.02 ± 0.13 μg of urease on the surface of the silicon wafer. Since both sides are coated, there is a total of 2.04 ± 0.18 μg of urease.

The coated silicon wafer was placed in a 1 cm^2 cuvette with an internal volume of 500 μL. The reduced volume was used so that the products of urea hydrolysis would be more concentrated than would be possible in a standard cuvette with an internal volume of 3 mL. The cuvette also contained 0.2 M urea and 10^{-6} M SNARF-X. Spectra were collected over a period of 1 h for the coated wafer and showed a gradual increase in the emission ratio of SNARF-X over time. An assay was also done with a blank consisting of bare silicon suspended in a solution of 0.2 M urea and 10^{-6} M SNARF-X in 66 mM phosophate buffer at

Can. J. Chem. Downloaded from www.nrcresearchpress.com by 195.246.54.202 on 09/08/12
For personal use only.

pH 7.4. No change was observed in the emission ratio of SNARF-X for the blank sample, which suggested that the change in the emission ratio in the urease–silicon sample was due to the reaction of urea with urease. The results clearly showed that there was a large signal present for the silicon wafer that was coated with urease. The bulk assay used concentrations of 5–20 μg mL^{-1} of urease in a volume of 3 mL, giving a total mass of 15–60 μg of urease. Thus the amount of urease studied in the surface-based assays was roughly 7-fold less than the amount used for the bulk assays. Nonetheless, the activity of the enzyme could easily be measured.

The specific activity of urease calculated for the adsorbed enzyme was 85.6 ± 7.5 units mg^{-1}. This value is slightly lower than the specific activity measured in solution (101.6 units mg^{-1} as in Table 1) or that stated by the supplier (105 units mg^{-1}), which indicates that some of the urease may have been denatured in the process of immobilization, or may have adsorbed with the catalytic site not exposed to solution. Another possibility is that the diffusion rate of urea to the adsorbed urease may have decreased since the urease was no longer distributed randomly in solution, thereby decreasing the apparent activity of the protein. It is not possible to determine which of the above factors is most directly responsible for the observed decrease in activity upon immobilization of urease. The decrease in the activity of immobilized urea indicates that the activity values measured from the surface are not necessarily absolute; however, comparison of relative activity values from different surfaces or from a single surface as a function of time is still possible, and can give information on parameters such as rates of denaturation, which are of greatest importance in the work described herein.

To confirm that the measured activity was not from protein present in bulk solution due to desorption from the surface, a silicon wafer that was coated with ca. 2 μg of urease was placed in a solution of 10^{-6} M SNARF-X in 66 mM phosphate buffer, left for 1 h, and then removed from the solution. The substrate was then added to the solution and the assay was run for 1 h. The results showed that there was no change in the emission ratio of SNARF-X, indicating that no significant desorption had occurred during the time period used for the assay. The thickness of the adsorbed urease layer was measured by ellipsometry both before and after the assay, showing thickness values of 12.3 ± 1.4 and 12.1 ± 0.9 nm, respectively. This measurement confirmed that the urease had not desorbed during the assay.

To confirm that the pH changes were indeed the result of an enzyme–substrate reaction, the urease was denatured prior to adsorption onto silicon. The denaturation process involved heating the enzyme for 1.5 h at a temperature range of 70–80°C. The thickness of an adsorbed coating of denatured urease was determined to be 8.2 ± 0.9 nm, corresponding to a mass of 1.4 ± 0.2 μg. The assay of the denatured urease was compared to a blank, and showed that no change in the ratio of emission of SNARF-X occurred over time. This result confirmed that the urease–urea reaction was responsible for the observed changes of pH.

Assay of urease covalently immobilized onto CIMs

The SNARF-X assay was sensitive enough to measure the activity of small amounts of an enzyme located on a surface, and was therefore used to measure the activity of a sample composed of urease that was linked onto a C-16 carboxylic acid membrane with the CDI activating agent. The membranes, both with and without immobilized urease, were characterized by ellipsometry and XPS. The results are given in Table 2. Two sets of samples were tested, one that had been examined by XPS before the assay, and the second, which had XPS measurements done only after the SNARF-X assays were complete. In the first case, angularly resolved measurements were done on the sample, and suggested that there was about 6.7 nm of urease on the surface, or about 60% coverage (see Table 2). The second set of samples was tested by XPS (at a single angle) only after the assays were done. The XPS studies again indicated a thickness of 6.7 nm of urease for each sample, while ellipsometry suggested a thickness of 5.7 nm for each sample.

Table 2 indicates that the thickness of the covalently immobilized membranes as measured by either ellipsometry or XPS differed by almost a factor of 2. The large discrepancies between the thickness values obtained for the membranes by ellipsometry and XPS are the result of the different assumptions of each technique when used for measurement of organic layers on inorganic substrates. The assumptions of the Drude equations, which are used to convert the ellipsometric Δ and Ψ to thickness values, are: (1) the samples are homogeneous, isotropic, non-absorbing and non-amplifying, (2) the films have uniform thickness and refractive index, (3) the sample and substrate are smooth, (4) the area of the film is many times its thickness, and (5) the boundaries between sample, substrate, and ambient are discrete and plane-parallel (20). Under optimum conditions in which all assumptions are valid, changes in thickness on the order of 0.1 nm can be detected while changes in refractive index on the order of 0.002 can be measured. In this work, the films that are measured do not strictly adhere to the assumptions of the Drude equations in that they are not isotropic, and thus the thickness values are accurate only to within 25% of the "true" value.

The thickness values measured by XPS used the ratio of the C(1*s*) peak of the protein and the Si(2*p*) peak of the substrate. The use of the C(1*s*) peak will introduce some inaccuracy into the thickness value owing to the presence of organic contamination. Airborne organic matter is known to adsorb to both hydrophilic and hydrophobic surfaces. In fact, it has been shown that an ultraclean surface prepared in ultrahigh vacuum will become coated with organic contaminants in a matter of seconds upon exposure to air, and that such contaminants are not removed when the sample is returned to an ultrahigh vacuum environment (21). Additional errors are introduced if the value used for the escape depth is not accurately known. The difficulty in establishing accurate escape depths and the problems with organic contamination result in the thickness values calculated by XPS being semi-quantitative at best. The thickness values obtained by XPS are therefore likely to be less accurate than those obtained by ellipsometry.

Fluorimetric assays were done over a period of 7 days on two covalently immobilized urease samples that were tested by XPS at a single angle only after the assays were done. Between assays, the samples were stored in phosphate buffer at 4°C. The activity values are given in Table 3. The SNARF-X assay was also done every 12 h over a period of 2 days for samples that were composed of urease adsorbed onto silicon. Ellipsometry measurements showed an initial thickness of 11.9 nm and a final thickness of 12.0 nm for the adsorbed protein layer, suggesting that the urease had not desorbed from the silicon, and leaving denaturation as the likely cause of the loss of activity.

The retention of activity of urease that was immobilized onto

TABLE 3. Activity of urease immobilized onto C-16 carboxylic acid membranes as a function of time. All values stated are averaged over three samples

Day	Activity of urease adsorbed on oxidized silicon (units mg^{-1})	Activity of urease immobilized on C-16 carboxylic acid membranes. Stored in buffer at 4°C (XPS done after assay) (units mg^{-1})
0	85.5 ± 7.5	[a]
0.5	20.7 ± 2.1	54 ± 8
1	3.3 ± 2.0	—
2	0	33 ± 6
7	0	8.8 ± 2.4

[a]The elapsed time from preparation of the sample to the first assay was about 12 h.

a C-16 carboxylic acid membrane, as compared to urease that was present on oxidized silicon with no spacer group, suggested that the presence of the C-16 acyl chains helped to decrease the rate of denaturation, but was unable to prevent significant denaturation over a period of a week. The results obtained from samples stored in solution are significant when compared to the results of Kallury et al. (4), which indicated that urease linked to carboxylic acid membranes with C-10 or C-23 acyl chains remained active for a period of about 7 days when stored dry. The similar rate of denaturation of samples that were hydrated and stored in dry conditions was not expected. These results suggest that linkage of urease to membranes composed of ionizable phospholipids should be attempted, since these have been shown to stabilize the activity of urease to the point where 95% activity remains after a period of 7 days when stored dry, with the half-life of the activity being on the order of months (4).

Conclusions

A fluorescence-based assay of enzyme activity was developed that was based on the emission of the probe seminaphtharhodafluor-X. This probe has two emission maxima, which shift in intensity relative to one another with changes of pH. The fluorescence-based assay was able to determine the activity of urease in bulk solution with an accuracy comparable to standard colourimetric assays. Urease was adsorbed onto silicon wafers or covalently linked onto the surface of a covalently immobilized carboxylic acid membrane with retention of some activity, thereby providing a completely stabilized monolayer–protein system. The SNARF-X assay used for samples of immobilized monolayers of enzyme (typically containing about 1 $\mu g\ cm^{-2}$ of protein) provided activity values accurate to within 10%. The fluorimetric assay suggested that the urease that was placed onto a C-16 carboxylic acid membrane had a high activity directly after covalent immobilization, but that the activity decreased substantially over a period of 7 days. The rate of denaturation of urease significantly limits the potential for development of biosensors based on this covalently immobilized enzyme.

Acknowledgements

We are grateful to the Natural Sciences and Engineering Research Council of Canada (NSERC) for financial support of this work. J.D.B. would also like to thank NSERC for the provision of a postgraduate fellowship.

1. M. Thompson and U.J. Krull. TrAC, Trends Anal. Chem. (Pers. Ed.) **3**, 173 (1984).
2. T.J. Thosas, I. Camins, and S.M. Angel. Anal. Chem. **59**, 2849 (1987).
3. L.D. Bowers. J. Am. Chem. Soc. **58**, 513A (1986).
4. K.M.R. Kallury, W.E. Lee, and M. Thompson. Anal. Chem. **64**, 1062 (1992).
5. M.J. Cooney, L.C. Shriver-Lake, T.L. Fare, and F.S. Ligler. Sens. Actuators, B: **B3**, 311 (1991).
6. F.V. Bright, T.A. Betts, and K.S. Litwiler. Anal. Chem. **62**, 1065 (1990).
7. B.J. Tromberg, M.J. Sepaniak, T. Vo-Dihn, and G.D. Griffin. Anal. Chem. **59**, 1226 (1987).
8. F.P. Anderson and W.G. Miller. Clin. Chem. **29**, 1582 (1988).
9. Z. Štefanac, M. Tomaškovic, and Z. Rakovic-Tresic. Anal. Lett. **2**, 197 (1969).
10. J.E. Whitaker, R.P. Haugland, and F.G. Prendergast. Anal. Biochem. **194**, 330 (1991).
11. J. Janata. Principles of chemical sensors. Plenum Press, New York. 1989.
12. D. Voet and J. Voet. Biochemistry. John Wiley and Sons, New York. 1990.
13. J.N. Demas and G.A. Crosby. J. Phys. Chem. **75**, 991 (1971).
14. F.L. McCracken. NBS Tech. Note (U.S.), **479** (1969).
15. J.D. Brennan, R.S. Brown, D. Foster, K.M.R. Kallury, and U.J. Krull. Anal. Chim. Acta, **255**, 73 (1991).
16. D. Ducharme, J.J. Max, C. Salesse, and R.M. Leblanc. J. Phys. Chem. **94**, 1925 (1990).
17. S.G. Schulman. *In* Modern fluorescence spectroscopy 2. *Edited by* E.L. Wehry. Plenum Press, New York. 1976. pp. 239–275.
18. O. Seksek, N. Henry-Toulmé, F. Sureau, and J. Bolard. Anal. Biochem. **193**, 49 (1991).
19. C.R. Cantor and P.R. Schimmel. Biophysical chemistry. Vol. 2. Freeman, San Francisco. 1980. p. 554.
20. R.M.A. Azzam and N.M. Bashara. Ellipsometry and polarized light. North-Holland Publishing Company, New York. 1977.
21. K. Mizuno, S. Maeda, and K. Suzuki. Anal. Sci. **7**, 345 (1991).

Can. J. Chem. Downloaded from www.nrcresearchpress.com by 195.246.54.202 on 09/08/12
For personal use only.

Trajectory study of the effect of energy barrier location on the energy disposal for the reaction $O(^3P) + Cl_2 \rightarrow OCl + Cl$

AGNIE M. KOSMAS
Department of Chemistry, University of Ioannina, GR 451 10 Ioannina, Greece

Received June 24, 1993

This paper is dedicated to Professor John C. Polanyi on the occasion of his 65th birthday

AGNIE M. KOSMAS. Can. J. Chem. **72**, 729 (1994).

The mode of partitioning of total energy available in the reaction $O(^3P) + Cl_2 \rightarrow OCl + Cl$ is investigated as a function of the initial collision energy, in correlation with Polanyi's adiabaticity rules, using a series of related LEPS-type potential energy functions. All surfaces possess a classical energy barrier of similar height located in the entrance valley of the reaction, but present a small, gradual displacement of the top of the barrier to later positions along the approach coordinate. Quasiclassical trajectory calculations on these surfaces indicate marked differences in the disposal of total energy and the dynamical behaviour of the reaction. Also the effect of excess reagent vibration is investigated.

AGNIE M. KOSMAS. Can. J. Chem. **72**, 729 (1994).

Utilisant une série apparentée de fonctions d'énergie potentielle de type LEPS, on a étudié le mode de partition de l'énergie totale disponible dans la réaction $O(^3P) + Cl_2 \rightarrow OCl + Cl$ en fonction de l'énergie de collision initiale, en corrélation avec les règles d'adiabaticité de Polanyi. Toutes les surfaces possèdent un barrière d'énergie classique de hauteur semblable, située à l'entrée de la vallée réactionnelle; toutefois, elles présentent un léger déplacement graduel du sommet de la barrière vers des positions ultérieures le long de la coordonnée d'approche. Des calculs de trajectoires quasiclassiques sur ces surfaces indiquent qu'il existe des différences importantes dans la façon de disposer de l'énergie totale et dans le comportement dynamique de la réaction. On a aussi étudié l'effet de la vibration du réactif en excès.

[Traduit par la rédaction]

Can. J. Chem. Downloaded from www.nrcresearchpress.com by 195.246.54.202 on 09/08/12
For personal use only.

1. Introduction

In a series of pioneering papers Polanyi and co-workers investigated in great detail the sensitive role of the location and the height of the energy barrier in the dynamics of elementary gas-phase chemical processes (1–4). Among the significant outcomes the effect of energy barrier location was proven very important in determining the mode of disposal of total energy available in the reaction products.

The reaction $O(^3P) + Cl_2 \rightarrow OCl + Cl$ has been studied extensively in discharge-flow systems (5–8) and in molecular beam experiments (9–11) and consequently represents a system suitable for theoretical investigation. No ab initio or any other information exists about the potential energy surface. It is a moderately exothermic reaction with a reaction exothermicity of 26.5 kJ/mol and an activation energy of 13.5 kJ/mol (12). In a previous classical trajectory study theoretical calculations of the total reaction cross section and the thermal reaction coefficient were carried out with good success. Also the simulation of the dynamical pattern of the reaction was examined using potential energy functions with quite different dynamical features with respect to the location of the classical energy barrier and the geometry of the minimum energy path configuration (13). Very good reproduction of the experimental differential cross sections $I(\theta, w)$, θ being the c.m. scattering angle and w the product relative velocity, and in particular of the interesting feature of forward scattered molecules having three times more kinetic energy than the wide angle scattering was accomplished when the reaction was assumed to take place on a PES with a collinear minimum energy path configuration and an energy barrier located in the entrance valley of the reaction. When the barrier was displaced towards the exit valley of the PES the dynamical pattern obtained was completely altered. On the other hand a bent transition state configuration did not advance the understanding of the dynamics over the collinear minimum energy configuration, a fact also observed in the trajectory study of the reaction $F + I_2 \rightarrow FI + I$ where a bent configuration did not improve the description of the cross section over the collinear geometry (14, 15).

The molecular beam experiments indicate that the reaction proceeds through a stripping mechanism for both low and high collision energies with a low fraction of total available energy deposited into product recoil energy, increasing as the collision energy rises. In the present work we employ the quasiclassical trajectory method to investigate the sensitive role of the location of the energy barrier in the mode of partitioning of the total energy available in the $O(^3P) + Cl_2 \rightarrow OCl + Cl$ reaction as a function of the collision energy, in correlation with Polanyi's adiabaticity rules (16–18). The calculations are carried out using a family of related LEPS-type PES, which all possess similar energetics in a collinear minimum energy path configuration and an energy barrier located in the entrance valley of the reaction but which present a gradual displacement of the saddle point location along the reaction coordinate. Average product translational distributions are calculated and compared with molecular beam results. Also the variation in average c.m. scattering angle and product vibrational energy distribution with increasing collision energy is studied and the influence of barrier position in the total reaction cross section is examined for a series of values of the initial kinetic energy. Finally, the effect of reagent vibrational energy in the disposal of total energy and the magnitude of the cross section is investigated.

2. PES and trajectory calculations

As already mentioned, no ab initio or any other information exists about the PES of the reaction $O(^3P) + Cl_2 \rightarrow OCl + Cl$. Only the ground-state surface has been reported to be reactive at the range of energies considered, so it is assumed that the reaction proceeds via a single adiabatic surface (10, 11, 13). A series of four PES, denoted A–D, were constructed using the generalized LEPS potential energy function, with a classical energy barrier of the same height, ~13.5 kJ/mol, located in the entrance valley of the reaction. By systematic variation of the

Can. J. Chem. Downloaded from www.nrcresearchpress.com by 195.246.54.202 on 09/08/12
For personal use only.

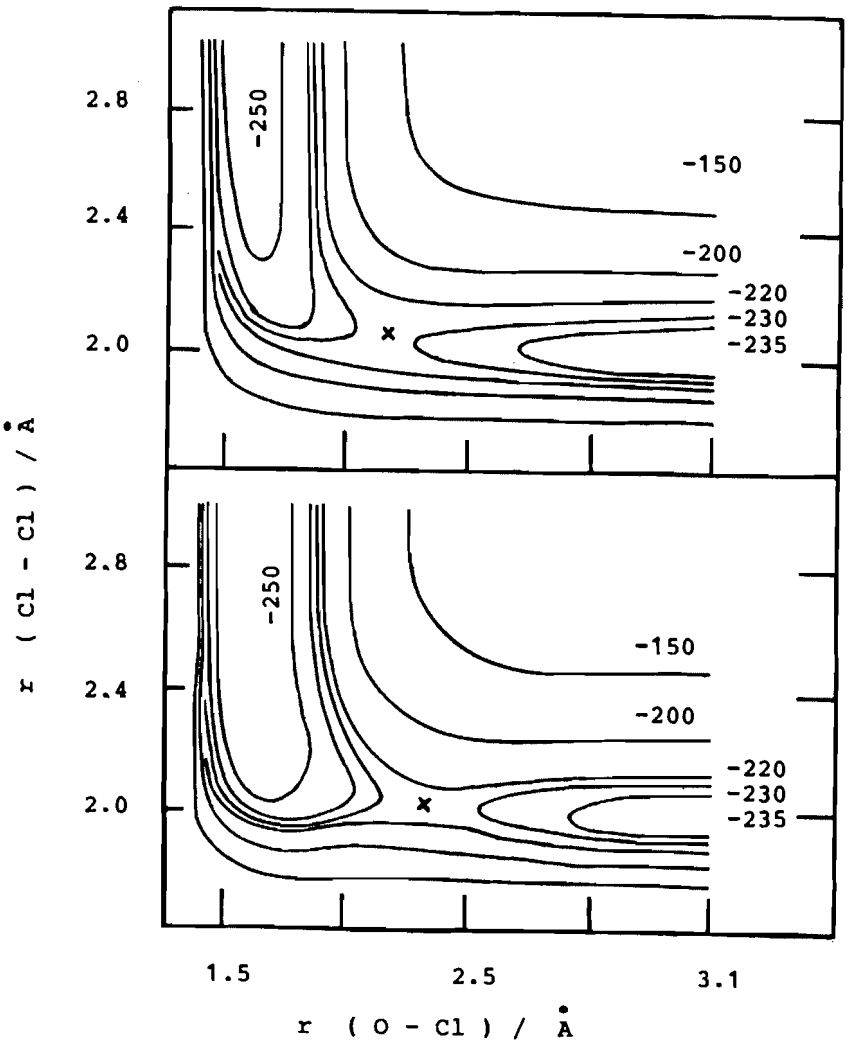

FIG. 1. Contour diagram of surfaces A (lower panel) and D (upper panel) for the collinear configuration. The numbers indicate values of potential energy in kJ/mol. The zero of energy corresponds to separated atoms. The marks indicate position of saddle point.

Sato parameters, S_{OCl} in the range −0.100–0.100 and S_{ClCl} in the range 0.000–0.300, the displacement of the saddle point along the reaction coordinate $r_1 = r$(O—Cl) was investigated and a contradictory correlation was found. Lowering the values of S(Cl–Cl) and raising the values of S(O–Cl) moves the barrier to later positions along the entrance valley. After several preliminary calculations the four surfaces were chosen so as to present a progressive shifting of the top of the barrier by 0.57 Å, 0.53 Å, 0.49 Å, and 0.45 Å with respect to the OCl equilibrium distance $r_{1e} = 1.57$ Å from surfaces A to D, respectively, while at the same $r_2 = r$(Br–Br) distance, equal to 2.02 Å in all cases. Surfaces A and D are depicted in Fig. 1 and the values of Sato parameters along with the saddle point dimensions are given in Table 1. In Fig. 2 the energy profiles of the reaction are given for all surfaces.

Trajectory calculations were performed for eight values of the initial collision energy E_T, using standard computational techniques (19). The diatomic was chosen initially as being in the zero vibrational level and the rotational level $J = 1$. For the lowest collision energy, $E_T = 13.5$ kJ/mol, 30 000 trajectories were computed for each of the four surfaces while for the higher values of the collision energy 20 000 trajectories for each surface were sufficient to obtain satisfactory statistics. Close to threshold enery and for surfaces A and D a second series of calculations were performed, assuming the diatomic as being in the $v = 1$ and $v = 2$ vibrational levels, 30 000 trajectories in each case, in order to examine the effect of excess reagent vibrational energy on the reaction cross section and the mode of disposal of the available energy. The maximum value of impact parameter was found the same in all cases in the study of the collisional energy effect, depending only on the value of E_T. The variation in b_{max} with increasing E_T is given in Fig. 3. Also displayed are

TABLE 1. Bond equilibrium distances, Sato parameters, and saddle point dimensions

	Surface			
	A	B	C	D
S(O–Cl)	−0.058	−0.032	−0.018	0.008
S(Cl–Cl)	0.280	0.269	0.157	0.084
r_1(O—Cl)/Å	2.14	2.10	2.06	2.02
r_2(Cl—Cl)/Å		2.02		
r_{1e}(O—Cl)/Å		1.57 (32)		
r_{2e}(Cl—Cl)/Å		1.99 (32)		

Can. J. Chem. Downloaded from www.nrcresearchpress.com by 195.246.54.202 on 09/08/12
For personal use only.

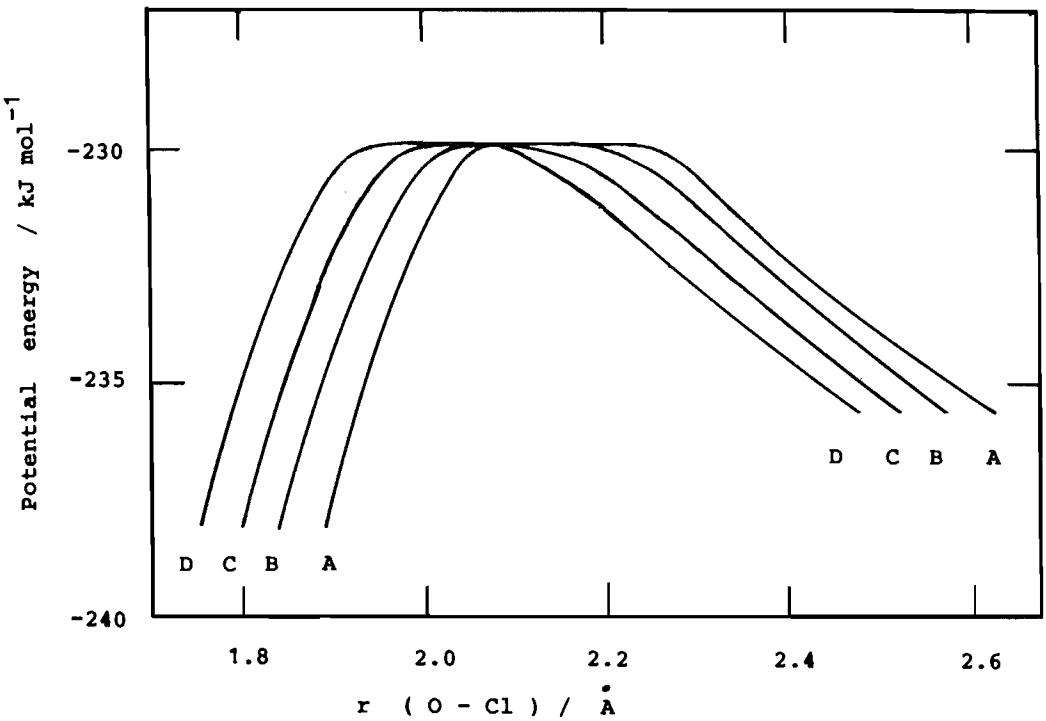

FIG. 2. Potential energy profile for all four surfaces vs. reaction coordinate.

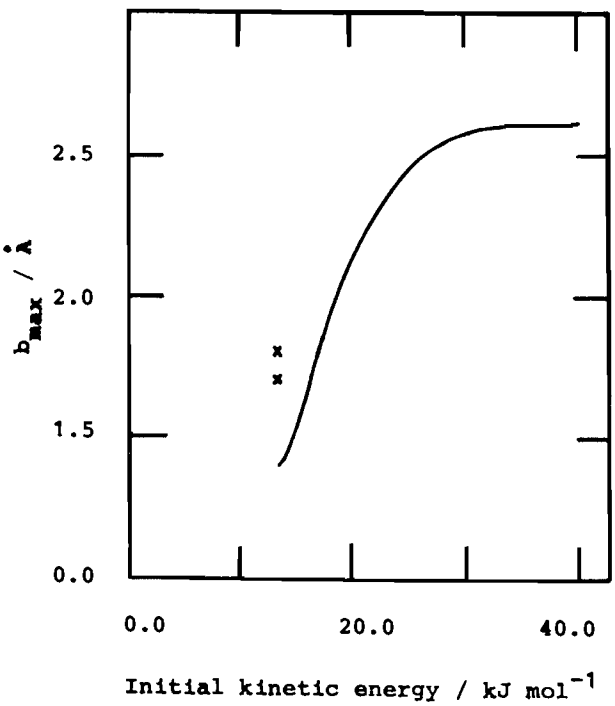

FIG. 3. Dependence of b_{max} on initial collision energy. The marks indicate b_{max} values for initial reagent vibration, the lower for $v = 1$ and the upper for $v = 2$.

the b_{max} values found appropriate in the study of the effect of excess reagent vibration.

The total energy, E_{tot}, available in an $O(^3P) + Cl_2$ collision, results from three contributions: the difference in binding energies, ΔD_0, the collision kinetic energy, E_T, and the internal energy of the diatomic molecule. It is assumed to be disposed exclusively into product recoil and internal energy.

$$[1] \quad E_{tot} = \Delta D_0 + E_T + E_{int} + E'_T = E'_{int}$$

where the prime quantities refer to products. Indeed, in all experimental studies only $^2P_{3/2}$ Cl atoms were ever detected. Also the contribution of $O(^3P)$ fine structure is assumed to be negligible in the study of energy disposal although this factor must be taken into account in the calculation of thermal reaction rate coefficient, as has been shown for the analogous reaction $O(^3P) + I_2 \rightarrow OI + I$ (20).

3. Results

In Fig. 4*a* the mean product recoil energy, $\langle E'_T \rangle$, and the average fraction of total energy deposited into product translational energy, $\langle f'_T \rangle$, are depicted vs. the initial kinetic energy of the reaction. Serious differences appear in the prediction of the amount of energy entering translation on each of the four PES. A set of parallel curves are obtained with a roughly linear dependence of product kinetic energy on rising collision energy and an approximate slope of 0.5. They predict, however, quite a different amount of energy disposed into translation close to threshold. Surface A directs a low amount of total energy into product translation in contrast to surface D, where enhanced product translation results, presumably from reaction through more compressed configurations. Also surfaces A, B, and C predict an increase in $\langle f'_T \rangle$, in accordance with the experimental results, while surface D approaches a reverse dependence. Indeed, it shows rather a slight decline in $\langle f'_T \rangle$ as E_T rises, indicating a total disagreement with the dynamical behaviour of the system in molecular beam experiments. From the other three surfaces, B shows better agreement at low E_T and A at high E_T although the experimental results are too limited to permit drawing definite conclusions.

A rising dependence of product translational excitation is assumed in several direct models for energy disposal (21–24) but they predict a faster rising fraction of total energy channeled

Can. J. Chem. Downloaded from www.nrcresearchpress.com by 195.246.54.202 on 09/08/12
For personal use only.

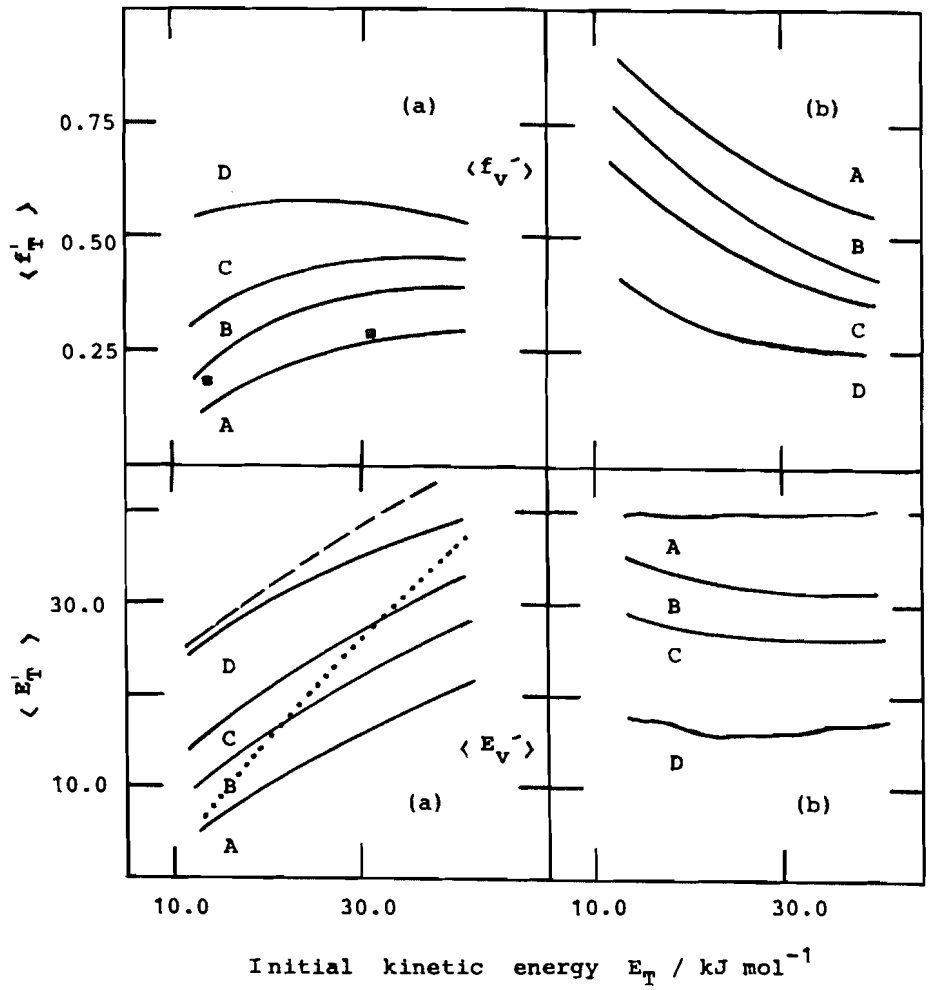

FIG. 4. (*a*) Mean product translational energy and average fraction of total energy transferred into product translation vs. initial collision energy. The marks indicate experimental points. Broken line represents the modified hard sphere model and dotted line the direct model with repulsive energy release. (*b*) Mean product vibrational energy and average fraction of total energy transferred into product vibration vs. initial collision energy.

into translation. For example, the modified hard sphere model with inclusion of conservation of angular momentum (25, 26) and the extension to the direct model with repulsive energy release (27, 28) are also displayed for comparison in Fig. 4*a*. In the first model the mean product translational energy is given by

$$[2]\quad \langle E'_T\rangle = \frac{(E_T + Q_{max})^2 - y^2 E_T{}^2}{36(E_T + Q_{max}) - 3yE_T}, \qquad E_T < Q_{max}/(y-1)$$

$$[3]\quad = (2/3)(E_T + Q_{max}), \qquad E_T > Q_{max}/(y-1)$$

where Q_{max} is the reaction exoergicity and $y = \mu/\mu'$ is the ratio of reduced masses of reactants and products. Good agreement is obtained with the results of surface D but the model assumes a faster rising amount of energy disposed into product translation. In the direct model with repulsive energy release the mean product kinetic energy is given by

$$[4]\quad \langle E'_T\rangle = [(\mu'/\mu)^{1/2} E_T{}^{1/2} + \sin\beta\, R^{1/2}]^2$$

where R is the repulsive energy release and $\cos^2\beta$ is the mass factor (29). Equation [4] reproduces the result of surface A at low E_T with $R = 4.8$ kJ/mol but again the model assumes a much faster rising amount of energy disposed into product translation with increasing E_T.

Figure 4*b* shows the mean product vibrational excitation and the average fraction of total energy, $\langle f'_v\rangle$, channeled into product vibration. In direct correlation with the translation excitation results, quite different amounts of energy are predicted to be transferred into product vibration for each surface, in the order A to D. On surface A most of the available energy around threshold is directed into product vibrational excitation while on D a low amount of energy enters product vibration. Concerning the dependence on E_T, all surfaces show analogous behaviour, i.e., the amount of total energy entering vibration changes very little or is similar to that transferred to vibration at the threshold region and independent of the collision energy. This behaviour is well demonstrated in Fig. 5 where product vibrational distributions are displayed for E_T equal to 13.5, 20.0, and 31.0 kJ/mol. In all cases the peak of the distribution moves to lower vibrational levels but becomes much broader since the mean product vibrational energy remains about constant for each surface, independent of E_T.

From the point of view of Polanyi's adiabaticity rules, surface A and, to a smaller extent, surfaces B and C seem to comply with the type of surface I (attractive surface) representing an

Can. J. Chem. Downloaded from www.nrcresearchpress.com by 195.246.54.202 on 09/08/12
For personal use only.

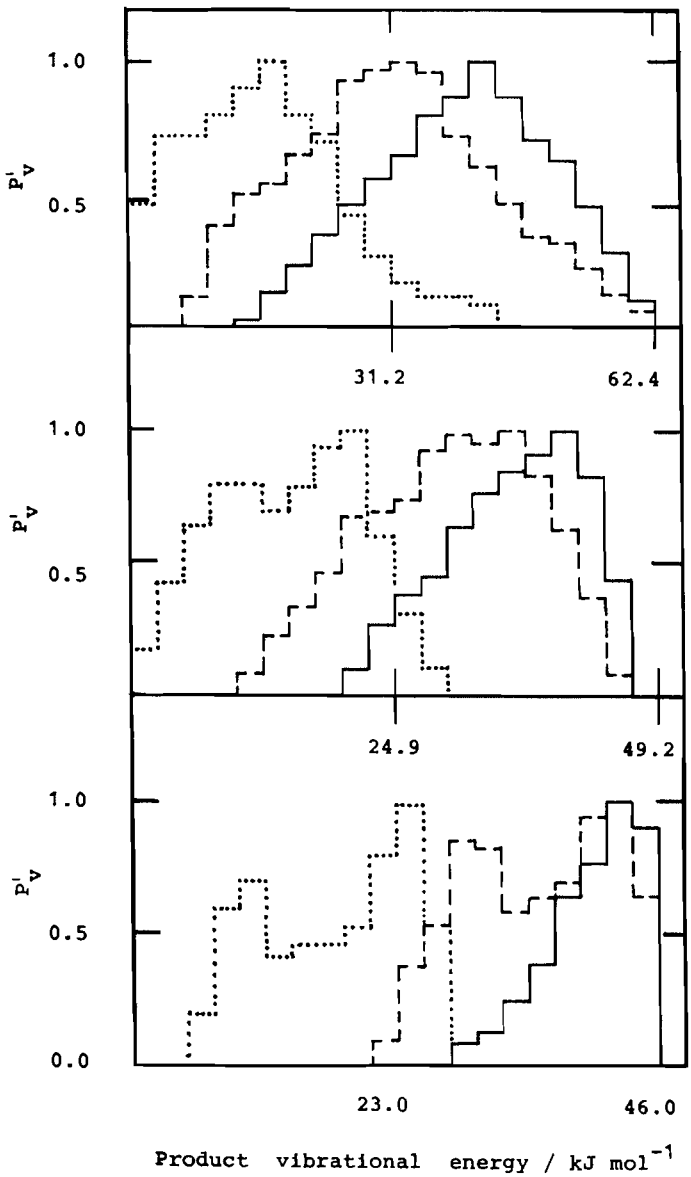

FIG. 5. Product vibrational distributions, arbitrarily normalized, for E_T = 13.5 kJ/mol (lower panel), 20.0 kJ/mol (middle panel), and 31.0 kJ/mol (upper panel) for surfaces A (—), B (– – – –), and D(·····).

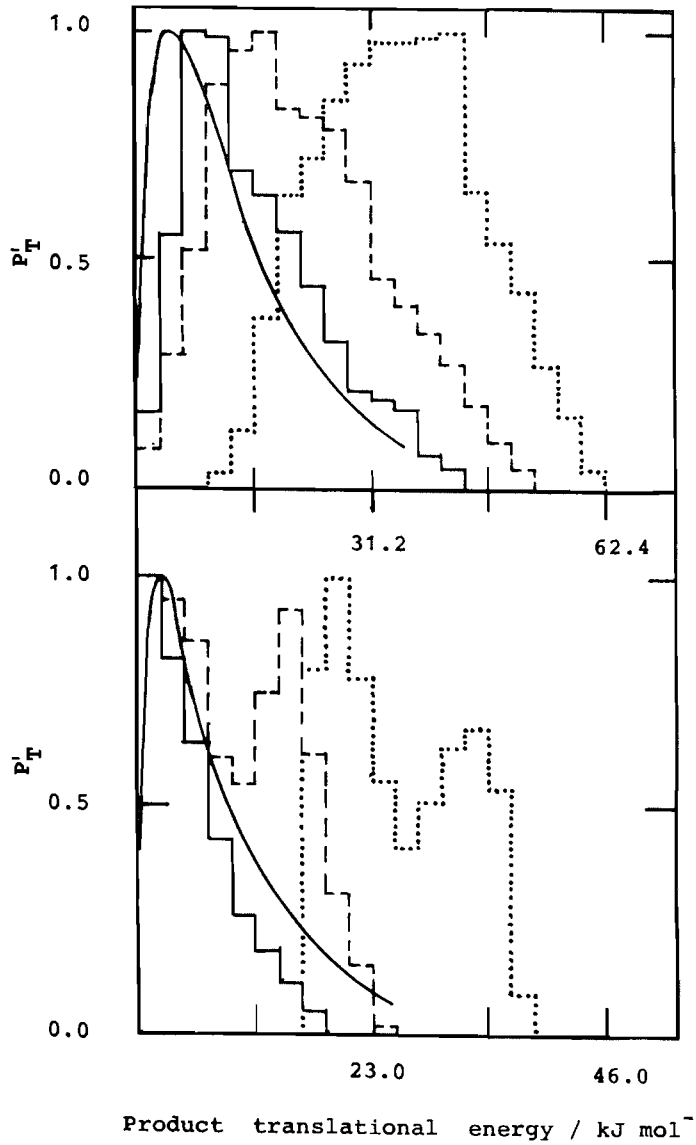

FIG. 6. Product translational distributions, arbitrarily normalized, for E_T = 13.5 kJ/mol (lower panel) and 31.0 kJ/mol (upper panel) for surfaces A (—), B (– – – –), and D(·····). Solid curves represent experimental data taken from refs. 10 and 11.

early barrier location (1, 2). Thus, on surface A for reagent kinetic energy near the threshold, reaction transposition appears to occur, i.e., the main fraction of total available energy is channeled into product vibration, $E_{tot} \rightarrow \Delta E'_v$. As the initial kinetic energy rises, the amount of energy deposited into vibration remains practically invariant while the excess collision energy ΔE_T leads to extra translational and rotational energy in the products:

$$[5] \quad \Delta E_T \sim \Delta E'_T + \Delta E'_{rot}$$

On the other hand, surface D approaches the behaviour of surface type II (repulsive surface) representing a late barrier although still along the approach coordinate at $r_1 = 2.02$ Å, i.e., displaced by 0.45 Å with respect to O–Cl equilibrium. Consequently, it predicts an unreasonably high fraction of total energy deposited into product recoil energy with low product vibrational excitation. Surfaces B and C seem to behave somewhere between surfaces A and D, predicting an equipartition between translation and vibration at high collision energies. Analogously, $\langle f'_v \rangle$ drops as the collision energy rises at a rate decreasing from A to D. Qualitatively this behaviour may be attributed to the stripping mechanism by which the reaction takes place while the old bond has not yet broken. The r_2 coordinate of the saddle point equals 2.02 Å, i.e., still very close to the Cl—Cl bond equilibrium distance r_{2e}. Apparently, the more extended the distance as the new bond is formed, the more vibrationally excited the products will be.

In Fig. 6 the product translational distributions from surfaces A, B, and D are compared to experimental average translational distributions observed at 13.5 and 31.0 kJ/mol in the molecular beam experiments of Grice and co-workers (10, 11). Good agreement is obtained for the results of surface A, which show that surface provides a satisfactory description of the translational energy profile of the reaction products.

Can. J. Chem. Downloaded from www.nrcresearchpress.com by 195.246.54.202 on 09/08/12
For personal use only.

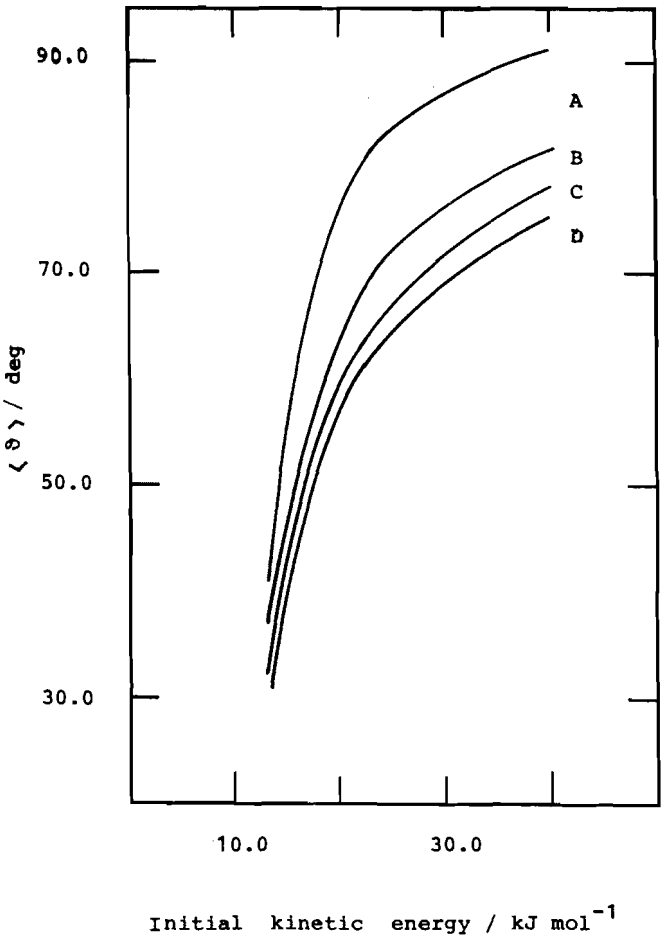

FIG. 7. Average c.m. scattering angle vs. initial kinetic energy.

The variation in average c.m. scattering angle, $\langle\theta\rangle$, vs. the initial kinetic energy of the reaction is shown in Fig. 7. All surfaces present the same pattern, i.e., mainly forward scattering at low collision energy with increasing tendency for sideways scattering as E_T rises, with surface A being the most demonstrative of this pattern. This general behaviour and, in particular, that of surface A is in good agreement with the considerable increase in wide angle scattering observed experimentally. The same effect is also clearly shown in Fig. 8 where detailed angular distributions are depicted for surfaces A, B, and D at E_T = 13.5 and 31.0 kJ/mol. The narrow distributions are typical of direct reactions and exclude the possibility of a shallow well in the potential energy function later along the reaction coordinate.

4. Effect of reagent vibrational excitation and cross sections calculations

In the second series of calculations the effect of reagent vibrational energy is investigated. In Table 2 the average amount of energy transferred into product translation and vibration is presented for surfaces A and D, assuming the diatomic to be in the v = 1 and v = 2 vibrational levels at a low collision energy E_T = 13.5 kJ/mol. These results are compared to the corresponding values in the v = 0 case where similar sums of kinetic and vibrational energies are provided initially. For surface A the reagent vibrational excitation seems to have a low effect on the mode of disposal of available energy, increasing slightly the mean energy transferred into product vibration. In contrast, due to the later barrier position on surface D, additional reagent vibrational excitation tends to remain as product vibration following the $\Delta V - \Delta V'$ adiabaticity rule. Thus, surface D changes markedly the mode of partitioning exhibited so far, showing the same tendency towards the behaviour of surface type II where excess reagent vibrational energy is channeled into product vibration once the late barrier is overcome.

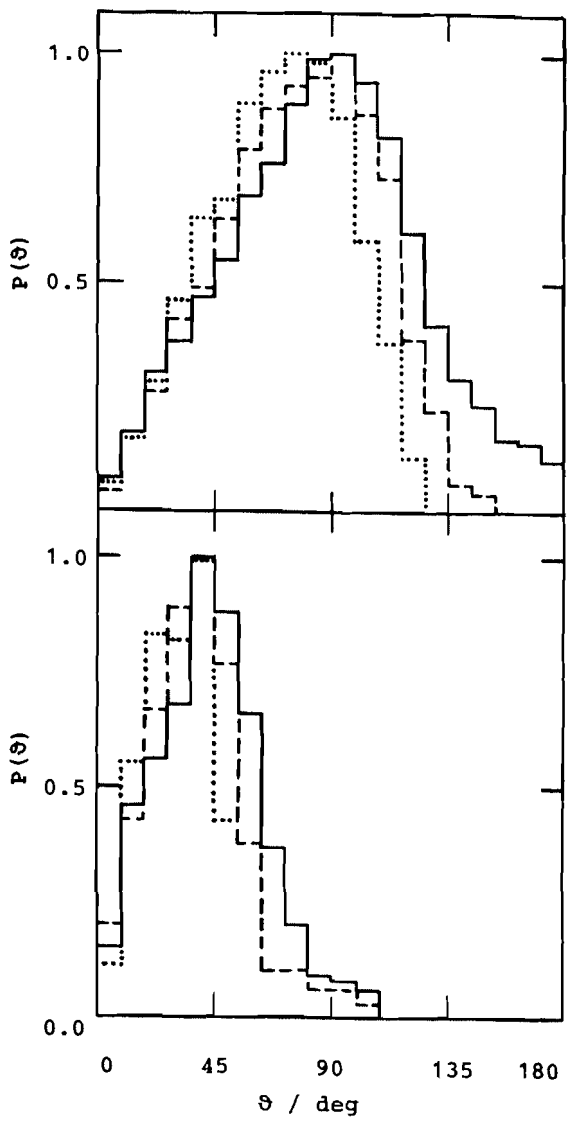

FIG. 8. Arbitrarily normalized angular distributions vs. cm scattering angle. Notation the same as in Fig. 6.

Table 3 shows the calculated cross sections for all surfaces and also for the cases v = 1 and v = 2. With the specified initial conditions employed here, the total reactive cross section at each particular collision energy depends only on E_T and was calculated as

$$[6] \quad \sigma_r = \pi b^2_{max} N_r(E_T)/N_{tot}(E_T)$$

where $N_r(E_T)$, $N_{tot}(E_T)$ are the number of reactive encounters and the total number of collisions at each E_T, respectively. The computed values are, on average, in good agreement with the experimental findings as deduced from thermal rate constant measurements. The thermal rate coefficient was found to follow the temperature dependence relation (6, 7)

TABLE 2. Average energy (kJ/mol) deposited into product translation and vibration

		Surface			
		A		D	
E_T/kJmol^{-1}	$E_v + E_T$/kJmol^{-1}	$\langle E'_T \rangle$	$\langle E'_v \rangle$	$\langle E'_T \rangle$	$\langle E'_v \rangle$
$v = 0$					
13.5	16.8	5.3	40.0	25.7	17.4
20.0	23.3	9.9	39.4	29.9	16.3
27.5	30.8	14.1	39.8	33.7	16.4
$v = 1$					
13.5	23.5	9.8	41.4	25.3	24.0
$v = 2$					
13.5	32.2	13.1	44.1	27.6	28.1

TABLE 3. Calculated total reactive cross sections in Å^2

	Surface			
E_T/kJmol^{-1}	A	B	C	D
$v = 0$				
13.5	0.10	0.17 ± 0.01[a]	0.17	0.16
17.0	1.00	1.19	1.15	1.13
20.0	1.99	2.48	2.41	2.14
24.0	3.63	2.81	3.56	3.43
27.5	4.66	4.86	4.71	4.48
31.0	5.59	5.80	5.68	5.47
36.0	6.62	6.72	6.31	6.16
40.0	7.45 ± 0.10	7.73	7.21	7.00
$v = 1$				
13.5	0.21 ± 0.01			0.39
$v = 2$				
13.5	0.51			0.93 ± 0.02

[a]The error limits on the reaction cross sections are given by the statistical error $\sigma_r[(N_{tot} - N_r)/N_{tot}N_r]^{1/2}$ (33).

[7] $\log k_1 = (9.76 \pm 0.18) - (13000 \pm 500)/(2.303RT)$

which corresponds to $\sigma_r = 0.25$ Å^2 for thermal conditions at $E_T = 13.5$ kJ/mol.

The main result that may be quoted at first sight from Table 3 is the significant increase in the magnitude of the cross section as the collision energy rises, following the general pattern of an exothermic reaction that proceeds on a surface with an energy barrier located in the entry valley. In addition, the cross section increases with E_T at a rate decreasing from surfaces B to D, in close correlation with the general trends observed in the mode of energy disposal, reconfirming the decreasing cabability of E_T to promote reaction as the barrier moves to later positions. However, a decline in σ_r is also observed when the barrier moves to earlier positions. Thus, closer inspection shows evidence of a maximum in the variation of the cross section with the displacement of the barrier position, the maximum value resulting from surface B. Indeed, preliminary trials with earlier and later barrier positions confirm this tendency. The maximum in σ_r variation should be expected since its location must reflect the barrier position in the true PES. The other interesting point is the insignificant increase in the cross section with reagent vibration, which complies with the typical behaviour of exothermic reactions. Finally, here again we must notice that surface D produces a larger increase in the cross section, with increasing reagent vibration, than does surface A, in agreement with the behaviour of repulsive-type surfaces where initial vibration is more effective in promoting reaction than translation.

5. Conclusion

The total energy disposal of the reaction $O(^3P) + Cl_2 \rightarrow OCl + Cl$ is examined with respect to energy barrier location in a series of quasiclassical trajectory calculations, using a family of related LEPS-type PES. The calculations have been performed for a series of values of the initial collision energy and the reagent vibration and show a radical change in the mode of energy disposal. Moving the barrier from $r_1 = 2.14$ Å to $r_1 = 2.02$ Å directs ~80% of total energy from product vibration to product translation. Thus, the results demonstrate the extreme sensitivity of the dynamical behaviour of the title reaction to the exact position of the energy barrier and the finest details of the PES that reflect the long-range repulsive forces that dominate the reaction.

Can. J. Chem. Downloaded from www.nrcresearchpress.com by 195.246.54.202 on 09/08/12
For personal use only.

The results produce good evidence that the true PES possesses a minimum energy barrier in a collinear transition state configuration located early along the approach coordinate. The dynamical behaviour seems to fluctuate between surfaces A and B. In view of these findings and in agreement with the experimental data, the simplest conclusion would be that the reaction takes place through interaction of the O atom unpaired p electron with the π electrons of the Cl_2 molecule in a stripping mechanism, in which no stable O—Cl—Cl intermediate is formed because of the strong orbital repulsion in the collinear configuration. The saddle point dimensions of surfaces A and B, 2.14 and 2.10 Å, respectively, are considerably larger than the equilibrium distance 1.57 Å of the OCl bond in OCl species or in dichlorine monoxide Cl_2O for which matrix isolation studies (30) produced a bond angle of 120° and a ClO bond distance of 1.587 Å. Therefore no PES involving intermediate formation of such species would be appropriate for the description of the reaction.

We conclude that the dynamics of the title reaction are adequately described by a surface intermediate between surfaces A and B where the early barrier position appears to account to a large extent for the long-range repulsive forces that govern the mechanism of the process. The dynamics suggested are consistent with collinear or near-collinear transition-state geometries, in accordance with the electronegativity ordering rule proposed by Herschbach and co-workers (31), which anticipates very low stability for a O—Cl—Cl intermediate where all atoms have similar, very high electronegativities.

1. J.C. Polanyi and W.H. Wong. J. Chem. Phys. **51**, 1439 (1969).
2. M.H. Mock and J.C. Polanyi. J. Chem. Phys. **51**, 1451 (1969).
3. J.C. Polanyi and N. Sathyamurthy. Chem. Phys. **33**, 287 (1978).
4. J.C. Polanyi and J.L. Schreiber. *In* Physical chemistry – an advanced treatise. Vol. 6. *Edited by* H. Eyring, W. Jost, and D. Henderson. Academic Press, New York. 1974.
5. H. Niki and B. Weinstock. J. Chem. Phys. **47**, 3249 (1967).
6. M.A.A. Clyne and J.A. Coxon. Trans. Faraday Soc. **62**, 2175 (1966).
7. J.N. Bradley, D.A. Whytock, and T.A. Zaleski. J. Chem. Soc. Faraday Trans. 1, **69**, 1251 (1973).
8. M.A.A. Clyne, P.B. Monkhouse, and L.W. Townsend. Int. J. Chem. Kinet. **8**, 425 (1976).
9. D.D. Parrish and D.R. Herschbach. J. Am. Chem. Soc. **95**, 6133 (1973).
10. P.A. Gorry, C.V. Nowikow, and R. Grice. Mol. Phys. **37**, 347 (1979).
11. R.J. Browett, J.H. Hobson, F.E. Davidson, and R. Grice. Mol. Phys. **43**, 113 (1981).
12. R.H. Krech, G.J. Diebold, and D.L. McFadden. J. Am. Chem. Soc. **99**, 4605 (1977).
13. A.M. Kosmas. J. Chem. Soc. Faraday Trans. **89**, 2999 (1993).
14. I.W. Fletcher and J.C. Whitehead. J. Chem. Soc. Faraday Trans. 2, **78**, 1165 (1982).
15. N.W. Keane, J.C. Whitehead, and R. Grice. J. Chem. Soc. Faraday Trans. 2, **85**, 1081 (1989).
16. D.S. Perry, J.C. Polanyi, and C.W. Wilson, Jr. Chem. Phys. **3**, 317 (1974).
17. B.A. Blackwell, J.C. Polanyi, and J.J. Sloan. Chem. Phys. **24**, 25 (1977).
18. J.C. Polanyi and N. Sathyamurthy. Chem. Phys. **37**, 259 (1979).
19. D.G. Truhlar and J.T. Muckerman. *In* Atom–molecule collision theory. *Edited by* R.B. Bernstein. Plenum Press, New York. 1979. Chap. 16.
20. A.M. Kosmas. J. Chem. Soc. Faraday Trans. **87**, 517 (1991).
21. A. Gonzalez-Urena. Adv. Chem. Phys. 213 (1987).
22. P.A. Kuntz. Mol. Phys. **23**, 1035 (1972); Trans. Faraday Soc. **66**, 2980 (1970).
23. H. Kaplan and D.R. Levine. Chem. Phys. **18**, 103 (1976).
24. R.D. Levine and R.B. Bernstein. Acc. Chem. Res. **7**, 393 (1974).
25. A. Gonzalez-Urena and F.J. Aoiz. Chem. Phys. Lett. **51**, 281 (1977).
26. L. Banares and A. Gonzalez-Urena. J. Chem. Phys. **93**, 6473 (1990).
27. A. Kafri, E. Pollak, R. Kosloff, and R.D. Levine. Chem. Phys. Lett. **33**, 201 (1975).
28. A. Kafri, Y. Shimoni, R.D. Levine, and S. Alexander. Chem. Phys. **13**, 323 (1976).
29. R.D. Levine and R.B. Bernstein. Molecular reaction dynamics and chemical reactivity. Oxford University Press, New York. 1987.
30. F.K. Chi and L. Andrews. J. Phys. Chem. **77**, 3062 (1973).
31. D.A. Dixon, D.D. Parrish, and D.R. Herschbach. Faraday Discuss. Chem. Soc. **55**, 385 (1973).
32. K.P. Huber and G. Herzberg. Molecular spectra and molecular structure, constants of diatomic molecules. van Nostrand Reinhold, New York. 1979.
33. L.M. Raff and D.L. Thomson. *In* Theory of chemical reaction dynamics. Vol. III. *Edited by* M. Baer. CRC Press, Boca Raton, Fla. 1985. Chap. 1.

Can. J. Chem. Downloaded from www.nrcresearchpress.com by 195.246.54.202 on 09/08/12
For personal use only.

Photolysis of ClNO adsorbed on MgO(100)

L. Hodgson,[1] G. Ziegler,[2] H. Ferkel, H. Reisler, and C. Wittig

Department of Chemistry, University of Southern California, Los Angeles, CA 90089-0482

Received June 28, 1993

This paper is dedicated to Professor John C. Polanyi on the occasion of his 65th birthday

L. Hodgson, G. Ziegler, H. Ferkel, H. Reisler, and C. Wittig. Can. J. Chem. **72**, 737 (1994).

The 365 nm pulsed laser photolysis of nitrosyl chloride adsorbed on a rough MgO(100) surface at 90 K has been studied. Mass spectrometric detection was used to record time-of-flight (TOF) spectra by monitoring Cl^+ and NO^+. These ions can derive from parent ClNO, which fragments completely in the mass spectrometer, as well as from Cl and NO photofragments. The TOF distributions are considerably slower than for the corresponding gas phase photodissociation process. NO was also detected state selectively by using resonance enhanced multiphoton ionization (REMPI), and a channel corresponding to direct adsorbate photolysis was identified. The state selective detection of NO molecules that emerge from the surface following photolysis shows unambiguously that their rotational degrees of freedom reflect the surface temperature (T_{rot} = 100–140 K), even at low coverages. At similar photolysis wavelengths, gas phase ClNO photodissociation is known to produce highly rotationally excited NO with a distinctive non-statistical distribution peaked at $J'' = 46.5$. Our studies suggest that, contrary to the gas-phase photolysis results, Cl and NO are not ejected rapidly following photolysis of surface-bound species on a repulsive potential energy surface. We postulate that ClNO grows in islands, with MgO defect sites serving as nucleation centers. Photofragment rotational and translational excitations are quenched efficiently due to strong attractive interactions that equilibrate NO to the surface temperature. Desorption of intact ClNO may also take place, but following (i.e., not during) the photolysis pulse. Such desorbed species can contribute to the TOF spectra, but not the REMPI spectra.

L. Hodgson, G. Ziegler, H. Ferkel, H. Reisler et C. Wittig. Can. J. Chem. **72**, 737 (1994).

Opérant à 90 K, on a étudié la photolyse à 365 nm, par laser pulsé, du chlorure de nitrosyle adsorbé sur du MgO(100) rugueux. On a utilisé la détection par spectrométrie de masse en temps de vol (TOF) pour détecter le Cl^+ et le NO^+. Ces ions peuvent provenir du ClNO parent qui se fragmente complètement dans le spectre de masse ainsi que des photofragments Cl et NO. Les distributions dans les spectres en TOF sont beaucoup plus lentes que dans le cas du processus correspondant de photodissociation en phase gazeuse. On a aussi détecté sélectivement divers états du NO en faisant appel à la résonance par ionisation multiphotonique améliorée (REMPI) et on a identifié un canal correspondant à une photolyse directe de la substance adsorbée. La détection sélective d'états des molécules de NO qui émergent de la surface à la suite de la photolyse démontre sans ambiguïté que leurs degrés de liberté de rotation sont des reflets de la température à la surface (T_{rot} = 100–140 K), même à de faibles taux de couverture. À des longueurs d'onde de photolyse semblables, il est connu que la photodissociation en phase gazeuse de ClNO conduit à du NO dont l'excitation rotationnelle est élevée et qui présente une distribution non-statistique distinctive avec un sommet à $J'' = 46{,}5$. Nos études suggèrent que, contrairement aux résultats en photolyse en phase gazeuse, le Cl et le NO, sur une surface d'énergie potentielle répulsive, ne sont pas éjectés rapidement après la photolyse d'espèces liées à la surface. On fait le postulat que le ClNO croît sous forme d'îles sur les défauts des sites du MgO qui servent de centres de nucléation. Les excitations de rotation et de translation du photofragment sont désactivés efficacement à cause des fortes interactions qui permettent au NO de s'équilibrer avec la température de la surface. Il est possible que la désorption de ClNO intact puisse aussi se produire après (et non pas durant) la pulsation photolytique. De telles espèces peuvent contribuer au spectre de TOF, mais pas auz spectres REMPI.

[Traduit par la rédaction]

I. Introduction

The use of ultraviolet lasers to initiate photochemical transformations at gas–surface interfaces is an area of both technological importance and scientific interest. Potential applications involve areas of long-standing investment such as catalysis (1) and the photochemical deposition and etching processes that are used widely in the microelectronics industry (2). Topics of scientific interest include understanding the myriad photoinduced processes that occur on surfaces and the influence of the surface on the photodissociationdynamics of the adsorbate.

The photochemistry of adsorbates on metal surfaces is often quite complicated (3, 4). Direct adsorbate photodissociation has been seen on a few metal substrates (3), but this is frequently not the case. The substrate can quench photoexcited adsorbates, thereby minimizing direct adsorbate photolysis. Additionally, the substrate competes for absorption of the ultraviolet light needed for adsorbate photolysis. Substrate absorption can lead to many different processes driven by photoemitted electrons, subvacuum level excitation, plasmon excitation, phonon excitation, etc. Reference 3 is an extensive review of the field of the photochemistry of adsorbates on metal surfaces.

Insulator surfaces typically transmit ultraviolet and visible light, making substrate-mediated processes less probable than on metal surfaces. This makes them better candidates for studying processes driven by adsorbate excitation. The direct photolysis of adsorbates on insulator surfaces has been seen in the following systems: CH_3Br (5–8), H_2S (6, 9), HBr (10, 11), HCl (11), OCS (12), C_2H_3Cl (13*a*), and NO_2 (13*b*) on LiF(001), CH_2I_2 on Al_2O_3 (14), $Fe(CO)_5$ on Al_2O_3 (15), thick polycrystalline layers of CH_3I on LiF(100) (16), C_6H_5I on LiF (17), CH_3I and CD_3I on MgO(100) (18) and NO_2 on Al_2O_3(1120) (19). In addition, the photodissociation of HBr (20) and CH_3Br (21) on LiF(001), IBr (22) and ICI (23) on MgO(001), and CH_3I on MgO(100) (18*c*) have been examined theoretically.

The detection of products in most of these systems has been achieved by using time-of-flight (TOF) mass spectroscopy, and information has been obtained regarding the different types of photochemical processes taking place and the geometries of the

[1]U.S. Department of Education Predoctoral Fellow.

[2]Present address: Böhringer, Mannheim, Germany.

Can. J. Chem. Downloaded from www.nrcresearchpress.com by 195.246.54.202 on 09/08/12
For personal use only.

Can. J. Chem. Downloaded from www.nrcresearchpress.com by 195.246.54.202 on 09/08/12
For personal use only.

molecules on the surface. Several groups have used resonance enhanced multiphoton ionization (REMPI) to detect reaction products (16–19). This has enabled photodissociation products to be detected unambiguously and state-selectively and, in certain cases, has enabled comparisons to be made with vibrational state distributions obtained from the photolysis of gas phase molecules (16, 18).

An important characteristic of most of the insulator systems studied previously has been the presence of two channels observed in TOF mass spectroscopy: a slow one corresponding to desorption of the parent molecule and a fast one corresponding to direct photolysis of the adsorbate. Different mechanisms for parent desorption were proposed: excitation of color centers leading to shock waves which cause desorption (5, 6, 8, 9, 12, 13), thermal heating (7), substrate quenching of excited adsorbates followed by desorption (17), explosive desorption (14, 16), and laser annealing where molecules in unstable sites desorb (15).

Another important issue is the pattern of adsorbate growth on the insulator surface. In metals, the adsorbate often wets the surface, since the surface–adsorbate bonds are much stronger than the adsorbate–adsorbate bonds (24). This is not always the case with inert insulators. For example, based on their temperature programmed desorption (TPD) data, Tabares et al. concluded that CH_3Br forms 3-dimensional islands on their 30 K LiF(001) surface (7). Harrison, et al. found that CH_3Br wets LiF(001), but at temperatures ~117 K (8), i.e., just below the desorption temperature. Polanyi and co-workers reported island formation for OCS (12*c*) and HBr (10, 11, 25) adsorbed at 85 K on LiF(001) and CH_3I on TiO_2 (26). In addition, they observed photoejection of HBr clusters (27) and photoreactions of HBr dimers (11).

ClNO was chosen for several reasons. Its gas phase photochemistry has been studied in great detail and exhibits several distinctive features (23–31). Dissociation takes place on a steep repulsive surface (28), and thus might occur before energy can be transferred to the surface. The NO product can be detected sensitively with REMPI, thereby providing unambiguous identification of NO photoproducts. In addition, rotational and vibrational state distributions can provide valuable dynamical information that is lacking in TOF studies. ClNO has a low bond dissociation energy (13 000 cm^{-1}) (29) and absorbs light throughout the visible and ultraviolet — spectral regions that are easily accessed with tunable dye lasers. The 300 K absorption spectrum consists of several broad absorption bands (32), which have recently been assigned (30). Its NO product state distributions, photofragment yield spectra, recoil anisotropy, rotational alignment, NO Λ-doublet populations and the nature of the orbitals involved in electronic transitions have been determined both experimentally and theoretically (28–31).

At 355 nm, gas phase ClNO is excited via a parallel transition, $S_3(2^1A') \leftarrow S_0(1^1A')$, yielding rotationally hot NO, i.e., $J''_{peak} = 46.5$ (29, 30). Almost all of the NO is in $v'' = 0$. Both NO spin–orbit states are nearly equally populated and there is a large propensity to form the Λ-doublet component that has its Π orbital perpendicular to the plane of NO rotation (29, 30). These signatures facilitate the determination of how the MgO crystal affects the photodissociation dynamics of adsorbed ClNO.

In the present study, ClNO adsorbed at 90 K on a *rough* MgO(100) surface was photolyzed at 365 nm. Species emanating from the surface were detected using a quadrupole mass spectrometer (QMS), and state distributions of NO fragments were determined by using two-photon, two-frequency laser ionization (REMPI). Single crystal MgO(100) is transparent to the 365 nm photolysis radiation, therefore substrate absorption and electron-induced processes seen on metal surfaces should be minimized. ClNO is weakly bound to the inert insulator surface, thus perturbation of its ground electronic potential energy surface should be slight. Due to this weak bond to the surface, island formation is likely. On the other hand, the nature of the electronically excited states of surface-bound ClNO is presently unknown. Specifically, these may interact more strongly with the substrate than does ground state ClNO. Therefore, we leave open the possibility that excited state dynamics of surface bound species differ qualitatively from those of their gas phase counterparts.

Following irradiation, TOF distributions are obtained by monitoring Cl^+ and NO^+. Since parent ClNO fragments completely in the mass spectrometer, yielding Cl^+ and NO^+, the TOF spectra contain contributions from ClNO molecules that desorb intact following irradiation, as well as from Cl and NO emerging from the surface. The TOF distributions are considerably slower than for the corresponding gas phase photodissociation process (28). This indicates a qualitative difference in the behavior of ClNO following photoexcitation. Specifically, there is no evidence for rapid ejection of products from the surface. The NO rotational distributions obtained by using REMPI are cold and can be fit with T_{rot} = 100–140 K, which differs greatly from the highly non-statistical gas phase distributions. These results, together with temperature programmed desorption (TPD) data, suggest that ClNO photolysis is dominated by strong attractive interactions with its surroundings and that ClNO aggregates as islands on the surface, nucleating around defect sites.

The main focus of the present paper is twofold: (*i*) demonstrating unambiguously the remarkable difference between the photophysics and photochemistry of adsorbed versus gas phase ClNO; and (*ii*) examining the possibility that nucleation and growth that takes place around defect sites are responsible for the observed differences.

II. Experimental

The experimental arrangement was described in detail elsewhere (33). Therefore only a brief description will be given, emphasizing modifications introduced for the photodissociation experiments. The vacuum system consisted of three chambers: a source chamber containing the molecular beam, a buffer chamber, and an ultrahigh vacuum (UHV) chamber. Figure 1 shows the UHV chamber, the major components being a rotatable sample manipulator equipped with liquid nitrogen cooling, two quadrupole mass spectrometers (UTI 100C), an Auger electron spectrometer (PHI 3017 with a 0.6% resolution CMA), a fast argon gun (Ion Tech), a channeltron electron multiplier (Galileo) for ion detection, a photolysis laser and a probe laser. The fast argon gun is not shown. The probe laser enters the chamber from below and ionizes NO 2–3 cm from the surface.

ClNO (Matheson, 99.2%) was purified in several freeze–pump–thaw cycles with a pentane slush (−131°C). The sample was stored at liquid nitrogen temperature and used in a darkened glass bulb. The crystal was dosed with ClNO using a pulsed molecular beam (Physik Instrumente). All experiments were performed at a backing pressure of 40–60 Torr neat ClNO. This low backing pressure was necessary to attain low coverages of the crystal, and to avoid clustering of ClNO in the molecular beam, which may become a problem with the greater cooling obtained at higher backing pressures. The coverage on the surface was varied by either changing the opening of the nozzle by controlling the voltage on the piezoelectric crystal, or by varying the dosing time, Δt. The product of Δt and the pressure increase in the

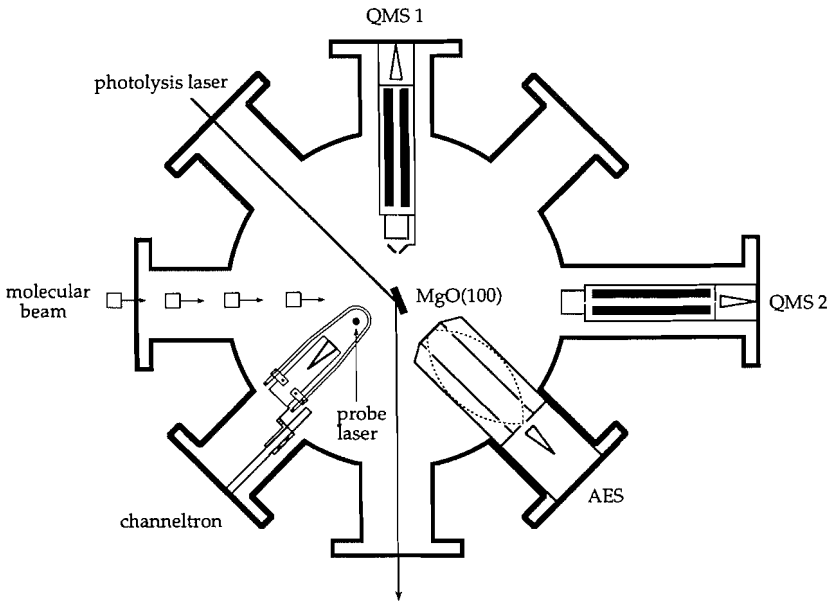

FIG. 1. Schematic of the UHV chamber for the adsorbate photolysis experiments. The photolysis radiation is incident on the MgO(100) crystal. The probe beam enters from below and ionizes NO 2–3 cm from the surface.

source chamber upon switching on the molecular beam, Δp, was proportional to coverage.

The MgO(100) crystal (Atomergic, $10 \times 10 \times 1$ mm^3) was cleaved and polished by the manufacturer. It was mounted on a molybdenum block which could be resistively heated to 800 K. Ideally, temperatures of ~1100 K would be needed for complete annealing. In our case, the surface can be characterized as clean but rough, exhibiting many steps, kinks, and vacancies. The surface temperature was measured using a chromel–alumel thermocouple attached to the molybdenum clamp of the sample holder. A temperature controller interfaced to a computer controlled the heating rate for the TPD experiments. The surface temperature was normally ramped at a rate of 0.5 K/s.

The surface was cooled with an open loop liquid nitrogen flow system. Liquid nitrogen flowed from a dewar outside the apparatus through an insulated feedthrough into the UHV chamber. Inside, flexible stainless steel bellows (connected to a small liquid nitrogen reservoir) and a sapphire plate joined the molybdenum surface holder to the reservoir. The sapphire acted as a thermal switch permitting cooling down to 90 K as well as high temperature annealing. Auger electron spectra (AES) of the MgO crystal could be taken at room temperature with a primary energy of 3 kV, but not always at liquid nitrogen temperature due to charging of the crystal. By reducing the primary energy to 800 eV, as suggested by Wei (34), reliable AES spectra could be obtained. Carbon was the main contaminant of the MgO crystal, as seen by the Auger spectrometer. This contamination was removed by fast argon atom bombardment (3 min, ~0.01 mA emission) followed by annealing (800 K, ~1 h). Auger spectroscopy is not very useful for quantitatively determining coverage if the molecules are weakly physisorbed, since the high energy electrons may cause desorption as well as dissociation.

A quadrupole mass spectrometer oriented in line with the ClNO molecular beam (QMS 2 in Fig. 1), was used to determine the composition of the direct molecular beam. The ion signals from the direct beam consisted of Cl^+ and NO^+ in a ratio of 1:5. Parent ClNO completely fragmented in the ionizer. Another mass spectrometer, QMS 1, collimated with ~5.5° angular resolution, was used to detect products in the TPD and TOF experiments. The surface to ionizer distance was 8.4 cm.

The photolysis laser was a XeCl excimer (Questek 2200) pumped dye laser system (Lambda Physik, FL 2002) operating at 365 nm. In order to obtain a uniform beam profile, the beam was expanded using a telescope and only the center portion was used. The laser beam diameter could be varied from 1 to 5 mm. For TOF measurements the laser beam diameter was 4–5 mm with energies of ~250 μJ. The photolysis laser entered and exited the UHV chamber through quartz windows.

The rotational state distribution of NO molecules leaving the surface after photolysis was measured by REMPI. The probe laser was a Nd:YAG pumped tunable dye laser system (Quanta-Ray DCR2/PDL1) that was frequency doubled and Raman shifted. The 226 nm photons (~4 μJ) excite the NO γ(0–0) transition and the 280 nm photons (~1 mJ) ionize the NO. The detection laser system was described in detail previously (33). The NO^+ ions were extracted from the ionization region and detected with a high sensitivity channeltron.

The determination of surface coverage on insulator surfaces by TPD is difficult. The difference in bond energies, i.e., between substrate–adsorbate and adsorbate–adsorbate is too small to produce a distinguishable break in the TPD spectra indicating the onset of multilayer coverage. The possibility of island growth further complicates the issue. In order to quantitatively determine the ClNO dosage in this experiment, a method commonly used for ionization gauge calibration was used. It makes use of the fact that the flux of molecules from a pressure stabilized reservoir through a known conductance into an evacuated chamber is fully computable (35). This flux calibration is reliable for molecules such as N_2 for which ionization gauge calibration factors are available. For a molecule such as ClNO, the flux must be calibrated through comparison with N_2.

The determination of the sticking probability was achieved by dosing the surface with a ClNO molecular beam, and comparing the background pressure in the UHV chamber when the surface was maintained alternately well below and well above the ClNO desorption temperature. The sticking probability is close to zero for temperatures higher than the desorption temperature. The pressure component due to the molecular beam decreased when the temperature of the surface was lowered beneath the desorption temperature, indicating that ClNO sticks to MgO. If all molecules that hit the surface are adsorbed, the molecular beam component would be zero. A reduction of the molecular beam contribution of 50% was obtained, indicating a sticking probability of ~50% at a surface temperature of 90 K. There were no indications that heating the surface affected the pumping speed due to the change in cold areas cryopumping the chamber. This is a reasonable assumption due to the small area of the surface.

III. Experimental results

A. *Temperature Programmed Desorption (TPD)*

TPD was used to help determine the nature of ClNO adsorption. In Fig. 2, the Cl^+ and NO^+ mass spectrometer signals ver-

Can. J. Chem. Downloaded from www.nrcresearchpress.com by 195.246.54.202 on 09/08/12
For personal use only.

Can. J. Chem. Downloaded from www.nrcresearchpress.com by 195.246.54.202 on 09/08/12
For personal use only.

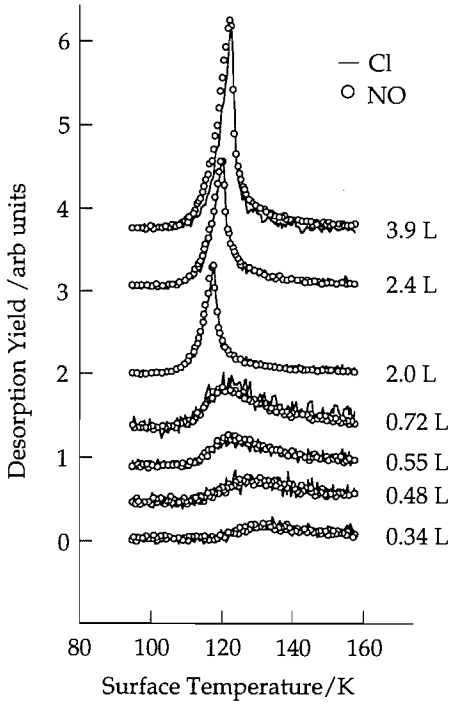

FIG. 2. TPD spectra of Cl^+ (lines) and NO^+ (circles) at different coverages with a heating rate of 0.5 K/s.

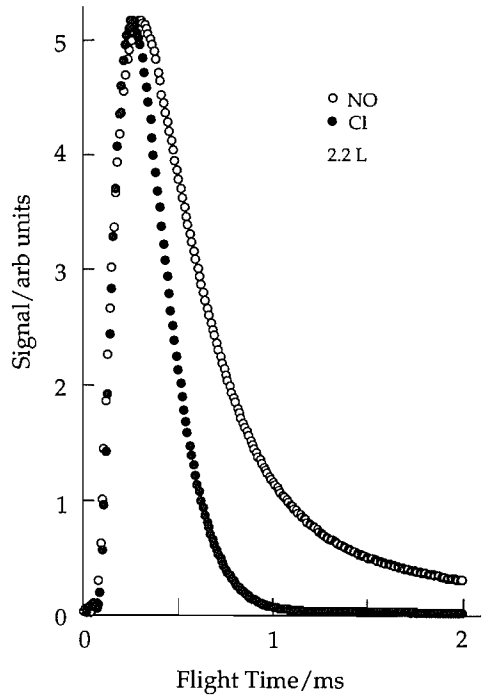

FIG. 3. Cl^+ (●) and NO^+(○) TOF signals after 365 nm photolysis of 2.2 L of ClNO adsorbed on MgO(100). Velocity dependent ionization efficiencies and ion flight times in the QMS have been taken into account. The signals were normalized to the same peak intensity.

sus temperature, obtained at a heating rate of 0.5 K/s, are shown for different coverages. In each case, the Cl^+ and NO^+ signals were normalized to the same height, and the curves are offset for clarity. As mentioned previously, parent ClNO cannot be seen due to complete fragmentation in the QMS. However, ClNO most likely adsorbs molecularly on MgO(100) since the desorption peaks for Cl^+ and NO^+ both occur at the same temperature. No other peaks were present in the TPD spectra, indicating that ClNO does not dissociate or react to form other molecules on the surface. It also does not thermally decompose during TPD and the sample is not contaminated, though NO cannot be completely eliminated because of an equilibrium between ClNO, NO, and Cl_2 (29). The main desorption peak for NO on MgO(100) was below the lowest temperatures attainable (~90 K), so its presence is restricted to defect sites.

B. TOF following laser irradiation

Samples with ClNO adsorbed on MgO(100) were irradiated at 365 nm and species that subsequently leave the surface were detected with the QMS. Cl^+ and NO^+ were the only ions seen in the mass spectrometer and no positive ions were seen with the ionizer off. TOF data were typically taken with the photolysis laser wavevector at 45° to the surface normal. Products were detected with the surface facing QMS 1. Signals from the first 3–4 laser shots were discarded.

The data presented in Fig. 3 show TOF distributions for a coverage of 2.2 L. Signals were corrected for the velocity dependent QMS detection efficiency and the ion flight times in the QMS. The Cl^+ and NO^+ signals are normalized to the same height and their risetimes are almost identical. The NO^+ signal exhibits a tail due to background NO; when this is subtracted the signal is essentially the same as that of Cl^+. Such data alone do not enable us to distinguish between ClNO molecules that reach the mass spectrometer intact, as opposed to Cl and NO fragments that travel from the surface to the mass spectrometer. Thus, we conclude that the TOF signals may include contributions from both desorbed parent ClNO and Cl and NO fragments generated in the photolysis of surface-bound ClNO. Details will be given in a future publication.

C. Photodissociation cross section of adsorbed ClNO

An upper limit to the ClNO photodissociation cross section can be obtained from the variation of the NO^+ signal versus the number of laser pulses, for specific initial coverages. Time integrated NO^+ signals were obtained with the surface normal pointing towards QMS 1. Signals decrease with the number of pulses directed at the same spot on the surface due to adsorbate depletion. This variation depends on initial coverage, as shown in Fig. 4*a*. The laser intensity was kept constant throughout these measurements.

Several conclusions can be drawn from the plots presented in Fig. 4. NO^+ signals only decrease exponentially at low coverages and for a modest number of laser firings. At higher coverages, they are almost constant. This suggests that species from the topmost layers are being released into the gas phase upon irradiation. If the total photoexcitation cross section, σ, is independent of coverage, the signal at low coverages is given by (3)

$$[1] \quad S = S_0 \exp(-n\sigma\Phi)$$

where S is assumed to be proportional to the surface coverage; S_0 is the corresponding signal for the first laser shot; Φ is the number of photons per unit area; and n is the number of laser pulses. Because of the likelihood that some parent molecules are desorbed intact from the surface, the parameter σ should be interpreted as an upper limit to the photodissociation cross section. From the slope of the low coverage curve shown in Fig. 4*b*,

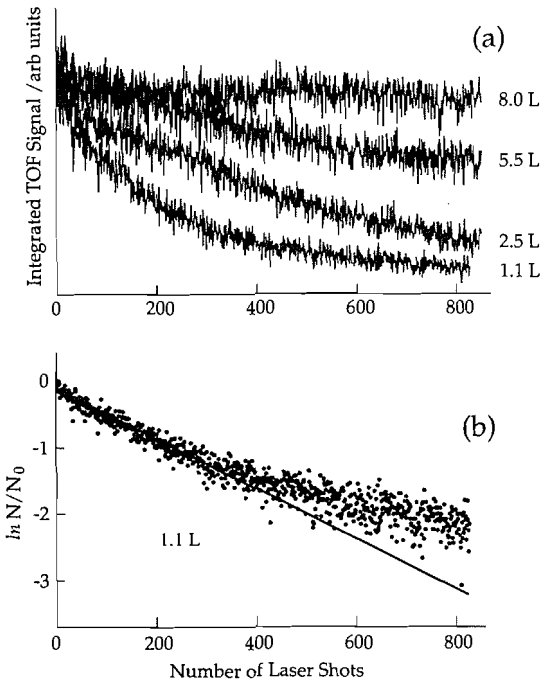

FIG. 4. Panel (*a*) shows the decrease in the time-integrated NO^+ TOF signal when ClNO is photolyzed at 365 nm at various coverages. Panel (*b*) is a semilogarithmic plot of the signal versus photon fluence at low coverages, from which an upper bound to the photodissociation cross section is obtained.

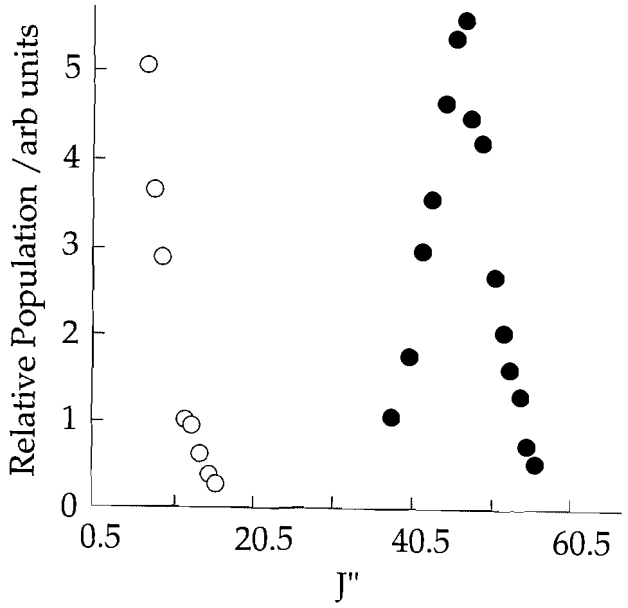

FIG. 5. Open circles: NO($v'' = 0$) rotational distribution from the 365 nm photolysis of ClNO adsorbed on MgO(100). Data are for the $R_{11} + Q_{21}$ branch of the lower energy $^2\Pi_{1/2}$ spin-orbit state; they can be fit with $T_{rot} \sim 140$ K. Filled circles: NO($v'' = 0$) rotational distribution from 355 nm photolysis of gas phase ClNO. Data are for the $Q_{11} + P_{21}$ branch of $^2\Pi_{1/2}$.

σ can be determined. This curve is not purely exponential, as can be seen from the deviation from a straight line after ~400 laser shots. Such deviation at longer times was also seen with $Fe(CO)_5$ adsorbed on Al_2O_3 (15). This probably arises because the laser beam is not spatially homogeneous: if the beam is more intense at the center, the signal will be dominated by this region initially, but as molecules at the center are depleted, contributions from the lower intensity wings will begin to dominate. From the initial slope we derive $\sigma \sim 4 \times 10^{-19}$ cm^2. As stated above, this is an upper limit to the ClNO absorption cross section, since parent molecules that desorb following irradiation contribute to the observed signal decrease just as if they had been dissociated. This upper bound can be compared to the known gas phase absorption cross section of approximately 0.8×10^{-19} cm^2 (32). Additionally, interference between the incident, transmitted, and reflected radiation was not taken into account (12). No pronounced surface-enhanced photodissociation was seen, as has been reported for rough metal surfaces (36, 37) and for OCS on unannealed LiF(001) (12*a*,*b*). We also note that the QMS samples a small solid angle (~5.5°), while for accurate cross section measurements all particles must be detected, i.e., angular distributions may vary with coverage, as noted by Polanyi and co-workers (9).

D. State-specific NO detection by REMPI

NO($v'' = 0$) rotational distributions were determined by using REMPI. A scan over transitions in the region 225.7–227.0 nm required about 800 points, averaging 10 shots per point. Thus, stability of the experimental conditions over 8000 shots of the photolysis laser was necessary. At low coverages, when the signal drops exponentially with each laser pulse, this requirement could not be fulfilled without replenishing the surface. For example, an initial coverage of about 1 L would be removed with 3000 laser shots.

By using the pulsed molecular beam as a doser, the crystal could be dosed between photolysis laser pulses, thereby maintaining a steady state of molecules on the surface during the measurement (5–13, 16, 38). The molecular beam and photolysis laser both operated at 10 Hz. Typical steady state surface coverages were 0.2–0.8 L. The stable signals obtained by using this alternating dose-and-desorb condition have proven to be invaluable for measurements of NO rotational distributions. With the surface positioned as shown in Fig. 1, rotationally resolved spectra were obtained under steady state conditions. Results are summarized as the open circles in Fig. 5 for a coverage of ~0.5 L. The time delay between the photolysis and probe laser was optimal at 150 μs. The data shown are for the $R_{11} + Q_{21}$ branch in the lower energy $^2\Pi_{1/2}$ spin orbit state. The NO rotational distributions corresponded to $T_{rot} = 100$–140 K — remarkably different from the hot NO rotational distributions seen in gas phase photolysis (29, 30) and reproduced in Fig. 5 (filled circles). No NO($v'' = 1$) was detected, paralleling the gas phase photolysis results, in which very little NO($v'' = 1$) is produced.

IV. Discussion

A. Evidence for adsorbate photodissociation

The results presented above indicate that the TOF and REMPI signals are a consequence of irradiating samples in which ClNO is adsorbed molecularly on MgO(100). We checked for contributions from gas phase ClNO photodissociation by the 365 nm photolysis laser, since the background pressure in the UHV chamber increased slightly when the molecular beam was on. With the molecular beam on and the crystal at 300 K (i.e., too high a temperature for ClNO to

Can. J. Chem. Downloaded from www.nrcresearchpress.com by 195.246.54.202 on 09/08/12
For personal use only.

adsorb), no signal was seen with the QMS, confirming that the observed signals are associated with molecules that are adsorbed on the crystal. The most convincing evidence against gas phase photodissociation, however, comes from the NO rotational distributions, which differed remarkably from those obtained in the gas phase photolysis of ClNO at any wavelength.

All signals depend linearly on 365 nm fluence over a large range of coverages, and therefore are not due to photodesorption of ClNO followed by its photolysis. Note that this rules out photodissociation of gaseous ClNO that is desorbed *within* the laser pulse, but leaves open the issue of ClNO that desorbs *following* the photoexcitation pulse. Signals were also checked for photodissociation of ClNO by the probe laser, since the absorption cross section of ClNO at 226 nm is a factor of 10^2 higher than at 365 nm (32). The laser signal depended on one photon each of the 226 and 280 nm radiations, confirming that absorption of the probe laser light by background ClNO is insignificant. This is also expected on the basis of the 226 nm photon fluence and the ClNO absorption cross section: only $\sim 10^{-4}$ of the ClNO will be photodissociated. The most conclusive evidence for direct photodissociation of adsorbed ClNO comes from the observation of NO by REMPI under conditions where photodissociation of desorbed ClNO is insignificant.

Preliminary experiments at other photolysis wavelengths are consistent with the suggestion that adsorbate photodissociation is taking place. Though fragments were detected following 475 nm photolysis (which coincides with the ClNO $S_1 \leftarrow S_0$ system), almost no signal was seen following irradiation in the weak $T_1 \leftarrow S_0$ system near 600 nm. At 600 nm, the cross section for gas phase ClNO photodissociation is small compared to 475 and 365 nm (32). It is also possible that surface and bulk defects, as well as photoproducts that remain bound to the surface (e.g., at defects), have absorptions that vary throughout these wavelength ranges.

B. Island formation

MgO(100) has many surface defects (predominantly oxygen vacancies) (39). Electrons can be trapped at these sites, creating states within the 7.8 eV band gap (40). States located 2.3 and 6 eV below the vacuum level have been seen by Henrich et al. using electron energy loss spectroscopy and were discussed in terms of oxygen vacancies and intrinsic surface effects (39). One indication of the existence of such defect states on the rough MgO(100) crystal used in the present experiments is the observation of a blue fluorescence upon electron bombardment. This fluorescence could be seen readily by the eye and was strongest for a clean MgO surface. After exposure to ClNO and desorption of ClNO by heating the surface ~150 K, the fluorescence disappeared and a small amount of chlorine could be seen on the surface with AES. This suggests that some ClNO dissociatively adsorbs on the surface with the chlorine occupying defect sites in the MgO crystal, most likely oxygen vacancies. These Cl atoms are strongly bound. They cannot be removed at temperatures as high as 800 K, but they can be removed with fast argon bombardment. Thus, it is possible that the nucleation center is a Cl atom attached to a defect.

The temperature at which exposures were carried out prior to TPD is only ~30 K lower than the main desorption peak at ~120 K. We assume that, following ClNO adsorption at 90 K, molecules are able to diffuse across the surface and may either find an unoccupied defect site, or may collide with other

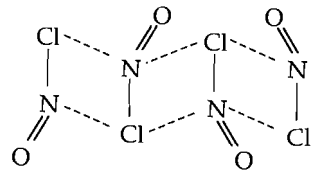

FIG. 6. Molecular solid of ONCl-II as proposed by Jones and Swanson (44).

so-called "walkers" (41), as well as with islands already formed. At higher exposures, defect-free areas become covered, presumably beginning with sites adjacent to the decorated defects. In this picture, adlayer growth over defect-free areas is in the form of two-dimensional islands and is nucleated by decorated defects. It should be mentioned that an island randomly formed on a defect-free area is not necessarily stable and can decay before exceeding the critical size to become stable (42). Therefore, the density on the surface during dosing can influence the ultimate size distribution of islands, at least at low coverage. Dosing the surface with a pulsed molecular source may cover the surface somewhat differently than a doser that maintains a constant density on the crystal after initiating the dosing procedure.

Desorption between 120 and 140 K is attributed to molecules evaporating from defect-free areas, perhaps at the edge of islands or dendrites. The desorption peak is seen to shift to lower temperatures with increasing coverage (Fig. 3). In general, such behavior of a TPD peak can be indicative of a variety of phenomena, including recombinative desorption (following dissociative adsorption), collision mediated desorption, and repulsive lateral interaction. Simulations of the TPD results indicate that the magnitude of the observed shift is consistent with each of these. At higher coverages, zeroth order desorption (typical of multilayers, clusters and chains of molecules) is seen.

Some information regarding ClNO aggregates can be obtained from spectroscopic studies of ClNO ices and thin films. Killough et al. (43) showed that in the range 85–190 K, ClNO ice exists as covalent dimers (ONCl-II), while in the range 74–85 K, an ionic phase exists (ONCl-I). Later, Jones and Swanson used infrared spectroscopy to study ClNO in matrices and thin films deposited on a cold CsI window (44). They suggested that ONCl-II consists of long chains with strong intermolecular covalent bonds, as shown in Fig. 6. This geometry agrees with *ab initio* calculations which show that nitrogen has a partial positive charge while chlorine and oxygen have partial negative charges (30). Formation of these chains leads to weakening of the Cl—NO bonds. The surface temperature of ~90 K used in our study is near the ONCl-I/ONCl-II phase transition. Dimer or chain formation is consistent with our observation of islands. However, if ClNO is ionic when adsorbed on the ionic MgO crystal, comparison to the gas phase photochemistry may be unjustified. A direct determination of the geometry and structure of ClNO on MgO(100) is clearly needed.

C. Rotational and translational energy distributions

As stated earlier, NO rotational distributions were very cold (100–140 K), i.e, close to the surface temperature. This differs markedly from the rotationally hot distributions seen in gas phase photodissociation.

As stated above, the TOF distributions observed mass spec-

Can. J. Chem. Downloaded from www.nrcresearchpress.com by 195.246.54.202 on 09/08/12
For personal use only.

Can. J. Chem. Downloaded from www.nrcresearchpress.com by 195.246.54.202 on 09/08/12
For personal use only.

trometrically may originate both from desorbed ClNO and photodissociation fragments. However, the observed distributions all correspond to species that are traveling much more slowly than in the case of gas phase photodissociation and there is no indication of a fast, instantaneous component. We note that the desorbates have average kinetic energies of ~10 meV, while in the gas phase photodissociation of ClNO, the Cl and NO fragments have 580 and 670 meV of translational energy, respectively, in the center-of-mass system. These values were obtained by assuming that 70% of the available energy goes into translation, as reported for the gas phase photolysis of ClNO at 347 nm by Busch and Wilson (28).

The observed cold translational and NO rotational energy distributions at nominal submonolayer coverages are consistent with island formation, where photofragments can experience strong, attractive interactions with other molecules in the island and the surface before escaping. Thus, their translational and rotational energies are quenched and are quite different from the products of gas phase photolysis. Similar TOF spectra were also seen with CH_3I on LiF (16) and HBr islands on LiF(001) (11) and interpreted in terms of products formed in lower layers which undergo many collisions before escaping. In the case of HBr, the H-atom TOF low energy tail increased with surface coverage.

It is surprising that other products (e.g., Cl_2) were not detected. In many systems, species other than the parent and photolysis products have been seen, indicating photoinitiated reaction (PRXN) on the surface (6, 9–11, 12*c*, 13, 17, 18). In these cases, surface-bound molecules are aligned due to interactions with the surface as well as each other and photolysis initiates reaction with an adjacent molecule. Attack angles and impact parameters are restricted, leading to a surface aligned PRXN.

It is known that the gas phase reaction $Cl + ClNO \rightarrow Cl_2 + NO$ has a large rate constant (45), and produces vibrationally excited NO (46). Thus, Cl_2 is potentially a PRXN product. However, no signal was observed at $m/e \cong 71$, indicating that the Cl^+ signals do not derive from Cl_2. Moreover, Cl_2 does not stay on the surface, since TPD spectra (to 200°C) taken after as many as 100 laser shots were identical to those taken with the photolysis laser off. The binding energy of Cl_2 to MgO has recently been calculated to be 4.1 kcal/mol (47). Thus, the photolysis laser does not initiate the formation of other products on the surface. The absence of a PRXN may result from the restricted geometries of surface-bound molecules. More work is needed to clarify this point.

Although the exact geometry of ClNO on the surface is unknown, it is reasonable that it lies flat on the surface, in analogy with the suggested geometry of its thin films on CsI surfaces (Fig. 6) (44). Consequently, photoproducts may be ejected preferentially in the plane of the surface. Since TOF products were typically detected along the surface normal, our observations may be biased toward molecules that undergo collisions. To examine this, TOF distributions were obtained with the detector at the surface normal and at 45° to the normal. Both measurements gave identical results. Though this is consistent with there being no surface order, it is also consistent with the surface being too rough for its plane to be well defined.

The TOF distributions obtained by Polanyi and co-workers for CH_3Br adsorbed on rough LiF also indicated slow products relative to smooth surfaces or gas phase photodissociation (6, 8). They attributed this to strong adsorption at different defect sites. The reduced translational energy was attributed to increased internal energy of the fragments and/or energy transfer to the surface, since bonding to the defect is strong. In our case, NO has *less* internal energy than in the corresponding case of gas phase photodissociation. After photodissociation the fragments may stick to the surface before desorbing. For example, Watson, NoorBatcha, and Lucchese (21), in trajectory simulations of the 222 and 193 nm photodissociation of CH_3Br on LiF(001), see a significant amount of sticking, especially on a rough surface. With our time resolution, it is not possible to determine if molecules stick briefly before desorbing.

Obviously the situation is complex and without knowing the geometry and nature of the surface-bound molecules it is imprudent to propose a complete model. It is unknown whether ClNO on the surface adsorbs in planar or non-planar geometries, and whether its structure is covalent, ionic, a molecular chain, or a 2- or 3-dimensional island. Presently experiments are being conducted to determine the nature of the bonding and the geometry of the molecules on the surface. In addition, experiments on smooth MgO crystals aimed at further establishing the role of defect sites are in progress in our laboratory (48). Preliminary results from these latter experiments confirm the interpretation suggested in this paper.

V. Conclusions

This study establishes that ClNO adsorbs molecularly on rough MgO(100) surfaces at 90 K. Following 365 nm laser irradiation, products due to ClNO photolysis are unambiguously identified by REMPI. TOF distributions indicate that only very slow species emanate from the surface. The NO^+ and Cl^+ mass spectrometer signals are probably due to both photodissociation and cracking of desorbed parent ClNO. The slow TOF distributions are remarkably different than gas phase photolysis, which yields high translational energies of products. NO rotational distributions reflect the surface temperature (T_{rot} = 100–140 K) and, again, are much colder than the corresponding gas phase distributions which peak at $J'' = 46.5$, suggesting that strong attractive interactions with the surface take place prior to desorption. Evidence points to ClNO island formation, with nucleation occurring around defect sites, but the nature and geometry of ClNO on the surface are presently unknown. One possibility is the chain-like structure observed by Killough et al. on cold CsI. Work is currently in progress to determine the geometry of ClNO on MgO(100), and the role of defects on the dissociation.

Acknowledgments

The authors thank Bruce Koel, Scott Powers, and Peter Blass for many helpful discussions and Jessie Chu and James Singleton for technical assistance. This research was supported by AFOSR.

1. T.J. Chuang. Surf. Sci. Rep. **3**, 1 (1983).
2. R.M. Osgood, Jr. Ann. Rev. Phys. Chem. **34**, 77 (1983).
3. X.-L. Zhou, X.-Y. Zhu, and J.M. White. Surf. Sci. Rep. **13**, 73 (1991).
4. X.-L. Zhou, X.-Y. Zhu, and J.M. White. Acc. Chem. Res. **23**, 327 (1990).
5. E.B.D. Bourdon, J.P. Cowin, I. Harrison, J.C. Polanyi, J. Segner, C.D. Stanners, and P.A. Young. J. Phys. Chem. **88**, 6100 (1984).
6. E.B.D. Bourdon, P. Das, I. Harrison, J.C. Polanyi, J. Segner, C.D. Stanners, R.J. Williams, and P.A. Young. Faraday Discuss. Chem. Soc. **82**, 343 (1986).
7. F.L. Tabares, E.P. Marsh, G.A. Bach, and J.P. Cowin. J. Chem. Phys. **86**, 738 (1987).

8. I. Harrison, J.C. Polanyi, and P.A. Young. J. Chem. Phys. **89**, 1475 (1988).
9. I. Harrison, J.C. Polanyi, and P.A. Young. J. Chem. Phys. **89**, 1498 (1988).
10. E.B.D. Bourdon, C.-C. Cho, P. Das, J.C. Polanyi, C.D. Stanners, and G.-Q. Xu. J. Chem. Phys. **95**, 1361 (1991).
11. C.-C. Cho, J.C. Polanyi, and C.D. Stanners. J. Chem. Phys. **90**, 598 (1989).
12. (*a*) St. J. Dixon-Warren, I. Harrison, K. Leggett, M.S. Matyjaszczyk, J.C. Polanyi, and P.A. Young. J. Chem. Phys. **88**, 4092 (1988); (*b*) K. Leggett, J.C. Polanyi, and P.A. Young. J. Chem. Phys. **93**,3645 (1990); (*c*) St. J. Dixon-Warren, K. Leggett, M.S. Matyjaszczyk, J.C. Polanyi, and P.A. Young. J. Chem. Phys. **93**, 3659 (1990); (*d*) J.C. Polanyi and P.A. Young. J. Chem. Phys. **93**, 3673 (1990).
13. (*a*) St. J. Dixon-Warren, M.S. Matyjaszczyk, J.C. Polanyi, H. Rieley, and J.G. Shapter. J. Phys. Chem. **95**, 1333 (1991); (*b*) St. J. Dixon-Warren, R.C. Jackson, J.C. Polanyi, H. Rieley, J.G. Shapter, and H. Weiss. J. Phys. Chem. **96**, 10983 (1992).
14. (*a*) T.J. Chuang and K. Domen. J. Vac. Sci. Technol. **A5**, 473 (1987); (*b*) K. Domen and T.J. Chuang. J. Chem. Phys. **90**, 3318 (1989); (*c*) T.J. Chuang and K. Domen. J. Vac. Sci. Technol. **B7**, 1200 (1989); (*d*) K. Domen and T.J. Chuang. Phys. Rev. Lett. **59**, 1484 (1987).
15. F.G. Celii, P.M. Whitmore, and K.C. Janda. J. Phys. Chem. **92**, 1604 (1988).
16. (*a*) J. Kutzner, G. Lindeke, K.H. Welge, and D. Feldmann. J. Chem. Phys. **90**, 548 (1989); (*b*) D. Feldmann, J. Kutzner, and K.H. Welge. *In* Springer Ser. Surf. Sci. Vol. 19. *Edited by* G. Betz and P. Varga. Springer-Verlag, Berlin. 1990.
17. E. Villa, J.A. Dagata, and M.C. Lin. J. Chem. Phys. **92**, 1407 (1990).
18. (*a*) K.A. Trentelman, H. Fairbrother, P.C. Stair, P.G. Strupp, and E. Weitz. J. Vac. Sci. Technol. **A9**, 1820 (1991); (*b*) K.A. Trentelman, D.H. Fairbrother, P.G. Strupp, P.C. Stair, and E. Weitz. J. Chem. Phys. **96**, 9221 (1992); (*c*) M.I. McCarthy, R.B. Gerber, K.A. Trentelman, P. Strupp, D.H. Fairbrother, P.C. Stair, and E. Weitz. J. Chem. Phys. **97**, 5168 (1992).
19. (*a*) T.J. Chuang, R. Schwarzwald, and A Mödl. J. Vac. Sci. Techol. **A9**, 1719 (1991); (*b*) T.J. Chuang. Lect. Notes Phys. **389**, 203 (1991).
20. Z.-H. Huang and H. Guo. J. Chem. Phys. **96**, 8564 (1992).
21. (*a*) J.M. Watson, I. NoorBatcha, and R.R. Lucchese. J. Chem. Phys. **96**, 7771 (1992); (*b*) Z.-H. Huang and H. Guo. J. Chem. Phys. **97**, 2110 (1992); (*c*) Z.-H. Huang and H. Guo. J. Chem. Phys. **98**, 3395 (1993).
22. M.I. McCarthy, R.B. Gerber, and M. Shapiro. J. Chem. Phys. **92**, 7708 (1990).
23. M.I. McCarthy and R.B. Gerber. J. Chem. Phys. **93**, 887 (1990).
24. M. Wortis. Phys. Today, **38**, S-22 (1985).
25. J.C. Polanyi, R.J. Williams, and S.F. O'Shea. J. Chem. Phys. **94**, 978 (1991).
26. V.P. Holbert. Ph.D. Thesis, Northwestern University. 1991.
27. C.-C. Cho, J.C. Polanyi, and C.D. Stanners. J. Phys. Chem. **92**, 6859 (1988).
28. G.E. Busch and K.R. Wilson. J. Chem. Phys. **56**, 3655 (1971).
29. A. Ogai, C.X.W. Qian, L. Iwata, and H. Reisler. Chem. Phys. Lett. **146**, 367 (1988).
30. Y.Y. Bai, A. Ogai, C.X.W. Qian, L. Iwata, G.A. Segal, and H. Reisler. J. Chem. Phys. **90**, 3903 (1989).
31. C.X.W. Qian, A. Ogai, L. Iwata, and H. Reisler. J. Chem. Phys. **92**, 4296 (1990).
32. C.F. Goodeve and S. Katz. Proc. R. Soc. London, A**172**, 432 (1939).
33. E. Kolodney, P.S. Powers, L. Hodgson, H. Reisler, and C. Wittig. J. Chem. Phys. **94**, 2330 (1991).
34. W. Wei. J. Vac. Sci. Techol. **A6**, 2576 (1988).
35. Leybold Vacuum Products, Inc. Product and vacuum technology reference book.
36. A. Nitzan and L.E. Brus. J. Chem. Phys. **75**, 2205 (1981).
37. (*a*) G.M. Goncher and C.B. Harris. J. Chem. Phys. **77**, 3767 (1982); (*b*) G.M. Goncher, C.A. Parsons, and C.B. Harris. J. Phys. Chem. **88**, 4200 (1984).
38. E. Hasselbrink, S. Jakubith, S. Nettesheim, M. Wolf, A. Cassuto, and G. Ertl. J. Chem. Phys. **92**, 3154 (1990).
39. V.E. Henrich and R.L. Kurtz. J. Vac. Sci. Technol. **18,** 416 (1981).
40. V.E. Henrich. *In* Advances in ceramics, Vol. 10. *Edited by* W.D. Kingery. Am. Chem. Soc. Columbus, OH. 1984.
41. M.C. Bartelt and J.W. Evans. Phys. Rev. B: Solid State, **46**, 12675 (1992).
42. J.A. Venables, G.D.T. Spiller, and M. Hanbrücken. Rep. Prog. Phys. **47**, 399 (1984).
43. P.M. Killough, B.I. Swanson, and S.F. Agnew. J. Phys. Chem. **93**, 7953 (1989).
44. L.H. Jones and B.I. Swanson. J. Phys. Chem. **95**, 86 (1991).
45. J.P.D. Abbatt, D.W. Toohey, F.F. Fenter, P.S. Stevens, W.H. Brune, and J.G. Anderson. J. Phys. Chem. *93*, 1022 (1989).
46. A.J. Grimley and P.L. Houston. J. Chem. Phys. **72**, 1471 (1980).
47. M.I. McCarthy and A.C. Hess. J. Chem. Phys. **96**, 6010 (1992).
48. H. Ferkel, L. Hodgson, J. Singleton, P.M. Blass, H. Reisler, and C. Wittig. To be published.

Can. J. Chem. Downloaded from www.nrcresearchpress.com by 195.246.54.202 on 09/08/12
For personal use only.

Optical–optical double resonance study of the $\tilde{B}(^1A_1)$ and $\tilde{a}(^3A_2)$ states of thiophosgene[1]

BENOIT SIMARD, VALERIE J. MACKENZIE,[2] AND PETER A. HACKETT
Inorganic Chemical Dynamics Group, Steacie Institute for Molecular Sciences, National Research Council of Canada, 100 Sussex Drive, Ottawa, ON K1A 0R6, Canada

AND

RONALD P. STEER
Department of Chemistry, University of Saskatchewan, Saskatoon, SK S7N 0W0, Canada

Received August 31, 1993

This paper is dedicated to Professor John C. Polanyi on the occasion of his 65th birthday

BENOIT SIMARD, VALERIE J. MACKENZIE, PETER A. HACKETT, and RONALD P. STEER. Can. J. Chem. **72**, 745 (1994).

The $\tilde{a}(^3A_2)$ and $\tilde{B}(^1A_1)$ states of jet-cooled thiophosgene (Cl_2CS) have been studied by optical–optical double resonance (OODR) spectroscopy. Two OODR schemes have been used to probe the $\tilde{B}(^1A_1)$ state. One scheme uses selected vibronic levels of the $\tilde{A}(^1A_2)$ state as the intermediate state, while the other uses the vibrationless and $2_1 3_1$ levels of the $\tilde{a}(^3A_2)$ state. All of the vibronic levels in the 33 980 – 35 600 cm^{-1} region can be rationalized with the following origin band and fundamentals: 0^0 = 34 277 cm^{-1}, ν_1 = 505 cm^{-1}, ν_2 = 470 cm^{-1}, ν_3 = 213 cm^{-1}, ν_6 = 249 cm^{-1}, 4^2 = 341 cm^{-1}, 4^4 = 627 cm^{-1}. The discrepancies among the various studies of the $\tilde{B}(^1A_1)$ state will be discussed and reconciled. It is conjectured that the $\tilde{B}(^1A_1)$ state potential along the C—S coordinate exhibits an asymmetric double-minimum potential resulting from the interaction of the $^1A_1$ states arising from the $(\pi^1_{CS}\ n^2_S\ \pi^{*1}_{CS})$ and $(\pi^2_{CS}\ n^0_S\ \pi^{*2}_{CS})$ configurations. The minimum corresponding to the $(\pi^1_{CS}\ n^2_S\ \pi^{*1}_{CS})$ configuration lies higher in energy and the principal decay mechanism for molecules pumped to its first few vibronic levels is fluorescence. On the other hand, molecules pumped to the minimum corresponding to the nominal $(\pi^2_{CS}\ n^0_S\ \pi^{*2}_{CS})$ configuration decay nonradiatively. The barrier height to inversion and the out-of-plane bending angle along the out-of-plane bending coordinate, ν_4, have been determined to be 945 cm^{-1} and 25°, respectively, by fitting quartic-quadratic and quadratic-Gaussian double-minimum potentials to the observed energy levels. The $\tilde{a}(^3A_2)$ state has been studied by a novel OODR scheme which uses the fluorescent vibrationless level of the $\tilde{B}(^1A_1)$ state to monitor $\tilde{a}(^3A_2)$–$\tilde{X}(^1A_1)$ transitions. A vibronic analysis has been carried out and the following origin band and fundamentals derived for the $\tilde{a}(^3A_2)$ state: 0^0 = 17 499 cm^{-1}, ν_1 = 923 cm^{-1}, ν_2 = 474 cm^{-1}, ν_3 = 247 cm^{-1}, 4^2 = 297 cm^{-1}, 4^4 = 560 cm^{-1}, 4^6 = 741 cm^{-1}. With the exception of a few corrections and additions, the results confirm the findings of previous studies, notably regarding the bent geometry and barrier height to inversion. An overall comparison of the data suggests that the wavenumber of ν_6 in the $\tilde{A}(^1A_2)$ state is 279 cm^{-1} instead of 189 cm^{-1}.

BENOIT SIMARD, VALERIE J. MACKENZIE, PETER A. HACKETT et RONALD P. STEER. Can. J. Chem. **72**, 745 (1994).

Faisant appel à la spectroscopie de double résonance optique – optique (DROO), on a étudié les états $\tilde{a}(^3A_2)$ et $\tilde{B}(^1A_1)$ du thiophosgène (Cl_2CS) refroidi par un jet. On a utilisé deux schémas de DROO pour examiner l'état $\tilde{B}(^1A_1)$. Un schéma utilise des niveaux vibroniques choisis de l'état $\tilde{A}(^1A_2)$ comme état intermédiaire, alors que l'autre fait appel aux niveaux sans vibration et $2_1 3_1$ de l'état $\tilde{a}(^3A_2)$. On peut rationaliser tous les états vibroniques de la région 33 980 à 35 600 cm^{-1} en utilisant la bande d'origine et les fondamentales suivantes: 0^0 = 34 277 cm^{-1}, ν_1 = 505 cm^{-1}, ν_2 = 470 cm^{-1}, ν_3 = 213 cm^{-1}, ν_6 = 249 cm^{-1}, 4^2 = 341 cm^{-1}, 4^4 = 627 cm^{-1}. On discute et on réconcilie les différences observées entre les divers études de l'état $\tilde{B}(^1A_1)$. On fait l'hypothèse que le potentiel de l'état $\tilde{B}(^1A_1)$ le long de la coordonnée C—S présente un potentiel à double minimum asymétrique résultant de l'interaction des états $^1A_1$ découlant des configurations $(\pi^1_{CS}\ n^2_S\ \pi^{*1}_{CS})$ et $(\pi^2_{CS}\ n^0_S\ \pi^{*2}_{CS})$. Le minimum correspondant à la configuration $(\pi^1_{CS}\ n^2_S\ \pi^{*1}_{CS})$ se trouve à une énergie plus élevée et le principal mécanisme de relaxation pour les molécules portées à leurs premiers niveaux vibroniques est la fluorescence. Par ailleurs, pour les molécules portées au minimum correspondant à la configuration nominale $(\pi^2_{CS}\ n^0_S\ \pi^{*2}_{CS})$, la relaxation ne se produit que d'une façon non radiative. En ajustant les potentiels de double minimum quartique/quadratique et quadratique/gaussien avec les niveaux d'énergie observés, on a déterminé que la hauteur de la barrière à l'inversion et l'angle de la déformation hors plan le long de la coordonnée ν_4 sont respectivement de 945 cm^{-1} et 25°. On a étudié l'état $\tilde{a}(^3A_2)$ par un nouveau schéma DROO qui fait appel au niveau fluorescent sans vibrations de l'état $\tilde{B}(^1A_1)$ pour déterminer les transitions $\tilde{a}(^3A_2)$–$\tilde{X}(^1A_1)$. On a effectué une analyse vibronique et on en a tiré la bande à l'origine et les fondamentales suivantes pour l'état $\tilde{a}(^3A_2)$: 0^0 = 17 499 cm^{-1}, ν_1 = 923 cm^{-1}, ν_2 = 474 cm^{-1}, ν_3 = 247 cm^{-1}, 4^2 = 297 cm^{-1}, 4^4 = 560 cm^{-1} et 4^6 = 741 cm^{-1}. À l'exception de quelques corrections et additions, les résultats confirment les résultats obtenus antérieurement, principalement en ce qui a trait à la géométrie inversée et à la hauteur de la barrière d'inversion. Une comparaison globale des données suggère que le nombre d'onde pour ν_6 de l'état $\tilde{A}(^1A_2)$ est 279 cm^{-1} au lieu de 189 cm^{-1}.

[Traduit par la rédaction]

I. Introduction

Thiophosgene (Cl_2CS) has been the subject of extensive spectroscopic and photophysical studies in both the gaseous and condensed phases (1–3). This molecule has also been the subject of a number of *ab initio* investigations (4–8). This remarkable interest arises from the facts that (*1*) unlike its carbonyl counterpart, Cl_2CS exhibits beautiful discrete electronic spectra, and (*2*) it fluoresces from both the first and second excited singlet states, in violation of Kasha's rule (9). This "anomalous" photophysical behavior, combined with its good thermodynamic stability (Cl_2CS is the only small thiocarbonyl that is commercially available) has made thiophosgene a prototypical species for both spectroscopic and dynamics studies. Despite this, there are still fundamental points about Cl_2CS that remain unclear. This paper addresses one unresolved ques-

[1]NRCC 37200.
[2]NRCC summer student 1992.

Can. J. Chem. Downloaded from www.nrcresearchpress.com by 195.246.54.202 on 09/08/12
For personal use only.

Can. J. Chem. Downloaded from www.nrcresearchpress.com by 195.246.54.202 on 09/08/12
For personal use only.

tion, namely, the energy level structure in the $\tilde{B}(^1A_1)$ state, a point that has been the subject of exciting debate for about 20 years. This paper will also present a reinvestigation of the $\tilde{a}(^3A_2)$ state by a scan up – scan down optical–optical double resonance technique (OODR), a simple variation of the usual OODR technique which has applications for any molecules requiring searches for new states or linkages between states.

II. Background

Thiophosgene belongs to the C_{2v} point group. The ground state structure has been accurately determined by microwave spectroscopy, which has revealed that the C═S and C—Cl bond lengths are 1.600 and 1.727 Å, respectively, and the S═C—Cl angle is 124.4° (10). The electron configuration giving rise to the ground state has been determined by photoelectron spectroscopy to be [core] $(11a_1)^2(7b_2)^2(3b_1)^2(12a_1)^2(2a_1)^2(8b_2)^2(13a_1)^2(4b_1)^2(9b_2)^2$, where the $11a_1$, $7b_2$, and $12a_1$ molecular orbitals (MO) contain the σ bonding electrons, the $3b_1$, $2a_2$, $8b_2$, and $13b_1$ MOs contain the chlorine lone pairs electrons, the $4b_1$ MO contains the π bonding electrons, and the $9b_2$ MO contains the sulfur lone pair electrons (11). The ground state is therefore of $^1A_1$ symmetry.

In all three excited states discussed below, the molecule is non-planar and non-rigid. Consequently it belongs to the non-rigid point group G_4 which is isomorphous with the C_{2v} representation. Thus, the symmetry arguments that should apply when discussing vibronic transitions are those of the C_{2v} point group.

The first excited singlet and triplet states arise from the promotion of a $9b_2$ electron to the $5b_1$ MO, and hence are of $^{1,3}A_2$ symmetries. Since the $5b_1$ MO is largely π* in character, this corresponds to a $\pi^* \leftarrow n$ electron promotion. The $\tilde{a}(^3A_2)$–$\tilde{X}(^1A_1)$ transition is spin-forbidden but gains appreciable intensity ($f \sim 10^{-6}$) owing to the $\tilde{a}(^3A_2)$–$\tilde{B}(^1A_1)$ interaction contained in the spin-orbit operator. Due to rapid nonradiative decay to the ground state, the $\tilde{a}(^3A_1)$ state does not exhibit measurable phosphorescence in the gas phase. For this reason this state has thus far been studied only by absorption spectroscopy. Our current understanding of its spectroscopy is mainly due to the room temperature work of Moule and Subramanian (12, 13), and Clouthier and Moule (14). Both studies are consistent with each other: the origin is placed at 17 491.9 cm^{-1}, the C—S bond length elongates from its ground state value by about 0.1 Å, the equilibrium out-of-plane bending angle is 32° and the inversion barrier height is 726 cm^{-1}. Only the antisymmetric Cl—C—Cl stretching mode (ν_5) was found to be inactive in the $\tilde{a}(^3A_2)$–$\tilde{X}(^1A_1)$ spectrum. The present work offers two advantages over the previous ones. First, due to supersonic cooling, all hot bands are eliminated so that assignment ambiguity is minimized. Second, the experimental scheme used here is much more sensitive and selective than prior ones so that vibronic features not observed before can be detected, thus providing greater insight into the $\tilde{a}(^3A_1)$ state.

The $\tilde{A}(^1A_2)$–$\tilde{X}(^1A_1)$ system is electronically forbidden but gains intensity through either magnetic dipole-induced interactions or vibronic mixings. The $\tilde{A}(^1A_2)$ state is very well-characterized spectroscopically (14, 15). Since this state is used only as an intermediate in the present study a detailed review of our current understanding of it will be omitted. The reader can refer to recent reviews. It suffices to know here that the extensive vibronic analyses of Brand *et al.* (15) together with the few minor reassignments of Clouthier and Moule (14) have been used to select the energies and symmetries of the intermediate levels in our OODR scheme. We consider the latter two works to be essentially accurate.

The second excited singlet state is of A_1 symmetry, and arises from the promotion of a $4b_1$ electron to the $5b_1$ MO. The $\tilde{B}(^1A_1) \leftarrow \tilde{X}(^1A_1)$ transition is therefore $\pi^* \leftarrow \pi$ in character, and results in lowering the C—S bond order from 2 to 1 and lengthening the equilibrium C—S bond length by about 0.5 Å. As a result, the $\tilde{B}$—$\tilde{X}$ band system is broad and the 0_0^0 band very weak with an estimated Franck–Condon factor of the order of 10^{-5}–10^{-6}. To compound the problem, the minimum in the $\tilde{B}(^1A_1)$ state potential is very shallow so that progressions can only be followed up to a few quanta.

Several attempts have been made to elucidate the electronic structure of the $\tilde{B}(^1A_1)$ state. The first vibronic analyses were reported by Duchesne (16) and Burnelle (17) in the late fifties. They assigned the absorption bands as being due to two distinct $\sigma^* \leftarrow n$ transitions; one located in the C—S group, the other in the C—Cl_2 group. The origin of the first system was located at 33 380 ± 468 cm^{-1} while the second was located at 36 045 cm^{-1}. Some 15 years later, Farnworth and King (18), on the basis of a medium resolution absorption spectrum showed that this interpretation was erroneous and correctly reinterpreted the spectrum in term of a $\pi^* \leftarrow \pi$, $^1A_1 \leftarrow \tilde{X}(^1A_1)$ transition. Their analysis indicated that the molecule is non-planar in the upper state with an out-of-plane angle of 20° and an inversion barrier of 126 cm^{-1}. The origin band was located at 36 007 cm^{-1}. Four years later, Oka et al. (19) from fluorescence quantum yield measurements and quenching effects showed that the origin band must lie to the red of 36 007 cm^{-1} and proposed the band at 35 112 cm^{-1} as the origin of the $\tilde{B}$–$\tilde{X}$ system. The self-quenching cross section, σ^2, for the vibronic levels lying near 35 000 cm^{-1} was determined to be of the order of 95 $Å^2$. In 1980, Judge and Moule (20) photographed the $\tilde{B}$–$\tilde{X}$ system at high enough resolution to resolve the splittings between the chlorine (35,35) and (35,37) isotopes of Cl_2CS. From these splittings, progressions in ν_1' (C—S stretch) and ν_4' and ν_4'' (out-of-plane bend) were assigned and the origin was moved again further to the red at 34 277 cm^{-1}. Their analysis was shown to be consistent with double minimum potentials along both the C—S stretching and out-of-plane bending coordinates. The inversion barrier heights along ν_1 and ν_4 were estimated to be 4855 and 729 cm^{-1}, respectively. Unfortunately, their analysis proved difficult as only 30% of the observed bands were assigned. More recently, Dixon and Western (21) attempted to locate the $\tilde{B}$–$\tilde{X}$ origin band unequivocally by using $\tilde{A}(^1A_2)$ as an intermediate state in an optical–optical double resonance scheme. A point that will be of great importance later is that their experiment was performed using a static cell filled with 0.5 Torr of Cl_2CS. By carefully selecting the vibronic levels of the $\tilde{A}(^1A_2)$ state the symmetries of the $\tilde{B}$ state levels were unequivocally determined. The lowest energy band of a_1 symmetry was observed at 33 991 cm^{-1} and this was proposed by Dixon and Western as the (new) origin band for the $\tilde{B}$–$\tilde{X}$ system. Progressions in ν_1, ν_2, ν_3, and ν_6 could be built on that origin but none of the derived vibrational frequencies were found to be in agreement with those proposed by Judge and Moule. A point that is particularly troubling is that Dixon and Western proposed that the out-of-plane bending mode is inactive in the OODR spectrum while Judge and Moule argued the contrary from the $\tilde{B}$–$\tilde{X}$ absorption spectrum. The disagreement is severe and has been causing great confusion among spectroscopists. This prompted Ludwiczak et al.

Can. J. Chem. Downloaded from www.nrcresearchpress.com by 195.246.54.202 on 09/08/12
For personal use only.

(22) to investigate the $\tilde{B}$–$\tilde{X}$ band system using a jet-cooled expansion so that the problem of hot bands could be eliminated, or, at least reduced to a minimum. Similar to Judge and Moule, they used the isotope effect as an aid to assign the spectrum. Their work showed unequivocally that the lowest energy cold band lies at 34 277 cm^{-1}, and since the isotope splitting within this band is small and negative, and that progressions could be built on it, they assigned the band as the origin band of the $\tilde{B}$–$\tilde{X}$ system in agreement with Judge and Moule. Ludwiczak et al. assign most of the observed bands in term of ν_1, ν_2, and ν_4, either alone or in combination. Several of the assignments are the same as those reported by Judge and Moule. The onset of predissociation was placed at 35 277 ± 50 cm^{-1} i.e. 1450 ± 50 cm^{-1} above the presumed zero point level in the $\tilde{B}$ state. Thus, the work of Ludwiczak et al. confirms that a major disagreement between the one-photon and sequential two-photon studies remains. In order to reconcile these studies Ludwiczak et al. suggested that the OODR study of Dixon and Western may have accessed an excited state other than $\tilde{B}(^1A_1)$. On the basis of the recent large scale MCD-CI calculations of Hachey et al. (8) on H_2CS, they further suggested that the $^1A_1$ state arising from the $\ldots\pi^2n^0\pi^{*2}$ configuration could be a potential candidate. This state is expected to have a long radiative lifetime, and under the experimental conditions used by Dixon and Western any molecules promoted to it may be collisionally transferred to the luminescent $\tilde{B}(^1A_1)$ state. This is a very interesting suggestion which warrants further investigation. The present OODR study has been carried out in a molecular beam under collision-free conditions so that both collision-induced phenomena and problem due to hot band absorption are eliminated.

III. Experimental procedure

The apparatus for producing a jet-cooled molecular beam is of standard design. A schematic diagram is shown in Fig. 1. The expansion chamber was a stainless steel high vacuum cube type cell mounted on an Edwards, model 250/2000, diffusion stack backed with a Varian, model SD 700, mechanical pump. The static pressure in the chamber was of the order of 1–2 × 10^{-7} Torr. A piezoelectric pulsed molecular beam valve constructed from the design of Proch and Trickl (23), was used to expand helium doped with about 6% thiophosgene (Aldrich, 97%). The sample was prepared as follows: the thiophosgene (10 mL) was placed in a 150 m stainless steel reservoir fitted with a dip-stick inlet and an outlet port located at the top of the reservoir, helium made to flow through the reservoir from the dip-stick inlet to the outlet in the direction of the valve, thus ensuring that the helium flow entrains a constant amount of thiophosgene to the nozzle. The backing pressure was 1 atm, and the nozzle orifice was 0.5 mm in diameter which, as shown in Fig. 2, was sufficient to eliminate most of the hot bands in the $\tilde{A}(^1A_2)$–$\tilde{X}(^1A_1)$ spectrum. The very few hot bands which remain are very weak. No band was detected to the red of the 4_0^1 band. This great cooling at rather mild expansion conditions is attributed to the high pulse intensity of the piezoelectric valve.

The pump laser was a Lumonics YM 1000 YAG operated at 10 Hz and tuned to its third harmonic (355 nm). The 350 mJ output was split into two equiergic beams in order to pump two dye lasers; a Lumonics HD 500, and a Lumonics HD 300. The former was used to pump thiophosgene from the ground state to either the $\tilde{A}(^1A_2)$ or the $\tilde{a}(^3A_2)$ state using either C 540 A or R 590 dye. The HD 300 dye laser was used to pump excited

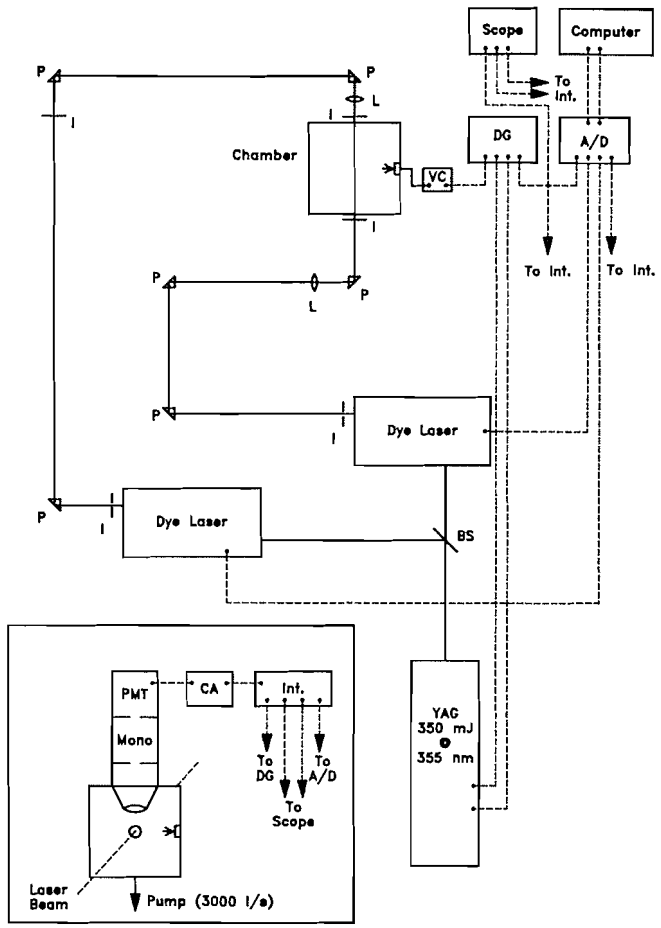

FIG. 1. Schematic diagram of the experimental arrangement. P, prism; I, iris; L, lens; BS, beam splitter; VC, valve controller; DG, delay generator; CA, current amplifier; Int, integrator.

thiophosgene from either $\tilde{A}(^1A_2)$ or $\tilde{a}(^3A_2)$ to the $\tilde{B}(^1A_1)$ state by using the R590, KR620, and DCM dyes. The two laser beams were made to counter-propagate, and overlap spatially and temporally in the center of the chamber. The pump and probe laser beams were focused in the chamber using a 25 cm and a 50 cm focal length lenses, respectively. The various delays were synchronized using a Stanford Research System, model DG 535 digital delay/pulse generator.

Fluorescence from thiophosgene was collected at right angles from the expansion and excitation axes by a biconvex, f/0.5, 5 cm focal length lens, was imaged at the slits of a 20 cm, Bausch and Lomb monochromator equipped with a 1200 lines/mm grating, and was viewed by a red sensitive RCA C31034 photomultiplier. The signal was sent to a Keithley, model 427 current amplifier, then to a home-built sample and hold integrator, and finally to the computer which also drives the dye lasers.

Laser wavelength calibration was effected using a Candela LS-1 laser spectrometer whose accuracy is specified to be 0.01 nm (approximatively 0.5 cm^{-1} at 500 nm). The calibration was often double-checked using neon atomic lines.

IV. Results and analysis

(A) Study of the $\tilde{B}(^1A_1)$ *state*

Two double resonance schemes have been used to probe the $\tilde{B}(^1A_1)$ state and these are shown in Fig. 3 as Schemes 1 and

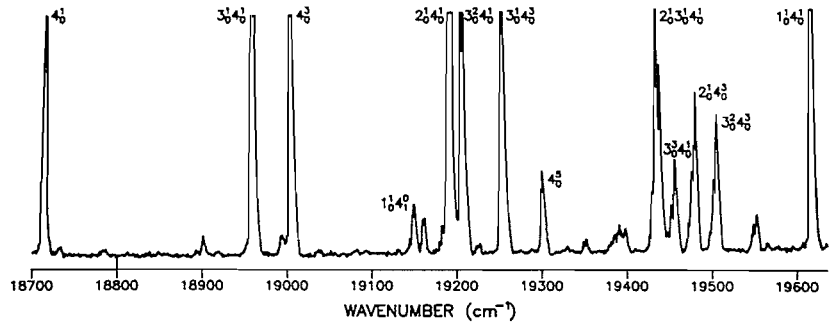

FIG. 2. Jet-cooled fluorescence excitation spectrum of the $\tilde{A}(^1A_2)$–$\tilde{X}(^1A_1)$ system of thiophosgene. The vertical axis is the intensity in arbitrary units.

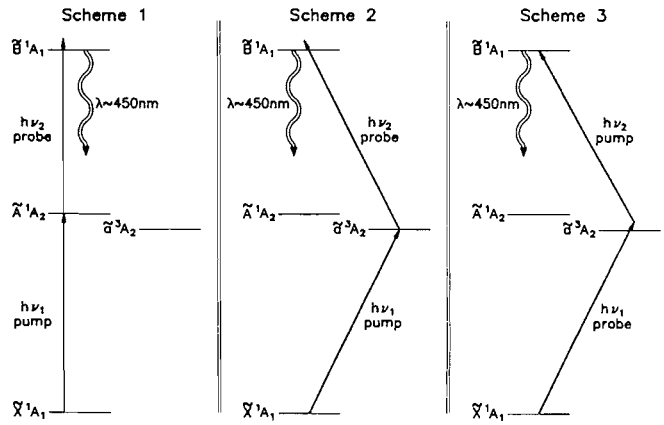

FIG. 3. Energy level diagrams showing the optical–optical double resonance schemes used in this work.

2. In Scheme 1, the molecules are PUMPed from the ground state to a specific vibronic level of the $\tilde{A}(^1A_2)$ state, and the PROBE laser is scanned so as to excite fluorescence from the $\tilde{B}(^1A_1)$ state. The vibronic levels of the $\tilde{A}(^1A_2)$ state that have been used are 4^1, 4^3, 4^5, 1^14^1, 3^14^1, 1^1, and 3^2. The first five of these are of $A_2 \otimes b_1 = b_2$ total vibronic symmetry while the last two are of $A_2 \otimes a_1 = a_2$ total symmetry. In Scheme 2, the molecules are PUMPed from the ground state to either the vibrationless or the 2^13^1 level of the $\tilde{a}(^3A_2)$ state, and the PROBE laser is scanned so as to excite fluorescence from the $\tilde{B}(^1A_1)$ state. In both schemes, the fluorescence is viewed at 450 nm which corresponds to the approximate maximum of the $\tilde{B} \rightarrow \tilde{X}$ emission.

Figures 4*a* and 4*b* show composite OODR spectra obtained by joining 100 cm^{-1} segments and using the 2^13^1 (Fig. 4*a*) and the vibrationless (Fig. 4*b*) levels of $\tilde{a}(^3A_2)$ as intermediate states. Figures 5, 6*a*, and 6*b* show composite OODR spectra obtained using the 1^1, and the 4^1 (Fig. 6*a*) and 1^14^1 (Fig. 6*b*) levels of the $\tilde{A}(^1A_2)$ state as intermediate states, respectively. In addition to the region covered by the latter spectra (Figs. 6*a* and *b*), the 33 580 – 33 945 cm^{-1} region was also investigated but no band was observed even when using the highest sensitivity available. It is clear from these spectra that the first vibronic band occurs at 34 277 cm^{-1} (Figs. 4 and 6). This band must therefore be connected to the vibrationless level of the $\tilde{B}$ state. Thus, we assign the vibronic level at 34 277 cm^{-1} as the vibrationless level of the $\tilde{B}$ state, in agreement with Judge and Moule, and Ludwiczak et al.

The band next highest in energy lies +213 cm^{-1} (34 490 cm^{-1}) from the origin. It is observed from the 4^1 and 1^1 levels of the $\tilde{A}$ state but is not observed from the vibrationless or the 2^13^1 level of the $\tilde{a}$ state. This wavenumber must be a fundamental and we assign it here as the wavenumber of the Cl—C—Cl bending mode (ν_3). In the ground state, $\nu_3 = 289$ cm^{-1} so that the $\tilde{B}/\tilde{X}$ ratio is 0.737 for this mode. In F_2CS (24) and ClFCS (25), the $\tilde{B}/\tilde{X}$ ratios are 0.760 and 0.728, respectively. The close correspondence makes the present assignment unequivocal. This band was also observed by Dixon and Western who assigned the upper state level as 2^13^1. Although this assignment is erroneous because of their mislocation of the origin, they correctly determined ν_3 to be 213 cm^{-1}.

Within the constraint of the C_{2v} point group, the 3^1 level of the $\tilde{B}$ state cannot be reached from the 1^1 level of the $\tilde{A}$ state but can from the 4^1 level. However, there is one means by which the band at 34 492 cm^{-1} can be observed from the 1^1 level of the $\tilde{A}$ state. If the separation between the $v = 0$ and $v = 1$ level of the out-of-plane bending mode (ν_4) in the $\tilde{B}$ state is very small (<0.5 cm^{-1}), then the separation between the 3^1 and 3^14^1 levels would be smaller than the experimental resolution. Thus, the level at 34 492 can also be assigned as 3^14^1. This assignment would be in agreement with the work of Judge and Moule, and Ludwiczak et al. who report a 0–1 separation of 0.11 cm^{-1} in mode 4 of the $\tilde{B}$ state.

The next highest wavenumber band lies at 34 525 cm^{-1}, +248 cm^{-1} from the origin. It is observed from the 4^1 and 1^1 levels of the $\tilde{A}$ state, and also from the 2^13^1 level of the $\tilde{a}$ state. Again, this separation must be a fundamental. We assign it here as the wavenumber of the Cl—C—Cl rocking mode, ν_6. In the ground state, $\nu_6 = 305$ cm^{-1}, so that the $\tilde{B}/\tilde{X}$ ratio is 0.813. This mode has not been reported to be active in F_2CS (24) and ClFCS (25), and comparisons with Cl_2CS are therefore not possible. A progression of up to 3 quanta can be found in the $\tilde{B}$–$\tilde{A}(4^1$ or $1^14^1)$–$\tilde{X}$ spectrum. Combination bands involving ν_3 and ν_6 can readily be found in the $\tilde{B}$–$\tilde{a}$–$\tilde{X}$ and $\tilde{B}$–$\tilde{A}(4^1$ or $1^14^1)$–$\tilde{X}$ spectra. The 34 525 cm^{-1} band was also observed by Dixon and Western who assigned the upper state level as 2^16^1. Again, this assignment is erroneous, and the 248 cm^{-1} interval in their spectrum has been incorrectly associated with ν_2.

The next band in the spectrum lies +341 cm^{-1} from the origin at 34 615 cm^{-1}. It is observed via the vibrationless or the 2^13^1 level of the $\tilde{a}$ state and also from the 4^1 (or 1^14^1) level of the $\tilde{A}$ state. This band was also observed by Ludwiczak et al. who assigned it as 4_0^2. This band was not observed directly by Judge and Moule but they did deduce a 341 cm^{-1} interval from combination differences which they associated with $2\nu_4$.

Can. J. Chem. Downloaded from www.nrcresearchpress.com by 195.246.54.202 on 09/08/12
For personal use only.

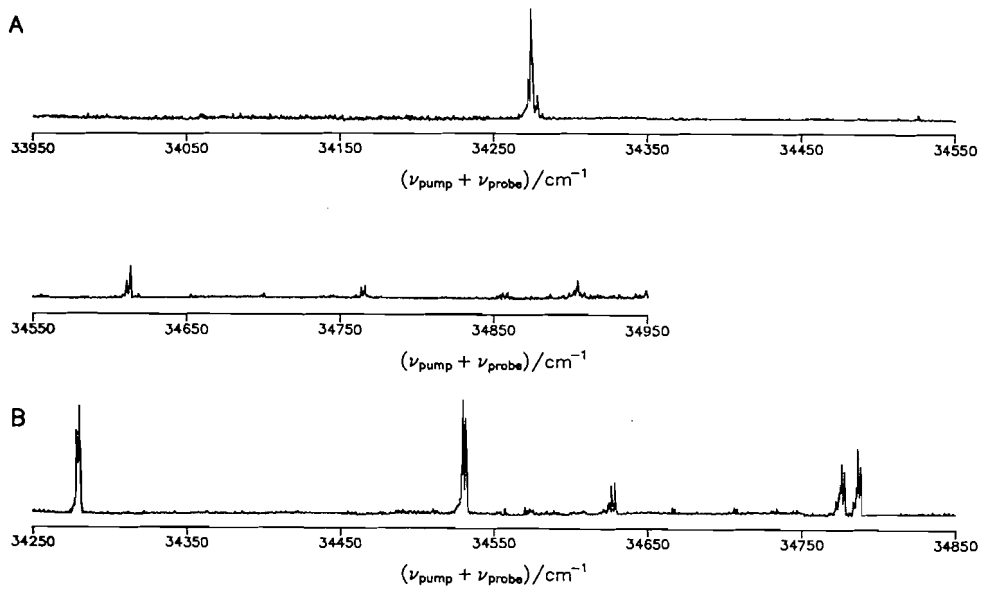

FIG. 4. (*A*) Jet-cooled $\tilde{B}(^1A_1,v')$–$\tilde{a}(^3A_2,2^13^1)$ –$\tilde{X}(^1A_1,0_0)$ optical–optical double resonance spectrum of thiophosgene in the 33 950 – 34 950 cm^{-1} region. The vertical axis is the intensity in arbitrary units. (*B*) same as (*A*) but using the 0^0 level of the $\tilde{a}(^3A_2)$ state as the intermediate state.

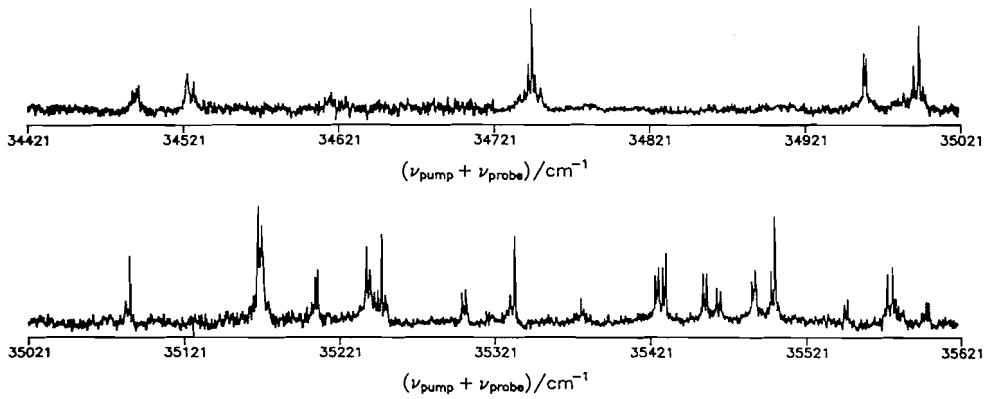

FIG. 5. Jet-cooled $\tilde{B}(^1A_1,v')$–$\tilde{A}(^1A_2,1^1)$ –$\tilde{X}(^1A_1,4_1)$ optical–optical double resonance spectrum of thiophosgene in the 34 421 – 35 621 cm^{-1} region. The vertical axis is the intensity in arbitrary units.

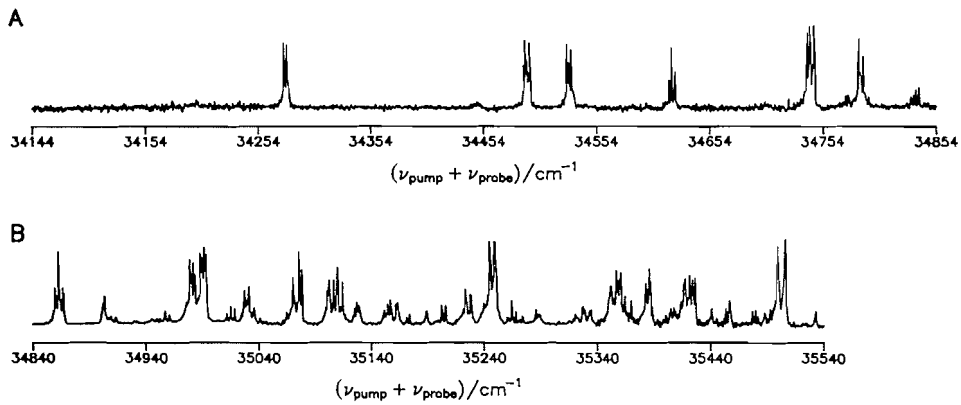

FIG. 6. (*A*) Jet-cooled $\tilde{B}(^1A_1,v')$–$\tilde{A}(^1A_2,4^1)$ –$\tilde{X}(^1A_1,0_0)$ optical–optical double resonance spectrum of thiophosgene in the 34 144 – 34 854 cm^{-1} region. The vertical axis is the intensity in arbitrary units. (*B*) same as (*A*) but using the 1^14^1 level of the $\tilde{A}(^1A_2)$ state as the intermediate state.

Can. J. Chem. Downloaded from www.nrcresearchpress.com by 195.246.54.202 on 09/08/12
For personal use only.

Can. J. Chem. Downloaded from www.nrcresearchpress.com by 195.246.54.202 on 09/08/12
For personal use only.

We agree with this assignment. This band was also observed by Dixon and Western who erroneously assigned the upper state level as $1^1 6^1$. The 341 cm^{-1} interval was established but was incorrectly associated with ν_1, the C—S stretching mode. Combination bands involving either ν_3 and ν_6 or both are readily found in the spectra.

The band at 34 747 cm^{-1} lies +470 cm^{-1} from the origin. It is observed only from the 1^1 level of the $\tilde{A}$ state. This band acts as a sub-origin for *all* the bands lying to the blue of it. We associate the 470 cm^{-1} interval with ν_2, the symmetric Cl—C—Cl stretching mode. In the ground state, its wavenumber is 505 cm^{-1}, so that the $\tilde{B}/\tilde{X}$ ratio is 0.930. This ratio compares very well with the corresponding ratios in F_2CS ($\tilde{B}/\tilde{X}$ = 0.926) (23) and ClFCS ($\tilde{B}/\tilde{X}$ = 0.964) (25). The band was not reported in the one-photon $\tilde{B}$–$\tilde{X}$ studies but was observed in the previous OODR study. However, Dixon and Western incorrectly assigned this $\tilde{B}$ state level as $2^1 3^1 6^1$ and they did not associate the 470 cm^{-1} interval with a fundamental.

At this point 70% of the observed bands have been assigned. The next lowest lying wavenumber band that has not yet been assigned lies +505 cm^{-1} (34 782 cm^{-1}) from the origin. It is observed only from the 4^1 level of the $\tilde{A}$ state. The band was observed by Judge and Moule, and Ludwiczak et al. in their one-photon $\tilde{B}$–$\tilde{X}$ studies and was assigned as 1^1_0. We agree with this assignment. Mode 1 is the C—S stretch. Its wavenumber in the $\tilde{X}$ state is 1139 cm^{-1}, so that the $\tilde{B}/\tilde{X}$ ratio is 0.443. This ratio compares very well with the corresponding one in ClFCS ($\tilde{B}/\tilde{X}$ = 0.450). Such a dramatic drop in the C—S wavenumber is expected because the bond order, which is nominally 2 in the ground state drops to 1 in the $\tilde{B}$ state. In the $\tilde{A}$ state, the bond order is nominally 1.5 and the C—S wavenumber 907 cm^{-1}. This band was also observed in the OODR study of Dixon and Western. However, they incorrectly assigned the $\tilde{B}$ state level as $3^1 6^2$ or $1^1 2^1 3^1$, and did not associate the 505 cm^{-1} interval with a fundamental.

Combination bands involving 1^1 with ν_2, ν_3, 4_2 and ν_6 are readily found in the spectra. At this point, only two bands remain to be assigned, and these lie +627 (34 904 cm^{-1}) and +828 cm^{-1} (35 103 cm^{-1}) from the origin. Both of them are observed from the 4^1 or $1^1 4^1$ level of the $\tilde{A}$ state. The former is also observed via the $2^1 3^1$ level of the $\tilde{a}$ state. The only plausible assignments for these intervals are 4^4 and 4^6. One may argue that the 627 cm^{-1} interval could be 5^1 but these would leave the 828 cm^{-1} band unassigned. Mode 5 is the antisymmetric Cl—C—Cl stretch. Its wavenumber in the ground state is 818 cm^{-1}. Assuming that the $\tilde{B}/\tilde{X}$ ratio is the same as for ν_6, then the wavenumber for ν_5 in the B state should be around 665 cm^{-1}.

All of the observed bands are now assigned. The assignments are given in Tables 1, 2, and 3. Table 4 summarizes the wavenumbers of the fundamentals and compares them with the corresponding ones in the $\tilde{X}$ and $\tilde{A}$ states.

(B) Study of the $\tilde{a}(^3A_2)$ *state*

The double resonance scheme that has been used to probe the $\tilde{a}(^3A_2)$ state is shown as Scheme 3 in Fig. 3. In this scheme the $\tilde{a}$–$\tilde{X}$ system is probed, and when absorption occurs the molecules are pumped to the vibrationless level of the $\tilde{B}(^1A_1)$ state. The absorption is detected by the occurrence of a fluorescence signal from the $\tilde{B}(^1A_1)$ $v = 0$ level. This requires that the total energy ($h\nu_{probe} + h\nu_{pump}$) be kept constant which is possible by scanning synchronously the probe laser up in energy and the pump laser down in energy. Since a signal is detected only when absorption from $\tilde{X}$ to $\tilde{a}$ occurs and since the $\tilde{B}$ state has the same symmetry as the $\tilde{X}$ state, the resulting fluorescence spectrum mimics the $\tilde{a}$–$\tilde{X}$ spectrum and would be similar to a phosphorescence excitation spectrum if the $\tilde{a}$ state were phosphorescent. The only difference would be in the relative intensity of individual vibronic bands because in the OODR experiment the $\tilde{B} \rightarrow \tilde{X}$ signal intensity is dictated by the product of the Franck–Condon factors $\tilde{a} \leftarrow \tilde{X}$ and $\tilde{B} \leftarrow \tilde{a}$, while in the one-photon $\tilde{a} \leftarrow \tilde{X}$ spectrum the intensity depends only on the $\tilde{a} \leftarrow \tilde{X}$ Franck–Condon overlap.

A portion of the spectrum is shown in Fig. 7. The wavenumber scale has a calibration error of +6 − 7 cm^{-1} compared with the work of Clouthier and Moule (14), and Moule and Subramaniam (12, 13). This spectrum is clear of hot bands from both the $\tilde{A}(^1A_2)$–$\tilde{X}(^1A_1)$ and $\tilde{a}(^3A_2)$–$\tilde{X}(^1A_1)$ systems. Rotating the laser field polarization by 90° produced no intensity change in the spectrum. The same wavenumber region has been re-

TABLE 1. Wavenumbers and assignment of the $\tilde{B}(^1A_1)$–$\tilde{a}(^3A_2)$–$\tilde{X}(^1A_1)$ OODR spectrum of thiophosgene, observed by pumping the 0^0 and $2^1 3^1$ levels of the $\tilde{a}(^3A_2)$ state

Wavenumber (cm^{-1})	Δ (cm^{-1})	Assignment[a]
34 277	0	0^0
34 524	247	6^1
34 615	338	4^2
34 702	425	3^2
34 769	492	6^2
34 861	584	$4^2 6^1$
34 904	627	4^4
34 949	672	$3^2 6^1$

[a]The labelling follows C_{2v} notation and refers to the $\tilde{B}(^1A_1)$ state vibronic levels.

TABLE 2. Wavenumbers and assignments of the $\tilde{B}(^1A_1)$–$\tilde{A}(^1A_2)$–$\tilde{X}(^1A_1)$ OODR spectrum of thiophosgene, observed by pumping the 1^1 level of the $\tilde{A}(^1A_2)$ state

Wavenumber (cm^{-1})	Δ (cm^{-1})	Assignment[a]
34 492	215	$3^1 4^1$
34 525	248	6^1
34 747	470	$2^1 4^1$
34 960	683	$2^1 3^1 4^1$
34 996	719	$2^1 6^1$
35 088	811	$2^1 4^3$
35 173	896	$2^1 3^2 4^1$
35 209	932	$2^1 3^1 4^1 6^1$
35 241	964	$2^1 4^1 6^2$
35 252	975	$1^1 2^1 4^1$
35 301	1024	$2^1 3^1 4^3$
35 335	1058	$2^1 4^2 6^1$
35 376	1099	$2^1 3^3 4^1$
35 423	1146	$2^1 3^2 6^1$
35 428	1151	$2^2 3^1 4^1$
35 456	1179	$2^1 3^1 4^1 6^2$
35 465	1188	$1^1 2^1 3^1 4^1$
35 489	1212	$2^1 6^3$
35 502	1225	$1^1 2^1 6^1$
35 550	1273	$2^1 3^1 4^2 6^1$
35 579	1302	$2^1 4^3 6^2$
35 603	1326	$2^1 3^4 4^1$

[a]The labelling follows C_{2v} notation and refers to the $\tilde{B}(^1A_1)$ state vibronic levels.

Can. J. Chem. Downloaded from www.nrcresearchpress.com by 195.246.54.202 on 09/08/12
For personal use only.

TABLE 3. Wavenumbers and assignments of the $\tilde{B}(^1A_1)$–$\tilde{A}(^1A_2)$–$\tilde{X}(^1A_1)$ OODR spectrum of thiophosgene, observed by pumping the 4_1 and 1_14_1 levels of the $\tilde{A}(^1A_2)$ state

Wavenumber (cm^{-1})	Δ (cm^{-1})	Assignment[a]
34 277	0	0^0
34 490	213	3^1
34 526	249	6^1
34 618	341	4^2
34 738	461	3^16^1
34 770	493	6^2
34 782	505	1^1
34 830	553	3^14^2
34 864	587	4^26^1
34 905	628	4^4
34 980	703	3^16^2
34 992	715	1^13^1
35 015	739	6^3
35 032	755	1^16^1
35 077	800	$3^14^26^1$
35 103	828	4^6
35 111	834	4^26^2
35 127	850	1^14^2
35 155	878	4^46^1
35 164	887	3^36^1
35 172	895	2^13^2
35 188	911	3^26^2
35 202	925	1^13^2
35 225	948	3^16^3
35 242	965	$1^13^16^1, 2^16^2$
35 257	980	1^12^1
35 278	1001	1^16^2
35 313	1036	3^14^6
35 320	1043	$3^14^26^2$
35 327	1050	$1^13^14^2$
35 344	1067	4^66^1
35 350	1073	4^26^3
35 376	1099	$1^14^26^1$
35 408	1131	3^36^2
35 414	1137	1^13^3
35 445	1168	3^26^3
35 492	1215	$1^13^16^2$
35 522	1245	3^24^6

[a]The labelling follows C_{2v} notation and refers to the $\tilde{B}(^1A_1)$ state vibronic levels.

peated three times with no significant change in the relative intensities. Most bands clearly show resolved splittings due to the three chlorine isotopomers of thiophosgene. These splittings have been a useful aid in assigning the spectrum.

The $\tilde{a}(^3A_2)$–$\tilde{X}(^1A_1)$ system gains its intensity by intensity borrowing from the strong $\tilde{B}$–$\tilde{X}$ system. This borrowing arises because the $\tilde{a}(^3A_2)$ state mixes with the $\tilde{B}(^1A_1)$ state through the spin-orbit operator. The selection rules should therefore resemble those for the $\tilde{B}(^1A_1)$–$\tilde{X}(^1A_1)$ system, namely that the C_{2v} point group applies and that the transition moment is z-polarized. For transitions originating from the vibrationless level of the ground state the vibrational symmetry of the $\tilde{a}(^3A_2)$ state must be a_1.

The five lowest wavenumber bands of the spectrum were also observed by Moule and Subramaniam, and Clouthier and Moule who assigned them as the 0_0^0, 3_0^1, 4_0^2, 2_0^1, 3_0^2 bands, respectively. We agree with these assignments.

The next two bands lie 534 cm^{-1} (18 033 cm^{-1}) and 560 cm^{-1} (18 059 cm^{-1}) from the origin, and have similar isotope splittings (see Table 5). The former was assigned as 4_0^4 while the latter was not observed in the previous two studies. The reason why this band was not observed before is not clear but it may be due to the fact that the 4_2^3 band (18 066 cm^{-1}) of the $\tilde{A}$–$\tilde{X}$ system overlaps this region. This hot band should be prominent under the experimental conditions used in the previous studies. Here, the substantial vibrational cooling provided by supersonic expansion makes the population of the 4_2 level too small to produce a measurable signal from the 4_2^3 transition. Furthermore, the isotope splittings clearly indicate that this is not the band observed here. There is only one plausible set of assignments for these bands; 4_0^4, and 6_0^2. Specific individual assignments are more difficult to make but on the basis on Franck–Condon envelope, we assign the band at 18 033 cm^{-1} as the 6_0^2 band, and the band at 18 059 cm^{-1} as the 4_0^4 band. This makes $\nu_6 = 267$ cm^{-1}, in reasonable agreement with expectation based upon the value of ν_6' for the $\tilde{B}(^1A_1)$ state (see Table 4).

The next band to be assigned lies 704 cm^{-1} (18 203 cm^{-1}) from the origin. It is the strongest band of the entire spectrum. It was assigned as the 4_0^6 band in the previous two studies but judged from its intensity, this assignment is difficult to sustain. The relative intensities of the 4_0^0, 4_0^2, and 4_0^4 bands are approximately 1, 2, 1, respectively. On that basis, the relative intensity of the 4_0^6 band should be <1. The relative intensity of the 18 203 cm^{-1} band is approximately 2.5. We prefer to assign this band as $2_0^13_0^1$ (although the isotope splitting appears slightly too small) and to leave the 4_0^6 assignment to the band at 18 240 cm^{-1}. The latter shows the expected intensity and isotope splitting. However, it partly overlaps with the 3_0^3 band and this may be the reason why it could not be extracted in the previous studies.

Based upon the Franck–Condon envelope of the 4_0^{2n} ($n = 0$, 1, 2, 3) progression, the 4_0^8 band should be observable. We thus tentatively assign the weak feature at 18 430 cm^{-1} as the 4_0^8 band.

Moule and Subramaniam assigned a feature lying at 18 749 cm^{-1} as the 1_0^1 band. Subsequently, Clouthier and Moule, using the powerful technique of magnetic rotation spectroscopy, showed that this assignment was in error, and that the 18 749 cm^{-1} band probably does not belong to the $\tilde{a}(^3A_2)$–$\tilde{X}(^1A_1)$ system. Indeed, in our study there is no band at this wavenumber (it should have appeared at 18 756 cm^{-1}). Clouthier and Moule observed no band that could be due to the activity of mode 1 alone but found an interval of ca. 923 cm^{-1} from combination bands that they associated with ν_1'. In our spectrum, there is a band of reasonable intensity that lies 918 cm^{-1} from the origin that has a small (perhaps negative) isotope shift and that has not otherwise been assigned. This band is therefore assigned as the 1_0^1 band.

The remaining bands can readily be assigned as combination bands. All the assignments are given in Table 5 along with the assignments from the previous two studies. The isotope shifts are accurate to about ± 0.5 cm^{-1}.

V. Discussion

There have been three recent attempts to rationalize the electronic structure of the $\tilde{B}(^1A_1)$ state. These are the 1980 $\tilde{B}$–$\tilde{X}$ absorption study of Judge and Moule, the 1986 OODR study of Dixon and Western, and the 1991 $\tilde{B}$–$\tilde{X}$ laser-induced fluorescence study of Ludwiczak et al. In each case the results were interpreted differently. The present work adds another in-

TABLE 4. Vibrational wavenumbers of thiophosgene in the $\tilde{X}(^1A_1)$, $\tilde{a}(^3A_2)$, $\tilde{A}(^1A_2)$, and $\tilde{B}(^1A_1)$ states

Mode	Description	$\tilde{X}(^1A_1)^a$	$\tilde{a}(^3A_2)$	$\tilde{A}(^1A_2)^a$	$\tilde{B}(^1A_1)^b$
$\nu_1(a_1)$	C—S stretch	1139	923[a]	907	505
$\nu_2(a_1)$	Cl—C—Cl sym. stretch	504	474[a]	480	470
$\nu_3(a_1)$	Cl—C—Cl bend	289	247[a]	245	213
$\nu_4(b_1)$	Out-of-plane bend	471	298[b,c]	280[c]	341[c]
$\nu_5(b_2)$	Cl—C—Cl antisym. stretch	818	—	—	—
$\nu_6(b_2)$	Cl—C—Cl rock	305	267[b]	189	249

[a]References 1 and 2.
[b]This work.
[c]0–2 separation.

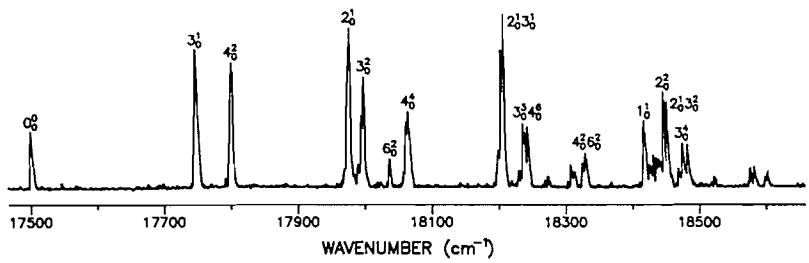

FIG. 7. Jet-cooled $\tilde{B}(^1A_1,0^0)$–$\tilde{a}(^3A_2,v')$–$\tilde{X}(^1A_1,0_0)$ optical–optical double resonance spectrum of thiophosgene in the 17 490 – 18 580 cm^{-1} region. The vertical axis is the intensity in arbitrary units.

TABLE 5. Wavenumbers and assignments of vibronic bands for the $\tilde{a}(^3A_2)$–$\tilde{X}(^1A_1)$ system of $^{35}Cl_2CS$

Wavenumber (cm^{-1})	Assignments			Δν	Isotope shift ν(35.35)–ν(35.37)
	This work	Refs. 12, 13	Ref. 14		
17 499	0_0^0	0_0^0	0_0^0	0	–0.5
17 745	3_0^1	3_0^1	3_0^1	246	1.6
17 796	4_0^2	4_0^2	4_0^2	297	0.8
17 972	2_0^1	2_0^1	2_0^1	473	2.1
17 993	3_0^2	3_0^2	3_0^2	494	3.3
18 033	6_0^2	4_0^4	4_0^4	534	1.4
18 059	4_0^4	N.R.[a]	N.R.	560	1.6
18 203	$2_0^1 3_0^1$	4_0^6	4_0^6	704	2.7
18 235	3_0^3	N.R.	N.R.	735	4.9
18 240	4_0^6	3_0^3	3_0^3	741	2.5
18 272	$3_0^1 6_0^2$	$3_0^1 4_0^4$	$3_0^1 4_0^4$	773	3.3
18 313	$3_0^1 4_0^4$	N.R.	N.R.	814	2.9
18 328	$4_0^2 6_0^2$	N.R.	N.R.	829	2.9
18 417	1_0^1	N.R.	N.R.	918	–0.5
18 430	4_0^8	N.R.	N.R.	931	3.3
18 446	2_0^2	N.R.	N.R.	947	4.1
18 451	$2_0^1 3_0^2$	$3_0^1 4_0^6$	$3_0^1 4_0^6$	952	5.3
18 475	3_0^4	N.R.	N.R.	976	6.0
18 482	$3_0^1 4_0^6$	1_0^1	N.R.	983	4.1
18 522	$2_0^1 3_0^1 4_0^2$	N.R.	N.R.	1023	3.5
18 583	$3_0^1 4_0^2 6_0^2$	N.R.	N.R.	1084	4.2
18 603	$4_0^4 6_0^2$	$2_0^3 3_1^0$	$2_0^3 3_1^0$	1104	2.9
18 666	$1_0^1 3_0^1$	N.R.	N.R.	1167	1.6
18 702	$2_0^1 3_0^3$	N.R.	N.R.	1203	7.2
18 721	$1_0^1 4_0^2$	N.R.	$1_0^1 4_0^2$	1222	—
18 896	$1_0^1 2_0^1$	$1_0^1 3_0^1$	$1_0^1 2_0^1$	1397	2.6
18 914	$1_0^1 3_0^2$	$2_0^1 3_0^1 4_0^6$	2_0^3	1415	3.2
19 132	$1_0^1 2_0^1 3_0^1$	N.R.	N.R.	1633	3.6
19 152	$1_0^1 3_0^3$	N.R.	N.R.	1653	—

[a]Not reported.

Can. J. Chem. Downloaded from www.nrcresearchpress.com by 195.246.54.202 on 09/08/12
For personal use only.

Can. J. Chem. Downloaded from www.nrcresearchpress.com by 195.246.54.202 on 09/08/12
For personal use only.

terpretation. It is clear that all these works must be reconciled if one wishes to consider the analysis satisfactory.

Comparison and reconciliation with the work of Dixon and Western (21) — Speculations about the $\tilde{B}(^1A_1)$ state potential

A comparison of our results with those of Dixon and Western shows that only 11 of the 23 bands observed by them are observed in the present study. These bands lie at 33 991, 34 203, 34 240, 34 331, 34 414, 34 452, 34 542, 34 577, 34 618, 34 663, 35 038, 35 122 cm^{-1}. It is clear that if we could find an explanation for these 12 "extra" bands, then the two studies would be reconciled. As mentioned before, the only conceptual difference between the two studies is that one has been performed in a cell at static pressure of 500 mTorr (Dixon and Western's) while the other (the present study) has been performed in a free-jet molecular beam apparatus at pressure below 5×10^{-5} Torr, i.e. in a collision-free environment. We therefore hypothesized that these 12 "extra" bands might be associated with transitions which (*1*) originated from excited vibrational levels of the ground state, or (*2*) resulted in some way from a "collision-assisted" process.

We have verified experimentally these hypotheses by using the molecular beam chamber as a static cell (simply by closing the gate valve to the diffusion pump) and by recording OODR spectra at various pressures in the regions of interest. Figure 8 shows a typical result for the 34 184 – 34 255 cm^{-1} region. It is clear that the bands near 34 200 and 34 230 cm^{-1} rapidly grow with increasing pressure. This is also the case for the band at 33 991 cm^{-1}. We have not performed the experiment for the other "extra" bands but it seems plausible that they also arise from (*1*) vibrationally excited molecules, or (*2*) molecules which have undergone collisions. Thus, excluding these transitions the work of Dixon and Western is entirely consistent with the present study. The origin is now unequivocally and firmly located at 34 277 cm^{-1} in agreement with the other work of both Judge and Moule, and Ludwiczak et al. We shall now examine these two explanations separately.

The first is the "hot band hypothesis". If a hot band underlies the cold band which is nominally being pumped, a second level lying higher in energy will be populated in addition to the preselected intermediate level, and this will produce an OODR signal at an apparent wavenumber below the true origin. In the present case, all of the 12 extra bands lie 286–289 cm^{-1} lower in energy than OODR bands observed under collision-free conditions. This interval corresponds approximately to the Cl—C—Cl bending wavenumber (ν_3) in the ground state. It is very tempting at this point to conclude that these 12 extra bands are the result of hot band overlap, but this would require that all seven of the $\tilde{A}(^1A_2)$–$\tilde{X}(^1A_1)$ vibronic bands selected by Dixon and Western are overlapped by hot bands involving ν_3''. Such coincidences are unlikely although near-coincidences exist for several of these bands. The closest agreements are between the 4_0^1 (18 716 cm^{-1}) and the $3_1^0 4_0^3$ (18 719 cm^{-1}) bands which lie 3 cm^{-1} apart, and the $4_0^1 6_1^1$ band (18 602 cm^{-1}) of the $\tilde{A}$–$\tilde{X}$ system and the $1_0^1 2_0^1 3_1^0$ band (18 600.5 cm^{-1}) of the $\tilde{a}$–$\tilde{X}$ system which lie only 1.5 cm^{-1} apart (using Clouthier and Moule's assignments (14)). The problem here is that it is not clear how much of the rotational structure of the underlying hot bands overlaps with the "targeted" bands considering that the laser linewidth in Dixon and Western's experiment was about 0.3 cm^{-1}. However, it seems clear that in these two cases

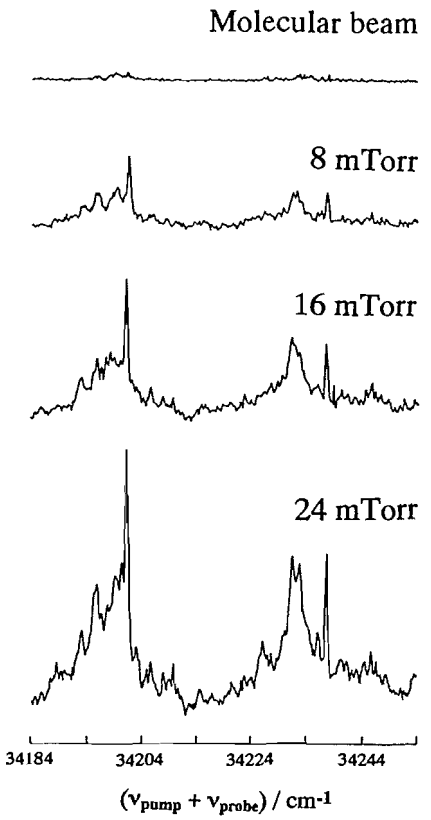

FIG. 8. Effect of pressure on the $\tilde{B}(^1A_1,v')$–$\tilde{A}(^1A_2,4^1)$ –$\tilde{X}(^1A_1,0_0)$ optical–optical double resonance spectrum of thiophosgene in the 34 184 – 34 254 cm^{-1} region. The vertical axis is the intensity in arbitrary units.

overlapping might be possible. The situation is less clear for the other 5 bands used by Dixon and Western. These bands are the $3_0^1 4_1^2$, and presumably the 4_1^0, 6_0^1, $3_0^1 4_1^0$, and $3_0^1 4_0^1$ bands (using Clouthier and Moule's assignments). Here potential hot bands should lie no closer than ±5–6 cm^{-1}. The problem here is that none of these bands have ever been observed in previous studies. For instance, the $2_0^1 3_1^0 4_0^1$ band should lie at +5 cm^{-1} from the 6_0^1 band but no such band has ever been reported despite the fact that the room temperature absorption spectrum is sparse in this region. In summary, some but not all of the extra bands might result from hot bands involving ν_3''.

The second explanation is the "dark state hypothesis" and the arguments run as follows. The experimental conditions and simple considerations clearly indicate that collision-assisted transitions occur once the molecules are excited in the final state i.e. after the absorption of the second photon. Collisional interactions in the intermediate state do not play an important role because the two laser pulses overlap both spatially and temporally. Furthermore, it was noticed by Dixon and Western that identical spectra were obtained when the probe laser was temporally overlapped with the pump beam and when it was delayed by 24 ns.

For collisions to occur, the excited molecules must be in real (as opposed to virtual) vibrational levels (prior to collisions). Regardless of whether the collisional interactions lead to vibrational activation, vibrational relaxation, direct passage through a barrier, or modification of the barrier, the laser wavenumbers at which the "collision-assisted" transitions are observed indicate the presence of real vibronic levels. Thus, there are non-fluorescent vibronic levels lying below the vibrationless

Can. J. Chem. Downloaded from www.nrcresearchpress.com by 195.246.54.202 on 09/08/12
For personal use only.

level of the fluorescent $\tilde{B}(^1A_1)$ state that can be easily populated from the $\tilde{A}(^1A_2)$ state. The presence of a "dark" state (DS) in the 295 nm region has already been established recently by Maciejewski et al. (26) from absorption measurements on Cl_2CS in perfluoroalkane solution at room temperature. The DS–$\tilde{X}$ oscillator strength has been estimated to be about 5×10^{-5} and the quantum yield of emission, $\phi_e \leq 10^{-8}$ under these conditions.

If the "dark" state seen by Maciejewski et al. is the one seen in the OODR studies then this state can be populated from both the $\tilde{X}(^1A_1)$ and $\tilde{A}(^1A_2)$ states, although our observations suggest that the DS—$\tilde{A}(^1A_2)$ oscillator strength is much larger than DS—$\tilde{X}$. This new piece of evidence supports the suggestion put forward by Maciejewski et al. that the identity of this "dark" state is of $^1A_1$ symmetry and is described in large measure by the $(\pi^2_{CS}\ n^0_S\ \pi^{*2}_{CS})$ configuration. If this suggestion is true, there should be two diabatic potential wells of $^1A_1$ symmetry along the C—S coordinate; one associated with the $(\pi^1_{CS}\ n^2_S\ \pi^{*1}_{CS})$ configuration whose minimum is at about 2.1 Å, and the other associated with the $(\pi^2_{CS}\ n^0_S\ \pi^{*2}_{CS})$ configuration whose minimum lies at somewhat larger internuclear distance. We now suggest that due to an avoided crossing, the resulting adiabatic potential of lower energy is described by an asymmetric double-minimum whose lower minimum corresponds to the minimum of the diabatic dark state, and whose higher minimum corresponds to the minimum of the diabatic fluorescent $\tilde{B}(^1A_1)$ state.

The existence of such an asymmetric double-minimum potential along the C—S coordinate would yield results consistent with the combined spectroscopic observations if the barrier separating the fluorescent from the dark minimum is of the appropriate height. Particularly, it would provide an explanation for the collision-assisted fluorescence. Consider a molecule pumped in a vibronic level lying in the "dark" minimum. If this level lies somewhat below the barrier but above the vibrationless level of the fluorescent minimum (here the $\tilde{B}(^1A_1)$ state) then collisions can transfer molecules to the fluorescent levels and consequently can make their detection possible by laser induced fluorescence. Obviously, in the absence of collision no transfer occurs and no fluorescence is detected as rapid non-radiative decay through other channels takes place.

We suggest that such a double-minimum potential along the C—S coordinate would explain the photophysical behavior of thiocarbonyls pumped to the $\tilde{B}(^1A_1)$ state. This is because the photophysical behavior of the $\tilde{B}(^1A_1)$ state now depends on the barrier height separating the fluorescent from the "dark" minimum. For instance, if the barrier height is very low then pumping the molecule to the $\tilde{B}(^1A_1)$ state minimum will not lead to fluorescence because the molecule will rapidly "flow" to the "dark" minimum which lies lower in energy. This is probably the situation which prevails in F_2CS which does not fluoresce from the $\tilde{B}(^1A_1)$ state but which nevertheless exhibits a discrete $\tilde{B}$–$\tilde{X}$ absorption spectrum.

The idea of a double-minimum potential along the C—S coordinate is not new. Indeed, Judge and Moule in their analysis of the $\tilde{B}$–$\tilde{X}$ absorption spectrum observed the doubling of some bands which they associated with the activity of mode 1, the C—S stretching mode, in a double-minimum potential. They fitted the energy levels to a symmetric double-minimum function represented by a Gaussian-type barrier function superimposed on a quadratic potential function, and obtained a barrier height of 4855 cm^{-1}. Unfortunately, the finding of Judge and Moule could not be corroborated by Ludwiczak et al. as they could not observe the inversion doublings seen by Judge and Moule presumably on account of poorer resolution. However, the data of Judge and Moule appears unquestionable.

TABLE 6. Comparisons between assignments of the vibronic levels of the $\tilde{B}(^1A_1)$ state of thiophosgene

Wavenumber (cm^{-1})	Assignment		Isotope shift[a] [ν(35,35)–ν(35,37)]
	Ref. 22	This work	
34 275	0^0	0^0	−0.4
34 616	4^2	4^2	2.6
34 771	2^1	6^2	2.0
34 781	1^1	1^1	1.4
34 960	4^4	2^13^1	5.5
35 105	2^14^2	4^6	5.0
35 111	1^14^2	4^26^2	4.2
35 258	2^2	1^12^1	4.1
35 268	1^2	N.O.[b]	3.4
35 278	4^6	1^16^2	—
35 430	2^14^4	2^23^1	—
35 444	1^14^4	$2^13^16^2$	7.2
35 579	2^24^2	$2^14^26^2$	6.5

[a]The isotope shifts are those of Ludwiczak et al. (22).
[b]N.O. = not observed.

Such a high barrier to inversion appears to be at odds with the evidence presented herein, although the idea of a double-minimum along the C—S coordinate is now firmly established. This discrepancy may be due to two effects. Firstly, it is possible that the model used by Judge and Moule overestimates the barrier height by several thousands wavenumbers. This is because their model assumes a symmetric double-minimum potential while the true potential is an asymmetric one. Their model also assumes that the diabatic potentials are well approximated by quartic functions which is certainly not the case here both because the fluorescent minimum is known to be very shallow and also because the two states in question are likely to be perturbed by nearby states. It is clear that the whole problem of fitting the double-minimum potential must be reviewed but this is beyond the scope of this paper. Secondly, it is also possible that the barrier height be modified upon collisions since intermolecular interaction is known in general to affect the shapes of potential wells. In the present case the two diabatic potentials arise from different electron configurations and hence will be affected differently by the collisional interaction. It is not difficult to imagine how such a process would yield a smaller barrier.

Since the 12 "extra" bands seen by Dixon and Western correspond to transitions terminating in the "dark" potential, it is therefore possible to use them to determine the wavenumbers of some fundamentals. Using the band at 33 991 cm^{-1} as a sub-origin, the following intervals are found; 212, 249, 340 and 627 cm^{-1}. These are sufficient to reproduce all twelve of these "extra" bands. Identical intervals were found in our OODR spectra and were ascribed to the activities of mode, 3, 4 (4^2 = 340 cm^{-1} and 4^4 = 627 cm^{-1}), and 6. Thus, the wavenumbers of these modes are the same in the fluorescent $^1A_1(\pi^1_{CS}\ n^2_S\ \pi^{*1}_{CS})$ and the "dark" $^1A_1(\pi^2_{CS}\ n^0_S\ \pi^{*2}_{CS})$ states. This is consistent with the fact that the transition is localized on the C—S moiety and the fact that the C—S bond order is nominally the same in both states. It would be interesting to verify this theoretically through *ab initio* calculations.

TABLE 7. Observed and calculated energy levels of thiophosgene excited in the out-of-plane bending potential of the $\tilde{B}(^1A_1)$ state

		Calculated	
v	Observed	Quartic-quadratic model	Quadratic-Gaussian model
0	0	0	0
1	$0.01 \leq v_1 \leq 0.15$[a]	0.007	0.072
2	341	341	341
3	342.9[b]	341.5	343.5
4	628	628	628
5	—	645	663
6	828	828	857
Parameters		$B = -9.4$ $A = 43.06$ cm^{-1}	$B = 3.9$ $\rho = 1.20$ $\nu_0 = 237.9_5$ cm^{-1}
Barrier height		951 cm^{-1}	928 cm^{-1}
Out-of-plane angle		25°	
Estimated structural parameters			C—S bond length = 2.1 Å C—Cl bond length = 1.727 Å S—C—Cl angle = 124.4°

[a]Reference 20.
[b]Reference 22.

Comparison with the work of Judge and Moule (20), and Ludwiczak et al. (22)

Having reconciled the two OODR studies, we now compare them with the one-photon $\tilde{B}$–$\tilde{X}$ studies of Judge and Moule, and Ludwiczak et al. It is clear that due to different selection rules, the number of features observed in the OODR studies is different from the number observed in the one-photon studies. However, with the exception of two which appear at 35 268 and 35 585 cm^{-1}, all cold bands that have been observed by Judge and Moule and Ludwiczak et al. in the 33 580 – 35 261 cm^{-1} region have also been observed in the present OODR study. The two features that have not been observed by OODR spectroscopy appear as the most intense features in the fluorescence excitation spectrum of Ludwiczak et al. These bands have been assigned by both groups as 1_0^2 (35 268 cm^{-1}) and $1_0^2 4_0^2$ (35 585 cm^{-1}) and we believe that these assignments are correct. Since the 1^1 and 4^2 levels are accessed in the OODR study, the only plausible reason for not accessing the 1^2 and $1^2 4^2$ levels is the poor Franck–Condon overlap with the 4^1 and $1^1 4^1$ levels of the $\tilde{A}(^1A_2)$ state. In the $\tilde{B}$–X system the Franck–Condon factors for the 1_0^2 and $1_0^2 4_0^2$ transitions are substantially larger because of the larger difference in the internuclear distances between the two states.

Among the 15 cold bands observed by Ludwiczak et al. in the 33 580 – 35 261 cm^{-1} region, only 5 (including the two bands not observed in the OODR experiment) share the same assignments as the corresponding bands in the OODR study. However, as shown in Table 6, most of the discrepancies are settled once the values of 470, 213, and 240 cm^{-1} for ν_2, ν_3, and ν_6, respectively, are introduced. The new assignments are entirely consistent with the selection rules for $\tilde{B}(^1A_1) \leftarrow \tilde{X}(^1A_1)$ transitions and are supported by the isotope splittings measured by Ludwiczak et al., with the exception of the band at 35 105 cm^{-1} which has an isotope splitting too small to support the 4^6 assignment proposed here. However, we maintain this assignment until the isotope splitting is corroborated by a new measurement.

Judge and Moule reported five cold bands in the wavenumber region covered by the present work. We agree with four of their assignments. Once the value of 248 cm^{-1} for ν_6 is introduced, complete agreement is obtained.

The double-minimum potential along the out-of-plane bending coordinate (ν_4) in the $\tilde{B}(^1A_1)$ state

It has been known for some time that upon occupation of the π^* orbital the molecule becomes bent. This behavior can be rationalized satisfactorily on the basis of Walsh's postulates, although vibronic couplings have been shown to play an important role. The out-of-plane angle and the barrier height to inversion can be derived by fitting a double-minimum function to the observed the energy levels. The present study places the 4^2, 4^4, and 4^6 levels at 341, 628, and 828 cm^{-1}, respectively. The energies of the 4^1, 4^3, and 4^5 levels could not be determined although it clearly appears that the 0–1 and 2–3 separations are very small; smaller than the experimental accuracy. However, the energies of the 4^1 and 4^3 levels can be determined from the data of Judge and Moule, and Ludwiczak et al. because they unambiguously determined the positions of the 4_1^1 and the 4_1^3 hot bands in their $\tilde{B}(^1A_1) \leftarrow \tilde{X}(^1A_1)$ spectra. Due to experimental inaccuracies, the energies of the 4^1 level is still not particularly well determined although it is clear from the work of Judge and Moule that it should be ≤ 0.15 cm^{-1}. The position of the 4^3 level is exclusively due to Ludwiczak et al. Two types of double-minimum functions have been fitted to these five energy levels and the results of the fits are presented in Table 7. One of these models is due to Laane (27) and consists of a quartic potential perturbed by a quadratic function while the other is due to Coon et al. (28) and consists of a quadratic potential superimposed by a Gaussian function. The details of these models can be found in the seminal papers of Laane (27), and Coon et al. (28).

The quadratic-Gaussian model appears to fit better than the quartic-quadratic one at $v \leq 3$ but the converse is observed for $v > 3$. In general both model give satisfactory agreement with experiment. The barrier height to inversion can be set at 845 ± 20 cm^{-1} while the out-of-plane angle is estimated to

Can. J. Chem. Downloaded from www.nrcresearchpress.com by 195.246.54.202 on 09/08/12
For personal use only.

Can. J. Chem. Downloaded from www.nrcresearchpress.com by 195.246.54.202 on 09/08/12
For personal use only.

about 25°. It is difficult to establish the accuracy of the latter because the necessary structural parameters of the $\tilde{B}(^1A_1)$ state are not known. In the present case, the C—Cl bond length and the S—C—Cl bond angle were assumed to be the same as the ground state values while the C—S bond length was set 0.5 Å longer than the ground state value. Should better structural parameters become available a new out-of-plane angle can be computed from the relation

$$\theta_{\text{out-of-plane}} = \frac{Q_{\text{minimum}}}{\mu^{1/2} r_{\text{C—S}}}$$

where $Q_{\text{minimum}} = 1.40 \times 10^{-20}$ g$^{1/2}$ cm, $r_{\text{C—S}}$ is the C—S bond length, and μ is the reduced mass; the latter being estimated from the following relation used by Coon et al. for H_2CO

$$\frac{1}{\mu} = \left(\frac{1}{M_S} + \frac{1}{M_C}\right) + \frac{2r_{\text{C—S}}}{M_C Z} + \left(\frac{1}{M_C} + \frac{1}{2M_{Cl}}\right)\frac{r_{\text{C—S}}^2}{Z^2}$$

where Z is the distance from the carbon atom to the line joining the two chlorine atoms.

The derived barrier height and out-of-plane angle may be compared to the $\tilde{a}(^3A_2)$ and $\tilde{A}(^1A_2)$ state values which are 726 cm^{-1} and 32°, and 620 cm^{-1} and 32°, respectively. The out-of-plane angle is therefore smaller in the $\tilde{B}(^1A_1)$ state than in the $\tilde{a}(^3A_2)$ and $\tilde{A}(^1A_2)$ states but the barrier to inversion is at least 220 cm^{-1} higher in the $\tilde{B}(^1A_1)$ state. This is not surprising since vibronic couplings are certainly more important in the $\tilde{B}(^1A_1)$ state than in the $\tilde{a}(^3A_2)$ and $\tilde{A}(^1A_2)$ states on account of the larger density of states in the neighborhood of the $\tilde{B}(^1A_1)$ state. This conclusion is borne out by the two-state calculations of Innes on H_2CO which show that the non-planarity is in large part attributable to vibronic couplings rather than solely to electronic effects (29).

The double-minimum potential along the out-of-plane bending coordinate (ν_4) in the $\tilde{a}(^3A_2)$ state

The barrier height to inversion and the out-of-plane angle in the $\tilde{a}(^3A_2)$ state were determined by Moule and Subramaniam by fitting a quadratic-Lorentzian potential to the ν_4' energy level structure established from their vibronic analysis of the $\tilde{a}(^3A_2) \leftarrow \tilde{X}(^1A_1)$ absorption spectrum. The present study performed with a novel OODR scheme challenges some of their assignments. In particular, the 4^4 and 4^6 levels have been placed at 560 and 741 cm^{-1} rather than 534 and 704 cm^{-1}, respectively. However, these changes have little effects on the barrier height and out-of-plane angle. In fact, it turns out that the new value for 4^6 enhances the quality of the fit done by Moule and Subramaniam, and consequently reaffirms the currently accepted structural parameters. However, the proposed new value for 4^4 diverges from the calculated by about 30 cm^{-1} while the divergence was only 5 cm^{-1} in the previous study. Nevertheless, we maintain our assignment because of the relative intensity of the 4_0^{2n} progression (*vide supra*).

Concerning the (ν_6) fundamental in the $\tilde{A}(^1A_2)$ state

An examination of Table 4 indicates that the vibrational frequencies of ν_1, ν_2, ν_3, and ν_4 in the $\tilde{a}(^3A_2)$ and $\tilde{A}(^1A_2)$ states are the same within 20 cm^{-1} but that the vibrational frequency of ν_6 differs by about 80 cm^{-1}. Furthermore, it is seen that $\nu_6(\tilde{a}(^3A_2))$ and $\nu_6(\tilde{B}(^1A_1))$ differ by only 18 cm^{-1}. This unexpected result makes the value of $\nu_6(\tilde{A}(^1A_2))$ dubious. It is clear from Table 4 that it should be of the order of 270 cm^{-1}. A careful examination of the jet-cooled $\tilde{A}(^1A_2) \leftarrow \tilde{X}(^1A_1)$ fluorescence excitation spectrum shown in Fig. 2 reveals the presence of a weak cold band near 18 995 cm^{-1}, just barely resolved from the strong 4_0^3 band which lies immediately to the blue. As this band is located close to the expected region we assign it as the 6_0^1 band and this makes $\nu_6 = 279$ cm^{-1}, in good agreement with expectation. It is unlikely that this band would have been observed in the previous studies because it nearly overlaps the 4_0^3 band.

VI. Conclusion

The $\tilde{B}(^1A_1)$ state of jet-cooled thiophosgene has been studied by optical–optical double resonance spectroscopy and all of the observed vibronic bands have been rationalized in terms of the activities of ν_1, ν_2, ν_3, ν_4, and ν_6. The discrepancies among the previous studies have been entirely reconciled. The $\tilde{B}(^1A_1)$ state is characterized by two double-minimum potentials; one along the C—S stretching coordinate and the other along the out-of-plane bending coordinate. The barrier to inversion along ν_4 and the out-of-plane angle have been determined to be 945 cm^{-1} and 25°, respectively. The double-minimum along ν_1 is particularly intriguing as one minimum leads to radiative decay while the other leads to rapid non-radiative decay. It is hoped that this study has opened the way to a greater understanding of the photophysics and photochemistry of thiophosgene and small thiocarbonyls in general. In particular, it would be rewarding to pursue this study by examining the details of the photophysics of thiophosgene excited in various part of the double-minimum surface along ν_1. Detailed photodissociation studies will also be very rewarding and are underway in our laboratory.

The $\tilde{a}(^3A_2)$ state has been probed by a novel and powerful optical–optical double resonance scheme which uses the fluorescent vibrationless level of the $\tilde{B}(^1A_1)$ state to monitor $\tilde{a}(^3A_2) \leftarrow \tilde{X}(^1A_1)$ absorption. A vibrational analysis has been performed and several reassignments have been proposed. These reassignments had little effect on the shape of the double-minimum potential along ν_4. The vibrational frequency of $\nu_6(\tilde{a}(^3A_2))$ has been determined for the first time. It is hoped that this novel OODR scheme will be used to probe non-fluorescent states by laser induced fluorescence or to determine the linkage between or parentage of states by using fluorescence or ionization techniques as means of detection.

Acknowledgments

P.A.H. and R.P.S. are grateful to the Network of Centres of Excellence in Molecular and Interfacial Dynamics, one of the 15 Networks of Centres of Excellence supported by the Government of Canada, for partial funding of this work. The authors are grateful to a referee for valuable comments.

1. R.P. Steer. Rev. Chem. Intermed. **4**, 1 (1981).
2. D.J. Clouthier and D.C. Moule. Topics in current chemistry. Vol. 150. Springer-Verlag, Berlin. 1989. p. 167.
3. A. Maciejewski and R.P. Steer. Chem. Rev. **93**, 67 (1993).
4. A. Kapur, R.P. Steer, and P.G. Mezey. J. Chem. Phys. **69**, 968 (1978).
5. A. Kapur, R.P. Steer, and P.G. Mezey. J. Chem. Phys. **70**, 745 (1979).
6. B. Simard, A.E. Bruno, P.G. Mezey, and R.P. Steer. Chem. Phys. **103**, 75 (1986).
7. W.-T. Chan and J. Goddard. Chem. Phys. Lett. **173**, 139 (1990).
8. M. Hachey, F. Grein, and R.P. Steer. Chem. Phys. Lett. **183**, 204 (1991).
9. M. Kasha. Faraday Discuss. Chem. Soc. **9**, 14 (1950).

10. J.H. Carpenter, D.F. Rimmer, J.G. Smith, and D.H. Whiffen. J. Chem. Soc. Faraday Trans. II, **71**, 1752 (1975).
11. D. Chadwick. Can. J. Chem. **50**, 737 (1972).
12. D.C. Moule and C.R. Subramaniam. Chem. Commun. 1340 (1969).
13. D.C. Moule and C.R. Subramaniam. J. Mol. Spectrosc. **48**, 336 (1973).
14. D.J. Clouthier and D.C. Moule. J. Mol. Spectrosc. **87**, 471 (1981).
15. J.C.D. Brand, J.H. Callomon, D.C. Moule, J. Tyrrell, and T.H. Goodwin. Trans. Faraday Soc. **61**, 2365 (1965).
16. J. Duchesne. J. Chem. Phys. **21**, 548 (1953).
17. L. Burnelle. J. Chem. Phys. **24**, 620 (1956).
18. E.R. Farnworth and G.W. King. J. Mol. Spectrosc. **46**, 419 (1973).
19. T. Oka, A.R. Knight, and R.P. Steer. J. Chem. Phys. **66**, 699 (1977).
20. R.H. Judge and D.C. Moule. J. Mol. Spectrosc. **80**, 363 (1980).
21. R.N. Dixon and C.M. Western. J. Mol. Spectrosc. **115**, 74 (1986).
22. M. Ludwiczak, D.R. Latimer, and R.P. Steer. J. Mol. Spectrosc. **147**, 414 (1991).
23. D. Proch and T. Trickl. Rev. Sci. Instrum. **60**, 713 (1989).
24. C.R. Lessard and D.C. Moule. Spectrochim. Acta, **29A**, 1085 (1973).
25. D.J. Clouthier, A.R. Knight, and R.P. Steer. J. Mol. Spectrosc. **83**, 148 (1980).
26. A. Maciejewski, M. Szymanski, and R.P. Steer. Chem. Phys. **165**, 101 (1992).
27. J. Laane. Appl. Spectrosc. **24**, 73 (1970).
28. J.B. Coon, N.W. Naugle, and R.D. Mckenzie. J. Mol. Spectrosc. **20**, 107 (1966).
29. K.K. Innes. J. Mol. Spectrosc. **99**, 294 (1983).

Can. J. Chem. Downloaded from www.nrcresearchpress.com by 195.246.54.202 on 09/08/12
For personal use only.

Non-adiabatic photodissociation dynamics of BrCl

JIANYING CAO, HANS-PETER LOOCK, AND CHARLES X.W. QIAN[1]

Department of Chemistry, University of Victoria, P.O. Box 3055, Victoria, BC V8W 3P6, Canada

Received July 7, 1993

This paper is dedicated to Professor John C. Polanyi on the occasion of his 65th birthday

JIANYING CAO, HANS-PETER LOOCK, and CHARLES X.W. QIAN. Can. J. Chem. **72**, 758 (1994).

Nozzle-cooled BrCl was excited with tunable laser radiation at selected wavelengths between 389 and 500 nm. The chlorine atomic fragments in their $Cl^*(^2P_{1/2})$ and $Cl(^2P_{3/2})$ state were stated-selectively probed by resonance-enhanced multiphoton ionization. The branching ratio $(Cl^*/(Cl + Cl^*))$ was measured as a function of the excitation wavelength. The relative Cl^* yield reaches a maximum at around $\lambda_{phot} = 460$ nm. Decomposition of these branching ratios into Cl and Cl^* photofragment yield spectra provides insight into the BrCl *B*-state $^3\Pi(0^+)$ non-adiabatic dissociation dynamics. Our results suggest that the dissociation mechanism involves non-adiabatic transitions among 0^+ potential energy curves.

JIANYING CAO, HANS-PETER LOOCK et CHARLES X.W. QIAN. Can. J. Chem. **72**, 758 (1994).

On a excité du BrCl refroidi à l'aide d'un rayonnement laser adjustable à diverses longueurs d'onde allant de 389 à 500 nm. Faisant appel à une ionisation multiphotonique rehaussée par résonance, on a examiné sélectivement les divers états des fragments atomiques du chlore dans leurs états $Cl^*(^2P_{1/2})$ et $Cl(^2P_{3/2})$. On a mesuré le rapport de branchement $(Cl^*/(Cl + Cl^*))$ en fonction de la longueur d'onde de l'excitation. Le rendement relatif de Cl^* atteint un maximum à environ $\lambda_{phot} = 460$ nm. La décomposition de ces rapports de branchement en spectres de rendement des photofragments Cl et Cl^* fournit des données sur la dynamique de la dissociation non-adiabatique de l'état *B*, $^3\Pi(0^+)$, du BrCl. Nos résultats suggèrent que le mécanisme de dissociation implique des transitions non-adiabatiques parmi les courbes d'énergie potentielle 0^+.

[Traduit par la rédaction]

Introduction

When two or more potential energy surfaces (PES) are involved in photodissociation processes, non-adiabatic interactions among these surfaces can influence the dynamics significantly. In particular, if at least one of the photofragments has a non-vanishing angular momentum, non-adiabatic transitions are most likely to be observed. In this situation, more than one exit channel is readily accessible so that, even if the dissociation was initiated on a single PES, the non-adiabatic interactions are unavoidable during the fragmentation process (1).

A simple example of non-adiabatic transitions is given when only two potential energy curves with an avoided crossing are involved (see, for example, ref. 2). If the kinetic energy near the interaction region is small, the dissociation will proceed adiabatically, i.e., the molecule stays on the initially prepared adiabatic curve throughout the dissociation. For significantly higher kinetic energy, the dissociation can proceed diabatically and the molecule jumps to the other potential energy curve.

In a realistic molecular system, however, several potential curves are normally involved. It is important to study the non-adiabatic transitions among these curves to understand the underlying fragmentation dynamics. With adequate kinetic energy, several exit channels can participate in the dissociation process. Such a problem presents a challenge to both the experimentalist and the theoretician.

BrCl photodissociation provides a unique opportunity to study the non-adiabatic interactions. Since both the chlorine and the bromine fragments have two spin-orbit states, there are four possible exit channels near the dissociation limit. From the UV and near-UV absorption spectrum (3) it was concluded that at least two excited states are involved. It is believed that the $^1\Pi(1)$ and the $^3\Pi(0^+)$ curves are responsible for the absorption in this region. Spectroscopy studies from several groups (4–6) have established the bound part of the $^3\Pi(0^+)$ curve. However, the repulsive part of both potential curves and the consequent dissociation dynamics remain to be investigated in detail.

[1]Author to whom correspondence may be addressed.

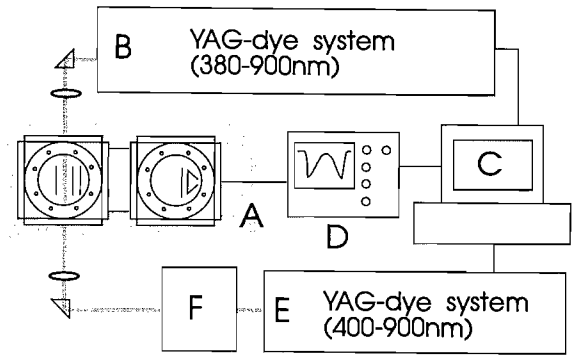

FIG. 1. Block diagram of the experimental setup: (A) the high-vacuum chambers house the TOF-MS grids and the molecular beam valve (not displayed); (B) photolysis laser; (C) computer and timing control; (D) digital oscilloscope; (E) probe laser system; (F) frequency doubler.

In this communication, we present our preliminary study of the BrCl UV and near-UV photodissociation dynamics. In particular, we report the chlorine spin-orbit state branching ratio $(Cl^*/(Cl+Cl^*))$ measured at different photolysis wavelengths. The implications of these measurements on the photodissociation dynamics and the non-adiabatic transitions among several exit channels are discussed.

Experimental

As shown schematically in Fig. 1, the experimental setup consists of two frequency tunable laser systems, a molecular beam source, and a time-of-flight mass spectrometer (TOF-MS). The molecular beam source and TOF-MS were mounted in a high-vacuum system with two differentially pumped chambers.

The output of a pulsed Nd:YAG laser pumped dye laser system (Continuum NY61 and ND60) was used as the photolysis light source. Different dye–solvent combinations enabled us to obtain an output at the desired wavelength. The frequency doubled output of another Nd:YAG laser pumped dye laser combination (Lumonics YM600, HD 500 and Hypertrak 1000 with a BBO crystal) was employed to probe the photofragments. A homemade pulsed (200 μs duration/pulse)

Can. J. Chem. Downloaded from www.nrcresearchpress.com by EESC ESCOLA DE ENGENHARIA on 09/08/12
For personal use only.

Can. J. Chem. Downloaded from www.nrcresearchpress.com by EESC ESCOLA DE ENGENHARIA on 09/08/12
For personal use only.

molecular beam valve (7) was used and the seeded beam was extracted by a 1-mm skimmer (Beamdynamics) 20 mm downstream. The TOF-MS used in our setup is of the two-stage Wiley–McLaren design (8) consisting of three stainless steel grids (95% transmittance/grid), a field-free region, and a microchannel-plate detector (Galileo FTD2003). The extraction region is defined by two grids that are separated by 17 mm and biased at 1995 V (repeller grid) and 1500 V (second grid). The acceleration region is 7 mm in length and is limited by this second grid and by a third grid that is held at ground potential. The detector is located in the second chamber at 521 mm distance from the interaction region. The signal from this detector was digitized by a digital oscilloscope (Tektronix 2440) and the data were then transferred to a 25 MHz/386 computer.

In a typical experiment the laser beams pass through the centre of the first vacuum chamber counterpropagating with respect to each other and at right angles to both the molecular beam and the TOF-MS axis. The photolysis beam (approx. 0.7 mJ/pulse) and the probe beam (approx. 0.05 mJ/pulse) were focussed with two 500-mm lenses to a spot of approximately 20 μm diameter in the interaction region. The timing in the experiment, i.e., the firing of the lasers, opening of the pulsed valve, and triggering of the digital oscilloscope, was controlled by a digital delay generator (EG&G 9650) in combination with a 10 channel pulse-delay computer card (Advantech PCL-830). The delay between the photolysis and probe laser was checked with a fast photodiode and set at 5 ns in our experiment.

BrCl was prepared by exposing 380 Torr (1 Torr = 133.3 Pa) of Cl_2 (Matheson) to an excess of liquid Br_2 and Br_2 vapour (Aldrich). The mixture of the gases was used after a 24 h waiting period. To assure that the reaction reached equilibrium an absorption spectrum was recorded and decomposed into the three components. The chemical equilibrium yields fractions of 55% BrCl, 26% Cl_2, and 19% Br_2. The contribution of Cl_2 dissociation to the TOF signal was estimated using these fractions and the known absorption probabilities (3). At the shortest wavelength used (i.e., 389 nm) Cl_2 contributes less than 8% to the signal when detecting the $Cl(^2P_{3/2})$ fragments and less than 1% in the case of the $Cl^*(^2P_{1/2})$ fragments. The influence of Cl_2 impurities is expected to be even less at longer wavelengths. Therefore further purification was superfluous. A 5% dilution of the sample in helium (Matheson, prepurified) was expanded into the vacuum chamber.

The photofragmentation of BrCl can yield bromine and chlorine fragments in their ($^2P_{3/2}$) (Cl or Br) ground states and (or) in their ($^2P_{1/2}$) (Cl* or Br*) spin-orbit excited states. The branching ratio (Cl*/(Cl+Cl*)) of the BrCl photodissociation was investigated at six different wavelengths between 389 and 500 nm. At each excitation wavelength the Cl* and Cl fragments were detected via 2+1 Resonance- enhanced Multiphoton Ionization (REMPI) at the vacuum wavelengths 235.204 and 235.338 nm, respectively. Furthermore the probe laser was scanned in 20 wavelength steps to cover the whole Doppler width of each ^{35}Cl REMPI line. At each photolysis/probe wavelength combination typically 20 laser shots were averaged. The resulting integrated intensities were then normalized with the different transition probabilities for the two states probed.

Under the condition that the ionization step is saturated, the two-photon transition probabilities for the $4p^2P_{1/2} \leftarrow 3p^2P_{1/2}(Cl^*)$ and $4p^2D_{3/2} \leftarrow 3p^2P_{3/2}(Cl)$ transitions used in our experiment were calculated. These calculations were performed assuming that (*a*) a pure L-S coupling scheme and (*b*) only the $3p^4 4s$ intermediate states are involved. The ratio of the calculated intensities of the two transitions is then Cl*/Cl = 0.9. This ratio was verified experimentally[2] and used to normalize the observed signals.

[2]The ratio Cl*/Cl = 0.9 was verified experimentally by measuring the ratio between the linestrengths of the $4p^2P_{1/2} \leftarrow 3p^2P_{1/2}(Cl^*)$ and $4p^2D_{3/2} \leftarrow 3p^2P_{1/2}(Cl^*)$ transitions. This ratio was determined to be 2.0 ± 0.5. Through division by the reported (1 : 2.5) ratio of the linestrengths of the $4p^2D_{3/2} \leftarrow 3p^2P_{1/2}(Cl^*)$ and $4p^2D_{3/2} \leftarrow 3p^2P_{3/2}(Cl)$ transitions (9), we found that the above number of 0.9 is accurate within our experimental limits.

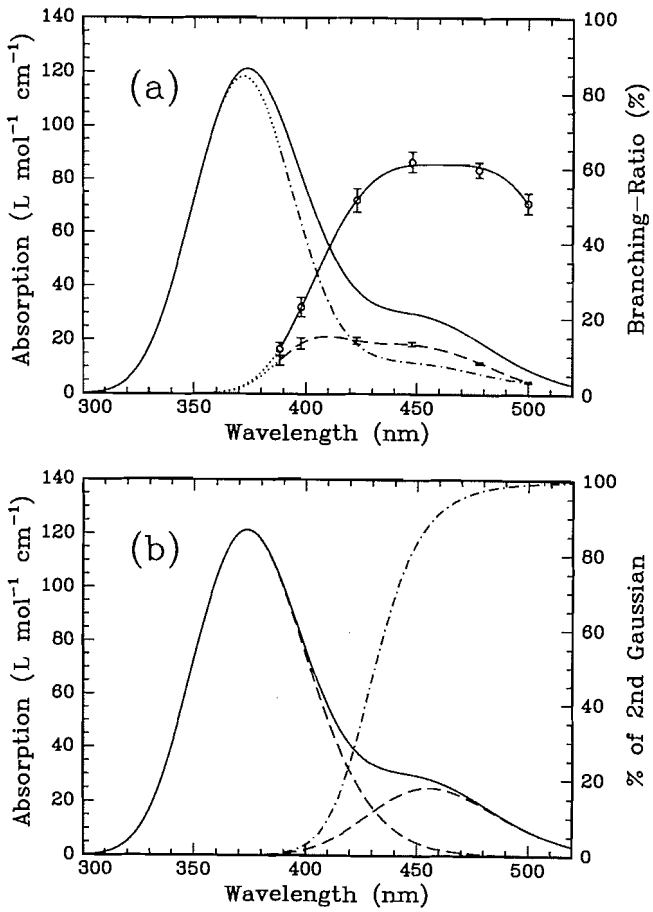

FIG. 2. (*a*) The percentage of the $Cl^*(^2P_{1/2})$ yield as a function of the photolysis wavelength (circles). A smooth curve is used to serve as a guide for the possible Cl* yield between these measurements. Also displayed is the absorption spectrum (solid line) obtained from ref. 3. By multiplying these two curves, the product yield spectra of the Cl* fragment (broken line) and similarly of the Cl fragment (dash-dotted line) were obtained. (*b*) The absorption spectrum of BrCl (solid line) and the two Gaussian curves in which it can be decomposed (broken lines). The percentage of the second Gaussian component is also included (dash-dotted line).

Results and discussion

In Fig. 2*a* the percentage of the Cl* yield from the BrCl photodissociation is displayed as a function of the photolysis wavelength. A smooth fitting curve with four parameters is used to serve as a guide for the possible Cl* yield between these measurements. Also displayed is the absorption spectrum obtained from ref. 3. By multiplication of the two curves one can obtain the product yield spectra of the Cl* fragment and similarly of the Cl fragment. These photofragment yield spectra are also included in Fig. 2*a*.

These results can be better understood in the context of the known exit-channel energetics and the potential energy curves. In the following paragraphs we will therefore describe them first.

Two to four exit channels are energetically accessible at the wavelengths we studied; these channels and their threshold energies, which were calculated based on the ground-state dissociation energy D_e from ref. 6, are listed below:

Can. J. Chem. Downloaded from www.nrcresearchpress.com by EESC ESCOLA DE ENGENHARIA on 09/08/12
For personal use only.

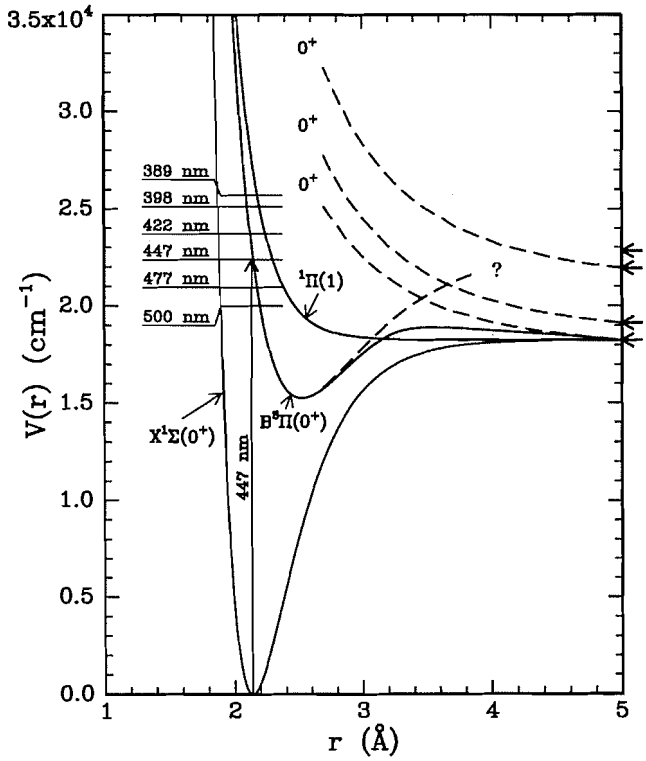

FIG. 3. Sketch of the potential energy curves of BrCl. Non-adiabatic interactions of the $^3\Pi(0^+)$ curve with other (0^+) states yield $Cl(^2P_{3/2})$ and $Cl^*(^2P_{1/2})$ fragments as discussed in the text. The photolysis laser wavelengths used in our experiment are displayed. The locations of the four exit channels are also indicated on the right axis.

$BrCl \rightarrow Br(^2P_{3/2}) + Cl(^2P_{3/2})$	555 nm	$E_{th} = 18022\ cm^{-1}$
$Br(^2P_{3/2}) + Cl^*(^2P_{1/2})$	529 nm	$E_{th} = 18903\ cm^{-1}$
$Br^*(^2P_{1/2}) + Cl(^2P_{3/2})$	461 nm	$E_{th} = 21707\ cm^{-1}$
$Br^*(^2P_{1/2}) + Cl^*(^2P_{1/2})$	443 nm	$E_{th} = 22588\ cm^{-1}$

The excited states responsible for the BrCl absorption in the region of 300–500 nm are believed to be the $^1\Pi(1)$ and the $^3\Pi(0^+)$ states. Drawn schematically in Fig. 3 are the ground state ($X^1\Sigma^+$), the B–$^3\Pi(0^+)$ state, and the $^1\Pi(1)$ state. The A–$^3\Pi(1)$ state, which lies below the B state, was not studied in detail previously and the role that it plays in the absorption was not clear.

The $^1\Pi(1)$ potential energy curve is repulsive near the Franck–Condon region but has a shallow minimum at large internuclear distance. The B state on the other hand has a well-defined minimum located at $r = 2.54$ Å (4) and a small barrier. The $^1\Pi(1)$ and the $^3\Pi(0^+)$ potential curves cross at $r \approx 3.05$ Å; this crossing is responsible for the near-threshold predissociation following excitation to the $^3\Pi(0^+)$ state (4–6). Based on the correlation diagram (10), adiabatic dissociation via the B state is expected to yield both the chlorine and the bromine fragments in their ground states. However, the diabatic dissociation limit was not clearly established. For instance, Clyne and Coxon concluded from semi-quantitative considerations that the diabatic dissociation limit should be Br + Cl* (11), whereas Tellinghuisen and co-workers recently noticed that the diabatic dissociation limit is less likely Br + Cl*, but possibly Br* + Cl (12).

The absorption spectrum was decomposed by Seery and Britton (3) into two Gaussian curves as displayed in Fig. 2*b*. However, these Gaussian curves cannot represent the partial absorption cross sections of the $^1\Pi(1)$ and the $^3\Pi(0^+)$ states, based on the following consideration. The onset of the second Gaussian curve is located around 430 nm whereas considerable amounts of Cl* fragments were observed even at 389 nm. From the correlation diagram (10) and the symmetry of the $^1\Pi(1)$ state it is unlikely that the $^1\Pi(1)$-state dissociation yields significant amounts of the Cl* fragments. The B-state absorption is therefore blue-shifted from the second Gaussian component. This implies, first, that the partial absorption from the $^1\Pi(1)$ state is narrower than expected from the first Gaussian curve, implying a more shallow excited state potential energy curve (13). Secondly, to explain the absorption at long wavelengths the introduction of a third excited state might become necessary. Since the only other allowed excited state lying below the B state is the A–$^3\Pi(1)$ state, this third contribution would then arise from A-state excitation.

As can be seen in Fig. 2*a*, at least two excited states contribute to the photofragment yield spectrum of the Cl fragment. At short wavelengths dissociation through the $^1\Pi(1)$ state is clearly favoured, while at wavelengths longer than 440 nm the $^3\Pi(0^+)$ state is dominant. It is also evident from Fig. 2*a* that dissociation through the $^1\Pi(1)$ state yields negligible amounts of the Cl* fragments, indicating that the dissociation is mainly adiabatic as described before. On the other hand, the dissociation via the B–$^3\Pi(0^+)$ state yields comparable amounts of Cl and Cl* fragments. This observation suggest that extensive non-adiabatic transitions among different potential energy curves are involved in the B-state dissociation. The shape of the branching ratio curve can be understood qualitatively based on the following consideration. In the short wavelength region the Cl* yield increases as the contribution of the B state to the absorption increases. In the long wavelength region there are two possible reasons for the decrease of the Cl* yield: (*a*) the extent of the B-state non-adiabatic interaction decreases with decreasing excitation energy and (*b*) the participation of the A state increases.

The shape of the Cl* yield curve is difficult to understand in the region between 400 and 470 nm, since apart from the maximum at 410 nm a shoulder appears at around 450 nm. If one considers that the Br* + Cl* channel opens at 443 nm and the Br + Cl* channel opens at 529 nm, a possible explanation for the observed Cl* yield curve involves contributions from both Br* + Cl* and the Br + Cl* channels.

In Fig. 3 we display the potential energy curves involved in the BrCl photodissociation according to our current understanding. Based on the correlation diagram (10) and spectroscopy studies (12) at least two (0^+) curves are expected to cross the $^3\Pi(0^+)$ state. The non-adiabatic interactions among these curves are responsible for the observed formation of Cl and Cl* fragments. The shape of the Cl* photofragment yield spectrum may give an indication for partial involvement of the Br* + Cl* channel. But even without this specific conclusion, the inclusion of non-adiabatic interactions in the photodissociation dynamics of BrCl is crucial, as we have demonstrated in this communication.

Further experiments as well as *ab initio* calculations are necessary to fully understand the details of the B-state photodissociation dynamics of BrCl. Direct measurements of the Br*/Br branching ratio are certainly desirable but are complicated by the large absorption cross section of Br_2 in this wavelength

region. Furthermore, these measurements will not allow the distinction between the Br* + Cl* and the Br* + Cl exit channels. However, photofragment TOF spectroscopy of the chlorine fragment provides information about the kinetic energy of the fragments and thereby about the participation of the four exit channels. These experiments are currently being carried out by our group.

Summary

The chlorine spin-orbit branching ratios for BrCl photodissociation were measured at several photolysis wavelengths between 389 and 500 nm. The branching ratios were used to determine the photofragment yield spectra of the Cl and the Cl* fragments. These measurements show that the B–$^3\Pi(0^+)$ state dissociation yields comparable amounts of Cl and Cl* fragments. The shape of the Cl* photofragment yield curve suggests the possible participation of the Br* + Cl* exit channel. Our results indicate that the B-state dissociation involves transitions among at least two (0^+) curves. Furthermore, from the onset of the Cl* formation it is implied that the A state contributes to the absorption in the long wavelength region. More experimental and theoretical studies are necessary to establish a detailed dissociation mechanism.

Acknowledgements

This work is supported by the Natural Sciences and Engineering Research Council of Canada, the Centres of Excellence in Molecular and Interfacial Dynamics, and the University of Victoria. The authors thank Dr. Y. Wang, Prof. W.J. Balfour, Prof. R.J. Le Roy, and a referee for helpful discussions and comments.

1. S.J. Singer, K.F. Freed, and Y.B. Band. J. Chem. Phys. **81**, 3064 (1984).
2. R.D. Levine and R.B. Bernstein. *In* Molecular reaction dynamics and chemical reactivity. Oxford University Press, New York. 1987.
3. D.S. Seery and D. Britton. J. Phys. Chem. **68**, 2263 (1964).
4. J.A. Coxon. J. Mol. Spectrosc. **50**, 142 (1974).
5. M.A.A. Clyne and I.S. McDermid. Faraday Discuss. Chem. Soc. **67**, 316 (1979).
6. J. Tellinghuisen. J. Chem. Phys. **89**, 6150 (1988).
7. D. Proch and T. Trickl. Rev. Sci. Instrum. **60**, 713 (1989).
8. W.C. Wiley and I.H. McLaren. Rev. Sci. Instrum. **26**, 1150 (1955).
9. Y. Matsumi, K. Tonokura, M. Kawasaki, G. Inoue, S. Satayapal, and R. Bersohn. J. Chem. Phys. **97**, 5261 (1992).
10. M.C. Heaven. Chem. Soc. Rev. **15**, 405 (1986).
11. M.A.A. Clyne and J.A. Coxon. Proc. R. Soc. London, A: **298**, 424 (1967).
12. S.W. Brown, C.J. Dowd, Jr., and J. Tellinghuisen. J. Mol. Spectrosc. **132**, 178 (1988).
13. J. Tellinghuisen. *In* Advances in chemical physics. Vol. 60. *Edited by* K.P. Lawley. John Wiley & Sons, New York. 1985. pp. 299–370.

Can. J. Chem. Downloaded from www.nrcresearchpress.com by EESC ESCOLA DE ENGENHARIA on 09/08/12
For personal use only.

Molecular beam kinetics: reactions of H and D atoms with alkali halides

P.E. SISKA[1] AND D.R. HERSCHBACH

Department of Chemistry, Harvard University, Cambridge, MA 02138, U.S.A.

Received August 26, 1993

This paper is dedicated to Professor John C. Polanyi on the occasion of his 65th birthday

P.E. SISKA and D.R. HERSCHBACH. Can. J. Chem. **72**, 762 (1994).

Angular distributions of alkali atoms produced in crossed-beam reactions of H and D atoms (at ~2800 K) with KF, CsF, KCl, CsCl, and KBr (at ~1100–1200 K) have been measured. For these systems, the reaction exoergicity varies from $\Delta D_0 \sim 17$ kcal/mol for H + KF to −4 kcal/mol for H + KBr; the thermal distribution of the reactant energy peaks near 12 kcal/mol with $E \sim 9$ kcal/mol in relative translation and $W \sim 3$ kcal/mol in vibration and rotation of the alkali halide. Kinematic analysis of the data is carried out by means of a least-squares procedure that includes averaging over the parent beam velocity distributions. The main results are (1) The reaction cross sections Q_r vary from ~1 to 30 Å^2. The magnitude correlates with ΔD_0 and with the identity of the halogen for a given alkali, decreasing as F → Cl → Br. For a given halogen, Q_r is 2–3 times larger for the Cs reaction than for K and about 2 times larger for D than for H. (2) Temperature-dependence measurements for the CsCl case indicate the activation energy (in excess of endoergicity) is near zero. (3) The preferred direction of the reactively scattered alkali atoms with respect to the incident alkali halide varies with the halogen, from mainly forward for the KBr reaction to more sideways for the KF and CsF reactions. (4) The partitioning of energy between product translation E' (M relative to HX) and internal excitation W' (vibration and rotation of HX) can only be roughly estimated; our data are consistent with $E' \sim W$ and $W' \sim E + \Delta D_0$ but a definitive analysis will require product velocity distributions or spectra. These results are discussed in terms of a dynamical model akin to Polanyi's DIPR model. This postulates that the motion of H or D is approximately separable from that of the heavier atoms and the preferred reaction geometry corresponds to a triangular H–X–M complex.

P.E. SISKA et D.R. HERSCHBACH. Can. J. Chem. **72**, 762 (1994).

On a mesuré les distributions angulaires des atomes alcalins produits dans des réactions à faisceaux croisés d'atomes de H et de D (à environ 2800 K) avec du KF, du CsF, du KCl, du CsCl et du KBr (à environ 1100–1200 K). Pour ces systèmes, l'exoergicité de la réaction varie de $\Delta D_0 \sim 17$ kcal/mol pour H + KF à −4 kcal/mol pour H + KBr; la distribution thermique de l'énergie des réactifs passe par un maximum vers 12 kcal/mol avec $E \sim 9$ kcal/mol pour la translation relative et $W \sim 3$ kcal/mol pour la vibration et la rotation des halogénures alcalins. On a effectué l'analyse cinématique des données à l'aide d'une méthode des moindres carrés qui implique de faire la moyenne des distributions de la vitesse du faisceau parent. Les résultats principaux sont : (1) les sections droites de la réaction varient de Q_r ~1 à 30 Å^2. Il existe une corrélation entre l'amplitude et le ΔD_0 ainsi qu'avec la nature de l'halogène d'un métal alcalin donné; elle diminue dans l'ordre F → Cl → Br. Pour un halogène donné, Q_r est trois fois plus important pour une réaction avec le Cs qu'avec le K et 2 fois plus important pour D que pour H; (2) les mesures de dépendance sur la température dans le cas du CsCl indiquent que l'énergie d'activation (en excès par rapport à l'endoergicité) est pratiquement égale à zéro; (3) la direction privilégiée des atomes alcalins dispersés par la réaction par rapport à l'halogénure alcalin incident varie avec l'halogène; alors qu'elle est principalement vers l'avant pour la réaction du KBr, elle est plus dirigée vers les côtés pour les réactions du KF et du CsF; (4) on ne peut faire qu'une évaluation très approximative de la partition de l'énergie entre la translation du produit, E' (M relatif à HX) et l'excitation interne, W' (vibration et rotation de HX); nos données sont en accord avec $E' \sim W$ et $W' \sim E + \Delta D_0$, mais une analyse définitive nécessitera des distributions de la vitesse des produits ou des spectres. On discute de ces résultats en fonction d'un modèle dynamique semblable au modèle DIPR de Polanyi qui fait l'hypothèse que le mouvement de H ou de D peut être séparé d'une façon approximative de celui des atomes plus lourds et que la géométrie réactionnelle privilégiée correspond à un complexe H–X–M triangulaire.

[Traduit par la rédaction]

Introduction

Reactions of hydrogen atoms with alkali halide molecules, H + MX → HX + M, invite study by virtue of the simple electronic structure of the reactants and the promise of instructive comparisons with other archetypical systems. Whereas the bonding change is *covalent* → *ionic* for the extensively studied "electron-jump" or "harpooning" reactions of alkali atoms with covalent halides (1), for the H + MX case the bonding change is *ionic* → *covalent* and might be viewed as "reverse harpooning."

In the entrance channel, the qualitative electronic structure has only one electron outside three closed-shell ions (H^+, M^+, X^-). This resembles the reactions of alkali atoms with alkali halides, which likewise have one electron outside three ion cores (M^+, M'^+, X^-). Beam experiments (2) and trajectory calculations (3) have shown the latter reactions go via a statistical collision complex. One-electron pseudopotential calculations (4) for several of these dialkali halide systems as well as *ab initio* calculations (5) for HLi_2 found that the potential energy surfaces contain deep basins (comparable to or exceeding the reaction exoergicity) for triangular configurations of the complex. For HXM systems, semiempirical surfaces (6) for nearly the full family (M = Li → Rb; X = F → I) as well as *ab initio* calculations (7) for HFLi find the dominant features are not basins but barriers. The geometry of the transition state and the location of the barrier (entrance or exit) shift with the halogen and are governed by the H—X distance at which the electron-jump occurs. The H + MX reaction dynamics can also be expected to show distinctive behavior because of the disparity of time scales for motion of the H atom relative to the heavy atoms (8).

By microreversibility, the hydrogen atom – salt reactions are related to M + HX → MX + H, the subject of a host of experiments and theoretical treatments, especially the Li + HF case (9). Experimental results for those systems include optical

[1]Present address: Department of Chemistry, University of Pittsburgh, Pittsburgh, PA 15260, U.S.A.

Can. J. Chem. Downloaded from www.nrcresearchpress.com by 195.246.54.202 on 09/08/12
For personal use only.

Can. J. Chem. Downloaded from www.nrcresearchpress.com by 195.246.54.202 on 09/08/12
For personal use only.

model parameters describing the dependence of reaction probability on collision energy and approach distance (10); on alignment of state-selected reagent molecules (11); variation of the total reaction cross section with collision energy (12) and vibrational (13) or rotational (14) excitation; and analysis of the velocity (15), rotational energy (16), and spatial orientation of angular momentum (17) of the reactively scattered salt molecules. For several M + HX systems, the electron-jump process has been directly observed, in collisional production of ion-pairs (18) and also in electron spin resonance spectra of a matrix-isolated σ^* radical corresponding to the HCl^-K^+ complex (19). By chemical extrapolation, Penning ionization systems such as He* + HCl (with He* acting as a "superalkali") likewise involve σ^* radicals (20).

Unfortunately, the interpretation of M + HX reactive scattering is severely handicapped by kinematic constraints that confine the MX product near the centroid (21). The preferred direction and speed of product recoil in the center-of-mass (cm) system are thus hard to discern from the laboratory data. Nearly isotropic recoil distributions were reported for the K + HBr and K + DBr reactions (15), but somewhat anisotropic, sideways-peaked distributions are also compatible with the data (22). The kinematic constraints were elegantly circumvented in a study of M + TBr reactions (23) by detecting the tritium atoms, which are not confined near the centroid. Sharply backward recoil of the T atoms with respect to the incident TBr was found, a "rebound" mechanism. Such an isotope effect is difficult to explain (24), and subsequent work suggests these results may be unreliable.[2] Microreversibility applied to H + MX offers another approach to this problem, as the kinematics of these reactions is favorable for study of the product recoil direction.

This paper presents angular distribution data for reactions of H and D atoms with five alkali halides. The product recoil distributions in the cm system are found to be quite anisotropic and to show a marked shift from dominantly sideways to forwards as the halogen is varied, F → Cl → Br. These shifts complement the results found for H + X_2 reactions (25), in which the product recoil distributions shift from backwards to sideways as Cl → Br → I, whereas for the H + M_2 reactions (26) the product recoil remains sideways as K → Rb → Cs. The special dynamical features pertinent to reaction of a light atom with a heavy molecule are exemplified by comparison with a model, akin to Polanyi's DIPR model (8), which postulates that the H atom motion is approximately separable from that of the heavy atoms. For this model, the product angular distribution is governed by the combined effects of anisotropy in the potential energy as a function of the molecular orientation and angular momentum constraints resulting from the mass disparity.

Experimental

Figure 1 shows the arrangement of beam sources and detector. The apparatus was essentially the same as in the H + M_2 study (26). The H atom beam was produced by thermal dissociation in a tungsten tube oven (27) (with 0.2 mm slit width) operated at ~2800 K and 1 Torr (= 133.3 Pa); the atom fraction in the beam was ~80%. The salt beam was produced by a double chamber oven (with exit slit 0.2 mm × 7 mm); the supply chamber temperature (~900–1200 K) was chosen to give a salt vapor pressure of ~1–10 Torr and the independently heated orifice chamber was kept ~80–120 degrees hotter to prevent condensation. The collimating slit was also kept at ~700 K to avert clogging. The background pressure in the collision chamber, due largely to ambient H_2 or D_2, was typically 1×10^{-6} Torr during runs.

The total scattering (M + MX) was detected with a Re surface ionization filament operated at ~1700 K, the reactive scattering (M atoms) with a Pt – 8% W alloy filament operated at ~1300 K and preconditioned by heating at ~1600 K for a few minutes in methane at 10^{-4} Torr to render the filament insensitive to alkali halides (28). Both filaments were ribbons, 0.03 mm thick and 0.76 mm wide. To employ phase-sensitive lock-in amplification, the hydrogen beam was modulated at 10 Hz by a two-blade chopper. The chopper was driven by a six-pole synchronous motor with 15 Hz input voltage to avoid pickup and a reference signal was provided by a light bulb and phototransistor on the chopper mount.

The fact that the reactively scattered M atoms can be measured directly on the "methanated" Pt alloy filament made these experiments feasible. For other alkali systems, the reactive scattering signal usually must be obtained as the small difference between the total and nonreactive scattering signals. This would fail for the H + MX systems, as the yield of alkali atoms is relatively small and appears near the salt beam. Here subtraction was still necessary to correct the Pt filament readings for the residual detection of salt molecules and to deduct from the Re readings the alkali atom contribution; however, in each case the difference signals are comparable to the original filament readings. The efficiency of the Re filament is taken as 100% for both M and MX; strong evidence for this is provided by comparison of data taken on W, Re, and Pt under a variety of conditions (29). If the detection efficiency of the "methanated" Pt filament is denoted by g, the reactive and nonreactive signals are related to the filament readings by

$$[1a] \quad I_M = (I_{Pt} - g_{MX} I_{Re})/(g_M - g_{MX})$$

$$[1b] \quad I_{MX} = (g_{MIRe} - I_{Pt})/(g_M - g_{MX})$$

The g_M factor varies appreciably with filament conditions but is roughly ~50% in our experiments, whereas g_{MX} is less than 1%, often much less (30). Thus, g_{MX} can be neglected in the denominators; g_M then enters only as a scale factor in eq. [1a] and thus need not be known to determine the shape of the M angular distribution. The g_{MX} factor was determined at the end of each run by comparing Pt and Re scans of the salt beam. The measured g_{MX} ranged from a maximum of 0.9% to less than 0.01%; the value varied from run to run but tended to correlate with the identity of the halogen (0.9% pertains to CsF, 0.01% to KBr). The work function of the "methanated" Pt filament, as monitored by the electron emission, did not show any appreciable or systematic changes. The Re filament, after prolonged operation in the ~10^{-6} Torr of ambient hydrogen, appeared to "fatigue" with loss of detection efficiency. Sometimes flashing in 10^{-4} Torr of oxygen would revive it, sometimes not. This problem was avoided by merely installing a new Re filament every few weeks.

Figure 2 shows the primary data, Pt and Re filament readings, for scattering of H and D with KX and CsX, where X = F, Cl, Br. For the potassium salts, which have smaller reaction cross sections, the two best sets of Pt data are included. In each case (except H + CsBr), the Pt signals clearly contain a contribution from reactively scattered alkali atoms. This makes the readings on Pt and Re quite different on the two sides of the salt beam. Also, the Pt signal usually falls off more gradually than the Re signal on the small-angle side, where most of the elastic scattering appears. No reactive scattering was observed for H + CsBr; since the reaction is endoergic by 9 kcal/mol, this result was expected. It provided a test of the detection scheme. When the Pt alloy ribbon was preconditioned by heating in oxygen to render it sensitive to MX, the signals obtained were superimposable on the Re data. When the Pt ribbon was preconditioned by heating in methane, the signals obtained were tiny (points at $\Theta = 80°$ and 82°) and after correction for the residual detection of MX (by use of the measured g_{MX} factor), no significant signal remained.

The H + CsF data are typical of the systems with the largest reactive signals. In he scattering zone, the H beam flux was ~10^{15} atoms cm^{-2} s^{-1} (derived from bolometer readings and calibrations (27)), the

[2]L.R. Martin has found in subsequent work with tritium systems that the experimental procedure of ref. 23 failed to give reproducible results (private communication).

Can. J. Chem. Downloaded from www.nrcresearchpress.com by 195.246.54.202 on 09/08/12
For personal use only.

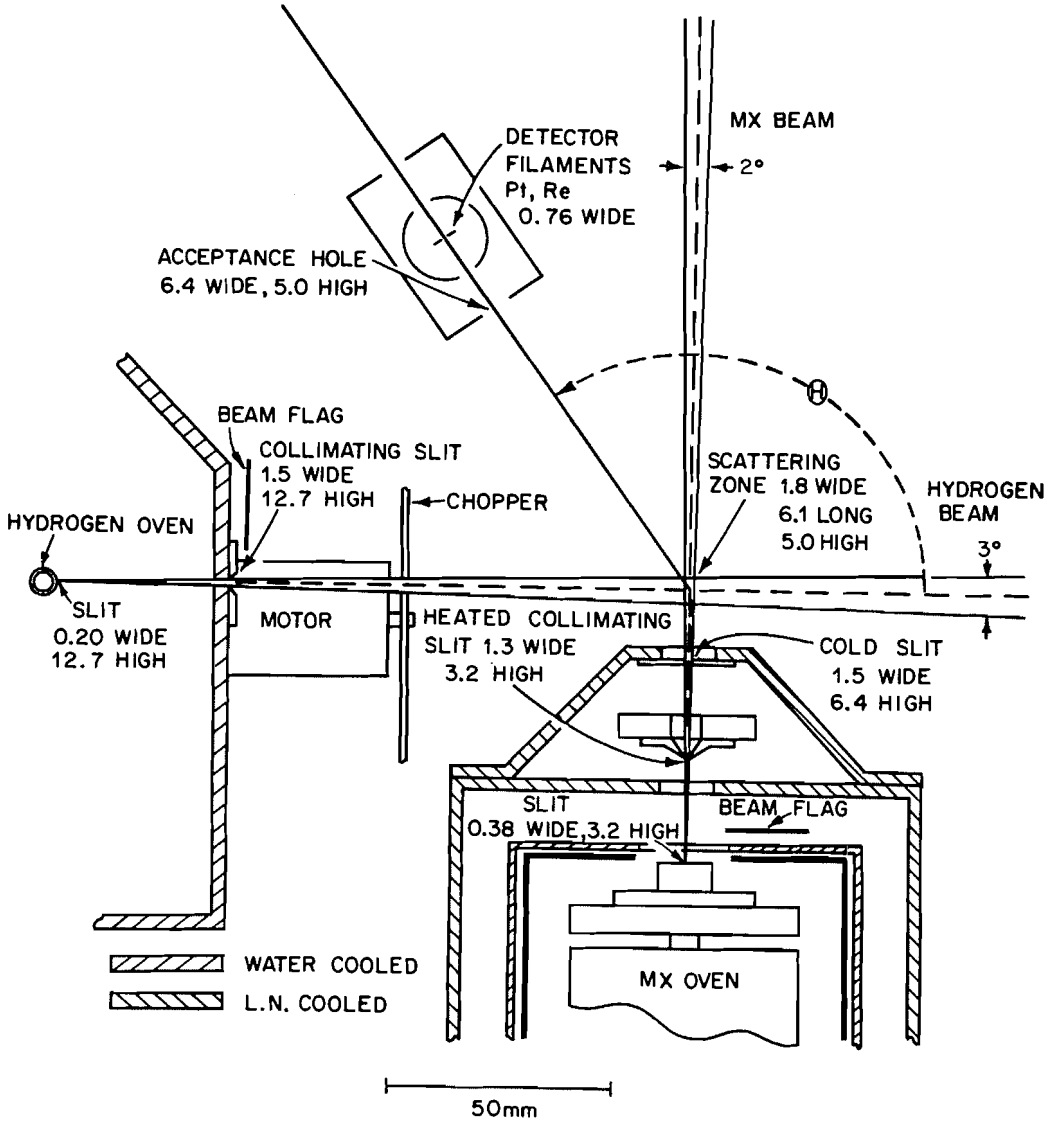

FIG. 1. Schematic of the crossed-beam apparatus. All dimensions are given in mm. Not shown are a bolometer detector (ref. 27) used to monitor the hydrogen atom beam and an additional surface ionization detector used to monitor the salt beam. The LAB scattering angle Θ specifies the direction of the product alkali atom with respect to the hydrogen beam.

salt beam flux was $\sim 2 \times 10^{15}$ molecules cm^{-2} s^{-1} (corresponding to a surface ionization signal of 3×10^{-6} A at the rotating detector). At Θ = 70°, the total scattered flux detected on the Re filament was $\sim 10^9$ molecules cm^{-2} s^{-1} (6×10^{-12} A), of which all but 5% was due to elastic scattering; the scattered flux detected on the Pt filament was 5×10^7 molecules cm^{-2} s^{-1} (3×10^{-13} A), of which about 80% was due to reactively scattered Cs atoms. The H + KBr case gave the smallest reactive signals observed; the salt beam flux and the total scattering at Θ = 70° were somewhat higher than above, but the Pt signal was about an order of magnitude less, with about 90% due to reactively scattered K atoms.

Nonreactive scattering

For these systems, the large mass ratio MX/H or MX/D severely handicaps kinematic transformation of the MX angular distribution data from the laboratory (LAB) to the center-of-mass (cm) system. An approximate transformation was carried out, however, in order to compare results for the nonreactive scattering by H, D, and He. Figure 3 illustrates the kinematic situation for the H + KBr case. The small sphere drawn about the tip of the centroid velocity vector $\boldsymbol{C}$ indicates the locus of the cm velocity $\boldsymbol{u}$ of KBr for purely elastic scattering. Since $|\boldsymbol{u}| < |\boldsymbol{C}|$, the KBr is confined to a narrow range of LAB angles Θ (between 72° and 90°, for the parent beam velocities corresponding to the diagram). In this range, two values of the cm scattering angle θ contribute at each LAB angle. The cm differential cross section $I_{cm}(\theta)$ thus is related to the observed LAB angular distribution by

$$[2] \quad I_{LAB}(\Theta) = J_i I_{cm}(\theta_i) + J_o I_{cm}(\theta_o)$$

The subscripts i and o refer to the inner and outer contributions (illustrated in Fig. 3) and J_i, J_o are the corresponding Jacobian factors for the LAB $\rightarrow$ cm transformation. For these systems, the inner contribution cannot be neglected as usual (29); the elastic scattering sphere is small enough to make J_i and J_o comparable, and usually $\theta_i < \theta_o$, so the inner portion is more intense. Also, the spread in $\boldsymbol{u}$ and $\boldsymbol{C}$ caused by the parent beam velocity distributions and imperfect collimation produces contributions to $I_{LAB}(\Theta)$ outside the nominal range allowed for the most probable beam velocities. To avoid resorting to stochastic calculations, we ignored the intensity in these outside regions as

Can. J. Chem. Downloaded from www.nrcresearchpress.com by 195.246.54.202 on 09/08/12
For personal use only.

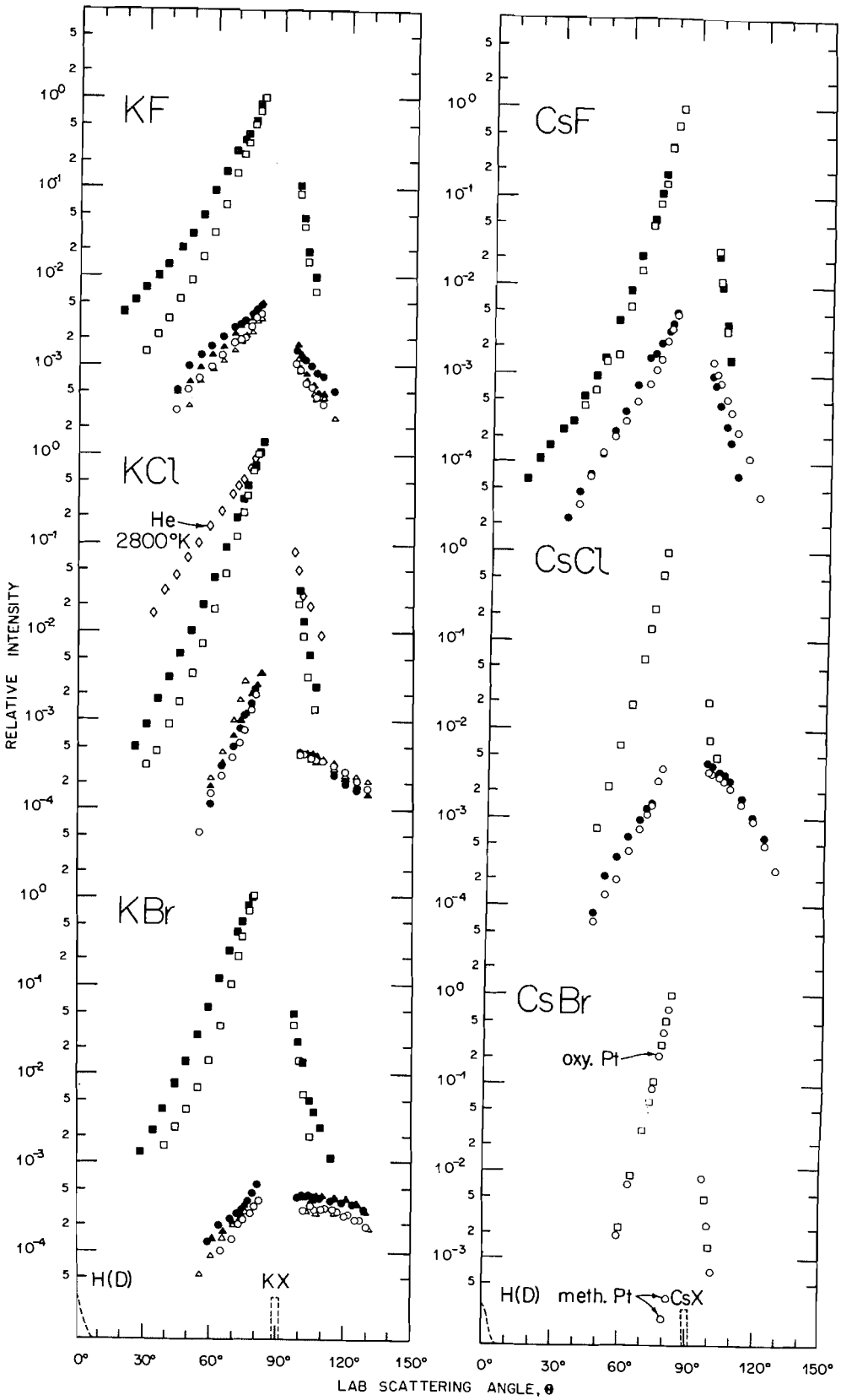

FIG. 2. Primary data collected on the Re (□, ■) and Pt (○, ●, △, ▲) filaments for scattering of six salts by H (open symbols) and D (filled symbols). For K salts, data are shown for two runs (circles and triangles). For KCl, data taken on Re (◇) are also shown for scattering by He; for CsBr, data were taken on Pt in both the oxygenated and methanated modes. The Re data are normalized so that the most intense H point for a given salt is unity, and the D data are also normalized to H at that point.

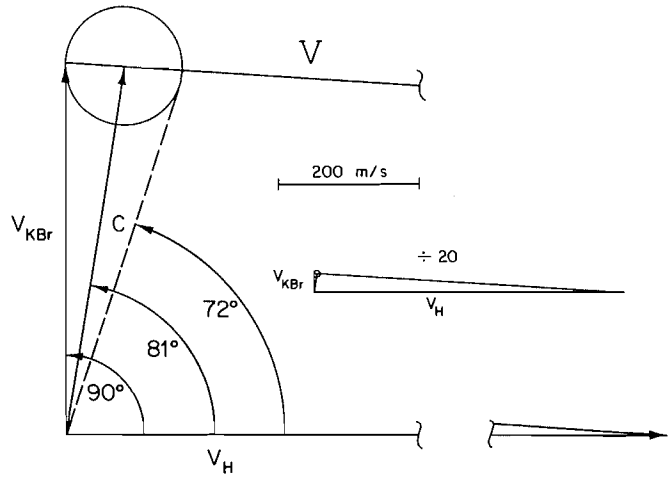

FIG. 3. Kinematic diagram for H + KBr elastic scattering: v_H and v_{KBr} are the most probable beam velocities; $\boldsymbol{C}$ the center-of-mass velocity; $\boldsymbol{V}$ the relative velocity; $\boldsymbol{u}$ the recoil velocity of KBr in the center-of-mass system. Circle shows locus of $\boldsymbol{u}$ vectors allowed by conservation of energy and momentum, which confine LAB elastic scattering within the range Θ = 72–90°. Portions of circle below and above $\boldsymbol{V}$ indicate the "inner" and "outer" branches, respectively, of the LAB → cm transformation. Inset on right shows complete diagram reduced by a factor of 20.

well as any inelastic contributions (probably minor) and derived $I_{cm}(\theta)$ from eq. [2] by a simple iterative procedure that makes use of the fact that the inner and outer branches come from the same function.

Figure 4 gives the resulting cm angular distributions of elastic scattering. Since in each case the most probable centroid velocity vector lies close to the salt beam, and accurate data could not be taken near the beam, most of the accessible LAB scattering transformed into the backward hemisphere ($\theta > 90°$) in the cm system. Two features are of interest:

1. In the LAB data for a given salt (Fig. 2, Re curves), collisions with D produce wider elastic scattering than those with H. The effect is most prominent for KF, the lightest target molecule, and becomes almost negligible for CsF. This is a kinematic isotope effect (seen in the H + M_2 data (26)), since the D atom carries $\sqrt{2}$ times more linear momentum than H at the same temperature. If the LAB → cm transformation were exact and the nonreactive scattering were solely elastic, the cm angular distributions (Fig. 4) for D and H should superimpose since both pertain to the same collision energy. The cm results indeed almost superimpose for each of the four salts studied.

2. The cm angular distributions show a rather strong decline in the $\theta > 90°$ region rather than the flat behavior expected for repulsive wall scattering. The similar decline found for He + KCl indicates that this is due largely to systematic bias introduced by the extensive velocity averaging and unfavorable kinematics. However, it is significant that with H or D the scattered KCl falls off more rapidly than with He; the extrapolated difference is a factor of 5 at θ = 180°, which corresponds to zero impact parameter. This difference can be attributed to reaction at small impact parameters that attenuates the wide-angle elastic scattering, as in K + HBr and other systems (10).

Reactive scattering

The analysis of the M atom scattering is not handicapped by kinematic constraints, since the mass ratio M/HX is comparable to unity, particularly for the potassium reactions. The data provide a fairly good determination of the cm angular distributions but only rough estimates of the product translational energy and total reaction cross sections.

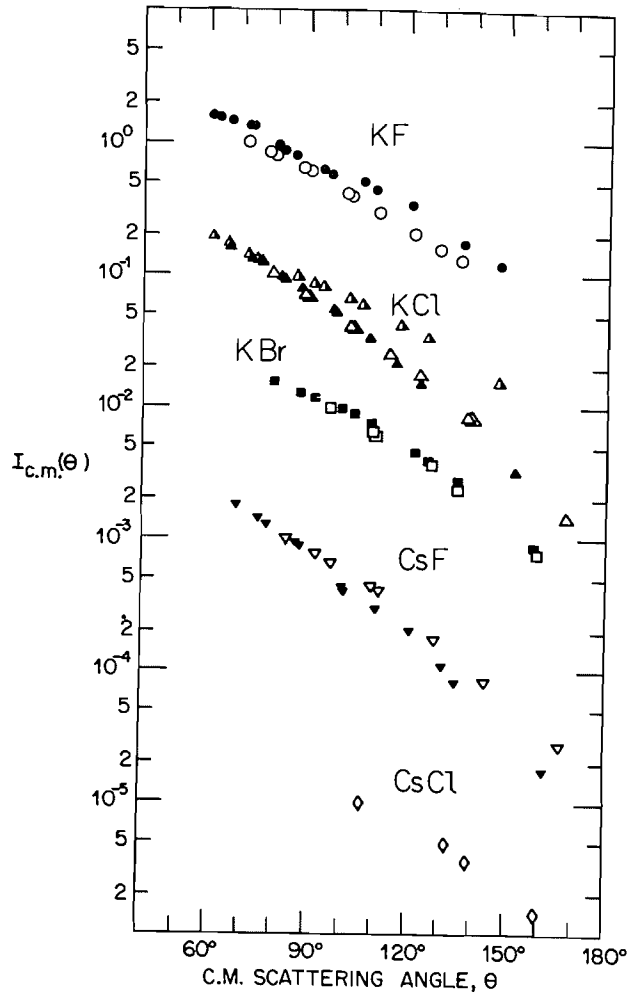

FIG. 4. Angular distributions (center-of mass system) for the elastic scattering of five salts by H (open symbols) and D (filled symbols). For KCl, points are included for scattering by He (half-filled symbols). Normalization for each salt is the same as in Fig. 2.

Product angular distributions

Figure 5 shows the LAB angular distributions of reactively scattered alkali atoms. Points within about ±10° of the salt beam had to be omitted because the correction for residual detection of MX in eq. [1] becomes large there. Likewise, points on the small-angle side ($\Theta < 90°$) of the salt beam have more scatter than on the large-angle side ($\Theta > 90°$), due to this correction. The peak positions and shapes of the alkali atom distributions are well determined, however. Also shown are the centroid angular distributions (21) (dashed curves) calculated from the parent beam velocity distributions. The reactive scattering is substantially broader than the centroid distribution in each case and it is displaced towards larger LAB angles, the displacement increasing as F → Cl → Br in the reactant salt. This trend is well outside experimental uncertainties. The shift to wider LAB angles indicates a preference in the cm system for recoil of the product M atoms into the forward hemisphere with respect to the incident MX molecules. By momentum conservation, the HX product molecules prefer the backward hemisphere.

Can. J. Chem. Downloaded from www.nrcresearchpress.com by 195.246.54.202 on 09/08/12
For personal use only.

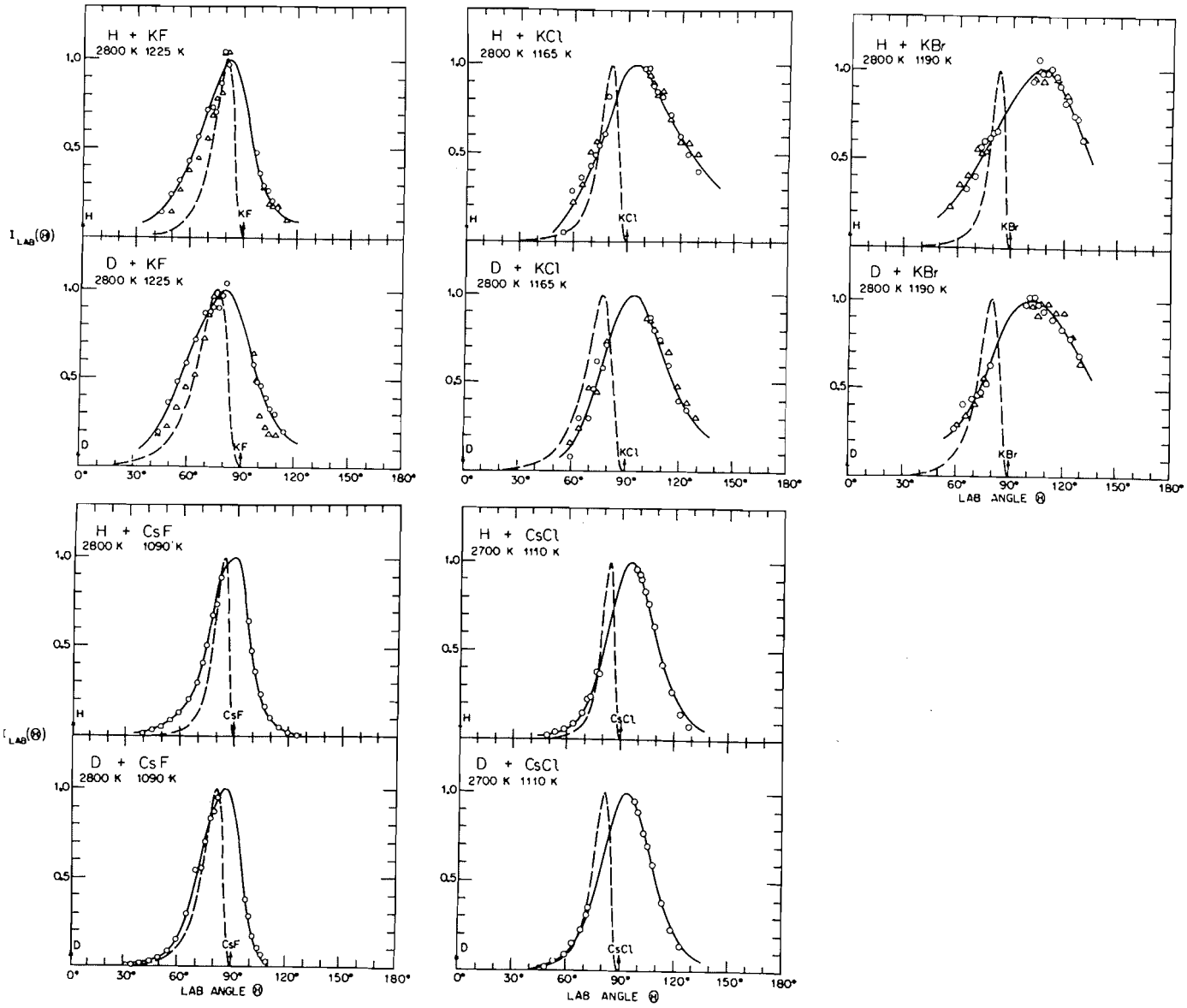

FIG. 5. Angular distributions (laboratory system) of M atoms from reactions of H and D with MX for five salts at the beam temperatures indicated. Ordinates are normalized to unity. Broken curves are centroid distributions; solid curves are calculated from a least-squares kinematic analysis.

The trend with change of the halogen might arise either from a systematic variation of (*i*) the product recoil velocity away from the centroid (small for F reactions, increasing for Cl and Br) or (*ii*) the preferred direction of recoil (more nearly sideways for F, increasingly forward for Cl and Br). A variation of recoil velocity opposite to that required by (*i*) seems likely, both because the reaction exoergicity is large for F reactions but much smaller for Cl and negative or Br, and because the product reduced mass is least for F reactions, most for Br. This is borne out by a kinematic analysis, which confirms that (*ii*) is responsible for the trend with halide.

The LAB → cm transformation was carried out as usual by an indirect procedure (29), since the lack of parent beam velocity analysis prevents a direct transformation. A separable form was assumed for the cm differential reaction cross section,

$$[3] \quad I_{cm}(\theta, u) = T(\theta)U(u)$$

The cm scattering angle for the M atom is defined such that $\theta = 0°$ at the direction of the incident MX beam and $\theta = 180°$ at the H or D beam; the cm velocity u pertains to recoil of the M atom away from the centroid. The angular factor was represented by the first six terms in a Legendre polynomial expansion, the recoil velocity factor by a Maxwellian flux distribution, of the form

$$[4] \quad U(u) = (u/\hat{u})^3 \exp 3/2[1 - (u/\hat{u})^2]$$

The most probable recoil velocity (denoted $\hat{u}$) was chosen by comparing trial calculations with the data, and the Legendre coefficients $(a_0, \ldots a_5)$ were determined by a least-squares method (31). The procedure involves computing LAB product velocity spectra at the desired angles, averaging over 36 combinations of parent beam velocities, and integrating these spectra to obtain the total flux at each LAB angle to be compared with

Can. J. Chem. Downloaded from www.nrcresearchpress.com by 195.246.54.202 on 09/08/12
For personal use only.

TABLE 1. Energy disposal[a]

	Salt				
	KF	CsF	KCl	CsCl	KBr
ΔD_0	17	15	2.2	−3.3	−4.0
$E'(E_-', E_+')$	9(2,30)	3(2,20)	12(3,14)	4(2,9)	2(1,4)
$W'(W_-', W_+')$	21(0,28)	24(7,25)	2(0,9)	5(0,7)	6(4,7)

[a]Energies in kcal/mol, for H reactions. Values of ΔD_0 for D reactions are higher (more positive) by 1.6, 1.3, 1.1 kcal/mol, respectively, for F → Cl → Br. Notation: $E'(E_-', E_+')$ indicates "nominal best-fit value (lower bound, upper bound)."

Can. J. Chem. Downloaded from www.nrcresearchpress.com by 195.246.54.202 on 09/08/12
For personal use only.

our data. Velocity analysis of hydrogen atom beams (25) and salt beams (32) under similar conditions indicates substantial deviations from effusive flow, both corresponding to Mach numbers near unity. An empirical number density distribution,

$$[5] \quad N(v) = (v/v^*)^n \exp(n/m)[1 - (v/v^*)^m]$$

was used for both beams, where $n = 8$, $m = 1$, and $v^* = 1.3(2\mathcal{R}T/\mathcal{M})^{1/2}$, with $\mathcal{R}$ the gas constant, T the source temperature (listed in Fig. 5), and $\mathcal{M}$ the molecular weight. The dependence of the cm cross section on initial collision energy was left implicit, since an appropriate functional form is not known and the spread in initial conditions is large. Trial calculations showed that the endoergicity of the KBr and CsCl reactions does not significantly affect the LAB → cm transformation, because the most probable initial collision energy much exceeds the endoergicity (cf. Table 1). The angular widths of the parent beams also proved to have negligible effect. Figure 5 includes the "best fits" (solid curves) to the LAB data obtained from this analysis.

Figure 6 gives the corresponding cm angular distributions, $T(\theta)$. Inspection of the fitting procedure indicates the peak positions are typically determined within about ±20°, but the wobbly structure seen in some of the curves is an artifact. It results from interpolation across the region obscured by the salt beam and Jacobian enhancement of contributions from low recoil velocities (31). However, three properties of qualitative interest appear reliable:

1. The cm product angular distributions for reaction of H and D with a given MX salt are the same, within the experimental resolution.

2. The cm distributions for K and Cs from a given halide show some similarity but the difference seen for the chloride case may be significant.

3. The cm distributions for a given alkali shift from sideways to forward peaking with change of the halogen atom from F → Cl → Br, in accord with the trend inferred from the LAB data.

For two kindred systems, the H + X_2 reactions (25) and the M + X_2 reactions (29), the shapes of the product angular distributions were found to depend primarily on the halogen atom. This holds at least approximately for H + MX, but it should be noted that here the product distributions also correlate with the reaction exoergicities (cf. Table 1). The substantially exoergic KF and CsF reactions give largely sideways scattering; the endoergic KBr and CsCl reactions give forward scattering; and the almost thermoneutral KCl case is intermediate.

Energy disposal in product modes

Energy conservation requires that

$$[6] \quad E' + W' = E + W + \Delta D_0$$

where E and W denote the reagent relative translational and internal excitation energies, primes pertain to the reaction products, and ΔD_0 is the difference in dissociation energies of the HX and MX bonds, measured from the ground vibration–rotation states. Due to the high kinetic energy of the H or D atoms produced by thermal dissociation ($E \sim 9$ kcal/mol) and the high temperatures needed to vaporize the alkali halides ($W \sim 3$ kcal/mol), the distribution of $E + W$ is nearly the same for all the reactions and is very broad. Figure 7 displays the accessible energy domains for the reactions of H or D with KX; those for the CsX reactions are quite similar. The reactions with KCl, CsCl, and KBr are nearly thermoneutral or slightly endoergic; thus, despite the high $E + W$, not much internal excitation of the product HX molecules can occur and usually the second vibrational level ($n = 2$) is out of reach. This is not so for the reactions with KF or CsF; there the exoergicity is sufficiently large to form HF with $n = 2$ or form DF with $n = 3$.

Table 1 lists values of ΔD_0 derived from bond strength data (33) and rough bounds for the product relative translational energy E' and internal energy W' obtained from our kinematic analysis. For these reactions the LAB → cm transformation is rather insensitive to the recoil velocity parameter $\hat{u}$ and since E' is proportional to $\hat{u}^2$, the energy disposal is therefore quite ill defined. We list the nominal best fit value obtained for E' with upper and lower bounds and the corresponding quantities for W' derived from eq. [6]. These values pertain to the H atom reactions; those for D agree within 1–2 kcal/mol in all cases.

Reaction models that uncouple the light-atom and heavy-atom modes in eq. [6], such as the spectator stripping model (34), give the simple propensity rules: $E' \sim W$ and $W' \sim E + \Delta D_0$. These agree well with the nominal E' and W' values of Table 1 for three cases, poorly for the other two, but the bounds are too broad to allow a significant test.

Temperature dependence

For the reactions of H and D with CsCl we carried out a study of the temperature dependence in order to determine the activation energy. This was done by measuring the reactive signal at a fixed LAB angle ($\Theta = 110°$) as a function of the hydrogen oven temperature. It was possible to remain at the same LAB angle because for the temperature range covered (2200–2800 K) the mean H atom velocity shifts by only ~10%; thus the LAB → cm transformation is affected very little (e.g., the θ scale shifts by <0.5°). Complete angle scans done for three different temperatures verified that the shape of the LAB angular distribution is invariant in this range. The change in the cm energy (or reagent translational temperature) is determined to better than 99% by the H atom LAB velocity distribution. Thus, we can employ the usual Arrhenius plot, shown in Fig. 8. The yield of

Can. J. Chem. Downloaded from www.nrcresearchpress.com by 195.246.54.202 on 09/08/12
For personal use only.

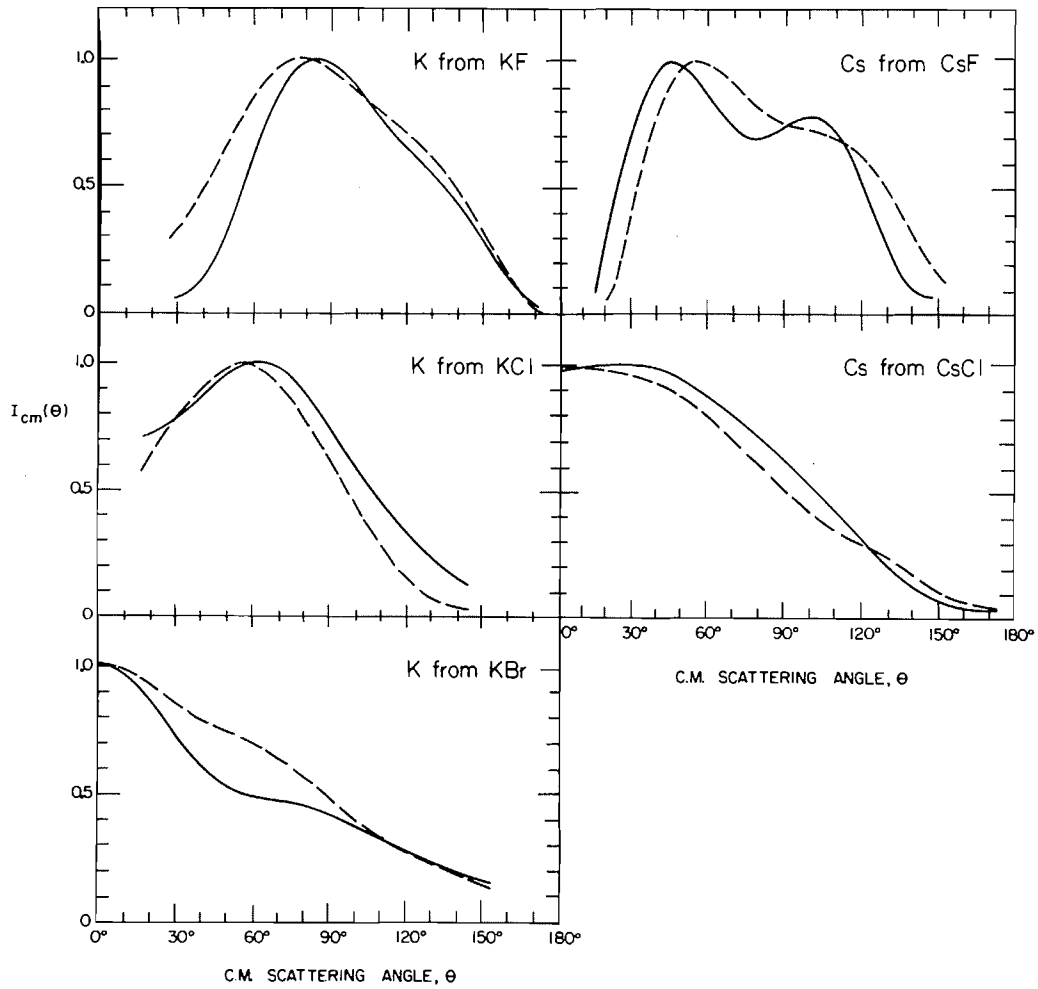

FIG. 6. Angular distributions (center-of-mass system) for product alkali atoms from H (—) and D (---) reacting with five salts. The cm scattering angle θ specifies the direction of the product alkali atom with respect to that of the reagent alkali halide beam.

reactively scattered Cs atoms was corrected for the variation of the percentage of H atoms in the reagent beam by normalizing to the bolometer signal. Since the H atom flux declines substantially with temperature, the uncertainties become sizable at the lower temperatures.

From the slope of the Arrhenius plot, the apparent activation energies are 5.7 and 4.5 kcal/mol, for the H and D reactions, respectively. Since these reactions are endoergic ($\Delta D_0 = -3.3$ and -2.0 kcal/mol for H and D, respectively), our data are consistent with a true activation energy of about $E_a = 2.5$ kcal/mol. An appreciably higher value cannot be accommodated unless the T dependence is assumed to become steeper as T decreases. However, within the error bars the data are also consistent with $E_a \sim 0$, as indicated by the dashed lines shown on the Arrhenius plot.

Total reaction cross section and isotope effect

The three methods usually used to determine the total reaction cross section (29) are not applicable to these reactions. Small-angle elastic scattering could not be observed, so we cannot normalize our data by use of the semiclassical small-angle scattering formula. Likewise, the lack of a complete elastic scattering distribution prevents normalizing to a theoretical value of the total scattering (nonreactive + reactive) cross section. The fact that attenuation of the salt beam could not be observed precludes normalizing to the total amount of MX scattered out of the reagent beam. The method resorted to here is less satisfactory than these usual normalization procedures, but seems adequate for determining the H/D isotope effect and gives at least a rough estimate of the magnitude of the reaction cross section.

The nonreactive scattering distributions of Fig. 4 can all be extrapolated without much ambiguity to 180°. Therefore we decided to normalize these data so that the magnitude of the nonreactive differential cross section there, $I_{cm}(nr; 180°)$ equals that for the hard-sphere cross section. The latter is given by $R^2/4$, where R denotes the sphere radius. This we take to be given by the sum of the covalent radius of the H atom (0.37 Å) and the average of the ionic radii of the M^+ and X^- ions. The resulting values of R, listed in Table 2, are smaller than for van der Waals radii, but seem more appropriate in view of the strongly ionic character of the alkali halide and the fairly high collision energy (0.4 eV). With such a normalization, and the experimentally determined ratio of elastic to reactive scattering, we can evaluate the cm reaction cross section Q_r in absolute units. This involves first integrating the cm angular distribution of reactive scattering, which is easily done using the functional forms specified in eq. [3], to obtain

Can. J. Chem. Downloaded from www.nrcresearchpress.com by 195.246.54.202 on 09/08/12
For personal use only.

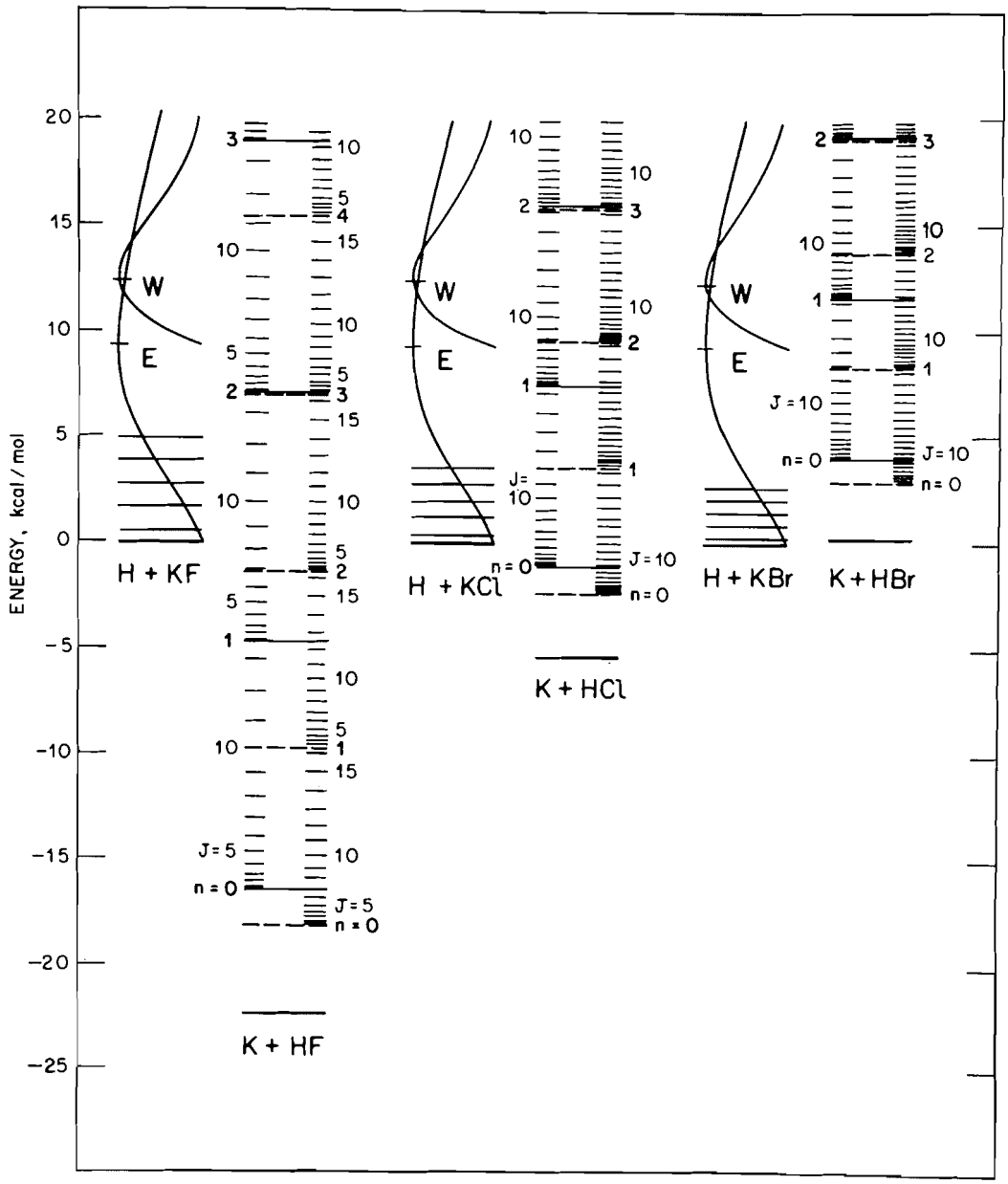

FIG. 7. Energy level diagram for reactants and products of H + KX → HX + K reactions. The curves show the distributions in translational (E) and internal (W) energies of the reactants. In each case, the origin for the W distribution is at the peak of the E distribution. Positions of the first five vibrational levels are indicated for KX and vibration-rotation levels are indicated for HX (left side) and DX (right sided) by the n and J quantum numbers. All levels are drawn in the harmonic oscillator – rigid rotor approximation. Zero of energy in each case pertains to reactants.

$$[7] \quad Q_r = 2\pi N \iint T(\theta)U(u) \sin\theta \, d\theta \, d\, u = 12.52 N a_0 \hat{u}$$

where the factor $12.52 \equiv 4\pi(2/9)\exp(3/2)$ and a_0 is the zeroth-order term in the Legendre expansion of the angular distribution; $\hat{u}$ is the most probable recoil velocity specified in eq. [4]. The normalization constant is given by

$$[8] \quad N = \left\{\frac{1}{4} R^2/[I_{cm}(nr; 180°)]_{rel}\right\} \times \{[I_{LAB}(r; \Theta_N)]_{rel}/[I_{LAB}(r; \Theta_N)]_{calc}\}$$

The subscript "rel" indicates arbitrary relative units; "calc" indicates the result computed from eq. [3] as if $N = 1$. The first bracketed factor converts the cm nonreactive scattering to absolute units, the second normalizes the cm differential reactive cross section to the same units. The LAB angle Θ_N at which N is determined is chosen in a region where the data are smooth; different choices gave consistent results.

Table 2 lists the R values and the total cross sections. The results for Q_r suffer from scatter in the raw data; from the subtraction required to correct the Pt data for nonreactive scattering; from uncertainties in the LAB → cm transformations for both nonreactive and reactive scattering (reflected in values of a_0 and $\hat{u}$); and from the estimation of R. Accordingly, the Q_r values obtained are uncertain by as much as a factor of 10 but likely provide an upper bound since in the first bracket of eq. [8] we neglect attenuation by reaction. The H/D isotope ratios for a

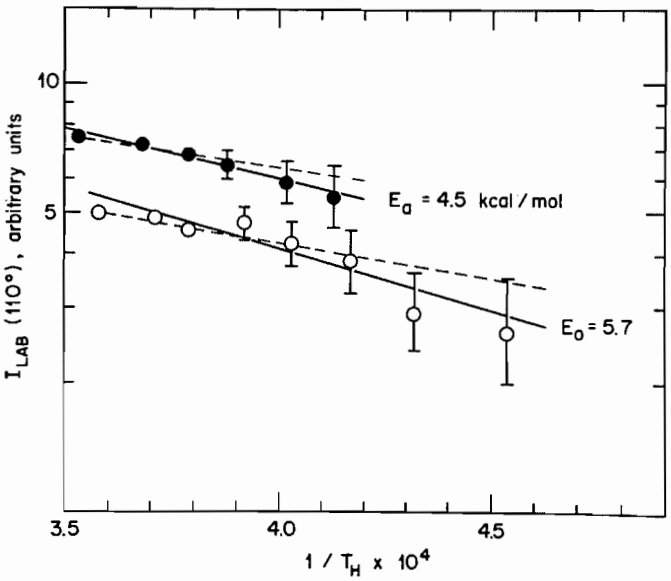

FIG. 8. Temperature dependence of the intensity of Cs atoms reactively scattered at 110° (LAB) from H (○) and D (●) + CsCl. Nominal activation energies are noted; these include the reaction endoergicity. Dashed lines indicate T dependence expected if true activation energy (in excess of endoergicity) is zero. Ordinate units are arbitrary, with data for the two reactions normalized to the ratio of total reaction cross sections.

TABLE 2. Total reaction cross sections[a]

	Salt				
	KF	CsF	KCl	CsCl	KBr
R	1.70	1.87	1.94	2.11	2.01
Q_r(H)	4	12	3	7	1.6
Q_r(D)	8	30	4	14	3

[a]Units are Å for R and Å^2 for Q_r.

given salt should, however, be reliably determined; we see that the cross section for the D reaction is consistently about twice as large as for the H reaction. The Cs/K ratio of the reaction cross sections for a given halide should also be much more reliable than the absolute values; this ratio is roughly 2–3 in favor of the Cs reaction.

Discussion

When a light atom attacks a pair of heavy ones, the large mass disparity fosters an approximate separability of the light atom motions. This has major consequences for the reaction dynamics, amply discussed and illustrated in previous trajectory studies (8, 35) and model treatments (8, 34). Here we consider chiefly features pertaining to the anisotropy of the product angular distributions. We also discuss how our results for H + MX relate to the reverse reactions, M + HX.

As a consequence of the mass disparity, the conservation law for the total angular momentum,

[9] $\mathcal{J} = \boldsymbol{L}' + \boldsymbol{J}' = \boldsymbol{L} + \boldsymbol{J}$

becomes approximately separable into two propensity rules: $\boldsymbol{L} \sim \boldsymbol{L}'$ and $\boldsymbol{J} \sim \boldsymbol{L}'$. For the H + MX case, the first of these holds because the initial orbital angular momentum $\boldsymbol{L}$ from motion of

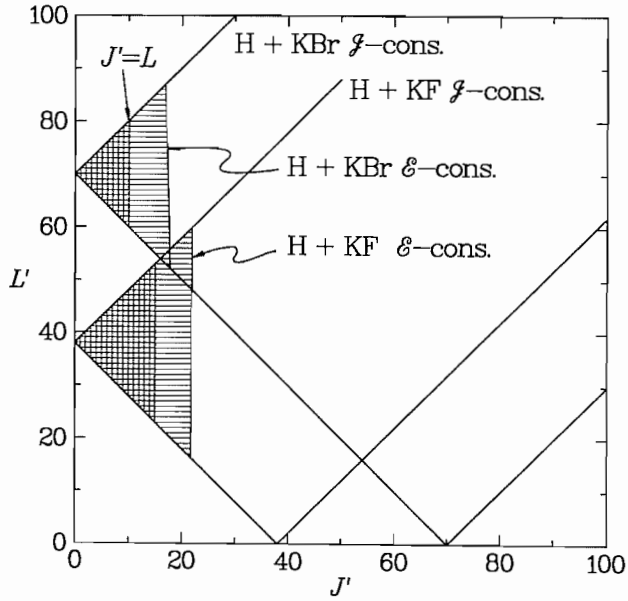

FIG. 9. Illustration of constraints imposed by the conservation laws on the partitioning of angular momentum between product orbital $\boldsymbol{L}'$ and rotational $\boldsymbol{J}'$ motion for the H + KF and H + KBr reactions. The magnitude of the total angular momentum $\mathcal{J}$ was taken to be the most probable $\boldsymbol{J}$ of the salt. The hatched triangular regions show the allowed $(\boldsymbol{L}', \boldsymbol{J}')$ range in each case, whereas the cross-hatched regions indicate the constraint imposed by the $\boldsymbol{J}' \approx \boldsymbol{L}$ model. For both reactions, the initial energy was 12 kcal/mol, corresponding to most probable $E + W = 9 + 3$ kcal/mol, from Fig. 7. The energy available to the products thus is about 29 kcal/mol for the KF reaction, and about 8 kcal/mol for the KBr reaction.

H with respect to MX tends to become the rotational momentum $\boldsymbol{J}'$ of the product HX molecule. Accordingly, the initial thermal rotational momentum $\boldsymbol{J}$ of the heavy-atom pair MX tends to persist as the orbital angular momentum $\boldsymbol{L}'$ of the M and HX products. In our experiments, typically $\boldsymbol{J} \gg \boldsymbol{L}$, by virtue of the high temperature and large moments of inertia of the salt molecules.

Figure 9 illustrates for the reactions of H with KF and KBr the constraints on the product $\boldsymbol{L}'$ and $\boldsymbol{J}'$ resulting from the mass disparity. This diagram was constructed in the usual way by combining the conservation laws for energy and angular momentum with a centrifugal barrier criterion (36). The magnitude of the total angular momentum $\mathcal{J}$ was approximated by the most probable J in a Boltzmann distribution for the salt molecule (38$\hbar$ for KF, 70$\hbar$ for KBr). The energy constraint was derived assuming no product vibrational excitation. An exit impact parameter also had to be assumed; this was chosen as 4 Å in each case, but the curves are insensitive to the choice within a sizable range (2–5 Å). The net result is a rather narrow allowed range for L' and J'. Also indicated is the somewhat narrower constraint imposed by $L = J'$, which takes the propensity rule noted under eq. [9] as an equality, in accord with an ultrasimple spectator stripping model (34).

The distribution of the direction of $\mathcal{J}$ as well as its magnitude is dominated by the rotation of the hot salt molecules. For our near-Maxwellian beam conditions, the spatial distribution of $\boldsymbol{J}$ is expected to be three-dimensionally isotropic (as opposed to that for $\boldsymbol{L}$, which is only isotropic in two dimensions). Even if correlations exist between the product angular momenta $\boldsymbol{L}'$ and $\boldsymbol{J}'$, the isotropy of the total $\mathcal{J}$ will obliterate any evidence of

Can. J. Chem. Downloaded from www.nrcresearchpress.com by 195.246.54.202 on 09/08/12
For personal use only.

Can. J. Chem. Downloaded from www.nrcresearchpress.com by 195.246.54.202 on 09/08/12
For personal use only.

such correlation in the product angular distributions. The fact that we observe decidedly anisotropic distributions implies that not all orientations of $\mathcal{J}$, and hence $\boldsymbol{J}$, are equally likely to produce reaction.

Anisotropic impulsive model

We consider a very simple dynamical model (commensurate with the modest quality of our data), which is akin to the spectator model (34) and other impulsive models (37), particularly Polanyi's DIPR model (8). In the sudden limit, the attacking light atom encounters a kinetically frozen target, the heavy molecule. A preferred reaction geometry would then select certain orientations of the molecule, corresponding to alignments of $\boldsymbol{J}$ that foster those orientations. For the prototypical collinear reaction intermediate, coplanar geometries and $\boldsymbol{J} \parallel \boldsymbol{L}$ are preferred. For strongly bent reaction complexes, broadside approach of the light atom and $\boldsymbol{J} \perp \boldsymbol{L}$ might be expected to dominate. When $\boldsymbol{J} \rightarrow \boldsymbol{L}'$, as in the spectator model, the latter case will give rise to predominantly sideways scattering of the reaction products.

The model adopted here, termed the anisotropic impulsive model (AIM), specifies a preferred angle of approach for the H atom, which is averaged over the spread in internal motion of the alkali halide. We enforce $\boldsymbol{L}' = \boldsymbol{J}$ by neglecting any contribution of $\boldsymbol{L}$ to the tangential motion of the products, but allow for an expected small repulsive energy release along the M—X axis. The final relative velocity $\boldsymbol{V}'$ of the products is decomposed into contributions from axial v_a and tangential v_t components. The axial velocity arises from combining the vibrational motion of MX and product repulsion, while the tangential motion is entirely due to MX rotation. Because these components are orthogonal, the Pythagorean relation $V'^2 = v_a^2 + v_t^2$ holds. However, this speed triangle may be oriented anywhere in space, so without further restrictions the angular distribution remains isotropic.

We introduce anisotropy by assigning a fixed orientation angle η of the MX axis with respect to the initial relative velocity $\boldsymbol{V}$, defined so that $\eta = 0$ when H approaches the halide end of the salt molecule. At zero impact, parameter η becomes identical with the polar angle γ between the relative separation vector and the MX axis. For a fixed η, the axial component v_a is fixed in direction along the MX axis, while v_t must lie in a plane perpendicular to this axis. A given $\boldsymbol{V}'$ defines a cone of height $V' \cos\theta$ and half-angle θ, where θ is the cm scattering angle of the M atom product. The edge of this cone may be reached by a range of (v_a, v_t) consistent with the triangle condition above; in general v_a may range from $v_< = V' \cos(\eta - \theta)$ to $v_> = V' \cos(\eta + \theta)$, so long as negative speeds do not result.

For this AIM, finding the cm intensity $I_{cm}(V',\theta)$ is chiefly a matter of compounding the component distributions, $P_a(v_a)$ and $P_t(v_t)$, over the range of velocities that contribute at (V',θ) to yield the desired distribution $P(V',\theta)$. This is done using the convolution relation (38)

$$[10] \quad P(V',\theta) = \int \mathrm{d}\, v_a \int \mathrm{d}\, v_t P_a(v_a) P_t(v_t) \delta(V' - [v_a^2 + v_t^2]^{1/2}) h(v_a - v_<) h(v_> - v_a)$$

where $\delta(x)$ is the Dirac delta function and $h(x)$ the unit step function. The cm intensity is then given by

$$[11] \quad I_{cm}(V',\theta) \propto \frac{V'}{\sin\theta} P(V',\theta)$$

The factor of V' converts P to a flux distribution, and $1/\sin\theta$ accounts for the polar enhancement due to azimuthal averaging. The P_a distribution is compounded (38) from the vibrational distribution $P_{vib}(v_{vib})$, taken as the Boltzmann average of the momentum–space harmonic oscillator wave functions, and the impulse distribution $P_i(v_i)$. For simplicity we choose $P_i(v_i) = \delta(v_i - v_{i0})$, making $P_a(v_a) = P_{vib}(v_a - v_{i0})$. The P_t distribution is taken as the classical rotational Boltzmann distribution P_{rot}, as appropriate for high-temperature heavy rotors. These choices allow the integrals in eq. [10] to be done analytically, yielding an expression for $P(V',\theta)$ in the form of a sum over the vibrational levels of integrals that are readily evaluated by recursion (22). Energy conservation places limits on the impulse velocity v_{i0}. If we define f_i as the fraction of the available energy $E + \Delta D_0$ delivered as product repulsion, then

$$[12] \quad v_{i0} = \left[f_i \frac{2}{\mu'} (E + \Delta D_0) \right]^{1/2}$$

where μ' is the product reduced mass. This completes the formulation.

Specifying η and f_i, along with experimental conditions, allows the calculation of I_{cm}, which can then be averaged over the initial beam velocity distributions and transformed into the LAB frame in the usual way. The AIM computer code (22) designed for this purpose also allows an average over a Gaussian distribution in η. Figure 10 compares specimen calculations of the LAB angular distributions with experiment. For the Cs salts, satisfactory fits were obtained just by varying η, with $f_i = 0$, owing in part to the missing central portion of the experimental data. For the K salts, where the kinematic resolution is better, specifying a small value for f_i greatly improved agreement with experiment. The effects of varying η and f_i are coupled; usually a nonzero f_i allows easier "steering" of the calculated curve into agreement with experiment by varying η. For the H + KBr system the effect of averaging over a range of η is also illustrated; the results indicate that the data are inconsistent with a broad range of orientations. Figure 11 gives the corresponding cm angular distributions. For the "best fit" values, $\eta = 80° \rightarrow 100° \rightarrow 110°$ for the salts as F → Cl → Br. The AIM analysis thus indicates that the preferred reaction geometry is roughly broadside, with only a relatively modest change with halogen. According to this model, much of the systematic increase in forward scattering of the products as F → Cl → Br is due to the angular momentum constraints, which reflect (cf. Fig. 9) both mass and energetic factors.

The $I_{cm}(\theta)$ distributions obtained from kinematic analysis and shown in Fig. 6 are probably more reliable than the AIM results of Fig. 11, because the model imposes additional constraints. However, the comparison serves to illustrate the limited resolution of $I_{cm}(\theta)$ provided by our experiments, since the AIM results account nearly as well for the LAB data (cf. Figs. 5 and 10). The most significant feature, exhibited by both the kinematic analysis and AIM, is that for all except the KF reaction the product alkali atoms appear predominantly in the forward hemisphere of the cm frame with respect to the direction of the alkali halide reagent.

Microreversibility aspects

Despite the host of studies devoted to M + HX reactions, the characterization of the reaction dynamics still suffers from many gaps and conflicts. Via microreversibility, our results for H + MX reactions add three pertinent items, concerning (1) the

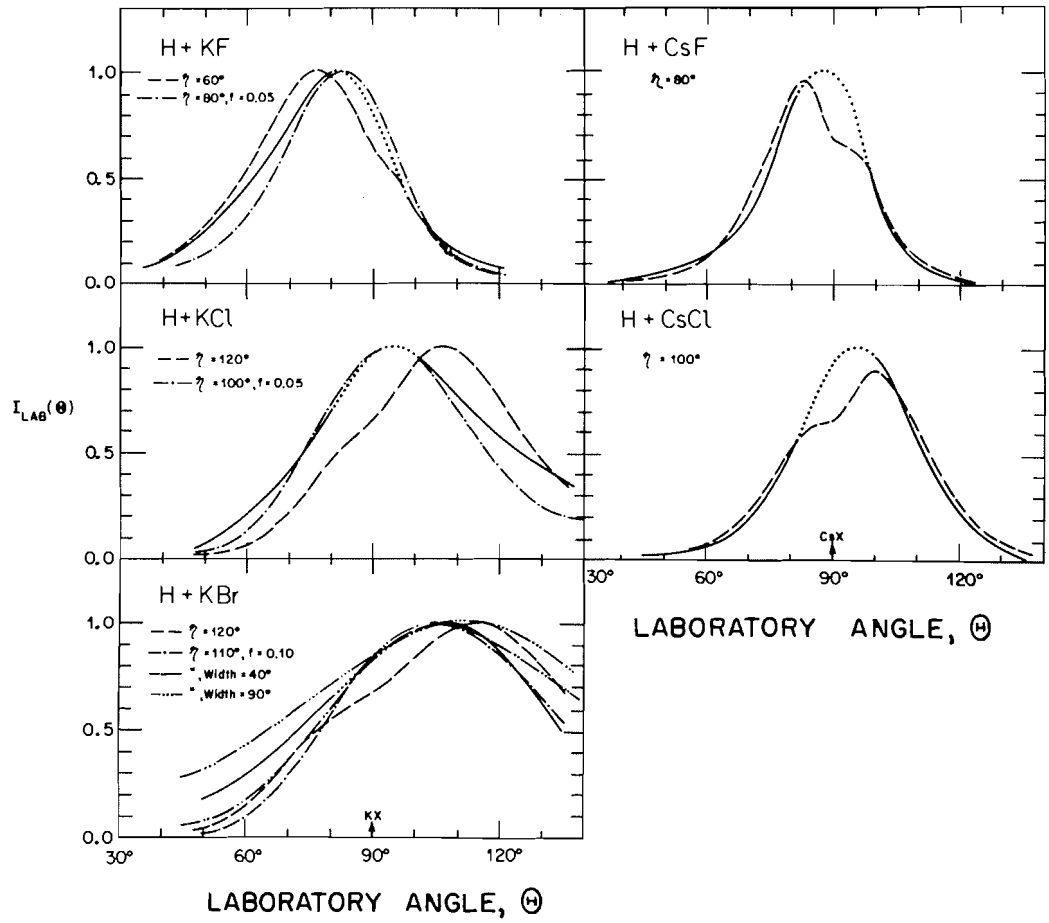

FIG. 10. Comparison of M atom laboratory angular distributions (solid curves) from reaction of H atoms with five salts with impulsive model calculations. Dotted portions of experimental curves indicate regions where data are lacking due to proximity of the parent salt beam.

product angular distributions; (2) the H/D isotope effect of the total reaction cross section; and (3) the Arrhenius activation energy. These items are our most reliable results, but we find that each brings out new questions rather than resolving old ones.

(1) The predominantly forward reactive scattering we observe for H or D + KBr corresponds, when all the cm velocity vectors are reversed, to forward scattering of KBr relative to the incident K direction in reactions with HBr or DBr. This contrasts with (*a*) the nearly isotropic (15) or slightly sideways (22) distributions reported for K + HBr and DBr and (*b*) the sharply backward reactive scattering (23) reported for K + TBr. The contrast may not be significant, as (*a*) is subject to intrinsically poor kinematic resolution and (*b*) may be vitiated by experimental error.[2] However, in our experiments, the peak of the thermal distribution of total energy (~8 kcal/mol re: K + HBr; cf. Fig. 7) is much higher than in (*a*) or (*b*), by typically about 6–7 kcal/mol. As exemplified by our AIM calculations, this energy is high enough to induce forward scattering unless reaction is inhibited by a sizable barrier. The threshold energy for reaction is only 0.4 kcal/mol (re: K + HBr), according to an optical model analysis of the nonreactive scattering (10), but at the low energies of (*a*) and (*b*) even such a small barrier can foster sideways or backward reactive scattering.

(2) We find the isotope ratio $Q_r(H + MX)/Q_r(D + MX) \simeq 0.5$ for all five reactions studied (Table 2) and no discernible isotope effect in the temperature dependence for the CsCl case (Fig. 8) beyond that due to endoergicity. For the reverse reaction, $Q_r(K + HX)/Q_r(K + DX) = 1.4 \pm 0.2$ was found (15), in good agreement with the ratio of 1.3 estimated from optical model analysis (10). This reversal in sense of the H/D isotope effect may again arise because the alkali atom experiments and ours differ markedly in the total energy and angular momentum supplied. Under our conditions, as seen in Fig. 7, the HBr/DBr product has a relatively large amount of energy available for rotation compared to that present in the HBr/DBr reagent in the K + HBr reaction. If the rotational levels are populated statistically, the greater number of available states for DBr (which goes roughly as the square root of the moment of inertia) might produce an isotope effect favoring D over H that would not occur under the conditions of the K + HBr reaction. It is striking that D is also favored over H by about a factor of 2 for reactions with alkali dimers (26).

(3) Our evidence that for H or D + CsCl the activation energy in excess of the endoergicity is near zero (Fig. 8) is qualitatively consistent with experimental results for K + HCl (E_a less than ~1 kcal/mol higher than the 2 kcal/mol endoergicity (12)) and K + HBr ($E_a \sim 0.4$ kcal/mol (10)). Barrier heights derived from a semiempirical valence bond treatment (6) are clearly much too high (~10–15 kcal/mol above zero-point endoergicities for K, Cs + HCl). Our data do not show the predicted increase with alkali atomic number nor any evidence for significant H atom tunneling, as E_a lacks an appreciable isotope effect.

Trajectory studies are needed to examine whether our items

Can. J. Chem. Downloaded from www.nrcresearchpress.com by 195.246.54.202 on 09/08/12
For personal use only.

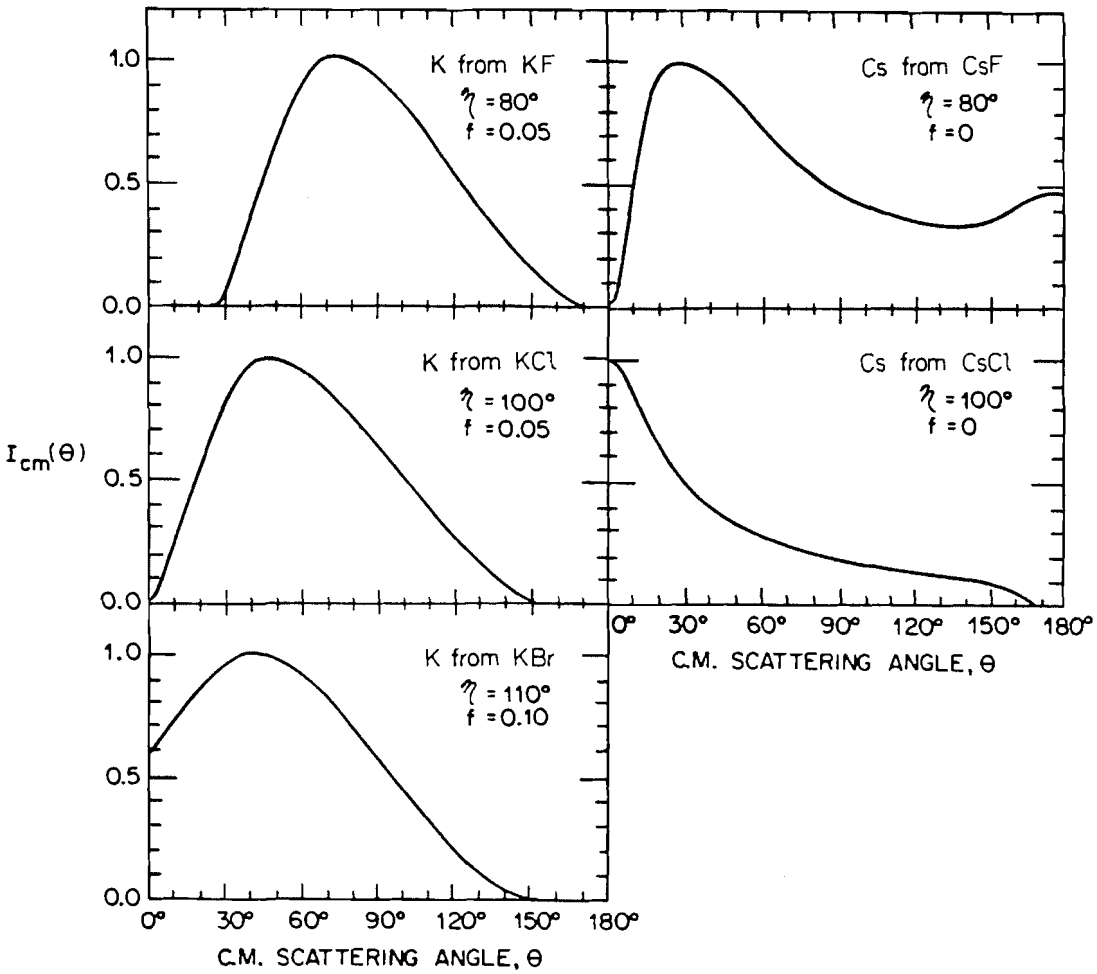

FIG. 11. Impulsive model results for M atom angular distributions in the cm system corresponding to Fig. 10 (dot-dashed curves for K, dashed for Cs).

(1)–(3) as well as the many other properties of M + HX systems now known can be reconciled with scaled versions of the available potential energy surfaces. Although several trajectory calculations have been carried out for the Li + HF system, most used a surface with poor asymptotic behavior that produced misleading results (39). This favorite reaction family deserves more comprehensive computer experiments, in the style pioneered by Polanyi (8), to search for what he likes to call "simple stories."

Acknowledgments

With joy we dedicate this paper to John Polanyi, in awe of his exquisite, insightful work and with gratitude for his inspiring example as scientist and citizen and for his warm friendship. We thank Yuan Lee, George Fisk, Walt Miller, Sanford Safron, Bill Stwalley, and Arendt Niehaus for many instructive suggestions; Doug Carlson for cheerful help with some of the experiments; and the National Science Foundation for financial support.

1. E.A. Gislason and J.G. Sachs. J. Chem. Phys. **62**, 2678 (1975), and work cited therein.
2. S. Stolte, A.E. Proctor, and R.B. Bernstein. J. Chem. Phys. **62**, 2506 (1975), and work cited therein.
3. G.H. Kwei, B.P. Boffardi, and S.F. Sun. J. Chem. Phys. **58**, 1722 (1973).
4. A.C. Roach and M.S. Child. Mol. Phys. **14**, 1 (1968); W.S. Struve. Mol. Phys. **25**, 777 (1973).
5. B.H. Cardelino, W.H. Eberhardt, and R.F. Borkman. J. Chem. Phys. **84**, 3230 (1986).
6. M. Shapiro and Y. Zeiri. J. Chem. Phys. **70**, 5264 (1979).
7. M.M.L. Chen and H.F. Schaefer III. J. Chem. Phys. **72**, 4376 (1980).
8. J.C. Polanyi. Science, **236**, 680 (1987), and work cited therein.
9. G.A. Parker, R.T. Pack, and A. Laganà. Chem. Phys. Lett. **202**, 75 (1993), and work cited therein.
10. J.R. Airey, E.F. Greene, K. Kodera, G.P. Reck, and J. Ross. J. Chem. Phys. **46**, 3287 (1967); E.F. Greene, L.F. Hoffman, M.W. Lee, J. Ross, and C.E. Young. J. Chem. Phys. **50**, 3450 (1969).
11. H.J. Loesch, E. Stenzel, and B. Wüstenbecker. J. Chem. Phys. **95**, 3841 (1991).
12. J.G. Pruett, F.R. Grabiner, and P.R. Brooks. J. Chem. Phys. **63**, 1173 (1975).
13. T.J. Odiorne, P.R. Brooks, and J.V.V. Kasper. J. Chem. Phys. **55**, 1980 (1971); F. Heismann and H.J. Loesch. Chem. Phys. **64**, 43 (1982).
14. B.A. Blackwell, J.C. Polanyi, and J.J. Sloan. Chem. Phys. **30**, 299 (1978); H.H. Dispert, M.W. Geis, and P.R. Brooks. J. Chem. Phys. **70**, 5317 (1979).
15. K.T. Gillen, C. Riley, and R.B. Bernstein. J. Chem. Phys. **50**, 4019 (1969); C.H. Becker, P. Casavecchia, P. Tiedemann, J.J. Valentini, and Y.T. Lee. J. Chem. Phys. **73**, 2833 (1980).
16. J.E. Mosch, S.A. Safron, and J.P. Toennies. Chem. Phys. Lett. **29**, 7 (1974).
17. D.S.Y. Hsu, N.D. Weinstein, and D.R. Herschbach. Mol. Phys. **29**, 257 (1975).

Can. J. Chem. Downloaded from www.nrcresearchpress.com by 195.246.54.202 on 09/08/12
For personal use only.

18. C.E. Young, R.J. Buehler, and S. Wexler. J. Chem. Phys. **61**, 174 (1974); S. Okada. Chem. Phys. Lett. **63**, 322 (1979).
19. D.M. Lindsay, M.C.R. Symons, D.R. Herschbach, and A.L. Kwiram. J. Phys. Chem. **86**, 3789 (1982).
20. P.E. Siska. Rev. Mod. Phys. **65**, 337 (1993).
21. S. Datz, D.R. Herschbach, and E.H. Taylor. J. Chem. Phys. **35**, 1549 (1961).
22. P.E. Siska. Ph.D. Thesis, Harvard University (1969).
23. L.R. Martin and J.L. Kinsey. J. Chem. Phys. **46**, 4834 (1967).
24. A.C. Roach. Chem. Phys. Lett. **6**, 389 (1970); D.G. Truhlar. J. Chem. Phys. **54**, 2635 (1970).
25. J.D. McDonald, P.R. LeBreton, Y.T. Lee, and D.R. Herschbach. J. Chem. Phys. **56**, 769 (1972).
26. Y.T. Lee, R.J. Gordon, and D.R. Herschbach. J. Chem. Phys. **54**, 2410 (1971).
27. M.A.D. Fluendy, R.M. Martin, E.E. Muschlitz, and D.R. Herschbach. J. Chem. Phys. **46**, 2172 (1967).
28. T.R. Touw and J.W. Trischka. J. Appl. Phys. **34**, 3635 (1963).
29. J.H. Birely, R.R. Herm, K.R. Wilson, and D.R. Herschbach. J. Chem. Phys. **57**, 993 (1967).
30. S. Datz and E.H. Taylor. J. Chem. Phys. **25**, 389, 395 (1956); G.H. Kwei, J.A. Norris, and D.R. Herschbach. J. Chem. Phys. **52**, 1317 (1970); K.T. Gillen and R.B. Bernstein. Chem. Phys. Lett. **5**, 275 (1970).
31. P.E. Siska. J. Chem. Phys. **59**, 6052 (1973).
32. W.B. Miller, S.A. Safron, and D.R. Herschbach. J. Chem. Phys. **55**, 113 (1973).
33. K.P. Huber and G. Herzberg. Molecular spectra and molecular structure IV. Constants of diatomic molecules. Van Nostrand, New York. 1978.
34. D.R. Herschbach. Appl. Phys. Suppl. **2** (Chemical Lasers), 128 (1965), and work cited therein.
35. S.K. Kim and D.R. Herschbach. Faraday Discuss. Chem. Soc. **30**, 159 (1987); S.K. Kim, S.C. Jeoung, A.L. Tan, and D.R. Herschbach. J. Chem. Phys. **95**, 3854 (1991).
36. J.C. Light. Faraday Discuss. Chem. Soc. **62**, 1372 (1967).
37. S.J. Riley, P.E. Siska, and D.R. Herschbach. Faraday Discuss. Chem. Soc. **67**, 27 (1979), and work cited therein.
38. J.H. Birely and D.R. Herschbach. J. Chem. Phys. **44**, 1690 (1966).
39. H.J. Loesch. Chem. Phys. **104**, 213 (1985), and work cited therein.

Can. J. Chem. Downloaded from www.nrcresearchpress.com by 195.246.54.202 on 09/08/12
For personal use only.

Addition of alkyl radicals to C_{60}. Part 3. The EPR spectra of R_3C_{60} radicals and a theoretical study of HC_{60} and H_3C_{60} radicals[1]

J.R. MORTON, F. NEGRI,[2] AND K.F. PRESTON

Steacie Institute for Molecular Sciences, National Research Council of Canada, 100 Sussex Drive, Ottawa, ON K1A 0R6, Canada

Received August 12, 1993

This paper is dedicated to Professor John C. Polanyi on the occasion of his 65th birthday

J.R. MORTON, F. NEGRI, and K.F. PRESTON. Can. J. Chem. **72**, 776 (1994).

The EPR spectra of a series of C_{60} adducts of the type R_3C_{60} are described and discussed. In every case, two of the three ligands are equivalent, leading to the conclusion that the R_3C_{60} radicals have a plane of symmetry. The unpaired electron distributions in mono- and trisubstituted-C_{60} radicals are computed with the help of the QCFF/PI and MNDO Hamiltonians. It is shown that the hyperfine constants predicted on the basis of the calculated spin densities reproduce well the values observed and suggest a reassignment of framework ^{13}C coupling constants in RC_{60}.

J.R. MORTON, F. NEGRI et K.F. PRESTON. Can. J. Chem. **72**, 776 (1994).

On décrit et on discute des spectres rpe d'une série d'adduits C_{60} du type R_3C_{60}. Dans tous les cas, deux des trois coordinats sont équivalents; ceci conduit à la conclusion que les radicaux R_3C_{60} possèdent un plan de symétrie. Utilisant des hamiltoniens QCFF/PI et MNDO, on a calculé les distributions de l'électron non paire dans les radicaux mono- et trisubstitués-C_{60}. On montre que les contantes hyperfines prédites sur la base des densités de spin calculées reproduisent bien les valeurs observées et elles suggèrent une réattribution des constantes de couplage du ^{13}C du squelette du RC_{60}.

[Traduit par la rédaction]

Can. J. Chem. Downloaded from www.nrcresearchpress.com by 195.246.54.202 on 09/08/12
For personal use only.

1. Introduction

Our first report (1) of alkyl radical addition to C_{60} concerned the detection by EPR spectroscopy of R_3C_{60} and R_5C_{60}, where R = the benzyl radical, $CH_2C_6H_5$. It seemed at the time that their precursor, $C_6H_5CH_2C_{60}$, and mono-adducts generally, would be difficult to detect because of their reactivity. Subsequent work (2–4) has shown however that, given the right conditions, a wide variety of monoalkyl- and monosilyl-C_{60} radicals can readily be detected. Curiously, it has proven difficult to detect further examples of those types of adducts first observed (R_3C_{60} and R_5C_{60}), in spite of the fact that multiple addition of methyl radicals (1) and hydrogen atoms (5) to C_{60} has been established by mass spectrometry.

In this article we present the EPR spectra of six radicals of general formula R_3C_{60}, including the prototype, H_3C_{60}, and we analyze the experimental results on the basis of quantum-chemical calculations of spin densities. In section 3.1 we show that the EPR spectra are accounted for by assuming an allyl-like structure for the R_3C_{60} radicals. In section 3.2 we present calculations of the spin density distribution for H_3C_{60} and HC_{60} radicals performed by using the semi-empirical QCFF/PI (6) and MNDO (7) Hamiltonians. Finally, the results of the calculations are analyzed and compared with the observed H and ^{13}C hyperfine couplings (hfc) in section 4.

2. Experimental

Pure C_{60} was purchased from Texas Fullerenes, Houston, TX. Reagents enriched in ^{13}C were purchased from CDN Isotopes Inc., Vaudreuil, Que. Saturated solutions (typically 0.003 molar) of C_{60} in various dried, degassed solvents were prepared and stored in a glove-box continuously flushed with dry argon. A 300 mm^3 aliquot of the stock solution was transferred to a 5 mm O.D. Suprasil™ EPR tube fitted with a greaseless stopcock. Other reagents were added to the sample with a microsyringe. The radicals which we identify as R_3C_{60} radicals were generated by UV photolysis of solutions containing dissolved C_{60} and a precursor of the radical R. The radicals R were generated by several methods (8), including photolysis of a ketone R_2CO, an aldehyde RCHO, a chloride RCl, or a bromide RBr (Table 1). Alternatively, an indirect method was used, involving photolysis of di-*tert*-butylperoxide, forming *tert*-butoxy radicals capable of abstracting a hydrogen atom from a hydrocarbon RH.

The solutions were photolysed with the focused light from a Schoeffel 1000 W high-pressure Hg/Xe lamp filtered though water to remove infrared radiation. The photolysis was carried out inside the cavity of the EPR spectrometer, a Varian E-12 instrument fitted with the usual accessories for readout of the temperature of the sample, the microwave frequency and the magnetic field strength. The spectrometer was also equipped with a multichannel analyser for signal/noise improvement. This device was obtained from Scientific Software Services, Bloomington, IL. The spectrometer was operated in the critically coupled mode, and it was necessary to vary the experimental conditions, particularly the temperature and microwave power, in order to optimise the spectra.

3. Results

3.1. *Identification of R_3C_{60} radicals*

It is apparent from the hyperfine interactions listed in Table 1 that three alkyl groups have attached themselves to the C_{60} surface, and that two of them (R) are equivalent and distinct from the third (R′). In five of the six cases, R = R′, and the hyperfine interactions associated with R are very much larger than the corresponding hyperfine interactions of R′. In the sixth case (photolysis of ^{13}C-enriched CCl_4/C_{60}) it seems probable (see below) that the unique ligand R′ is different from the other two.

We have explained elsewhere (3) that the icosahedral symmetry of C_{60} is lowered to C_s by the addition of a single ligand R. In seeking a structure for trialkyl-C_{60} radicals, we are clearly dealing with a similar situation: a species belonging to the C_s point group. Only under this assumption can we accommodate two equivalent ligands R (lying on either side of the symmetry plane), and a unique ligand R′ (lying on the symmetry plane). The structure we propose for trialkyl-C_{60} radicals is shown in Fig. 1. It conforms to the requirements of C_s symmetry, with the symmetry plane passing through R′, C_6, and C_1.

[1]NRCC No. 37230.

[2]Permanent address: Dipartimento di Chimica "G. Ciamician", Università di Bologna, 40126 Bologna, Italy.

TABLE 1. Hyperfine interactions of $R_2R'C_{60}$ radicals

R	R′	Hyperfine interactions[a]	(G)[b]	T/K
H	H	2H = 18.7	1H = 0.9	200[c]
CH_3	CH_3	6H = 0.20	3H = 0.06	440[d]
CF_3	CF_3	6F = 0.36		300[e]
CCl_3	Cl	2C = 16.4	1Cl = 0.61	375[f]
CBr_3	CBr_3	2C = 20.1	1C = 4.6	355[g]
$C_6H_5CH_2$	$C_6H_5CH_2$	2C = 9.70	1C = 1.75	323[h]
		2C = 19.8[i,j]	1C = 13.1[j,k]	

[a]All g-factors lay in the range 2.0022–2.0024 unless otherwise stated.
[b]Hyperfine interactions originate with R or R′ unless otherwise specified.
[c]0.5 millimole CH_3CHO in 350 mm^3 methyl cyclohexane/C_{60}.
[d]20 mm^3 $(CH_3)_2CO$ in 350 mm^3 *tert*-butylbenzene/C_{60}.
[e]0.5 millimole CF_3H and 10 mm^3 di-*tert*-butylperoxide in 300 mm^3 benzene/C_{60}.
[f]350 mm^3 99% ^{13}C-enriched CCl_4/C_{60}.
[g]5 mg 99% ^{13}C-enriched CBr_4 in 350 mm^3 benzene/C_{60}, g = 2.0100.
[h]5 mm^3 di-*tert*-butylperoxide in 350 mm^3 99% α-^{13}C-enriched toluene/C_{60} (ref. 1).
[i]C_2 and $C_{2'}$ on the C_{60} surface.
[j]Relative intensities of ^{13}C satellite not established with certainty.
[k]C_1, C_{12}, and $C_{12'}$ on the C_{60} surface, see Table 5 and the discussion in the text.

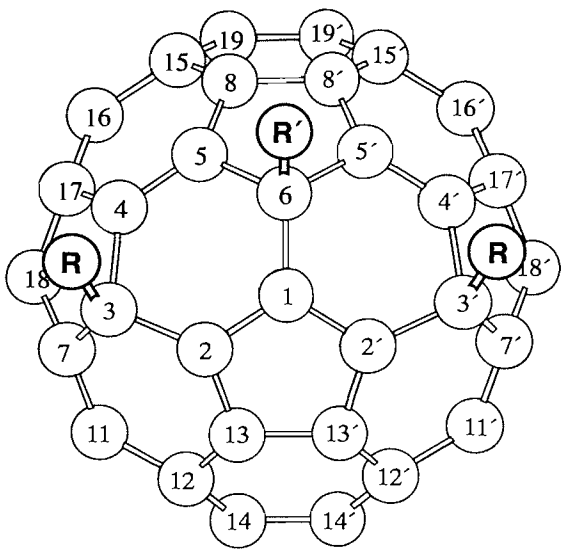

FIG. 1. Atom numbering for the R_3C_{60} radicals. In RC_{60}, R is on C_6 only.

It is interesting to note that this structure is also supported by calculations of the HC_{60} spin density distribution which have recently appeared in the literature (10–13). In fact, most of the theoretical results predict relatively large spin density on the C_3 and $C_{3'}$ carbons of HC_{60} (H on C_6). As a consequence, these positions are particularly reactive and are likely to promote the formation of the H_3C_{60} isomer shown in Fig. 1. Because of the substituents' position, the spin density distribution of the latter radical is expected to be qualitatively similar to that of an allyl radical (9). This deduction is supported by recent MNDO calculations of its unpaired electron distribution (10). Thus, in contrast to monoalkyl-C_{60} radicals, which have a $^2A'$ ground state, trialkyl-C_{60} radicals have a $^2A''$ ground state.

The spectrum of tribenzyl-C_{60} was so powerful that ^{13}C hyperfine structure could be detected in natural abundance,

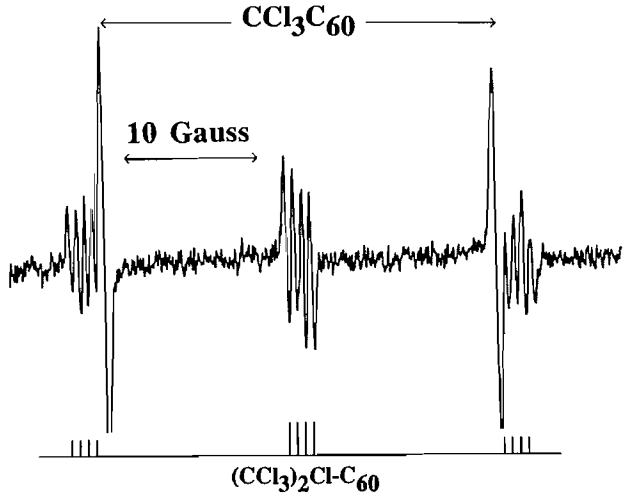

FIG. 2. The EPR spectrum of ^{13}C-enriched $(CCl_3)_2ClC_{60}$ and CCl_3C_{60} in CCl_4 at 325 K.

hyperfine interactions of 19.8, 13.1, and 9.7 Gauss (G) being observed (1). Using toluene enriched in ^{13}C on the α carbon atom, it was seen that the 9.7 G hyperfine interaction originated with the equivalent R (= $^{13}CH_2C_6H_5$) groups, and that there was a smaller interaction of 1.75 G due to R′ (also $^{13}CH_2C_6H_5$). The remaining hyperfine interactions were assigned to C_1 (13.1 G) and C_2, $C_{2'}$ (19.8 G) on the C_{60} surface. This assignment was made by comparison of these hyperfine interactions with those of the allyl radical itself: C_1 = 17.2 G, $C_2 = C_{2'}$ = 21.9 G (9). The correlation between the ^{13}C data of the allyl radical and of tribenzyl-C_{60} confirmed that an allyl-like structure for the latter is a reasonable assumption.

In the case of $(CBr_3)_3C_{60}$, ^{13}C enrichment established the presence of three CBr_3 ligands, two of one kind and one of another, characteristic of an allyl configuration. The same is true of the spectrum of $(CF_3)_3C_{60}$: six equivalent ^{19}F nuclei nuclei have 0.36 G hyperfine interactions (the terminal CF_3 groups), those of the central CF_3 group being unresolved. For R = CCl_3 however, ^{13}C enrichment indicated that R′ was *not* CCl_3 since the expected (small) ^{13}C interaction was not present; instead a hyperfine interaction with a single Cl nucleus was observed. We conclude, therefore, that the spectrum is that of $(CCl_3)_2ClC_{60}$. The initially formed adducts are presumably ClC_{60} and CCl_3C_{60}. The latter was observed, and is stable in the dark (Fig. 2). The former has never been observed. Presumably, ClC_{60} reacts rapidly with chlorine atoms to form diamagnetic products, but when it reacts with CCl_3 radicals $(CCl_3)_2ClC_{60}$ is formed. It, too, is stable with the UV off (Fig. 2). It would appear that the stability of CCl_3C_{60} and $(CCl_3)_2ClC_{60}$ is due to shielding of their reaction sites by the bulky CCl_3 group(s).

It has been suggested that C_{60} or derivatives thereof are present in interstellar space (14, 15) and that hydrogenated C_{60} molecules are carriers of the diffuse interstellar bands in the visible (16) and ultra-violet (17) regions of the spectrum. If it turns out that fullerenes generally, and C_{60} in particular, are present in the interstellar medium, it is possible that the zero-field emissions of HC_{60} and H_3C_{60} eventually will be detectable by radiotelescopes. The zero-field emission of HC_{60} is at 94 MHz (18), a not particularly convenient region of the spectrum, being in the middle of the FM broadcast band. In H_3C_{60} the two equivalent protons have hyperfine interactions of 18.6 G, or 52.1 MHz. The zero-field emission of the $F = 1.5 \rightarrow 0.5$ transition

Can. J. Chem. Downloaded from www.nrcresearchpress.com by 195.246.54.202 on 09/08/12
For personal use only.

TABLE 2. Computed bond lengths (Å) for the HC_{60} and H_3C_{60} radicals

	H_3C_{60}		HC_{60}			
Parameter	QCFF/PI[a]	MDK[b]	QCFF/PI[a]	PW[c]	MDK[b]	CG[d]
C_1C_2	1.425	1.41	1.443	1.46	1.44	1.498
C_2C_3	1.481	1.49	1.417	1.43	1.38	1.362
C_3C_4	1.532	1.53	1.478	1.47	1.47	1.497
C_4C_5	1.396	1.37	1.403	1.43	1.37	1.359
C_5C_6	1.542	1.53	1.541	1.54	1.53	1.546
C_1C_6	1.482	1.50	1.492	1.52	1.49	1.548
C_3C_7	1.549	1.53	1.459		1.45	1.453
C_7C_{11}	1.404	1.37	1.420		1.39	1.381
$C_{11}C_{12}$	1.480	1.47	1.467		1.45	1.452
$C_{12}C_{13}$	1.405	1.38	1.412		1.38	1.379
C_2C_{13}	1.447	1.46	1.474		1.46	1.452
C_5C_8	1.446	1.44	1.443	1.45	1.44	1.448
C_8C_{15}	1.417	1.39	1.422	1.42	1.39	1.381
$C_{15}C_{16}$	1.448	1.45	1.456	1.47	1.45	1.450
$C_{16}C_{17}$	1.415	1.39	1.413	1.42	1.39	1.379
C_4C_{17}	1.446	1.44	1.463	1.46	1.45	1.454
$C_{17}C_{18}$	1.461	1.45	1.469		1.46	1.462
C_7C_{18}	1.442	1.44	1.472		1.46	1.462
$C_{12}C_{14}$	1.462	1.45	1.469		1.46	1.464
$C_{15}C_{19}$	1.477		1.473	1.48		
$C_{13}C_{13'}$	1.459	1.45	1.455		1.45	1.464
$C_{14}C_{14'}$	1.426	1.39	1.411		1.38	1.375
$C_8C_{8'}$	1.459	1.45	1.461	1.50	1.45	1.464
$C_{19}C_{19'}$	1.407		1.408	1.39		

[a]This work.
[b]Reference 10.
[c]Reference 11.
[d]Reference 13.

will therefore be at $1.5 \times 52.1 = 78$ MHz, just outside the FM band and therefore a more attractive proposition to radioastronomers.

3.2. *Radical structures and spin density distributions*

Among the fullerenyl radicals, HC_{60} has been the subject of a considerable number of theoretical studies (10–13, 19), most of which deal with the stability of the exo-radical and the interpretation of the observed μSR spectrum of MuC_{60}. The structures obtained by semi-empirical (10, 11) or *ab initio* methods (12, 13) indicate a localization of the distortion close to the hydrogen atom. A more extensive analysis of the addition of H and F to C_{60} and the stability of polysubstituted-C_{60} has been recently published by Matsuzawa and co-workers (10), who studied up to penta-substituted derivatives using the MNDO Hamiltonian. The authors also compare in a qualitative way calculated spin densities with observed EPR data. However, no attempt has been made to analyze the H and ^{13}C hfc observed for RC_{60} and R_3C_{60}, on the basis of quantum-chemical calculations.

The aim of this study is to show that the spin density distributions calculated for both radicals are consistent with the corresponding EPR spectra. To this end we have calculated the equilibrium structures and unpaired electron distributions of the two prototype radicals, HC_{60} and H_3C_{60}, using a modified version (20) of the QCFF/PI program (6). This model is based on the σ–π separation and uses a quantum chemical scheme only for the π electrons, while it simulates the σ electrons by an empirical potential. The modified version (20) adopted here can perform Half-Electron Self Consistent Field (HE-SCF) calculations (21) followed by Configuration Interaction (CI) for electronic states of any multiplicity. Recently, it was used to produce fairly accurate structures and vibrational frequencies for C_{60} (22), C_{70} (23), and C_{60}^{6-} (24).

The equilibrium structures of the ground state of the two radicals were obtained by using the HE-CI method. Test calculations, performed with various CI dimensions, indicated that the ground configuration is the only determinant that contributes significantly to the ground-state wavefunction (coefficient = 0.99). Hence, all calculations were performed by including a rather small number of determinants. The calculated bond lengths showing the largest deviations from the equilibrium C_{60} structure (1.411 Å and 1.471 Å (22)) are presented in Table 2. Inspection of Table 2 shows that the structures predicted by QCFF/PI are essentially similar to those obtained by previous calculations (10–13). A comparison of the structures calculated for the HC_{60} and H_3C_{60} radicals indicates, as expected, that the distortion of the latter introduced by the additional two hydrogen atoms is larger than for HC_{60}. However, in agreement with MNDO results (10), the distortion is still mainly localized close to the hydrogen atoms.

The spin density distributions listed in Table 3 were calculated for the optimized structures of the two radicals using the QCFF/PI and the MNDO wavefunctions, both obtained by the HE-CI procedure. Because of the RHF nature of the orbitals employed in the calculations only positive, i.e. α spin densities are obtained and spin-polarization contributions are not included. As a consequence, the spin densities shown in Table 3 represent a lower limit for the true positive spin population. However, we are confident that the relative values of the predicted densities are reliable: model calculations on the cyclohexadienyl radical assign 0.42 and 0.26 to the *para* and *ortho* carbon atoms, respectively. Although the absolute values are

Can. J. Chem. Downloaded from www.nrcresearchpress.com by 195.246.54.202 on 09/08/12
For personal use only.

TABLE 3. Spin densities calculated by QCFF/PI and MNDO for the HC_{60} and H_3C_{60} radicals

	HC_{60}				H_3C_{60}		
	QCFF/PI[a]	MNDO[a]	PW[b]	MDK[c]	QCFF/PI[a]	MNDO[a]	MDK[c]
C_1	0.259	0.296[d]	0.298	0.32			
C_2					0.234	0.255[d]	0.27
C_3	0.134	0.144	0.138	0.14			
C_4						0.003	0.01
C_5	0.027	0.033	0.033	0.04	0.001		
C_6							
C_7	0.007	0.003			0.024	0.021	0.02
C_8							
C_{11}	0.056	0.056	0.054	0.05			
C_{12}	0.011	0.007		0.01	0.124	0.113	0.10
C_{13}	0.022	0.019	0.021	0.02	0.011	0.012	0.01
C_{14}	0.003	0.002			0.047	0.041	0.04
C_{15}	0.021	0.015	0.015	0.01			
C_{16}	0.008	0.003					
C_{17}	0.022	0.012	0.014	0.01	0.002	0.001	
C_{18}	0.008	0.007		0.01			
C_{19}	0.007	0.005			0.001		
R[e]						0.012	0.01
R'[e]		0.021		0.03			

[a]This work.
[b]Reference 11.
[c]Reference 10.
[d]For C atoms total $p + s$ contributions are listed. The s contribution is always smaller than 0.001.
[e]R = R' = H.

underestimated by ~20%, the ratio of the two densities, 1.6, compares very well with the ratio of the experimentally deduced spin densities (1.5) (25, 26).

The HC_{60} spin densities listed in Table 3 indicate that the unpaired electron is localized in the neighborhood of the hydrogen atom, with the largest contribution on C_1 followed by C_3 and $C_{3'}$. These predictions are in close agreement with previous semi-empirical calculations (10, 11) and with recent *ab initio* studies (12, 13), although the latter predict an even larger localization on C_1. Among the several calculations, only the PRDDO/UHF results (19) indicate a spin density delocalized over the entire ball. We obtained a similar result by using the MNDO/UHF wavefunction to calculate spin densities, but the spin contamination was so large that the predictions are deemed completely unreliable.

It is interesting to note, as shown in Table 3, that the spin densities calculated by us (columns 1, 2 in Table 3) are very close to those calculated using the MNDO Hamiltonian combined with an RHF approach, and the ROHF (10) or the UHF (11) geometries. Since UHF/MNDO (11) ROHF/MNDO (10) and our HECI/QCFF/PI geometries are somewhat different, this indicates that the spin density distribution is almost independent of the structure, for a relatively large range of HC_{60} structures.

As expected, the spin distribution of H_3C_{60} is rather different from that predicted for HC_{60}. As in the allyl radical itself, the spin density is mainly located on C_2 and $C_{2'}$. However, the calculations also predict a considerable contribution on C_{12} and $C_{12'}$ carbon atoms. As for HC_{60}, our results for H_3C_{60} agree with those obtained at the MNDO-optimized geometry (10). It is worth noting that the prediction of a considerable spin density on C_{12} and $C_{12'}$ provides an explanation for the R_3C_{60} reactivity leading to the formation of the observed penta-substituted R_5C_{60} cyclopentadienyl radicals (1).

4. Discussion

In the previous section we have shown that the results of our calculations provide a picture of the spin density distribution that is in close agreement with most of the studies appearing in the literature. The considerable number of theoretical studies and the qualitative agreement among the predictions made by different methods encourage us to analyze more closely the extent to which the calculated spin densities can account for the experimentally observed hfc.

One of the problems addressed here is the spin population carried by C_1, C_5, and $C_{5'}$, atoms identified by the usual Kekulé formulations as primary locations for the unpaired spin in HC_{60} and its derivatives. There would appear to be a discrepancy between the amount of unpaired electron on these nuclei predicted by the calculations and deduced from EPR experiments (1). A second problem pertains to the spin population on C_2 and $C_{2'}$ in H_3C_{60}. The magnitude of the observed hfc seems to indicate that the spin population on these atoms should be close to that of the allyl radical, while calculations indicate a smaller amount.

In the first part of this section we attempt to shed some light on this subject by establishing a correlation between the observed hfc of mono- and tri-substituted-C_{60} derivatives. In the second part of the discussion we show that the results predicted by the calculations are indeed in satisfactory agreement with the observed H and ^{13}C hfc, and that they suggest a possible reassignment of some of the observed hyperfine interactions to different nuclei.

The proton in HC_{60} (H on C_6) is a "β proton" vis-a-vis the spin-carrying (α) carbons C_1, C_5 and $C_{5'}$. Many years ago Whiffen (27) pointed out that the correct procedure for predicting the β-proton hyperfine splitting in organic π radicals with multiple spin-bearing α carbons is to square the sum of the α-carbon coefficients in the SOMO before multiplying by the conversion factor Q_H:

Can. J. Chem. Downloaded from www.nrcresearchpress.com by 195.246.54.202 on 09/08/12
For personal use only.

TABLE 4. Comparison of hyperfine splittings (/G) of the central atom of R in $R_2R'C_{60}$ radicals with those of R in RC_{60} radicals

RC_{60}	a_{1R} in RC_{60}	R_3C_{60}	a_{2R} in $R_2R'C_{60}$
HC_{60}	33.1	H_3C_{60}	18.7
$C_6H_5CH_2C_{60}$	14.9	$(C_6H_5CH_2)_3C_{60}$	9.70
CCl_3C_{60}	29.6	$(CCl_3)_2ClC_{60}$	16.4
CBr_3C_{60}	35.3	$(CBr_3)_3C_{60}$	20.1

$$[1] \quad a_H = Q_H \times \left[\sum_o c_o\right]^2$$

where the subscripts indicate that the summation covers only atoms *ortho* to C—H. An identical equation in a_C and Q_C applies to ^{13}C in a ^{13}C—C_{60} configuration. Attention has been recently drawn to Whiffen's relation by Percival and co-workers (11) who compared computed spin densities and observed hyperfine interactions in fullerenyl radicals. The empirical equation [1] has indeed a theoretical justification and it is a legitimate extension of the McConnell relation (28) for those nuclei that bear a fraction of the unpaired electron because of the hyperconjugation effect (29). By applying relation [1] to the hfc of the mono- and trisubstituted-C_{60} radicals, we can obtain a qualitative estimate of $[\Sigma_o c_o]^2$ for the SOMO of the two radicals. The value of Q_H for a β-proton eclipsed by the semi-occupied $2p$ orbital on the adjacent carbon is ca. 50 G (30). In HC_{60} the proton is required by the structure to eclipse $2p$ orbitals whether on C_1, C_5, or $C_{5'}$. Bearing in mind the distinction between organic π-radicals and HC_{60}, we note that with a_{1H} = 33 G in HC_{60}, a Q_H of 50 G implies $(c_1 + 2c_5)^2$ = 0.66, indicating a considerable dispersal of the unpaired spin away from these carbons (c_1 and c_5 SOMO coefficients have the same sign). If we use the hydrogen hyperfine splittings of H_3C_{60} (18.7 G) and the same Q_H we obtain a value of 0.37 for $(c_2 + c_4 + c_7)^2$ which indicates a significant delocalization of the unpaired electron for trisubstituted-C_{60} radicals also.

Besides the actual magnitude of $[\Sigma_o c_o]^2$, which depends on the value assumed for Q_H or Q_C, eq. [1] provides a useful relation between the hfc observed for mono- and trisubstituted-C_{60} radicals. The values of a_{1H}, a_{2H}, a_{1C}, and a_{2C} for R = H and various alkyls are listed in Table 4. Plotting a_{1H} or a_{1C} against a_{2H} or a_{2C} gives the graph shown in Fig. 3, where the data points are fitted to a least-squares straight line whose slope is 1.99 ± 0.10. According to eq. [1], and with the reasonable assumption that the Q_X (X = H, C) constants are the same for mono- and trisubstituted-C_{60} radicals, the value of the slope in Fig. 3 indicates that

$$[2] \quad \frac{(c_1 + 2c_5)^2}{(c_2 + c_4 + c_7)^2} = \sim 2$$

for all the observed pairs of radicals. An obvious explanation of this experimental result is that the distribution of the unpaired electron on the C_{60} surface is substantially independent of the chemical nature of the substituent, and that, to a good approximation, it is determined only by the number and position of the substituents.

The latter observation is of some relevance: first, it indicates that calculations performed for the prototype radicals can be used to interpret the EPR spectra of other mono- or trisubstituted-C_{60} radicals. Second, it provides a criterion with which to assess the reliability of the theoretical predictions. A primary requirement of the calculations is that they lead to a value of ratio [2] close to 2.

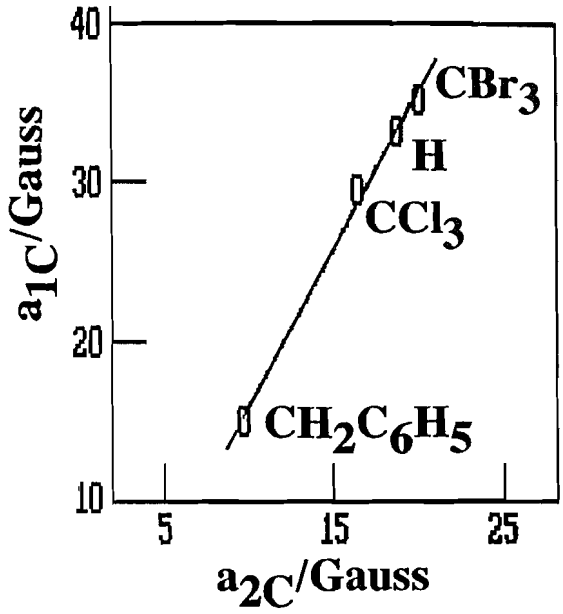

FIG. 3. Graph of a_{1H} and a_{1C} in HC_{60} and RC_{60} radicals against a_{2H} and a_{2C} in H_3C_{60} and R_3C_{60} radicals. The line is a least-squares fit to the data. The labels beside each point identify the ligands H and R.

It is interesting to note that a ratio of 2 would be obtained by assuming the most simplistic distribution of the unpaired electron for the two radicals, namely 1.0 spin density on C_1 for HC_{60} and 0.5 on C_2 and $C_{2'}$ for H_3C_{60}. As a consequence, if we assume that the unpaired electron in H_3C_{60} is localized only on C_2 and $C_{2'}$, as the comparison between hfc for H_3C_{60} and the allyl radical would suggest, and we assume a 0.58 spin density (9) on each of the two nuclei, we are led to the conclusion that the HC_{60} spin density on C_1 should be close to 1.2, a value not compatible with the observed isotropic $^{13}C_1$ hyperfine coupling (17.8 G). This supports the results of the calculations, which predict some delocalization of the unpaired electron for both radicals.

To evaluate relation (2) we employ the spin densities obtained by the QCFF/PI method. As already pointed out, these spin densities are very close to those obtained here and in previous studies (10, 11), using the MNDO Hamiltonian. However, we choose to use the QCFF/PI wavefunction because it conforms more strictly to the assumption of a perturbative description of the hyperconjugation effect implicit in eq. [1]. In fact, spin densities are calculated by QCFF/PI only for the sp^2 carbon atoms, since only p electrons are described quantum-chemically by the method. On the other hand, MNDO calculates spin densities for all the atoms. In terms of perturbation theory, QCFF/PI densities are obtained from a zero order wavefunction, without the inclusion of the perturbation due to the hydrogen atoms, which is described by eq. [1]. On the other hand, MNDO spin densities do include the perturbation, i.e., they account for the hyperconjugation effect, and thus for the appearance of a non-zero spin density in the $1s$ hydrogen and $2s$ carbon orbitals.

By using the c_o coefficients deduced from columns 1 and 5 in Table 3 we obtain $[\Sigma_o c_o]^2$ = 0.70 for HC_{60}. For H_3C_{60}, $[\Sigma_o c_o]^2$ = 0.41 (by including only C_2 and C_7 contributions) or $[\Sigma_o c_o]^2$ = 0.39 (by including also the negative contribution of

Can. J. Chem. Downloaded from www.nrcresearchpress.com by 195.246.54.202 on 09/08/12
For personal use only.

TABLE 5. Experimental and computed ^{13}C hyperfine interactions for the C_{60} surface of RC_{60} and R_3C_{60} radicals

	RC_{60}		R_3C_{60}	
	Calc[a]	Exp[b]	Calc[a]	Exp[c]
C_1	19.7	17.8	−9.7	13.1[d]
C_2	−8.5	8.9	17.6	19.8
C_3	10.0	9.4		
C_4	−3.7	4.5[e]	−0.1	
C_5	2.1	3.6[e]	0.1	
C_6		5.6		
C_7	−3.5	4.0[e]	1.9	
C_8	−1.0		—	
C_{11}	3.9	5.6[e]	−3.4	
C_{12}	−0.8		8.3	13.1[d]
C_{13}	1.0		−6.8	
C_{14}	−0.1		−0.1	
C_{15}	1.2	2.4[e]	—	
C_{16}	−0.3		−0.1	
C_{17}	1.3	2.4[e]	0.1	
C_{18}	—		−0.8	
C_{19}	—		—	

[a]QCFF/PI spin densities are used, from columns 1 and 5 in Table 3.
[b]From ref. 3.
[c]This work.
[d]See discussion in the text.
[e]Tentative assignment.

the coefficient of atom C_4, bearing a spin density of 0.0003). Hence, the predicted ratio (2) is 1.71 or 1.82, respectively, in very good agreement with the slope of Fig. 3, and, in particular, in excellent agreement with the experimental ratio a_{1H}/a_{2H} = 1.77.

Similar values for the ratio of coefficients squared in relation [2] are obtained by using the spin densities on the C_{60} surface calculated by the MNDO method. In addition, MNDO results provide a double check by means of the predicted H 1*s* spin densities, which are directly proportional to the H hfc. The ratio of the 1*s* H spin densities listed in Table 3, 0.021/0.012 = 1.75, is also in excellent agreement with the experimental value of a_{1H}/a_{2H}. Although the absolute values of these spin densities are underestimated, it is worth noting that this tendency of the semi-empirical method can be corrected by scaling the calculated spin densities. In fact, a similar calculation for the cyclohexadienyl radical predicts a spin density of 0.032 on the β proton. Hence, the calculated ratio of the β proton hfc in cyclohexadienyl and that of HC_{60} is 0.032/0.021 = 1.52 which compares very well with the ratio of the observed hfc: 48 G/ 33 G = 1.45.

The above discussion indicates that the calculated spin distributions account for the observed H and ^{13}C—C_{60} hfc of RC_{60} and R_3C_{60}. We have also estimated the hfc of the C_{60} carbon atoms using the Karplus–Fraenkel relation (31)

$$[3]\quad a_C = \left(S^C + \sum_{i=1}^{3} Q^C_{CC'}\right)\rho^\pi + \sum_{i=1}^{3} Q^C_{C'C}\rho^\pi_i$$

and assuming $Q^C_{CC'} = -20.9$ G, $Q^C_{CC'} = 30.0$ G (32) and the standard value of −12.7 G for the S_C parameter. We use the above values for the former two parameters, deduced for bond lengths of 1.50 Å (32), according to most of the calculated bond lengths close to the substituents. Inspection of the computed hfc, listed in Table 5, shows a close agreement with the experimental data, also listed in Table 5: the largest hfc of both radicals are satisfactorily reproduced by the calculations. In particular, the computed hyperfine splittings indicate that one of the two hfc observed at ~9 G for HC_{60} and previously assigned to C_5 should be reassigned to C_2. It is interesting to note that a similar conclusion is also supported by recent *ab initio* calculations (12, 13). Although these calculations predict too large a hfc for C_1, they indicate similar hfc for atoms C_2 and C_3. In addition, comparison of the calculated hfc of H_3C_{60}, listed in Table 5, indicates that the hyperfine splitting observed at 13.1 G may arise from carbons (C_1, C_{12}, $C_{12'}$) that are accidentally equivalent. The experimental determination of the sign of the hyperfine splittings will be of crucial importance to substantiate the reassignments proposed here. Relative sign determination for H and ^{13}C is possible, in principle, by muon level-crossing (26) or ENDOR experiments. The consistency of the present results is of particular importance since it indicates that semi-empirical predictions of the spin distributions for such large systems are reliable.

1. P.J. Krusic, E. Wasserman, P.N. Keizer, J.R. Morton, and K.F. Preston. Science, **254**, 1183 (1991).
2. J.R. Morton, K.F. Preston, P.J. Krusic, S.A. Hill, and E. Wasserman. J. Phys. Chem. **96**, 3576 (1992).
3. J.R. Morton, K.F. Preston, P.J. Krusic, and E. Wasserman. J. Chem. Soc. Perkin Trans. 2, 1425 (1992).
4. P.N. Keizer, J.R. Morton, K.F. Preston, and P.J. Krusic. J. Chem. Soc. Perkin Trans. 2, 1041 (1993).
5. J.A. Howard. Chem. Phys. Lett. **203**, 540 (1993).
6. A. Warshel and M. Karplus. J. Am. Chem. Soc. **94**, 5612 (1972); A. Warshel and M. Levitt. Quantum chemistry program exchange No. 247, Indiana University.
7. M.J.S. Dewar and W. Thiel. J. Am. Chem. Soc. **99**, 4899 (1977); M.J.S. Dewar and W. Thiel. J. Am. Chem. Soc. **99**, 4907 (1977); M.J.S. Dewar, M.L. McKee, and H.S. Rzepa. J. Am. Chem. Soc. **100**, 3607 (1978); M.J.S. Dewar and J.J.P. Stewart. Quantum chemistry program exchange No. 506, Indiana University.
8. D. Griller. Magn. Reson. Rev. **5**, 1 (1979).
9. H.J. McManus, R.W. Fessenden, and D.M. Chipman. J. Phys. Chem. **92**, 3778 (1988).
10. N. Matsuzawa, D.A. Dixon, and P.J. Krusic. J. Phys. Chem. **96**, 8317 (1992).
11. P.W. Percival and S. Wlodek. Chem. Phys. Lett. **196**, 317 (1992).
12. T.A. Claxton and S.F.J. Cox. Chem. Phys. Lett. **207**, 31 (1993).
13. T.A. Claxton and J. Graham. J. Phys. Chem. **97**, 4621 (1993).
14. J.P. Hare and H.W. Kroto. Acc. Chem. Res. **25**, 106 (1992).
15. H.W. Kroto and M. Jura. Astron. Astrophys. **263**, 275 (1992).
16. A. Webster. Mon. Not. R. Astr. Soc. **255**, 41p (1992).
17. A.S. Webster. Mon. Not. R. Astr. Soc. **257**, 750 (1992).
18. J.R. Morton, K.F. Preston, P.J. Krusic, and L.B. Knight. Chem. Phys. Lett. **204**, 481 (1993).
19. S.K. Estreicher, C.D. Latham, M.I. Heggie, R. Jones, and S. Öberg. Chem. Phys. Lett. **196**, 311 (1992).
20. F. Zerbetto, M.Z. Zgierski, F. Negri, and G. Orlandi. J. Chem. Phys. **89**, 3681 (1988); F. Negri, G. Orlandi, A.M. Brouwer, F.W. Langkilde, and R. Wilbrandt. J. Chem. Phys. **90**, 5944 (1989).
21. M.J.S. Dewar, J.A. Hashmall, and C.J. Venier. J. Am. Chem. Soc. **90**, 1953 (1968).
22. F. Negri, G. Orlandi, and F. Zerbetto. Chem. Phys. Lett. **144**, 31 (1988); F. Negri, G. Orlandi, and F. Zerbetto. Chem. Phys. Lett. **190**, 174 (1992).
23. F. Negri, G. Orlandi, and F. Zerbetto. J. Am. Chem. Soc. **113**, 6037 (1991).
24. F. Negri, G. Orlandi, and F. Zerbetto. Chem. Phys. Lett. **196**, 303 (1992).
25. R.W. Fessenden and R.H. Schuler. J. Chem. Phys. **38**, 773 (1963).

Can. J. Chem. Downloaded from www.nrcresearchpress.com by 195.246.54.202 on 09/08/12
For personal use only.

26. R.F. Kiefl, P.W. Percival, J-C. Brodovitch, S-K. Leung, D. Yu, K. Venkateswaran, and S.F.J. Cox. Chem. Phys. Lett. **143**, 613 (1988).
27. D.H. Whiffen. Mol. Phys. **6**, 223 (1963).
28. H.M. McConnell. J. Chem. Phys. **24**, 632 (1956).
29. R. Bersohn. J. Chem. Phys. **24**, 1066 (1956).
30. R.W. Fessenden and R.H. Schuler. J. Chem. Phys. **39**, 2147 (1963).
31. M. Karplus and G.K. Fraenkel. J. Chem. Phys. **35**, 1312 (1961).
32. H.L. Strauss and G.K. Fraenkel. J. Chem. Phys. **35**, 1738 (1961).

Can. J. Chem. Downloaded from www.nrcresearchpress.com by 195.246.54.202 on 09/08/12
For personal use only.

Bond energies for cationic bare metal hydrides of the first transition series: a challenge to density functional theory

TOM ZIEGLER AND JIAN LI

Department of Chemistry, University of Calgary, Calgary, AB T2N 1N4, Canada

Received July 19, 1993

This paper is dedicated to Professor John C. Polanyi on the occasion of his 65th birthday

TOM ZIEGLER and JIAN LI. Can. J. Chem. **72**, 783 (1994).

Density functional methods based on the Local Density Approximation (LDA) and its nonlocal extensions (LDA/NL) are used to calculate the bond energies, as well as the bond lengths and vibrational frequencies of the high spin, open shell first-row transition metal hydride cations MH^+. The $D_{298}(M^+—H)$ LDA/NL bond energies are in good agreement with experiment for the early transition metals with errors within 5 kcal/mol. However, the error increases to 6–13 kcal/mol for the late metal hydrides. An analysis based on atomic properties such as 4*s* ionization potentials and 4*s* to 3*d* promotion energies revealed that the large error in bonding energies among the late transition metals can be attributed to an overestimation of the exchange energy in the DFT schemes. It is shown that a simple remedy, based on a thermodynamic cycle, can improve the agreement between experimental and theoretical bond energies. However, simple cationic bare metal complexes such as MH^+ remains a challenge to approximate DFT.

TOM ZIEGLER et JIAN LI. Can. J. Chem. **72**, 783 (1994).

On a utilisé des méthodes de densité fonctionnelle basées sur l'approximation de la densité locale (LDA) et ses extensions non locales (LDA/NL) pour calculer les énergies de liaison, ainsi que les longueurs de liaison et les fréquences vibrationnelles de spin élevé, des cations, MH^+, des hydrures des métaux de transition de la première rangée avec une couche ouverte. Les énergies de liaison $D_{298}(M^+—H)$ LDA/NL sont en bon accord (avec des erreurs inférieures à 5 kcal/mol) avec les résultats expérimentaux pour les premiers métaux de transition. Une analyse basée sur les propriétés atomiques telles que les potentiels d'ionisation 4*s* et les énergies de promotion de 4*s* à 3*d* révèlent que l'erreur importante dans les énergies de liaison observée avec les derniers métaux de transition peut être attribuée à une surévaluation de l'énergie d'échange dans les schémas DFT. On montre qu'un remède simple, basée sur un cycle thermodynamique, peut améliorer la concordance entre les énergies de liaison expérimentales et théoriques. Toutefois, avec des complexes métalliques cationiques simples, tels que MH^+, l'approximation du DFT demeure un défi.

[Traduit par la rédaction]

I. Introduction

Accurate data on metal–hydrogen (and metal–carbon) bonds are essential for a quantitative assessment of reaction enthalpies in organometallic processes and might even help addressing mechanistic issues. The efforts to obtain accurate bond enthalpies in this field was pioneered by Skinner (1*a*), Pilcher and Skinner (1*b*), Halpern (1*c*), and Connor (1*e*). Since then, organometallic thermochemistry has grown into a vast body of data with the aid of an impressive arsenal of experimental methods. This development has most recently been reviewed by Simoes and Beauchamp (1*d*).

Theoretical methods have had considerable success in providing accurate data on bond strength of small organic molecules. Thus, Pople and co-workers (2, 3) have recently shown that enthalpies of formation for small organic molecules can be calculated within chemical accuracy (± 2 kcal mol^{-1}) in the "Gaussian-1" (G1) as well as the revised "Gaussian-2" (G2) methods. Bond dissociation energies for simple diatomic metal hydrides can also be calculated to the same degree of accuracy (4). However, G2 calculations on larger organic molecules, let alone transition metal complexes, are still impractical.

Becke (5) has in a series of seminal papers, shown that methods based on Density Functional Theory (6, 7) (DFT) afford bond energies of nearly the same quality as the G2 *ab initio* technique. Becke's investigation made use of a DFT approach in which the Local Density Approximation (LDA) (8, 9) has been augmented by nonlocal (10–15) corrections, LDA/NL. DFT-based calculations on bond energies for small organic molecules have also been carried out by others (16).

The LDA/NL method has recently been implemented at the self-consistent level (17) and applied to molecular structures (18). It was demonstrated (17, 23) that nonlocal corrections greatly improves the accuracy of metal–ligand and metal–metal bond distances. Studies on transition state structures have also been carried out by the nonlocal method (19). DFT-based methods have in addition been applied successfully to studies on IR spectra of main group molecules (20) and transition metal complexes (21).

Our knowledge of metal–hydride (and metal–alkyl) bond dissociation energies comes from studies of two distinctly different classes of compounds. The first involves 18-electron RML_n systems where the metal centre is coordinatively saturated by ancillary ligands other than the R group. The second class comprises bare metal complexes, M—R, in which the metal centre is coordinatively unsaturated. The 18-electron systems have a direct bearing on the kind of compounds normally studied in organometallic chemistry. However, only a few experimental M—R bond energies are available from this category. We have in previous studies (22, 23) validated the nonlocal method with respect to the sparse experimental data from 18-electron systems. It was concluded that the LDA/NL scheme for this type of compounds afford M—R bond energies within ± 5 kcal/mol of experiment.

The number of accurate M—R bond energies among the coordinatively unsaturated M—R complexes is large in comparison to the saturated 18-electron systems, thanks to several new experimental gas phase techniques developed over the last decade (1*d*, 24). However, there has been surprisingly few (25) DFT-based calculations on bare atom complexes in spite of their small size, and no systematic evaluation has been undertaken on the ability of DFT methods to reproduce experimental findings for this class of compounds.

Can. J. Chem. Downloaded from www.nrcresearchpress.com by EESC ESCOLA DE ENGENHARIA on 09/08/12
For personal use only.

TABLE 1. The electron affinities[a,c] of first row transition metal cations

	Sc^+	Ti^+	V^+	Cr^+	Mn^+	Fe^+	Co^+	Ni^+	Cu^+
HFS	5.62	5.69	5.94	6.00	6.17	7.02	7.40	7.81	8.33
LDA	6.50	6.86	7.18	7.32	7.54	8.20	8.57	8.92	9.40
LDA + B + P	6.44	6.75	7.06	7.19	7.38	8.13	8.34	8.71	9.20
Exp[b]	6.56	6.83	7.14	7.28	7.44	7.87	8.28	8.67	9.04

[a]All energies in eV.
[b]The experimental values are taken from Moore's table (37) and averaged over the $(2J + 1)$ spin–orbit states.
[c]Corresponding to the $3d^{n-2}4s^1 \rightarrow 3d^{n-2}4s^2$ process.

We shall here consider the smallest of the bare metal complexes, the MH^+ hydrides. We shall demonstrate that bond energies in these systems are poorly described by the existing DFT-based methods for hydrides of late transition metals, in contrast to M—L bond strength among the saturated 18-electron complexes. The error sources will further be analysed by performing calculations on the electron affinities and $4s$ to $3d$ promotion energies of the cations, M^+. The main objective of this study has been to point to a series of molecules that can serve as a testing ground for improvements of the existing DFT-based methods.

II. Computational details and basic theory

The reported calculations were all carried out by utilizing the HFS-LCAO program system A-MOL, developed by Baerends et al. (26, 27*a*) and vectorized by Ravenek (27*b*). The numerical integration procedure applied for the calculations was developed by te Velde et al. (28). The geometry optimization procedure was based on the method implemented by Versluis and Ziegler (29). Vibrational frequencies were evaluated from force constants calculated by numerical differentiation of the energy gradients (20*e*). The electronic configurations of the molecular systems were described by an uncontracted triple-ζ STO basis set (30) on the metal ($3d$, $4s$, and $4p$) as well as a double-ζ STO basis set (30*b*) on hydrogen ($1s$). Hydrogen were given an extra polarization function: $2p_H$ ($\zeta_{2p} = 2.0$). The $1s^2 2s^2 2p^6$ configuration on the metal centers was assigned to the core and treated by the frozen-core approximation. A set of auxiliary (31) s, p, d, f, and g STO functions, centered on all nuclei, was used to fit the molecular density and present Coulomb and exchange potentials accurately in each SCF cycle.

We have compared results from different levels of DFT. The simplest is the Xα or Hartree–Fock–Slater scheme (8) in which the exchange correlation energy is approximated by Slater's exchange expression from the homogeneous electron gas without considering the corresponding correlation term. In the Local Density Approximation (LDA) (9*a*), both exchange and correlation from the homogeneous electron gas are included based on the parametrization due to Vosko et al. (9*b*). Stoll et al. (32) have pointed out that the LDA approximation exaggerate correlation between electrons of the same spin. They have suggested that this correlation be removed altogether. Two nonlocal corrections will be considered. The first is the exchange correction due to Becke (13*d*), and the second Perdew's (14*c*) correction to correlation. We shall refer to the scheme included Becke's and Perdew's corrections as LDA + B + P. The two nonlocal corrections take into account that the density in atoms and molecules is inhomogeneous. Perdew's correction removes, in addition, the deficiencies in the original LDA scheme pointed out by Stoll et al. (32). The application of approximate density functional theory to organometallic chemistry has been reviewed recently (6, 33).

The state energies for molecules and atoms were evaluated by the multiplet method due to Ziegler et al. (34) using nonspherical densities (35) and a complex representation (36) of the orbitals. As examples, the ^4F state of $Ti^+(4s^1 3d^2)$ was described by the state function $|\bar{4}_s^+ 3\bar{d}_2^+ 3\bar{d}_1^+|$ whereas the $^3\Phi$ state of TiH^+ is represented by $|\bar{\sigma}^+ \bar{\sigma}^- \bar{\phi}_2^+ \bar{\pi}_1^+|$.

III. Results and discussion

The formation of MH^+ from M^+ and H involves the pairing of an electron on M^+ of, say, α-spin with an electron on H of β-spin. The pair will be situated in a M—H σ-bonding orbital, σ_{MH}. The additional electrons on M^+ are only slightly perturbed as MH^+ is formed and remain in d-based orbitals retaining their spin polarisation. The energetics of this spin-pairing process have several contributions. In the first place, the spin pairing increases the stabilisation due to the correlation energy between electrons of opposite spins by $\Delta E_{XC}^{\alpha\beta}$. Further, the number of interacting electrons of the same spin are going to increase in those cases where the metal has additional electron of β-spin. This will be the case for late transition metals, Fe–Cu, and results in a stabilising contribution, $\Delta E_{XC}^{\beta\beta}$, from the exchange part of the exchange-correlation energy. Also, the formation of σ_{MH} might constitute a transfer of charge between M^+ and H or between $4s$ and $3d$. In the first case, we have a stabilising charge transfer contribution, ΔE_{ct}, in the second a stabilising polarisation contribution, ΔE_{pol}.

It is clear from the discussion above that the M—H bond formation is influenced by several factors, and that an accurate determination of the M—H bond energy will require a balanced description of all these factors. We shall now examine how well the different factors are represented in DFT-based methods by comparing atomic energy differences from experiments with the corresponding values evaluated with various levels of DFT theory. The atomic calculations are particularly appropriate since the electronic structure of MH^+ is largely atomic in nature (4*a–d*). Further, atomic studies will allow us to study several of the factors mentioned above, one at a time.

Electron affinities

Table 1 displays the electron affinities (37), A_I, for M^+ anions of the first transition series corresponding to the process

$$[1] \quad 3d^{n-2}4s^1 + e^- \rightarrow 3d^{n-2}4s^2$$

It follows from the discussion above that A_I should have a positive contribution from $\Delta E_{XC}^{\alpha\beta}$ as the $4s^2$ electron pair is formed. There will in addition be a positive contribution to A_I from $\Delta E_{XC}^{\beta\beta}$ among the late transition metals, Fe–Cu, as the

Can. J. Chem. Downloaded from www.nrcresearchpress.com by EESC ESCOLA DE ENGENHARIA on 09/08/12
For personal use only.

TABLE 2. The 4*s* to 3*d* promotion energies[a,b] of first-row transition metal cations

	Sc^+	Ti^+	V^+	Cr^+	Mn^+	Fe^+	Co^+	Ni^+	Cu^+
HFS	0.66	−0.26	−0.88	−1.78	2.37	0.22	−0.41	−1.59	−2.98
LDA	0.49	−0.39	−1.07	−1.76	1.28	0.20	−0.73	−1.86	−3.33
LDA + B + P	0.47	−0.33	−0.97	−1.80	1.25	0.05	−0.85	−1.75	−3.02
Exp[c]	0.60	0.10	−0.33	−1.52	1.81	0.25	−0.43	−1.08	−2.81

[a]Energies in eV.
[b]Corresponding to the process $3d^{n-1}4s^1 \rightarrow 3d^n$.
[c]The experimental values are taken from Moore's table (37) and averaged over the $(2J + 1)$ spin–orbit states.

Can. J. Chem. Downloaded from www.nrcresearchpress.com by EESC ESCOLA DE ENGENHARIA on 09/08/12
For personal use only.

added electron of, say, β spin, interacts with *d*-electrons of the same spin-polarization on M^+. Thus, the process in eq. [1] is in many ways analogous to the formation of MH^+.

Table 1 reveals that the simple HFS scheme (8) underestimates all electron affinities. This is to be expected since the HFS method completely neglects electron correlation between electrons of different spins, and thus lacks the positive contribution to A_I from $\Delta E_{XC}^{\alpha\beta}$. In the LDA case $\Delta E_{XC}^{\alpha\beta}$ is present and we see an increase in the calculated values for A_I. For the early to middle transition metal cations, Sc^+ to Mn^+, the LDA values are in good agreement with experiment. The average deviation is only 0.05 eV. These are the elements for which the contribution from $\Delta E_{XC}^{\beta\beta}$ is absent since the captured electron has a spin polarization different from that of the valence electrons on M^+. Thus, it would seem that LDA provides an accurate estimate of $\Delta E_{XC}^{\alpha\beta}$. On the other hand, the affinities calculated by LDA for the late transition metal cations, Fe^+–Cu^+, are too large. For these elements $\Delta E_{XC}^{\beta\beta}$ becomes important, and we attribute the deviation between theory and experiment to an overestimation of the exchange term $\Delta E_{XC}^{\beta\beta}$. The size of $\Delta E_{XC}^{\beta\beta}$ is to a first approximation, proportional to the number of electrons on M^+ of the same spin as that of the captured electron, and that is mostly likely why the gap between experiment and theory increases from Fe^+ to Cu^+.

Becke's nonlocal exchange correction (13*d*) combined with Perdew's nonlocal correlation correction (14*d*), LDA + B + P, are seen to reduce the calculated electron affinities, Table 1, and improve the agreement with experiment for the late transition metals. Thus, the mean deviation for Fe^+—Cu^+ is reduced from 0.35 eV in the LDA case to 0.12 eV in the LDA + B + P case. However, the affinities remain too large due to an overestimation of $\Delta E_{XC}^{\beta\beta}$. The deviation between experiment and theory would increase by 0.1 eV if relativistic correction were taken into account according to estimates by Kutzler and Painter (35). It is thus clear that nonlocal corrections to the exchange (13*d*) only in part are able to correct the substantial error in the LDA exchange energy.

Kutzler and Painter (35) have previously studied the same series. Their LDA and LDA/NL results are quite similar to ours although they used the nonlocal functional due to Langreth and Mehl (10). However, Kutzler and Painter did not provide an interpretation of their data in terms of $\Delta E_{XC}^{\alpha\beta}$ and $\Delta E_{XC}^{\beta\beta}$. This interpretation is needed here in order to understand the MH^+ results.

Kutzler and Painter (35) have also calculated electron affinities in which a 3*d* orbital is occupied. They found in this case even larger deviations from experiment. It seems that the exchange between electrons in 3*d* orbitals is even more exaggerated than the exchange between electrons in, respectively, 3*d* and 4*s* orbitals. This has already been noted by Gunnarson and Jones (38).

Promotion energies

We have calculated the promotion energy E_{4s-3d} corresponding to the process

[2] $3d^{n-1}4s^1 \rightarrow 3d^n$

for the series of first row transition metal cations. A comparison of calculated and experimental (37) promotion energies should enable us to judge how well DFT-based methods are able to evaluate the term ΔE_{pol} discussed above.

Of the two configurations $3d^{n-1}4s^1$ and $3d^n$, the first is favored by having the smallest electron–electron repulsion whereas $3d^n$ has the most stabilizing exchange energy, at least in the cases where $3d^{n-1}4s^1$ and $3d^n$ have the same numbers of electrons with α and β spins, respectively. Both trends can be attributed to the fact that exchange as well as Coulomb interactions between electrons in the compact *d*-orbitals are stronger than the same interactions between electrons in 4*s* and 3*d* orbitals, respectively, with different radial extents (4*a*).

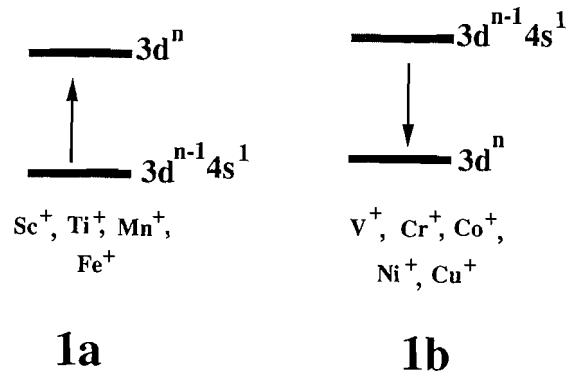

SCHEME 1

The Sc^+, Ti^+, Mn^+, and Fe^+ cations have a $3d^{n-1}4s^1$ ground state, **1***a*, and thus a positive E_{4s-3d} promotion energy, Table 2, whereas V^+, Cr^+, Co^+, Ni^+, and Cu^+ all have a $3d^n$ ground state, **1***b*, with a negative promotion energy, Table 2 (Scheme 1). The HFS method is seen to underestimate E_{4s-3d} for Ti^+ and Fe^+ with the $3d^{n-1}4s^1$ ground state configuration, **1***a*. The inclusion of correlation, LDA, does not change the calculated values much since the $3d^{n-1}4s^1$ and $3d^n$ configurations have the same number of electrons with α and β spins, respectively.

It appears that the local methods have a bias in favor of $3d^n$ over $3d^{n-1}4s^1$ (Table 2). The bias comes from the exchange energy which is overestimated for both configuration, but most in the $3d^n$ case. This is so (38) since the exchange between electrons in 3*d* orbitals is even more exaggerated than the exchange between electrons in 3*d* and 4*s* orbitals, respectively, as already pointed out by Gunnarsson and Jones (38).

TABLE 3. Bond energies (kcal/mol) of first-row transition metal hydride cations MH^+

	ScH^+	TiH^+	VH^+	CrH^+	MnH^+	FeH^+	CoH^+	NiH^+	CuH^+
Ground states	$^2\Delta$	$^3\Phi$	$^4\Delta$	$^5\Sigma$	$^6\Sigma$	$^5\Delta$	$^4\Phi$	$^3\Delta$	$^2\Sigma$
	(001)	(011)	(021)	(022)	(122)	(123)	(133)	(143)	(144)
HFS	41.7	37.4	32.6	35.7	31.3	43.8	49.9	42.1	28.2
LDA	65.4	60.7	56.1	47.8	58.7	59.2	59.3	52.8	41.6
LDA + B + P	61.2	57.0	53.1	39.6	53.3	59.0	55.7	49.2	35.0
Exp[b]	57 ± 2	54 ± 2	48 ± 1	33 ± 2	49 ± 3	50 ± 1	47 ± 1	40 ± 2	22 ± 3

[a]The numbers in parentheses (*xyz*) represent the occupation numbers of nonbonding electrons in σ, π, and δ orbitals, respectively.
[b]Reference 1*d*.

It also follows from Table 2 that nonlocal corrections, LDA + B + P, do little to improve the agreement with experiment. Thus these corrections are not able to correct the imbalance in the exchange energies between the $3d^{n-1}4s^1$ and $3d^n$ configurations introduced by the local methods. The same conclusion has been reached by Kutzler and Painter (35).

For the V^+, Cr^+, Co^+, Ni^+, and Cu^+ systems with the $3d^n$ ground state configuration, **1***b*, we see again that HFS favors the $3d^n$ compared to $3d^{n-1}4s^1$. The E_{4s-3d} promotion energies are all too negative, and this trend is not significantly changed by either LDA or the nonlocal LDA + B + P scheme, Table 2.

We shall shortly see how the bias introduced by the local methods in favor of $3d^n$ over $3d^{n-1}4s^1$ is carried over into the DFT description of the electronic structure in MH^+.

The D(M^+—H) bond energy in MH^+

We define the electronic bonding energy $D_e(M^+—H)$ of MH^+ as

$$[3]\quad D_e(M—H^+) = E(MH^+, \text{ground state}) - E(M^+, \text{ground state}) - E(H, {}^2S)$$

For $D_0(M^+—H)$ the vibrational zero point energy correction has been added to $D_e(M—H^+)$. Additional standard rotational, vibrational, and translational corrections were added to evaluate $D_{298}(M^+—H)$ which can be compared directly with experiment (1*d*). The calculated $D_{298}(M^+—H)$ values are compared to experiment in Table 3. The ground state electronic configurations determined by the DFT methods, Table 3, correspond to those obtained previously by Ohanessian and Goddard (4*a*).

We find that the HFS method underestimates $D_{298}(M^+—H)$ for the entire series, and we attribute this to the lack of correlation. Thus, the HFS method completely neglects the positive contribution to $D_{298}(M^+—H)$ from $\Delta E_{XC}^{\alpha\beta}$ due to the pairing of the two electrons in σ_{MH}. This is analogous to the underestimation of A_I by the HFS method due to the neglect of $\Delta E_{XC}^{\alpha\beta}$ from the electron pairing in the $4s^2$ shell.

The $\Delta E_{XC}^{\alpha\beta}$ term is included in the LDA approach and we now find, as expected, an increase in the calculated bond energies. Unfortunately, this increase leads to overbinding, even among the early to middle transition systems. It is a general observation that LDA provides bond energies that are too large (6*a*). In fact, the nonlocal corrections (10–14), LDA + B + P, were introduced in order to remedy this shortcoming. The factors responsible for the overbinding have been analysed by Tschinke and Ziegler (39).

The inclusion of nonlocal correction, LDA + B + P, reduces all calculated bond energies, Table 3, and bring the $D_{298}(M^+—H)$ values for the early to middle transition metals in acceptable agreement with experiment. The bond energies for these systems are now determined with the same accuracy (±5 kcal/mol) as the M—L bond strengths among saturated 18-electron complexes.

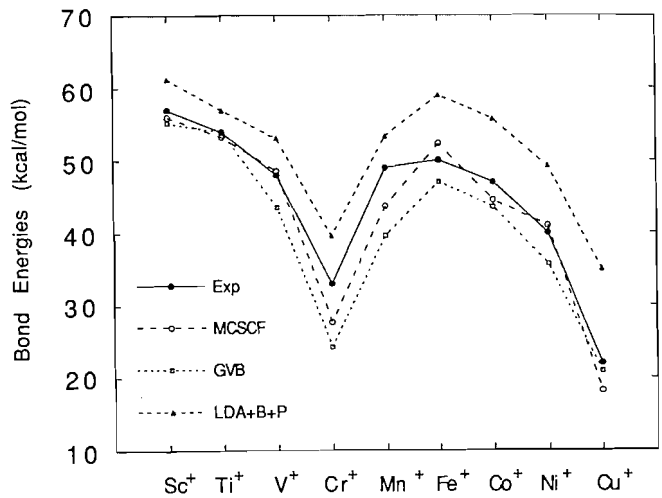

FIG. 1. Calculated and experimental bonding energies for first-row transition metal hydride cations.

However, we note a substantial overbinding at the end of the series for FeH^+, NiH^+, CoH^+, and CuH^+, even after the inclusion of nonlocal corrections. We attribute the overbinding for the late transition metal hydrides to an overestimation of $\Delta E_{XC}^{\beta\beta}$ from the exchange interaction between the electron on hydrogen and the electrons on M^+ of the same spin-polarisation. The situation is quite similar to that encountered for the electron affinities of M^+ among the late transition metal cations Fe^+ to Cu^+, where A_I was overestimated due to an exaggerate contribution from $\Delta E_{XC}^{\beta\beta}$. We shall suggest a possible remedy for this shortcoming after a comparison of our calculations with results from other theoretical studies (4*a*, 4*c*).

Figure 1 depicts LDA + B + P bonding energies together with experimental data and results from GVB (4*a*) as well as MCPF (4*c*) calculations. It can be seen from Fig. 1 that the bonding energies decrease from ScH^+ to CrH^+, jump up at MnH^+, and decrease again from FeH^+ to CuH^+. Ohanessian and Goddard (4*a*) explained this double-valley picture in terms of exchange energy loss (4*b*), which reflects the important role of nonbonding electrons. The DFT-based methods as well as the GVB and MCPF schemes are all able to reproduce the double valley trend. We note further that the GVB and MCPF methods underestimate $D_{298}(M^+—H)$ in contrast to the LDA + B + P method where the calculated bond energies, as already discussed, are too large.

Can. J. Chem. Downloaded from www.nrcresearchpress.com by EESC ESCOLA DE ENGENHARIA on 09/08/12
For personal use only.

Can. J. Chem. Downloaded from www.nrcresearchpress.com by EESC ESCOLA DE ENGENHARIA on 09/08/12
For personal use only.

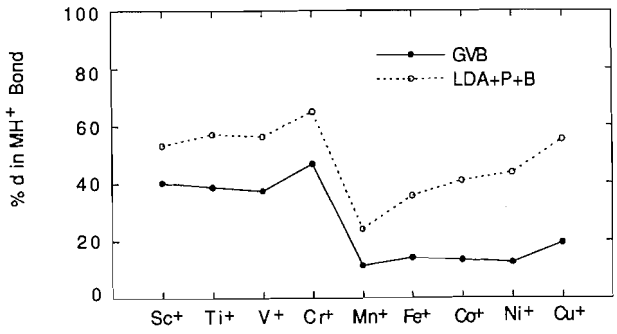

FIG. 2. Percentages of $3d$ orbital character in the M^+—H σ orbital of first-row transition metal hydride cations. Only GVB and LDA + B + P values are shown.

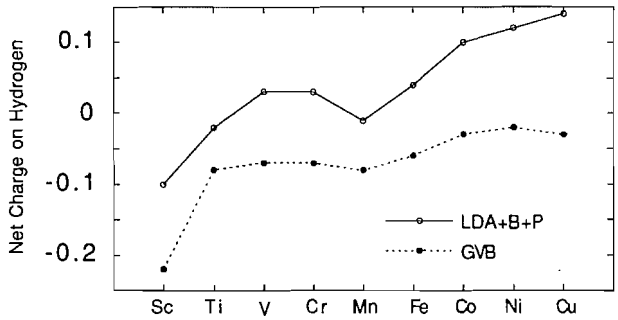

FIG. 3. Total charge on hydrogen in the M^+—H σ orbital of first-row transition metal hydride cations. Only GVB and LDA + B + P values are shown.

The nature of the M^+—H bond can be analysed by investigating the composition of the σ_{MH} orbital. Figure 2 displays the percent contribution to σ_{MH} from the d orbital in the case of the LDA + B + P and GVB (4*a*) methods. The two schemes exhibit the same trends along the series. However, the DFT scheme tends consistently to put more electrons in the d orbital. We can rationalise this by the bias towards the d^n configuration discussed previously. The bias is in particular noticeable for the late transition metals Fe to Cu, Fig. 2. The MCPF method (5) gives a d percentage similar to that of the GVB scheme for early transition metals. For the later transition metals MCPF provides a d percentage between GVB and LDA + B + P. Pettersson et al. (5) attributed the difference between GVB and MCPF to a better description of the $3d$–$3d$ correlation in the latter method.

Figure 3 displays the charge on hydrogen throughout the series as a measure of the polarisation in the M—H bond. Data are given for GVB as well as LDA + B + P. The trends are the same for the two methods with more charge on hydrogen at the beginning of the series among the electropositive early transition metals and less charge at the end among the more electronegative late transition metals. However, in absolute terms the GVB and LDA + B + P results differ. The GVB scheme has a negative charge on hydrogen throughout the series whereas LDA + B + P has hydrogen positively charged with the exception of Sc and Ti. We note in particular the increase in the positive charge on hydrogen for the late transition elements Fe–Cu and attribute it again to the energy stabilisation of the d-orbitals.

Protonation energies and revised bond energies

As a remedy for reducing the large error in the calculated bond energies for FeH^+ to CuH^+, one might consider the following thermodynamic cycle

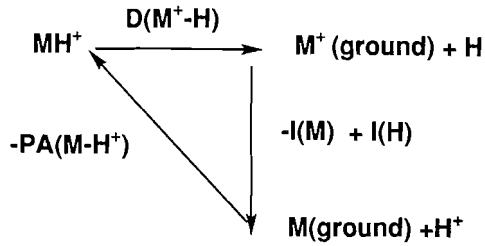

2

SCHEME 2

The cycle in Scheme 2 allows us to express $D(M^+—H)$ as

[4] $D(M^+—H) = PA(M—H^+) + I(M) - I(H)$

The protonation process for the late transition metals does not change the number of interacting electrons of the same spin or opposite spin, in contrast to the formation of MH^+ from H and M^+. Thus, $PA(M—H^+)$ should be determined more accurately than $D(M^+—H)$ since the error from $\Delta E_{XC}^{\beta\beta}$ is absent.

The theoretical $PA(M—H^+)$ values reported in Table 4 correspond to the process

[5] $M(\text{exp. ground state}) + H^+ \rightarrow MH^+(\text{ground state}) - PA(M—H^+)$

and they were calculated (see footnote to Table 4) as

[6] $$PA(M—H^+)_{est} = E_{cal}(MH^+) - E_{cal}(M, \text{LDA + B + P ground state}) + E_{exp}(M, \text{LDA + B + P ground state}) - E_{exp}(M, \text{exp. ground state}) - E_{cal}(H^+)$$

We see from Table 4 that the average deviation between estimated, eq. [6], and experimental $PA(M—H^+)$ values is as low as 3.5 kcal/mol.

We can next recalculate the $D(M^+—H)$ bond energies according to

[7] $D(M^+—H)_{est} = PA(M—H^+)_{est} + I_{exp}(M) - I_{exp}(H)$

The error in the estimated bond energies has now decreased to within 5 kcal/mol, Table 4.

The rather *ad hoc* procedure introduced in this section can not hide the fact that the present generation of approximate DFT methods has serious deficiencies. It is clear that new approximate functional will have to give a more accurate account of $\Delta E_{XC}^{\beta\beta}$ in atoms and the related bare metal complexes.

Bond lengths and frequencies in MH^+

The optimized M^+—H bond lengths and calculated vibrational frequencies are displayed in Tables 5 and 6. Since no experimental data are available, we have to compare the DFT results with high quality *ab initio* calculation.

The bond lengths calculated by the various DFT methods are quite similar, in particular for LDA and LDA + P + B. The DFT

TABLE 4. Protonation energies of Fe—Cu and bond energies of FeH^+—CuH^+[a]

		FeH^+	CoH^+	NiH^+	CuH^+
PA(M—H^+)	LDA + B + P[c]	186.2	185.6	175.8	154.8
	Exp[b]	182	179	177	157
$D_{298}(M^+—H)$	LDA + B + P[d]	52.1	51.5	36.5	17.7
	Exp[b]	50 ± 1	47 ± 1	40 ± 2	22 ± 3

[a]All energies in kcal/mol.
[b]Reference 1*d*.
[c]Calculated according to eq. [6]. Experiment and LDA + B + P have the same ground states for Cu:$[3d^{10}4s^1; {}^2S]$ and Fe:$[3d^64s^2; {}^5D]$. For Co and Ni, the LDA + B + P ground states are $[3d^84s^1; {}^4F]$ and $[3d^94s^1; {}^3D]$ whereas the experimental are $[3d^74s^2; {}^4F]$ and $[3d^84s^2; {}^3F]$, respectively.
[d]Calculated according to eq. [7].

TABLE 5. M^+—H bond lengths (Å) of first-row transition metal hydrid cations

	ScH^+	TiH^+	VH^+	CrH^+	MnH^+	FeH^+	CoH^+	NiH^+	CuH^+
HFS	1.767	1.728	1.645	1.590	1.613	1.558	1.532	1.474	1.495
LDA	1.756	1.684	1.632	1.588	1.573	1.557	1.531	1.473	1.493
LDA + B + P	1.795	1.689	1.646	1.589	1.573	1.556	1.533	1.473	1.494
GVB[a]	1.810	1.730	1.662	1.602	1.702	1.653	1.606	1.561	1.513
MCPF[b]	1.834	1.740	1.661	1.604	1.652	1.603	1.547	1.487	1.445

[a]Reference 4*a*.
[b]Reference 4*c*.

TABLE 6. Vibrational frequencies of MH^+ (cm^{-1})

	ScH^+	TiH^+	VH^+	CrH^+	MnH^+	FeH^+	CoH^+	NiH^+	CuH^+
HFS	1714	1686	1777	1833	1801	1990	1932	2063	1800
LDA	1732	1836	1825	1872	1983	2002	1943	2083	1879
LDA + B + P	1580	1736	1732	1795	1874	1885	1815	1940	1791
GVB[a]	1631	1696	1749	1818	1570	1657	1631	1728	1793
MCPF[b]	1566	1705	1671	1882	1740	1805	1888	2004	2050

[a]Reference 4*a*.
[b]Reference 4*c*.

distances are in general shorter than the bond lengths obtained from *ab initio* GVB (4*a*) and MCPF (4*c*) calculations. This is consistent with the fact that the DFT bond energies are too large whereas the *ab initio* bond strength are underestimated.

From ScH^+ to CuH^+, the DF bond lengths decrease monotonically while the *ab initio* bond lengths exhibit a peak at MnH^+. The peak has been attributed (4*a*) to a half-filled 3*d* shell at Mn^+.

The vibrational frequencies obtained by LDA and post-LDA methods compare well with *ab initio* results. Remarkably, the LDA + B + P values are somewhat close to those obtained by the MCPF method. The post-LDA corrections trend to decrease the frequencies.

IV. Concluding remarks

We have carried out DFT-based calculations on the cationic bare metal hydrides, MH^+, for the first transition series. It has been demonstrated that $D_{298}(M^+—H)$ values evaluated by the nonlocal LDA + B + P method are overestimated for the early to middle transition metals. However, the error of ±5 kcal is comparable to that observed in calculation on M—L bond energies among saturated 18-electron complexes.

The $D_{298}(M^+—H)$ bond energies calculated by the nonlocal method for the late transition metals are much larger, with a maximum of 13 kcal/mol for CuH^+. We have further shown that the large error can be attributed to an overestimation of the exchange by the DFT-based methods. The error in the exchange energy is also responsible for the large *d*-population in the MH^+ systems compared to *ab initio* results.

Acknowledgements

This investigation was supported by the Natural Sciences and Engineering Research Council of Canada (NSERC). We gratefully acknowledge the donors of the Petroleum Research Fund, administered by the American Chemical Society (ACS-PRF # 27023-AC3). J.L. thanks NSERC for an International Research Fellowship and L. Deng and E. Folga for many useful discussions.

1. (*a*) H.A. Skinner. J. Chem. Thermodyn. **10**, 309 (1978); (*b*) G. Pilcher and H.A. Skinner. *In* The chemistry of the metal carbon bond. *Edited by* F.R. Hartley and S. Patai, Wiley, New York. 1982. Chapt. 2; (*c*) J. Halpern. J. Pure Appl. Chem. **51**, 2171 (1979); (*d*) J.A. Martinho Simoes and J.L. Beauchamp. Chem. Rev. **90**, 629 (1990), (*e*) J.A. Connor. Top. Curr. Chem. **71**, 71 (1977).
2. J.A. Pople, M. Head-Gordon, D.J. Fox, K. Raghavachari, and L.A. Curtiss. J. Chem. Phys. **90**, 5622 (1989).
3. L.A. Curtiss, K. Raghavachari, G.W. Trucks, and J.A. Pople. J. Chem. Phys. **93**, 2537 (1990).
4. (*a*) G. Ohanessian and W.A. Goddard III. Acc. Chem. Res. **23**, 386

Can. J. Chem. Downloaded from www.nrcresearchpress.com by EESC ESCOLA DE ENGENHARIA on 09/08/12
For personal use only.

(1990); (*b*) J.B. Schilling, W.A. Goddard III, and J.L. Beauchamp, J. Am. Chem. Soc. **108**, 582 (1986); (*c*) L.G. Pettersson, C.W. Bauschlicher, Jr., and S.R. Langhoff. J. Chem. Phys. **87**, 481 (1987); (*d*) J.B. Schilling, W.A. Goddard III, and J.L. Beauchamp. J. Phys. Chem. **91**, 5616 (1987); (*e*) J.F. Harrison and E. Alvarado-Swaisgood. J.Phys. Chem. **92**, 2757 (1988); (*f*) E. Alvarado-Swaisgood and J.F. Harrison. J. Phys. Chem. **89**, 5198 (1985); (*g*) A. Mavridis and J.F. Harrison. J. Chem. Soc. Faraday Trans. II, **85**, 1391 (1985); (*h*) E. Alvarado-Swaisgood, J. Allison, and J.F. Harrison. J. Phys. Chem. **89**, 2517 (1985); (*i*) M. Sodupe, J.M. Lluch, A. Oliva, F. Illas, and J. Rubio. J. Chem. Phys. **90**, 6436 (1989); (*j*) J. Anglada, P.J. Bruna, and F. Grein. J. Chem. Phys. **92**, 6732 (1990); (*k*) M.L. McKee. J. Am. Chem. Soc. **112**, 2601 (1990); (*l*) J.K. Perry, G. Ohanessian, and W.A. Goddard III. J. Phys. Chem. **97**, 5238 (1993).

5. A.D. Becke. J. Chem. Phys. (*a*) **98**, 1372 (1993); (*b*) **98**, 5648 (1993).
6. (*a*) T. Ziegler. Chem. Rev. **91**, 651 (1991); (*b*) J.K. Labonowsky and J. Andzelm (*Editors*). *In* Density functional methods in chemistry. Springer-Verlag, New York. 1991.
7. (*a*) R.G. Parr and W. Yang. *In* Density-functional theory of atoms and molecules. Oxford University Press, New York. 1989; (*b*) E.S. Kryachko and E.V. Ludena. *In* Density functional theory of many electron systems. Kluwer Press, Dordrecht. 1990; (*c*) R.M. Dreizler and E.K.U. Gross. *In* Density functional theory. Springer, Heidelberg. 1990.
8. J.C. Slater. Adv. Quantum Chem. **6**, 1 (1972).
9. (*a*) O. Gunnarson and I. Lundquist. Phys. Rev. **B10**, 1319 (1974); (*b*) S.J. Vosko, L. Wilk, and M. Nusair. Can. J. Phys. **58**, 1200 (1980).
10. D.C. Langreth and M.J. Mehl. Phys. Rev. **B28**, 1809 (1983).
11. A.D. Becke. Int. J. Quantum Chem. **27**, 1915 (1983).
12. A.D. Becke. J. Chem. Phys. **84**, 4524 (1986).
13. A.D. Becke. (*a*) Phys. Rev. **A33**, 2786 (1988); (*b*) Am. Chem. Soc. Symp. Ser. Vol. 394. Washington. 1989. (*c*) Int. J. Quantum Chem. **S23**, 599 (1989); (*d*) Phys. Rev. **A38**, 2398 (1988).
14. (*a*) A.E. DePristo and J.D. Kress. J. Chem. Phys. **86**, 1425 (1987); (*b*) J.P. Perdew. Phys. Rev. Lett. **55**, 1655 (1985); (*c*) J.P. Perdew. Phys. Rev. **B33**, 8822 (1986); Erratum, Phys. Rev. **B34**, 7406 (1986); (*d*) L.C. Wilson and M. Levy. Phys. Rev. **B41**, 12930 (1990); (*e*) C. Lee, W. Yang, and R.G. Parr. Theochem. **163**, 305 (1987).
15. V. Tschinke and T. Ziegler. Can. J. Chem. **67**, 460 (1988).
16. (*a*) J. Andzelm and E. Wimmer. J. Chem. Phys. **96**, 1280 (1992); (*b*) F. Sim, A. St-Amant, I. Papai, and D.R. Salahub. J. Am. Chem. Soc. **114**, 4391 (1992); (*c*) P.M.W. Gill, B.G. Johnson, J.A. Pople, and M.J. Frisch. Int. J. Quantum Chem. **S27**, 319 (1992).
17. (*a*) L. Fan and T. Ziegler. J. Chem. Phys. **94**, 6057 (1991); (*b*) R. Fournier. J. Chem. Phys. **98**, 8041 (1993); (*c*) P. Mlynarski and D.R. Salahub. Phys. Rev. B: Solid State, **43**, 1399 (1991).
18. L. Fan and T. Ziegler. J. Chem. Phys. **95**, 7401 (1991).
19. (*a*) L. Fan and T. Ziegler. J. Am. Chem. Soc. **114**, 10890 (1992); (*b*) T.K. Woo, E. Folga, and T. Ziegler. Organometallics, **12**, 1289 (1993); (*c*) E. Folga and T. Ziegler. Organometallics, **12**, 324 (1993).
20. (*a*) L. Fan and T. Ziegler. J. Chem. Phys. **96**, 9005 (1992); (*b*) A. Bérces and T. Ziegler. J. Chem. Phys. **98**, 4793 (1993); (*c*) A. Bérces and T. Ziegler. J. Chem. Phys. Lett. **203**, 592 (1993); (*d*) N.C. Handy, P.E. Maslen, R.D. Amos, J.S. Andrews, C.W. Murray, and G.J. Laming. Chem. Phys. Lett. **197**, 506 (1992); (*e*) L. Fan, L. Versluis, T. Ziegler, E.J. Baerends, and W. Ravenek. Int. J. Quantum Chem. **S22**, 173 (1988); (*f*) I. Papai, A. St-Amant, R. Fournier, and D.R. Salahub. Int. J. Quantum Chem. **S23**, (1989).
21. (*a*) L. Fan and T. Ziegler. J. Phys. Chem. **96**, 6937 (1992); (*b*) C. Sosa, J. Andzelm, E. Wimmer, K.D. Dobbs, and D.A. Dixon. J. Phys. Chem. **96**, 6630 (1992).
22. (*a*) V. Tschinke and T. Ziegler. *In* Density matrices and density functionals. *Edited by* R. Erdahl and V.H. Smith, Jr. Reidel, Dordrecht. 1987. p. 189; (*b*) T. Ziegler, V. Tschinke, and A.D. Becke. J. Am. Chem. Soc. **109**, 1351 (1987); (*c*) T. Ziegler, W. Cheng, E.J. Baerends, and Ravenek. Inorg. Chem. **27**, 3458 (1988); (*d*) T. Ziegler, V. Tschinke, E.J. Baerends, J.G. Snijdes, and W. Ravenek. J. Phys. Chem. **93**, 3050 (1989); (*e*) T. Ziegler, V. Tschinke, L. Versluis, E.J. Baerends, and W. Ravenek. Polyhedron, **7**, 1625 (1988); (*f*) T. Ziegler, V. Tschinke, and C. Ursenbach. J. Am. Chem. Soc. **109**, 4825 (1987); (*g*) L. Versluis and T. Ziegler. J. Am. Chem. Soc. **112**, 6163 (1990); (*h*) T. Ziegler and V. Tschinke. *In* Bonding energetics in organometallic compounds. Am. Chem. Soc. Symp. Ser. No. 428. *Edited by* T. Marks. Am. Chem. Soc. Washington, DC. 1990.
23. E. Folga and T. Ziegler. J. Am. Chem. Soc. **115**, 5169 (1993).
24. (*a*) P.B. Armentrout and J.L. Beauchamp. Acc. Chem. Res. **22**, 315 (1989); (*b*) P.B. Armentrout. *In* Gas phase inorganic chemistry. *Edited by* D.H. Russell. Plenum, New York. 1989.
25. (*a*) D.R. Salahub. *In Ab initio* methods in quantum chemistry — II. *Edited by* K.P. Lawley.Wiley, New York. 1987. (*b*) E. Broclawik and D.R. Salahub. Int. J. Quantum Chem. **S26**, 393 (1992); (*c*) S.M. Mattar and W.D. Hamilton. J. Phys. Chem. **96**, 8277 (1992); (*d*) S.M. Mattar. J. Phys. Chem. **97**, 3171 (1993).
26. E.J. Baerends, D.E. Ellis, and P. Ros. Chem. Phys. **2**, 41 (1973).
27. (*a*) E.J. Baerends. Ph.D. Thesis. Vrije Universiteit, Amsterdam. 1975; (*b*) W. Ravenek. *In* Algorithms and applications on vector and parallel computers. *Edited by* H.J.J. te Riele, Th.J. Dekker, and H.A. van de Vorst. Elsevier, Amsterdam. 1987.
28. (*a*) P.M. Boerrigter, G. te Velde, and E.J. Baerends. Int. J. Quantum Chem. **33**, 87 (1988); (*b*) G. te Velde and E.J. Baerends. J. Comput. Phys. **99**, 84 (1992).
29. L. Versluis and T. Ziegler. J. Chem. Phys. **88**, 322 (1988).
30. (*a*) G.J. Snijders, E.J. Baerends, and P. Vernooijs. At. Nucl. Data. Tables, **26**, 483 (1982); (*b*) P. Vernooijs, G.J. Snijders, and E.J. Baerends. Slater type basis functions for the whole periodic system. Internal report, Free University of Amsterdam, The Netherlands. 1981.
31. J. Krijn and E.J. Baerends. Fit functions in the HFS-method. Internal Report (in Dutch), Free University of Amsterdam, The Netherlands. 1984.
32. H. Stoll, E. Golka, and H. Preuss. Theor. Chim. Acta, **49**, 143 (1978).
33. (*a*) T. Ziegler and V. Tschinke. Am. Chem. Soc. Symp. Ser. **428**, 277 (1990); (*b*) T. Ziegler, J.G. Snijders, and E.J. Baerends. Am. Chem. Soc. Symp. Ser. **383**, 322 (1989); (*c*) T. Ziegler, V. Tschinke, and L. Versluis. NATO ASI Series, **C176**, 189 (1986); (*d*) T. Ziegler. J. Pure Appl. Chem. **63**, 873 (1991); (*e*) T. Ziegler. NATO ASI Series, **C367**, 357 (1992); (*f*) T. Ziegler and L. Versluis. Adv. Chem. Ser. **230**, 75 (1992).
34. T. Ziegler, A. Rauk, and E.J. Baerends. Theor. Chim. Acta **43**, 261 (1977).
35. F.W. Kutzler and G.S. Painter. Phys. Rev. B: Solid State, **43**, 6865 (1991).
36. J.P. Perdew and A. Zunger. Phys. Rev. B: Solid State, **23**, 5048 (1981).
37. C.E. Moore. Atomic energy level. Nat. Bur. Stand. Washington, DC. 1958.
38. O. Gunnarson and R.O. Jones. Phys. Rev. B: Solid State, **31**, 7588 (1985).
39. V. Tschinke and T. Ziegler. Theor. Chem. Acta, **81**, 65 (1991).

Can. J. Chem. Downloaded from www.nrcresearchpress.com by EESC ESCOLA DE ENGENHARIA on 09/08/12
For personal use only.

Infrared chemiluminescence in a mixed reaction situation: F + CH_4 and F + $CHCl_3$

M. Maneshkarimi and H. Heydtmann[1]

Institut für Physikalische und Theoretische Chemie der J.W. Goethe Universität, Marie Curie Str. 11, D-60439 Frankfurt am Main, Germany

Received June 29, 1993

This paper is dedicated to Professor John C. Polanyi on the occasion of his 65th birthday

M. Maneshkarimi and H. Heydtmann. Can. J. Chem. **72**, 790 (1994).

Infrared chemiluminescence from the product molecule HF (DF) was observed for the F + CH_4(CD_4) and F + $CHCl_3$ reactions under low-pressure flow conditions. The reactions with methane and deuterated methane showed the well-known vibrational inversion effect. For the mixed reaction situation F + CH_4(CD_4) + $CHCl_3$ it can be shown by switching between CH_4 and CD_4 that no special relaxation effects are present. The HF (DF) spectra can be explained by results from the isolated reactions. A non-inverted distribution was confirmed for F + $CHCl_3$.

M. Maneshkarimi et H. Heydtmann. Can. J. Chem. **72**, 790 (1994).

On a observé de la chimiluminescence infrarouge à partir des molécules produites HF (DF) au cours des réactions H + CH_4(CD_4) et F + $CHCl_3$ effectuées dans des conditions de faibles pressions d'écoulement. Les réactions avec le méthane et avec le méthane deutére présentent l'effet bien connu d'inversion vibrationnelle. Pour la situation de la réaction mixte F + H + CH_4(CD_4) + $CHCl_3$, on peut montrer, en passant du CH_4 au CD_4 qu'il n'existe pas d'effet de relaxation spécial. On peut expliquer les spectres HF (DF) par les résultats de réactions isolées. On a pu confirmer la présence d'une distribution qui n'est pas inversée pour F + $CHCl_3$.

[Traduit par la rédaction]

Introduction

For more than 25 years IR chemiluminescence has been an accepted technique to obtain information about the reaction dynamics of elementary processes (1). Chemiluminescence studies of F atom reactions with polyatomic hydrides are numerous (1–3) because the product molecule HF is especially suitable for such experiments (high Einstein coefficients for the rotational–vibrational states, fundamental band emission in an experimentally well-accessible range).

Two different types of experiment have been used in the past. The so-called arrested relaxation (AR) technique using a low-pressure, fast flow system was introduced by Polanyi (1) and is also used in this work (4). The second technique, flowing afterglow (FA), employs a carrier gas in a fast flow system and hence the reactions take place at distinctly higher pressures, typically at about 1 Torr (133 Pa). Both methods have been used for many reactions and, in a comparative study from the Kansas and the Frankfurt laboratories, some of these results have been reported together (2, 5). The results are usually presented as vibrational distributions of the HF molecule and these vibrational distributions are in most cases independent of the method used. Thus there is good agreement between the work of several laboratories for the reaction

[1] $F + CH_4 \rightarrow HF\ (v \leq 3) + CH_3$

which was measured in Frankfurt by the AR technique to yield: $N_{v=1} : N_{v=2} : N_{v=3} = 0.16 : 0.74 : 0.10$. This reaction has a recommended rate constant at 298 K of 6.64×10^{-11} cm^3 molecule^{-1} s^{-1} (6) and also serves as a standard here.

Another reaction used in the reported work is

[2] $F + CD_4 \rightarrow DF\ (v \leq 4) + CD_3$

Its rate constant at standard conditions is reported to be 4.24×10^{-11} cm^3 molecule^{-1} s^{-1} (6). Remarkable differences were noted for the reaction

[3] $F + CHCl_3 \rightarrow HF\ (v \leq 4) + CCl_3$

for which FA yielded (2): $N_{v=1} : N_{v=2} : N_{v=3} : N_{v=4} = 0.22 : 0.32 : 0.37 : 0.09$ and AR gave rise to a mean distribution (with F_2 as a precursor of F-atoms) $N_{v=1} : N_{v=2} : N_{v=3} = 0.72 : 0.23 : 0.5$ (2).

Nazar and Polanyi (3) were the first to report IR chemiluminescence data for this reaction. They used very low molecular flows but their total flow rate was in the range 2.5–20 μmol s^{-1}. The vibrational distributions documented in Table 4 of their paper depended somewhat on the flow conditions, but are qualitatively equal to the ones quoted above, i.e., $N_{v=1} > N_{v=2} > N_{v=3}$.

The presence of only one microscopic reaction channel, namely, direct H-abstraction on a ps time scale, was proposed by us for the FA conditions. A second microscopic channel (F-atom addition and slow elimination of HF from the primary complex) was additionally introduced to explain the AR results (2). Unexpectedly, these revealed a lack of inversion between the vibrational levels $v = 1$ and $v = 2$ as well as between $v = 2$ and $v = 3$. It was argued that both microscopic channels are present, but that the addition–elimination channel predominates. The addition–elimination is suppressed under FA conditions by stabilization of the addition complex. The assumption of two distinct reaction channels was corroborated by the disagreement between the rate constants for eq. [3]. Clyne et al. determined the rate constant $k_{298} = 0.42 \times 10^{-11}$ cm^3 molecule^{-1} s^{-1} (7, 8), whereas Setser and his group arrived at $k_{298} = 0.14 \times 10^{-11}$ cm^3 molecule^{-1} s^{-1} from observation of the IR emission (2).

Some doubts, however, remained whether special relaxation effects may take place in this system. Such effects have been discussed before for similar experimental conditions concerning the reaction F + HBr (9). This work presents new results using an inlet system of three concentric nozzles, with which competitive reactions could be studied. Competitive hydrogen abstractions from two RH compounds, which both yield HF

[1]Author to whom correspondence may be addressed.

Can. J. Chem. Downloaded from www.nrcresearchpress.com by 195.246.54.202 on 09/08/12
For personal use only.

Can. J. Chem. Downloaded from www.nrcresearchpress.com by 195.246.54.202 on 09/08/12
For personal use only.

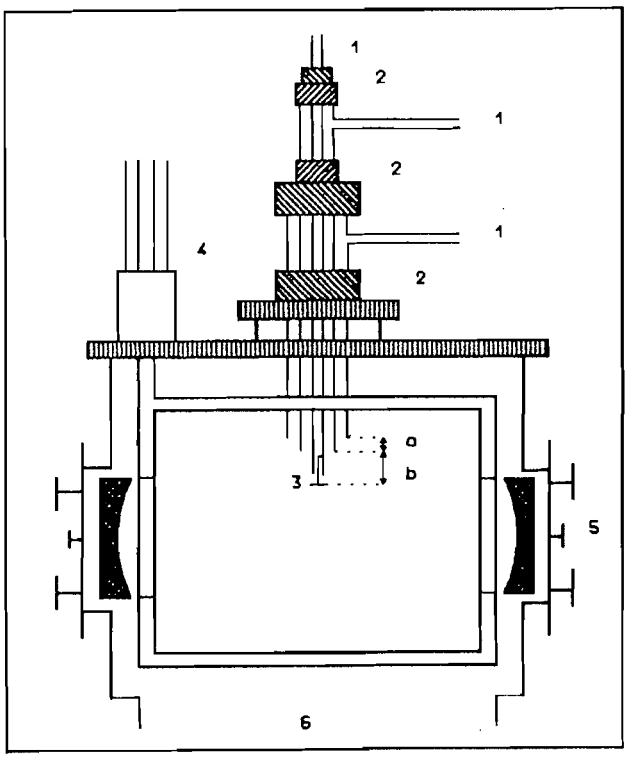

FIG. 1. Schematic view of the reaction vessel with new inlet design. 1: Inlet tubes for reagents. 2: Stainless steel flange. 3: Deflector plate. 4: Liquid nitrogen cooling system. 5: White cell arrangement. 6: Outlet to pump.

products, should reveal such an effect, because if strong relaxation occurs it must occur for HF from *both* reactions. Reaction [3] is very suitable for such a study in this system because no interference from secondary reactions has to be feared. The results indeed confirm that under arrested vibrational relaxation conditions at low pressure a different vibrational distribution for the HF product molecules ensues, distinct from the one found for higher pressures (FA conditions).

Experimental

All experiments were performed in an apparatus similar to the one used before (4), the only major change being a new inlet system, which is similar to the one described by Sloan and co-workers (9, 10). A schematic picture of this setup is given in Fig. 1. The reaction vessel is pumped by an effective diffusion pump (pumping capacity 5000 L/s). The inlet system consists of three concentric quartz tubes, which can be moved relative to each other. The tubes are connected to each other by Swagelok joints made from stainless steel. This system is fixed to a lid that closes the reaction vessel on the top side but mobility relative to the lid was also provided for. The tubes were covered with Teflon (PTFE-Spray, Safematic Nidda, Germany) in order to avoid wall reactions, especially atom recombinations.

The central tube (nozzle 1) has an internal diameter of 0.8 cm and is equipped with a deflector plate for lateral injection of hydrocarbon into a stream of F atoms. The idea was to effect thorough mixing of the gases before the center of the White cell was reached by the flowing gas. The next tube, which has an internal diameter of 1.5 cm, forms the annular nozzle 2, the outermost tube with an internal diameter of 2.6 cm is the annular nozzle 3. F atoms could be produced in all three inlet tubes by flowing CF_4 or F_2 inside those tubes and fitting a microwave cavity on the outside; 2450 MHz and a power of 90 W were used. The White cell, with mirrors 12 cm in diameter, collects the infrared light emitted from the HF (DF) molecules from a volume near the horizontal plane in the middle of the vessel. The reaction volume is surrounded by a cold wall (77 K) to effect complete wall relaxation of vibrationally excited hydrogen fluoride.

For taking the spectra an FTIR instrument (BIORAD) was used. The adopted resolution was usually 2 cm^{-1}. The crude spectra were treated in the usual manner. The total concentration of emitting HF, G_I, was measured for each run by adding the heights of all lines (after corrections by Einstein coefficients and instrument function). This sum was expressed relative to thermal emission at a selected wavelength from the background signal. G_1 gave valuable qualitative information, for example, finding the best nozzle arrangement. Also subtraction of spectra was exercised and played a very important role in this work. This was only done for experiments that were performed under similar conditions on the same day; essentially only methane was exchanged for deuterated methane. The subtraction was done line by line using the corrected spectra. The usefulness of this procedure will become clear in discussing the results shown in Table 2.

Results

1. The F + CH_4 reaction

Table 1 gives results of some of the many experiments performed to test our new inlet system. Experiment 1 shows that with retracted nozzles 1 and 2 a condition can be reached where relaxation is extensive and the signal becomes too low to be measurable. Under these circumstances most of the reaction enthalpy must have been transformed to translational energy by the time HF arrived in the central plane of the White cell. Radiational relaxation can be considered negligible as stated in our earlier work (4) because of the high pumping capacity. Relaxation due to gas collisions and wall collisions must be very effective with this special configuration of our new nozzle system. Changing the inflow of CF_4 from nozzle 2 to nozzle 3 yields a signal that shows relaxation (expts. 2 and 3) but certainly the effective reaction volume has moved downward. Satisfactory populations are reached in experiment 10 since the N_v ratios are the same as in the best of our earlier experiments. In this experiment perhaps some rotational relaxation has happened but this is of no interest for our present paper.

Some remarks are useful concerning the rotational structure. The rotational distribution for HF (v = 1, 2) is, for the most favorable flow conditions, not very different from the Boltzmann shape (see Fig. 1 of ref. 5): the distributions both peak at $J = 2$, but higher populations for $J \geq 7$ are observed. This feature is also true for F + $CHCl_3$. A Boltzmann distribution at 300 K reaches very low populations beyond $J = 6$. In conclusion, little relaxation of rotational states is necessary to reach the Boltzmann shape. Secondly, relaxation is observed for the higher J levels but is so slow that non-Boltzmann rotational populations exist under all conditions of our experiments.

Runs 4, 5, 6, and 8 show intermediate cases with occurrence of slight vibrational relaxation. Experiments 7 and 9 are included because they show that the choice of the precursor molecule, CF_4 or F_2, is of no relevance to the results. However, the signal intensity G_I of no. 7 compared to no. 6 and of no. 9 compared to no. 8 is much stronger due to a better yield of F atoms from the fluorine gas. Experiments 11 and 12 show the effect of added argon ([Ar]/[CH_4] = 10). In no. 11 argon was mixed with the CH_4 flow into nozzle 1; in no. 12 argon was introduced separately into the external nozzle 3. Especially in the former case relaxation is observed due to a high Ar partial pressure in the local reaction volume.

Other experiments, which are not described in detail, were concerned with the vertical position of the total inlet system. As for the reaction F + CH_4, the highest intensities were measured

TABLE 1. The experiments with configuration effect. The tube extending farthest downward is about at the same level as the upepr rim of the White cell mirrors

No.	Configuration[a]	Flow [μmol/s] $CF_4(F_2)/CH_4$	G_I	HF distribution $v = 1$	$v = 2$	$v = 3$
1	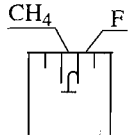	5/15	—	—	—	—
2	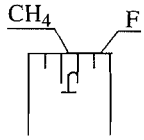	2.5/7.44 = A	0.41	0.47	0.43	0.10
3		7.44/7.44 = B	1.3	0.45	0.46	0.09
4	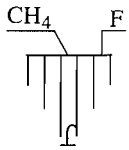	A	0.84	0.33	0.49	0.18
5		B	1.4	0.30	0.56	0.14
6	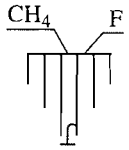	A	0.89	0.31	0.60	0.09
7			(3.7)[b]	(0.27)[b]	(0.60)[b]	(0.13)[b]
8		B	1.6	0.27	0.65	0.08
9			(4.3)[b]	(0.27)[b]	(0.64)[b]	(0.09)[b]
10	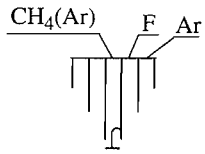	4/4 = C	0.78	0.16	0.72	0.12
11		4/4 + $Ar_{noz\ 1}$ = D	2.9	0.29	0.63	0.08
12		4/4 + $Ar_{noz\ 3}$ = E	1.5	0.20	0.71	0.09

[a]Distances of nozzle tip, see Fig. 1: Expts. 4–12, $a = b = 0.5$ cm. Expt. 1–3, $a = -1.3$ cm and $b = +0.5$ cm. Inner nozzle = no. 1, middle nozzle = no. 2, and outer nozzle = no. 3.
[b]Refers to F_2 as a precursor for F atoms.

when the nozzle system was moved about 1 cm downward as compared with the conditions of Table 2.

2. The F + $CHCl_3$ reaction

The first experiments were of the same kind as those described in greater detail for the F + CH_4 system. Two experiments showing results for F + $CHCl_3$ only, namely, nos. 2 and 10, are included in Table 2. These two experiments differ in the choice of the precursor molecule, but they yield about the same distribution. The precursor effect was more noticeable in our former experiments (2). As described before, other experiments tested the effect of the vertical position of the entire nozzle system. For the reaction F + $CHCl_3$ a better signal was achieved for a rather high (upward) position of this system, higher than actually used in Table 2. The position chosen was equal to the position in experiments 4–12 of Table 1. This position was considered a good compromise between the best position found for the two molecular reagents.

The main results are based on experiments that used flows in all three concentric nozzles; such experiments are illustrated by the results in Table 2. For understanding, it is important to realize that chloroform is always added to the central nozzle 1, methane, always to nozzle 3. Experiment 1, Table 2, for example, has the central nozzle not in use, i.e., shut off. In this manner CH_4 is introduced differently than in the experiments in section 1, but the resulting vibrational distribution (see expt. 1) still shows strong inversion between levels 1 and 2. The first four lines of Table 2 show the results for the separate reactions [1] and [3], both reactions in competition, and finally competitive results for reactions [2] and [3]. The amounts of CD_4 and (or) $CHCl_3$ added were chosen as reported in order to create roughly the same reaction rate as for methane; in other words, the smaller rate constants were compensated by higher partial pressures. That this expectation is met can be seen from the G_I values. As expected, experiments 2 and 4 of the table under discussion render very similar distributions and also show comparable HF emission intensities. CD_4 in experiment 4 was added to create similar flow conditions and to investigate the relaxation effects of $CHCl_3$ on DF and of CD_4 on HF. The relaxation effect for the latter is negligible as can be seen from the results of experiments 2 and 4. For the former case the evaluation of the DF distribution ($N_{v=1} : N_{v=2} : N_{v=3} : N_{v=4} = 0.13 : 0.16 : 0.56 : 0.15$) shows that the large excess of $CHCl_3$ and the reaction product of [3] has only a small effect. The differences (3 − 4) were obtained by subtraction of absolute line intensities as described in detail in the experimental section. Similar differences were extracted from the spectra of experiments 5–8 with different CF_4 flows. Experiments 9–12 are parallel to experi-

Can. J. Chem. Downloaded from www.nrcresearchpress.com by 195.246.54.202 on 09/08/12
For personal use only.

TABLE 2. Switching experiments for the system F/$CHCl_3$. A = $CF_4/CH_4/CHCl_3$, B = $CF_4/CD_4/CHCl_3$. Nozzle positions as shown for expts. 6–9 in Table 1; $CHCl_3$ flow in inner nozzle (no. 1). CF_4 through middle nozzle (no. 2), and CH_4 flow in outer nozzle (no. 3)

No.	Reaction and flow [μmol/s]	HF distribution G_1	$v = 1$	$v = 2$	$v = 3$
1	CF_4/CH_4 = 4/4	4.7	0.30	0.56	0.14
2	$CF_4/CHCl_3$ = 4/65	2.4	0.50	0.37	0.13
3	A_1 = 4/4/65	3.6	0.41	0.46	0.13
4	B_1 = 4/8/55	2.7	0.47	0.39	0.14
	Difference (3 – 4)	—	0.20	0.61	0.19
5	A_2 = 8/4/75	3.8	0.42	0.47	0.11
6	B_2 = 8/8/70	2.9	0.46	0.39	0.15
	Difference (5 – 6)	—	0.20	0.66	0.14
7	A_3 = 2/4/70	2.5	0.44	0.44	0.12
8	B_3 = 2/8/70	1.6	0.49	0.39	0.12
	Difference (7 – 8)	—	0.25	0.58	0.17
9	F_2/CH_4 = 4/4	3.5	0.31	0.58	0.11
10	$F_2/CHCl_3$ = 4/70	4.8	0.54	0.38	0.08
11	A_{F2} = 4/4/65	4.3	0.43	0.48	0.09
12	B_{F2} = 4/8/70	5.5	0.49	0.39	0.12
	Difference (11 – 12)	—	0.26	0.62	0.12

ments 1–4 but with F_2 as a precursor molecule. Also, here CD_4, DF, and CD_3 radicals have no special effect on the HF vibrational distribution.

Figures 2*a* and 2*b* visualize the change in distributions for HF $v = 1$, $v = 2$, and $v = 3$ in these switching experiments and also give the subtraction results.

Discussion

In the earlier paper of Wickramaaratchi et al. (2) the difficulty in obtaining agreement between the work of two laboratories using the same method was discussed extensively. In an AR apparatus there is the possibility of gas phase relaxation of excited species whenever the concentrations of relaxing species are too high. It must be remembered that radicals are also present and that the relaxation effects of these radicals is difficult to assess. Furthermore, wall relaxation, especially at the warmer parts of the reaction vessel, cannot be entirely excluded; this type of relaxation necessarily varies with construction of the reaction vessel.

As already emphasized in the results section, there is no significant mutual effect of reactions [2] and [3] when these reactions are mixed (experiments 4, 6, 8, and 12 of Table 2). The procedure of subtracting spectra of two competitive experiments, as described before and documented for four cases in Table 2, shows that a distribution is obtained in each case that resembles very closely the primary HF distribution from reaction [1]. It must be borne in mind that relative populations of an experiment are already uncertain by 10%, therefore the distribution obtained by subtraction must have an even larger error.

We conclude that reactions [1] and [3] studied simultaneously in the same reaction vessel and under suitable conditions do not influence each other. Hence the reaction F + $CHCl_3$ at low pressure produces HF with a primary vibrational distribution without any inversion and the main features of this vibrational distribution are not due to relaxation effects. If relaxation occurred, relaxed difference spectra would be expected. There is no doubt also that the FA experiments, which were carefully planned and performed, yield reliable results. We propose that different microscopic processes occur under different conditions and that the explanation attempted before (2) still is the best solution. It is strongly recommended that molecular beam experiments be performed in order to clarify the detailed dynamics of reaction [3].

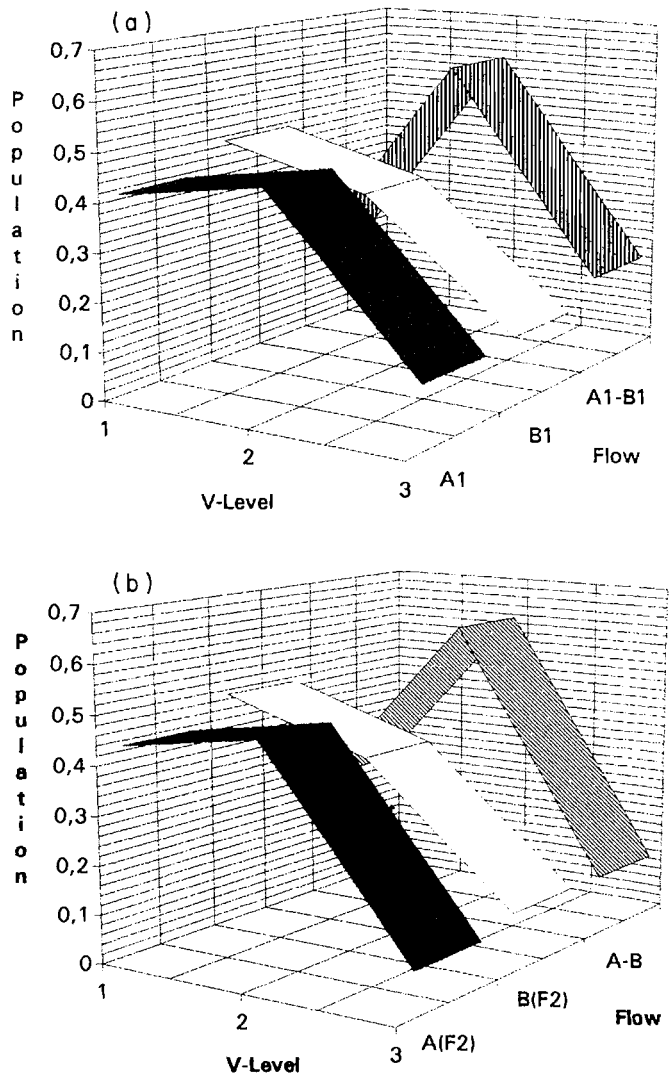

FIG. 2. HF vibrational distributions from the $CH_4/CHCl_3$ switching experiments. The flow conditions are defined in Table 2: (*a*) experiments 3 and 4; (*b*) experiments 11 and 12.

Acknowledgement

The financial support of this work by the Deutsche Forschungsgemeinschaft (DFG) is gratefully acknowledged.

1. (*a*) J.C. Polanyi (Nobel lecture). Chem. Sci. **27**, 229 (1987); (*b*) J.C. Polanyi. Angew. Chem. **99**, 981 (1987).
2. M.A. Wickramaaratchi, D.W. Setser, B. Hildebrandt, B. Körbitzer, and H. Heydtmann. Chem. Phys. **94**, 109 (1985).
3. M.A. Nazar and J.C. Polanyi. Chem. Phys. **55**, 299 (1981).
4. B. Dill and H. Heydtmann. Chem. Phys. **35**, 161 (1978).
5. M.A. Wickramaaratchi, D.W. Setser, B. Hildebrandt, B. Körbitzer, and H. Heydtmann. Chem. Phys. **84**, 105 (1984).

Can. J. Chem. Downloaded from www.nrcresearchpress.com by 195.246.54.202 on 09/08/12
For personal use only.

6. D.L. Baulch, J. Duxbury, S.J. Grant, and D.C. Montague. J. Phys. Chem. Ref. Data, **10**, Suppl. 1, 1 (1981).
7. M.A.A. Clyne, D.J. McKenney, and R.F. Walker. Can. J. Chem. **51**, 3596 (1973).
8. M.A.A. Clyne and W.S. Nip. Int. J. Chem. Kinet. **10**, 383 (1978).
9. P.M. Aker, D.J. Donaldson, and J.J. Sloan. J. Phys. Chem. **90**, 3110 (1986).
10. D.J. Donaldson and J.J. Sloan. Can. J. Chem. **61**, 906 (1983).

Can. J. Chem. Downloaded from www.nrcresearchpress.com by 195.246.54.202 on 09/08/12
For personal use only.

Two-dimensional sublimation of CO_2 on NaCl(100) with molecular reorientation as revealed by polarization infrared spectroscopy

J. HEIDBERG,[1] E. KAMPSHOFF, R. KÜHNEMUTH, AND O. SCHÖNEKÄS

Institut für Physikalische Chemie und Elektrochemie der Universität Hannover, Callinstr. 3-3A, D-30167 Hannover, Germany.

Received August 30, 1993

This paper is dedicated to Professor John C. Polanyi on the occasion of his 65th birthday

J. HEIDBERG, E. KAMPSHOFF, R. KÜHNEMUTH, and O. SCHÖNEKÄS. Can. J. Chem. **72**, 795 (1994).

Two-dimensional sublimation of CO_2 on NaCl(100), prepared by cleaving a single crystal in situ under ultrahigh vacuum, was observed by polarization Fourier transform infrared spectroscopy. At the transition pressure $p_t(T) < 1 \times 10^{-10}$ mbar in the temperature range $45 \leq T/\mathrm{K} \leq 75$ the 2D solid and the ideal 2D lattice gas coexist in a 2D thermodynamic equilibrium. The temperature dependence of the spreading pressure $\pi(T)$ of the coexisting 2D lattice gas yields the enthalpy of the 2D sublimation $\Delta H_S^{2D} = (3.0 \pm 0.1)$ kJ/mol. In the two-dimensional sublimation reorientation of the CO_2 molecules takes place; both the polar and the azimuthal molecular angles change.

J. HEIDBERG, E. KAMPSHOFF, R. KÜHNEMUTH et O. SCHÖNEKÄS. Can. J. Chem. **72**, 795 (1994).

On a observé, par spectroscopie infrarouge à transformation de fourier polarisée, la sublimation bi-dimensionnelle du CO_2 sur du NaCl(100) préparé par clivage in situ d'un cristal unique sous vide très poussé. À la pression de transition $p_t(T) < 1 \times 10^{-10}$ mbar dans l'intervalle de température allant de $45 \leq T/\mathrm{K} \leq 75$ le solide 2D et le réseau 2D gazeux idéal coexistent dans un équilibre thermodynamique 2D. L'effet de la température sur l'étalement de la pression $\pi(T)$ des réseaux 2D gazeux coexistants donne l'enthalpie de la sublimation 2D $\Delta H_S^{2D} = (3{,}0 \pm 0{,}1)$ kJ/mol. Il se produit une réorientation des molécules de CO_2 dans la sublimation bi-dimensionnelle; les deux angles polaire et azimutale changent.

[Traduit par la rédaction]

Introduction

In physisorption, the weak interaction between molecules and solids has been studied for many years. A new topic is the stereodynamics of chemical reactions between surface-aligned and oriented physisorbed molecules (1). This paper reports on the thermodynamics of a two-dimensional phase transition with molecular reorientation as revealed by polarization infrared spectroscopy. The system studied is CO_2 physisorbed on NaCl(100), which can be considered a model for physisorption. It has become important also in geology, in sea spray chemistry, as well as in industrial applications and waste technology. Rock salt in the extended North German salt domes contains, besides the brine inclusions and water from the associated hydrated minerals, primary gases adsorbed on the crystal boundaries or trapped in inclusions. Knowledge of the behaviour of such primary gases as CO_2, CH_4, H_2O, and HCl is essential when planning the safety aspects for a final repository of radioactive waste in the salt domes (2). To model the behaviour of these simple gases in the salt domes, studies of the gas adsorption on NaCl(100) under well-defined conditions are necessary. Especially those thermodynamic measurements yielding adsorption isotherms, heats of adsorption, and two-dimensional phase transitions give insight into the gas–surface interaction. The results can also be used to describe migration processes along the salt surfaces.

It is well known that physisorption systems such as small molecules and rare gas atoms on single crystal surfaces can undergo two-dimensional (2D) phase transitions. They have been studied both experimentally and theoretically for several years (3–5). Only a few methods are suitable for highly sensitive detection of a 2D lattice gas at very low coverages ($\theta \leq 0{,}01$). One of these methods, thermal energy He scattering, has been used to study the system Xe–Pt(111) (6). The heat of 2D vaporization could be measured directly from the temperature-dependent density of the coexisting 2D lattice gas, but also independently as the difference between the isoteric heats of adsorption of the coexisting 2D phases (6). High-resolution Fourier transform infrared (FTIR) spectroscopy of adsorbed molecules can yield additional information concerning, for example, adsorption geometries and lateral adsorbate interaction, especially dynamic dipole–dipole coupling within the adlayer. Recent examples are CO–Ru(001) (7) and PF_3–Pt(111) (8). In these systems coexistence of 2D lattice gas and 2D islands could be detected, but thermodynamic quantities like heats of adsorption and 2D phase transition were not derived.

Here we present results of polarized FTIR spectroscopy of the adsorption system CO_2–NaCl(100). This adsorption system has become the object of many investigations in recent years (9–17). In our group a two-dimensional phase transition at pressure $p_t(T)$ within the adsorbate has been observed on NaCl(100) samples prepared in air (11). With the integrated absorption of the asymmetric ν_3 stretching vibration as a measure of the surface coverage θ, two adsorbate phases can be distinguished. At $p < p_t$ the 2D lattice gas is the stable phase, the CO_2 molecules being oriented parallel to the surface as derived from the polarization dependency of the single ν_3 absorption band (11). This result is in full agreement with several theoretical calculations (11, 17). At pressures $p_t \leq p \leq p_0$ (p_0 being the vapor pressure of 3D-solid CO_2 at temperature T), the 2D solid is observed, indicated by a characteristic ν_3 doublet. In combination with isotope dilution experiments (11), low-energy electron diffraction (LEED) (18), and helium atom scattering (HAS) results (19) we derived a (2×1) monolayer structure for the 2D solid. Within the framework of the experimental data two independent theoretical models, namely spectra simulation and calculation of the minimum of the potential energy, give details on the structure (15). The unit cell with symmetry *pg* contains two energetically equiv-

[1]Author to whom correspondence may be addressed. Phone: (0511) 762-2288; Fax: (0511) 762-4009.

Can. J. Chem. Downloaded from www.nrcresearchpress.com by 195.246.54.202 on 09/08/12
For personal use only.

Can. J. Chem. Downloaded from www.nrcresearchpress.com by 195.246.54.202 on 09/08/12
For personal use only.

alent molecules, which are tilted by 34° ± 5° with respect to the surface. The projections of neighbouring translationally inequivalent molecules onto the surface enclose an angle of 80° ± 5°. The ν_3 doublet results from a correlation field within the adsorbate. Other IR studies gave comparable results (12, 20).

Even more interesting spectral and thermodynamic features are measured on NaCl(100) prepared by cleaving a single crystal in situ under ultrahigh vacuum. All IR absorptions become remarkably sharper and hence more intense since they retain the same integrated absorptions as on air-cleaved samples. The ν_2 bending vibration of the 2D solid CO_2, being split into a quartet as a result of a combined site symmetry and correlation field splitting, has an instrument-limited linewidth of only 0.04 cm^{-1} at a sample temperature of 5 K, which is the sharpest reported absorption of an adsorbate (14). More detailed thermodynamic information about the adsorbate is also available now. In particular, the coexistence of 2D lattice gas and 2D solid that was not detected in the adsorption measurements on air-cleaved NaCl(100) samples is now observable. Hence it is now possible to measure directly the two-dimensional sublimation equilibrium within the adsorbate.

Experimental

The results reported below were performed in an experimental setup that will be described here briefly. A more detailed description is given in refs. 11 and 16. The setup consists of an FTIR spectrometer (Bruker IFS 113v with transfer optics according to Heidberg, Hoge, Warskulat), an UHV chamber, and an external detector compartment. The UHV chamber contains a liquid helium cryostat and the cleavage device, consisting of anvil and blade, for the NaCl samples. The temperatures reported were measured by Au(Fe)/NiCr and NiCr/Ni thermocouples mounted to the sample and sample holder. The CO_2 pressure was determined by a quadrupole mass spectrometer, taking into account the total pressure given by an ion gauge, which was calibrated against a spinning rotor gauge. The interferogram was monitored by a liquid nitrogen cooled InSb detector. We used an angle of (50 ± 1)° for the incident IR light, which was polarized by means of a wire-grid polarizer. The adsorption isotherms were measured with $^{13}C^{16}O_2$ to avoid overlap of the adsorbate signal with rovibrational transitions of atmospheric $^{12}C^{16}O_2$ present in the residual gas of the interferometer and the detector compartment. The thermodynamics of the adsorbate was found to be independent of the CO_2 isotope used, within the error limits (11). Isotope contamination of $^{13}C^{16}O_2$ by $^{13}C^{16}O^{18}O$ and $^{13}C^{18}O_2$ is present in the gas and in the adsorbate. This influences the linewidth and peak absorption of the main component due to vibrational coupling between the same isotopic species within the ordered 2D solid CO_2 on NaCl(100) (11). On the other hand the integrated absorption, which was calculated for all isotopes, is not affected. We can therefore neglect this spectral effect within this thermodynamic study.

Results and discussion

The systematic thermodynamic investigation of the adsorption of CO_2 on NaCl(100) started by measuring several adsorption isotherms. Some of these isotherms at sample temperatures 87, 91, 93, and 96.3 K are displayed in Fig. 1. Every isotherm shows a characteristic shape with a vertical step at pressure $p = p_t(T)$ indicating the two-dimensional first-order phase transition within the adsorbate. Adsorption isotherms calculated according to the Fowler–Guggenheim model for localized adsorbates (21) are also displayed. The corresponding fit parameters, which are not needed in this work, will be discussed elsewhere. Experimental details will be described using the isotherm at 91 K. In Fig. 2 some of the ν_3 spectra measured at 91 K are shown to explain the spectral features connected with the pressure-dependent behaviour of the adsorbate. It should be mentioned that in Fig. 2 only the ν_3 region of the isotope $^{13}C^{16}O_2$ is displayed. All other isotopes present in the 3D gas phase were also detected in the adsorbate and have been taken into account in the determination of the surface coverage. The first signal observable at lowest coverages is a broad, polarization-independent absorption at 2276 cm^{-1} with a full width at half maximum (FWHM) of 4–6 cm^{-1}. Increasing the CO_2 pressure enlarges the FWHM of this absorption to 10–15 cm^{-1}. This signal appears to be different at each NaCl(100) sample used and therefore is attributed to CO_2 adsorbed on surface defects, mainly steps. The bonding and localization of this adsorbate species is probably the strongest. In comparison to the integrated absorption of the full monolayer, the integrated adsorption due to defects was determined to be between 0.01 and 0.11 for the different samples used. The area of this signal is only weakly dependent upon pressure; it grows slowly over more than two orders of magnitude in pressure. From $p \approx 0.1p_t$ to $p = p_t$ a single sharp absorption at 2278.9 cm^{-1} with a FWHM <0.4 cm^{-1} was detected (e.g., top spectra in Fig. 2). Its integrated absorption increases linearly with the CO_2 pressure. This observation proves the validity of the 2D ideal gas law (21). The single peak is therefore in concert with the absence of any spectral coupling effects attributed to the 2D lattice gas phase of CO_2 on NaCl(100). From the polarization dependency of this signal the parallel orientation of the molecules in the 2D lattice gas with respect to the surface can be derived, as predicted from theoretical calculations (11, 17). At pressure $p = p_t = 4 \times 10^{-8}$ mbar (1 bar = 100 kPa) the ν_3 spectra change remarkably, indicating the onset of the 2D phase transition accompanied by a reorientation of the CO_2 molecules and distinct changes of both polar and azimuthal molecular angles. As can be seen in Fig. 2, two additional absorptions at 2283.0 and 2275.0 cm^{-1} with FWHM 1.5 and 1.9 cm^{-1} appear along with the absorption of the 2D lattice gas. The integrated absorptions of these two signals increase, whereas the absorption of the 2D lattice gas decreases (see Fig. 2). During the phase transition the density of both coexisting phases remains constant. The density ρ of the 2D lattice gas is given by the number of 2D lattice gas molecules per NaCl(100) unit cell not occupied by the 2D solid. The density of the 2D solid is equal to the density of the full monolayer at $p = 10p_t(T)$ as inferred from a complete lineshape analysis. At the end of the condensation process the coverage of the surface has changed from about $\theta \approx 0.01$ to $\theta \approx 0.95$ of the full monolayer at constant pressure p_t. Even after several hours at $p = p_t$ the absorption of the 2D solid stayed at the value of $\theta \approx 0.95$. Only further increase of the CO_2 pressure by about one order of magnitude resulted in an increase of the coverage up to $\theta = 1$. Above p_t we find the well-known ν_3 doublet of 2D solid CO_2 on NaCl(100) for over two magnitudes of pressure. The structure and dynamic behaviour of this phase have been described elsewhere (14–16). Further increase of the CO_2 pressure to $p \geq p_0$ leads to new IR absorptions corresponding to multilayer formation.

We now want to view the 2D phase transition in more detail. As can be seen in the spectra, both phases coexist at $p = p_t(T)$. Taking into account the structural details known about the phases from our recent work, the arrangement displayed in Fig. 3 describes this coexistence. The enthalpy of the 2D sublimation can be determined by the following procedure.

We prepared the adsorbate at $\theta \approx 0.15$ on both the front and back face of the crystal by dosing with a capillary at substrate

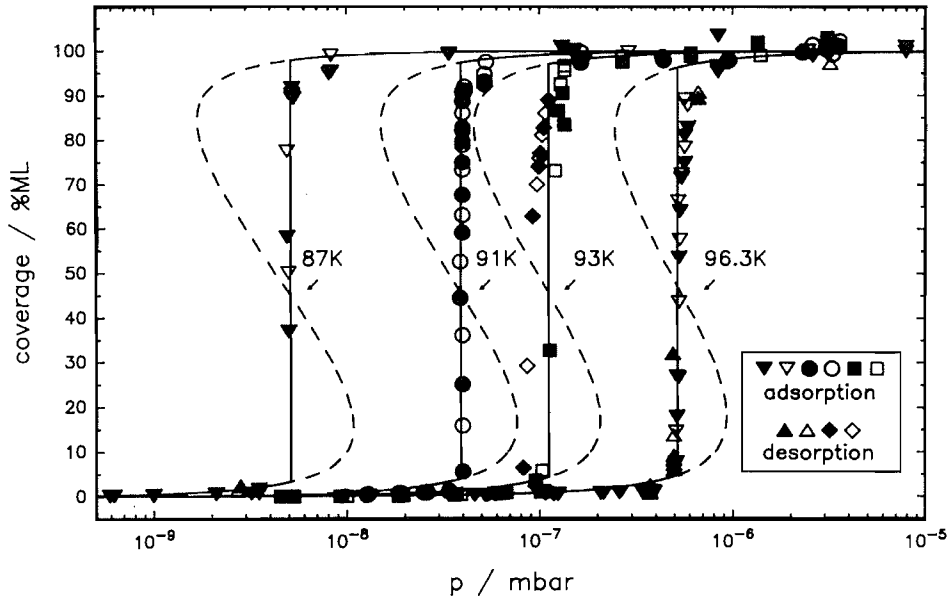

FIG. 1. Adsorption isotherms of $^{13}C^{16}O_2$ on NaCl(100) (UHV-cleaved) at 87 K, 91 K, 93 K, and 96.3 K with fits according to the Fowler–Guggenheim model. The surface was prepared by cleaving a single crystal in situ under ultrahigh vacuum. Coverages were determined from *p*- (full symbols) and *s*-polarized spectra (open symbols).

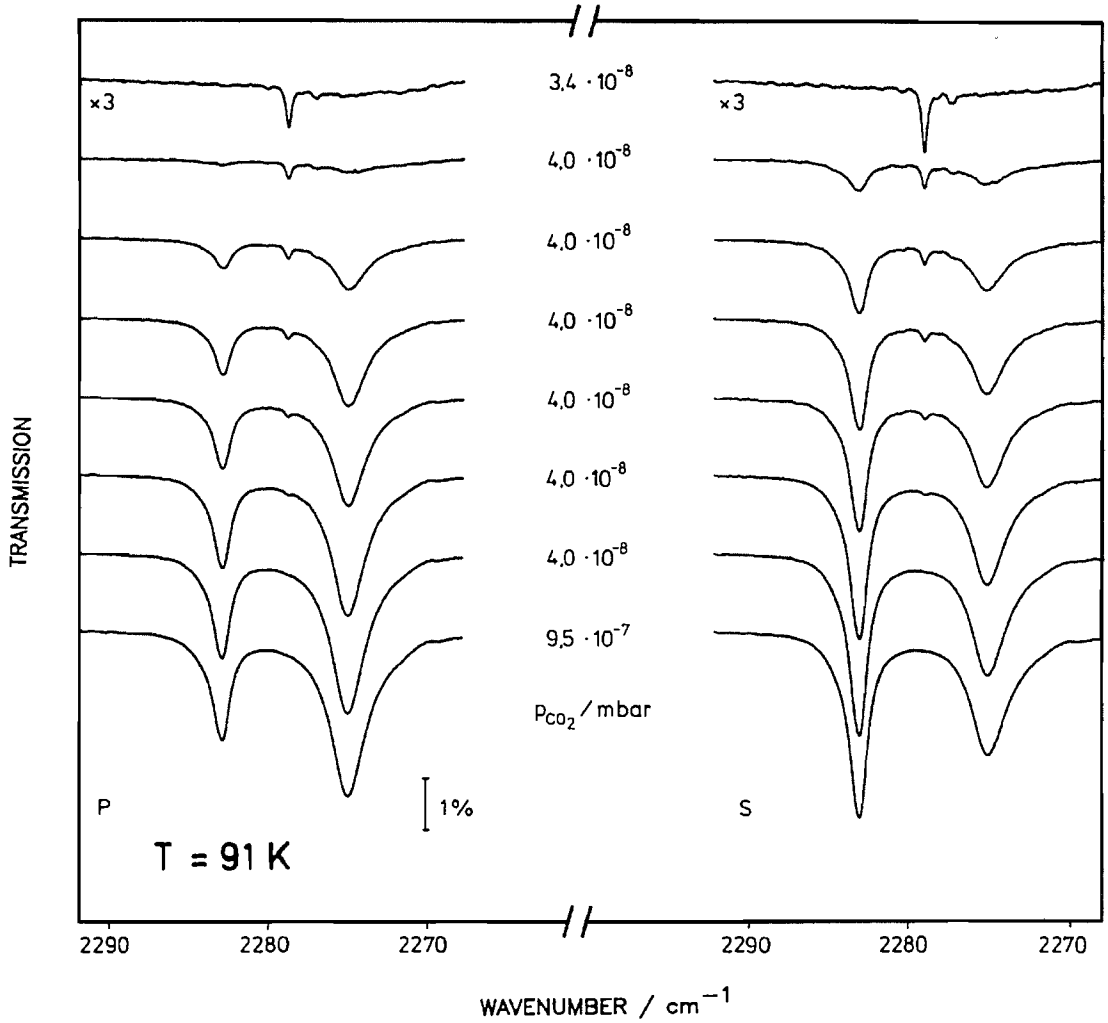

FIG. 2. The *p*- and *s*-polarized FTIR spectra of $^{13}C^{16}O_2$ on NaCl(100) (UHV-cleaved) at 91 K: 2D lattice gas (top), 2D solid (bottom), and coexistence of these phases. All spectra were measured with a resolution of 0.16 cm^{-1} and calculated from the interferogram using a Blackman–Harris apodisation function and a zero-filling factor of two. Note the increased ordinate scaling by a factor 3 in the top spectra.

Can. J. Chem. Downloaded from www.nrcresearchpress.com by 195.246.54.202 on 09/08/12
For personal use only.

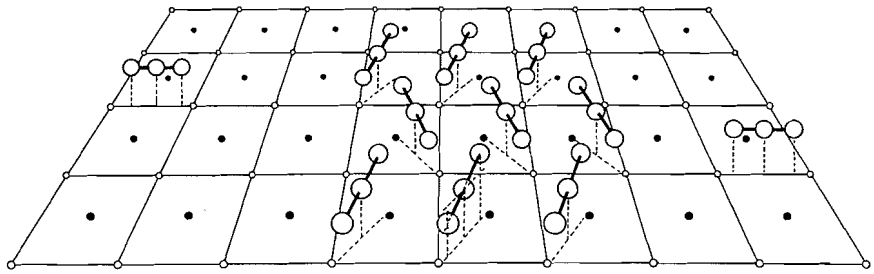

FIG. 3. Model of the coexisting 2D lattice gas and 2D solid CO_2 on NaCl(100).

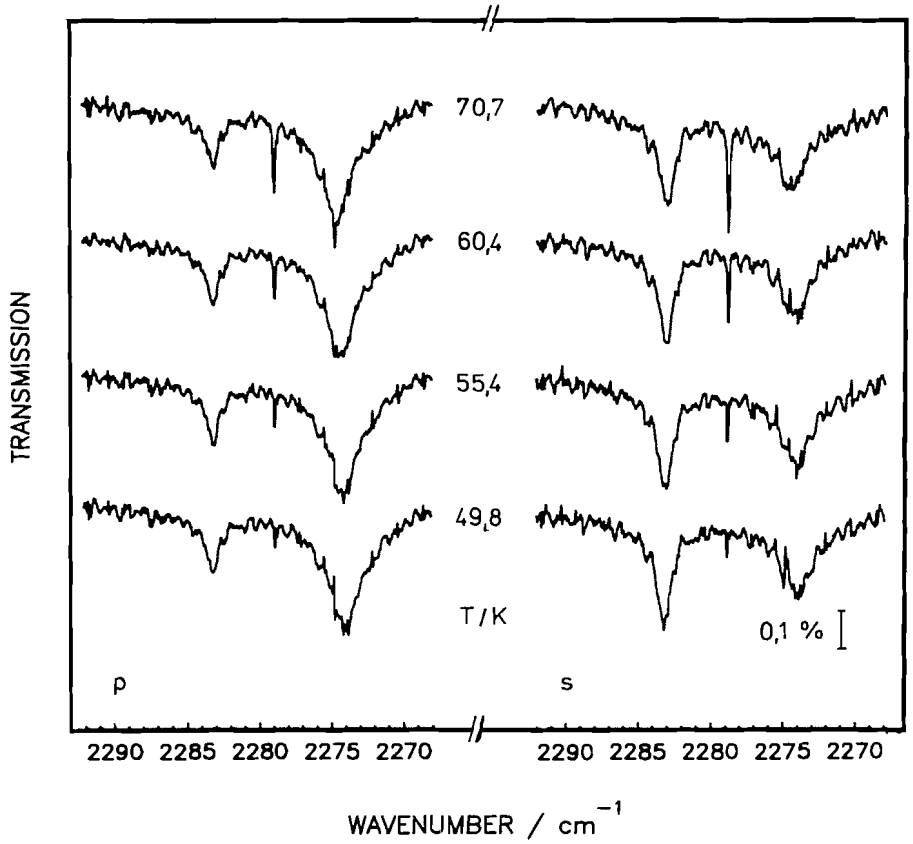

FIG. 4. Temperature-dependent p- and s-polarized FTIR spectra of $^{13}C^{16}O_2$ on NaCl(100) (UHV-cleaved) at constant coverage $\Theta \approx 0.15$ ($\Theta_{DEFECT} \approx 0.08$, $\Theta_{GAS} + \Theta_{SOLID} \approx 0.07$).

temperature $T = 77$ K and a CO_2 background pressure of $p < 2 \times 10^{-11}$ mbar. The adsorbate consists of the 2D lattice gas and the 2D solid in thermodynamic equilibrium, as well as of CO_2 molecules adsorbed at defects ($\theta_{DEFECT} \approx 0.08$). The 2D lattice gas density at temperature T is not affected by θ_{DEFECT}. For a given adsorbent θ_{DEFECT} was constant at different temperatures and their transition pressures $p_t(T)$ as derived from the adsorption isotherms for $T \geq 87$ K. Isosteric decrease of the substrate temperature leads to formation of the 2D solid, whereas the absorption of the 2D lattice gas becomes smaller (Fig. 4). This effect is reversible when heating up the sample. For each temperature the density ρ of the 2D lattice gas on the (100) terraces can be calculated from the coverages θ_{GAS} and θ_{SOLID}:

$$[1] \qquad \rho = \Theta_{GAS}/(1 - \Theta_{SOLID})$$

Both coverages are derived from the integrated absorptions of the corresponding ν_3 signals for a given polarization, corrected by the absorption of CO_2 adsorbed at surface defects:

$$[2] \qquad \Theta_{GAS} = \frac{fA_{GAS}}{A_{ML} - A_{DEFECT}}$$

$$[3] \qquad \Theta_{SOLID} = \frac{A_{SOLID}}{A_{ML} - A_{DEFECT}} = \frac{A_{TOTAL} - A_{DEFECT} - A_{GAS}}{A_{ML} - A_{DEFECT}}$$

A_{GAS}, A_{ML}, A_{TOTAL}, A_{DEFECT}, and A_{SOLID} denote the integrated absorptions over the ν_3 spectral region at a given polarization of the 2D lattice gas, the full monolayer (= saturated coverage at $p = 10p_t(T)$), the submonolayer under study, the adsorbate at defects, and the 2D solid, respectively. The factor f, determined from the Fresnel equations, takes into account the different orientations of the CO_2 molecules in the 2D lattice gas and the 2D solid. The effect on f of the dipole–dipole

Can. J. Chem. Downloaded from www.nrcresearchpress.com by 195.246.54.202 on 09/08/12
For personal use only.

HEIDBERG ET AL.

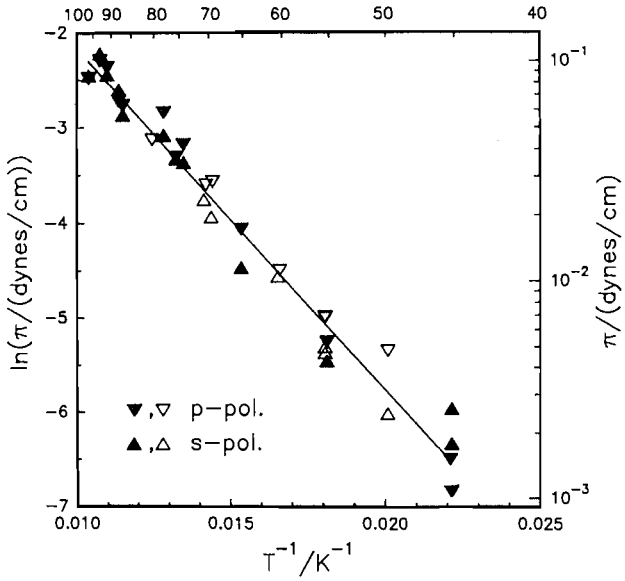

FIG. 5. 2D Clausius–Clapeyron plot of the spreading pressure π of the coexisting 2D lattice gas with temperature T for the 2D sublimation of CO_2 on NaCl(100) (UHV-cleaved). Data points were measured with decreasing (full symbols) and increasing temperature (open symbols).

coupling and the electronic screening in the 2D solid can be neglected, as shown by calculation of the complete line shapes using the gas phase values for the vibrational and electronic polarizibilities.

An exponential increase of density ρ of the coexisting 2D lattice gas with T is observed. Using the value of ρ, the spreading pressure π can be also calculated using the 2D ideal gas equation [4] (21):

$$[4] \qquad \pi = \rho kT/\beta$$

$\beta = a_0^2$ denotes the area of the substrate unit cell with $a_0 = 3.96$ Å for NaCl(100). A 2D Clausius–Clapeyron plot (Fig. 5) gives the enthalpy ΔH_S^{2D} of the 2D sublimation (22):

$$[5] \qquad \left(\frac{\partial \ln \pi}{\partial 1/T}\right)_{\text{coex}} = -\frac{\Delta H_S^{2D}}{R}$$

The slope of this plot yields $\Delta H_S^{2D} = (3.0 \pm 0.1)$ kJ/mol. Analyzing adsorption isosteres, the isosteric heats of adsorption for the 2D lattice gas and the 2D solid on NaCl(100) have been determined as $q_{st}^g = (32.4 \pm 1.1)$ kJ/mol and $q_{st}^s = (35.6 \pm 1.3)$ kJ/mol, respectively (23). The difference between these two values agrees very well with ΔH_S^{2D} determined directly from the spectra measured at coexistence of 2D lattice gas and 2D solid.

Considering these results, FTIR spectroscopy appears again as a well-suited nondestructive method to study physisorption systems like CO_2 on NaCl(100). Structural, dynamic, and thermodynamic information about the adsorbate can be derived from the IR spectra.

As is well known, in three-dimensional space the triple point of CO_2 lies above 100 kPa, so that the solid sublimes and the 3D liquid cannot exist at normal atmospheric pressure. Further work is directed to a better understanding of the 2D phase equilibria, its basis, the 2D phase rule, and the concept of chemical component in the adsorbate CO_2 on NaCl(100). The existence of a 2D critical point for the 2D sublimation should be examined.

Acknowledgements

We thank Prof. Dr. H. Gies, Dr. N. Jockwer, and Dr. J. Moenig for helpful discussions. Financial support by Land Niedersachsen, the Fonds der Chemischen Industrie, and the Deutsche Forschungsgemeinschaft (DFG) is gratefully acknowledged. Some of the results reported are part of a cooperation with the Forschungszentrum für Umwelt und Gesundheit (GSF).

1. J.C. Polanyi. Faraday Discuss. Chem. Soc. **84**, 1 (1987). J.C. Polanyi and H.H. Rieley. *In* Dynamics of gas–surface interactions. *Edited by* C.T. Rettner and M.N.R. Ashfold. The Royal Society of Chemistry, Letchworth. 1991. p. 329.
2. N. Jockwer and S. Gross. Mater. Res. Soc. Symp. Proc. **50**, 587 (1985); N. Jockwer. *In* Scientific basis for nuclear waste management. Vol. 3. Plenum Publishing Company, New York. 1981.
3. Á. Thomy, X. Duval, and J. Regnier. Surf. Sci. Rep. **1**, 1 (1984).
4. B.N.J. Persson. Surf. Sci. Rep. **15**, 1 (1992).
5. H.J. Kreuzer and S.H. Payne. Surf. Sci. **198**, 235 (1988).
6. B. Poelsema, L.K. Verheij, and G. Comsa. Phys. Rev. Lett. **51**, 2410 (1983). B. Poelsema, L.K. Verheij, and G. Comsa. Surf. Sci. **152/153**, 851 (1985).
7. H. Pfnür, D. Menzel, F.M. Hoffmann, A. Ortega, and A.M. Bradshaw. Surf. Sci. **93**, 431 (1980); H. Pfnür and D. Menzel. Surf. Sci. **148**, 411 (1984).
8. S. Liang and M. Trenary. J. Chem. Phys. **89**, 3323 (1988). V.K. Agrawal and M. Trenary. J. Chem. Phys. **95**, 6962 (1991).
9. J. Heidberg and D. Hoge. Surf. Sci. **189/190**, 448 (1987).
10. J. Heidberg, E. Kampshoff, H. Stein, H. Weiss, and M. Warskulat. Microchim. Acta, **2**, 105 (1988); J. Heidberg, D. Hoge, K. Stahmer, H. Stein, M. Venschott, M. Warskulat, and H. Weiss. Vacuum, **38**, 275 (1988).
11. J. Heidberg, E. Kampshoff, O. Schönekäs, H. Stein, and H. Weiss. Ber. Bunsen-Ges. Phys. Chem. **94**, 112 (1990); **94**, 118 (1990); **94**, 127 (1990).
12. O. Berg and G.E. Ewing. Surf. Sci. **220**, 207 (1989); O. Berg, R. Disselkamp, and G.E. Ewing. Surf. Sci. **277**, 8 (1992).
13. J. Heidberg, E. Kampshoff, R. Kühnemuth, O. Schönekäs, H. Stein, and H. Weiss. Surf. Sci. Lett. **226**, L43 (1990).
14. J. Heidberg, E. Kampshoff, R. Kühnemuth, O. Schönekäs, and M. Suhren. J. Electron Spectrosc. Relat. Phenom. **54/55**, 945 (1990).
15. J. Heidberg, E. Kampshoff, R. Kühnemuth, and O. Schönekäs. Surf. Sci. **251/252**, 314 (1991).
16. J. Heidberg, E. Kampshoff, R. Kühnemuth, and O. Schönekäs. Surf. Sci. **269/270**, 120 (1992).
17. J. Heidberg, R.D. Singh, and C.F. Chen. Z. Phys. Chem. NF, **110**, 135 (1978); J. Heidberg and R.D. Singh. J. Electron Spectrosc. Relat. Phenom. **39**, 163 (1986).
18. J. Schimmelpfennig, S. Fölsch, and M. Henzler. Surf. Sci. **250**, 198 (1991).
19. D. Schmicker, J.P. Toennies, R. Vollmer, and H. Weiss. J. Chem. Phys. **98**, 10096 (1993).
20. W. Chen and W.L. Schaich. Surf. Sci. **220**, L733 (1989).
21. S. Ross and J.P. Olivier. On physical adsorption. Interscience Publishers, New York. 1964.
22. T.L. Hill. J. Chem. Phys. **76**, 3327 (1982).
23. J. Heidberg, E. Kampshoff, R. Kühnemuth, and O. Schönekäs. Surf. Sci. **272**, 306 (1992).

Can. J. Chem. Downloaded from www.nrcresearchpress.com by 195.246.54.202 on 09/08/12
For personal use only.

Phase-plane geometries in enzyme kinetics

SIMON J. FRASER[1] AND MARC R. ROUSSEL

Chemical Physics Theory Group, Department of Chemistry and Scarborough College, University of Toronto, Toronto, ON M5S 1A1, Canada

Received June 23, 1993

This paper is dedicated to Professor John C. Polanyi on the occasion of his 65th birthday

SIMON J. FRASER and MARC R. ROUSSEL. Can. J. Chem. **72**, 800 (1994).

The transient and steady-state behaviour of the reversible Michaelis–Menten mechanism [R] and Competitive Inhibition (CI) mechanism is studied by analysis in the phase plane. Usually, the kinetics of both mechanisms is simplified to give a modified Michaelis–Menten velocity expression; this applies to the CI mechanism with excess inhibitor and to mechanism [R] in the product inhibition limit. In this paper, [R] is treated *exactly* as a plane autonomous system of differential equations and its true (dynamical) steady state is described by a line-like slow manifold $\mathcal{M}$. Initial velocity experiments for [R] no longer strictly correspond to the hyperbolic law (as in the irreversible Michaelis–Menten mechanism) and this leads to corrections to the standard integrated rate law. Using a new analysis, the slow dynamics of the CI mechanism is reduced from a three-dimensional system to a planar system. In this mechanism transient decay collapses the trajectory flow onto a two-dimensional "slow" surface Σ; motion on Σ can be treated *exactly* as projected dynamics in the plane. This projected flow may differ in important ways from that of two-step mechanisms, e.g., it may lack a proper steady state. The relevance of these more accurate dynamical descriptions is discussed in relation to experimental design and metabolic function.

SIMON J. FRASER et MARC R. ROUSSEL. Can. J. Chem. **72**, 800 (1994).

Nous présentons une analyse du mécanisme Michaelis–Menten réversible [R] et du mécanisme d'inhibition compétitive (CI) dans le plan de phase. Normalement, on simplifie les équations différentielles découlant de ces deux mécanismes par l'approximation de l'état stationaire; la vitesse réactionelle est ainsi mise dans la forme de Michaelis et Menten. Par contre, nous démontrons que le mécanisme [R] est exactement descriptible par un système d'équations différentielles planaire possédant une courbe intégrale (la courbe intégrale lente, $\mathcal{M}$) qu'approchent toutes les autres solutions après la période transitoire. Dans un traitement exact, la vitesse initiale ne décrit plus nécessairement une courbe hyperbolique, même pour le mécanisme de Michaelis et Menten; nous présentons une méthode pour obtenir les corrections et en dérivons les premiers termes. Les équations différentielles du mécanisme d'inhibition compétitive peuvent aussi être réduites à un système planaire puisque le mode transitoire le plus rapide porte un point dans l'espace de phase à la surface intégrale lente Σ. Le mouvement d'un point représentatif sur Σ peut donc être projeté sur un plan de phase. L'écoulement projeté peut cependant être très différent de ce qu'on retrouve dans le cas d'un mécanisme vraiment planaire comme [R]. Par exemple, il peut n'y avoir aucune courbe intégrale lente en tant que telle. L'analyse exacte de la cinétique que nous prônons a d'importantes conséquences, et pour les expériences exécutées en laboratoire, et pour notre entendement du métabolisme.

Can. J. Chem. Downloaded from www.nrcresearchpress.com by 195.246.54.202 on 09/08/12
For personal use only.

1. Introduction

The coupled ordinary differential equations (ODEs) of all two-step stoichiometric reaction mechanisms can be reduced to plane autonomous systems (1). Even three-step mechanisms can be reduced to planar flows if a transient mode is removed by adiabatic elimination (2). This procedure of "planarization" of the full system produces an accurate global picture of the system's slow time evolution.[2] Representations of this kind are important because they expose conceptual errors in the analysis of standard, supposedly well-understood mechanistic models, and they can also provide accurate solutions to the governing ODEs. The dynamics of these planar systems is often richer than the standard picture permits. The importance of this aspect of enzyme kinetics has been emphasized by Walter (3).

In this paper, we apply dynamical systems analysis to the transient and steady-state kinetics of two *inhibition* models in enzyme kinetics: the reversible Michaelis–Menten mechanism [R], and the Competitive Inhibition (CI) mechanism.

Mechanism [R] corresponds to the reaction scheme (4):

$$\text{[R]} \qquad \mathrm{E + S \underset{k_{-1}}{\overset{k_1}{\rightleftharpoons}} C \underset{k_{-2}}{\overset{k_2}{\rightleftharpoons}} P + E}$$

where E is enzyme, S substrate, C = ES enzyme–substrate complex, and P is product. In [R], product P competes with substrate S for the active site on the enzyme. Note that the irreversible Michaelis–Menten mechanism [I] (5), which lacks any inhibition effects, corresponds to taking the limit $k_{-2} \to 0$; this gives

$$\text{[I]} \qquad \mathrm{E + S \underset{k_{-1}}{\overset{k_1}{\rightleftharpoons}} C \overset{k_2}{\rightarrow} P + E}$$

Since [I] is a particular case of [R], the analysis for [R] can immediately be specialized to [I] by taking the limit $k_{-2} \to 0$. Both [I] and [R] have two reaction steps and therefore two independent concentrations.

Competitive inhibition is usually modelled by the following mechanism

$$\text{[CI]} \qquad \begin{aligned} &\mathrm{E + S \underset{k_{-1}}{\overset{k_1}{\rightleftharpoons}} C \overset{k_p}{\rightarrow} E + P} \qquad \text{[I]} \\ &\mathrm{E + I \underset{k_{-2}}{\overset{k_2}{\rightleftharpoons}} H} \qquad \text{[Inh]} \end{aligned}$$

where I is an inhibitor species and H (= EI) is enzyme–inhibitor complex (4); microscopically, the (inert) inhibitor

[1]Author to whom correspondence may be addressed. Telephone: (416)-978-4650. FAX: (416)-978-8775. E-mail: sfraser@alchemy.chem.utoronto.ca

[2]Here planarization implies that the dynamical description of the *slow* time evolution of the system is projected onto a plane, so information about initial conditions and transient motion is eliminated in this description.

Can. J. Chem. Downloaded from www.nrcresearchpress.com by 195.246.54.202 on 09/08/12
For personal use only.

molecule I competes with substrate S for the active site. The catalysis [I], which is just the irreversible Michaelis–Menten reaction, has two degrees of freedom and the inhibition step [Inh] has one, so the evolution of the CI mechanism has three independent concentrations.

The quasi-steady-state velocity expression for both these mechanisms can, in suitable limits, be written in the form

$$v = \frac{V_{max}[S]}{K_M(1 + [I]/K_i) + [S]}$$

where V_{max} is the maximal reaction velocity, [S] substrate and [I] "inhibitor" concentration, K_M the Michaelis constant, and K_i the inhibitor constant. Alternatively, this formula for v can be written as the standard hyperbolic law

$$v = \frac{V_{max}[S]}{K_M^{app} + [S]}$$

where K_M^{app} is the apparent Michaelis constant. In the case of mechanism [R] this phenomenological formula describes the product-inhibition limit, where the product P can sequester free enzyme E to form a complex, but this complex cannot regenerate substrate S. In the CI mechanism, I represents a true inhibitor whose (total) concentration must be sufficiently large for this steady-state expression to hold. We will examine the relationship of such approximate expressions to precise and often more realistic dynamical descriptions where these approximations break down. Thus our study provides a sound mathematical framework for *in vivo* biochemical reactions, where enzyme, substrate, and inhibitor concentrations are often comparable (6). The dynamical consequences of this living environment cannot be inferred just from a knowledge of the "asymptotic" parameters V_{max} and K_M. For example, dynamical effects in the CI mechanism caused by changes in total inhibitor concentration have been studied by Straus and Goldstein (7).

To understand the hyperbolic law in a broader dynamical context some history of earlier steady-state theory is helpful. In biochemical systems, rate laws are obtained by formal linear modelling of nonlinear equations of motion. The underlying linear approach appeared in the nineteenth century (8), and the adaptation of this method to nonlinear enzyme systems was made famous by the work of King and Altman (9). However, since dynamical variables appear in the rate coefficients in this method the system is effectively non-autonomous: some procedure must be introduced to account for the time dependence of the formal rate-coefficient matrix of the quasi-linear scheme. Unless this is done there is no hope of producing a systematic, convergent procedure of reaching the true steady-state solution (slow time evolution) of the ODEs governing the system. Indeed, a related form of perturbation theory for chemical reactions was introduced by Hirschfelder (10). He described an approximate perturbation treatment of the evolution of a model bimolecular mechanism although he did not indicate how to extend his method to a convergent procedure for complete steady-state solution of this mechanism. Singular perturbation methods did tackle this problem in a systematic way (11). However, not all chemical reactions separate into "inner" and "outer" solutions in the clean way required by singular perturbation theory, nor is the "small parameter" uniquely determined even in stiff systems (12). An unambiguous way of resolving all these difficulties is to carry out a global analysis of the trajectory flow in the geometrical setting of the phase space, Γ, of species concentrations. To demonstrate the power and insight provided by this geometrical approach we study the [R] and CI mechanisms, which can both be reduced to plane autonomous systems. These mechanisms display unusual features and show that standard steady-state analysis breaks down easily.

In the global, geometrical picture, chemical kinetics is viewed as a flow governed by ODEs in Γ (13–17). In the simplest case relaxation in such systems corresponds to a cascade through a set of smooth, nested structures of decreasing dimension so that in the final stages of relaxation the representative point for the system moves on a *two-dimensional surface* $\Sigma(\subset \Gamma)$, then traverses a *line*, the slow manifold $\mathcal{M}(\subset \Sigma)$, and finally comes to rest at the stable equilibrium $\mathcal{P}(\in \mathcal{M})$. Experimentally this cascade corresponds to relaxation processes in the physically accessible part Γ^+ of Γ. Certainly in all closed, stoichiometric two-step systems the simple picture just described holds; this is demonstrated by our treatment of mechanism [R]. In contrast, for some parameter regimes in the CI mechanism, this hierarchical collapse is interrupted (18): the system flow no longer simply contracts from flow on a surface to flow on a line; instead the line-like motion may occur on disconnected pieces separated by a region where the motion is intrinsically two-dimensional.

To carry out a global analysis, a combination of mathematical tools must be used: functional equations, perturbation methods, and linearized analysis. To begin, the motion can be formally separated into "fast" and "slow" variables, as in center manifold theory (19–21). By writing the fast variables as smooth functions of the slow variables and introducing the velocity components defined by the governing ODEs, *differential equations*[3] for the system's invariant manifolds[4] are obtained. These differential equations are rearranged to give *functional equations* for the invariant manifolds. If such a functional equation defines a contraction, mapping its solution can be found exactly by iteration (13–17, 21). Geometrically, this solution corresponds to an invariant manifold which rapidly "attracts" the surrounding flow. The equations for the slow manifold $\mathcal{M}$ contain far more "kinetic" information than the usual Steady-State Approximation (SSA) or Equilibrium Approximation (EA) formulas. Similarly, the equation for the surface Σ contains more information than the usual linearized analysis for transient relaxation. To complement this global method, a linearized analysis of the flow (Jacobian) at the equilibrium point determines local bifurcation structure. Finally, perturbation methods provide closed formulas for limiting cases. Together, these techniques allow us to build a complete and essentially exact dynamical picture of the system. And this picture overcomes the errors and limitations of the standard steady-state analysis.

In recent years several new theoretical approaches to nonlinear kinetics have been developed. These have arisen from an interest in the time evolution of large sets of coupled reactions, particularly gas-phase reactions in flames (22). Turányi et al. (23) considered general methods for testing the accuracy of the quasi-steady-state approximation in such cases. In a re-

[3]These differential equations are ODEs for the line-like slow manifold $\mathcal{M}$ and partial differential equations for the slow surface Σ.

[4]A manifold is invariant if it is transformed (continuously) into itself under the flow, i.e., for any point $x_0 = x(0)$ in the manifold, its image $x(t, x_0)$ after time t lies in the manifold.

Can. J. Chem. Downloaded from www.nrcresearchpress.com by 195.246.54.202 on 09/08/12
For personal use only.

cent paper Li et al. (24) used singular perturbation methods to determine approximate lumping schemes for some important nonlinear biochemical models; their method can, in principle, be used to describe the transient and steady-state kinetics for large chemical systems.[5] However, they point out that there is no general method for finding global invariant manifolds for nonlinear reactions. The description of the slow time evolution of the systems they consider can ultimately be related to geometrical structures, i.e., surface-like or line-like slow manifolds. In the present paper we use iteration methods to solve the functional equations and so determine the corresponding (slow) invariant manifolds. It may even be convenient to expand the functional equation if it contains a radical (branch point) or if we are interested in a solution near an irreversible limit. However, this is not the only method for solving such functional equations or for finding invariant manifolds. As we have previously shown, such structures can be determined either numerically (25) or by perturbation theory (15, 18).

The scheme of the paper follows:

In Sect. 2 we discuss mechanism [R]. For [R] the functional equation for the slow manifold is formally quadratic, and in the irreversible limit becomes a singular perturbation problem. We treat this case carefully to demonstrate the differences between the reversible [R] and irreversible [I] cases. We show that reversibility produces corrections to the usual steady-state initial velocity and integrated rate law formulas for mechanisms [I] and [R].

In Sect. 3 we treat a planar model of the CI mechanism. While this mechanism can be reduced exactly to a three-dimensional system, most of its interesting dynamics can be captured by a planar system, including the bifurcations accompanying the appearance of a global steady state. This cautions against the uncritical use of methods that *assume* the existence of such a global steady state.

In Sect. 4 we compare our results with the standard treatment and discuss the experimental implications of our analysis, arguing that improved methods would yield a far clearer interpretation of relaxation and steady-state kinetics.

2. Reversible Michaelis–Menten mechanism [R]

The phase-space analysis of the kinetics of the reversible mechanism [R] (25) is now developed; this leads through a singular perturbation treatment to the corresponding irreversible mechanism [I] (14, 15, 17).

The system of coupled ODEs for [R] is

$$[1] \qquad \dot{e} = -k_1 es + (k_{-1} + k_2)c - k_{-2}ep$$

$$[2] \qquad \dot{c} = k_1 es - (k_{-1} + k_2)c + k_{-2}ep$$

$$[3] \qquad \dot{s} = -k_1 es + k_{-1}c$$

$$[4] \qquad \dot{p} = k_2 c - k_{-2}ep$$

Since there are *four* species in this system the corresponding phase space is four-dimensional; we write $\Gamma = \Gamma_4 = s \times c \times e \times p$.[6] However, there are also *linear* constants of the motion: adding eqs. [2], [3], and [4] gives

$$\dot{c} + \dot{s} + \dot{p} = 0$$

which integrates to

$$[5] \qquad c + s + p = m_s$$

where m_s is the conserved total substrate concentration.[7] Similarly, adding eqs. [1] and [2] gives

$$\dot{e} + \dot{c} = 0$$

which integrates to

$$[6] \qquad e + c = m_e$$

where m_e is the conserved total enzyme concentration. The existence of these two linear constants of the motion means that there is a *planar* two-dimensional coset[8] parameterized by m_s and m_e, say $\Gamma_2(m_s, m_e) \subset \Gamma_4$, to which the corresponding family of trajectories is restricted. Two natural projections exist for the flow in $\Gamma_2(m_s, m_e)$, namely, those onto $s \times c$ and onto $s \times p$. The $(s \times p)$ representation formally preserves the symmetry of mechanism [R] but the $(s \times c)$ representation is related to previous work (14, 15, 17) and also to the way that experimentalists discuss enzyme kinetics, so this representation will be used here. Therefore, introducing eqs. [5] and [6] into eqs. [2] and [3] gives the plane autonomous system

$$[7] \qquad \dot{c} = k_1(m_e - c)s - (k_{-1} + k_2)c + k_{-2}(m_e - c)(m_s - s - c)$$

$$[8] \qquad \dot{s} = -k_1(m_e - c)s + k_{-1}c$$

This system, which is fully equivalent to the original four-dimensional system [1]–[4], is now used to give a description of the slow time evolution for mechanism [R].[9]

2.1 Standard approximations and equilibria of mechanism [R]

The SSA is obtained by setting $\dot{c} = 0$ in eq. [7]; this gives a quadratic equation for c whose "negative" branch corresponds to the SSA, i.e., the $(\dot{c} = 0)$ isocline or c nullcline. The equation for this nullcline can be reduced to the first-order perturbation expression

$$[9] \qquad c_{SSA}(s; \eta) = \frac{m_e s}{s + K_S} + \eta \frac{m_e K_S}{(s + K_S)^2}\left(m_s - s - \frac{m_e s}{s + K_S}\right) + O(\eta^2)$$

where η is the rate constant ratio

$$\eta = \frac{k_{-2}}{k_1}$$

and

$$K_S = \frac{k_{-1} + k_2}{k_1}$$

[5]Reference 24 contains many references to the early lumping methods used in chemical engineering and to the recent developments of this method applied to nonlinear systems.

[6]This space is given the usual Euclidean metric: if P_1 and P_2 are two points in Γ_4, then the distance function d between them is given by $d(P_1, P_2) = [(s_1 - s_2)^2 + (c_1 - c_2)^2 + (e_1 - e_2)^2 + (p_1 - p_2)^2]^{1/2}$.

[7]Because of the symmetry in mechanism [R] this could equally well be called "total product" concentration.

[8]This coset is *not* a linear manifold (subspace) since it does not contain the origin of Γ_4.

[9]The fast motion, from any initial condition, can be obtained by Taylor series methods. This method is discussed in ref. 25.

Can. J. Chem. Downloaded from www.nrcresearchpress.com by 195.246.54.202 on 09/08/12
For personal use only.

is the Michaelis constant for the forward reaction S $\longrightarrow$ P.[10] For $\eta = 0$, eq. [9] gives the c nullcline for mechanism [I], i.e.,

$$c_{SSA}(s;\, 0) = \frac{m_e s}{s + K_S}$$

The EA corresponds to the ($\dot{s} = 0$) isocline or s nullcline, obtained by setting $\dot{s} = 0$ in eq. [8]:

$$[10] \qquad c_{EA}(s) = \frac{m_e s}{s + K_1}$$

where K_1 is the "equilibrium" constant for the first step in [R], so

$$K_1 = \frac{k_{-1}}{k_1}$$

Evidently, K_S and K_1 can be related by

$$K_S = K_1 + \epsilon$$

where

$$\epsilon = \frac{k_2}{k_1}$$

Note that c_{EA} is independent of η.[11] The graphs of SSA and EA are shown in Fig. 1 together with the phase trajectories. These trajectories all move into a trapping region lying between the SSA and EA nullclines, towards a unique trajectory, the slow manifold $\mathcal{M} = \mathcal{M}(\eta)$, which represents the true *dynamical steady state* of [R].

The disappearance of the reversible step in going from [R] to [I] produces important changes in the global topology of the flow; both singular and non-singular effects occur and these are related to the two branches of the quadratic equation(s) underlying mechanism [R]. This important feature is omitted in standard treatments of [R] but is central to a procedure for systematic improvement to these standard treatment. The basic quadratic character is most simply illustrated by a discussion of the behaviour of the equilibria in [R].

It is evident from the flow pattern in Fig. 1 that the EA and SSA nullclines intersect at two equilibria (●): The (lower) physical equilibrium $\mathcal{P}_+ = \mathcal{P}_+(\eta)$ is *stable* and its position moves smoothly as $\eta \longrightarrow 0$; the (upper) unphysical equilibrium $\mathcal{P}_- = \mathcal{P}_-(\eta)$ is *unstable* and its position moves in a singular way (to infinity) as $\eta \longrightarrow 0$. These equilibria of mechanism [R] are given by setting $\dot{c} = \dot{s} = 0$ in eqs. [7] and [8]. This gives a quadratic equation in s (or c) with solutions $s_\pm$ (or $c_\mp$); the root s_+ corresponds to the physical equilibrium and s_- to the unphysical equilibrium in $s \times c$. To $O(\eta)$ the physical

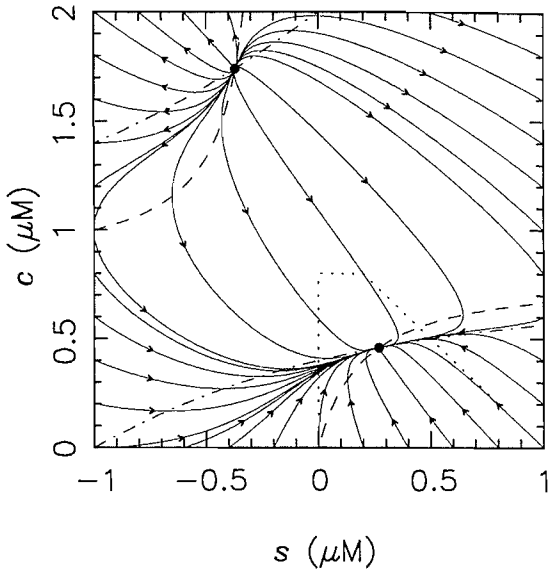

FIG. 1. Trajectories for the reversible Michaelis–Menten mechanism at: $m_e = 8.0 \times 10^{-7}$ M, $m_s = 1.0 \times 10^{-6}$ M, $k_1 = 1.0 \times 10^7$ M^{-1} s^{-1}, $k_{-1} = 2.0$ s^{-1}, $k_2 = 1.0$ s^{-1}, $k_{-2} = 5.0 \times 10^6$ M^{-1} s^{-1}. The flow pattern is shown near both equilibria $\mathcal{P}_\pm$ indicated by ●. Arrows indicate the direction of the flow. The upper left ● marks the unstable node $\mathcal{P}_-$; this is a "source" of the trajectory flow. The lower right ● marks the stable node $\mathcal{P}_+$; this is a "sink" for the trajectory flow. The broken curves (– –) are the two branches of the hyperbola corresponding to the EA. The flow crosses the EA branches vertically everywhere. The dot-dash curves (– · – ·) are the two (nearly hyperbolic) branches corresponding to the SSA. The flow crosses these curves horizontally everywhere. The dotted trapezium (· · ·) in the lower right corner shows the boundary of the physical domain. Note how the flow becomes trapped between the EA and SSA nullclines near the stable equilibrium $\mathcal{P}_+$.

equilibrium $\mathcal{P}_+(\eta)$ is located in $s \times c$ at[12]

$$s_{eq}^+ = s_+(\eta) = \eta \frac{K_1 m_s}{\epsilon}, \qquad c_{eq}^+ = \eta \frac{m_e m_s}{\epsilon}$$

in $\Gamma_2 = s \times c$. As $\eta \longrightarrow 0$ the position of $\mathcal{P}_+(\eta)$ moves smoothly to the origin of $s \times c$. Its position vector can easily be extended to $\Gamma(m_e, m_s) \subset \Gamma_4$ using the constants of the motion, m_s and m_e. Thus the two remaining coordinates of $\mathcal{P}_+(\eta)$ in Γ_4 are

$$e_{eq}^+ = m_e \left(1 - \eta \frac{m_s}{\epsilon}\right), \quad p_{eq}^+ = m_s \left[1 - \eta \frac{(m_e + K_1)}{\epsilon}\right]$$

The overall equilibrium constant K_{eq} is defined by

$$K_{eq} = \frac{k_1 k_2}{k_{-1} k_{-2}} = \frac{p_{eq}^+}{s_{eq}^+}$$

so that, formally to $O(\eta^0)$,

$$K_{eq}(\eta) = \frac{p_{eq}^+(\eta)}{s_{eq}^+(\eta)} = \frac{\epsilon}{\eta K_1} + O(\eta^0)$$

[10]For the reversible case, $\eta > 0$, the SSA nullcline given by eq. [9] is *not* the lower branch of a rectangular hyperbola. In standard initial velocity experiments, the initial condition is $s(0) = m_s$ (variable), $e(0) = m_e$ (constant), and $p(0) = 0$. The set of experimental results corresponds to recording data for the event $\dot{c} = 0$ on every sample trajectory, i.e., to crossing the non-hyperbolic SSA nullcline. This implies that curvature can appear in any of the standard linearized plots. This possibility has not been discussed in the literature.

[11]It is useful to think of η and ϵ as small parameters, since we are interested in the case where the rate of product formation is intrinsically small, i.e., k_2 is small and therefore ϵ is small. Also, we consider the limit where the recombination of product with enzyme becomes vanishingly small, i.e., k_{-2} and therefore η both tend to zero.

[12]The sign +/− on $\mathcal{P}_\pm(\eta)$ denotes the physical/unphysical equilibrium, not the branch of the quadratic equation: in the quadratic equation for $c(\eta)$, the branch $c_-(\eta)$ corresponds to the physical solution and the branch $c_+(\eta)$ to the unphysical solution, whereas the opposite is true for $s(\eta)$.

Can. J. Chem. Downloaded from www.nrcresearchpress.com by 195.246.54.202 on 09/08/12
For personal use only.

but, in fact, the $O(\eta^{-1})$ term is exactly K_{eq}; it can be extended to give the Haldane (26) relation for mechanism [R].

The behaviour of the flow near equilibrium is governed by the first-order decay exponents there. For nearly all initial conditions the relevant exponent will be the one with smaller magnitude. For example, in the irreversible mechanism [I] this decay constant or eigenvalue is commonly written as V_{max}/K_M, i.e., $k_2 m_e/K_S$ here, but this is only approximate. We show later that the correction depends on m_e/K_S for mechanism [I]. We now tackle the dynamics near equilibrium by linearizing the ODEs there.

The linearized stability analysis at $\mathcal{P}_+(\eta)$ is carried out as follows. In the neighbourhood of an equilibrium, the equation of motion is

$$\frac{d}{dt}\begin{pmatrix}\delta c\\ \delta s\end{pmatrix} = \begin{pmatrix}\frac{\partial \dot c}{\partial c} & \frac{\partial \dot c}{\partial s}\\ \frac{\partial \dot s}{\partial c} & \frac{\partial \dot s}{\partial s}\end{pmatrix}\begin{pmatrix}\delta c\\ \delta s\end{pmatrix}$$

At $\mathcal{P}_+(\eta)$ the Jacobian in this equation can be written as

$$J(\eta) = J_0 + \eta J_1$$

where

$$J_0 = \begin{pmatrix}-(k_{-1}+k_2) & k_1 m_e\\ k_{-1} & -k_1 m_e\end{pmatrix}$$

is the Jacobian at the origin, i.e., $\mathcal{P}_+(0)$, and

$$J_1 = \frac{1}{\epsilon}\begin{pmatrix}-[k_{-1}m_s + k_2(m_s+m_e)] & -m_e(k_1 m_s + k_2)\\ k_{-1}m_s & k_1 m_e m_s\end{pmatrix}$$

is the perturbation matrix.

The eigensystem of J_0 is easily constructed. The eigenvalues are

[11]
$$\lambda_\pm = \frac{-(k_{-1}+k_2+k_1 m_e) \pm \sqrt{(k_{-1}+k_2+k_1 m_e)^2 - 4k_1 k_2 m_e}}{2}$$

with left eigenvectors

$$\langle \pm| = \left(1, \frac{k_{-1}+k_2+\lambda_\pm}{k_{-1}}\right)$$

and right eigenvectors

$$|\pm\rangle = \left(\frac{k_1 m_e + \lambda_\pm}{k_{-1}}, 1\right)^T$$

where ^{T} indicates the transpose (column) vector. Then, using the usual Rayleigh–Schrödinger procedure (27), to $O(\eta)$ the perturbed eigenvalues are

$$\lambda_\pm(\eta) = \lambda_\pm + \eta\frac{\langle \pm| J_1 |\pm\rangle}{\langle \pm|\pm\rangle}$$

and the perturbed right eigenvectors are

$$|\pm;\eta^1\rangle = |\pm\rangle + \eta\frac{|\mp\rangle\langle\mp| J_1|\pm\rangle}{\langle\mp|\mp\rangle(\lambda_\pm - \lambda_\mp)}$$

As usual, these $O(\eta)$ eigenvectors give an $O(\eta^2)$ leading correction to the eigenvalues. The perturbed left eigenvectors are

$$\langle \pm;\eta^1| = \langle\pm| + \eta\frac{\langle\pm| J_1|\mp\rangle\langle\mp|}{(\lambda_\pm - \lambda_\mp)\langle\mp|\mp\rangle}$$

These formulas for the perturbed left and right eigenvectors preserve normalization and orthogonalization to $O(\eta)$ so that $\langle \pm;\eta^1|\pm;\eta^1\rangle = \langle\pm|\pm\rangle + O(\eta^2)$ and $\langle\pm;\eta^1|\mp;\eta^1\rangle = 0 + O(\eta^2)$.

Similarly, to $O(\eta)$, the unphysical equilibrium $\mathcal{P}_-(\eta)$ is located in $s \times c$ at

$$s_{eq}^- = s_-(\eta) = -K_1\left(1 + \eta\frac{m_e}{\epsilon}\right),$$

$$c_{eq}^- = \frac{\epsilon}{\eta} + m_e + m_s + K_1 - \eta\frac{m_s m_e}{\epsilon}$$

and the additional coordinates in Γ_4 are

$$e_{eq}^- = -\frac{\epsilon}{\eta} - m_s - K_1 + \eta\frac{m_s m_e}{\epsilon},$$

$$p_{eq}^- = -\frac{\epsilon}{\eta} - m_e + \eta\frac{m_e(m_s + K_1)}{\epsilon}$$

This unstable equilibrium moves to infinity as $\eta \to 0$, and in principle this singular motion leads to interesting changes in the directional behaviour of the vector field "at infinity" as $\eta \to 0$. Since there is no unperturbed solution for $\mathcal{P}_-(\eta)$ at $\eta = 0$ we have to solve the eigensystem directly (see Lefschetz, ref. 1, Chap. 9).

2.2 Slow manifold integrated rate law for mechanism [R]

We now consider the problem of finding the slow manifold for mechanism [R] and to the related question of solving the steady-state equation of motion to get the integrated rate law (28).

Dividing eq. [7] by eq. [8] gives the trajectory equation

$$c' = \frac{\dot c}{\dot s} = \frac{dc}{ds}$$

$$= \frac{k_1(m_e - c)s - (k_{-1}+k_2)c + k_{-2}(m_e - c)(m_s - s - c)}{-k_1(m_e - c)s + k_{-1}c}$$

where $(.)' \equiv d(.)/ds$. This can be rearranged[13] to give the following quadratic functional equation

[12] $$\eta c^2 - [(s + K_1)(1 + c') + \epsilon + \eta(m_s + m_e - s)]c + m_e s(1 + c') + \eta m_e(m_s - s) = 0$$

The formal solution of eq. [12] is

[13]This differential equation can be also solved by the perturbation method discussed in refs. 15 and 18 but here we consider the perturbation expansion of the functional equation itself since we are interested in the way the solution coalesces with the irreversible case as $\eta \to 0$.

[13] $$c_{\pm}(s;\eta) = \frac{1}{2\eta}\left\{(s+K_1)(1+c')+\epsilon+\eta(m_s+m_e-s)\pm\sqrt{[(s+K_1)(1+c')+\epsilon+\eta(m_s+m_e-s)]^2-4\eta[m_e s(1+c')+\eta m_e(m_s-s)]}\right\}$$

This is the fundamental equation arising from our analysis, since the iterative or perturbation solution of its "negative" branch gives a sequence of functions that converges to a limit function, $c_{-}^{*}(s;\eta)$ say, which is the formula for the slow manifold $\mathcal{M}$ for mechanism [R]. Equation [13] can be rewritten as

[14] $$c_{\pm}(s;\eta) = \frac{B_0+\eta B_1 \pm \sqrt{[B_0+\eta B_1]^2-4\eta(C_0+\eta C_1)}}{2\eta}$$

where

$$B_0 = (s+K_1)(1+c')+\epsilon$$

$$B_1 = m_s + m_e - s$$

$$C_0 = m_e s(1+c')$$

$$C_1 = m_e(m_s - s)$$

Equations [13] and [14] are exact. Since the formal solution $c_{\pm}(s;\eta)$ is two-branched the perturbation treatment of eq. [14] is now developed to identify the "physical" and "unphysical" branches and to expose the relation between the reversible and irreversible cases.[14]

At small η the functional equation [14] presents a singular perturbation problem, or at least a problem where the "positive" branch $c_{+}(s;\eta)$, which is $O(\eta^{-1})$, behaves in a singular way as $\eta \to 0$ and where the "negative" branch $c_{-}(s;\eta)$, which is $O(\eta^{0})$, behaves normally as $\eta \to 0$. For small η, the positive branch of eq. [14] gives

$$c_{+}(s;\eta) = \frac{B_0}{\eta} + B_1 - \frac{C_0}{B_0} + O(\eta)$$

so

$$\lim_{\eta\to 0} c_{+}(s;\eta) = \infty$$

Similarly the negative branch gives

[15] $$c_{-}(s;\eta) = \frac{C_0}{B_0} + \eta\left(\frac{C_1}{B_0} - \frac{C_0 B_1}{B_0^2} + \frac{C_0^2}{B_0^3}\right) + O(\eta^2)$$

Thus, as $\eta \to 0$, c_{-} reduces to the functional equation for mechanism [I], i.e.,

$$\lim_{\eta\to 0} c_{-}(s;\eta) = c_{-}(s;0) = \frac{C_0}{B_0} = \frac{m_e s(1+c')}{(s+K_1)(1+c')+\epsilon}$$

which has been studied before (14, 15, 17, 25). The c_{-} branch therefore gives the physically relevant solution, i.e., the slow manifold $\mathcal{M}$ for mechanism [R]. Since this equation is only accurate to $O(\eta)$, it is solved approximately. The solution procedure will be considered after the meaning of the SSA and EA has been discussed in relation to eq. [15].

The functional equation [15] gives an interesting meaning to the SSA and EA. Any *horizontal* line $c(s)$ = const. implies $c' = 0$ so that the image of this line under the functional equation is the SSA, i.e., the c nullcline which trajectories cross *horizontally*.[15] Similarly, any *vertical* line implies $c'(s) = \infty$ so its image under the functional equation is the EA, i.e., the s nullcline which trajectories cross *vertically*. In fact it is very convenient to use the formula for the EA or the SSA as a starting function for finding the equation for $\mathcal{M}$ iteratively under eq. [15].

There are other interesting limits for eq. [13]. In the product inhibition case, which is a type of irreversible inhibition (29), formally, at least, the first step becomes irreversible, so $k_{-1} \to 0$. In the van Slyke–Cullen case (30) both steps are irreversible, i.e., $k_{-1} = k_{-2} = 0$. The change in trajectory flow as the kinetics approaches the product inhibition limit is shown in Fig. 2; here all the parameters except k_{-1} are the same as in Fig. 1. In Fig. 2*a*, k_{-1} is small but non-zero. Notice that the EA lies (in part) near to the c axis, because "equilibrium" between C and E + S is less and less easily achieved as k_{-1} decreases. Figure 2*b* shows the product inhibition limit, obtained formally by setting $k_{-1} = 0$ in mechanism [R].[16] The s nullcline has become the union of the lines $s = 0$ and $c = m_e$; the equilibrium point has migrated to the c axis. The product inhibition limit, $k_{-1} \to 0$, changes the flow in the physical region, whereas the reduction of [R] to [I], as $k_{-2} \to 0$, also changes the global flow structure, e.g., $\mathcal{P}_{-}(\eta) \to \infty$ as $\eta \to 0$.

We now turn to the problem of finding the integrated rate law or progress curve for mechanism [R]. Geometrically the progress curve is identified with the slow manifold and dynamically it corresponds to progress along this manifold.

Usually, the integrated rate law is derived from the SSA, but the functional equation [15] allows improved expressions to be obtained. The additional corrections that arise become larger as the reaction progresses and so are increasingly important in the middle and late stages of reaction. Indeed, these corrections are what distinguish the structure of $\mathcal{M}$, which underlies the integrated rate law, from the structure of the SSA or c nullcline, which underlies initial velocity experiments.

Since the dynamical steady state of mechanism [R] corresponds to progress along $\mathcal{M}$, a sequence of approximations to the integrated rate law can be found from the corresponding sequence of formulas for $\mathcal{M}$. To get such sequences, eq. [15] is written as an iterative scheme; this scheme defines a contraction mapping on a space of smooth functions with fixed

[14]The branch point associated with the radical in the functional equation [13] can cause difficulties in functional iteration.

[15]In agreement with this interpretation, eq. [9], which is the perturbation expansion to $O(\eta)$ of the exact solution of the quadratic equation for the SSA nullcline, is also the image of any horizontal line, $c(s)$ = const, under eq. [15] which is the functional equation to $O(\eta)$ for $\mathcal{M}$ for mechanism [R].

[16]It has been remarked in ref. 4 that in more realistic models of the product inhibition limit, intermediate complexes should be considered.

Can. J. Chem. Downloaded from www.nrcresearchpress.com by 195.246.54.202 on 09/08/12
For personal use only.

Can. J. Chem. Downloaded from www.nrcresearchpress.com by 195.246.54.202 on 09/08/12
For personal use only.

point $c_-^*(s;\eta)$, so that $\mathcal{M} = \text{graph}\{c_-^*(s;\eta)\}$. In fact, from its form, eq. [15] maps rational functions into rational functions so $c_-^*(s;\eta)$ is approximated by an infinite sequence of convergent rational functions.[17] The formulas for $c_{EA}(s;\eta)$ in eq. [10] and for $c_{SSA}(s;\eta)$ in eq. [9] represent the EA and SSA respectively in the $s \times c$ plane. These are first approximations to the formula for $\mathcal{M}$ and they improve as $s \longrightarrow \infty$. However, they are not necessarily good in the crossover region from zeroth order to first order kinetics (where [R] really has no order). An improved approximation for $\mathcal{M}$ is obtained by introducing $c'_{EA}(s;\eta)$ in the right of eq. [15] to get a straightforward if lengthy $O(\eta)$ perturbation solution. Similarly, $c'_{SSA}(s;\eta)$ can be put on the right of eq. [15] to get some of the $O(\eta^2)$ correction for $\mathcal{M}$ as well.

For mechanism [R] slow (dynamical steady-state) motion is intrinsically one-dimensional, so the evolution equation is

$$[16] \qquad \dot{s} = -k_1(m_e - c_-^*(s;\eta))s + k_{-1}c_-^*(s;\eta)$$

where c_-^* is the formula for $\mathcal{M}$ or a good approximation to it.[18] If $c_{SSA}(s;0)$ is used in eq. [16] (which is separable) we get the standard integrated rate law for mechanism [I], i.e.,

$$[17] \qquad V_{max}t = s(0) - s(t) + K_S \ln\left[\frac{s(0)}{s(t)}\right]$$

where $V_{max} = m_e k_2$. Rigorously speaking, eq. [17] describes constrained evolution along the SSA or c nullcline for mechanism [I]. At $\eta = 0$, the long-time behaviour of this equation is dominated by the divergent logarithmic term, which predicts that

$$s(t) \sim \exp\left(-\frac{V_{max}}{K_S}\,t\right)$$

or, equivalently,

$$\lim_{t\to\infty} -\frac{\ln s(t)}{t} = \frac{V_{max}}{K_S}$$

This behaviour should be compared with the result predicted by eq. [11] for the asymptotic decay exponent, which is

$$[18] \qquad \lim_{t\to\infty} -\frac{\ln s(t)}{t} = -\lambda_+ \approx \frac{V_{max}}{K_S}\left(1 - \frac{m_e}{K_S}\right)$$

so there is an $O(m_e)$ correction to the decay eigenvalue. This result can be recovered from a more accurate description of the motion along the slow manifold. Thus, using the first iterate of $c_{EA}(s)$ under eq. [15] in eq. [16] gives

$$[19] \qquad V_{max}t = s(0) - s(t) + K_S \ln\left[\frac{s(0)}{s(t)}\right] + m_e \ln\left[\frac{s(0)}{s(t)}\right] + m_e \ln\left[\frac{s(t)+K_1}{s(0)+K_1}\right]$$
$$+\frac{\eta}{\epsilon}\left\{K_S s + [(K_1 - m_s)K_S + m_e K_1]\ln s + m_e \epsilon \ln(s + K_S) + \frac{K_1 K_S m_s}{s}\right\}\Bigg|_{s(0)}^{s(t)}$$

The first three terms in the first line comprise the standard formula for mechanism [I]. The fourth and fifth $O(m_e)$ terms are iterative corrections under eq. [15]. The first line implies that K_S is the Michaelis constant and that the fourth term is the $O(m_e)$ correction in eq. [18] to the decay eigenvalue λ_+ of eq. [11]. Depending on parameter values and data-fitting procedures in experiments, this correction to the decay eigenvalue can be important at long times, i.e., near the equilibrium of the system. The second line in eq. [19] is the correction, proportional to η/ϵ, as in s_{eq}^+ etc., for the reversible step which changes [I] into [R].

Setting $k_{-1} = 0$ in eq. [19], implying that $K_1 = 0$, gives the product inhibition result for the integrated rate law as

$$[20] \qquad V_{max}^{PI}t = s(0) - s(t) + \epsilon \ln\left[\frac{s(0)}{s(t)}\right]$$
$$+ \eta[s - m_s \ln s + m_e \ln(s + \epsilon)]\Big|_{s(0)}^{s(t)}$$

At $\eta = 0$ this corresponds to van Slyke–Cullen integrated rate law and gives the decay eigenvalue as $\lambda_+ \approx -k_1 m_e$ in this limit.

[17]Since each iteration creates a higher degree polynomial in the numerator and denominator of this sequence of rational functions, the limit is a transcendental function.

[18]For an approach that provides a general formalism for treating the transient (fast) and slow motion together as a singular perturbation problem see ref. 24.

The perturbation solutions discussed above are only approximate since they arise from the $O(\eta)$ approximation to the functional equation for the slow manifold. To get very accurate formulas for $\mathcal{M}$ (when η is large) the exact relation [13] must be used. The c_- branch of this functional equation possesses the contraction mapping property under iteration, which automatically guarantees that sequences of iterates converge to a unique fixed-point function $c_-^*(s;\eta)$, i.e., the formula for the slow manifold (trajectory) $\mathcal{M}(\eta)$ for mechanism [R].

3. Planarized competitive inhibition mechanism

We now discuss the CI mechanism because its dynamics can be reduced to a planar system after the elimination of a fast transient. Nevertheless, relaxation in the CI mechanism still shows several distinct relaxation regimes (18), and we study the one displaying the richest transient behaviour.

We write this motion using c, s, and i as dynamical variables with total enzyme $m_e = e + c + h$ and total inhibitor $m_i = i + h$ as conserved variables. Thus the rate equations for the CI mechanism (Scheme [CI]) are

$$\dot{s} = -k_1 s(m_e - c - m_i + i) + k_{-1}c$$
$$[21] \qquad \dot{c} = k_1 s(m_e - c - m_i + i) - (k_{-1} + k_p)c$$
$$\dot{i} = -k_2 i(m_e - c - m_i + i) + k_{-2}(m_i - i)$$

Important changes in transient behaviour described by the system [21] take place as the total amount of inhibitor, m_i, is reduced. (These effects could also be detected experimentally.)

Can. J. Chem. Downloaded from www.nrcresearchpress.com by 195.246.54.202 on 09/08/12
For personal use only.

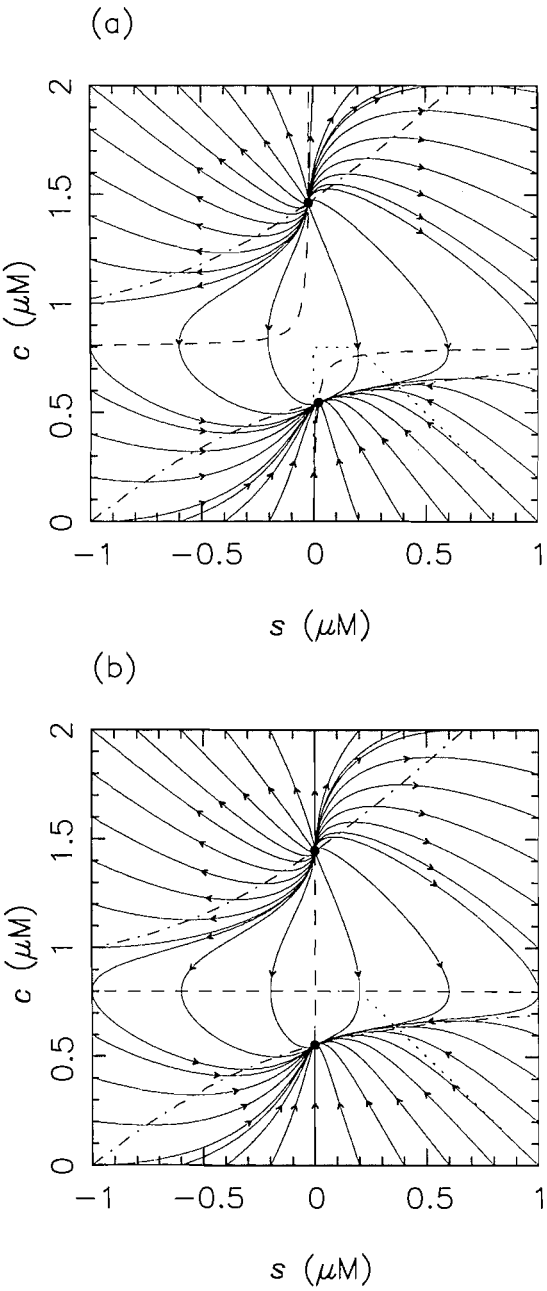

FIG. 2. The changes in the flow for mechanism [R] approaching the product inhibition limit ($k_{-1} \rightarrow 0$) are shown. All parameters are the same as in Fig. 1 apart from k_{-1}; the various curves and regions have the same meaning. (*a*) Flow for $k_{-1} = 0.1\ s^{-1}$ (which is smaller than that in Fig. 1). Note how the EA (--) has become sharply bent. (*b*) Flow for $k_{-1} = 0.0\ s^{-1}$. This is the product inhibition limit. Note how the EA has become a degenerate hyperbola, i.e., the straight lines formed by the *c* and *s* axes. The equation for the *s* nullcline (cf. eq. [8]) factors in this limit.

At very large m_i, at least one of the two concentrations i and h must be large so the equilibration in step [Inh] is faster than the steps in reaction [I] and corresponds to the fastest transient. Total inhibitor concentration m_i can be reduced until the relaxations in [Inh] and [I] occur at comparable rates; this signals crossover behaviour that occurs at $m_i = m_i^{(2)}$ in the notation of ref. 18. For values of $m_i < m_i^{(2)}$ the equilibration in reaction [I] is the fastest step at large s. However, at small s, unusual relaxation dynamics can arise from competition between the

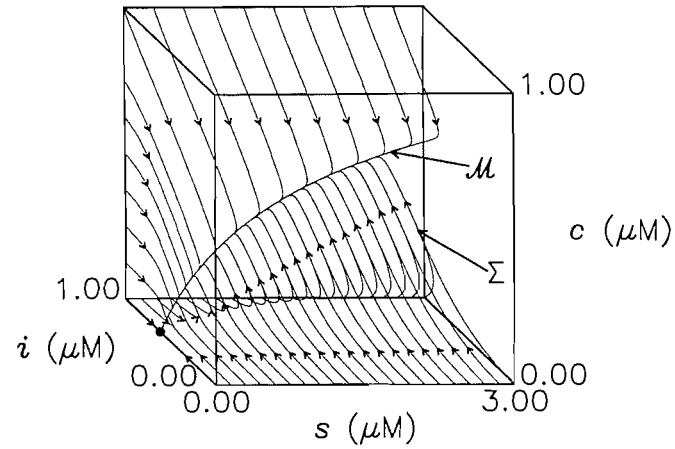

FIG. 3. Some trajectories for the CI mechanism at: $m_e = 1.0 \times 10^{-6}$ M, $m_i = 1.0 \times 10^{-6}$ M, $k_1 = 1.0 \times 10^7\ M^{-1}\ s^{-1}$, $k_{-1} = 10.0\ s^{-1}$, $k_2 = 8.0 \times 10^7\ M^{-1}\ s^{-1}$, $k_{-2} = 80.0\ s^{-1}$, $k_p = 1.0\ s^{-1}$. Arrows indicate the direction of the flow. Note how the trajectories first approach a well-defined (sloping) surface Σ before moving towards the slow manifold $\mathcal{M} \subset \Sigma$. A representative point on $\mathcal{M}$ follows this unique trajectory to the equilibrium point on the i axis, indicated by ●.

first-order decay in the catalysis [I] and the equilibration in step [Inh]. It is the regime $m_i < m_i^{(2)}$ that we study.

For $m_i < m_i^{(2)}$, the fast transient decay in the three-dimensional phase space $\Gamma = s \times c \times i$ corresponds to collapse of the trajectory flow onto a two-dimensional surface Σ. This relaxation is shown in Fig. 3. The surface Σ intersects the $s \times i$ plane in the i axis and has a single-valued projection onto this plane.

These geometrical characteristics correspond to the fact that the equilibration in reaction [I] is fast so that c is a "fast" or entrained variable (2). Thus the geometry of the medium velocity or slow dynamics in Σ is captured by projection onto the $s \times i$ phase plane.

To simplify the description of the dynamics we move the origin of the coordinate system to the equilibrium of the system [21] at

$$s_{eq} = 0$$

[22] $$c_{eq} = 0$$

$$i_{eq} = \tfrac{1}{2}\{m_i - m_e - K_i + \Delta_i^{1/2}\}$$

where the discriminant

[23] $$\Delta_i = (m_e + m_i + K_i)^2 - 4m_e m_i$$

is always positive and

$$K_i = \frac{k_{-2}}{k_2}$$

is the dissociation or inhibitor constant for the complex H = EI. Using displacement dynamical variables defined by

$$s = s_{eq} + \delta s$$

[24] $$c = c_{eq} + \delta c$$

$$i = i_{eq} + \delta i$$

and the additional equilibrium coordinate

$$e_{eq} = \tfrac{1}{2}\{m_e - m_i - K_i + \Delta_i^{1/2}\}$$

Can. J. Chem. Downloaded from www.nrcresearchpress.com by 195.246.54.202 on 09/08/12
For personal use only.

the system [21] can be written as

$$\delta\dot{s} = -k_1 e_{eq}\delta s + k_{-1}\delta c + k_1\delta s(\delta c - \delta i)$$

[25] $$\delta\dot{c} = k_1 e_{eq}\delta s - (k_{-1} + k_p)\delta c - k_1\delta s(\delta c - \delta i)$$

$$\delta\dot{i} = -[k_2(i_{eq} + e_{eq}) + k_{-2}]\delta i + k_2 i_{eq}\delta c + k_2\delta i(\delta c - \delta i)$$

To find the equation for the surface function $\phi = \phi_\Sigma$ for Σ, we write

[26] $$\delta c = \phi(\delta s, \delta i)$$

and differentiate with respect to time to get

[27] $$\delta\dot{c} = \frac{\partial\phi}{\partial\delta s}\delta\dot{s} + \frac{\partial\phi}{\partial\delta i}\delta\dot{i}$$

Substituting eqs. [25] and rearranging gives the functional equation for ϕ as

[28] $$\phi(\delta s, \delta i) = \frac{\delta s(e_{eq} + \delta i)\left(1 + \frac{\partial\phi}{\partial\delta s}\right) + \alpha\delta i(i_{eq} + e_{eq} + \delta i + K_i)\frac{\partial\phi}{\partial\delta i}}{\epsilon + (\delta s + K_E)\left(1 + \frac{\partial\phi}{\partial\delta s}\right) + \alpha(i_{eq} + \delta i)\frac{\partial\phi}{\partial\delta i}}$$

where[19]

$$\epsilon = k_p/k_1$$

$$K_E = k_{-1}/k_1$$

$$K_S = K_E + \epsilon$$

$$\alpha = k_2/k_1$$

Notice that eq. [28] has no explicit time dependence since the underlying ODEs are autonomous. We find the fixed-point function $\phi^*(\delta s, \delta i)$ of eq. [28] iteratively: taking $\phi_0 = $ const. on the right of eq. [28] gives $\partial\phi_0/\partial\delta s = \partial\phi_0/\partial\delta i = 0$ so that ϕ_1, the iterate of ϕ_0 under eq. [28], is

[29] $$\delta c = \phi_1(\delta s, \delta i) = \frac{\delta s(e_{eq} + \delta i)}{\delta s + K_S}$$

Replacing δc with ϕ_1 in the system [25] gives the (projected) plane autonomous system

[30] $$\delta\dot{s} = -k_1 e_{eq}\delta s + k_{-1}\frac{\delta s(e_{eq} + \delta i)}{\delta s + K_S} + k_1\delta s\left[\frac{\delta s(e_{eq} + \delta i)}{\delta s + K_S} - \delta i\right]$$

$$\delta\dot{i} = -[k_2(i_{eq} + e_{eq}) + k_{-2}]\delta i + k_2 i_{eq}\frac{\delta s(e_{eq} + \delta i)}{\delta s + K_S} + k_2\delta i\left[\frac{\delta s(e_{eq} + \delta i)}{\delta s + K_S} - \delta i\right]$$

The flow of this plane autonomous system near its equilibrium at $(\delta s_{eq}, \delta i_{eq}) = (0, 0)$ imitates the quasi-planar flow on Σ near equilibrium, where only the linear terms contribute. However, the system [30] also captures important features of the dynamics far from equilibrium and so provides a faithful global model. For, expanding eq. [28] asymptotically at large δs shows that eq. [29] is asymptotically correct to $O(\delta s^0)$, so that the planarized representation of the system [30] is correct to this order also. This argument shows that the velocity components $\{\delta\dot{s}, \delta\dot{i}\}$ are never large on Σ, i.e., they are $O(\delta s^0)$. Also, in the far-from-equilibrium regime the surface function ϕ_1 has a hyperbolic-law contribution and also an important cross-term $\delta i\delta s$. If the form for ϕ_1 is simplified in any way, important features of the (true) flow on Σ are *lost* in the planarized representation, so in some sense the functional form of the system [30] provides a *minimal model* of the relaxed flow in the underlying system.[20] We now analyse this planar model flow.

Figure 4 shows the deformation of the flow defined by the planarized velocity functions [30] as the experimental parameter m_i is varied. For some values of the rate constants, a region of complex eigenvalues and eigenvectors of the Jacobian $\boldsymbol{J} = \partial\{\dot{s}, \dot{c}, \dot{i}\}/\partial\{s, c, i\}$ interrupts the slow manifold. This important property is associated with the breakup of the line-like slow manifold in the CI mechanism (18), behaviour that differs geometrically from that of any stoichiometric two-step system. However, the imitation of these changes in flow structure on Σ in a planar system is a great simplification over the full three-dimensional description since the eigensystem at equilibrium can be easily solved. This means that the defective character of the flow at the bifurcation value of m_i can be understood. We now examine this.

In the neighbourhood of equilibrium, the planarized system gives the following linearized equation of motion

[31]

$$\frac{d}{dt}\begin{pmatrix}\delta s\\ \delta i\end{pmatrix} = \begin{pmatrix}-\frac{k_p e_{eq}}{K_S} & 0\\ \frac{k_2 i_{eq} e_{eq}}{K_S} & -[k_2(i_{eq} + e_{eq}) + k_{-2}]\end{pmatrix}\begin{pmatrix}\delta s\\ \delta i\end{pmatrix}$$

where the Jacobian matrix of the velocity functions [30] has been evaluated at the equilibrium ($\delta s = \delta i = 0$) to give the matrix $\boldsymbol{J}_{eq}$ in eq. [31]. Since $\boldsymbol{J}_{eq}$ is in lower triangular form, its eigenvalues, $\lambda_{1,2}$ say, are equal to the diagonal elements. Therefore the characteristic equation takes the form $|\boldsymbol{J}_{eq} - \lambda\boldsymbol{I}| = (\lambda_1 - \lambda)(\lambda_2 - \lambda)$, where the eigenvalue

$$\lambda_1 = -\frac{k_p e_{eq}}{K_S}$$

has right eigenvector

[32] $$\boldsymbol{u}_1 = (\delta s_1, \delta i_1)^T = \left(\frac{K_S[k_2(i_{eq} + e_{eq}) + k_{-2}] - k_p e_{eq}}{k_2 i_{eq} e_{eq}}, 1\right)^T$$

and the eigenvalue

$$\lambda_2 = -[k_2(i_{eq} + e_{eq}) + k_{-2}]$$

has eigenvector

[33] $$\boldsymbol{u}_2 = (\delta s_2, \delta i_2)^T = (0, 1)^T$$

[19]This notation is identical with that in ref. 18. This is slightly modified from that in Sect. 2 of the present paper.

[20]The asymptotic expansion of the functional equation [28] in powers of δs^{-1} implies that the starting function $\phi_0 = e_{eq} + \delta i$ gives a version of ϕ_1 that is asymptotically correct to $O(\delta s^{-1})$ as $\delta s \to \infty$. However, the additional terms in this version of ϕ_1 are not required to capture the dynamical and bifurcation behaviour discussed here.

Can. J. Chem. Downloaded from www.nrcresearchpress.com by 195.246.54.202 on 09/08/12
For personal use only.

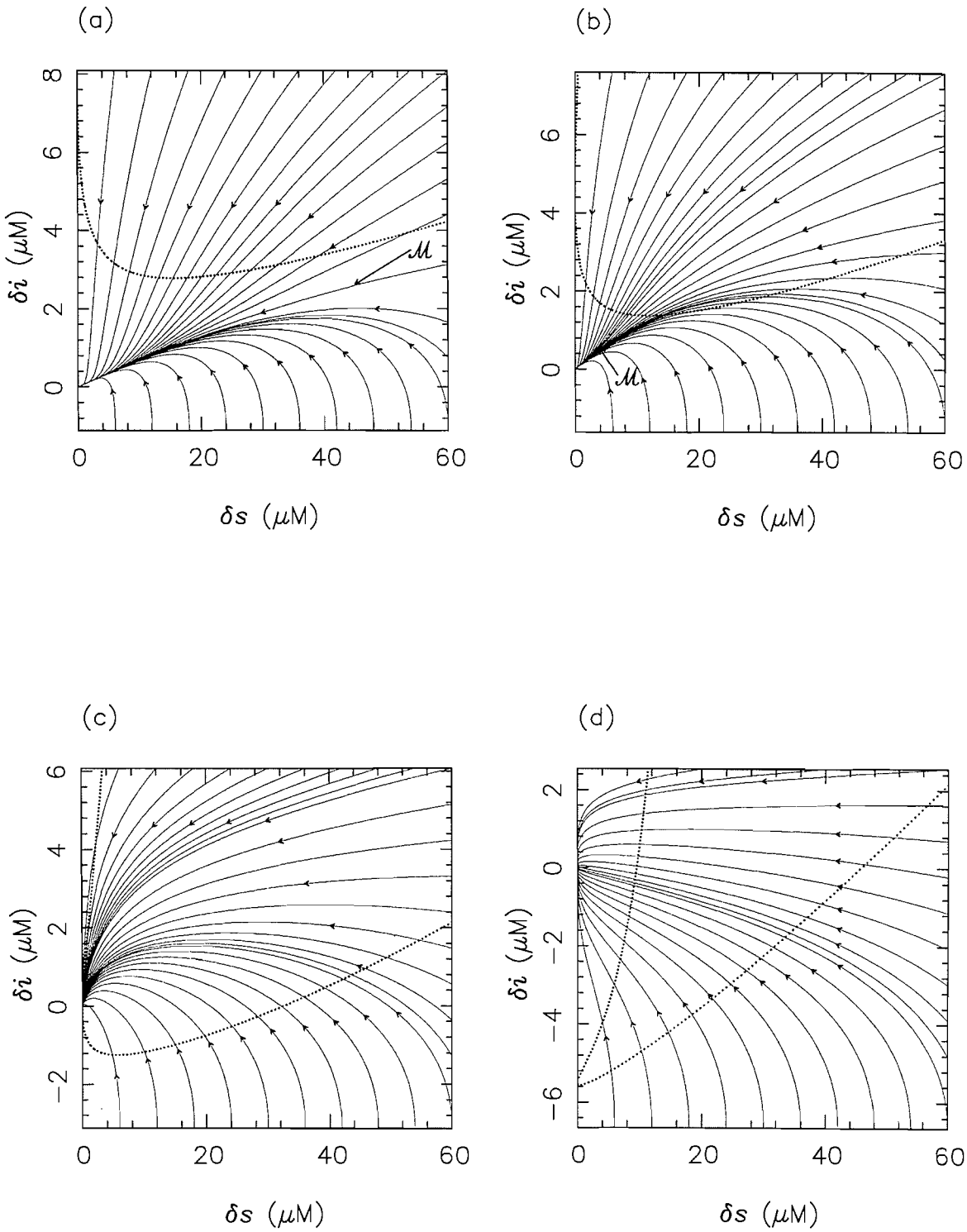

FIG. 4. The panels in this figure represent the change in the planarized flow pattern as m_i decreases through the bifurcation value $m_i^{(1)}$. Arrows represent the flow direction and the equilibrium is always at the origin in the displacement coordinates δi and δs. Locally the slow manifold $\mathcal{M}$ at the equilibrium $\delta s = \delta i = 0$ changes from a direction pointing into the interior of the physical region to the direction of the i axis. Different relaxation scenarios for the CI mechanism are illustrated. In all panels $m_e = 9.2 \times 10^{-6}$ M, $k_1 = 4.6 \times 10^7$ M^{-1} s^{-1}, $k_{-1} = 42.0$ s^{-1}, $k_2 = 2.2 \times 10^6$ M^{-1} s^{-1}, $k_{-2} = 43.0$ s^{-1}, and $k_p = 710.0$ s^{-1}. In each case, the flow on Σ, for the full system (cf. eq. [25]) projected onto $s \times i$ is indistinguishable from the planarized flow shown by the full system. (*a*) Flow for $m_i = 1.5 \times 10^{-4}$ M $> m_i^{(1)}$. At large m_i, $\mathcal{M}$ is well defined and lies in the interior of the physical region. The dotted curve is the boundary of the region (upper right) of complex eigenvalues for the Jacobian of the flow; this curve does not intersect $\mathcal{M}$. (*b*) Flow for $m_i = 1.0 \times 10^{-4}$ M $> m_i^{(1)}$. The complex-eigenvalue region intersects $\mathcal{M}$. The segment of $\mathcal{M}$ lying between the complex-eigenvalue region and the equilibrium is indicated. (*c*) Flow for $m_i = 4.4 \times 10^{-5}$ M $= m_i^{(1)}$. At this bifurcation (crossover) value for m_i, the boundary of complex-eigenvalue region just touches the equilibrium (origin) and there is only one relaxation eigenvector along the δi axis ($\mathcal{M}$ locally) in this, the defective, case. (*d*) Flow for $m_i = 1.0 \times 10^{-5}$ M $< m_i^{(1)}$. Below the bifurcation value of m_i, the "slow" direction is the δi axis ($\mathcal{M}$ locally). The "fast" direction is nearly the δs axis. The complex-eigenvalue region now separates the neighbourhood of the equilibrium from the large δs (asymptotic) region.

Can. J. Chem. Downloaded from www.nrcresearchpress.com by 195.246.54.202 on 09/08/12
For personal use only.

i.e., the i axis. Clearly, the eigenvalues of $\boldsymbol{J}_{eq}$ are always real for physically reasonable parameter values. When $\lambda_1 = \lambda_2$, which occurs at $m_i = m_i^{(1)}$ in the notation of ref. 18, there is only *one* eigenvector and the eigensystem is defective. This degenerate case is not structurally stable, since any small parameter change removes the degeneracy.[21] The triangular form of $\boldsymbol{J}_{eq}$ means that lifting this degeneracy produces a discontinuity in the motion of the slowest relaxation direction:

1. For $m_i > m_i^{(1)}$, $\lambda_2 < \lambda_1 < 0$, and, figuratively speaking, the slow eigenvector $\boldsymbol{u}_1$ in eq. [32] points towards equilibrium from inside the physical part of $s \times i$.

2. As $m_i \rightarrow m_i^{(1)}$, $\boldsymbol{u}_1$ rotates towards the i axis, i.e., $\boldsymbol{u}_2$, and at $m_i = m_i^{(1)}$ (the defective case) $\lambda_2 = \lambda_1 < 0$ and $\boldsymbol{u}_1 = \boldsymbol{u}_2$ from eqs. [32] and [33], i.e., the i axis has become the slow eigenvector.

3. For $m_i < m_i^{(1)}$, $\lambda_1 < \lambda_2 < 0$, and the i axis, i.e., $\boldsymbol{u}_2$ given by eq. [33], remains the slow eigenvector. Thus the *velocity of rotation* of the slow direction changes abruptly as m_i passes through $m_i^{(1)}$.

We now compare the eigenvalues of the planarized system with those of the underlying three-dimensional system [25]. This can be understood geometrically.

1. The "fast" transient eigenvalue and its eigenvector, which is transversal to Σ, describe the rapidly decaying mode eliminated by planarization, so this mode has no analogue in the planarized system.

2. The $s \times i$ plane and the surface Σ both contain the i axis (as long as m_i is not too large (18)), so near equilibrium they have a wedge-like intersection with the i axis as the "hinge" or edge. Consequently, the i axis and the corresponding eigenvalue λ_2 are invariant under planarization and comprise a common eigensystem of the full and planarized systems.

3. Provided ϕ^* representing Σ is known accurately, the remaining eigenvalue of the full system and the projection of its eigenvector onto $s \times i$ will be close to λ_1 and $\boldsymbol{u}_1$, respectively, of the planarized systems. Accordingly, the approximation ϕ_1 for ϕ^* gives $\lambda_1 = -k_p e_{eq}/K_S$. This compares well with the corresponding eigenvalue in Σ called λ_+ in ref. 18. When e_{eq}/K_S is small, $\lambda_+ = -k_p e_{eq}/(e_{eq} + K_S)$, which is close to λ_1. Similarly, the inclination of the surface Σ to the plane $s \times i$ at the equilibrium point is given by $\partial\phi_1/\partial\delta s = e_{eq}/K_S$, so the wedge-angle arctan (e_{eq}/K_S) will be small when $\lambda_1 \approx \lambda_+$.

Broadly speaking, motion in the planar system always corresponds to attraction to $\mathcal{M}$ at large s but this segment of $\mathcal{M}$ may stop before equilibrium is reached. The final approach towards equilibrium is then along the i axis. The functional equation for the surface Σ is a single scalar equation in the partial derivatives of two independent variables (16), whereas the functional equation for $\mathcal{M}$ is a vector equation in the ordinary derivatives of (the same) two variables.

The planarized motion and bifurcation discussed above are illustrated in Fig. 4. The panels in this figure show the change in the planarized flow pattern as m_i passes through the crossover value $m_i^{(1)}$. Locally the slow manifold at the equilibrium $\delta s = \delta i = 0$ moves from a position that points into the interior of the physical region to a fixed position lying along the i axis.

4. Discussion

We have examined two important enzyme inhibition mechanisms whose evolution can be treated as two-variable dynamical systems in the phase plane. These particular reaction schemes have not been treated thoroughly before and we have been able to give a complete description of their transient and steady-state kinetics. Although these mechanisms are different chemically they were treated by the same overall mathematical strategy. Algebraically, this approach combines local linearization with global functional equation methods; geometrically it relates local flow features to global "scattering" structures in phase space.

For the first example, the reversible Michaelis–Menten mechanism [R], the standard treatment obtains approximate expressions for the steady-state velocity and the integrated rate law (28). We have related these expression to the standard steady-state approximation for the irreversible mechanism [I], and have given first correction terms using functional iteration. This procedure is systematic and converges to the exact dynamical steady state, the slow manifold, so that additional corrections can be directly obtained. Because the underlying geometry of the phase flow is used to obtain our functional equations, the resulting formulas possess the *same* formal structure as the standard SSA and EA, in contrast to expressions from singular perturbation theory (11). In our procedure the slow dynamics is restricted by a constraint equation to a curve in the phase plane. And because it is a systematic, convergent method, it generates a sequence of such curves that accumulates at the slow manifold. This limit curve contains exact information about the slow time evolution of mechanism [R]. This convergent procedure should be compared with the standard treatment where important errors arise. These errors come from failure to use all conserved total concentrations, or approximate use of such conservation laws.[22] This omission has either lead to geometrically ambiguous formulas or it has prevented systematic improvement because the underlying equations are not properly closed. This is also related to the failure to argue consistently even when using the standard SSA or EA. In either of these approximations one differential equation is replaced by an algebraic constraint — this implies a perfectly respectable dynamical system. However, it is commonly assumed that the conserved variables in the constrained system are the same as those for the full system of differential equations. This assumption is *false*, and in the treatment of the reversible mechanism [R] it leads to inconsistencies. Formulas obtained under the flawed assumption cannot be used as a basis for a more accurate treatment.

We now outline an experimental procedure justified by our analysis. Normally, experimentalists treat mechanisms [I] and [R] by different procedures, particularly if they believe that the reversible step in [R] is important. In the product inhibition limit it is also reasonable to treat the first step in [R] as irreversible, so that product inhibition is just a special case of [R]. In [I] the flow structure is determined by the values of the specific rate constants (fixed at fixed temperature) and a *disposable* constant m_e, the total enzyme concentration. Since an experiment is begun with separate samples of E and S it is natural to work at fixed m_e. However, in mechanism [R]

[21]The chemical example of defectiveness given here should be compared to critical damping in mechanical systems. In this case the eigensystem is also defective but the Jacobian is not in lower triangular form. Consequently, the eigenvalues also depend on the off-diagonal elements and the defective case separates a regime of real eigenvalues from one with complex eigenvalues. This fundamental difference arises from the fact that mechanical systems have an inertial term whereas chemical systems do not.

[22]This omission appears in some of the books in ref. 4.

Can. J. Chem. Downloaded from www.nrcresearchpress.com by 195.246.54.202 on 09/08/12
For personal use only.

($k_{-2} > 0$), and the product inhibition case ($k_{-2} > 0, k_{-1} = 0$), total substrate m_s must also be fixed to correspond to the same underlying phase-space structures in a series of experiments. This condition is not satisfied in initial velocity experiments as they are normally performed for [R] since the initial condition is $\{s(0) = m_s, c(0) = m_e, p(0) = 0\}$ (at $t = 0$); the starting value $s(0) = m_s$ in this initial condition is varied from experiment to experiment, which changes the underlying slow manifold $\mathcal{M}(m_s)$ and nullclines. In contrast, working at fixed m_s and m_e fixes these structures. This suggests that using these total concentration constraints would improve statistical fitting of data from repeated experiments using either initial velocities or progress curves.

The second example of competitive inhibition is a three-step mechanism, governed by a three-dimensional system of ODEs, which displays varied transient behaviour (7, 18). For example, at intermediate inhibitor concentrations, imitating those often found *in vivo* (6), the ODEs of the CI mechanism can be reduced to a planar system[23] because there is fast relaxation from the "volume" of phase space towards a smoothly curved "slow" surface Σ with a *single-valued* projection on some (Euclidean) plane, which is $s \times i$ here; the dynamics in this plane can be given exactly in terms of the velocities of its natural coordinates, $\dot{s}$ and $\dot{i}$, and the equation $c = \phi(s, i)$ of the slow surface Σ. Relaxation in this system displays more interesting dynamics than the two-step mechanism [R]. For some parameter values, the slow manifold in the planarized CI mechanism consists of two pieces separated by a region where the motion is intrinsically two-dimensional. (Such behaviour is not found in [R] or any other two-step mechanisms because in such cases the slow manifold is a single, infinite curve connecting the asymptotic regime to the stable equilibrium.) The intrinsically two-dimensional behaviour of the CI flow is associated with small-magnitude, complex-conjugate eigenvalues (with negative real part) for the flow Jacobian in the local linearization of the velocity field. In contrast, the one-dimensional behaviour on the bits of the slow manifold is connected with a unique (real) smallest magnitude eigenvalue in this linearization. These features allow a precise description to be given of the breakdown of steady-state methods in experiments on the CI mechanism. But we argue that it is just this regime, inaccessible to standard analysis, which is of most interest in living systems, because enzyme and inhibitor concentrations are often comparable *in vivo* and just these circumstances encourage the replacement of the usual one-dimensional steady state by intrinsically two-dimensional behaviour. The fixed phase-space structures, e.g., Σ, studied here underlie the behaviour of open systems in which the metabolic pathway flux corresponds to high local concentrations of enzyme (6).

The entire dynamics of these planar systems, and indeed higher dimensional systems, can be studied by the same mathematical methods. Principally, functional equation methods are used because they define contraction mappings that converge rapidly to the phase-space structure underlying the "slow" dynamics, namely, the slow-transient surface Σ or slow manifold $\mathcal{M}$. Furthermore, this method is formally very simple because it depends on differentiation, and is in the same general class as the standard steady-state methods. Thus these standard results make their appearance on the way to getting the exact answer. However, the CI study shows that even approximate solutions contain most of the essential ingredients of the exact dynamics and that these features can be displayed in a global, consistent geometrical way.

Finally, it should be noted that functional equations are solvable by both the analytic treatment given here and by numerical methods. A numerical treatment may be required in the case of mechanisms with third- or higher-order steps and may be used in dealing with mechanisms with a large number of independent concentrations. However, algebraic manipulators such as Maple make feasible a semi-numerical approach in which explicit functional equations are numerically iterated. A fully numerical implementation of our functional equation method is perfectly feasible as it requires only techniques used in implicit-method ODE solvers.

[23]Planarization is always possible in the CI mechanism because oscillatory transients never arise (31). The particular case studied is one of two possible planar regimes: One exists at high inhibitor concentration, and the other at low or intermediate inhibitor concentration. This difference is determined by the orientation of Σ in Γ, which may affect the choice of projected variables.

Acknowledgements

This work was supported by the Natural Sciences and Engineering Research Council (NSERC) of Canada. M.R.R. was supported by an Ontario Graduate Scholarship during the preparation of this manuscript. We would also like to thank Jerry Kresge for many helpful conversations.

1. S. Lefschetz. Differential equations: geometric theory. Dover, New York. 1977; V.I. Arnold. Ordinary differential equations. MIT Press, Cambridge, Mass. 1978; W. Kaplan. Ordinary differential equations. Addison–Wesley, London. 1958.
2. H. Haken. Synergetics: an introduction. Springer, New York. 1978; Advanced synergetics. Springer, New York. 1983; A. Fernández and O. Sinanoğlu. J. Math. Phys. **25**, 406 (1984); J. Math. Phys. **25**, 2576 (1984); A. Fernández. Phys. Rev. A, **32**, 3070 (1985).
3. C. Walter. Steady-state applications in enzyme kinetics. Ronald, New York. 1965.
4. J.T.-F. Wong. Kinetics of enzyme mechanisms. Academic, New York. 1975; I.H. Segel. Enzyme kinetics: behavior and analysis of rapid equilibrium and steady-state enzyme systems. Wiley, New York. 1975; K.J. Laidler and P.S. Bunting. The chemical kinetics of enzyme action. Clarendon, Oxford. 1973; A. Cornish-Bowden. Principles of enzyme kinetics. Butterworths, London. 1976; H.J. Fromm. Initial rate enzyme kinetics. Springer, New York. 1975; H. Gutfreund. Enzymes: physical principles. Wiley, New York. 1972; S. Ainsworth. Steady-state enzyme kinetics. University Park, Baltimore, Md. 1977.
5. A.J. Brown. J. Chem. Soc. **81**, 373 (1902); V. Henri. C.R. Acad. Sci. **135**, 916 (1902); L. Michaelis and M.L. Menten. Biochem. Z. **49**, 333 (1913).
6. P.A. Srere. Science, **158**, 936 (1967); A. Sols and R. Marco. Curr. Topics Cell. Regul. **2**, 227 (1970); M. Laurent and N. Kellershohn. J. Mol. Biol. **174**, 543 (1984); G.F. Betts and D.K. Srivastava. J. Theor. Biol. **151**, 155 (1991).
7. O.H. Straus and A. Goldstein. J. Gen. Physiol. **26**, 559 (1943); A. Goldstein. J. Gen. Physiol. **27**, 529 (1944).
8. G. Kirchhoff. Ann. Phys. Chem. **72**, 497 (1874).
9. E.L. King and C. Altman. J. Phys. Chem. **60**, 1375 (1956).
10. J.O. Hirschfelder. J. Chem. Phys. **26**, 271 (1957).
11. F.G. Heineken, H.M. Tsuchiya, and R. Aris. Math. Biosci. **1**, 95 (1967); S.I. Rubinow and J.L. Lebowitz. J. Am. Chem. Soc. **92**, 3888 (1970); C.C. Lin and L.A. Segel. Mathematics applied to deterministic problems in the natural sciences. Macmillan, New York. 1974. Chaps. 9, 10; J.D. Murray. Lectures on nonlinear-differential-equation models in biology. Clarendon Press, Oxford. 1977. Chap. 1.
12. C.W. Gear. Numerical initial value problems in ordinary dif-

ferential equations. Prentice-Hall, Englewood Cliffs, N.J. 1971; J.D. Lambert. Computational methods in ordinary differential equations. Wiley, New York. 1973.
13. S.J. Fraser. J. Chem. Phys. **88**, 4732 (1988).
14. A.H. Nguyen and S.J. Fraser. J. Chem. Phys. **91**, 186 (1989).
15. M.R. Roussel and S.J. Fraser. J. Chem. Phys. **93**, 1072 (1990).
16. M.R. Roussel and S.J. Fraser. J. Chem. Phys. **94**, 7106 (1991).
17. M.R. Roussel and S.J. Fraser. J. Phys. Chem. **95**, 8762 (1991).
18. M.R. Roussel and S.J. Fraser. J. Phys. Chem. **97**, 8316 (1993).
19. N. Chafee. J. Differential Equations, **4**, 661 (1968).
20. J. Hale. Ordinary differential equations. Wiley, New York. 1969. Chap. 7.
21. J. Carr. Applications of centre manifold. Appl. Math. Sci. **35**, Springer, New York. 1981.
22. A.S. Tomlin, M.J. Pilling, T. Turányi, J.H. Merkin, and J. Brindley. Combust. Flame, **91**, 107 (1992); U. Maas and S.B. Pope. Combust. Flame, **88**, 239 (1992).
23. T. Turányi, A.S. Tomlin, and M.J. Pilling. J. Phys. Chem. **97**, 163 (1993).
24. G. Li, A.S. Tomlin, and H. Rabitz. J. Chem. Phys. **99**, 3562 (1993).
25. M.R. Roussel. M.Sc. Thesis, University of Toronto, 1990.
26. J.B.S. Haldane. Enzymes. MIT Press, Cambridge. 1965 (reprint of 1930 book originally published by Longmans Green and Company).
27. L.I. Schiff. Quantum mechanics. McGraw–Hill, New York. 1968.
28. B.A. Orsi and K.F. Tipton. Methods Enzymol. **63**, 159 (1979).
29. R. Kitz and I.B. Wilson. J. Biol. Chem. **237**, 3245 (1962).
30. D.D. van Slyke and G.E. Cullen. J. Biol. Chem. **19**, 141 (1914).
31. U. Ryde-Pettersson. Eur. J. Biochem. **194**, 431 (1990).

Can. J. Chem. Downloaded from www.nrcresearchpress.com by 195.246.54.202 on 09/08/12
For personal use only.

Molecular dynamics study of the surface diffusion of large adsorbates: III. Role of adsorbate shape

YEHUDA ZEIRI

Department of Physics, Nuclear Research Center – Negev, P.O. Box 9001, Beer-Sheva 84190, Israel

Received July 7, 1993

This paper is dedicated to Professor John C. Polanyi on the occasion of his 65th birthday

YEHUDA ZEIRI. Can. J. Chem. **72**, 813 (1994).

The present study is dedicated to the investigation of the relationship between the surface diffusion mechanism of large adsorbates and the adsorbate shape. Three different shapes of model adsorbates were examined: linear chains, branched chains, and cyclic molecules. It was found that the surface diffusion mechanism of linear and branched chain adsorbates is quite similar, while a markedly different diffusion mechanism is observed for cyclic adsorbates. For all types of adsorbates the temperature dependence of the diffusion coefficient was found to obey an Arrhenius expression. The results of the simulations have shown good qualitative agreement with the available experimental data.

YEHUDA ZEIRI. Can. J. Chem. **72**, 813 (1994).

Cette étude porte sur la relation existant entre le mécanisme de diffusion en surface des gros adsorbats et la forme de l'adsorbat. On a examiné trois modèles d'adsorbats de forme différente : des molécules à chaîne linéaire, des molécules à chaîne ramifiée et des molécules cycliques. On a trouvé que le mécanisme de diffusion en surface des molécules à chaîne linéaire est tout à fait semblable à celui des molécules à chaîne ramifiée, tandis qu'on observe un mécanisme de diffusion nettement différent pour les adsorbats de forme cyclique. Pour tous les types d'adsorbats, on a trouvé que l'effet de la température obéit à une expression d'Arrhénius. Les résultats des simulations révèlent un bon accord qualitatif avec les données expérimentales disponibles.

[Traduit par la rédaction]

Can. J. Chem. Downloaded from www.nrcresearchpress.com by 195.246.54.202 on 09/08/12
For personal use only.

1. Introduction

The characterization of the transition state in various gas phase processes involving molecular systems has been a major research topic in a number of laboratories. During the past two decades Professor J.C. Polanyi and co-workers made major contributions to this field. However, the unique assignment of a transition state along the path of a system from initial to final configurations is not always possible. In the following we shall demonstrate a situation where the large number of degrees of freedom in a molecular system prevents the assignment of a unique transition state. In particular, we shall examine in detail the motion of large adsorbates along a solid surface. It will be argued that for such systems a more realistic description of the surface diffusion is in terms of a large sequence of energy barriers associated with the motion of the adsorbate along the surface.

The surface diffusion of adsorbed species plays an important role in many processes related to the chemistry and physics of gas–surface interactions. Surface diffusion constitutes a direct probe of the adsorbate–surface and adsorbate–adsorbate interaction potentials (see, for example, ref. 1). Moreover, the mobility of adsorbates may constitute the rate-limiting step in many technologically important processes. Hence, a detailed understanding of the surface diffusion mechanism in various systems is highly desirable.

It is well established that for small adsorbates the surface diffusion may be described as a random walk of the ad particle among the various adsorption sites on the surface (1). Such a description seems to be suitable for adsorbates whose size is small compared to the magnitude of the surface unit cell. In such systems it is usually possible to define adsorption sites that are, in many cases, associated with high symmetry sites in the surface unit cell (strongest adsorbate–surface bonds). The minimum energy path between two neighboring adsorption sites usually shows the existence of an energy barrier that is assigned as the activation energy for the diffusion process or transition state. The magnitude of this activation energy, E_{diff}, is determined by the nature of the adsorbate–surface interaction. In most cases, the magnitude of E_{diff} is larger than the thermal energy of the system, kT (where k is the Boltzmann constant and T is the system temperature). As a result, the motion of the ad particle along the surface can be described as a sequence of random jumps among the adsorption sites. Since in most situations $E_{diff} \gg kT$ these jumps can be considered as rare events.

This situation may change markedly if the size of the adsorbate is large compared with the surface unit cell. These type of systems include the adsorption of polyatomic molecules onto single crystal surfaces. For such systems the terms "best adsorption site" and "transition state" cannot be defined uniquely. In other words, it is expected, due to the large number of degrees of freedom in the system, that many of the possible configurations will correspond to similar adsorbate–surface binding energies. The transition between two neighboring adsorption sites, in this subspace of configurations, may pass through an activation barrier. Thus, the motion of the adsorbate along the solid surface may be associated with a sequence of energy barriers instead of a single well-defined transition state. Hence, a sequence of barriers is expected to dominate the diffusive motion of the adsorbate along the surface. In many systems, the energy difference between these barriers may be of the order of kT. In such systems the surface diffusion of large adsorbates cannot be described any longer as a random walk process but should be viewed as a quasi-continuous motion along the surface.

Recently, George and co-workers (2) discussed the results of experimental surface diffusion studies of a number of n-alkanes on a Ru(001) surface. In addition, studies of the surface diffusion of cycloalkanes as well as other isomers were reported by the same group (3). The surface diffusion coefficient, D, of these adsorbates was measured using the laser-induced thermal desorption (LITD) method (4). These studies indicated that the variation of D as a function of temperature, for all the ad-molecules investigated, could be described by an Arrhenius behavior. It was found that the values of E_{diff} obtained for

Can. J. Chem. Downloaded from www.nrcresearchpress.com by 195.246.54.202 on 09/08/12
For personal use only.

n-alkanes increased linearly with the carbon chain length, while in most cases the pre-exponential factors remained nearly constant (2, 3).

Moreover, temperature-programmed desorption (TPD) measurements have shown that the activation energy for desorption, E_{des}, also increases linearly as a function of the chain length, while the corrugation ratio, $\Omega = E_{diff}/E_{des}$, remains practically constant. In addition, it was found that in most cases D is coverage independent (i.e., for *n*-alkanes (2), for cyclopropane and cyclohexane (3*a*), and for isopentane (3*c*)) while strong coverage dependence of the surface diffusion was observed for cyclopentane (3*a*) and neopentane (3*b*). Based on these experimental results, George and co-workers suggested that the surface diffusion of such polyatomic adsorbates can be described by a concerted motion of the ad-particles along the surface (2, 3).

These experimental studies have stimulated a number of theoretical investigations whose goal was to obtain understanding of the mechanism that describes the surface diffusion of large adsorbates. In earlier studies (5) we utilized the molecular dynamics (MD) approach for simulations of the surface diffusion of large *n*-alkane-like adsorbates on a W(100) surface. These calculations were aimed to investigate the influence of chain length (5*a*) and chain stiffness (5*b*) on the mechanism by which large adsorbates move along a solid surface. In the following we shall refer to these studies as paper I and paper II, respectively. The MD results suggested a nonlinear scaling between E_{diff} and the chain length. Moreover, it was found that for long chains (containing $n = 10$ or more carbons) the surface diffusion process can be described as a sequential motion of segments of the adsorbed species, while for short chains, $n = 3$ and 6, concerted motion, suggested by the experimental data, represents a reliable description of the surface diffusion.

Another theoretical study (6) utilized MD simulations to investigate the conformations associated with the diffusional motion of *n*-pentane on a metallic surface. These calculations were performed using potential functions similar to those used in papers I and II except for the interaction among the chain atoms. For the latter, a more realistic potential, including angular terms related to the rotation of neighboring bonds, was used. The results of this study (6) suggested that the *n*-pentane exhibits a number of well-defined conformations during its concerted motion along the surface. The number of observed conformations was found to depend on the symmetry of the solid surface, while the transition between the various conformations could be described as a rare event.

The next section contains a brief description of the theoretical model used in the present study, while Sect. 3 is devoted to description and discussion of the results. A short summary is given in the last section.

2. The theoretical model

The present study is an extension of papers I and II. The goal in this investigation was to examine the relationship between the surface diffusion mechanism of large adsorbates and the shape of the adsorbed species. We have considered the low coverage limit where the interactions among the adsorbates can be ignored. Hence, this study includes simulations of the surface diffusion of single adsorbates. Five different shapes of model adsorbates were considered: linear and branched chains with $n = 6$ and $n = 10$ and a ring with $n = 6$. In the following we shall refer to these model adsorbates as: *n*-hexane, *n*-decane, isohexane, isodecane, and cyclohexane, respectively. The different adsorbates considered are shown schematically in Fig. 1.

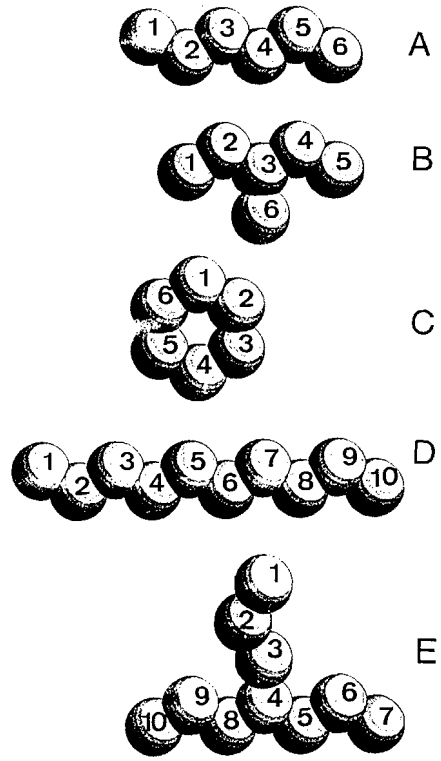

FIG. 1. Schematic description of the various adsorbates investigated.

The details of the calculations in the present study are similar to those described in papers I and II (5). The generalized Langevin approach, GLE (7, 8), was used to describe the thermal motion of the solid surface. The primary zone was described by 169 W atoms arranged in a single layer of 13 × 13 atoms. The rest of the solid was represented by 221 fictitious particles that surrounded the primary zone. These were attached to primary zone atoms whose bonds to atoms outside the primary zone were truncated. For each type of adsorbate 20 trajectories were calculated at any given temperature. Termination of the trajectory occurred if the maximum number of integrating steps was reached (i.e., 40 000 steps, which corresponds to 40 ps) or if the adsorbate migrated outside the region spanned by the primary zone. At the beginning of each trajectory the adsorbate–surface system was allowed to thermalized for a period of about 4–5 ps. The thermalization period was terminated when the average kinetic energy of the system reached the predefined system temperature. The momentary positions and velocities at the end of the thermalization period were used as initial conditions for the trajectory.

The potential function describing the various interactions in the system was constructed as a sum of three terms:

$$[1] \quad V(\boldsymbol{R}, \boldsymbol{X}, \boldsymbol{S}) = V_{SLAB}(\boldsymbol{R}, \boldsymbol{S}) + V_{AD-S}(\boldsymbol{R}, \boldsymbol{X}) + V_{AD}(\boldsymbol{X})$$

where $\boldsymbol{R}$, $\boldsymbol{X}$, and $\boldsymbol{S}$ represent the position vectors of the primary zone atoms, the adsorbate atoms, and the fictitious particles, respectively.

The three terms in eq. [1] correspond to the interaction among the primary zone particles (W atoms and fictitious particles), interaction between the adsorbate and the surface, and

Can. J. Chem. Downloaded from www.nrcresearchpress.com by 195.246.54.202 on 09/08/12
For personal use only.

the interaction among the atoms constituting the adsorbate, respectively. The functional form of these three terms was taken to be identical to those used in papers I and II. In the evaluation of the last term, $V_{AD}(X)$, we used the parameters that correspond to "stiff" chains in ref. 5*b*. The only modification of the potential in the present calculations, as compared to those of papers I and II, is related to the parameters used to evaluate the adsorbate–surface interaction term, V_{AD-S}. In the present simulations the binding energy used in the Lennard–Jones potentials was $\epsilon_{RX} = 0.7$ kcal/mol as opposed to 0.722 kcal/mol used in papers I and II. The result of this minor modification is a small decrease in the calculated values of E_{diff} as will be discussed below. For a more detailed description of the MD approach and the potential functions used the reader is referred to ref. 5.

3. Results and discussion

3.1. Pre-exponentials and activation energies

For all the adsorbates discussed below we performed simulations at four different temperatures, $T = 300$, 450, 600, and 800 K. This range of T was chosen to be able to obtain reliable diffusion coefficients during the limited time that could be simulated using the MD approach. The diffusion coefficient for any given adsorbate and system temperature was calculated using the Einstein formula (9):

$$[2] \quad D_{t\to\infty} = \frac{1}{4}\langle[\boldsymbol{X}_{CM}(t_0 - t) - \boldsymbol{X}_{CM}(t_0)]^2\rangle_{Nt}/t$$

where $\boldsymbol{X}_{CM}$ is the adsorbate center-of-mass position vector and $\langle\ldots\rangle_{Nt}$ represents an average over time steps. For a given adsorbate and surface temperature the diffusion coefficient was obtained as an average over the 20 trajectories calculated.

An Arrhenius form was assumed for the dependence of D on T. The results for the five adsorbates considered are shown in Fig. 2. These results clearly indicate that the dependence of D on T obeys an Arrhenius form. These data allow the extraction of the pre-exponential factor, D_0, and the activation energy for diffusion, E_{diff}. These quantities, as obtained from the data shown in Fig. 2, are summarized in Table 1. Inspection of the observed D_0 and E_{diff} values shows that for the three adsorbates with $n = 6$ there is some spread in the pre-exponential factor; however, considering the errors in the calculated values of D_0, these quantities are practically identical (exhibiting at most a factor of two in the corresponding D values). A somewhat larger spread is observed in the values of E_{diff}. Here, we find that *n*-hexane and isohexane exhibit almost identical activation energies for diffusion, while the corresponding value for cyclohexane is much smaller. Note that this difference in the magnitude of E_{diff} results in an order of magnitude difference in the corresponding values of the diffusion coefficients. Similar qualitative behavior of D_0 and E_{diff} for different shapes of adsorbates was observed experimentally (3). In addition, the activation energies for desorption obtained for the various hexane-like adsorbates are very similar and decrease in the order *n*-hexane > isohexane > cyclohexane. As a result, the corrugation ratios for *n*-hexane and isohexane are identical while that of cyclohexane is somewhat smaller. Similar examination of the results obtained for the two adsorbates with $n = 10$ indicates that the linear and branched chains exhibit different D_0, as well as different E_{diff} and E_{des} values. However, the variation of the two activation energies is such that the corrugation ratio of these two adsorbates remains practically constant.

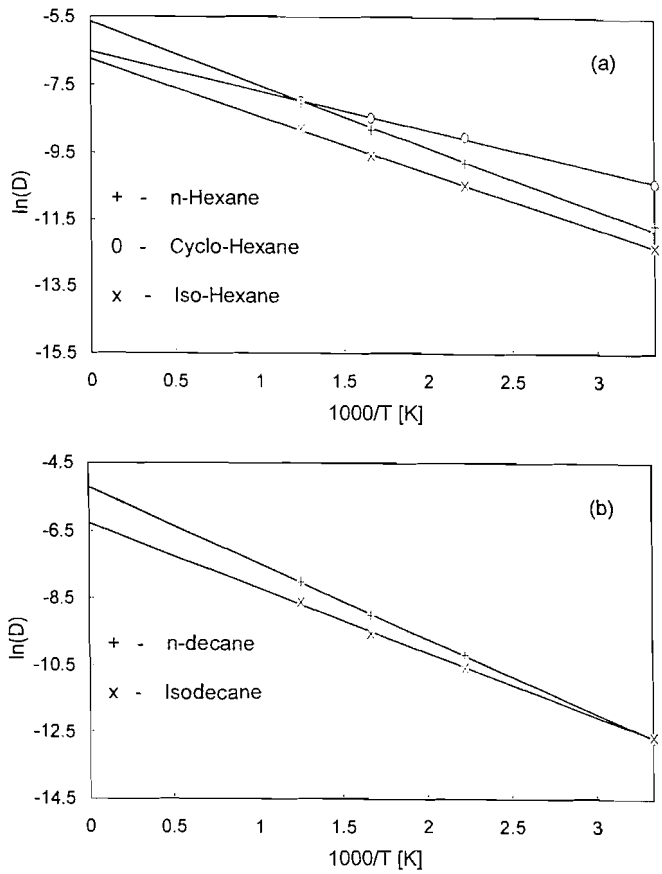

FIG. 2. Arrhenius plots of the surface diffusion coefficients for: (*a*) three different shapes of hexane-like molecules and (*b*) two different shapes of decane-like molecules.

TABLE 1. Calculated values of D_0, E_{diff}, E_{des}, and Ω for the various adsorbates considered. The units used for the pre-exponential factor are cm^2/s and for the activation energies kcal/mol

Adsorbate	$D_0 \times 10^4$	E_{diff}	E_{des}	Ω
n-Hexane	17.9 ± 4.1	3.4 ± 0.2	11.1 ± 0.1	0.31
Isohexane	7.9 ± 2.3	3.3 ± 0.2	10.6 ± 0.1	0.31
Cyclohexane	9.8 ± 2.4	2.3 ± 0.2	10.1 ± 0.1	0.23
n-Decane	36.4 ± 7.0	4.5 ± 0.15	17.1 ± 0.1	0.26
Isodecane	12.7 ± 3.1	3.8 ± 0.10	16.1 ± 0.1	0.24

The results of the hexane-like adsorbates indicate that both *n*-hexane and isohexane move along the surface according to a similar mechanism, while cyclic adsorbates move according to a different mechanism. Moreover, the surface diffusion mechanism for larger adsorbates (*n*-decane and isodecane) seems to be different than that of the hexane-like molecules. In the following we shall discuss the detailed surface diffusion mechanism of these model adsorbates.

3.2. Surface diffusion mechanism: hexane-like adsorbates

Let us first consider the three different hexane-like adsorbates. The mean square end-to-end distances, R^2_{ete} (5), for typical trajectories of *n*-hexane and isohexane at $T = 800$ K are shown in Fig. 3. For the linear chain R^2_{ete} is defined between atoms 1 and 6 while for isohexane this quantity corresponds to the distance between atoms 1 and 5 (see Figs. 1*a* and 1*b*). Inspection of these results shows that the magnitude of R^2_{ete} for

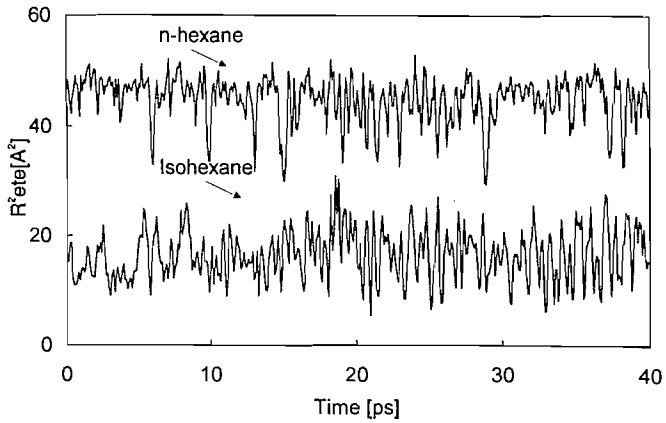

FIG. 3. Variation of the mean square end-to-end distance during typical trajectories of *n*-hexane and isohexane at $T = 800$ K. Note that the results associated with *n*-hexane were shifted by 15.0 Å^2.

both adsorbates fluctuates rapidly around the mean values (29.6 ± 0.1 Å^2 for *n*-hexane and 16.1 ± 0.1 Å^2 for isohexane). For both adsorbates one can observe instances during which the magnitudes of R^2_{ete} are quite a bit smaller (or larger in the case of isohexane) than the average values. These correspond to various bent (or stretched) configurations of the adsorbates on the surface. It should be noted that the lifetime of these bent/stretched configurations is similar for both adsorbates, of the order of 0.5–2.0 ps. Animation of a number of typical trajectories for these two adsorbates indicated that during most of the simulation their motion can be described as a concerted motion of the molecule as a whole. However, occasionally these adsorbates can be found, for a short duration, in a highly bent (or stretched) configuration.

Two configurations are demonstrated in Fig. 4 for the isohexane-like molecule. These configurations correspond to the most stable and most unstable (largest and smallest adsorbate–surface binding, respectively) configurations found in a typical trajectory of the isohexane molecule. It is clear that the stable configurations are associated with an adsorbate that is practically parallel to the solid surface (Figs. 4*a* and 4*c*) while the high-energy unstable conformations correspond to adsorbates whose molecular plane is basically normal to the surface (Figs. 4*b* and 4*d*). Note that this type of high-energy configuration (like the one shown in Fig. 4) is quite rarely observed and occurs mainly at the higher T values investigated.

Similar examinations of R^2_{ete} for the cyclohexane-like adsorbate (corresponding to distances of opposite atoms in the ring) have shown that this quantity is practically constant during the trajectory. This is evidence that the molecular shape is not distorted appreciably even at high surface temperatures. The animation of some typical trajectories for cyclohexane-like adsorbate suggested that the surface diffusion of such molecules is dominated by two types of basic rotational motion. The first, and most frequent one, corresponds to the rotation of the adsorbate in a plane parallel to the surface around an axis that is normal to the surface and points through the center of mass of the molecule. This rotational motion is coupled to a translational movement of the molecule along the surface. Hence, the net result is that, during the motion of the molecule center of mass along the solid surface, the orientation of the atoms changes with respect to the location of the center of mass of the adsorbate. In the following we shall term this type of rotational motion as "in-plane rotation" and use the abbreviation IPR. It

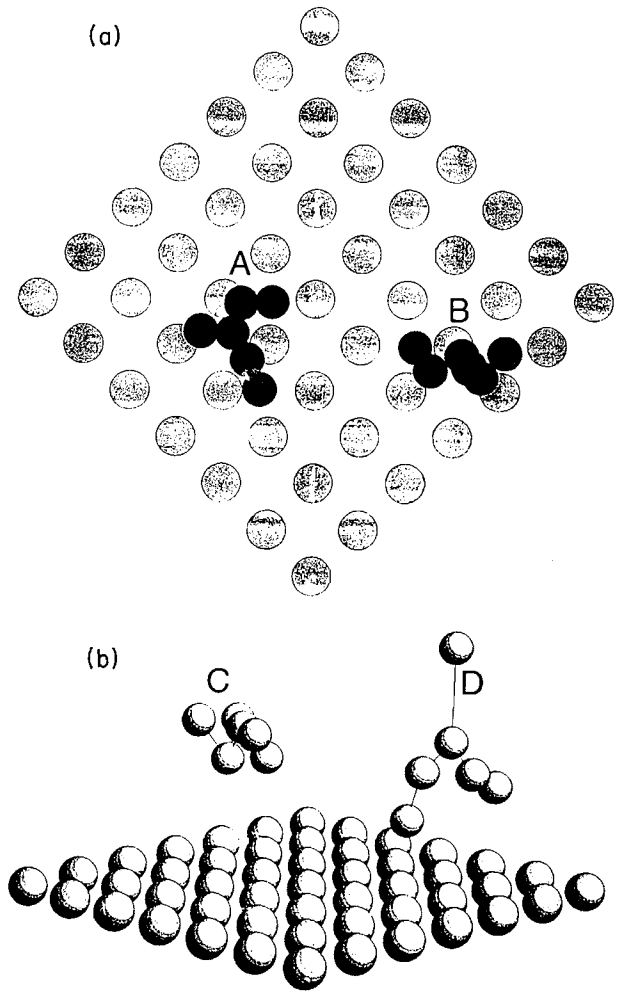

FIG. 4. Top and side views of the configurations associated with the most stable ((*a*) and (*c*)) and most unstable ((*b*) and (*d*)) configurations obtained during a typical trajectory of isohexane-like adsorbate at $T = 600$ K. Note that the normal adsorbate–surface distances were scaled by a factor of 1.5.

has to be noted that during most of the simulated period the molecular plane (the plane containing the adsorbate, which is basically planar, see Fig. 1*c*) is practically parallel to the solid surface.

The second type of rotational motion is related to a flip of the molecular plane around an axis that is parallel to the surface. The transition state in such a movement corresponds to a configuration where the molecular plane is normal to the solid surface. We shall term this type of rotation "flip over" and designate it by FO.

The energy barrier for the in-plane rotation is determined by the surface corrugation as seen by the adsorbate, while the activation energy for a flip-over movement corresponds to an extensive weakening of the adsorbate–surface binding. It should be noted that geometries in which the molecular plane is normal to the surface were also observed prior to a desorption event. Since a large activation energy is associated with the FO movement, it may be viewed as a rare event compared to the IPR motion, and the probability of its occurrence is expected to be a sensitive function of the surface temperature. Both rotational motions described above may be regarded as a concerted motion of the adsorbate as a whole.

Can. J. Chem. Downloaded from www.nrcresearchpress.com by 195.246.54.202 on 09/08/12
For personal use only.

Can. J. Chem. Downloaded from www.nrcresearchpress.com by 195.246.54.202 on 09/08/12
For personal use only.

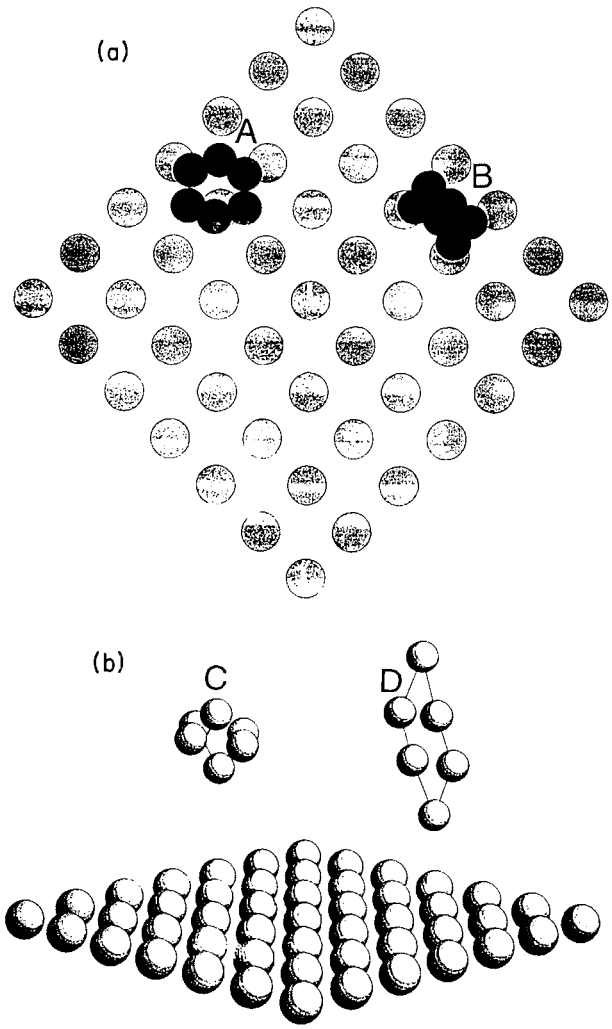

FIG. 5. Same as in Fig. 4 for a cyclohexane-like adsorbate at T = 800 K.

The adsorption configurations of cyclohexane for the strongest and weakest molecule–surface binding during a typical trajectory are shown in Fig. 5. Inspection of these results shows that "good" adsorption configurations of the cyclohexane are those in which the molecule is adsorbed parallel to the surface as shown in Figs. 5*a* and 5*c*. The configuration associated with weak adsorbate–surface binding coincides in this case with the transition state during a flip-over movement, Figs. 5*b* and 5*d*. At this configuration only three atoms of the cyclohexane are strongly interacting with the surface while the other three are located farther away and have only a small contribution to the adsorbate–surface binding.

To obtain a more quantitative description of these rotational motions we monitored two quantities during the evolution of the trajectories. The first corresponds to the distance (along the surface normal) between the molecular center of mass and the surface plane. The second quantity was the azimuthal angle of one of the ring atoms relative to the position of the molecular center of mass. The results obtained in two typical trajectories at T = 300 and 800 K are shown in Fig. 6. At the low temperature, T = 300 K, the average distance between the molecular center of mass and the surface, Z(c.m.), is 2.5 Å. Oscillations around this average value are clearly seen, Fig. 6*a*, where the largest amplitude observed is approximately 0.25 Å. The corresponding variation in the azimuthal angle of one of the ring atoms is shown in Fig. 6*b*. No flip-over movements were detected during this trajectory.

TABLE 2. Calculated values of the average angular velocity of adsorbed cyclohexane. Units of temperature are in degrees K while the angular velocity is given in terms of rad/s

T	$\omega_R(\times 10^{-13})$
300	1.08 ± 0.025
450	1.34 ± 0.032
600	1.61 ± 0.053
800	1.83 ± 0.047

Inspection of the corresponding results at the high temperature, Figs. 6*c* and 6*d*, shows that at some instances large-amplitude oscillations in Z(c.m.) are observed (i.e., ΔZ(c.m.) ≈ 0.75 Å) together with a major variation of the azimuthal angle during the trajectory. Careful examination of Fig. 6*d* shows that a highfrequency rotational motion, associated with the IPR movements, is superimposed on a low-frequency and large amplitude rotation that is related to the FO movements. In particular, near t = 10 and 17 ps the cyclohexane performed two flip-over movements that are manifested by large-magnitude oscillations in Z(c.m.), Fig. 6*c*, together with a corresponding rapid change in the azimuthal angle from approximately 270° to 90°, Fig. 6*d*. Hence, at T = 800 K, the high thermal energy manifests itself by the occurrence of combinations of the two rotational motions. Comparison of the results in Figs. 6*b* and 6*d* shows that the frequency of the oscillations associated with the IPR motion increases as a function of the surface temperature.

To demonstrate this point, we used the variation of the azimuthal angle to calculate the average angular velocity, ω_R, of the cyclohexane at the various surface temperatures considered. The calculated values of ω_R are summarized in Table 2. Inspection of these results shows that ω_R increases monotonically with elevation of the surface temperature. Since the adsorbate is in thermal equilibrium with the substrate, the increase in ω_R as a function of T is directly related to the increased thermal energy in the system. As a result, at elevated T values larger portions of the available configuration space are sampled by the adsorbate during its trajectory. Moreover, the thermal fluctuations of the adsorbed molecule at high surface temperatures is expected to result in an increased frequency by which the adsorbate–surface geometries (which correspond to energy barriers associated with the IPR motion) are sampled. Hence, the IPR movements, which dominate the adsorbate motion at low temperatures, are expected to become more rapid at higher surface temperatures. In addition, at elevated temperature the FO movements become more probable. It should be emphasized that the high T values used in the present study were required because of the short period during which the dynamics of large adsorbate surface diffusion could be simulated using the MD approach. It is believed that the mechanisms governing the diffusional motion of large adsorbates, as observed in these calculations, constitute a qualitatively accurate description of the process. Namely, both IPR and FO movements do occur at any surface temperature; the only question is what are the probabilities associated with each one of these types of motion. The MD simulations suggest that the probability for the IPR motion is much larger than that of the FO movement for temperatures at which the experiments are performed. However, even at such

Can. J. Chem. Downloaded from www.nrcresearchpress.com by 195.246.54.202 on 09/08/12
For personal use only.

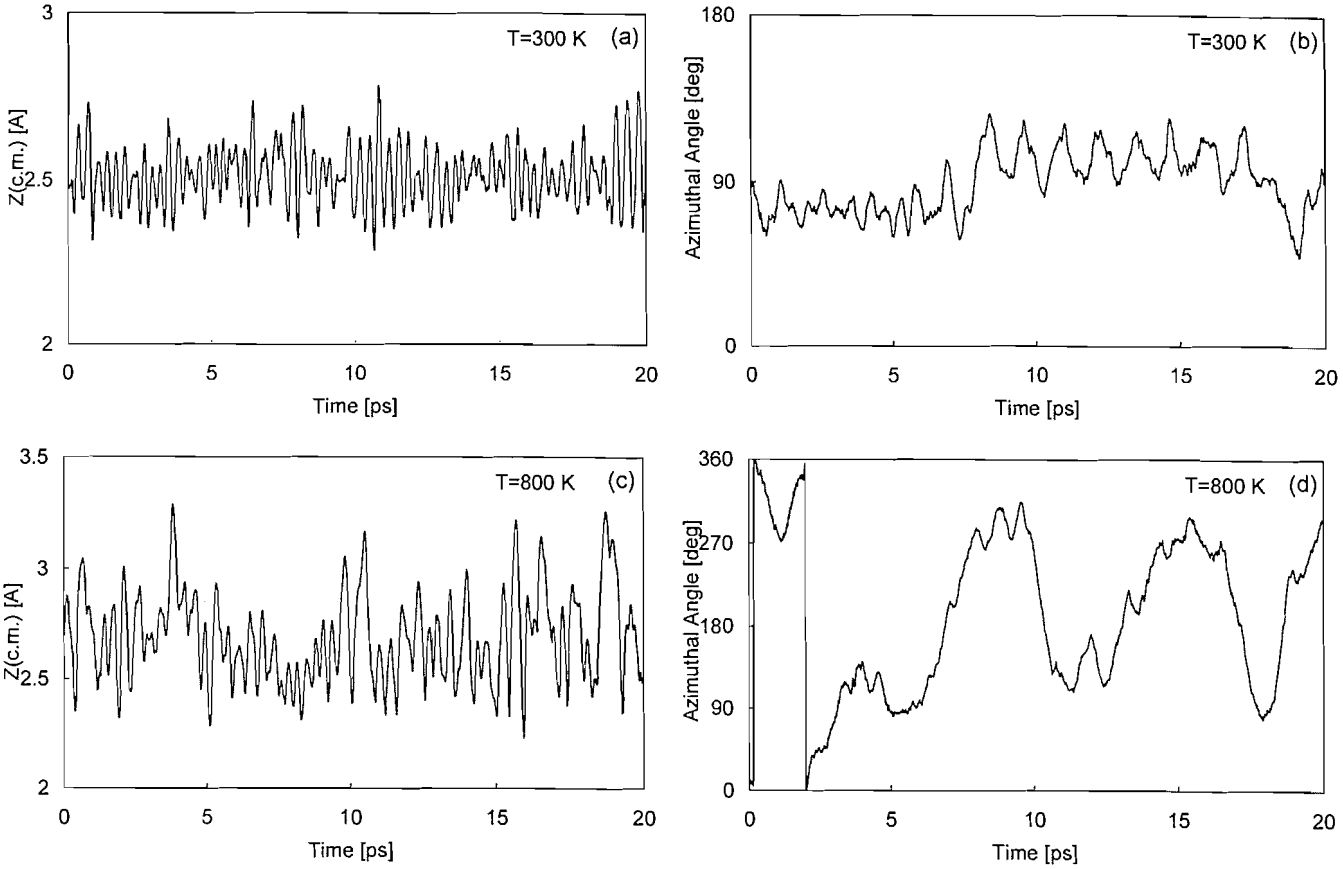

FIG. 6. Variation of the center of mass normal position, Z(c.m.), ((*a*) and (*c*)) and of the azimuthal angle associated with an atom in the ring ((*b*) and (*d*)) during typical trajectories of cyclohexane at two surface temperatures, $T = 300$ K ((*a*) and (*b*)) and $T = 800$ K ((*c*) and (*d*)).

low T values, non-zero probability is expected for the occurrence of the FO-type motion (during the experimental time scale).

3.3. *Surface diffusion mechanism: decane-like adsorbates*

Next we shall examine the mechanism that dominates the surface diffusion of the larger adsorbates. Inspection of Table 1 shows that the calculated values of both E_{diff} and E_{des} for *n*-decane and isodecane are larger than those obtained for the hexane-like adsorbates. However, the decreased corrugation ratio for these adsorbates indicates that the variation of the energy barrier for diffusion with adsorbate size is not linear. This nonlinear relationship between E_{diff} and the adsorbate size has been discussed in papers I and II. Comparison of the activation energies for diffusion obtained for linear and branched adsorbates shows that the influence of the molecular shape is much more pronounced for these larger molecules (as compared to the case of $n = 6$). This pronounced difference between *n*-decane and isodecane is related to the change in the mechanism dominating the surface diffusion of the larger adsorbates as compared to the various hexane-like molecules.

The results presented in papers I and II suggested that the surface diffusion mechanism of adsorbates the size of hexane (or smaller) is dominated by a concerted motion of the adsorbed species, while in the case of larger adsorbates a mechanism associated with segmental motion is dominant. Two basic segmental movements of large adsorbates, termed edge rotation, ER, and central segment rotation, CSR, were identified (5). Hence, the differences between the surface diffusion of *n*-decane and isodecane will be discussed with relation to this segmental mechanism.

The variation of the mean square end-to-end distance during two typical trajectories of *n*-decane and isodecane is shown in Fig. 7. In the case of isodecane, Fig. 7*b*, the various R^2_{ete} correspond to the distances between atoms 1–7, 7–10, and 1–10, respectively (see Fig. 1*e*). Inspection of the results for *n*-decane, Fig. 7*a*, shows that the adsorbate is occasionally "trapped" in highly bent configuration during its motion along the surface. These bent configurations are manifested by a large decrease in the value of R^2_{ete} (upper curve in Fig. 7*a*). The lifetimes of such bent configurations vary in the range of 1–5 ps. The mean square difference of the normal distance between the chain ends, R^2_{ete}(N), is also shown in Fig. 7*a* (bottom curve). It is clear that some of the bent configurations are related to large R^2_{ete}(N) values. This correlation between R^2_{ete}(N) and R^2_{ete}, together with the results discussed in papers I and II, manifests the role of the segmental movements during the surface diffusion of *n*-decane. Comparison of these results with the variation of R^2_{ete} for isodecane, Fig. 7*b*, shows some marked differences. First, the frequency at which the bent configurations occur in the case of isodecane is noticeably larger than that for *n*-decane. In addition, the lifetimes associated with these bent configurations are shorter than the corresponding value for *n*-decane.

The R^2_{ete} values, associated with bent conformations of different "end pairs" in the case of isodecane, are in many cases highly correlated. This correlation is due to the shape of the adsorbate; for example, if one end of the molecule performs an ER movement it is expected that one R^2_{ete} value associated with

Can. J. Chem. Downloaded from www.nrcresearchpress.com by 195.246.54.202 on 09/08/12
For personal use only.

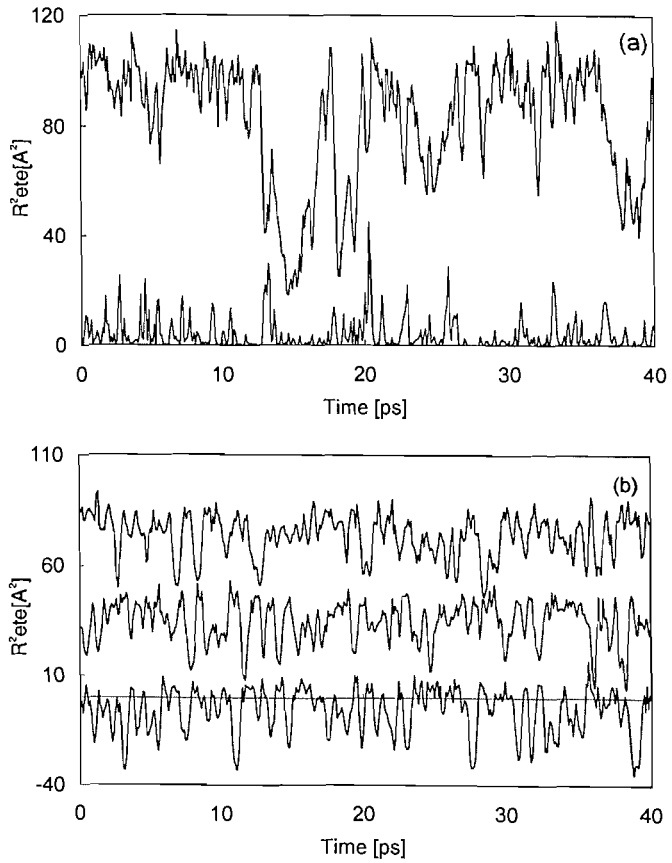

FIG. 7. Variation of the mean square end-to-end distance during two typical trajectories of *n*-decane (*a*) and isodecane (*b*). In the case of *n*-decane the top curve represents R^2_{ete}, while the mean square difference of the end-to-end normal distance (multiplied by 5.0) is also shown (bottom curve). In the case of isodecane, the three curves correspond to the variation of R^2_{ete} between atoms: 1–7 (top curve, shifted by 40 Å^2), 7–10 (middle curve), and 1–10 (bottom curve, shifted by −40 Å^2). For the definition of this numbering see Fig. 1*e*.

this end will increase while the other will decrease. These differences between *n*-decane and isodecane suggest that the edge rotation type of movements dominates the surface diffusion of isodecane while both ER and CSR segmental movements (and their combinations) contribute in the case of *n*-decane. Two geometries of isodecane are illustrated in Fig. 8. Here, top and side views of the configurations corresponding to the largest (Figs. 8*a* and 8*c*) and smallest (Figs. 8*b* and 8*d*) values of isodecane–surface binding, in a typical trajectory, are shown. It is clear that the low binding configuration is related to a situation in which a segment of the adsorbate is elevated during an edge rotational movement. The size of the segment that performs the ER motion is dictated by the shape of the isodecane. It is expected that during a CSR movement the isodecane should reach a geometry similar to the one shown in Fig. 4*d* for isohexane. Such a configuration corresponds to a large decrease in the adsorbate–surface binding and has a very low probability at the *T* values examined here. Hence, it was never observed in the present simulations.

This difference in the details of the surface diffusion mechanism of these two types of adsorbates results in the observed discrepancy in the calculated E_{diff} values. Inspection of the animation of typical trajectories, for both adsorbates, supports the conclusions of the discussion presented above.

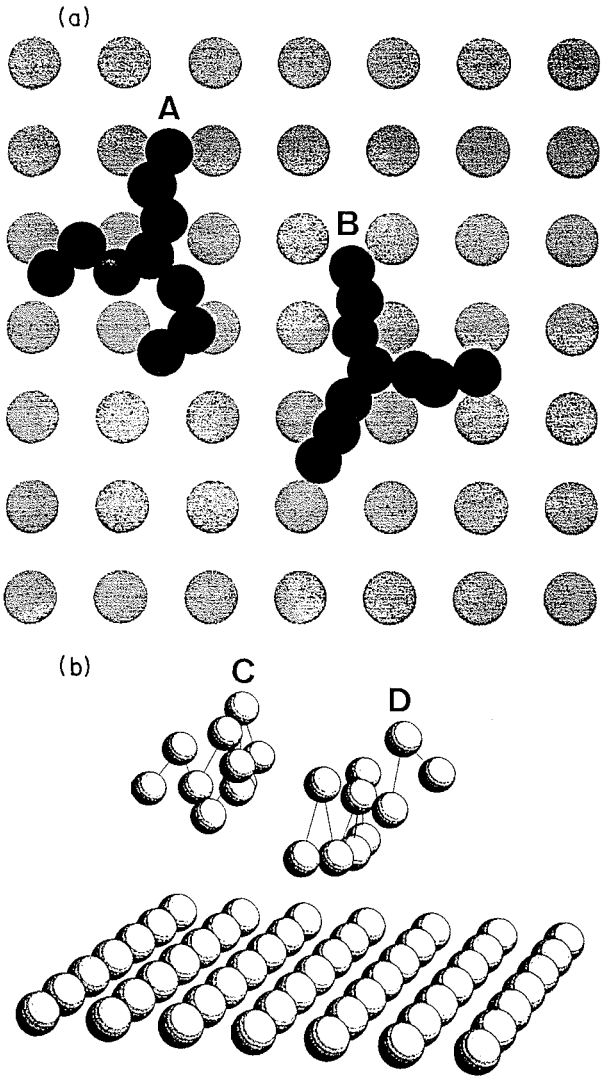

FIG. 8. Same as in Fig. 4 for a isodecane-like adsorbate at T = 450 K.

4. Summary

Molecular dynamics simulations were performed to examine the relationship between the surface diffusion mechanism and the adsorbate shape. It was found that the surface diffusion of medium size adsorbates, such as various shapes of hexane, can be described in terms of a concerted motion of the adsorbed species. This is in agreement with the experimental results. In addition, the variation of the calculated pre-exponential factors and the activation energies for surface diffusion as a function of adsorbate shape were found to be in good qualitative agreement with the experimental observations.

The simulations have shown that the mechanism by which cyclic adsorbates move along the surface can be attributed to two basic rotational movements, which were termed in-plane-rotation and flip over. The first type of rotational motion, IPR, is the dominant one while the FO movements are rare events that involve the motion across relatively high activation energy barriers. Hence, the FO-type movement becomes more frequent at elevated surface temperatures.

For larger adsorbates the surface diffusion mechanism was found to be dominated by segmental movements. This is in accordance with previous theoretical results (5). Once the seg-

mental motion dominates the diffusion along the surface, branched chains were found to diffuse more quickly than linear chains. This difference is associated with the natural division of such adsorbates into small segments dictated by the shape of branched molecules. In the case of branched adsorbates the "edge rotational" movements were found to be the most important, while, for linear chains, combinations of ER and CSR were found to dominate their surface diffusion mechanism.

1. (*a*) G. Ehrlich and K. Stolt. Annu. Rev. Phys. Chem. **30**, 603 (1980); (*b*) D.A. King. J. Vac. Sci. Technol. **17**, 241 (1980); (*c*) A.G. Naumovets and Y.S. Vedula. Surf. Sci. Rep. **4**, 365 (1985); (*d*) R. Gomer. Rep. Prog. Phys. **53**, 917 (1990).
2. J.L. Brand, M.V. Arena, A.A. Deckert, and S.M. George. J. Chem. Phys. **92**, 5136 (1990).
3. (*a*) C.H. Mak, B.G. Koehler, and S.M. George. J. Vac. Sci. Technol. A: **6**, 856 (1988); (*b*) E.D. Westre, M.V. Arena, A.A. Deckert, J.L. Brand, and S.M. George. Surf. Sci. **233**, 293 (1990); (*c*) M.V. Arena, A.A. Deckert, J.L. Brand, and S.M. George. J. Phys. Chem. **94**, 293 (1990); (*d*) J. Chem. Phys. **94**, 4001 (1991).
4. (*a*) S.M. George, A.M. DeSantolo, and R.B. Hall. Surf. Sci. **159**, L425 (1985); (*b*) C.H. Mak, J.L. Brand, A.A. Deckert, and S.M. George. J. Chem. Phys. **85**, 1676 (1986); (*c*) C.H. Mak, B.G. Koehler, J.L. Brand, and S.M. George. J. Chem. Phys. **87**, 2340 (1987); (*d*) C.H. Mak, J.L. Brand, B.G. Koehler, and S.M. George. Surf. Sci. **191**, 108 (1987).
5. (*a*) D. Cohen and Y. Zeiri. J. Chem. Phys. **97**, 1531 (1992); (*b*) Surf. Sci. **274**, 173 (1992).
6. M. Silverberg. J. Chem. Phys. In press.
7. (*a*) S.A. Adelman and J.D. Doll. J. Chem. Phys. **61**, 4242 (1974); (*b*) S.A. Adelman. J. Chem. Phys. **71**, 4471 (1979); (*c*) J.C. Tully. J. Chem. Phys. **73**, 1975 (1980); **73**, 6333 (1980); (*d*) R.R. Lucchese and J.C. Tully. Surf. Sci. **137**, 570 (1983).
8. (*a*) Y. Zeiri, J.J. Low, and W.A. Goddard. J. Chem. Phys. **84**, 2408 (1986); (*b*) Y. Zeiri and R.R. Lucchese. J. Chem. Phys. **94**, 4055 (1991); (*c*) Surf. Sci. **264**, 197 (1992).
9. (*a*) M. Bishop, M.H. Kalos, and H.L. Frisch. J. Chem. Phys. **70**, 1299 (1979); (*b*) D.C. Rapaport. J. Chem. Phys. **71**, 3299 (1979); (*c*) W. Bruns and R. Bansal. J. Chem. Phys. **74**, 2064 (1981); (*d*) J. Luque, J. Santamaria, and J.J. Freire. J. Chem. Phys. **91**, 584 (1989).

Can. J. Chem. Downloaded from www.nrcresearchpress.com by 195.246.54.202 on 09/08/12
For personal use only.

Bound–free $B\ ^2\Sigma^+ - X\ ^2\Pi$, $A\ ^2\Sigma^+$ emission in the BAr van der Waals complex

EUNSOOK HWANG AND PAUL J. DAGDIGIAN
Department of Chemistry, The Johns Hopkins University, Baltimore, MD 21218, U.S.A.

AND

MILLARD H. ALEXANDER
Department of Chemistry, The University of Maryland, College Park, MD 20742, U.S.A.

Received July 29, 1993

This paper is dedicated to Professor John C. Polanyi on the occasion of his 65th birthday

EUNSOOK HWANG, PAUL J. DAGDIGIAN, and MILLARD H. ALEXANDER. Can. J. Chem. **72**, 821 (1994).

Spectrally resolved bound–free fluorescence emission spectra for the excitation of several vibrational levels in the excited $B\ ^2\Sigma^+$ electronic state of the van der Waals molecule ^{11}BAr are presented. This excited state emits to the ground $X\ ^2\Pi$ and low-lying $A\ ^2\Sigma^+$ states, both of which correlate with the ground state atomic asymptote B($2p\ ^2P$) + Ar. Because of the large differences in equilibrium internuclear separations, the emission occurs mainly to the repulsive walls. In order to gain more information on this portion of the potential energy curves, the experimental emission spectra were compared with simulated spectra derived from *ab initio* calculated B–Ar interaction potentials. The simulated spectra reproduce the experimental spectra well if the lower-state potential energy curves are shifted slightly inward. This discrepancy is consistent with our previous observation that the *ab initio* calculations slightly overestimate the vibrationally averaged internuclear separation, which we determined experimentally. This reflects the difficulty of accurately calculating weak van der Waals interaction energies.

EUNSOOK HWANG, PAUL J. DAGDIGIAN et MILLARD H. ALEXANDER. Can. J. Chem. **72**, 821 (1994).

On a mesuré les spectres d'émission de fluorescence, résolus en fonction des espèces liées et libres, pour l'excitation de plusieurs niveaux vibrationnels de l'état électronique excité $B\ ^2\Sigma^+$ de la molécule de van der Waals ^{11}BAr. Cet état excité émet vers les états fondamentaux ($X\ ^2\Pi$) ou presque ($A\ ^2\Sigma^+$) qui assurent tous les deux une corrélation avec l'asymptote de l'état fondamental atomique B($2p\ ^2P$) + Ar. À cause des grandes différences dans les séparations d'équilibre internucléaires, l'émission se produit principalement vers les surfaces répulsives. Afin d'obtenir plus d'information sur cette partie des courbes d'énergie potentielle, on a comparé les spectres d'émission expérimentaux avec les spectres simulés par des calculs *ab initio* des potentiels d'interaction B–Ar. Si les courbes d'énergie potentielle de l'état de basse énergie est légèrement déplacé vers l'intérieur, les spectres simulés reproduisent bien les spectres expérimentaux. La différence est en accord avec l'observation antérieure selon laquelle les calculs *ab initio* surestiment légèrement la séparation internucléaire vibrationnelle moyenne qui est déterminée expérimentalement. Ceci reflète la difficulté de calculer d'une façon précise les faibles interactions de van der Waals.

[Traduit par la rédaction]

Can. J. Chem. Downloaded from www.nrcresearchpress.com by EESC ESCOLA DE ENGENHARIA on 09/08/12
For personal use only.

Introduction

Supersonic beam and laser spectroscopic methods have been extensively employed to observe transitions between bound vibrational levels of weakly bound diatomic metal – rare gas van der Waals complexes, as illustrated by recent representative studies involving metals in a number of chemical groups (1–17). With the resulting derived spectroscopic data, considerable information has been obtained on the attractive portions of the potential energy curves of the ground and excited electronic states. It would also be interesting to extract similar information on the repulsive parts of these curves from analysis of continuum spectra.

In a recent paper (17), we reported a collaborative experimental and theoretical study of the BAr van der Waals complex. This metal – rare gas complex contains the lightest element of the group 13 family and has a relatively small number of electrons so that accurate electronic structure calculations could be carried out for the ground and excited electronic states of this system. Similar all-electron calculations on other weakly bound metal – rare gas complexes have performed (18–21). A number of the complexes of heavier members of this series (AlRg, InRg) have been spectroscopically studied by other groups (11–16). In our study of BAr, we observed (17), using laser fluorescence excitation of a pulsed supersonic beam, a progression of ^{11,10}BAr bands in the $B\ ^2\Sigma^+ - X\ ^2\Pi_{1/2}$ system, which correlates with the boron atomic $3s\ ^2S - 2p\ ^2P$ transition. The experimental parameters were compared with the results of *ab initio* calculations of the BAr $X\ ^2\Pi$, $A\ ^2\Sigma^+$, and $B\ ^2\Sigma^+$ potential energy curves. In order to obtain accurately the interaction energies of this weakly bound system, multireference, internally contracted, configuration-interaction calculations were carried out.

There was reasonable agreement between the experimental and theoretical results. For the $X\ ^2\Pi$ ground state, the average internuclear separation in the ground vibrational level, defined as $R_0 = [\langle R^{-2}\rangle_{v=0}]^{-1/2}$, was predicted by the calculations to be ~0.1 Å larger than that derived from the experimental B_0'' rotational constant. The experimental Λ doubling parameter p_0'' for the $X\ ^2\Pi$ state was found to be reasonably well reproduced by a theoretical modeling of this parameter. The Λ doubling in the $X\ ^2\Pi$ state arises from spin–orbit and coriolis interactions with $^2\Sigma^{\pm}$ states (22), and the spectroscopic parameter p_0'' is most sensitive to the average separation of the $X\ ^2\Pi$ state and the primarily repulsive $A\ ^2\Sigma^+$ state, both of which correlate with the ground B($2p\ ^2P$) + Ar asymptote. In contrast to our calculation (17), an earlier complete active space self-consistent field (CASSCF) calculation on BAr did not recover any of the weak binding in the BAr $X\ ^2\Pi$, $A\ ^2\Sigma^+$, and $B\ ^2\Sigma^+$ states (23), because dispersion interactions were not included.

More extensive data on the BAr excited $B\ ^2\Sigma^+$ state, consisting of term values and rotational constants for several vibrational levels of two isotopomers, were experimentally obtained so that it was possible to assign v' vibrational quantum numbers and to generate an RKR potential for this state (17). One of the more interesting features of our experimental BAr fluorescence

Can. J. Chem. Downloaded from www.nrcresearchpress.com by EESC ESCOLA DE ENGENHARIA on 09/08/12
For personal use only.

excitation spectrum was that the last two bands in the v' progression were broadened and showed no rotationally resolved features. This suggests that the highest observed vibrational levels are quasibound and that the potential energy curve of the $B\ ^2\Sigma^+$ state has a barrier at long range. In similar fashion, the *ab initio* calculations on this electronic state also exhibited a barrier. The electronic structure of this state is difficult to describe accurately, and the most extensive calculations were able to recover only ~40% of the experimentally estimated dissociation energy of ca. 1 100 cm^{-1}. An estimate of the barrier height of ~140 cm^{-1} was obtained by comparing the experimental widths for the highest two vibrational levels with Lorentzian line widths calculated with a combined experimental and scaled theoretical $B\ ^2\Sigma^+$ potential energy curve. The presence of barriers has been inferred in the corresponding $B\ ^2\Sigma^+$ states of heavier group 13 – rare gas complexes (12, 15, 16).

In the present paper, we report spectrally resolved bound–free fluorescence emission spectra for the excitation of several vibrational levels in the excited $B\ ^2\Sigma^+$ electronic state. Because of the large difference in the equilibrium internuclear separation between the $X\ ^2\Pi$ and $B\ ^2\Sigma^+$ states, this emission occurs mainly to the repulsive wall of the lower state, as well as to the $A\ ^2\Sigma^+$ state. Thus, comparison of the experimental emission spectra with simulated spectra calculated using *ab initio* potential energy curves will provide additional information on the repulsive regions of the X and A potentials, which are not probed by bound–bound spectroscopy.

While continuum spectra have long been known in molecular spectroscopy (24), they have not been widely employed to determine repulsive potential energy curves. In recent years, methodologies have been developed for the inversion of continuum spectra to yield such repulsive curves (25–27). The wavenumbers of the extrema in the spectra determine the potential energy curves, while intensity information can be used to derive the transition moment function. Fawzy et al. (28) have recently reported such a study for the determination of the repulsive potential in the InAr van der Waals molecule. Fortuitously, this system also involves a group 13 metal – rare gas complex and is a higher homologue of BAr. The InAr $X\ ^2\Pi$ spin–orbit splitting is much greater than that in BAr so that the $B\ ^2\Sigma^+ - X_1\ ^2\Pi_{1/2}$, $X_2\ ^2\Pi_{3/2}$ emissions are resolved. It was possible to invert the experimental data to obtain a pointwise repulsive potential for the InAr($X_1\ ^2\Pi_{1/2}$) state (28). Overlapping of the $B\ ^2\Sigma^+ - X\ ^2\Pi_{3/2}$ and $B\ ^2\Sigma^+ - A\ ^2\Sigma^+$ emission prevented extraction of the repulsive potentials of the lower states of these transitions by this inversion method. Bound–free spectra involving excitation of the $^3\Sigma^+$ state correlating with the Hg($7\ ^3S_1$) + M asymptote have been observed in optical–optical double resonance studies of the HgAr (29) and HgNe (30) van der Waals molecules. As in the $B\ ^2\Sigma^+$ states of the group 13 – rare gas complexes, these states have barriers in their potential energy curves.

Because of the spectral overlap of the B–X and B–A emissions and the availability of high-quality *ab initio* calculations for the relevant electronic states in BAr (17), we have taken a different approach for the analysis of our experimental BAr bound–free emission spectra. Rather, we will compare them with simulated spectra derived using the *ab initio* repulsive potentials. The adequacy of these potentials will be judged by how well the simulated and experimental spectra agree. As already anticipated by the difference between the experimental and *ab initio* vibrationally averaged internuclear separations R_0 (17), it will be necessary to shift the repulsive potentials of the lower $X\ ^2\Pi$ and $A\ ^2\Sigma^+$ states inward to get good agreement. This comparison is facilitated by the availability of a potential energy curve for the upper $B\ ^2\Sigma^+$ state which reliably reproduces spectroscopic observations connected with this state (17).

Experimental apparatus

The apparatus employed for the experimental portion of this work was a modification of the apparatus which we previously employed (17) for the observation of the BAr $B\ ^2\Sigma - X\ ^2\Pi_{1/2}$ transition.

Boron atoms were produced by 193 nm photolysis of diborane diluted 150:1 in a Ar/He mixture, and the van der Waals complex was formed in the supersonic expansion from a pulsed valve (General Valve series 9). The nozzle orifice diameters of 0.2 and 0.5 cm were employed, and the backing gas pressure was 5–7 atm. The chamber in which the molecular beam was generated was pumped by an unbaffled 10 in. diffusion pump. The ArF excimer photolysis laser (Lambda Physik EMG101MSC) was focused with a 30 cm f. l. lens at the tip of the nozzle, and the pulse energy was approximately 2 mJ. At high excimer laser pulse energies, the beam temperature (as measured by the B atom $^2P_{1/2,3/2}$ spin–orbit population ratio) was found to increase, with a decrease (17) in the intensity of the BAr spectral features. The positions of the nozzle and the focused laser spot could be independently adjusted while the chamber was evacuated.

Boron atoms and BAr van der Waals complexes were detected 1.5 cm downstream of the nozzle with a frequency-doubled dye laser (Lambda Physik LPD3002E) scanning the wavelength region around the boron atom $3s\ ^2S \leftarrow 2p\ ^2P$ transition near 249.8 nm. The laser line width in these experiments was 0.3 cm^{-1}. The dye laser was fired at a variable delay after the photolysis laser to allow for the molecular transit time from the photolysis to the detection zones. For the recording of dispersed emission spectra, the laser-excited fluorescence was imaged with a telescope onto a 0.25 m Fastie-Ebert spectrometer (Jarrell–Ash 82-410, operated in second order at a spectral bandpass of 1 nm) and detected through an order-sorting filter (Schott UG-5) by a photomultiplier (EMI 9813QB), whose output was directed to a gated integrator (Stanford Research Systems SRS250) and then to a chart recorder and/or laboratory computer. Wavelength calibration was verified with Hg atomic lines and the ultraviolet laser radiation.

Experimental results

Dispersed emission spectra were taken for excitation of the ^{11}BAr($B\ ^2\Sigma^+$) $v' = 5$–8 vibrational levels. The excited vibrational levels $v' = 5$–7 were prepared by tuning the laser to the Q_1 head of the respective $B\ ^2\Sigma^+ - X\ ^2\Pi_{1/2}$ (v',0) band. Figure 1 presents the spectra obtained. To gauge the importance of dye laser scattered light and emission excited by the photolysis laser alone, we also took spectra with the dye laser tuned off atomic or molecular features. The spectra shown in Fig. 1 have been corrected for the transmission of the order-sorting filter, and the background emission has been subtracted. In the worst case, the dye laser scattered light contributed at most 5% (for $v' = 5$) to the integrated signal of the near resonant emission feature; for higher v' levels, this background was even less. The excimer laser induced emission was also considerably smaller than the laser scattered light signal.

The undulatory behavior of the spectra reflect interferences between the upper state vibrational and lower state continuum wave functions. Each panel in Fig. 1 has a similar qualitative appearance. The displacements of corresponding extrema in the spectra appear at smaller displacements from the excitation wavenumber with increasing v'. This reflects the tendency for the emission to occur at larger internuclear separations, and hence to lower parts of the lower state repulsive walls, as v' increases. We found from our previous theoretical study (17) of BAr($X\ ^2\Pi$) that this state had three bound vibrational levels.

Can. J. Chem. Downloaded from www.nrcresearchpress.com by EESC ESCOLA DE ENGENHARIA on 09/08/12
For personal use only.

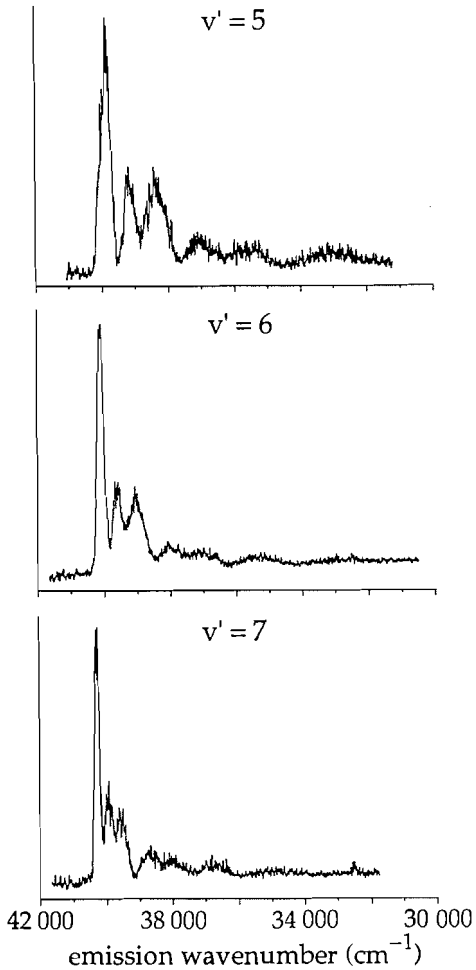

FIG. 1. Experimental dispersed emission spectra for excitation of the ^{11}BAr($B\ ^2\Sigma^+$) $v' = 5$–7 vibrational levels.

The spacings between these levels are considerably smaller than our spectral resolution and the emissions to these bound levels, which occur on the high-wavenumber side of the strong near-resonant feature, are not resolved. The fraction of the radiative decay to these bound levels is quite small because of the poor overlap of the $B\ ^2\Sigma^+$ and $X\ ^2\Pi$ bound vibrational wave functions. The spin–orbit splitting in the $X\ ^2\Pi$ state (17) is even smaller than the vibrational spacings and is also not resolved.

For $v' = 8$, the laser was tuned to the peak of the rotationally unresolved feature. Figure 2 displays the spectrum obtained in this case. This emission spectrum has a different qualitative character from those shown in Fig. 1, consisting mainly of emission near the excitation wavenumber. In the laser fluorescence excitation spectrum (17), no rotational structure could be discerned in the $B\ ^2\Sigma^+ - X\ ^2\Pi_{1/2}$ (8,0) band, in contrast to lower bands in the progression. This broadening was found to be due to predissociation of the $v' = 8$ level through the barrier in the excited state. From comparison of the experimental spectra with simulated spectra, the predissociation width was estimated to be ~ 2 cm^{-1}. The predissociation rate derived from this width is considerably greater than the radiative decay rate (approximately equal to the atomic B $3s\ ^2S \rightarrow 2p\ ^2P$ decay rate of ca. 2×10^8 s^{-1} (see below)), and the $v' = 8$ vibrational level is expected to decay primarily through predissociation. This process leads to the formation of electronically excited B($3s\ ^2S$) atoms, which decay through the $3s\ ^2S \rightarrow 2p\ ^2P$ transition, leading to the strong

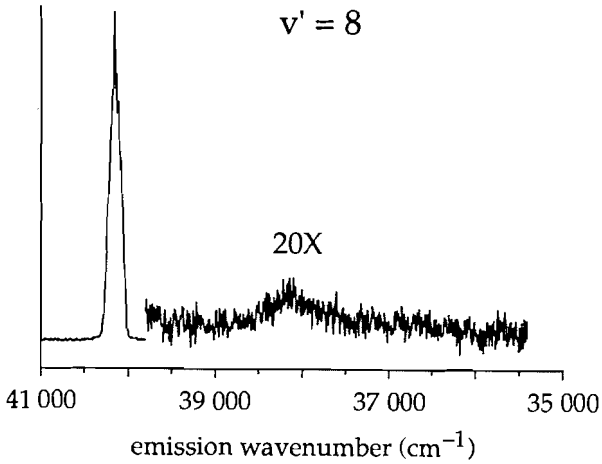

FIG. 2. Experimental dispersed emission spectrum for excitation of the ^{11}BAr($B\ ^2\Sigma^+$) $v' = 8$ vibrational level. The signal in the spectral region to the red of 39 800 cm^{-1} has been amplified by a factor of 20.

atomic feature observed in the emission spectrum and the lack of the undulatory *molecular* features seen in Fig. 1.

Theoretical calculations and simulation of the emission spectra

In order to gauge the reliability of the *ab initio* potential energy curves for the lower BAr electronic states, the experimental dispersed emission spectra presented above are compared with simulated spectra generated using these curves. The continuum emission intensity for the radiative decay of electronically excited BAr($B\ ^2\Sigma^+$, v') at photon energy $h\nu$ is proportional to

$$[1] \quad I(h\nu) \propto |\langle B\ ^2\Sigma^+, v'|\mu|E\rangle|^2$$

where $|B\ ^2\Sigma^+, v'\rangle$ is the vibrational wave function of the electronically excited level, $|E\rangle$ is the lower state continuum wave function, and μ is the electronic transition moment. The energy E equals $E(B\ ^2\Sigma^+, v') - h\nu$, where $E(B\ ^2\Sigma^+, v')$ is the excited state energy relative to the B($2p\ ^2P$) + Ar asymptote. The continuum wave function in eq. [1] is taken as energy normalized (31), i.e.

$$[2] \quad \lim_{R\rightarrow\infty} |E\rangle = (2\mu_{BAr}/\pi\hbar^2 k)^{1/2} \sin(kR - l\pi/2 + \eta)$$

where k is the asymptotic wave vector, μ_{BAr} is the B—Ar reduced mass, l is the orbital angular momentum, and η is the phase shift.

As discussed above, the $B\ ^2\Sigma^+$ excited levels can decay to both the $X\ ^2\Pi$ and $A\ ^2\Sigma^+$ states, so that the B–X and B–A continuum emission spectra will overlap. We must properly weight the relative contributions from these two transitions. We define the electronic transition dipole moments according to the modern convention (32) as

$$[3] \quad \mu(B - X) = \langle B\ ^2\Sigma^+(\Lambda = 0)|\mu_{-1}|X\ ^2\Pi(\Lambda = +1)\rangle$$

and

$$[4] \quad \mu(B - A) = \langle B\ ^2\Sigma^+(\Lambda = 0)|\mu_0|A\ ^2\Sigma^+(\Lambda = 0)\rangle$$

In terms of the Cartesian components of the molecular orbitals, these can be expressed as

Can. J. Chem. Downloaded from www.nrcresearchpress.com by EESC ESCOLA DE ENGENHARIA on 09/08/12
For personal use only.

[5] $\mu(B - X) = -\langle B\sigma|\mu_x|X\pi_x\rangle$

and

[6] $\mu(B - A) = \langle B\sigma|\mu_z|A\sigma\rangle$

In the atomic limit, in which the electronic wave functions of the $X\ ^2\Pi$ and $A\ ^2\Sigma^+$ states are described as boron atomic $2p_{x,y}$ and $2p_z$ orbitals, respectively, the magnitudes of the *B–X* and *B–A* transition moments would be equal.

While several $B\ ^2\Sigma^+$ rotational levels are excited by the dye laser, only levels of low rotational angular momentum are prepared. Excitation of the Q_1 head with a dye laser radiation of 0.3 cm^{-1} bandwidth prepares BAr($B\ ^2\Sigma^+$) molecules with $J' = 0.5–2.5$ (17). Moreover, the possible change of the total angular momentum J can be only 0 or ± 1 upon radiative decay. Accordingly, a centrifugal potential was not added to the potential energy curves. Test calculations were carried out for nonzero nuclear angular momentum N (assumed to be the same for the upper and lower states). The computed emission spectra for $N = 0$ and 10 were found to be virtually identical.

Since the spin–orbit splitting is not resolved in the $X\ ^2\Pi$ state, we can sum over the spin–orbit levels. However, the rotational/fine-structure states do play a role in that the sum over the allowed final angular momentum quantum numbers affects the relative intensities of the *B–X* and *B–A* emissions. With the above convention (32) for the transition moments, the sum of the rotational intensity factors over all possible final orbital and electronic angular momentum quantum numbers out of a given $B\ ^2\Sigma^+$ level equals 4 $(2J' + 1)$ for the $B\ ^2\Sigma^+ - X\ ^2\Pi$ transition and 2 $(2J' + 1)$ for the $B\ ^2\Sigma^+ - A\ ^2\Sigma^+$ transition. Thus, the intensities calculated from eq. [1] for the former transition must be multiplied by factor of 2 relative to the latter.

In order to calculate BAr emission spectra, we employed a hybrid potential for the upper $B\ ^2\Sigma^+$ potential energy curve consisting of the experimental RKR curve around the minimum, the long-range *ab initio* potential scaled to match the RKR energy at the outer $v' = 7$ turning point, and an R^{-12} extrapolation at short range. This potential, which is described in detail in our previous paper (17) on BAr, yielded resonance widths for the quasibound $v' = 8$ and 9 levels which were in reasonable agreement with experimentally estimated widths and reproduced well the observed $B\ ^2\Sigma^+$ vibrational energy spacings (17).

The potential energy curves for the lower $X\ ^2\Pi$ and $A\ ^2\Sigma^+$ electronic states were those obtained from our *ab initio* calculations (17). Additional, equivalent calculations were carried out at shorter internuclear distances to extend the repulsive walls of these curves, as well as to generate additional long-range points. As described in detail previously (17), CASSCF (33) calculations with three electrons in four active orbitals (2*s* and 2*p* of B) were performed, using state averaging (34–36) to obtain a single set of CASSCF orbitals for the $X\ ^2\Pi_x$, $X\ ^2\Pi_y$, and $A\ ^2\Sigma^+$ states. Multireference, internally contracted, configuration-interaction (MR-CI) calculations were then carried out. The effect of higher-order excitations was estimated with the multi-reference averaged coupled-pair functional method (MR-ACPF) of Gadnitz and Alrichs (37). The calculations were performed with the MOLPRO suite of *ab initio* programs (38). Table 1 lists the full set of calculated interaction energies for the $X\ ^2\Pi$ and $A\ ^2\Sigma^+$ states. The top panel of Fig. 3 shows the *X*, *A*, and *B* potential energy curves. On the scale of this figure, the wells in the curves are not evident. The avoided crossing of *A* and *B* states seen in this figure occurs well inside the inner turning points of the $B\ ^2\Sigma^+$ vibrational levels so that it will not affect the calculated emission spectra.

TABLE 1. Calculated MR-ACPF B + Ar interaction energies (in cm^{-1})

R (bohr)	$X^2\Pi$	$A^2\Sigma^+$
3.00	26192.66	50339.24
3.50	12942.47	34907.02
4.00	6437.12	19226.77
4.50	2933.88	9792.25
5.00	1161.72	4734.70
5.50	352.60	2174.93
6.00	27.91	939.95
6.50	−77.39	357.74
6.75	−92.14	204.31
7.00	−94.48	104.58
7.25	−89.94	41.35
7.50	−82.01	2.62
8.00	−63.45	−31.88
8.50	−46.79	−38.34
9.00	−33.88	−34.54
9.50	−24.45	−28.04
10.00	−17.74	−21.73
11.00	−9.68	−12.49
12.00	−5.54	−7.17
14.00	−2.09	−2.61
16.00	−0.91	−1.09
18.00	−0.43	−0.51
20.00	−0.23	−0.26
25.00	−0.06	−0.06

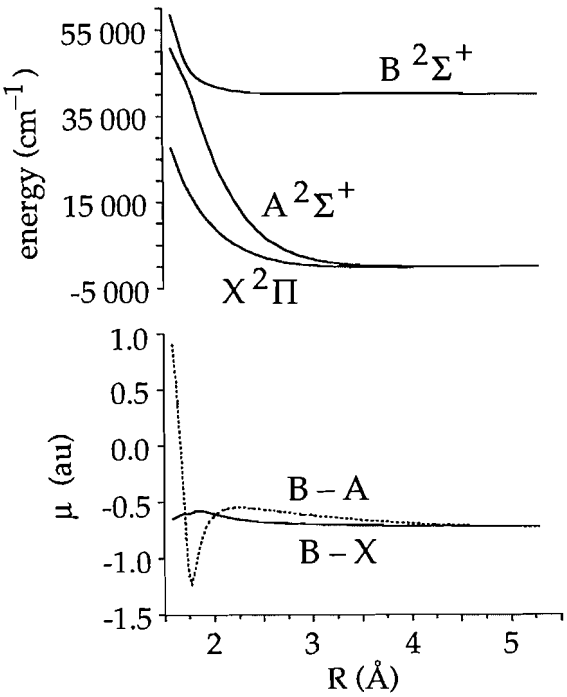

FIG. 3. Top panel: calculated MR-ACPF potential energy curves for the $X\ ^2\Pi$, $A\ ^2\Sigma^+$, and $B\ ^2\Sigma^+$ states. Bottom panel: calculated CASSCF *B–X* and *B–A* electronic transition moment functions.

The CASSCF calculations described above were also used to calculate *B–X* and *B–A* electronic transition moments as a function of the internuclear separation. The values of these transition moments are presented in Table 2 and displayed in the bottom panel of Fig. 3. It can be seen that the equality of these

TABLE 2. Calculated CASSCF BAr electronic transition moments (in au)

R (bohr)	B–X	B–A
3.00	−0.6546	0.9061
3.50	−0.5828	−0.9151
4.00	−0.6334	−0.5653
4.50	−0.6690	−0.5571
5.00	−0.6857	−0.5844
5.50	−0.6954	−0.6122
6.00	−0.7023	−0.6365
7.00	−0.7122	−0.6748
8.00	−0.7171	−0.7007
9.00	−0.7181	−0.7153
10.00	−0.7173	−0.7217

transition moments, expected for the atomic limit, is reasonably well obeyed over most of the significant range of internuclear separations. From the magnitude of the transition moments extrapolated to infinite separation (0.72 au), we estimate the radiative lifetime of the B($3s\ ^2S$) state to be 4.9 ns, or an oscillator strength of 0.063 for the $3s$–$2p$ transition. This is in reasonable agreement with the range of oscillator strengths reported from various experiments (0.055 (39), 0.090 (40), 0.062 (41), 0.087 (42) and calculations (0.067 (43), 0.069 (44)). Below $R \sim$ 2.6 Å, the BAr B–A transition moment varies rapidly and changes sign, because of the avoided crossing of the lowest two $^2\Sigma^+$ electronic states.

The simulated spectra were obtained by calculating the B–X and B–A intensities with eq. [1] as a function of E. The bound $B\ ^2\Sigma^+$ vibrational wave functions and the continuum $X\ ^2\Pi$ and $A\ ^2\Sigma^+$ wave functions were computed by Numerov integration (see, for example, ref. 45) of a one-dimensional Schrödinger equation. The integral in eq. [1] was then computed numerically using spline fits of the *ab initio* transition moments.

Figure 4 compares the experimental emission spectrum obtained for the excitation of the $B\ ^2\Sigma^+\ v' = 6$ vibrational level with simulated spectra. It can be seen in the top panel of Fig. 4 that this simulation does not predict well the energies at which the extrema in the emission spectrum occur. Specifically, the extrema are predicted to appear at energies (relative to the B($2p\ ^2P$) + Ar atomic asymptote) too large as compared with the experimental energies. This suggests that the repulsive walls of the *ab initio* potentials are appearing at too large internuclear separations. This discrepancy is consistent with our previous observation (17) that the *ab initio* vibrationally averaged internuclear separation R_0 is larger than our experimental estimate by ~0.1 Å.

We have investigated whether simple changes in the lower state *ab initio* potential energy curves could bring the experimental and simulated spectra into better agreement. In the lower panels of Fig. 4, we compare the $v' = 6$ experimental emission spectrum with simulated spectra for which the $X\ ^2\Pi$ and $A\ ^2\Sigma^+$ potential energy curves were both shifted inward by 0.1 and 0.2 Å. After a shift of only 0.1 Å the extrema are still predicted to occur at too high energy. However, with a shift of 0.2 Å we reproduce well the locations of the extrema and the relative intensities in the experimental spectrum.

The relative contributions of the B–X and B–A transitions are indicated in the simulated spectra displayed in Fig. 4. It can be seen that only the former (both bound–free and bound–bound transitions) contributes to the intense near-resonant peaks. Moreover, the maxima at ~600 and 1200 cm^{-1} are also peaks in

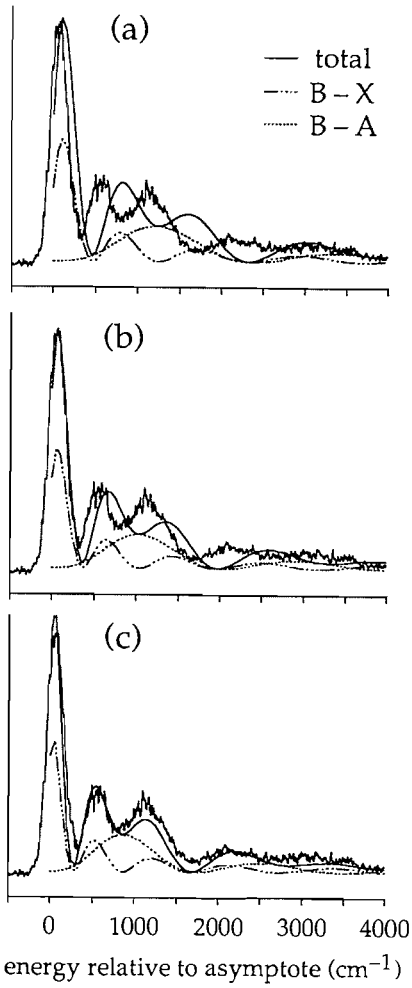

FIG. 4. Comparison of the experimental $v' = 6$ emission spectrum with simulated spectra with (*a*) no, (*b*) a 0.1 Å, and (*c*) a 0.2 Å inward shift of the $X\ ^2\Pi$ and $A\ ^2\Sigma^+$ potential energy curves. The contributions of the B–X and B–A transitions to the spectrum are separately indicated. As discussed in the text, the B–X intensity must be multiplied by 2 in the simulated total emission spectrum. For clarity, the spectra have been truncated at energies 4000 cm^{-1} above the B($4p\ ^2P$) + Ar asymptote.

the B–X emission. The first B–A maximum, which results from a constructive interference involving the overlap of the outer lobe of the $B\ ^2\Sigma^+$ vibrational wave function with the inner lobe of the $A\ ^2\Sigma^+$ continuum wave function, appears between these two peaks. The B–A transition does not contribute at smaller energies because $A\ ^2\Sigma^+$ potential energy curve is more repulsive than that of the $X\ ^2\Pi$ state.

Figure 5 presents a comparison of the experimental spectra for excitation of $v' = 5$ and 7 with simulated spectra calculated using 0.2 Å shifted $X\ ^2\Pi$ and $A\ ^2\Sigma^+$ potentials. As with $v' = 6$, the agreement of experimental and simulated spectra is quite good.

As discussed above, we found (17) from bound state spectroscopy that the average value of the B—Ar distance, as measured by the quantity R_0, was predicted by the *ab initio* potentials to be ~0.1 Å larger than the experimental estimate, obtained from the measured X state rotational constant B_0. A uniform translation of the X state potential curve inward by 0.2 Å lowers the calculated value of R_0 by 0.165 Å, to 3.538 Å, now in somewhat better agreement with the experimental value of

Can. J. Chem. Downloaded from www.nrcresearchpress.com by EESC ESCOLA DE ENGENHARIA on 09/08/12
For personal use only.

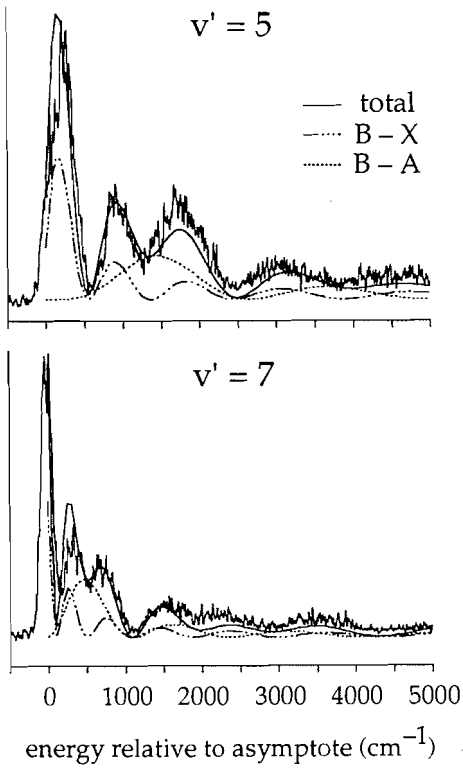

FIG. 5. Comparison of the experimental $v' = 5$ and 7 emission spectra with simulated spectra for which the $X\ ^2\Pi$ and $A\ ^2\Sigma^+$ potential energy curves were shifted inward by 0.2 Å. The contributions of the *B–X* and *B–A* transitions to the spectrum are separately indicated. As discussed in the text, the *B–X* intensity must be multiplied by 2 in the simulated total emission spectrum.

R_0 (3.606 ± 0.007 Å). This implies that perfect agreement with experiment would require a modification of the *ab initio* potential energy curves that is more complex than a simple shift.

Discussion

The present paper demonstrates clearly that bound–free emission spectra, originating from an excited state of a molecular van der Waals complex down to the repulsive wall of the electronic ground state, can provide detailed information on the repulsive wall of the latter. This region is not probed directly in conventional laser excitation fluorescence spectroscopy. Since molecular van der Waals complexes are usually prepared in supersonic jets, so that the internal energy is small, measurable absorption usually takes place out of only the lowest vibrational level of the complex. Thus, fluorescence excitation spectroscopy of van der Waals complexes provides information on the ground state potential energy only in the vicinity of the bottom of the well.

The present study on BAr and the previous investigation (28) of InAr shows that dispersed bound–free fluorescence emission spectra can provide significant information on the repulsive wall of the ground electronic state of the complex. In the present case, where two electronic states correlate with the electronic ground state of the atomic asymptote, the features seen in the emission spectra are primarily sensitive to the least repulsive of the ground state potential energy curves ($X\ ^2\Pi$) and provide relatively little information on the more repulsive ($A\ ^2\Sigma^+$) curve. Similarly, Fawzy et al. (28) were able to carry out a semiclassical inversion of their data to yield a pointwise representation of the ground InAr($X_1\ ^2\Pi_{1/2}$) potential energy curve but were not able to obtain such complete information on the two states ($X_2\ ^2\Pi_{3/2}, A\ ^2\Sigma^+$) correlating with the spin–orbit excited asymptote In($5p\ ^2P_{3/2}$) + Ar.

Fawzy et al. (28) also employed the intensities of the maxima in their InAr bound–free spectra to estimate the $B\ ^2\Sigma^+ - X_1\ ^2\Pi_{1/2}$ transition moment function. They found that this function is approximately a constant over the range 2.9 to 3.8 Å. This constancy is consistent with the idea that the metal atom chromophore in such a weakly bound molecule is essentially unaffected by the presence of the rare gas atom until rather small internuclear separations, as is shown by our calculated BAr *B–X* and *B–A* transition moment functions, displayed in Fig. 3.

The present study demonstrates conclusively that our *ab initio* potentials for the two lowest electronic states of BAr, which correlate with the ground state atomic asymptote [B($2p\ ^2P$) + Ar], are a bit too repulsive. Shifting them inward slightly (~0.2 Å) led to a much better simulation of the experimental spectra. In fact, the calculations will certainly also underestimate the depth of the van der Waals well, for which no correction was made in the present simulation. A more complex scaling of the *ab initio* curves was not attempted here. This would certainly become justified, were additional experimental information, in particular the positions of the excited vibrational levels of the $X\ ^2\Pi$ state, to become available.

Acknowledgements

This research was supported by the Air Force Office of Scientific Research under Grant No. AFOSR-91-0363. Millard Alexander is grateful to Hans-Joachim Werner for his invaluable technical support for the *ab initio* calculations. The assistance of David Varley in the experiments is gratefully acknowledged.

1. C.J. Lee, M.D. Havey, and R.P. Meyer. Phys. Rev. A: Gen. Phys. **43**, 77 (1991).
2. E. Zanger, V. Schmatloch, and D. Zimmermann. J. Chem. Phys. **88**, 5396 (1988).
3. R.P. Bennett, J.G. McCaffery, and W.H. Breckenridge. J. Chem. Phys. **92**, 2740 (1990).
4. C. Jouvet, C. Lardeux-Dedonder, S. Martrenchard, and D. Solgadi. J. Chem. Phys. **94**, 1759 (1991).
5. R. Bobkowski, M. Czajkowski, and L. Krause. Phys. Rev. A: Gen. Phys. **41**, 243 (1990).
6. R.R. Bennett and W. H. Breckenridge. J. Chem. Phys. **96**, 882 (1992).
7. I. Wallace, J.G. Kaup, and W.H. Breckenridge. J. Phys. Chem. **95**, 8060 (1991).
8. M.-C. Duval, O. Benoist-d'Azy, W.H. Breckenridge, C. Jouvet, and B. Soep. J. Chem. Phys. **85**, 6324 (1986).
9. T. Tsuchizawa, K. Yamanouchi, and S. Tsuchiya. J. Chem. Phys. **89**, 4646 (1988).
10. C. Ledonder-Lardeux, C. Jouvet, M. Richard-Viard, and D. Solgadi. J. Chem. Phys. **92**, 2828 (1990).
11. J.M. Gardiner and M.I. Lester. Chem. Phys. Lett. **137**, 301 (1987).
12. C.L. Callender, S.A. Mitchell, and P.A. Hackett. J. Chem. Phys. **90**, 5252 (1989).
13. M.J. McQuaid, J.L. Gole, and M.C. Heaven. J. Chem. Phys. **92**, 2733 (1990).
14. Z. Fu, S. Massick, J.G. Kaup, O.Benoist-d'Azy, and W.H. Breckenridge. J. Chem. Phys. **97**, 1683 (1992).
15. S.A. Heidecke, Z. Fu, J.R. Colt, and M.D. Morse. J. Chem. Phys. **97**, 1692 (1992).
16. C.L. Callender, S.A. Mitchell, and P.A. Hackett. J. Chem. Phys. **90**, 2535 (1989).

Can. J. Chem. Downloaded from www.nrcresearchpress.com by EESC ESCOLA DE ENGENHARIA on 09/08/12
For personal use only.

17. E. Hwang, Y.-L. Huang, P.J. Dagdigian, and M.H. Alexander. J. Chem. Phys. **98**, 8484 (1993).
18. R.P. Saxon, R.E. Olson, and B. Liu. J. Chem. Phys. **67**, 2692 (1977).
19. B. Pouilly, B.H. Lensfield, and D.R. Yarkony. J. Chem. Phys. **80**, 5089 (1984).
20. G. Chalsinski and J. Simons. Chem. Phys. Lett. **148**, 289 (1988).
21. J.A. Boatz, K.L. Bak, and J. Simons. Theor. Chim. Acta, **83**, 209 (1993).
22. H. Lefebvre-Brion and R.W. Field. Perturbations in the spectra of diatomic molecules. Academic Press, New York. 1986.
23. P.R. Taylor. Chem. Phys. Lett. **105**, 79 (1986).
24. G. Herzberg. Molecular spectra and molecular structure. I. Spectra of diatomic molecules. D. Van Nostrand, Princeton. 1950. Chap. VII.
25. R.J. LeRoy, R.G. Macdonald, and G. Burns. J. Chem. Phys. **65**, 1485 (1976).
26. M.S. Child, H. Essén, and R.J. LeRoy. J. Chem. Phys. **78**, 6732 (1983); R.J. LeRoy, W.J. Keogh, and M.S. Child. J. Chem. Phys. **89**, 4564 (1988).
27. R.J. LeRoy. Comput. Phys. Commun. **52**, 383 (1989).
28. W.M. Fawzy, R.J. LeRoy, B. Simard, H. Niki, and P.A. Hackett. J. Chem. Phys. **98**, 140 (1993).
29. M.-C. Duval, O. Benoist-d'Azy, W.H. Breckenridge, C. Jouvet, and B. Soep. J. Chem. Phys. **85**, 6324 (1986).
30. M. Okunishi, K. Yamanouchi, K. Onda, and S. Tsuchiya. J. Chem. Phys. **98**, 2675 (1993).
31. M.S. Child. *In* Specialist periodical reports. Molecular spectroscopy. The Chemical Society, London. 1974. p. 466.
32. E.E. Whiting, A. Schadee, J.B. Tatum, J.T. Hougen, and R.W. Nicholls. J. Mol. Spectrosc. **89**, 249 (1980).
33. P.J. Knowles and H.-J. Werner. Chem. Phys. Lett. **115**, 259 (1985).
34. R.N. Diffenderfer and D.R. Yarkony. J. Phys. Chem. **86**, 5098 (1982).
35. B.H. Lengsfield. J. Chem. Phys. **77**, 4073 (1982).
36. H.-J. Werner and W. Meyer. J. Chem. Phys. **74**, 5794 (1981).
37. R.J. Gadnitz and R. Alrichs. Chem. Phys. Lett. **143**, 413 (1988).
38. MOLPRO is a package of *ab initio* programs written by H.-J. Werner and P.J. Knowles, with contributions from J. Almlöf, R. Amos, S. Elbert, W. Meyer, E.A. Reinsch, R. Pitzer, and A. Stone.
39. L. Bergström, J. Bromander, R. Buchta, L. Ludin, and L. Martinson. Phys. Lett. **28A**, 721 (1969).
40. J. Bromander. Phys. Scr. **4**, 61 (1971).
41. M.W. Smith and W.L. Wiese. Astrophys. J. **23**, Suppl. 196 (1971).
42. J.A. Kernahan, E.H. Pinnington, A.E. Livingston, and D.J.G. Irwin. Phys. Scr. **12**, 319 (1976).
43. A.W. Wiese. Phys. Rev. **188**, 119 (1969).
44. R.K. Nesbet. Phys. Rev. A: Gen. Phys. **14**, 1065 (1976).
45. K. Smith. The calculation of atomic collision processes. Wiley-Interscience, New York. 1971. pp. 60–71.

Can. J. Chem. Downloaded from www.nrcresearchpress.com by EESC ESCOLA DE ENGENHARIA on 09/08/12
For personal use only.

Proton transfer dynamics on highly attractive potential energy surfaces: Induced repulsive energy release in O^- + HF at high collision energies

M.A. CARPENTER, M.T. ZANNI, D.J. LEVANDIER,[1] D.F. VARLEY,[2] AND J.M. FARRAR[3]

Department of Chemistry, University of Rochester, Rochester, NY 14627, U.S.A.

Received August 30, 1993

This paper is dedicated to Professor John C. Polanyi on the occasion of his 65th birthday

M.A. CARPENTER, M.T. ZANNI, D.J. LEVANDIER, D.F. VARLEY, and J.M. FARRAR. Can. J. Chem. **72**, 828 (1994).

We present the angular and kinetic energy distributions for the products of the proton transfer reaction $O^- + HF \rightarrow OH + F^-$ at center-of-mass collision energies of 45.0 and 55.8 kJ mol^{-1} (0.47 and 0.58 eV, respectively). At both collision energies, the product angular distributions show forward–backward symmetry, characteristic of the decay of a transient complex living at least several rotational periods. The product kinetic energy distributions show structure that is clearly attributable to the formation of OH in $v' = 0$, 1, and 2. The kinetic energy distribution for a single vibrational state of OH is equivalent to the rotational state distribution for that state. At the higher collision energy, the product kinetic energy distribution shows a clear angular dependence, from which we infer a transition to more direct dynamics involving low impact parameter collisions that access the repulsive wall of the potential surface in bent geometries. The vibrational energy in the products decreases with increasing collision energy, with f_V', the fraction of available energy appearing in vibration, decreasing from 0.28 to 0.22 over the reported collision energy range. We attribute this behavior to a transition from mixed energy release of a **Heavy + Light–Heavy** collision system dominated by the strong attractive well to induced repulsive energy release as the system reaches the low energy repulsive wall of the potential energy surface.

M.A. CARPENTER, M.T. ZANNI, D.J. LEVANDIER, D.F. VARLEY et J.M. FARRAR. Can. J. Chem. **72**, 828 (1994).

On a mesuré les distributions d'énergie angulaire et cinétique des produits de la réaction de transfert de proton $O^- + HF \rightarrow OH + F^-$ au centre de énergies de collision massique, soit 45,0 et 55, 8 kJ mol^{-1} (0.47 et 0.58 eV respectivement). Aux deux énergies de collision, les distributions angulaires du produit présentent une symétrie avant/arrière qui est caractéristique d'un décomposition d'un complexe transitoire qui vit au moins plusieurs périodes de transition. Les distributions d'énergie cinétique du produit montrent une structure qui est clairement attribuable à la formation de OH dans $v' = 0$, 1 et 2. La distribution de l'énergie cinétique pour un seul état vibrationnel de OH est équivalente à la distribution de l'état rotationnel de cet état. À des énergies de collision plus élevées, la distributuion de l'énergie cinétique du produit présente une dépendance angulaire bien marquée à partir de laquelle on peut déduire la présence d'une transition vers une dynamique plus directe impliquant des collisions à faible paramètre d'impact qui atteignent la mur répulsif de la surface de potentiel des géométries recourbées. L'énergie vibrationnelle des produits diminue avec une augmentation de l'énergie de collision, alors que f_V', la fraction d'énergie disponible apparaissant dans la vibration, diminue de 0,28 à 0,22 pour la plage d'énergie de collision rapportée. On attribue ce comportement à une transition d'une perte d'énergie mixte d'un système de collision **Lourd + Léger–Lourd** sous la domination d'un puits d'attraction important vers une perte d'énergie par répulsion induite lorsque le système atteint le faible mur d'énergie répulsive de la surface d'énergie potentielle.

[Traduit par la rédaction]

Introduction

The study of gas phase ion–molecule reactions has applications ranging from electrical discharges, atmospheric chemistry, and combustion processes to plasma chemistry and etching in semiconductor systems. (1) The development of techniques for investigating ionic reactions has proceeded rapidly in the last several years, (see, for example, ref. 2) with special emphasis on understanding the dynamics of such collisions, i.e., energy disposal, direct vs. complex mechanisms, and preferred collision geometries. The study of gas phase proton transfer reactions has been particularly active, with a variety of techniques including molecular beams (3–5), drift and selected ion flow tubes (6, 7), infrared emission (8, 9), and laser-induced fluorescence (LIF) (10, 11) applied to this class of chemical interactions over collision energies from thermal to those approaching covalent bond strengths. It has been particularly fruitful to compare dynamics of ionic systems with those of analogous neutral systems. For example, a comparison of product state distributions in reactions such as F^- and F with hydrogen halides, e.g., F^- + HCl with F + HCl (8, 9, 12), has shown that the vibrational state distributions for the ionic and neutral processes are remarkably similar despite the fact that the ionic system has a deep potential energy well. The pioneering work of Polanyi and co-workers (13, 14) has provided the conceptual basis for understanding these results, namely that the kinematic effect of the **Heavy + Light–Heavy** mass combination dominates energy partitioning and collision dynamics. In proton transfer reactions in particular, the angle between the entrance and exit channels of the potential energy surface in scaled and skewed coordinates (15) is quite small, near 20° for particle transfer between bases of moderate mass. Trajectory studies by Polanyi and collaborators (16–19) on such surfaces have shown that product energy release is determined more by the initial conditions of a trajectory than by details of the potential surface itself. At low collision energies, these studies show that reaction occurs through the mechanism of "mixed energy release", in which proton transfer occurs when both the breaking bond in the reagents and the bond forming in the products are extended. Reagent translation appears in product vibration in collisions governed by mixed energy release. Furthermore, a comparison of energy partitioning in systems exhibiting mixed energy release at low collision energies with results taken at enhanced translational

[1]Present address: Department of Chemistry, State University of New York, Stony Brook, NY 11794, U.S.A.

[2]Present address: Department of Chemistry, Johns Hopkins University, Baltimore, MD 21218, U.S.A.

[3]Author to whom correspondence should be addressed.

Can. J. Chem. Downloaded from www.nrcresearchpress.com by 195.246.54.202 on 09/08/12
For personal use only.

Can. J. Chem. Downloaded from www.nrcresearchpress.com by 195.246.54.202 on 09/08/12
For personal use only.

energy shows an effect Polanyi terms "induced repulsive energy release", in which incremental reagent translation appears in product translation. This effect arises as collisions sample the low energy repulsive wall of the potential surface with both the breaking and forming bonds compressed.

In this paper, we present crossed beam measurements on the proton transfer system (heats of formation are from ref. 20)

[1] $O^- + HF \rightarrow OH + F^-$ $\Delta H° = -46$ kJ mol^{-1}

at center-of-mass collision energies of 45.0 kJ mol^{-1} (0.47 eV) and 55.8 kJ mol^{-1} (0.58 eV). We have already reported on the results of this system at the lower collision energy (21, footnote 4). In this paper, we present a more complete analysis of the lower energy results, as well as results at a higher energy that complement our understanding of **Heavy + Light–Heavy** dynamics, particularly in light of the concepts of mixed energy release and induced repulsive energy release as conceptualized by Polanyi.

Previous studies of this system by Hamilton et al. (10) in thermal energy flow tube measurements and more recent drift tube studies by Knutsen et al. (11) have yielded product state distributions over an expanded range of incident kinetic energies up to 22 kJ mol^{-1}. Those studies showed that, relative to the thermal energy reference data, incremental translation appears to be partitioned preferentially into product vibration. Knutsen et al. have interpreted these observations as a consequence of the attractive well on the potential surface, estimated from *ab initio* calculations to be 187 kJ mol^{-1} relative to the reagents (22). The drift tube experiments showed that the fraction of the total available energy appearing in product vibration increases linearly with increasing translation up to 15 kJ mol^{-1}, consistent with mixed energy release on the **Heavy + Light–Heavy** potential energy surface. Our crossed beam work at 45 kJ mol^{-1} showed that this linear trend began to break down as a larger fraction of incremental reagent translation appeared in product translation, consistent with Polanyi's notion of induced repulsive energy release. We commented that the enhanced translation in the crossed beam experiments may allow collisions to move out of the deep ion-induced dipole potential well and onto the low energy repulsive wall. We noted that at higher energies, we would expect this trend to continue, with product vibrational excitation decreasing significantly as the low energy repulsive wall transforms reagent translation into product translation on the highly skewed O^- + HF potential energy surface.

In this paper, we report on higher energy measurements and demonstrate clearly that incremental translation begins to probe the low energy repulsion. We also show that the product energy distributions have a strong angular dependence, despite evidence that the reaction proceeds through a collision complex living a significant fraction of a rotational period. The observations provide a more detailed signature for reactions undergoing a transition from collision complex-mediated to direct dynamics.

Experimental

The crossed beam apparatus used for this study has been described in detail in previous work (3, 4, 23). We produced O^- ions by electron impact on N_2O at a pressure of ~0.01 torr. Following acceleration and magnetic mass analysis, the ion beam was collimated to 1–2° by electrostatic optics. The neutral beam was produced by passing 500 torr of He through a sample bulb containing HF held at −45°C with an acetonitrile/liquid N_2 bath. At this temperature the HF vapor pressure is ~40 torr. The mixture was expanded through a 0.07 mm nozzle, collimated to 2° by a 1 mm electroformed skimmer and 3.5 mm square aperture, modulated at 30 Hz to allow for background correction, and allowed to pass into the collision chamber where it intersects the collimated ion beam. Products were detected as a function of laboratory angle, energy and mass using a rotatable electrostatic energy analyzer – quadrupole mass filter equipped with a dual microchannel plate ion detector. The resolution of the energy analyzer is 0.07 eV in the laboratory coordinate system. The energy scale was calibrated in a separate experiment by resonant charge transfer from NO^- also produced by electron impact on N_2O, to NO expanded supersonically in the crossed beam.

We collected F^- product flux distributions as function of laboratory kinetic energy at selected laboratory angles, measuring an angular distribution by integrating the signal over energy to normalize the data. Energy and angular distributions were measured with a multichannel scaler implemented with CAMAC modular electronics. In this study, we measured product fluxes at 20 to 26 angles over the laboratory scattering angle range from –2° to 112° measured relative to the ion beam direction. At each angle, reactive fluxes were binned into 80 kinetic energy channels, giving a total of 1600 to 2080 data points for each experiment from which to construct the center of mass kinetic energy and angular distributions.

Results

The experiments were performed at collision energies of 45.0 and 55.8 kJ mol^{-1}. Figure 1 shows experimental data at the higher collision energy, along with the results of an iterative deconvolution data analysis program we describe later. The kinematic Newton diagram at the bottom of the figure shows the concentric circles corresponding to the formation of F^- *in concert with* OH in specific vibrational states with quantum numbers $v' = 0$, 1, and 2. The laboratory speeds at which these vibrational states appear for a given laboratory scattering angle are marked in the figure, showing clear correspondence with the structure in the experimental data. Our analysis of these data is directed toward extracting angular and kinetic energy distributions for product formation, vibrational state populations, and characteristics of the OH rotational state distributions within each vibrational state.

Analysis

In our earlier report on this system (21), we employed the integration fitting method for analyzing the center-of-mass cross sections. This method assumes that the center-of-mass cross section, $I_{c.m.}(u,\theta)$, defined in terms of the center-of-mass speed u and scattering angle θ, can be written as a product function of center-of-mass speed distributions $f^{v'}(u)$ and angular distribution functions $g^{v'}(\theta)$ for each vibrational state. The center-of-mass scattering angle θ is defined such that F^- products moving in the direction of the initial HF projectile in the center-of-mass are defined to scatter through 0°.[5] With this definition, forward scattered F^- products correspond to large impact parameter collisions. The function data $f^{v'}(u)$ and $g^{v'}(\theta)$

[4]The collision energy we reported in ref. 21 has been revised upward by 10% owing to a more accurate procedure for calibrating the energy zero of our detection system.

[5]Note that this definition of scattering angles is the opposite of our usual definition, employed in ref. 21, in which the incident ion direction in center of mass coordinates defines forward scattering. The definition employed in this paper is more physically intuitive, since the direction of the product we detect, F^-, is referred to the center of mass direction of HF, from which F^- originates.

Can. J. Chem. Downloaded from www.nrcresearchpress.com by 195.246.54.202 on 09/08/12
For personal use only.

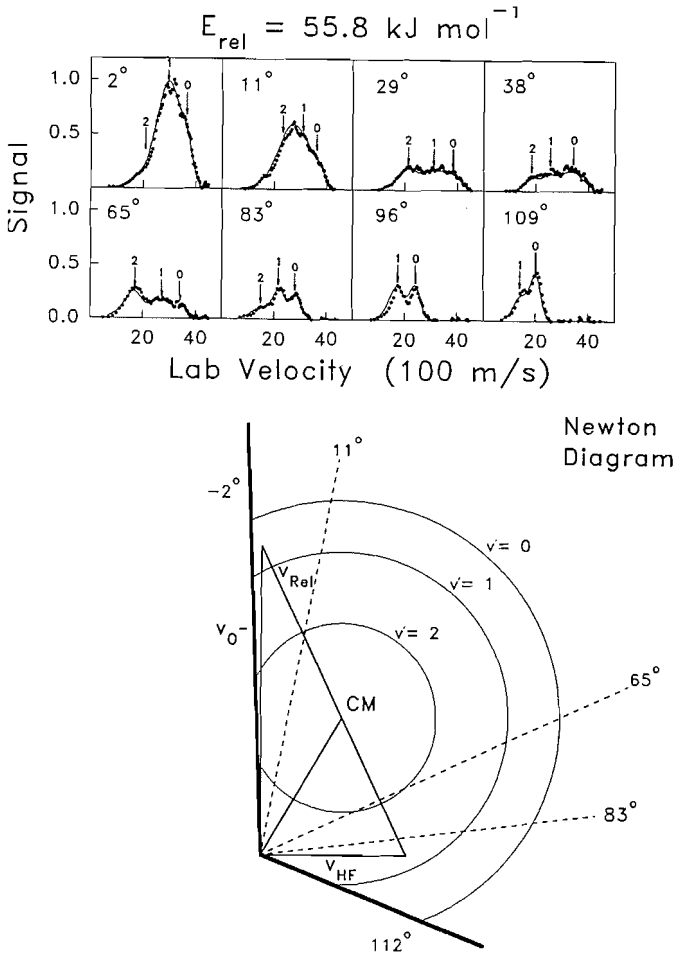

FIG. 1. Experimental F^- reactive flux data and Newton diagram for O^- + HF reactive collisions at a relative energy of 55.8 kJ mol^{-1}. The experimental data points (····) have been transformed to velocity space for comparison with the results of kinematic calculations (——), and the vertical arrows indicate the velocities at which the corresponding OH vibrational states appear in the fluxes.

depend on a small parameter set that is optimized to fit the laboratory data when the center-of-mass data are transformed to the laboratory. This procedure yielded a satisfactory fit to the data, although the intensities produced by the calculations were significantly smaller than experiment for wide laboratory scattering angles near the HF beam. We discovered that the assumption of separation of the variables u and θ in the center-of-mass cross section was responsible for this discrepancy, which became increasingly important with increasing collision energy. We therefore applied the iterative deconvolution procedure of Siska (26), in which we invert transformation relation [2]

$$[2] \quad I_{lab}(v,\Theta) = \sum_{i=1}^{N} f_i I_{c.m.}(u_i,\theta) \frac{v^2}{u_i^2}$$

while deconvoluting the dispersion in the initial beam velocities. This procedure yields a grid of center-of-mass intensities $I_{c.m.}(u_i,\theta)$ defined on the set of points in laboratory velocity space at which the experimental data were acquired. When transformed to the laboratory with suitable averaging over initial beam conditions the center-of-mass intensities $I_{c.m.}(u,\theta)$ recover the laboratory data with a standard deviation of 4%. The

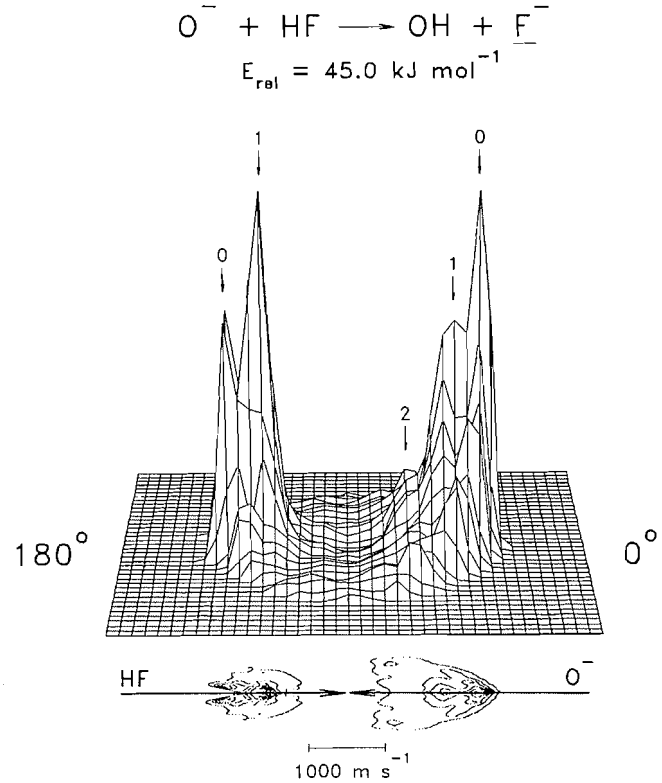

FIG. 2. Barycentric polar flux axonometric plots and contour projections for the F^- product in the O^-+ HF reaction at a collision energy of 45.0 kJ mol^{-1}. Structure in the flux plot corresponds to contributions from OH produced v' = 0, 1, and 2 as labelled.

center-of-mass intensity grid is intrinsically nonseparable in the variables u and θ. The center-of-mass intensities that we obtain in this way provide a more faithful reproduction of the laboratory data than those constructed from integration fitting. We employ a linear bivariate interpolation algorithm to calculate values of the deconvoluted flux on a Cartesian grid in the center-of-mass velocity space. In Figs. 2 and 3, we present three dimensional axonometric representations of the center-of-mass scattering fluxes for F^- production at both collision energies. The data plotted in these figures are the results of pointwise deconvolution of the experimental data, and embody the noise of the original data, amplified by the deconvolution procedure.

The three dimensional flux maps shown in Figs. 2 and 3 have peaks at 0° and 180° in center-of-mass coordinates, showing clear symmetry about 90°. Flux distributions with this symmetry are generally diagnostic of the decay of a transient complex living at least several rotational periods (25, 26), supporting calculations that predict the existence of an O^-·HF complex stable relative to O^- + HF by 187 kJ mol^{-1} (22). In the decay of such a transient complex, the products "forget" the direction of initial reagent approach and the energy distributions are independent of scattering angle. Nevertheless, the fact that we observed a strong angular dependence to the product state distributions implies that the collision complex model is not quantitatively applicable, a point we address in detail below.

The strong nonseparability of the data in u and θ implies that portraying the product kinetic energy distribution by integrating the center-of-mass fluxes over the full range of scattering angles $0° \leq \theta \leq 180°$ will result in a significant loss of dynamical information. In order to visualize the strong angular depen-

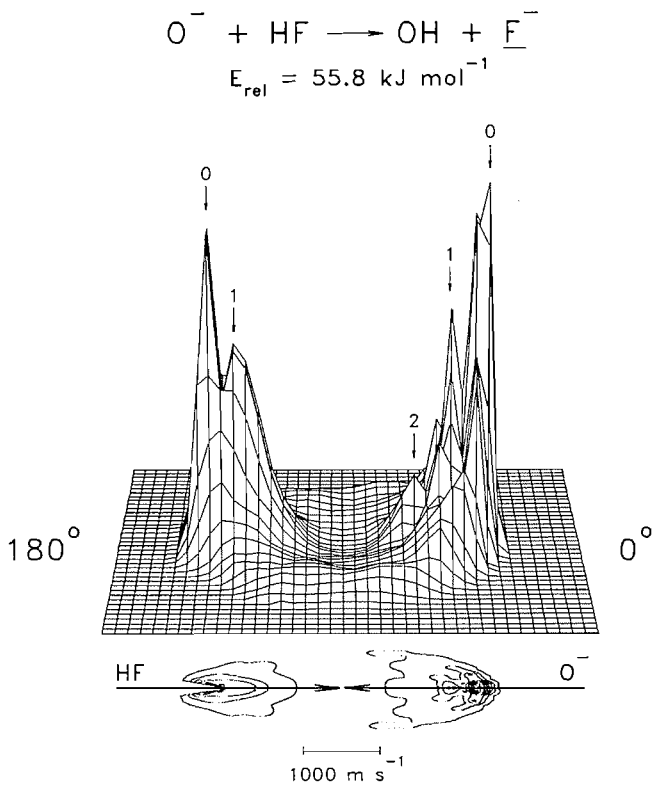

FIG. 3. Barycentric polar flux axonometric plots and contour projections for the F^- product in the O^- + HF reaction at a collision energy of 55.8 kJ mol^{-1}. Structure in the flux plot corresponds to contributions from OH produced in $v' = 0$, 1, and 2 as labelled.

dence of the product energy distributions, we have divided the full angular scattering range $0° \leq \theta \leq 180°$ into n smaller bins, each of width $180°/n$, and have computed the partial kinetic energy distribution for the kth bin by integration over the appropriate angular range:

$$[3] \quad P_k(E'_T) \propto u^{-1} \int_{(k-1)(\pi/n)}^{k(\pi/n)} I(u,\theta) \sin\theta \, d\theta \text{ for } 1 \leq k \leq n$$

In Figs. 4 and 5, we show kinetic energy distributions obtained by dividing the angular range into six bins. In the lower collision energy experiment, shown in Fig. 4, the product recoil distributions show a weak dependence on angular range, but the resolution of the distributions into contributions from individual vibrational states is roughly constant, independent of angular range. The relative contributions from the OH vibrational state populations reflect the fact that the angular distributions are state dependent. The near constancy of the widths of the individual components reflects the independence of product rotational excitation on scattering angle.

At the higher collision energy, the product recoil distributions shown in Fig. 5 have a much stronger angular dependence. F^- scattering in the angular range from 30° to 180° results in kinetic energy distributions that can be resolved into three components, but the individual components are quite broad. In contrast, however, the vibrational states are much more completely resolved for F^- scattered in the angular range from 0° to 30°, this observation indicates that the distributions of OH rotational energy for each vibrational state are significantly narrower for such collisions. F^- products scattered in the forward hemisphere relative to incoming HF correspond to collisions in which O^- strips a proton from HF, the F^- product following the initial HF direction, and OH recoiling in the opposite direction. The implications of this observation are that such collisions take place over fairly narrow ranges of impact parameter. The product recoil distributions show that OH formation through direct stripping collisions becomes increasingly important as the collision energy is raised. This behaviour is characteristic of collisions on potential surfaces with strong attractive components.

It is possible to use the angle-dependent kinetic energy distributions for each vibrational state to estimate OH rotational population distributions (27). Because our experiments lack rotational resolution, estimating the rotational distribution from a continuous kinetic energy distribution for the production of a single vibrational level is only of limited validity. Nevertheless, estimates of the mean rotational excitation for each vibrational state as well as the widths of the distributions provide information diagnostic of the potential surface. At the lower collision energy of 45 kJ mol^{-1}, the product rotational state distributions are angle independent. For OH in $v' = 0$ and 1, the most probable J' is approximately 15, decreasing to 12 in $v' = 2$. These quantum numbers correspond to rotational energies of 54 and 35 kJ mol^{-1} respectively. In energy space, the full widths at half maximum of the distributions are 30 kJ mol^{-1} for $v' = 0$ and 1, decreasing to 20 kJ mol^{-1} for $v' = 2$.

At the higher collision energy of 55.8 kJ mol^{-1}, the widths of the product rotational state distributions have a significant angular dependence, although the most probable energies are reasonably independent of angle. For backward angles, OH is formed with most probable J' values between 13 and 15 independent of vibrational state. The widths of these distributions decrease monotonically with increasing vibration: for OH in $v' = 0$, the rotational distribution is 70 kJ mol^{-1} wide, decreasing to ~50 kJ mol^{-1} for $v' = 1$ and 40 kJ mol^{-1} for $v' = 2$. In the forward direction, corresponding to stripping collisions, the widths of the rotational distributions are significantly narrower than for the backward direction, ranging from 30 kJ mol^{-1} for $v' = 0$ and 1 to 22 kJ mol^{-1} for $v' = 2$. Corresponding numbers for backward scattering are more than a factor of two larger. The principal trend in the experimental data is the development of much broader distributions in OH rotation for backward scattered F^- products. Collisions yielding such products correspond to low impact parameter encounters. In the collinear limit, proton transfer would result in F^- scattered through 180°; larger impact parameters result in sideways-peaked product distributions, until large impact parameters result in stripping collisions.

The angular distributions for the individual vibrational states of the products can be obtained by integrating the center-of-mass fluxes over the appropriate ranges of speeds. Those distributions are shown in Figs. 6 and 7. At the lower collision energy, the angular distributions for forming OH in $v' = 0$ and 1 show forward–backward symmetry, indicative of a collision complex contribution to the scattering. The $v' = 2$ state, formed only 5 kJ mol^{-1} above threshold, has an asymmetric angular distribution favoring forward scattering, corresponding to a stripping collision through a large impact parameter. At the higher collision energy, the angular distributions for all three states of OH show approximate forward backward symmetry. The $v' = 2$ state is now formed 16 kJ mol^{-1} above threshold, and the asymmetry we observed earlier is now gone.

The vibrational state populations for OH ($v' = 0$, 1, and 2), reported in Table 1, were extracted numerically from the exper-

Can. J. Chem. Downloaded from www.nrcresearchpress.com by 195.246.54.202 on 09/08/12
For personal use only.

Can. J. Chem. Downloaded from www.nrcresearchpress.com by 195.246.54.202 on 09/08/12
For personal use only.

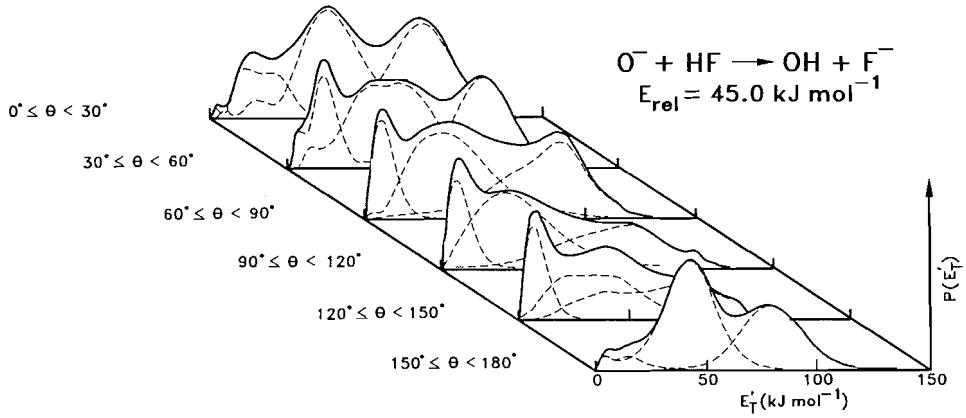

FIG. 4. Angular dependent partial recoil energy distribution $P_k(E_T')$ at a collision energy of 45.0 kJ mol^{-1}, computed by integrating center of mass fluxes over angular ranges indicated. Dashed curves correspond to distributions of individual vibrational states $v' = 2$, 1, and 0, in order of increasing *translational* energy.

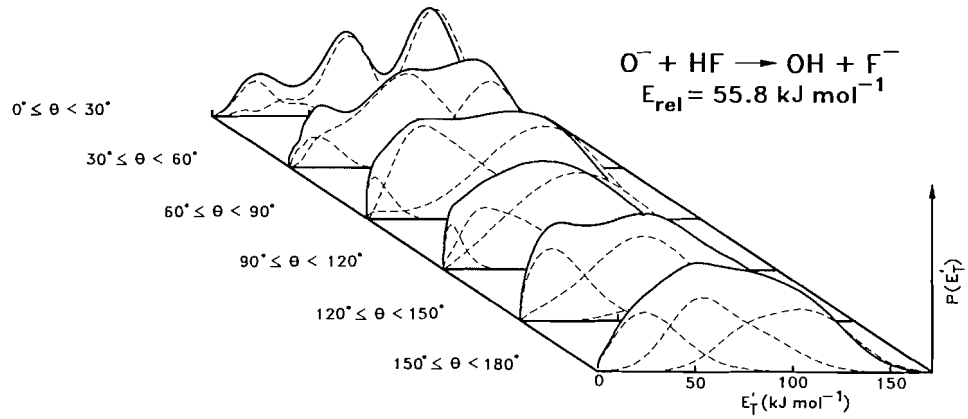

FIG. 5. Angular dependent partial recoil energy distributions $P_k(E_T')$ at a collision energy of 55.8 kJ mol^{-1}, computed by integrating center of mass fluxes over angular ranges indicated. Dashed curves correspond to distributions of individual vibrational states $v' = 2$, 1, and 0, in order of increasing *translational* energy.

TABLE 1. OH vibrational state populations

v'	Experimental 45 kJ mol^{-1}	Phase space	Experimental 55.8 kJ mol^{-1}	Phase space
0	0.45 ± 0.025	0.64	0.53 ± 0.025	0.58
1	0.45 ± 0.025	0.32	0.40 ± 0.02	0.33
2	0.04 ± 0.02	0.04	0.07 ± 0.02	0.09

imental data by decomposing the structure in the data into contributions from individual vibrational states and transforming the data to the center-of-mass using the iterative deconvolution procedure. The resultant center-of-mass fluxes were then integrated over appropriate ranges of u and θ to yield vibrational state probabilities. In the integration-fitting procedure we employed in our earlier report on this system, we assumed relative vibrational state populations in the center-of-mass system, varying the amplitudes and shapes of the recoil distributions for each state to fit the data. The method did not correctly recover all of the flux in $v' = 0$ or 1. The iterative deconvolution procedure recovers the experimental data more faithfully, but more accurate state population estimates require a set of data covering all center-of-mass space. Inspection of the contour plots of Figs. 2 and 3 indicates that a "wedge" of intensity is missing near 180°, comprised primarily of flux in OH ($v' = 0$). In order to estimate the $v' = 0$ vibrational state population, we assumed

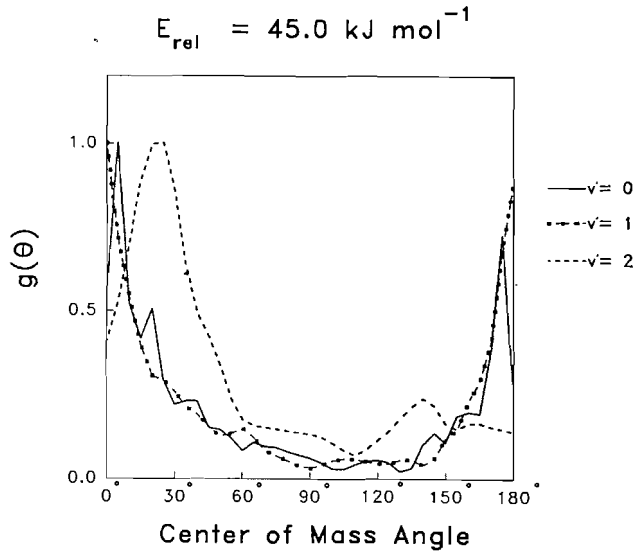

FIG. 6. Center of mass state-resolved angular distributions for OH ($v' = 0$, 1, and 2) at a collision energy of 45.0 kJ mol^{-1}.

that the wedge intensity across the gap was constant and equal to the value of the flux at the apex of the wedge. Such an approximation may underestimate the flux into $v' = 0$, making

Can. J. Chem. Downloaded from www.nrcresearchpress.com by 195.246.54.202 on 09/08/12
For personal use only.

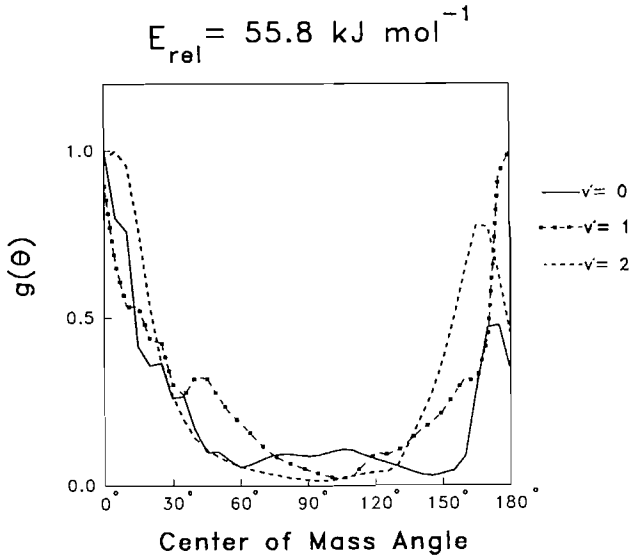

FIG. 7. Center of mass state-resolved angular distributions for OH ($v' = 0$, 1, and 2) at a collision energy of 55.8 kJ mol^{-1}.

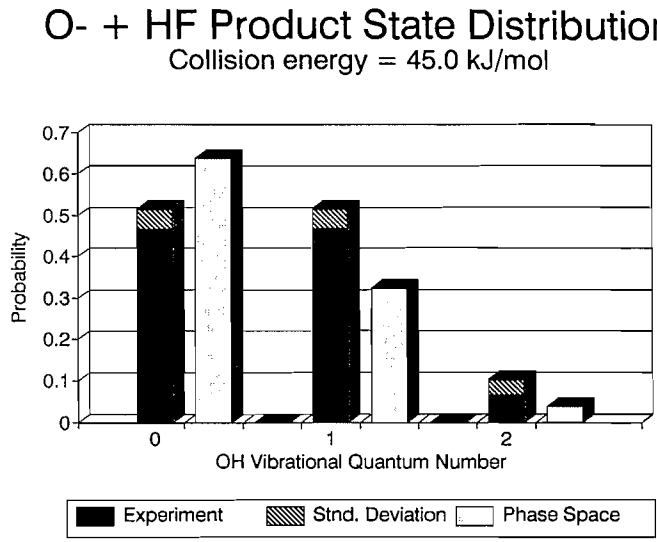

FIG. 8. OH product vibrational state populations, compared with statistical phase space theory calculations as described in the text, for a collision energy of 45.0 kJ mol^{-1}. Experimental range shown corresponds to one standard deviation.

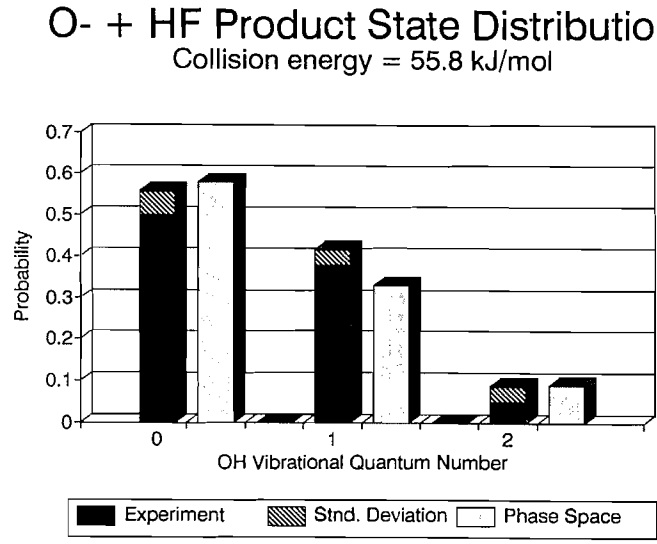

FIG. 9. OH product vibrational state populations, compared with statistical phase space theory calculations as described in the text, for a collision energy of 55.8 kJ mol^{-1}. Experimental range shown corresponds to one standard deviation.

our estimates of the amount of energy appearing in product vibrational excitation an upper limit. Reasonable estimates for the missing flux indicate that our reported value for the $v' = 0$ state population may be low by a few percentage points at most, underscoring our claim that our tabulated state populations result in upper limits on the product vibrational excitation.

The evidence we have presented from angular distribution measurements for the participation of a transient collision complex living several rotational periods has motivated us to compare the measured vibrational product state distributions with the results of angular momentum conserving statistical phase space theory calculations (28). The calculations are performed by evaluating the number of OH product quantum levels accessible from an O^-·HF complex with specified total angular momentum; the total energy accessible to the products is the sum of the collision energy and the reaction exothermicity, 91.0 and 101.8 kJ mol^{-1} for the two collision energies reported here. Angular momentum partitioning in the exit channel is determined by the centrifugal barrier of the separating products. The total angular momentum is computed by assuming a Langevin thermal rate and an $E^{-1/2}$ dependence of the reactive cross section. This estimate yielded a value of $70\hbar$ at both energies. The product state populations vary by less that 1% for $10\hbar$ variations in the total angular momentum. That comparison is made both in Table 1 and in Figs. 8 and 9. At the lower collision energy for which results are shown in Fig. 8, the deviations between experiment and theory are significant, with more $v' = 1$ and less $v' = 0$ formed than predicted by theory. We have already commented (21) that this preference for product vibrational excitation is a reflection of specific nonstatistical dynamics on the O^- + HF potential surface in which the long range attraction in the entrance channel accelerates the reagents together in a manner that mimics a direct reaction. At the higher collision energy, less energy appears in product vibration. The experimental distribution more closely approximates phase space theory, although the reaction shows significant evidence of deviating from collision complex behavior. As we discuss later, the partitioning of excess translation into product translation reflects the accessibility of the low energy repulsion as collision energy increases.

The critical issue in understanding how energy dependent trajectories probe the potential energy surface in this study comes from assessing how incremental translational energy is partitioned into product vibration. Figure 10 shows a plot of the average value of the fraction of the total energy in product vibration, $f_{V'}$, as a function of the total energy. The variable $f_{V'}$ is defined as follows:

$$[4] \quad f_{V'} = \sum_{v'=0}^{2} P_{v'} E_{v'} E_{\text{total}}$$

In this expression, $P_{v'}$ is the probability of populating the v' quantum state of OH and E_{total} is the total energy accessible to the system, defined by the sum of reagent collision and internal energy and reaction exothermicity as follows:

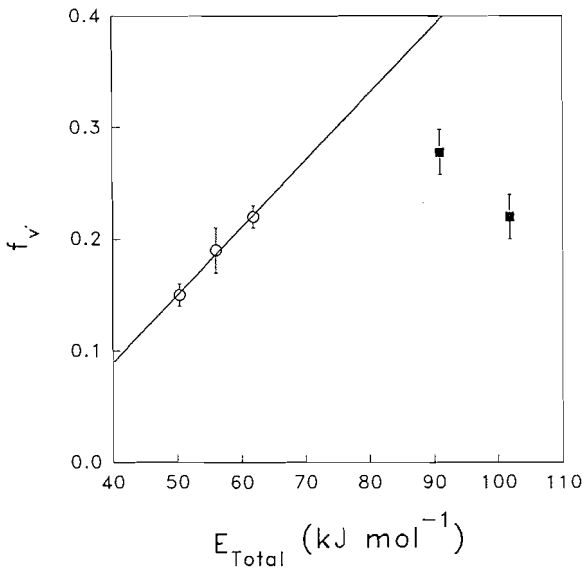

FIG. 10. Fraction of total energy in product vibration, $f_{V'}$, vs total available energy E_{total}. The three lower energy points are from refs. 10, 11 at collision energies of 3.8, 9.6, and 15.4 kJ mol^{-1}, while the filled symbols (■) correspond to the collision energies of the present study.

$$[5] \quad E_{total} = E_{rel} + E_{vib} + E_{rot} - \Delta H^\circ$$

This expression employs mean values when there exists a distribution in energy. HF reagents in the drift tube studies have a significant thermal rotational energy contribution while HF reagents produced by seeded supersonic expansion in the present experiments are rotationally cold. The graph shows data from the drift tube studies as well as from the experiments reported here and illustrates a number of important points. In the lower collision energy experiments done in flow tubes at collision energies up to 15 kJ mol^{-1} (E_{total} = 62 kJ mol^{-1}), $f_{V'}$ increases linearly with collision energy, consistent with mixed energy release. At 45 kJ mol^{-1} collision energy (E_{total} = 91 kJ mol^{-1}), the value of $f_{V'}$ continues to increase but departs from linearity as less of the incremental reagent translation appears to be partitioned into product vibration than at the lower energies. That trend is underscored in the highest collision energy experiment, as $f_{V'}$ now decreases, indicating that an even higher fraction of the incremental translational energy of the reagents appears in product translation. The data thus suggest that trajectories explore new portions of the potential energy surface at these higher collision energies.

Discussion

We have commented in our earlier study of the O^- + HF system that a discussion of energy partitioning on a specific potential surface must be concerned with two issues: *baseline* energy partitioning at a specific reference energy, e.g., thermal; and the effect of *incremental* energy, either in the form of internal or translational excitation, on the baseline. Previous studies on **Heavy + Light–Heavy** reaction systems show that the dynamics are dominated by kinematics rather than specific features of the potential energy surface itself. The extensive trajectory studies of Polanyi and co-workers (16–19) shows that reactive collisions on such highly skewed surfaces are direct, with a strong propensity to cut the corner separating the entrance and exit valleys. These motions correspond to light atom transfer from configurations extended from equilibrium bond lengths with little momentum transfer to the departing heavy atoms, yielding reaction products that are highly vibrationally excited. The thermal energy studies of ref. 10 on the O^- + HF system are also consistent with baseline energy partitioning into product vibration via this mechanism of mixed energy release.

The concept of "induced repulsive energy release" was introduced by Polanyi and co-workers to address partitioning of incremental translational energy on **Heavy + Light-Heavy** potential surfaces (12). In this picture, reactive trajectories with excess translation penetrate far into the "corner" of the highly skewed potential surface where both the forming and breaking bonds are compressed. The trajectory moves into the exit valley with little motion perpendicular to the reaction coordinate, yielding products with high translational excitation. Depending on the extent to which the collision geometry in the corner is bent, the nascent products will partition some of the incident translation into product rotation. The trajectory therefore explores a new portion of the potential surface relative to reference trajectories at lower energies.

The deep potential well of the O^- + HF system, estimated from *ab initio* calculations to lie 187 kJ mol^{-1} below the reagents, adds new factors to the nature of mixed energy release on **Heavy + Light-Heavy** potential energy surfaces. In the flow and drift tube studies of refs. 10 and 11, a fourfold increment in relative translational energy from 3.8 to 15.4 kJ mol^{-1} results in a linear increase in the fraction of the total energy appearing in product vibration, shown in Fig. 10. As we noted in our previous discussion, this linear increase is consistent with corner cutting trajectories and mixed energy release. Because the increment in translational energy is only 6% of the O^-·HF well depth, these reactive trajectories explore essentially the same regions of the potential energy surface over the full collision energy range, and thus "induced repulsive energy release" does not apply. Energy partitioning mimics the mixed energy release case where proton transfer occurs in geometries in which both breaking and forming bonds are extended.

At the higher collision energies of the beam experiments, 45.0 and 55.8 kJ mol^{-1}, the increments in translation over the thermal energy baseline collision energy are 41 and 52 kJ mol^{-1}, respectively, representing 22 to 28% of the O^-·HF well depth. In this case, the incremental energy allows collisions to access additional regions of the potential energy surface, in particular the repulsive wall. Corner cutting trajectories are less important in this energy regime as high translation in conjunction with the highly skewed nature of the **Heavy + Light–Heavy** potential surface forces trajectories past the well and onto the low energy repulsive wall. The fact that collisions at these higher energies show significant deviations from statistical behavior in the product vibrational state distributions with an enhanced propensity to partition reagent translation into product translation supports the claim that at these energies, the influence of the well in the reaction dynamics is giving way to low energy repulsive forces.

Induced repulsive energy release may impart a significant torque on the newly formed product as the three atom collision system moves from the corner into the exit channel. Trajectory studies by Polanyi and co-workers (12) have demonstrated that this effect manifests itself as a partitioning of incremental reagent translation into product translation and rotation: $\Delta T \rightarrow \Delta T' + \Delta R'$. Although buffer gas collisions in the thermal energy measurements (10, 11) prevent the determination of product

Can. J. Chem. Downloaded from www.nrcresearchpress.com by 195.246.54.202 on 09/08/12
For personal use only.

rotational energies and therefore do not give us a baseline for rotational energy, the constancy of nascent product rotational excitation in our own data suggests that incremental translation appears primarily in product translation, with product rotational angular momenta of no more than 12–15$\hbar$. However, a very distinct broadening of the rotational energy distributions for low impact parameter encounters appears in the higher collision energy data. The widths of the rotational distributions for these collisions are approximately twice as large as for products scattered into the opposite hemisphere. For such low impact parameter collisions, the acceleration of the approaching reagents by the long range attraction projects the system onto the low energy repulsive wall in bent configurations. Such collisions have a clear direct character and further suggest that the distribution of low impact parameters contributes to the widths of the rotational distributions, an important probe of the potential energy surface. Such trajectories are truly diagnostic of the transition from collision complex mediated dynamics to direct, impulsive collisions.

Conclusions

The work we have reported here represents one of the most detailed dynamical studies of a simple ion–molecule reaction presented to date. Product angular distributions indicate that the strong attractive potential of the approaching reagents plays a dominant role in the dynamics by controlling energy partitioning of the transient O^-·HF complex. Nevertheless, vibrational product state distributions are in clear disagreement with Phase Space theory, in that more OH is formed in $v' = 1$ and less in $v' = 0$, than predicted by theory. The product kinetic energy distributions for single vibrational states have been analyzed for the OH rotational energy distributions. The results show that OH is formed with $J' \sim 12$–$15\hbar$, roughly independent of vibrational state. The widths of the rotational state distributions undergo a marked broadening at the higher collision energy for low impact parameter collisions, suggesting that such collisions are direct, and that a distribution of bent geometries on the low energy repulsive wall of the surface determines the partitioning of reagent translation into product translation and rotation. Such a picture is consistent with the onset of induced repulsive energy release as collisions sample the low energy repulsive wall.

The data presented for this reaction are comparable in detail to those for the $F + H_2$ reaction (29). The extensive energy dependent internal energy distributions as well as state-specific angular distributions will provide critical tests for *ab initio* potential energy surfaces as well as dynamics calculated on such surfaces. We hope that this system will become a benchmark for low energy proton transfer systems.

Acknowledgements

We gratefully acknowledge the United States Department of Energy Division of Chemical Sciences for support of this work. J.M.F. is grateful to Professors Franco Vecchiocattivi and Piero Casavecchia and Dr. Nadia Balucani of the University of Perugia for helpful conversations. Travel support from a NATO Grant for International Collaboration in Research is also gratefully acknowledged. M.T.Z. thanks the University of Rochester for support through the Advantage Scholars Internship Program. M.A.C. also thanks the University of Rochester for support as a Sherman Clarke Fellow. We also wish to acknowledge Professor Stephen Leone for encouragement and helpful conversations on this system.

1. State-selected and state-to-state ion–molecule reaction dynamics. Part 1: Experiment. *Edited by* C.Y. Ng and M. Baer; Part 2: Theory. *Edited by* M. Baer and C.Y. Ng. Vol. LXXXII. *In* Advances in chemical physics. Wiley-Interscience, New York. 1992.
2. J.M. Farrar and W.H. Saunders, Jr. (*Editors*). Techniques for the study of ion–molecule reactions. Wiley-Interscience, New York. 1988.
3. D.F. Varley, D.J. Levandier, and J.M. Farrar. J. Chem. Phys. 96 8806 (1992).
4. D.J. Levandier, D.F. Varley, and J.M. Farrar. J. Chem. Phys. 97, 4008 (1992).
5. C.–L. Liao, R. Xu, G.D. Flesch, M. Baer, and C.Y. Ng. J. Chem. Phys. 93, 4818 (1990).
6. R.R. Squires, V.M. Bierbaum, J.J. Grabowski, and C.H. DePuy. J. Am. Chem. Soc. 105, 5185 (1983).
7. J.M. Van Doren, S.E. Barlow, C.H. DePuy, and V.M. Bierbaum. Int. J. Mass Spectrom. Ion Proc. 109, 305 (1991).
8. J.C. Weisshaar, T.S. Zwier, and S.R. Leone. J. Chem. Phys. 75, 4873 (1981).
9. A.O. Langford, V.M. Bierbaum, and S.R. Leone. J. Chem. Phys. 83, 3913 (1985).
10. C.E. Hamilton, M.A. Duncan, T.S. Zwier, J.C. Weisshaar, G.B. Ellison, V.M. Bierbaum, and S.R. Leone. Chem. Phys. Lett. 94, 4 (1983).
11. K. Knutsen, V.M. Bierbaum, and S.R. Leone. J. Chem. Phys. 96, 298 (1992).
12. A.M.G. Ding, L.J. Kirsch, D.S. Perry, J.C. Polanyi, and J.L. Schreiber. Faraday Discuss. Chem. Soc. 55, 252 (1973).
13. J.C. Polanyi. Acct. Chem. Res. 5, 161 (1972).
14. J.C. Polanyi. Science, 236, 680 (1987).
15. H. Eyring and M. Polanyi. Z. Physik. Chem. B12, 279 (1931).
16. K.G. Anlauf, J.C. Polanyi, W.H. Wong, and K.B. Woodall, J. Chem. Phys. 49, 5189 (1968).
17. K.G. Anlauf, P.J. Kuntz, D.H. Maylotte, P.D. Pacey, and J.C. Polanyi. Faraday Discuss. Chem. Soc. 44, 183 (1967).
18. D.H. Maylotte, J.C. Polanyi, and K.B. Woodall. J. Chem. Phys. 57, 1547 (1972).
19. C.A. Parr, J.C. Polanyi, and W.H Wong. J. Chem. Phys. 58, 5 (1973).
20. S.G. Lias et al. J. Phys. Chem. Ref. Data 17, Suppl. 1 (1988).
21. D.J. Levandier, D. F. Varley, M.A. Carpenter, and J.M. Farrar. J. Chem. Phys. 99, 148 (1993).
22. S.E. Bradforth, D.W. Arnold, R.B. Metz, A. Weaver, and D.M. Neumark. J. Phys. Chem. 95, 8066 (1991).
23. R.M. Bilotta, F.N. Preuninger, and J.M. Farrar. J. Chem. Phys. 73, 1637 (1980).
24. P.E. Siska. J. Chem. Phys. 59, 6052 (1973).
25. R.D. Levine and R.B. Bernstein. Molecular reaction dynamics and chemical reactivity Oxford, New York. 1987. pp. 412–417.
26. W.B. Miller, S.A. Safron, and D.R. Herschbach. Faraday Discuss. Chem. Soc. 44, 108 (1967).
27. D.M. Neumark, A.M. Wodtke, G.N. Robinson, C.C. Hayden, and Y.T. Lee. J. Chem. Phys. 82, 3045 (1985).
28. P. Pechukas, J.C. Light, and C. Rankin. J. Chem. Phys. 44, 794 (1966).

Can. J. Chem. Downloaded from www.nrcresearchpress.com by 195.246.54.202 on 09/08/12
For personal use only.

Microtube flowing coulometry[1]

LIFENG CHEN,[2] CHRISTA L. COLYER,[3] MUTHONI G. KAMAU, JAN C. MYLAND, KEITH B. OLDHAM,[4] AND PETER G. SYMONS
Trent University, Peterborough, ON K9J 7B8, Canada

Received July 20, 1993

This paper is dedicated to Professor John C. Polanyi on the occasion of his 65th birthday

LIFENG CHEN, CHRISTA L. COLYER, MUTHONI G. KAMAU, JAN C. MYLAND, KEITH B. OLDHAM, and PETER G. SYMONS. Can. J. Chem. **72**, 836 (1994).

An aqueous solution containing supporting electrolyte and a small concentration of an electroactive analyte is allowed to flow, under a gravitational head, through a polarized platinum tube. The tube is narrow enough that, during their few seconds of residence time within the tube, virtually all the analyte molecules are able to diffuse to the tube wall and be electrolytically destroyed. The analyte concentration is accurately calculable, when the applied voltage and head are optimized, from the measured flow rate of the solution and the steady-state electric current, the latter being background-corrected by subtracting the current under no-flow conditions. Though the detailed theory is complicated, the principles of the method and its experimental realization are straightforward.

LIFENG CHEN, CHRISTA L. COLYER, MUTHONI G. KAMAU, JAN C. MYLAND, KEITH B. OLDHAM et PETER G. SYMONS. Can. J. Chem. **72**, 836 (1994).

On permet à une solution aqueuse contenant un électrolyte de support et une faible concentration d'un produit à analyser électroactif de s'écouler, par gravitation, à travers un tube de platine polarisé. Le tube est suffisamment étroit pour que, durant les quelques secondes où elles sont présentes dans le tube, pratiquement toutes les molécules du produit à analyser sont capables de diffuser vers la paroi du tube et d'être détruites électrolytiquement. Quand on optimise le voltage appliqué et la gravitation, on peut calculer avec précision la concentration du produit à analyser à partir de la mesure de la vitesse d'écoulement de la solution et du courant électrique à l'état stationnaire; on corrige ce dernier pour le bruit de fond en soustrayant le courant observé lorsqu'il n'y a pas d'écoulement. Même si la théorie détaillée est complexe, les principes de la méthode et sa réalisation expérimentale sont simples.

[Traduit par la rédaction]

Introduction

In analytical coulometry the analyte is quantitatively removed from solution by exhaustive electrolysis. The original analyte concentration c^b is then calculated by the formula

$$[1] \qquad c^b = \frac{Q}{nFV}$$

from two measured quantities (the total electric charge Q and the sample volume V) and two known constants (Faraday's constant F and the number n of electrons involved in the electrode reaction). Coulometry with the potential controlled electronically was introduced by Hickling (1) in 1942; by 1975, a review (2) of this topic cited almost 700 references. Since that time coulometry continues to hold its place in the repertoire of electroanalytical techniques, though rival amperometric methods have stolen most of the limelight.

Even when diffusion is augmented by convective transport, exhaustive electrolysis is a slow process. Because the electrolysis time increases with the cell volume, researchers have striven to reduce V, leading to such developments as thin-layer coulometry (3). A difficulty that is then encountered is in delineating the boundary of the electrolysis zone and in measuring its volume accurately. These obstacles are overcome by allowing the analyte solution to flow slowly and steadily through the cell: the electrolysis zone boundary is no longer important, and the measurement of a small volume is replaced by the easier task of measuring a slow flow rate (dV/dt). The analyte concentration is now calculable from the steady-state current I by the formula

$$[2] \qquad c^b = \frac{I}{nF(dV/dt)} = \frac{I}{nFf}$$

which may be obtained from eq. [1] by differentiation. Henceforth we shall use f, instead of dV/dt, to denote the constant flow rate. Equation [2] provides the basis of flowing coulometry. Note that, even though the measured electrical variable is now the *current*, the technique is appropriately named "flowing *coulo*metry" (4) because its principles are closer to those of classical coulometry than they are to standard amperometric methods. Flowing coulometry has been practiced for many years, a review (5) of the technique appearing as early as 1966.

In this article we describe experiments in which, driven by a gravitational head, a solution of an electroactive analyte flows through a narrow cylindrical metal tube, which serves to define the solution's flow rate. During its few seconds of residence time within the tube, effectively *all* the analyte is able to diffuse to the tube's inner wall, where it is oxidized or reduced. Because of the inherent slowness of diffusion, this rapid removal of a solute by electrolysis is possible only in the *micro*bore metal tubing that has recently become available commercially. Studies of electrochemical processes within platinum and gold tubes of considerably wider bores were pioneered by Blaedel and co-workers (6) a quarter of a century ago, and have continued in this area (7).

[1]Dedicated to John Charles Polanyi, a brilliant scientist and former classmate of the corresponding author, on the occasion of the 65th anniversary of his birth.

[2]Present address: Department of Chemical Engineering, Queen's University, Kingston, ON K7L 3N6, Canada.

[3]Ph.D. Candidate in the Trent-Queen's Graduate Program in Chemistry, Queen's University, Kingston, ON K7L 3N6, Canada.

[4]Author to whom correspondence may be addressed (telephone: (705) 748-1336; facsimile: (705) 748-1625; E-mail: KOldham@Trent U.CA).

Can. J. Chem. Downloaded from www.nrcresearchpress.com by 195.246.54.202 on 09/08/12
For personal use only.

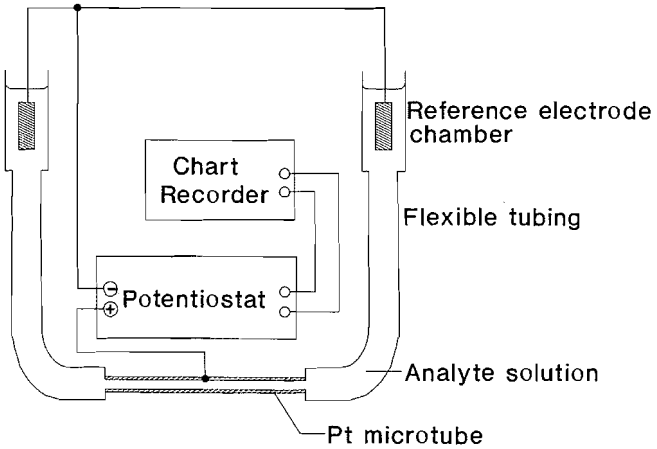

FIG. 1. Diagram showing the essential features of the microtube flowing coulometry apparatus.

A simplified diagram of our apparatus is shown in Fig. 1. Solution containing the analyte $[Fe(CN)_6]^{4-}$ (aq) is allowed to flow through a platinum microtube under an adjustable gravitational head. The tube functions as an anode and two commoned cathodes are mounted in the inlet and outlet chambers. With a suitable potential applied across the cell, the steady-state current is measured both with flow (I_f) and without (I_{nf}). The latter measurement is treated as a nonfaradaic "background", the difference $I_f - I_{nf}$ replacing I in eq. [2]. Accordingly, the analyte concentration can be calculated from

$$[3] \qquad c^b = \frac{I_f - I_{nf}}{nFf}$$

the flow rate f being measured in a separate experiment under identical conditions.

Theory

No-flow case

First, we address the question of how rapidly diffusion to the wall can remove an electroactive solute from the interior of a tube *in the absence of flow*. It is this process that governs the decay of the faradaic current in the non-flowing phase. In a cylindrical coordinate system, with r denoting radial distance from the tube's axis, diffusion is governed by Fick's second law in the form (8)

$$[4] \qquad \frac{\partial}{\partial t} c(r, t) = D\left(\frac{\partial^2}{\partial r^2} + \frac{1}{r}\frac{\partial}{\partial r}\right) c(r, t)$$

Here D is the diffusivity (diffusion coefficient) of the electroactive species and c is its concentration, which is a function of position r and time t. A solution to eq. [4] is sought subject to the condition that the concentration equals its original (bulk) value c^b initially:

$$[5] \qquad c(r, 0) = c^b$$

and the two boundary conditions

$$[6] \qquad c(R, t > 0) = 0$$

where R is the inner radius of the tube, and

$$[7] \qquad \frac{\partial c}{\partial r}(0, t) = 0$$

TABLE 1. The residual analyte fraction as a function of time. τ equals Dt/R^2 and ε is equal to $\exp(-5.78\tau)$

τ	$\frac{N(t)}{\pi c^b R^2}$
0	1
Small	$1-4\sqrt{\tau/\pi}$
0.001	0.930
0.002	0.901
0.005	0.845
0.01	0.784
0.02	0.701
0.05	0.548
0.0630	0.500
0.1	0.394
0.2	0.218
0.5	0.0384
0.733	0.0100
1	0.0021
2	7×10^{-6}
Large	$\varepsilon/1.446$
∞	0

Equation [7] is a consequence of the cylindrical symmetry, while eq. [6] applies if concentration polarization is total, i.e., if the potential applied to the tube is sufficiently large that the analyte is immediately destroyed on reaching the wall.

The solution to the mathematical problem posed by eqs. [4]–[7] is addressed in Appendix A. Our present interest is in the rate at which the number $N(t)$ of moles of solute within a cross section of the tube decreases with time. $N(t)$ has the mol m^{-1} unit and its initial value is $\pi c^b R^2$.

As discussed in the appendix, the amount remaining after time t is given by the equivalent expressions

$$[8] \qquad \frac{N(t)}{\pi c^b R^2} = \begin{cases} 1 - 4\sqrt{\dfrac{\tau}{\pi}} + \tau + \sqrt{\dfrac{\tau^3}{9\pi}} + \dfrac{\tau^2}{8} + \cdots \\ \dfrac{\exp(-5.783\tau)}{1.446} + \dfrac{\exp(-30.47\tau)}{7.618} + \cdots \end{cases}$$

where τ symbolizes Dt/R^2. This ratio is just the fraction of the original analyte that remains after time t. Table 1 lists some values of this quantity, calculated with the aid of one or other of the series in eq. [8], as a function of the dimensionless parameter Dt/R^2. Note that half the analyte has disappeared by the time 0.0630 R^2/D, and that 99% has been removed by 0.733 R^2/D. The latter characteristic time will be denoted t_{99}:

$$[9] \qquad t_{99} = 0.733\frac{R^2}{D} \approx (1.5 \times 10^9 \text{ s m}^{-2})R^2$$

The final expression in eq. [9] assumes a diffusivity of 5×10^{-10} m^2 s^{-1}, which is a typical value for the hexacyanoferrate(II) ion in a variety of aqueous solutions (9–12). Using the same value of D, Table 2 lists the 99%-removal times for tubes of various radii. Notice that, for a tube of 50 μm internal radius, as used in our experiments, depletion is predicted to be virtually complete in 4 s.

Electric current for the no-flow case

Here we address the question of the magnitude of the current

Can. J. Chem. Downloaded from www.nrcresearchpress.com by 195.246.54.202 on 09/08/12
For personal use only.

TABLE 2. Times required to remove 99% of an analyte ($D = 5 \times 10^{-10}$ m^2 s^{-1}) from a static solution by electrolysis at the wall of a cylindrical tube of radius R

R	t_{99}
10 μm	0.15 s
20 μm	0.6 s
50 μm	4 s
0.10 mm	15 s
0.20 mm	1.0 min
0.50 mm	6 min
1.0 mm	24 min

that flows after a microtube, originally containing a solution with an electroactive analyte concentration c^b, is held at a potential sufficient to cause total concentration polarization at the inner surface of the tube. Let $I(t)$ denote this current at a time t after polarization and $Q(t)$ be the corresponding charge. The latter is related by Faraday's law to the total decrease in the amount of analyte:

$$[10] \qquad \int_0^t I(t)\,dt = Q(t) = nF[\pi c^b R^2 - N(t)]Z$$

where Z is the length of the tubular electrode. An expression for this quantity, namely

$$[11] \qquad \frac{Q(t)}{\pi nFc^bR^2Z} = \begin{cases} 4\sqrt{\dfrac{\tau}{\pi}} - \tau - \sqrt{\dfrac{\tau^3}{9\pi}} - \dfrac{\tau^2}{8} - \cdots \\ 1 - \dfrac{\exp(-5.783\tau)}{1.446} - \dfrac{\exp(-30.47\tau)}{7.618} \\ \qquad\qquad - \cdots \end{cases}$$

follows immediately from eqs. [8] and [10].

Differentiation of eq. [11] with respect to t produces the two equivalent expressions

$$[12] \qquad \frac{I(t)}{\pi nFc^bDZ} = \begin{cases} \dfrac{2}{\sqrt{\pi\tau}} - 1 - \sqrt{\dfrac{\tau}{4\pi}} - \dfrac{\tau}{4} - \dfrac{25}{48}\sqrt{\dfrac{\tau^3}{\pi}} \\ \qquad\qquad - \cdots \\ 4\exp(-5.783\tau) + 4\exp(-30.47\tau) \\ \qquad +4\exp(-74.89\tau) + \cdots \end{cases}$$

for the current where, as before, $\tau = Dt/R^2$. Table 3 lists values of the normalized $I(t)$ and $Q(t)$ calculated with the aid of the last two equations.

Flowing solution

When we turn to the case in which the solution flows through the tube, the general problem enters three dimensions with the introduction of an axial z direction. We choose a z axis such that $0 < z \leq Z$, $0 \leq r < R$ corresponds to space within the hollow cylindrical electrode occupied by solution, as illustrated in Fig. 2, whereas $z < 0$, $0 \leq r < R$ corresponds to undepleted solution in a coaxial entry tube that is a geometric continuation of the hollow electrode.

Let $v_z(r)$ be the velocity of flow in the z direction, being independent of z and t but a function r such that

$$[13] \qquad 2\pi \int_0^R r v_z(r)\,dr = f$$

TABLE 3. Normalized charge $Q(t)$ and its derivative $I(t)$ at selected values of the parameter τ, which equals Dt/R^2. ε is again equal to $\exp(-5.78\tau)$

τ	$\dfrac{I(t)}{\pi nFc^bDZ}$	$\dfrac{Q(t)}{\pi nFc^bR^2Z}$	Notes
0	∞	0	Initial
Small	$2/\sqrt{\pi\tau}$	$4\sqrt{\tau/\pi}$	Limiting form
0.001	34.7	0.0704	
0.002	24.2	0.0989	
0.005	14.9	0.155	
0.010	10.2	0.216	
0.020	6.93	0.299	
0.050	3.97	0.452	
0.063	3.40	0.500	50% depletion
0.100	2.44	0.606	
0.200	1.27	0.782	
0.500	0.222	0.962	
0.733	0.0577	0.990	99% depletion
1.000	0.0123	0.998	
2.000	4×10^{-5}	$1 - 7 \times 10^{-6}$	
Large	4ε	$1 - \varepsilon/1.446$	Limiting form
∞	0	1	Final

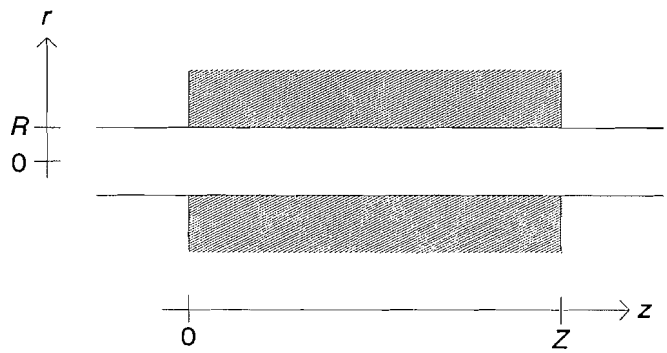

FIG. 2. Schematic diagram showing coordinate system of the microtube.

Then eq. [4] becomes modified to

$$[14] \qquad \frac{\partial}{\partial t}c(r, z, t) = D\left(\frac{\partial^2}{\partial r^2} + \frac{1}{r}\frac{\partial}{\partial r} + \frac{\partial^2}{\partial z^2}\right)c(r, z, t) - v_z(r)\frac{\partial}{\partial z}c(r, z, t)$$

by the introduction of terms representing diffusion and convection in the z dimension.

Because our interest is confined to the steady state, the left-hand term in eq. [14] may be set to zero. We also plan to ignore the $\partial^2 c/\partial z^2$ term. This is easily justified in the context of the parameters adopted in our experiments because the Z dimension of the tube exceeds the R dimension by a factor of 2000. Concentration gradients in the z dimension will therefore be minuscule in relation to $\partial c/\partial r$ values. With these simplifications eq. [14] may be rearranged to

$$[15] \qquad \frac{\partial}{\partial z}c(r, z) = \frac{D}{v_z(r)}\left(\frac{\partial^2}{\partial r^2} + \frac{1}{r}\frac{\partial}{\partial r}\right)c(r, z)$$

A solution to this differential equation must also obey the

Can. J. Chem. Downloaded from www.nrcresearchpress.com by 195.246.54.202 on 09/08/12
For personal use only.

Can. J. Chem. Downloaded from www.nrcresearchpress.com by 195.246.54.202 on 09/08/12
For personal use only.

prevailing boundary conditions. Since fresh solution enters the electrode tube at $z = 0$ then

$$[16] \qquad c(r, 0) = c^{b}$$

If concentration polarization is total then

$$[17] \qquad c(R, z > 0) = 0$$

and due to the cylindrical symmetry of the tube

$$[18] \qquad \frac{\partial c}{\partial r}(0, z) = 0$$

The similarity of these three boundary conditions to those in eqs. [5]–[7] for the no-flow problem is evident.

Electric current in steady-state flow

The prime measurement in microtube flowing coulometry is the steady-state current I that flows after the dissipation of the transient behaviour, which occurs when the flow first starts. We need to be able to predict what this current should be for a tube of any dimensions R, Z and for any flow rate f. There are (at least) three possible approaches to the calculation of the current:

(*a*) From the flux of analyte at the walls of the tube, via the equation

$$[19] \qquad \frac{I}{nF} = 2\pi RD \int_0^Z \left[\frac{\partial}{\partial r} c(r, z)\right]_{r=R} \mathrm{d}z$$

This is the standard method used by electrochemists to calculate voltammetric currents.

(*b*) From the equation

$$[20] \qquad \frac{I}{nF} = -2\pi \int_0^Z \int_0^R r v_z(r) \frac{\partial}{\partial z} c(r, z)\, \mathrm{d}r\, \mathrm{d}z$$

which we derive by the following argument. Consider the element of solution between the planes z and $z + \mathrm{d}z$. Analyte enters this element at a rate (mol s^{-1}) given by

$$[21] \qquad 2\pi \int_0^R r v_z(r) c(r, z)\, \mathrm{d}r$$

and leaves at a rate given by a similar equation in which $c(r, z+\mathrm{d}z)$ replaces $c(r, z)$. The difference between these two rates, which again may be expressed analogously to eq. [21] but with $-(\partial/\partial z)c(r, z)\mathrm{d}z$ replacing $c(r, z)$, represents the rate at which analyte is lost by electrolysis at the wall segment of length $\mathrm{d}z$. Equation [20] then follows by z-integration.

(*c*) By ignoring the distribution of analyte in the body of the tube and employing the equation

$$[22] \qquad \frac{I}{nF} = c^{b} f - 2\pi \int_0^R r v_z(r) c(r, Z)\, \mathrm{d}r$$

The two right-hand terms are the rate of entry (mol s^{-1}) of analyte into the electrode tube across the $z = 0$ plane and its rate of exit across the $z = Z$ plane.

Though they appear very distinct, the three methods are equivalent. Nevertheless, from a computational viewpoint, one may be much easier to implement, in certain circumstances, than the others.

Uniform flow

In this section we assume that the solution flows uniformly down the tube, so that the flow velocity is independent of the radial position. In that event

$$[23] \qquad v_z(r) = v_z = \frac{f}{\pi R^2}$$

where f is the volume flow rate. The differential equation [15] then becomes

$$[24] \qquad \frac{\partial}{\partial z} c(r, z) = \frac{R^2}{K}\left(\frac{\partial^2}{\partial r^2} + \frac{1}{r}\frac{\partial}{\partial r}\right) c(r, z)$$

where K is a characteristic length equal to $f/\pi D$. Comparison with eq. [4] shows this problem to be strictly equivalent to the no-flow problem, the time dimension in the static case being replaced by the distance dimension z in the steady-state uniform-flow problem. Because z is measured from the inlet end of the tube, it is related to t in the no-flow case by the equivalence

$$[25] \qquad z = \frac{KD}{R^2} t = \frac{f}{\pi R^2} t$$

Hence, by analogy with expressions [8],

$$[26] \qquad \frac{N(z)}{\pi c^{b} R^2} = \begin{cases} 1 - 4\sqrt{\dfrac{\zeta}{\pi}} + \zeta + \sqrt{\dfrac{\zeta^3}{9\pi}} + \dfrac{\zeta^2}{8} + \cdots \\ \dfrac{\exp(-5.783\zeta)}{1.446} + \dfrac{\exp(-30.47\zeta)}{7.618} + \cdots \end{cases}$$

where $\zeta = z/K$ and is equivalent to τ. The significance of $N(z)$ remains as before: it is the total amount of the analyte in a cross section of the tube. It can be defined by

$$[27] \qquad N(z) = 2\pi \int_0^R r c(r, z)\mathrm{d}r$$

and has the mol m^{-1} unit.

To find the current, we shall adopt method (*b*) of the previous section. Because we are treating $v_z(r)$ as independent of r, the inner integral in eq. [20] becomes

$$[28] \qquad -2\pi v_z \int_0^R r \frac{\partial}{\partial z} c(r, z)\, \mathrm{d}r = -v_z \frac{\mathrm{d}}{\mathrm{d}z} N(z)$$

in light of definition [27]. Accordingly, making reference again to eq. [20], we find the simple expression

$$[29] \qquad \frac{I(Z)}{nF} = -v_z \int_{z=0}^{z=Z} \mathrm{d}N = v_z[\pi c^{b} R^2 - N(Z)] = f c^{b}\left[1 - \frac{N(Z)}{\pi c^{b} R^2}\right]$$

so that, when the expansions [26] are used, the result

$$[30] \qquad \frac{I(Z)}{nFfc^{b}} = \begin{cases} 4\sqrt{\dfrac{Z}{\pi K}} - \dfrac{Z}{K} - \sqrt{\dfrac{Z^3}{9\pi K^3}} - \dfrac{Z^2}{8K^2} - \cdots \\ 1 - \dfrac{\exp(-5.783Z/K)}{1.446} - \dfrac{\exp(-30.47Z/K)}{7.618} - \cdots \end{cases}$$

Can. J. Chem. Downloaded from www.nrcresearchpress.com by 195.246.54.202 on 09/08/12
For personal use only.

emerges for the current. Notice, by comparison with eq. [11], that the *current* in the uniform-flow case is the analogue of the *charge* in the no-flow experiment.

The length of tube needed to capture 99% of the analyte is easily found by analogy with eq. [9], as

$$[31] \qquad Z_{99} = 0.733\,K \approx (5 \times 10^8\ \mathrm{s\ m^{-2}})f$$

if the flow is regarded as uniform. For example, the 10 cm length of the tube used in our experiments is predicted, according to this model, to capture at least 99% of the analyte provided that the uniform-flow rate does not exceed 2×10^{-10} m^3 s^{-1}, or 0.2 μL s^{-1}.

Complete solution for uniform flow

Another interpretation of the quantity $N(z)$ is that $N(z)/\pi R^2$ represents the average concentration

$$[32] \qquad c_{\mathrm{avg}}(z) = \frac{N(z)}{\pi R^2} = \frac{2}{R^2}\int_0^R rc(r, z)\,\mathrm{d}r$$

of the analyte at the plane $z = z$. As we have seen, this information is adequate to calculate the salient experiment parameter, the current. However, it is also of interest to determine how the concentration varies as a function of r.

To address this question, we return to eq. [24] and solve it, along with its attendant boundary conditions [16]–[18], by the method of "separation of variables." Details of the solution have been relegated to Appendix B and here we present only the final result:

$$[33] \qquad c(r, z) = 2c^{\mathrm{b}}\sum_{k=1}^{\infty}\frac{\mathrm{J}_0\left(\frac{j_{0,k}r}{R}\right)\exp\left(-\frac{j_{0,k}^2 z}{K}\right)}{j_{0,k}\mathrm{J}_1(j_{0,k})}$$

where $\mathrm{J}_0(\ )$ and $\mathrm{J}_1(\ )$ are Bessel functions and $j_{0,k}$ denotes the kth zero of J_0.

It is quite easy to demonstrate that, substituted into eq. [19], this complete solution leads via method (*a*) to the same current expressions as in eq. [30] by method (*b*). However, conclusions may be reached from eq. [33] that were inaccessible by route (*b*). For example, we can argue that when z is large enough, only the $k = 1$ term contributes significantly to the summation in eq. [33] and then the concentration profile in the tube is that of a zeroth-order Bessel function, namely:

$$[34] \qquad c(r, \text{large } z) = 1.602\,c^{\mathrm{b}}\mathrm{J}_0\left(\frac{2.405r}{R}\right)\exp\left(-\frac{5.783z}{K}\right)$$

This approximation is certainly valid at Z_{99}; in fact it is useful beyond about Z_{50}, the plane at which half the analyte has been removed.

Poiseuille flow

Though it has provided an easily tractable model, the assumption of uniform flow is not valid for a gravitational head, though it is applicable when electroosmosis provides the driving force. In the cylindrical tube of our experiments the flow profile is not flat with an r-independent axial velocity v_z; instead, once a streamlined flow regime is established, the local velocity is dependent parabolically on the radial coordinate

$$[35] \qquad v_z(r) = \frac{2(R^2 - r^2)}{\pi R^4}f$$

This means that the solution moves more slowly than average in the annular region $(R/\sqrt{2}) < r \leq R$ and faster than average in the central core $0 \leq r < (R/\sqrt{2})$. As a result, the concentration profiles become skewed compared with those in the uniform-flow case, and capture at the wall is less efficient.

When eq. [35] replaces eq. [23], the differential equation to be solved becomes

$$[36] \qquad \frac{\partial}{\partial z}c(r, z) = \frac{R^2}{2K(1 - r^2/R^2)}\left(\frac{\partial^2}{\partial r^2} + \frac{1}{r}\frac{\partial}{\partial r}\right)c(r, z)$$

instead of eq. [24]. The boundary conditions [16]–[18] remain unchanged. This set of equations may be solved by a procedure, described in Appendix C, which closely parallels that used in the uniform-flow problem. The solution, however, is much more complicated. It is

$$[37] \qquad c(r, z) = c^{\mathrm{b}}\sum_{k=1}^{\infty}A_k\mathrm{E}_k\left(\frac{r}{R}\right)\exp\left(-\frac{2(2\nu_k + 1)^2 z}{K}\right)$$

where $\mathrm{E}_k(\rho)$ denotes the Graetz function (ref. 13, p. 204), which we have defined by

$$[38] \qquad \mathrm{E}_k(\rho) = \mathrm{L}_{\nu_k}((4\nu_k + 2)\rho^2)\exp(-(2\nu_k + 1)\rho^2)$$

ν_k is the kth zero of the Graetz function which satisfies the equality $\mathrm{L}_{\nu_k}(4\nu_k + 2) = 0$, where $\mathrm{L}_{\nu_k}(\ )$ is the Laguerre function. The first four values of ν_k are listed in Appendix C. The coefficients A_k are given by the ratio of two integrals

$$[39] \qquad A_k = \frac{\int_0^1 \rho(1 - \rho^2)\mathrm{E}_k(\rho)\,\mathrm{d}\rho}{\int_0^1 \rho(1 - \rho^2)\mathrm{E}_k^2(\rho)\,\mathrm{d}\rho}$$

where ρ is used to denote the r/R ratio. Values of $A_1, \ldots, A_4$ are listed in Appendix C.

As with the uniform-flow problem, the exponential terms in eq. [37] ensure such rapid convergence for large Z that only the $k = 1$ summand is needed, so that

$$[40] \qquad c(r, \text{large } Z) = c^{\mathrm{b}}A_1\mathrm{E}_1\left(\frac{r}{R}\right)\exp\left(-\frac{2(2\nu_1 + 1)^2 Z}{K}\right)$$

We plan to use method (*c*) to calculate the current and, because our experimental interest is in using tubes long enough that almost all the analyte is captured, Z will be restricted to values large enough that eq. [40] is adequate. The current, then, is given by

$$[41] \qquad \frac{I(Z)}{nF} = c^{\mathrm{b}}f - 4c^{\mathrm{b}}f \times \exp\left(-\frac{2(2\nu_1 + 1)^2 Z}{K}\right)A_1\int_0^1 \rho(1 - \rho^2)\mathrm{E}_1(\rho)\,\mathrm{d}\rho$$

where use has been made of eqs [22], [35], and [40]. Notice that the integral in this equation is identical with the numeratorial integral in the $k = 1$ version of eq. [39]. If follows that

$$[42] \qquad \frac{I(Z)}{nFfc^{\mathrm{b}}} = 1 - 4\frac{\Lambda^2}{\Omega}\exp\left(-\frac{2(2\nu_1 + 1)^2 Z}{K}\right)$$

Can. J. Chem. Downloaded from www.nrcresearchpress.com by 195.246.54.202 on 09/08/12
For personal use only.

where Λ and Ω are the definite integrals

$$[43] \qquad \Lambda = \int_0^1 \rho(1-\rho^2)E_1(\rho)\,d\rho = 0.1387$$

and

$$[44] \qquad \Omega = \int_0^1 \rho(1-\rho^2)E_1^2(\rho)\,d\rho = 0.09393$$

that we have evaluated numerically (ref. 14, Sect. A7) and found to have the values cited.

Finally, therefore, we can calculate the current under Poiseuille flow from the numerical equation

$$[45] \qquad \frac{I(Z)}{nFfc^b} = 1 - 0.8191 \exp\left(-\frac{3.657Z}{K}\right)$$

provided Z exceeds $0.14K$. If this is not the case, more than one exponential term must be included, the first two being

$$[46] \qquad \frac{I(Z)}{nFfc^b} = 1 - 0.8191 \exp\left(-\frac{3.657Z}{K}\right) - 0.09753 \exp\left(-\frac{22.30Z}{K}\right) - \cdots$$

Note the similarity of this result to the second alternative in eq. [30].

The length of tube needed to capture 99% of the analyte is easily found by making use of eq. [45]. 99% capture corresponds to only 1% of the analyte exiting the tube and thus the second right-hand terms in eqs. [41] and [45] must be equal to 0.01. These terms have this value at

$$[47] \qquad Z_{99} = 1.205K \approx (8 \times 10^8 \text{ s m}^{-2})f$$

To ensure that virtually all of the analyte will suffer electrolysis during its passage through the tube, and that eq. [2] will be valid, Z must be greater than Z_{99}. Notice the surprising result that expression [47] does not involve the tube radius.

As is evident in eqs. [31] and [47], the planar and Poiseuille flow regimes give different results for the calculation of Z_{99} or the flow rate. By assuming Poiseuille flow, the tube must be longer or the flow rate slower by a factor of 1.64 than that predicted by planar flow. Table 4 lists values of the parameter $\pi DZ/f$ needed to capture a certain percentage of the analyte for each flow profile. The ratio of this parameter for Poiseuille and planar flow decreases as the percentage captured increases.

Flow rate

Equation [47] may be interpreted as prescribing a maximum flow rate, which we may also regard as the optimal flow rate

$$[48] \qquad f_{opt} = \frac{\pi DZ_{99}}{1.205}$$

because it makes the most efficient use of the tube as an electrode. With the values $D = 5 \times 10^{-10}$ m^2 s^{-1} and $Z = 0.100$ m appropriate to our experiments, an optimal flow rate of 1.3×10^{-10} m^3 s^{-1} is predicted. Flow rates that are greater than this optimal value permit unelectrolyzed analyte to pass through the tube, while lower flow rates leave a portion of the wall area unused, with the consequential penalty of unnecessarily large ohmic polarizations and background currents.

TABLE 4. Values for the ratio $\pi DZ/f$ needed to capture a percentage of the analyte for both the planar and Poiseuille flows

Percent captured	$\left(\frac{\pi DZ}{f}\right)_{plr}$	$\left(\frac{\pi DZ}{f}\right)_{Poi}$	Ratio of Poiseuille to planar
50.0	0.0629	0.138	2.19
80.0	0.215	0.386	1.80
90.0	0.334	0.575	1.72
95.0	0.454	0.765	1.69
99.0	0.733	1.205	1.64
99.9	1.131	1.834	1.62
100	∞	∞	1.58

However, as the bulk concentration c^b increases, so does the current density and ohmic overvoltage. To counteract the lack of total concentration polarization may then require a flow rate slower than f_{opt}.

Poiseuille's law relates the flow rate by the equation

$$[49] \qquad f = \frac{\pi R^4 dgh}{8\eta Z}$$

to the gravitational head h that drives the solution through the tube. Here g is the acceleration (9.806 m s^{-2}) caused by gravity, while d and η are, respectively, the density and viscosity of the solution. Using values (997.1 kg m^{-3} and 8.904×10^{-4} kg m^{-1} s^{-1}) of d and η appropriate to pure water at 25°C, we calculate from eqs. [48] and [49] that the optimal head is

$$[50] \qquad h_{opt} = (6.05 \times 10^{-7} \text{ m s}) \frac{Z^2 D}{R^4}$$

for aqueous solutions whose density and viscosity are not significantly different from those of the solvent. Experimentally convenient tube lengths lie in the range 20–100 mm. Table 5, based on eq. [50], lists the optimal heads for this range of lengths and an analyte of diffusivity 5×10^{-10} m^2 s^{-1}. Notice that it is only for a tube of inner radius in the vicinity of 50 μm that an optimal gravitational head exists which is both practically attainable and accurately measurable. It was these considerations, as well as the cost and commercial availability of platinum microtube, that dictated our choice (100 mm length and 50 μm internal radius) of experimental tube dimensions. Of course, forces other than gravitational could be used to drive the solution through the tube, but gravity is simple and reliable.

Experimental

The microtube and other apparatus

A platinum microtube was supplied by Goodfellow (Cambridge, United Kingdom), with nominal dimensions of 100 mm length, 0.40 mm outside diameter, and 0.15 mm wall thickness. Flow rates of water through the tube were measured to be in excess of the predictions of Poiseuille's equation, possibly because the inner radius is larger than the nominal 50 μm. An 8% tolerance in the tube diameter would explain our findings.

To protect the fragile microtube, it was mounted within a stainless-steel support tube by means of Teflon ferrules. Detail of one end of the assembly is shown in Fig. 3; the other end is identical. After assembly, electrical contact to the microtube was achieved by placing small pieces of Wood's metal and a copper wire into a hole previously drilled through the wall of the stainless-steel tube; after heating with

TABLE 5. Optimal heads calculated for solutions flowing through tubes of the stated radii and lengths 20–100 mm

R	h_{opt}
10 μm	12–302 m
20 μm	0.76–19 m
50 μm	19–484 mm
0.10 mm	1.2–30 mm
0.20 mm	0.075–1.9 mm
0.50 mm	1.9–48 μm
1.0 mm	0.12–3.0 μm

a hot-air gun, the fusible metal formed a conducting bond between the copper wire and the two tubes. When not in use, the microtube was stored with its bore filled with distilled water.

The mounted microtube was positioned horizontally and connected by flexible Tygon tubing to two chambers. Each chamber was adapted from the plastic barrel of a graduated 1 cm^3 disposable hypodermic syringe, whereby accurate flow-rate measurements could be made. In the flowing coulometric studies, these chambers also accommodated the reference electrodes, which were constructed from porous silver foil, previously anodized to acquire a coating of AgCl or Ag_2SO_4.

The entire apparatus has total bilateral symmetry about the midplane of the microtube. To achieve flow, one of the reference chambers was raised an appropriate distance above the other, the head being accurately measured.

Solutions

The reaction chosen for study was the oxidation of the hexacyanoferrate(II) ion

$$[51] \qquad [Fe(CN)_6]^{4-}(aq) \rightarrow e^- + [Fe(CN)_6]^{3-}(aq)$$

in aqueous solution. An oxidation was chosen in preference to a reduction to avoid interference from, and the necessity to remove, dissolved oxygen. Solutions of known concentrations in the range 0.025–10.00 mM were prepared daily from weighted quantities of $K_4Fe(CN)_6 \cdot 3H_2O$ (BDH, Toronto) and stock solutions of supporting electrolyte.

Four different supporting electrolytes were employed: (*a*) 2.50 M KCl (BDH, Toronto); (*b*) 2.00 M KNO_3 (Baker, Phillipsburg, N.J.) plus 0.50 M KCl; (*c*) 1.80 M K_2SO_4 (BDH, Toronto); and (*d*) 1.00 M H_2SO_4 (Caledon, Georgetown). All reagents were analytical grade and were used as received. Similar results were obtained for all four solutions, with (*d*) giving a wider range of useful voltages (and therefore being used more often) than the other three, presumably because of its higher conductivity. However, the hexacyanoferrate(II) ion underwent a slow decomposition in the acidic medium (*d*), as evidenced by the buildup of a pale-blue colouration, so that fresh solutions needed to be prepared more frequently with this particular supporting electrolyte.

Solutions were not degassed, though this procedure might have eliminated the occasional anomalous behaviour that we attribute to bubble formation within the microtube. Experiments were performed at an ambient temperature of 23 ± 2°C.

Procedure

The levels in the two chambers were carefully adjusted to be equal and the system was left for a few minutes to reach a no-flow condition before any electrical signal was applied.

The simple electrical circuit is illustrated in Fig. 1. Because separate reference and counter electrodes would have been pointless, the potentiostat (Pine Instruments model RDE3) was operated in a two-electrode mode, generating a preset constant potential difference ΔE that was applied to the microtube with respect to the twin silver/silver salt electrodes. The separate currents flowing from the two reference electrodes were not monitored; instead the total current was measured and displayed as a function of time on an XY-chart recorder.

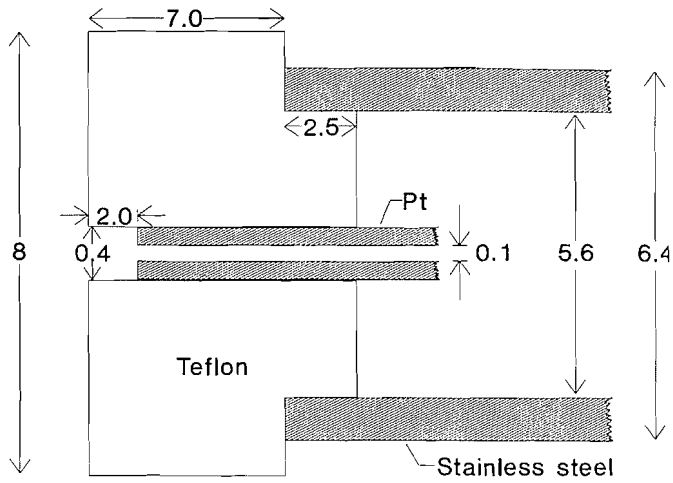

FIG. 3. Detail, not to scale, of one end of the microtube mount. All dimensions are in millimetres.

At every value of ΔE applied, the tube was "conditioned" before measuring the steady-state current under flow or no-flow conditions. This process, believed to involve the equilibration of the oxide layer, required the potential to be applied for some minutes to the tube filled with non-flowing analyte solution. After conditioning, the tube was flushed with fresh analyte solution, by gravitational flow, and the chambers returned to their original, levelled positions before commencing the experiment proper.

The current during the phase of the experiment with levelled chambers, initially very large, declined steeply and after several minutes acquired a constant no-flow value I_{nf}. This steady-state condition was allowed to persist for a further 60 s, to allow an accurate determination of I_{nf}.

One of the chambers was then raised to a predetermined level, so that flow suddenly commenced. As the exhausted solution within the tube was replaced by new analyte-containing solution, the current increased, but it eventually settled to a new constant value I_f, as a flowing steady-state regime became established in the tube. The I_f current was carefully measured from the chart record and the quantity $(I_f - I_{nf})/nFf$ was then evaluated; this, according to eq. [3], should be equal to the bulk analyte concentration.

Results and discussion

In our procedure, the I_{nf} current is measured under conditions of no-flow and after an interval so long that all the hexacyanoferrate(II) ion initially present has had ample time to reach the wall and be oxidized. This current therefore contains no component arising from reaction [51]; it is solely "background" current arising from imperfectly understood steady-state processes occurring at the platinum/solution interface. Because there is no change in applied potential between the measurement of the I_{nf} and I_f currents, it is believed that the background current remains virtually unchanged when flow is commenced. Therefore the subtraction $I_f - I_{nf}$ is designed to correct for the background. If the subtractive correction is efficient, then eq. [3] will hold subject to two provisos: that the applied voltage ΔE is large enough, and the flow rate small enough, to ensure complete depletion. Figure 4 shows a typical current-versus-time trace, in which the two measured currents are identified.

Using a solution of known composition and standard flow rate, a typical series of experiments consisted of repeating the procedure described above with a steadily increasing ΔE. Table 6 presents values of the quantity $(I_f - I_{nf})/nFf$ calculated for many experimental series, with $[Fe(CN)_6]^{4-}$ concentra-

Can. J. Chem. Downloaded from www.nrcresearchpress.com by 195.246.54.202 on 09/08/12
For personal use only.

TABLE 6. Measured values[a] of the quantity $(I_f - I_{nf})/nFf$ as functions of c^b, ΔE, and f for solutions of $[Fe(CN)_6]^{4-}$ in 1.00 M H_2SO_4

	ΔE/mV							
c^b/mM	600	700	800	900	1000	1100	1200	$f/10^{-11}$ m^3 s^{-1}
0.0250	0.0242	0.0258	0.0248	0.0273	0.0287			14.0
0.0500	0.0454	0.0502	0.0512	0.0532	0.0531			14.0
0.100	0.0924	0.0961	0.0988	0.1000	0.1020			10.9
0.200	0.197	0.200	0.205	0.210	0.214	0.215		10.9
0.500	0.409	0.482	0.494	0.499	0.519	0.528		10.9
1.00		0.927	1.013	1.016	1.052			7.31
2.00		1.56	1.83	1.98	2.00	2.01		7.31
5.00			4.44	4.92	5.05	5.13		3.54
10.00			6.56	8.09	9.35	9.95	10.02	3.54

[a]Each table entry represents the average of at least three replications. The relative standard deviation associated with each entry averages 1.2% and never exceeds 3.7%.

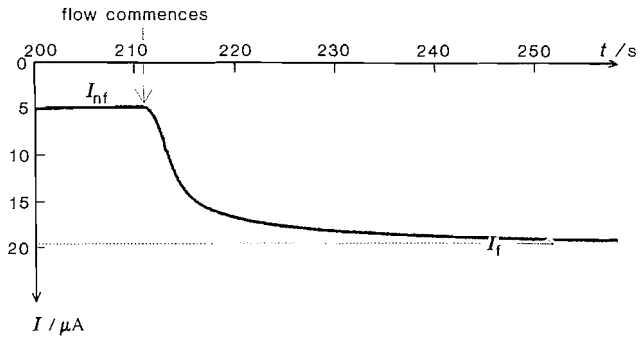

FIG. 4. Typical chart record, showing a no-flow current of 5 μA and a flow current of 19.5 μA. Experimental conditions: 2.00 mM $Fe(CN)_6^{4-}$ in 1.00 M H_2SO_4; ΔE = 1000 mV; f = 7.31 × 10^{-11} m^3 s^{-1}.

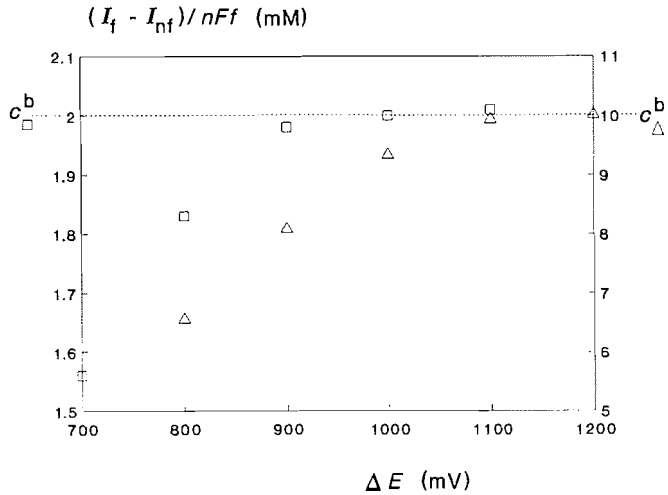

FIG. 5. Experimentally determined values of $(I_f - I_{nf})/nFf$ as a function of applied potential difference for a 2.00 mM (□) and a 10.00 mM (△) $[Fe(CN)_6]^4$ solution prepared in 1.00 M H_2SO_4, with flow rates of 7.31 × 10^{-11} and 3.54 × 10^{-11} m^3 s^{-1}, respectively.

tions ranging from 0.025 to 10.00 mM (in 1.00 M H_2SO_4) and solution flow rates ranging from 3.54 × 10^{-11} to 1.40 × 10^{-10} m^3 s^{-1}. The experimental series for the 2.00 mM and 10.00 mM table entries are illustrated in Fig. 5.

From the table it is evident that there was incomplete "capture" of the hexacyanoferrate(II) ion at applied potentials of less than 700 mV, regardless of bulk concentration or solution flow rate. At the lowest analyte concentrations, complete capture proved possible with a flow rate of 1.40 × 10^{-10} m^3 s^{-1} or less, which is in excellent agreement with the theoretical optimal flow rate of 1.3 × 10^{-10} m^3 s^{-1}. At higher concentrations, however, lower flow rates and (or) higher cell voltages were needed. We interpret this effect as arising from ohmic drop within the solution (15). Calculations that will be published elsewhere show that the currents flowing through the tube at the highest concentrations lead to *IR* products on the order of volts, effectively shutting off the central region of the tube. The tube acts as if it were shorter and, in consequence, slower flow rates are needed.

In Fig. 5, for example, applied potentials in the range of 900–1100 mV with a flow rate of 7.31 × 10^{-11} m^3 s^{-1} gave $(I_f - I_{nf})/nFf$ values within 1% of the true analyte concentration for a 2.00 mM $[Fe(CN)_6]^{4-}$ solution. However, for a solution five times more concentrated, a slower flow rate (3.54 × 10^{-11} m^3 s^{-1}) and higher potential range (1100–1200 mV) were required to obtain $(I_f - I_{nf})/nFf$ values within 1% of the true bulk concentration.

The principles upon which microtube flowing coulometry rest are simple and elegant. Once the microtube is mounted, the apparatus is uncomplicated and easy to use. The only measurements needed are of electric current and volume flow rate and, since these are made in the steady state, high accuracy is attainable. Though the detailed theory of the method is elaborate, the success of analysis by microtube flowing coulometry is independent of these theoretical details.

There are, however, a number of drawbacks to the technique. Sensitivity is limited by the background current, though we have made successful measurements down to the submillimolar level. The possibility of reducing background currents by using a gold microtube in experiments similar to those cited herein remains to be investigated. Studies have not been made with mixtures of electroactive species but, because of the need to apply extra voltage to overcome the considerable position-dependent ohmic polarization, it is unlikely that the method will display noteworthy selectivity. Yet another disadvantage is the need to work with solutions that confer high conductivity.

Acknowledgements

We thank Ken Fowler and Miroslav Švestka for their help and encouragement. The generous financial support of the

Can. J. Chem. Downloaded from www.nrcresearchpress.com by 195.246.54.202 on 09/08/12
For personal use only.

Natural Sciences and Engineering Research Council of Canada is deeply appreciated.

1. A. Hickling. Trans. Faraday Soc. **38**, 27 (1942).
2. J.E. Harrar. *In* Electroanalytical chemistry. Vol. 8. *Edited by* A.J. Bard. Dekker, New York. 1975.
3. A.J. Bard and L.R. Faulkner. Electrochemical methods. Wiley, New York. 1980. p. 406.
4. K.B. Oldham and J.C. Myland. Fundamentals of electrochemical science. Academic Press, Inc., San Diego. 1994. p. 156.
5. A.J. Bard. Anal. Chem. **38**, 88R (1966).
6. W.J. Blaedel et al. Anal. Chem. **35**, 2100 (1963); **39**, 1065 (1967); **43**, 1538 (1971); **49**, 1563 (1977).
7. S.Y. Mo and Y.S. Fung. Chin. Chem. Lett. **2**, 719 (1991).
8. D.D. Macdonald. Transient techniques in electrochemistry. Plenum Press, New York. 1977. p. 48.
9. J. Heyrovský and J. Küta. Principles of polarography. Academia, Prague. 1966.
10. R.N. Adams. Electrochemistry at solid electrodes. Dekker, New York. 1969. p. 219.
11. L. Sinru, J. Osteryoung, J.J. O'Dea, and R.A. Osteryoung. Anal. Chem. **60**, 1135 (1988).
12. A.M. Keightley, J.C. Myland, K.B. Oldham, and P.G. Symons. J. Electroanal. Chem. **322**, 25 (1992).
13. J. Newman. *In* Electroanalytical chemistry. Vol. 6. *Edited by* A.J. Bard. Dekker, New York. 1973.
14. J. Spanier and K.B. Oldham. An atlas of functions. Hemisphere, Washington, and Springer, Berlin. 1987.
15. R. Alkire and A.A. Mirarefi. J. Electrochem. Soc. **120**, 1507 (1973).
16. G.M. Murphy. Ordinary differential equations and their solutions. Van Nostrand, Princeton. 1960.
17. L. Graetz. Ann. Phys. Chem. **18**, 79 (1883); **25**, 337 (1885).
18. M. Abramowitz. J. Math. Phys. **32**, 184 (1953).

Can. J. Chem. Downloaded from www.nrcresearchpress.com by 195.246.54.202 on 09/08/12
For personal use only.

Appendix A

The initial condition [5] is incorporated when eq. [4] is Laplace transformed to the second-order differential equation

$$[A1] \qquad \frac{d^2\bar{c}}{dr^2} + \frac{1}{r}\frac{d\bar{c}}{dr} = \frac{s\bar{c}}{D} - \frac{c^b}{D}$$

of which the general solution (ref. 16, p. 339) is

$$[A2] \qquad \bar{c}(r, s) = \frac{c^b}{s} + A(s)I_0\left(r\sqrt{\frac{s}{D}}\right) + B(s)K_0\left(r\sqrt{\frac{s}{D}}\right)$$

where $I_0(\ )$ and $K_0(\ )$ are the zeroth-order instances of the hyperbolic Bessel and the Basset functions (ref. 14, Chaps. 49 and 51) respectively. Arbitrary functions of the Laplace variable s are represented by the coefficients $A(s)$ and $B(s)$; the forms adopted by these coefficients for the present problem may be deduced from the boundary conditions [6] and [7]. One finds $A(s) = -c^b/[sI_0(R\sqrt{s/D})]$ and $B(s) = 0$ and accordingly

$$[A3] \qquad \bar{c}(r, s) = \frac{c^b}{s}\left[1 - \frac{I_0\left(r\sqrt{\frac{s}{D}}\right)}{I_0\left(R\sqrt{\frac{s}{D}}\right)}\right]$$

The total amount of solute in a cross section of the tube is

$$[A4] \qquad N(t) = 2\pi\int_0^R rc(r, t)\,dr$$

and, by the integration (ref. 14, formula 49:10:7) of expression [A3] with respect to r, the transform of this quantity is found to be

$$[A5] \qquad \bar{N}(s) = 2\pi\int_0^R r\bar{c}(r, s)\,dr = \frac{\pi c^b R^4}{D}\left[\frac{1}{\sigma} - \frac{2I_1(\sqrt{\sigma})}{\sqrt{\sigma^3}\,I_0(\sqrt{\sigma})}\right]$$

where σ is used as an abbreviation for R^2s/D and $I_1(\ )$ denotes the first-order hyperbolic Bessel function (ref. 14, Chap. 49).

Though equation [A5] cannot be inverted to a closed algebraic form, expansions are possible that permit two expressions for $N(t)$ to be found, at least one of which is valid at any instant. By using asymptotic expansions (ref. 14, formulas 49:6:4 and 49:6:5) of the hyperbolic Bessel functions in eq. [A5], and performing a synthetic division, one finds

$$[A6] \qquad \frac{D\bar{N}(s)}{\pi c^b R^4} = \frac{1}{\sigma} - \frac{2}{\sqrt{\sigma^3}} + \frac{1}{\sigma^2} + \frac{1}{4\sqrt{\sigma^5}} + \frac{1}{4\sigma^3} + \frac{25}{64\sqrt{\sigma^7}} + \cdots$$

which inverts to

$$[A7] \qquad \frac{N(t)}{\pi c^b R^2} = 1 - 4\sqrt{\frac{\tau}{\pi}} + \tau + \sqrt{\frac{\tau^3}{9\pi}} + \frac{\tau^2}{8} + \frac{5}{24}\sqrt{\frac{\tau^5}{\pi}} + \cdots$$

where $\tau = Dt/R^2$. Because the series on which it is based are only asymptotically convergent, eq. [A7] is strictly valid only in the $t \longrightarrow 0$ limit; nonetheless, it may be used to generate accurate numerical values provided that t is not too large.

Alternatively, one may exploit an infinite product expansion of the zeroth-order hyperbolic Bessel function by writing

$$[A8] \qquad \frac{I_1(\sqrt{\sigma})}{2\sqrt{\sigma}I_0(\sqrt{\sigma})} = \frac{d[\ln I_0(\sqrt{\sigma})]}{d\sigma} = \left(\frac{d}{d\sigma}\right) \ln \prod_{k=1}^{\infty} \left[1 + \frac{\sigma}{j_{0,k}^2}\right]$$

Here $j_{0,k}$ denotes the kth zero of the zeroth-order Bessel function (ref. 14, Sect. 52:9), of which the first few values are $j_{0,1} = 2.4048$, $j_{0,2} = 5.5201$, $j_{0,3} = 8.6537$, $j_{0,4} = 11.7915$. Thereby, eq. [A5] can be converted to

$$[A9] \qquad \frac{D\bar{N}(s)}{\pi c^b R^4} = \left(\frac{1}{\sigma}\right)\left[1 - \sum_{k=1}^{\infty} \frac{4}{\sigma + j_{0,k}^2}\right] = \sum_{k=1}^{\infty} \frac{4}{j_{0,k}^2(\sigma + j_{0,k}^2)}$$

in which the second equality holds because $\Sigma(1/j_{0,k}^2) = 1/4$. Inversion to

$$[A10] \qquad \frac{N(t)}{\pi c^b R^2} = 4\sum_{k=1}^{\infty} \frac{\exp(-j_{0,k}^2\tau)}{j_{0,k}^2}$$

is now readily achieved. Except when τ is very small, this series converges very rapidly. In fact, one term is often adequate.

Equations [A7] and [A10] lead directly to eq. [8] of the main text.

Appendix B

Define $\rho = r/R$ and $\zeta = z/K$, so that eq. [24] becomes

$$[B1] \qquad \frac{\partial}{\partial\zeta} c(\rho, \zeta) = \left(\frac{\partial^2}{\partial\rho^2} + \frac{1}{\rho}\frac{\partial}{\partial\rho}\right) c(\rho, \zeta)$$

and the boundary conditions [16]–[18] become

$$[B2] \qquad c(\rho, 0) = c^b$$

$$[B3] \qquad c(1, \zeta) = 0$$

and

$$[B4] \qquad \frac{\partial c}{\partial\rho}(0, \zeta) = 0$$

A solution of the form

$$[B5] \qquad c(\rho, \zeta) = c^b \sum_{k=1}^{\infty} A_k G_k(\rho) H_k(\zeta)$$

is assumed where each unknown function $G_k(\rho)$ is independent of ζ and is defined such that

$$[B6] \qquad G_k(0) = 1$$

and similarly each $H_k(\zeta)$ function is independent of ρ and satisfies

$$[B7] \qquad H_k(0) = 1$$

If [B5] satisfies [B1], then so does any constant multiplied by each summand. Hence $G_k(\rho)H_k(\zeta)$ satisfies [B1] and when this is substituted for $c(\rho, \zeta)$ one finds

Can. J. Chem. Downloaded from www.nrcresearchpress.com by 195.246.54.202 on 09/08/12
For personal use only.

$$[B8] \quad \frac{1}{H_k(\zeta)}\frac{d}{d\zeta}H_k(\zeta) = \frac{1}{G_k(\rho)}\left[\frac{d^2}{d\rho^2} + \frac{1}{\rho}\frac{d}{d\rho}\right]G_k(\rho) = -\lambda_k^2$$

The third equality stems from the fact that since the left-hand side is independent of ρ and the right-hand side is independent of ζ, they must each equal the same constant, $-\lambda_k^2$. Thus

$$[B9] \quad \frac{d}{d\zeta}H_k(\zeta) = -\lambda_k^2 H_k(\zeta)$$

so that

$$[B10] \quad H_k(\zeta) = (\text{const})\exp(-\lambda_k^2\zeta)$$

but, because of [*B*7], the constant must be unity. Therefore

$$[B11] \quad H_k(\zeta) = \exp(-\lambda_k^2\zeta)$$

The right-hand side of [*B*8] leads to

$$[B12] \quad \frac{d^2G_k(\rho)}{d\rho^2} + \frac{1}{\rho}\frac{dG_k(\rho)}{d\rho} + \lambda_k^2 G_k(\rho) = 0$$

which is an example of Bessel's equation (ref. 16, p. 338) whose solution is of the form

$$[B13] \quad G_k(\rho) = UJ_0(\lambda_k\rho) + VY_0(\lambda_k\rho)$$

where $J_0(\ )$ and $Y_0(\ )$ are zeroth-order Bessel and Neumann functions and U and V are constants. However, because $J_0(0) = 1$ and $Y_0(0) = \infty$, we must choose $U = 1$ and $V = 0$ to satisfy [*B*6]. Hence:

$$[B14] \quad G_k(\rho)H_k(\zeta) = J_0(\lambda_k\rho)\exp(-\lambda_k^2\zeta)$$

To satisfy boundary condition [*B*3]

$$[B15] \quad J_0(\lambda_k)\exp(-\lambda_k^2\zeta) = 0$$

requires that λ_k be one of the zeros of the zeroth-order Bessel function. If λ_k is the kth zero then $\lambda_1 = j_{0,1}$, $\lambda_2 = j_{0,2}$, etc. as given in Appendix A.

G_k and H_k are now identified but A_k must still be found. Substitution of condition [*B*2] into [*B*5] gives

$$[B16] \quad 1 = \sum_{k=1}^{\infty} A_k G_k(\rho) = \sum_{k=1}^{\infty} A_k J_0(j_{0,k}\rho)$$

Multiplying each side of [*B*16] by $\rho J_0(j_{0,K}\rho)$ where $j_{0,K}$ is one particular value of the $j_{0,k}$'s and integrating from 0 to 1 gives

$$[B17] \quad \int_0^1 \rho J_0(j_{0,K}\rho)\,d\rho = \sum_{k=1}^{\infty} A_k \int_0^1 \rho J_0(j_{0,K}\rho)J_0(j_{0,k}\rho)d\rho$$

Due to the orthogonality of Bessel functions (ref. 14, Sect. 52:14) the right-hand integral is zero except when $k = K$, in which case we have

$$[B18] \quad \int_0^1 \rho J_0^2(j_{0,K}\rho)d\rho = \frac{1}{2}J_1^2(j_{0,K})$$

Moreover the left-hand integral evaluates to $[J_1(j_{0,K})]/j_{0,K}$. Therefore

$$[B19] \quad A_K = \frac{2}{j_{0,K}J_1(j_{0,K})}$$

which gives values of $A_1 = 1.602$, $A_2 = -1.065$, $A_3 = 0.851$, etc. The final expression for the concentration is thus

$$[B20] \quad c(\rho, \zeta) = 2c^b \sum_{k=1}^{\infty} \frac{J_0(j_{0,k}\rho)\exp(-j_{0,k}^2\zeta)}{j_{0,k}J_1(j_{0,k})}$$

Can. J. Chem. Downloaded from www.nrcresearchpress.com by 195.246.54.202 on 09/08/12
For personal use only.

Appendix C

Following a procedure that parallels that in Appendix B, a solution identical in form to [*B*5] is assumed to be a solution to the Poiseuille flow problem governed by the differential equation

$$[C1] \qquad \frac{\partial}{\partial\zeta}c(\rho,\zeta)=\frac{1}{2(1-\rho^2)}\left(\frac{\partial^2}{\partial\rho^2}+\frac{1}{\rho}\frac{\partial}{\partial\rho}\right)c(\rho,\zeta)$$

After the variables are separated, the dual equations are

$$[C2] \qquad \frac{2}{H_k(\zeta)}\frac{d}{d\zeta}H_k(\zeta)=\frac{1}{(1-\rho^2)G_k(\rho)}\left[\frac{d^2}{d\rho^2}+\frac{1}{\rho}\frac{d}{d\rho}\right]G_k(\rho)$$

This time it is more convenient to let the separation constant be $-(4\nu_k+2)^2$, rather than $-\lambda_k^2$. The ζ-dependent function is found to be

$$[C3] \qquad H_k(\zeta)=\exp(-2(2\nu_k+1)^2\zeta)$$

while the ρ-dependent function must satisfy the differential equation

$$[C4] \qquad \frac{d^2G_k(\rho)}{d\rho^2}+\frac{1}{\rho}\frac{dG_k(\rho)}{d\rho}+(4\nu_k+2)^2(1-\rho^2)G_k(\rho)=0$$

A change of independent variable from ρ to $\Upsilon=(4\nu_k+2)\rho^2$ and of dependent variable from $G_k(\rho)$ to $S_k(\Upsilon)=G_k(\rho)\exp(\Upsilon/2)$ converts [*C*4] into

$$[C5] \qquad \Upsilon\frac{d^2S_k(\Upsilon)}{d\Upsilon^2}+(1-\Upsilon)\frac{dS_k(\Upsilon)}{d\Upsilon}+\nu_kS_k(\Upsilon)=0$$

which is a form of Laguerre's equation (ref. 16, p. 330).

Equation [*C*5] is solved by the Laguerre function (ref. 14, Sect. 23:14) of degree ν_k and we therefore postulate that the appropriate solution to [*C*5] is

$$[C6] \qquad S_k(\Upsilon)=(\text{constant})\,L_{\nu_k}(\Upsilon)$$

or equivalently

$$[C7] \qquad G_k(\rho)=(\text{constant})\exp(-(2\nu_k+1)\rho^2)L_{\nu_k}((4\nu_k+2)\rho^2)$$

Because Laguerre functions of zero argument equal unity, the "constant" must itself be unity in order that condition [*B*6] be satisfied.

Therefore, putting the two functions together

$$[C8] \qquad G_k(\rho)H_k(\zeta)=L_{\nu_k}((4\nu_k+2)\rho^2)\exp(-(2\nu_k+1)\rho^2-2(2\nu_k+1)^2\zeta)$$

Boundary condition [*B*3] demands that

$$[C9] \qquad 0=L_{\nu_k}(4\nu_k+2)\exp(-(2\nu_k+1)-2(2\nu_k+1)^2\zeta)$$

Since ζ is a variable, this condition can only be met by certain specific values of ν_k for which $L_{\nu_k}(4\nu_k+2)=0$. The first such zero occurs close to 0.1761; the second, third, and fourth are $\nu_2\approx 1.1698$, $\nu_3\approx 2.1683$, and $\nu_4\approx 3.1678$, etc. As k increases the values approach $\nu_k=k-5/6$. Accurate values of these special orders are not available in the literature and $\nu_1, \nu_2, \ldots \nu_{20}$ were therefore calculated from the hypergeometric representation of the Laguerre function (ref. 14, Sect. 18:14). These values agree with less precise results published elsewhere (17, 18, 13).

G_k and H_k are now identified and again it only remains to find the A_k's. The first equality in [*B*16] holds so that

$$[C10] \qquad 1=\sum_{k=1}^{\infty}A_kL_{\nu_k}((4\nu_k+2)\rho^2)\exp(-(2\nu_k+1)\rho^2)$$

$$=\sum_{k=1}^{\infty}A_kE_k(\rho)$$

Can. J. Chem. Downloaded from www.nrcresearchpress.com by 195.246.54.202 on 09/08/12
For personal use only.

where we use $E_k(\rho)$ as a convenient abbreviation. The orthogonality procedure may again be used. The $E_k(\rho)$ functions are mutually orthogonal on the interval 0 to 1 with a weighting factor of $\rho(1-\rho^2)$ (ref. 13, p. 200). Therefore, on multiplying both sides of [C10] by $\rho(1-\rho^2)E_K(\rho)$ one obtains

$$[C11] \quad \int_0^1 \rho(1-\rho^2)E_K(\rho)\,d\rho = \sum_{k=1}^{\infty} A_k \int_0^1 \rho(1-\rho^2)E_K(\rho)E_k(\rho)\,d\rho$$

$$= A_K \int_0^1 \rho(1-\rho^2)E_K^2(\rho)\,d\rho$$

after integration. The left-hand integral has been found to evaluate to

$$[C12] \quad \int_0^1 \rho(1-\rho^2)E_K(\rho)\,d\rho = \frac{2\nu_K L_{\nu_K-1}(4\nu_K+2)\exp(-\lambda_K/2)}{4\nu_K+2}$$

but since the right-hand integral has to be evaluated numerically, both integrals were so evaluated and gave for the first four values of A_k: $A_1 = 1.476$, $A_2 = -0.8061$, $A_3 = 0.5888$, and $A_4 = -0.4759$.

Appendix D: glossary of symbols

A_k	summation constant
$A(s)$, $B(s)$	arbitrary functions of the Laplace variable (mol m^{-3} s)
c	local analyte concentration (mol m^{-3})
c^b	original (bulk) analyte concentration (mol m^{-3})
$c_{avg}(z)$	average concentration at the plane $z = z$ (mol m^{-3})
d	density of solution (kg m^{-3})
D	analyte diffusivity (m^2 s^{-1})
$E_k(\rho)$	the kth Graetz function
F	Faraday's constant (96485 C mol^{-1})
f	flow rate (m^3 s^{-1})
f_{opt}	optimal flow rate (m^3 s^{-1})
$G_k(\rho)$	kth undimensionalized function of the radial coordinate
g	gravitational acceleration (m s^{-2})
$H_k(\zeta)$	kth undimensionalized function of the axial coordinate
h	hydrostatic head (m)
h_{opt}	optimal hydrostatic head (m)
I	electric current (A)
I_{nf}, I_f	experimental steady-state no-flow and flow currents (A)
$I_0(\ )$, $I_1(\ )$	hyperbolic Bessel functions of zeroth, first order
$J_0(\ )$, $J_1(\ )$	Bessel functions of zeroth, first order
$j_{0,k}$	kth zero of the zeroth-order Bessel function
$K_0(\ )$	zeroth-order Basset function
K	characteristic length equal to $f/\pi D$ (m)
k	summation or product index
$L_{\nu_k}(\ )$	Laguerre function of degree ν_k
$N(t)$	amount of analyte in a cross section of the tube at time t (mol m^{-1})
$N(z)$	amount of analyte in a cross section of the tube at position z (mol m^{-1})
n	number of electrons involved in the electrode reaction
Q	total charge (C)
R	inner radius of microtube (m)
r	radial coordinate (m)
$S_k(\rho)$	kth undimensionalized function of the radial coordinate
s	Laplace variable (s^{-1})
t	time (s)
t_{99}	time at which 99% of the analyte has been consumed (s)
U, V	arbitrary constants of integration
V	sample volume (m^3)
$v_z(r)$	flow velocity (m s^{-1})
$Y_0(\ )$	zeroth-order Neumann function
Z	tube length (m)
Z_{99}, Z_{50}	tube lengths needed to consume 99% or 50% of the analyte (m)
z	axial coordinate (m)
ΔE	applied potential difference (V)

Can. J. Chem. Downloaded from www.nrcresearchpress.com by 195.246.54.202 on 09/08/12
For personal use only.

ϵ	abbreviation used in Tables 1 and 3
ζ	abbreviation for z/K or $\pi Dz/f$
η	viscosity of solution (kg m^{-1} s^{-1})
Λ, Ω	integrals defined by eqs. [43] and [44]
λ_k	kth constant used in Appendix B, equal to $j_{0,k}$
ν_k	kth zero of the Graetz function
π	Archimedes' constant (3.1416)
ρ	abbreviation for the ratio r/R
σ, τ	abbreviations for R^2s/D, Dt/R^2
Υ	abbreviation for $(4\nu_k + 2)\rho^2$

An overbar denotes the Laplace transform of the barred quantity, the units of which are augmented by s.

Can. J. Chem. Downloaded from www.nrcresearchpress.com by 195.246.54.202 on 09/08/12
For personal use only.

Multiple potential surfaces and movable energy barriers in the chemiluminescent reaction Mn + $SnCl_4$

DALE L. HERBERTSON,[1] DAVID A. NEWNHAM,[2] AND MARTIN R. LEVY[3]

Department of Chemical and Life Sciences, University of Northumbria at Newcastle, Ellison Building, Ellison Place, Newcastle upon Tyne NE1 8ST, U.K.

Received July 5, 1993

This paper is dedicated to Professor John C. Polanyi on the occasion of his 65th birthday

DALE L. HERBERTSON, DAVID A. NEWNHAM, and MARTIN R. LEVY. Can. J. Chem. **72**, 850 (1994).

A laser-ablated pulsed beam of Mn atoms, in various long-lived states, has been employed to determine excitation functions for the reactions Mn + $SnCl_4$ → MnCl* ("blue," "green," "red") + $SnCl_3$. The data all show a sharp rise at low energies, followed by an equally rapid fall, but they differ in the initial thresholds and the rate at which $\sigma(E_T)$ approaches zero. Analysis in terms of a multiple line-of-centres model (Levy, Res. Chem. Kinet. **1**, 163 (1993)) indicates that each excitation function is unique, and is due to reaction of only one Mn reagent state — most probably the first metastable state, a^6D_J. This suggests a strong symmetry control in the entrance channel of the reaction, at least; that is, the Mn atom approaches along the C_3 axis of $SnCl_4$, so that the symmetry corresponding to the spatial configuration of the odd *d* electron is retained. In two cases, "blue" and "red," if not all, the luminescing MnCl* state seems to be produced on a surface that does not directly correlate with the reagents. As collision energy increases in each case, the reaction transition state seems to shift *forward* into the entrance valley, a result attributed to restricted access to the exit valley.

DALE L. HERBERTSON, DAVID A. NEWNHAM et MARTIN R. LEVY. Can. J. Chem. **72**, 850 (1994).

On a utilisé un faisceau pulsé d'atomes de Mn, obtenus par ablation au laser et présents dans divers états de longue durée, pour déterminer les fonctions d'excitation de la réaction Mn + $SnCl_4$ → MnCl* («bleu», «vert» ou «rouge») + $SnCl_3$. Les données indiquent toutes une augmentation importante des basses énergies suivie par une baisse aussi rapide; elles diffèrent toutefois par leurs seuils initiaux et par la vitesse à laquelle $\sigma(E_T)$ approche de zéro. Une analyse en fonction du modèle à plusieurs raies centrales (Levy, Res. Chem. Kinet. **1**, 163 (1993)) indique que chaque fonction d'excitation est unique et qu'elle est causée par la réaction d'un seul état réactif du Mn, probablement le premier état métastable, a^6D_J. Ceci suggère la présence d'un contrôle important par la symétrie dans le canal d'entrée de le réaction, au moins que l'atome de Mn approche par l'axe C_3 du $SnCl_4$, de façon à ce que la symétrie correspondant à la configuration spaciale de l'électron *d* célibataire est maintenue. Dans au moins deux cas, «bleu» et «rouge», l'état MnCl* luminescent semble être produit sur une surface qui n'est pas en corrélation directe avec les réactifs. Lorsque l'énergie de collision augmente dans chaque cas, l'état de transition de la réaction semble se déplacer vers *l'avant*, dans la vallée d'entrée; ce résultat est attribué à un accès limité à la vallée de sortie.

[Traduit par la rédaction]

Introduction

Among the many contributions of John Polanyi to reaction dynamics, a classic series of papers (1–8) deals with the consequences of different energy barrier locations. By performing trajectory calculations on model thermoneutral surfaces, he and his colleagues have shown that the position of the *crest* of the barrier plays a significant role. Thus, if the crest lies in the entrance valley ("surface I"), translational energy in excess of the barrier leads to reaction, while vibration does not, whereas the opposite holds if the crest is in the exit valley ("surface II"). This behaviour is readily understood in terms of the motion of a sliding mass along the reaction coordinate: for surface I, linear momentum along the approach direction R_{AB} is needed to overcome the barrier, while, for surface II, momentum along the product distance R_{BC} (i.e., reagent vibration) helps the system to turn the corner and to surmount the barrier. However, for a given basic surface, the results are modified to a certain extent by mass effects: thus the combination **L** + **HH** (**L** = light atom, **H** = heavy atom) effectively skews and scales the surface so that the barrier shifts to a later position, accentuating the behaviour on I while moderating that on II, whereas **H** + **HL** shows the opposite behaviour since the barrier is effectively shifted further forward.

Calculations on exothermic reactions (with much lower barriers) show that both excess translation and vibration enhance reaction, but the translation is much more effective (9). On the other hand, endothermic reactions (with higher barriers) are predicted generally to require vibrational excitation (10) (this would be expected from microscopic reversibility if the corresponding exothermic reaction disposed its energy into vibration). It has been concluded (10) that substantially exothermic reactions have the crest of the barrier along R_{AB}, while substantially endothermic reactions have the crest along R_{BC}.

Later papers of the series (6–8) have nonetheless shown that substantially endothermic reactions do require a minimum reagent translational energy in addition to the vibrational energy. This lower limit corresponds to the magnitude of the repulsive energy release in the reverse, exothermic direction, and therefore provides a measure of the energy required to overcome that part of the barrier that lies along the endothermic coordinate of approach. This result has been confirmed by calculations on surfaces with "sudden" and "gradual" rises to the crest. The greater availability of translational energy for barrier crossing on gradual surfaces seems to correlate not only with a greater fraction of the barrier along the endothermic coordinate of approach, but also with a more gradual curvature of the repulsive wall of the potential at short internuclear distances.

While a number of experimental studies, e.g., K + HCl, HF (v = 0,1) (11) and Ba + N_2O (n_2 = 0,1) (12–14) have addressed

[1]Present address: Heaton Manor School, Jesmond Park West, Newcastle upon Tyne NE7 7DP, U.K.

[2]Present address: Space Science Division, Rutherford Appleton Laboratory, Chilton, Didcot, Oxon OX11 0QX, U.K.

[3]Author to whom correspondence may be addressed.

Can. J. Chem. Downloaded from www.nrcresearchpress.com by 195.246.54.202 on 09/08/12
For personal use only.

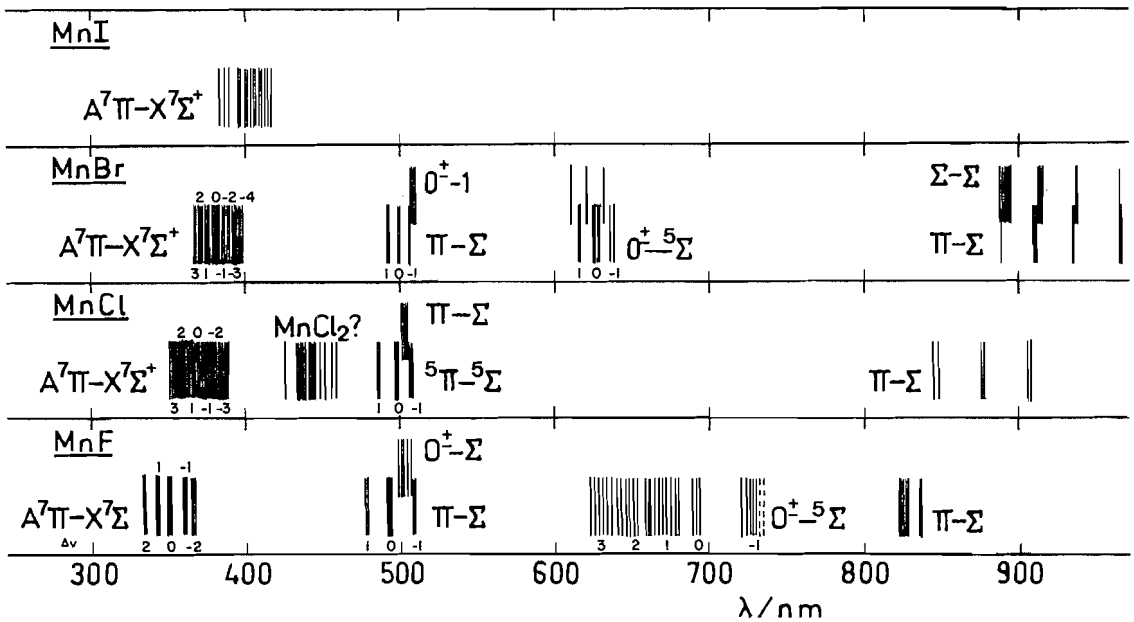

FIG. 1. Schematic representation of the known electronic spectroscopy of the Mn monohalides (28–31). The bands marked $MnCl_2$? have been reported only once, by Mesnage in 1930 (29), and he suggested that they might not be due to MnCl. The possible attribution to $MnCl_2$ is due to Pearse and Gaydon (31).

the relative role of translational and vibrational energy in promoting reaction, the foregoing conclusions about the disposition of barrier crests on substantially exothermic and endothermic potential surfaces do not seem to have received any critical examination. In particular, while the conclusions may well be appropriate for single potential surfaces, it is not clear that they can apply when multiple surfaces interact, for example, in reactions that are substantially exothermic to ground state products but endothermic to formation of electronically excited species. Likewise, relatively little attention has been given to determining either the position of the barrier crest relative to the repulsive wall, or the degree of curvature in the threshold region. However, following a recent survey and reinterpretation, by one of us (15), of a large number of translational excitation functions for chemical reactions, it is becoming clear that such information is already available, albeit in somewhat crude form. In addition, there appears to be a whole class of reactions for which the position of the barrier crest effectively sampled by trajectories is not fixed, but shifts *forward* into the entrance valley as collision energy increases. The present paper shows how the chemiluminescent reactions of Mn atoms with $SnCl_4$ fall into the latter category.

Over the past years, considerable effort at this laboratory has been directed towards the investigation of chemiluminescent reactions of Mn atoms in various long-lived states. Laser ablation of a solid metal target has been employed to generate a pulsed beam of Mn atoms, and thereby to measure the collision energy dependences of the following processes:

$$Mn + N_2O, O_2, NO_2, CO_2, SO_2 \rightarrow MnO^*(A^6\Sigma^+)$$

(refs. 16, 17)

$$Mn + D_2 \rightarrow MnD^*(d^5\Pi) \text{ (ref. 18)}$$

$$Mn + CH_4, C_2H_2, C_2H_4, C_2H_6, C_3H_6, 1\text{-}C_4H_8,$$
$$1\text{-}C_4H_{10}, c\text{-}C_5H_{12} \rightarrow MnH^*(A^7\Pi, d^5\Pi) \text{ (ref. 19)}$$

In all these cases, analysis of the excitation functions in terms of microcanonical transition state theory (MTST) (20) indicates that chemiluminescence derives from only a very small number of metal atom states, most commonly the first excited state, a^6D_J, although ground-state a^6S atoms appear to responsible in $Mn + N_2O$ (16), while very highly excited states seem to be the active species with D_2 and the smallest hydrocarbons.

The extension of such studies to reactions with halogen-containing molecules is a logical next step. By analogy with alkali (21–26) and alkaline earth (27) atom reactions, $Mn + SnCl_4$ would appear to be a useful starting point for such investigations. However, two problems arise: firstly, many of the manganese monohalide bands are not well characterized, and, secondly, the exoergicity of the fully ground state reaction

$$[1] \quad Mn + SnCl_4 \rightarrow MnCl + SnCl_3$$

is not known, as the $SnCl_3$—Cl bond strength has not been determined.

Figure 1 shows schematically the state of published Mn monohalide electronic spectroscopy, which dates from the 1960s at the latest (28–31). Several band systems are known for each molecule, from the ultraviolet to the infrared, although some seem to be absent or even questionable. By comparison with MnH (32–34), septuplet and several quintet band systems are to be anticipated but, of those shown in the figure, only the UV system has been definitely assigned, as $A^7\Pi \rightarrow X^7\Sigma^+$ (a far UV system not shown on the figure, and designated $B^7\Sigma^+ \rightarrow X^7\Sigma^+$, has also been detected for MnF and MnCl). For the rest, analysis of the vibrational (and in some cases rotational) structure has allowed a number of vibrational constants, ν_{00} values (Table 1) and probable term symbols of the participating state pairs to be deduced, but neither the exact identify of the *lower* state of the transition, nor its excitation energy, is known. If, however, these band systems can be detected from the reaction $Mn + SnCl_4$, and the translational thresholds determined, then upper limits can be placed on the excitations, providing the Mn

Can. J. Chem. Downloaded from www.nrcresearchpress.com by 195.246.54.202 on 09/08/12
For personal use only.

Can. J. Chem. Downloaded from www.nrcresearchpress.com by 195.246.54.202 on 09/08/12
For personal use only.

TABLE 1. Assigned MnX transitions 300–900 nm (28, 30)

Molecule	Band system	$h\nu_{00}$/kJ mol^{-1}
MnF	$A^7\Pi$–$X^7\Sigma^+$	341
	Π–Σ	243
	$0^{\pm}$–Σ	~239
	$0^{\pm}$–$^5\Sigma$	173
	Π–Σ	146
MnCl	$A^7\Pi$–$X^7\Sigma^+$	323
	Π–Σ	241
	Π–Σ	~239
	Π–Σ	137
MnBr	$A^7\Pi$–$X^7\Sigma^+$	315
	$^5\Pi$–$^5\Sigma$	239
	$0^{\pm}$–I	~235
	$0^{\pm}$–$^5\Sigma$	190,196
	Π–Σ	128
	Σ–Σ	128
MnI	$A^7\Pi$–$X^7\Sigma$	~297

TABLE 2. Gaseous enthalpies of formation (kJ mol^{-1}) at 298 K (37) (A = Si, Ge, Sn, Cl)

Element	ACl_4	ACl_3	ACl_2	A
Si	−664.8	−393.1	−168.6	+450.0
Ge	−495.8	−320.8	−171.0	+374.0
Sn	−471.5	?	−197.9	+301.5
Cl	—	—	—	+121.9

reagent states and the ground-state reaction exothermicity are known.

In the previous work on K, Rb, Cs + $SnCl_4$, Wilson, Riley and Herschbach (21, 22) assumed an $SnCl_3$—Cl bond energy of ~315 kJ mol^{-1}, i.e, one quarter of the enthalpy of atomization of $SnCl_4$ (35). By contrast, Behrens et al. (26), in studying the Li reaction, used the significantly lower value of ~230 kJ mol^{-1}, recommended by Oldershaw and Robinson (36) following flash photolysis studies of $SnCl_4$ decomposition. For the present purposes, this disagreement is simply too broad. However, a new (and arguably more reliable) estimate of the $SnCl_3$—Cl bond energy can be obtained by considering the enthalpy changes for the processes

[2] $ACl_4(g) \rightarrow ACl_3(g) + Cl(g)$

[3] $\frac{1}{2}ACl_4(g) \rightarrow \frac{1}{2}ACl_2(g) + Cl(g)$

[4] $\frac{1}{4}ACl_4(g) \rightarrow \frac{1}{4}A(g) + Cl(g)$

where A = Si, Ge, or Sn. Enthalpies of formation (at 298 K) have now been obtained (37) for all the relevant species except $SnCl_3$, and are listed in Table 2, while Fig. 2 shows the result of plotting the data for reactions [2] and [3] against those for reaction [4]. It can be seen that, as the central atom gets heavier, not only do the enthalpy changes for eqs. [2]–[4] decrease, but the gap between the values for eqs. [2] and [3] also falls. Extrapolation of the ΔH_2 data suggests a value for Sn ~263 kJ mol^{-1}, i.e., very close to that for ΔH_3, and, with one proviso that will be discussed below, this can be taken as the effective $SnCl_3$—Cl bond energy. The extrapolation is crude, but it seems unlikely from the trends that the missing ΔH_2 value should be any more than 5 kJ mol^{-1} higher than this. In fact, in deriving their value

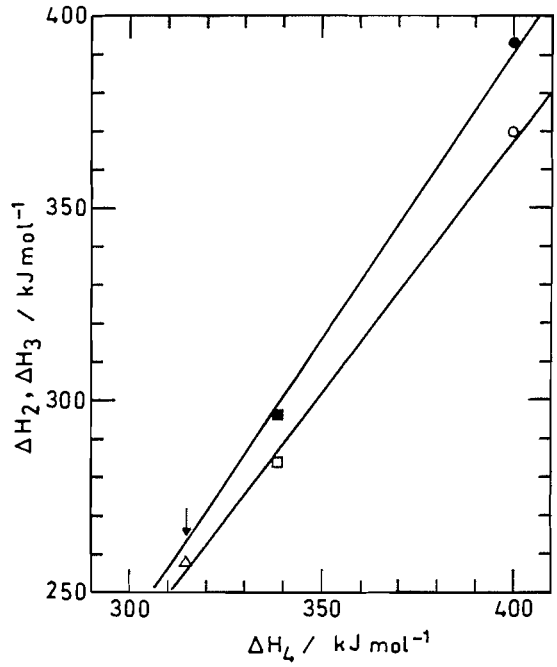

FIG. 2. Estimate of $D(SnCl_3$—Cl) by plotting enthalpy changes for reaction (2), $ACl_4 \rightarrow ACl_3$ + Cl (solid symbols), and reaction [3], $\frac{1}{2}ACl_4 \rightarrow \frac{1}{2}ACl_2$ + Cl (hollow symbols), against reaction [4], $\frac{1}{4}ACl_4 \rightarrow \frac{1}{4}A$ + Cl, for A = Si(●, ○), Ge(■, □), Sn(Δ). The ΔH values plotted were calculated from enthalpies of formation given in Table 2 (37). The tip of the arrow represents the preferred ΔH_3 value deduced for A = Sn.

TABLE 3. Mn state excitations (39) (with spin-orbit splitting)

State	E_i/kJ mol^{-1}
a^6S	0
a^6D_J	207 ± 4
z^8P_J	222 ± 2
a^4D_J	281 ± 2

for $D(SnCl_3$—Cl), Oldershaw and Robinson (37) *assumed* that it would be approximately equal to $D(SnCl_3$—Cl); the higher value here stems entirely from the enthalpy of atomization of $SnCl_2$ being less than deduced by Oldershaw and Robinson.

Using this derived value, and the known MnCl bond energy of 357 kJ mol^{-1} (38), we calculate ΔD_0 ~ 94 kJ mol^{-1} for reaction [1]. For ground state atoms, this is clearly insufficient to excite any of the MnCl band systems in Fig. 1 and Table 1, unless translational energy is supplied. However, some of the band systems might be produced without a translational threshold, if their lower states are not themselves highly excited, and if metastable Mn atoms are the reagents. The excitation energies of the lowest Mn metastable states are listed in Table 3 (39).

Experimental

A full description of the apparatus has been given previously (16, 17). Briefly, a pulsed beam of Mn atoms and ions, of wide velocity range and comprising various long-lived electronic states (including the ground state), is produced by focusing the Q-switched output (~10 ns) of a Nd:YAG laser at 1.064 μm directly onto a solid metal target in vacuo. The beam is collimated by a small aperture in the focusing mir-

Can. J. Chem. Downloaded from www.nrcresearchpress.com by 195.246.54.202 on 09/08/12
For personal use only.

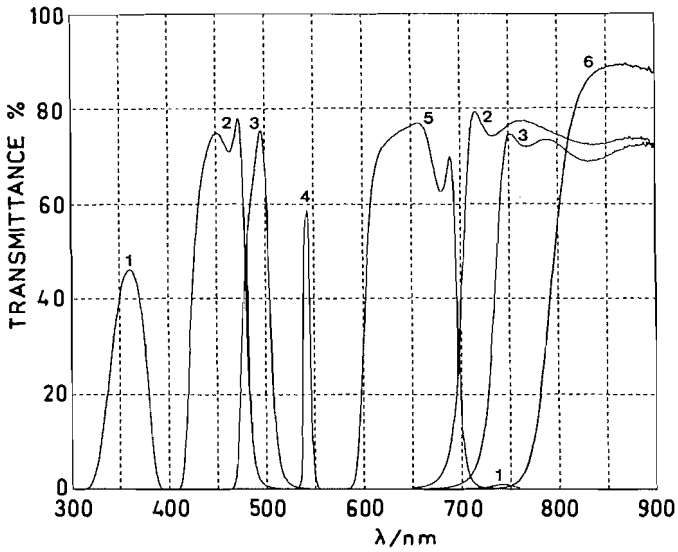

FIG. 3. Transmission curves of the various filters used: 1, 320–390 nm (ultraviolet); 2, 418–490 nm (blue); 3, 470–510 nm (green); 4, 540 nm narrow band (for Mn beam emission); 5, 590–690 nm (red); 6, >750 nm (infrared).

ror, stripped of ions by a d.c. electric field, and passed into a separate vacuum chamber containing a low pressure of $SnCl_4$ reactant gas. Here the beam is monitored, after a 282-mm flight path from the target, by emission at ~540 nm from the metastable $Mn^*(z^8P_J)$ states, whose radiative lifetimes, ~82 and ~122 μs (16), are of a similar order to the flight times. A beamsplitter and an appropriate broadband filter allow simultaneous detection of chemiluminescence at the same point. Signals from the two monitoring photomultipliers are amplified, acquired alternately into the two channels of a transient digitizer, and then averaged over 255 laser shots each to generate time profiles $I(t)$, $I_r(t)$ for beam emission and chemiluminescence, respectively. In these experiments, data have been obtained at both 5 MHz and 2 MHz digitizing rates, the latter allowing measurement (over 1024 channels maximum) to much longer flight times, i.e., to much lower collision energies.

The transmission curves of the various filters employed are displayed in Fig. 3. OX1 ("Chance's glass") and 750 nm cut-on filters, respectively, were used in the (unsuccessful) attempts to detect emission in the MnCl $A^7\Sigma^+ \rightarrow X^7\Sigma^+$ ("ultraviolet") and infrared Π–Σ band systems; in the other cases, combinations of short-pass and cut-on filters were necessary. To simplify the following discussion, we label these remaining band systems by the colours of the filter combinations used: "blue" (418–490 nm), "green" (470–510 nm), and "red" (590–690 nm). As shown in the figure, the blue and green filter transmissions overlap, but exchange of cut-on filters showed that no significant chemiluminescence occurred in the 470–490 nm region. The emissions that were detected are therefore more correctly described as concentrated in the 418–470 and 490–510 nm regions, respectively. The additional transmission of these filter combinations in the far red and infrared parts of the spectrum likewise caused no problem: as remarked above, no infrared chemiluminescence was detected, and while red emission was found, none could been seen through the blue and green filters when the short wavelength transmission was blocked out.

Figure 4 shows typical beam and chemiluminescence time profiles, obtained at the 5 MHz digitizing rate. As before (16, 17), such data were transformed to relative cross section σ by taking ratios point by point, and correcting for the different detection efficiencies and the radiative decay of the emitting Mn^* ($z^8P_{7/2,5/2}$) substates:

$$[5] \quad \sigma(t) \propto (I_r(t)\Gamma(t)t)/I(t)$$

Here $\Gamma(t)$ is the weighted exponential decay factor of the emitting J-substates (described in ref. 16), and the factor t enters because the beam signal represents number density rather than flux. This procedure

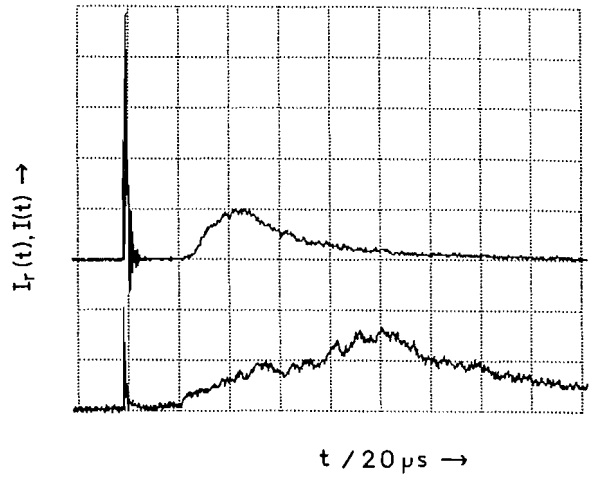

FIG. 4. Typical time profiles of $Mn(z^8P_J \rightarrow a^6S)$ beam emission (upper) and Mn + $SnCl_4$ blue luminescence (lower), each averaged over 255 laser shots. Vertical sensitivity is respectively 10 and 5 mV/division, with fullscale resolution 128 point. Horizontal resolution is 1024 point, the start of the initial spike in both traces indicating the time zero.

assumes that all Mn states start with the same velocity distribution, a reasonable assumption in view of the ~80 000 K temperature of the laser-produced Mn plasma (16). Leaving aside for the moment the spread of $SnCl_4$ collision velocities in this beam-gas configuration, the *nominal* collision velocity is equal to x/t, where x is the distance (282 mm) from the target; and the *nominal* collision energy E_T^0 is given by

$$[6] \quad E_T^0 = \tfrac{1}{2}\mu(x/t)^2$$

Equations [5] and [6] can thus be used to generate relative chemiluminescence cross sections $\sigma(E_T^0)$. However, from an individual pair of data traces such as those in Fig. 4, the overall noise in σ is generally quite large, due to the small magnitude and erratic nature of the primary signals, particularly at long delay times. The excitation functions that are presented below are therefore the result of adding together relative cross sections derived from a substantial number of pairs of data traces. In addition, the Doppler broadening at each nominal collision energy E_T^0 means that $\sigma(E_T^0)$ differs somewhat from the *true* excitation function $\sigma(E_T)$, particularly in the threshold region $E_T \approx E_0$. However, as demonstrated previously (17), this deviation can be rigorously accounted for in the data analysis.

As before, the solid Mn target was electrolytic quality. $SnCl_4$ (BDH) was degassed at liquid nitrogen temperature before admission to the reaction chamber. Typical pressures measured by the Penning gauge were ~$(1–2) \times 10^{-3}$ Torr (0.13–0.27 Pa) but, as the gauge was calibrated only for nitrogen, the true pressure may have been as much as a factor of 10 less. At the highest pressures, some attenuation of the beam was evident, but since both beam and luminescence were detected at the same point, this was assumed to be unimportant.

Results and analysis

As remarked above, no emission could be detected in the ultraviolet or infrared band systems, but signal was indeed found in the blue, green, and red filter regions. In addition, and in common with many other collision partners (16, 18, 19, 40–42), $SnCl_4$ was observed to give rise to $Mn^*(z^6P \rightarrow a^6S)$ collision-induced emission at ~403 nm; however, discussion of that process will be reserved to a subsequent paper (41).

Figure 5 shows excitation functions $\sigma(E_T^0)$ for emissions in the blue, green, and red spectral regions, derived from time profiles recorded, at 0.2 μs digitizing intervals, to 180 μs maximum delay time (i.e., minimum energy $E_T^0 \sim 56$ kJ mol^{-1}). To

Can. J. Chem. Downloaded from www.nrcresearchpress.com by 195.246.54.202 on 09/08/12
For personal use only.

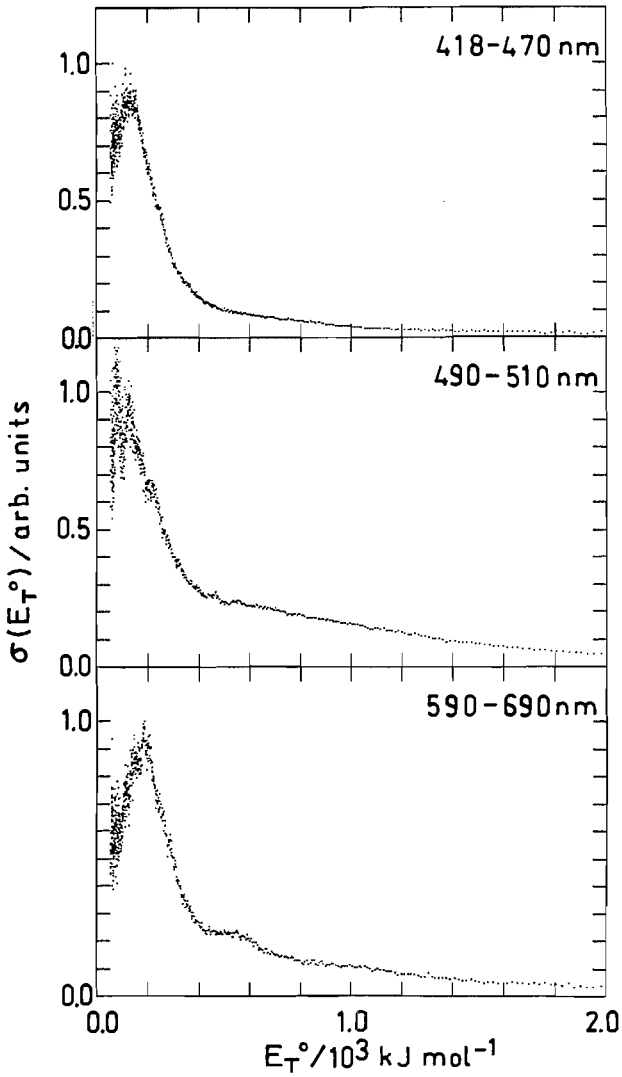

FIG. 5. Excitation functions, $\sigma(E_T^0)$, for production of emission in the wavelength regions indicated, in collisions of Mn atoms with $SnCl_4$. Point-to-point resolution corresponds to 0.2 μs delay, and the data therefore start at only $E_T^0 \sim 56$ kJ mol^{-1} . The excitation functions are arbitrarily normalized to unity at their maximum.

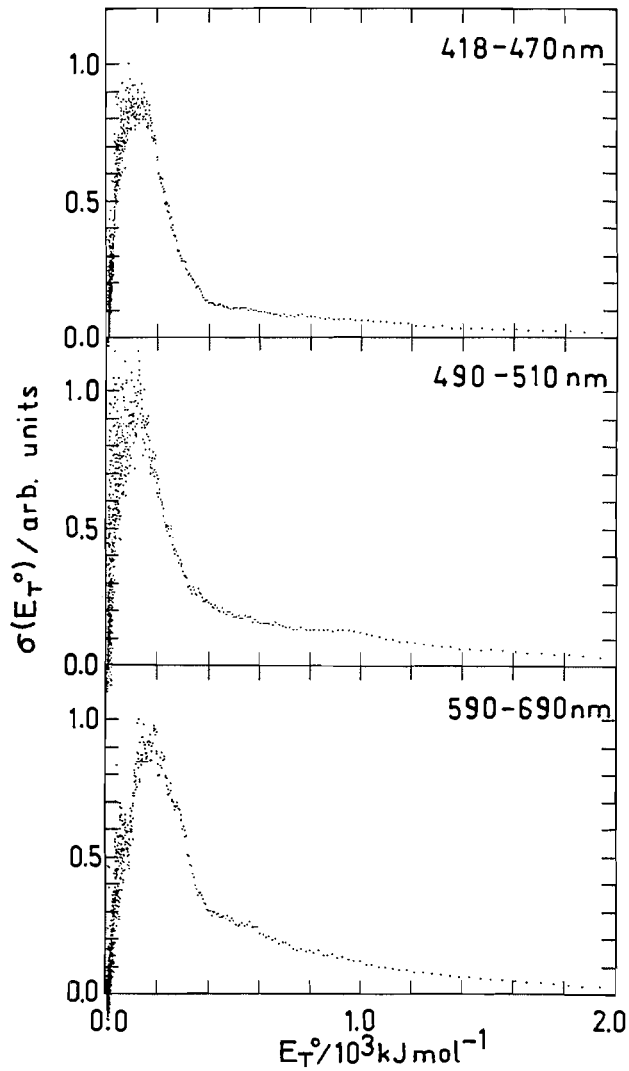

FIG. 6. Same as in Fig. 5, but recorded at 0.5 μs resolution. The data now extend down to $E_T^0 \sim 9$ kJ mol^{-1}.

generate these, some 9200, 45 000, and 17 000 laser shots were required, respectively. Absolute comparison of the peak cross sections is unfortunately not straightforward, as the scattering gas pressure could not be held constant over the large number of runs (of 255 shots per channel) required to generate data of satisfactory quality. However, a crude comparison at 102.4 μs delay (~172 kJ mol^{-1}, close to the peak cross section), taking into account the varying quantum efficiency of the photomultiplier, yielded relative intensities of ~1.0:1.5:5.0 for the green, red, and blue emissions, respectively. That the blue signal is by far the largest is clear from the different numbers of shots required, and from the different signal-to-noise ratios still remaining, in Fig. 5.

The excitation functions all show the same basic form, rising rapidly to a peak in the range ~150–200 kJ mol^{-1}, and falling off rapidly thereafter. There are differences, however, in the rate at which the cross sections approach zero as E_T^0 increases: in particular, the fall-off starts latest for the red signal, and both the green and red excitation functions seem to show a pronounced shoulder. However, as all three show significant noise at low energies (i.e., long times) and thresholds below the minimum energy achieved, the behaviour up to and including the peak cross section remains somewhat ambiguous.

To resolve this issue, the experiments were repeated at 0.5 μs digitizing intervals. This was not adopted as a routine measure since the laser focussing conditions necessary to sustain the Mn beam at significant magnitudes in the range ~200–500 μs could only be achieved, and then fleetingly, for a fresh mirror and Mn target combination. However, after strenuous efforts, it was possible to accumulate data of satisfactory quality over some 9200 laser shots in each spectral region. The results, displayed in Fig. 6, are in general noisier than those of Fig. 5, in part because of the smaller number of laser shots, but also because of the reduced chance of capturing individual photons at the slower digitizing rate. Nonetheless, the data do now extend to detectable thresholds and, within the noise, the measured excitation functions achieved at the different digitizing rates agree quite well. For the green emission, the shoulder/peak ratio is somewhat smaller than at 0.2 μs, but this discrepancy must be regarded as a consequence of the substantial difference in the number of laser shots employed (~9200 instead of ~45 000).

Can. J. Chem. Downloaded from www.nrcresearchpress.com by 195.246.54.202 on 09/08/12
For personal use only.

In past work from this laboratory (17, 18, 40), the initial rise part of such excitation functions has been analysed in terms of the microcanonical transition state theory (MTST) approach of González Ureña (20):

$$[7] \quad \sigma(E_T) = \sigma_0(E_T - E_0)^n/E_T$$

where E_0 is the threshold, and n is a small number representing the active modes at the critical transition state. In principle, the analysis involves transforming eq. [7] to the yield function form

$$[8] \quad Y(E_T) = \sigma(E_T)E_T = \sigma_0(E_T - E_0)^n$$

and plotting $Y^{1/n}$ against E_T for different values of n until the best linearity is achieved. In practice, however, as noted above, the beam-gas configuration measures an effective cross section $\sigma(E_T^0)$ at *nominal* collision energy E_T^0, with collision energy spread introducing a degree of threshold curvature in the linear $Y^{1/n}$ plot. Nonetheless, the curvature can be modeled analytically for integral values of n (17). By this means it was found that, in the reactions $Mn^*(a^6D_J) + O_2$, NO_2, CO_2, SO_2 (17), n = 2–3 at relatively low energies, but $n = 1$ at higher energies. This indicates a potential well before the exit transition state, but one whose influence on the transition state dynamics diminishes as collision energy increases.

In the present case, yield functions $Y(E_T^0)$ for the threshold regions of the three different emissions, i.e, calculated from the cross sections of Fig. 6, are displayed in Fig. 7. The initial linear behaviour is quite clear, showing that the data follow the line-of-centres form ($n = 1$), from thresholds of 10 ± 2, 15 ± 2, and 22 ± 1 kJ mol^{-1}, respectively. Despite the noise on the cross-section data, the yield function plots define the thresholds extremely tightly, especially when the requirement to fit the threshold curvature (see below, Fig. 10) as well as the linear part is taken into account. Not only does the conversion to yield function reduce the relative noise, but the reduced energy interval at long delay times means that the functionality becomes better defined as E_T^0 decreases towards E_0. The error limits given here indicate *absolute* possible maximum and minimum values for each threshold, pushed to the limit of consistency with the data. Although the blue and green thresholds are relatively close, it has not proved possible to reconcile them satisfactorily with any single intermediate value.

The significant higher energy differences in Fig. 7 lend support to the observation of different thresholds. The green plot is linear up to ~140 kJ mol^{-1}, the red emission shows a second threshold at ~105 kJ mol^{-1}, whereas the blue plot displays a "step," with a sharp upward break near 30 kJ mol^{-1}, followed by a *linear* fall-off from ~40 kJ mol^{-1}. While the red break at ~105 kJ mol^{-1} also appears on the 0.2 μs yield function (not shown), the step in the blue emission is at such low energies that it is not even hinted at in the 0.2 μs data. The reality of this feature was confirmed by adding separately 3 groups of 6 files, instead of the 18 previously summed together; although the noise is higher, the step clearly appears in each group.

Space considerations limit our presentation of the yield functions to the threshold region only. However, at energies beyond the range of Fig. 7, all plots display a sharp downward break, while further, opposite, slope changes occur at higher energies still. This, together with the peculiar behaviour of the blue data at E_T^0 ~ 30–40 kJ mol^{-1}, has prompted the question of what may be responsible, and whether in general there is a suitable

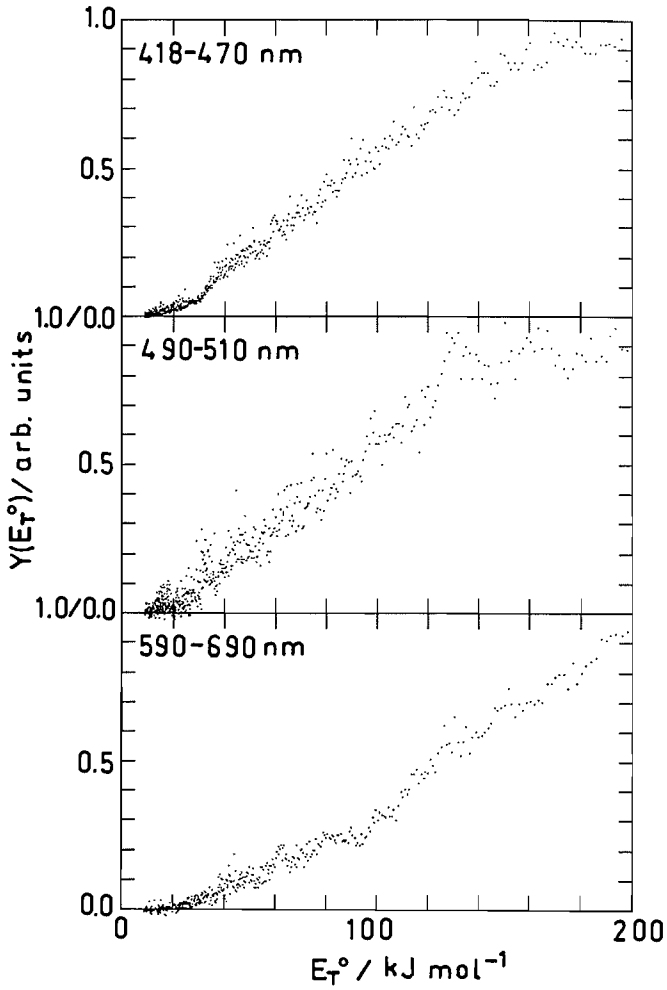

FIG. 7. Yield functions $Y(E_T^0)$ for the threshold region, calculated from the data of Fig. 6 (again arbitrary normalization).

functional form that may be employed to analyse the fall-off for each of these excitation functions. In fact, such a procedure has recently been proposed by one of us (15). It takes the form

$$[9] \quad \sigma(E_T) \sim \Sigma\sigma_k(1 - E_k/E_T)$$

where $k = 0, 1, 2,...$ and σ_k ($k > 0$) may be negative. Each term in the series only contributes from its threshold E_k, and the asymptotic sign allows for initial $n > 1$ behaviour by each individual component. This result has proved highly successful in analysing a large number of excitation functions in the scientific literature, revealing two major classes of fall-off from an initial rise (15).

In "simple" cases, generally only two terms contribute, with $|\sigma_1| \leq \sigma_0$; eq. [9] may then be written, for $E_T > E_1$, as

$$[10] \quad \sigma(E_T) \sim \pi P_0 R_0^2(1 - E_0/E_T) - \pi P_0 P_1 R_1^2(1 - E_1/E_T)$$

Here, as illustrated in Fig. 8, the first term represents reaction, with probability P_0 and line-of-centres energy $\geq E_0$, at internuclear distance R_0, while the second represents *recrossing*, with probability P_1, as the system penetrates with line-of-centres energy $\geq E_1$ to internuclear distance R_1, and is reflected from the repulsive wall of the potential. Since $P_1 \leq 1$, and recrossing

Can. J. Chem. Downloaded from www.nrcresearchpress.com by 195.246.54.202 on 09/08/12
For personal use only.

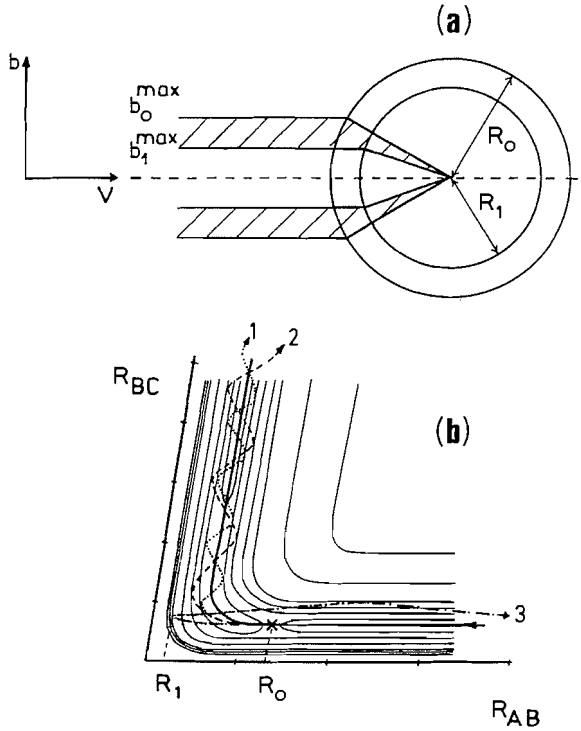

FIG. 8. (*a*) Simple excitation function fall-off model (15). R_0, R_1 are the line-of-centres internuclear distances at which, respectively, reaction and depletion occur; b_0^{max}, b_1^{max} are the respective maximum impact parameters for the two processes at a given relative velocity *V*. (*b*) Schematic of A + BC → AB + C potential surface shape and dynamics consistent with this model. The bold line indicates the minimum energy path, with saddle point × at R_0, while trajectories 1, 2, and 3 have increasing energy in excess of the barrier. Recrossing occurs when trajectories can penetrate as far the repulsive wall of the potential at R_1.

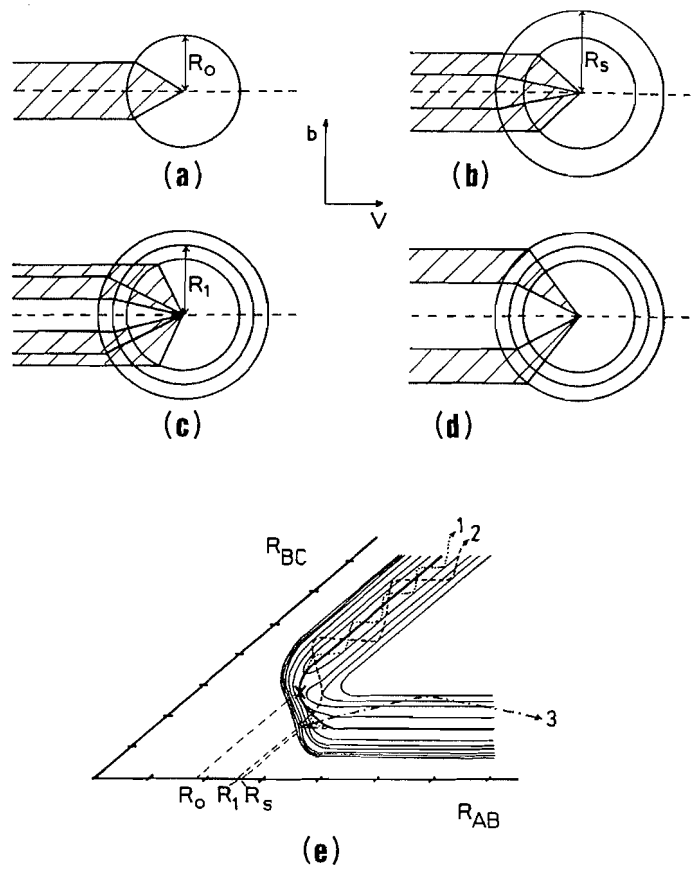

FIG. 9. Complex excitation function fall-off model (15). (*a*) At low collision energy, reaction only occurs at R_0. (*b*) As E_T increases, the transition state for reaction shifts *forward* to R_s at low impact parameters, but the overall cross section is not affected. (*c*) At higher energies, depletion starts at R_1. (*d*) At higher energies still, σ starts to rise again, as reaction at R_s can now occur at impact parameters greater than R_0. (*e*) Schematic of potential surface features consistent with the above behaviour: as before, the bold line represents the minimum energy path; 1, 2, and 3 are trajectories with progressively higher collision energy; and × is the saddle point.

requires that $R_1 \leq R_0$, the relative slopes σ_0 and $(\sigma_0 + \sigma_1)$ of the bilinear yield plot may then be analysed, to give $P_1 \geq |\sigma_1/\sigma_0|$, or $R_1/R_0 \geq |\sigma_1/\sigma_0|^{1/2}$. Among others, the reactions K + C_2H_5Br (43), Sr + HF (44), and Xe*($^3P_{2,0}$) + HCl (45) fall into this category.

A number of reactions, however, follow more complex behaviour. In essence, this is characterized by a three-term series (at least),

$$[11] \quad \sigma(E_T) \sim \sigma_0(1 - E_0/E_T) + \sigma_1(1 - E_1/E_T) + \sigma_2(1 - E_2/E_T)$$

with each term again only contributing above its threshold. As before, $\sigma_1 < 0$; but in this case $|\sigma_1/\sigma_0| > 1.0$, implying recrossing occurs at greater internuclear distances than reaction! The third, positive, term is, however, significant, suggesting that above E_2 the equation should really be written as

$$[12] \quad \sigma(E_T) \sim \sigma_s(1 - E_s/E_T) + \sigma_1(1 - E_1/E_T)$$

where $\sigma_s = (\sigma_0 + \sigma_2)$ and $E_s = (\sigma_0 E_0 + \sigma_2 E_2)/(\sigma_0 + \sigma_2)$. As shown in Fig. 9, the rapid depletion is then understood in terms of the reaction transition state having already *shifted forward*, from R_0 to a distance R_s, at line-of-centres energy E_s. This shift, however, can only lead to an increase in $\sigma(E_T)$ once $\sigma_s(E_T - E_s) > \sigma_0(E_T - E_0)$, i.e., $E_T > E_2$. Such an interpretation can of course only be valid if the calculated value of $E_s < E_1$, but this does indeed appear to be the case for such reactions as Ba + $N_2O(n_2 = 1)$ (13, 14) and K + CH_3I (46–48). Relative internuclear distances R_s/R_0 and R_1/R_0 have thereby been deduced from the multilinear yield functions found in those reactions (15). The shift has been identified with a restricted access to the exit valley, so that, as collision energy increases, trajectories "cut" the corner and effectively sample an earlier barrier. Such a situation might occur if R_{BC} needs to stretch a little before reaction takes place, and if there is insufficient time for this to occur at elevated collision energies. At higher energies still, there will be even less time, so access to the exit valley is completely blocked off, and depletion occurs at internuclear distances of $\sim R_s$.

In the present cases, the shapes of the excitation and yield functions suggest that the reactions fall for the most part into the second category, although, as noted, the blue emission shows an "early" fall-off that is more reminiscent of the "simple" depletion behaviour. There is, however, an additional complication in that, in principle, several Mn states could generate the observed luminescence, giving rise to several independent production and depletion thresholds. We reserve discussion of this issue to the next section, and concentrate here on determining whether the excitation functions can be modelled and, if so, the parameters of the fit.

TABLE 4. Parameters of the analysis (energies E_k in kJ mol^{-1})

Emission	k	0	1	2	3	4
Blue	σ_k	0.44 ± 0.07	3.40 ± 1.18	−(2.88 ± 1.26)	−(1.37 ± 0.018)	0.337 ± 0.018
	E_k	10 ± 2	36 ± 2	40 ± 1	158 ± 3	393 ∓ 13
Green	σ_k	0.83 ± 0.035	−(0.925 ± 0.025)	0.165 ± 0.005	−(0.123 ± 0.004)	
	E_k	15 ± 2	150 ∓ 5	390 ± 10	955 ∓ 15	
Red	σ_k	0.81 ± 0.03	0.47 ∓ 0.03	−(1.73 ± 0.03)	0.61 ± 0.03	−(0.205 ± 0.005)
	E_k	22 ± 1	100 ± 5	200 ± 5	400 ∓ 10	535 ± 15

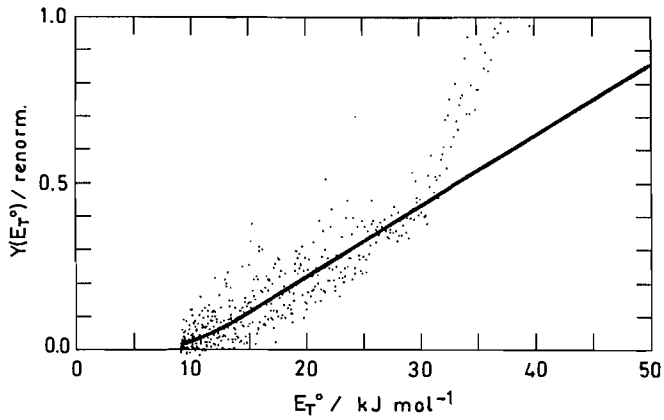

FIG. 10. Magnification of the blue yield function in Fig. 7, showing the line-of-centres "best fit" to the initial rise. The renormalized linear scale corresponds to an expansion factor of ~7.5. The derived initial threshold is ~10 kJ mol^{-1}, but collision energy spread in the beam-gas configuration leads to the curvature shown. Likewise, the true threshold corresponding to the break at ~30 kJ mol^{-1} is in fact ~36 kJ mol^{-1}.

The procedure that has been adopted is essentially an iterative one: first, as shown in Fig. 10, the threshold energy dependence of $Y(E_T^0)$ is fitted to a line-of-centres form, modified by collision energy spread; next, depending on whether $Y(E_T^0)$ shows an upward or downward break from this behaviour, a new yield function is generated by respectively subtracting, or subtracting *from*, the extrapolated form of the fitting; and then the process starts again. In this way, each section of the plot is fitted in turn. However, because the 0.5 μs data are of inferior quality at higher energies, they have only been used to determine the threshold behaviour, and these results have then been employed as starting points for the 0.2 μs analysis.

The σ_k, E_k parameters derived from this procedure are displayed in Table 4. The numbers of pairs in each case, 5 for the blue and red data, and 4 for the green, match the numbers of different slope regions of the yield plots. With the exception of the step in the blue data, all of these slope regions extend over a considerable collision energy range, and, indeed, no satisfactory fitting could be obtained in any of the excitation functions with a smaller number of parameter pairs. The uncertainties given in the table were obtained from repeated trials of the procedure, starting with the maximum and minimum possible E_0 values already given above. The direction of the ± or ∓ signs in the table generally indicates the correlations between successive terms, i.e., a "high" estimate of σ_k will tend to be compensated by a corresponding "low" estimate (or "high" negative estimate) or σ_{k+1}. However, for the blue excitation function the step at ~36 kJ mol^{-1} is so sharp, and the resulting threshold curvature so substantial, that the correlation between the $k = 0$ and $k = 1$ terms is small and, if anything, in the opposite direction. The substantial uncertainty in σ_1 (and hence in σ_2) in this system derives principally from the sharpness and short range of the step; but since the sum $(\sigma_0 + \sigma_1 + \sigma_2)$ is well defined from the yield plot, the uncertainties on the higher terms are much smaller.

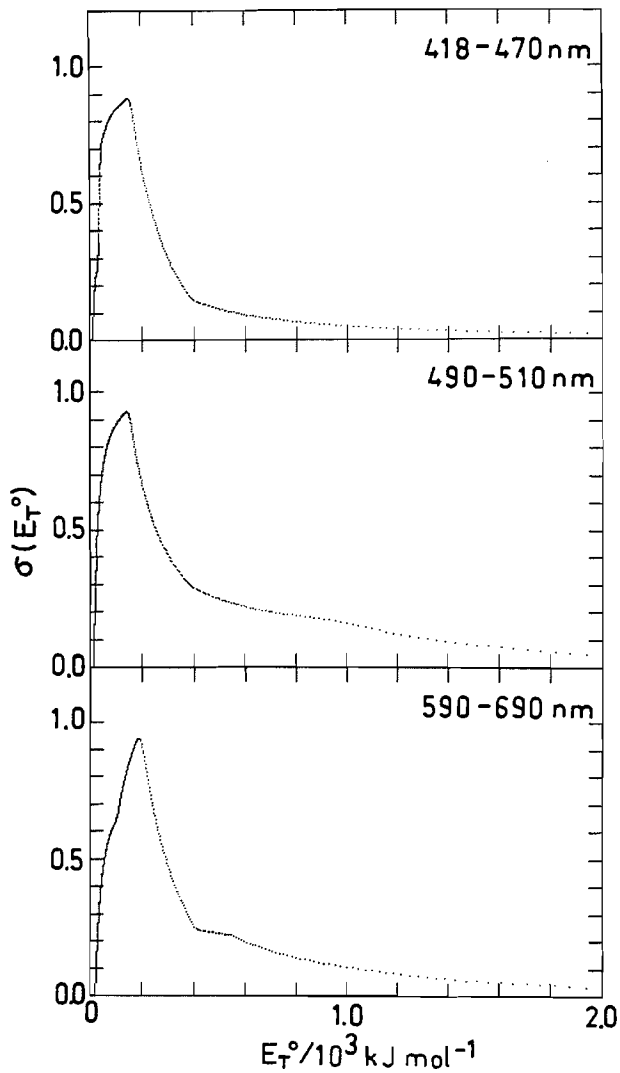

FIG. 11. "Best-fit" excitation functions derived from the parameters given in Table 3, and including the effect of collision energy spread. As with the original data, the separation between data points decreases as collision energy decreases. The apparent steps at low collision energy are merely artefacts of the printer resolution.

The shapes of the "best" excitation function fits (calculated at the E_T^0 value of each data point in Fig. 6) are shown in Fig. 11.

Can. J. Chem. Downloaded from www.nrcresearchpress.com by 195.246.54.202 on 09/08/12
For personal use only.

Can. J. Chem. Downloaded from www.nrcresearchpress.com by 195.246.54.202 on 09/08/12
For personal use only.

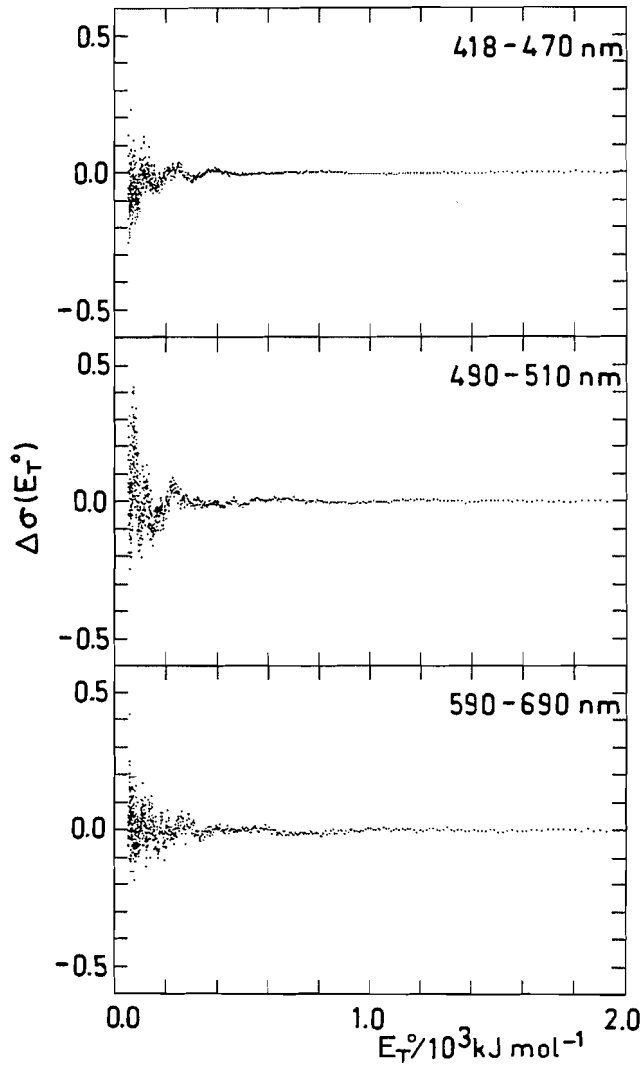

FIG. 12. Residual plots $\Delta\sigma(E_T^0)$ of the deviations between the experimental excitation functions in Fig. 5, and the derived model functions in Fig. 11, to the same scale.

It was not sensible to include such fits in Figs. 5 or 6, since the individual data points are very close together, and most would disappear under the fit. However, to show the quality of agreement, Fig. 12 displays the residual plots representing the difference between the data of Fig. 5 and the calculated excitation functions. Clearly the average deviation is virtually zero across the whole collision energy range. The noise at low energy reflects the noise on the original excitation functions, which are at their largest in that energy range.

Discussion

1. Product and reagent state excitations

The first point to be made about the measured excitation functions is that each is unique. Although the data in Fig. 5 (and Fig. 6) appear superficially similar, the parameters in Table 4 make the differences clear. It is true that there appear to be some correspondences in blue and green E_k values in Table 4, i.e., (10,15), (158,150), and (393,380); but the relative magnitudes of the corresponding σ_k values are quite different: ~0.65 (at E_0 = 12–13), ~1.4, and ~2.2, respectively. Besides, it is important not to take a subset of the parameters in isolation. In terms of the multiple line-of-centres/movable barriers approach outlined above, the sum $\Sigma\ \sigma_k$ can be expected to take values between significantly positive and slightly negative, depending on the degree of depletion and the relative positions of the barriers (e.g., R_1 could even slightly exceed R_s in Fig. 9). For each complete excitation function, we find that $\Sigma\ \sigma_k$ is indeed ~0, but, for the blue data, $(\sigma_0 + \sigma_3 + \sigma_4) \sim -0.54$, which is excessively negative. The correspondences in E_k values between the blue and green data must therefore be regarded as reflecting similarities, rather than *identities*, between the potential surfaces involved.

The uniqueness of the excitation functions, and the correspondence of emission regions with the known MnX spectroscopy, means that the emitters in all cases are almost certainly MnCl* molecules, in *different* electronically excited states. In confirmation of this conclusion, we and other workers have found some or all of the same emissions, again with different excitation functions, in collisions of Mn atoms with $SiCl_4$, CF_4, SF_6, Br_2, ICl, $GeCl_4$, $TiCl_4$, S_2Cl_2, and SO_2Cl_2 (41, 42). MnX_2* (or MnXY*) cannot entirely be eliminated as the blue emitting species, but it seems unlikely that such a product would be detected from so many reactions (in fact, from all except Mn + $GeCl_4$ (42).

Each excitation function also appears to result from reaction of only a single Mn electronic state. As noted above, an upward break in the yield function could represent the observed onset of either a new process (e.g., a shift forward in the transition state location, or an increase in reaction probability) or the contribution of a less excited Mn state to the chemiluminescence, but the magnitude of the fall-off in each case is so large that the latter must be eliminated. It is highly unlikely that chemiluminescent reaction from two different Mn states should start to be depleted from the same threshold energy.

Given that only one Mn state contributes in each case, it is instructive to consider what that might be. Analogously to the reactions with oxygen-containing molecules (17), the threshold E_0 for chemiluminescence is given by

$$[13]\quad E_0 = D_0(SnCl_3\text{—}Cl) - \bar{E}_{v,r}(SnCl_4) - E_i(Mn^*) - D_0(MnCl^*) + E_i(MnCl^*) + E_b$$

where $\bar{E}_{v,r}$ = the average vibration-rotation energy in $SnCl_4$, E_i = electronic excitation, and E_b = the excess barrier over the endothermicity for reaction. As noted in the Introduction, $D_0(SnCl_3\text{—}Cl)$ is not well known, and, in fact, the value estimated above, ~263 kJ mol^{-1}, is strictly an enthalpy change, determined at 298 K rather than at absolute zero. However, since the excitation functions all follow n = 1 MTST functionality, i.e., two-body behaviour, we can assume that the bulk of the $SnCl_4$ vibration-rotation energy at 298 K does not contribute to overcoming any barrier, but is retained in the $SnCl_3$ product. Thus, by restricting the partitioning of E_b only to product translation or to MnCl* vibrational excitation, we can ignore $\bar{E}_{v,r}(SnCl_4)$, and assume $D_0(SnCl_3\text{—}Cl) \sim 263$ kJ mol^{-1}. Equation [13] then becomes

$$[14]\quad E_0 \geq E_i(MnCl^*) - E_i(Mn^*) - 94\ \text{kJ mol}^{-1}$$

A lower limit to $E_i(MnCl^*)$ is given by $h\nu_{00}$ in each case: ~266 kJ mol^{-1} for the blue emission (assuming λ_{00} = 450 nm); ~240 kJ mol^{-1} for the green bands (Table 1 (28)); and, by analogy with MnF (Table 1 (28)), ~173 kJ mol^{-1} for the red bands.

Can. J. Chem. Downloaded from www.nrcresearchpress.com by 195.246.54.202 on 09/08/12
For personal use only.

Substitution of $E_0 = 10$, 15, and 22 kJ mol^{-1}, as appropriate, into eq. [14] then shows that $E_i(Mn^*) \geq 162$, 131, and 57 kJ mol^{-1}, respectively.

Clearly, from Table 3, ground-state Mn atoms cannot be responsible for any of the observed reactions but, in the absence of further information, any of the metastable states listed could be. In any case, since a^6D_J atoms were found to be the most active species in the Mn + O_2, NO_2, CO_2, SO_2 chemiluminescent reactions (17), it would be very surprising if they did not play a role here. On the other hand, participation from z^8P_J atoms should be disfavoured since, as discussed below, the MnCl* emitters are likely to be quintet states, or components thereof, whose production from Mn*(z^8P_J) + $SnCl_4$ would violate spin conservation. That process could happen if the reaction proceeded via a potential well, so that the octet $MnClSnCl_3$ intermediate had a lifetime long enough to cross over to a sextet surface; but the excitation functions suggest that such a feature is absent, since they display $n = 1$ MTST functionality and since (as discussed below) the transition state at low collision energies lies at relatively short internuclear distances, i.e., towards the exit channel.

On the other hand, a contribution from Mn*(a^4D_J) atoms cannot a priori be excluded, since they were implicated in Mn + O_2, CO_2, SO_2 (though *not* Mn + NO_2) (17) and since production of excited quintet states of MnCl* would certainly be spin-allowed. However, as remarked above, the present data can only be understood in terms of a single reagent state in each case. If that state were a^4D_J, then one would expect production of at least some of the MnCl* band systems to be *exoergic*, opening up the possibility of negative thresholds. Among all the many chemiluminescent Mn atoms so far studied, whether with oxygen (16, 17), hydrogen- (18, 19) or halogen- (41, 42) containing molecules, the only one observed to have a negative threshold is Mn + NO_2, and there a^6D_J atoms alone were deduced to be the reagent species, with $n \sim 2.5$ functionality (17). Quite highly excited Mn states do seem to be involved in some of the MnH-producing reactions, but in all these cases the processes remain endoergic, displaying significant thresholds. Thus, although we cannot completely exclude a^4D_J atoms (or, for that matter, higher metastable states) in the present reaction, it seems highly likely that the sole progenitors of all three MnCl* band systems observed here are Mn*(a^6D_J) atoms.

If that is indeed the case, then the absence of any contribution from z^8P_J or a^4D_J is something of a problem, especially as z^8P_J atoms should (as shown below, Fig. 14) correlate with MnCl*($A^7\Pi$), which is not observed here. However, while MnX*($A^7\Pi \rightarrow X^7\Sigma$) luminescence has been observed in Mn + SF_6 (41), SO_2Cl_2 (42), and $TiCl_4$ (42), and z^8P_J atoms may well be the reagent, such emission is a relatively rare occurrence, and it may well be that in most cases ground-state products are preferred. As for a^4D_J atoms, collision-induced dissociation is possible, since the electronic excitation exceeds the (derived) $SnCl_3$—Cl bond energy.

If the a^6D_J state is accepted as the reagent species, then eq. [14] can be used to obtain *upper limits* to the excitation of the emitting MnCl* product states. Inserting $E_i(Mn^*) = 207$ kJ mol^{-1}, from Table 3, leads to $E_i(MnCl^*) < 311$, 316, and 323 kJ mol^{-1} for the *upper* states of the blue, green, and red emissions, respectively. By subtracting $h\nu_{00}$ from these energies, we then obtain $E_i(MnCl^*) < 45$, 76, and 150 kJ mol^{-1} for the respective excitations of the *lower* states of the transitions. Clearly these values would be modified if a more accurate estimate of $D_0(SnCl_3$—Cl) could be obtained, or if a more excited Mn metastable state turns out to be the active species. However, it is noteworthy that these upper excitations are all comparable to that of the $A^7\Pi$ state, 323 kJ mol^{-1} (28). This tallies with the Mn + SF_6 (41), SO_2Cl_2 (42), and $TiCl_4$ (42) results, where the thresholds for MnX*($A^7\Pi$) production suggest that it lies above the blue, green, and red emitting states. Of course, the true excitations may be well below 323 kJ mol^{-1}, since production of each emitting state may involve a different value of the excess barrier E_b.

2. Chemiluminescence mechanism

Before considering the processes leading to chemiluminescence, it is necessary to discuss the possible identities of the red, green, and blue states, whose maximum excitations we have just deduced. While the MnCl blue system is something of an enigma, the likely term symbols of the green and red emitting states can be inferred from the analysis by Hayes (28), which has already been summarized in Fig. 1 and Table 1. Although Hayes did not find any red band system for MnCl, his observation of comparable systems for MnF and MnBr strongly suggests that the red emission found here should have the same character, viz. $0^{\pm}$–$^5\Sigma$. The MnF and MnBr spectra do not indicate which of these terms is the upper level of the transition, but $0\pm$ must be preferred since such case (*c*) coupling would be much more likely at higher excitations (28). The upper limit of 323 kJ mol^{-1} determined above for the red emitting state would tend to be consistent with this conclusion.

Hayes found two band systems in the green part of the spectrum, both Π–Σ in character. One, which spans the range 485.0–508.2 nm, is almost certainly $^5\Pi$–$^5\Sigma$; while the other also has "a multiplicity of at least five" (28). Since the vibrational constants ω_e', ω_e'' for each are quite different, it seems unlikely that they are separate components of the same system. It has not been possible to separate the bands in the present experiments, but it is clear that only a single green system is produced; whichever it is, it must be $^5\Pi$–$^5\Sigma$ in character.

Further insight into the likely states involved might be gained by comparison with MnH (32–34), which displays band systems near 416, 450, 480, 566, 847, 939, and 1060 nm. The 566 nm system has been assigned to the $A^7\Pi$–$X^7\Sigma^+$ transition; but the $a^5\Sigma^+$ state lies only ~20 kJ mol^{-1} above the ground state (49, 50), and it has now been shown (33, 34) that the 480, 847, and 1060 systems are due to the $d^5\Pi$–$a^5\Sigma^+$, $c^5\Sigma^+$–$a^5\Sigma^+$, and $b^5\Pi_i$–$a^5\Sigma^+$ transitions, respectively. Similar transitions in MnX would not be unreasonable, although, from the $A^7\Pi$–$X^7\Sigma^+$ comparison, they might well be shifted to shorter wavelengths. In that case we would expect some of the band systems, at least, to have the same ω_e'' values. Unfortunately, Hayes' data (28), albeit incomplete, do not support this. The only coincidences that might be present are between ω_e'' for the higher energy green $^5\Pi$–$^5\Sigma$ bands, and ω_e' for one of the infrared systems (Π–Σ for MnCl, Σ–Σ for MnBr).

Strictly, however, we ought to compare MnX to the isoelectronic FeO. The molecular orbital diagram, after Merer (51), is shown in Fig. 13. In MnX, the ground state is formally ...$8\sigma^2 3\pi^4 1\delta^2 9\sigma^1 4\pi^2 10\sigma^1$, $^7\Sigma^+$, which corresponds to one electron in each of the orbitals that carries over from the metal atom *d* orbitals. The 10σ orbital, however, is strongly antibonding, and low-lying quintet states result from pairing the electron into the 1δ, 9σ, or 4π orbitals. For these excited states, the molecule may therefore be regarded as Mn^{+*}(...$3d^6$, a^5D_J) X^-, the differ-

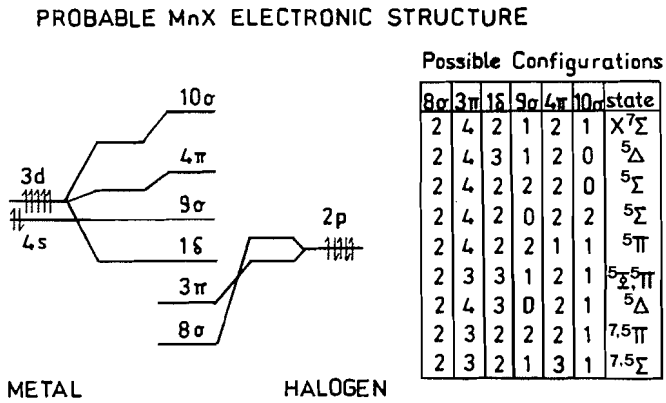

8σ	3π	1δ	9σ	4π	10σ	state
2	4	2	1	2	1	$X^7\Sigma$
2	4	3	1	2	0	$^5\Delta$
2	4	2	2	2	0	$^5\Sigma$
2	4	2	0	2	2	$^5\Sigma$
2	4	2	2	1	1	$^5\Pi$
2	3	3	1	2	1	$^5\Sigma,^5\Pi$
2	4	3	0	2	1	$^5\Delta$
2	3	2	2	2	1	$^{7,5}\Pi$
2	3	2	1	3	1	$^{7,5}\Sigma$

FIG. 13. Probable MnX electronic structure, after Merer (51) (for the isoelectronic FeO). The halogen atomic orbitals, and the molecular orbital numbering, strictly refer to X = F (or O); however, no substantial differences in comparable molecular orbital energies are anticipated for X = Cl, Br, I.

ent possible locations of the odd *d* electron determining the term symbol. In FeO, the ground state is in fact the $\Omega = 4$ component of the $^5\Delta_i$ multiplet, $..8\sigma^2 3\pi^4 1\delta^3 9\sigma^1 4\pi^2$, ~2 kJ mol^{-1} below the $a^7\Sigma^+$ state, and ~48 kJ mol^{-1} below the $A^5\Sigma^+$ state ($...8\sigma^2 3\pi^4 1\delta^2 9\sigma^2 4\pi^2$) (51). By analogy, therefore, MnX should also possess a low-lying $^5\Delta$ state, as well as $^5\Sigma^+$.

The diagram also illustrates another important expectation for MnX, the possibility of "charge-transfer" configurations, in which an electron is displaced from an orbital predominantly located on X (or O), into one of the partially filled *d*-type orbitals located on the metal. Indeed, FeO (51) shows a $C^5\Pi/B^5\Phi$ charge-transfer complex, with configuration $...8\sigma^2 3\pi^3 9\sigma^1 1\delta^3 4\pi^2 10\sigma^1$, 118–129 kJ mol^{-1} above the ground state; and a strong, highly irregular orange emission, which may also be a charge-transfer system. (The FeO $D^5\Delta$ multiplet, however, at ~214–222 kJ mol^{-1}, seems to involve the non-charge-transfer configuration $...8\sigma^2 3\pi^4 1\delta^3 4\pi^2 10\sigma^1$.) Because of the strength of the MnCl blue emission here, and the lack of structure found by Mesnage (29), it is tempting to speculate that it too might involve a transition from a charge-transfer upper state to a $^5\Delta$ lower state. Certainly, as indicated above, both the blue and green emission bands have quite low-lying lower states, and if the green lower state, at ≤76 kJ mol^{-1}, is $^5\Sigma$, then it would not be unreasonable for the blue lower state, at ≤45 kJ mol^{-1}, to be $^5\Delta$. As already remarked, these excitations might well be even lower if chemiluminescence production involves excess barriers.

Whatever the specific upper and lower term symbols in each band system, it is clear that there must be a considerable number of excited MnCl states at accessible energies — so many, in fact, that Mn*(a^6D_J) atoms are unlikely to correlate directly with most of the upper states of the emission bands detected. Production of chemiluminescence must therefore involve mixing between potential surfaces or between vibrational manifolds of the MnCl product. Since, in principle, a multitude of such mixings may be occurring, a full understanding of the reaction requires knowledge not only of the identities of the various "dark" and luminescent product channels, but of the branching ratios and their dependence on the individual substates of the Mn*(a^6D_J) multiplet.

For chemiluminescence, however, the uniqueness of the excitation functions presented here shows that the mixing must be

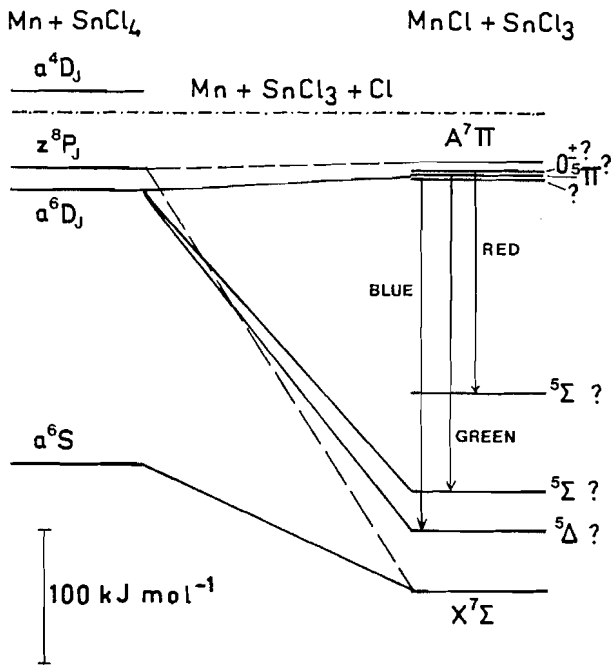

FIG. 14. Possible form of the electronic state correlation diagram for Mn + $SnCl_4$, consistent with the results obtained. The diagram is likely to be incomplete, owing to the fragmentary knowledge of the electronic spectroscopy of both MnCl and $SnCl_3$.

highly selective, i.e, the effective potential surface that leads to each observed emission must be quite distinct. Given the similarity in initial thresholds, and the likely overlap between the vibrational manifolds of the blue, green, and red states, this selectivity suggests some degree of symmetry control. From Fig.13, that would appear to require conservation of *d* electron configuration in the entrance channel, i.e., between Mn*(a^6D_J) + $SnCl_4$ and Mn^{+}*(a^6D_J) + $SnCl_4^-$, the first step to production of electronically excited Mn^+Cl^-. This can only occur if chemiluminescence results from reaction along the C_3 axis: Mn approach along any other direction would mix spatially de- generate *d* orbital configurations with the odd electron in different locations, thereby promoting more than one product state. As the reactive collision evolves, the initial configuration could be lost by mixing between different potential surfaces, but, in view of the selectivity observed, it seems most likely that the mixing will be restricted to surfaces (or vibrational manifolds) that retain the *symmetry* corresponding to the initial configuration, i.e., Σ–Σ, Π–Π, Δ–Δ, or components thereof.

The overall conclusions on energetics and state correlations are schematically summarized in Fig. 14. The term symbols of the different emitting states have been tentatively assigned, on the basis of Hayes' results, but these must be regarded as speculative, since the present work has not addressed the detailed spectroscopy. In any case, the diagram cannot be the complete picture, as no excited electronic states of $SnCl_3$ are represented and as the infrared MnCl band system has been omitted; indeed, investigations of a number of other reactions (41, 42) suggest that the infrared system connects two of the lowest-lying MnCl states. Nonetheless, Fig. 14 does at least provide a possible framework for rationalizing the current observations. It suggests, as discussed below, that the green emission ($^5\Pi? \rightarrow {}^5\Sigma?$) is produced on a surface that directly correlates with Mn*(a^6D_J) + $SnCl_4$, but conversely, that the blue and red emissions will

Can. J. Chem. Downloaded from www.nrcresearchpress.com by 195.246.54.202 on 09/08/12
For personal use only.

Can. J. Chem. Downloaded from www.nrcresearchpress.com by 195.246.54.202 on 09/08/12
For personal use only.

only result from mixing with surfaces leading to lower lying $^5\Sigma$ or $^5\Delta$ states.

3. Transition states and potential surface shapes

One of the most remarkable features of the present results is the degree to which the multiple line-of-centres model is able to fit the data. Originally developed (15) as an approximate approach to rationalizing data from reactions taking place on single potential surfaces, the model has now demonstrated its applicability to situations where many surface interactions are anticipated. This cuts across the accepted wisdom that the velocity dependence of surface crossing is significant in determining the collision-energy dependence of the cross section. The results show that, in the present cases, such dependence is predominantly discontinuous, i.e, at given line-of-centres energies, the transition state location shifts, or the efficiency of crossing changes, or a competing process begins. The yield functions would show significant curvature if the efficiency of surface crossing depended continuously on velocity.

Following the procedure outlined above, in relation to eqs. [9]–[12], we can interpret the parameters in Table 4 to derive energies and relative internuclear distances of the various critical transition states. We pursue this here with some detail not only to illustrate the possible dynamics consistent with the data, but also to prevent misconceptions and pitfalls in future applications of the procedure. Care is required since any error in determining one pair of parameters generates a comparable but opposite error in the next pair in the series. However, as stated above, subsequent pairs of parameters may well have higher precision: e.g., in the green excitation function the large uncertainty in σ_1 generates an opposite uncertainty in σ_2; but $(\sigma_0 + \sigma_1 + \sigma_2)$, and thus σ_3, are quite well defined. It turns out that most of the derived internuclear distance ratios are fairly insensitive to the uncertainties in the values of the parameters given in Table 4.

All three excitation functions seem to involve, at some energy, a shift forward in the transition state location. The green data reveal this most straightforwardly. From the parameters derived, it seems that the shift occurs at $E_s \simeq 77$ kJ mol^{-1}, and that $R_s/R_0 \simeq 1.09$. Depletion then begins at $E_1 \simeq 150$ kJ mol^{-1}, and $R_1/R_0 \simeq 1.06$; but the internuclear distance at which this takes place also shifts forward, to $R_d/R_0 \simeq 1.12$, at $E_d \simeq 245$ kJ mol^{-1}. In fact, E_s and E_d are strictly upper limits; the true thresholds could be significantly lower if the shift is also accompanied by an initial difference in functionality, i.e., $n > 1$ in eq. [7].

The red excitation function is more complex in that σ_1 is positive. As noted above, this must correspond to some new process — an increase in reaction probability, due to the opening up of a new path, and (or) a shift in the transition state location. If the latter is exclusively the case, then the parameters in Table 4 imply that the shift, to $R_s/R_0 \simeq 1.26$, occurs at $E_s \simeq 51$ kJ mol^{-1}, and is followed by a further shift, to $R_{s'}/R_0 \simeq 1.53$, at $E_{s'} \simeq 163$ kJ mol^{-1}. Depletion likewise begins at $E_2 \simeq 195$ kJ mol^{-1}, and $R_2/R_0 \simeq 1.46$, and shifts forward to $R_d/R_0 \simeq 1.55$ at $E_d \simeq 231$ kJ mol^{-1}. These seem excessively large changes.

On the other hand, if the rise at ~100 kJ mol^{-1} is caused by the opening up of a new path, then the subsequent rapid fall (σ_2) and secondary rise (σ_3) indicate that it must at least have the same entrance channel as the original path. In the extreme case of an increase in reaction probability *at the same internuclear distance*, then the excitation function in the range $E_T \sim$ 100–195 kJ mol^{-1} should be written as

$$[15a] \quad \sigma(E_T) = \pi(P_0 R_0^2(1 - 22/E_T) + \pi(P_1 - P_0)R_0^2(1 - 100/E_T)$$

$$[15b] \quad = \pi(P_1 R_0^2(1 - 100/E_T) + \pi(P_0 R_0^2(78/E_T)$$

where $P_0 < P_1 \leq 1.0$. In terms of Figs. 8 and 9, reaction can now be visualized as occurring with probability P_1 at low impact parameters, and with probability P_0 at high impact parameters. From Table 4, there will then still be a forward shift in transition state location at $E_s \simeq 164$ kJ mol^{-1}, but now to $R_s/R_0 \simeq 1.22$, a similar value to that found for the green data. The relative internuclear distances for depletion are now $R_2/R_0 \simeq 1.16$ and $R_d/R_0 \simeq 1.23$.

Such behaviour does, however, have consequences for the subsequent detail of the excitation and yield functions. Instead of a single break at $E_T = E_3$, there should be a first upward break when

$$[16] \quad \pi R_s^2(E_T - 164) = \pi R_0^2(E_T - 100)$$

i.e., when reaction at R_s with probability P_1 starts to overtake reaction at R_0 with probability P_0; and then a second, but much smaller, upward break should occur when

$$[17] \quad \pi R_s^2(E_T - 164) = \pi R_0^2(E_T - 22)$$

i.e., when reaction at R_0 is completely overtaken. These collision energies turn out to be ~290 and ~460 kJ mol^{-1}, respectively. There is no clear evidence for such thresholds, whether from the excitation function, from the extrapolated yield plot (not shown), or from the residual plot in Fig. 12. However, as collision energy spread would broaden the threshold behaviour, it is conceivable that the changes may lie within the noise on the data.

It seems more likely, however, that any increase in reaction probability should also be accompanied by a shift inwards in the transition state location — i.e, the system has sufficient line-of-centres energy to penetrate to, say, an avoided crossing that allows a greater probability of reaching the exit valley. Equation [15*a*] should then be written

$$[18] \quad \sigma(E_T) = \pi P_0 R_0^2(1 - 22/E_T) + \pi(P_1 - P_0)R_1^2(1 - 100/E_T)$$

where $R_1 < R_0$. From σ_0 and σ_1 we then get $(P_1/P_0 - 1)(R_1^2/R_0^2) \simeq 0.58$, i.e., $P_1/P_0 < 1.58$. In this case, the yield function should still show two upward breaks at higher collision energy, but, depending on the relative magnitudes of P_0, P_1 and R_0, R_1, R_s, these two could again be indistinguishable (within the noise) from the single break found in the analysis.

This last possibility might well apply if, as suggested above, reaction takes place on a potential surface that does not directly correlate with the emitting MnCl* state. At low collision energies, chemiluminescence would then only occur as a result of exit channel interactions or overlap of vibrational manifolds between the directly produced, and the observed, states. At a given collision energy, the mixing — whether in the potential surfaces or in the MnCl product — would become more efficient; and then, at higher energies still, there would be the shift forward in the transition state location, due to restricted access to the exit valley, as found for the green emission. If that is indeed the case, then the rela-

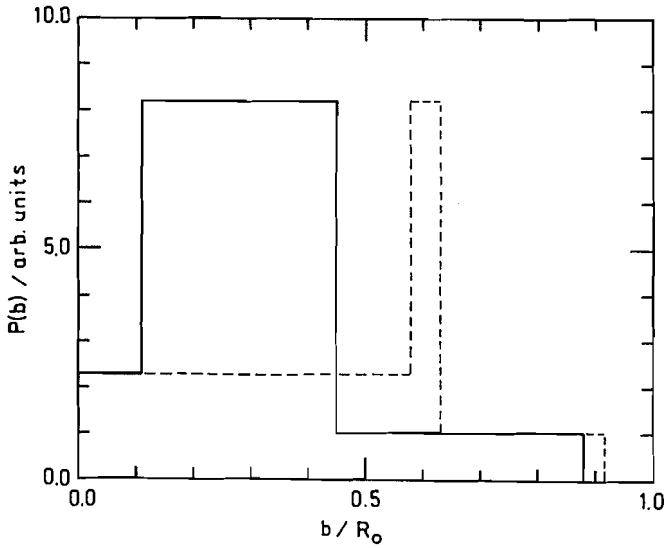

FIG. 15. Derived shape of the opacity function for production of blue MnCl chemiluminescence, calculated for $E_T = 45$ kJ mol^{-1} (solid line) and $E_T = 60$ kJ mol^{-1} (dashed line). The horizontal axis is normalized to unity at $b = R_0$, the internuclear distance corresponding to the transition state on the potential surface.

tive simplicity of the green excitation function suggests that, as illustrated in Fig. 14, it perhaps reflects reaction on a potential surface that correlates directly with the MnCl* emitting state.

The blue yield function is the most complex of all three in Fig. 7. The rise and fall-off in the narrow energy range $E_T \sim$ 36–40 kJ mol^{-1} is so sharp that an experimental artefact was originally suspected; however, since the behaviour appears on each of the data subsets, it must be considered genuine. In view of this, the further rapid depletion from ~158 kJ mol^{-1}, and the subsequent rise from ~393 kJ mol^{-1}, also present a problem: the former implies that the transition state for reaction has shifted forward, but the latter functionality, added to the other positive terms, suggests $E_s \sim$ 60–80 kJ mol^{-1}, i.e., above the ~40 kJ mol^{-1} initial threshold for depletion!

This conundrum can, however, be resolved if we consider that the changes between ~36 and ~40 kJ mol^{-1} correspond to first an increase, then a decrease, in reaction probability with increasing line-of-centres energy. Very crudely, P can then be regarded as taking relative values $\sim\sigma_0$:$(\sigma_0 + \sigma_1)$:$(\sigma_0 + \sigma_1 + \sigma_2)$, i.e., ~1.0:(8.5 ± 1.5):(2.3 ± 0.3), from thresholds ~10, 36, and 40 kJ mol^{-1}, respectively. As E_T increases, $P(b)$ will then assume, equally crudely, the form illustrated in Fig. 15, becoming finally a step with a "spike" superimposed on it. If P remains at the final, low-impact parameter, value when the reaction transition state shifts forward, then, as in Fig. 9, the effect on $\sigma(E_T)$ will not immediately be obvious. At higher energies there should, as discussed for the red emission, be some changes in the slopes of the excitation and yield function plots when reaction at R_s overtakes both the spike and the lower reactivity beyond it; but, because the initial thresholds are in such a narrow energy range, such behaviour could easily be lost in the noise and collision energy spread, and be indistinguishable from the rise threshold at ~393 kJ mol^{-1}.

On this basis, we can write, for the excitation function in the range 40–158 kJ mol^{-1}, the effective single expression

$$[19a]\quad \sigma(E_T) = (0.44 \pm 0.07)\{1 - (10 \pm 2)/E_T\} + (3.40 \pm 1.18)\{1 - (36 \pm 2)/E_T\} - (2.88 \pm 1.26)\{1 - (40 \pm 1)/E_T\}$$

$$[19b]\quad = (0.96 \pm 0.015)\{1 - (12.5 \pm 1.6)/E_T\},$$

the low overall uncertainties in eq. [19*b*] resulting from direct modelling of the yield function in the range $E_T^0 \sim$ 40–100 kJ mol^{-1}. Combination with the $k = 4$ rise term then leads to the conclusion that $R_s/R_0 = 1.16 \pm 0.02$ at $E_s \simeq 111$ kJ mol^{-1}, a similar shift to that deduced for the green and red emissions. The relative internuclear distance for depletion at ~158 kJ mol^{-1} is then $R_d/R_0 = 1.17 \pm 0.02$, again of the same order.

The unusual form of $P(b)$ displayed in Fig. 15 begs the question of whether it is at all physically reasonable. Such a rapid change in reaction probability with impact parameter, or collision energy, is in fact characteristic of a sharp "resonance," of the sort that has been much discussed, from the theoretical standpoint, for H-atom transfer reactions (52). However, the present reaction deals with Cl-atom transfer, and the resonances that are found in 3-dimensional quantal calculations are much narrower than the present spike, and in any case predicted to be washed out by the averaging over all partial waves leading to reaction (52).

One recent experimental result does, however, show that data of the type presented here may not be that unusual. In a high-resolution measurement of the reaction Ca*($^1D_2$) + HCl → CaCl*(A, B) + H, González Ureña and co-workers (53) have found three clear, but progressively diminishing, steps in $\sigma(E_T)$ in the range E_T = 18.5–23.5 kJ mol^{-1}. The authors suggest that the steps are associated with the opening up of internal transition states, corresponding to bending motion, that become available as total energy increases.

It is not the function of the present paper to comment on the Ca*($^1D_2$) + HCl results. However, here there is no definitive evidence for more than one step, although such behaviour might well be hidden by the noise, especially if the second, third, etc. steps are much smaller than the first. In addition, whatever the number of steps, transition state bending motion is unlikely to be the cause in such a large system as Mn + $SnCl_4$. A possible explanation, which is consistent with the deduction above that reagents and observed products are unlikely to correlate directly, is that there is a narrow range of collision energies where there is strong mixing between the potential surface initially sampled, and that leading directly to blue chemiluminescence. Ultimately, as with the red excitation function, the increase in reaction probability is relatively modest; but what is different here is the high efficiency of mixing in a narrow energy range. The situation parallels the sort of predissociation observed in electronic spectroscopy, where a dissociative potential curve mixes with the bound curve of the upper electronic state of the transition. Here, however, the mixing leads to an enhanced access to the blue MnCl product, not to dissociation.

Whatever the exact route from reactants to products, it is clear that the effective potential surfaces for these chemiluminescent reactions differ significantly from those for ground-state alkali and alkaline earth atoms with $SnCl_4$ (21–27). In the latter cases, angular scattering measurements suggest that reaction proceeds on a surface with a significant potential well, corresponding to a stable $M^+SnCl_4^-$ intermediate; but here the

Can. J. Chem. Downloaded from www.nrcresearchpress.com by 195.246.54.202 on 09/08/12
For personal use only.

Can. J. Chem. Downloaded from www.nrcresearchpress.com by 195.246.54.202 on 09/08/12
For personal use only.

interactions appear to be completely repulsive, with no indications of a well before the exit transition state (i.e., $n = 1$ in eq. [7] always). This result is at first surprising, considering that $Mn^*(a^6D_J)$ atoms should have an ionization potential of 7.43 – 2.15 = 5.28 eV, i.e., comparable to that of $Na(3^2S)$ and $Ba(6^1S)$. However, this corresponds to the process $...3d^64s^1 \rightarrow ...3d^54s^1(Mn^+, a^5S)$, whereas the discussion above has suggested that, for chemiluminescence, the *d*-orbital configuration is initially sustained. In fact, the excitation energy of the $...3d^6$, a^5D_J state of Mn^+ is 1.8 eV (174.5 kJ mol^{-1}) (54), so the ionization potential that we need to take is 7.08 eV. Even allowing for a significant $SnCl_4$ electron affinity, it is clear that the $Mn^*(a^6D_J) + SnCl_4$ and $Mn^{+*}(a^5D_J) + SnCl_4^-$ potentials will cross only at very short internuclear distances, i.e., the interaction is likely to be quite repulsive. Indeed, while the red and blue emissions seem to arise from mixing between potential surfaces or product state manifolds, it is quite conceivable that the thresholds we are observing are true activation barriers, even for those lower-lying product states. If in addition there is a significant stretching of the Sn—Cl equilibrium bond length on electron transfer, as might be expected, then we can see that restricted access to the exit channel might well also arise, as suggest above.

Conclusions

Our analysis of the shapes of the excitation functions for the chemiluminescent Mn + $SnCl_4$ reaction provides us with interesting insights into the potential surfaces involved, and their interactions. In all cases it appears that $Mn^*(a^6D_J)$ atoms are the reagents, but the uniqueness of each excitation function suggests that there is a strong symmetry control. This means that, in the entrance channel at least, the symmetry corresponding to the spatial configuration of the odd *d* electron must be retained, and chemiluminescence result from approach of the Mn atom along the C_3 axis of $SnCl_4$.

In two cases, red and blue, if not all, the luminescing MnCl* state appears to be produced on a surface that does not correlate directly with the reagents. This result is consistent with predictions based on the known, but fragmentary, MnX spectroscopy, and comparison with MnH and FeO, which suggests a large number of relatively low-lying states. At the lowest energies, the red and blue luminescences most probably derive from mixing of vibrational manifolds of MnCl* *states* of the same symmetry, whereas, at higher energies, the mixing appears to be between *surfaces* with Mn^+ configurations of the same symmetry.

In all cases the transition state for reaction seems to shift forward, into the approach coordinate, with increasing collision energy. In the simplest terms, we might consider that this is a case of the barrier crest moving from the exit valley to the entrance valley. However, the notion of barrier crest requires some care when dealing with interacting potential surfaces. At low energies the crest for production of the red and blue emissions, at least, may simply correspond to the threshold for the onset of exit channel mixing. At higher energies, the mixing appears to be between potential surfaces; and since there is no evidence for a well before the transition state, the interaction is likely to occur within the repulsive wall of both potentials. In this circumstance, the barrier crest cannot be represented simply as a saddle point on a contour plot of potential energies, especially as trajectories may double back on themselves once they have made the transition between the surfaces. Even when, at higher energies still, the transition state shifts forward, the concept of barrier crest remains problematic, as the effective barrier no longer lies on the minimum energy path. In both these circumstances, the dynamics are likely to be quite different from those on the relatively simple potential surfaces employed in John Polanyi's pioneering trajectory studies. In particular, there should be changes in the observed dynamics when the transition state shifts or when depletion begins. It would therefore be intriguing to disperse the chemiluminescence from the Mn + $SnCl_4$ reaction, and determine the MnCl* vibrational distributions as a function of collision energy.

Acknowledgements

We thank the Science and Engineering Research Council for the equipment grant which enabled this research to be carried out, the *Canadian Journal of Chemistry* for soliciting this contribution, and an unknown referee for helpful and stimulating comments. It is a great pleasure to be able to participate in this birthday tribute to John Polanyi.

1. J.C. Polanyi and W. H. Wong. J. Chem. Phys. **51**, 1439 (1969).
2. M.H. Mok and J.C. Polanyi. J. Chem. Phys. **51**, 1451 (1969).
3. M.H. Mok and J.C. Polanyi. J. Chem. Phys. **53**, 4588 (1970).
4. B.A. Hodgson and J.C. Polanyi. J. Chem. Phys. **55**, 4745 (1971).
5. D.S. Perry and J.C. Polanyi. Can. J. Chem. **50**, 3916 (1972).
6. J.C. Polanyi. Acc. Chem. Res. **5**, 161 (1972).
7. D.S. Perry, J.C. Polanyi, and C.W. Wilson, Jr. Chem. Phys. **3**, 317 (1974).
8. J.C. Polanyi and N. Sathyamurthy. Chem. Phys. **33**, 287 (1978).
9. J.C. Polanyi and N. Sathyamurthy. Chem. Phys. **37**, 259 (1979).
10. J.C. Polanyi and J.L. Schreiber. *In* Physical chemistry: an advanced treatise. Vol. VIA. *Edited by* W. Jost. Academic Press, London. 1974. p. 383.
11. F. Heismann and H.J. Loesch. Chem. Phys. **64**, 43 (1982).
12. H. Jalink, F. Harren, D. van den Ende, and S. Stolte. Chem. Phys. **108**, 391 (1986).
13. H. Jalink, M.H.M. Janssen, M. Geijberts, S. Stolte, D.H. Parker, and J.Z.W. Wang. *In* Selectivity in chemical reactions. *Edited by* J.C. Whitehead. Reidel, Dordrecht. 1988.
14. D.H. Parker, H. Jalink, and S. Stolte. Faraday Discuss. Chem. Soc. **81**, 184 (1988).
15. M.R. Levy. Res. Chem. Kinet. **1**, 163 (1993).
16. M.R. Levy. J. Phys. Chem. **93**, 5195 (1989).
17. M.R. Levy. J. Phys. Chem. **95**, 8491 (1991).
18. M.R. Levy. Faraday Discuss. Chem. Soc. **91**, 168 (1991).
19. M.R. Levy. Manuscript in preparation.
20. A González Ureña. Mol. Phys. **52**, 1145 (1984).
21. K.R. Wilson and D.R. Herschbach. J. Chem. Phys. **49**, 2676 (1968).
22. S.J. Riley and D.R. Herschbach. J. Chem. Phys. **58**, 27 (1973).
23. J.C. Whitehead, D.R. Hardin, and R. Grice. Mol. Phys. **23**, 787 (1972).
24. D.D. Parrish and R.R. Herm. J. Chem. Phys. **49**, 5544 (1968).
25. D.D. Parrish and R.R. Herm. J. Chem. Phys. **51**, 5467 (1969).
26. R. Behrens, Jr., R.R. Herm, and C.M. Sholeen. J. Chem. Phys. **65**, 4791 (1976).
27. R.R. Herm, S.M. Lin, and C.A. Mims. J. Chem. Phys. **77**, 2931 (1973).
28. W. Hayes. Proc. Phys. Soc. London, Sect. A: **68**, 1097 (1955), and references therein.
29. P. Mesnage. Ann. Phys. **12**, 5 (1939).
30. S.V.K. Rao, S.P. Reddy, and P.T. Rao. Proc. Phys. Soc. **79**, 741 (1962).
31. R.W.B. Pearse and A.G. Gaydon. The identification of molecular spectra. 4th ed. Chapman Hall, London. 1976.
32. T.E. Nevin. Proc. Roy. Ir. Acad. **48**, 1 (1942).

33. W.J. Balfour. J. Chem. Phys. **88**, 5242 (1988).
34. W.J. Balfour, O. Launila, and L. Klynning. Mol. Phys. **69**, 443 (1990).
35. T.L. Cottrell. The strength of chemical bonds. Butterworths, London. 1958.
36. G.A. Oldershaw and K. Robinson. J. Chem. Soc. A: 2963 (1971).
37. O. Knacke, O. Kubaschewski, and K. Hesselmann. Thermochemical properties of inorganic substances. Springer Verlag, Berlin. 1991.
38. K. Huber and G. Herzberg. Constants of diatomic molecules. Van Nostrand, New York. 1979.
39. J. Sugar and C. Corliss. J. Phys. Chem. Ref. Data, **14**, Suppl. 2, 388 ff (1985).
40. M.R. Levy. J. Phys. Chem. **95**, 8500 (1991).
41. D.L. Herbertson, D.A. Newnham, and M.R. Levy. Manuscript in preparation.
42. T.J. Hughes, B.K. Bagral, S.J. Murphy, and M.R. Levy. Manuscript in preparation.
43. V. Herrero, V. Sáez Rábanos, and A. González Ureña. J. Phys. Chem. **88**, 2339 (1984).
44. A Gupta, D.S. Perry, and R.N. Zare. J. Chem. Phys. **72**, 6250 (1980).
45. K. Johnson, J.P. Simons, P.A. Smith, C. Washington, and A. Kvaran. Mol. Phys. **57**, 255 (1986).
46. M.E. Gersh and R.B. Bernstein. J. Chem. Phys. **55**, 4661 (1971); **56**, 6131 (1972).
47. A.M. Rulis and R.B. Bernstein. J. Chem. Phys. **57**, 5497 (1972).
48. K.T. Wu, H.F. Pang, and R.B. Bernstein. J. Chem. Phys. **68**, 1064 (1978).
49. A.E. Stevens, C.S. Feigerle, and W.C. Lineberger. J. Chem. Phys. **78**, 5420 (1983).
50. A.E. Stevens Miller, C.S. Feigerle, and W.C. Lineberger. J. Chem. Phys. **87**, 1549 (1987).
51. A.J. Merer. Annu. Rev. Phys. Chem. **40**, 407 (1989).
52. G.C. Schatz, D. Sokolovski, and J.N.L. Connor. Faraday Discuss. Chem. Soc. **91**, 17 (1991), and references therein.
53. M. Menéndez, M. Garay, E. Verdasco, and A. González Ureña. J. Chem. Soc. Faraday Trans. **89**, 1493 (1993).
54. S.M. Younger, J.R. Fuhr, G.A. Martin, and W.L. Wiese. J. Phys. Chem. Ref. Data, **7**, 495 (1978).

Can. J. Chem. Downloaded from www.nrcresearchpress.com by 195.246.54.202 on 09/08/12
For personal use only.

Dynamics of $I^*(^2P_{1/2})$ production in the ultraviolet photodissociation of alkyl iodides

S. Uma and Puspendu Kumar Das[1]

Department of Inorganic and Physical Chemistry, Indian Institute of Science, Bangalore 560 012, India

Received July 5, 1993

This paper is dedicated to Professor John C. Polanyi on the occasion of his 65th birthday

S. Uma and Puspendu Kumar Das. Can. J. Chem. **72**, 865 (1994).

The relative quantum yields, ϕ^*, for the production of $I^*(^2P_{1/2})$ at 266, 280, and ~305 nm are reported for a series of primary alkyl iodides using the technique of two-photon laser-induced fluorescence for the detection of $I(^2P_{3/2})$ and $I^*(^2P_{1/2})$ atoms. Results are analyzed by invoking the impulsive energy disposal model, which summarizes the dynamics of dissociation as a single parameter. Comparison of our data with those calculated by a more sophisticated time-dependent quantum mechanical model is also made. Near the red edge of the alkyl iodide *A* band, absorption contribution from the $^3Q_1$ state is important and the dynamics near the $^3Q_0$–$^1Q_1$ curve-crossing region seem to be influenced by the kinematics of the dissociation process.

S. Uma et Puspendu Kumar Das. Can. J. Chem. **72**, 865 (1994).

On a déterminé les rendements quantiques relatifs, ϕ^*, pour la production de $I^*(^2P_{1/2})$ à 266, 280 et environ 305 nm, pour une série d'iodures d'alkyles primaires; pour ce faire, on a utilisé la technique de fluorescence à deux photons induite au laser pour la détection des atomes de $I(^2P_{3/2})$ et de $I^*(^2P_{1/2})$. On a analysé les résultats en invoquant le modèle de disposition de l'énergie impulsive qui résume les dynamiques de dissociation en un seul paramètre. On a effectué une comparaison de nos résultats avec ceux calculés à l'aide d'un modèle plus sophistiqué de mécanique quantique dépendant du temps. Au niveau de la limite du rouge de l'absorption de la bande *A* de l'iodure d'alkyle, la contribution de l'état $^3Q_1$ est importante et la dynamique près de la région du croisement de la courbe $^3Q_0$–$^1Q_1$ semble être influencée par la cinématique du processus de dissociation.

[Traduit par la rédaction]

Introduction

Photodissociation dynamics of simple alkyl iodides in the *A* band arising from $n \rightarrow \sigma^*$ ($X \rightarrow A$) transition has been of interest over the last two decades. This is mainly because alkyl iodides offer an unique opportunity to understand key factors such as radical size (CH_3, C_2H_5, C_3H_7, etc.), substitution (CH_3, CF_3, etc.), and structure (primary, secondary, and tertiary) that affect their photodissociation dynamics. Subsequent to the measurement of magnetic circular dichroism (MCD) spectra of CH_3I by Gedanken and Rowe (1), several groups (2–16) came up with a variety of techniques to investigate the dynamics of alkyl iodide photodissociation. Riley and Wilson (2) and Dzvonik et al. (3) simultaneously carried out photodissociation experiments on CH_3I using the time-of-flight (TOF) technique. From the results, they concluded that at 260 nm the transition dipole is predominantly parallel to the C—I bond ($^3Q_0 \leftarrow {}^1A_1$) and the dissociation leads to $I(^2P_{1/2})$ (will be called I* from now) and $CH_3^{\cdot}$ radicals as major products. Later Sparks et al. (4) carried out another TOF experiment on CH_3I at 266 nm; they extracted the ν_2 (umbrella mode of CH_3) vibrational distribution of CH_3 fragments from the spectrum and found that it peaked at $v = 2$. Hermann and Leone (5) measured the infrared emission from CH_3 radicals produced from CH_3I at 248 and 266 nm. Their results at 266 nm agreed well with those of Sparks et al. (4). At 248 nm the vibrational distribution was again found to peak at $v = 2$, which differed from the theoretical results of Shapiro and Bersohn (6) who had predicted the product distribution maximum at $v = 4$ at that wavelength. In 1984, a new TOF experiment on methyl iodide at 248 nm was carried out by van Veen et al. (7). They found two peaks in the spectrum corresponding to $I(^2P_{3/2})$ (will be called I from now) and I* products and both the convoluted vibrational distributions peaked at $v = 2$. Brewer et al. (8) measured the quantum yield of I* production for a series of alkyl iodides at 248 nm using a two-photon laser-induced fluorescence (TPLIF) detection scheme for both I and I* atoms. Photofragmentation of CH_3I at 248 nm was studied by Barry and Gorry (9); they observed the ν_2 vibrational distribution to peak at $v = 2$ for the I* channel, and to extend up to $v = 8$ for the I channel. Using the TPLIF technique, Godwin et al. (10) measured the quantum yield for production of I and I* for a series of alkyl iodides at 248 nm. They observed that the I* yield or the dynamics of I* production varies with the alkyl radical size, substitutions on α- and β-carbon atoms, and structure. Using a diode laser to probe the dissociation dynamics of CH_3I at 266 nm, Hess et al. (11) measured the I* quantum yield as 0.73 ± 0.04. At 229.4 nm Penn et al. (12) also found that I* is the major product from CH_3I. In 1989 Ogorzalek Loo et al. (13) looked again at the vibrational distribution of CH_3 at 266 nm using the multiphoton ionization technique for detecting CH_3 fragments in their vibrational states. They predicted that $v = 0$ is the most populated umbrella vibration in CH_3 fragments, in disagreement with the results obtained by Sparks et al. (4). The authors (13) ascribed the difference to contamination by vibrationally excited CH_3I in the latter experiment. The I* yield increases with increasing vibrational excitation in the methyl fragment and the estimated net yield is 0.56, which is lower than the value measured by other direct techniques.

In this work we report ϕ^*, the relative quantum yield for I* production (i.e., $\phi^* = [I^*]/([I] + [I^*])$), for a series of simple alkyl iodides at three different dissociation wavelengths: 266, 280, and ≃305 nm. The resulting atomic fragments $I(^2P_{3/2})$ and $I^*(^2P_{1/2})$ have been probed directly using the TPLIF technique (8). At ≃305 nm I and I* atoms were produced by the same pulse that was used for probing. From now on the experiments at 266 and 280 nm wavelengths will be referred to as pump–probe experiments and that at ≃305 nm as a single laser experiment. We discuss our results in the light of a classical Landau–Zener model and compare them with recent theoretical and experimental results obtained by other groups.

[1]Author to whom correspondence may be addressed. FAX: 91-080-3341683.

Can. J. Chem. Downloaded from www.nrcresearchpress.com by 195.246.54.202 on 09/08/12
For personal use only.

TABLE 1. Relative quantum yield (ϕ^*) of I* production at different dissociation wavelengths

Molecule	ϕ^* ≃305 nm	ϕ^* 280 nm	ϕ^* 266 nm
Methyl iodide	0.43 ± 0.01	0.69 ± 0.02	0.79 ± 0.02
Ethyl iodide	0.39 ± 0.02	0.60 ± 0.02	0.73 ± 0.02
n-Propyl iodide	0.35 ± 0.02	0.56 ± 0.02	0.66 ± 0.02
n-Butyl iodide	0.30 ± 0.02	0.50 ± 0.03	0.64 ± 0.03
Isobutyl iodide	0.35 ± 0.02	0.56 ± 0.03	0.71 ± 0.01

Experimental setup

The apparatus used in our experiments has been described in detail elsewhere (17). Briefly, a sample gas is contained at 50–70 mTorr (1 Torr = 133.3 Pa) in a stainless steel cell that is pumped continuously by a diffusion pump and the pressure monitored by an MKS Baratron gauge (model 122A). The pump and the probe lasers are crossed perpendicular inside the chamber and the signal is detected at the third perpendicular direction. The fourth harmonic of a Nd-YAG laser (DCR-3G, Spectra Physics) was used for dissociation at 266 nm (≃19 mJ/pulse) whereas the second harmonic of a Nd:YAG pumped dye laser was employed for the photolysis experiments at 280 nm (≃5 mJ/pulse). A typical delay of 400 ns between the pump and the probe lasers was maintained to avoid collisional relaxation of the nascent fragments. The resulting iodine atoms were detected by the technique of TPLIF using another doubled dye laser ("probe" laser) output (≃0.5 mJ/pulse). In the case of ≃305 nm dissociation, the probe laser alone was used but with tight focussing by a 5-in. focal length Suprasil lens at the center of the cell. The VUV fluorescence was detected through a MgF_2 window by a solar blind PMT (Thorn EMI, model 9423B). The space between the window and the PMT was continuously flushed with dry nitrogen. The signal was amplified (×25) by a preamplifier (SRS 440) and averaged in a gated boxcar averager (SRS 250), the output of which was fed to a strip-chart recorder for display. The alkyl iodides were obtained commercially or prepared by standard procedures. All the iodides were decolorized with 10% sodium bisulfite solution, dried on anhydrous $MgSO_4$, and fractionally distilled prior to each experiment.

Results

The VUV emission spectra were recorded by scanning the probe laser across the two-photon absorption lines of I (304.7 nm) and I* (306.7 nm). Typical TPLIF spectra of I* and I are shown in Fig. 1. The relative quantum yield, ϕ^*, was determined directly from the spectra. Here we took the experimental signal intensities S and S^* as being directly proportional to [I] and [I*], respectively. Since our ϕ^* value of 0.79 for CH_3I at 266 nm agrees very well with the same (0.76) found by Riley and Wilson (2) by photofragment spectroscopy, no calibration was done to our raw data.

The quantum yields for I* production obtained at three different wavelengths are listed in Table 1. For the pump–probe experiments, the signal varies linearly with the pump laser power (Fig. 2*a*). For all pump–probe experiments care was taken to reduce the probe-alone contribution to ≤2%. In the single laser experiment the very small difference in the absorption coefficients at 304.7 and 306.7nm is neglected. A power dependence study shows that three photons are involved in the process (Fig. 2*b*), implying that one photon is utilized for the dissociation and two subsequent photons for probing the iodine fragments.

Discussion

The *A* band in the absorption of alkyl iodides arising from a

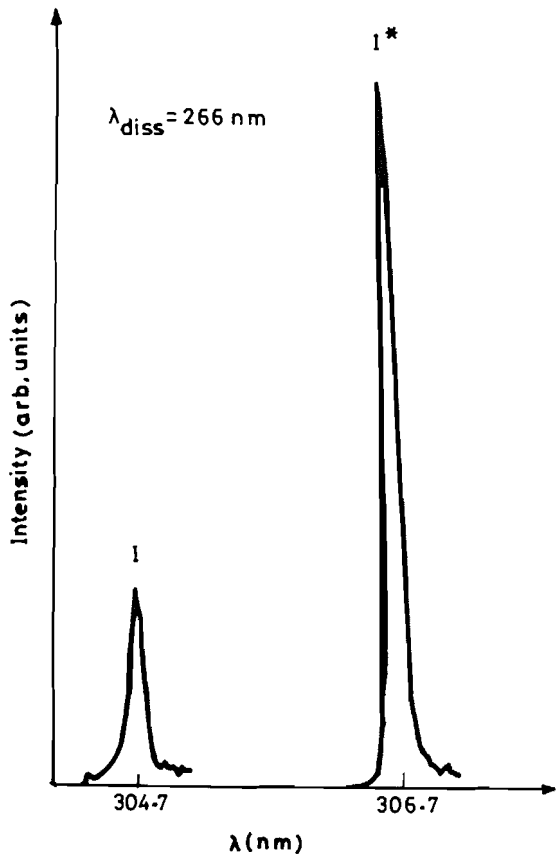

FIG. 1. Typical TPLIF spectra of I and I* from CH_3I dissociation at 266 nm.

$n \rightarrow \sigma^*$ transition is strongly localized on the C—I bond. Gedanken and Rowe (1) resolved that *A* band using MCD. The three possible transitions are labelled according to Mulliken (18) as $^1Q_1 \leftarrow N$, $^3Q_1 \leftarrow N$, and $^3Q_0 \leftarrow N$. The first two transitions are perpendicular transitions leading to the formation of I, whereas the third is a parallel transition that leads to I*. Figure 3 displays a schematic one-dimensional potential energy diagram showing all these states. The electronic transition at 266 and 280 nm is mainly to the $^3Q_0$ state but a significant amount of I atoms (Table 1) are produced by a curve-crossing mechanism from $^3Q_0$ to $^1Q_1$. At these wavelengths no significant contribution is made by the $^3Q_1$ state, as pointed out by Gedanken and Rowe (1). The energy disposal at these two wavelengths may be best described by a simple classical model suggested by Godwin et al. (10). In their model the I* quantum yield is described by the probability of staying on the initial $^3Q_0$ state as,

$$[1] \quad \phi^* = \exp(-2\pi V_{12}^2/\hbar|\Delta F|v) = \exp(-\zeta/v)$$

where V_{12} is the coupling term between the $^3Q_0$ and $^1Q_1$ states, ΔF is the difference in their gradients at the crossing point, and v is the velocity through the crossing point. Further, they grouped the unknowns V_{12} and ΔF into one parameter to determine if it remains the same for a series of related alkanes. Hence the problem is simplified to the extent of finding the velocity at the crossing point. For this the translational energy (E_t) at the asymptotic limits is calculated using a quasidiatomic model and is given by

$$[2] \quad E_t = (\mu_{CI}/\mu_{RI})E_{avl}$$

Can. J. Chem. Downloaded from www.nrcresearchpress.com by 195.246.54.202 on 09/08/12
For personal use only.

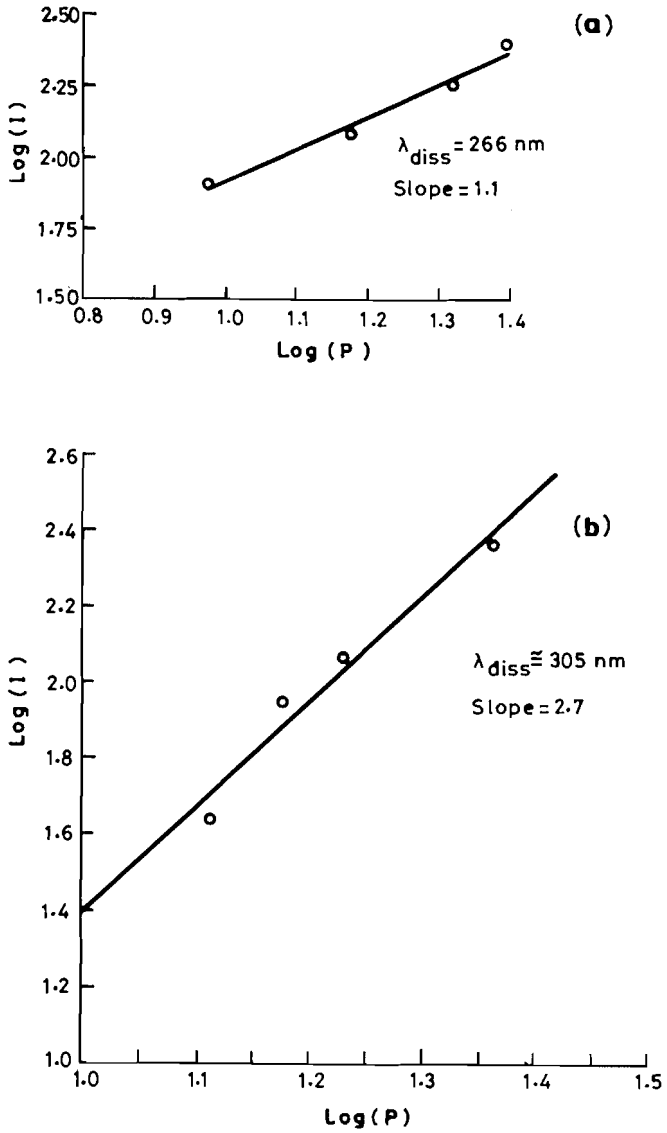

FIG. 2. (*a*) A log–log plot of the pump laser (266 nm) power and the iodine atom signal intensity for the pump–probe experiment. (*b*) A log–log plot of the probe laser power and the iodine atom signal intensity for the single laser experiment. The slope gives the laser power dependence of the signal in each case.

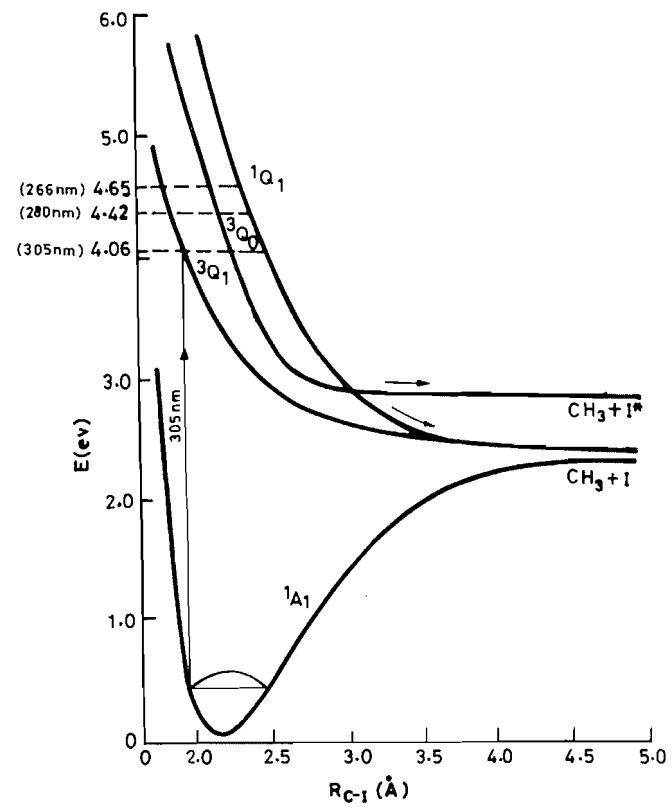

FIG. 3. Schematic potential energy surfaces for the alkyl iodides showing only the important states.

where μ_{CI} is the reduced mass of C and I, μ_{RI} the reduced mass of the radicals R and I, and E_{avl} is the available energy, which is $h\nu - D_0^0 - E_{so}$ with ν being the excitation frequency, D_0^0 the dissociation energy of the C—I bond at 0 K, and E_{so} is the iodine spin-orbit excitation energy. Now E_t must be linearly related to the translational energy at the crossing point and the proportionality constant, if any, may again be absorbed within the parameter ζ. Thus the final expression for ϕ^* becomes,

$$[3] \quad \phi^* = \exp\left[-\mu_{RI}\zeta/(2\,\mu_{CI}\,E_{avl})^{1/2}\right]$$

We have used this model at 266 and 280 nm and find reasonable fits to the experimental points with ζ being 670 m/s and 970 m/s, respectively (Figs. 4*a* and 4*b*). It is worth noting that although a single parameter describes the dynamics on the upper potential energy surfaces, most of the actual information (i.e., the coupling between the potential energy surfaces and the C—I bond length at the crossing point) is actually hidden in this parameter, as pointed out by Lao et al. (14). However, a detailed model to describe the dynamics will be complicated and computationally demanding. Also the predictive power of all such calculations will rely on the accuracy of the potential energy surfaces used. The quantum yield of I* at ~305 nm was not treated in this manner since at this wavelength I is the major product, which cannot be explained on the basis of the initial excitation to the $^3Q_0$ state. But if we look carefully at the different components of the *A* band, this is not at all surprising. Similar to the mechanism proposed by Hwang and El-Sayed (19, 20) in the case of CF_3I dissociation, at this wavelength the initial absorption in alkyl iodides is not mainly confined to the $^3Q_0$ state. The low-energy $^3Q_1$ state carries a significant transition strength (since the total absorption cross section at this wavelength is very small) and produces mainly the ground state I product through a direct dissociation mechanism. Therefore, production of I atoms at this wavelength may be attributed to the direct dissociation from the $^3Q_1$ state as well as curve crossing between the $^3Q_0$ and $^1Q_1$ states. However, it is clear from Table 1 that the extent of these two mechanisms varies as one goes from methyl to isobutyl iodide.

The trend reversal in the ϕ^* values in going from *n*-butyl iodide to isobutyl iodide may be explained qualitatively by considering the increased inductive and hyperconjugative effects in the latter. Since the excitation is localized on the C—I bond, the electronic charge distribution around this bond is likely to affect the dynamical outcome. V_{12} is unlikely to change in the family of primary alkyl iodides since it is directly proportional to the iodine spin-orbit splitting. But depending on the net charge on the β-carbon atom, the internuclear distance where the crossing occurs may be altered. Our results indicate a higher curve-crossing probability (i.e., lower I* yield) for *n*-butyl iodide than

Can. J. Chem. Downloaded from www.nrcresearchpress.com by 195.246.54.202 on 09/08/12
For personal use only.

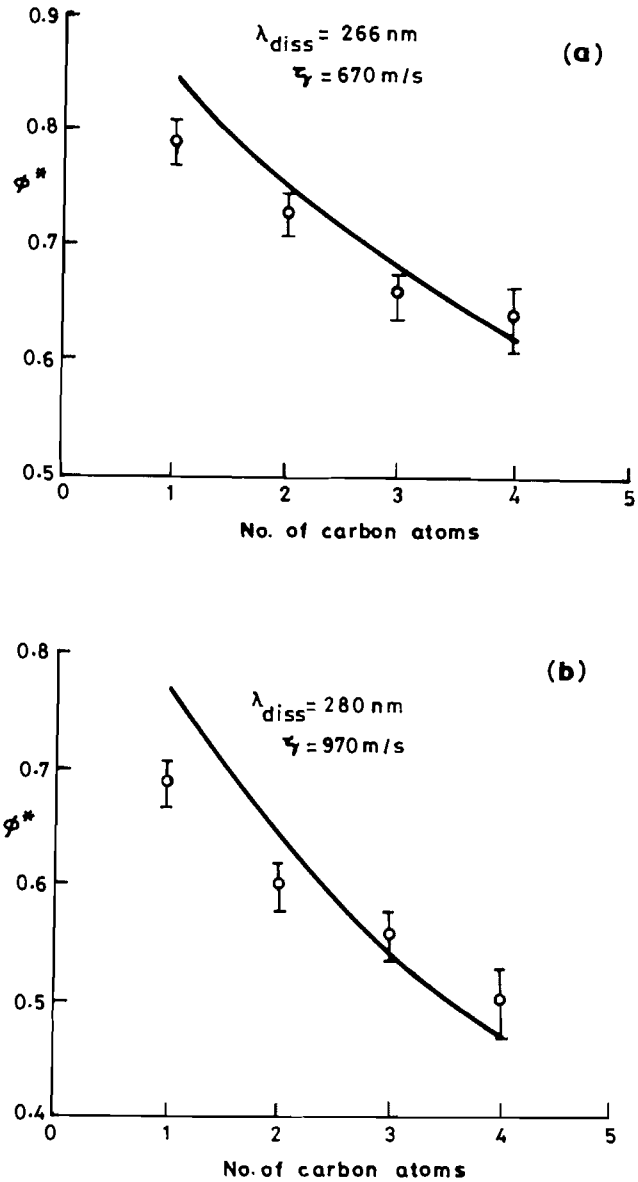

FIG. 4. I* quantum yields at (*a*) 266 nm, and (*b*) 280 nm as a function of number of carbon atoms in the alkyl radical. Solid lines are fits obtained from eq. [3] with ζ values shown on the respective curves.

for isobutyl iodide assuming similar crossing velocities for both.

Recently Guo and Schatz (21–23) carried out three-dimensional quantum mechanical calculations based on the fast Fourier transform method developed by Kosloff and Kosloff (24). Using the potential energy functions and the nonadiabatic coupling between the $^3Q_0$ and $^1Q_1$ states from Yabushita and Morokuma (25), they predicted the I* quantum yield as a function of dissociation wavelength. We have compared our experimental I* yields from CH_3I with Guo's (23) calculations (Fig. 5) and find that the trend is better reproduced when initial excitation is only to the $^3Q_0$ state. However, in his calculation the internal energy distribution in the methyl fragments is better reproduced when excitation to both $^3Q_0$ and $^1Q_1$ states is considered. We find that around 266 nm (near the absorption maxima of the *A* band) the I* yield reaches a maximum and drops much faster at longer wavelengths. The formation of I dominates at ≃305 nm, which is in apparent contradiction to the calculated results (23),

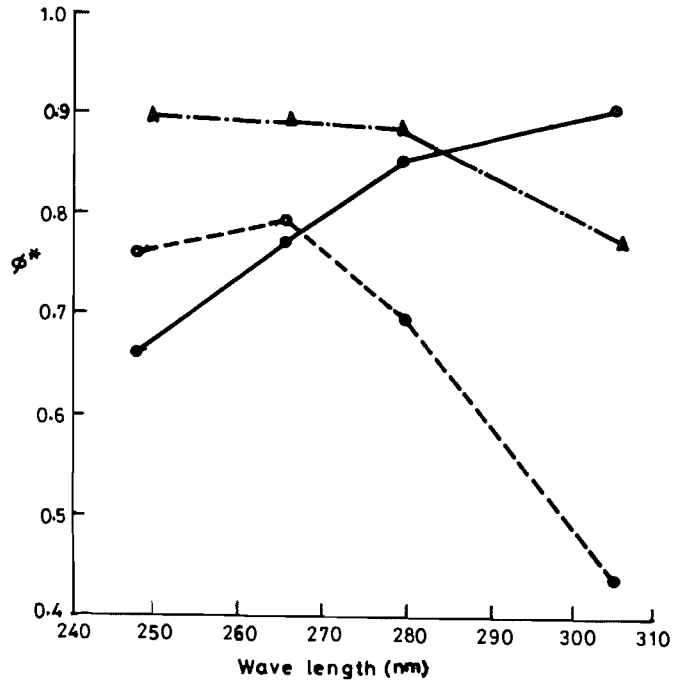

FIG. 5. Comparison of ϕ^* obtained from a full three-dimensional quantum mechanical calculation (adapted from ref. 23) with initial excitation to the $^3Q_0$ state (dot-dash line), with initial excitation to both $^3Q_0$ and $^1Q_1$ states (solid line), and experiments (dotted line). The experimental ϕ^* values at 248 nm are taken from ref. 8.

which predict a much higher I* yield at that wavelength. This discrepancy may be attributed to the fact that the contribution of the $^3Q_1$ state, which is important above 300 nm, has not been included in the above model. Insofar as the effects of substitution, size, and structure on the dynamics of primary alkyl iodide series in the ultraviolet are concerned, treatment by a full three-dimensional sophisticated model would be difficult and a semiclassical model with an accurate potential energy function might be an easier alternative to obtain a good dynamical picture for these molecules.

Conclusion

From the determination of the I* yields at ≃305-, 280-, and 266-nm dissociation of a series of alkyl iodides, it appears that the iodine atom in the spin-orbit excited state is the major product over the *A* band of alkyl iodides except near the red wing. Substantial contribution from the low-energy transition, $^3Q_1 \leftarrow N$, cannot be *undermined* at ≃300 nm absorption. Also, substitutions at the α- as well as the β-carbon atoms will alter the dynamics at the upper potential energy surfaces slightly.

Although a classical impulsive model is useful in describing the dynamics in one dimension, most of the details are lost in such a treatment. An appropriate full three-dimensional quantum mechanical model that contains contributions from all three excited states (i.e., $^1Q_1$, $^3Q_0$, and $^3Q_1$) may better explain the photodissociation dynamics in these molecules. What are more difficult to understand are the effects of substitution, size, and structure of the alkyl radicals on the coupling between the $^3Q_0$ and $^1Q_1$ states and the C—I distance where these two states cross. We hope that future work in this direction will better answer some of these questions.

Acknowledgements

We would like to thank Mr. P.V. Ramakrishnan for designing

Can. J. Chem. Downloaded from www.nrcresearchpress.com by 195.246.54.202 on 09/08/12
For personal use only.

the pulse divider–delay generator circuit for us. Generous financial support from the Director, Indian Institute of Science, the Department of Science & Technology, Govt. of India, and the Department of Atomic Energy, Govt. of India, for this project is gratefully acknowledged.

1. A. Gedanken and M.D. Rowe. Chem. Phys. Lett. **34**, 39 (1975).
2. S.J. Riley and K.R. Wilson. Faraday Discuss. Chem. Soc. **53**, 132 (1972).
3. M. Dzvonik, S. Yang, and R. Bersohn. J. Chem. Phys. **61**, 4408 (1974).
4. R.K. Sparks, K. Shobatake, L.R. Carlson, and Y.T. Lee. J. Chem. Phys. **75**, 3838 (1981).
5. H.W. Herman and S.R. Leone. J. Chem. Phys. **76**, 4766 (1982).
6. M. Shapiro and R. Bersohn. J. Chem. Phys. **73**, 3810 (1980).
7. G.N.A. van Veen, T. Baller, A.E. de Vries, and N.J.A. van Veen. Chem. Phys. **87**, 405 (1984).
8. P. Brewer, P. Das, G. Ondrey, and R. Bersohn. J. Chem. Phys. **79**, 720 (1983).
9. M.D. Barry and P.A. Gorry. Mol. Phys. **52**, 461 (1984).
10. F.G. Godwin, P.A. Gorry, P.M. Hughes, D. Raybone, T.M. Watkinson, and J.C. Whitehead. Chem. Phys. Lett. **135**, 163 (1987).
11. W.P. Hess, S.J. Kohler, H.K. Haugen, and S.R. Leone. J. Chem. Phys. **84**, 2143 (1986).
12. S.M. Penn, C.C. Hayden, K.J.C. Muyskens, and F.F. Crim. J. Chem. Phys. **89**, 2909 (1988).
13. R. Ogorzalek Loo, H.P. Haerri, G.E. Hall, and P.L. Houston. J. Chem. Phys. **90**, 4222 (1989).
14. K.Q. Lao, M.D. Person, P. Xayariboun, and L.J. Butler. J. Chem. Phys. **92**, 823 (1990).
15. T.F. Hunter and K.S. Kristjansson. Chem. Phys. Lett. **58**, 291 (1978).
16. D.W. Chandler, J.W. Thoman, Jr., M.H.M. Janssen, and D.H. Parker. Chem. Phys. Lett. **156**, 151 (1989).
17. S. Uma and P.K. Das. Curr. Sci. **65**, 307 (1993).
18. R.S. Mulliken. Phys. Rev. **50**, 1017 (1936).
19. H.J. Hwang and M.A. El-Sayed. J. Chem. Phys. **94**, 4877 (1991).
20. H.J. Hwang and M.A. El-Sayed. J. Phys. Chem. **96**, 8728 (1992).
21. H. Guo and G.C. Schatz. J. Chem. Phys. **93**, 393 (1990).
22. H. Guo. J. Chem. Phys. **96**, 2731 (1992).
23. H. Guo. J. Chem. Phys. **96**, 6629 (1992).
24. D. Kosloff and R. Kosloff. J. Comput. Phys. **52**, 35 (1983).
25. S. Yabushita and K. Morokuma. Chem. Phys. Lett. **153**, 3130 (1988).

Can. J. Chem. Downloaded from www.nrcresearchpress.com by 195.246.54.202 on 09/08/12
For personal use only.

Electron impact studies of autoionizing states in CO_2 using a multi-angle parallel detection electron spectrometer

A.T. WEN, D. TREMBLAY,[1] B. TREMBLAY, AND D. ROY[2]

Laboratoire de physique atomique et moléculaire, Département de physique, Pavillon Vachon, Université Laval, Cité universitaire, Québec, QC G1K 7P4, Canada

Received July 12, 1993

This paper is dedicated to Professor John C. Polanyi in honor of his 65th birthday

A.T. WEN, D. TREMBLAY, B. TREMBLAY, and D. ROY. Can. J. Chem. **72**, 870 (1994).

The MAPDESS, a multi-angle-detector electron scattering spectrometer, has been adapted to electron ejection measurements. A study of autoionization from Rydberg states has been carried out for the neutral linear molecule CO_2 in the continuum region 15–19 eV by low-energy electron impact. Observations have been made of structure due to excitation of these states by slow electron scattering and their decay by ejection of electrons. A multi-angle parallel detection technique has been used and this has enabled some CO_2 autoionizing states resulting from non-dipole transitions to be observed clearly. The major features appearing in the ejected electron spectra of CO_2 have tentatively been classified and (or) assigned in terms of autoionization to the ground ionic state ***X***, from highly excited electronic states corresponding to the "Tanaka progression I" and "Tanaka–Ogawa" Rydberg series converging to the ionic ***A*** state, as well as from the Henning "sharp" and "diffuse" series, along with the forbidden $np\sigma_u$ series, converging to the ***B*** state. In addition to the features already known, new features have been observed, and they seem to be rather sensitive to electron impact energies employed. Strong relative intensity variations are observed at the different impact energies, and marked angular effects are also found in the ejected electron spectra.

A.T. WEN, D. TREMBLAY, B. TREMBLAY et D. ROY. Can. J. Chem. **72**, 870 (1994).

Le MAPDESS, un spectromètre à détection multiple conçu pour la diffusion différentielle d'électrons, a été utilisé pour des mesures d'électrons éjectés par impact d'électrons. Nous avons réalisé une étude de l'autoionisation de la molécule linéaire CO_2 impliquant les états de Rydberg situés dans la région 15–19 eV. Les spectres obtenus reflètent l'excitation de ces états par collisions d'électrons lents et leur désexcitation par l'éjection d'électrons. Grâce à la technique utilisée impliquant des électrons projectiles lents et la détection en parallèle à angles multiples, il est possible d'observer certains états autoionisants résultant de transitions non dipolaires. Les principales singularités se manifestant dans les spectres d'électrons éjectés font l'objet de classements et d'attributions en termes de l'autoionization vers l'état fondamental ***X*** de l'ion, à partir des états correspondant à la progression I de Tanaka et des séries de Rydberg de Tanaka–Ogawa convergeant vers l'état ***A*** de l'ion, ainsi que des séries «sharp» et «diffuse» de Henning et de la série interdite $np\sigma_u$ convergeant vers l'état ***B***. De nouvelles singularités particulièrement sensibles à l'énergie d'impact sont observées. Suivant l'énergie d'impact, de grandes variations relatives d'intensité sont observées et des effets très marqués de dépendance angulaire se manifestent dans les spectres d'électrons éjectés.

1. Introduction

The ubiquitous carbon dioxide molecule has historically attracted substantial attention in molecular physics and life sciences because of its abundance and importance in planetary atmospheres and living systems. In particular, spectroscopists and theorists have long been interested in CO_2 as a prototype for photon/electron–molecule collision studies in linear triatomic molecules. Today, CO_2 has in many ways become the paradigm of a single polyatomic molecule in molecular spectroscopy.

The valence electronic structure of CO_2, in the energy region 7–20 eV, has been the subject of considerable experimental investigation by various techniques, such as photon absorption (1–4), photoelectron spectroscopy (5–7), photoionization efficiency spectroscopy (8–10), and electron impact spectroscopy (11–15). Both photoionization (8) and electron energy loss (15) spectra of CO_2 have revealed rich autoionization structures in the first 8 eV above the lowest ionization onset. Some of the structures have been identified as highly excited Rydberg states (4, 15, 16) (e.g., "Henning diffuse" and "sharp" series converging to $B^2\Sigma_u^+$, $v = 0$, ionic state of CO_2^+ (1, 2)), whereas the origin of others remains a mystery. There is now tangible evidence that autoionization can make a major contribution to the ionization cross section for molecules, especially at low energies just above the ionization energy (10). This is particularly remarkable in the near threshold region of the total photoabsorption and photoionization cross sections for diatomic and small polyatomic molecules. For the former, the autoionization processes can in practice dominate the total ionization picture (17, 18).

Although the autoionizing states of CO_2 in the energy region of 15–19 eV have been obtained by various means (2, 3, 8, 12, 18) and studied carefully by optical (6, 19) and electron impact (15) excitation, it is still fair to state that some of the autoionizing features unveiled by those electron spectroscopies mentioned above have not yet been assigned firmly. Against this background of experimental activity, it is worthwhile to reexamine this energy sector using a different approach, such as ejected electron spectroscopy, in which the ejected electrons of autoionization are energy analyzed directly. This complementary information may help to clarify the previous investigations and the mechanism of autoionizing processes in CO_2. It is this consideration as well as a long-standing interest in low-energy electron impact spectroscopy of linear triatomic molecules that has motivated the present study.

Despite a substantial amount of work on CO_2 by means of various spectroscopies for more than half a century, no ejected electron spectroscopy of CO_2 has, to our knowledge, been reported thus far. This may partially reflect the fact that measurements on the electron ejection of autoionizing states arising from photon or electron impact are in general beset by many intrinsic difficulties, and the resulting spectral data are normally rather rich and complicated, and consequently difficult to interpret (20). We recently employed a technique of detecting the

[1]Present address: Hôpital de l'Hôtel-Dieu de Québec, Québec, Qué.
[2]Author to whom correspondence may be addressed.

Can. J. Chem. Downloaded from www.nrcresearchpress.com by 195.246.54.202 on 09/08/12
For personal use only.

Can. J. Chem. Downloaded from www.nrcresearchpress.com by 195.246.54.202 on 09/08/12
For personal use only.

ejected electrons induced by low-energy (20–55 eV) electron excitation with an energy resolution of about 30 meV, and would like to report some of our observations of autoionizing transitions in CO_2. The advantage of ejected electron measurements is that the spectral structure can be ascribed directly to autoionization. In other words, if the initial Rydberg states in the two-step process are already identified, then the kinetic energies of ejected electrons directly determine the final ionic states. In addition, the energy and angular distributions of ejected electrons may yield some information on the decay modes, branching ratios, and the symmetry of the autoionizing states. The use of the low-energy electron scattering method often opens more transition paths than photoabsorption owing to the considerable relaxation of selection rules and therefore enables us to investigate some autoionizing states that are inaccessible by photon excitation, as was demonstrated clearly in some electron excitation studies of CO_2 (13, 15).

The four outermost occupied molecular orbitals (MOs) of CO_2 in its $D_{\infty h}$ ground state configuration are ... $(4\sigma_g)^2(3\sigma_u)^2(1\pi_u)^4(1\pi_g)^4$, with their ionization energies (E_I) decreasing from $4\sigma_g$ to $1\pi_g$. It is known that the $4\sigma_g$, $3\sigma_u$, and $1\pi_g$ MOs are relatively nonbonding and they display only rather narrow peaks in the photoelectron spectrum (5, 7). The $1\pi_u$ is, however, a strong bonding orbital in the valence region and gives rise to a broad photoelectron band that embraces at least seven vibrational levels. The latest photoelectron spectroscopy data (7) provide the $X^2\Pi_g$ ground ionic state ($\Omega_{3/2}$) with an E_I of 13.778 eV, 19.5 meV lower than its spin-orbit partner ($\Omega_{1/2}$); $A^2\Pi_u$ ($\Omega_{3/2}$) with an E_I at 17.314 eV, just 11.9 meV apart from its $\Omega_{1/2}$; $B^2\Sigma_u^+$ at 18.077 eV and $C^2\Sigma_g^+$ 19.394 eV. Rydberg series leading to each of these limits have been observed, among which are the "Tanaka progressions I/II," "Tanaka–Ogawa," and "Lindholm" series converging to the ionic state A (2–4, 6, 8); the two Henning series mentioned earlier and a forbidden $np\sigma_u$ series converging to the B state (1, 2, 15); two absorption (one is much stronger than the other) and an emission series converging to the C state (2). Molecular spectroscopy of CO_2 indicates that both $A^2\Pi_u$ and $B^2\Sigma_u^+$ states are strongly perturbed as a result of Renner–Teller, spin-orbit, and vibronic interactions, while the $C^2\Sigma_g^+$ is highly unstable and may rapidly undergo predissociation (21, 22). Quite noticeably, the excitation spectrum beyond the first threshold is characterized by deep autoionization structures (6, 15, 18). As far as is currently known, this autoionization is of the electronic type, and originates largely from autoionizing Rydberg states, such as autoionization of the Tanaka–Ogawa and two Henning series to the ground ionic state X in its (000) and (100) vibrational levels (18, 19).

The autoionizing Rydberg states of a molecule may be thought of as an excited ionic core plus an excited electron in a Rydberg-like orbital. Electronic autoionization takes place between this Rydberg state and the ionization continuum of a lower electronic state of the ion, and hence belongs to a process of pure Coulomb interaction. It has been recognized, in addition to radiation decay, as another major de-excitation channel of a highly electronic excited state. This de-excitation is usually fast and efficient, since typical autoionization lifetimes are only $10^{-15} - 10^{-13}$ s. The occurrence of electronic autoionization favours Rydberg states of low n^*, because the higher Rydberg states have a smaller probability of being initially formed by absorption, and hence a smaller probability of subsequently autoionizing (10). There are also selection rules for autoionization of this sort, namely, $\Delta J = 0$, $\Delta L = 0$, and $\Delta S = 0$ for LS coupling and no parity change. In other words, two electrostatically interacting states must have identical symmetry (23). However, this does not necessarily mean that autoionizing transitions have been restricted to a small group of electronic excited states because of these selection rules. On the contrary, a great number of the total final states, molecular ion plus electron of ejection, may meet the symmetry demand of the initial autoionizing Rydberg state. This is due to the fact that the departing electron, such as photoelectrons, can carry practically any kind of symmetry and angular momentum away from the ion. Obviously, studying the symmetry of the outgoing electrons may result in determining the symmetry character of the Rydberg series if one knows the symmetry of the ion that the ejected Rydberg electron has just left behind. This is one reason why tremendous effort, both experimental and theoretical, has been made for years in studying the angular distributions of electrons of emission.

Using a newly constructed multi-angle parallel detection electron spectrometer, we also measured the angular distributions of ejected electrons for CO_2 autoionization, and present here some results that show that the intensities and shapes of autoionization lines vary at different ejection angles and are quite sensitive to incident electron energies as well. These data might potentially be of significance in helping to classify the energy level structure in the autoionizing region of CO_2 and (or) to determine the quantum numbers specifying Rydberg states. In addition, some new features not seen in previous experiments of low-energy electron impact excitation (15) were obtained and they appear to be favoured by low-energy-induced electron ejection. Therefore, the present results complement those of the other researchers mentioned above.

2. Experimental

The experiment was performed with a multi-angle parallel detection electron scattering spectrometer (MAPDESS for short) recently constructed in this laboratory. A schematic side view of this MAPDESS is displayed in Fig. 1; its major features have been discussed in detail elsewhere (24). For a better understanding of the present measurements, the following gives a brief account of this novel electrostatic electron spectrometer.

A well-defined electron beam, formed in the electron gun chamber and energy-selected by the monochromator of a standard 127° cylindrical deflector, is directed towards the collision center by the double-zoom lenses, deflectors, and an electron collimator, to cross at 90° with a beam of a gaseous target emanating from a narrow gas-inlet capillary. After collision, the scattered electrons of selected energy will, with the guidance of an annular lens, pass through the hemispherical analyzer and finally reach the channel electron multipliers.

The energy analyzer, the main piece of the MAPDESS, is a truncated spherical mirror that is symmetric with respect to the scattering center. Its ring-shaped exit is coupled to 19 channel multipliers, thus allowing parallel multichannel detection. Therefore, this spectrometer can directly give the angular distribution of an energy-resolved scattering event at 19 different angles separated by 8°, from 18° to 162°, with respect to the incident electron beam. With an angular resolution of ~3°, the overall energy resolution can be 25 meV, obtained with a monochromated beam in electron energy loss measurements at the analyzer pass energy of 7 eV.

Since the early work of Comer and Read in 1972 (25), refinements of the techniques involving detection of the ejected electrons have been made (26). The kinetic energy of the electron ejected from an autoionizing state, unlike the energies of inelastically scattered electrons, is independent of the incident electron energy (provided that the post-collision interaction is negligible here). This signifies that the

Can. J. Chem. Downloaded from www.nrcresearchpress.com by 195.246.54.202 on 09/08/12
For personal use only.

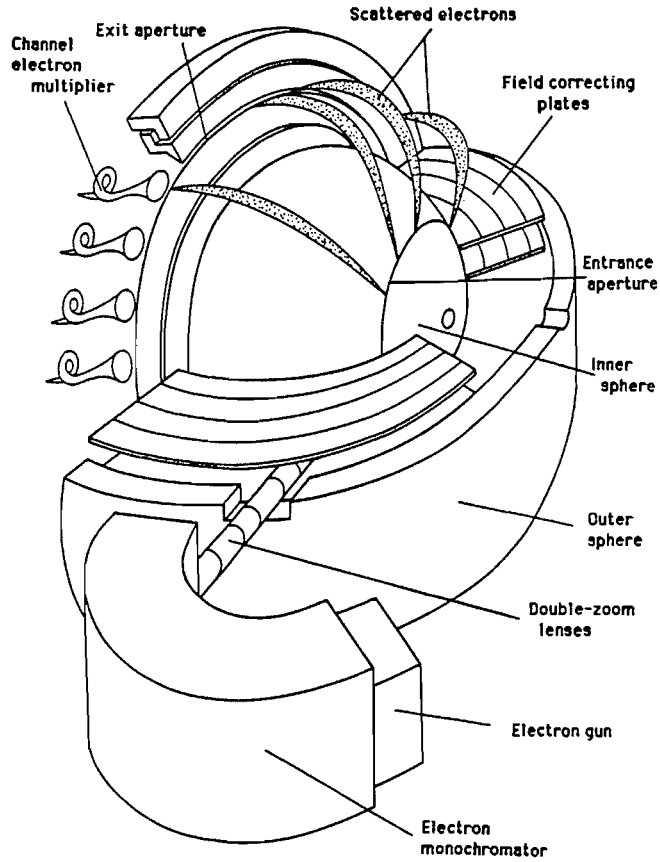

FIG. 1. Schematic three-dimensional view of the MAPDESS.

incident electron beam can be formed from a high-intensity gun, instead of a monochromator, and used directly, as good energy resolution is required solely in the analyzer. This is exactly the case in the present experiment. In fact, the monochromator in Fig. 1 was dismounted for our measurements for the ejection spectra. The energy resolution in this case was approximately 30 meV for the ejection experiment, slightly lower than before. This was already insufficient to observe directly the spin-orbit splitting of the CO_2^+ $X^2\Pi_g$ state, which is only about 19.5 meV (7).

As discussed previously (26), there are two basic modes of measuring an ejected electron spectrum, i.e., either at constant incident energy, measuring the electron yield as a function of energy loss (mode I), or a constant energy loss, measuring the yield as a function of ejection energy (mode II). For clarity, let us review briefly some main points of the early description (26). If the analyzer of an unmonochromated spectrometer receives electrons of various kinetic energies E_k from the collision center at a constant incident energy E_i (mode I), an energy loss spectrum may be obtained by sweeping E_l (sweeping the potential applied to the analyzer V_l in reality, since $E_l = eV_l$) and consequently E_k through the relation

$$[1] \quad E_l = E_i - E_k$$

In the case of autoionization, the kinetic energy of an ejected electron is given by

$$[2] \quad E_{ej} = E^* - E_I$$

where E^* is the energy of an excited Rydberg state. To detect the ejected electrons, one must have $E_{ej} = E_k$, which yields

$$[3] \quad E_l = E_I + E_{ex}$$

where E_{ex} ($= E_i - E^*$) denotes the excess energy of the incident electron relative to the Rydberg state. Thus, through these relations, one may find that mode I can also be used to detect the ejected electrons. On the other hand, by operating the gun and analyzer in the constant energy loss mode (mode II), in which only the incident electron energy is swept, with E_l being kept constant, it is possible to separate the ejected electron spectra from the simpler energy loss spectra. Mode II was utilized in the present work to avoid the possibility of energy loss structure appearing in the ejection spectrum. According to the above equations, one may determine the ejection energy scale by calibrating the incident energy and the energy loss. In this study, however, the energy loss scale was determined by the cutoff feature of the zero kinetic energy in the energy loss spectrum. The fine adjustment of the calibration was achieved by careful alignment of a prominent spectral peak with a spectroscopically well-known excitation line.

The main vacuum chamber containing the spectrometer has a background pressure of about 8×10^{-8} Torr (1 Torr = 133.3 Pa) using an efficient turbo-molecular pumping system. The spectra were recorded at sample pressures of the order of only 5×10^{-6} Torr. This improves the stability of the electron optics and of the instrument. The pressure in the collision region, however, was two orders of magnitude higher owing to the directed nature of the gas inlet jet. The CO_2 sample used was purchased commercially from Liquid Air, with a stated minimum purity of 99.98%, and therefore was taken directly from the lecture bottle without further purification.

3. Results and discussion

3.1 Ejected electron spectra

The three electron ejection spectra of CO_2, exhibiting the systematic change in intensity of features under different experimental conditions, are depicted in Fig. 2. They are representative of the many spectra that were recorded under various incident electron energies (20–55 eV). As explained in the experimental section, these spectra were taken under conditions of the constant energy-loss mode (mode II), which gives a range of incident energies for each spectrum in Fig. 2 from the top to the bottom as follows:

(1) $E_i = 25.0 \rightarrow 29.0$ eV $\quad E_l = 25.0$ eV
(2) $E_i = 30.0 \rightarrow 34.0$ eV $\quad E_l = 30.1$ eV
(3) $E_i = 50.9 \rightarrow 54.9$ eV $\quad E_l = 51.3$ eV

Each spectrum presented here is in fact the sum of 19 spectra recorded simultaneously at every 8° between 18° and 162°. This is somehow parallel to the photoelectron partial cross section for various molecular orbitals in the absorption spectrum that is obtained by integrating angle-resolved differential cross sections over all accessible angles. The strong varying ionization continuum (combined with low-energy electron background) present in the original data has, for clarity, been subtracted following the procedure proposed by Carbonneau et al. (27). Yet, this causes valleys between the peaks to appear as dips in our spectra, which have no real physical significance. The yield of ejected electrons is plotted in arbitrary units of electrons versus ejection kinetic energy, which covers the range from 0.7 eV up to a kinetic energy of 4.7 eV, the energy sector that falls into the region where autoionizing transitions in CO_2 occur most actively amongst the electronic states.

It has been found that the electron ejection features in Fig. 2, which correspond directly to autoionization, are remarkably similar to those appearing in some electron energy loss spectra of CO_2 that were obtained in this laboratory (15, 28), as can be seen in Fig. 3. Here, an ejected electron spectrum summed over all angles was plotted in the inset in order to compare directly with the energy loss spectra recorded in the constant incident

Can. J. Chem. Downloaded from www.nrcresearchpress.com by 195.246.54.202 on 09/08/12
For personal use only.

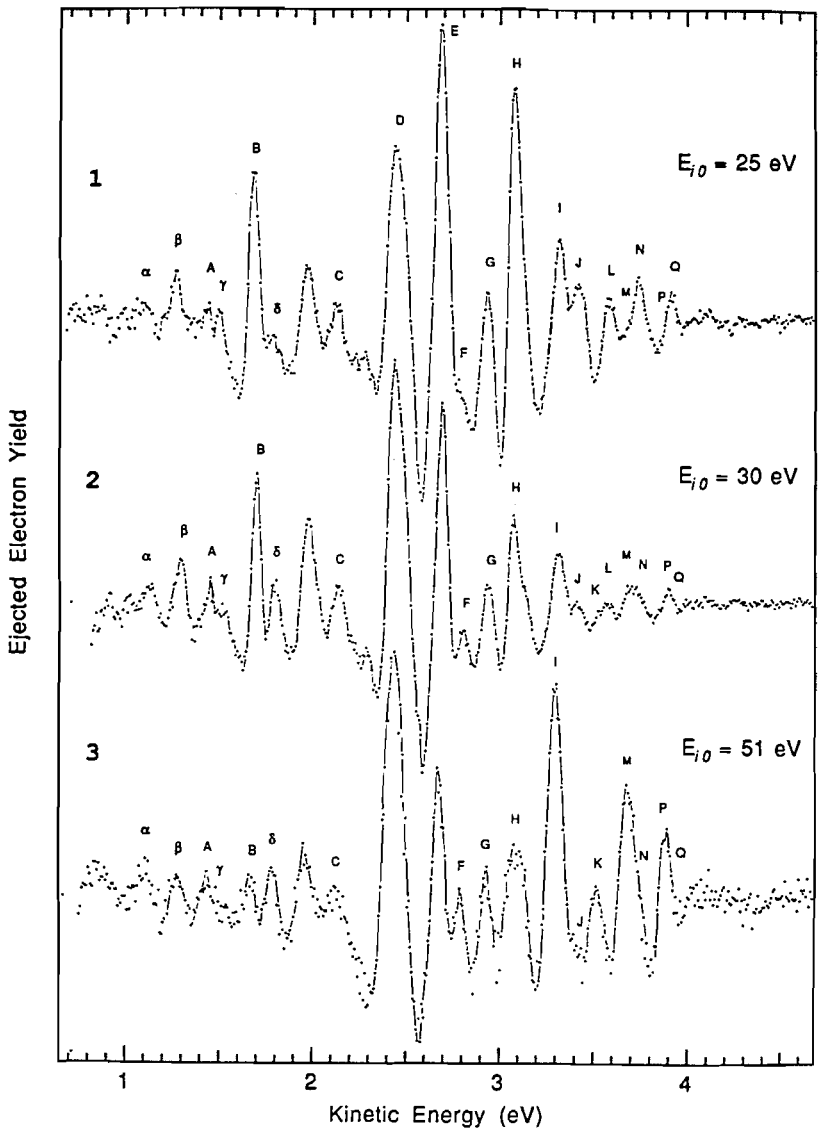

FIG. 2. Ejected electron spectra of CO_2 recorded at various incident electron energies (E_i) and excess energies (E_{ex}), where the incident energy was ramped up to 4 eV above the initial E_{i0} while keeping the energy loss fixed (see the text for details). Each spectrum is in fact the sum of 19 angle-resolved spectra recorded in parallel at every 8° between 18° and 162°. The analyzer energy resolution is approximately 30 meV. Features designated by letters correspond to those observed in the electron energy loss spectra in Fig. 3. Several features labelled by Greek letters are not present in the energy-loss spectra.

energy mode (mode I) for the region showing prominent autoionizing bands. The inset spectrum, which was acquired by scanning the incident energy (mode II) from 40.0 eV to 42.0 eV while fixing the energy loss at 40.0 eV, has seemingly been resolved slightly better than its energy loss counterpart of about 30 meV stated resolution. Figure 3 illustrates one attractive characteristic of ejected electron spectroscopy. The nice and consistent correlation of the features between the ejection spectrum and the energy loss spectrum leaves no doubt that the two techniques are describing the same autoionization zone in CO_2; otherwise, the features would not appear at the same relative position on both spectra. Thus, the same labelling system of features in the energy loss spectrum was adopted to the ejection spectra in Fig. 2 to facilitate the following spectral analysis.

3.2 Energy, intensity, and shape

Although Figs. 2 and 3 show that each of the autoionizing Rydberg series appearing in the excitation spectrum may find its counterpart in the ejection spectrum, this does not make it much easier to unambiguously determine the spectral features observed in ejection. This is because ejection spectroscopy provides us merely with the energy difference between an initial autoionizing state and a final ionic state (see eq. [2]), i.e., the kinetic energy of ejection is known, whereas the two states are not. Unless one of the two coupled states is certain, no decisive assignment can be given in general. Even if an assignment is made, it may not be the unique one, since several possible transitions may sometimes produce the same or very similar ejection energy, which closely matches the energy of the feature determined. Thus, the observation of ejected electrons does cause one complication that is not present in photon or electron excitation experiments, that is, the possible occurrence of one single line in the ejection spectrum corresponding to several autoionizing transitions. This undoubtedly gives rise to some uncertainty in the assignments. Therefore, some of the assignments given have only suggestive significance.

Can. J. Chem. Downloaded from www.nrcresearchpress.com by 195.246.54.202 on 09/08/12
For personal use only.

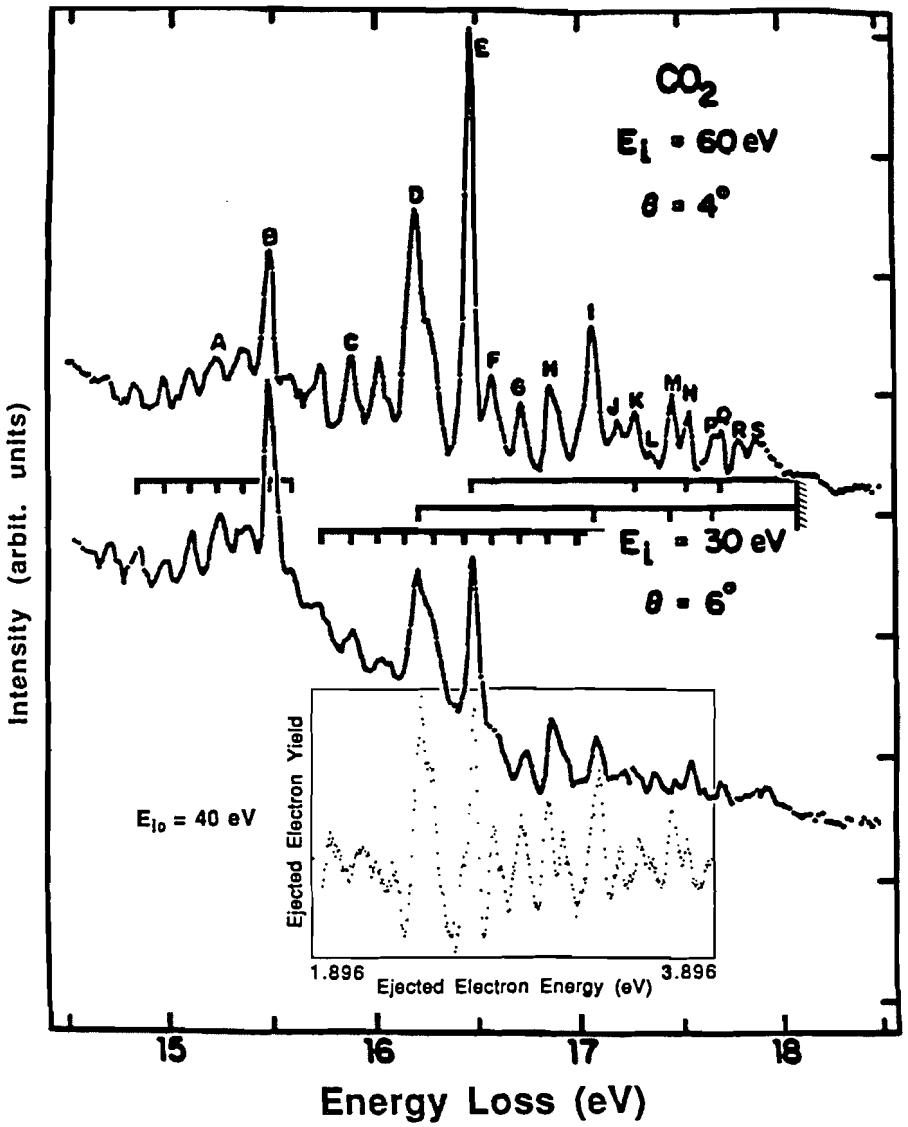

FIG. 3. Electron energy-loss spectra of CO_2 in the energy region 14.5–18.5 eV (taken from ref. 15). The spectra were recorded in the constant incident energy mode at scattering angles of 4° and 6°, and the overall energy resolution of the spectrometer was around 30 meV. The inset presented here is an integrated ejected electron spectrum to illustrate the spectral similarity between absorption and emission. The ejection spectrum was obtained by scanning the incident energy between 40 and 42 eV.

The kinetic energies and proposed assignments of the major spectral features in the ejected electron spectra of CO_2 are listed in Table 1. Since many autoionizing lines are closely spaced or even overlapped in this region and their intensities vary with the incident energy, which makes it sometimes difficult to accurately determine the energy position of features from a single spectrum, Table 1 includes only the features labelled in Fig. 2 as well as those whose positions can be recognized in the different spectra and (or) with reasonable certainty. The tabulated assignments are based, in addition to the previous results of excitation or ionization studies, chiefly on the energy match between the measured kinetic energy and the energy difference between the neutral Rydberg state and the final ionic state. In a few cases, assignments are made in such a way that they are reasonable in the sense that the corresponding autoionizing transitions are in accord with our spectroscopical "intuition" as well as spectroscopically reasonable population analysis results. The autoionizing lines observed in the present study can be identified as members of different Rydberg series, and six Rydberg series have been considered to be present in our ejected electron spectra. Each of these series will be discussed as follows.

3.2.1. Tanaka progression I

This series was identified initially by Henning (1) and was also observed as one of two weak ultraviolet absorption bands by Tanaka et al. (2), who called it the first progression but gave no explanation of it. Lindholm (4) assigned it to the first member of a forbidden Rydberg series ($np\sigma_u\ ^1\Pi_g$) converging to the $A^2\Pi_u$ ionic state of CO_2^+, whose higher members remain unknown up to the present time. In the ejected electron spectra of Fig. 2, this series appears in the low kinetic energy region, starting at the feature α and ending up around the δ. Apparently, the progression looks clearer and sharper under conditions of lower incident electron energies (see spectra 1 and 2), especially at peaks β and B, suggesting their character as optically forbidden transitions. This is consistent with the electron excitation results of Hubin-Franskin et al. (15), who observed, in addition to the impact-energy dependence, the strong angular

TABLE 1. Kinetic energies (eV) and proposed assignments for features in the ejected electron spectrum of CO_2

Major feature	Kinetic energy (eV)	$\tilde{A}$ state Ryds decay to $\tilde{X}$		$\tilde{B}$ state Ryds decay to $\tilde{X}$			$\tilde{C}$ state Ryds (nf_u) $\delta = 0.05$ decay	
		Tanaka Progs I $(np\sigma_u)^a$	T-O series $(ns\sigma_g)^b$	$R_B(np\sigma_u)^c$	H-D series $(nd\sigma_g)^d$	H-S series $(ns\sigma_g)^e$	to $\tilde{B}^f$	to $\tilde{X}^f$
	0.85 (2)[g]						$n = 5$, 18.846 → 18.077 0.769	
	0.91 (1)						$n = 6$, 19.007 → 18.077 0.930	
α	1.085 (8)	$v' = 0$, 14.866 → 13.778(000)[h] 1.088						
	1.184 (7)	$v' = 1$, 15.002 → 13.778 1,224 $v' = 2$, 15.108 → 13.93(100) 1.177						
β	1.300 (7)	$v' = 2$, 15.108 → 13.778 1.330 $v' = 3$, 15.235 → 13.931 1.304						
A	1.452 (7)	$v' = 3$, 15.235 → 13.778 1.457						
γ	1.508 (7)	$v' = 6$, 15.594 → 14.084(200) 1.510						
	1.580 (9)	$v' = 4$, 15.361 → 13.778 1.583						
B	1.700 (5)	$v' = 5$, 15.477 → 13.778 1.699			$n = 3$, 15.491 → 13.778 1.713			
δ	1.772 (7)	$v' = 6$, 15.594 → 13.833(010) 1.761						
	1.820 (8)	$v' = 6$, 15.594 → 13.778 1.816						
	1.974 (5)		$n = 4$, $v' = 0$, 15.751 → 13.778 1.973					
C	2.116 (5)		$n = 4$, $v' = 1$, 15.894 → 13.778 2.116					
	2.252 (7)		$n = 4$, $v' = 2$, 16.031 → 13.778 2.253					
	2.292 (7)		$n = 4$, $v' = 3$, 16.165 → 13.866(010) 2.299					
	2.388 (8)		$n = 4$, $v' = 3$, 16.165 → 13.778 2.387					
D	2.436 (4)				$n = 3$, 16.214 → 13.778 2.436			
	2.524 (8)		$n = 4$, $v' = 4$, 16.303 → 13.778 2.525					
	2.660 (8)		$n = 5$, $v' = 0$, 16.439 → 13.778 2.661					

Can. J. Chem. Downloaded from www.nrcresearchpress.com by 195.246.54.202 on 09/08/12
For personal use only.

TABLE 1. (*concluded*)

Major feature	Kinetic energy (eV)	$\tilde{A}$ state Ryds decay to $\tilde{X}$		$\tilde{B}$ state Ryds decay to $\tilde{X}$			$\tilde{C}$ state Ryds (nf_u) $\delta = 0.05$ decay	
		Tanaka Progs I ($np\sigma_u$)[a]	T-O series ($ns\sigma_g$)[b]	$R_B(np\sigma_u)$[c]	H-D series ($nd\sigma_g$)[d]	H-S series ($ns\sigma_g$)[e]	to $\tilde{B}$[f]	to $\tilde{X}$[f]
E	2.700 (5)					$n = 4$, 16.483 → 13.778 2.705		
F	2.804 (7)		$n = 5$, $v' = 1$, 16.582 → 13.778 2.804					
G	2.940 (5)		$n = 5$, $v' = 2$, 16.723 → 13.778 2.945					
H	3.086 (4)		$n = 5$, $v' = 3$, 16.857 → 13.778 3.079	$n = 4$, 16.877 → 13.778 3.099				
	3.150 (5)	??						
	3.240 (8)		$n = 5$, $v' = 4$, 16.998 → 13.778 3.220					
			$n = 5$, $v' = 4$, $\Omega_{1/2}$ 17.039 → 13.797(000) 3.242					
I	3.300 (5)				$n = 4$, 17.073 → 13.778 3.295			
	3.360 (8)		$n = 5$, $v' = 5$, 17.137 → 13.778 3.359					
J	3.418 (6)		$n = 6$, $v' = 3$, 17.201 → 13.778 3.423					
K	3.503 (7)		$n = 6$, $v' = 4$, 17.281 → 13.778 3.503			$n = 5$, 17.282 → 13.778 3.504		
	3.525 (6)		$n = 6$, $v' = 4$, $\Omega_{1/2}$ 17.317 → 13.797 3.520					
L	3.574 (6)			$n = 5$, 17.354 → 13.778 3.576				
M	3.690 (6)		$n = 6$, $v' = 5$, 17.477 → 13.778 3.699		$n = 5$, 17.458 → 13.778 3.680			
N	3.770 (8)					$n = 6$, 17.540 → 13.778 3.762		
	3.840 (10)		$n = 6$, $v' = 6$, 17.616 → 13.778 3.838	$n = 6$, 17.608 → 13.778 3.830				
P	3.876 (6)				$n = 6$, 17.657 → 13.778 3.879			
Q	3.924 (10)		$n = 6$, $v' = 7$, $\Omega_{1/2}$ 17.730 → 13.797 3.933			$n = 7$, 17.700 → 13.778 3.922		
	3.996 (10)				$n = 7$, 17.768 → 13.778 3.990			
	4.080 (12)		$n = 6$, $v' = 8$, $\Omega_{1/2}$ 17.864 → 13.797 4.067		$n = 8$, 17.844 → 13.778 4.066		$n = 3$, 17.866 → 13.778 4.088	

[a]See ref. 2.
[b]See ref. 3.
[c]See ref. 15.
[d]See refs. 10 and 28.
[e]See ref. 10.
[f]See refs. 2, 6, 19, and 28.
[g]Errors in final figures in parentheses.
[h]Unless indicated by $\Omega_{1/2}$, the final state of autoionization means the ground state $X^2\prod(\Omega = 3/2)$ of CO_2. This is also applicable to the $A^2\prod_g$ ionic state. CO_2 has three fundamental modes of vibration: the symmetric-stretch mode (1, 0, 0); the bending mode (0, 1, 0); and the asymmetric-stretch mode (0, 0, 1). (v_1, v_2, v_3) indicates the vibrational level of the molecular ion.

Can. J. Chem. Downloaded from www.nrcresearchpress.com by 195.246.54.202 on 09/08/12
For personal use only.

Can. J. Chem. Downloaded from www.nrcresearchpress.com by 195.246.54.202 on 09/08/12
For personal use only.

dependence of this series, indicating a sort of u–u symmetry-forbidden excitation. In terms of the energy shift and the band-shape change in their threshold excitation, Hubin-Franskin et al. even considered the possibility of excitation of a triplet state $^3\Pi_g$ for this first member ($3p\sigma_u$) of the series. In the ejection spectra, the intensity and line shape of peaks β and B vary more noticeably with incident energy, and they have been attributed to the involvement of more than one line under the peak, as indicated in Table 1.

It should be pointed out that some of the features (e.g., γ) have been assigned to electronic autoionization occurring between the $3p\sigma_u$ Rydberg state converging to the v'th vibrational level of the $A^2\Pi_u$ state and the continuum of the $X^2\Pi_g$ state in its v''th vibrational level, since there is no restriction in this regard (23) (although the vibrational intensity distribution in the final ionic states may follow the pattern predicted by the Smith (29) model, which shows that if autoionization dominates the photoionization process in small molecules, such as O_2, the distribution depends only upon Franck–Condon factors connecting the autoionizing Rydberg and final ionic states). However, the considered vibrational levels of the $X^2\Pi_g$ state are only those that have exhibited a reasonable intensity in the CO_2 photoelectron spectrum (5, 7) to be in accord with their probability of being populated. Though less than 1 eV, this energy region has been considered to be very complicated. Baer and Guyon (6) had to propose the excitation to two, rather than one, electronic states in this region to fit the rich structure displayed in their threshold photoelectron spectrum. Interestingly, among the two series they proposed, only the one they believed to originate from the vibrational development of the excited $X^2\Pi_g$ ionic state (i.e., resonance autoionization with ejection of low-energy electrons) is in agreement with our data. Besides the features already studied by electron excitation (15), a few new ones were observed here, and they are given in Table 1.

3.2.2. Tanaka–Ogawa series

This is an optically allowed Rydberg series and each member of the series is composed of a long and strong vibrational progression with a maximum intensity around $v' = 3$ owing to excitation of the symmetric-stretching mode in CO_2. Discovered by Tanaka–Ogawa, the series was classified by Fridh et al. (16) as the $ns\sigma_g$ Rydberg series with quantum defect of 1.18, converging to the $A^2\Pi_u$ ionic state. Because of the profound ν_1 vibrational development of the $A^2\Pi_u$ state itself, stemming from the remarkable change of molecular geometry in ionization of the neutral ground state to the A ionic state, many high-level Rydberg members have already reached deep inside the $A^2\Pi_u$ continuum. The series may therefore be expected to appear as a major progression of Rydberg bands extending through the entire ejection spectrum beyond 1.9 eV. However, the higher n^* Rydberg levels are less likely to be observed in the ejection spectrum here because of insufficient energy resolution. The first Rydberg member to appear in our spectra is a relatively intense peak just below peak C (see Fig. 2). It, along with peak C, has a rather stable shape in the incident energy range under investigation. Yet the peak next to C on the higher energy side has an unusual low intensity compared to the energy-loss spectrum presented in the top of Fig. 2. Although the $v' = 3$ level of the $4s\sigma_g$ Rydberg state, which is supposed to have the highest intensity in the progression, seems to be overshadowed by the illustrious peak D of the Henning series, two other vibrational levels of this state between peaks D and E give rise to a strong appearance (as a visible shoulder) in the inset of Fig. 3.

The remaining members of this series are labelled by the letters F, G, H, J, K, M, and Q; among them, features G and J are the relatively pure Tanaka–Ogawa Rydberg states and somehow show a weak dependence of the series on the incident energy in this region. The dramatic change in intensity of peak H is believed to be associated with another Rydberg series, to be discussed below. Finally, on account of the spin-orbit coupling, each series is in fact made up of two bands that coverage towards the $\Omega = 3/2$ and $\Omega = 1/2$ ionization limits of the $A^2\Pi_u$ state. In a few cases, the members of the series converging to the $\Omega = 1/2$ limit have been considered in our assignments, since they can apparently give a better energy match to the kinetic energy of an autoionizing line, as has been shown in Table 1. Again, several weak features have been identified and their possible corresponding autoionizing transitions are listed in the table.

There also exists another fairly weak but visible (in photoabsorption (3) and photoion yield spectra (8)) progression (5 levels) in parallel with the $n = 4$ member of the Tanaka–Ogawa Rydberg series. This "additional progression" of Tanaka and Ogawa (3), emerging at 15.80 eV, has been considered as the first member ($n = 3$) of a Rydberg series of $nd\delta_g$ excitation by Lindholm (4), based on its quantum defect being about 0.00. Although the series, referred to often today as the Lindholm Rydberg series, has tentatively been extended by McCulloh (8) to the $n = 4$ progression (merely 2 levels at best, however), its other members have remained undefined until now. Because of limitations in the energy resolution, the Lindholm progression is not resolved by our spectrometer and, consequently, the series has been left out altogether. However, it should be borne in mind that, since the Lindholm series occurs closely in parallel with the Tanaka–Ogawa series in the energy region of 15.8–16.9 eV, it may play a role in shaping the autoionization peaks appearing in this region.

3.2.3. Optically forbidden series R_B

This series was first observed by Cvejanovic et al. (14) and was extended to a higher energy area by Hubin-Franskin et al. (15). Three Rydberg states of the series, which are indicated by the letters B, H, and L in Fig. 3, have been determined so far by the low-energy electron impact technique. The differential cross sections of these three states intensify at lower incident electron energies, and vary with the scattering angles, strongly signifying the occurrence of a symmetry-forbidden transition. With a quantum defect of 0.70, the series has been assigned to the $np\lambda_u$ Rydberg series, possibly by symmetry σ_u, converging to the $B^2\Sigma_u^+$ ionic state (15). The forbidden character of this series is also manifested in our ejected electron spectra of Fig. 2. Throughout the three spectra of different incident energies, the peak intensity of the series changes spectacularly, from a pronounced peak (B and H in spectrum 1) to a weak feature (B in spectrum 3) or to a featureless background (L in spectrum 3). The striking intensity enhancement of peaks B and H in spectrum 1 has been attributed to the enhanced population of the initial autoionizing levels using the low-energy electron impact. The exceptional height of peak H may suggest the participation of some other states adjacent to H, such as Rydberg states of the Tanaka–Ogawa (or perhaps plus the Lindholm) series, which apparently also gain some intensity in this energy region, as mentioned earlier. Another piece of evidence supporting this

Can. J. Chem. Downloaded from www.nrcresearchpress.com by 195.246.54.202 on 09/08/12
For personal use only.

idea comes from the inset ejection spectrum in Fig. 3. The spectrum reveals that at the present resolution there exist at least two lines under the envelope of peak H. The line of higher energy has a kinetic energy of 3.150 eV, and there is no other reasonable autoionizing transition that could produce an electron ejection energy of such a value. We have no adequate explanation for this at the moment. It is possible that the 3.150 eV peak is the real line that belongs to the $np\sigma_u$ forbidden series, while the peak on the low-energy side of it (3.086 eV) may be the 5th Rydberg member of the Tanaka–Ogawa $ns\sigma_g$ series converging to the $v' = 3$ vibrational level of the $A^2\Pi_u$ state, judging from its distance to peak G, which is approximately equal to the separation between peaks G and F, as well as from its height, which is the highest in the vibrational development, being in harmony with the photon absorption observation (3).

3.2.4. Henning diffuse series

This series, together with the Henning sharp one to be discussed later, is the oldest Rydberg absorption series discovered in CO_2 by Henning (1). Based on the quantum defect of ~0.31, obtained by the photoabsorption studies of Tanaka et al. (2) and Tanaka and Ogawa (3), the diffuse series was designated initially by Lindholm (4) as an $nd\sigma_g$ Rydberg series, converging to the $B^2\Sigma_u^+$ ionic state. But it was revised later to an $ns\sigma_g$ excitation, upon assuming the quantum defect to be 1.31 rather than 0.31 (16). However, the electron impact work performed in this laboratory (28) shows that the quantum defect of this series is just about 0.30, in rather good agreement with the result of Tanaka and Ogawa (3). Therefore, the former designation ($nd\sigma_g$) is, in our view, preferable on every ground.

The Henning diffuse Rydberg series gives rise to an intense as well as broad autoionization structure in the photoabsorption (6, 18, 19) and electron excitation (15) spectra, at least for the low-energy members. This structure, consisting of the features D, I, M, and P, can also be seen readily in the ejected electron spectra of Figs. 2 and 3, as it dominates each of the spectra. The peak intensity of the series, too, does vary with incident electron energies, but it is enhanced at high incident energy, consistent with the typical behaviour of symmetry-allowed transitions. This effect is particularly noticeable in spectrum 3, where all members of the series gain substantial intensities and virtually overtake their counterparts in the Henning sharp series (features E, N, and Q), and even more, peak I has become more intense than E. This is in sharp contrast to the situation in the electron energy loss spectra (15) (see also Fig. 3), where the cross section of peak E always appears to be larger than that of D and this has led to the conclusion (19) that the Henning sharp Rydberg state represented by peak E is involved in other electronic configurations. We consider that the intensity increase in the Henning diffuse Rydberg series may be associated with the enhanced relative cross section of the initial autoionizing levels at higher impact energies and the coupling between these initial neutral states and the final ionic state. It is possible also that there occurs an increased contribution from other Rydberg series, such as the Tanaka–Ogawa Rydberg series, or perhaps the Lindholm series (4), which runs closely with the Henning series throughout this energy region, since the bands of different n and v values gradually become quite close in energy and even overlap as n increases.

3.2.5. Henning sharp series

Its quantum defect, also determined by Tanaka et al. (2) and Tanaka and Ogawa (3), is approximately 0.93. This number agrees well with the typical quantum defects of $\sigma \rightarrow ns\sigma$ transitions in some small molecules, and hence has led Lindholm (4) to classify the sharp series as an $ns\sigma_g$ excitation series, converging to the same limit as the diffuse series. The classification was reviewed later, however, because the first 3*s* member (near 84.0 nm) was not present in McCulloh's photoion yield spectrum (8). The final designation was then $nd\pi_g$, after the quantum defect was chosen to be almost zero (16). It is interesting to note here that the electron energy loss spectra of CO_2 also provide the sharp series with the quantum defect of 1.05 (28) and, as a result, the series has tentatively been assigned to the $ns\sigma_g$ Rydberg series (15, 28). This is in excellent accord with the result from the fluorescence polarization work by Poliakoff et al. (30), which shows that, like the diffuse series, the sharp one also possesses $^1\Sigma_u^+$ electronic character. On the basis of additional supporting material from the theoretical calculations of Dittman et al. (31), Dehmer (32) suggested that it might be necessary to revise the $nd\pi_g$ designation of Fridh et al. (16). As for the missing 3*s* member, we consider that the 14.682 eV (84.45 nm) peak in our energy loss spectra (15, 28) (see also the first feature in Fig. 3) may be related to this $n = 3$ member. Though anomalously weak in intensity, the peak is not unlikely to be the first member of the sharp series, as this series might have its intensity maximum at $n = 6$ (33). Thus there is meagre evidence to favour the classification of the Henning sharp series as the $nd\pi_g$ excitation.

The $n = 4$ member of the Henning sharp series has in most cases been an outstanding feature in photoabsorption as well as photoionization (6, 8, 18). As can also be seen from the top electron energy loss spectrum in Fig. 3, there, it is peak E that dominates the spectrum and is followed by the other members of the series: the features K, N, and Q. Like peak D of the diffuse series, peak E can also be made to shrink markedly into a background-like feature in the electron energy-loss spectrum under dipole-forbidden conditions (15, 28). Yet this is seemingly not quite the case in the ejected electron spectra. We have observed that the peak intensity associated with peaks E, N, and Q of the sharp series is, instead of shrinking, enhanced as the incident electron energy decreases (see Fig. 2). Such behaviour appears to parallel that observed for optically forbidden transitions in the electron energy loss spectra. This is quite different from the situation we have just met in the Henning diffuse series, implying strongly that these two Henning series bear a different type of substructure and symmetry in nature. A further piece of supporting evidence comes from Fig. 4, which presents the angular distributions of the ejected electrons. In Fig. 4, we see that the autoionizing transition probability of the sharp- series peak E evidently prefers the large ejection angles, which is totally opposite to that of the diffuse-series peak D. We have not been able to carry out a detailed analysis of such remarkable behaviour in intensity at this point. However, the dissimilarity of the two intensity distributions plausibly reflects differences of configurational interaction between these two Henning series and the final $X^2\Pi_g$ continuum states. It has been suggested that the peak E of extraordinary intensity cannot be a pure Rydberg state and contains instead a considerable contribution from unresolved bands related to its neighbouring states (6, 19). The $n = 5$ member of the Tanaka–Ogawa Rydberg series (and perhaps the Lindholm progression as well), with its vibrational levels surrounding peak E, could be a reasonable candidate for such a

Can. J. Chem. Downloaded from www.nrcresearchpress.com by 195.246.54.202 on 09/08/12
For personal use only.

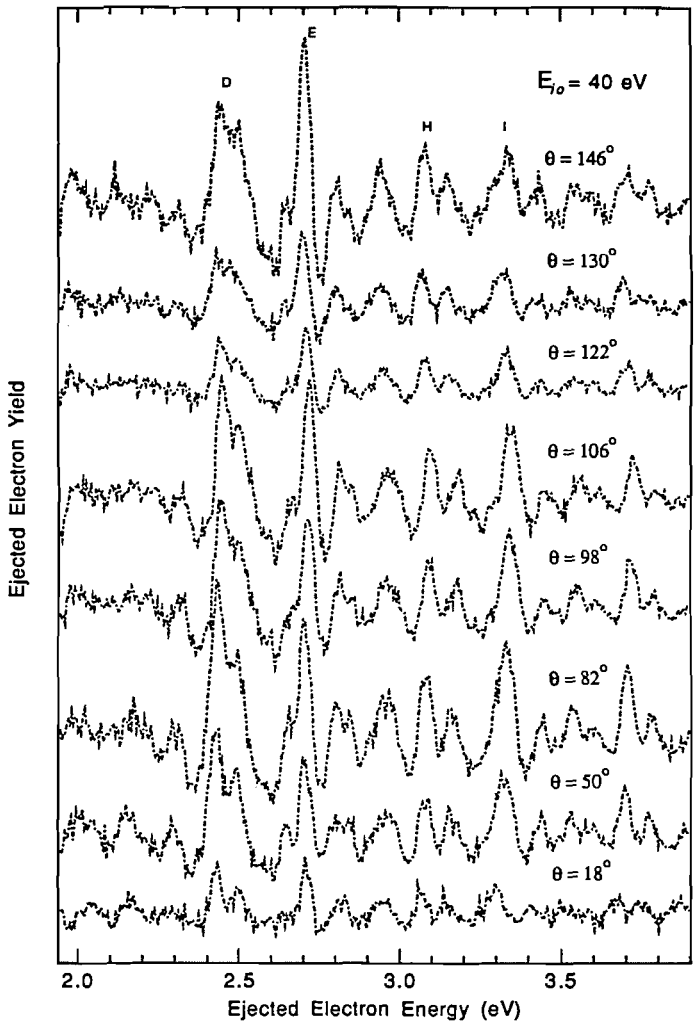

FIG. 4. Ejected electron spectra of CO_2, the sum of which gives rise to the inset presented in Fig. 3, showing the angular behaviour of ejection. For clarity, only 8 representatives are sampled here of the 19 spectra obtained simultaneously by the spectrometer in the constant incident energy mode, as specified in Fig. 3. Each spectrum is plotted to actual height relative to the other spectra to illustrate the probability of autoionizing transitions at different ejection angles.

neighbouring state. Close inspection of spectrum 1 in this region shows that there may exist some strong interaction between the E Rydberg state and the vibrational levels (e.g., the feature F) of the 5th Tanaka–Ogawa series. This could be correlated to the "complex resonance" phenomenon observed in the diatomic molecule N_2 (34, 35).

One more point that should be singled out for recognition is that, unlike the other members of the same series, the $n = 5$ member of the Henning sharp series (feature K) behaves in rather different fashion in Fig. 2. It peaks in spectrum 3 but vanishes in spectrum 1. Again, this behaviour may have something to do with the Tanaka–Ogawa series. In spectrum 1, we assume that the 5th Rydberg state might interact strongly with the high-lying members of the Tanaka–Ogawa series and its electronic character has been distributed over many surrounding levels, resulting in its disappearance from the spectrum. Lacking such interaction, the 5th state emerges as an isolated peak in spectrum 3. It is clear that further careful study will be needed before these phenomena present in our spectra can fully be understood, and other related data, experimental as well as theoretical, will be helpful in this regard.

3.2.6. Rydberg nf_n *series*

This series, along with the other two, was initially observed by Tanaka et al. (2) as a weak absorption Rydberg series that converges to the ionization limit of the $C^2\Sigma_g^+$ ionic state. It was once interpreted by Lindholm (4) as a series of forbidden transitions to $nd\pi_g$ Rydberg states, but such an assignment was criticized by McCulloh (8) because of the absence of the $n = 3$ member (≈69.4 nm) in his photoionization efficiency spectrum. It was then reassigned by Fridh et al. (16) to an allowed nf_u excitation series. However, more recent work of Baer and Guyon (6) claims that an extra sharp autoionization feature of 17.936 eV (69.125 nm) revealed by threshold photoelectron spectroscopy may be associated with the missing $n = 3$ member, and an electron energy loss spectrum recorded in this laboratory (28) shows also that this member appears at 17.886 eV (69.320 nm). This *weak* absorption series has a strong showing in the low energy electron excitation measurements, and its relative cross section is even larger than that of the other absorption series (the third Rydberg series in this region is just an emission series). With the determined quantum defect $\delta = 0.02$, the weak series has been considered as excitation to either $nd\pi_g$ or nf_u Rydberg states (28). Based upon their work of partial photoionization cross section on these three series converging to the $C^2\Sigma_g^+$ state, Hubin-Franskin et al. (19) indicated that the three series autoionize only to the lower ***B*** and ***X*** ionic states. Therefore, we consider that three weak features at the ends of our ejected electron spectra may originate from this sort of autoionization, based mostly upon the transition energies being able to match well the observed kinetic energies. Their assignments are given in Table 1. Considering the nature of the weak absorption as well as the competition from possible predissociation (8, 21, 22), the weak intensity displayed by these autoionizing transitions is fairly understandable.

3.3 Angular behaviour of ejection

The inset ejection spectrum in Fig. 3 is actually the sum of 19 angle-resolved ejected electron spectra that were measured in parallel by the MAPDESS at 19 different angles separated by 8° and ranging from 18° to 162° with respect to the incident electron beam. It represents only the energy distribution of the electrons and a somewhat crude integral behaviour of electrons ejected from various autoionizing states, irrespective of the angle at which the emitted electrons were detected. Therefore, much information about the symmetry about the ejected electrons and (or) the two interacting states in autoionization has been ignored. Eight representative components of the inset spectrum are sampled in Fig. 4 to demonstrate the angular distribution of ejected electrons among the various autoionizing states. Without any normalization and (or) correction of the detector efficiency, each spectrum is plotted to actual height relative to the other spectra to illustrate the probability of autoionizing transitions at different ejection angles. A glance at Fig. 4 shows the drastic change in intensity of some major autoionizing lines as the angle increases: lines D and E, for instance, whose intensities have been virtually inverted, suggesting that the Henning series they represent, respectively, have different electronic character in origin. In terms of a relatively rough estimate, the Henning diffuse series reaches its maximum intensity around 80° at the initial incident energy of 40 eV, whereas the Henning sharp

Can. J. Chem. Downloaded from www.nrcresearchpress.com by 195.246.54.202 on 09/08/12
For personal use only.

series has its best at 146°. This would have been seen more clearly by plotting the ejected electron yield versus the ejection angle in polar coordinates. In fact, with the 19 points obtained at every incident energy the angular dependence of ejected electrons could be mapped out in a polar plot for each autoionizing state to show its angular behaviour in emission, if the angular dependence of the detector efficiency was properly calibrated. The results should be informative and helpful in determining the wave type and symmetry of the outgoing electrons.

It is obvious from Fig. 4 that the ejected electrons are not isotropically distributed. In general, the electrons leave the randomly oriented, excited CO_2 molecule preferentially in certain directions, and precisely, they favour relatively large angles. We have found the maxima in ejected electron intensity between 80° and 110° with respect to the incident electron beam direction, and low electron yield in the forward angles for every single incident energy measurement. The ejection yield at 146° is always prominently large compared to its neighbours, but the yield is, without exception, extremely low at the three angles of 34°, 58° and 162°. Interestingly, the angle 58° is merely a few degrees away from the so-called magic angle (54.74°), at which the measured photoelectron current is directly proportional to the integrated cross section, regardless of the incident photon polarization and the photoelectron angular distribution. This may serve as a simple example of showing that the behaviour of ejected electrons in autoionization differs in many aspects from that of photoelectrons in direct ionization. However, the significant effect of autoionization on the photoelectron angular asymmetry parameter β has been noted in the study of photoelectron angular distributions in CO_2 (36, 37).

4. Summary

Using a gas-phase electron scattering spectrometer capable of the multiangle parallel detection of electrons departing from the collision center, we have, with the incident electron energy varying from 20 to 55 eV and the angular range between 18° and 162°, measured the energy and angular distributions of electrons ejected from CO_2 autoionizing Rydberg states lying in the continuum region 15–19 eV. The results show that the ejected electrons arising from diverse autoionizing states are quite sensitive to the low incident electron energies utilized and their yields have strong angular dependence. A careful examination of the ejected electron spectra recorded has led to the identification of some new features not present in the electron energy loss spectra and they have tentatively been assigned. Of all the Rydberg series observed, two of the most prominent are the Henning diffuse and sharp series. It was found that they exhibit remarkably different responses to the alteration of the incident energy and the angle. The different geometries of the Rydberg states and a different mechanism of coupling to the $X^2\Pi_g$ ground ionic state have been considered responsible for such behaviour. We have also noted that there apparently exists fairly strong interaction between the Tanaka–Ogawa Rydberg series and the Henning series, which may result in the change of autoionizing lines in intensity and shape. The present study should provide new and valuable information on the molecular spectroscopy and the dynamic interaction associated with the electron–molecule collision of CO_2.

Acknowledgments

The authors are grateful to M.J. Hubin-Franskin for discussions and suggestions, to L.J. Dubé for reading the manuscript, and to D. Dubé, J. Parent, and S. Chamberland for technical assistance. This work was financially supported in part by the Natural Sciences and Engineering Research Council of Canada (NSERC/CRSNG), Fonds FCAR du Québec, and the Network of Centers of Excellence (NCE) programme. D.R. is a member of the Centre de Recherches sur les Propriétés des Interfaces et la Catalyse (CERPIC) and the Network of Centers of Excellence on Molecular and Interfacial Dynamics (CEMAID/CEDMI).

1. H.S. Henning. Ann. Phys. **13**, 599 (1932).
2. Y. Tanaka, A.S. Jursa, and F.J. LeBlanc. J. Chem. Phys. **32**, 1199 (1960).
3. Y. Tanaka and M. Ogawa. Can. J. Phys. **40**, 879 (1962).
4. E. Lindhom. Ark. Fys. **40**, 125 (1969).
5. I. Reinech, C. Nohre, R. Maripuu, P. Lodin, S.H. Al-Shamma, H. Veenhuizen, L. Karlsson, and K. Siegbahn. Chem. Phys. **78**, 311 (1983).
6. T. Baer and P.M. Guyon. J. Chem. Phys. **85**, 4765 (1986).
7. L.S. Wang, J.E. Reutt, Y.T. Lee, and D.A. Shirley. J. Electron Spectrosc. **47**, 167 (1988).
8. K.E. McCulloh. J. Chem. Phys. **59**, 4250 (1973).
9. R. Freg, B. Gotchev, O.F. Kalman, W.B. Peatman, H. Pollak, and E.W. Schlag. Chem. Phys. **21**, 89 (1977).
10. J. Berkowitz. Photoabsorption, photoionization and photoelectron spectroscopy. Academic Press, New York. 1979.
11. E.N. Lassetre, A. Skerbele, M.A. Dillon, and K.J. Ross. J. Chem. Phys. **48**, 5066 (1968).
12. M. Krauss, S.R. Mielczarek, D. Neumann, and C.E. Kuyatt. J. Geophys. Res. **76**, 3733 (1971).
13. R.I. Hall, A. Chutjian, and S. Trajmar. J. Phys. B: At. Mol. Phys. **6**, L264 (1973).
14. S. Cvejanovic, J. Jureta, and D.C. Cvejanovic. J. Phys. B: At. Mol. Phys. **18**, 2541 (1985).
15. M.J. Hubin-Franskin, J. Delwiche, B. LecLerc, and D. Roy. J. Phys. B: At. Mol. Opt. Phys. **21**, 3211 (1988).
16. C. Fridh, L. Asbrink, and E. Lindholm. Chem. Phys. **27**, 169 (1978).
17. P.M. Dehmer and W.A. Chupka. J. Chem. Phys. **62**, 4525 (1975).
18. M.J. Hubin-Franskin, J. Delwiche, P. Morin, M.Y. Adam, I. Nenner, and P. Roy. J. Chem. Phys. **81**, 4246 (1984).
19. M.J. Hubin-Franskin, J. Delwiche, and P.M. Guyon. Z. Phys. D: At. Mol. Clusters, **5**, 203 (1987).
20. J.A. Baxter, P. Mitchell, and J. Comer. J. Phys. B: At. Mol. Phys. **15**, 1105 (1982).
21. L.C. Lee and D.L. Judge. J. Chem. Phys. **57**, 4443 (1972).
22. J.H.D. Eland and J. Berkowitz. J. Chem. Phys. **67**, 2782 (1977).
23. H. Lefèbvre-Brion and P.W. Field. Perturbation in the spectra of diatomic molecules. Academic Press, New York. 1986.
24. D. Roy, D. Tremblay, and D. Dubé. J. Electron Spectrosc. **62**, 787 (1990); D. Tremblay, D. Dubé, and D. Roy. Rev. Sci. Instrum. **60**, 879 (1989).
25. J. Comer and F.H. Read. J. Electron Spectrosc. **1**, 3 (1972/73).
26. D. Roy and D. Tremblay. Rep. Prog. Phys. **53**, 1621 (1990).
27. R. Carbonneau, E. Bolduc, and P. Marmet. Can. J. Phys. **51**, 505 (1973).
28. B. Leclerc. Ph.D. Thesis, Université Laval (1985).
29. A.L. Smith. Philos. Trans. R. Soc. Lond. A: **268**, 169 (1970).
30. E.D. Poliakoff, J.L. Dehmer, A.C. Parr, and G.E. Leroi. J. Chem. Phys. **77**, 5243 (1982).
31. P.M. Dittman, D. Dill, and J.L. Dehmer. Chem. Phys. **78**, 405 (1983).
32. P.M. Dehmer. J. Chem. Phys. **83**, 24 (1985).
33. G.R. Cook, P.H. Metzger, and M. Ogawa. J. Chem. Phys. **44**, 2935 (1966).
34. A. Giusti-Suzor and H. Lefèbvre-Brion. Phys. Rev. A, **30**, 3057 (1984).

35. P.M. Dehmer, P.J. Miller, and W.A. Chupka. J. Chem. Phys. **80**, 1030 (1984).
36. T.A. Carlson and G.E. McGuire. J. Electron Spectrosc. **1**, 209 (1972).
37. F.A. Grimm, J.D. Allen, Jr., T.A. Carlson, M.O. Krause, D. Mehaffy, P.R. Keller, and J.W. Taylor. J. Chem. Phys. **75**, 92 (1982).

Can. J. Chem. Downloaded from www.nrcresearchpress.com by 195.246.54.202 on 09/08/12
For personal use only.

Structural and substituent effects on the ketene infrared stretching frequency

MICHAEL A. MCALLISTER AND THOMAS T. TIDWELL
Department of Chemistry, University of Toronto, Toronto, ON M5S 1A1, Canada

Received July 18, 1993

This paper is dedicated to Professor John C. Polanyi on the occasion of his 65th birthday

MICHAEL A. MCALLISTER and THOMAS T. TIDWELL. Can. J. Chem. **72**, 882 (1994).

The frequencies and intensities of the ketene asymmetric stretching vibration near 2100 cm^{-1} for a series of substituted ketenes and fulvenones have been calculated using *ab initio* molecular orbital methods. Comparisons of the calculated values with experimentally determined results show reasonably good agreement in most cases, with a typical deviation of ± 10 cm^{-1} between the measured and calculated values. A test of a correlation proposed by Gano and Jacob (Spectrochim. Acta, **43***A*, 1023 (1987)) of the frequencies with substituent field and resonance parameters F and R shows a modest correlation coefficient of 0.86, with no significant dependence on R. These results are consistent with enhancements of ketene infrared absorption frequencies by interaction of substituents with the negative charge density at C_β of ketenes, as indicated by the resonance structure $R\bar{C}H—C{\equiv}O^+$. The calculated intensities I (km/mol) for non-π acceptor substituents are correlated with the group electronegativities X by the relationship $I = 1841.6 - 305.7X$ ($r = 0.94$). The π-acceptor substituents show exaltations of the intensities, and the results are interpreted as showing an enhancement of intensities by electropositive substituents increasing the normal ketene dipole directed towards oxygen, and an opposite effect by π-acceptor substituents delocalizing the negative charge at C_β.

MICHAEL A. MCALLISTER et THOMAS T. TIDWELL. Can. J. Chem. **72**, 882 (1994).

Utilisant des méthodes *ab initio* d'orbitales moléculaires, on a calculé les fréquences et les intensités de la vibration d'élongation asymétrique du cétène près de 2100 cm^{-1} d'une série de cétènes et de fulvénones substitués. Des comparaisons des valeurs calculées avec les valeurs obtenues expérimentalement présentent une bonne corrélation dans la plupart des cas; la déviation typique entre les valeurs calculées et expérimentales est de 10 cm^{-1}. Une évaluation d'une corrélation proposée par Gano et Jacob (Spectrochim, Acta, **43***A*, 1023 (1993)) entre les fréquences et les paramètres F (champ du substituant) et R (résonance) présente un modeste coefficient de corrélation (0,86) et aucune dépendance significative sur R. Ces résultats sont en accord avec les augmentations des fréquences d'absorption des cétènes en infrarouge lorsqui'ils sont soumis à l'influence de substituants portant une densité de charge négative sur le C_β, tel que représenté par la structure de résonance $R\bar{C}HC{\equiv}O^+$. On a établi une corrélation entre les intensités calculées, I (km/mol), pour les substituants accepteurs non-π et les électronégativités de groupe, X; la relation est $I = 1841{,}6 - 305{,}7X$ ($r = 0{,}94$). Les substituants accepteurs-π présentent des augmentations des intensités et on interprète les résultats comme une preuve d'une augmentation des intensités par les substituants électropositifs dû à une augmentation du dipôle normal du cétène dirigé vers l'oxygène et d'un effet opposé par les substituants accepteurs-π qui délocalisent la charge négative sur le C_β.

[Traduit par la rédaction]

Introduction

The characteristic carbonyl stretching frequency in the infrared spectra of ketenes near 2100 cm^{-1} is frequently utilized for the detection of these elusive intermediates (1), and is especially useful because the measurements can be made under a wide variety of conditions necessary for observing the ketenes ranging from the gas phase to matrix isolated samples at low temperatures. Analysis of the infrared spectra and assignment of the principal bands has been carried out for ketene itself (2), and for some haloketenes (3*a*–*d*) and silylketenes (3*e*). *Ab initio* calculations at the MP2 level (2*c*) give good agreement with the experimental IR spectrum of ketene.

Despite the frequent use of IR in ketene detection this technique has seldom been used in ketene identification. One reason for this is that ketenes defy systematic experimental study, because the representative types of ketenes have widely different properties, so that different techniques and conditions are needed for the preparation of different ketenes, and the measurements must often be made *in situ*. Moreover, it is not only often difficult to prepare these transient species and measure their spectra, but the absorption frequencies are highly medium dependent, so that to be useful, data sets must be obtained under the same conditions. For example, Moore and Pimental (2*b*) found the C═O stretch of ketene occurs at 2151, 2142, and 2133 cm^{-1} in the gas phase, an Ar matrix, and the solid, respectively, and values for $CCl_2{=}C{=}O$ of 2160, and 2155 have been found in the gas phase and Ar matrix (3*b*, *d*).

Because of the paucity of consistent data there has not been much progress in the investigation of the effect of substituents on the ketene carbonyl stretching frequencies. This is in contrast to the situation with ketones, where large sets of data are available, and there have been detailed correlation analysis of the effects of substituents on stretching frequencies in both aliphatic and aromatic compounds (4).

Gano and Jacob (5*a*) recently addressed the question of substituent effects on ketene stretching frequencies, and analyzed data for a set of four symmetrically disubstituted ketenes $R_2C{=}C{=}O$ (R = H, Cl, CN, and CH_3) for which stretching frequencies were measured in argon matrices, together with a value estimated for R = CF_3 in the matrix, based on gas phase data. These data were correlated using Hammett-type substituent parameters, specifically the field effect parameter F and the resonance effect parameter R, as originally derived by Swain and Lupton (6), by eq. [1].

$$[1] \quad \nu(cm^{-1}) = 24F + 30R + 2142$$

This limited data set gave a rather good correlation, and this was used to predict stretching frequencies for a number of other ketenes. However, so far it appears that none of these predictions has been checked experimentally. The correlation suggests that the C═O stretching frequency is increased both by inductive and resonance electron withdrawal by the substituents, and this is consistent with the expectation that the resonance con-

Can. J. Chem. Downloaded from www.nrcresearchpress.com by EESC ESCOLA DE ENGENHARIA on 09/08/12
For personal use only.

Can. J. Chem. Downloaded from www.nrcresearchpress.com by EESC ESCOLA DE ENGENHARIA on 09/08/12
For personal use only.

tributor **1***A* of ketenes would be favored by electron acceptors, and would lead to higher frequencies (5*a*). The normal polarity of ketenes is as shown in **1***B*, as shown by the dipole moments, which are enhanced by electropositive groups R, and reduced by electronegative or π-acceptor groups (10a).

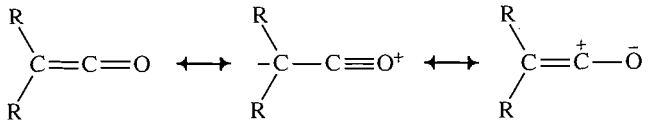

1 **1***A* **1***B*

Other data in support of the hypothesis that stabilization of the resonance structure **1***A* by electron-withdrawing substituents leads to increased infrared stretching frequencies are the reported values in 1,2-dichloroethane of diarylketenes $(4\text{-}XC_6H_4)_2C{=}C{=}O$ of 2096, 2100, and 2109 cm^{-1} for X = MeO, H, and O_2N, respectively (5*b*). The increase in the frequency as the acceptor power increases from MeO to H to O_2N is small, but is in the order expected.

The Swain–Lupton treatment of substituent effects has been criticized (7), but an authoritative recent survey of Hammett substituent parameters (8) utilizes modified values of these constants as consistent with current understanding of the field, and reports values for 530 substituents. However, the lack of sufficient ketene data restricts a thorough test of eq. [1].

The question of the effect of substituents on the intensities of infrared vibrations has also been widely studied, particularly for aromatic ring vibrations (4*a*, 9*a*,*b*), and also for the frequencies of carbonyl groups, alkenes, nitriles, and C—H bonds (4*a*, 9*c*–*e*). However, the relationship between infrared frequencies and intensities has been little explored, and there have been measurements of ketene intensities (3*a*), but no systematic study.

The use of *ab initio* molecular orbital calculations provides an attractive alternative approach to the problem of substituent effects on ketene infrared frequencies and intensities. We have previously applied this method to the calculation of the structure and energies of a large number of ketenes (10*a*–*c*) and have found that the stabilizing effect of substituents on ketenes can be correlated by the substituent group electronegativities (10*d*).

These studies have now been extended to the calculation of the infrared stretching frequencies of a large number of ketenes, including mono- and disubstituted species, and some fulvenones and cycloalkylideneketenes (10*b*) for which frequencies have been determined experimentally. An advantage of this approach is that a large number of ketenes of diverse structural types can be considered, and the calculated values all apply to the same medium, namely the gas phase. The validity of the calculations can be tested by comparison to experimental values, for which a reasonable number of gas phase values are available, and the intensities of the absorptions can also be calculated.

Computational methods

Ab initio molecular orbital calculations were carried out for a variety of ketenes using the GAUSSIAN 90 and GAUSSIAN 92 (11*a*) series of programs on Hewlett-Packard 9000-750 and IBM RS/6000-530 minicomputers. All geometries were gradient optimized using the split-valence 6-31G* basis set (11*b*,*c*). There were no geometrical constraints during the optimization, except in the case of fulvenones, for which the ring systems were constrained to planarity. The orders (number of negative diagonal elements of the Hessian matrix) of all critical points were determined at the HF/6-31G* level by analytical differential of the restricted Hartree–Fock wave function and were found to be zero in all cases except for difluorotrifulvenone, divinylketene, heptafulvenone, and trimethyleneketene, which all have order 1 (one). Geometries optimized at MP2/6-31G* were also order checked at that level of theory. The frozen core approximation was not used.

Results and discussion

As a test of the reliability of the calculations, in Table 1 are listed the calculated frequencies for disubstituted and monosubstituted ketenes for which comparative experimental data are available (12, 13), or for which frequencies were predicted by Gano and Jacob (5*a*). Also included for comparison are frequencies calculated by molecular mechanics (MM3) (5*c*). In Table 2 are listed the frequencies calculated at the HF/6-31G* level for 27 monosubstituted ketenes, as well as their calculated intensities. For 19 of these the frequencies for geometries optimized at the MP2/6-31G* level are also given. In Table 3 are listed calculated experimental frequencies for fulvenones, cycloalkylideneketenes, and model compounds.

Comparison of the calculated frequencies for distributed ketenes to the available experimental values (Table 1) show that for ketenes $M_2C{=}C{=}O$ (M = H, Cl, CN, and Me) there is rather good agreement, with the largest deviation (17 cm^{-1}) for M = Cl. However, for M = F and M = NH_2 the deviations of the *ab initio* calculated frequencies from those calculated from their correlation by Gano and Jacob (5*a*) are large (73 and 54 cm^{-1}, respectively). The two methods are not in agreement for these ketenes, and while the *ab initio* methods give satisfactory agreement for the available experimental data for both monosubstituted (*vide infra*) and disubstituted ketenes, until experimental data become available it cannot be determined which method has the best predictive value for these two cases.

There are nine monosubstituted ketenes for which comparisons of the calculated frequencies with gas phase experimental frequencies can be made, and one other for which a solution measurement is available (Table 1). The differences range from 0 to 30.7 cm^{-1}, with an average deviation of 13 cm^{-1}.

There are five examples in Table 1 for which comparisons are available with frequencies calculated by MM3 molecular mechanics calculated values (5*c*), and for all but $Me_2C{=}C{=}O$ these agree to within 12 cm^{-1}. However, the MM3 parameters were adjusted to fit values derived from *ab initio* MP2/4-31G** calculations, except for $Me_2C{=}C{=}O$, and so the agreement is not unexpected.

In Table 3 there are three conjugated fulvenone examples in which the calculated and experimental values can be compared, and in all cases the agreement is excellent. Thus for pentafulvenone two bands are observed experimentally due to matrix effects (12*a*), at 2130 and 2133 cm^{-1}, while the calculated position is 2125 cm^{-1}. For heptafulvenone the calculated and experimental values are both 2103 cm^{-1}, although independent experimental structure proof of the identity of the species giving the absorption at 2103 cm^{-1} is lacking (12*d*). The theoretical and experimental (in a matrix) frequencies determined by others (12*e*) for the thiafulvenone ylide **4** give excellent agreement.

Dimethyleneketene (**2**) (12*b*,*c*) and trimethyleneketene (**3**) (12*c*) each show two bands experimentally, with a 10 cm^{-1} dif-

TABLE 1. Comparison of *ab initio* calculated IR stretching frequencies and observed valeus

$M_2C{=}C{=}O$			$MCH{=}C{=}O$			
M	$\nu(cm^{-1})_{calc}$ [a]	$\nu(cm^{-1})_{obs}$ [b]	M	$\nu(cm^{-1})_{calc}$ [a]	$\nu(cm^{-1})_{obs}$ [b]	Reference
H	2140.6	2142	H	2140.6	2151[f]	2*b*
	(2135.5)[c]			(2130.2)[e]		
F	2226.3	(2142)[d]	F	2168.9	2142.2[f]	3*a*
Cl	2172	2155		(2167.1)[c]		
	(2160.5)[c]			(2118.3)[e]		
CN	2181.5	2180	Cl	2159.1	2141.4[f]	3*a*
Me	2120.4	2128		(2155.1)[c]		
	(2182.8)[c]			(2127.2)[e]		
NH_2	2130.0	(2076)[d]	CH_3	2132.0	2130[g]	13*a*
				(2120.0)[e]	2132[f,h]	
			$CH_2{=}CH$	2124.6	2130	13*c*
				(2112.9)[e]		
			Ph	2119.3	(2250)[i]	13*d*
			HO	2145.5	2136[j]	13*e*
				(2109.7)[e]		
			SiH_3	2112.2	2112[k]	3*e*
				(2116.5)[e]		
			O=CH	2142.2	2137[f,l]	13*f*
				(2116.3)[e]		
			c-Pr	2130.3	2110[m]	13*g*

[a] HF/6-31G* scaled by 0.9.
[b] Matrix, ref. 5*a*, unless indicated.
[c] Calculated by MM3, ref. 5*c*.
[d] Predicted from correlation derived in ref. 5*a*.
[e] MP2/6-31G*.
[f] Gas phase.
[g] In THF.
[h] EtCH=C=O, ref. 13*b*.
[i] Derived from the photoelectron spectrum.
[j] MeO (matrix).
[k] Me_3Si.
[l] $O{=}C(CH_3)$.
[m] 2,2-Dimethylcyclopropyl (in pentane).

Can. J. Chem. Downloaded from www.nrcresearchpress.com by EESC ESCOLA DE ENGENHARIA on 09/08/12
For personal use only.

ference between independent measurements for **2** (Table 3). These are matrix values and it has also been observed that matrix values change with temperature, and so it is difficult to select a standard basis for comparison. The theoretically determined values are within 18 and 7 cm^{-1} for the highest of the experimental values.

In total 17 comparisons between experimental and calculated IR frequencies are available, with an average deviation of 12.9 cm^{-1}. It may be concluded that the *ab initio* calculated values are of significant predictive value for the determination of ketene frequencies within these limits, and can be utilized for the examination of the origin of substituent effects on the frequencies.

Correlation of the frequencies calculated at the HF/6-31G* level with the field and resonance parameters of the substituents (8) is given by eq. [2], with a correlation coefficient $r = 0.87$. The coefficient of the resonance term is indistinguishable from zero within the precision of the correlation, and field effects alone give an equally good correlation, eq. [3] ($r = 0.86$), as shown in Fig. 1. For the smaller set of substituents for which frequencies were obtained for MP2/6-31G* optimized geometries (Table 2) the correlation of the frequencies with the field effect parameter was much poorer.

$$[2] \quad \nu = 2119 + 91(\pm 13)F - 6(\pm 9)R$$

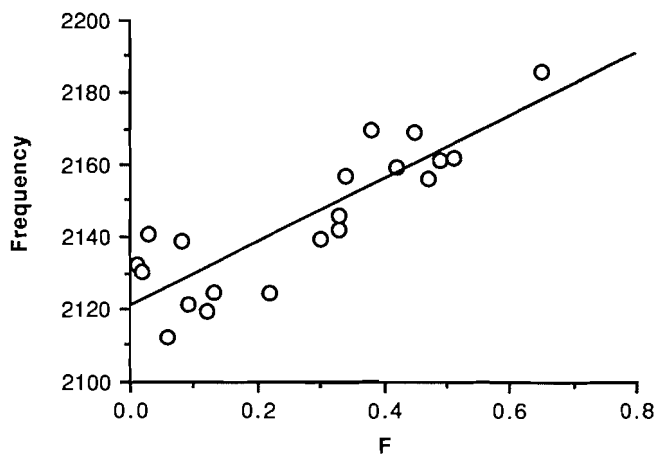

FIG. 1. Correlation of ketene HF/6-31G* calculated stretching frequencies (cm^{-1}) with substituent field effect constants *F*.

$$[3] \quad \nu = 2120 + 88F$$

We have previously (10*a*) used group electronegativities X_{BE} (10*d*) for the correlation of substituent effects on ketene stabilization, and in Fig. 2 a plot of ketene stretching frequencies versus group electronegativities is shown. This plot permits the inclusion of the additional groups Li, Na, BeH,

Can. J. Chem. Downloaded from www.nrcresearchpress.com by EESC ESCOLA DE ENGENHARIA on 09/08/12
For personal use only.

TABLE 2. Calculated infrared ketene stretching frequencies (ν), intensities (I), and substituent parameters X, F, and R for MCH=C=O

M	ν(cm^{-1})[a,b]	ν(cm^{-1})[c,d]	I(km/mol)[a]	I(km/mol)[c]	X[e]	F[f]	R[f]
H	2140.6	2130.2	917.5	403.4	2.20	0.03	0.00
Li	2023.2	2047.6	1527.0	855.9	1.00		
BeH	2100.2	2096.8	1232.1	751.7	1.47		
BH_2	2119.2	2111.6	1341.2	702.5	1.93		
CH_3	2132.0	2120.0	996.9	440.3	2.56	0.01	−0.18
NH_2	2139.0	2096.8	885.0	361.6	3.10	0.08	−0.74
OH	2145.5	2109.7	735.8	284.4	3.64	0.33	−0.70
F	2168.9	2118.3	600.0	208.9	4.00	0.45	−0.39
Na	2010.4	1985.7	1549.3	610.7	1.00		
MgH	2066.7	2083.0	1492.2	832.3	1.33		
AlH_2	2096.8	2099.8	1457.0	815.7	1.62		
SiH_3	2112.2	2116.5	1252.8	684.7	1.91	0.06	0.04
PH_2	2121.1	2113.9	1220.4	596.4	2.17	0.09	−0.04
SH	2139.1	2121.2	1122.3	489.2	2.63	0.30	−0.15
Cl	2159.1	2127.2	925.5	353.6	3.05	0.42	−0.19
CF_3	2169.7		1253.5		2.71	0.38	0.16
c-Pr	2130.3		1184.9		2.57	0.02	−0.23
HC≡C	2124.6	2128.4	1232.1	545.7	2.66	0.22	0.01
HC=O	2142.1	2116.3	1171.9	623.2	2.60	0.33	0.09
N=O	2161.2	2145.0	1235.3		3.12	0.49	0.42
NO_2	2185.9		1054.3		3.22	0.65	0.13
CO_2H	2157.0		1101.6		2.63	0.34	0.11
CH_2=CH	2124.6	2112.9	1528.0	665.8	2.58	0.13	−0.17
CN	2162.2		1253.5		2.69	0.51	0.15
NC	2156.0		1165.3		3.26	0.47	0.02
C_6H_5	2119.3		1494.5		2.58	0.12	−0.13
CH_2=C=CH	2126.1		1711.3		2.58		

[a]HF/6-31G*//HF/6-31G*.
[b]Scaled by 0.9.
[c]MP2/6-31G*//MP2/6-31G*.
[d]Scaled by 0.95.
[e]Group electronegativity, ref. 10*d*.
[f]Field and resonance parameters, ref. 8.

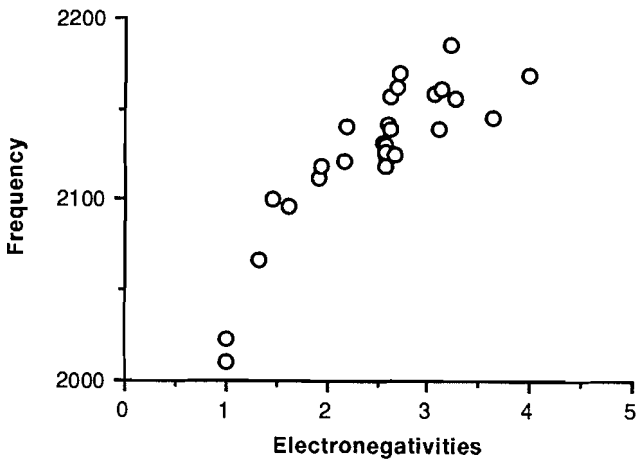

FIG. 2. Plot of ketene HF/6-31G* calculated stretching frequencies (cm^{-1}) versus group electronegativities X.

MgH, BH_2, and AlH_2, for which F and R parameters are not available. A definite trend is seen, but there is no useful linear correlation.

A good correlation is found between the infrared intensities **I** and group electronegativities for the first 17 entries in Table 2, which are generally non-π acceptor substituents. For the HF/6-31G* level calculations the correlation is I (kcal/mol) = 1841.6 − 305.7X, r = 0.94 (Fig. 3), while at the MP2/6-31G* level, for 15 substituents, the correlation is I (kcal/mol) = 1128.3 − 240.8X, r = 0.985. It was not practical to carry out calculations at the higher level for many additional substituents. This enhancement of the IR intensity by electropositive substituents may be attributed to the interaction of the substituent with the asymmetrical vibration of the C=C=O moiety. This vibration, depicted as **2***A* and **2***B*, causes a large change in the dipole moment during the vibration, and this gives rise to the strong ketene band (4*a*). The normal dipole moment of ketones is toward the negatively charged oxygen as represented by resonance structure **1***B*, which corresponds to the vibrational structure **2***B*, and electropositive substituents would augment this interaction.

2*A* **2***B*

Inclusion of the latter 10 substituents in Table 2 in the plot of intensity versus electronegativity results in positive deviations of the calculated intensities from the defined correlation, as shown by closed circles on Fig. 3. These substituents (NO_2, NO, NC, CN, HC≡C, CH_2=CH, CH_2=C=CH, CO_2H, CHO, and Ph) can act as π acceptors, which can interact strongly with the vibrational structure **2***A*, which has enhanced

TABLE 3. HF/6-31G* *ab initio* calculated IR frequencies (cm^{-1}) and matrix measured values (in parentheses)

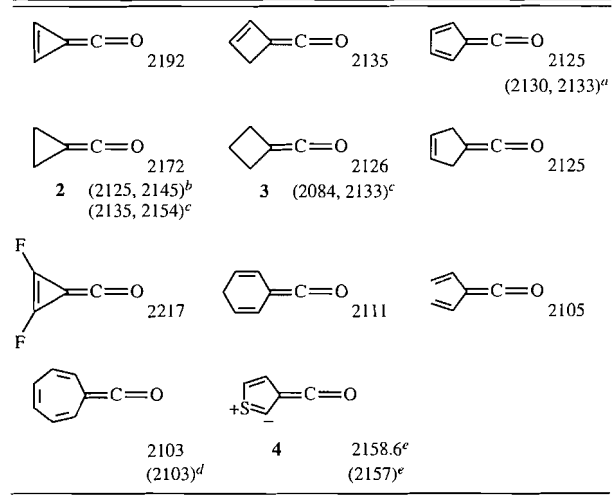

[a]Reference 12*a*.
[b]Reference 12*b*.
[c]Reference 12*c*.
[d]Reference 12*d*.
[e]Reference 12*e*.

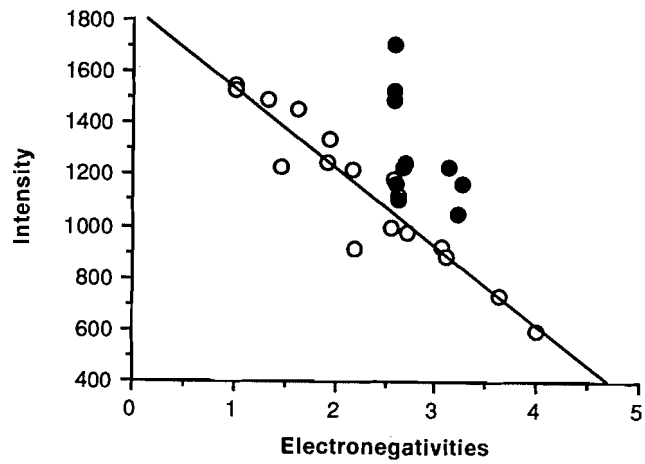

FIG. 3. Correlation of ketene HF/6-31G* calculated intensities (Int. km/mol) with group electronegativities *X* (open circles, for first 17 entries in Table 2; closed circles, remaining 10 entries).

C—C single bond character, and a polarity corresponding to **1***A*, with positive charge on oxygen and negative charge on C_β. The π acceptor group could delocalize this negative charge as in the structure **3** for vinylketene, which has been proposed (13*c*) as leading to the low observed dipole moment of this ketene. Such an interaction could enhance the dipole moment change during the vibration, and thereby increase the intensity.

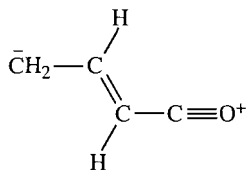

3

Thus the ketene vibrational intensities are enhanced by both electropositive and by π-acceptor substituents, and the same effects have been proposed to stabilize ketenes (10*a*). There is no strong correlation of the infrared intensities and frequencies, and as noted above the field effect of the substituents appears to be a major contributor to the latter. There is also no correspondence between the *ab initio* calculated intensities and similarly calculated dipole moments, which have been reported previously (10*a*), as the former are determined by the changes in dipole moment during the vibration (4*a*).

In conclusion *ab initio* calculated frequencies for the characteristic vibrations of both monosubstituted and disubstituted ketenes give reasonable predictions of the experimental values. A test of a reported correlation of ketene frequencies with substituent field and resonance parameters shows that field parameters alone are sufficient for the correlation, which is however of limited predictive value. There is a good correlation of calculated intensities with substituent group electronegativities, and there is a further effect of enhancement of the intensities by π acceptor groups.

Acknowledgement

Financial support by the Natural Sciences and Engineering Research Council of Canada is gratefully acknowledged.

1. (*a*) J.W. Munson. *In* The chemistry of ketenes, allenes and related compounds. *Edited by* S. Patai. Wiley, New York. 1980. Chap. 5; (*b*) W. Runge. Prog. Phys. Org. Chem. **13**, 315 (1981).
2. (*a*) W.F. Arendale and W.H. Fletcher, J. Chem. Phys. **26**, 793 (1956); (*b*) C.B. Moore and G.C. Pimentel. Chem. Phys. **38**, 2816 (1963); (*c*) J. Leszczynski and J.S. Kwiatkowski. Chem. Phys. Lett. **201**, 79 (1993); (*d*) J.L. Duncan, A.M. Ferguson, J. Harper, and K.H. Tonge. J. Mol. Spectrosc. **125**, 196 (1987).
3. (*a*) G. Davidovics, M. Monnier, and A. Allouche. Chem. Phys. **150**, 395 (1991); (*b*) M.C.L. Gerry, W. Lewis-Bevan, and N.P.C. Westwood. Can. J. Chem. **63**, 676 (1985); (*c*) V.N. Khabashesku, A.K. Mal'tsev, I. Bertoti, T. Sekei, and O.M. Nefedov. Dokl. Akad. Nauk SSSR, **293**, 924 (1987); (*d*) M. Torres, J. Ribo, A. Clement, and O.P. Strausz. Nouv. J. Chim. **5**, 351 (1981); (*e*) L.L. Shchukovskaya, A.I. Kol'tsov. A.N. Lazarev, R.I. Pal'chik. Dokl. Akad. Nauk SSSR, **179**, 892 (1968).
4. (*a*) K. Kiss-Eröss. *In* Comprehensive analytical chemistry. Vol. VI. *Edited by* G. Svehla. Elsevier, New York. 1976. Chap. 6; (*b*) R.D. Topsom. Prog. Phys. Org. Chem. **16**, 193 (1987); (*c*) C. Laurence, M. Berthelot, M. Lucon, M. Helbert, D.G. Morris, and J.-F. Gal. J. Chem. Soc., Perkin Trans. 2, 705 (1984); (*d*) J.-F. Gal, D.G. Morris, and M. Rouillard. J. Chem. Soc., Perkin Trans. 2, 1287 (1992); (*e*) R.N. Jones, W.F. Forbes, and W.A. Mueller. Can. J. Chem. **35**, 504 (1957); (*f*) T.G. Traylor and J.C. Ware. J. Am. Chem. Soc. **89**, 2304 (1967); (*g*) R. Stewart and K.C. Teo. Can. J. Chem. **58**, 2491 (1980); (*h*) P.G. Gassman and T.T. Tidwell. Acc. Chem. Res. **16**, 279 (1983).
5. (*a*) J.E. Gano and E.J. Jacob. Spectrochim. Acta, **43A**, 1023 (1987); (*b*) A. Melzer, and E.F. Jenny. Tetrahedron Lett. 4503 (1968); (*c*) E.L. Stewart and J.P. Bowen. J. Comput. Chem. **13**, 1125 (1992).
6. (*a*) C.G. Swain and E.C. Lupton, Jr. J. Am. Chem. Soc. **90**, 4328 (1968); (*b*) G.C. Swain, S.H. Unger, N.R. Rosenquist, and M.S. Swain. J. Am. Chem. Soc. **105**, 492 (1983); (*c*) C.G. Swain. J. Org. Chem. **49**, 2005 (1984).
7. (*a*) W.F. Reynolds and R.D. Topsom. J. Org. Chem. **49**, 1989 (1984); (*b*) A.J. Hoefnagel, W. Oosterbeek, and B.M. Wepster. J. Org. Chem. **49**, 1993 (1984); (*c*) M. Charton. J. Org. Chem. **49**, 1997 (1984).
8. C. Hansch, A. Leo, and R.W. Taft. Chem. Rev. **91**, 165 (1991).
9. (*a*) R.T.C. Brownlee, R.E.J. Hutchinson, A.R. Katritzky, T.T. Tid-

Can. J. Chem. Downloaded from www.nrcresearchpress.com by EESC ESCOLA DE ENGENHARIA on 09/08/12
For personal use only.

well, and R.D. Topsom. J. AM. Chem. Soc. **90**, 1757 (1968); (*b*) A.R. Katritzky and R.D. Topsom. Angew. Chem. Intern. Ed. Engl. **9**, 87 (1970); (*c*) L.W. Deady, P.M. Harrison, and R.D. Topsom. Spectrochim. Acta, **31A**, 1671 (1975); (*d*) O. Exner and K. Bocek. Coll. Czech. Chem. Commun. **38**, 50 (1973); (*e*) G.P. Ford, A.R. Katritzky, and R.D. Topsom. J. Chem. Soc. Perkin Trans. 2, 1378 (1975).

10. (*a*) L. Gong, M.A. McAllister, and T.T. Tidwell. J. Am. Chem. Soc. **113**, 6021 (1991); (*b*) M.A. McAllister and T.T. Tidwell. J. Am. Chem. Soc. **114**, 5362 (1992); (*c*) A.D. Allen, J. Andraos, A.J. Kresge, M.A. McAllister, and T.T. Tidwell. J. Am. Chem. Soc. **14**, 1878 (1992); (*d*) R.J. Boyd and S.L. Boyd. J. Am. Chem. Soc. **114**, 1652 (1992).
11. (*a*) M.J. Frisch, G.W. Trucks, M. Head-Gordon, P.M.W. Gill, M.W. Wong, J.B. Foresman, B.G. Johnson, H.B. Schlegel, M.A. Robb, E.S. Replogle, R. Gomperts, J.L. Andres, K. Raghavachari, J.S. Binkley, C. Gonzales, R.L. Martin, D.J. Fox, D.J. DeFrees, J. Baker, J.J.P. Stewart, and J.A. Pople. GAUSSIAN 92, Gaussian Inc., Pittsburg, PA, 1992; (*b*) W.J. Hehre, L. Radom, P. von R. Schleyer, and J.A. Pople. *Ab initio* molecular orbital theory. Wiley–Interscience, New York 1986; (*c*) P.C. Hariharan and J.A. Pople. Theoret. Chim. Acta, **28**, 213 (1973).
12. (*a*) M.S. Baird, I.R. Dunkin, N. Hacker, M. Poliakoff, and J.J. Turner. J. Am Chem. Soc. **103**, 5190 (1981); (*b*) G.J. Baxter, R.F.C. Brown, F.W. Eastwood, and K.J. Harrington. Tetrahedron Lett. 4283 (1975); (*c*) R. Leung-Toung and C. Wentrup, J. Org. Chem. **57**, 4850 (1992); (*d*) R.J. McMahon and O.L. Chapman. J. Am. Chem. Soc. **108**, 1713 (1986); (*e*) J.H. Teles, B.A. Hess, Jr., and L.J. Schaad. Chem. Ber. **125**, 423 (1992).
13 (*a*) C.C. McCarney and R.S. Ward. J. Chem. Soc. Perkin Trans. 1, 1600 (1975); (*b*) J.W. Coomber, J.N. Pitts, Jr., and R.R. Schrock. Chem. Commun. 190 (1968); (*c*) R.D. Brown, P.D. Godfrey, and M. Woodruff. Austr. J. Chem. **32**, 2103 (1979); (*d*) R. Sammynaiken and N.P.C. Westwood. J. Chem. Soc. Perkin Trans. 2, 1987 (1989); (*e*) R. Leung-Toung and C. Wentrup. Tetrahedron, **48**, 7641 (1992); (*f*) D.W. Emerson, R.L. Titus, and R.M. Gonzalez. J. Org. Chem. **56**, 5301 (1991); (*g*) W.C. Agosta and A.B. Smith, III. J. Am. Chem. Soc. **93**, 5513 (1971).

Can. J. Chem. Downloaded from www.nrcresearchpress.com by EESC ESCOLA DE ENGENHARIA on 09/08/12
For personal use only.

The dynamics of the reaction of $O(^1D)$ with HBr studied by crossed molecular beams and time-resolved Fourier transform spectroscopy

N. BALUCANI, L. BENEVENTI, P. CASAVECCHIA, AND G.G. VOLPI
Dipartimento di Chimica, Università di Perugia, 06100 Perugia, Italy

AND

E.J. KRUUS AND J.J. SLOAN
Department of Chemistry, University of Waterloo, Waterloo, ON N2L 3G1, Canada

Received July 13, 1993

This paper is dedicated to Professor John C. Polanyi on the occasion of his 65th birthday

N. BALUCANI, L. BENEVENTI, P. CASAVECCHIA, G.G. VOLPI, E.J. KRUUS and J.J. SLOAN. Can. J. Chem. **72**, 888 (1994).

The reaction $O(^1D)$ + HBr has been investigated by the crossed molecular beams and infrared chemiluminescence methods in an effort to characterize the dynamics of both possible reactive channels. The angular and velocity distribution of the BrO product from the $O(^1D)$ + HBr → BrO + H pathway have been obtained in crossed beam experiments at collision energies, E_c, of 5.0 and 14.0 kcal/mol. The product center-of-mass angular distribution is found to be almost backward–forward symmetric at both E_c, with backward scattering being slightly favored, from which it is deduced that two processes contribute to this channel: a dominant one occurring via formation of a long-lived complex, following $O(^1D)$ insertion, and another one occurring via direct abstraction of the halogen atom and giving rise to a rebound dynamics. The large fraction (≈50%) of available energy released into translation indicates the existence of a potential barrier for H-displacement in the exit channel. From energy and angular momentum conservation arguments, it is inferred that BrO is formed rotationally very hot in the lowest vibrational levels of both $^2\Pi_{3/2}$ and $^2\Pi_{1/2}$ electronic states. The initial vibrational distribution of the OH product from the $O(^1D)$ + HBr → OH + Br channel has been measured using fast time-resolved Fourier transform spectroscopy. The vibrational distribution is strongly inverted, from which it is deduced that the HOBr intermediate dissociates very rapidly, before energy randomization occurs. A lower limit to the branching ratio of the relative cross sections for the BrO + H and OH + Br channels is derived ($\sigma(BrO + H)/\sigma(OH + Br) \geq 0.16 \pm 0.07$) and compared to recent bulk work. The dynamical results for the overall reaction are discussed with reference to the relevant singlet and triplet potential energy surfaces and possible molecular configurations involved. Comparison with the dynamics of the ground state reaction $O(^3P)$ + HBr → OH + Br is carried out also, to examine the effect of electronic excitation on the dynamics of the reactions of atomic oxygen with hydrogen halides.

N. BALUCANI, L. BENEVENTI, P. CASAVECCHIA, G.G. VOLPI, E.J. KRUUS et J.J. SLOAN. Can. J. Chem. **72**, 888 (1994).

Dans le but de caractériser les dynamiques des deux vois réactionnelles possibles, on a étudier la réaction $O(^1D)$ + HBr par des méthodes de faisceaux moléculaires croisés et de chimiluminescence infrarouge. On a obtenu les distributions angulaires et de la vélocité du produit BrO provenant de la voie $O(^1D)$ + HBr → BrO + H à l'aide des expériences de faisceaux croisées, à des énergies de collision, E_c, de 5,0 et 14,0 kcal/mol. On a trouvé qu'aux deux E_c la distribution du masse du produit est pratiquement symétrique pour les deux directions même si la diffusion vers l'avant est légèrement favorisée; on en déduit que les deux processus contribuent à cette voie: un processus dominant qui se produit par la formation d'un complexe de longue durée après l'insertion du $O(^1D)$ et un autre qui se produit par un enlèvement direct de l'atome d'halogène et qui donne lieu à une dynamique de rebondissement. La plus grande partie de l'énergie disponible (environ 50%) est transmise sous forme de translation et ceci suggère l'existence d'une barrière de potentiel pour le déplacement du H dans la voie de sortie. Sur la base d'arguments relatifs à la conservation de l'énergie et du moment angulaire, on en déduit que le BrO se forme rotationnellement très chaud dans le états de vibration les plus bas des états électroniques $^2\Pi_{3/2}$ et $^2\Pi_{1/2}$. On a mesuré la distribution vibrationnelle initiale du OH produit par la voie $O(^1D)$ + HBr → OH + Br en faisant appel à de la spectroscopie par transformation de Fourier rapide et résolue en fonction du temps. La distribution vibrationnelle est fortement inversée et, sur cette base, on déduit que l'intermédiaire HOBr se dissocie très rapidement, avant qu'une distribution au hasard ne se produise. On a déduit une limite inférieure pour le rapport des branchements des sections droites relatives des voies BrO + H et OH + Br ($\sigma(BrO + H)/\sigma(OH + Br) \geq 0{,}16 \pm 0{,}07$) et on l'a comparée à celle obtenue au cours d'un travail récent. On discute des résultats dynamiques de la réaction globale en faisant référence aux surfaces d'énergie potentielle singulet et triplet appropriées et aux configurations moléculaires qui pourraient être impliquées. Afin de pouvoir examiner l'effet de l'excitation électronique sur la dynamique des réactions de l'oxygène atomique avec les halogénures d'hydrogène, on a aussi effectué une comparaison avec la dynamique de la réaction de l'état fondamental $O(^3P)$ + HBr → OH + Br.

[Traduit par la rédaction]

Introduction

The reactions of atomic oxygen, both in the ground state $O(^3P)$ and the first electronically excited state $O(^1D)$, with hydrogen halides are of interest in determining the impact of halogen compounds on the chemistry of the stratosphere, particulary with regard to the ozone layer. Also, these reactions occur in the combustion chemistry of halogenated compounds, for example in their use as fire extinguishers. From a fundamental point of view, they comprise a class of three-atom reactions which are amenable to detailed experimental and theoretical investigation. While rate constants as a function of temperature have been measured for the series of the $O(^3P)$ + HX (X = Cl, Br, I) reactions (1–5), only the room temperature rate constants have been determined for the reactions $O(^1D)$ + HCl, HBr, and HF (6, 7). Upon electronic excitation, the rate constant at room temperature increases by six and four orders of magnitude for HCl and HBr, respectively. The reactions of $O(^1D)$ with most compounds occur with near gas kinetic frequency, including those with halogenated molecules (8, 9). This is due to the fact that $O(^1D)$ reactions take place on singlet potential energy sur-

Can. J. Chem. Downloaded from www.nrcresearchpress.com by 195.246.54.202 on 09/08/12
For personal use only.

Can. J. Chem. Downloaded from www.nrcresearchpress.com by 195.246.54.202 on 09/08/12
For personal use only.

faces with virtually zero activation energy, in contrast to $O(^3P)$ reactions which proceed on triplet surfaces with significant activation energies.

While the microscopic dynamics of $O(^3P)$ reactions with simple molecules have been investigated for a number of years, studies on the reactions $O(^3P)$ + HX (X = Cl, Br) have been reported only recently by Zare and co-workers (10, 11). In the series $O(^1D)$ + HX, only studies on the reaction dynamics with HCl have been reported (12–15). The reactions $O(^3P, ^1D)$ + HCl have also received significant theoretical attention (16*a–c*). No dynamical information is available on the next reaction of the series, namely $O(^1D)$ + HBr.

Dynamical studies of $O(^1D)$ reactions with simple molecules address the important issue of the role of electronic excitation on reaction dynamics. While there has been a long-standing interest in the collisional removal rates of electronically excited atoms (17), only recently has the effect of atomic electronic excitation on the dynamics of A + BC reactions been tackled in crossed beams, using laser excitation of alkali and alkali-earth atoms, in a series of elegant crossed beam experiments by Lee and co-workers (18) and other researchers (19). There has been less work on this effect for non-metal atoms in A + BC reactions. A direct comparative study for the reaction $O(^3P, ^1D)$ + H_2S using crossed beams has been reported recently (20, 21). In this context, new dynamical studies of $O(^1D)$ reactions alone can provide the basis for indirect comparisons for those cases where dynamical studies involving $O(^3P)$ are already available. This is the case of the reaction between atomic oxygen and hydrogen bromide to be examined in the present report.

Bromine contributes significantly to the loss of stratospheric ozone. It is believed to account for nearly one third of the yearly Antarctic ozone loss in the austral spring (22) and for a sizeable fraction of the mid-latitude ozone decline over the last decade (23). The reason for the high contribution of bromine in spite of its much lower (about 1/100) concentration with respect to chlorine is that it is predominantly in "active" forms (compounds which react with ozone directly) in the stratosphere whereas Cl is often in the form of inactive, or "reservoir" compounds. For example, reactions with H_2 and CH_4 which convert active Br into HBr are endoergic, and reservoir molecules such as HBr and $BrONO_2$ are much less stable than the corresponding Cl-containing molecules. Current atmospheric models suggest that the dominant form of bromine in the stratosphere is BrO, a form catalytically active towards ozone destruction. Formation of BrO is a likely pathway in the reactions of $O(^1D)$ with bromocarbons, following direct abstractions or insertion (24). These reactions are faster than the analogous ones with chlorocarbons. BrO formation can arise from the reaction of $O(^1D)$ with HBr also, where the HBr comes from UV photoelimination processes involving hydrobromocarbons.

The reaction of $O(^1D)$ with HBr can be considered prototypical of the reactions of $O(^1D)$ with brominated compounds. The reaction can proceed via two competing pathways:

$$O(^1D) + HBr \rightarrow \begin{cases} \rightarrow OH + Br & \Delta H_0^0 = -60.5 \text{ kcal/mol} \quad [1a] \\ \rightarrow BrO + H & \Delta H_0^0 = -14.0 \text{ kcal/mol} \quad [1b] \end{cases}$$

Also, there is a physical quenching channel:

$$O(^1D) + HBr \rightarrow O(^3P) + HBr \qquad \Delta H_0^0 = -45.4 \text{ kcal/mol} \quad [1c]$$

All products of reaction [1] are catalytically active species in ozone chemistry. A single occurrence of this reaction can initiate the two catalytic cycles (25):

$$\begin{aligned} OH + O_3 &\rightarrow HO_2 + O_2 \\ HO_2 + O &\rightarrow OH + O_2 \\ \hline \textit{net}: \; O_3 + O &\rightarrow 2O_2 \end{aligned}$$

and

$$\begin{aligned} Br + O_3 &\rightarrow BrO + O_2 \\ BrO + O &\rightarrow Br + O_2 \\ \hline \textit{net}: \; O_3 + O &\rightarrow 2O_2 \end{aligned}$$

each of which removes a molecule of ozone and regenerates the reagent radical on each occurrence of the cycle. Furthermore, BrO from reaction [1*b*] can disproportionate (26):

$$BrO + BrO \rightarrow BrO_2 + Br$$

$$BrO + BrO \rightarrow Br_2 + O_2$$

where the unstable BrO_2 species decomposes to Br + O_2 and Br_2 is readily photolyzed to atomic bromine. Therefore, both reactions convert BrO to Br, which starts the catalytic cycle again. Bromine atoms are also regenerated from the very rapid reaction with NO (26):

$$BrO + NO \rightarrow Br + NO_2$$

The bromine–chlorine radical coupling reaction

$$BrO + ClO \rightarrow Br + ClO_2$$

is also important in the stratospheric budget of halogenated species (27). Finally, H-atoms from reaction [1*b*] can react rapidly with ozone (28):

$$H + O_3 \rightarrow OH + O_2$$

creating catalytically active OH.

A recent kinetic study (7) has established that the total rate constant for $O(^1D)$ removal by HBr is very large ($k_{298} = 1.48 \times 10^{-10}$ cm^3 molecule^{-1} s^{-1}) and has estimated the branching ratio for reaction [1*a*] and [1*b*] to be $k(1b)/k(1a) \leq 0.05$. The finding that the H-displacement pathway is a minor channel in the reaction of $O(^1D)$ with HBr is somewhat surprising since the analogous reaction with HCl was found to proceed with a similar rate, but the corresponding of channel [1*b*] was estimated (7, 15) to account for about one third of the overall reaction.

Once the total rate constant is established, it becomes important to determine the branching ratio among the possible reaction pathways and the detailed dynamics of the overall reaction. Knowledge of the energy partitioning behavior of the possible reaction channels is important, because the fate of the products in subsequent reactions depends to a large extent upon their state of excitation. For instance, vibrationally excited hydroxyl radicals can undergo reactions with ozone which are not energetically accessible to ground state OH:

$$OH\,(v = 3) + O_3 \rightarrow OH(v = O) + O(^3P) + O_2$$

and

Can. J. Chem. Downloaded from www.nrcresearchpress.com by 195.246.54.202 on 09/08/12
For personal use only.

$$OH\ (v = 1) + O_3 \rightarrow H + 2O_2$$

Finally, the electronic to vibrational energy transfer occurring in the physical quenching channel creates vibrationally excited HBr which can undergo subsequent reactions as well.

This analysis indicates that a dynamical study of reaction [1] may be very useful from both practical and fundamental points of view.

In this work, we report the results of the first direct dynamical investigation of reaction [1]. We employ two sophisticated complementary experimental techniques: the fast time-resolved Fourier-transform infrared chemiluminescence method is used to unravel the dynamics of the H-abstraction channel [1*a*] leading to OH formation, while the crossed molecular beams scattering method with mass spectrometric detection is used to characterize the dynamics of the H-displacement channel [1*b*], which leads to the formation of BrO. The latter also provides an estimate of the lower limit for the ratio of the cross sections for branching into channels [1*b*] and [1*a*]. We found it essential to use both of these powerful and complementary techniques to obtain a complete picture of the reaction dynamics of $O(^1D)$ with HBr. In this context, we note that the combination of molecular beams and low pressure infrared chemiluminescence techniques has provided much of the basis for our present understanding of molecular reaction dynamics. This was recognized by the award of the 1986 Nobel prize for chemistry to D.R. Herschbach, Y.T. Lee, and J.C. Polanyi. Professors Herschbach and Lee pioneered molecular beams methods, and Professor Polanyi developed infrared chemiluminescence for this purpose. It is our pleasure to dedicate this paper to Professor Polanyi on the occasion of his sixty-fifth birthday.

The paper is organized as follows: in Section II we will describe the configuration of the spectroscopic and scattering experiments. The results will be presented in Section III and the discussion will follow in Section IV.

II. Experimental

A. The crossed molecular beams experiment

The scattering experiments were carried out on the universal crossed molecular beam apparatus of Perugia, which is an implementation for reactive scattering studies of the high-resolution machine previously used for measuring elastic and total (elastic + inelastic) differential cross section for atom–atom and atom–molecule collisions (29). The apparatus has been described in detail elsewhere (21, 29), and only a brief description necessary to understand the present experiments is given here. Two well-collimated supersonic beams of the reactants, after two stages of differential pumping, are crossed at 90° under single-collision conditions in a large scattering chamber maintained below 5×10^{-7} mbar. The reaction products are detected by an electron bombardment ionization quadrupole mass-spectrometer which can rotate in the plane of the two beams around their intersection axis (i.e., around the collision region). The ionizer is mounted on a liquid nitrogen cooled OFHC copper chamber, which is kept in the 10^{-11} mbar region by extensive ion-, turbo-, and cryo-pumping and represents the innermost region of a triply differentially pumped ultra-high-vacuum rotatable chamber.

The seeded supersonic atomic oxygen beams, containing $O(^1D)$ and ground-state $O(^3P)$, were generated by a high-pressure, radio-frequency (rf) discharge nozzle source similar in design to that described by Sibener et al. (30) and which has been optimized for $O(^1D)$ production (15, 20, 21). Two $O(^1D)$ beams with different translational energies were produced in order to vary the relative collision energy of the experiment. By discharging 350 mbar of a 5% O_2 in helium gas mixture through a 230 μm diameter quartz nozzle at 250 W of rf power, a beam with peak velocity of 2962 m/s and speed ratio of 6.4 was obtained. By discharging 350 mbar of a 5% O_2 in neon gas mixture through a 260 μm diameter quartz nozzle at 290 W of rf power a beam with peak velocity of 1715 m/s and speed ratio of 5.8 was produced. The angular divergence is 2.3° in both cases. Using the fast and slow beams of $O(^1D)$, relative collision energies, E_c, of 14.0 and 5.0 kcal/mol, respectively, were obtained (see below). Due to very efficient coupling of the rf power to the plasma, high degrees of molecular dissociation are achieved (>80% and >90% with the helium and neon mixture, respectively). The oxygen beams contain a very large fraction of ground-state $O(^3P)$, but this species does not interfere as the collision energies of our experiments are not sufficient to overcome the strong endoergicity of the reaction $O(^3P) + HBr \rightarrow BrO + H$ (ΔH = 31.4 kcal/mol).

Supersonic beams of HBr were generated by expanding pure HBr at a stagnation pressure of 1 bar through a 100 μm diameter stainless-{2}steel nozzle kept at about 510 K to prevent significant cluster formation. For the experiment at E_c = 14.0 kcal/mol the peak velocity was 616 m/s, while slightly different experimental conditions gave a peak velocity of 599 m/s for the experiment at E_c = 5.0 kcal/mol. Speed ratios were about 9 and the angular divergence 2.9° in both cases. Because of the significant rotational cooling during supersonic expansion (a rotational temperature of about 25 K is estimated assuming equilibrium between translational and rotational degrees of freedom), the HBr molecules in the beam are expected to be in the lowest few rotational states of the ground vibrational level and therefore the internal energy of the molecular reactant contributes negligibly (<0.2 kcal/mol) to the total available energy.

Angular distributions of products of reaction [1*b*] were obtained by taking at least 5 scans of 100 s counts at each angle. The HBr beam was modulated at 160 Hz by a tuning-fork chopper for background subtraction. Velocity analysis of the beams was carried out by conventional "single-shot" time-of-flight (TOF) techniques, using a high-speed multichannel scaler and a CAMAC data acquisition system controlled by a personal computer.

Velocity distributions of products were obtained at 13 different angles at E_c = 14.0 kcal/mol and at five different angles at E_c = 5.0 kcal/mol using the cross-correlation TOF technique (31) with four 127-bit pseudorandom sequences. High-time resolution was achieved by spinning the TOF disk, located at the entrance of the detector, at 393.7 Hz corresponding to a dwell time of 5 μs/channel. The flight length was 23.6 cm. Counting times varied from 30 to 120 min depending upon the signal intensity.

B. The time-resolved infrared chemiluminescence experiment

The internal energy distributions in the products of reaction [1*a*] were obtained by measuring their vibrationally- and rotationally-resolved infrared chemiluminescence emission spectra under conditions in which negligible collisional thermalization of these distributions had occurred. In addition, subsequent collisional energy transfer processes were also observed. Both of these results were obtained using fast time-resolved Fourier transform spectroscopy (FTRFTS) with a conventional low pressure infrared chemiluminescence apparatus.

The infrared chemiluminescence apparatus consists of a 25 cm diameter cylindrical stainless steel reaction chamber equipped with two sets of multipass mirrors on axes which are both perpendicular to the axis of the chamber. One set of mirrors passes light from a KrF excimer laser back and forth four times through the reaction zone at the centre of the chamber. The other set collects the emission from the reaction products and focuses it into a Michelson interferometer. The chamber is evacuated through a 38 cm diameter cryobaffle and a 30 cm diameter gate valve by a 5000 L/s diffusion pump. The gate valve is adjusted to maintain the desired pressure (approximately 3×10^{-2} mbar) during the experiments. A dry-ice-cooled copper baffle is also located inside the reaction zone to improve cryopumping and reduce both the thermal and optical background created by the excimer laser light.

Ozone and HBr enter the chamber from the top, are mixed thoroughly by a Teflon baffle just inside the inlet, and flow downward

Can. J. Chem. Downloaded from www.nrcresearchpress.com by 195.246.54.202 on 09/08/12
For personal use only.

between the multipass mirrors. The ozone is photodissociated by the 248 nm light from the KrF excimer laser, a modified Lumonics model TE-860-4 laser, which produced about 20 mJ/pulse at 330 Hz, the repetition rate required by the experiment.

The photodissociation forms $O(^1D)$ (90%) and $O(^3P)$ (10%) with relative translational energies of about 10 and 37 kcal/mol, respectively (32), in the frame of reference of the HBr collision. As mentioned earlier, the activation energy for the reaction of HBr with $O(^1D)$ is nearly zero, and that of the $O(^3P)$ reaction is about 3 kcal/mol (2–4). In principle, therefore, we cannot rule out the possibility that both electronic states of oxygen created in the photolysis contribute to the *initial* OH product observed in these experiments. We note in passing that this potential interference is possible with *all* experiments which use photodissociation of O_3 to generate $O(^1D)$, unless a very large excess of buffer gas be used to thermalize the translationally hot reagents. If buffer gas is used, however, the results could be compromised by partial thermalization of the reaction products by the buffer gas. To our knowledge, there is no clear experimental resolution to these conflicting effects of adding buffer gas for reagent thermalization.

The interfering reaction with $O(^3P)$ would have to occur at its first collision after the photolysis, because most of the excess translational energy would be lost on the first collision. The presence of translationally hot $O(^3P)$, however, may not be important to the results reported here, for several reasons: first, it is a minor constituent (<10%) of the photodissociation products. Second, the reactive cross sections of processes such as this decrease at the extremely high relative translational energy of the $O(^3P)$ atom (33, 34) and finally, increased reagent translational energy causes reduced product vibrational excitation in reactions such as this (35). This latter effect, in the case of the reaction reported here, causes the OH from the $O(^3P)$ reaction to be created predominantly in the lowest vibrational levels. In contrast to this, the results which we shall describe in the later sections, show that the OH is actually created in very high vibrational levels, consistent with the distribution expected from the $O(^1D)$ reaction.

The partial pressures of each of the O_3 and HBr were maintained at about 0.01 mbar, so the average gas kinetic collision time of the OH with the background gases during the experiments was about 4 μs. The first spectrum was recorded at a time delay of 20 μs *before* the photolysis laser pulse. Thereafter, spectra were recorded at 40 μs intervals until 540 μs after the photolysis pulse. The first measurement which contained signal from the reaction, therefore, was recorded 20 μs, or about 5 gas kinetic collisions, after the initiation of the reaction, and subsequent measurements were spaced at intervals of about 10 gas kinetic collisions.

The time-resolved Fourier transform apparatus used in these experiments was described previously (36). The algorithm, based on continuous-scan Fourier transform spectroscopy, was compared with other similar methods in a previous publication (37). The particular data acquisition configuration used in these experiments was a CAMAC-based PDP 11/83 processor with a LeCroy model 8818 transient digitizer. This was a prototype instrument; it was replaced recently by a VME-based system (38) which uses hardware built in our laboratory, and a Motorola 68040 processor.

The data acquisition system which we developed for our implementation of FTRFTS operates with any commercial continuous-scan Michelson interferometer. For the experiments reported here, we used the interferometer from a Nicolet 7199 FTS instrument, which had been slightly modified for this application. The data acquisition system produces time-resolved spectra by triggering the excitation source (the KrF laser in the present case) at a precisely-measured time with respect to the zero crossing of the He/Ne laser, then triggering the A/D which samples the infrared interferogram at several (precisely-measured) times which are delayed with respect to the time at which the excitation source is triggered. In our implementation, a single scan of the interferometer collects all of the time-delayed interferograms; it is not necessary to interleave data points collected during different interferometer scans into the same interferogram. This point is important in experiments which have systematic noise or instabilities, because the latter can create spectroscopic artifacts if used with the interleaving or "stroboscopic" method. This point is discussed in more detail in ref. 37.

III. Results and analysis

The two experimental techniques employed for the present studies are not equally sensitive for detecting the products of the two possible reactive pathways. The crossed molecular beams technique is more suitable for investigating the H-displacement channel, while the infrared chemiluminescence method is very sensitive to the H-abstraction channel leading to OH product. Under the experimental conditions of the scattering study we were able to observe only the BrO product from reaction [1*b*], while the signal from the kinematically unfavored OH, produced in the reaction channel [1*a*], was <0.01 of the signal from BrO measured at $m/e = 95$. On the basis of linear momentum conservation, in fact, the light OH from the strongly exothermic channel [1*a*] will travel very fast and will be spatially distributed in a very broad laboratory range, while the very heavy BrO from the significantly less exothermic channel [1*b*] will have a much lower center-of-mass (c.m.) velocity and will be confined in a narrow lab angular range around the c.m. This leads to a strong enhancement of the BrO number density in the lab frame with respect to that of OH. From our failure to detect the OH only a lower limit for the ratio of the relative cross sections for the two reaction channels could be estimated (see below). Instead, the OH channel can be easily examined by using spectroscopic techniques such as chemiluminescence emission, which is most sensitive to vibrationally excited species having high Einstein transition probabilities, such as diatomic hydrides. This technique, when coupled with the sensitivity and high resolving power of Fourier transform spectroscopy, can detect less than 10^{10} emitters/(quantum state cm^3) in the infrared.

A. The reactive scattering results: center-of-mass angular and energy distributions of the BrO product

The angular distributions of the BrO product, detected at $m/e = 95$, for the collision energies of 14.0 and 5.0 kcal/mol are shown in Fig. 1. The error bars are of the order of the size of the dots. Product counting rates were 1500 c/s and 500 c/s at the high and low E_c, respectively, with signal-to-noise above 100 using 100 s counting times. The solid lines in Fig. 1 show the calculated best-fit (see below). The product time-of-flight distributions of the two energies are reported in Figs. 2 and 3 together with the results of the best-fit calculations (see below). The TOF distributions have been normalized to the relative intensities at each angle. The angular distributions show some structure around the c.m., with a shoulder at angles $> \Theta_{c.m.}$ higher than at angles $< \Theta_{c.m.}$. The TOF spectra at the highest E_c display also some bimodality at angles close to the center-of-mass. This fact and the fairly large width of the lab angular distributions suggest that the product translational energy distribution peaks away from zero and that the fraction of available energy released in translation is large.

Data at both energies were analyzed by using a forward convolution trial-and-error fitting technique in which the c.m. angular and energy distributions are input as trial functions (39, 40). The corresponding laboratory angular and TOF distributions are then calculated and compared to the experimental data. The experimental resolution broadening, due to the TOF disk and detector slit sizes, disk velocity, and ionizer length, and spread in beam velocities and angular divergences, is taken into account. The original trial function is adjusted and the process

Can. J. Chem. Downloaded from www.nrcresearchpress.com by 195.246.54.202 on 09/08/12
For personal use only.

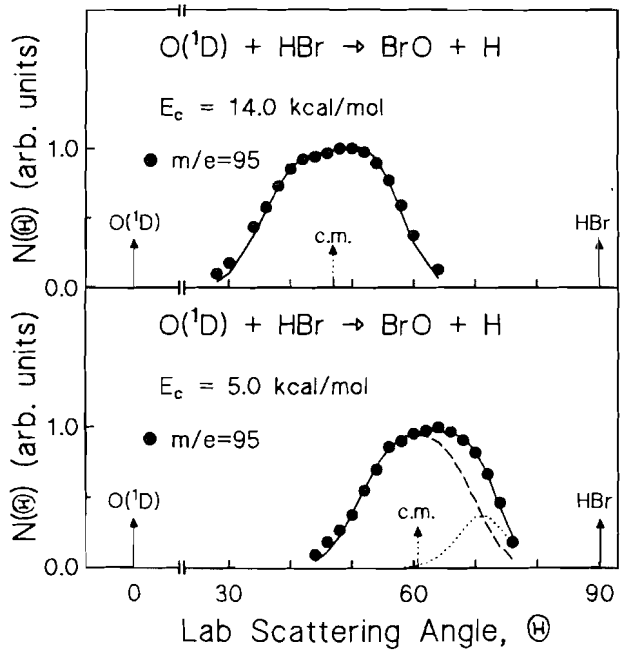

FIG. 1. Laboratory angular distribution of the BrO product from the $O(^1D)$ + HBr reaction at two different collision energies, E_c. Solid lines: calculation with best-fit c.m. translational energy and angular distributions of Fig. 4. In the lower panel, dashed and dotted lines represent the contribution of the long-lived complex mechanism and the rebound mechanism, respectively (see text).

repeated until a satisfactory fit is obtained to both the TOF spectra and the angular distributions. The energy dependence of the reaction cross section has been taken into account in the data analysis. For a reaction without threshold and dominated by long-range forces in the entrance channel, the centrifugal barrier model (41) predicts a decrease of the cross section with the relative collision energy and, therefore, an $E^{-1/3}$ dependence has been used.

The c.m. product flux distribution is assumed to be separable into the product of a translational energy and angular part:

$$I_{c.m.}(\theta, E') = T(\theta) \times P(E')$$

Data at the highest E_c could be fitted in this way. The best fit calculations to the experimental angular and TOF distributions are shown as solid lines in Figs. 1 and 2, respectively. Figure 4 shows the resultant c.m. angular distribution, $T(\theta)$, and translational energy distribution, $P(E'_T)$. The final result of the data fitting analysis is a c.m. contour map of product flux as a function of angle and product recoil energy (40). After a straightforward transformation to convert the flux distribution from an energy space to a velocity space, the c.m. contour map $I_{c.m.}(\theta, u)$, where u is the c.m. product velocity, is represented in polar form in Fig. 5, where a 3-D perspective is also given. The $P(E'_T)$ distribution is very broad and peaks at about 18 kcal/mol, beyond the exothermicity, extending up to the limits of energy conservation (see Fig. 4*b*). The average product translational energy

$$\langle E'_T \rangle = \sum P(E'_T)E'_T / \sum P(E'_T)$$

is about 49% of the total available energy, E_{tot}, which, under the present experimental conditions, is the sum of the relative collision energy and the reaction exoergicity.

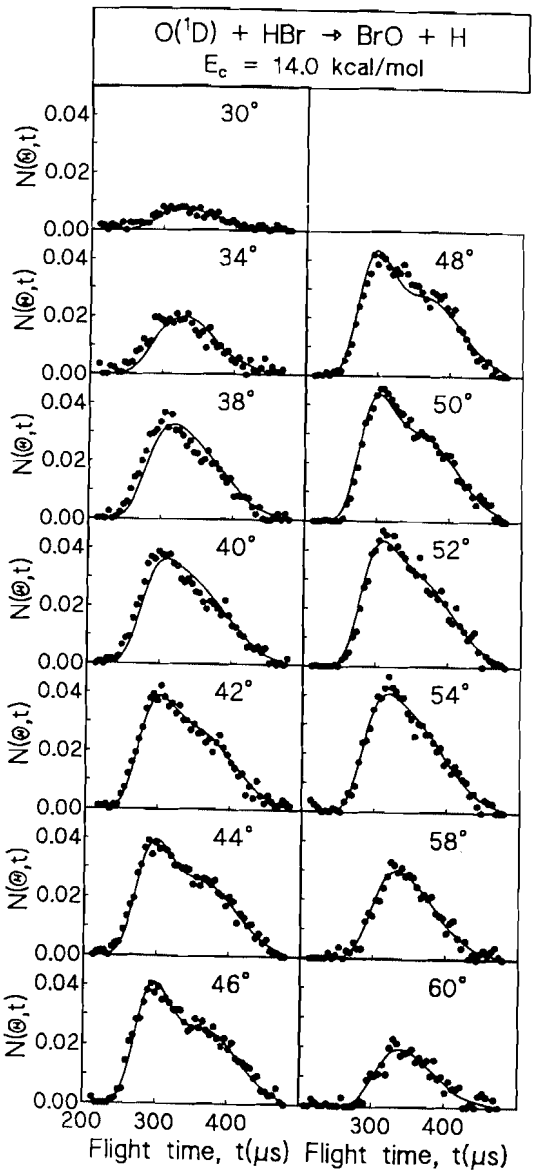

FIG. 2. Time-of-flight spectra of the BrO product at the indicated laboratory angles for the collision energy of 14.0 kcal/mol. The time scale is absolute, the ion flight time and electronic offsets having been taken into account. The distributions are normalized to the relative intensities at each angle. Solid lines: calculation with best-fit c.m. translational energy and angular distributions of Fig. 4.

The transformation of the c.m. flux $I_{c.m.}(\theta, u)$ to laboratory number density $N(\Theta)$ is given by (40):

$$N(\Theta) = (v/u^2)I_{c.m.}(\theta, u)$$

The effect of the Jacobian v/u^2 for the coordinate transformation is seen in the strong enhancement of the low energy product. While the product flux actually peaks fairly well removed from the c.m. vector on the relative velocity axis (see Fig. 5), the observed lab signal, which is proportional to $N(\Theta)$ does not show a pronounced dip around the c.m. The c.m. angular distribution is not backward–forward symmetric, as one would expect if the reaction were proceeding through a long-lived complex, i.e., a complex with a lifetime of several rotational periods (42). A slightly favored backward scattering (with re-

Can. J. Chem. Downloaded from www.nrcresearchpress.com by 195.246.54.202 on 09/08/12
For personal use only.

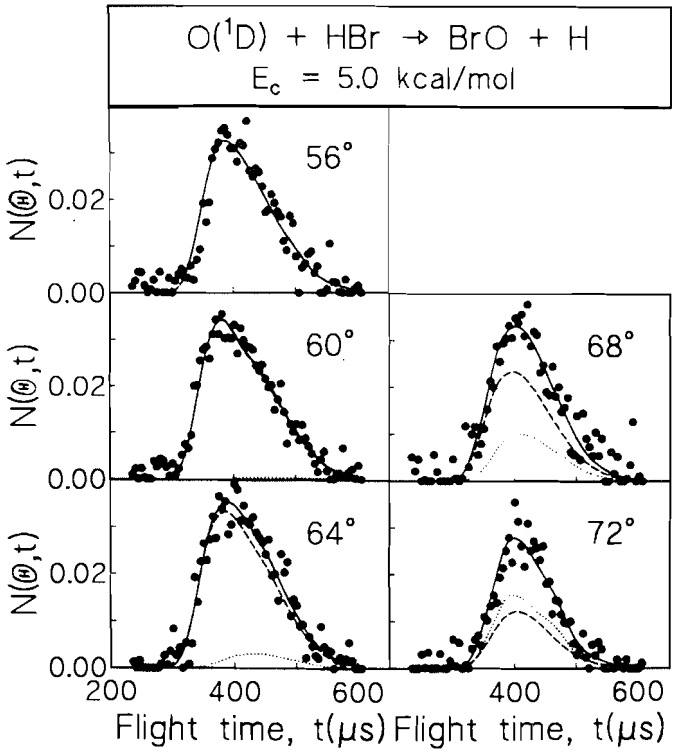

FIG. 3. As for Fig. 2, but for the collision energy of 5.0 kcal/mol. Dashed lines: contribution from long-lived complex mechanism. Dotted lines: contribution from direct rebound mechanism. Solid lines: total fit to the data according to eq. [2] (see text) with c.m. functions of Fig. 5.

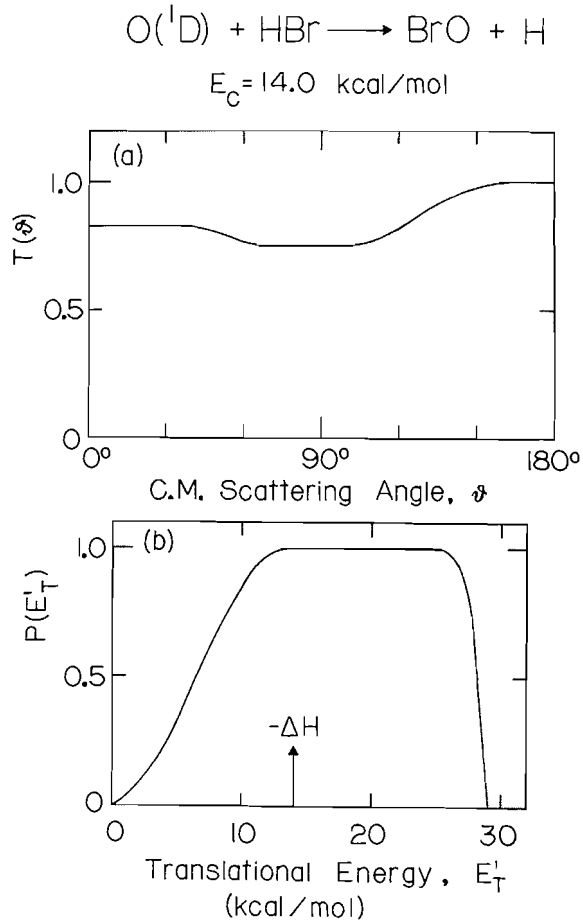

FIG. 4. Best-fit center-of-mass product angular (*a*) and translational energy (*b*) distributions at E_c = 14.0 kcal/mol. The reaction exoergicity ($-\Delta H$) is indicated.

spect to the O atom direction) is noted, well outside the uncertainty. A symmetric $T(\theta)$ would give a calculated symmetric lab angular distribution, while experimentally there is more intensity in the backward direction. This is similar to what was found in the homologous reaction of $O(^1D)$ with HCl (15), where the $T(\theta)$ was interpreted as arising from the superposition of a dominant backward–forward component, following the decomposition of a persistent complex, with a backward component due to a direct rebound interaction. The peaking at the poles ($\theta = 0°$ and 180°) with respect to $\theta = 90°$ provides information about the disposal of the total angular momentum into product rotation (42). In the present case a very weak polarization is found (see Fig. 4(*a*)), weaker than in the case of $O(^1D)$ + HCl. As it will be discussed below, this is consistent with the expected trend of the product rotational excitation.

The data at the lowest E_c could not be fitted quantitatively with single uncoupled c.m. angular and translational energy distributions, although it was possible to reproduce all the qualitative features. In particular, it was not possible to fit the intensity of the angular distribution at angles larger than $\Theta_{c.m.}$. The data could only be fitted by invoking two different reaction micromechanisms, the same two micromechanisms which we believe to be involved at the higher energy: a dominant one involving formation of a long-lived complex with fairly high translational energy release, and a second, backward scattered mechanism with a very high translational energy release. Direct backward scattering attributable to steric effects and accompanied by strong repulsion in the exit channel has been observed in bimolecular reactions (43). The c.m. flux in energy space was parametrized according to:

$$[2] \quad I_{c.m.}(\theta, E') = T_1(\theta) \times P_1(E') + \alpha \times T_2(\theta) \times P_2(E')$$

where the parameter α weights the contribution of the backward component. The best fit to the data at E_c = 5.0 kcal/mol is shown in Figs. 1 and 3 as a continuous line; the two separate contributions from the two micromechanisms are indicated by the dashed and dotted lines. The corresponding best-fit c.m. functions are depicted in Fig. 6. The component corresponding to direct backward scattering accounts for 15% ($\alpha = 0.15 \pm 0.03$) of the overall H-displacement channel, and leads to a larger translational energy release than the micromechanism corresponding to the decay of a long-lived HOBr complex. Within the uncertainty of our determination, the symmetric $T(\theta)$ is isotropic, suggesting a high degree of rotational excitation. The $P(E'_T)$ distributions of the two micromechanisms indicate that at low E_c as well, a large fraction of the total available energy is channeled into translation. The average product translational energy, $\langle E'_T \rangle$, is 48% of the total available energy for the mechanism associated with the formation of a long-lived complex and 77% for the direct rebound mechanism.

A fit attempting to disentangle the contribution of the two possible processes was also carried out at E_c = 14.0 kcal/mol. Using c.m. angular distributions which are similar, and of comparable relative weight, to those found for the low E_c case, it was possible to reach a slightly better fit than that obtained using the single components of Fig. 4. The two resulting $P(E'_T)$

Can. J. Chem. Downloaded from www.nrcresearchpress.com by 195.246.54.202 on 09/08/12
For personal use only.

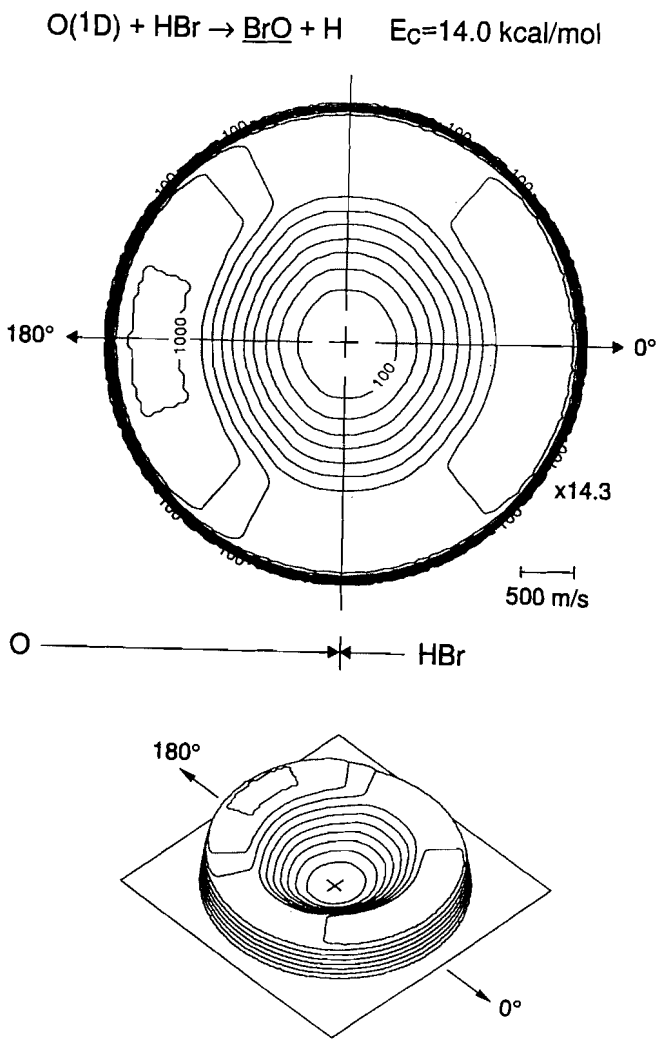

FIG. 5. Top: center-of-mass polar flux (velocity-angle) contour maps of BrO product at a relative collision energy of 14.0 kcal/mol. Bottom: three-dimensional representation of reactive flux intensity at E_c = 14.0 kcal/mol.

distributions, however, were actually overlapping each other. Because of this, we did not feel that an analysis in terms of two components was warranted.

B. The infrared-chemiluminescence results: energy partitioning in the BR + OH channel

A selection of the time-dependent emission spectra recorded using the FTRFTS system is shown in Fig. 7. All of the lines in these spectra can be assigned to the fundamental bands of either OH or HBr. The emission from about 2700 to about 3500 cm^{-1} is from OH, while that from 2350 to 2600 cm^{-1} is from HBr. The spectral resolution is about 0.4 cm^{-1}, which is high enough to resolve all vib-rotational lines in the spectra of OH and HBr, as well as the OH spin doublets and some of the OH lambda doublets. The populations of all vib-rotational states were calculated from the intensities of the corresponding emission lines, using known OH Einstein transition probabilities (44). The zero of the experiment's timescale is defined by the KrF laser pulse which creates the $O(^1D)$; time increases from the bottom of the figure to the top. The bottom spectrum was recorded at 20 μs (about five gas kinetic collisions) after the KrF laser, and the remaining spectra in the figure were recorded at 60 μs (15 collisions), 100 μs (25 collisions), 140 μs (35 collisions), 180 μs (45 collisions), and 220 μs (55 collisions) after time = 0. The OH spectra recorded at the earliest times have their greatest populations in the highest vibrational levels, indicating that the reaction creates OH with a strongly inverted vibrational distribution. We found (14) the same shape for the vibrational distribution of the $O(^1D)$ + HCl reaction, a result which was confirmed in later LIF measurements (13). Both the OH emission intensity and its average vibrational excitation decay smoothly after the first observation until the emission ceases to be observable at 300 μs. This temporal behaviour indicates that OH is a primary reaction product. In contrast to this, the HBr emission intensity is nearly zero in the earliest spectrum, but rises smoothly and slowly at the same time when the OH intensity is falling. This contrasting temporal behaviour shows that the OH and HBr arise from two different processes. All species which are produced directly in the $O(^1D)$ + HBr reaction are present in the earliest observation. This includes all of the OH and a very small amount of vibrationally excited HBr produced in the physical quenching of $O(^1D)$, which has been reported to occur in 20% of the $O(^1D)$ + HBr collisions (7). We observed HCl emission from the analogous process in our study of the $O(^1D)$ + HCl system, and were able to determine the branching ratio directly in that case. We found that the HCl is created with a strongly inverted vibrational distribution by this physical quenching process. In the present study, however, there was no evidence of HBr($v' > 1$) emission in the earliest spectrum. As a consequence, we were not able to determine the branching ratio or the HBr internal energy distribution. The only HBr emission

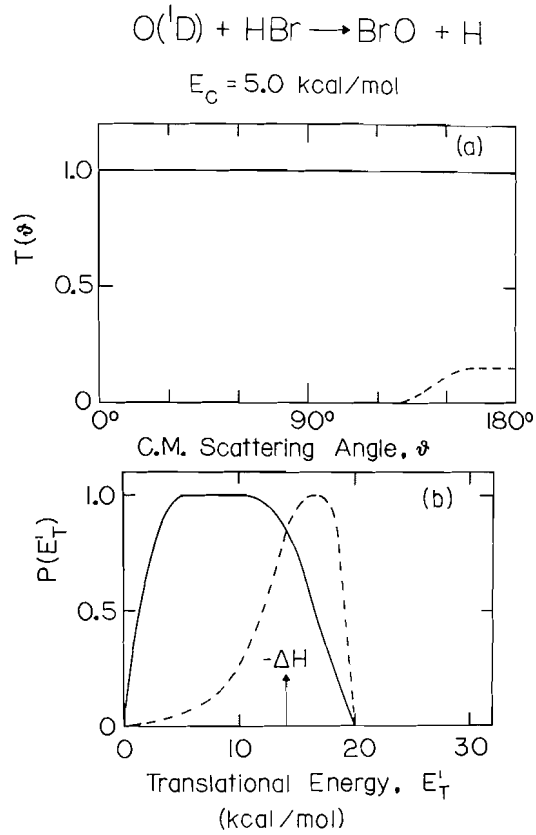

FIG. 6. As in Fig. 4, but at E_c = 5.0 kcal/mol. Solid lines: c.m. functions for the mechanisms via long-lived complex. Dashed lines: c.m. functions for the direct rebound mechanism. The c.m. angular distributions (*a*) for the two different mechanisms are in the same scale.

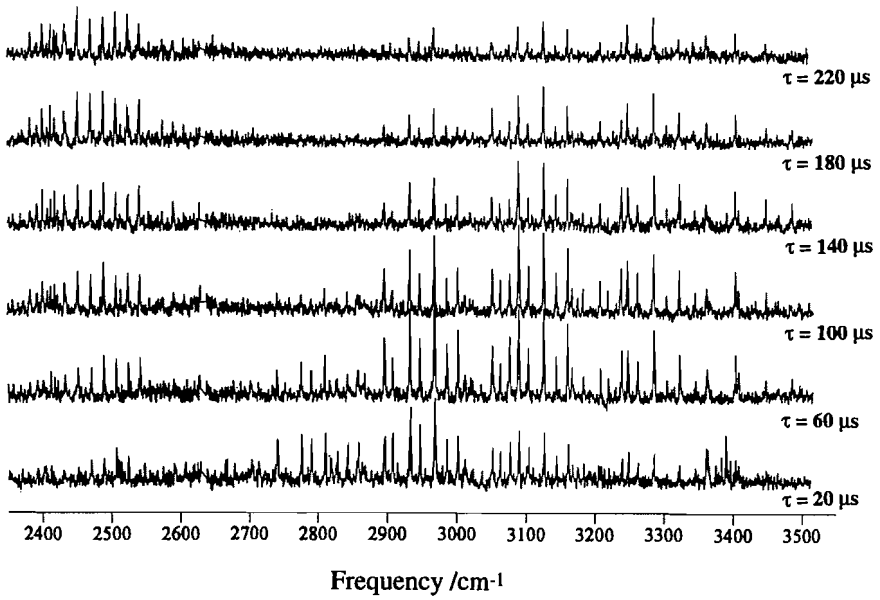

FIG. 7. Time-resolved spectra of the OH product from the $O(^1D)$ + HBr reaction recorded at 40 μs intervals, beginning at 20 μs (bottom) and continuing to 220 μs (top) after the creation of the $O(^1D)$.

Can. J. Chem. Downloaded from www.nrcresearchpress.com by 195.246.54.202 on 09/08/12
For personal use only.

evident in the first spectrum is five transitions of the HBr($v' = 1 \rightarrow 0$) band. The intensity of this emission increases continuously in later spectra. The HBr($v' = 1$), however, is not created in the physical quenching reaction. It is the result of a secondary V–V process between the vibrationally excited OH, created in the reaction, and the remaining HBr($v = 0$) which did not participate in the original reaction:

$$OH(v) + HBr(v = 0) \rightarrow OH(v' < v) + HBr(v = 1)$$

We have also seen this behaviour in the case of the $O(^1D)$/HCl experiments. In both cases, the V–V process is exothermic — the vibrational spacing of OH ($\omega_e = 3738\ cm^{-1}$) is larger than either that of HCl ($\omega_e = 2990\ cm^{-1}$) or HBr ($\omega_e = 2649\ cm^{-1}$) — and it is also quite fast. Since we have no direct measurements of the reagent concentrations, we cannot extract quantitative information about the kinetics of this energy transfer. It is possible to estimate the order of magnitude of the rate constant, however, based on estimated concentrations and the rate of rise of the HBr emission. We estimate the total concentration of vibrationally excited OH to be on the order of 10^{-5} mbar; we know that the concentration of HBr($v = 0$) is about 10^{-2} mbar, and from the rate of increase of the HBr($v = 1$) emission, we estimate that the rate constant for this process must be of the order of $10^6\ mbar^{-1}\ s^{-1}$.

Assignment of the spectra shows that the OH vibrational levels are very highly excited, and show strong population inversion, with population almost to the energetic limit. Because of the large spin–orbit splitting of the Br atom, about 3678 cm^{-1}, the energetic limit on the OH excitation depends on the electronic state of the Br atom. For the OH created in conjunction with the $Br(^2P_{1/2})$ excited state, this limit is OH($v' = 6$), while for that created with the $Br(^2P_{3/2})$ ground state, it is OH($v' = 8$). In contrast, the OH spin–orbit splitting is very small; the $OH(^2\Pi_{1/2})$ excited state is only about 123 cm^{-1} above the $OH(^2\Pi_{3/2})$ ground state.

Examination of the spectra shows that the highest vibrational level which we observe in the $OH(^2\Pi_{1/2}; v')$ manifold is ($v' = 6$). The highest level observed in the $OH(^2\Pi_{3/2})$ ground state manifold, however, is ($v' = 5$). The fact that the excited spin–orbit state has higher vibrational excitation than the ground spin–orbit state is somewhat unusual. It may, however, give information about the preferred reaction pathway, and we shall return to this point later, in the Discussion section.

The OH rotational distributions recorded in our earliest-time spectrum showed slight suprathermal excitation. We believe, however, that these are not the true initial rotational distributions, because rapid rotational energy transfer had probably modified the rotational populations substantially, even at the time of the first spectrum (which corresponds to five gas kinetic collisions). Based on the behaviour we have observed (14, 45, 46) in other experiments involving vibrationally excited OH in collisions with molecules like O_3 and HCl, we estimate that the OH rotational degree of freedom would be partially thermalized after five gas kinetic collisions, and completely thermalized at the second observation, which corresponds to about fifteen collisions.

In this experiment, OH vibrational energy transfer is very much slower than its rotational deactivation, and we believe that virtually no vibrational deactivation had occurred at the time of the initial observation. Vibrational deactivation does occur, however, during our observation time. The data show that the total vibrational inversion is lost after about 250 μs (50–60 gas kinetic collisions). Furthermore, the gases are continuously being pumped through the observation zone, so the OH emission signal becomes too weak to see shortly after this time, at about 300 μs.

The temporal behaviour of the OH vibrational populations is shown in Fig. 8. Each vibrational population is the sum of the rotational populations for that vibrational level. As indicated earlier, we believe that the initial vibrational distribution is that shown for the first time delay. The distribution is collisionally deactivated thereafter in a way which is characteristic of this kind of process. In this vibrational deactivation pattern, which we saw also in the $O(^1D)$ + HCl reaction, the highest vibrational level created by the reaction decreases with time monotonically

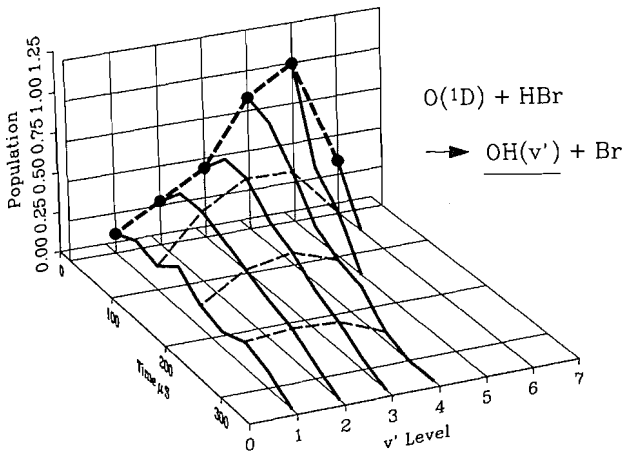

FIG. 8. The evolution of the OH vibrational distribution with time. The initial distribution (recorded at 20 μs) is shown as dots connected by a heavy dashed line. Dashed lines also connect subsequent distributions spaced at 80 μs intervals.

and more rapidly than the lower levels. The populations of the lower levels first increase, then decrease with time. The rates of increase and decrease are fastest for the higher levels and become slower as the vibrational level decreases. Superimposed on this process is a monotonic decrease in the populations of all levels, due to their removal from the observation zone. This overall behaviour constitutes a vibrational "cascading" process in which the predominant collisional deactivation is $\Delta v = -1$. In this process, the initial increase in the vibrational population of each intermediate vibrational level (v) predominantly arises from deactivation of the level immediately above it ($v + 1$), which has a larger population due to the initial population inversion. The population buildup in level (v), in turn, increases the rate of population of the level below it, until the increase with time of the latter is faster than its decrease due to all other processes.

As a consequence of this set of circumstances, the rise and decay of the lower levels is slower than the corresponding processes for the higher levels because the lower levels are fed from an increasingly larger pool of higher levels, and more deactivation steps are involved in their population as the vibrational quantum number decreases. We have modelled the behaviour of such a "cascade" deactivation process for OH collisional relaxation in the products of the reaction $O(^1D) + H_2S \rightarrow OH(v) + HS$. We achieved a reasonable fit using only $\Delta v = -1$ processes (46).

C. The branching ratio $\sigma(BrO + H)/\sigma(OH + Br)$

The mass spectrometric detection of the product OH from channel [1*a*] is, in crossed beams, kinematically very unfavored, since in the c.m. frame, the following relationship holds:

$$u_{OH} = -(m_{Br}/m_{OH})u_{Br}$$

where u is the c.m. velocity and m the mass, and therefore OH will be scattered in a very wide lab angular range. Kinematically it is more favorable to detect the Br atom than the OH counterpart; but, unfortunately, Br^+ produced from dissociative ionization, under electron impact in the detector, of elastically scattered HBr represents a severe complication. We have estimated upper limits for the signal at $m/e = 17$ (OH) and $m/e = 79$ (Br) with respect to the signal at $m/e = 95$ (BrO) by performing TOF measurements at the c.m. angle and have obtained that $(m/e = 17)/(m/e = 95) \leq 0.01$ and $(m/e = 79)/(m/e = 95) \leq 0.05$. Since the absolute intensities of the reactant beams, the exact size of the collision volume, and the detection efficiency are not known, absolute reaction cross sections cannot be derived directly in the present experiment. These parameters, however, do not change during the course of an experiment, and therefore the branching ratio between the two reaction channels can be calculated from the ratio of the relative cross sections, corrected for the ionization cross sections of the products, and their fragmentation patterns and relative transmission through the quadrupole mass filter. The branching ratio, defined as the ratio of the total reaction cross section, $\sigma(ClO + H)$ and $\sigma(OH + Br)$ for channels [1*b*] and [1*a*] is obtained as follows (see also ref. 47):

$$\frac{\sigma(BrO + H)}{\sigma(OH + Br)} = \frac{\sigma^0(BrO + H)}{\sigma^0(OH + Br)} \cdot \frac{\sigma^{ion}(OH)}{\sigma^{ion}(BrO)}$$

where $\sigma^0(BrO + H)$ and $\sigma^0(OH + Br)$ are the apparent cross sections derived from the signal at m/e 95 and 17 and from the ratio of the integrals of the angular and translational energy distributions in the c.m. frame, in which the masses of the different products are taken into account.

A slightly forward-peaked c.m. angular distribution, as obtained from classical trajectory studies (16*b*) for the related $O(^1D) + HCl$ reaction, was assumed for the OH channel and a translational energy distribution, reflecting the degree of internal excitation measured in the infrared-chemiluminescence experiments (see above), was used. The ionization cross sections of OH and BrO, $\sigma^{ion}(OH)$ and $\sigma^{ion}(BrO)$, are approximated using the method of Fitch and Sauter (48) based on polarizability values. The fragmentation pattern under 100 eV electron bombardment was assumed to be the same for the two diatomic species. The transmission of the quadrupole mass filter has been determined to be constant in the range of masses under consideration. The ratio between the cross sections σ for formation of BrO and OH was then calculated to be $\sigma(BrO + H)/\sigma(OH + Br) \geq 0.05$ using the upper limit of the OH/BrO ratio and $\sigma(BrO + H)/\sigma(OH + Br) \geq 0.16 \pm 0.07$ using that of the Br/BrO ratio. The latter value is more reliable, because of the higher sensitivity to the heavier Br atom than to OH. The estimated uncertainty reflects the uncertainty in the c.m. functions (especially $T(\theta)$) assumed for the OH + Br channel, in the ratio of the ionization cross sections and in the fragmentation ratios. For the $O(^1D) + HCl$ reaction (15) it was found $\sigma(ClO + H)/\sigma(OH + Cl) \geq 0.34 \pm 0.10$. However, we note that, under the same experimental conditions, the signal at the BrO mass was 2.5 times larger than the signal at the ClO mass, and even accounting for the 30% larger ionization cross sections of BrO, this leads us to conclude that the cross sections for the channel XO + H are comparable for X = Cl and X = Br. The results for X = Br are in contrast to recent bulk estimates (7), while they were in agreement for X = Cl.

IV. Discussion

In Fig. 9 we show the energy level and correlation diagram which are relevant to the following discussion. The energy levels are only known for the reagents, products, and the ground state of HOBr. No experimental or theoretical information is available for the excited states of the two isomeric forms, HOBr and HBrO, and not even for the ground state of HBrO; in the diagram, therefore, these states have been indicated with

Can. J. Chem. Downloaded from www.nrcresearchpress.com by 195.246.54.202 on 09/08/12
For personal use only.

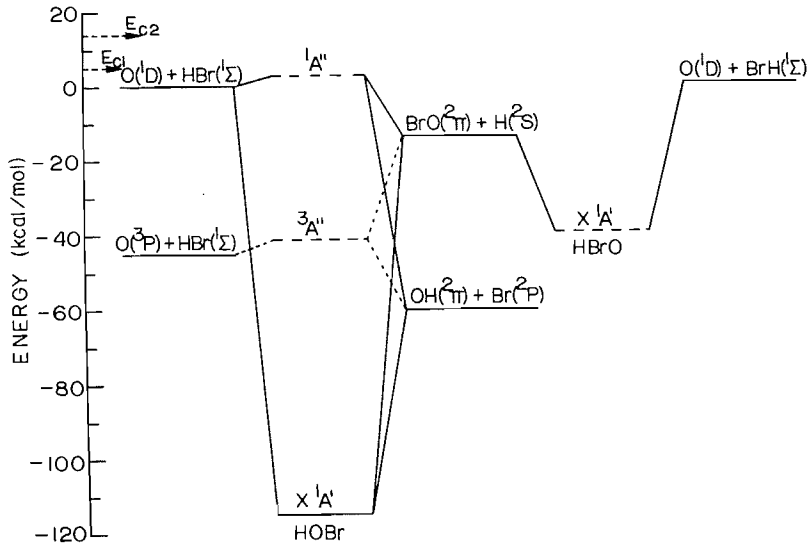

FIG. 9. The energy level and correlation diagram for the $O(^3P,^1D)$ + HBr system. The energies of the HOBr $^3A'$ and $^1A''$ states and of the HBrO X^1A' state (indicated with dashed lines) are not known: the energy of $^3A''$ has been put equal to the activation barrier for the triplet reaction and the others have been drawn by analogy with the related $O(^1D)$ + HCl system (see ref. 15). E_{c1} and E_{c2} indicate the experimental relative collision energies of the scattering study.

dashed lines by analogy with the homologous O + HCl system, for which SCF-CI calculations have been carried out by Bruna et al. (16*a*). Of the two lowest excited singlet states of HOBr, $^1A''$ and $^1A'$, we have assumed that only the $^1A''$ state (represented in the figure) is accessible at the experimental energies and only the ground state of the HBrO isomer may be energetically involved, in analogy with O + HCl (see ref. 15). In Fig. 9, E_{c1} and E_{c2} represent the relative translational energies of the reagents in the low E_c and high E_c scattering experiments, respectively; in the infrared chemiluminescence experiment the maximum energy accessible to the products is about 10 kcal/mol, which is near the average of E_{c1} and E_{c2}. The reaction involving ground state oxygen is also portrayed in Fig. 9, where the triplet ground state surface, $^3A''$, has been located on the energy scale at the value of the experimental activation barrier (about 3.4 kcal/mol) of the $O(^3P)$ + HBr reaction (2–4).

For a detailed discussion of the product energy partitioning it will also be useful to refer to Fig. 10, where the fine structure levels of the products are specified. As can be seen, the electronically adiabatic correlations in the $O(^3P,^1D)$ + HBr system are relatively complex. For the ground state reaction three spin–orbit states of the reagent $O(^3P_{2,1,0})$ are coupled to two $^2P_{3/2,1/2}$ states of the Br atom and two $^2\Pi_{3/2,1/2}$ states of OH. However, assuming linear geometry ($C_{\infty V}$) and with Ω (the projection of the total electronic angular momentum along the internuclear axis), the good quantum number, being conserved, the $^3A''$ ground state triplet surface ($^3\Pi_{2,1,0+,0-}$ in the $C_{\infty V}$ geometry) adiabatically correlates only with the $OH(^2\Pi_{3/2,1/2}) + Br(^2P_{3/2})$ manifold (49, 50). For the excited state reaction, the reagent $O(^1D_2)$ is coupled to two $^2\Pi_{3/2,1/2}$ states of BrO for the H-displacement channel and to two $^2P_{3/2,1/2}$ states of Br and two $^2\Pi_{3/2,1/2}$ states of OH for the H abstraction channel. However, again the X^1A' ($^1\Sigma^+$ in the $C_{\infty V}$ geometry) ground state singlet surface correlates adiabatically only with $OH(^2\Pi_{3/2}) + Br(^2P_{3/2})$ and with $BrO(^2\Pi_{1/2}) + H(^2S_{1/2})$, while the first excited singlet $^1A''$ state ($^1\Pi_1$ in the $C_{\infty V}$ geometry) correlates adiabatically with $OH(^2\Pi_{1/2}) + Br(^2P_{3/2})$ and $BrO(^2\Pi_{3/2}) + H(^2S_{1/2})$ (see ref. 49). Because of the several curve crossings which occur, one may reasonably expect that the product state partitioning is controlled by nonadiabatic couplings in the entrance and/or exit channel regions of the potential energy hypersurface. If the OH forming reaction channel was to proceed adiabatically, no excited $Br(^2P_{1/2})$ should be formed. Unfortunately, this is not probed in our experiments. We note, however, that very recent work by Matsumi et al. (49) on the homologous $O(^1D)$ + HCl reaction found a fine structure branching ratio of product chlorine atoms $Cl(^2P_{1/2})/Cl(^2P_{3/2})$ of 0.20 at a collision energy of 7.6 kcal/mol. Some $Br(^2P_{1/2})$ may well be formed also in the reaction with HBr, although the significantly larger (about 4 times) spin–orbit splitting of Br with respect to Cl suggests a weaker nonadiabatic interaction and consequently a smaller fine structure branching ratio. We note that formation of spin–orbit excited $Br(^2P_{1/2})$ in the amount of about 6% was inferred in a study of the $O(^3P)$ + HBr reaction (10). Nonadiabatic effects should instead be larger in the ground state manifold $OH(^2\Pi_{3/2,1/2}) + Br(^2P_{3/2})$, where the OH fine structure splitting is relatively very small (123 cm^{-1}). Indeed, the spin–orbit levels of OH are populated nearly statistically in the $O(^1D)$ + HCl reaction (13, 14). The same has been found for the $O(^3P)$ + HBr reaction (10) and it is reasonable to expect a similar results for the $O(^1D)$ + HBr reaction as well. The present chemiluminescence study indicates a nearly statistical $OH(^2\Pi_{1/2})/OH(^2\Pi_{3/2})$ ratio (see below).

A. $O(^1D) + HBr \rightarrow OH + Br$

The predominant mode of energy release in this channel is into vibration in the OH product. The observed OH vibrational distribution is strongly inverted, peaking in OH($v' = 5$). The normalized OH vibrational distribution is $P_{OH}(v' = 1{:}2{:}3{:}4{:}5{:}6) = 0.04{:}0.10{:}0.14{:}0.28{:}0.32{:}0.12$. The uncertainty in the normalized population of each level is about ± 0.02. Assuming a negligible population in OH($v' = 0$), which seems justified by the shape of the observed distribution, this indicates that the reaction releases 56% of the available reagent energy into vibration in this channel. In this calculation, the total available energy is taken to be the exoergicity of the reaction forming all products

Can. J. Chem. Downloaded from www.nrcresearchpress.com by 195.246.54.202 on 09/08/12
For personal use only.

Can. J. Chem. Downloaded from www.nrcresearchpress.com by 195.246.54.202 on 09/08/12
For personal use only.

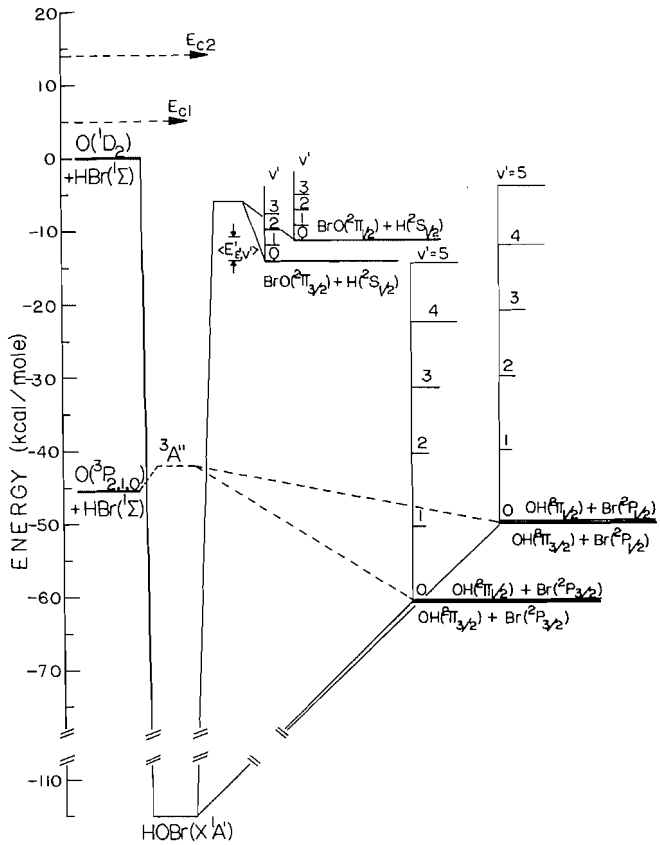

FIG. 10. Detailed energy level and correlation diagram for the $O(^3P,^1D)$ + HBr system: the fine structure states of the products are indicated. $\langle E_{\epsilon',v'} \rangle$ indicates the average fraction of total available energy which is estimated (see Discussion section B.1) to be released into electronic and vibrational degrees of freedom for the scattering experiment at E_{c1} = 5.0 kcal/mol.

in their ground states, 60.5 kcal/mol, plus the relative translational energy in the $O(^1D)$ + HBr collision, about 10 kcal/mol. We note that the entire population of the OH(v' = 6) level is due to the $OH(^2\Pi_{1/2})$ component. Within the signal-to-noise ratio of our measurements, we observe no population for the $OH(^2\Pi_{3/2}$; v' = 6) state. We shall comment on this result later in this section.

This energy partitioning pattern is similar to that found for other similar reactions of $O(^1D)$. The reactions with H_2, CH_4, H_2S, and HCl all produce OH with substantial vibrational excitation (14, 45, 46, 51, 52). In particular, the OH vibrational distribution created by the reaction with HCl is virtually the same as that observed for the HBr reaction. These reactions all share several similarities. They all involve the transfer of a hydrogen atom to $O(^1D)$, from third bodies which have a range of masses, over potential energy surfaces which all have very similar shapes. One of the most important features shared by the potential energy surfaces for all of these reactions is a relatively deep minimum corresponding to a strongly-bound intermediate having the general form H—O—R. (In the present case, although the energy of the other possible bound intermediate, HBrO, is not known, it is unlikely to be as stable as HOBr.) The mass combinations of these reactions also appear to have an influence on the dynamics. The primary effect in this regard is the transfer of a light atom between two heavier entities. In our previous work (14) on the $O(^1D)$ + HCl reaction, we argued that the timescale of the interaction is governed by the relatively slow motion of the heavier atoms, while the motion of the H atom is much faster. The relative masses of the R fragments also appear to be important. We find, for example, that the OH vibrational excitation created by the $O(^1D)$ reactions with HCl, H_2S, and HBr is very much larger than it is for the reactions with H_2 and CH_4. The H_2S reaction channels 60% of the available energy into OH vibration (46); the percentages for the HCl and HBr reactions are 67% and 56% respectively (14, this work). The reactions with H_2 and CH_4 channel only about 40–45% of the energy into OH vibration (45, 51, 52). In the CH_4 reaction, it has been suggested (52) that the additional degrees of freedom play a role in the low vibrational excitation, by introducing a component of energy randomization, which competes with the dissociation. This process was suggested to be responsible for bimodality which was observed in the energy distribution of that reaction. In the case of the HBr reaction, of course, no bimodality in the energy distribution was observed.

The highly specific energy disposal into OH vibration exhibited by the reactions involving the heavy R fragments implies that these occur on a very short timescale — much shorter than the time required for statistical energy partitioning among the product modes. In this sense, we consider these reactions to have direct dynamics. By this, we do not mean to imply that the geometry of the collision is necessarily collinear or that the H atom is transferred at a large distance without significant interaction between the $O(^1D)$ and the other heavy entity. It does imply, however, that the timescale of the interaction must be very short.

We observe nearly statistical population of the spin–orbit states for the lowest five OH vibrational levels created in the $O(^1D)$ + HBr reaction. (By statistical, we mean that the population is proportional to the spin degeneracy, $2J + 1$; we neglect the energy contribution, which is small by comparison with the exoergicity of the reaction.) Averaged over the vibrational levels OH(v' = 1–5), the ratio of the spin–orbit populations which we observe is $OH(^2\Pi_{3/2})/OH(^2\Pi_{1/2}) = 2.2 \pm 0.2$. We found a similar result in the $O(^1D)$ + HCl reaction (14).

In contrast to the lower vibrational levels, we find that the highest observed vibrational level, OH(v'= 6), has a greater population for the $OH(^2\Pi_{1/2})$ excited spin–orbit state, than for the $OH(^2\Pi_{3/2})$ ground state. This is an unusual result. Park et al. (13) determined sublevel populations for the $O(^1D)$ + HCl reaction. They reported a propensity for production of the OH $\Pi(A')$ sublevel; the ratio $\Pi(A')/\Pi(A'') = 2.0$. The $\Pi(A')$ sublevel correlates with the $HOCl(^1A')$ intermediate, indicating that the $(^1A'')$ intermediate does not participate much in the reaction. In the $O(^1D)$ + HX reactions, the $HOX(^1A')$ intermediate correlates adiabatically only with the $OH(^2\Pi_{3/2})$ state while the $OH(^2\Pi_{1/2})$ state correlates with the higher energy $HOX(^1A'')$ intermediate (49). Our result, therefore, indicates that the OH(v' = 6) level results predominantly from reaction via the higher energy $HOBr(^1A'')$ intermediate.

This result is dynamically reasonable in view of the fact that the interaction via the $HOBr(^1A'')$ state is predominantly repulsive. It does not have the potential energy minimum of the $(^1A')$ ground state (see Fig. 9). Reaction on the upper state, therefore, should be more impulsive and have a shorter duration than that on the ground state. This, in turn, could create higher vibrational excitation in the diatomic product. The effect of the higher vibrational excitation on the probability of curve crossing, and hence the reason for the lack of $OH(^2\Pi_{3/2}$; v' = 6) in the

Can. J. Chem. Downloaded from www.nrcresearchpress.com by 195.246.54.202 on 09/08/12
For personal use only.

products, cannot be determined without a more detailed knowledge of the shapes of the potential surfaces involved. The information available to us presently, however, indicates that reaction via the lower ($^1A'$) intermediate creates less OH vibrational excitation than reaction on the excited state surface.

B. $O(^1D) + HBr \rightarrow BrO + H$

The derived angular and translational energy distributions of the BrO product in the c.m. frame allow an evaluation of the dynamical influence of the potential energy surface as well as the kinematic constraints for this reaction channel.

1. Product energy distributions

A dominant feature of this reaction channel is the large fraction of available energy released into translation. The $P(E'_T)$ distributions shown in Figs. 4*b* and 6*b* indicate that for both collision energies the average product translational energy is about 50% of E_{tot} and even larger for the range of reactive collisions associated with the rebound dynamics. Classical trajectory studies on model surfaces for the **H + HL → HH + L** (**H** — Heavy; **L** — Light) mass combination have shown that the presence of a late barrier to reaction results in large amounts of energy in translation (53). The presence of a barrier in the exit channel is reported in *ab initio* SCF-CI calculations (16*a*) for the dissociation of HOCl/HClO into ClO + H, both in the ground state (X^1A') potential of HClO and the first excited state ($^1A''$) potentials of HOCl and HClO. It is reasonable to expect the presence of these features also in the strictly related HOBr/HBrO system.

The remaining 50% of available energy will be in internal degrees of freedom (electronic, vibrational, and rotational) and, on the basis of the conservation of the total angular momentum (42), it is expected to be mostly in product rotational excitation. In fact, for the specific mass combination, as a consequence of the much smaller reduced mass of the products (0.990 amu) with respect to that of the reagents (13.37 amu), $\boldsymbol{L} \gg \boldsymbol{L}'$, where $\boldsymbol{L}$ and $\boldsymbol{L}'$ are the initial and final orbital angular momenta, and the final rotational angular momentum, $\boldsymbol{j}'$, is about equal to $\boldsymbol{L}$, since the initial $\boldsymbol{j}$ is very small with respect to $\boldsymbol{L}$ in view of the fact that the HBr reagent molecules are formed in a supersonic expansion, where considerable rotational cooling occurs. As a consequence, $\boldsymbol{L}$ and $\boldsymbol{L}'$ are not expected to be correlated, which determines the observed isotropic shape of the c.m. angular distribution. We recall that for a reaction which proceeds through the formation of a long-lived complex, one will observe a symmetric c.m. angular distribution sharply polarized at $\theta = 0°$ and $\theta = 180°$ if $\boldsymbol{L}$ and $\boldsymbol{L}'$ are parallel or antiparallel; this situation occurs only when the product molecules are not rotationally excited or when M' (the projection of the total angular momentum $\boldsymbol{J}$ along the final recoil velocity v') is null (42). When part of the total $\boldsymbol{J}$ is removed as $\boldsymbol{j}'$ (i.e,, when rotation excitation of the product molecules occurs) and M' is not null, $\boldsymbol{L}$ and $\boldsymbol{L}'$ are weakly correlated and the sharp polarization of $T(\theta)$ at the poles is lost, while the backward–forward symmetry is maintained. In general, when no geometric constraints are present in the collision complex, there will be a distribution of M' and, therefore, dissociation of a complex leading to highly excited products will lead to an isotropic, or nearly isotropic, $T(\theta)$. This appears to be the case observed here (see Figs. 4–6). For the collision energy E_c = 5.0 kcal/mol, very little energy remains for electronic and vibrational excitation, since ≈50% is released in translation and high rotational excitation also occurs. Assuming $j' = L$, one calculates an average product rotational energy, $\langle E'_R \rangle$, of 6.3 kcal/mol. The spin–orbit splitting of $BrO(^2\Pi_{3/2,1/2})$ is 2.8 kcal/mol and the vibrational spacing about 2.1 kcal/mol (54). This suggest that BrO can mainly be formed in the lowest few vibrational levels of the ground $^2\Pi_{3/2}$ electronic state, or in the ground vibrational level of the ground $^2\Pi_{3/2}$ and first electronically excited $^2\Pi_{1/2}$ states (see Fig. 10). Unfortunately, the present experiment does not probe the relative population of the fine structure levels of $BrO(^2\Pi)$. Considering the relatively small spin–orbit splitting of $BrO(^2\Pi)$, which is comparable to that in atomic chlorine, we may reasonably expect that extensive nonadiabatic coupling occurs and that both fine structure components of BrO are populated in the reaction. For E_c = 14.0 kcal/mol similar arguments apply, but now a little more energy will be available for more vibrational excitation of the products.

2. Angular distributions

The $T(\theta)$ in Figs. 4(*a*) and 6(*a*) contain a significant amount of information. At E_c = 5.0 kcal/mol the dominant $T(\theta)$ is symmetric about 90°. Though this symmetry in principle is possible in a direct interaction, it is very likely the result of the formation of a H—O—Br complex with a lifetime longer than its rotational period. At this relatively low E_c, this is not surprising due to the known complex stability of about 115 kcal/mol with respect to the $O(^1D)$ and HBr reactants (ref. 55*a*, the heat of formation of HOBr (ΔH_f^0 = 19 ± 2 kcal/mol) is taken from ref. 55*b*, and that of BrO (ΔH_f^0 = 32 ± 0.6 kcal/mol) from ref 55*c*). The isotropy of the $T(\theta)$ has been rationalized in terms of angular momentum disposal, which leads to highly rotationally excited products and an isotropic distribution of $\boldsymbol{L}'$ (see previous section). The lack of correlation between $\boldsymbol{L}$ and $\boldsymbol{L}'$ is not surprising in this case since the large reactive cross section indicates no geometric constraint in the entrance channel. A small, but significant, portion of reactive collisions lead, at E_c = 5.0 kcal/mol, to backward scattering with a very high degree of product translational excitation. The corresponding $T(\theta)$ is completely confined in the backward hemisphere and peaks at $\theta = 180°$ (see dotted line in Fig. 6(*a*)) and the average fraction of available energy released in translation is very large (about 77%); this implies that collinear, or nearly collinear, encounters at small impact parameters are taking place and leading to the formation of products after passing through a high exit barrier. In this picture the oxygen atom approaches collinearly (or within a narrow cone of acceptance) from the halogen atom side and the configuration involved is O—Br—H (see Fig. 9). It should be noted that trajectory studies (53, 56) on a late barrier surface, for all mass combinations, show a tendency toward backward scattering, in agreement with our observation. From the above, it can be argued that at E_c = 5.0 kcal/mol the reaction takes place by a direct mechanism for very small impact parameters within a narrow angle of orientations and by an insertion mechanism leading to the formation of a long-lived complex for all other impact parameters and orientations. The latter is the dominant micromechanism and is likely to involve the ground state potential energy surface X^1A' of HOBr, although also the X^1A' surface of HBrO cannot be ruled out. The rebound micromechanism is expected to involve the ground X^1A' surface of HBrO (see Fig. 9).

The results obtained at the higher E_c = 14.0 kcal/mol corroborate the above interpretation. In fact, both the $P(E'_T)$ and $T(\theta)$ distributions shown in Fig. 4 can be seen as the superposition of two distributions which can be associated with the same micro-

Can. J. Chem. Downloaded from www.nrcresearchpress.com by 195.246.54.202 on 09/08/12
For personal use only.

mechanisms operative at E_c = 5.0 kcal/mol. The $T(\theta)$ is almost backward–forward symmetric, but with more intensity in the backward direction. The $P(E'_T)$ appears to be the envelope of the two $P(E'_T)$ reported in Fig. 6(*b*). As already mentioned, an analysis of the data at this higher E_c in terms of two micromechanisms required the parameter α in eq. [2] to be also 0.15, as at the lower E_c. This seems to suggest that the relative contribution of the two micromechanisms does not vary with E_c, at least in the investigated range. The steric requirement appears to be the dominant factor: when $O(^1D)$ approaches within a narrow cone on the halogen side at small impact parameters, a direct rebound mechanism is operative; for all other orientations and range of impact parameters the reactants are driven into the deep $HOBr(X^1A')$ well following $O(^1D)$ insertion into the H—Br bond and giving rise to the formation of a long-lived collision complex which can undergo H—OBr bond fission because of the high energy content.

The very different dynamics observed for the OH- and BrO-forming channels may be ascribed to the different role played by the different singlet surfaces and the different configurations of the reaction intermediate. A more efficient trapping into the deep potential well of the singlet intermediate seems to be the explanation for the formation of a long-lived complex in the H-displacement process (reaction [1*b*]; this is favored by the significantly lower exoergicity with respect to the H-abstraction process and by the presence of a potential barrier in the exit channel (see Fig. 10).

No clear indication about a possible role of singlet–triplet surface crossing has been obtained in this study. While this will be responsible for the physical quenching of $O(^1D)$ to $O(^3P)$ by HBr, we can only speculate that it may also be involved in the OH-forming channel, as the observation that the OH internal energy distribution from the excited state reaction resembles that of the ground state reaction would suggest (see below). In this regard, recent work by Wategaonkar and Setser (57) on the H + OCl reaction, using infrared chemiluminescence in a fast flow reactor, should be noted. These authors measured the branching to OH + Cl and HCl + $O(^3P)$ with both sets of products being accessed from a bound singlet intermediate. The formation of the $O(^3P)$ + HCl was related to a singlet–triplet surface crossing in the exit channel of the HClO configuration.

A full dynamic description of $O(^1D)$ reactions, which have the characteristics of releasing a very large amount of energy into a strongly bound intermediate, needs to take into account the stability of the singlet intermediate and of its possible isomers, the exoergicity of the process, the multiplicity of the electronic state of the product and the mass combination of the reagents. The present experimental results should facilitate attempts to model the dynamics of the $O(^1D)$ + HX reactions using realistic potential energy surfaces.

C. Comparison with $O(^3P)$ + HBr → OH + Br

The reaction of ground state oxygen with HBr is known to be about four orders of magnitude slower than the reaction of electronically excited oxygen, with the room temperature rate constant being $k_{298} = 3.4 \times 10^{-14}$ cm^{-3} molecule^{-1} s^{-1} and the activation energy of about 3.4 kcal/mol (2–4). In Figs. 9 and 10 the energy level and correlation diagram are also shown for $O(^3P)$. An early ESR flow-tube study found that the OH product vibrational distribution was very strongly inverted (58). More recently, a very detailed dynamical study was performed by Zare and co-workers (10) and a quantitative measure of the product internal energy disposal was provided. It was found that on the average, for collision energies up to 6 kcal/mol, about 75% of the available energy appears as internal (vibrational + rotational) excitation of the OH product, with very strong vibrational and rotational inversion. The OH(v = 0, 1, 2) states were found to be populated in the ratio of (0:9:1) and the dominant product channels are those rotational levels in OH(v = 1) and OH(v = 2) approximately thermoneutral with respect to the reagents. In order to explain an anomaly in the OH(v = 1) rotational distribution it was proposed that 6% of the outcome of the reaction involved the excited state $Br(^2P_{1/2})$ + $OH(^2\Pi)$ channel (see Fig. 10). The results were rationalized in terms of a direct abstraction mechanism and supported by classical trajectory calculations, which for the $O(^3P)$ + HBr mass combination (**H** + **LH′** → **HL** + **H′**) predict that a large fraction of the kinetic energy available will appear as internal excitation. This is the result of kinematic influences of the PES. The trajectory calculations have shown, in fact, that vibrational excitation arises because of the so-called "corner-cutting" trajectories where the dynamics are dominated by the rapid motion of the light H-atom relative to the heavy atoms. It should be noted, however, that these trajectory studies make use of a single PES, and nonadiabatic effects are therefore neglected. It was concluded (10) that the rotational excitation of the OH product derives from the repulsive interaction in the breaking of the OH—Br (Light—Heavy) bond. The transition state geometry is quite bent and this imparts a large torque on the departing OH moiety with efficient conversion of the repulsive energy into product rotation.

The similarity of the OH energy distribution from the reaction: $O(^1D)$ + HBr → OH + Br to that of the $O(^3P)$ reaction suggests the possibility that some $O(^1D)$/HBr collisions which begin on the $^1A'$ surface may switch to the $^3A''$ surface in the entrance channel and finish the reaction on the triplet surface. This spin–orbit crossing is an intriguing possibility which has been puzzling dynamicists for some time. It is known that the physical quenching of $O(^1D)$ to $O(^3P)$ by HBr, which accounts for about 20% of all $O(^1D)$ + HBr collisions at room temperature (7), involves a singlet–triplet crossing. So far, however, there is no direct evidence that this surface crossing also forms OH in $O(^1D)$ reactions with any species. The most commonly accepted mechanism for this is the insertion of $O(^1D)$ into the H—Br bond on the $^1A'$ surface to form a vibrationally hot HOBr complex, which fragments very rapidly within a few bending vibrations into OH + Br. This insertion mechanism is consistent with the observation of the stabilized complex in the $O(^1D)$ + HX (X = Cl, Br), reactions, when these occur in an argon matrix (59). We note parenthetically that the observation of high rotational excitation in the products of the gas phase reaction, to which we have referred earlier, does not contradict the insertion mechanism because Monte Carlo simulations of the $O(^1D)$ + HCl reaction using a statistical model suggest (60) that the high OH rotational excitation arises from angular momentum constraints and has no unique dynamical origin.

It has been noted that the energy partitioning of both the ground state and excited state reactions resembles that of the direct abstraction reaction of F with HBr (34, 61). The observation, however, of a marked propensity for production of the $\Pi(A')$ λ component in the OH product of the $O(^1D)$ + HCl reaction (13) implies that the half-filled π orbital of OH lies preferentially oriented in its rotational plane and remains in the plane of the dissociating triatomic complex. This fact led to the con-

clusion that only the ground $HOCl(X^1A')$ state is involved in the reaction (13). This finding suggests that a possible role of the $^3A''$ state in the reaction with HBr is precluded as well, since the overall dynamics does not seem to change appreciably when HCl is replaced by HBr.

A clarification of the possible role of single–triplet surface crossings and of the similarity with the F + HX reactions has to await the results of dynamical calculations on reliable potential energy surfaces. Finally, it should be noted that the $O(^3P, ^1D)$ + HX systems are good candidates for studies investigating the role of multiple potential surfaces and nonadiabatic effects on chemical reaction dynamics.

Acknowledgements

N.B., L.B., P.C., and G.G.V. gratefully acknowledge financial support from the Italian "Consiglio Nazionale delle Ricerche — Progetto Finalizzato Chimica Fine" and "Ministero Università e Ricerca Scientifica". J.J.S. gratefully acknowledges financial support from the Natural Sciences and Engineering Research Council of Canada. Several aspects of the research reported here were made possible by a NATO collaborative grant (CRG. 920549) between P.C. and J.J.S.

1. A.R. Ravishankara, G. Smith, R.T. Watson, and D.D. Davis. J. Phys. Chem. **81**, 220 (1977).
2. R.D.H. Brown and I.W.M. Smith. Int. J. Chem. Kinet. **7**, 301 (1975); **10**, 1 (1978).
3. D.L. Singleton and R.J. Cvetanovic. Can. J. Chem. **56**, 2934 (1978).
4. B.S. Agrawalla, A.S. Manocha, and D.W. Setser. J. Phys. Chem. **85**, 2873 (1981); D.F. Nava, S.R. Bosco, and L.J. Stief. J. Chem. Phys. **78**, 2443 (1983).
5. K. Mahmud, J.S. Kim, and A. Fontijn. J. Phys. Chem. **94**, 2994 (1990).
6. J.A. Davidson, C.M. Sadowski, H.I. Schiff, G.E. Streit, C.J. Howard, D.A. Jennings, and A.L. Schmeltekopf. J. Chem. Phys. **64**, 57 (1976); J.A. Davidson, H.I. Schiff, G.E. Streit, J.R. McAfee, A.L. Schmeltekopf, and C.J. Howard. J. Chem. Phys. **67**, 5021 (1977).
7. P.H. Wine, J.R. Wells, and A.R. Ravishankara. J. Chem. Phys. **84**, 1349 (1986).
8. K. Schofield. J. Photochem. **9**, 55 (1978).
9. K. Schofield. J. Phys. Chem. Ref. Data, **8**, 25 (1979); R.E. Hine and J.T. Herron. Prog. Reaction Kinet. **8**, 1 (1985); R.J. Cvetanovic and D.L. Singleton. Rev. Chem. Intermediates, 5, 183 (1984); M.C. Lin. *In* Reactions of small transient species. *Edited by* M.A.A. Clyne and A. Fontijn. Academic, London. 1983.
10. K.G. McKendrick, D.J. Rakestraw, R. Zhang, and R.N. Zare. J. Phys. Chem. **92**, 5530 (1988).
11. D.J. Rakestraw, K.G. McKendrick, and R.N. Zare. J. Chem. Phys. **87**, 7341 (1987); K.G. McKendrick, D.J. Rakestraw, and R.N. Zare. J. Chem. Soc. Faraday Discuss. **84**, 39 (1987).
12. A.C. Luntz. J. Chem. Phys. **73**, 5393 (1980).
13. C.R. Park and J.R. Wiesenfeld. Chem. Phys. Lett. **163**, 230 (1989).
14. E.J. Kruus, B.I. Niefer, and J.J. Sloan. J. Chem. Phys. **88**, 985 (1988).
15. N. Balucani, L. Beneventi, P. Casavecchia, and G.G. Volpi. Chem. Phys. Lett. **180**, 34 (1991).
16. (*a*) P.J. Bruna, G. Hirsch, S.D. Peyerimhoff, and R.J. Buenker. Can. J. Chem. **57**, 1839 (1979); (*b*) R. Schinke. J. Chem. Phys. **80**, 5510 (1984); (*c*) H. Kornweitz, A. Persky, I. Schechter, and R.D. Levine. Chem. Phys. Lett. **169**, 489 (1990); H. Koizumi and G.C. Schatz. J. Chem. Phys. **95**, 6421 (1991); V. Aquilanti, S. Cavalli, G. Grossi, V. Pellizzari, M. Rosi, A. Sgamellotti, and F. Tarantelli. Abstracts XI Int. Symposium on Gas Kinetics, Assisi (Italy), September 1990, p. O26.
17. X. Yang and P.J. Dagdigian. Chem. Phys. Lett. **200**, 217 (1992), and references therein.
18. J.M. Mestdagh, B.A. Balko, M.H. Covinsky, P.S. Weiss, M.F. Vernon, H. Schmidt, and Y.T. Lee. Faraday Discuss. Chem. Soc. **84**, 145 (1987); A.G. Suits, H. Hou, H.F. Davis, Y.T. Lee, and J.M. Mestdagh. J. Chem. Phys. **95**, 8178 (1991); A.G. Suits, H. Hou, H.F. Davis, and Y.T. Lee. J. Chem. Phys. **96**, 2777 (1992).
19. J.-M. L'Hermite, G. Rahmat, and R. Vetter. J. Chem. Phys. **95**, 3347 (1991) and references therein; M. Menendez, M. Garay, E. Verdasco, and A. Gonzales Urena. J. Chem. Soc. Faraday Trans. **89**, 1493 (1993); M. Garay, M. Menendez, E. Verdasco, J. Castano, and A. Gonzales Urena. J. Phys. Chem. **97**, 5836 (1993); C.T. Rettner and R.N. Zare. J. Chem. Phys. **77**, 2416 (1982); R. Duren, U. Lackschewitz, and S. Milosevic. Chem. Phys. **126**, 81 (1988); F.X. Gadea, J.M. L'Hermite, G. Rahmat, and R. Vetter. Chem. Phys. Lett. **151**, 183 (1988); J. Cuvellier, P. de Pujo, J.M. Mestdagh, P. Meynadier, J.P. Visticot, J. Berlande, and A. Binet. J. Chem. Phys. **90**, 7050 (1989).
20. N. Balucani, L. Beneventi, P. Casavecchia, D. Stranges, and G.G. Volpi. J. Chem. Phys. **94**, 8611 (1991); Faraday Discuss. Chem. Soc. **91**, 147 (1991); Faraday Discuss. Chem. Soc. **91**, 147 (1991); Faraday Discuss. Chem. Soc. **91**, 383 (1991).
21. P. Casavecchia, N. Balucani, and G.G. Volpi. *In* Research in chemical kinetics. Vol. 1. *Edited by* R.G. Compton and G. Hancock. Elsevier, Amsterdam. 1993. In press.
22. R.J. Salawitch, S.C. Wofsky, and M.B. McElroy. Planet. Space Sci. **36**, 213 (1988); S. Salomon, Nature, **347**, 347 (1990).
23. Scientific assessment of ozone depletion: 1991, WMO/UNEP report. 1992.
24. J.E. Thompson and A.R. Ravishankara. Int. J. Chem. Kinet. **25**, 479 (1993).
25. J.G. Anderson. Ann. Rev. Phys. Chem. **38**, 489 (1987).
26. A.A. Turnipseed, J.W. Birks, and J.G. Calvert. J. Phys. Chem. **94**, 7477 (1990).
27. A.J. Hills, R.J. Cicerone, J.G. Calvert, and J.W. Birks. J. Phys. Chem. **92**, 853 (1988); R.R. Friedl and S.P. Sander. J. Phys. Chem. **93**, 4756 (1989).
28. D.L. Baulch, R.A. Cox, P.J. Crutzen, R.F. Hampson, Jr., J.A. Kerr, J. Troe, and R.T. Watson. J. Phys. Chem. Ref. Data, **11**, 327 (1982).
29. L. Beneventi, P. Casavecchia, and G.G. Volpi. J. Chem. Phys. **85**, 7011 (1986); *In* Electronic and atomic collisions. Invited Papers XVII ICPEAC, Brisbane. 1991, *Edited by* W.R. MacGillivary, I.E. McCarthy, and M.C. Standage. IOP, Bristol. 1992. p. 527 and references therein; L. Beneventi, P. Casavecchia, G.G. Volpi, C.R. Bieler, and K.C. Janda. J. Chem. Phys. **98**, 178 (1993).
30. S.J. Sibener, R.J. Buss, C.Y. Ng, and Y.T. Lee. Rev. Sci. Instrum. **51**, 167 (1980).
31. K. Sköld. Nucl. Instr. Methods, **63**, 114 (1968).
32. R.K. Sparks, L.R. Carlson, K. Shobotake, M.L. Kowalczy, and Y.T. Lee. J. Chem. Phys. **72**, 1401 (1980); J.J. Valentini. Chem. Phys. Lett. **96**, 395 (1983); T. Kinugawa, T. Sato, T. Arikawa, Y. Matsumi, and M. Kawasaki. J. Chem. Phys. **93**, 3289 (1990).
33. P. Andresen and A.C. Luntz. J. Chem. Phys. **72**, 5842 (1980); A.C. Luntz and P. Andresen. J. Chem. Phys. **72**, 5851 (1980).
34. J.W. Hepburn, K. Liu, R.G. MacDonald, F.J. Northrup, and J.C. Polanyi. J. Chem. Phys. **75**, 3353 (1981).
35. A.M.G. Ding, L.J. Kirsch, D.S. Perry, J.C. Polanyi, and J.L. Schreiber. Faraday Discuss. Chem. Soc. **55**, 252 (1973); P.A. Berg and J.J. Sloan. Unpublished results.
36. P.M. Aker and J.J. Sloan. *In* Time-resolved vibrational spectroscopy. Springer proceedings in physics. Vol. 4. *Edited by* A. Labereau and M. Stockburger. Springer, Berlin. 1985; J.J. Sloan, P.M. Aker, and B.I. Niefer. Proc. SPIE, **669**, 169 (1986).
37. E.J. Kruus and J.J. Sloan. *In* Advances in spectroscopy. Vol. 18. Time-resolved spectroscopy. *Edited by* R.J.H. Clark and R.E. Hester. John Wiley and Sons. 1989. Chapt. 5.
38. P.A. Berg and J.J. Sloan. Rev. Sci. Instrum. **64**, 2508 (1993).

Can. J. Chem. Downloaded from www.nrcresearchpress.com by 195.246.54.202 on 09/08/12
For personal use only.

39. R.J. Buss. Ph.D. Thesis, University of California, Berkeley. 1979. LBL-9057.
40. Y.T. Lee. *In* Atomic and molecular beam methods. *Edited by* G. Scoles. Oxford University, New York. 1987. Vol. 1.
41. R.D. Levine and R.B. Bernstein. Molecular reaction dynamics. Oxford Univ. Press, Oxford. 1974. p. 44.
42. W.B. Miller, S.A. Safron, and D.R. Herschbach. Discussion Faraday Soc. **44**, 108 (1967).
43. T.P. Parr, A. Freedman, R. Behrens, and R.R. Herm. J. Chem. Phys. **67**, 2181 (1977); S.-M. Lin, C.A. Mims, and R.R. Herm. J. Phys. Chem. **77**, 569 (1973).
44. S.R. Langhoff, H.-J. Werner, and P. Rosmus. J. Mol. Spectrosc. **118**, 507 (1986).
45. P.M. Aker, J.J.A. O'Brien, and J.J. Sloan. J. Chem. Phys. **84**, 745 (1986).
46. E.J. Kruus, B.I. Niefer, and J.J. Sloan. J. Photochem. Photobiol. A: Chem. **57**, 419 (1991).
47. A.M. Schmoltner, P.M. Chu, and Y.T. Lee. J. Chem. Phys. **91**, 5365 (1989).
48. W.L. Fitch and A.D. Sauter. Anal. Chem. **55**, 832 (1983).
49. Y. Matsumi, K. Tonokura, M. Kavasaki, K. Tsuji, and K. Obi. J. Chem. Phys. **98**, 8330 (1993).
50. S.J. Singer, K.F. Freed, and Y.B. Band. Adv. Chem. Phys. **61**, 1 (1985).
51. P.M. Aker. Ph.D. Thesis, Carleton University, Ottawa, Canada. 1986; P.M. Aker and J.J. Sloan. J. Chem. Phys. **85**, 1412 (1986); J.E. Butler, R. Glen MacDonald, D.J. Donaldson, and J.J. Sloan. Chem. Phys. Lett. **95**, 183 (1983).
52. C.R. Park and J.R. Wiesenfeld. J. Chem. Phys. **95**, 8160 (1991).
53. J.C. Polanyi and J.L. Schreiber. *In* Physical chemistry: an advanced treatise. Vol. 6A. *Edited by* W. Jost. Academic Press, New York. 1974. p. 383.
54. M.K. Gilles, M.L. Polak, and W.C. Lineberger. J. Chem. Phys. **96**, 8012 (1992).
55. (*a*) L.M. Loewnstein and J.C. Anderson. J. Phys. Chem. **91**, 2993 (1987); (*b*) S.W. Benson. Thermochemical kinetics. 2nd ed. Wiley and Sons, New York. 1976. p. 292; (*c*) H. Okabe. Photochemistry of small molecules. Wiley and Sons, New York. 1978. p. 376.
56. P.J. Kuntz. *In* Dynamics of molecular collisions. Part B. *Edited by* W.H. Miller. Plenum, New York. 1976.
57. S.J. Wategaomkar and D.W. Setser. J. Chem. Phys. **90**, 6223 (1989).
58. J.E. Spencer and G.P. Glass. Int. J. Chem. Kinet. **11**, 97 (1977).
59. I. Schwager and A. Arkell. J. Am Chem. Soc. **89**, 6006 (1967).
60. K. Rynefors, P.A. Elofson, and L. Holmid. Chem. Phys. **100**, 53 (1985).
61. K. Tamagake, D.W. Setser, and J.P. Sung. J. Chem. Phys. **73**, 2203 (1980); B.S. Agrawalla and D.W. Setser. J. Phys. Chem. **90**, 2450 (1986).

Can. J. Chem. Downloaded from www.nrcresearchpress.com by 195.246.54.202 on 09/08/12
For personal use only.

A coupled channel hyperspherical scattering study of the Cl + HCl → ClH + Cl reaction: cumulative and state-selected probabilities, integral cross sections, and product rotational distributions

GEORGE C. SCHATZ[1]
Theoretical Chemistry Group, Argonne National Laboratory, Argonne, IL 60439, U.S.A.

AND

D. SOKOLOVSKI AND J.N.L. CONNOR
Department of Chemistry, University of Manchester, Manchester M13 9PL, England

Received August 31, 1993

This paper is dedicated to Professor John C. Polanyi on the occasion of his 65th birthday

GEORGE C. SCHATZ, D. SOKOLOVSKI, and J.N.L. CONNOR. Can. J. Chem. **72**, 903 (1994).

We present accurate quantum results for the Cl + HCl → ClH + Cl reaction using a coupled channel hyperspherical coordinate method (denoted CCH). A semiempirical extended London–Eyring–Polanyi–Sato potential energy surface is employed. In our calculations, the body-fixed z projection quantum number Ω in the rotational basis set has been truncated at $\Omega_{max} = 2$, since this is sufficient to give converged results near to, and above, the reaction threshold (total energies E in the range 0.40–0.60 eV). We compare our results with earlier work using the centrifugal sudden hyperspherical (CSH) method, in which only $\Omega = 0$ is included in the basis; other features of the calculations are identical. At $E = 0.40$ eV, where reactivity is low, the CCH($\Omega_{max} = 2$) and CSH($\Omega = 0$) degeneracy averaged reaction probabilities, integral cross sections and product rotational distributions are mostly in excellent agreement. This agreement deteriorates with increasing E, such that at $E = 0.60$ eV, the CCH($\Omega_{max} = 2$) cumulative reaction probability is approximately twice its CSH($\Omega = 0$) counterpart. Even at $E = 0.40$ eV there are some important differences between CCH($\Omega_{max} = 2$) and CSH($\Omega = 0$) concerning m_j-resolved reaction probabilities. In addition, there are differences in the relative contributions of "tight bend" and "nearly free-rotor" mechanisms to the reaction probabilities and product rotational distributions, with the "nearly free-rotor" mechanism dominant in all cases.

GEORGE C. SCHATZ, D. SOKOLOVSKI et J.N.L. CONNOR. Can. J. Chem. **72**, 903 (1994).

On présente des résultats quantiques précis obtenus pour la réaction Cl + HCl → ClH + Cl en faisant appel à une méthode de coordonnées hypersphériques à canal couplé (dénotée CCH). On emploie une surface d'énergie potentielle semi-empirique de London–Eyring–Polanyi–Sato étendue. Dans nos calculs, le nombre quantique Ω de la projection z du corps fixé dans l'ensemble rotationnel de base a été tronqué au niveau de $\Omega_{max} = 2$ parce que ce niveau est suffisant pour obtenir des résultats convergents au niveau du, et au-dessus du, niveau limite de la réaction (énergies totales, E, allant de 0,40 à 0,60 eV). On compare nos résultats avec ceux d'un travail antérieur en utilisant la méthode centrifuge devant soudainement hypersphérique (CSH) dans laquelle on n'inclut que $\Omega = 0$ dans la base alors que les autres caractéristiques des calculs sont identiques. Au niveau de $E = 0{,}40$ eV où la réactivité est faible, les méthodes CCH($\Omega_{max} = 2$) et CSH($\Omega = 0$) sont en excellent accord pour prédire les probabilités moyennes de réactions causées par une dégénérescence, les sections droites intégrales et les distributions rotationnelles du produit. L'accord devient moins bon lorsqu'on augmente la valeur de E; par exemple, lorsque $E = 0{,}60$, la probabilité réactionnelle cumulative selon CCH($\Omega_{max} = 2$) est environ deux fois plus grande que celle prédite par la méthode CSH($\Omega = 0$). Même au niveau de $E = 0{,}40$, il existe quelques différences importantes entres les méthodes CCH($\Omega_{max} = 2$) et CSH($\Omega = 0$) concernant les probabilités réactionnelles résolues selon m_j. De plus, il existe des différences dans les contributions relatives des mécanismes "courbure serrée" et "rotor pratiquement libre" aux probabilités réactionnelles et aux distributions rotationnelles des produits; le mécanisme à "rotor pratiquement libre" est dominant dans tous les cas.

[Traduit par la rédaction]

I. Introduction

The reaction

$$Cl + HCl \rightarrow ClH + Cl$$

is a prototype for heavy–light–heavy (**HLH**) atom-exchange reactions, an area of research pioneered by John Polanyi. As such, the Cl + HCl reaction has been the subject of numerous theoretical investigations, including studies of its potential energy surface (reviewed in refs. 1, 2), quasiclassical trajectory calculations (reviewed in ref. 3), and quantum dynamics computations (reviewed in refs. 4, 5). There have also been experimental measurements, in particular of thermal rate coefficients (reviewed in ref. 6)[2] and of transition state photodetachment spectra (reviewed in ref. 7).

Interest in the quantum dynamics of Cl + HCl has evolved through a number of stages. The early collinear calculations of Bondi et al. (8) computed accurate reaction probabilities and studied the diagonally corrected vibrationally adiabatic hyperspherical (DIVAH) approximation (8). Then various three dimensional quantum approximations were developed and applied, such as the centrifugal sudden distorted wave (CSDW) method (9). In recent years, a significant amount of work has used the centrifugal sudden hyperspherical (CSH) technique (ref. 10, reviewed in ref. 5). In this technique, the Schrödinger equation is first solved exactly for the case where the total angular momentum quantum number is zero ($J = 0$) using a coupled channel (CC) method, and then the CS approximation is used to generate results for $J > 0$, so that partial wave sums can be evaluated. In the CSH method, Ω, the quantum number for the body-fixed z projection of the total angular momentum, is fixed for each coupled-channel calculation, and

[1]Permanent address: Department of Chemistry, Northwestern University, Evanston IL 60208-3113, U.S.A.

[2]On p. 4406, ref. 6, $R_s = 2.80677\,a_0$ should read $R_s = 2.80677$ Å.

Can. J. Chem. Downloaded from www.nrcresearchpress.com by 195.246.54.202 on 09/08/12
For personal use only.

Can. J. Chem. Downloaded from www.nrcresearchpress.com by 195.246.54.202 on 09/08/12
For personal use only.

then summed over in order to calculate cross sections and rate coefficients.

For a reaction with a minimum barrier height in the collinear geometry, it is the $\Omega = 0$ state which has the largest reaction probability at energies close to the threshold for reaction. Most CSH calculations have therefore been restricted to $\Omega = 0$, with adiabatic bend and related approximations used to perform the sum over Ω (11). Note that many of the commonly used semiempirical potential energy surfaces for Cl + HCl also possess collinear saddle points, although *ab initio* calculations show that the saddle point configuration is bent (6, 12).

In this paper, we present the first results of coupled channel hyperspherical (CCH) calculations for Cl + HCl in which states with different values of Ω are allowed to couple. Although the rotational basis set we use does not include all possible Ω's (the maximum value for Ω is $\Omega_{max} = 2$), the results should be almost converged at the energies we have studied. Of course, convergence with respect to other features of the vibration/rotation basis set has already been demonstrated in our CSH($\Omega = 0$) calculations (5, 10), so the present results should be free of basis set truncation errors.

The main impediment in the present calculations has been computational. For each J, the size of the coupled-channel basis set grows significantly in going from a CSH($\Omega = 0$) to a CCH($\Omega_{max} = 2$) calculation (from 80 states for CSH($\Omega = 0$) to a maximum of 364 states for CCH($\Omega_{max} = 2$) at $E = 0.60$ eV). In addition, a large number of partial waves must be included (up to $J_{max} = 140$ in the present applications). There are also significant disk storage needs (~1 GByte) associated with the intermediate files used during the calculations. Memory is also required to store the scattering information for later analysis (~0.3 GBytes). Our calculations would not be feasible without the Ω_{max} truncation of the allowed values of Ω in the rotational basis set, since the maximum allowed value for Ω is much larger than $\Omega_{max} = 2$.

This Ω_{max} truncation approach has previously been used by Launay et al. in studies of the H + H_2, F + H_2, He + H_2^+, and Cl + H_2 reactions (13). Our application is similar, except that we use Delves' hyperspherical coordinates (14) and a body-fixed representation in which the quantization axis is taken along the atom–diatom Jacobi vector in each arrangement channel. In this approach, Ω-coupling arises in two ways (15): (*a*) from the centrifugal operator for each arrangement channel, and (*b*) from the transformation of coordinates between the reagent and product arrangement channels. For Cl + HCl, the coupling present in the centrifugal operator is generally weak because different Ω's correspond to different bending states of the ClH-Cl saddle point complex, which are approximately separated by the 0.07 eV (600 cm^{-1}) saddle point harmonic bending energy. In contrast, the coupling that arises from the coordinate transformation can be weak or strong, depending on the angle between the reagent and product Jacobi vectors and on the value of J. For Cl + HCl, we are aided by the fact that the **HLH** mass combination and the potential energy surface greatly favor reaction through geometries where the reagent and product helicity axes are approximately antiparallel, i.e., the reagent atom–diatom Jacobi vector is approximately antiparallel to the corresponding product Jacobi vector because the center-of-mass of the **HL** diatom lies close to the **H** atom. If these two vectors were exactly antiparallel, as occurs for the collinear configuration, the coupling would vanish for all J, which makes it likely that the coupling is weak for the real system.

TABLE 1. CCH partial wave cumulative reaction probability $P^J(E)$ as a function of Ω_{max} for $J = 10$ using a small basis in each arrangement channel, $v = 0$ and $j = 0$–3

	$P^J(E)$			
	E/eV = 0.40		E/eV = 0.50	
Ω_{max}	Even parity	Odd parity	Even parity	Odd parity
0	0.0832	0	0.9974	0
1	0.0854	0.0022	1.0328	0.0356
2	0.0855	0.0023	1.0329	0.0357
3	0.0855	0.0023	1.0329	0.0357

Section II presents some computational details of our CCH calculations. Section III contains our results, including the J dependence of cumulative and state selected reaction probabilities, the energy dependence of integral cross reactions and probabilities, and product rotational distributions. Our conclusions are in Section IV.

II. Calculations

The potential surface used in all our calculations is the semiempirical extended LEPS (London–Eyring–Polanyi–Sato) function developed by Bondi et al. (8). This BCMR surface has been used in many earlier studies (1–5, 8–11, 16, 17), and a recent comparison with large scale accurate *ab initio* calculations (12) indicates that it is fairly realistic even though it has a collinear saddle point. In addition, thermal rate coefficients calculated by the CSH($\Omega = 0$) method for the BCMR surface are in good agreement with experiment (5, 11).

The CCH method employed for the dynamics calculations has been described in detail previously (10, 17, 18) with the exception of the truncated Ω_{max} procedure. The CCH method expands the wavefunction in a set of vibration–rotation basis functions, defined in terms of Delves' hyperspherical coordinates for each of the two arrangement channels, i.e., reagents and products. The variable describing rotational motion in Delves' coordinates is just the usual Jacobi angle, so a free diatomic rotor basis is used, labelled by the quantum numbers j and Ω. Here Ω is the projection quantum number along the body-fixed z axis for both the total angular momentum quantum number J and the rotational angular quantum number momentum j, which means that the constant $|\Omega| \leq \min(j, J)$ applies in the absence of truncation. In the truncated version, the constraint is modified to $|\Omega| \leq \min(j, J, \Omega_{max})$ where $\Omega_{max} \geq 0$ is chosen large enough to converge the reaction probabilities, as will be illustrated below. The vibrational part of the basis set is defined using numerically determined solutions of a reference potential which changes with hyperradius such that it merges with the isolated diatomic potential at long range.

Table 1 shows the convergence of the CCH partial wave cumulative reaction probability, $P^J(E)$ with Ω_{max} for $J = 10$ at $E = 0.40$ and 0.50 eV, using a relatively small basis ($v = 0$, $j = 0$–3 for each arrangement channel) where it is possible to include all Ω's (denoted $\Omega_{max} = 3$). $P^J(E)$ is the sum over all open reagent and product states of the state-to-state reaction probability, and E is the total energy relative to the minimum of the Cl + HCl potential. At $E = 0.40$ eV, which is just at the threshold for reaction, $P^J(E)$ for $\Omega_{max} = 0$ is already within 3% of the full CCH value for even parity, while $\Omega_{max} = 1$ gives essentially exact results. At $E = 0.50$ eV, the partial

TABLE 2. CCH($\Omega_{max} = 2$) and CSH($\Omega = 0$) cumulative reaction probabilities, integral cross sections, and product rotational energy partitioning

	Value for E/eV =				
Property	0.40	0.45	0.50	0.55	0.60
	(a) CCH($\Omega_{max} = 2$) using partial waves J = 0(1)3, 10(10)60, 80(20)140				
$P(E)$	78.1	22.9×10^2	78.6×10^2	20.3×10^3	41.6×10^3
$\hat{j}_0$	9	10	11	12	12
$Q_{0\hat{j}}(E)/a_0^2$	0.021	0.32	0.73	1.97	2.27
$\langle j' \rangle_{0\hat{j}}$	8.1	8.7	10.1	11.0	10.9
	(b) CSH($\Omega = 0$) using partial waves J = 0(1)3, 10(10)60, 80(20)140				
$P(E)$	83.1	23.8×10^2	61.1×10^2	10.8×10^3	17.6×10^3
$\hat{j}_0$	9	10	10	12	12
$Q_{0\hat{j}}(E)/a_0^2$	0.024	0.35	0.43	0.79	0.83
$\langle j' \rangle_{0\hat{j}}$	8.1	8.7	9.1	10.0	9.5
	(c) CSH($\Omega = 0$) using partial waves J = 0(5)140[a]				
$P(E)$	85.4	24.4×10^2	66.3×10^2	12.2×10^3	19.6×10^3
$\hat{j}_0$	9	10	10	12	12
$Q_{0\hat{j}}(E)/a_0^2$	0.025	0.36	0.48	0.85	0.96
$\langle j' \rangle_{0\hat{j}}$	8.1	8.7	9.0	10.1	9.6

[a] J = 0(1)100 at E = 0.40 eV, J = 0(5)100 at E = 0.45 eV, and J = 0(5)110 at E = 0.50 eV.

wave cumulative reaction probability is much larger, but the $\Omega_{max} = 0$ result is in error by only 4% and $\Omega_{max} = 2$ is fully converged.

In the more extensive calculations reported in the next section, we used a basis consisting of three vibrations, with j_{max} = 19, 13, and 5 for v = 0, 1, and 2, respectively. For $J = 0$ this results in 40 states for each of the two arrangement channels, giving a total of 80 states. This is the same basis set that we used in our previous CSH($\Omega = 0$) calculations (5, 10). For the CCH calculations with $\Omega_{max} = 2$, for $J \geq 2$, the basis set contains 222 and 142 functions for the two parity components. The calculations were performed for J = 0(1)3, 10(10)60, 80(20)140 at E = 0.40 (0.05) 0.60 eV. Linear interpolation of the reaction probabilities was employed to evaluate partial wave sums. We tested this procedure by using our earlier CSH($\Omega = 0$) reaction probabilities to calculate cross sections on two grids: (a) the same coarse grid employed in the CCH($\Omega_{max} = 2$) calculations, and (b) a finer grid consisting of every J for E = 0.40 eV and every 5th J for other energies. Comparison of the two sets of cross sections generally indicates convergence to within 14% (see Table 2). Unfortunately, it is difficult to calculate accurate scattering matrix elements and hence differential cross sections by this interpolation method, so we will not consider angular distributions in this paper. Note also that the energy range E = 0.40–0.60 eV does not include the transition state resonance analyzed in ref. 10.

III. Results

A. Definitions

The reaction probability P is labelled by the total angular momentum quantum number J and by the initial and final quantum numbers (v, j, m_j) and (v', j', m_j') respectively, where m_j is the reagent P-helicity quantum number, which initially is identical to $-\Omega$, and m_j' is the corresponding product quantum number, identical to Ω' (15). The integral reactive cross section Q is labelled by these same initial and final state quantum numbers. Q and P are related by the partial wave sum:

$$Q_{vjm_j \to v'j'm_j'}(E) = \frac{\pi}{k_{vj}^2} \sum_{J=0}^{\infty} (2J+1) P^J_{vjmj \to v'j'm_j'}(E)$$

where k_{vj} is the initial translational wavenumber. Degeneracy averaged cross sections are then defined by

$$Q_{vj \to v'j'}(E) = \frac{1}{2j+1} \sum_{m_j=-j}^{j} \sum_{m_j'=-j'}^{j'} Q_{vjmj \to v'j'm_j'}(E)$$

together with the cross section summed over final states

$$Q_{vj}(E) = \sum_{v'j'} Q_{vj \to v'j'}(E)$$

We will also consider the reaction probability summed over final states

$$P^J_{vjm_j}(E) = \sum_{v'j'm_j'} P^{J'}_{vjm_j \to v'j'm_j'}(E)$$

and its degeneracy average

$$P^J_{vj}(E) = \frac{1}{2j+1} \sum_{m_j} P^J_{vjm_j}(E)$$

as well as the partial wave cumulative reaction probability $P^J(E)$ given by

$$P^J(E) = \sum_{vjm_j} \sum_{v'j'm_j'} P^J_{vjm_j \to v'j'm_j'}(E)$$

where the summations are over all open initial and final rovibrational states. The sum over partial waves of $P^J(E)$ is the cumulative reaction probability $P(E)$, so that,

$$P(E) = \sum_{J=0}^{\infty} (2J+1) P^J(E)$$

Can. J. Chem. Downloaded from www.nrcresearchpress.com by 195.246.54.202 on 09/08/12
For personal use only.

Can. J. Chem. Downloaded from www.nrcresearchpress.com by 195.246.54.202 on 09/08/12
For personal use only.

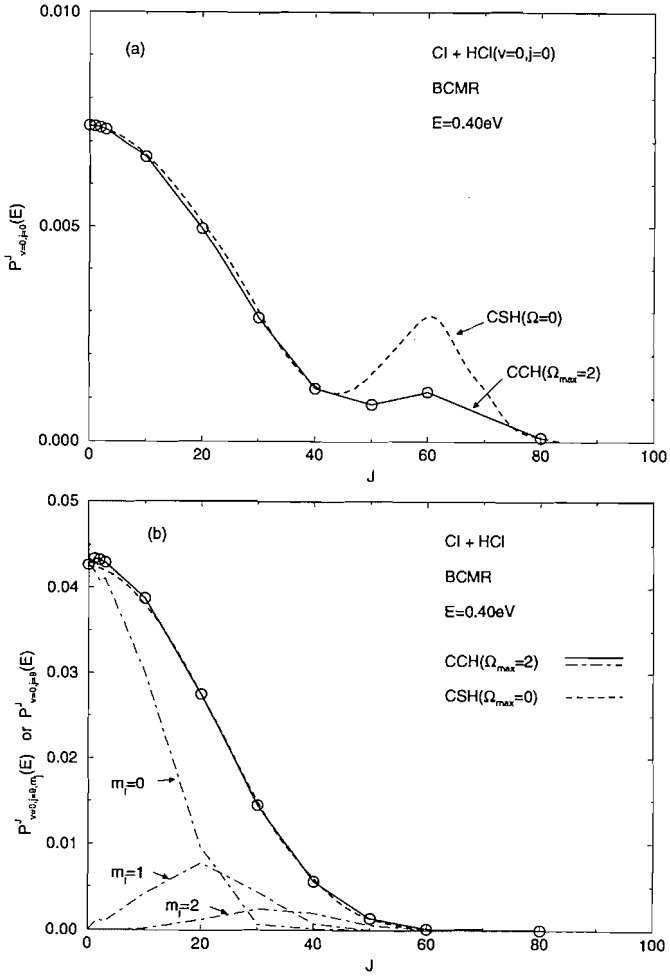

FIG. 1. Reaction probability versus J at $E = 0.40$ eV: (*a*) $P^J_{00}(E)$ with CCH($\Omega_{max} = 2$) (circles and solid curve) and CSH($\Omega = 0$) (dashes), (*b*) $P^J_{09}(E)$ with CCH($\Omega_{max} = 2$) (circles and solid curve) and CSH($\Omega = 0$) (dashes). Also shown are $P^J_{09m_j}(E)$ for CCH($\Omega_{max} = 2$) with $m_j = 0$, 1, 2 (dash–dot). Note that $P^J_{09-m_j}(E) = P^J_{09m_j}(E)$.

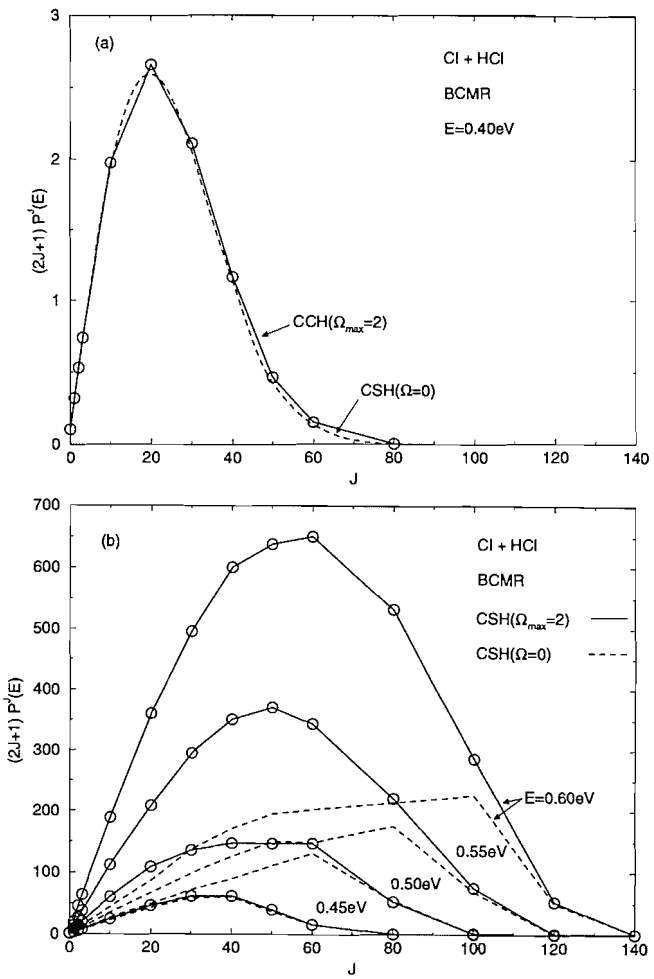

FIG. 2. $(2J + 1)P^J(E)$ versus J, showing CCH($\Omega_{max} = 2$) (circles and solid curves) and CSH($\Omega = 0$) (dashes). The energies are (*a*) $E = 0.40$ eV and (*b*) $E = 0.45$, 0.50, 0.55, and 0.60 eV.

The cumulative reaction probability is important for the reaction dynamics, because thermal rate coefficients may be obtained from a Boltzmann average of $P(E)$; however, we will not calculate thermal rate coefficients here, because the energy range over which CCH($\Omega_{max} = 2$) cross sections have been obtained is too limited for an accurate evaluation of the Boltzmann average.

B. J dependence of reaction probabilities

Figure 1 shows the J dependence of five CCH($\Omega_{max} = 2$) reaction probabilities at $E = 0.40$ eV. In Fig. 1*a* we plot $P^J_{vj}(E)$ vs. J for $v = 0, j = 0$, while in Fig. 1*b* are drawn $P^J_{vjm_j}(E)$ vs. J for $v = 0, j = 9, m_j = 0, 1, 2$ together with the degeneracy averaged reaction probability $P^J_{vj}(E)$ for $v = 0, j = 9$. Note that $P^J_{vj-m_j}(E) = P^J_{vjm_j}(E)$. Figure 2 shows $(2J + 1)P^J(E)$ vs. J at $E = 0.40$ eV (Fig. 2*a*) and at $E = 0.45$, 0.50, 0.55, 0.60 eV (Fig. 2*b*). We also plot the corresponding CSH($\Omega = 0$) probabilities in Figs. 1 and 2.

The most important result in Figs. 1 and 2 is that the CCH($\Omega_{max} = 2$) and CSH($\Omega = 0$) degeneracy averaged and cumulative reaction probabilities are in good agreement for nearly all J at $E = 0.40$ and 0.45 eV. At higher E, the CCH($\Omega_{max} = 2$) probabilities grow larger than CSH($\Omega = 0$) until at $E = 0.60$ eV the ratio CCH($\Omega_{max} = 2$)/CSH($\Omega = 0$) is 2–3 for $J = 30$–90 in Fig. 2*b*. At $E = 0.40$ eV, Fig. 1*b* indicates excellent agreement between the $v = 0, j = 9$ degeneracy averaged probabilities, even though values of $m_j \neq 0$ make a significant contribution to the CCH($\Omega_{max} = 2$) sum over m_j. The $v = 0, j = 0$ probabilities in Fig. 1*a* also agree closely, apart from the peak near $J = 60$ which is much larger for CSH($\Omega = 0$).

The $J = 60$ peak in Fig. 1*a* has previously (5) been connected with a minor part of the reaction mechanism on the BCMR potential surface in which relatively low rotor j states of the reagents react through a nearly collinear transition state, to produce low rotor j' states in the products. This "tight bend" mechanism is distinct from the dominant reaction pathway which involves nearly free rotational motion up to, and down from, the saddle point. This second "nearly-free rotor" mechanism favors reaction from high rotor j states (3, 16), and is thus the only significant mechanism involved in Fig. 1*b* where $j = 9$. However, in Fig. 1*a*, where $j = 0$, the first mechanism controls the high J peak, and we see that this is less pronounced in the CCH($\Omega_{max} = 2$) curve. A simple explanation for this result is that in a CCH calculation, it is possible to make transitions out of $\Omega = 0$ initial states (which dominate the reactivity in either mechanism) to $\Omega' \neq 0$ states, as the reaction occurs. This forces the reaction to follow noncollinear

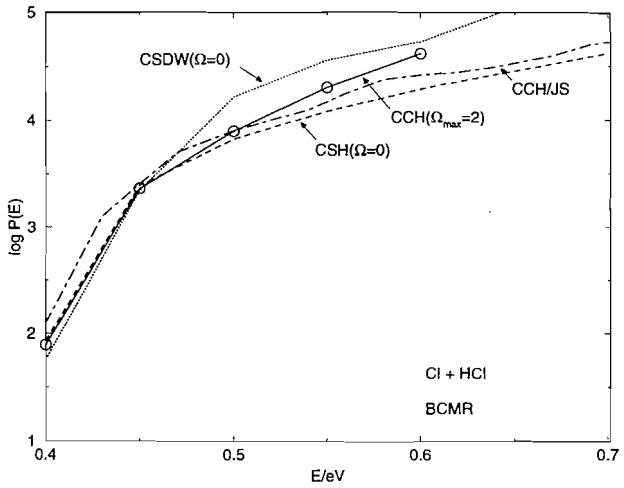

FIG. 3. log $P(E)$ versus E, showing CCH($\Omega_{max} = 2$) (circles and solid curve), CCH/JS (dash dot), CSH($\Omega = 0$) (dashes) and CSDW($\Omega = 0$) (dots).

geometries, because there is a centrifugal potential for $\Omega' \neq 0$ which makes the collinear geometry less accessible. Since the "tight bend" mechanism requires nearly collinear geometries, one thus expects it to be less important in a CCH calculation than in CSH($\Omega = 0$).

Note that the "tight bend" mechanism makes no significant contribution to the J dependence of $(2J+1)P^J(E)$ in Fig. 2, and as a result, the CCH($\Omega_{max} = 2$) and CSH($\Omega = 0$) curves are in good agreement at $E = 0.40$ eV. At higher E, the contributions of $\Omega \neq 0$ and $\Omega' \neq 0$ become important as is evident from Fig. 2*b*, and the CCH($\Omega_{max} = 2$) and CSH($\Omega = 0$) curves are close only in the $J = 0$ and large J limits.

C. Energy dependence of cross sections and probabilities

Table 2 shows the cumulative reaction probability $P(E)$ at the five energies we have done calculations, together with three other quantities: (*1*) the reactive section $Q_{0\hat{j}}(E)$ summed over final states for the reagent state $v = 0$ and $j = \hat{j}_0$, (*2*) $\hat{j}_0$, which is the value of j that has the largest $v = 0$ cross section, and (*3*) $\langle j' \rangle_{0\hat{j}}$, the average product rotational quantum number associated with reagent state $v = 0$, $j = \hat{j}_0$. The entries in this table labelled (*a*) and (*b*) show CCH ($\Omega_{max} = 2$) and CSH($\Omega = 0$) results using the same coarse grid of partial waves. Entry (*c*) reports CSH($\Omega = 0$) results calculated from the finer partial wave grids that were used in our earlier work (5). Figure 3 shows $P(E)$ vs. E for the CCH($\Omega_{max} = 2$) and CSH($\Omega = 0$) calculations, as well as for two other approximations (5), namely (*a*) CCH/JS, a J-shifted $\Omega = 0$ calculation (11) in which only CCH($J = 0$) calculations are done, and (*b*) CSDW($\Omega = 0$), centrifugal sudden distorted wave (9, 16) calculations.

There are three significant conclusions to be drawn from Table 2 and Fig. 3, namely: (*1*) The two sets of CSH($\Omega = 0$) results for $P(E)$ and $Q_{0\hat{j}}(E)$ (i.e., from the finer and coarser partial wave grids) are in good agreement, differing by 4% at $E = 0.40$ eV and 14% at $E = 0.60$ eV. This indicates the accuracy to be expected for the CCH($\Omega_{max} = 2$) results due to the linear interpolation of the partial waves. (*2*) At $E = 0.40$ and 0.45 eV, the CCH($\Omega_{max} = 2$) and CSH($\Omega = 0$) $P(E)$ are in close agreement (6% at $E = 0.40$ eV and 4% at $E = 0.45$ eV). This is the expected result at low E, where only the $\Omega = 0$ ground bending state of the saddle

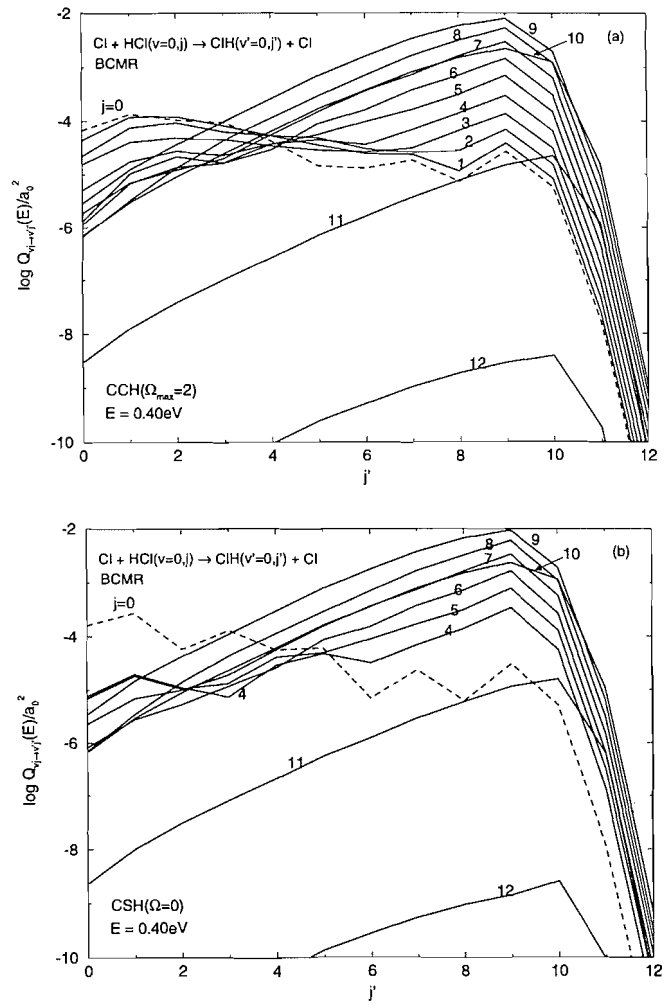

FIG. 4. log $Q_{vj \to v'j'}(E)$ versus j' at $E = 0.40$ eV for $v = v' = 0$ and j in the range between 0 and 12: (*a*) CCH($\Omega_{max} = 2$) results, with the $j = 0$ result displayed using a dashed curve; (*b*) CSH($\Omega = 0$) results, with $j = 1$–3 omitted for clarity of presentation and a dashed curve used for $j = 0$.

point complex contributes to tunnelling through the barrier. At higher E, the CCH($\Omega_{max} = 2$) and CSH($\Omega = 0$) $P(E)$ diverge, differing by a factor of 2.4 at $E = 0.60$ eV. This presumably reflects the contribution of excited bending states to the reaction probabilities. (*3*) Of the three approximate $P(E)$ shown in Fig. 3, it is the CSH($\Omega = 0$) $P(E)$ that agrees best with CCH($\Omega_{max} = 2$) at low E. At higher E, none of the approximate theories include states with $\Omega \neq 0$, so agreement is not expected. Note that CSDW($\Omega = 0$) predicts an even higher $P(E)$ than CCH($\Omega_{max} = 2$), but this is probably due to the breakdown of first order perturbation theory, rather than omission of states with $|\Omega| > 0$.

D. Product rotational energy distributions

Figure 4 shows the logarithm of the state-to-state integral cross section log $Q_{vj \to v'j'}(E)$ versus j' at $E = 0.40$ eV for $v = v' = 0$. The CCH($\Omega_{max} = 2$) cross sections are plotted in Fig. 4*a*, and the CSH($\Omega = 0$) results in Fig. 4*b*. All energetically open rotational states ($j = 0$–12 and $j' = 0$–12) have been included. We note that in both plots, the dominant behavior in the rotational distributions (seen for $j = 5$–12) is an approximately exponential increase up to a maximum at $j' = 9$ or 10, followed by an exponential decrease for $j' > 10$.

Can. J. Chem. Downloaded from www.nrcresearchpress.com by 195.246.54.202 on 09/08/12
For personal use only.

Can. J. Chem. Downloaded from www.nrcresearchpress.com by 195.246.54.202 on 09/08/12
For personal use only.

As a result, the average value of j', denoted by $\langle j' \rangle_{0\hat{j}}$ for $j = \hat{j}_0$ in Table 2, is close to the peak value of j'.

For $j = 0$–4, the rotational distributions also have a peak or shoulder at low j', in addition to the $j' = 9$ peak. This behavior is seen in both CCH($\Omega_{max} = 2$) and CSH($\Omega = 0$), although the CSH($\Omega = 0$) cross sections also oscillate with j', somewhat obscuring the overall trend. (We have omitted the $j = 1$–3 curves from the CSH($\Omega = 0$) plot because of overlapping oscillations.) In ref. 5, we discussed the low j' peak in the CSH($\Omega = 0$) results, arguing that it may be due to the "tight bend" reaction mechanism discussed earlier, since one expects this mechanism to be more important for low j and j'. Figure 4*a* shows that this same mechanism is present in the CCH($\Omega_{max} = 2$) cross sections, though reduced in magnitude. In ref. 5 we noted that the oscillations in the $j = 0$ curve in Fig. 4*b* could be the result of numerical artifacts. However, an alternative explanation is that they are due to interference between the "tight bend" and "nearly-free rotor" reaction mechanisms discussed previously. If so, then one would expect a smaller interference in the CCH($\Omega_{max} = 2$) results in Fig. 4*a* (as observed) because scattering into channels with $|\Omega| > 0$ or $|\Omega'| > 0$ is more important in one mechanism than in the other.

IV. Conclusions

We have presented CCH($\Omega_{max} = 2$) cumulative and state selected reaction probabilities, integral cross sections, and product rotational distributions for the Cl + HCl reaction on the BCMR potential surface, and comparisons with the CSH($\Omega = 0$), CSDW($\Omega = 0$), and CCH/JS approximations. Our calculations allow an assessment of the accuracy of this earlier work. Much of what we have seen in the new results had been anticipated in the earlier work, in particular, that the cross sections near the reaction threshold are well approximated by CSH($\Omega = 0$). However, as E increases, the CCH($\Omega_{max} = 2$) cross sections increase more rapidly than do CSH($\Omega = 0$). This can be rationalized using the adiabatic bend approximation, but note that even at $E = 0.40$ eV, states with $|\Omega| > 0$ and $|\Omega'| > 0$ make a significant contribution to the CCH($\Omega_{max} = 2$) m_j-resolved cross sections (see Fig. 1*b*). The good agreement between CSH($\Omega = 0$) and CCH($\Omega_{max} = 2$) for degeneracy averaged quantities in this case suggests that Ω does not have to be conserved in order for CSH($\Omega = 0$) to be accurate. What remains to be seen is whether inclusion of states with $|\Omega| > 0$ in CSH will give accurate results at higher E, where the CSH($\Omega = 0$) results are inaccurate.

V. Acknowledgements

This research was supported by the U.S. Department of Energy, Division of Chemical Sciences, under Contract W-31-109-ENG-38 and by the U.K. Science and Engineering Research Council. The computations were carried out at the National Energy Research Supercomputer Center (Livermore, U.S.A.), the National Center for Supercomputing Applications (University of Illinois, U.S.A.), and the Manchester Computing Centre, U.K.

1. G.C. Schatz. *In* Advances in molecular electronic structure theory. Vol. 1. Calculation and characterization of molecular potential energy surfaces. *Edited by* T.H. Dunning, Jr. JAI Press, Greenwich. 1990. pp. 85–127.
2. G.C. Schatz. Rev. Mod. Phys. **61**, 669 (1989).
3. J.N.L. Connor and W. Jakubetz. *In* Supercomputer algorithms for reactivity, dynamics and kinetics of small molecules. Proceedings of the NATO Advanced Research Workshop, Colombella di Perugia, Italy. 30 Aug. – 3 Sept. 1988. *Edited by* A. Laganà. Kluwer, Dordrecht. 1989. pp. 395–411.
4. G.C. Schatz. Annu. Rev. Phys. Chem. **39**, 317 (1988).
5. G.C. Schatz, D. Sokolovski, and J.N.L. Connor. *In* Advances in molecular vibrations and collision dynamics. Vol. 2B. Quantum reactive scattering. *Edited by* J.M. Bowman. JAI Press, Greenwich. 1994. pp. 1–26.
6. B.C. Garrett, D.G. Truhlar, A.F. Wagner, and T.H. Dunning, Jr. J. Chem. Phys. **78**, 4400 (1983).
7. D.M. Neumark. Annu. Rev. Phys. Chem. **43**, 153 (1992).
8. D.K. Bondi, J.N.L. Connor, J. Manz, and J. Römelt. Mol. Phys. **50**, 467 (1983); D.K. Bondi, J.N.L. Connor, B.C. Garrett, and D.G. Truhlar. J. Chem. Phys. **78**, 5981 (1983).
9. G.C. Schatz, B. Amaee, and J.N.L. Connor. Chem. Phys. Lett. **132**, 1 (1986); Comput. Phys. Commun. **47**, 45 (1987); J. Phys. Chem. **92**, 3190 (1988); J. Chem. Phys. **92**, 4893 (1990); J. Chem. Phys. **93**, 5544 (1990).
10. G.C. Schatz, D. Sokolovski, and J.N.L. Connor. J. Chem. Phys. **94**, 4311 (1991); Faraday Discuss. Chem. Soc. **91**, 17 (1991); W. Jakubetz, D. Sokolovski, J.N.L. Connor, and G.C. Schatz. J. Chem. Phys. **97**, 6451 (1992); J.N.L. Connor, P. McCabe, D. Sokolovski, and G.C. Schatz. Chem. Phys. Lett. **206**, 119 (1993).
11. Q. Sun, J.M. Bowman, G.C. Schatz, J.R. Sharp, and J.N.L. Connor. J. Chem. Phys. **92**, 1677 (1990).
12. M.A. Vincent, J.N.L. Connor, M.S. Gordon, and G.C. Schatz. Chem. Phys. Lett. **203**, 415 (1993).
13. J.M. Launay and M. Le Dourneuf. Chem. Phys. Lett. **163**, 178 (1989); Chem. Phys. Lett. **169**, 473 (1990); J.M. Launay. Theor. Chim. Acta **79**, 183 (1991); B. Lepetit and J.M. Launay. J. Chem. Phys. **95**, 5159 (1991); J.M. Launay and S.B. Padkjaer. Chem. Phys. Lett. **181**, 95 (1991); S.E. Branchett, S.B. Padkjaer, and J.M. Launay. Chem. Phys. Lett. **208**, 523 (1993); J.M. Launay and M. Le Dourneuf. *In* Electronic and atomic collisions, Proceedings of the Seventeenth International Conference on the Physics of Electronic and Atomic Collisions. Brisbane, Australia, 10–16 July 1991. *Edited by* W.R. MacGillivray, I.E. McCarthy, and M.C. Standage. Hilger, Bristol. 1992. pp. 549–558; J.M. Launay. *In* Dynamical processes in molecular physics. First EPS Southern European School of Physics. Avila, Spain. 1–14 September 1991. *Edited by* G. Delgado-Barrio. Institute of Physics Publishing, Bristol. 1993. pp. 97–120.
14. L.M. Delves. Nucl. Phys. **9**, 391 (1959); **20**, 275 (1960).
15. A. Kuppermann, G.C. Schatz, and J.P. Dwyer. Chem. Phys. Lett. **45**, 71 (1977).
16. B. Amaee, J.N.L. Connor, J.C. Whitehead, W. Jakubetz, and G.C. Schatz. Faraday Discuss. Chem. Soc. **84**, 387 (1987).
17. G.C. Schatz. Chem. Phys. Lett. **150**, 92 (1988); **151**, 409 (1988).
18. H. Koizumi and G.C. Schatz. *In* Advances in molecular vibrations and collision dynamics. Vol. 1A. *Edited by* J.M. Bowman and M.A. Ratner. JAI Press, Greenwich. 1991. pp. 139–164.

Hybridization properties of oligoarabinonucleotides

PAUL APOSTOLOS GIANNARIS AND MASAD JOSÉ DAMHA[1]

Department of Chemistry, McGill University, Montreal, QC H3A 2K6, Canada

Received September 8, 1993

This paper is dedicated to Professor John C. Polanyi on the occasion of his 65th birthday

PAUL APOSTOLOS GIANNARIS and MASAD JOSÉ DAMHA. Can. J. Chem. **72**, 909 (1994).

3′-Phosphoramidite derivatives of arabinocytidine, arabinoadenosine, and arabinouridine were prepared and used for the solid-phase synthesis of oligoarabinonucleotides (arabinonucleic acid, or ANA). Thermal denaturation analysis and gel mobility shift assays were used to investigate the interaction between ANA and complementary DNA and RNA. In general, the ANA/DNA and ANA/RNA complexes exhibited melting temperatures comparable to those of the corresponding DNA/DNA and DNA/RNA complexes. Thus the inversion of stereochemistry at the C2′ of ribonucleotides does not have a negative effect on interaction with natural sequences. In fact, in complexes with poly dT, oligoarabinoadenylates displayed greater hybridization affinity than oligoriboadenylates. In summary, we observed that (*i*) ara(Ap)$_7$A interacted favourably with poly rU and poly dT; (*ii*) ara(Cp)$_7$C formed a stable complex with poly rG; (*iii*) ara(Up)$_7$U did not bind with complementary poly rA; and (*iv*) the mixed oligoarabinonucleotide ara(UCU UCC CUC UCC C) formed complexes with complementary DNA and RNA. Hybridization was observed between the phosphorothioatelinked arabinoadenylate ara(Aps)$_7$A and poly rU and poly dT; however, this binding was weaker than that between the phosphorothioate-linked deoxyriboadenylate d(Aps)$_7$A and poly rU and poly dT. Both ara(Aps)$_7$A and its deoxy analog d(Aps)$_7$A displayed significant and similar resistance to digestion by snake venom phosphodiesterase.

PAUL APOSTOLOS GIANNARIS et MASAD JOSÉ DAMHA. Can. J. Chem. **72**, 909 (1994).

On a effectué la synthèse des dérivés 3′-phosphoramidite de l'arabinocytidine, de l'arabinoadénosine et de l'arabinouridine et on les a utilisés pour la synthèse en phase solide d'oligoarabinonucléotides (acide arabinonucléique, AAN). On a utilisé une analyse de dénaturation thermique et des essais de déplacements par mobilité sur gel pour étudier les interactions entre l'AAN et des ADN et ARN complémentaires. En général, les complexes AAN/ADN et AAN/ARN présentent des températures de fusion semblables à celles des complexes correspondants ADN/ADN et ADN/ARN. L'inversion de stéréochimie au niveau C2′ des ribonucléotides n'a donc pas d'effet négatif sur l'interaction avec les séquences naturelles. En fait, dans les complexes contenant des poly dT, les oligoarabinoadénylates présentent une affinité d'hybridation plus grande que celle des oligoriboadénylates. En résumé, on a observé que (*i*) l'ara(Ap)$_7$ interagit favorablement avec les poly rU et poly dT; (*ii*) que l'ara(Cp)$_7$C forme un complexe stable avec le poly rG; (*iii*) que l'ara(Up)$_7$U ne se lie pas avec le poly rA complémentaire et (*iv*) que l'oligoarabinonucléotide mixte ara(UCU UCC CUC UCC C) forme des complexes avec les ADN et ARN complémentaires. On a observé une hybridation entre l'arabinoadénylate ara(Aps)$_7$A lié au phosphorothioate et les poly rU et poly dT; toutefois, cette interaction est plus faible que celle entre le désoxyriboadénylate d(Aps)$_7$A lié au phosphorothioate et les poly rU et poly dT. L'ara(Aps)$_7$ ainsi que son analogue désoxy, d(Aps)$_7$A, présentent tous les deux une résistance importante et semblable à la digestion par la phosphodiestéase du venin de serpent.

[Traduit par la rédaction]

Introduction

The antisense approach to gene regulation requires oligonucleotides that exhibit stability against degradation by cellular enzymes and the ability to hybridize complementary DNA or RNA targets with good affinity and specificity. Short oligodeoxyribonucleotides can function as antisense oligomers (1) although their utility is limited by nucleolytic degradation in vivo (2). Various modified oligomers including those bearing modified phosphodiester linkages (3), non-phosphate linkages (4), and 2′,5′- rather than 3′-5′-phosphodiester linkages (5) have been designed in an attempt to increase nuclease resistance without severely hindering the ability to hybridize target DNA or RNA (for reviews of this area, see ref. 6). In addition, oligomers incorporating modified nucleoside units including α-nucleosides (7), L-deoxyribo and L-ribonucleosides (8, 9), glyceronucleosides (10), 4′-thionucleosides (11), carbocyclic nucleosides (12), and 2′-O-alkyl nucleosides (13) have also been explored as possible antisense agents.

Oligonucleotides containing the sugar D-arabinose (arabinonucleic acids, or ANA) (Scheme 1) have not been investigated as antisense agents, except for one reported example of an oligomer of 1-α-D-arabinofuranosyl thymidine (14). This may be due in part to the inherent difficulties in ANA synthesis, which, as in RNA synthesis (15), necessitates the differential chemical protection of the 2′ and 3′ hydroxyl groups. In the original work by Wechter, oligoarabinonucleotide synthesis was carried out without 2′-OH protection, resulting in mixtures of 2′,5′- and 3′,5′-linked nucleotides (16). There had been two other major strategies in the synthesis of 3′,5′-linked arabinonucleotides. The first and most widely used strategy makes use of 5′,2′-O-protected arabinonucleotides as precursors, which upon phosphorylation of the remaining 3′-hydroxyl function affords a suitable building block for the synthesis of arabinonucleotides (17–19). The problem with this approach is that of selective protection of the 2′-hydroxyl function, a very difficult requirement because of its orientation towards the hindered β face of the sugar. In practice, this is accomplished by first masking the 5′- and 3′-OH groups with a disiloxane bridging group, then protecting the 2′-hydroxyl, and finally deblocking the disiloxane function so that 5′-trityl and 3′-phosphate moieties can be introduced (17, 18). The second strategy is limited to pyrimidine arabinonucleotides, as they require formation of O^2-2′-anhy-

[1]Author to whom correspondence may be addressed. Tel: (514) 398-7552. Fax: (514) 398-3797. E-Mail: Damha@omc.lan.mcgill.ca.

Can. J. Chem. Downloaded from www.nrcresearchpress.com by 195.246.54.202 on 09/08/12
For personal use only.

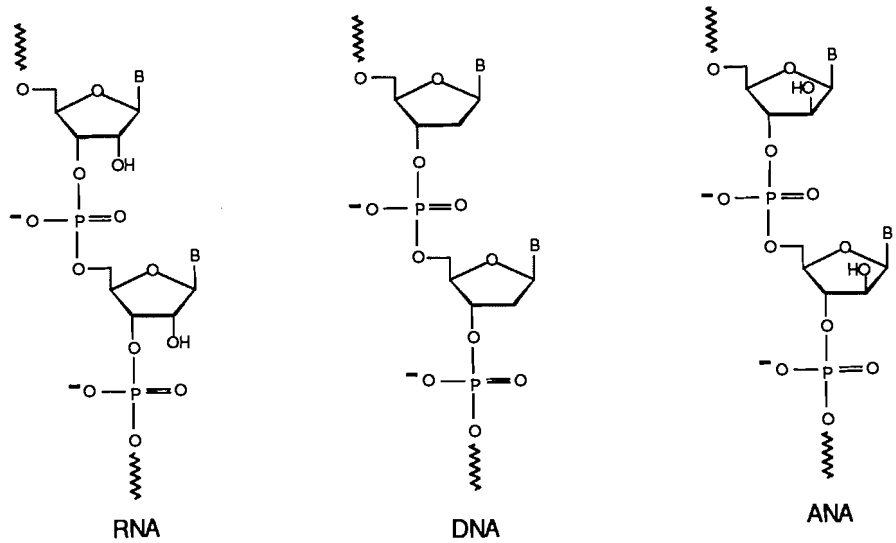

SCHEME 1

dronucleoside synthons, and this strategy is therefore rarely used (20). We thought that the best way to deal with the 2′-OH group was to block it only *after* the desired moieties of 5′- and 3′-positions had been introduced. This was readily achieved by sequential and regioselective tritylation (at 5′), phosphoramidation (at 3′), and acetylation (at 2′) of arabinonucleosides. The resulting 5′-tritylated arabinonucleoside 2′-*O*-acetyl-3′-*O*-phosphoramidites proved to be very useful synthons for the solid-phase synthesis of short arabinoadenylates and uridylates (21). Pfleiderer and co-workers have also made useful advances in using solid-phase phosphoramidite chemistry to make an all-β-D-arabinose "transfer ANA" molecule (22).

Arabinonucleosides have found application as antiviral (23) and antitumor (24) agents and, in particular, arabinofuranosyl cytosine (araC) has been found to be very effective in the treatment of leukemia (25). Although very little is known about the mechanism of action, its activity appears to be associated with its misincorporation into DNA (26). Mikita and Beardsley reported that the presence of araC at the 3′-terminus of a DNA primer strand results in a reduction in the rate of addition of the next nucleotide unit in vitro (27). Similarly, a single internucleotide araC insertion into an oligomer serving as the template strand hindered the function of certain polymerases, affecting, as a result, the process of replication in vitro (27). Whether these observations reflect differences in the structure of the complexes formed by normal DNA and those formed by oligomers containing araC is not clear. X-ray diffraction analysis of the self-complementary DNA oligomer d(CCAGGCaraCTGG) demonstrated that this oligomer forms a duplex with B-DNA conformation with only small conformational perturbations (28). However, molecular modeling studies have indicated that serious steric clashes may occur between the 2′-OH and neighboring atoms when araC is placed into the RNA strand of a DNA/RNA duplex (27). Altona and co-workers prepared self-complementary d(CGaraCTAGCG) to investigate the structural implications of an araC insertion into DNA by NMR analysis (29–31). They discovered that under certain conditions this oligomer exclusively adopts a hairpin structure whereas the unmodified DNA adopts a B-BNA type duplex. AraC incorporation into an alternating dC-dG sequence d(CGaraCGCG) has been shown to facilitate the B to Z conversion (32). Very little is known about the thermal stability of DNA chimeras containing 1-β-D-arabinonucleosides. A self-complementary DNA oligomer containing a single araC insert exhibited a somewhat lower melting temperature (T_m) (2°C/araC substitution) than the unmodified DNA (18) and no interaction was observed between a short oligomer of araU and poly rA (20*a*). In this work we prepared a series of 1-β-D-arabinonucleic acids and show, for the first time, that these oligomers can form stable complexes with complementary single-stranded DNA and RNA.

Results and discussion

Preparation of N^4*-benzoyl-5′-O-monomethoxytritylarabinocytidine-2′-O-acetyl-3′-O-N,N-diisopropyl-β-cyanoethylphosphoramidite* **5**

The title compound was prepared in good yield by acetylation of the 2′-OH *after* protection of the 4-amino and 5′- and 3′-hydroxyl groups (Scheme 2). Thus, 1-β-D-arabinofuranosylcytosine was first protected at the 5′-OH (monomethoxytrityl) and N^4 (benzoyl) positions, affording **3** in 60% combined yield. The protected arabinocytidine **3** was then phosphitylated with *N,N*-diisopropyl-β-cyanoethylphosphonamidic chloride, resulting in mainly **4** (77% yield). The free 2′-OH of **3** also reacted with the phophitylating reagent, although to a much lesser extent as indicated by additional very faint spots in the TLC plate. Compound **4** was produced as a pair of diastereoisomers that could be easily separated by silica gel column chromatography. The position of the phosphoramidite moiety on **4** was established by ^{13}C NMR. The spectrum clearly shows that the C4′, C3′, and C2′ resonances are coupled to phosphorus whereas that of C1′ is not, the two-bond $J(^{13}C3'–^{31}P)$ value being the greatest (Fig. 1). Furthermore, the greatest downfield shift in ^{13}C resonance of the arabinose sugar of **4** relative to the unphosphitylated derivative **3** was observed for C3′, identifying it as the carbon where the phosphoramidite moiety is attached. Subsequent 2′-O-acetylation of one diastereoisomer of **4** afforded the key activated monomer **5** in 87% yield.

Compound **5** was also obtained in a separate synthesis from ribocytidine. The key step in this approach was the inversion of the C2′-OH by strong heating with diphenyl carbonate – water in DMF (33) (Scheme 3). Under the reaction conditions, the initial 2′,3′-cyclic carbonate intermediate **7** reacts intramolecularly, forming 2,2′-cycloanhydride **8** which is subsequently

Can. J. Chem. Downloaded from www.nrcresearchpress.com by 195.246.54.202 on 09/08/12
For personal use only.

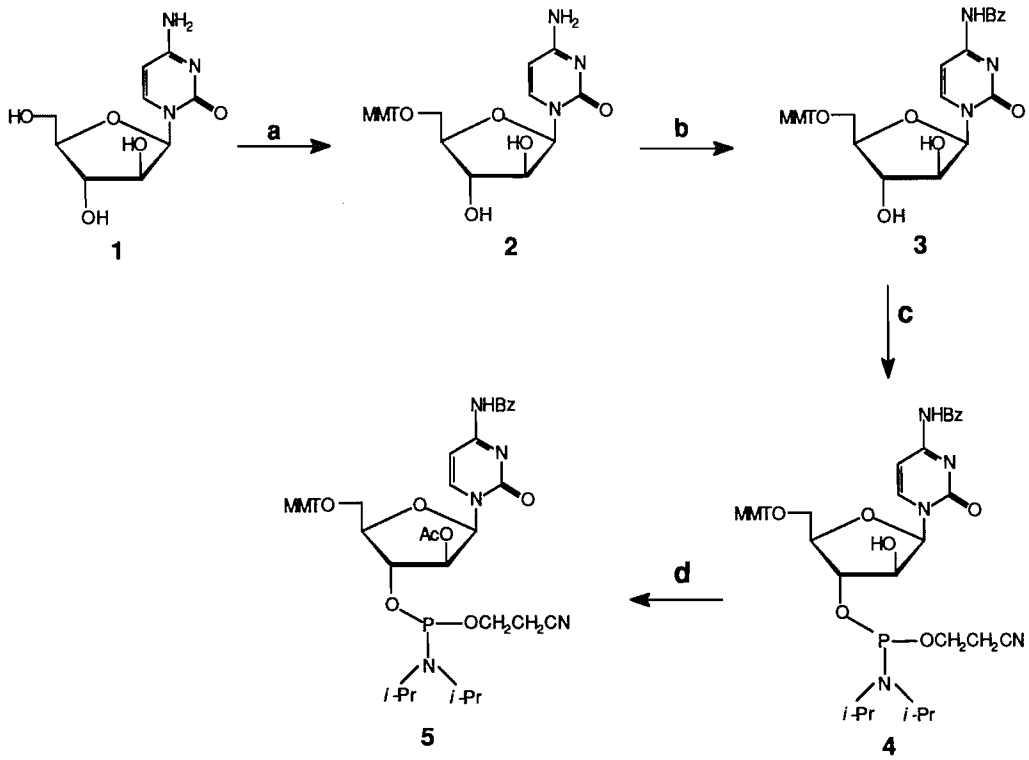

SCHEME 2

(a) MMT-Cl/pyridine, 22 h (79%); (b) (i) trimethylsilyl chloride/pyridine, 30 min; (ii) benzoyl chloride/pyridine, 2 h ; (iii) 29% ammonia, water, 0°C, 25 min (73%); (c) $(iPr_2N)P(OCH_2CH_2CN)Cl$/diisopropylethylamine/THF, 90 min (77%); (d) acetic anhydride/DMAP/diisopropylethylamine, 45 min (87%).

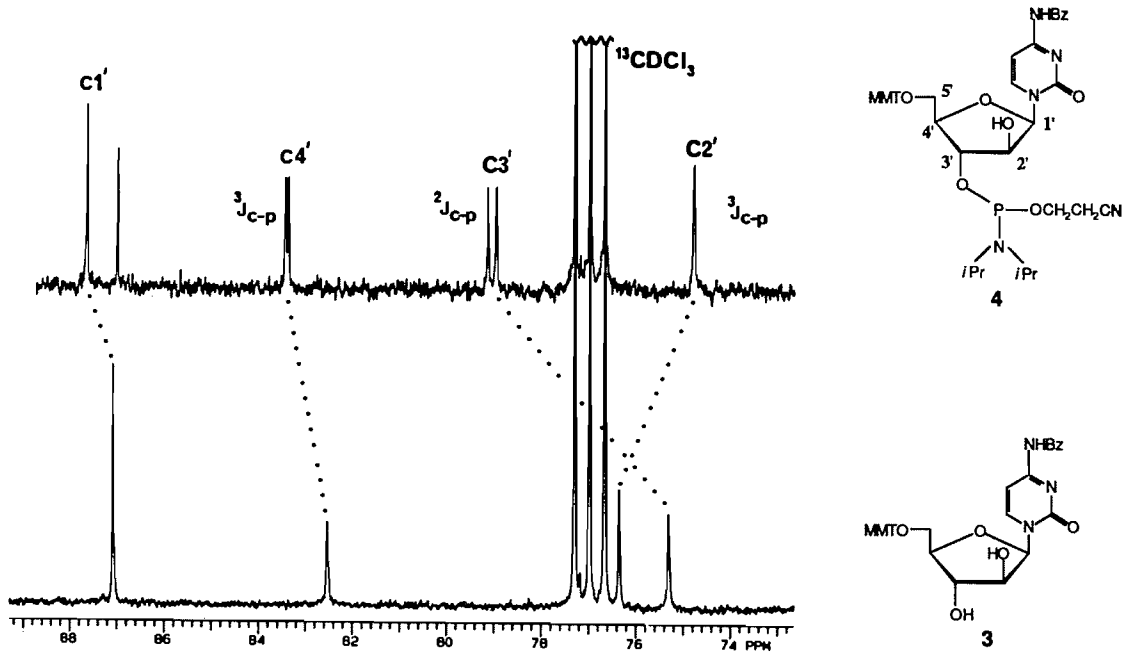

FIG. 1. ^{13}C NMR (DEPT, $CDCl_3$) spectra of arabinocytidine phosphoramidite **4** (one diastereoisomer) and arabinonucleoside **3**.

opened, producing a mixture of arabinocytidine and the starting material in a ratio of 9:1 (TLC, ethanol–water 1:1). These 2′ epimers could not be separated at this stage. They were, however, fully separated by silica gel chromatography after partial protection of the sugar (5′-MMT) and base (4-NH-Bz) moieties. Subsequent phosphitylation and acetylation of **3** afforded **5** in 65% combined yield.

Synthesis and characterization of oligoarabinonucleotides

Oligoarabinonucleotides were synthesized with an Applied Biosystems DNA/RNA synthesizer (model 381A) using amidite **5**, and analogous araU and araA 3′-*O*-(cyanoethyl)phosphoramidites (20). Oligomers were prepared on a 1.0 μmol scale employing "trityl on" synthesis cycle (60 s coupling time) and long-chain alkylamine controlled-pore glass (LCAA-CPG)

Can. J. Chem. Downloaded from www.nrcresearchpress.com by 195.246.54.202 on 09/08/12
For personal use only.

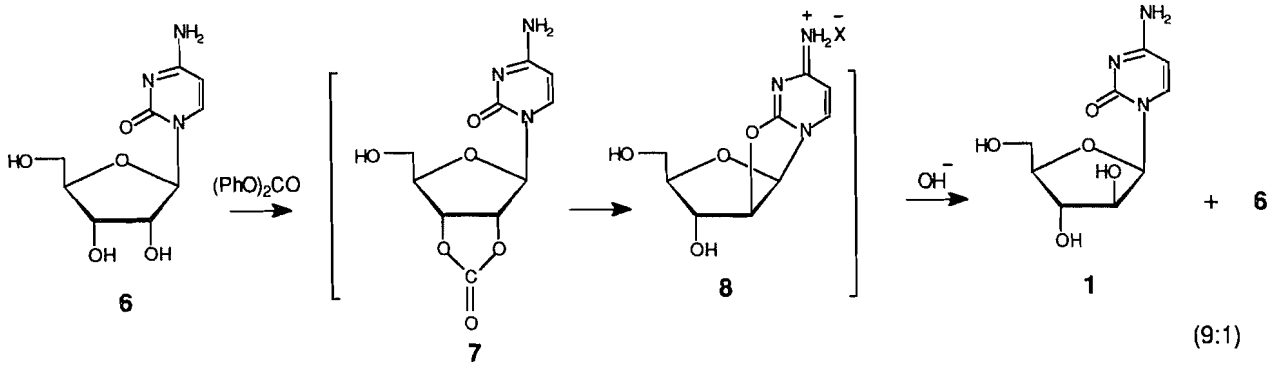

SCHEME 3

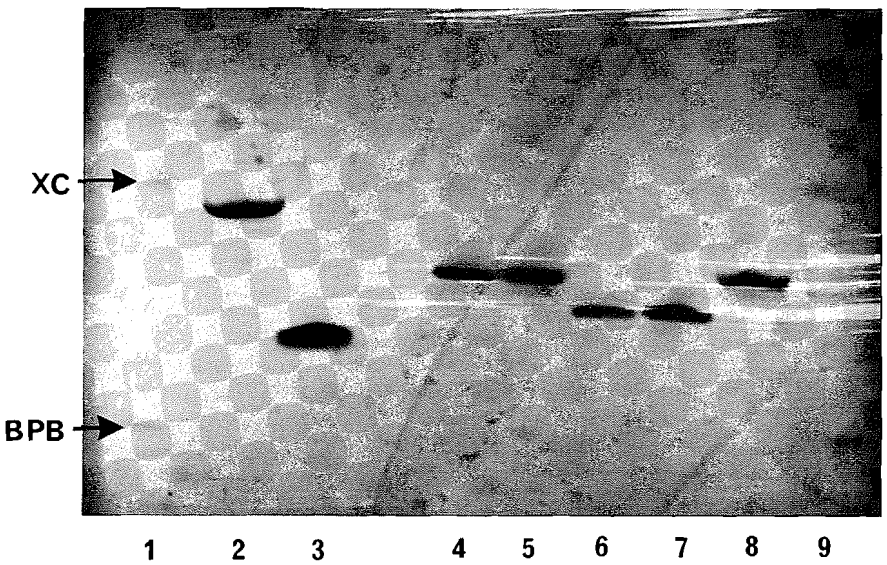

FIG. 2. Polyacrylamide gel electrophoresis (16%, denaturing) of oligoarabinonucleotides. Lanes: (1) xylene cyanol and bromophenol blue; (2) $d(Tp)_{14}T$; (3) $d(Tp)_4T$; (4) crude $ara(Cp)_9C$; (5) pure $ara(Cp)_9C$; (6) crude $ara(Cp)_7C$; (7) pure $ara(Cp)_7C$; (8) $ara(Cp)_9C$ treated with 0.1 N KOH for 24 h; (9) xylene cyanol and bromophenol blue.

bearing 3′-terminal arabinonucleosides. The coupling efficiency was routinely greater than 98% as monitored by the release of the MMT cation. RNA (34) and DNA (35) oligomers were prepared by standard means. Deprotection of sugar and phosphate moieties with concomitant release of oligomers from the glass support was accomplished by a single ammonia treatment (29% NH_4OH, 55°C, 8 h). The terminal trityl group was cleaved with trifluoroacetic acid during purification with a reversed phase OPC® cartridge (Applied Biosystem), and in the case of araC oligomers it was removed prior to purification by polyacrylamide gel electrophoresis (PAGE). Purity of ANA oligomers was verified by analytical gel electrophoresis and was determined to be greater than 95% (Fig. 2). No other bands that would indicate poor monomer coupling or branch formation were detected (21). The ANA, DNA, and RNA sequences prepared for this study are shown in Table 1.

The integrity of the oligoarabinonucleotides was established by chemical and enzymatic degradation with subsequent analysis of the nucleotide–nucleoside mixtures by polyacrylamide gel electrophoresis (PAGE). Oligoarabinonucleotides are expected to be resistant to base conditions since the *trans* relationship of the 2′-OH with respect to the 3′,5′-phosphodiester linkage prevents participation of the 2′-OH in intranucleotide cleavage. This stability has been previously observed for 3′,5′-linked dinu-

TABLE 1. Oligonucleotides prepared for binding studies

Oligonucleotide sequences	Designation
Normal oligomers	
5′-r(AAA AAA AA)	$r(Ap)_7A$
5′-r(UUU UUU UU)	$r(Up)_7U$
5′-r(CCC CCC CC)	$r(Cp)_7C$
5′-r(CCC CCC CCC CCC CC)	$r(Cp)_{14}C$
5′-d(AAA AAA AA)	$d(Ap)_7A$
5′-d(TTT TTT TT)	$d(Tp)_7T$
5′-d(CCC CCC CC)	$d(Cp)_7C$
5′-r(CCC UCU CCC UUC U)	r(U/C)-13-mer
5′-r(AGA AGG GAG AGG G)	r(A/G)-13-mer
5′-d(AGA AGG GAG AGG G)	d(A/G)-13-mer
Oligoarabinonucleotides	
5′-ara(AAA AAA AA)	$ara(Ap)_7A$
5′-ara(UUU UUU UU)	$ara(Up)_7U$
5′-ara(CCC CCC CC)	$ara(Cp)_7C$
5′-ara(CCC UCU CCC UUC U)	ara(U/C)-13-mer
Phosphorothioates	
5′-d(AsAsAs AsAsAs AsAs)	$d(Aps)_7A$
5′-ara(AsAsAs AsAsAs AsAs)	$ara(Aps)_7A$

Can. J. Chem. Downloaded from www.nrcresearchpress.com by 195.246.54.202 on 09/08/12
For personal use only.

TABLE 2. Binding of oligoarbinonucleotides with complementary DNA and RNA homopolymers[a]

Complex	T_m (%H) 100 mM NaCl	T_m (%H) 1.0 M NaCl
poly rU/ribo(Ap)$_7$A	23.0 (43)	57.6 (43)
ara(Ap)$_7$A	24.5 (25)	50.7 (28)
d(Ap)$_7$A	21.8 (29)	57.5 (30)
d(Aps)$_7$A	19.7 (29)	55.0 (30)
ara(Aps)$_7$A	12.1 (34)	44.1 (36)
poly dT/ribo(Ap)$_7$A	14.8 (25)	28.0 (38)
ara(Ap)$_7$A	25.5 (36)	52.6 (35)
d(Ap)$_7$A	27.0 (30)	65.0 (35)
d(Aps)$_7$A	19.6 (30)	57.7 (35)
ara(Aps)$_7$A	12.2 (12)	44.7 (35)
poly rA/ribo(Up)$_7$U		23.0 (30)
ara(Up)$_7$U		—
d(Up)$_7$U		25.0 (20)

[a]Equimolar mixtures on a per base basis were used. T_m's are ±0.5°C. Buffer: 10 mM sodium phosphate with [NaCl] as indicated. —, not observed. Hyperchromicity values (%H) are presented in parentheses relative to the initial temperature reading.

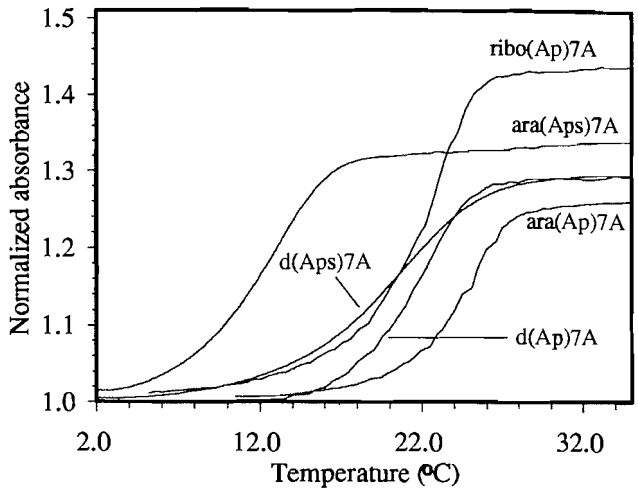

FIG. 3. Thermal denaturations of poly rU:oligomer complexes. Equimolar mixtures (per residue basis) of poly rU and each oligomer indicated below were prepared and denatured in 100 mM NaCl, 10 mM Na_2HPO_4, pH 7.0. Thermal denaturation curves for the mixtures of poly rU with phosphodiester-linked oligomers r(Ap)$_7$A, d(Ap)$_7$A, and ara(Ap)$_7$A as well as phosphorothioate-linked oligomers ara(Aps)$_7$A and d(Aps)$_7$A are shown normalized to their respective first temperature reading. T_m and %H values for these melts are tabulated in Table 2.

cleoside monophosphates of arabinocytidine (16), arabinouridine and arabinoadenosine (21), as well as for the trinucleotide ara-(ApApA) (17). The oligoarabinonucleotides prepared in this study were also found to be completely stable to treatment with 0.1 N KOH for 24 h (Fig. 2, compare lanes 2 and 4 with 7), whereas the corresponding oligoribonucleotides were completely degraded under these conditions (data not shown).

The arabinonucleotides displayed some stability against cleavage by snake venom phosphodiesterase (SVPDE). For example, only 5–10% hydrolysis of ara(Ap)$_7$A, ara(Cp)$_7$C, and ara(Up)$_7$U was detected during incubation of these oligomers with SVPDE at 37°C for 45 min, whereas oligoribonucleotides were completely degraded within 5 min under the same conditions (PAGE). The oligoarabinonucleotides, however, did not exhibit any significant stability, relative to ribonucleotides, when incubated with other nucleases. For example, treatment with the endonucleases Nuclease P1 and Ribonuclease S1, or the 5′-exonuclease calf spleen phosphodiesterase, resulted in degradation of both ara and ribo oligomers within 45 min at 37°C. Digestion with spleen phosphodiesterase served also to establish a 3′,5′-phosphodiester connectivity within the oligoarabinonucleotides, since 2′,5′-linked arabinonucleotides (16) and 2′-5′-linked oligoribonucleotides (5, 16) are not hydrolyzed by this enzyme.

The phosphorothioate-linked oligomers ara(Aps)$_7$A and d(Aps)$_7$A were characterized by incubation with SVPDE at 37°C for 16 h followed by analysis of the digest by HPLC. Under these conditions, less than 20% of ara(Aps)$_7$A and d(Aps)$_7$A was degraded whereas phosphodiester-linked d(Ap)$_7$A was completely degraded within 10 min. The increased stability of the phosphorothioate-linked oligomers d(Aps)$_7$A and ara(Aps)$_7$A, relative to d(Ap)$_7$A, is consistent with related work that shows that phosphorothioate-linked DNA (36) and phosphorothioate linked RNA (37) are more resistant to nuclease activity than normal DNA and RNA strands.

Interaction of oligoarabinonucleotides with complementary DNA and RNA

In the presence of poly dT and 100 mM NaCl, the oligoarabinoadenylate ara(Ap)$_7$A exhibits a melting temperature approximately equal to, or significantly higher than, the corresponding natural oligomers d(Ap)$_7$A and r(Ap)$_7$A (Table 2, Fig. 3). In addition, at 100 mM NaCl, the T_m of the complex formed between ara(Ap)$_7$A and poly rU was marginally higher than those values observed for the complexes d(Ap)$_7$A):(poly rU) and r(Ap)$_7$A):(poly rU) (Table 2, Fig. 3). The stoichiometry of complexes of ara(Ap)$_7$A and r(Ap)$_7$A with poly rU was determined in each case to be 2U:1A (triplex) from UV mixing curves (1 M NaCl at 20°C) (38).[2] All these results suggest that *the inversion of stereochemistry at the C2′ of ribonucleotides usually does not have a strong positive or negative effect on interaction with natural sequences, and that the 2′-OH group of ANA does not usually hinder the formation of ANA/DNA and ANA/RNA complexes.* In fact, the significantly higher T_m observed for complexes ara(Ap)$_7$A:poly dT and ara(Ap)$_7$A:poly rU relative to complexes r(Ap)$_7$A:poly dT and r(Ap)$_7$A:poly rU indicates that the 2′-OH of ANA exerts, in this case, a stabilizing effect.[3] Oligoribonucleotides containing modifications at the 2′-position, including 2′-*O*-methyl (13, 39), 2′-fluoro (40), 2′-*O*-allyl (41), 2′-*O*-ethyl (42), and 2′-*O*-propyl (42), generally exhibit higher T_m than their respective unmodified oligomers in the interaction with complementary RNA. This being the case, it would be of interest to determine whether the stabilizing effect exerted by 2′-substituents in ribonucleotides will also be evident for 2′-O-modified arabinonucleotides.

To study the effect of base sequence on complex stability, the interaction of oligoarabinonucleotide ara(5′-CCC UCU CCC UUC U-3′) (abbreviated ara(U/C)-13-mer) with complementary RNA (r(A/G)-13-mer) and DNA (d(A/G)-13-mer) was

[2]1Py:1Pu mixtures were used in the hybridization assays of ara(Ap)$_7$A and poly dT and polyrU. We later determined that poly rU interacts with ara(Ap)$_7$A with a 2U:1A stoichiometry. We have also observed that mixtures of 1Py:1Pu and 2Py:1Pu (Pu = adenylates and Py = poly rU) give the same T_m values within experimental error.

[3]We make this statement with caution since ΔT_m may not reflect $\Delta\Delta G^0$.

Can. J. Chem. Downloaded from www.nrcresearchpress.com by 195.246.54.202 on 09/08/12
For personal use only.

TABLE 3. Binding of ara(U/C)-13-mer and ara(Cp)$_7$C

Oligonucleotide complex	T_m (%H)[a] CsCl 50 mM	T_m (%H) NaCl 200 mM
r(AG)-13-mer/r(U/C)-13-mer	65 (18)	75 (16)
/ara(U/C)-13-mer	48 (14)	53 (12)
/d(T/C)-13-mer	55 (16)	64 (15)
d(AG)-13-mer/r(U/C)-13-mer	41 (13)	50 (13)
/ara(U/C)-13-mer	11 (8)	18 (5)
/d(T/C)-13-mer	48 (16)	53 (16)
poly rG/ribo(Cp)$_7$C	73.2 (10)	77.5 (15)
ara(Cp)$_7$C	58.1 (4)	57.0 (5)
d(Cp)$_7$C	64.1 (4)	64.5 (5)
ara(Cp)$_{14}$C	85.0 (6)	83.4 (6)

[a] T_m are ±0.5°C for melts with poly rG, and ±1.0°C for all other melts (due to broad transitions). Hyperchromicity values (%H) are presented in parentheses relative to the absorbance reading at 20°C. Buffer: 10 mM sodium phosphate pH 7 with [CsCl] or [NaCl] as indicated. Equimolar mixtures (2.5 μmol in each strand) were used.

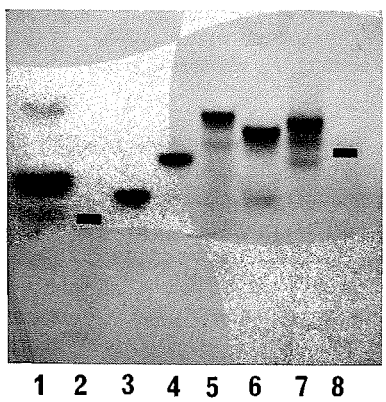

FIG. 4. Mobility shift assay of ara(U/C)-13-mer complex with RNA on non-denaturing PAGE (24%). Mixtures of approximate equimolar strand concentrations (2.0 μmol in each strand) in lanes 5–7. Single strands (ss) are shown in lanes 2–4, and 8. Lanes: (1) xylene cyanol and bromophenol blue; (2) ss r(U/C)-13mer; (3) ss d(T/C)-13-mer; (4) ss ara(U/C)-13-mer; (5) (r(U/C)-13-mer):(r(A/G)-13-mer); (6) (d(T/C)-13-mer):(r(A/G)-13-mer); (7) (ara(U/C)-13-mer):(r(A/G)-13-mer); (8) ss r(A/G)-13-mer. The mobility of the bands in lanes 2 and 8 have been highlighted for clarity. T_m values for these complexes are listed in Table 3.

investigated by UV thermal denaturation analysis (Table 3). All of the complexes listed in Table 3 showed similar broad cooperative transitions at 260 nm indicative of complex formation while the single strands, run on their own, exhibited only linear increases in absorbance.[4] In 200 mM NaCl, the ANA/RNA complex ara(U/C)-13-mer):(r(A/G)-13-mer) exhibited a T_m of 53°C, while the melting temperatures of the analogous RNA/RNA (T_m = 75°C) and DNA/RNA (T_m = 64°C) complexes were significantly higher. A mobility shift PAGE assay was used to confirm the formation of these complexes. Figure 4 clearly

[4] The only exception is r(A/G)-13-mer, which self-associates (ref. 5). The self-association of this oligomer can be largely eliminated by heating the sample to 90°C for 30 min before measurements. Longer heating times are not recommended as this may result in significant degradation.

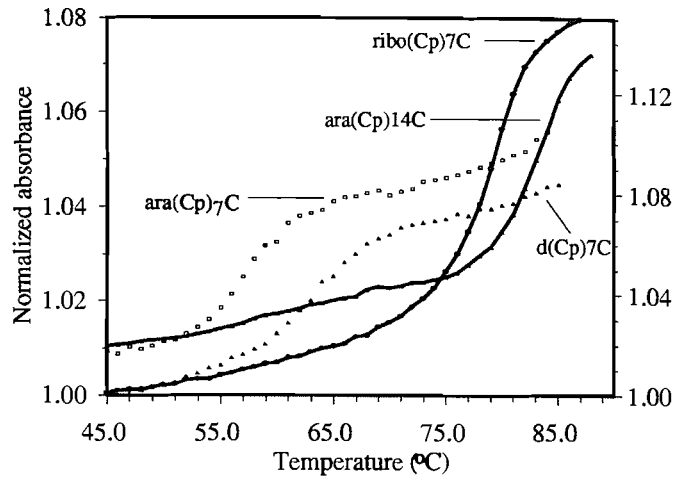

FIG. 5. Thermal denaturations for (oligomer):(poly rG) complexes in 200 mM NaCl, 10 mM Na_2HPO_4, pH 7.0. Curves for the interaction of r(Ap)$_7$A, d(Cp)$_7$C, ara(Cp)$_7$C, and ara(Cp)$_{14}$C are shown normalized to their respective absorbance readings at 20°C. Curves for complexes (poly rG):(ara(Cp)$_7$C) and (poly rG):(ara(Cp)$_{14}$C) are offset for clarity and the curve for (poly rG):(r(Cp)$_7$C) is plotted using the *y*-axis on the right part of the graph. T_m and %H values are tabulated in Table 3.

shows that an equimolar mixture of ara(U/C)-13-mer and r(A/G)-13-mer resulted in the formation of a new band migrating much more slowly than the component single strands (compare lane 7 to 4, and 8) and with very similar mobility to the slow bands in lanes 5 and 6, which represent the complexes (r(U/C)-13-mer):(r(A/G)-13-mer) and (d(A/G)-13-mer):(r(A/G)-13-mer). Hybridization was observed between ara(U/C)-13-mer and d(A/G)-13-mer (T_m = 18°C), although this was significantly weaker than that observed between r(U/C)-13-mer with d(A/G)-13-mer (T_m = 53°C).

Oligoarabinonucleotide ara(Cp)$_7$C forms a stable complex with poly rG in 200 mM NaCl, exhibiting a T_m of 57.0°C. This represents a reduction in T_m of 20° and 7.5° relative to, respectively, the control complexes (r(Cp)$_7$C):(poly rG) and (d(Cp)$_7$C):(poly rG) (Table 3, Fig. 5). The hyperchromic effect observed for (ara(Cp)$_7$C):(poly rG) (5 %H) was similar to that of (d(Cp)$_7$C):(poly rG) (5 %H) and significantly lower than that for the interaction between r(Cp)$_7$C with poly rG (15 %H). This observation may indicate that base stacking in (ara(Cp)$_7$C):(poly rG) is more closely related to that in (d(Cp)$_7$C):(poly rG) than in (r(Cp)$_7$C):(poly rG). As expected, a mixture of poly rG and a longer araC oligomer, namely ara(Cp)$_{14}$C, exhibited a higher T_m and %H relative to ara(Cp)$_7$C, confirming the interaction between araC and riboG residues.

In contrast to our previous finding that ara(Ap)$_7$A forms stable complexes with complementary RNA and DNA, we were unable to detect the formation of a complex between ara(Up)$_7$U and poly rA. There was no cooperative transition at 260 nm upon heating a mixture of ara(Up)$_7$U and poly rA (1 M NaCl), whereas under similar conditions we observed transitions for the melting of (r(Up)$_7$U):(poly rA) and (d(Tp)$_7$T):(poly rA) (Table 2). This observation is consistent with the work of Provenzale and Nagyvary, who showed that short oligomers of araU did not bind with poly rA under conditions where poly rU/poly rA formed (20*a*). It is possible that ara(Up)$_7$U binds to poly rA but the T_m value of the complex is too low to be detected.

Can. J. Chem. Downloaded from www.nrcresearchpress.com by 195.246.54.202 on 09/08/12
For personal use only.

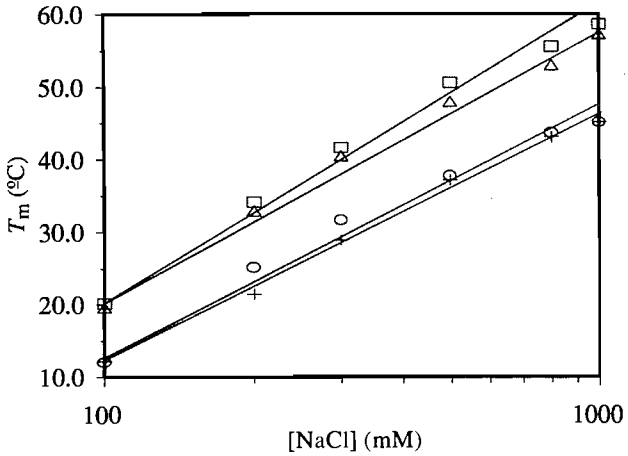

FIG. 6. Effect of increasing [NaCl] concentration on T_m for the complexes of phosphorothioate-linked oligoadenylates with poly dT and poly rU. Log [NaCl] versus T_m curves for the complexes (□) (poly dT):(d(Aps)$_7$A); (△) (poly rU):(d(Aps)$_7$A); (○) (poly rU):(ara(Aps)$_7$A); (+) (poly dT):(ara(Aps)$_7$A).

Interaction of the phosphorothioate ara(Aps)$_7$A with poly dT and poly rU

Replacement of the normal internucleotide linkage in ara(Ap)$_7$A with phosphorothioate linkages had a destabilizing effect on the complexes formed with poly rU and poly dT. For example, in 100 mM NaCl, the T_m of the complex (ara(Aps)$_7$A):(poly rU) was 12.4°C lower than that of the "all"-phosphodiester complex (ara(Ap)$_7$A):(poly rU) (Table 2). Similarly, ara(Aps)$_7$A gave a depressed T_m value when annealed to poly dT. It is clear from Fig. 4 and the data presented in Table 2 that the destabilizing effect resulting from phosphorothioate substitution in ara(Ap)$_7$A is significantly greater than in d(Ap)$_7$A. This destabilization was observed over a large range of ionic conditions (100 mM – 1 M NaCl) as illustrated in the plots of T_m vs. log [NaCl] (Fig. 6). Despite their enhanced nuclease stability, the weak hybridization affinity of phosphorothioate oligoarabinonucleotides may limit their use as antisense agents or as probes. However, we point out that the stability of complexes formed by phosphorothioate oligodeoxynucleotides is known to be sequence dependent.[5,6] Thus, to fully assess the binding potential of phosphorothioate ANA, oligomers of mixed base composition need to be investigated.

Conclusions

ANA oligomers can readily be prepared by the conventional solid-phase methodology employing phosphoramidite chemistry. Oligoarabinonucleotides were found to hybridize with complementary RNA and DNA exhibiting T_m's comparable to, and in some cases greater than, the corresponding unmodified oligomers. Although the ANA oligomers were susceptible to cleavage by certain nucleases, their stability under cellular conditions remains to be determined. Phosphorothioate-linked oligoarabinoadenylates exhibit characteristics normally observed for phosphorothioate DNA and RNA oligomers, for instance, significant stability against SVPDE cleavage and, in the case of ara(Aps)$_7$A, reduced T_m's when hybridized to complementary ssDNA and RNA relative to the unmodified ara(Ap)$_7$A. Our findings that ANA can form stable complexes with both ssDNA and RNA are very encouraging for those hoping to use sugar-modified antisense oligonucleotides as antisense agents or as probes. We are currently evaluating the effect of mixed base composition and 2′-modification (e.g., alkylation) on the ability of ANA to complex with both single- and double-stranded DNA and RNA.

[5]Generally, incorporation of phosphorothioate linkages at the 5′-side of a purine residue results in less destabilization of duplexes relative to when they are placed at the 5′-side of pyrimidines; this is particularly true in phosphorothioate d(AT) and d(GC) systems (43).

[6]Phosphorothiate substitution within (dTpT) is more destabilizing than substitution within (dCpC) oligomers (44).

Experimental

General procedures, chemicals, and reagents

THF was distilled from sodium benzophenone ketyl. Dimethylformamide (DMF), pyridine, and *N,N*-diisopropylethylamine were dried by stirring over CaH_2 followed by distillation under reduced pressure, and were stored over activated 4Å molecular sieves. Dichloromethane was distilled from P_2O_5. Acetonitrile was stirred in P_2O_5 and distilled from calcium hydride. Acetic anhydride was distilled and stored over magnesium turnings. Silylated ribonucleoside 3′-(cyanoethyl)phophoramidites were obtained from Dalton Chemical Laboratories, Inc. (Toronto, Ont.). DNA cyanoethyl phosphoramidite monomers, long-chain alkylamine controlled-pore glass (LCAA-CPG) bearing deoxyribonucleosides, tetraethylthiuram disulfide (TETD), and all other ancillary reagents for DNA/RNA/ANA synthesis were obtained from Applied Biosystems (Toronto, Ont.). LCAA-CPG bearing ribonucleosides or arabinonucleosides were prepared as previously described (45). *N*^{6}-benzoyl-5′-*O*-monomethoxytritylarabinoadenosinesine-2′-*O*-acetyl-3′-*O*-*N,N*-diisopropyl-β-cyanoethylphosphoramidite and 5′-*O*- monomethoxytrityllarabinouridine-2′-*O*-acetyl-3′-*O*-*N,N*-diisopropyl-β-cyanoethylphosphoramidites used in ANA synthesis were prepared according to Damha et al. (21). Cytidine, arabinocytidine, poly dT, poly rU, poly rG, and poly rA were used as obtained from Sigma Chemical Co (St. Louis, Mo.). Polyacrylamide gel electrophoresis reagents were obtained from Bio-Rad (Toronto, Ont.). HPLC grade solvents were purchased from Caledon (Toronto).

Preparation of N^4*-benzoyl-5′-*O*-monomethoxytritylarabinocytosine-2′-*O*-acetyl-3′-*O-N,N*-diisopropyl-β-cyanoethylphosphoramidite* ***5***

1. From 1-β-D-arabinofuranosylcytosine ***1***

Synthesis of 5′-O-monomethoxytritylarabinocytidine ***2***. Arabinocytidine **1** (18.0 mmol, 4.4 g) was coevaporated with pyridine (3 × 10 mL) and dissolved in dry pyridine (20 mL). Monomethoxytrityl chloride (19.8 mmol, 6.1 g) was added and the solution stirred at room temperature for 10 h, at which time a further 800 mg (0.1 equiv.) of monomethoxytrityl chloride was added and the mixture was allowed to stir for an additional 12 h. The mixture was evaporated to near dryness, dissolved in dichloromethane, and washed first with a solution of 5% sodium bicarbonate (100 mL) followed by brine (100 mL). The organic layer was dried over sodium sulfate and coevaporated with a solution of 10% dichloromethane in toluene (2 × 50 mL) to remove residual pyridine. This crude mixture was purified by silica gel chromatography by elution with dichloromethane–ethanol 85:15, affording 7.0 g (79% yield) of pure **2**. TLC (CH_2Cl_2/EtOH, 8:2) R_f 0.42; ($CHCl_3$/EtOH, 7:3) R_f 0.67. UV (95% EtOH/H_2O) λ_{max}: 230, 275 nm; λ_{min}: 224, 252 nm. ^{1}H NMR (acetone-d_6, 500 MHz) δ: 7.2–7.5 (m, 14, aryl trityl), 6.24 (d, 1, $J_{H1'-H2'}$ = 3.91 Hz, H1′), 4.34 (t, 1, H2′), 4.18 (t, 1, H3′), 4.07 (m, 1, H4′), 3.79 (s, 3, OCH_3), 3.45 (m, 2, H5′), 3.41 (m, 2, H5″).

N^4*-Benzoyl-5′-*O*-monomethoxytritylarabinocytidine* ***3***. Monomethoxytritylarabinocytidine **2** (10.9 mmol, 5.65 g) was coevaporated with pyridine (2 × 30 mL) and dissolved in pyridine (40 mL). Trimethylchlorosilane (54.8 mmol, 6.9 mL) was added to the solution over a period of 5 min and the mixture was stirred at ambient temperature (30 min) until all the starting material had reacted (TLC: dichlo-

Can. J. Chem. Downloaded from www.nrcresearchpress.com by 195.246.54.202 on 09/08/12
For personal use only.

Can. J. Chem. Downloaded from www.nrcresearchpress.com by 195.246.54.202 on 09/08/12
For personal use only.

romethane/ethanol 8:2). Benzoyl chloride (54.9 mmol, 6.4 mL) was added via syringe over a 5 min period. TLC analysis (dichloromethane/ethanol 8:2), 2 h later, indicated that less than 5% of non-benzoylated trisilylated product (R_f 0.76) remained. The reaction flask was immersed in an ice bath and water (5 mL) was added, followed by a solution of 29% ammonia (5 mL) 10 min later. After 15 min of stirring, the "thick" mixture was evaporated to near dryness, dissolved in dichloromethane (30 mL), and washed with water (30 mL). The organic layer was dried over sodium sulfate and the solvent was evaporated. The brown gum was coevaporated with toluene (2 × 30 mL) and purified twice by silica gel chromatography by elution with 5% ethanol–dichloromethane, affording 4.9 g (73% yield) of pure **3**. TLC: (CH_2Cl_2/EtOH 9:1) R_f 0.33; (EtOAc/EtOH, 9:1) R_f 0.63; (EtOAc) R_f = 0.13. UV (95% EtOH/H_2O, nm) λ_{max}: 230, 257, 307; λ_{min}: 224, 245, 286. ^{1}H NMR ($CDCl_3$, 200 MHz) δ: 3.73 (s, 3, OCH_3), 3.45 (m, 2, H5′), 4.04 (m, 1, H4′), 4.31 (t, 1, H3′), 4.61 (t, 1, H2′), 6.21 (d, 1, $J_{H1'-H2'}$ = 4.85 Hz, H1′), 7.0–7.5 (m, 14, aryl trityl), 7.4–7.7 (m, 5, aryl benzoyl). MS (FAB-NBA) *m/e*: 620 (MH^+, 5.3%), 273 ($MMTr^+$, 100%), 228 (6.0%), 216 (HCy^{Bz} + H^+, 31.0%).

N^4-*Benzoyl-5′-O-monomethoxytritylarabinocytidine-3′-O-N,N-diiso-propyl*-β-cyanoethylphosphoramidite **4**. To a dry hypovial under argon was aded dry THF (30 mL), dry diisopropylethylamine (35.5 mmol, 6.2 mL), and the nucleoside derivative **3** (4.5 mmol, 8.8 g). *N,N*-Diisopropyl-β-cyanoethylphosphonamidic chloride (9.8 mmol, 2.2 mL) was added dropwise over 20 min. At the 90 min mark, ethyl acetate (prewashed with a solution of 5% sodium bicarbonate) (100 mL) was added and the mixture transferred to a separator funnel where it was washed with brine (4 × 100 mL) and dried over sodium sulfate. Removal of the solvent afforded 1.15 g of a white crystalline foam. TLC analysis (TLC: EtOAc/CH_2Cl_2/Et_3N 48:48:4) indicated a >95% completed reaction. The crude product was purified by silica gel chromatography by elution with CH_2Cl_2/hexanes/triethylamine 50:45:5, yielding both diastereoisomers of compound **4** in 77% combined yield. Physical properties of fast diastereoisomers: TLC (EtOAc/CH_2Cl_2/Et_3N, 48:48:4) R_f 0.62. ^{1}H NMR ($CDCl_3$, 100 MHz) δ: 8.12 (d, 1, H6, J_{H6-H5} = 2.4 Hz), 7.3–7.5 (H5, overlap with trityl), 6.14 (d, 1, $J_{H1'-H2'}$ = 4.98 Hz, H1′), 4.53 (2 × dd, 1, H2′, $J_{H2'-H3'} \cong J_{H1'-H2'}$ = 3.4 Hz), 4.29–4.34 (2 × dd, 1, H3′, $J_{H2'-H3'} \cong J_{H3'-H4'}$ = 3.9 Hz), 4.13–4.16 (m, 1, H4′), 3.4 (m, 2, H5′, H5″), 3.75 (s, 3, OCH_3), 1.17 (d, 6, i-Pr), 1.10 (d, 6, i-Pr). ^{13}C NMR ($CDCl_3$, 100 MHz) δ: 143.65 (s, C6), 113.2 (s, C5), 87.21 (s, C1′), 83.23 (d, C4′), 77.88 (d, C3′), 75.17 (d, C2′), 62.59 (s, C5′). ^{31}P NMR ($CDCl_3$, 80 MHz) δ: 150.60. Physical properties of slow diastereoisomer: TLC (EtOAc/CH_2Cl_2/Et_3N, 48:48:4) 0.48. ^{1}H NMR ($CDCl_3$, 100 MHz) δ: 8.10 (d, 1, H6, J_{H6-H5} = 2.3 Hz), 7.3–7.5 (H5, overlap with trityl), 6.25 (d, 1, $J_{H1'-H2'}$ = 4.03 Hz, H1′), 4.57 (2 × dd, 1, H2′, $J_{H2'-H3'} \cong J_{H1'-H2'}$ = 2.9 Hz), 4.30 (2 × dd, 1, H3′, $J_{H2'-H3'} \cong J_{H3'-H4'}$ = 3.5 Hz), 4.15 (m, 1, H4′), 3.4 (m, 2, H5′, H5″), 3.78 (s, 3, OCH_3), 1.13 (d, 6, i-Pr). ^{13}C NMR ($CDCl_3$, 100 MHz) δ: 86.98 (s, C1′), 83.42 (d, C4′), 78.95 (d, C3′), 74.79 (d, C2′), 62.90 (s, C5′). ^{31}P NMR ($CDCl_3$, 80 MHz) δ: 150.80. MS (FAB-NBA) *m/e*: 820 (MH^+, 6.9%), 602 ([MH^+ − $CNCH_2CH_2OP(OH)$(i-Pr)$_2$], 17.9%), 273 ($MMTr^+$, 100%), 216 (HCy^{Bz} − H^+, 33.9%), 201 ($CNCH_2CH_2OP$(i-Pr)$_2^+$, 46.3%).

N^4-*Benzoyl-5′-O-monomethoxytritylarabinocytosine-2′-O-acetyl-3′-O-N,N-diisopropyl*-β-cyanoethylphosphoramidine **5**. To a dry hypovial containing the slow diastereoisomer of **4** (1.1 mmol, 900 mg) and dimethylaminopyridine (0.4 mmol, 53 mg) were added dry THF (5 mL) and diisopropylethylamine (8.7 mmol, 1.5 mL). Acetic anhydride (4.4 mmol, 450 μL) was added over 1 min and the solution was stirred for 45 min since TLC analysis ((CH_2Cl_2/EtOAc/Et_3N, 1:1) R_f 0.63) indicated that all of the starting material had reacted. Ethyl acetate (prewashed with a solution of 5% sodium bicarbonate) (25 mL) was added and the mixture transferred to a separator funnel where it was washed with brine (5 × 100 mL) and dried over sodium sulfate. Removal of the solvent produced **5** as a white crystalline foam in 87% yield. TLC (EtOAc/CH_2Cl_2/Et_3N, 48:48:4) R_f 0.63. ^{1}H NMR ($CDCl_3$, 400 MHz) δ: 7.96 (d, 1, H6, J_{H6-H5} = 2.4 Hz), 7.3–7.5 (H5, overlap with trityl), 6.33 (d, 1, H1′, $J_{H1'-H2'}$ = 4.21 Hz), 5.45 (2 × dd, 1, H2′, $J_{H2'-H3'} \cong J_{H1'-H2'}$ = 3.2 Hz), 4.40 (2 × dd, 1, H3′, $J_{H2'-H3'} \cong J_{H3'-H4'}$ = 3.2 Hz), 4.25 (m, 1, H4′), 3.70 (s, 3, OCH_3), 3.42 (2 × dd, 1, H5″, $J_{H5'-H5''}$ = 10.2 Hz, $J_{5''-H4'}$ = 4.4 Hz), 3.36 (2 × dd, 1, H5′, $J_{H5'-H5''}$ = 10.2 Hz, $J_{H5'-H4'}$ = 5.6 Hz), 1.74 (s, 3, $COCH_3$). ^{31}P NMR ($CDCl_3$, 80 MHz) δ: 151.26. MS (FAB-NBA) *m/e*: 862 (MH^+, 1.6%), 644 ([MH^+ − $CNCH_2CH_2OP(OH)$(i-Pr)$_2$], 4.3%), 273 ($MMTr^+$, 100%), 216 (HCy^{Bz} + H^+, 14.5%), 201 ($CNCH_2CH_2OP$(i-Pr)$_2^+$, 14.0%).

2. *From cytidine*

A stirred mixture of cytidine (48.7 mmol, 11.8 g), diphenyl carbonate (73.4 mmol, 13.3 g), dimethylformamide (20 mL), and water (50 mmol, 0.9 mL) was heated at 150°C for 15 min and the resulting dark solution was poured, with stirring, into 120 mL of ether. The gummy yellow precipitate formed was washed with cold ether (3 × 50 mL). Two new compounds with a relative intensity of 9:1 were evident by TLC (isopropyl/ammonia/water, 55:35:10, R_f 0.66 and 0.56). This crude mixture was coevaporated (3 × 30 mL) and dissolved in dry pyridine (20 mL). Monomethoxytrityl chloride (31.2 mmol, 9.6 g) (1.3 equivalents based on 50% yield of **2**) was added and the solution stirred for 19 h at room temperature. Analysis by TLC showed the formation of two compounds (CH_2Cl_2/EtOH, 8:2, R_f 0.49 and 0.33) with a relative intensity of 1:9, respectively. The mixture was evaporated to near dryness, dissolved in dichloromethane, washed first with a solution of 5% sodium bicarbonate (100 mL) followed by brine (100 mL), and dried over sodium sulfate. Approximately one half of this mixture (5.8 mmol, 3.0 g), was coevaporated (2 × 30 mL) and dissolved in pyridine (40 mL). Trimethylchlorosilane (29.0 mmol, 3.6 mL) was added and the solution was stirred at ambient temperature for 20 min, at which time benzoyl chloride (29.5 mmol, 3.45 mL) was introduced via syringe. TLC analysis (CH_2Cl_2/EtOH 9:1), 2 h later, indicated that less than 5% of the starting material remained. The mixture was then cooled by immersing in an ice bath; water (5 mL) was added, followed 10 min later by a solution of 29% ammonia (5 mL). After 15 min of stirring, the "thick" mixture was evaporated to near dryness, dissolved in dichloromethane (30 mL), and washed with water (30 mL). The organic layer was dried over sodium sulfate and the solvent evaporated. The brown gum was coevaporated with toluene (2 × 30 mL) and purified twice by silica gel chromatography, eluting first with dichloromethane (750 mL) followed by 5% EtOH/CH_2Cl_2, and affording pure **3** in 26% yield from cytidine. Preparation of **5** from this point on was as described in the previous section.

Solid-phase synthesis and purification of oligonucleotides

Oligoribonucleotides were prepared and purified as previously described (34). DNA oligomers were prepared and purified by the "trityl on" method (35). ANA oligomers were prepared on a 1.0 μmol scale employing "trityl on" synthesis cycle (60 s coupling time). Deprotection of sugar and phosphate moieties with concomitant release of oligomers from the glass support was accomplished by a single ammonia treatment (55°C, 8 h). The terminal trityl group was cleaved with trifluoroacetic acid during purification with reversed phase OPC® cartridges (Applied Biosystems). Oligoarabinocytidines were purified by polyacrylamide gel electrophoresis (PAGE). Phosphorothioate-linked DNA and ANA were prepared using tetraethylthiuram disulfide (TETD) as the sulfurizing reagent. After each coupling the glass beads were exposed to TETD (instead of iodine–water) for 10 min and then washed *extensively* with dry acetonitrile. Phosphorothioate oligomers were deblocked and purified as for the normal (phosphate) sequences.

Polyacrylamide mobility shift assays

Experiments were carried out as previously described (5).

Enzyme resistance assay

Incubations of oligomers with nucleases and analysis of the digests by PAGE were carried out as described (21). Analysis of the SVPDE digests of ara(Aps)$_7$A and d(Aps)$_7$A by HPLC was carried out on a Waters instrument equipped with dual 501 pumps, a 480 UV detector, and a 740 Data module. A Whatman Patrisil ODS-2 (10 μm, 4.6 × 250 mm) column was used with a linear elution gradient 0–50% over 30 min (solvent A: 20 mM KH_2PO_4 pH 5.5; solvent B: methanol).

Melting temperature (T_m) measurements

Thermal denaturations were performed on a Varian–Cary 1 UV spectrophotometer equipped with a Peltier thermal unit. Equimolar mixtures (2.5 μmol in each strand) of complementary oligomers were allowed to equilibrate at 40°C for 20 min, followed by slow cooling (over 20–30 min) to the start temperature prior to starting (runs involving poly rG or poly rA were heated to 80°C for 20–30 min). Thermal denaturation curves were recorded at 1 min intervals at 260 nm while the temperature was ramped at a rate of 0.5°C/min. The curves were analyzed by the first derivative method to obtain T_m values. Hyperchromicity (*%H*) is reported with respect to the initial absorbance in each curve. T_m versus log NaCl data was obtained as follows: first denaturation was run in 100 mM NaCl; upon completion, the sample was cooled slowly to 40°C; an appropriate amount of NaCl crystals was added to increase the salt concentration to the next level, samples were then cooled to the start temperature, and denatured again. This process was repeated for all salt concentrations. No correction for volume was made. Stoichiometry was determined by the method of continuous variation (38) as previously described (5).

Acknowledgements

We gratefully acknowledge financial support from the Natural Sciences and Engineering Research Council of Canada (NSERCC), the Canadian Foundation for AIDS Research (CANFAR), McGill University, and the University of Toronto. M.J.D. acknowledges a post-graduate fellowship received from the Ministry of Colleges and Universities, Government of Ontario (John Polanyi Prize in Chemistry, 1989).

1. (*a*) P.C. Zamecnik and M.L. Stephenson. Proc. Natl. Acad. Sci. U.S.A. **75**, 280 (1978); (*b*) M.L. Stephenson and P.C. Zamecnik. Proc. Natl. Acad. Sci. U.S.A. **75**, 285 (1978); (*c*) P.C. Zamecnik, J. Goodchild, Y. Taguchi, and P.S. Sarin. Proc. Natl. Acad. Sci. U.S.A. **83**, 4143 (1986); (*d*) C.J. Markus-Sekura, A.M. Woerner, K. Shinozuka, G. Zon, and G.V. Quinnan. Nucleic Acids Res. **15**, 5749 (1987).
2. E. Wickstru. J. Biochem. Biophys. Methods, **13**, 97 (1986).
3. (*a*) P.S. Miller. *In* Oligodeoxynucleotides, antisense inhibitors of gene expression. *Edited by* J.S. Cohen. Macmillan, Houndsmills and London. 1989. pp. 79–95; (*b*) C.A. Stein and J.S. Cohen. *In* Oligodeoxynucleotides, antisense inhibitors of gene expression. *Edited by* J.S. Cohen. Macmillan, Houndsmills and London. 1989. pp. 97–117; (*c*) B. Froehler, P. Ng, and M. Matteucci. Nucleic Acids Res. **16**, 4831 (1988); (*d*) W.S. Marshall and M.H. Caruthers. Science, **259**, 1564 (1993).
4. (*a*) J. Cormier and K.K. Ogilvie. Nucleic Acids Res. **16**, 4583 (1988); (*b*) E.P. Stirchak, J.E. Summerton, and D.D. Weller. J. Org. Chem. **52**, 4202 (1987); (*c*) M. Matteucci. Nucleosides Nucleotides, **10**, 231 (1991); (*d*) B. Musicki and T.S. Widlanski. Tetrahedron Lett. **32**, 1267 (1991); (*e*) S.H. Kawai, D. Wang, P.A. Giannaris, M.J. Damha, and G. Just. Nucleic Acids Res. **21**, 1473 (1993); (*f*) B. Meng, S.H. Kawai, D. Wang, G. Just, P.A. Giannaris, and M.J. Damha. Angew. Chem. Int. Ed. Engl. **32**, 729 (1993).
5. P.A. Giannaris and M.J. Damha. Nucleic Acids Res. **21**, 4742 (1993).
6. (*a*) P.D. Cook. Anti-Cancer Drug Des. **6**, 585 (1991); (*b*) E. Ulhmann and A. Peyman. Chem. Rev. **90**, 543 (1990); (*c*) C. Hélène and J.-J. Toulmé. Biochim. Biophys. Acta, **99**, 1049 (990); (*d*) J.S. Cohen (*Editor*). Oligodeoxynucleotides, antisense inhibitors of gene expression. Macmillan, Houndsmills and London. 1989; (*e*) G. Zon. Pharm. Res. **5**, 539 (1988).
7. (*a*) F. Debart, B. Rayner, G. Degols, and J.-L. Imbach. Nucleic Acids Res. **20**, 1193 (1992); (*b*) F. Morvan, B. Rayner, J.-L. Imbach, S. Thenet, J.-R. Bertrand, J. Paoletti, C. Malvy, and C. Paoletti. Nucleic Acids Res. **15**, 3421 (1987).
8. (*a*) M.J. Damha, P.A. Giannaris, P. Marfey, and L.S. Reid. Tetrahedron Lett. **32**, 2573 (1991); (*b*) S. Fujimori and K. Shudo. J. Am. Chem. Soc. **112**, 7436 (1990); (*c*) M.L. Capobianco, A. Garbesi, F. Arcamone, B. Maschera, and G. Palu. Nucleic Acids Res. Symp. Ser. **24**, 2587 (1991).
9. G.W. Ashley. J. Am. Chem. Soc. **114**, 9731 (1992).
10. K.C. Schneider and S.A. Benner. J. Am. Chem. Soc. **112**, 453 (1990).
11. L. Bellon, J.-L. Barascut, G. Maury, G. Divita, R. Goody, and J.-L. Imbach. Nucleic Acids Res. **21**, 1587 (1993).
12. (*a*) M. Perbost, M. Lucas, and C. Charvis. Biochem. Biophys. Res. Commun. **165**, 742 (1989); (*b*) J. Sagi, A. Szemzo, J. Szecsi, and L. Otvos. Nucleic Acids Res. **18**, 2133 (1991).
13. B.S. Sproat, A.I. Lamond, B. Beijer, P. Neumer, and U. Ryder. Nucleic Acids Res. **17**, 3373 (1989); (*b*) E.A. Lesnik, C.J. Guinosso, A.M. Kawasaki, H. Sasmor, M. Zounes, L.L. Cummins, D.J. Ecker, P.D. Cook, and S.M. Freir. Biochemistry, **32**, 7832 (1993); (*c*) M. Cotten, B. Oberhauser, H. Brunear, A. Holzner, G. Issakides, C.R. Noe, G. Schaffner, E. Wagner, and M. Birnstiel. Nucleic Acids Res. **19**, 2629 (1991).
14. A.D. Adams, C.R. Petrie, and R.B. Meyer, Jr. Nucleic Acids Res. **19**, 3647 (1991).
15. (*a*) K.K. Ogilvie, A.L. Schifman, and C.L. Penney. Can. J. Chem. **57**, 2230 (1979); (*b*) K.K. Ogilvie, S.L. Beaucage, A.L. Schifman, N.Y. Theriault, and K.L. Sadana. Can. J. Chem. **56**, 2768 (1978); (*c*) R.T. Pon and K.K. Ogilvie. Nucleosides Nucleotides, **3**, 485 (1984); (*d*) N. Usman, K.K. Ogilvie, M.-Y. Jiang, and R.J. Cedergren. J. Am. Chem. Soc. **109**, 7845 (1987).
16. W.J. Wechter. J. Med. Chem. **10**, 762 (1967).
17. C. Gioeli, J.B. Chattopadhyaya, A.F. Drake, and B. Oberg. Chem. Scr. **19**, 13 (1982).
18. G.P. Beardsley, T. Mikita, M. Klaus, and A.L. Nussbaum. Nucleic Acids Res. **16**, 9165 (1988).
19. (*a*) K.K. Ogilvie, D.P.C. McGee, S.M. Boisvert, G.H. Hakimelahi, and Z.A. Proba. Can. J. Chem. **61**, 1204 (1983); (*b*) D.P.C. McGee. M.Sc. thesis, McGill University, Montreal, Canada (1981).
20. (*a*) G. Provenzale and J. Nagyvary. Biochemistry, **9**, 1744 (1970); (*b*) J. Nagyvary and G. Provenzale. Biochemistry, **8**, 4769 (1969); (*c*) K.K. Ogilvie and D. Iwacha. Can. J. Chem. **48**, 862 (1970); (*d*) G. Schramman. Angew. Chem. Int. Ed. Engl. **6**, 460 (1967).
21. M.J. Damha, N. Usman, and K.K. Ogilvie. Can. J. Chem. **67**, 831 (1989).
22. (*a*) M. Resmini and W. Pfleiderer. Helv. Chim. Acta, **76**, 158 (1993); (*b*) W. Pfleiderer. 10th Int. Roundtable: Nucleosides and Nucleotides, Park City, Utah, Sept 16, 1992.
23. (*a*) E.J. Reist, P.A. Sturm, R.Y. Pong, M.J. Tanga, and R.W. Sidwell. *In* Nucleotide analogues as antiviral agents. *Edited by* J.C. Martin. American Chemical Society, Washington, D.C. 1989. pp. 17–34; (*b*) J.L. Rideout, D.W. Henry, and L.M. Beacham III (*Editors*). Nucleosides, nucleotides and their biological activity. Academic Press, New York. 1983, and references therein.
24. R.S.K. Young and G.A. Fischer. Biochem. Biophys. Res. Commun. **32**, 23 (1968).
25. (*a*) M.J. Keating, K.B. McCredie, G.P. Bodey, T.L. Smith, E. Gehan, and E.J. Freieich. J. Am. Med. Assoc. **248**, 2481 (1982); (*b*) D.W. Kufe and D.R. Springs. Semin. Oncol. **12**, 34 (1985); (*c*) E. Frei III, J. Bickers, M. Lane, W. Leary, and R. Tally. Cancer Res. **29**, 1325 (1969).
26. (*a*) N.R. Cozzarelli. Annu. Rev. Biochem. **46**, 641 (1977); (*b*) A. Fridland. Biochemistry, **16**, 5308 (1977).
27. T. Mikita and G.P. Beardsley. Biochemistry, **27**, 4698 (1988).
28. (*a*) Y-G. Gao, G.A. van der Marel, J.H. van Boom, and A.H.-J. Wang. Biochemistry, **30**, 9922 (1991).
29. J.M.L. Pieters, E. de Vroom, G.A. van der Marel, J.H. van Boom, and C. Altona. Eur. J. Biochem. **184**, 415 (1989).
30. J.M.L. Pieters, E. de Vroom, G.A. van der Marel, J.H. van Boom, T.M.G. Koning, R. Kaptein, and C. Altona. Biochemistry, **29**, 788 (1990).
31. E. de Vroom, H.C.P.F. Roelen, C.P. Saris, T.N.W. Budding, G.A. van der Marel, and J.H. van Boom. Nucleic Acids Res. **16**, 2987 (1988).

Can. J. Chem. Downloaded from www.nrcresearchpress.com by 195.246.54.202 on 09/08/12
For personal use only.

32. M.-K. Teng, Y.-C. Liaw, G.A. van der Marel, J.H. van Boom, and A.H.-J. Wang. Biochemistry, **28**, 4923 (1989).
33. (*a*) J. Beránek, T.J. Delia, and P. Drašar. Collect. Czech. Chem. Commun. **42**, 1588 (1976); (*b*) K.K. Ogilvie. Carbohydrate Res. **24**, 210 (1972).
34. M.J. Damha and K.K. Ogilvie. *In* Protocols for oligonucleotide and analogs: synthesis and properties, methods in molecular biology. *Edited by* S. Agrawal. The Humana Press Inc., Totowas, N.J. 1993. pp. 81–114.
35. M.J. Gait (*Editor*). Oligonucleotide synthesis: a practical approach. IRL Press, Oxford. 1984.
36. C.A. Stein, C. Subasinghe, K. Shinozuka, and J.S. Cohen. Nucleic Acids Res. **16**, 3209 (1988).
37. (*a*) F. Morvan, B. Rayner, and J.-L. Imbach. Tetrahedron Lett. **49**, 7149 (1990); (*b*) S. Agrawal, J.Y. Tang, D. Sun, P.S. Sarin, and P.C. Zamecnik. Ann. N.Y. Acad. Sci. **660**, 3 (1992).
38. (*a*) P. Job. Anal. Chim. Acta, **9**, 113 (1928); (*b*) D.S. Pilch, C. Levenson, and R. Shafer. Proc. Natl. Acad. Sci. U.S.A. **87**, 1942 (1990).
39. (*a*) H. Inoue, Y. Hayase, M. Asaka, A. Imura, S. Iwai, K. Miura, and E. Ohtsuka. Nucleic Acids Res. **16**, 165 (1985).
40. A.M. Kawasaki, M.D. Casper, S.M. Freier, E.A. Lesnik, M.C. Zounes, L.L. Cummins, C. Gonzalez, and P.D. Cook. J. Med. Chem. **36**, 831 (1993).
41. A.M. Iribarren, B.S. Sproat, P. Neuner, I. Sulston, U. Ryder, and A.I. Lamond. Proc. Natl. Acad. Sci. U.S.A. **87**, 7747 (1990).
42. E.A. Lesnik, C.J. Guinosso, A.M. Kawasaki, H. Sasmor, M. Zounes, L.L. Cummins, D.J. Ecker, P.D. Cook, and S.M. Freier. Biochemistry, **32**, 7832 (1993).
43. (*a*) J.W. Suggs and D.A. Taylor. Nucleic Acids Res. **13**, 5707 (1985); (*b*) L. Kibler-Herzog, G. Zon, B. Uznaski, G. Whittier, and W.D. Wilson. Nucleic Acids Res. **19**, 2979 (1991); (*c*) L.J.P. Latimer, K. Hampel, and J.S. Lee. Nucleic Acids Res. **17**, 1549 (1989); (*d*) F. Eckstein and T.M. Jovin. Biochemistry, **22**, 4546 (1983); (*e*) T.M. Jovin, J.J. van de Sande, D.A. Zarling, D.J. Arndt-Jovin, F. Eickstein, H.H. Füldner, C. Greider, I. Grieger, E. Hamori, B. Kalisch, L.P. McIntosh, and M. Robert-Nicoud. Cold Springs Harbor Symp. Quant. Biol. **47**, 143 (1983).
44. C.A. Stein, C. Subasinghe, K. Shinozuka, and J.S. Cohen. Nucleic Acids Res. **16**, 3209 (1988).
45. M.J. Damha, P.A. Giannaris, and S.V. Zabarylo. Nucleic Acids. Res. **18**, 3813 (1990).

Can. J. Chem. Downloaded from www.nrcresearchpress.com by 195.246.54.202 on 09/08/12
For personal use only.

Cooperative mechanisms for the H + ICl reaction and their significance for the K + ICl experiment

ANTONIO LAGANÀ,[1] OSVALDO GERVASI, AND STEFANO CROCCHIANTI
Dipartimento di Chimica, Università di Perugia, Perugia, Italy

ERNESTO GARCIA AND GUILLERMO OCHOA DE ASPURU
Departamento de Química Física, Universidad del Pais Vasco, Vitoria, Spain

AND

JOSÉ M. ALVARIÑO
Departamento de Química Física, Facultad de Química, Universidad de Salamanca, Salamanca, Spain

Received July 18, 1993

This paper is dedicated to Professor John C. Polanyi on the occasion of his 65th birthday

ANTONIO LAGANÀ, OSVALDO GERVASI, STEFANO CROCCHIANTI, ERNESTO GARCIA, GUILLERMO OCHOA DE ASPURU, and JOSÉ M. ALVARIÑO. Can. J. Chem. **72**, 919 (1994).

To characterize the dynamics of halogen centre reactions, we have investigated the H + ICl system. In particular, we have focused our attention on the importance of indirect atom–diatom reactivity in determining the macroscopic and microscopic branching of a reaction. An analysis of opacity functions and trajectory plots evaluated for different collision angles and isotopic variants evidenced the occurrence of cooperative reactive mechanisms in which an atom of the target diatom favours reaction with the other end of the molecule. Two limiting cooperative mechanisms were singled out and associated with different ranges of the impact parameter. A generalization of these findings to heavier systems has been performed by considering the ^{39}H + ICl reaction. Calculated properties of the model were found to agree with values measured for the K + ICl reaction.

ANTONIO LAGANÀ, OSVALDO GERVASI, STEFANO CROCCHIANTI, ERNESTO GARCIA, GUILLERMO OCHOA DE ASPURU et JOSÉ M. ALVARIÑO. Can. J. Chem. **72**, 919 (1994).

Dans le but de caractériser la dynamique des réactions de centres halogénés, on a étudié le système H + ICl. On a focalisé notre attention sur l'importance de la réactivité indirecte atome–diatome dans la détermination des branches macroscopique et microscopique d'une réaction. Une analyse des fonctions d'opacité et des courbes des trajectoires évaluées pour différents angles de collision et diverses variations isotopiques mettent en évidence la mécanismes de réaction coopérative dans lesquels un atome d'un diatome cible favorise la réaction avec l'autre extrémité de la molécule. On a singularisé deux mécanismes coopératifs limites et on les a associés à divers sections différentes du paramètre d'impact. On a réalisé une généralisation de ces résultats à des systèmes plus lourds en considérant la réaction ^{39}H + ICl. On a trouvé que les propriétés calculées pour le modèle sont en accord avec les valeurs mesurées pour la réaction K + ICl.

[Traduit par la rédaction]

1. Introduction

The rationalization of the dynamics of halogenic centre reactions is of particular interest because indirect paths to reaction (1) (defined as reactive paths leading to a final product partner differing from the atom to which the attack was initially directed) can be singled out. In principle, indirect reactive mechanisms can occur for various kinds of reactions including those collinearly dominated at low collision energy (2). In particular, however, indirect paths to products were found to play an important role for some reactions involving halogenic diatomic targets such as the F + I_2 (3, 4) and F + ICl (5, 6) reactions.

The Potential Energy Surface (PES) of the F + I_2 reaction exoergic and has two wells associated with colinear intermediates: an early (FII) and a late (IFI) one. A peculiar property of the F + I_2 reaction is that the opacity function has been found not to show the usual stepwise shape common to several exoergic reactive processes. The opacity function is, in fact, negligible at small impact parameters (b), it increases with b to reach a maximum at around b = 3 Å, and then it falls quite rapidly. These characteristics were rationalized in terms of a migration of the attacking atom F from the iodine of the first attack to the next one at large values of the impact parameter b. Such a mechanism was found to lead to a larger rotational and a smaller vibrational product excitation (compared with "non-migratory" ones) though the overall product internal energy is about the same.

The heteronuclear nature of the target molecule in the F + ICl reaction offers a means for linking indirect attacks to macroscopic branching (i.e., the yield ratio between different products). In particular, in ref. 6 it was pointed out that the migration of F between I and Cl plays an important role in determining the branching ratio and that the products have more translation and less vibration than those of non-migratory collisions.

A suitable prototype for this type of reactions is H + ICl. Because of the light mass of the impinging atom. H + ICl reactive collisions explore in detail the potential energy surface around the target molecule and, as a result, they allow an exhaustive description of possible paths to reaction. In particular, it is possible to distinguish microscopic branching (alternative reaction paths giving the same product with different energetic properties) from macroscopic branching (alternative reaction paths giving different products) and find out their contribution to reactivity.

An experimental (7) and a theoretical (8) study of this reaction was carried out by Polanyi and co-workers. In an attempt to generalize their conclusions to similar systems we have performed an extended classical trajectory study of the H + ICl reaction and its isotopic variant with the hydrogen artificial

[1]Author to whom correspondence may be addressed.

Can. J. Chem. Downloaded from www.nrcresearchpress.com by 195.246.54.202 on 09/08/12
For personal use only.

Can. J. Chem. Downloaded from www.nrcresearchpress.com by 195.246.54.202 on 09/08/12
For personal use only.

heavy isotope ^{39}H. This reaction has been considered as a model for K + ICl for which angular and time-of-flight distributions have been obtained for both KI and KCl products (9, 10).

The paper is organized as follows: Calculated reactive properties of the H + ICl reaction are reported in Sect. 2 by paying special attention to the competition between alternative paths to reaction. In Sect. 3 a first rationalization of the results is carried out by analysing the opacity functions. In Sect. 4 a graphical analysis of the reactive trajectories is performed to classify the different types of migratory trajectories. In Sect. 5 analogies between K + ICl and H + ICl are investigated by discussing the ^{39}H + ICl reaction and comparing calculated quantities with experimental data.

2. Competing paths for the H + ICl reaction

As already mentioned, the H + ICl system was first investigated by Polanyi and Skrlac (7). They not only measured macroscopic branching by detecting both the HI and the HCl product, but they also found evidence for microscopic branching by obtaining bimodal distributions for the HCl product. These experimental findings were rationalized by carrying out quasiclassical trajectory calculations on a LEPS PES (8).

To understand in more detail the reactive dynamics of this system, we carried out trajectory calculations at both a translational temperature of 300 K and a collision energy of 2 kcal/mol. Differences in the calculated cross sections were found (11) to be related to the contrasting energy dependence of the collinear reactive probability for the following two processes:

[1] $H + ICl \rightarrow HCl + I$

[2] $H + ICl \rightarrow HI + Cl$

In fact, when H approaches ICl collinearly from the Cl side ($\Phi_I = 0°$. Φ_I is defined as the angle formed by the HI and ICl bonds that, thanks to the large mass of I, coincides with the one formed by the atom diatom displacement and the ICl bond), reaction to form HCl occurs by surmounting an early barrier of about 1.6 kcal/mol. (See the lower panel of Fig. 1 where the LEPS PES used has been plotted as a function of the Bond Order coordinates (12).) Collinear approaches of the H atom from the I side ($\Phi_I = 180°$) are shown in the upper panel of Fig. 1. These collisions do not go through a reaction barrier and are driven by a long-range attractive tail. A small well (associated with the formation of the HICl intermediate) occurs in the exit channel before the asymptote of the HI product channel is reached. This channel is 32.6 kcal/mol less exoergic than that leading to the formation of the HCl product. Accordingly, the collinear reactive probability for process [1] is zero at low collision energy and rises steeply to unity at threshold to decrease again at much higher collision energy. By contrast, the collinear reactive probability for process [2] shows no appreciable threshold and decreases with the collision energy.

However, on releasing the constraint of reacting along a line, the reactive outcome may differ (13). To investigate this aspect in detail, the calculations were repeated for a wide range of initial conditions. In Figs. 2 and 3 quasiclassical cross sections are shown for processes [1] and [2], respectively, calculated at $\Phi_I = 180°$, 135°, 90°, 45°, and 0° and E_c from 0.5 to 6 kcal/mol. For all the calculations the reactant ICl molecule was set at the ground rovibrational state ($v = j = 0$).

The short-dashed line of Fig. 2 is a plot of the reactive cross section calculated for process [1] when H attacks from the Cl side starting with a collinear HClI geometry ($\Phi_I = 0°$) and the value of the impact parameter b is chosen randomly (i.e., the velocity vector is not constrained along the line connecting the three atoms). As expected, the calculated cross section when plotted as a function of the collision energy has the typical shape of that of barrier-controlled reactions: there is no reactivity at low translational energy while, once past the threshold (whose location is usually closely related to the vibrationally adiabatic barrier) the reactive cross section rises significantly. When the angle Φ_I increases, the repulsive contribution to the potential associated with Cl is compensated by the long-range attractive tail associated with I. As a result, at low translation energies, H attacks slide sideways towards Cl, lowering or even eliminating threshold effects (cross sections calculated at $\Phi_I = 45°$, 90°, and 135° are also shown in Fig. 2 as dashed-dotted, dotted, and long-dashed curves, respectively). This is still true for $\Phi_I = 180°$ (solid curve) collisions for which the below-the-threshold value of the cross section is particularly large even if attacks to Cl occur from the opposite (I) side. Such a cooperative (intracatalytic) effect of I in enhancing the reaction of H with Cl, when low translation energy collisions take place from the I side, implies also that the impinging H atom has a lower chance of reacting with Cl at higher collision energy. In this case, in fact, the additional momentum induced by the I attractive tail reduces the interaction time between H and Cl (as will be seen in more detail for process [2]).

Plots of the cross section for process [2] are given in Fig. 3. In this case, almost all curves have the same decreasing trend with collision energy owing to the fact that a larger translational energy reduces the interaction time between H and I. This is in line with what has been found for collinear collisions taking place from the I side. However, at a given translational energy, attacks slightly more displaced towards the Cl end ($\Phi_I = 135°$ and 90°, given as long-dashed and dotted curves) are more reactive than those taking place at $\Phi_I = 180°$ (solid line) because the impinging atom is partially slowed down by the repulsive nature of the potential on the Cl side (an intracatalytic effect of Cl). Yet, when a trajectory passes too close to Cl (as for $\Phi_I = 45°$ and 0°; dashed-dotted and short-dashed lines, respectively), the repulsive effect becomes dominant, especially at low translational energies, and repels the incoming atom. As a matter of fact, reaction with I taking place from the opposite side ($\Phi_I = 0°$; short-dashed line) leads to a threshold effect as for barrier-controlled reactions.

3. Opacity functions and migratory trajectories

As for F + I_2 and F + ICl, the reactive behaviour of H + ICl could be rationalized in terms of migratory trajectories (i.e., by assuming that the reaction occurs via the formation of a temporary intermediate in which H binds to an atom of the target molecule different from the final product partner). A clear fingerprint of a migratory mechanism is believed to be the anomalous (inverted as a function of b) shape of the opacity function (4, 6). Yet the opacity functions calculated for H + ICl at collision energies typical of the experiment do not show a definite inverted shape, implying that, for this reaction, migration is not the dominant reactive mechanism.

To investigate this feature in more detail, we calculated fixed angle opacity functions. A synoptic view of the opacity functions of process [1] (dotted line) and process [2] (solid line) calculated at $\Phi_I = 180°$, 135°, 90°, 45°, and 0° (from the left to the

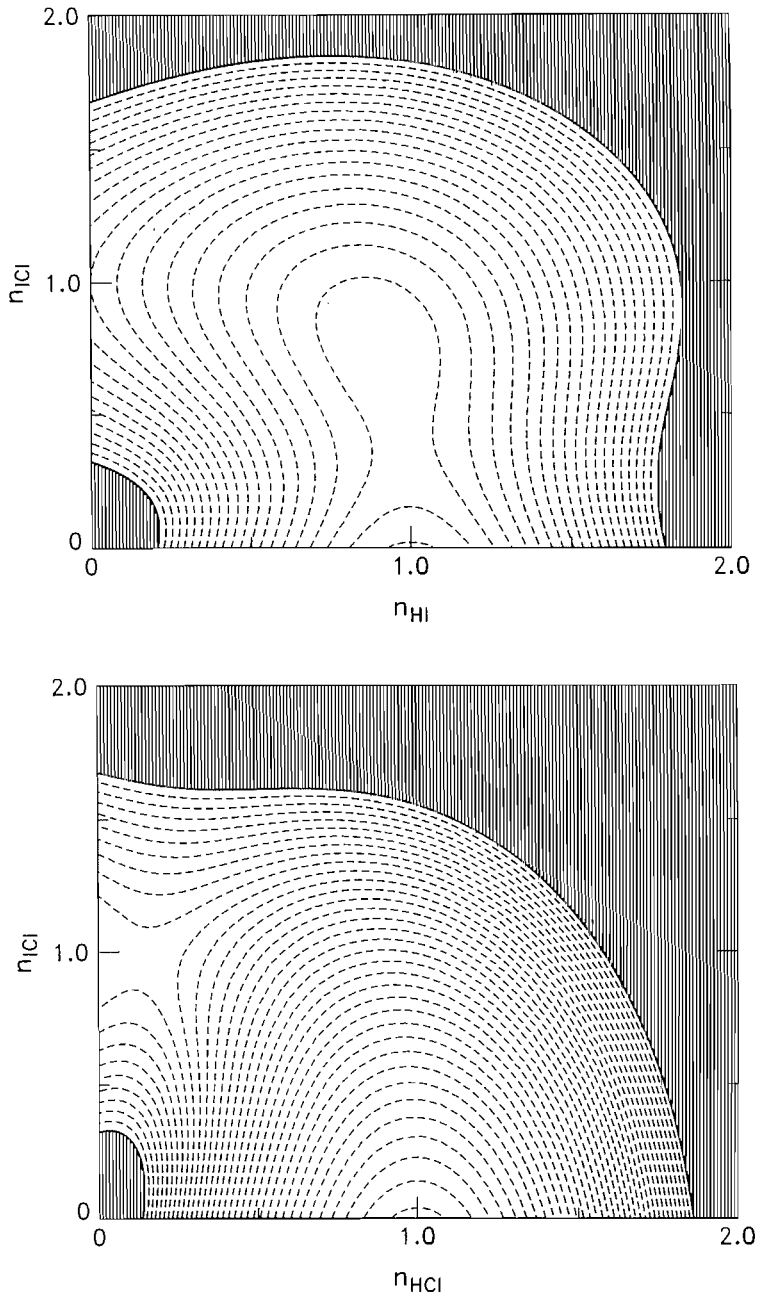

FIG. 1. Isoenergetic contours of the H + ICl potential energy surface used for the calculations plotted as a function of the n_{HI} and n_{ICl} bond order variables and $\Phi_I = 180°$ (upper panel) and as a function of the n_{HCl} and n_{ICl} bond order variables and $\Phi_{Cl} = 180°$ (lower panel). Energy cuts have been taken every 0.23 kcal/mol.

right-hand side panels) and E_e = 1, 2, 3, 4, 5, 6 kcal/mol (from the bottom panel up) is given in Fig. 4. The zero opacity function calculated at $\Phi_I = 0°$ and E_c = 1 kcal/mol (right panel of the bottom row) indicates that at low collision energy the barrier to reaction located on the Cl side prevents H from reaching the product valley of both processes [1] and [2], leading, as a consequence, to a threshold effect. By contrast, for higher Φ_I values (i.e., when attacks pass closer to I) reaction can take place even at such low (smaller than the collinear HClI barrier) energy thanks to the different (attractive instead of repulsive) nature of the potential energy path to reaction. The attractive nature of the reaction path at $\Phi_I = 0°$ manifests itself in a "non-negligible" reactive probability centred on large b values (left panel) due to less direct reaction mechanisms. In this case, in fact, direct attacks with small b are unproductive because they are made too fast by the attractive tail of the potential. For intermediate Φ_I values, when moving right from $\Phi_I = 180°$ to lower Φ_I values, smaller impact parameters increasingly contribute to the opacity function, indicating that for both processes [1] and [2] more direct encounters, with small values of b, become reactive.

When translational energy becomes larger than the barrier to reaction, (see for example the second row from the bottom where opacity functions calculated at E_c = 2 kcal/mol are shown), collisions occurring at $\Phi_I = 0°$ (Cl side) also have enough energy to access the HCl product valley. Accordingly, the related opacity function has the usual stepwise shape typical of direct, barrier-controlled reactions (i.e., it is unity until the

Can. J. Chem. Downloaded from www.nrcresearchpress.com by 195.246.54.202 on 09/08/12
For personal use only.

Can. J. Chem. Downloaded from www.nrcresearchpress.com by 195.246.54.202 on 09/08/12
For personal use only.

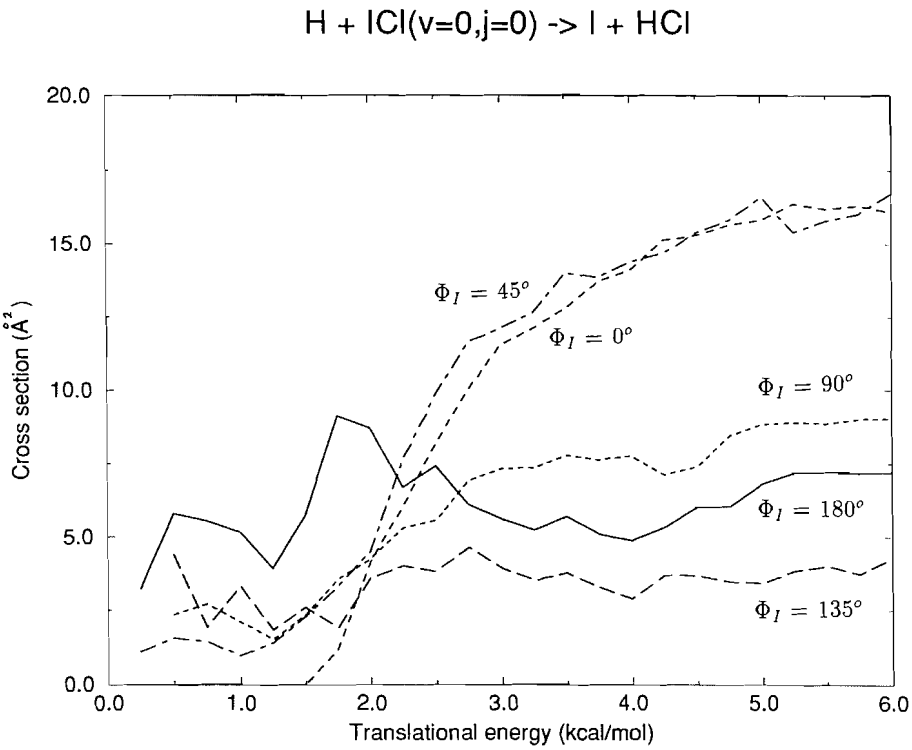

FIG. 2. Fixed Φ_I reactive cross section for the H + ICl → HCl + I process calculated at Φ_I = 0°, 45°, 90°, 135°, and 180° (short-dashed, dashed-dotted, dotted, long-dashed, and solid lines, respectively) plotted as a function of the collision energy.

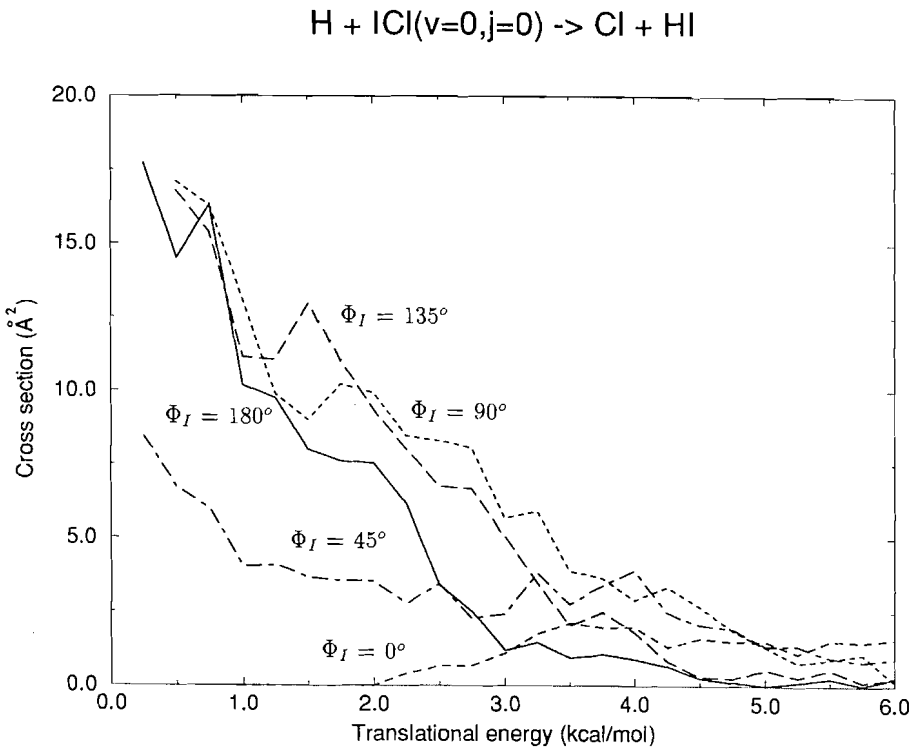

FIG. 3. As in Fig. 2 for the H + ICl → HI + Cl process.

energy component along the line of centres is sufficient to overtake the barrier relative to the corresponding collision angle (14). Again, when Φ_I = 180°, most of the reactivity is indirect and takes place at large b values. Only when moving to smaller Φ_I values do smaller impact parameters contribute to reactivity. Though this is true for both processes [1] and [2], it is the formation of HI that makes the best use of the availability for reaction of a broader range of impact parameters.

When the collision energy rises to 3 kcal/mol (see the third row of the figure) direct (Φ_I = 0°) reactivity with Cl (right

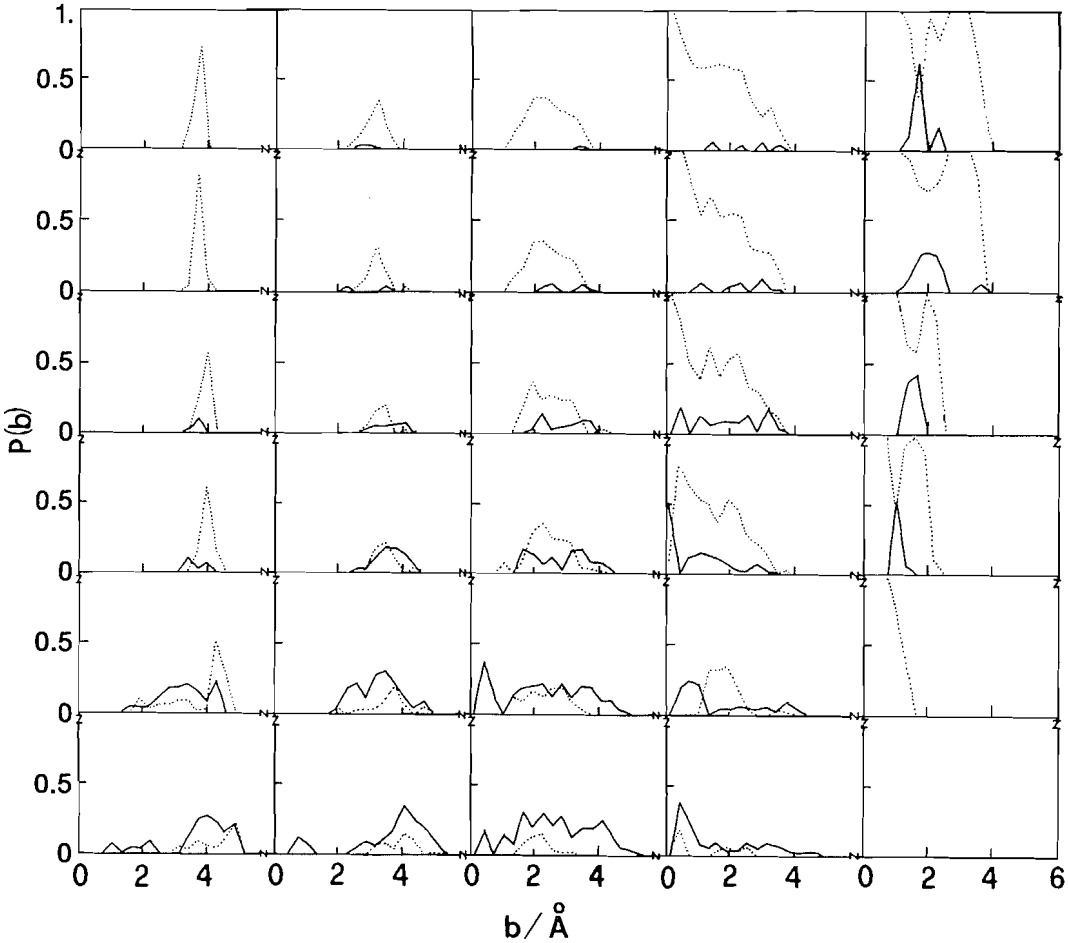

FIG. 4. Opacity functions for process [1] (dotted line) and process [2] (solid line) calculated at $\Phi_I = 180°, 135°, 90°, 45°, 0°$ (from the left to the right panel) and $E_c = 1, 2, 3, 4, 5, 6$ kcal/mol (from the lowest to the highest panel) plotted as a function of b.

panel) benefits from a larger availability of collision energy that is highly efficient in promoting this type of reactive mechanism. As a result, the opacity function extends to larger b values. However, there is a limited small interval of b values for which reactivity of process [1] drastically decreases in favour of that of process [2], which suddenly switches on. In other words, the opacity function plot indicates that there are particular combinations of b and E_c for which reactive attacks on Cl transform into reaction with I, implying a clear migration of H from Cl to I.

Such a situation is not confined to $E_c = 3$ kcal/mol. In fact, the same property is shown by opacity functions calculated at $\Phi_I = 0°$ for $E_c = 4$, 5, and 6 kcal/mol (respectively, the right panel of the three upper rows of the figure). The increase of the collision energy cuts out the contribution to reactivity of process [2] while that of process [1] increases thanks to direct reactivity (small impact parameters) at small Φ_I values and indirect reactivity (large impact parameters) at large Φ_I values.

In conclusion, the analysis of the opacity function suggests that there are clear cooperative (intracatalytic) effects through which an atom of the interhalogenic molecule helps its diatomic partner to react with H. The analysis has also singled out two extreme cases of cooperative mechanisms: One takes place mainly at moderate b values and requires (in a sequence) a close interaction between the incoming atom and both ends of the target molecule. The other takes place at large b values and is associated with a longer range interaction with the target molecule.

4. A graphical analysis of migratory trajectories

To get a better understanding of the dynamical characteristics of cooperative mechanisms, we undertook a graphical analysis of the reactive trajectories. The analysis was restricted to $\Phi_I = 0°$ and 180°, for which the two opposite prototypical cooperative mechanisms were singled out when inspecting the calculated opacity functions. At given values of E_c and Φ_I, the impact parameter was gradually increased from zero to quite large values. This allowed us to investigate the effect of making the velocity vector increasingly point away from the line of centres. Because of the choice of dealing only with initially "non-rotating" reactant molecules, it has been possible to represent the trajectories using daisy plots.

Daisy plots of five typical trajectories calculated at small, medium, and large values of b are shown in Figs. 5–9.

Small impact parameter reactive encounters are direct (i.e., H heads directly onto the atom to which, eventually, it will finally bind, while the other atom is gradually released from the opposite side). An example of this type of direct reactive encounters is given in Fig. 5 for process [1], i.e., for H reacting with Cl after attacking on the Cl side ($\Phi_I = 0°$). As shown by the figure, when the H atom (circles) comes close to Cl (squares) with enough collision energy to overtake the barrier to reaction, it links to the chlorine atom to form a stable HCl bond. Because of the negligible value of the impact parameter, HCl rotates very slowly while it moves away from the triatomic centre of mass (that for H + ICl essentially coincides with the atom I). As result, when

Can. J. Chem. Downloaded from www.nrcresearchpress.com by 195.246.54.202 on 09/08/12
For personal use only.

Can. J. Chem. Downloaded from www.nrcresearchpress.com by 195.246.54.202 on 09/08/12
For personal use only.

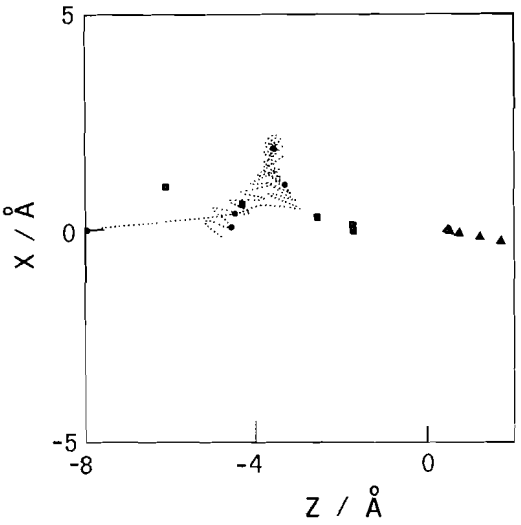

FIG. 5. Daisy plot for a trajectory of the H + ICl → HCl + I process having a small impact parameter.

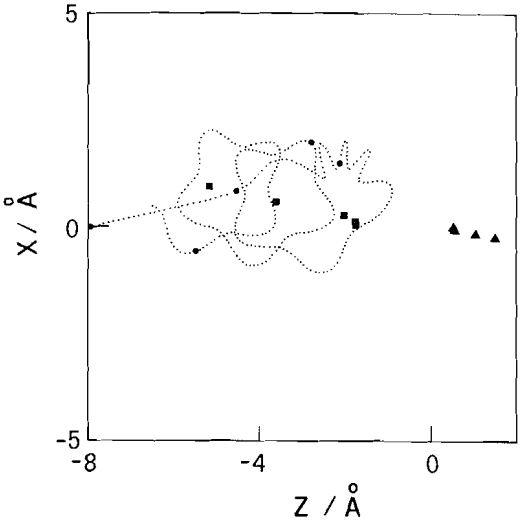

FIG. 6. As in Fig. 5 for a trajectory with moderate impact parameter.

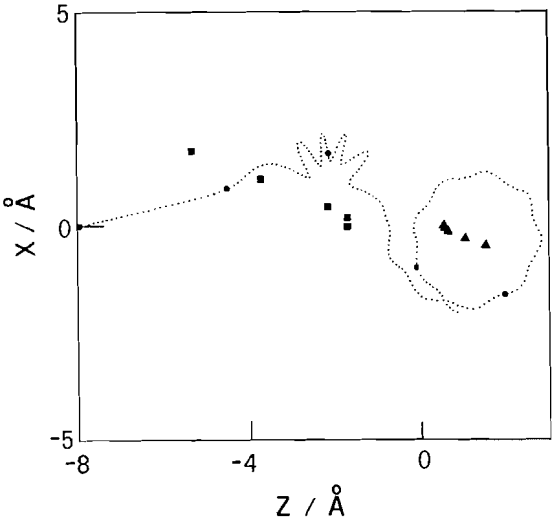

FIG. 7. As in Fig. 6 for a trajectory of the H + ICl → HI + Cl (BRB) process.

H ends up facing I (triangles), the internuclear distance has become so large that the interaction is negligible. A similar situation can occur for attacks taking place from the I side. In this case, however, there is no barrier to reaction. Therefore, the attractive tail of the potential can accelerate the impinging atom so much that the interaction time becomes too short to lead to reaction. Yet, when these small impact parameter collisions succeed in reaching the product valley, the rotation is again so slow that, by the time H ends up facing Cl, this atom has already moved far enough to make the interaction negligible.

At moderate impact parameters, the insertion dynamics becomes much richer and the energy flow increasingly involves rotations. As a matter of fact, when the atom attacks from the Cl side with a moderate impact parameter and enough energy to overtake the reaction barrier, it binds to Cl, leading to a significant rotational component in HCl. As a result, the H atom, after oscillating a few times around Cl, ends up facing the I atom when the internuclear distance is still short enough to lead to a strong interaction. This may generate two possible reactive outcomes: (*a*) the interaction with I pulls ahead the H atom into a faster HCl rotation (see Fig. 6); (*b*) the interaction with I strips out the H atom to form rotationally excited HI (see Fig. 7).

Both cases lead to rotationally excited products as a result of the conversion of the reactant orbiting motion into the product rotational motion. However, while in the first case there is a direct transfer of the reactant orbiting motion into the product rotational motion, in the second case a pure Bind–Release–Bind (BRB) migratory mechanism takes place. Such a mechanism offers a clear rationale for the complementarity shown by the $\Phi_I = 0°$ opacity functions for processes [1] and [2] (see the higher energy right panels of Fig. 4) at moderate *b* values. We also found evidence for a BRB migratory mechanism when the attack takes place from the I side. However, the effect was not unambiguous, not only because the whole process is disfavoured by the lower reactivity of process [2] at high energy but also because of cooperative effects taking place at larger impact parameter (and, therefore, more significantly contributing to the cross section).

The contribution of cooperative mechanisms other than BRB is also evidenced by the graphical study of the trajectories. In this case, the long-range attractive tail of the potential (due to the I atom) balances the escape component of the velocity of the impinging H atom. This kind of orbiting capture prevents H from missing the target and makes it available for a closer interaction with the target diatom. At this point, H can react either with Cl or I according to the particular combination of momenta characterizing that point of the collision. Illustrative cases of the two alternative reactive possibilities for this type of Orbit-And-Bind (OAB) mechanism are given in Figs. 8 and 9 for processes [1] and [2], respectively. In the first case, the orbiting results in H binding to the opposite Cl atom while in the second case H binds to I after bouncing back (twice) from Cl.

5. A model for the K + ICl reaction

To investigate the possibility of generalizing the above findings to heavier systems we made the mass of the H atom 39 times heavier (i.e., we considered the artificial hydrogen isotope ^{39}H). In other words, we took the $^{39}H + ICl \rightarrow {}^{39}HCl + I$ (process [3]) and $^{39}H + ICl \rightarrow {}^{39}HI + Cl$ (process [4]) reactions as a model for K + ICl → KCl + I (process [5]) and K + ICl → KI + Cl (process [6]), respectively. Such a choice was motivated

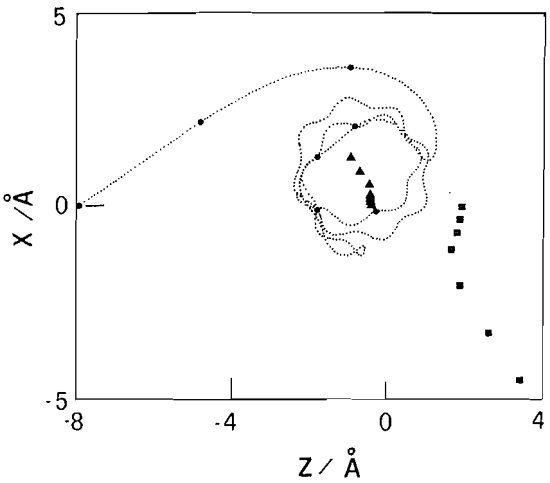

FIG. 8. As in Fig. 6 for a OAB trajectory (large impact parameter).

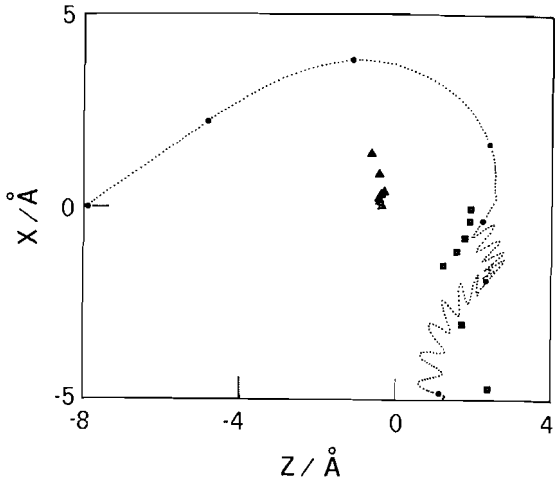

FIG. 9. As in Fig. 7 for a OAB trajectory (large impact parameter).

by the availability of recent crossed molecular beam data (9).

The collision angle Φ_I was either selected randomly or fixed to a given value according to the experimental quantity being considered. The remaining initial conditions were taken, as usual, from a pseudorandom selection with the exception of those fixed by the experiment. In particular, rotational and vibrational energies were selected to give rotational and vibrational temperatures of 14 and 300 K, respectively, while the collision energy was set at 38 kcal/mol. Under these experimental conditions the measured branching ratio between processes [5] and [6] is 4:1. The experiment also finds that product energy distributions are bimodal and migratory mechanisms are so important that *"KCl is formed favourably when the K atom approaches the molecule from the I end and vice versa the formation of KI is enhanced when K hits the Cl end."*

Though the adopted model is rather crude (it completely neglects the differences between the electronic structures of KICl and HICl) our calculations are in satisfactory agreement with measured data. At E_c = 38 kcal/mol, in fact, the calculated value for the branching ratio is about 3:1, only slightly less favourable to the formation of KCl than the experiment. Another favourable comparison of the calculations with the experiment is the energy dependence of the branching ratio. The experiment[2] indicates that the branching ratio increases with energy. The calculations reproduce this finding. In more detail, the trajectory calculations find that, while the cross section of process [3] increases with energy, that of process [4] decreases with energy and, therefore, they cooperate in increasing the branching ratio when energy increases. Such behaviour leads, at low collision energy, to an inversion of the branching ratio.

Again, to understand in more detail the effect of the collision energy on the efficiency of the different processes, we calculated cross sections at fixed angles and at different values of the collision energy. The values of these cross sections are plotted in Figs. 10 and 11 for collision energies ranging from 0 to 6 kcal/mol. The two figures show that by increasing the mass of the impinging atom most of the low-energy structure obtained for H + ICl disappears. The reactive cross section has the expected decreasing trend of reactions without barriers when the product is KI while it has the more familiar post-threshold rise with energy when the product is KCl. An interesting feature of the trajectory results is that, despite the fact that the K atom is heavy, there is a significant contribution of migratory mechanisms to reactivity as can be seen from Figs. 9 and 10. The calculations agree with the experiment also in finding that product energy distributions are bimodal for both processes [3] and [4].

However, there is a key point that the calculations seem unable to reproduce. As already mentioned, oriented beam measurements find that the system systematically favours the reactivity with the opposite end of the reactant molecule. On the contrary, as in the case of the H + ICl reaction, our calculations indicate that, though migratory mechanisms are very important in building up the reactivity of K + ICl, the largest contribution to the reactivity comes from the formation of the product with the ICl end facing the side of the attacking K. Further calculations are in progress to find out possible causes for the discrepancy and to extend the investigation to more complex interhalogenic targets, such as halons.

6. Concluding remarks

By carrying out quasiclassical trajectory calculations for the H + ICl reaction over an extended range of collision energies, it has been possible to rationalize the reactive behaviour of halogenic reaction centres and reproduce experimental findings. In particular, we have been able to calculate the energy dependence of the reactive cross section and find a rationale for the observed branching ratio. Reactive probabilities calculated at different values of the angle of approach have allowed an analysis of the dependence of the efficiency of the competing reactive mechanisms as a function of the impact parameter. The impact parameter was found to play a key role not only in discriminating direct form indirect processes but also in determining the dynamics of the cooperative reactive attacks.

In more detail, by carrying out a graphical analysis of the trajectories it has been found that, at moderate impact parameter, cooperative mechanisms take place via a binding of the impinging atom to the closest end of the diatom. This mechanism produces enough rotational energy to bring the impinging atom in close contact with the other end of the diatomic molecule before the formed molecule is able to escape. As a result of such a close interaction, the formed diatom can either exit highly rotationally excited or rupture to form a new (different) bond. How-

[2]H.J. Loesch. Private communication.

Can. J. Chem. Downloaded from www.nrcresearchpress.com by 195.246.54.202 on 09/08/12
For personal use only.

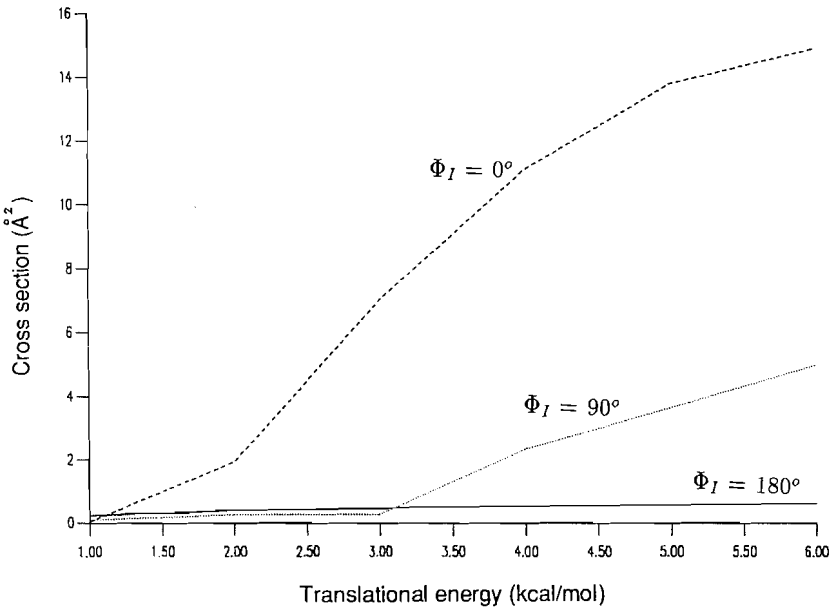

FIG. 10. Fixed Φ_I reactive cross section for the $^{39}H + ICl \rightarrow {}^{39}HCl + I$ process calculated at $\Phi_I = 0°$, 90°, and 180° (dashed, dotted, and solid lines, respectively) plotted as a function of the collision energy.

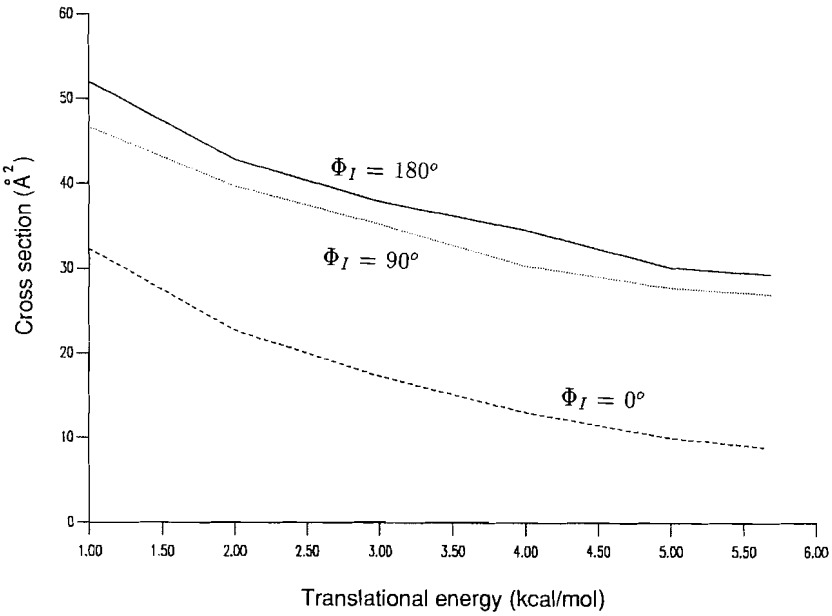

FIG. 11. As in Fig. 10 for the $^{39}H + ICl \rightarrow {}^{39}HI + Cl$ process.

ever, in this case too, the product molecule is formed in a highly excited rotational state.

By contrast, at large b values the cooperative mechanism takes place through an orbiting-like capture of the impinging atom and subsequent formation of a bond with either reaction partner.

We have also investigated the possibility of extending our findings to heavier attacking atoms by modeling the K + ICl reaction as an isotopic variant of the H + ICl reaction. For this system it was found that the lower mobility of the K atom does not prevent migratory mechanisms from occurring. It was also found that the heavier mass of the impinging atom causes the calculated cross section to have a smooth energy dependence and leads to agreement with the measured branching ratio. In addition, calculations were able to predict a bimodal translational energy distribution. On the contrary, though rationalizing the importance of cooperative reactivity, these calculations were unable to agree with the experimentally observed preference of the impinging atom to react with the opposite end of the target molecule.

7. Acknowledgments

The authors acknowledge financial support from the Italian Comitato Nazionale delle Ricerche (CNR) (Progetti Finalizzati), the Spanish Direccion General Investigacíon Científica y Tecnológia (DGICYT) (grant PS-89-0160), the Integrated

Can. J. Chem. Downloaded from www.nrcresearchpress.com by 195.246.54.202 on 09/08/12
For personal use only.

Spain–Italy Action (grant HI-93-012), the Environment project of the European Community (contract EV5V-CT92-0230), and a grant from the Basque government.

1. J.M. Alvariño, M.L. Hernandez, J.J. Margarido, and A. Laganà. J. Chem. Phys. **93**, 1082 (1990); A. Laganà, M. Dini, E. Garcia, J.M. Alvariño, and M. Paniagua. J. Phys. Chem. **95**, 8379 (1991).
2. I. Schechter, R.D. Levine, and R.B. Bernstein. J. Phys. Chem. **91**, 5466 (1987).
3. N.C. Firth, N.W. Keane, D.J. Smith, and R. Grice. Faraday Discuss. Chem. Soc. **84**, 53 (1987); **84**, 111 (1987); B. Girard, N. Billy, and J. Vigue. Faraday Discuss. Chem. Soc. **84**, 65 (1987); J. Chem. Phys. **88**, 2342 (1988).
4. N.W. Keane, J.C. Whitehead, and R. Grice. J. Chem. Soc. Faraday Trans. 2, **85**, 1081 (1989); I.W. Fletcher and J.C. Whitehead. J. Chem. Soc. Faraday Trans. 2, **78**, 1165 (1982); **80**, 985 (1984); M.I. Urrecha, F. Castano, and I. Iturbe. J. Chem. Soc. Faraday Trans. 2, **82**, 1077 (1986).
5. L. Stein, J. Wanner, H. Figger, and H. Walker. Ber. Bunsen-ges. Phys. Chem. **82**, 1275 (1978); T. Trikl and J. Wanner. J. Chem. Phys. **78**, 6091 (1983); K. Wageman, J. Wanner, and X.K. Zeng. Faraday Discuss. Chem. Soc. **84**, 115 (1987); N.C. Firth, D.J. Smith, and R. Grice. Mol. Phys. **61**, 859 (1987).
6. M.I. Urrecha, J. Serna, and I. Iturbe. Chem. Phys. **154**, 85 (1991); M.I. Urrecha and I. Iturbe. Mol. Phys. **75**, 763 (1992).
7. J.C. Polanyi and W.J. Skrlac. Chem. Phys. **23**, 167 (1977).
8. J.C. Polanyi, J.L. Schreiber, and W.J. Skrlac. Faraday Discuss. Chem. Soc. **67**, 66 (1979).
9. H.J. Loesch and J. Moller. J. Chem. Phys. **97**, 9016 (1992).
10. H.J. Loesch and A. Remscheid. J. Chem. Phys. **93**, 4779 (1990).
11. J.M. Alvariño and A. Laganà. J. Phys. Chem. **91**, 5487 (1987).
12. A. Laganà. J. Chem. Phys. **95**, 2216 (1991); A. Laganà, G. Ferraro, E. Garcia, O. Gervasi, and A. Ottavi. Chem. Phys. **168**, 341 (1992).
13. A. Laganà, J.M. Alvariño. and L.M. Quintales. Faraday Discuss. Chem. Soc. **91**, 343 (1991); L.M. Quintales. Tesina de Licenciadura, Salamanca (1986).
14. R.D. Levine and R.B. Bernstein. Molecular reaction dynamics and chemical reactivity. Oxford University Press, New York. 1987.

Can. J. Chem. Downloaded from www.nrcresearchpress.com by 195.246.54.202 on 09/08/12
For personal use only.

Quantum chemical shape: new density domain relations for the topology of molecular bodies, functional groups, and chemical bonding

PAUL G. MEZEY

Mathematical Chemistry Research Unit, Department of Chemistry and Department of Mathematics and Statistics, University of Saskatchewan, SK, S7N 0W0 Canada

Received November 5, 1993

This paper is dedicated to Professor John C. Polanyi on the occasion of his 65th birthday

PAUL G. MEZEY. Can. J. Chem. **72**, 928 (1994).

A density domain (DD) is the formal body enclosed by a molecular isodensity contour (MIDCO) surface. Individual nuclear neighborhoods and various formal molecular fragments can be regarded as fuzzy moieties of electron densities, dominated by one or several nuclei. Such a fuzzy fragment involves a whole range of density values, hence it cannot be described by a single MIDCO, but it can be represented by a sequence of density domains. Within the chemically important range of density values, there are only a *finite number of topologically different bodies of density domains*. In the Density Domain Approach, chemical bonding is described by the interfacing and mutual interpenetration of local fuzzy charge density clouds. The bonding between fragments of a molecule is characterized by a finite sequence of density domains within a wide range of density values and by the correponding sequence of topological patterns of the mutual interpenetration of these fragments. In earlier works, the DD approach was advocated as an alternative to the conventional "skeletal model" of chemical bonding. The classically motivated line diagrams as representatives of bonding are replaced by the pattern of interpenetration of fuzzy fragment bodies at various density thresholds. In this study, novel DD relations are described, suitable for a quantum chemical characterization of functional groups, the local shape properties of such groups, and their contributions to global molecular shape.

PAUL G. MEZEY. Can. J. Chem. **72**, 928 (1994).

Un domaine de densité (DD) est l'ensemble formel entouré par une surface de contour d'isodensité moléculaire (MIDCO). On peut considérer que les environnements moléculaires individuels et divers fragments moléculaires formels sont des portions diffuses des densités électroniques, dominées par un ou plusieurs noyaux. Un tel fragment diffus implique un ensemble de valeurs de densité et on ne peut donc le décrire par une seule MIDCO; il peut toutefois être représenté par une séquence de domaines de densité. Dans le domaine chimiquement important des valeurs de densité, il n'existe qu'un *nombre fini de corps topologiquement différents de domaines de densité*. Dans l'approche du domaine de densité, on décrit la liaison chimique par l'interface et l'interpénétration mutuelle de nuages locaux de densité de charge diffuse. On caractérise la liaison entre les fragments d'une molécule par une séquence finie de domaines de densité ayant un grand éventail de valeurs de densité et par la séquence correspondante de patrons topologiques d'interpénétration mutuelle de ces fragments. Dans des travaux antérieurs, l'approche du DD avait été proposée comme une alternative au «modèle du squelette» conventionnel de la liaison chimique. On remplace les diagrammes linéaires proposés d'une façon classique pour représenter les liaisons par le patron d'interpénétration des corps de fragments diffus, à diverses limites de densité. Dans ce travail, on décrit de nouvelles relations de DD appropriées pour une caractérisation, par chimie quantique, des groupes fonctionnels, des propriétés locales des formes de tels groupes et de leurs contributions à la forme moléculaire globale.

[Traduit par la rédaction]

1. Introduction

Reaction topology (1) and molecular topology (2) are the two main branches of a research program aimed at a topological reformulation of the fundamentally classical, geometrical, models of chemistry. The basic principle of the topology program is the notion that on the molecular level, where quantum mechanics plays a prominent role, geometrical concepts are no longer the ideal tools, and topology, a generalization of geometry, provides better models of reality. Most of our traditional chemical concepts have evolved within a classical mechanical framework, based on macroscopic geometrical analogies. The spectacular development of quantum chemistry has made most of its impact in areas of chemistry where classical models are reliable enough for the interpretation of results, such as the calculation of three-dimensional structural diagrams, theoretical bond lengths, and bond angles. These very concepts, however, have inherent limitations. It is well accepted that the concept of precise electronic positions within a molecule has no utility; however, the concept of precise nuclear positions within a molecule is still in use as a practical but ultimately misleading classical approximation. In the strict sense, the Heisenberg uncertainty relation applies to electrons as well as to nuclei, and neither electronic position nor nuclear position within a molecule is meaningful in a quantum mechanical model. Conventionally, precise bond lengths and bond angles rely on a formal determination of nuclear positions, hence none of the formal structural parameters of bond lengths and bond angles is fully compatible within quantum mechanics. It is, however, not easy to escape from the conventional "skeletal" image of a chemical bond as a line between nuclear positions where the bond length is the distance between two nuclei. In fact, it is still a common practice in chemistry to search for classical interpretations and to equate understanding with finding some macroscopic classical analogy. Such analogies have only limited value and can become rather misleading, since many important properties of molecules and reactions, such as quantized molecular vibrations and the contribution of tunneling to the propagation of reactions through energy barriers, are not directly observable in the more familiar macroscopic phenomena. For the understanding of these properties, the conventional "skeletal" image of chemical bonding is more an impediment than a help. By contrast, more of the fundamental aspects of bonding within formal "bodies" of molecules can be described by molecular isodensity contour (MIDCO) surfaces. However, a single MIDCO surface, another geometrical construction, is insufficient by itself to reflect all the essential details of the electron distribution. Therefore,

Can. J. Chem. Downloaded from www.nrcresearchpress.com by 195.246.54.202 on 09/08/12
For personal use only.

Can. J. Chem. Downloaded from www.nrcresearchpress.com by 195.246.54.202 on 09/08/12
For personal use only.

the fuzzy density domains are characterized not by individual MIDCOs but by *topological equivalence classes* of MIDCOs. This offers an alternative approach for the description of bonding within molecular "bodies," where the conflict with quantum mechanics is avoided (2).

Topological theories and models have an increasingly important role in studies of molecular shape and similarity (3). Besides their role in reformulating some of the basic notions, the topological analysis, quantification, and numerical evaluation of molecular shape similarity have important practical applications, for example, in modern drug design and molecular engineering (4–6). In this report some topological rules influencing the patterns of density domains will be discussed.

2. Molecular isodensity contours (MIDCOs)

For simplicity, we shall first consider the semiclassical models of a formal, static, nuclear arrangement for each molecule. For a given electronic state, the nuclear arrangement K has a dominant influence on the shape of the formal body of molecular electron distribution $\rho(\boldsymbol{r})$. The molecular charge density function $\rho(\boldsymbol{r})$ can be determined experimentally from X-ray diffraction experiments (7, 8), and can be calculated by quantum chemical methods, for example, by the standard quantum chemistry programs (9) or by approximate methods designed for large molecules (10).

We shall regard electron distributions as functions $\rho(\boldsymbol{r}, K)$ of the nuclear arrangement K. It is common to regard the set of all possible nuclear arrangements K of a given stoichiometry as a formal nuclear configuration space. This space is provided with a proper distance function $d(K, K')$ for any two nuclear arrangements K and K', turning the configuration space into a metric space M. Note, however, that the nuclear configuration space M is not a vector space and cannot be turned into one (1).

The molecular potential energy (of a specified electronic state), as a function of the nuclear arrangements K, is a hypersurface $E(K)$ over this space M (1). Chemical species can be associated with various open sets (catchment regions) of the given energy hypersurface, a model that relaxes the classical constraints of rigid nuclear geometry and avoids the conflict with the Heisenberg uncertainty relation (1). Similarly, the 3D electronic density of a specified electronic state can be regarded as a function $\rho(\boldsymbol{r}, K)$ defined over the nuclear configuration space M, and molecular shape can be associated with an entire family of $\rho(\boldsymbol{r}, K)$ charge density distributions occurring within a catchment region (2).

A *molecular isodensity contour surface*, MIDCO, of nuclear configuration K and density threshold a is denoted by $G(a, K)$, and is defined as

$$[1] \quad G(a, K) = \{\boldsymbol{r}: \rho(\boldsymbol{r}, K) = a\}$$

that is, as the collection of all points of the 3D space where the electronic density is equal to the constant a. If a single, formal nuclear configuration K is considered, and if this is evident from the context, then symbol K can be suppressed in the notation, and one may simply write

$$[2] \quad G(a) = \{\boldsymbol{r}: \rho(\boldsymbol{r}) = a\}$$

The electronic density $\rho(\boldsymbol{r})$ is a continuos function; consequently, the set of all points $\boldsymbol{r}$ fulfilling eq. [2] does form a continuous surface.

In the strict sense, the electronic charge density function $\rho(\boldsymbol{r})$ becomes zero only at infinite distance from the nuclei of the molecule. However, $\rho(\boldsymbol{r})$ converges rapidly to zero already at short distances, becoming negligible at about 8–10 Å from the nearest nucleus. The electronic density is approximately localized within a close neighborhood of the nuclei. It is justified to regard only those regions of the 3D space as "belonging" to the molecule of nuclear configuration K, where the electronic density $\rho(\boldsymbol{r})$ is larger than some small threshold. By taking a sufficiently small threshold value a, an approximate *molecular body* can be defined as the collection $F(a, K)$ of all those points $\boldsymbol{r}$ of the 3D space where the electronic density is greater than the threshold a,

$$[3] \quad F(a, K) = \{\boldsymbol{r}: \rho(\boldsymbol{r}, K) > a\}$$

Using the conventional mathematical terminology, these points $\boldsymbol{r}$ are said to form a *level set* $F(a, K)$, with respect to the threshold level a. Note that *negative* charge means a *positive* value for the density function $\rho(\boldsymbol{r}, K)$. Again, if the formal nuclear configuration K is evident from the context, then symbol K can be suppressed, and one may write

$$[4] \quad F(a) = \{\boldsymbol{r}: \rho(\boldsymbol{r}) > a\}$$

According to definitions [3] and [4], those points $\boldsymbol{r}$ of the 3D space where the value of the electronic density function is equal to the threshold,

$$[5] \quad \rho(\boldsymbol{r}) = a$$

do not belong to the level set $F(a)$. One may adopt alternative definitions and include all points $\boldsymbol{r}$ of the 3D space where eq. [5] holds. Such domains of the 3D space, including *all the points and all the boundary points* of the level sets $F(a)$, are, of course, closely related to the level sets $F(a)$ themselves and are of special importance. These domains, providing a natural representation of chemical bonding in molecules, are the *density domains* (2, 11), denoted by $DD(a)$, or by $DD(a, K)$, if the nuclear configuration K is also specified. These density domains are defined as

$$[6] \quad DD(a, K) = \{\boldsymbol{r}: \rho(\boldsymbol{r}, K) \geq a\}$$

or, if the formal nuclear configuration K is evident from the context, then symbol K can be suppressed, and one may write

$$[7] \quad DD(a) = \{\boldsymbol{r}: \rho(\boldsymbol{r}) \geq a\}$$

If molecular charge densities were macroscopic clouds of various densities, then a density domain $DD(a)$ could be visualized as the object seen if one's eyes were adjusted to notice only densities equal to or higher than the threshold a. By readjusting one's eyes, density domains of lower and lower threshold values could be seen.

The shape and size of a level set $F(a, K)$ depend on the choice of the threshold value a. Instead of selecting an arbitrary value for a, it is more meaningful to consider a whole *range* of possible a values for the electronic density level sets $F(a, K)$ and for the related MIDCOs $G(a, K)$ and density domains $DD(a, K)$. It is not necessary to consider very high a values, occurring only in the vicinity of heavy nuclei. Also, by taking a small but non-

Can. J. Chem. Downloaded from www.nrcresearchpress.com by 195.246.54.202 on 09/08/12
For personal use only.

zero lower limit for the a values, one can avoid considering level sets where a single, common envelope surface encloses two, essentially independent, molecules of large but finite distance from one another.

As one of their important applications, MIDCOs are used in molecular similarity analysis. The resulting techniques of precise, nonvisual, algorithmic description of molecular shape and numerical evaluation of molecular similarity are based on the general GSTE principle of treating Geometrical Similarity as Topological Equivalence (2, 12–14). Most computer implementations of the GSTE principle are based on the Shape Group Methods (SGM) (15–18): these are algebraic–topological shape analysis techniques using the homology groups of molecular surfaces truncated according to some local curvature criterion. The GSHAPE 90 computer program (19), based on the shape groups, uses *ab initio* or semiempirical electron densities as input, and performs nonvisual shape analysis and similarity evaluation of molecular sequences. The GSTE principle has also been the basis of other topological methods, where families of alternative geometrical models with equivalent topological features are used for characterization (2, 12–14). Various combinations of geometrical and topological techniques provide numerical measures of molecular shape similarity (2, 12–14).

3. The "Late–Early Rule" of the density domain approach (DDA) to chemical bonding

The conventional formal chemical bonds of a molecule are usually modeled by lines interconnecting the nuclei and represent only a molecular skeleton. However, a bond skeleton cannot fully describe the molecular body and the shape of the molecule. In reality, a molecule is a three-dimensional object held together by the fuzzy body of the electron charge distribution. Chemical bonding is not constrained to a set of lines or narrow bonding channels in space; actual chemical bonding involves a broad interfacing of molecular fragments. A more detailed description of chemical bonding must take into account the 3D fuzzy electron distribution of the molecular body. The family of all topologically distinct density domains are objects that describe in detail the actual buildup of electronic densities within molecules. Furthermore, if the shape analysis is extended to the individual density domains, then additional fine details of electron densities can be distinguished.

Density domains $DD(a, K)$, level sets $F(a, K)$, and MIDCOs $G(a, K)$ are related in a simple way:

$$[8] \quad DD(a, K) = F(a, K) \cup G(a, K)$$

A density domain $DD(a, K)$ can be regarded as a formal *molecular body at an electronic density threshold* a *and nuclear configuration* K. In general, such a $DD(a, K)$ body may be a single piece or it may be a collection of several disconnected pieces $DD_i(a, K)$, called the *maximum connected components* of $DD(a, K)$:

$$[9] \quad DD(a, K) = \bigcup_i DD_i(a, K)$$

Of course, if the body $DD(a, K)$ has a single piece, then $DD(a, K)$ is the same as its single maximum connected component $DD_1(a, K)$,

$$[10] \quad DD(a) = DD_1(a)$$

According to the precise terminology, the $DD_i(a, K)$ maximum components of the $DD(a, K)$ body are the density domains of the molecule at density threshold value a. Conventionally, the term "domain" should be applied only to a single maximum component. However, for simplicity, the term "density domain" is also used for the union in eq. [9].

A MIDCO $G(a, K)$ is also the union of its maximum connected components $G_i(a, K)$:

$$[11] \quad G(a, K) = \bigcup_i G_i(a, K)$$

For any fixed density threshold a, the patterns of the $DD_i(a, K)$ density domains and the patterns of their respective boundary surfaces, the MIDCOs $G_i(a, K)$, provide the same shape information.

In general, one may study the electron density buildup in a molecule by taking an initial high-density threshold a_{max} and gradually decreasing this threshold to a small enough value a such that all the nuclei of the molecule are enclosed by a single MIDCO $G(a)$.

If the nuclear configuration K is fixed and obvious from the context, it can be omitted from the notation. It is useful, however, to indicate the nuclei enclosed by each maximum connected component, that is, by each density domain $DD_i(a)$. If the nuclei A, B, etc., are enclosed within a density domain $DD_i(a_j)$ at a threshold a_j, then the detailed notation $DD_i(a_j, A, B, \ldots)$ can be used.

For example, consider a semiclassical model and the three topologically distinguishable sets of density domains of the equilibrium nuclear arrangement of the methane molecule. At a high density threshold a_1 there is electronic density only near the carbon nucleus, hence there is only a single density domain; at this density threshold a_1 the set of density domains has a single element,

$$[12] \quad \{DD_1(a_1, C)\}$$

At a medium-density threshold a_2, electronic density appears simultaneously about the four hydrogen nuclei (as follows from symmetry), and there are five separate density domains. That is, the set of density domains has five elements,

$$[13] \quad \{DD_1(a_2, C), DD_2(a_2, H), DD_3(a_2, H), DD_4(a_2, H), DD_5(a_2, H)\}$$

At a low enough threshold a_3, the methane molecule has a single density domain that contains all five nuclei C, H, H, H, and H. At this density threshold a_3 the set of density domains has a single element,

$$[14] \quad \{DD_1(a_3, C, H, H, H, H)\}$$

For a detailed illustration, we shall use the ethanol molecule at a nuclear configuration K approximating its equilibrium nuclear geometry, and the electronic density results obtained in a study on the relations between acidity and molecular shape near protonic moieties (20). A sequence of topologically different sets of density domains of the ethanol molecule, CH_3CH_2OH, is shown in Figs. 1–3, as calculated using a 6-31G* basis set, the GAUSSIAN 90 [9] *ab initio*, and the GSHAPE 90 (19) molecular shape analysis programs. Some of the extreme high-density domains are not shown in these figures:

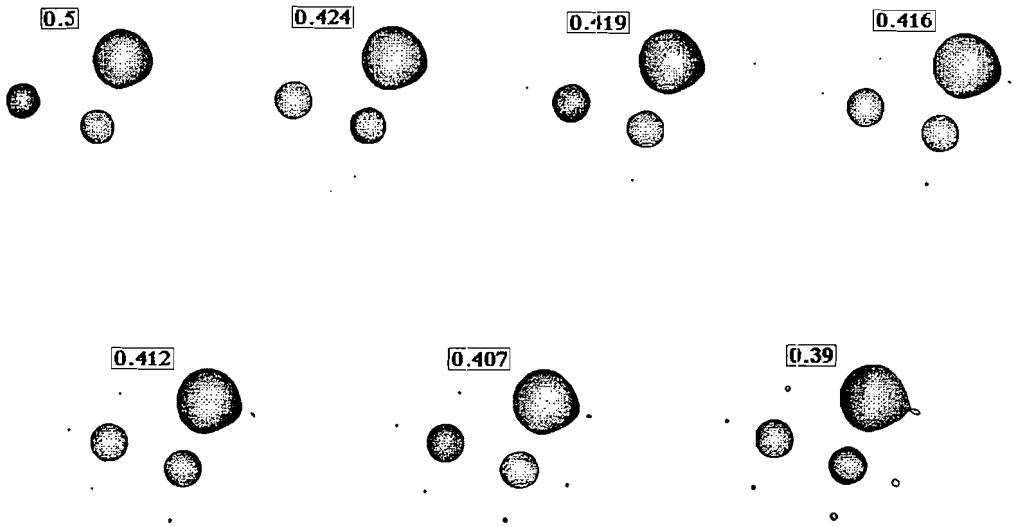

FIG. 1. The topologically different high-threshold density domains of the ethanol molecule CH_3CH_2OH, calculated using a 6-31G* basis set, the GAUSSIAN 90 (9) *ab initio*, and the GSHAPE 90 (19) molecular shape analysis programs.

the density domain $DD_1(a_1, O)$ of the oxygen atom that appears first at a high-density threshold and the next topologically distinct $DD(a)$ pattern of the pair of methyl carbon and oxygen atoms $DD_1(a_2, C)$, $DD_2(a_2, O)$ are not shown in these figures.

The first $DD(a)$ pattern shown in Fig. 1 is the set of the three density domains of the heavy nuclei, that is, the family

$$[15] \quad \{DD_1(a_1, C), DD_2(a_1, C), DD_3(a_1, O)\}$$

where the threshold parameter is $a_1 = 0.5$ au. The density domain $DD_3(a_1, O)$ of the oxygen atom is the bulkiest, reflecting an accumulation of electronic density due to the largest nuclear charge and the highest electronegativity of oxygen among these atoms. This pattern is followed by others showing the sequential appearance of the various hydrogen density domains. According to the calculations, at the $a_j = 0.407$ threshold density all nuclear neighborhoods are present as density domains, and one obtains the family

$$[16] \quad \{DD_1(a_j, H), DD_2(a_j, H), DD_3(a_j, H), DD_4(a_j, H), DD_5(a_j, H), DD_6(a_j, H), DD_7(a_j, C), DD_8(a_j, C), DD_9(a_j, O)\}$$

The last pattern on this figure shows the first merger of density domains in the above sequence of gradually decreasing thresholds. This merger occurs at the threshold value of $a_j = 0.390$, where the density domain of the OH proton links up with that of the oxygen atom. The following family of density domains is obtained:

$$[17] \quad DD_1(a_j, H), DD_2(a_j, H), DD_3(a_j, H), DD_4(a_j, H), DD_5(a_j, H), DD_6(a_j, C), DD_7(a_j, C), DD_8(a_j, O, H)$$

These domains collectively represent the formal ("dismembered") molecular body $DD(a_j)$ at the density threshold $a_j = 0.390$.

This pattern is our first example for the formation of a density domain of a typical *functional group*, the OH group. The corresponding density domain $DD_8(0.390, O, H)$ serves as a density-based justification for assigning a separate identity to the OH functional group and for regarding it as a chemical entity. For the OH group there exists a whole range $[a', a'']$ of density threshold values within which the O and H nuclei are surrounded by MIDCOs, separating them from all the other nuclei of the ethanol molecule. This criterion, the existence of a MIDCO that separates a family a nuclei from all other nuclei of a molecule, has been used for the identification and a detailed characterization of the functional groups of chemistry (11).

Not every actual density domain $DD_i(a_j)$ and the nuclei enclosed by it can be transferred from one molecule to another without altering the topology of the density domain. Nevertheless, the DD approach provides a physically motivated criterion for what molecular moiety, at the given density threshold a, can be regarded to have a well-defined identity. This justifies a generalization of the usual chemical concept of functional groups. According to this generalized concept, a collection of all nuclei within a density domain $DD_i(a_j)$, together with the density domain itself, can be regarded as a functional group of the molecule at the density threshold a_j.

This approach can be regarded as a physically motivated choice (11) within the general scheme (21) for the identification and analysis of functional groups of various molecular arrangements within the nuclear configuration space M. If a MIDCO separates a group of nuclei from the rest of the nuclei of the molecule, this indicates a chemical linkage among the local charge densities surrounding these given nuclei that is more prominent than the linkage between this group and the rest of the molecule. This is a property expected from most functional groups of chemistry. Nevertheless, the Density Domain concept of functional group does not necessarily coincide in each case with the concept conventionally used by chemists. Furthermore, the calculated Density Domains are dependent on the level of quantum chemical methods used. Consequently, in the analysis of calculated functional groups, the quality of the calculated charge density (e.g., basis set specification, such as 6-31G*) should also be indicated, especially for density domains at the high threshold ranges.

In the process of generating density domains of gradually decreasing threshold a, the most acidic proton of the ethanol

Can. J. Chem. Downloaded from www.nrcresearchpress.com by 195.246.54.202 on 09/08/12
For personal use only.

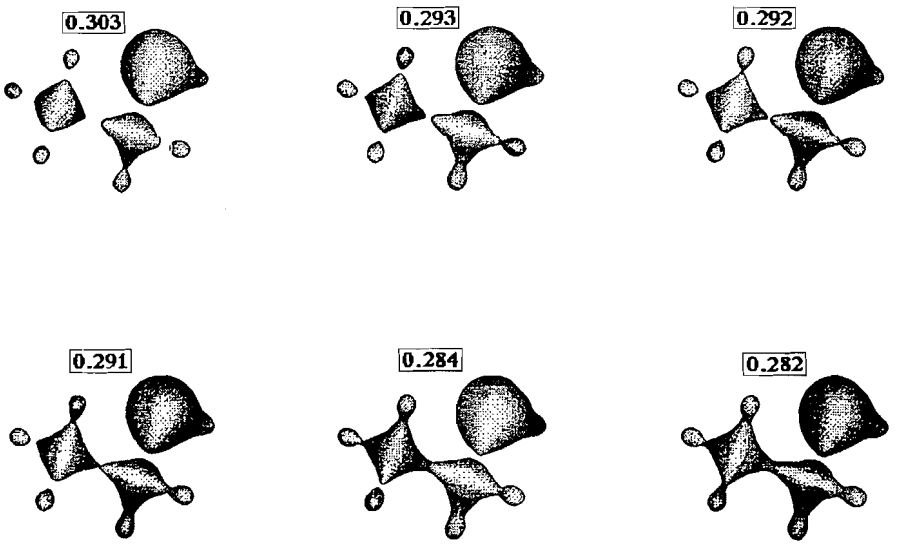

FIG. 2. The topologically different medium-threshold density domains of the ethanol molecule CH_3CH_2OH, calculated using a 6-31G* basis set, the GAUSSIAN 90 (9) *ab initio*, and the GSHAPE 90 (19) molecular shape analysis programs.

Can. J. Chem. Downloaded from www.nrcresearchpress.com by 195.246.54.202 on 09/08/12
For personal use only.

molecule loses its separate density domain first. This is the merger of the highest density threshold. The minimal electronic charge density is of the highest value between this proton and another nucleus (the oxygen nucleus) of the molecule. This is only in an apparent conflict with the fact that, as the most acidic proton of the molecule, this is the proton most easily donated to proton acceptors. The explanation of this apparently counterintuitive pattern is explained by the high electronegativity and the resulting, more extensive, high-density domain about the oxygen nucleus. The high electron density cloud about the oxygen engulfs this particular proton, resulting in the highest density threshold "bridgehead" between a proton and another nucleus of this molecule.

This observation can be combined with another: the density domain of the OH proton appears relatively late in the process of gradually decreasing the density threshold. Of course, this fact can also be justified by the high electronegativity of oxygen: the electron density is "siphoned away" by the oxygen; consequently, the nearby proton has a chance for the formation of a density domain only at a lower level of density.

The above two observations represent a rather general trend. Consider a molecule with a set of identical nuclei A and, for simplicity, assume that A is single valenced in the classical sense. Hydrogen nuclei are typical examples. The density domain of a nucleus A that appears late (that is, at a low-density threshold) is likely to join a neighboring density domain early (at a density threshold higher than the DDs of most of the other nuclei of type A). We may state this observed trend as a formal rule. This trend, called the "Late–Early Rule," can be stated as follows.

The Late–Early Rule:

If the threshold density is gradually decreased in a density domain analysis of a given molecule, then the order of joining of various individual density domains of a given atom type A to neighboring density domains tends to be the reversed order of their appearance.

This Late–Early Rule is justified by electronegativity considerations: a higher electronegativity neighbor of A is likely to delay the appearance of the density domain of A to a lower density threshold, and also likely to have a more extensive charge density cloud about it; hence an early joining of the density domains of the neighbor and A is likely. In effect, this density domain exists in a narrower threshold interval that is contained within the corresponding intervals of other density domains containing the same nucleus type A.

One may state this trend using the expected inclusion relations of the electron density threshold intervals where the density domains exist as separate entities. Order the nuclei of type A according to the order of increasing effective electronegativity of the neighbor nuclei involved in the *first* merger of the density domains of nuclei of type A:

$$[18] \quad A^{(k)},\ k = 1, 2, \ldots q$$

Accordingly, the effective electronegativity of nucleus $B^{(1)}$, that is, the first nucleus to share its density domain with that of $A^{(1)}$, is the lowest, whereas the effective electronegativity of nucleus $B^{(q)}$, that is, the first nucleus to share its density domain with that of $A^{(q)}$, is the highest.

Denote by (a_k, a'_k) the interval of density thresholds where a separate density domain exists for nucleus $A^{(k)}$. Then the trend expressed by the Late–Early Rule is equivalent to the following, ideal, sequence of inclusion relations:

$$[19] \quad (a_1, a'_1) \supset (a_2, a'_2) \supset (a_3, a'_3) \supset \ldots \supset (a_k, a'_k) \ldots \supset (a_q, a'_q)$$

The above inclusion relations of the Late–Early Rule are not always followed in a strict sense; however, it is the expected trend. In some examples the extreme case of the Late–Early Rule applies: the density domain of $A^{(q)}$ of a neighbor $B^{(q)}$ of highest electronegativity exists in the narrowest threshold interval, contained within the corresponding intervals of all other density domains of the same nucleus type A. That is, the last domain that appears is the first to join a neighbor. A special case of the Late–Early Rule, as applied to protonic density domains, has been called the Last–First Rule (2). The Late–Early Rule, introduced above, is a generalization of the Last–First Rule.

4. There is no methyl group in the ethanol molecule (according to the density domain functional group criterion)

In Fig. 2 additional mergers of density domains are displayed

Can. J. Chem. Downloaded from www.nrcresearchpress.com by 195.246.54.202 on 09/08/12
For personal use only.

as the density threshold is further reduced. The next two topologically distinct set of density domains are represented by the threshold values of $a_j = 0.303$ and $a_{j'} = 0.293$, corresponding to the two-step merger of methylenic carbon and the two methylenic hydrogen density domains. The resulting two families are the set of seven density domains

[20] $\{DD_1(a_j, H), DD_2(a_j, H), DD_3(a_j, H), DD_4(a_j, H), DD_5(a_j, C), DD_6(a_j, C, H), DD_7(a_j, O, H)\}$

and the set of the six density domains,

[21] $\{DD_1(a_{j'}, H), DD_2(a_{j'}, H), DD_3(a_{j'}, H), DD_4(a_{j'}, C), DD_5(a_{j'}, C, H, H), DD_6(a_{j'}, O, H)\}$

respectively.

The $DD(a_{j'})$ pattern at $a_{j'} = 0.293$ shows the presence of a methylenic (CH_2) functional group, represented by the density domain $DD_5(a_{j'}, C, H, H)$, occurring simultaneously with the hydroxyl group, represented by $DD_6(a_{j'}, O, H)$. Both of these groups have separate chemical identity *within* the ethanol molecule if one accepts the density domain criterion, since there exists a MIDCO that separates the carbon and the two hydrogen nuclei from all other nuclei of the ethanol molecule, and the same holds for the nuclei of the OH moiety. This justifies regarding both the methylene and hydroxyl groups as functional groups within the ethanol molecule. The terminal CH_3 moiety is still disconnected at this density threshold value of $a_{j'} = 0.293$.

The next topologically significant change is the merger of the carbon density domain of the CH_3 moiety (formal methyl group) with one of the corresponding hydrogen density domains. One obtains the density domain family

[22] $\{DD_1(a_j, H), DD_2(a_j, H), DD_3(a_j, C, H), DD_4(a_j, C, H, H), DD_5(a_j, O, H)\}$

as shown by the $DD(a_j)$ body at the threshold $a_j = 0.292$.

The next topological change is of special interest: the merger between the $DD_3(a_j, C, H)$ and $DD_4(a_j, C, H, H)$ domains of the previous density threshold. This merger results in a new family of density domains at the threshold $a = 0.291$:

[23] $\{DD_1(a, H), DD_2(a, H), DD_3(a, C, H, C, H, H), DD_4(a, O, H)\}$

The density domain $DD_3(a, C, H, C, H, H)$ of this family is of special significance: its occurrence clearly shows that the terminal CH_3 moiety (formal methyl group) cannot have a separate density domain. In the given nuclear configuration of the ethanol molecule (and also within an entire topological range of the nuclear configuration space) there exists no MIDCO surface separating the nuclei of the terminal CH_3 moiety from all other nuclei of the molecule.

We may rephrase this observation: *according to the given 6-31G* level of quantum chemical calculations, the methyl group does not appear as a formal functional group of separate identity within the ethanol molecule.* As a density domain functional group, there is no methyl group in the ethanol molecule. This result is in good agreement with chemical practice: few organic chemists would attempt to use ethanol as a methylating agent, that is, as a source of methyl group for incorporation into another molecule to be synthesized.

The next topological change is shown at the threshold value of $a = 0.284$ au. The family of density domains obtained is

[24] $\{DD_1(a, H), DD_2(a, C, H, H, C, H, H), DD_3(a, O, H)\}$

where the pattern of $DD_2(a, C, H, H, C, H, H)$ is of special interest: its shape indicates a "trans disconnected" arrangement. The hydrogen density domain $DD_1(a, H)$ with a dihedral angle near 180° with the density domain $DD_3(a, O, H)$ of the OH functional group has the lowest electron density, indicating differences of formal acidities of the terminal H atoms. These results are similar to those derived from overtone spectra on the nonequivalence of CH bonds (22–28).

The $DD_1(0.284, H)$ density domain joins $DD_2(0.284, C, H, H, C, H, H)$ if the threshold is lowered to $a = 0.282$. The new DD family making up the molecular body DD(0.282) consists of only two density domains,

[25] $\{DD_1(0.282, C, H, H, H, C, H, H), DD_2(0.282, O, H)\}$

The existence of the new density domain $DD_1(0.282, C, H, H, H, C, H, H)$ indicates that the ethyl group is a density domain functional group of the ethanol molecule. The density domains $DD_1(0.282, C, H, H, H, C, H, H)$ and DD_2 (0.282, O, H) of the ethyl functional group and the hydroxyl functional group, respectively, have separate identities at this density threshold value. The presence of the ethyl and the hydroxyl groups in the ethanol molecule is well reflected in the conventional name of the molecule: ethyl alcohol.

Figure 3 shows the next important topological change: the merger of the ethyl and hydroxyl density domains, shown at a threshold value of $a = 0.265$. The family DD(0.265) of density domains has only a single member,

[26] $\{DD_1(0.265, C, H, H, H, C, H, H, O, H)\}$

This last topological change concludes the *bonding sequence* as specified by the topological sequence of gradually interconnected families of density domains. This bonding sequence provides a detailed three-dimensional description of bonding in the ethanol molecule.

At this and any lower density threshold, the nuclei of the molecule are enclosed by a single density contour. In particular, no fragmentation of density domains of the ethanol molecule can occur at lower thresholds. However, further important shape changes occur at lower threshold values; some of the typical shapes are shown for the threshold interval ranging from $a = 0.200$ to $a = 0.004$, leading to an eventual spherical shape at very low densities.

All the different shapes below the $a = 0.265$ threshold represent the same topological molecular body of a single density domain,

[27] $DD(a) = DD_1(a)$

These bodies correspond to a topological ball.

5. A classification of density domains

In each molecule, the bonding pattern shows some characteristic density ranges where typical shape features occur. Never-

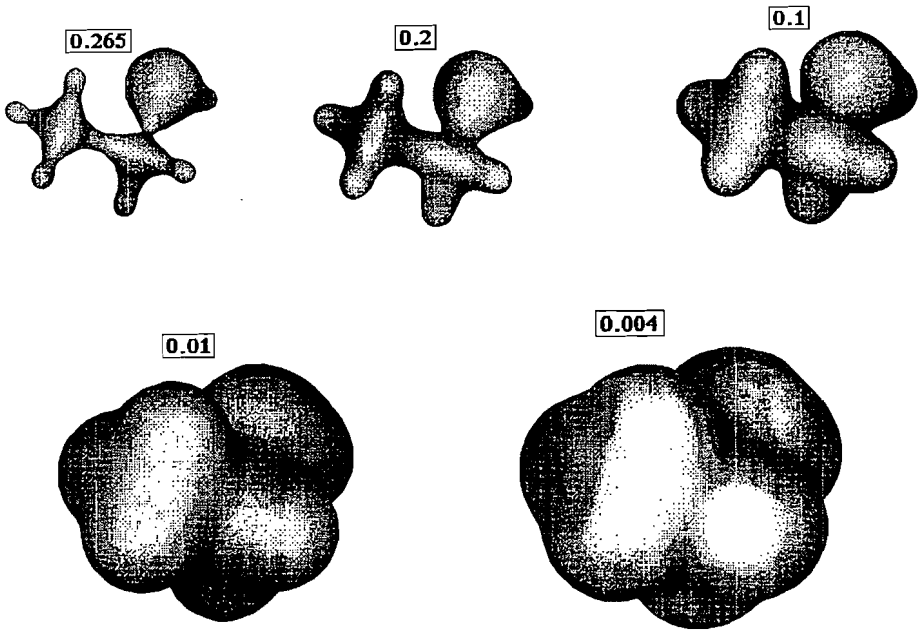

FIG. 3. The topologically different low-threshold density domains of the ethanol molecule CH_3CH_2OH, calculated using a 6-31G* basis set, the GAUSSIAN 90 (9) *ab initio*, and the GSHAPE 90 (19) molecular shape analysis programs.

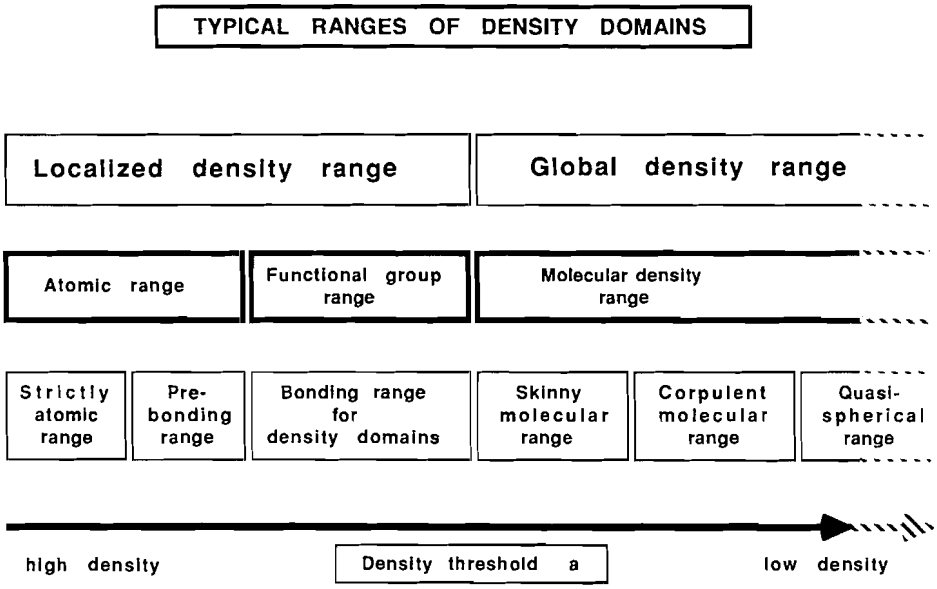

FIG. 4. A classification of types of density domains according to the ranges of the electron density threshold *a*.

theless, there are some important general trends in the entire range of possible density threshold values, valid for all molecules (2). These trends provide a classification of density domains according to various ranges of the density threshold parameter *a*, as illustrated in Fig. 4.

We shall consider a gradual decrease of the density threshold *a*, starting with a high value (2). Within the high-density range of the threshold *a*, only individual nuclear neighborhoods appear as disconnected density domains, that is, there is precisely one nucleus within each density domain that appears. The density range where this holds can be referred to as the *atomic range*. In a lower density range some nuclear neighborhoods join to form density domains containing two or more nuclei, but not all nuclei of the molecule are contained in a common density domain. In this density range one finds the various functional groups as individual entities; hence this range is called the *functional group range*. In this range the bonding pattern (interconnection pattern) of the density domains is revealed; consequently, this range is also called the *bonding range for density domains*. In a lower density range the essential molecular pattern of bonding is established, and all nuclei of the molecule are found within a common density domain. This range is called the *molecular density range*.

The atomic range is subdivided into two subranges. In the *strictly atomic range* all the atomic density domains are convex, whereas in the *prebonding range* at least one density domain is no longer convex, as it "reaches out" to join a neighboring density domain.

The molecular density range also contains some subranges. At the high threshold values within the molecular range, the

Can. J. Chem. Downloaded from www.nrcresearchpress.com by 195.246.54.202 on 09/08/12
For personal use only.

density domains often have some local "neck" regions: there is at least one topological belt or some other multiply connected set on the surface of the density domain along which the surface is not locally convex. Within this density subrange the molecular body is "skinny," and this range is referred to as the *skinny molecular range*. At lower densities no such neck regions occur, but one usually finds at least one local nonconvex region along the surface of the density domain. If this occurs, then the corresponding subrange is called the *corpulent molecular range*. At very low densities the density domains of all molecules (even those of long-chain molecules) are convex. The corresponding range is called the *quasi-spherical molecular range*.

The atomic and the functional group ranges together can be regarded as the *localized range*, and the molecular density range can be regarded as the *global density range*.

The example of the ethanol molecule shown in Figs. 1–3 illustrates the above classification scheme.

Summary

Following an introduction to the concepts, notations, and methods of Density Domain analysis of chemical bonding, a new rule, the Late–Early Rule, has been suggested for the distribution and persistence of density domains within various intervals of density thresholds of molecules. The observations have plausible explanations based on simple electronegativity arguments. Application of Density Domain analysis to the ethanol molecule indicates that no separate electron density envelope exists for the formal terminal methyl group; by this criterion, the electron density distribution does not justify regarding the terminal CH_3 moiety as a formal functional group.

Whereas the emphasis in this study has been on global topological properties of formal molecular bodies, alternative methods are available for detailed shape analysis. The shape changes of each density domain can be described in detail by considering local curvature variations and subdividing the surfaces according to various curvature domains. An algebraic characterization of these shapes can be given (2), using the Shape Group Method (SGM), introduced earlier (15, 16). A detailed shape analysis of individual molecular orbitals, as compared to the density domains, is expected to provide information on reactivity of molecules. This approach, using the *most delocalized orbital representations* (29), will be the subject of a forthcoming study.

Acknowledgements

This work was supported by both strategic and operating research grants from the Natural Sciences and Engineering Research Council of Canada, and by additional financial assistance from the Computational Chemistry Laboratory of the Upjohn Company.

1. P.G. Mezey. Potential energy hypersurfaces. Elsevier, Amsterdam. 1987.
2. P.G. Mezey. Shape in chemistry: an introduction to molecular shape and topology. VCH, New York. 1993.
3. M.A. Johnson and G.M. Maggiora (*Editors*). Concepts and applications of molecular similarity. Wiley, New York. 1990.
4. W.G. Richards. Quantum pharmacology. Butterworths, London. 1983.
5. P.M. Dean. Molecular foundations of drug–receptor interaction. Cambridge University Press, New York. 1987.
6. R. Hoffmann and P. Laszlo. Angew. Chem. Int. Ed. Engl. **30**, 1 (1991).
7. P. Coppens and M.B. Hall (*Editors*). Electron distribution and the chemical bond. Plenum, New York and London. 1982.
8. S. Fliszár. Charge distributions and chemical effects. Springer, New York. 1983.
9. M.J. Frisch, M. Head-Gordon, G.W. Trucks, J.B. Foresman, H.B. Schlegel, K. Raghavachari, M.A. Robb, J.S. Binkley, C. González, D.J. Defrees, D.J. Fox, R.A. Whiteside, R. Seeger, C.F. Melius, J. Baker, R.L. Martin, L.R. Kahn, J.J.P. Stewart, S. Topiol, and J.A. Pople. GAUSSIAN 90; Carnegie–Mellon Quantum Chemistry Publishing Unit, Pittsburgh, Pa. 1990.
10. P.D. Walker and P.G. Mezey. J. Am. Chem. Soc. **115**, 12423 (1993).
11. P.G. Mezey. J. Chem. Inf. Comput. Sci. **32**, 650 (1992).
12. P.G. Mezey. *In* Concepts and applications of molecular similarity. *Edited by* M.A. Johnson and G.M. Maggiora. Wiley, New York. 1990.
13. P.G. Mezey. "Molecular Surfaces", *In* Reviews in computational chemistry. *Edited by* K.B. Lipkowitz and D.B. Boyd. VCH Publishers, New York. 1990.
14. P.G. Mezey. *In* The role of computational models and theories in biotechnology. *Edited by* J. Bertran. Kluwer Academic Publishers, Dordrecht. 1992.
15. P.G. Mezey. Int. J. Quantum Chem. Quant. Biol. Symp. **12**, 113 (1986).
16. P.G. Mezey. J. Comput. Chem. **8**, 462 (1987).
17. P.G. Mezey. Int. J. Quantum Chem. Quant. Biol. Symp. **14**, 127 (1987).
18. P.G. Mezey. J. Math. Chem. **2**, 299 (1988).
19. P.D. Walker, G.A. Arteca, and P.G. Mezey. Program GSHAPE 90; Mathematical Chemistry Research Unit, University of Saskatchewan, Saskatoon, Canada, 1990.
20. P.D. Walker, L. Raju, K. Gilbertson, and P.G. Mezey. (to be published).
21. J.-E. Dubois and P.G. Mezey. Int. J. Quantum Chem. **43**, 647 (1992).
22. B.R. Henry. Acc. Chem. Res. **29**, 429 (1987).
23. D.J. Swanton and B.R. Henry. J. Chem. Phys. **86**, 4801 (1987).
24. H. Kjaergaard, H. Yu, B.J. Schattka, B.R. Henry, and A.W. Tarr. J. Chem. Phys. **93**, 6239 (1990).
25. K.M. Gough, B.R. Henry, B.J. Schattka, and T.A. Wildman. J. Phys. Chem. **95**, 1579 (1991).
26. M.G. Sowa, B.R. Henry, and Y. Mizugai. J. Phys. Chem. **95**, 7659 (1991).
27. H. Kjaergaard, B.R. Henry, and A.W. Tarr. J. Chem. Phys. **94**, 5844 (1991).
28 H. Kjaergaard and B.R. Henry. J. Chem. Phys. **96**, 4841 (1992).
29. J. Pipek and P.G. Mezey. J. Chem. Phys. **90**, 4916 (1989).

Can. J. Chem. Downloaded from www.nrcresearchpress.com by 195.246.54.202 on 09/08/12
For personal use only.

The meaning of "adiabatic"

KEITH J. LAIDLER
Department of Chemistry, University of Ottawa, Ottawa, ON K1N 6N5, Canada

Received May 20, 1993

This paper is dedicated to Professor John C. Polanyi on the occasion of his 65th birthday

KEITH J. LAIDLER. Can. J. Chem. **72**, 936 (1994).

In chemical kinetics the word "adiabatic" has come to refer to a process in which there is no change of quantum state, a meaning that has no connection with the thermodynamic meaning or with the etymology of the word. This usage is traced to early discussions of *reversible adiabatic* processes in classical and quantum mechanics, processes that came to be referred to simply as adiabatic.

KEITH J. LAIDLER. Can. J. Chem. **72**, 936 (1994).

En cinétique chimique, le mot «adiabatique» se réfère aujourd'hui à un processus dans lequel il n'y a pas de changement d'état quantique, une signification qui n'a aucune relation avec le sens thermodynamique ou avec l'étymologie du mot. On peut retracer l'origine de ce nouvel usage dans les premières discussions des processus *adiabatiques réversibles* de la mécanique classique ou quantique auxquels on a fini par se référer simplement adiabatiques.

[Traduit par la rédaction]

Can. J. Chem. Downloaded from www.nrcresearchpress.com by 195.246.54.202 on 09/08/12
For personal use only.

Introduction

In chemical kinetics the word "adiabatic" has long been used to refer to a chemical reaction in which the products remain in the same quantum state as the reactants. This usage has created some puzzlement as it does not seem to have, and indeed does not in fact have, any connection with the etymology of the word adiabatic, or with the appropriate use of the word in thermodynamics. The word adiabatic means "not passing through," and in thermodynamics refers to a condition imposed on a system, a condition that prevents any passage of heat into or out of the system. In its kinetic usage the word relates not to a condition imposed on the system, but rather to an inherent property of a chemical process, namely its tendency under certain conditions to occur without any change in quantum states.

A consideration of how the kinetic meaning of adiabatic developed is of some interest in the history of science, and is also instructive in leading to a better understanding of some of the fundamental principles of statistical mechanics and quantum mechanics. The trail begins with a paper (1) published in 1866 by Ludwig Boltzmann, in which he mistakenly claimed to have derived the second law of thermodynamics on the basis of classical mechanics. Within a few years, thanks to his study of Clerk Maxwell's papers, he had realized that his argument was invalid, and that the second law must be explained along statistical lines. In his 1868 paper, however, he had considered a reversible adiabatic process, and it is from that argument that the winding and sometimes indistinguishable trail eventually led, through several false turns, to the inappropriate use of the word adiabatic in modern kinetics.

"Adiabatic" as used in thermodynamics

The word adiabatic was first used in 1858 by W.J.M. Rankine (2), and it derives from the Greek prefix α- (a-), not, δια (dia), through, and βαινιν (bainen), to pass. Although it was Rankine who first used the word, the *concept* of an adiabatic process, in which no heat enters or leaves the system, is stated clearly in Carnot's famous memoir (3) of 1824, and in Clapeyron's mathematical treatment of Carnot's cycle (4), which involves two isothermal and two adiabatic steps.

"Adiabaticity" in classical mechanics

Boltzmann was 22 years old in 1866 when he wrote his paper entitled "On the mechanical meaning of the second law of thermodynamics" (1). In it he claimed to have given a "purely analytical, completely general, proof of the second law of thermodynamics." By 1868 he had realized that his arguments were ill-conceived, and in that year he published a paper of great importance (5), which initiated his pioneering contributions to statistical mechanics. This contribution owed much to an important paper by Clerk Maxwell (6) on the distribution of speeds in gases. Others, however, notably Rudolf Clausius (7, 8) and Coloman (or Kálmán) Szily von Nagy-Szigeth (9–11), continued to maintain the view that the second law can be proved on the basis of mechanics.

Although Boltzmann's 1866 paper was invalid, it did involve a principle that was later helpful in leading to an understanding of the quantum theory. Boltzmann considered a somewhat artificial model for a gas in which the molecules undergo a periodic motion of frequency ν. He then proved that if the gas were subjected to a *reversible adiabatic change* the ratio of the energy E to the frequency ν would remain constant. In their later papers Clausius and Szily also considered reversible adiabatic changes, agreeing with Boltzmann's conclusion that E/ν remains constant. It was at about that time that the word *action* began to be applied to the quantity E/ν.

Subsequently a number of other workers stressed this invariance of E/ν. In 1902, for example, Lord Rayleigh, in a treatment (12) of the pressure of radiation, considered a simple pendulum consisting of a bob and a string. By means of a small ring round the string its length could be altered, and as the string becomes shorter the frequency of the pendulum increases. Rayleigh proved that if the ring is lowered extremely slowly (i.e., the process is carried out reversibly) work is done on the system and the energy of the pendulum increases in exact proportion to the frequency; in other words the action, E/ν, remains constant. If, on the other hand, the ring is lowered rapidly just at the moment that the string is vertical, no work is done; the frequency increases but the energy remains constant, so that the action is no longer unchanged. Other treatments of the same principle in relation to other situations were given by Andrade (13), Morton (14), and Bhatnagar and Kothari (15).

"Adiabatic invariance" in quantum theory

Paul Ehrenfest was particularly effective in his writings on

Can. J. Chem. Downloaded from www.nrcresearchpress.com by 195.246.54.202 on 09/08/12
For personal use only.

the fundamentals of mechanics (16–19), and he laid special emphasis on this constancy of E/ν, in both classical and quantum mechanics. In one paper (16*a*), published in 1911, he extended the principle of invariance of E/ν in classical systems, for processes that are extremely slow, to apply to motions other than harmonic motions, to which the principle had previously been restricted. He also extended the argument to quantized systems, showing that when the parameters of a system in a particular quantum state are changed slowly, the system remains in the same quantum state. In this same paper he proved rigorously that, since E/ν is the only property that remains constant if one brings about a very slow change in the system, this is the only property that can be quantized. It should be remarked that although as a matter of convenience we speak of the quantization of energy — and this terminology has been sanctioned by Einstein and Planck among many others — it is, strictly speaking, the action (E/ν) that is quantized. Planck in fact referred to his constant h (= E/ν) as the *elementary quantum of action.*

Ehrenfest's analysis in this 1911 paper (16) threw light on a difficulty that was troubling many of the leading physicists of the time. The laws of classical mechanics had been well worked out to deal with energy transfers that occur when molecules collide. What, however, would be the situation if energies are quantized? This matter was brought up at the First Solvay Congress, held in Brussels at the end of October, 1911, only a couple of weeks after Ehrenfest's paper appeared. H.A. Lorenz, then professor at Leiden and in the following year to be succeeded there by Ehrenfest himself, posed a simple question of fundamental importance. He imagined a pendulum oscillating in a particular quantum state, and asked what would happen to the quantized state if the string were shortened. Ehrenfest had not been invited to attend the Congress but, according to the report of the Congress, Einstein immediately and unhesitatingly answered that *if the length were changed infinitely slowly,* the energy would remain equal to $h\nu$. It is known that Einstein had by that time read Ehrenfest's paper (16*a*),[1] and he was probably also familiar with Rayleigh's treatment of the classical problem.

Although the emphasis had always been on the *slowness* of the processes, it was shortly after this meeting that the constancy of E/ν began to be referred to as "adiabatic invariance." This expression was apparently first used in print by Einstein in a paper (20) that appeared in 1914. This usage by Einstein is acknowledged in papers by Ehrenfest (19) which appeared in 1916. The English version of these papers, which appeared in the *Philosophical Magazine*, was entitled "Adiabatic invariants and the theory of quanta," and on page 502 appears the following significant passage:

> "By changing the parameters ... in an infinitely slow way, a given motion $\beta(a)$ may be transformed into another motion $\beta(a')$. This special type of influencing upon the system may be called "*a reversible adiabatic affection*", the motion $\beta(a)$ and $\beta(a')$ being *adiabatically related to each other* [his italics]"

Much the same is said in the Dutch versions of the paper. The key word "reversible" disappeared in the second part of this sentence, and was also omitted in latter discussions of the problem. In some of these later treatments one meets anomalous phrases like "...if a process occurs adiabatically, i.e., very slowly...". The emphasis should, of course, be on the reversibility and not on the adiabaticity; the same effect would be obtained if the process were reversible and *isothermal.* The important point, as stressed by Einstein at the Solvay Congress, is that processes must be *slow* in order for quantum states to be preserved. In spite of this, the inappropriate word adiabatic came to be used.

[1]Reference 16*a* appeared in October, 1911, and the fact that Einstein had read it before the Solvay Congress, which occurred at the end of October, is known from the fact that he referred to it in a letter to his friend M. Besso dated 21st October, 1911.

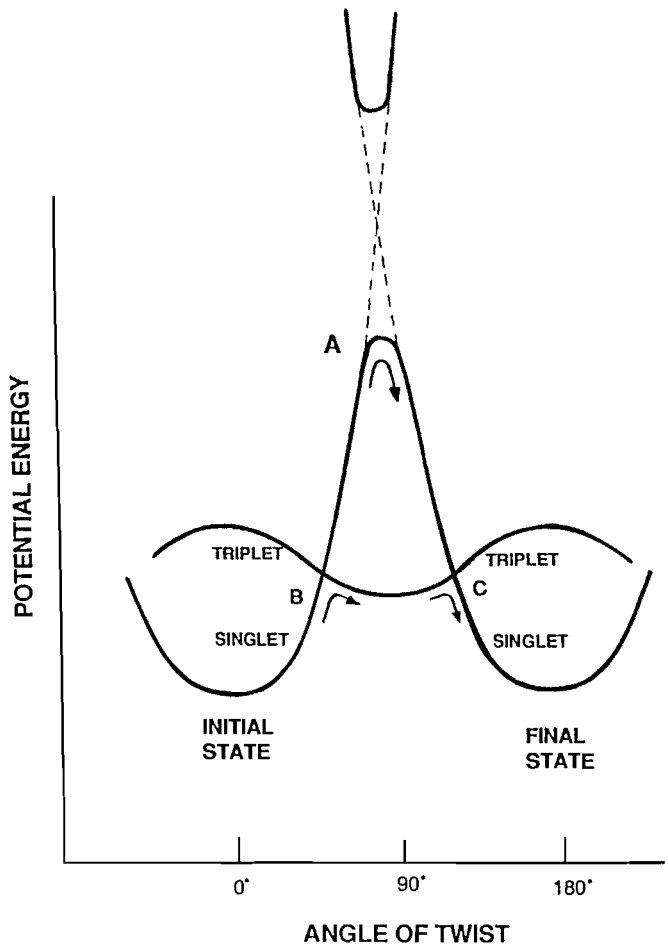

FIG. 1. Schematic potential-energy diagram for the *cis–trans* isomerization of a substituted ethylene.

"Adiabaticity" in chemical kinetics

The modern use of the word adiabatic in chemical kinetics is consistent with the usage introduced by Einstein and Ehrenfest. The first use in kinetics appears to have been by Fritz London (21) in 1928, in connection with his approximate quantum-mechanical expression for the energy of the H...H...H complex, an intermediate in the H + H_2 reaction. In discussing this problem London suggested that many chemical reactions proceed "adiabatically," by which he meant that there is no abrupt jump from one quantum state to another.

Reactions that are not adiabatic in this sense are referred to as diabatic or nonadiabatic. Examples of nonadiabatic reactions are the *cis–trans* isomerizations of certain substituted ethylenes. Figure 1 shows a schematic potential-energy profile (22) for such a system, the energy being plotted against the angle of twist about the double bond. There is a triplet excited state having a minimum corresponding to a twist of 90° so that there are two alternative reaction paths. The system may remain in a singlet state throughout and proceed via point A, where there is a crossing of two singlet states; this process is referred to as adi-

Can. J. Chem. Downloaded from www.nrcresearchpress.com by 195.246.54.202 on 09/08/12
For personal use only.

abatic. Alternatively, the system may cross to the triplet state at B and cross to the singlet state at C; this is the non-adiabatic process. The adiabatic process has a higher activation energy than the non-adiabatic process, but has a normal pre-exponential factor, since there is little restriction to passing from a singlet state to another singlet state. The non-adiabatic process has a lower activation energy but a lower pre-exponential factor because of the difficulty in crossing from a singlet to a triplet state. The evidence for the *cis-trans* isomerizations is that the pre-exponential factors are abnormally low by a factor of about 10^{-3}: this factor, referred to as the *transmission coefficient* for the reaction, reflects the low probability of transition between singlet and triplet states.

Systems approaching B in Fig. 1 do so at various speeds. According to the principles enunciated by Ehrenfest and Einstein, systems moving very slowly will inevitably remain in the triplet state, but these will have insufficient energy to reach C and will therefore not undergo isomerization. Systems moving more rapidly will have a significant possibility of jumping into the triplet state where they will probably undergo a number of vibrations before passing into the product state. The details are obviously a matter of great complexity.

The word adiabatic has also been used in kinetics in a more specialized sense: a reaction in which the system remains in the same vibrational state has been said to be "vibrationally adiabatic." In conventional transition-state theory (23, 24) the initial and activated states are treated quantum mechanically, but the passage over the col is treated classically. Also, in the earlier dynamical treatments of the motion of systems over potential-energy surfaces, the initial states are quantized but the actual motion follows classical laws (25), so that the products do not appear in their appropriate quantum states. Some attempts have been made to develop extensions of conventional transition-state theory in which the motions are constrained to remain in quantum states (26, 27), and these have been referred to as adiabatic transition-state treatments. In a number of publications Polanyi and co-workers have dealt with the theory (28) of this type of adiabaticity and have provided examples (29). Other treatments consistent with this type of adiabaticity have been put forward by Garrett and Truhlar (30), and by Quack and Tröe (31, 32) who have proposed an "adiabatic channel model," which is a detailed version of adiabatic transition-state theory.

The word adiabatic in its kinetic sense also appears in Marcus's theory of unimolecular gas reactions (33, 34), often referred to as Rice–Ramsperger–Kassel–Marcus (RRKM) theory. Certain types of energy residing in a molecule are regarded as inactive or adiabatic; what is meant is that energy of this type remains in the same quantum state during reaction and therefore makes no contribution to the rearrangement of bonds that occurs during reaction. The zero-point energy is adiabatic in this sense, as is the energy of overall translation and rotation, since this energy is preserved when the energized molecule becomes an activated complex. Other energies, such as some vibrational energies, are said in RRKM theory to be active or non-adiabatic.

Discussion

It is evident that besides being used in kinetics in a sense that is different from the thermodynamic sense, the words adiabatic, diabatic, and non-adiabatic are used in different ways by different writers on kinetics. It is obviously of the greatest importance that whenever the words are used in kinetics they should be clearly defined. It should also be noted that the words are often used not to describe the way in which a reaction is believed to proceed, but rather the approximation that is being used in the theoretical treatment of the reaction.

1. L. Boltzmann. Sitzungsber. Akad. Wiss. Wien, **53**, 195 (1866).
2. W.J.M. Rankine. A manual of applied mechanics. London and Glasgow. 1859.
3. S. Carnot. Réflections sur la puissance motrice du feu. Bachelier, Paris. 1824.
4. B.P.E. Clapeyron. J. Éc. Polytech. **14**, 153 (1834).
5. L. Boltzmann. Sitzungsber. Akad. Wiss. Wien, **58**, 517 (1868).
6. J. Clerk Maxwell. Philos. Mag. **157**, 49 (1867).
7. R. Clausius. Sitzungsber. Niederrhein. Ges. Bonn, 114 (1870); (Poggendorff's) Ann. Phys. Chem. [2], **141**, 124 (1870); English version in Philos. Mag. [5], **40**, 122 (1870), and reproduced in S.G. Brush. Kinetic theory. Vol. 1. Pergamon Press, Oxford. 1965.
8. R. Clausius. (Poggendorff's) Ann. Phys. Chem. [2], **142**, 433 (1871); English version in Philos. Mag. [5], **42**, 161 (1871).
9. C. Szily. (Poggendorff's) Ann. Phys. Chem. [2], **145**, 295 (1872); English version in Philos. Mag. [4], **43**, 339 (1872).
10. C. Szily. (Poggendorff's) Ann. Phys. Chem. [2], **149**, 74 (1873); English version in Philos. Mag. [4], **46**, 426 (1873).
11. C. Szily. (Poggendorff's) Ann. Phys. Chem. Ergänz. **7**, 154 (1876); English version in Philos. Mag. [5], **1**, 22 (1876); **2**, 254 (1876).
12. Lord Rayleigh (J.W. Strutt). Philos. Mag. **3**, 338 (1902).
13. E.N. da C. Andrade. The structure of the atom. 3rd ed. G. Bell, London. 1923. pp. 198–206.
14. W.B. Morton. Philos. Mag. [7], **8**, 186 (1929).
15. P.L. Bhatnagar and D.S. Kothari. Indian J. Phys. **16**, 272 (1942).
16. (*a*) P. Ehrenfest. Ann. Phys. [4], **36**, 91 (1911); (*b*) Martin J. Klein (*Editor*). Paul Ehrenfest: Collected scientific papers. North Holland, Amsterdam. 1959.
17. P. Ehrenfest and T. Ehrenfest. Begriffliche Grundlagen der statische Auffassung in der Mechanik. *In* Encyklopädie der Mathematische Wissenschaften. B.G. Teubner, Leipzig, IV, 2, II, Heft 6. 1911; English translation by M.M.J. Moravczik in P. and T. Ehrenfest. The conceptual foundations of the statistical approach in mechanics. Cornell University Press, Ithaca, N.Y. 1959; reprinted by Dover Publications, New York. 1990.
18. P. Ehrenfest. Proc. Amsterdam Acad. **16**, 591 (1913).
19. P. Ehrenfest. Versl. Akad. Wet. Amsterdam, **25**, 412 (1916); English translation in Proc. Amsterdam Acad. **19**, 576 (1916); condensed English version with change of title in Philos. Mag. [6], **33**, 500 (1917).
20. A. Einstein. Verh. Dtsch. Phys. Ges. **16**, 820 (1914).
21. F. London. *In* Probleme der modernen Physik. Sommerfeld Festschrift. F. Hirtzel, Leipzig. 1928.
22. J.L. Magee, W. Shand, and H. Ering. J. Am. Chem. Soc. **63**, 677–688 (1941).
23. H. Eyring. J. Chem. Phys. **3**, 107 (1935).
24. M.G. Evans and M. Polanyi. Trans. Faraday Soc. **31**, 875 (1935).
25. K. Karplus, R.N. Porter, and R.D. Sharma. J. Chem. Phys. **43**, 3259 (1965).
26. D.G. Truhlar. J. Chem. Phys. **53**, 2041 (1970).
27. A. Tweedale and K.J. Laidler. J. Chem. Phys. **53**, 2045 (1970).
28. C.A. Parr, J.C. Polanyi, and W.H. Wong. J. Chem. Phys. **58**, 5 (1973), and later publications.
29. L.T. Cowley, D.S. Hone, and J.C. Polanyi. Chem. Phys. Lett. **12**, 144 (1971), and later publications.
30. B.C. Garrett and D.G. Truhlar. J. Chem. Phys. **83**, 1052 (1979), and later publications.
31. M. Quack and J. Tröe. Ber. Bunsen-Ges. Phys. Chem. **79**, 170 (1975).
32. M. Quack and J. Tröe. Theor. Chem. (N.Y.), **6B**, 199 (1981).
33. R.A. Marcus. J. Chem. Phys. **20**, 359 (1952).
34. G.M. Wieder and R.A. Marcus. J. Chem. Phys. **37**, 1835 (1962).

Accidental conical intersections in $H_2Cl^+(^1A')$

PHILIP J. KUNTZ AND W. NEIL WHITTON
Hahn–Meitner-Institut (Berlin) GmbH, Glienicker Str. 100, D-14 109 Berlin, Germany
AND
IVANA PAIDAROVÁ AND RUDOLF POLÁK
J. Heyrovský Institute of Physical Chemistry, Academy of Sciences of the Czech Republic, Dolejškova 3, 182 23 Prague 8 Czech Republic

Received July 18, 1993

This paper is dedicated to Professor John C. Polanyi on the occasion of his 65th birthday

PHILIP J. KUNTZ, W. NEIL WHITTON, IVANA PAIDAROVÁ, and RUDOLF POLÁK. Can. J. Chem. **72**, 939 (1994).

Conical intersections in C_s, C_{2v}, and linear configurations for the $^1A'$ states of the H_2Cl^+ molecule are investigated with the help of a 10 × 10 model Hamiltonian matrix in a valence-bond basis. The line of intersection (*linea*) between states 2 and 3 is traced from one end point, an intersection between two states of $^1B_2$ symmetry in a C_{2v} configuration, to the other end point, an intersection between two $^1\Sigma^+$ states in a linear H—H—Cl configuration. The *linea* consists of 5 branches having symmetries C_s, C_s, $C_{\infty v}$, C_{2v}, and C_s. A *linea* between states 3 and 4 starting at a crossing of $^1\Sigma^+$ and $^1\Pi$ states in a linear $C_{\infty v}$ configuration consists of three branches (C_s, C_{2v}, C_s) leading to the asymptotic region Cl + H_2. The starting point of linea 3/4 is connected to the asymptotic region H + HCl via a *linea* in the linear configuration. *Lineae* of C_s symmetry could be found by examining the eigenvalues of the Hessian matrix of second derivatives along a line of intersection in a higher symmetry (C_{2v} or linear), a useful method for locating accidental intersections that lends itself readily to *ab initio* calculations. The existence of the *lineae* could be related to physical properties of the molecule, such as the dipole moment, indicating that the model Hamiltonian does reflect the true physical behaviour.

PHILIP J. KUNTZ, W. NEIL WHITTON, IVANA PAIDAROVÁ et RUDOLF POLÁK. Can. J. Chem. **72**, 939 (1994).

Faisant appel à un hamiltonien matriciel modèle de 10 × 10, dans une base de liaison de valence, on a examiné les intersections coniques des configurations C_s, C_{2v} et linéaires des états $^1A'$ de la molécule de H_2Cl^+. La ligne d'intersection (*linea*) entre les états 2 et 3 est tracée à partir d'un point terminal, une intersection entre deux états de symétrie $^1B_2$ de configuration C_{2v} vers un autre point terminal, une intersection entre deux états $^1\Sigma^+$ dans une configuration linéaire H—H—Cl. La *linea* comporte cinq branches de symétries C_s, C_s, $C_{\infty v}$, C_{2v}, et C_s. Une *linea* entre les états 3 et 4, qui commence à un croisement des états $^1\Sigma^+$ et $^1\Pi$ dans une configuration linéaire $C_{\infty v}$, comporte trois branches (C_s, C_{2v} et C_s) et elle conduit à la région asymptotique Cl + H_2. Le pont de départ de la *linea* 3/4 est relié à la région asymptotique H + HCl par le biais d'une *linea* de configuration linéaire. On peut trouver des *lineae* de symétrie C_s en examinant les valeurs propres de la matrice hessiane des deuxièmes dérivés le long d'une ligne d'intersection dans une symétrie plus élevée (C_{2v} ou linéaire); il s'agit d'une méthode utile pour localiser des intersections accidentelles qui se prêtent facilement à des calculs *ab initio*. On peut relier l'existence de *linea* aux propriétés physiques de la molécule, comme le moment dipolaire; ceci indique que l'hamiltonien modèle est un reflet du comportement physique réel.

[Traduit par la rédaction]

Introduction

In this paper we use a diatomics-in-molecules (DIM) model Hamiltonian matrix to map some of the lines of accidental conical intersections in the $^1A'$ states of H_2Cl^+. By accidental, we mean intersections of states from the *same* irreducible representation of the symmetry group of the molecule. The classic paper by Longuet-Higgins in 1975 (1) appears to be definitive as to the existence of such intersections and their dimensionality. Since then, these intersections have become well established both from the theoretical and computational perspectives (2–12) and have important implications for the theory of reaction dynamics (13–22). Within a specified area, the *existence* of a conical intersection can be demonstrated without actually *locating* it, if one exploits the geometric phase factor (Berry's phase): the eigenvectors of the intersecting states change their signs on being transported in a closed curve around the point of intersection (23–28). This also serves to verify that a located point is in fact a bona fide intersection, for there are always numerical limitations preventing one's finding the *exact* intersection. This procedure, applied some time ago (29), was recently used to verify the existence of a conical intersection for high level *ab initio* MCSCF wave functions (2, 3). The first work to locate a conical intersection using large-scale CI wave functions was recently reported (5), in which it is shown that calculation of the Hessian matrix of second derivatives (5, 30) together with the use of Lagrange multipliers (31, 32) permits one to follow the line of intersection very well.

We have used a modification of the Hessian matrix technique to follow some of the lines of accidental intersections, which we shall refer to here as *lineae*, over as much of their entire lengths as possible. Although the DIM valence bond model is simplistic compared with the recent *ab initio* work, it has the advantage of being applicable over the whole of the configuration space of the molecule, allowing us to follow the *lineae* out to large internuclear separations and thus enabling us to map the behaviour of the *lineae* over most of the regions of interest. Our interest (33) in the H_2Cl^+ molecule-ion stems from a study (34) of the ion–molecule reactions:

[1] $$H^+ + HCl \rightarrow H + HCl^+(X\ ^2\Pi)$$

[2] $$H^+ + HCl \rightarrow H + HCl^+(A\ ^2\Sigma^+)$$

The reagents in these reactions correspond to the second $^1A'$

[1]Author to whom correspondence may be addressed. FAX: (030) 8062 2434; e-mail kuntz@vax.hmi.d400.de

Can. J. Chem. Downloaded from www.nrcresearchpress.com by 195.246.54.202 on 09/08/12
For personal use only.

Can. J. Chem. Downloaded from www.nrcresearchpress.com by 195.246.54.202 on 09/08/12
For personal use only.

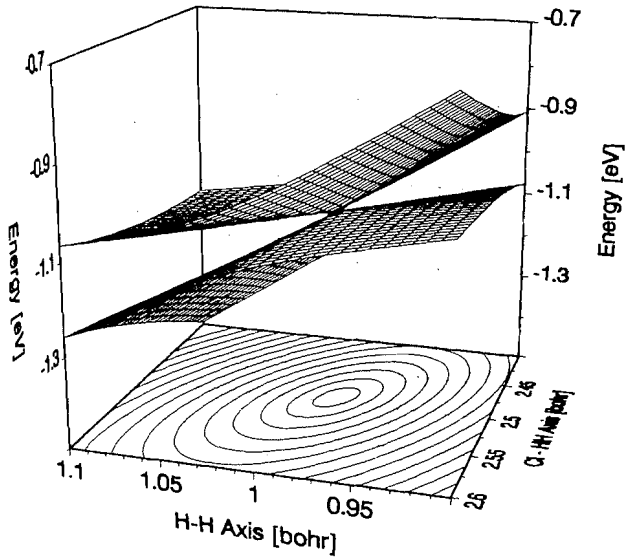

FIG. 1. Conical intersection for potential energy surfaces 2 and 3. r(H—H) = 6 bohr. The position of the Cl atom is referred to a coordinate system with origin in the HH bond midpoint. The energy of each surface is shown by the two cross-hatched sheets, the energy difference by the projections onto the plane.

eigenstate of the H_2Cl^+ molecule; the products correspond to the first and third $^1A'$ eigenstates, respectively. Both reaction paths may proceed via non-adiabatic mechanisms in regions of avoided crossings. In the reaction leading to the *excited* state products, H + $HCl^+(A\ ^2\Sigma^+)$, the avoided crossing region happens to be associated with an accidental conical intersection between the second and third eigenstates in C_s geometrical configurations. This was discovered when the contours for the *difference* in energy between the second and third eigenvalues were plotted for a fixed distance of the H_2 molecule, as in Fig. 1, which shows the two surfaces and the contour map of the energy difference between them. The H_2 bond distance, r(H—H), is held fixed at 6 bohr (1 bohr = 52.9 pm); the direction of the H_2 bond serves to define one of the axes of the plane. The other axis is the line perpendicular to the bond midpoint in the plane of the molecule. The projected contours are characteristic of a conical intersection, the existence of which was verified by computing the change in the geometric phase of the eigenvectors on circumscribing the intersection point.

The work presented here is a continuation of an earlier investigation on conical intersections in the H_2Cl^+ molecule-ion (35), where we only succeeded in calculating a small segment of the *linea* corresponding to the intersection mentioned above, a segment of a second *linea* for eigenvalues 2 and 3, and a third one for states 3 and 4. The existence of these *lineae* in the strong interaction region of the potential energy surface was tentatively related to the crossing of the diatomic curves of the $HCl(X\ ^1\Sigma^+)$ and $HCl^+(A\ ^2\Sigma^+)$ states in the asymptotic region H + HCl, and this in turn was shown to have some relationship to the charge distribution in the molecule. These ideas are reinforced by the present study. In addition, we are now able to follow the *lineae* along their entire lengths and can conclude that they terminate in a united-atom limit, in an asymptotic region, or in a point of higher symmetry. We show that the two segments of the 2/3 *lineae* of the previous work are actually part of a single extended *linea* which is made up of C_s, C_{2v}, and linear parts. The local behaviour of the *lineae* can be related to the crossings that occur in the various diatomic curves in the asymptotic regions corresponding to the separation of one of the atoms from the rest of the molecule. We demonstrate how a C_s *linea* might be located by following *lineae* in higher symmetries.

Computations

The model Hamiltonian

The model Hamiltonian (10 basis functions from 6 valence-bond (VB) structures) is described in earlier work (33) on the first three eigenstates of the H_2Cl^+ molecule-ion; information of relevance to the conical intersections appears in a later paper (35). The basis functions are obtained from spin-coupled direct products of the following set of atomic basis functions: Cl^-, $Cl^+(^3P_g)$, $Cl^+(^1D_g)$, $Cl^+(^1S_g)$, $Cl^+(^2P_u)$, H^+, and $H(^2S_g)$. These suffice to represent the $^1A'$ states of the triatomic molecule and they allow for charge transfer (ionicity) in H_2Cl^+ and in the HCl and HCl^+ fragments. The Hamiltonian matrix elements are evaluated in the diatomics-in-molecules (DIM) approximation: each matrix element is expressed in terms of the atomic and diatomic fragment matrices in the same basis, making use of the rotation matrices associated with the atomic basis functions. The first derivatives of the matrix elements are obtained analytically; the second derivatives are obtained from these numerically.

Since the potential energy surfaces have been described in detail (33), we shall not discuss them here. It should be noted that the DIM model was developed for the region of strong interaction between all three atoms — the behaviour at extremely short range (corresponding to much higher energy) is rather arbitrary. At very long range, the surfaces all approach their correct asymptotic limits but there are some spurious crossings in the diatomic curves, at least for the $H_2^+(X\ ^2\Sigma_g^+)$ and $H_2^+(^2\Sigma_u^+)$ fragments. Crossings in the HCl interactions at ≈7.5 bohr may also be spurious. The crossing of states 2 and 3 for r(H—Cl) = 4.2685 bohr is, however, a real phenomenon, and plays an important role in determining the loci of the *lineae*.

Finding the intersections

The previous work was plagued by numerical difficulties, which prevented us from finding the complete *lineae*. We see now that this was due mainly to our taking one of the internuclear distances, r(H—H), as the parameter describing the *linea* in 3-space, a method similar to that used by Manaa and Yarkony (30, 5). While this is a perfectly good procedure over part of the *linea*, it breaks down in regions where the *linea* is nearly perpendicular to the r(H—H) coordinate, since the plane in which the local search for the intersection is carried out is then nearly identical with the plane containing the *linea*. This is illustrated in Fig. 2. The *linea* cuts the base plane in two points, making it difficult not only to determine the exact point of intersection but also to calculate the geometric phase factor for verification: as the points coalesce, the line circumscribing the point may accidentally include *both* intersection points, leading to a zero phase factor. To remedy this deficiency, we now take the distance *along* the *linea* as the parameter, or progress variable, a procedure that guarantees that the search for the intersection will be carried out in a plane nearly perpendicular to the *linea*, as it should be. Accordingly, each line of intersection, or *linea*, is defined parametrically in

Can. J. Chem. Downloaded from www.nrcresearchpress.com by 195.246.54.202 on 09/08/12
For personal use only.

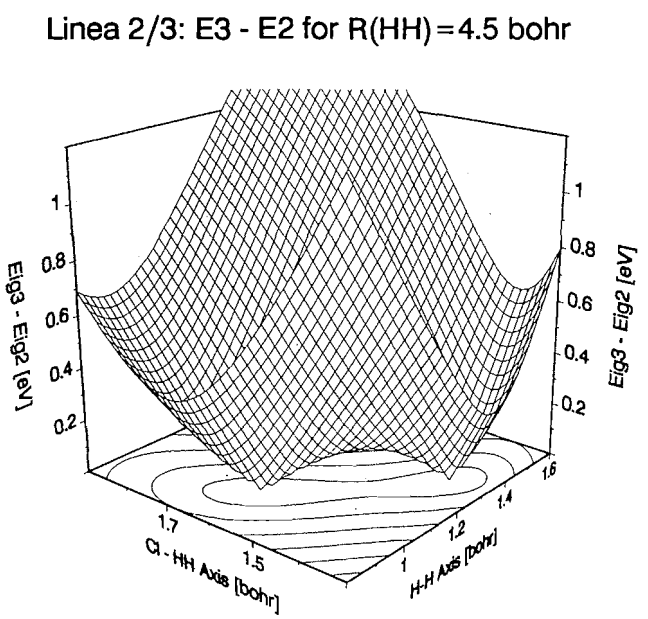

FIG. 2. Energy difference between states 2 and 3 in a region where the *linea* is nearly parallel to the base plane; the projections of this difference are shown as contours in the base plane. The coordinate system is as in Fig. 1 with r(H—H) = 4.5 bohr.

a space of "body-fixed" coordinate, $(u(\lambda), v(\lambda), w(\lambda))$ in terms of the progress variable, λ. The Cartesian coordinates (with respect to a fixed origin in space) for the atoms 1 (H), 2 (H), and 3 (Cl) are given in terms of the body-fixed coordinates as (0, 0, 0), (0, 0, w), and (u, 0, v). The two internuclear distances r(H—Cl) (denoted by r_a and r_b) and the distance r(H—H) (denoted by r_{ab}) are related to these coordinates by

$$[3] \qquad r_a = \sqrt{u^2 + (v - w)^2}$$

$$[4] \qquad r_b = \sqrt{u^2 + v^2}$$

$$[5] \qquad r_{ab} = w$$

To find the point of conical intersection of two eigenstates, E_1 and E_2, one starts with a point lying as close as possible to the *linea*. From such an approximate starting point, the position of the intersection can be found by searching in the plane perpendicular to the direction of the *linea* for the minimum in the *square* of the difference in energy, $S = (E_2 - E_1)^2$, an analytic function. Having found an exact point on the *linea*, successive points in the positive and negative sense of the *linea* direction can be found in a stepwise fashion until the endpoints of the *linea* are reached.

Crucial to this strategy is finding the *linea* direction. This is estimated by computing the Hessian matrix, D, of the second partial derivatives of the function S with respect to the body-fixed coordinates (u, v, w):

$$[6] \qquad D_{ij} = \left(\frac{\partial^2 S}{\partial \eta_i \partial \eta_j}\right)$$

where η_i is one of u, v, w. The matrix D is diagonalized to obtain the eigenvalues, e, and the eigenvectors, c: $Dc = ce$. Since the function S is identically zero at all points on the *linea*, the first and second derivatives are also zero along the direction of the *linea*, which implies that at least one of the eigenvalues of the Hessian matrix will be zero. The eigenvector corresponding to this eigenvalue, the column vector c_1, is then the direction of the *linea* at the point. The other two eigenvectors, c_2 and c_3, provide unit vectors perpendicular to the *linea*. In terms of the row vector (1, 1, 1) in (u, v, w) space, three local unit vectors spanning configuration space can be defined as

$$[7] \qquad \hat{I} = (1, 1, 1)c_1$$

$$[8] \qquad \hat{J} = (1, 1, 1)c_2$$

$$[9] \qquad \hat{K} = (1, 1, 1)c_3$$

The c_i are arranged in increasing order of the absolute values of their corresponding eigenvalues. Points in the neighbourhood of a given point, $Q \equiv (u, v, w)$, are defined in terms of three "Hessian variables" (λ, h_1, h_2):

$$[10] \qquad Q' = Q + \lambda\hat{I} + h_1\hat{J} + h_2\hat{K}$$

The eigenvalues of the Hamiltonian, E_1 and E_2, are considered to be functions of the Hessian variables. The strategy for propagating the *linea* from a point Q_0 to a neighbouring point Q_λ consists of the following steps:

1. Estimate the position of the next point on the *linea* by going a small step λ in the *linea* direction: $Q'_\lambda = Q_0 + \lambda\hat{I}$. ($\lambda$ is the "progress variable", or parameter of the *linea*.)

2. From the approximate point, Q'_λ, find the exact point, Q_λ, by minimizing the function $S(\lambda; h_1, h_2)$ with respect to the two "Hessian variables" h_1, h_2, holding λ fixed. h_1 and h_2 span the space perpendicular to the direction of the *linea*.

3. At the exact point Q_λ, find the new unit vectors $\hat{I}$, $\hat{J}$, $\hat{K}$ by diagonalizing the Hessian matrix at that point.

Step 2, minimizing the function S, may be unsuccessful, especially at large internuclear distances, where whole groups of eigenvalues are nearly degenerate, and at points where the wave functions corresponding to the two intersecting states change their character abruptly, causing the *linea* to execute a sharp turn in configuration space. In this case, step 2 must be repeated with smaller values of the progress variable, λ, until the *linea* is out of the difficult region. Even then, failure of the method can still occur if two nearly parallel *lineae* approach each other, for then there are two zeros of the function S that lie very close to each other. Special numerical methods would then be needed. This procedure worked very well for most cases investigated here, allowing determination of the point of intersection to within a relative error in the energy of better than 10^{-9}. It is more efficient and much more reliable than the methods used in our previous work (35), the chief reason being that the *linea* is defined in terms of a progress variable along a locally determined direction, rather than along some arbitrary global coordinate, although the latter method can be successful over much of the *linea* (30). All of the intersections were verified by computing the geometric phase factor on transporting the eigenvector of the lower state around the intersection in the plane spanned by the Hessian variables. (Note that the *lineae* must either be closed curves or must extend to infinity in order that it be unambiguous whether a given closed curve encircles a *linea* or not. All of the curves discussed here do in fact satisfy this condition.)

A special difficulty arises when there is near degeneracy of

Can. J. Chem. Downloaded from www.nrcresearchpress.com by 195.246.54.202 on 09/08/12
For personal use only.

the lowest Hessian eigenvalue with some of the others. This occurs, for example, when two *lineae* meet each other (e.g., when a *linea* of C_s symmetry meets a *linea* of higher symmetry). In such a case, it is necessary to form a linear combination of the corresponding Hessian eigenvectors so as to project out the unwanted direction. For a *linea* of C_s symmetry, it is convenient to define a *local direction*, $\hat{t}$, which is the direction connecting the two most recently determined points on the *linea*. The matrix of the projector onto $\hat{t}$ is then

$$[11] \qquad P_t = \begin{pmatrix} t_1^2 & t_1 t_2 \\ t_1 t_2 & t_2^2 \end{pmatrix}$$

where $t_i = \hat{t} \cdot c_i$. The desired direction of the *linea* is then obtained from

$$[12] \qquad \hat{l} = (1, 1, 1)(c_1, c_2)p$$

where p is the (column) eigenvector of P_t corresponding to the largest eigenvalue.

For a *linea* in C_{2v} configuration space, a slightly modified procedure is needed: symmetry coordinates are defined as

$$[13] \qquad X = u$$

$$[14] \qquad Y = (2w + v)/\sqrt{5}$$

$$[15] \qquad Z = (w - 2v)/\sqrt{5}$$

Two of these, X and Y, span the C_{2v} space when $Z = 0$, so that if $\hat{t}$ be taken as the unit vector $\hat{Z}$ and the eigenvector p be taken to correspond to the *smallest* eigenvalue of the projector, then eq. [12] eliminates the non-C_{2v} component from the estimated *linea* direction. A similar procedure obtains for a *linea* in linear configurations: the nonlinear component, X, must be projected out. In following a C_s *linea* in regions where it approaches close to a *linea* of higher symmetry, the desired direction is that which has the highest projection onto the component perpendicular to the higher symmetry: $\hat{t} = Z$ for approach to C_{2v} and $\hat{t} = X$ for approach to the linear configuration.

This method of handling degeneracies turns the difficulties experienced earlier (35) to an advantage: not only does it allow a determination of a specified *linea* even when it is in the neighbourhood of *lineae* of differing symmetry, but it can also be used as a diagnostic for the presence of C_s *lineae*, which are normally quite difficult to find. This is illustrated in Fig. 3, which shows the logarithm of the Hessian eigenvalues along C_{2v} branches of *lineae* 2/3 and 3/4. The lowest eigenvalue should, of course, be zero, as explained above. The second eigenvalue is degenerate with the first at the positions marked with C_s. (Note that the C_{2v} branch of *linea* 3/4 is a closed curve.) Hence, it is possible to locate a line of conical intersection in C_s configurations by investigating the behaviour of the Hessian eigenvalues along lines of intersection in higher symmetry. The latter lines can often be determined very easily from contour diagrams of the energy difference between states belonging to different irreducible representations. This procedure lends itself readily to *ab initio* calculations. The two spikes marked "mini C_s" show places where a C_s *linea* makes a small loop away from the C_{2v} symmetry and then returns. We have not investigated this feature further; we mention it only to illustrate the sensitivity of the method for locating *lineae* of accidental intersections.

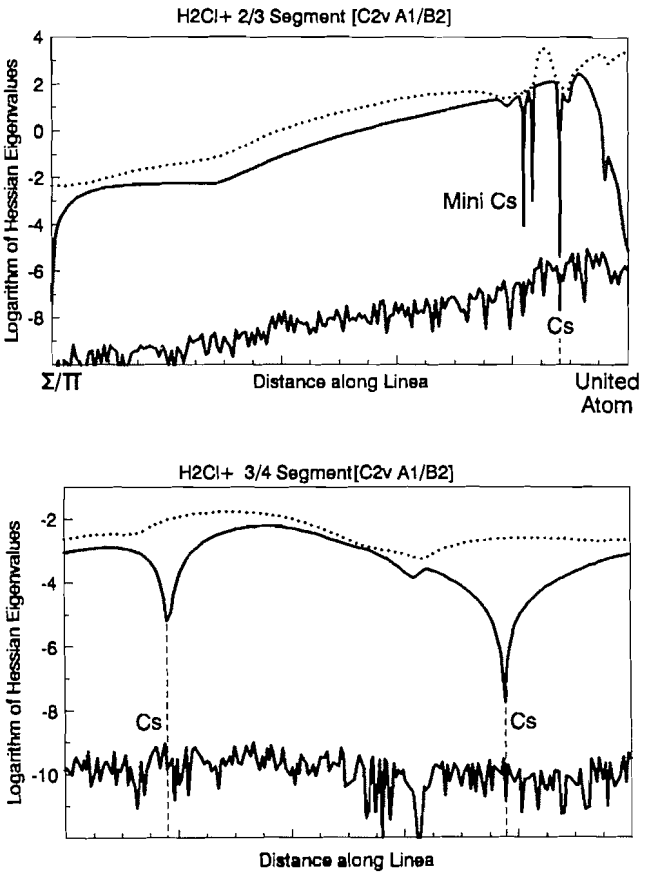

FIG. 3. Logarithm of the 3 Hessian eigenvalues along the C_{2v} branches of *linea* 2/3 (top) and *linea* 3/4 (bottom). The abscissae are in arbitrary units and run over the whole length of the C_{2v} branches shown in Figs. 4 and 6. The positions where the C_{2v} *lineae* intersect with the C_s *linea* are indicated by "C_s". The 3/4 branch is a closed loop: see the projection in Fig. 6.

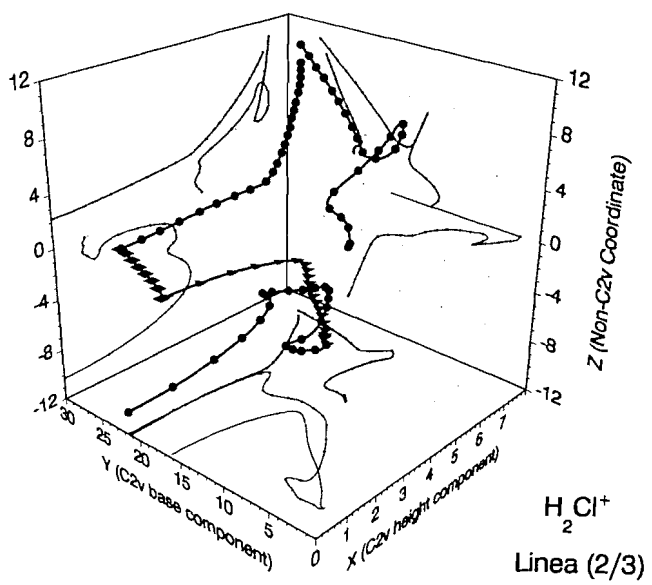

FIG. 4. *Linea* 2/3 referred to C_{2v} symmetry coordinates. The C_s branches are marked with circles, the C_{2v} branch (in the plane $Z = 0$) with triangles, and the linear branch (in the plane $X = 0$) with squares. The C_s projections onto the planes are marked with circles, the other projections are unmarked.

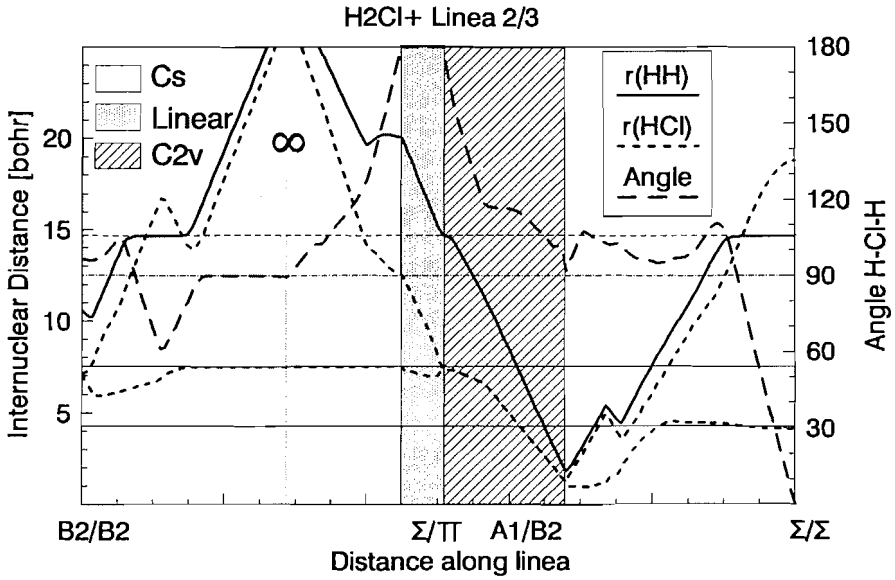

FIG. 5. *Linea* 2/3. Internuclear distances (HH solid lines, HCl short dashed lines) and the H—Cl—H angle (long dashes) as a function of the distance (in arbitrary units) along the *linea*. The C_{2v} and linear regions are emphasized by means of the hatched and dotted backgrounds, respectively. The special points (r(H—Cl) = 4.269 and 7.5185 bohr; r(H—H) = 14.672 bohr) are indicated by thin horizontal lines, solid for HCl, dashed for HH. At the vertical line marked with ∞, the first and second C_s branches approach the asymptotic region H + HCl.

Results

In this work, we are mainly interested in the *lineae* of C_s symmetry. Nevertheless, it is necessary to consider *lineae* of higher symmetry as well, for we have found that the C_s variety proceed until they arrive at one of four types of end point: (*i*) the point at infinity (i.e., one of the asymptotic regions of the potential energy surface, (*ii*) a united atom limit — one, two, or three of the internuclear distances approach zero, (*iii*) a C_{2v} configuration, or (*iv*) a linear configuration. The *lineae* are therefore either closed curves or extend to infinity. In cases (*iii*) and (*iv*) there are two possibilities depending on whether the two intersecting states belong to the same irreducible representation of the higher symmetry state or not. If they do, the C_s *linea* terminates, since in general there cannot be a *line* of intersection in a collinear or C_{2v} subspace (the non-crossing rule!), so that the terminating point is indeed an endpoint. Otherwise, it is usual for the endpoint of the C_s *linea* to lie on a line of intersection in the higher symmetry subspace. This makes it possible for two C_s *lineae* to be connected via higher symmetry *lineae*.

In Fig. 4 the intersection between states 2 and 3, *linea* 2/3, is displayed as a line in 3-space referred to the C_{2v} symmetry coordinates (X, Y, Z) (see eqs. [14] and [15]). This coordinate system is advantageous because the symmetry of each branch of the *linea* is immediately evident: linear configurations must lie in the YZ plane, $X = 0$, and C_{2v} configurations in the XY plane, $Z = 0$. The five branches of the *linea* are represented by thick lines with symbols on them: circles for C_s, triangles for C_{2v}, and squares for linear symmetry. The projections of the C_s branches on each of the three coordinate planes are also shown, as well as two of the projections of the C_{2v} branch (the third projection is just a line in the on the X-axis since the whole curve lies in the XY plane). The internuclear distances and the H—Cl—H angle along *linea* 2/3 are displayed in the companion diagram, Fig. 5. This *linea* starts at an isolated C_{2v} point, where the intersection is between two states of $^1B_2$ symmetry. It follows a C_s branch to the point at infinity corresponding to the asymptotic region H + HCl with angle H—Cl—H = 90° and r(H—Cl) ≈ 7.517 bohr, a distance very close to, but less than, the crossing between two states in the isolated HCl molecule, r(H—Cl) = 7.5185 bohr. At infinity, this branch meets another one with r(H—Cl) = 7.520 bohr (slightly greater than the asymptotic crossing distance), also of C_s symmetry, which proceeds towards the YZ plane to a point of intersection between $^1\Sigma^+$ and $^1\Pi$ states in the linear configuration H—Cl—H. The collinear branch is part of a *linea* that connects a point at infinity, again having r(H—Cl) ≈ 7.517 bohr, with the $D_{\infty h}$ point having r(H—Cl) = 7.386 bohr. The latter point is also the endpoint of a C_{2v} *linea*, which goes to a united atom limit, r(H—H) → 0, r(H—Cl) → 1.524 bohr. Just before reaching this limit, the C_{2v} branch meets another C_s branch at the point r(H—H) = 1.859 bohr, r(H—Cl) = 1.292 bohr. The final branch proceeds to negative values of Z, eventually terminating in a collinear H—H—Cl configuration where there is an intersection of two $^1\Sigma^+$ states for r(H—H) = 14.672 bohr, r(H—Cl) = 4.142 bohr. These values lie very close to curve crossings in the isolated molecules H_2 and HCl: 14.672 and 4.2685 bohr, respectively. The curve crossings in the isolated molecules, collected in Table 1, are indicated by thin horizontal lines in Fig. 5.

TABLE 1. Crossing points in the diatomic curves

Molecule	State indices	Crossing (bohr)	Description of states	
HCl	2/3	4.2685	$HCl^+(A\ ^2\Sigma^+)$	$HCl(X\ ^1\Sigma^+)$
HCl	2/3	7.5185	$HCl^+(A\ ^2\Sigma^+)$	$HCl^+(^2\Pi)$
HCl	3/4	7.4067	$HCl(X\ ^1\Sigma^+)$	$HCl^+(^2\Pi)$
HCl	4/5	7.328	$HCl(^1\Pi)$	$HCl^+(^2\Pi)$
H_2	3/4	14.6704	$H_2^+(X\ ^2\Sigma_g^+)$	$H_2^+(^2\Sigma_u^+)$

Conical intersections between states 3 and 4 are presented in Fig. 6 and its companion Fig. 7. This *linea* consists of three branches. It starts in a linear configuration H—Cl—H with r(H—H) = 12.57 bohr and r(H—Cl) = 5.63 bohr. From there it goes via a C_s *linea* to a C_{2v} point with r(H—H) =

Can. J. Chem. Downloaded from www.nrcresearchpress.com by 195.246.54.202 on 09/08/12
For personal use only.

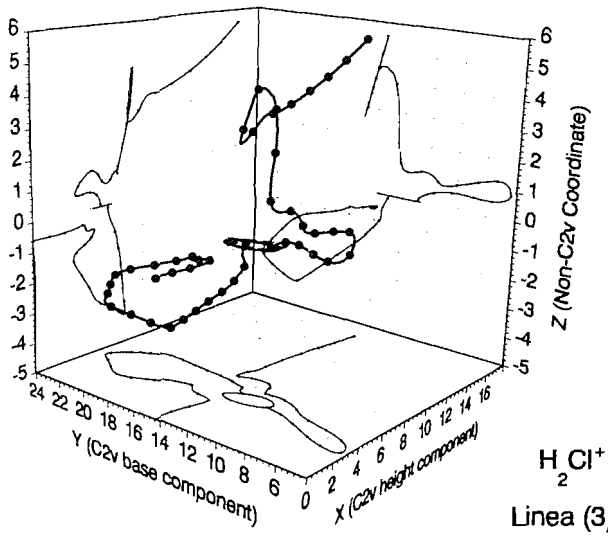

FIG. 6. *Linea* 3/4 referred to C_{2v} symmetry coordinates. The C_s branches are marked with circles, the C_{2v} branch (in the plane $Z = 0$) with triangles. The linear branches (in the plane $X = 0$) leading to the asymptotic region H + HCl are not shown. The C_s projections onto the planes are marked with circles, the other projections are unmarked.

11.63 bohr and r(H—Cl) = 7.85 bohr. The latter lies on a C_{2v} *linea* that is the closed curve for which the Hessian eigenvalues of Fig. 3 were computed. A second C_s branch leaves this curve at the point r(H—H) = 9.73 bohr and r(H—Cl) = 6.79 bohr, and proceeds to the point at infinity corresponding to Cl + H_2 with r(H—H) = 14.672 bohr. One could perhaps allow the existence of a fourth branch going from the starting linear configuration alone a linear line of $^1\Sigma^+$–$^1\Pi$ intersections in two directions, one leading to the point of infinity with r(H—Cl) = 7.43 bohr and the other to the point at infinity with r(H—Cl) = 0.89 bohr, both values of r(H—Cl) corresponding to crossings in the isolated molecule. To avoid clutter, this branch is not shown in the diagrams. Information about the branches of the *lineae* is collected in Table 2.

A few calculations were carried out with a second model Hamiltonian differing from the first only in the $H_2^+(X\ ^2\Sigma_g^+)$ and $H_2^+(^2\Sigma_u^+)$ long-range interactions. The main model has a spurious crossing of these curves at r(H—H) = 14.672 bohr, as shown in Table 1. In the second model, this crossing was removed, altering the locus of the *lineae* at long range (see C_s-b in Table 2). This was done in order to confirm the notion that the accidental crossings in the diatomic curves are intimately bound up with the existence and behaviour of the accidental intersections at finite distances.

Discussion

Using the eigenvalues of the Hessian matrix as a tool for determining the direction(s) of *lineae* near a given point, we have succeeded in tracing out the lines of intersections (2/3) and (3/4) in their entirety. The *lineae* reported in the previous work have been verified and extended and we have shown that they are segments of the *lineae* reported here (with minor differences owing to a slightly different numerical representation of the long-range interactions). In addition, a connecting C_s segment was found by inspecting the Hessian eigenvalues along the *lineae* of higher symmetry, demonstrating that such a method may be of use in searching for C_s *lineae* in other systems.

The shape of the *lineae* is not at all smooth: the figures show that the internuclear distances can change abruptly as a function of the distance along the *linea*. Closer inspection reveals that there are certain "special" values of the distances at which this occurs. In fact, these special values lie very close to points of intersection of the diatomic curves in the asymptotic region. The most important of these are collected in Table 1: at r(H—Cl) = 4.2685 bohr, there is a crossing between the HCl($X\ ^1\Sigma^+$) and HCl$^+$($A\ ^2\Sigma^+$) states; at r(H—Cl) = 7.4067 bohr and r(H—Cl) = 7.5185 bohr there are crossings of the HCl$^+$($^2\Pi$) state with the HCl($X\ ^1\Sigma^+$) and HCl$^+$($A\ ^2\Sigma^+$) states, respectively; at r(H—H) = 14.672 bohr, the $H_2^+(^2\Sigma_u^+)$ state crosses with the $H_2^+(X\ ^2\Sigma_g^+)$ state (a spurious crossing due to inaccuracies in the diatomic input). These crossings play an important role in governing the shape of the various *lineae* because, in the neighbourhood of these points, the character of the adiabatic states changes abruptly. Now the line of intersection is usually associated with some property of the molecule (e.g., the charge distribution), which in turn depends upon the weights of the valence-bond structures in the wave function, and these change abruptly in the region of the crossings. This results in the *linea* undergoing a sharp change in direction in order to stay in a region that preserves the character of the wave function. For example, in Fig. 7, in the region where the progress variable leaves the C_{2v} area heading toward ∞, the lower r(H—Cl) distance increases steadily until it arrives in the neighbourhood of the value 7.39, where, as seen from Table 1, there are several successive crossings because the HCl$^+$($^2\Pi$) state intrudes upon the scene. At values of r(H—Cl) < 7.386, the dominant valence-bond structures in states 3 and 4 of the polyatomic molecule involve the HCl($X\ ^1\Sigma^+$) and HCl($^1\Pi$) states of the diatomic HCl whereas, at larger values, it is the HCl($X\ ^1\Sigma^+$) and HCl$^+$($^2\Pi$) states. At 7.4067 bohr, the latter two states merely change their order but then, at r(H—Cl) = 7.5185 bohr, the wave function would shift to involve the HCl($X\ ^1\Sigma^+$) and HCl$^+$($A\ ^2\Sigma^+$) states. To avoid this, the progress of the smaller HCl distance is arrested temporarily until the H_2 distance increases to a crossing region between the $H_2^+(X\ ^2\Sigma_g^+)$ and $H_2^+(^2\Sigma_u^+)$ states, where the increase in r(H—H) is arrested, allowing r(H—Cl) to increase again. The crossing in the H_2^+ molecule is spurious in our model; if we remove this crossing, then the increase in r(H—H) is not arrested and r(H—Cl) remains at a value of 7.5 bohr. Similar behaviour is seen for *linea* 2/3 in Fig. 5, but for r(H—Cl) $\approx$ 4.265 bohr. This behaviour is very suggestive of an influence of some sort of symmetry associated with the *linea* itself but we have not been able to identify it as yet. Further study utilizing a simpler model would perhaps clarify the behaviour of the intersections.

The use of model potential energy surfaces, in particular the LEPS model, in the study of chemical dynamics has been extremely useful in uncovering the salient features of many systems and has formed the basis for very widely applicable generalizations such as Polanyi's rules. We are therefore hopeful that this work also may be useful in understanding the overall behaviour of accidental conical intersections. Our results are based on a fairly accurate semi-empirical model that gives a very good representation of the shape of the surfaces and the regions of crossing of the first three surfaces in the strong bonding region: the results at very short range and very long range (e.g., >8 bohr) are not reliable, so the *exact* loci of the *lineae* are certainly questionable. Nevertheless, the nature of the accidental intersections and the fact of their existence is, in our opinion, reliable. The main features appear to be robust in the intermediate range. We do not believe

Can. J. Chem. Downloaded from www.nrcresearchpress.com by 195.246.54.202 on 09/08/12
For personal use only.

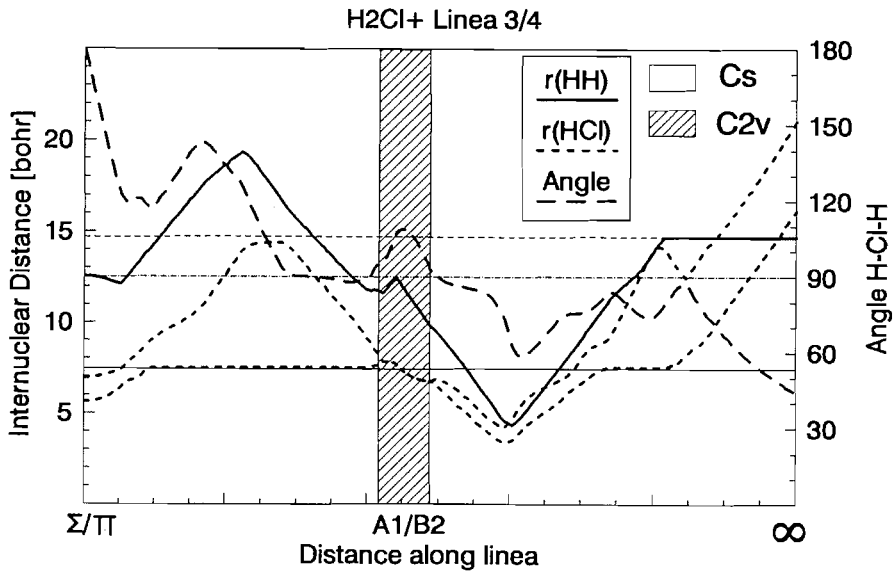

FIG. 7. *Linea* 3/4. Internuclear distances (HH solid lines, HCl short dashed lines) and the H—Cl—H angle (long dashes) as a function of the distance (in arbitrary units) along the *linea*. The C_{2v} region is emphasized by means of the hatched background. The special points (r(H—Cl) = 4.269 and 7.5185 bohr; r(H—H) = 14.672 bohr) are indicated by thin horizontal lines, solid for HCl, dashed for HH.

TABLE 2. *Linea* branches (distances in bohr; 1 bohr = 52.9 pm)

Linea	Branch	First endpoint		Second endpoint	
2/3	C_s	H—Cl—H $C_{2v}(^1B_2/^1B_2)$	r(H—H) = 10.58 r(H—Cl) = 7.10	H + ClH r(H—Cl) = 7.517	Angle H—Cl—H = 90°
2/3	C_s	H—Cl—H $C_{\infty v}(^1\Sigma^+/^1\Pi)$	r(H—H) = 20.08 r(H—Cl) = 7.512	H + ClH r(H—Cl) = 7.520	Angle H—Cl—H = 90°
2/3	$C_{\infty v}$	HCl + H $C_{\infty v}(^1\Sigma^+/^1\Pi)$	r(H—Cl) = 7.517	H—Cl—H $D_{\infty h}(^1\Sigma^+/^1\Pi)$	r(H—H) = 14.772 r(H—Cl) = 7.386
2/3	C_{2v}	r(H—H) → 0 $C_{2v}(^1A_1/^1B_2)$	r(H—Cl) = 1.524	H—Cl—H $D_{\infty v}(^1\Sigma^+/^1\Pi)$	r(H—H) = 14.772 r(H—Cl) = 7.386
2/3	C_s	H—Cl—H $C_{2v}(^1A_1/^1B_2)$	r(H—H) = 1.859 r(H—Cl) = 1.292	H—H—Cl $C_{\infty v}(^1\Sigma^+/^1\Sigma_+)$	r(H—H) = 14.672 r(H—Cl) = 4.142
3/4	C_s	H—Cl—H $C_{2v}(^1A_1/^1B_2)$	r(H—H) = 11.628 r(H—Cl) = 7.848	H—CL—H $C_{\infty v}(^1\Sigma^+/^1\Pi)$	r(H—H) = 12.566 r(H—Cl) = 5.630
3/4	C_{2v}	H—Cl—H $C_{2v}(^1A_1/^1B_2)$	Closed loop		
3/4	C_s	H—Cl—H $C_{2v}(^1A_1/^1B_2)$	r(H—H) = 9.733 r(H—Cl) = 6.789	Cl + H_2	r(H—H) = 14.672
3/4	C_s-b	H—Cl—H $C_{2v}(^1A_1/^1B_2)$	r(H—H) = 9.733 r(H—Cl) = 6.789	H—Cl—H $C_{2v}(^1A_1/^1B_2)$	r(H—H) = 11.423 r(H—Cl) = 7.844

that the C_s *linea* result solely from neglect of terms in the Hamiltonian. The intersections occur for very good physical reasons and are evidently related to the crossing of diatomic curves in the asymptotic region. Note that such crossings do not of themselves imply the existence of conical intersections at finite distances and they are not necessarily connected with them by a *linea*; for that, it is necessary that the direction of the *linea*, as determined by the Hessian eigenvectors, lead from the point at infinity to finite configurations. This is not the case in a molecule such as H_3^+, even though the first two states cross in the same manner as the second and third states of H_2Cl^+. The reason is simply that, at large distances, the interaction is such that the Hessian eigenvector with the lowest eigenvalue is tangential to a large circle drawn around the H_2 molecule. In H_2Cl^+, there is a dipole moment in the HCl molecule and charge transfer in HCl^+. It is then clear that for the configuration H^+ + HCl, the proton can approach the HCl molecule perpendicular to the bond axis in such a way that there is no net ionic interaction (at large distances the covalent interaction is negligible); the approach of an H atom to HCl^+ entails very little interaction at large distances, so that the difference in energy between the two states corresponding to these valence-bond structures can be kept equal to the value at infinity. But the latter is zero if there is a curve crossing! This is precisely the explanation for the behaviour of *linea* 3/4 in the left part of Fig. 7. Thus, the conical intersections observed here are the result of the physical aspects of the model and not of the simplifications that have gone into it, whereby the latter undoubtedly also play a role in determining the exact topology of the *lineae*.

In summary, by using a model Hamiltonian, we have been able to study some of the accidental conical intersections in the H_2Cl^+ molecule in fair detail and have shown their connection with symmetry-allowed intersections and with the behaviour of diatomic interaction potentials. Such model calculations ought to be an aid in finding the location of these intersections with

Can. J. Chem. Downloaded from www.nrcresearchpress.com by 195.246.54.202 on 09/08/12
For personal use only.

more precise methods. In particular, searching for degeneracy in the Hessian matrix eigenvalues along lines of symmetry-allowed intersections provides a powerful way of uncovering the whereabouts of accidental intersections if they exist at all in the molecule under investigation. The methods here could also be extended to molecules of more than three atoms, where the existence of accidental degeneracies is even more probable.

Acknowledgement

We should like to thank the Stabsabteilung Internationale Beziehungen for supporting this project. This work was also partially supported by the grant agency of the Czech Republic, Project No. 203/93/1129.

1. H.C. Longuet-Higgins. Proc. R. Soc. London Ser. A: **344**, 147 (1975).
2. S.S. Xantheas, S.T. Elbert, and K. Ruedenberg. J. Chem. Phys. **93**, 7519 (1990).
3. S.S. Xantheas, G.J. Atchity, S.T. Elbert, and K. Ruedenberg. J. Chem. Phys. **94**, 8054 (1991).
4. G.J. Atchity, S.S. Xantheas, and K. Ruedenberg. J. Chem. Phys. **95**, 1862 (1991).
5. M. Riad Manaa and D.R. Yarkony. J. Chem. Phys. **93**, 4473 (1990).
6. C.A. Mead. J. Chem. Phys. **70**, 2276 (1979).
7. T. Pacher, C.A. Mead, L.S. Cederbaum, and H. Köppel. J. Chem. Phys. **91**, 7057 (1989).
8. E.R. Davidson, W.T. Borden, and J. Smith. J. Am. Chem. Soc. **100**, 3299 (1978).
9. V. Bonačić-Koutecký, J. Koutecký, and J. Michl. Angew. Chem. Int. Ed. Engl. **26**, 170 (1987).
10. F. Bernardi, S. De, M. Olivucci, and M.A. Robb. J. Am. Chem. Soc. **112**, 1737 (1990).
11. J.E. Avron, A. Raveh, and B. Zur. Rev. Mod. Phys. **60**, 873 (1988).
12. M.V. Berry and M. Wilkinson. Proc. R. Soc. London Ser. A: **392**, 15 (1984).
13. F. Bernardi, M. Olivucci, and M.A. Robb. Acc. Chem. Res. **23**, 405 (1990).
14. B. Goss Levi. Phys. Today, **46**, 17 (1993).
15. Y.S.M. Wu and A. Kuppermann. Chem. Phys. Lett. **201**, 178 (1993).
16. R.L. Whetten, G.S. Ezra, and E.R. Grant. Annu. Rev. Phys. Chem. **36**, 277 (1985).
17. J.C. Lorquet, D. Dehareng, C. Sannen, and G. Raşeev. J. Chim. Phys. **77**, 719 (1980).
18. M. Desouter-Lecomte, B. Leyh-Nihant, M.T. Praet, and J.C. Lorquet. J. Chem. Phys. **86**, 7025 (1987).
19. C.A. Mead. *In* Mathematical frontiers in computational chemical physics. *Edited by* D.G. Truhlar. Springer, New York. 1987. Chap. 1, pp. 1–17.
20. U. Manthe and H. Köppel. J. Chem. Phys. **93**, 1658 (1990).
21. U. Manthe and H. Köppel. J. Chem. Phys. **93**, 345 (1990).
22. C.A. Mead and D.G. Truhlar. J. Chem. Phys. **70**, 2284 (1979).
23. M.V. Berry. Proc. R. Soc. London Ser. A: **392**, 45 (1984).
24. M.V. Berry. Phys. Today, **43**, 34 (1990).
25. J.W. Zwanziger, M. Koenig, and A. Pines. Annu. Rev. Phys. Chem. **41**, 601 (1990).
26. A.J. Stone. Proc. R. Soc. London Ser. A: **351**, 141 (1976).
27. R. Jackiw. Comments At. Mol. Phys. **21**, 71 (1988).
28. S.P. Keating and C.A. Mead. J. Chem. Phys. **82**, 5102 (1985).
29. A.J.C. Varandas, J. Tennyson, and J.N. Murrell. Chem. Phys. Lett. **61**, 431 (1979).
30. M. Riad Manaa and D.R. Yarkony. J. Chem. Phys. **97**, 715 (1992).
31. D.R. Yarkony. J. Phys. Chem. **97**, 4407 (1993).
32. M. Riad Manaa and D.R. Yarkony. J. Phys. Chem. **97**, 4989 (1993).
33. P.J. Kuntz, A.C. Roach, and D.M. Hirst. J. Phys. Chem. **95**, 8364 (1991).
34. Th. Glenewinkel-Meyer, Ch. Ottinger, P. Rosmus, and H.J. Werner. Chem. Phys. **152**, 409 (1991).
35. P.J. Kuntz and W.N. Whitton. J. Chem. Phys. **95**, 5149 (1991).

Can. J. Chem. Downloaded from www.nrcresearchpress.com by 195.246.54.202 on 09/08/12
For personal use only.

Femtosecond real-time probing of reactions. XIV. Rydberg states of methyl iodide

HUA GUO[1] AND AHMED H. ZEWAIL

Arthur Amos Noyes Laboratory of Chemical Physics,[2] California Institute of Technology, Pasadena, CA 91125, U.S.A.

Received October 7, 1993

This paper is dedicated to Professor John C. Polanyi on the occasion of his 65th birthday

HUA GUO and AHMED H. ZEWAIL. Can. J. Chem. **72**, 947 (1994).

The elementary reaction dynamics of methyl iodide in two Rydberg states leading to an iodine and a methyl radical occur on the femtosecond time scale (M.H. Janssen, M. Dantus, H. Guo, and A.H. Zewail. Chem. Phys. Lett. **214**, 281 (1993)). In this article, we consider the dynamics of this elementary process which involves both the Rydberg and valence states. Direct comparisons are made between theory and experiment with special focus on the following observations: large isotope effects, mode dependence of the predissociation rates, and coherence effects. The quantal molecular dynamics in two-dimensions show that the initial wave packet motion occurs along a vibrational mode involving the light atoms accompanied by transitions from the Rydberg state to the repulsive state; subsequent dynamics on the dissociative state lead to the C—I bond cleavage. The theoretical calculations also give the decay behavior of the Rydberg states with lifetimes in agreement with those observed in the femtosecond experiments. Moreover, the large isotope effect in observed predissociation rates of CH_3I and CD_3I has been successfully reproduced by the same model. The two-dimensional dynamics underscore the shortcomings of a one-dimensional picture in which the C—I serves as the sole reaction coordinate. The model presented here offers a viable mechanism for the dynamics of these Rydberg states.

HUA GUO et AHMED H. ZEWAIL. Can. J. Chem. **72**, 947 (1994).

La dynamique de la réaction élémentaire de l'iodure de méthyle dans les deux états de Rydberg conduit à des radicaux iode et méthyle dans un temps de l'ordre de la femtoseconde (M.H. Janssen, M. Dantus, H. Guo et A.H. Zewail. Chem. Phys. Lett. **214**, 281 (1993)). Nous considérons dans cet article la dynamique de ce processus élémentaire qui implique à la fois les états de Rydberg et la valence. On a comparé directement la théorie et l'expérimentation en mettant l'accent spécialement sur les observations suivantes: un large effet isotopique, l'influence du mode sur la vitesse de prédissociation et les effets de cohérence. La dynamique moléculaire quantique en deux dimensions montre que le mouvement du paquet d'ondes initial se produit le long d'un mode vibrationnel impliquant les atomes légers accompagné des transitions à partir des états de Rydberg jusqu'à l'état de répulsion; les dynamiques subséquentes relatives à l'état de dissociation conduisent au clivage de la liaison C—I. Les calculs théoriques donnent également la dégradation des états de Rydberg avec des temps de vie correspondant à ceux observés dans les expériences de l'ordre de la femtoseconde. De plus, le même modèle a permis de reproduire avec succès, le large effet isotopique dans les vitesses de prédissociation observées du CH_3I et du CD_3I. La dynamique bi-dimensionnelle met en évidence les défauts d'une image monodimensionnelle dans laquelle la liaison C—I représente la seule coordonnée de la réaction. Les modèles présentés offrent un mécanisme viable pour la dynamique de ces états de Rydberg.

[Traduit par la rédaction]

1. Introduction

The elementary processes of dissociation in methyl iodide (CH_3I) and its deuterated isotope (CD_3I) have been the subject of intensive investigations, both experimentally and theoretically. Most studies, guided by the theoretical analysis of Mulliken and Teller (1), were concerned (2–32) with the first absorption band which is structureless from 350 to 190 nm with a peak at 260 nm (2). This so-called A band arises from an electronic transition from a non-bonding $5p\pi$ orbital to a C—I antibonding σ orbital ($n \rightarrow \sigma^*$). Due to the strong spin–orbit coupling of iodine, five electronic states are formed in this manifold. They are, according to Mulliken (1), $^1Q_1(\Pi)$, $^3Q_2(\Delta)$, $^3Q_1(^3\Pi)$, $^3Q_{0+}(^3\Sigma^+)$, and $^3Q_{0-}(^3\Sigma^-)$. Since all the five states are repulsive in the C—I coordinate, the absorption of photon results in prompt fragmentation of methyl iodide. Both real-time measurements (3) and photofragment anisotropy analyses (4) have shown that the dissociation time in the A band is of the order of 100 fs.

The dissociation products from the *A* state excitation include both the ground and excited spin–orbit states of the iodine atom and methyl radical in its ground electronic state (5–8). the ro-vibrational state distributions of the methyl radical have been determined using various experimental techniques. It has been shown that the majority of dissociation energy is channeled into the translational recoil of the fragments and a relatively small portion of the excess energy is disposed into the umbrella bending (ν_5) of the methyl fragment (9–16) and its rotation about the axis perpendicular to the C_3 axis (14, 17, 18). Resonance Raman studies of the dissociation process have demonstrated the involvement of various vibrational modes in the process of fragmentation (19–23).

The dissociation from the A band is reasonably well understood theoretically. *Ab initio* potential energy surfaces have been calculated for the A band states (24, 25). It has been suggested (26) that the dissociation dynamics of CH_3I can be modeled by a collinear triatomic model where the umbrella bend of the CH_3 moiety can be approximated by a stretch between C and H_3. This approximation seems to be adequate for simulating most experimentally observed data. Both quantal (26–29) and classical (30–32) dynamical studies based on this model have been reported and the agreement between the two is generally very promising. Very recently, one of us (33) has reported a three-dimensional quantal study of the dissociation of methyl iodide in the A band, using the *ab initio* potential energy surfaces calculated by Morokuma and co-workers (25). Both the rotational and vibrational distributions of the methyl fragments as well as the I^* yield are in good agreement with latest experimental data (14–18).

[1]On leave from Department of Chemistry, University of Toledo, Toledo, OH 43606, U.S.A.

[2]Contribution No. 8869.

Can. J. Chem. Downloaded from www.nrcresearchpress.com by ESC ESCOLA DE ENGENHARIA on 09/08/12
For personal use only.

Can. J. Chem. Downloaded from www.nrcresearchpress.com by EESC ESCOLA DE ENGENHARIA on 09/08/12
For personal use only.

In this work, we focus on the dissociation dynamics of several Rydberg states which have higher absorption bands. Despite the vast literature on the A band dissociation, there is little known about the Rydberg states. The Rydberg character of the series can be largely attributed to transitions from a $5p$ orbital to a higher atomic Rydberg orbital, such as $6s$ or $6p$, of the iodine atom (1). The Rydberg series starts at 200 and 184 nm with two distinct bands, known as the B and C bands (34, 35). Both absorption bands are the result of an excitation of a non-bonding $5p\pi$ electron to the first Rydberg orbital ($6s$) of the iodine atom. The strong spin–orbit coupling at the iodine atom causes the splitting of the ion core into $^2E_{1/2}$ and $^2E_{3/2}$ in C_{3v} or $^2\Pi_{1/2}$ or $^2\Pi_{3/2}$ in $C_{\infty v}$, and interactions between the core and Rydberg electron yield five electronic states in two groups separated by approximately 5000 cm^{-1} (1). The B band is derived from the two lower states with a $^2E_{3/2}$ ion core, and the other three states (two are near degenerate) with a $^2E_{1/2}$ ion core are responsible for the C band. Traditionally (36), these states are named as the [1], [2], [3], and [4] states of the $6s$ transition. Similar arguments apply to higher Rydberg absorption bands which are originated from excitations of a non-bonding $5p\pi$ electron to higher Rydberg orbitals of iodine, such as $6p$ and $7s$, etc. In general, each Rydberg manifold splits into two bands characterized by the $^2E_{3/2}$ and $^2E_{1/2}$ ion cores with two distinguishable states for each band. Similar rules apply to the CH_3I^+ ion which can be loosely considered as a Rydberg state with the Rydberg electron infinitely far from the ion core.

The absorption spectra of these Rydberg states have been recorded by several groups (36–44). Felps et al. (36) have measured the one-photon absorption spectra of the B and C bands and extracted frequencies of various modes from the spectra. Resonance enhanced multiphoton ionization (REMPI) and other methods have also been employed to obtain the absorption spectra of methyl iodide (37–43). In particular, Vaida et al. (39–41) have examined the absorption of CH_3I and its clusters with a special interest on the effect of the cluster induced potential shift on the predissociation (42).

The higher $5p\pi \rightarrow 6p$ transitions near 170 and 150 nm have been investigated by Gedanken et al. (44) using (2 + 1) REMPI and by Tsukiyama et al. (45) using fluorescence spectroscopy. Similar to the $5p\pi \rightarrow 6s$ transitions, two bands with a separation of 5000 cm^{-1} were observed. The assignment of the vibronic transitions in this region was made by Gedanken et al. (44). In a recent study by Dobber et al. (46), who used both picosecond and nanosecond REMPI spectroscopy coupled with photoelectron spectroscopy (PES), a comprehensive analysis has led to the reassignment of the $6p$ and $7s$ Rydberg manifolds. These authors (46) were able to identify the feature near 311 nm (155.5 nm in two photons) as the band origin of the $5p\pi \rightarrow 7s$ transition, instead of the ν_6 overtone of the $5p\pi \rightarrow 6p$ transition assigned previously (44).

From the above studies, it has been realized that the transitions from the ground state to various Rydberg states are rather vertical. The vibrational progressions are short and the band origins usually represent the strongest transitions. This is because the Rydberg excitation (including the ionization) from a non-bonding orbital ($5p\pi$) does not significantly alter the molecular geometry of the molecule (or ion). As a result, the vibrational frequencies as well as the equilibrium geometry of various Rydberg states are very similar to those of the ground electronic state (37, 38, 44, 46, 47). All the Rydberg features of methyl iodide are significantly broadened. The broadening is associated with the predissociation of these Rydberg states since the line width is less than the vibrational spacing.

The rates of predissociation have been deduced for the first two Rydberg states (the B and C bands) using various techniques. An early photofragment anisotropy analysis at 193 nm (48) estimated that the lifetime of CH_3I is approximately 150 fs. Ziegler and co-workers (49) have deduced the lifetimes of the B (50–52) and C (53) Rydberg states by monitoring the depolarization ratio of Raman scattering, in which the average rotation of the molecule is utilized as an effective clock. The lifetimes of the B and/or C Rydberg states obtained by these authors range from 10^2 to 10^3 fs and the lifetime data exhibit strong isotopic and mode selectivities (51). For instance, it was found (51) that the lifetime of CD_3I is a factor of two longer than that of CH_3I. Recently, information on lifetimes was also obtained from the direct measurement of the absorption profile, as reported by Syage (43).

Large discrepancies were found among reported lifetimes in the *B* and *C* states. For example, Sapers and Donaldson (38) reported a much faster predissociation rate for the first ν_3 (C—I stretch) overtone in the B band than the band origin. This conclusion was advanced to explain the observation that the ν_3 feature is present in the dimer but disappears in the monomer. Wang and Ziegler (51), from the Raman analysis of the same system, concluded that the decay rate of the first ν_3 overtone is much slower than both the band origin and the second ν_3 overtone. A simple Franck–Condon model was proposed by these authors to rationalize the experimental findings (51). Both results (38, 51), although in opposite directions, pointed to strong mode specificity in the predissociation of methyl iodide Rydberg states. The latest study on the same system (43), however, reported very weak mode-specific predissociation rates for the band origin and the first ν_3 overtone.

Theoretically, the predissociation of Rydberg states of methyl iodide have been studied by several groups. Donaldson et al. (54) reported classical trajectory studies on the predissociation in the B band. These authors utilized empirical potential energy surfaces to investigate the dissociation dynamics and the influence of the cluster on the curve crossing process. Wang and Ziegler (51) proposed a simple Franck–Condon model to interpret their findings of slow predissociation rate of the ν_3 overtone (see above). These studies have not addressed the femtosecond quantum dynamics and, in particular, the large isotope and coherence effects in the predissociation.

Real-time studies of the Rydberg state dynamics of methyl iodide in a molecular beam have been reported using femtosecond transition-state spectroscopy (FTS) (55). In these studies (56, 57), a molecular beam of methyl iodide was excited by a femtosecond (fs) pulse near the $6p$–$7s$ manifold (by two photons) and subsequently ionized by another fs pulse. The resulting parent (CH_3I^+) or fragment ions (CH_3^+ and I^+) were detected in a time-of-flight mass spectrometer. The ionization pulse was delayed from the excitation pulse so that the dynamics of the Rydberg state could be probed with femtosecond resolution. The transients show that the decay of the Rydberg states is on the femtosecond time scale. For example, the $6p[4]$ band origin was found to decay with a lifetime of 178 fs (56, 57). The experiment also shows that there is a strong isotope effect; the lifetime of CD_3I is at least two times longer than that of the CH_3I. Mode specificity in predissociation dynamics was found to be weak in the energy range studied, as the first ν_3 overtone decays only slightly faster than the band origin (57).

Can. J. Chem. Downloaded from www.nrcresearchpress.com by EESC ESCOLA DE ENGENHARIA on 09/08/12
For personal use only.

To examine the predissociation dynamics on the femtosecond time scale, we have initiated quantum mechanical studies of these Rydberg states in one and two dimensions (57, 58). Classical mechanics and one-dimensional models are not adequate for reasons discussed below. Our preliminary results in two dimensions show that the large isotope effect in the predissociation of the Rydberg states can be attributed to the involvement of the C—H_3 stretch in the dissociation pathway. The experimentally measured transients for the band origin of the $5p\pi \rightarrow 6p[4]$ transitions were nicely reproduced for both CH_3I and its deuterated isotope CD_3I.

In this contribution, we provide a full account of this two-dimensional quantum mechanical model, focusing on the acute isotope effect in dynamics, mode selectivity, and coherence effects. We discuss the nature of the Rydberg-valence state coupling and the non-adiabatic transition dynamics along the reaction coordinate. This paper is organized as follows. In Section II, a brief description of the experimental results is given. In Section III, we discuss the rationale for the newly developed empirical potential energy surfaces for both the Rydberg and dissociative states, and the time-dependent quantum mechanical method used in our calculations. In Section IV, the results from the calculation are presented. The implication of the results and general features of the Rydberg dynamics are discussed in the Section IV.

II. Experimental

As mentioned earlier and detailed elsewhere (56, 57), the Rydberg levels of CH_3I and CD_3I were selectively excited via a femtosecond coherent two-photon absorption. The dynamics of the Rydberg states were then probed by a temporally delayed pulse which ionizes the parent molecule to its ions. This femtosecond pump–probe scheme (with mass resolution) is different from previous REMPI studies using nanosecond or picosecond lasers (44–46). It is well known that the A band states, which serve as the intermediate states for the two-photon excitation ladder, are strongly dissociative with a lifetime of ~100 fs (3–5). Therefore, unless the pulse duration is comparable with or shorter than the dissociation time of the A states, the two-photon transition will be overwhelmed by the one-photon dissociation in lower A band. This phenomenon is clearly illustrated in the nanosecond REMPI studies of methyl iodide (44, 46) where the spectra are contaminated by sharp transitions of the iodine atoms produced from the A band fragmentation. Such a behavior is avoided in the REMPI using femtosecond pulses.

Femtosecond transients were taken at several pump wavelengths (57). Here, we concentrate on three of them, i.e., transitions to the band origin and first ν_3 overtone of the $6p[4]^2E_{1/2}$ Rydberg state and to the band origin of the $7s[1]^2E_{3/2}$ Rydberg state. The three transitions have two-photon excitation energies of 63 493 cm^{-1} (λ_{pump} = 315 nm), 63 958 cm^{-1} (λ_{pump} = 312.5 nm) and 64 230 cm^{-1} (λ_{pump} = 311.5 nm), respectively. The ionization laser has a wavelength of 618 nm. Figure 1 presents the absorption spectrum of methyl iodide (CD_3I) in this spectral region with the assignments by Dobber et al. (46). Two types of pump pulses with different bandwidths were used in the experiment (57). Their excitation bandwidths are 1.5 and 3.5 nm at ~320 nm, respectively. With the broad bandwidth pump pulse, it is possible to excite two vibronic bands coherently, which may lead to interesting dynamics (57), as discussed below.

The transients measured using narrow bandwidth pump pulses can be fitted to single exponential functions, from which the lifetime of the Rydberg state can be obtained. Table 1 lists the lifetimes of individual Rydberg states for both CH_3I and CD_3I. It is clear that no mode selectivity in the lifetime of the $6p[4]^2E_{1/2}$ state is weak in the energy range studied. The lifetime of the band origin (178 fs) is only slightly longer than that of the first ν_3 overtone (141 fs) of $6p[4]^2E_{1/2}$ Rydberg state. The FTS measurements have also been made for the deuterated methyl iodide. It was found that the decay time of CD_3I is generally a factor of two or more slower than that of CH_3I, as shown in Fig. 2*a*.

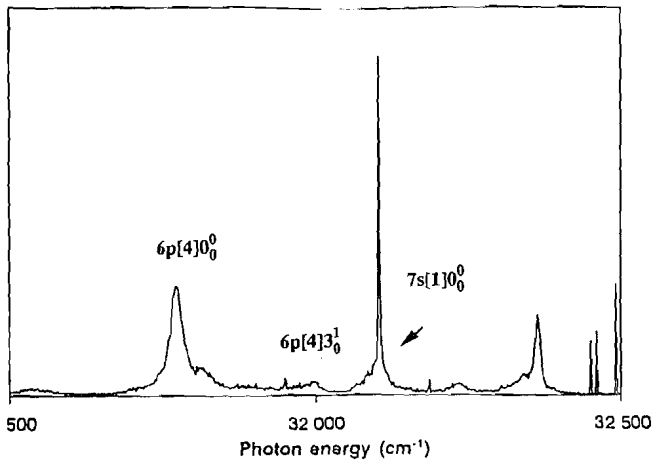

FIG. 1. Experimental Rydberg state absorption spectrum of the CD_3I near 64 000 cm^{-1} (adopted from Dobber et al. (46)). Note that the sharp feature near 32 100 cm^{-1} is due to an atomic iodine transition and is irrelevant to the molecular Rydberg absorption.

TABLE 1. Experimental lifetimes of Rydberg levels

λ^a (nm)	Level[b]	Lifetimes (fs) CH_3I	Lifetimes (fs) CD_3I
315.0/b	$6p[4]0_0^0$	178	333
314.7/n	$6p[4]0_0^0$	183	—
312.7/n	$6p[4]3_0^1$	141	—
312.0/b	$\{6p[4]3_0^1 + 7s[1]0_0^0\}$	141	414
311.3/n	$7s[1]0_0^0$	115	—

[a]Letters n and b denote narrow and broad bandwidths of the pump pulses, respectively.

[b]The vibrational modes of CH_3I are defined as follows (34): the symmetric C—H_3 stretch (ν_1), the umbrella C—H_3 bend (ν_2), the C—I stretch (ν_3), the antisymmetric C—H_3 stretch (ν_4), the CH_3 deformation (ν_5), and the I—C—H_3 bend (ν_6).

The broadening of the pump pulse bandwidth does not significantly alter the lifetime of the band origin of the $6p[4]^2E_{1/2}$ Rydberg state (57). When the broad bandwidth pulse was tuned to 311 nm, however, the experimental transient could not be fitted to a single exponential (see Fig. 2*b*). It seems that the transient contains a double peak structure or a damped oscillatory structure with a frequency of 7×10^{12} Hz (Δt = 140 fs) at the initial stage of the dynamics. A similar effect has been found for the same Rydberg feature of the deuterated methyl iodide. It should be noted that the broad bandwidth pulse covers coherently both the first ν_3 overtone of the $6p[4]^2E_{1/2}$ state and the band origin of the $7s[1]^2E_{3/2}$ state, which have an energy separation of 240 cm^{-1} (see Fig. 1). This point will be discussed in more detail later when we discuss the coherence effect.

III. Theoretical model

A one-dimensional model was recently proposed to simulate the observed femtosecond dynamics of methyl iodide Rydberg predissociation (58). In this model, only the C—I coordinate was considered and the predissociation dynamics were modeled by non-adiabatic transitions from the Rydberg state to a dissociative state using a quantum mechanical method. The results indeed showed a slightly slower predissociation rate for the deuterated methyl iodide than that of CH_3I, but the cal-

Can. J. Chem. Downloaded from www.nrcresearchpress.com by EESC ESCOLA DE ENGENHARIA on 09/08/12
For personal use only.

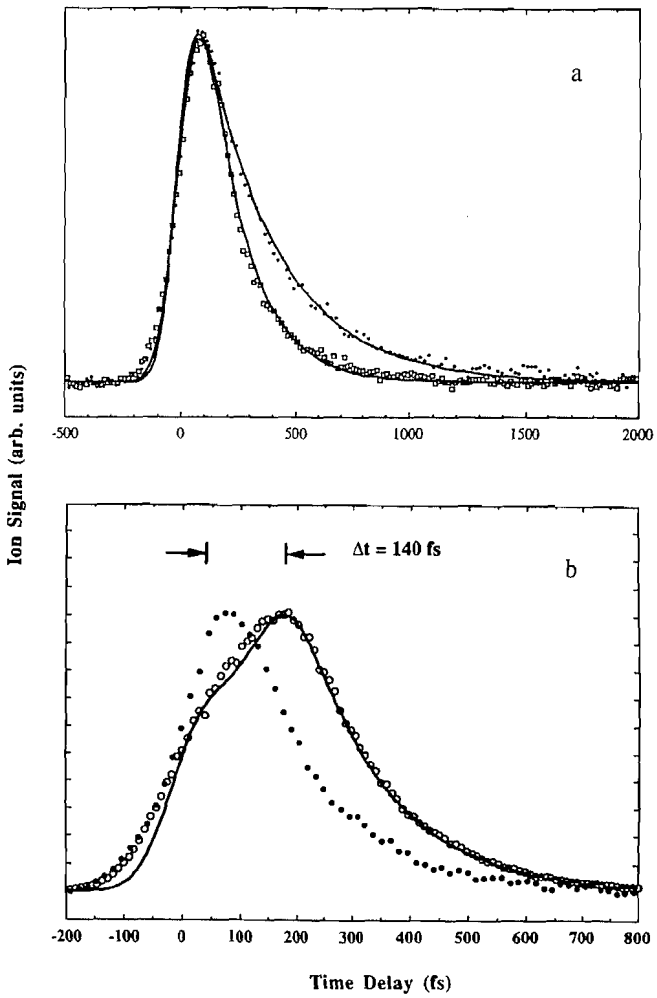

FIG. 2. Femtosecond transients obtained (*a*) for 315 nm two photon excitation for CH_3I (open square) and CD_3I (filled circles) (adopted from Dantus et al. (56)), and (*b*) for 312 nm two-photon excitation of CH_3I (adopted from Janssen et al. (57)). A transient has been superimposed (filled circles) in (*b*) to highlight the large difference in shape occurring when the $6p[4]\ 3_0^1$ and $7s[1]\ 0_0^0$ modes are overlapped by the excitation-laser bandwidth (see text).

culated isotope effect was significantly smaller than the ratio found experimentally. The implication is that the C—I mode may not be the major contributor of the initial predissociation reaction pathway. This can be readily understood in terms of the ratio of the reduced masses of the deuterated and hydrogenated methyl iodide species, which is 1.18. The significant isotope effect indicates the involvement of modes other than the dissociating C—I coordinate. One possibility is that the molecule dissociates through a barrier involving light atom (H or D) tunneling. An overall slowdown of the deuterated predissociation dynamics is hence expected because the tunneling probability decreases exponentially with mass.

We in this work propose a new predissociation mechanism for the CH_3I Rydberg states by including another nuclear mode. Our choice of the additional mode is the ν_1 vibration, i.e., the symmetries C—H_3 stretch (58). The reduced mass of the C—H_3 mode is 1.67 times smaller than that of C—D_3, which may result in a large isotope effect. It should be pointed out that the choice of the ν_1 mode is to some extent arbitrary because the dissociation may well involve one or many other modes that have large mass differences, such as the antisymmetric C—H_3 stretch (ν_4) or umbrella bend (ν_5) modes, etc. Our purpose here is to illustrate the importance of the multidimensional effect on the predissociation dynamics. There is some evidence indicating the involvement of the ν_1 mode in the predissociation. For example, resonance Raman measurements (50–53) on lower B and C Rydberg states concluded that the excitation in the C—H_3 symmetric stretch leads to much faster decay rates for both CH_3I and CD_3I. Photofragmentation experiments (48, 60) also found significant excitation of the fragment C—H vibration and even cleavage of a C—H bond during the dissociation for photon wavelengths shorter than 170 nm. In the next subsection we will develop empirical potential energy surfaces for both the Rydberg and dissociative states for the CH_3I system based on these arguments. The dynamical calculations on these potential energy surfaces will be detailed in the second subsection.

A. Potential energy surfaces

The existing *ab initio* calculations of methyl iodide potential energy surfaces (24, 25) are mainly concerned with the low-lying A manifold and the ground electronic state. Information on the Rydberg potential energy surfaces is mostly from spectroscopic data. It is well known from absorption studies that the potential energy surfaces of the Rydberg states are very similar to that of the ground state. The normal frequencies of the Rydberg states are found to be comparable with those on the ground state (36, 44, 46). The similarities between the ground and Rydberg states of methyl iodide indicate that the Rydberg transitions have little impact on the molecular parameters of the CH_3I ion core. Such a phenomenon is due to the fact that the Rydberg transition is from a non-bonding orbital ($5p\pi$) to an atomic orbital (6*s*, 6*p*, or 7*s* etc.).

Throughout this work, we will limit ourselves to a two-dimensional model which involves both the C—I (ν_3) and C—H_3 (ν_1) vibrational modes. Empirical potential energy surfaces are developed to possess certain important features which will result in an accurate reproduction of experimental findings. For instance, the intersection between the Rydberg state and the repulsive state (i.e. the seam) is arranged in such a way that the isotope effect in the predissociation can be correctly represented. We have manipulated the potentials so that the seam is perpendicular to the C—H_3 coordinate in the Franck–Condon region, rather than to the C—I dissociation mode as assumed in the one-dimensional calculations (58). Thus, the dissociation is more likely to proceed along the C—H_3 coordinate at the beginning of the dissociation. Subsequent dissociation will then lead to the C—I bond cleavage. The resulting reaction pathway therefore involves both the C—I and C—H_3 modes and the dissociation should show a much larger isotope effect due to the significantly larger differences in both the reduced mass and zero point energy during the initial pr dissociation dynamics. The nature of similar reaction path been addressed recently in the work of Nikitin and co-wor (59).

For the sake of simplicity, the potential energy surfa the ground state, the Rydberg state and the repulsive s all written as sums of two one-dimensional potentials. aration of modes in the model potential energy surfa not affect the dynamics because the potentials are relative to each other. The ground electronic st energy surface consists of a Morse function in ordinate (R) and a quadratic potential for C— (*r*):

TABLE 2. Parameters of potential energy surfaces (atomic units[a])

Parameter	Value	Parameter	Value	Parameter	Value	Parameter	Value	Parameter	Value
D_1	0.08741	R_{01}	4.1688	r_{01}	2.0503	α_1	0.9150	ϵ_1	-0.2893
D_2	0.07153	R_{02}	4.2576	r_{02}	2.0503	α_2	0.8295	ϵ_2	0.0000
D_3	18.3673	R_{03}	0.0	r_{03}	2.5503	α_3	1.30	ϵ_3	-0.1044
						α_{23}	0.50		
D_{23}	0.028					$k_{01} = k_{02} = k_{03} = 0.8066$			

[a]1.0 Å = 1.8898 au (Bohr), 1.0 eV = 0.03675 au (Hartree).

$$[1] \qquad V_1 = D_1\{1 - \exp[-\alpha_1(R - R_{01})]\}^2 + \tfrac{1}{2}k_1(r - r_{01})^2 + \epsilon_1$$

Similar form of potential energy function is given for the Rydberg state:

$$[2] \qquad V_2 = D_2\{1 - \exp[-\alpha_2(R - R_{02})]\}^2 + \tfrac{1}{2}k_2(r - r_{02})^2 + \epsilon_2$$

The Morse potential of the Rydberg state is slightly different from that of the ground state, reflecting changes in molecular parameters. The C—H_3 potential, on other hand, is chosen to be identical to that of the ground state. The selection of the potential parameters is consistent with the absorption spectrum of Rydberg states of methyl iodide (44, 46), as shown below.

There is little known about the nature of the dissociative state which interacts with the Rydberg state. This dissociative state is "optically dark" and information from *ab initio* calculations is sketchy. There are some suggestions that it may be one of the five A band states (57). For the zeroth order, we assume that it is repulsive in the C—I coordinate and bound in the C—H_3 coordinate. An exponential function is used for the C—I mode and a harmonic oscillator potential is adopted for the C—H_3 mode:

$$[3] \qquad V_3 = D_3 \exp[-\alpha_3(R - R_{03})] + \tfrac{1}{2}k_3(r - r_{03})^2 + \epsilon_3$$

The C—H_3 potential in eq. [3] has the same force constant as the ground state, but is shifted from the ground state C—H_3 equilibrium geometry. Such a shift enables the dissociative state to form an intersection with the Rydberg state in the direction perpendicular to the C—H_3 coordinate. As discussed earlier, the location of the intersection is vital in simulating the experimentally observed isotope effect. As shown in the one-dimensional calculations (58), the alternative would be an intersection perpendicular to the C—I coordinate, which would only produce a limited isotope effect. It should be pointed out that this potential energy surface is not expected to give the correct asymptotic properties of the CH_3 fragment. However, this deficiency would have little effect on the Rydberg dynamics which occurs at relatively small C—I distances.

The parameters of all the three potential energy surfaces are given in Table 2. The potential energy surfaces of both the bound Rydberg and dissociative states are plotted in Fig. 3. The intersection between the two potential energy surfaces is nearly perpendicular to the C—H_3 coordinate, as shown in the figure. Three dimensional view of the lower adiabatic potential energy surface is also given in Fig. 3*b*.

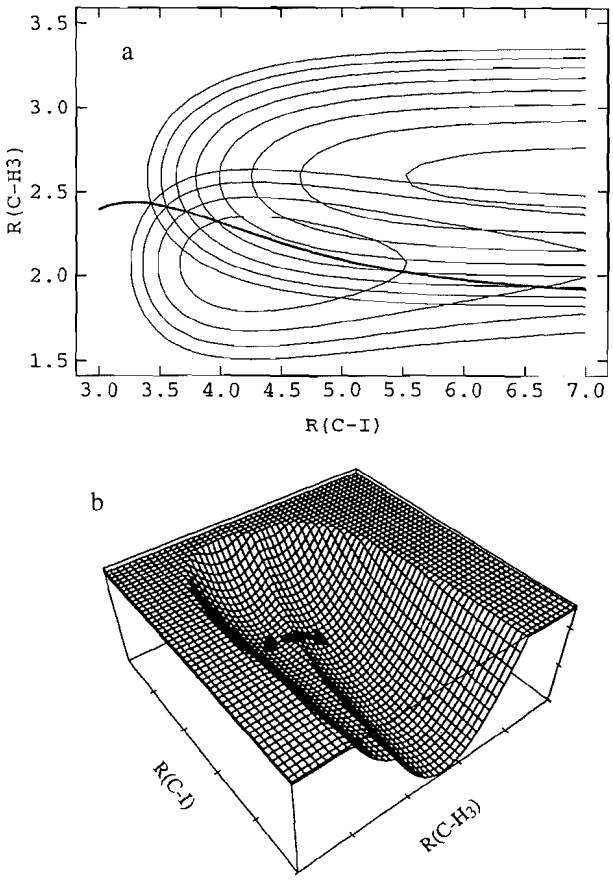

FIG. 3. (*a*) Diabatic potential energy surfaces of the $6p[4]^2E_{1/2}$ Rydberg state and the dissociative state. The intersection (seam) of the two potential energy surfaces is also given with a heavy black line. The energy interval of the contours is 0.03 au. (*b*) Three dimensional view of the lower adiabatic potential energy surface. The C—I and C—H_3 coordinates are from (3.0, 1.0) to (6.0, 4.0) au. The Franck–Condon region is showed by the black spot and the minimal energy path is indicated by the arrow.

B. Time-dependent quantum mechanical theory

Theoretical studies of the femtosecond dynamics have been reported by many groups (see, e.g., refs. 61–71). In this work, we employ a time-dependent quantum mechanical description of such a process. The nuclear Hamiltonian of the methyl iodide Rydberg system including the light–molecular interaction is given in a diabatic representation (58):

$$[4] \qquad \mathbf{H} = \begin{bmatrix} \mathbf{h}_{11} & \mathbf{h}_{12} & \mathbf{0} & \mathbf{0} \\ \mathbf{h}_{12}^* & \mathbf{h}_{22} & \mathbf{h}_{23} & \mathbf{h}_{24} \\ \mathbf{0} & \mathbf{h}_{23}^* & \mathbf{h}_{33} & \mathbf{0} \\ \mathbf{0} & \mathbf{h}_{24}^* & \mathbf{0} & \mathbf{h}_{44} \end{bmatrix}$$

Can. J. Chem. Downloaded from www.nrcresearchpress.com by EESC ESCOLA DE ENGENHARIA on 09/08/12
For personal use only.

Can. J. Chem. Downloaded from www.nrcresearchpress.com by EESC ESCOLA DE ENGENHARIA on 09/08/12
For personal use only.

where the asterisk denotes complex conjugate. There are at least four states involved in the pump-probe experiment (57). An additional state is needed when the electronic coherence effect is studied. The ground electronic state (state 1) is coupled radiatively ($\mathbf{h}_{12}$) with the Rydberg state (state 2). The non-adiabatic or radiationless interaction ($\mathbf{h}_{23}$) between the Rydberg state and the dissociative state (state 3) is responsible for the predissociation. The dynamics on the Rydberg state are probed by a delayed pulse ($\mathbf{h}_{24}$) which promotes the molecule to the ion state (state 4). The diagonal terms in the Hamiltonian matrix consist of the kinetic and potential energy operators:

$$[5] \qquad \mathbf{h}_{ii} = \frac{\mathbf{p}_R^2}{2\mu_R} + \frac{\mathbf{p}_r^2}{2\mu_r} + V_i(R, r)$$

where V_i are the diabatic potential energy surfaces defined in the last subsection; μ_R and μ_r are appropriate reduced masses for the two coordinates. The overall rotation of the parent molecule is not included in our model since the dissociation time of the Rydberg states is much shorter than the rotational period. Other degrees of freedom of methyl iodide are also assumed to be separable from the reaction coordinates and not considered here. The off-diagonal matrix terms representing the non-adiabatic coupling are given by the coupling potential:

$$[6] \qquad \mathbf{h}_{23} = V_{23} = D_{23} \exp[-\alpha_{23}R]$$

The potential parameters for the non-adiabatic coupling are given in Table 2.

Within the dipole and classical electromagnetic field approximations (63, 67, 72), the light-molecular interactions are given by

$$[7] \qquad \begin{aligned} \mathbf{h}_{12} &= A_{12}(t) \exp(i\omega_{12}t) \\ \mathbf{h}_{24} &= A_{24}(t-\tau) \exp(i\omega_{24}t) \end{aligned}$$

where ω_{12} and ω_{24} are the photon frequencies of the pump and probe pulses, respectively. τ denotes the time delay between the pump and probe pulses. The pre-exponential factor $A(t)$ consists of the appropriate transition dipole moment and the temporal shape of the pulse. The transition dipole moments are assumed to be constants of the nuclear coordinates (Condon approximation) because of the lack of information on their coordinate dependence. The laser pulses are assumed to have a Gaussian functional form (63):

$$[8] \qquad A(t-t_0) = A_0 \exp[-\beta(t-t_0)^2/2]$$

Where β determines the temporal width of the pulse and t_0 determines the time of the pulse.

The overall dynamics of the pump-probe process can be obtained by solving the time-dependent Schrödinger equation (atomic units are used hereafter) (58, 63, 67)]:

$$[9] \qquad i\frac{\partial}{\partial t}\begin{bmatrix}\varphi_1\\ \varphi_2\\ \varphi_3\\ \varphi_4\end{bmatrix} = \begin{bmatrix}\mathbf{h}_{11} & \mathbf{h}_{12} & \mathbf{0} & \mathbf{0}\\ \mathbf{h}_{12}^* & \mathbf{h}_{22} & \mathbf{h}_{23} & \mathbf{h}_{24}\\ \mathbf{0} & \mathbf{h}_{23}^* & \mathbf{h}_{33} & \mathbf{0}\\ \mathbf{0} & \mathbf{h}_{24}^* & \mathbf{0} & \mathbf{h}_{44}\end{bmatrix}\begin{bmatrix}\varphi_1\\ \varphi_2\\ \varphi_3\\ \varphi_4\end{bmatrix}$$

where φ_i are the nuclear wavefunctions on individual electronic states. Initially, only the ground state is populated and wavefunctions on all other states are assumed to be zero. The highly oscillatory phase factor in the radiative coupling (i.e., $\exp(i\omega t)$) can be absorbed into the wavefunction. The effect of this operation is to raise the ground state potential by the amount ω_{12} and lower the ion state potential by ω_{24} (63). Therefore, the radiative coupling can be effectively regarded as a time-dependent non-adiabatic coupling. Such a treatment not only avoids oscillations introduced by the field, which may substantially increase the number of temporal steps in numerical integration, but also simplifies the Schrödinger equation dramatically.

It is instructive to rewrite the Schrödinger equation in the integral form. For the Rydberg state, for example, its temporal evolution can be described by:

$$[10] \qquad \begin{aligned} \varphi_2(t) &= -i\int_{-\infty}^{t} dt' e^{[-i\mathbf{h}_{22}(t-t')]}[\mathbf{h}_{12}\varphi_1(t') \\ &\quad + \mathbf{h}_{23}\varphi_3(t') + \mathbf{h}_{24}\varphi_4(t')] \\ &= -i\int_{-\infty}^{t} dt' e^{[-i\mathbf{h}_{22}(t-t')]}[A_{12}(t')\varphi_1(t') \\ &\quad + V_{23}\varphi_3(t') + A_{24}(t'-\tau)\varphi_4(t')] \end{aligned}$$

The population of the Rydberg state as initial $t \rightarrow -\infty$ is zero. The first term in the integrand represents the transfer of population from the ground state to the Rydberg state while the pump pulse is switched on. Population is subsequently lost to the dissociative state via the non-adiabatic coupling V_{23}. When the probe pulse is switched on at time τ, some population is transferred to the ion state, which is represented by the third term. If the laser field is considered to be weak, a perturbative approach can be adopted (65, 69, 72). Under such circumstances, the ground state can be, to the first order, approximated by a stationary state and the population transferred back from the Rydberg state is negligible.

The experimentally measured ion transient signal is considered to be proportional to the asymptotic population of the ion state at different delay times. In our calculations, however, we have imposed an approximation that the ionization photon is on resonance with the energy gap between the Rydberg state and the ion state. Therefore, the ion state population at various delay times (the transient) is directly proportional to the temporal population on the Rydberg state except for a numerical factor representing the pulse shape (69). Photo-induced ionization processes are often considered as a Franck–Condon event. Since the electron ejected by the photon may carry different kinetic energies, even with the same ionization photon wavelength, its treatment requires special care (73, 74). Limited test calculations with all four states have been carried out and the transients obtained are almost identical to the temporal population of the Rydberg state. Another approximation in our calculations is the treatment of the pump pulse. We have assumed that the Rydberg state is prepared by a single photon whereas two coherent photons were used in the experiment to reach the Rydberg state. This simplification should not significantly affect the calculated results, other than the usual change in the pulse width and coherence width with multiphoton processes.

The numerical solution of the time-dependent Schrödinger equation was carried out on a two-dimensional grid. The temporal propagation of the coupled differential equations was accompanied by using a short iterative Lanczos (SIL) method (75). In the SIL method, a N-dimensional Krylov subspace

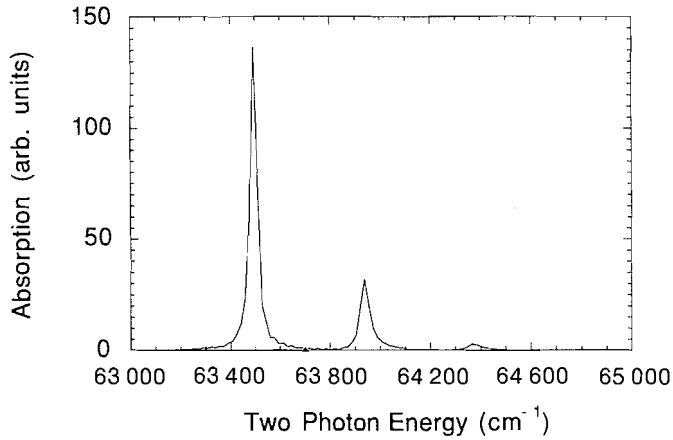

FIG. 4. Calculated absorption spectrum of the $6p[4]^2E_{1/2}$ Rydberg state of CH_3I using the model potential energy surfaces. The spectrum shows the strongest absorption is at the band origin and the ν_3 progression is weak.

spanned by $\mathbf{H}^N\Psi$ is constructed by the Lanczos recursion scheme. The propagator is then obtained from the eigenvalues and diagonalization matrix of effective Hamiltonian matrix in the subspace. It has been shown (75) to be efficient in dealing with both the time-dependent and time-independent Hamiltonians.

The evaluation of $\mathbf{H}\Psi$ was carried out in two steps. The action of the potential energy operator on the wavefunction can be readily obtained by multiplying the two at each grid point. The action of the kinetic energy operator was calculated in momentum space where the kinetic energy operator is diagonal. The wavefunction transformation between coordinate and momentum representations was carried out by using a fast Fourier transform (FFT) method (76). In order to avoid reflection on the edges of the grid, a damping scheme (77) was used at large R to eliminate the wave packet on the dissociative state. Since we are interested in the population decay on the bound Rydberg state, the damping at large C—I distances would not affect our simulation.

IV. Results and discussion

We used in the calculations a grid of 256 × 32 (R, r) points covering a rectangular region from (3.5, 1.0) to (7.5, 4.0) bohr. The temporal interval is 0.5 fs with an eight-dimensional Krylov space for the SIL propagator. The starting point of the propagation is −300 fs and the pump pulse is centered at 0 fs. The laser pulse was chosen to have an 80 fs temporal width (FWHM). The laser field strength was arbitrarily chosen to simulate a weak field scenario. Convergence tests have been conducted with respect to the sizes of both spatial and temporal grids.

A. Absorption, isotope effect, and mode selectivity

Figure 4 is the calculated absorption spectrum of the $6p[4]^2E_{1/2}$ Rydberg state of CH_3I. The spectrum was calculated from the Fourier transform of the autocorrelation function of the Rydberg state with a delta-function excitation pulse (78, 79). The energy resolution of the spectrum is approximately 17 cm^{-1} which corresponds to 2 ps of propagation. The calculated spectrum shows an intensive absorption near 63 500 cm^{-1} and two much weaker overtone excitations near 63 950 and 64 400 cm^{-1}, respectively, in good agreement with experiment (44, 46). Note that the equilibrium geometry

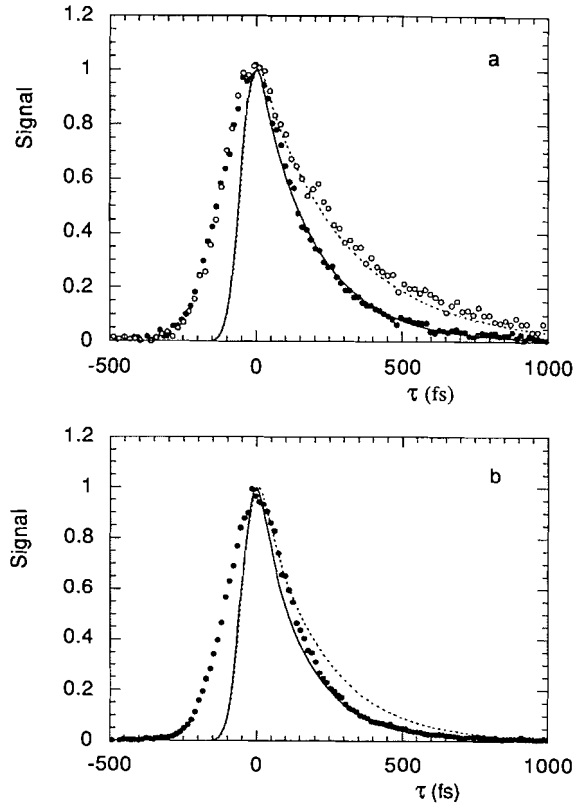

FIG. 5. Calculated femtosecond transient of the $6p[4]\ 0_0^0$ (*a*) and $6p[4]\ 3_0^1$ (*b*) Rydberg levels for both CH_3I (solid line) and CD_3I (dashed line). The experimental data (filled and open circles for CH_3I and CD_3I, respectively) are also given.

of the Rydberg state is shifted to a larger R relative to that of the ground state. The difference in the equilibrium geometry of the two states changes the Franck–Condon overlap and results in a weak progression in ν_3. No progression in the ν_1 mode is observed because the Rydberg state has the same C—H_3 potential as the ground state.

The transients of the first two vibrational levels of the $6p[4]^2E_{1/2}$ Rydberg state for both CH_3I and CD_3I are given in Fig. 5 together with corresponding experimental data. All the curves are normalized to unity and the zero time is arbitrarily chosen. The top panel is for the band origin of the $6p[4]^2E_{1/2}$ Rydberg state. The calculated decay curves not only fit the experimental transients, they also correctly reproduce the isotope effect observed in the experiment. The agreement between the two-dimensional model calculations and the experiments of CD_3I is particularly encouraging since our potential parameters were only adjusted to fit the CH_3I transient. Comparison with previous one-dimensional calculations (58) strongly supports the argument that the significant isotope effect is due to the involvement of tunneling of the light atoms during predissociation. The lower panel in Fig. 5 gives the transients of the first overtone of the ν_3 mode on the $6p[4]^2E_{1/2}$ Rydberg state. Experimental data are only available for the CH_3I species. The agreement again is rather satisfactory. The calculated results support the experimental observation that the ν_3 vibrational overtone predissociates slightly faster than the band origin.

Figure 6 shows a cut of the potential energy surfaces along the C—H_3 coordinate at the groundstate equilibrium C—I distance. The CH_3I low-lying vibrational levels of both the $6p[4]^2E_{1/2}$ and $7s[1]^2E_{3/2}$ Rydberg states also plotted in the

Can. J. Chem. Downloaded from www.nrcresearchpress.com by EESC ESCOLA DE ENGENHARIA on 09/08/12
For personal use only.

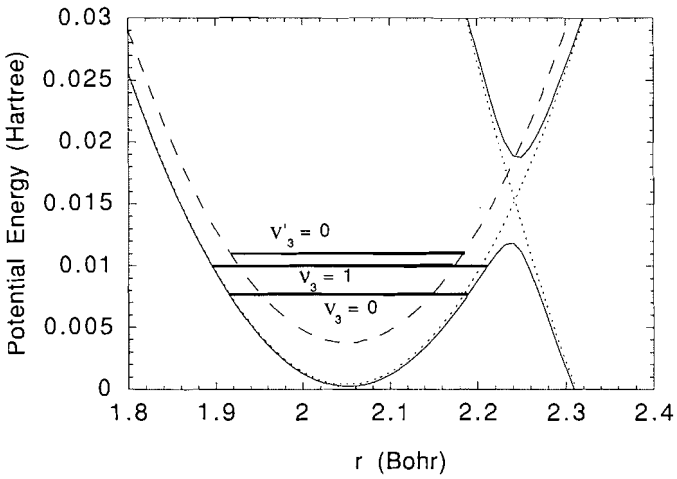

FIG. 6. Potential energy surface cuts in the C—H_3 coordinate at the ground state C—I equilibrium geometry. The dotted (the $6p[4]$ Rydberg and dissociative states) and dashed (the $7s[1]$ Rydberg state) lines are diabatic surfaces. The solid lines represent adiabatic surfaces formed between the $6p[4]$ Rydberg and dissociative states. Vibrational levels on the two Rydberg states are also given. Both the isotope effect and mode selectivity can be explained in the adiabatic picture (see text).

figure. The $6p[4]^2E_{1/2}$ Rydberg state intersects with the dissociative state at $r = 2.25$ au and they form two adiabatic surfaces due to the non-adiabatic coupling between the two states. It was found from our calculations that the coupling is significant so that the transition from the Rydberg state to the dissociative state is best described in the adiabatic representation. At the intersection, as shown in Fig. 6, the coupling is approximately 700 cm^{-1}. In order to reach the dissociation channel, the system has to tunnel through a barrier formed by the lower adiabatic surface. Since the deuterated methyl iodide has a much larger reduced mass in the r coordinate, it is more difficult to penetrate the barrier to dissociate. Furthermore, the CD_3I vibrational levels (not shown in the figure) are lower than their CH_3I counterparts because of the smaller zero point energy. The width of the barrier at these levels is thus relatively broader. Both factors contribute to the overall slowdown of the CD_3I predissociation.

The accelerated predissociation rate for the first ν_3 overtone can also be interpreted using the picture of Fig. 6. It can be clearly seen from the figure that the vibrational level for the first ν_3 overtone is much closer to the top of the barrier so that it is much easier to penetrate the barrier and dissociate. However, the increase in predissociation rate is small because the averaged kinetic energy is largely in the C—I direction.

B. Wave packet dynamics

As we indicated earlier in this paper, the model potential energy surfaces were developed in such a way that the predissociation proceeds initially along the C—H_3 coordinate and then leads to CH_3 and I. Indeed, the wave packet dynamics clearly show these characteristics of the potential energy surfaces. Snapshots of the decaying wave packet of CH_3I at 0, 10, 20, and 30 fs are plotted in Fig. 7. The lower *adiabatic* potential energy surface is also given in the background (heavy contours). In order to show the immediate propagation at short times, we used a delta function pulse for the excitation of the wave packet from the ground state. The wave packet shown in Fig. 7 is a sum of the wave packet modules on both the Rydberg and dissociative states. The wave packet is initially prepared on the Rydberg state, in the small well on the adiabatic surface (Fig. 7*a*).

In the first ten femtoseconds, the movement of the wave packet is mostly along the CH_3 coordinate (Fig. 7*b*) because the barrier to direct C—I bond cleavage is very high. The wave packet therefore chooses to make non-adiabatic transitions from the Rydberg state to the dissociative state along the C—H_3 coordinate. The part of the wave packet that escapes from the shallow well immediately experiences strong forces in both the C—H_3 and C—I directions. As a result, the wave packet starts to oscillate in the C—H_3 direction and accelerate down hill towards the dissociation of the C—I bond (Fig. 7*c* and *d*). These transitions are responsible for the decay of the Rydberg population shown in Fig. 5. It was found that there is no population recurrence in the Rydberg state and the decay can be readily fitted by an exponential function. The wave packet at large C—I distances is damped in the calculation since we are only interested in the dynamics of the parent CH_3I Rydberg state.

The oscillation in the C—H_3 coordinate will eventually lead to the excitation of the CH_3 fragment and such a motion is the analog of transition-state resonances (80). In the extreme cases, the excitation can result in the C—H bond cleavage. Although the asymptotic CH_3 internal energy is not of interest in this study, the strong oscillation in the C—H_3 mode is consistent with experimental observations of large vibrational excitation of the CH_3 fragment (48, 60).

C. Coherence effects

Finally, we would like to discuss the possible existence of coherence in the sufficiently broad bandwidth excitation near 312 nm (57). As shown in Fig. 2, the transient at 312 nm seems to have two peaks with a shift or an "oscillation period" of 140 fs. This frequency coincides with the energy difference between the $\nu_3 = 1$ vibrational level on the $6p[4]^2E_{1/2}$ Rydberg state and the $\nu_3 = 0$ level on the $7s[1]^2E_{3/2}$ Rydberg state. Since both vibrational levels could be coherently excited by a single pulse, there is a possibility that they may retain the coherence for some time provided that these two states are properly coupled. In this section, we will attempt to model coherence effects using wave packet dynamics.

The key in preparing a wave packet is to coherently excite more than one quantum state. In other words, these quantum states have to be excited by photons with the same phase. This was not possible experimentally until the introduction of the femtosecond lasers since only on this time scale a coherent nuclear wave packet could be formed at a given nuclear geometry (55). On a given potential, coherence can be manifested in a number of ways. For example, it has been shown in the case of I_2 (81) that a coherent wave packet can be prepared on an excited state by a femtosecond pulse and probed by another femtosecond pulse at a delayed time via either fluorescence (81) or ionization (56). The wave packet oscillates between the two turning points of the potential energy curve and its motion can be described by classical (82) and quantum (83) mechanics. The wave packet is a coherent superposition of adjacent vibrational eigenstates, and since each vibrational state has different energy, interferences among these states lead to time-dependent motion of the packet. The wave packet dephases gradually due to the anharmonicity of the potential. The time period for the wave packet to return to the original internuclear separation is determined by the energy differences

Can. J. Chem. Downloaded from www.nrcresearchpress.com by EESC ESCOLA DE ENGENHARIA on 09/08/12
For personal use only.

Can. J. Chem. Downloaded from www.nrcresearchpress.com by EESC ESCOLA DE ENGENHARIA on 09/08/12
For personal use only.

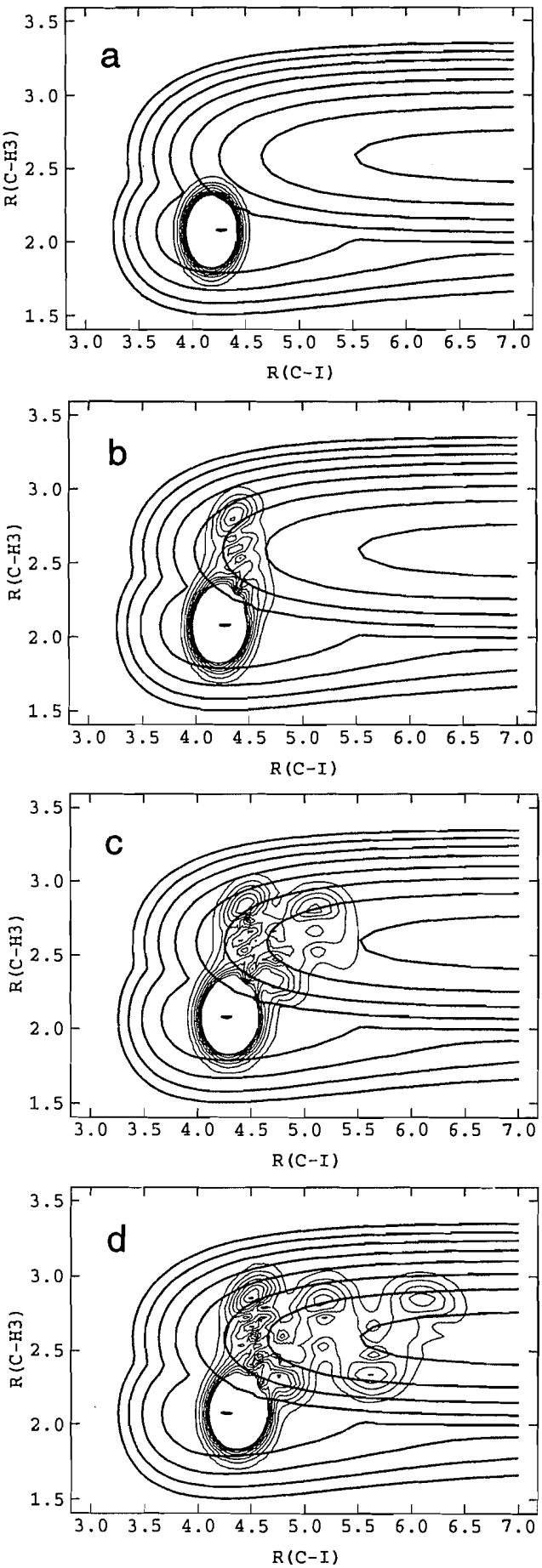

between adjacent levels. This type of coherence is universal to all processes involving elementary nuclear motions on various types of potentials (55).

Coherence can also exist between two states with different electronic characters provided they are appropriately coupled. In the case of methyl iodide, the band origin of the $7s[1]^2E_{3/2}$ state is only 240 cm^{-1} higher than the first ν_3 overtone on the $6p[4]^2E_{1/2}$ state. This can be seen from Fig. 6 where the vibrational levels are plotted with the potential energy surfaces of the $7s$ (dashed line) and $6p$ (dotted line) states. We have carried out calculations with two phase-locked ($\Delta\phi = 0$) femtosecond pulses tuned respectively to the two vibrational levels on the two Rydberg states. The transition dipole moment of the $7s[1]$ state was assumed to be a factor of two smaller than that of the $6p[4]$ state, in accordance with the experimental absorption spectrum (44, 46). Appropriate modifications of the Schrödinger equation were needed to include an extra state and two pump pulses. Although the two Rydberg states are not directly coupled, both of them are coupled with the dissociative state. Because of the energy difference between the two levels, interferences may arise and cause oscillations or quantum beats in the populations of the Rydberg states, which is reminiscence of the vibrational coherence in I_2. The calculated populations of both Rydberg levels are plotted with respect to time for both CH_3I (Fig. 8*a*) and CD_3I (Fig. 8*b*). It can be clearly seen that there is an oscillation with a frequency of approximately 140 fs throughout the decay of both CH_3I and CD_3I. Our calculated results give a reasonable account on the oscillatory feature observed in experiment although they are unable to offer a quantitative agreement, particularly at longer times. The disappearance of the oscillation in the later part of the dissociation is probably due to dephasing in a larger dimensional space which is not considered here.

One approximation we made in the calculations was to neglect the ionization pulse. Our rationale is based on the lack of knowledge of the ion state and the Franck–Condon nature of an ionization process. It should be pointed out that the oscillatory structure may also be attributed to the ionization process. Two ionization pathways exist during the probe process. One pathway is via the $6p[4]$ state while the other is via the $7s[1]$ state. Since the two Rydberg levels are prepared coherently by the pump pulse, the total ion signal is a square of the amplitude sum for the two pathways. Interferences will be important if the two pathways have comparable amplitudes. Furthermore, the energy difference of 240 cm^{-1} between the two Rydberg levels may survive the ionization and leads to the oscillations in the ion population in the first hundred femtoseconds (84, 85). The role played by the ionization in femtosecond pump-probe experiments certainly needs a more detailed analysis. It would be interesting to experimentally resolve the phase shift as the system executes the motion between the two states, in analogy with the experiment on iodine (86) and with the experiments on phase-shifted quantum beats for IVR studies (87).

FIG. 7. Snapshots of wave packet at 0 (*a*), 10 (*b*), 20 (*c*), and 30 (*d*) fs after a delta-function pulse excitation to the $6p[4]$ state. The heavy contours are the adiabatic potential energy surface formed by the Rydberg and repulsive states. The dissociation proceeds first along the C—H_3 vibrational coordinate and then to the C—I dissociation coordinate.

Can. J. Chem. Downloaded from www.nrcresearchpress.com by EESC ESCOLA DE ENGENHARIA on 09/08/12
For personal use only.

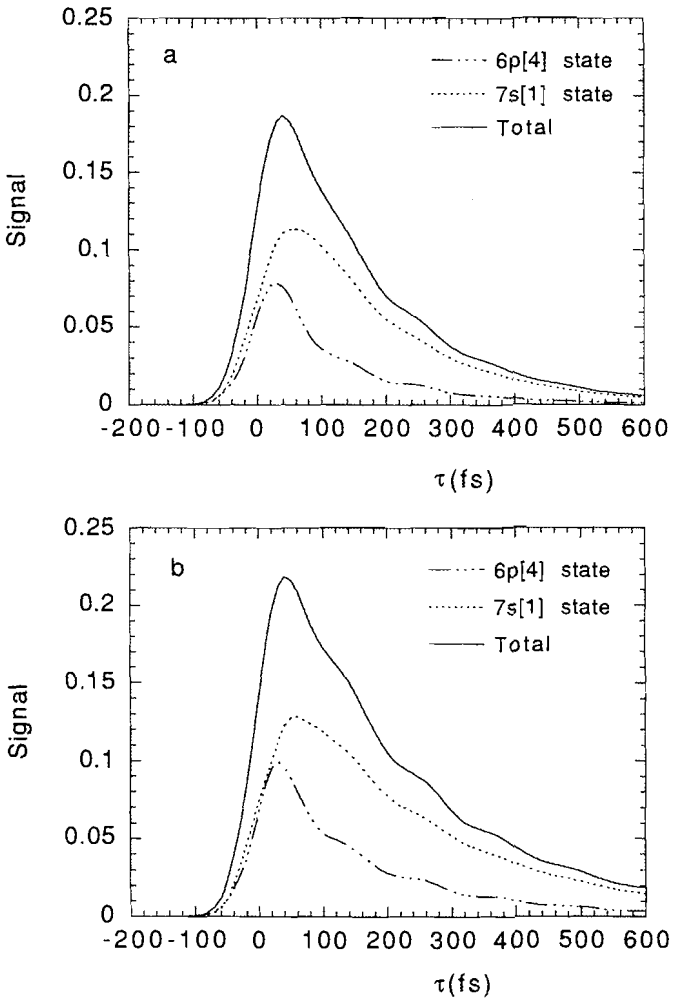

FIG. 8. Calculated transients for the broad bandwidth pulse excitation at 312 nm. Both the $6p[4]$ 3_0^1 and $7s[1]$ 0_0^0 Rydberg levels are excited coherently by the pulse. Oscillations with approximately 140 fs can be seen for both CH_3I (upper panel) and CD_3I (lower panel). The solid lines represent the total ion signal which is a sum of the signals from the two Rydberg states.

V. Conclusion

In summary, the femtosecond dynamics of Rydberg states, associated with the process of bond breakage in methyl iodide, involves more than one nuclear degree of freedom. This conclusion is based on experimental evidence of large isotope effects in the dissociation rate, which is indicative of the involvement of light atom tunneling in the dissociation. A two-dimensional model of the Rydberg predissociation dynamics of both methyl iodide and its deuterated isotope is advanced to account for the isotope effect, mode selectivity and coherence effects.

The two degrees of freedom involved in the model calculations are the C—I and C—H_3 coordinates. It is found that the predissociation of a methyl iodide Rydberg state involves non-adiabatic transitions to a dissociative state. Because the intersection between the Rydberg and dissociative states is perpendicular to the C—H_3 coordinate, the wave packet is forced to tunnel through the adiabatic barrier formed by the intersection and then dissociates. Since the predissociation involves tunneling of light atoms, a classical treatment of the dynamics becomes inappropriate. The calculations successfully reproduce the experimental observations and emphasize the importance of multidimensionality of the reaction pathway and the involvement of hydrogen (deuterium) atoms during the bond cleavage. We have also addressed the coherence effect induced by a broad bandwidth pump pulse. Although the model gives all the major features of the experimental results, it should be realized that the actual dynamics may involve many degrees of freedom. However, the present description may be sufficient for describing the elementary Rydberg state dynamics on the femtosecond scale.

For the future work, it would be advantageous to carry out *ab initio* calculations of the potential energy surfaces of the Rydberg and dissociative states of methyl iodide, which may help us to quantify the effect of the multidimensionality on the wave packet dynamics and on the non-adiabatic coupling. It would also be desirable to investigate the dynamics in the lower B and C bands in real-time in order to resolve some apparent controversies. Studies on this and other systems should be important to a broad class of Rydberg state dynamics, especially that the femtosecond time and mass resolutions make it possible to selectively isolate the elemental steps before long time events become operative.

Acknowledgments

This article is dedicated to John C. Polanyi, a colleague and friend, whose visionary and insightful work continues to inspire researchers in a number of areas covering science and humanity; it has certainly influenced the contribution reported here.

This work was funded by the donors of Petroleum Research Fund, administered by the American Chemical Society, by the National Science Foundation (CHE-9116501) to H.G., and by AFOSR to A.H.Z. Stimulating discussions with Marcos Dantus, Maurice Janssen and Volker Engel are gratefully acknowledged.

1. R.S. Mulliken. Phys. Rev. **47**, 413 (1935); R.S. Mulliken. Phys. Rev. **61**, 277 (1942); R.S. Mulliken and E. Teller, Phys. Rev. **61**, 283 (1942).
2. A. Gedanken and M.D. Rowe. Chem. Phys. Lett. **34**, 39 (1975).
3. J.L. Knee, L.R. Khundkar, and A.H. Zewail. J. Chem. Phys. **83**, 1996 (1985).
4. M.K. Dzvonik, S. Yang, and R. Bersohn. J. Chem. Phys. **61**, 4408 (1974).
5. S.J. Riley and K.R. Wilson. Faraday Discuss. Chem. Soc. **53**, 132 (1972).
6. T.F. Hunter and K.S. Krestjansson. Chem. Phys. Lett. **58**, 291 (1978).
7. P. Brewer, P. Das, G. Ondrey, and R. Bersohn. J. Chem. Phys. **79**, 720 (1983).
8. W.P. Hess, S.J. Kohler, H.K. Haugen, and S.R. Leone. J. Chem. Phys. **84**, 2143 (1986).
9. M.D. Barry and P.A. Gorry. Mol. Phys. **52**, 461 (1984).
10. G.N.A. van Veen, T. Baller, A.E. de Vries, and N.J.A. van Veen. Chem. Phys. **87**, 405 (1984).
11. S.L. Baughcum and S.R. Leone. J. Chem. Phys. **72**, 6531 (1980).
12. R.K. Sparks, K. Shobatake, L.R. Carlson, and Y.T. Lee. J. Chem. Phys. **75**, 3838 (1981).
13. H.W. Hermann and S.R. Leone. J. Chem. Phys. **76**, 4766 (1982).
14. R. Ogorzalek Loo, H.-P. Haerri, G.E. Hall, and P.L. Houston. J. Chem. Phys. **90**, 4222 (1989).
15. G.E. Hall, T.J. Sears, and J.M. Frye. J. Chem. Phys. **75**, 6234 (1989).
16. T. Suzuki, H. Kanamori, and E. Hirota. J. Chem. Phys. **94**, 6607 (1991).

Can. J. Chem. Downloaded from www.nrcresearchpress.com by EESC ESCOLA DE ENGENHARIA on 09/08/12
For personal use only.

17. J.F. Black and I. Powis. J. Chem. Phys. **89**, 3986 (1988); Chem. Phys. **125**, 375 (1988); I. Powis and J.F. Black. J. Phys. Chem. **93**, 2461 (1989),
18. D.W. Chandler, J.W. Thomas, Jr., M.H.M. Janssen, and D.H. Parker. Chem. Phys. Lett. **156**, 151 (1989); M.H.M. Janssen, D.H. Parker, G.O. Sitz, S. Stolte, and D.W. Chandler. J. Phys. Chem. **95**, 8007 (1991).
19. D. Imre, J.L. Kinsey, A. Sinha, and J. Krenos. J. Phys. Chem. **88**, 3956 (1984).
20. M.O. Hale, G.E. Galica, S.G. Glogover, and J.L. Kinsey. J. Phys. Chem. **90**, 4997 (1986).
21. K.Q. Lao, M.D. Person, P. Xayariboun, and L.J. Butler. J. Chem. Phys. **92**, 823 (1990).
22. G.E. Galica, B.R. Johnson, J.L. Kinsey, and M.O. Hale. J. Phys. Chem. **95**, 7994 (1991).
23. P.G. Wang and L.D. Ziegler. J. Phys. Chem. In press.
24. M. Tadjeddine, J.P. Flament, and C. Teichteil. Chem. Phys. **118**, 45 (1987).
25. Y. Amatatsu, K. Morokuma, and S. Yabushita. J. Chem. Phys. **94**, 4858 (1991).
26. M. Shapiro and R. Bersohn. J. Chem. Phys. **73**, 3810 (1980).
27. M. Shapiro. J. Phys. Chem. **90**, 3644 (1986).
28. H. Guo and G.C. Schatz. J. Chem. Phys. **93**, 393 (1990).
29. H. Guo, K.Q. Lao, G.C. Schatz, and A.D. Hammerich. J. Chem. Phys. **94**, 6562 (1991).
30. S.-Y. Lee and E.J. Heller. J. Chem. Phys. **76**, 3035 (1982).
31. S.K. Gray and M.S. Child. Mol. Phys. **51**, 189 (1984).
32. R.L. Sundberg, D. Imre, M.O. Hale, J.L. Kinsey, and R.D. Coalson. J. Phys. Chem. **90**, 5001 (1986).
33. H. Guo. Chem. Phys. Lett. **187**, 360 (1991); J. Chem. Phys. **96**, 6629 (1992).
34. G. Herzberg. Molecular spectra and molecular structure. Vol. 3. Krieger, Malabar. 1991.
35. M.B. Robin. Higher electronic states of polyatomic molecules. Vol. 1. Academic, New York. 1974.
36. S. Felps, P. Hochmann, P. Brint, and S.P. McGlynn. J. Mol. Spectros. **59**, 355 (1976).
37. D.H. Parker, R. Pandolfi, P.R. Stannard, and M.A. El-Sayed. Chem. Phys. Lett. **45**, 27 (1980).
38. S.P. Sapers and D.J. Donaldson. Chem. Phys. Lett. **173**, 257 (1990).
39. S.P. Sapers, V. Vaida, and R. Naaman. J. Chem. Phys. **88**, 3638 (1988).
40. D.J. Donaldson, V. Vaida, and R. Naaman. J. Chem. Phys. **87** 2522 (1987); J. Phys. Chem. **92**, 1204 (1988).
41. V. Vaida, D.J. Donaldson, S.P. Sapers, and R. Naaman. J. Chem. Soc. Faraday Trans. **86**, 2043 (1990).
42. V. Vaida, D.J. Donaldson, S.P. Sapers, R. Naaman, and M.S. Child. J. Phys. Chem. **93**, 513 (1989).
43. J.A. Syage. Chem. Phys. Lett. **212**, 124 (1993); J.A. Syage and J. Steadman. J. Phys. Chem. **94**, 7343 (1990).
44. A. Gedanken, M.B. Robin, and Y. Yafet. J. Chem. Phys. **76**, 4798 (1982).
45. K. Tsukiyama, B. Katz, and R. Bersohn. Chem. Phys. Lett. **124**, 309 (1986).
46. M.R. Dobber, W.J. Buma, and C.A. de Lange. J. Chem. Phys. **99**, 836 (1993).
47. K. Lao, M.D. Person, T. Chou, and L.J. Butler. J. Chem. Phys. **89**, 3463 (1988).
48. G.N.A. van Veen, T. Baller, and A.E. de Vries. Chem. Phys. **97**, 179 (1985).
49. L.D. Ziegler, Y.C. Chung, P.G. Wang, and Y.P. Zhang. J. Phys. Chem. **94**, 3394 (1990).
50. P.G. Wang, Y.P. Zhang, C.J. Ruggles, and L.D. Ziegler. J. Chem. Phys. **92**, 2806 (1990).
51. P.G. Wang and L.D. Ziegler. J. Chem. Phys. **95**, 288 (1991).
52. D.J. Campbell and L.D. Ziegler. J. Chem. Phys. **98**, 150 (1993).
53. D.J. Campbell and L.D. Ziegler. Chem. Phys. Lett. **201**, 159 (1993).
54. D.J. Donaldson, M.S. Child, and V. Vaida. J. Chem. Phys. **88**, 7410 (1988).
55. A.H. Zewail. Science, **242**, 1645 (1988); Faraday Discuss. Chem. Soc. **91**, 207 (1991).
56. M. Dantus, M.H.M. Janssen, and A.H. Zewail. Chem. Phys. Lett. **181**, 281 (1991).
57. M.H.M. Janssen, M. Dantus, H. Guo, and A.H. Zewail. Chem. Phys. Lett. **214**, 281 (1993).
58. H. Guo. Chem. Phys. Lett. **193**, 527 (1992).
59. E.E. Nikitin and M. Ya. Ovchinnikova. Chem. Phys. **138**, 45 (1989).
60. R.E. Continetti, B.A. Balko, and Y.T. Lee. J. Chem. Phys. **89**, 3383 (1988).
61. Faraday Discuss. Chem. Soc. **91** (1991); J. Phys. Chem. (1993); special issue on Femtochemistry.
62. R. Bersohn and A.H. Zewail. Ber. Bunsen-Ges. Phys. Chem. **92**, 373 (1988); R.B. Bernstein and R.B. Zewail. J. Chem. Phys. **90**, 829 (1989).
63. S.O. Williams and D.G. Imre. J. Phys. Chem. **92**, 6648 (1988); **92**, 6636 (1988).
64. V. Engel, H. Metiu, R. Almeida, R.A. Marcus, and A.H. Zewail. Chem. Phys. Lett. **152**, 1 (1988).
65. V. Engel and H. Metiu. J. Chem. Phys. **90**, 6116 (1989); **91**, 1596 (1989).
66. S.E. Choi and J.C. Light. J. Chem. Phys. **90**, 2593 (1989).
67. R. Heather and H. Metiu. Chem. Phys. Lett. **157**, 505 (1989).
68. H. Metiu and V. Engel. J. Chem. Phys. **93**, 5693 (1990).
69. V. Engel. Comp. Phys. Comm. **63**, 228 (1991).
70. S. Chapman and M.S. Child. J. Phys. Chem. **95**, 578 (1991).
71. M. Gruebele, G. Roberts, and A.H. Zewail. Phil. Trans. R. Soc. London, **A332**, 223 (1990).
72. R. Loudon. The quantum theory of light. Oxford University Press, Oxford. 1983.
73. V. Engel. Chem. Phys. Lett. **178**, 130 (1991).
74. M. Seel and W. Domcke. Chem. Phys. Lett. **151**, 59 (1991); J. Chem. Phys. **95**, 7806 (1991).
75. C. Leforestier, R. Bisseling, C. Cerjan, M.D. Feit, R. Friesner, A. Guldberg, A. Hammerich, G. Jolicard, W. Karrlein, H.D. Meyer, N. Lipkin, O. Roncero, and R. Kosloff. J. Comput. Phys. **94**, 59 (1991).
76. D. Kosloff and R. Kosloff. J. Comput. Phys. **52**, 35 (1983).
77. R. Heather and H. Metiu. J. Chem. Phys. **86**, 5009 (1987).
78. E.J. Heller. J. Chem. Phys. **68**, 2066 (1978).
79. R. Schinke. Photodissociation dynamics. Cambridge University Press, Cambridge. 1993.
80. S. Pedersen, L. Bañares, and A.H. Zewail. J. Chem. Phys. **97**, 8801 (1992).
81. R.M. Bowman, M. Dantus and A.H. Zewail. Chem. Phys. Lett. **161**, 297 (1989); M. Dantus, R.M. Bowman, and A.H. Zewail. Nature, **343**, 737 (1990).
82. R. Bernstein and A.H. Zewail. Chem. Phys. Lett. **170**, 321 (1990).
83. M. Gruebele, G. Roberts, M. Dantus, R.M. Bowman, and A.H. Zewail. Chem. Phys. Lett. **166**, 459 (1990); M. Gruebele and A.H. Zewail. J. Chem. Phys. **98**, 883 (1993).
84. T. Baumert, V. Engel, C. Meier, and G. Gerber. Chem. Phys. Lett. **200**, 488 (1993).
85. V. Engel, T. Baumert, C. Meier, and G. Gerber. Z. Phys. In press.
86. R.M. Bowman, M. Dantus, and A.H. Zewail. Chem. Phys. Lett. **174**, 546 (1990).
87. P. Felker and A.H. Zewail. Phys. Rev. Lett. **53**, 501 (1984); Adv. Chem. Phys. **70**, 265 (1988).

Two-color coherent control with SEP preparation: electronic branching in Na_2 photodissociation

JEFFREY DODS AND PAUL BRUMER[1]

Chemical Physics Theory Group, Department of Chemistry, University of Toronto, Toronto, ON M5S 1A1, Canada

AND

MOSHE SHAPIRO

Department of Chemical Physics, The Weizmann Institute of Science, Rehovot, Israel 76100

Received August 24, 1993

This paper is dedicated to Professor John C. Polanyi on the occasion of his 65th birthday

JEFFREY DODS, PAUL BRUMER, and MOSHE SHAPIRO. Can. J. Chem. **72**, 958 (1994).

Extensive control over relative product yields is shown to result from weak laser photodissociation in a two-color coherent control scenario. Photodissociation takes place from a superposition state prepared by stimulated emission pumping. The method allows for control in the presence of laser phase jumps by using four-wave mixing to prepare the required laser frequencies. The near UV photodissociation of Na_2, resulting in the Na(3*s*) + Na(4*s*) and the Na(3*s*) + Na(3*d*) products, is used to illustrate the method.

JEFFREY DODS, PAUL BRUMER et MOSHE SHAPIRO. Can. J. Chem. **72**, 958 (1994).

On démontre que les rendements relatifs en produit peuvent être fortement contrôlés par une photodissociation faible au laser dans un scénario de contrôle cohérent en deux couleurs. La photodissociation se produit par un état de superposition préparé par un pompage stimulé d'émission. La méthode permet de réaliser un contrôle en présence de sauts de phase du laser en utilisant un mélange de quatre ondes pour préparer les fréquences laser requises. Pour illustrer la méthode, on utilise la photodissociation dans le proche UV du Na_2 qui conduit aux produits Na(3*s*) + Na(4*s*) et Na(3*s*) +Na(3*d*).

[Traduit par la rédaction]

1. Introduction

The past few decades have seen enormous progress in our understanding of the detailed dynamics of chemical reactions, and J.C. Polanyi's pioneering leadership in this area is widely acclaimed. This knowledge base has allowed recent progress (1, 2) towards an essential goal of practical chemistry, control over chemical reactions. Our technique of coherent radiative control (1) affords a method of controlling molecular dynamics by exploiting quantum interference phenomena. For example, in photodissociation of a molecule at energy E where a number of products are present, control over relative product yield can be achieved by introducing two or more simultaneous excitation routes. Varying the intensity and relative phases of the lasers used to excite the molecule allows one to directly alter the interference between these routes and hence to directly alter the reaction yield.

Thus far we have devised a number of scenarios that rely upon this interference principle and that utilize either CW or pulsed laser excitation sources. Here we introduce a specific scenario, which embellishes our first control scheme (3) and which allows us to bypass deleterious incoherence effects due to laser jitter.[2] Briefly, the scheme involves two steps: preparation of a molecular superposition state by stimulated emission pumping (SEP), followed by photodissociation after a suitable time delay. If the frequencies used are prepared by an appropriate nonlinear mixing scheme then we show that the method is insensitive to any laser jitter inherent in the light sources. In the next section we give a more detailed overview of the control scheme. Subsequent sections describe the details of the method and give applications to the photodissociation of Na_2.

2. One photon vs. one photon coherent control

2.1 Overview

The first coherent control scenario (3) considered the photodissociation, at energy E, of a molecule in a superposition of two bound states $|E_1\rangle$ and $|E_2\rangle$. The ratio of dissociation products could be varied by altering the relative phase and intensity of two coherent sources, of frequencies $(E - E_i)/\hbar\,(i = 1, 2)$. In addition, we demonstrated, through a quantitative study of products in methyl iodide dissociation, that the range of product control can be extensive. A subsequent study of the utility of this scenario in the presence of collisions (5) showed that control survived over a reasonable temperature range.

In this paper we demonstrate that by preparing the initial state in a specific fashion we are able to construct an experimental scheme that is readily implemented and that minimizes deleterious effects due to laser jitter. In addition, the method allows for the preparation of superposition states where $(E_2 - E_1)$ can be large, aiding in the supression of uncontrollable competitive photodissociation routes.

Briefly, we propose to use a frequency ω_0 to pump two dye lasers at frequencies ω_1 and ω_2. The quantity $\hbar\,(\omega_1 - \omega_2)$ is chosen equal to $(E_j - E_i)$, the energy difference between $|E_j\rangle$ and $|E_i\rangle$, two vib-rotational levels on the ground electronic surface. The molecule (see Fig. 1) is then irradiated with ω_1 and ω_2 light for a fixed time period, resulting in preparation of the superposition state via stimulated emission pumping (6). After some selected time delay the molecule is photodissociated with two frequencies $(\omega_0 + \omega_1)$ and $(\omega_0 + \omega_2)$ prepared by mixing the ω_1 and ω_2 beams with ω_0 in a nonlinear crystal. Simultaneous excitation to energy E results, with interference effects controlled by the relative intensity and phases of the two routes. Phase jitter effects are eliminated and uncontrollable satellite contributions can be minimized, as discussed below.

2.2 Superposition preparation

Consider the molecule, defined by Hamiltonian H_m with eigenstates $|E_j\rangle$ of energy E_j, which is subject to the time-dependent perturbation $V(t)$. The standard solution (7) is given by the wavefunction $|\psi(t)\rangle$:

[1]Author to whom correspondence may be addressed.

[2]For an alternate two-photon vs. two-photon control scheme for overcoming interference loss due to phase jumps and thermal effects see ref. 4.

Can. J. Chem. Downloaded from www.nrcresearchpress.com by 195.246.54.202 on 09/08/12
For personal use only.

[1] $$|\psi(t)\rangle = \sum_j a_j(t)|E_j\rangle \exp(-iE_jt/\hbar)$$

where

[2] $$a_j(t) \equiv \langle E_j|\psi^{\mathrm{I}}(t)\rangle = \langle E_j|\mathbf{T}\exp\left(-\frac{i}{\hbar}\int_{t_0}^{t} V^{\mathrm{I}}(t')\mathrm{d}t'\right)|\psi(t_0)\rangle$$

Here $\mathbf{T}$ is the time-ordering operator and $V^{\mathrm{I}}(t)$ and $|\psi^{\mathrm{I}}(t)\rangle$ denote the perturbation and wavefunction in the interaction representation. That is

[3] $$|\psi(t)\rangle = \exp(-iH_{\mathrm{m}}t/\hbar)|\psi^{\mathrm{I}}(t)\rangle$$

and

$$V^{\mathrm{I}}(t) = \exp(iH_{\mathrm{m}}t/\hbar)V(t)\exp(-iH_{\mathrm{m}}t/\hbar)$$

In the case of SEP preparation, $V(t)$ describes the influence of two laser fields with frequencies ω_1 and ω_2, and amplitudes ϵ_1, ϵ_2, i.e.,

[4] $$V(t) = -d_{\epsilon_1}\epsilon_1(\omega_1)\cos(\omega_1t + \phi_1) - d_{\epsilon_2}\epsilon_2(\omega_2)\cos(\omega_2t + \phi_2)$$

Here the d_{ϵ_i} is the component of the transition dipole moment operator along the direction of the ith linearly polarized electric field. Expanding the exponential function in eq. [2] in a power series, truncating after the third term, and assuming the initial state $|\psi(t_0)\rangle$ to be the ith vibration–rotation level of the ground electronic state with no population in states $|E_j\rangle \neq |E_i\rangle$, allows us to rewrite eq. [2] as

[5] $$a_j(t) = \langle E_j|1 - \frac{i}{\hbar}\int_{t_0}^{t} V^{\mathrm{I}}(t')\mathrm{d}t' - \frac{1}{2\hbar^2}\int_{t_0}^{t}V^{\mathrm{I}}(t')\mathrm{d}t'\int_{t_0}^{t'}V^{\mathrm{I}}(t'')\mathrm{d}t''|E_i\rangle$$

Both the first and second matrix elements are zero, the first by orthogonality and the second (the first-order, one-photon transition) because the transition between $|E_i\rangle$ and $|E_j\rangle$, which belong to the same electronic surface, is assumed dipole forbidden.

To evaluate the third term we insert complete sets of states between the integrals. We can limit consideration to a particular vibration–rotation level of an intermediate electronic state (denoted $|E_{\mathrm{N}}\rangle$) if ω_1 and ω_2 are tuned to resonance. Choosing ω_1 resonant with the $E_i \longrightarrow E_{\mathrm{N}}$ transition and ω_2 with the stimulated $E_{\mathrm{N}} \longrightarrow E_j$ emission, we can rewrite eq. [2] as

[6] $$a_j(t) = -\frac{1}{2\hbar^2}\int_{t_0}^{t}\mathrm{d}t'\exp\big(i(E_j - E_{\mathrm{N}})t'/\hbar\big)\langle E_j|V(t')|E_{\mathrm{N}}\rangle\int_{t_0}^{t'}\mathrm{d}t''\exp\big(i(E_{\mathrm{N}} - E_i)t''/\hbar\big)\langle E_{\mathrm{N}}|V(t'')|E_i\rangle$$

Substituting the explicit form of $V(t)$ we obtain, in the rotating wave approximation (i.e., retaining absorption of $|E_i\rangle$ to $|E_{\mathrm{N}}\rangle$ and emission from $|E_{\mathrm{N}}\rangle$ to $|E_j\rangle$), that

[7] $$a_j(t) = \frac{1}{4\hbar^2}\int_{t_0}^{t}\mathrm{d}t'\exp\big(i(E_j - E_{\mathrm{N}} + \hbar\omega_2)t'/\hbar + i\phi_2\big) \times\epsilon_2(\omega_2)\langle E_j|d_{\epsilon_2}|E_{\mathrm{N}}\rangle\int_{t_0}^{t'}\mathrm{d}t''\exp(i(E_{\mathrm{N}} - E_i - \hbar\omega_1)t''/\hbar - i\phi_1)\epsilon_1(\omega_1)\langle E_{\mathrm{N}}|d_{\epsilon_1}|E_i\rangle$$

Evaluating the integrals gives

[8] $$a_j(t) = \frac{1}{8\hbar^2}(t - t_0)^2\epsilon_1(\omega_1)\epsilon_2(\omega_2)\langle E_j|d_{\epsilon_2}|E_{\mathrm{N}}\rangle\langle E_{\mathrm{N}}|d_{\epsilon_1}|E_i\rangle\exp(i(\phi_2 - \phi_1))$$

[9] $$\equiv a_j^{\mathrm{p}}\exp(i(\phi_2 - \phi_1 + \beta_{ij}))$$

where a_j^{p} denotes the absolute magnitude of the post-preparation coefficient of state $|E_i\rangle$ and β_{ij} is the phase of $\langle E_j|d_{\epsilon_2}|E_{\mathrm{N}}\rangle\langle E_{\mathrm{N}}|d_{\epsilon_1}|E_i\rangle$. Equation [1] therefore acquires the explicit form

[10] $$|\psi(t)\rangle = |E_i\rangle\exp(-iE_it/\hbar) + a_j^{\mathrm{p}}\exp(i(\phi_2 - \phi_1 + \beta_{ij} - E_jt/\hbar))|E_j\rangle$$

Equation [10] neglects the term in $|E_{\mathrm{N}}\rangle$, which is justified if, as below, subsequent photodissociation from $|E_{\mathrm{N}}\rangle$ is negligible due to poor Franck–Condon factors.

It is convenient to begin the photodissociation at time zero. To allow this we shift the zero of time by starting the SEP preparation step at time $-(T + \tau_{\mathrm{p}})$ and terminating it at time $-T$. The molecular state at the time the SEP preparation is completed ($t = -T$) is then

[11] $$|\psi(-T)\rangle = |E_i\rangle + a_j^{\mathrm{p}}\exp(i(\phi_2 - \phi_1 + \beta_{ij}))|E_j\rangle$$

and the state at a time just before the turn on of the photodissociation laser is

[12] $$|\psi(0)\rangle = |E_i\rangle\exp(-iE_iT/\hbar) + a_j^{\mathrm{p}}\exp(i(\phi_2 - \phi_1 + \beta_{ij}))|E_j\rangle\exp(-iE_jT/\hbar)$$

Can. J. Chem. Downloaded from www.nrcresearchpress.com by 195.246.54.202 on 09/08/12
For personal use only.

Thus the final outcome of the molecular preparation step leaves the molecule in a superposition of bound states with phases dictated by relative laser phase and time delay before the photodissociation pulse. Note also that the molecular state has acquired the relative laser phase $(\phi_2 - \phi_1)$, with positive phase contribution ϕ_2 from emission and negative, $-\phi_1$, from absorption. Below we will see that the form of these phases is crucial to the coherent control scheme.

2.3 Photodissociation of the superposition state

Consider now photodissociation of the prepared superposition state of eq. [12] by two CW lasers of frequency $\omega_{E_i} = (E - E_i)/\hbar$ and $\omega_{E_j} = (E - E_j)/\hbar$ (or by pulses containing these frequencies):

$$[13] \qquad \epsilon(t) = \epsilon_4(\omega_{E_i}) \cos(\omega_{E_i} t + \phi_4) + \epsilon_3(\omega_{E_j}) \cos(\omega_{E_j} t + \phi_3)$$

To obtain the photodissociation amplitudes $b(Enq|t \rightarrow \infty)$ we expand the wavefunction as

$$[14] \qquad |\psi(t)\rangle = \sum_i c_i(t)|E_i\rangle \exp\left(-\frac{i}{\hbar} E_i t\right) + \sum_{nq} \int \mathrm{d}E' b(E'nq|t)|E'nq^-\rangle \exp\left(-\frac{i}{\hbar} E' t\right)$$

and solve for $b(Enq|t)$. Here $|Enq^-\rangle$ are incoming scattering wave functions which asymptotically go to products at energy E in arrangement channel q and internal quantum numbers n; in diatomics, n is simply the scattering angle vector $\hat{\mathbf{k}}$. Assuming the fields are sufficiently weak we have $c_i(t) = a_i^0$ at all times and, at long times, (3):

$$[15] \qquad \left(\frac{\hbar}{i\pi}\right) b(Enq|t \rightarrow \infty) = \epsilon_4(\omega_{E_i})\langle Enq^-|d_{\epsilon_4}|E_i\rangle \exp(-i(\phi_{\omega_{E_i}} + E_i T/\hbar)) + a_j^0 \epsilon_3(\omega_{E_j})\langle Enq^-|d_{\epsilon_3}|E_j\rangle \exp(i(\phi_2 - \phi_1 + \beta_{ij} - \phi_{\omega_{E_j}} - E_j T/\hbar))$$

with $E = E_i + \hbar\omega_{E_i} = E_j + \hbar\omega_{E_j}$. The probability of forming product in product channel q at energy E is given by $P(q;E) = \lim_{t\rightarrow\infty} \sum_n |b(Enq|t)|^2$. This assumes a convenient form if we introduce the notation

$$[16] \qquad d_{44}^q = \int \mathrm{d}\hat{\mathbf{k}} |\langle Enq^-|d_{\epsilon_4}|E_i\rangle|^2$$

$$[17] \qquad d_{33}^q = \int \mathrm{d}\hat{\mathbf{k}} |\langle Enq^-|d_{\epsilon_3}|E_j\rangle|^2$$

$$[18] \qquad d_{34}^q = |d_{34}^q| \exp(i\alpha_{34}^q) = \int \mathrm{d}\hat{\mathbf{k}} \langle E_j|d_{\epsilon_3}|Enq^-\rangle\langle Enq^-|d_{\epsilon_4}|E_i\rangle$$

Expanding the square in $|b(Enq|t)|^2$ allows us to write the yield $R(q;E)$ to observe products in channel q, with energy E as

$$[19] \qquad R(q;E) = \frac{P(q;E)}{P(q;E) + P(q';E)}$$

with

$$[20] \qquad P(q;E) \propto d_{44}^q + x^2 d_{33}^q + 2x|d_{34}^q| \cos(\Phi + \beta_{ij} + \alpha_{34}^q)$$

Here we have left out proportionality factors irrelevant to R and have introduced the notation:

$$[21] \qquad \Phi = \phi_{\omega_{E_i}} - \phi_{\omega_{E_j}} + \phi_2 - \phi_1 + (E_i - E_j)T/\hbar$$

$$[22] \qquad x = \frac{a_j^0 \epsilon_3(\omega_{E_j})}{\epsilon_4(\omega_{E_i})}$$

Equation [20] comprises three terms, direct photodissociation of levels $|E_i\rangle$ and $|E_j\rangle$ plus an interference term between these routes. It is evident from eq. [20] that changing either x or Φ will result in a variation in the probability $P(q;E)$. Both variables comprise experimentally controllable parameters including the relative phases and intensities of the excitation sources in both steps, as well as the time delay T between preparation and dissociation. Varying these control parameters in the laboratory allows direct control over the interference term and hence over the product distribution.

Additional photodissociation at energies other than E, the so-called satellite contributions, also occur. These correspond to the photodissociation of $|E_i\rangle$ by absorption of ω_{E_j} to energy $E + E_i - E_j$ and the photodissociation of $|E_j\rangle$ by absorption of ω_{E_i} to energy $E + E_j - E_i$. Since there is only one pathway to each of these energies, they correspond to uncontrolled photodissociation pathways. However, this scenario allows large $(E_i - E_j)$ so that these absorptions may be placed outside of the continuum absorption range.

2.4 Countering phase incoherence

Relying on independent lasers for state creation and subsequent photodissociation has serious disadvantages. Specifically, if the four relative laser phases within Φ are unstable or uncorrelated then phase fluctuations during the interaction of the molecule with four independent lasers can lead to extensive phase averaging. Such phase averaging destroys the coherence vital to coherent control. However, a simple experimental scenario resolves this problem. In particular, consider using a single CW laser of frequency ω_0 to pump two dye lasers at frequencies ω_1 and ω_2. The associated laser phases are denoted ϕ_0, ϕ_1, and ϕ_2. The three frequencies are chosen such that $(\omega_0 + \omega_1) = \omega_{E_i}$, $(\omega_0 + \omega_2) = \omega_{E_j}$. If ω_1 and ω_0, as

Can. J. Chem. Downloaded from www.nrcresearchpress.com by 195.246.54.202 on 09/08/12
For personal use only.

Can. J. Chem. Downloaded from www.nrcresearchpress.com by 195.246.54.202 on 09/08/12
For personal use only.

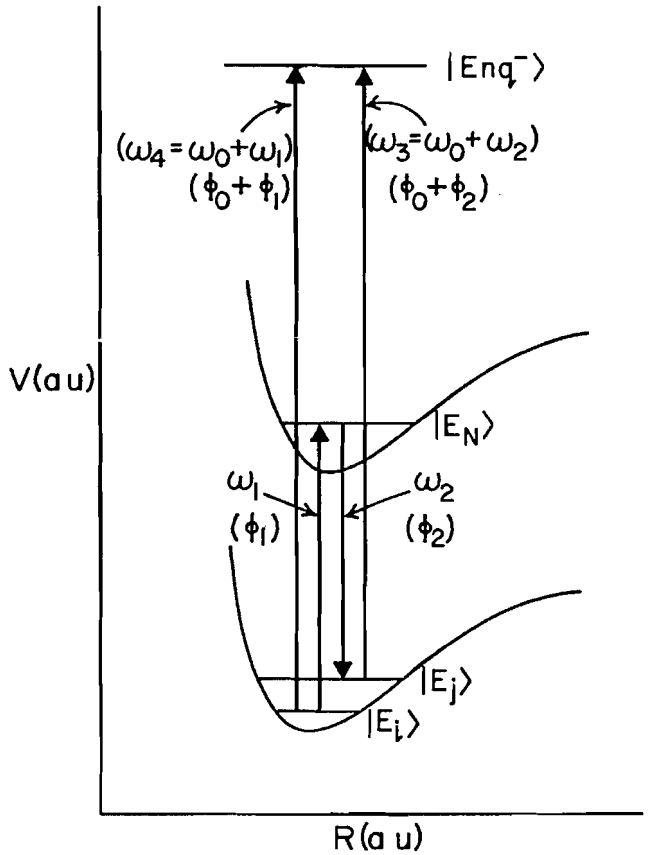

FIG. 1. Schematic of the coherent control scenario. The phase of route one (excitation by $\omega_0 + \omega_1$) imparts to the continuum state $\phi_0+\phi_1$. Similarly, the phase imparted in route two (ω_1, ω_2) preparation followed by $\omega_0+\omega_2$ dissociation equals $(\phi_1-\phi_2+\phi_0+\phi_2) = (\phi_0+\phi_1)$.

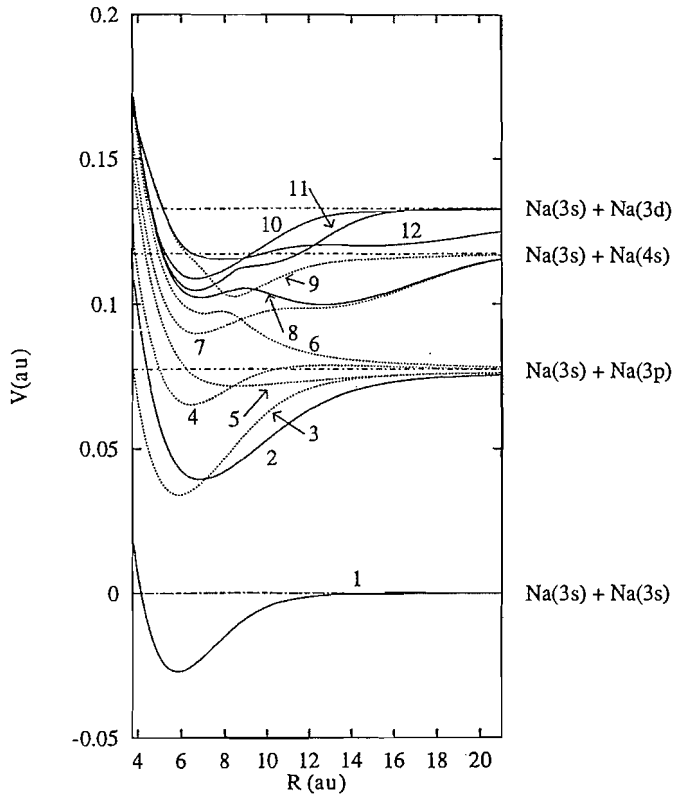

FIG. 2. The most relevant Na_2 potential curves are shown: $(1)^1\Sigma_g$, $(2)^1\Sigma_u$, $(3)^3\Pi_u$, $(4)^1\Pi_u$, $(5)^1\Pi_g$, $(6)^3\Sigma_u$, $(7)^1\Sigma_g$, $(8)^1\Sigma_u$, $(9)^3\Sigma_u$, $(10)^1\Pi_u$, $(11)^3\Pi_u$, $(12)^1\Sigma_u$, Additional states included in the computation but omitted here for clarity are as follows: one $^1\Sigma_g$, two $^3\Sigma_g$, and one $^3\Pi_g$, which are asymptotic to the Na(3*s*) + Na(3*p*) product, and one $^3\Sigma_g$ state that is asymptotic to the Na(3*s*) + Na(4*s*) product.

well as ω_2 and ω_0, are mixed in a nonlinear crystal then the created frequencies $(\omega_0+\omega_1) = \omega_{E_i}$ and $(\omega_0+\omega_2) = \omega_{E_j}$ have phases $\phi_0+\phi_1$ and $\phi_0+\phi_2$, respectively.

With this mode of frequency preparation the phase Φ assumes the form:

$$[23] \quad \Phi = \phi_{\omega_{E_i}} - (\phi_1 - \phi_2 + \phi_{\omega_{E_j}}) + (E_i - E_j)T/\hbar$$

$$[24] \quad = (\phi_0 + \phi_1) - (\phi_1 - \phi_2 + \phi_0 + \phi_2) + (E_i - E_j)T/\hbar$$

$$[25] \quad = (E_i - E_j)T/\hbar$$

Thus the phase difference between the two routes is independent of the laser phases and, in particular, independent of the fluctuations in the laser sources.

An enlightening qualitative picture of the phases associated with the two excitation routes to dissociation is shown in Fig. 1. Route one to dissociation is excitation from level $|E_i\rangle$ via $\epsilon_4(\omega_{E_i})$; the created state acquires the phases $[-(\phi_0 + \phi_1)]$. Route two is a three-photon route, from $|E_i\rangle$ to $|E_N\rangle$ to $|E_j\rangle$ to the continuum. Phase accumulated along this route is $[-\phi_1 + \phi_2 - (\phi_0 + \phi_2)] = [-(\phi_0 + \phi_1)]$. Hence both excitation routes result in the same accumulated phase and the phase difference between them cancels.

Laboratory control over the phase then corresponds to varying T or, if preferred, deliberately introducing an additional phase delay between the two routes. We therefore extend the definition of Φ to include any experimentally introduced additional phase delay.

3. Results

Although this control scheme is applicable to a wide range of molecules, it is convenient to choose a particular system, e.g., Na_2, to demonstrate the method. We first consider some photodissociation amplitudes characteristic of the energy range of interest. Appendix A provides additional details on the nature of these calculations; below we will discuss only the qualitative results of the photodissociation and the coherent control of products Na(3*s*) + Na(4*s*) vs. Na(3*s*) + Na(3*d*).

3.1 Na_2 photodissociation

A total of 17 Na_2 electronic states (8) were included in the computation. The 12 curves contributing most significantly are shown in Fig. 2, with the remainder omitted for clarity of presentation. Those which are dipole coupled to the ground state (9), and which are in the energy range of interest, are shown using solid lines. Since the ground state of Na_2 is a $^1\Sigma_g$, only singlets of ungerade symmetry are dipole coupled to this state. A small spin-orbit coupling does mix singlet states with triplets; only one triplet state need concern us in this study, the $^3\Pi_u$ curve numbered 11. Also shown are typical frequencies used to apply the coherent control scenario discussed above to this system. The low-lying potentials leading to the Na(3*s*) + Na(3*p*) and Na(3*s*) + Na(3*s*) have negligible Franck–Condon factors for the photodissociation energies of interest, but are necessary for the computation of the SEP preparation step.

Can. J. Chem. Downloaded from www.nrcresearchpress.com by 195.246.54.202 on 09/08/12
For personal use only.

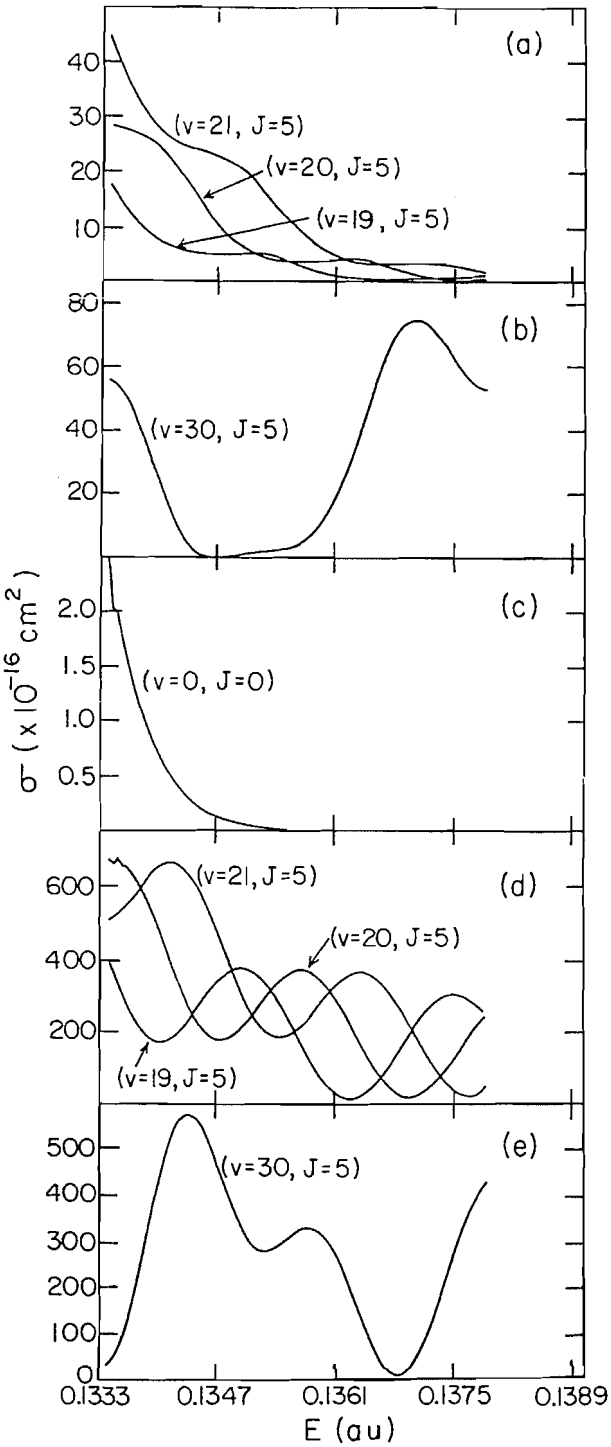

FIG. 3. Photodissociation cross sections into Na(3*s*) + Na(4*s*) from $J = 5$, (*a*) $v = 19, 20, 21$; (*b*) $v = 30$. Photodissociation cross sections into Na(3*s*) + Na(3*d*) vs. photon energy from Na_2; (*c*) into $v = 0$, $J = 0$; (*d*) $J = 5$, $v = 19, 20$, and 21; and (*e*) $v = 30$.

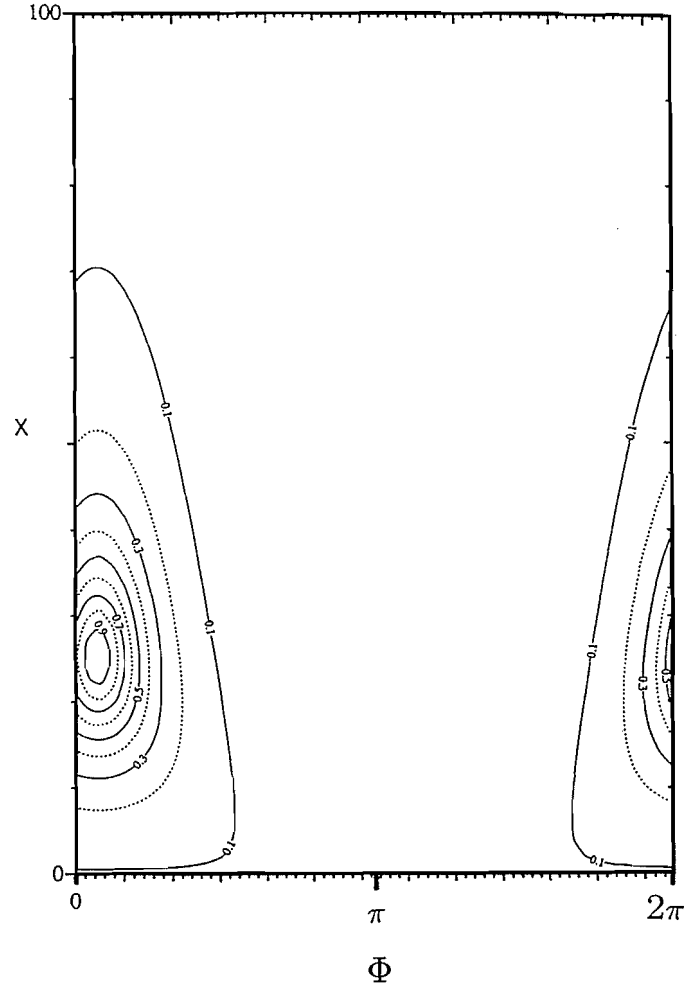

FIG. 4. Contours of constant $R(4s; E)$. The ordinate is the parameter x and the abscissa is the relative phase Φ. The control map is for the initial superposition of $v = 24$, $J = 0$ with $v' = 27$, $J = 0$.

Our computations show that the Na_2 photodissociation cross section to the Na(3*s*) + Na(4*s*) channel is extremely small for vibrational states $v = 0$ to $v = 15$. This is due to the large bond length of the ground $(1)^1\Sigma_g$ state of Na_2, resulting in a small overlap between the $v = 0$ to $v = 15$ levels and the state $[(8)^1\Sigma_u]$ leading to the Na(3*s*) + Na(4*s*) products. This low cross section is in contrast with the Na(3*s*) + Na(3*d*) channel cross section, which has a detectable magnitude starting with photodissociation of the Na_2 $v = 0$ state due to adequate overlap with the $(12)^1\Sigma_u$ state. The cross section for both channels increases as v increases. Figure 3 shows selected Na_2 photodissociation cross sections.

Figure 3*a* shows typical cross sections to the Na(3*s*) + Na(4*s*) product channel. Adjacent bound states are seen to give similar cross sections. For $v = 19$ to $v = 21$, the decrease in cross section as photolysis energy increases is due to diminishing Franck–Condon factors on the repulsive wall of the excited surfaces. But $v = 30$ (Fig. 3*b*) has a different structure because the turning point of the bound state is outside the turning point of the excited state repulsive wall. A minimum is seen at about 0.1347 au of photon energy, followed by a peak at 0.1370 au.

Sample results for the Na(3*s*) + Na(3*d*) channel are shown in Figs. 3*c*–*e*. The vibrationless level of the $(1)^1\Sigma_g$ state of Na_2 has a Na(3*s*) + Na(3*d*) channel cross section that decays rapidly (Fig. 3*c*). By $v = 10$ the cross section develops clear oscillations, but by $v = 30$ (Fig. 3*e*) the oscillatory structure is no longer clear because there is significant interference from the Franck–Condon factors of the two strongly participating singlet states, the $(12)^1\Sigma_u$ and the $(10)^1\Pi_u$ states. This is in

Can. J. Chem. Downloaded from www.nrcresearchpress.com by 195.246.54.202 on 09/08/12
For personal use only.

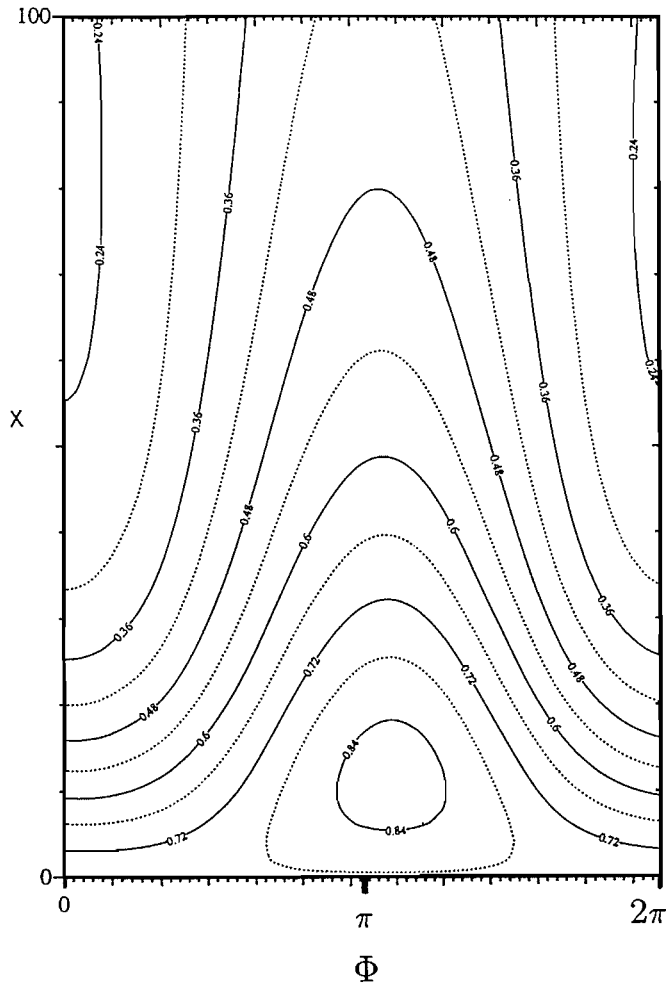

FIG. 5. As in Fig. 4 but with $J = 5$.

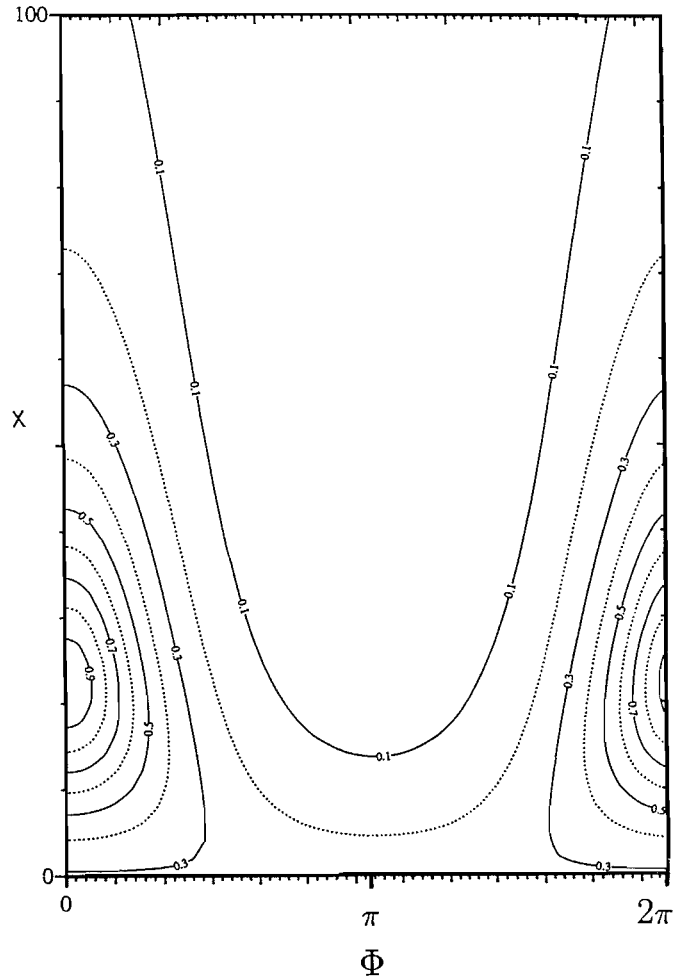

FIG. 6. As in Fig. 4 but with $J = 10$.

contrast with the results in Fig. 3*d* where the oscillatory structure is clear and where only one excited state, the $(12)^1\Sigma_u$, dominates the photodissociation. This state has a distinctly different location of its inner repulsive wall in the region of the Na(3*s*) + Na(3*d*) channel threshold.

3.2 Coherent control of Na_2

Here we consider control over the fractional yield of the $q \equiv$ Na(3*s*) + Na(4*s*) vs. the $q' \equiv$ Na(3*s*) + Na(3*d*) channels. The vanishingly small cross section to produce Na(3*s*) + Na(4*s*) for lower vibrational states prevents us from using low vibrational states for coherent control purposes. Below we describe control starting with the higher vibrational states ($v \geq 24$), which, if desired, can be experimentally created by the SEP pumping or by adiabatic passage techniques (10). We will use the availability of such techniques to our advantage by assuming that control can begin with the molecule in a high vibrational level of the ground electronic state.

Assume, for example, that we can begin the control experiment with the molecule in $v = 24$ and J_i, $M_i = 0$, where the latter denotes the angular momentum of the *i*th state and its *z*-projection. A survey (11) of Franck–Condon factors between this state and vib-rotational states of the $(2)^1\Sigma_u$ state shows that a superposition state comprising the $(v = 24, J = 0)$, and $(v = 27, J = 0)$ states could be conveniently formed via an $|E_N\rangle$ state with $v = 14$, $J = 1$. This corresponds to the choice $\hbar\omega_1 = 12\,883$ cm^{-1} and $\hbar\omega_2 = 12\,538$ cm^{-1}. Control results at $E = 29\,672$ cm^{-1} are shown in Fig. 4 where we plot $R(4s;E)$, the fractional yield of 4*s* as a function of the control parameters *x* and Φ. The figure shows contours of constant $R(4s;E)$ and indicates that the branching ratio can be varied between 10 and 90% by varying *x* and Φ. The maximum Na(4*s*) yield is at $\Phi \sim 0.2\pi$ radians and the amplitude factor $x \sim 25$.

Figures 5 and 6 show results for initial states with higher rotational quantum numbers for which *M* averaging has been performed. Figure 5 shows results for the superpositions $(v = 24, J = 5)$, and $(v = 27, J = 5)$ at the slightly higher energy $E = 30\,046$ cm^{-1}. Control of the Na(4*s*) yield has been somewhat reduced (ranging from 0.24 to 0.84) relative to the case shown in Fig. 4. This is accompanied by a shift in the maximum in the Na(4*s*) yield to $\Phi \sim 3.5\pi$ radians and $x \sim 10$. The $J_i = J_j = 10$ case (Fig. 6) shows very similar results to the $J_i = J_j = 0$ situation, with the range of control of 0.1–0.9 now restored.

As an example of the observed behavior of other combinations of bound state pairs, consider the case where the molecule is in the $v = 27$, $J = 0$ plus $v = 31$, $J = 0$ state, pumped via the intermediate $v = 21$, $|E_N\rangle$ state. This corresponds to using $\hbar\omega_1 = 13\,268$ cm^{-1} and $\hbar\omega_2 = 12\,837$ cm^{-1}. The resultant $R(4s;E)$ control map at $E = 29\,607$ cm^{-1}

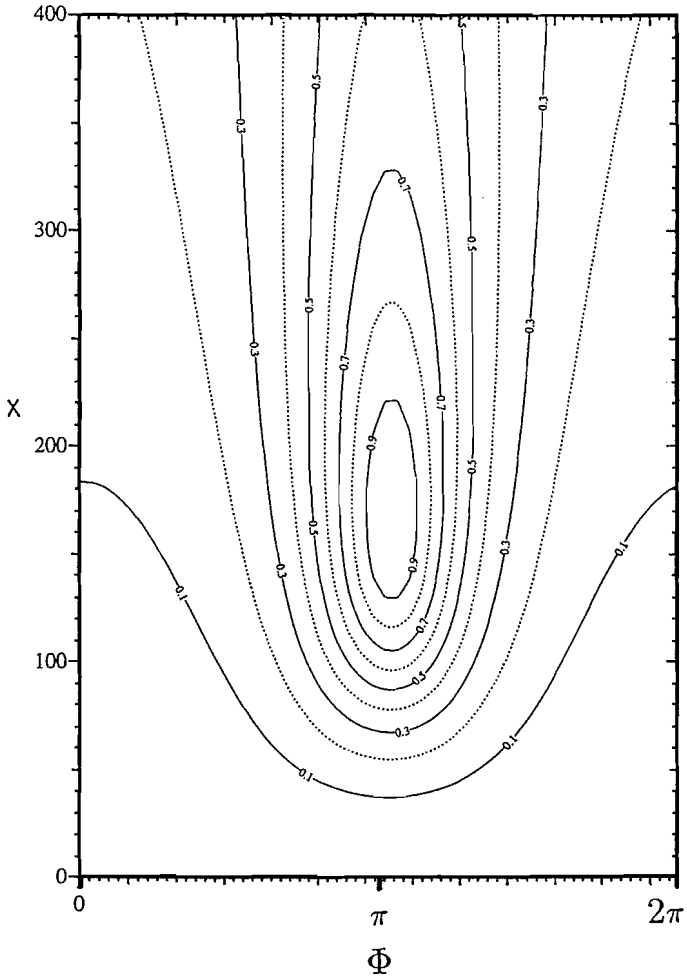

FIG. 7. As in Fig. 4 but with $v = 27$, and $v = 31$.

is shown in Fig. 7. The observed range of control is large, with the maximum in the Na(4*s*) yield appearing at very large x. This is a consequence of the relatively small Franck–Condon factor between the intermediate state and $v = 31$. That is, if one of the excitation paths has a much weaker cross section, the electric field carrying that component to the continuum must be increased to compensate, resulting in large x.

4. Conclusion

We have proposed a SEP one photon vs. one photon coherent control scheme with a number of experimental advantages. Specifically, the scenario allows minimization of effects due to laser jitter and reduction of effects due to uncontrolled satellites. The scenario shows the possibility of a wide range of control, as demonstrated in computations on electronic branching in the photodissociation of Na_2.

Acknowledgements

This work was supported by the U.S. Office of Naval Research and by the Ontario Laser and Lightwave Research Centre.

1. P. Brumer and M. Shapiro. Acc. Chem. Res. **22**, 407 (1989); Annu. Rev. Phys. Chem. **42**, 257 (1992), and references therein.
2. S.A. Rice. Science, **258**, 412 (1992); W.S. Warren, H. Rabitz, and M. Dahleh. Science, **259**, 1581 (1993).
3. P. Brumer and M. Shapiro. Chem. Phys. Lett. **126**, 541 (1986).
4. Z. Chen, P. Brumer, and M. Shapiro. J. Chem. Phys. **98**, 6843 (1993).
5. M. Shapiro and P. Brumer. J. Chem. Phys. **90**, 6179 (1989).
6. C.E. Hamilton, J.L. Kinsey, and R.W. Field. Annu. Rev. Phys. Chem. **37**, 493 (1986).
7. P. Roman. Advanced quantum theory. Addison-Wesley, Reading, Mass. 1965.
8. G. Jeung. J. Phys. B: At. Mol. Phys. **16**, 4289 (1983); A. Schmidt. Ph.D. Dissertation, Univ. Kaiserslautern, Germany.
9. H. Lefebvre-Brion and R.W. Field. Perturbations in the spectra of diatomic molecules. Academic Press, Orlando, Fla. 1986.
10. U. Gaubatz, P. Rudecki, S. Shiemann, and K. Bergmann. J. Chem. Phys. **92**, 5363 (1990).
11. J. Dods. M.Sc. Dissertation, University of Toronto (1992).
12. I. Levy and M. Shapiro. J. Chem. Phys. **89**, 2900 (1988).
13. M. Shapiro and R. Bersohn. Annu. Rev. Phys. Chem. **33**, 409 (1982).
14. M. Shapiro and G.G. Balint-Kurti. Chem. Phys. **61**, 137 (1981), and references therein.

5. Appendix: Computational details

The bound–bound matrix elements, $\langle E_j|d|E_N\rangle\langle E_N|d|E_i\rangle$ that appear in $P(q;E)$ are calculated using uniform semiclassical wave functions.

To solve for the photodissociation amplitude, a considerable amount of manipulation is required. Here we only state the relevant results of the formulation (12, 13).

The amplitude $\langle Enq^-|d|E_i\rangle$ is obtained in accord with the method of Levy and Shapiro (12). Specifically we expand in partial waves

$$[A1] \quad \langle Enq^-|d|E_i\rangle \equiv \langle Enq^-|d|E_i, J_i, M_i\rangle$$

$$= \frac{\sqrt{2\mu k_n}}{h} \sum_{J,p,\lambda\geq 0} \begin{pmatrix} J & 1 & J_i \\ -M_i & 0 & M_i \end{pmatrix} \sqrt{2J+1}\, \mathcal{D}^{J,p}_{\lambda,M_i}(\phi_k, \theta_k, 0)\mathrm{t}(EJp\lambda q|E_iJ_i)$$

where $\hat{\mathbf{k}} = (\phi_k, \theta_k)$ is the direction of the recoiling fragments and λ is the magnitude of the electronic angular momentum about the internuclear axis. The $\mathcal{D}^{J,p}_{\lambda,M_i}$ are the parity-adapted rotation matrices defined, with parity $p = \pm 1$ as:

$$[A2] \quad \mathcal{D}^{J,p}_{\lambda,M_i} = t_\lambda[\mathcal{D}^{J}_{\lambda,M_i} + p\mathcal{D}^{J}_{-\lambda,M_i}]$$

Can. J. Chem. Downloaded from www.nrcresearchpress.com by 195.246.54.202 on 09/08/12
For personal use only.

where $t_\lambda = \sqrt{\frac{1}{2}}$ for $\lambda \neq 0$ and $t_\lambda = \frac{1}{2}$ for $\lambda = 0$. The quantity $\mathbf{t}$ is the reduced matrix element for photodissociation.

$$[A3] \quad \mathbf{t}(EJp\lambda q|E_iJ_i) = (-1)^\lambda t_\lambda \sqrt{(2J+1)(2J_i+1)} \begin{pmatrix} J & 1 & J_i \\ -\lambda & \lambda & 0 \end{pmatrix} (1 + p(-1)^{J+1+J_i}) \times \sum_\xi \int \mathrm{d}\, R\Phi_\xi^{*(J,p-)}(R)(\xi|d|g)\Phi_{E_i}^{J_i}(R)$$

Here the sum over ξ is over all the electronic states that correlate with the same final channel. The $(\xi|d(R)|g)$ matrix element is the electronic transition dipole moment between the ground state and the ξth state. The quantity $\Phi_\xi^{(J,p-)}(R)$ is the radial nuclear scattering wave function in electronic state's ξ and $\Phi_{E_i}^{J_i}(R)$ is the radial nuclear bound wavefunction with energy E_i.

The $\mathbf{t}$ matrix element is computed using the artificial channel method (14).

To calculate the probability $P(q; E)$ requires repeated use of this explicit form. For example, to calculate the first term d_{44}^q, we expand the $\mathcal{D}_{\lambda,M_i}^{J,p}$ and perform the integration over the scattering angle $\hat{\mathbf{k}}$ to arrive at:

$$[AA4] \quad d_{44}^q = \frac{8\pi\mu k_n}{\hbar^2} \sum_{J,p,\lambda\geq 0} \begin{pmatrix} J & 1 & J_i \\ -M_i & 0 & M_i \end{pmatrix}^2 |\mathbf{t}(EJp\lambda nq|E_iJ_i)|^2$$

Similarly, the other terms in $P(q; E)$ are given by:

$$[AA5] \quad d_{33}^q = \frac{8\pi\mu k_n}{\hbar^2} \sum_{J,p,\lambda\geq 0} \begin{pmatrix} J & 1 & J_j \\ -M_j & 0 & M_j \end{pmatrix}^2 |\mathbf{t}(EJp\lambda q|E_jJ_j)|^2$$

and

$$[AA6] \quad d_{34}^q = \frac{8\pi\mu k_n}{\hbar^2} \sum_{J,p,\lambda\geq 0} \begin{pmatrix} J & 1 & J_i \\ -M_i & 0 & M_i \end{pmatrix} \begin{pmatrix} J & 1 & J_j \\ -M_j & 0 & M_j \end{pmatrix} \mathbf{t}(EJp\lambda q|E_iJ_i)\mathbf{t}^*(EJp\lambda q|E_jJ_j)$$

In general, the sums over J extend over $J_i - 1$, J_i, $J_i + 1$ except for the $J_i = 0$ case for which there is only the $J = 1$ term.

Can. J. Chem. Downloaded from www.nrcresearchpress.com by 195.246.54.202 on 09/08/12
For personal use only.

Controlled variation of boundary-activated ion fragmentation processes in a quadrupole ion trap

RAYMOND E. MARCH[1] AND MARK R. WEIR[2]
Department of Chemistry, Trent University, Peterborough, ON K9J 7B8, Canada

FRANK A. LONDRY
Department of Physics, Trent University, Peterborough, ON K9J 7B8, Canada

SILVIA CATINELLA AND PIETRO TRALDI
Consiglio Naxionale delle Ricerche, Corso Stati Uniti, 4, Padova, Italy 35020

AND

JOHN A. STONE AND W. BRADLEY JACOBS
Department of Chemistry, Queen's University, Kingston, ON K7L 3N6, Canada

Received August 24, 1993

This paper is dedicated to Professor John C. Polanyi on the occasion of his 65th birthday

RAYMOND E. MARCH, MARK R. WEIR, FRANK A. LONDRY, SILVIA CATINELLA, PIETRO TRALDI, JOHN A. STONE, and W. BRADLEY JACOBS. Can. J. Chem. **72**, 966 (1994).

Fragmentation in a quadrupole ion trap of each of two isomeric molecular ions, obtained from 4-nitro-*o*-xylene and 4-nitro-*m*-xylene, has been investigated. It is demonstrated that the degree of fragmentation may be controlled by prolongation of both the duration for which the working point of the mass-selected species is held in the vicinity of a stability boundary and a prior collisional cooling period. The extent of fragmentation has been found to increase as the working point is held near the $\beta_z = 0$ stability boundary while the relative abundances of fragment ions can be varied with the duration of the collisional cooling period. Under appropriate conditions for 4-nitro-*o*-xylene, >94% of the isolated ions can be fragmented; <5% of the ions are lost from the ion trap while 1% remain intact. As 99% of the charge of the fragmented ions is retained in the ion trap, the overall optimum efficiency of boundary-activated dissociation is >93%; the corresponding efficiency for 4-nitro-*m*-xylene is 74%. 50% of the selected ions can be fragmented in ≤3 ms. The results are compared with collision-activated dissociation studies carried out with a triple stage quadrupole–hexapole–quadrupole instrument. This technique of boundary-activated dissociation provides a general procedure which does not require careful tuning of the instrument as is required for the more commonly-used technique of resonance excitation.

RAYMOND E. MARCH, MARK R. WEIR, FRANK A. LONDRY, SILVIA CATINELLA, PIETRO TRALDI, JOHN A. STONE et W. BRADLEY JACOBS. Can. J. Chem. **72**, 966 (1994).

On a étudié la fragmentation de deux ions moléculaires, obtenus à partir des 4-nitro-*o*-xylène et 4-nitro-*m*-xylène, dans un piège à ions quadripolaires. On a démontré que le degré de fragmentation peut être contrôlé par une prolongation à la fois de la période préalable de refroidissement collisionnel et de la durée pour laquelle le point de travail des espèces de masse choisie est maintenue dans les environs d'une frontière de stabilité. On a trouvé que le degré de fragmentation augmente lorsque le point de travail est maintenu près de la frontière de stabilité $\beta_z = 0$ alors que les abondances relatives des ions fragments peuvent être amenées à varier avec la durée de la période de refroidissement collisionnel. Pour le 4-nitro-*o*-xylène dans des conditions appropriées, >94% des ions isolés peuvent être fragmentés; <5% des ions sont perdus du piège à ions et 1% demeure intact. Comme 99% de la charge des ions fragmentés sont retenus dans le piège à ions, l'efficacité optimale globale de la dissociation activée par la frontière est >93%; l'efficacité correspondante pour le 4-nitro-*m*-xylène est de 74%. Près de 50% des ions choisis peuvent être fragmentés en ≤3 ms. On compare ces résultats avec ceux d'études de dissociations activées par des collisions et effectuées à l'aide d'une appareil à trois stades quadripolaire–hexapolaire–quadripolaire. Cette technique de la dissociation activée par la frontière fournit une méthode générale qui ne requiert pas un ajustement aussi rigoureux que celui exigé pour la technique habituelle de l'excitation par résonance.

[Traduit par la rédaction]

Introduction

The quadrupole ion trap has been shown to be highly effective for performing tandem mass spectrometry (MS/MS) experiments (1, 2). An essential element of tandem mass spectrometry is the quiescent period when the amplitude of the RF drive potential is held constant, following a process of mass-selection, and the isolated reactant ion species is allowed to undergo unimolecular and/or bimolecular reactions which, in the widest sense, will include cluster formation, photo-dissociation (3, 4), collisions with surfaces (5), pulsed axial activation (6), and resonance excitation. The vast majority of ion trap MS/MS data has been obtained with an auxiliary RF potential, or "tickle" (7) voltage, applied across the end-cap electrodes and oscillating at a frequency resonant with a component of the secular motion of a chosen and isolated ion species. However, the "tickle" frequency must be carefully tuned to the secular frequency of the ion if high fragmentation efficiencies are to be obtained and this tuning procedure is experimentally difficult for transient species, such as those eluting from a chromatographic inlet. A general procedure for ion activation which does not require such careful tuning would, therefore, be useful for ion trap tandem mass spectrometry.

[1]To whom correspondence should be addressed

[2]Present address: Department of Chemistry, University of Calgary, Calgary, Alberta, Canada.

Can. J. Chem. Downloaded from www.nrcresearchpress.com by 195.246.54.202 on 09/08/12
For personal use only.

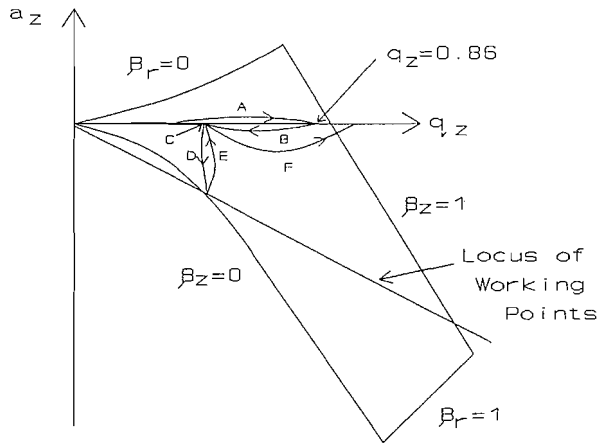

FIG. 1. Stability diagram in a_z, q_z space for the quadrupole ion trap showing the four boundaries at which $\beta_z = 0$ and 1, and $\beta_r = 0$ and 1. The movement of the working point of a chosen ion species is described by the path ABCDEF. Ion ejection was carried out at q_z = 0.86, as shown. The locus of all working points during boundary-activated dissociation is shown also.

Two such ion activation methods which employ DC pulses rather than resonance excitation have been reported recently. When short-duration, fast-rising DC pulses of amplitude ca. 350 V are applied to both end-cap electrodes, ions impinge upon the end-cap electrodes and interact with the surfaces (5). For example, in the dissociation of the pyrene molecular ion, *m/z* 202, the fragment ion of *m/z* 122 was observed; while the relative abundance of this fragment was but 0.2%, observation of this fragment is significant in that its appearance energy is some 17 eV. A related method of pulsed axial activation has been reported from the same laboratory (6); here, ion activation was observed using fast DC pulses applied to one end-cap electrode only. The amount of internal energy deposited, which can be controlled directly by variation of the amplitude of the pulse, has been estimated to exceed 10 eV in the dissociation of the *n*-butylbenzene molecular ion and 13 eV for dissociation of $W(CO)_6^{+\cdot}$ to W^+. Dissociation efficiencies ranged from 50% at low internal energy deposition to 5% at maximum internal energy deposition. In the high internal energy regime, collisions with an electrode surface may occur.

A further ion activation–method proposed in 1991 (8) has attracted considerable attention (9–13). This method is based on the interaction of mass-selected ions with the high fields derived from the RF drive potential; this interaction causes acceleration of the ion which is dissociated following activation in collisions with the buffer gas. The interaction of the ions with the high fields is brought about experimentally by choosing values of the stability parameters (1) a_z and q_z such that the working point of the ion species is located close to the boundary of the stability diagram (Fig. 1); it is for this reason that this method has been described as "boundary activation", or "boundary-activated dissociation" (BAD). BAD is, therefore, a mass-selective collisional process which does not require the careful tuning of a tickle voltage. Curcuroto et al. (11) found that internal energy deposition at a boundary exceeded that observed by tickling, yet Creaser and O'Neill (13) found that energy deposition in BAD was generally lower than that for optimized CAD.

The positioning of the working point of a given ion species close to a boundary of the stability diagram has implications for the trajectory stability of other ion species stored simultaneously in the ion trap. Let us recall that, under all operating conditions of the ion trap, the locus of working points of stored ions is a straight line passing through the origin of the stability diagram in a_z, q_z space. When the working point of a given ion species is moved to the $\beta_z = 1$ boundary the trajectories of ions having lower mass/charge, *m/z*, ratios become unstable and such ions are lost from the trap. When the working point of the same ion species is moved subsequently close to the $\beta_z = 0$ boundary, the trajectories of ions having higher *m/z* ratios become unstable and these ions are lost from the trap leaving the given ion species isolated in the ion trap. When the working point is held in the vicinity of the $\beta_z = 0$ boundary for some milliseconds, the isolated ion species undergoes BAD following activating collisions with helium buffer gas; fragment ions are formed which can be detected during a normal analytical scan of the instrument, and the locus of the working points (during BAD) of all ion species is shown in Fig. 1. Thus ion isolation carried out in two consecutive steps, as described above, can be followed immediately by a non-resonant excitation process leading to fragmentation of the isolated ion species.

In simulation studies (14) of consecutive ion isolation (15), it was found that a period of collisional cooling of a given ion species, prior to moving the working point close to the $\beta_z = 0$ boundary, had a profound effect on the amount of energy that an ion could absorb from the RF field without the ion being lost in a collision with an electrode. Consequently, it was hypothesized that the fragmentation pattern obtained by BAD would be affected by a period of collisional cooling also. This hypothesis was tested experimentally using 2,6-dimethyl-9-methoxy-4*H*-pyrrole[3,2,1,-*ij*]quinoline-4-one, synthesized and purified as described elsewhere (16). This compound was selected on the basis of the availability of a large amount of mass spectrometric data (11, 17); in retrospect, it was not the best choice as the activation energies of the fragmentation channels are not known. However, at that time, the marked effects of variation of cooling time prior to BAD were not known also. Upon BAD, at a helium buffer gas pressure of ca. 1×10^{-3} Torr, four fragment ion species were observed, two of which had not been observed with tickle excitation (18, 19). Furthermore, when the cooling period was varied from 0–450 μs, the fragment ion relative abundances varied in a fashion reminiscent of that exhibited in an energy-breakdown curve.

We report here a study of the effects of variation of the duration of each of collision cooling and boundary-activated dissociation on the mass-selected isomeric molecular ions of 4-nitro-*o*-xylene and 4-nitro-*m*-xylene, together with a comparison of collision-activated dissociation (CAD) carried out with a triple stage (QhQ) instrument comprised of two quadrupole mass filters with an intervening hexapole collision cell. Again, the choice of compound was not the best, but an inter-laboratory study is now underway of five compounds selected on the basis of known thermochemistry.

Experimental

The ion trap experiments were carried out with a modified Varian Saturn I Ion Trap Detector operated with dipolar resonance ejection at a fixed frequency of 416.5 kHz to give mass-selective ejection at q_z = 0.86 during the analytical scan. The modified Saturn I instrument was controlled by a data acquisition programme which had been written in a combination of C and assembler. Scan functions, which describe the temporal variations of electrode potentials during each experiment, were customized to perform CAD experiments utilizing BAD with or

Can. J. Chem. Downloaded from www.nrcresearchpress.com by 195.246.54.202 on 09/08/12
For personal use only.

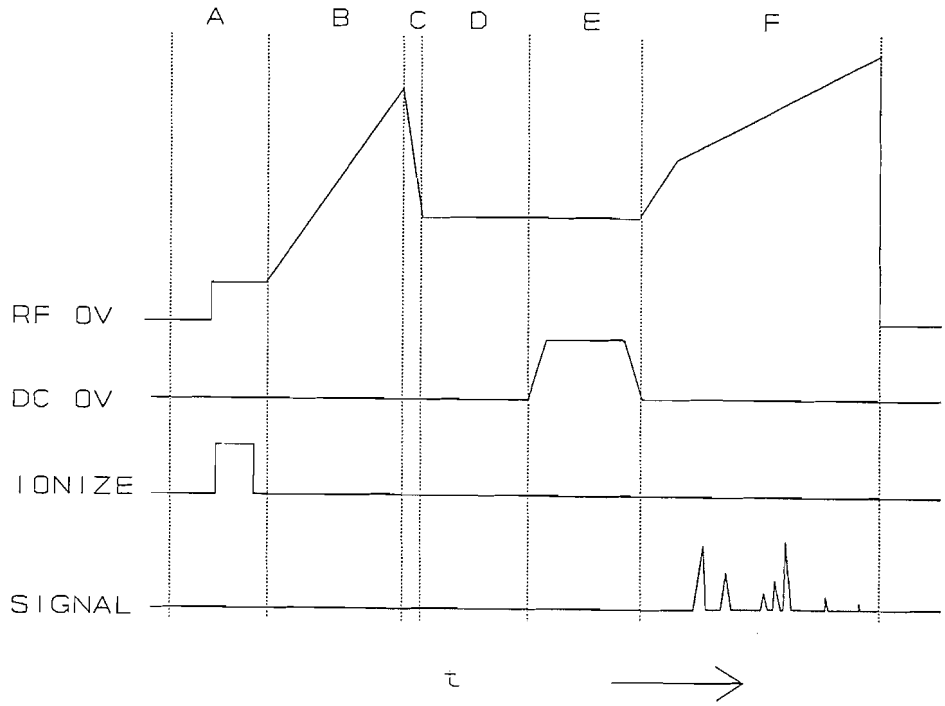

FIG. 2. The scan function for ion isolation and boundary-activated dissociation. The segments are described in the text.

without a period of collisional cooling; a typical scan function for a consecutive isolation/BAD experiment is shown in Fig. 2. The corresponding effect on the working point of the chosen ion species is shown in Fig. 1: here, the initial RF ramp (A) moved the working point of the chosen ion species close to $q_z = 0.86$ whereupon all lower mass ions were ejected; the RF amplitude was ramped down (B) to place the chosen ion's working point at C where a cooling period could be incorporated into the scan function; a DC pulse was applied (D) to move the working point to the vicinity of the $\beta_z = 0$ boundary; at the end of the DC plateau duration, the DC pulse was removed (E) and was followed by an analytical scan (F).

The ion trap was operated in pulsed mode, that is, ionization was effected with a pulse of 70 eV electrons (segment A in Fig. 2), after which the RF level was increased to eject ions of low *m/z* values at $q_z = 0.86$ using axial modulation (segment B). The q_z value of the chosen ion species was established by ramping the RF level to the appropriate value (segment C). Segment D represents a collisional cooling period of variable duration, which was followed by a DC ramp (segment E) to move the working point of the chosen ion species to the vicinity of the $\beta_z = 0$ boundary and to eject ions of higher *m/z* values. The DC level was maintained for a variable period, then reduced to zero and followed by a mass-instability scan of the RF voltage. Collision-activated dissociation mass spectra were obtained by co-adding 500 microscans. The absolute partial pressures of 4-nitro-*o*-xylene (m.p. 30–31°C) and 4-nitro-*m*- xylene (m.p. 9°C) in the ion trap were not known. Concentrations of these compounds were adjusted by varying the temperature of the inlet system to obtain an ion count of ca. 20 000 ions with an ionization period of 1000 μs. The helium pressure in the manifold measured with a Bayard–Alpert ionization gauge corrected for helium sensitivity was ca. 0.1×10^{-3} Torr; the helium pressure in the ion trap is ca. ten times that in the manifold. Under these conditions, collisions of ions with helium atoms are much more frequent than with parent molecules.

The QhQ instrument was a VG Quattro (Fisons Instruments, Altringham, England). Ions were formed by 70 eV electron ionization, selected by a first quadrupole, dissociated in the middle hexapole collision cell and analyzed by a second quadrupole. The collision gas was argon and the energy of the incident ion beam was determined by the potential difference between the ion source and the collision cell. Collision-activated dissociation mass spectra was obtained by multichannel accumulation of data from ca. 20–30 scans.

Results and discussion

4-Nitro-o-xylene

The fragmentation scheme for the molecular ion of 4-nitro-*o*-xylene is given in eq. [1]

$$\begin{aligned} C_6H_3(CH_3)_2NO_2^{+\cdot} &\rightarrow 121^+ + NO^{\cdot} \qquad (ortho) \\ &\rightarrow 106^{+\cdot} + NO^{\cdot} + CH_3^{\cdot} \\ &\rightarrow 105^+ + NO_2^{\cdot} \\ &\rightarrow 93^+ + NO^{\cdot} + CO \\ &\rightarrow 91^+ + NO^{\cdot} + CH_2O \end{aligned} \qquad [1]$$

In Table 1 are shown the results of a number of experiments in which following ejection of ions of lower *m/z* ratio the working point for the molecular ion of 4-nitro-*o*-xylene, *m/z* 151, was moved from the q_z axis to the vicinity of the $\beta_z = 0$ boundary and then returned to the q_z axis, at a constant value of $q_z = 0.3$. The abundances were reproducible to within 1% of abundances in excess of 20%, and up to 5% for lower abundances. Throughout this work, reference is made to the base condition wherein there was no cooling period and the DC plateau duration was zero. However, the imposition and removal of a positive DC pulse takes a finite time which is estimated as ca. 1 ms. As the duration of this "zero" DC plateau is not known precisely, all stated values of DC plateau duration refer to the additional duration of the DC plateau. Following the "zero" plateau duration, it was observed during the subsequent analytical scan that 95.2% of the total ion signal was due to the molecular ion and the remainder was due to four fragment ion species, *m/z* 121, 105, 93, and 91. The amplitude of the DC pulse was selected such that the total ion signal was not significantly less (>95%) than the signal due to the molecular ion in the absence of the DC pulse, yet traces of fragment ions could be detected.

Can. J. Chem. Downloaded from www.nrcresearchpress.com by 195.246.54.202 on 09/08/12
For personal use only.

TABLE 1. 4-Nitro-*o*-xylene ion abundances following boundary-activated dissociation expressed as percentages of the total ion abundance with "zero" DC plateau duration and zero cooling; $q_z = 0.3$

	m/z 151	*m/z* 121	*m/z* 106	*m/z* 105	*m/z* 93	*m/z* 91	Σ
0[a]; 0[b]	95.2	4.1	0	0.2	0.3	0.2	100
15; 0	1.4	38.2	0.7	1.4	3.0	1.6	46.3
15; 50	1.8	35.2	1.6	1.2	2.5	1.5	43.8
15; 100	2.1	32.2	2.4	1.0	2.1	1.3	41.1

[a]Plateau duration in milliseconds.
[b]Collisional cooling duration in milliseconds.

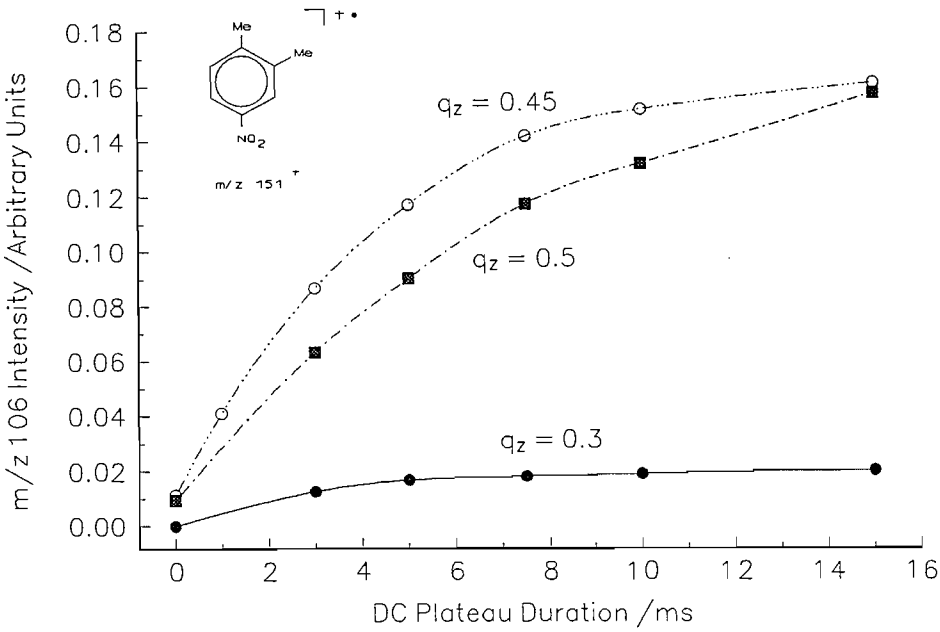

FIG. 3. Boundary-activated dissociation; variation of the degree of fragmentation of $M^{+\cdot}$ of 4-nitro-*o*-xylene to *m/z* 106 with DC plateau duration (in excess of "zero" duration) for three values of q_z:

These conditions were appropriate for the removal of (hypothetical) ions of higher *m/z* ratio; the total ion signal was used as a basis for comparison with those obtained with a finite pre-cooling and/or a plateau duration. As the DC plateau duration was increased to 15 ms, the relative abundance of the molecular ion fell dramatically (to 1.4%); approximately half of the molecular ions were lost from the ion trap, while half were dissociated among all of the previously-observed dissociation channels together with a new channel to form *m/z* 106. The dominant dissociative channel showed the loss of NO˙ to form *m/z* 121. According to Beynon et al. (20), *m/z* 151 dissociates via two competitive unimolecular mechanisms with similar activation energies. One channel leads to *m/z* 121 with a resonance-stabilized aryloxy cation structure while the other channel proceeds through a three-membered epoxide intermediate resulting in relatively unstable *m/z* 121 ions. When the experiment was repeated with a cooling period of 50 ms, each of the original dissociative channel products showed slight decreases in relative abundance, the overall ion signal was lowered, yet the molecular ion abundance and that of *m/z* 106 increased somewhat. These results indicate that formation of *m/z* 106 is favoured under these conditions but the retention of other fragment ions is impaired. This trend is continued when the cooling period is increased to 100 ms.

The entire series of experiments was repeated at $q_z = 0.45$. At zero cooling and "zero" DC plateau duration, the mass spectrum was not dissimilar from that obtained earlier. A trace of fragment ion *m/z* 106 was observed here, while no signal was detected for *m/z* 91. Again upon allowing a plateau duration of 15 ms, the relative abundance of the molecular ion fell dramatically to 0.7% but, under these conditions, there was high retention of ions within the trap in that 99.2% of the original total ion abundance was retained. Once more, the principal fragment ion species was *m/z* 121 (73.8%); the other species detected were *m/z* 106, 105, 93, and 91. Upon the addition of cooling periods of 50 and 100 ms, the system reacted in a very interesting manner. The total ion abundance fell only slightly to 97.6% at the longer cooling time, showing that evaporative ion losses are minimal at the higher value of $q_z = 0.45$. Fragment ion species of *m/z* 121, 105, and 93 declined in relative abundance while those of *m/z* 106 and 91 increased. These results, wherein ions with lower *m/z* ratios are observed with greater abundance at the expense of ions of higher *m/z* ratios, suggested that fragmentation reaction channels of relatively high activation energies become more competitive with those of lower activation energies as the cooling period is increased. The more an ion is cooled, the greater is the internal energy which may be acquired subsequently by the ion so that, upon unimolecular fragmentation, fragmentation channels of greater activation energy are accessed.

The effect of DC plateau duration on the fragmentation of the

Can. J. Chem. Downloaded from www.nrcresearchpress.com by 195.246.54.202 on 09/08/12
For personal use only.

TABLE 2. 4-Nitro-*o*-xylene ion abundances following boundary-activated dissociation expressed as percentages of the total ion abundance with "zero" DC plateau duration and zero cooling; $q_z = 0.45$

	m/z 151	*m/z* 121	*m/z* 106	*m/z* 105	*m/z* 93	*m/z* 91	Σ
0[a]; 0[b]	92.2	6.4	0.3	0.3	0.8	0	100
15; 0	0.7	73.8	4.4	3.4	8.0	8.9	99.2
15; 50	1.1	69.3	9.8	3.1	6.7	9.4	99.4
15; 100	1.6	61.7	16.8	2.7	5.2	9.6	97.6

[a]As for Table 1.
[b]As for Table 1.

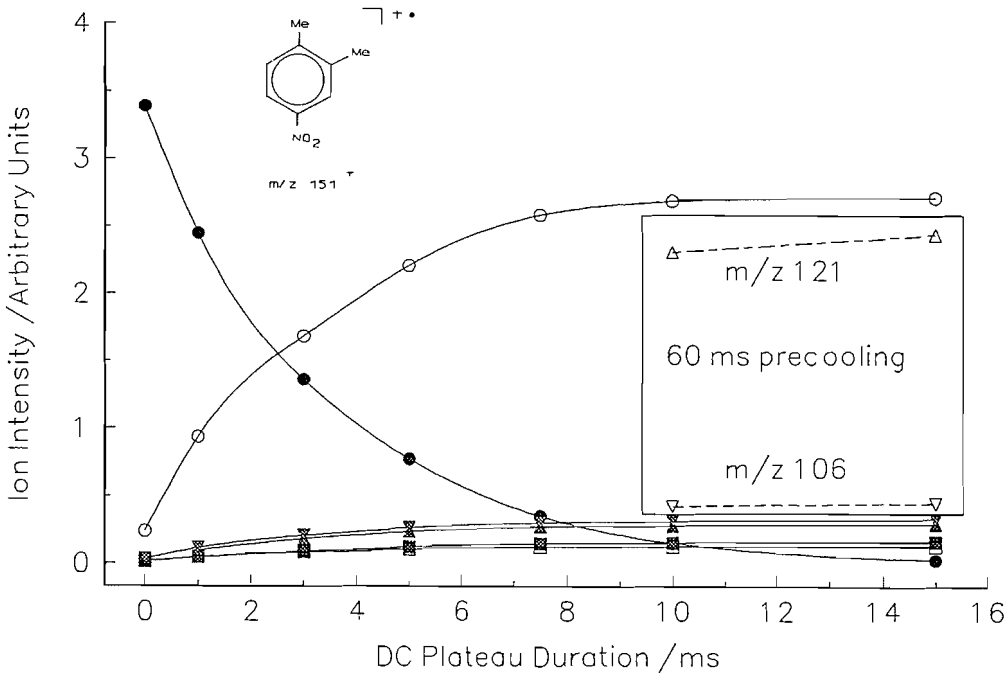

FIG. 4. Boundary-activated dissociation; variation of fragmentation of $M^{+\cdot}$ of 4-nitro-*o*-xylene and formation of fragment ions with DC plateau duration (in excess of "zero" duration) at $q_z = 0.45$. The effects of a cooling period of 60 ms on the relative abundances of *m/z* 121 and *m/z* 106 are shown in the inset. Total ion retention at the end of 15 ms of DC plateau is 97%.

molecular ion of 4-nitro-*o*-xylene to *m/z* 106 by loss of NO˙ and CH_3˙ is shown in Fig. 3 for three values of q_z. The results obtained at $q_z = 0.3$ show that the maximum yield of *m/z* 106 is reached after some 7.5 ms, at this point virtually all of the molecular ions either had been dissociated or ejected from the trap. At $q_z = 0.45$, fragmentation to *m/z* 106 continues throughout the observation time of 15 ms at which point virtually all of the molecular ions had been dissociated; there was no ion loss under these conditions. Note that the intensities of *m/z* 106 for 15 ms of DC plateau duration at $q_z = 0.3$ and $q_z = 0.45$ correspond to the appropriate abundances shown in Tables 1 and 2, respectively. At $q_z = 0.5$, the final degree of fragmentation to *m/z* 106 is similar to that obtained at $q_z = 0.45$. Although the field which the molecular ion experiences is greater at the higher value of q_z, the initial rate of fragmentation at $q_z = 0.5$ is lower than that at $q_z = 0.45$; a probable explanation for this observation is that the proximity of the working point to the $\beta_z = 0$ boundary differed slightly in these two experiments.

The influence of DC plateau duration on the abundances of the 4-nitro-*o*-xylene molecular ion and fragment ions at $q_z = 0.45$ is shown in Fig. 4. This value for q_z was chosen to maximize both fragmentation and the mass range of daughter ions which could be stored. Total ion retention at the end of 15 ms of DC plateau is 97%. Also shown here is the effect of 60 ms of cooling. The principal dissociative channel enhanced by cooling is that in which *m/z* 106 is formed (by loss of NO˙ + CH_3˙), and at the expense of *m/z* 121 (formed by loss of NO˙).

In Fig. 5 it is seen that the relative abundance of the *m/z* 106 ion increases linearly with the duration of both DC plateau and cooling period. The possibility of a direct relationship between *m/z* 121 and *m/z* 106 arose as it had been observed in earlier work that *m/z* 502, as produced by electron impact from perfluorotri-*n*-butylamine, exists in a long-lived metastable state and, when isolated in the ion trap, undergoes unimolecular fragmentation without additional excitation. However, when *m/z* 121 was isolated and subjected to BAD for 20 ms, the only signals observed were those due to *m/z* 93 and 91, of approximately equal intensity, and presumably through losses of CO and CH_2O, respectively. By chance, here was a situation wherein an excited ion dissociated via two reaction channels with equal weighting without the benefit of a cooling period. Thus an opportunity was afforded for examining the effects, if any, of cooling mass-selected ions which upon 20 ms of BAD showed similar rate constants for two quite dissimilar rearrangement reactions. The effects of up to 100 ms of cooling mass-selected *m/z* 121 ions on the ratio of the product ions, *m/z* 91 and *m/z* 93,

Can. J. Chem. Downloaded from www.nrcresearchpress.com by 195.246.54.202 on 09/08/12
For personal use only.

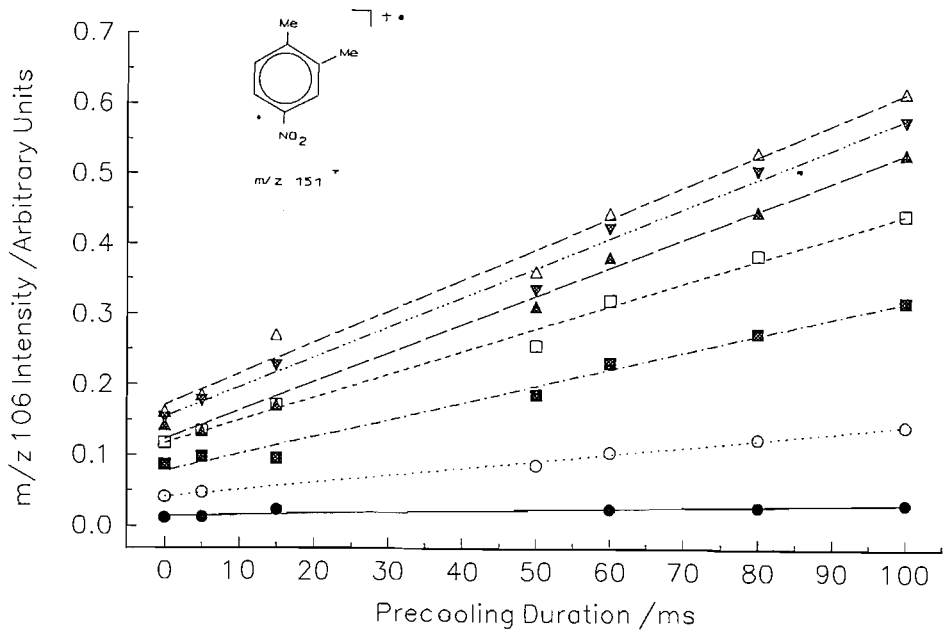

FIG. 5. Boundary-activated dissociation at $q_z = 0.45$; variation of the relative abundance of the *m/z* 106 fragment ion produced from $M^{+\cdot}$ of 4-nitro-*o*-xylene with the duration of a cooling period. Data are shown for each of seven DC plateau durations, as follows: ●, "zero" plateau duration; ○, 5 ms; ■, 15 ms; □, 50 ms; ▲, 60 ms; ▼, 80 ms; △, 100 ms.

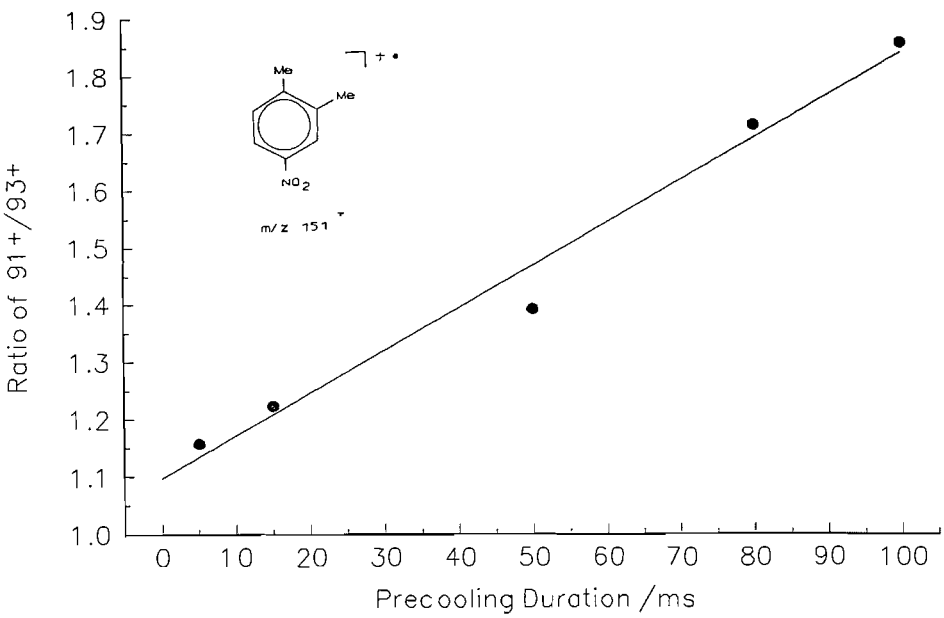

FIG. 6. Boundary-activated dissociation of *m/z* 121 from 4-nitro-*o*-xylene; variation of the intensity ratio of the product ions, *m/z* 91 and 93, with the duration of a cooling period.

are shown in Fig. 6. The signal intensity ratio for *m/z* 91 and *m/z* 93 increased as the cooling period was extended, so that, after 100 ms of cooling the abundance ratio *m/z* 91/*m/z* 93 was double that in the absence of cooling. Thus, on the basis of our understanding of the results to date, it would appear that the activation energy for the formation of *m/z* 91 exceeds that for formation of *m/z* 93. This hypothesis was confirmed by the dissociation of *m/z* 121 in a triple stage quadrupole instrument: here, at each of two collision energies, the signal intensity of *m/z* 91 was less than that of *m/z* 93; the abundance ratio *m/z* 91/*m/z* 93 was 1:7 at a collision energy of 10 eV and 1:4 at 100 eV.

Parenthetically, once appropriate values for q_z (0.45) and the DC pulse amplitude (95 V) had been chosen, tandem mass spectrometry was performed facilely up to $(MS)^5$ using the existing software.

4-Nitro-m-*xylene*

Fragmentation of the 4-nitro-*m*-xylene molecular ion differs significantly from that of the *ortho* isomer, as is shown in eq. [2]

$$\text{[2]}\quad \begin{aligned} C_6H_3(CH_3)_2NO_2^{+\cdot} &\rightarrow 135^{+\cdot} + O \qquad (\textit{meta}) \\ &\rightarrow 134^{+} + OH^{\cdot} \\ &\rightarrow 106^{+\cdot} + NO^{\cdot} + CH_3^{\cdot} \\ &\rightarrow 105^{+} + NO_2^{\cdot} \end{aligned}$$

Can. J. Chem. Downloaded from www.nrcresearchpress.com by 195.246.54.202 on 09/08/12
For personal use only.

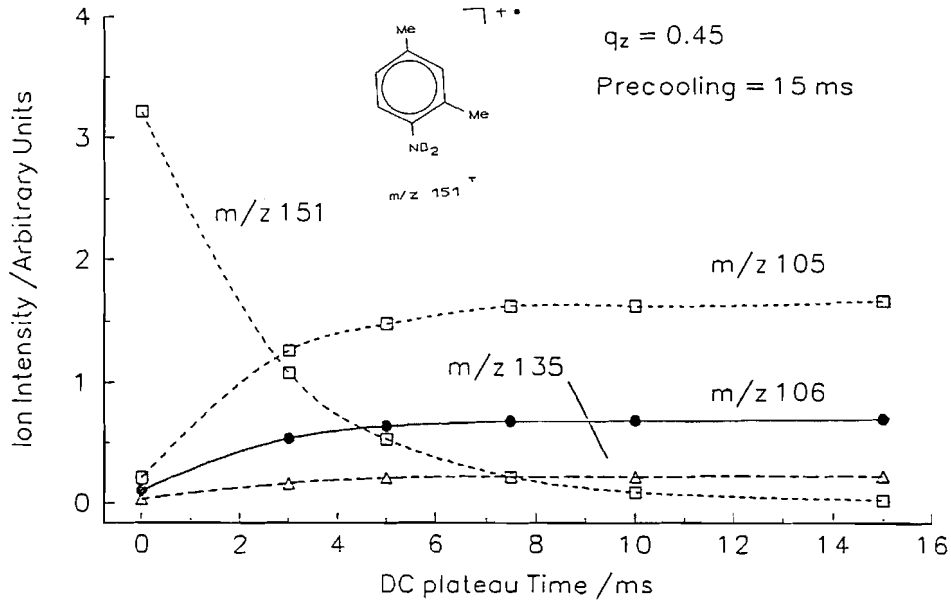

FIG. 7. Boundary-activated dissociation; variation of the relative abundances of $M^{+\cdot}$ of 4-nitro-*m*-xylene and fragment ions with DC plateau duration (in excess of "zero" duration), at $q_z = 0.45$, and with 15 ms of cooling.

TABLE 3. 4-Nitro-*m*-xylene ion abundances following boundary-activated dissociation expressed as percentages of the total ion abundance with "zero" DC plateau duration and zero cooling; $q_z = 0.3$

	m/z 151	*m/z* 135	*m/z* 134	*m/z* 106	*m/z* 105	Σ
0[a]; 0[b]	94.3	0.9	1.3	0.9	2.6	100
15; 0	0.9	2.8	2.1	4.6	14.6	25.0
15; 50	1.0	2.9	2.4	5.0	15.6	26.9

[a]As for Table 1.
[b]As for Table 1.

TABLE 4. 4-Nitro-*m*-xylene ion abundances following boundary-activated dissociation expressed as percentages of the total ion abundance with "zero" DC plateau duration and zero cooling; $q_z = 0.45$

	m/z 151	*m/z* 135	*m/z* 134	*m/z* 106	*m/z* 105	Σ
0[a]; 0[b]	83.9	1.0	1.3	4.7	9.1	100
15; 0	0.8	6.6	2.4	19.9	48.2	77.9
15; 50	0.8	6.4	2.6	19.8	47.1	76.7
15; 80	0.8	6.5	2.7	19.6	46.1	75.7

[a]As for Table 1.
[b]As for Table 1.

The above series of experiments was repeated with the molecular ion of 4-nitro-*m*-xylene at both $q_z = 0.3$ and 0.45; the results are shown in Tables 3 and 4, respectively. At $q_z = 0.3$ and with zero cooling and "zero" DC plateau, the results obtained were similar to those for 4-nitro-*o*-xylene, except that the fragments were different; in place of *m/z* 121, 93, and 91, ions of *m/z* 135 and 134 were observed. Upon introducing a plateau duration of 15 ms, 75% of the ions were lost from the trap, the relative abundance of the molecular ion fell to 0.9% but that of each of the four fragment ion species was increased. When a cooling period of 50 ms was introduced, the relative abundances of all of the ion species were increased slightly, and the total ion signal increased accordingly.

The results shown in Table 3 indicate that, with finite plateau duration and cooling period, only half the number of fragment ions from the *meta* isomer remain in the trap compared with those of the *ortho* isomer at $q_z = 0.3$. As the experimental conditions were the same for each isomer, then the degrees of internal energy enhancement must have been comparable for the isomeric molecular ions, thus a lowered retention of ions indicates that evaporation of *meta* isomer molecular ions exceeds fragmentation and that the activation energies of the dissociative reaction channels are greater than those for the *ortho* isomer.

The results shown in Table 4 were obtained for the *meta* isomer at $q_z = 0.45$. Under zero cooling and DC plateau conditions, some 16.1% of the molecular ion dissociated to form the four fragment ion species. When the DC plateau duration was extended to 50 ms, the molecular ion was almost fully dissociated; the major fragmentation channels were those which led to the formation of *m/z* 105 and 106 in the abundance ratio 5:2. The insertion into the scan function of cooling periods of 50 and 80 ms duration had virtually no effect on the relative ion abundances.

From these results, the duration (15 ms) of the DC plateau is sufficient to bring about almost complete dissociation of the molecular ion. The influence of a cooling period here is small, at best; at $q_z = 0.3$, the relative abundances of all fragment ions were enhanced a little with a cooling period of 50 ms, while at $q_z = 0.45$, only the *m/z* 134 fragment ion relative abundance was enhanced. The total ion retention at $q_z = 0.45$ may be low due to formation of *m/z* 77 fragment ions which would not be detected under these conditions (*vide infra*); however, at $q_z = 0.3$, where such ions would have been detected, none were observed.

Variation of the relative abundances of the 4-nitro-*m*-xylene molecular ion and fragment ions with DC plateau duration at $q_z = 0.45$ and with 15 ms of cooling is shown in Fig. 7. Once more, the rapid decrease in molecular ion relative abundance continues smoothly throughout the period of observation. As dissociation of the molecular ion is virtually complete after 10 ms at the DC plateau with 69% ion retention, clearly BAD is compatible with the requirements for rapid ion dissociation on

Can. J. Chem. Downloaded from www.nrcresearchpress.com by 195.246.54.202 on 09/08/12
For personal use only.

Can. J. Chem. Downloaded from www.nrcresearchpress.com by 195.246.54.202 on 09/08/12
For personal use only.

the gas chromatographic time-scale, as reported earlier by Creaser and O'Neill (13). A DC plateau duration of only 2.7 ms is required for 50% dissociation; the corresponding time in Fig. 4 is 2.2 ms. The dominant fragment ion species is *m/z* 105 formed by loss of $NO_2^{\cdot}$.

The mechanism for BAD involves the action of the RF trapping field on the selected ion species when its working point is moved to the vicinity of the $\beta_z = 0$ stability boundary. The ions are both accelerated by the field and moved axially away from the centre of the ion trap whereupon they experience multiple collisions with helium buffer gas, acquire internal energy in these collisions and, in the limit, either dissociate due to their internal energy or escape from the trapping field once their kinetic energy exceeds the trapping potential. The proximity of the mass-selected ion working point to the $\beta_z = 0$ boundary, which is determined by the magnitude of the DC voltage applied to the ring electrode (at a given q_z) determines, in turn, both the degree of ion loss and the rate of ion dissociation. The magnitude of the DC voltage was chosen such that <5% of the total charge was lost when the DC voltage was applied and removed immediately, that is, with zero plateau time. Upon extending the plateau time under ideal conditions (see Table 2), more than 99% of mass-selected ions are lost either by dissociation (with 98.5% retention of fragment ions) or by ejection (0.8%) from the trap. Thus the optimum BAD efficiency (defined as the sum of the fragment ion signal intensities divided by the initial mass-selected ion signal intensity) for 4-nitro-*o*-xylene is >93%. For 4-nitro-*m*-xylene, the efficiency is >74%. Creaser and O'Neill (13), using a plateau time of 50 ms, reported a fragmentation efficiency (defined as the sum of the product ions divided by the sum of the product ions plus the residual precursor ions) of 99.2% for diethylbenzene and 8.9% for benzothiophene. Despite the low fragmentation efficiency for benzothiophene, the product ions permitted the presence of benzothiophene in a complex diesel matrix to be confirmed.

The locus of the working points of the fragment ions is a line passing through the origin of the stability diagram and the working point (near the $\beta_z = 0$ boundary) of the selected ion species. Thus the fragment ions' working points all lie at higher q_z and lower a_z values; yet these ions do not experience the high RF field experienced by the selected ion species, rather they appear to be focused collisionally towards the centre of the trap from which they are detected with high efficiency.

When BAD is carried out at $q_z = 0.45$, the mass range of daughter ions which may be trapped is limited by the intersection of the locus of working points with the $\beta_z = 1$ boundary which occurs at $q_z \approx 1.1$. Thus for the example of a mass-selected ion of *m/z* 151 subjected to BAD at $q_z = 0.45$, the mass range of daughter ions which may be trapped extends to *m/z* 62. Ions of lower *m/z* ratio are lost from the trap. In order to analyze, or detect, all of the ions stored, it is necessary to reduce the DC and RF voltages incrementally so as to maintain the working point of *m/z* 62 ions within the stability diagram. In the work described here, the daughter ion mass range is limited by two factors: firstly, the DC voltage was reduced in one step (thus placing all of the working points on the q_z axis) and, secondly, the analytical scan was carried out with axial modulation (that is, resonant ejection) at $q_z = 0.86$. Note that, in practice, resonant mass-selective instability occurs at $q_z = 0.9014$, rather than the intersection of the q_z axis and the $\beta_z = 1$ boundary for which the theoretical value of $q_z = 0.908$. Thus the daughter ion mass range in the experiments described above with BAD of *m/z* 151 at $q_z = 0.45$ extended to *m/z* 79 only.

The mechanism proposed for the cooling effect is based on the earlier simulation study (14) and the experimental observations. When ions have undergone a process of isolation, either by the concurrent or consecutive process, their trajectories fill a volume of several cubic millimeters near the centre of the trap. As their working point approaches the $\beta_z = 0$ boundary for the BAD, there is a competition between internal energy increase which will lead to dissociation and kinetic energy increase which will lead to ion loss. The moderating effects of ion/buffer gas collisions are negligible under BAD conditions. In an extreme case, when an ion is accelerated by the field and suffers few if any collisions it can acquire sufficient kinetic energy that its trajectory exceeds the physical limits of the trap so that it strikes an electrode and is lost. Clearly, the lower the trapping potential (at low q_z values) the greater will be the number of ions which are lost this way. When the volume filled by ion trajectories is reduced by momentum-dissipating collisions with buffer gas while the working point is maintained on the q_z axis, ion kinetic energies are lowered and the ions reside closer to the bottom of the trapping pseudo-potential well. When the working point is moved subsequently to the boundary, the accelerations experienced by the ions tightly focused near the centre of the trap are much reduced because the RF trapping field is smaller near the centre of the trap. As the ions are moved gradually from the trap centre and gain kinetic energy, collisions with buffer gas atoms lead to an accumulation of internal energy, but now the competition between acquisition of internal energy and kinetic energy is in favour of the former as ions suffer more collisions at low kinetic energy. Thus ion internal energy increases under conditions which are not conducive to acceleration to kinetic energies sufficiently great that ion trajectories exceed the physical limits of the trap. This mechanism is shown schematically in Fig. 8. In Fig. 8(*a*) are shown five Maxwell–Boltzmann-type (assumed) distributions of ion kinetic energies; the ordinate is the energy scale. The solid line corresponds to the distribution of nascent ions formed by electron impact. In Fig. 8(*b*), a trapping potential well in the axial dimension is shown on the same arbitrary energy scale. As the ions are subjected to a cooling period, their Maxwell–Boltzmann-type distributions of ion kinetic energies move towards the foot of the diagram so that the ions reside closer to the bottom of the potential well.

Thus far, the cooling period has been treated simply as one in which ion momentum is lost but it is equally possible that, during this period of kinetic cooling, ion internal energy increases just as it appears to do during the initial stages of BAD.

If we assume an activation energy of 5 eV and a collision rate with helium of 20 000 s^{-1}, then the average internal energy increment per collision during excitation may be calculated. Some 50% of selected ions can be dissociated by BAD in 2.6 ms; during that time, an ion experiences, on the average, 52 collisions thus the average internal energy increment is 0.1 eV. The transfer of 0.1 eV requires an ion kinetic energy of at least 4 eV, based on target and projectile masses of 4 u and 151 u, respectively. An ion kinetic energy of 4 eV is not unduly large and, as simulation studies (14) have shown that ions can acquire of the order of 100 eV while their working point is close to a boundary of the stability diagram, this ion kinetic energy requirement may even be increased several-fold. However, this model requires that the average net increase, per collision, in ion inter-

TABLE 5. Electron impact (70 eV) partial mass spectra of 4-nitro-*o*-xylene and 4-nitro-*m*-xylene

4-Nitro-*o*-xylene				4-Nitro-*m*-xylene			
m/z	Relative abundance	*m/z*	Relative abundance	*m/z*	Relative abundance	*m/z*	Relative abundance
151	100	103	47.45	151	14.33	103	40.56
135	1.39	93	8.57	135	7.06	93	2.23
134	2.16	92	2.32	134	78.36	92	3.92
121	26.88	91	18.11	121	2.10	91	19.66
106	5.35	79	53.86	106	38.07	79	90.61
105	75.64	78	16.40	105	13.32	78	29.88
104	—	77	78.32	104	15.92	77	100

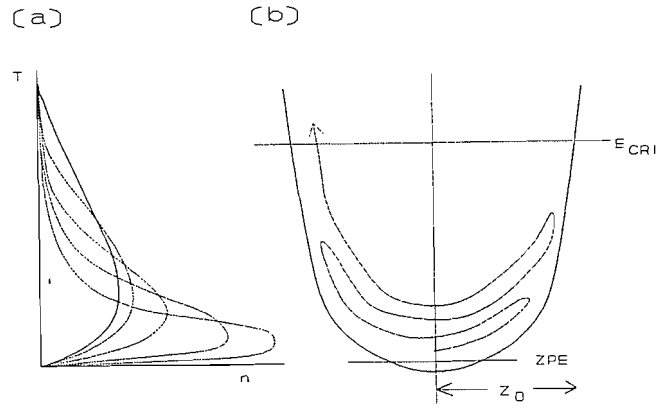

FIG. 8. Schematic representation of collisional cooling. (*a*), five Maxwell–Boltzmann-type (assumed) distributions of ion kinetic energies; the ordinate is the energy scale. The solid line corresponds to the distribution of nascent ions formed by electron impact; dashed lines represent successively cooler distributions (as the maximum in each curve moves to lower energies) brought about by collisions with buffer gas atoms. (*b*), a trapping potential well in the axial dimension shown on the same arbitrary energy scale. As ions are cooled, they reside closer to the bottom of the potential well.

nal energy due to ion activation and ion de-activation during BAD is 0.1 eV.

In summary, it is proposed that during the cooling period ion kinetic energy and axial (and radial) excursions of ions from the trap centre are reduced, as has been shown by simulation (14). Also during the cooling period, when an ion undergoes momentum-dissipating and focusing collisions with helium buffer gas, ion internal energy may be enhanced moderately. Prolongation of the cooling period without the intercession of BAD failed to produce ion fragmentation. Thus, unlike BAD, cooling alone is insufficient to bring about dissociation in the ions studied to date. Upon BAD, the effect of helium buffer gas is to expand ion axial excursions (though from much reduced values compared with those for ions which had not been cooled). As ion excursions from the trap centre increase, ion motion is influenced strongly by the RF trapping field so that ion kinetic energy increases. In turn, ion internal energy increases rapidly so as to access, or access more readily, reaction channels with higher energies of activation. In combination with BAD, cooling can enhance access to reaction channels.

Comparison with results from a QhQ instrument

An attempt has been made to compare the fragmentation patterns of 4-nitro-*o*-xylene and 4-nitro-*m*-xylene obtained with the ion trap under conditions of BAD with cooling with those obtained with a QhQ instrument. Two types of mass spectra were obtained with the QhQ. Firstly, 70 eV electron impact mass spectra were obtained: the mass spectra of the two isomers differ substantially as can be seen from Table 5; the molecular ion is the base peak for the *ortho* isomer, whereas the base peak for the *meta* isomer is *m/z* 77. Secondly, collision-activated dissociation mass spectra were obtained for the molecular ion of each isomer using argon as the collision gas. The collision energy of the mass-selected molecular ions was varied over the range 10–100 eV and, for one isomer, the effects of an increase in the collision gas pressure were investigated. The relative fragment ion abundances of the QhQ daughter ion mass spectra, electron impact mass spectrum and ion trap daughter ion mass spectrum for the *ortho* and *meta* isomers are shown in Tables 6 and 7, respectively.

From a comparison of the data shown in Tables 6 and 7, the patterns of fragment ion relative abundances obtained with the ion trap show some degree of similarity with both EI mass spectra and with daughter ion mass spectra obtained at collision energies of 100 eV, in general agreement with an earlier comparison (18). Yet these comparisons are far from satisfactory if the intent is to use the QhQ data in order to assign a crude "collision energy" to the ion trap data. In Table 6, a major fragment ion in the ion trap is *m/z* 106 which is not observed at all in the QhQ daughter ion spectra; while this species is observed in the QhQ EI mass spectrum, its relative abundance can be accounted for entirely as the ^{13}C-containing analogue of *m/z* 105. Furthermore, *m/z* 103 is not observed at all in the ion trap yet it is almost invariably observed in QhQ spectra.

A major difference between the mass spectra obtained with the QhQ and those obtained with the ion trap, as shown in Tables 6 and 7, is the relative abundance of the mass-selected ion undergoing dissociation after completion of the dissociation processes. For example, at collision gas pressures of 0.30, 0.75, 1.0, and 1.8 mTorr, the fractional survival of mass-selected *m/z* 151 ions was 0.78, 0.50, 0.37, and 0.18, respectively; these results were obtained with a collision energy of 100 eV. In the ion trap, where the pressure of collision gas is ca. 0.2 mTorr, the mass-selected ion is almost fully dissociated. Clearly, the mass-selected ions experience very different conditions: in the QhQ, ions are accelerated initially then suffer a single collision (or very few) with the target gas in which part of the ion kinetic energy is converted to internal energy whereupon the ion eventually undergoes unimolecular dissociation; in the ion trap, the kinetic energization process is interspersed with many collisional events by which ion internal energy is accumulated incrementally. It is then not entirely unexpected that the fragmentation patterns obtained from such widely-differing pro-

Can. J. Chem. Downloaded from www.nrcresearchpress.com by 195.246.54.202 on 09/08/12
For personal use only.

TABLE 6. Partial mass spectra of 4-nitro-*o*-xylene. Comparison of relative abundances of selected fragment ions obtained with (*i*) a triple stage quadrupole (QhQ) instrument with variation of collision energy and collision gas pressure, (*ii*) electron impact with the QhQ, and (*iii*) ion trap operated with a DC plateau duration of 15 ms and a cooling period of 100 ms

	Relative abundance (percentage abundances)					
	QhQ					Ion trap
m/z	100 eV[a,b]	100 eV[a,c]	50 eV[a,d]	10 eV[a,e]	EI[f]	$q_z = 0.45$[g]
121	54	40	55	75	14.8	64.3
106	—	—	—	—	2.9	17.5
105	34	43	36	22	41.5	2.8
103	5	6	2	—	26.1	—
93	5	7	5	3	4.7	5.4
91	2	4	2	—	10.0	10.0

[a]Collision energy.
[b]89% of the products was undissociated *m/z* 151 (average of two runs).
[c]Collision gas pressure increased; 73.4% of the products was undissociated *m/z* 151.
[d]94.3% of the products was undissociated *m/z* 151.
[e]95.5% of the products was undissociated *m/z* 151.
[f]70 eV electrons.
[g]0.8% of the products was undissociated *m/z* 151.

TABLE 7. Partial mass spectra of 4-nitro-*m*-xylene. Comparison of relative abundances of selected fragment ions obtained with (*i*) a QhQ instrument with variation of collision energy, (*ii*) electron impact with the QhQ, and (*iii*) ion trap operated with a DC plateau duration of 15 ms and a cooling period of 80 ms

	Relative abundance (percentage abundances)			
	QhQ			Ion trap
m/z	100 eV[a,b]	10 eV[a,c]	EI[d]	$q_z = 0.45$[e]
135	—	—	3.3	8.7
134	90.4	100	36.5	3.6
106	6.8	—	17.7	26.2
105	2.1	—	6.2	61.5
104	0.7	—	7.4	—
103	—	—	18.8	—
93	—	—	1.0	—
91	—	—	9.1	—

[a]Collision energy.
[b]77.5% of the products was undissociated *m/z* 151.
[c]85% of the products was undissociated *m/z* 151.
[d]70 eV electrons.
[e]0.8% of the products was undissociated *m/z* 151.

cesses are so different. Not only do the patterns of relative abundances differ but, in some cases, the same ion species are not observed in both methods, yet all of the fragment ion species observed are observed in the EI mass spectra.

Conclusions

Boundary-activated dissociation can afford a highly efficient and rapid method for dissociation of mass-selected ions of the compounds examined with, under appropriate conditions, almost total retention of daughter ion fragments. A DC plateau duration of some 10–15 ms is sufficient to cause the fragmentation of ≥90% of the isolated ion species. BAD can be applied facilely to successive generations of ions. The addition of a cooling period appears to bring about significant changes in the fragmentation patterns which are more marked for the *ortho* isomer molecular ion than for that from the *meta* isomer. These changes invariably show enhanced signal relative abundances for ions of lower *m/z* ratio and suggest that channels having higher activation energies are accessed in this manner. A change in the BAD abundance ratio of grand-daughter ions from an isolated daughter ion species was observed to be dependent upon the duration of a cooling period.

Acknowledgements

The authors gratefully acknowledge the financial assistance of Varian Associates Inc., the Natural Sciences and Engineering Research Council of Canada, and Trent University.

1. R.E. March and R.J. Hughes. Quadrupole storage mass spectrometry. Chemical Analysis Series. Vol. 102. Wiley Interscience, New York. 1989.
2. J.N. Louris, R.G. Cooks, J.E.P. Syka, P.E. Kelley, G.C. Stafford, Jr., and J.F.J. Todd. Anal. Chem. **59**, 1677 (1987).
3. A.B. Young, R.E. March, and R.J. Hughes. Can. J. Chem. **63**, 2324 (1985).
4. J.N. Louris, J.E. Brodbelt, and R.G. Cooks. Int. J. Mass Spectrom. Ion Processes, **75**, 345 (1987).
5. S.A. Lammert and R.G. Cooks. J. Am. Soc. Mass Spectrom. **2**, 487 (1991).
6. S.A. Lammert and R.G. Cooks. Rapid Commun. Mass Spectrom. **6**, 528 (1992).
7. J.E. Fulford, D.-N. Hoa, R.J. Hughes, R.E. March, R.F. Bonner, and G.J. Wong. J. Vac. Sci. Technol. **17**, 829 (1980).
8. C. Paradisi, J.F.J. Todd, P. Traldi, and U. Vettori. Org. Mass Spectrom. **27**, 251 (1992).
9. C. Paradisi, J.F.J. Todd, and U. Vettori. Org. Mass Spectrom. **27**, 1210 (1992).
10. C.S. Creaser and K.E. O'Neill. Second European Meeting on Tandem Mass Spectrometry. Warwick, U.K. July 1992.
11. O. Curcuroto, S. Fontana, P. Traldi, and E. Celon. Rapid Commun. Mass Spectrom. **6**, 322 (1992).
12. L.S. Matthews. M.Sc. Thesis, University of East Anglia, U.K. 1992.
13. C.S. Creaser and K.E. O'Neill. Org. Mass Spectrom. **28**, 564 (1993).
14. R.E. March, M. Tkaczyk, F.A. Londry, and R.L. Alfred. Int. J. Mass Spec. Ion Processes, **25**, 9 (1993).

Can. J. Chem. Downloaded from www.nrcresearchpress.com by 195.246.54.202 on 09/08/12
For personal use only.

15. J. Gronowska, C. Paradisi, P. Traldi, and U. Vettori. Rapid Commun. Mass Spectrom. **4**, 306 (1990); C.E. Ardanaz, P. Traldi, U. Vettori, J. Kavka, and F. Guidugli. Rapid Commun. Mass Spectrom. **5**, 5 (1991).
16. A. Castellin, A. Chilin, P. Rodighiero, and A. Guiotto. To be published.
17. S. Fontana, O. Curcuruto, P. Traldi, A. Castellin, A. Chilin, P. Rodighiero, and A. Guiotto. Org. Mass Spectrom. **27**, 1255 (1992).
18. R.E. March, M.R. Weir, F.A. Londry, S. Catinella, P. Traldi, J.A. Stone, and B. Jacobs. Proc. 41st ASMS Conf. Mass Spectrometry and Allied Topics, San Francisco, CA, June 1993. p. 446*a*.
19. R.E. March, M.R. Weir, F.A. Londry, S. Catinella, P. Traldi, J.A. Stone, and B. Jacobs. Rapid Commun. Mass Spectrom. **7**, 929 (1993).
20. J.H. Beynon, M. Bertrand, and R.G. Cooks. J. Am. Chem. Soc. **95**, 1739 (1973).

Can. J. Chem. Downloaded from www.nrcresearchpress.com by 195.246.54.202 on 09/08/12
For personal use only.

Near ultraviolet photolysis of phosphine studied by H atom photofragment translational spectroscopy

IAN R. LAMBERT, GREGORY P. MORLEY,[1] DAVID H. MORDAUNT, MICHAEL N.R. ASHFOLD,[2] AND RICHARD N. DIXON
School of Chemistry, University of Bristol, Bristol BS8 1TS, U.K.

Received June 29, 1993

This paper is dedicated to Professor John C. Polanyi on the occasion of his 65th birthday

IAN R. LAMBERT, GREGORY P. MORLEY, DAVID H. MORDAUNT, MICHAEL N.R. ASHFOLD, and RICHARD N. DIXON. Can. J. Chem. **72**, 977 (1994).

We report time-of-flight measurements of the H atom fragments arising in the photodissociation of phosphine at three near ultraviolet excitation wavelengths — 218.2 nm, 221.6 nm, and 228.0 nm. For these wavelengths, energetic considerations dictate that ground state $PH_2(\tilde{X})$ fragments must be the partner product of the primary photolysis event. The measured H atom kinetic energy distributions indicate that internal excitation of these partner fragments accounts for the major part ($\geqslant$62%) of the available energy, in excess of that required to break the H—PH_2 bond, provided by the photon. Inspection of the poorly resolved structure evident near the peak of the H atom kinetic energy distribution suggests the presence of substantial bending excitation and *a*-axis rotational excitation in the PH_2 partner fragment. The H atom kinetic energy distribution also shows clear evidence of atoms arising from secondary photolysis of the primary $PH_2(\tilde{X})$ fragments. This secondary photo-dissociation is observed to show a marked anisotropy, consistent with a perpendicular photo-excitation of the $PH_2(\tilde{X})$ fragment. Arguments are presented which indicate that the secondary photolysis leads both to the formation of PH(X) fragments, carrying high levels of rotational excitation, and to the three-body atomisation process.

IAN R. LAMBERT, GREGORY P. MORLEY, DAVID H. MORDAUNT, MICHAEL N.R. ASHFOLD et RICHARD N. DIXON. Can. J. Chem. **72**, 977 (1994).

On a effectué des mesures en temps de vol des atomes d'hydrogène, sous la forme de fragments provenant de la photodissociation de la phosphine à trois longueurs d'onde d'excitation — 218,2, 221,6 et 228,0 nm — proches de l'ultraviolet. Pour ces longueurs d'onde, des considérations énergétiques dictent que les fragments $PH_2(\tilde{X})$ de l'état fondamental doivent être les produits partenaires de la photolyse primaire. Les distributions de l'énergie cinétique mesurées pour les atomes d'hydrogène indiquent que l'excitation interne de ces fragments partenaires tient compte de la plus grande partie ($\geqslant$62%) de l'énergie disponible à partir du photon, ce qui est supérieur à l'énergie requise pour briser la liaison H—PH_2. Un examen minutieux de la structure mal résolue présente près du pic de la distribution de l'énergie cinétique des atomes d'hydrogène suggère la présence d'une excitation importante de déformation et d'une excitation rotationnelle le long de l'axe *a* du fragment partenaire PH_2. La distribution de l'énergie cinétique des atomes d'hydrogène montre des preuves de la présence d'atomes provenant d'une photolyse secondaire des fragments $PH_2(\tilde{X})$ primaires. L'observation de cette photodissociation secondaire démontre la présence d'une anisotropie marquée qui est en accord avec une photoexcitation du fragment $PH_2(\tilde{X})$. On présente des arguments indiquant que la photolyse secondaire conduit à la formation de fragments PH(X) portant des niveaux élevés d'excitation rotationnelle ainsi qu'au processus d'atomisation à trois corps.

[Traduit par la rédaction]

Introduction

The ultraviolet (UV) and vacuum ultraviolet (VUV) photochemistry of phosphine is of interest for several reasons. From a commercial viewpoint, PH_3 is an important component in the growth of InP, GaP, terniary and quarternary semiconductors by metalorganic chemical vapour deposition (MOCVD) methods (1, 2). Reports have appeared suggesting that such microelectronic device fabrication processes may be enhanced by the presence of UV laser radiation (3). An understanding of phosphine photochemistry is also important, given that PH_3 is a significant constituent of the reducing atmospheres of some of the outer planets, notably Jupiter and Saturn (4–7). Finally, at the most fundamental level, it is of interest to look for parallels between the primary photochemistry of PH_3 and that of its far more extensively studied first row homologue, ammonia.

The electronic absorption spectra of PH_3 and NH_3 show many similarities. In both cases the longest wavelength ($\tilde{A}$–$\tilde{X}$) absorption feature is associated with electronic promotion from the highest occupied lone pair orbital (of a_2'' symmetry in the planar D_{3h} limit) to an excited orbital that is reasonably approximated as an *ns* Rydberg orbital (n = 3 and 4, respectively, in the case of NH_3 and PH_3) in the vertical Franck–Condon region. In NH_3, this excitation is accompanied by a planar ← pyramidal change in the equilibrium geometry of the nuclear framework. Analysis of the first band in the photoelectron spectrum of PH_3, however, indicates that the equilibrium configuration of the ground state of the PH_3^+ ion is slightly nonplanar, with an angle of ~15° between any one P—H bond and the plane defined by the remaining PH_2 moiety (8). *Ab initio* calculations (9) suggest a similar non-planarity for the first excited $\tilde{A}^1A_1$ (C_{3v}) state of PH_3. In both molecules, elongation of one N—H (P—H) bond causes the excited *ns* orbital to acquire substantial antibonding valence character and, ultimately, to evolve to the 1*s* orbital of the atomic hydrogen fragment. *Ab initio* calculations of the potential energy surface for the first excited singlet electronic state of NH_3 — the $\tilde{A}^1A_2''$ state — reveal a small potential energy barrier in the H_2N---H dissociation coordinate, the magnitude of which increases with bending away from planarity (10–12). Because of this barrier, the pure bending vibrational levels of the $\tilde{A}^1A_2''$ state of ammonia are quasi-bound and the $NH_3(\tilde{A}^1A_2'' \leftarrow \tilde{X}^1A_1')$ absorption spectrum shows a progression of predissociation broadened vibronic bands involving excitation of ν_2' (the excited state out-of-plane bending mode) (11, 13–16).

The corresponding $\tilde{A}$–$\tilde{X}$ transition in PH_3 appears as a broad continuous absorption, centred around 180 nm but extending to

[1]Present address: Physikalisch-Chemisches Institut der Universität Zürich, Winterthurerstrasse 190, CH-8057, Zürich, Switzerland.

[2]To whom correspondence may be addressed.

Can. J. Chem. Downloaded from www.nrcresearchpress.com by 195.246.54.202 on 09/08/12
For personal use only.

Can. J. Chem. Downloaded from www.nrcresearchpress.com by 195.246.54.202 on 09/08/12
For personal use only.

wavelengths ~230 nm (17–21). This lack of any discernable vibronic structure is consistent with the *ab initio* calculations of Müller et al. (9), which show only a small barrier (less than the zero-point energy associated with a P—H stretching vibration) in the H_2P---H exit channel of the $\tilde{A}^1A_1$ state potential. The corresponding first excited triplet state of PH_3 (the $\tilde{a}^3A_1$ state) is also predicted (9) to be unbound with respect to the ground state products H + $PH_2(\tilde{X})$ — a result consistent with the diffuse appearance of the $\tilde{a}^3A_1 \leftarrow \tilde{X}^1A_1$ transition in the electron energy loss spectrum of PH_3 (22). Several of the higher excited states of PH_3 are sufficiently resistant to predissociation that they show resolved vibronic (but not rotational) structure (18, 20, 23). This structure has been explained in terms of a number of overlapping progressions, involving excitation of the ν_2 mode as expected on Franck–Condon grounds, but the lack of rotational resolution has hampered definitive symmetry assignments for these (presumed) Rydberg excited states.

The photochemistry of NH_3 following excitation to its $\tilde{A}^1A_2''$ state has been much studied. The ensuing dissociation dynamics, and thus the ultimate energy disposal, has been shown to be greatly influenced by the presence of a conical intersection, in the H_2N---H dissociation coordinate at extended C_{2v} geometries, between the parent ground ($\tilde{X}$) and first excited ($\tilde{A}$) state surfaces. Early studies of NH_3 photolysis following excitation within its $\tilde{A}$–$\tilde{X}$ absorption system showed the resulting H atoms to be translationally "cool" (24), and the accompanying $NH_2(\tilde{X})$ fragments to be highly internally excited — as evidenced by the (at the time) unintelligibly complex appearance of the resulting $NH_2(\tilde{A}$–$\tilde{X})$ laser induced fluorescence (LIF) spectrum (25). Such conclusions were reiterated in a more recent study of the Doppler lineshape of the resulting H atom photofragments (26). However, any quantitative understanding of the energy disposal in this dissociation, and its specific dependence on parent quantum state, had to await the development of the technique of H atom photofragment translational spectroscopy by Welge and co-workers (27–32). The time-of-flight (TOF) spectra of the H atoms resulting from photodissociation of NH_3 following excitation to each of a number of vibronic levels of the $\tilde{A}^1A_2''$ state showed well resolved struture. Analysis of this structure revealed a strong propensity for the partner $NH_2(\tilde{X})$ fragments to be formed with little vibrational excitation, but with large amounts of rotational excitation, specifically concentrated about the *a*-inertial axis (28–30). Such product rotational energy disposal can be directly correlated to the effects of the conical intersection, in the H_2N---H dissociation channel, through which the dissociating $NH_3(\tilde{A})$ molecules must pass in order to reach the H + NH_2 asymptote (28–30, 33). Finally, given detailed knowledge of the identities and energies of these high angular momentum states of the $NH_2(\tilde{X})$ products it has since proved possible to assign their LIF excitation spectra and thereby deduce improved bending potential energy functions for both the ground $\tilde{X}^2B_1$ and first excited $\tilde{A}^2A_1$ states of the NH_2 radical (34).

No such high resolution studies of the primary photochemistry of PH_3 have been reported. Given $D_0(H_2P—H) = 28\,850 \pm 150\ cm^{-1}$ (35), we can deduce the following threshold wavelengths for forming ground and excited state PH_2 fragments in the photodissociation of PH_3:

[1] $PH_3 + h\nu \rightarrow PH_2(\tilde{X}^2B_1) + H \qquad \lambda \leq 347$ nm

[2] $\qquad\qquad PH_2(\tilde{A}^2A_1) + H \qquad \lambda \leq 212$ nm

In addition, the following PH forming fragmentation channels also satisfy the requirements of spin and energy conservation following excitation within the $\tilde{A}$–$\tilde{X}$ absorption band of PH_3 (36):

[3] $PH_3 + h\nu \rightarrow PH(a^1\Delta) + H_2 \qquad \lambda \leq 404$ nm

[4] $\qquad\qquad PH(b^1\Sigma^+) + H_2 \qquad \lambda \leq 316$ nm

[5] $\qquad\qquad PH(X^3\Sigma^-) + H + H \qquad \lambda \leq 187$ nm

[6] $\qquad\qquad PH(c^1\Pi) + H_2 \qquad \lambda \leq 181$ nm

We recognise that the quoted wavelength thresholds for the H_2 elimination pathways (which correspond to the thermodynamic thresholds) are likely to be too long, since these processes almost certainly have an associated activation barrier. Indeed, there is by now reasonable consensus that dissociation [1] is the dominant primary process following excitation within the parent $\tilde{A}$–$\tilde{X}$ absorption band. Kley and Welge (37) observed transient absorptions due to both PH_2 and PH radicals in their respective ground states (but none due to PH fragments in their metastable $a^1\Delta$ electronic state) following broadband flash photolysis using wavelengths longer than 195 nm. Their observation that the strengths of these absorptions grew with time delay and with increasing pressure of added inert gas led to the suggestion that the nascent PH_2 and PH fragments were formed with considerable internal (or, possibly, electronic) excitation. Di Stefano et al. (38, 39) have reported measurements of the spontaneous fluorescence from electronically excited $PH_2(\tilde{A})$ and PH(*b*) fragments as a function of parent excitation wavelength, thereby obtaining fluorescence excitation spectra for these two photofragments. No emission from PH(*b*) fragments was identified for excitation wavelengths longer than ~147 nm (39), thereby indicating negligible rôle for dissociation channel [4] at the excitation wavelengths employed in the present study. $PH_2(\tilde{A}$–$\tilde{X})$ photofragment fluorescence has been detected following PH_3 photolysis at wavelengths as long as 208 nm (38). This particular fluoresence excitation spectrum provides a fairly faithful replication of the parent PH_3 absorption spectrum at energies up to the first ionisation limit (125.6 nm (35)) but the estimated quantum yield for dissociation [2] was never greater than ~2%. Two later studies have attempted to shed further light on the detailed energy disposal within the nascent PH_2 fragments following PH_3 photolysis at the ArF laser wavelength, 193.3 nm. In the first of these Sam and Yardley (40) observed fluorescence from electronically excited $PH_2(\tilde{A})$ and PH(*A*) photoproducts. The latter were deduced to arise from a two-photon excitation process which, by analogy with ammonia (41), we can surmise involves the initial formation of highly internally excited $PH_2(\tilde{X})$ fragments which themselves undergo secondary photolysis. Most recently, Wittig and co-workers (42) reinvestigated this photo-dissociation process using the technique of velocity aligned Doppler spectroscopy (VADS). Analysis of the VADS lineshapes of the resulting H atom photofragments confirmed that most of the available energy was partitioned into (unspecified) internal excitation of the $PH_2(\tilde{X})$ partner ($\langle E_{int} \rangle \sim 14\,000\ cm^{-1}$). The deduced shape of the $PH_2(\tilde{X})$ fragment internal energy distribution was seen to be in good accord with that predicted by a simple density of states (prior) calculation, leading these authors to suggest that statistical factors may play an important role in this dissociation (42).

Here we report the first application of the technique of H

Can. J. Chem. Downloaded from www.nrcresearchpress.com by 195.246.54.202 on 09/08/12
For personal use only.

atom photofragment translational spectroscopy to the near UV photo-dissociation of a jet-cooled sample of PH_3. We have specifically chosen to study this photolysis at wavelengths (218–228 nm) in the low energy tail of the $PH_3(\tilde{A}–\tilde{X})$ electronic absorption-wavelengths for which, by analogy with ammonia, we might expect the simplest pattern of fragment internal energy disposal. Dissociation channels [1], [3], and [4] are the only energetically-allowed processes following one photon absorption at these wavelengths. Of these, only channel [1] will yield the H atoms to which our experiment is sensitive but, as summarised above, the quantum yields for processes [3] and [4] are believed to be minimal at these energies. Our results confirm the importance of the primary dissociation channel [1], yielding $PH_2(\tilde{X})$ fragments with very high levels of internal excitation. Even with the high intrinsic resolution of our present experiment the total fragment kinetic energy spectrum is essentially continuous, although some partially resolved structure is evident at the highest PH_2 internal energies. Partly by analogy with previous studies of the near UV photolysis of NH_3, we attribute this structure to selective formation of fragments with high levels of *a*-axis rotational angular momentum. The total fragment kinetic energy spectrum also shows clear evidence of H atoms arising from secondary photolysis of the primary $PH_2(\tilde{X})$ fragments; the partner PH fragments are deduced to be formed via a perpendicular photoexcitation, with an anisotropic distribution of recoil velocities and with large amounts of internal (presumably rotational) energy.

Experimental

The photofragment translational spectrometer and the laser systems used to effect the photodissociation and to "tag" the resulting atomic H photofragments have been described previously (43–45); only key features will be summarised here. A skimmed pulsed supersonic beam of PH_3 (BOC, Electra II grade, stated purity 99.999%) seeded in argon (5% mixing ratio, total stagnation pressure of ~1 bar) is crossed at 90° by the output of the various pulsed laser systems used to effect the photolysis and to "tag" the nascent H atom photoproducts. The recoil kinetic energy distribution of these tagged atoms is determined by measuring their collision free times-of-flight (TOF) to a detector (a Johnston multiplier, type MM1-SG) positioned along the third orthogonal axis with its front face 425.7 mm distant from the interaction region.

The experiment employs three pulsed laser systems. Near UV photolysis was brought about using an Nd–YAG pumped dye laser system (JK Lasers HY-750 plus Quanta-Ray PDL-2) operating at selected wavelengths in the range 545–585 nm. This dye laser output was frequency doubled and then mixed with the residual 1064 nm fundamental radiation of the Nd–YAG laser to yield radiation at 218.2 nm (45 826 cm^{-1}), 221.6 nm (45 112 cm^{-1}), and 228.0 nm (43 855 cm^{-1}), respectively. The resulting near UV radiation was directed through a polarisation rotator (Newport RFU $\frac{1}{2}$ Fresnel rhomb) and then focussed (75 cm f.l. lens) so as to intercept the output of the pulsed molecular beam in the centre of the interaction region. "Tagging" the H photofragments involves promoting them, via a double resonant excitation, to high Rydberg states (principal quantum number $n \sim 70$) lying just below the ionization threshold. In our experiment this is achieved using one Nd–YAG pump laser (Continuum YG 682-10) and two dye lasers. The first of these is employed to generate the Lyman-*a* radiation (corresponding wavenumber 82 259 cm^{-1}) required in order to excite the H ($2p \leftarrow 1s$) transition. The dye laser itself operates at ~554.9 nm, its output is mixed with the residual 1064 nm fundamental output of the Nd–YAG laser in a KDP crystal, and the resulting near UV radiation (at ~364.6 nm) is then frequency tripled, in krypton, to produce the required radiation at 121.6 nm. The second dye laser (Spectron SL4000G) operates with the dye LDS 720 to produce light at ~730 nm. This is frequency doubled (in a DCDA crystal) to yield the UV radiation required to further promote the H ($n = 2$) atoms to levels close to the ionisation limit. The UV and VUV beams are focussed into the interaction region (crossing angle ~6°) so as to spatially and temporally overlap the focussed output of the photolysis laser. Rydberg atoms excited in this way "fly" from the interaction volume; those that happen to recoil along the TOF axis are field ionised immediately prior to striking the Johnston multiplier. A pair of suitably biased annual electrodes (providing a field strength ~2 V mm^{-1}) positioned on either side of the interaction region ensure that any ions formed by the initial laser excitations are extracted at source and thus do not contribute to the measured TOF spectrum. The output from the multiplier is amplified and sent to one channel of a digital storage oscilloscope (LeCroy 9450, 350 MHz bandwidth) for visual display. The signal is also transferred on a shot by shot basis, via a parallel interface, to an IBM PS/2 for accumulation and subsequent data processing.

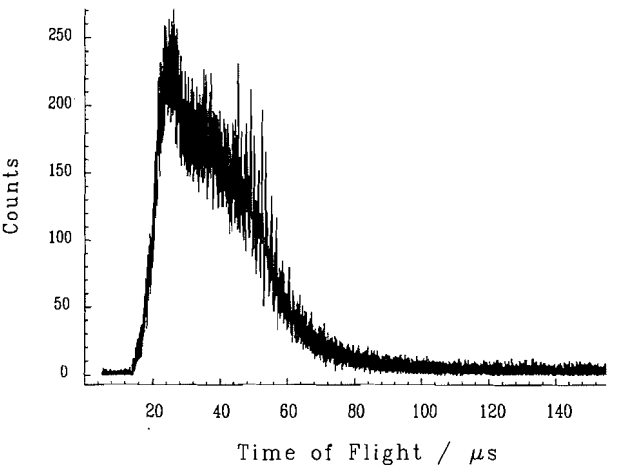

FIG. 1. H Rydberg atom TOF spectrum resulting from photolysis of a jet-cooled sample of PH_3 using 218.2 nm laser radiation, linearly polarised with ϵ_{phot} aligned parallel to the TOF axis.

Results

Figure 1 shows an H Rydberg atom TOF spectrum resulting from photolysis of a jet-cooled PH_3 sample using 218.2 nm radiation, linearly polarised with its electric vector (ϵ_{phot}) aligned parallel to the TOF axis. Figure 2*a* shows the same data, transformed to a plot of total fragment kinetic energy using the conversion

$$[7] \quad E_{kin,total} = E_{kin,H} + E_{kin,PH_2} = \frac{1}{2} m_H \left[1 + \frac{m_H}{m_{PH_2}}\right] \left(\frac{d}{t_H}\right)^2$$

where t_H is the measured H atom TOF and d is the flight distance (425.7 mm). Also indicated on this spectrum (by the arrow) is the maximum fragment kinetic energy (~17 000 cm^{-1}) that is allowed by energy conservation assuming that the observed H atoms arise solely from dissociation channel [1]. Even a cursory inspection of Fig. 2*a* is sufficient to reveal that some H atoms are formed with kinetic energies that exceed this presupposed maximum. The partially resolved structure evident around the maximum of this distribution is shown on an expanded scale in the inset.

The corresponding spectrum recorded with ϵ_{phot} aligned perpendicular to the TOF axis is shown in Fig. 2*b*. It shows the same partially resolved fine structure near the distribution maximum and, once again, the formation of some H atoms with kinetic energies in excess of what is possible simply from 218.2 nm photolysis of PH_3 via primary dissociation pathway [1]. Even more noteworthy, however, is the secondary maxi-

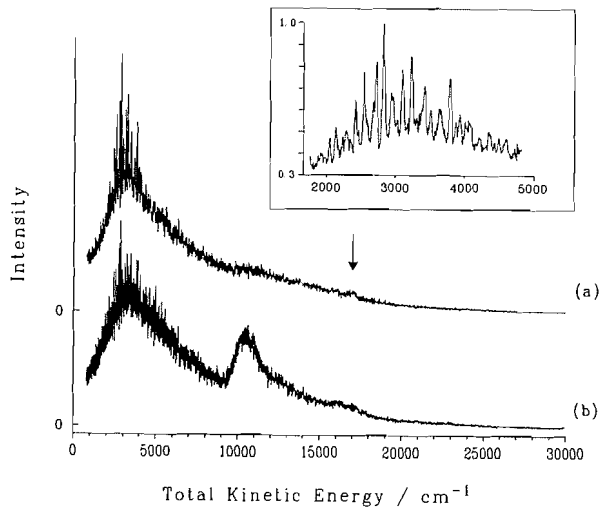

FIG. 2. Total kinetic energy spectrum of the fragments resulting from photolysis of a jet-cooled sample of PH_3 at 218.2 nm with ϵ_{phot} aligned (*a*) parallel and (*b*) perpendicular to the TOF axis. The incompletely resolved structure around the peak of (*a*) is displayed again, in the inset, with an offset baseline and on a four times expanded energy scale. The kinetic energy scales on these spectra are appropriate for the case of an H atom recoiling from a PH_2 fragment, as defined in eq. [7].

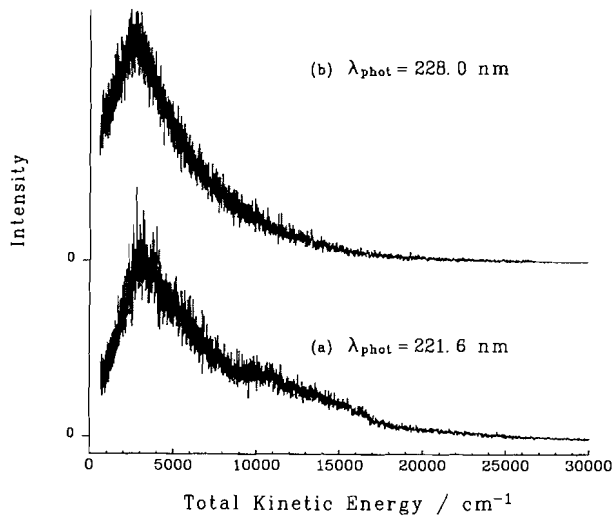

FIG. 3. Total kinetic energy spectrum of the fragments resulting from photolysis of PH_3 at (*a*) 221.6 nm and (*b*) 228.0 nm. In both cases ϵ_{phot} was aligned parallel to the TOF axis. The horizontal scale is appropriate for the case of an H atom recoiling from a PH_2 fragment, as defined in eq. [7].

mum in this kinetic energy distribution, peaking at $E_{kin} \sim 10\,000$ cm^{-1}. The relative importance of this secondary maximum was observed to increase as the energy of the UV photolysis laser was increased. The total fragment kinetic energy spectra obtained at both of the longer excitation wavelengths investigated (221.6 and 228.0 nm) were found to be of generally similar profile; see Fig. 3. Checks were made to ensure that the fastest atoms did not derive from PH_3 photolysis by the Lyman-α probe radiation. Certainly, at our highest Lyman-α intensities we were able to detect an abundance of H atoms resulting from 121.6 nm photodissociation of PH_3, the TOF spectrum of which was dominated by "slow" atoms and had an overall shape not dissimilar to that obtained using the near UV wavelengths (e.g. Fig. 1). Converting this TOF spectrum to a spectrum of total fragment kinetic energy is complicated by the multiplicity of H atom forming dissociation channels that are energetically possible using a 121.6 nm photon; even the four body atomisation process is exoergic by ~2800 cm^{-1} at this wavelength! However, TOF spectra such as that shown in Fig. 1 were recorded under conditions where the VUV photon flux had been reduced to the point where the H atom TOF signal resulting solely from Lyman-α dissociation of PH_3 was negligible. (This is most simply achieved by increasing the pressure of krypton in the tripling cell, and thereby degrading the third harmonic generation efficiency.)

As we show below, both the angular dependent secondary peak in the total fragment kinetic energy spectrum, and the yield of H atoms with kinetic energies greater than can be derived simply from the one photon dissociation of PH_3 at 218.2 nm, can be most easily explained in terms of secondary photolysis of the nascent $PH_2(\tilde{X})$ fragments. Such a suggestion is not entirely original (40, 42). It is also reminiscent of the photochemistry reported recently for the SH/SD(X) fragments resulting from near UV photodissociation of H_2S and D_2S (45, 46).

Discussion

The primary photolysis: $PH_3 \rightarrow PH_2(\tilde{X}) + H$

H atoms attributable to secondary photolysis are most evident in spectra recorded with ϵ_{phot} perpendicular to the TOF axis so, in order to focus on the primary step, we first concentrate attention on spectra such as those shown in Figs. 2*a* and 3 which were derived from experiments in which ϵ_{phot} was aligned parallel to the TOF axis. Quantifying the observed energy disposal is complicated by any underlying H atom signal resulting from secondary photolysis and by the fact that our measured distributions do not extend down to zero kinetic energy. Nonetheless we are able to make a reasonable estimate of the "centre of gravity" of the distribution of H atoms with kinetic energies less than the 17 000 cm^{-1} maximum permitted, by energy conservation, from the primary photolysis step. Thus we can estimate that internal excitation of the nascent PH_2 fragments accounts for at least 62% of the available energy (i.e. the energy provided by the photolysis photon in excess of that required to break the H—PH_2 bond). The general form of this distribution is pleasingly similar to that deduced by Wittig and co-workers (42) from analysis of the VADS lineshapes of the H atoms resulting from photolysis of a room temperature sample of phosphine at 193.3 nm. The observation that the form of this earlier distribution was in reasonable accord with that predicted using a prior calculation (i.e. with a model which assumes that the probability for dissociating to yield a PH_2 fragment with a particular internal energy is dependent upon the PH_2 vibrational state density at that particular energy) led these authors to enquire whether this photodissociation process should be viewed as an example of a "statistical" fragmentation (42). Such a process would be somewhat surprising given the demonstrable role of dynamics in establishing the product energy disposal in the corresponding photofragmentation of NH_3 (28–30). The present results, particularly the partially resolved structure around the maximum in the total kinetic energy spectrum, suggest that such is not the case.

Fragmentation channel [2] would be an endoergic process at the excitation wavelengths used in the present experiment. It thus follows that the fine structure apparent in the total kinetic energy spectrum must be associated with the formation of

Can. J. Chem. Downloaded from www.nrcresearchpress.com by 195.246.54.202 on 09/08/12
For personal use only.

Can. J. Chem. Downloaded from www.nrcresearchpress.com by 195.246.54.202 on 09/08/12
For personal use only.

ground state PH_2 fragments in a very specific subset of the total density of rovibrational eigenstates existing at internal energies $\sim$14 000 cm^{-1}. However, definitive assignment of this structure is hampered by the lack of spectroscopic data concerning high rovibrational levels of the ground electronic state of PH_2. Spectroscopy involving thermalised PH_2 samples (47–49), supplemented by *ab initio* theory (50), has yielded the following vibrational and rotational parameters for the $\tilde{X}\,^2B_1$ state of PH_2:

$$\nu_1 = 2330\ cm^{-1} \qquad A_0 = 9.132\ cm^{-1}$$

$$\nu_2 = 1102\ cm^{-1} \qquad B_0 = 8.084\ cm^{-1}$$

$$\nu_3 = 2495\ cm^{-1} \qquad C_0 = 4.215\ cm^{-1}$$

but the rotational analyses are based on transitions involving levels with $N \leqslant 9$ and $K_a \leqslant 8$ only (49).

To proceed further with the assignment we again compare and contrast this fragmentation process with that for ammonia. Photodissociation of NH_3 following excitation at the long wavelength end of its $\tilde{A}$–$\tilde{X}$ transition yields $NH_2(\tilde{X})$ fragments, primarily in their vibrationless level and in the specific subset of rotational states that have $N \sim K_a$. The observed propensity for *a*-axis rotational excitation of the molecular fragment has been rationalised in terms of the Franck–Condon excitation of out-of-plane bending motion in the parent molecule, amplified by the presence of the deep conical intersection between the $\tilde{A}$ and $\tilde{X}$ states of the parent at planar configurations in the H---NH_2 exit channel, through which the dissociating molecule must pass in order to yield ground state fragments (28–30). The physics of PH_3 dissociation following excitation to its $\tilde{A}\,^1A_1$ state must show many parallels. As in NH_3, the dominant forces acting on the nuclei following electronic excitation will tend to promote out-of-plane motion and simultaneous elongation of one P—H bond. Dissociation to the ground state H + $PH_2(\tilde{X})$ products will require the molecule to pass through a near planar geometry as it traverses the region of the conical intersection in the exit channel. Given this scenario, specific excitation of *a*-axis rotational motion in the resulting $PH_2(\tilde{X})$ fragments would seem to be inevitable. However, a comparison between the geometries of the ground ($\tilde{X}$) and excited ($\tilde{A}$) states of ammonia and phosphine and of the resulting ground state NH_2 and PH_2 fragments indicates that we should also expect substantially more bending excitation in the $PH_2(\tilde{X})$ products. Such has been proposed previously (40, 42), and is based on a consideration of the much greater change in the equilibrium bond angle of the surviving PH_2 moiety as the PH_3 molecule evolves from its excited $\tilde{A}$ state ($\hat{HPH} \sim 114°$ (9)) to the ground state product ($\hat{HPH} \sim 92°$ (47–49)).

Rigorous confirmation of this proposed energy disposal would require knowledge of the eigenvalues of the rotational levels with $N \sim K_a$ for the various ν_2 bending vibrational levels of $PH_2(\tilde{X})$. Such data are not yet available, but can be estimated given a realistic model for the PH_2 ground state bending potential function. This we have attempted to do, treating PH_2 as a "semi-rigid" bender (51) and including the strong Renner–Teller interaction between its $\tilde{A}$ and $\tilde{X}$ states for $K_a > 0$. In this method the centrifugal energy and the Renner–Teller interaction terms for each value of K_a are added to the Born–Oppenheimer potential energy functions to yield a single effective Hamiltonian for the bending motion in the $\tilde{A}$ and $\tilde{X}$ states. The eigenvalues of this Hamiltonian are the substate origins $G(\nu_2, K_a)$ for the two states, to which can be added the complete manifold of rotational energy levels derived using the usual perturbation theory approach. We used this Hamiltonian as formulated by Duxbury and Dixon (51), together with a potential energy function derived by least squares fitting to existing term values for levels of the $\tilde{A}$ and $\tilde{X}$ states of PH_2 (47–49), to calculate term values for all ground state levels with $N = K_a$, $\nu_2 \leq 7$ and total energy less than that of the first excited $\tilde{A}^2A_1$ state (i.e. $E_{int} \leqslant$ 18 000 cm^{-1}). Unfortunately, these calculations do not provide any single, unambiguous interpretation of the fine structure peaks evident at internal energies $\sim$14 000 cm^{-1} in Fig. 2. This is not particularly surprising given the paucity of spectroscopic data available for fitting the ground state potential function. What is encouraging, however, is the fact that several pairs and sequences of peaks are observed with separations similar to the predicted eigenvalue spacings, thus lending support to our expectation that the observed fine structure will ultimately prove to be explicable in terms of a number of overlapping progressions of levels with $N \sim K_a$.

Secondary photolysis

From kinetic energy spectra such as that shown in Fig. 2*a* we conclude that the primary photolysis of PH_3 at 218.2 nm results in $PH_2(\tilde{X})$ fragments with internal energies spanning the entire range from zero up to the maximum available energy ($\sim$17 000 cm^{-1}), peaking at $E_{int} \sim$ 14 000 cm^{-1}. This distribution is shown schematically in Fig. 4*a*. How should we picture the secondary photolysis of these $PH_2(\tilde{X})$ fragments? Given the angular anisotropy of the resulting H atom photofragments we must conclude that the dissociation occurs on a timescale that is fast compared to the timescale for rotation. Notwithstanding the large amount of internal excitation within the primary fragments, our observation that the maximum yield of secondary H atoms occurs when ϵ_{phot} is orthogonal to the TOF axis is most readily explained by assuming a perpendicular (i.e. $^2A_1 \leftarrow \tilde{X}^2B_1$) excitation in the PH_2 fragment. There is no available experimental information concerning the higher excited electronic states of the PH_2 radical but, given the close similarity between the first ionisation potentials of PH_2 and PH_3 (35), it is reasonable to suppose that the first Rydberg absorption of PH_2 (i.e. the $^2A_1 \leftarrow \tilde{X}\,^2B_1$ transition associated with the $4sa_1 \leftarrow 2b_1$ electron promotion) will fall in the same wavelength range as the $\tilde{A}$–$\tilde{X}$ transition of PH_3. As with other hydride molecules we might also anticipate that this first nominal "Rydberg" state of PH_2 actually has substantial antibonding valence character (19). The one reported *ab initio* calculation for this second $^2A_1$ excited state of PH_2 suggests that such a picture may be overly simplistic. Specifically, Gu et al. (52) have calculated the form of the bending potential for the 2^2A_1 state (with both bonds held fixed at their ground state separation, $R_{P—H}$ = 0.1418 nm) and found it to have a linear equilibrium configuration, at which geometry the wavefunction shows minimal Rydberg character. However, the reported bending potential curve (52) is not just a simple parabolic function; rather it shows a point of inflection at $\hat{HPH} \sim 120°$ suggestive of an avoided crossing between bent (largely Rydberg) and linear (predominantly valence) diabatic functions of $^2A_1$ symmetry. Only future, more extensive, calculations will reveal to what extent, if at all, this result is conditioned by the somewhat restricted basis set employed.

We now turn to consider the possible products of the secondary photodissociation. Figure 4*b* shows the population distribution of the nascent $PH_2(\tilde{X})$ fragments raised in energy by

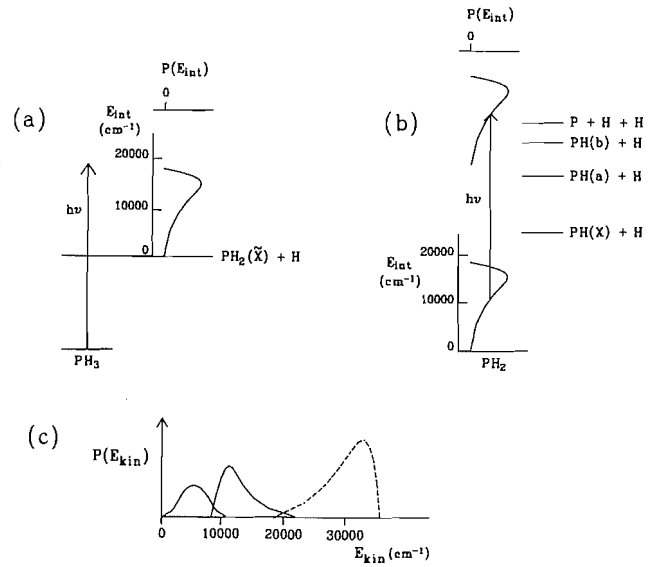

FIG. 4. Schematic illustration of various possible forms of the kinetic energy distribution of the H atoms resulting from secondary photolysis of the $PH_2(\tilde{X})$ fragments arising in the near UV photodissociation of PH_3. (*a*) depicts the general form of the experimentally observed internal distribution, $P(E_{int})$, of the primary $PH_2(\tilde{X})$ fragments. (*b*) shows the energy of this distribution of PH_2 fragments *after absorption of a near UV photolysis photon*, relative to the various H + PH dissociation thresholds. This clearly shows that *if* the major dissociation pathway were to yield internally cold ground state PH fragments then the partner H atoms would of necessity possess a highly excited, inverted kinetic energy distribution (dashed curve in (*c*)). In actuality, we deduce the kinetic energy distribution of these secondary H atoms to be of the form shown by the solid curves in (*c*), which we interpret in terms of the sum of two distinct contributions derived from dissociation pathways yielding (*i*) very highly rotationally excited PH(X) fragments and (*ii*) three atomic fragments — see text for further details.

absorption of one UV photolysis photon. Were we to assume that this photo-excitation (and the subsequent dissociation) occurs with an efficiency that is independent of the degree of internal excitation in the nascent PH_2 fragment and that the dissociation results in the formation of just *ground* state PH fragments *with little internal excitation* then, given D_0(H—PH) = 25 950 ± 700 cm^{-1} (35), we would expect the H atom photoproducts resulting from 218.2 nm photolysis of the $PH_2(\tilde{X})$ fragments to have a kinetic energy distribution that was a mirror image of that arising from the primary dissociation, i.e. a distribution which starts at $E_{kin} \sim 20\,000$ cm^{-1} and peaks at kinetic energies around 34 000 cm^{-1} (i.e. as shown by the dashed curve in Fig. 4*c*). The distribution of secondary fragments we observe is very different: it contains some fast fragments, but peaks at kinetic energies ~10 000 cm^{-1} and then falls off at still lower kinetic energies.

The following H atom forming decomposition pathways are available to a $PH_2(\tilde{X})$ fragment *in its zero-point level* following absorption of a 218.2 nm photon:

[8] $PH_2(\tilde{X}) + h\nu(218.2\text{ nm}) \rightarrow PH(X^3\Sigma^-) + H \quad KE \leqslant 19\,900\text{ cm}^{-1}$

[9] $\rightarrow PH(a^1\Delta) + H \quad KE \leqslant 12\,200\text{ cm}^{-1}$

[10] $\rightarrow PH(b^1\Sigma^+) + H \quad KE \leqslant 4\,700\text{ cm}^{-1}$

However, we know that the nascent $PH_2(\tilde{X})$ fragments formed in the primary photolysis step actually have a most probable kinetic energy of ~14 000 cm^{-1} and a maximum kinetic energy ~17 000 cm^{-1}. If some or all of this internal excitation of the PH_2 fragments can be partitioned into recoil of the secondary photodissociation products then the maximum kinetic energies quoted above need to be increased accordingly. In addition, further decomposition pathways become energetically allowed if we include the PH_2 internal excitation in the overall energy balance, e.g.:

$PH_2(\tilde{X}, E_{int} = 14\,000\text{ cm}^{-1}) + h\nu(218.2\text{ nm})$

[11] $\rightarrow PH(A^3\Pi) + H \quad KE \leqslant 4\,300\text{ cm}^{-1}$

[12] $\rightarrow P(^4S) + H + H \quad KE \sim 9\,200\text{ cm}^{-1}$

The present data do not allow unambiguous identification of the products of the secondary photolysis, but the following interpretation appears to be consistent with most of the available observations. We propose that dissociation of the highly internally excited $PH_2(\tilde{X})$ fragments yields PH fragments predominantly, if not exclusively, in their ground electronic state and carrying very high levels of internal (principally rotational) excitation. Extensive vibrational excitation of the PH product is considered less likely given the similar P—H bond lengths in PH_2 and PH. Product rotation, however, can be envisaged arising as a carry over both of the *a*-axis rotational motion and large amplitude bending in the photo-excited PH_2 molecule. The three-body fragmentation [2] represents the ultimate of this mode of dissociation, in which the centrifugal forces acting in the photo-excited PH_2 fragment are sufficient to induce rupture of both P—H bonds; the most probable partitioning of the surplus energy in such a three-body dissociation would have the two H atoms each recoiling with roughly half of the available energy.

Such an interpretation is consistent with the observed kinetic energy distribution of the secondary photolysis products. It accounts for the way in which the secondary H atom yield increases with decreasing kinetic energy up to the point where the PH(X) partner is itself unstable. At this threshold the experimental spectrum shows a discontinuity in the H atom yield. This, too, is reasonable since the simultaneous three body dissociation (12) is not restricted to follow one or other of the H---PH exit valleys on the excited state potential, and will tend to favour an equitable sharing of the available energy between the two recoiling H atoms. Dissociations proceeding via [12] are thus presumed to contribute to the broad underlying maximum centred at $E_{kin} \sim 5000$ cm^{-1}. (Such a model of the secondary dissociation process is reminiscent of that occurring in H_2S and D_2S following excitation to the $\tilde{B}^1A_1$ surface (31, 45).) The solid curves in Fig. 4*c* illustrate the expected forms of the distributions arising from these two secondary decomposition pathways. Experimentally, of course, we will measure the sum of the two, superimposed upon the kinetic energy spectrum of the H atoms arising from the primary photolysis of the PH_3 parent molecules. Our interpretation is consistent with the early observation of Kley and Welge (37), that absorption due to ground state PH(X) fragments arising in the near UV flash photolysis of PH_3 increases with increasing pressure and/or time delay; such would be expected as the highly internally excited PH(X) fragments are collisionally relaxed. Lastly, we note that our exclusion of any major role for dissociation pathways [9] and [10] (a conclusion based largely on the fact that the $a^1\Delta$ and

Can. J. Chem. Downloaded from www.nrcresearchpress.com by 195.246.54.202 on 09/08/12
For personal use only.

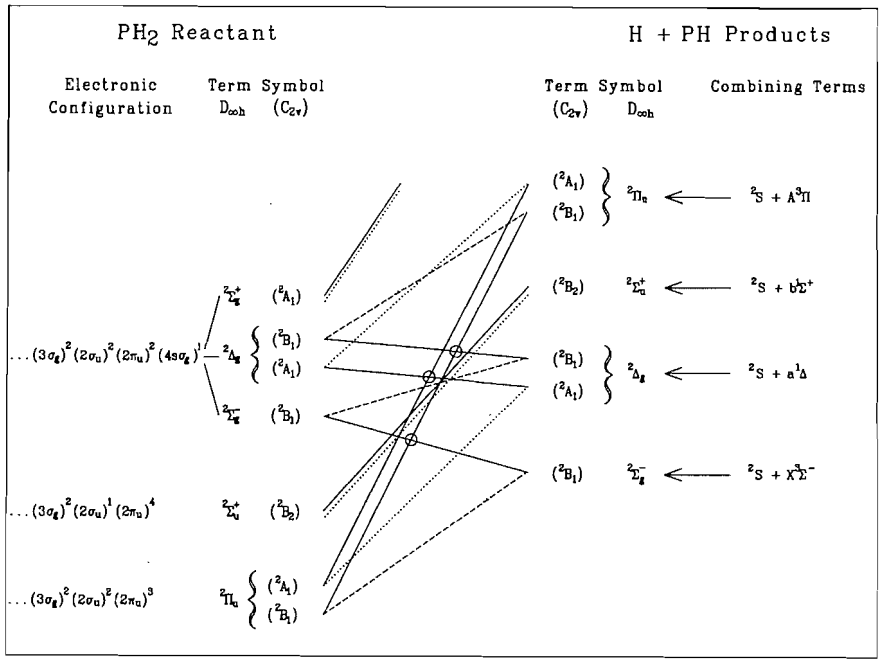

FIG. 5. Correlation diagram linking electronic states of PH_2 with those of the H + PH fragments. The states are defined in the linear and bent C_{2v} limits. Correlations in the linear limit are shown by the solid tie lines (—), the circles indicate regions of avoided crossing in the C_{2v} limit, whilst the dashed lines (... and --- for A' and A'' states, respectively) show the correlations appropriate to the lower (C_s) symmetry prevailing during the $PH_2 \rightarrow PH + H$ dissociation process.

$b^1\Sigma^+$ excited states of PH both correlate to excited states of the phosphorus atom and are thus less obviously able to account for the observed discontinuity in the H atom kinetic energy spectrum) is consistent with the fact that there have been no reports of absorption associated with PH(a) fragments following PH_3 photolysis in the near ultraviolet (37), nor of fluorescence from PH(b) photofragments following PH_3 photolysis at 193.3 nm (40).

Finally, we should give brief consideration to possible mechanisms for the secondary photodissociation process. Figure 5 shows a correlation diagram linking electronic states of PH_2 and the H + PH products resulting from simple P—H bond fission in the linear, bent (C_{2v}) and asymmetric bent (C_s) limits. In no case does the photoprepared 2^2A_1 state of PH_2 (pictured here as one component of the 4s Rydberg state having $^2\Delta_g$ symmetry in the linear limit) correlate diabatically with the ground state products. In the linear limit the natural correlation appears to be with the low lying metastable $a^1\Delta$ state of the PH product, whilst in the point group of lowest symmetry (C_s) the 2^2A_1 state correlates with the $A^3\Pi$ excited state of PH; i.e. product channel [11], which at the present excitation wavelengths is exoergic only for the most internally excited PH_2 fragments. Clearly, any mechanism advanced to explain fragmentation to *ground* state products must provide a means of coupling between A' and A'' surfaces. Renner–Teller (electronic Coriolis) and spin–orbit coupling are two such mechanisms. Both would be capable of mixing the $^2A_1$ and $^2B_1$ components of the $^2\Delta_g$ state, particularly at geometries where the two states are near degenerate; i.e. at or close to the linear configuration. In the present case, however, the PH_2 primary products are believed to be formed with high levels of a-axis rotational excitation. Such excitation must inevitably cause strong centrifugal distortion away from the a-axis (34) with the result that the photoexcited PH_2 fragments will never have the opportunity to sample near linear configurations. However, given these high levels of a-axis rotation in the PH_2 fragment and the corresponding magnitude of the effective coupling operator $2AKL_z$, electronic Coriolis mixing is still expected to be important wherever there is an accidental degeneracy. Further, Λ will be a poor quantum number for PH_2 at these strongly bent geometries. Thus it is unlikely that such mixings will occur only between levels of the $^2A_1$ and $^2B_1$ Renner–Teller components of the $^2\Delta_g$ state. Rather we expect similar mixing whenever there is an accidental degeneracy between levels of the photo-excited $^2A_1(^2A')$ state of PH_2 and those belonging to neighbouring states of $^2B_1(^2A'')$ symmetry. Provided K(K_a) is high, therefore, we anticipate that population transfer to the ground state surface will be a facile process — as indeed our interpretation of the H atom kinetic energy spectrum and, particularly, the deduced recoil anisotropy shows it to be.

Conclusions

In this paper we present time-of-flight spectra for the H atom fragments arising following excitation of jet-cooled PH_3 molecules in the long wavelength tail of its near ultraviolet $\tilde{A}$–$\tilde{X}$ absorption system. Energy conservation requires that the partner molecular fragments arising in the primary photolysis step are, of necessity, PH_2 fragments in their electronic ground state. The measured H atom kinetic energy distributions are broad, and show only poorly resolved structure. Nonetheless they suffice to indicate that the $PH_2(\tilde{X})$ fragments carry substantial internal excitation — at least 62% of the available energy. Analogy with ammonia — the photochemistry of which has been studied in much greater detail — suggests that bending vibrational motion and a-axis rotation are both important contributors to this internal excitation.

The H atom translational energy spectra also show clear evidence of H atoms arising from secondary photodissociation of the primary $PH_2(\tilde{X})$ fragments. These secondary photoproducts show a marked anisotropy, the angular dependence of which can be understood if the photo-excitation of the PH_2 moiety is

Can. J. Chem. Downloaded from www.nrcresearchpress.com by 195.246.54.202 on 09/08/12
For personal use only.

assumed to involve a perpendicular transition. The kinetic energy spectrum of the secondary H atoms indicates that, following photo-excitation, the primary PH_2 fragments dissociate both by single P—H bond cleavage — yielding an H atom together with a highly rotationally excited ground state $PH(X)$ fragment — and via a three-body fragmentation process, forming H + H + $P(^4S)$ atoms. Electronic Coriolis mixing is advanced as the most likely mechanism for coupling the photo-excited PH_2 fragments with these ground state product channels.

Acknowledgements

Once again it is a pleasure to acknowledge the generous help and inspiration of Professor K.H. Welge, Dr. L. Schnieder and their colleagues at Universität Bielefeld. We are also grateful to SERC — for equipment grants, for a post-doctoral fellowship (to I.R.L.) and research studentships (to G.P.M. and D.H.M.), and to the Laser Support Facility at the SERC Rutherford Laboratory for the loan of the photolysis laser system.

1. J. Hwang, P. Pianetta, C.K. Shih, W.E. Spicer, Y.C. Pao, and J.S. Harris, Jr. Appl. Phys. Lett. **51**, 1632 (1978).
2. N.K. Singh, A.J. Murrell, and J.S. Foord. Surf. Sci. **274**, 341 (1992).
3. T. Sugino, H. Ito, and J. Shirafuji. Jpn. J. Appl. Phys. (Part 2), **29**, L1771 (1990); Electron. Lett. **26**, 1750 (1990).
4. R.P. Wayne. Chemistry of atmospheres. 2nd ed. Clarendon Press, Oxford. 1991.
5. K.S. Noll and H.P. Larson. Icarus, **89**, 168 (1991).
6. F. Chen, D.L. Judge, and C.Y.R. Wu. J. Geophys. Res. **96**, 17519 (1991).
7. C.A. Griffith. Icarus, **98**, 82 (1992).
8. R. Maripuu, I. Reineck, H. Ågren, W. Nian-Zu, J.M. Rong, H. Veenhuizen, S.H. Al-Shamma, L. Karlsson, and K. Siegbahn. Mol. Phys. **48**, 1255 (1983).
9. J. Müller, H. Ågren, and S. Canuto. J. Chem. Phys. **76**, 5060 (1982).
10. R. Runau, S.D. Peyerimhoff, and R.J. Buenker. J. Mol. Spectrosc. **68**, 253 (1977).
11. P. Rosmus, P. Botschwina, H.J. Werner, V. Vaida, P.C. Engelking, and M.I. McCarthy. J. Chem. Phys. **86**, 6677 (1987).
12. M.I. McCarthy, P. Rosmus, H.J. Werner, P. Botschwina, and V. Vaida. J. Chem. Phys. **86**, 6693 (1987).
13. K. Watanabe. J. Chem. Phys. **22**, 1564 (1954).
14. A.D. Walsh and P.A. Warsop. Trans. Faraday Soc. **57**, 345 (1961).
15. V. Vaida, W. Hess, and J.L. Roebber. J. Phys. Chem. **88**, 3397 (1984).
16. M.N.R. Ashfold, C.L. Bennett, and R.J. Stickland. Comm. At. Mol. Phys. **19**, 181 (1987).
17. A.D. Walsh and P.A. Warsop. Adv. Mol. Spectrosc. **2**, 383 (1962).
18. C.M. Humphries, A.D. Walsh, and P. Warsop. Discuss. Faraday Soc. **35**, 148 (1963).
19. M.B. Robin. Higher excited states of polyatomic molecules. Academic Press, New York. Vols. 1 and 2. 1974; Vol. 3. 1985.
20. T.J. Xia, C.Y.R. Wu, and D.L. Judge. Phys. Script. **41**, 870 (1990).
21. A.M. Halpern and B.R. Ramachandran. J. Mol. Spectrosc. **151**, 26 (1992).
22. M.B. Arfa and M. Tronc. Chem. Phys. **155**, 143 (1991).
23. M.N.R. Ashfold, R.J. Stickland, and B. Tutcher. Mol. Phys. **65**, 1455 (1988).
24. R.A. Back and S. Koda. Can. J. Chem. **55**, 1387 (1977).
25. V.M. Donnelly, A.P. Baronavski, and J.R. McDonald. Chem. Phys. **43**, 271 (1979).
26. B. Koplitz, Z. Xu, and C. Wittig. Chem. Phys. Lett. **137**, 505 (1987).
27. H.J. Krautwald, L. Schnieder, K.H. Welge, and M.N.R. Ashfold. Faraday Discuss. Chem. Soc. **82**, 99 (1986).
28. J. Biesner, L. Schnieder, J. Schmeer, G. Ahlers, X. Xie, K.H. Welge, M.N.R. Ashfold, and R.N. Dixon. J. Chem. Phys. **88**, 3607 (1988).
29. J. Biesner, L. Schnieder, G. Ahlers, X. Xie, K.H. Welge, M.N.R. Ashfold, and R.N. Dixon. J. Chem. Phys. **91**, 2901 (1989).
30. M.N.R. Ashfold, R.N. Dixon, S.J. Irving, H.-M. Koeppe, W. Meier, J.R. Nightingale, L. Schnieder, and K.H. Welge. Phil. Trans. R. Soc. London A, **332**, 375 (1990).
31. L. Schnieder, W. Meier, K.H. Welge, M.N.R. Ashfold, and C.M. Western. J. Chem. Phys. **92**, 7027 (1990).
32. M.N.R. Ashfold, I.R. Lambert, D.H. Mordaunt, G.P. Morley, and C.M. Western. J. Phys. Chem. **96**, 2938 (1992).
33. R.N. Dixon. Mol. Phys. **68**, 263 (1989).
34. R.N. Dixon, S.J. Irving, J.R. Nightingale, and M. Vervloet. J. Chem. Soc. Faraday Trans. **87**, 2121 (1991).
35. J. Berkowitz, L.A. Curtiss, S.T. Gibson, J.P. Greene, G.L. Hillhouse, and J.A. Pople. J. Chem. Phys. **84**, 375 (1986).
36. M.N.R. Ashfold, M.T. Macpherson, and J.P. Simons. Top. Curr. Chem. **86**, 1 (1979).
37. D. Kley and K.H. Welge. Z. Naturforsch. Teil A, **20**, 124 (1965).
38. G. Di Stefano, M. Lenzi, A. Margani, A. Mele, and C.N. Xuan. J. Photochem. **7**, 335 (1977).
39. G. Di Stefano, M. Lenzi, A. Margani, and C.N. Xuan. J. Chem. Phys. **68**, 959 (1978).
40. C.L. Sam and J.T. Yardley. J. Chem. Phys. **69**, 4621 (1978).
41. R.D. Kenner, R.K. Browarzik, and F. Stuhl. Chem. Phys. **121**, 457 (1988).
42. D. Baugh, B. Koplitz, Z. Xu, and C. Wittig. J. Chem. Phys. **88**, 879 (1987).
43. G.P. Morley, I.R. Lambert, M.N.R. Ashfold, K.N. Rosser, and C.M. Western. J. Chem. Phys. **97**, 3157 (1992).
44. D.H. Mordaunt, I.R. Lambert, G.P. Morley, M.N.R. Ashfold, R.N. Dixon, C.M. Western, L. Schnieder, and K.H. Welge. J. Chem. Phys. **98**, 2054 (1993).
45. G.P. Morley, I.R. Lambert, D.H. Mordaunt, S.H.S. Wilson, M.N.R. Ashfold, R.N. Dixon, and C.M. Western. J. Chem. Soc. Faraday Trans. **89**, 3865 (1993).
46. R.E. Continetti, B.A. Balko, and Y.T. Lee. Chem. Phys. Lett. **182**, 400 (1991).
47. R.N. Dixon, G. Duxbury, and D.A. Ramsay. Proc. R. Soc. London A, **296**, 137 (1967).
48. J.-M. Berthou, B. Pascat, H. Guenebaut, and D.A. Ramsay. Can. J. Phys. **50**, 2265 (1972) and references therein.
49. F.W. Birss, G. Lessard, B.A. Thrush, and D.A. Ramsay. J. Mol. Spectrosc. **92**, 269 (1982).
50. M. Peric, R.J. Buenker, and S.D. Peyerimhoff. Can. J. Chem. **57**, 2491 (1979).
51. G. Duxbury and R.N. Dixon. Mol. Phys. **43**, 255 (1981) and references therein.
52. J. Gu, M. Huang, F. Kong, and S. Liu. Theochem. **60**, 39 (1989).

Can. J. Chem. Downloaded from www.nrcresearchpress.com by 195.246.54.202 on 09/08/12
For personal use only.

Semiclassical study of sudden approximations for rotationally inelastic scattering of Ar+HF

JAMES J.C. BARRETT AND HOWARD R. MAYNE[1]
Department of Chemistry, University of New Hamphire, Durham, NH 03824-3589, U.S.A.

MARK KEIL[1]
Department of Physics and Astronomy, University of Oklahoma, Norman, OK 73019-0225, U.S.A.
AND
LESLIE J. RAWLUK
Department of Science, Grande Prairie Regional College, Grande Prairie, AL T8V 4C4, Canada

Received July 30, 1993

This paper is dedicated to Professor John C. Polanyi on the occasion of his 65th birthday

JAMES J.C. BARRETT, HOWARD R. MAYNE, MARK KEIL, and LESLIE J. RAWLUK. Can. J. Chem. **72**, 985 (1994).

"Exact" quantum close coupled (CC) and infinite-order sudden approximation (IOSA) calculations have been carried out for the Ar + HF system on an accurate potential energy surface. The differential cross sections from the IOSA calculations show marked differences from the CC results. We find that the energy sudden component of the IOSA breaks down in a different manner for small and large impact parameters, significantly shifting and distorting the state-to-state differential cross sections. We also find that the centrifugal sudden approximation alone reproduces all features of the full semiclassical calculations quite faithfully. Through the use of several rotational sudden approximations, including a semiclassical version of the IOSA, we identify how the differences between the CC and IOSA results arise.

JAMES J.C. BARRETT, HOWARD R. MAYNE, MARK KEIL et LESLIE J. RAWLUK. Can. J. Chem. **72**, 985 (1994).

On a effectué des calculs quantiques en couplage fermé « exact » (CC) et dans l'approximation soudaine d'ordre infini (IOSA) pour le système Ar + HF, sur une surface d'énergie potentielle précise. Les sections droites différentielles obtenues par les calculs IOSA présentent des différences importantes par rapport à celles obtenus par CC. On a trouvé que la composante énergétique soudaine de l'approximation IOSA se répartit d'une façon différente suivant les paramètres d'impact petits ou grands et qu'il en résulte un déplacement et une distorsion des sections droites différentielles d'un état à un autre. On a aussi trouvé que l'approximation centrifuge soudaine permet de reproduire fidèlement, toute seule, toutes les caractéristiques des calculs semiclassiques complets. Utilisant plusieurs approximations rotationnelles soudaines, y compris une version semiclassique de IOSA, on a pu identifier l'origine des différences entre les méthodes CC et IOSA.

[Traduit par la rédaction]

I. Introduction

One of the first attempts to systematize rate constants for state-to-state rotational relaxation was made by Polanyi and Woodall over two decades ago (1), as a by-product of measuring state-resolved populations in chemiluminescent reactions producing hydrogen halide products. The early success of their "exponential gap" scaling rule lay in its ability to correlate rate constants for a wide variety of systems. More detailed measurements however, especially differential cross sections, could not be explained by a two-parameter empirical model. Instead, these more detailed studies began to reveal the dynamical role of the potential energy surface for rotational energy transfer.

In the last decade, scattering studies have been joined by high-resolution spectroscopic studies on weakly-bound van der Waals molecules. Whenever accessible, experimental high resolution spectroscopy has always provided the most accurate source of information on intermolecular forces, including those for van der Waals molecules (2). In particular, accurate potential energy surfaces have been obtained using these techniques for weakly-bound rare gas + hydrogen halide systems (3, 4). However, such measurements are sensitive primarily to those parts of the potential capable of supporting bound states. Repulsive regions of the potential surface can only be obtained by rather extensive extrapolations of the spectroscopic information. In contrast, state-to-state scattering experiments, especially differential cross sections (DCS), probe the repulsive wall of the potential directly (5, 6). Such experiments can help characterize the potential for purely repulsive or very weakly attractive systems (6).

It is clear from the above that scattering measurements and spectroscopy tend to provide complementary information on the potential. Spectroscopic data for the Ar+HF system have been used by Hutson (3) to obtain a potential of excellent quality (7) in the attractive region, hereafter referred to as the "Hutson H6" potential. Scattering data, in the form of final state selected DCS from crossed molecular beam experiments on Ar+HF, have also recently been obtained (8). In order to analyze these experiments, "exact" quantum mechanical close-coupled (CC) inelastic scattering calculations have been carried out (9) using the Hutson H6 potential energy surface (3). When the results were transformed to the laboratory scattering frame, and averaged over the experimental conditions, the agreement was found to be quite good for the low final rotational states, $j' \leq 2$. The comparison of the CC results with the experimental DCS for the higher rotational states was poor (9). This is not surprising, since large Δj transitions are due primarily to collisions which sample the repulsive wall of the potential (10, 11), and this is the portion of the potential not directly probed by the spectroscopic studies. Again it is clear that spectroscopic and scattering results are best combined to determine attractive and repulsive regions of the potential surface.

Nevertheless, scattering results are not necessarily insensi-

[1]To whom correspondence may be addressed.

Can. J. Chem. Downloaded from www.nrcresearchpress.com by 195.246.54.202 on 09/08/12
For personal use only.

Can. J. Chem. Downloaded from www.nrcresearchpress.com by 195.246.54.202 on 09/08/12
For personal use only.

tive to the attractive portions of the potential. In the earlier study (9), we conducted calculations to determine the sensitivity of the scattering to various features of the potential. It was found that the state-to-state DCS, particularly for the $j = 0 \rightarrow j' = 0$ and $j = 0 \rightarrow j' = 1$ transitions, displayed novel features with interference characteristics of quantum mechanical origin (9). Using the CC method, it was shown that these DCS were very sensitive to changes in both the attractive well and the repulsive wall. Further work on this system using a semiclassical approach (12) showed in more detail how the attractive and repulsive regions of the potential strike a particular balance in producing the novel features observed in the CC calculations, features that are entirely absent from the fully classical results.

For predominantly repulsive systems, the theoretical technique most successful in extracting information on the potential energy surface has been the infinite order sudden approximation (IOSA) (13, 14). This approximation has also been invaluable in obtaining a physical understanding of rotational excitation due to scattering from a hard anisotropic core (11, 15). The success of the IOSA in fitting repulsive potentials is due to the following: the method is computationally fast; and, in conjunction with an additional semiclassical approximation (11, 16), it links the local surface topography with the dynamics. Unfortunately, it is likely that the IOSA performance is poorest for precisely those rare gas + hydrogen halide (HX) van der Waals systems best characterized spectroscopically. Not only is the energy sudden criterion violated by the large HX rotational spacings, but the centrifugal sudden criterion is also rendered suspect the by attractiveness of the potential energy surface. In view of the IOSA's difficulties, the unambiguous, global determination of a strongly attractive, anisotropic potential surface, such as that for Ar+HF scattering, poses a theoretical challenge.

Accordingly, calculations on the Hutson H6 Ar+HF potential were carried out using the IOSA and compared with CC data (9). The results were disappointingly poor, at least quantitatively, in the sense that they failed to reproduce the "exact" CC results at the state resolved level, thus prohibiting the use of the IOSA in systematically improving even the repulsive region of the potential. Since the IOSA is such a frequently used tool in the analysis of rotationally inelastic scattering (11) it would be beneficial to better understand these discrepancies between the IOSA and CC results. In particular, we use previously developed semiclassical methods (12, 17) herein to understand the origins of these deviations. There have previously been a few systematic studies of decoupling approximations within a time-dependent framework (17–19). Perhaps the most comprehensive such work was that on the classical limit of decoupling (20).

In section II, we present the computational methods employed in this study. In particular, we detail the semiclassical method together with the decoupling and sudden approximations used. In section III, we compare the semiclassical CC and IOSA results. We further relate features in the CC and IOSA DCS to oscillations in the semiclassical opacity functions. This leads us to introduce a two-state model of the semiclassical method. This simplification elucidates shortcomings of the IOSA occurring even for low impact parameters (i.e. repulsive collisions). Finally, we examine the time-dependent evolution of the system to explain the failure of the IOSA for high impact parameters. Concluding remarks are made in section IV.

II. Calculations

IIA. Time-independent methods

The time-independent close-coupled (CC) calculations using the HIBRIDON package of molecular scattering programs have been described elsewhere in detail (9, 21). The infinite order sudden approximation (IOSA) calculations are carried out using the standard l-initial convention (13, 14).

IIB. Time-dependent methods

The time-dependent methods employed here are less standard than the time-independent methods. We therefore describe the time-dependent semiclassical (or classical path) method in some detail. In addition, we give explicit formulations for a hierarchy of approximations leading ultimately to the semiclassical version of the IOSA. The methods have been reviewed previously (17, 19, 22).

In the semiclassical approximation for rotationally inelastic collisions (23) we take advantage of the mass discrepancy between the translational and internal coordinates of the collision system. In this case we are scattering a hydrogenic diatom (HF) from a heavy rare gas atom (Ar). In this problem the translational reduced mass, given by

$$[1] \qquad M = \frac{m_{\mathrm{Ar}}(m_{\mathrm{F}} + m_{\mathrm{H}})}{m_{\mathrm{Ar}} + m_{\mathrm{F}} + m_{\mathrm{H}}}$$

is large. Therefore, the relative motion can reasonably be treated classically. Conversely the rotational degrees of freedom of the hydrogenic HF must be treated quantum mechanically to give accurate dynamics.

The motion for the translational coordinate is governed by Hamilton's equations of motion. In Cartesian coordinates these are given by

$$[2] \qquad \dot{\mathbf{R}} = \frac{\partial H_{\mathrm{cl}}}{\partial \mathbf{P}}; \quad \dot{\mathbf{P}} = -\frac{\partial H_{\mathrm{cl}}}{\partial \mathbf{R}}$$

where $\mathbf{R}$ is the displacement of the atom from the diatom center of mass, and $\mathbf{P}$ is its conjugate momentum. The classical Hamiltonian for the translational motion is given by

$$[3] \qquad H_{\mathrm{cl}} = \frac{P^2}{2M} + \langle V(\mathbf{R}) \rangle$$

where $\langle V(\mathbf{R}) \rangle$ is an appropriate average of the potential energy over the internal coordinates (24).

Propagation of the rotational degrees of freedom is achieved by solving the time-dependent Schrödinger equation for the internal state wave function (25)

$$[4] \qquad i\hbar \frac{\mathrm{d}|\Psi(t)\rangle}{\mathrm{d}t} = \hat{H}_{\mathrm{q}}|\Psi(t)\rangle$$

where $\hat{H}_{\mathrm{q}}$ is the quantum Hamiltonian for a rigid rotor in a time-dependent external field, $\hat{V}(t)$. The time dependence of $\hat{H}_{\mathrm{q}}$ arises from the external field as

$$[5] \qquad \hat{H}_{\mathrm{q}} = \hat{H}_0 + \hat{V}(t)$$

where $\hat{H}_0$ is the zeroth order Hamiltonian for an unperturbed rigid rotor. We expand the wave function for the system in an appropriate basis set (i.e. the eigenstates of $\hat{H}_0$, the spherical harmonics) so that

$$[6] \qquad |\Psi(t)\rangle = \sum_l c_l(t)|l\rangle \exp(-iE_l t/\hbar)$$

Can. J. Chem. Downloaded from www.nrcresearchpress.com by 195.246.54.202 on 09/08/12
For personal use only.

with $c_l(t)$ being the time-dependent expansion coefficient for the lth rotational state, $|jm\rangle$, and E_l is the energy associated with the j rotational level of the lth state. The time-dependent quantum equations of motion are then given by

$$[7] \qquad i\hbar\,\dot{c}_k = \sum_l c_l V_{kl}(t) \exp(i\omega_{kl}t)$$

where

$$[8] \qquad V_{kl}(t) = \langle k|\hat{V}(t)|l\rangle$$

and

$$[9] \qquad \omega_{kl} = \frac{E_k - E_l}{\hbar}$$

We shall refer to eq. [7] as being the "full" semiclassical treatment, or simply "SC". The integral in eq. [8] is given by

$$[10] \qquad V_{kl}(t) = \int d\hat{\mathbf{r}} Y^*_{j'm'}(\hat{\mathbf{r}})\hat{V}(\mathbf{R}(t), \hat{\mathbf{r}})Y_{jm}(\hat{\mathbf{r}})$$

where $\mathbf{R}(t)$ is the atom–diatom displacement vector as a function of time from the classical part of the calculation and $\hat{\mathbf{r}}$ is the diatom bond unit vector. The classical and quantum degrees of freedom are propagated simultaneously.

The potential energy operator, $\hat{V}$, taken as the interaction potential, $V(R, \gamma)$, is a function of R and γ only. R is the length of the vector $\mathbf{R}(t)$ and γ is the angle between $\hat{\mathbf{r}}$ and $\mathbf{R}(t)$. In the classical trajectory, $\mathbf{R}$ is described in space-fixed coordinates (26). In this study $V(R, \gamma)$ is taken as the Hutson H6 potential for Ar+HF ($v = 0$) (3). This potential is selected over several other surfaces (27) because it has been shown in previous work (9) to best reproduce scattering features experimentally observed in rotationally resolved differential cross sections (8). It has also been very useful in extending further spectroscopic studies (28).

The time-dependent probability of finding the system in some rotational state, k, is given by

$$[11] \qquad P_k(t) = |c_k(t)|^2$$

The final probability is taken as $t \rightarrow \infty$. In our semiclassical treatment a trajectory is started at some impact parameter, b, and run until the final rotational state probability is constant to three decimal places. Since we are not concerned with resolving the m-sublevels, the quantum opacity function for a given final rotational level, $P_{j'}(b)$, is given as the sum

$$[12] \qquad P_{j'}(b) = \sum_{m'=-j'}^{j'} |c_{j'm'}|^2$$

The scattering angle, θ, for a trajectory is given as the angle between the initial and final classical relative momentum vectors, $\mathbf{P}$ and $\mathbf{P}'$, respectively. The classical deflection function, $\theta(b)$, is obtained from a set of trajectories calculated for an elastic collision between the Ar and HF. The $\langle V(R)\rangle$ used in the classical trajectory calculation is taken as the spherical average of the H6 potential. It has been suggested that an "Ehrenfest" average of the potential (22, 23), given by

$$[13] \qquad \langle V(R(t))\rangle = \langle \Psi(t)|V(\mathbf{R}(t), \hat{\mathbf{r}})|\Psi(t)\rangle$$

be used in the classical trajectory. We have employed this method in our calculations and find that using the spherical average of the potential shows no significant difference between the deflection or opacity functions from an Ehrenfest average calculation, but with a substantial savings in computational time.

From the quantum opacity function for elastic and inelastic transitions and the classical deflection function for the scattering angle, we calculate the DCS using

$$[14] \qquad \frac{d\sigma_{j'}(\theta)}{d\bar{\omega}} = \frac{1}{\sin\theta} \sum_i b_i P_{j'}(b_i) \left|\frac{d\theta}{db}\right|^{-1}_i$$

where b_i is the impact parameter leading to the particular scattering angle, θ. In the sum over i, there is one trajectory for $\theta > |\theta_r|$, whereas three trajectories contribute for $\theta \leq |\theta_r|$, where θ_r is the classical rainbow angle (29). The problems associated with using this classical definition of the DCS are well known (30); however, we find this method to be sufficient in our application.

The first of the approximations to the full SC dynamics that we introduce is the "energy sudden" approximation (31, 32). This approximation is based on the assumption that all rotational energy levels are degenerate, i.e. $E_k = E_l$. In this case, $\omega_{kl} = 0$ and eq. [7] reduces to

$$[15] \qquad i\hbar\,\dot{c}_k = \sum_l c_l V_{kl}(t)$$

We will refer to this as the semiclassical energy-sudden approximation (SC-ES). While this approximation does not lead to a significant savings in computational time, we will see in the following section that the SC-ES does allow for the investigation of the exact nature of any differences between the IOSA and a fully coupled calculation of the scattering dynamics.

In order to implement the decoupling approximations, we introduce body-fixed (BF) coordinates (33), in which the BF vector, $\hat{\mathbf{z}}$, is chosen to lie along the internuclear separation vector, $\mathbf{R}$. In this case, the time-dependent equations of motion are given by

$$[16] \qquad i\hbar\,\dot{c}_{j'm}(t) = \sum_j c_{jm}(t)\langle j'm|V(t)|jm\rangle \exp(i\omega_{j'j}t)$$

(Note that due to the axial symmetry of the potential, only $\Delta m = 0$ transitions are allowed.) Because of the similarity of this method to the time-independent coupled-states approximation (34), we shall denote the results from eq. [16] as the semiclassical coupled-states (SC-CS) approximation. Essentially, the approximation involved in going from the full semiclassical theory to the SC-CS approximation, in which the m-sublevels are decoupled, is equivalent to the "centrifugal sudden" approximation (13, 35).

The final approximation required to produce a coupling scheme in the time-dependent, semiclassical regime equivalent to the IOSA is to incorporate the energy sudden approximation into eq. [16]. Thus, the time-dependent equivalent of the IOSA is given by

$$[17] \qquad i\hbar\,\dot{c}_{j'm}(t) = \sum_j c_{jm}(t)\langle j'm|V(t)|jm\rangle$$

We shall refer to this result as the SC-IOS approximation. In all

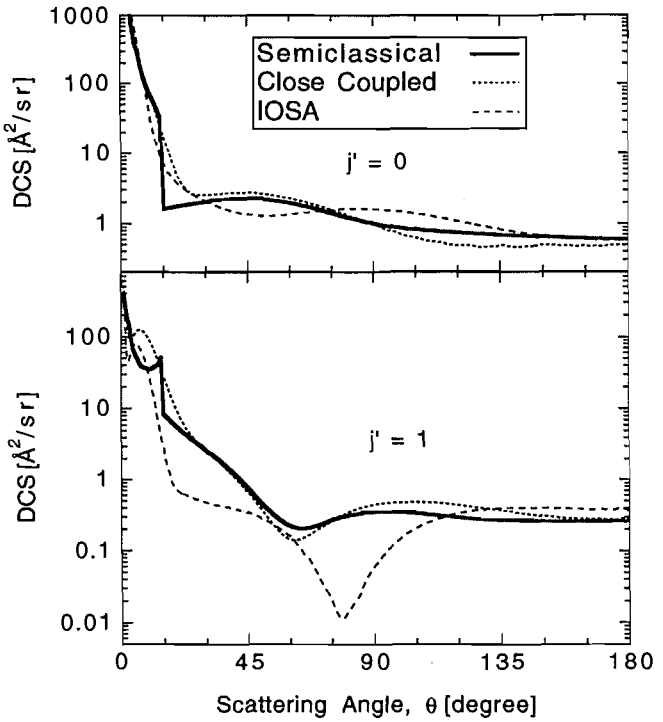

FIG. 1. Differential cross sections for Ar+HF ($j = 0$) $\longrightarrow$ Ar + HF ($j' = 0, 1$) calculated using the full semiclassical, quantum CC and IOSA formalisms. Relative collision energy, $E_{coll} = 135$ meV. Note that the CC and IOSA results have been smoothed using a 2° angular averaging function to suppress high frequency oscillations.

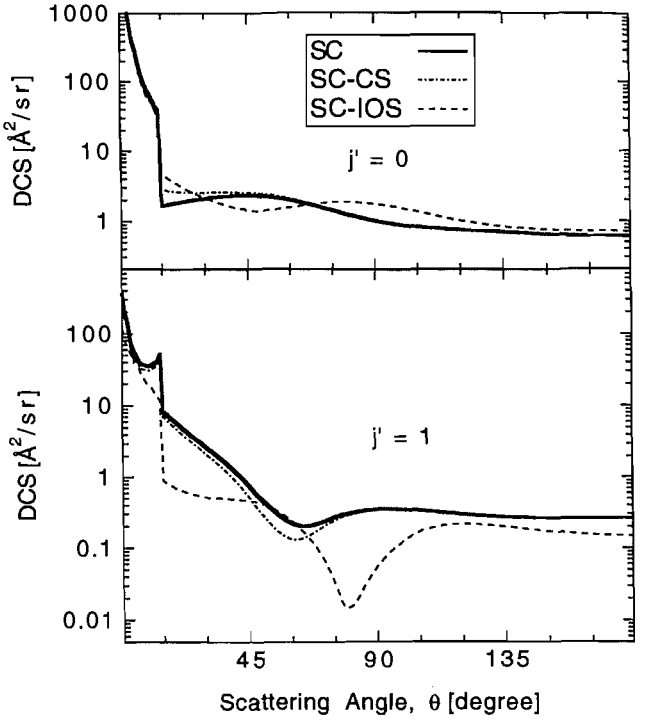

FIG. 2. Differential cross sections calculated using the full semiclassical method and indicated approximations. Collision energy and initial rotational state are in Fig. 1.

of the semiclassical methods the time-dependent equations are solved using a standard fourth-order Runge–Kutta integrator. We concentrate our efforts in this paper on the transitions out of an initial state $|j = 0, m = 0\rangle$ at a single collision energy of 135 meV, the nominal collision energy of the scattering experiment (8, 9). In all cases, a 2° angular averaging is imposed upon the calculated results to obviate features as yet inaccessible to these experiments.

III. Results and discussion

The DCS calculated using the "exact" CC, IOSA, and full semiclassical methods at a collision energy of 135 meV are shown in Fig. 1. The most notable features of the CC DCS have been discussed elsewhere (9, 12). To summarize: (*1*) the rainbow, expected at 7°, in the elastic $0 \longrightarrow 0$ DCS is suppressed whereas this feature is present in the $0 \longrightarrow 1$ DCS; (2) there is a broad shoulder in the $0 \longrightarrow 0$ DCS at $\theta \sim 40$–$70°$ with a concomitant dip in the $\theta \longrightarrow 1$ DCS centered near $\theta \sim 60°$. It has been shown (9) that these features have a quantum mechanical origin. Away from the rainbow angle, there is good agreement between the semiclassical DCS and the CC results indicating that the full semiclassical model provides an reasonable description of the collision dynamics (12).

The IOSA DCS shows features qualitatively similar to those in the CC DCS. For instance, the rainbow in the $0 \longrightarrow 0$ DCS is suppressed in this approximation, whereas the $0 \longrightarrow 1$ DCS does show a rainbow. In addition, there is a shoulder in the $0 \longrightarrow 0$ DCS, but in the IOSA the feature has shifted out to scattering angles near $\theta \sim 90°$. The accompanying dip in the $0 \longrightarrow 1$ DCS is also shifted to the same region.

In Fig. 2 we compare the full semiclassical calculations of the DCS with those using the SC-CS and the SC-IOS approximations. It is seen that the full and CS semiclassical results are in very good agreement, so that the SC-CS approximation reproduces the CC DCS rather well for this case. In contrast, the SC-IOS differs markedly from the SC results. The shoulder/dip features in the SC-IOS DCS are shifted to higher scattering angles. In fact, the SC-IOS greatly resembles the results from the time-independent IOSA calculation. To emphasize the similarity, we compare the DCS from the IOSA with those from the SC-IOS treatment in Fig. 3. The agreement is very good, with the exception of an indication of the rainbow in the SC-IOS elastic DCS. (In the rainbow region, a "primitive" semiclassical approximation like eq. [14] is expected to fail catastrophically (36)).

We now examine the collision dynamics within each of the approximations more closely. We take advantage of the time-dependent semiclassical framework, in which we can examine the contributions from individual impact parameters and the role of the potential as the trajectory evolves in time. We use these attributes to analyze the discrepancies between the fully-coupled SC and the SC-IOS calculations and relate these back to the differences between the quantum CC and IOSA results.

We first examine opacity functions from the full SC calculation and from each of the more approximate methods, shown in Figs. 4*a*–*d*. The opacity functions for the full SC (Fig. 4*a*) and the SC-CS (Fig. 4*b*) are almost identical, with the most marked difference being a somewhat smaller $P_l(b)$ near the maximum at $b = 7$ bohr in the SC-CS. This translates into an excellent agreement between the full SC and SC-CS DCS of Fig. 2. Comparing the opacity functions from the SC-ES (Fig. 4*c*) and SC-IOS (Fig. 4*d*) with Fig. 4*a*, we immediately see a dramatic difference attributable to the ES approximation.

The most obvious difference between the SC-ES and the full SC opacity functions is in the impact parameter region, $5.5 < b < 8.0$ bohr. However, a far more noticeable effect on

Can. J. Chem. Downloaded from www.nrcresearchpress.com by 195.246.54.202 on 09/08/12
For personal use only.

Can. J. Chem. Downloaded from www.nrcresearchpress.com by 195.246.54.202 on 09/08/12
For personal use only.

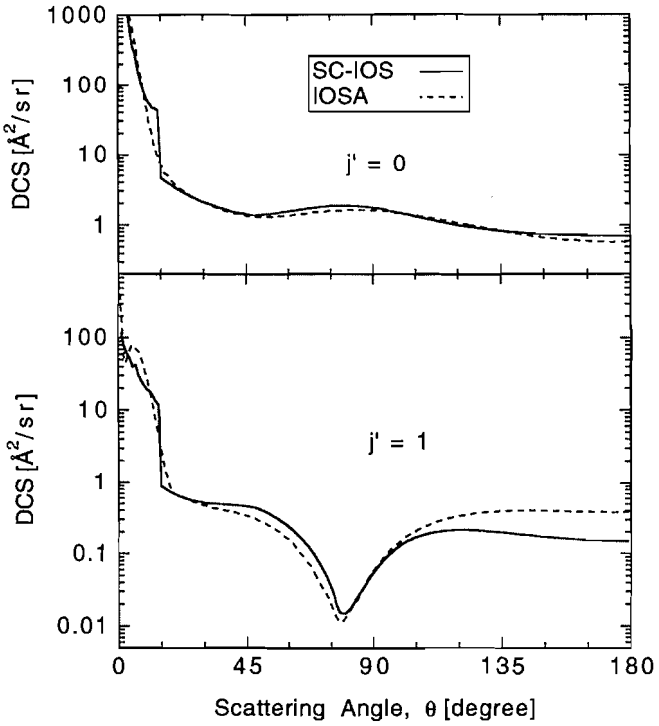

FIG. 3. Comparison of DCS from the time-independent quantum IOSA and the semiclassical IOS approximations.

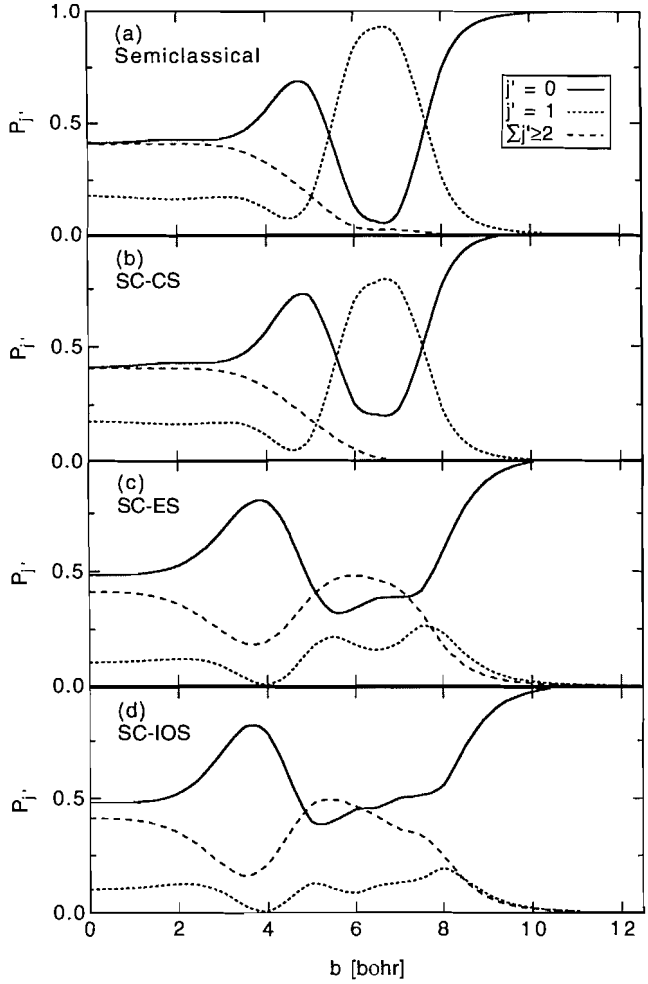

FIG. 4. Opacity functions for Ar+HF ($j = 0$) $\longrightarrow$ Ar + HF (j') from: (*a*) the full semiclassical method; (*b*) SC-CS; (*c*) SC-ES; and (*d*) SC-IOS. The summation refers to the total transition probability into rotational states $j' \geq 2$.

the observed DCS comes from the more subtle difference in the range, $3.5 < b < 5.5$ bohr, as we shall explain below. In this region, the peak and dip seen, respectively, in the $P_0(b)$ and $P_1(b)$ functions are shifted to a slightly lower b in the SC-ES (and SC-IOS) opacity functions. To highlight this shift we plot, in Fig. 5, the opacity functions for $j' = 0$ only. We also show the deflection function in this plot to indicate the scattering angles at which the features in the opacity functions manifest themselves in the DCS. The DCS is obtained from the opacity and deflection functions using eq. [14]. It is clear that a maximum in the opacity function, in the region where $\theta(b)$ is single valued, will account for a peak or "shoulder" in the DCS. (Scattering angles less than the rainbow angle, θ_r, result from impact parameters $b > 6$ bohr. In this region the effect of changes in the $P_{j'}(b)$ on the DCS is less obvious since three impact parameters contribute to the DCS.) From Fig. 5 we recognize that the shift of the $P_0(b)$ peak to lower impact parameter will cause the "shoulder" feature in the $j' = 0$ DCS to shift out to higher scattering angles. The shift in the $P_0(b)$ peak from $b = 4.5$ bohr to $b = 4.0$ bohr is responsible for the shift of the shoulder in the $0 \longrightarrow 0$ DCS in the IOSA of Fig. 1. Note that, although the $P_0(b)$ has a larger value in the SC-IOS, it occurs at a lower b value. This reduced b-weighting (see eq. [14]) compensates for the increased peak height and the shoulders are seen to have comparable intensities.

Complementary arguments are used to explain the more dramatic dip in the $0 \longrightarrow 1$ DCS observed between the CC and the IOSA. In Fig. 6 we plot the opacity functions for $j' = 1$ from each of the SC approximations. As with the peak in $P_0(b)$, the dip in $P_1(b)$ is shifted to lower impact parameters in the SC-IOS as compared to the dip in the full SC opacity function. We can also see in Fig. 6 that the dip in the SC-IOS $P_1(b)$ is deeper than in the SC model. The combination of these two features — the shift to lower impact parameter and the smaller $P_1(b)$ — result in the deep hole observed for the $0 \longrightarrow 1$ IOSA DCS in Fig. 1.

We have now established a connection between the opacity functions calculated from the various SC approximations and the features observed in the CC and IOSA DCS. We now go on to discuss the origins of the differences observed in the opacity functions calculated using the SC and SC-ES methods. Looking at Figs. 5 and 6 we see that there are two distinct regions in the opacity functions. In the low impact parameter region, $b < 5.5$ bohr, the SC and SC-ES results are qualitatively similar. However, in the high impact parameter region, $b > 5.5$ bohr, the opacity functions differ quite dramatically. We take this impact parameter, $b = 5.5$ bohr, as the division point for our discussion because of the qualitative difference between the opacity functions in these regions.

Further investigation of the dynamics reveals that a qualitative change in the coupling potential, $V_{kl}(t)$, occurs in the region of the dividing point, $b = 5.5$ bohr. This is illustrated for $V_{00}(t)$ and $V_{01}(t)$ in Fig. 7. The $V_{kl}(t)$ changes from a function which has attractive and repulsive portions to one which is solely attractive. We discuss the scattering dynamics in these two impact parameter regions in the sections below.

IIIA. Low impact parameter region

As stated above, the shift in the shoulder/hole feature to

Can. J. Chem. Downloaded from www.nrcresearchpress.com by 195.246.54.202 on 09/08/12
For personal use only.

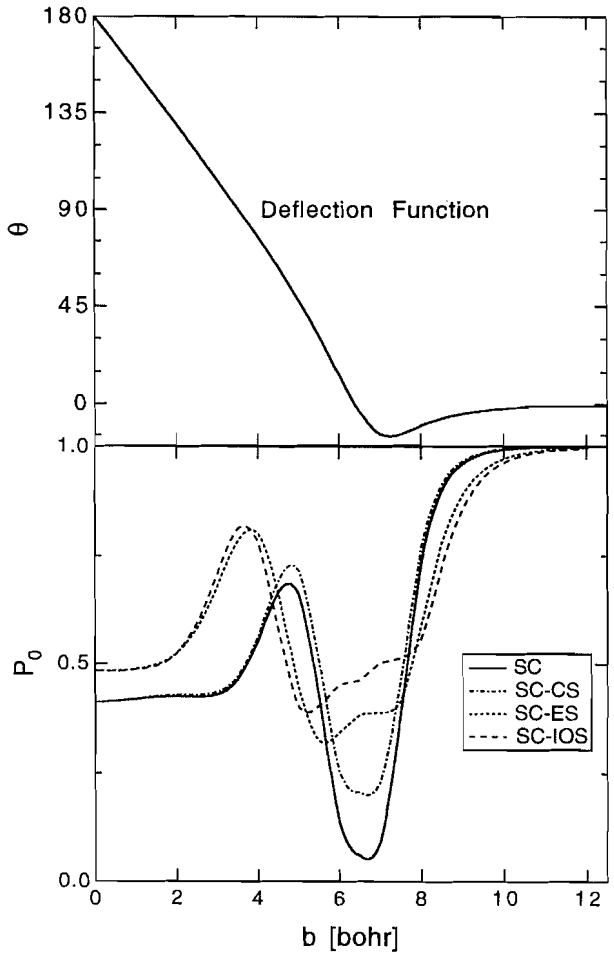

FIG. 5. Upper panel: Classical deflection function for elastic Ar+HF ($0 \rightarrow 0$) collision on the Hutson H6 ($v = 0$) surface, used in calculating each of the semiclassical DCS. Lower panel: Comparison of the $j' = 0$ opacity functions from each of the semiclassical approximations.

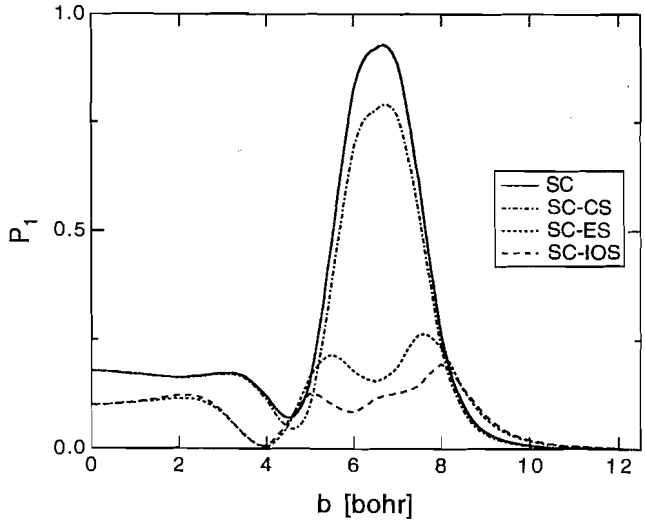

FIG. 6. Comparison of the opacity functions for Ar+HF ($j = 0$) $\rightarrow$ Ar + HF ($j' = 1$) from each of the semiclassical approximations.

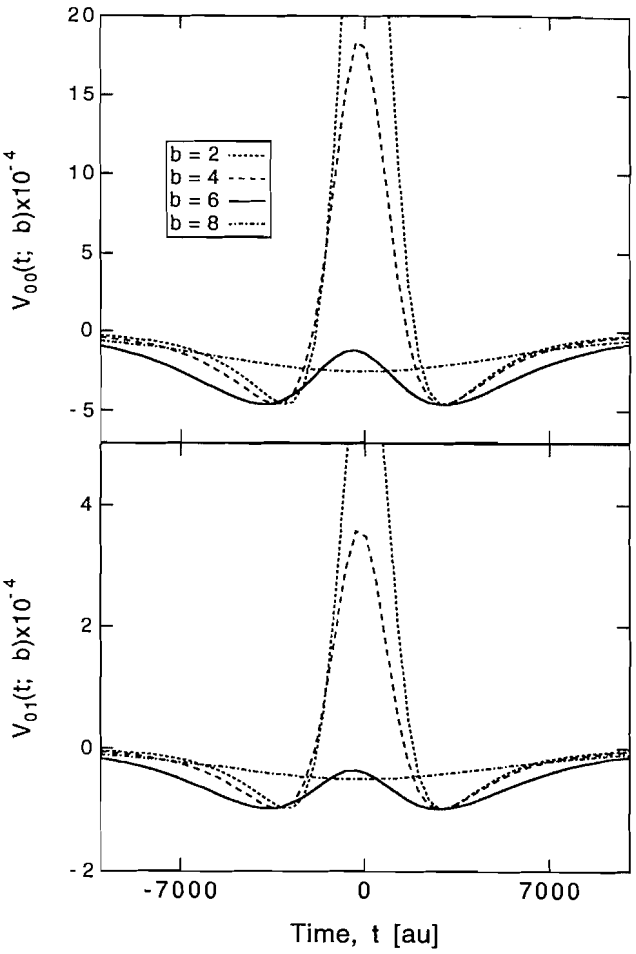

FIG. 7. Time-dependent coupling potentials at several impact parameters, b. The upper panel shows $\langle 00|V(t)|00\rangle$, denoted $V_{00}(t; b)$. The lower panel shows $\langle 00|V(t)|10\rangle$, denoted $V_{01}(t; b)$.

higher scattering angles in the IOSA is caused by a related shift of the peak in the $P_0(b)$ to lower impact parameters in the SC-IOS calculations. In a previous publication Barrett et al. (12) employed a "two-state model" to suggest that the shoulder/hole feature in the $j' = 0$ and 1 DCS was due to a balance between the repulsive and attractive parts of the potential energy surface. A two-state model was justified in the previous study by noting that: (*1*) There is a strong coupling between the $j = 0$ and $j = 1$ states, denoted by the near mirror imaging of the $P_0(b)$ in the $P_1(b)$; that is, as the $P_0(b)$ increases or decreases, the $P_1(b)$ displays a complementary decrease or increase; (*2*) The transition probabilities for the system are dominated by the transitions $0 \rightarrow 0$ and $0 \rightarrow 1$; these two final states comprise 70% or more of the total transition probability at all impact parameters.

The equations of motion for the two-state model, within the SC-CS approximation, are given by

$$[18a] \quad i\hbar\,\dot{c}_0(t) = c_0(t)V_{00}(t) + c_1(t)V_{01}(t)\exp(i\omega_{01}t)$$

$$[18b] \quad i\hbar\,\dot{c}_1(t) = c_0(t)V_{01}(t)\exp(i\omega_{10}t) + c_1(t)V_{11}(t)$$

Note that $V_{10}(t) = V_{01}(t)$. By recognizing (12) that the $V_{00}(t)$ and $V_{11}(t)$ are very similar during the course of the time evolution and by further recognizing (12) that the $V_{01}(t)$ has roughly

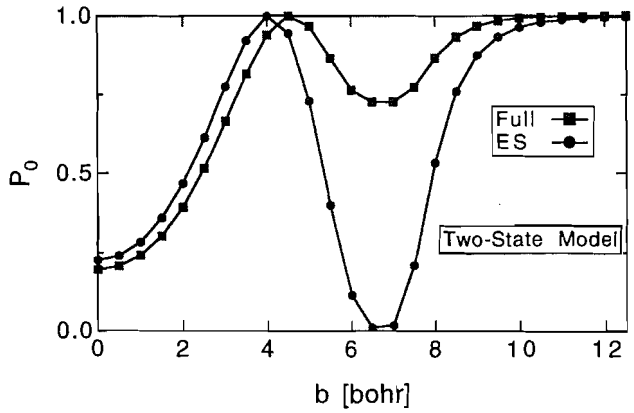

FIG. 8. Opacity functions from a two-state model of the Ar+HF collision dynamics. "Full" indicates use of eqs. [20]; "ES" indicates use of eqs. [21].

the same functional form as $V_{00}(t)$, but with a smaller magnitude, we make the following simplifications to eqs. [18]: (*1*) We substitute $V_{00}(t)$ for $V_{11}(t)$; (*2*) We employ a parameter to determine the coupling between the 0 and 1 states. In doing this we replace $V_{01}(t)$ with $\epsilon V_{00}(t)$, where ϵ is the coupling parameter less than 1. Using these simplifications in eqs. [18] we obtain

$$[19a] \quad i\hbar\,\dot{c}_0(t) = V_{00}(t)\big(c_0(t) + \epsilon c_1(t)\exp(i\omega_{01}t)\big)$$

$$[19b] \quad i\hbar\,\dot{c}_1(t) = V_{00}(t)\big(\epsilon c_0(t)\exp(i\omega_{10}t) + c_1(t)\big)$$

as the basic equations for the fully coupled two-state model. As in a previous work (12) we use, as a reasonable estimate to the true coupling potential, and ϵ value of 0.2 to analyze the scattering dynamics of the fully coupled system.

We may further simplify the two-state model by incorporating the ES approximation into eqs. [19] to obtain

$$[20a] \quad i\hbar\,\dot{c}_0(t) = V_{00}(t)\big(c_0(t) + \epsilon c_1(t)\big)$$

$$[20b] \quad i\hbar\,\dot{c}_1(t) = V_{00}(t)\big(\epsilon c_0(t) + c_1(t)\big)$$

as the "energy sudden" two-state model. We now use the simplified two-state models of eqs. [19] and [20] to explore the effects of the ES approximation on the scattering dynamics. In Fig. 8 we plot the opacity function for $j' = 0$ from the two-state model with and without the ES approximation. It is evident that the $P_0(b)$ are similar up to $b \sim 5.0$ bohr. The only significant difference is a slight shift of the energy sudden curve to lower impact parameters. Qualitatively, this is just what is observed in Fig. 5: both methods which employ the energy sudden approximation have their first maximum in $P_0(b)$ at lower b values than those calculations which have non-zero energy spacings. This shift to lower b in that impact parameter region where the scattering is sideways is just what is required to shift the shoulder in the $0 \rightarrow 0$ DCS to higher scattering angles, as was observed in the IOSA of Fig. 1. Thus the two-state model reproduces this trend very well. We analyze this shift further below.

One advantage of the two-state model is that it is simple to analyse. In particular, there are only two state coefficients to consider, $c_0(t)$ and $c_1(t)$, and the scattering dynamics reduce to

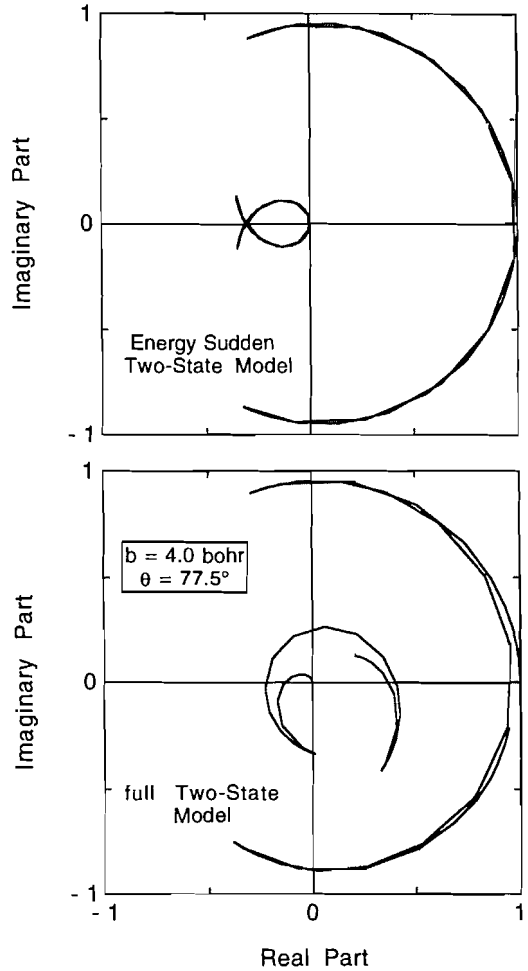

FIG. 9. Time evolution of the expansion coefficients c_0 and c_1 from the full (lower panel) and ES (lower panel) two state models at impact parameter, $b = 4.0$ bohr. Initially, $c_0 = (1, 0)$, $c_1 = (0, 0)$. Thus the outer curve describes the evolution of c_0, the inner curve c_1. The V_{00} potential controlling the dynamics is shown in Fig. 7. The initial sense of motion is counter-clockwise. At $t = -2400$ au, V_{00} changes sign, as does the sense of motion. The next reversal occurs at $t = 2400$ au.

the time-evolution of these two states. We plot trajectories of these coefficients in Fig. 9. The upper panel shows the time-evolution of the system using the energy sudden formulation (eqs. [20]); the lower panel shows the evolution of the full two-state model (eqs. [19]). In order to explain the motion in these plots we note that for $\epsilon = 0$ (i.e. no coupling between the states) the equations of motion are

$$[21] \quad \dot{c}_i = \frac{-ic_iV_{00}}{\hbar} \qquad (i = 0,\ 1)$$

By writing $c_i = |c_i|\exp(i\phi_i)$, where $\phi_i = \arg(c_i)$, substituting into eq. [21], and equating the real and imaginary parts we obtain:

$$[22] \quad \frac{\mathrm{d}}{\mathrm{d}t}|c_i| = 0; \qquad \frac{\mathrm{d}}{\mathrm{d}t}\phi_i = \frac{-V_{00}}{\hbar}$$

Thus motion in this case is pure rotation in the complex plane. A negative coupling potential leads to counter-clockwise rotation in the complex plane; a positive V_{00} gives clockwise

Can. J. Chem. Downloaded from www.nrcresearchpress.com by 195.246.54.202 on 09/08/12
For personal use only.

rotation. Furthermore, for the $\epsilon = 0$ case, the equations may be solved explicitly to give

$$[23] \qquad c_i(t) = c_i(-\infty) \exp\left(-i \int_{-\infty}^{t} \mathrm{d}t' V_{00}(t')/\hbar\right)$$

as the time-evolution for the states. The integral in eq. [23] is known as the action integral (17, 22).

We consider next the effect of c_j ($j \neq i$) on c_i when c_i is negligible. In this case we have

$$[24] \qquad i\hbar\, \dot{c}_i(t) = c_j(t)\epsilon V_{00}(t) \exp(\pm i\omega_{01}t)$$

where the +(−) applies to $i = 0(1)$. An alternative expression for eq. [24] gives the change in c_i, δc_i, as

$$\begin{aligned}[25] \delta c_i(t) = \dot{c}_i(t)\delta t &= (\delta t \hbar^{-1} \epsilon V_{00}(t)|c_j(t)|) \\ &\quad \times \exp\left[i\left(\phi_j - \frac{\pi}{2} \pm \omega_{01}t\right)\right] \\ &= \{\delta t \hbar^{-1}\epsilon |V_{00}(t)||c_j(t)|\} \\ &\quad \times \exp\left[i\left(\phi_j - \mathrm{sign}\,(V_{00}(t))\frac{\pi}{2} \pm \omega_{01}t\right)\right]\end{aligned}$$

The term within the braces { } is always positive. Thus, when ω_{01} is zero (i.e. in the ES approximation), the change in c_i due to a nonzero c_j is a complex number rotated $\pi/2$ from c_j on the clockwise or counter-clockwise side depending on the sign of V_{00}.

The two-state model was utilized in an earlier study (12) to explain the presence of the shoulder in the $0 \rightarrow 0$ DCS. We briefly reiterate some of our earlier findings to explain the difference between the two-state model with and without the ES approximation. Referring to the upper panel in Fig. 9, we see that the $c_0(t)$ returns to its initial value of (1, 0) twice during the collision. In fact, it is clear that the net action for this trajectory is almost exactly zero. That is, at this impact parameter the attractive and repulsive parts of the potential exactly balance each other on the incoming and outgoing portions of the classical path. We can see that initially $c_0(t)$ rotates in a counter-clockwise sense until the repulsive part of the potential is reached. At this point the potential becomes positive and $c_0(t)$ retraces its initial path. Note that during this trajectory, the c_1 term always remains small and the evolution of the states is essentially governed by the simplification given in eq. [21]. The rotation of $c_0(t)$ continues to a point conjugate to the position where the repulsive part of the potential was entered. As the trajectory goes back into the attractive part of the potential, and V_{00} goes negative, the cycle is completed by $c_0(t)$ retracing its path once more back to a point near (1, 0). It is this balancing between the attractive and repulsive parts of the potential — which leads to the zero action — that is responsible for the quantum feature seen near $\theta = 40$–$70°$ in the CC DCS in Fig. 1.

Now examine the lower panel in Fig. 9. The motion begines as in the two-state energy sudden case. However, instead of the change in c_1 being directed along a vector $\pi/2$ to the direction of c_0, the motion is pushed further in the counter-clockwise direction due to the presence of the ω_{01} term. This motion is exemplified by eq. [25]. When the potential becomes positive, instead of retracing itself, as with the ES model, the c_1 in the full model is pulled out further. That is, the rotation rate in the clockwise direction is slowed by the non-zero ω_{01}. As the particles separate on the outgoing path of the trajectory, the c_1 is again pulled in the counter-clockwise direction and spirals toward the origin. The trajectory once more produces a nearly null action; however, the inclusion of the non-zero frequency, ω_{01}, has slightly shifted the phase of the coefficients. Thus the overall trend of the $c_i(t)$ motion is similar in the two models, but the asymptotic values of the c_i are slightly shifted. This accounts for the shift of the shoulder/hole feature observed in the CC and IOSA DCS.

IIIB. High impact parameter region

We now discuss the scattering dynamics in the impact parameter range, $5.5 < b < 8.0$ bohr. Because this impact parameter range lies in the rainbow scattering region, changes in the opacity functions have a less obvious effect on the shape of the DCS, but have a large effect on the integral cross section. This region also shows the greatest difference between the opacity functions of the full SC calculation and the SC-IOS, and understanding this difference is important to identifying any shortcomings in the IOS approximation.

At the higher impact parameters ($b > 5.5$ bohr) the potential is attractive during the full time-evolution of the system. That is, the trajectory never encounters the repulsive part of the potential. Examination of Fig. 8 shows that the two-state model does not reporduce the trends in the opacity functions of the SC or SC-IOS. This is very intriguing because in this impact parameter range the asymptotic values of the expansion coefficients, (that is, the opacity functions of Fig. 4*a*) show that >90% of the total probability is in the $j' = 0$ and 1 rotational states if the full dynamics are employed. In addition, Fig. 4*d* reveals that for the SC-IOS ~50% of the final state probability is in $j' \geq 2$. In light of this, we see that the two-state model is inappropriate for an understanding of the energy sudden dynamics in this impact parameter region. Accordingly, we set it aside and return to the multi-state methods.

Examination of Figs 4*a* and 4*b* shows that at impact parameters greater than 5.5 bohr, transitions to the higher rotational states (i.e. $j' \geq 2$) do not occur when ω_{kl} is non-zero. This is due to the energetic separation of the states which manifests itself through the $\exp(i\omega_{kl}t)$ term, which is included in the full SC and in the SC-CS. The effect of the frequency term is most easily seen, perhaps, if one considers the first order perturbation theory limit (37) of the time-dependent scattering:

$$[26] \qquad P_{j'} = \left| \int_{-\infty}^{\infty} \mathrm{d}t V_{0j'}(t) \exp(i\omega_{0j'}t) \right|^2 \hbar^{-2}$$

This has the form of the Fourier transform of the interaction potential. In general, for simple $V_{0j'}(t)$, this term will decrease as $\omega_{0j'}$ increases; that is, the low frequency terms will dominate. Since in the impact parameter region of interest here — high b — $V_{0j'}(t) < 0$ for all time, this is expected to hold. Clearly, the sudden approximation of setting $\omega_{0j'}$ to zero removes this frequency dependence, and the probabilities of all transitions become solely a function of the action integral for the $0 \rightarrow j'$ transition.

Figures 4*c* and 4*d* show that a substantial component of the total transition probability is in $j' \geq 2$ for the SC-ES and SC-IOS approximations. We also see from Fig. 4 that the major differences between the SC and the SC-IOS in the high impact parameter region result from making the ES approximation. Because of this, we focus on the differences between the full SC and SC-ES methods.

Can. J. Chem. Downloaded from www.nrcresearchpress.com by 195.246.54.202 on 09/08/12
For personal use only.

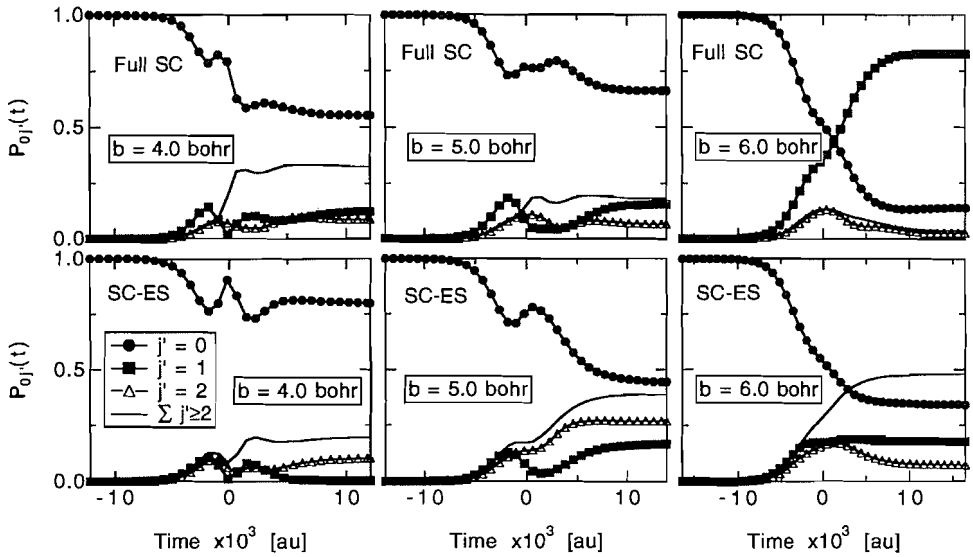

FIG. 10. Time evolution of rotational state probability from the full SC and the SC-ES models. In both cases the summation refers to the total probability for rotational states, $j' \geq 2$. Note different time scales for each impact parameter.

In Fig. 10 we plot the rotational state probability as a function of time, $P_{j'}(t)$, for the SC and SC-ES models at several impact parameters. At the lower impact parameters the time-dependent probability for $j' = 0$ and $j' = 1$ are quite similar in both models, as expected from our previous analysis. The summed probabilities into rotational states $j' \geq 2$ are also similar; however, the SC-ES overestimates the probability into $j' = 2$. As we move to higher impact parameters (e.g. $b = 5.0$ bohr), again the $j' = 0$ and 1 probabilities are similar in the two methods, but it is now becoming clear that the SC-ES is greatly overestimating the transition probability into the higher rotational states.

By $b = 6$ bohr, the dynamics exhibited by the SC and the SC-ES are quite different. The reason for this should be clear from the above discussion. In this impact parameter interval, the interaction potentials (see Fig. 7) are purely non-positive. Thus, the "sudden" action can accumulate monotonically along the trajectory. This is not necessarily the case for all $V_{0j'}$, but it certainly explains the generally poor performance of the SC-ES in this region. For instance, in the SC method the $P_1(t)$ increases steadily from its initial value of zero to become the dominant transition. In the SC-ES the $P_1(t)$ increases on the incoming part of the trajectory, as in the full SC method, however the $P_1(t)$ reaches its asymptotic value by the mid-point of the trajectory. In both methods the $P_2(t)$ increases steadily and reaches a maximum near the turning point of the trajectory, then falls off to $P_2(t) < 0.1$. The difference between the methods is that in the full SC the $P_2(t)$ (along with the continued decrease in $P_0(t)$) relinquishes much of the flux to $P_1(t)$. In the SC-ES, however, because of the removal of the exp $(i\omega_{kl}t)$ term the states $j' > 2$ begin to dominate the total transition probability.

This is the impact parameter region where the IOS approximation performs most poorly. By overestimating the transition probability into the higher rotational states, the IOS approximation no longer provides an adequate representation of the true collision dynamics. It is generally accepted that the IOSA is poor when the scattering is dominated by a strongly attractive potential (11). Our time-dependent pictures provides a rather striking illustration of this.

Conclusions

In this paper we have explored the collision dynamics for Ar+HF using several computational approaches. We presented time-independent quantum mechanical CC and IOSA results calculated on the Hutson H6 potential for the Ar+HF ($v = 0$) system at a collision energy of 135meV out of an initial rotational state, $|j = 0, m = 0\rangle$. The differential cross sections obtained using the IOSA differ markedly from the CC differential cross sections. The origin of this discrepancy was investigated using several time-dependent semiclassical methods. With this approach, the effect of each of the decoupling approximations on the dynamics was explored. The intuitive advantage of the time-dependent methods over the time-independent methods, is that the local (rather than the global) effects of the potential on the scattering dynamics can be observed.

From this work it was found that the biggest deviation of the IOSA from the "exact" CC calculations is due to the inclusion of the energy sudden approximation. Further, it was found that the energy sudden approximation "failed" differently for different impact parameter regions. For $b < 5.5$ bohr, in which the repulsive part of the potential is sampled and backwards and sideways scattering dominate, the opacity functions obtained from the SC-IOS are qualitatively similar to those obtained using the fully coupled SC method. While this qualitative agreement is encouraging, the quantitative differences are sufficiently great to shift features in the DCS by as much as 30°.

An analysis of the time dependence of the dynamics in this low impact parameter region was facilitated by the use of a two-state model calculation. The model data agreed well with the SC calculations, and revealed the same trends on the inclusion of the ES approximation. The model revealed that at one impact parameter in this range the net action along the classical trajectory will be zero. In the model with the energy sudden approximation included it was found that the zero action trajectory leads to a transition probability for $0 \rightarrow 0$ of essentially unity — necessarily a maximum. With the ES approximation absent, the trend is similar but the maximum shifts slightly to higher impact parameters.

In the impact parameter range $b > 5.5$ bohr, the SC-ES

Can. J. Chem. Downloaded from www.nrcresearchpress.com by 195.246.54.202 on 09/08/12
For personal use only.

Can. J. Chem. Downloaded from www.nrcresearchpress.com by 195.246.54.202 on 09/08/12
For personal use only.

method performs badly when compared to the full SC. The two-state model is no longer appropriate in this region to study the sudden approximation, since it is clear that the energy sudden approximation allows access to higher product rotational states than occur in the full calculation. At these higher impact parameters, the trajectory experiences exclusively an attractive potential. It is the presence of the attractive potential and the energy sudden approximation that artificially couples the system to high j' states in the IOSA; this does not occur to as great an extent for a replusive encounter.

Finally, we make some remarks on the universality of our findings. As its name implies, the accuracy of the "sudden" approximation depends on the time scales involved during the collision. At the collision energy used here, the collision time is on the order of 2×10^4 au. This is comparable with the classical rotational period for an HF molecule in its $j = 1$ state, 3.354×10^4 au. Therefore, for the system at hand, the IOSA is unlikely to be accurate, even for the $j = 0 \rightarrow j' = 1$ transition, at collision energies less than 1 eV. Similarly, one would expect the sudden approximation to perform better in calculations with lighter rare gas atoms, but worse with heavier ones. Our findings here and previously (9) indicate that the IOSA is unlikely to prove a useful tool in improving potential surfaces for rare gas+hydrogen halide scattering for the experimental conditions presently accessible.

Dedication and acknowledgements

It is a pleasure to dedicate this paper to Professor John C. Polanyi on the occasion of his 65th birthday. We (H.R.M. and M.K.) first became interested in the problem of rotational energy transfer while enjoying post-doctoral fellowships in Professor Polanyi's group. We had earlier contributed to experiments showing anomalously large $j = 0 \rightarrow j' = 1$ integral cross sections for collisions of HF with several rare gases. Such integral cross sections were first measured in Professor Polanyi's laboratories a decade ago (38).

In addition to acknowledging Professor Polanyi's sponsorship of our earlier work, we would like to thank a number of our contemporaries at Toronto, all of whom worked on the "yellow machine" or *inside* the "red machine": Jack Barnes, Ray Kutina, Kenji Honma, Dan Thomas and Dave Wrigley.

Acknowledgment is made to the donors of the Petroleum Research administered by the American Chemical Society, for support to H.R.M. of this research. M.K. also wishes to thank the donors of the Petroleum Research administered by the American Chemical Society for support of this research.

1. J.C. Polanyi and K.B. Woodall. J. Chem. Phys. **56**, 1563 (1972).
2. J.M. Hutson. Annu. Rev. Phys. Chem. **41**, 123 (1990) and references therein.
3. J.M. Hutson. J. Chem. Phys. **96**, 6752 (1992).
4. C.M. Lovejoy and D.J. Nesbitt. J. Chem. Phys. **91**, 2790 (1989).
5. M. Faubel. J. Chem. Phys. **81**, 5559 (1984).
6. S.D. Jones, J.E. Shirley, M.T. Vonk, C.F. Giese and W.R. Gentry, J. Chem. Phys. **97**, 7831 (1992); A.G. Suits, L.S. Bontuyan, P.L. Houston, and B.J. Whitaker. J. Chem. Phys. **96**, 8618 (1992); P.L. Jones, E. Gottwald, U. Hefter, and K. Bergmann. J. Chem. Phys. **78**, 3838 (1983); U. Hefter, P.L. Jones, A. Mattheus, J. Witt, K. Bergmann, and R. Schinke. Phys. Rev. Lett. **46**, 915 (1981); K. Bergmann, U. Hefter, A. Mattheus, and J. Witt. Chem. Phys. Lett. **78**, 61 (1981); J.A. Serri, A.M. Morales, W. Moskowitz, D.E. Pritchard, C.H. Becker, and J.L. Kinsey. J. Chem. Phys. **72**, 6304 (1980); K. Bergmann, U. Hefter, and J. Witt. J. Chem. Phys. **72**, 4777 (1980); M. Faubel, K.H. Kohl, J.P. Toennies, K.T. Tang, and Y.Y. Yung. Faraday Discuss. Chem. Soc. **73**, 205 (1982); U. Buck, F. Huisken, J. Schleusener, and H. Pauly. Phys. Rev. Lett. **38**, 680 (1977); W.R. Gentry and C.F. Giese. J. Chem. Phys. **67**, 5389 (1977).
7. M.A. Dvorak, S.W. Reeve, W.A. Burns, A. Grushow, and K.R. Leopold. Chem. Phys. Lett. **185**, 399 (1991); C.M. Lovejoy, J.M. Hutson and D.J. Nesbitt. J. Chem. Phys. **97**, 8009 (1992); H.-C. Chang, F.-M. Tao, W. Klemperer, C. Healey, and J.M. Hutson. J. Chem. Phys. **99**, 9337 (1993).
8. L.J. Rawluk, Y.B. Fan, Y. Apelblat, and M. Keil. J. Chem. Phys. **94**, 4205 (1991).
9. L.J. Rawluk, M. Keil, M.H. Alexander, H.R. Mayne, and J.J.C. Barrett. Chem. Phys. Lett. **202**, 293 (1993).
10. H.R. Mayne and M. Keil. J. Phys. Chem. **88**, 883 (1984).
11. R. Schinke and J.M. Bowman. *In* Dynamics of molecular collisions. *Edited by* J.M. Bowman. Springer, Berlin. 1982. Chap. 4.
12. J.J.C. Barrett, H.R. Mayne, and M. Keil. J. Chem. Phys. **100**, 304 (1994).
13. R.T. Pack. J. Chem. Phys. **60**, 633 (1974).
14. G.A. Parker and R.T. Pack. J. Chem. Phys. **68**, 1585 (1978).
15. H.J. Korsch and R. Schinke. J. Chem. Phys. **75**, 3850 (1981).
16. H.J. Korsch and R. Schinke. J. Chem. Phys. **73**, 1222 (1980).
17. A.S. Dickinson. Comput. Phys Commun. **17**, 51 (1979).
18. A.P. Clark, A.S. Dickinson, and D. Richards. Adv. Chem. Phys. **36**, 63 (1977).
19. G.G. Balint-Kurti. International review of science, physical chemistry. Ser. 2. Vol. 1. *Edited by* W. Byers Brown. Butterworth, London. 1975. p. 285.
20. T. Mulloney and G.C. Schatz. Chem. Phys. **45**, 213 (1980).
21. HIBRIDON M.H. Alexander, D.E. Manolopoulos, H.-J. Werner, and B. Follmeg, with contributions from P.F. Vohralik, D. Lemoine, G. Corey, B. Johnson, T. Orlikowski, W. Kearney, A. Berning, A. Degli-Esposti, C. Rist, and P. Dagdigian.
22. G.D. Billing. Comput. Phys. Rep. **1**, 237 (1989).
23. R.B. Gerber and R. Alimi. Isr. J. Chem. **31**, 383 (1991).
24. A.E. DePristo. J. Chem. Phys. **78**, 1237 (1983).
25. D. Bohm. Quantum theory. Dover Publication, Inc., New York. 1989. Chap. 18. pp. 407–409.
26. A.M. Arthurs and A. Dalgarno. Proc. R. Soc. London Ser. A: Math. Phys. Sci. **256**, 540 (1960).
27. J.M. Hutson and B.J. Howard. Mol. Phys. **45**, 791 (1982); C. Douketis, J.M. Hutson, B.J. Orr, and G. Scoles. Mol. Phys. **52**, 763 (1984); D.J. Nesbitt, M.S. Child, and D.C. Clary. J. Chem. Phys. **90**, 4855 (1989).
28. S. Green and J.M. Hutson. J. Chem. Phys. **100**, 891 (1994).
29. R.D. Levine and R.B. Bernstein. Molecular reaction dynamics and chemical reactivity. Oxford University Press, New York. 1987. p. 861.
30. M.S. Child. Molecular collision theory. Academic Press, New York. 1974. pp. 141–148.
31. D. Chase. Phys. Rev. **104**, 838 (1956).
32. J.M. Bowman and S.C. Leasure. J. Chem. Phys. **66**, 288 (1977).
33. C.F. Curtiss and F.T. Adler. J. Chem. Phys. **20**, 249 (1952); G. Gioumousis and C.F. Curtiss. J. Math. Phys. **2**, 96 (1961); L.W. Hunter and C.F. Curtiss. J. Chem. Phys. **58**, 3884 (1973); M. Pattengill. J. Chem. Phys. **66**, 5042 (1977).
34. P. McGuire. Chem. Phys. Lett. **23**, 575 (1973); P. McGuire and D.J. Kouri. J. Chem. Phys. **60**, 2488 (1974); Y. Shimoni and D.J. Kouri. J. Chem. Phys. **65**, 706 (1976); D.J. Kouri. *In* Atom–molecule collision theory. *Edited by* R.B. Bernstein. Plenum Press, New York. 1979. Chapt. 9.
35. D. Secrest. J. Chem. Phys. **62**, 710 (1975).
36. M.V. Berry and K.E. Mount. Rep. Prog. Phys. **35**, 315 (1972).
37. G.C. Schatz and M.A. Ratner. Quantum mechanics in chemistry. Prentice Hall, Engelwood Cliffs. N.J. 1993. p. 60.
38. J.A. Barnes, M. Keil, R.E. Kutina, and J.C. Polanyi. J. Chem. Phys. **72**, 6306 (1980); **76**, 913 (1982).

Transition state spectroscopy with electrons as studied by 3D-trajectory calculations of the reaction $He^+ + Br_2^- \rightarrow He^+Br^- + Br$

HARALD MORGNER[1] AND HUBERT SEIBERLE[2]

Fakultät für Physik der Universität Freiburg, Hermann-Herder-Str.3, D-79104 Freiburg, Germany

Received September 8, 1993

This paper is dedicated to Professor John C. Polanyi on the occasion of his 65th birthday

HARALD MORGNER and HUBERT SEIBERLE. Can. J. Chem. **72**, 995 (1994).

We investigate electron emission from the interaction of metastable helium He($1s2s$; 2^3S) with Br_2 molecules. A small part of the electron energy spectrum is due to direct Penning ionization, giving rise to spectral features familiar from photoionization of Br_2. However, the dominant contribution to electron emission originates from a collision complex that can be described as ion pair state He^+–Br_2^-. In analogy to a collision between the alkali atom Li($2s$) and Br_2, which leads via Li^+–Br_2^- to salt formation LiBr + Br, this system can be viewed as undergoing a chemical reaction to He^+Br^- Br. Of course, no stable products He^+Br^- can be produced in this way since the large recombination energy of He^+ causes autoionization to He + Br^+ + e^-. On the other hand, this situation is ideal if one wishes to study spectroscopically the transition state of a chemical reaction, in our case the development of the system from He($1s2s$) + Br_2 to (He^+Br^-) + Br. Neither of the separate reaction partners is able to emit electrons. During the encounter the lifetime against autoionization is so short that decay into the ionized channel cannot occur long after the chemical reaction is complete. Thus, electron emission is confined to the lifetime of the reaction complex. Accordingly, the electron energy spectrum contains information exclusively on the transition state with no blending by emission from educts or products as could be the case in optical spectroscopy. As a case study we carry out 3D-trajectory calculations on the collision complex He^+–Br_2^-, monitoring the energy distribution of emitted electrons throughout the lifetime of the complex. We find that the electron energy spectrum varies strongly from the initial to the final stages of the ongoing chemical reaction.

HARALD MORGNER et HUBERT SEIBERLE. Can. J. Chem. **72**, 995 (1994).

On a étudié l'émission électronique provenant de l'interaction de l'hélium métastable, He($1s2s$; 2^3S) avec les molécules de Br_2. Une faible partie du spectre d'énergie électronique est dû à l'ionisation de directe de Penning qui donne lieu aux caractéristiques spectrales bien connues de la photoionistion du Br_2. Toutefois, la contribution la plus importante á l'émission d'électrons tire son origine d'un complexe de collision que l'on peut décrire comme un état de paire d'ions He^+–Br_2^-. Par analogie avec la collision entre un atome du métal alcalin Li($2s$) avec le Br_2 qui conduit à la formation de sel, LiBr + Br, par le biais du Li^+–Br_2^-, on peut considérer que ce système subit une réaction chimique conduisant au He^+Br^- Br. On ne peut toutefois pas obtenir de produit He^+Br^- stable de cette façon puisque la grande énergie de recombinaison du He^+ provoque son autoionisation en He + Br^+ + e^-. Par ailleurs, cette situation est idéale pour quelqu'un quiv veut étudier l'état de transition d'une réaction chimique d'une façon spectroscopique, dans notre cas la réaction allant de He($1s2s$) + Br_2 à (He^+Br^-) + Br. Aucun des partenaires de chacune des deux réactions séparées n'émet d'électrons. Au cours de la rencontre, le temps de vie en fonction de l'autoionisation est tellement faible que la dcroissance par la voie ionisée ne peut pas se produire longtemps aprs que la réaction chimique se soit complétée. L'émission d'électrons est donc limitée au temps de vie du complexe réactionnel. Il en découle que le spectre d'énergie électronique ne contient que de l'information relative à l'état de transition, sans mélange avec des émissions d'éduits ou de produits comme c'est le cas en spectroscopie optique. À titre d'exemple, on a effectué des calculs de la trajectoire tridimensionnelle du complexe de collision He^+–Br_2^- en examinant la distribution d'énergie des électrons émis pendant toute la duré de vie du complexe. On a trouvé que le spectre d'énergie électronique varie fortement de l'étape initiale à l'étape finale de la réaction chimique qui se produit.

[Traduit par la rédaction]

1. Introduction

It certainly has always been, and still is, a challenge for the spectroscopist to observe a chemical reaction not via the ready products but by monitoring information from the collision complex itself, i.e., from the ongoing reaction. If attempted by optical spectroscopy the odds seem to be strongly against such an enterprise: the lifetime against photon emission ($\sim 10^{-8}$ s) is orders of magnitude larger than the typical duration of a collision ($\sim 10^{-13}$–10^{-12} s) with the consequence that low signal, large background, and blending by emission from educts or products represent a severe problem. In spite of these difficulties, John Polanyi has for many years pursued this goal (1–3) and inspired others, both experimentalists (4) and theorists (5).

It has been proposed by Polanyi to designate the object of this type of spectroscopy as the "transition state" (1) and to understand by this term not one point in the space of nuclear motion but "the range of configurations encountered en route from reactant to product." Since one of us (H.M.) learned about the idea of "transition state spectroscopy" in 1984 (6), we began to interpret experimental data on Penning electron spectroscopy with this goal in mind (7, 8) and thus gave a new direction to an already existing activity (9). There is, of course, no general relationship between Penning electron spectroscopy and chemical reactions. However, for selected cases the link is rather direct. As an example, we discuss the process

$$[1] \qquad Li + Br_2 \rightarrow (Li^+ + Br_2^-) \rightarrow LiBr + Br$$

which can be considered a prototype chemical reaction. The intermediate collision complex, denoted here as ion pair state, would be the object of our curiosity in the context of transition state spectroscopy. Essentially the same situation can occur as a consequence of the encounter of metastable helium $He^*(1s2s)$ with a halogen molecule

[1]Author to whom correspondence should be addressed. Present address: Institut für Experimentalphysik, Universität Witten/Herdecke, Stockumer Str. 10, D-58448 Witten, Germany.

[2]Present address: F. Hoffmann-LaRoche Ltd., Roche LC Research Department, CH-4002 Basel, Switzerland.

Can. J. Chem. Downloaded from www.nrcresearchpress.com by 195.246.54.202 on 09/08/12
For personal use only.

Can. J. Chem. Downloaded from www.nrcresearchpress.com by 195.246.54.202 on 09/08/12
For personal use only.

[2a] $He^*(1s2s) + Br_2 \rightarrow He + Br_2^+ + e^-$

[2b] $\rightarrow (He^+ + Br_2^-) \rightarrow He + Br + Br^+ + e^-$

A third type of process, namely excitation transfer with subsequent autoionization of the superexcited target molecule, is known for $He^* + Cl_2$ (7, 9, 10) but apparently is insignificant for $He^* + Br_2$ (8).

In the processes [2a] and [2b], the metastable atom plays a twofold role. Firstly, it carries a fairly large amount of excitation energy (~20 eV), which can lead in a direct Penning process to ionization of the target molecule, reaction [2a]. The resulting electron energy spectrum is essentially the same as that obtained in photoionization. Secondly, He^* is an atom with a 2s valence electron and thus a species that undergoes chemical reactions as readily as $Li(1s^22s)$. This latter feature is the basis of our approach. As in reaction [1], the transition from the covalent to the ion pair state is possible. It is even, by far, the dominant process and it is known that reaction [2a] is enabled only by symmetry conservation that prohibits ion pair formation in the isosceles triangle conformation of the nuclei (10). The collision complex $He^+ + Br_2^-$ will develop in time to (He^+Br^-) and Br, just as in process [1]. The important, and for our purpose crucial, aspect is, however, that the recombination energy of He^+ (24.587 eV) is so large that the collision complex lies in the autoionization continuum throughout its time evolution. Consequently, electrons will be emitted from this transition state system.

Since the lifetime against autoionization can be as short as 10^{-16} s, the probability for electron emission during the lifetime of the collision complex is almost unity. This is indeed a very different situation compared to photon emission spectroscopy. Together with the fact that the separated reaction partners He^* and Br_2 are not able to autoionize, this confines the emission of electrons to the lifetime of the collision complex, an ideal situation for the purpose of transition state spectroscopy.

As is usual in this field, calculations that model the dynamics of the system are needed in order to retrieve the information from the experimental data. We carry out trajectory calculations for the three-body system $He^+ + Br_2^-$ using a potential surface constructed in the framework of "diatoms in molecules." The electronic transition probability is described by analytical functions, the parameters of which had to be determined. The extent of agreement between measured and calculated electron energy spectra serves as an indication that the dynamics of the nuclear motion in the collision complex as well as its decay via ionization is properly described in the calculations. The progress of the present study over a preceding study (8) on $He^* + Br_2$ can be indicated by considering several aspects:

1. In ref. 8 we described the potential surface of the collision complex $(He^+ + Br_2^-)$ by only two coordinates, namely, the separation between He and the center of mass of Br_2 and the distance between the bromine atoms. Thus, the chemical reaction proper cannot be accounted for without changing the meaning of the coordinates in the course of the time evolution of the complex (7).

2. The fact that the transition $He^* + Br_2 \rightarrow He^+ + Br_2^-$ is symmetry forbidden if He^* is in the middle plane of the Br atoms is fully accounted for in our model. This restricts the starting conformations for the time evolution of the complex $(He^+ + Br_2^-)$.

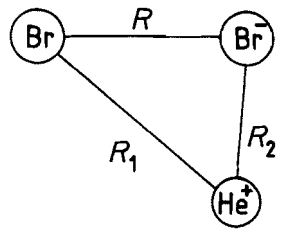

FIG. 1. Coordinate system for the description of the He^+–Br_2^- potential surface. The z-axis coincides with the Br—Br internuclear axis. He^+ lies in the (x, z) plane, which renders the nuclear y-coordinates identically zero. Both angles β_i are measured against the positive direction of the z-axis. For the orientation of the corresponding orbitals at sites 1 and 2 we have chosen the convention that they are identical except for a translation along the z-axis by the distance R.

3. The electron energy spectrum depends not only on the energy of the collision complex but, as well, on the energy of the ionized system after electron emission. Here, we have introduced a more realistic description by incorporating the complete set of Br_2^+ potential curves.

We find the interesting result that the spectrum of emitted electrons varies drastically in the course of the chemical reaction going on. Secondly, we observe a distinct correlation between the motion of He^+ and the relative motion of the two Br nuclei even if we average over all trajectories taken into account.

This paper is organized as follows: in Sect. 2, the potential surfaces and the electronic transitions are discussed and their description within this paper are given. The algorithm for the trajectory calculations and the hierarchy of electronic transitions are treated in the subsequent section. In the last section we present as our main result the link between the shape of the electron energy spectrum and the dynamics of the system $He^+ + Br_2^-$.

2. Potential surfaces and transition probabilities

2.a. He^+–Br_2^- potential surface

The potential surface of the triatomic system $He^+(^2S)$, $Br(^2P)$, and $Br^-(^1S_0)$ is described by a perturbation method within the concept of "diatoms in molecules." Spin is neglected in the treatment. Figure 1 explains the coordinate system. We distinguish two sites for bromine atoms. The total state of the triatomic is described as the superposition of two states that are defined by assigning the full excess charge of Br_2^- to only one bromine atom. State 1 is defined by having the neutral bromine at site 1 and $Br^-(^1S_0)$ at site 2. State 2 is defined by the reverse positions of Br and Br^-. We have to consider three pairs of atoms. We start with the potentials of Br_2^-. From ref. 11 we take the potentials of the ground state $^2\Sigma_u^+$ and three excited states which have, in increasing energetic order, the symmetries $^2\Pi_g$, $^2\Pi_u$, and $^2\Sigma_g^+$. We interpret the difference between gerade and ungerade states as being caused by symmetric splitting of an unperturbed state due to an exchange matrix element $V_{12}(R)$ and get

$$
\begin{aligned}
V(\Sigma_u^+|R) &= V^{\Sigma}(R) + V_{12}^{\Sigma}(R) \\
V(\Sigma_g^+|R) &= V^{\Sigma}(R) - V_{12}^{\Sigma}(R) \\
V(\Pi_g|R) &= V^{\Pi}(R) - V_{12}^{\Pi}(R) \\
V(\Pi_u|R) &= V^{\Pi}(R) + V_{12}^{\Pi}(R)
\end{aligned}
\qquad [3]
$$

TABLE 1. Information on LiBr (12) and parameters for the He^+–Br^- interaction potential $U(R_i)$. The zero of $U(R_i)$ corresponds to $He^+ + Br^-$ at infinite separation

LiBr	D_e[LiBr → Li + Br]	=	4.335 eV
	D_e[LiBr → $Li^+ + Br^-$]	=	6.363 eV
	R_e	=	$4.1 a_0$
	ω_e	=	563.1 cm^{-1}

He^+Br^-

$$U(R_i) = \begin{cases} D(e^{2y} - 2e^{y}) \\ \quad \text{with } y = \beta(1 - R_i/R_e) & R_i < R_s \\ -\dfrac{27.211}{R_i} - \dfrac{1}{2}\dfrac{\alpha}{R_i^4} & R_i \geq R_s \end{cases}$$

with

D = 6.363 eV
R_e = 4.1 a_0
β = 1.624
α = 502.4 a_0^3
R_s = 5.3267 a_0

The signs follow from our convention that the orientation of corresponding orbitals at sites 1 and 2 is identical, which means that the orbitals can be transformed into each other by a mere translation along the internuclear axis. It follows that $V_{12}^{\Sigma}(R) < 0$ and $V_{12}^{\Pi}(R) > 0$.

The interaction between $He^+(^2S)$ and $Br^-(^1S_0)$ is spherically symmetric. The potential is described at long range by the Coulomb potential plus an induction term arising from the polarizability of Br^-. At shorter distances we make use of information on the ground state of LiBr. From ref. 12 we obtain the equilibrium distance r_e, the potential well depth with respect to dissociation into neutrals D_e[Li + Br], and the energy of the vibrational quantum ω_e = 563.1 cm^{-1}. Combining the quoted information allows us to give a substantial estimate of the He^+–Br^- potential at all relevant separations. Numerical values are found in Table 1. Below, this potential is denoted by $U(R_i)$ where i refers to the site of the negative ion Br^-.

To zeroth order we neglect the influence of He^+ on the neutral Br atom. There is, however, the possibility that the presence of He^+ causes mixing of the Br_2^- states that have pure Π or Σ symmetry with respect to the Br–Br^- axis. Thus, the presence of He^+ influences the Br_2^- subsystem in two respects: the degree to which the He^+ polarizes the Br_2^- by dragging the excess negative charge to the bromine at the site closer to He^+, and the extent to which the Π states of Br_2^- contribute. This latter information should in principle have impact on the ionization process. We lack, however, sufficiently detailed knowledge on the ionization process to exploit this information (cf. Sect. 2.*d*). Further, we found that the degree of polarization of Br_2^- as mentioned above is well described by using only the $Br_2^-(^2\Sigma_u, {}^2\Sigma_g)$ states as basis states. This reduces the energy matrix of He^+–Br_2^- to a 2 × 2 matrix

$$[4] \qquad \begin{bmatrix} V^{\Sigma}(R) + U(R_2) & V_{12}^{\Sigma}(R) \\ V_{12}^{\Sigma}(R) & V^{\Sigma}(R) + U(R_1) \end{bmatrix}$$

The results reported below were obtained with this simplified matrix. It can be diagonalized analytically and thus saves a fair amount of computer time.

The lowest eigenvalue of this matrix is employed as the He^+–Br_2^- potential surface

$$[5] \qquad V(R_1, R, R_2) = V^{\Sigma}(R) + \frac{U(R_1) + U(R_2)}{2} - \{0.25(U(R_1) - U(R_2))^2 + V_{12}^{\Sigma}(R)\}^{1/2}$$

The related eigenvector is (a_1, a_2) with

$$[6] \qquad a_1 = \left\{ \left(\frac{V^{\Sigma}(R) + U(R_2) - V(R_1, R, R_2)}{V_{12}^{\Sigma}(R)} \right)^2 + 1 \right\}^{-1/2}$$

$$a_2 = a_1 \frac{V(R_1, R, R_2) - V^{\Sigma}(R) - U(R_2)}{V_{12}^{\Sigma}(R)}$$

a_i is the amplitude of the state describing the situation with the neutral Br atom at site i and the negative ion Br^- at the opposite site.

2.b. Transition $He^* + Br_2 \rightarrow He^+ + Br_2^-$

Within the concept of "diatoms in molecules" we consider explicitly the electron transition between two atoms He^*+Br → $He^+ + Br^-$. We describe the transition matrix element as (13)

$$V_{c \rightarrow i}(R_i) = DR_i \exp(-R_i C_{inv})$$

with

$$C_{inv} = \left(\frac{IP[He^*]}{2} \right)^{1/2} + \left(\frac{EA[Br]}{2} \right)^{1/2}$$

$$D = IP[He^*] \cdot EA[Br]\ C_{inv}$$

$$IP[He^*] = 0.175 \text{ au}$$

$$EA[Br] = 0.124 \text{ au}$$

The total electronic transition matrix element is then

$$[7] \qquad V_{c \rightarrow i}(R_1, R, R_2) = \sum_{i=1}^{2} V_{c \rightarrow i}(R_i) a_i \cos \beta_i$$

with a_i being the component of the eigenvector of $He^+ + Br_2^-$ defined above. For the case in which He forms an isosceles triangle with the two bromine atoms, our above-defined convention leads to $a_1 = a_2$ and $\cos \beta_1 = -\cos \beta_2$. Thus, the definition of $V_{c \rightarrow i}(R_1, R, R_2)$ prohibits covalent to ion pair transitions in the isosceles conformation of the nuclei as required by symmetry arguments (10).

The transition rate is obtained as

$$[8] \qquad W_{c \rightarrow i}(R_1, R, R_2) = 2\pi \rho(R) \frac{V_{c \rightarrow i}^2(R_1, R, R_2)}{\hbar}$$

The weighting factor $\rho(R)$ is the normalized probability function for finding the $Br_2(v = 0)$ molecule at internuclear separation R.

2.c. Br_2^+ potential curves

In the final state of the collision complex, i.e., after the emission of an electron, we have the system He + Br + Br^+. We simplify the treatment by neglecting the interaction of the bromine atoms with the ground state rare gas He for all nuclear conformations. Thus, the final state is fully described by the molecular states of Br_2^+. In a previous publication (8) we

Can. J. Chem. Downloaded from www.nrcresearchpress.com by 195.246.54.202 on 09/08/12
For personal use only.

Can. J. Chem. Downloaded from www.nrcresearchpress.com by 195.246.54.202 on 09/08/12
For personal use only.

collected information on those states of Br_2^+ that are accessible by photoionization, i.e., by a one-electron process, from the ground state. In the present study, however, we have to consider ionization via an intrinsic two-electron process from the negative ion Br_2^- state.

Consequently, we must be aware that no propensity rule such as Koopman's theorem favours ionization into the known $Br_2^+(X, A, B, C)$ states, but that in principle all possible molecular states of Br_2^+ could be populated. Hence we have tried to estimate the Br_2^+ states in such a way that the energy positions of all states are represented more realistically than by only the four states X, A, B, C. On the other hand, we tried to avoid unnecessary speculations. We make use of a simple perturbation ansatz for the molecular states, spin not being taken into account.

For the Br^+ atom with its two-hole orbitals labelled a and b we define the set of states

$$|lm; l_a m_a l_b m_b\rangle = C(l_a l_b l; m_a m_b m)|l_a m_a\rangle|l_b m_b\rangle$$

with C( ) denoting the Clebsch–Gordon coefficients.

The states of the neutral atom Br(P) we denote by the set $|l_c m_c\rangle$. Projection quantum numbers are meant with reference to the Br–Br axis. The angular momenta l_a, l_b, l_c are unity since they refer to atomic p-hole orbitals. The tensor product of both sets is used as basis for Br_2^+.

The electrostatic interactions between the three-hole orbitals are treated pairwise. The interatomic interactions a, c and b, c are described by the operators O_{ac} and O_{bc}. To keep the number of parameters small we employ only the diagonal elements

$$[9] \qquad O_{m_a m_c} = \langle m_a' m_c'|O_{ac}|m_a m_c\rangle \delta_{m_a,m_a'} \delta_{m_c,m_c'}$$

and likewise for the operator O_{bc}. If O_{ac} were the Coulomb operator it would follow from ref. 14 that O_{mamc} depends on the absolute values $|m_a|$ and $|m_c|$ only. By assuming the same property for the operator O_{ac} we reduce the number of unknown matrix elements of O_{ac} and O_{bc} to three: O_{00}, O_{10}, O_{11}. The matrix element of interatomic interaction $O = O_{ac} + O_{bc}$ is then in the above chosen basis.

$$[10] \qquad \langle l'm'm_a'; m_c'|O_{ac} + O_{bc}|lmm_a; m_c\rangle$$
$$= C(11l'; m_a m - m_a m) C(11l; m_a m - m_a m) \{O_{|m_a|,|m_c|} + O_{|m-m_a|,|m_c|}\}$$

Note that this matrix is not diagonal in l, which has the values 1, 2, 0 for the three states of the bromine ion $Br^+(^3P, {}^1D, {}^1S)$.

The operator that controls the interaction between the hole orbitals within the ion Br^+ is diagonal in l, independent of m, and does not act on the neutral Br atom. Thus, we can write its matrix elements as

$$[11] \qquad \langle l'm'm_a'; m_c'|A|lmm_a; m_c\rangle = \langle l|A|l\rangle \delta_{l,l'}, \delta_{m,m'}, \delta_{m_a,m_a'} \delta_{m_c,m_c'}$$

Following ref. 14 this can be parametrized as

$$\langle l|A|l\rangle = \begin{cases} -5F_2 & (l = 1) \\ 1F_2 & (l = 2) \\ 10F_2 & (l = 0) \end{cases}$$

with $F_2 = 0.207$ eV.

The gerade–ungerade splitting is described by the exchange operator V^{ex}, which we conceive to consist of three summands that act on either of the three-hole states. The matrix elements of this operator are

$$[12] \qquad \langle lmm_a; m_c|V^{ex}|lmm_a; m_c\rangle$$
$$= C(11l; m_a m - m_a m)^2 \{\langle m_a|V_a^{ex}|m_a\rangle + \langle m - m_a|V_b^{ex}|m - m_a\rangle + \langle m_c|V_c^{ex}|m_c\rangle\}$$
$$= C(11l; m_a m - m_a m)^2 \{V_{|m_a|}^{ex} + V_{|m-m_a|}^{ex} + V_{|m_c|}^{ex}\}$$

In the above equation the bra vectors refer to a situation where Br and Br^+ have exchanged their position compared to the meaning of the ket vectors.

$V_1^{ex}(R)$, i.e., the g–u splitting of the π-orbitals, can be calculated from the energy separation between the known Br_2^+ potentials $V(X^2\Pi_g)$ and $V(A^2\Pi_u)$ via

$$V_1^{ex}(R) = \tfrac{1}{2}[V(A^2\Pi_u|R) - V(X^2\Pi_g|R)]$$

This is justified by the fact that both Br_2^+ states can be considered as being created from their parent state $Br_2(X^1\Sigma_g)$ by a one-electron process. Removal of a $2\pi_g$ electron leads to the $X^2\Pi_g$ state and a $(2\pi_u)^{-1}$ hole forms Br_2^+ in the $A^2\Pi_u$ state.

Lack of information on Σ_u states of Br_2^+ prohibits a similar approach for the g–u splitting of the σ-orbitals. To help this situation we make use of a rule of thumb that holds roughly for many molecules tested during the preparation of a paper on molecular rare gas ions (15), even though it was not used in ref. 15. This rule states that the ratio of exchange matrix elements of p-orbitals in σ-symmetry and in π-symmetry can be roughly equated to the internuclear separation in atomic units.

$$\frac{V_0^{ex}}{V_1^{ex}} = -\frac{R}{a_0}$$

with R in atomic units. The minus sign results from our convention that like orbitals at each atom are defined as being identical except for translation.

We count four unknown parameters that we have introduced in the above treatment:

$$O_{00}(R),\ O_{10}(R),\ O_{11}(R), \text{ and } V_1^{ex}(R)$$

On the other hand we can employ as known quantities the potential curves of the four spinless Br_2^+ states

$$V(X^2\Pi_g|R),\ V(A^2\Pi_u|R),\ V(B^2\Sigma_g|R), \text{ and } V(C^2\Sigma_g|R)$$

Information, including analytical expressions for these potential curves, has been collected in ref. 8. As pointed out before, V_1^{ex} can be determined in a straightforward way from the difference between the $A^2\Pi_u$ and $X^2\Pi_g$ potentials. The other three quantities have to be determined by evaluation of three coupled linear equations.

We are now in the position to compute all Br_2^+ states dissociating to Br(^2P) and $Br^+(^3P, {}^1D, {}^1S)$. Inclusion of spin could be done in a straightforward way (14) but has been omitted since spin is not taken into account in our treatment of the ionization process. The calculated potential curves are displayed

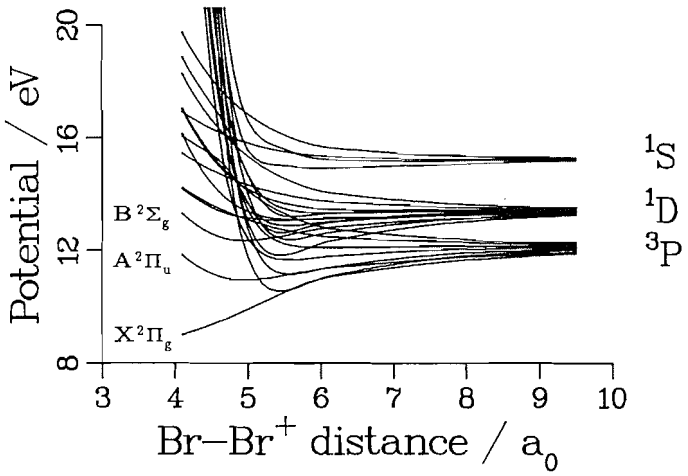

FIG. 2. Potential curves of the Br_2^+ states. Calculated without spin using the parametrization discussed in the text. The equilibrium separation for the lowest $Br_2^+(X^2\pi_g)$ state is $r_e = 4.145a_0$. For our trajectory calculations only distances larger than the equilibrium separation of the neutral Br_2 ($r_e = 4.311a_0$) are relevant. The calculation is not meant to predict individual unknown states of Br_2^+ but to give a reasonable estimate of the range of energies spanned by Br_2^+ as a function of internuclear separation R.

in Fig. 2. The states $X^2\Pi_g$, $A^2\Pi_u$, and $B^2\Sigma_g$ are indicated. The potential curve of $C^2\Sigma_g$ is buried under a wealth of other states.

We would like to emphasize that this calculation is not meant to predict individual states of Br_2^+ but rather to give a reasonable estimate of the range of energies spanned by the Br_2^+ states as a function of internuclear separation.

2.d. Transition $He^+ + Br + Br^- \rightarrow He + Br + Br^+ + e^-$

Because of the large recombination energy of He^+, the system $He^+ + Br + Br^-$ lies in the ionization continuum of $He + Br + Br^+ + e^-$. The rate for electron emission

$$W(R_1, R, R_2) = 1/\hbar\,\Gamma(R_1, R, R_2)$$

in connection with the dynamics of nuclear motion governs the probability that a conformation (R_1, R, R_2) contributes to the observed electron energy spectrum.

Again, we rely on the concept of "diatoms in molecules" in parametrizing the autoionization width $\Gamma(R_1, R, R_2)$. For ionization to take place, two electrons have to move: one electron tunnels from bromide into the 1*s* hole of He^+. The excess energy is transferred to a second bromine electron, which is emitted. We assume the first electron to originate from Br^- rather than from Br. This is plausible for two reasons: firstly, the 4*p* orbitals of the negative ion are far more extended than those at the neutral ion; secondly, the bromine atom closest to He^+ will always have the larger fraction of the negative charge due to polarization, thus rendering the influence of the system $He^+ + Br$ less significant than that of the $He^+ + Br^-$. Further, we assume that the emitted electron starts from the same bromine atom as the first one. This is certainly true during the later stages of the reaction when the distance between the two bromine atoms has reached large values, but we employ this concept for all nuclear conformations. It follows that the autoionization width of the whole complex $He^+ + Br + Br^-$ can be built up from the properties of the diatomic system

$$He^+ + Br^- \rightarrow He + Br^+(^3P, {}^1D, {}^1S) + e^-$$

Even though this is a two-electron process, we use the analytical form from ref. 13 for the electronic matrix element

$$H_{el}(l|R_j) = \begin{cases} D_P \cdot R_j \exp(-R_j/C_P) & \text{for } Br^+(^3P), \\ & \text{i.e., } l = 1 \\ D_D \cdot R_j \exp(-R_j/C_D) & \text{for } Br^+(^1D, {}^1S), \\ & \text{i.e., } l = 2, 0 \end{cases}$$

The four parameters D_P, C_P, D_D, and C_D are varied in the course of the calculation to fit the experimental electron energy spectrum. We found that the population of the final states $Br^+(P)$ and $Br^+(D)$ have to be described by different sets of parameters. The state $Br^+(^1S)$ is of lesser importance, since at larger Br–Br distance it is too high in energy to allow electron emission and at smaller Br–Br separations its effect is diluted in the many molecular Br_2^+ states. Population of $Br^+(S)$ is satisfactorily described by the parameters chosen for $Br^+(D)$. In this model, the autoionization width is written as

$$\Gamma(R_1, R, R_2) = \sum_I \Gamma(I|R_1, R, R_3)$$

with the partial widths being expressed as

$$[13] \qquad \Gamma(I|R_1, R, R_2) = \sum c_{I,l}{}^2 (a_1{}^2 H_{el}{}^2(l, R_2) + a_2{}^2 H_{el}(l, R_1))^2$$

The index I refers to the Br_2^+ states discussed above and the coefficients $c_{I,l}$ are the weighting factors of the ionic states $Br^+(l = 1, 2, 0)$. The coefficients a_i are familiar from the definition of the $He^+ + Br + Br^-$ potential surface and depend on all three nuclear distances R_1, R, R_2. The incoherent summing over the two contributions of the wavefunction of $He^+ + Br + Br^-$ has been employed since the lack of information about the angular distribution of the emitted electrons does not allow us to consider symmetry restrictions in the electron emission process without introducing further parameters. Because there is neither a basis to determine these parameters nor the need to take care of electron angular distributions we have chosen the form of eq. [13] to describe the ionization probability. Unfortunately, the numerical values of the four parameters D_P, D_D, C_P, C_D cannot be supplied. In the seven years that elapsed between carrying out the calculations and writing this paper, these values were lost and a new determination would require repeating the extended calculations. We would like to state, however, that the implicit effect of these parameters is clearly visible in the results presented: the relative weight of events taking place in early and late stages of the development of the collision complex reflects the prefactors D_P and D_D, and the spatial distribution for the ionization events to take place is intricately connected to the characteristic distances C_P and C_D.

3. Trajectory calculations

The calculations are carried out for the collision energy between He^* and Br_2 of $E_{coll} = 70$ meV, which represents the mean value that we use for comparison in the experiment.

In the laboratory frame we define a coordinate system in the following way: a plane is defined by the center of mass of the Br_2 molecule and the initial position and initial velocity of the projectile He^*. The *z*-axis goes through the center of mass of Br_2 and is parallel to the He^* velocity. The initial

Can. J. Chem. Downloaded from www.nrcresearchpress.com by 195.246.54.202 on 09/08/12
For personal use only.

Can. J. Chem. Downloaded from www.nrcresearchpress.com by 195.246.54.202 on 09/08/12
For personal use only.

distance between He* and the target center of mass is $13a_0$, which is sufficiently large to exclude reactions. As a first step a random number generator selects the orientation of the axis of the target molecule by two angles, one with respect to the z-axis and one with reference to the plane defined above. Further, the impact parameter of He* with respect to the Br_2 center of mass is chosen from the interval $0 < b \leq b_{max}$ such that the values of b^2 are randomly distributed. The maximum impact parameter is set to $b_{max} = 11a_0$ since crossing into the ion pair state $He^+ + Br_2^-$ is insignificant beyond this value. Note that this coordinate system differs from the one used to define the electronic properties. Evaluation of potential energies and transition amplitudes in the trajectory calculations require a coordinate transformation.

The nuclear motion of the system He^*+Br_2 is then described by a straight trajectory of He* with Br_2 remaining fixed in space. This simplified treatment of molecular dynamics is justified by the fact that it is applied only for large projectile–target separations. However, along this trajectory the coupling to the ion pair configuration

$$He^* + Br_2 \rightarrow He^+ + Br_2^-$$

as expressed in Sect. 2.*b* is monitored. If the integrated transition probability exceeds 10%, the motion in the $He^* + Br_2$ channel is interrupted and a new trajectory is started in the potential surface of the system $He^+ + Br_2^-$, as discussed in Sect. 2.*a*. Nuclear motion is then propagated by means of the Gear integrator (16). We employ the code used by Gerlich et al. (17). We had to add, of course, the subroutines that handle decay into final states $He+Br_2^+ + e^-$. This is a straightforward task that has been done before (7–9). During every time step ($\Delta t = 0.25 \times 10^{-14}$ s) the transition probabilities in the Br_2^+ states as defined in Sect. 2.*c* are evaluated according to Sect. 2.*d* and the corresponding contributions to the electron energy spectrum stored. If the total ionization probability along the trajectory has risen above 0.95 the trajectory is stopped.

Then the program switches back into the system $He^* + Br_2$ and continues the interrupted trajectory until again a 10% probability for transition into the ion pair state $He^+ + Br_2^-$ is accumulated, and so forth until the survival probability in the $He^* + Br_2$ trajectory is below 0.05.

4. Results

In Fig. 3*a* we show the experimental electron energy spectrum that results from the reaction of $He^*(2^3S)$ with Br_2 (18). We reproduce here only the range of electron energies up to 6.2 eV since the features at larger energies are due to direct Penning ionization into the $Br_2^+(X, A)$ states. As discussed above, this process [2*a*] has no bearing on the question of transition state spectroscopy. The population of $Br_2^+(B^2\Sigma_g^+)$ via process [2*a*] could, in principle, show up in the spectrum. Its energy position is given by the difference between the excitation energy of $He(2^3S)$ and the vertical ionization potential of the $B^2\Sigma_g^+$ state as $19.8 - 14.6 = 5.2$ eV. Comparison with the HeI photoelectron spectrum reveals, however, that such a conbution must be extremely small (18). Thus, we can consider the spectrum in Fig. 3*a* as being caused by electron emission from the reaction complex $He^+ + Br_2^-$. Figure 3*b* displays, for comparison, our calculated spectrum. Even though the agreement is not perfect within the very small experimental error, the similarity is such that the essential features of the dynamics of the system are apparently reproduced in the calculation. The

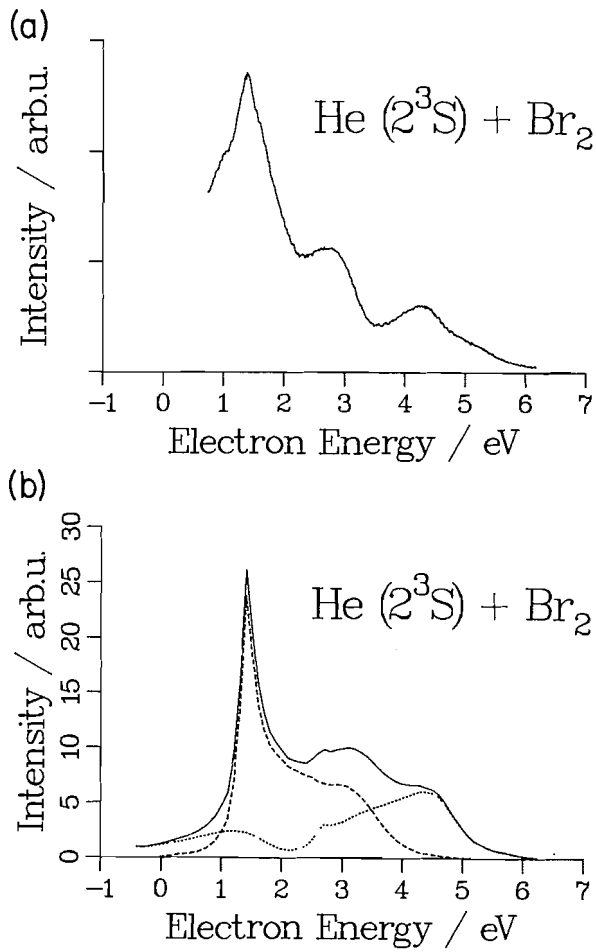

FIG. 3. (*a*) Experimental electron energy spectrum from the reaction of $He(2^3S)$ with Br_2, adopted from ref. 18. Only the energy range below 6.2 eV, which originates from the collision complex He^+–Br_2^-, is shown, i.e., after the covalent to ion pair transition $He^* + Br_2 \rightarrow He^+$–$Br_2^-$ has taken place. Further discussion is in the text. (*b*) Calculated spectrum. Best fit with respect to the parameters of the autoionization width as defined in Sect. 2.*d*. The contributions related to $Br^+(P, D)$ are shown separately. Dotted line: $Br^+(P)$; broken line $Br^+(D)$. Further explanation is in the text.

respective contributions of the spectrum that can be related to the population of $Br^+(P)$ and $Br^+(D)$ states are indicated. In the nomenclature of Sect. 2.*c* this means that the populations of basis states containing $|l = 1, m\rangle$ and $|l = 2, m\rangle$ are separately stored in the calculation. As mentioned in Sect. 2.*d*, the states containing $|l = 0\rangle$ hardly play a role. Some energy considerations allow us to illustrate the gross features of Fig. 3*b*. If we use $He + Br_2(v = 0)$ as zero of the energy scale, the system He^*+Br_2 starts with an electronic energy of 19.819 eV, which is the excitation energy of $He^*(2^3S)$. Since dissociation of Br_2 requires $D_2[Br_2] = 1.99$ eV (8), the subsystem He^+Br^- can be formed with a maximum energy of 17.83 eV in the course of the process $He^* + Br_2 \rightarrow He^+Br_2^- \rightarrow He^+Br^- + Br$ in the limit of small relative kinetic energy between He* and Br_2. On the other hand, the minimum value of the He^+Br^- potential (cf. Table 1) can be computed from the atomic energy values IP[He*] = 4.768 eV and EA[Br] = 3.364 eV (8) to be 14.86 eV. Accordingly, the autoionization of the subsystem He^+Br^- into a given state $He + Br^+(P, D, S)$ should have an electron energy spread of $17.83 - 14.86 = 2.97$ eV. Population of the $Br^+(^1D)$ state (IP = 13.34 eV) should lead

Can. J. Chem. Downloaded from www.nrcresearchpress.com by 195.246.54.202 on 09/08/12
For personal use only.

to electron energies between 1.52 and 4.49 eV. The respective boundaries for the $Br^+(^3P)$ state are 2.77 and 5.74 eV. Inspection of Fig. 3*b* shows that the major features of the calculated spectra lie in the quoted energy regimes. However, some parts of the spectra are distinctly outside the given bounds. In particular, the prominent peak at ~1.4 eV electron energy, which is associated with formation of the $Br^+(^1D)$ state, is just below the lower bound of 1.52 eV. This indicates that the autoionization of the subsystem He^+Br^- is not a sufficient description of the process and that the binding energy between all three atoms plays a role: if the binding energy is smaller in the final state than in the neutral precursor, the energy of the emitted electron is smaller than the quoted lower bound and vice versa.

The attempt to visualize the nuclear motion is shown in Fig. 4 in a manner used before in ref. 19. The trajectories chosen lie in one plane and the coordinates of the three nuclei are given within this plane for several time steps. The trajectories are followed from the instant when transition from the covalent $He^* + Br_2$ into the ion pair state has occurred until the total probability for electron emission exceeds 0.95. The starting positions of the nuclei are denoted by an octagon. At every 15th time step other symbols indicate the acquired nuclear positions. This is meant to give an impression of the simultaneous motion of the three particles. It can be observed that the two bromine nuclei separate monotonically in time whereas the helium ion oscillates with a large amplitude. The mass ratio between He and Br keeps the corresponding oscillations of the nearest Br atom on a very small, but visible, amplitude. We observe that at, or shortly after, the third close encounter between helium and either of the bromine atoms the trajectory is stopped, which indicates that its survival probability is below 5%. At this instant, we find that the separation between the halide nuclei has become rather large and, further, that it is clearly decided to which of the Br atoms the helium has formed a bond. In other words the chemical reaction

$$He^+ + Br_2^- \rightarrow He^+Br^- + Br$$

is visibly completed. This shows that the process of electron emission is fast enough to be confined to the transition state but slow enough to go on until the characteristic features of the exit channel can clearly be identified. In Fig. 4*a* we have a situation where the He^+ attack occurs at the same Br atom with which a bond is formed later on. A different type of trajectory is depicted in Fig. 4*b*. Here the light projectile switches after the first encounter to the other bromine atom, to stay there until the bond is stabilized. The difference between these pathways has been observed before (20) in the analysis of the reaction of hydrogen atoms with heteronuclear halogen molecules and has been given the name "microscopic branching." Its occurrence was found to show up in a bimodal distribution of rotational states of the hydrogen halides formed in the reaction. This, of course, is not the realm of "transition state spectroscopy" but rather the spectroscopy of reaction products. In our case, identification of microscopic branching is made difficult by the fact that the target molecule is homonuclear. The trajectories in Fig. 4, however, show features familiar from ref. 20. The rotational excitation is clearly larger in Fig. 4*b*, i.e., after the helium has switched sites. This should enhance the centrifugal forces and, indeed, the minimum distance between He and Br during the second and third encounters in Fig. 4*b* is larger ($3.24a_0$) than in the first close encounter in Fig. 4*b* and in all three encounters in Fig. 4*a* ($2.97a_0$). Since the electron energy

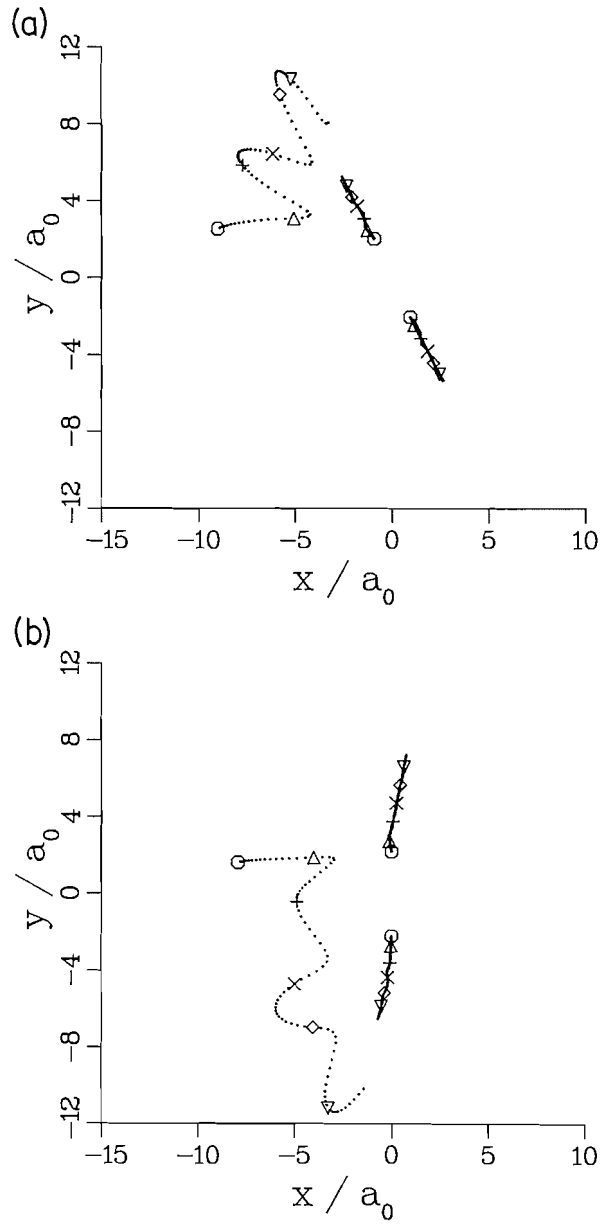

FIG. 4. Trajectories of the He^+–Br_2^- complex. The octagons indicate the positions of He and the two Br atoms right after electron transfer from He^* to Br_2. Time evolution of the system is visualized by dots for every time step. Same symbols for the nuclear positions refer to the same time. (*a*) Example of a trajectory where He^+ stays near the bromine first encountered; (*b*) example of a trajectory where He^+ switches to the other Br atom after first encounter.

depends strongly on the internuclear separation, it is to be expected that the effect should be observable experimentally. To study the problem more carefully in a calculation like ours, one had to store the electron energy spectra for both types of trajectories separately. Unfortunately, we neglected to do so, not being aware of the question at the time the calculations were carried out. It is interesting to note in this context that electron energy spectra from reactions of He^* with heteronuclear halogen molecules (18) can be understood as linear combinations of the spectra from the respective homonuclear halogens only as concerns the gross features. A careful inspection of the spectra shows (18) that the different details of the reaction dynamics have a district influence of the experimental data.

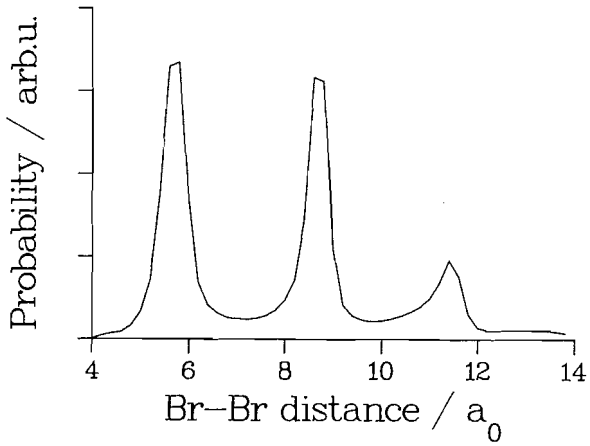

FIG. 5. Ionization probability as function of Br–Br separation. Averaged over all trajectories. The maxima of the ionization probability arise from the first, second, and third close encounters of the He^+ ion with either of the Br atoms. Since the Br–Br separation varies monotonically with time the ionization probability would exhibit the maxima as well if plotted as function of time.

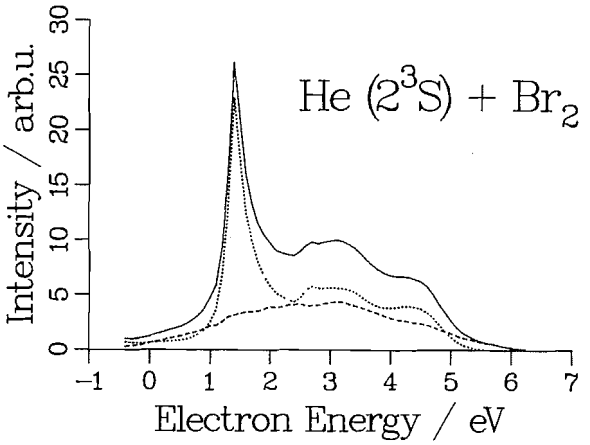

FIG. 6. Electron energy spectrum composed from the contributions during the first encounter (dashed line) and the second and third encounters (dotted line).

The fact that the autoionization width Γ (cf. Sect. 2.*d*) increases with decreasing distance between helium and either of the bromine atoms results in enhanced electron emission during close encounters. Thus, one expects a cyclic ionization activity as a function of time for a given trajectory. We found, however, that even if we average over all trajectories with initial conditions as described in Sect. 2 we have a surprisingly well-structured behaviour. In Fig. 5 we have plotted the ionization probability averaged over all trajectories as a function of Br–Br separation. The latter varies monotonically with time as seen in Figs. 4*a* and *b*. This finding allows us to plot separately the electron energy distributions that originate from different encounters. In Fig. 6 we show how the calculated electron energy spectrum is composed of the contribution from the first encounter and the contributions from the second and third encounters, the latter ones being very similar. The first encounter can be conceived as reaction between the projectile helium and a molecular target. At the corresponding Br–Br distance of $\sim 5.8a_0$ the Br_2^+ states (cf. Fig. 2) represent a broad and rather evenly populated energy band, giving rise to an unstructured electron energy distribution. On the other

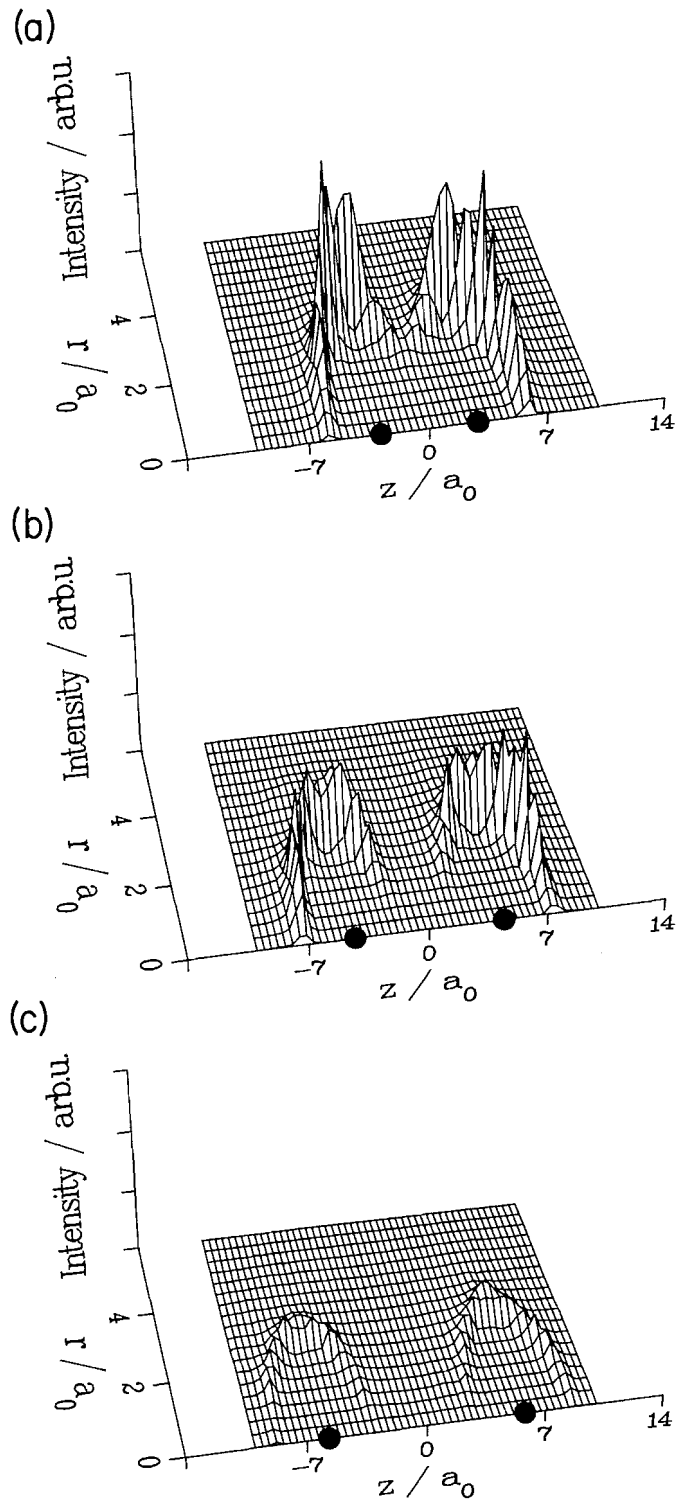

FIG. 7. Ionization probability as a function of He^+ position. The He^+ position is given in a system of cylindrical coordinates. Its z-axis coincides with the Br–Br axis. r measures the separation between He^+ and the z-axis. (*a*) First encounter; (*b*) second encounter; (*c*) third encounter. For further explanation, see text.

hand, the following encounters occur with the second Br atom being at a distance of almost $9a_0$ or more. Here, electron emission occurs with a much narrower distribution of final states. Accordingly, the electron energy distribution is distinctly more structured and contains the peak at ~1.4 eV electron energy that is characteristic for the halogen species involved (18). The

Can. J. Chem. Downloaded from www.nrcresearchpress.com by 195.246.54.202 on 09/08/12
For personal use only.

main process leading to this peak is ionization into the $Br^+(^1D)$ state, as can be seen in Fig. 3*b*. The large Br–Br separation suggests understanding this feature as being essentially due to autoionization of the subsystem He^+Br^-. The limits of this concept have already been pointed out in the discussion of Fig. 3*b*. Nonetheless, this concept provides the framework to explain why formation of the $Br^+(^1D)$ state, but not of $Br^+(^3P)$, is associated with a sharp peak: ionization into the $Br^+(^1D)$ state takes place with large probability at separations near the minimum of the He^+–Br^- potential curve $U(R_i)$ whereas the population of the $Br^+(^3P)$ state is confined to smaller He^+–Br^- separations. This is caused by a different R_i dependence of the corresponding electronic matrix elements, discussed in Sect. 2.*d*. In terms of the parameters given in Sect. 2.*d* this means that $C_P < C_D$.

As a result of the analysis we note that the electron energy spectrum varies drastically between the initial and final stages of the observed chemical reaction

$$He^+ + Br_2^- \rightarrow He^+Br^- + Br$$

Thus, this type of spectroscopy has the potential for direct observation of the time evolution of the "transition state."

To make visible which parts of the nuclear conformation space are probed by electron emission, we display the ionization probability as a function of the He^+ position. Figures 7*a*, *b*, *c* refer to the first, second, and third encounters, respectively. Again we can observe how the target behaviour varies from that of a molecular entity to that of two individual atoms. The low ionization activity at $z = 0$ in Fig. 7*a* is a result of the geometrical constraint on covalent to ion pair transition mentioned in Sect. 2.*b*.

Acknowledgements

We are most grateful to C. Schlier and O. Brass, who made the computer code for the trajectory calculations available to us and supported us in the initial stages of the calculations. The computations were carried out in the Computing Center of the University of Freiburg. This work was financially supported by the Deutsche Forschungsgemeinschaft.

1. J.C. Polanyi. Faraday Discuss. Chem. Soc. **67**, 129 (1979).
2. P. Arrowsmith, S.H.P. Bly, P.E. Charters, and J.C. Polanyi. J. Chem. Phys. **79**, 283 (1983).
3. J.C Polanyi and R.J. Wolf. J. Chem. Phys. **75**, 5951 (1981).
4. T.C. Maguire, P.R. Brooks, and R.F. Curl, Jr. Phys. Rev. Lett. **50**, 1918 (1983).
5. V. Engel und R. Schinke. Chem. Phys. Lett. **122**, 103 (1985).
6. J.C. Polanyi. Spectroscopy of the transition state. Gordon Research Conf. on Atomic and Molecular Interactions, Wolfeboro, N.H. 1984. Chairman: P.E. Siska.
7. A. Benz and H. Morgner. Mol. Phys. **57**, 319 (1986).
8. A. Benz and H. Morgner. Mol. Phys. **58**, 223 (1986).
9. W. Kischlat and H. Morgner. Z. Phys. A: At. Nucl. **312**, 305 (1983).
10. O. Leisin, H. Morgner, and H. Seiberle. Mol. Phys. **56**, 349 (1985).
11. P.W. Tasker, G.G. Balint-Kurti, and R.N. Dixon. Mol. Phys. **32**, 1651 (1976).
12. K.P. Huber and G. Herzberg. Molecular spectra and molecular structure. IV. Constants of diatomic molecules. Van Nostrand, New York. 1979.
13. R.E. Olson, F.T. Smith, and E. Bauer. Appl. Opt. **10**, 1848 (1971).
14. E.U. Condon and G.H. Shortley. The theory of atomic spectra. Cambridge University Press, Cambridge. 1963.
15. D. Hausamann and H. Morgner. Mol. Phys. **54**, 1085 (1985).
16. C.W. Gear. SIAM Num. Anal. **2**, 69 (1964).
17. D. Gerlich, U. Nowotny, C.H. Schlier, and E. Teloy. Chem. Phys. **47**, 245 (1980).
18. K. Beckmann, O. Leisin, and H. Morgner. Mol. Phys. **59** 829 (1986).
19. J.C. Polanyi, J.L. Schreiber, and W.J. Skrlac. Faraday Discuss. Chem. Soc. **67**, 66 (1979).
20. J.C. Polanyi and W.J. Skrlac. Chem. Phys. **23**, 167 (1977).

Can. J. Chem. Downloaded from www.nrcresearchpress.com by 195.246.54.202 on 09/08/12
For personal use only.

1993 Syntex Award Lecture
Photomedicine and photodynamic therapy[1]

DAVID DOLPHIN[2]

Department of Chemistry, University of British Columbia, 2036 Main Mall, Vancouver, BC V6T 1Z1, Canada

Received June 4, 1993

DAVID DOLPHIN. Can. J. Chem. **72**, 1005 (1994).

Photodynamic therapy (PDT) involves the treatment of diseased tissue and cells using a photosensitizer and visible light. Such photomedical treatments have been known since the time of the ancient Egyptians but it was only just this year that this therapeutic modality was made available to modern medicine with the approval, in Canada, of Photofrin® for the treatment of bladder cancer. This paper reviews PDT with an emphasis on drug development, particulary for the second generation drugs, especially BPDMA (benzoporphyrin derivative-mono acid), which is now in human clinical trials.

DAVID DOLPHIN. Can. J. Chem. **72**, 1005 (1994).

La thérapie photodynamique (TPD) implique le traitement des tissus et des cellules malades en utilisant un photosensibilisateur et la lumière visible. De tels traitements photomédicaux sont connus depuis le temps des anciens Egyptiens, mais la médecine moderne n'a eu accès à cette modalité thérapeutique que cette année seulement avec l'approbation, au Canada, de la Photofine® pour le traitement du cancer de la vessie. Cet article revoit la TPD en mettant l'emphase sur la mise au point des médicaments, particulièrement pour la deuxième génération de médicaments et spécialement la BPDMA (le dérivé mono-acide de la benzophorphyrine) qui est à l'essai clinique chez les humains.

[Traduit par la Rédaction]

Photomedicine has been practiced since at least the time of the ancient Egyptians (1). Psoralins from orally ingested plants accumulated in the skin and when activated by sunlight brought about repigmentation of the skin. This 4000-year-old treatment for vitilago is still used today with psoralins and UV exposure and represents the best known treatment even though it has only limited success. Indeed, a number of skin diseases, including acne, eczema, herpes simplex, and psoriasis, have been treated in a similar manner.

Niels Finsen won the Nobel Prize in Medicine in 1903 for his treatment of cutaneous tuberculosis by UV radiation. However, the most promising areas of photomedicine are those that use a photosensitizer. Indeed, it was believed in the 19th century that all efficacious drugs were colored and while this belief led to the discovery of the sulfa drugs (Prontosil is an azo dye) it was not until the beginning of the 20th century that the medicinal properties of photosensitizers were explored. Raab (2) in 1900 showed that acridine dyes and light effectively killed *Paramecia*. In 1925 Policard (3) examined the ability of porphyrins, including hematoporphyrin (**1**), to produce a phototoxic effect.

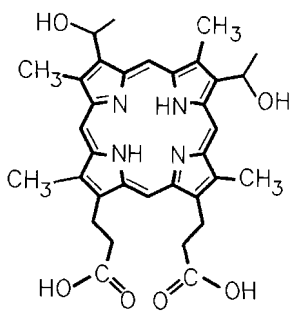

1

Mayer-Betz injected himself with 200 mg of hematoporphyrin (4) and suffered no ill effects until he exposed himself to sunlight, whereupon he suffered extreme swelling and remained photosensitive for several months. Similar accumulation of porphyrins in the skin of porphyric patients may cause severe skin necrosis upon exposure to strong light (5). Auler and Banzer in 1946 (6) showed that hematoporphyrin accumulated in cancerous tissues and, since it exhibits strong fluorescence, its localization into neoplastic and rapidly dividing tissue could be quantitatively assessed (7).

Hematoporphyrin derivative HpD was first prepared by Schwartz and co-workers and its potential as a radiosensitizer was examined (8), but in 1964 Lipson et al. showed that HpD preferentially accumulated in cancerous tissue rather than in the surrounding healthy tissue (9–11). Interest in photomedicine and particulary photodynamic therapy (PDT) was rekindled when Dougherty (12) showed that HpD could be purified by gel exclusion chromatography, which removed monomeric porphyrins. The remaining oligomeric material is known as Photofrin® (**2**) and Quadra Logic Technologies, Vancouver (QLT), in partnership with Lederle Laboratories have just received a notice of Compliance from the Canadian Health Protection Branch for the use of Photofrin® in the treatment of superficial bladder cancer.

Photodynamic therapy (PDT) requires that the photoactive agent first absorb a photon of a specific wavelength and in general the action spectra correlate well with the absorption spectra. As can be seen from the modified Yablonski diagram in Fig. 1, the first excited singlet state (S_1) can fluoresce or this excited state can participate in an electron transfer process with a biological substrate, resulting in the photobleaching of the photosensitizer and modification (destruction/inactivation) of the substrate. This is known as a Type I photoprocess (13). PUVA (psoralin, 8-methoxypsoralin, plus UV radiation using UVA) relies on this photochemistry where the psoralin is believed to undergo photoaddition to thymidine bases of DNA (14). In addition to being the most widely used treatment of psoriasis, PUVA also gives rise to cutaneous cancers (15). Photosynthesis using reduced porphyrins (chlorophylls, bacteriochlorophylls) makes use of a Type I process but the initially oxidized "porphyrin", at the reaction center, is reduced by another porphyrin

[1]This Syntex Award Lecture was delivered by Professor Dolphin at the Annual Conference of the Canadian Society for Chemistry, Sherbrooke, Quebec, June 2, 1993.

[2]David Dolphin is the NSERC Industrial Research Chairholder in Photodynamic Technologies at the University of British Columbia and Vice President, Technology Development, at Quadra Logic Technologies Inc., Vancouver.

Can. J. Chem. Downloaded from www.nrcresearchpress.com by EESC ESCOLA DE ENGENHARIA on 09/08/12
For personal use only.

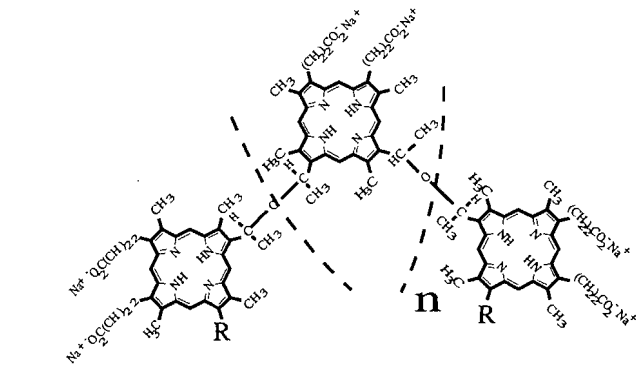

R = HO–CH(CH$_3$)– or –CH=CH$_2$ and n = 0-7

PHOTOFRIN® (Profimer Sodium) **(2)**

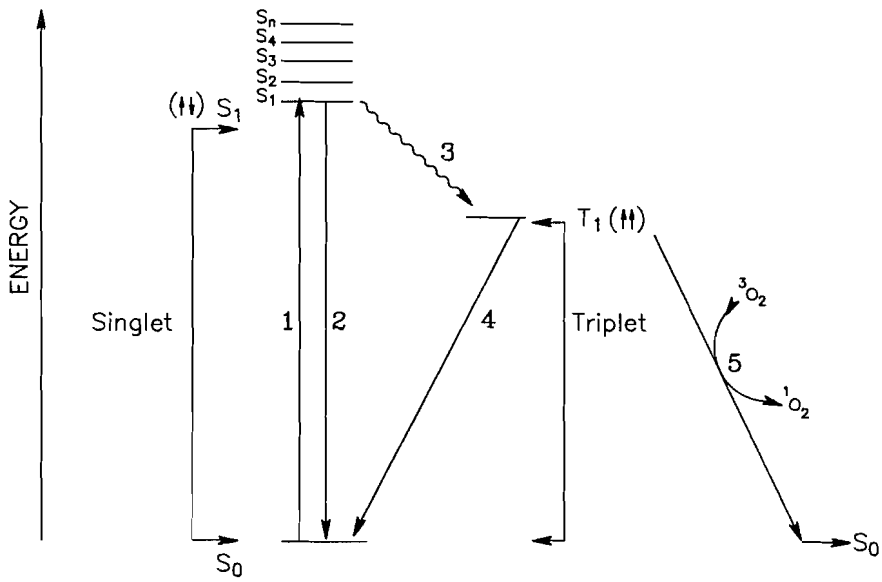

1 – Absorption – Depends upon extinction coefficient and wavelength
2 – Fluorescence – Lifetime depends on molecular interactions
3 – Intersystem crossing
4 – Phosphorescence
5 – Conversion of triplet oxygen $^3O_2$ to singlet oxygen $^1O_2$

FIG. 1. Modified Yablonski diagram.

(cytochrome) such that no net destruction of the photoactive species occurs.

A second, and far more interesting, photochemical process known as a Type II photoprocess results in the conversion of stable triplet oxygen ($^3O_2$) to the short-lived but highly reactive (toxic) singlet oxygen ($^1O_2$). This reaction occurs, as shown in Fig. 1, when the S_1 state of the photosensitizer undergoes intersystem crossing to its first excited triplet state (T_1) followed by a triplet–triplet reaction with $^3O_2$ to regenerate the photosensitizer in its ground state and singlet oxygen.

Singlet oxygen has a lifetime of ~6 μs in water and a little longer in lipid and cell membranes, which means that it cannot diffuse more than a single cell length. Singlet oxygen is a powerful, fairly indiscriminant, oxidant that reacts with a variety of biological molecules and assemblies. As shown in Fig. 2, oxygen atom transfer can result in the oxidation of both carbon and sulfur and in the formation of hydroperoxides from a variety of substrates including cholesterol and phosopholipids. The site of the greatest accumulation of the phototoxin may not define the site of cell death since, while a single oxidation of an amino acid in a protein may results in the shutdown of critical biological process (16–18), greater destruction of less critical sites may be required for cell death. Be that as it may, Oleinick and colleagues (19) have shown that, in vitro, cells die by apoptosis[3]

[3]Apoptosis is programmed cell death involving endonucleosis and chromatin condensation.

Can. J. Chem. Downloaded from www.nrcresearchpress.com by EESC ESCOLA DE ENGENHARIA on 09/08/12
For personal use only.

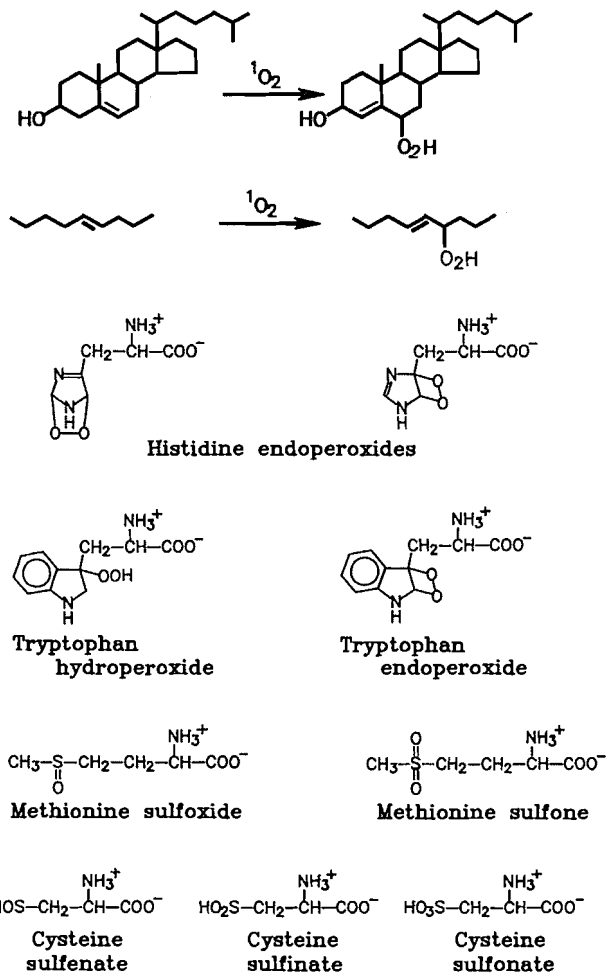

FIG. 2. Typical examples of the reactions of singlet oxygen with biomolecules.

after PDT. A dramatic example of cell membrane damage is shown in Fig. 3. This damage was observed (20) using BPDMA, which is discussed below.

Since most photosensitizers currently in clinical trials for PDT (21) have quantum yields for singlet oxygen production of ~0.5 or higher, considerable amounts of singlet oxygen can be produced when the photosensitizer is illuminated with light of the appropriate wavelength. The penetration of light through tissue is attenuated by a number of factors but absorption and scattering are the most important in limiting the penetration depth for effective treatment. Heme proteins account for most of the absorption of light in the visible region. Since this drops off rapidly beyond 550 nm, the effective depth of penetration doubles in going from 550 to 630 nm (where Photofrin® is activated) and doubles again in going to 700 nm. However, beyond 700 nm only an additional 10% increase in penetration is achieved by moving into the infrared (Fig. 4). The clinical activation of Photofrin® at 630 nm was chosen since it has an absorption band there (albeit weak) that is stronger than the absorption of oxyhemoglobin at that wavelength (Fig. 5).

Porphyrins (**3**) (Fig. 6) are 18π-electron aromatic macrocycles that exhibit characteristics optical spectra with a very strong π–π* transition around 400 nm (known as the Soret band) and four Q-bands in the visible region. As can be seen in Fig. 6, two of the peripheral double bonds, in opposite pyrrolic rings, are crossed conjugated and are not required to maintain aromaticity. Thus reduction of one or both of these cross-conjugated double bonds (to give chlorins (**4**) and bacteriochlorins (**5**) maintains aromaticity but the change in symmetry results in bathochemically shifted Q-bands with high extinction coefficients (Fig. 6). Nature uses these optical properties of the reduced porphyrins to harvest solar energy via photosynthesis with chlorophylls and bacteriochlorophylls as both antennae and reaction center pigments. The long-wavelength absorptions of these chromophores naturally led to explorations of their use as phototoxins in PDT where they have exhibited some interesting properties (22, 23). Nevertheless, the complexity of these natural pigments and the considerable problems in their isolation, separation, and purification add to the difficulties in their development for clinical use. Moreover, chlorins and bacteriochlorins, by virtue of their di- and tetrahydro reduction states, can be readily oxidized back to the parent porphyrin accompanied by the loss of their long-wavelength absorption bands. This potential lack of stability has led us to examine other ways of producing stable chlorin-like chromophores.

Protoporphyrin IX as its iron complex (heme) is the prosthetic group of heme proteins and is thus readily available from a number of animal sources. As a result of the cross-conjugated nature of the peripheral double bonds it seemed likely that one of these double bonds and a conjugated vinyl group of protoporphyrin IX might act as a diene in a Diels–Alder reaction (24).

When protoporphyrin IX dimethyl ester (**6**) is treated with a strong dienophile such as tetracyanoethylene, both 2 + 2 and 2 + 4 cycloadditions take place on either or both rings A and B (Scheme 1) (24). Acetylene dicarboxylic ester, on the other hand, brings about a Diels–Alder reaction at either ring A or B but we have not seen reaction at both rings (25). The initially formed cycloadducts (**7,8**) are 1,4-cyclohexadienes having strong absorptions at 666 nm consistent with their chlorin-like chromophores (Fig. 7). Treatment of the 1,4-diene with triethylamine tautomerizes it to the 1,3-diene (**9**). This conjugated chlorin absorbs at 686 nm and turns out to be a kinetically controlled product having a cis arrangement of the angular methyl and methoxycarbonyl groups. Treatment of this *cis*-1,3-diene or the original 1,4–dienes with 1,5–diazobicyclo[5.4.0]undec-5-ene (DBU) generates the thermodynamically more stable *trans* product (**11**). X-ray crystallography confirms the structure and stereochemical assignments made from previous NMR studies (Fig 8) (26). The *cis* and *trans* isomers both exhibit strong absorption around ~690 nm (Fig. 7). Prolonged treatment of the 1,3-dienes with TEA eliminates the angular methyl group and generates the benzoporphyrin (**10**), which has a characteristic porphyrin spectrum (Fig. 7).

Hydrolysis of the dimethyl ester in concentrated HCl leaves the ester groups on the exocyclic ring intact owing to steric hindrance experienced by the group close to the angular methyl and the conjugation of the other. The propionic esters do hydrolyze to give a mixture of the diacid (**14**) and the two regioisomeric monacid monoesters (**12, 13**). Cytotoxicity studies using the diacid showed that it was 10–70 times more cytotoxic than hematoporphyrin against a variety of normal and malignant cell lines (27). Surprisingly, a comparison of the phototoxicity of the monoacids showed that they were five times more cytotoxic than the corresponding diacids (28) for both the ring A and ring B analogs (Fig. 9). We choose to proceed towards clinical trials using the two regioisomeric monoacids of the ring A analog (**12** and **13**) that we call BPDMA (benzoporphyrin derivative ring

Can. J. Chem. Downloaded from www.nrcresearchpress.com by EESC ESCOLA DE ENGENHARIA on 09/08/12
For personal use only.

Can. J. Chem. Downloaded from www.nrcresearchpress.com by EESC ESCOLA DE ENGENHARIA on 09/08/12
For personal use only.

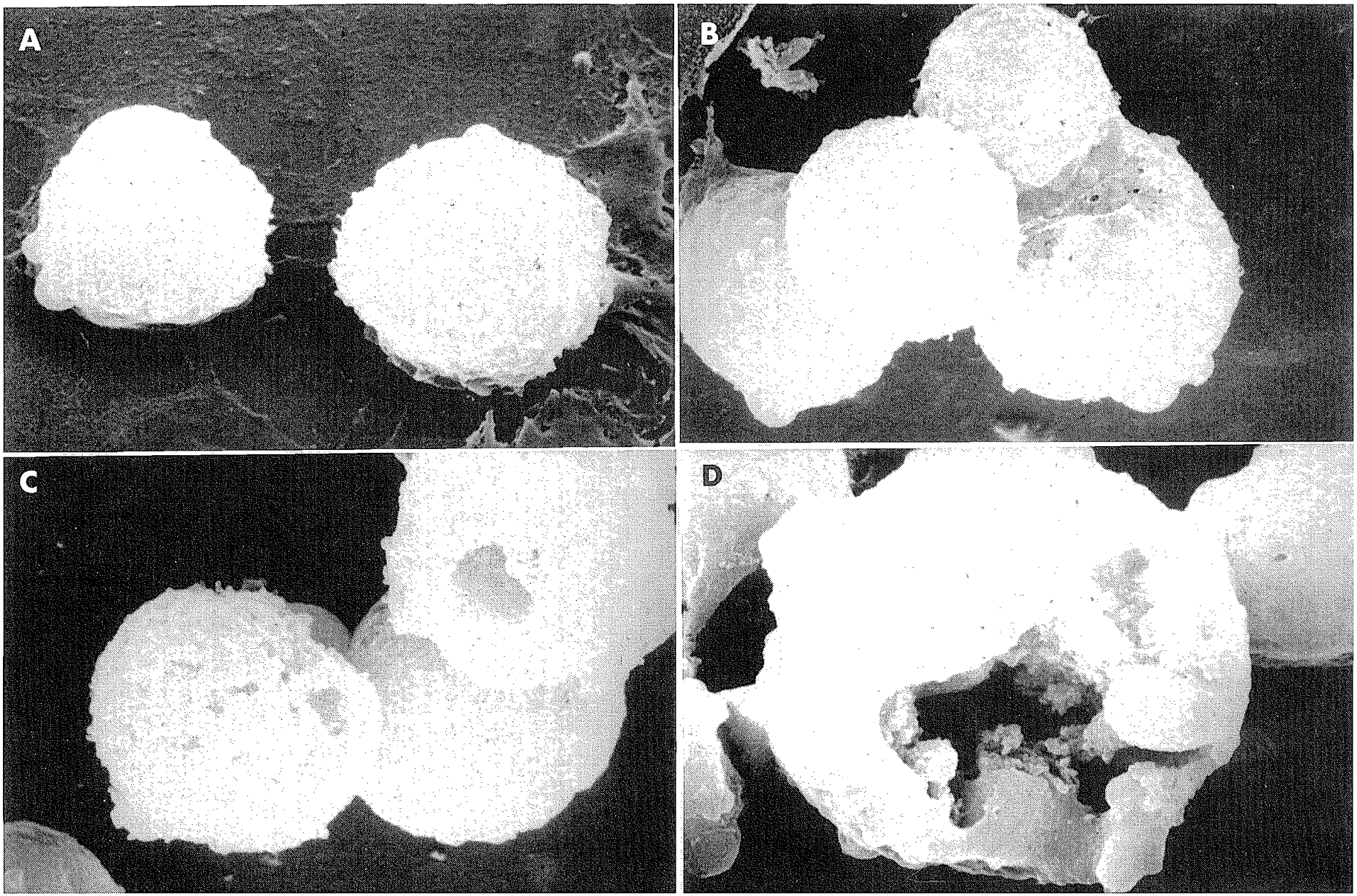

FIG. 3. Feline T cells were treated with 2 μg/mL of BPDMA and light. A: uninfected cells and light show no damage; B, infected (with FelV) cells after early treatment with light show small holes in the membrane, as light treatment continues, the holes increase in size (C) until the membrane eventually appears to be completely destroyed (D). Reprinted by permission form Blood Cells (20).

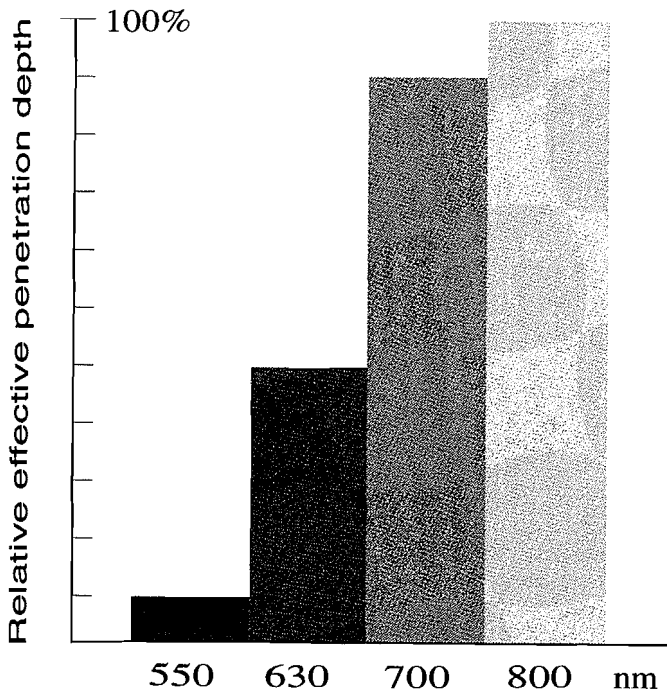

FIG. 4. Relative depth of penetration, in muscle, of light of various wavelengths.

A mono acid), whose optical spectrum (Fig. 10) shows a maximum absorption at the wavelength (~690 nm) where blood has a minimum absorption.

While BPDMA does not show specific affinity for tumors, it exhibits significantly higher concentrations in tumors than in the surrounding healthy tissues (29). BPDMA localized in tumors better than in other tissues except liver, kidney, and

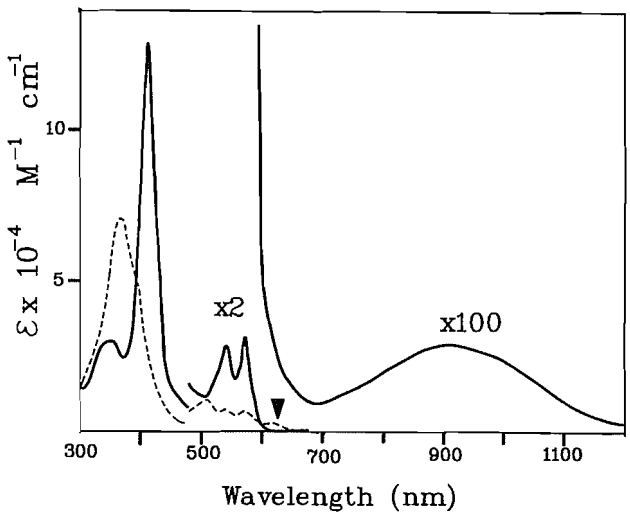

FIG. 5. Optical spectra of oxyhemoglobin (——) and Photofrin® (- - - -).

spleen. BPDMA is a chemically stable powerful phototoxin (its quantum yield for singlet oxygen is 0.46 (30)); however, before proceeding with the extremely expensive and time- consuming preclinical studies needed before a health board will issue an IND (investigation of a new drug), which allows the undertaking of human clinical trials, one is well advised to examine the extent of prolonged skin photosensitivity.

Photofrin® causes skin photosensitivity in patients for 4–6 weeks after treatment. This is a minor side effect compared to those experienced with chemotherapy or radiation therapy; nevertheless, a successful second generation phototoxin for PDT must exhibit dramatically reduced skin photosensitivity compared to Photofrin®. As can be seen from Fig. 11, compounds **12**, **13**, and **14** all showed rapidly decreasing skin photo-

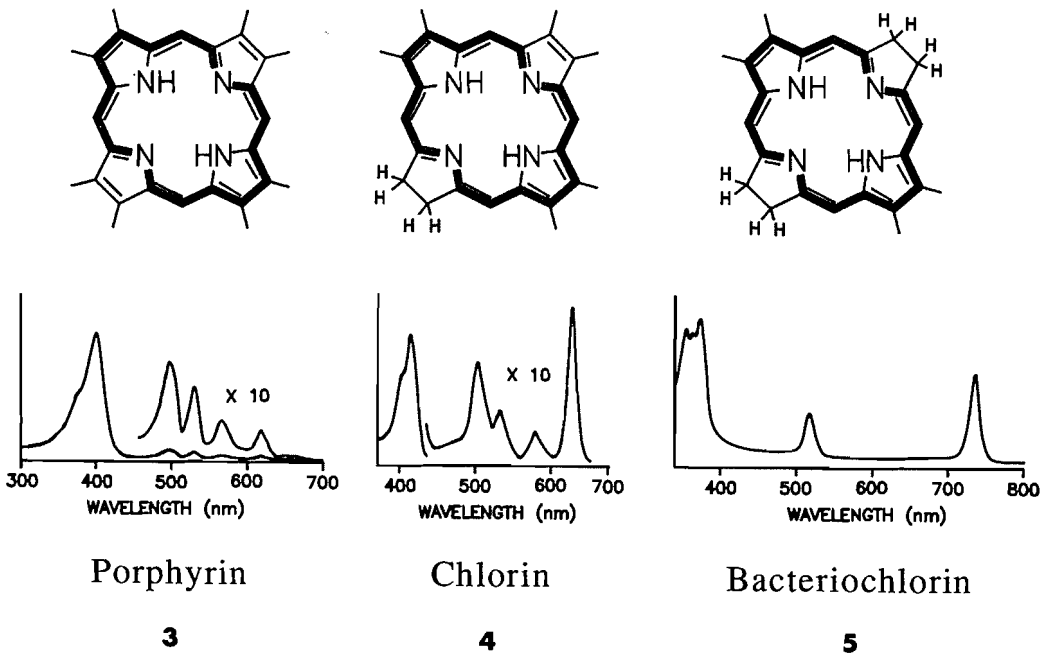

FIG. 6. Structures of the porphyrin (**3**), chlorin (**4**), and bacteriochlorin (**5**) macrocycles. The cross-conjugated double bonds in **3** can be reduced, leaving the dihydro (**4**) and tetrahydro (**5**) analogs aromatic. Increasing reductions result in an increasing bathochromic shift of the lowest energy absorption band.

Can. J. Chem. Downloaded from www.nrcresearchpress.com by EESC ESCOLA DE ENGENHARIA on 09/08/12
For personal use only.

Can. J. Chem. Downloaded from www.nrcresearchpress.com by EESC ESCOLA DE ENGENHARIA on 09/08/12
For personal use only.

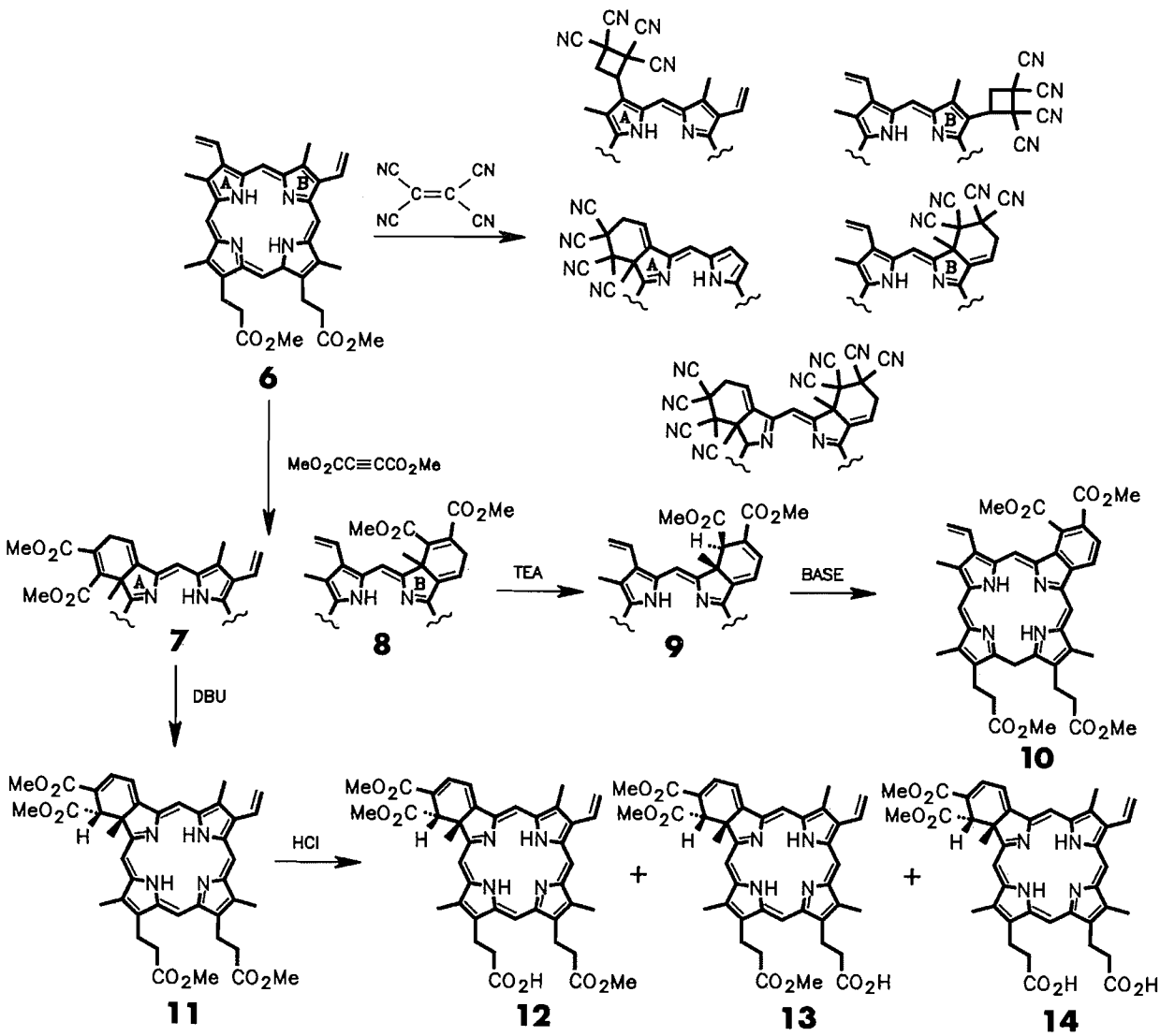

SCHEME 1

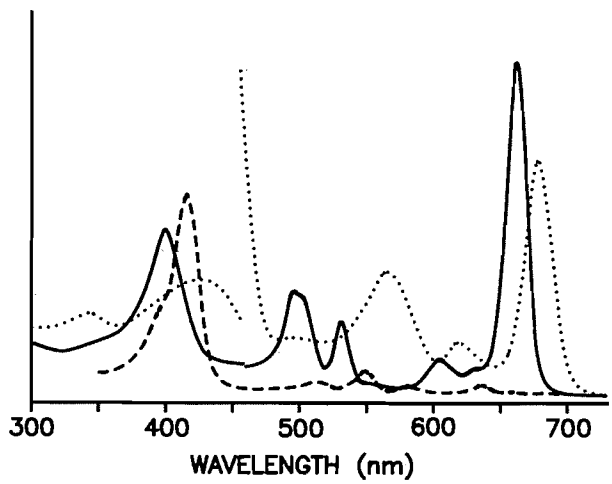

FIG. 7. Optical spectra of the 1,4-diene (**7**, • • • •), the 1,3-diene (**11**, ——), and the benzoporphyrin (**10**, - - - -).

sensitivity compared to Photofrin®, and after 72 skin photosensitivity had almost returned to normal with the monoacids. At this stage we were anxious to see if this minimal skin photosensitivity would also be seen with humans.

BPDMA is virtually insoluble in water and it has been formulated in unilamellar liposomes to make it water soluble. There is evidence to suggest that tumor selectivity with hydrophobic photosensitizers may be mediated by plasma proteins, especially low-density lipoproteins (LDL) (31–33). BPDMA associates predominantly with LDL (34) and, when preassociated with LDL improved delivery to tumors in a mouse tumor model was seen (35). The unilamellar liposomes rapidly deliver the BPDMA to the lipoprotein fraction when placed in serum, and PDT in a mouse tumor model showed that the liposomally formulated material accumulated more rapidly when delivered in this fashion than when injected in DMSO/PBS (36).

As long as a phototoxin preferentially accumulates in diseased tissue, or in a pathogen, then differential damage occurs when the system is illuminated. Under such conditions an appropriate drug dose – light energy combination can be found whereby the diseased tissue or pathogen can be destroyed without causing irreversible damage to healthy tissues. Photobleaching (37), a type I photoprocess that occurs more readily in vivo than in pure organic or aqueous solvents, may assist in minimizing damage to healthy tissue if photobleaching of low concentrations of the phototoxin in healthy tissue is complete

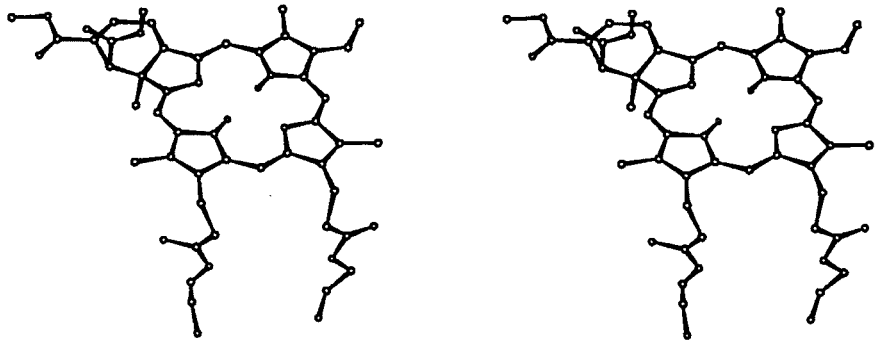

FIG. 8. X-ray structure of a BPD derivative drawn by Biosym's InsightII.

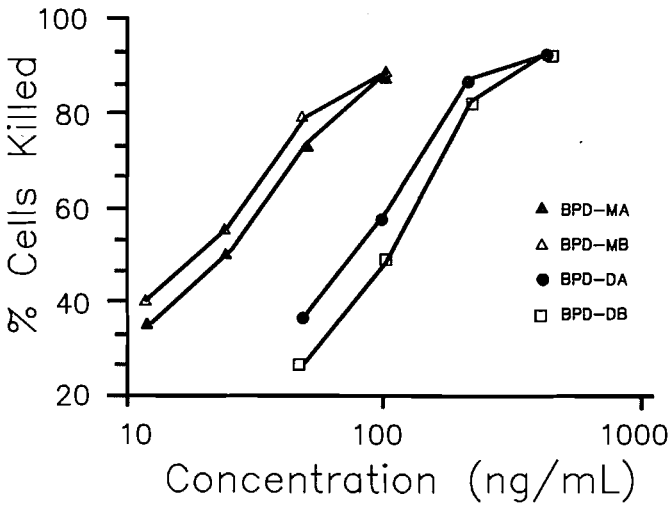

FIG. 9. In vitro cytotoxicity BPDMA (**12** and **13**, ▲), the corresponding monoacid monoester derivatives of the ring B analog ( ), the diacid (**14**, ●), and the analogous ring B diacid (□) examined under the same conditions (28).

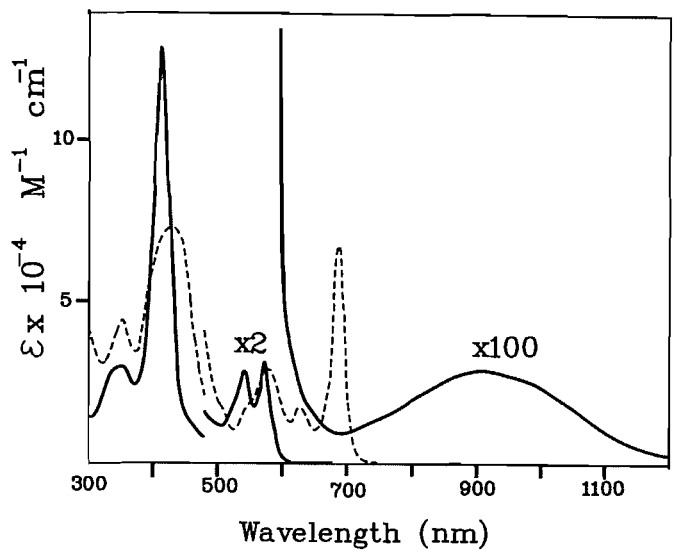

FIG. 10. Optical spectra of oxyhemoglobin (——) and BPDMA (- - - -).

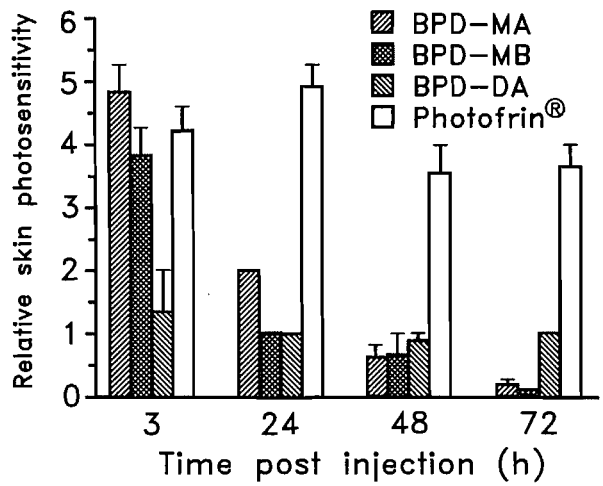

FIG. 11. Skin photosensitivity in mice following i.v. injection of the photosensitizers (4 mg/kg) and exposure to white light (95 J/cm^2). Severe damage resulting in eschar formation was scored as 5 (47). Compounds are described in Fig. 9.

before irreversible damage can take place. Photofrin® and BPDMA photobleach at similar rates.[4]

While we are just beginning to understand the mechanisms by which phototoxins biodistribute, few structure–activity relationships are known. Nevertheless, BPDMA has a great propensity to accumulate in diseased cells and in the neovasculature of hypoproliferic tissues. Measurements of biodistribution are aided by the strong fluorescence at 690 nm shown by BPDMA (Fig. 12). Fluorescence-activated cell-sorting (FACS) analysis following excitation in the UV at 420 nm showed dramatic differences between several leukemic cell lines, leukemic clinical isolates, and normal bone marrow cells incubated with BPDMA (38). Indeed BPDMA shows great potential for the ex-vivo purging of residual tumor cells in autologous bone marrow grafts. A four-log elimination of tumor cells occurred after a 1-h incubation with 75 ng/mL BPDMA followed by exposure to white light; at the same time pluripotent stems, the progenitors for all hemopoietic cells, survived the purging regime (39). Human clinical trial using BPDMA to purge leukemic autolysis grafts will begin this year under the direction of QLT.

Numerous viruses, pathogenic to humans, contain an outer hydrophobic membrane (envelope). Included amongst these viruses are cytomegatovirus (CMV), herpes simplex virus (HSV), several of the hepatitis viruses, and retroviruses such as the human T cell leukemic virus (HTLV) and human immunodeficiency virus (HIV). These, and other viruses, may be transmitted in transfused blood but it has been shown, using

[4]W.R. Potter. Personal communication.

Can. J. Chem. Downloaded from www.nrcresearchpress.com by EESC ESCOLA DE ENGENHARIA on 09/08/12
For personal use only.

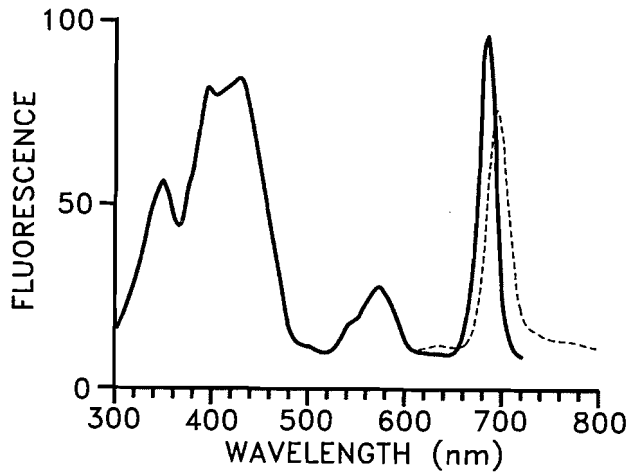

FIG. 12. Fluorescence (- - - -) excitation (——) spectrum of BPDMA.

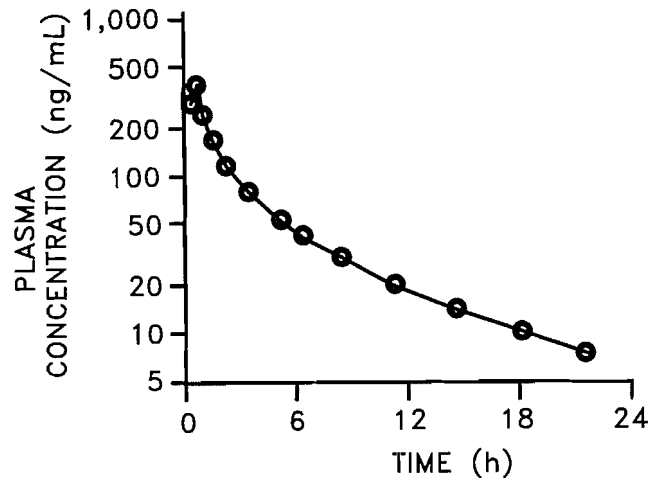

FIG. 13. Plasma concentrations of BPDMA in patients following an i.v. infusion of the drug at 2.5 mg/kg.

vesicular stomatitis virus (VSV) and feline leukemia virus (FeLV) as models, that BPDMA and light were effective in eliminating both cell-free virus and virally infected cells while at the same time leaving the red cells apparently undamaged (20, 40). Further studies have shown that BPDMA is effective for the elimination of both free and virally infected leukocytes in whole blood from virally infected humans under conditions that appeared to spare both the red cells and uninfected leukocytes (41). On the basis of these results and other preclinical studies, QLT plan to initiate clinical trials for the extracorporeal treatment of HIV-infected patients. The benefits of reducing the viral load must await the results of the clinical trials. In addition to reducing the viremia, other immunologic effects may be found as were observed after PDT with Photofrin®. Immunosuppression, as indicated by sensitivity to dinitrofluorobenzene (42), was observed in mice after PDT and an increase in chronic inflammatory cells was observed in patients after treatment for bladder cancer using Photofrin®. Moreover, the release of cytokines such as interleukin-1b and -2 and the release of tumor necrosis factor by macrophages (43, 44) and of thromoxane (45) have all been observed shortly after PDT.

While several second generation drugs are in clinical trials (21), the most advanced and most promising is BPDMA, which is being used on a number of cutaneous cancers including basal cell carcinoma, metastatic breast and gastrointestinal carcinomas, and metastatic amelanotic melanoma as well as for the treatment of psoriasis. At the present time the drug is infused in doses ranging from 1.5 to 5.0 mg/kg and light doses, administered 3 h later, have ranged from 25 to 150 J/cm^2. More than 70 cutaneous tumors have been treated and followed for several months after treatment. Complete responses were observed for the higher drug and light doses, and overall tumor responses of greater than 60% has been recorded (46). These exciting and promising results are being paralleled in the treatment of psoriasis where only a few patients have so far been treated.

We noted above that any successful second generation photosensitizer must exhibit minimally prolonged skin photosensitivity if it is to be successful in the clinic. The pharmacokinetic profile for BPDMA in human serum concentrations is shown in Fig. 13 where rapid clearance from the system is clearly observed. This decrease in serum levels is paralleled by a lowering of skin photosensitivity with time. A major purpose of the first phase of the clinical trial was a measurement of skin photosensitivity, and extensive studies using UVA and visible light from a solar simulator (using a filtered xenon arc lamp) have been carried out (46). Marked skin photosensitivity was observed shortly after treatment but photosensitivity shows a logarithmic decrease with time and it is expected that skin photosensitivity will return to normal (pre-BPDMA infusion) within 1–2 days at the expected clinical dose of BPDMA.

BPDMA thus seems to be meeting all of the necessary and hoped-for requirements of a successful second generation photosensitizing drug and, as the only non-mutagenic, non-carcinogenic, non-(dark) toxic anti-cancer drug known, we anticipate its use in a variety of clinical situations.

Acknowledgements

This work was supported by the Natural Sciences and Engineering Research Council of Canada (NSERC) and Quadra Logic Technologies Inc.

1. M.F. Edelson. Sci. Am. **259**, 68 (1988).
2. O. Raab. Z. Biol. **19**, 524 (1900).
3. A. Policard. C.R. Hebd. Soc. Biol. **91**, 1422 (1924).
4. The physiological effects of radiation energy. *Edited by* H. Laurens. Tudor Press, New York. 1933.
5. L. Eales. *In* The porphyrins. Vol. VI. *Edited by* D. Dolphin. Academic Press Inc., New York. 1979. p. 663.
6. H. Auler and G. Banzer. Z. Krebsforsch. **53**, 65 (1942).
7. F.H.J. Frigge, G.S. Wieland, and L.O.J. Mungariello. Proc. Soc. Exp. Biol. Med. **68**, 640 (1948).
8. T.J. Dougherty, B.W. Henderson, S. Schwartz, J.W. Winkelman, and R.L. Lipson. *In* Photodynamic therapy. *Edited by* B.W. Henderson and T.J. Dougherty. Marcel Dekker Inc., New York. 1992. p. 1.
9. R.L. Lipson, E.J. Blader, and E.M. Olsen. J. Natl. Cancer Inst. **26**, 1 (1961).
10. R.L. Lipson, M.J. Gray, and E.J. Blades. Proc. IX Int. Cancer Congr. 9th, Tokyo. 1966. p. 393.
11. T.J. Dougherty. Cancer Res. **38**, 2628 (1988).
12. T.J. Dougherty. Photochem. Photobiol. **46**, 569 (1987).
13. E.I. Kapinus, M.M. Weksankia, V.P. Starzi, V.I. Boghillo, and I.I. Dilung. J. Chem. Soc. Faraday Trans. 2, **81**, 631 (1985).
14. J.A. Parrish, T.B. Fitzpatrick, L. Tanenbaum, and M.A. Puthak. N. Engl. J. Med. **291**, 1207 (1974).
15. J.H. Epstein. *In* The sciences of photobiology. *Edited by* K.C. Smith. Plenum Press, New York. 1989. p. 155.

Can. J. Chem. Downloaded from www.nrcresearchpress.com by EESC ESCOLA DE ENGENHARIA on 09/08/12
For personal use only.

16. E. Ben-Hur, A. Orenstein, A. Livinc, and I. Rosenthal. Laser Life Sci. **3**, 255 (1990).
17. K.J.A. Davies, S.W. Lin, and R.E. Pacitici. J. Biol. Chem. **262**, 9914 (1987).
18. C. Prinsze, T.M.A.R. Dubbelman, and J. Van Steveninck. Biochim. Biophys. Acta, **1038**, 152 (1990).
19. M.L. Agarwal, M.E. Clay, E.J. Harvey, H.H. Evans, and N.L. Oleinick. Cancer. Res. **51**, 5993 (1991).
20. J. North, H. Neyndorff, D. King, and J.G. Levy. Blood Cells, **18**, 129 (1992).
21. E.D. Sternberg and D. Dolphin. J. Clin. Laser Med. Surgery. In press.
22. R.P. Allen, D. Kessel, R.S. Tharratt, and N. Volz. *In* Photodynamic therapy and biomedical lasers. *Edited by* P. Spinelli, M. Dal Fante, and R. Marchesini. Elsevier Science Publishers B.V., The Netherlands. 1992. p. 441.
23. K.M. Smith, S.-J. Lee, F.-Y. Shian, R.K. Pandey, and N. Jagerovic. *In* Photodynamic therapy and biomedical lasers. *Edited by* P. Spinelli, M. Dal Fante, and R. Marchesini. Elsevier Science Publishers B.V., The Netherlands. 1992. p. 769.
24. V. Scherrer Pangka, A.R. Morgan, and D. Dolphin. J. Org. Chem. **51**, 1094 (1986).
25. R.K. DiNello and D. Dolphin. J. Org. Chem. **45**, 5196 (1980).
26. E.D. Sternberg, S. Rettig, and D. Dolphin. Manuscript in preparation.
27. A.M. Richter, B. Kelly, J. Chow, D.J. Liu, G.H.N. Towers, D. Dolphin, and J.G. Levy. J. Natl. Cancer Inst. **79**, 1327 (1987).
28. A.M. Richter, E. Waterfield, A.K. Jain, E.D. Sternberg, D. Dolphin, and J.G. Levy. Photochem. Photobiol. **52**, 495 (1990).
29. A.M. Richter, S. Cerruti-Sola, E.D. Sternberg, D. Dolphin, and J.G. Levy. J. Photochem. Photobiol. B: **5**, 231 (1990).
30. E.D. Sternberg, D. Dolphin, R. Scurlock, M. Rougee, and R. Bensasson. Photochem. Photobiol. In press.
31. G. Jori, E. Beltramini, E. Reddi, B. Salvato, A. Pagnan, L. Ziron, L. Tomio, and T. Tsanov. Cancer Lett. **24**, 291 (1984).
32. D. Kessel. Cancer Lett. **33**, 183 (1986).
33. P. Morliere, E. Kohen, J.P. Reyftmann, R. Santus, et. al. Photochem. Photobiol. **46**, 183 (1987).
34. B. Allison, P.H. Pritchard, Richter, A.M., and J.G. Levy. Photochem, Photobiol. **46**, 501 (1990).
35. B. Allison, E. Waterfield, A.M. Richter, and J.G. Levy. Photochem. Photobiol. **54**, 709 (1991).
36. A.M. Richter, E. Waterfield, A.K. Jain, A.J. Canaan, B.A. Allison, and J.G. Levy. *In* Photodynamic therapy and biomedical lasers. *Edited by* P. Spinelli, M. Dal Fante, and R. Marchesini. Elsevier Science Publishers B.V., The Netherlands. 1992. p. 549.
37. L.O. Svaasand and W.R. Potter. *In* Photodynamic therapy. *Edited by* B.W. Henderson and T.J. Dougherty. Marcel Dekker Inc., New York. p. 369.
38. C.H.M. Jamieson, W.N. McDonald, and J.G. Levy. Leuk. Res. **14**, 209 (1990).
39. R.M. Lemoli, T. Igarashi, M. Knizewski, L. Acabu, A. Richter, A. Jain, D. Mitchell, J. Levy, and S.C. Galati. Blood, **81**, 793 (1993).
40. J. North, S. Freeman, J. Overbaugh, J. Levy, and R. Lansman. Transfusion, **32**, 121 (1992).
41. J. North, R. Coombs, and J. Levy. *In* Photodynamic therapy and biomedical lasers. *Edited by* P. Spinelli, M. Dal Fante, and R. Marchesini. Elsevier Science Publishers B.V., The Netherlands. 1992. p. 103.
42. C.A. Elmets and K.D. Brown. Cancer Res. **46**, 1608 (1986).
43. S. Evans, W. Matthews, R. Perry, D. Fraker, J. Norton, and H.I. Pass. J. Natl. Cancer Inst. **82**, 34 (1990).
44. D.A. Bellnier. Photochem. Photobiol. **8**, 203 (1991).
45. V.H. Fingar, T.J. Wieman, and K.W. Dunk. Cancer Res. **50**, 2599 (1990).
46. H. Lui, L. Hruza, N. Kollias, J. Wimberly, V. Salvatori, and R.R. Anderson. Proc. SPIE — Int. Soc. Opt. Eng. **1876**, 147 (1993).
47. A.M. Richter, S. Yip, E. Waterfield, P.M. Logan, C.E. Stonecker, and J.G. Levy. Photochem. Photobiol. **53**, 281 (1991).

Can. J. Chem. Downloaded from www.nrcresearchpress.com by EESC ESCOLA DE ENGENHARIA on 09/08/12
For personal use only.

1992 Lemieux Award Lecture
Studies related to the penicillin receptor[1]

SAUL WOLFE[2]
Department of Chemistry, Simon Fraser University, Burnaby, BC V5A 1S6, Canada

Received June 3, 1993

SAUL WOLFE. Can. J. Chem. **72**, 1014 (1994).

The relative antibacterial activities of penicillins and cephalosporins are discussed in terms of their differing abilities to complex to and react with penicillin-binding proteins. The insights gained from such an analysis are being used to attempt the design of new kinds of structures targeted to the penicillin receptor. Details of such design, and examples of several new classes of compounds suggested by this work, are described. Some of these compounds exhibit interesting antibacterial activity.

SAUL WOLFE. Can. J. Chem. **72**, 1014 (1994).

On discute des activités antibactériennes relatives des pénicillines et des céphalosporines en fonction de leurs facilités relatives de se complexer à et de réagir avec les protéines qui lient les pénicillines. On utilise les connaissances acquises par une telle analyse pour essayer d'imaginer de nouvelles sortes de structures pouvant s'associer au récepteur de la pénicilline. On décrit les détails d'un tel développement et on présente des exemples de nouvelles classes de composés qui ont été suggérées par ce travail. Un certain nombre de ces composés présentent une activité antibactérienne intéressante.

[Traduit par la Rédaction]

An introduction to "Sugar Ray"

I first met Professor Lemieux in Ottawa in the spring of 1955, in a "temporary" womens' barrack that had been built for the Second World War. The barrack had been converted to the chemistry building of the University of Ottawa by two carpenters named Lemieux and Anet, with the assistance of the Oblate Fathers of the University. Three months later I returned to Ottawa, with a Master's degree from the University of Toronto, as the Department's (and Lemieux's) first Ph.D. student. It is difficult to convey to today's colleagues and students the conditions under which organic chemistry students were required to work in Toronto at that time; but as a result of my experience in that environment, I was apprehensive about how I was expected to behave in the presence of my supervisor, and how I should address him. When I sought advice on this matter, it was suggested that I should refer to Professor Lemieux as "Sugar Ray".

The last time I related this story in public, I attributed the advice to Frank Anet, whom I was introducing at one of the frequent Lemieux symposia. Frank was dumbfounded, insisted that he would not have used such a description, and that this sobriquet would never have occurred to him. In any event, he argued, scientific precision would have been better served at that time by the name "Maltose Ray" or Sucrose Ray".

I have many people to thank for the Lemieux Award, including the individuals who, without my knowledge, nominated and selected me. But the person who has to accept the greatest responsibility is Professor Lemieux himself. He is the father of my career. What I learned from him is that research can be exciting and great fun, if one works hard, is prepared to take some risks, and always treats the work seriously, but never oneself. He encouraged me to have ideas, and he taught me how to develop ideas and to devise ways to test them. In view of his lifelong influence upon every aspect of what I do, I would like to take this opportunity to urge those referees of my papers and grant applications, or those members of audiences who are outraged by my work, to consider directing their outrage in future to Lemieux and not to me.

Amel Menotti and Bristol Laboratories

After he completed his PhD in 1946, Professor Lemieux joined Wolfrom's group at Ohio State as a Bristol Laboratories Fellow. This Fellowship had been created by Dr. Amel Menotti, who was then, and for many years afterwards, Vice President and Scientific Director of Bristol. Ten years later, when the antibiotic kanamycin was discovered in Umezawa's laboratory in Japan, as a result of research also supported by Bristol (1), Lemieux was asked to help with the elucidation of its structure. The student who worked on the structure of kanosamine was Ning-Jo Chü (2), with whom I was at that time sharing an apartment.

I learned about Bristol Laboratories from Paul Chü and, in 1959, when I could not find work in Canada, I wrote to Bristol. On Professor Lemieux's recommendation, Dr. Menotti offered me a position. 6-Aminopenicillanic acid (6-APA) (**1**), the nucleus of penicillin (**2**), had just become available as a result of research at Beecham Laboratories (3), and Beecham and Bristol were collaborating on the synthesis and evaluation of the many new semisynthetic penicillins that were now accessible via chemical acylation of the amino group of 6-APA. The nucleus itself has no antibacterial activity, but every semisynthetic penicillin is biologically active, the magnitude and nature of the activity depending on the nature of R.

Diastereomeric penicillins

By the summer of 1960, a first set of lead structures had been identified, and these compounds were undergoing development. Among them were three (**3***b*, **3***c*, and **4***b*) in which the side-chain carboxylic acid had a stereogenic centre at the α-carbon. In each case, when the penicillins were prepared from the resolved acids, one of the diastereomers was found to be 5 to 10 times more active than the other against a range of organisms. In the case of α-aminopenicillin G (**3***b*), which later became known as ampicillin, and α-hydroxypenicillin G (**3***c*), the side-chain acid having the *R*-configuration gave the more active penicillin, but with α-methylpenicillin V (**4***b*), which later became known as phenethicillin, the *S*-acid offorded the more active penicillin.

[1]This work was presented as the Lemieux Award Lecture at the 75th Annual Conference of the Canadian Society for Chemistry, Edmonton, June 1, 1992.

[2]Holder of a Canada Council Killam Research Fellowship 1990–1992.

Can. J. Chem. Downloaded from www.nrcresearchpress.com by EESC ESCOLA DE ENGENHARIA on 09/08/12
For personal use only.

Can. J. Chem. Downloaded from www.nrcresearchpress.com by EESC ESCOLA DE ENGENHARIA on 09/08/12
For personal use only.

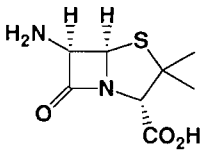

1

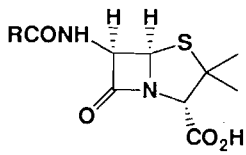

2

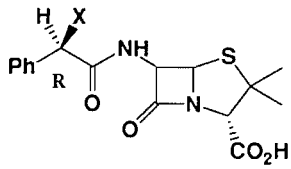

3*a* X = H Penicillin G
3*b* X = NH_2 Ampicillin
3*c* X = OH

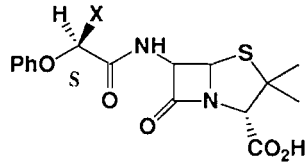

4*a* X = H Penicillin V
4*b* X = CH_3 Phenethicillin

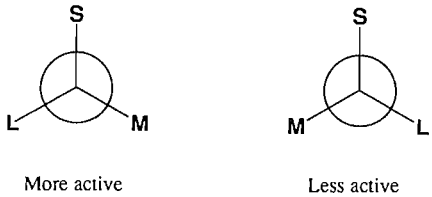

More active Less active

5

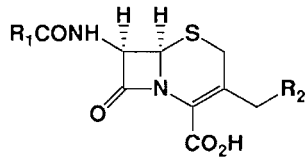

6

When Joe Lein, Alex Gourevitch, and I examined the structures of these compounds, we found that, despite the differences in absolute configuration, in each case the side chain acid that led to the more active penicillin had the small, medium, and large substituents arranged in a clockwise sense when these were viewed along the C_α-COOH bond (**5**). Our 1961 paper reporting this observation was my first publication in the field. (4), but the questions that it raised, and my attempts to pursue these questions, have occupied my attention continuously since that time.

The earliest work on semisynthetic penicillins coincided with Abraham and Newton's completion of the structure proof of Cephalosporin C (**6**; R^1 = δ-D-α-aminoadipyl; R^2 = OAc) (5). It is evident, upon examination of **2** and **6**, that penicillins and cephalosporins have a number of structural and stereochemical features in common. They also have the same mechanism of action (6), and they are formed in nature from the same amino acid and peptide precursors (7). Although the original data base for the small–medium–large effect in the side chains of penicillins was three, numerous others have been added since (8), with no exceptions, and the effect is also seen in the side chains of cephalosporins (9).

Lock and key interactions

In 1894, Emil Fisher wrote that, for a chemical reaction to take place between an enzyme and its substrate, these must fit together like a lock and a key (10). I believe that I first learned of this idea in Lemieux's graduate course in carbohydrate chemistry. One way to apply the concept to the action of an enzyme, or the interaction of a drug with its receptor, is to think of the opening of a lock as a two-stage process: in the first stage, the key fits into the lock; in the second, the key turns and opens the lock. As I will explain later, I now find it useful to treat the first stage as analogous to the formation of an enzyme–substrate complex (eq. [1]), that is, the "fit" of a drug to its receptor, and the second stage as related to k_{cat}, that is, the "reactivity" of a drug with its receptor. Understanding a lock and key relationship therefore requires an understanding of both fit and reactivity.

$$[1]\quad E + S \rightleftharpoons ES \xrightarrow{k_{cat}} P$$

"fit" *"reactivity"*

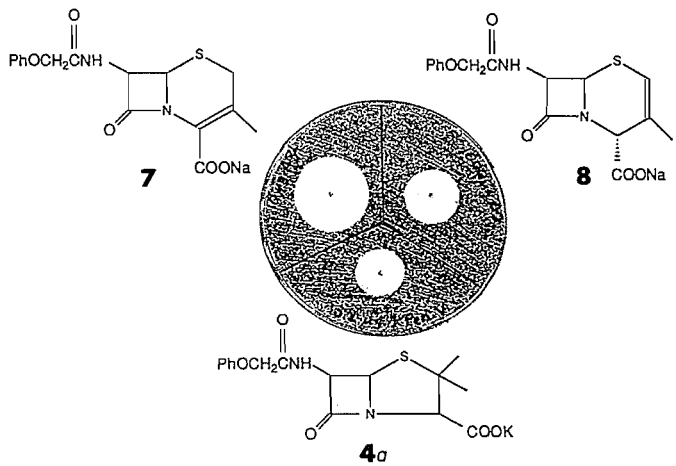

7 **8** **4***a*

FIG. 1. Zones of inhibition, versus a sensitive strain of *S. aureus*, using the potassium salt of penicillin V (**4***a*), the sodium salt of desacetoxycephalosporin V (**7**), and the sodium salt of Δ^2-desacetoxycephalosporin V (**8**). The amounts of material on this plate are: **4***a*, 0.1 μg; 7, 5 μg; **8**, 500 μg.

Figure 1 shows zones of inhibition for penicillin V (**4***a*), desacetoxycephalosporin V (**7**), and the Δ^2-isomer of desacetoxycephalosporin V (**8**), against a strain of *Staphylococcus aureus* isolated at Vancouver General Hospital. The relative amounts of material required to achieve the same inhibition are **4***a*: 1; **7**: 50; **8**: 5000. Is the Δ^3-cephalosporin less active than the penicillin because it has a poorer fit or because it is inherently less reactive? If an imperfect substrate exhibits a poorer fit, how is its reactivity affected? It has been argued (11*a*, 11*b*, 11*c*) that "reacting molecules have to be in a particular position relative to each other in order to undergo reaction and that they bind to the active site of (an) enzyme in this favourable mutual orientation" (11*d*). Does this view imply that there is a *perfect* substrate for which the *optimum* "particular positions" achieved by the reacting atoms of an enzyme–substrate complex can be determined? What are the kinetic consequences of deviations from these positions?

The early work of Eschenmoser and co-workers (11*e*), King and McGarrity (11*f*), and Lok and Coward (11*g*), and more recent work by Beak (11*h*) on endocyclic methyl transfer (e.g.,

Can. J. Chem. Downloaded from www.nrcresearchpress.com by EESC ESCOLA DE ENGENHARIA on 09/08/12
For personal use only.

PENICILLIN BINDING PROTEINS (PBP'S)

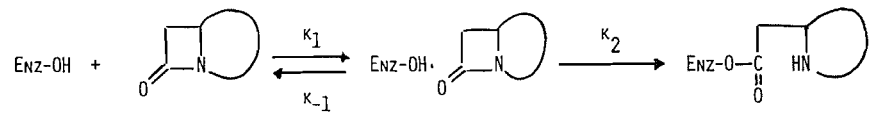

SCHEME 1

TABLE 1. Kinetic data for the hydrolyses of some β-lactam compounds by hydroxyl ions, and for the reactions of the ame compounds with an exocellular PBP from *Streptomyces* R61.[a]

	k_2/K_m (M^{-1} s^{-1})	OH^- (M^{-1} s^{-1})	K_m (mM)	k_2 (s^{-1})
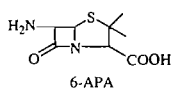 6-APA	0.2 (1)	0.15 (1)	0.8 (1)	0.0002 (1)
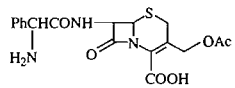 Cephaloglycine	22 (110)	0.90 (6)	0.4 (0.5)	0.009 (45)
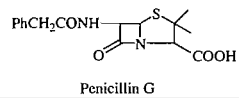 Penicillin G	13000 (65 000)	0.50 (3.3)	13 (16)	180 (900 000)

[a]Data from ref. 12.

9), provides helpful insights on this point. When the length of the chain separating N and L is too short, the geometrical requirements of an intramolecular S_N2 reaction cannot be achieved, and only intermolecular methyl transfer is then observed. King found that there is an intramolecular component in the case of **10**, but not in the case of **11**, and was able to estimate that endocyclic methyl transfer is at least 200 times slower in the latter case.

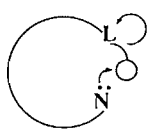

9

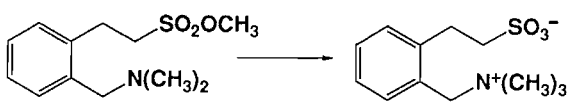

10

11

At the molecular level the catalytic efficiency of an enzyme is given by the ratio k_2/K_m, where $K_m = (k_{-1} + k_2)/k_1$. For the process summarized in Scheme 1, the units of k_2/K_m are M^{-1} s^{-1}, which corresponds to a second order rate constant. As will be seen later, this scheme describes the initial stages of the reactions of penicillins and cephalosporins with penicillin-binding proteins (PBP's); the chemical reaction measured by k_2 is the acylation of the hydroxyl group of a serine residue by the β-lactam ring. As summarized in Table 1, for an exocellular PBP from *Streptomyces* R61, which has been studied in some detail (12), the catalytic efficiencies towards 6-APA, cephaloglycine, and penicillin G are 0.2, 22, and 13 000. The corresponding second-order rate constants for nonenzymatic hydrolysis by OH^- are 0.15, 0.90, and 0.50. There is no correlation between the trends in the enzymatic and nonenzymatic rate constants, but this could simply mean that hydrolysis by OH^- does not properly simulate the chemical reaction measured by k_2. The trends in k_2 and K_m are somewhat more revealing, and one might conclude that it is rather important to understand the mechanism of the acylation step.

None of this was known in 1960. At that time we thought that the bicyclic nucleus of a penicillin or cephalosporin provided the fit, and that the side chain was needed to turn on the activity. But if every side chain turns on activity, how can the *configuration* in the side chain affect activity by an order of magnitude? What are the conformations of diastereomeric penicillins? How are epimers distinguished by the penicillin receptor? What is this receptor? Would answers to such questions lead to the design of novel structural types that would mimic the action of penicillin? Figure 2 shows zones of inhibition against *Escherichia coli* exhibited by penicillin V and one such compound. The structure of this compound and the reasoning that led to its synthesis will be presented later.

It was my good luck that Dr. Menotti believed in taking risks. He took a personal interest in the questions that I was asking in 1960, and decided to give me the freedom to pursue them on a

Can. J. Chem. Downloaded from www.nrcresearchpress.com by EESC ESCOLA DE ENGENHARIA on 09/08/12
For personal use only.

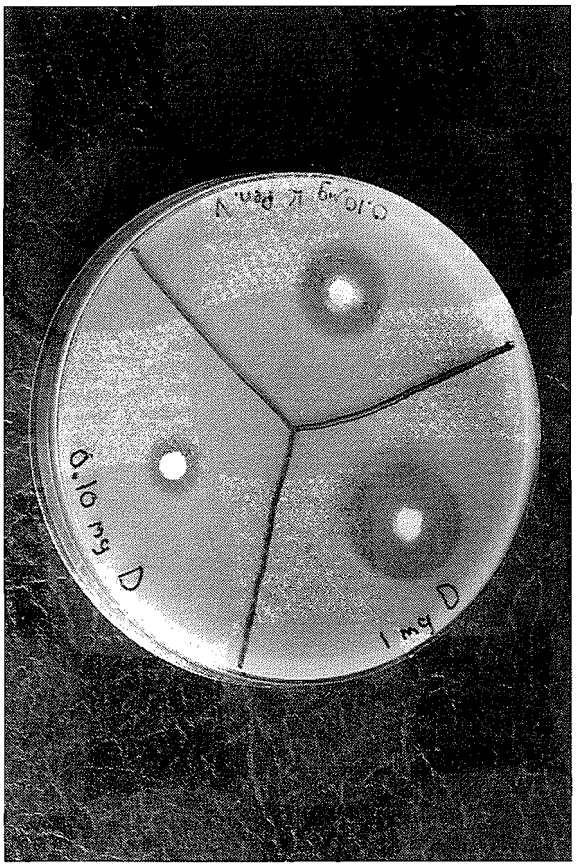

FIG. 2. Zones of inhibition, versus a sensitive strain of *S. aureus,* using 0.1 μg of penicillin V, and 0.1 and 1.0 mg of **20** (see text).

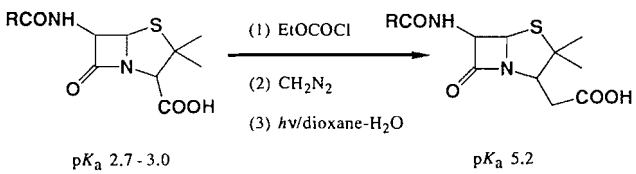

SCHEME 2

full-time basis. He also asked Joe Lein, Irv Hooper, and Merle Pindell, the heads of the microbiology, biochemistry, and pharmacology groups, to help me read the literature of their disciplines.

Moving to Queen's. Sulfur-free penicillin derivatives

He then did much more. When Bob McIntosh persuaded me to move to Queen's in 1961, Bristol offered the University a substantial unrestricted gift to equip my laboratory, and Dr. Menotti personally travelled to Kingston to persuade John Deutsch to allow Bristol to fund my work directly. This funding continued for more than 10 years, until Dr. Menotti's retirement.

From discussions with Merle Pindell I learned that optimum absorption and blood levels are found for carboxylic acids when these have pK_a's above 5. Penicillins have pK_a's between 2.7 and 3.0. We thought that the pK_a would be raised if the carboxyl group were moved away from the thiazolidine ring. Photochemical Arndt–Eistert homologation successfully gave homopenicillin G and homopenicillin V (Scheme 2), both of which were obtained crystalline as their potassium salts. Both had pK_a's of 5.2. Although, in each case the in vitro activity was

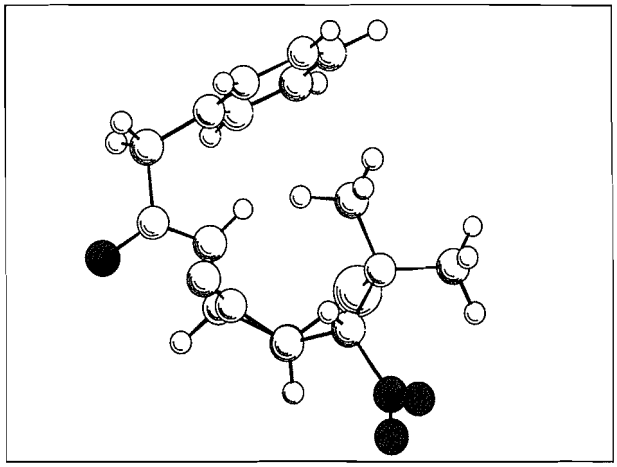

FIG. 3. Crystal structure of penicillin G. The carboxyl group and the carbonyl oxygen of the amide side chain occupy the convex face of the bicyclic system (shaded). The aromatic side chain is on the concave face of the molecule.

less than 1% of that of the parent penicillin, high or prolonged blood levels could lead to much better activity in vivo. Merle Pindell's group therefore proceeded to in vivo trials. All members of a control group of animals survived treatment with homopenicillins, but all of the infected animals died.[3]

It was already known that a free carboxyl group is essential for in vitro activity of penicillins. Indeed, by 1961, all of the obvious changes around the periphery of the bicyclic nucleus had been carried out, always with loss of activity. In addition, Sheehan's total synthesis (13) and the later work of Vanderhaeghe and coworkers (14) had shown that, of the eight stereoisomers of penicillin, only the natural isomer is active. From our experiments with homopenicillins we now knew that, if the carboxyl group engages in binding to a penicillin receptor, this group must be positioned precisely with respect to at least one other binding site in the molecule.

Although we did not realize it at the time, there was evidence regarding the nature of the second binding site. Phthalimidopenicillin (**12**), which lacks an N-H in the side chain, is at least 300 times less active than penicillin G, and it could not be excluded that the observed activity arises from hydrolysis to the phthalamic acid, which does occur at pH 7.5 (15).

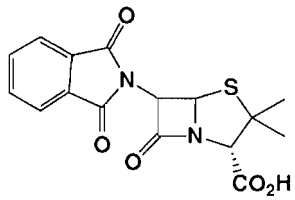

12

Figure 3 shows the crystal structure of penicillin G (16). In the crystal structures of all penicillins and cephalosporins, the carboxyl group and the amide oxygen of the side chain occupy the convex face of the bicyclic system; the amide N-H is on the concave face. Since the solution conformation was not known, we supposed that it is the same as the crystal structure, and that the exposed amide oxygen complexes to the penicillin receptor.

[3]S. Wolfe and M.H. Pindell. Unpublished results (1961).

R.U. Lemieux

July 6, 1960.

The nuclear magnetic resonance spectra for 6-aminopenicillanic acid and eleven of its N-acyl derivatives are reproduced in figure 1. The spectra were measured in heavy water, 20-30% solution, using a high resolution Varian spectrometer operating at 60 Mc/s. The chemical shifts were established using the side-band technique and are reproducible to better than 1%. All chemical shifts are from the signal arising from the H_2O signal.

FIG. 4. Extract from a report written by R.U. Lemieux in 1960.

This is consistent with the requirement that, for antibacterial activity to be achieved, an acyl group must be attached to the amino group of 6-APA. In the phthalimido compound, the N-H is replaced by a carbonyl carbon, and both carbonyl carbons are attached to a benzene ring. We thought that the steric hindrance thus created on the concave face of the molecule would result in rotation about the C6—N bond, and cause the complexing oxygen to move away from its optimum position.

We used the same reasoning 5 years later when Leigh, at ICI Laboratories, reported that *N*-methylpenicillin V is 1000 times less active than penicillin V (17). However, it must also be recognized that the conversion of penicillin V to *N*-methylpenicillin V and the conversion of 6-APA to phthalimidopenicillin lead to compounds that no longer have an *N-H* in the side chain. The possibility that it is the amide *hydrogen*, and not the carbonyl *oxygen*, which interacts with the penicillin receptor did not occur to me for more than 25 years. This idea will be pursued later, but we may note here that an important difference between 6-APA and an *N*-acylated 6-APA derivative is that the amino nitrogen of 6-APA is a hydrogen-bond acceptor, but the amide N—H of a penicillin is a hydrogen-bond donor.

Another relevant result from this early period was provided by Professor Lemieux. During the winter of 1956–1957, we had heard a lecture by Harold Bernstein on the subject of the nmr spectrum of phenanthrene. He had found, using compounds that Leonard Leitch had labelled with deuterium, that the 4,5-hydrogens are shifted downfield by 1 ppm; and in that lecture what became known as the ring current effect was discussed for the first time. By 1960 this effect was sufficiently well established that we thought we might be able to learn how the benzene rings were oriented in the ampicillin (**3***b*) and phenethicillin (**4***b*) diastereomers by examination of the chemical shifts of the methyl groups. We did not yet have an nmr spectrometer at Bristol, but Professor Lemieux did, in Ottawa. Figure 4 is the introduction to his report, reproduced here to illustrate how spectra were obtained at that time. We were able to supply the *R* and *S* isomers of α-methylpenicillin V; each isomer exhibited nonequivalent methyl groups in the thiazolidine ring, but the chemical shifts of these methyl groups were the same in both isomers. A few months later we obtained our own spectrometer, and were able to examine the spectra of the isomers of α-amino and α-hydroxypenicillin G. They also showed no difference in the chemical shifts of the methyl groups. I did not return to this matter for 25 years.

From Joe Lein and Irv Hooper I learned that penicillin acts on growing bacteria by inhibiting the formation of their cell walls, that all bacterial cell walls contain *N*-acetylmuramic acid (**13**) (18), and that penicillin-treated cells of *S. aureus* had been found by Park (19) to accumulate a number of uridine nucleotides, e.g., **14**, in which a short peptide chain is attached to the carboxyl group of the *N*-acetylmuramic acid. The pK_a of *N*-acetylmuramic acid is 2.6, almost the same as that of penicillin.

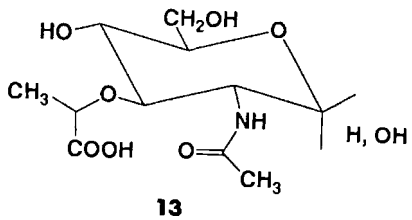

13

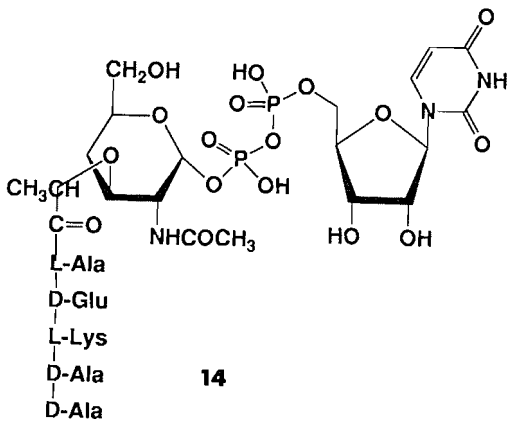

14

Since *N*-acetylmuramic acid had been found only in bacterial cells and in certain rickettsiae, and penicillin is toxic to bacterial cells and the same rickettsiae, our first idea was that penicillin is a structural analog of *N*-acetylmuramic acid, and blocks its incorporation into the cell wall. Figure 5, which dates from 1960, shows the model that was proposed following inspection of molecular models. In this figure the bold lines denote the matching parts of the two molecules. In terms of this model, the fusion of a second ring to the β-lactam achieves conformational constraint, but the presence of sulfur in this second ring would not be essential for this constraint. The β-lactam ring is thereby positioned properly with respect to, and acylates a functional group at, the active site.

Can. J. Chem. Downloaded from www.nrcresearchpress.com by EESC ESCOLA DE ENGENHARIA on 09/08/12
For personal use only.

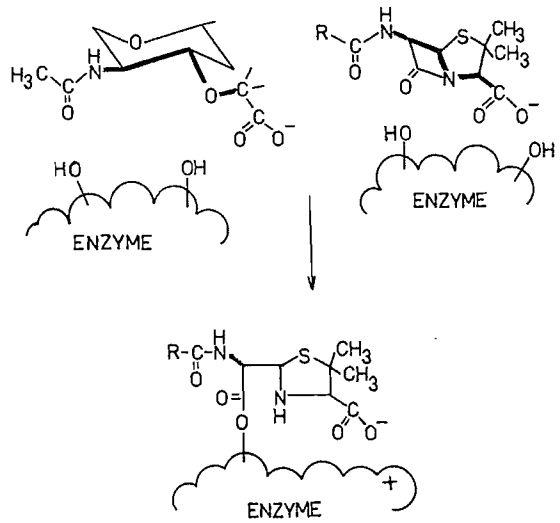

FIG. 5. An early model purporting to demonstrate a structural relation between *N*-acetylmuramic acid and penicillin as a basis for the action of the antibiotic.

One of the predictions of this model is that replacement of the sulfur atom of penicillin by other atoms, e.g., oxygen, carbon, nitrogen, selenium, should not lead to loss of activity. This was the project I took to Queen's. The first Bristol postdoctoral fellow was Dick Stoodley, who had just completed a Ph.D. in carbohydrate chemistry with J.K.N. Jones. Six months after he began, I showed him a paper that had just appeared in Nature, with the title "A Structural Similarity Between *N*-Acetylmuramic Acid and Penicillin as a Basis for Antibiotic Action" (20). Collins and Richmond, at the National Institute for Medical Research, at Mill Hill, had independently reached, and published, the hypothesis on which my entire synthetic programme was based.

My recollection is that Stoodley was crushed, but I was excited: Mill Hill was a major laboratory, and many of Alexander Fleming's contemporaries worked there. My ideas might, therefore, not be entirely without value. I wrote to John Collins, and was informed that they were not pursuing a synthetic programme based on their model. He later spent several months in Kingston, and invited me to London and then Edinburgh, where he introduced me to Henry Arnstein, Dorothy Hodgkin, Mark Richmond, and Richard Ambler, who was the first to determine the sequence of a penicillin-recognizing enzyme.

The work on sulfur-free penicillin derivatives continued for more than 10 years before any of it was published. We could do this for two reasons: through Dr. Menotti, the support from Bristol was assured; and, so far as I knew, no other laboratory in the world was engaged in similar chemistry. The conversion of a penicillin into a 1-oxacephem was reported at the Quebec CIC Conference in 1972, and followed up with six papers during the next 2 years (21).

Unfortunately for me, Saul was a King of Israel, but Moses was a prophet and, unlike Moses Gomberg (Fig. 6), I was unable to reserve this field for myself (22). By the time of the IUPAC natural products meeting in Ottawa in 1974, I was able to show a slide listing over 40 laboratories now working on nuclear-modified penicillins. Soon afterwards (Fig. 7), Woodward's synthesis of penems (23), and the discovery of thienamycin (24), clavulanic acid (25), the nocardicins (26), and the monobactams (27) attracted many more workers to the field.

One of these groups was directed by Wataru Nagata at the

BY M. GOMBERG.

Received October 2, 1900.

[PRELIMINARY PAPER.]

SOME time ago I published a method of preparing tetraphenylmethane. The yield was rather small and I was obliged to study the solubilities, composition, molecular weight, and the nitro derivative on about 0.5 gram of the hydrocarbon. The stereochemical interest attached to this compound has induced me to take up the subject once more, in the hope of obtaining larger yields. I have, therefore, gone over most of the methods which have been tried by others for the preparation of tetraphenylmethane. My results, while differing in detail from those published by others, agree in the main,—the hydrocarbon could not be obtained by the usual reactions. One of the main proofs advanced by me for the constitution of tetraphenylmethane was that it furnished a tetranitro derivative which gave no colored salts with alcoholic potash, while most of the less phenylated methanes do respond to this test. To prove whether

This work will be continued and I wish to reserve the field for myself.

UNIVERSITY OF MICHIGAN,
CHEMICAL LABORATORY,
August, 1900.

FIG. 6. "I wish to reserve the field for myself."

Shionogi Pharmaceutical Company, in Osaka. During a period of 5 years they synthesized many oxacephems, and discovered and developed an industrial synthesis of the compound now known as latamoxef (**15**), which has been in clinical use since about 1980 (28). In 1979, Dr. Nagata invited me to meet with Shionogi's oxacephem team. There were so many people in the room that I knew it was time to leave this field.

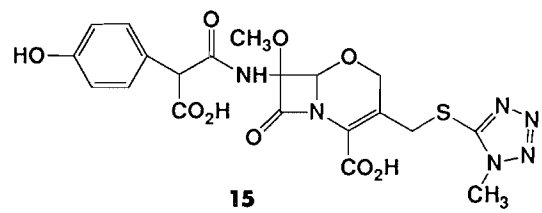

15

Penicillin-recognizing enzymes

However, I had also known for some time that the *N*-acetylmuramic acid hypothesis, on which our oxacephem work was founded, is not correct. The early research of Park has been continued to the present day, mainly by Park's co-worker Strominger (29), by Strominger's co-worker Ghuysen (30), and by Ghuysen's collaborator Frère (31). Strominger showed, in the early 1960's, that the incorporation of the *N*-acetylmuramic acid pentapeptide into cell walls leads to a linear polymer containing alternating units of the muramyl peptide and *N*- acetylglucosamine, and that this reaction is not blocked by penicillin (32). Later work revealed that the wall consists of a cross-linked polymer in which the terminal D-alanine is lost and the penultimate D-alanine is linked to the terminal amino group of lysine, through a pentaglycine bridge. The key observation was made by Tipper and Strominger in 1965 (33), namely, that it is this final, cross-linking, step that is blocked by penicillins and cephalosporins. These workers therefore suggested that penicillin is a structural analog of *N*-acyl-D-ala-D-ala. This hypothesis remains valid today.

Figure 8 is taken from the 1966 thesis of my student Syed

Can. J. Chem. Downloaded from www.nrcresearchpress.com by EESC ESCOLA DE ENGENHARIA on 09/08/12
For personal use only.

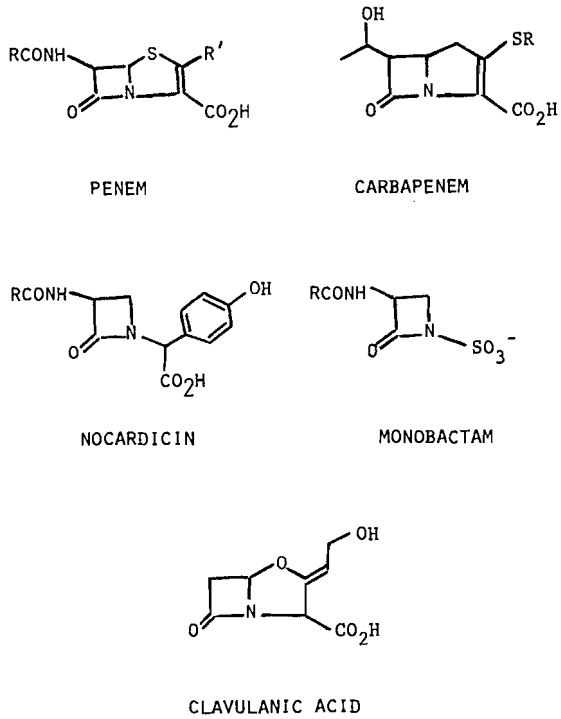

FIG. 7. Some biologically and clinically important classes of β-lactam compounds.

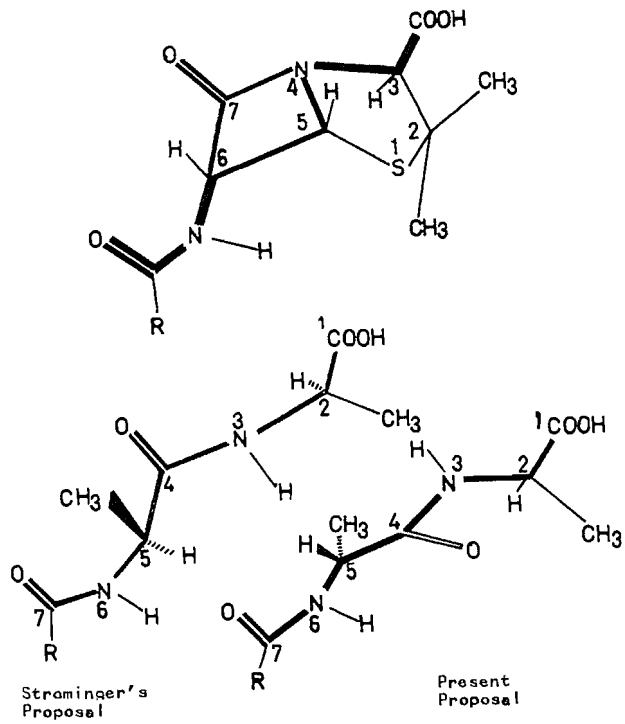

FIG. 8. Strominger's 1965 proposal and Hasan's 1966 proposal regarding the structural relationship between *N*-acyl-D-ala-D-ala and penicillin: in the former, atoms 3, 4, 7, 6 of penicillin correspond to atoms 2, 3, 4, 5 of the peptide; in the latter, atoms 3, 4, 5, 6 of penicillin correspond to atoms 2, 3, 4 5 of the peptide.

TABLE 2. Values of k_2 and k_3 for penicillin G[a]

k_2 (s^{-1})	k_3 (s^{-1})	Enzyme
180	1.4×10^{-4}	PBP from *S.* R61
4090	3610	Lactamase from *Bacillus cereus*
173	96	Lactamase from *S. aureus*
2800	1500	Lactamase from *E. coli*

[a]Reference 34.

Hasan. It shows the skeleton of *N*-acyl-D-ala-D-ala in the conformation proposed by Strominger, and in the one that we preferred at that time, superimposed on the skeleton of penicillin. Since the sulfur atom is not essential to the analogy in either proposal, our synthetic objectives remained valid.

All penicillin-recognizing enzymes are serine proteases, which differ in their kinetic behaviour and, to some extent, in their constitutions. Whether a β-lactam compound acylates and thereby inactivates the enzyme, or is hydrolyzed and thereby is itself inactivated, depends on the relative magnitudes of k_2 and k_3 of eq. [2]. When $k_2 \gg k_3$, the enzyme is termed a penicillin-binding protein, as noted earlier; when $k_2 \approx k_3$, the enzyme is a β-lactamase. Table 2 illustrates, for penicillin G, the kinetic differences between the two types of enzyme (34).

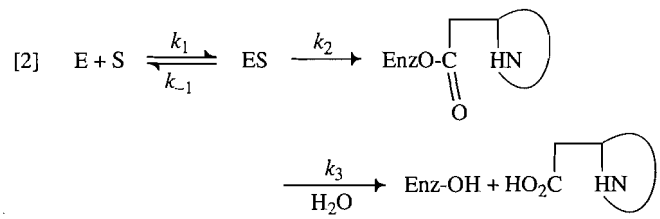

All penicillin-recognizing enzymes contain the sequence Ser-X-X-Lys at the active site (35). Several β-lactamases and one PBP, from *Streptomyces* R61, have been crystallized (36). The β-lactamases have a second lysine residue, and also arginine and glutamate in the vicinity of the active site. The roles of these residues in the formation of the initial complex and in the hydrolysis of the acyl enzyme are currently under intensive study in a number of laboratories, using site-directed mutagenesis and X-ray crystallography (37). The β-lactamases also have up to five water molecules in the vicinity of the active site.

In the PBP from *Streptomyces* R61 the serine and lysine side chains of the Ser-X-X-Lys tetrad are on the same side of the molecule, and Ghuysen and Frère have suggested, based on pH-dependence experiments (38), that the terminal amino group of this lysine residue is charge-paired to the carboxyl group of the antibiotic.

The action of the trypsin serine proteases involves a charge relay mechanism (39), in which close contact between the carboxyl group of aspartic acid, the imidazole ring of histidine, and the hydroxyl group of the active site serine act to deprotonate this hydroxyl group, which then adds to the carbonyl group of the substrate. The resulting charged tetrahedral intermediate is stabilized by hydrogen bonding in the so-called oxyanion hole (40).

An Asp-His-Ser catalytic triad is not seen in the PBP crystal structure. There is a histidine residue whose imidazole ring is ca. 5 Å away from the serine hydroxyl group (41), and mutagenesis and pH-dependence studies suggest that this residue facilitates the positioning of the antibiotic in the active site (42).

Can. J. Chem. Downloaded from www.nrcresearchpress.com by EESC ESCOLA DE ENGENHARIA on 09/08/12
For personal use only.

Can. J. Chem. Downloaded from www.nrcresearchpress.com by EESC ESCOLA DE ENGENHARIA on 09/08/12
For personal use only.

These findings may mean that the hydrogen atom of the serine hydroxyl group is involved directly in the chemical reaction.

Theoretical studies

As a result of observations by Erwin Buncel (43) and the work of Arvi Rauk, one of my first students (44), we decided in 1964 to try to learn how to carry out and interpret ab initio molecular orbital calculations, with Imre Csizmadia as our mentor. Between 1964 and 1980, Rauk's pioneering work on sulfur-containing carbanions was continued and extended by a series of outstanding students: Luis Tel, Mike Whangbo, Berny Schlegel, Dave Mitchell, and Albert Stolow (45).

During the same period, numerous papers appeared in the literature describing molecular orbital calculations on simple β-lactam compounds and, in some cases, reactions of β-lactam compounds with hydride ion. However, I did not believe that knowledge of the angles at a β-lactam nitrogen atom, or the bond order between this atom and the adjacent carbonyl group, or the charge at the carbonyl group, or the arbitrary positioning of an arbitrary nucleophile with respect to this group, had any relevance to how penicillin binds to and reacts with its receptor, if this receptor were not also taken into account in the analysis. However, it was not possible to contemplate molecular orbital calculations on a protein receptor. Molecular mechanics programmes for peptides were available, but in the early 1980's these seemed to consist of black boxes with no published documentation of the algorithms employed, or the origins of parameters. Allinger's MM2 programme was fully documented (46), but was restricted to 100 atoms, and there were no parameters for peptides or β-lactam antibiotics. Scheraga's fully documented ECEPP programme (47) produced peptide structures and coordinates, but ultimately was limited by its use of fixed bond lengths and bond angles.

I thought that the problem was intractable, until Mario Pinto wondered whether one could use ab initio calculations to obtain unknown force constants, and torsional and electrostatic parameters for MM2. This would produce a "Scaled Quantum Mechanical Force Field" (48). At the time we decided to pursue this idea, CHARMM (49), AMBER (50), and MACROMODEL (51) had not yet appeared in the literature, and Allinger's peptide parameters had not yet been published (52).

Eventually we greatly expanded the dimensions of MM2 (53), and determined and tested MM2 parameters for peptides (53), penicillins (54), and cephalosporins (55), as well as the new structures described later. For small molecules, a rather complete conformational analysis is feasible, using the dihedral driver of MM2, but this strategy is impractical for a peptide. The conceptual breakthrough was made by Stephen Bruder and Kiyull Yang, who devised a random number strategy that screens hundreds of thousands of torsional isomers, using ECEPP, minimizes several hundred low-energy structures of this set, and then automatically converts these to the MM2 format for final minimization of all bond lengths, bond angles, and dihedral angles (56).

All of the results that will now be described have been obtained using the bulk dielectric constant to treat the solvent. Most workers, including Professor Lemieux (57), regard this as an unacceptable assumption. However, our decision to proceed in this manner, at least for the present, was based on the data seen in Table 3, which refer to the solvent dependence of the conformations of the alanyl dipeptide, and are in agreement with experiment.

Figure 9 shows *A*, the crystal structure of penicillin G, after minimization with a dielectric constant of 78.5, and also a conformation (*B*) calculated to be 3 kcal/mol lower in energy than the crystal structure. Also shown are *C*, the calculated conformations of *N*-methylpenicillin G, *D*, the ampicillin epimer having the D (more active) and *E*, the epimer having the L (less active) configuration in the side chain (58). The most significant difference between *A* and *B* is the orientation of the amide bond of the side chain: in the optimized structure the N-H moves to the convex face, and the C=O to the concave face of the molecule.

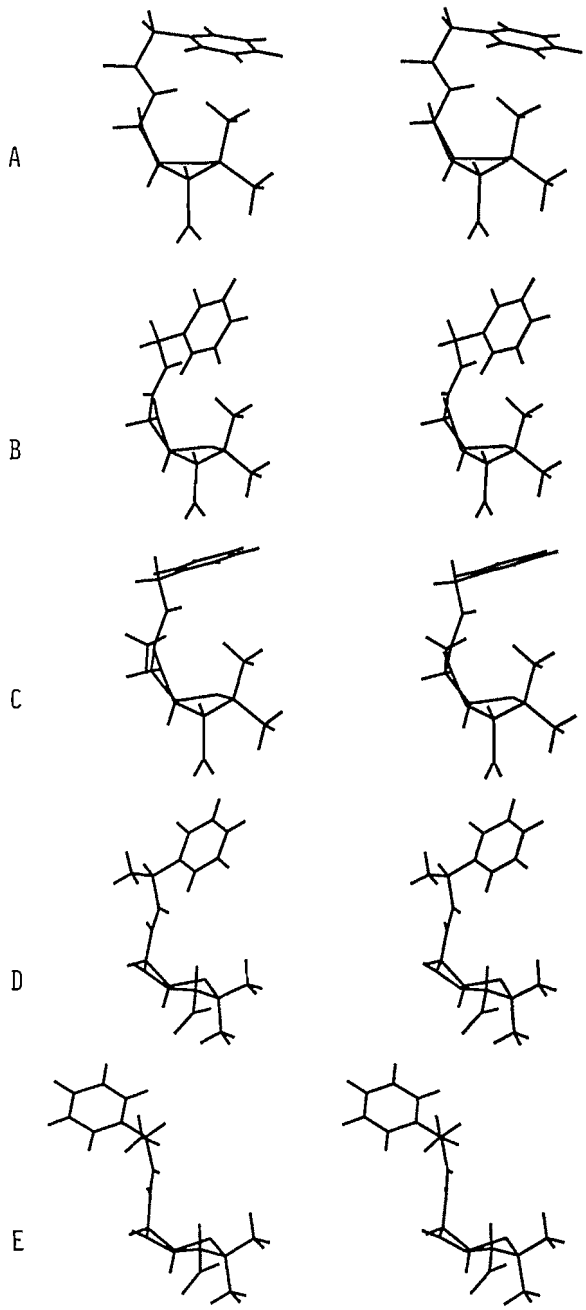

FIG. 9. Stereoscopic views along the N4—C5 bond. (*A*) Crystal structure of penicillin G after MM2 minimization (54); (*B*) calculated global minimum of penicillin G; (*C*) calculated global minimum of *N*-methylpenicillin G; (*D*) calculated global minimum of the more active D epimer of ampicillin; (*E*) calculated global minimum of the less active L epimer of ampicillin.

For the evolution of our thinking, the most important compu-

Can. J. Chem. Downloaded from www.nrcresearchpress.com by EESC ESCOLA DE ENGENHARIA on 09/08/12
For personal use only.

TABLE 3. Calculated relative energies of the different conformations of AcNH-CH(CH_3)-CONHCH_3 in chloroform and in water, using the bulk dielectric constant of the solvent

	Dielectric constant (D)	
Conformation	4.8	78.5
C_7^{eq}	0.00[a]	0.21
α_R	0.67	0.00
α'	0.82	0.26
C_5	0.85	0.46
P_{II}	1.13	0.23
α_L	1.24	0.62
C_7^{ax}	1.33	0.97

[a]In kcal/mol.

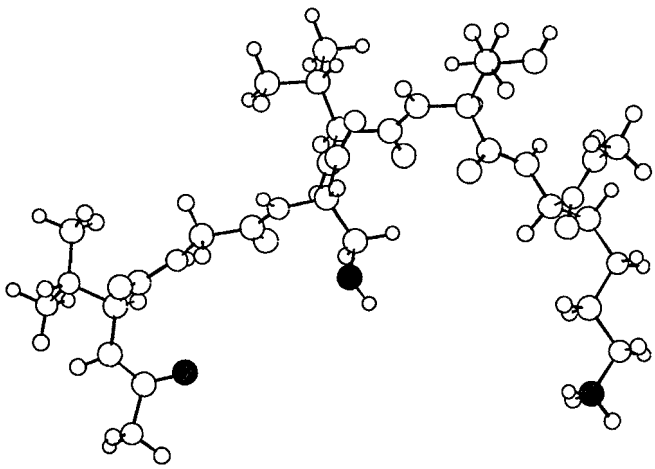

FIG. 10. A computer-generated model of the active site of a penicillin-binding protein having the sequence val-gly-ser-val-thr-lys. The model shows close contact, on the concave face, between the serine hydroxyl, the lysine amino, and an end group (shaded).

tational observation was that, in *N*-methylpenicillin G (*C*), the methyl group occupies the same position as the N-H of penicillin G; but the latter is an active compound, and *N*-methylpenicillins are inactive as antibacterial agents (17). Eventually we concluded that the convex face of penicillin must be binding to its receptor, and that the carboxyl group and the amide N-H are engaged in primary binding to this receptor.

To obtain a model of a penicillin receptor, we selected the sequence around the active site of *Streptomyces* R61, i.e., Ac-Val-Gly-Ser-Val-Thr-Lys-NHMe, for examination by the Bruder–Yang strategy (56).We assumed that we were seeking a low-energy conformation in which the terminal amino group of lysine is 6–8 Å from the serine hydroxyl oxygen. Following a preliminary search of 200 000 structures and examination of 50 low-energy structures we found the conformation shown in Fig. 10. The serine oxygen – lysine nitrogen distance in this structure is 8.5 Å. These reactive sites are on the concave face of the structure, which also includes an amide carbonyl group. It now seemed reasonable to try to form a supermolecule in which the amide N-H of penicillin G was hydrogen-bonded to the amide C=O of the receptor model, and the carboxyl group of the antibiotic was hydrogen-bonded to the terminal amino group of the lysine residue. Kiyull Yang wrote a computer programme that creates a supermolecule by specification of two intermolecular hydrogen bonds, minimizes the energy of this supermolecule

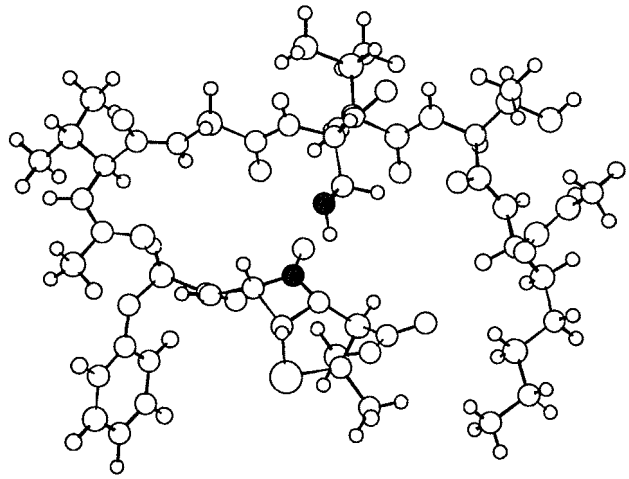

FIG. 11. Docking of penicillin V to the active site model of Fig. 10. Formation of hydrogen bonds between CO_2^- and NH_3^+, and between amide N-H and valine C=O, results in close contact between the serine hydroxyl group of the receptor and the convex face of the β-lactam ring of the antibiotic. The serine oxygen and β-lactam carbonyl carbon are shaded.

and the two hydrogen-bonding distances, and creates the input file for a full MM2 minimization (58).

In the case of the global minimum of penicillin G, this procedure led to the structure shown in Fig. 11, in which the serine oxygen is positioned on the convex face of penicillin, 3.8 Å from the carbon atom to which it will become bonded. Significantly, the higher energy crystal conformation of penicillin G produces a lower energy complex (Fig. 12), in which the serine hydroxyl group is also on the convex face of the molecule, and again positioned over the β-lactam ring. We believe that, had only the crystal structure been available to us, we would have expected the amide N-H to be buried in the interior of the molecule, and would not have examined its participation in the complexation.

Figure 13 shows **7**, **8**, and **16**, the 4-epi isomer of **8**, docked to the model of the penicillin receptor (55). In each case we observe the same kind of relationship between the serine hydroxyl group and the convex face of the antibiotic.

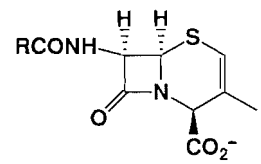

16

When we published the structures of some of these computer-generated complexes in 1988 (58), there was already in the literature a 1983 structure (Fig. 14), based on the experimental crystal structure of the *Streptomyces* R61 enzyme (59). In this 1983 structure, the serine hydroxyl group is clearly seen to be positioned on the *concave face* of the bicyclic system. Subsequently, however, Kelly and Knox (60) proposed a rather different structure for the cephalosporin complex (Fig. 15). A close relationship between the carboxyl group of the antibiotic and the terminal amino group of the lysine residue of the Ser-X-X-Lys tetrad can now be seen and, significantly, the hydroxyl oxygen of the active site serine *occupies the convex face of the molecule*, as in all of our theoretical structures.

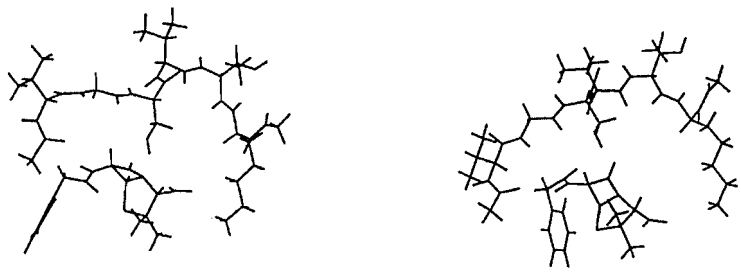

FIG. 12. Docking of the crystal structure of penicillin G and also of the minimized structure of penicillin G to the active site model of Fig. 10, using the protocol of Fig. 11. The higher energy crystal structure forms a lower energy complex.

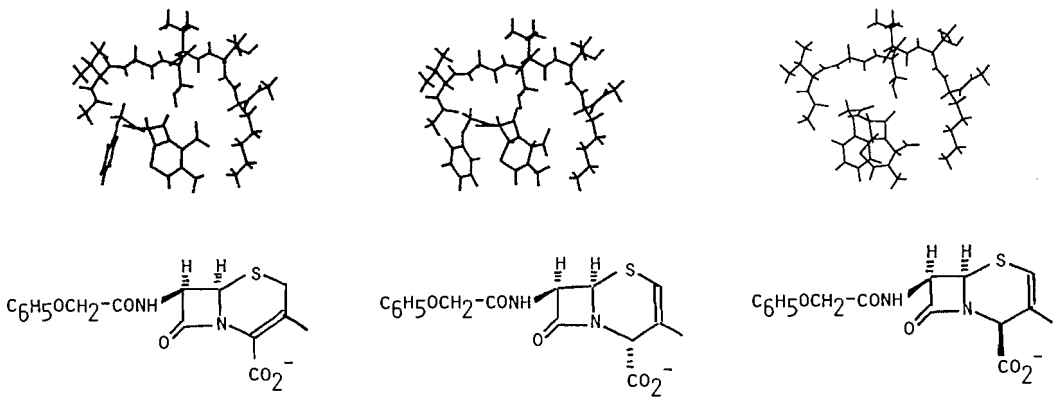

FIG. 13. Docking of the cephems **7**, **8**, and **16** to the active-site model of Fig. 10, as in Fig. 11, showing the similar relationship in each case between the serine hydroxyl group of the receptor and the convex face of the antibiotic.

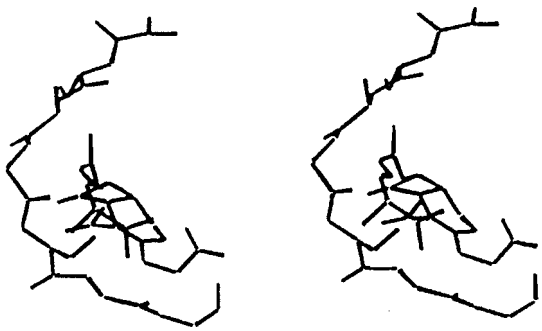

FIG. 14. A 1983 proposal, based on an experimental crystal structure, showing the hydroxyl group of serine attacking the concave face of a cephalosporin (from ref. 59).

Neutral alcoholysis of β-lactam compounds: the role of water

How is the C-O-H group acylated by the N-C=O moiety of a β-lactam ring when these are oriented with respect to each other as depicted in Fig. 16? Although the O..C=O angle is correct (61), the geometry of Fig. 16 is not consistent with a mechanism involving an initial addition to the carbonyl group to form a tetrahedral intermediate; such a mechanism would require attack by O-C from the direction *anti* to C=O, and not *syn* as seen in the figure. In fact, the acylation mechanism suggested by Fig. 16 is an unprecedented one, in which C—O and N—H bond formation are concerted with the cleavage of the β-lactam bond.

It is known, from the work of Michael Page (62), that the chemical hydrolysis of penicillin G exhibits the pH dependence shown in Fig. 17. In the acid region, there is rate-determining protonation of the β-lactam nitrogen, from the convex face of the molecule; in the alkaline region, nucleophilic addition of HO^- to the carbonyl group is rate determining. There are no experimental data for the biologically relevant region pH 6–8, and, with Fig. 16 in mind, we decided to search for a neutral mechanism in which the two reactions merge.

Figure 18 shows transition structures, fully optimized by ab initio calculations at the 3-21G level (63), for the reaction of methanol with *N*-methylazetidinone via the unprecedented pathway involving *N*-protonation, and also via an *O*-protonated pathway, which leads to the tetrahedral intermediate. Each of these structures possesses one and only one imaginary frequency, and represents a genuine transition state. An *N*-protonated process therefore exists, at least at this computational level. More importantly, on the basis of one-point calculations at the correlated MP2/6-31G* level, the *N*-protonated transition structure is 7.84 kcal/mol lower in energy than its *O*-protonated isomer!

Figure 19 shows the fully optimized 3-21G* transition structures for the reaction of the bicyclic penam (thiazolidine-β-lactam) nucleus with methanol via the *N*-protonated pathway, an *O*-protonated pathway from the convex face, and

Can. J. Chem. Downloaded from www.nrcresearchpress.com by EESC ESCOLA DE ENGENHARIA on 09/08/12
For personal use only.

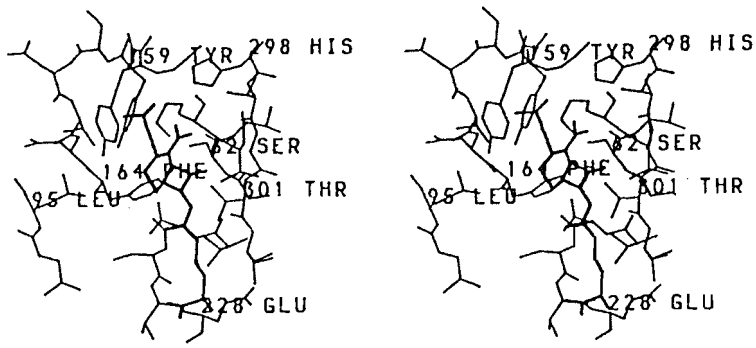

FIG. 15. A 1989 proposal, based on the same crystal structure as Fig. 14, but now showing the hydroxyl group of serine attacking the convex face of a cephalosporin (from ref. 60).

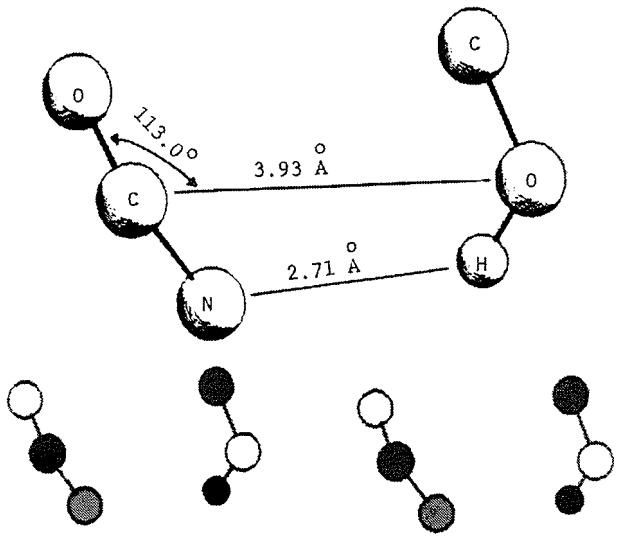

FIG. 16. A closeup view of the relationship between the serine C-O-H and β-lactam N–C=O in the calculated complex between penicillin G and the receptor model of Fig. 10 (from ref. 58).

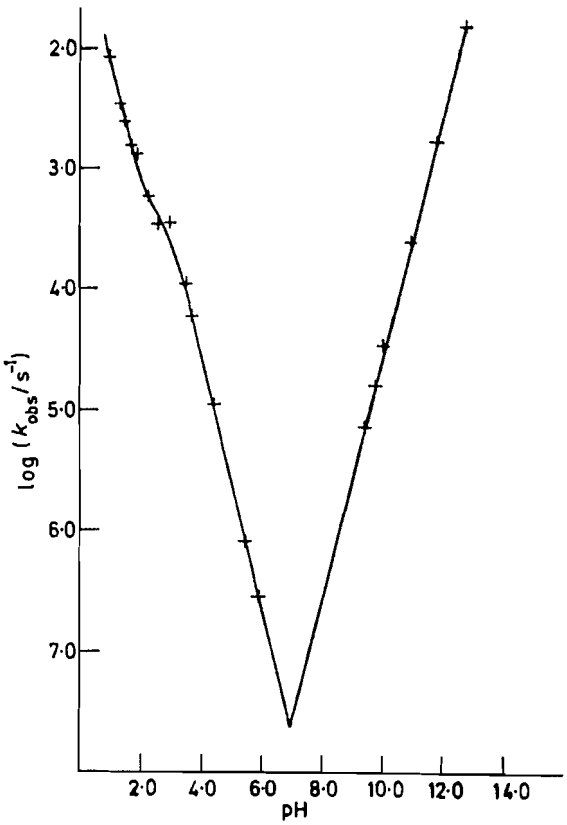

FIG. 17. pH dependence of the chemical hydrolysis of penicillin G (from ref. 62).

an *O*-protonated pathway from the concave face (63). Again, on the basis of the one-point MP2/6-31G* energies, the *N*-protonated pathway is preferred over either *O*-protonated pathway by almost 8 kcal/mol; in the *O*-protonated pathway, attack from the convex face is 2 kcal/mol lower in energy than attack from the concave face. The different orientations of the methyl group in the *O*-protonated and *N*-protonated mechanisms should also be noted.

It would be proper to object at this stage that these computational results are irrelevant, because they refer to the gas phase, in which the four-centred processes seen in Figs. 18 and 19 are enforced by the absence of water. However, the chemical reactions of β-lactam compounds with penicillin-recognizing enzymes also take place in an environment that is almost solvent free. Although the water content at the active site of the PBP is not known to us, as noted earlier β-lactamases contain at least one water molecule in this region. Accordingly, we decided to examine the effect of one water molecule on the different reactions of methanol with β-lactam compounds.

Figure 20 shows 3-21G transition structures for the reaction of methanol with *N*-methylazetidinone, with the addition of one water molecule (63). The significant results are that the *N*-protonated pathway is preferred by over 9 kcal/mol, and that the water molecule has a substantial catalytic effect on both reactions, over 10 kcal/mol.

These are very difficult structures to determine at this computational level, and we believed that it was not feasible to go further. However, for reasons that will soon be clear, it became necessary to examine the catalytic effect of water on the reaction of methanol with a C3-carboxypenam (63). The structures shown in Fig. 21 required more than 6 months to find, and are fully optimized at 3-21G*. The *N*-protonated pathway proceeds via a termolecular complex, which precedes the transition state along the reaction coordinate. The transition structure resembles the one for *N*-methylazetidinone.

We were surprised to find that the C···O distance in the termolecular complex is 3.8 Å, the same as in the molecular mechanics structures seen earlier. Accordingly, Dr. Yang modified the molecular mechanics docking programme to allow a water molecule to be included at the active site. In the case of penicillin V, this led to the structure shown in Fig. 22 which, in truncated form, is shown, together with the ab initio structure,

Can. J. Chem. Downloaded from www.nrcresearchpress.com by EESC ESCOLA DE ENGENHARIA on 09/08/12
For personal use only.

Can. J. Chem. Downloaded from www.nrcresearchpress.com by EESC ESCOLA DE ENGENHARIA on 09/08/12
For personal use only.

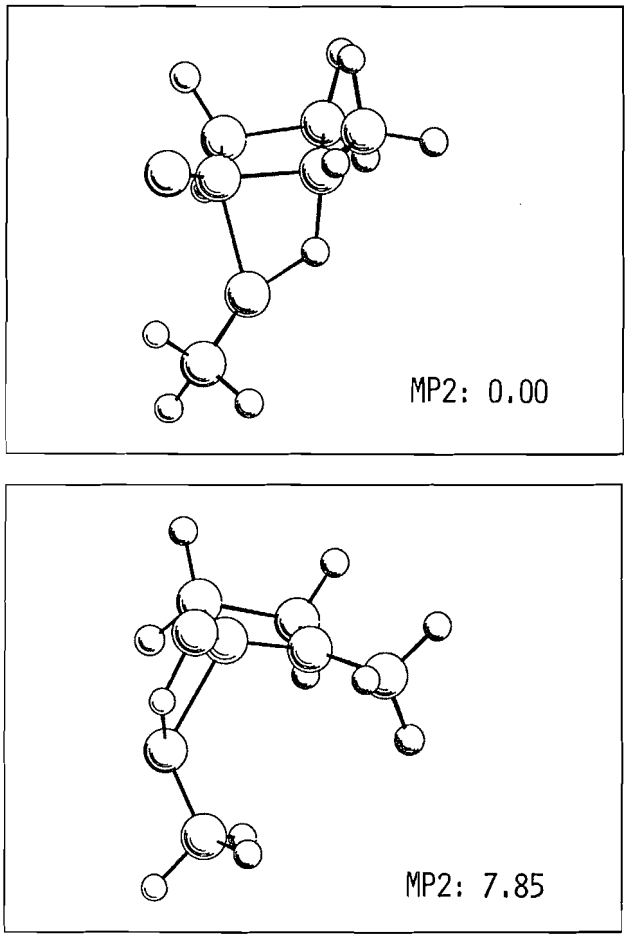

FIG. 18. Transition structures for the reaction of methanol with *N*-methylazetidinone via *N*-protonated (top) and *O*-protonated pathways (bottom). The structures are optimized at 3-21G; the relative energies are obtained at MP2/6-31G*//3-21G.

in Fig. 23. The two structures are obtained in entirely different ways, and we believe Fig. 23 suggests that the function of the enzyme is to orient the reacting molecules on the proper reaction coordinate for the most favourable chemical reaction. We also believe that this conclusion is consistent with the views expressed earlier (11).

Combining "fit" with "reactivity." Semiempirical calculations

We now wish to understand how differences in the fit to, and reactivity with, a penicillin-binding protein produces differences in antibacterial activity. We propose to compare the fits using the root-mean-square differences in the positions of the N-C=O and C-O-H atoms of different complexes, relative to their positions in a standard substrate. Reactivities could be compared if activation energies for the neutral alcoholysis of the β-lactam ring could be computed as a function of extensive structural variation of the system.

Ab initio calculations would not be practical in the latter case. Semiempirical computations would be feasible, but the results would have to be compatible with the three ab initio benchmarks determined above, viz., (*i*), in four-centred reactions of methanol with the β-lactam ring system, the *N*-protonated pathway is preferred over the *O*-protonated pathway; (ii) *O*-protonated attack from the convex face of a bicyclic system is

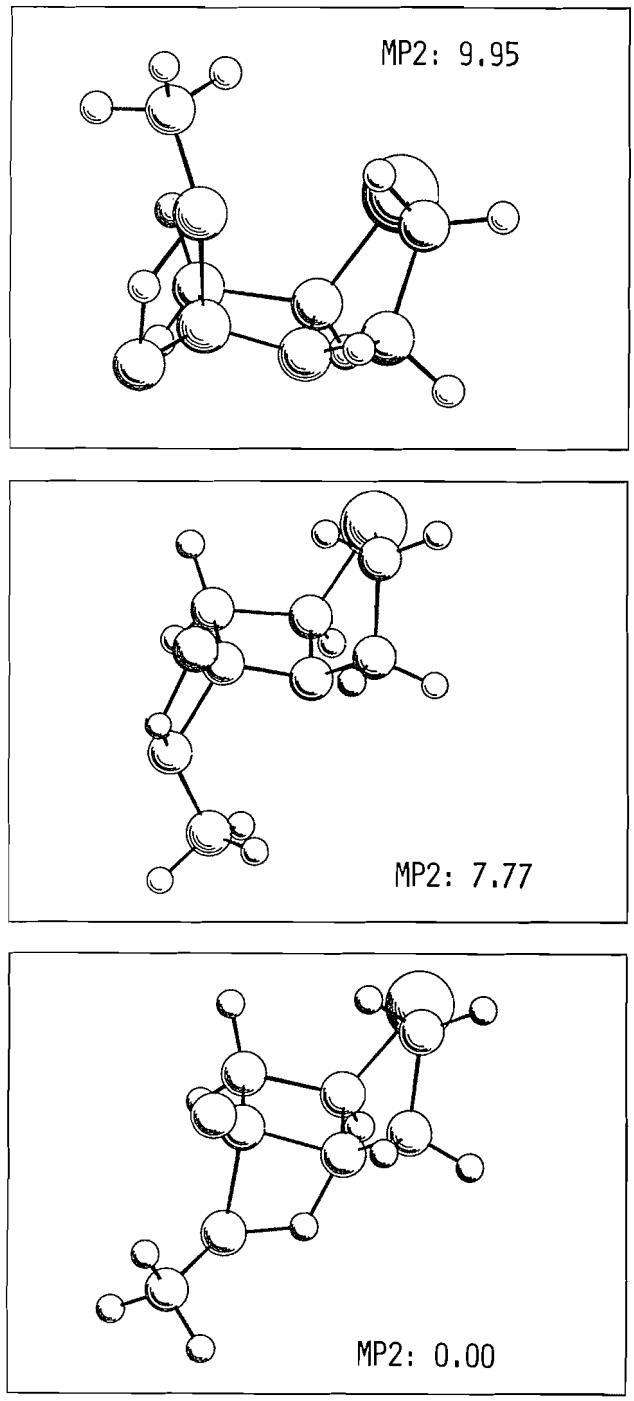

FIG. 19. Transition structures for the reaction of methanol with the penam ring system via *N*-protonated (bottom), *exo*-*O*-protonated (centre), and *endo*-*O*-protonated pathways (top). The structures are optimized at 3-21G*; the relative energies are obtained at MP2/6-31G*// 3-21G*.

preferred over attack from the concave face; (*iii*) in reactions that include water, the water has a catalytic effect.

As shown in Table 4 (55), of the several semiempirical possibilities, namely, AM1, MNDO, MNDO/M, PM3, and MINDO/3, only MINDO/3 reproduces the ab initio trends for the four-centred reactions. Accordingly, MINDO/3 was used for a systematic study of structure–reactivity relationships. Each line of Fig. 24 compares the relative reactivities of a series of related structures, expressed as $\Delta\Delta E^{\ddagger}$, to the parent penam

TABLE 4. Relative energies of four-centred transition structures for the reaction of methanol with a fused β-lactam-thiazolidine (kcal/mol)

Reaction	MP2/6-31G*//3-21G*	MINDO/3	MNDO	AM1	MNDO/M	PM3
N-attack	0.00	0.00	7.38	10.84	10.39	11.19
O-attack (convex)	7.77	4.80	0.00	0.00	0.00	0.00
O-attack (concave)	9.95	5.54	6.62	5.19	6.43	3.90

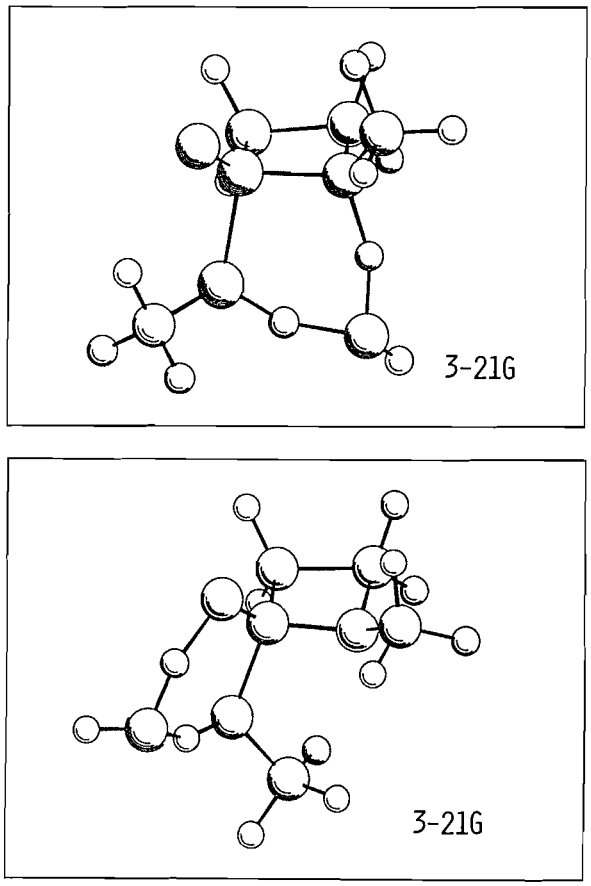

FIG. 20. Effect of water on the reaction of methanol with *N*-methylazetidinone by the *N*-protonated (top) and *O*-protonated pathways (bottom). The catalytic effect of the water molecule is 10 kcal/mol.

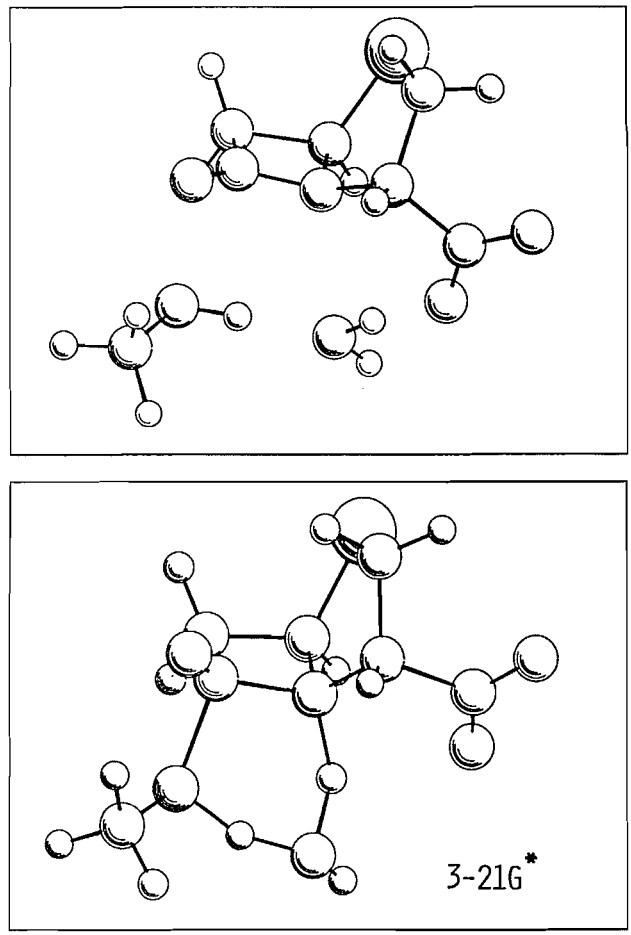

FIG. 21. Reactant complex and transition structure computed at 3-21G* for the attack of methanol upon 3α-carboxypenam, with catalysis by one water molecule.

ring system. Line 3 suggests that the attachment of a carboxyl group on the convex face, corresponding to the natural penicillin configuration, increases the reactivity, but the epimer is less reactive. Line 2 suggests that the Δ^3-cephem nucleus is inherently less reactive than the penicillin nucleus; isomerization of the double bond decreases the reactivity further. Attachment of the methyl groups decreases the reactivity, unless an α-carboxyl group is also present (line 4). The reactivities of the nucleus alone and of a fully functionalized penicillin are almost the same (line 5).

Turning to the effect of water, we found that only AM1 correctly predicts catalysis. All other semiempirical procedures predict inhibition. Accordingly, using AM1, we began to extend the data of Fig. 24 to include the effect of water (Fig. 25). The trends in lines 1 and 2 of Fig. 24 and 25 are the same. However, with the carboxypenams (line 3), the AM1 mechanism changes.[4]

Proceeding from the separated reactants, there are now two intermediates, two transition structures, and the hydrolyzed product. The first intermediate is the termolecular complex (Fig. 26). Although, superficially, the AM1 and ab initio complexes seem to resemble one another, they differ in an important way, because of a known artifact of AM1: with AM1, water molecules incorrectly tend to form bifurcated hydrogen bonds (64). Because of the bifurcated water–carboxylate geometry in the AM1 complex, what ensues resembles a proton shuttle triggered by the carboxylate anion (Fig. 27). One proton moves

[4]S. Wolfe and C.-K. Kim, Unpublished results.

Can. J. Chem. Downloaded from www.nrcresearchpress.com by EESC ESCOLA DE ENGENHARIA on 09/08/12
For personal use only.

Can. J. Chem. Downloaded from www.nrcresearchpress.com by EESC ESCOLA DE ENGENHARIA on 09/08/12
For personal use only.

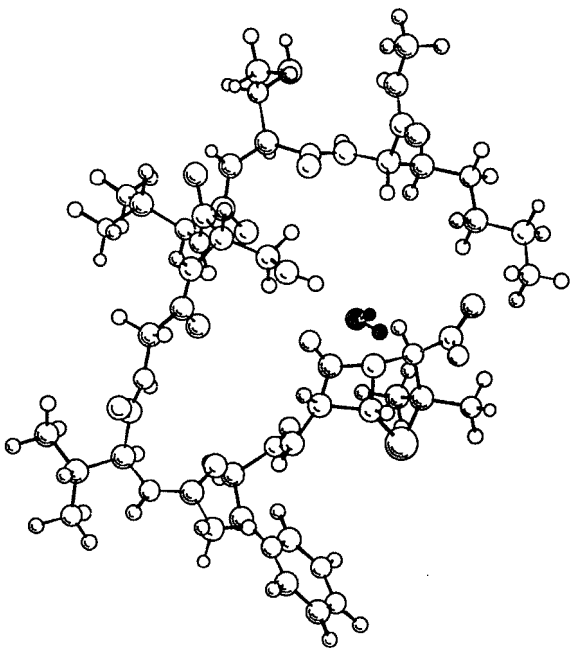

FIG. 22. Incorporation of one water molecule (filled circles) in the drug–receptor complex of Fig. 11.

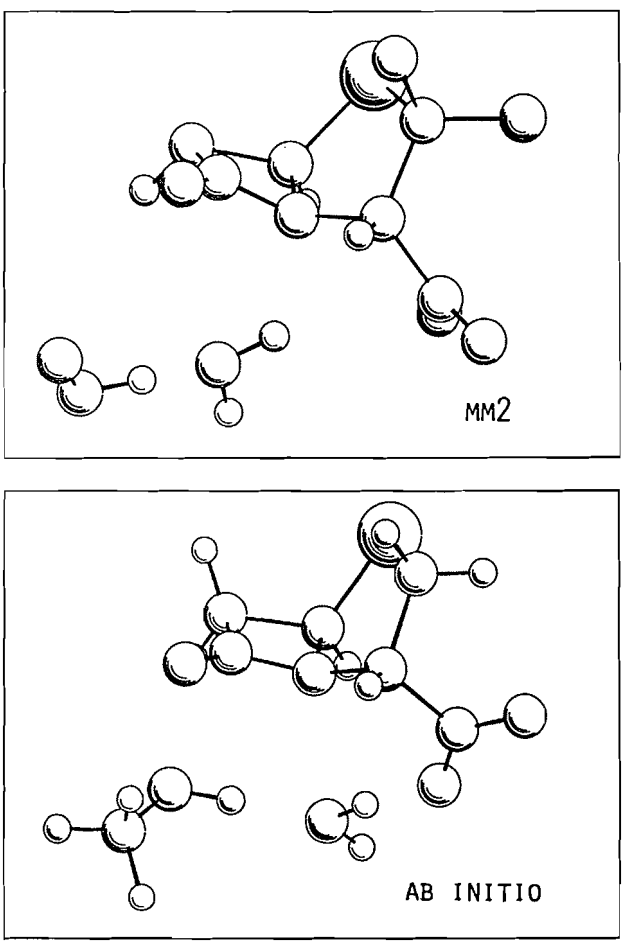

FIG. 23. A closeup view of the serine C-O-H, water, carboxypenam relationship in Fig 22 (top), and the ab initio reactant complex of Fig. 21 (bottom).

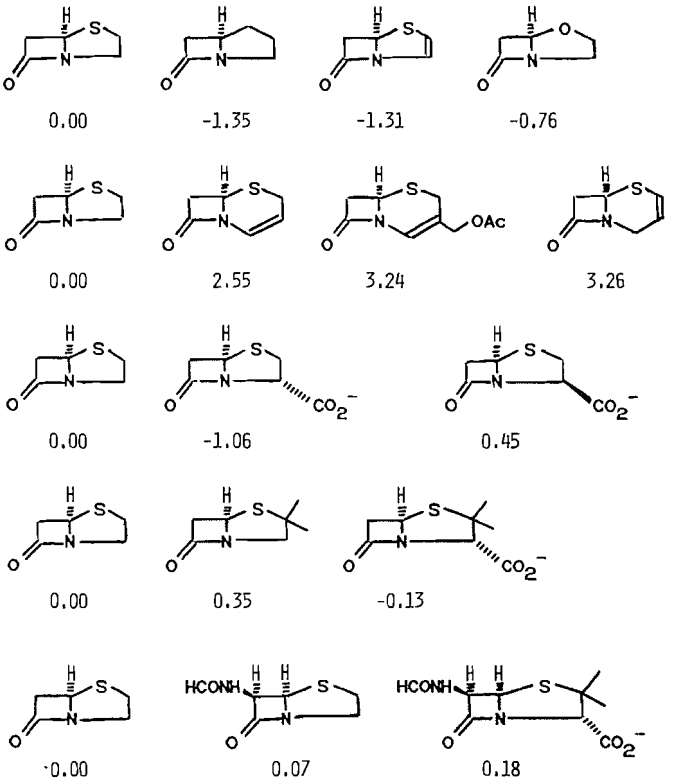

FIG. 24. Calculated MINDO/3 activation energies, relative to the penam skeleton, for the reaction of methanol with various β-lactam compounds via an *N*-protonated pathway.

TABLE 5. Calculated fits[a] and reactivities[b] relative to penicillin V (**4***a*) for the interaction of Δ^3-cephem V (**7**), 4α-Δ^2-cephem V (**8**), and 4α-Δ^2-cephem V (**16**) with the penicillin receptor model (Fig. 10)

Compound	$\Delta\Delta E^{\ddagger}$ (kcal/mol)	RMS (Å)
4*a*	0.00	0.000
7	2.81	0.103
8	1.94	0.684
16	4.65	0.252

[a]Refers to the root-mean-square deviation of the coordinates of the serine C-O-H and the β-lactam N—C=O in the complexes, from those of penicillin V.
[b]Refers to MINDO/3 calculations of the reactions of methanol with 3α-carboxypenam in the case of **4***a*, Δ^3-cephem-4-carboxylate in the case of **7**, 4α-Δ^2-cephemcarboxylate in the case of **8** and 4β-Δ^2-cephemcarboxylate in the case of **16**.

from water to the carboxylate anion, a second proton moves from methanol to water, and the methoxide ion adds to the carbonyl group to form a tetrahedral intermediate; the formation of this intermediate is rate determining. In the product-determining step, a proton is transferred from the carboxyl group to nitrogen, and a new bifurcated hydrogen bond is created.

Although the mechanism depicted in Fig. 27 seems interesting, the ab initio calculations described earlier show that a multistep mechanism does not occur. These findings reemphasize that semiempirical calculations on complex chemical processes must be interpreted with caution.

Table 5 summarizes the "fits" and "reactivities" exhibited by a Δ^3-cephem, a 4α-Δ^2-cephem, and a 4β-Δ^2-cephem, each carrying the penicillin V side chain, compared to penicillin V itself (55). The reactivities are based on MINDO/3 calculations of the four-centred processes.

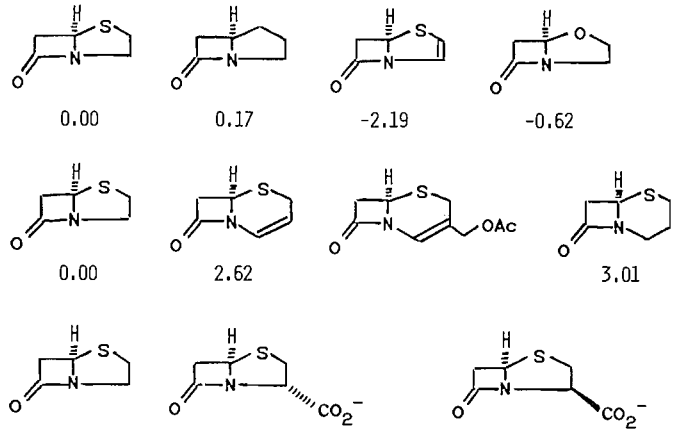

FIG. 25. Calculated AM1 activation energies, relative to the penam skeleton, for the reaction of methanol with various β-lactam compounds via an *N*-protonated pathway, with catalysis by one water molecule.

As mentioned earlier, the Δ^3-cephem is 50 times less active, and the 4α-Δ^2-cephem, which equilibrates with the Δ^3-cephem in solution, is 5000 times less active that the penicillin.The 4β epimer had been predicted by Noal Cohen to be active (65), but a compound of this type proved to be inactive when synthesized at Ciba–Geigy (66). According to Table 5, the Δ^3-cephem has a slightly different fit than the penicillin, and it is inherently less reactive. With a carboxyl group on the convex face of the molecule, the 4α-Δ^2-cephem is more reactive than the Δ^3-cephem, but it has a significantly poorer fit. In the 4β epimer, the fit is greatly improved, at the expense of an inherent decrease in reactivity.

Targeting the penicillin receptor

We believed that this kind of analysis provided, for the first time, sufficient insight into what is happening at the penicillin receptor to allow the design of new kinds of compounds having structures and reactivities targeted to this receptor. As depicted in Fig. 28, the target should have functional groups able to hydrogen-bond to the amino and carbonyl groups of the receptor model. Positioned between these two groups, and oriented properly in relation to them, the target structure should contain a functional group that will fit to the hydroxyl group of serine, and exhibit a four-centred relationship with this group.

On the basis of MINDO/3 calculations of four-centred methanolysis mechanisms, cyclic imines appeared to be significantly more reactive than β-lactams, and their reactivity could be varied by variation of the size of the ring and the nature of any additional substituents (67). Accordingly, we wished to synthesize a molecule possessing a cyclic C=N group, to react with the hydroxyl group of serine, a carboxyl group able to complex to the amino group of lysine, and a hydroxyl group positioned to hydrogen-bond to the carbonyl oxygen of the receptor model. Since the distances between these groups, and also the dihedral angles about the bonds separating them, were known from, eg. Fig. 11–13, potential candidates could be screened initially by inspection of molecular models. For promising structures, MM2 parameters were determined, and the compounds were calculated and docked to the model of the penicillin receptor.

The strategy led to **17** as a candidate for synthesis (67). However, model experiments soon revealed that **18** could, in principle, adopt any of three tautomeric structures: the imine **18***a*; the endocyclic enamine **18c**; or the exocyclic enamine **18***b*.Only enamine **18***c* could be detected by nmr in all solvents examined. Therefore it was necessary to block the formation of this tautomer. When this was accomplished by the introduction of methyl groups at C2, two tautomeric structures (e.g., **19***a* and **19b**) remained possible. Although the position of equilibrium between **19***a* and **19***b* was solvent dependent, the side chain of **19***b* is seen to be a masked aldehyde and, when **19***a* was generated from its silylated derivative, the compound proved to be highly unstable.

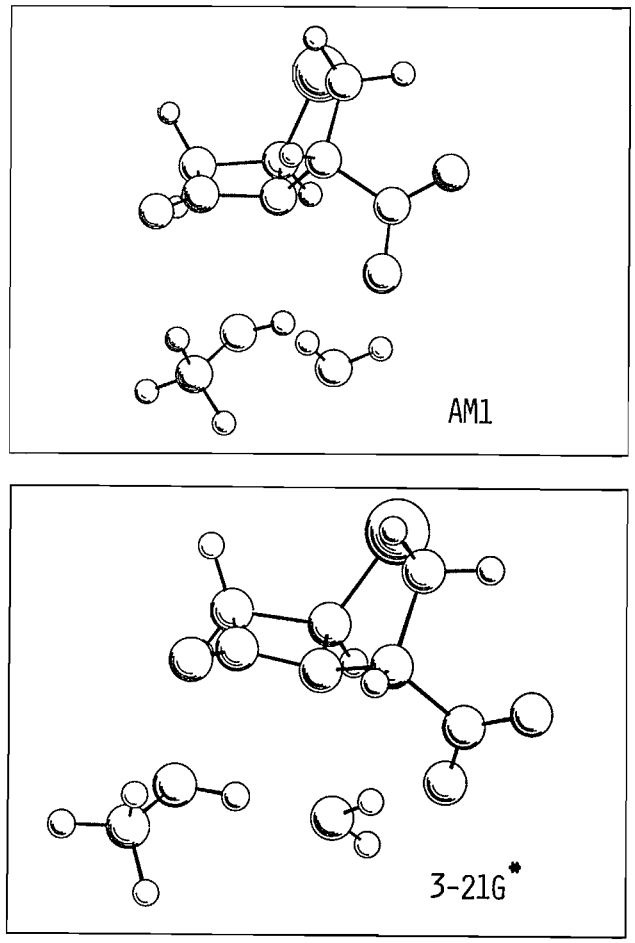

FIG. 26. Primary complex for the reaction of methanol with 3α-carboxypenam, catalyzed by one water molecule, as calculated by AM1 (top) and ab initio 3-21G* (bottom). The AM1 structure has bifurcated hydrogen bonds between the water molecule and a carboxylate oxygen.

Accordingly it became necessary to move the hydroxyl group one position further away from the nucleus. The resulting structure (**20**), for which Fig. 29 represents one conformation of the 3*S*, 8*R* isomer complexed to the model of the penicillin receptor, seemed to exhibit an acceptable fit.

The first synthesis of **20** began with the homoallylic alcohol **21** and D-serine. The alcohol was converted to the mercaptoketone **22** by successive silylation, permanganate oxidation, mesylation, and sulfuration. The amino acid was converted to the D-β-lactone **23** by the method of Vederas and co-workers (68). Condensation of **22**, as its lithium salt, with **23**, followed by deprotection with formic acid, then yielded 3*S*-**20** as a mixture of epimers at C8. As seen in Figs. 1 and 2, this material exhibited antibacterial activity versus *S. aureus* comparable to that of the Δ^2-cephem **8.**

Can. J. Chem. Downloaded from www.nrcresearchpress.com by EESC ESCOLA DE ENGENHARIA on 09/08/12
For personal use only.

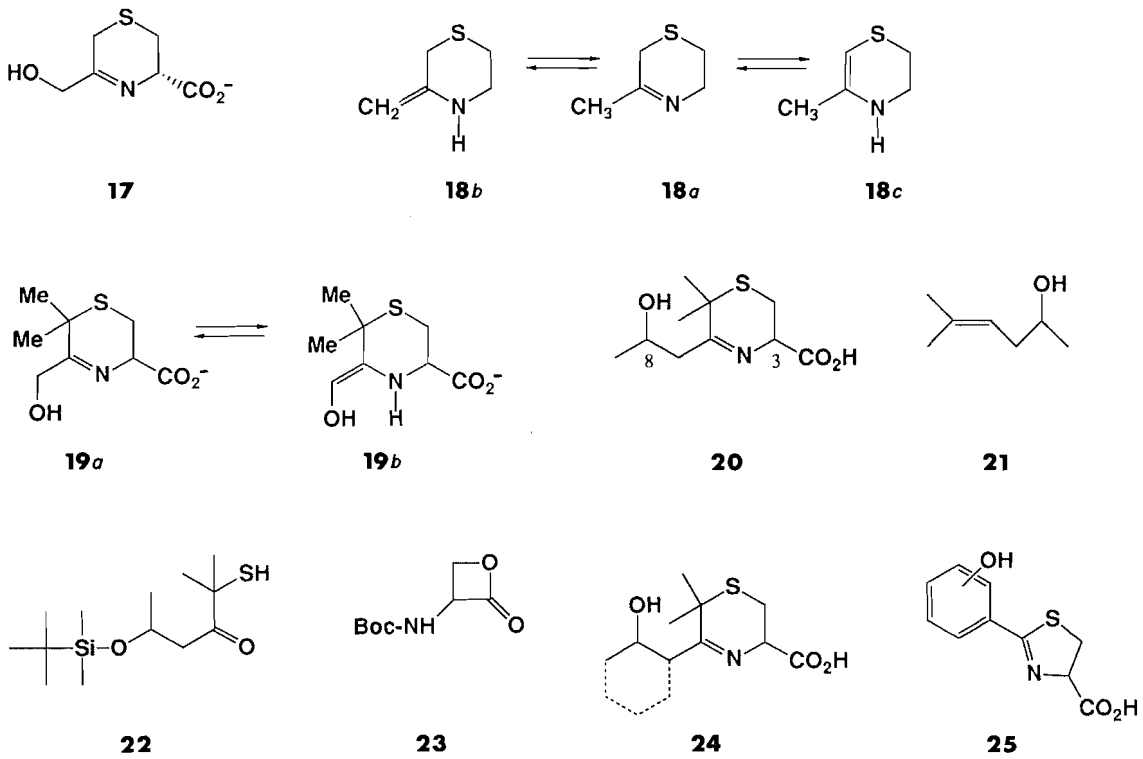

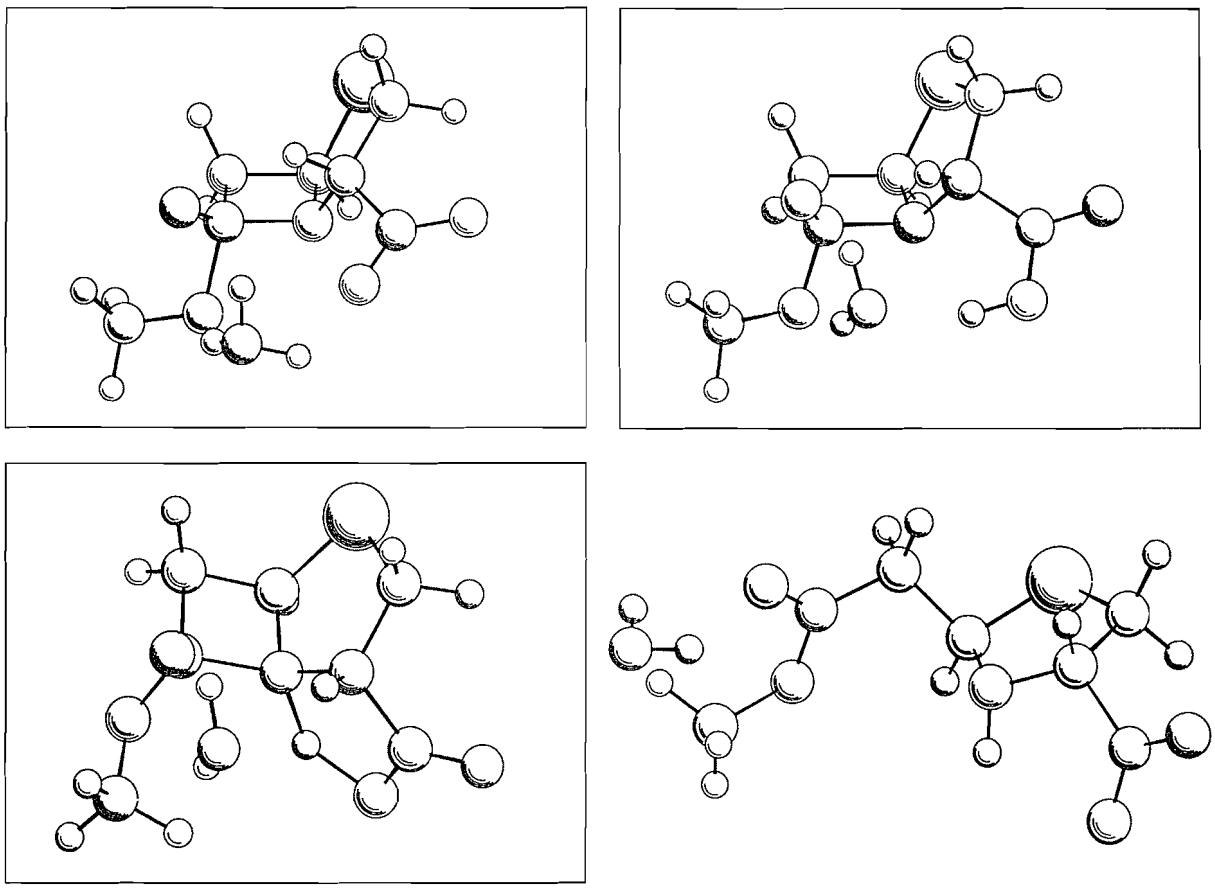

FIG. 27. AM1 coordinate for the reaction of methanol with 3α-carboxypenam, catalyzed by one water molecule. Starting with the bifurcated hydrogen-bonded complex of Fig. 26, the process proceeds over a rate-determining transition state (upper left), to an intermediate (upper right), and then over a product-determining transition state (lower left).

Can. J. Chem. Downloaded from www.nrcresearchpress.com by EESC ESCOLA DE ENGENHARIA on 09/08/12
For personal use only.

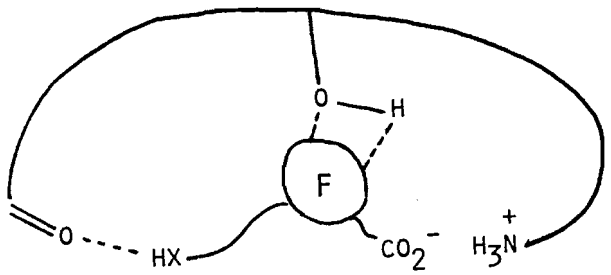

FIG. 28. Requirements for the design of a compound targeted to the penicillin receptor (see text).

Significantly, when the synthesis was repeated starting with L-serine, to yield 3*R*-**20** as a mixture of epimers at C8, this material was found to be inactive at the concentration employed in Fig. 2. This suggests that the activity observed in the 3*S* series is probably not the result of a generalized bactericidal effect of structure **20**, but, rather, is associated with a more specific "fit" to a receptor by the isomers having the 3*S* configuration

In subsequent work (69), sterospecific syntheses of the four stereoisomers of **20** were devised, and the activity of the 3*S* series and lack of activity in the 3*R* series were confirmed. The side-chain epimers were found to have comparable activity.

Although the activities of these first examples of designed antibacterial agents were low, we were encouraged by the fact that the activities of Δ^2-cephems are also low, but only one structural change is needed to convert the latter into the clinically important Δ^3-cephems. Therefore, the syntheses of 3*S*-**20** were scaled up to provide sufficient material for more detailed microbiological and toxicological studies. However, we now found that we could not crystallize the compounds. During these crystallization attempts, the nmr spectra became progressively more complex, *but the antibacterial activity remained.*

This situation was clarified by HPLC, which revealed that the degraded material consists of at least five components, each of which is active, and rapidly reequilibrates with the others. The major component was found to have structure **20** (67).

These complications led us to consider the general structure **24**, which can be regarded as a variant of **20** in which the labile aldol side chain is replaced by an aromatic ring or, as an alternative, a structure such as **25**. The latter compounds are accessible in one step, reaction of an aryl nitrile with cysteine (70), and Fig. 30 suggests that an ortho hydroxyl group would provide an acceptable fit to the receptor model. In Fig. 30, which refers to the L isomer of 2-(*o*-hydroxyphenyl)-thiazoline-4-carboxylic acid, the attack of the serine can be seen to be *syn* to the carboxyl group, as in penicillins and cephalosporins. In the case of the D isomer (not shown), the serine attack is *anti* to the carboxyl group. We found thiazolines having the general structure **25** to be stable for several days in water solvent, and antibacterial activity was observed with both enantiomers. The activity of the D isomer was comparable to that of 3*S*-**20**, but the L isomer appeared to be significantly more active.

We do not yet know the mechanisms of action of **20** and **25**, and will have to be prepared for the possibility that the reasoning which led to the syntheses of these compounds is flawed. However, the hypothesis depicted in Fig. 5 was also flawed, but this led to sulfur-free penicillins, and resulted in the discovery of the oxacephems. If, with the aid of the current theoretical model, we discovered (or rediscovered (71)) a useful lead structure, the model will have served its purpose. Thus, after our theoretical and experimental work on the isomers of **25** was complete, we learned that the L isomer is a known compound, dihydroeruginoic acid, which has been patented as a medicinal agent against Gram positive fungi, moulds, and newcastle disease virus (71).

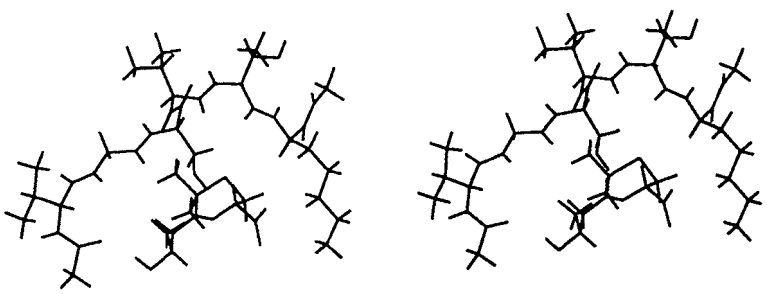

FIG. 29. Stereoscopic view of **20** complexed to the receptor model. The hydroxyl group of serine is positioned over the C=N of **20**.

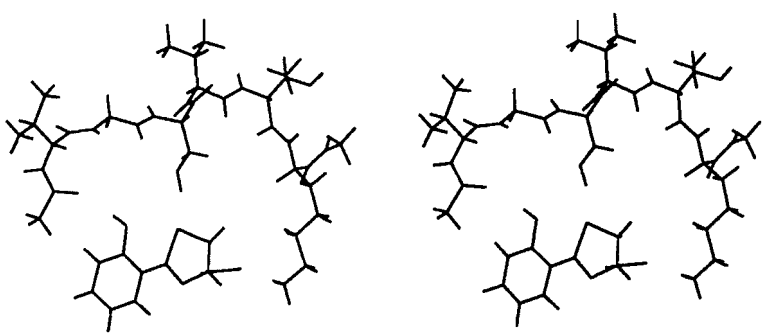

FIG. 30. Stereoscopic view of L-**25** complexed to the receptor model, which suggests that an *ortho* hydroxyl group in the aromatic ring provides an acceptable fit.

Can. J. Chem. Downloaded from www.nrcresearchpress.com by EESC ESCOLA DE ENGENHARIA on 09/08/12
For personal use only.

Can. J. Chem. Downloaded from www.nrcresearchpress.com by EESC ESCOLA DE ENGENHARIA on 09/08/12
For personal use only.

Acknowledgments

The work reported here has been funded at various times by Bristol Laboratories, National Research Council (NRC) and Natural Sciences and Engineering Research Council (NSERC) Operating and Equipment Grants, the Atkinson Foundation of Toronto, the Killam Foundation, Robert Bender, Queen's University, and Simon Fraser University.

I sincerely thank all of the colleagues and co-workers, named in the text and in the references, who contributed to the development of these ideas during a period of 33 years.

I thank Bob McIntosh, Don Heyding, Duncan Sinclair, and the staff of the Office of Research Services at Queen's University for their many years of friendship and support.

I am particularly indebted to Cam Oehlschlager. In 1990 he persuaded his colleagues in the Chemistry Department and the senior administrators of Simon Fraser University that I was still capable of useful research. He then built for me a beautiful office and laboratory, provided me with a computer 30 times more powerful than the one I had been using, and placed me among an exciting and dedicated group of young organic, inorganic, polymer, and biochemistry faculty, with whom I have been able to interact extensively. Much of the recent work I have described was carried out in the intensive research environment that can now be found at SFU.

1. T. Takeuchi, T. Hikiji, K. Nitta, S. Yamazuki, S. Abe, H. Takayama, and H. Umezawa. J. Antibiot. Ser. A, **10**, 107 (1957).
2. M.J. Cron, D.L. Evans, F.M. Palermiti, D.F. Whitehead, I.R. Hooper, P. Chü, and R.U. Lemieux. J. Am Chem. Soc. **80**, 4741 (1958).
3. F.R. Batchelor, F.P. Doyle, J.H.C. Nayler, and G.N. Rolinson. Nature, **183**, 257 (1959).
4. A. Gourevitch, S. Wolfe, and J. Lein. Antimicrob. Agents Chemother. 576 (1961).
5. E.P. Abraham and G.G.F. Newton. Biochem. J. **79**, 373 (1961).
6. J.P. Duguid. Edinburgh Med. J. **53**, 401 (1945); J.R. Edwards and J.D. Park J. Bacteriol. **99**, 459 (1969); H.J. Rogers. Nature, **213**, 31 (1969).
7. H.R.V. Arnstein and D. Morris. Biochem. J. **76**, 357 (1960); P.A. Fawcett, P.B. Loder, M.J. Duncan, T.J. Beesley, and E.P. Abraham. J. Gen. Microbiol. **79**, 293 (1973); G. Banko, A.L. Demain, and S. Wolfe. J. Am. Chem. Soc. **109**, 2858 (1987).
8. J. Hoogmartens, E. Roets, G. Janssen, and H. Vanderhaeghe. J. Chromatog. **244**, 299 (1982).
9. L.P. Marrelli. *In* Cephalosporins and penicillins. Chemistry and biology. *Edited by* E.H. Flynn. Academic Press, New York. 1972. p. 609.
10. E. Fisher. Ber. Dtsch. Chem. Ges. **27**, 2985 (1894).
11. *(a)* D.E. Koshland, Jr. J. Theor. Biol. **2**, 75 (1962); *(b)* F.M. Menger. Tetrahedron, **39**, 1013 (1983); *(c)* Acc. Chem. Res. **26**, 206 (1993); *(d)* W.P. Jencks. Catalysis in chemistry and enzymology. Dover, New York. 1987. p.19; *(e)* L. Tenud, S. Farook, J. Seibl, and A. Eschenmoser. Helv. Chim. Acta, **53**, 2059 (1970); *(f)* J.F. King and M.J. McGarrity. J. Chem. Soc. Chem. Commun. 1140 (1979); *(g)* R. Lok and J.K. Coward. Bioorg. Chem. **5**, 169 (1975); *(h)* P. Beak. Acc. Chem. Res. **25**, 215 (1992).
12. J.-M. Frère and B. Joris. Crit. Rev. Microbiol. **11**, 299 (1985).
13. J.C. Sheehan and K.R. Henery-Logan. J. Am. Chem Soc. **81**, 5838 (1959).
14. R. Busson, P.J. Claes, and H. Vanderhaeghe. J. Org. Chem. **41**, 2556 (1976).
15. S. Wolfe and S.K. Hasan. Can. J. Chem. **48**, 3572 (1970).
16. G.J. Pitt. Acta Crystallogr. 770 (1952).
17. T. Leigh. J. Chem. Soc. 3616 (1965).
18. C.S. Cummins and H. Harris. J. Gen. Microbiol. **14**, 583 (1956); J.L. Strominger, J.T. Park, and R.E. Thompson J. Biol. Chem. **234**, 3263 (1959); H.R. Perkins and H.J. Rogers. Biochem. J. **72**, 647 (1959).
19. J.T. Park. J. Biol. Chem. **194**, 855 (1952); **194**, 877 (1952); **194**, 897 (1952).
20. J.F. Collins and M.H. Richmond. Nature, **195**, 142 (1962).
21. S. Wolfe, W.S. Lee, G. Kannengiesser, and J.-B. Ducep. Can. J. Chem. **50**, 2894 (1972); S. Wolfe, W.S. Lee, J.-B. Ducep, and G. Kannengiesser. Can. J. Chem. **50**, 2898 (1972); S. Wolfe, J.-B. Ducep, G. Kannengiesser, and W.S. Lee. Can. J. Chem. **50**, 2902 (1972); S. Wolfe and M.P. Goeldner. Tetrahedron Lett. 5131 (1973); S. Wolfe, J.-B. Ducep, K.-C. Tin, and S.-L. Lee. Can. J. Chem. **52**, 3996 (1974); S. Wolfe, S.-L. Lee, J.-B. Ducep, G. Kannengiesser, and W.S. Lee. Can. J. Chem. **53**, 497 (1975).
22. M. Gomberg. J. Am. Chem. Soc. **22**, 757 (1900).
23. I. Ernest, J. Gosteli, C.W. Greengrass, W. Holick, D.E. Jackman, H.R. Pfaendler, and R.B. Woodward. J. Am. Chem. Soc. **100**, 8214 (1978).
24. G. Albers-Schonberg, B.H. Arison, O.D. Hensens, J. Hirshfield, K. Hoogsteen, E.A. Kaczka, R.E. Rhodes, J.S. Kahan, F.M. Kahan, R.W. Ratcliffe, E. Walton, L.J. Ruswinkle, R.B. Morin, and B.G. Christensen. J. Am. Chem. Soc. **100**, 6481 (1978).
25. T.T. Howarth, A.G. Brown, and T.J. King. Chem. Commun. 266 (1976).
26. H. Aoki, H. Sakai, M. Kohsaka, T. Konomi, J. Hosoda, Y. Kubochi, E. Eguchi, and H. Imanaka. J. Antibiot. **29**, 492 (1976).
27. A. Imada, K. Kitano, K. Kitaka, M. Muroi, and M. Asai. Nature, **289**, 590 (1981); R.B. Sykes, C.M. Cimarusti, D.P. Bonner, K. Bush, D.M. Floyd, N.H. Georgopapadakou, W.H. Koster, W.C. Liu, W.L. Parker, P.A. Principe, M.L. Rathnum, W.A. Slwsarchyk, W.H. Treo, and T.S. Wells. Nature, **291**, 489 (1981).
28. W. Nagata. *In* Current trends in organic synthesis. *Edited by* H. Nozaki. Pergamon Press, New York. 1983. p. 83.
29. D.J. Waxman and J.L. Strominger. Annu. Rev. Biochem. **52**, 825 (1983).
30. J.-M. Ghuysen, J.-M. Frère, M. Leyh-Bouille, and O. Dideberg. *In* β-Lactam antibiotics. Mode of action, new developments, and future prospects. *Edited by* M.R.J. Salton and G.D. Shockman. Academic Press, New York. 1981. p. 127; J.-M. Ghuysen. Annu. Rev. Microbiol. **45**, 37 (1991).
31. J.-M Frère, B. Joris, F. Jacob, A. Matagne, D. Monnaie, M. Jamin, M. Hadonou, C. Bourguignon-Bellefroid, L. Varetto, J.-M. Wilkin, A. Dubus, C. Damblon, M. Adam, P. Ledent, F. De Meester, and M. Galleni. *In* Bioorganic chemistry in healthcare and technology. *Edited by* U.K. Pandit and F.C. Alderweireldt. Plenum Press, New York. 1991. p. 161.
32. J.S. Anderson, M. Matsuhashi, M.A. Haskin, and J.L. Strominger. Proc. Natl. Acad. Sci. U.S.A. **53**, 881 (1965); M. Matsuhashi, C.P. Dietrich, and J.L. Strominger. Proc. Natl. Acad. Sci. U.S.A. **54**, 587 (1965).
33. D.J. Tipper and J.L. Strominger. Proc. Natl. Acad. Sci. U.S.A. **54**, 1133 (1965).
34. H. Christensen, M.T. Martin, and S.G. Waley. Biochem. J. **266**, 853 (1990).
35. R.A. Nicholas, J.L. Strominger, H. Suzuki, and Y. Hirota. J. Bacteriol. **164**, 456 (1985); J.-M. Ghuysen, J.-M. Frère, M. Leyh-Bouille, M. Nguyen-Distèche, and J. Coyette. Biochem J. **235**, 159 (1986); B. Joris, P. Ledent, O. Dideberg, E. Fonzé, J. Lamotte-Brasseur, J.A. Kelly, J.-M. Ghuysen, and J.-M. Frère. Antimicrob. Agents Chemother. **35**, 2294 (1991).
36. J.A. Kelly, J.R. Knox, P.C. Meows, G.J. Hite, J.B. Bartolone, H. Zhao, B. Joris, J.-M. Frère, and J.-M. Ghuysen, J. Biol. Chem. **260**, 6449 (1985); O. Dideberg, P. Charlier, J.-P. Wéry, P. Dehottay, J. Dusart, T. Erpicum, J.-M. Frère, and J.-M. Ghuysen. Biochem J. **245**, 911 (1987); O. Herzberg and J. Moult. Science, **236**, 694 (1987); D.C. Phillips, A. Cordero-Borboa, B.J. Sutton, and R.J. Todd. Pure Appl. Chem. **59**, 279 (1987); O. Herzberg, G. Kapadia, B. Blanco, T.S. Smith, and A. Coulson. Biochemistry, **30**, 9503 (1991); J.R. Knox and P.C. Moews. J. Mol. Biol. **220**, 435 (1991); O. Herzberg. J. Mol. Biol. **217**, 701 (1991); C.

Can. J. Chem. Downloaded from www.nrcresearchpress.com by EESC ESCOLA DE ENGENHARIA on 09/08/12
For personal use only.

Jelsch, F. Lenfant, J.M. Masson, and J.P. Samama. FEBS Lett. **299**, 135 (1992).
37. L.M. Ellerby, W.A. Escobar, A.L. Fink, C. Mitchinson, and J.M. Wells. Biochemistry, **29**, 5797 (1990); W.A. Escobar, A.K. Tan, and A.L. Fink. Biochemistry, **30**, 10783 (1991); L. Varetto, F. de Meester, D. Monnaie, J. Marchand-Brynaert, G.Dive, F. Jacob, and J.-M. Frère. Biochem. J. **278**, 801 (1991); F. Jacob-Dubuisson, J. Lamotte-Brasseur, O. Dideberg, B. Joris, and J.-M. Frère. Protein Eng. **4**, 811 (1991); H. Adachi, M. Ishiguro, S. Imajoh, T. Ohta, and H. Matsuzawa. Biochemistry, **31**, 430 (1992); J. Lamotte-Brasseur, F. Jacob-Dubuisson, G. Dive, J.-M. Frère, and J.-M. Ghuysen. Biochem. J. **282**, 189 (1992); N.C. Strynadka, H. Adachi, S.E. Jensen, K. Johns, A. Sielecki, C. Betzel, K. Sutoh, and M.N.G. James. Nature, **359**, 700 (1992); J.R. Knox, P.C. Moews, W.A. Escobar, and A.L. Fink. Protein Eng. **6**, 11 (1993).
38. L. Varetto, J.-M. Frère, M. Nguyen-Distèche, J.-M. Ghuysen, and C. Houssier. Eur. J. Biochem. **162**, 525 (1987).
39. J. Kraut. Annu. Rev. Biochem. **46**, 331 (1977); T.A. Steitz and R.G. Shulman. Annu. Rev. Biophys. Bioeng. **11**, 419 (1982); R.L. Schowen. *In* Molecular structure and energetics. *Edited by* J.F. Liebman and A. Greenberg. VCH Publishers, New York. 1988. p.119.
40. R. Henderson. J. Mol. Biol. **54**, 341 (1970); S.N. Rao, U.C. Singh, P.A. Bash, and P.A. Kollman. Nature, **328**, 551 (1987); B.P. Murphy and R.F. Pratt. Biochem. J. **256**, 669 (1988); R. Ménard, J. Carrière, P. Laflamme, C. Plouffe, H.E. Khouri, T. Vernet, D.C. Tessier, D.Y. Thomas, and A.C. Storer. Biochemistry, **30**, 8924 (1991).
41. D.B. Boyd, J.N. Snoddy, and H.-S. Lin. J. Comput. Chem. **12**, 635 (1991).
42. A.M. Hadonou, M. Jamin, M. Adam, B. Joris, J. Dusart, J.-M. Ghuysen, and J.-M. Frère. Biochem. J. **282**, 495 (1992).
43. E. Buncel, E.A. Symons, and A.W. Zabel. Chem. Commun. 173 (1965).
44. A. Rauk, E.Buncel, R.Y. Moir, and S. Wolfe. J. Am. Chem. Soc. **87**, 5498 (1965); S. Wolfe and A. Rauk. Chem. Commun. 778 (1966).
45. A. Rauk, S. Wolfe, and I.G. Csizmadia. Can. J. Chem. **47**, 113 (1969); S. Wolfe, A. Rauk, L.M. Tel, and I.G. Csizmadia. J. Chem. Soc. B, 136 (1971); S. Wolfe. Acc. Chem. Res. **5**, 102 (1972); M.-H. Whangbo, H.B. Schlegel, and S. Wolfe. J. Am Chem. Soc. **99**, 1296 (1977); S. Wolfe, M.-H. Whangbo, and D.J. Mitchell. Carbohydr. Res. **69**, 1 (1979); M.-H. Whangbo and S. Wolfe. Isr. J. Chem. **20**, 36 (1980); S. Wolfe, D.J. Mitchell, and H.B. Schlegel. J. Am. Chem. Soc. **103**, 7692 (1981); **103** 7694 (1981); S. Wolfe, A. Stolow, and L.A. LaJohn. Can. J. Chem. **62**, 1470 (1984).
46. N.L. Allinger and Y. Yuh. QCPE, **12**, 395 (1980).
47. F.A. Momany, R.F. McGuire, A.W. Burgess, and H.A. Scheraga. J. Phys. Chem. **79**, 2361 (1975); C. Pottle, M.S. Pottle, R.W. Tuttle, R.J. Kinch, and H.A. Scheraga. J. Phys. Chem. **87**, 1883 (1983); ECEPP, QCPE No. 454, Bloomington, Ind.
48. C.E. Blom and C. Altona. Mol. Phys. **31**, 1377 (1976); M.J.S. Dewar, G.P. Ford, M.L. McKee, H.S. Rzepa, W. Thiel, and Y. Yamaguchi, J. Mol. Struct. **43**, 135 (1978); P. Pulay, G. Fogarasi, G. Pongor, J.E. Boggs, and A. Vargha. J. Am. Chem. Soc. **105**, 7037 (1983); G. Fogarasi and P. Pulay. Annu. Rev. Phys. Chem. **35**, 191 (1984).
49. B.R. Brooks, R.E. Bruccolleri, B.D. Olafson, D.J. States, S. Swaminathan, and M. Karplus. J. Comput. Chem. **4**, 187 (1983).
50. P.K. Weiner and P.A. Kollman. J. Comput. Chem. **2**, 287 (1981); S.J. Weiner, P.A. Kollman, D.A. Case, U.C. Singh, C. Ghio, G. Alagona, S. Profeta, Jr., and P. Weiner. J. Am. Chem. Soc. **106**, 765 (1984); S.J. Weiner, P.A. Kollman, D.T. Nguyen, and D.A. Case, J. Comput. Chem. **7**, 230 (1986).
51. F. Mohamadi, N.G.J. Richards, W.C. Guida, R. Liskamp, M. Lipton, C. Caufield, G. Chang, T. Hendrickson, and W.C. Still. J. Comput. Chem. **11**, 440 (1990).
52. J.-H. Lii, S. Gallion, C. Bender, H. Wikström, N.L. Allinger, K.M. Flurchick, and M.M. Teeter. J. Comput. Chem. **10**, 503 (1989).
53. S. Wolfe, D.F. Weaver, and K. Yang. Can. J. Chem. **66**, 2687 (1988).
54. S. Wolfe, M. Khalil, and D.F. Weaver. Can. J. Chem. **66**, 2715 (1988).
55. S. Wolfe and T. Hoz. Can. J. Chem. **72**, 1044 (1994).
56. S. Wolfe, S. Bruder, D.F. Weaver, and K. Yang. Can. J. Chem. **66**, 2703 (1988).
57. H. Beierbeck and R.U. Lemieux. Can. J. Chem. **68**, 820 (1990).
58. S. Wolfe, K. Yang, and M. Khalil. Can. J. Chem. **66**, 2733 (1988).
59. J.A. Kelly. *In* The target of penicillin. *Edited by* R. Hakenbeck, J.-V. Höltje, and H. Labischinski. Walter de Gruyter, Berlin. 1983. p. 387.
60. J.A. Kelly, J.R. Knox, H. Zhao, J.-M. Frère, and J.-M. Ghuysen. J. Mol. Biol. **209**, 281 (1989).
61. H.B. Bürgi, J.D. Dunitz, and E. Shefter. J. Am. Chem. Soc. **95**, 5066 (1973); H.B. Bürgi and J.D. Dunitz. Acc. Chem. Res. **16**, 153 (1983).
62. M.I. Page Acc. Chem. Res. **17**, 144 (1984); M.I. Page. Adv. Phys. Org. Chem. **23**, 165 (1987).
63. S. Wolfe, C.-K. Kim, and K. Yang. Can. J. Chem. **72**, 1033 (1994).
64. C.J. Marsden, B.J. Smith, J.A. Pople, H.F. Schaefer III, and L. Radom. J. Chem. Phys. **95**, 1825 (1991).
65. N.C. Cohen. J. Med. Chem. **26**, 259 (1983).
66. N.C. Cohen, I. Ernest, H. Fritz, H. Fuhrer, G. Rihs, R. Scartazzini, and P. Wirz. Helv. Chim. Acta, **70**, 1967 (1987).
67. S. Wolfe, H. Jin, K. Yang, C.K. Kim, and E. McEachern. Can. J. Chem. **72**, 1051 (1994).
68. L.D. Arnold, R.G. May, and J.C. Vederas. J. Am. Chem. Soc. **110**, 2237 (1988).
69. S. Wolfe, C. Zhang, B.D. Johnston, and C.K. Kim. Can. J. Chem. **72**, 1066 (1994).
70. G.L. Eggleton, D.R. Bushman, D.W. Whitlock, D.K. Pugh, and K.L. Chance. J. Chem. Eng. Data, **29**, 351 (1984).
71. M. Matsui and Y. Yamada. Chem. Abstr. **79**, 92205c (1973).

Ab initio molecular orbital calculations on the neutral hydrolysis and methanolysis of azetidinones, including catalysis by water. Relationship to the mechanism of action of β-lactam antibiotics

SAUL WOLFE,[1,2] CHAN-KYUNG KIM,[2] AND KIYULL YANG[3]

Department of Chemistry, Queen's University, Kingston, ON K7L 3N6, Canada, and Department of Chemistry, Simon Fraser University, Burnaby, BC V5A 1S6, Canada

Received August 24, 1993

SAUL WOLFE, CHAN-KYUNG KIM, and KIYULL YANG. Can. J. Chem. **72**, 1033 (1994).

The docking of penicillins to a computer model of the active site of the penicillin-binding protein of *Streptomyces* R61 produces structures that exhibit a four-centred interaction between the O-H of a serine residue and the (O)C-N of the β-lactam ring. If such a structure is a stationary point on the reaction coordinate for the acylation of the serine OH by the β-lactam carbonyl group, the acylation mechanism would appear to consist of O—C and H—N bond formation, concerted with the cleavage of the C—N bond. The existence of this "N-protonation" mechanism, and the energetics of this mechanism in comparison to the usual "O-protonation" pathway in which proton transfer to oxygen and addition to the carbonyl group *precede* C—N bond fission, have been examined by ab initio MO calculations on the neutral hydrolysis and methanolysis of *N*-methylazetidinone, penam, and penam-3α-carboxylate. The geometries of reactants and transition structures have been optimized fully at the 3-21G or 3-21G* levels, the existence of transition structures has been confirmed by vibrational analysis, thermochemical data have been computed, and the one-point energies of all structures have been determined at the MP2/6-31G* level. The N-protonation mechanism is found to exist with all substrates, and to be preferred over the O-protonation mechanism by over 5 kcal/mol. The activation energies are 5 kcal/mol lower in the bicyclic penam than in the monocyclic *N*-methylazetidinone, and attack from the convex face is preferred over attack from the concave face. The introduction of a 3α-carboxylate group, as in penicillin itself, results in an additional 5 kcal/mol decrease in activation energy. The origins of these trends are discussed. Since the active sites of some penicillin-recognizing enzymes contain at least one water molecule, catalysis of the foregoing reactions by one water molecule has also been examined. The catalysis amounts to over 10 kcal/mol in both the N- and O-protonation mechanisms, and the preference for the N-protonation mechanism is maintained. It is concluded that penicillin complexes to its receptor in such a manner as to allow acylation of the active site serine residue to proceed via the energetically most favourable mechanism.

SAUL WOLFE, CHAN-KYUNG KIM et KIYULL YANG. Can. J. Chem. **72**, 1033 (1994).

L'arrimage de pénicillines au modèle sur ordinateur du site actif de la protéine de liaison de la pénicilline du *Streptomyces* R61 fournit des structures qui présentent une interaction à quatre centres entre le O-H de la sérine et le (O)C-N du noyau β-lactame. Si une telle structure est un point stationnaire sur les coordonnées réactionnelles de l'acylation du OH de la sérine par le groupe carbonyle du β-lactame, il semblerait que le mécanisme d'acylation comporterait la formation de liaisons O—C et H—N concertée avec un clivage de la liaison C—N. L'existence de ce mécanisme de «N-protonation» et les énergies impliquées dans ce mécanisme, par comparaison avec la voie usuelle de «O-protonation» dans laquelle le transfert d'un proton à l'oxygène et l'addition sur le group carbonyles *précèdent* la fission de la liaison C—N, ont été étudiées par des calculs d'OM ab initio pour l'hydrolyse neutre et pour la méthanolyse de la *N*-méthylazétidinone, du péname et du péname-3α-carboxylate. On a pleinement optimisé les géométries de réactifs et des structures de transition aux niveaux 3-21G ou 3-21G*, on a confirmé l'existence de structures de transition par une analyse vibrationnelle, on a calculé les données thermochimiques et on a déterminé les énergies ponctuelles de toutes les structures au niveau MP2/6-31G*. On a trouvé que le mécanisme de N-protonation existe pour tous les substrats et qu'il est préféré au mécanisme par O-protonation par plus de 5 kcal/mol. Les énergies d'activation sont 5 kcal/mol plus faible dans le péname bicyclique que dans la N-méthylazétidinone monocyclique et que l'attaque par la face convexe est préférée à l'attaque par la face concave. L'introduction d'un groupe carboxylique en position 3α, comme il en existe un dans la pénicilline elle-même, réduit encore une fois l'énergie d'activation par un autre 5 kcal/mol. On discute des origines de ces tendances. Puisque les sites actifs de certains enzymes qui reconnaissent les pénicillines contiennent au moins une molécule d'eau, on a aussi examiné la catalyse par une molécule d'eau des réactions mentionnées plus haut. La catalyse par l'eau des mécanismes de N- et de O-protonation correspond à 10 kcal/mol et la préférence pour le mécanisme par N-protonation est maintenu. On en conclut que la pénicilline se complexe à son récepteur d'une façon telle que l'acylation du site actif de la sérine pourra se faire par le mécanisme énergétiquement le plus favorable.

[Traduit par la Rédaction]

Introduction

β-Lactam antibiotics function by covalent bonding to the active site serine residue of one or more of a group of enzymes termed penicillin-binding proteins (PBP's) (1). These enzymes serve to complete bacterial cell wall synthesis by a cross-linking of peptidoglycan chains, and they are essential to the cells (2).

The simplest kinetic description of the reaction between a PBP and a β-lactam antibiotic is given in eq. [1], where **1** is a generalized structure. Since the PBP is regenerated in the deacylation step, useful antibacterial activity is considered (3) to require $k_3/K \geq 1000\ M^{-1}\ s^{-1}$, and $k_4 \leq 1 \times 10^{-4}\ s^{-1}$.

Using the serine- and lysine-containing active site hexapeptide of a D-alanyl carboxypeptidase-transpeptidase of *Streptomyces* R61 (4) as a model of a PBP, and a test series of nine penicillins (**2**), ranging from the highly active penicillin G (R = $PhCH_2$, R′ = H) to the biologically inactive 6α-methylpenicillin G (R = $PhCH_2$, R′ = Me), we have studied the complexation step of eq. [1] (5). In each case, the assumptions that the lock and key

[1]Canada Council Killam Research Fellow, 1990–1992.

[2]Simon Fraser University.

[3]Present address: Department of Chemical Education, Gyeongsang National University, Chinju 660-701, Republic of Korea.

Can. J. Chem. Downloaded from www.nrcresearchpress.com by ESC ESCOLA DE ENGENHARIA on 09/08/12
For personal use only.

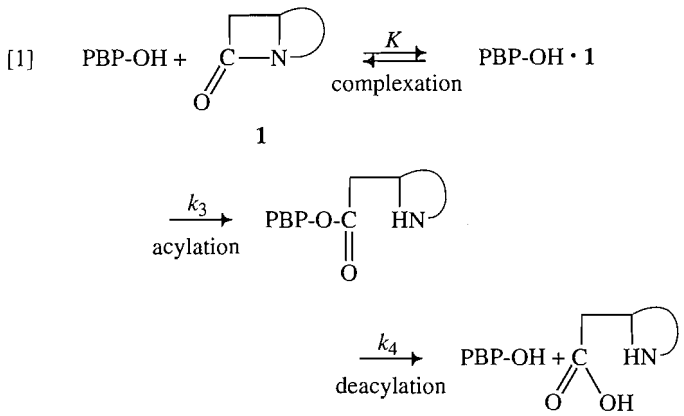

(6) interactions take place on the convex face of penicillin, and involve hydrogen bonding to the C3-carboxyl group and the side chain N-H, lead to a close contact in the complex between the hydroxyl oxygen of the serine and C7 of the penicillin (Fig. 1 (5)). The same relationship between the serine hydroxyl group and the β-lactam ring is seen in complexes formed from the experimental crystal structure of the *Streptomyces* R61 enzyme (7). The O—C7 distances and O—C7=O angles of Fig. 1 are appropriate for the attack of a nucleophile upon a carbonyl group (8), and variations in these parameters can be correlated qualitatively with variations in antibacterial activity.

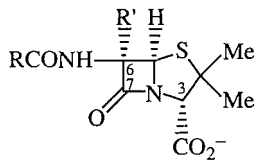

2

As a first step in the possible extension of these qualitative observations to more quantitative structure–activity predictions, we sought an understanding of the mechanism of the acylation step, and the nature of its transition structure. The PBP of *Streptomyces* R61 is an atypical serine peptidase, because a histidine residue does not appear to participate in the acyl transfer (9). This could mean that the hydroxyl hydrogen is involved directly in the reaction. For example, if the four-centred relationship between O-H of serine and C7-N of the β-lactam ring that is seen in Fig. 1 represents the geometry of a stationary point on a reaction coordinate, the indicated reaction should be C7—O bond formation and H → N proton transfer, concerted with the cleavage of the β-lactam bond. The existence of such a mechanism in the neutral hydrolysis of formamide has been discussed recently (10).

The geometry of Fig. 1 is reminiscent of that found in *gas phase* additions of alcohols to carbonyl groups (11), in which a cyclic process is enforced by the absence of solvent. There are significant differences, however: the process suggested by Fig. 1 involves proton transfer to *nitrogen*, not oxygen; also, the bond lengths of Fig. 1 (C—O = 3.6–4.4 Å; N—H = 2.7–4.3 Å (5)) are much longer than the C—O and O—H bond lengths (1.67–1.69 Å and 1.41–1.45 Å, respectively) in the four-centred transition states of the addition of alcohols to aldehydes (11*a*). As will be seen later, the longer bond lengths of Fig. 1 are compatible with the presence of a catalytic water molecule in the complex.

The hydrolysis and alcoholysis of β-lactam compounds have received much experimental (12) and theoretical (13) attention. In water solvent above pH 8, the rate-determining step in the hydrolysis of penicillin G is addition to the carbonyl group to form a tetrahedral intermediate; below pH 6, there is rate-determining proton transfer to the β-lactam nitrogen, from the convex face of the molecule (14). Hydrolysis is extremely slow in the (biologically relevant) pH range 6–8 (15), and the possible existence of a molecular mechanism in this region is not established. Likewise, all previous theoretical studies of β-lactam hydrolysis or alcoholysis have focused on anionic addition to the β-lactam carbonyl group.

Using ab initio molecular orbital (MO) theory, with full geometry optimization and vibrational characterization of all reactant and transition structures at the 3-21G or 3-21G* levels (16), followed by single point MP2/6-31G* calculations of the energies of these structures (17), we have now examined the neutral hydrolysis and methanolysis of monocyclic and bicyclic azetidinones. In the initial stage of the work the objectives were to determine whether ab initio MO theory supports the existence of four-centred transition structures in the reactions of *N*-methylazetidinone (**3**), penam (**4**), and penam-3α-carboxylate (**5**), and which four-centred structure (N-protonated, O-protonated, *exo*-attack, *endo*-attack) is energetically preferred.

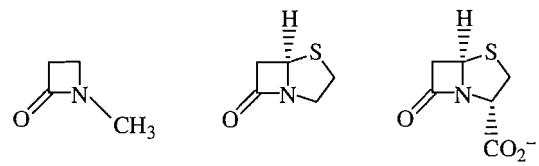

3 4 5

These calculations describe gas phase reactions, and some authors (10*b*, 11*b*) suggest that this is a valid way to treat the hydrophobic environment at the active site of an enzyme. However, we have noted recently (18) that the magnitude of the secondary kinetic isotope effect in an enzymatic methyl transfer reaction is not compatible with the desolvation argument.

Although the crystal structure of the *Streptomyces* R61 PBP has been discussed extensively (4, 7), the water content of its active site is not known. This information is, however, available for two related penicillin-recognizing enzymes, β-lactamases from *S. aureus* (19) and from *B. licheniformis* (20). The two structures (P3BLM and P4BLM, respectively) were retrieved from the Brookhaven Protein Data Bank, and the number of water molecules in the vicinity of the active site Ser70 hydroxyl oxygen was determined. In the case of the *S. aureus* enzyme (P3BLM), there were 3 water molecules ca. 3 Å, 4 water molecules 4–5 Å, and 16 water molecules 5–10 Å from the serine hydroxyl oxygen. In the *B. licheniformis* structure, there were 2 water molecules ca. 2–3 Å, 2 water molecules 4–5 Å, and 12 water molecules 5–10 Å from the serine hydroxyl oxygen. The closest contacts in the two cases are shown in Fig. 2.

Accordingly, in the second stage of the work, the effect of one water molecule on the N- and O-protonated pathways was examined, using **3** and **5** as substrates.

Calculations were performed using GAUSSIAN 86 (21), GAUSSIAN 90 (22), or GAUSSIAN 92 (23). Thermochemical quantities ($\Delta H^{\ddagger}$, $\Delta S^{\ddagger}$, and $\Delta G^{\ddagger}$) were calculated by standard procedures (24), from the output of these programmes.

Results and discussion

*Uncatalyzed Reactions of H_2O and MeOH with **3**, **4**, and **5***

Energies

Table 1 summarizes the 3-21G (3-21G*) and the MP2/

Can. J. Chem. Downloaded from www.nrcresearchpress.com by EESC ESCOLA DE ENGENHARIA on 09/08/12
For personal use only.

Can. J. Chem. Downloaded from www.nrcresearchpress.com by EESC ESCOLA DE ENGENHARIA on 09/08/12
For personal use only.

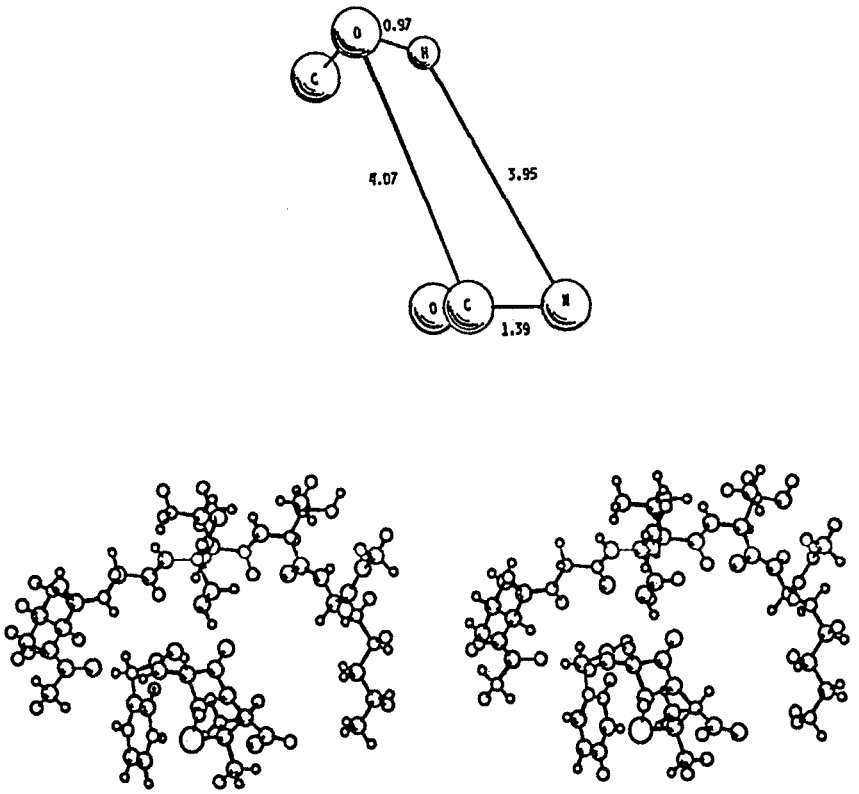

FIG. 1. Theoretically generated (5) complex of the crystal structure of penicillin G with a model of the active site hexapeptide of the PBP from *Streptomyces* R61. Inset: a closeup view of the relationship in the complex between the C-O-H of the serine residue of the peptide, and the N-C═O of the β-lactam ring.

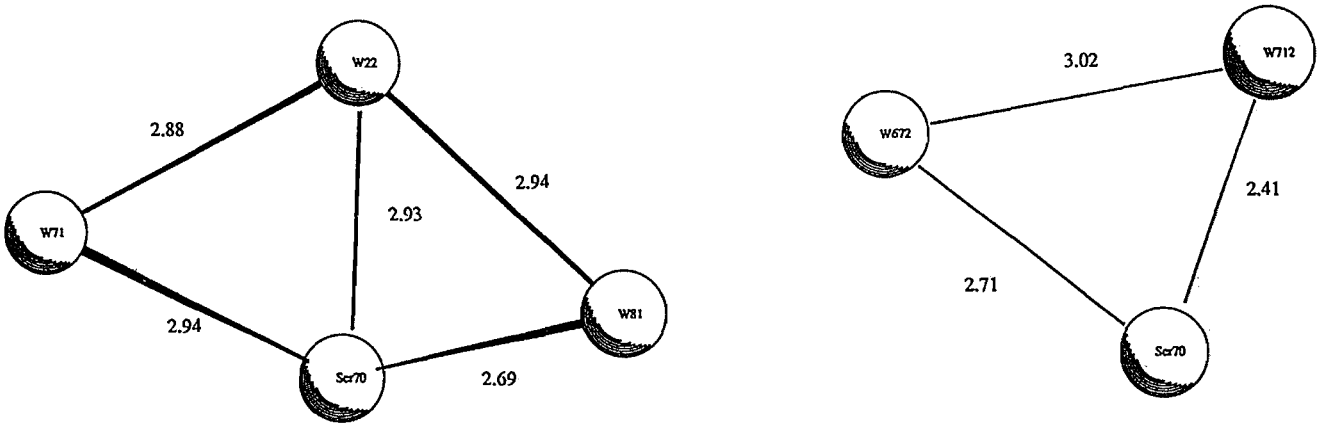

S. aureus *B. licheniformis*

FIG. 2. Left: the γ oxygen atom of the active site serine residue in the crystal structure of a β-lactamase from *S. aureus*, and the positions of the oxygen atoms of the three closest water molecules. Right: the γ oxygen of the active site serine residue in the crystal structure of a β-lactamase from *B. licheniformis*, and the positions of the oxygen atoms of the two closest water molecules. Distances are in ångstroms.

6-31G*//3-21G (3-21G*) energies of **3**, **4**, **5**, H_2O, CH_3OH, the hydrogen-bonded complexes between **3**, **4**, **5** and water or methanol, and the N-protonated and O-protonated four-centred transition structures. Table 2 collects the energy differences calculated from these data.

With the monocyclic *N*-methylazetidinone **3** as the substrate, the N-protonation mechanism is favoured by at least 5 kcal mol^{-1} in the reaction with water, and also in the reaction with methanol. This preference does not depend on how the activation energy is expressed (electronic energy ($\Delta E^{\ddagger}$), enthalpy ($\Delta H^{\ddagger}$), or free energy ($\Delta G^{\ddagger}$)), or on how the activation energy is measured (from the separated reactants, or from the hydrogen-bonded complexes). The $\Delta E^{\ddagger}$ and $\Delta H^{\ddagger}$ are higher when calculated from the hydrogen-bonded complexes, because these are stabilized relative to the separated reactants. However, there is a compensating entropic effect, because the pre-association of reactants in these complexes significantly reduces the unfavorable entropies of activation of these cyclic

Can. J. Chem. Downloaded from www.nrcresearchpress.com by EESC ESCOLA DE ENGENHARIA on 09/08/12
For personal use only.

TABLE 1. Calculated energies of the optimized structures of water, methanol, **3–5**, the reactant complexes formed from water or methanol with **3–5**, and the transition structures for the hydrolysis and methanolysis of the β-lactam rings of **3–5** via four-centred N-protonation (N) or O-protonation (O) pathways

Species	Mechanism	Energy[a] 3-21G (3-21G*[b])	Energy[a] MP2/6-31G*//3-21G (3-21G*[b])
Water		−75.58596	−76.19648
Methanol		−114.39802	−115.34538
3		−283.25056	−285.69281
3·H_2O (C)[c]	N	−358.84617	−361.89716
3·H_2O (C)	O	−358.85389	−361.90316
3·MeOH (C)	N	−397.66589[d]	−401.05325
3·MeOH (C)	O	−397.66589[d]	−401.05325
3·H_2O (ǂ)[e]	N	−358.78041	−361.82919
3·H_2O (ǂ)	O	−358.77139	−361.81822
3·MeOH (ǂ)	N	−397.59540	−400.98687
3·MeOH (ǂ)	O	−397.58517	−400.97437
4		−716.56990	−721.32221
4·MeOH (ǂ)	N	−830.92542	−836.62323
4·MeOH (ǂ)	O[f]	−830.91226	−836.61085
4·MeOH (ǂ)	O[g]	−830.90642	−836.60737
5		−902.55894	−908.86327
5·MeOH (C)	N	−1016.99681	
5·MeOH (ǂ)	N	−1016.92274	

[a]In atomic units (1 au = 627.5 kcal mol^{-1}).
[b]The 3-21G* basis set was used for all calculations on penam systems.
[c]Refers to the hydrogen-bonded complex formed between the reactants.
[d]The N- and O-protonation processes proceed via the same complex.
[e]Refers to a transition structure.
[f]Refers to attack from the convex face of the bicyclic system.
[g]Refers to attack from the concave face of the bicyclic system.

TABLE 2. Activation energies and thermochemical data for the reactions of water or methanol with **3–5**[a,b]

Reaction	Mechanism	3-21G (3-21G*) $\Delta E^{ǂ}$	3-21G (3-21G*) $\Delta H^{ǂ}$	3-21G (3-21G*) $\Delta S^{ǂ}$	3-21G (3-21G*) $\Delta G^{ǂ}$	MP2/6-31G*//3-21G (3-21G*) $\Delta E^{ǂ}$
3 + H_2O	N	35.21	36.27	−39.29	47.98	37.71
	N	*41.27*	*40.23*	*−13.20*	*44.17*	*42.65*
	O	40.87	41.33	−37.99	52.66	44.60
	O	*51.77*	*49.86*	*−11.62*	*53.32*	*53.30*
3 + MeOH	N	33.37	33.11	−42.60	45.81	32.20
	N	*44.23*	*42.30*	*−12.54*	*46.04*	*41.65*
	O	39.79	38.73	−38.75	50.28	40.05
	O	*50.65*	*47.92*	*−8.69*	*50.51*	*49.50*
4 + MeOH	N	26.67	26.53	−43.59	39.52	27.84
	O[c]	34.93	34.59	−42.24	47.18	35.60
	O[d]	38.59	38.03	−43.50	51.00	37.79
5 + MeOH	N	21.47	20.93	−39.28	32.64	

[a]Energies are in kcal mol^{-1}; entropies are in cal mol^{-1} deg^{-1}; free energies refer to standard state 298 K and 1 atm.
[b]Data in italics refer to the energy differences between transition structures and hydrogen-bonded complexes. All other data refer to energy differences between transition structures and separated reactants.
[c]Refers to attack of methanol from the convex face of the molecule.
[d]Refers to attack of methanol from the concave face of the molecule.

processes. Consequently the free energies of activation are virtually the same, whether these are based on the separated reactants, or on the complexes.

The preference for the N-protonation mechanism is maintained with the bicyclic compound **4** as the substrate but, compared to **3**, the activation energies of both mechanisms are lower by ca. 5 kcal/mol^{-1}. An additional 5 kcal/mol^{-1} reduction in activation energy is seen with **5**, which has the 3α-carboxylate group of penicillin. In the case of the O-protonation mechanism, attack from the convex face of **4** is preferred by at least 2 kcal/mol^{-1} over attack from the concave face. The energy differences just discussed are necessary benchmarks for the evaluation of any semiempirical molecular orbital treatment of these reactions (25).

Geometries

Figure 3 shows **3** and the N- and O-protonated transition structures for the reactions of **3** with water and with methanol.

Can. J. Chem. Downloaded from www.nrcresearchpress.com by EESC ESCOLA DE ENGENHARIA on 09/08/12
For personal use only.

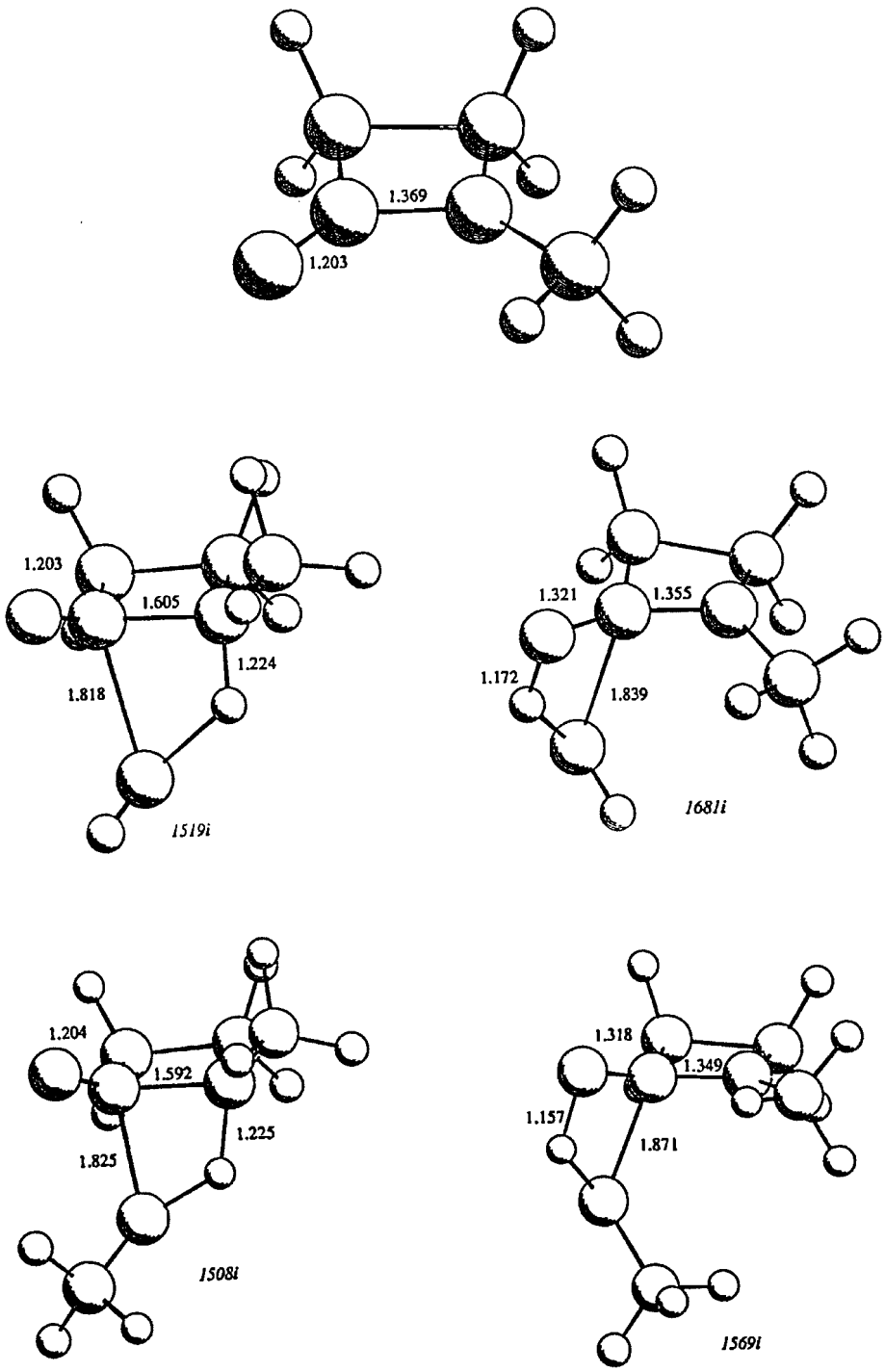

FIG. 3. Top: calculated structure of N-methylazetidinone (**3**). Centre left: N-protonation transition structure for the hydrolysis of **3**. Centre right: O-protonation transition structure for the hydrolysis of **3**. Lower left: N-protonation transition structure for the methanolysis of **3**. Lower right: O-protonation transition structure for the methanolysis of **3**.

Figure 4 shows **4** and the transition structures for the N- and O-protonated reactions of **4** with methanol. Figure 5 shows **5** and the transition structure for the N-protonation reaction **5** with methanol.[4] The imaginary frequencies of the various transition structures are included in Figs. 3–5.

There is no obvious relationship between the N—C and C═O β-lactam bond lengths and the relative reactivities of **3–5**. The N—C and C═O bond lengths calculated for the bicyclic **5** (1.377 and 1.205 Å, respectively) are very close to those found in penicillin crystal structures (1.380 and 1.210 Å, respectively (26)), and not very different from those calculated for the monocyclic **3**. In **4**, the N—C bond is longer (1.405 Å) and the C═O bond is shorter (1.195 Å).

A relationship between the planarity of a β-lactam nitrogen and the ease of hydrolysis of the ring was first discussed by

[4]Full details of the geometries of all structures calculated in this work are available as Supplementary Data, and may be purchased from the Depository of Unpublished Data, Documentary Delivery, CISTI, National Research Council Canada, Ottawa, Canada K1A 0S2.

Can. J. Chem. Downloaded from www.nrcresearchpress.com by EESC ESCOLA DE ENGENHARIA on 09/08/12
For personal use only.

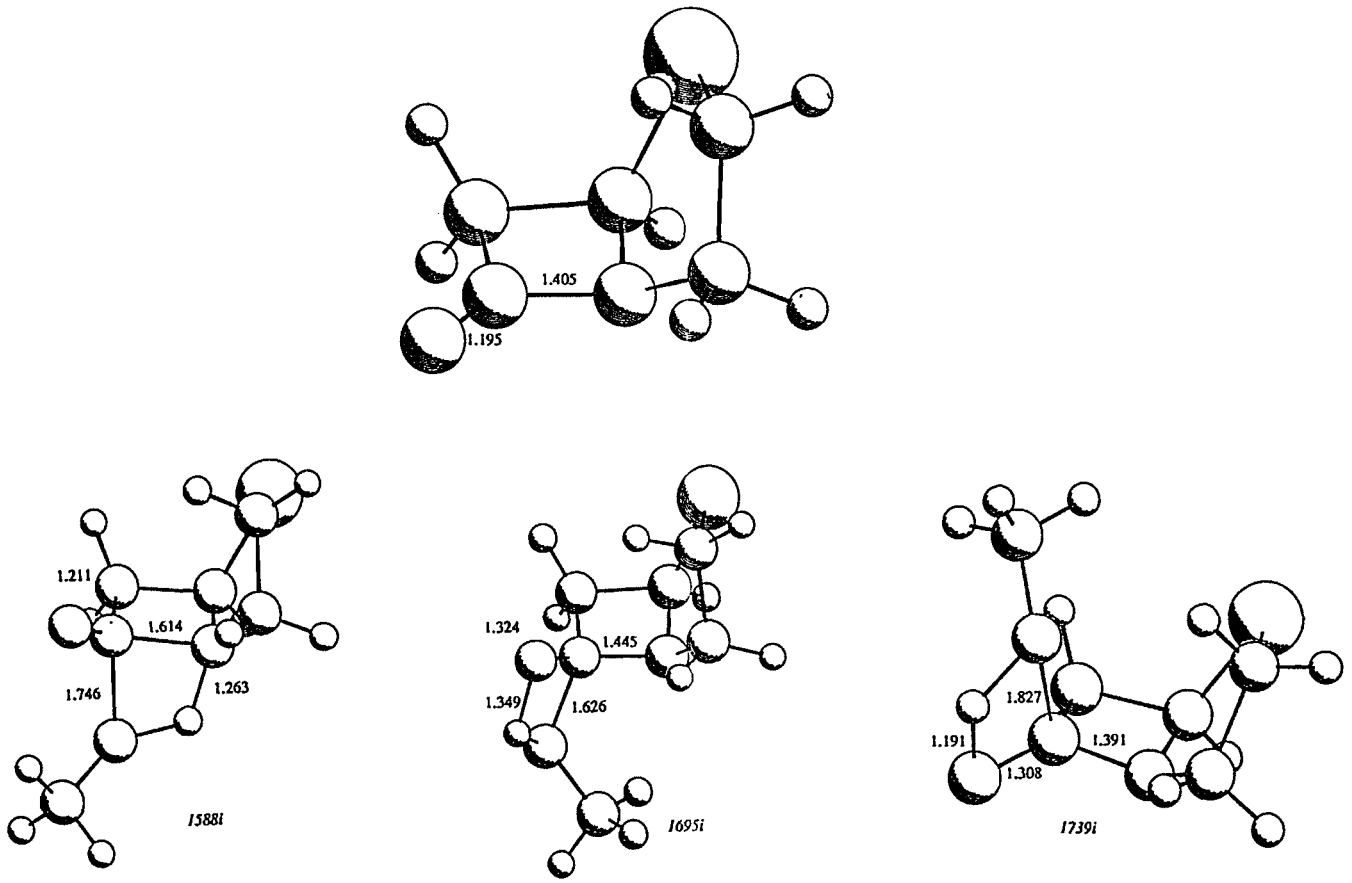

FIG. 4. Top: calculated structure of penam (**4**). Lower left: N-protonation transition structure for the methanolysis of **4**. Lower centre: O-protonation transition structure for the methanolysis of **4** from the convex face. Lower right: O-protonation transition structure for the methanolysis of **4** from the concave face.

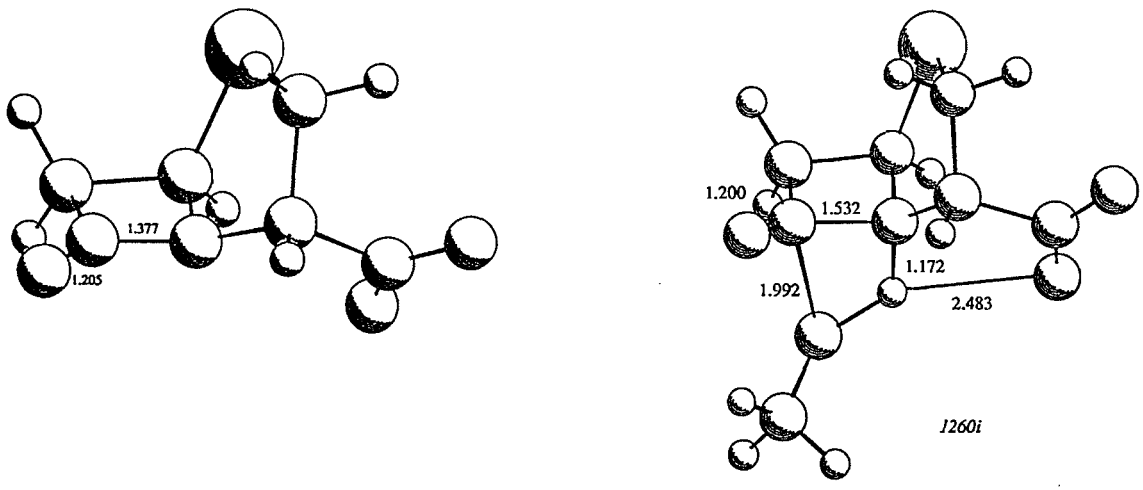

FIG. 5. Left: calculated structure of penam-3α-carboxylate (**5**). Right: N-protonation transition structure for the methanolysis of **5**.

Woodward (27). Subsequent workers sought relationships between the planarity at this centre, as measured by the sum of the angles at nitrogen, and the antibacterial activity of a β-lactam antibiotic (28). In **3–5**, the sum of the angles at the β-lactam nitrogen atoms are 360.0°, 336.1°, and 344.6°, respectively. The value for **4** is the same as that found in the crystal structure of penicillin G (335.8° (5)). The greater reactivity of **4** over **3** calculated in this work is consistent with the nonplanarity argument, but the enhanced reactivity of **5** over **4** implies that other effects are also operative.

Examination of O···C (i) and H···N (ii) bond formation, and β-lactam bond cleavage (iii) in the N-protonation transition structures for the methanolyses of **3** and **4** suggests that (i) and (iii) are more advanced with the more reactive (and more pyramidal at nitrogen) substrate **4**, and (ii) is more advanced in the planar (at nitrogen) substrate **3**. In the N-protonation transition

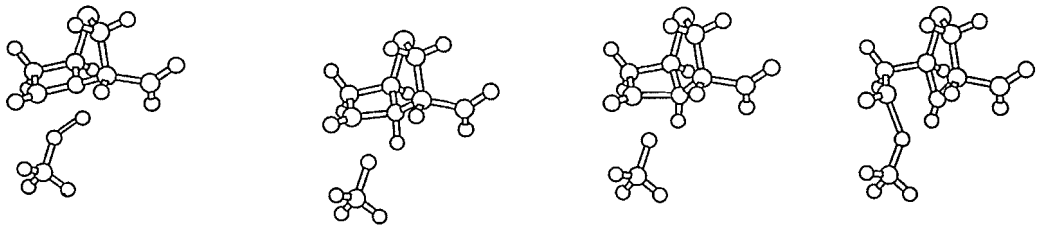

FIG. 6. A series of views, using the computer program XMol (29), of the vibrations that are associated with the imaginary frequency of the N-protonation transition structure for the methanolysis of **5**.

TABLE 3. Calculated energies of the reactant complexes and transition structures for the hydrolysis of **3** and the methanolyses of **3** and **5** via N-protonation and O-protonation pathways, with catalysis by one water molecule

Species	Mechanism	Energy[a] 3-21G (3-21G*)	Energy[a] MP2/6-31G*//3-21G (3-21G*)
3·H_2O·H_2O (C)[b]	N	−434.45927	−438.10897
3·H_2O·H_2O (≠)[c]	N	−434.41263	−438.05411
3·H_2O·H_2O (C)	O	−434.47214	−438.11777
3·H_2O·H_2O (≠)	O	−434.42150	−438.05054
3·MeOH·H_2O (C)	N	−473.27047	−477.25872
3·MeOH·H_2O (≠)	N	−473.22557	−477.20819
3·MeOH·H_2O (C)	O	−473.28336	−477.26773
3·MeOH·H_2O (≠)	O	−473.23111	−477.20271
5·MeOH·H_2O (C)	N	−1092.61961	−1100.45846
5·MeOH·H_2O (≠)	N	−1092.55401	−1100.39486
5·MeOH·H_2O (C)	O	−1092.59289	−1100.44095
5·MeOH·H_2O (≠)	O	−1092.55134	−1100.37912

[a]In atomic units.
[b]Refers to the ternary hydrogen-bonded complex formed from the reactants.
[c]Refers to a transition structure.

structure of the most reactive substrate **5**, the proton transfer to nitrogen is nearly complete; in addition, there is a significant change in the magnitude of the imaginary frequency. Figure 6 displays the vibrations associated with this imaginary frequency, using the programme XMol (29). From left to right these depict an inversion motion of the β-lactam nitrogen, proton transfer, continued inversion at nitrogen with strengthening of the nascent N—H bond, and a further nitrogen movement with cleavage of the N—C bond and C—O bond formation. All of these effects seem to be the result of an attractive interaction, on the convex face of the molecule, between the carboxylate anion and the proton-in-flight.

The differences in (i) and (ii) in the N-protonation and O-protonation mechanisms do not seem to be sufficient to explain the energetic preference for the former reaction. However, it is evident from Fig. 3 that the two mechanisms lead to different positions of the R group of the R-O-H moiety with respect to the methyl group of *N*-methylazetidinone: in the O-protonation mechanism there is a 1,3-eclipsing interaction between R and Me. In the O-protonation mechanism from the convex face of **4** there is close contact between the methyl group of methanol and C4 of the thiazolidine ring.

Catalysis by water of the hydrolysis and methanolysis of 3 and 5

Table 3 summarizes the 3-21G (3-21G*) and MP2/6-31G*// 3-21G (3-21G*) energies of the termolecular complexes (C) and transition structures (≠) that are formed by the N-protonation and O-protonation mechanisms of water-catalyzed hydrolysis and methanolysis of **3**, and methanolysis of **5**. The energy differences calculated from these data, and from the appropriate data of Table 1, are collected in Table 4. The termolecular complexes and transition structures formed in the different mechanisms are shown in Figs. 7–12.

From the $\Delta E^{\neq}$ and $\Delta H^{\neq}$ calculated at 3-21G (3-21G*), one might conclude from Table 4 that the ternary complexes are stabilized relative to the separated reactants by ca. 20 kcal/mol^{-1} in the N-protonation mechanism and ca. 25 kcal mol^{-1} in the O-protonation mechanism. However, these large stabilization energies are the result of the incomplete description of the separated reactants that is achieved when a relatively small basis set such as 3-21G or 3-21G* is used. This is termed basis set superposition error (BSSE) (30), which has been discussed extensively in connection with calculations on water clusters (31). The BSSE leads to energies of separated reactants that are artificially too high, causing $\Delta E^{\neq}$ and $\Delta H^{\neq}$ to be too low or even negative, when these are calculated from the separated reactants.

Because of the BSSE, it is more reliable to compare absolute energies of isomeric transition structures, especially when these are obtained at the MP2/6-31G* level. In a recent study of the hydration of formaldehyde actively catalyzed by one, two, and three molecules of water (32), very similar activation energies were computed at MP2/6-31G*//MP2-6-31G* and MP2/ 6-31G*//3-21G, because the geometries calculated at 3-21G and at MP2/6-31G* are not very different.

An alternative way to deal with the BSSE problem is to compute all stationary points of a reaction with the same basis set. This is the situation when the activation energies are calculated

Can. J. Chem. Downloaded from www.nrcresearchpress.com by EESC ESCOLA DE ENGENHARIA on 09/08/12
For personal use only.

TABLE 4. Activation energies and thermochemical data for the water-catalyzed hydrolysis of **3** and the water-catalyzed methanolyses of **3** and **5**[a,b]

Reaction	Mechanism	3-21G (3-21G*) $\Delta E^{\ddagger}$	$\Delta H^{\ddagger}$	$\Delta S^{\ddagger}$	$\Delta G^{\ddagger}$	MP2/6-31G*//3-21G (3-21G*) $\Delta E^{\ddagger}$
3 + H_2O	N	6.18	9.65	−75.33	32.11	19.87
	N	*29.27*	*27.10*	*−12.79*	*30.92*	*34.43*
	O	0.61	4.59	−75.75	27.18	22.11
	O	*31.78*	*29.82*	*−13.45*	*33.83*	*42.19*
3 + MeOH	N	5.63	7.78	−78.41	31.16	16.62
	N	*28.18*	*25.74*	*−15.44*	*30.34*	*31.71*
	O	2.15	4.60	−78.94	28.14	20.06
	O	*32.98*	*30.47*	*−15.43*	*35.07*	*40.80*
5 + MeOH	N	−6.96	−5.15	−80.25	18.77	6.44
	N	*41.16*	*37.92*	*−11.82*	*41.44*	*39.91*
	O	−5.28	−2.64	−78.51	20.76	16.32
	O	*26.07*	*23.83*	*−15.27*	*28.38*	*38.80*

[a]Energies are in kcal mol^{-1}; entropies are in cal mol^{-1} deg^{-1}; free energies refer to standard state 298 K and 1 atm.
[b]Data in italics refer to the energy differences between transition structures and hydrogen-bonded complexes. All other data refer to energy differences between transition structures and separated reactants.

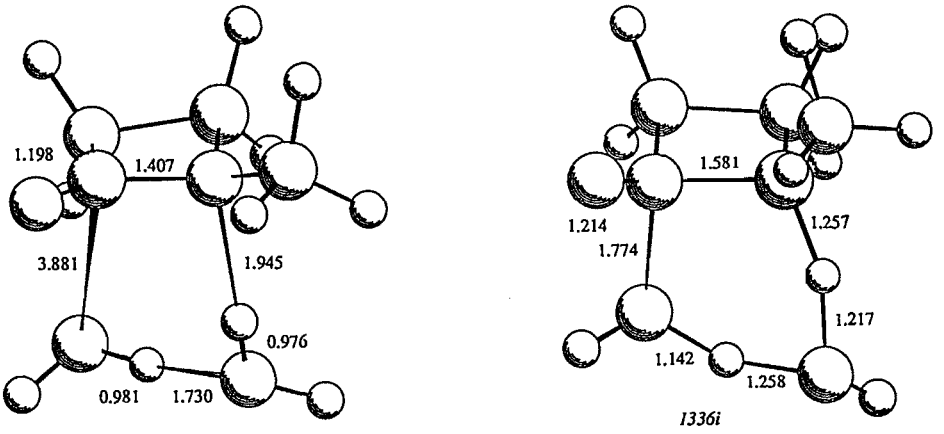

FIG. 7. Calculated reactant complex (left) and transition structure (right) for the hydrolysis of **3** by the N-protonation mechanism, with catalysis by one water molecule.

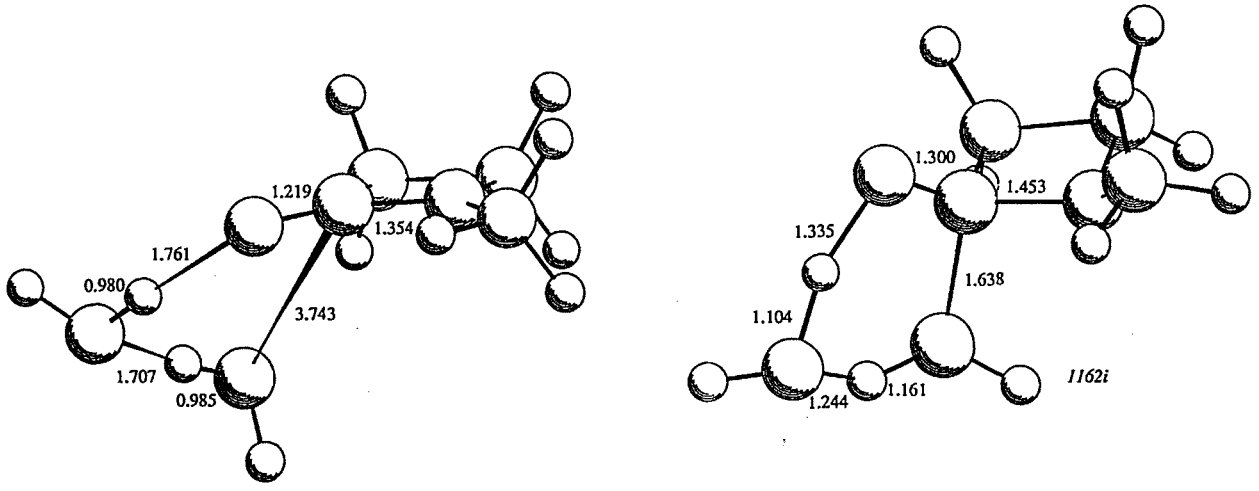

FIG. 8. Calculated reactant complex (left) and transition structure (right) for the hydrolysis of **3** by the O-protonation mechanism, with catalysis by one water molecule.

Can. J. Chem. Downloaded from www.nrcresearchpress.com by EESC ESCOLA DE ENGENHARIA on 09/08/12
For personal use only.

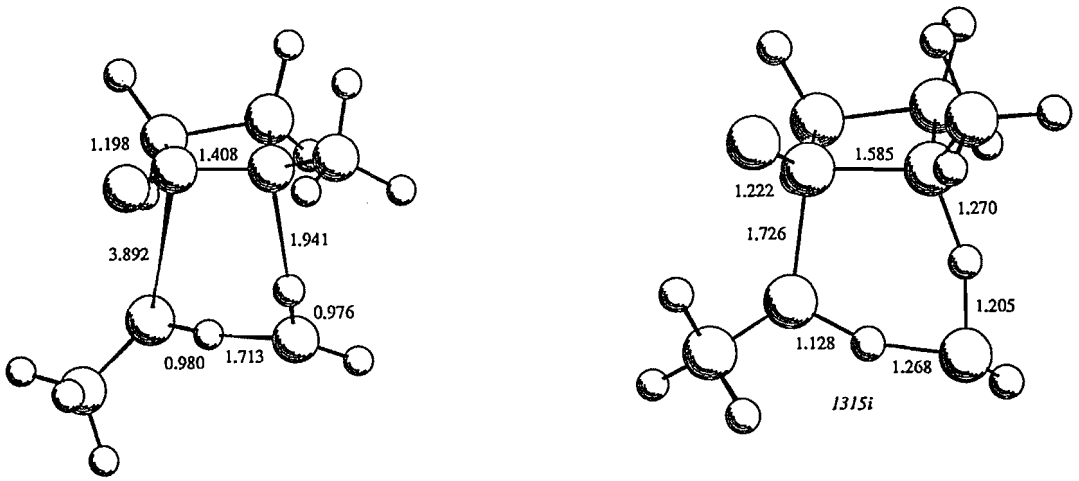

FIG. 9. Calculated reactant complex (left) and transition structure (right) for the methanolysis of **3** by the N-protonation mechanism, with catalysis by one water molecule.

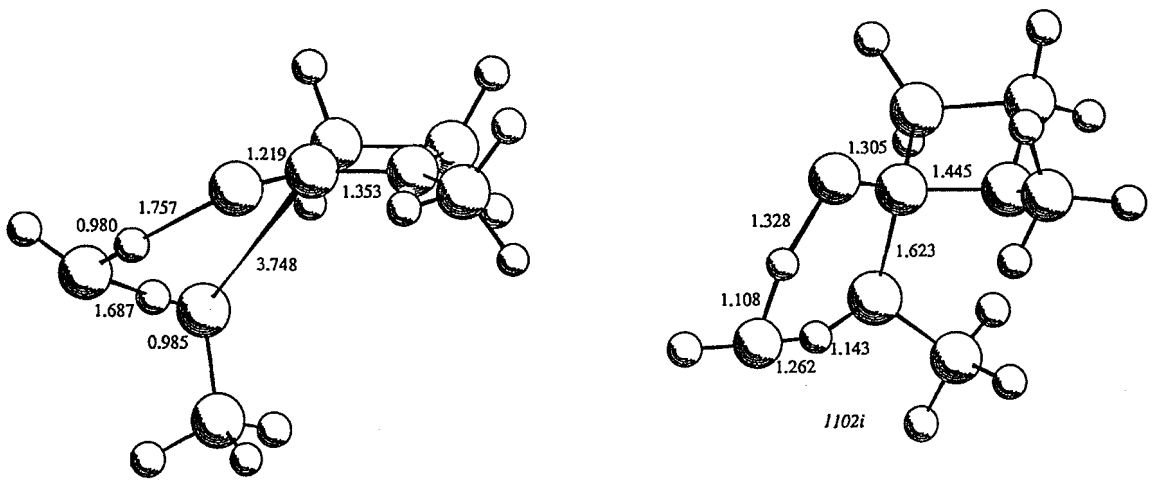

FIG. 10. Calculated reactant complex (left) and transition structure (right) for the methanolysis of **3** by the O-protonation mechanism, with catalysis by one water molecule.

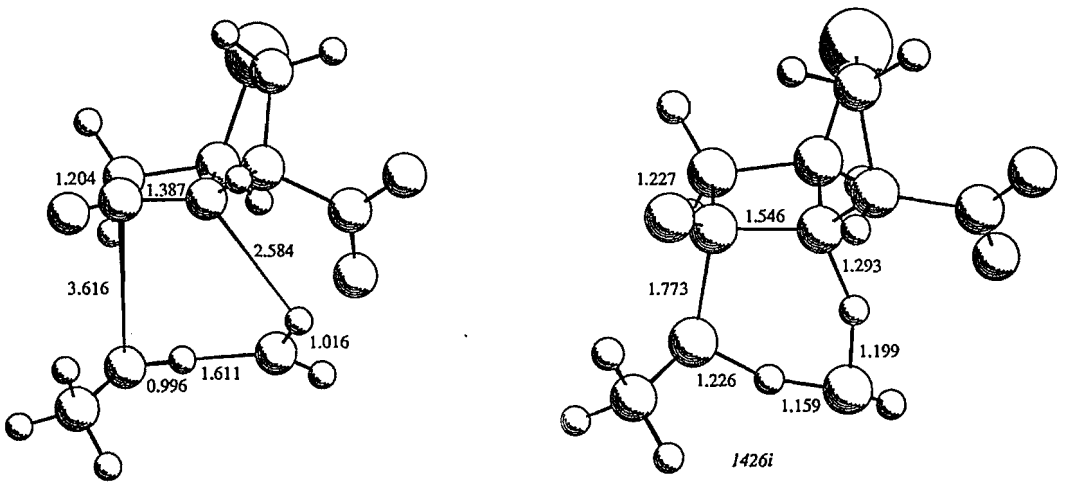

FIG. 11. Calculated reactant complex (left and transition structure (right) for the methanolysis of **5** by the N-protonation mechanism, with catalysis by one water molecule. Note that in the complex the catalytic water molecule is hydrogen bonded to one of the carboxylate oxygens, and not to nitrogen.

Can. J. Chem. Downloaded from www.nrcresearchpress.com by EESC ESCOLA DE ENGENHARIA on 09/08/12
For personal use only.

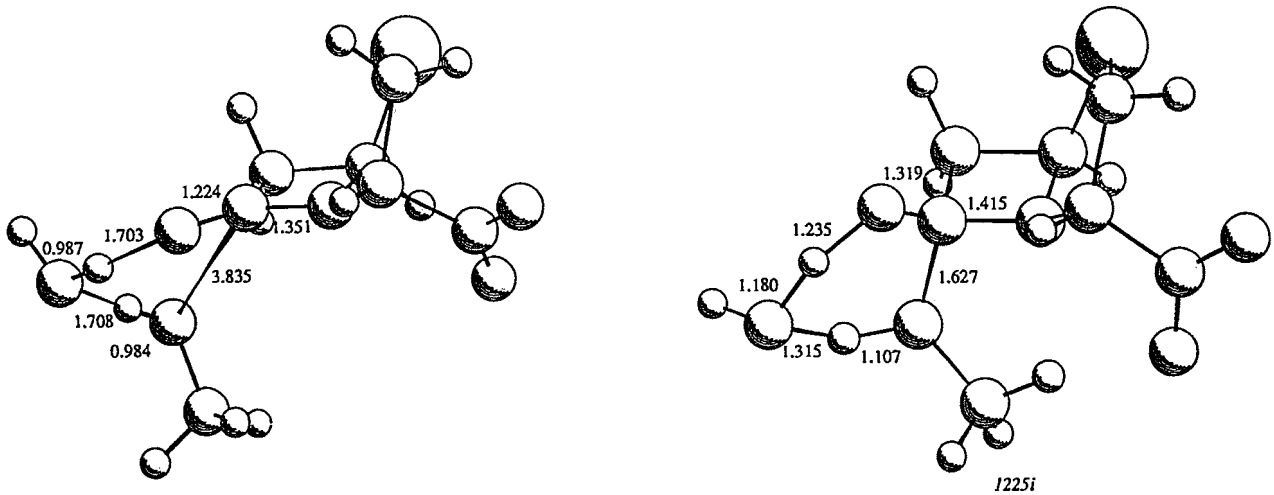

FIG. 12. Calculated reactant complex (left) and transition structure (right) for the methanolysis of **5** by the O-protonation mechanism, with catalysis by one water molecule.

from the ternary complexes, and for these entries of Table 4 it can be seen that the numbers in the first and last columns of Table 4 are not very different.

Unfortunately, as can be seen in Fig. 11, the water molecule of the termolecular complex of **5** with methanol and water is calculated to be hydrogen bonded to the carboxylate anion, and not to the β-lactam nitrogen. The energy of this complex is therefore much too low, leading to an artificially high 3-21G* N-protonation barrier. In this case the only reliable $\Delta E^{\ddagger}$ are those calculated from the separated reactants.

With this qualification, it is clear from the last column of Table 4 that the preference for the N-protonation mechanism is 2–4 kcal mol^{-1} when calculated from the separated reactants, and 7–8 kcal mol^{-1} when calculated from the complexes.

It is also clear than one water molecule has a pronounced catalytic effect, *amounting to at least 10 kcal* mol^{-1}, on the neutral hydrolysis and methanolysis of azetidinones.[5]

A most interesting feature of the geometries shown in Figs. 7 and 9 is the ca. 3.9 Å O···C=O distance in the hydrogen-bonded complexes. This is reminiscent of the 4.1 Å O···C=O distance seen in Fig. 1, and the 3.6–4.4 Å range of values mentioned in the Introduction (5) for the distance, in the docked complexes, between the hydroxyl oxygen of serine and the carbon atom of the β-lactam carbonyl group.

This observation suggests that the O—H/C(O)—N distances in the "enzyme"–substrate complexes are longer than those of four-centred transition structures in order to allow a water molecule to be accommodated. The addition of this water molecule would then create a Ser-O-H/H-O-H/N-C=O geometry that is identical to the geometry of the stationary point of the chemical reaction.

These findings raise many questions. For example, (*i*) can an enzyme exert its catalytic effect by causing a termolecular reactant complex to be assembled in the proper geometry, thereby reducing the unfavorable entropy of activation associated with a termolecular reaction? (*ii*) does the "fit" of a substrate to an enzyme cause reacting groups to be organized into a geometry that can be computed ab initio? (*iii*) is the kinetic behaviour of different substrates of an enzyme determined by the degree to which the reactive site geometries of their enzyme–substrate complexes can attain the geometry of the calculated "perfect fit"? (*iv*) can an understanding of "fit" be used in drug design?

Answers to these questions are currently being sought (32, 33). Regardless of the eventual conclusions of those studies, the principal results of the present work are the conclusions that penicillin complexes with its receptor in such a way as to allow the most favourable mechanism for acylation of the active site serine to be attained, and that this mechanism can consist of a one-step water-catalyzed cleavage of the β-lactam bond, with proton transfer to nitrogen.

[5]NOTE ADDED IN PROOF: We have now found that a *second* water molecule has a small inhibitory effect.

Acknowledgements

The authors thank the Natural Sciences and Engineering Research Council of Canada for financial support, and Simon Fraser University for generous provision of computer resources.

1. D.J. Waxman and J.L. Strominger. Annu. Rev. Biochem. **52**, 825 (1983).
2. B.G. Spratt. J. Gen. Microbiol. **129**, 1247 (1983).
3. J.M. Ghuysen, J.M. Frère, M. Leyh-Bouille, J. Coyette, C. Duez, B. Joris, J. Dusart, M. Nguyen-Distèche, O. Dideberg, P. Charlier, J.R. Knox, J.A. Kelly, P.C. Moews, and M.L. DeLucia. *In* Beta-lactam antibiotics. *Edited by* S. Mitsuhashi. Japan Scientific Societies Press, Tokyo. 1981. p. 185.
4. J.A. Kelly, J.R. Knox, P.C. Moews, G.J. Hite, J.B. Bartolone, H. Zhao, B. Joris, J.-M. Frère, and J.-M. Ghuysen. J. Biol. Chem. **260**, 6449 (1985).
5. S. Wolfe, K. Yang, and M. Khalil. Can. J. Chem. **66**, 2733 (1988).
6. E. Fischer. Ber. Dtsch. Chem. Ges. **27**, 2985 (1894).
7. J.A. Kelly, J.R. Knox, H. Zhao, J.-M. Frère, and J.-M. Ghuysen. J. Mol. Biol. **209**, 281 (1989).
8. H.-B. Bürgi and J.D. Dunitz. Acc. Chem. Res. **16**, 153 (1983).
9. L. Varetto, J.-M. Frère, M. Nguyen-Distèche, J.-M. Ghuysen, and C. Houssier. Eur. J. Biochem. **162**, 525 (1987); A.M. Hadonou, M. Jamin, M. Adam, B. Joris, J. Dusart, J.-M. Ghuysen, and J.-M. Frère. Biochem. J. **282**, 495 (1992).
10. (*a*) T. Oie, G.H. Loew, S.K. Burt, J.S. Binkley, and R.D. MacElroy. J. Am. Chem. Soc. **104**, 6169 (1982); **105**, 2221 (1983); (*b*) J.P. Krug, P.L.A. Popelier, and R.F.W. Bader. J. Phys. Chem. **96**, 7604 (1992).
11. (*a*) I.H. Williams, D. Spangler, G.M. Maggiora, and R.L. Schowen. J. Am. Chem. Soc. **107**, 7717 (1985); (*b*) M.J.S. Dewar and

Can. J. Chem. Downloaded from www.nrcresearchpress.com by EESC ESCOLA DE ENGENHARIA on 09/08/12
For personal use only.

D.M. Storch. Proc. Natl. Acad. Sci. U.S.A. **82**, 2225 (1985); (*c*) S. Hoz, K. Yang, and S. Wolfe. J. Am Chem. Soc. **112**, 1319 (1990).
12. M.I. Page. Adv. Phys. Org. Chem. **23**, 165 (1987).
13. W.C. Topp and B.G. Christensen. J. Med. Chem. **17**, 342 (1974); D.B. Boyd, R.B. Hermann, D.E. Presti, and M. Marsh. J. Med. Chem. **18**, 408 (1975); H.-D. Holtje. Arch. Pharm. **309**, 26 (1976); D.B. Boyd. Proc. Natl. Acad. Sci. U.S.A. **74**, 5239 (1977); R. Virudachalam and V.S.R. Rao. Int. J. Pept. Protein Res. **10**, 51 (1977); N.V. Joshi, R. Virudachala, and V.S.R. Rao. Curr. Sci. **47**, 933 (1978); D.B. Boyd. J. Med. Chem. **22**, 533 (1979); C. Petrongolo, G. Ranghino, and R. Scordamaglia. Chem. Phys. **45**, 279 (1980); C. Petrongolo, E. Pescatori, G. Ranghino, and R. Scordamaglia, Chem. Phys. **45**, 291 (1980); C. Petrongolo and G. Ranghino. Theor. Chim. Acta, **54**, 239 (1981); T.K. Vasudevan and V.S.R. Rao, Biopolymers, **20**, 865 (1981); D.B. Boyd. Ann. N.Y. Acad. Sci. **367**, 531 (1981); C. Glidewell and G.S.M. Mollison. J. Mol. Struct. **72**, 3 (1981); N.V. Joshi and V.S.R. Rao. J. Biosci. **4**, 209 (1982); T.K. Vasudevan and V.S.R. Rao. Curr. Sci. **51**, 402 (1982); T.K. Vasudevan and V.S.R. Rao. Int. J. Biol. Macromol. **4**, 219 (1982); **4**, 347 (1982); V.S.R. Rao and T.K. Vasudevan. CRC Crit. Rev. Biochem. **14**, 173 (1983); S. Vishveshwara and V.S.R. Rao. J. Mol. Struct. (Theochem), **92**, 19 (1983); V.S.R. Rao. *In* The target of penicillin. *Edited by* R. Hackenbeck, J.-V. Holtje, and H. Labischinski. Walter de Gruyter, Berlin. 1983. p. 359; L. Lu, J. Liu, F. Du, and W. Hua. J. Mol. Struct. (Theochem), **206**, 17 (1990); G. Ranghino. Gazz. Chim. Ital. **121**, 509 (1991); J. Weinberg, A. Donescu, V.E. Sahini, and M. Cojocaru. Rev. Roum. Chim. **36**, 417 (1991); J. Lamotte-Brasseur, G. Dive, O. Dideberg, P. Charlier, J.-M. Frère, and J.-M. Ghuysen. Biochem. J. **279**, 213 (1991); K. Nahm. Bull. Kor. Chem. Soc. **12**, 674 (1991); A. Nangia. J. Mol. Struct. (Theochem), **251**, 237 (1991); J. Frau, J. Donoso, F. Muñoz, and F.G. Blanco. J. Mol. Struct. (Theochem), **251**, 205 (1991); J. Lamotte-Brasseur, F. Jacob-Dubuisson, G. Dive, and J.-M. Frère. Biochem. J. **282**, 189 (1992); J. Frau, J. Donoso, F. Muñoz, and F.G. Blanco. J. Comput. Chem. **13**, 681 (1992); B. Fernández, L. Carballeira, and M.A. Rios. Biopolymers, **32**, 97 (1992); A. Nangia. Proc. Ind. Acad. Sci. **105**, 131 (1993).
14. M.L. Sinott. Adv. Phys. Org. Chem. **24**, 113 (1988).
15. N.P. Gensmantel, E.W. Gowling, and M.I. Page. J. Chem. Soc. Perkin Trans. 2, 335 (1978).
16. J.S. Binkley, J.A. Pople, and W.J. Hehre. J. Am. Chem. Soc. **102**, 939 (1980); W.J. Pietro, M.M. Francl. W.J. Hehre, D.J. DeFrees, J.A. Pople, and J.S. Binkley. J. Am. Chem. Soc. **104**, 5039 (1982).
17. W.J. Hehre, L. Radom, P.v.R. Schleyer, and J.A. Pople. Ab initio molecular orbital theory. Wiley–Interscience, New York. 1986.
18. R.J. Boyd, C.-K. Kim, Z. Shi, N. Weinberg, and S. Wolfe. J. Am. Chem. Soc. **115**, 10147 (1993).
19. O. Herzberg. J. Mol. Biol. **217**, 701 (1991).
20. J.R. Knox and P.C. Moews, J. Mol. Biol. **220**, 435 (1991).
21. M.J. Frisch, J.S. Binkley, H.B. Schlegel, K. Raghavachari, C.F. Melius, R.L. Martin, J.J.P. Stewart, F.W. Bobrowicz, C.M. Rohlfing, L.R. Kahn, D.J. DeFrees, R. Seeger, R.A. Whiteside, D.J. Fox, E.M. Fluder, and J.A. Pople. GAUSSIAN 86. Carnegie-Mellon Quantum Chemistry Publishing Unit, Pittsburgh, Pa. 1984.
22. M.J. Frisch, M. Head-Gordon, G.W. Trucks, J.B. Foresman, H.B. Schlegel, K. Raghavachari, M.A. Robb, J.S. Binkley, C. Gonzalez, D.J. DeFrees, D.J. Fox, R.A. Whiteside, R. Seeger, C.F. Melius, J. Baker, R.L. Martin, L.R. Kahn, J.J.P. Stewart, S. Topiol, and J.A. Pople. GAUSSIAN 90. Gaussian, Inc., Pittsburgh, Pa. 1990.
23. M.J. Frisch, G.W. Trucks, M. Head-Gordon, P.M.W. Gill, M.W. Wong, J.B. Foresman, B.G. Johnson, H.B. Schlegel, M.A. Robb, E.S. Replogle, S. Gomperts, J.L. Andres, K. Raghavacharan, J.S. Binkley, C. Gonzalez, R.L. Martin, D.J. Fox, D.J. DeFrees, J. Baker, J.J.P. Stewart, and J.A. Pople. GAUSSIAN 92, Revision B. Gaussian, Inc. Pittsburgh, Pa. 1992.
24. S.S. Shaik, H.B. Schlegel, and S. Wolfe. Theoretical aspects of physical organic chemistry. The S_N2 mechanism. Wiley–Interscience, New York. 1992. pp. 80–84.
25. S. Wolfe and T. Hoz. Can. J. Chem. **72**, 1044 (1994).
26. S. Wolfe, M. Khalil, and D.F. Weaver. Can. J. Chem. **66**, 2715 (1988).
27. R.B. Woodward, A. Neuberger, and N.R. Trenner. *In* The chemistry of penicillin. *Edited by* H.T. Clarke, J.R. Johnson, and R. Robinson. Princeton University Press, Princeton, N.J. 1949. p. 415.
28. R.M. Sweet. *In* Cephalosporins and penicillins: chemistry and biology. *Edited by* E.H. Flynn. Academic Press, New York. 1972. p. 280; R.B. Woodward. Philos. Trans. R. Soc. London, B: **289**, 239 (1980).
29. XMol. Version 1.3.1. Minnesota Supercomputer Center, Inc., Minneapolis, Minn. 1993.
30. N.R. Kestner. J. Chem. Phys. **48**, 4557 (1968); S.F. Boys and F. Bernardi. Mol. Phys. **19**, 55 (1970).
31. G. Alagona and C. Ghio. J. Comput. Chem. **11**, 930 (1990); E.P.F. Lee and J.M. Dyke. Mol. Phys. **73**, 375 (1991); S.M. Cybulski and G. Chalasinski. Chem. Phys. Lett. **197**, 591 (1992); A. Vibók and I. Mayer. Int. J. Quantum Chem. **43**, 801 (1992); J.G.C.M. van Duijneveldt-van de Rijdt and F.B van Duijneveldt. J. Chem. Phys. **97**, 5019 (1992).
32. S. Wolfe and C.-K. Kim. J. Am. Chem. Soc. Submitted.
33. S. Wolfe, H. Jin, K. Yang, C.-K. Kim, and E. McEachern. Can. J. Chem. **72**, 1051 (1994); S. Wolfe, C. Zhang, B.J. Johnson and C.-K. Kim. Can. J. Chem. **72**, 1066 (1994).

Can. J. Chem. Downloaded from www.nrcresearchpress.com by EESC ESCOLA DE ENGENHARIA on 09/08/12
For personal use only.

A semiempirical molecular orbital study of the methanolysis of complex azetidinones. A combined MM and QM analysis of the interaction of Δ^2- and Δ^3-cephems with the penicillin receptor

SAUL WOLFE[1,2] AND TOVA HOZ[3]

Department of Chemistry, Queen's University, Kingston, ON K7L 3N6, Canada, and Department of Chemistry, Simon Fraser University, Burnaby, BC V5A 1S6, Canada

Received August 24, 1993

Can. J. Chem. Downloaded from www.nrcresearchpress.com by EESC ESCOLA DE ENGENHARIA on 09/08/12
For personal use only.

SAUL WOLFE and TOVA HOZ. Can. J. Chem. **72**, 1044 (1994).

The semiempirical molecular orbital procedures MINDO/3, MNDO, MNDO/M, AM1, and PM3 have been used to examine possible mechanisms and modes of attack of methanol on penam, the bicyclic ring system of penicillin. These mechanisms include a one-step process in which C—O bond formation from the convex face of the molecule and proton transfer to the β-lactam nitrogen are concerted with the cleavage of the N—C(O) bond (the N-protonated pathway), and two O-protonated pathways, viz., addition to the β-lactam carbonyl group from the convex face and from the concave face of the bicyclic ring system. Only MINDO/3 reproduces the ab initio MP2/6-31G*//3-21G* trends, that the N-protonated pathway is energetically preferred over either O-protonated pathway, and, in the latter, attack from the convex face is slightly preferred over attack from the concave face. MINDO/3 has, therefore, been used for a systematic examination of the reactions of many substituted and unsubstituted β-lactam-containing ring systems with methanol. The N-protonated structure created by attack of the alcohol from the convex face of the molecule is always preferred, and structure–reactivity relationships are observed that parallel structure–activity relationships of β-lactam antibiotics. MINDO/3 has also been used to compute a scaled quantum mechanical force field for Δ^2- and Δ^3-cephems. This has allowed parameters to be proposed for Δ^2- and Δ^3-cephems in the force field of Allinger's MMP2(85) programme that complement earlier parameterizations of the program for penicillins and peptides. The availability of these parameters has led to the development of a protocol for the analysis of the differences in the antibacterial activities of penicillins and cephalosporins. The analysis is based on a combination of "fit" and "reactivity" at the site of action. Fit is determined from the geometry that results when the β-lactam compound is complexed to a hexapeptide model of the penicillin receptor, in particular, the four-centred interaction between C-O-H of the active site serine residue and (O)C-N of the azetidinone ring. Reactivity is derived from MINDO/3 calculations of $\Delta E^{\neq}$ for the reaction of methanol with the different ring systems via the N-protonated pathway. Δ^3-Cephalosporins are suggested to be inherently less active than penicillins because they are inherently less *reactive*. Δ^2-Cephalosporins containing a 4α-oriented carboxyl group are much less active than Δ^3-cephalosporins because they have a much poorer *fit*. The 4β epimers of these Δ^2-cephalosporins are much less active than Δ^3-cephalosporins because they are much less *reactive*.

SAUL WOLFE et TOVA HOZ. Can. J. Chem. **72**, 1044 (1994).

On a utilisé les méthodes de calculs d'orbitales moléculaires semiempiriques MINDO/3, MNDO, MNDO/M, AM1 et PM3 pour étudier les mécanismes possibles et les modes d'attaque du méthanol sur le péname, le système bicyclique de la pénicilline. Ces mécanismes incluent le processus en une étape au cours duquel la formation d'une liaison C—O à partir de la face convexe de la molécule et le transfert de proton à l'azote du β-lactame se font d'une façon concertée avec le clivage de la liaison N—C(O) (la voie N-protonée) ainsi que deux voies O-protonées, à savoir l'addition au groupe carbonyle du β-lactame à partir de le face convexe ou de la face concave du système bicyclique. Seuls les calculs MINDO/3 ont permis de reproduire les tendances des calculs ab initio MP2/6-31G*//3-21G* selon lesquels la voie N-protonée est d'une point de vue énergétique préférée aux deux voies O-protonées et, dans ces derniers cas, l'attaque par la face convexe est légèrement préférée à une attaque par la face concave. On a donc utilisé les calculs MINDO/3 pour examiner d'une façon systématique les réactions du méthanol avec plusieurs systèmes cycliques de β-lactames substitués et non substitués. La structure N-protonée créée par l'attaque de l'alcool sur la face convexe de la molécule est toujours privilégiée et on a observé des relations structure–activité qui sont parallèles aux relations structure–activité d'antibiotiques de β-lactames. On a aussi utilisé des calculs MINDO/3 pour calculer un champ de force de mécanique quantique pour les Δ^2- et Δ^3-céphèmes. On a ainsi pu proposer des paramètres pour les Δ^2- et Δ^3-céphèmes dans le champ de force du programme MMP2(85) d'Allinger qui sert de complément aux paramétrisations antérieures du programme pour les pénicillines et les peptides. La disponibilité de ces paramètres a conduit au développement d'un protocole pour l'analyse des différences dans les activités antibactériennes des pénicillines et des céphalosporines. L'analyse est basée sur une combinaison d'«ajustement» et de «réactivité» au site de l'action. L'ajustment est déterminé à partir des géométries qui sont obtenues lorsque le composé β-lactame se complexe à un hexapeptide modèle du récepteur de la pénicilline, en particulier, l'interaction à quatre centres entre le C-O-H de la sérine du site actif et le (O)C-N du noyau de l'azétidinone. La réactivité est déterminée par des calculs MINDO/3 du $\Delta E^{\neq}$ pour la réaction du méthanol avec divers systèmes cycliques par le biais de la voie N-protonée. Il est suggéré que les Δ^3-céphalosporines sont d'une façon inhérente moins actives que les pénicillines parce qu'elles sont d'une façon inhérente moins *réactives*. Les Δ^2-céphalosporines contenant un groupe carboxyle orienté en 4α sont beaucoup moins actives que les Δ^3-céphalosporines parce qu'elles s'*ajustent* beaucoup plus mal. Les épimères 4β de ces Δ^2-céphalosporines sont moins actifs que les Δ^3-céphalosporines parce qu'ils sont beaucoup moins *réactifs*.

[Traduit par la Rédaction]

---

[1]Canada Council Killam Research Fellow, 1990–1992.

[2]Simon Fraser University.

[3]Present address: Department of Chemistry, Bar Ilan University, Ramat Gan, Israel.

TABLE 1. Relative energies (kcal/mol) of four-centred transition structures[a] in the reaction of methanol with penam, a fused β-lactam thiazolidine compound

Reaction	MP2/6-31G*//3-21G*	MINDO/3	MNDO	MNDO/M	AM1	PM3
N-Attack	0.00	0.00	7.38	10.39	10.84	11.19
O-Attack (convex)	7.77	4.80	0.00	0.00	0.00	0.00
O-Attack (concave)	9.95	5.54	6.62	6.43	5.19	3.90

[a]All transition structures have been characterized by vibrational analysis, and exhibit one imaginary frequency.

Introduction

Cephalosporins (**1**) are related to penicillins (**2**) structurally (1), biosynthetically (2), and in their mechanism of action (3). This mechanism includes complexation of the antibiotic to the active site of a penicillin binding protein (PBP) (4) (Step 1), followed by acylation of a serine hydroxyl group of this enzyme by the β-lactam carbonyl group (5) (Step 2).

We have recently studied Step 1 (6) for a series of penicillins, using a computer-derived model of the active site hexapeptide (Ac-Val[1]-Gly[2]-Ser[3]-Val[4]-Thr[5]-Lys[6]-NHMe) of a PBP from *Streptomyces* R61 (7). Examination of the geometry of the interaction between the serine O-H and the β-lactam N-C(O) in these complexes led to the suggestion that Step 2 may involve protonation of the β-lactam nitrogen concerted with C7—O bond formation. Support has now been obtained for the existence and, indeed, energetic preference for this mechanism (8) in the gas phase, and also in the presence of a catalytic water molecule (9).

These findings lead to the idea that the differing antibacterial activities exhibited by different β-lactam-containing ring systems are determined, inter alia, by their different "fits" to the PBP (Step 1), and their different intrinsic "reactivities" towards alcoholysis via an N-protonated transition structure (Step 2). The present work is concerned with an examination of the "fits" and "reactivities" associated with the penicillin, Δ^2-cephalosporin, and Δ^3-cephalosporin classes of β-lactam compounds bearing the common side chain R = $PhOCH_2CONH$ of penicillin V.

Cephalosporins undergo a facile $\Delta^3 \rightleftarrows \Delta^2$ isomerization, to give equilibrium mixtures in which the *biologically inactive* Δ^2 isomer (**3**) predominates (10). Several kinds of explanations have been advanced to account for this loss of activity (11). The majority of the earlier proposals had focused on the apparent stability of Δ^2-cephems towards *basic* hydrolysis (11*a*), but in an important contribution, Cohen (11*b*) argued that the problem resides in the fit of such compounds to the penicillin receptor, and that an improved fit might be achieved by 4-*epi*-Δ^2-cephems (**4**). However, compounds of this type have since been found also to be inactive (12).

Results and discussion

A semiempirical molecular orbital treatment of "reactivity"

As a measure of the different "reactivities" of different β-lactam containing ring systems, we wished to compute $\Delta E^{\ddagger}$ for the four-centred reaction of methanol with the N-C(O) groups of these compounds. Because of the large number of $\Delta E^{\ddagger}$ computations that were required, ab initio methods were not feasible, and a semiempirical approach was sought from among MINDO/3 (13), MNDO (14), MNDO/M (15), AM1 (16), and PM3 (17). The decision regarding which of these would be most reliable was based on the ab initio benchmark of ref. 9: at the MP2/6-31G*//3-21G* level, transition structure **5**, which involves attack from the convex face of the molecule and proton transfer to the β-lactam nitrogen, is 7.77 kcal/mol more stable than transition structure **6**, which involves attack from the convex face of the molecule and proton transfer to the carbonyl oxygen; **6** is, in turn, 2.18 kcal/mol more stable than transition structure **7**, in which addition to the carbonyl group takes place from the concave face of the molecule. As can be seen in Table 1, only MINDO/3 captures the ab initio trends.

TABLE 2. Calculated $\Delta\Delta E^{\ddagger}$ (kcal/mol, MINDO/3) relative to penam for the methanolyses of β-lactam compounds via N-protonated transition structures[a]

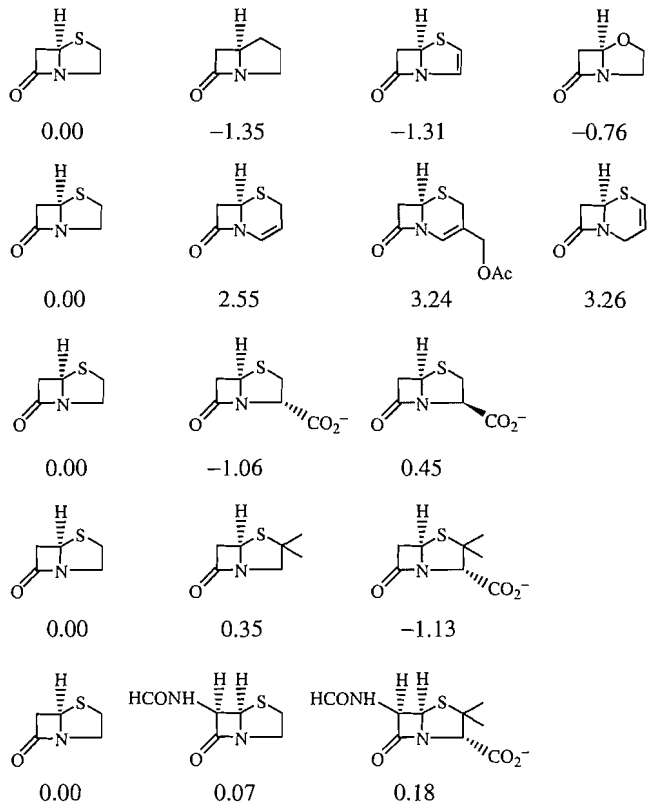

[a]See footnote *a* of Table 1.

Structure–activity and structure–"reactivity" relationships

Table 2 summarizes the calculated activation energies ($\Delta\Delta E^{\ddagger}$, MINDO/3, kcal/mol relative to penam) for the methanolyses of a number of bicyclic azetidinones. Each row of Table 2 examines the effect of a different kind of structural change on the $\Delta E^{\ddagger}$ of penam, the parent compound. The data are discussed row by row:

1. The relative reactivities are carbapenam > penem > oxap-

Can. J. Chem. Downloaded from www.nrcresearchpress.com by EESC ESCOLA DE ENGENHARIA on 09/08/12
For personal use only.

TABLE 3. Calculated $\Delta\Delta E^{\ddagger}$ (kcal/mol, MINDO/3) relative to **8** for the methanolyses of carboxy-substituted cephalosporins via a four-centred N-protonated transition structure[a]

Substrate	$\Delta\Delta E^{\ddagger}$
8	0.00
9	1.94
10	2.81
11	4.65
12	2.08
13	3.50
14	8.04
15	8.33

[a]See footnote *a* of Table 1.

enam > penam. Oxapenicillins (18) and penems (19) having the C3 and C6 substituents of penicillins are known to have antibacterial activity; although the carbapenam ring system is known (20), carbapenicillins have not yet been reported.

2. In the comparison of the penam and cephem ring systems, the relative reactivities are penam >> Δ^3-cephem > Δ^2-cephem, acetoxymethyl-Δ^3-cephem. With a common acylamino side chain, penicillins are an order of magnitude more active than acetoxymethyl-Δ^3-cephalosporins and the latter are, in general, an order of magnitude more active than 3-methyl-Δ^3-cephems (21); as already mentioned, Δ^2-cephems are inactive.

3. Introduction of the C3α-carboxyl group enhances the reactivity. We suggest that the carboxyl group assists the methanolysis through hydrogen bonding, because epimerization (C3β) decreases the reactivity significantly.

4. Introduction of C2-methyl substituents decreases the reactivity, unless a C3α-carboxyl group is present.

5. The 6β-acylamino substituent has almost no effect on the reactivity. Consequently, the chemical reactivity of a penicillin differs only slightly from that of the parent penam.

Figure 1 shows stereoscopic views of three isomeric transition structures for the methanolysis of the β-lactam ring of formylpenicillin. A is the N-protonated transition structure; B is the O-protonated transition structure for attack from the convex face; C is the O-protonated transition structure for attack for the concave face. The relative energies of the structures are A: 0.00 kcal/mol; B, 7.36 kcal/mol; C, 9.73 kcal/mol.[4]

The trend seen on line 3 of Table 1 is also present in 4α-carboxy and 4β-carboxy-Δ^2-cephems. Table 3 gives $\Delta E^{\ddagger}$ relative to 2,2-dimethyl-3α-carboxypenam (**8**) for the methanolysis of the β-lactam rings of cephems via N-protonated transition structures. The relative reactivities are: penam (**8**) > Δ^2-cephem (**9**) > Δ^3-cephem (**10**) > 4-*epi*-Δ^2-cephem (**11**). The stereoisomers **9** and **11** exhibit a 2.71 kcal/mol difference in $\Delta E^{\ddagger}$. If this difference reflects the hydrogen-bonding assistance provided for attack from the convex face of the molecule by an α-oriented carboxylate group, the reactivity of **11** might be improved by the introduction of a new hydrogen-bonding donor atom onto this convex face. Possible sites for such a substituent include 4α and 7α (see **9** for numbering), and Table 3 includes the results obtained for the 7α-methoxy (**12**), 4α-carboxy (**13**), 7α-fluoro (**14**), and 4α-methoxy (**15**) compounds. Depending on their "fits", the "reactivities" calculated for **12** and **13** could make acylamino-substituted derivatives of these compounds interesting.

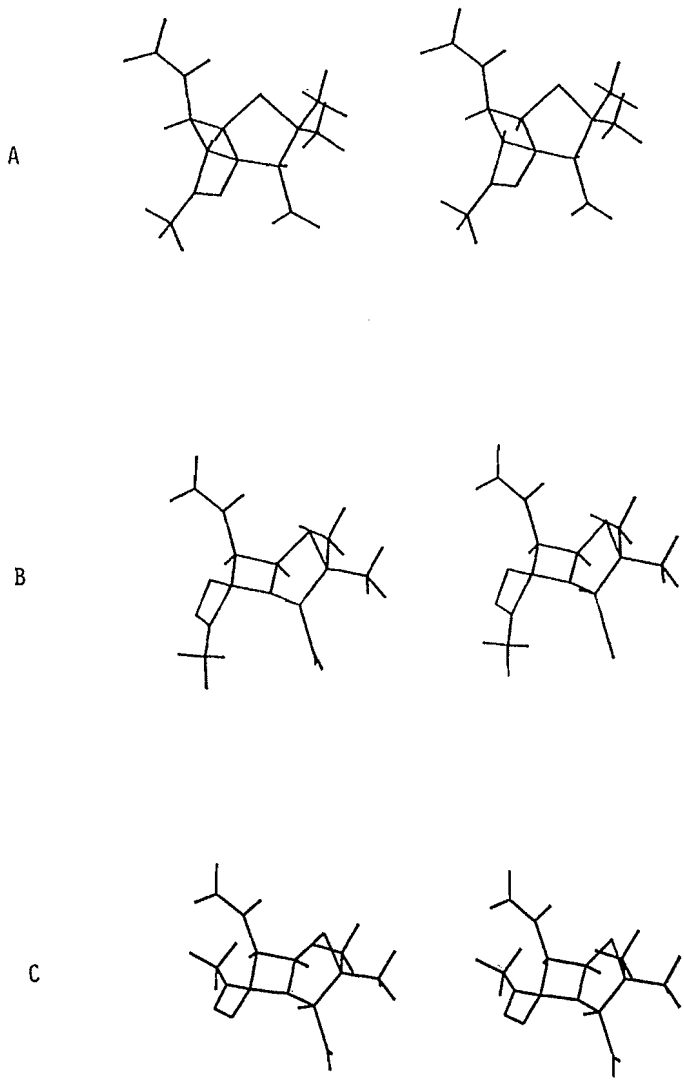

FIG. 1. (*a*) N-protonated transition structure for the methanolysis of N-formylpenicillin; (*b*) O-protonated transition structure for the methanolysis of N-formylpenicillin from the convex face; (*c*) O-protonated transition structure for the methanolysis of N-formylpenicillin from the concave face. All structures have been optimized fully using MINDO/3.

Ceparam, a parameterization of cephalosporins for MMP2(85)

A prerequisite to the treatment of the "fit" of cephalosporins to our hexapeptide model of the penicillin receptor is the establishment of parameters for the molecular mechanics force field of MMP2(85) (22), comparable in quality to MMPEN (23), the parameterization of this force field for penicillins. In the case of MMPEN, torsional and electrostatic parameters were determined computationally (24, 25), van der Waals parameters were taken from MMP2(85), and stretching and bending parameters were available from crystallographic data and the experimental force fields of 2-azetidinone and thiazolidine. An analogous strategy was envisaged for cephalosporins, but the paucity of crystallographic information and absence of vibra-

[4]All of the primary data (geometries, parameters) of this article are available as supplementary data, and may be purchased from the Depository of Unpublished Data, Documentary Delivery, CISTI, National Research Council Canada, Ottawa, Canada K1A 0S2.

Can. J. Chem. Downloaded from www.nrcresearchpress.com by EESC ESCOLA DE ENGENHARIA on 09/08/12
For personal use only.

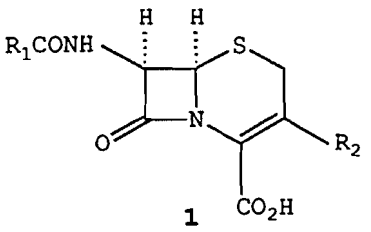
1

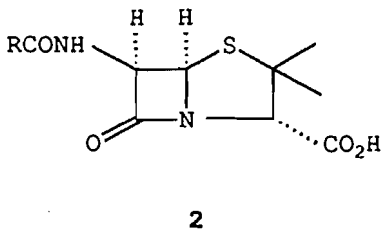
2

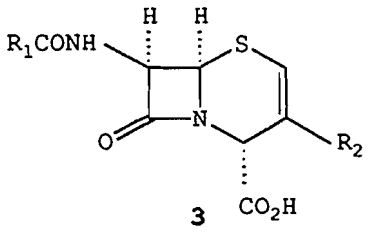
3

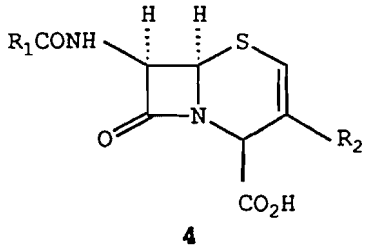
4

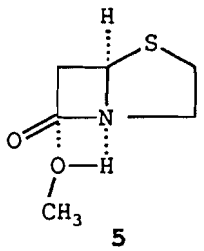
5

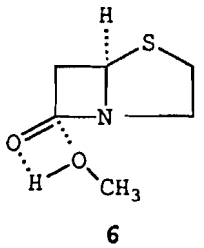
6

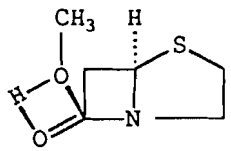
7

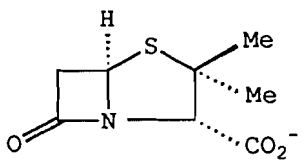
8

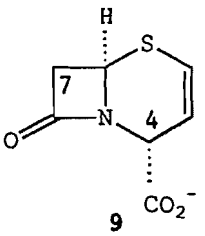
9

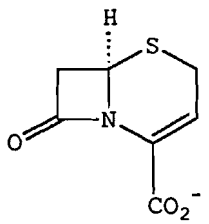
10

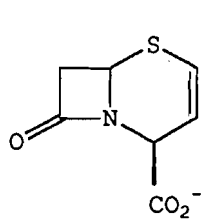
11

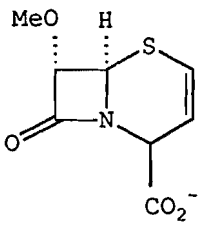
12

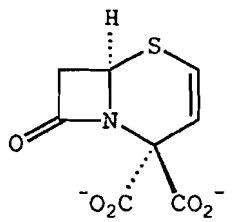
13

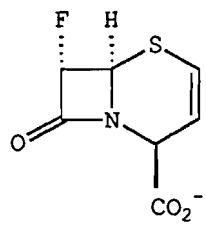
14

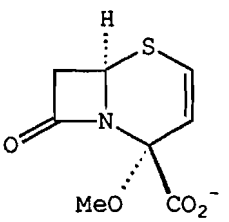
15

tional data for dihydrothiazines necessitated a scaled quantum mechanical (SQM) (26) approach to obtain the stretching and bending parameters.

Using MINDO/3, the internal coordinates of the optimized geometries of 3-methyl-Δ^2- and 3-methyl-Δ^3-cephem were distorted one at a time (27)[5] in both positive and negative directions by 0.01 Å for bond stretching, and 1.0° for angle bending, while the rest of the molecule was allowed to relax, and the force constants were calculated numerically. Scaling factors were determined by inspection of calculated and experimental results for cyclohexene (28), cyclobutane (29), azetidine (30), 2-azetidinone (31), thiazolidine (32), propene (33), 1-propenethiol (34), and allylamine (35), and are included with the supplementary data.[4]

As a preliminary test of the SQM computational strategy, the stretching and bending parameters of the penicillin nucleus were calculated, using MINDO/3. Introduction of these parameters into MMPEN (23) in place of the previous experimentally derived parameters (31, 32) allowed the crystal structure of penicillin G to be reproduced exactly.

Completion of the parameterization then followed established procedures (23). The final refinements of the torsional parameters were performed by trial and error, until the rms

[5]The AMPAC program (16) was used in conjunction with Essén's algorithm.

Can. J. Chem. Downloaded from www.nrcresearchpress.com by EESC ESCOLA DE ENGENHARIA on 09/08/12
For personal use only.

Can. J. Chem. Downloaded from www.nrcresearchpress.com by EESC ESCOLA DE ENGENHARIA on 09/08/12
For personal use only.

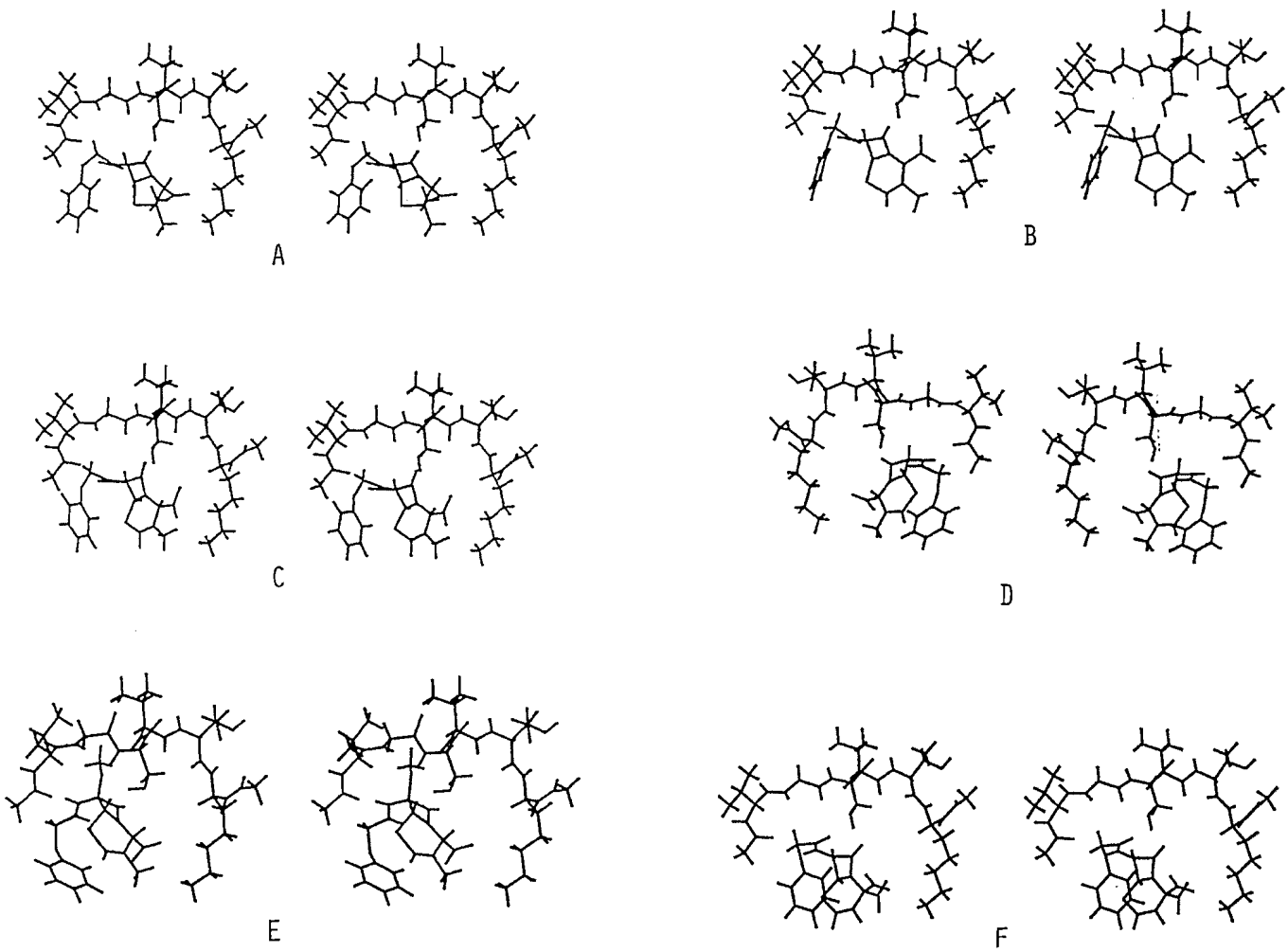

FIG. 2. A. Stereoscopic view of the complex formed between penicillin V (**18**) and a model of the penicillin receptor. B. Stereoscopic view of the complex formed from **19**. C. Stereoscopic view of the complex formed from **17**. D. Stereoscopic view of the complex formed from **20**. E. Stereoscopic view of the complex formed from **21**. F. Stereoscopic view of the complex formed from **22**.

deviations from the experimental crystal structures of **16** (36) and **17** (37) were less than 0.4 Å in each case.

Fitting penicillin V and cephalosporin V analogs to the receptor model

Figure 2 shows stereoscopic views of the complexes formed between our model of the penicillin receptor (6) and: A, penicillin V (**18**); B, 3-methyl-Δ^3-cephalosporin V (**19**); C, 3-methyl-Δ^2-cephalosporin V (**17**); D, 3-methyl-4-*epi*-Δ^2-cephalosporin V (**20**); E, 3-methyl-4-*epi*-7α-methoxy-Δ^2-cephalosporin V (**21**); F, 3-methyl-4,4-dicarboxy-Δ^2-cephem (**22**). To obtain these complexes (6), hydrogen bonding was assumed between the carboxyl group of the β-lactam compound and the terminal amino group of Lys^6, and between the side-chain N-H and the Val^1 end group, a preliminary minimization was performed using a simplified van der Waals and electrostatic force field, and the Cartesian coordinates of the resulting supermolecule were then employed as input to MMP2(85).

The docking of several conformations of each of the β-lactam compounds was examined and, in each case, the lowest energy complex was achieved from the global minimum of the uncomplexed structure. In the global minima of **17**, **19**, and **20**, the conformations of the dihydrothiazine rings are the same as in the crystal structures, but Ar···S interactions (38) cause compact conformations of the side chains to be preferred, as already noted for penicillins (23).

TABLE 4. Root-mean-square (rms) differences (Å), relative to penicillin V, of the Cartesian coordinates of the O-H atoms of serine and the C(O)-N atoms of the azetidinone ring in complexes of β-lactam compounds with a model of the penicillin receptor (column 2). Activation energies (MINDO/3, kcal/mol, from Table 3), relative to **8**, for the reaction of azetidinones with methanol (column 3). The product of rms × $\Delta\Delta E^{\ddagger}$ (column 4)

Substrate	rms	$\Delta\Delta E^{\ddagger}$	rms × $\Delta\Delta E^{\ddagger}$
18	0.000	0.00	0.00
19	0.103	2.81	0.29
17	0.684	1.94	1.33
20	0.252	4.65	1.17
21	0.482	2.08	1.00
22	0.543	3.50	1.90

Inspection of Fig. 2 illustrates, in each case, the *exo* orientation and four-centred nature of the interaction between C-O-H of serine and (O)C-N of the azetidinone Table 4 lists the rms differences (in Å), relative to penicillin V, of the Cartesian coordinates of the O-H/C-N interaction. The fit of the 4-*epi*-

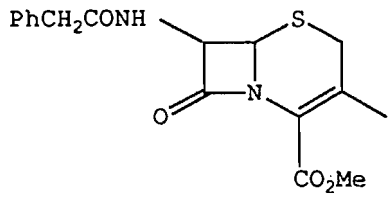

16

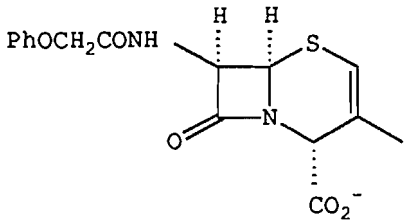

17

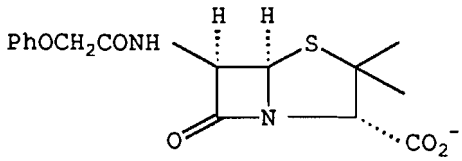

18

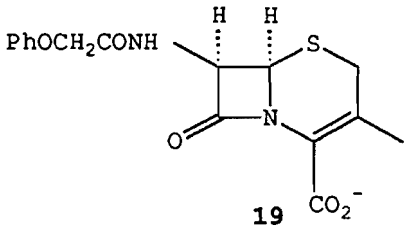

19

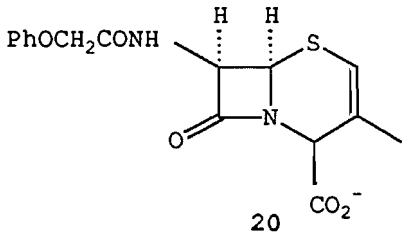

20

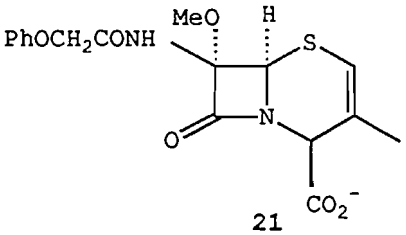

21

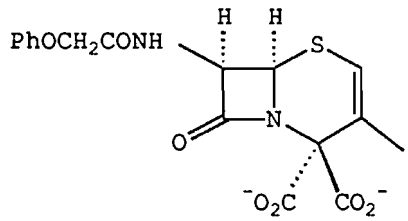

22

Δ^2-cephem **20** to the model of the penicillin receptor is much better than that of the Δ^2-cephem **17**, *as predicted by Cohen* (11*b*). Table 4 also includes $\Delta\Delta E^{\ddagger}$, relative to penicillin, for the various compounds, as well as the *product* rms $\times$ $\Delta\Delta E^{\ddagger}$, which appears to order **17–20** in the order of their antibacterial activities. Based on this quantity, **17** is inactive because of its poorer fit, and **20** is inactive because of its reduced chemical reactivity. Taken together, the "fits" and "reactivities" of **21** and **22** suggest that **21** may be more active, and **22** less active than previously described Δ^2-cephems. Experimental tests of these conclusions, as well as syntheses of novel structures based on the analysis developed herein, are in progress.

Acknowledgements

This research was supported by the Natural Sciences and Engineering Research Council of Canada. The authors thank Queen's University and Simon Fraser University for generous allocation of computer resources.

1. E.H. Flynn (*Editor*). Cephalosporins and penicillins. Chemistry and biology. Academic Press, New York. 1972.
2. S. Wolfe, A.L. Demain, S.E. Jensen, and D.W.S. Westlake, Science, **226**, 1386 (1984); J.E. Baldwin and E.P. Abraham. Nat. Prod. Reps. 129 (1988).
3. D.J. Waxman and J.L. Strominger. *In* Chemistry and biology of β-lactam antibiotics. Vol. 3. *Edited by* R.B. Morin and M. Gorman. Academic Press, New York. 1982. p. 209.
4. D.J. Waxman and J.L. Strominger. Annu. Rev. Biochem. **52**, 825 (1983).
5. R.R. Yocum, D.J. Waxman, J.R. Rasmussen, and J.L. Strominger. Proc. Natl. Acad. Sci. U.S.A. **76**, 2730 (1979).
6. S. Wolfe, K. Yang, and M. Khalil. Can. J. Chem. **66**, 2733 (1988).
7. J.A. Kelly, J.R. Knox, P.C. Moews, G.J. Hite, J.B. Bartolone, H. Zhao, B. Joris, J.-M. Frère, and J.-M. Ghuysen. J. Biol. Chem. **260**, 6449 (1985).
8. I.H. Williams, D. Spangler, G.M. Maggiora, and R.L. Schowen. J. Am. Chem. Soc. **107**, 7717 (1985); M.J.S. Dewar. Enzyme, **36**, 8 (1986).
9. S. Wolfe, C.-K. Kim, and K. Yang. Can. J. Chem. **72**, 1033 (1994).
10. S. Mobashery and M. Johnston. J. Org. Chem. **51**, 4723 (1986), and references cited therein.
11. (*a*) J.-M. Frère, J.A. Kelly, D. Klein, and J.-M. Ghuysen. Biochem. J. **203**, 223 (1982), and references cited therein; (*b*) N.C. Cohen. J. Med. Chem. **26**, 259 (1983).

Can. J. Chem. Downloaded from www.nrcresearchpress.com by EESC ESCOLA DE ENGENHARIA on 09/08/12
For personal use only.

12. N.C. Cohen, I. Ernest, H. Fritz, H. Fuhrer, G. Rihs, R. Scartazzini, and P. Wirz. Helv. Chim. Acta, **70**, 1967 (1987).
13. R.C. Bingham, M.J.S. Dewar, and D.M. Lo. J. Am. Chem. Soc. **97**, 1285 (1975).
14. M.J.S. Dewar and W. Thiel. J. Am. Chem. Soc. **99**, 4899 (1977).
15. A.A. Bliznyuk and A.A. Voityuk. J. Mol. Struct. (THEOCHEM), **164**, 343 (1988).
16. M.J.S. Dewar, E.G. Zoebisch, E.F. Healy, and J.J.P. Stewart. J. Am. Chem. Soc. **107**, 3902 (1985).
17. J.J.P. Stewart. J. Comput. Chem. **10**, 221 (1989).
18. L.D. Cama and B.G. Christensen, Tetrahedron Lett. 4233 (1978).
19. I. Ernest, J. Gosteli, C.W. Greenglass, W. Holick, D.E. Jackman, H.R. Pfaendler, and R.B. Woodward. J. Am. Chem. Soc. **100**, 8214 (1978).
20. M.D. Bachi, R. Breiman and H. Meshulam. J. Org. Chem. **48**, 1439 (1983).
21. J.R.E. Hoover. *In* Antibiotics containing the beta-lactam structure. Part II. *Edited by* A.L. Demain and N.A. Solomon. Springer-Verlag, Berlin. 1983. Chap. 14.
22. N.L. Allinger. MMP2(85). Available from Quantum Chemistry Program Exchange, Bloomington, Ind.
23. S. Wolfe, M. Khalil, and D.F. Weaver. Can. J. Chem. **66**, 2715 (1988).
24. A.J. Hopfinger and R.A. Pearlstein. J. Comput. Chem. **5**, 486 (1984).
25. S.J. Weiner, P.A. Kollman, D.T. Nguyen, and D.A. Case. J. Comput. Chem. **7**, 230 (1986); B.R. Brooks, R.E. Bruccoleri, B.D. Olafson, D.J. States, S. Swaminathan, and M. Karplus. J. Comput. Chem. **4**, 187 (1983).
26. C.E. Blom and C. Altona. Mol. Phys. **31**, 1377 (1976); M.J.S. Dewar, G.P. Ford, M.L. McKee, H.S. Rzepa, W. Thiel, and Y. Yamaguchi. J. Mol. Struct. **43**, 135 (1978); P. Pulay, G. Fogarasi, G. Pongor, J.E. Boggs, and A. Vargha. J. Am. Chem. Soc. **105**, 7037 (1983); G. Fogarasi and P. Pulay. Annu. Rev. Phys. Chem. **35**, 191 (1984); R.A. Shaw, C. Ursenbach, A. Rauk, and H. Wieser. Can. J. Chem. **66**, 1318 (1988); M. Ruiz-Pastrana, J.M. Hernando, and E. Velasco. J. Mol. Struct. (THEOCHEM), **166**, 279 (1988).
27. H. Essén. J. Comput. Chem. **4**, 136 (1983).
28. N. Neto, C. Di Lauro, E. Castellucci and S. Califano. Spectrochim. Acta, Part A: **23A**, 1763 (1967).
29. G. Bánhegyi, G. Fogarasi, and P. Pulay. J. Mol. Struct. **89**, 1 (1982).
30. H. Günther, G. Schrem, and H. Oberhammer. J. Mol. Spectrosc. **104**, 152 (1984).
31. K. Hanai, Y. Maki, and A. Kuwae. Bull. Chem. Soc. Jpn. **58**, 1367 (1985).
32. M. Guilliano, G. Mille, T. Avignon, and J. Chouteau. Raman Spectrosc. **7**, 214 (1978).
33. C.E. Blom and C. Altona. Mol. Phys. **34**, 177 (1977).
34. J.N. Macdonald, N.L. Owen, and M. Rosolini. J. Mol. Struct. **159**, 229 (1987).
35. K. Yamanouchi, T. Matsuzawa, K. Kuchitsu, Y. Hamada, and M. Tsuboi. J. Mol. Struct. **126**, 305 (1985).
36. P. Domiano, M. Nardelli, A. Balsamo, B. Macchia, F. Macchia, and G. Meinardi. J. Chem. Soc. Perkin Trans. 2, 1082 (1978).
37. R.M. Sweet and L.F. Dahl. J. Am. Chem. Soc. **92**, 5489 (1970).
38. M. Lebl, E.E. Sugg, and V.R. Hruby. Int. J. Pept. Protein Res. **29**, 40 (1987), and references cited therein.

Can. J. Chem. Downloaded from www.nrcresearchpress.com by EESC ESCOLA DE ENGENHARIA on 09/08/12
For personal use only.

Interactive design and synthesis of a novel antibacterial agent[1]

SAUL WOLFE,[2,3] HAOLUN JIN,[4] KIYULL YANG,[5] CHAN-KYUNG KIM, AND ERNEST MCEACHERN[6]

Department of Chemistry, Simon Fraser University, Burnaby, BC V5A 1S6, Canada, and Department of Chemistry, Queen's University, Kingston, ON K7L 3N6, Canada

Received June 22, 1993

SAUL WOLFE, HAOLUN JIN, KIYULL YANG, CHAN-KYUNG KIM, and ERNEST MCEACHERN. Can. J. Chem. **72**, 1051 (1994).

β-Lactam compounds act on penicillin-recognizing enzymes via acylation of the hydroxyl group of an active site serine. When the resulting acyl enzyme is kinetically stable, as in the case of a penicillin-binding protein (PBP), the biosynthesis of a bacterial cell wall is inhibited, and death of the organism results. The de novo design of an antibacterial agent targeted to a PBP might be possible if the three-dimensional structural requirements of the equilibrium (i.e., *fit*) and catalytic (i.e. *reactivity*) steps of the aforementioned enzymatic process could be determined. For a model of the active site of a PBP from *Streptomyces* R61, the use of molecular mechanics calculations to treat "fit," and ab initio molecular orbital calculations to treat "reactivity," leads to the idea that the carboxyl group (G_1) and the amide N-H (G_2) of the antibiotic are hydrogen bonded to a lysine amino group and a valine carbonyl group in the enzyme–substrate complex. These two hydrogen bonds place the serine hydroxyl group on the convex face of the antibiotic, in position for attack on the β-lactam ring by a neutral reaction, catalyzed by water, that involves a direct proton transfer to the β-lactam nitrogen. Molecular orbital calculations of structure–reactivity relations associated with this mechanism suggest that C═N is bioisosteric to the β-lactam N-C(═O), comparable to a β-lactam in its reactivity with an alcohol, and that the product RO(C-N)H is formed essentially irreversibly ($-\Delta E > 10$ kcal/mol). Accordingly, structures containing a G_1 and a G_2 separated by a C═N, and positioned in different ways with respect to this functional group, have been synthesized computationally and examined for their ability to fit to the PBP model. This strategy identified a 2*H*-5,6-dihydro-1,4-thiazine substituted by hydroxyl and carboxyl groups as a target for chemical synthesis. However, exploratory experiments suggested that the C═N of this compound equilibrates with endocyclic and exocyclic enamine tautomers. This required that the C2 position be substituted, and that the hydroxyl group not be attached to the carbon atom adjacent to the C═N. These conditions are met in a 2,2-dimethyl-3-(2-hydroxypropyl)-1,4-thiazine, which also exhibits the necessary fit to the PBP model. Two epimers of this compound have been synthesized, from D- and L-serine. The compound derived from L-serine is not active. The compound derived from D-serine exhibits antibacterial activity, but is unstable, and binding studies with PBP's have not been performed. It is hoped that these studies can be carried out if modification of the lead structure leads to compounds with improved chemical stability.

SAUL WOLFE, HAOLUN JIN, KIYULL YANG, CHAN-KYUNG KIM et ERNEST MCEACHERN. Can. J. Chem. **72**, 1051 (1994).

Les β-lactames agissent sur les enzymes qui reconnaissent la pénicilline par le biais d'une acylation du groupe hydroxyle d'un site actif de la sérine. Lorsque l'enzyme acylé qui en résulte est cinétiquement stable, comme dans le cas d'une pénicilline se liant à une protéine (PBP), la biosynthèse d'une paroi de la cellule bactérienne est inhibée et la mort de l'organisme s'en suit. Le «design» de novo d'un agent antibactérien orientée vers une PBP peut être possible s'il est possible de déterminer les besoins structuraux des étapes d'équilibre (à savoir l'*ajustement*) et catalytique (à savoir la *réactivité*) des processus enzymatiques mentionnés plus haut. Pour un modèle du site actif d'une PBP du *Streptomyces* R61, l'utilisation de calculs de mécanique moléculaire pour examiner l'adjustement et des calculs d'orbitales moléculaires ab initio pour traité de la «réactivité» conduisent à la suggestion que, dans le complexe enzyme–substrat, le groupe carboxyle (G_1) et le groupe amide (G_2) de l'antibiotique sont reliés à un groupe amino de la lysine et à un groupe carbonyle de la valine par des liaisons hydrogènes. Ces deux liaisons hydrogènes placent le groupe hydroxyle de la sérine sur la face convexe de l'antibiotique, dans une position permettant une attaque sur le noyau β-lactame par une réaction neutre, catalysée par l'eau, qui implique un transfert direct de proton à l'azote du β-lactame. Des calculs d'orbitales moléculaires des relations structure–réactivité associées avec ce mécanisme suggèrent que le C═N est bioisostérique avec le β-lactame, N-C(═O), comparable au β-lactame en ce qui a trait à sa réactivité avec un alcool, et que le produit RO(C-N)H se forme d'une façon qui est essentiellement irréversible ($-\Delta E > 10$ kcal/mol). Sur cette base, on a synthétisé par ordinateur des structures contenant les groupes G_1 et G_2 séparés par un C═N et placés dans des positions diverses par rapport à ce groupe fonctionnel et on a examiné leur habilité à s'insérer dans le modèle PBP. Cette stratégie a permis d'identifier une 2*H*-5,6-dihydro-1,4-thiazine substituée par des groupes hydroxyles et carboxyles comme cibles pour une synthèse chimique. Toutefois, des essais préliminaires ont suggéré que le C═N de ce composé serait en équilibre avec les énamines endocycliques et exocycliques tautomères. Cette caractéristique nécessite que la position C2 soit substituée et que le groupe hydroxyle ne soit pas attaché au carbone adjacent du C═N. On rencontre ces conditions dans une 2,2-diméthyl-3-(2-hydroxypropyl)-1,4-thiazine qui présente aussi les qualités requises pour s'insérer dans le modèle PBP. On a synthétisé deux épimères de ce composé à partir des D- et L-sérine. Le composé dérivé de la L-sérine n'est pas actif. Le composé dérivé de la D-sérine présente une activité antibactérienne, mais il est instable et on n'a pas pu effectuer d'études de liaisons avec les PBP. On espère que ces études pourront être effectuées sur des modifications de cette structure qui auraient une meilleure stabilité chimique.

[Traduit par la Rédaction]

[1]This paper is dedicated to the twin patriarchs of alkaloid synthesis and biosynthesis in Canada, David B. MacLean and Ian D. Spenser, on the occasion of their retirements from McMaster University.

[2]Canada Council Killam Research Fellow, 1990–1992.

[3]Simon Fraser University.

[4]Present address: BioChem Pharma Inc., 531 Blvd. des Prairies, Laval, QC H7V 1B7, Canada.

[5]Permanent address: Department of Chemical Education, Gyeongsang National University, Chinju 600-701, Republic of Korea.

[6]Present address: Department of Chemistry, University of British Columbia, Vancouver, B.C.

Can. J. Chem. Downloaded from www.nrcresearchpress.com by ESC ESCOLA DE ENGENHARIA on 09/08/12
For personal use only.

Can. J. Chem. Downloaded from www.nrcresearchpress.com by EESC ESCOLA DE ENGENHARIA on 09/08/12
For personal use only.

Introduction

β-Lactam antibiotics interact with their target enzymes in three stages (Scheme 1) (1). In the first stage, the antibiotic (**A**) "fits" reversibly (k_1, k_{-1}) to the enzyme (**E**-OH), to form an enzyme–substrate complex (**E**-OH·**A**). Then OH, the hydroxyl group of a serine residue, "reacts" (k_2), and is acylated by the β-lactam carbonyl group. In the final stage, the acyl-enzyme (**E**-OCOR) is hydrolysed (k_3). This regenerates **E**-OH, and produces an inactive degradation product of the antibiotic.

When $k_3 \ll k_2$, Scheme 1 leads to inactivation of the enzyme, and an enzyme that exhibits these kinetics is termed a penicillin-binding protein (PBP) (2). The inactivation of a PBP comprises a killing mechanism, because these enzymes play an essential role in the biosynthesis of bacterial cell walls. When the biosynthesis is interrupted, the wall is weakened, becomes permeable to water, and the cell swells, bursts, and dies. On the other hand, if k_3 is large in Scheme 1, it is the substrate that is inactivated; an enzyme having this property is termed a β-lactamase (3), and its presence, or its ability to be induced when an organism is challenged by a β-lactam antibiotic, are primarily responsible for bacterial resistance to these antibiotics.

Theoretical considerations: "fit" and "reactivity"

We have recently discussed the abilities of penicillins (**1**) and cephalosporins (**2**) to "fit" to a computer-generated model (Fig. 1) of the peptide Ac-Val[1]-Gly[2]-Ser[3]-Val[4]-Thr[5]-Lys[6]-NHMe (**3**) (4). This peptide contains the residues that surround the active site serine of a PBP from *Streptomyces* R61, which has been studied in some detail (5). Since (*i*) structure–activity and conformation–activity relationships project important roles for the carboxyl group and the amide N-H of a β-lactam antibiotic in its interaction with a PBP (4); (*ii*) pH-dependence studies suggest that the carboxyl group of the antibiotic is charge-paired to the terminal amino group of Lys[6] (5*b*); (*iii*) in **3**, the carbonyl group of Val[1] and the Ser[3] and Lys[6] side chains are in proximity, we "fit" β-lactam antibiotics to **3** with one hydrogen bond from the side-chain N-H to the carbonyl group of Val[1], and a second hydrogen bond from the amino group of Lys[6] to the carboxyl group.

When this docking strategy is used to "fit" the crystal structure of penicillin G (6) to **3**, the complex which results (Fig. 2) has the Ser[3] hydroxyl group positioned on the convex face of the bicyclic molecule, poised for attack on the β-lactam group. The positions of the C-O-H and N-C=O reacting groups of Fig. 2 with respect to one another (C-O approximately *syn* to C=O, and O-H approximately *syn* to N-C on the convex face) are the same as those seen in the most recent modelling of a β-lactam antibiotic into the active site of the *crystal structure* of the *Streptomyces* R61 PBP (7). However, there is a mechanistic problem associated with these structures, because addition to the carbonyl group to form the expected tetrahedral intermediate of β-lactam alcoholysis cannot occur from a geometry in which C-O and C=O are *syn* to one another.

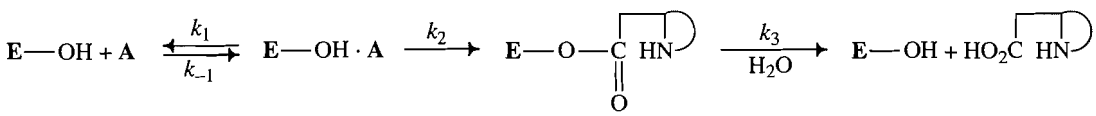

SCHEME 1

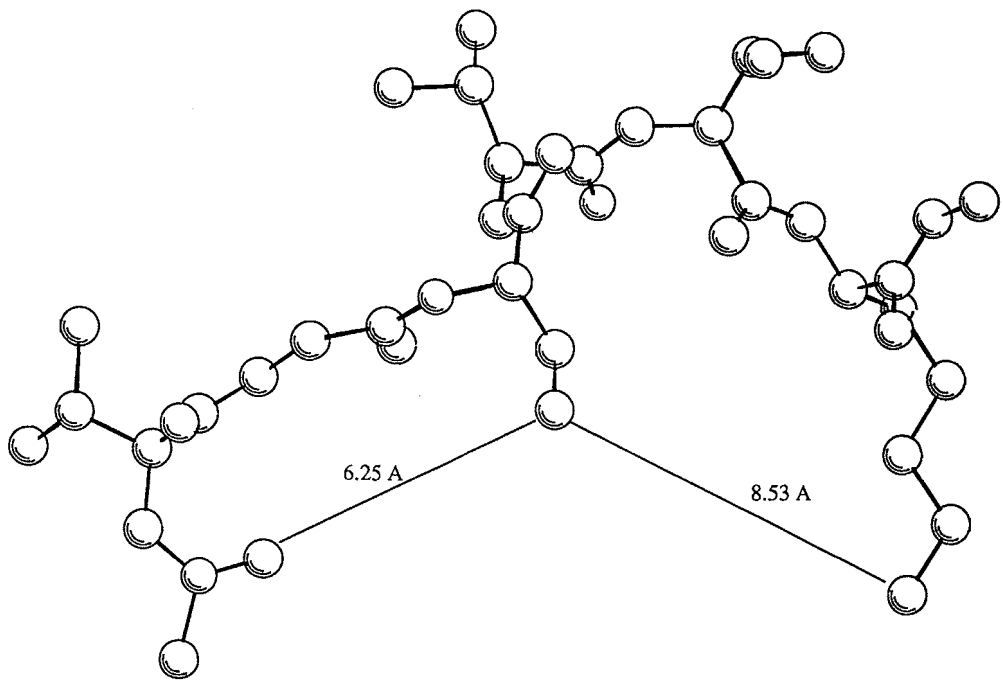

FIG. 1. A computer-generated model of the active site of a penicillin-binding protein having the sequence val-gly-ser-val-thr-lys. The model shows close contact, on the concave face, between the serine hydroxyl, the lysine amino, and a valine carbonyl.

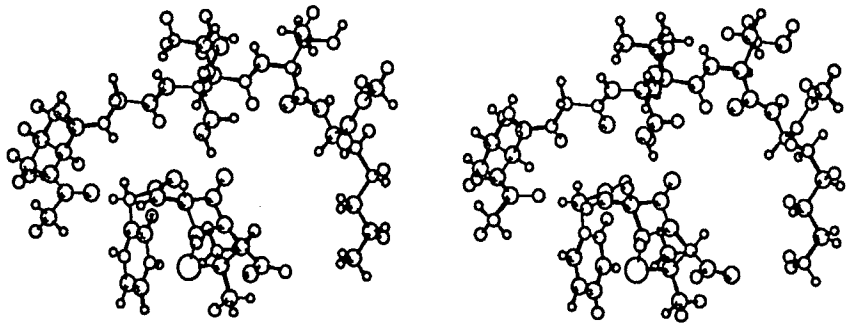

FIG. 2. Docking of the crystal structure of penicillin G to the active site model of Fig. 1. The creation of hydrogen bonds between the carboxyl group of the antibiotic and the amino group of lysine, and between the amide N-H of the antibiotic and the valine carbonyl, results in close contact between the serine hydroxyl group and the convex face of the penicillin.

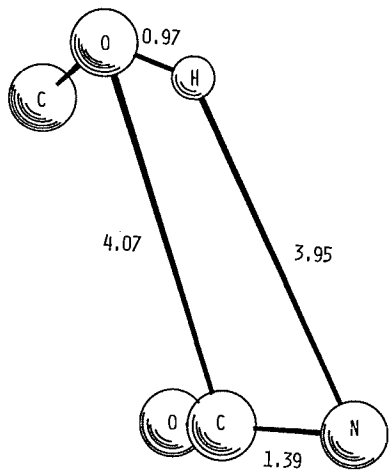

FIG. 3. A closeup view of the C-O-H/N-C=O relationship in Fig. 2.

The nature of the problem is seen more clearly in Fig. 3, a closeup view of the C-O-H/N-C=O relationship in Fig. 2. This arrangement of the reacting groups suggests that the "reactivity" step of Scheme 1, which produces the acyl-enzyme, involves C=O bond formation and proton transfer to nitrogen, *concerted with the fission of the β-lactam bond.* As we report elsewhere (8), ab initio MP2/6-31G*//3-21G* calculations (9) of the neutral hydrolysis and alcoholysis of *N*-methylazetidinone (**4**) and penam (**5**) confirm that a concerted mechanism, with proton transfer to nitrogen, exists, and is 5–10 kcal/mol energetically more favorable than addition to the carbonyl group, with proton transfer to oxygen. In addition, attack on **5** from the convex face is more favourable than attack from the concave face.

What emerges from this theoretical analysis of the first two steps of Scheme 1 is the idea that a β-lactam antibiotic "fits" to a PBP in such a way as to permit acylation of a hydroxyl group via the mechanistically and energetically most favourable chemical "reaction". The realization that the action of the enzyme involves both "fit" and "reactivity" (10) is a variation of Emil Fischer's lock and key analogy (11), in which a key fits into a lock, and then turns to open the lock.

The methanolysis of **4** exhibits significant catalysis by one water molecule (8). In this case, based on 3-21G calculations, the reaction proceeds via a ternary complex (Fig. 4), whose C-OH/N-C=O/H-O-H bond lengths are highlighted in Fig. 5.

If the water molecule is deleted from Fig. 5, what remains resembles Fig. 3. This suggests that the structure of Fig. 3 is

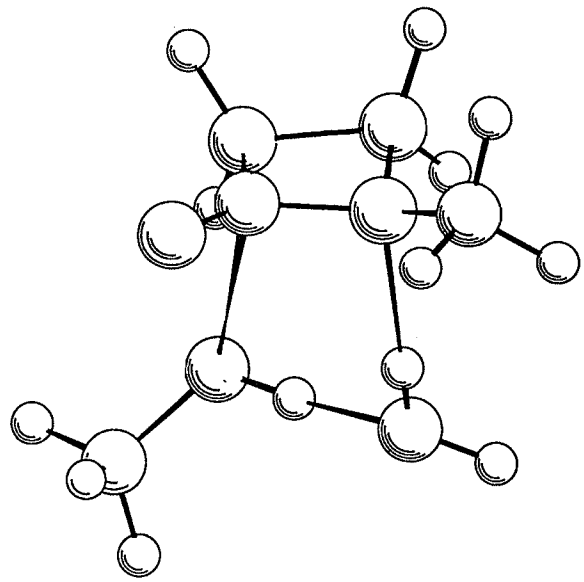

FIG. 4. Ab initio (3-21G) structure of the complex formed on the reaction coordinate when the reaction of methanol with *N*-methylazetidinone is catalyzed by one molecule of water.

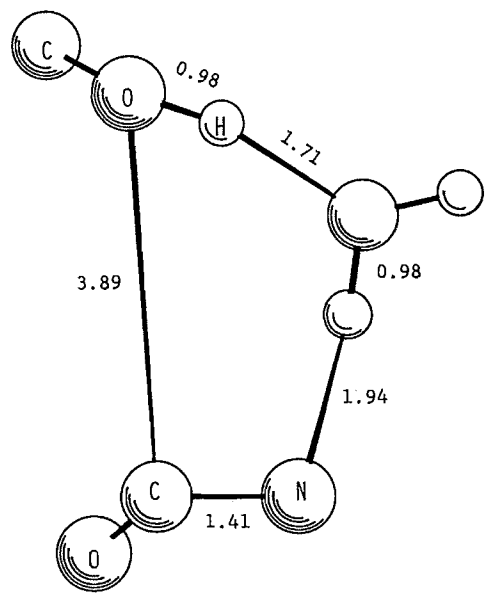

FIG. 5. A closeup view of the C-O-H/N-C=O/H-O-H bond lengths of the reactant complex of Fig. 4.

Can. J. Chem. Downloaded from www.nrcresearchpress.com by EESC ESCOLA DE ENGENHARIA on 09/08/12
For personal use only.

Can. J. Chem. Downloaded from www.nrcresearchpress.com by EESC ESCOLA DE ENGENHARIA on 09/08/12
For personal use only.

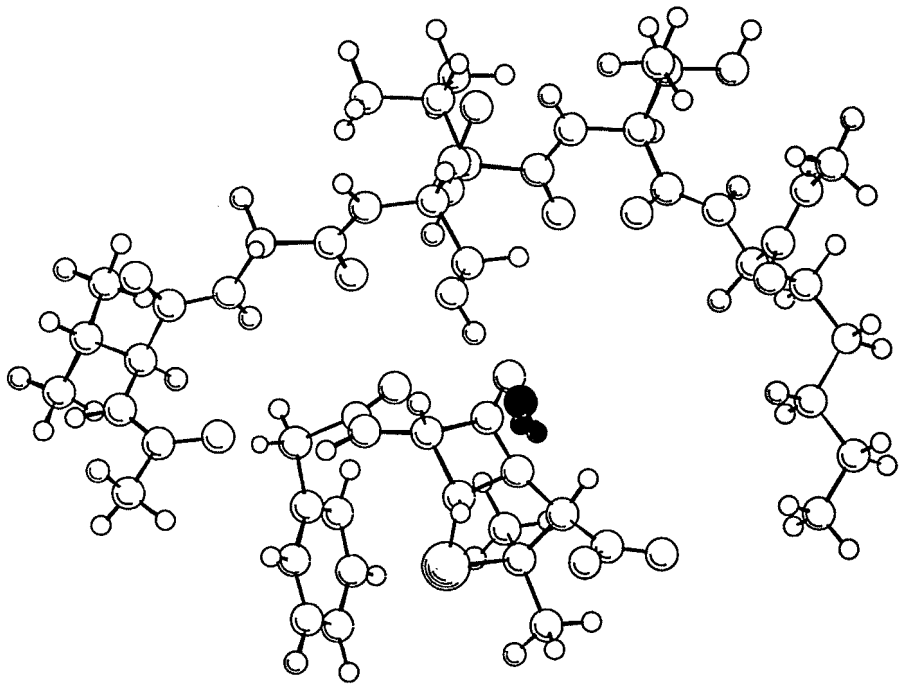

FIG. 6. Addition of one water molecule to the complex of penicillin G with the receptor model. The water molecule is in the centre of the structure.

able to accommodate a water molecule, and that at least one water molecule should also be included in the active site of Fig. 2. This would be consistent with the limited information concerning water in the active sites of β-lactamase crystal structures (12). Based on these considerations, the program developed to obtain the supermolecule of Fig. 2 (4) was modified[6] to allow a third molecule, in this case, water, to be included, with the result shown in Fig. 6 and, in close-up, in Figs. 7 and 8.

It is important to emphasize that the (nearly identical) Figs. 5 and 8 are obtained in very different ways. Figure 5, an ab initio result, is a closeup view of a stationary point on a reaction coordinate; Fig. 8, a molecular mechanics result, is a closeup view of an "enzyme"–water–substrate complex. Because of its ability to assemble the reactants in the proper manner, the "enzyme" has overcome the entropic disadvantage of a termolecular process.

Targeting a PBP

We wish to use the insights gained from the work just described to attempt the de novo design of a molecule that will "fit" to the active site of a PBP in the same manner as penicillin, "react" with the hydroxyl group of the active site serine through a geometry similar to that seen in Figs. 3 or 8, and exhibit antibacterial activity (13). As depicted in Fig. 9, our synthetic objective should possess a carboxyl group or its bioisosteric equivalent (G_1), to interact with the Lys^6 amino group of **3**, and also a hydrogen-bonding donor group X-H (G_2), to interact with the Val^1 carbonyl group of **3**. The distance between G_1 and G_2 can be determined from, e.g., the corresponding distance in the crystal structure of penicillin G.

The formation of the hydrogen bonds to G_1 and G_2 must now cause a functional group 𝔽 to be oriented into a four-centred relationship with respect to the serine hydroxyl group (cf. Fig. 3). A decision concerning the choice of 𝔽 is possible if a functional group can be found that reacts with a hydroxyl group via a four-centred geometry, possibly with catalysis by water, and with an activation energy comparable to that exhibited by a β-lactam. The search for 𝔽 was carried out computationally.

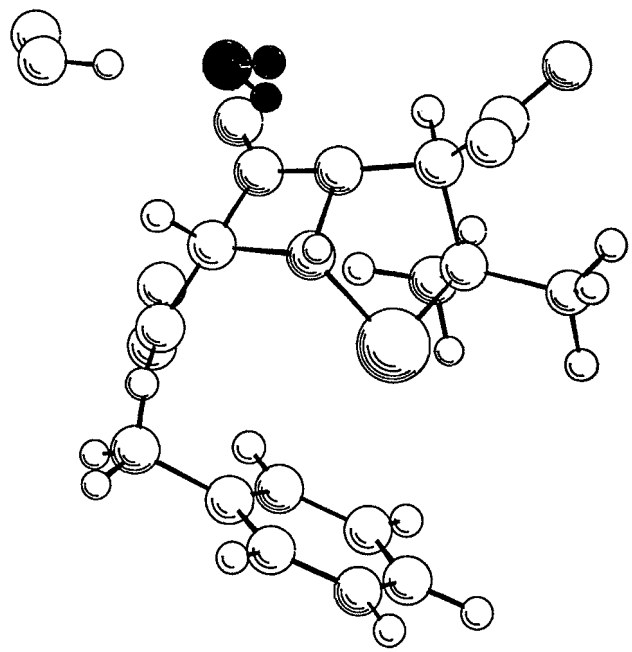

FIG. 7. Truncation of the structure of Fig. 6, showing the C-O-H of serine and the water molecule on the convex face of the penicillin.

Figure 10 is the N-protonated transition structure calculated, using MINDO/3, for the four-centred reaction of 2,2-dimethyl-3α-carboxypenam (**6**) with methanol. The activation energy of this reaction is 49.6 kcal/mol, 7.6 kcal/mol lower than that required for the alternative process of addition to the β-lactam carbonyl group. This trend is typical. As discussed elsewhere (14), MINDO/3, but not MNDO, MNDO/H, AM1,

[6]K. Yang and S. Wolfe. To be published.

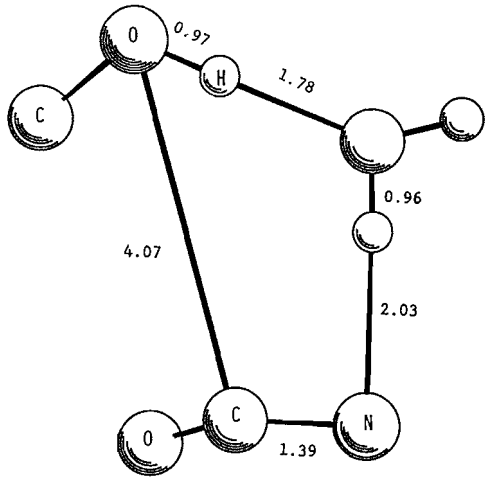

FIG. 8. A closeup view of the C-O-H/N-C=O/H-O-H bond lengths in Figs. 6 and 7.

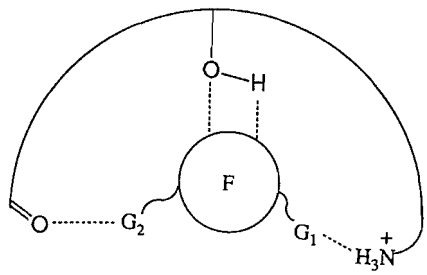

FIG. 9. Targeting the penicillin receptor.

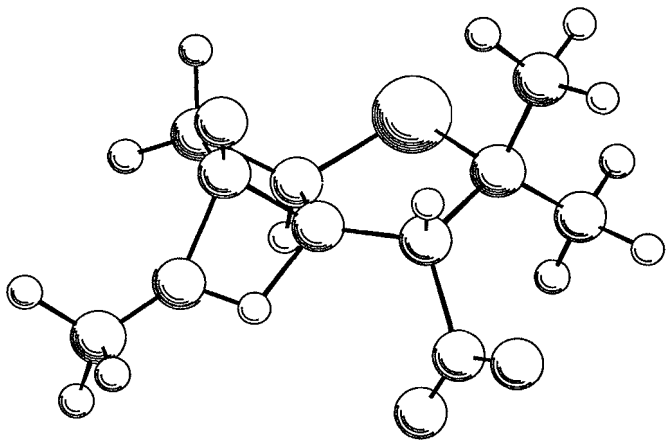

FIG. 10. MINDO/3 transition structure for the methanolysis of 2,2-dimethyl-3α-carboxypenam.

or PM3 reproduces the ab initio findings concerning the relative energies of the N- and O-protonated reaction pathways. In addition, MINDO/3 calculations of the activation energies for the methanolyses of azetidinones provide structure–reactivity trends that parallel the trends in the structure–activity relations of penicillins and cephalosporins (14). Therefore, the MINDO/3 semiempirical procedure was used for a preliminary survey of more general relationships between structure and four-centred reactivity towards methanol.

Table 1 lists the activation energies calculated for the four-centred reactions of methanol with the β-lactam (N-C=O), γ-lactam (N-C=O), β-lactone (O-C=O), γ-lactone

TABLE 1. Calculated activation energies (kcal/mol, MINDO/3), relative to 2,2-dimethyl-4-carboxypenam (6), for the neutral methanolysis of various compounds via a four-centred mechanism

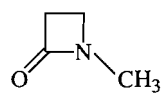	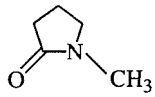	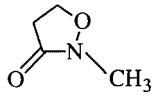
4.90 (N)	9.70 (N)	11.05 (N)
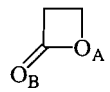	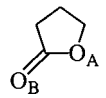	
A 18.10 B 8.28	A 22.98 B 12.05	
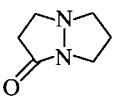	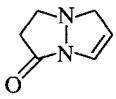	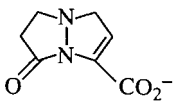
10.52 (N)	10.52 (N)	9.92 (N)

TABLE 2. Calculated activation energies (kcal/mol, MINDO/3), relative to **6**, for the four-centred attack of methanol on some C=N containing compounds

		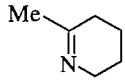		
−18.35	−15.33	−8.32	−14.09	−20.99

(O-C=O), oxazolidinone (O-N-C=O) (13*f*, 13*g*, 13*h*), and pyrazolidinone (N-N-C=O) (13*d*, 13e) functional groups, relative to the 49.6 kcal/mol calculated for **6**. The designations N, A, and B in Table 1 refer to the site to which the O-H proton of methanol is added. All of the compounds of Table 1 are calculated to be less reactive than **6**.

On the other hand, the data of Table 2 suggest that the imino group (C=N) is inherently more reactive towards methanol than the β-lactam ring of **6**, and that the reactivity of this group can be varied by variation of the ring size and the nature of the substituents.

The reactivities of several cyclic imines with methanol, with and without catalysis by water, were therefore examined more closely, using the 3-21G basis set for ab initio geometry optimizations, followed by one-point calculations of energies at the MP2/6-31G* level. In Fig. 11, A and B are the reactant complex and transition structure for the four-centred reaction with pyrroline, which produces the carbinolamine ether E; C and D are stereoscopic views of the complex and transition structure of the water-catalyzed process.

Table 3 summarizes the calculated reactivities towards methanol of *N*-methylazetidinone, 1-pyrroline, 2-oxazoline, 2-thiazoline, and also *N*-methyloxazolidinone. The first and second columns of Table 3 give the energy differences between separated reactants and transition structures for the uncatalyzed and catalyzed reactions; the third column shows the energy differences between the ternary reactant complexes and the transition structures of the catalyzed reactions.

The enhanced C=N reactivity predicted by the four-centred

Can. J. Chem. Downloaded from www.nrcresearchpress.com by EESC ESCOLA DE ENGENHARIA on 09/08/12
For personal use only.

Can. J. Chem. Downloaded from www.nrcresearchpress.com by EESC ESCOLA DE ENGENHARIA on 09/08/12
For personal use only.

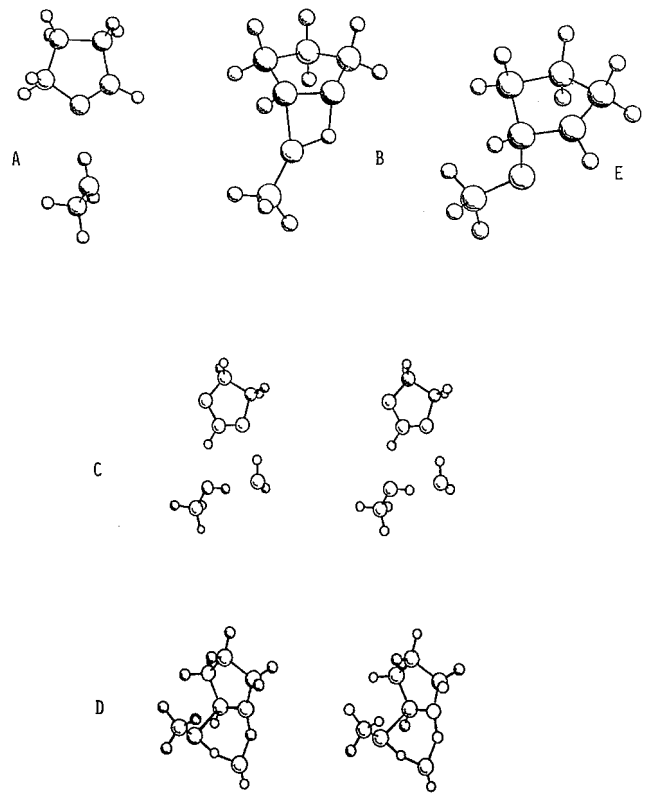

FIG. 11. Ab initio (3-21G) structures for the reaction of methanol with 1-pyrroline. A: reactant complex for the four-centred reaction. B: transition structure of the four-centred reaction. C: reactant complex for the water-catalyzed reaction. D: Transition structure of the water-catalyzed reaction. E: the carbinolamine ether product of the reaction.

TABLE 3. Ab initio activation energies[a] for the reaction of methanol with *N*-methylazetidinone (**4**),[b] 1-pyrroline, 2-oxazoline, 2-thiazoline, and *N*-methyl-1,2-oxazolidin-3-one (**A**)

Substrate	$\Delta E^{\ddagger}$ for reaction with: Methanol[c]	Methanol + water[d]	ΔE
4[e]	32.20[f]	16.62[f] (31.71)[g]	
1-Pyrroline[e]	40.42[f]	11.58[f] (33.25)[g]	−16.16[h]
2-Oxazoline[e]	39.86[f]	13.97[f] (35.45)[g]	
2-Thiazoline[i]	41.32[f]	— —	
A	29.37[f]	— —	

[a]In kcal/mol.
[b]Proton transfer to the β-lactam nitrogen.
[c]Four-centred reaction. See, e.g., Fig. 10.
[d]Reaction catalyzed by water. See, e.g., Fig. 4.
[e]MP2/6-31G*//3-21G calculations.
[f]Refers to the energy difference between separated reactants and transition structure.
[g]Data in parentheses refer to the energy difference between reactant complex and transition structure. See, e.g., C and D of Fig. 11.
[h]Energy change for MeOH + 1-pyrroline → 2-methoxy-1,3-oxazolidine.
[i]MP2/6-31G*//3-21G* calculations.

MINDO/3 calculations of Table 2 is not reproduced by the four-centred ab initio calculations of Table 3. In the β-lactam N-C=O, the lone pair of N and the π-orbital of C=O are approximately parallel, and the formation of the N—H and C—O bonds of the four-centred structure in a *syn* manner is not inhibited. In N=C, however, the lone pair of N and the

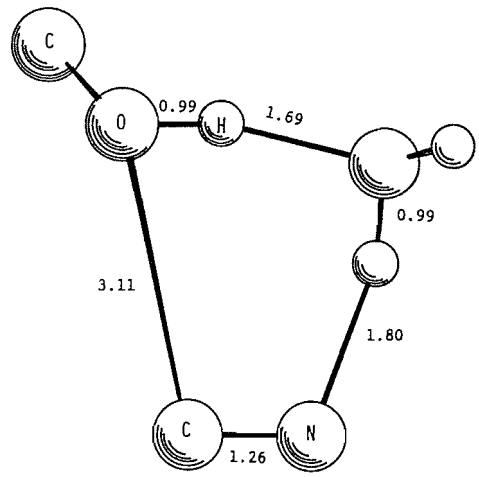

FIG. 12. A closeup view of the C-O-H/C=N/H-O-H bond lengths in the reactant complex C of Fig. 11.

π-orbital of N=C are approximately perpendicular, and *syn* formation of the N—H and C—O bonds is more difficult. This effect is taken into account in the ab initio calculations, but not by MINDO/3 (15). As can be seen in D of Fig. 11, the catalytic water molecule is important, because it allows the H-N-C-O dihedral angle to increase. The trends in the second and third columns of Table 3 are therefore more reliable than the four-centred trends, and suggest that the *bioreactivity* of C=N should be comparable to that of the β-lactam N-C=O. As seen in Fig. 12, the C=N group is also *bioisosteric* to N-C=O; this figure is a closeup view of the C-O-H/C=N/H-O-H bond lengths in C (Fig. 11), and can be compared to Fig. 5.

The final column of Table 3 contains the important result that the formation of a carbinolamine ether is an exoergic process. This means that the capture of a hydroxyl group by an imine function will be effectively irreversible, a necessary requirement for a compound targeted to a penicillin receptor. Furthermore, since the final deacylation step of Scheme 1 has no counterpart in the case of a carbinolamine ether, the incorporation of C=N into a properly designed compound could lead to the inhibition of both PBP's *and* β-lactamases.

It should be emphasized that the role of water could not be examined in the MINDO/3 calculations of Tables 1 and 2, because MINDO/3 does not treat intermolecular hydrogen bonds well, and predicts that water *inhibits* all of these processes (10). In addition, although AM1 correctly predicts catalysis, the use of AM1 for a systematic analysis of the catalyzed reactions fails for other reasons (10). Nevertheless, despite all of these limitations of the semiempirical calculations, these calculations do agree with the ab initio identification of C=N as a candidate for 𝔽.

In this connection, a referee has commented that excessive reliance on the MINDO/3 calculations of Table 1 would not have identified the X-N-C=O functionality of oxazolidinones (X = OR) and pyrazolidinones (X = NR_2) as potential candidates for 𝔽, and the existence of antibacterial agents containing these ring systems and targeted towards penicillin-binding proteins (13*d*, 13*e*, 13*f*, 13*g*, 13*h*) would not have been predicted.

The reason for the failure of MINDO/3 in the case of molecules having adjacent electron pairs (15) is that the neglect of one-centre overlap in the INDO procedure causes N—N (N—O) bonds to be too short and R-N-N (R-N-O) angles to be too large. The molecules then behave as though they have an

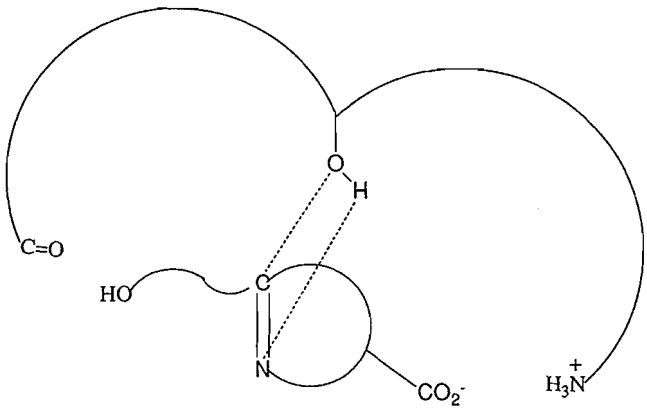

FIG. 13. Updated requirements for the targeting of the penicillin receptor.

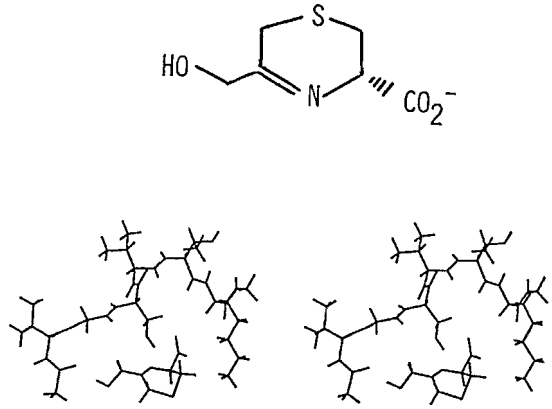

FIG. 14. Stereoscopic view of the initial synthetic target **7**, showing the *S* enantiomer docked to the penicillin receptor model.

electron-withdrawing substituent attached to a planar nitrogen, and proton transfer to this nitrogen becomes more difficult. As seen in the final entry of Table 3, the 6.15 kcal/mol reactivity preference for *N*-methylazetidinone over *N*-methyloxazolidinone that is predicted by MINDO/3 (Table 1) has been reversed at MP2/6-31G*//3-21G, to a 2.83 kcal/mol preference for the reaction of *N*-methyloxazolidinone. Clearly, ab initio calculations should be given priority in future computational studies related to 𝔽.

The identification of C=N as our current candidate for 𝔽 allowed Fig. 9 to be revised to Fig. 13, in which G_1 is CO_2^-, and G_2 is OH, and it was now necessary to create the desired spatial relationship between G_1, C=N, and G_2. This was done, crudely at first, by inspection of molecular models. For example, based on the dihedral angles in penicillin G, a compound having the part structure H-O-C1-C2=N-C3-CO_2^- would require O-C-C=N and C=N-C-C dihedral angles of −155° and +155°, respectively. Structures in which C1 and C3, or C2 and C3 were connected by different sized rings were, therefore, examined; these, in turn, suggested other possibilities.

A more careful conformational analysis of each candidate structure identified in this way was then performed, using MM2 (28). Previously unknown MM2 parameters were found, where necessary, using established procedures (14, 16). The parameters thus determined for the compounds to be discussed below are available as Supplementary Material.[7]

Each candidate was docked to **3** via the two hydrogen bonds already noted, and the relationship between the C=N of the candidate and the O-H of Ser^3 in the resulting complex was examined. This procedure eventually identified a number of targets for synthesis, and a programme directed towards the 2*H*-5,6-dihydro-1,4-thiazine **7** (cf Fig. 14), was initiated. Because it was known (17) that dihydrothiazines exhibit imine–enamine tautomerism (e.g., **8***a–c*), some preliminary experiments were necessary to assess the possible complications resulting from such tautomerism.

Preliminary Synthetic Studies

The reaction of L-cysteine with 1-benzoyloxy-3-chloropropanone (**9**), prepared in three steps from epichlorohydrin (18), produced an unstable product from which, after esterification with diazomethane, only the enamine **10** could be isolated. The same compound was obtained when **9** was reacted with the methyl ester of cysteine. Attempts to shift the double bond of **10** were not successful.

After numerous variations of the above synthesis had been examined, a compound with the gross structure **12***a* was isolated from the reaction of L-cysteine methyl ester with methyl bromoacetoacetate (**11**). However, this compound is a special case, since its ^{1}Hmr spectrum is consistent with the zwitterion structure **12***b* (no side-chain CH_2, but N^+-H at 9.00 and C=C-H at 4.63 ppm).

It was concluded that these 5,6-dihydro-1,4-thiazines prefer the 4H-tautomeric structure **8***b* and that, to avoid this structure, it would be necessary to place substituents at C2. The original objective **7** was, therefore, modified to **13***a*, which is the cyclodehydration product of **14***a*.

Scheme 2 summarizes the synthesis of the fully protected cysteine derivative **14***b*. Bromination of methyl isopropyl ketone afforded **15**, which was oxidized to **16** with lead tetraacetate, and then thiolated to **17** with triethylamine – hydrogen sulfide. Condensation of the lithium salt of **17** with the Vederas lactone **18** (19) proceeded smoothly to yield the acid **14***c*, and thence **14***b*.

Removal of the *tert*-butoxycarbonyl protecting group of **14***b* with anhydrous formic acid (20) led directly to the protected dihydrothiazine **13***b*. That cyclization had taken place in the desired manner was immediately apparent from the observation of ^{1}Hmr coupling, through the C=N double bond, between the exocyclic methylene protons and H5.

Unfortunately, **13***b* was not stable, and decomposed completely within 1 day to acetic acid and the thiazine **19** (Scheme 3). This decomposition may proceed by 1,4-elimination of acetic acid from **13***b*, to form **20**, which tautomerizes to **19**. The alternative tautomerization, from **13***b* to **21**, could not be observed. However, the experiments summarized in Scheme 4 demonstrate that the latter process does occur. Lithium hydroxide hydrolysis of **14***b*, and remethylation, afforded **14***d*, which was silylated to **14***e*. The deprotection of **14***e* with formic acid did not proceed as with **14***b*; instead the product was the exocyclic enamine **22**, and not the dihydrothiazine **13***c*. Treatment of **14***d* with formic acid gave a complex reaction mixture from which no identifiable product could be isolated.

The imine tautomer is sometimes stable

The observations summarized so far seem to be consistent

[7]Supplementary data may be purchased from: The Depository of Unpublished Data, Documentary Delivery, CISTI, National Research Council Canada, Ottawa, Canada K1A 0S2.

Can. J. Chem. Downloaded from www.nrcresearchpress.com by EESC ESCOLA DE ENGENHARIA on 09/08/12
For personal use only.

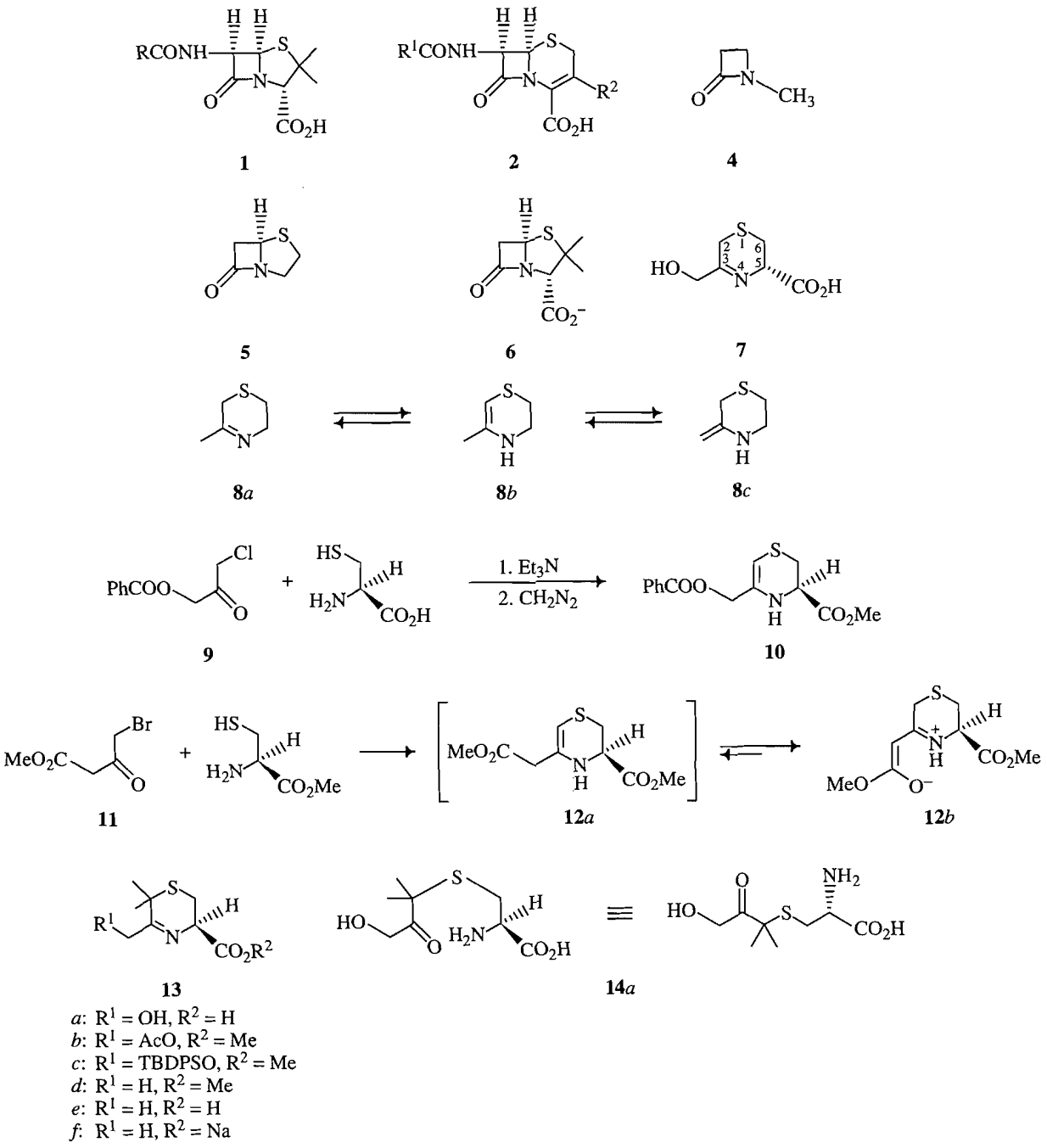

a: R^1 = OH, R^2 = H
b: R^1 = AcO, R^2 = Me
c: R^1 = TBDPSO, R^2 = Me
d: R^1 = H, R^2 = Me
e: R^1 = H, R^2 = H
f: R^1 = H, R^2 = Na

with prior work (17): in the C2-unsubstituted system the endocyclic enamine is the preferred tautomeric structure; when this structure is blocked by the introduction of methyl groups, the relative stabilities of the imine and exocyclic enamine structures depend upon the nature of R^1 of **13**. This latter point was examined further with the deoxy compound **13***d*, prepared from the bromoketone **15** by thiolation, condensation with **18** as in Scheme 2, methylation, and deprotection with formic acid.

The imine structure **13***d* was readily identified by the 2.0 Hz coupling between H5 and the C3 methyl protons. Only this structure could be observed in pure chloroform solvent, and the compound appeared to be stable for at least several days. In one preparation, however, the chloroform was not pure, and **13***d* underwent complete rearrangement to the enamine tautomer **23***a* in 1 day (N-H at 5.20 Hz; C=CH_2 singlets at 4.59, 4.60 Hz).

A knowledge of the chemical shifts of **23***a* proved useful in the next set of experiments. Hydrolysis of **13***d* to the acid **13***e* was successful, using lithium hydroxide. Only the imine tautomer of the sodium salt **13***f* could be observed in D_2O solvent during a period of 3 days at room temperature. However, during this period, the C3 methyl protons underwent hydrogen–deuterium exchange. The solution of **13***f* was lyophilized at this point, and the compound was redissolved in H_2O. Because of the isotope effect, the original spectrum of **13***f* required 5 days to reappear fully. At no time during these experiments in D_2O and H_2O was any other compound (e.g., **23***b*) observable by nmr.

The simplest explanation of these observations is that the imine–enamine equilibrium **13***f* ⟶ **23***b* lies on the side of the imine tautomer in water, and this leads to the exchange of the methyl protons in a deuterated solvent.

Can. J. Chem. Downloaded from www.nrcresearchpress.com by EESC ESCOLA DE ENGENHARIA on 09/08/12
For personal use only.

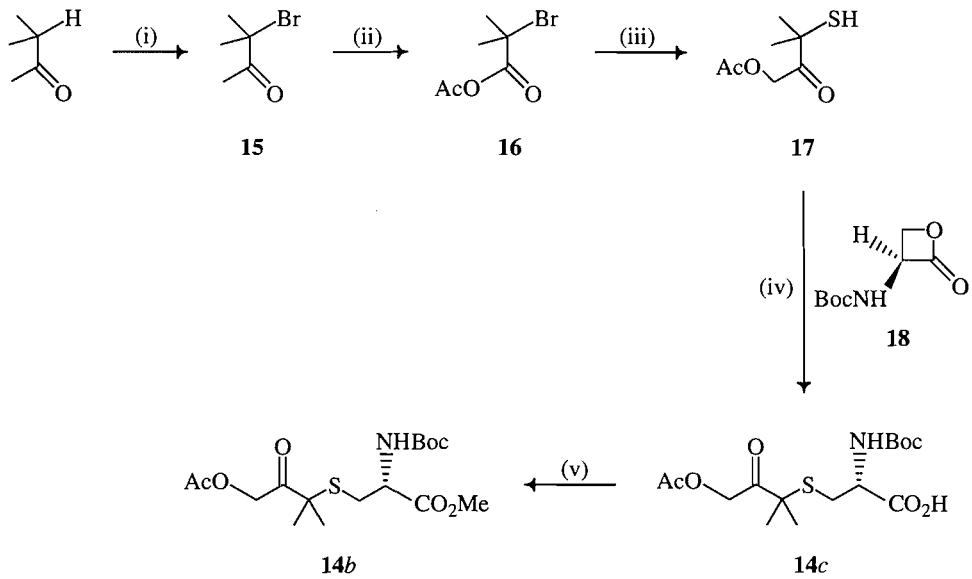

SCHEME 2: (i) Br_2, KCl, H_2O, *hν*; (ii) HOAc, LTA, 100°C; (iii) CH_2Cl_2, Et_3N, H_2S, –20°C; (iv) LDA, DMF–THF, –60°C; (v) CH_2N_2

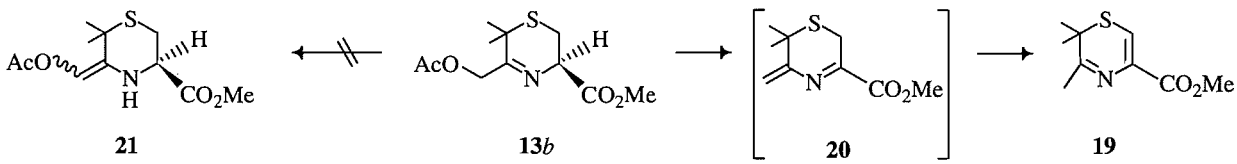

SCHEME 3

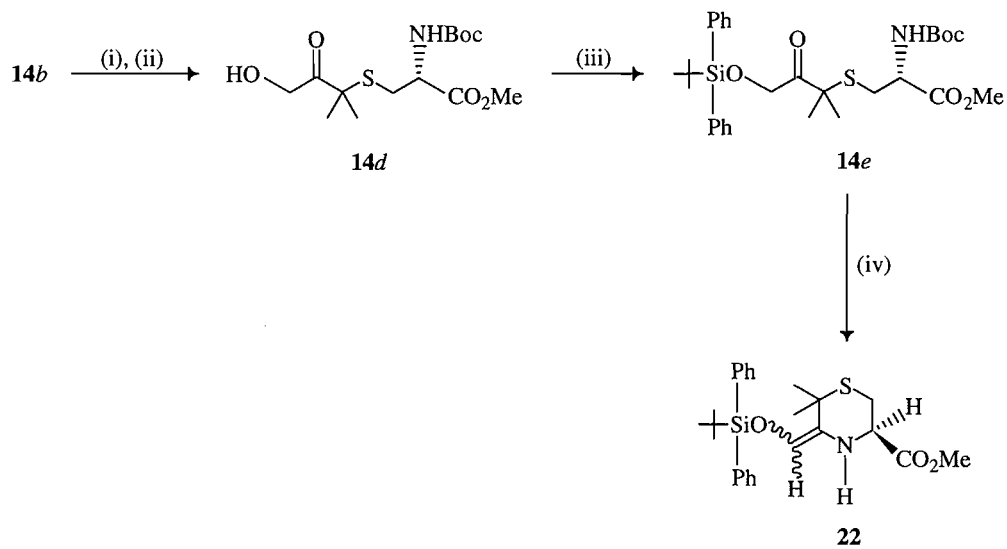

SCHEME 4: (i) LiOH; (ii) CH_2N_2; (iii) $(Ph)_2Si(Cl)$—, pyridine, $AgNO_3$; (iv) HCO_2H

Interaction of theory and synthesis: the 2-hydroxypropyl side chain

It was now clear that the desired ring system could be attained, and the imine tautomer maintained in water solvent. However, it was also clear that the molecule does not tolerate oxygen on the carbon atom adjacent to the C=N double bond. The hydroxyl group of **13***a* would therefore have to be repositioned. Replacement of the hydroxymethyl side chain of **13***a* by

Can. J. Chem. Downloaded from www.nrcresearchpress.com by EESC ESCOLA DE ENGENHARIA on 09/08/12
For personal use only.

Can. J. Chem. Downloaded from www.nrcresearchpress.com by EESC ESCOLA DE ENGENHARIA on 09/08/12
For personal use only.

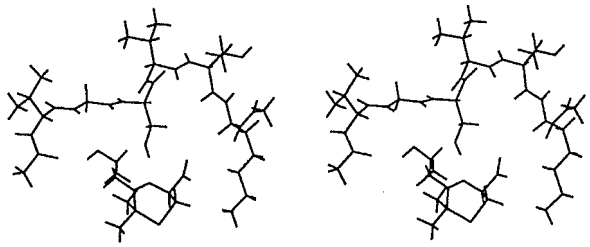

FIG. 15. Stereoscopic view showing one of the conformations of one of the stereoisomers of **26** docked to the penicillin receptor model.

a hydroxyethyl side chain leads to **24**. However, this compound is, formally, the primary product of the reaction of the enamine **25** with formaldehyde, and was feared to be unstable with respect to the reverse of the latter process. The hydroxypropyl side chain (**26**) was, therefore, examined.

Figure 15 is a stereoscopic view of the structure obtained by docking **3** to one of the conformations of the 3**S**,8**R** isomer of **26** (21). This structure is compatible with the formal design requirement depicted in Fig. 13, and the synthesis of **26**, the cyclodehydration product of **27** ($R^1 = R^2 = H$), was undertaken.

Based on the preliminary studies already described, it was expected that **27** would be accessible from the reaction of the mercaptoketone **28** with **18**, and that **28** could be synthesized from the ketol **29**. If an olefin-to-ketol oxidation **30** → **29** could be achieved, the starting materials for the synthesis of **26** would then be 5-methyl-4-hexen-2-ol (**30**, R = H) and serine. Since the racemic bromide **31** was known from the work of Julia et al. (22), the first synthesis of **26** was directed towards the 3**R** and 3**S** isomers, starting with **31** and, respectively, L- and D-serine.

The bromide **31** was converted, via the acetate (**30**, R = OAc) and alcohol (**30**, R = OH), to the *tert*-butyldimethylsilyl (*t*-BDMS) compound (**30**, R = *t*-BDMS). As shown in Scheme 5, the key olefin-to-ketol transformation was accomplished

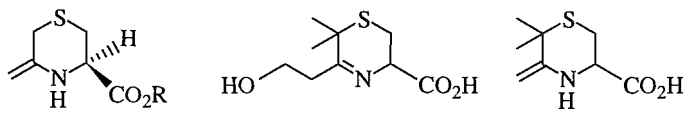

23

a: R = Me
b: R = Na^+

24

25

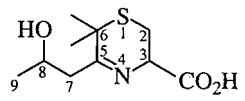

26

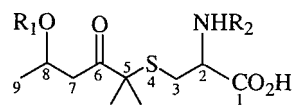

27

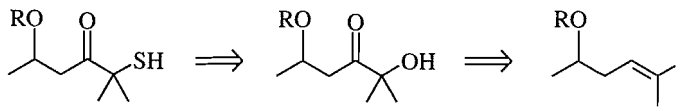

28 **29** **30**

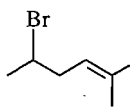

31

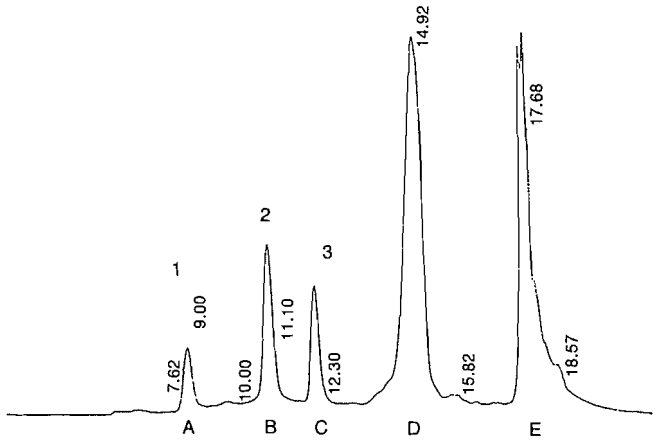

FIG. 16. HPLC examination of **26**. Peak D has the assigned structure.

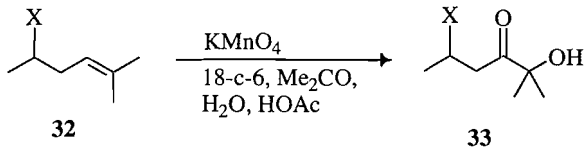

32 **33**

SCHEME 5

using potassium permanganate (23). Although the reaction conditions are rather special, this is a general reaction, which usually proceeds in 70–80% yield.[8]

The silylated ketol **29** (R = *t*-BDMS) was converted to the thiol **28** (R = *t*-BDMS), following activation as the mesylate and, as the lithium salt, **28** reacted with D- and L-**18** to produce the 2**S** and 2**R** isomers of **27** (R^1 = *t*-BDMS, R^2 = *t*-Boc) in over 80% yield.

In addition to **27** (R^1 = *t*-BDMS), the compounds **27** (R^1 = Ac) and **27** (R^1 = *tert*-butyldiphenylsilyl) were also synthesized. The latter two did not undergo clean removal of the *t*-Boc protecting group. Formic acid treatment of the acetate or trifluoroacetic acid treatment of the *tert*-butyldiphenylsilyl ether resulted in concomitant elimination of the C8 substituent of **27**. On the other hand, treatment of **27** (R^1 = *t*-BDMS) with formic acid led to the removal of both protecting groups, and cyclization to **26**.

The 3**R** and 3**S** epimers of **26**, synthesized separately from L- and D-serine, are not particularly stable. Figure 16 is the analytical chromatogram obtained, using an acetonitrile–water gradient with detection at 250 nm, for a sample of the amorphous sodium salt of 3**S**-**26**, after this had been maintained at 0°C for several weeks, or at room temperature for 1 day. The peak labelled D comprises ca. 45% of the mixture, and is also the initial product of the deprotection of **27**; the nmr and high-resolution mass spectra of D confirm structure **26**. Each of the peaks seen in Fig. 16 begins to reappear after several hours when the sodium salt of **26** is dissolved in water. The bioassay of **26** was, therefore, carried out as soon as possible after the isolation of the compound, and always within 1 day.

Bioassay of 26S and 26R: 26S is an antibacterial agent

The bioassay of **26S** and **26R** was carried out at 37°C using

[8]H. Jin and S. Wolfe. To be published. See also ref. 29.

TABLE 4. Inhibition of *S. aureus* by the thiazine **27**[a]

Amount (mg)	Zone of Inhibition (mm)
0.05	6.0
0.10	8.5
1.0	19
1.0	18

[a]Potassium penicillin V (0.10 μg) gives a 13 mm zone of inhibition.

4.0 mm filter discs, loaded with known weights of material, and placed on (*i*) *Sarcina lutea* seeded plates prepared by Mr. Dennis Muncey, Department of Microbiology, Queen's University; (*ii*) *Escherichia coli* seeded plates prepared by Dr. G.J. Delisle, Hotel Dieu Hospital, Kingston; (*iii*) penicillin sensitive *Staphylococcus aureus* plates prepared by Dr. J.A. Smith, Vancouver General Hospital.

The *R* isomer, synthesized from L-serine, did not exhibit activity against any of these organisms, in amounts up to 1000μg. At this level, the *S* isomer showed activity against all of the organisms. Direct comparisons with authentic antibiotics indicated that **26S** has 1/800 the activity of penicillin G versus *S. lutea*, and 1/10 the activity of cephalexin versus *E. coli*. As seen in Table 4, inhibition of *S. aureus* could be observed using 50 μg of **26S.**

Although the activity thus observed with the *S* isomer of **26** is extremely modest in comparison to that of penicillin G, as a lead structure representing the prototype of a designed antibacterial agent, **26S** is already comparable to a Δ^2-cephalosporin (10), which requires only one structural change (Δ^2 to Δ^3 isomerization) to become a useful antibiotic. Furthermore, the much lower activity of the *R* isomer of **26** suggests that **26S** is not a general bactericidal agent, but functions via a three-dimensional fit to a specific receptor. An understanding of the nature of this fit will require bioassay data for each of the four stereoisomers of **26**, and, eventually, kinetic studies of the reactions of these compounds with penicillin-recognizing enzymes. The syntheses and bioassays of the four stereoisomers of **26** are reported in an accompanying paper (21). However, because of its chemical instability, binding studies with **26** are not currently planned, unless systematic modification of the lead structure is unable to improve the stability.

Experimental

General experimental

All syntheses with sulfur-containing compounds were performed under dry nitrogen. Anhydrous magnesium sulfate was used routinely as a drying agent. Melting points were determined on a Fisher–Johns apparatus, and are uncorrected. Solvents were distilled before use and dried, as necessary, by literature procedures. Optical rotations were obtained on Perkin Elmer 141 or Rudolph Automatic polarimeters. Infrared (ir) spectra were recorded on a Perkin–Elmer 599B spectrometer. Nuclear magnetic resonance (nmr) spectra were run at 400 MHz on Bruker WM or Bruker AM spectrometers. High-resolution mass spectra refer to direct inlet EI measurements on a Kratos MS50 Spectrometer.

Analytical thin-layer chromatography was carried out on precoated Merck Silica Gel 60 F-254 plates with aluminium backing. Spots were observed under short-wavelength ultraviolet light, or were visualized with iodine vapour, ninhydrin, or ceric sulfate. Preparative layer chromatography (plc) was performed on Silica gel 60 F-254 precoated 20 × 20 cm plates (layer thickness 2mm) or, alternatively, glass plates were coated with a slurry of Macherey Nagel silica gel G-HR and calcium sulfate. Flash chromatography was carried out with 230–400 mesh Merck silica gel. The high-performance liquid chromatography (HPLC) system consisted of an M600 gradient module, U6K universal sample injector, 486 tunable absorbance detector, 170 sample loader, M746 data module, and fraction collector plus diverter valve, all from Waters. Analytical work was carried out using a 8 × 10 10-μm 125 Å μBondapak column. Preparative work was performed using a 25 × 10 10-μm 125 Å μBondapak column, with a loading of 25 mg per run. Acetonitrile and methanol for HPLC analyses were HPLC grade. Water for HPLC was collected through a Millipore purifier and degassed prior to use.

Elemental analyses are by M.K. Yang on a Carlo Erba model 1106 elemental analyzer at Simon Fraser University.

Theoretical

Ab initio molecular orbital calculations were carried out using GAUSSIAN 86 (24), GAUSSIAN 90 (25), or GAUSSIAN 92 (26). Semiempirical molecular orbital calculations were performed using AMPAC Version 2.1, kindly provided by Professor M.J.S. Dewar, or MOPAC Version 6.0 (27). Molecular mechanics calculations employed an extensively locally modified version of MMP2(85) (28). Docking of two molecules to form an intermolecular complex was accomplished as follows: first, preliminary MM2 calculations were carried out on these molecules to obtain, for predetermined conformations of each, their input data files. Then the numbering of the atoms that had been selected to engage in intermolecular hydrogen bond formation was determined. Next, the energy of the supermolecule created by these hydrogen bonds was minimized to produce an MM2 input file for the supermolecule. The docking of three molecules was carried out in two steps: in the first, the strategy just described was employed to dock two of the three molecules. Then the third molecule was added, using the appropriate numbers to identify the atoms engaging in the hydrogen bonds. Structures are drawn using a locally modified version of CHEMGRAF. We thank Dr. David Watkin, Oxford University, for a copy of the source code of this programme.

*Synthesis of the endocyclic enamine **10***

A solution of epichlorohydrin (10 mL) in water (10 mL) containing *p*-toluenesulfonic acid (50 mg) was refluxed for 9 h, cooled, neutralized by addition of sodium bicarbonate (22 mg), and distilled under reduced pressure. After removal of the water, 2-chloropropane-1,2-diol (9.3 g) was collected at 55°/2 Torr (1 Torr = 133.3 Pa). A solution of this diol (1.1 g, 10 mmol) in methylene chloride (10 mL) was cooled in an ice-bath, and treated successively with triethylamine (2.09 mL, 1.52 g, 15 mmol) and benzoyl chloride (1.16 mL, 1.40 g, 10 mmol). After 1 h, additional methylene chloride (10 mL) was added, and the solution was washed successively with water (2 × 10 mL), 0.1 N hydrochloric acid (2 × 10 mL), saturated sodium bicarbonate (1 × 10 mL), water (1 × 10 mL), and saturated sodium chloride (1 × 10 mL), dried, and evaporated. The crude monobenzoate (1.89 g, 8.8 mmol) was used directly in the next step. It was dissolved in methylene chloride (30 mL), and pyridinium chlorochromate (PCC) (9.5 g) was added in portions. The reaction mixture was stirred at room temperature for 6 h and additional PCC (5.0 g) was then added. Stirring was continued for 30 h. The mixture was then filtered, and after washing with methylene chloride (2 × 10 mL), the combined filtrates were washed successively with 0.5 N hydrochloric acid (2 × 10 mL), saturated sodium bicarbonate (2 × 10 mL), water (1 × 10 mL), and saturated sodium chloride (1 × 10 mL), dried, and evaporated. The residue was chromatographed on 5 g of silica gel. Successive elution with 10, 15, 25, and 50% ethyl acetate – hexane yielded 483 mg of the crystalline chloroketone **9** mp 94°C (lit. (18) mp 94°C).

To a solution of L-cysteine (12.1 mg, 0.1 mmol) in methanol (0.3 mL) were added consecutively triethylamine (28 μL, 0.2 mmol), dimethylformamide (DMF) (0.1 mL), and a solution of **9** (21.3 mg, 0.1 mmol) in DMF (0.2 mL). After 10 min, acetic acid (6 μL) was added, followed by ethereal diazomethane until the yellow colour per-

Can. J. Chem. Downloaded from www.nrcresearchpress.com by EESC ESCOLA DE ENGENHARIA on 09/08/12
For personal use only.

Can. J. Chem. Downloaded from www.nrcresearchpress.com by EESC ESCOLA DE ENGENHARIA on 09/08/12
For personal use only.

sisted. After an additional 10 min, ethyl acetate (5 mL) was added, and the reaction mixture was washed successively with water (2 × 5 mL) and saturated sodium chloride (1 × 5 mL), dried, and concentrated to yield 26 mg of crude product. This was purified by plc (silica gel, methylene chloride:ethyl acetate:acetic acid, 1.2:0.8:0.1, one elution) to give 7 mg, (24%) of **10**, $[\alpha]_D^{25}$ 172 (*c* 5, MeOH); ^{1}Hmr ($CDCl_3$), δ: 8.06 (2H, d, 7 Hz), 7.59 (1H, t, 7 Hz), 7.48 (2H, t, 7 Hz), 6.06 (1H, br, N-H), 5.50 (1H, C═C-H), 4.96 (1H, d, 12 Hz, O-C-H), 4.89 (1H, d, 12 Hz, O-C-H), 4.53 1H, d, 12 Hz, N-C-H), 3.87 (3H, s, ester), 3.35 (1H, d, 12 Hz, S-C-H), 2.31 (1H, t, 12 Hz, S-C-H). Decoupling experiments established that the protons at δ 4.53 and 3.35 are not coupled.

In a second experiment, the methyl ester hydrochloride of L-serine (207 mg, 1.2 mmol), in methanol (2 mL), was cooled in an ice-bath and triethylamine (336 μL, 2.4 mmol) and a solution of **9** (256 mg, 1.2 mmol) in dimethylformamide (3.7 mL) were added. The clear solution was stirred for 35 min, and then concentrated under reduced pressure to remove most of the methanol. Methylene chloride (50 mL) was added, and the resulting solution was washed successively with saturated sodium bicarbonate (2 × 10 mL), water (2 × 10 mL), and saturated sodium chloride (1 × 10 mL), dried, and evaporated. The residue was chromatographed on silica gel (11 g); successive elution with 10, 15, 30, 40, 50, and 60% acetone–hexane afforded, in the latter eluate, 48 mg (14%) of **10**.

*Synthesis of the zwitterionic imine **12**b*

Ketene dimer (1.05 g, 12.5 mmol, purified by distillation at 48–54°C/90 Torr) was dissolved in carbon tetrachloride (8 mL), cooled in an ice-bath, and a solution of bromine (2.0 g, 12.5 mmol, freshly treated with concentrated sulfuric acid), in carbon tetrachloride (5 mL) was added dropwise. Stirring was continued for 5 min, and methanol (0.6 mL, 0.47 g, 14.8 mmol) was then added. After 10 min, the reaction mixture was washed with water until the aqueous washings were neutral (3 × 10 mL), and then successively with saturated sodium bicarbonate (1 × 10 mL), water (1 × 5 mL), and saturated sodium chloride (1 × 5 mL), dried, and concentrated to yield 1.95 g of the bromoacetoacetate **11**.

The methyl ester hydrochloride of L-serine (17.2 mg, 0.1 mmol), in methanol (0.1 mL), was cooled in an ice-bath, and **11** (19.5 mg, 0.1 mmol), in methanol (1.1 mL), was added. The solution was stirred, allowed to warm to room temperature, and, after 30 min, triethylamine (28 μL, 0.2 mmol) was added. After 10 h, the solvent was removed and the residue, in methylene chloride (15 mL), was washed successively with saturated sodium bicarbonate (1 × 5 mL), water (1 × 5 mL), and saturated sodium chloride (1 × 5 mL). The solvent was dried and evaporated, and the product purified by chromatography on a column containing 1.5 g of silica gel. Elution with 20% ethyl acetate–hexane afforded 10 mg (43%) of ***12b***; ^{1}Hmr ($CDCl_3$), δ: 9.00 (1H, br, N^+-H), 4.63 (1H, s, C═C-H), 4.27 (1H, dd, 4, 9 Hz, N-C-H), 3.82 (3H, s), 3.66 (3H, s), 3.36 (1H, d, 14 Hz, S-C-H), 3.29 (1H, dd, 4, 14 Hz, S-C-H), 3.17 (1H, d, 14 Hz, S-C-H), 3.02 (1H, dd, 9, 14 Hz, S-C-H).

*Synthesis of **14**b*

*A. Preparation of the thiol **17***

Methyl isopropyl ketone (15 mL, 140 mmol) was added to a solution of potassium chloride (1.1 g, 14.8 mmol) in water (9.6 mL). The mixture was stirred, warmed to 60°C, and illuminated with a 350-W tungsten lamp mounted beside the flask. Bromine (11.9 g, 74.4 mmol) was then added dropwise. When the colour of the first few drops had disappeared, the heating bath was replaced by a cold water bath, and the 350-W bulb was replaced by a 60-W bulb. Addition of bromine was continued at a rate sufficient to maintain the internal temperature at 40–45°C. When the addition was complete (25 min), the reaction mixture was allowed to stand for 2 h and the organic phase was then separated, washed with water – magnesium oxide, and dried over anhydrous calcium chloride. Fractional distillation afforded 7.0 g (30%) of **15**, bp 82–86°C/145 Torr; ^{1}Hmr ($CDCl_3$), δ: 2.36 (3H, s), 1.77 (6H, s).

The bromoketone **15** (4.65 g, 28 mmol) was dissolved in glacial acetic acid (40 mL), and freshly recrystallized lead tetraacetate (12.5 g, 28.2 mmol) was added. The mixture was heated at 100°C, with stirring, for 2 h and cooled to room temperature. Ethylene glycol (2 mL) was then added to destroy unreacted lead tetraacetate. The reaction mixture was diluted with ether (100 mL), washed successively with 10% sodium carbonate, water, and saturated sodium chloride, dried, and evaporated. The residue was distilled, and the fraction boiling at 57–60°C/120 Torr was further purified by chromatography (silica gel, 5% → 10% → 15% ether–hexane) to give the bromoketoacetate **16** (750 mg, 11%); ^{1}Hmr ($CDCl_3$), δ: 5.16 (2H, s), 2.13 (3H, s), 1.87 (6H, s).

Triethylamine (140 μL) was added to methylene chloride (3 mL). The solution was cooled to −20°C, and gaseous hydrogen sulfide was introduced during 10 min. Then the bromoketoacetate **16** (200 mg), in methylene chloride (1.0 mL), was added dropwise with stirring during 10 min. The yellow solution was diluted with methylene chloride (30 mL), washed successively with 2 N hydrochloric acid, water, and saturated sodium chloride, dried over anhydrous sodium sulfate, and evaporated to yield the mercaptoketoacetate **17** (145 mg, 96%); ^{1}Hmr ($CDCl_3$), δ: 5.16 (2H, s), 2.18 (3H, s), 1.57 (6H, s) 1.55 (1H, s).

*B. Preparation of the β-lactone **18***

To triphenylphosphine (258 mg, 0.98 mmol) in dry tetrahydrofuran (1.0 mL) was added dropwise with stirring at −78°C a solution of dimethylacetylenedicarboxylate (144 mg, 0.99 mmol) in tetrahydrofuran (1.0 mL). The white slurry was maintained at −78°C for 10 min, and a solution of Boc-L-serine (184 mg, 0.90 mmol) in tetrahydrofuran (1.0 mL) was added dropwise. The temperature was maintained at −78°C for 20 min and the reaction mixture was then allowed to warm to room temperature (2 h). The solvent was removed and the residue was chromatographed on silica gel. Elution with 15% → 22% → 30% → 35% ethyl acetate – hexane afforded the β-lactone **L-18**. ^{1}Hmr ($CDCl_3$), δ: 5.29 (1H, br), 4.92 (1H, br), 4.34 (2H, br), 9.07 (9H, s). Anal. calcd. for $C_8H_{13}NO_4$: C 51.33, H 6.99, N 7.48; found: C 51.59, H 7.05, N 7.62.

*C. Reaction of **17** with **18***

To a solution of **17** (79.6 mg, 0.45 mmol) in dry degassed dimethylformamide (1.5 mL) was added dropwise a solution of lithium diisopropylamide (0.8 mmol) in tetrahydrofuran (1.5 mL). The addition was carried out under nitrogen at −60°C. The reaction mixture was allowed to warm to −25°C during 50 min, cooled again to −55°C, and a solution of **18** (56.4 mg, 0.30 mmol) in dry degassed dimethylformamide (0.5 mL) was added dropwise. When the addition was complete, the mixture was warmed to −20°C, stirred for 25 min, and then diluted with ethyl acetate (30 mL) and washed with 0.5 N hydrochloric acid (2 mL). The aqueous layer was extracted with ethyl acetate (2 × 10 mL) and the combined organic extracts were washed with water (2 × 5 mL) and saturated sodium chloride (1 × 5 mL), dried, and evaporated. The oily residue was purified by preparative layer chromatography on a 10 × 20 cm plate coated with silica gel, using methylene chloride:ethyl acetate:acetic acid (1.7:0.3:0.05) as eluant to give ***14c*** (77 mg, 70%); ^{1}Hmr ($CDCl_3$), δ: 5.43 (1H, br), 5.20 (1H, d, 18 Hz), 5.04 (1H, d, 18 Hz), 4.46 (1H, br), 2.97 (1H, br), 2.78, 2.74 (1H, dd, 4.5, 9.0 Hz), 2.17 (3H, s), 1.48 (3H, s), 1.47 (3H, s), 1.44 (9H, s).

The acid ***14c*** (77 mg) was dissolved in methylene chloride (10 mL) and treated at 0°C with an ethereal solution of diazomethane. The solvent was removed and the residue was purified on a 5 × 10 cm silica gel plate using hexane:ethyl acetate (1.4:0.6) as eluant to give the ester ***14b*** (48.2 mg); ^{1}Hmr ($CDCl_3$), δ: 5.32 (1H, br d, N-H), 5.15 (1H, d, 11 Hz, O-C-H), 5.07 (1H, d, 11 Hz, O-C-H), 4.48 (1H, br q, N-C-H), 3.76 (3H, s,ester), 2.91 (1H, dd, 4, 12 Hz, S-C-H), 2.74 (1H, dd, 5.5, 12 Hz, S-C-H), 2.17 (3H, s, Ac), 1.48 (3H, s, C-Me), 1.47 (3H, s, C-Me), 1.44 (9H, s, *t*-Boc).

*Deprotection and cyclization of **14**b. Formation of **13**b and **19***

The methyl ester acetate ***14b*** (3.7 mg) was treated at room temperature with anhydrous formic acid (0.2 mL). After 10 min, the solution was frozen and the solvent removed by lyophilization to give ***13b***;

Can. J. Chem. Downloaded from www.nrcresearchpress.com by ESC ESCOLA DE ENGENHARIA on 09/08/12
For personal use only.

^{1}Hmr ($CDCl_3$), δ: 4.82 (1H, q, 1.8, 14.3 Hz, O-C-H coupled to O-C-H and N-C-H), 4.71 (1H, q, 2.4, 14.3 Hz, O-C-H coupled to O-C-H and N-C-H), 4.56 (1H, td, 1.8, 2.4, 7.8 Hz, N-CH), 3.79 (3H, s, ester), 2.94 (2H, d, 7.8 Hz), 2.14 (3H, s, Ac), 1.36 (6H, s, C-Me). During a period of 24 h, the spectrum of **13***b* gradually disappeared, and the spectra of **19** and acetic acid (2.09 ppm) appeared; ^{1}Hmr of **19** ($CDCl_3$), δ: 7.29 (1H, q, S-C-H coupled to C═C-Me), 3.86 (3H, s, ester), 2.29 (3H, d, N═C-Me), 1.36 (6H, s, C-Me).

*Conversion of **14**b to the exocyclic enamine **22***

The ester **14***b* (46 mg), in tetrahydrofuran (1 mL), was treated at room temperature with 0.25 M lithium hydroxide (0.4 mL). After 25 min an additional 0.4 mL of lithium hydroxide was added. The mixture was stirred for 35 min and then diluted with ethyl acetate (10 mL) and washed with 0.5 N hydrochloric acid (2 × 5 mL). The aqueous layer was extracted with ethyl acetate (2 × 5 mL) and the combined organic extracts were washed with water (1 × 5 mL), followed by saturated sodium chloride (1 × 5 mL), dried, and evaporated. The residue was dissolved in the minimum of methylene chloride, treated with ethereal diazomethane, concentrated, and the residue was purified on a 10 × 20 cm silica gel plate. Elution with hexane:ethyl acetate (1.4:0.6) gave **14***d* (14.4 mg); ^{1}Hmr ($CDCl_3$), δ: 5.22 (1H, br), 4.58 (2H, d), 4.48 (1H, br), 3.75 (3H, s), 3.06 (1H, br), 2.92 (1H, br), 2.74 (1H, dd, 5, 11 Hz), 1.46 (9H, s), 1.44 (6H, s).

To a solution of **14***d* (5 mg, 0.015 mmol) in freshly dried pyridine (0.2 mL) were added successively silver nitrate (3.4 mg, 0.02 mmol) and *tert*-butyldiphenylchlorosilane (6.3 mg, 0.023 mmol). The solution was stirred for 15 min at room temperature. The solvent was then removed and the product was purified by preparative layer chromatography to give **14***e* (5.5 mg); ^{1}Hmr ($CDCl_3$), δ: 7.69 (4H, m), 7.41 (6H, m), 5.07 (1 H, br), 4.70 (2H, s), 4.41 (1H, br), 3.72 (3H, s), 2.70 (1H, dd, 6, 15 Hz), 2.55 (1H, dd, 6, 15 Hz), 1.43 (9H, s), 1.28 (3H, s), 1.26 (3H, s), 1.10 (9H, s).

The silylated ester **14***e* (5 mg) was treated at room temperature with formic acid (0.2 mL). After 33 min the reaction mixture was frozen and the solvent was removed by lyophilization to yield the enamine **22**. ^{1}Hmr ($CDCl_3$), δ: 8.31 (1H, br, N-H), 7.69 (4H, m, Ar), 7.40 (6H, m, Ar), 5.90 (1H, s, C═C-H) 4.65 (1H, br, N-C-H), 3.79 (3H, s, ester), 3.17 (1H, dd, 10, 15 Hz, S-C-H), 3.00 (1H, dd, 3, 15 Hz, S-C-H), 1.49 (3H, s, C-Me), 1.31 (3H, s, C-Me), 1.08 (9H, s, *t*-Bu).

*Synthesis of the deoxythiazine **13**d*

To methylene chloride (3 mL), saturated with hydrogen sulfide, were added successively at −20°C triethylamine (0.33 mL, 0.24 g, 2.36 mmol) and the bromoketone **15** (330 mg, 2.0 mmol). The reaction was complete in 10 min, and the thiol (101 mg) was isolated as described above for **17**, and used directly in the next step.

To the thiol (38 mg, 0.32 mmol), in dimethylformamide (1 mL), was added dropwise at −55°C 1.0 mL of a 0.64 M solution of lithium diisopropylamide in tetrahydrofuran. The temperature was allowed to rise to −20°C during 45 min, then lowered again to −55°C, and **18** (30 mg, 0.16 mmol), in dimethylformamide (0.4 mL), was added. Stirring was continued at −20°C for 25 min, and the reaction mixture was then worked up as described above for **14***c*. The product was purified by plc (silica gel, 0.5 mm thickness, 10 × 20 cm plate, methylene chloride: ethyl acetate:acetic acid 1.7:0.3:0.05, one elution), to give 43.5 mg (89%) of the cysteine derivative Me-CO-C(Me)$_2$-S-CH$_2$-CH(NHBoc)-CO_2H.

This acid (20 mg), in methylene chloride (0.5 mL), was treated with ethereal diazomethane. The reaction was instantaneous. The solvent was removed and the residue purified by plc (silica gel, 10 × 20 cm, hexane – ethyl acetate 1.4:0.6, one elution) to give the methyl ester (18 mg); ^{1}Hmr ($CDCl_3$), δ: 5.19 (1H, d, 4 Hz, N-H), 4.48 (1H, br, N-C-H), 3.73 (3H, s, ester), 2.82 (1H, dd, 5, 16 Hz, S-C-H), 2.73 (1H, dd, 7, 16 Hz), 2.26 (3H, s, Me-CO), 1.41 (9H, s, Boc), 1.39 (6H, s, C-Me).

The methyl ester (14 mg) was dissolved in anhydrous formic acid (0.4 mL) and the solution was maintained at room temperature for 50 min. The solvent was then removed by lyophilization, and the product was purified by plc (alumina, 10 × 20 cm, methylene chloride:ethyl acetate 0.8:1.2, two elutions) to give the thiazine **13***d*; ^{1}Hmr ($CDCl_3$), δ: 4.48 (1H, ddq, 2.0, 5.0, 8.8 Hz, N-C-H coupled to S-C-H, S-C-H, and N═C-Me), 3.81 (3H, s, ester), 2.88 (1H, dd, 5.0, 14.2 Hz, S-C-H), 2.94 (1H, dd, 8.8, 14.2 Hz), 2.10 (1H, d, 2.0 Hz, N═C-Me coupled to N-C-H), 1.52 (3H, s, CMe), 1.47 (3H, s, C-Me).

The thiazine **13***d* was relatively stable. However, one $CDCl_3$ solution underwent isomerization to the enamine **23***a*; ^{1}Hmr, δ: 5.20 (1H, br s, N-H), 4.60 (1H, s, C═C-H), 4.59 (1H, s, C═C-H), 4.51 (1H, m), 3.77 (3H, s, ester), 2.94 (1H, dd, 5.0, 13 Hz), 2.77 (1H, dd, 5.8, 13 Hz), 1.47 (3H, s, C-Me), 1.46 (3H, s, CMe).

*Hydrolysis of **13**d*

The methyl ester (1.3 mg, 0.0055 mmol) was treated at 0°C with methanol (0.2 mL) and 0.5 M lithium hydroxide (80 μL). After 20 min, 1 M sulfuric acid (17.25 μL) was added, the methanol was removed under reduced pressure, and the remaining solvent was removed by lyophilization. For nmr studies the residue was dissolved in 0.6 mL of a solution prepared from 4 mg of sodium bicarbonate and 1.0 mL of D_2O; ^{1}Hmr of **13***f* (D_2O), δ: 4.12 (1H, br), 2.87 (1H, q, 4.9, 14 Hz), 2.78 (1H, q, 7.3, 14 Hz), 1.95(3H, br, exchanges), 1.37 (3H, s), 1.35 (3H, s).

*Synthesis of **26**. Biologically active series*

*A. Synthesis of the bromide **31***

A solution of ethyl 2-methylcyclopropanecarboxylate (5.0 g, 38.9 mmol) in dry ether (5 mL) was added dropwise, with stirring under nitrogen, to the Grignard reagent prepared from magnesium turnings (1.935 g, 0.080 g-atom) and methyl iodide (12.43 g, 87.6 mmol) in dry ether (42 mL). The addition required 30 min; stirring was continued for 2.75 h at room temperature and then for 2 h under reflux. The reaction mixture was cooled in an icebath and saturated ammonium chloride (10 mL) was added, with stirring. The layers were separated and the aqueous layer was extracted with ether (2 × 20 mL). The combined organic phase was dried, evaporated, and the residue distilled at 132–136°C to give the tertiary alcohol product (4.24 g, 95%).

To this alcohol (4.24 g, 37 mmol), cooled in an ice-bath, was added ice-cold 48% hydrobromic acid (15 mL). The mixture was shaken vigorously in the ice-bath for 30 min. The two layers were then separated, the aqueous layer extracted with hexane (2 × 20 mL), and the combined organic phase was washed successively with saturated bicarbonate (2 × 10 mL), water (2 × 10 mL), and saturated sodium chloride (2 × 10 mL), dried over anhydrous sodium sulfate, and evaporated. Distillation afforded 3.72 g (60%) of the bromide **31**, bp 46–54°C/10 Torr; ^{1}Hmr ($CDCl_3$) δ: 5.18 (1H, br t), 4.11 (1H, q), 2.59 (1H, m), 2.51 (1H, m), 1.72 (3H, s), 1.68 (3H, d, 8 Hz), 1.62 (3H, s).

*B. Conversion of **31** to **30** (R = Ac)*

To a solution of the bromide **31** (3.72 g, 21 mmol) in glacial acetic acid (20 mL) was added potassium acetate (3.1 g, 31.6 mmol). The mixture was heated under reflux for 12 h, cooled, and poured into water (30 mL). Extraction with ether (3 × 30 mL), followed by successive washing of the organic phase with saturated sodium carbonate, water, and saturated sodium chloride, drying, and evaporation at room temperature yielded the acetate 2.82 g (85%); ^{1}Hmr ($CDCl_3$), δ: 5.10 (1H, br t), 4.88 (1H, q, 6 Hz), 2.30 (1H, m), 2.19 (1H, m), 2.02 (3H, s), 1.71 (3H, br s), 1.62 (3H, br s), 1.20 (3H, d, 6 Hz).

C. Hydrolysis of the acetate

The acetate (320 mg, 2.05 mmol) was dissolved in methanol (2 mL) and treated dropwise with a 1.5 M solution of potassium hydroxide in methanol (1.38 mL). The reaction mixture was allowed to stand for 6 h and was then neutralized with 1.5 M methanolic hydrogen chloride, and the solvent was removed. The residue was dissolved in methylene chloride, and this solution was washed successively with water and saturated sodium chloride, dried, and evaporated to give the alcohol **30**

Can. J. Chem. Downloaded from www.nrcresearchpress.com by EESC ESCOLA DE ENGENHARIA on 09/08/12
For personal use only.

(R = H) (208 mg, 99%); ^{1}Hmr ($CDCl_3$) δ: 5.14 (1H, tq, 1.5, 8 Hz), 3.79 (1H, sextet, 6 Hz), 2.16 (2H, br t, 7.5 Hz), 1.72 (3H, br s), 1.63 (3H, br s), 1.18 (3H, d, 6 Hz).

D. tert-*Butyldimethylsilylation of the alcohol* ***30*** *(R = H)*

The alcohol (312 mg, 2.73 mmol) was dissolved in dimethylformamide (2 mL) and to this solution were added successively *tert*-butyldimethylchlorosilane (535 mg, 3.55 mmol), pyridine (0.29 mL, 284 mg, 3.59 mmol), and silver nitrate (603 mg, 3.55 mmol). The mixture was stirred for 2 h and then filtered. The insoluble material was triturated with ether (20 mL) and the combined organic material was washed successively with saturated sodium bicarbonate, water, and saturated sodium chloride, dried, and evaporated to give the silylated compound **30** (R = *t*-BDMS) (620 mg, 100%); ^{1}Hmr ($CDCl_3$), δ: 5.13 (1H, br t), 3.77 (1H, m), 2.17 (1H, m), 2.08 (1H, m), 1.69 (3H, br s), 1.60 (3H, br s), 1.11 (3H, d, 6.1 Hz), 0.88 (9H, s), 0.05 (3H, s), 0.03 (3H, s).

E. Permanganate oxidation of the silylated alcohol. Preparation of the ketol ***29*** *(R = t-BDMS)*

The olefin **30** (R = *t*-BDMS) (624 mg, 2.73 mmol) was dissolved in acetone (3 mL) and 18-crown-6 (100 mg, 0.27 mmol) and acetic acid (0.16 mL) were added successively followed, dropwise, by a solution of potassium permanganate (603 mg, 3.82 mmol) in water (7.5 mL). The mixture was stirred for 1 h and then diluted with methylene chloride (50 mL). The organic phase was washed successively with 20% sodium bisulfite, 0.5 N hydrochloric acid, saturated sodium bicarbonate, water, and saturated sodium chloride, dried, and evaporated. The residue was subjected to flash chromatography on silica gel (7 g). Elution with 4 → 15% ethyl acetate – hexane gave 479 mg (70%) of **29** (R = *t*-BDMS); ^{1}Hmr ($CDCl_3$), δ: 4.42 (1H, m), 3.95 (1H, s), 2.83 (1H, dd, 7.6, 16.0 Hz), 2.47 (1H, dd, 4.8, 16.0 Hz), 1.34 (3H, s), 1.33 (3H, s), 1.18 (3H, d, 6.1 Hz), 0.84 (9H, s), 0.06 (3H, s), 0.02 (3H, s). Mass spectrum (CI, isobutane, *m/e*): 261 (M + 1). Anal. calcd. for $C_{13}H_{28}O_3Si$: C 59.95, H 10.84; found: C 59.78, H 10.99.

F. Mesylation of ***29*** *(R = t-BDMS)*

To a solution of the ketol (478 mg, 1.83 mmol) in methylene chloride (6 mL) were added successively triethylamine (0.76 mL, 4.0 mmol) and methanesulfonyl chloride (0.24 mL, 3.1 mmol). The reaction mixture was stirred for 5 h at room temperature and then diluted with methylene chloride (80 mL). The solution was washed successively with water, 0.5 N hydrochloric acid, saturated sodium bicarbonate, water, and saturated sodium chloride, dried, and evaporated. Flash chromatography on silica gel (3 g) and elution with 7% → 8% → 9% → 10% ethyl acetate – hexane gave the mesylate Me-CH(O*t*BDMS)-CH_2-CO-CH(Me)$_2$-OSO_2CH_3 (432 mg, 70%); ^{1}Hmr ($CDCl_3$), δ: 4.40 (1H, m), 3.11 (3H, s), 2.94 (1H, dd, 7.5, 17.3 Hz), 2.59 (1H, dd, 4.6, 17.3 Hz), 1.68 (3H, s), 1.63 (3H, s), 1.18 (3H, d, 6.1 Hz), 0.84 (9H, s), 0.07 (3H, s), 0.02 (3H, s).

G. Synthesis of the thiol ***28*** *(R = t-BDMS)*

Methylene chloride (5 mL) was saturated with hydrogen sulfide at −20°C, and triethylamine (0.14 mL, 1 mmol) and a solution of the above mesylate (233 mg, 0.5 mmol) were added successively. The solution was stirred for 10 min at −20°C and for 45 min at −20° to 0°C, and was then diluted with methylene chloride (30 mL), washed successively with 0.5 N hydrochloric acid, water, and saturated sodium chloride, dried, and evaporated to give, after drying at 0.1 Torr, the silylated mercaptan **28** (R = *t*-BDMS) (170 mg, 85%); ^{1}Hmr ($CDCl_3$), δ: 4.37 (1H, m), 2.98 (1H, dd, 5, 11 Hz), 2.63 (1H, dd, 4, 11 Hz), 1.98 (1H, s), 1.49 (3H, s), 1.48 (3H, s), 1.17 (3H, d, 6 Hz), 0.84 (9H, s), 0.05 (3H, s), 0.01 (3H, s). Mass spectrum (CI, *m/e*): 277 (M^+). Anal. calcd. for $C_{13}H_{28}O_2SSi$: C 56.47, H 10.21; found: C 56.25, H 10.07.

H. Coupling of the thiol ***28*** *(R = t-BDMS) with* ***D-18****: 27 (R^1 = t-BDMS, R^2 = Boc)*

Under nitrogen, the mercaptan **28** (100 mg, 0.36 mmol) was dissolved in degassed dimethylformamide (1.0 mL). The solution was cooled to −55°C and treated with 0.46 mL of a solution of lithium diisopropylamide prepared from *n*-butyllithium (0.8 mL of a 1.6 M hexane solution) and diisopropylamide (0.36 mL, 0.259 g, 2.56 mmol) in degassed tetrahydrofuran (0.8 mL). The reaction mixture was stirred at −45°C for 30 min, and a solution of the β-lactone **D-18** (56.8 mg, 0.30 mmol) in degassed dimethylformamide (0.8 mL) was added. The mixture was stirred at −30°C for 20 min, then diluted with methylene chloride (10 mL), and washed with 0.5 N hydrochloric acid. The aqueous layer was extracted with methylene chloride (2 × 5 mL) and the combined organic extracts were washed with water, then saturated sodium chloride, dried, and evaporated. The residue was dried under high vacuum and purified by flash chromatography (silica gel, 4 g; 0% → 8% ethyl acetate – methylene chloride (1% acetic acid)) to give the coupled product **27** (R^1 = *t*-BDMS, R^2 = Boc) having the *S* configuration at C2 in 89% yield; ^{1}Hmr ($CDCl_3$), δ (one isomer): 5.28 (1H, br t), 4.48 (1H, br), 4.32 (1H, m), 2.83, 2.71 (2H, m), 2.71, 2.62 (2H, m), 1.44 (6H, s), 1.16 (3H, d, 6 Hz), 0.85 (9H, s), 0.05 (3H, s), 0.00 (3H, s). The nmr spectrum shows a 1:1 mixture of epimers in the 2-hydroxypropyl side chain. Anal. calcd. for $C_{21}H_{41}NO_6SSi$: C 54.40, H 8.91, N 3.02; found: C 54.16, H 8.72, N 2.96.

I. Formation and characterization of 3S- ***26***

To **27** (R^1 = *t*-BDMS, R^2 = Boc) (22.7 mg, 0.049 mmol) was added formic acid (0.3 mL). The solution was shaken for 20 min at room temperature and the solvent was then removed by lyophilization. The residue was dissolved in a mixture of ether (3 mL) and water (1 mL). The ether phase was extracted with water (1 mL), and the combined aqueous phase was neutralized with 5% sodium bicarbonate and lyophilized to give **26** (5 mg, 40%) as a mixture of epimers in the 2-hydroxypropyl side chain; ir (KBr, cm^{-1}): 3422 (OH), 1696 (C=O), 1636 (C=N); ^{1}Hmr (D_2O), δ: 4.23 (1H, m), 3.80 (1H, m), 3.30 (1H, q), 2.70–2.85 (3H, m), 1.40 (6H, s), 1.15 (3H, d). High-resolution mass spectrum (*m/e*): 231.0924 (M^+), 213.0823 (M − H_2O).

Acknowledgements

Support of this research by the Operating and Equipment Grants programmes of the Natural Sciences and Engineering Research Council of Canada (NSERC), by Simon Fraser University, and by the Killam Programme of the Canada Council is gratefully acknowledged. The authors also thank the referees for their careful reading of the manuscript, and constructive comments.

1. J.-M. Frère, M. Nguyen-Distèche, J. Coyette, and B. Joris. *In* The chemistry of β-lactams. *Edited by* M.I. Page. Blackie Academic and Professional, London. 1992. p. 148.
2. D.J. Waxman and J.L. Strominger. Annu. Rev. Biochem. **52**, 825 (1983).
3. H. Christensen, M.T. Martin, and S.G. Waley. Biochem. J. **266**, 853 (1990).
4. S. Wolfe, K. Yang, and M. Khalil. Can. J. Chem. **66**, 2733 (1988).
5. (*a*) J.M. Frère and B. Joris. Crit. Rev. Microbiol. **11**, 299 (1985); (*b*) L. Varetto, J.-M. Frère, M. Nguyen-Distèche, J.M. Ghuysen, and C. Houssier. Eur. J. Biochem. **162**, 525 (1987); (*c*) J.A. Kelly, J.R. Knox, P.C. Moews, G.J. Hite, J.B. Bartolone, H. Zhao, B. Joris, J.-M. Frère, and J.-M. Ghuysen. J. Biol. Chem. **260**, 6449 (1985).
6. G.J. Pitt. Acta Crystallogr. 770 (1952).
7. J.A. Kelly, J.R. Knox, H. Zhao, J.-M. Frère, and J.-M. Ghuysen. J. Mol. Biol. **209**, 281 (1989).
8. S. Wolfe, C.-K. Kim and K. Yang. Can. J. Chem. **72**, 1033 (1994).
9. W.J. Hehre, L. Radom, P.v.R. Schleyer, and J.A. Pople. Ab initio molecular orbital theory. Wiley, New York. 1986.
10. S. Wolfe. Can. J. Chem. Can. J. Chem. **72**, 1014 (1994).
11. E. Fischer. Ber. Dtsch. Chem. Ges. **27**, 2985 (1894).
12. O. Dideberg, P. Charlier, J.-P. Wery, P. Dehottay, J. Dursart, T.

Erpicum, J.-M. Frère, and J.-M. Ghuysen. Biochem. J. **245**, 911 (1987); O. Herzberg and J. Moult. Science, **236**, 694 (1987); J.R. Knox and P.C. Moews. J. Mol. Biol. **220**, 435 (1991); N.C.J. Strynadka, H. Adachi, S.E. Jensen, K. Johns, A. Sielecki, C. Betzel, K. Sutoh, and M.N.G. James. Nature, **359**, 700 (1992); J.R. Knox, P.C. Moews, W.A. Escobar, and A.L. Fink. Protein Eng. **6**, 11 (1993).

13. For reviews of attempts to target the penicillin receptor, see: (*a*) J. Marchand-Brynaert and L. Ghosez. *In* Recent progress in the chemical synthesis of antibiotics. *Edited by* M. Ohno and G. Lukais. Springer-Verlag, Berlin. 1990. p. 729; (*b*) B. Pirotte, J. Delarge, J. Coyette, and J.-M. Frère. J. Antibiot. **44**, 844 (1991); (*c*) J.E. Baldwin, G.P. Lynch, and J. Pitlik. J. Antibiot. **44**, 1 (1991); (*d*) L.N. Jungheim and R.J. Ternansky. *In* The chemistry of β-lactams. *Edited by* M.I. Page. Blackie Academic and Professional, London. 1992. p. 306; (*e*) D.B. Boyd. J. Med. Chem. **36**, 1443 (1993). For additional examples based on anaturally occurring compound targeted to the penicillin receptor, see: (*f*) H. Ono and S. Harada. *In* Biochemistry of peptide antibiotics: Recent advances in the biotechnology of β-lactams and microbial bioactive peptides. *Edited by* H. Kleinkauf and H. von Döhren. Walter de Gruyter, Berlin. 1990. p. 131; (*g*) J.E. Baldwin, C. Lowe, and C.J. Schofield. Tetrahedron Lett. **31**, 2211 (1990); (*h*) Y. Ueda, L.B. Crast, Jr., A.B. Mikkilineni, and R.A. Partyka. Tetrahedron Lett. **32**, 3767 (1991).
14. S. Wolfe and T. Hoz. Can. J. Chem. **72**, 1044 (1994).
15. R.C. Bingham, M.J.S. Dewar, and D.H. Lo. J. Am. Chem. Soc. **97**, 1302 (1975); M.J.S. Dewar and W. Thiel. J. Am. Chem. Soc. **99**, 4907 (1977).
16. S. Wolfe, D.F. Weaver, and K. Yang. Can. J. Chem. **66**, 2687 (1988); S. Wolfe, M. Khalil, and D.F. Weaver. Can. J. Chem. **66**, 2715 (1988).
17. A.K. Bose, V. Sudarsanam, B. Anjaneyulu, and M.S. Manhas. Tetrahedron, **25**, 1191 (1969); F. Asinger, H. Offermanns, and D. Neuray. Liebigs Ann. Chem. **739**, 32 (1970); F. Asinger, A. Saus, and D. Neuray. Liebigs Ann. Chem. **759**, 121 (1972); M.D. Ennis and M.E. Baze. Tetrahedron Lett. **29**, 6533 (1988); M. Sainsbury. *In* Comprehensive heterocyclic chemistry. Vol. 3. *Edited by* A.R. Katritzky and C.W. Rees. Pergamon Press, Oxford. 1984. p. 995.
18. R.W. Pero, P. Babiarz-Tracy, and T.P. Fondy. J. Med. Chem. **20**, 644 (1977).
19. L.D. Arnold, R.G. May, and J.C. Vederas. J. Am. Chem. Soc. **110**, 2237 (1988).
20. S.E. Jensen, D.W.S. Westlake, R.J. Bowers, C.F. Ingold, M. Jouany, L. Lyubechansky, and S. Wolfe. Can. J. Chem. **62**, 2712 (1984).
21. S. Wolfe, C. Zhang, B.D. Johnston, and C.-K. Kim. Can. J. Chem. Can. J. Chem. **72**, 1066 (1994).
22. M. Julia, S. Julia, and J.A. du Chaffault. Bull. Soc. Chim. Fr. 1735 (1960).
23. S. Wolfe, C.F. Ingold, and R.U. Lemieux. J. Am. Chem. Soc. **103**, 938 (1981); S. Wolfe and C.F. Ingold. J. Am. Chem. Soc. **105**, 7755 (1984).
24. M.J. Frisch, J.S. Binkley, H.B. Schlegel, K. Raghavachari, C.F. Melius, R.L. Martin, J.J.P. Stewart, F.W. Bobrowicz, C.M. Rohlfing, L.R. Kahn, D.J. Defrees, R. Seeger, R.A. Whiteside, D.J. Fox, E.M. Fluder, and J.A. Pople. GAUSSIAN 86; Gaussian, Inc., Pittsburgh, Pa. 1986.
25. M.J. Frisch, M. Head-Gordon, G.W. Trucks, J.B. Foresman, H.B. Schlegel, K. Raghavachari, M.A. Robb, J.S. Binkley, C. Gonzalez, D.J. Defrees, D.J. Fox, R.A. Whiteside, R. Seeger, C.F. Melius, J. Baker, R.L. Martin, L.R. Kahn, J.J.P. Stewart, S. Topiol, and J.A. Pople. GAUSSIAN 90. Gaussian, Inc., Pittsburgh, Pa. 1990.
26. M.J. Frisch, G.W. Trucks, M. Head-Gordon, P.M.W. Gill, M.W. Wong, J.B. Foresman, B.G. Johnson, H.B. Schlegel, M.A. Robb, E.S. Replogle, R. Gomperts, J.L. Andres, K. Raghavachari, J.S. Binkley, C. Gonzalez, R.L. Martin, D.J. Fox, D.J. Defrees, J.Baker, J.J.P. Stewart, and J.A. Pople. GAUSSIAN 92, Revision A. Gaussian, Inc., Pittsburgh, Pa. 1992.
27. J.J.P. Stewart. MOPAC. Version 6.00. QCPE 455. Bloomington, Ind.
28. N.L. Allinger. MMP2(85). QCPE. Bloomington. Ind.
29. N.S. Srinivasan and D.G. Lee. Synthesis, 520 (1979).

Can. J. Chem. Downloaded from www.nrcresearchpress.com by EESC ESCOLA DE ENGENHARIA on 09/08/12
For personal use only.

Synthesis of the stereoisomers of a novel antibacterial agent and interpretation of their relative activities in terms of a theoretical model of the penicillin receptor

SAUL WOLFE,[1] CAIJUN ZHANG, BLAIR D. JOHNSTON, AND CHAN-KYUNG KIM
Department of Chemistry, Simon Fraser University, Burnaby, BC V5A 1S6, Canada

Received August 25, 1993

SAUL WOLFE, CAIJUN ZHANG, BLAIR D. JOHNSTON, and CHAN-KYUNG KIM. Can. J. Chem. **72**, 1066 (1994).

2,2-Dimethyl-3-(2′-hydroxypropyl)-5-carboxy-Δ^3-1,4-thiazine (**1**) is a designed antibacterial agent. Based on an analysis of how penicillin complexes to and reacts with a model of a penicillin-binding protein, **1** contains a functional group (C═N) that can react with a serine hydroxyl group of the receptor according to the putative reaction Enz-OH + C═N → Enz-O-C-NH. Compound **1** also contains additional substituents that are designed to position the O-H and C═N groups relative to one another in the enzyme–substrate complex in a geometry that attempts to reproduce the optimum geometry of approach of two such reactants. A most important assumption is that this optimum geometry can be computed ab initio. In a first preparation of **1**, (±)-5-methyl-4-hexene-2-ol (**2**) was converted to the lithium salt of (±)-2-mercapto-2-methyl-5-*tert*-butyldimethylsiloxy-3- hexanone (**7**), which was condensed with the *N*-*tert*-butoxycarbonyl-D- and L-serine-β-lactones (**3**). The synthesis was completed by deprotection with formic acid and cyclization in water. The *R* and *S* enantiomers of **2** have now been obtained, and the absolute configuration of the alcohol established, by reaction of the *R*- and *S*-propylene oxides with an organometallic reagent prepared from β,β-dimethylvinyl bromide. The *R* alcohol has also been secured by lipase-catalyzed transesterification with trifluoroethyl butyrate, and chemical hydrolysis of the trifluoroethyl ester. The *R* and *S* enantiomers of **2** were converted to the *R* and *S* enantiomers of **7**, and these were condensed with the *R* and *S* enantiomers of **3** to yield each of the stereoisomers of the chemically unstable **1** in ca. 95% optically pure form. Antibacterial activity resides in the 5*S*,8*R* and 5*S*,8*S* isomers. These findings are shown to be consistent with the theoretical model. It is hoped that the stability of the lead structure **1** can be improved, to allow binding experiments with penicillin recognizing enzymes to proceed.

SAUL WOLFE, CAIJUN ZHANG, BLAIR D. JOHNSTON et CHAN-KYUNG KIM. Can. J. Chem. **72**, 1066 (1994).

La 2,2-diméthyl-3-(2′-hydroxypropyl)-5-carboxy-Δ^3-1,4-thiazine (**1**) devrait être une agent antibactérien. Sur la base d'une analyse du mécanisme de complexation et de réaction de la pénicilline avec un modèle d'une protéine se liant à la pénicilline, **1** contient un groupe fonctionnel (C═N) qui peut réagir avec un groupe hydroxyle de la sérine du récepteur suivant la réaction Enz-OH + C═N → Enz-O-C-NH. Le composé **1** contient aussi des substituants additionnels choisis pour orienter les groupes O-H et C═N l'un par rapport à l'autre dans le complexe enzyme–substrat dans une géométrie qui essaye de reproduire la géométrie optimale de l'approche de deux tels réactants. Une hypothèse très importante est que cette géométrie optimale peut être calculée ab initio. Dans une première préparation du composé **1**, on a transformé le (±)-5-méthyl-hex-4-èn-2-ol (**2**) en sel de lithium de la (±)-2-mercapto-2-méthyl-5-*tert*-butyldiméthylsiloxyhexan-3-one (**7**) qui a été condensée avec les *N*-*tert*-butoxycarbonyl-D- et L-sérine-β-lactones (**3**). On a complété la synthèse par une déprotection à l'aide d'acide formique et une cyclisation dans l'eau. On a maintenant obtenu les énantiomères *R* et *S* du composé **2** et on a déterminé la configuration absolue de l'alcool par réaction avec les oxydes de propylène *R* et *S* avec un réactif organométallique préparé à partir du bromure de β,β-diméthylvinyle. On a aussi préparé l'alcool *R* par une transestérification catalysée par la lipase avec du butyrate de trifluoroéthyle, suivi d'une hydrolyse chimique de l'ester trifluoroéthyle. On a transformé les énantiomères *R* et *S* du composé **2** en énantiomères *R* et *S* du composé **7** et on a condensé ces derniers avec les *R* et *S* du composé **3** pour obtenir chacun des stéréoisomères du produit **1** (qui est chimiquement instable) sous des formes qui sont environ 95% optiquement pures. On retrouve de l'activité antibactérienne avec les isomères 5*S*,8*R* et 5*S*,8*S*. On montre que ces résultats sont en accord avec le modèle théorique. On espère, dans le but de permettre des études de liaison avec des enzymes qui reconnaissent la pénicilline, qu'il sera possible d'augmenter la stabilité de la structure **1**.

[Traduit par la Rédaction]

Introduction

β-Lactam antibiotics act on their target enzymes (penicillin-binding proteins, PBP's) by acylation of the hydroxyl group of an active site serine residue (1). The reaction is believed to proceed within a complex in which the hydroxyl group and a water molecule are properly positioned for attack on the N—C bond of the β-lactam N-C═O (2). The necessary geometry is achieved by hydrogen bonding of the carboxyl group (G_1) and side-chain N-H (G_2) of the antibiotic to complementary amino and carbonyl groups of the PBP (3).

We have proposed (4) that the N═C bond of an imine is bioisosteric to the N—C bond of the β-lactam group, and comparable to a β-lactam in its bioreactivity towards a hydroxyl group. A compound intended to fit to, and react with, the penicillin receptor in the same manner as penicillin itself might, therefore, contain an imine group properly positioned with respect to a G_1 and a G_2. A reconciliation of these structural requirements with the chemical properties of dihydrothiazines suggested compound **1** as an example of a designed antibacterial agent. As summarized in Scheme 1 (4), the synthesis of **1** was accomplished starting with the racemic alcohol **2**, prepared by a literature route from ethyl 2-methylcyclopropanecarboxylate (5), and the chiral lactones **3**, prepared by a literature route from D- and L-serine (6). The compound having stereostructure **1***a*, derived from D-serine, is an antibacterial agent; the isomer **1***b* is not active.

In the present work, new syntheses of **2** and of its *R* and *S* enantiomers, as well as an enzymatic resolution of **2**, have been carried out, and the strategy of Scheme 1 has then been followed to produce each of the four stereoisomers of **1**. Although these compounds are chemically unstable, the activity of the **1***a*

[1]Canada Council Killam Research Fellow 1990–1992.

Can. J. Chem. Downloaded from www.nrcresearchpress.com by EESC ESCOLA DE ENGENHARIA on 09/08/12
For personal use only.

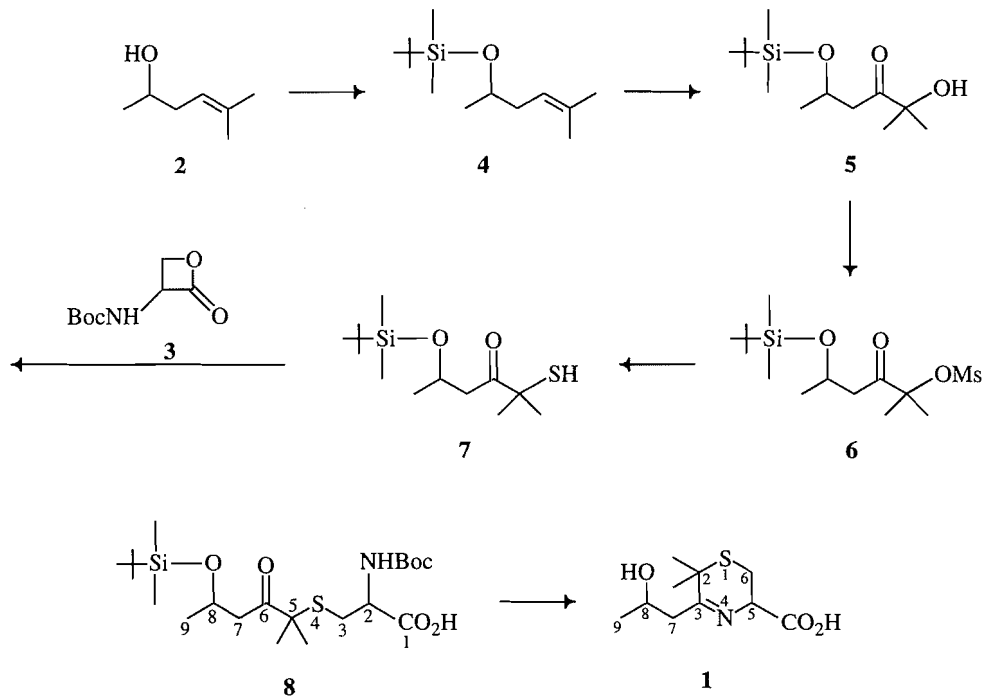

SCHEME 1

1*a* **1***b*

stereostructure has been confirmed, and it has been found that the hydroxypropyl side-chain epimers have the same activity. Analysis of these observations has led to new insights into the meaning of "fit," as applied to an enzyme–substrate complex, a definition of "fit," and a relationship between a biological property (antibacterial activity) and the "fits" exhibited by different stereoisomers.

Results and discussion

Syntheses

The addition of racemic propylene oxide (**9**) to the organometallic reagent **10**, prepared from β,β-dimethylvinyl bromide (7) by successive treatment with magnesium and then cuprous iodide (8), afforded the racemic alcohol **2** in 80% yield (eq. [1]).

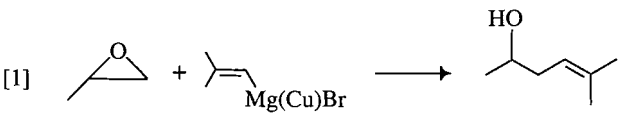

[1]

9 **10** **2**

The *R* and *S* enantiomers of **2** were, therefore, accessible from the *R* and *S* enantiomers of propylene oxide. These were prepared from ethyl L-lactate by (*a*) tosylation, reduction with borane – dimethyl sulfide, and treatment with base to obtain *R*-propylene oxide, $[\alpha]_D^{23}$ +7.32 (*c* 2.5, CH_2Cl_2) (9); or (*b*) reduction with lithium aluminium hydride, reaction with 45% hydrogen bromide in acetic acid, and treatment with base to obtain *S*-propylene oxide, $[\alpha]_D^{20}$ −7.57 (*c* 1.6, CH_2Cl_2) (10) (Scheme 2).

The reaction of the *R*-epoxide with **10** gave *R*-**2**, $[\alpha]_D^{21}$ −11.74 (*c* 3.15, CH_2Cl_2); *p*-nitrobenzoate: $[\alpha]_D^{21}$ −31.5 (*c* 1.3, CH_2Cl_2). The *S*-epoxide reacted analogously to give *S*-**2**, $[\alpha]_D^{21}$ +11.75 (*c* 1.6, CH_2Cl_2); *p*-nitrobenzoate: $[\alpha]_D^{21}$ +31.90 (*c* 0.94, CH_2Cl_2).

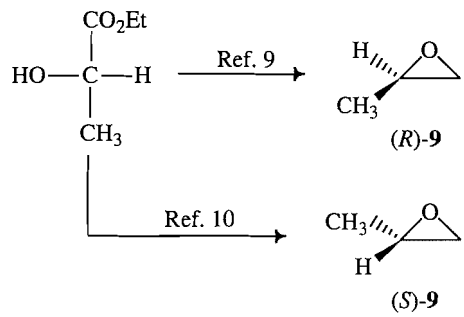

SCHEME 2

Alternatively, trifluoroethyl butyrate and the racemic alcohol **2** were stirred in ether with porcine pancreatic lipase (11) until 50% conversion to the *n*-butyl ester of **2** had occurred (Scheme 3). The unreacted alcohol recovered from the kinetic resolution at this stage was the expected (11) *S* enantiomer, $[\alpha]_D^{21}$ +9.2 (*c* 2.1, CH_2Cl_2). Hydrolysis of the *R* ester gave *R*-**2** of high optical purity, $[\alpha]_D^{21}$ −11.95 (*c* 2.0, CH_2Cl_2).

Racemic **2** and the optically active alcohols prepared by the epoxide route and by kinetic resolution were then converted to their Mosher esters (12) by reaction with the acid chloride (13) of *R*-(+)-α-methoxy-α-(trifluoromethyl)-phenylacetic acid (MTPA). Examination of the ^{19}F and ^1Hmr spectra of the various **2**-MTPA esters indicated that optical purities were best determined by integration of the methyl doublets of the Me-CHX- moiety at δ =1.258 (*R* epimer) and 1.326 (*S* epimer) in the ^1Hmr spectrum. Except for the *S* alcohol from the kinetic resolution, all optically active samples of **2** exhibited >97% enantiomeric excess (ee). The syntheses of the stereoisomers of **1** were therefore continued using *S*-**2** from the epoxide route,

Can. J. Chem. Downloaded from www.nrcresearchpress.com by EESC ESCOLA DE ENGENHARIA on 09/08/12
For personal use only.

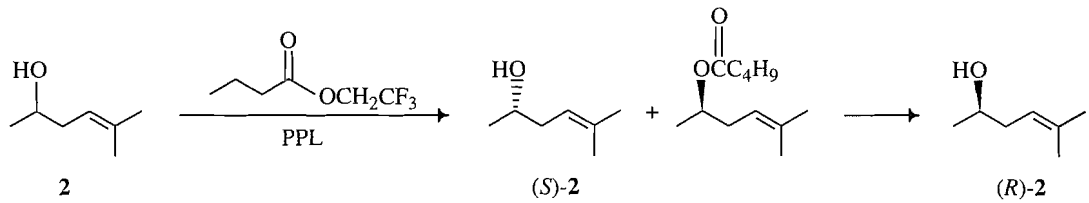

SCHEME 3

TABLE 1. Rotations ($[\alpha]_D$, degrees) of the enantiomers of **2–7** (Scheme 1)[a]

Compound	Isomer	Rotation
2	**R**	−11.74
	S	+11.75
3	**R**	+10.91
	S	−10.81
4	**R**	−5.04
	S	+5.04
5	**R**	−32.0
	S	+32.2
6	**R**	−10.1
	S	+10.6
7	**R**	−33.5
	S	+33.3

[a]All rotations are in CH_2Cl_2.

R-**2** from the kinetic resolution, *S*-**3** from L-serine, and *R*-**3** from D-serine.

Table 1 summarizes the rotations of **2–7** in the *R* and *S* series (Scheme 1). Coupling of the lithium salts of *R*- and *S*-**7** with *R*- and *S*-**3** yielded the four stereoisomers of **8**, each of which was obtained in analytically pure form. The structures and rotations of the isomers of **8** are shown in Table 2, which includes the structures and rotations of the four stereoisomers of **1** prepared from **8** by deprotection with formic acid, cyclization in water, and purification by preparative HPLC (4). Each of the isomers of **1** is believed to be ca. 95% stereochemically pure.

Figure 1 shows the zones of inhibition versus *Staphylococcus aureus* produced by 0.1 μg of penicillin V and by 1.0 mg of each of the isomers of **1**. It is evident that the activity of **1** resides in the isomers having the *S* configuration at C5, as noted earlier in stereostructure **1***a*. The activities of the 5*S*,8*S* and 5*S*,8*R* isomers appear to be the same. The active isomers of **1** have only about 1/1000 the activity of penicillin V, but these activities are already comparable to that of a Δ^2-cephalosporin (2). Although Δ^2-cephalosporins are too weakly active to be useful antibiotics, one structural change, a shift of the nuclear double bond, yields the clinically important Δ^3-cephalosporins. We hope that the lead structure **1** can also be modified to improve its activity and chemical stability. Increased chemical stability will facilitate the planning of binding experiments with penicillin-recognizing enzymes.

Theoretical considerations

The antibacterial activity of a penicillin is the end result of the ability of the compound to reach, and then fit to and acylate, a PBP. As a result of the "fit", the hydroxyl group of the active site serine residue and the N—C bond of the β-lactam N-C=O are so positioned with respect to one another that a catalytic water molecule can complete the structure of the complex in which the acylation reaction occurs. Figure 2 illustrates this point. Structure A (4) is a closeup view of the C-O-H/H-O-H/N-C=O geometry in the complex formed between the crystal structure of penicillin G (**11**), a water molecule, and **12**, a hexapeptide model of the penicillin receptor (3). To form this complex, G_1, the carboxyl group of the antibiotic, was hydrogen bonded to the terminal amino group of a lysine residue of **12**, labelled N, and G_2, the side-chain N-H of the antibiotic, was hydrogen bonded to a carbonyl oxygen of **12**, labelled V. Structure B (4) is a closeup view of the C-O-H/H-O-H/N-C=O geometry in the ab initio (3-21G) complex that proceeds to the transition state of the water-catalyzed methanolysis of *N*-methylazetidinone. There is an obvious resemblance between A and B, and the root-mean-square deviation (rms) between the six atoms of the cyclic portions of the two structures is 0.24 Å. This value (rms = 0.24 Å) can be regarded as a theoretical measure of the *optimum fit* for penicillin.

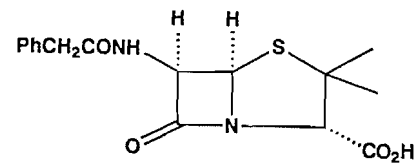

11

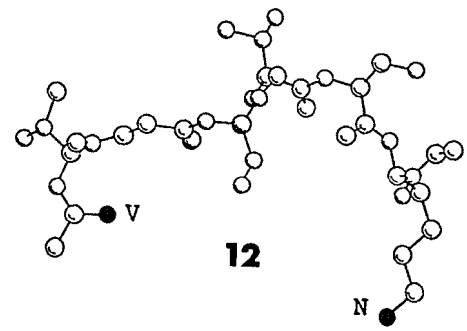

12

If **1** has the same mechanism of action as penicillin (*a point not yet proven experimentally*), the chemical reaction that serves as the analog of acylation by the β-lactam ring is addition of the serine hydroxyl group to the C=N bond. For such a reaction, Fig. 3, the 3-21G reactant complex of the water-catalyzed reaction of methanol with 1-pyrroline (4) is the structure to which the fit to the PBP can be compared. In practice, the "fits" discussed below are based on the four-centred relationship between O-H and C=N (shown, for the 3-21G structure, as an insert in Fig. 3).

Figure 4 shows one of the conformations of the 5*S*,8*S* isomer

Can. J. Chem. Downloaded from www.nrcresearchpress.com by EESC ESCOLA DE ENGENHARIA on 09/08/12
For personal use only.

TABLE 2. Rotations ($[\alpha]_D$, degrees) of the stereoisomers of **8**[a] and of **1**[b]

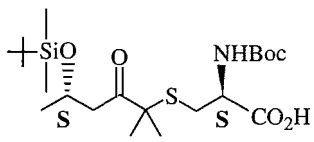	+27.2°	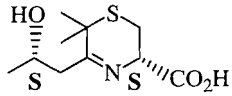	+155°
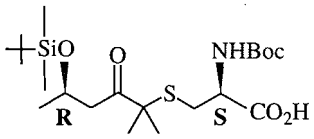	−33.0°	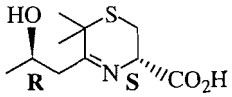	−75°
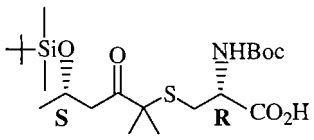	+33.9°	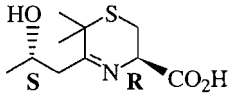	+73°
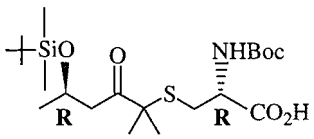	−26.9°	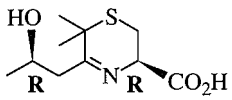	−155°

[a]In CH_2Cl_2.
[b]In 50% acetone – water.

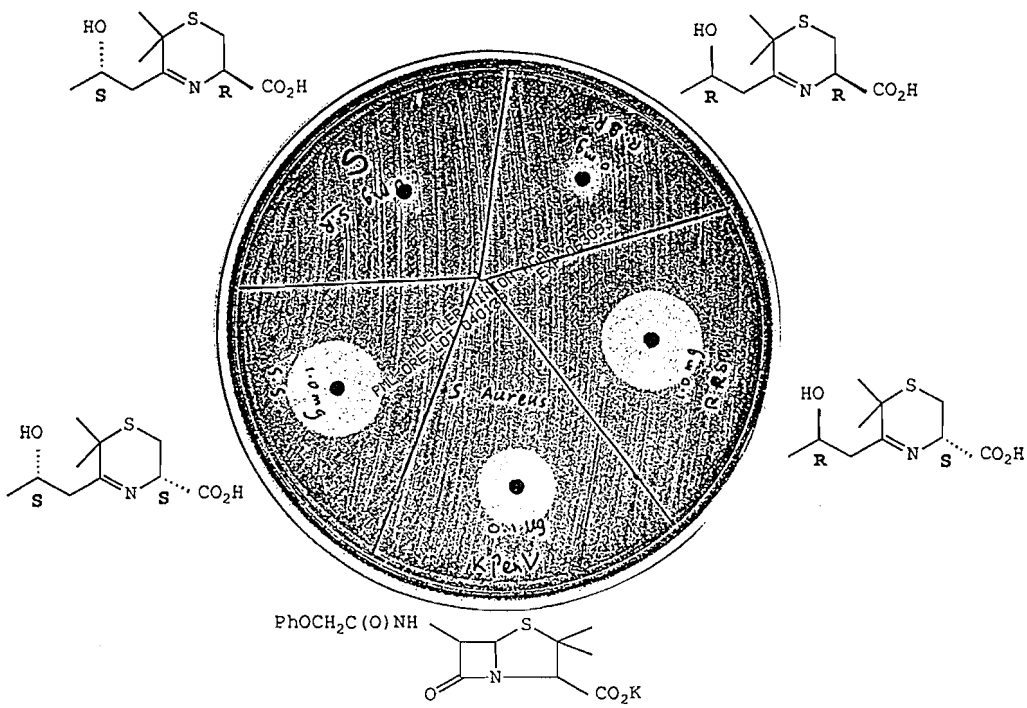

FIG. 1. Zones of inhibition produced on *S. aureus* by penicillin V (0.1 μg), and by the stereoisomers of **1** (1 mg).

of **1**. Sixteen initial orientations of G_1 (CO_2^-) and G_2 (O-H) of this structure with respect to the amino (N) and carbonyl (V) groups of **12** were minimized (3, 4) to produce, as the lowest energy structure, the complex shown in Fig. 5. The four-centred relationship between O-H and C=N in this complex is shown as an insert in the figure. *The rms deviation between the four-centred inserts of Figs. 3 and 5 is 0.37 Å.*

Ten conformations of the *RR/SS* diastereomer and seven conformations of the *RS/SR* diastereomer of **1**, corresponding to torsion about the *C5—C6*, *C3—C7*, *C7—C8*, and *C8—O* bonds, were generated using the dihedral driver of MMP2 (85) (14), and the energies of these structures were minimized. Each of the 34 *RR*, *SS*, *RS*, and *SR* structures was then docked to **12**, as described above, the energies of the docked structures were minimized, and the rms deviations from the four-centred relationship of Fig. 3 were determined. Table 3 summarizes the relative energies of the *RR/SS* conformations, and the rms deviations exhibited by the *RR* and *SS* complexes. Table 4 con-

Can. J. Chem. Downloaded from www.nrcresearchpress.com by EESC ESCOLA DE ENGENHARIA on 09/08/12
For personal use only.

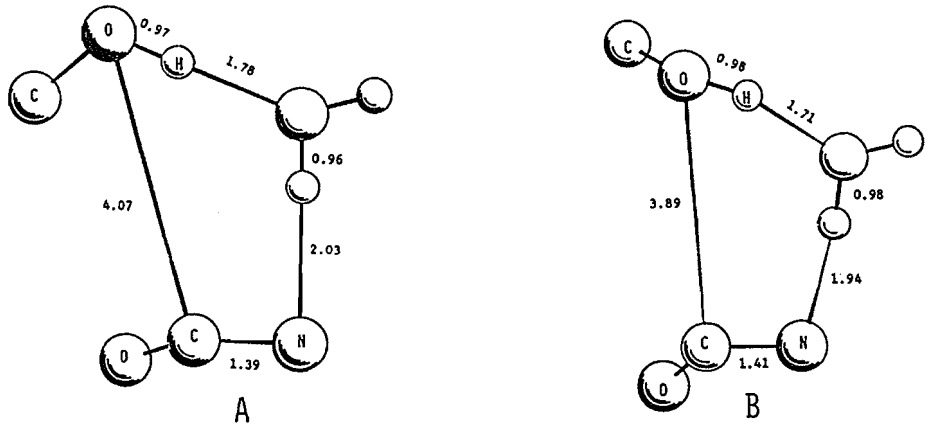

FIG. 2. (A) A closeup view of the C-O-H/H-O-H/N-C=O geometry in the complex of the crystal structure of penicillin G and a water molecule with **12**, Ac-NH-Val-Gly-Ser-Val-Thr-Lys-NHMe. (B) A closeup view of the C-O-H/H-O-H/N-C=O geometry in the stationary point, computed at 3-21G, that is formed when methanol reacts with *N*-methylazetidinone in the presence of one water molecule. The RMS deviation between the two structures is 0.24 Å.

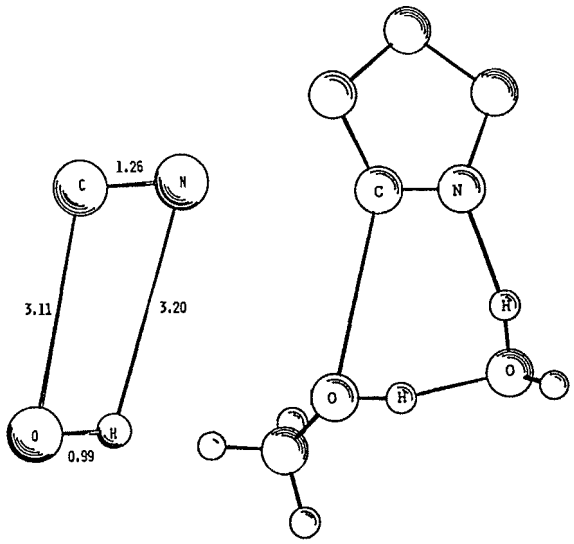

FIG. 3. The stationary point, computed at 3-21G, showing the complex that is formed when methanol reacts with 1-pyrroline in the presence of one water molecule (some hydrogens have been deleted for clarity). Inset: a closeup view of the O-H/C=N geometry in this complex.

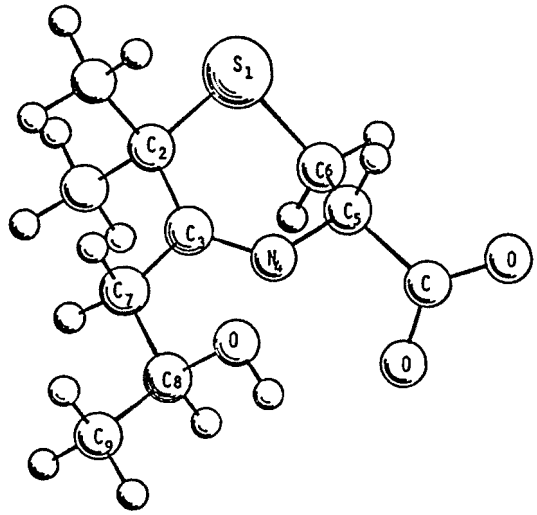

FIG. 4. One of the conformations of the 5*S*,8*S* isomer of **1**. The structure is conformation 2 of Table 3.

tains the analogous data for the *RS/SR* conformations and the *RS* and *SR* complexes. The structure shown in Fig. 4 is conformation 2 of Table 3.

Referring to Table 3, we observe that conformations 1–6 and conformation 8 of the *SS* isomer exhibit better fits to the receptor model than do any of the conformations of the *RR* isomer. In Table 4 we observe that the fit of conformation 3 of the *SR* isomer is better than that of any conformation of the *RS* isomer, and the same as that of conformations 1, 2, and 8 of the *RR* isomer.

With "fit" defined as the deviation between the geometry accessible to the reacting groups in the "enzyme"–substrate complex and the geometry of the stationary point (reactant complex) of the reaction itself, the ordering of these fits is

$$\text{penicillin G} > (5S,8S = 5S,8R) > 5R,8S > 5R,8R$$

This ordering of fits is reminiscent of the ordering of relative antibacterial activities seen in Fig. 1.

There are several practical and mechanistic consequences if binding experiments with penicillin-recognizing enzymes support the connection between theory and experiment that has been developed here. The existence of a quantitative definition of "fit", and also of a relationship between the "fit" exhibited by a candidate structure and its putative antibacterial activity, will narrow the choice of compounds to be selected for synthesis.

As was evident in Fig. 2, our definition of "fit" is based on the geometry of an "enzyme"–substrate complex, not a transition structure. This idea appears to be in conflict with the belief that transition state stabilization is the origin of enzymic catalysis (15). The relationships between ground state and transition state effects (16), and related questions (17), will have to be addressed in the next phase of this research.

Experimental

General

General experimental procedures have been summarized in ref. 4.

*(R)-Propylene oxide (+)-**9***

This was prepared from ethyl L-lactate (9); $[\alpha]_D^{23}$ +7.32 (*c* 2.5, CH_2Cl_2); ir (film): 2994.5, 1407.0, 1265.2, 1022.9, 949.8, 828.9 cm^{-1}; ^{1}Hmr ($CDCl_3$), δ: 1.29 (3H, d, 5.2 Hz, CH_3), 2.40 (1H, dd, 5.0, 2.7 Hz, CH_2), 2.72 (1H, dd, 5.0, 5.0 Hz, CH_2), 2.95 (1H, m, CH).

Can. J. Chem. Downloaded from www.nrcresearchpress.com by EESC ESCOLA DE ENGENHARIA on 09/08/12
For personal use only.

TABLE 3. Calculated relative energies of different conformations of the *RR/SS* diastereomer of **1** and, for the complexes formed by the *RR* and *SS* enantiomers with **12**, the root-mean-square deviations of the O-H/C=N coordinates from those of the ab initio complex of Fig. 3[a]

Conformation of the *RR/SS* isomer	Relative energy	RMS	
		5*R*,8*R* Complex	5*S*,8*S* Complex
1	0.00	1.99	0.38
2	0.00	1.92	0.37
3	0.10	0.65	0.54
4	0.69	1.51	0.47
5	0.69	1.28	0.50
6	0.78	1.31	0.47
7	0.89	0.61	1.08
8	0.90	0.77	0.37
9	1.22	0.81	1.63
10	1.87	0.76	1.08

[a]Root-mean-square (RMS) data are in angstrom. Energies are in kcal/mol, using MMP2(85). See refs. 3 and 4 for details of the method and for listings of parameters.

TABLE 4. Calculated relative energies of different conformations of the *RS/SR* diastereomer of **1** and, for the complexes of the *RS* and *SR* enantiomers with **12**, the root-mean-square deviations of the O-H/C=N coordinates from those of the ab initio complex of Fig. 3[a]

Conformation of the *RS/SR* isomer	Relative energy	RMS	
		5*S*,8*R* Complex	5*R*,8*S* Complex
1	0.00	1.26	1.00
2	0.40	1.14	0.81
3	0.42	0.38	0.90
4	0.57	0.66	1.18
5	0.77	1.04	0.65
6	1.04	0.54	0.61
7	1.41	0.76	0.42

[a]See footnote *a* of Table 3.

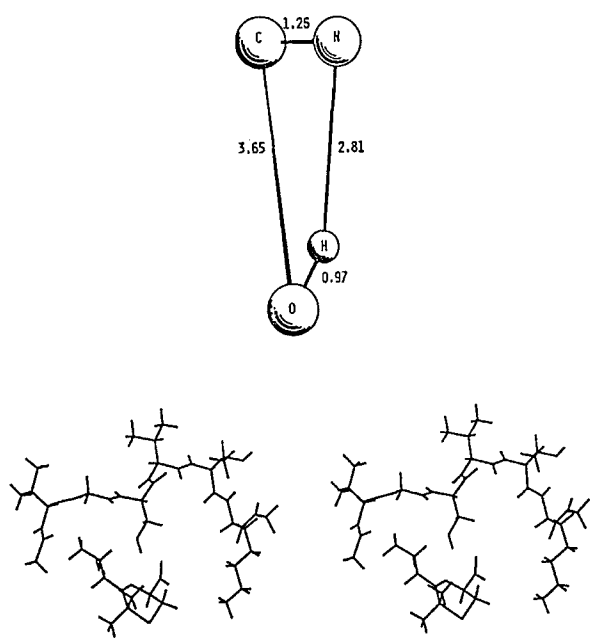

FIG. 5. Stereoscopic view of the complex formed between the structure of Fig. 4 and the model of the penicillin receptor. Inset: a closeup view of the O-H/C=N geometry in this complex. The RMS deviation between the insets of Figs. 3 and 5 is 0.37 Å.

*(S)-Propylene oxide (−)-***9**

This compound was also prepared from ethyl L-lactate (10); $[\alpha]_D^{20}$ −7.57 (*c* 1.58, CH_2Cl_2) (lit. (14) $[\alpha]_D^{20}$ −7.77 (*c* 0.032, $CHCl_3$)); ir (film): 2994.8, 1407.2, 1265.3, 1023.1, 949.8, 828.8 cm^{-1}; ^{1}Hmr ($CDCl_3$), δ: 1.29 (3H, d, 5.2 Hz, $CHCH_3$), 2.42 (1H, dd, 5.0, 2.7 Hz, CHH), 2.72 (1H, dd, 5.0, 5.0 Hz, CHH), 2.95 (1H, m, $CHCH_3$).

(R)-5-Methyl-4-hexene-2-ol (−)-2

A solution of bromine (150 mL, 465.3 g, 2.9 mol) in methylene chloride (500 mL) was cooled in an ice-bath, stirred, and isobutylene was bubbled in slowly. When the bromine colour disappeared the solvent was removed, and the residue was distilled to give 433.4 g (69%) of 1,2-dibromo-2-methylpropane, bp 46–48°/20 Torr (1 Torr = 133.3 Pa); ^{1}Hmr ($CDCl_3$), δ: 1.87 (6H, s), 4.86 (2H, s). The dibromide (84.0 g, 0.39 mol) was added dropwise over 45 min at 100°C to a solution of potassium hydroxide (30 g, 0.53 mol) in ethylene glycol (100 mL) in a flask set up for distillation. The reaction was terminated when the distillation temperature reached 90°C. The two phases of the distillate were transferred to a separatory funnel with the aid of methylene chloride (5 mL), and the lower phase was separated, dried over anhydrous calcium chloride, and distilled to yield 41.8 g (80%) of β,β-dimethylvinyl bromide (7), bp 90–92°C; ^{1}Hmr ($CDCl_3$), δ: 1.78 (6H, d), 5.87 (1H, m).

Tetrahydrofuran (30 mL) was stirred under nitrogen with magnesium turnings (2.0 g, 82 mg-atom). A crystal of iodine and 0.2 mL of 1,2-dibromoethane were added, the mixture was refluxed until the iodine colour had disappeared, and β,β-dimethylvinyl bromide (5.58 g, 4.2 mL, 41 mmol) in tetrahydrofuran (10 mL) was added drop-

Can. J. Chem. Downloaded from www.nrcresearchpress.com by EESC ESCOLA DE ENGENHARIA on 09/08/12
For personal use only.

Can. J. Chem. Downloaded from www.nrcresearchpress.com by EESC ESCOLA DE ENGENHARIA on 09/08/12
For personal use only.

wise over 30 min. The reaction mixture was refluxed for 3 h, cooled to room temperature, and the supernatant was transferred to a fresh flask. The solution was cooled to −30°C, dry cuprous iodide (0.16 g, 8 mmol) was added in one portion, the mixture was stirred for 15 min, and a solution of (*R*)-propylene oxide (2.0 g, 2.4 mL, 34.4 mmol) in tetrahydrofuran (20 mL) was then added dropwise during 1 h. When the addition was complete, the mixture was warmed to room temperature, stirred for 4 h, and poured onto rapidly stirred saturated ammonium chloride (150 mL). The organic layer was separated and the blue aqueous layer was extracted with ether (3 × 20 mL). The combined organic extract was washed with saturated sodium chloride (2 × 50 mL), dried over anhydrous magnesium sulfate, evaporated, and distilled to give 3.12 g (79%) of a colourless oil, bp 65–70°/20 Torr; $[\alpha]_D^{21}$ −11.74 (*c* 3.15, CH_2Cl_2); ir (film): 3362.0, 2969.5, 2926.8, 1716.0, 1455.8, 1375.9, 1121.8, 1078.3 cm^{-1}; ^{1}Hmr ($CDCl_3$), δ: 1.18 (3H, d, 6.7 Hz, $CHCH_3$), 1.63 (1H, s, O*H*), 1.63 (3H, s, CCH_3), 1.72 (3H, s, CCH_3), 2.16 (2H, dd, 7.5, 7.5 Hz, $CHCH_2CH$), 3.79 (1H, m, C*H*OH), 5.15 (1H, m, C*H*═C); ms (*m/e*, CI): 114 ($M^+ + 1$), 97 ($M^+ - H_2O$).

(S)-5-Methyl-4-hexene-2-ol (+)-2

This compound was prepared from (*S*)-propylene oxide in 80% yield; $[\alpha]_D^{21}$ +11.75 (*c* 1.6, CH_2Cl_2); ir (film): 3362.0, 2969.5, 2926.8, 1716.0, 1455.8, 1375.9, 1121.8, 1078.3 cm^{-1}; ^{1}Hmr ($CDCl_3$), δ: 1.18 (3H, d, 6.7 Hz), 1.63 (1H, s), 1.63 (3H, s), 1.72 (3H, s), 2.16 (2H, dd, 7.5, 7.5 Hz), 3.79 (1H, m), 5.15 (1H, m); ms (*m/e*, CI): 114 ($M^+ + 1$), 97 ($M^+ - H_2O$).

Resolution of 5-methyl-4-hexene-2-ol

A mixture of trifluoroethanol (20.6 g, 15.0 mL, 206 mmol), butyric anhydride (31.9 g, 23.0 mL, 202 mmol), and *p*-toluenesulfonic acid monohydrate (0.3 g) was stirred and heated to reflux under nitrogen. When the temperature of the vapour reached 105°C, the reflux condenser was replaced by a distillation head and rapid distillation was performed. The material boiling to 130°C was collected and redistilled through a 20-cm Vigreux column to give a central fraction of trifluoroethyl butyrate, bp 105–115°C, 33.2 g (90%); ir (film): 2972.4, 2881.3, 1762.4, 1713.0, 1413.7, 1282.9, 1169.9, 1102.5 cm^{-1}; ^{1}Hmr ($CDCl_3$), δ: 1.00 (3H, t, 7.2 Hz, $CH_2CH_2CH_3$), 1.71 (2H, m, $CH_2CH_2CH_3$), 2.43 (2H, t, 7.0 Hz, $CH_2CH_2CH_3$), 4.49 (2H, q, 8.3 Hz, CH_2CF_3); ms (*m/e*): 170 (M^+), 155 ($M^+ - CH_3$).

5-Methyl-4-hexen-2-ol (10.66 g, 93.3 mmol), trifluoroethyl butyrate (18.8 g, 110 mmol), dry ether (55 mL), and Porcine Pancreatic Lipase (E.C. 3.1.1.3, Sigma crude preparation lipase, type 2, no. L-3126, 8.2 g) were stirred in a 250-mL flask protected from moisture. The progress of the reaction was monitored by gas chromatography (GC). When this indicated that 50% of the alcohol had been esterified, the reaction was terminated by filtration. The filtrate was concentrated and the residue distilled to give (*S*)-(+)-5-methyl-4-hexen-2-ol, 4.87 g (46%), bp 65–75°C/17 Torr, and the trifluoroethyl ester of (*R*)-5-methyl-4-hexen-2-ol, 4.07 g (24%), bp 80–95°C/17 Torr. The ester (4.07 g, 21.7 mmol), in 1.0 M methanolic potassium hydroxide (50 mL, 50 mmol), was refluxed for 50 min. The solvent was removed and the residue was triturated with ether (3 × 20 mL). This extract was washed with saturated sodium chloride (2 × 20 mL), dried over anhydrous magnesium sulfate, and evaporated. Distillation afforded 1.5 g (69%) of (*R*)-(−)-5-methyl-4-hexen-2-ol, bp 60–70°C/15 Torr. For (*S*)-(+)-5-methyl-4-hexen-2-ol (ee = 65%): $[\alpha]_D^{21}$ +9.19 (*c* 2.1, CH_2Cl_2); ir (film): 3362.0, 2969.5, 2926.8, 1716.0, 1455.8, 1375.9, 1121.8, 1078.3 cm^{-1}; ^{1}Hmr ($CDCl_3$), δ: 1.18 (3H, d, 6.7 Hz), 1.63 (1H, s), 1.63 (3H, s), 1.72 (3H, s), 2.16 (2H, dd, 7.5, 7.5 Hz), 3.79 (1H, m), 5.15 (1H, m); ms (*m/e*, CI): 114 ($M^+ + 1$), 97 ($M^+ - H_2O$). For (*R*)-(-)-5-methyl-4-hexane-2-ol (ee = 97%): $[\alpha]_D^{21}$ −11.95 (*c* 2.05, CH_2Cl_2); ir (film): 3362.0, 2969.5 2926.8, 1716.0, 1455.8, 1375.9, 1121.8, 1078.3 cm^{-1}; ^{1}Hmr ($CDCl_3$), δ: 1.18 (3H, d, 5.7 Hz), 1.63 (1H, s), 1.63 (3H, s), 1.72 (3H, s), 2.16 (2H, dd, 7.5, 7.5 Hz), 3.79 (1H, m), 5.15 (1H, m); ms (*m/e*, relative intensity, CI): 114 ($M^+ + 1$), 97 ($M^+ - H_2O$).

(R)-(−)-5-Methyl-4-hexen-2-ol p-*nitrobenzoate*

p-Nitrobenzoyl chloride (80 mg, 0.47 mmol) was added to a solution of (*R*)-(−)-5-methyl-4-hexen-2-ol (50 mg, 0.44 mmol, from epoxide) in pyridine (2 mL). The solution was stirred at room temperature for 3 h, and then poured into water (5 mL). The aqueous layer was extracted with ether (2 × 5 mL), and this extract was washed successively with 5% sodium bicarbonate (2 × 5 mL) and saturated sodium chloride (2 × 5 mL), dried over anhydrous magnesium sulfate, and evaporated. The syrup was purified by flash chromatography on silica gel (10% ethyl acetate – hexane, 50 mL) to give 80.1 mg (73%) of material, mp 47.0–48.0°C after recrystallization from methanol; $[\alpha]_D^{21}$ −31.5 (*c* 1.30, CH_2Cl_2); ir (film): 3113.8, 2976.1, 1714.8, 1607.7, 1528.6, 1450.6, 1353.5, 1274.4, 1105.8, 1056.1 cm^{-1}; ^{1}Hmr ($CDCl_3$), δ: 1.36 (3H, d, 6.3 Hz, $CHCH_3$), 1.63 (3H, s, CCH_3), 1.70 (3H, s, CCH_3), 2.34 (1H, m, $CHCH_2CH$), 2.45 (1H, m, $CHCH_2$), 5.16 (1H, m, $OCHCH_3$), 5.16 (1H, m, C*H*═C), 8.19 (2H, m), 8.28 (2H, m); ms (*m/e*, CI): 264 ($M^+ + 1$). Anal. calcd. for $C_{14}H_{17}O_4N$: C 63.86, H 6.51, N 5.32; found: C 64.08, H 6.58, N 5.27.

(S)-(+)-5-Methyl-4-hexen-2-ol p-*nitrobenzoate*

This compound was prepared from (*S*)-(+)-5-methyl-4-hexen-2-ol (50 mg, 0.44 mmol, from epoxide); mp 47.0–48.0°C, $[\alpha]_D^{21}$ +31.90 (*c* 0.94, CH_2Cl_2); ir (film): 3113.8, 2976.1, 1714.8, 1607.7, 1528.6, 1450.6, 1353.5, 1274.4, 1105.8, 1056.1 cm^{-1}; ^{1}Hmr ($CDCl_3$), δ: 1.36 (3H, d, 6.3 Hz), 1.63 (3H, s), 1.70 (3H, s), 2.34 (1H, m), 2.45 (1H, m), 5.16 (1H, m), 5.16 (1H, m), 8.19 (2H, m), 8.28 (2H, m); ms (*m/e*, CI): 264 ($M^+ + 1$). Anal. calcd. for $C_{14}H_{17}O_4N$: C 63.86, H 6.51, N 5.32; found: C 64.06, H 6.54, N 5.19.

Mosher esters of 5-methyl-4-hexen-2-ol

(R)-5-Methyl-4-hexen-2-ol, (S)-α-methoxy-α-(trifluoromethyl)-phenylacetate

A mixture of 4-dimethylaminopyridine (DMAP, 18 mg, 0.15 mmol) and triethylamine (100 μL) in methylene chloride (0.5 mL) was treated with (*R*)-**2** (17 mg, 0.15 mmol, from epoxide), and 30 μL (40.5 mg, 0.16 mmol) of (+)-MTPA-chloride was added. The solution was stirred at room temperature for 2 h and the reaction was then quenched by addition of 3 drops of water. The mixture was passed through a short plug of silica gel (1.5 cm, 20% ethyl acetate in hexane as eluent) to yield 40.3 mg (82%) of an oil; ^{1}Hmr ($CDCl_3$), δ: 1.258 (3H, d, 6.3 Hz, $CHCH_3$), 1.48 (3H, s, CCH_3), 1.76 (3H, s, CCH_3), 2.17 (1H, m, $CHCHHCH$), 2.42 (1H, m, $CHCHHCH$), 3.55 (3H, s, OCH_3), 3.55 (1H, m, $CHCH_3$), 5.10 (1H, m, C*H*═C), 7.43 (3H, m) 7.53 (2H, m), ee 98%.

(S)-5-Methyl-4-hexen-2-ol, (S)-α-methoxy-α(trifluoromethyl)-phenylacetate

This compound was prepared from (**S**)-**2** (17 mg, 0.15 mmol, from epoxide); ^{1}Hmr ($CDCl_3$), δ: 1.326 (3H, d, 6.3 Hz, $CHCH_3$), 1.53 (3H, s, CCH_3), 1.63 (3H, s, CCH_3), 2.20 (1H, m, $CHCHHCH$), 2.33 (1H, m, $CHCHHCH$), 3.55 (3H, s, OCH_3), 3.56 (1H, m, $CHCH_3$), 5.13 (1H, m, C*H*═C), 7.43 (3H, m), 7.53 (2H, m), ee 97.2%.

*(R)-2-*tert*-Butyldimethylsiloxy-5-methyl-4-hexene (R)-4*

A solution of (*R*)-**2** (2.721 g, 23.83 mmol, $[\alpha]_D^{21}$ −11.95), DBU (0.7 mL, 0.713 g, 4.7 mmol), and triethylamine (3.2 mL, 2.32 g, 24.2 mmol) in methylene chloride (150 mL) was cooled in an ice-bath, and *tert*-butyldimethylsilyl chloride (5.75 g, 38.1 mmol) was added in three portions during 10 min. The reaction mixture was stirred overnight while warming to room temperature, and then poured into 150 mL of water. The aqueous phase was extracted with ether (3 × 30 mL) and the combined organic layers were washed with 0.5 N hydrochloric acid (30 mL), saturated sodium bisulfate (2 × 30 mL) and saturated sodium chloride (2 × 30 mL), dried over anhydrous magnesium sulfate, and evaporated. The residue was distilled to give 3.42 g (62%) of a colourless liquid, bp 61–65°C/0.1 Torr; $[\alpha]_D^{23.5}$ −5.04 (*c* 1.19, CH_2Cl_2); ir (film): 2940, 2915, 2842, 1464, 1455, 1370, 1250, 1130, 1089, 1005, 840, 776 cm^{-1}; ^{1}Hmr ($CDCl_3$), δ: 0.033 (3H, s, $SiCH_3$), 0.050 (3H, s, $SiCH_3$), 0.88 (9H, s, $SiC(CH_3)_3$), 1.11 (3H, d, 6.1 Hz, $CHCH_3$), 1.692 (3H, s, CCH_3), 1.694 (3H, s, CCH_3), 2.06 (1H,

Can. J. Chem. Downloaded from www.nrcresearchpress.com by ESC ESCOLA DE ENGENHARIA on 09/08/12
For personal use only.

m, CHCH*H*CH), 2.16 (1H, m, CHC*H*HCH), 3.77 (1H, m, C*H*CH_3), 5.13 (1H, m, C*H*=C).

*(S)-2-*tert*-Butyldimethylsiloxy-5-methyl-4-hexene (S)-4*

This compound was prepared from (*S*)-**2**, $[\alpha]_D^{21}$ +11.75); bp 62–66°C/0.i Torr; $[\alpha]_D^{22}$ +5.04 (*c* 1.80, CH_2Cl_2); ir (film): 2940, 2915, 2842, 1464, 1455, 1370, 1250, 1130, 1089, 1005, 840,776 cm^{-1}; ^{1}Hmr ($CDCl_3$), δ: 0.033 (3H, s), 0.050 (3H, s), 0.88 (9H, s), 1.11 (3H, d, 1.6 Hz), 1.692 (3H, s), 1.694 (3H, s), 2.06 (1H, m), 2.16 (1H, m), 3.77 (1H, m), 5.13 (1H, m).

*(R)-2-Hydroxy-2-methyl-5-*tert*-butyldimethylsiloxy-3-hexanone (R)-5*

A mixture of (*R*)-**4** (5.85 g, 25.4 mmol, $[\alpha]_D^{24}$ −5.04), reagent grade acetone (115 mL), water (43 mL), and acetic acid (4.75 mL) was stirred at room temperature, and a solution of potassium permanganate (6.0 g, 38.0 mmol) in water (25 mL) and acetone (93 mL) was added quickly. The reaction mixture was stirred for 1.5 h and then poured onto saturated sodium bisulfite (500 mL). The aqueous phase was extracted with ether (4 × 60 mL), and the combined organic extracts were washed successively with saturated sodium bicarbonate (2 × 50 mL) and saturated sodium chloride (2 × 60 mL), dried over anhydrous magnesium sulfate, and concentrated. The residue was purified by flash chromatography on silica gel (5% and 14% ethyl acetate in hexane) to yield 5.85 g (88%) of a colourless liquid; $[\alpha]_D^{21}$ −32.05 (*c* 1.56, CH_2Cl_2); ir (film): 3480.3, 2957.8, 2857.5, 1711.7, 1472.2, 1375.5, 1255.7, 1136.4, 1078.8, 1004.5, 836.2 cm^{-1}; ^{1}Hmr ($CDCl_3$), δ: 0.017 (3H, s, SiCH_3), 0.063 (3H, s, SiCH_3), 0.840 (9H, s, SiC(CH_3)$_3$), 1.179 (3H, d, 6.1 Hz, CHCH_3), 1.328 (3H, s, CCH_3), 1.339 (3H, s, CCH_3), 2.474 (1H, dd, 16.0, 4.8 Hz, CHCH*H*CO), 2.834 (1H, dd, 16.0, 7.6 Hz, CHC*H*HCO), 4.39 (1H, m, C*H*CH_3); ms (*m/e*, CI): 261 (M^+ + 1), 243 (M^+ − H_2O), 159. Anal. calcd. for $C_{13}H_{28}O_3Si$: C 59.95, H 10.84; found: C 59.78, H 10.99.

*(S)-2-Hydroxy-2-methyl-5-*tert*-butyldimethylsiloxy-3-hexanone (S)-5*

This compound was obtained in 88% yield from (*S*)-**4** having $[\alpha]_D^{22}$ +5.04: $[\alpha]_D^{23}$ +32.2 (*c* 1.42, CH_2Cl_2); ir (film): 3480.3, 2957.8, 2857.5, 1711.7, 1472.2, 1375.5, 1255.7, 1136.4, 1078.8, 1004.5, 836.2 cm^{-1}; ^{1}Hmr ($CDCl_3$), δ: 0.017 (3H, s), 0.063 (3H, s), 0.840 (9H, s), 1.179 (3H, d, 6.1 Hz), 1.328 (3H, s), 1.339 (3H, s), 2.474 (1H, dd, 16.0, 4.8 Hz), 2.834 (1H, dd, 16.0, 7.6 Hz), 4.39 (1H, m); ms (*m/e*, CI): 261 (M^+ + 1), 243 (M^+ − H_2O), 159. Anal. calcd. for $C_{13}H_{28}O_3Si$: C 59.95, H 10.84; found: C 60.09, H 10.70.

*(R)-2-Methyl-2-methanesulfonyloxy-5-*tert*-butyldimethylsiloxy-3-hexanone (R)-6*

A mixture of *R*-**5** (1.10 g, 4.2 mmol, $[\alpha]_D^{21}$ −32.1) and triethylamine (1.0 mL, 7.1 mmol) in methylene chloride (150 mL) was stirred in an ice-water bath, and methanesulfonyl chloride (0.5 mL, 6.3 mmol) in methylene chloride (10 mL) was added dropwise. The reaction mixture was stirred at 0–10°C for 5 h and then poured onto water (150 mL). The organic layer was separated and the aqueous layer was extracted with methylene chloride (3 × 50 mL). The combined organic extracts were washed with 0.5 N hydrochloric acid (20 mL), saturated sodium bicarbonate (2 × 60 mL), and saturated sodium chloride (2 × 60 mL), dried over anhydrous magnesium sulfate, and concentrated. The residue was flash chromatographed on silica gel (20% ethyl acetate in hexane) to yield 1.12 g (79%) of a colourless liquid, $[\alpha]_D^{21}$ −10.1 (*c* 3.16, CH_2Cl_2); ir (film): 2957.5, 2856.8, 2360.1, 1706.8, 1471.9, 1373.9, 1255.5, 1138.3, 1079.8, 1006.1 cm^{-1}; ^{1}Hmr ($CDCl_3$), δ: 0.016 (3H, s, SiCH_3), 0.069 (3H, s, SiCH_3), 0.840 (9H, s, SiC(CH_3)$_3$), 1.184 (3H, d, 6.1 Hz, CHCH_3), 1.633 (3H, s, CCH_3), 1.675 (3H, s, CCH_3), 2.589 (1H, dd, 17.3, 4.6 Hz, CHCH*H*CO), 2.941 (1H, dd, 17.3, 7.5 Hz, CHC*H*HCO), 3.113 (3H, s, OCH_3), 4.40 (1H, m, C*H*CH_3).

*(S)-2-Methyl-2-methanesulfonyloxy-5-*tert*-butyldimethylsiloxy-3-hexanone (S)-6*

This compound was prepared in 78% yield from (*S*)-**5** having $[\alpha]_D^{23}$ +32.2: $[\alpha]_D^{21}$ +10.6 (*c* 1.22, CH_2Cl_2); ir (film): 2957.5, 2856.8, 2360.1, 1706.8, 1471.9, 1373.9, 1255.5, 1138.3, 1079.8, 1006.1 cm^{-1}; ^{1}Hmr ($CDCl_3$), δ: 0.016 (3H, s), 0.069 (3H, s), 0.840 (9H, s), 1.184 (3H, d, 6.1 Hz), 1.633 (3H, s), 1.675 (3H, s), 2.589 (1H, dd, 17.3, 4.6 Hz), 2.941 (1H, dd, 17.3, 7.5 Hz), 3.113 (3H, s), 4.40 (1H, m).

*(R)-2-Mercapto-2-methyl-5-*tert*-butyldimethylsiloxy-3-hexanone (R)-7*

Triethylamine (4.75 mL) was added to methylene chloride (60 mL). The solution was stirred, cooled to −15°C, and hydrogen sulfide was passed in for 20 min. Then a solution of *R*-**6** (3.93 g, 11.6 mmol, $[\alpha]_D^{23}$ −10.1) in methylene chloride (20 mL) was added dropwise with stirring during 30 min. The reaction mixture was stirred at −15 to 0°C for 5 h with continuous introduction of hydrogen sulfide, and was then poured onto water (100 mL). The organic layer was separated and the aqueous layer was extracted with methylene chloride (3 × 50 mL). The combined organic extract was washed with 0.5 N hydrochloric acid (20 mL), water (2 × 50 mL), and saturated sodium sulfate (2 × 60 mL), dried over anhydrous magnesium sulfate, and concentrated. Chromatography on silica gel (10% ethyl acetate in hexane) yielded 2.58 g (80%) of a colourless liquid; $[\alpha]_D^{21}$ −33.5 (*c* 1.01, CH_2Cl_2); ir (film): 2929.7, 2856.9, 1707.0, 1461.8, 1374.0, 1255.4, 1137.9, 1079.6, 1005.8 cm^{-1}; ^{1}Hmr ($CDCl_3$), δ: 0.011 (3H, s, SiCH_3), 0.056 (3H, s, SiCH_3), 0.844 (9H, s, SiC(CH_3)$_3$), 1.18 (3H, d, 6.0 Hz, CHCH_3), 1.484 (3H, s, CCH_3), 1.521 (3H, s, CCH_3), 1.98 (1H, s, S*H*), 2.626 (1H, dd, 16.0, 5.2 Hz, CHCH*H*CO), 2.980 (1H, dd, 16.0, 7.2 Hz, CHC*H*HCO), 4.36 (1H, m, C*H*CH_3); ms (*m/e*): 277 (M^+), 245 (M^+ − SH). Anal. calcd. for $C_{13}H_{28}O_2SSi$: C 56.47, H 10.21; found: C 56.34, H 10.28.

*(S)-2-Mercapto-2-methyl-5-*tert*-butyldimethylsiloxy-3-hexanone (S)-7*

This compound was prepared in 78% yield from (*S*)-**6** having $[\alpha]_D^{21}$ +10.6: $[\alpha]_D^{21}$ +33.3 (*c* 1.02, CH_2Cl_2); ir (film): 2929.7, 2856.9, 1707.0, 1461.8, 1374.0, 1255.4, 1137.9, 1079.6, 1005.8 cm^{-1}; ^{1}Hmr ($CDCl_3$), δ: 0.011 (3H, s), 0.056 (3H, s), 0.844 (9H, s), 1.18 (3H, d, 6.0 Hz), 1.484 (3H, s), 1.521 (3H, s), 1.98 (1H, s), 2.626 (1H, dd, 16.0, 5.2 Hz), 2.980 (1H, dd, 16.0, 7.2 Hz), 4.36 (1H, m); ms (*m/e*): 277 (M^+), 245 (M^+ − SH). Anal. calcd. for $C_{13}H_{28}O_2SSi$: C 56.47, H 10.21; found: C 56.52, H 10.02.

N-tert-*Butoxycarbonyl-*D*-serine-*β*-lactone (R)-3*

A solution of triphenylphosphine (2.006 g, 7.65 mmol) in anhydrous tetrahydrofuran (30 mL) was stirred under nitrogen, cooled to −78°C, and dimethylazodicarboxylate (0.9 mL, 1.19 g, 8.2 mmol) was added dropwise during 10 min. The mixture was stirred for an additional 10 min, and a solution of freshly dried *N-t*-Boc-D-serine (1.20 g, 5.85 mmol) in tetrahydrofuran (30 mL) was added dropwise during 25 min. Stirring was continued at −78°C for 30 min, and for an additional 3 h after the cooling bath had been removed. The solvent was then removed under reduced pressure, and the residue was chromatographed on silica gel (35% ethyl acetate in hexane) to give the product (0.638 g, 58%), mp 117.5–118.5°C; $[\alpha]_D^{21}$ +10.91 (*c* 1.10, CH_2Cl_2); ir (KBr): 3360, 3032, 2978, 1844, 1680, 1534, 1370, 1290 cm^{-1}; ^{1}Hmr (acetone-d_6), δ: 1.40 (9H, s, *t*-Bu), 4.404 (2H, m, CH_2), 4.454 (1H, m, CH), 5.214 (1H, m, NH); ms (*m/e*, CI): 188 (M^+ + 1), 132 (M^+ − *t*-Bu). Anal. calcd. for $C_8H_{13}NO_4$: C 51.33, H 6.99, N 7.48; found: C 51.60, H 6.96, N 7.53.

N-tert-*Butoxycarbonyl-*L*-serine-*β*-lactone (S)-3*

This compound was prepared in 57% yield from *N-t*-Boc-L-serine; mp 117.5–118.5°C (lit. (6) mp 119.5–120.5°C); $[\alpha]_D^{21}$ −10.8 (*c*, 0.93, CH_2Cl_2); $[\alpha]_D^{21}$ −26.4 (*c* 0.53, CH_3CN) (lit. (6) $[\alpha]_D^{22}$ −26.7 (*c* 1, CH_3CN); ir (KBr): 3360, 3032, 2978, 1844, 1680, 1534, 1370, 1290 cm^{-1}; ^{1}Hmr (acetone-d_6), δ: 1.40 (9H, s), 4.404 (2H, m), 4.454 (1H, m), 5.214 (1H, m); ms (*m/e*, CI): 188, 132. Anal. calcd. for $C_8H_{13}NO_4$: C 51.33, H 6.99, N 7.48; found: C 51.59, H 7.05, N 7.62.

*(2R,8R)-2-*tert*-Butoxycarbonylamino-4-thia-5,5-dimethyl-6-oxo-8-*tert*-butyldimethylsiloxynonanoic acid (2R,8R)-8*

A solution of (*R*)-**7** (322 mg, 1.165 mmol, $[\alpha]_D^{21}$ −33.5) in dry tet-

Can. J. Chem. Downloaded from www.nrcresearchpress.com by EESC ESCOLA DE ENGENHARIA on 09/08/12
For personal use only.

rahydrofuran (15 mL) was cooled to −40°C, stirred, and 1 N lithium diisopropylamide (1.20 mL, 1.2 mmol, freshly prepared at −40°C under nitrogen by addition of 1.0 mL of 2.5 M ethereal *n*-butyllithium to 1.5 mL of a 1:2 v:v solution of diisopropylamine in tetrahydrofuran) was added dropwise. Then *N-tert*-butoxycarbonyl-L-serine-β-lactone (*S*-**3**) (224 mg, 1.19 mmol, $[\alpha]_D^{21}$ −10.81) in tetrahydrofuran (10 mL) was added dropwise. The mixture was stirred at −40 to −5°C for 6 h, and was then diluted with methylene chloride (100 mL) and washed with 0.5 N hydrochloric acid (20 mL). The organic layer was separated and the aqueous layer was extracted with methylene chloride (3 × 25 mL). The combined organic extract was washed with water (2 × 25 mL) and with saturated sodium chloride (2 × 30 mL), dried over anhydrous magnesium sulfate, and concentrated. The residue was purified by flash chromatography on silica gel (9% methanol in methylene chloride) and then by preparative layer chromatography (silica gel, thickness 1.0 mm, 20 × 20 cm plate) to give 84 mg (16%) of (2*R*,8*R*)-**8**; $[\alpha]_D^{24}$ −26.9 (*c* 0.45, CH_2Cl_2); ir (film): 2929.7, 2856.9, 1707.0, 1461.8, 1374.0, 1255.4, 1137.9, 1079.6, 1005.8 cm^{-1}; ^{1}Hmr ($CDCl_3$), δ: 0.005 (3H, s, $SiCH_3$), 0.055 (3H, s, $SiCH_3$), 0.862 (9H, s, $SiC(CH_3)_3$), 1.165 (3H, d, 6.0 Hz, $CHCH_3$), 1.459 (15H, s, $OC(CH_3)_3$ and $C(CH_3)_2$), 2.598 (1H, dd, 5.4 Hz, 16 Hz, CHCH*H*CO), 2.76 (2H, m, SCH_2CH), 2.949 (1H, dd, 7.3 Hz, 16 Hz, CHC*H*HCO), 4.157 (1H, m, SCH_2CH), 4.327 (1H, m, $OCHCH_3$), 5.523 (1H, m, N*H*); ms (*m/e*, relative intensity): 277 (60), 245 (100), 219 (11), 187 (20), 159 (62). Anal. calcd. for $C_{21}H_{41}O_6SSi$: C 54.39, H 8.91, N 3.02; found: C 54.13, H 9.00, N 2.89.

*(2*R,*8*S*)-2-*tert-*Butoxycarbonylamino-4-thia-5,5-dimethyl-6-oxo-8-*tert-*butyldimethylsiloxynonanoic acid (2*R,*8*S*)-8***

This compound was prepared from (*S*)-**7** (0.230 g, 0.832 mmol, $[\alpha]_D^{21}$ +33.3) and *N-tert*-butoxycarbonyl-L-serine-β-lactone (0.197 g, 1.0 mmol, $[\alpha]_D^{21}$ −10.81). The product (51.4 mg, 11%) was purified as described above; $[\alpha]_D^{24}$ +33.9 (*c* 1.12, CH_2Cl_2); ir (film): 2929.7, 2856.9, 1707.0, 1461.8, 1374.0, 1255.4, 1137.9, 1079.6, 1005.8 cm^{-1}; ^{1}Hmr ($CDCl_3$), δ: 0.007 (3H, s), 0.047 (3H, s), 0.846 (9H, s), 1.161 (3H, d, 6.0 Hz), 1.442 (15H, s), 2.563 (1H, dd, 5.4 Hz, 16.3 Hz), 2.77 (2H, m), 2.905 (1H, dd, 7.3 Hz, 16.3 Hz), 4.332 (1H, m), 4.489 (1H, m), 5.250 (1H, m); ms (*m/e*, relative intensity): 277 (60), 245 (100), 219 (11), 187 (20), 159 (62). Anal. calcd. for $C_{21}H_{41}O_6SSi$: C 54.39, H 8.91, N 3.02; found: C 54.59, H 8.77, N 3.22.

*(2*S,*8*R*)-2-*tert-*Butoxycarbonylamino-4-thia-5,5-dimethyl-6-oxo-8-*tert-*butyldimethylsiloxynonanoic acid (2*S,*8*R*)-8***

This compound was prepared from (*R*)-**7** (0.245 g, 0.9 mmol, $[\alpha]_D^{24}$ −33.0) and *N-tert*-butoxycarbonyl-D-serine-β-lactone (0.198 g, 1.05 mmol, $[\alpha]_D^{21}$ +10.91). The product (94.0 mg, 23%) was purified as described above; $[\alpha]_D^{24}$ −33.0 (*c* 0.46, CH_2Cl_2); ir (film): 2929.7, 2856.9, 1707.0, 1461.8, 1374.0, 1255.4, 1137.9, 1079.6, 1005.8 cm^{-1}; ^{1}Hmr ($CDCl_3$), δ: 0.003 (3H, s), 0.057 (3H, s), 0.843 (9H, s), 1.162 (3H, d, 6.0 Hz), 1.419 (15H, s), 2.604 (1H, dd, 5.4 Hz, 16.3 Hz), 2.81 (2H, m), 2.947 (1H, dd, 7.3 Hz, 16.3 Hz), 4.110 (1H, m), 4.325 (1H, m), 5.592 (1H, m); ms (*m/e*, relative intensity): 277 (60), 245 (100), 219 (11), 187 (20), 159 (62). Anal. calcd. for $C_{21}H_{41}O_6SSi$: C 54.39, H 8.91, N 3.02; found: C 54.40, H 8.80, N 2.97.

*(2*S,*8*S*)-2-*tert-*Butoxycarbonylamino-4-thia-5,5-dimethyl-6-oxo-8-*tert-*butyldimethylsiloxynonanoic acid (2*S,*8*S*)-8***

This compound was prepared from (*S*)-**7** (0.245 g, 0.9 mmol, $[\alpha]_D^{21}$ +33.3) and *N-tert*-butoxycarbonyl-D-serine-β-lactone (0.200 g, 1.07 mmol, $[\alpha]_D^{21}$ +10.91). The product (60.0 mg, 15%) was purified as described above; $[\alpha]_D^{24}$ +27.2 (*c* 0.81, CH_2Cl_2); ir (film): 2929.7, 2856.9, 1707.0, 1461.8, 1374.0, 1255.4, 1137.9, 1079.6, 1005.8 cm^{-1}; ^{1}Hmr ($CDCl_3$), δ: 0.006 (3H, s), 0.056 (3H, s), 0.843 (9H, s), 1.163 (3H, d, 6.0 Hz), 1.442 (15H, s), 2.602(1H, dd, 5.4 Hz, 16.3 Hz), 2.78 (2H, m), 2.968 (1H, dd, 7.3 Hz, 16.3 Hz), 4.173 (1H, m), 4.312 (1H, m), 5.490 (1H, m); ms (*m/e*, relative intensity): 277 (60), 245 (100), 219 (11), 187 (20), 159 (62). Anal. calcd. for $C_{21}H_{41}O_6SSi$: C 54.39, H 8.91, N 3.02; found: C 54.47, H 8.75, N 3.12.

*(5*R,*8*R*)-2,2-Dimethyl-3-(2′-hydroxypropyl)-5-carboxy-Δ^3-1,4-thiazine (5*R,*8*R*)-1***

The acid (2*R*,8*R*)-**8** (20.0 mg, 0.043 mmol, $[\alpha]_D^{24}$ −26.9) was dissolved in methylene chloride (0.5 mL), and 1.0 mL of 98% formic acid and one drop of 1,3-propanedithiol were added. The solution was stirred at room temperature for 10 h. The solvent was then removed under high vacuum, and the residue was treated with ether (5 mL) and water (5 mL). The ether layer was extracted with water (2 × 5 mL). The combined aqueous extracts were neutralized to pH 8 with 5% sodium bicarbonate and lyophilized to yield 20 mg of white solid. This was dissolved in 4.0 mL of water, and purified by HPLC, using the following conditions: detection at 254 nm; sensitivity 1.0 AUS; injection volume 1.0 mL; flow rate 10.0 mL/min; gradient elution with water–acetonitrile. Collection of the fraction with retention time 9.87 min yielded 2.5 mg (25%) of (5*R*,8*R*)-**1**; $[\alpha]_D^{24}$ −155 (*c* 0.045, 50% acetone–water); ir (film): 3421.7, 2972.4, 1751.5, 1686.1, 1636.7, 1388.2, 1074.3 cm^{-1}; ^{1}Hmr (D_2O), δ: 1.18 (3H, d, 6.2 Hz, $CHCH_3$), 1.39 (6H, s, $C(CH_3)_2$), 2.68 (1H, m, CHCH*H*C=N), 2.84 (2H, m, SCH_2CH), 2.97 (1H, m, CHC*H*HC=N), 4.24 (1H, m, SCH_2CH), 4.53 (1H, m, $CHCH_2C$=N); ms (*m/e*): 231 (M^+).

*(5*S,*8*R*)-2,2-Dimethyl-3-(2′-hydroxypropyl)-5-carboxy-Δ^3-1,4-thiazine (5*S,*8*R*)-1***

This compound was prepared from (2*S*,8*R*)-**8** (20.0 mg, 0.043 mmol, $[\alpha]_D^{24}$ −33.0). The crude product (21.0 mg) was purified by HPLC to yield 3.1 mg (31%) of (5*S*,8*R*)-**1**; $[\alpha]_D^{24}$ −75 (*c* 0.080, 50% acetone–water); ir (film): 3421.7, 2972.4, 1751.5, 1686.1, 1636.7, 1388.2, 1074.3 cm^{-1}; ^{1}Hmr (D_2O), δ: 1.16 (3H, d, 6.2 Hz), 1.45 (6H, s), 2.75 (1H, m), 2.82 (2H, m), 2.93 (1H, m), 4.23 (1H, m), 4.52 (1H, m); ms (*m/e*): 231 (M^+).

*(5*R,*8*S*)-2,2-Dimethyl-3-(2′-hydroxypropyl)-5-carboxy-Δ^3-1,4-thiazine (5*R,*8*S*)-1***

This compound was prepared from (2*R*,8*S*)-**8** (20.0 mg, 0.043 mmol, $[\alpha]_D^{24}$ +33.9). The crude product (20.5 mg) was purified by HPLC to give 3.0 mg (30%) of (5*R*,8*S*)-**1**; $[\alpha]_D^{24}$ +73 (*c* 0.060, 50% acetone–water); ir (film): 3421.7, 2972.4, 1751.5, 1686.1, 1636.7, 1388.2, 1074.3 cm^{-1}; ^{1}Hmr (D_2O), δ: 1.18 (3H, d, 6.0 Hz), 1.45 (6H, s), 2.68 (1H, m), 2.84 (2H, m), 2.97 (1H, m), 4.22 (1H, m), 4.53 (1H, m); ms (*m/e*): 231 (M^+).

*(5*S,*8*S*)-2,2-Dimethyl-3-(2′-hydroxypropyl)-5-carboxy-Δ^3-1,4-thiazine (5*S,*8*S*)-1***

This compound was prepared from (2*S*,8*S*)-**8** (20.0 mg, 0.043 mmol, $[\alpha]_D^{24}$ +27.2). The crude product (19.8 mg) was purified by HPLC to yield 2.4 mg (24%) of (5*S*,8*S*)-**1**; $[\alpha]_D^{24}$ +155 (*c* 0.055, 50% acetone–water); ir (film): 3421.7, 2972.4, 1751.5, 1686.1, 1636.7, 1388.2, 1074.3 cm^{-1}; ^{1}Hmr (D_2O), δ: 1.19 (3H, d, 6.2 Hz), 1.456 (6H, s), 2.68 (1H, m), 2.84 (2H, m), 2.97 (1H, m), 4.22 (1H, m), 4.32 (1H, m); ms (*m/e*): 231 (M^+).

Acknowledgements

This research was supported financially by the Natural Sciences and Engineering Research Council of Canada, and by Simon Fraser University.

1. J.-M. Frère, M. Nguyen-Distèche, J. Coyette, and B. Joris. *In* The chemistry of β-lactams. *Edited by* M.I. Page. Blackie Academic and Professional, London. 1992. p. 148.
2. S. Wolfe. Can. J. Chem. **72**, 1014 (1994).
3. S. Wolfe, K. Yang, and M. Khalil. Can. J. Chem. **66**, 2733 (1988).
4. S. Wolfe, H. Jin, K. Yang, C.-K. Kim, and E. McEachern. Can. J. Chem. **72**, 1051 (1994).
5. M. Julia, S. Julia, and J.A. du Chaffault. Bull. Soc. Chim. Fr. 1735 (1960).
6. L.D. Arnold, T.H. Kalantar, and J.C. Vederas. J. Am. Chem. Soc. **107**, 7105 (1985).
7. E.A. Braude and E.A. Evans. J. Chem. Soc. 3328 (1955).

8. C. Huynh, F. Derguini-Boumechal, and G. Linstrumelle. Tetrahedron Lett. 1503 (1979).
9. B. Seuring and D. Seebach. Helv. Chim. Acta, **60**, 1175 (1977).
10. M.K. Ellis and B.T. Golding. Org. Synth. **63**, 140 (1985).
11. G. Kirchner, M.P. Scollar, and A.M. Klibanov. J. Am. Chem. Soc. **107**, 7072 (1985); T.M. Stokes and A.C. Oehlschlager. Tetrahedron Lett. **28**, 2091 (1987); B. Morgan, A.C. Oehlschlager, and T.M. Stokes. Tetrahedron, **47**, 1611 (1991).
12. J.A. Dale, D.L. Dull, and H.S. Mosher. J. Org. Chem. **34**, 2543 (1969).
13. Y. Gao, R.M. Hanson, J.M. Klunder, S.Y. Ko, H. Masamune, and K.B. Sharpless. J. Am. Chem. Soc. **109**, 5765 (1987).
14. R.G. Ghirardelli. J. Am. Chem. Soc. **95**, 4987 (1973).
15. L. Pauling. Chem. Eng. News, **24**, 1375 (1946); Nature, **161**, 707 (1948).
16. L. Mandolini. Adv. Phys. Org. Chem. **22**, 1 (1986); X. Duan and S. Scheiner. J. Am. Chem. Soc. **114**, 5849 (1992).
17. F.M. Menger. Biochemistry, **31**, 5368 (1992); Acc. Chem. Res. **26**, 206 (1993).

Can. J. Chem. Downloaded from www.nrcresearchpress.com by EESC ESCOLA DE ENGENHARIA on 09/08/12
For personal use only.

Partial molar volumes of some drugs in water and ethanol at 35°C

M. IQBAL[1] AND M. ASGHAR JAMAL
Department of Chemistry, Bahauddin Zakariya University Multan, Pakistan 60800

AND

MAQSOOD AHMED AND BASHIR AHMED
Department of Pharmacy, Bahauddin Zakariya University Multan, Pakistan 60800

Received September 1, 1992[2]

M. IQBAL, M. ASGHAR JAMAL, MAQSOOD AHMED, and BASHIR AHMED. Can. J. Chem. **72**, 1076 (1994).

Partial molar volumes, V^0, of six drugs, mostly anaesthetics, viz., cinchocaine HCl, lidocaine HCl, mepivacaine HCl, procaine HCl, propranolol HCl, tetracaine HCl, in water and ethanol, calculated from precision densities obtained at 35°C from a vibrating tube densitometer, are reported in this work. The data represent the smaller volumes of drug molecules in ethanol than in water. Volume contribution of hydrochloride part were calculated and excluded from V^0 to assess the volume of free base component of the solutes. Volumes of free bases were also found smaller in ethanol, although much closer to those in water. The differences in volumes are interpreted as due to hydrophobicity of solutes. Relative hydrophobicities were estimated from volumes of transfer from aqueous to organic media. Correlation of V^0 with van der Waal volumes are also reported. The hydrophobicity of these compounds is proposed to play a key role in the resulting drug action. Possible mechanism of drug binding with the membrane structure is also discussed.

M. IQBAL, M. ASGHAR JAMAL, MAQSOOD AHMED et BASHIR AHMED. Can. J. Chem. **72**, 1076 (1994).

Utilisant des densités mesurées avec précision à 35°C, à l'aide d'un densimètre à tube vibrant, on a calculé les volumes molaires partiels, V^0, de six drogues, principalement des anesthésiques, à savoir les chlorhydrates de cinchocaïne, de lidocaïne, de mépivacaïne, de procaïne, de propranalol et de tétracaïne, dans l'eau et l'éthanol. Les données représentent des volumes plus faibles des molécules de drogues dans l'éthanol que dans l'eau. On a calculé la contribution au volume de la portion chlorhydrate et, dans le but d'évaluer le volume de la portion de la base libre dans les solutés, on l'a exclue de la valeur de V^0. On a trouvé que les volumes des bases libres sont aussi plus petites dans l'éthanol que dans l'eau, même s'ils sont maintenant plus proches que ceux dans l'eau. On attribue les différences dans les volumes à l'hydrophobicité des solutés. On a évalué les hydrophobicités relatives à partir des volumes de transfert de solutions aqueuses à des solutions organiques. On rapporte aussi une corrélation entre V^0 et les volumes de van der Waal. On suggère que l'hydrophobicité de ces composés joue un rôle important dans l'activité de ces composés comme drogues. On discute aussi du mécanisme possible de fixation de la drogue avec les structures membranaires.

[Traduit par la Rédaction]

Can. J. Chem. Downloaded from www.nrcresearchpress.com by EESC ESCOLA DE ENGENHARIA on 09/08/12
For personal use only.

Introduction

Solute–solvent interactions play an important role in a variety of phenomena. In bio-physical chemistry, drug interaction is a subject of intensive studies, involving complex molecular mechanisms. Despite years of investigations, many important drug actions and their mechanisms are not fully understood. Structure activity relationship is one of the most common rationale presented for explaining drug reactions. In cases such as certain hormones, antibiotic and peptide actions, amphiphilicity in molecular structure is considered to be a key factor in the overall drug mechanism (1, 2). Knowledge about mechanism of anaesthesia is also clouded in mystery despite years of intensive studies (3). The role of volume property, however, is considered important in connection with this phenomenon. According to the concept of critical volume of anaesthesia (4, 5), nerve conduction is blocked when drug molecules enter the lipid bilayer and causes expansion in the membrane structure to a critical volume level. The disordering of bilayer structure, resulting from volumetric expansion, causes the disfunctioning of the membrane transport property and the blockage of nerve conduction. An important evidence in favour of this concept is given in terms of the observed reversal of anaesthesia under applied pressure (4).

Since volume is an additive property, gross changes in the volume of a system can be assessed by comparing the volume of the system with those of its components. Moreover, volumetric data often lead to interpretations in terms of molecular interactions within the system. Volumetric data of drugs, lipid bilayers, and membrane proteins can provide clues to the interactions occurring in cellular fluids. Recent literature on the volumetric properties of drugs and other materials of biological importance shows increasing interest by a number of workers in this area of study (6–10).

This work is part of a study of molecular interactions in drug-substrate systems using thermodynamic methods. Partial molar volumes of six drug compounds, mostly anesthetics, are calculated from experimental densities in water and ethanol (aqueous and organic media) at 35°C, using a vibrating tube electronic densitometer. The data are discussed in terms of relative solvation of these compounds in both solvents. Relative hydrophobicity of solutes and aspects of structural features viz-a-viz drug action are also discussed.

Experimental

Materials and method

Drugs used in this study are as follows: (*1*) cinchocaine HCl (Orgamol, Fabrication de Products Chimiques Evionnaz, Suisse, Batch No. 96682); (*2*) lidocaine HCl (from Co. Farmaceutical Milanese, S.p.a. 20151 Milano-viagallarate, Italy); (*3*) mepivaciane HCl (Orgamol, Fabrication de Products Chimiques Evionnaz, Suisse, Batch No. 89012); (*4*) procaine HCl (E. Merck USP lot 7467); (*5*) propranolol HCl (Sigma lot No. 33F-0495); (*6*) Tetracaine

[1]To whom correspondence should be addressed.
[2]Revision received October 14, 1993.

TABLE 1. Volumetric data of hydrochloride salts at 35°C

Compounds	In water: Concentration range (mol kg^{-1})	In water: V_w^0 (cm^3 mol^{-1})	In ethanol: Concentration range (mol kg^{-1})	In ethanol: V_e^0 (cm^3 mol^{-1})
Cinchocain HCl	0.008–0.074	326.63 ± 0.15	0.022–0.149	311.67 ± 0.79
Lidocaine HCl	0.010–0.099	240.21 ± 1.24	0.020–0.199	223.31 ± 0.52
Mepivacaine HCl	0.013–0.140	245.84 ± 0.64	0.025–0.200	233.65 ± 3.70
Procaine HCl	0.010–0.140	226.63 ± 0.15[a]	0.019–0.199	205.82 ± 2.22
Propranalol HCl	0.010–0.080	246.09 ± 0.20[b]	0.010–0.059	230.63 ± 0.03
Tetracaine HCl	0.011–0.140	266.60 ± 0.01	0.019–0.199	254.56 ± 0.86

[a] V_w^0 at 25°C = 225.84 cm^3 mol^{-1} from ref. 9.
[b] V_w^0 at 25°C = 245.14 cm^3 mol^{-1} from ref. 9.

HCl (Orgamol, Fabrication de Products Chimiques Evionnaz, Suisse, Batch No. 96573).

Samples were purified by recrystallising from ethanol–water mixtures. Densities of aqueous and ethanolic solutions were measured at 35°C, using a vibrating tube electronic densitometer (11) (Anton Paar DMA 60/602), capable of an accuracy to $\pm 2 \times 10^{-6}$ g cm^{-3}. Calibration of densitometer was done using literature densities of water (12) and 2-propanol (13). Temperature control was maintained by a HETO circulating thermostat which provides an accuracy to better than ±0.01°C. Temperature calibration was done with respect to the triple point of water. Water used in the experimentation was doubly distilled, deionised, and degassed. Absolute ethanol (Merck) was used directly as the organic solvent.

Results and discussion

Apparent molal volumes (ϕ_v cm^3 mol^{-1}) were first calculated using the following equation:

$$[1] \quad \phi_v = \frac{1000(d_0 - d)}{mdd_0} + \frac{M}{d}$$

where d, d_0, m, and M are the densities of solution, solvent, molality, and the relative molar mass of solute, respectively. Apparent molar volume data for these compounds in water were checked for possible changes arising from proton ionisation and disproportionation reactions, etc. (10, 14, 15). The corrections in ϕ_v due to such reactions were found to be within experimental error and are thus ignored.

ϕ_v data were found to vary linearly and were fitted to the following equation using a weighted least squares fit programme.

$$[2] \quad \phi_v + \phi_v^0 + S_v m^x$$

where ϕ_v^0, the first coefficient of fit, is the apparent molal volume at infinite dilution and S_v is the second coefficient of fit. Values of x were taken as 1/2 and 1, for data in water and ethanol, respectively (to take into account the electrolytic character of solutes in water). Errors in the apparent molal volumes ($\delta\phi_v$) were computed and used as weighting parameters in the least squares fit computation of ϕ_v^0 (10, 16). Values of ϕ_v^0 obtained from the fitting procedure were taken to be partial molal volumes, V^0, of the respective compounds, and are shown in Table 1.

It is seen that the volumes of these drugs in water, V_w^0, are higher than those in ethanol, V_e^0, the difference ranging from 10 to 20 cm^3 mol^{-1}. A rough correlation was also found between V^0 and molar mass of these compounds. Values of correlation coefficients were found to be 0.6761 and 0.7085 in water and ethanol, respectively. Studies made in the past on model compounds (polar, non-polar, amphiphilic, etc.) have shown that the volumes of water-soluble compounds are generally smaller in aqueous medium than in nonaqueous medium (17, 18). Present data, however, show an opposite trend implying a behaviour similar to that of water-insoluble (hydrophobic) compounds.

Using the principle of volume additivity, the volume of a hydrochloride salt, V^0(BHCl), can be taken as the sum of the volume of free base, V^0(B), and that of HCl, V^0(HCl).

$$[3] \quad V^0(\text{BHCl}) = V^0(\text{B}) + V^0(\text{HCl})$$

The volume contribution of the free base component, which would be of much greater significance to a pharmacologist, could best be obtained from direct experimentation of free base solutes. We, however, could not obtain experimental data for free bases due to a shortage in materials. Instead, we attempted calculations of V^0(B), using V^0(HCl) data from the literature. One of the methods is to subtract the partial molar volume of pure HCl in the given solvent from V^0(BHCl). In water, at 35°C, we derived this value to be = 17.90 cm^3 mol^{-1} (17). Another method provides more realistic estimates of V^0(HCl) in compounds of similar structure. Recent volumetric data of neurotransmitter drugs in water by Shahidi (9) shows that the value of V^0(HCl) in these cases varies from 11 to 14.5 cm^3 mol^{-1} at 25°C. It is found to be on the low side (11 cm^3 mol^{-1}) when the amino group is at the terminus whereas for molecules with the amino group away from the terminus and within the alkyl chain, the value of V^0(HCl) is found to be ≃14.5 cm^3 mol^{-1}. In our case, since the amino group is away from the terminus and within the alkyl chains, we can choose the higher value with a further increment of 0.5 cm^3 mol^{-1}, on account of the higher temperature of the system (35°C) and an anticipated less hydration (due to more complex structures). Considering the expandability of HCl and the complexity of molecular structure of these solutes, this increment is reasonable in the present calculations. Therefore, using V^0(HCl) = 15.0 cm^3 mol^{-1} in eq. [3], one gets the volumes of free base components in water, V_w^0(B), as shown in Table 2.

In the case of ethanol, there were no data for similar compounds and no other realistic estimates of V^0(HCl), available. We therefore resorted to calculating V^0(B) using partial molar volumes of pure HCl in ethanol. At 25°C, this value is reported to be 3.00 cm^3 mol^{-1} (17). However, we have allowed an incre-

Can. J. Chem. Downloaded from www.nrcresearchpress.com by ESC ESCOLA DE ENGENHARIA on 09/08/12
For personal use only.

Can. J. Chem. Downloaded from www.nrcresearchpress.com by EESC ESCOLA DE ENGENHARIA on 09/08/12
For personal use only.

Cinchocaine HCl

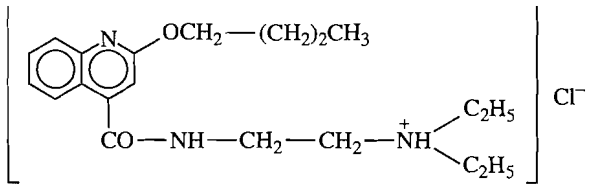

Lidocaine HCl

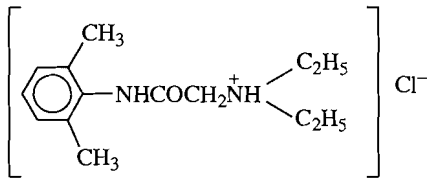

Mepivacaine HCl

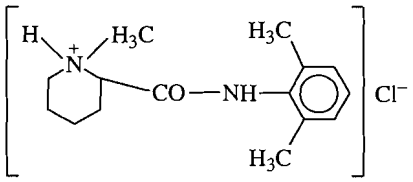

Procaine HCl

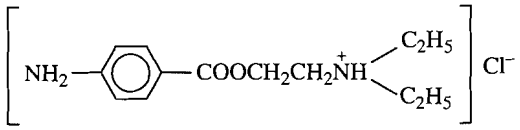

Propranolol HCl

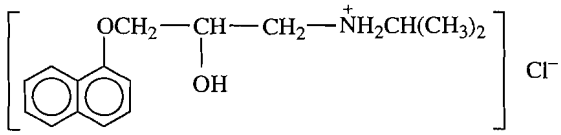

Tetracaine HCl

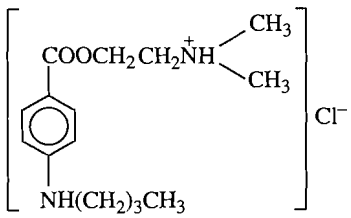

FIG. 1. Molecular structure of the compounds studied.

ment of 0.2 cm^3 mol^{-1} when we are applying this to eq. [3] using the above argument. In other words, V^0(HCl) = 3.2 cm^3 mol^{-1} and the volumes of free bases calculated are reported in Table 2 as V_e^0(B).

Tables 1 and 2 show that while V^0(BHCl) values differ by 10 to 20 cm^3 mol^{-1}, the difference in V^0(B) is much smaller (0.2 to 9 cm^3 mol^{-1}). Volumes of transfer from aqueous to ethanolic medium, V_{tr} (= $V_w^0 - V_e^0$), were calculated and found to be positive as shown in Table 1. For mepivacaine and tetracaine, the V_{tr}^0 values fall within the experimental error, implying nearly the same volumes of free base molecules in both solvents. The positive values of V_{tr}^0 for all compounds, however, show a trend in the data that can be discussed in terms of the solvation of these compounds.

Smaller volumes of hydrochloride salts and their free base moieties in ethanol can be interpreted in terms of more intensive solvation of these solutes in ethanol than in aqueous medium. This also implies a hydrophobic character for these compounds despite some of their apparent hydrophilic properties. Although there are certain polar sites such as, —O—, $\equiv N^+-$, etc., present in these molecules (Fig. 1), they also contain alkyl chains, aromatic rings, and other hydrophobic groups. The net character of the molecule resulting from the complex interactions of various sites seems to render the molecule virtually hydrophobic.

Van der Waal volumes, V_v, of these solutes were also calculated from group contributions, using Bondi's data (19). Correlation between V^0 and V_v were obtained using the well known

TABLE 2. Calculated volumetric data of free bases at 35°C

Compounds	$V_w^0(B)^a$	$V_e^0(B)^a$	V_{tr}^a
Cinchocaine	311.63	308.47	3.16
Lidocaine	225.21	220.11	5.10
Mepivacaine	230.84	230.45	0.39
Procaine	211.63	202.62	9.01
Propranolol	231.09	227.43	4.46
Tetracaine	251.60	251.36	0.24

[a]In units of $cm^3\ mol^{-1}$.

equation (20) [4]

$$[4] \quad V^0 = aV_v + b$$

a and b for the hydrochloride salts were found to be 1.601 ± 0.033 and −20.754 ± 5.727 in water and 1.657 ± 0.059 and −46.045 ± 9.476 in ethanol. For free bases, these values are a = 1.601 ± 0.032, b = −59.151 ± 6.200 in water and a = 1.657 ± 0.060, b = −73.470 ± 9.342 in ethanol.

The compounds studied in this work are known for their anaesthetic action in terms of specific duration, strength, selectivity of action, side effects, etc. (21–26). Figure 1 shows that an important structural feature of these compounds is the presence of hydrophobic and hydrophilic domains separated by an intervening alkyl chain. The hydrophilic group is generally a tertiary or secondary amine while the major hydrophobic residue is often an aromatic ring. Amino nitrogen of the hydrophilic portion is generally separated from the aromatic segment by a distance of 4 to 6 bonds in the aliphatic chain. This structural feature appears to be a key factor in the anaesthetic action of these drugs, supporting the theory that the anaesthetic is dependent on a structure–activity relationship (27).

The hydrophobicity of these compounds may well play a crucial role in the resulting drug reaction. It can be argued that the hydrophobic force supplements the structure–activity relationship in that these molecules tend to bind in a site-specific manner. The hydrophilic and hydrophobic parts of the drug match with the specific counter sites on the membrane. The hydrophilic part of the drug molecule (—$N^+\tilde{N}$) being anchored to the polar head group of the lipid chain (or at some suitable site on the imbedded protein), pushes the hydrophobic tail into the bilayer grease. The submerging of hydrophobic part into the lipid chain structure then causes a subsequent fluidization of the organised membrane resulting into a volume expansion and hence a blockage of the ion transport.[3]

[3]A complete set of tables of experimental data showing molalities, densities, and ϕ_v values for the compounds studied may be purchased from: the Depository of Unpublished Data, Document Delivery, CISTI, National Research Council Canada, Ottawa, Canada K1A 0S2.

Acknowledgement

We are grateful to Dr. Inamul Haq Incharge, Quality Control Department, Federal Ministry of Health, Islamabad, for gifts of drug samples. Financial grant from National Scientific and Research Development Board (NSRDB) for the purchase of DMA 60/602 assembly is gratefully acknowledged.

1. D. Fukushima, E.T. Kaiser, F.J. Kezday, D.J. Kroom, J.P. Kupferberg, and S. Yokoyama. Ann. N.Y. Acad. Sci. **348**, 366 (1980).
2. E.T. Kaiser and F.J. Kezday. Science, **223**, 249 (1984).
3. S.J. Slater, K.J.A. Cox, J.V. Lombardi, C. Ho, M.B. Kelly, E. Rubin, and C.D. Stubbs. Nature, **364**, 82 (1993).
4. S. Roth. Ann. Rev. Pharmacol. Toxicol. **19**, 1959 (1979).
5. N.P. Frank and W.R. Leib. Nature, **292**, 248 (1981).
6. S. Katz, R.G. Shinaberry, E.L. Heck, and W. Squire. Biochemistry, **19**, 3805 (1980).
7. D. Causon, J. Gettin, J. Gormally, R. Greenwood, N. Natarajan, and E. Wyn-Jones. J. Chem. Soc. Faraday. Trans. I, **77**, 143 (1981).
8. J.D. Pandey, K. Mishra, A. Shukla, and R.D. Rai. Can. J. Chem. **65**, 303 (1987).
9. F. Shahidi. Can. J. Chem. **65**, 1924 (1987).
10. M. Iqbal and R.E. Verall. Can. J. Chem. **67**, 727 (1989).
11. O. Kratky, H. Leopold, and H. Stabinger. Angew. Phys. **27**, 273 (1978).
12. G.S. Kell. J. Chem. Eng. Data, **20**, 97 (1975).
13. M. Sakurai. J. Soln. Chem. **17**, 267 (1988).
14. S. Cabani, V. Mollica, L. Lepori, and S.T. Lobo. J. Phys. Chem. **81**, 982 (1977).
15. M.V. Kaulgud, M.R. Awode, and A. Shrivastava. Ind. J. Chem. **19A**, 295 (1980).
16. H.S. Harned and B.B. Owen. The physical chemistry of electrolyte solutions. 3rd ed. Reinhold, New York. 1958. p. 358.
17. F.J. Millero. Chem. Rev. **71**, 147 (1971).
18. I.N. Basumallick and R.K. Mohanty. Indian J. Chem. **29**, 647 (1990).
19. A. Bondi. J. Phys. Chem. **68**, 441 (1964).
20. A. Terasawa, H. Itsuki, and S. Arakawa. J. Phys. Chem. **79**, 2345 (1975).
21. A.N. Martin, J. Swarbrick, J. Cammarata, and K. Chun. Physical Pharmacy. Lea and Febiger, Philadelphia, Pa. 1969.
22. Remington's Pharmaceutical Sciences. 17th ed. Mack Easton, Pa. 1985.
23. Merck manual diagnosis and therapy. 12th ed. Merck Sharp and Dohm, Rahway, NJ. 1972.
24. C. Davidson. *In* Fundamentals of drug metabolism and drug deposition. The Williams and Wilkens Co., Baltimore, U.S.A. 1975.
25. The Pharmaceutical Codex. 11th ed. Pharmaceutical Press, London. 1979.
26. R.H. Girdwood. Clinical pharmacology. 23rd ed. 1976. Chapts. 4, 8, 9.
27. S.P. Gupta. Chem. Rev. **91**, 1100 (1991).

Can. J. Chem. Downloaded from www.nrcresearchpress.com by EESC ESCOLA DE ENGENHARIA on 09/08/12
For personal use only.

Activities of dilute NiO in $Na_2O{\cdot}2SiO_2$ by electromotive force measurements[1]

P.J. TUMIDAJSKI

Materials Laboratory, Building M-20, National Research Council of Canada, Ottawa, ON K1A 0R6, Canada

Received July 20, 1993

P.J. TUMIDAJSKI. Can. J. Chem. **72**, 1080 (1994).

The thermodynamic properties of dilute NiO in $Na_2O{\cdot}2SiO_2$ for $X_{NiO} < 0.0125$ have been investigated in the temperature range 1073–1173 K by emf measurements using the electrochemical cell

$$Ni_{(s)}|NiO_{(s)}|ZrO_2\text{–}CaO||Ni_{(s)}|NiO$$

where *NiO* denotes a solution with $Na_2O{\cdot}2SiO_2$. It was found that for $X_{NiO} < 0.003$ the solutions obey Henry's law. The Henrian activity coefficients and the related dilute solution thermodynamic properties based on the solid NiO standard state are reported.

P.J. TUMIDAJSKI. Can. J. Chem. **72**, 1080 (1994).

Utilisant une celle électrochimioque

$$Ni_{(s)}|NiO_{(s)}|ZrO_2\text{–}CaO||Ni_{(s)}|NiO$$

dans laquelle *NiO* indique une solution de $Na_2O{\cdot}2SiO_2$ et faisant appel à des mesures de fem, on a étudié les propriétés thermodynamiques du NiO en solution dilué ($X_{NiO} < 0{,}0125$) dans du $Na_2O{\cdot}2SiO_2$, à des températures allant de 1073 à 1173 K. On a trouvé que, pour $X_{NiO} < 0{,}003$ les solutions obéissent à la loi de Henry. On rapporte les coefficients d'activité de Henry et les propriétés thermodynamiques apparentées des solutions diluées qui sont basées sur l'état de référence du NiO solide.

[Traduit par la Rédaction]

Introduction

Despite the industrial and theoretical significance of NiO slags, there is a paucity of accurate thermodynamic data for these systems. The thermodynamic properties of NiO in calcium and sodium silicates have been studied (1–4). However, the thermodynamic properties of dilute solutions of NiO in silicate slag have not heretofore been reported. It was the purpose of the present study to investigate dilute solutions of NiO ($X_{NiO} < 0.0125$) in $Na_2O{\cdot}2SiO_2$. Dilute solutions are ideally suited for understanding the effects of complex formation in silicates and the relationships between structure and thermodynamic properties. Furthermore, fundamental slag studies aid in the understanding and optimization of industrial pyrometallurgical processes.

Experimental

The electrochemical cell is an oxygen concentration cell described as

$$(RE)\ Ni_{(s)}|NiO_{(s)}|ZrO_2\text{–}CaO||Ni_{(s)}|NiO\ (WE)$$

where *NiO* denotes a solution with $Na_2O{\cdot}2SiO_2$. The cell design is given in Fig. 1. The cell consisted of two independent and isolated half-cell compartments and a solid electrolyte. The solid electrolytes were 46 cm long by 6 mm o.d. tubes with closed ends. The tubes were ZrO_2 stabilized with 5 mol% CaO. The imperviousness of the tubes was checked with a helium leak tester. The only mass transfer through the electrolyte was the electrochemical transfer of oxide anions. The reference electrode (RE) consisted of a spectrographically pure Ni wire immersed in an equimolar mixture of Ni and NiO powders. The working electrode (WE) was a Ni wire which dipped into the slag. The slag was contained in a zirconia crucible. There was minimal evidence of chemical attack of the crucibles and electrolyte tubes after several days of exposure. The entire cell was contained in a 5 cm o.d. quartz tube.

The cell was assembled and heated slowly to 500°C. Vacuum was applied to the WE and RE compartments. After 3 h the glass tubes from the electrode compartments were flame-sealed; then the temperature was increased to 800°C. Eight hours were required for cell voltage to stabilize which indicated that equilibrium was established. The cell response to temperature change was immediate. However, temperature cycling and polarization tests were done to confirm reversibility. For the latter, 1 mA was passed through the cell in each direction using an external d.c. source. In each case, the cell voltage returned to the original value in less than a minute. Runs for each composition lasted 2 days. Temperatures were measured with a Pt versus Pt 13% Rh thermocouple. All voltages were recorded with a high imput impedance $6\frac{1}{2}$ digit digital multimeter (Hewlett-Packard Model 3468B).

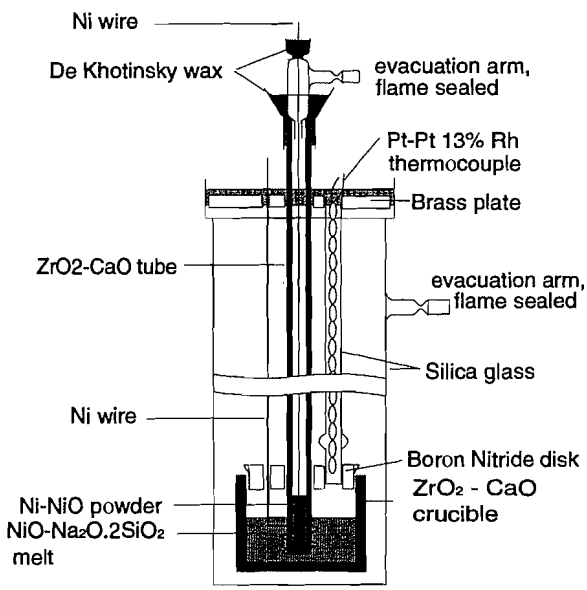

FIG. 1. Experimental electrochemical cell.

The method adopted for the preparation of the slags was to initially make $Na_2O{\cdot}2SiO_2$, and then to melt it with NiO. The $Na_2O{\cdot}2SiO_2$ was produced by melting in a platinum crucible a mixture of Na_2CO_3 and SiO_2. After 48 h, the slag was homogeneous. When the presence

[1]NRCC No. 36922.

Can. J. Chem. Downloaded from www.nrcresearchpress.com by ESC ESCOLA DE ENGENHARIA on 09/08/12
For personal use only.

Can. J. Chem. Downloaded from www.nrcresearchpress.com by EESC ESCOLA DE ENGENHARIA on 09/08/12
For personal use only.

of CO_2 bubbles was considerable, the slag was ground and remelted. Subsequently, $Na_2O{\cdot}2SiO_2$ and NiO were melted together at 1050°C for 48 h. The ternary slags were homogeneous and slightly purple in color. The intensity of the color varied according to the NiO content. Samples were finely ground and stored in a desiccator. The exact composition of NiO in $Na_2O{\cdot}2SiO_2$ was confirmed by the dimethylglyoxime wet chemical technique.

The chemical reactions for the NiO concentration cell are as follows:

[1*a*] RE: $NiO_{(s)} + 2e^- = Ni_{(s)} + O^{2-}_{RE}$

[1*b*] Transference through ZrO_2–CaO: $O^{2-}_{RE} = O^{2-}_{WE}$

[1*c*] WE: $Ni_{(s)} + O^{2-}_{WE} = NiO + 2e^-$

[1] Overall: $NiO_{(solid,a=1)} = NiO_{solution,a<1)}$

where *NiO* denotes a solution with $Na_2O{\cdot}2SiO_2$. The corresponding Nernst equation is,

$$[2] \quad E_{cell} = -\frac{R\cdot T}{2\cdot F}\ln a_{NiO\ (solid\ standard\ state)} = -\frac{R\cdot T}{2\cdot F}\ln \gamma_{NiO} - \frac{R\cdot T}{2\cdot F}\ln X_{NiO}$$

where E_{cell} is the measured cell voltage at temperature T, R is the universal gas constant, and F is the Faraday constant. A plot of E_{cell} against $\ln X_{NiO}$ should be linear with a slope of $R\cdot T/2\cdot F$.

Results and discussions

Table 1 summarizes the measured cell voltages which have been expressed as least-squares lines of the form $E = A + BT$, where E represents the cell voltage in mV, and T is the thermodynamic temperature in Kelvin. The correlation coefficients in Table 1 indicate that the plots of cell voltage versus temperature are linear. The estimate for the standard deviation of cell potential for the regression of cell potential on temperature is approximately 3 mV for all compositions. Figure 2 is the variation of the cell voltage versus temperature for all the compositions studied. The experimental data are well represented by the linear least squares lines as indicated.

The Nernst plots for 1073, 1173 and 1273 K, as expressed by eq. [2], are given in Fig. 3. The experimental data indicate a two-electron reaction, as expected. Linear regression analysis for the Nernst plots gave correlation coefficients of almost unity for all cases. The linearity of the plots indicates that the dilute solutions of NiO in $Na_2O{\cdot}2SiO_2$ obey Henry's law.

The NiO activities based on the solid standard state, and calculated with eq. [2], are summarized in Table 2 for 1073, 1173, and 1273 K. The NiO activities based on the liquid standard state were not reported because reliable data for the heat of fusion for NiO is unavailable. It can be seen from Table 2 that the NiO activities deviate positively from the ideal behavior (i.e., $a_i = X_i$, for all X_i's). The structural interpretations of the activity deviations is highly speculative when the standard state is the solid and will not be pursued. Also included in Table 2 are the dilute solution properties. The Henrian activity coefficients were calculated with eq. [3].

$$[3] \quad \left.\frac{\partial a_{NiO}}{\partial X_{NiO}}\right|_{X_{NiO}\to 0} = \gamma^0_{henrian}$$

The relationship is depicted graphically for 1173 K in Fig. 4. The activity coefficients follow Henry's law for $X_{NiO} < 0.003$; and for this composition range the solutions can be considered

TABLE 1. E_{cell} versus temperature[a] for the NiO–$Na_2O{\cdot}2SiO_2$ system

X_{NiO}	E_{cell}/mV	Correlation coefficient
0.0125	−234.89 ± 0.2929·T	0.9997
0.0100	−222.89 ± 0.2876·T	0.9998
0.0050	−203.67 ± 0.2958·T	0.9991
0.0010	−194.45 ± 0.3555·T	0.9989
0.00075	−158.26 ± 0.3323·T	0.9990

[a]Thermodynamic temperature (T) in Kelvin.

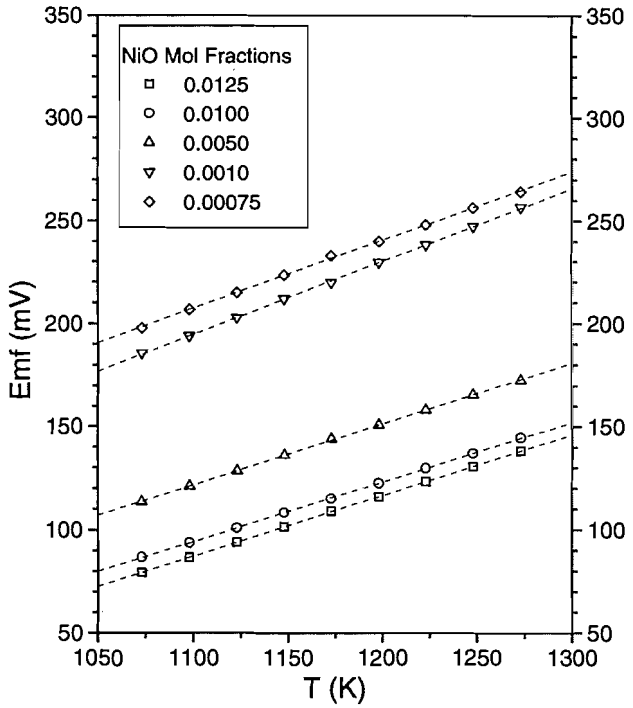

FIG. 2. Temperature dependence of measured cell voltages.

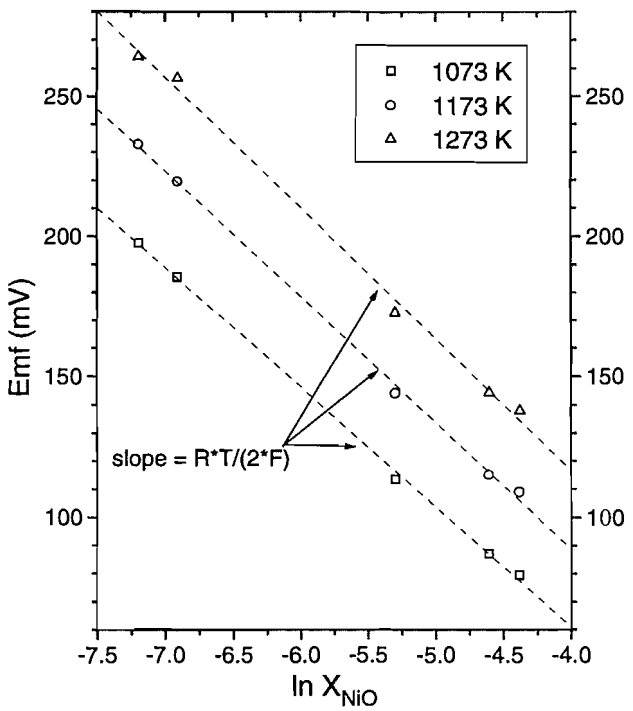

FIG. 3. Nernst plots for 1073, 1173, and 1273 K.

TABLE 2. Thermodynamic properties[a] for the NiO–$Na_2O{\cdot}2SiO_2$ system

T/K	X_{NiO}	a_{NiO}	γ_{NiO}	$\Delta\bar{H}$/kJ mol^{-1}	$\Delta\bar{G}^{xs}$/kJ mol^{-1}	$\Delta\bar{S}$/J mol^{-1} K^{-1}
1073	0.0125	0.180	14.4	45	24	20
	0.0100	0.153	15.3	43	24	17
	0.0050	0.086	17.2	39	25	13
	0.0010	0.0181	18.1	38	26	11
	0.00075	0.0139	18.6	40	26	12
	∞ dilution		19.1	37	26	10
1173	0.0125	0.116	9.3	45	22	20
	0.0100	0.103	10.3	43	23	17
	0.0050	0.058	11.6	39	24	13
	0.0010	0.013	13.0	38	25	11
	0.00075	0.010	13.3	40	25	12
	∞ dilution		13.6	37	25	10
1273	0.0125	0.081	6.5	45	20	20
	0.0100	0.072	7.2	43	21	17
	0.0050	0.043	8.6	39	23	13
	0.0010	0.0093	9.3	38	24	11
	0.00075	0.0081	9.33	40	24	12
	∞ dilution		9.96	37	24	10

[a]Based on the solid standard state.

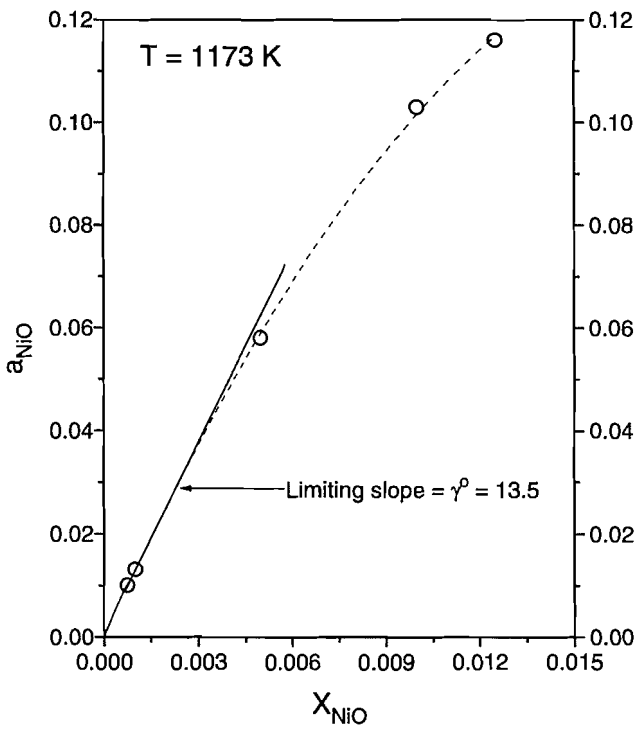

FIG. 4. Concentration dependence of NiO activities at 1173 K, and determination of the Henrian activity coefficient.

to be exactly Henrian (i.e. activity coefficients are compositionally independent and not equal to unity). The uncertainty in the reported activity coefficient values is estimated to be ±5%. The partial enthalpy, entropy, and excess free energy of mixing for NiO based on the solid standard state are also reported in Table 2. The values were calculated according to eq. [4] to eq. [6].

$$[4] \qquad \overline{\Delta H} = \frac{\partial(R \cdot \ln \gamma_{NiO})}{\partial(1/T)}$$

$$[5] \qquad \overline{\Delta H}^{xs} = R \cdot T \cdot \ln \gamma_{NiO}$$

$$[6] \qquad \overline{\Delta S} = -\frac{\partial(R \cdot \ln \gamma_{NiO})}{\partial(T)}$$

The error in the values of enthalpies and excess free energies is approximately ±3 kJ mol^{-1}, while the error for the entropies is ±3 J mol^{-1} K^{-1}. The enthalpies and entropies are considered to be temperature independent over the limited temperature range of the experiments.

1. A.L. Lacy and J.A. Pask. J. Am. Cer. Soc. **53**, 559 (1970).
2. J.M. Duke and A.J. Naldrett. Geol. Asso. Can. Mineral. Assoc. Can. Program Abstr. **2**, 16 (1977).
3. I.H. Campbell, A.J. Naldrett and P.L. Roeder. Can. Mineral. **17**, 495 (1979).
4. E.B. Pretorius and A. Muan. J. Am. Ceram. Soc. **75**, 1490 (1992).

Can. J. Chem. Downloaded from www.nrcresearchpress.com by EESC ESCOLA DE ENGENHARIA on 09/08/12
For personal use only.

Solvent effects on the reactivity of solvated electrons with ions in isobutanol/water mixed solvents

RUZHONG CHEN, YURIS AVOTINSH,[1] AND GORDON R. FREEMAN[2]
Chemistry Department, University of Alberta, Edmonton, AB T6G 2G2, Canada

Received July 20, 1993

RUZHONG CHEN, YURIS AVOTINSH, and GORDON R. FREEMAN. Can. J. Chem. **72**, 1083 (1994).

The effective reaction radii κR_r, where R_r is the reactive encounter radius and κ is the probability of reaction per encounter, for e_s^- with H_s^+, $NH_{4,s}^+$, Ag_s^+, Cu_s^{2+}, and $NO_{3,s}^-$ are all 0.7 ± 0.1 nm in isobutanol containing 10–20 mol% water. The value remains at 0.7 ± 0.1 nm for H_s^+, Ag_s^+, and Cu_s^{2+} in pure isobutanol, and for the two transition metal ions in pure water solvent. The value for $NO_{3,s}^-$ reduces to 0.35 nm in pure isobutanol and pure water solvents, whereas for H_s^+ and $NH_{4,s}^+$ in pure water solvent it is only 0.14 nm and 2.6×10^{-5} nm, respectively. The low reactivity of $NH_{4,s}^+$ with e_s^- in water is attributed to the symmetry of the hydrogen-bonded solvation structure of NH_4^+ in water, and the higher reactivity of H_s^+ ($OH_{3,s}^+$) is attributed to the lower symmetry of its hydrogen-bonded solvation structure. The NH_4^+ and OH_3^+ ions have no low-lying orbital for an electron to occupy, so either reaction occurs by proton transfer to the electron site or the neutral species must decompose. We suggest that the proton transfer or the decomposition of the neutral species is facilitated by an unsymmetrical solvation structure.

Reaction of e_s^- in $Al(ClO_4)_3$ solutions in water is due mainly to H_s^+ from hydrolysis of Al_s^{3+}, and partly to partially hydroxylated aluminum(III) species. Reaction of e_s^- with Al_s^{3+} itself appears to be negligible in water. The reactivity of the solutions of $Al(ClO_4)_3$ in isobutanol-rich solvents is 3–5 times greater than that in water.

In pure C_1 to C_4 1-alcanol solvents the value of $k_2(e_s^- + NO_{3,s}^-)$ increases linearly with the dielectric relaxation time τ_1 of the solvent. In these solvents the probability of permanent capture per encounter increases approximately as the square of the encounter duration.

RUZHONG CHEN, YURIS AVOTINSH et GORDON R. FREEMAN. Can. J. Chem. **72**, 1083 (1994).

On a déterminé que dans de l'isobutanol contenant de 10 à 20% d'eau, les rayons efficaces de réaction, κR_r, où R_r est le rayon de rencontre réactif et κ est la probabilité de réaction par rencontre, des entités e_s^- avec H_s^+, $NH_{4,s}^+$, Ag_s^+, Cu_s^{2+} et $NO_{3,s}^-$ son tous égaux à 0,7 ± 0,1. La valeur demeure 0,7 ± 0,1 nm pour H_s^+, Ag_s^+ et Cu_s^{2+} dans l'isobutanol pur et pour les ions des deux métaux de transition dans l'eau pure. La valeur pour $NO_{3,s}^-$ diminue à 0,35 nm dans l'isobutanol pur et l'eau pure alors que, pour le H_s^+ et le $NH_{4,s}^+$ dans l'eau pure, les valeurs sont respectivement 0,14 nm et $2,6 \times 10^{-5}$ nm. On attribue la faible réactivité du $NH_{4,s}^+$ avec les e_s^- dans l'eau à la symétrie de la structure de solvatation comportant des liaisons hydrogènes du $NH_{4,s}^+$ dans l'eau et on attribue la réactivité plus élevée des H_s^+ ($OH_{3,s}^+$) à la symétrie plus faible de sa structure de solvatation comportant une liaison hydrogène. Les ions NH_4^+ et OH_3^+ n'ont aucune orbitale de bas niveau pour accommoder un électron; la réaction se produit donc par un transfert de proton vers un site d'électron ou les espèces neutres doivent se décomposer. On suggère que le transfert de proton ou la décomposition d'espèces neutres est rendu plus facile par une structure de solvatation qui n'est pas symétrique.

La réaction des e_s^- dans des solutions de $Al(ClO_4)_3$ dans l'eau est principalement due aux H_s^+ provenant de l'hydrolyse des Al_s^{3+} et, en partie, à des espèces d'aluminium(III) partiellement hydroxylées. La réactivité des solutions de $Al(ClO_4)_3$ dans des solvants riches en isobutanol est de trois à cinq fois plus grande que dans l'eau.

Dans des solvants formés d'alcanols purs contenant de un à quatre atomes de carbone, la valeur de $k_2(e_s^- + NO_{3,s}^-)$ augmente d'une façon linéaire avec le temps de relaxation diélectrique, τ_1, du solvant. Dans ces solvants, la probabilité d'une capture permanente par rencontre augmente par un facteur approximativement égal au carré de la durée de rencontre.

[Traduit par la Rédaction]

Introduction

The present article continues the studies of solvated electron reactions with ions in mixed solvents (1), in this case isobutanol/water.

The reactions of solvated electrons (e_s^-) are usually electron transfer reactions (2). Possible exceptions are $e_s^- + ROH \rightarrow H + RO_s^-$ and $e_s^- + ROH_{2,s}^+ \rightarrow H + ROH$ in water and alcohols, where a proton from a solvating —OH or $—OH_2^+$ group might transfer to the site of the electron (3). Proton transfer to the "cavity" of the electron site might avoid the work needed to create a new site for the H atom if the electron were to transfer first, followed by decomposition of the transient ROH^- or ROH_2. The electron and proton are both elementary particles, but the former has a much smaller mass and, other things being equal, would have a larger transfer probability. Protons have larger mobilities than do electrons in water and alcohols, which means that the transport mechanisms are different.

For electron transfer between two species A and B in liquid media one may write

$$[1a] \qquad A_s + B_s \rightleftharpoons [A_s, B_s]$$

$$[1b] \qquad [A_s, B_s] \rightarrow C_s + D_s$$

where the subscript s signifies "solvated". The first step represents the random diffusion of two reactants, which by chance encounter each other and thereby form an [encounter pair], and which might diffuse apart again. The second step represents electron transfer within the encounter pair, which might involve thermal activation of the solvated species A_s and B_s in concert (4, 5).

The overall second order reaction rate constant k_2 may be represented by

[1] Present address: Faculty of Chemistry, Stuchka Latvian State University, Gorkii St., 48, 226013 Riga, Latvia.

[2] To whom correspondence should be addressed.

Can. J. Chem. Downloaded from www.nrcresearchpress.com by EESC ESCOLA DE ENGENHARIA on 09/08/12
For personal use only.

Can. J. Chem. Downloaded from www.nrcresearchpress.com by EESC ESCOLA DE ENGENHARIA on 09/08/12
For personal use only.

$$[2] \qquad \frac{1}{k_2} = \frac{1}{k_{1a}} + \frac{1}{K_{1a}k_{1b}} = \frac{1}{k_d} + \frac{1}{K_{1a}k_r}$$

where $k_d = k_{1a}$ = diffusion controlled upper limit of the reaction rate constant, $K_{1a} = k_{1a}/k_{-1a}$, and $k_r = k_{1b}$ = rate of formation of products from encounter pairs. The value of K_{1a} is typically 10^{-5} m^3/mol.

We analyze large values of k_2 from the viewpoint of the Smoluchowski–Debye model (1, 6):

$$[3] \qquad k_2 \approx k_d = 4\pi N_A(D_A + D_B)R_r f$$

where N_A = Avogadro's constant, D_A and D_B are diffusion coefficients, R_r is the average center-to-center distance between A and B when electron transfer occurs, and f is a factor that accounts for the effect of the coulombic interaction between the reactants on their probability of diffusing to within a distance R_r of each other.

The relative contributions of k_d and k_r to limiting the observed reaction rate are reflected in the ratio k_2/k_d. If $k_2 \approx k_d$, then $K_{1a}k_r \gg k_d$; if $k_2 = 0.5\,k_d$, then $K_{1a}k_r \approx k_d$; if $k_2 \ll k_d$, then $k_2 \approx K_{1a}k_r$. We have introduced the probability κ that reaction occurs during the lifetime of an encounter pair (1). Then,

$$[4] \qquad k_2 = \kappa k_d = 4\pi N_A(D_A + D_B)\kappa R_r f$$

For example, when $\kappa \leq 0.10$, then $K_{1a}k_r \leq k_d/9$. We evaluate solvent effects on k_2/f. Partial information is obtained about the diffusion coefficients of ionic reactants by measuring molar conductances of the reactant electrolyte solutions.

Experimental

Materials

Isobutanol (Aldrich, 99+%, Spectrophotometric Grade, Gold Label) was dried for one week on Davison Molecular Sieves (3 Å), then treated for one day under UHP argon (99.999%, Liquid Carbonic Canada Ltd.) with sodium borohydride (2 g/L) at 330 K. The alcohol was then fractionally distilled under argon, through an 80 × 2.3 cm column packed with glass helices, discarding the first 20% and last 40%. The middle 40% portion was collected and stored in a flask under argon. The water content, measured by Karl–Fisher titration, was 0.05 mol%. The solvated electron half-life after a 100 ns pulse of 340 fJ (2.1 MeV) electrons (4 J/kg) at 298 K was about 10 μs.

Singly distilled water was further purified in a Barnstead Nanopure II ion exchange system. The half-life of solvated electrons after a 100 ns pulse of 340 fJ electrons (4 J/kg) was about 12 μs.

The following chemicals were obtained from Aldrich: lithium nitrate (99.999%, gold label), ammonium nitrate (99.999%), ammonium perchlorate (99.8%), lithium perchlorate (reagent grade), copper(II) perchlorate (98%, reagent grade), and aluminum(III) perchlorate (98%, reagent grade). Silver perchlorate (reagent grade) was from Strem. After opening a bottle, it was stored in a vacuum desiccator that contained P_2O_5.

Perchloric acid (70 wt%, in water) was obtained from Fisher Scientific.

The salts and acid were used as received.

Techniques

Butanol/water mixed solvents were prepared in a 1000 cm^3 volumetric flask, by volume measurements at 298 K.

Solid solutes were weighed into 25 cm^3 volumetric flasks and dissolved in the mixed solvent to get the stock solution. Sample solutions were made by diluting aliquots of stock solution, using syringes or volumetric pipettes. Perchloric acid samples were prepared through several steps of dilution from the 70 wt% solution, and the concentrations were checked with the calibrated pH meter.

Four to six sample solutions with different concentrations were prepared for each solute. The solutions were poured into 10 mm Spectrosil optical cells, deaerated by bubbling with UHP argon, and sealed. All components of the solution were of low volatility, so their concentration changed negligibly during bubbling.

Electrons were produced by pulse radiolysis. The radiation was a 100 ns pulse of 340 fJ (2.1 MeV) electrons, delivering a dose of ~4 Gy(J/kg). The number of pulses per sample was 2 or 3 at each temperature, and the number of temperatures per sample was 4 or 5. A pure solvent sample was part of each series, so the effect of the ~3×10^{-3} mol/m^3 of aldehyde produced during three pulses would not affect the value of k_2 obtained from the slope of the plot of k_{obs} against added solute concentration.

The light source was a 1000 W Xe arc lamp (Optical Radiation Co., model XLN) contained in a lamp housing (Photochemical Research Assoc., model PRA ALH220). A Bausch and Lomb monochromator housing, type 33-86-25, was used with the grating type 33-86-03 (700–1000 nm), and a Corning filter type CS-2-64 (700–1000 nm). The light intensity reaching the detector was controlled by adjusting the slits on the monochromator. The wavelength of the analyzing light was 850 nm with bandwidth 9 nm, to obtain an optimal absorption signal.

The silicon detector (pin photodiode SGD 040) was sensitive over the wavelength range 400–1100 nm. The 3 to 97% response time of the detector, amplifier and transient digitizer (Tektronix R7912) was 6 ns. The signal to noise ratio of the differential amplifier (Tektronix 7A13) was increased by using the 5 MHz filter, which gave a system response time of 96 ns.

The cell holder in the thermostated box was repeatedly rotated full cycles clockwise and counterclockwise between pulse measurements, to obtain a temperature uniformity of ±0.1 K within the box.

The decay half-life of the solvated electron absorption was computed as a function of time after each pulse, and recorded on the absorption trace (1*b*). The first order decay constants were plotted against solute concentration, and second order rate constants obtained from the slope of the line. At high concentrations in butanol the plots were curved due to ionic strength effects, in which case initial slopes were used.

Electrical conductivity measurements were made as described earlier (1*a*).

pH measurements were made with a Fisher Accumet digital pH/ion meter (model 520) with a glass indicating electrode (Fisher No. 13-639-3) and a reference electrode (Fisher No. 13-639-52). The meter was calibrated with two standard buffer solutions at 298 K, SO-B-108 (pH = 7.00 ± 0.01) and SO-B-98B (pH = 4.00 ± 0.01).

Results and discussion

Physical properties

Isobutanol is not miscible with water in the composition range 45.4–97.8 mol% water at 298 K (7). Reaction rate constants were measured in solvents that contained the following mol% water: 0.0, 10.0, 20.0, 35.0, 45.0, 98.0, 100.0. Values of the viscosities of the mixed solvents were obtained from ref. 8, and of the relative permittivities at 298 K from ref. 9.

Rate constants

Arrhenius plots of k_2 for $LiNO_3$, NH_4NO_3, NH_4ClO_4, $AgClO_4$, $HClO_4$, and $Cu(ClO_4)_2$ in the mixed solvents are given in Figs. 1–4. The symbols that represent the different solvent compositions are listed in Table 1.

The precision of k_2 values is 5–10% in pure water solvent and 10–15% in mixed and pure alcohol solvents.

Due to the low solubilities of NH_4ClO_4 and NH_4NO_3 in pure

Can. J. Chem. Downloaded from www.nrcresearchpress.com by EESC ESCOLA DE ENGENHARIA on 09/08/12
For personal use only.

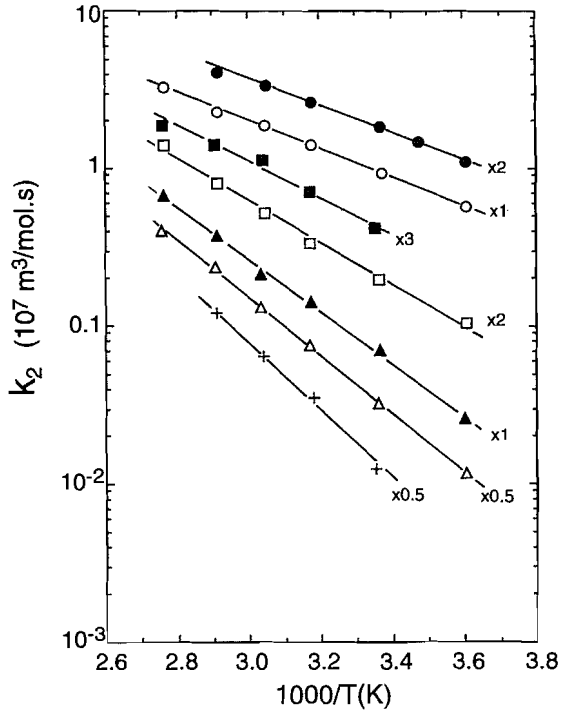

FIG. 1. Arrhenius plots of k_2 of e_s^- reactions with lithium nitrate in isobutanol/water mixed solvents. Symbols are explained in Table 1. To separate the lines, the values of k_2 have been multiplied by the factors indicated.

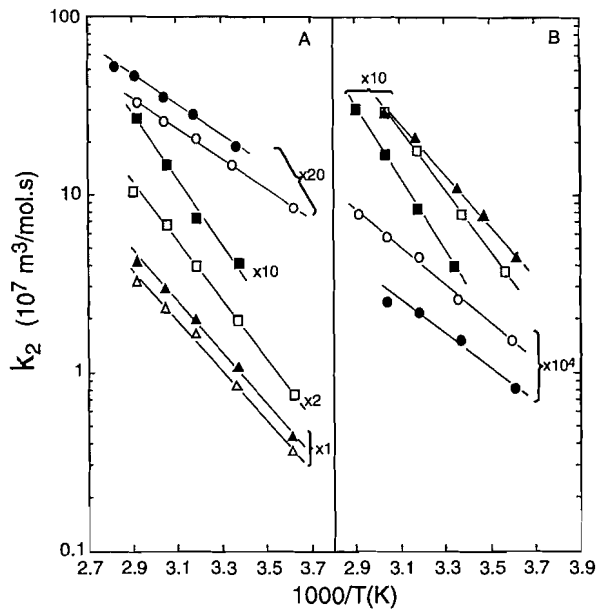

FIG. 2. Arrhenius plots of k_2 of e_s^- reactions with ammonium nitrate (*A*) and ammonium perchlorate (*B*) in isobutanol/water solvents. Symbols are explained in Table 1. The values of k_2 have been multiplied by the factors indicated. Data for $NH_{4,s}^+$ in (*B*) in 100 and 98 mol% of water have been corrected for reaction of H_s^+ from $NH_{4,s}^+$ dissociation (see text).

isobutanol, and of NH_4ClO_4 in the 10 mol% water mixture, these values of k_2 could not be measured.

The observed rate of electron reaction in NH_4ClO_4 solutions in 100 and 98 mol% water was affected by reaction of e_s^- with H_s^+ obtained from the dissociation (1*a*)

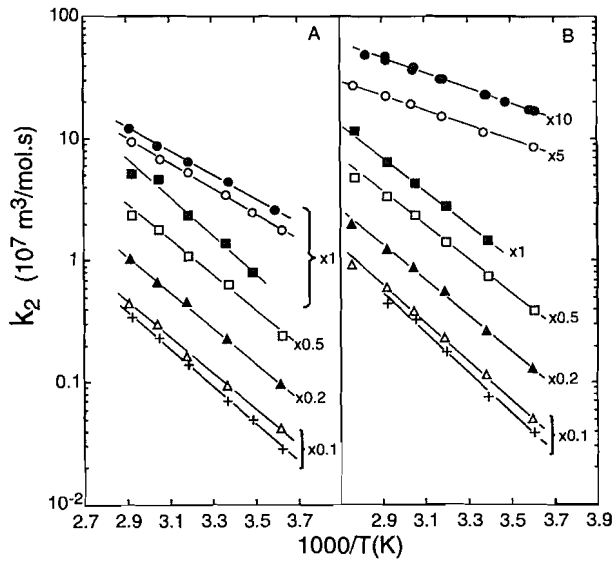

FIG. 3. Arrhenius plots of k_2 of e_s^- reactions with silver perchlorate (*A*) and perchloric acid (*B*) in isobutanol/water solvents. Symbols are explained in Table 1. Values of k_2 have been multiplied by the factors indicated.

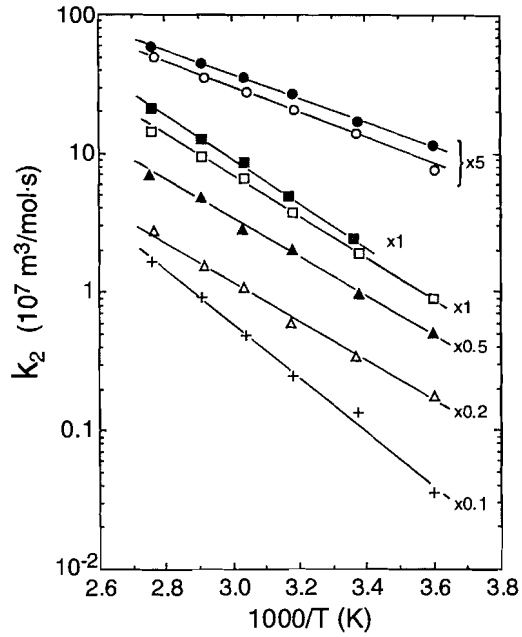

FIG. 4. Arrhenius plots of k_2 of e_s^- reactions with copper(II) perchlorate in isobutanol/water solvents. Symbols are explained in Table 1. Values of k_2 have been multiplied by the factors indicated.

TABLE 1. Symbols in Figs. 1–4

Symbol	mol% H_2O	Symbol	mol% H_2O
+	0	■	45
△	10	○	98
▲	20	●	100
□	35		

Can. J. Chem. Downloaded from www.nrcresearchpress.com by EESC ESCOLA DE ENGENHARIA on 09/08/12
For personal use only.

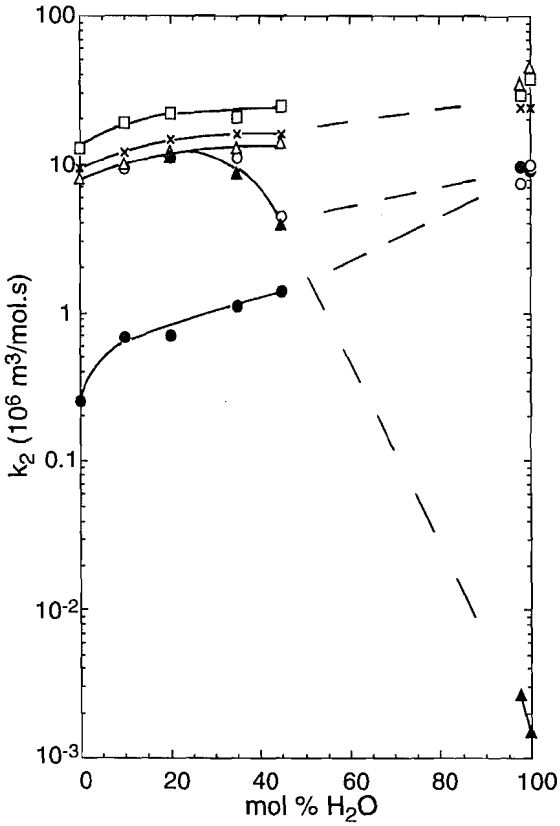

FIG. 5. Solvent composition dependence of k_2 at 298 K in isobutanol/water solvents. ● $LiNO_3$, ○ NH_4NO_3, ▲ NH_4ClO_4, △ $AgClO_4$, × $HClO_4$, □ $Cu(ClO_4)_2$.

[5] $$NH^+_{4,s} \rightleftharpoons NH_3 + H^+_s$$

[6] $$[H^+] = (K_a[NH^+_{4,s}])^{0.5}$$

Values of the dissociation constant K_a of $NH^+_{4,s}$ are only known for pure water solvent (1*a*), but they are a reasonable approximation for the 98 mol% water solvent as well. The values of $k_2(e^-_s + NH^+_{4,s})$ were calculated from the slopes of plots of $(k_{obs} - k_2[H^+_s])$ against the concentration of undissociated $NH^+_{4,s}$, where k_2 is the rate constant for $(e^+_s + H^+_s)$ in the appropriate solvent. The corrections are ~50% at 277 K and ~80% at 328 K; the values of $k_2(e^-_s + NH^+_{4,s})$ are very low in these solvents.

In the alcohol-rich solvents the values of $k_2(e^-_s + NH^+_{4,s})$ are so high that, unless K_a is >10× the value in pure water solvent, the corrections for $k_2[H^+_s]$ are negligible. The values of k_2 in alcohol-rich solvents were taken directly from the slopes of plots of k_{obs} against added $[NH^+_{4,s}]$.

The overall rate constants at 297 K for reaction of e^-_s with $Li^+_s + ClO^-_{4,s}$ are 100 ± 20 m^3/mol.s in water and <40 m^3/mol.s in isobutanol. Thus the rate constants of e^-_s with the ions Li^+_s and $ClO^-_{4,s}$ are negligible by comparison with those with $NO^-_{3,s}$, $NH^+_{4,s}$, H^+_s, Ag^+_s, and Cu^{2+}_s.

Figure 5 displays the solvent composition dependence of k_2 at 298 K for $NO^-_{3,s}$, $NH^+_{4,s}$, H^+_s, Ag^+_s, and Cu^{2+}_s, and for $NH^+_{4,s}$ and $NO^-_{3,s}$ in combination. As found in other mixed solvents (1*a*), the reaction of e^-_s with $NH^+_{4,s}$ is 4 orders of magnitude faster in the alcohol-rich solvent than in pure water solvent. The low reactivity in water is attributed (1*b*) to a symmetric

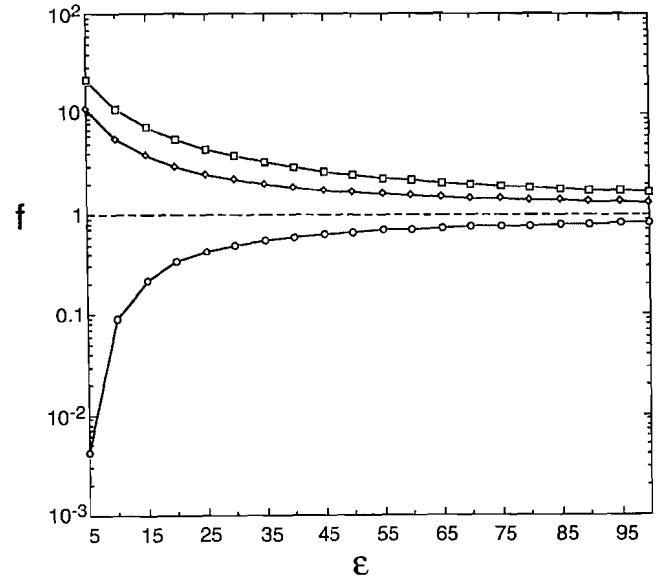

FIG. 6. Dielectric permittivity dependence of the Debye factor f at 298 K. □ $z = +2$ and ◇ $z = +1$, using $R_r = 1.0$ nm; ○ $z = -1$, using $R_r = 1.5$ nm.

structure of NH^+_4 hydrogen bonded into the structure of water, which would tend to spread out the positive charge and reduce the electron affinity of the ion. The reaction might actually happen by proton transfer to the electron site (3). In alcohol, NH^+_4 is unsymmetrically solvated, which evidently facilitates either electron attachment and the subsequent decomposition of $NH_4 \rightarrow H + NH_3$ (1*b*), or approach of the electron site and proton transfer to it.

The observed rate constants for NH_4NO_3 solutions are mainly due to $NO^-_{3,s}$ in the water-rich region and to $NH^+_{4,s}$ in the alcohol-rich region.

The Debye factor f

The coulombic interaction between e^-_s and a reactant of charge $z\xi$ increases their probability of approach to within the distance R_r if z is positive, and decreases it if z is negative (ref. 6; Fig. 6):

[7] $$f = \frac{U(R_r)}{k_B T}\left[\exp\left(\frac{U(R_r)}{k_B T}\right) - 1\right]^{-1}$$

where $U(R_r)$ is the potential energy of interaction between the reactants at center-to-center distance R_r, and k_B is Boltzmann's constant. For the electron and ion,

[8] $$U(R_r) = -\frac{z\xi^2}{4\pi\epsilon_0\epsilon R_r}$$

where ϵ_0 is the permittivity of vacuum, and ϵ is the relative permittivity of the medium between the electron and ion.

The estimated value of f depends on the choice of values of ϵ and R_r. Some authors used the hydrated ion radius for R_r (10), which seems too small for solvated electron reaction with a solvated ion (4). The van der Waals diameter of a water molecule is 0.29 nm (footnote 3). To use the bulk value of ϵ for water one would need at least three water molecules

[3]Reference 11. $r_{vdW} = \left(\frac{3}{4\pi N_A} \cdot \frac{b}{4}\right)^{1/3} = 4.63 \times 10^{-9}\, b^{1/3}$.

Can. J. Chem. Downloaded from www.nrcresearchpress.com by EESC ESCOLA DE ENGENHARIA on 09/08/12
For personal use only.

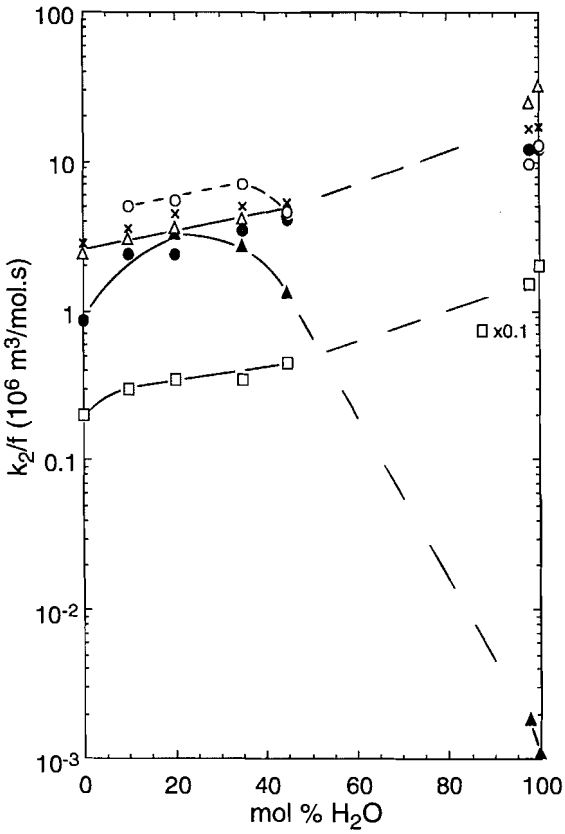

FIG. 7. Solvent composition dependence of k_2/f at 298 K in isobutanol/water solvents. See Table 2 for values of f. Symbols as in Fig. 5. To separate the lines, some values of k_2/f have been multiplied by the factors indicated.

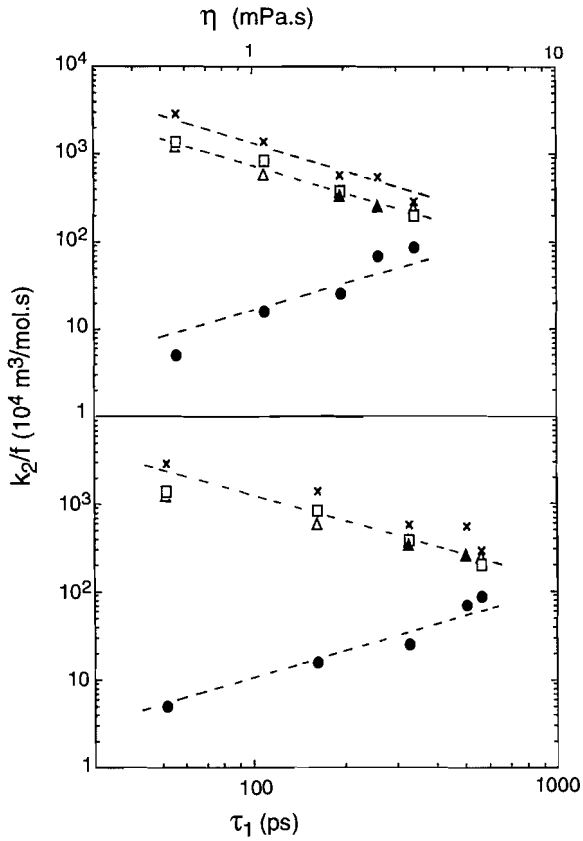

FIG. 8. k_2/f in pure primary C_1–C_4 alcohol solvents at 298 K, as functions of viscosity η and dielectric relaxation time τ_1. Symbols as in Fig. 5. References for k_2: C_1 and C_2 (14); C_3 (1*b*, 15); C_4 (1*a* and present work, data for H^+ in 1-BuOH, unpublished data measured by the authors). Solvent properties: η (12); τ_1 (13). The dashed lines have slopes of 1.0.

between the reactants (one polarized by each reactant, and one relatively free), so $\epsilon = 78$ would require $R_r \geq 0.9$ nm. We took $R_r = 1.0$ nm for reaction of e_s^- with positive ions. The repulsion between a negative ion and an electron makes it somewhat more difficult for them to approach each other closely, so we took $R_r = 1.5$ nm for reaction of e_s^- with anions and used the bulk value of the static dielectric constant of the solvent. Values of f at 298 K are shown as functions of ϵ and z in Fig. 6. Values of f at other temperatures were not calculated because the variation of ϵ with temperature is not known for the mixed solvents.

The solvent composition dependences of k_2/f at 298 K are shown in Fig. 7. When adjusted for the coulombic interactions in this way, the rate constants k_2/f are all similar and increase with increasing water content. Exceptions are the low values for $e_s^- + NO_{3,s}^-$ in pure alcohol solvent and $e_s^- + NH_{4,s}^+$ in water, which are inefficient reactions (1). The points for ammonium nitrate are higher than the rest because both ions are reactants; the overall k_2 was partitioned between $NH_{4,s}^+$ and $NO_{3,s}^-$ using the ratio of ammonium perchlorate and lithium nitrate rate constants, then each part was divided by the appropriate f, and the results added to obtain an overall k_2/f.

Comparisons of k_2/f *in other primary alcohols*

Alcohols that have longer alkyl groups have lower molecular diffusion rates, indicated by the higher shear viscosities η (12), and lower molecular rotation rates, indicated by the longer dielectric relaxation times τ (13). The changes of k_2/f with η and τ for reactions of e_s^- with a number of cations and anions in a series of primary alcohol solvents (1, 14, 15) are shown in Fig. 8.

Reactions of e_s^- with the positive ions (H_s^+, $NH_{4,s}^+$, Ag_s^+, Cu_s^{2+}) display values of k_2/f that vary approximately as η^{-1} and τ^{-1} (Fig. 8). The correlation with η^{-1} and the near equality of the values for the different ions indicates that the reactions in alcohol solvents are essentially diffusion-controlled (16*a*). The somewhat larger rate constants for H_s^+ are due to the proton-hopping mechanism of diffusion (16*b*).

For the e_s^- reaction with $NO_{3,s}^-$ the value of k_2/f increases as η^{+1} (Fig. 8) so the diffusion process [1*a*] is not rate limiting. The duration of an encounter between a pair of reactants increases with increasing η; the multistep reaction that results in the permanent capture of e_s^- by $NO_{3,s}^-$ (1) evidently becomes more probable as the encounter duration increases, in spite of the fact that the rate of new encounters decreases. This indicates that the probability of reaction per encounter increases approximately as the square of the encounter duration.

There is a correlation between the viscosity and the longest dielectric relaxation time τ_1 in alcohols (Fig. 9). The correlation of k_2/f for $(e_s^- + NO_{3,s}^-)$ with τ_1^{+1} is better than that with η^{+1} (Fig. 8), which we do not yet understand. The line through the points in Fig. 9 intersects the η axis, which indicates that the rounder shaped alcohol molecules (methanol) can rotate more freely (small τ) than they can bump past each other (η). This might mean that the duration of an e_s^- encounter with a $NO_{3,s}^-$ is determined by the molecular dipole rotation time.

Can. J. Chem. Downloaded from www.nrcresearchpress.com by EESC ESCOLA DE ENGENHARIA on 09/08/12
For personal use only.

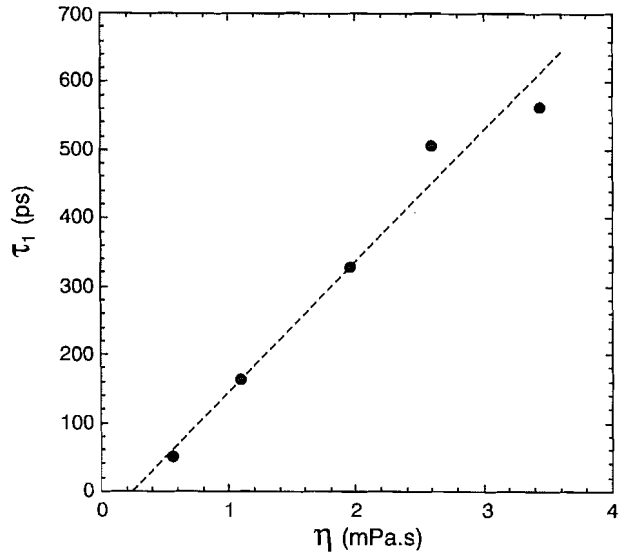

FIG. 9. Dielectric relaxation time τ_1 (13*a*, *b*) of primary C_1–C_4 alcohols at 298 K, as a function of viscosity η (12). The dashed line represents $\tau_1/\text{ps} = 192\ (\eta - 0.24)/\text{mPa s}$.

Dipole reorientation must accompany charge migration in polar solvents, because of the large polarization energy of the solvent molecules around the ion or electron.

Electrical conductivities and effective reaction radii (κR_r)

The diffusion coefficients in eq. [4] are related to the molar electrical conductivities λ ($S \cdot m^2/mol$) of the respective ions (16*b*). However, the conductivities of solvated electrons in the mixed solvents are not known, so the ionic conductivities Λ_0 of the dilute reactant electrolyte solutions are used as an approximation. The ratios of the conductance of e_s^- (17) to that of the various reactant ions (18) in water are known and are roughly assumed to have similar values in the mixed solvents (15):

$$[9] \qquad \lambda(e_s^-) + \lambda(B^z)/z^2 \approx 1.8\Lambda_0/z$$

where z is the number of charges on the reactant in B^z, Λ_0 is the molar conductivity of its electrolyte solutions at low concentration, and the factor 1.8 has an average deviance of ±0.2 for the present solutes in water. By rearranging eq. [4] and making appropriate use of eq. [9] one can obtain (15*b*):

$$[10] \qquad \kappa R_r \approx 1 \times 10^{-16} z k_2/fT\Lambda_0$$

The solvent composition dependences of Λ_0 of the reactant electrolytes at 298 K, and of the approximate values of κR_r at 298 K, are shown in Figs. 10 and 11, respectively. The rate parameters are listed in Table 2. In most cases the concentrations of salts are ≤0.2 mol/m³ for k_2 and Λ measurements, so ion pairing is negligible. The low reactivity of NH_4ClO_4 in water required concentrations up to 100 mol/m³ for measurement of k_2, and the same concentration range was used for Λ measurement; the Debye–Hückel–Onsager equation (16*c*) describes the Λ data, so ion pairing is negligible.

Most of these values of κR_r are relatively insensitive to solvent composition. The greatest exception is for $NH_{4,s}^+$, which is only 10^{-4} times as reactive in water as in isobutanol. The next largest exception is for H_s^+, which is only 0.2 times as reactive in pure water solvent as in the alcohol-rich solvents;

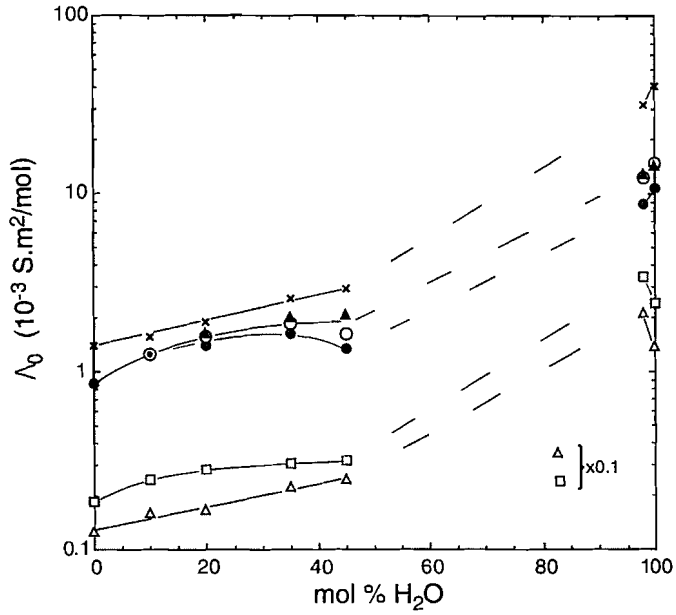

FIG. 10. Solvent composition dependences of the molar conductivities Λ_0 of dilute electrolyte solutions at 298 K in isobutanol/water solvents. Symbols as in Fig. 5. Some values of Λ_0 have been multiplied by the factors indicated.

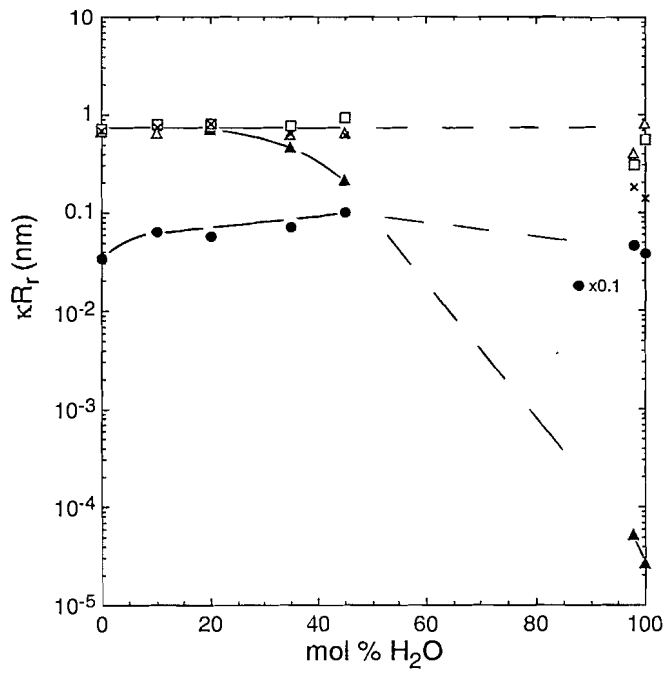

FIG. 11. Solvent composition dependences of κR_r, eq. [10], at 298 K in isobutanol/water solvents. Symbols as in Fig. 5. Some values of κR_r have been multiplied by the factors indicated.

this supports the previous conclusion that reaction of e_s^- with H_s^+ in water is 0.2 times slower than diffusion controlled (19, 20), and that the reaction is diffusion controlled in alcohol.

Activation energies E_2 *and* E_Λ

The Arrhenius temperature coefficients E_2 and E_Λ of reaction and conductance neare 298 K are plotted against solvent composition in Fig. 12. The most remarkable feature is the large increase of E_Λ upon addition of 2 mol% of isobutanol to the aqueous solutions of $AgClO_4$ and $Cu(ClO_4)_2$, as seen on

TABLE 2. Rate parameters for reaction of solvated electrons with solvated ions in isobutanol/water at 298 K

ϵ[a]	η[b] (10^{-3} Pa · s)	mol% H_2O	f[c]	k_2 (10^6 m^3/mol · s)	k_2/f (10^6 m^3/mol · s)	E_2[d] (kJ/mol)	Λ_0[e] (10^{-3} S·m^2/mol)	E_Λ^f (kJ/mol)
					$NO_{3,s}^-$[g]			
78.5	0.89	100	0.78	9.2	12	16	10.8	15
73.0	1.30	98	0.77	9.6	12	17	8.7	20
19.8	3.25	45	0.34	1.4	4.1	24	1.35	25
18.4	3.15	35	0.31	1.1	3.5	28	1.63	23
17.6	3.13	20	0.29	0.70	2.4	32	1.40	23
17.5	3.20	10	0.29	0.69	2.4	35	1.25	21
17.6	3.40	0	0.29	0.25	0.86	41	0.86	19
					$NH_{4,s}^+$, $NO_{3,s}^-$[h]			
		100	0.78	10	13	16	14.8	18
		98	0.77	7.4	9.6	17	12.3	19
		45	[h]	4.5	4.6	35	1.64	22
		35		11	7.0	32	1.88	22
		20		11	5.4	29	1.58	22
		10		9.3	5.0	28	1.26	23
					$NH_{4,s}^+$[i]			
		100	1.40	0.0015	0.0011	20	14.0	16
		98	1.43	0.0026	0.0018	21	12.5	20
		45	3.01	3.9	1.3	36	2.05	25
		35	3.20	8.6	2.7	32	1.98	24
		20	3.32	11	3.3	29	1.61	23
					Ag_s^+[j]			
		100	1.40	45	32	18	13.4	15
		98	1.43	35	24	20	21.0	22
		45	3.01	14	4.7	29	2.43	24
		35	3.20	13	4.1	28	2.20	23
		20	3.32	12	3.6	28	1.62	23
		10	3.34	10	3.0	28	1.57	23
		0	3.32	8.0	2.4	30	1.22	23
					H_s^+[k]			
		100	1.40	24	17	12	40.3	10
		98	1.43	24	17	12	31.5	12
		45	3.01	16	5.3	27	2.95	18
		35	3.20	16	5.0	26	2.58	21
		20	3.32	15	4.5	27	1.91	22
		10	3.34	12	3.6	29	1.56	23
		0	3.32	9.5	2.9	30	1.41	24
					Cu_s^{2+}[l]			
		100	1.88	38	20	16	24.3	16
		98	1.96	29	15	17	34.3	24
		45	5.68	25	4.4	31	3.15	26
		35	6.11	21	3.4	27	3.04	24
		20	6.38	22	3.4	26	2.84	24
		10	6.42	19	3.0	27	2.48	24
		0	6.38	13	2.0	36	1.88	25

[a] Static dielectric permittivity, ref. 9.
[b] Viscosity, ref. 8.
[c] Debye factor.
[d] Arrhenius temperature coefficient of k_2 at 298 K.
[e] Molar conductivity of the salt solutions at concentrations <0.2 mol/m^3.
[f] Arrhenius temperature coefficient of Λ_0 at 298 K.
[g] $NO_{3,s}^-$ in $LiNO_3$ solutions, concentrations 0.02–0.4 mol/m^3.
[h] $NH_{4,s}^+$ and $NO_{3,s}^-$ in NH_4NO_3 solutions, concentrations 0.02–0.2 mol/m^3. The value of f was calculated according to $z = -1$ ($NO_{3,s}^-$) in 100 and 98 mol% H_2O; in the other compositions, k_2/f was calculated from the proportionate contributions of each ion and the appropriate f and summed.
[i] $NH_{4,s}^+$ in NH_4ClO_4 solutions, concentrations 2–170 mol/m^3 for mol% H_2O of 100 and 98; 0.02–0.2 mol/m^3 for mol% H_2O of 45, 35, and 20.
[j] Ag_s^+ in $AgClO_4$ solutions, concentrations 0.01–0.08 mol/m^3.
[k] H_s^+ in $HClO_4$ solutions, concentrations 0.01–0.07 mol/m^3.
[l] Cu_s^{2+} in $Cu(ClO_4)_2$ solutions, concentrations 0.01–0.1 mol/m^3.

Can. J. Chem. Downloaded from www.nrcresearchpress.com by EESC ESCOLA DE ENGENHARIA on 09/08/12
For personal use only.

Can. J. Chem. Downloaded from www.nrcresearchpress.com by EESC ESCOLA DE ENGENHARIA on 09/08/12
For personal use only.

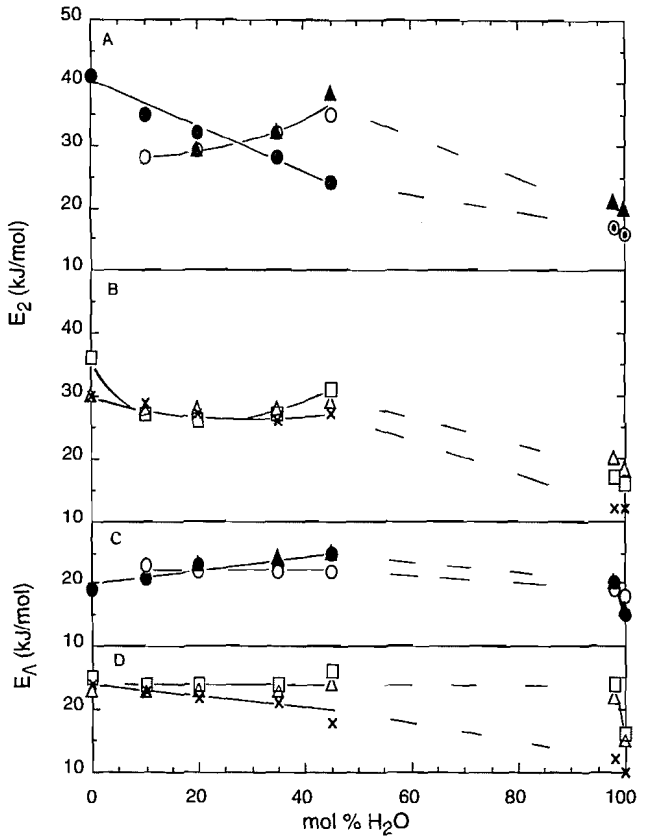

FIG. 12. Solvent composition dependences of the activation energies E_2 of e_s^- reactions, and E_Λ of conductance, near 298 K in isobutanol/water solvents. Symbols as in Fig. 5. *A*, *C*: $LiNO_3$, NH_4NO_3, and NH_4ClO_4. *B*, *D*: $AgClO_4$, $HClO_4$, and $Cu(ClO_4)_2$.

the right-hand side of Fig. 12*D*. This effect is reproducible and corresponds to an increase in conductivity at 298 K (Fig. 10), which contrasts with the decrease of conductivity of the other aqueous solutions when 2 mol% of isobutanol was added (Fig. 10). The decrease of Λ and relatively small increase of E_Λ of the other solutions is due to the increased η upon addition of 2 mol% of alcohol to water (Table 2). The *increase* of Λ and large increase of E_Λ of the $AgClO_4$ and $Cu(ClO_4)_2$ solutions is attributed to an increase of hydrolysis of metal ions, perhaps by complexation of Cu^{2+} and Ag^+ with the alcohol. The increase of Λ with T is reproducible with different heating times. It is not due to oxidation of the alcohol by ClO_4^-, and is worth a separate study. A pH meter would have to be calibrated for each solvent and temperature.

The Arrhenius temperature coefficients of the e_s^- reactions in pure water solvent are 2 ± 2 kJ/mol greater than those of conductance of the electrolyte solutions; this difference is essentially the mean thermal agitation energy $RT = 2.5$ kJ/mol, since conductance is driven by the electric field, whereas diffusion is driven by thermal energy. The values of E_2 in pure water solvent are 3 ± 1 kJ/mol lower than the temperature coefficient of solvated electron diffusion, 20 kJ/mol (17). The exception is $(e_s^- + H_s^+)$, where $E_2 = 12$ kJ/mol equals the temperature coefficient of proton diffusion in water near 298 K (ref. 17; Table 2, $E_\Lambda(H_s^+ + ClO_{4,s}^-) + 2.5$ kJ/mol).

In the alcohol-rich mixed solvents E_2 is ~6 kJ/mol greater than E_Λ for the transition metal ions Ag^+ and Cu^{2+} and the acidic ions H_s^+ and $NH_{4,s}^+$, indicating a need for a slightly greater agitation energy to react. At the miscibility edge of 45 mol% water, $(E_2 - E_\Lambda)$ for the acidic ions increases to ~12 kJ/mol, possibly indicating that e_s^- and the acidic ions are selectively solvated by different components of the solvent, or that they are selectively solvated in the same component but separated by a microstructure of the other component.

The effect of greatest magnitude is the opposite changes of E_2 and E_Λ for the $LiNO_3$ solutions on going from pure isobutanol to the water solubility edge at 45 mol% water (Figs. 12*A* and *C*): E_2 decreases from 41 to 25 kJ/mol while E_Λ increases from 19 to 25 kJ/mol. Thus, $E_2 - E_\Lambda = 22$ kJ/mol in pure isobutanol solvent, but it decreases upon addition of water, reaching zero at the water solubility limit of 45 mol%, and remains at essentially zero in pure water solvent. Electron capture by NO_3^- is clinched by subsequent reaction of the initial NO_3^{2-}; the reaction is evidently a relatively easy protonation by water in pure water solvent, but involves a more difficult reaction of the alcohol in alcohol solvent (1).

A plot of $(E_2 - E_\Lambda)$ against E_Λ for the various solvent compositions breaks the data into alcohol-rich and water-rich regions, which have been demonstrated in greater detail for other alcohols by plots of k_2 against η at 298 K (21, 22). The $(E_2 - E_\Lambda)$ plot is therefore not shown.

Alcohol/water mixed solvents form composite structures, as indicated by their thermodynamic properties (23). Dilute solutions of electrolytes in mixtures near the critical 2-phase composition might have properties characteristic of nanoemulsions. The study of liquids and of liquid solutions for their own sake has reached the beginning of a new cycle of great interest and value to general science.

Effective radii R_d for mutual diffusion

We obtain further insight into eqs. [4] and [10] by considering R_d. The Stokes radius R_d for mutual diffusion of ions i and j in an electrolyte solution is (16*a*)

$$[11] \qquad R_d = \left(\frac{1}{R_{di}} + \frac{1}{R_{dj}}\right)^{-1} = 8.62 \times 10^{-16}/\eta \left(\frac{\lambda_i}{z_i^2} + \frac{\lambda_j}{z_j^2}\right)$$

In our case, $i = e_s^-$ and $j =$ reactant ion. As discussed earlier, values of $\lambda_{e_s^-}$ are not available for the mixed solvents, so we use the approximation $[\lambda_{e_s^-} + (\lambda_j/z_j^2)] \approx 1.8\Lambda_0/z_j$, hence

$$[12] \qquad R_d \approx 5 \times 10^{-16} z_j/\eta\Lambda_0$$

where Λ_0 is the molar conductance of dilute solutions of the electrolyte that contains reactant ion j.

The solvent composition dependences of R_d are shown in Fig. 13. Equation [12] emphasizes the more mobile ion. In water the mobility of e_s^- (17, 24) is greater than that of all the ions we studied except H_s^+; the last has a high mobility due to a solvent-structure-dependent proton hopping mechanism (16*b*). This is why R_d for $HClO_4$ is only 14 pm, while the rest are in the vicinity of 45 pm in pure water solvent.

The apparent decrease of R_d for $AgClO_4$ and $Cu(ClO_4)_2$ from 43 pm in pure water to 20 pm in 98 mol% water (Fig. 13) supports the suggestion that the increase of Λ_0 and E_Λ of these solutions upon addition of 2 mol% of isobutanol to water is caused by complexation of the Ag^+ and Cu^{2+} ions by the alcohol, and acid dissociation of the complex ion: for example,

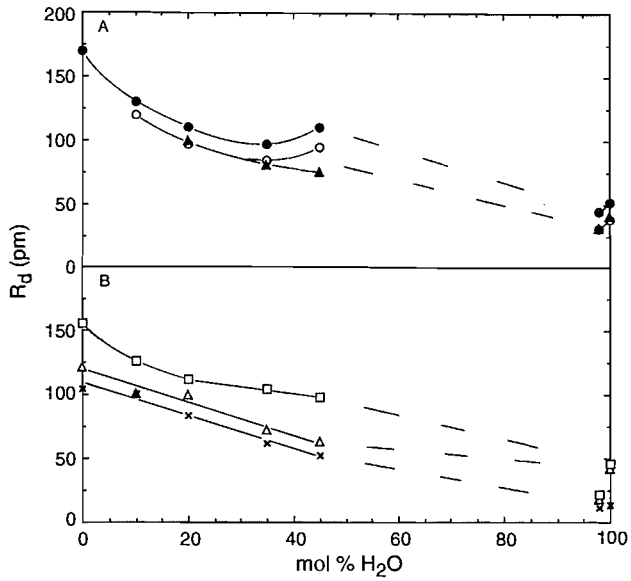

FIG. 13. Solvent composition dependence of R_d, eq. [12], at 298 K in isobutanol/water mixed solvents. Symbols as in Fig. 5. *A*: $LiNO_3$, NH_4NO_3, and NH_4ClO_4. *B*: $AgClO_4$, $HClO_4$, and $Cu(ClO_4)_2$.

[13] $[Ag(ROH)_2]_s^+ \rightleftharpoons [(ROH)AgOR]_s + H_s^+$

This is why the dashed lines do not acknowledge the apparent decrease of R_d in Fig. 13 or of κR_r in Fig. 11 for Ag^+ or Cu^{2+} on going from 100 to 98 mol% water. These ions hydrolyse to a small extent even in pure water solvent (Table 4-1, p. 50 of ref. 25), which was detectable with the pH meter. However, addition of 2 mol% (10 vol.%) of isobutanol to the water or to the dilute salt solutions did not change their indicated pH's appreciably (±0.03 units), possibly due to an effect of the alcohol on the electrode.

The fact that R_d for $H^+ClO_4^-$ is also smaller in pure alcohol and the mixed solvents than R_d for the other electrolytes (Fig. 13), indicates that proton hopping also occurs in those solvents. The ratio $R_d(H^+ClO_4^-)/R_d$ (other salts) ≈ 0.3 in water and is usually ~0.6 in isobutanol, so proton hopping is less efficient in alcohol than in water. However, $Ag^+ClO_4^-$ has an exceptionally high conductance in alcohol solvents (Fig. 13 and ref. 15*b*), which again suggests that reaction [13] occurs.

The larger values of R_d for electrolytes in alcohol than in water are attributed to the larger size of the solvating molecules that attach to the ions.

Reactions of e_s^- in $Al(ClO_4)_3$ solutions

The reaction rate of e_s^- with Al_s^{3+} cannot be measured directly, because Al_s^{3+} hydrolyses extensively (25). The identities of the species present in aluminum salt solutions at different pH's are not well known, because the hydrolysed ions can form charged clusters and polymers (25–28). For example, Rubin and co-workers studied the influence of pH on clustering and coagulation in Al(III) solutions, and concluded that in acidic aqueous solutions the main species in equilibrium are Al_s^{3+}, $AlOH_s^{2+}$, and a polymer $[Al_8(OH)_{20}]_s^{4+}$. However, for the very dilute, natural pH solutions of $Al(ClO_4)_3$ used in our work, we only consider two equilibria (25, 28):

[14] $[(H_2O)_6Al]_s^{3+} \rightleftharpoons [(H_2O)_5AlOH]_s^{2+} + H_s^+,\ K_{14}$

[15] $[(H_2O)_5AlOH]_s^{2+} \rightleftharpoons [(H_2O)_4Al(OH)_2]_s^+ + H_s^+,\ K_{15}$

where K_{14} and K_{15} are the equilibrium constants.

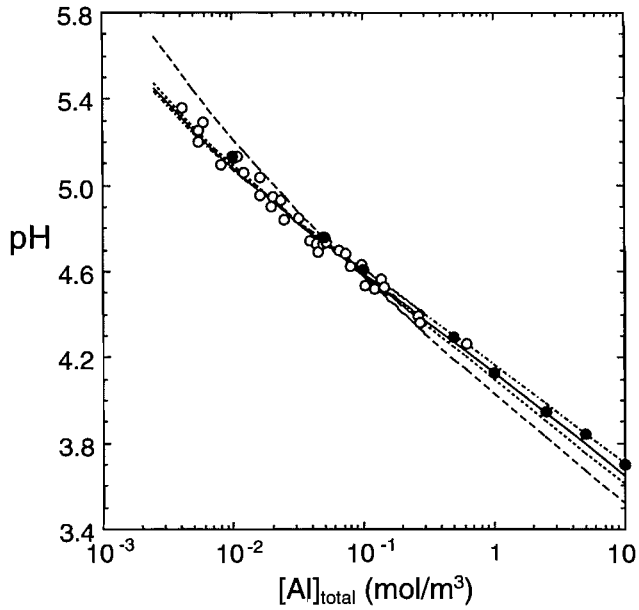

FIG. 14. pH of $Al(ClO_4)_3$ aqueous solutions at 298 K as a function of concentration of aluminum(III) added. ○ present measurements; ● ref. 28. — calculated for reactions [14] and [15], with $K_{15}/K_{14} = 2$ and $K_{14} = 4.7\times10^{-3}$ mol/m^3; - - - $K_{15}/K_{14} = 0$ and $K_{14} = 9.6\times10^{-3}$ mol/m^3; ··· $K_{15}/K_{14} = 1$ and $K_{14} = 6.0\times10^{-3}$ mol/m^3; - · - · - · $K_{15}/K_{14} = 4$ and $K_{14} = 3.5\times10^{-3}$ mol/m^3.

Measured values of pH of aqueous $Al(ClO_4)_3$ solutions at 298 K are plotted against added Al(III) concentration in Fig. 14, along with data from ref. 28. The e_s^- reaction rate constant data were obtained at $Al(ClO_4)_3$ concentrations <0.10 mol/m^3, but pH was also measured at higher concentrations to sort out the hydrolysis equilibria. We attempted to fit the data in Fig. 14 by selecting a value of K_{15}/K_{14} and adjusting the value of K_{14} to give calculated pH values as near as possible to the experimental values. Curves for $K_{15}/K_{14} = 0$, 1, 2, and 4 are shown in Fig. 14, and the corresponding values of K_{14} are given in the legend. The best fit was obtained with $K_{15}/K_{14} = 2$ and $K_{14} = 4.7\times10^{-3}$ mol/m^3, which corresponds to $pK_{14} = 5.33$ and $pK_{15} = 5.03$. The dashed line for $K_{15}/K_{14} = 0$ corresponds to the single stage hydrolysis with $pK = 5.02$ reported earlier (25). Figure 14 confirms that multistep hydrolysis (25–28) is significant even at these low concentrations.

Measured half-lives of e_s^- in these solutions gave the first-order k_{obs} values displayed in Fig. 15. These values were corrected for reaction of e_s^- with H_s^+, using the measured pH values and $k_2(e_s^- + H_s^+) = 2.4\times10^7$ m^{3}mol.s. The net reaction rate with aluminum species is represented by $(k_{obs} - 2.4\times10^7[H_s^+])$; the curve is sublinear (Fig. 15). The net reaction rate also gives sublinear curves when plotted against the equilibrium values of $[Al_s^{3+}]$ or $[HOAl_s^{2+}]$; it gives a superlinear curve when plotted against $[(HO)_2Al_s^+]$. It appears that e_s^- does not react appreciably with Al_s^{3+}, but that it reacts with a partially hydroxylated species with a rate constant $k_2 > 3\times10^6$ m^3/mol.s.

An early report of $k_2(e_s^- + Al_s^{3+}) = 2\times10^6$ m^3/mol.s in water at room temperature, at pH = 6.8 (29*a*), is unclear, because at pH = 6.8 hydrated alumina precipitates. We observed the e_s^- reaction rate in the aluminum perchlorate "solutions" at pH = 6.4 to be the same as that in aqueous $H_2PO_4^-/HPO_4^{2-}$ buffer at that pH. Anbar and Hart might have obtained pH = 6.8 with $H_2PO_4^-/HPO_4^{2-}$ buffer (29*b*) in which case the

Can. J. Chem. Downloaded from www.nrcresearchpress.com by EESC ESCOLA DE ENGENHARIA on 09/08/12
For personal use only.

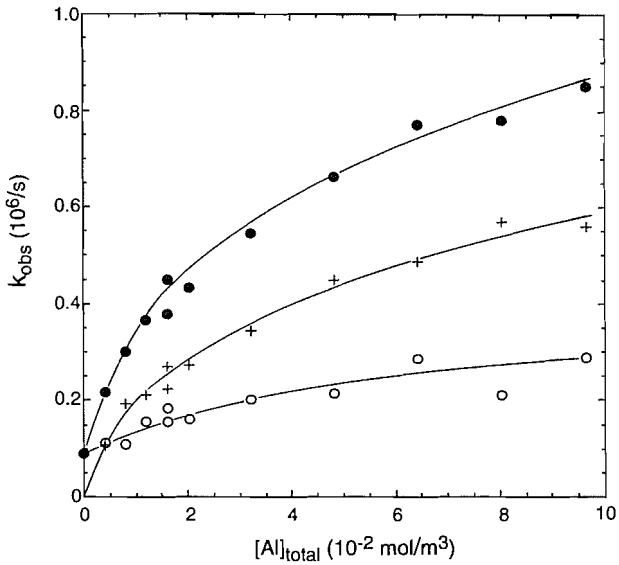

FIG. 15. k_{obs} of e_s^- reactions in $Al(ClO_4)_3$ aqueous solutions as a function of concentration of aluminum(III) added. ●, experimentally measured k_{obs}; +, 2.4×10^7 $[H_s^+]$, with $[H_s^+]$ from pH measurement; ○ ($k_{obs} - 2.4 \times 10^7[H^+]$).

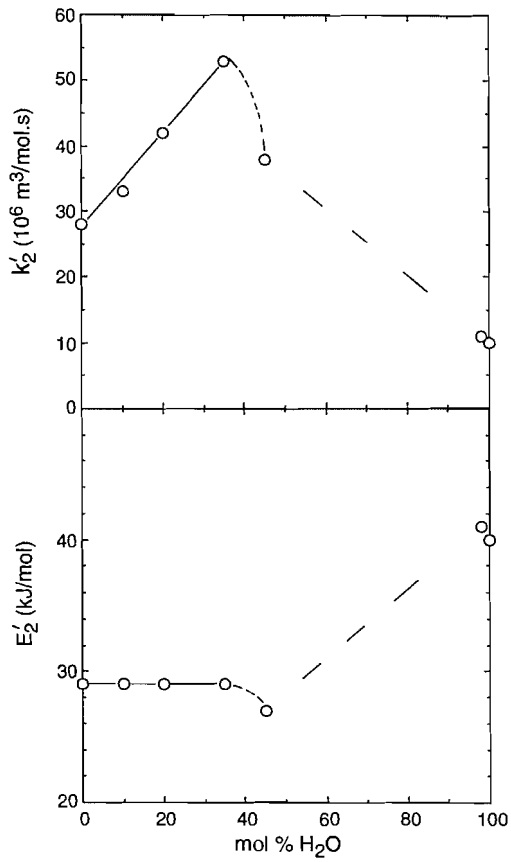

FIG. 16. Solvent composition dependences of rate constants k_2' and Arrhenius temperature coefficients E_2' for reaction of e_s^- in aluminum perchlorate solutions at 298 K. See text.

observed reaction rate could have been due to the $H_2PO_4^-$. We obtained $k_2(e_s^- + H_2PO_4^-) = 1.2 \times 10^4$ m^3/mol.s at $[H_2PO_4^-] = 72$ mol/m^3 and pH = 6.42 at 298 K, whereas Anbar and Hart (29*c*) reported 0.8×10^4 m^3/mol.s at $[H_2PO_4^-] = 100$ mol/m^3 and pH = 7.1 at room temperature.

We could not measure $[H_s^+]$ in the alcoholic solvents. Uncorrected values of k_2' obtained from plots of k_{obs} against added $[Al(ClO_4)_3]$ and the corresponding Arrhenius temperature coefficients E_2' are displayed against solvent composition in Fig. 16. The relatively low values of k_2' and high values of E_2' in pure water and 98 mol% water solvents indicate that the hydrolysis reactions, possibly [14] and [15], have activation energies of about 20 kJ/mol. The higher values of k_2' and lower E_2' in the isobutanol-rich solvents indicate that either the acid dissociation constants of the solvated Al_s^{3+} are higher in these solvents, or that the solvated ions themselves are more reactive with e_s^-.

Acknowledgements

We thank the Natural Sciences and Engineering Research Council for financial assistance, and the personnel of the Radiation Research Centre at the University of Alberta for aid with electronics and for maintaining the equipment.

1. (*a*) R. Chen and G.R. Freeman. Can. J. Chem. **71**, 1303 (1993); (*b*) T.B. Kang and G.R. Freeman. Can. J. Chem. **71**, 1297 (1993).
2. E.J. Hart and M. Anbar. The hydrated electron. Wiley-Interscience, New York. 1970.
3. (*a*) G.L. Bolton, M.G. Robinson, and G.R. Freeman. Can. J. Chem. **54**, 1177 (1976); (*b*) P. Han and D.M. Bartels. J. Phys. Chem. **96**, 4899 (1992).
4. R.A. Marcus. J. Chem. Phys. **24**, 966 (1956).
5. M.D. Newton and N. Sutin. Ann. Rev. Phys. Chem. **35**, 437 (1984).
6. P. Debye. Trans. Electrochem. Soc. **82**, 265 (1942).
7. J.M. Sorensen and W. Arlt. Liquid–liquid equilibrium data collection, DECHEMA Chem. Data Series. Frankfurt. 1979. p. 245.
8. P.C. Senanayake and G.R. Freeman. Can. J. Chem. **65**, 2441 (1987).
9. A.C. Brown and D.J.G. Ives. J. Chem. Soc. II. 1608 (1962).
10. A.J. Elliot, D.R. McCracken, G.V. Buxton, and N.D. Wood. J. Chem. Soc. Faraday Trans. **86**, 1539 (1990).
11. R.C. Weast (*Editor*). Handbook of chemistry and physics. 70th ed. CRC Press, Boca Raton, FL. 1989. p. D-190.
12. R.W. Gallant. Physical properties of hydrocarbons. Vol. 1. Gulf Publishing, Houston, TX. 1968.
13. (*a*) J. Barthel, K. Bachhuber, R. Buchner, and H. Hetzenauer. Chem. Phys. Lett. **165**, 369 (1990); (*b*) H. Sato, H. Nakamura, K. Itoh, and K. Higasi. Chem. Lett. Chem. Soc. Jpn. 1167 (1985); (*c*) F. Buckley and A.A. Maryott. Tables of dielectric dispersion data for pure liquids and diluted solutions. NBS Circular 589. Washington, D.C. 1958.
14. C.C. Lai and G.R. Freeman. J. Phys. Chem. **94**, 4891 (1990).
15. S.A. Peiris and G.R. Freeman. (*a*) Can. J. Phys. **68**, 940 (1990); (*b*) Can. J. Chem. **69**, 157 (1991).
16. P.W. Atkins. Physical chemistry. 4th ed. Freeman, New York. 1990. (*a*) pp. 763–766; (*b*) pp. 754–757; (*c*) p. 760.
17. K.H. Schmidt, P. Han, and D.M. Bartels. J. Phys. Chem. **96**, 199 (1992).
18. A.L. Horvath. Handbook of aqueous electrolyte solutions. Wiley, New York. 1985. pp. 262–263.
19. M. Anbar. Adv. Chem. Ser. **50**, 55 (1965).
20. K.N. Jha and G.R. Freeman. J. Chem. Phys. **48**, 5480 (1968).
21. P.C. Senanayake and G.R. Freeman. J. Phys. Chem. **91**, 2123 (1987).
22. Y. Maham and G.R. Freeman. Can. J. Chem. **66**, 1706 (1988).
23. B. Marongiu, I. Perino, R. Monaci, V. Solinas, and S. Torrazza. J. Mol. Liq. **28**, 229 (1984).
24. G.R. Freeman. *In* Kinetics of nonhomogeneous processes. *Edited by* G.R. Freeman. Wiley-Interscience, New York. 1987. p. 80.
25. J.P. Hunt. Metal ions in aqueous solution. Benjamin, New York. 1963. Chap. 4.

Can. J. Chem. Downloaded from www.nrcresearchpress.com by EESC ESCOLA DE ENGENHARIA on 09/08/12
For personal use only.

26. J. Bjerrum, G. Schwarzenbach, and L.G. Sillen. Stability constants of metal-ion complexes, with solubility products of inorganic substances. Part II: Inorganic ligands. Chemical Society, London. 1958. pp. 20–21; and references therein.
27. A.J. Rubin. Aqueous-environmental chemistry of metals. Ann Arbor Science Publishers, Ann Arbor, MI. 1976. Chap. 9.
28. C.R. Frink and M. Peech. Inorg. Chem. **2**, 473 (1963).
29. (*a*) M. Anbar and E.J. Hart. J. Phys. Chem. **69**, 973 (1965); (*b*) J.K. Thomas, S. Gordon, and E.J. Hart. J. Phys. Chem. **68**, 1524 (1964); (*c*) M. Anbar and E.J. Hart. Adv. Chem. Ser. **81**, 79 (1968).

Can. J. Chem. Downloaded from www.nrcresearchpress.com by EESC ESCOLA DE ENGENHARIA on 09/08/12
For personal use only.

Déplacements homolytiques intramoléculaires : 20. Influence de la nature de la fonction peroxyde sur la décomposition induite de peroxydes δ-insaturés

B. MAILLARD[1]

Laboratoire de chimie organique et organométallique, associé au Centre national de la recherche scientifique, Unité de recherche associée n° 35, Université Bordeaux I, 351 cours de la Libération, F-33405 Talence Cedex, France

ET

X. LUBEIGT, M-J. BOURGEOIS ET E. MONTAUDON[1]

Institut du Pin – Laboratoire de chimie appliquée, Université Bordeaux I, 351 cours de la Libération, F-33405 Talence Cedex, France

Reçu le 31 mars 1993

B. MAILLARD, X. LUBEIGT, M-J. BOURGEOIS et E. MONTAUDON. Can. J. Chem. **72**, 1094 (1994).

La décomposition des dérivés peroxydiques δ-insaturés CH_2=$CH(CH_2)_3OY$ (Y = O*t*Bu, $OCMe_2Ph$, OCOEt, $OCMe_2OMe$) dans divers solvants conduit à un hétérocycle et éventuellement un peroxyde adduit. La substitution homolytique intramoléculaire (S_Hi), responsable de la formation du cycle, dépend de la stabilité de la liaison O—Y. Celle-ci est déterminée par analyse calorimétrique différentielle des homologues saturés. Une estimation de la constante de vitesse de la S_Hi à 60°C est donnée pour Y = O*t*Bu, $OCMe_2Ph$.

B. MAILLARD, X. LUBEIGT, M-J. BOURGEOIS, and E. MONTAUDON. Can. J. Chem. **72**, 1094 (1994).

Induced decomposition of δ-unsaturated peroxidic derivatives CH_2=$CH(CH_2)_3OY$ (Y = O*t*Bu, $OCMe_2Ph$, OCOEt, $OCMe_2OMe$) in various solvents yields a heterocycle and, in some cases, a peroxidic adduct. Intramolecular homolytic substitution (S_Hi) leading to the cyclic ether is highly dependent on the thermal stability of the peroxidic linkage. The rate constant was determined at 60°C for Y = O*t*Bu, $OCMe_2Ph$.

Depuis plusieurs années notre recherche s'est développée dans la définition des paramètres gouvernant la décomposition induite des composés peroxydiques insaturés afin de permettre des applications synthétiques de ce type de réaction. Au cours de ce travail, nous avons observé une première fois (1) l'influence de la nature du groupe lié à l'atome d'oxygène sur la compétition existant après addition du radical Z à la double liaison de dérivés peroxydiques de l'acide hex-5-énoïque. Lorsque la réaction est effectuée dans le cyclohexane (ZH = C_6H_{12}), si Y est un groupe *tert*-butoxyle, le seul produit de la réaction est le perester, tandis que si Y est un groupe hex-5-énoyloxyle, seule la δ-lactone est formée (figure 1, $n = 3$).

Par ailleurs au cours de l'étude du mécanisme de décomposition induite du perpent-4-énoate de *tert*-butyle (2) nous avons été amenés à remplacer le groupe *tert*-butoxyle par d'autres (Y = CH_2Ph, OCOR, NR_2) qui paraissaient susceptibles d'être expulsés par attaque intramoléculaire du radical résultant de l'addition du radical Z sur la double liaison (figure 1, $n = 2$). Seuls le perester de *tert*-butyle (Y = O*t*Bu) et le peroxyde de diacyle (Y = OCOR) ont conduit à la formation de la γ-lactone résultant de la substitution homolytique intramoléculaire (S_Hi) du groupe Y.

Cet ensemble de résultats semblait indiquer que la S_Hi se fait d'autant plus facilement que la liaison O—Y est plus faible. Nous avons voulu analyser ce phénomène en étudiant le comportement de différents dérivés peroxydiques, issus de l'hydroperoxyde de pent-5-ényle, qui présentent des stabilités thermiques différentes. En effet, il existe une corrélation entre ce paramètre et la force de la liaison O—Y rompue au cours de l'homolyse. Les modèles choisis pour effectuer cette étude sont les suivants :

CH_2=$CH(CH_2)_3O$—O*t*Bu **1***a* CH_2=$CH(CH_2)_3O$—$OCMe_2Ph$ **1***b*

CH_2=$CH(CH_2)_3O$—OC(O)Et **1***c* CH_2=$CH(CH_2)_3O$—$OCMe_2OMe$ **1***d*

[1]Auteurs à qui adresser toute correspondance.

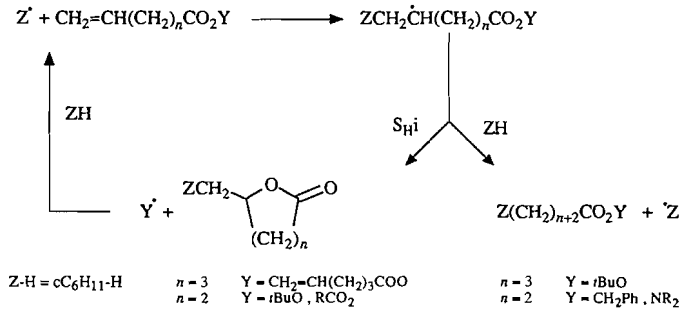

FIG. 1

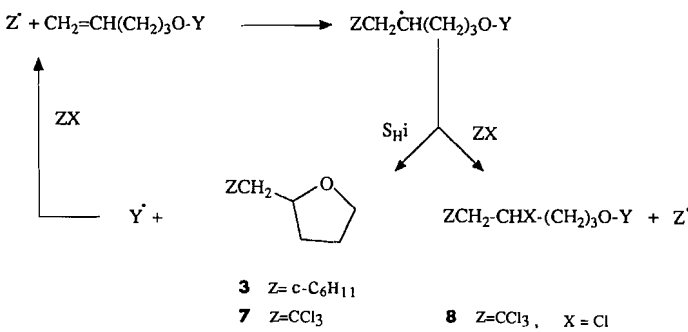

FIG. 2

Dans ces conditions, l'hétérocycle susceptible de se former sera le même dérivé tétrahydrofuranique (figure 2).

1. Définition des conditions de réaction

Les premières études ont été réalisées en utilisant le cyclohexane comme substrat ZH. Le rapport ZH/peroxyde a été fixé à 50/1, comme dans le travail relatif à la stéréochimie de la formation des tétrahydrofurane (3).

L'addition doit être réalisée à une température telle que la perte des composés peroxydiques **1** par thermolyse soit

Can. J. Chem. Downloaded from www.nrcresearchpress.com by ESC ESCOLA DE ENGENHARIA on 09/08/12
For personal use only.

TABLEAU 1. Addition radicalaire[a,b] du cyclohexane aux composés peroxydiques **1**

n°	Y	Peroxyde résiduel	**3**	**4**	**5**	**6**	Bilan
1*a*	O*t*Bu	10	70	9	4		93
1*b*	$OCMe_2Ph$	[c]	36	6	4		46
1*c*	OC(O)Et	7	40	8	4	30	89
1*d*	$OCMe_2OMe$	25	44	6	4		79

[a]Rapports molaires solvant/**1**/PDCE : 50/1/0,5; 60°C; 10 h.
[b]Rendements déterminés par CPG par rapport au peroxyde mis en jeu.
[c]**1***b* ne peut pas être mis en évidence dans nos conditions d'analyse.

minimisée, la réaction radicalaire étant déclenchée par la dégradation d'un amorceur annexe. Le choix de ce dernier dépend de la stabilité thermique des composés **1**. Une étude qualitative par DSC des composés saturés correspondants $CH_3(CH_2)_4O$—Y, **2**, en solution 0,1 mol/L dans le phtalate de dibutyle indique que la décomposition débute à 115°C pour **2***a* et **2***b*, 65°C pour **2***c* et 105°C pour **2***d*. Ceci montre que la stabilité de la liaison O—Y augmente dans le sens :

$$\underset{\mathbf{2}c}{\text{O—OCOEt}} < \underset{\mathbf{2}d}{\text{O—OCMe}_2\text{OMe}} < \underset{\mathbf{2}a}{\text{O—O}t\text{Bu}}, \underset{\mathbf{2}b}{\text{O—OCMe}_2\text{Ph}}$$

Nous avons donc choisi d'amorcer les additions radicalaires à 60°C par le perdicarbonate de diéthyle (PDCE). Des essais préliminaires ont montré que les meilleurs rendements en 2-cyclohexylméthyl tétrahydrofurane, **3**, (figure 2, Z—X = cC_6H_{11}—H) sont obtenus pour un rapport molaire PDCE/**1** = 0,5.

En conclusion, les conditions de réaction sont les suivantes : chauffage d'un mélange cyclohexane/**1**/PDCE (rapports molaires 50/1/0,5) à 60°C durant 10 h.

2. Addition de radicaux cyclohexyle

Les produits obtenus au cours des additions radicalaires du cyclohexane aux composés peroxydiques **1** sont présentés dans le tableau 1.

À côté de l'éther cyclique **3** dont la formation est décrite dans la figure 2 (Z = cC_6H_{11}), on identifie dans tous les cas : (*i*) l'éther de cyclohexyle et de pent-4-ényle, issu de l'attaque de la liaison O—O par le radical cyclohexyle (figure 3). Compte-tenu des faibles rendements d'obtention de ce produit, nous n'avons pas cherché les produits du type $C_6H_{11}Y$, qui pourraient se former de la même manière, d'autant plus que, dans les milieux réactionnels, tous les composés présents en quantités importantes ont été identifiés; (*ii*) le carbonate d'éthyle et de (2-tétrahydrofuryl) méthyle, **5**, formé par addition du radical éthoxycarbonyloxyle issu de l'amorceur au dérivé peroxydique **1** (figure 4).

Dans le cas particulier du perpropionate de pent-4-ényle, **1***c*, on observe la présence du 2-propyl tétrahydrofurane, **6**, formé par décomposition induite du perester par le radical éthyle (figure 5). Cette réaction, secondaire ici, peut présenter une excellente voie d'accès à des 2-alkyl tétrahydrofuranes.

La différence de comportement des radicaux éthoxycarbonyloxyle et propionyloxyle s'explique par une plus grande vitesse de décarboxylation de ces derniers (4, 5).

Notons que si le bilan en produits identifiés est compris

FIG. 3

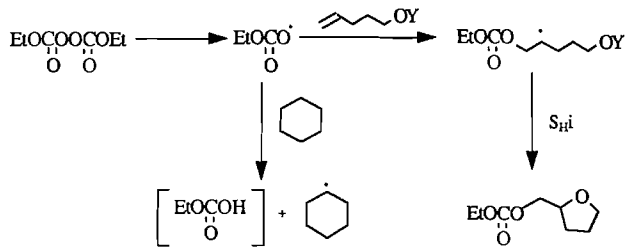

FIG. 4

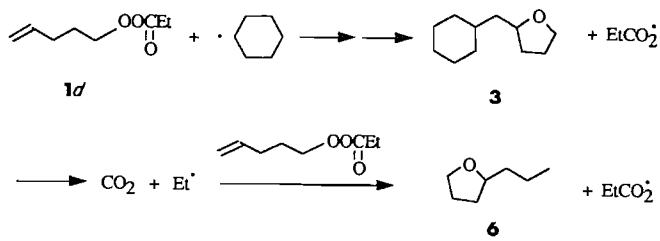

FIG. 5

entre 79 et 93% pour les peroxydes **1***a*, **1***c* et **1***d*, il est loin d'être complet pour le peroxyde **1***b*, même en considérant que le mélange réactionnel peut contenir du peroxyde initial.

Si l'on compare les rapports hétérocycles formés (**3** + **5** + **6**)/composé peroxydique consommé, le classement des aptitudes des divers composés peroxydiques insaturés à conduire à un éther cyclique est :

$$\underset{\mathbf{1}d}{\text{O—OCMe}_2\text{OMe}} < \underset{\mathbf{1}a}{\text{O—O}t\text{Bu}}, \underset{\mathbf{1}c}{\text{O—OCOEt}}$$

le peroxyde **1***b* ne pouvant être classé, puisqu'il n'est pas possible de savoir s'il a été totalement consommé. Il ne semble donc y avoir aucune corrélation entre ce classement et celui de la stabilité des liaisons O—O des composés peroxydiques saturés **2**, précédemment établi.

Cependant, ces conclusions peuvent traduire davantage l'intervention de nombreuses réactions secondaires que l'influence de la nature de la liaison O—O sur la réaction étudiée. C'est pourquoi, une autre méthodologie devra être développée.

Can. J. Chem. Downloaded from www.nrcresearchpress.com by EESC ESCOLA DE ENGENHARIA on 09/08/12
For personal use only.

Can. J. Chem. Downloaded from www.nrcresearchpress.com by EESC ESCOLA DE ENGENHARIA on 09/08/12
For personal use only.

3. Addition de radicaux trichlorométhyle

Une définition efficace de l'influence de la force de la liaison O—O sur la facilité de la S_Hi nécessite la recherche de conditions dans lesquelles il pourrait y avoir compétition entre la S_Hi et une réaction de transfert; cette dernière serait utilisée comme réaction étalon.

Le choix du milieu réactionnel pour cette étude doit être basé sur les remarques suivantes : (*i*) le radical Z doit s'additionner efficacement sur la double liaison; (*ii*) le radical Z doit avoir plusieurs sources ZX pour lesquelles la constante de vitesse de transfert de X à un radical alkyle secondaire est connue; ces composés doivent aussi transférer aisément l'atome X aux radicaux Y ou à ceux qui en découlent.

Les dérivés de type CCl_3—X satisfont à ces conditions. L'utilisation d'un précurseur des espèces trichlorométhyle plutôt qu'un autre, voire d'un mélange, permet d'obtenir des proportions relatives d'hétérocycle **7** et de peroxyde adduit **8** variables (figure 2, Z—X = CCl_3—X). En effet, les vitesses d'attaque du radical alkyle secondaire sur le dérivé halogéné devraient varier fortement selon la nature de l'atome X, si l'on se base sur les constantes de vitesse suivantes :

X = H $k_H = 2{,}54 \times 10^2\ M^{-1}\ s^{-1}$ (37°C) pour un radical *tert*-butyle (6)

X = Cl $k_{Cl} = 4{,}9 \times 10^4\ M^{-1}\ s^{-1}$ (37°C) pour un radical *tert*-butyle (6)

X = Cl $k_{Cl} = 1{,}9 \times 10^5\ M^{-1}\ s^{-1}$ (60°C) pour un radical cyclohexyle (7)

X = Br $\frac{k_{Br}}{k_{Cl}} = 1600$ pour un radical cyclohexyle (8)

soit $k_{Br} = 3 \times 10^8\ M^{-1}\ s^{-1}$ (60°C).

Les réactions sont réalisées comme indiqué dans la section 1, à savoir : chauffage à 60°C durant 10 h. Compte tenu de la nature des solvants et afin de piéger l'eau et les acides pouvant se former ou présents initialement, les décompositions sont effectuées, sous agitation, en présence de sulfate et de carbonate de sodium anhydres (9). Les rapports molaires solvant/peroxyde/PDCE/Na_2SO_4/Na_2CO_3 utilisés sont 50/1/0,5/0,1/0,2.

(a) Constantes de vitesse des S_Hi

Dans la mesure où l'hétérocycle **7** et le peroxyde adduit **8** sont stables dans les conditions de réaction et d'analyse, la détermination de leurs proportions relatives, à faible taux de conversion du peroxyde **1**, permet d'accéder à la constante de vitesse de la S_Hi.

En effet compte-tenu de la compétition étudiée (figure 2, Z—X = CCl_3—X), on peut écrire les équations cinétiques :

$$\frac{d[\mathbf{7}]}{dt} = k_{S_Hi}[R^\cdot]$$

$$\frac{d[\mathbf{8}]}{dt} = k_X[R^\cdot][CCl_3X]$$

soit après intégration :

$$\frac{[\mathbf{7}]}{[\mathbf{8}]} = \frac{k_{S_Hi}}{k_X}\,\frac{1}{[CCl_3X]}$$

ou $$k_{S_Hi} = k_X[CCl_3X]\,\frac{[\mathbf{7}]}{[\mathbf{8}]}$$

Peroxyde de tert*-butyle et de pent-4-ényle,* **1***a*

La décomposition de **1***a* dans CCl_4 conduit à un mélange hétérocycle–peroxyde adduit dans lequel l'hétérocycle est très minoritaire. L'utilisation d'un solvant tel que $CHCl_3$, dans lequel le transfert de X (H) est moins rapide, permet de favoriser la formation de ce dernier; mais dans ces conditions le peroxyde adduit n'est pas obtenu. Des réactions ont donc été réalisées, à l'échelle analytique, dans des mélanges $CHCl_3$/CCl_4 utilisés dans les rapports molaires : 90/10; 80/20; 70/30; 60/40; 50/50, contenant respectivement : 1,25; 2,4; 3,55; 4,6; 5,65 moles de CCl_4 par litre. Le peroxyde de *tert*-butyle et de 4,6,6,6-tétrachlorohexyle, **8***a*, et le 2-(2,2,2-trichloroéthyl) tétrahydrofurane, **7**, sont dosés par CPG; la validité du dosage est testée par l'analyse de mélanges synthétiques de mêmes compositions. Les résultats sont rassemblés dans la figure 6.

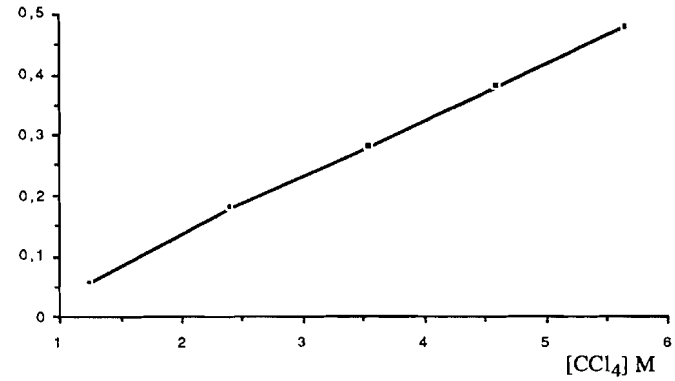

FIG. 6. Effet de la concentration en CCl_4 sur la distribution des produits de réaction.

Compte-tenu de l'équation cinétique précédemment établie, la pente de la droite $[\mathbf{8}a]/[\mathbf{7}] = f([CCl_4])$ représente le rapport k_{Cl}/k_{S_Hi}. Des valeurs expérimentale ($k_{Cl}/k_{S_Hi} = 0{,}08$) et bibliographique (7) ($k_{Cl} = 1{,}9 \times 10^5\ M^{-1}\ s^{-1}$ pour un radical alkyle secondaire à 60°C), on peut déduire : $k_{S_Hi} = 2{,}4 \times 10^6\ s^{-1}$. Notons que les résultats obtenus lors de l'addition de CCl_4 à **1***a* (10) nous avaient conduits à une estimation de l'ordre de $10^6\ s^{-1}$, à 110°C.

Peroxyde de cumyle et de pent-4-ényle, **1**b

Contrairement au cas précédent, la détection en CPG du peroxyde adduit **8***b*, de masse moléculaire plus élevée, est impossible. Une estimation de la constante de vitesse de la S_Hi a alors été réalisée à partir des produits isolés. La décomposition de **1***b* dans CCl_4 conduit, après chromatographie liquide–solide, à 25% d'hétérocycle **7** et 15% de peroxyde de cumyle et de 4,6,6,6-tétrachlorohexyle, **8***b*. Dans l'hypothèse où ces deux composés ont été totalement récupérés, on estime $k_{S_Hi} \sim 3 \times 10^6\ s^{-1}$.

Can. J. Chem. Downloaded from www.nrcresearchpress.com by EESC ESCOLA DE ENGENHARIA on 09/08/12
For personal use only.

TABLEAU 2. Addition radicalaire[a] de solvants polyhalogénés aux composés peroxydiques **1**

n°	Y	7 Rdt (%)[b]	Solvant CCl_4	Solvant $BrCCl_3$
1*a*	O*t*Bu	<2	99	1
1*b*	$OCMe_2Ph$	<2	99	1
1*c*	OC(O)Et	6	0	100
1*d*	$OCMe_2OMe$	<2	90	10

[a]Rapports molaires solvant/**1**/PDCE/Na_2SO_4/Na_2CO_3 : 50/1/0,5/0,1/0,2; 60°C : 10 h.
[b]Présence décelée par CPG (limite de détection de **7**, ~2%).

Perpropionate de pent-4-ényle, **1***c, et peroxyde de (1-méthoxy-1-méthyl) éthyle et de pent-4-ényle,* **1***d*

Les peroxydes adduits **8***c* et **8***d*, beaucoup plus fragiles que leurs homologues **8***a* et **8***b* (cf. peroxydes saturés dans section 1), n'ayant pu être préparés en raison de leur instabilité, il n'a pas été possible de les identifier lors des décompositions de **1***c* et **1***d*. Par conséquent une estimation de la constante de vitesse de la substitution homolytique ne peut être donnée.

(b) Classement des réactions de S_Hi en fonction des groupes Y

S'il ne nous est pas possible pour tous les composés peroxydiques **1** de déterminer la quantité de peroxyde adduit formé, il devrait être relativement facile de définir à partir de quelles proportions et de quel mélange de solvants précurseurs de radicaux $^{\cdot}CCl_3$ la réaction de S_Hi n'a plus lieu, en suivant la disparition de **7**.

Les réactions ont tout d'abord été effectuées dans le tétrachlorure de carbone afin de situer la réaction de S_Hi relativement au transfert. Dans ce solvant, **7** est identifié dans tous les cas. Afin de favoriser l'étape de transfert, des quantités croissantes de $BrCCl_3$ ont été ajoutées au CCl_4. Les proportions limites des deux solvants halogénés permettant d'éliminer la formation de **7** ont pu être définies (tableau 2).

Les résultats de cette étude montrent que la facilité de la S_Hi évolue donc dans le sens :

$$\underset{\mathbf{1}a}{O\text{—}OtBu},\ \underset{\mathbf{1}b}{O\text{—}OCMe_2Ph},\ <\ \underset{\mathbf{1}d}{O\text{—}OCMe_2OMe}\ <\ \underset{\mathbf{1}c}{O\text{—}OCOEt}$$

Si l'on compare ce classement à celui des stabilités des composés peroxydiques saturés correspondant, on observe une bonne concordance générale. Toutefois, ces résultats doivent être considérés avec une certaine précaution en raison de l'absence de bilans réactionnels au cours des analyses.

Conclusion

Cette étude a permis de montrer que le classement des composés peroxydiques vis à vis de la S_Hi :

$$O\text{—}OtBu,\ O\text{—}OCMe_2Ph,\ <\ O\text{—}OCMe_2OMe\ <\ O\text{—}OCOEt$$

semble suivre l'ordre inverse de stabilité des fonctions peroxydiques :

$$O\text{—}OCOEt\ <\ O\text{—}OCMe_2OMe\ <\ O\text{—}OtBu,\ O\text{—}OCMe_2Ph$$

Une estimation de la constante de vitesse de la S_Hi ($\sim 10^6$ s^{-1} à 60°C) n'a été possible qu'à partir de **1***a* et **1***b*, du fait de l'instabilité des peroxydes adduits susceptibles de se former dans les autres cas.

Partie expérimentale

Techniques analytiques

L'analyse des produits de réaction par chromatographie en phase gazeuse a été effectuée sur les appareils suivants : Intersmat IGC 112 F (ionisation de flamme, gaz vecteur : azote), équipé de colonnes en acier inox de 2 mm de diamètre intérieur : OV 17 (10% sur Chromosorb W HP, 80/100 mesh, longueur 1,5 m), FFAP (10% sur Chromosorb W AW, 80/100 mesh, longueur 2 m) et Carbowax 20 M (5% sur Chromosorb W DMCS, 80/10 mesh, longueur 3 m); Delsi DI 200 (ionisation de flamme, gaz vecteur : azote), équipé de colonnes capillaires en silice fondue : CP Sil 5 CB (longueur 25 m, diamètre intérieur 0,32 mm) et BP 20 (longueur 25 m, diamètre intérieur 0,22 mm). Ces appareils sont associés à un intégrateur Intersmat 1CR-1B donnant les temps de rétention et les surfaces des pics. Les dosages ont été effectués par la méthode de l'étalon interne.

Les spectres RMN ^1H ont été enregistrés sur des appareils Perkin–Elmer R 24B fonctionnant à 60 MHz et Bruker AC 250 fonctionnant à 250 MHz. Tous les composés étudiés sont en solution dans le tétrachlorure de carbone, en présence de TMS ou de benzène comme référence interne. Les spectres RMN ^{13}C ont été enregistrés dans des solutions de chloroforme deutéré sur un appareil Bruker AC 250 fonctionnant à 62,9 MHz.

Les spectres de masse ont été réalisés sur un spectromètre à simple focalisation VG Micromass 16F, couplé avec un chromatographe en phase gazeuse Intersmat IGC 121M.

Techniques réactionnelles

Les réactions sont effectuées par chauffage à 60°C, durant 10 h, de mélanges constitués par le solvant, le composé peroxydique et l'amorceur (perdicarbonate de diéthyle, PDCE) dans les rapports molaires 50/1/0,5. Lorsqu'il s'agit de solvants halogénés, du sulfate et du carbonate de sodium sont ajoutés dans les rapports molaires 0,1/0,2, et le milieu réactionnel est agité magnétiquement. Les conditions propres à chaque expérience sont rappelées dans les tableaux de la partie théorique.

(a) Études analytiques : 2 cm^3 de solution sont introduits dans une ampoule de 10 cm^3. Celle-ci, fermée hermétiquement, est placée sur un agitateur magnétique chauffant équipé d'un bain d'huile thermostaté. Les rendements sont déterminés par CPG directement sur le mélange réactionnel selon la méthode de l'étalon interne.

(b) Études préparatives : 90 cm^3 de solution sont introduits dans un autoclave en acier de 125 cm^3 que l'on place dans une étuve préalablement chauffée à 60°C ou sur un agitateur magnétique chauffant équipé d'un bain d'huile thermostaté. Après élimination du solvant, les hétérocycles sont isolés par distillation (appareil classique ou microfour tubulaire). Les peroxydes adduits sont isolés par chromatographie liquide–solide sur gel de silice. Les structures sont déterminées par les techniques spectroscopiques habituelles.

Matières premières

(a) Amorceur

Le *perdicarbonate de diéthyle* est synthétisé selon la référence 11.

(b) Peroxydes de dialkyle

Ils sont préparés à partir du 5-bromopent-1-ène (12) ou du 1-bromopentane et des hydroperoxydes de *tert*-butyle ou de cumyle selon la référence 13. *Peroxyde de* tert*-butyle et de pent-4-ényle,* **1***a* : décrit dans la référence 10. *Peroxyde de cumyle et de pent-4-ényle,* **1***b* : purifié sur silice; Rdt = 75%; n_D^{20} = 1,4975. RMN ^1H (ppm) : 7,7–6,9, m, 5H (H Ar); 6,2–4,6, m, 3H (CH_2=CH); 3,8, t (J = 8 Hz), 2H (CH_2O); 2,3–1,6, m, 4H (CH_2CH_2); 1,5, s, 6H ($(CH_3)_2C$). *Peroxyde de* tert*-butyle et de pentyle,* **2***a* : décrit dans la référence 13. *Peroxyde de cumyle et de pentyle,* **2***b* : purifié sur silice; Rdt = 65%; n_D^{20} = 1,4868. RMN ^1H (ppm) : 7,6–6,9, m, 5H (H Ar); 3,8, t (J = 8 Hz), 2H (CH_2O); 2,3–0,9, m, 15H (autres H). Litt. (14) $Eb_{0,01}$ = 46–47°C.

Can. J. Chem. Downloaded from www.nrcresearchpress.com by EESC ESCOLA DE ENGENHARIA on 09/08/12
For personal use only.

(c) Peresters

Ils sont synthétisés selon la référence 15 à partir du chlorure de propanoyle et des hydroperoxydes correspondants, eux-mêmes préparés selon la référence 16 à partir du pent-4-én-1-ol (17) et du pentanol, via leur mésylate (18). *Perpropionate de pent-4-ényle,* **1***c* : purifié sur silice; Rdt = 58%; n_D^{20} = 1,4300. RMN ^{1}H (ppm) : 6,1–4,7, m, 3H (CH_2=CH); 4,1, t (J = 8 Hz), 2H (CH_2O); 2,6–1,6, m, 6H (autres CH_2); 1,1, t (J = 8 Hz), 3H (CH_3). *Perpropionate de pentyle,* **2***c* : purifié sur silice; Rdt = 63%; n_D^{20} = 1,4158. RMN ^{1}H (ppm) : 4,1, t (J = 8 Hz), 2H (CH_2O); 2,3, q (J = 8 Hz), 2H (CH_2CH_3); 2–0,8, m, 12H (autres H).

(d) Peroxycétals

Ils sont préparés selon la référence 19 à partir de 2-méthoxypropène et des hydroperoxydes correspondants en milieu acide. *Peroxyde de (1-méthoxy-1-méthyl) éthyle et de pent-4-ényle,* **1***d* : Rdt = 60%; n_D^{20} = 1,4275; Eb_5 = 48°C. RMN ^{1}H (ppm) : 6,2–4,7, m, 3H (CH_2=CH); 3,9, t (J = 8 Hz), 2H (CH_2O); 3,1, s, 3H (CH_3O); 2,5–1,3, m, 4H (CH_2CH_2); 1,25, s, 6H (($CH_3)_2C$). *Peroxyde de (1-méthoxy-1-méthyl) éthyle et de pentyle,* **2***d* : Rdt = 48%; n_D^{20} = 1,4116; Eb_{10} = 61°C. RMN ^{1}H (ppm) : 3,9, t (J = 8 Hz), 2H (CH_2O); 3,2, s, 3H (CH_3O); 1,8–0,8, m, 9H (autres H); 1,25, s, 6H (($CH_3)_2C$).

Produits de réactions

2-Cyclohexylméthyl tétrahydrofurane, ***3*** : n_D^{20} = 1,4721; $Eb_{0,35}$ = 77°C (litt. (20) $Eb_{0,1}$ = 45°C). RMN ^{1}H (ppm) : 4,2–3,5, m, 3H (H en α de O); 2,25–1, m, 17H (autres H). Principaux pics du spectre de masse (*m/z*, abondance) : 41 (35); 43 (30); 55 (21); 71 (100).

Ether de cyclohexyle et de pent-4-ényle, ***4*** : un échantillon de référence a été synthétisé selon la référence 21 : Une solution de 0,05 mol de cyclohexanol dans son volume de HMPT est additionnée goutte à goutte à 0,05 mol de NaH recouvert de HMPT. Un fort dégagement gazeux se produit. À la fin de celui-ci, on ajoute 0,05 mol de 5-bromopent-1-ène en solution dans son volume de HMPT, puis le milieu réactionnel est chauffé 3 h à 70°C. Après refroidissement, la solution est versée sur la glace, puis acidifiée avec HCl 10%. La phase organique est extraite à l'éther, lavée à l'eau jusqu'à neutralité puis séchée sur sulfate de sodium anhydre. Après élimination du solvant, l'éther obtenu est purifié par distillation; Rdt = 35%; n_D^{20} = 1,4511; Eb_3 = 104°C. RMN ^{1}H (ppm) : 6,1–4,7, m, 3H (CH_2=CH); 4–3,7, m, 3H (H en α de O); 2,1–1, m, 14H (autres H). Principaux pics du spectre de masse (*m/z*, abondance) : 41 (38); 44 (32); 57 (100); 67 (25); 82 (52).

Carbonate d'éthyle et de (2-tétrahydrofuryl) méthyle, ***5*** : un échantillon de référence a été synthétisé : 0,056 mol de chloroformiate d'éthyle diluée dans 5 cm^3 d'éther est additionnée, goutte à goutte, à une solution comprenant 0,05 mol de 2-tétrahydrofuryl méthanol, 0,056 mol de pyridine et 20 cm^3 d'éther, maintenue à 0°C. La réaction est poursuivie 2 h après la fin de l'addition, puis le mélange réactionnel est filtré et le solvant éliminé par évaporation. Le carbonate cyclique est distillé; Rdt = 80% n_D^{20} = 1,4320; $Eb_{0,3}$ = 90°C. RMN ^{1}H (ppm) : 4,4–3,2, m, 7H (H en α de O); 3,2–1,6, m, 4H (CH_2CH_2); 1,3, t, (J = 8 Hz) 3H(CH_3). Principaux pics du spectre de masse (*m/z*, abondance) : 28 (30); 43 (28); 71 (100).

2-Propyl tétrahydrofurane, ***6*** : un échantillon de référence a été synthétisé : 0,14 mol de propène est dissoute dans une solution de 2,8 mol de THF et 0,008 mol de peroxyde de di-*tert*-butyle. Cette préparation introduite dans un autoclave en acier est mise à réagir durant 10 h à 140°C. Le propyl tétrahydrofurane est isolé par distillation; n_D^{20} = 1,4220; Eb_{80} = 95°C. (litt. (22) Eb_{773} = 135°C).

2-(2,2,2-Trichloroéthyl)-tétrahydrofurane, ***7*** (10) : n_D^{20} = 1,4919; $Eb_{0,3}$ = 54°C. RMN ^{1}H (ppm) : 4,3–3,5, m, 3H (CH_2OCH); 2,6–1,3, m, 6H (autres CH_2). Principaux pics du spectre de masse (*m/z*, abondance) : 27 (20); 29 (18); 39 (18); 41 (33); 42 (21); 43 (35); 71 (100).

Peroxyde de tert*-butyle et de 4,6,6,6-tétrachlorohexyle,* ***8***a (10) : n_D^{20} = 1,4719. RMN ^{1}H (ppm) : 4,7–3,7, m, 3H (CHCl, CH_2O); 3,3–3,1, m, 2H (CH_2CCl_3); 2,3, 1,3, m, 4H (CH_2CH_2); 1,2, s, 9H (*t*Bu).

Peroxyde de cumyle et de 4,6,6,6-tétrachlorohexyle, ***8***b : n_D^{20} = 1,5225. RMN ^{1}H (ppm) : 7,5–7, m, 5H (H Ar); 4,2–3,5, m, 3H (CHCl, CH_2O); 3,3–3, m, 2H (CH_2CCl_3); 2–1,5, m, 4H (CH_2CH_2); 1,5, s, 6H (2 CH_3).

1. B. Maillard, A. Kharrat et C. Gardrat. Nouv. J. Chim. **10**, 259 (1986).
2. B. Maillard, A. Kharrat et C. Gardrat. Nouv. J. Chim. **11**, 7 (1987).
3. E. Montaudon, X. Lubeigt et B. Maillard. J. Chem. Soc. Perkin Trans. 1, 1531 (1991).
4. J. Chateauneuf, J. Lusztyk, B. Maillard et K.U. Ingold. J. Am. Chem. Soc. **110**, 6727 (1988).
5. R. Kaptein. Advances in free radical chemistry. Vol. 5. *Édité par* G.H. Williams. Elech Science, Londres. Chap. 5, pp. 346, 1 et 75.
6. M.G. Katz, A. Horowitz et L.A. Rajenbach. Int. J. Chem. Kinet. **7**, 183 (1975).
7. P.G. Frith et K.A. McLauglan. J. Chem. Soc. Faraday Trans. 2, 87 (1976)
8. B. Giese et K. Keller. Chem. Ber. **112**, 1743 (1979).
9. E. Montaudon et R. Kappes. Bull. Soc. Chim. Fr. Sous presse.
10. M.J. Bourgeois, B. Maillard et E. Montaudon. Tetrahedron, **42**, 5309 (1986).
11. F. Strain, W.E. Bissinger, W.R. Dial, H. Rudoff, B.J. De Witt, H.C. Stevens et J.H. Langston. J. Am. Chem. Soc. **72**, 1254 (1950).
12. G.A. Kraus et K. Landgrebe. Synthesis, 885 (1984).
13. M.J. Bourgeois, E. Montaudon et B. Maillard. Synthesis, 700 (1989).
14. V.V. Federova, A.T. Menyailo, T.G. Narozhenko et N.F. Sarafanova Izv. Vyssh. Uchebn. Zaved. Khim. Teknol. **13**, 1308 (1970); Chem. Abstr. **74**, 42067 (1971).
15. N.A. Milas et D.M. Surgenor. J. Am. Chem. Soc. **68**, 642 (1946).
16. S. Dykstra et H.S. Mosher. J. Am. Chem. Soc. **79**, 3474 (1957).
17. L.A. Brooks et H.R. Snyder. Org. Synth. **25**, 84 (1945).
18. A. Sekera et C.S. Marvel. J. Am. Chem. Soc. **55**, 345 (1933).
19. E.S. Huyser et D.E. Ordway. J. Org. Chem. **44**, 777 (1979).
20. M. Agorrody, E. Montaudon et B. Maillard. Can. J. Chem. **65**, 2694 (1987); E.E. Schweizer, W.S. Creasy, K.K. Light et E.T. Shaffer. J. Org. Chem. **34**, 212 (1969).
21. H. Normant et Y.T. Cuvigny. Bull. Soc. Chim. Fr. 1866 (1965).
22. R. Paul. Bull. Soc. Chim. Fr. **5**, 1053 (1938); E. Montaudon, J. Thépénier et R. Lalande. J. Heterocycl. Chem. **16**, 113 (1979).

Rate constants for cyanate hydrolysis to urea: A Raman study

NANPING WEN AND MURRAY H. BROOKER[1]

Chemistry Department, Memorial University of Newfoundland, St. John's, NF A1B 3X7, Canada

Received September 1, 1992[2]

NANPING WEN and MURRAY H. BROOKER. Can. J. Chem. **72**, 1099 (1994).

Raman spectra of aqueous solutions of potassium cyanate have been obtained at suitable time intervals. It was found that the peaks attributed to cyanate became less intense, while the peaks attributed to urea, carbamate and carbonate, centred at 1003, 1034, and 1065 cm^{-1}, respectively, enhanced greatly with the passage of time. Further Raman spectroscopic studies revealed that the cyanate ion hydrolysed slowly and spontaneously at room temperature. Urea, carbamate, and carbonate were formed even without additional ammonium. Raman intensity measurements were used to monitor species concentrations as a function of time. The results suggested a complicated hydrolysis process: the hydrolysis of cyanate ion to form carbonate and ammonium, a rearrangement type reaction of aqueous cyanate ion with aqueous ammonium to formed urea, and an equilibrium reaction of carbonate and ammonium to form carbamate. The initial hydrolysis of cyanate with pure water was found to be first order with rate constant $k_1 = (2.67 \pm 0.53) \times 10^{-4}$ min^{-1} at 22°C. The reaction of cyanate with aqueous ammonium was found to be second order with rate constant $k_2 = (4.64 \pm 0.93) \times 10^{-4}$ $mol^{-1} \cdot L \cdot min^{-1}$. The equilibrium reaction of carbonate and ammonium to form carbamate was very fast. Urea and carbamate were formed in parallel reactions. It was not possible to convert urea to carbamate or carbamate to urea at room temperature.

NANPING WEN et MURRAY H. BROOKER. Can. J. Chem. **72**, 1099 (1994).

On a déterminé les spectres Raman de solutions aqueuses de cyanate de potassium à divers intervalles de temps. On a trouvé que l'intensité des raies d'absorption attribuées au cyanate diminuent avec le temps alors que celles des raies dues à l'urée, au carbamate et au carbonate, centrées respectivement à 1003, 1034 et 1065 cm^{-1}, augmentent considérablement avec le temps. D'autres études par spectroscopie Raman ont révélé que, à la température ambiante, l'ion cyanate s'hydrolyse lentement et spontanément. Il y a formation d'urée, de carbamate et de carbonate, même sans addition d'ion ammonium supplémentaire. On a utilisé des mesures d'intensité en Raman pour déterminer d'une façon quantitative les concentrations des diverses espèces en fonction du temps. Les résultats suggèrent l'existence d'un processus d'hydrolyse compliqué; l'hydrolyse de l'ion cyanate pour former du carbonate et de l'ammonium, une réaction ressemblant à un réarrangement de l'ion cyanate aqueux avec de l'ammonium aqueux conduisant à de l'urée et une réaction d'équilibre du carbonate et de l'ammonium pour former du carbamate. On a trouvé que l'hydrolyse initiale du cyanate dans l'eau pure est du premier ordre avec une constante de vitesse de $k_1 = (2{,}67 \pm 0{,}53) \times 10^{-4}$ min^{-1}, à 22°C. On a trouvé que la réaction du cyanate avec l'ammonium aqueux est du deuxième ordre, avec une constante de vitesse $k_2 = (4{,}64 \pm 0{,}93) \times 10^{-4}$ $mol^{-1} \cdot L \cdot min^{-1}$. La réaction d'équilibre du carbonate et de l'ammonium pour former du carbamate est très rapide. L'urée et le carbonate se forment par des réactions parallèles. À la température ambiante, il n'a pas été possible de transformer de l'urée en carbamate ou du carbamate en urée.

[Traduit par la Rédaction]

1. Introduction

Wöhler (1) first synthesised urea in 1828 by evaporation to dryness a mixture of aqueous ammonium sulphate and potassium cyanate. It has long been supposed that the ammonium cyanate produced in the metathesis reaction rearranged into urea although the mechanism has been the subject of much debate (2). As part of a comprehensive study (3) of aqueous solutions of small molecules which contain N, C, O, and H the Raman spectrum KOCN has been measured for the aged aqueous phase. A full account of band assignments, Fermi resonance, and hydration of aqueous cyanate has been presented elsewhere (3, 4).

Several previous studies (5, 6) indicated that the spectrum of the potassium cyanate aqueous solution changed with the passage of time. After aqueous cyanate had stood a few days, new peaks were observed. Williams (5) and Cleveland (6) have reported evidence of cyanate hydrolysis and assigned the new peaks to ammonium, carbonate, and bicarbonate ions formed by hydrolysis reactions ([1] and [2]).

[1] $$KOCN + 3H_2O \rightarrow KHCO_3 + NH_4OH$$

[2] $$2KOCN + 4H_2O \rightarrow K_2CO_3 + (NH_4)_2CO_3$$

However, the present study on aged aqueous potassium cyanate revealed the presence of urea, carbamate, and carbonate formed by hydrolysis (reaction [3]). Urea was formed even in the absence of additional ammonium.

[3] $$3OCN^- + 3H_2O \rightarrow H_2NCOO^- + H_2NCONH_2 + CO_3^{2-}$$

There was no evidence to suggest the presence of bicarbonate or ammonium ions in the aged solutions although small quantities of these ions would be expected since aqueous carbamate has been shown to exist in equilibrium with ammonium, carbonate, and bicarbonate (3, 7). Addition of potassium cyanate to aqueous ammonium chloride resulted in a much greater yield in urea.

2. Experimental

The spectroscopic measurements were carried out on a Coderg PHO Raman spectrometer after sample excitation with a INNOVA 70-4 argon ion laser operating at approximately 1300 mW output in the 488.0 nm wavelength line. The usual right angle scattering geometry was employed with the incident light vertically polarized and the scattered light analyzed with polaroid film to give the $I_{\parallel}[x(zz)y]$ and $I_{\perp}[x(zx)y]$ scattering geometries. A quarter-wave plate before the entrance slit served to compensate for the grating polarization preference. Raman wavenumber calibration was achieved with the plasma lines of the laser, but when required a narrow-bandpass interference filter was used to remove the unwanted plasma lines. The spectral slit widths of the double monochromator were set at 2.0 cm^{-1}, which is sufficiently narrow to avoid the need for a slit correction to the band-shape. The Raman scattering light was detected with a PMT cooled to −30°C, integrated with a photon counter and processed with a

[1]To whom correspondence should be addressed.

[2]Revision received October 22, 1993.

Can. J. Chem. Downloaded from www.nrcresearchpress.com by EESC ESCOLA DE ENGENHARIA on 09/08/12
For personal use only.

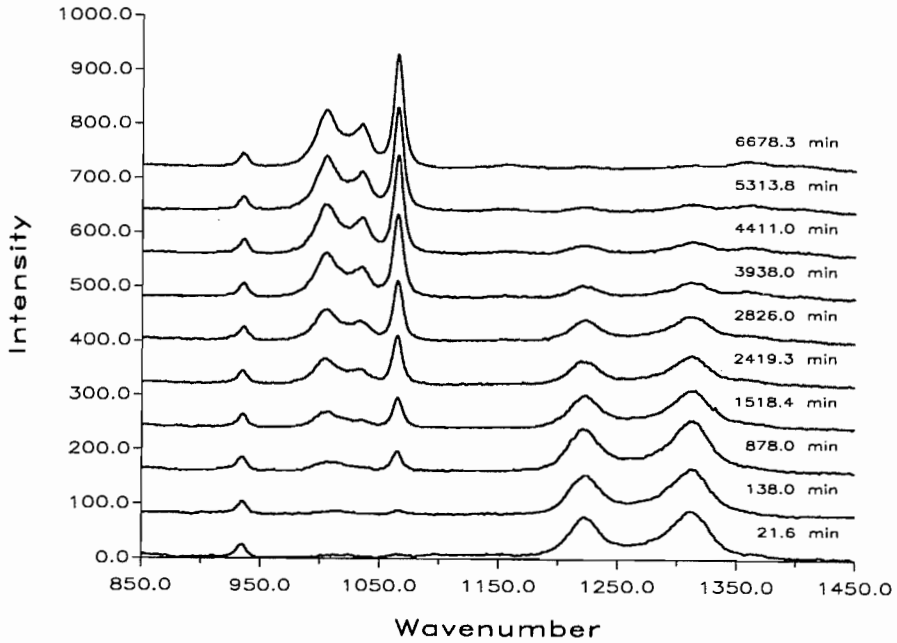

FIG. 1. Raman spectra of 2.48 mol·L^{-1} KOCN at 22°C at different times. A 0.0500 mol·L^{-1} concentration of ClO_4^- has been added as an internal intensity standard.

home-built box-car averager interfaced to the Memorial University VAX 8800 computer. The scan rate was 50 cm^{-1} min^{-1} and two data points were collected per wavenumber. Spectra were smoothed twice with a Savitsky–Golay three-point smoothing function. Curve resolution of overlapped bands and calculations of band half-width and intensity were achieved with a standard computer fitting program CURVEFIT originally developed by Pitha and Jones (8–10) for infrared spectroscopy and subsequently modified by Brooker and Rice (11) for Raman spectroscopy (BASIC language, VAX/VMS version).

All chemicals were reagent grade used without further purification. Potassium cyanate was obtained from BDH Chemical Ltd. Aqueous solutions were prepared with distilled water. The aqueous solutions of potassium cyanate contained a measured amount of $NaClO_4$ (0.0500 mol·L^{-1}) and the 935 cm^{-1} band of ClO_4^- was used as an internal intensity standard for the quantitative study. Samples were sealed-off in quartz tubing (4 mm in outsider diameter and approximately 15 cm in length) under their own vapour pressure to avoid loss of ammonia and carbon dioxide gases which are decomposition products of carbamic acid. The aqueous samples were routinely centrifuged for 5 min to settle dust particles. The Raman spectra of the fresh aqueous solutions were obtained immediately. Samples were then stored in a lightproof place. Additional Raman studies were made after suitable intervals. No special effort was made to control the temperatures of the samples for such long time periods; however the samples were measured and stored in a room at a well-controlled ambient temperature of 22 ± 0.5°C.

3. Results and discussion

Hydrolysis of cyanate to urea

The Raman spectrum of aqueous potassium cyanate solutions changed considerably with the passage of time (Fig. 1). In the spectrum of a freshly prepared potassium cyanate aqeuous solution intense bands appeared at 1223 and 1310 cm^{-1} due to $2\nu_2$ and ν_1 in Fermi resonance (3, 4). Several hours after the solution was prepared the bands centred at 1223 and 1310 cm^{-1} became less intense, while the new bands appearing at 1003, 1034, and 1065 cm^{-1} greatly increased in intensity with the passage of time. After about 10 days the intensities of the new bands reached a maximum and the bands due to cyanate were no longer detectable. As an aid to the assignments the Raman spectra between 300 and 2300 cm^{-1} of a 2.0 mol·L^{-1} potassium cyanate solution aged in ordinary aqueous solution (curve *a*) and aged in deuterium aqueous solution (curve *b*) were measured (Fig. 2).

Williams (5) and Cleveland (6) suggested that the new bands in the spectrum of potassium cyanate aged in ordinary aqueous solution arose from the carbonate, bicarbonate, and ammonium, which were formed by hydrolysis of potassium cyanate (reactions [1] and [2]). There can be no doubt that the band at 1065 cm^{-1} is due to the $\nu_1(A_1')$, CO_3^{2-} symmetric stretch. However, there was no evidence to suggest the presence of peaks due to bicarbonate or ammonium as suggested by Williams and Cleveland. The characteristic peaks for bicarbonate (12) and ammonium (13) are at 1017, $\nu_5(A')$, the C—OH stretching of bicarbonate ion, and 1450 cm^{-1}, the N—H antisymmetric stretching, $\nu_3(F_2)$, of ammonium ion, respectively. It was possible to identify the urea and carbamate ion as the source of the peaks at 1003 and 1034 cm^{-1} by comparison with spectra of known samples. The urea assignments were confirmed by the presence of bands due to $(ND_2)_2CO$ at 991 and 889 cm^{-1} in the spectrum (Fig. 2) of the sample hydrolysed in D_2O. These assignments were in excellent agreement with the results obtained by Yamaguchi et al. (14) for pure urea-d_4. Although the band due to carbamate-h_2 was identified in the spectrum of the KOCN hydrolysed in H_2O, a comparable band due to carbamate-d_2 was not detected for KOCN dissolved in D_2O. The difference between the present results and those of Cleveland and Williams can be accounted for by the experimental differences in the sample control. In the present work the samples were maintained in sealed tubes which did not allow ammonia gas to escape. An aged sample (sealed) of 2.0 mol·L^{-1} potassium cyanate aqueous solution had a pH value of about 10 when hydrolysis was complete. At this pH there should be a considerable amount of ammonia but because of the presence of carbonate an equilibrium reaction resulted and carbamate was formed. If the solution were exposed to atmosphere the carbamate solution would lose ammonia slowly and would become more acidic.

Can. J. Chem. Downloaded from www.nrcresearchpress.com by ESC ESCOLA DE ENGENHARIA on 09/08/12
For personal use only.

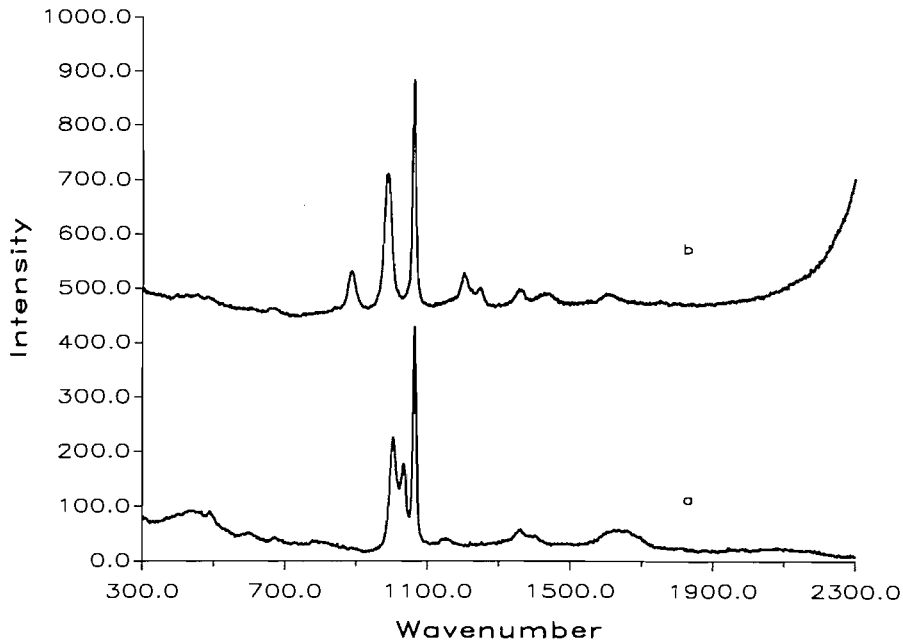

FIG. 2. Raman spectra of (*a*) an aged normal aqueous solution of 2.0 mol·L^{-1} KOCN; (*b*) an aged deuterium aqueous solution of 2.0 mol·L^{-1} KOCN, both at 22°C.

In 1828 Wöhler (1) synthesised urea by adding ammonium sulphate solution to potassium cyanate solution and evaporating the mixture to dryness. Normally, it is assumed that ammonium cyanate was prepared in an ion-pair reaction [4]

[4] $$NH_4^+ + OCN^- \rightarrow NH_4OCN$$

followed by rearrangement of ammonium cyanate to form urea (reaction [5]).

[5] $$NH_4OCN \rightarrow NH_2CONH_2$$

The nature and mechanism of this reaction is not fully understood. The mechanism for the formation of urea in the Wöhler synthesis was the subject of considerable debate in the early period (15–19). It has been shown that both the ionic and the molecular mechanisms conform to the same rate law because of the equilibrium acid–base reactions for ammonium, ammonia, and cyanate, cyanic acid with an overall equilibrium constant, K.

[6] $$NH_4^+ + OCN^- \rightarrow H_2NCONH_2$$

[7] $$\text{Rate} = kC_{NH_4^+}C_{OCN^-}(\gamma_\pm)^2$$

[8] $$NH_3 + HOCN \rightarrow H_2NCONH_2$$

[9] $$\text{Rate} = k'KC_{NH_3}C_{HOCN}(\gamma_\pm)^2$$

In 1961, Frost and Pearson (2) concluded that the two mechanisms were equally supported by the available kinetic evidence and would be indistinguishable through kinetic studies. However, Moelwyn-Hughes (20) did not agree with Frost and Pearson's conclusion and proposed that the ionic mechanism was indicated because of the similarity between the pre-exponential term in the Arrhenius equation for the Wöhler reaction with the same term for the ionic reaction of HCO_3^- protonation; both values are higher by a factor of at least 100 than the value generally found for reactions between neutral molecules in solution.

In the present study Raman spectra of aged aqueous solutions of a mixture 2.0 mol·L^{-1} ammonium chloride with 2.0 mol·L^{-1} potassium cyanate were measured and compared to a 2.0 mol·L^{-1} solution of pure urea (curves *a* and *b* in Fig. 3). The very strong band at 1003 cm^{-1} was due to the $\nu_4(A_1)$, NCN symmetric stretching, of urea (14). The urea has been characterized not only by the 1003 cm^{-1} band but also by the 1158, $\nu_3(A_1)$, NH_2 wagging, 1597, $\nu_2(A_1)$, NH_2 rocking, and 1662 cm^{-1}, $\nu_1(A_1)$, CO stretching, bands of urea (14). The band at 1034 cm^{-1}, of medium intensity and overlapping with the 1003 cm^{-1} band of urea (Fig. 1), was assigned to the ν_5, NH_2 symmetric rock, of H_2NCOO^- (21). Raman investigations of aqueous ammonium carbonate solutions (3, 7) showed that carbamate ion was a major equilibrium species but urea was not formed in this system.

[10] $$CO_3^{2-} + NH_4^+ \rightleftarrows H_2NCOO^- + H_2O$$

The carbamate ion has also been characterized by Raman bands at 563, ν_{12} torsion about the C—N axis, and 1405 cm^{-1}, ν_3 C—N stretching (21). These additional characteristic frequencies of carbamate ion have also been detected in the Raman spectrum of aged aqueous potassium cyanate (Fig. 3*c*).

There was no doubt that the new band at 1065 cm^{-1} with strong intensity (Figs. 1–3) was due to carbonate, as suggested by Williams and Cleveland. The presence of carbonate was clearly indicated by the characteristic peaks at 676 cm^{-1} $\nu_4(E')$, 1065 cm^{-1} $\nu_1(A_1')$, and a weak broad peak at 1380 cm^{-1} $\nu_3(E')$. The frequencies, half-widths, and depolarization ratios for these bands were all identical to those of the pure aqueous sodium carbonate.

It was concluded that the new bands at 1003, 1034, and 1065 cm^{-1} (Figs. 1–3) were due to $\nu_4(A_1)$, NCN symmetric stretching, of urea, ν_5, NH_2 symmetric rock, of carbamate, and $\nu_1(A_1')$, CO symmetric stretching, of carbonate, respectively. Clearly, urea, carbamate, and carbonate were formed

Can. J. Chem. Downloaded from www.nrcresearchpress.com by EESC ESCOLA DE ENGENHARIA on 09/08/12
For personal use only.

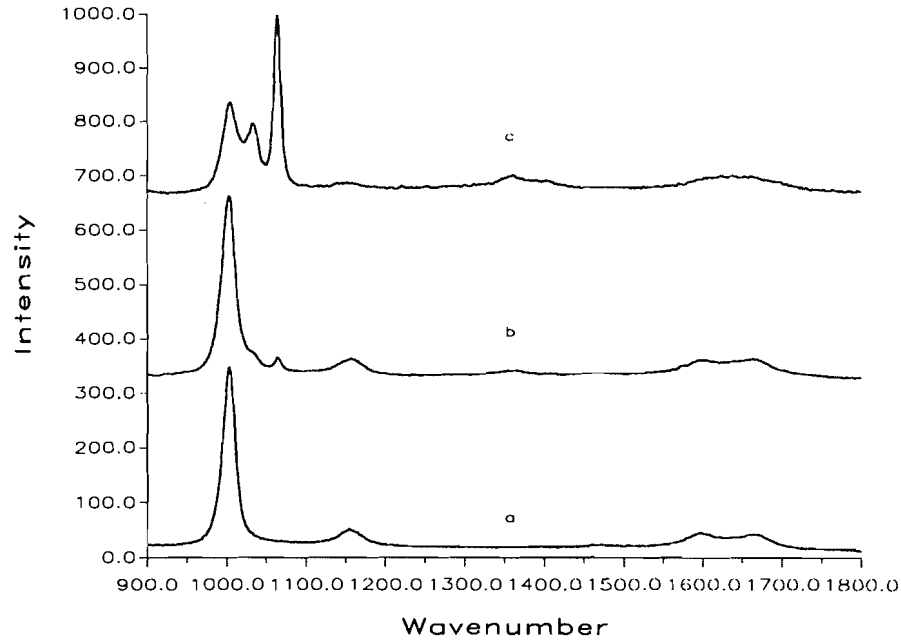

FIG. 3. Raman spectra of (*a*) an 2.0 mol·L^{-1} urea aqueous solution; (*b*) an aged aqueous solution of 2.0 mol·L^{-1} KOCN and 2.0 mol·L^{-1} NH_4Cl; (*c*) an aged aqueous solution of 2.0 mol·L^{-1} KOCN, all at 22°C.

by cyanate hydrolysis (reaction [11]).

[11] $$3OCN^- + 3H_2O \rightarrow H_2NCONH_2 + H_2NCOO^- + CO_3^{2-}$$

The rate of cyanate hydrolysis

The preliminary studies described above revealed that the cyanate ions underwent hydrolysis to form urea, carbamate and carbonate slowly and spontaneously, even without additional ammonium and the reaction took place at room temperature. The possible hydrolysis processes might be as follows:

[12] $$OCN^- + 2H_2O \rightarrow CO_3^{2-} + NH_4^+$$

[13] $$OCN^- + NH_4^+ \rightarrow H_2NCONH_2$$

[14] $$CO_3^{2-} + NH_4^+ \rightleftarrows H_2NCOO^- + H_2O$$

The overall reaction is

[15] $$3OCN^- + 3H_2O \rightarrow H_2NCONH_2 + H_2NCOO^- + CO_3^{2-}$$

In the first reaction, cyanate ion undergoes hydrolysis to produce carbonate and ammonium ions. Since there is a large excess of water in the reaction mixture, the concentration of water remains virtually constant throughout the course of the hydrolysis. Under this condition the change in the amount of water present in the solution has no effect on the rate. Therefore the rate of cyanate ion hydrolysis might be expressed as a first order reaction (eq. [16]).

[16] $$\text{Rate}_I = -\frac{dC_{OCN^-}}{dt} = k_1 C_{OCN^-}$$

where Rate_I is the rate of cyanate ion hydrolysis (eq. [12]). One can show from eq. [16] that

[17] $$\log C_{OCN^-} = -\frac{k_1 t}{2.303} + \log C_{0,OCN^-}$$

where log is the common or base 10 logarithms, C_{0,OCN^-} and C_{OCN^-} are the concentrations of cyanate ion at times $t = 0$ and $t = t$, respectively. Therefore if the reaction is first order a plot of log C_{OCN^-} versus t would give a straight line with a slope of $-k_1/2.303$. The rate constant k_1 can be determined.

Kinetic measurements were carried out for different concentrations of potassium cyanate. The results indicated that the hydrolysis of cyanate ion in pure water (eq. [12]) was very slow (e.g., for a 2.0 mol·L^{-1} KOCN aqueous solution complete reaction took about 10 days at room temperature). From the kinetic measurements it was found that the rate at which cyanate ion hydrolysed in dilute aqueous solution was directly proportional to the cyanate concentration for about the first 4000 min after sample preparation. An example will serve to illustrate the progress of the reaction with time.

The Raman spectrum of a 2.48 mol·L^{-1} KOCN aqueous solution changed with the passage of time (Fig. 1). The use of the 934 cm^{-1} band of ClO_4^- as an internal intensity reference permitted quantitative measurements of the concentration (C) from the integrated band intensities (I) through the relationship $I = JC$, where J is the molar scattering coefficient. It proved convenient to measure the increase in product concentrations: carbonate, carbamate, and bicarbonate because the cyanate bands were weak, broad, and complicated by Fermi resonance. Cyanate concentration measured at each time period are listed in Table 1, where the concentration of the cyanate ion, C_{OCN^-}, for each measurement was obtained by subtracting the concentrations of urea, carbamate, and carbonate from the initial concentration of cyanate ion.

[18] $$C_{OCN^-} = C_{0,OCN^-} - C_{H_2NCONH_2} - C_{H_2NCO_2^-} - C_{CO_3^{2-}}$$

$C_{H_2NCONH_2}$, $C_{H_2NCO_2^-}$, and $C_{CO_3^{2-}}$ were calculated from the relative integrated intensities of the 1003, 1034, and 1065 cm^{-1} bands obtained in each kinetic measurement and the corresponding $J_{H_2NCONH_2}$, $J_{H_2NCO_2^-}$, and $J_{CO_3^{2-}}$ values (0.481, 0.403, and 0.375 L·mol^{-1}) (3). $J_{CO_3^{2-}} = 0.375 \pm 0.019$ and $J_{H_2NCONH_2} = 0.481 \pm 0.024$ L·mol^{-1} were obtained from in-

Can. J. Chem. Downloaded from www.nrcresearchpress.com by EESC ESCOLA DE ENGENHARIA on 09/08/12
For personal use only.

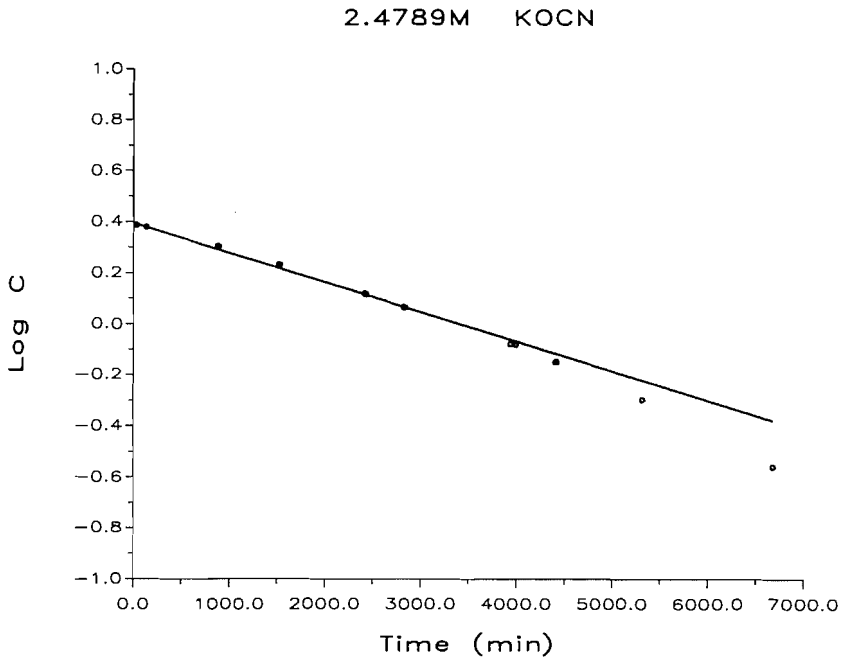

FIG. 4. A plot of log C_{OCN^-} against t for 2.48 mol·L^{-1} KOCN aqueous solution.

TABLE 1. Kinetic data for hydrolysis of a 2.48 mol·L^{-1} KOCN aqueous solution at 22°C

t (min)	C_{OCN^-} (mol·L^{-1})	log C_{OCN^-}
21.6	2.444	0.3882
34.0	2.443	0.3879
138.0	2.394	0.3792
878.0	2.020	0.3053
891.0	2.014	0.3040
1518	1.708	0.2325
1531	1.705	0.2316
2419	1.309	0.1168
2433	1.302	0.1145
2826	1.165	0.06636
2839	1.161	0.06472
3938	0.834	−0.07904
3993	0.829	−0.08129
4411	0.711	−0.1484
4423	0.709	−0.1492
5314	0.505	−0.2966
6678	0.275	−0.5600
∞	0.0000	—

tensity measurements of the 1065 cm^{-1} band of carbonate (in a series of aqueous sodium carbonate solutions) relative to the 934 cm^{-1} band of the perchlorate internal standard and for the 1003 cm^{-1} band of aqueous urea in an analogous procedure. The value of $J_{H_2NCOO^-} = 0.403 \pm 0.040$ L·mol^{-1} was obtained in a similar manner from intensity measurements of the 1034 cm^{-1} band of carbamate ion in aqueous ammonium carbamate solutions (a correction for the presence of carbonate and bicarbonate was required). The log C_{OCN^-} versus t plot (Fig. 4) gave a straight line with a slope of $-(1.158 \pm 0.231) \times 10^{-4}$ at $t < 4000$ min. The first order rate constant was determined from the slope of the line, $k_1 = (2.67 \pm 0.53) \times 10^{-4}$ min^{-1}. The half-life of the hydrolysis was 2600 (±520) min and was independent of the initial concentration of the cyanate ion.

For the second process, reaction of cyanate ion with ammonium to produce urea (eq. [13]), the rate might be considered as follows

$$[19] \qquad \text{Rate}_2 = -\frac{dC_{OCN^-}}{dt} = k_2 C_{OCN^-} C_{NH_4^+}$$

where Rate$_2$ is the rate of cyanate ion aqueous rearrangement reaction with ammonium (eq. [13]). In this case the initial concentrations of cyanate and ammonium were equal. They remained equal as the reaction proceeds if there were no competing reactions. The integrated rate equation for the second order reaction is then,

$$[20] \qquad \frac{1}{C_{OCN^-}} - \frac{1}{C_{0,OCN^-}} = k_2 t$$

If the reaction is second order the plot of $1/C_{OCN^-}$ versus t will give a straight line with a slope k_2.

To assess the above proposal Raman spectroscopy was used to study the reaction rates for solutions with constant concentration of cyanate and different concentrations of ammonium chloride. In an aqueous solution of cyanate also containing ammonium the hydrolysis reaction was much faster than that in a solution of potassium cyanate in water only (e.g., for a 2.0 mol · L^{-1} KOCN with 2.0 mol · L^{-1} NH_4Cl aqueous solution complete reaction took about 3 days at room temperature). Furthermore, the addition of ammonium to aqueous cyanate resulted in a much greater yield of urea. A second order reaction was indicated by the fact that when the concentration of cyanate was kept constant the rate was directly proportional to the concentration of ammonium. The greater the amount of ammonium, the faster the rate. Clearly, ammonium was one of the reactants and the reaction of cyanate ion with ammonium could be an elementary step.

For example, the Raman spectra measured at different elapsed time for the 2.47 mol·L^{-1} KOCN with 2.47 mol·L^{-1} NH_4Cl aqueous solution at room temperature showed that urea was formed (Fig. 5). The corresponding kinetic data have been listed in Table 2. For the graph of $1/C_{OCN^-}$

Can. J. Chem. Downloaded from www.nrcresearchpress.com by EESC ESCOLA DE ENGENHARIA on 09/08/12
For personal use only.

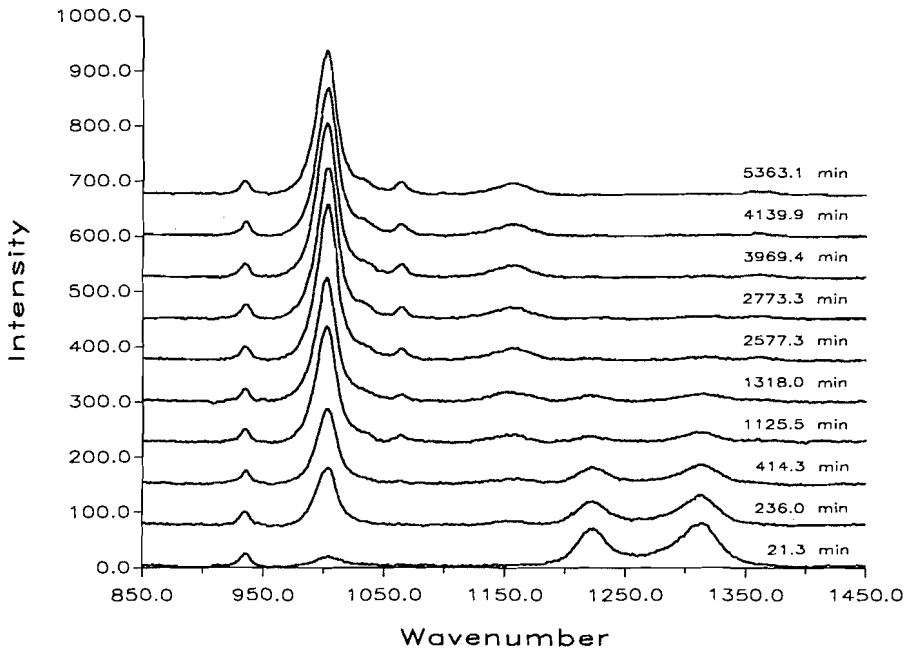

FIG. 5. Raman spectra of a solution of 2.47 mol·L^{-1} KOCN and 2.47 mol·L^{-1} NH_4Cl at 22°C at different times. A 0.0500 mol·L^{-1} $NaClO_4$ has been added as an internal intensity standard.

plotted versus t (Fig. 6) the points lie close to a straight line. These results confirmed that the kinetics were second order. The rate constant was equal to the slope of the line $k_2 = (4.64 \pm 0.93) \times 10^{-4}$ mol^{-1} · L · min^{-1}.

For the third process (eq. [14]), carbonate and ammonium react to produce carbamate.

[21] $$CO_3^{2-} + NH_4^+ \rightleftarrows H_2NCOO^- + H_2O$$

This reaction has been shown to be a fast exchange reaction. The carbonate and ammonium were found to be in equilibrium with carbamate. The equilibrium has been discussed in detail (3, 7). The amount carbonate and ammonium at equilibrium was essentially controlled by the pH. It was found that when the cyanate ion hydrolysis was complete, the aqueous solution had a pH value of about 10. At this pH the major species present are carbonate and carbamate, not bicarbonate.

The characteristic band of bicarbonate has been identified at 1017 cm^{-1}, $\nu_5(A')$ C—OH stretching (12). It was found that there was a small amount of bicarbonate (1017 cm^{-1}) in the early stage of the reaction (the curves at t = 21.6 min in Fig. 1). The presence of bicarbonate at the initial stage of hydrolysis can be explained by the fact that the hydrolysis of potassium cyanate in pure water initially gives a pH value of about 9. At this pH the carbonate ion produced in the first stage of cyanate hydrolysis (eq. [12]) was in equilibrium with bicarbonate. A detectable amount of bicarbonate was found in the early stage of hydrolysis but as NH_4^+ was consumed to produce urea the pH value increased and the equilibrium between the carbonate and bicarbonate shifted to favour the formation of the carbonate.

[22] $$CO_3^{2-} + H_2O \rightleftarrows HCO_3^- + OH^-$$

which then increased the formation of the carbamate.

[23] $$CO_3^{2-} + NH_4^+ \rightleftarrows H_2NCOO^- + H_2O$$

The hydrolysis of a mixture of 2.0 mol·L^{-1} potassium cyanate with 2.0 mol·L^{-1} aqueous ammonia was also studied by Raman measurements. It was found that the rate of cyanate hydrolysis was slower than the rate of cyanate hydrolysis in pure water although more ammonia was added. In this case the principal product was carbonate, not urea. The pH value for a mixture of 2.0 mol·L^{-1} potassium cyanate and 2.0 mol·L^{-1} ammonia was about 12. At this pH value, the concentration of ammonium ion free to react would only be 10^{-3} mol·L^{-1} initially. This small amount of ammonium ion had a negligible influence on the rate of cyanate hydrolysis. The fact that the rate of cyanate hydrolysis in aqueous ammonia was slower than that in pure water or that in ammonium chloride solution indicated that the reaction to produce urea is not just a nucleophilic attack of NH_3 at the C of OCN^-.

The kinetic Raman measurements were also carried out for a 2.0 mol·L^{-1} potassium cynate with additional sodium hy-

TABLE 2. Kinetic data for the reaction of 2.47 mol·L^{-1} KOCN and 2.47 mol·L^{-1} NH_4Cl aqueous solution at 22°C

t (min)	C_{OCN^-} (mol·L^{-1})	$\frac{1}{C_{OCN^-}}$
21.3	2.256	0.4433
33.6	2.220	0.4504
236.0	1.713	0.5836
248.7	1.675	0.5969
414.3	1.518	0.6586
1125	1.099	0.9100
1142	1.0793	0.9265
1318	0.941	1.063
2577	0.621	1.610
2773	0.577	1.734
3969	0.444	2.255
4140	0.426	2.349
4153	0.425	2.349
5363	0.341	2.929
∞	0.0000	—

Can. J. Chem. Downloaded from www.nrcresearchpress.com by ESC ESCOLA DE ENGENHARIA on 09/08/12
For personal use only.

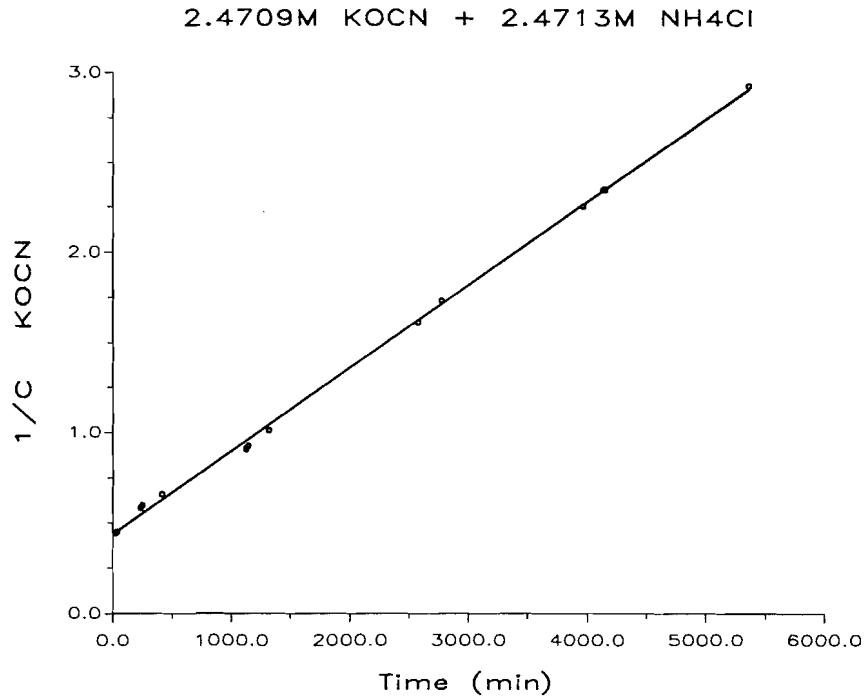

FIG. 6. The plot of $1/C_{OCN^-}$ against t for 2.47 mol·L^{-1} NH_4Cl aqueous solution.

TABLE 3. Summary of reaction parameters for cyanate hydrolysis kinetics at 22°C

Parameter	$OCN^- + H_2O = CO_3^{2-} + NH_4^+$	$OCN^- + NH_4^+ = H_2NCONH_2$
C_{0,OCN^-}	2.48 mol·L^{-1}	2.47 mol·L^{-1}
C_{0,NH_4^+}		2.47 mol·L^{-1}
Plot	$\log C_{OCN^-} \sim t$	$\frac{1}{C_{OCN^-}} \sim t$
Slope	$-(1.158 \pm 0.231) \times 10^{-4}$	$(4.64 \pm 0.93) \times 10^{-4}$
k	$(2.67 \pm 0.53) \times 10^{-4}$ min^{-1}	$(4.64 \pm 0.93) \times 10^{-4}$ mol^{-1}·L·min^{-1}
$t_{1/2}$	2600 ± 500 min	873 ± 175 min

droxide (0.050 mol · L^{-1}) aqueous solution. The result indicated that the rate of cyanate hydrolysis in sodium hydroxide solution is much slower than that in pure water. When sodium hydroxide was added, the pH of this solution was about 13. At this high pH, the ammonium/ammonia ratio was 3.6×10^{-4} to 1. The free ammonium ion concentration produced from the first step of cyanate hydrolysis (eq. [12]) was reduced. With this low concentration of ammonium ion, the rate of cyanate rearrangement with ammonium to form urea (eq. [13]) was significantly reduced even when compared to cyanate hydrolysis in pure water.

From an overall view, the hydrolysis of cyanate ion is a complex process which contains a consecutive reaction, a parallel reaction, and a chemical equilibrium system. Careful consideration of cyanate ion hydrolysis in pure water indicated that when the concentration of cyanate ion, C_{OCN^-}, was not too low and the reaction time, t, was not too long (e.g., in the case of $C_{0,OCN^-} = 2$ mol·L^{-1}, $t < 4000$ min), the concentration of NH_4^+ produced by cyanate ion hydrolysis, $OCN^- + H_2O \rightarrow NH_4^+ + CO_3^{2-}$, was relatively low and the consumption of the cyanate ion by reacting with ammonium, $OCN^- + NH_4^+ \rightarrow H_2NCONH_2$, was relatively small. The effect of competition by the parallel reaction, $OCN^- + NH_4^+ \rightarrow H_2NCONH_2$, was not sufficient to cause deviation from first order kinetics. It is important to notice that urea was produced throughout the course of the reaction (Fig. 1). Nevertheless the initial part of log C_{OCN^-} versus t plot for cyanate ion hydrolysis in pure water (Fig. 4) was presented as a straight line. Therefore hydrolysis of the cyanate ion in pure water appears to be a first order reaction with the rate-determining step given by eq. [12]. When the reaction time was greater than 4000 min, $t > 4000$ min, the effect of competition by the parallel reaction, $OCN^- + NH_4^+ \rightarrow H_2NCONH_2$, increased and the concentration of cyanate decreased at a faster rate (Fig. 4).

For hydrolysis of potassium cyanate with additional ammonium chloride the concentration of added NH_4^+ was much higher than the concentration of NH_4^+ produced by cyanate hydrolysis, $OCN^- + H_2O \rightarrow NH_4^+ + CO_3^{2-}$. In addition, the rate constant of cyanate ion hydrolysis in pure water was much slower than the rate constant of the reaction of cyanate ion with ammonium. Since, $k_1 \ll k_2$, the $1/C_{OCN^-}$ versus t plot (Fig. 6) was a straight line.

The rate constants and half-lives for the reactions are presented in Table 3.

Can. J. Chem. Downloaded from www.nrcresearchpress.com by EESC ESCOLA DE ENGENHARIA on 09/08/12
For personal use only.

4. Conclusion

The rate constants have been determined for two parallel reactions that occur when cyanate undergoes hydrolysis. The initial stages of cyanate hydrolysis generate carbonate, bicarbonate, carbamate, and ammonium ions. The excess cyanate then reacts with ammonium to produce urea. The present studies cannot be directly compared to previous work because the previous work was performed at higher temperatures (because the reaction was so slow for conventional methods) and in open vessels. However, the results are in reasonable agreement with the values calculated from the kinetic parameters obtained at higher temperatures. The present work confirmed that the rate was directly proportional to the concentration of ammonium rather than ammonia and tends to support the ionic mechanism argued by Moelwyn-Hughes. The parallel reaction to produce carbamate has been shown to be important. The present study demonstrated that Raman spectroscopy can be employed to monitor both the reactants and the products associated with cyanate ion hydrolysis.

5. Acknowledgments

This work was supported in part by a grant from the Natural Science and Engineering Research Council of Canada. One of the authors (N.W.) gratefully acknowledges the support of a Memorial University of Newfoundland Graduate Student Fellowship.

1. F. Wöhler. Ann. Phys. Chem. **12**, 253 (1828).
2. A.A. Frost and R.G. Pearson. Kinetics and mechanism (A study of homogeneous chemical reactions. 2nd ed. John Wiley and Sons, Inc., New York. 1961.
3. N. Wen. Ph.D. Thesis. Chemistry Department, Memorial University of Newfoundland, St. John's, NF, Canada. 1993.
4. M.H. Brooker and N. Wen. Can. J. Chem. **71**, 1764 (1993).
5. D. Williams. J. Am. Chem. Soc. **62**, 2442 (1940).
6. F.F. Cleveland. J. Am. Chem. Soc. **63**, 622 (1941).
7. M.H. Brooker, J. Hand, and N. Wen. Raman studies of aqueous carbonate, bicarbonate and carbamate equilibria. Proceedings of the International Conference on Raman Spectroscopy, XI, London, England. *Edited by* R.J.H. Clark and D.A. Long. Wiley, Chichester. 1988.
8. J. Pitha and R.N. Jones. Can. J. Chem. 44, 3031 (1966).
9. J. Pitha and R.N. Jones. Can. J. Chem. 45, 2347 (1967).
10. J. Pitha and R.N. Jones. National Research Council of Canada Bulletins, No. 12, 2nd ed., in Vol. 2 of "Optimization methods of fitting curves to infrared band envelopes. *Edited by* R.N. Jones. National Research Council of Canada, Ottawa. 1968.
11. M.H. Brooker and B. Rice. Chemistry Department, Memorial University of Newfoundland, St. John's, Newfoundland, Canada A1B 3X7.
12. A.R. Davis and B.G. Oliver. J. Solution Chem. **1**(4), 329 (1972).
13. K. Mitsui and T. Ukaji. Research Reports of Ikutoku Tech. Univ., B-1, 89 (1976).
14. A. Yamaguchi, T. Miyazawa, T. Shimanouchi, and S. Mizushima. Spectrochim Acta, **10**, 170 (1958).
15. J. Walker and F.J. Hambly. J. Chem. Soc. **67**, 746 (1895).
16. F.D. Chattaway and D.L. Chapman. J. Chem. Soc. **101**, 170 (1912).
17. J.C. Werner. J. Chem. Soc. **103**, 1010 (1913).
18. E.E. Walker. Proc. R. Soc. A, **87**, 539 (1912).
19. J. Walker and S.A. Kay. J. Chem. Soc. **71**, 489 (1897).
20. E.A. Moelwyn-Hughes. The chemical statistics and kinetics of solutions. Academic Press, London. 1971.
21. D.L. Frasco. J. Chem. Phys. **41**, 2134 (1964).

Can. J. Chem. Downloaded from www.nrcresearchpress.com by EESC ESCOLA DE ENGENHARIA on 09/08/12
For personal use only.

Interligand interaction in ternary complexes of Zn(II) and Cd(II) with dipeptides and aminoacids[1]

ALEXANDER VARGHESE VAIDYAN AND PABITRA K. BHATTACHARYA

Department of Chemistry, Faculty of Science, M.S. University of Baroda, Baroda 390002, India

Received June 11, 1993

ALEXANDER VARGHESE VAIDYAN and PABITRA K. BHATTACHARYA. Can. J. Chem. **72**, 1107 (1994).

The stability constants of binary and ternary complexes [MA], [MA_2], and [MAL] (where M = Zn(II) on Cd(II); A = glycylglycine, glycyl L-alanine, glycyl L-leucine; L = α-alanine phenylalanine, tyrosine, tryptophan, or L-listidine) in aqueous medium have been determined potentometrically at 25°C and an ionic strength of 0.2 M $NaClO_4$ (0.2 mol dm^{-3}) using a computer system. It is observed that Δ log *K* of MAL complexes has low negative or positive values. Probable reasons have been discussed.

ALEXANDER VARGHESE VAIDYAN et PABITRA K. BHATTACHARYA. Can. J. Chem. **72**, 1107 (1994).

Faisant appel à la potentiométrie, opérant à 25°C, dans un milieu aqueux de force ionique 0,2 M de $NaClO_4$ (0,2 mol dm^{-3}), et utilisant un logiciel d'ordinateur, on a déterminé les constantes de stabilité de complexes binaires et tertiaires [MA], [MA_2] et [MAL] dans lesquels M = Zn(II) ou Cd(II), A = glycylglycine, glycyl-L-alanine ou glycyl-L-leucine et L = α-alanine, phénylalanine, tyrosine, tryptophane ou L-histidine. On a observé que les valeurs du Δ log *K* des complexes MAL sont faibles, avec des signes négatifs ou positifs. On discute des causes de ces résultats.

[Traduit par la Rédaction]

Introduction

It is well known that Zn(II) ion is an integral component of many proteins and is indispensable for their catalytic function and structural stability (1). The biological roles of zinc(II) have been well reviewed (2–6) and seem dominated by its ability to assume distorted four- or five-coordinated structures in enzymes. In biological system, the metal ion is bound to two different ligands at various stages and there are various factors that stabilize these ternary complexes (7). Flexible intramolecular interligand interaction between the non-coordinating groups of the two ligands is the most important factor (8, 9). For the interaction, non-coordinating side groups on the two ligands should be suitably oriented to achieve effective overlap (10, 11). In the case of Zn(II) complexes with tetrahedral geometry, hydrophobic interaction between non-coordinated side groups of two ligands are more pronounced than in square planar Ni(II) or Cu(II) complexes (12), and hence Δ log *K* will be less negative or more positive in Zn(II) complexes than in Cu(II) or Ni(II) complexes.

Complexes of aminoacids and oligopeptides are involved in the exchange and the transport mechanism of trace metal ions in the human body (13). Hence it is worthwhile to study ternary complexes of Zn(II) and Cd(II) involving dipeptides and aminoacids. The MAL complexes, where M = Zn(II) or Cd(II); A = glycyl glycine (gg), glycyl L-alanine (ga), or glycyl L-leucine (gl); and L = α-alanine (ala), phenylalanine (phe), tyrosine (tyr), tryptophan (trp), or L-histidine (hist) have been studied.

Experimental

All the reagents used were of A.R. grade. Potentiometric titrations were carried out in aqueous medium at 25°C and at an ionic strength of 0.2 mol dm^{-3} ($NaClO_4$). The perchlorate solutions of Zn(II) and Cd(II) were prepared and standardized by titration with EDTA solution.

The formation constants for the ternary systems were computed from the titration data in which concentrations of metal, dipeptides (A), and aminoacids (L) were in the ratio 1:1:1, 1:2:2, and 1:3:3. Titrations were done against a standard alkali (ca. 0.2 M NaOH). A summary of the other experimental parameters for the Zn(II) and Cd(II) binary and mixed ligand systems is given below:

Summary of experimental parameters

Ligand systems
- (*a*) 0.02 M $HClO_4$:0.004 M ligand A:0.176 M $NaClO_4$
- (*b*) 0.02 M $HClO_4$:0.006 M ligand A:0.174 M $NaClO_4$

Binary systems
- (*a*) 0.02 M $HClO_4$:0.002 M $Zn(ClO_4)_2$/$Cd(ClO_4)_2$ 0.004 M ligand A:0.174 M $NaClO_4$
- (*b*) 0.02 M $HClO_4$:0.002 M $Zn(ClO_4)_2$/$Cd(ClO_4)_2$ 0.006 M ligand A:0.172 M $NaClO_4$

Mixed ligand systems
- (*a*) 0.02 M $HClO_4$:0.002 M $Zn(ClO_4)_2$/$Cd(ClO_4)_2$ 0.002 M ligand A:0.002 M ligand L:0.174 M $NaClO_4$
- (*b*) 0.02 M $HClO_4$:0.002 M $M(ClO_4)_2$ where M = Zn(II) or Cd(II) 0.004 M ligand A:0.004 M ligand L:0.170 M $NaClO_4$
- (*c*) 0.02 M $HClO_4$:0.002 M $M(ClO_4)_2$:0.006 M ligand A: 0.006 M ligand L:0.168 M $NaClO_4$

Ionic strength, electrolyte 0.2 mol dm^{-3}, $NaClO_4$
Experimental method: pH titration using Orion ionanalyser/901
Accuracy: 0.001 pH unit; calibrated with buffer pH 4, pH 7, and pH 9
pH range: protonation 3.00–8.0
pH range: M(II) complexation: 5.5–7.5 for Zn(II)
M(II) complexation: 5.5–8.5 for Cd(II)
Temperature: 25°C
Method of calculation: SCOGS (14)
Species considered: protonation. AH_2, AH, LH_2, LH, and LH_3 in case of histidine

M(II) binary system:
AH_2, AH, ZnA, ZnA_2, and ZnA(OH) for Zn(II)
LH_2, LH, ZnL, ZnL_2, and protonated ZnLH where L = histidine
In case of Cd(II) binary system, AH_2, AH, CdA, CdA_2, LH_2, LH, CdL,CdL_2

M(II) mixed-ligand system:
Zn(II) ternary complexes
AH_2, AH, LH_2, LH, ZnA, ZnA_2, ZnA(OH), ZnL, ZnL_2, ZnAl ZnLH where L is histidine
Cd(II) ternary complexes
AH_2, AH, LH_2, LH, CdA, CdL, and CdAL

The total volume of the solution was adjusted to 50 cm^3 by adding double distilled water. Titrations for each set of solutions were carried

[1]This paper is published without authors' proofreading of the galleys.

Can. J. Chem. Downloaded from www.nrcresearchpress.com by EESC ESCOLA DE ENGENHARIA on 09/08/12
For personal use only.

Can. J. Chem. Downloaded from www.nrcresearchpress.com by EESC ESCOLA DE ENGENHARIA on 09/08/12
For personal use only.

out twice to check reproducibility. The refined values of the protonation constants have been used as fixed parameters for the refinement of binary complexes and the values of protonation constants and the binary constants have been used as fixed parameters for the refinements of mixed ligand species. The protonation constants and formation constants of binary and mixed ligand complexes, and their $\Delta \log K$ values are listed in Tables 1 and 2.

Results and discussion

It was reported earlier that in the complex [ZnA], where A = glycylglycine or glycinamide (15), the ligand binds to the metal ion through N-amino and O-peptide donor groups, as in the case of CuA at low pH. For the copper dipeptide system, the formation of CuA_{-H} was also observed at high pH, with coordination from N-amino and deprotonated peptide N (16, 17). However, in the case of Zn(II) dipeptide systems, it has been reported that species ZnA_{-H} is not of much significance (18). In the bis species ZnA_2, the dipeptide coordinates from amino-nitrogen and peptide oxygen. Similarly, we found the presence of the CdA and CdA_2 species with the dipeptide bound to the Cd(II) ion through N-amino and O-peptide groups.

In the binary system containing Zn(II), the equilibrium reaction such as $Zn + A + H_2O \rightleftharpoons ZnA(OH) + H^+$, was assumed to exist and the equilibrium constant

$$K = [ZnA(OH)][H^+]/[Zn^{2+}][H_2O]$$

could be refined. However, it is to be noted that an equilibrium due to deprotonation of peptide nitrogen in the presence of metal ion may exist. This reaction of the dipeptide with the cation, resulting in the formation of ZnA_{-H} and the liberation of proton, is similar to the above equilibrium reaction in which zinc hydroxy species is formed. Thus the formation of ZnA_{-H} species at high pH cannot be ruled out. However, the value of the constant K^M_{MA} for the formation of ZnA calculated without taking into account the formation of ZnA(OH) is very close to the value obtained by taking into account the formation of this species. This is because, as seen in the calculated concentration of the species, the percentage of ZnA(OH) formed in the pH range of calculation is not very significant. In the case of Cd(II) system, taking the formation of CdA(OH) into account does not affect the results, showing that the hydroxy species is not formed. The values of binary constants reported here are comparable with the literature values (18).

The formation of a ternary complex may take place through simultaneous binding of the metal ion with the ligands: $M + A + L \rightleftharpoons MAL$. The constants K^M_{MAL} were calculated and are reported in the Table 2.

In the ternary complexes, an equilibrium, $M^{2+} + A + L + H_2O = MA(OH)L + H^+$ was also considered, but its equilibrium constant could not be refined. Hence, no formation of MA(OH)L was considered in the case of both Zn(II) and Cd(II) ternary complexes. The stability of the ternary complexes has been evaluated in terms of $\Delta \log K$.

$$\Delta \log K = \log K^M_{MAL} - (\log K^M_{MA} + \log K^M_{ML})$$

It can also be represented as

$$\Delta \log K = \log K^M_{MAL} - \log K^M_{ML}$$

$$\Delta \log K = \log K^M_{MAL} - \log K^M_{MA}$$

Deviation in $\Delta \log K$ has been calculated by assuming error

TABLE 1. Protonation constants of free ligands and formation constants of binary complexes in aqueous medium t = 25°C, I = 0.2 (mol dm^{-3}) ($NaClO_4$)[a]

System	p	q	r	s	log β	S.D.
Zn–gg	0	1	0	1	7.992	0.020
	0	1	0	2	11.034	0.030
	1	1	0	0	3.745	0.010
	1	1	0	−1	−3.556	0.030
	1	2	0	0	6.610	0.020
Zn–ga	0	1	0	1	8.073	0.030
	0	1	0	2	11.102	0.020
	1	1	0	0	3.789	0.020
	1	1	0	−1	−3.968	0.010
	1	2	0	0	6.650	0.030
Zn–gl	0	1	0	1	8.071	0.020
	0	1	0	2	11.174	0.030
	1	1	0	0	3.858	0.010
	1	1	0	−1	−4.052	0.050
	1	2	0	0	6.751	0.040
Zn–ala	0	0	1	1	9.661	0.020
	0	0	1	2	11.760	0.010
	1	0	2	0	5.330	0.010
	1	0	2	0	9.701	0.030
Zn–Phe	0	0	1	1	9.214	0.010
	0	0	1	2	11.251	0.020
	1	0	1	0	4.785	0.008
	1	0	2	0	9.264	0.010
Zn–tyr	0	0	1	1	9.074	0.010
	0	0	1	2	10.961	0.010
	1	0	1	0	4.634	0.020
	1	0	2	0	9.010	0.020
Zn–trp	0	0	1	1	9.448	0.030
	0	0	1	2	11.451	0.010
	1	0	1	0	4.835	0.020
	1	0	2	0	9.653	0.030
Zn–L-hist	0	0	1	1	8.932	0.010
	0	0	1	2	15.009	0.030
	1	0	1	1	11.623	0.020
	1	0	1	0	6.514	0.010
	1	0	2	0	12.010	0.020
Cd–gg	1	1	0	0	2.920	0.030
	1	2	0	0	5.420	0.009
Cd–ga	1	1	0	0	2.990	0.010
	1	2	0	0	5.531	0.020
Cd–gl	1	1	0	0	3.005	0.030
	1	2	0	0	5.554	0.010
Cd–ala	1	0	1	0	5.038	0.030
	1	0	2	0	8.562	0.010
Cd–Phe	1	0	1	0	4.505	0.010
	1	0	2	0	8.100	0.020
Cd–tyr	1	0	1	0	4.415	0.020
	1	0	2	0	7.790	0.030
Cd–trp	1	0	1	0	4.551	0.010
	1	0	2	0	8.690	0.020
Cd–L-hist	1	0	1	0	5.545	0.010
	1	0	2	0	10.152	0.030

[a] p, q, r, s are the stoichiometric coefficients corresponding to M(II), A, L, and H^+

TABLE 2. The overall formation of ternary complexes in aqueous medium; t = 25°C, I = 0.2 mol dm^{-3} ($NaClO_4$)

System	p	q	r	s	log β	S.D.	Δ log K	S.D.
Zn.gg.ala	1	1	1	0	8.854	0.010	−0.221	0.017
Zn.gg.phe	1	1	1	0	8.693	0.020	0.163	0.023
Zn.gg.tyr	1	1	1	0	8.768	0.009	0.389	0.024
Zn.gg.trp	1	1	1	0	8.910	0.020	0.330	0.030
Zn.gg.hist	1	1	1	0	16.801	0.030	1.433	0.030
	1	1	1	0	10.874	0.010	1.615	0.017
Zn.ga.ala	1	1	1	0	8.826	0.020	−0.293	0.030
Zn.ga.phe	1	1	1	0	8.594	0.020	0.020	0.030
Zn.ga.tyr	1	1	1	0	8.641	0.010	0.218	0.030
Zn.ga.trp	1	1	1	0	8.823	0.020	0.199	0.036
Zn.ga.hist	1	1	1	0	16.912	0.040	1.500	0.048
	1	1	1	0	10.794	0.020	0.491	0.030
Zn.gl.ala	1	1	1	0	8.901	0.010	−0.287	0.017
Zn.gl.phe	1	1	1	0	8.605	0.010	−0.038	0.017
Zn.gl.tyr	1	1	1	0	8.712	0.010	0.220	0.024
Zn.gl.trp	1	1	1	0	8.92	0.020	0.227	0.030
Zn.gl.hist	1	1	1	0	16.915	0.040	1.434	0.045
	1	1	1	0	10.837	0.010	0.465	0.017
Cd.gg.ala	1	1	1	0	7.301	0.020	−0.657	0.037
Cd.gg.phe	1	1	1	0	7.205	0.010	−0.220	0.017
Cd.gg.tyr	1	1	1	0	7.374	0.020	0.039	0.030
Cd.gg.trp	1	1	1	0	7.400	0.010	−0.071	0.017
Cd.gg.hist	1	1	1	0	9.114	0.030	0.649	0.033
Cd.ga.ala	1	1	1	0	7.435	0.010	−0.593	0.033
Cd.ga.phe	1	1	1	0	7.262	0.020	−0.233	0.024
Cd.ga.tyr	1	1	1	0	7.316	0.010	−0.089	0.024
Cd.ga.trp	1	1	1	0	7.456	0.010	−0.085	0.017
Cd.ga.hist	1	1	1	0	8.932	0.020	0.397	0.024
Cd.gl.ala	1	1	1	0	7.368	0.030	−0.675	0.052
Cd.gl.phe	1	1	1	0	7.221	0.020	−0.289	0.037
Cd.gl.tyr	1	1	1	0	7.268	0.020	−0.152	0.041
Cd.gl.trp	1	1	1	0	7.425	0.010	−0.131	0.033
Cd.gl.hist	1	1	1	0	8.930	0.030	0.380	0.043

propagation, and shown in Table 2. Δ log K can be described as the difference in the strength of binding of the ligand to the free metal ion and the metal ion already bound to another ligand. The tendency of metal ions to bind with a ligand decreases with increase in the number of ligands because of statistical, electrostatic, and steric factors. Hence, K^{M}_{MAL} should be less than K^{M}_{ML} and Δ log K should be negative. In the case of MAL complexes, where L = α-alanine (ala) or phenylalanine (phe), Δ log K was found to be negative. This can be accounted for by considering the electrostatic repulsion between the aminoacid anion and dipeptide anion. However, it is less negative than what is expected, when one takes into consideration the repulsion between the aminoacid anion and dipeptide anion. This can be due to the intramolecular hydrogen bonding between carboxylate groups of dipeptide and the amino group of the aminoacid (19). Furthermore, it was observed that when L = tryptophan (trp) or tyrosine (tyr), Δ log K is either less negative or positive.

This observation can be explained as follows. The aminoacids are coordinated from the aminocarboxylate end, whereas the indole and hydroxyphenyl group of tryptophan and tyrosine are free. The less negative or positive Δ log K values for the complexes may be due to hydrogen bonding between the indole NH of tryptophan or the hydroxyphenyl OH group of tyrosine and the free carboxylate oxygen of the dipeptides as indicated in the case of copper complexes (17). This results in the equilibrium of the mixed ligand complex formation reaction M + A + L $\rightleftharpoons$ MAL to proceed more to the right, resulting in higher values of log K^{M}_{MAL} and more positive Δ log K. It is, however, observed that the Δ log K values for Zn(II) complexes are less negative than those for the corresponding Cu(II) complexes. This may be attributed to the fact that intramolecular ligand–ligand interaction is enhanced in tetrahedral Zn(II) or Cd(II) complexes, leading to a larger shift of the equilibrium to the right and therefore resulting in less negative or positive Δ log K values. Non-covalent interaction in Zn(II) complexes, dependent on the geometrical coordination requirements of the metal ion, has been suggested by Rizzarelli and co-workers (20–22) and in our earlier investigation (23). It is, however, observed that for the Cd(II) complexes Δ log K values are more negative than those for Zn(II) complexes. This may be because Cd(II) complexes take up an octahedral geometry more easily than Zn(II) complexes, resulting in a smaller amount of H-bonding and a less amount of the CdAL complex formed. H-Bonding interaction in Zn(II) complexes are shown in Fig. 2.

In the case of Zn(II) histidine (L) – dipeptide (A) mixed system, ZnALH and ZnAL species were obtained in addition to the binary species ZnA, ZnL, and ZnLH. In the Cd(II) – histidine (L) – dipeptide (A) system, on the other hand, only [CdAL] species was detected, no [CdALH] formation was observed more-

Can. J. Chem. Downloaded from www.nrcresearchpress.com by EESC ESCOLA DE ENGENHARIA on 09/08/12
For personal use only.

Can. J. Chem. Downloaded from www.nrcresearchpress.com by EESC ESCOLA DE ENGENHARIA on 09/08/12
For personal use only.

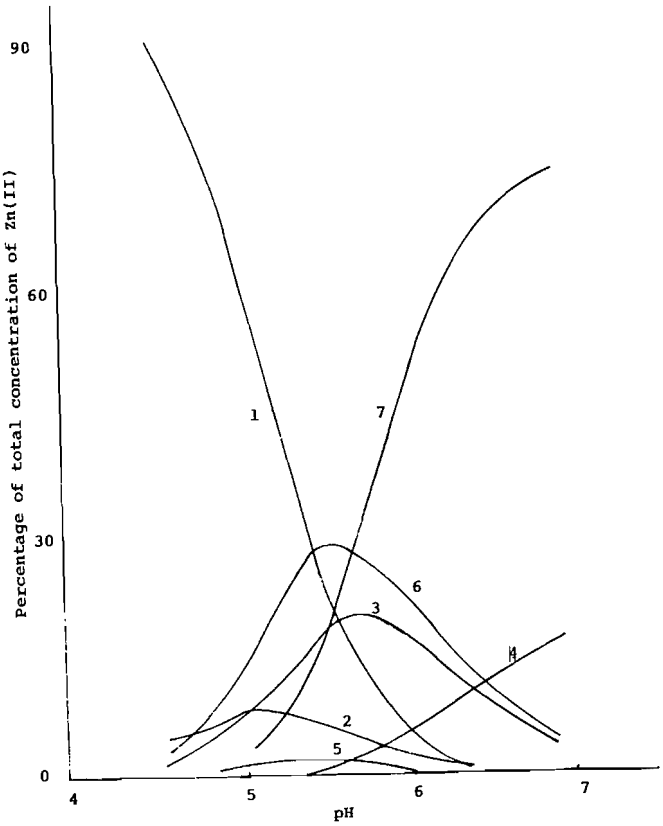

FIG. 1. Distribution of species of Zn–Gly–Gly (A) – Hist (L) – system at M:A:L ratio of 1:2:2: (*1*) free Zn(II), (*2*) ZnLH, (*3*) ZnL, (*4*) ZnL_2, (*5*) ZnA, (*6*) ZnLHA (*7*) ZnAL.

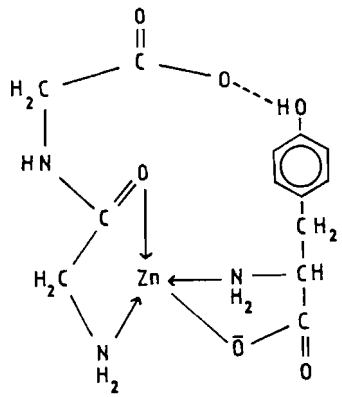

FIG. 2. Proposed structure for [Zn(Gly, Gly) (tyr)].

over, in the binary system, only the formation of CdL has been reported and no CdLH is formed (18).

For the ZnALH species, which is formed at lower pH, coordination of histidine occurs through the amino carboxylate end and the imidazole nitrogen remains protonated. Δ log *K* values for all ZnALH complexes are positive, indicating higher stability. This can be explained by the fact that the protonated histidine is neutral and does not repel the incoming dipeptide anion. Furthermore, there is H-bonding between the free protonated imidazole or histidine and the non-coordinated carboxylate group of the dipeptide (17). These two effects enhance the stability of the ternary species.

In the case of the MLA species where M = Zn(II) or Cd(II), histidine may coordinate through amino nitrogen and imidazole nitrogen, and the carboxylate group is free, as in the copper or nickel system at high pH. The Δ log *K* values for MAL complexes, when L is histidinate, is more positive than when L is α-alanine or phenylalanine. This is because in the MA–histidine system, there is a possibility of double hydrogen bonding. First the free carboxylate group of dipeptide may be involved in hydrogen bonding with the amino group of histidine, as in case of other M-dipeptide – amino acid complexes. Furthermore, the free carboxylate group of histidine can form a hydrogen bond with the amino group of dipeptide. This double hydrogen bonding results in an enhanced stability of the ternary complex and hence Δ log *K* is positive. It is thus observed that using the same solvent in the binary and ternary systems, the relative stabilization of ternary complexes varies depending on the extent of intramolecular interligand interaction between the noncoordinating side groups of the ligands.

1. D. Keilin and T. Mann. Biochemistry, **34**, 1163 (1940).
2. M.F. Dunn. Struct. Bonding (Berlin), **23**, 61 (1975).
3. A. Galdes and H.A.O. Hill. *In* Inorganic biochemistry. *Edited by* H.A.O. Hill. Specialist Periodical Report, Chemical Society of London. 1979. p. 317 ff.
4. A.M. Cheh and J.B. Neilands. Struct. Bonding (Berlin), **29**, 123 (1976).
5. R.H. Prince. Adv. Inorg. Chem. Radiochem. **22**, 349 (1979).
6. S. Lindskog. Struct. Bonding (Berlin), **8**, 153 (1970).
7. H. Sigel (*Editor*). Metal ions in biological systems. Vol. 2. 1973; Vol. 13. 1981.
8. N. Emanuel and P.K. Bhattacharya. Indian J. Chem. **24A**, 498 (1985).
9. P. Chaudhari and H. Sigel. J. Am. Chem. Soc. **99**, 3142 (1977).
10. C. Helene and G. Lancelot. Prog. Biophys. Mol. Biol. **39**, 1 (1982).
11. T.M. Lohman, P.L. DeHaseth, and M.T. Record, Jr. Biochemistry, **19**, 3522 (1980).
12. P. Amico, P. Bonome, R. Cali, V. Cucinotta, P.G. Daniele, G. Ostacoli, and E. Rizzarelli. Inorg. Chem. **28**, 3555 (1989).
13. S. Lau and B. Sarkar. Can. J. Chem. **53**, 710 (1975).
14. (*a*) I.G. Sayce. Talanta, **15**, 1397 (1968); (*b*) I.G. Sayce. Talanta, **18**, 653 (1971); (*c*) I.G. Sayce and V.S. Sharma. Talanta, **19**, 831 (1972).
15. M.S. Nair, M. Santappa, and P. Natarajan. Indian J. Chem. **19A**, 672 (1980).
16. V. Manjula, D. Chakraborty, and P.K. Bhattacharya. Indian J. Chem. **29A**, 577 (1990).
17. D. Chakraborty and P.K. Bhattacharya. J. Inorg. Biochem. **39**, 1 (1990).
18. A.E. Martell and M. Smith. Critical stability constants. Vol. 1. Plenum Press, New York. 1974.
19. (*a*) M.S. Nair, K. Venkatachelapathi, and M. Santappa. J. Chem. Soc. Dalton Trans. 555 (1982); (*b*) D.W. Christiansen and R.S. Alexander. J. Am. Chem. Soc. **111**, 6412 (1989).
20. G. Arena, R. Cali, V. Cucinotta, S. Musumeci, E. Rizzarelli, and S. Sammartano. J. Chem. Soc. Dalton Trans. 1271 (1983).
21. G. Arena, R. Cali, V. Cucinotta, S. Musumeci, E. Rizzarelli, and S. Sammartano. Thermochim. Acta, **74**, 77 (1984).
22. G. Arena, R. Cali, V. Cucinotta, S. Musumeci, E. Rizzarelli, and S. Sammartano. J. Chem. Soc. Dalton Trans. 1651 (1984).
23. A. Varghese and P.K. Bhattacharya. J. Inorg. Biochem. **46**, 223 (1992).

Excess enthalpies of some (1-propanol + methyl *tert*-butyl ether + C_6-hydrocarbon) ternary systems at 298.15 K

SHEMIN ZHU, SHUBAO SHEN, GEORGE C. BENSON, AND BENJAMIN C.-Y. LU
Department of Chemical Engineering, University of Ottawa, Ottawa, ON K1N 6N5, Canada
Received July 29, 1993

SHEMIN ZHU, SHUBAO SHEN, GEORGE C. BENSON, and BENJAMIN C.-Y. LU. Can. J. Chem. **72**, 1111 (1994).

Calorimetric measurements of excess enthalpies are reported for the three ternary systems (1-propanol + methyl *tert*-butyl ether + (*n*-hexane, or 2,3-dimethylbutane, or cyclohexane)) at 298.15 K. Smoothing equations, fitted to the results, were used to construct constant enthalpy contours on a Roozeboom diagram for each of the systems.

SHEMIN ZHU, SHUBAO SHEN, GEORGE C. BENSON et BENJAMIN C.-Y. LU. Can. J. Chem. **72**, 1111 (1994).

On a effectué des mesures calorimétriques d'enthalpies en excès pour trois systèmes ternaires (propan-1-ol + oxyde de méthyle et de *tert*-butyle + (*n*-hexane ou 2,3-diméthylbutane ou cyclohexane)) à 298,15 K. On a utilisé des équations atténuées, ajustées aux résultats, pour construire, pour chaque système, des contours d'enthalpie constante sur un diagramme de Roozeboom.

[Traduit par la Rédaction]

Can. J. Chem. Downloaded from www.nrcresearchpress.com by EESC ESCOLA DE ENGENHARIA on 09/08/12
For personal use only.

The use of alkanols and ethers as gasoline additives has led to an increased interest in the thermodynamic properties of their mixtures with hydrocarbons. Recently we have been studying the excess thermodynamic properties of ternary systems of the type (alkanol + ether + hydrocarbon) (1, 2). As a continuation of those investigations, we have determined the excess molar enthalpies of three ternary systems of the type (1-propanol + methyl *tert*-butyl ether + a C_6-hydrocarbon) where the C_6-hydrocarbon is *either* *n*-hexane, or 2,3-dimethylbutane, or cyclohexane.

Experimental

Component liquids

Anhydrous 1-propanol (PrOH) and methyl *tert*-butyl ether (MTBE) were obtained from the Aldrich Chemical Co. Pure Grade *n*-hexane (*n*-C_6), 2,3-dimethylbutane (*br*-C_6), and cyclohexane (*c*-C_6) were obtained from the Phillips Chemical Co. All of these materials had stated purities exceeding 99 mol%. Their densities, measured at 298.15 K in an Anton-Paar digital densimeter, were 799.64, 735.56, 655.04, 657.13, and 774.04 kg m^{-3} for PrOH, MTBE, *n*-C_6, *br*-C_6, and *c*-C_6, respectively. These are in reasonable agreement with the values 799.75, 735.3, 654.84, 657.02, and 773.89 kg m^{-3}, compiled by the TRC (3, 4).

Calorimetric measurements

Excess molar enthalpies H_m^E at 298.15 ± 0.005 K were measured in an LKB flow microcalorimeter. Details of the equipment and its operation have been described previously (5, 6). In studying the ternary systems, the excess molar enthalpy $H_{m,1+23}^E$ was measured for several pseudo-binary systems in which component 1 (PrOH) was added to binary mixtures of components 2 (MTBE) and 3 (*n*-C_6, or *br*-C_6, or *c*-C_6) having a fixed mole ratio x_2/x_3. These binaries were prepared by weighing. The excess molar enthalpy $H_{m,123}^E$ of the ternary system is then given by the relation

$$[1] \qquad H_{m,123}^E = H_{m,1+23}^E + (1 - x_1)H_{m,23}^E$$

where $H_{m,23}^E$ is the excess molar enthalpy of the particular (MTBE + C_6-hydrocarbon) binary. Over most of the PrOH mole fraction range, the errors of $H_{m,1+23}^E$ are about 0.5% or 2 J mol^{-1}, whichever is larger. Errors in the mole fractions of the ternary mixtures are estimated to be less than 5×10^{-4}.

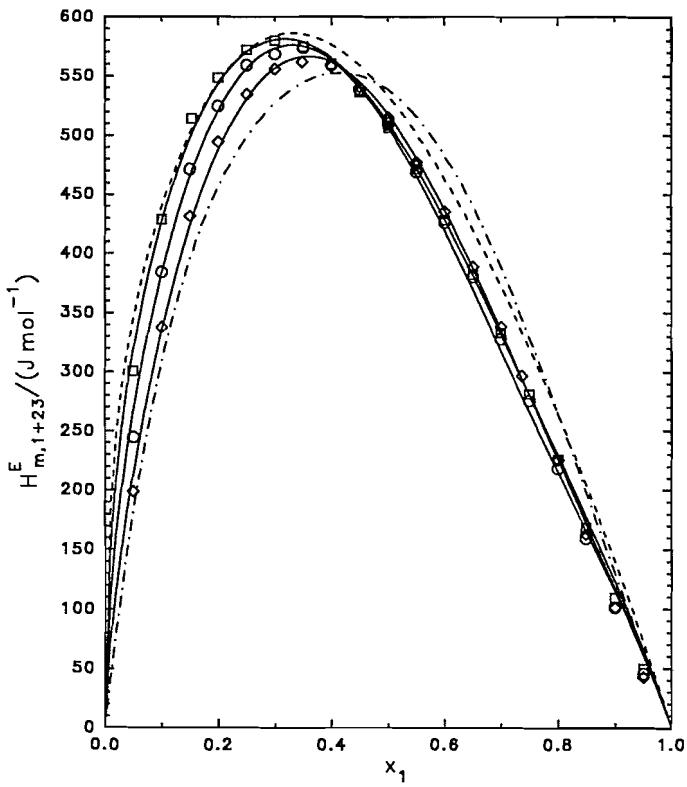

FIG. 1. Excess molar enthalpies $H_{m,1+23}^E$ at 298.15 K for the addition of PrOH to binary mixtures of MTBE and *n*-C_6 to form $x_1C_3H_7OH + x_2(CH_3)_3COCH_3 + x_3CH_3(CH_2)_4CH_3$. Experimental results: □, $x_2/x_3 = 0.3333$; ○, $x_2/x_3 = 0.9992$; ◇, $x_2/x_3 = 3.0000$. Curves: -·-, $x_3 = 0$, from ref. 1; ---, $x_2 = 0$, from ref. 10; —, calculated from eqs. [2] and [3] with $H_{m,T}^E$ from the footnote of Table 1.

Results and discussion

Tables 1–3 summarize the experimental values of $H_{m,1+23}^E$ measured for the three ternary systems. Included in these tables are the corresponding values of $H_{m,123}^E$ calculated from eq. [1], using the smooth representations of $H_{m,23}^E$ reported previously

Can. J. Chem. Downloaded from www.nrcresearchpress.com by EESC ESCOLA DE ENGENHARIA on 09/08/12
For personal use only.

TABLE 1. Experimental excess molar enthalpies $H^E_{m,1+23}$ at 298.15 K for the addition of PrOH to (MTBE + *n*-C_6) to form $\{x_1C_3H_7OH + x_2(CH_3)_3COCH_3 + x_3CH_3(CH_2)_4CH_3\}$, and values of $H^E_{m,123}$ calculated from eq. [1] using $H^E_{m,23}$ from ref. 7

x_1	$H^E_{m,1+23}$[a] / J mol^{-1}	$H^E_{m,123}$ / J mol^{-1}	x_1	$H^E_{m,1+23}$[a] / J mol^{-1}	$H^E_{m,123}$ / J mol^{-1}	x_1	$H^E_{m,1+23}$[a] / J mol^{-1}	$H^E_{m,123}$ / J mol^{-1}
			$x_2/x_3 = 0.3333$, $H^E_{m,23}$/(J mol^{-1}) = 279.9					
0.0500	300.9	566.8	0.4000	560.3	728.3	0.7000	333.3	417.3
0.1001	429.1	681.0	0.4501	536.6	690.5	0.7501	281.2	351.2
0.1532	514.5	751.5	0.5000	508.5	648.5	0.8000	225.6	281.6
0.2000	549.0	772.9	0.5003	506.6	646.5	0.8500	168.7	210.7
0.2500	572.1	782.0	0.5502	471.9	597.7	0.9000	109.7	137.7
0.3000	580.2	776.0	0.6000	428.5	540.4	0.9500	50.0	64.0
0.3499	574.9	756.9	0.6501	382.4	480.3			
			$x_2/x_3 = 0.9992$, $H^E_{m,23}$/(J mol^{-1}) = 369.5					
0.0500	244.6	595.6	0.4003	559.8	781.3	0.6999	328.1	439.0
0.1000	384.3	716.8	0.4503	539.0	742.1	0.7501	275.3	367.7
0.1500	471.4	785.4	0.5000	510.2	695.0	0.8002	217.9	291.8
0.1999	525.0	820.6	0.5002	512.4	697.1	0.8499	159.5	215.0
0.2501	559.0	836.0	0.5498	469.3	635.6	0.9000	101.6	138.6
0.3000	568.6	827.2	0.6001	426.3	574.0	0.9500	46.0	64.4
0.3500	574.1	814.3	0.6499	380.5	509.9			
			$x_2/x_3 = 3.0000$, $H^E_{m,23}$/(J mol^{-1}) = 275.3					
0.0501	199.0	460.5	0.4001	558.4	723.6	0.7001	338.4	420.9
0.1001	337.8	585.6	0.4503	540.8	692.1	0.7372	297.0	369.4
0.1501	431.7	665.7	0.5001	515.3	653.0	0.8001	225.3	280.3
0.2000	494.7	714.9	0.5501	475.0	598.8	0.8500	163.0	204.3
0.2502	534.7	741.1	0.5501	477.3	601.1	0.9000	101.5	129.0
0.3000	555.9	748.6	0.5999	435.8	545.9	0.9500	42.9	56.7
0.3480	562.1	741.6	0.6503	389.0	485.3			

[a]Ternary term for representation of $H^E_{m,1+23}$ by eqs. [2] and [3]: $H^E_{m,T}$/(J mol^{-1}) = $x_1x_2x_3(3708.5 - 18394.5x_1 - 7227.7x_2 + 32249.1x_1^2 + 41410.5x_1x_2 - 365.5x_2^2 - 29684.8x_1^3 - 50083.2x_1^2x_2)$, s = 8.6.

TABLE 2. Experimental excess molar enthalpies $H^E_{m,1+23}$ at 298.15 K for the addition of PrOH to (MTBE + *br*-C_6) to form $\{x_1C_3H_7OH + x_2(CH_3)_3COCH_3 + x_3(CH_3)_2CHCH(CH_3)_2\}$, and values of $H^E_{m,123}$ calculated from eq. [1] using $H^E_{m,23}$ from ref. 8

x_1	$H^E_{m,1+23}$[a] / J mol^{-1}	$H^E_{m,123}$ / J mol^{-1}	x_1	$H^E_{m,1+23}$[a] / J mol^{-1}	$H^E_{m,123}$ / J mol^{-1}	x_1	$H^E_{m,1+23}$[a] / J mol^{-1}	$H^E_{m,123}$ / J mol^{-1}
			$x_2/x_3 = 0.3334$, $H^E_{m,23}$/(J mol^{-1}) = 235.4					
0.0499	298.2	521.9	0.4502	506.6	636.1	0.7000	301.1	371.8
0.0500	305.0	528.7	0.4502	511.0	640.5	0.7001	300.8	371.5
0.1001	424.9	636.7	0.4999	475.6	593.3	0.7500	252.5	311.4
0.1001	426.8	638.7	0.5000	474.5	592.2	0.7501	257.8	316.6
0.1499	469.3	669.4	0.5000	480.7	598.4	0.7998	205.1	252.2
0.1500	471.5	671.6	0.5000	480.9	598.6	0.8000	200.6	247.7
0.2001	509.5	697.8	0.5499	441.7	547.6	0.8500	148.2	183.5
0.2501	533.1	709.6	0.5500	437.6	543.5	0.8500	152.6	187.9
0.3000	544.3	709.1	0.6000	395.8	490.0	0.9000	99.9	123.5
0.3501	543.2	696.2	0.6000	400.9	495.0	0.9000	95.9	119.4
0.3999	531.1	672.4	0.6499	349.7	432.1	0.9500	44.5	56.3
0.4002	527.7	668.9	0.6500	356.8	439.2	0.9500	48.4	60.1

TABLE 2 (*concluded*)

x_1	$H^E_{m,1+23}$[a] / J mol^{-1}	$H^E_{m,123}$ / J mol^{-1}	x_1	$H^E_{m,1+23}$[a] / J mol^{-1}	$H^E_{m,123}$ / J mol^{-1}	x_1	$H^E_{m,1+23}$[a] / J mol^{-1}	$H^E_{m,123}$ / J mol^{-1}
			x_2/x_3 = 1.0007, $H^E_{m,23}$/(J mol^{-1}) = 307.9					
0.0500	245.5	538.0	0.4001	528.0	712.7	0.7000	314.3	406.6
0.1000	390.4	667.4	0.4501	513.5	682.8	0.7498	260.9	337.9
0.1500	456.6	718.3	0.4999	492.3	646.2	0.7998	207.3	268.9
0.2000	496.0	742.3	0.5001	494.6	648.5	0.8500	150.8	197.0
0.2501	519.5	750.3	0.5500	454.0	592.5	0.9000	95.3	126.1
0.3000	536.1	751.6	0.6000	414.0	537.1	0.9500	43.3	58.7
0.3500	532.8	732.9	0.6500	366.3	474.0			
			x_2/x_3 = 2.9903, $H^E_{m,23}$/(J mol^{-1}) = 226.8					
0.0501	201.8	417.3	0.4000	546.2	682.3	0.7000	341.7	409.8
0.1000	341.0	545.1	0.4500	538.8	663.6	0.7501	285.1	341.8
0.1500	417.9	610.7	0.5002	516.8	630.2	0.8001	225.5	270.8
0.2000	477.9	659.3	0.5002	515.6	628.9	0.8500	163.4	197.4
0.2500	509.4	679.5	0.5500	484.0	586.1	0.9000	103.1	125.8
0.3000	529.9	688.7	0.6000	442.4	533.2	0.9500	46.3	57.7
0.3500	545.7	693.1	0.6500	397.7	477.1			

[a]Ternary term for representation of $H^E_{m,1+23}$ by eqs. [2] and [3]: $H^E_{m,T}$/(J mol^{-1}) = $x_1x_2x_3$(2843.2 − 13152.8x_1 − 5106.5x_2 + 26271.8x_1^2 + 11110.4x_1x_2 + 1927.1x_2^2 − 28760.2x_1^3), s = 6.1.

TABLE 3. Experimental excess molar enthalpies $H^E_{m,1+23}$ at 298.15 K for the addition of PrOH to (MTBE + c-C_6) to form {$x_1C_3H_7OH$ + $x_2(CH_3)_3COCH_3$ + $x_3C_6H_{12}$}, and values of $H^E_{m,123}$ calculated from eq. [1] using $H^E_{m,23}$ from ref. 9

x_1	$H^E_{m,1+23}$[a] / J mol^{-1}	$H^E_{m,123}$ / J mol^{-1}	x_1	$H^E_{m,1+23}$[a] / J mol^{-1}	$H^E_{m,123}$ / J mol^{-1}	x_1	$H^E_{m,1+23}$[a] / J mol^{-1}	$H^E_{m,123}$ / J mol^{-1}
			x_2/x_3 = 0.3335, $H^E_{m,23}$/(J mol^{-1}) = 370.4					
0.0500	297.9	649.8	0.3998	571.9	794.2	0.7000	350.9	462.0
0.1000	435.1	768.5	0.4500	552.3	756.1	0.7501	295.6	388.2
0.1500	507.9	822.8	0.5001	523.1	708.3	0.8000	240.7	314.8
0.2001	555.5	851.8	0.5001	523.8	709.0	0.8500	181.5	237.0
0.2500	579.2	857.0	0.5499	488.5	655.2	0.9000	121.2	158.2
0.2999	590.7	850.1	0.5998	447.6	595.8	0.9500	59.3	77.8
0.3498	588.0	828.9	0.6502	400.5	530.1			
			x_2/x_3 = 0.9993, $H^E_{m,23}$/(J mol^{-1}) = 465.5					
0.0500	243.4	685.6	0.3999	550.8	830.2	0.7001	332.1	471.7
0.1000	383.7	802.6	0.4498	533.0	789.1	0.7498	276.9	393.4
0.1499	457.0	852.7	0.4999	512.5	745.3	0.7999	220.3	313.4
0.1999	516.5	889.0	0.5001	512.8	745.5	0.8500	162.1	231.9
0.2500	548.8	898.0	0.5500	475.5	685.0	0.9000	104.9	151.5
0.3001	561.1	886.9	0.6000	433.3	619.5	0.9500	49.5	72.8
0.3501	557.7	860.2	0.6500	384.1	547.1			
			x_2/x_3 = 2.9920, $H^E_{m,23}$/(J mol^{-1}) = 331.7					
0.0500	203.1	518.2	0.3999	558.7	757.8	0.7000	347.4	446.9
0.1000	341.4	639.9	0.4501	542.6	725.0	0.7499	290.4	373.3
0.1499	435.2	717.1	0.5003	519.8	685.6	0.8000	230.7	297.0
0.2001	499.9	765.2	0.5500	487.1	636.3	0.8500	169.0	218.7
0.2504	543.8	792.5	0.6003	446.1	578.7	0.9000	107.9	141.1
0.3000	558.9	791.1	0.6500	399.0	515.1	0.9500	49.0	65.6
0.3501	566.5	782.1						

[a]Ternary term for representation of $H^E_{m,1+23}$ by eqs. [2] and [3]: $H^E_{m,T}$/(J mol^{-1}) = $x_1x_2x_3$(5790.9 − 22102.2x_1 − 15877.5x_2 + 27649.4x_1^2 + 27668.3x_1x_2 + 11966.3x_2^2 − 28228.4x_1^3), s = 8.2.

Can. J. Chem. Downloaded from www.nrcresearchpress.com by EESC ESCOLA DE ENGENHARIA on 09/08/12
For personal use only.

Can. J. Chem. Downloaded from www.nrcresearchpress.com by EESC ESCOLA DE ENGENHARIA on 09/08/12
For personal use only.

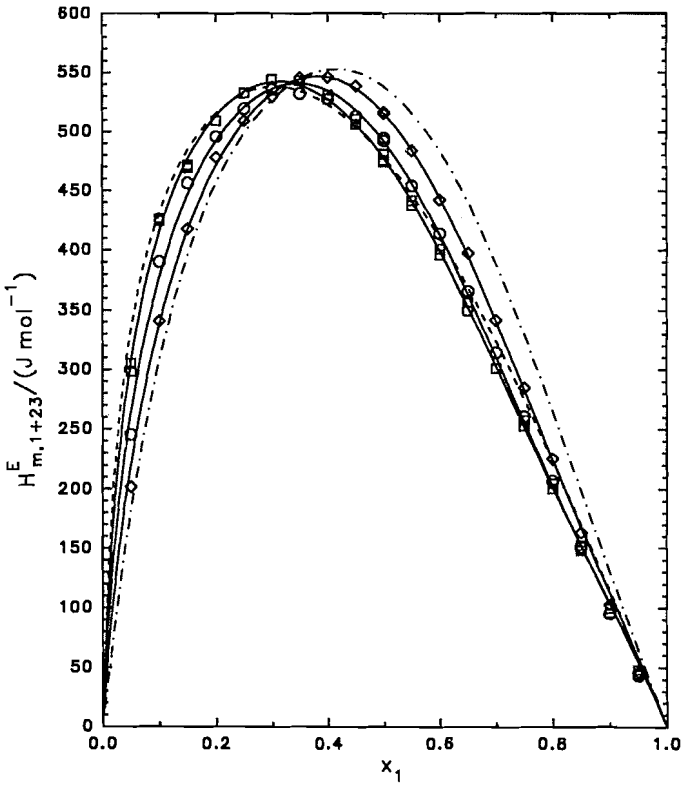

FIG. 2. Excess molar enthalpies $H^E_{m,1+23}$ at 298.15 K for the addition of PrOH to binary mixtures of MTBE and *br*-C_6 to form $x_1C_3H_7OH + x_2(CH_3)_3COCH_3 + x_3(CH_3)_2CHCH(CH_3)_2$. Experimental results: □, $x_2/x_3 = 0.3334$; ○, $x_2/x_3 = 1.0007$; ◇, $x_2/x_3 = 2.9903$. Curves: ---, $x_3 = 0$, from ref. 1; ---, $x_2 = 0$, from ref. 8; —, calculated from eqs. [2] and [3] with $H^E_{m,T}$ from the footnote of Table 2.

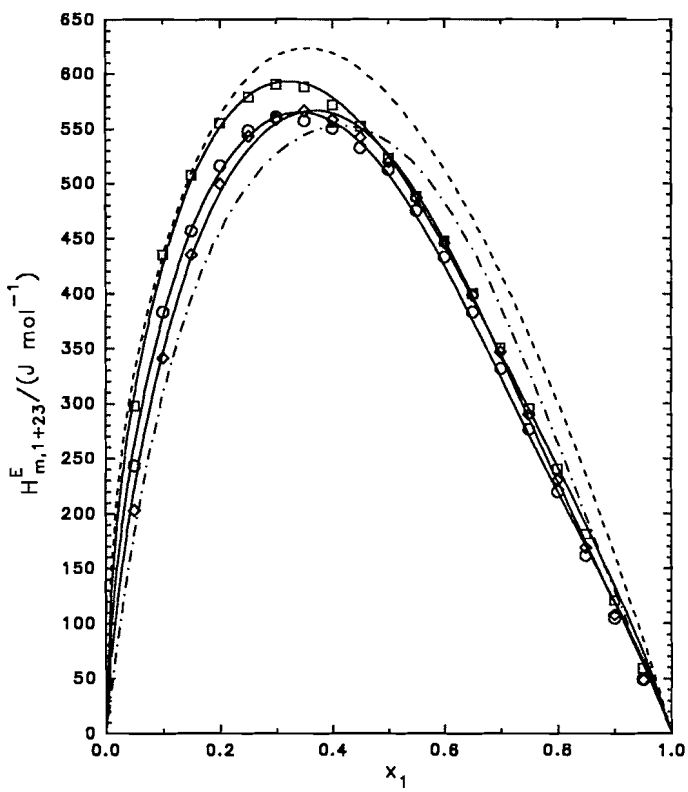

FIG. 3. Excess molar enthalpies $H^E_{m,1+23}$ at 298.15 K for the addition of PrOH to binary mixtures of MTBE and *c*-C_6 to form $x_1C_3H_7OH + x_2(CH_3)_3COCH_3 + x_3C_6H_{12}$. Experimental results: □, $x_2/x_3 = 0.3335$; ○, $x_2/x_3 = 0.9993$; ◇, $x_2/x_3 = 2.9920$. Curves: ---, $x_3 = 0$, from ref. 1; ---, $x_2 = 0$, from ref. 11; —, calculated from eqs. [2] and [3] with $H^E_{m,T}$ from the footnote of Table 3.

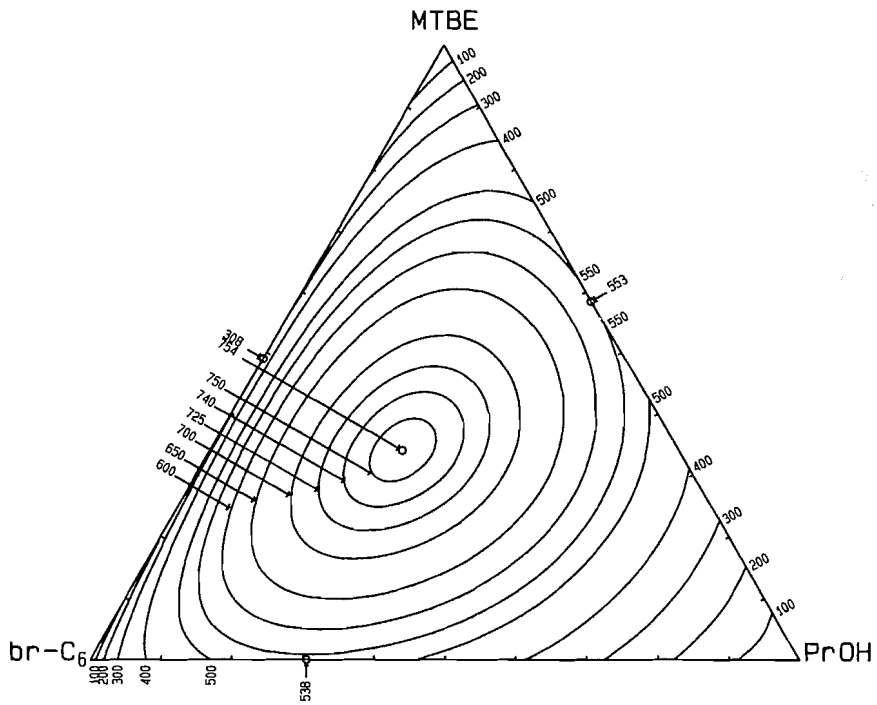

FIG. 4. Contours for constant values of the excess molar enthalpy $H^E_{m,123}/(J\ mol^{-1})$ of the (PrOH + MTBE + *br*-C_6) system at 298.15 K, calculated from eqs. [1]–[3] using $H^E_{m,T}$ from the footnote of Table 2.

for (MTBE + n-C_6) (7), (MTBE + br-C_6) (8), and (MTBE + c-C_6) (9). The $H^E_{m,1+23}$ results are plotted in Figs. 1–3. Also shown for each system are curves for the cases $x_2 = 0$ and $x_3 = 0$, taken from the literature: (PrOH + MTBE) (1), (PrOH + n-C_6) (10), (PrOH + br-C_6) (8), and (PrOH + c-C_6) (11).

As in our previous work (1, 2, 7, 9, 10), the values of $H^E_{m,1+23}$ were represented as a sum of binary terms (12) with an added ternary contribution

$$[2] \qquad H^E_{m,1+23} = \left(\frac{x_2}{1-x_1}\right)H^E_{m,12} + \left(\frac{x_3}{1-x_1}\right)H^E_{m,13} + H^E_{m,T}$$

and following Morris et al. (13), the form

$$[3] \qquad H^E_{m,T} = x_1x_2x_3(c_0 + c_1x_1 + c_2x_2 + c_3{x_1}^2 + c_4x_1x_2 + c_5{x_2}^2 + c_6{x_1}^3 + \cdots)$$

was adopted for the ternary term. For each system, the values of the parameters c_k were determined by the method of least squares, and the results of the analyses are given in the footnotes of Tables 1–3, along with the standard deviations s of the representations. Curves calculated using these representations are shown in Figs. 1–3.

Equations [1]–[3] were used to calculate constant $H^E_{m,123}$ contours on Roozeboom diagrams for each of the systems. These are very similar to each other and to those found for the ethanol systems studied previously (2). The plot for (PrOH + MTBE + br-C_6) in Fig. 4 typifies the behaviour of $H^E_{m,123}$ for the present systems. In all cases, a maximum of $H^E_{m,123}$ occurs near the centroid of the triangle. The locations and values of the maxima (x_1, x_2, $H^E_{m,123}$/(J mol^{-1})) are (0.2683, 0.3438, 836), (0.2713, 0.3397, 754), and (0.2491, 0.3181, 899) for the present n-C_6, br-C_6, and c-C_6 systems, respectively.

Acknowledgement

The financial support of the Natural Sciences and Engineering Research Council of Canada (NSERC) is gratefully acknowledged.

1. S. Zhu, S. Shen, G.C. Benson, and B.C.-Y. Lu. Fluid Phase Equilib. **22**, 1073 (1993).
2. S. Zhu, S. Shen, G.C. Benson, and B.C.-Y. Lu. J. Solution Chem. In press.
3. TRC thermodynamic tables — non-hydrocarbons. Thermodynamics Research Center, Texas A & M University System, College Station, TX. 1988. pp. a-5030, a-6040.
4. TRC thermodynamic tables — hydrocarbons. Thermodynamics Research Center, Texas A & M University System, College Station, TX. 1988. pp. a-1010, a-1140, a-2050.
5. R. Tanaka, P.J. D'Arcy, and G.C. Benson. Thermochim. Acta, **11**, 163 (1975).
6. F. Kimura, G.C. Benson, and C.J. Halpin. Fluid Phase Equilib. **11**, 245 (1983).
7. L. Wang, G.C. Benson, and B.C.-Y. Lu. Thermochim. Acta, **213**, 83 (1993).
8. L. Wang, G.C. Benson, and B.C.-Y. Lu. J. Chem. Thermodyn. **24**, 1305 (1992).
9. S. Zhu, S. Shen, G.C. Benson, and B.C.-Y. Lu. Thermochim. Acta. In press.
10. L. Wang, G.C. Benson, and B.C.-Y. Lu. J. Chem. Eng. Data, **37**, 403 (1992).
11. F. Veselý, P. Uchytil, M. Zábranský, and J. Pick. Coll. Czech. Chem. Commun. **44**, 2869 (1979).
12. C.C. Tsao and J.M. Smith. Chem. Eng. Prog. Symp. Ser. No. 7, **49**, 107 (1953).
13. J.W. Morris, P.J. Mulvey, M.M. Abbott, and H.C. Van Ness. J. Chem. Eng. Data, **20**, 403 (1975).

Can. J. Chem. Downloaded from www.nrcresearchpress.com by EESC ESCOLA DE ENGENHARIA on 09/08/12
For personal use only.

Rate constant and activation energy determination for reaction of $e^-_{(aq)}$ and $^{\cdot}OH$ with 2-butanone and propanal[1]

STEPHEN P. MEZYK

AECL Research, Research Chemistry Branch, Whiteshell Laboratories, Pinawa, MB R0E 1L0, Canada

and

Radiation Laboratory, University of Notre Dame, South Bend, IN 46556, U.S.A.

Received September 27, 1993

STEPHEN P. MEZYK. Can. J. Chem. **72**, 1116 (1994).

The techniques of pulse radiolysis and absorption spectroscopy have been used to determine kinetic parameters for $e^-_{(aq)}$ and $^{\cdot}OH$ reaction with 2-butanone and propanal. The temperature dependent rate constants for hydrated electron reaction are given by $\ln k(T) = (28.96 \pm 0.06) - (1970 \pm 20)/T$ (2-butanone, 275–343 K), and $\ln k(T) = (29.2 \pm 0.2) - (2160 \pm 50)/T$ (propanal, 275–310 K), where the given uncertainties are 1σ and only represent precision, and the rate constants are in units of M^{-1} s^{-1}. For hydroxyl radical reaction over the same temperature ranges, $\ln k(T) = (25.32 \pm 0.02) - (1460 \pm 40)/T$ (2-butanone) and $\ln k(T) = (32.73 \pm 0.03) - (3310 \pm 100)/T$ (propanal).

STEPHEN P. MEZYK. Can. J. Chem. **72**, 1116 (1994).

On a utilisé des techniques de radiolyse pulsée et de spectroscopie d'absorption pour déterminer les paramètres cinétiques des réactions de $e^-_{(aq)}$ et de $^{\cdot}OH$ avec la butan-2-one et le propanal. Les constantes de vitesse dépendantes de la température pour la réaction de l'électron hydraté sont données $\ln k(T) = (28{,}96 \pm 0{,}06) - (1970 \pm 20)/T$ (butan-2-one, 275–343 K) et $\ln k(T) = (29{,}2 \pm 0{,}2) - (2160 \pm 50)/T$ (propanal, 275–310 K), pour lesquelles les incertitudes sont données par 1σ et ne représentent que la précision et les constantes de vitesses sont en unités de M^{-1} s^{-1}. Pour la réaction du radical hydroxyle aux mêmes températures, $\ln k(T) = (25{,}32 \pm 0{,}02) - (1460 \pm 40)/T$ (butan-2-one) et $\ln k(T) = (32{,}73 \pm 0{,}03) - (3310 \pm 100)/T$ (propanal).

[Traduit par la Rédaction]

Introduction

The hazard of radioactive iodine release to the atmosphere, following a nuclear reactor accident, has greatly stimulated the study of the radiation-induced chemistry of iodine-containing species (1). As large quantities of water are also expected to be released in most accidents at water-cooled reactors, a good knowledge of the aqueous chemistry of iodine is necessary for an adequate understanding of its behaviour under these conditions. To date, a large body of information on the mechanisms and rate constants for inorganic iodo-species reaction with a variety of free radicals in solution has been collected (2).

The high radiation fields also expected to be present have been shown to significantly affect the iodine chemistry that occurs (3). Of particular interest are the reactions that lead to the formation of low molecular weight iodoalkanes (4). These species are more volatile, and thus harder to contain than inorganic forms of iodine. Although qualitative demonstration of their formation in irradiated iodide or iodine solutions containing organic impurities has been reported (5–7), there is very little quantitative information on rate constants or mechanisms presently available.

A systematic investigation of this process has recently been initiated, using 2-butanone (MEK) as a prototypical organic impurity (8). The steady state irradiation of MEK solutions has been shown to produce a large number of product species (9). Thus, to ensure a complete understanding of this radiolytic process, the confirmation of proposed mechanistic schemes by computer modelling is required. Such modelling is dependent on accurate rate constant data being available for the aqueous radiolysis species reaction with MEK and its subsequent radiolytic products.

Rate constants for the reaction of water radiolysis intermediates with MEK, and some of its radiolysis products, have not previously been accurately determined. Hence the measurement of kinetic parameters for these compounds has been initiated. This paper reports the experimental determination of the rate constants and activation energies for the reaction of $e^-_{(aq)}$ and $^{\cdot}OH$ with MEK and propionaldehyde (propanal).

Experimental

Solutions of MEK (Aldrich HPLC grade, 99.5%+) and propanal (Aldrich 99%+) were prepared by pipetting the neat liquid into known volumes of Millipore filtered water, which had been fully deoxygenated by bubbling with N_2O or N_2. Some solutions had their pH adjusted to ~5.2 by addition of 10^{-2} M sodium phosphate (monobasic, Anachemica A.C.S. reagent); the rate constants obtained under these conditions were the same as from unbuffered solutions. More acidic solutions were prepared by addition of $HClO_4$ (Baker Analyzed).

The electron pulse radiolysis facilities at the Radiation Laboratory, University of Notre Dame, were used for all these experiments. This system has been described in detail elsewhere (10). The solution flow rate was adjusted so that each irradiation was performed on a fresh sample. Dosimetry was performed using N_2O saturated 10^{-2} M KSCN (Fischer certified) with typical doses of ~600 rads/10 ns pulse.

Experiments at non-ambient temperatures were performed by flowing the room temperature solutions through a short, temperature-controlled condenser tube immediately before irradiation (11). The exact solution temperature was measured by a thermocouple placed directly above the irradiation cell. The temperature stability of this method was found to be better than ±0.5°C.

Results and discussion

Reaction of hydrated electron

The irradiation of N_2-saturated solutions containing 1.0 M *t*-butanol and MEK allows the reaction

$$e^-_{(aq)} + CH_3CH_2COCH_3 \rightarrow CH_3CH_2C(CH_3)O^{\cdot -}$$

[1]The research described herein was supported by the Office of Basic Energy Sciences of the Department of Energy. This is Contribution No. NDRL 3646 from the Notre Dame Radiation Laboratory. Financial assistance was provided by AECL Research.

Can. J. Chem. Downloaded from www.nrcresearchpress.com by EESC ESCOLA DE ENGENHARIA on 09/08/12
For personal use only.

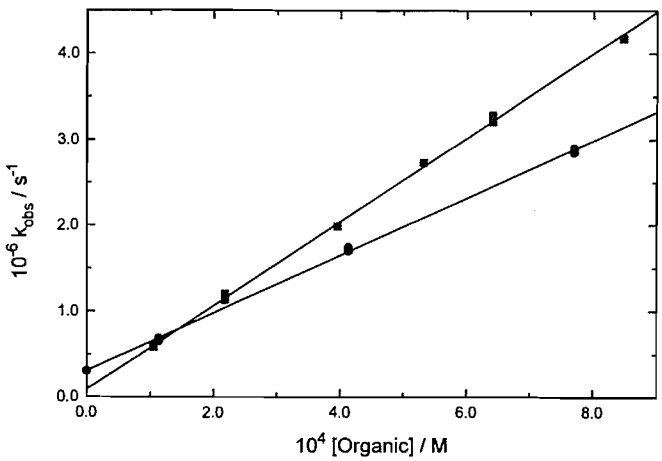

FIG. 1. Rate constant determination for $e^-_{(aq)}$ reaction with MEK (■, 23.0°C) and propanal 23.3 (●, 23.3°C).

to be studied in isolation. The rate constant for this reaction was measured by observing the change in decay of the hydrated electron at 600–650 nm, as a function of the MEK concentration over the range (1–10) × 10^{-4} M. To ensure that monochromator second order effects and solution photolysis were minimized, a Corning 0-54 cut-off filter was placed between the monitoring lamp and the solution.

Typical results from this study are shown in Fig. 1, for a temperature of 23.0°C. A rate constant of $(4.9\pm0.1)\times10^9$ M^{-1} s^{-1} was obtained, significantly slower than the only previous measurement indirectly obtained for room temperature liquid MEK (12) of 1.2×10^{11} M^{-1} s^{-1}.

These experiments were repeated across the temperature range 1.5–70°C, and the individual rate constants obtained are given in Table 1. From the Arrhenius expression,

$$k = Ae^{-E_a/RT}$$

plotted in Fig. 2, the measured activation energy for this reaction is 16.4 ± 0.2 kJ mol^{-1}, with a corresponding pre-exponential factor, $A = (3.8 \pm 0.2) \times 10^{12}$ M^{-1} s^{-1}. These values are in very good agreement to those measured for acetone (13), where an activation energy of 15 kJ mol^{-1} and an A factor of 3.29×10^{12} M^{-1} s^{-1} were obtained over the temperature range 3–47°C.

Similar experiments were conducted for propanal and for this compound, a value of $(3.36\pm0.06)\times10^9$ M^{-1} s^{-1} was obtained at 23.3°C, (Fig. 1), in good agreement with the previous determination of 4.1×10^9 M^{-1} s^{-1} at room temperature (14). By varying the temperature over the range 2–37°C (values given in Table 1), an activation energy of 18.0 ± 0.4 kJ mol^{-1} was obtained (Fig. 2), with an A factor of $(4.8\pm1.0)\times10^{12}$ M^{-1} s^{-1}. The close agreement of the measured Arrhenius parameters for MEK, propanal, and acetone suggests that the hydrated electron reaction mechanism of addition to the oxygen atom (2) is the same for all three compounds.

Reaction of hydroxyl radical

The direct rate constant measurement for the reaction

$$^{\bullet}OH + CH_3CH_2COCH_3 \rightarrow H_2O + CH_3COC^{\bullet}HCH_3$$

was not possible, as the irradiation of N_2O saturated MEK solutions over the pH range 2.0–7.0 produced no change in absorbance over the wavelength range 250–800 nm. Thus this

TABLE 1. Rate constant measurements for $e^-_{(aq)}$ and $^{\bullet}OH$ reaction with MEK and propanal at various temperatures

		10^{-9} k/M^{-1} s^{-1}	
Reaction	T/°C	This work	Other values[a]
$e^-_{(aq)}$ + MEK	1.5	2.97 ± 0.01	120
	10.0	3.7 ± 0.2	
	23.0	4.9 ± 0.1	
	34.5	6.3 ± 0.2	
	41.5	7.3 ± 0.2	
	57.1	9.7 ± 0.2	
	70.0	12.5 ± 0.7	
$e^-_{(aq)}$ + propanal	2.0	1.87 ± 0.01	4.1
	12.6	2.50 ± 0.04	
	23.3	3.36 ± 0.06	
	36.8	4.48 ± 0.09	
$^{\bullet}OH$ + MEK	1.5	0.490 ± 0.005	0.9
	13.5	0.590 ± 0.001	
	24.4	0.734 ± 0.008	
	41.5	0.936 ± 0.009	
	66.5	1.35 ± 0.07	
$^{\bullet}OH$ + propanal	2.5	1.01 ± 0.02	—
	13.5	1.64 ± 0.03	
	24.6	2.39 ± 0.06	
	39.5	4.25 ± 0.04	

[a]Room temperature values.

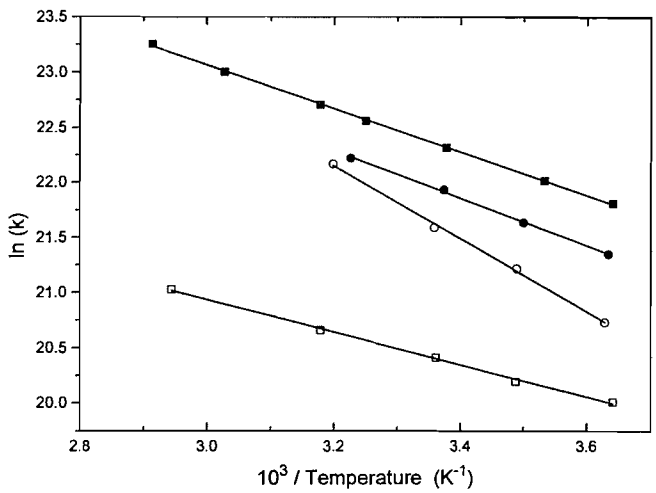

FIG. 2. Activation energy determinations: $e^-_{(aq)}$ reaction with MEK (■) and propanal (●); $^{\bullet}OH$ reaction with MEK (□) and propanal (○).

rate constant was determined by competition kinetics, using SCN^- as the reaction standard. This reaction

$$^{\bullet}OH + SCN^- \rightarrow SCNOH^{\bullet -}$$

was chosen to allow direct comparison to the only previous rate constant determination for hydroxyl radical reaction with MEK (15), and because its temperature dependence has been characterized by the expression (16)

$$[1] \qquad \ln k(T) = (29.6 \pm 0.6) - (1900 \pm 190)/T$$

over the range of this study.

Stock solutions of 1.01×10^{-4} M SCN^- buffered at pH 5.2 were irradiated and the $(SCN)_2^{\bullet -}$ absorption at 472 nm

Can. J. Chem. Downloaded from www.nrcresearchpress.com by EESC ESCOLA DE ENGENHARIA on 09/08/12
For personal use only.

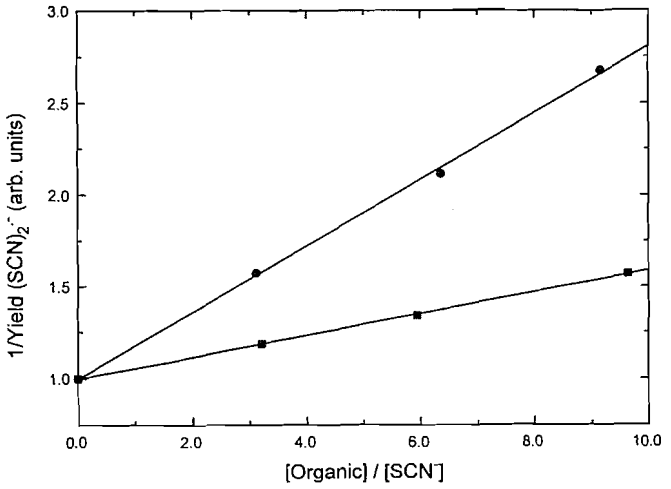

FIG. 3. Competition kinetics determination of the rate constant for reaction of ·OH, with MEK (■, 24.4°C) and propanal (●, 24.6°C), for 1.01×10^{-4} M SCN^- solutions at pH 5.2.

measured. The addition of MEK, over the concentration range $(1–10) \times 10^{-4}$ M, caused the intensity of the peak absorbance to decrease. Assuming that the initial ·OH radical yield is the same in both solutions, the standard competition kinetics equation

$$\frac{1}{[SCN]_2^{\cdot-}} = 1 + \frac{k_{MEK}[MEK]}{k_{SCN^-}[SCN^-]}$$

predicts that a plot of $1/\text{Yield}(SCN)_2^{\cdot-}$ vs. $[MEK]/[SCN^-]$ should give a straight line of slope k_{MEK}/k_{SCN^-}. The values obtained for MEK at 24.4°C are shown in Fig. 3, and an excellent straight line of slope 0.0599 ± 0.0007 was obtained. Based on the calculated rate constant (16) of 1.22×10^{10} M^{-1} s^{-1} for ·OH with SCN^- at this temperature, this corresponds to a rate constant for ·OH reaction with MEK of $(7.34 \pm 0.08) \times 10^8$ M^{-1} s^{-1}. This value is slightly lower than the previously determined rate constant of 9×10^8 M^{-1} s^{-1} (15).

Concern has been raised previously (17) about a potential problem with this procedure in that the formation of $(SCN)_2^{\cdot-}$ involves the intermediate formation of SCN· and $SCNOH^{\cdot-}$ (18–20). If either of these species can oxidise MEK, then less $(SCN)_2^{\cdot-}$ will be formed, leading to an artificially high rate constant for ·OH reaction with MEK.

To determine whether such interfering reactions occurred for MEK, the experimental $(SCN)_2^{\cdot-}$ formation curves obtained at 24.4°C (shown in Fig. 4) were modelled by the following reaction scheme,

$$e^-_{(aq)} + N_2O + H_2O \rightarrow {}^{\cdot}OH + N_2 + {}^-OH \qquad k = 8.9 \times 10^9\ M^{-1}\ s^{-1} \quad (2)$$

$$^{\cdot}OH + SCN^- \rightarrow SCNOH^{\cdot-} \qquad k = 1.22 \times 10^{10}\ M^{-1}\ s^{-1} \quad (16)$$

[2] $SCNOH^{\cdot-} \rightarrow SCN^{\cdot} + {}^-OH \qquad k_2$

[3] $SCN^{\cdot} + SCN^- \rightarrow (SCN)_2^{\cdot-} \qquad k_3$

[4] $(SCN)_2^{\cdot-} \rightarrow SCN^{\cdot} + SCN^- \qquad k_4$

$$^{\cdot}OH + MEK \rightarrow MEK^{\cdot} + {}^-OH \qquad k = 7.34 \times 10^8\ M^{-1}\ s^{-1}$$

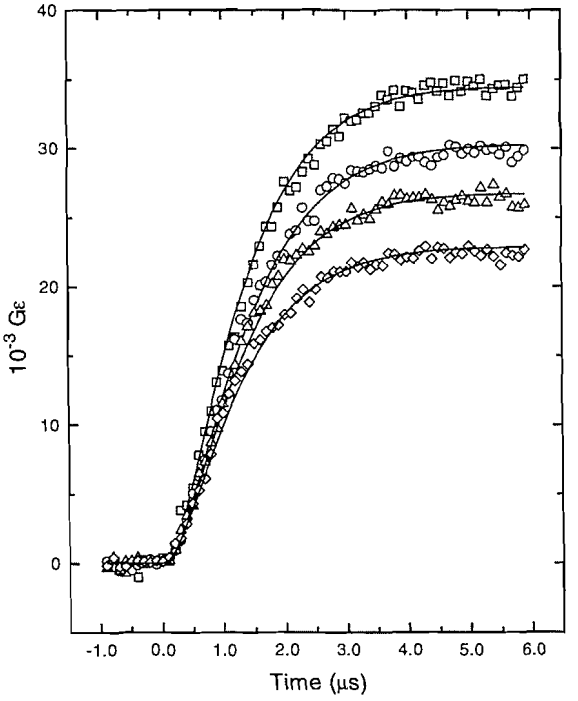

FIG. 4. Comparison of experimental and calculated $(SCN)_2^{\cdot-}$ growth kinetics observed at 472 nm with added MEK concentrations of 0.00 (□), 3.25 (○), 6.01 (△), and 9.71 (◇) $\times 10^{-4}$ M at 24.4°C. Solid lines are calculated based on model described in text.

using the FACSIMILE (21) modelling program. The values of the rate constants, k_2–k_4, and the total yield of $(SCN)_2^{\cdot-}$ were fitted to the experimental data, with average values of $G\epsilon = 34\,500 \pm 200$, $k_2 = (1.57 \pm 0.04) \times 10^9$ s^{-1}, $k_3 = (1.23 \pm 0.07) \times 10^{10}$ M^{-1} s^{-1} and $k_4 = (1.51 \pm 0.05) \times 10^4$ s^{-1} obtained. These rate constants are in general agreement with previously determined values of $>5 \times 10^7$ s^{-1} (19), $\sim 6 \times 10^9$ M^{-1} s^{-1} (16), and $\sim 3 \times 10^4$ s^{-1} (16), respectively (the latter two literature values have extremely large error, and can only be considered correct to their order of magnitude). Using the values of this study, the temporal profiles for the different MEK concentrations were calculated, and these are also shown in Fig. 4. The excellent agreement seen suggests that no additional reactions are occurring in this system.

Additional evidence was obtained by modelling the effects of adding the hypothetical oxidising reactions

[5] $SCNOH^{\cdot-} + MEK \rightarrow MEK^{\cdot} + SCN^- + {}^-OH \qquad k_5$

[6] $SCN^{\cdot} + MEK \rightarrow MEK^{\cdot} + SCN^- \qquad k_6$

[7] $MEK^{\cdot} + SCN^- \rightarrow SCN^{\cdot} + MEK \qquad k_7$

to the original reaction mechanism. These calculated temporal profiles, for a MEK concentration of 9.71×10^{-4} M, are shown in Fig. 5. It was found that including reaction [5], with a reaction rate constant of $k_5 \leq 5.0 \times 10^9$ M^{-1} s^{-1}, had no effect on the $(SCN)_2^{\cdot-}$ growth profile. However, if reaction [6] occurred with the same rate constant, then the yield of $(SCN)_2^{\cdot-}$ was considerably reduced, and the $(SCN)_2^{\cdot-}$ growth rate was far faster. In contrast, the effect of including reaction [7] was to increase the yield, and make the overall growth significantly slower.

Based on these findings, it is believed that there are no

Can. J. Chem. Downloaded from www.nrcresearchpress.com by EESC ESCOLA DE ENGENHARIA on 09/08/12
For personal use only.

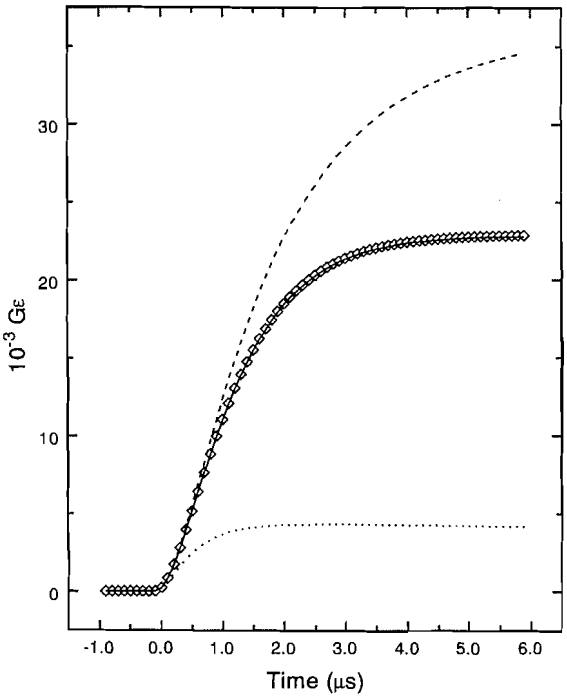

FIG. 5. Calculated $(SCN)_2^{\bullet -}$ growth kinetics for 9.71×10^{-4} M MEK solutions containing no additional oxidation reactions (◇), $SCNOH^{\bullet -}$ oxidation of MEK with $k_5 = 5.0 \times 10^9$ M^{-1} s^{-1} (—); $^{\bullet}SCN$ oxidation of MEK with $k_6 = 5.0 \times 10^9$ M^{-1} s^{-1} (···) and MEK$^{\bullet}$ oxidation of SCN^- with $k_7 = 5.0 \times 10^9$ M^{-1} s^{-1} (- - -).

oxidation reactions from $SCN^{\bullet}$ or $SCNOH^{\bullet -}$ occurring for MEK.

Rate constants for MEK reaction with $^{\bullet}OH$ were obtained at various temperatures (see Table 1) and the calculated Arrhenius plot is also shown in Fig. 2. For this reaction a value of $E_a = 12.2 \pm 0.3$ kJ mol^{-1} was obtained, with an A factor of $(1.00 \pm 0.02) \times 10^{11}$ M^{-1} s^{-1}.

Analogous SCN^- competition experiments were also performed for propanal. The rate constant determined at 24.6°C, $(2.39 \pm 0.06) \times 10^9$ M^{-1} s^{-1} (Fig. 3) is faster than measured for $^{\bullet}OH$ reaction with MEK. The experimental temporal profiles for different propanal concentrations were also modelled at this temperature, and again showed that no extraneous oxidation reactions need to be considered. Rate constant determinations at different temperatures gave the activation energy and pre-exponential factors for propanal as 27.5 ± 0.8 kJ mol^{-1} and $(1.63 \pm 0.05) \times 10^{14}$ M^{-1} s^{-1}, respectively, (individual values shown in Table 1 and Fig. 2).

These higher E_a and A Arrhenius parameters suggest that either a different $^{\bullet}H$ atom is being abstracted from propanal, or that the β carbon C—H bond strength is larger than in MEK. At present, *ab initio* calculations and EPR experiments are being performed to investigate these two possibilities.

Acknowledgements

The author would like to thank Dr. H.W. Richter for her assistance in operating the temperature control system used in this study.

1. T.J. Thompson and J.G. Beckerley (*Editors*). The technology of nuclear reactor safety. MIT Press, Cambridge. 1973.
2. G.V. Buxton, C.L. Greenstock, W.P. Helman, and A.B. Ross. J. Phys. Chem. Ref. Data, **17**, 513 (1988).
3. A.C. Vikis (*Editor*). Proceedings of the 3rd CSNI Workshop on Iodine Chemistry in Reactor Safety. AECL Research Report, AECL-9923. 1989.
4. J. Paquette and B.L. Ford. Radiat. Phys. Chem. **36**, 353 (1990).
5. E.C. Beahm, Y.-M. Wang, S.J. Wisbey, and W.E. Shockley. Nucl. Technol. **78**, 34 (1987).
6. J.B. Lutz and J.L. Kelly. Nucl. Technol. **80**, 431 (1987).
7. S. Ono, N. Fujita, K. Fujiwara, H. Mochizuki, H. Shiraishi, and K. Ishigure. Proc. Int. Conf. Water Chemistry of Nuclear Reactor Systems 4. British Nuclear Energy Society, London. 1986.
8. C.A. Chuaqui and J.M. Ball. 4th Meeting of the European Severe Accident Chemistry Group ENEL/CRTN, Milano, December 1992.
9. S.M.S. Akhtar, R.J. Woods, and J.A.E. Bardwell. Int. J. Radiat. Phys. Chem. **7**, 603 (1975).
10. R.H. Schuler, A.L. Hartzell, and B. Behar. J. Phys. Chem. **85**, 192 (1981).
11. H.W. Richter, K.P. Madden, and I. Duncanson. To be published.
12. A.V. Vannikov, E.I. Mal'tsev, and A.V. Rudnev. Proceedings of the Tihany Symposium Radiation Chemistry Vol. 1. 3rd ed. 1971. p. 157.
13. C.C. Lai and G.R. Freeman. J. Phys. Chem. **94**, 302 (1990).
14. A.M. Afanassiev, K. Okazaki, and G.R. Freeman. J. Phys. Chem. **83**, 1244 (1979).
15. G.E. Adams, J.W. Boag, J. Currant, and B.D. Michael. Pulse radiolysis. *Edited by* M. Ebert, J.P. Keene, A.J. Swallow, and J.H. Baxendale. Academic Press, NY. 1965. p. 131.
16. M. Chin and P.H. Wine. J. Photochem. Photobiol. Chem. **69**, 17 (1992).
17. S.R. Logan and G.A. Salmon. Radiat. Phys. Chem. **24**, 593 (1984).
18. J.H. Baxendale, P.L.T. Bevan, and D.A. Stott. Trans. Faraday Soc. **64**, 2389 (1968).
19. D.H. Ellison, G.A. Salmon, and F. Wilkinson. Proc. R. Soc. A, **328**, 23 (1972).
20. D. Behar, P.L.T. Bevan, and B.D. Michael. Trans. Faraday Soc. **61**, 1417 (1965).
21. A.R. Curtis and W.P. Sweetenham. Harwell Research Report, AERE-R 12805. 1987.

Can. J. Chem. Downloaded from www.nrcresearchpress.com by EESC ESCOLA DE ENGENHARIA on 09/08/12
For personal use only.

Protonation/deprotonation energetics of uracil, thymine, and cytosine in water from e.m.f./spectrophotometric measurements

SONALI GANGULY AND KIRON K. KUNDU[1]
Physical Chemistry Laboratories, Jadavpur University, Calcutta-700 032, India
Received March 19, 1993

SONALI GANGULY and KIRON K. KUNDU. Can. J. Chem. **72**, 1120 (1994).

The protonation/deprotonation constants for uracil (U) (pK_1 and pK_2), thymine (T) (pK_1) and cytosine (C) (pK_1 and pK_2) in water have been determined from emf measurements of Harned–Ehler type cells comprising H_2 and Ag–AgI electrodes at five equidistant temperatures ranging from 15–35°C. The pK_a values were fitted in the temperature equation $pK_a = AT^{-1} + B + CT$ by the method of least squares and the standard free energies (ΔG^0), entropies (ΔS^0), and enthalpies (ΔH^0) of protonation/deprotonation processes in water were evaluated using the values of the coefficients A, B, and C of the respective acids. The second step deprotonation constant for T was determined using precise spectrophotometric method. The results have been duly compared with the existing literature data and are also shown to derive important reflections on the sites of protonation/deprotonation in the light of pK values of some acids and bases of comparable functional groups and especially the entropies of protonation/deprotonation of the key DNA–RNA base molecules.

SONALI GANGULY et KIRON K. KUNDU. Can. J. Chem. **72**, 1120 (1994).

Utilisant des mesures de fém de cellules de type Harned Ehler comportant des électrodes H_2 et Ag–AgI effectuées à cinq températures équidistantes allant de 15 à 35°C, on a déterminé les constantes de protonation/déprotonation de l'uracile (U) (pK_1 et pK_2), de la thymine (T) (pK_1) et de la cytosine (C) (pK_1 et pK_2) dans l'eau. Faisant appel à la méthode des moindres carrés, on a ajusté les valeurs de pK_a dans l'équation de température: $pK_a = AT^{-1} + B + CT$; utilisant les valeurs des coefficients A, B et C, on a aussi évalué les énergies libres (ΔG^0), les entropies (ΔS^0) et les enthalpies (ΔH^0) standards des processus de protonation/déprotonation des acides respectifs dans l'eau. Utilisant une méthode spectrophotométrique précise, on a calculé la deuxième constante de déprotonation de T. On a comparé les résultats avec ceux rapportés dans la littérature et, en se basant sur les valeurs de pK_a de quelques acides et de quelques bases portant des groupes fonctionnels comparables et spécialement sur les valeurs des entropies de protonation/déprotonation de molécules clés des bases ADR–ARN, on peut tirer des indications importantes sur les sites de protonation/déprotonation.

[Traduit par la Rédaction]

Introduction

It is well known that a living organism is an open, self regulating, self reproducing and developing heterogeneous system whose most important functional substances are biopolymers, proteins, and nucleic acids (1). In fact, the latter biopolymers are the principal constituents of chromosomes which are responsible for the key living process, namely "biogenesis" — the basis for self-reproduction, development, and propagation of life itself. Also, it is the nucleic acids which dictate the structure and properties of living cells and organisms in the final analysis and specify the genetic programme of protein synthesis.

The principal chain of nucleic acids consists of alternating phosphoric acid (P) units and a sugar moiety. Attached to each of the sugar unit is one heterocyclic nitrogeneous base and this type of sequence is repeated n times. The nitrogeneous heterocyclic bases are derivatives of pyrimidines and purines. Uracil (U), thymine (T), and cytosine (C) are the principal pyrimidine "bases" present in DNA's and RNA's. Because of the structural features all these heterocyclic nitrogeneous bases display "tautomerism" and variable proton accepting and donating propensity and hence the varied energetics of protonation/deprotonation. Energetics of these important biochemical molecules will help us understand the primary roles of RNA's and DNA's on various biological processes. The structures of U, T, and C are illustrated in Fig. 1.

Literature survey (2, 3) reveals that some of the desired data in water are no doubt available. However, we consider most of these protonation/deprotonation constant data to be lacking in precision. These data either are based on half-neutralization

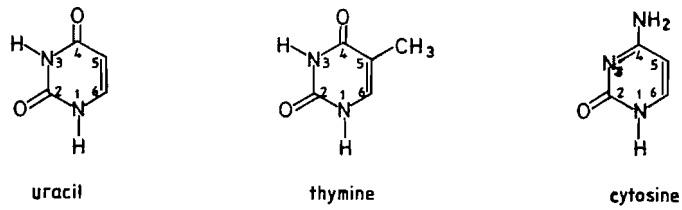

FIG. 1. Structures of uracil, thymine, cytosine.

point (hnp) determination of pH-titration curves using glass (H^+) and aqueous saturated calomel electrodes SCE (W) or hydrogen–calomel electrodes forming cells with liquid junction, or spectrophotometric methods based on isosbestic points using different pH solutions. Moreover, since the experiments were done under a variety of temperature, ionic strength, and solvent conditions, their results are hardly comparable and lack in true thermodynamic precision and physical significance. Furthermore, until now there have been no deprotonation constant and thermodynamic quantities reported for the second step deprotonation constant for T and U, respectively.

This paper reports our findings on protonation/deprotonation constants and related true thermodynamic quantities for U, T, and C as determined by the most precise method by measuring the emf's. We used Harned–Ehler (4) type galvanic cells without liquid junctions comprising Pt, H_2 (g, 1 atm) and Ag–AgI electrodes and buffers of different ionic strengths and did the measurements at five equidistant temperatures ranging from 15–35°C. Notably, preliminary studies with Ag–AgCl electrode exhibited perceptible drifts in emf values with time especially in the case of the free base C containing an amino group possibly because of the formation of Ag^+–amine complex with this compound. The same tendency was however found to be

[1]To whom correspondence should be addressed.

Can. J. Chem. Downloaded from www.nrcresearchpress.com by EESC ESCOLA DE ENGENHARIA on 09/08/12
For personal use only.

Can. J. Chem. Downloaded from www.nrcresearchpress.com by EESC ESCOLA DE ENGENHARIA on 09/08/12
For personal use only.

completely absent in the case of Ag–AgI electrodes due to the lower solubility of AgI as compared to AgCl. Since the effect of hydrolysis was very high in the case of second step deprotonation of T, pK_2 of T cannot be evaluated by emf method and so precise spectrophotometric method was adopted.

The Harned–Ehler type cells used for the determination of various pK_a's and related energetics are [A]–[D].

For $p(K_1)_{H_2A}$ of U, T:

[A] Pt, H_2 (g, 1 atm)/$H_2A(m_1)$, $NaHA(m_2)$, $KI(m_3)$/AgI–Ag

For $p(K_2)_{HA^-}$ of U:

[B] Pt, H_2 (g, 1 atm)/$NaHA(m_1)$, $Na_2A(m_2)$, $KI(m_3)$/AgI–Ag

For $p(K_1)_{H_2A^+}$ of C:

[C] Pt, H_2 (g, 1 atm)/$H_2A^+I^-(m_1)$, $HA(m_2)$, $KI(m_3)$/AgI–Ag

For $p(K_2)_{HA}$ of C:

[D] Pt, H_2 (g, 1 atm)/$HA(m_1)$, $NaA(m_2)$, $KI(m_3)$/AgI–Ag

Experimental

U (grade U-0750), T (grade T-0376), and C (grade C-3506) were all from Sigma and used without further pretreatment. These biochemicals assayed 99% by UV spectroscopy (5, 6). Water was triply distilled and stored in a CO_2-free atmosphere. KI (GR, E Merck) was used after drying at 150°C and then stored in a vacuum desiccator for about 12 h. Stock NaOH (GR, E Merck) solution was prepared and its molality was obtained by alkalimetric titration. For the determination of pK_1 and pK_2 for U, pK_1 for T, and pK_2 for C, cell solutions of different ionic strengths were prepared in well stoppered Jena bottles by mixing appropriate weighed amounts of the "base" under study, KI, NaOH solution, and triply distilled water. For determining pK_1 for C, distilled HI acid (GR, E Merck) was used instead of alkali solution. The method of HI distillation was similar to that as described earlier (*7a*).

For determining the pK_2 of T, buffers containing T and NaOH solution (0.5–5 M) were prepared in a closed chamber fluxed with pure nitrogen to avoid CO_2.

Emf method

The emf's of the cells were measured using a Leeds and Northrup K_4-potentiometer fitted with a moving coil galvanometer (Cambridge Instrument Co.) as the null point detector. Ag–AgI electrodes were of the thermal type and prepared by the method described earlier (*7a*). General experimental procedures including the preparation of H_2(Pt) electrodes and the measurement of emf were similar to those described elsewhere (7). The Ag–AgI electrodes were introduced after 1 h discharge of hydrogen gas through the cells. The equilibrium was attained in 3–4 h. When the emf readings stayed constant to about ±0.1 mV for 1 h, it was assumed that equilibrium had been reached. The readings were first taken at 15°C and then successively at higher temperatures at 5°C intervals. The readings at 25°C when back checked after 35°C agreed to within ±0.3 mV.

Spectrophotometry

A Perkin Elmer Lambda 3A UV/VIS spectrophotometer was used to measure the absorbances of each buffer solution at wavelength = 280 nm (5, 6).

Results

The measured emf's of cells [A]–[D] at different temperatures after due correction to $p_{H_2} = 1$ atm gave the values of E. These E values and the corresponding molalities of KI, H_2A, NaHA for cell [A], KI, NaHA, Na_2A for cell [B], KI, $H_2A^+I^-$, HA for cell [C], and KI, HA, NaA for cell [D] for each of the solvent mixtures are given in Table 1.

The values of pK_1 and pK_2 for U, pK_1 for T, and pK_1 and pK_2 for C were obtained using the functions pK_1' and pK_2' as defined by eqs. [1] to [4].

---

[1] $$pK_1(U, T) = (E - E^0)/k + \log (m_{I^-} m_{H_2A}/m_{HA^-}) + \log (\gamma_{I^-}\gamma_{H_2A}/\gamma_{HA^-})$$

$$pK_1'(U, T) = (E - E^0)/k + \log [m_3(m_1 + m_{OH^-})/(m_2 - m_{OH^-})] = pK_1(U, T) + f(\mu)$$

where

[1′] $$\log m_{OH^-} = \log K_W + p_WH$$

$$p_WH = -\log a_{H^+}\gamma_{OH^-} \approx -\log a_{H^+}\gamma_{I^-} = (E - E^0)/k + \log m_{I^-} \qquad \text{(ref. 8)}$$

and $k = 2.3026\ RT/F$ and μ (ionic strength) $= m_2 + m_3$.

[2] $$pK_2(U) = (E - E^0)/k + \log (m_{I^-} m_{HA^-}/m_{A^{2-}}) + \log (\gamma_{I^-}\gamma_{HA^-}/\gamma_{A^{2-}})$$

$$pK_2'(U) = (E - E^0)/k + \log [m_3(m_1 + m_{OH^-})/(m_2 - m_{OH^-})] + 2S_f(\mu d_0)^{1/2}$$

$$= pK_2(U) + f(\mu)$$

where m_{OH^-} is given by [1′], $\mu = m_1 + 3m_2 + m_3 - m_{OH^-}$, S_f (Debye–Hückel constant) $= 1.824 \times 10^6\ (\epsilon_s T)^{-3/2}$, ϵ_s = dielectric constant of the solvent (ref. 8).

[3] $$pK_1(C) = -\log (m_{H^+} m_{HA}/m_{H_2A^+}) - \log (\gamma_{HA}\gamma_{H^+}/\gamma_{H_2A^+})$$

$$pK_1'(C) = -\log [m_{H^+}(m_2 + m_{H^+})/(m_1 - m_{H^+})] = pK_1(C) + f(\mu)$$

where $-\log (m_{H^+}) = (E - E^0)/k + \log (m_{I^-}) - 2S_f(\mu d_0)^{1/2}$ (ref. 9) and $\mu = m_1 + m_3$.

[4] $$pK_2(C) = (E - E^0)/k + \log (m_{I^-} m_{HA}/m_{A^-}) + \log (\gamma_{I^-}\gamma_{HA}/\gamma_{A^-})$$

$$pK_2'(C) = (E - E^0)/k + \log [m_3(m_1 + m_{OH^-})/(m_2 - m_{OH^-})] = pK_2(C) + f(\mu)$$

where m_{OH^-} is given by eq. [1′] and $\mu = m_2 + m_3$.

TABLE 1. EMF values at different temperatures for different cell solutions in pure water for protonation/deprotonation constant of U, T, and C

μ	$m_1 \times 10^3$ (mol kg^{-1})	$m_2 \times 10^3$ (mol kg^{-1})	$m_3 \times 10^3$ (mol kg^{-1})	emf (V) 15°C	20°C	25°C	30°C	35°C
U: $pK_1 = (pK_a)_{H_2A}$; $m_1 = m_{H_2A}$, $m_2 = m_{HA^-}$, $m_3 = m_{I^-}$								
0.0111	6.4	7.5	3.6	0.5421	0.5465	0.5504	0.5542	0.5585
0.0206	3.8	6.7	13.9	0.5195_5	0.5230	0.5264	0.5295	0.5338
0.0302	4.2	7.5	22.7	0.5075	0.5125	0.5148	0.5177	0.5214
0.0412	7.6	13.4	27.8	0.5031	0.5068	0.5101	0.5138	0.5165
0.0504	7.1	12.5	37.9	0.4960	0.4998	0.5027_5	0.5060	0.5092
0.0616	11.4	20.0	41.6	0.4946	0.4981	0.5012	0.5042	0.5076
0.0810	11.4	20.1	60.9	0.4866	0.4897	0.4930	0.4958	0.4982
U: $pK_2 = (pK_a)_{HA^-}$; $m_1 = m_{HA^-}$, $m_2 = m_{A^{2-}}$, $m_3 = m_{I^-}$								
0.0471	5.0	14.9	11.3	0.6760	0.6781	0.6804_5	0.6830_5	0.6855
0.0609	6.4	19.2	14.5	0.6756	0.6777	0.6799	0.6825	0.6850_5
0.0703	7.4	22.2	15.7	0.6768	0.6789	0.6813	0.6838	0.6864
0.0803	8.4	25.1	19.0	0.6749	0.6769	0.6791_5	0.6816	0.6841_5
0.0954	9.9	29.7	22.5	0.6745_5	0.6764	0.6784_5	0.6810	0.6837
0.1120	11.8	35.4	24.6	0.6762	0.6779	0.6799	0.6826	0.6853
0.1253	13.3	39.8	26.6	0.6769	0.6785	0.6805	0.6830	0.6858
0.1408	14.8	44.2	30.7	0.6757	0.6771	0.6788	0.6816	0.6843
T: $pK_1 = (pK_a)_{H_2A}$; $m_1 = m_{H_2A}$, $m_2 = m_{HA^-}$, $m_3 = m_{I^-}$								
0.0100	7.5	7.1	2.9	0.5697	0.5742	0.5791	0.5832	0.5879
0.0197	17.4	15.3	4.4	0.5597	0.5622	0.5668	0.5712	0.5758
0.0358	20.1	16.8	19.0	0.5207	0.5246	0.5286	0.5320	0.5357
0.0452	20.0	17.0	28.2	0.5115	0.5150	0.5188	0.5222	0.5256
0.0583	19.9	17.0	41.3	0.5026	0.5060	0.5092	0.5128	0.5163
0.0688	19.6	17.2	51.6	0.4977	0.5012	0.5041	0.5072	0.5100_5
0.0775	19.8	17.2	60.3	0.4836_5	0.4970	0.5004	0.5034	0.5062
0.0934	20.0	17.1	76.3	0.4775_5	0.4906	0.4936	0.4970	0.4997
C: $pK_1 = (pK_a)_{H_2A^+}$; $m_1 = m_{H_2A^+}$, $m_2 = m_{HA}$, $m_3 = m_{I^-}$								
0.0102	10.2	9.1	10.2	0.2378	0.2398	0.2413	0.2426	0.2431
0.0202	15.0	13.8	20.2	0.2225	0.2244	0.2255	0.2266	0.2272
0.0308	20.1	17.9	30.8	0.2118	0.2126	0.2138	0.2150	0.2160
0.0417	19.6	18.3	41.7	0.2059	0.2066	0.2077	0.2084	0.2092
0.0570	19.9	18.0	57.0	0.1970	0.1982	0.1990	0.1998	0.2005
0.0713	21.1	17.3	71.3	0.1889	0.1904	0.1909	0.1916	0.1919
0.0787	20.5	17.6	78.7	0.1873	0.1886	0.1892	0.1896	0.1901
0.0964	20.0	17.7	96.4	0.1824	0.1838	0.1844	0.1846	0.1850
C: $pK_2 = (pK_a)_{HA}$; $m_1 = m_{HA}$, $m_2 = m_{A^-}$, $m_3 = m_{I^-}$								
0.0109	7.2	7.8	3.1	0.6798	0.6834	0.6860	0.6888	0.6919
0.0242	13.7	16.1	8.1	0.6669	0.6708	0.6730	0.6758	0.6789
0.0337	21.5	28.4	5.3	0.6853_5	0.6888	0.6921	0.6956	0.6988
0.0450	21.9	28.1	16.9	0.6563	0.6596	0.6620	0.6650	0.6679
0.0537	21.8	28.1	25.6	0.6459	0.6486	0.6515	0.6538	0.6567
0.0675	21.6	28.3	39.2	0.6352	0.6388	0.6404_5	0.6428	0.6453_5
0.0852	21.8	28.0	57.2	0.6257	0.6280	0.6304_5	0.6328	0.6353_5
0.0949	21.7	28.3	66.6	0.6222	0.6245	0.6270	0.6292	0.6314

In the above equations m and γ denote the molality and molal activity coefficients of the species involved. The standard state is so chosen that at infinite dilution in the solvent water γ_i of any species i is equal to unity. The required $(E^0)_{Ag-AgI}$ values in water at different temperatures were known from the literature (7). The involved activity coefficients in water are approximated by the Debye–Hückel limiting law $-\log \gamma_i = S_f z_i^2 (\mu d_0)^{1/2}$ where μ = molal ionic strength of the cell solution, z_i = charge of the species involved and S_f = Debye–Hückel constant. Since pK_1' for C is around 4, pK_1's for U, T and pK_2's for U, C are above 9, due corrections for m_{H^+} (9) and m_{OH^-} (8) have been made, respectively. The pK values at different temperatures were obtained from linear fit of the type $pK' = pK + b\mu$ and their values are listed in Table 2. These pK's were fitted into Harned-Robinson type expression (10)

$$[5] \qquad pK = AT^{-1} + B + CT$$

by the method of least squares. The thermodynamic parameters ΔG^0, ΔS^0, ΔH^0 accompanying the protonation/deprotonation of the acids were evaluated using the following relationships that involve the coefficients of eq. [5]

$$[6] \qquad \Delta G^0 = 2.3026R[A + BT + CT^2]$$

$$[7] \qquad \Delta S^0 = -2.3026R[B + 2CT]$$

Can. J. Chem. Downloaded from www.nrcresearchpress.com by EESC ESCOLA DE ENGENHARIA on 09/08/12
For personal use only.

TABLE 2. Values of pK_a with standard deviation of the various nucleic acid bases in pure water at different temperatures[a]

Nucleic acid bases	Parameter	Value 15°C	20°C	25°C	30°C	35°C
U	pK_1	$9.57_5 \pm 0.004$	9.46 ± 0.001	9.36 ± 0.002	9.26 ± 0.002	$9.16_5 \pm 0.004$
	pK_2	13.88 ± 0.002	13.60 ± 0.002	$13.49_5 \pm 0.002$	$13.30 \pm 0.002_5$	$13.14_5 \pm 0.003$
T	pK_1	10.07 ± 0.001	$9.96 \pm 0.001_5$	9.86 ± 0.002	$9.75_5 \pm 0.001$	9.66 ± 0.002
C	pK_1	4.75 ± 0.002	4.69 ± 0.003	4.63 ± 0.003	4.57 ± 0.003	$4.50 \pm 0.001_5$
	pK_2	12.55 ± 0.001	12.40 ± 0.004	12.25 ± 0.002	12.10 ± 0.003	11.95 ± 0.002

[a]Correlation coefficient for $pK_{1,U} = pK_{2,U} = pK_{1,T} = pK_{1,C} = pK_{2,C} = 1$ at different temperatures.

TABLE 3. Values of A, B, C and relevant energetics ΔG^0, ΔS^0, and ΔH^0 (molal scale) with standard deviations for different nucleic acid bases at 25°C

Nucleic acid bases	A/K	B	C/K^{-1}	ΔG^0/kJ mol^{-1}	ΔS^0/J K^{-1} mol^{-1}	ΔH^0/kJ mol^{-1}
			1st step dissociation			
U	3425 (±19)	−7.52 (±0.13)	0.01808 (±0.00002)	53.41 ± 0.01	-62.4 ± 1.0	34.8 ± 0.3
			2nd step dissociation			
	12276 (±3)	−58.40 (±0.05)	0.10294 (±0.00001)	76.86 ± 0.01	$-57.1 \pm 0.8_5$	$59.8 \pm 0.2_5$
			1st step dissociation			
T	2254 (±13)	0.87 (±0.09)	0.00478 (±0.00015)	56.25 ± 0.01	-71.2 ± 0.5	35.0 ± 0.2
			1st step dissociation			
C	−374 (±5)	10.81 (±0.03)	−0.01652 (±0.00006)	26.43 ± 0.01	-18.4 ± 1.0	21.0 ± 0.3
			2nd step dissociation			
	−106 (±1)	21.79 (±0.01)	−0.03079 (±0.00001)	69.94 ± 0.01	-65.7 ± 0.9	50.4 ± 0.3

[8] $$\Delta H^0 = 2.3026R[A - CT^2]$$

The values of ΔG^0, ΔS^0, and ΔH^0 so obtained and the values of constants A, B, and C are presented in Table 3. The maximum uncertainties in ΔG^0, ΔS^0, and ΔH^0 as calculated by Please's method (11) are ±0.03 kJ mol^{-1}, ±1 J K^{-1} mol^{-1}, and ±0.3 kJ mol^{-1}, respectively.

pK_2 for T at 25°C was obtained from the following relationship

[9] $$H_- = p(K_a)_{HA^-} + \log [C_{A^{2-}}/C_{HA^-}]$$
$$= p(K_a)_{HA^-} + \log [(A - A_a)/(A_b - A)]$$

where H_- is the acidity function of the solution (12*a*), A = absorbance of each buffer solution, A_a = absorbance corresponding to the most acidic form, A_b = absorbance corresponding to the most alkaline form at λ_{max} = 280 nm. At $\log [(A - A_a)/(A_b - A)] = 0$, $p(K_a)_{HA^-} = H_-$. The values of H_- for different strengths of NaOH solutions are taken from the literature (12*b*, 13). The linear plot of H_- against $\log [(A - A_a)/(A_b - A)]$ is shown in Fig. 2. The results are presented in Table 4.

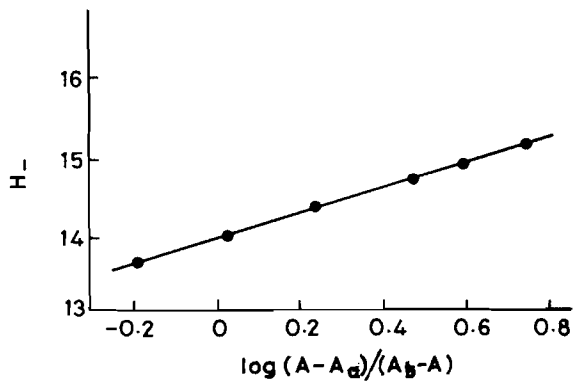

FIG. 2. Variation of H_- with $\log [(A - A_a)/(A_b - A)]$.

Discussion

Ultraviolet and ultrasonic absorption studies (6, 14) indicate that U and T primarily exist in the lactam form in an aqueous solution. However, in the alkaline solution two ionizations were detected: that of the 2-hydroxyl group characterised by pK_1 and that of the 4-hydroxyl group for pK_2. The pK_a values

Can. J. Chem. Downloaded from www.nrcresearchpress.com by EESC ESCOLA DE ENGENHARIA on 09/08/12
For personal use only.

Can. J. Chem. Downloaded from www.nrcresearchpress.com by EESC ESCOLA DE ENGENHARIA on 09/08/12
For personal use only.

TABLE 4. Spectrophotometric data for pK_2 of thymine at 25°C

C_{NaOH}/M^a	A^a	$H_-{}^{a,b}$	$\log [(A - A_a)/(A_b - A)]$
0.0001	0.23	—	—
0.5	0.47	13.71	−0.18
1.0	0.54	14.02	0.03
2.0	0.61	14.37	0.24
3.0	0.68	14.65	0.48
4.0	0.71	14.95	0.60
5.0	0.74	15.20	0.75
10.0	0.83	—	—

[a] C, concentration; A, absorbance; H_-, acidity function.
[b] References 12*b*, 13.

for T are slightly higher which is perhaps due to the presence of —CH_3 group at 5 position. The possible stepwise ionizations involved in the cases of U and T are summarised in Scheme 1.

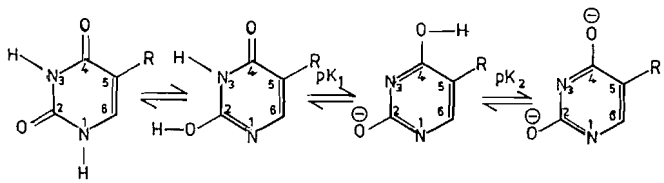

SCHEME 1

The site of ionization from the protonated form of C(CH^+) is still a subject of controversy. From reports based on n.m.r. data (15, 16), calorimetry (17) and resemblance of enthalpy of ionization (ΔH^0) of CH^+ and protonated pyridine (PyH^+) (ref. 3), some previous workers are of the opinion that (*A*) represents CH^+. On the contrary, potentiometric, spectrophotometric, and ultrasonic studies (14, 18) and similarity of pK_a values of CH^+ and protonated aniline ($PhNH_3^+$) (19) led to suggest that (*B*) (Scheme 2) is the protonated form of C. A perusal of the

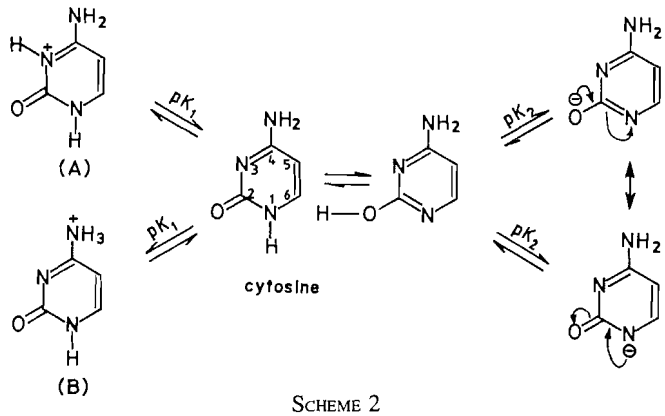

SCHEME 2

comparison of the related thermodynamic data of CH^+, PyH^+, and $PhNH_3^+$ at 25°C as given below

	CH^+	PyH^+	$PhNH_3^+$
ΔH^0/kJ mol^{-1}	21.5 (ref. 3)	20.1 (ref. 3)	30.4 (ref. 3)
ΔG^0/kJ mol^{-1}	26.4	30.0 (ref. 20)	26.4 (ref. 20)
$T\Delta S^0$/kJ mol^{-1}	−4.9	−9.9	4.1

seemingly fails to distinguish which of the forms really stanc for CH^+. However, based on ultrasonic absorption studies o proton transfer reaction in acidic range, Zana et al. believe that —NH_2 group of C is the favourable site of protonatior [form (B)]. The possible ionization step considered for CH^+ is depicted in Scheme 2.

Since ultrasonic absorption studies of proton transfer reactions in alkaline range shows no absorption maximum, Zana et al. conclude that C molecule does not contain lactam group. Therefore, as per Scheme 2, the lactim form of C is predominantly involved in yielding the extractable proton in alkaline range.

The observed protonation/deprotonation constants for U, T, and C and the related energetics at 25°C are compared (Table 5) with some literature data based on various methods.

The small negative magnitude of the entropy change accompanying the first step deprotonation of C, ΔS_1^0(C) and the large negative magnitude of ΔS_2^0(C) can be probably explained from the nature of the equilibria involved. Thus in the first step ionization of protonated C which is a charge transfer process:

$$H_2A^+ + H_2O \overset{K_1}{\rightleftharpoons} H_3O^+ + HA$$

ΔS_1^0(C) is given by eq. [10] (refs. 21, 22).

$$[10] \qquad \Delta S_1^0(C) = (\bar{S}^0_{H_3O^+} - \bar{S}^0_{H_2O}) + (\bar{S}^0_{HA} - \bar{S}^0_{H_2A^+})$$

$\bar{S}_i^0$ being the standard entropy per mole of i. In the second step ionization which involves charge separation:

$$HA + H_2O \overset{K_2}{\rightleftharpoons} H_3O^+ + A^-$$

ΔS_2^0(C) in represented by eq. [11]

$$[11] \qquad \Delta S_2^0(C) = (\bar{S}^0_{H_3O^+} - \bar{S}^0_{H_2O}) + (\bar{S}^0_{A^-} - \bar{S}^0_{HA})$$

Since H_3O^+ carrying a charge must be solvated, there is an increase in orderliness and therefore a decrease in entropy relative to H_2O, i.e. $\bar{S}^0_{H_3O^+} < \bar{S}^0_{H_2O}$. For a similar reason $\bar{S}^0_{H_2A^+} < \bar{S}^0_{HA}$ and hence the small negative magnitude of ΔS_1^0(C) as the two terms in parentheses in eq. [10] almost nullify each other. Similarly, in the case of deprotonation of HA, as $\bar{S}^0_{A^-} < \bar{S}^0_{HA}$ and $\bar{S}^0_{H_3O^+} < \bar{S}^0_{H_2O}$ the resulting ΔS_2^0(C) should be large negative as observed.

In the case of U, the dissociation processes involved are $H_2A \overset{K_1}{\rightleftharpoons} H^+ + HA^-$ and $HA^- \overset{K_2}{\rightleftharpoons} H^+ + A^{2-}$ and the corresponding entropy changes are given by eqs. [12] and [13].

$$[12] \qquad \Delta S_1^0(U) = (\bar{S}^0_{H_3O^+} - \bar{S}^0_{H_2O}) + (\bar{S}^0_{HA^-} - \bar{S}^0_{H_2A})$$

and

$$[13] \qquad \Delta S_2^0(U) = (\bar{S}^0_{H_3O^+} - \bar{S}^0_{H_2O}) + (\bar{S}^0_{A^{2-}} - \bar{S}^0_{HA^-})$$

Now, from Born-type electrostatic effect (23) one expects $\Delta S_2^0(U) < \Delta S_1^0(U)$. However, the observed data show just the reverse as $\Delta S_2^0(U) = -57.1$ J K^{-1} mol^{-1} and $\Delta S_1^0(U) = -62.4$ J K^{-1} mol^{-1}. Evidently Born-type electrostatic effect is not the sole contributing factor. In fact, as indicated earlier (24), $\bar{S}^0(i)$ for any species i can be visualized as the sum of several effects, viz.

TABLE 5. Comparison of pK_1 and pK_2 values and related thermodynamic quantities for U, T, and C in water at 25°C

Source	Method[a]	pK_1	ΔG_1^0/kJ mol^{-1}	ΔS_1^0/J K^{-1} mol^{-1}	ΔH_1^0/kJ mol^{-1}	pK_2	ΔG_2^0/kJ mol^{-1}	ΔS_2^0/J K^{-1} mol^{-1}	ΔH_2^0/kJ mol^{-1}
			Uracil						
Present study	emf method	9.36	53.4	−62.4	34.8	13.49_5	76.9	−57.1	59.8
Izatt et al. (3)	C, pH titn.	9.46	54.0	−70.7	32.9	—	—	—	—
Nakanishi et al. (31)	Spectrophotometry, pH titn.	9.51	54.3	—	—	—	—	—	—
Levene et al. (32)	Electrometric titn.	9.28	53.0	—	—	13.56	77.4	—	—
Shugar and Fox (6)	Spectrophotometry	—	—	—	—	>13	—	—	—
			Thymine						
Present study	emf method (for pK_1), spectrophotometry (for pK_2)	9.86	56.3	−71.2	35.0	13.96	79.7	—	—
Izatt et al. (3)	C, pH titn.	9.90	56.5	−75.3	34.1	—	—	—	—
Shugar and Fox (6)	Spectrophotometry	—	—	—	—	>13	—	—	—
			Cytosine						
Present study	emf method	4.63	26.4	−18.4	21.0	12.25	69.9	−65.7	50.4
Izatt et al. (3)	C, pH titn.	4.58	26.1	−15.5	21.5	12.15	69.4	−71.1	48.1
Suchorukow et al. (33)	Spectrophotometric, T	4.50	25.7	−15.5	21.0	11.82	67.5	−71.6	46.0
Levene et al. (32)	Electrometric titn.	4.60	26.3	—	—	12.16	69.4	—	—

[a]C, calorimetry; T, temperature variation.

Can. J. Chem. Downloaded from www.nrcresearchpress.com by EESC ESCOLA DE ENGENHARIA on 09/08/12
For personal use only.

[14] $$\bar{S}^0(i) = \bar{S}^0_{int}(i) + \bar{S}^0_{cav}(i) + \bar{S}^0_{disp}(i) + \bar{S}^0_{dd}(i)$$

$$\text{or } \bar{S}^0_B(i) + \bar{S}^0_{str}(i)$$

where $\bar{S}^0_{int}(i)$ stands for the entropy due to intrinsic structure of the species, $\bar{S}^0_{cav}(i)$ that associated with the formation of cavity required for accommodation of the species in the solvent, $\bar{S}^0_{disp}(i)$ that for dispersion effect, $\bar{S}^0_{dd}(i)$ due to dipole–dipole interaction in case of non-ionic species and $\bar{S}^0_B$ for Born-type electrostatic effect for ionic species and $\bar{S}^0_{str}(i)$ is that associated with the change in the order–disorder of solvent molecules adjacent to the dissolved species. As the contributions from ion–dipole and ion – induced dipole interactions are bereft of dielectric constants and other temperature dependent terms (23, 25), the entropy contributions for those terms are zero. From eqs. [12] to [14] we can write

[15] $$\Delta S_2^0(U) - \Delta S_1^0(U) = \bar{S}^0(A^{2-}) - 2\bar{S}^0(HA^-) + \bar{S}^0(H_2A)$$

$$= \bar{S}^0_B(A^{2-}) - 2\bar{S}^0_B(HA^-) + \bar{S}^0_{dd}(H_2A) + \Delta S^0_{str}$$

as the intrinsic, cavity, and dispersion terms are likely to be cancelled for the species HA, A^-, and A^{2-}. In eq. [15], ΔS^0_{str} stands for $\bar{S}^0_{str}(A^{2-}) - 2\bar{S}^0_{str}(HA^-) + \bar{S}^0_{str}(H_2A)$. Now, although the Born and dipole–dipole interaction terms are tentatively computable by the relevant expressions (23, 25), it is hardly feasible to account for the difference of $\Delta S_2^0(U) - \Delta S_1^0(U) = 5.3$ J K^{-1} mol^{-1} unless ΔS^0_{str} is realized. This is formidably difficult for these species.

To gain a better insight into the relative solvation behavior of the anions, especially those involved in the first step ionization process, we calculate the enthalpy of formation of A^- ($\Delta H_f^0(A^-)$ and HA^- ($\Delta H_f^0(HA^-)$. In the case of U, T, and C, the following equilibria for the thermodynamics of solute–solvent interaction can be considered:

$$HA\ (solid) \rightleftharpoons HA\ (soln)$$

and

$$H_2A\ (solid) \rightleftharpoons H_2A\ (soln)$$

Enthalpy of ionization, ΔH_{ion}, for the above equilibria can be ascribed as

[16] $$\Delta H_{ion}(HA) = \Delta H^0_{f,soln}(H^+) + \Delta H^0_{f,soln}(A^-) - \Delta H^0_{f,soln}(HA)$$

and

[17] $$\Delta H_{ion}(H_2A) = \Delta H^0_{f,soln}(H^+) + \Delta H^0_{f,soln}(HA^-) - \Delta H^0_{f,soln}(H_2A)$$

Enthalpy of solution, ΔH_{soln}, can be written as

[18] $$\Delta H_{soln}(HA) = \Delta H^0_{f,soln}(HA) - \Delta H^0_{f,solid}(HA)$$

and

[19] $$\Delta H_{soln}(H_2A) = \Delta H^0_{f,soln}(H_2A) - \Delta H^0_{f,solid}(H_2A)$$

Again

$$\Delta H^0_{f,soln}(H^+) = \tfrac{1}{2} D(H_2) + I(H) + \Delta H_{hydr}(H^+)$$

$$= 659.4 \text{ kJ mol}^{-1}.$$

where $D(H_2)$ (ref. 26) stands for the dissociation energy of H_2 molecule, $I(H)$ (ref. 26) that for ionization energy of H atom and $\Delta H_{hydr}(H^+)$ (ref. 25) is the enthalpy change associated with the transfer of H^+ from gaseous state to solution.

Adding eqs. [16] and [18] and substituting the values for

$\Delta H^0_{f,soln}(H^+)$, $\Delta H^0_{f,soln}(HA)$ (27, 28), and $\Delta H_{soln}(HA)$ (29), we get the enthalpy of formation of the anion of C in solution, i.e. $\Delta H^0_{f,soln,C}(A^-) = -832.5$ kJ mol^{-1}. Similarly for U and T, $\Delta H^0_{f,soln,U}(HA^-) = -1019.6$ kJ mol^{-1} and $\Delta H^0_{f,soln,T}(HA^-) = -1062.9$ kJ mol^{-1}.

From the negative magnitude of $\Delta H^0_{f,soln}(A^-$ or $HA^-)$ it is apparent that the heats of formation of the anions A^- and HA^- of the pyrimidine bases in water are, as expected, highly negative. Furthermore, the relative increasing order of $|\Delta H^0_{f,soln,C}(A^-)| < |\Delta H^0_{f,soln,U}(HA^-)| < |\Delta H^0_{f,soln,T}(HA^-)|$ suggests that the anion of T is more solvated in water than the same for U and C. This behavior is also in accordance with what is expected from charge density distribution (30) and the fact that the methyl group of T is slightly more stabilized by water due to the structuring of water molecules about this hydrophobic group.

Acknowledgement

Thanks to UGC, Govt. of India, New Delhi, for financial assistance under COSIST Programme to the Department of Chemistry, Jadavpur University.

1. M.A. Volkenstein. Biophysics, Mir Publications, Moscow. 1983. p. 15.
2. (*a*) R. Phillips. Chem. Rev. **66**, 501 (1966); (*b*) Biochemistry, **9**, 2022 (1970).
3. R.M. Izatt, J.C. Christensen, and J.H. Rytting. Chem. Rev. **71**, 439 (1971).
4. H.S. Harned and R.W. Ehlers. J. Am. Chem. Soc. **54**, 1350 (1932).
5. M. Windholz (*Editor*). The Merck index. 10th ed. Merck and Co., Rahway, NJ. 1983.
6. D. Shugar and J.J. Fox. Biochim. Biophys. Acta, **9**, 199 (1952).
7. (*a*) K.K. Kundu, D. Jana, and M.N. Das. Electrochim. Acta, **18**, 75 (1973); (*b*) K.K. Kundu and K. Mazumdar. J. Chem. Soc. Trans. I, **71**, 1422 (1975).
8. H.S. Harned and B.B. Owen. The physical chemistry of electrolyte solutions. 3rd ed. Reinhold, New York. 1958. p. 650.
9. S. Glasstone. An introduction to electrochemistry. D. Van Nostrand Co. Inc., Princeton, NJ. 1942. p. 320.
10. H.S. Harned and R.A. Robinson. Trans. Faraday Soc. **36**, 973 (1940).
11. N.W. Please. Biochem. J. 196 (1954).
12. (*a*) C.H. Rochester. Rev. 511 (1966); (*b*) Acidity functions. Academic Press, London. 1970. p. 237.
13. R.H. Boyd. *In* Solute–solvent interactions. *Edited by* J.F. Coetzee and C.D. Ritchie. Marcel Dekker, New York. 1969. p. 192.
14. J. Lang, J. Strum, and R. Zana. (*a*) J. Phys. Chem. **77**, 2329 (1973); (*b*) J. Phys. Chem. **78**, 80 (1974); (*c*) Biopolymers, **10**, 2639 (1971).
15. C.D. Jardetzky and O. Jandetzky. J. Am. Chem. Soc. **82**, 222 (1960).
16. O. Jardetzky, P. Pappas, and N.G. Wade. J. Am. Chem. Soc. **85**, 1657 (1963).
17. J.J. Christensen, J.H. Rytting, and R.M. Izatt. J. Chem. Soc. B, 1643 (1970).
18. S. Lewin and D.A. Humphreys. J. Chem. Soc. B, 210 (1966).
19. J.J. Fox, D. Van Praag, I. Wempen, I.L. Doerr, L. Cheong, J.E. Knoll, M.L. Eidinoff, A. Bendich, and G.B. Brown. J. Am. Chem. Soc. **81**, 178 (1959).
20. R.C. Weast (*Editor*). Handbook of chemistry and physics. 67th ed. The Chemical Rubber Co., U.S.A. 1986.
21. K.K. Kundu, P.K. Chattopadhyay, and M.N. Das. J. Chem. Soc. B, 2034 (1972).
22. H. Talukdar, S.P. Rudra, and K.K. Kundu. Ind. J. Chem. **27A**, 764 (1988).
23. J. O'M Bockris and A.K.N. Reddy. Modern electrochemistry. Vol. 1. Plenum Press, New York. 1970.
24. S. Sinha and K.K. Kundu. Ind. J. Chem. **32A**, 1 (1993).
25. Y. Marcus. Ion solvation. John Wiley and Sons Ltd., Chichester. 1985. p. 37.
26. W.M. Latimer. Oxidation states. 2nd ed. Prentice-Hall, NJ. 1961, p. 30.
27. S.R. Wilson, I.D. Watson, and G.N. Malcolm. J. Chem. Thermodyn. **11**, 911 (1979).
28. M. Nabavian, R. Sabbah, R. Chastel, and M. Laffitte. J. Chim. Phys. Phys.-Chim. Biol. **74**, 115 (1977).
29. R.L. Benoit and M. Frechette. Thermochim. Acta, **126**, 155 (1988).
30. J.I. Fernandez-Alonso. *In* Advances in chemical physics. Vol. VII. *Edited by* J. Duchesne. Interscience Publishers, London. 1964. p. 52.
31. K. Nakanishi, N. Suzuki, and F. Yamazaki. Bull. Chem. Soc. Jpn. **34**, 53 (1961).
32. P.A. Levene, L.W. Bass, and H.S. Simms. J. Biol. Chem. **70**, 229 (1926).
33. B.T. Suchorukow, V.I. Poltew, and L. Blumenfeld. Abh. Deut. Akad. Wiss. Berlin, Kl. Med. 381 (1964).

Can. J. Chem. Downloaded from www.nrcresearchpress.com by ESC ESCOLA DE ENGENHARIA on 09/08/12
For personal use only.

Thiobenzoates of lead (II) and bismuth (III). The crystal and molecular structures of $(AsPh_4)$ $[Pb(SOCPh)_3]$ and $Pb(SOCPh)_2(S_2CP\{c\text{-}C_6H_{11}\}_3)$[1]

THOMAS R. BURNETT, PHILIP A.W. DEAN,[2] AND JAGADESE J. VITTAL[2]

The Department of Chemistry, University of Western Ontario, London, ON N6A 5B7, Canada

Received August 10, 1993

THOMAS R. BURNETT, PHILIP A.W. DEAN, and JAGADESE J. VITTAL. Can. J. Chem. **72**, 1127 (1994).

The compounds $M(SOCPh)_n$ (M = Pb, n = 2; M = Bi, n = 3) have been prepared by the reaction of $M(OAc)_n$ or $M(SPh)_n$ with a slight excess of PhCOSH in MeOH. The ligands $PhCOS^-$, $(c\text{-}C_6H_{11})_3PCS_2$ and $(c\text{-}C_6H_{11})_3PO$ solubilize $Pb(SOCPh)_2$ in solvents in which it is otherwise poorly soluble. Neither Ph_3P nor Ph_3P increase the solubility of $Pb(SOCPh)_2$ and none of the above five ligands enhance the solubility of very poorly soluble $Bi(SOCPh)_3$. Solubilization of the Pb(II) compound is due in each case to a 1:1 reaction as shown by the isolation of $(Ph_4As)(SOCPh)_3]$ (**1**) and $Pb(SOCPh)_2(S_2CP\{c\text{-}C_6H_{11}\}_3)$ (**2**), and by a multi-NMR (^{31}P, ^{207}Pb) study of the system Pb(SOCPh) : $(c\text{-}C_6H_{11})_3PO$ (in which unidentified more ligand-rich species are also formed). **1** and **2** have been characterized by multi-nuclear magnetic resonance spectroscopy (^{13}C, ^{31}P, ^{207}Pb, as appropriate) and by single crystal X-ray diffractometry techniques at –50°C. The compound $\mathbf{1}.CH_2Cl_2$ (= **1′**) crystallizes in the triclinic space group $P\bar{1}$ with Z = 2. The crystal data for **1′** are a = 13.395(4), (b) = 16.585(3), c = 11.582(3) Å, α = 88.03(2), β = 112.34(2), γ = 113.00(2)°, V = 2171(1) Å^3, ρ_{calcd} (ρ_{obsd}) = 1.663 (1.65(3)) g cm^{-3}, R_F = 0.038, R_w = 0.035. In the $[Pb(SOCPh)_3]^-$ anion the Pb—S distances are in the range 2.703(3) – 2.763(2) Å. The primary coordination geometry around Pb is trigonal pyramidal (PbS_3 kernel). There are four additional weaker interactions with oxygen atoms, one from each ligand and one a bridging interaction that links the anions in a centrosymmetric dimer. The Pb—O distances are in the range 2.879(6) – 3.298(7) Å. Compound **2** crystallizes in the monoclinic space group, $P2_1/c$ with Z = 4. The crystal data for **2** are, a = 17.039(2), b = 11.834(2), c = 18.965(3) Å, β = 116.44(1)°, V = 3424(1) Å^3, ρ_{calcd} (ρ_{obsd}) = 1.621 (1.61(3)) g cm^{-3}, R_F = 0.034, R_w = 0.029. The $(c\text{-}C_6H_{11})_3PCS_2$ ligand binds in an anisobidentate manner and the primary coordination geometry around Pb in the neutral molecule is trigonal pyramidal, the primary Pb—S distances in the PbS_3 kernel being 2.626(2), 2.755(2), and 2.885(2) Å. The weakly bound sulfur of the $(c\text{-}C_6H_{11})_3PCS_2$ acts as a bridge, again producing a centrosymmetric dimer. In addition to the two weak interactions to sulfur (3.350(2), 3.639(2) Å) there are also two involving the oxygens of the $PhCOS^-$ ligands (2.626(5), 3.002(5) Å).

2 is the first complex containing a ligand of the type R_3PCS_2 bound to a Main Group element.

THOMAS R. BURNETT, PHILIP A.W. DEAN et JAGADESE J. VITTAL. Can. J. Chem. **72**, 1127 (1994).

On a préparé les composés $M(SOCPh)_n$ (M = Pb, n = 2; M = Bi, n = 3) en faisant réagir le $M(OAc)_n$ ou le $M(SPh)_n$ avec un léger excès de PSCOSH dans du MEOH. Les ligands $PhCOS^-$, $(c\text{-}C_6H_{11})_3PCS_2$ et $(c\text{-}C_6H_{11})_3PO$ solubilisent le composé $Pb(SOCPh)_2$ dans des solvants qui ne le dissolvaient que faiblement. Le Ph_3P et le Ph_3P n'augmentent pas la solubilité du $Pb(SOCPh)_2$ et les cinq ligands mentionnés ci-dessus n'améliorent aucunement la solubilité du composé $Bi(SOCPh)_3$ très faiblement soluble. La solubilisation du composé Pb(II) est due, dans chaque cas, à une réaction 1:1 comme le démontrent les diverses études en rmn des noyaux multiples (^{31}p et du $^{207}Pb^{31}$) du système Pb(SOCPh) : $(c\text{-}C_6H_{11})_3PO$ (dans lequel il se forme également des espèces plus riches en ligands que l'on n'a pas identifiées) et également le fait que l'on a pu isoler les composés $(Ph_4As)[Pb(SOCPh)_3]$ (**1**) et $Pb(SOCPh)_2(S_2CP\{c\text{-}C_6H_{11}\}_3)$ (**2**). On a caractérisé les composés **1** et **2** par la spectroscopie de résonnance des noyaux multiples (^{13}C, ^{31}P et du ^{207}Pb selon le cas) et par les techniques de diffraction de rayons x sur un monocristal à –50°C. Le composé $\mathbf{1}.CH_2Cl_2$ (=**1′**) appartient au groupe d'espace triclinique $P\bar{1}$ avec Z = 2, a = 13,395(4), (b) = 16,585(3), (c) = 11,582(3) Å, α = 88,03(2), β = 112,34(2), γ = 113,00(2)°, V = 2171(1) Å^3, $\rho_{calculé}$ ($\rho_{observé}$) = 1,663 (1,65(3)) gcm^{-3}, R_F = 0,038, R_w = 0,035. Dans l'anion $[Pb(SOCPh)_3]^-$ les distances Pb—S se situent dans l'intervalle 2,703(3) – 2,763(2) Å. La géométrie de coordination primaire autour du Pb est trigonale pyramidale (dans le noyau PbS_3). Il y a quatre faibles interactions additionnelles avec les atomes d'oxygène, une à partir de chaque ligand et une autre interaction en position de pont qui lie les anions dans un dimère centrosymétrique. Les distances Pb—O se situent dans l'intervalle de 2,879(6) – 3,298(7) Å. Le composé **2** appartient au groupe d'espace monoclinique $P2_1/c$ avec Z = 4, a = 17,039(2), b = 11,834(2), c = 18,965(3) Å, β = 116,44(1)°, V = 3424(1) Å^3, $\rho_{calculé}$ ($\rho_{observé}$) = 1,621 (1,61(3)) g cm^{-3}, R_F = 0,034, R_w = 0,029. Le ligand $(c\text{-}C_6H_{11})_3PCS_2$ est lié de façon anisobidentate et la géométrie de coordination primaire autour du Pb dans la molécule neutre est trigonale pyramidale, les distances primarires Pb—S dans le noyau PbS_3 étant 2,626(2), 2,755(2) et 2,885(2) Å. La faible liaison soufre du composé $(c\text{-}C_6H_{11})_3PCS_2$ sert de pont, produisant un dimère centrosymétrique. En plus de ces deux faibles interactions dues au soufre (3,350(2), 3,639(2) Å) il y a également deux autres interactions impliquant l'oxygène des ligands de type $PhCOS^-$ (2,626(5), 3,002(5) Å.

Le complexe **2** est le premier à contenir un ligand du type R_3PCS_2 lié à un élément du group principal.

[Traduit par la Rédaction]

Introduction

Monothiocarboxylates are an interesting class of ligands containing both a soft sulfur donor site and a hard oxygen donor site (1, 2). The presence of two types of donor sites can lead to aggregation of soft and hard metal centres. This is shown, for example, in the recently reported (3) structure of trinuclear $[Na(CdSOCPh_3)_2]^-$. In this anion the relatively soft Cd(II) is bound strongly to sulfur atoms while the hard Na(I) is attached to oxygen atoms.

Evidently use of $RCOS^-$ ligands might lead to a variety of unusual bimetallics species. However, extension of this chemistry to include soft Main Group metal centres is hampered by the dearth of information that is available about even the relevant *simple* metal monothiocarboxylates (1, 2). Therefore, as a contribution to this area we describe here the synthesis and some properties of $Pb(SOCPh)_2$ and $Bi(SOCPh)_3$. As part of

[1]Taken in part from the Honours Research Thesis of Thomas R. Burnett: University of Western Ontario, 1993.

[2]Authors to whom correspondence may be addressed.

Can. J. Chem. Downloaded from www.nrcresearchpress.com by EESC ESCOLA DE ENGENHARIA on 09/08/12
For personal use only.

Can. J. Chem. Downloaded from www.nrcresearchpress.com by ESC ESCOLA DE ENGENHARIA on 09/08/12
For personal use only.

this study, we have isolated both ($AsPh_4$) [$Pb(SOCPh)_3$] and $Pb(SOCPh)_2(S_2CPCy_3)$[3] and characterized them by NMR spectroscopy and X-ray structural analysis. Complexes of R_3PCS_2 with transition metals have become well-established over the last two decades (for a recent paper, see ref. 4), but as far as we are aware $Pb(SOCPh)_2(S_2CPCy_3)$ represents the first example of a complex of this type of ligand with a Main Group element.

Experimental

Material and general procedures

All starting materials were of reagent grade and were used as received, except that triphenylphosphine was recrystallized from ethanol. Literature methods were used from the synthesis of $Bi(OAc)_3$ (5), $Bi(SPh)_3$ (6), $Pb(SPh)_2$ (7), $Ph_4As[Pb(SPh)_3]$ (8), and Ph_2S_2(9). $KMnO_4$ oxidation of the phosphine in Me_2CO (10) was used to produce both $OPPh_3$ and $OPCy_3$.

Solvents for use in synthesis or the preparation of NMR samples were dried by standing over 3A molecular sieves. Before use with thiolates or thiobenzoates they were thoroughly deoxygenated with Ar. Syntheses were carried out by Schlenk-type techniques or in an Ar-filled glovebag.

$Pb(SOCPh)_2$

(*A*) To a stirred solution of $Pb(OAc)_2.3H_2O$ (5.17 g, 13.6 mmol) in 30 mL of eythanol thiobenzoic acid (5.5 mL, 46.8 mmol) was added slowly. A thick suspension of yellow precipitate appeared immediately. A small amount of brown contaminant, presumably PbS,[4] formed unless the PhCOSH was added below the surface by syringe. The mixture was stirred for 2 h to ensure complete reaction. The thick suspension was then centrifuged, the supernatant liquid was removed, and the solid was washed three times with cold ethanol, with recentrifugation between washings. In the final cycle the supernatant liquid was colourless. The product was dried under vacuum. Yield: 5.31 g (81.1%). *Anal.* calcd. for $C_{14}H_{10}O_2PbS_2$: C 34.91, H 2.08; found: C 35.01, 35.11; H 1.83, 1.94.

(*B*) To a suspension of $Pb(SPh)_2$ (3.73 g, 8.8 mmol) in ethanol (60 mL) thiobenzoic acid (2.4 mL, 20.3 mmol) was added below the surface using a syringe. The bright yellow suspension became much paler in colour. Thereafter, the procedure was as described in synthesis (*A*). Yield: 4.06 g(95.9%). *Anal.* found: C 34.87 H 1.97. The IR spectrum (Nujol mull) showed that $Pb(SPh)_2$ (ν(C—S) $\approx$ 730 cm^{-1}) was absent.

$Bi(SOCPh)_3$

(*A*) This procedure followed method (*A*) used for $Pb(SOCPh)_2$ except that $Bi(OAc)_3$ was used in place of $Pb(OAc)_2$, and the amount of PhCOSH was a slight excess over the required PhCOSH:Bi ratio of 3:1. Yield of the pale yellow product: 92%. *Anal.* calcd. for $C_{21}H_{15}BiO_3S_3$: C 40.65, H 2.42; found: C 40.16, 39.97; H 2.14, 2.28.

(*B*) This synthesis was similar to synthesis (*B*) used for $Pb(SOCPh)_2$ except that $Pb(SPh)_2$ was replaced by $Bi(SPh)_3$. The amount PhCOSH was adjusted accordingly. Yield: 95%. *Anal.* found: C 40.57, H 2.16. The IR spectrum showed that $Bi(SPh)_3$ (ν(C—S) $\approx$ 730 cm^{-1}) was absent.

$(Ph_4As)[Pb(SOCPh)_3]$ (1)

(*A*) Thiobenzoic acid (0.49 mL, 4.1 mmol) was added to a solution of NaOMe produced by adding sodium metal (0.10 g, 4.3 mmol) to methanol (5 mL). The resulting solution of NaSOCPh was added to a stirred suspension of $Pb(SOCPh)_2$ (1.0 g, 2.1 mmol) in methanol (20 mL), causing dissolution of the lead compound to give a green solution. When a solution of $(AsPh_4)Cl.H_2O$ (0.88 g, 2.1 mmol) in MeOH (30 mL) was added, initially there was precipitation of a yellow solid, but this disappeared quickly in the solution to give, finally, a brown oil and a yellow supernatant solution. The yellow solution was decanted from the oil, and water (ca. 60 mL) was added to it until a trace of pale yellow solid persisted. The mixture was refrigerated and produced pale yellow crystals, which were separated by filtration under Ar and dried in vacuo. The product was recrystallized from Me_2CO:H_2O (3:2 v:v), isolated by filtration, and dried.

The brown oil produced a grey solid when 10 mL of water was added. This solid was dried under vacuum then dissolved in Me_2CO. The solution was filtered using a fine frit. The filtrate was treated in the same way as the yellow supernatant liquid to yield another crop of the pale yellow crystals. Combined yield: 67% (1.39 g). *Anal.* calcd. $C_{45}H_{35}AsO_3PbS3$: C 53.92, H 3.49; found: C 54.02, H 3.38 (crystals from original yellow solution). ^1H NMR ($(CD_3)_2CO$, 293 K): 7.0–7.6, 8.0–8.17 (anion); 7.7–8.0 (cation); Ph_{cation}/Ph_{anion} = 4/3. ^{13}C NMR ($CDCl_3$, 293 K): 143.9 (C_1), 128.9 ($C_{2,6}$ or $C_{3,5}$), 128.3 ($C_{2,6}$ or $C_{3,5}$), 132.0 (C_4), 204.6 (Ph*C*OS) [anion]; 122.1 (C_1), 134.3 ($C_{2,6}$), 131.9 ($C_{3,5}$), 135.4 (C_4) [cation].

(*B*) This procedure was generally similar to that used to synthesize $Ph_4As[Pb(SPh)_3]$ (8). A solution of NaSOCPh in methanol was prepared as in route (*A*), using thiobenzoic acid (1.7 mL, 14.5 mmol) and sodium metal (0.3 g, 13.0 mmol). This solution was added to a stirred solution of $Pb(NO_3)_2$ (1.42 g, 4.3 mmol) in 5 mL of water producing a brown-coloured supernatant liquid and a beige precipitate. A solution of $(AsPh_4)Cl.H_2O$ (1.85 g, 4.4 mmol) in methanol (30 mL) was stirred into the mixture resulting in a faint yellow supernatant liquid and brown precipitate. A 100-mL volume of water was added to this solution producing more brown precipitate and causing the supernatant liquid to become colourless. The precipitate was allowed to settle and the supernatant liquid removed by decantation. The brown solid was washed twice with ethanol and dried under vacuum. Acetone (ca. 30 mL) was added to the solid. Undissolved material was removed with a fine frit and water was added to the filtrate until a yellow precipitate persisted. This solution was refrigerated and pale yellow crystals resulted. When separated by filtration and dried the crystals had a beige colour and when examined under a microscope they were found to contain a mixture of pale yellow crystals and a very fine brown contaminant, presumably PbS. A second recrystallization from a 3:2 acetone:water mixture resulted in crystals with the same contaminant present. The sample was purified using a column of Kieselgel 60 silica gel (18 cm long, 1 cm id).[5] A solution of all of the isolated material in Me_2CO (ca. 20 mL) was passed through the column, followed by a 5-mL wash of acetone. The solvent was removed from the eluate producing an oil. This oil produced pale yellow crystals from an acetone–water solution. Yield: 29.3% (1.26 g). The identity of this material with that produced by method (*A*) was confirmed by ^1H, ^{13}C, and ^{207}Pb NMR.

$Pb(SOCPh)_2(S_2CPCy_3)$ (2)

To a suspension of $Pb(SOCPh)_2$ (0.48 g, 1.0 mmol) in CS_2 (40 mL) was added S_2CPCy_3 (0.36 g, 1.1 mmol), gradually, with continuous stirring. The mixture became deep red in colour as the solids dissolved. The small amount of solid remaining after ca. 20 min was removed using a medium frit. A two-thirds reduction in the volume of the filtrate was achieved under a stream of Ar. The concentrated mixture was refrigerated overnight to promote crystallization. Using a pipette, most of the supernatant liquid was separated from the crystals so produced. Then the red–brown crystals were isolated by filtration, washed with cold CS_2, and dried under a flow of argon. The volume of the separated supernatant liquid was reduced by about one half under an Ar stream and the solution refrigerated again. Once again the crystals produced were separated by filtration, washed, and dried. This procedure was repeated until no more crystalline material was formed. Combined yield: 48% (0.40 g). *Anal.* Calcd. for $C_{33}H_{43}O_2PPbS_4$: C 47.30, H 5.14, S 15.30; found: C 47.11, 47.29; H 4.69, 4.88; S 15.12, 15.21.

NMR spectra

All spectra were measured at ambient probe temperature. The ^1H

[3]Cy = *c*-C_6H_{11}.

[4]We observe that PbS forms when the vapor of PhCOSH comes in contact with $Pb(OAc)_2$/EtOH.

[5]A shorter column would have sufficed.

TABLE 1. Crystal data and experimental details[a]

Parameter			Value	
			1′	**2**
Compounds			$C_{45}H_{35}As_1O_3Pb_1S_3.CH_2Cl_2$	$C_{33}H_{43}O_2P_1Pb_1S_4$
Formula weight			1087.06	838.18
Crystal system, space group			Triclinic, $P\bar{1}$	Monoclinic, $P2/_1/c$
Cell dimensions	a	=	13.395(4)	17.039(2) Å
	b	=	16.585(3)	11.834(2) Å
	c	=	11.582(3)	18.965(3) Å
	α	=	88.03(2)°	
	β	=	112.34(2)°	116.44(1)°
	γ	=	113.00(2)°	
Temperature			−50°C	
Cell volume (Å^3), Z			2171(1), 2	3424(1), 4
Density, g cm^{-3}, obsd., calcd.				1.65(3), 1.6631.61(3), 1.621
F(000)			1063	1661
Diffractometer, monochromator			Enraf-Nonius CAD4F; graphite	
Radiation, wavelength (Å)			MoKα, 0.71073	
Absorption coefficient (cm^{-1})			47.5	52.7
No. of observation, variables			4513($I \geq 2.5\sigma(I)$), 196	4405($I \geq 2.5\sigma(I)$), 287
Final model; R_F and R_w			0.038, 0.035	0.034, 0.029
GoF			2.53	3.37

[a] $R_F = \Sigma(\|F_o\| - F_c\|)/\Sigma|F_o|$; $R_w = [\Sigma w(\|F_o\| - |F_c\|)^2/\Sigma w|F_o|]^{1/2}$ and GoF = $[\Sigma w (\|F_o\| - |F_c\|)^2/(\text{number of reflections} - \text{number of parameters})]^{1/2}$.

NMR spectra were measured using a Varian Gemini-200 or XL-300 spectrometer and referenced using the solvent residual signal ($\delta_H(CD_3)(CHD_2)CO$) = 2.04). The ^{13}C spectra were measured using a broad-banded Varian Gemini-200 or Varian XL300 spectrometer depending upon the probe size to be used (10 mm or 5 mm), and referenced to the solvent signal ($\delta_c(CDCl_3)$ = 77.0). The ^{31}P and ^{207}Pb[6] NMR spectra were obtained with the broad-banded Varian Gemini-200 with and without ^1H-decoupling, respectively, and with no ^2D field/frequency lock (field drift is negligible, <0.04 and <0.02 ppm/day for ^{31}P and ^{207}Pb, respectively). In these cases samples were prepared in 10 mm od NMR tubes with concentrations expressed in terms of mass of solute/volume of solvent. They were referenced by sample interchange with 85% H_3PO_4 and 1.0 *M* $Pb(NO_3)_2$(aq), respectively. For the latter reference δ_{Pb}(1.0 *M* $Pb(NO_3)_2$(aq)) = $\delta_{Pb}(PbMe_4$(toluene)) + 2961 ppm (12); in the text δ_{Pb} are given relative to the $PbMe_4$ standard. The ^{31}P and ^{207}Pb NMR chemical shifts are thought to be reproducible to ±0.1 and ±2 ppm, respectively.

IR spectra

All IR spectra were measured as mulls between KBr windows using a Nicolet 205 FTIR spectrometer.

X-ray structure determination

Crystals of **1** (as the CH_2Cl_2 solvate, **1′** (see below)) suitable for X-ray analysis were obtained by diffusing Et_2O into a solution of **1** in CH_2Cl_2. Suitable crystals of **2** were obtained during the synthesis described above.

The crystals **1′** and **2** were examined by a similar experimental procedure. An overview is given below and crystal data are summarized in Table 1. The crystal densities were measured by the neutral buoyancy method in mixtures of CCl_4 and 1,2-$C_2H_4Br_2$. Crystal **1′** was losing solvent at room temperature and hence measurements were made at −50°C. For comparison, the data collection of crystal **2** was also carried out at −50°C. In both cases data were collected on an Enraf-Nonius CAD4F diffractometer using graphite monochromated Mo Kα radiation (13). Photo and automatic indexing routines, followed by least squares fits of 21 accurately centered reflections gave cell constant and an orientation matrix. Intensity data were recorded in ω mode at variable scan speeds (1.50 to 4.12 deg min^{-1}), and a scan width of 0.70 + 0.35 tan θ with a maximum time per datum of 45 s. Background measurements were made by extending the scan by 25% on each side. Standard reflections were monitored every 120 min of X-ray exposure time. The faces of the data crystals were indexed and the distances among them were measured under a Filar microscope for Gaussian absorption correction which was made using the routine "abso". The data were processed using the NRCVAX crystal structure programs (14) running on a SUN 3/80 workstation. The structure solutions and the refinements were done by full-matrix least-squares techniques on F. The structures were solved using the program SHELXS-86 (15) and subsequent difference Fourier techniques. Anisotropic thermal parameters were assigned to all the atoms except for the phenyl rings and were refined. The hydrogen atoms were placed in ideal positions (C—H = 1.08 Å) and their thermal parameters were taken to be 10% larger than those of the attached carbon atoms.

Crystal 1′

A crystal of suitable size (0.1 × 0.1 × 0.2 × mm) was obtained by cleaving a rod-like crystal along (201) plane. In all 6201 reflections in the 2θ range 0–45° ($-45 \leq h \leq 1, -17 \leq k \leq 17, -12 \leq l \leq 12$) and 32 repetitions of the standards were recorded. The crystal used for data collection has 11 faces. The indices are {0,1,0}, {1,$\bar{1}$,$\bar{1}$}, ($\bar{1}$,1,$\bar{1}$), ($\bar{1}$,$\bar{1}$,1), (1,0,$\bar{1}$), (2,0,1), (0,$\bar{1}$,$\bar{1}$), (0,1,$\bar{1}$), and ($\bar{1}$,2,0). The minimum and maximum transmissions factors are 0.548 and 0.768. The space group $P\bar{1}$ was assumed for the triclinic system. The refinement converged for 196 parameters and 4513 ($I \geq 2.5\sigma(I)$) observations at R_F = 0.038, R_w = 0.035 and Gof = 2.53 using the weighting scheme based on counting statistics. In the final difference Fourier synthesis ranges from 1.66 to −0.84 e Å^{-3}. The top two peaks have the electron density greater than 1.0 e Å^{-3}. The top two peaks have the electron density greater than 1.0 e Å^{-3} and are associated with Pb at distances 1.26 and 1.34 Å respectively. The largest Δ/σ = 0.037.

Crystal 2

A blood-red crystal of suitable size (0.27 × 0.29 × 0.41 mm) was obtained by cleaving a plate along the (100) and (100) planes. The initial orientation matrix and the monoclinic cell were obtained from 25

[6] ^{207}Pb, 22.6% natural abundance, spin, I = 1/2, receptivity relative to ^{13}C, D^C = 11.4 (ref. 11).

Can. J. Chem. Downloaded from www.nrcresearchpress.com by EESC ESCOLA DE ENGENHARIA on 09/08/12
For personal use only.

Can. J. Chem. Downloaded from www.nrcresearchpress.com by EESC ESCOLA DE ENGENHARIA on 09/08/12
For personal use only.

reflections using the routines SEARCH and INDEX. The cell reduction program indicated a C-centered orthorhombic cell. The Laue check on a limited number of reflections suggested *mmm* symmetry. On the basis of these observations the intensity data were collected initially in a C-centered orthorhombic cell ($a = 33.985(13)$, $b = 17.047(5)$, $c = 11.838(4)$ Å, $Z = 8$). At the end of the data collection, an inspection of all the absorption corrected data showed that the systematic absences and symmetry-related reflections did not reflect the crystal system or the space group chosen. The data and the cell were transformed to a monoclinic system using the matrix transformation [0,–1,0, 0,0,1, –0.5,0.5,0], and it was found that the crystal belonged to the Laue group *2/m* (based on an observation of symmetry equivalent reflections) with the space group $P2_1/c$ from the systematic absences (16) ($h0l$, $l = 2n + 1$ and $0k0$, $k = 2n + 1$). However, the data collection was completed on the old C-centered orthorhombic cell ($-40 \leq h \leq 1$, $-20 \leq k \leq 20$, $-14 \leq l \leq 14$) in the 2θ range 0–50°. The data were processed, corrected for absorption and finally transformed to the monoclinic cell using the above-mentioned transformation matrix. The new cell data are $a = 17.039(2)$, $b = 11.834(2)$, $c = 18.965(3)$ Å, $\beta = 116.44(1)°$ (centering from 21 high angles in the 2θ range 24.1 to 30.2°), $Z = 4$. All the numbers reported here belong to the monoclinic cell. In all 10163 reflections were recorded, of which 6015 are unique reflections. The crystal used for data collection was seven faces with indices {1,0,0}, {0,1,0}, {$\bar{1}$,0,2}, and ($\bar{1}$,0,1). The minimum and maximum transmission factors are 0.2458 and 0.3445. In the final cycles, the refinement of 287 parameters and 4405 ($I \geq 2.5\sigma(I)$) observations, gave convergence at $R_F = 0.034$, $R_w = 0.029$, and GoF = 3.37 using the weighting scheme based on counting statistics. In the final difference Fourier synthesis ranges 1.00 to –1.26 e Å^{-3}. The top peak was 1.05 Å from Pb. The largest $\Delta/\sigma = 0.065$. The secondary extinction coefficient was refined to 0.636 (17).

The experimental details and crystal data are shown in Table 1, the positional and B_{iso} thermal parameters are given in Tables 2 and 3 for **1′** and **2** respectively. Tables of anisotropic thermal parameters, hydrogen atom positional parameters, selected dihedral and torsional angles have been included in the depository materials.[7]

Elemental analysis

Elemental microanalyses were carried out by Guelph Chemical Laboratories Ltd.

Results and discussion.

$Pb(SOCPh)_2$ and $Bi(SOCPh)_3$

These compounds can be synthesized in excellent yields by the following simple routes (M = Pb, $n = 2$; M = Bi, $n = 3$):

[1] $M(OAc)_n + n\text{PhCOSH} \xrightarrow{\text{MeOH}} M(SOCPh)_n + n\text{HOAc}$

[2] $M(SPh)_n + n\text{PhCOSH} \xrightarrow{\text{MeOH}} M(SOCPh)_n + n\text{PhSH}$

A minor complication is the gas phase reaction between thiobenzoic acid and the slurry of metal acetate or benzenethiolate, but this can be prevented by addition of the acid below the surface of the slurry.

Both salts are insoluble in most common solvents, pointing to polymeric structures. However, they are soluble in DMF. At 294 K the ^{207}Pb NMR spectrum of a saturated solution of $Pb(SOCPh)_2$ in DMF consists of a very broad line ($\Delta_{\nu 1/2} \approx 2000$ Hz) with $\delta_{Pb} \approx 740$. At 213 K, no ^{207}Pb signal was observed for the solution. There is evidently an exchange process and no information can be obtained on the nature of the species present.

[7]Copies may be purchased from Document Delivery, the Depository of Unpublished Data, CISTI, National Research Council Canada, Ottawa, ON, Canada K1A OS2.

TABLE 2. Atomic parameters x, y, z, and B_{iso} for $(AsPh_4)[Pb(SOCPh)_3]\cdot CH_2Cl_2$, **1′**

Atom	x	y	z	B_{iso}[a]
Pb	0.15815(4)	0.17043(3)	0.01462(4)	2.49(2)
S(1)	0.06276(24)	0.29416(17)	–0.01262(23)	3.43(16)
S(2)	0.02692 (25)	0.10263 (16)	–0.23101(24)	3.49(18)
S(3)	0.32213(25)	0.28175(18)	–0.06931(28)	4.18(19)
O(1)	0.2598(6)	0.3308(4)	0.1843(6)	3.86(43)
O(2)	0.0447(7)	–0.0271(4)	–0.1006(6)	4.64(51)
O(3)	0.3811(6)	0.1622(4)	0.0532(6)	4.13(49)
C(1)	0.1759(8)	0.3501(6)	0.1313(8)	2.70(59)
C(2)	0.0078(8)	–0.0050(6)	–0.2057(9)	2.75(61)
C(3)	0.4075(8)	0.2231(6)	–0.0089(8)	2.76(59)
C(11)	0.1687(5)	0.4257(3)	0.1933(5)	2.28(19)
C(12)	0.2582(4)	0.4671(4)	0.3110(5)	2.97(21)
C(13)	0.2562(4)	0.5363(4)	0.3740(4)	3.48(22)
C(14)	0.1648(5)	0.5641(3)	0.3193(5)	3.52(22)
C(15)	0.0753(4)	0.5227(4)	0.2016(5)	3.50(22)
C(16)	0.0773(4)	0.4535(4)	0.1386(4)	3.17(21)
C(21)	–0.0562(5)	–0.0746(3)	–0.3170(5)	2.41(19)
C(22)	–0.0624(5)	–0.1596(4)	–0.2976(4)	3.26(22)
C(23)	–0.1170(5)	–0.2256(3)	–0.4000(6)	4.04(24)
C(24)	–0.1654(5)	–0.2066(4)	–0.5219(5)	4.00(24)
C(25)	–0.1593(5)	–0.1216(4)	–0.5414(4)	3.69(23)
C(26)	–0.1047(5)	–0.0556(3)	–0.4389(6)	3.25(22)
C(31)	0.5231(4)	0.2500(4)	–0.0230(6)	2.62(20)
C(32)	0.6082(5)	0.2224(3)	0.0572(5)	3.19(21)
C(33)	0.7168(5)	0.2486(4)	0.0474(5)	3.66(23)
C(34)	0.7403(4)	0.3024(4)	–0.0425(6)	4.20(25)
C(35)	0.6552(6)	0.3301(3)	–0.1226(5)	4.11(24)
C(36)	0.5466(5)	0.3039(4)	–0.1129(5)	3.63(23)
Cation				
As	0.27891(8)	0.83058(6)	0.50273(8)	1.97(6)
C(41)	0.2647(5)	0.8921(3)	0.3614(4)	1.94(18)
C(42)	0.2269(5)	0.8479(2)	0.2423(5)	2.15(18)
C(43)	0.2197(5)	0.8943(3)	0.1389(4)	2.45(19)
C(44)	0.2502(5)	0.9851(3)	0.1545(4)	2.74(20)
C(45)	0.2879(5)	1.0293(2)	0.2736(5)	2.58(20)
C(46)	0.2952(5)	0.9828(3)	0.3770(4)	2.22(18)
C(51)	0.3174(5)	0.9055(3)	0.6456(4)	2.02(18)
C(52)	0.2289(4)	0.9037(3)	0.6824(5)	2.79(20)
C(53)	0.2577(5)	0.9594(4)	0.7883(5)	3.43(22)
C(54)	0.3751(5)	1.0169(3)	0.8575(4)	3.35(22)
C(55)	0.4637(4)	1.0186(3)	0.8206(5)	3.40(22)
C(56)	0.4348(4)	0.9629(4)	0.7147(5)	2.76(20)
C(61)	0.1333(4)	0.7354(3)	0.4774(5)	2.13(18)
C(62)	0.0339(5)	0.7167(3)	0.3654(4)	2.66(20)
C(63)	–0.0719(4)	0.6452(4)	0.3488(4)	3.27(22)
C(64)	–0.0782(4)	0.5924(3)	0.4444(6)	3.60(23)
C(65)	0.0212(5)	0.6111(3)	0.5565(5)	3.77(23)
C(66)	0.1270(4)	0.6825(4)	0.5730(4)	3.19(22)
C(71)	0.3996(4)	0.7902(3)	0.5307(5)	1.86(17)
C(72)	0.4510(5)	0.7992(3)	0.4438(4)	2.80(20)
C(73)	0.5404(5)	0.7700(4)	0.4653(5)	3.40(22)
C(74)	0.5783(4)	0.7319(4)	0.5737(5)	3.11(21)
C(75)	0.5269(5)	0.7229(3)	0.6606(4)	2.66(20)
C(76)	0.4375(5)	0.7521(3)	0.6391(4)	2.66(20)
Solvent				
C(10)	0.5375(11)	0.4956(7)	0.1887(11)	6.01(88)
Cl(1)	0.6323(3)	0.4566(2)	0.1724(4)	8.26(28)
Cl(2)	0.5767(3)	0.5448(2)	0.3349(3)	7.19(28)

[a]B_{iso} is the mean of the principal axes of the thermal ellipsoid.

Can. J. Chem. Downloaded from www.nrcresearchpress.com by EESC ESCOLA DE ENGENHARIA on 09/08/12
For personal use only.

TABLE 3. Atomic parameters x, y, z, and B_{iso} for $Pb(SOCPh)_2(S_2CPCy_3)$, **2′**

Atom	x	y	z	B_{iso}[a]
Pb	0.16305(2)	0.09654(3)	0.02128(2)	2.60(2)
P	−0.12310(13)	0.09762(18)	−0.25250(10)	2.01(10)
S(1)	0.21810(16)	0.31738(17)	0.03100(13)	3.61(13)
S(2)	0.25239(19)	0.04194(18)	−0.05634(14)	4.75(16)
S(3)	0.03926(14)	0.19239(17)	−0.12648(12)	3.05(11)
S(4)	−0.01475(16)	−0.04070(17)	−0.10814(13)	3.58(13)
O(1)	0.3123(4)	0.1690(4)	0.1331(3)	4.18(34)
O(2)	0.2830(4)	−0.1034(5)	0.0562(3)	4.32(37)
C(1)	0.3072(5)	0.2685(6)	0.1126(4)	2.82(47)
C(2)	0.3010(5)	−0.0729(6)	0.0036(4)	2.82(45)
C(3)	−0.0288(5)	0.0803(6)	−0.1566(4)	2.23(40)
C(111)	−0.1915(5)	0.2175(6)	−0.2502(4)	1.89(38)
C(112)	−0.2187(5)	0.2025(6)	−0.1844(4)	2.43(44)
C(113)	−0.2865(5)	0.2932(6)	−0.1916(4)	3.06(49)
C(114)	−0.2480(5)	0.4130(7)	−0.1901(5)	3.46(50)
C(115)	−0.2192(5)	0.4257(6)	−0.2541(5)	2.72(46)
C(116)	−0.1510(5)	0.3360(6)	−0.2476(4)	2.43(46)
C(121)	−0.0827(5)	0.1300(5)	−0.3249(4)	2.14(42)
C(122)	−0.1572(5)	0.1424(6)	−0.4077(4)	2.62(44)
C(123)	−0.1229(5)	0.1844(7)	−0.4628(4)	3.35(50)
C(124)	−0.0487(6)	0.1128(7)	−0.4624(5)	3.65(53)
C(125)	0.0257(5)	0.0976(7)	−0.3785(4)	3.06(45)
C(126)	−0.0090(5)	0.0523(6)	−0.3233(4)	2.75(44)
C(131)	−0.1928(5)	−0.0295(6)	−0.2747(4)	1.99(40)
C(132)	−0.2886(5)	−0.0108(6)	−0.3345(5)	2.90(45)
C(133)	−0.3421(5)	−0.1173(7)	−0.3366*5)	3.43(47)
C(134)	−0.3026(6)	−0.2243(7)	−0.3542(5)	3.58(53)
C(135)	−0.2068(6)	−0.2372(6)	−0.2981(5)	3.59(56)
C(136)	−0.1539(5)	−0.1329(6)	−0.2975(4)	2.26(41)
C(11)	0.3809(3)	0.3470(4)	0.1588(3)	2.47(16)
C(12)	0.4422(4)	0.3128(3)	0.2335(3)	3.85(19)
C(13)	0.5119(3)	0.3837(4)	0.2790(2)	4.24(20)
C(14)	0.5203(3)	0.4888(4)	0.2498(3)	3.50(18)
C(15)	0.4590(3)	0.5230(3)	0.1750(3)	3.34(18)
C(16)	0.3893(3)	0.4522(4)	0.1295(2)	2.67(16)
C(21)	0.3670(3)	−0.1396(4)	−0.0138(3)	3.27(18)
C(22)	0.3796(3)	−0.2534(4)	0.0074(3)	3.74(19)
C(23)	0.4376(4)	−0.3183(3)	−0.0093(3)	3.96(20)
C(24)	0.4829(3)	−0.2694(4)	−0.0473(3)	5.37(24)
C(25)	0.4703(3)	−0.1556(5)	−0.0685(3)	5.10(23)
C(26)	0.4123(4)	−0.0906(3)	−0.0517(3)	3.89(18)

[a] B_{iso} is the mean of the principal axes of the thermal ellipsoid.

Addition of donor ligands

The addition of strong donor ligands has been found to solubilize dimeric $Ni_2(SOCPh)_4.EtOH$ (17) and the presumed- polymeric thiobenzoates of Pd(II) and Pt(II) (18). These earlier findings and the solubility of both $Pb(SOCPh)_2$ and $Bi(SOCPh)_3$ in the strong donor solvent (19) DMF, suggested that solubilization of the Pb(II) and Bi(III) salts might be achieved by the addition of appropriate ligands.

None of the ligands $PhCOS^-$, Cy_3PCS_2, Cy_3PO, Ph_3PO, or PPh_3 increased the solubility of $Bi(SOCPh)_3$ in any of the solvents in which it was otherwise insoluble. However, more positive results were obtained for $Pb(SOCPh)_2$ as described next.

(i) $Pb(SOCPh)_2$:$SOCPh^-$

Addition of one mole equivalent of $PhCOS^-$ to $Pb(SOCPh)_2$ in MeOH leads to the formation of $[Pb(SOCPh)_3]^-$ (reaction [3]). The new anion has been isolated in good yield as the $AsPh_4^+$ salt, **1**. Alternatively, **1** may be synthesized from $Pb(NO_3)_2$ and excess $PhCOS^-$ in methanol:water (reaction[4]). In this case the yield is poor. A brown solid, presumably PbS, is formed concurrently and it is tedious to separate this from the $AsPh_4^+$ salt.

$$[3]\quad Pb(SOCPh)_2 + PhCOS^- \xrightarrow{MeOH} [Pb(SOCPh)_3]^-$$

$$[4]\quad Pb^{2+} + 3PhCOS^- \xrightarrow{MeOH:H_2O} [Pb(SOCPh)_3]^-$$

The salt **1** is soluble in Me_2CO, MeCN, CH_2Cl_2, $CHCl_3$, and DMF. The ^{207}Pb NMR chemical shifts (and approximate linewidths[8]) at 294 K and a concentration of 0.025 mol per L of solvent are at 1463 (13 Hz), 1422 (15 Hz), and 1422 (280 Hz) in Me_2CO, MeCN, and DMF, respectively, at 294 K. These indicate the presence of the same species in each solvent, allowing for solvent effect on δ_{Pb}, which are expected to be large. The relatively large value of $\Delta\nu_{1/2}$ found for the DMF solution may indicate exchange broadening caused by the onset of dissociation.

^{207}Pb NMR chemical shifts found for mixtures of $(Ph_4As)[Pb(SPh)_3]$ and excess PhCOSH or $(PhCOS)_2$ show that the $[Pb(SOCPh)_3]^-$ anion is also being formed according to reactions [5] and [6].

$$[5]\quad [Pb(SPh)_3]^- + 3PhCOS \rightarrow [Pb(SOCPh)_3]^- + 3PhSH$$

$$[6]\quad [Pb(SPh)_3]^- + (3/2)\,(PhCOS)_2 \rightarrow [Pb(SOCPh)_3]^- + (3/2)Ph_2S_2$$

For reaction [5] in $CHCl_3$ $\delta_{Pb}(\Delta\nu_{1/2}) = 1414$ (≈140 Hz), while for reaction [6] in Me_2CO, $\delta_{Pb}(\Delta\nu_{1/2}) = 1466$ (≈10 Hz).

The ^{207}Pb resonance of $[Pb(SOCPh)_3]^-$ is considerably more shielded than those found (8, 20) for various anions $[Pb(SR)_3^-]$, e.g. 2868 ppm for $(Ph_4As)[Pb(SPh)_3]^-$ in $CHCl_3$ at 296 K (8). The same phenomenon has been observed (3) for $[Cd(SOCPh)_3]^-$ vs. $[Cd(SR)_3]^-$ and has been taken to indicate a significant interaction of the metal with the oxygen of the $PhCOS^-$ ligand. The structure of $[Pb(SOCPh)_3]^-$, discussed below, shows that there is indeed an interaction with the oxygens in this anion.

(ii) $Pb(SOCPh)_2$:S_2CPCy_3

$Pb(SOCPh)_2$ is poorly soluble in CS_2, but becomes very soluble in the presence of S_2CPCy_3. From these mixtures a red–brown (blood red as larger crystals) 1:1 adduct can be obtained in moderate yield. The solubility of these crystals in CS_2 is much less than that attainable in the initial (presumably supersaturated) solution.

The formation of $Pb(SOCPh)_2(S_2CPCy_3)$ is associated with a deshielding of the ^{31}P NMR signal of S_2CPCy_3: $\delta_P = 23.8$ and $\Delta\delta_P$ (= δ_P(complex) − δ_P(free ligand)) = 9.9 for solutions in CS_2 at 294 K. Clearly binding between the S_2CPCy_3 and the lead center persists in solution. The ^{207}Pb NMR spectrum of the 1:1 adduct in CS_2 gives $\delta_{Pb}(\Delta\nu_{1/2}) = 1288$ (≈220 Hz) for a saturated solution in CS_2 (< 0.025 mol/L of CS_2). It is tempting to conclude from the similar ^{207}Pb NMR chemical shifts of $Pb(SOCPh)_2$ and $[Pb(SOCPh)_3]^-$ that there is a similarity of structure, and X-ray analysis (see below) does reveal a common

[8] The values of $\Delta\nu_{1/2}$ are upper limits, since the values generally increase with time, presumably due to minor temperature fluctuations coupled with a high temperature effect on δ_{Pb}.

Can. J. Chem. Downloaded from www.nrcresearchpress.com by EESC ESCOLA DE ENGENHARIA on 09/08/12
For personal use only.

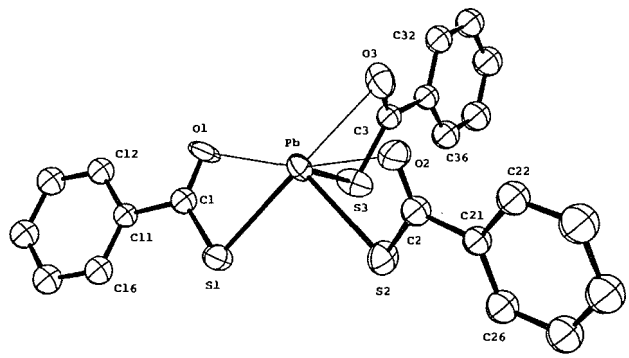

FIG. 1. A view of the anion in **1′** and the atom numbering scheme. Atoms are drawn as 50% probability thermal ellipsoids and hydrogen atoms have been omitted for clarity.

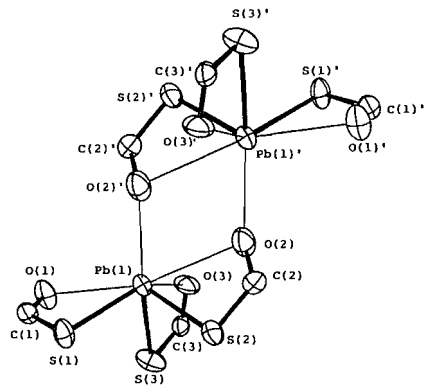

FIG. 2. The dimeric interaction between the anions in **1′**.

PbS_3 primary kernel. Such logic may be simplistic, however, since the ^{207}Pb chemical shift of $Pb(SOCPh)_2(OPCy_3)$ is also similar (see below).

(iii) $Pb(SOCPh)_2$:$PPCy_3$

Addition of $OPCy_3$ (but not the weaker donor $OPPh_3$, or PPh_3 itself) solubilizes $Pb(SOCPh)_2$ in Me_2CO. The lead salt is completely soluble at a 1:1 ratio. A titration using ^{31}P NMR confirms this reactant ratio for $Pb(SOCPh)_2/OPCy_3 \geq 1$.[9] The complex $Pb(SOCPh)_2(OPCy_3)$ is characterized by $\delta_P = 58.2$, deshielded as expected (22) relative to free $OPCy_3$ ($\delta_P = 48.8$), and $\delta_{Pb}(\Delta\nu^{1/2}) = 1335(\approx 890\ Hz^7)$ at 294 K. (These values were measured with $Pb(SOCPh)_2/OPCy_3 \leq 1$ for ^{31}P, and with $Pb(SOCPh)_2/OPCy_3 = 2$ and 0.05 mol of $OPCy_3$ per L of acetone for ^{207}Pb.)

An alternative formulation of the product as $[Pb(OPCy_3)_3][Pb(SOCPh)_3]_2$ is ruled out by δ_{Pb}. For $[Pb(OPCy_3)_3]^{2+}$ $\delta_{Pb} \approx -1142$ (relative to $PbMe_4$(toluene)) for a solution in SO_2(1) at 203 K (22). Combined with $\delta_{Pb}([Pb(SOCPh)_3]^-)$, this leads to $\delta_{Pb} \approx 590$ for $[Pb(OPCy_3)_3][Pb(SOCPh)_3]_2$, assuming fast exchange (only one signal is observed in the ^{207}Pb NMR spectrum). Even allowing for temperature and medium effects on δ_{Pb}, which are expected to be large, this is quite different from the value of δ_{Pb} observed.

Structure of $(AsPh_4)[Pb(SOCPh)_3]$. CH_2Cl_2 (1′)

The crystal structure consists of discrete cations, anions occurring as centrosymmetric dimers, and a molecule of solvent (CH_2Cl_2). The Pb and As are separated by 6.59 Å. The shortest interionic distance of 2.307 Å is H(44)...O(3) [x, $(1 + y)$, $(1 + z)$].

Figure 1 shows a view of the $[Pb(SOCPh)_3]^-$ anion and gives the atomic numbering scheme used. Figure 2 shows the coordination spheres of the lead atoms in the centrosymmetric dimer that the anions form. The Pb...Pb distance in the dimer is 5.509(2) Å. Listed in Table 4 are selected bond distances and angles. Those of the cation and solvent molecule are unexceptional and are not discussed further.

The immediate coordination sphere of each lead atom contains three sulfur atoms and three oxygen atoms from three chelating thiobenzoate ligands. The three Pb—S distances are significantly different and cover the range 2.706(3) – 2.764(3) Å. The shortest Pb—S distance just touches on the range of Pb—S distances found for primary interactions in Pb(II) complexes with simple terminal mono- and di-thiolates (2.554(4) to 2.696(3) Å (8, 23)). However, they all fall into the range that has been established from the shorter Pb—S bonds to the anisobidentate ligands that are found in Pb(II) complexes of dithiocarbamates (24), xanthates (25, 26) and dithiophosphates (27) (2.673(4) to 2.946(3) Å). The S—Pb—S angles are irregular and cover the range 85.02(9)–90.75(8)°. For comparison, S—Pb—S angles for the $Pb(SPh)_3^-$ anion are 90.32(4) – 96.14(5)° in the $AsPh_4^+$ salt (8) and 89.7(1) – 102.7(1)° in the $N^nPr_4^+$ salt (23*a*) and the angles between the three shorter Pb—S distances in $[Pb(S_2COEt)_3]^-$ are 84.38(8)–89.80(9)°(26).

The Pb—O distances are 2.879(6), 2.905(7), and 3.113(6) Å. The longest is associated with the bridging interaction, Pb—O(2)[a], 3.298(7) Å. All four Pb—O distances are less than the sum of the van der Waals radii, 3.5 Å (28). They are, however, significantly longer than those found for the primary bonds in simple carboxylates of Pb(II), for which Pb—O distances to the bidentate ligands fall in the range 2.32(2)–2.74(1) Å (29). Thus the Pb—O distances in the present case represent secondary interactions.

In the $PhCOS^-$ ligands, the C—O distances range from 1.219(11) to 1.235(11) Å, the C—S distances from 1.721(10) to 1.739(9) Å, and the S—C—O angles from 122.1(7) to 123.5(7)°. These values are comparable to those found in $(Me_4N)[Na(CdSOCPh_3)_2]$ (3), $[Ni(SOCPh)_2]_2$.EtOH (30), and $(PhCOS)_2$ (31).

It is possible to consider the coordination geometry around Pb as being based primarily on a pyramidal PbS_3 kernel of the VSEPR type AX_3E. The weaker Pb—O interactions then occur around the region that is occupied by the lone pair electrons, as occurs in the dimer of $[Pb(SOCOEt)_3]^-$ also (26). The geometry of the overall PbS_3O_4 kernel in the dimer of $[Pb(SOCPh)_3]^-$ is remarkably similar to that of the overall SbS_3O_4 kernel found in polymeric $Sb(SOCMe)_3$ (32). Earlier authors (26) have commented that the structures of Pb(II) complexes are "strikingly reminiscent" of their Sb(III) and Bi(III) analogues.

It is important to note that although the Pb—O bonds of $[Pb(SOCPh)_3]^-$ are secondary in the solid state, the ^{207}Pb NMR chemical shift of the anion (as discussed above) suggests that Pb—O bonding remains important for the anion in solution. A reviewer has suggested that a different structure with stronger Pb—O bonding may occur in solution.

[9]At $Pb(SOCPh)_2/OPCy_3 < 1$, δ_P is less shielded than expected for $Pb(SOCPh)_2(OPCy_3)$ and excess $OPCy_3$ undergoing fast exchange. Evidently more than one $OPCy_3$ can coordinate to Pb, but we were unable to identify the ligand-rich species formed. We note that there is evidence for $[Pb(OPPh_3)_n]^{2+}$ ($n > 3$) are known (ref. 21).

TABLE 4. Bond distances (Å) and angles (deg) for $(AsPh_4)[Pb(SOCPh)_3]\cdot CH_2Cl_2$, **1′**

Bond	Distance	Bond	Distance
Pb(1)—S(1)	2.764(3)	Pb(1)—S(2)	2.706(3)
Pb(1)—S(3)	2.740(3)	Pb(1)—O(1)	2.879(6)
Pb(1)—O(2)	3.113(6)	Pb(1)—O(2)[a]	3.298(7)
Pb(1)—O(3)	2.905(7)	S(1)—C(1)	1.739(9)
S(2)—C(2)	1.733(10)	S(3)—C(3)	1.721(10)
O(1)—C(1)	1.219(11)	O(2)—C(2)	1.230(11)
O(3)—C(3)	1.235(11)	C(1)—C(11)	1.518(11)
C(2)—C(21)	1.488(10)	C(3)—C(31)	1.506(11)
As(1)—C(41)	1.886(5)	As(1)—C(51)	1.881(5)
As(1)—C(61)	1.891(4)	As(1)—C(71)	1.897(7)
C(10)—Cl(1)	1.702(14)	C(10)—Cl(2)	1.701(12)

Bonds	Angle	Bonds	Angle
S(1)—Pb(1)—S(2)	90.75(8)	S(1)—Pb(1)—S(3)	88.85(9)
S(1)—Pb(1)—O(1)	55.01(13)	S(1)—Pb(1)—O(2)	131.18(15)
S(1)—Pb(1)—O(2)[a]	93.00(14)	S(1)—Pb(1)—O(3)	139.34(14)
S(2)—Pb(1)—S(3)	85.02(9)	S(2)—Pb(1)—O(1)	141.56(14)
S(2)—Pb(1)—O(2)	52.97(14)	S(2)—Pb(1)—O(2)[a]	91.86(13)
S(2)—Pb(1)—O(3)	101.92(15)	S(3)—Pb(1)—O(1)	78.12(16)
S(3)—Pb(1)—O(2)	114.98(15)	S(3)—Pb(1)—O(2)[a]	176.39(13)
S(3)—Pb(1)—O(3)	54.68(13)	O(1)—Pb(1)—O(2)	163.71(18)
O(1)—Pb(1)—O(2)[a]	105.47(18)	O(1)—Pb(1)—O(3)	96.05(19)
O(2)—Pb(1)—O(2)[a]	61.54(18)	O(2)—Pb(1)—O(3)	85.04(19)
O(2)a—Pb(1)—O(3)	124.51(17)	Pb(1)—S(1)—C(1)	87.5(3)
Pb(1)—S(2)—C(2)	94.5(3)	Pb(1)—S(3)—C(3)	89.5(3)
Pb(1)—O(1)—C(1)	93.9(5)	Pb(1)—O(2)—Pb(1)[a]	118.5(2)
Pb(1)—O(2)—C(2)	89.0(5)	Pb(1)[a]—O(2)—C(2)	115.8(6)
Pb(1)—O(3)—C(3)	93.4(6)	S(1)—C(1)—O(1)	122.7(7)
S(1)—C(1)—C(11)	118.3(6)	O(1)—C(1)—C(11)	119.0(7)
S(2)—C(2)—O(2)	123.5(7)	S(2)—C(2)—C(21)	118.4(6)
O(2)—C(2)—C(21)	118.2(8)	S(3)—C(3)—O(3)	122.1(7)
S(3)—C(3)—C(31)	119.7(6)	O(3)—C(3)—C(31)	118.0(8)
C(41)—As(1)—C(51)	110.2(2)	C(41)—As(1)—C(61)	110.6(2)
C(41)—As(1)—C(71)	108.5(3)	C(51)—As(1)—C(61)	106.4(3)
C(51)—As(1)—C(71)	109.9(3)	C(61)—As(1)—C(71)	111.1(2)
C(1)—C(11)—C(12)	117.0(6)	C(1)—C(11)—C(16)	123.0(5)
C(2)—C(21)—C(22)	118.3(5)	C(2)—C(21)—C(26)	121.7(6)
C(3)—C(31)—C(32)	119.3(6)	C(3)—C(31)—C(36)	120.7(6)
As(1)—C(41)—C(42)	120.4(4)	As(1)—C(41)—C(46)	119.6(3)
As(1)—C(51)—C(52)	120.2(3)	As(1)—C(51)—C(56)	119.8(5)
As(1)—C(61)—C(62)	121.3(4)	As(1)—C(61)—C(66)	118.7(3)
As(1)—C(71)—C(72)	120.2(4)	As(1)—C(71)—C(76)	119.8(5)
Cl(1)—C(10)—Cl(2)	116.1(7)		

[a]Symmetry equivalents ($-x$, $-y$, $-z$).

Structure of $Pb(SOCPh)_2$ (S_2CPCy_3) (2)

The crystal structure of this compound shows that it is essentially molecular. Figure 3 shows a molecule and gives the numbering scheme used. However, the molecules are linked together as dimers through a long interaction, Pb—S(4)[a], 3.639(2) Å, that is just within the sum of the van der Waals radii, 3.80 Å (28). A dimer is shown in Fig 4. Within the dimer, the Pb...PB distance is 5.723 Å. Selected bond distances and angles are given in Table 5.

In the $Pb(SOCPh)_2(S_2CPCy_3)$ molecule, the primary bonding is to three sulfur atoms, one from each ligand. The bonding of the two thiobenzoate ligands differs. One, ligand(1), has a Pb—S distance (2.755(2) Å) that places it within the range of primary Pb—S distances observed for $[Pb(SOCPh)_3]^-$, and a Pb—O distance (2.626(5) Å) significantly shorter than the Pb—O distances observed in the anion. The other ligand(2), has a Pb—S distance (2.626(2) Å) that is shorter than the corresponding distances in the anion, while the Pb—O distance (3.002(5) Å) is within the appropriate range of the anion.

The S_2CPCy_3 ligand is bound in an anisobidentate manner, with Pb—S distances 2.885(2) and 3.350(2) Å. The shorter of these places it within the range of primary Pb—S distances found for dithiocarbamates, xanthates, and dithiophosphates (see above). The longer of the Pb—S distances places it outside the range observed for the weaker bonds of the anisobidentate ligands in these compounds (2.83(4)–3.232(10) Å (24–27)). Still, it is significantly less than the Pb—S(4)[a] bridging distance or the van der Waals distance. The weak bridging interaction of S(4) seems insufficient to account for the discrepancy between Pb—S(3) and Pb—S(4), which we attribute instead to the propensity of Pb(II) to form a pyramidal PbS_3 primary kernel.

The Pb—S(4) interaction, though weak, may be significant.

Can. J. Chem. Downloaded from www.nrcresearchpress.com by EESC ESCOLA DE ENGENHARIA on 09/08/12
For personal use only.

TABLE 5. Selected bond distances (Å) and angles (deg) for $Pb(SOCPh)_2(S_2CPCy_3)$, **2**

Bond	Distance	Bond	Distance
Pb—S(1)	2.755(2)	Pb—S(2)	2.626(2)
Pb—S(3)	2.885(2)	Pb—S(4)	3.350(2)
Pb—S(4)[a]	3.639(2)	Pb—O(1)	2.626(5)
Pb—O(2)	3.002(5)	P—C(3)	1.826(7)
P—C(111)	1.849(7)	P—C(121)	1.830(7)
P—C(131)	1.845(7)	S(1)—C(1)	1.715(8)
S(2)—C(2)	1.728(8)	S(3)—C(3)	1.685(7)
S(4)—C(3)	1.660(7)	O(1)—C(1)	1.231(9)
O(2)—C(2)	1.220(9)	C(1)—C(11)	1.494(9)
C(2)—C(21)	1.526(10)	C(111)—C(112)	1.523(9)
C(111)—C(116)	1.554(10)	C(112)—C(113)	1.537(10)
C(113)—C(114)	1.557(11)	C(114)—C(115)	1.506(10)
C(115)—C(116)	1.537(10)	C(121)—C(122)	1.524(10)
C(121)—C(126)	1.547(10)	C(122)—(123)	1.491(10)
C(123)—C(124)	1.519(11)	C(124)—C(125)	1.541(11)
C(125)—C(126)	1.511(10)	C(131)—C(132)	1.534(11)
C(131)—C(136)	1.542(9)	C(132)—C(133)	1.545(11)
C(133)—C(134)	1.539(11)	C(134)—C(13)	1.507(13)
C(135)—C(136)	1.526(11)		

Bonds	Angle	Bonds	Angle
S(1)—Pb—S(2)	90.34(7)	S(1)—Pb—S(3)	76.82(6)
S(1)—Pb—S(4)	132.76(6)	S(1)—Pb—S(4)[a]	115.24(6)
S(1)—Pb—O(1)	57.2(1)	S(1)—Pb—O(2)	123.7(1)
S(2)—Pb—S(3)	84.72(7)	S(2)—Pb—S(4)	91.77(7)
S(2)—Pb—S(4)[a]	154.38(6)	S(2)—Pb—O(1)	86.5(1)
S(2)—Pb—O(2)	54.7(1)	S(3)—Pb—S(4)	56.45(5)
S(3)—Pb—S(4)[a]	98.99(6)	S(3)—Pb—O(1)	133.0(1)
S(3)—Pb—O(2)	131.0(1)	S(4)—Pb—S(4)[a]	70.11(5)
S(4)—Pb—O(1)	170.0(1)	S(4)—Pb—O(2)	94.8(1)
S(4)[a]—Pb—O(1)	108.2(1)	S(4)[a]—Pb—O(2)	107.4(1)
O(1)—Pb—O(2)	76.1(2)	C(3)—P—C(111)	110.3(3)
C(3)—P—C(121)	108.3(3)	C(3)—P—C(131)	109.1(3)
C(111)—P—C(121)	108.0(3)	C(111)—P—C(131)	106.4(3)
C(121)—P—C(131)	114.7(3)	Pb—S(1)—C(1)	83.0(3)
Pb—S(2)—C(2)	93.0(3)	Pb—S(3)—S(4)	69.67(6)
Pb—S(3)—C(3)	96.6(2)	Pb—S(4)—Pb[a]	109.89(6)
Pb—S(4)—S(3)	53.88(5)	Pb—S(4)—C(3)	81.2(3)
Pb[a]—S(4)—C(3)	116.7(3)	Pb—O(1)—C(1)	98.6(5)
Pb—O(2)—C(2)	88.9(4)	S(1)—C(1)—O(1)	121.2(6)
S(1)—C(1)—C(11)	119.7(5)	O(1)—C(1)—C(11)	119.1(6)
S(2)—C(2)—O(2)	123.3(6)	S(2)—C(2)—C(21)	116.6(5)
O(2)—C(2)—C(21)	120.0(6)	P—C(3)—S(3)	114.7(4)
P—C(3)—S(4)	119.6(4)	S(3)—C(3)—S(4)	125.7(4)
P—C(111)—C(112)	110.8(5)	P—C(111)—C(116)	114.7(5)
C(112)—C(111)—C(116)	111.9(5)	C(111)—C(112)—C(113)	109.6(6)
C(112)—C(113)—C(114)	109.9(6)	C(113)—C(114)—C(115)	111.2(6)
C(114)—C(115)—C(116)	111.9(6)	C(111)—C(116)—C(115)	108.2(6)
P—C(121)—C(122)	112.0(5)	P—C(121)—C(126)	115.8(5)
C(122)—C(121)—C(126)	111.9(6)	C(121)—C(122)—C(123)	110.4(6)
C(122)—C(123)—C(124)	113.3(6)	C(123)—C(124)—C(125)	111.7(6)
C(124)—C(125)—C(126)	111.1(6)	C(121)—C(126)—C(125)	109.9(6)
P—C(131)—C(132)	114.6(5)	P—C(131)—C(136)	113.4(5)
C(132)—C(131)—C(136)	110.9(6)	C(131)—C(132)—C(133)	108.8(6)
C(132)—C(133)—C(134)	111.6(6)	C(133)—C(134)—C(135)	111.7(6)
C(134)—C(135)—C(136)	112.0(7)	C(131)—C(136)—C(135)	108.5(6)
C(1)—C(11)—C(12)	118.0(5)	C(1)—C(11)—C(16)	122.0(4)
C(2)—C(21)—C(22)	118.1(6)	C(2)—C(21)—C(26)	121.9(5)

[a]Symmetry equivalents ($-x$, $-y$, $-z$).

Can. J. Chem. Downloaded from www.nrcresearchpress.com by EESC ESCOLA DE ENGENHARIA on 09/08/12
For personal use only.

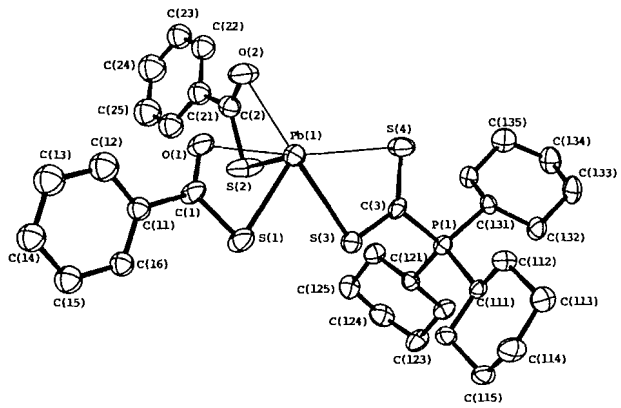

FIG. 3. A view of the $Pb(SOCPh)_2(S_2CPCy_3)$ molecule in **2** and the atom numbering scheme. Atoms are drawn as 50% probability thermal ellipsoids and hydrogen atoms have been omitted for clarity.

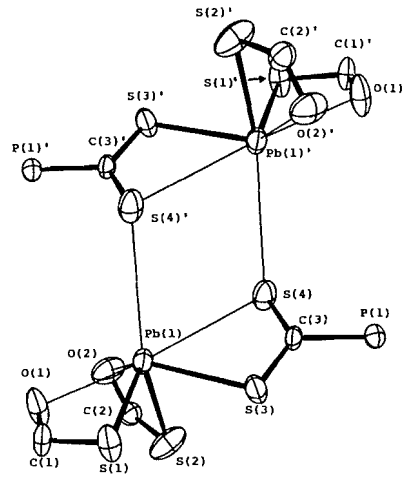

FIG. 4. The dimeric interaction between the molecules in **2**.

The difference between the Pb—S(3) and Pb—S(4) distances is less than the 1.241 Å difference between the two Pt—S distances in *cis*-$[Pt(C_6F_6)_2\{SC(S)PCy_3\}(CO)]$ where the S_2CPCy_3 ligand is considered monodentate (33). Two other structural features suggest a significance for Pb—S(4). First, the difference between the two C—S distances of the S_2CPCy_3 ligand, Δr(C—S), for $(Pb(SOCPh)_2(S_2CPCy_3)$ is smaller than that found in *cis*-$[Pt(C_6F_6)_2\{\eta^1\text{-}SC(S)PCy_3\}(CO)]$ (33), though probably larger than that found in $[Pt(C_6F_5)_2\eta^2\text{-}S_2CPCy_3)]$ (33). Second, the S—C—S angle of the carbodithioate moiety in the lead complex falls between those of the Pd and Pt complexes just mentioned.

Considering the angles subtended at Pb by the sulfurs that are strongly bound, the angle S(1)—Pb—S(2) between the sulfur atoms of the thiobenzoates is 90.34(7)°, larger than the S—Pb—S angles involving a thiobenzoate and S_2CPCy_3 (76.82(6) and 84.72(7)°). The reason for this discrepancy is not clear, but we note that even in $[Pb(S_2COEt)_3]^-$, where all three ligands are identical, there is significant variation in the S—Pb—S angles (84.38(8)–89.80(9)°) (26).

As is the case for $[Pb(SOCPh)_3]^-$ and other structures already discussed, the secondary interactions in $Pb(SOCPh)_2(S_2CPCy_3)$ (with O(1), O(2), S(4), and S(4)^a) take place in the "open" region expected to be occupied by the lone pair on a molecule of the VSEPR type AX_3E.

Each of the four-membered rings Pb,S(1),O(1),C(1), Pb,S(2),O(2),C(2), and Pb,S(3),S(4),C(3) is planar within experimental error. The dihedral angle between the first and last of these planes is particularly small, 10.8(2)°, perhaps due to the approach of the bridging sulfur, S(4)^a.

The complex **2** is the first of a Main Group element with an R_3PCS_2 ligand. However, apart from the features discussed above, the structure of the S_2CPCy_3 ligand in the Pb(II) complex is comparable to those where this ligand acts as a $2e^-$- or $4e^-$-donor to a transition metal (33)[10]. Factors that may contribute to the stability of the S_2CPR_3 ligand in the Pb(II) complex include the relative "softness" (34) of the metal center (reflected here by strong bonding to the S atoms and weak bonding to the O atoms of $PhCOS^-$) and a symbiotic relationship (35) between the S_2CPCy_3 and the S-bound $PhCOS^-$ ligands already present.[11] In any event, there seems no reason to believe that the lead complex is unique. Indeed the absence of R_3PCS_2 complexes of the Main Group elements may simply be due to lack of attention. Accordingly, we plan to explore this area further.

Conclusions.

The compounds $Pb(SOCPh)_2$ and $Bi(SCOPh)_3$ can be prepared by reaction of PhCOSH with the appropriate metal acetate or benzenethiolate. The ligands $PhCOS^-$, Cy_3PCS_2, and Cy_3PO form 1:1 complexes with $Pb(SOCPh)_2$ causing solubilization of the lead compound in solvents in which it is otherwise insoluble. Neither Ph_3P nor Ph_3PO increase the solubility of $Pb(SOCPh)_2$ and none of the five ligands enhance the solubility of very poorly soluble $Bi(SOCPh)_3$.

Single crystal X-ray analyses of (Ph_4As) $[Pb(SCOPh)_3]$ and $Pb(SOCPh)_2(S_2CP\{c\text{-}C_6H_{11}\}_3)$ show that in both cases the primary coordination kernal is PbS_3 with a trigonal pyramidal geometry. The complex with Cy_3PCS_2 is the first for any ligand of the type R_3PCS_2 with a Main group element.

Acknowledgements.

Funding for this work was provided by this department and by the Natural Sciences and Engineering Council of Canada through a Research Grant to P.A.W.D. Within this department, Susan England provided expert assistance in obtaining some of the NMR spectra and Professor N.C. Payne kindly allowed J.J.V. use of the X-ray and computing facilities.

1. J.A. Cras and J. Willemse. *In* Comprehensive coordination chemistry. Vol. 2. *Edited by* G. Wilkinson, R.G. Gillard, and J.A. McCleverty. Pergamon, Oxford. 1987. Chap. 16.4.
2. B.J. McCormick, R. Beremon, and D. Baird. Coord. Chem. Rev. **54**, 99 (1984).
3. J.J. Vittal and P.A.W. Dean. Inorg. Chem. **32**, 791 (1993).
4. J. Cuyas, D. Miguel, J.A. Perez-Martinez, V. Riera, and J. Garcia-Granda. Polyhedron, **11**, 2713 (1992).
5. W. Rigby. J. Chem. Soc. 794 (1951).
6. M.E. Peach. J. Inorg. Nucl. Chem. **41**, 1390 (1979).

[10]Other bonding modes are known with transition metals (ref. 4).

[11]We note that in complexes of monothiocarbamates, the S atoms tend to occupy mutually adjacent positions, but the reasons for this are not well understood (ref. 2). In the present complex one interligand S...S distance, S(1)...S(3), 3.5056 Å, is less than the sum of the van der Waals radii, 3.6 Å (ref. 28). This relatively short distance may represent an interaction that stabilizes the particular combination of ligands present, albeit weakly

Can. J. Chem. Downloaded from www.nrcresearchpress.com by EESC ESCOLA DE ENGENHARIA on 09/08/12
For personal use only.

7. R.A. Shaw and M. Woods. J. Chem. Soc. (A), 1561 (1971).
8. P.A.W. Dean, J.J. Vittal, and N.C. Payne. Inorg. Chem. **23**, 4232 (1984).
9. L. Field. *In* Organic chemistry of sulfur. *Edited by* S. Oae. Plenum, New York. 1977. Chap. 7.
10. K. Isslieb and K. Brack. Z. Anorg. Allgem. Chem. **277**, 258 (1954).
11. R.K. Harris. Nuclear magnetic resonance spectroscopy. Pitman, London. 1983. p. 230.
12. R.K. Harris, J.D. Kennedy, and W. McFarlane. *In* NMR and the periodic table. *Edited by* R.K. Harris and B.E. Mann. Academic, London. 1978. Chap. 10 and references therein.
13. CAD4 diffractometer manual. Enraf-Nonius: Delft, the Netherlands. 1988.
14. E.J. Gabe, Y. Le Page, J-P. Charland, and F.C. Lee. J. Appl. Cryst. **22**, 384 (1989).
15. G.M. Sheldrick. Shelxs-86, structure solving program. University of Gottingen, F.D.R. 1986.
16. International tables for crystallography. Vol. A, D. Reidel Publishing Co. Boston. 1983.
17. J.A. Goodfellow and T.A. Stephenson. Inorg. Chim. Acta, **41**, 19 (1980).
18. J.A. Goodfellow, T.A. Stephenson, and M.C. Cornock. J. Chem. Soc. Dalton Trans. 1195 (1978).
19. V. Gutmann. The donor–acceptor approach to molecular interactions. Plenum, New York. 1978.
20. J.J.I. Arsenault and P.A.W. Dean. Can. J. Chem. **61**, 1516 (1983).
21. P.A.W. Dean, D.D. Phillips, and L. Polensek. Can. J. Chem. **59**, 50 (1981).
22. P.A.W. Dean. Can. J. Chem. **60**, 2921 (1982).
23. (*a*) G. Christou, K. Folting, and J.C. Hufman. Polyhedron, **3**, 1247 (1984); (*b*) P.B. Hitchcock, M.F. Lappert, B.J. Samways, and E.L. Weinberg. J. Chem. Soc. Chem. Commun. 1492 (1981); P.A.W. Dean, J.J. Vittal, and N.C. Payne. Inorg. Chem. **24**, 3594 (1985).
24. H. Iwasaki and H. Hagihara. Acta Crystallogr. Sect. B, **28**, 507 (1972); M. Ito and H. Iwasaki. Acta Crystallogr. Sect. B, **36**, 443 (1980); H. Iwasaki. Acta Crystallogr. Sect. B, **36**, 2138 (1980).
25. H. Hagihara and S. Yamashita. Acta Crystallogr. **21**, 350 (1966); H. Hagihara, Y. Watanabe, and S. Yamashita. Acta Crystallogr. Sect. B, **24**, 960 (1968); H. Hagihara, N. Yoshida, and Y. Watanabe. Acta Crystallogr. Sect. B, **25**, 1775 (1969).
26. S.G. Hardin, P.C. Healy, W.G. Mumme, A.H. White, and G. Winter. Austral. J. Chem. **35**, 2423 (1982).
27. T. Ito. Acta Crystallogr. Sect. B, **28**, 1034 (1972); S.L. Lawton and G.T. Kokotailo. Inorg. Chem. **11**, 363 (1972).
28. A. Bondi. J. Phys. Chem. **68**, 441 (1964).
29. J. Canonne and G. Nowogrocki. Acta Crystallogr. Sect. B, **37**, 686 (1981); R.K. Rajaram and J.K. Mohona Rao. Z. Kristallogr. **160**, 225 (1982); C. Houttemane, J.C. Boivin, D.J. Thomas, P.G. Harrison, and A.T. Steel. J. Organomet. Chem. **239**, 105 (1982); C. Gaffney, P.G. Harrison, and T.J. King, J. Chem. Soc. Dalton Trans. 1061 (1982), R.G. Bryant, V.P. Chacko, and M.C. Etter. M.C. Inorg. Chem. **23** 3580 (1984).
30. G.A. Melson, P.T. Greene, and R.F. Bryan. Inorg. Chem. **9**, 1116 (1970).
31. G.C. Rout, T. Seshasayee, T. Subrahmanyan, and G. Aravamudan. Acta. Crystallogr. Sect. C, **39**, 1387 (1983).
32. M. Hall and D.B. Sowerby. J. Chem. Soc. Dalton Trans. 1292 (1980).
33. R. Uson, J. Fornies, M.A. Uson, J.F. Yague, P.G. Jones, and K. Meyer-Base. J. Chem. Soc. Dalton Trans. 947 (1986).
34. R.G. Pearson. J. Am. Chem. Soc. **85**, 3533 (1963).
35. C.K. Jorgensen. Inorg. Chem. **3**, 1201 (1969).

Can. J. Chem. Downloaded from www.nrcresearchpress.com by EESC ESCOLA DE ENGENHARIA on 09/08/12
For personal use only.

On the mechanism of alkaline hydrogen peroxide oxidation of the lignin model *p*-hydroxyacetophenone

MARTIN B. HOCKING[1] AND JOHN P. CROW[2]

Department of Chemistry, University of Victoria, Victoria, BC V8W 3P6, Canada

Received July 6, 1993

MARTIN B. HOCKING and JOHN P. CROW. Can. J. Chem. **72**, 1137 (1994).

The oxidation of *p*-hydroxyacetophenone by a small excess of alkaline hydrogen peroxide has been found to be an autocatalysed process in which hydroquinone monoacetate and the peracetate ion are generated and consumed at similar rates. The reaction proceeds at a maximum rate when the base concentration is about 0.3 M. A chain-type mechanism that involves peracetate as the oxidizing agent is proposed for the reaction that explains the observed dependence of rate on base concentration. At high pH *o*-hydroxyacetophenone reacts by the same mechanism, whereas *m*-hydroxyacetophenone does not react with hydrogen peroxide under these conditions.

MARTIN B. HOCKING et JOHN P. CROW. Can. J. Chem. **72**, 1137 (1994).

On a trouvé que l'oxydation de la *p*-hydroxyacétophénone par un léger excès de peroxyde d'hydrogène alcalin est un processus autocatalysé dans lequel le monoacétate de l'hydroquinone et l'ion peracétate sont générés et consommés à des vitesses relativement semblables. La réaction se produit avec une vitesse maximale lorsque la concentration de la base est d'environ 0,3 M. On suggère que le mécanisme est de type «en chaîne» et qu'il implique le peracétate comme agent oxydant; ce mécanisme explique la relation entre la vitesse de la réaction et la concentration de la base. À des pH plus élevés, l'*o*-hydroxyacétophénone réagit par le même mécanisme alors que, dans ces conditions, la *m*-hydroxyacétophénone ne réagit pas avec le peroxyde d'hydrogène.

[Traduit par la Rédaction]

Introduction

Aromatic hydroxyketones and other compounds with oxygen atoms *para* to unsaturated groups are of interest relevant to the bleaching of wood pulp, because they contain chromophores similar to those found in lignin (1, 2). Investigation of the oxidation reactions of compounds of this type gives information on the processes that are likely to occur during the bleaching of wood pulp. It has long been accepted that the initial step in the hydrogen peroxide oxidation of an aromatic *o*- or *p*-hydroxyketone under alkaline conditions is the nucleophilic attack of the carbonyl carbon atom of the ketone by the hydroperoxide anion (3, 4). This is followed by a Baeyer–Villiger type rearrangement to give an ester that may react further, depending on conditions (Scheme 1).

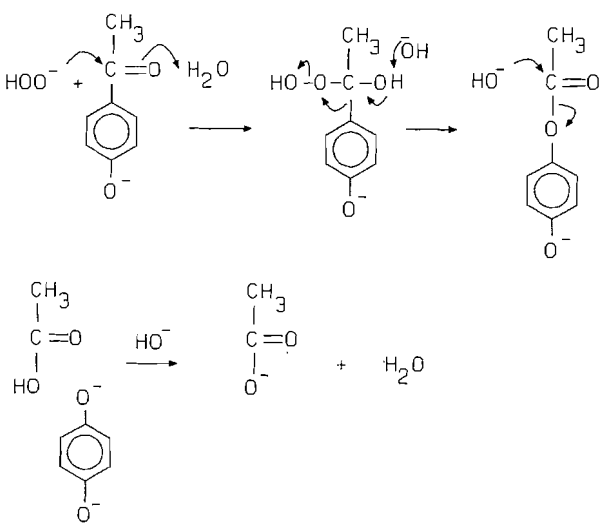

SCHEME 1

Hocking (5) showed earlier that the rate of reaction of the lignin model *p*-hydroxyacetophenone (*p*HAP) with a 100-fold excess of aqueous alkaline hydrogen peroxide depended on the concentration of hydrogen peroxide to the power 1.4. Under different conditions they detected and isolated hydroquinone monoacetate (HMA) as an intermediate in the reaction. Normally this ester is hydrolysed during the reaction to the final products hydroquinone and the acetate ion (6). They also noted that concentrations of reactant *p*HAP and product acetate could be monitored by NMR from their methyl resonances since these were sharp, upfield from water and separated by about 0.6 ppm. To try to clarify the role of the intermediate HMA in the mechanism, we have now extended the study of the alkaline peroxide oxidation of hydroxyketones in aqueous solution to situations in which the hydrogen peroxide is in 2–10 times excess, conditions that more closely resemble the stoichiometric to 6 times excess, peroxide to carbonyl content, typically used in the bleaching of wood pulp (7).

Results and discussion

The fractions of the original amount of a 0.29 mmol sample of *p*HAP left during its reaction with 1.44 mmol of hydrogen peroxide in the presence of sodium hydroxide or sodium carbonate in 1.2 mL of aqueous solution at 30°C was determined from the relative peak heights of the proton methyl resonances of the *p*HAP reactant and the acetate product (Scheme 1). Hydroquinone, the aromatic product, did not rapidly undergo significant further reaction under the conditions used. The reaction was predictable and the results were surprisingly consistent from one kinetic run to the next. No evidence of oxygen formation, which could indicate the presence of free radicals, was seen, probably because phenols are effective free radical scavengers.

Figure 1 shows the rate curve for this reaction in the presence of 0.30 mmol of base. Examples of the raw concentration data used to draw the graphs in Figs. 1 and 3 are given in Table 1. In both sodium carbonate and sodium hydroxide solutions the reaction has an induction period, which was very helpful for the monitoring method used, followed by a period when the reac-

[1]Author to whom correspondence should be addressed.

[2]Present address: Department of Chemistry, College of New Caledonia, 3330-22nd Avenue, Prince George, BC V2N 1P8, Canada.

Can. J. Chem. Downloaded from www.nrcresearchpress.com by EESC ESCOLA DE ENGENHARIA on 09/08/12
For personal use only.

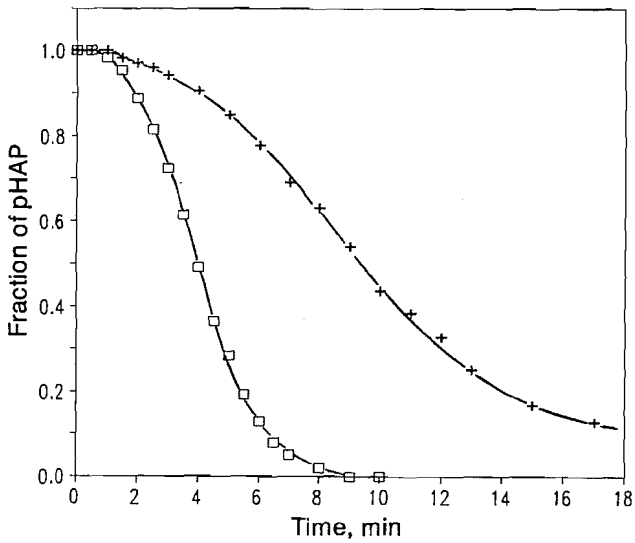

FIG. 1. Fraction of initial amount of *p*HAP remaining vs. time on oxidation of 0.29 mmol of *p*HAP with 1.44 mmol H_2O_2 in 1.2 mL of aqueous 0.25 M base at 30°C. +, for sodium hydroxide, run 3; □, for sodium carbonate, run 12.

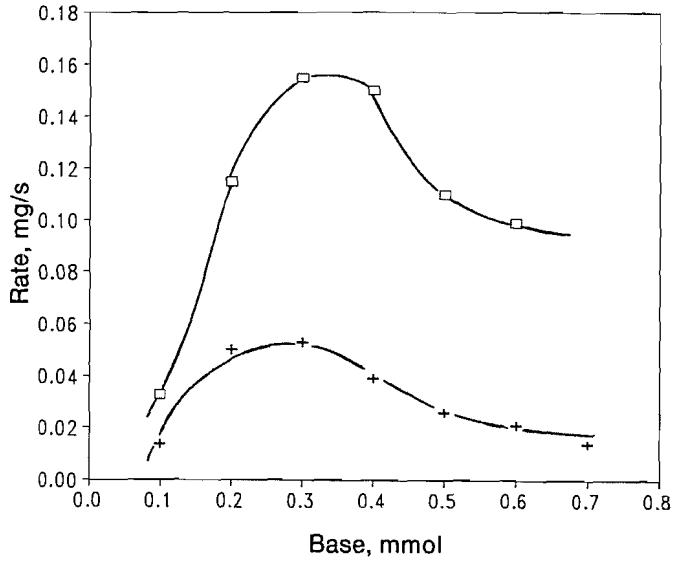

FIG. 2. Rate of oxidation of 0.29 mmol of *p*HAP with 1.44 mmol of hydrogen peroxide in 1.2 mL of aqueous base at 30°C. +, for sodium hydroxide runs 1–8; □, for sodium carbonate, runs 9–15.

TABLE 1. Effect of additives on the fraction of initial *p*HAP left for the reaction of 40 mg of *p*HAP (0.29 mmol) with 1.44 mmol of H_2O_2 and 0.30 mmol of NaOH, in a total volume of 1.2 mL at 30°C

	Fraction[a] of *p*HAP left with the following additives			
Time (min)	None, run 3	Hydroquinone (9.1 μmol), run 21	HMA (9.1 μmol), run 22	Sodium peracetate (9.1 μmol), run 24
0	1.000	1.000	1.000	1.000
1	1.000	1.000	0.919	0.882
2	0.962	0.984	0.818	0.750
3	0.943	0.967	0.727	0.603
4	0.907	0.935	0.615	0.485
5	0.850	0.865	0.477	0.338
6	0.778	0.818	0.383	0.228
7	0.692	0.730	0.304	0.161
8	0.632	0.666	0.216	0.128
9	0.540	0.581	0.174	
10	0.436	0.484	0.132	
11	0.385	0.421	0.101	
12	0.326	0.341		
13	0.250	0.274		
15	0.166	0.241		
17	0.127	0.143		

[a]Values of (*p*HAP methyl peak height)/(sum of *p*HAP methyl and acetate methyl peak heights) were calculated to three significant figures and are accurate to two figures. Estimated error in fraction data is ±4%.

tion occurs at a relatively constant rate. The rate of reaction was taken to be the slope of the linear portion of the rate curve in milligrams of *p*HAP per second. A series of kinetic runs with various initial concentrations of reactants gave similarly shaped rate curves, although the induction period varied from 1 to 7 min. The rate, which was reproducible to within ±5% for the same set of conditions, depended on the nature of the base used and the initial concentration of reactants. Values of rates obtained are given in Table 2.

The curves plotted in Fig. 2, for the reaction of 0.29 mmol of *p*HAP with 1.44 mmol of hydrogen peroxide in various molar concentrations of aqueous base, show that the rate is invariably greater in sodium carbonate than sodium hydroxide solution, and that there is an optimum base concentration for each base to obtain the maximum rate. Interestingly this parallels the observed behaviour of alkaline hydrogen peroxide in the bleaching of wood pulp, which also shows an optimum base concentration for maximum effectiveness (7, 8).

Sigmoidal-shaped rate curves similar to the ones in Fig. 1 are characteristic of reactions that are autocatalysed and depend on the presence of an intermediate generated during the induction period by the reaction. To determine the nature of the intermediate, the oxidation reactions were repeated in the presence of various additives. Addition of magnesium sulphate, which is commonly used as a stabilizer in pulp bleaching (7), or the reaction products acetate and hydroquinone had little effect on the rate. However, addition to the reaction mixture of either hydroquinone monoacetate or sodium peracetate in amounts of about 0.5 mol% of the hydrogen peroxide concentration eliminated the induction period and increased the rate somewhat.

Figure 3 shows the reactant remaining during the same reactions (0.29 mmol *p*HAP, 1.44 mmol peroxide, and 0.30 mmol NaOH in 1.2 mL solution at 30°C) with and without the presence of 0.0054 mmol of sodium peracetate added at the start of the reaction at the same time as the hydrogen peroxide.

An extension of earlier NMR studies confirmed that HMA and other phenyl esters, such as hydroquinone diacetate and acetyl salicylate, in the presence of alkaline hydrogen peroxide are hydrolysed to phenols and peracetate rather than acetate (6). That peracetate was produced was confirmed by both ^1H and ^{13}C NMR (Table 3). However, peracetate possesses limited stability in the alkaline solutions used. Its slow decay to acetate could be followed by ^1H NMR scans at 5-min intervals; under the conditions used for the kinetic runs, half of a sample of peracetate had decomposed to acetate within 10 min. Hofman et al. have studied the hydrolysis by alkaline hydrogen peroxide of various *N*- and *O*-acetyl esters and found that peracetate, rather than acetate, is the major hydrolysis product (10). Clearly the

Can. J. Chem. Downloaded from www.nrcresearchpress.com by EESC ESCOLA DE ENGENHARIA on 09/08/12
For personal use only.

TABLE 2. Summary of measured data for the oxidation of *o*HAP and *p*HAP in 1.2 mL of aqueous solution at 30°C using proportions of reactants given

Run	Hydroxyketone[a]	Base[b]	Hydrogen peroxide[a]	Additives[a,c]	Rate[d] (mg/s)	Induction period[e]	Initial pH[f]
1	0.29 *p*	0.10 H	1.44		0.014		
2	0.29 *p*	0.20 H	1.44		0.050		8.5
3	0.29 *p*	0.30 H	1.44		0.052		9.4
4	0.29 *p*	0.30 H	1.44		0.052		
5	0.29 *p*	0.40 H	1.44		0.039		10.7
6	0.29 *p*	0.50 H	1.44		0.026		11.5
7	0.29 *p*	0.60 H	1.44		0.021		11.9
8	0.29 *p*	0.70 H	1.44		0.014		
9	0.29 *p*	0.10 C	1.44		0.033		7.9
10	0.29 *p*	0.20 C	1.44		0.12		8.7
11	0.29 *p*	0.30 C	1.44		0.16		9.3
12	0.29 *p*	0.30 C	1.44		0.15		
13	0.29 *p*	0.40 C	1.44		0.14		9.7
14	0.29 *p*	0.50 C	1.44		0.11		9.8
15	0.29 *p*	0.60 C	1.44		0.099		
16	0.29 *p*	0.40 C	2.16		0.17		
17	0.29 *p*	0.40 C	2.88		0.18		
18	0.15 *p*	0.40 C	1.44		0.033		
19	0.44 *p*	0.40 C	1.44		0.23		
20	0.29 *p*	0.30 C	1.44	0.050 Mg	0.057		
21	0.29 *p*	0.30 H	1.44	0.0091 Hq	0.051		
22	0.29 *p*	0.30 H	1.44	0.0066 HMA	0.071	No	
23	0.29 *p*	0.30 H	1.44	0.0132 HMA	0.12	No	
24	0.29 *p*	0.30 H	1.44	0.0054 Pa	0.087	No	
25	0.29 *p*	0.40 H	1.44	0.0091 Hq	0.033		
26	0.29 *p*	0.40 H	1.44	0.0074 Ac	0.036		
27	0.29 *p*	0.40 H	1.44	0.0132 HMA	0.041	No	
28	0.29 *p*	0.60 C	1.44	0.0066 HMA	0.10	No	
29	0.29 *p*	0.60 C	1.44	0.0054 Pa	0.089	No	
30	0.29 *o*	0.60 H	0.72		0.5 (est)	No	
31	0.29 *p*	0.60 H	0.72		0.011		
32	0.29 *o*	0.90 H	0.72		0.042		
33	0.29 *o*	0.90 H	0.72	0.0054 Pa	0.076	No	
34	0.25 *p*	0.40 H	0.0	0.27 Pa	2.8* (est)	No	

[a]Reactant and additive quantities are given in millimoles. *p* = *p*HAP, *o* = *o*HAP.
[b]H = sodium hydroxide, C = sodium carbonate. Quantities are given in millimoles.
[c]Additives: Mg = magnesium sulphate; Hq = hydroquinone; Ac = sodium acetate; HMA = hydroquinone monoacetate; Pa = sodium peracetate; none where none specified.
[d]Rate is the slope of the linear portion of the rate curve, except for the asterisk where the rate is calculated from the slope of 1/(fraction of *p*HAP left) vs. time. est reactions were too fast to allow accurate determination of the rate.
[e]All runs had an induction period, except where noted.
[f]The pH was measured at the start of the reaction for the runs given.

peracetate ion, generated from hydroquinone monoacetate and hydrogen peroxide, is the active oxidizing agent in this autocatalysed reaction. A probable mechanism for the reaction that fits the observed requirements is shown in Scheme 2.

The key sequence of reactions in the mechanism proposed is the nucleophilic attack of peracetate on the carbonyl carbon of *p*HAP, followed by rearrangement of the peroxy adduct to hydroquinone monoacetate. This is hydrolysed by the hydroperoxide anion to hydroquinone and another peracetate ion that continues the oxidation cycle. The peracetate concentration rapidly builds up to a steady state, resulting in the constant rate observed in these reactions.

The reaction went only slightly faster, 0.17 vs. 0.14 mg *p*HAP per second, when the initial amount of hydrogen peroxide was increased to 2.16 mmol in run 16 from 1.44 mmol in run 13. When the initial amount of *p*HAP was increased from 0.29 mmol in run 13 to 0.44 mmol in run 19, the reaction rate increased markedly from 0.14 to 0.23 mg/s. These observations would indicate that step 4 in the mechanism, attack of peracetate on the hydroxyketone, is slower than step 3, hydrolysis of HMA by hydroperoxide anion to peracetate.

The mechanism presented is also supported by the results of the reaction of *p*HAP with an equivalent amount of peracetate in slightly basic solution (run 34 in Table 2). This reaction has no induction period and, with a rate of 2.8 mg/s, was 70 times faster than the rate observed for the oxidation of *p*HAP with hydrogen peroxide. These characteristics meant that the reaction of *p*HAP with peracetate was particularly difficult to follow by the NMR method used and reliable numerical data were hard to obtain, hence information on the rate of the reaction was of doubtful value.

Ogata and Sawaki (11) reported that the oxidation of hydroxyketones by peroxybenzoic acid is a second-order process, so it is likely that the oxidation of *p*HAP by peracetate, a similar process, also follows second-order kinetics. When the reaction between *p*HAP and peracetate in sodium hydroxide

Can. J. Chem. Downloaded from www.nrcresearchpress.com by EESC ESCOLA DE ENGENHARIA on 09/08/12
For personal use only.

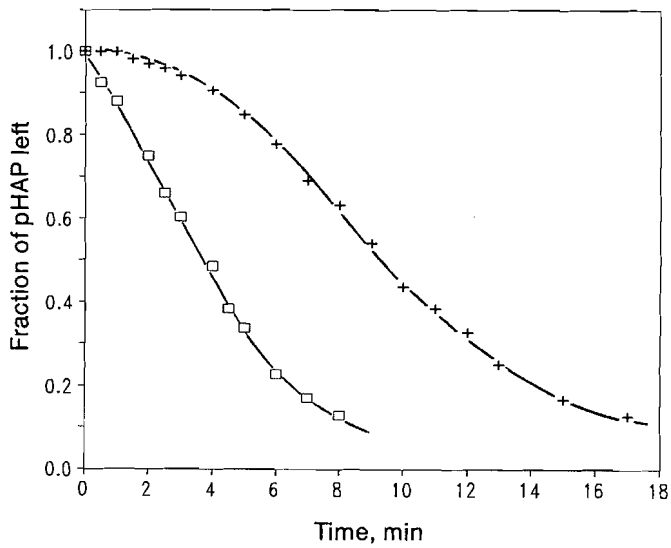

FIG. 3. Fraction of 0.29 mmol of *p*HAP remaining during oxidation by 1.44 mmol hydrogen peroxide in 1.2 mL of solution containing 0.3 mmol of sodium hydroxide at 30°C. +, without other additives, run 3; □, with 5.4 μmol of added peracetate, run 24.

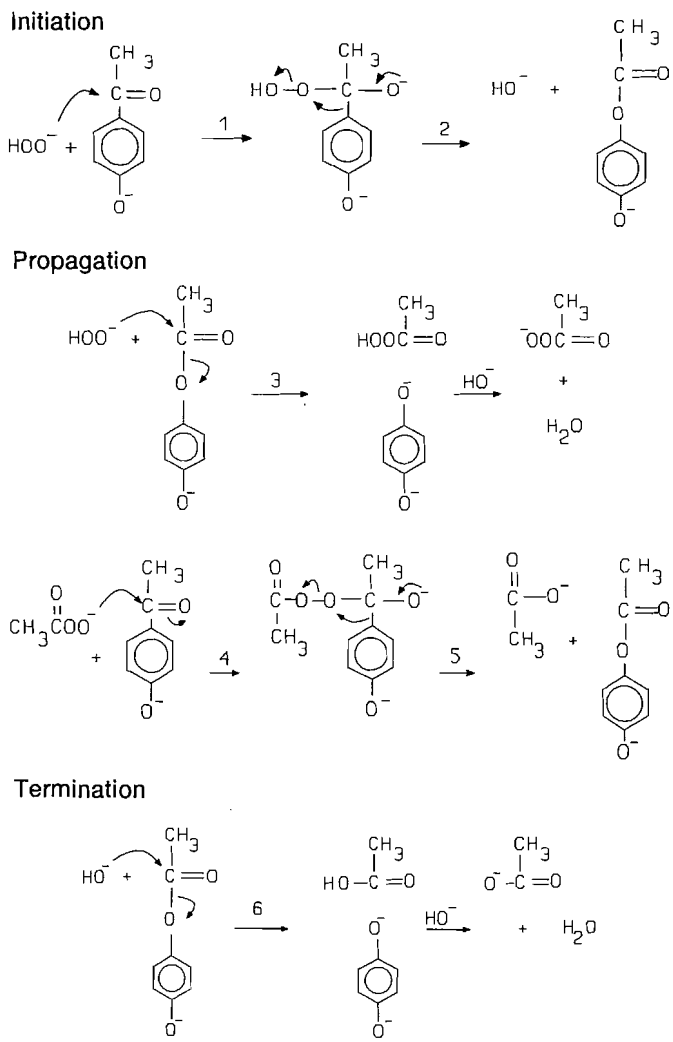

SCHEME 2. Proposed mechanism for the hydrogen peroxide oxidation of *p*HAP which produces and uses peracetate.

solution at pH 8 was scaled up and subsequently extracted with ether, it was possible to obtain crystals of HMA in 10% yield. NMR scans of this reaction mixture prior to extraction showed much larger concentrations of HMA present (by far the largest peak) in addition to hydroquinone and acetate ions, but rapid hydrolysis of the rather labile HMA under the basic conditions used decreased the actual recovery of solid product. High-amplification NMR scans of the reaction mixture of *p*HAP and hydrogen peroxide used earlier in the kinetic runs showed small methyl resonances at the shifts expected for peracetate and HMA, in addition to those of reactant and product. The elimination of the induction period by initial addition of peracetate, the known formation of peracetate from hydrogen peroxide and HMA, and the fast reaction of peracetate and *p*HAP strongly support the proposed mechanism.

Previous studies of the reaction of *o*HAP with alkaline hydrogen peroxide showed that the reaction is fast at low pH, but much slower at pHs over 12 (11, 12). The reaction between 0.3 mmol of *o*HAP and 0.72 mmol of hydrogen peroxide in the presence of 0.9 mmol (0.75 M) of sodium hydroxide in a total volume of 1.2 mL was quite slow and found to have an induction period that was removed when peracetate was added at the start of the reaction. It seems probable that under these conditions the *ortho* isomer also reacts by a mechanism similar to that proposed earlier for the *para* isomer. When the concentration of sodium hydroxide was decreased to 0.5 M (0.6 mmol of NaOH added), this reaction was much faster; it was essentially complete in 90 s (e.g., runs 32 and 30 in Table 2). This was too fast to quantitatively measure by the NMR method used, nor could an induction period be detected under these conditions. Therefore, it is likely that the fast oxidation of *o*HAP proceeds via a different mechanism, one that does not require generation of peracetate, when the base concentration is lower.

*m*HAP, which is much less reactive than the *ortho* and *para* isomers for electronic reasons, did not react with either hydrogen peroxide or peracetate in dilute aqueous sodium hydroxide.

The mechanism proposed for the reaction of *p*HAP with alkaline hydrogen peroxide explains the observed dependence of the rate on base type and concentration. Base is required to ensure significant dissociation of hydrogen peroxide to the hydroperoxide anion required for the cleavage of hydroquinone monoacetate to peracetate and hydroquinone. Hydroxide ions, when present in excess of the amount required to produce the hydroperoxide anion, can hydrolyse HMA to hydroquinone and acetate and so will compete with the hydroperoxide anion for the available HMA, causing a lower steady-state concentration of both HMA and peracetate and hence a slower reaction. Thus, we would expect the rate of ketone oxidation to be greater in aqueous sodium carbonate, which provides sufficient alkalinity without a high concentration of hydroxide ions, than in aqueous sodium hydroxide solution. This explanation would also predict that there should be an optimum base concentration for maximum rate as is observed, rather than a progressive increase of rate with base concentration.

Interpretation of the relevance of these results to the brightening reactions of softwood mechanical pulps is complex (13, 14). As seen with the model compound here, there is an optimum ratio of sodium hydroxide to pulp for any given peroxide:pulp ratio to achieve maximum brightness. However, this is not so much rate related as a factor of residual hydroxide ion concentration (or pH) at the time that the peroxide component of the brightening system used is exhausted. Too high a pH at this stage promotes pulp-darkening reactions.

Can. J. Chem. Downloaded from www.nrcresearchpress.com by EESC ESCOLA DE ENGENHARIA on 09/08/12
For personal use only.

TABLE 3. Summary of experimentally observed NMR shift data

Substances	^{1}H NMR (ppm)[a]	^{13}C NMR (ppm)[b]
Sodium acetate	1.9	20.2 (CH_3), 176.5 (CO)
Sodium peracetate	2.1	16.7 (CH_3), 172.6 (CO)
Hydroquinone	6.9	(115.6, 149.7)[c]
Hydroquinone monoacetate	2.3, 7.0d (J = 1 Hz)	
HMA + H_2O_2[d]	2.1, 2.3, 6.9, 7.0d (J = 1 Hz)	
HMA + H_2O_2 + Na_2CO_3[e]	2.1, 6.9	16.7, 20.2, 116.2 148.8, 172.6, 176.6
*p*HAP	2.5, 6.7d, 7.7d (J = 10 Hz)	
Runs 3 (high amplitude)	1.9, 2.1, 2.3, 2.5 (CH_3 only)	

[a]All ^{1}H NMR spectra were measured on 10-ppm sweep widths at 30°C on a Perkin Elmer R-32 continuous wave spectrometer at 90 MHz in 2% aqueous solution relative to an external TMS standard in $CDCl_3$. d, doublet.

[b]^{13}C NMR shifts were referenced to TMS, were measured on 188-ppm sweep width in aqueous solution at ambient temperature on a Bruker AMX 360 FT spectrometer at 90.568 MHz locked to an internal D_2O reference, and are nonquantitative. Collection parameters for the sodium acetate and sodium peracetate spectra: acquisition time, 0.623 s; relaxation delay, 0.100 s; recycle time, 0.723 s; from 700 transients. Collection conditions for the oxidation mixture spectrum (footnote *e*) were as follows: acquisition time, 0.819 s; relaxation delay, 0.100 s; recycle time, 0.919 s, for a total of 3300 transients.

[c]From ref. 9; in dimethyl sulphoxide.

[d]21.5 mg HMA in 1 mL of D_2O and 0.2 mL of 7.2 M H_2O_2.

[e]21.5 mg HMA in 1 mL of D_2O and 0.2 mL of 7.2 M H_2O_2, and 0.2 mL of 1 M Na_2CO_3.

It is also difficult to directly translate the promising rate measurements of *p*HAP oxidation in aqueous sodium carbonate to the brightening reactions of mechanical pulps. Decreased brightness gains of 1–1.5 points, but with improved brightness stability, has been reported from tests of partial replacement of sodium hydroxide by sodium carbonate in the peroxide brightening of spruce chemithermomechanical pulp (CTMP) (15). Full replacement of sodium carbonate has also been reported to yield equivalent final brightness with aspen CTMP, while also providing superior peroxide stabilization and consequent higher peroxide residuals (16). Our model compound rate findings confirm the need evident from these results to further explore the benefits to be achieved by optimized conditions for sodium carbonate replacement in the peroxide-based bleaching of wood pulps.

Experimental

Commercial *p*HAP and *m*HAP were purified by recrystallization from toluene and then water before use. Hydroquinone monoacetate was obtained as previously described (5). Commercial peracetic acid (32%) was analyzed for acid equivalence by titration with sodium hydroxide solution, for peroxide concentration by titration with permanganate solution (17), and for total oxidizing ability by addition of potassium iodide and subsequent titration with thiosulphate (18). The concentration of commercial 30% hydrogen peroxide was checked by addition of iodide and then titration with aqueous thiosulphate solution (18). It was diluted with distilled and deionized water to make its concentration 7.2 M before use.

^{1}H NMR spectra and the quantitative work for the kinetic runs were carried out on aqueous solutions at 30°C on a Perkin Elmer R-32 continuous wave spectrometer at 90 MHz. ^{13}C spectra were run at ambient temperature at 90.568 MHz on a Bruker AMX 360 FT NMR spectrometer. Values of pH were measured on a Metrohm 632 pH meter standardized at pH 9.18. Mass spectra were run on a Finnigan 3300 quadrupole GC–MS system spectrometer.

Kinetic experiments

The starting amount of hydroxyketone (usually 40 mg, 0.29 mmol) was dissolved in the required volume of 1.0 M base. The required amount of distilled, deionized water was added so that the final volume after all additions would be 1.2 mL for all kinetic runs. The solution was placed in the spectrometer in a 5-mm NMR tube and allowed to reach 30°C. The required amount (usually 0.2 mL) of 7.2 M hydrogen peroxide solution (1.44 mmol) was added to the sample, timing was started, and the mixture was shaken for 5 s. NMR scans of the methyl peaks in the region of 2.6–1.8 ppm were made every 30 or 60 s as the HAP methyl resonance decreased in size, while that of the acetate increased. In most cases the sum of the two peak heights stayed remarkably constant (about 80 mm) during the run. The fraction of reactant remaining was calculated from the relative peak heights. Previous studies had indicated that the peak height was a reliable measure of the relative amount of substance in solution (5, 12). Occasionally impurities caused decomposition of the peroxide to oxygen, which resulted in a rapid loss of resolution and collapse of the methyl resonances. Additives, when used, were dissolved in the appropriate amount of water and added to the mixture immediately after the hydrogen peroxide solution. To prevent premature decomposition of the peracetic acid, it was diluted and neutralized immediately before use by adding 0.1 mL of it to 10 mL of 0.122 M NaOH solution. One tenth of a millilitre of this diluted solution contained 0.0054 mmol of neutralized peracetate ion.

Preparation of HMA from peracetate and pHAP

*p*HAP (500 mg) was dissolved in 6 mL of 1 M NaOH. To this was added 6 mL of 1 M NaOH containing 1 mL of peracetic acid. The pH was adjusted to 8 by addition of a few more drops of NaOH solution. The mixture was stirred for 15 min at room temperature and then extracted with three 10-mL portions of diethyl ether. The combined extracts were dried with anhydrous sodium sulphate and the ether was evaporated under reduced pressure. The residual oil was pumped on a vacuum line for 1 h. The residue was extracted with two 60-mL portions of hot hexane, which were allowed to cool very slowly (24 h) to −10°C. The yield was very variable, during several repetitions; 45–100 mg of crystalline HMA was obtained, mp 55–58°C (lit. (19) mp 61–63°C). The ^{1}H NMR spectrum was identical to that of authentic material. The chemical ionization mass spectrum showed peaks at 154 (M + 1), 181 (M + 29), and 193 (M + 41).

Acknowledgements

Financial assistance from the University of Victoria and the College of New Caledonia towards completion of this project is gratefully recognized.

1. M.B. Hocking. Modern chemical technology and emission control. Springer-Verlag, Berlin 1985.

Can. J. Chem. Downloaded from www.nrcresearchpress.com by EESC ESCOLA DE ENGENHARIA on 09/08/12
For personal use only.

2. F.E. Brauns. Chemistry of lignin. Academic Press, New York. 1952.
3. C.A. Bunton. *In* Peroxide reaction mechanisms. *Edited by* J.O. Edwards. Interscience, New York. 1962. p. 14.
4. J.B. Lee and B.C. Uff. Q. Rev. Chem. Soc. **21**, 429 (1967).
5. M.B. Hocking and J.H. Ong. Can. J. Chem. **55**, 102 (1977).
6. M.B. Hocking, M. Ko, and T.A. Smyth. Can. J. Chem. **56**, 2646 (1978).
7. M. Solinas. Pulp Pap. Can. **77**, 50 (1976).
8. P.A. Wright, Y.A. Ginting, and J. Abbot. J. Wood Chem. Technol. **12**, 111 (1992).
9. C.J. Pouchert and J. Behnke. The Aldrich library of ^{13}C and ^{1}H FT NMR spectra. Vol. I. The Aldrich Chemical Company, Milwaukee. 1993. p. 304.
10. J. Hofman, G. Just, W. Pritzkow, and H. Schmidt. J. Prakt. Chem. **334**, 293 (1992).
11. Y. Ogata and Y. Sawaki. J. Org. Chem. **37**, 2953 (1972).
12. M.B. Hocking, K. Bhandari, B. Shell, and T.A. Smyth. J. Org. Chem. **47**, 4208 (1982).
13. G. Gellerstedt, H.-L. Hardell, and E.-L Lindfors. Acta Chem. Scand. Ser. B. **34**, 669 (1980).
14. D.G. Holah and C. Heitner. J. Pulp Pap. Sci. **18**, J161 (1992).
15. A.W. Rudie, T.J. McDonough, F. Rauh, R.J. Klein, J.L. Parker, and S.A. Heimburger. J. Pulp Pap. Sci. **19**, J47 (1993).
16. S. Heimburger, F. Rauh, and R. Klein. Sodium carbonate replacement of caustic soda during chlorine-free bleaching. 2nd Non-Chlorine Bleaching Conference, Hilton Head, S.C. March 15–18, 1993.
17. W.C. Smit. Recl. Trav. Chim. Pays-Bas, **49**, 675 (1930).
18. C.W. Wilson and D.W. Wilson. Comprehensive analytical Chemistry. Vol. IC. Van Nostrand, New York. p. 277.
19. C.A. Bunton and J. Hellyer. J. Am. Chem. Soc. **89**, 6252 (1967).

Can. J. Chem. Downloaded from www.nrcresearchpress.com by EESC ESCOLA DE ENGENHARIA on 09/08/12
For personal use only.

The preparation of 1,2,3,5-dithiadiazolium chlorides from the reaction of nitrile sulphides with thiazyl chloride

JOHN N. BRIDSON,[1] STEVEN B. COPP, MELBOURNE J. SCHRIVER,[2] AND SHUGUANG ZHU
Department of Chemistry, Memorial University, St. John's, NF A1B 3X7, Canada
AND
MICHAEL J. ZAWOROTKO[1]
Department of Chemistry, Saint Mary's University, Halifax, NS B3H 3C3, Canada
Received September 28, 1993

JOHN N. BRIDSON, STEVEN B. COPP, MELBOURNE J. SCHRIVER, SHUGUANG ZHU, and MICHAEL J. ZAWOROTKO. Can. J. Chem. **72**, 1143 (1994).

Adamantyl-1,3,4-oxathiazol-2-one has been prepared for the first time and from it 1-adamantyl nitrile sulphide has been generated. Characterisation data are presented, including the X-Ray crystal structure of the oxathiazolone. (Crystal data for $C_{12}H_{15}NO_2S$: monoclinic, space group $P2_1/c$, a = 11.334(2) Å, b = 7.344(1) Å, c = 14.373(2) Å, β = 107.74(1)°, V = 1139.5(3) Å^3, Z = 4, R = 0.042). The planar heterocyclic ring is similar to structures observed in the gas phase for other oxathiazolone derivatives. The nitrile sulphide was reacted with dimethyl-acetylene dicarboxylate *in situ* to give an isothiazole derivative. The X-Ray crystal structure of 3-adamantyl-4,5-bis(methoxycarbonyl)-isothiazole has been obtained. (Crystal data for $C_{17}H_{21}NO_4S$: monoclinic, space group $P2_1/n$, a = 7.305(4) Å, b = 7.339(4) Å, c = 31.552(4) Å, β = 92.75(3)°, V = 1690(1) Å^3, Z = 4, R = 0.079). A general cycloaddition reaction was discovered between the nitrile sulphides and thiazyl chloride to give 1,2,3,5-dithiadiazolium chlorides. The structure of the new 4-adamantyl-1,2,3,5-dithiadiazolium chloride was confirmed by reduction to the 4-adamantyl-1,2,3,5-dithiadiazolyl for which the X-Ray crystal structure has been determined. (Crystal data for $C_{11}H_{15}N_2S_2$: monoclinic, space group $C2$, a = 10.284(4) Å, b = 8.651(2) Å, c = 13.669(2) Å, β = 112.83(1)°, V = 1120.9(4) Å^3, Z = 4, R = 0.042). The radical adopts a twisted dimer structure in the solid state which is similar to the structures observed for other alkyl derivatives.

JOHN N. BRIDSON, STEVEN B. COPP, MELBOURNE J. SCHRIVER, SHUGUANG ZHU et MICHAEL J. ZAWOROTKO. Can. J. Chem. **72**, 1143 (1994).

On a préparé l'adamantyl-1,3,4-oxathiazol-2-one pour la première fois et on l'a utilisé pour générer la sulfure de 1-adamantyl nitrile. On présente les données ayant servi à sa caractérisation, y compris la structure de l'oxathiazolone déterminée par diffraction des rayons X. Les données cristallines pour $C_{12}H_{15}NO_2S$ sont les suivantes: cristaux monocliniques, groupe d'espace $P2_1/c$, avec a = 11,334(2), b = 7,344(1) et c = 14,373(2) Å, β = 107,74(1)°, V = 1139,5(3) Å^3, Z = 4 et R = 0,042. Le noyau hétérocyclique planaire est semblable à celui observé pour les structures en phase gazeuse pour d'autres dérivés oxathiazolone. Le sulfure de nitrile réagit avec l'acétylènedicarboxylate de diméthyle *in situ* et fournit un dérivé isothiazole. On a détermine la structure du 3-adamantyl-4,5-bis(méthoxycarbonyl)isothiazole par diffraction des rayons X. Les données cristallines pour $C_{17}H_{21}NO_4S$ sont les suivantes: cristaux monocliniques, groupe d'espace $P2_1/n$, avec a = 7,305(4), b = 7,339(4), c = 31,552(4) Å, β = 92,75(3)°, V = 1690(1) Å^3, Z = 4 et R = 0,079. On a découvert une réaction générale de cycloaddition des sulfures de nitrile avec le chlorure de thiazyle qui conduit à des chlorures de 1,2,3,5-dithiadiazolium. On a confirmé la structure du nouveau chlorure de 4-adamantyl-1,2,3,5-dithiadiazolium par réduction en 4-adamantyl-1,2,3,5-dithiadiazolyle dont on a déterminé la structure par diffraction des rayons X. Les données cristallines pour $C_{11}H_{15}N_2S$ sont les suivantes: cristaux monocliniques, groupe d'espace C_2, avec a = 10,282(4), b = 8,651(2), c = 13,669(2) Å, β = 112,83(1)°, V = 1120,9(3) Å^3, Z = 4 et R = 0,042. À l'état solide, le radical adopte une structure dimère déformée semblable à celles des structures observées pour d'autres dérivés alkyles.

[Traduit par la Rédaction]

Introduction

The chemistry of the heavier elements from Groups 15 and 16 has often been dominated by either metathetical or non-specific, low yield reactions. In contrast, the organic chemistry of carbon has provided chemists with a number of general, high yield reactions that can reliably be used in the synthesis of new molecules. These reactions are often controlled by subtle electronic features of the molecules involved and the products of the reactions are usually predictable. The Diels-Alder and 1,3–dipolar cycloaddition reactions are classic examples of these types of synthetically useful processes that dominate organic synthesis. It has generally been thought that the ability of carbon to form π bonds is a phenomenon unique to the first row elements and that the heavy Main Group elements would not participate in similar processes. The recent preparation of a number of molecules that contain stable π bonds to the heavier elements of Groups 15 and 16 (1) suggests that the chemistry of carbon may be a template for the discovery of new areas of Main Group chemistry.

The 1,3-dipole cycloaddition reaction has been used in recent years in the preparation of a number of new heterocyclic systems (2, 3). In these reactions, molecules that incorporate π bonds to the pnictogens and chalcogens have acted as both the dipole and the dipolarophile. Propargyl-allenyl 1,3-dipoles often feature elements of Groups 16 and 17 in the π manifold, however, those that incorporate third and fourth period elements are rare and usually unstable. The nitrile sulphides **1** which are an unstable family of 1,3-dipoles that contain a sulphur–nitrogen π bond have been the subject of several recent reviews (4, 5). They are typically generated *in situ* from precursor oxathiazolone heterocycles **2** in the presence of a dipolarophile to give five-membered ring heterocycles.

The nitrile sulphides have been shown to decompose to the

[1]For correspondence regarding crystallography.
[2]For correspondence regarding chemistry (phone (709) 737-8744, facsimile (709) 737-3702, electronic mail mschriver@kean.ucs.mun.ca).

Can. J. Chem. Downloaded from www.nrcresearchpress.com by EESC ESCOLA DE ENGENHARIA on 09/08/12
For personal use only.

Can. J. Chem. Downloaded from www.nrcresearchpress.com by EESC ESCOLA DE ENGENHARIA on 09/08/12
For personal use only.

corresponding nitriles and elemental sulphur. The nitrile oxides (R—C≡N—O), a related family of 1,3-dipoles, can be isolated in the presence of sterically protective groups such as mesityl (—$C_6H_2(Me)_3$) or "super mesityl" (—$C_6H_2(t\text{-butyl})_3$) (4). The extreme steric protection offered by these groups has also been used in Main Group chemistry in the isolation of new π systems. It has been shown, however, that Main Group π systems such as the phosphaalkynes (R—C≡P) can also be stabilised by substitution with saturated alkyl groups (such as *t*-butyl, —C_4H_9) or cage hydrocarbons (such as adamantyl, —$C_{10}H_{15}$) (2). Nitrile sulphides, or the precursor molecules from which they are generated, that would be stabilised by extreme steric protection or substitution with cage hydrocarbons have not been prepared or generated.

In this work we will investigate the possible stabilisation of the nitrile sulphide moiety by substitution with an adamantane group. The preparation and the solid state structure of the adamantyl derivative of the precursor oxathiazolone **2***c* is described and is the first reported crystal structure of any member of this family of heterocycles. The cycloaddition chemistry of this new nitrile sulphide to the carbon–carbon and sulphur–nitrogen triple bonds to give isothiazole **3** and 1,2,3,5-dithiadiazolium **4** derivatives respectively is presented. The solid state structure of the isothiazole adduct **3** between adamantyl nitrile sulphide and dimethyl acetylene dicarboxylate [DMAD] is presented. The structure of the 4-adamantyl-1,2,3,5-dithiadiazolyl radical, generated by the reduction of **4c** is also described.

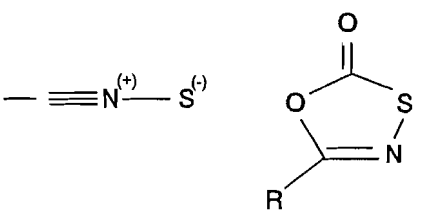

1

2a R = t-butyl
2b R = phenyl
2c R = adamantyl

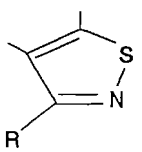

3

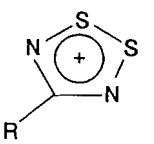

4

Experimental

General procedures

Reagents used in synthesis ($C_6H_5C(O)NH_2$, $C_4H_9C(O)Cl$, $C_{10}H_{15}C(O)Cl$, $CH_3CO_2CCCO_2CH_3$ (DMAD), and $(C_6H_5)_3Sb$) were purchased from Aldrich and used as received. The amides $C_4H_9C(O)NH_2$ and $C_{10}H_{15}C(O)NH2$ were prepared from the acid chlorides following standard literature procedures (6). $(NSCl)_3$ was prepared as described in ref. 7. Solvents were refluxed with the appropriate drying agent (C_6H_5Cl (CaH_2), $C_6H_5CH_3$ (Na), CH_2Cl_2 (CaH_2)) and distilled under nitrogen prior to use. Air sensitive compounds were handled under a nitrogen atmosphere. Solids were manipulated in a Vacuum Atmospheres nitrogen-filled glove box. Melting points were determined on a Mel-Temp II melting point apparatus and are uncorrected. Elemental analyses were carried out at Canadian Microanalytical Service Ltd., Delta, British Columbia, Canada. IR spectra were recorded from Nujol mulls on KBr plates using a Mattson Polaris FT-IR instrument. NMR spectra were recorded on a General Electric 300 MHz instrument [^1H, ^{13}C] or on a Bruker AMX400 MB instrument (^{14}N) (at the Atlantic Regional Magnetic Resonance Center). Chemical shifts are reported in ppm (high frequency positive) relative to internal standards (^1H, ^{13}C: TMS) and external standards (^{14}N:CH_3NO_2). Mass spectra were recorded on a VG Micromass 7070HS double focusing spectrometer. Molecular orbital calculations were made using the Hyperchem (version III) suite of semi-empirical programs from Autodesk operating on a 80486 based IBM compatible computer. Molecules were subjected to a full geometry optimisation (Polak-Ribiere conjugate gradient) prior to single point calculation of the molecular orbitals.

Preparation and characterisation data

$C_{10}H_{15}$—$\overline{COC(O)SN}$ 2c

Neat chlorocarbonylsulfenyl chloride, ClC(O)SCl (28.0 g, 221.4 mmol) was added to a mixture of toluene (~150 mL) and adamantyl amide, $C_{10}H_{15}C(O)NH_2$ (20.8 g, 116.0 mmol) under nitrogen to give a clear yellow solution over a white solid. The solution was brought to reflux (at which point the solid dissolved) and maintained at that temperature for three hours. The resulting yellow–brown solution was poured into a crystallizing dish and allowed to evaporate to dryness to give a dark brown crystalline solid (25.6 g) which was transferred to a sublimation apparatus and heated to 90°C [10^{-3} mmHg] for 20 h to give a white sublimed solid (24.8 g) and a non-sublimed brown residue. The white solid was recrystallised from hexanes to give clear, colourless plate shaped crystals of $C_{10}H_{15}$—$\overline{COC(O)SN}$ (16.3 g, 68.7 mmol, 59.2%), mp 79–81°C, IR (cm^{-1}): 1809 (sh), 1766 (s), 1594 (ms), 1236 (m), 1101 (w), 1072 (m), 996 (ms), 907 (ms), 570(w). NMR, ^1H δ: 2.09, 1.96, 1.76 ^{13}C δ(assign.): 174.8 (C=O), 167.3 (C_{het}), 38.9 (CH_2), 38.5 (C_{quat}), 36.1 (CH_2), 27.5 (CH) ^{14}N δ($\Delta v^{1/2}$ Hz) –160 (950). Mass spectrum [IE, 70 eV] *m/e* (%, assign.): 237 (12, $C_{10}H_{15}COC(O)SN$), 193 (1, $C_{10}H_{15}CNS$), 161 (12, $C_{10}H_{15}CN$), 135 (100, $C_{10}H_{15}$), 95 (24), 79 (18), 41 (16). Anal. calcd.: C 60.73, H 6.37, N 5.90; found: C 59.27, H 6.27, N 5.71.

$C_{10}H_{15}$—$\overline{CNSC(CO_2CH_3)C(CO_2CH_3)}$ 3

5-Adamantyl-1,3,4-oxathiazol-2-one, $C_{10}H_{15}$—$\overline{COC(O)SN}$ (2.4 g, 10.0 mmol) was dissolved in chlorobenzene (~25 mL) and added dropwise to a refluxing mixture of chlorobenzene (~25 mL) and DMAD, $CH_3CO_2CCCO_2CH_3$ (1.5 g, 10.7 mmol). The addition was conducted under nitrogen and complete addition required 5 h. The reaction mixture was refluxed for 20 h to give a light brown solution from which an oily yellow brown solid (2.6 g) was recovered by solvent evaporation and exhaustive evacuation. The solid was dissolved in $CHCl_3$ and passed through a column (silica gel, 60 mesh) to give a light–yellow solid (1.9 g) which was transferred to a subli mation apparatus and heated to 50°C [10^{-3} mmHg] for several days. The yellow-white solid (0.94 g) which sublimed to the cold finger was shown to be a mixture of the product **3** and $C_{10}H_{15}$—CN by NMR and mass spectroscopy. The non-sublimed yellow-white solid was shown to be pure isothiazole **3** (0.90 g, 2.68 mmol, 26.8%). The product was recrystallised from $CHCl_3$ to give clear colourless plate shaped crystals of $C_{10}H_{15}$—$\overline{CNSC(CO_2CH_3)C(CO_2CH_3)}$, mp 117.5–118.5°C, IR ($cm^{-1}$): 1739 (s), 1531 (m), 1336 (w), 1271 (ms), 1245 (ms), 1133 (m), 1016 (m), 983 (w), 801 (w), 777 (w). NMR, ^1H δ(#H): 3.97/3.90 (6H, OCH_3), 2.06 (9H), 1.75(6H) ^{13}C δ(assign.): 175.5 (C=O), 166.3 (C=O), 159.5(C_{het}), 154.6(C_{het}),132.8(C_{het}), 53.0/52.8 (OCH_3), 40.8 (CH_2), 40.4 (C_{quat}), 36.4 (CH), 28.4 (CH_2) ^{14}N δ($\Delta v^{1/2}$ Hz) –87 (2500). Mass spectrum (IE, 70 eV) *m/z* (%, assign.): 335 (84, $C_{10}H_{15}$-$CNSC(CO_2CH_3)C(CO_2CH_3)$ M^+ , 320 (100, $M^+ - CH_3$), 304 (27, $M^+ - CH_3O$), 303 (27, $M^+ - CH_3OH$), 276 (16, $M^+ - CH_3CO_2$), 275 (24, $M^+ - CH_3CO_2H$), 245 (22), 79 (21), 41 (25). Anal. calcd.: C 60.88, H 6.31, N 4.18, S 9.56; found: C 60.43, H 6.28, N 4.18, S 8.7.

Generation of NSCl in C_6H_5Cl

A solution of $(NSCl)_3$ (0.243 g, 3.00 mmol NSCl) in C_6H_5Cl (~3

TABLE 1. Experimental data for the reaction of R—$\overline{COC(O)SN}$ **2** and NSCl

R—$\overline{COC(O)SN}$ (g, mmol)	$(NSCl)_3$ (g, mmol[a])	R—CN (g, mmol, %)	R—$\overline{CNSSN}^+Cl^-$ (g, mmol, %)	Elemental analysis element calcd. (obsc.)
C_4H_9—COC(O)SN (6.37, 40.01)	3.98, 48.77		4.375, 22.24, 56	C 30.53(30.55) H 32.60(33.19) N 14.24(14.27) S 32.60(33.19)
C_4H_9—COC(O)SN[b] (6.43, 40.39)	6.50, 79.74		1.318, 6.70, 17	
C_6H_5—COC(O)SN (7.21, 40.25)	4.11, 50.42	1.45, 14.06, 35	2.983, 8.29, 21[c]	C 41.17(40.33) H 2.53(2.47) N 11.71(11.70) S 26.80(26.39)[c]
$C_{10}H_{15}$—COC(O)SN (9.61, 40.49)	4.09, 50.17	3.11, 19.28, 48	5.795, 21.09, 52[d]	C 48.07(47.65) H 5.50(5.35) N 10.19(10.02) S 23.33(19.86)

[a]The number given is the millimolar equivalents of NSCl.

[b]An alternate procedure was used in this preparation. The oxathiazolone was dissolved in C_6H_5Cl (~25 mL) and added dropwise to a refluxing solution of $(NSCl)_3$ in C_6H_5Cl (~75 mL) under nitrogen. The subsequent procedure was as described above.

[c]The product of this reaction was a partial C_6H_5Cl solvate. The elemental analysis is most consistent with a compound of composition C_6H_5—$CN_2S_2^+Cl^-$·$0.2C_6H_5Cl$. The % yield and the elemental analysis are calculated with respect to this partial solvate.

[d]This derivative has not been reported in the literature. $C_{10}H_{15}$—$\overline{CNSSN}^+Cl^-$, mp 260–263°C (decomp.), IR; Nujol mull, KBr plates, cm^{-1}: 1672 (w), 1308 (ms), 1261 (m), 1117 (m), 1102 (m), 1019 (w), 899 (m), 891 (m), 857 (m), 800 (w), 714 (ms). Mass Spectrum [IE, 70 eV] *m/e* (%, assign.): 239 (9, $C_{10}H_{15}$—$CNSSN^+$), 160 (6, $C_{10}H_{14}CN^+$?), 135 (4, $C_{10}H_{15}^+$), 104 (1, $CNSSN^+$), 62 (36), 59 (16), 45 (86), 44 (30), 41 (11), 36 (15), 32 (22, S^+), 28 (100, N_2^+)

mL) under N_2 was prepared in a 10 mm o.d. NMR tube fitted with a J. Young, Teflon in glass valve. The solution was immediately examined at room temperature by ^{14}N NMR spectroscopy. Three resonances were observed at 330 ppm (NSCl), −72 ppm (N_2) and −262 ppm ($(NSCl)_3$, assignments based on ref. 8). The two higher frequency resonances were not large enough to reliably allow concentration analysis by integration. The solution was then heated to reflux (135°C) for 10 min and then cooled to room temperature. The ^{14}N NMR spectrum of this solution contained the same three resonances, however, the NSCl and N_2 resonances were of much greater intensity and approximately equal integration. The resonance due to $(NSCl)_3$ was observed but could not be reliably analyzed by integration. The solution was heated further but massive precipitation of a yellow solid occurred and the solution became murky, consistent with decomposition. It was also observed when the tube was opened that a significant increase in pressure had occurred.

Reaction of R-$\overline{COC(O)SN}$ 2 with NSCl

A solution of the oxathiazolone **2** (~40 mmol) and $(NSCl)_3$ (~50 mmol NSCl) in C_6H_5Cl (~100 mL) was heated at reflux for 20 h under nitrogen. The reaction mixtures were typically observed to pass from an initial clear yellow colour through green and dark brown stages to eventually resolve to a clear orange solution over a yellow–orange solid. The air-sensitive, yellow–orange solid was removed by filtration, ground to a fine powder and transferred to a sublimation apparatus where it was heated to 100°C (10^{-3} mmHg) to attempt to remove solvent of crystallisation and sulphur. The resultant non-sublimed yellow white solids were then identified as 1,2,3,5-dithiadiazolium chlorides by comparison of their infrared spectra with published spectra, mass spectroscopy and elemental analysis. All pertinent experimental data are given in Table 1. The C_6H_5Cl solution containing the soluble products from the original reaction mixture was fractionally distilled to give the solvent and nitrile (R = —C_6H_5) or a red–black viscous liquid from which the nitrile could be removed by sublimation (R = $C_{10}H_{15}$, 20 h, 100°C, 10^{-3} mmHg). The nitriles were identified by comparison of the infrared and NMR spectra with published spectra.

Reaction of $C_{10}H_{15}$—CN with NSCl

A mixture of $C_{10}H_{15}$—CN (1.629 g, 10.10 mmol) and $(NSCl)_3$ (0.862 g, 10.57 mmol NSCl) was dissolved in C_6H_5Cl (~75 mL) and heated to reflux under nitrogen for 20 h. The initial reaction mixture was a clear light yellow colour that went through dark green and opaque black phases until it resolved to a deep red–orange solution. Filtration of the solution did not reveal undissolved solids. The solvent was reduced by distillation to a volume of approximately 10 mL and allowed to remain at r.t. overnight after which a small amount of a colourless crystalline solid was recovered by filtration (0.07 g). The colourless crystalline solid was shown to be pure, unreacted nitrile by IR and NMR spectroscopy. Further reduction in the volume of the solution gave an intractable red–brown tar-like solid.

$C_{10}H_{15}$—$\overline{CNSSN}$, 8

A mixture of $C_{10}H_{15}$—$\overline{CNSSN}^+Cl^-$ (6.355 g, 23.12 mmol) and $(C_6H_5)_3Sb$ (4.99 g, 14.13 mmol] was dissolved in CH_2Cl_2 (~75 mL) under nitrogen. An immediate reaction occurred to give an opaque blue–black solution which was stirred overnight. The solvent was removed by evacuation to give a blue-black solid which was washed with pentane and transferred to a sublimation tube. The solid was heated to 60°C [10^{-3} mmHg] for several days. This sublimation gave a crop of large (>2mm) plate-shaped, purple–black crystals of $C_{10}H_{15}$—$\overline{CNSSN}$ (2.447 g, 10.22 mmol, 44%), mp 78–80°C. IR (cm^{-1}): 1673 (w), 1580 (m), 1306 (w), 1252 (ms), 1177 (w), 998 (w), 722 (ms), 610 (w). Mass spectrum [IE, 70 eV] m/e (%, assign.): 239 (100, $C_{10}H_{15}CNSSN$), 160 (59, $C_{10}H_{14}CN$?), 135 (41, $C_{10}H_{15}$), 104 (12, CNSSN), 93 (24), 79 (36, HSNS ?), 46 (12, NS), 41 (34). Elemental anal., element calcd.(obs.): C 55.19(51.95), H 6.32(6.31), N 11.70(10.76), S 26.79(28.95).

X-ray data collection, solution and refinement

All pertinent crystallographic data are summarised in Table 2. (**2c**) Data were collected at room temperature (17 ± 1°C)on an Enraf-Nonius CAD-4 diffractometer (MoK_α, $\lambda = 0.70930$ Å, graphite monochromator) using the ω scan mode. No significant decay of three standard reflections was observed during data collection. Unit cell parameters were obtained from 24 reflections with 2θ angle in the range of 28.00–40.00 degrees. The choice of space group was based on systematically absent reflections. Data were corrected for Lorentz and polarisation effects. Scattering factors were taken from the International Tables for X-ray Crystallography (9). An empirical absorbtion correction was made based on a series of ψ scans which resulted in minimum and maximum transmission factors of 0.817602 and 0.988848 respectively. Hydrogen atoms were treated as follows: methylene hydrogen atoms were placed in calculated positions with $D_{C\text{-}H}$= 1.08 Å; methyne hydrogen atoms were located via difference Fourier map inspection. Hydrogen atoms were given temperature factors based on the carbon atoms to which they are bonded and fixed

Can. J. Chem. Downloaded from www.nrcresearchpress.com by EESC ESCOLA DE ENGENHARIA on 09/08/12
For personal use only.

Can. J. Chem. Downloaded from www.nrcresearchpress.com by EESC ESCOLA DE ENGENHARIA on 09/08/12
For personal use only.

TABLE 2. Crystallographic data

Formula	$C_{12}H_{15}NO_2S$	$C_{17}H_{21}NO_4S$	$C_{11}N_{15}N_2S_2$
fw	237.31	335.42	239.37
Space group	$P2_1/c$	$P2_1/n$ (#14)	$C2$ (#5)
a, Å	11.334(2)	7.305(4)	10.284(4)
b, Å	7.344(1)	7.339(4)	8.651(2)
c, Å	14.373(2)	31.552(4)	13.669(2)
β, deg	107.74(1)	92.75(3)	112.83(1)
V, Å^3	1139.5(3)	1690(1)	1120.9(4)
Z	4	4	4
F(000)	504	712	508
D_{calcd}, g cm^{-3}	1.38	1.318	1.418
Size, mm	0.40 × 0.33 × 0.15	0.40 × 0.30 × 0.20	0.40 × 0.35 × 0.10
μ, cm^{-1}	2.60	18.25	4.24
Max 2θ, deg	44.9	120.2	49.9
Reflections:			
Measured	1571	2995	1113
Unique	1485	2750	1049
Observed	1085[a]	1988[b]	971[b]
Parameters	145	233	131
R[c]	0.039	0.072	0.038
R_w[d]	0.042	0.079	0.042
GoF	3.14	4.38	2.10

[a] $I_o > 2.5\sigma(I_o)$.
[b] $I_o > 3\sigma(I_o)$.
[c] $R = \Sigma||F_o| - |F_c||/\Sigma|F_o|$.
[d] $R_w = [\Sigma(w(|F_o| - |F_c|)^2/\Sigma(w|F_o|)^2]^{1/2}$.

during least squares refinement. All crystallographic calculations were effected with the PC version of NRCVAX (10) implemented on a 80486 based IBM compatible computer. Fractional atomic coordinates and isotropic thermal parameters are given in Table 3 and selected bond distances and angles are given in Table 6. Supplementary material (anisotropic thermal parameters and structure factors) is available.[3]

Data were collected at room temperature (26 ± 1°C) on a Rigaku AFC6S diffractometer (**3**: CuK_α, λ = 1.54178 Å; **8**: MoK_α, λ = 0.70930 Å, graphite monochromator) and a 2KW sealed tube generator. Cell constants and an orientation matrix for the data collection were obtained from a least squares refinement using the setting angles of 20 carefully centered reflections in the range 48.2 < 2θ < 50.6 degrees for **3** and 18 reflections in the range 38.32 < 2θ <49.67 degrees for **8**. The space groups were determined based on the systematic absences, packing considerations and a statistical analysis of intensity distribution. The data were collected using the ω–2θ scan technique to a maximum of 2θ value of 120.2° for **3** and 49.9° for **8**. The intensities of three representative reflections which were measured after every 150 reflections remained constant throughout data collection indicating crystal and electronic stability. The crystal of **8** was cut to size from a larger crystal resulting in a highly irregular shape. An absorption correction, using the program DIFABS (11), was applied to both **3** (which resulted in transmission factors ranging from 0.61 to 1.15) and **8** (which resulted in transmission factors ranging from 0.79 to 1.69). The data were corrected for Lorentz and polarisation effects. The structure was solved by direct methods. The non-hydrogen atoms were refined anisotropically. Neutral atom scattering factors were taken from Cromer and Waber (9). In the structure of **8** the hydrogen atoms were initially placed in calculated positions assuming bond lengths of 0.95 Å, then allowed to refine, with very little result. They were subsequently fixed again and so are included but not refined in the final rounds of least squares calculations. The isotropic thermal parameters of the hydrogen atoms were set 20% greater than the bonded carbons. The structure of **3** collected and solved normally, but a second partial image of the skeleton rotated by 60° appeared in the difference maps. Attempts to locate all the atoms were unsuccessful, but the three atoms bonded to the pivotal carbon atom showed up clearly in both major and minor images (which exist in a ratio of 7:3) permitting placement of the missing atoms in calculated positions. Diagrams and data are given here for the major orientation of the adamantyl group. Details of the minor orientation are provided as supplementary material. The hydrogen atom positions were initially calculated assuming bond lengths of 0.95 Å and isotropic thermal parameters 20% greater than the bonded partner.

TABLE 3. Fractional atomic coordinates and isotropic thermal parameters for compound **2c**

Atom	x/a	y/b	z/c	$B_{(eq)}$
S	0.4719(1)	0.4013(2)	0.22348(8)	3.92(5)
O1	0.2628(2)	0.3929(4)	0.0945(2)	3.8(1)
O2	0.2901(3)	0.1538(4)	0.1978(2)	5.4(2)
N	0.4259(3)	0.5699(4)	0.1388(2)	3.5(2)
C1	0.3300(4)	0.2900(6)	0.1744(3)	3.7(2)
C2	0.3277(4)	0.5435(5)	0.0804(3)	3.0(2)
C3	0.2606(3)	0.6617(5)	−0.0033(2)	3.0(2)
C4	0.1379(3)	0.7305(5)	0.0121(3)	3.3(2)
C5	0.0677(3)	0.8500(5)	−0.0749(2)	3.5(2)
C6	0.0374(4)	0.7377(6)	−0.1691(3)	3.7(2)
C7	0.1577(4)	0.6717(6)	−0.1855(3)	3.7(2)
C8	0.2291(3)	0.5504(5)	−0.0990(3)	3.5(2)
C9	0.2372(4)	0.8350(6)	−0.1929(3)	4.2(2)
C10	0.1474(4)	1.0129(6)	−0.0816(3)	4.1(2)
C11	0.2681(4)	0.9460(6)	−0.0981(3)	4.0(2)
C12	0.3409(4)	0.8266(6)	−0.0114(3)	3.9(2)

[3]The supplementary material can be purchased from the Depository of Unpublished Data, Document Delivery, CISTI, National Research Council Canada, Ottawa ON K1A 0S2, Canada.

Tables of atomic positional parameters, bond distances and bond angles for $C_{12}H_{15}NO_2S$, $C_{17}H_{21}NO_4S$, and $C_{11}H_{15}N_2S_2$ have also been deposited with the Cambridge Crystallographic Data Centre, and can be obtained on request from The Director, Cambridge Crystallographic Data Centre, University Chemical Laboratory, 12 Union Road, Cambridge, CB2 1EZ, U.K.

Can. J. Chem. Downloaded from www.nrcresearchpress.com by EESC ESCOLA DE ENGENHARIA on 09/08/12
For personal use only.

TABLE 4. Fractional atomic coordinates and isotropic thermal parameters for compound **3**

Atom	*x/a*	*y/b*	*z/c*	$B_{(eq)}$
S(1)	0.2558(2)	0.2425(2)	0.39813(4)	6.00(7)
O(1)	0.5761(5)	0.5226(6)	0.2919(1)	7.6(2)
O(2)	0.7726(5)	0.3198(5)	0.3205(1)	6.4(2)
O(3)	0.4189(5)	0.1100(5)	0.2862(1)	7.3(2)
O(4)	0.2184(5)	−0.0143(5)	0.3280(1)	6.5(2)
N(1)	0.3742(5)	0.4100(5)	0.4202(1)	5.7(2)
C(1)	0.5023(6)	0.4686(6)	0.3951(1)	4.3(2)
C(2)	0.5054(6)	0.3734(6)	0.3557(1)	4.1(2)
C(3)	0.3739(6)	0.2403(6)	0.3534(1)	4.5(2)
C(4)	0.6329(6)	0.6160(6)	0.4122(1)	4.2(2)
C(5)	0.554(1)	0.715(1)	0.4500(3)	6.9(4)
C(6)	0.701(1)	0.851(1)	0.4720(3)	6.3(4)
C(7)	0.867(1)	0.750(1)	0.4819(2)	5.9(4)
C(8)	0.947(1)	0.662(1)	0.4460(2)	5.7(4)
C(9)	0.8078(8)	0.521(1)	0.4272(2)	5.1(3)
C(10)	0.682(1)	0.756(1)	0.3785(2)	7.7(4)
C(11)	0.837(1)	0.893(1)	0.3961(2)	6.2(4)
C(12)	0.741(1)	0.987(1)	0.4330(4)	9.1(5)
C(13)	0.992(1)	0.786(1)	0.4137(2)	6.8(4)
C(14)	0.6194(7)	0.4163(7)	0.3189(1)	5.0(2)
C(15)	0.886(1)	0.347(1)	0.2839(3)	9.7(4)
C(16)	0.3427(7)	0.1068(7)	0.3181(1)	5.0(2)
C(17)	0.180(1)	−0.156(1)	0.2963(2)	8.4(4)

TABLE 5. Fractional atomic coordinates and isotropic thermal parameters for compound **8**

Atom	*x/a*	*y/b*	*z/c*	$B_{(eq)}$
S(1)	0.2017(1)	0.5186	0.48443(9)	3.62(5)
S(2)	0.1550(1)	0.3481(2)	0.57331(9)	3.37(5)
N(1)	0.1994(4)	0.6582(5)	0.5646(3)	3.3(2)
N(2)	0.1430(4)	0.4664(4)	0.6611(3)	3.1(1)
C(1)	0.1689(4)	0.6150(6)	0.6474(3)	2.8(2)
C(2)	0.1699(4)	0.7350(6)	0.7282(3)	2.7(2)
C(3)	0.1295(5)	0.6631(6)	0.8147(4)	3.6(2)
C(4)	0.1309(5)	0.7852(7)	0.8960(4)	3.9(2)
C(5)	0.0253(6)	0.9124(7)	0.8404(4)	4.7(2)
C(6)	0.0659(5)	0.9858(7)	0.7547(4)	4.0(2)
C(7)	0.0643(5)	0.8655(7)	0.6730(3)	3.5(2)
C(8)	0.3181(4)	0.8083(6)	0.7807(3)	3.2(2)
C(9)	0.3187(5)	0.9301(6)	0.8613(3)	3.6(2)
C(9)	0.3187(5)	0.9301(6)	0.8613(3)	3.6(2)
C(10)	0.2141(6)	1.0571(6)	0.8053(4)	4.3(2)
C(11)	0.2789(5)	0.8557(7)	0.9471(3)	3.8(1)

The hydrogen atoms were calculated independently and the minor set was copied into a data file already holding the major set. The image of the major orientation is good and well refined with all heavy atoms set anisotropic. All calculations for the structures of **3** and **8** were performed using the TEXSAN crystallographic software package (12) using a VAX 3100 work station. Fractional atomic coordinates and isotropic thermal parameters for **3** and **8** are given in Tables 4 and 5 respectively and selected bond distances and angles are given in Tables 7 and 8 respectively. Supplementary material (anisotropic thermal parameters and structure factors, 60 pages) is available.[3]

Results and discussion

Preparation, characterisation and structure of 5-adamantyl-1,3,4-oxathiazol-2-one, 2c

The generation of nitrile sulphides *in situ* from oxathiazolone heterocycles 2 is a well established reaction (5). If the nitrile sulphide is not trapped by a dipolarophile it will immediately decompose to a nitrile and sulphur. In fact stable, isolable nitrile sulphides have never been prepared. The preparation of the heterocyclic precursor is a general and near quantitative cycloaddition reaction involving the elimination of two equivalents of HCl from the reaction of an amide with chlorocarbonyl sulfenyl chloride. A wide variety of aromatic derivatives and a smaller number of alkyl derivatives of this heterocycle have been prepared via this route, however, the

TABLE 6. Selected bond lengths (Å) and angles (deg) in $C_{10}H_{15}$—$\overline{COC(O)SN}$, **2c**

Bond	Lengths	Bonds	Angles
S—N	1.687(3)	N—S—C(1)	93.5(2)
S—C(1)	1.750(4)	S—N—C(2)	109.6(3)
O(1)—C(1)	1.392(5)	C(1)—O(1)—C(2)	112.0(3)
O(1)—C(2)	1.377(5)	S—C(1)—O(1)	106.5(3)
O(2)—C(1)	1.188(5)	S—C(1)—O(2)	131.4(3)
N—C(2)	1.272(5)	O(1)—C(1)—O(2)	122.1(4)
C(2)—C(3)	1.491(5)	O(1)—C(2)—N	118.4(3)
C(3)—C(4)	1.557(5)	O(1)—C(2)—C(3)	115.0(3)
C(3)—C(8)	1.545(5)	N—C(2)—C(3)	126.6(3)
C(3)—C(12)	1.541(5)	C(2)—C(3)—C(4)	109.4(3)
C(4)—C(5)	1.536(5)	C(2)—C(3)—C(8)	109.4(3)
C(5)—C(6)	1.532(5)	C(2)—C(3)—C(12)	110.5(3)
C(5)—C(10)	1.519(6)	C(4)—C(3)—C(8)	108.9(3)
C(6)—C(7)	1.531(6)	C(4)—C(3)—C(12)	109.2(3)
C(7)—C(8)	1.543(5)	C(8)—C(3)—C(12)	109.3(3)
C(7)—C(9)	1.524(6)		
C(9)—C(11)	1.534(6)		
C(10)—C(11)	1.539(6)		
C(11)—C(12)	1.542(6)		

TABLE 7. Selected bond lengths (Å) and angles (deg) in $C_{10}H_{15}$—$\overline{CSNC(C(O)CH_3)C}(C(O)CH_3)$, **3c**

Bond	Lengths	Bonds	Angles
S(1)—N(1)	1.645(4)	N(1)—S(1)—C(3)	94.7(2)
S(1)—C(3)	1.690(4)	N(14)—O(2)—C(15)	114.0(4)
O(1)—C(14)	1.186(6)	C(16)—O(4)—C(17)	115.4(4)
O(1)—C(15)	1.470(9)	N(1)—C(1)—C(2)	114.0(4)
O(3)—C(16)	1.176(6)	N(1)—C(1)—C(4)	117.6(4)
O(4)—C(16)	1.318(6)	C(2)—C(1)—C(4)	128.3(4)
O(4)—C(17)	1.461(8)	C(1)—C(2)—C(3)	110.8(4)
N(1)—C(1)	1.323(6)	C(1)—C(2)—C(14)	127.6(4)
C(1)—C(2)	1.429(6)	C(3)—C(2)—C(14)	121.7(4)
C(1)—C(4)	1.524(6)	S(1)—C(3)—C(2)	109.5(3)
C(2)—C(3)	1.370(6)	S(1)—C(3)—C(16)	124.3(3)
C(2)—C(14)	1.494(6)	C(1)—C(3)—C(16)	126.2(4)
C(3)—C(16)	1.491(6)	C(1)—C(4)—C(5)	111.0(4)
C(4)—C(5)	1.532(9)	C(1)—C(4)—C(9)	106.7(3)
C(4)—C(9)	1.512(7)	C(1)—C(4)—C(10)	113.1(4)
C(4)—C(10)	1.534(9)	C(5)—C(4)—C(9)	108.8(4)
C(5)—C(6)	1.60(1)	C(5)—C(4)—C(10)	109.5(5)
C(6)—C(7)	1.44(1)	C(9)—C(4)—C(10)	107.6(5)
C(6)—C(12)	1.62(1)		
C(7)—C(8)	1.45(1)		
C(8)—C(9)	1.55(1)		
C(8)—C(13)	1.42(1)		
C(10)—C(11)	1.59(1)		
C(11)—C(12)	1.55(1)		
C(11)—C(13)	1.47(1)		

TABLE 8. Selected bond lengths (Å) and angles (deg) in $C_{10}H_{15}$—CNSSN, **8**

Bond	Lengths	Bonds	Angles
S(1)—S(2)	2.083(2)	S(2)—S(1)—N(1)	93.8(1)
S(1)—N(1)	1.637(4)	S(1)—S(2)—N(2)	94.9(1)
S(2)—N(2)	1.618(4)	S(1)—N(1)—C(1)	115.4(3)
N(1)—C(1)	1.340(6)	S(2)—N(2)—C(1)	115.3(3)
N(2)—C(1)	1.340(6)	N(1)—C(1)—N(2)	120.7(4)
C(1)—C(2)	1.513(6)	N(1)—C(1)—C(2)	119.2(4)
C(2)—C(3)	1.529(6)	N(2)—C(1)—C(2)	120.1(4)
C(2)—C(7)	1.546(6)	C(1)—C(2)—C(3)	111.0(4)
C(2)—C(8)	1.547(6)	C(1)—C(2)—C(7)	109.9(3)
C(3)—C(4)	1.530(6)	C(1)—C(2)—C(8)	110.3(3)
C(4)—C(5)	1.526(7)	C(3)—C(2)—C(7)	109.0(4)
C(4)—C(11)	1.533(6)	C(3)—C(2)—C(8)	108.8(3)
C(5)—C(6)	1.526(7)	C(7)—C(2)—C(8)	107.9(4)
C(6)—C(7)	1.523(7)		
C(6)—C(10)	1.538(7)		
C(8)—C(9)	1.523(6)		
C(9)—C(10)	1.520(7)		
C(9)—C(11)	1.527(6)		

Atoms	Distance
S(1)—N(2)	3.355(4)
S(1)—N(1)	3.425(4)
S(1)—S(2)	3.439(2)
S(2)—S(2)	3.036(3)
S(2)—N(1)	3.269(4)

adamantyl derivative has not been reported. The preparation of 5-adamantyl-1,3,2-oxathiazol-2-one, **2***c*, from adamantyl amide and chlorocarbonyl sulfenyl chloride in hot toluene produced a mixture of products that was largely the desired heterocycle, sulphur and adamantyl nitrile. The two latter products are undoubtedly produced by the decomposition described above. Unfortunately, when the reaction was run for longer periods at a lower temperature (to prevent decomposition) the product that was obtained was contaminated with the amide and was isolated in lower yield. Therefore, the preparation was typically conducted at 100°C in toluene and the product had to be purified by sublimation (to remove tarrish impurities), filtered on a silica gel column and then recrystallised several times to give a pure product. Significant amounts of the heterocyclic product remained in the mother liquors and the non-crystalline crusts removed during the recrystallisation process. The pure crystalline solid was observed to acquire a distinct light violet colour when left exposed to light on the bench. This change in colour did not lead to any changes in the observed physical (mp) or spectroscopic (^{1}H, ^{13}C NMR, and IR) properties.

The identity of this new derivative of the oxathiazolone heterocycle family was established by spectroscopic and ultimately by crystallographic methods. The ^{13}C NMR of derivatives of this heterocyclic family have two characteristic resonances at 174.2 ± 0.6 ppm [C^2, C=O] and 162 ± 5.2 ppm (C^5) (R = —CH_3, —C_4H_9, —$C_{10}H_{15}$, —C_6H_5). The identity of the product is confirmed by the mass spectrum which gives the expected molecular ion and the fragments generated by loss of CO_2, S, and CN in sequence.

The solid state structure of **2***c* is shown in Fig. 1. The oxathiazolone rings are planar and apparently unassociated in the solid state with no significant intermolecular contacts. This is

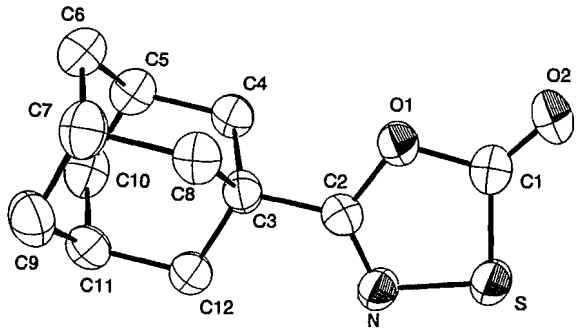

FIG. 1 ORTEP view of $C_{10}H_{15}$—COC(O)SN **2***c*.

the first report of the solid state structure of any derivative of this the oxathiazol-2-one family, however, there have been reports of the gas phase structures of two derivatives (R = H, CH_3) (13). The solid state and gas phase structures are not significantly different ($\Delta \geq 3\sigma$).The result of a bond order analysis based on the Pauling (14) and Nyberg equations (15) is summarised in **5** and is consistent with π bonds which are not significantly delocalised to adjacent atoms. The adamantyl moiety and the bond to the bridgehead carbon are identical to those reported in the literature for other small molecules.

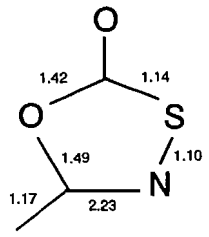

5

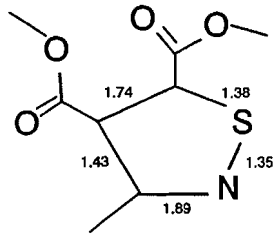

6

Cycloaddition reaction of adamantyl nitrile sulphide with DMAD

Dimethyl acetylene dicarboxylate (DMAD) is a powerful dipolarophile due to its exceptional stability and excellent electronic properties for participation in cycloaddition reactions (4). Most known nitrile sulphides have been reacted with DMAD and give the expected isothiazole heterocycles in varying yields. This is an important route to an industrially significant family of heterocycles which are used in the pesticide and pharmaceutical industries (16).

The reaction of **2***c* with DMAD in refluxing chlorobenzene produced a mixture of the isothiazole, nitrile, and sulphur with unreacted DMAD. To separate the components of this mixture a process of vacuum drying, filtration and finally sublimation was required. The sublimation must be conducted at low tem peratures, for both the nitrile and the isothiazole readily sublime but the higher molecular mass of the isothiazole product allows recovery a pure compound as a non-sublimed solid that can be recrystallised from a blend of hexanes and chloroform. The separation of the adamantyl nitrile from the product is again a problem that has only partially been solved and a significant fraction of the product remains in the form of a mixture. Column chromatography using a variety of solvent combinations did not give adequate separation of the two species. The identity of the pure product is clearly established by spectroscopy and unequivocally confirmed by X-ray crystallography. The ^{1}H and ^{13}C NMR spectra of isothiazoles and

Can. J. Chem. Downloaded from www.nrcresearchpress.com by EESC ESCOLA DE ENGENHARIA on 09/08/12
For personal use only.

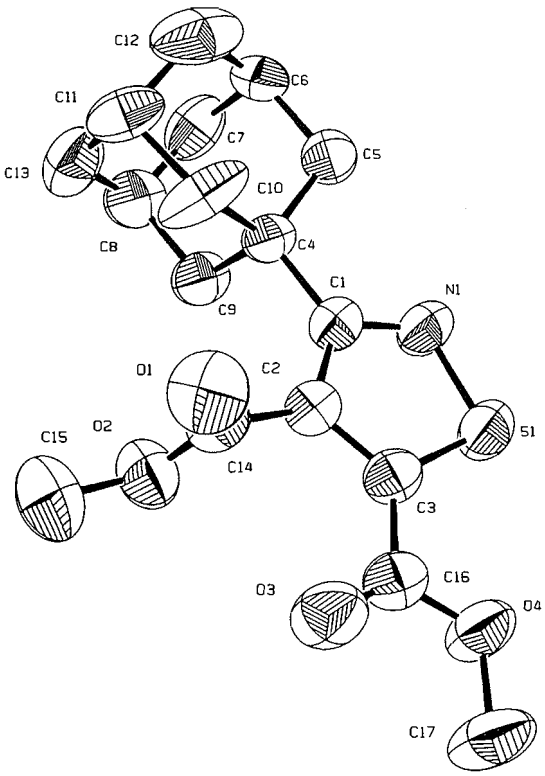

FIG. 2 ORTEP view of $C_{10}H_{15}$—CNSC(C(O)OCH$_3$)C(C(O)OCH$_3$) **3**.

DMAD cycloadducts have been compiled (16) and generally show two resonances in the range 155 ± 11 ppm (this work: 159.5 and 154.6 ppm) and a third resonance in the range 128 ± 18 ppm (this work: 132.0 ppm) for the three endocyclic carbon atoms. The spectra of 3 are also consistent with the DMAD molecule incorporated into the five membered ring [IR: strong carbonyl band at 1739 cm^{-1}, ^{1}H NMR: two OCH$_3$ resonances at 3.97 and 3.90 ppm, ^{13}C NMR: two OCH$_3$ resonances at 53.1 and 52.9 ppm and two C=O resonances at 175.5 and 166.3 ppm). The identity of the product is confirmed by the mass spectrum which gives the expected molecular ion and the fragments generated by loss of Me, OMe, and CO_2Me in sequence.

The solid state structure and the unit cell of **2***c* are shown in Figs. 2 and 3, respectively. The isothiazole heterocycles are apparently unassociated in the solid state with no significant intermolecular contacts. Solid state structures that contain DMAD cycloadducts or isothiazole heterocycles have been reported but the structure of the new compound **3** is the first structure of an isothiazole that is a cycloadduct of DMAD or that is substituted by an adamantyl group. The structure (bond lengths, bond angles, and substituent orientation) is consistent with those reported for molecules that contain DMAD, isothiazole or adamantyl moieties. However, the carbon–sulphur bonds (C3—S1: 1.690(4) Å, reported average: 1.720 Å) and the carbon–carbon (C1 and C2: 1.429(6) Å, reported average 1.454 Å) bonds are significantly shorter than the related bonds in previously reported isothiazole structures (16). These observations may be due to the influence of π bond delocalisation to the methyl carboxylate moieties. A bond order analysis of the isothiazole ring is given in **6** and confirms that there is significant π bond delocalisation in the isothiazole ring. Banisters treatment of such π systems (17) indicates that the isothiazole ring is a 6π system (3C (3 πe$^-$) + N (1 πe$^-$) + S (2 πe$^-$)) and is therefore a pseudo Hückel 4*n* + 2 aromatic system.

The general cycloaddition reaction of nitrile sulphides with thiazyl chloride

Thiazyl halides (N≡S—X, X = F, Cl) are well known in sulphur–nitrogen chemistry for their high reactivity and predictable behaviour in cycloaddition reactions (8, 18). A number of methods have been reported for the generation of these species (19). The formal sulphur–nitrogen triple bond in the thiazyl halide molecule has been used in both Diels–Alder and 1,3-dipolar cycloaddition reactions to give heterocyclic products in high yield.

The thiazyl chloride monomer is known to be intimately involved with its trimer $(NSCl)_3$ in solution and it has been reported using ^{14}N NMR spectroscopy that the equilibrium between the monomer and the trimer is strongly dependant on the solvent polarity and temperature (8). We have shown using ^{14}N NMR that the trimer is soluble in chlorobenzene and that at room temperature only trace amounts of the monomer can be detected. At the reflux temperature of chlorobenzene how ever, only trace amounts of the trimer are present and that the equilibrium is effectively shifted entirely in favour of the monomer. Decomposition of the sample at this temperature is rapid, leading to insoluble solids and nitrogen. Therefore, hot solutions of $(NSCl)_3$ in chlorobenzene can be used as a synthetic equivalent to a solution of NSCl but the stability of the solution is low and the *in situ* reaction must occur quickly if significant yields of product are to be expected. Therefore, it was proposed that the *in situ* reaction of NSCl and a nitrile sulphide in refluxing chlorobenzene could give a cycloadduct resulting from the reaction of the 1,3-dipole with the sulphur–nitrogen triple bond. This reaction has not been previously reported.

The general reaction of nitrile sulphides with thiazyl chloride were carried out in refluxing chlorobenzene and the products recovered by filtration and sublimation (to remove solvent and nitrile impurities). The cycloaddition reaction between these two species could give heterocycles of the 1,2,3,5-dithiadiazolium, **4**, or 1,3,2,4-dithiadiazolium, **7**, families. These cations are expected from this reaction because the autoionisation reaction to generate a 6π cationic system as a chloride salt is known to be energetically favourable (17).

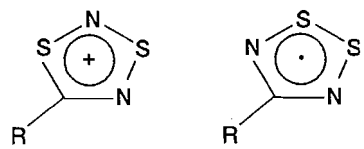

7 8

The products recovered from these reactions were shown to be derivatives of the 1,2,3,5-dithiadiazolium cation (4) in reasonable yields (typically ~50%). The salt 4b was recovered as a partial solvate (4b$^+$Cl$^-$·(1/5)C_6H_5Cl) which could not be reduced to a lower solvate by the sublimation procedures used for the other derivatives. Therefore, these reactions represent a new, general route to dithiadiazolium chloride salts. The generation of heterocyclic radicals (1,2,3,5-dithiadiazolyl, **8**) with potentially useful conductivity properties from these salts has been of intense interest to Main Group chemists (20). A number of methods have been reported for their preparation and indeed this family of heterocyclic cations appears to represent a "thermodynamic sink" in heterocyclic carbon–sulphur—

Can. J. Chem. Downloaded from www.nrcresearchpress.com by EESC ESCOLA DE ENGENHARIA on 09/08/12
For personal use only.

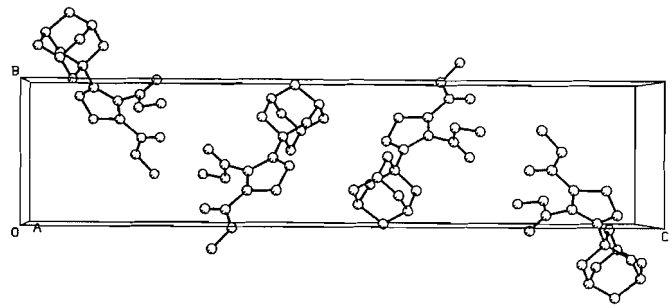

FIG. 3 PLUTO view of the unit cell of $C_{10}H_{15}$—CNSC(C(O)OCH$_3$)C(C(O)OCH$_3$) **3**.

nitrogen chemistry. To demonstrate that the reactions reported here must involve the cycloaddition of the nitrile sulphide, adamantyl nitrile was reacted with $(NSCl)_3$ under the conditions used for these cycloaddition reactions. The reaction did not give a isolable sample of the dithiadiazolium salt **4***c*$^+$Cl$^-$ even though it has been reported that nitriles react with $(NSCl)_3$ to give dithiadiazolium salts under milder reaction conditions (21). This demonstrates that the reaction environment leading to the decomposition of the nitrile sulphide to nitrile and sulphur does not provide for a significant enhancement of the yield of the reaction. Additionally, it was shown that the highest yields are obtained for reactions in which the oxathiazol-2-one precursor is intimately mixed with the thiazyl chloride (Table 1). It has been reported that higher yields of reactions involving nitrile sulphides are observed when the dipole (nitrile sulphide) is slowly added to a dilute solution of a large excess of the dipolarophile (π bond) (5). In these reactions however, the thermal instability of the thiazyl chloride monomer in the reaction environment condemns such a procedure to lower yields. The thermal instability of thiazyl chloride in refluxing chlorobenzene would appear to be the most significant factor in limiting this reaction.

The dithiadiazolium chlorides generated in this work were identified by infrared and mass spectroscopy and elemental analysis. The mass spectra of these species contained peaks assignable to the expected molecular cations and a fragmentation pattern consistent with sequential loss of a S_2N fragment and the substituent from the heterocycle. The infrared and mass spectra of two derivatives (R = C_6H_5 and C_4H_9) have been reported previously. The hitherto unknown adamantyl derivative has spectroscopic and physical properties that are consistent with those of other alkyl derivatives of this family. The insolubility of these salts and their high thermal stability make them difficult to fully characterise, therefore the adamantyl salt 4c was reduced to the new radical 4-adamantyl-1,2,3,5-dithiadiazolyl, **8**. The protocol established by Oakley and co-workers for the reduction and purification of these heterocycles was followed in which the salt was reacted with triphenyl antimony in methylene chloride and the solvent removed to give an opaque black solid which was washed with pentane and then purified by sublimation (22). The large purple–black crystals were identified as the radical **8** by mass spectroscopy, elemental analysis, and X-ray crystallography. The strongest peak in the mass spectrum of this radical is the molecular ion which is likely due to the volatility and stability of this radical.

The solid state structure of **8** is shown in Figure 4 and the contents of the unit cell of **8** is shown in Fig. 5. A bond order analysis of the dithiadiazolyl ring is given in **9** and the π bond

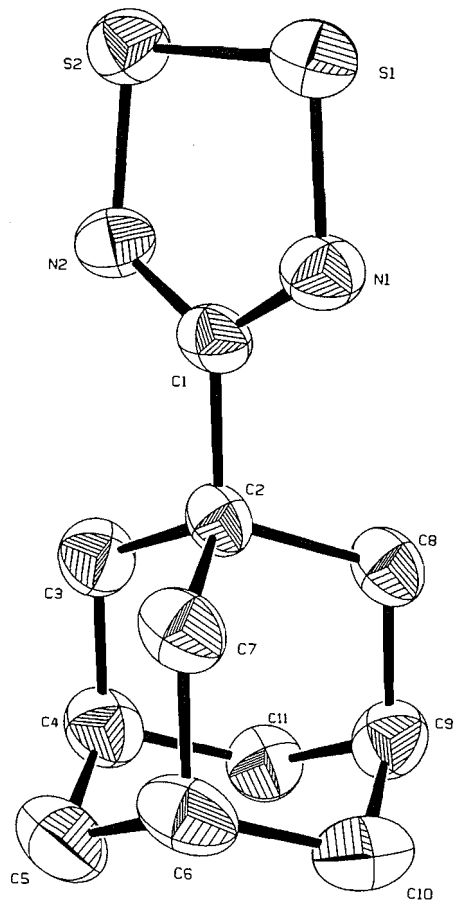

FIG. 4 ORTEP view of $C_{10}H_{15}$-CN_2S_2 **8**.

delocalisation that is expected in the 7π heterocycle is observed. To date, the crystal structures of five mono-functional dithiadiazolyl radical dimers have been reported (R = —CH_3 (23), —CF_3 (24), —$N(CH_3)_2$ (25), —C_6H_5 (26), —*p*-C_6H_5(CN) (27)) and their solid state structures have been recently reviewed (25). The structure of the adamantyl dithiadiazolyl derivative presented here is congruous with the reported structures. The heterocycle is planar and the bond distances and angles within the ring are not significantly different from the mean values reported for this ring system (25).

In this structure the dithiadiazolyl heterocycles are associated into roughly co-planar dimer units in which the rings are rotated approximately 90° from a "*cis*" structure **12** with the most significant intermolecular contacts occurring between the sulphur atoms (S(2)—S(2): 3.036(3) Å). Secondary inter-

Can. J. Chem. Downloaded from www.nrcresearchpress.com by EESC ESCOLA DE ENGENHARIA on 09/08/12
For personal use only.

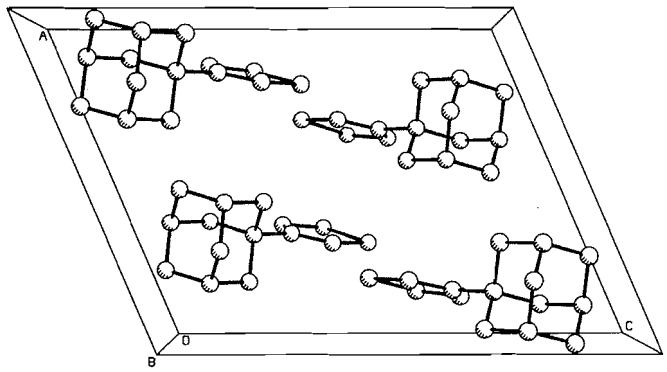

FIG. 5 PLUTO view of the unit cell of $C_{10}H_{15}$—CN_2S_2 **8** showing the orientation of the dimer units.

molecular contacts are observed between the sulphur and nitrogen atoms (shortest contact S(2)—N(1): 3.269(4) Å). This essentially co-planar twisted conformation **11** is observed in the methyl, trifluoromethyl, and dimethyl-amino derivatives of this radical family. Theoretical studies have been used to show that the conformation of the dimer can be changed from **10** to **11** to **12** with only small changes in the total energy of the system (24). It has been suggested that the actual orientation

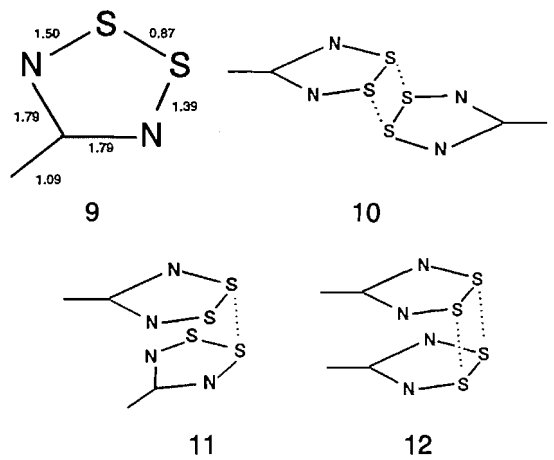

of the dimer may be primarily a result of simple packing forces (20). With this in mind, we proposed that the adamantyl derivative may adopt the *trans* conformation **12** of the dimer to minimise steric interactions between the bulky substituent groups. The *trans* conformation has only been reported for the cyano-phenyl derivative in which secondary interactions involving the sulphur atoms and the cyano group made this the preferred conformation. The structure of **8** is the first of a dithiadiazolyl radical that is substituted with a cage hydrocarbon. It is apparent that the rigidity and steric influence of the large adamantyl moiety has not significantly affected the structure from that observed for smaller alkyl substituents. The preference of alkyl derivatives of this ring system for the twisted dimer structure suggests that the *cis* **10** and *trans* **12** structures observed for the phenyl and cyano-phenyl derivatives, respectively, are the result of electronic differences that involve the delocalisation of charge or π bonding into the substituent. The fact that the twisted conformation **11** was found to be the structure of the adamantyl dimer suggests that this structure may indeed be a minimum between the higher energy dimer conformations **10** and **12**.

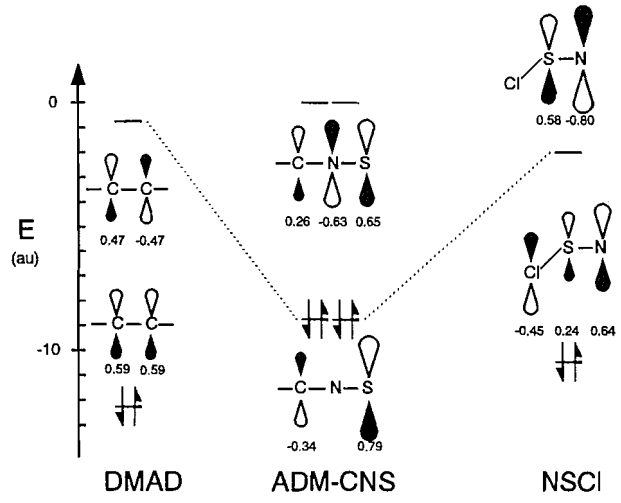

FIG. 6 Energy levels of the π frontier orbitals of DMAD, $C_{10}H_{15}$—CNS and NSCl indicating the most significant HOMO–LUMO pairs. The numbers are the values of the eigenvector coefficients.

Theoretical considerations

The cycloaddition reaction of propargyl allenyl type 1,3-dipoles [R—A≡B—C] with π bonds has been extensively investigated and reviewed (4). There has, however, been only a limited number of studies on the theoretical aspects of nitrile sulphide cycloadditions (28). The frontier molecular orbitals (HOMO: Highest Occupied Molecular Orbital, LUMO: Lowest Unoccupied Molecular Orbital) of a number of nitrile sulphides and π bonds were calculated at the semi-empirical level (PM3) and the results are given in Table 9. The inter-atomic distances were set by the default values in the program and fully geometry optimised at the PM3 level prior to the single point calculation of the molecular orbitals. The substitution of the nitrile sulphide with alkyl groups slightly stabilises the π LUMO more than the π HOMO therefore decreasing the HOMO-gap with increasing substituent size. The composition and energies of the frontier π orbitals of a nitrile sulphide with DMAD and thiazyl chloride are shown in Fig. 6. The π frontier orbitals are of the appropriate orientation to allow a symmetry allowed cycloaddition reaction to occur with the π bonds. The difference in energy of the nitrile sulphide HOMO and the π bond LUMO is consistently and significantly smaller than the complementary HOMO–LUMO pair. This is consistent with calculations reported for both nitrile oxides and nitrile sulphides (4, 28). The incorporation of elements with high electronegativity into the π manifold acts to stabilise the π orbitals with respect to the frontier orbitals of the dipolarophile.

These data in Table 9 indicate that substitution of nitrile sulphides with alkyl groups minimizes the energy difference of the critical HOMO–LUMO pair. When the nitrile sulphide is substituted with an aryl group the π HOMO and π LUMO of the nitrile sulphide have substantial contributions from the 2p orbitals on the carbons of the aromatic ring. This delocalisation of the π orbitals may act to stabilise the nitrile sulphide but it does not enhance the interactions of the frontier orbitals. Our experimental results show that the reaction of the alkyl substituted nitrile sulphides gives the thiazyl chloride cycloadduct in higher yield (54 ± 2%) than the aryl substituted derivative (17%). This may be due to the ability of the alkyl nitrile sulphides to successfully undergo cycloaddition to the thermally

Can. J. Chem. Downloaded from www.nrcresearchpress.com by EESC ESCOLA DE ENGENHARIA on 09/08/12
For personal use only.

TABLE 9. PM3 eigen values (ν) and eigen vectors (λ) for some nitrile sulphides and π bonds

	π Frontier orbitals			
	π HOMO[b]		π LUMO[b]	
Molecule[a]	ν (au)	λ	ν (au)	λ
H—C≡N—S	−9.18[c]	S 0.90 C −0.90	−0.11[c]	S 0.23 N −0.56 C 0.59
CH_3—C≡N—S	−8.97[c]	S 0.71 C −0.31	−0.06[c]	S 0.24 N −0.57 C 0.58
C_4H_9—C≡N—S	−8.93[c]	S 0.65 C −0.28	+0.04[c]	S 0.26 N −0.64 C 0.66
$C_{10}H_{15}$—C≡N—S	−8.90[c]	S 0.79 C −0.34	+0.07[c]	S 0.26 N −0.63 C 0.65
C_6H_5—C≡N—S	−8.80	S 0.85 C[d] −0.36	−0.01[c]	S 0.27 N −0.65 C[d] 0.67
DMAD	−12.19	C 0.59 C 0.59	−0.77	C 0.58 C −0.58 C[d] 0.67
N≡S—Cl	−10.52	N 0.64 S 0.24 Cl −0.45	−1.92[c]	N −0.80 S 0.58

[a]Molecular geometry calculated by PM3 geometry optimisation. Bond distances in nitrile sulphides: S—N 1.65 Å, N≡C 1.17 Å. Bond distance in DMAD: C≡C 1.19. Bond distances and angle in NSCl: N≡S 1.35 Å, S—Cl 2.00 Å, N—S—Cl 108.5°.

[b]Values quoted for λ are for np_z orbitals (C,N $2p_z$ S,Cl $3p_z$).

[c]Degenerate orbital.

[d]The value quoted is for the carbon in the —C≡N—S moiety. Other carbon atoms in the phenyl substituent make significant contributions to this orbital (λ > 0.2).

unstable thiazyl chloride π bond faster than the aryl substituted derivative.

The calculated charges on the atoms in *t*-butyl nitrile sulphide and thiazyl chloride are shown in 13. The cycloaddition reaction to produce a sulphur-sulphur and a carbon-nitrogen bond is preferred electrostatically to the complementary cycloaddition which would produce carbon–sulphur and nitrogen–sulphur bonds. This is also supported thermodynamically in a bonds broken – bonds formed thermochemical analysis which indicates that generation of the 1,2,3,5-dithiadiazolium heterocycle is preferred by ~56 $kJmol^{-1}$ over the 1,3,2,5-dithiadiazolium alternative (if one assumes that the values for bond delocalisation and autoionisation are the same for both cations).

The π structure of the nitrile sulphides is very similar to that reported for the SNS^+ cation (3). The lower symmetry of the nitrile sulphides and the incorporation of carbon into the π manifold would appear to make the frontier orbitals of the nitrile sulphides asymmetric and of higher energy. Nevertheless, in both species the dominant frontier orbital interaction is the same and one would expect their cycloaddition chemistries to be very similar.

These calculations indicate that the cycloaddition of nitrile sulphides with thiazyl chloride are symmetry allowed processes

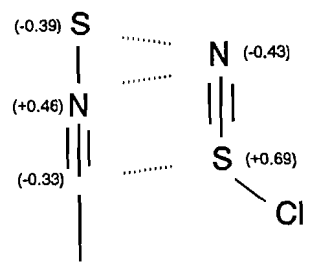

13

that are driven by the HOMO (NSCl) - LUMO (RCNS) frontier molecular orbital pair. The thermal instability of the thiazyl sulphide creates a situation where the best nitrile sulphide derivatives for cycloaddition will be substituted with saturated alkyl groups. Aryl substitution may stabilise the nitrile sulphide itself but the cycloaddition is dependant on highly reactive 1,3-dipoles to give significant yields. It may yet be possible to isolate a stable nitrile sulphide by substitution with sterically protective aromatic substituents such as mesityl or super mesityl but they may also be less reactive in similar cycloaddition reactions.

Can. J. Chem. Downloaded from www.nrcresearchpress.com by EESC ESCOLA DE ENGENHARIA on 09/08/12
For personal use only.

Acknowledgements

We thank the Natural Sciences and Engineering Research Council of Canada, Saint Mary's University and Memorial University of Newfoundland for financial support. M.J.S thanks Dr. D.J. Burnell and Dr. A.R. Stein for many helpful discussions.

1. A.H. Cowley and N.C. Norman. Prog. Inorg. Chem. **34**, 1 (1986); R. West, M.J. Fink and J. Michl. Science Washington D.C.), **214**, 1343 (1981); M. Drager, J. Escudie, C. Couret, H. Ranivonjotova and J. Satge, Organometallics, **7**, 1010 (1988).
2. M. Regitz. Chem. Rev. **90**, 191 (1990).
3. S. Parsons, J. Passmore, M.J. Schriver, and X. Sun. Inorg. Chem. **30**, 3342 (1991).
4. A. Padwa (*Editor*) 1,3-Dipolar cycloaddition chemistry. John Wiley and Sons, New York, 1984.
5 R.M. Paton. Chem. Soc. Rev. **18**, 33 (1989); C. Wentrup and P. Kambouris. Chem. Rev. **91**, 365 (1991).
6. B.S. Furniss, A.J. Hannaford, P.W.G. Smith and A.R. Tatchell. Vogel's textbook of practical organic chemistry. 5th ed. John Wiley and Sons, New York. 1989.
7. W.L. Jolly and K.D. Maguire. Inorg. Synth. **9**, 102 (1967).
8. J. Passmore and M.J. Schriver. Inorg. Chem. **27**, 2749 1988).
9. D.T. Cromer and J.T. Waber. *In* International tables for X-ray crystallography. Vol. IV. Kynoch Press, Birmingham. 1974. Table 2.2B (Present Distributer: Kluwer Academic Publishers, Dordrecht and Boston.)
10. E.J. Gabe, Y. Le Page, J-P. Charland, F.L. Lee and P.S. White. J. Appl. Crystallogr. **22**, 384, (1989).
11. N. Walker and D. Stuart, Acta Crystallogr. **A39**, 158 (1983).
12. TEXSAN - TEXRAY Structure Analysis Package. Molecular Structure Corporation, 1985.
13. B. Bak, O. Neilsen, H. Svanholt, A. Almenningen, O. Bastiansen, L. Fernholt, G. Gundersen, C.J. Neilsen, B.N. Cyvin, and S. Cyvin. Acta Chem. Scand. **32A**, 1005 (1978); B. Bak, O. Neilsen, H. Svanholt, A. Almenningen, O. Bastiansen, G. Braathen, L. Fernholt, G. Gundersen, C.J. Neilsen, B.N. Cyvin and S. Cyvin. Acta Chem. Scand. **36A**, 283 (1982).
14. L. Pauling. The nature of the chemical bond. 3rd ed. Cornell University Press, Ithaca. 1960.
15. S.C. Nyburg. J. Cryst. Mol. Struct. **3**, 331 (1973).
16. D.L. Pain, B.J. Peart, and K.R.H. Woolridge. Isothiazoles and their benzo derivatives. *In* Comprehensive hetrocyclic chemistry. *Edited by* A.R. Katritsky and C.W. Rees. Pergamon Press, New York. 1984. Sect. **4.17**, p. 131.
17. H.G. Heal. The inorganic heterocyclic chemistry of sulphur, nitrogen and phosphorus. Academic Press, London. 1980, and references therein.
18. D.K. Padma and R. Mews. Z. Naturforsch. B: Chem. Sci. **42**, 699 (1987); W. Bludssus and R. Mews. J. Chem. Soc. Chem. Commun. 35 (1979).
19. R.L. Patton and W.L. Jolly. Inorg. Chem. **9**, 1079 (1970); A. Apblett, A.J. Banister, D. Biron, A.G. Kendrick, J. Passmore, M. Schriver, and M. Stojanac. Inorg. Chem. **25**, 4451 (1986).
20. A.W. Cordes, R.C. Haddon and R.T. Oakley. *In* The chemistry of inorganic ring systems. *Edited by* R. Steudel. Elsevier, Amsterdam. 1992. p. 295; A.J. Banister and J.M. Rawson. *In* The chemistry of inorganic ring systems. *Edited by* R. Steudel, Elsevier, Amsterdam, 1992. p. 323.
21. A. Apblett and T. Chivers. Inorg. Chem. **28**, 4544 (1989).
22. A.W. Cordes, R.C. Haddon, R.G. Hicks, D.K. Kennepohl, R.T. Oakley, L.F. Schneemeyer and J.V. Waszczak. Inorg. Chem. **32**, 1554 (1993).
23. A.J. Banister, M.I. Hansford, Z.V. Hauptman, S.T. Wait and W. Clegg. J. Chem. Soc. Dalton Trans. 1705 (1989).
24. H-U. Höfs, J.W. Bats, R. Gleiter, G. Hartmann, R. Mews, M. Eckert-Maksić, H. Oberhammer, and G. Sheldrick. Chem. Ber. **118**, 3781 (1985).
25. A.W. Cordes, J.D. Goddard, R.T. Oakley and N.P.C. Westwood. J. Am. Chem. Soc. **111**, 6147 (1989).
26. A. Vegas, A. Pérez-Salazar, A.J. Banister, and R.G. Hey. J. Chem. Soc. Dalton Trans. 1812 (1980).
27. A.W. Cordes, R.C. Haddon, R.G. Hicks, R.T. Oakley and T.T.M. Palstra. Inorg. Chem. **31**, 1802 (1993).
28. M.C. McKie, Ph.D. Thesis, University of Edinburgh, 1988, and references therein.

Can. J. Chem. Downloaded from www.nrcresearchpress.com by EESC ESCOLA DE ENGENHARIA on 09/08/12
For personal use only.

Structural studies of organoboron compounds. LX.[1] Reaction of sterically hindered arylboronic acids with 2-(hydroxyamino)alkanols. Crystal and molecular structure of 2-mesityl-6,6-pentamethylene-1,3-dioxa-4-aza-2-boracyclohexane

WOLFGANG KLIEGEL[2] AND GOTTFRIED LUBKOWITZ

Institut für Pharmazeutische Chemie der Technischen Universität Braunschweig, Beethovenstrasse 55, 38106 Braunschweig, Germany

AND

STEVEN J. RETTIG AND JAMES TROTTER[2]

Department of Chemistry, University of British Columbia, 2036 Main Mall, Vancouver, BC V6T 1Z1, Canada

Received August 31, 1993

WOLFGANG KLIEGEL, GOTTFRIED LUBKOWITZ, STEVEN J. RETTIG, and JAMES TROTTER. Can. J. Chem. **72**, 1154 (1994).

Three 2-(hydroxyamino)alkanols have been reacted with sterically hindered arylboronic acids, $ArB(OH)_2$. When Ar = *o*-tolyl, 1:2 condensates having bicyclic structures are formed but when Ar = mesityl (2,4,6-$(CH_3)_3C_6H_2$), 1:1 condensates having six-membered cycloboronate structures result. These 1:1 condensates represent the first examples of *N*-unsubstituted 1,3-dioxa-4-aza-2-boracyclohexane derivatives. An X-ray analysis of one example provides unambiguous proof of the structure. Crystals of 2-mesityl-6,6-pentamethylene-1,3-dioxa-4-aza-2-boracyclohexane, **3***c*, are monoclinic, $a = 11.076(9)$, $b = 23.94(2)$, $c = 13.414(9)$ Å, $\beta = 109.40(5)°$, $Z = 8$, space group $P2_1/n$. The structure was solved by direct methods and refined by full-matrix least-squares procedures to $R = 0.051$ and $R_w = 0.058$ for 2037 reflections with $I \geq 3\sigma(F^2)$.

WOLFGANG KLIEGEL, GOTTFRIED LUBKOWITZ, STEVEN J. RETTIG et JAMES TROTTER. Can. J. Chem. **72**, 1154 (1994).

On a fait réagir trois 2-(hydroxyamino)alcanols avec des acides arylboroniques stériquement empêchés, $ArB(OH)_2$. Lorsque Ar = *o*-tolyle, il se forme de produits de condensation 1 : 2 de structures bicycliques; toutefois, lorsque Ar = mésityle (2,4,6-$(CH_3)_3C_6H_2$), les produits de condensation sont de nature 1 : 1 et il s'agit de cycloboronates à six chaînons. Ces produits de condensation 1 : 1 représentent les premiers exemples de dérivés 1,3-dioxa-4-aza-2-boracyclohexanes non *N*-substitués. Une analyse d'un exemple par diffraction des rayons X fournit une preuve non ambiguë de la structure. Les cristaux du 2-mésityl-6,6-pentaméthylène-1,3-dioxa-4-aza-2-boracyclohexane, **3***c*, sont monocliniques, groupe d'espace $P2_1/n$, avec $a = 11,076(9)$, $b = 23,94(2)$ et $c = 13,414(9)$ Å, $\beta = 109,40(5)°$ et $Z = 8$. On a résolu la structure par des méthodes directes et on l'a affinée par la méthode des moindres carrés jusqu'à des valeurs de $R = 0,051$ et $R_w = 0,058$ pour 2037 réflexions avec $I \geq 3\sigma(F^2)$.

[Traduit par la Rédaction]

Introduction

2-(Hydroxyamino)alkanols **1** react with phenylboronic acid to give eight-membered heterocyclic pyroboronates **2** (Ar = C_6H_5) that are stabilized by transannular N–B coordination (1–3). These bicyclic compounds are obtained even if only one molar equivalent of phenylboronic acid is applied. The six-membered cycloboronates **3** or their dimers **4** could not be isolated in these cases. Since the formation of cyclic arylboronates from 1,3-diol compounds is generally well known, and the structures of several six-membered cycloboronates have been established by X-ray crystallographic analyses (ref. 4, and references therein), we attempted to achieve the synthesis of **3** by impeding the formation of the bicyclic ring skeleton through steric hindrance via the introduction of one or two *ortho* methyl groups into the phenylboronic acid.

The application of *o*-tolylboronic acid, however, did not lead to the monoarylboronates **3** but gave instead compounds containing two molecules of the arylboronic acid each. Elemental analyses and infrared and nmr spectra suggest bicyclic structures for **2***a–c*, like those established for **2** ($R^1 = R^2 = H$, $R^3 = R^4 = CH_3$, Ar = C_6H_5) (1) and the *N*-benzyl derivative **5** (5) by X-ray structure analyses. The ^{11}B nmr spectrum of **2***b* shows two signals of nearly equal peak area at $\delta(Et_2OBF_3) = 11.7$ and 30.7 ppm, indicating tri- and tetravalent boron atoms, respectively (6). These values correspond to the shifts of 13.3 and 28.0 ppm observed in the spectrum of the *N*-substituted bicyclic pyroboronate **5**, which possesses two different states of boron hybridization (5). It can therefore be assumed that the *o*-tolylboronates **2***a–c* have a comparable bicyclic pyroboronate structure.

In contrast to the above results, elemental analyses and ^1H nmr spectra suggested that the reaction of **1** with mesitylboronic acid gave 1:1 condensation products having the monocyclic structure **3**. The N—H stretching vibration in the infrared spectra of **3***a–c* appears between 3160 and 3290 cm^{-1}, different from the N—H absorptions in the infrared spectra of **2***a–c* which appear between 3050 and 3100 cm^{-1}, as observed for the bicyclic phenylboronates **2** (Ar = C_6H_5) (1–3). The shift of the N—H absorption bands in **3***a–c* to higher frequencies (by 100–200 cm^{-1}) corresponds to a decreased positive charge at the hydroxylamine nitrogen atom in a type **3** compound lacking the transannular N–B coordination.

As expected, the ^{11}B nmr spectrum of **3***c* displays only one signal at $\delta(Et_2OBF_3) = 29.3$ ppm, indicating a trivalent (sp^2) boron moiety. In the solid state, however, a dimeric association product of the type **4** cannot be excluded. The phenylboronate of an *N*-methyl derivative of **1** (R^1 = Me, $R^2 = R^3 = R^4 = H$) exists as a type **4** BONBON dimer in the crystalline state and displays a main ^{11}B nmr signal at 27.2 ppm in solution (5). The spectroscopic data do not unambiguously exclude a five-membered arylboronate of the type **6**[3] nor its *N*-oxide tautomer **7**

[1]Previous paper in this series: ref. 12.

[2]Authors to whom correspondence may be addressed.

[3]The O—H stretching vibrations in the infrared spectra of *N*-hydroxyoxazolidines (which are related to **6**) are found between 3250 and 3280 cm^{-1}.

Can. J. Chem. Downloaded from www.nrcresearchpress.com by EESC ESCOLA DE ENGENHARIA on 09/08/12
For personal use only.

Can. J. Chem. Downloaded from www.nrcresearchpress.com by EESC ESCOLA DE ENGENHARIA on 09/08/12
For personal use only.

that could dimerize to the BONBON compound **8** (at least in the solid state). To distinguish between the structural possibilities **3**, **4**, **6**, and **8** in the solid state, a structure analysis of compound **3***c*, which yielded the most suitable crystals, was undertaken.

Experimental

8,8-Dimethyl-3,5-di(o-tolyl)-2,4,6-trioxa-1-azonia-3-bora-5-boratabicyclo[3.3.0]octane, ***2a***

2-(Hydroxyamino)-2-methylpropanol, **1***a* (7) (0.21 g, 2 mmol) and *o*-tolylboronic acid (0.54 g, 4 mmol) are dissolved in 20 mL of benzene and refluxed for 1 h using a Dean–Stark trap for continuous removal of water. The solvent is distilled off in vacuo and the solid residue crystallized from toluene, yielding 0.60 g (93%) of colorless crystals, mp 144–146°C (dec.). Infrared (KBr): 3060 (N—H), 1600 (aryl C═C) cm^{-1}; ^1H nmr (90 MHz, $CDCl_3$/TMS), δ (ppm): 1.25 and 1.33 (s and s, $C(CH_3)_2$), 2.40 and 2.56 (s and s, 2 aryl-CH_3), 3.57 (q, O-CH_2), 6.98–7.35 (m, NH and 6 aromatic H), 7.54–7.88 (m, 2 aromatic H). Anal. calcd. for $C_{18}H_{23}B_2NO_3$: C 66.93, H 7.18, N 4.34; found: C 66.63, H 7.28, N 4.02.

7,8,8-Trimethyl-3,5-di(o-tolyl)-2,4,6-trioxa-1-azonia-3-bora-5-boratabicyclo[3.3.0]octane, ***2b***

3-(Hydroxyamino)-3-methyl-2-butanol, **1***b* (7) (0.24 g, 2 mmol), and *o*-tolylboronic acid (0.54 g, 4 mmol) are reacted as described for **2***a*, yielding 0.64 g (94%) of colorless crystals, mp 167–168°C (dec.). Infrared (KBr): 3100 (N—H), 1600 (aryl C═C) cm^{-1}; ^1H nmr (90 MHz, $CDCl_3$/TMS), δ (ppm): 1.07 and 1.36 (s and s, $C(CH_3)_2$), 1.26 (d, J = 6 Hz, O-C-CH_3), 2.42 and 2.57 (s and s, 2 aryl-CH_3), 3.95 (q, J = 6 Hz, CH-O), 6.58 (s, exchangeable, NH), 6.95–7.34 (m, 6 aromatic H), 7.61–7.86 (m, 2 aromatic H); ^{11}B nmr (64 MHz, $CDCl_3/Et_2OBF_3$), δ (ppm): 11.7 ($w_{1/2}$ = 214 Hz) and 30.7 ($w_{1/2}$ = 514 Hz); ratio of peak areas 1:1. Anal. calcd. for $C_{19}H_{25}B_2NO_3$: C 67.71, H 7.48, B 6.42, N 4.16; found: C 67.84, H 7.47, B 6.28, N 4.37.

7,7-Pentamethylene-3,5-di(o-tolyl)-2,4,6-trioxa-3-bora-5-boratabicyclo[3.3.0]octane, ***2c***

1-(Hydroxyaminomethyl)cyclohexanol, **1***c* (7) (0.30 g, 2 mmol), and *o*-tolylboronic acid (0.54 g, 4 mmol) are reacted as described for **2***a*, yielding 0.67 g (92%) of colorless crystals, mp 188–189°C. Infrared (KBr): 3050 (N—H), 1600 (aryl C═C) cm^{-1}; ^1H nmr (90 MHz, DMSO-d_6/TMS), δ (ppm): 1.1–1.9 (m, $(CH_2)_5$), 2.34 and 2.52 (s and s, 2 aryl-CH_3), 3.00 and 3.47 (q, AB-system, N-CH_2), 6.94–7.33 (m, 6 aromatic H), 7.51–7.70 (m, 2 aromatic H), 10.91 (d, J = 5 Hz, exchangeable, NH). Anal. calcd. for $C_{21}H_{27}B_2NO_3$: C 69.47, H 7.50, N 3.86; found: C 69.34, H 7.67, N 4.04.

2-Mesityl-5,5-dimethyl-1,3-dioxa-4-aza-2-boracyclohexane, ***3a***

2-(Hydroxyamino)-3-methyl-2-propanol, **1***a* (0.32 g, 3 mmol), and mesitylboronic acid (0.49 g, 3 mmol) are refluxed in 20 mL of benzene for 1 h using a Dean–Stark trap for continuous removal of water. After evaporation of the solvent in vacuo the oily residue is dissolved in a small quantity of petroleum ether and cooled down until crystallization yields 0.51 g (73%) of colorless crystals, mp 88°C. Infrared (KBr): 3160 (N—H), 1610 (aryl C═C) cm^{-1}; ^1H nmr (90 MHz, $CDCl_3$/TMS), δ (ppm): 1.29 (s, $C(CH_3)_2$), 2.24 (s, 2 aryl-*p*-CH_3), 2.39 (s, aryl-*o*-CH_3), 3.83 (s, O-CH_2), 5.43 (s, br, exchangeable, NH), 6.74 (s, 2 aromatic H). Anal. calcd. for $C_{13}H_{20}BNO_2$: C 66.98, H 8.65, B 4.64, N 6.01; found: C 67.05, H 8.80, B 4.54, N 6.15.

2-Mesityl-5,5,6-trimethyl-1,3-dioxa-4-aza-2-boracyclohexane, ***3b***

3-(Hydroxyamino)-3-methyl-2-butanol, **1***b* (0.36 g, 3 mmol), and mesitylboronic acid (0.49 g, 3 mmol) are reacted as described for **3***a*, yielding 0.51 g (69%) of colorless crystals, mp 54°C. Infrared (KBr): 3180 (N—H), 1610 (aryl C═C) cm^{-1}; ^1H nmr (90 MHz, $CDCl_3$/TMS), δ (ppm): 1.16 and 1.24 (s and s, $C(CH_3)_2$), 1.25 (d, J = 7 Hz, O-C-CH_3), 2.22 (s, aryl-*p*-CH_3), 2.38 (s, 2 aryl-*o*-CH_3), 4.10 (q, J = 7 Hz, O-CH), 5.40 (s, br, exchangeable, NH), 6.73 (s, 2 aromatic H). Anal. calcd. for $C_{14}H_{22}BNO_2$: C 68.04, H 8.97, N 5.67; found: C 68.08, H 8.97, N 5.72.

TABLE 1. Crystallographic data[a]

Compound	**3***c*
Formula	$C_{16}H_{24}BNO_2$
fw	273.18
Crystal system	Monoclinic
Space group	$P2_1/n$
a, Å	11.076(9)
b, Å	23.94(2)
c, Å	13.414(9)
β°	109.40(5)
V, Å^3	3355(4)
Z	8
ρ_{calc}, g/cm^3	1.082
F(000)	1184
Radiation	Mo-K_α
μ, cm^{-1}	0.65
Crystal size, mm	0.30 × 0.35 × 0.45
Transmission factors (relative)	0.77–1.00
Scan type	ω–2θ
Scan range, deg in ω	0.89 + 0.35 tan θ
Scan speed, deg/min	8
Data collected	$+h$, $+k$, $\pm l$
$2\theta_{max}$, deg	50
Crystal decay	Negligible
Total reflections	5112
Total unique reflections	4834
R_{merge}	0.049
Reflections with $I \geq 3\sigma(F^2)$	2037
No. of variables	398
R	0.051
R_w	0.058
gof	2.24
Max Δ/σ (final cycle)	0.13
Residual density e/Å^3	−0.16 to 0.20

[a]Temperature 294 K, Rigaku AFC6S diffractometer, Mo-K_α (λ = 0.71069 Å) radiation, graphite monochromator, takeoff angle 6.0°, aperture 6.0 × 6.0 mm at a distance of 285 mm from the crystal, stationary background counts at each end of the scan (scan/background time ratio 2:1, up to 8 rescans), $\sigma^2(F^2) = [S^2(C + 4B) + (0.03F^2)^2]/Lp^2$ (S = scan rate, C = scan count, B = normalized background count), function minimized $\Sigma w(|F_o| - |F_c|)^2$ where $w = 4F_o^2/\sigma^2(F_o^2)$, $R = \Sigma||F_o| - |F_c||/\Sigma|F_o|$, $R_w = (\Sigma w(|F_o| - |F_c|)^2/\Sigma w|F_o^2|^2)^{1/2}$, and gof = $[\Sigma w(|F_o| - |F_c|)^2/(m - n)]^{1/2}$. Values given for R, R_w, and gof are based on those reflections with $I \geq 3\sigma(F^2)$.

2-Mesityl-6,6-pentamethylene-1,3-dioxa-4-aza-2-boracyclohexane, ***3c***

1-(Hydroxyaminomethyl)cyclohexanol, **1***c* (0.44 g, 3 mmol), and mesitylboronic acid (0.49 g, 3 mmol) are reacted as described for **3***a*, yielding 0.60 g (73%) of colorless crystals, mp 79–80°C. Infrared (KBr): 3290 (N—H), 1610 (aryl C═C) cm^{-1}; ^1H nmr (90 MHz, $CDCl_3$/TMS), δ (ppm): 1.23–1.97 (m, $(CH_2)_5$), 2.24 (s, aryl-*p*-CH_3), 2.36 (s, 2 aryl-*o*-CH_3), 3.16 (s, N-CH_2), 6.09 (s, br, exchangeable, NH), 6.47 (s, 2 aromatic H); ^{11}B nmr (64 MHz, $CDCl_3/Et_2OBF_3$), δ (ppm): 29.3 ($w_{1/2}$ = 280 Hz). Anal. calcd. for $C_{16}H_{24}BNO_2$: C 70.35, H 8.86, B 3.96, N 5.13; found: C 70.36, H 8.91, B 4.10, N 5.28. Crystals suitable for X-ray analysis were obtained by slow recrystallization from petroleum ether.

X-ray crystallographic analysis of ***3c***

Crystallographic data appear in Table 1. The final unit-cell parameters were obtained by least squares on the setting angles for 25 reflections with 2θ = 20.2–24.5°. The intensities of three standard reflections, measured every 200 reflections throughout the data collection, showed only small random fluctuations. The data were pro-

Can. J. Chem. Downloaded from www.nrcresearchpress.com by EESC ESCOLA DE ENGENHARIA on 09/08/12
For personal use only.

TABLE 2. Final atomic coordinates (fractional) and B_{eq} (Å^2)[a]

Atom	x	y	z	B_{eq}	occ.
O(1)	0.685(1)	0.1329(4)	0.2597(6)	6.4(4)	0.60
O(1A)	0.718(1)	0.1231(6)	0.330(1)	6.0(6)	0.40
O(2)	0.5175(3)	0.0824(1)	0.2933(2)	5.6(2)	
O(3)	0.1693(7)	0.0542(3)	0.2153(6)	6.2(4)	0.60
O(3A)	0.203(1)	0.0425(5)	0.292(1)	6.1(5)	0.40
O(4)	0.0180(3)	0.0896(1)	0.2921(2)	5.3(1)	
N(1)	0.7139(6)	0.0811(3)	0.2153(6)	5.6(4)	0.60
N(1A)	0.768(1)	0.0652(6)	0.332(1)	8.0(7)	0.40
N(2)	0.2220(7)	0.1111(3)	0.2278(7)	7.5(4)	0.60
N(2A)	0.2743(9)	0.0889(5)	0.348(1)	6.7(6)	0.40
C(1)	0.6953(6)	0.0352(3)	0.2685(6)	7.6(3)	
C(2)	0.5598(4)	0.0284(2)	0.2691(4)	5.0(2)	
C(3)	0.5553(5)	−0.0110(2)	0.3556(4)	7.8(3)	
C(4)	0.5767(8)	−0.0719(3)	0.3304(7)	11.0(4)	
C(5)	0.4786(8)	−0.0886(3)	0.227(1)	12.4(5)	
C(6)	0.4881(5)	−0.0509(3)	0.1395(5)	9.5(4)	
C(7)	0.4683(4)	0.0107(2)	0.1637(4)	7.0(3)	
C(8)	0.5358(4)	0.1849(2)	0.3319(4)	4.7(2)	
C(9)	0.5561(4)	0.1993(2)	0.4367(5)	5.6(3)	
C(10)	0.5068(6)	0.2484(3)	0.4602(4)	6.9(3)	
C(11)	0.4365(6)	0.2842(2)	0.3853(6)	7.0(3)	
C(12)	0.4149(5)	0.2701(2)	0.2811(5)	7.0(3)	
C(13)	0.4637(5)	0.2212(2)	0.2536(4)	5.8(3)	
C(14)	0.6339(5)	0.1617(2)	0.5250(4)	8.9(3)	
C(15)	0.3840(6)	0.3386(2)	0.4122(6)	11.0(4)	
C(16)	0.4334(6)	0.2071(2)	0.1381(5)	9.9(4)	
C(17)	0.2197(6)	0.1335(3)	0.3189(6)	8.3(4)	
C(18)	0.0869(4)	0.1417(2)	0.3266(4)	5.1(2)	
C(19)	0.0063(5)	0.1874(2)	0.2559(4)	7.5(3)	
C(20)	0.0519(6)	0.2447(2)	0.2953(6)	9.8(4)	
C(21)	0.0580(7)	0.2533(2)	0.4088(6)	10.0(4)	
C(22)	0.1421(6)	0.2087(3)	0.4800(5)	9.1(4)	
C(23)	0.0932(5)	0.1508(2)	0.4394(4)	6.8(3)	
C(24)	−0.0117(4)	−0.0087(2)	0.2232(4)	4.5(2)	
C(25)	−0.1001(4)	−0.0169(2)	0.1221(4)	4.8(2)	
C(26)	−0.1706(4)	−0.0655(2)	0.0980(4)	5.5(2)	
C(27)	−0.1576(5)	−0.1066(2)	0.1713(5)	5.6(3)	
C(28)	−0.0698(5)	−0.0987(2)	0.2723(4)	6.0(3)	
C(29)	0.0031(4)	−0.0510(2)	0.2983(4)	5.0(2)	
C(30)	−0.1235(5)	0.0286(2)	0.0396(4)	7.0(3)	
C(31)	−0.2373(5)	−0.1600(2)	0.1452(5)	8.7(3)	
C(32)	0.0961(5)	−0.0442(2)	0.4090(4)	8.5(3)	
B(1)	0.5863(6)	0.1292(3)	0.3028(5)	5.5(3)	
B(2)	0.0668(5)	0.0464(2)	0.2546(5)	5.4(3)	

[a] $B_{eq} = (8/3)\pi^2\Sigma\Sigma U_{ij} a_i^* a_j^* (\mathbf{a}_i \cdot \mathbf{a}_j)$.

cessed,[4] and corrected for Lorentz and polarization effects and for absorption (empirical, based on azimuthal scans for three reflections).

The structure was solved by direct methods, the coordinates of the non-hydrogen atom being determined from an *E*-map or from subsequent difference Fourier syntheses. There are two crytallographically independent molecules in the asymmetric unit. The thermal parameters of the N-O moieties of the six-membered heterocyclic rings of both of the independent molecules suggested conformational disordering. Split-atom anisotropic models were employed for the atoms N(1), N(2), O(1), and O(3), the site occupancy factors being adjusted as the refinement progressed to result in approximately equal thermal parameters for the two components of each disordered atom. It is likely that the disorder extends beyond the modeled regions and therefore some of the derived geometrical parameters may be affected. The paucity of significant data along with probable separations of component atoms that are below the limits of resolution, however, preclude modeling of this probable extended disorder. Non-hydrogen atoms were refined with anisotropic thermal parameters. The hydrogen atoms were fixed in idealized positions (N—H/C—H distances normalized to 0.98 Å, $B_H = 1.2\ B_{\text{bonded atom}}$, least-squares fit to difference map positions for the methyl groups, N-H orientation based on difference map positions). A correction for secondary extinction was applied, the final value of the extinction coefficient being $8.1(3) \times 10^{-7}$. Neutral atom scattering factors for all atoms and anomalous dispersion corrections for the non-hydrogen atoms were taken from the *International Tables for X-Ray Crystallography* (8). Final atomic coordinates and equivalent isotropic thermal parameters, bond lengths, and bond angles appear in Tables 2–4, respectively. Stereoviews of the two independent **3***c* molecules are shown in Fig. 1, and the packing arrangement is shown in Fig. 2. Hydrogen atom parameters, anisotropic thermal

[4] TEXSAN/TEXRAY structure analysis package (Version 5.1), Molecular Structure Corp. 1985.

TABLE 3. Bond lengths (Å) with estimated standard deviations

Atom	Atom	Distance	Atom	Atom	Distance
O(1)	N(1)	1.46(1)	C(8)	B(1)	1.546(7)
O(1)	B(1)	1.40(1)	C(9)	C(10)	1.376(6)
O(1A)	N(1A)	1.49(2)	C(9)	C(14)	1.510(7)
O(1A)	B(1)	1.38(1)	C(10)	C(11)	1.352(7)
O(2)	C(2)	1.448(5)	C(11)	C(12)	1.380(7)
O(2)	B(1)	1.337(6)	C(11)	C(15)	1.519(7)
O(3)	N(2)	1.469(9)	C(12)	C(13)	1.389(7)
O(3)	B(2)	1.413(8)	C(13)	C(16)	1.509(7)
O(3A)	N(2A)	1.42(1)	C(17)	C(18)	1.522(6)
O(3A)	B(2)	1.42(1)	C(18)	C(19)	1.526(6)
O(4)	C(18)	1.454(5)	C(18)	C(23)	1.506(6)
O(4)	B(2)	1.341(6)	C(19)	C(20)	1.497(7)
N(1)	C(1)	1.362(8)	C(20)	C(21)	1.516(8)
N(1A)	C(1)	1.20(1)	C(21)	C(22)	1.526(8)
N(2)	C(17)	1.343(9)	C(22)	C(23)	1.522(7)
N(2A)	C(17)	1.23(1)	C(24)	C(25)	1.397(6)
C(1)	C(2)	1.512(6)	C(24)	C(29)	1.399(6)
C(2)	C(3)	1.510(6)	C(24)	B(2)	1.559(7)
C(2)	C(7)	1.501(6)	C(25)	C(26)	1.379(6)
C(3)	C(4)	1.533(8)	C(25)	C(30)	1.512(6)
C(4)	C(5)	1.51(1)	C(26)	C(27)	1.364(6)
C(5)	C(6)	1.51(1)	C(27)	C(28)	1.394(6)
C(6)	C(7)	1.541(7)	C(27)	C(31)	1.528(6)
C(8)	C(9)	1.391(6)	C(28)	C(29)	1.376(6)
C(8)	C(13)	1.392(6)	C(29)	C(32)	1.509(6)

parameters, torsion angles, intermolecular contacts, least-squares planes, and measured and calculated structure factor amplitudes are included as supplementary material.[5]

Results and discussion

The structure analysis confirms the six-membered cycloboronate structure **3***c* for the product of the reaction of **1***a* with mesitylboronic acid. The spectroscopic data for compounds **3***a* and **3***b* indicate that these materials have structures analogous to that of **3***c*, and, to the best of our knowledge, represent the first *N*-unsubstituted 1,3-dioxa-4-aza-2-boracyclohexane derivatives to be reported. *N*-Substituted BONCCO ring systems of this type have been reported for the phenylboronates **9** (9), and, as a conformational variant, in the BONBON dimer of 4,6-dimethyl-2-phenyl-1,3-dioxa-4-aza-2-boracyclohexane (type **4**) (5). In the present case the formation of a dimeric associate **4** is probably impeded by steric effects associated with the *B*-mesityl group. The *o*-methyl groups would have substantial steric interactions with the cyclohexane moiety at C-6 (crystallographic numbering C(2) and C(18) for the two independent molecules, Fig. 1) as well as with the N-H hydrogen atom. A similar example of steric hindrance between mesityl *o*-methyl groups and the N-H hydrogen can be clearly seen in a model of a bicyclic pyroboronate with *B*-mesityl substituents (type **2**, Ar = 2,4,6-$(CH_3)_3C_6H_2$), and may be the reason that this type of compound is not formed. The steric hindrance is less restrictive with *B*-*o*-tolyl groups which do not prevent the formation of the generally favored pyroboronate **2**, as demonstrated by the examples **2***a–c*.

In the solid state structure of **3***c* (Fig. 2) the two independent molecules are connected in alternating linear chains extending along the *a* axis by intermolecular N—H···O hydrogen bonds (N(1)—H(1)···O(4)(1 + *x*, *y*, *z*), N(1A)—H(1A)···O(4)(1 + *x*, *y*, *z*), N(2)—H(25)···O(2), and N(2A)—H(25A)···O(2); H···O = 2.27, 2.09, 2.26, and 2.05 Å; N···O = 3.168(9), 3.021(11), 3.185(8), and 3.045(12) Å; N—H···O = 154, 171, 157, and 167°; respectively).

The six-membered BONCCO boronate rings in **3***c* have irregular, "semiplanar", C(1)/C(17) sofa conformations similar to the BONCCO ring systems in **9** (9), the BONCNO ring systems in **10** (4, 10), and to those in other six-membered cycloboronate rings (ref. 4, and references therein). In each of the two independent molecules, the disorder generates two different sofa conformations that have opposite chiralities at the asymmetric (presumably pyramidal) nitrogen atoms. This arrangement of the disordered portions of the rings allows for the formation of hydrogen bonds involving both disorder components, the hydrogen bonding parameters (above) actually being more favorable for the lower-occupancy moieties.

A partial double bond character of the O—B bonds resulting from O—B $pp(\pi)$ back-donation is in accord with the near planarity about the sp^2-hybridized boron atoms, as noted for many boronic acid esters. The bond angle sums at the trivalent boronate B atoms (357.8 and 357.6° (involving O(1) and O(3), respectively), 354.7 and 353.1° (involving O(1A) and O(3A), respectively)) suggest slight pyramidalization at B(1) and B(2), but it is highly probable that this is an artifact of the disorder. The differences between the two O—B bond lengths in each boronate moiety of **3***c*, 0.063(13) and 0.072(13) Å, are similar to those observed in the compounds of type **9** (9). The O—B bond from the alcoholate ligand is the shorter one in each case, probably as a consequence of a better $p(\pi)$ donor quality relative to that of the hydroxylamine ligand in **3***c* and the hydroxamate ligand in **9**.

The orientation of the mesityl rings with respect to the sp^2-boron coordination planes is roughly perpendicular, the angles between normals to the BO_2C and mesityl mean planes being 79.4 and 83.8° for the major, and 84.0 and 77.9° for the minor components at B(1) and B(2), respectively. The O-B-C-C torsion angles involving the ordered oxygen atoms O(2) and O(4) are all near 90° while those involving the disordered oxygen atoms (O(1), O(1A), O(3), and O(3A)) range from 57° to 75°. A similar, near perpendicular, orientation of the *B*-mesityl group has been found in the mesitylboronate **10***a* with a dihedral angle between normals to the aromatic ring and boron coordination mean planes of 87.2° (4). In a phosphorus analog of borazine with considerable aromatic character, $(MesBPC_6H_{11})_3$, the *B*-mesityl groups are also oriented perpendicular to the plane of the B_3P_3 ring (11). The steric hindrance that results from *ortho*-methyl groups presumably forces the aryl ring out of a resonance-favored coplanarity with the boronate ester group in these cases. The mean B—C(aryl) bond length in **3***c* (1.553 Å) does not differ significantly from that in the mesitylboronate **10***a* (1.560(2) Å) (4), and is slightly shorter than the mean B—C(aryl) bond length in $(MesBPC_6H_{11})_3$ (1.575(8) Å) (11).

The spiro-connected cyclohexane moieties at C(2) and C(18) in the two independent molecules of **3***c* have slightly distorted chair conformations with the boronate ester groups in equatorial

[5]Supplementary material mentioned in the text may be purchased from the Depository of Unpublished Data, Document Delivery, CISTI, National Research Council Canada, Ottawa, Canada K1A 0S2.

Tables of hydrogen atom coordinates and bond lengths and angles involving hydrogen atoms have also been deposited with the Cambridge Crystallographic Data Centre and can be obtained on request from The Director, Cambridge Crystallographic Data Centre, University Chemical Laboratory, 12 Union Road, Cambridge CB2 1EZ, U.K.

Can. J. Chem. Downloaded from www.nrcresearchpress.com by EESC ESCOLA DE ENGENHARIA on 09/08/12
For personal use only.

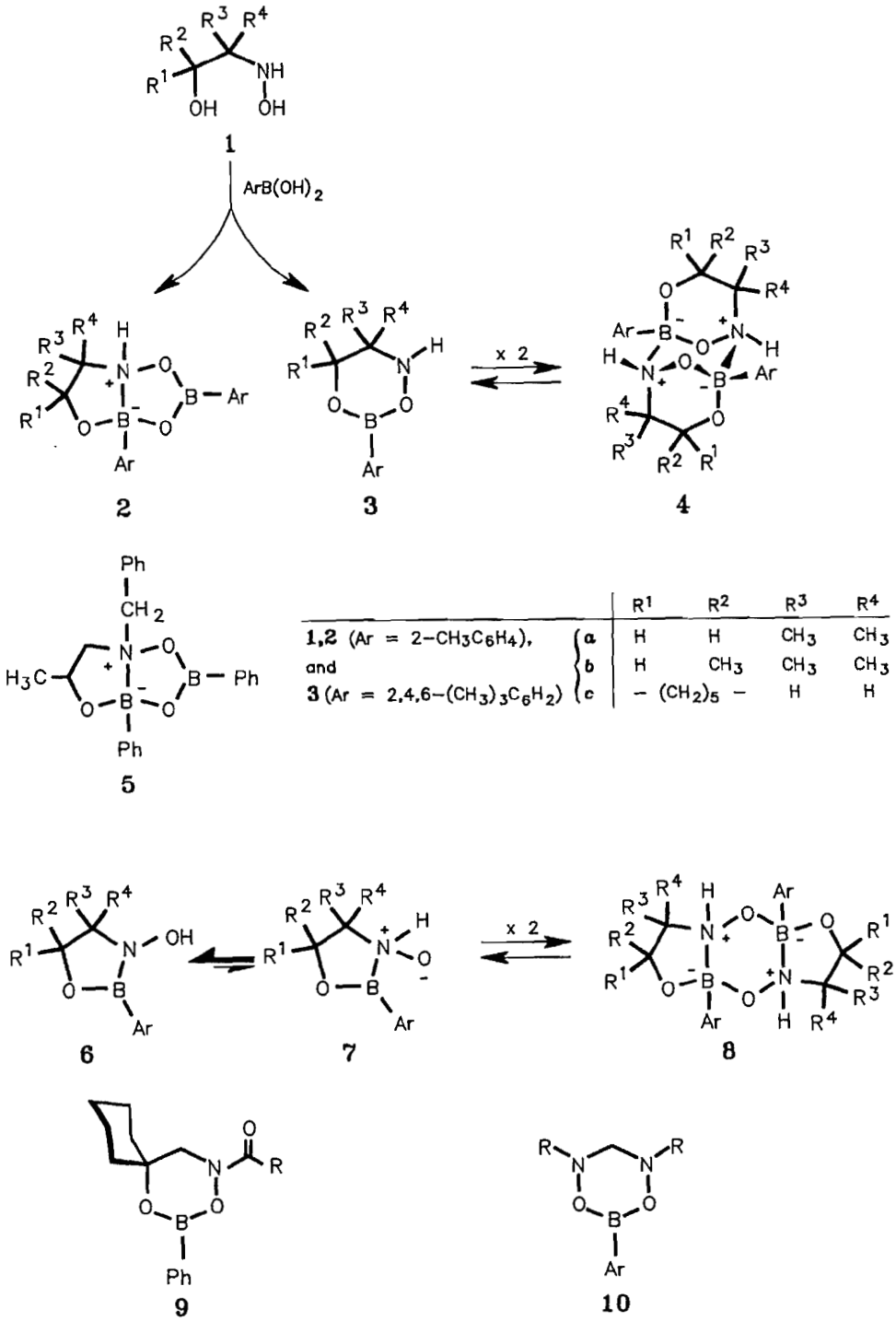

		R^1	R^2	R^3	R^4
1,2 (Ar = 2-$CH_3C_6H_4$), and **3** (Ar = 2,4,6-$(CH_3)_3C_6H_2$)	*a*	H	H	CH_3	CH_3
	b	H	CH_3	CH_3	CH_3
	c	$-(CH_2)_5-$		H	H

a R = $C(OH)(C_6H_5)_2$
b R = $C(OBF_2)(C_6H_4\text{-}4\text{-}OCH_3)_2$

a R = $C(CH_3)_2CN$, Ar = 2,4,6-$(CH_3)_3C_6H_2$
b R = $C(C_6H_5)CH_2NO_2$, Ar = C_6H_4-4-OCH_3

SCHEME 1

Can. J. Chem. Downloaded from www.nrcresearchpress.com by EESC ESCOLA DE ENGENHARIA on 09/08/12
For personal use only.

Can. J. Chem. Downloaded from www.nrcresearchpress.com by EESC ESCOLA DE ENGENHARIA on 09/08/12
For personal use only.

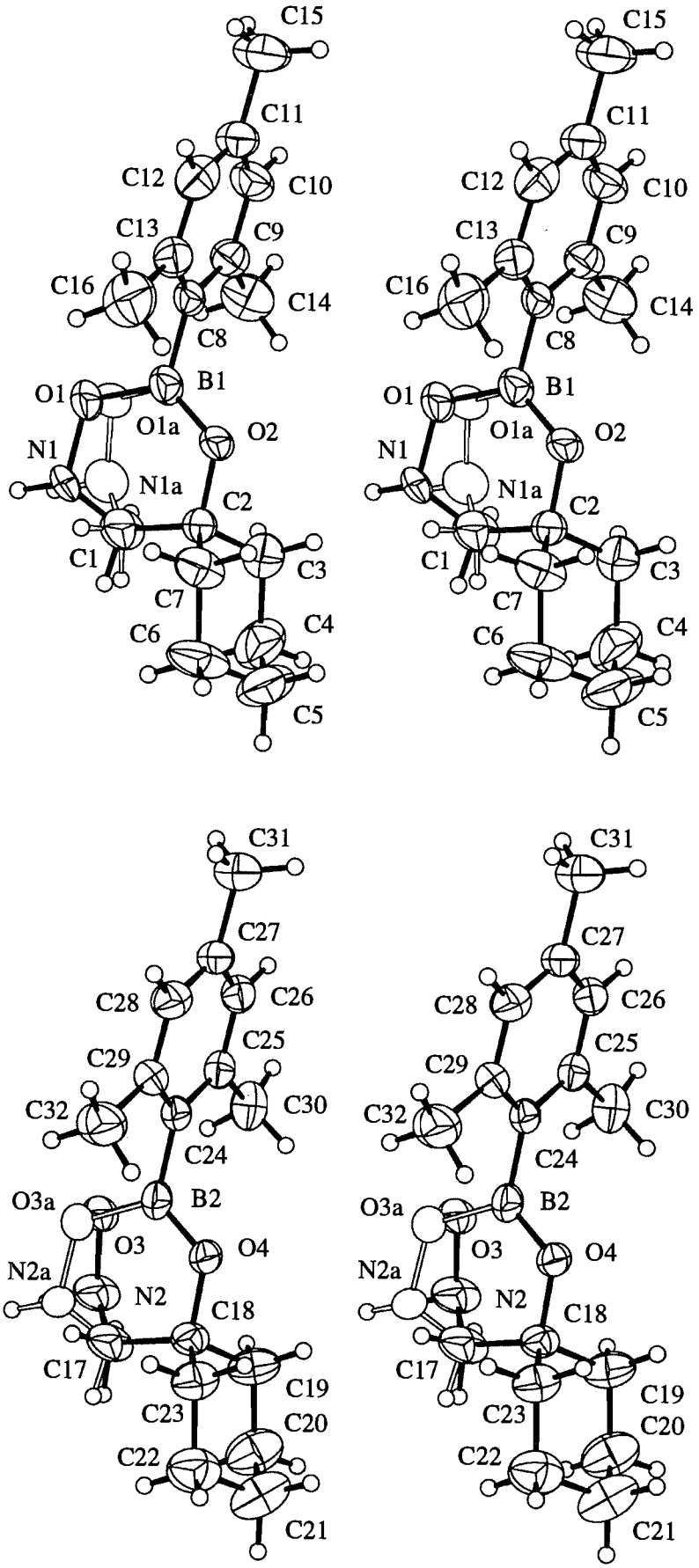

FIG. 1. Stereoview of the two independent molecules of **3***c*; 33% probability thermal ellipsoids are shown for the non-hydrogen atoms.

TABLE 4. Bond angles (deg) with estimated standard deviations

Atom	Atom	Atom	Angle	Atom	Atom	Atom	Angle
N(1)	O(1)	B(1)	114.9(7)	C(8)	C(9)	C(10)	120.0(5)
N(1A)	O(1A)	B(1)	117(1)	C(8)	C(9)	C(14)	120.2(5)
C(2)	O(2)	B(1)	123.5(4)	C(10)	C(9)	C(14)	119.8(5)
N(2)	O(3)	B(2)	114.7(6)	C(9)	C(10)	C(11)	123.0(5)
N(2A)	O(3A)	B(2)	118.2(9)	C(10)	C(11)	C(12)	117.5(5)
C(18)	O(4)	B(2)	123.1(4)	C(10)	C(11)	C(15)	122.6(6)
O(1)	N(1)	C(1)	112.4(6)	C(12)	C(11)	C(15)	120.0(7)
O(1A)	N(1A)	C(1)	112(1)	C(11)	C(12)	C(13)	121.6(5)
O(3)	N(2)	C(17)	110.4(6)	C(8)	C(13)	C(12)	120.1(5)
O(3A)	N(2A)	C(17)	113(1)	C(8)	C(13)	C(16)	120.7(5)
N(1)	C(1)	C(2)	114.3(6)	C(12)	C(13)	C(16)	119.1(6)
N(1A)	C(1)	C(2)	119.7(8)	N(2)	C(17)	C(18)	115.1(6)
O(2)	C(2)	C(1)	107.5(4)	N(2A)	C(17)	C(18)	118.4(8)
O(2)	C(2)	C(3)	106.8(4)	O(4)	C(18)	C(17)	106.6(4)
O(2)	C(2)	C(7)	107.2(4)	O(4)	C(18)	C(19)	106.2(4)
C(1)	C(2)	C(3)	111.0(5)	O(4)	C(18)	C(23)	106.7(4)
C(1)	C(2)	C(7)	112.8(5)	C(17)	C(18)	C(19)	115.4(5)
C(3)	C(2)	C(7)	111.3(4)	C(17)	C(18)	C(23)	111.3(5)
C(2)	C(3)	C(4)	112.2(5)	C(19)	C(18)	C(23)	110.1(4)
C(3)	C(4)	C(5)	109.8(6)	C(18)	C(19)	C(20)	112.2(5)
C(4)	C(5)	C(6)	110.0(6)	C(19)	C(20)	C(21)	112.1(5)
C(5)	C(6)	C(7)	111.0(5)	C(20)	C(21)	C(22)	110.3(5)
C(2)	C(7)	C(6)	111.7(4)	C(21)	C(22)	C(23)	110.1(5)
C(9)	C(8)	C(13)	117.9(4)	C(18)	C(23)	C(22)	112.5(4)
C(9)	C(8)	B(1)	121.2(5)	C(25)	C(24)	C(29)	118.3(4)
C(13)	C(8)	B(1)	120.9(5)	C(25)	C(24)	B(2)	121.9(5)
C(29)	C(24)	B(2)	119.8(5)	C(28)	C(29)	C(32)	119.3(5)
C(24)	C(25)	C(26)	120.4(4)	O(1)	B(1)	O(2)	121.0(6)
C(24)	C(25)	C(30)	120.2(4)	O(1)	B(1)	C(8)	116.5(6)
C(26)	C(25)	C(30)	119.3(5)	O(1A)	B(1)	O(2)	116.9(7)
C(25)	C(26)	C(27)	121.6(4)	O(1A)	B(1)	C(8)	117.5(7)
C(26)	C(27)	C(28)	118.4(4)	O(2)	B(1)	C(8)	120.3(5)
C(26)	C(27)	C(31)	121.6(5)	O(3)	B(2)	O(4)	120.8(5)
C(28)	C(27)	C(31)	120.0(5)	O(3)	B(2)	C(24)	117.1(5)
C(27)	C(28)	C(29)	121.3(4)	O(3A)	B(2)	O(4)	115.4(6)
C(24)	C(29)	C(28)	120.0(4)	O(3A)	B(2)	C(24)	118.0(6)
C(24)	C(29)	C(32)	120.6(4)	O(4)	B(2)	C(24)	119.7(4)

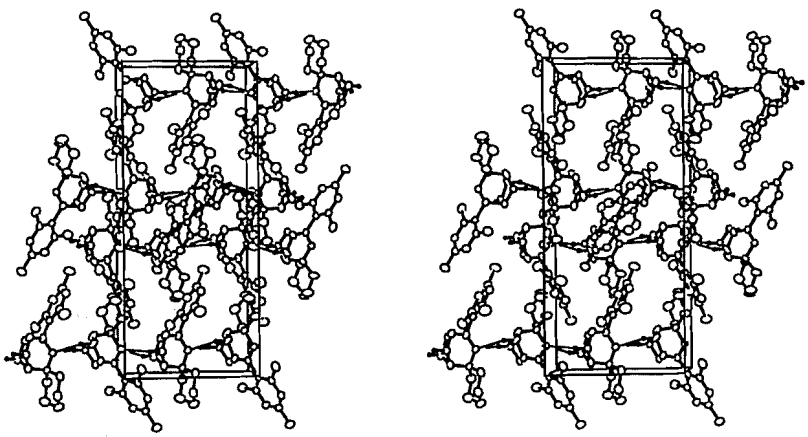

FIG. 2. Stereoview along the *c* axis of the packing arrangement and hydrogen bonding of **3***c*.

Can. J. Chem. Downloaded from www.nrcresearchpress.com by EESC ESCOLA DE ENGENHARIA on 09/08/12
For personal use only.

positions. This arrangement was noted for the related spiro compounds **9** (9).

The most obvious differences between the bond lengths of the *N*-unsubstituted and the *N*-acylated BONCCO rings of **3***c* and **9**, respectively, are those involving the nitrogen atoms. The N—O distance in **3***c* (mean 1.465 Å) is distinctly longer than those in **9***a* (1.401(1) Å) and **9***b* (1.402(3) Å). The intra-annular C—N bonds in **3***c* (mean 1.353 Å) appear to be considerably shorter than the corresponding bonds in **9***a* (1.448(2) Å) and **9***b* (1.440(4) Å) (9), but in this case imperfect modeling of the disorder (see Experimental) may be partially responsible even though some shortening is expected. The distances between the resolved, disordered, N and O atoms are almost certainly more realistic.

Acknowledgments

We thank the Natural Sciences and Engineering Research Council of Canada and the Fonds der Chemischen Industrie, Frankfurt am Main, for financial support. We are grateful to the Chemische Institute der Technischen Universität Braunschweig for running the ^{11}B nmr and mass spectra.

1. S.J. Rettig, J. Trotter, W. Kliegel, and H. Becker. Can. J. Chem. **54**, 3142 (1976).
2. W. Kliegel and H. Becker. Chem. Ber. **110**, 2090 (1977).
3. W. Kliegel, B. Enders, and H. Becker. Liebigs Ann. Chem. 1712 (1982).
4. W. Kleigel, G. Lubkowitz, S.J. Rettig, and J. Trotter. Can. J. Chem. **69**, 234 (1991).
5. W. Kliegel, G. Lubkowitz, S.J. Rettig, and J. Trotter. Can. J. Chem. **70**, 2809 (1992).
6. (*a*) H. Nöth and B. Wrackmeyer. Nuclear magnetic resonance spectroscopy of boron compounds. Springer-Verlag, Berlin. 1978; (*b*) B. Wrackmeyer. Annu. Rep. NMR Spectrosc. **20**, 61 (1988); (*c*) A. Siedle. Annu. Rep. NMR Spectrosc. **20**, 205 (1988).
7. W. Kliegel and H. Becker. Chem. Ber. **110**, 2067 (1977).
8. International Tables for X-Ray Crystallography. Vol. IV. Kynoch Press, Birmingham, U.K. (present distributor: Kluwer Academic Publishers, Dordrecht, The Netherlands). 1974. pp. 99–102 and 149.
9. W. Kliegel, L. Preu, U. Schumacher, S.J. Rettig, and J. Trotter. Can. J. Chem. **70**, 1176 (1992).
10. W. Kliegel, G. Lubkowitz, S.J. Rettig, and J. Trotter. Can. J. Chem. **69**, 1227 (1991).
11. H.V.R. Dias and P.P. Power. Angew. Chem. **99**, 1320 (1987).
12. W. Kliegel, G. Lubkowitz, S.J. Rettig, and J. Trotter. Can. J. Chem. **71**, 2129 (1993).

Can. J. Chem. Downloaded from www.nrcresearchpress.com by EESC ESCOLA DE ENGENHARIA on 09/08/12
For personal use only.

Unusual Weiss–Cook condensation of dimethyl 2,3-dioxobutanedioate and dimethyl 3-oxoglutarate[1]

GHISLAIN DESLONGCHAMPS,[2] DANIEL MINK, PAUL D. BOYLE, AND NINA SINGH
Department of Chemistry, University of New Brunswick, Fredericton, NB E3B 5A3, Canada

Received May 17, 1993

GHISLAIN DESLONGCHAMPS, DANIEL MINK, PAUL D. BOYLE, and NINA SINGH. Can. J. Chem. **72**, 1162 (1994).

The Weiss–Cook condensation of dimethyl 2,3-dioxobutanedioate with two equivalents of dimethyl 3-oxoglutarate in aqueous bicarbonate produces an "abnormal" product, pentamethyl *cis*-3-(carbomethoxymethyl)-3,7-dihydroxy-2-oxabicyclo-[3.3.0]oct-7-ene-1,4,5,6,8-pentacarboxylate **7**, whose structure has been determined by X-ray crystallography. Krapcho decarbomethoxylation (sodium chloride, aqueous dimethyl sulfoxide, 140°C) of this compound produces dimethyl *cis*-3,7-dioxobicyclo[3.3.0]octane-1,5-dicarboxylate **4** in quantitative yield. These results suggest that compound **7** may be the product of a kinetically controlled reaction pathway involving 4-hydroxypent-2-en-1-one intermediate **5**. Heating of **7** in dimethyl sulfoxide may have promoted thermodynamic equilibration to a Weiss–Cook product, which then decarbomethoxylated to produce **4**.

GHISLAIN DESLONGCHAMPS, DANIEL MINK, PAUL D. BOYLE et NINA SINGH. Can. J. Chem. **72**, 1162 (1994).

La condensation de Weiss–Cook du 2,3-dioxobutanedioate de diméthyle avec deux équivalents du 3-oxoglutarate de diméthyle effectuée dans une solution aqueuse de bicarbonate conduit à un produit «anormal», le *cis*-3-(carbométhoxyméthyl)-3,7-dihydroxy-2-oxabicyclo[3.3.0]oct-7-ène-1,4,5,6,8-pentacarboxylate de pentaméthyle, **7**, dont on a déterminé la structure par diffraction des rayons X. Soumis à une décarbométhoxylation de Krapcho (chlorure de sodium, diméthylsulfoxyde aqueux, 140°C), ce composé conduit au *cis*-3,7-dioxobicyclo[3.3.0]octane-1,5-dicarboxylate de diméthyle avec un rendement quantitatif. Ces résultats suggèrent que le composé **7** est probablement le produit d'une voie réactionnelle contrôlée d'une façon cinétique et impliquant la 4-hydroxypent-2-én-1-one **5** comme intermédiaire. Le chauffage du composé **7** dans le diméthylsulfoxyde a probablement provoqué un équilibre thermodynamique vers un produit de Weiss–Cook qui par une décarbométhoxylation conduit au produit **4**.

[Traduit par la Rédaction]

Introduction

The Weiss–Cook reaction, involving the condensation of two equivalents of 3-oxoglutarate with one equivalent of an α-dicarbonyl compound, has been widely used for the convergent synthesis of polyquinanes and polyquinenes (1). The general mechanism for this reaction is thought to involve a series of aldol condensations, dehydrations, and Michael reactions (2).

Our research group has been engaged in the design and synthesis of new abiotic receptors capable of selective binding of neutral organic targets via a tandem of complementary hydrogen-bonding and hydrophobic interactions. During preliminary work, a 1,5-difunctionalized 3,7-dioxobicyclo[3.3.0]-octane was sought that could be readily obtained via the Weiss–Cook reaction. In this paper, we wish to report an unusual Weiss–Cook condensation product between dimethyl 3-oxoglutarate **2** and dimethyl 2,3-dioxobutanedioate **1** and its conversion to the desired compound **4**.

Results and discussion

One of the starting materials for our receptor synthesis was dimethyl *cis*-3,7-dioxobicyclo[3.3.0]octane-1,5-dicarboxylate **4**. The synthesis of **4** has already been reported (3) and involves Weiss–Cook condensation (aqueous $NaHCO_3$) of one equivalent of α-dicarbonyl **1** with two equivalents of 3-oxoglutarate **2**, followed by Krapcho decarbomethoxylation (4) (NaCl, aqueous DMSO, 140°C) of the resulting hexaester **3** to produce bicyclic diester **4** (Scheme 1). Compound **1** was obtained by treating dihydroxytartrate with methanolic HCl.

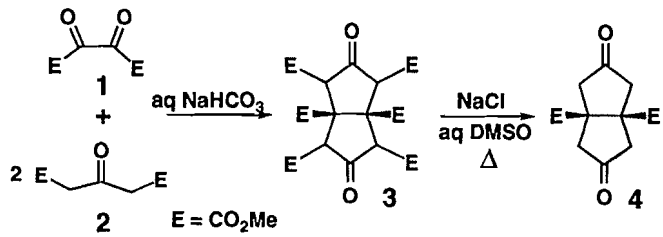

SCHEME 1

In an attempt to optimize the procedure,[3] we sought to pinpoint which step gave the poorest yield.

Work-up of the Weiss–Cook reaction had produced a syrupy product containing a crystalline material and was assumed to contain condensation product **3**. Trituration of the crude product with ether, followed by filtration, enabled the isolation of a white crystalline material in 26.2% overall yield (from dihydroxytartrate), thought to be condensation product **3**. The mother liquor was shown to contain unreacted **2**. The other reaction products were presumably hydrophilic enough to be lost during the extractive work-up.

The UV spectrum of the crystals suggested the presence of an enolized β-ketoester (λ_{max} = 247, ϵ = 14 900). The ^1H nmr spectrum gave support for an enol proton (δ 10.66) but also showed six nonequivalent methyl ester singlets, an alcohol (δ 6.17), and an AB quartet centered at δ 3.12. The nmr spectrum could not be correlated to any of the possible tautomers of **3**. At this point it was believed that the crystals were simply a by-product of the Weiss–Cook reaction. In fact, X-ray crystallographic analysis showed that the crystalline condensation

[1]Dedicated to Professor Pierre Deslongchamps on the occasion of his being awarded the 1994 R.U. Lemieux Award.

[2]Author to whom correspondence may be addressed. Telephone: (506) 453-4792. FAX: (506) 453-4599.

[3]The reported yield for the overall conversion of dihydroxytartrate to **4** was only 18% and, in our hands, we could reproducibly increase this yield to only 26%.

Can. J. Chem. Downloaded from www.nrcresearchpress.com by EESC ESCOLA DE ENGENHARIA on 09/08/12
For personal use only.

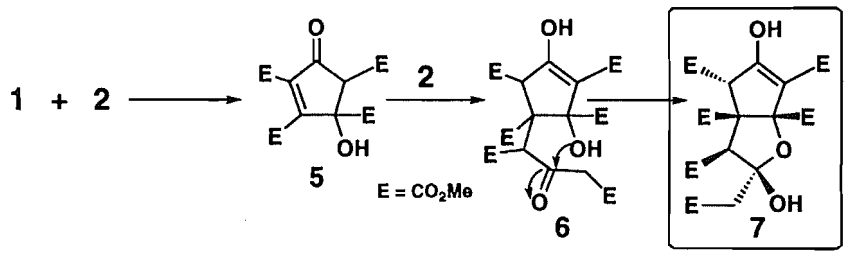

SCHEME 2

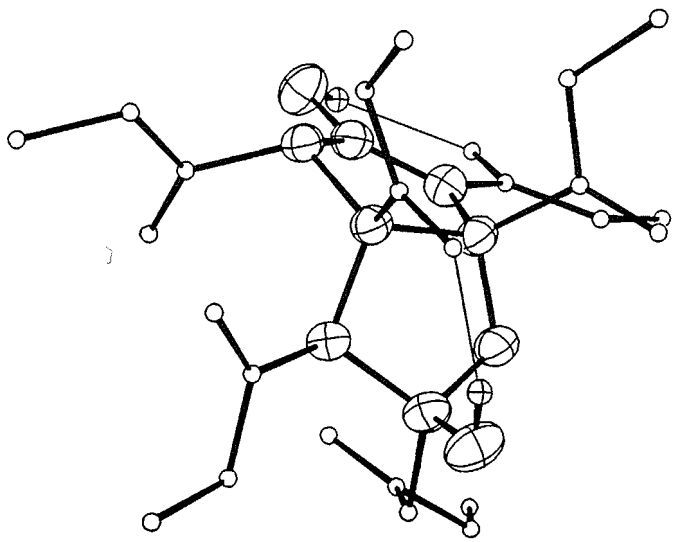

SCHEME 3. ORTEP diagram of compound **7**. Side-chain atoms are represented by spheres of arbitrarily small radii. Hydrogens attached to carbons were omitted for clarity.

product was not the anticipated compound **3** but, instead, compound **7** (Schemes 2 and 3).

This abnormal Weiss–Cook product would have most likely been produced via the intermediacy of the 4-hydroxycyclopent-2-en-1-one 1:1 adduct **5**. 4-Hydroxycyclopent-2-en-1-one derivatives have been suggested to be important intermediates in the Weiss–Cook condensation at both high and low pH (1*a*, 2*b*, 5). Michael addition of a second molecule of 3-oxoglutarate to intermediate **5** followed by intramolecular cyclization of the resulting 2:1 adduct **6** could have produced hemiketal **7**.

The isolation of compound **7** gives additional support to the reaction sequence proposed by Weiss and Cook (2*b*), which involved the formation of 4-hydroxycyclopent-2-en-1-ones as key intermediates. Interestingly, hemiketal **7** must arise from a different mechanism than that which generates the hemiketal in the 1:1 adduct of camphorquinone and 3-oxoglutarate (2*b*).[4,5]

[4]An alternate mechanism can be proposed which involves O-alkylation by the enol during the final Michael addition (instead of C-alkylation). Although the O-alkylation can be rationalized based on stereoelectronic principles (6), this mechanism can be disregarded since it later necessitates hydration of the resulting enol ether, a step that is less likely to occur in bicarbonate solution.

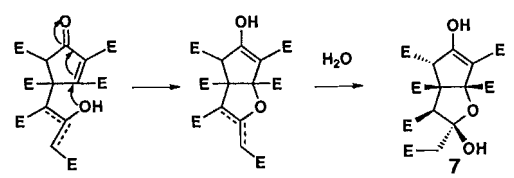

Could "abnormal" Weiss–Cook product 7 be in fact the true precursor to diketone 4?

To test this hypothesis, compound **7** was subjected to Krapcho's decarbomethoxylation conditions (NaCl, aqueous DMSO, 140°C, 4 h), which resulted in diketone **4** being isolated in quantitative yield! Since the overall yield for the conversion of dihydroxytartrate to diketone **4** was 26%, this result indicated that virtually *all* of diketone **4** had been produced via the intermediacy of compound **7**.

One must then assume that, under the Krapcho decarbomethoxylation conditions, compound **7** somehow underwent ring opening and recyclization to generate a bicyclo[3.3.0]octane carbocycle (such as **3**), which would have subsequently decarbomethoxylated to produce **4** (Scheme 4). There are many plausible pathways to the formation of **4** from **7** and we are only illustrating the simplest one. We have been unable to isolate intermediates such as hexaesters **8** and **3** from the crude decarbomethoxylation mixture. It is worth noting that decarbomethoxylation of two of the methyl esters in an intermediate such as **8** (i.e., asterisks on **8**) could not have preceded the ring closure or else the cyclization would have involved Michael addition of an unactivated ketone, in bicarbonate solution.

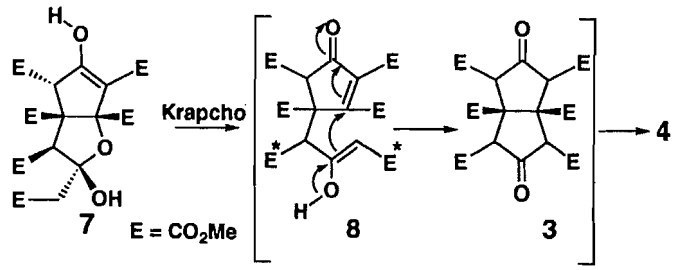

SCHEME 4

Weiss–Cook condensations are generally carried out under equilibration conditions such that the thermodynamically favored C-alkylated adduct (as in **3**) is the product obtained. It is reasonable to assume that the cyclization of precursor **6** (Scheme 2) to form hemiketal **7** was kinetically preferred over the elimination of the tertiary hydroxyl that would have led to hexaester **3**. In our particular case, the tertiary hydroxyl in compound **6** presumably does not undergo elimination as readily as one might expect because of the presence of an electron-withdrawing ester at the ring junction[6] and because of developing steric repulsion between adjacent ester groups. Elimination of

[5]Although of a different type, another interesting case of abnormal Weiss–Cook condensation was recently reported (7).

[6]Varying the electron density on the β-carbon does not seem to hamper the Michael addition itself (8).

Can. J. Chem. Downloaded from www.nrcresearchpress.com by EESC ESCOLA DE ENGENHARIA on 09/08/12
For personal use only.

the tertiary hydroxyl group in **6** (instead of hemiketal formation) would have set up one final Michael addition to produce a "normal" Weiss–Cook carbocycle. Upon heating, hemiketal **7** could have readily undergone ring opening and elimination to revert to an acyclic precursor such as **8**, allowing proper channeling to a thermodynamically more stable compound (such as **3**) that cleanly produced diketone **4** upon decarbomethoxylation.

Our findings add strong support to the 4-hydroxycyclopent-2-en-1-one pathway of the Weiss–Cook condensation since compound **7** can be readily rationalized as the kinetic product obtained along this mechanistic route. The conversion of **7** into **4** can also be rationalized by a thermodynamic equilibration of **7** followed by decarbomethoxylation of the resulting bicyclo[3.3.0]octane carbocycle.

Experimental

The nmr spectra were recorded on a Varian Unity-400 spectrometer with $CDCl_3$ as solvent. High-resolution mass spectra (EI) were run on a Kratos MS50 mass spectrometer.

Abnormal Weiss–Cook adduct 6

The crude Weiss–Cook condensation mixture was prepared as described (3) using 100 g (0.44 mol) of disodium dihydroxytartrate. Trituration with ether and filtration afforded 56.5 g (26.2%) of compound **6** as white crystals: mp 175–177°C (from CH_3OH); uv (EtOH): λ_{max} = 247, ϵ = 14 900; ir ($CHCl_3$): 3600, 2960, 1755, 1690, 1455, 1350 cm^{-1}; ^1H nmr δ: 10.66 (br s, 1H), 6.17 (s, 1H), 5.09 (s, 1H), 4.69 (s, 1H), 3.85 (s, 3H), 3.731 (s, 3H), 3.726 (s, 3H), 3.71 (s, 3H), 3.70 (s, 3H), 3.53 (s, 3H), 3.18 (A of AB q, J = 15.4, 1H), 3.07 (B of AB q, J = 15.4, 1H), minor enolic form also visible at 10.5, 4.87, 3.65, 3.64, 3.61, and 3.59; ^{13}C nmr δ: 174.28, 171.07, 170.51, 169.22, 168.29, 167.95, 167.70, 106.09, 103.67, 94.06, 64.70, 55.65, 54.26, 53.32, 52.89, 52.66, 52.04, 51.92, 51.51, 41.67, minor enolic form also visible at 170.96, 168.17, 65.02, 54.64, 52.39, 51.73. Exact Mass calcd. for $C_{20}H_{24}O_{15}$ ($M^+ - H_2O$): 486.1009; found: 486.1084.

Dimethyl cis-3,7-dioxobicyclo[3.3.0]octane-1,5-dicarboxylate 4 from compound 7

A solution of **7** (56.5 g, 0.112 mol), NaCl (6.86 g, 0.118 mol), and water (25.2 mL) in DMSO (95 mL) was heated at 140°C for 4 h. After cooling to room temperature, water (150 mL) was added and the mixture was extracted with $CHCl_3$ (7 × 100 mL), washed with saturated $NaHCO_3$ solution (4 × 50 mL) and water (3 × 50 mL), and dried over Na_2SO_4. Evaporation of solvents afforded 30.0 g (quantitative) of diketone **4**, which crystallized upon standing.

X-ray crystallography of compound 7

The structural analysis of **7** was uneventful. Compound **7** shows interesting C-H···O hydrogen bonding. An in-depth analysis of this structure will be the subject of a forthcoming paper that will include a full complement of crystallographic details.[7]

Supplementary material available

400-MHz ^1H, ^{13}C, and HETCOR nmr spectra of compound **7** as well as crystallographic data have been deposited.[8]

Acknowledgements

We thank the Natural Sciences and Engineering Research Council of Canada, the University of New Brunswick, and the Maritime Provinces Higher Education Commission for financial support. N.S. wishes to thank NSERC for an undergraduate summer research fellowship. We also wish to thank Professor Zdenek Valenta for helpful discussions.

1. (*a*) X. Fu and J.M. Cook. Aldrichimica Acta, **25**, 43 (1992); (*b*) A.K. Gupta, X. Fu, J.P. Snyder, and J.M. Cook. Tetrahedron, **47**, 3665 (1991).
2. (*a*) R. Mitschka, J. Oehldrich, K. Takahashi, J.M. Cook, U. Weiss, and J.V. Silverton. Tetrahedron, **37**, 4521 (1981); (*b*) S. Yang-Lan, M. Mueller-Johnson, J. Oehldrich, D. Wichman, U. Weiss, and J.M. Cook. J. Org. Chem. **41**, 4053 (1976).
3. P. Camps and M. Figueredo. Can. J. Chem. **62**, 1184 (1984).
4. A.P. Krapcho and A.J. Lovey. Tetrahedron Lett. 957 (1972).
5. (*a*) G. Kubiak, J.M. Cook, and U. Weiss. J. Org. Chem. **49**, 561 (1984); (*b*) S.H. Bertz, W.O. Adams, and J.V. Silverton. J. Org. Chem. **46**, 2828 (1981); (*c*) O. Campos and J.M. Cook. J. Heterocycl. Chem. **14**, 711 (1977).
6. J.E. Baldwin and L.I. Kruse. J. Chem. Soc. Chem. Commun. 233 (1977).
7. L.A. Paquette, G.E. Underliner, and J.C. Gallucci. J. Org. Chem. **57**, 3512 (1992).
8. G. Kubiak and J.M. Cook. Tetrahedron Lett. 2163 (1985).

[7]P.D. Boyle and G. Deslongchamps. Manuscript in preparation.

[8]These data can be purchased from: The Depository of Unpublished Data, Document Delivery, CISTI, National Research Council Canada, Ottawa, ON K1A 0S2, Canada.

The crystallographic data have also been deposited with the Cambridge Crystallographic Data Centre, and can be obtained on request from The Director, Cambridge Crystallographic Data Centre, University Chemical Laboratory, 12 Union Road, Cambridge, CB2 1EZ, U.K.

Can. J. Chem. Downloaded from www.nrcresearchpress.com by EESC ESCOLA DE ENGENHARIA on 09/08/12
For personal use only.

Studies on the interaction of selenite and selenium with sulphur donors. Part 1. 2-Mercaptoethanol[1]

W. Amaratunga, O. Chaudry, and J. Milne[2]

Ottawa Carleton Chemistry Institute, Department of Chemistry, University of Ottawa, Ottawa, ON K1N 6N5, Canada

Received August 12, 1993

W. Amaratunga, O. Chaudry, and J. Milne. Can. J. Chem. **72**, 1165 (1994).

Raman spectroscopy and proton and ^{77}Se NMR have been used to show that selenous acid reacts with 2-mercaptoethanol (HOC_2H_4SH), according to Ganther's reaction (H.E. Ganther, Biochemistry, **7**, 2898 (1968)).

$$H_2SeO_3 + 4HOC_2H_4SH \rightarrow HOC_2H_4SSC_2H_4OH + HOC_2H_4SSeSC_2H_4OH + 3H_2O$$

The bis(hydroxyethylthio)selenide decomposes readily in strongly acidic and moderately basic solution to selenium and disulfide,

$$HOC_2H_4SSeSC_2H_4OH \rightarrow Se + HOC_2H_4SSC_2H_4OH$$

Selenium dissolves in excess hydroxyethylmercaptide to give the catenated anion, $HOC_2H_4SSe^-$

$$HOC_2H_4S^- + Se = HOC_2H_4SSe^-$$

Air oxidation of this equilibrium mixture yields disulfide and selenium. Formation of the hydroxyethylthioselenide is endothermic ($\Delta H = 0.66 \pm 0.02$ kJ mol^{-1}).

W. Amaratunga, O. Chaudry et J. Milne. Can. J. Chem. **72**, 1165 (1994).

On a utilisé la spectroscopie Raman el la rmn du proton et du ^{77}Se pour montrer que l'acide sélénieux réagit avec le 2-mercaptoéthanol ($HOCH_2.CH_2SH$) selon la réaction de Ganther (H.E. Ganther, Biochemistry, **7**, 2898 (1968)).

$$H_2SeO_3 + 4HOC_2H_4SH \rightarrow HOC_2H_4SSC_2H_4OH + HOC_2H_4SSeSC_2H_4OH + 3H_2O$$

Le bis(hydroxyéthylthio)séléniure se décompose facilement en milieu acide fort et en solution basique modérée pour donner du sélénium et du disulfure,

$$HOC_2H_4SSeSC_2H_4OH \rightarrow Se + HOC_2H_4SSC_2H_4OH$$

Le sélénium se dissout dans l'excès d'hydroxyéthylmercapture pour donner le caténo-anion, $HOC_2H_4SSe^-$

$$HOC_2H_4S^- + Se = HOC_2H_4SSe^-$$

Une oxydation à l'air de ce mélange à l'équilibre fournit le disulfure et du sélénium. La formation de l'hydroxyéthylthiosélénure est endothermique ($\Delta H = 0{,}66 \pm 0{,}02$ kJ mol^{-1}).

[Traduit par la Rédaction]

Introduction

Thiols react with selenous acid generally, according to reaction [1]

[1] $H_2SeO_3 + 4\ RSH \rightarrow RSSeSR + RSSR + 3H_2O$

Bis(alkythio)selenides exhibit variable stability depending upon pH and the concentration of any excess RSH present (2, 3). The decomposition reaction has been shown to yield elemental selenium and disulfide generally (1*b*),

[2] $RSSeSR \rightarrow RSSR + Se$

although exceptions have been reported (4, 5). Reactions [1] and [2] combined are the basis of a turbidimetric method of analysis for selenium, using 2-mercaptoethanol (3). Excess 2-mercaptoethanol was found to cause precipitated selenium to redissolve and this was attributed to the formation of a zero valent selenium complex with the ligand, having the formula $Se(HOC_2H_4SH)_6$.

Neither bis(hydroxyethylthio)selenide nor the zero valent selenium complex with 2-mercaptoethanol have been characterized and, as part of our continuing studies on Se(II) species (6), we initiated a study of the interaction of 2-mercaptoethanol and selenous acid.

Experimental

Selenium dioxide (Aldrich) was analyzed by potentiometric titration and found to be 91.3% SeO_2 (8.7% H_2O). The chemical was used directly, allowing for this analysis. 2-Mercaptoethanol (BDH) was analyzed iodometrically (7),

[3] $2HOC_2H_4SH + I_3^- \rightarrow HOC_2H_4SSC_2H_4OH + 2HI + I^-$

and found to be 98.8% pure in agreement with the proton NMR spectrum, which showed the presence of a trace of disulfide. Oxygen-free distilled water was used as a solvent for all reactions. Solutions of the disulphide for spectroscopic studies were prepared at ambient temper-

[1]This paper is dedicated to the memory of a valued colleague, Professor J.L. Roustan.

[2]Author to whom correspondence should be addressed.

Can. J. Chem. Downloaded from www.nrcresearchpress.com by ESC ESCOLA DE ENGENHARIA on 09/08/12
For personal use only.

Can. J. Chem. Downloaded from www.nrcresearchpress.com by EESC ESCOLA DE ENGENHARIA on 09/08/12
For personal use only.

ature by reactions [3] as well as by using air oxidation of basic solutions of the thiol and hydrogen peroxide oxidation. Bis(hydroxyethylthio)selenide was prepared by multiple extraction of the insoluble yellow oil produced by reaction [1]. Disulfide is more soluble in water than bis(hydroxyethylthio)selenide and may be extracted using water adjusted to pH 5.0. In a typical preparation, 3.9 g of SeO_2 (0.036 mol) were dissolved in 10 mL distilled water and 10 mL of 2-mercaptoethanol (0.14 mol) were added dropwise with stirring and cooling. After a few minutes a yellow oil settled from the solution. The oil mixture of disulfide and bis(hydroxyethylthio)selenide of 9 mL volume, was extracted 15 times with 2.0 mL portions of dilute HCl (pH = 5.0) and then pumped free of water. Bis(hydroxyethylthio)selenide recovered (0.5 mL; 6% yield) was free of disulfide as shown by the absence of a proton signal at 2.5 ppm ($CDCl_3$). The product was found to be stable to laser light at 647.1 nm but subject to decomposition at basic pH, in the presence of excess thiol or in strongly acidic solutions. Similar findings regarding the stability of bis(thio)selenides have been reported previously (2, 3). Attempts to purify bis(hydroxyethylthio)-selenide by crystallization, distillation, and chromatographic methods failed.

Raman spectra were recorded, using a Jobin-Yvon Ramanor HG2 monochromator with a Princeton Applied Instruments photon counter. The spectra were excited with a Krypton ion laser operating at 647.1 nm. Slits were fixed at 1600 μ, giving a resolution of 6 cm^{-1} at 1000 cm^{-1}.

The ^{77}Se NMR spectra were recorded using a Bruker AMX 500 spectrometer, operating at 95.47 MHz, with a 90° tip angle and a 1 s pulse delay. Proton spectra were recorded on both Varian T60 and Gemini 200 machines. ^{13}C NMR spectra were recorded on the Gemini 200 machine. The chemical shifts for H_2O solutions were measured unlocked by sample replacement. Field drift was found to be within the accuracy of the quoted chemical shifts over the time span of the experiments. In the case of sample No. 10, Table 2, 10% D_2O by volume was added as lock and the H_2O signal at 4.8 ppm was suppressed. All sample concentrations were in the molar range. The proton chemical shifts are referred to TMS. The ^{77}Se chemical shifts are referenced to pure dimethyl selenium via an external secondary standard of saturated H_2SeO_3 in H_2O (8). The reference for ^{13}C NMR was internal tetramethylsilane. The mass spectrum was measured with VG 7070E spectrometer. Equilibrium constants were determined by gravimetry.

Results and discussion

Bis(hydroxyethylthio)selenide formation

Raman spectroscopy

The Raman spectra of 2-mercaptoethanol, the bis(hydroxyethylthio)selenide, the disulfide formed by oxidation of mercaptoethanol, and the products of the reaction of a 4:1 2-mercaptoethanol/selenous acid mixture are given in Fig. 1 and the observed frequencies up to 1000 cm^{-1} are given in Table 1. The strongest band observed for 2-mercaptoethanol is the CS stretching mode at 662 cm^{-1}. This band shifts to lower frequency by 20 cm^{-1} on oxidation to the disulphide (reaction [3]) and a stronger band appears at 512 cm^{-1}. The frequency and intensity of this peak supports its assignment to the SS stretching mode. The SS stretching frequency for S_2Cl_2 and S_2Br_2 appear at 540 and 529 cm^{-1}, respectively (9). The insoluble yellow oil produced from a 4:1 2-mercaptoethanol/selenous acid mixture in water gives a Raman spectrum consistent with the reaction.

$$[4]\quad H_2SeO_3 + 4HOC_2H_4SH \rightarrow HOC_2H_4SSC_2H_4OH + HOC_2H_4SSeSC_2H_4OH + 3H_2O$$

The spectrum has three characteristic bands at 512, 642, 820 cm^{-1} due to disulfide and seven bands due to bis(hydroxyethylthio)selenide, the most characteristic of which is the symmetric stretching mode of the —SSeS— moiety in the molecule, arising at 399 cm^{-1}. The spectrum of pure bis(hydroxyethylthio)selenide exhibits this strong band at 399 cm^{-1} and the sum of the spectra of the disulfide and the selenide accounts for all the bands in the 4:1 HOC_2H_4SH/H_2SeO_3 mixture. No evidence for the formation of thiosulfonate, as observed for some sterically hindered thiols (4), was found. The assignments of the observed peaks to the two species formed in the mixture is given in Table 1. The nearest analogous structural unit to that of the angular —SSeS— moiety for which Raman spectra are reported is the $SeCl_2$ molecule (10). In this case the symmetric and asymmetric stretching modes are found at 412 and 381 cm^{-1}, which supports the assignment of these modes at 399 and 373 cm^{-1} in the bis(hydroxyethylthio)selenide.

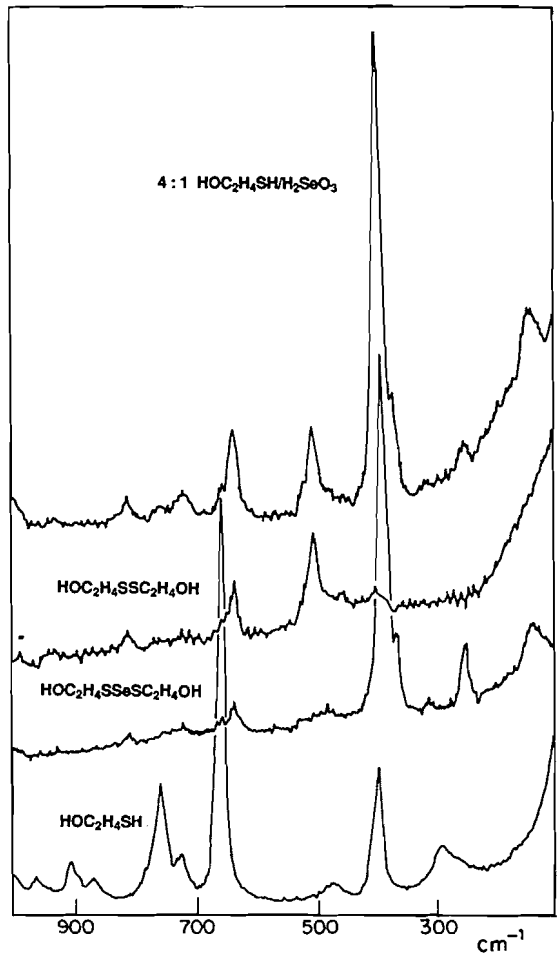

FIG. 1. Raman spectra of HOC_2H_4SH, $HOC_2H_4SSeSC_2H_4OH$, $HOC_2H_4SSC_2H_4OH$ and 4:1 molar ratio aqueous HOC_2H_4SH/H_2SeO_3.

The pale yellow aqueous supernatant in the 4:1 2-mercaptoethanol/selenous acid mixture also exhibited the 642, 512, and 399 cm^{-1} bands showing the presence of the —SS— and —SSeS— species. However, the SSeS band at 399 cm^{-1} was only three times the intensity of the SS stretching band, compared to six times, in the spectrum of the oil, indicating that the —SSeS— species was relatively more soluble in the oil than in the aqueous phase.

Mass spectrometry

The mass spectrum of pure bis(hydroxyethylthio)selenide

TABLE 1. Raman frequencies for neat HOC_2H_4SH, 1.0 M $HOC_2H_4SSC_2H_4OH$ in water, neat $HOC_2H_4SSeSC_2H_4OH$, and the oil produced from a 4:1 HOC_2H_4SH/H_2SeO_3 molar mixture in water

Neat HOC_2H_4SH	Neat $HOC_2H_4SSeSC_2H_4OH$	1.0 M $HOC_2H_4SSC_2H_4OH$	4:1 mol ratio HOC_2H_4SH/H_2SeO_3	Origin[a]
—	147(2, br)	—	145(2)	RSSeSR[b]
—	256(2)	—	258(1)	RSSeSR
265(1)	—	—	—	—
290(1)	—	—	—	—
—	372(2)(ν_{SSe}, a)	—	373(1, sh)	RSSeSR
—	396(10)(ν_{SSe}, s)	—	399(10)	RSSeSR and Trace RSSR?
400(3)	—	—	—	—
—	—	405(2)	—	—
—	—	462(1)	462(0)	RSSR
478(1)	—	—	—	—
—	480(0, br)	—	—	—
—	—	512(10)(ν_{SS})	512(2)	RSSR
—	641(1)(ν_{CS})	642(6)(ν_{CS})	642(2)	RSSeSR and RSSR
—	661(0)	662(0)	663(0, sh)	RSSR and RSSeSR
662(10)(ν_{CS})	—	—	—	—
—	725(0)	—	729(1)	RSSeSR
726(1)	—	—	—	—
761(3)	—	—	—	—
—	762(0)	—	762(0)	RSSeSR
—	818(0)	820(1)	820(1)	RSSR
870(1)	—	—	—	—
908(1)	—	—	—	—
965(1)	—	—	—	—

[a]Origin of peaks in the spectrum of the 4:1 HOC_2H_4SH/H_2SeO_3 solution.
[b]R = HOC_2H_4.

TABLE 2. Proton NMR of HOC_2H_4SH, $HOC_2H_4S^-$, $HOC_2H_4SSC_2H_4OH$, and $HOC_2H_4SSeSC_2H_4OH$

Sample no.	Species	Solvent	Chemical shifts (ppm)[a] δ_1	δ_2	δ_3	δ_4	J_{23} (Hz)[a]
1	HOC_2H_4SH[b]	neat	4.90	3.93	2.87	1.89	6.5
2	HOC_2H_4SH[c]	$CDCl_3$	2.95	3.72	2.68	1.48	6.1
3	HOC_2H_4SH	H_2O(1.0 M)	[d]	3.85	2.80	1.93	6.4
4	$HOC_2H_4S^-$	H_2O(1.0 M)	[d]	3.69	2.61	—	8.0
5	$(HOC_2H_4S)_2$[e]	H_2O(1.0 M)	[d]	4.1	3.1	—	6.5
6	$(HOC_2H_4S)_2$	$CDCl_3$	2.5	3.9	2.9	—	5.9
7	$(HOC_2H_4S)_2Se$	$CDCl_3$	3.3	3.96	3.20	—	5.8
8	$(HOC_2H_4S)_2Se$	Oil[f]	5.0	4.21	3.49	—	6.2
	and $(HOC_2H_4S)_2$			4.11	3.18	—	6.2
9	$(HOC_2H_4S)_2Se$	sat'd in H_2O	[d]	4.1	3.4	—	6.0
	and $(HOC_2H_4S)_2$			4.0	3.1	—	6.1
10	$HOC_2H_4SSe^-$	H_2O(c_{RS^-} = 1.0 M)	[d]	3.90	2.95	—	—
	and $HOC_2H_4S^-$			3.62	2.65	—	7.6

[a]δ_1: H on O; δ_2: H on C bonded to O; δ_3: H on C bonded to S; δ_4: H on S.
[b]J_{12} = 5.5 Hz; J_{34} = 8.1 Hz.
[c]J_{12} not observed; J_{34} = 8.4 Hz.
[d]Rapid exchange with solvent.
[e]HOC_2H_4SH oxidized by SeO_2 (at pH = 1.0), I_2, or H_2O_2.
[f]Insoluble yellow oil layer from 4:1 HOC_2H_4SH/H_2SeO_3 mixture.

exhibits a five line group of peaks clustered around mass 234, which is the mass of the selenide with ^{80}Se, the most abundant isotope. The five lines are the highest mass lines in the spectrum and have, in increasing order of mass, the intensities 8.5(230), 6(231), 21(232), 42.5(234), and 10(236) (mass numbers in parentheses). This is the order of intensity expected for the masses of the selenides formed with the distribution of isotopes in natural abundance. In addition, strong peaks are observed for the fragments: C_2H_3 (27/35); CH_2OH (31/50); CHS (45/100); C_2H_3S (59/74); SC_2H_4OH (77/20); CSe (92/21); SeS (112/18); $(HOC_2H_4)_2S$ (154/13); $(CH_2S)_2Se$ (172/30).

NMR spectroscopy

The proton chemical shifts and coupling constants for HOC_2H_4SH, $HOC_2H_4S^-$, $HOC_2H_4SSC_2H_4OH$, $HOC_2H_4SSeSC_2H_4OH$, and $HOC_2H_4SSe^-$ are given in Table 2. The proton NMR spectrum of pure mercaptoethanol (Sample No. 1) consists of four signals, in order of increasing shielding, 4.90

Can. J. Chem. Downloaded from www.nrcresearchpress.com by EESC ESCOLA DE ENGENHARIA on 09/08/12
For personal use only.

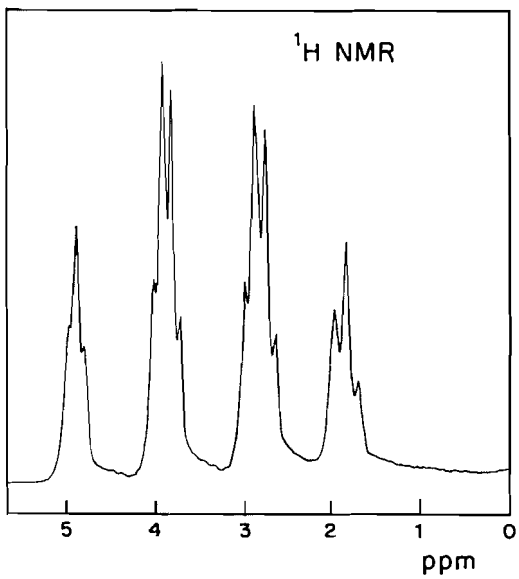

FIG. 2. Proton NMR spectrum of neat HOC_2H_4SH.

(H on O), 3.93 (H on C bound to O), 2.87 (H on C bound to S), and 1.89 (H on S) with relative intensities of 1:2:2:1 respectively, as shown in Fig. 2. Only three-bond couplings are apparent in the spectrum with the hydrogen on carbon signals, appearing as overlapped triplets, which resemble quartets. The chemical shifts for hydrogen on carbon and hydrogen on sulfur as well as the coupling constant for the two types of protons on carbon are similar for 2-mercaptoethanol in aqueous solution but coupling with protons on O and S is eliminated due to exchange of these protons with solvent. The spectrum of 2-mercaptoethanol dissolved in $CDCl_3$ shows hydrogen on carbon and hydrogen on sulfur resonances all slightly more shielded than for the aqueous solutions but the hydrogen on oxygen resonance moves 2 ppm upfield with the breakdown, in $CDCl_3$, of the relatively strong hydrogen bonding of H_2O and HOC_2H_4SH.

Deprotonation of 2-mercaptoethanol gives the mercaptide ion, $HOC_2H_4S^-$ ($pK_a(HOC_2H_4SH)$ = 9.61 (11)). The NMR spectrum exhibits no characteristic hydrogen on sulfur resonance and the hydrogen on carbon signals (1:1 relative intensities) are more shielded than in the parent acid, due to greater negative charge on these protons. The proton NMR spectrum of solutions of 2-mercaptoethanol oxidized with SeO_2 (weakly basic conditions), I_3^- and H_2O_2 with oxidant/HOC_2H_4SH stoichiometries of 1:4, 1:2, and 1:2 respectively, do not show a signal, corresponding to hydrogen bound to sulfur and oxidation to the disulfide is complete via reactions [3], [5], and [6].

[5] $H_2O_2 + 2HOC_2H_4SH \rightarrow HOC_2H_4SSC_2H_4OH = 2H_20$

[6] $H_2SeO_3 + 4HOC_2H_4SH \rightarrow 2HOC_2H_4SSC_2H_4OH + Se + 3H_2O$

Reaction [6] is the basis of a turbidimetric analysis for selenium(IV) (3). The hydrogen on carbon chemical shifts of the disulfide (1:1 relative intensities) are less shielded than those of HOC_2H_4SH and $HOC_2H_4S^-$, reflecting the greater degree of oxidation of the system.

Under weakly acid conditions (pH < 7), 4:1 mixtures of 2-mercaptoethanol and selenous acid do not yield elemental selenium (reaction [6]) but proceed according to reaction [4]. At the concentrations used in this work aqueous and oil layers were formed and the proton NMR spectra of both layers showed four triplets, two of which correspond, in chemical shifts and J_{23} coupling constant, to the spectrum of the disulfide and the remaining two of which must be due to the bis(hydroxyethylthio)selenide, as shown in Table 2. The relative intensities of the disulfide and selenide signals in the aqueous layer show that the disulfide is more soluble in water than the selenide and this is the basis of the method isolation of the selenide. The hydrogens on carbon next to sulfur bound to selenium are deshielded with respect to the comparable hydrogens of other species studied in the same solvent, by the presence of selenium bound to sulphur, which is the reverse of what might be expected, if Se is considered to be more metallic than S.

The ^{77}Se NMR spectrum of bis(hydroxyethylthio)selenide in acetone exhibits a chemical shift of 691.1 ppm. In the oil, which is a mixture of selenide and sulfide, containing a small amount of water, the shift is 690.5 ppm and in aqueous 4:1 HOC_2H_4SH/H_2SeO_3 solutions, 684.5 ppm. All signals are narrow ($w_{1/2} \sim$ 0.5 ppm.) These peaks lie at the high end of the chemical shift range for RSSeSR species (2). No coupling to the methylene protons was observed. The ^{13}C NMR spectrum of the bis(thio)selenide dissolved in chloroform exhibits only two peaks at δ = 41.2 ppm (carbon bound to sulfur) and 60.5 ppm (carbon bound to oxygen). No ^{77}Se–^{13}C coupling was observed probably because ^2J(SeC) is small compared to the baseline width of the 41.2 ppm line (30 Hz) and low relative intensity of the expected doublet. Two bond coupling in the CCSe chain of alkyl selenides is of the order of 12 Hz (12) and, if coupling over the CSSe chain were comparable, it would not be observed.

According to ^{77}Se NMR, the addition of base to solutions of the bis(hydroxyethylthio)selenide results in complete decomposition to selenium and disulfide.

[7] $HOC_2H_4SSeSC_2H_4OH \rightarrow HOC_2H_4SSC_2H_4OH + Se$

Excess base causes disproportionation of Se, according to

[8] $(2n + 1)Se + 6OH- = 2Se_n^{2-} + SeO_3^{2-} + 3H_2O$

The ^{77}Se NMR spectrum of a 4:1 $Na[HOC_2H_4S]/H_2SeO_3$ solution ($c(Na[HOC_2H_4S]$ = 2.83 M) shows signals at 1273 and –461 ppm due to the presence of SeO_3^{2-} ($\delta(Me_2Se)$ = 1272.6 ppm (8)) and Se^{2-} ($\delta(Me_2Se)$ = –435 ppm in ethylenediamine (13)). No signals due to polyselenides were observed in this solution and further work will be required to clarify the exact stoichiometry of this reaction.

Hydroxyethylthioselenide ion, $HOC_2H_4SSe^-$

The dissolution of elemental selenium in a solution of hydroxyethylmercaptide produces a deep brown coloured solution. The colour has been attributed to the formation of a zero valent selenium complex of the type $Se(HOC_2H_4SH)_6$ (3). It is also possible that disproportionation, according to reaction [8], could be the cause of the Se solubility and colour formation but reaction [8] only becomes extensive at hydroxide ion concentrations above 1 M (14). Hydroxide ion concentrations in these experiments and in previous work (3) did not exceed 0.01 M. In view of the tendency of chalcogen species to catenate, a likely cause of the selenium solubility in mercaptide solutions is the reaction,

Can. J. Chem. Downloaded from www.nrcresearchpress.com by EESC ESCOLA DE ENGENHARIA on 09/08/12
For personal use only.

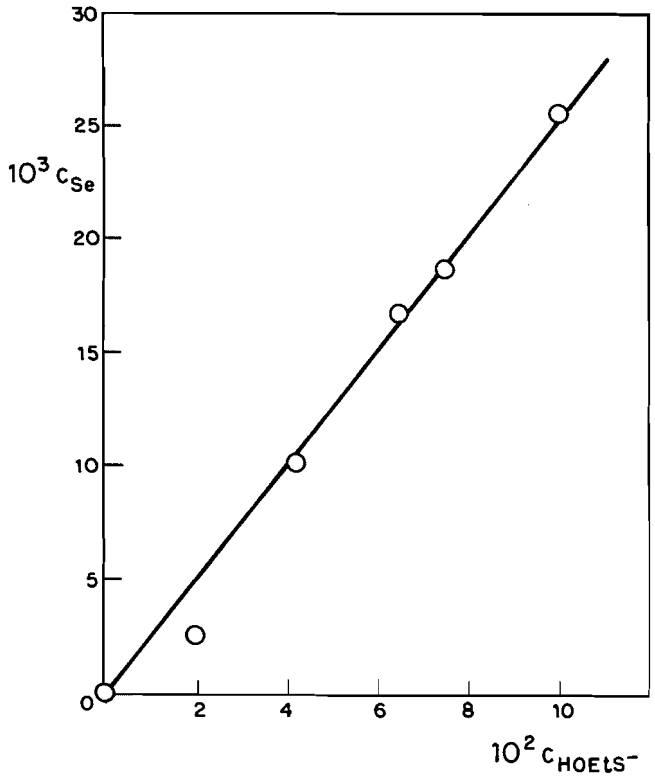

FIG. 3. Selenium solubility, c_{Se}, dependence on mercaptide concentration, $c(HOC_2H_4S^-)$, at 23°C.

[9] $Se + HOC_2H_4S^- = HOC_2H_4SSe^-$

A plot of mercaptide concentration, $c(HOC_2H_4S^-)$, against selenium solubility, c(Se), at 25°C, shown in Fig. 3, shows a linear dependance, which excludes $Se(HOEtSH)_6$ as a possibility and supports solubility due to equilibrium [9]. The lowest mercaptide concentration point shows a low value of c(Se) due to the susceptibility of the basic mercaptide solutions to air oxidation. The formation constant for equilibrium [9] is found to be 0.33 ± 0.06 at 23°C.

The Raman spectra of aqueous solutions of 1.0 M $Na[SC_2H_4OH]$ before and after saturation with selenium are listed in Table 3. After saturation with selenium the pH of the solution was 9.68. Calculation from the K_a for HOC_2H_4SH and K for equilibrium [9] shows that the concentrations of HOC_2H_4SH, $HOC_2H_4S^-$, and $HOC_2H_4SSe^-$ are respectively 0.39, 0.47, and 0.14 M. From these estimated concentrations, the Raman peaks have been assigned to the various species present, as given in Table 3. The SeS stretching mode for the $HOC_2H_4SSe^-$ anion, which is expected to be one of the most intense bands in the spectrum, in spite of the low relative concentration, appears at 382 cm^{-1}.

The proton NMR spectrum of a 2.0 M $Na[SC_2H_4OH]$ solution saturated with elemental selenium shows, in addition to the equal intensity triplets of the $HOC_2H_4S^-$ ion, two additional broad signals ($w_{1/2}$ = 18 Hz) of equal intensity, due to the selenium containing anion. No coupling between the different protons on carbon is observed for this species, which may be a result of restricted rotation about the C—C bond due to a steric effect of the attached Se. As in the case of bis(hydroxyethylthio)selenide, the hydrogens on carbon are deshielded, compared to the disulfide, by the attachment of Se to S. The ^{77}Se NMR spectrum of a 1.0 M $Na[SC_2H_4OH]$ solution saturated with selenium consists of a broad signal at 243 ppm ($w_{1/2}$ = 30 ppm), indicating that moderately fast Se exchange is occurring in these solutions, and a very weak peak at 1297 ppm ($w_{1/2}$ = 3 ppm) due to selenite (8). Relative concentrations of these species, estimated from peak intensities, are 300:1 $HOC_2H_4SSe^-$/Se(IV). The selenite arises from a small amount of selenium disproportionation, according to equilibrium [8]. No peaks for any Se_n^{2-} species (13) were observed in the spectrum and this is probably due to a combination of their weakness and breadth. The $HOC_2H_4SSe^-$ anion is probably undergoing exchange with these polyselenide species and this accounts for the breadth of the $HOC_2H_4SSe^-$ signal.

TABLE 3. Raman spectra of 1.0 M $Na[SC_2H_4OH]$ before and after saturation with elemental selenium

1.0 M $Na[SC_2H_4OH]$	1.0 M $Na[SC_2H_4OH]$ saturated with Se[a]	Origin[b]
166(1, sh)	165(0, sh)	RS^-
228(1, sh)	247(7)	$RSSe^-$ and RS^-
—	269(7)	$RSSe^-$ and RSH
—	382(10, br)[c]	$RSSe^-$, RS^- & RSH
403(8)	—	RS^-
515(3)	505(2)[d]	RS^-
650(1, sh)	640(3, sh)	RS^-
666(5)	658(10)	$RSSe^-$, RS^- and RSH
756(10)	745(4)	$RSSe^-$, RS^- and RSH
830(0)	813(0)	$RSSe^-$ and RS^-
989(6)	988(1, br)	$RSSe^-$ and RS^-

[a]Solution pH = 9.68.
[b]R = HOC_2H_4.
[c]ν_{SeS}.
[d]This peak may be in part due to disulfide produced by air oxidation.

TABLE 4. Variation of K for equilibrium [9] with temperature

T (K)[a]	K
288.0	0.208
293.0	0.278
296.0	0.333
300.0	0.431
303.0	0.536

[a]Temperature control, ±0.2°C.

The solubility of selenium in $HOC_2H_4S^-$ solutions increases with temperature, as shown in Table 4. A plot of ln K vs. $1/T$ yields $\Delta H = 0.66 \pm 0.02$ kJ mol^{-1}, $\Delta S = -7 \pm 1$ J mol^{-1} deg^{-1}, $\Delta G = 2.8 \pm 0.4$ kJ mol^{-1}. The formation of the SeS bond in these solutions is endothermic and the negative entropy change is consistent with the loss in translational degrees of freedom with formation of the $HOC_2H_4SSe^-$ ion.

Mercaptide solutions are subject to slow oxidation (15). The addition of elemental selenium to the solutions accelerates the process. No signals due to the disulfide were detected in the proton NMR spectrum of a 0.10 M $Na[SC_2H_4OH]$ solution after bubbling oxygen for 15 min. However, such a solution saturated with elemental selenium gave a detectable amount of red selenium after bubbling oxygen for 15 min. The oxidation product was identified by NMR as the disulfide.

Can. J. Chem. Downloaded from www.nrcresearchpress.com by EESC ESCOLA DE ENGENHARIA on 09/08/12
For personal use only.

[10] $2H_2O + 4HOC_2H_4SSe^- + O_2 \rightarrow 2HOC_2H_4SSC_2H_4OH + 4Se + 4OH^-$

Selenium apparently catalyses the oxidation to disulfide. The selenite ion has also been shown to act as a catalyst in the oxidation of thiols to disulfides (16). In view of the ease of reduction of Se(IV) to elemental selenium in basic thiol solution, it is possible that Se is the actual catalyst in this process also.

Conclusion

Selenous acid or selenite are readily reduced by thiols. In moderately acid solution 2-mercaptoethanol reacts quantitatively with Se(IV) to give bis(hydroxyethylthio)selenide and the corresponding disulfide. Bis(hydroxyethylthio)selenide decomposes in strongly acidic and moderately basic solutions (pH > 7) to elemental selenium and disulfide (1*b*, 3). No evidence for disporportionation of the bis(hydroxyethylthio)-selenide to selenite and selenium (and mercaptide) as has been suggested for protein bis(thio)selenides (5) has been found. Excess mercaptide dissolves the selenium formed in the decomposition of the bis(thio)selenide to yield $HOC_2H_4SSe^-$ ion. Solutions of this ion are oxidized by oxygen to give selenium and disulfide. Selenium acts as a catalyst for the oxidation of $OC_2H_4S^-$ to the disulfide.

Acknowledgements

The authors thank Energy, Mines and Resources Canada and the Natural Sciences and Engineering Research Council for financial support. We also thank William Lear and Dr. Glen Facey for recording some of the Raman and NMR spectra.

1. (*a*) E.P. Painter. Chem. Rev. **28**, 179 (1941); (*b*) H.E. Ganther. Biochemistry, **7**, 2898 (1968).
2. D.L. Rabenstein and K.-S. Tan. Magn. Reson. Chem. **26**, 1079 (1988).
3. H. Afsar, I. Tor, and R. Apak. Analyst, **114**, 1315 (1989).
4. J.L. Kice, D.M. Wilson, and J.M. Espinola. J. Org. Chem. **56**, 3520 (1991).
5. K.J. Jenkins. Can. J. Biochem. **46**, 1417 (1968).
6. M. Lamoureux and J. Milne. Polyhedron, **9**, 589 (1990).
7. S.D. Nogare. Organic sulfur groups. *In* Organic analysis. Vol. 1. *Edited by* J. Mitchell, I.M. Kolthoff, E.S. Proskauer, and A. Weissberger. Interscience, New York. 1953. p. 343.
8. J. Milne. Magn. Reson. Chem. **31**, 652 (1993).
9. R. Forneris and C.E. Hennies. J. Mol. Struct. **5**, 449 (1970).
10. J. Milne. Polyhedron, **4**, 65 (1985).
11. D.J. Hupe and W.P. Jencks. J. Am. Chem. Soc. **99**, 450 (1977).
12. W. Nakanishi, S. Hayashi, H. Tukada, and H. Iwamura. J. Phys. Org. Chem. **3**, 358 (1990).
13. M. Bjorgvinsson and G.J. Schrobilgen. Inorg. Chem. **30**, 2540 (1991).
14. Gmelins Handbuch, Sys. No. 10, Selen, Part A, Verlag Chemie, Weinheim. 1942. p. 248.
15. G. Capozzi and G. Modena. Oxidation of thiols. *In* The chemistry of the thiol group. Part 2. *Edited by* S. Patai. John Wiley, London. 1974. p. 818.
16. C.C. Tsen and A.L. Tappel. J. Biol. Chem. **233**, 1230 (1958).

Can. J. Chem. Downloaded from www.nrcresearchpress.com by EESC ESCOLA DE ENGENHARIA on 09/08/12
For personal use only.

Alkene adducts of cyclic thiazenes. Identification of *exo* and *endo* addition of 1,3,2,4,6-dithiatriazines to 1,5-norbornadiene by 2-D NMR methods and the crystal structure of a single molecule in which both modes of addition are displayed

RENÉ T. BOERÉ,[1] JOHN A. ENG, AND KATHRYN PREUSS
Department of Chemistry, University of Lethbridge, Lethbridge, AB T1K 3M4, Canada

MASOOD PARVEZ
Department of Chemistry, University of Calgary, Calgary, AB T2N 1N4, Canada

AND

C.D. BRYAN AND A.W. CORDES
Department of Chemistry and Biochemistry, University of Arkansas, Fayetteville, AR 72701, U.S.A.

Received September 17, 1993

RENÉ T. BOERÉ, JOHN A. ENG, KATHRYN PREUSS, MASOOD PARVEZ, C.D. BRYAN, and A.W. CORDES. Can. J. Chem. **72**, 1171 (1994).

4-CF_3—C_6H_4—CN_3S_2, **1**, forms symmetrical sulfur-bound adducts with norbornene (NBE), norbornadiene (NBD), and 1-heptene (C_7H_{14}), which were studied by ^1H, ^{13}C, COSY-45, and HETCORR NMR. **1**·NBE exists in solution in a single isomeric form which corresponds to that found in the solid state for 4-CH_3O—C_6H_4—CN_3S_2·NBE by single-crystal X-ray diffraction: orthorhombic, $P2_12_12_1$ with $Z = 4$, $a = 10.224(3)$, $b = 10.369(5)$, $c = 14.075(5)$. $R = 0.0475$ and $R_w = 0.0492$ for 634 data. **1**·NBD exists in solution in two isomeric forms which are not interchangeable. One of these corresponds to that found in the NBE adduct, i.e. *exo* addition; the other is the first example of *endo* addition. Two *bis* adducts of stoichiometry NBD·**21** have been prepared and separated. They are isomers exhibiting *exo-exo* and *exo-endo* addition. The structure of the latter was confirmed by X-ray diffraction: orthorhombic, *Pcab* with $Z = 8$, $a = 7.816(2)$, $b = 17.264(3)$, $c = 36.842(5)$. $R = 0.068$ and $R_w = 0.106$ for 1506 data. **1**·C_7H_{14} exists as a mixture of *syn* and *anti* isomers. NMR structure parameters derived here have been applied to published data on over 15 thiazene NBE and NBD adducts.

RENÉ T. BOERÉ, JOHN A. ENG, KATHRYN PREUSS, MASOOD PARVEZ, C.D. BRYAN et A.W. CORDES. Can. J. Chem. **72**, 1171 (1994).

Le 4-CF_3—C_6H_4—CN_3S_2 (**1**) réagit avec le norbornène (NBE), le norbornadiène (NBD) et le hept-1-ène (C_7H_{14}) pour donner des adduits symétriques liés par le soufre; on a étudié ces adduits par rmn ^1H, ^{13}C, COSY-45 et HETCORR. En solution, l'adduit **1**·NBE existe sous la forme d'un seul isomère qui correspond à celui trouvé pour l'état solide, par diffraction des rayons x sur un cristal unique du 4-CH_3O—C_6H_4—CN_3S_2·NBE: cristaux orthorhombiques, groupe d'espace $P2_12_12_1$, avec a = 10,224(3), b = 10,369(5) et c = 14,075(5), $Z = 4$ et R = 0,0474 et R_w = 0,0492 pour 634 réflexions. En solution, l'adduit **1**·NBD existe sous deux formes isomères qui ne sous pas interchangeables. L'une d'elles correspond à celle observée pour l'adduit avec le NBE, à savoir une addition *exo*; l'autre est le premier exemple d'une addition *endo*. On a préparé et séparé les deux bis-adduits de stoechiométrie NBD·**21**. Ce sont des isomères correspondant à des additions *exo-exo* et *exo-endo*. On a confirmé la structure du dernier par diffraction des rayons x: cristaux orthorhombiques, groupe d'espace *Pcab*, avec a = 7,816(2), b = 17,264(3) et c = 36,842(5), $Z = 8$ et R = 0,068 et R_w = 0,106 pour 1506 réflexions. L'adduit **1**·C_7H_{14} existe sous la forme d'un mélange des isomères *syn* et *anti*. On a appliqué les paramètres de structure rmn obtenus avec ces composés à quinze adduits thiazène–NBE ou –NBD.

[Traduit par la Rédaction]

Introduction

The study of inorganic heterocycles containing conjugated —S—N— units has been greatly assisted by their ability to form, sometimes reversibly, adducts with alkenes (1–13). These have commonly been olefins which are activated by reason of ring strain, of which the most used has been norbornadiene (NBD), although there are a few examples where norbornene (NBE) (12) or dicyclopentadiene (9, 13) have been employed. The resulting adducts facilitate the chemical analysis of unstable rings and ring fragments, are often highly crystalline and allow X-ray structure determination of the parent ring system, sometimes before the parent rings are structurally characterized (1). For certain rings, for example salts of $S_3N_3^+$ (12), only the adducts have been characterized. Mass spectra of alkene adducts usually only show molecular peaks for the components.

Compared to other thiazene compounds, 1,3,2,4,6-dithiatriazines form particularly strong adducts with alkenes, making them especially suitable for a study of alkene addition. These additions are probably similar to 1,3-dipolar cycloaddition reactions (14). The high affinity of dithiatriazines for alkenes can be attributed to the strongly anti-aromatic 8π electronic structure of the parent ring system (2, 15). In the case of the directly-bound trifluoromethyl dithiatriazine, $CF_3CN_3S_2$, even unactivated olefins such as ethene and butenes form stable cycloadducts (13) (Scheme 1).

NMR spectroscopy of the alkene adducts is usually possible, and over the years a large amount of NMR data on such systems has been published (see Table 4). However, the assignments of the published NMR spectra have often been in error. These errors are easily corrected by the use of 2-D NMR, in particular ^1H-^1H COSY and ^1H-^{13}C HETCORR methods.

In the course of our study of aryl dithiatriazines we noted indications of isomers in the NMR spectra of their NBD adducts, and therefore chose to use NBE to derivatize them (16). Only single solution species were observed for the NBE adducts by NMR. In this paper we report on a detailed investigation of the alkene adducts of aryl dithiatriazines, focusing on 4-$CF_3C_6H_4CN_3S_2$, **1** (Scheme 1), a choice determined by the

[1]Author to whom correspondence may be addressed: telephone 403-329-2045; FAX 403-329-2057; Internet BOERE@HG.ULETH.CA.

Can. J. Chem. Downloaded from www.nrcresearchpress.com by EESC ESCOLA DE ENGENHARIA on 09/08/12
For personal use only.

Can. J. Chem. Downloaded from www.nrcresearchpress.com by EESC ESCOLA DE ENGENHARIA on 09/08/12
For personal use only.

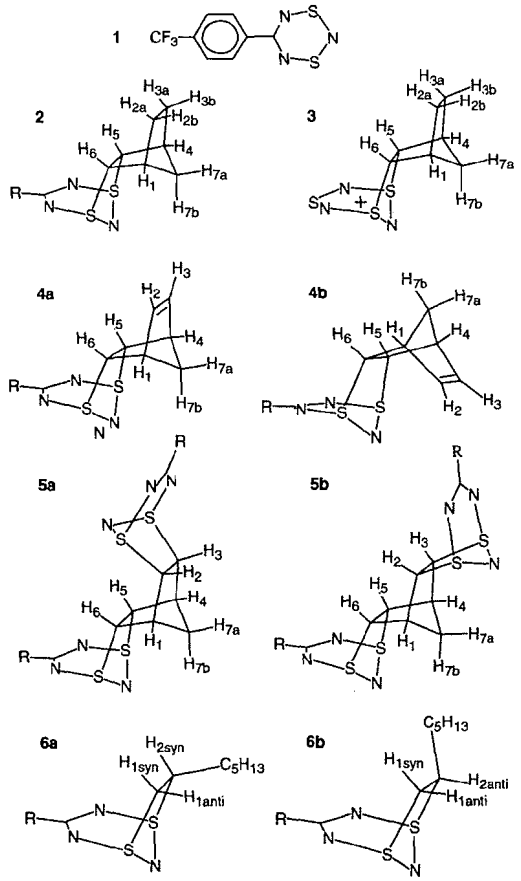

SCHEME 1. Structures of **1–6** as calculated on the model compounds with R = H by the MNDO method. The labeling of the H atoms is shown as they are used in the discussion of the NMR spectra and in Tables 4–6.

suitable solubility properties of its adducts. Using 2-D NMR we have made reliable assignments of the ^1H and ^{13}C spectra of their NBD and NBE adducts (**4** and **2**, respectively). We also provide an assignment of the previously unpublished ^1H NMR spectrum of the closely related $[S_3N_3{\cdot}NBE]^+$ adduct, **3** (12). Adducts **4** exist in two isomeric forms, which are not interchangeable in solution. There are four possible structures for such adducts which are consistent with the chemical shifts and symmetry of the NMR spectra, and with known crystallographic structures for related complexes. These possibilities are shown in Scheme 2. The NMR data we report here allow us to assign the two observed isomers conclusively to the *syn-exo* and *syn-endo* geometries. These assignments have been corroborated by MNDO calculations on model compounds.

In view of the relatively high thermal stability of NBD adducts of dithiatriazines, we speculated on the possibility of *bis* addition using both the double bonds in a single NBD molecule. We report here that such adducts can indeed be prepared, and that they also exist in two isomeric forms, which can be isolated and separated. The isomers have been shown to contain *exo-endo* (**5***a*) and *exo-exo* (**5***b*) addition modes by 2-D NMR methods. The identity of the *exo-endo* isomer has been confirmed by a single-crystal X-ray structure determination. We have also demonstrated that **1** forms stable adducts with the unactivated olefin 1-heptene in two isomeric forms **6***a* and **6***b*. The isomers have been conclusively identified from their NMR spectra.

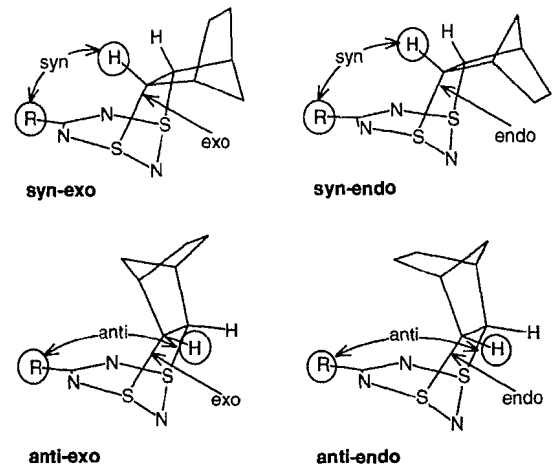

SCHEME 2. The four possible geometries of norbornane–dithiatriazine attachment which are consistent with the observed plane of symmetry in the adducts. The nomenclature used to describe the isomers is defined here.

Experimental section

Starting materials and general procedures

1 and **2** were prepared as reported previously (16). The $AlCl_4^-$ salt of **3** was prepared by the literature method (12). 1,5-Norbornadiene, norbornene, and 1-heptene (Aldrich) were obtained commercially and used as received. $AlCl_3$ (Aldrich) was vacuum sublimed before use and handled in a glove box. CH_3CN was double-distilled from P_2O_5 and CaH_2. SO_2 (Matheson) was stored over molecular sieves (4 Å) in a glass bulb fitted with a Rotaflo stopcock. Unless otherwise indicated, all procedures were performed under an atmosphere of purified N_2 using a dry-box, Schlenk-ware, and vacuum-line techniques. Infrared spectra were recorded on a Bomem MB102 Fourier transform spectrometer as Nujol mulls between CsI plates and are reported in the 1600–200 cm^{-1} region only, unless otherwise indicated. NMR spectra were recorded on a Bruker AC-F 250 MHz FT spectrometer. Mass spectra were recorded by the Mass Spectrometry Centre, University of Alberta. Elemental analyses were performed by MHW Laboratories, Phoenix, Az.

Preparation of 4-$CF_3C_6H_4CN_3S_2{\cdot}C_7H_8$, 4

To a suspension of **1** (0.21 g, 0.80 mmol) in 3 mL CH_3CN was added 2.0 mL (excess) 1,5-norbornadiene. After several hours stirring, the brown colour faded to give a clear solution. Removal of solvent *in vacuo* followed by recrystallization from a minimum volume of hot CH_3CN and cooling to 0°C gave colourless plates, mp 179–181°C. Yield 0.15 g (0.42 mmol, 53%). Anal. calcd. for $C_{15}H_{12}F_3N_3S_2$: C 50.69, H 3.40, N 11.82, S 18.04; found: C 50.57, H 3.67, N 11.91, S 18.18. IR (1600–250 cm^{-1} region) 1514 (w), 1427 (s), 1319 (s), 1261 (w), 1161 (m), 1124 (m), 1099 (m), 1064 (m), 1016 (m), 983 (w), 923 (w), 868 (m), 856 (m), 787 (m), 763 (m), 702 (m), 678 (m), 657 (w), 592 (w), 551 (m), 536 (s), 480 (s), 462 (s), 426 (m), 384 (m), 368 (w), 282 (m). Mass spectrum, *m/z* 355 ($CF_3C_6H_4CN_3S_2{\cdot}C_7H_8^+$, 3%), 336 ($CF_2C_6H_4CN_3S_2{\cdot}C_7H_8^+$, 2%), 263 ($CF_3C_6H_4CN_3S_2^+$, 100%), 249 ($CF_3C_6H_4CN_2S_2^+$, 3%), 217 ($CF_3C_6H_4CN_2S^+$, 35%), 171 ($CF_3C_6H_4CN^+$, 6%), 152 ($CF_2C_6H_4CN^+$, 10%), 91 ($C_7H_7^+$, 25%).

Preparation of (4-$CF_3C_6H_4CN_3S_2)_2{\cdot}C_7H_8$, 5

In a typical reaction, 0.450 g (1.71) mmol of **1** was suspended in 15 mL of CH_3CN, and 92.3 μL (0.855 mmol) of 1,5-norbornadiene was added by micropipette. The reaction was heated to 63°C in an oil bath for 4 h, until all the brown starting material had been consumed. The resulting solution was yellow–brown in colour, and usually contained a small amount of colourless solids. The solution was filtered hot. The solid collected from the hot filtration was rinsed with cold CH_3CN and dried *in vacuo* to give 0.07 g (0.15 mmol, 13% yield) of **5***a*. On cooling

Can. J. Chem. Downloaded from www.nrcresearchpress.com by EESC ESCOLA DE ENGENHARIA on 09/08/12
For personal use only.

the filtrate to room temperature, 0.20 g of crystalline solid precipitated, which was filtered off. After reducing the volume to one-half, redissolving, and cooling back to room temperature, a further 0.06 g of this material could be recovered for a total yield of 0.26 g (0.42 mmol, 49% yield) of **5***b*.

5*a*:

Recrystallized from warm CH_3CN, loss of dithiatriazine at 178°C, mp 188°C. Anal. calcd. for $C_{23}H_{16}F_6N_6S_4$: C 44.65, H 2.61, N 13.58; found: C 44.42, H 2.88, N 13.69. IR (1600–250 cm^{-1} region) 1427 (s), 1319 (vs), 1269 (w), 1169 (s), 1138 (s), 1105 (s), 1067 (s), 1017 (m), 916 (w), 858 (m), 806 (w), 783 (w), 764 (m), 721 (m), 677 (m), 538 (w), 523 (m), 498 (w), 459 (w), 413 (w). Mass spectrum, *m/z* 355 ($CF_3C_6H_4CN_3S_2{\cdot}C_7H_8^+$, 3%), 336 ($CF_3C_6H_4CN_3S_2{\cdot}C_7H_8^+$, 3%), 263 ($CF_3C_6H_4CN_3S_2^+$, 100%), 217 ($CF_3C_6H_4CN_2S^+$, 23%), 187 ($CF_3C_6H_4CNSH_2^+$, 11%), 172 ($CF_3C_6H_4CNH^+$, 11%), 152 ($CF_2C_6H_4CN^+$, 15%), 91 ($C_7H_7^+$, 33%), 69 ($CF_3^+$, 33%), 46 ($SN^+$, 48%).

5*b*:

Recrystallized from 2:1 $CHCl_3$/hexanes, loss of dithiatriazine at 138°C, mp 158°C. Anal. calcd. for $C_{23}H_{16}F_6N_6S_4$: C 44.65, H 2.61, N 13.58; found: C 44.58, H 2.66, N 13.59. IR (1600–250 cm^{-1} region) 1427 (s), 1317 (vs), 1167 (s), 1134 (s), 1067 (s), 1016 (m), 916 (w), 858 (m), 804 (w), 789 (w), 763 (m), 737 (w), 702 (w), 679 (m), 594 (w), 548 (m), 520 (w), 467 (w), 415 (w), 328 (w), 278 (w). Mass spectrum, *m/z* 355 ($CF_3C_6H_4CN_3S_2{\cdot}C_7H_8^+$, 3%), 336 ($CF_2C_6H_4CN_3S_2{\cdot}C_7H_8^+$, 3%), 263 ($CF_3C_6H_4CN_3S_2^+$, 100%), 217 ($CF_3C_6H_4CN_2S^+$, 19%), 187 ($CF_3C_6H_4CNSH_2^+$, 11%), 172 ($CF_3C_6H_4CNH^+$, 16%), 152 ($CF_2C_6H_4CN^+$, 14%), 91 ($C_7H_7^+$, 42%), 46 ($SN^+$, 52%).

*Preparation of 4-$CF_3C_6H_4CN_3S_2{\cdot}C_7H_{14}$, **6***

To a suspension of **1** (0.13 g, 0.50 mmol) in 5 mL CH_3CN was added 0.5 mL (excess) 1-heptene. After several hours stirring at 45°C, the brown colour faded to give a clear solution. Removal of solvent *in vacuo* followed by extraction with pentane, filtration, and concentration of the filtrate to 30 mL gave the product on cooling to –30°C as colourless plates, mp 114–117°C. A second crop could be won by concentration of the mother liquor and cooling again. Yield 0.07 g (0.19 mmol, 39%) of a mixture of **6***a* and **6***b*. No attempt was made to separate the isomers. Anal. calcd. for $C_{15}H_{18}F_3N_3S_2$: C 49.85, H 5.02, N 11.63; found: C 49.61, H 5.12, N 11.57. IR (1600–250 cm^{-1} region) 1377 (s), 1300 (m), 1170 (m), 1134 (s), 1101 (m), 1068 (m), 1016 (m), 966 (m), 916 (w), 866 (m), 800 (w), 765 (m), 744 (w), 721 (w). Mass spectrum, *m/z* 342 ($CF_2C_6H_4CN_3S_2{\cdot}C_7H_{14}^+$, 1%), 263 ($CF_3C_6H_4CN_3S_2^+$, 67%), 249 ($CF_3C_6H_4CN_2S_2^+$, 16%), 217 ($CF_3C_6H_4CN_2S^+$, 19%), 203 ($CF_3C_6H_4CNS^+$, 8%), 171 ($CF_3C_6H_4CN^+$, 31%), 152 ($CF_2C_6H_4CN^+$, 32%), 92 ($S_2N_2^+$, 34%), 46 ($SN^+$, 100%).

NMR studies

NMR samples were prepared in 5 mm tubes using $CDCl_3$ as the solvent (except for **3**). The $AlCl_4^-$ salt of **3**, which is quite insoluble in common NMR solvents, was dissolved in SO_2 in a tube insert constructed of 4 mm Pyrex tubing, which was sealed under vacuum. This 4 mm tube was fitted into a round-bottom 5 mm NMR tube, and the small remaining space was filled with C_6D_6 which acted as a lock for the NMR spectrometer. The top of the nmr tube was sealed against the walls of the insert with a small amount of Teflon plumbers tape. With this sample we were able to obtain standard COSY-45 and HETCORR spectra using the automated software included with the Bruker spectrometer.

Crystal structure determinations

The crystal structures of **2***b* (at Calgary) and **5***a* (at Arkansas) were determined using Enraf-Nonius CAD-4 diffractometers. At an intermediate stage in the refinement of the structure of **2***b*, a difference map revealed a few maxima consistent with the positions of the hydrogen atoms. H atoms were included in the subsequent cycles of refinement at geometrically idealized positions (C—H 0.95 Å) and with a fixed overall isotropic temperature factor. Calculated H atom positions were used for **5***a*. Crystals of **5***a* were extremely thin and tended to cleave parallel to the flat side. These were the best crystals we could obtain after much effort (see Results and discussion section).

Scattering factors used at Calgary were those of Cromer and Mann (17) and Stewart, Davidson, and Simpson (18), and allowance was made for anomalous dispersion (19); at Arkansas the values from the International tables for crystallography, Vol. 4, were used. Computer programs used at Calgary included SHELX'76 (20) and ORTEP II (21); at Arkansas NRC386, a PC version of NRCVAX (22). Experimental details for both structures are summarized in Table 1, fractional coordinates and U_{eq} in Table 2, and important interatomic distances in Table 3.[2] ORTEP diagrams showing the atom numbering scheme are found in Figs. 1 and 3.

Computational methods

The computational studies were performed on NBE, NBD, and 1-heptene adducts of the model dithiatriazine HCN_3S_2. The HyperChem suite of programs was employed (23) running under Windows on a 486/66 MHz Intel-based personal computer. In this method, the molecule is drawn on the computer screen, and a default three dimensional structure is calculated by the program. This crude geometry is refined by molecular mechanics using the MM+ force field (proprietary to HyperChem, but based on Alinger's MM2). Full geometry optimizations were then performed using HyperChem's implementation of MNDO (using RHF wavefunctions and Polak–Ribiere conjugate gradients, with convergence set at RMS of 0.1 kcal mol^{-1}).[3] HyperChem does not use symmetry constraints during geometry minimizations, relying instead on a close starting geometry from the molecular mechanics minimization. The energy of the model adducts are reported in Table 7 as enthalpies of formation. The absolute heats of formation have little meaning, but the relative energies for a series of isomers can be usefully compared. The reliability of these MNDO calculations was assessed by comparison of the bond lengths and angles with crystal structures of adducts containing these fragments (for example, those of **2***b*, **5***a*, and $PhCN_3S_2{\cdot}$NBD (24). In all cases excellent agreement was observed between the calculated (gas phase) structures and the crystallographically determined structures in solids.

Results and discussion

Structures of NBE adducts

The NBE adducts of the aryl dithiatriazines reported in our previous work (16), in contrast to their NBD derivatives, have NMR spectra consistent with a single species in solution. The NMR parameters of two such derivatives, $CF_3C_6H_4CN_3S_2{\cdot}C_7H_{10}$, **2***a*, and $CH_3OC_6H_4CN_3S_2{\cdot}C_7H_{10}$, **2***b*, are included in Table 4. The solution NMR spectra of these two, and all the other derivatives we have prepared, are virtually identical. However, **2***b* formed crystals suitable for an X-ray crystallographic structure determination. This structure is a necessary

[2]Tables of bond lengths and angles (S1, S5, and S6), anisotropic thermal parameters (S2 and S7), calculated H atom positions (S3 and S8) and observed and calculated structure factors (S4 and S9) for the crystal structure may be purchased from the Depository of Unpublished Data, Document Delivery, CISTI, National Research Council of Canada, Ottawa, ON K1A 0S2, Canada.

Tables of bond lengths and angles have also been deposited with the Cambridge Crystallographic Data Centre and can be obtained on request from: The Director, Cambridge Crystallographic Data Centre, University Chemical Laboratory, 12 Union Road, Cambridge, CB2 1EZ, U.K.

[3]HyperChem has implemented the MNDO method (along with several other semi-empirical methods), but has re-written the original FORTRAN code in C and C++. These calculations are therefore not directly comparable to those from other popular packages containing MNDO. In order to facilitate comparison of the methods, the authors are providing MOPAC-style **Z**-matrix files of the minimized adduct geometries. These may be obtained from the corresponding author by E-Mail as file "ALKTHIA.TXT".

TABLE 1. Summary of crystal data, intensity collection, and structure refinement for **2***b* and **5***a*

Parameter	Value		
	2*b*		**5***a*
Formula	$C_{15}H_{17}N_3OS_2$		$C_{23}H_{16}F_6N_6S_4$
Formula weight	319.44		618.65
Crystal system		Orthorhombic	
Space group	$P2_12_12_1$		*Pcab*
a, Å	10.224(3)		7.816(2)
b, Å	10.369(5)		17.264(3)
c, Å	14.075(5)		36.842(5)
V, Å^3	1492.1		4971(2)
Z	4		8
d_c, g cm^{-3}	1.422		1.65
Crystal dimension (mm)	0.188 × 0.125 × 0.129		0.58 × 0.28 × 0.10
Cell determination, reflections	25		25
Cell determination, 2θ range, deg	10–15		16–20
Radiation, Mo Kα, Å	λ = 0.71069		λ = 0.71073
Temperature, K	293		295
Scan technique	ω–2θ		ω–2θ
Scan speed, deg min^{-1}	0.67–4.0		4–16 (in ω)
Scan width, deg	0.70 + 0.35 tan θ		1.0 + 0.35 tan θ
2θ range, deg	4–54		4–44
h, *k*, *l*, ranges	0,13; 0,13; 0,17		0, 8; −18, 0; −38, 38
Drift of standards, %	Insignificant		1.5
μ, mm^{-1}	0.307		0.44
Absorption correction	None		Empirical ψ scans
Absorption, range			0.89–1.00
Total reflections	1938		6013
Unique reflections	1867		3039
Data with $I > 3\sigma(I)$	634		1506
R for merge			0.060
Solution method		Direct methods	
Parameters refined	194		352
R	0.0474		0.068
R_w	0.0492		0.106
GOF	3.358		1.76
Largest Δ/σ	<0.1		0.007
Extinction correction	None		None
Final difference map, e Å^{-3}	−0.24, +0.30		−0.5(1), +0.4(1)
F(000)	672		2511.6
H atom treatment		Idealized positions (C—H = 0.95 Å)	

starting point for our analysis, since there have previously been no X-ray structures of NBE adducts of dithiatriazines.

The structure of the adduct in the solid state, presented in Fig. 1, shows *syn-exo* geometry. The labels for the possible isomeric structures are depicted in Scheme 2, and are based on the standard organic nomenclature for fused rings (25). We consider the adducts to be comprised of three central fused rings: the 6-membered dithiatriazine portion, the five-membered C_2S_2N portion, and the 6-membered ring of the norbornene or norbornadiene. The protons attached to the fused C_2 fragment may then be located *syn* or *anti* to the substituent at the 5-position of the dithiatriazine ring. At the same time, the S atoms are located either in *endo* or *exo* positions on the bicyclic hydrocarbon.

The *syn-exo* geometry has been observed in numerous thiazene adducts of the related olefin NBD, for example (24), as well as in the NBE adduct of $S_3N_3^+$ (12). In this geometry, there is a close approach of H_{7b} to the unique nitrogen atom (N1 in Fig. 1), which is tipped out of the plane of CNSSN atoms. (This tipping is a consequence of re-hybridization at S, and has been noted previously (2); it does not seem to be *caused* by the proximity of H_{7b}.)

Table 4 presents the ^{1}H NMR assignments of the NBE and NBD adducts. These are based on a combination of well-known Karplus angle and W-coupling relationships in rigid hydrocarbon compounds (26). All the expected ^{1}H—^{1}H correlation peaks in the COSY-45, as well as the ^{1}H—^{13}C correlations in the HETCORR spectra were observed. On this basis, most of the signals could be unambiguously assigned; any exceptions to this generalization are noted in the table.

Table 4 also tabulates a chemical shift difference parameter, Δδ, for the bridge methylene protons H_{7a} and H_{7b}. In free NBE, this parameter is 0.25 ppm, reflecting the difference in environment of H_{7a} facing a C—C single bond and H_{7b} facing the double bond, while in the adducts **2** Δδ = 0.93 ppm. We believe that the large increase in this parameter, which is primarily caused by a downfield shift in the resonance frequency of H_{7b}, is due to through-space deshielding of H_{7b} caused by its proximity to the apical N atom of the dithiatriazine ring. The expected *reverse* effect on the ^{13}C resonance of C_7 is consistent with this interpretation. This observation gives us a great deal of confidence that the solution structure of **2** is similar to the solid-state structure in the crystal. We thus identify a value of Δδ ≈ 1 ppm with the

Can. J. Chem. Downloaded from www.nrcresearchpress.com by EESC ESCOLA DE ENGENHARIA on 09/08/12
For personal use only.

Can. J. Chem. Downloaded from www.nrcresearchpress.com by EESC ESCOLA DE ENGENHARIA on 09/08/12
For personal use only.

TABLE 2. Final positional and equivalent isotropic thermal parameters of **2b**[a] and **5a**[b]

(*a*) **2b**

Atom	*x*	*y*	*z*	U_{eq}[c]
S1	1.0540(3)	1.0481(3)	0.2623(3)	72(2)
S2	0.8052(3)	1.0113(3)	0.2460(2)	68(2)
O	1.0445(9)	0.7039(8)	−0.2414(7)	87(6)
N1	0.9117(10)	1.1242(8)	0.2654(8)	84(7)
N2	0.8385(8)	0.9402(10)	0.1449(6)	68(7)
N3	1.0723(9)	0.9792(10)	0.1576(6)	65(6)
C1	0.9646(12)	0.9356(10)	0.1176(9)	54(8)
C2	1.0142(10)	0.9086(11)	0.3376(9)	58(7)
C3	0.8631(9)	0.8919(11)	0.3314(8)	47(7)
C4	0.8199(10)	0.9091(11)	0.4319(9)	58(7)
C5	0.8610(11)	0.7874(13)	0.4878(9)	70(9)
C6	1.0128(12)	0.7994(13)	0.4910(9)	77(9)
C7	1.0367(12)	0.9330(12)	0.4438(8)	62(8)
C8	0.9150(10)	1.0085(11)	0.4727(8)	73(7)
C9	0.9845(10)	0.8805(11)	0.0223(9)	51(8)
C10	0.8824(12)	0.8104(11)	−0.0207(10)	64(8)
C11	0.8981(11)	0.7532(12)	−0.1086(10)	61(8)
C12	1.0151(14)	0.7585(13)	−0.1554(9)	70(9)
C13	1.1159(12)	0.8269(12)	−0.1136(9)	70(9)
C14	1.0984(11)	0.8855(10)	−0.0258(9)	59(8)
C15	0.9509(18)	0.6164(15)	−0.2774(10)	120(14)

[a]Atomic numbering scheme as defined in Fig. 1.
[b]Atomic numbering scheme as defined in Fig. 3.
[c]U_{eq} (× 10^3 Å^2) = $(U = U_{22} + U_{33})/3$.

(*b*) **5a**

Atom	*x*	*y*	*z*	B_{eq}
S1	0.8590(5)	0.41276(24)	0.17282(10)	3.10(18)
S2	1.0198(5)	0.30243(21)	0.13838(10)	3.09(18)
S3	1.3500(5)	0.46108(23)	0.25180(10)	3.12(17)
S4	1.4840(5)	0.33442(24)	0.22568(11)	3.29(18)
F1	0.1937(21)	0.4650 (12)	−0.0074 (4)	12.0 (11)
F2	0.127 (3)	0.3555 (14)	0.0060 (6)	21.2 (19)
F3	0.300 (3)	0.3814 (13)	−0.0333 (5)	14.9 (14)
F4	1.0746(24)	0.2115 (8)	0.4429 (4)	11.5 (10)
F5	1.0778(23)	0.1067 (8)	0.4126 (4)	10.9 (10)
F6	1.2991(21)	0.1496 (10)	0.4339 (4)	11.3 (10)
N1	0.7399(15)	0.4225 (8)	0.1356 (3)	3.7 (6)
N2	0.8927(18)	0.3216 (8)	0.1043 (3)	4.0 (6)
N3	0.9159(16)	0.3220 (7)	0.1762 (3)	3.7 (6)
N4	1.2864(16)	0.4102 (7)	0.2866 (3)	3.3 (6)
N5	1.3922(16)	0.2902 (7)	0.2614 (3)	3.3 (6)
N6	1.5325(15)	0.4232 (8)	0.2367 (3)	3.7 (6)
C1	0.250 (4)	0.3954 (17)	0.0008 (6)	7.8 (15)
C2	0.3947(24)	0.3927 (12)	0.0263 (5)	4.8 (10)
C3	0.4242(21)	0.4544 (11)	0.0480 (5)	4.5 (9)
C4	0.5477(21)	0.4501 (11)	0.0753 (4)	4.2 (9)
C5	0.6428(22)	0.3832 (9)	0.0783 (4)	3.6 (8)
C6	0.6197(25)	0.3199 (10)	0.0548 (5)	4.7 (9)
C7	0.491 (3)	0.3273 (11)	0.0291 (4)	5.0 (10)
C8	0.7718(20)	0.3747 (9)	0.1082 (4)	2.9 (7)
C9	1.1574(19)	0.3865 (8)	0.1383 (4)	2.8 (7)
C10	1.0618(17)	0.4542 (8)	0.1566 (4)	2.6 (6)
C11	1.1884(18)	0.4837 (7)	0.1844 (4)	2.7 (7)
C12	1.3562(20)	0.4703 (8)	0.1643 (4)	3.2 (7)
C13	1.3303(16)	0.3832 (8)	0.1593 (3)	2.4 (7)
C14	1.2952(18)	0.3540 (7)	0.1979 (4)	3.1 (7)
C15	1.2041(18)	0.4247 (8)	0.2161 (4)	3.0 (7)
C16	1.3188(18)	0.3342 (9)	0.2867 (4)	2.8 (7)
C17	1.2743(18)	0.2920 (10)	0.3209 (4)	2.9 (8)
C18	1.2232(25)	0.3313 (10)	0.3520 (5)	4.9 (10)
C19	1.181 (3)	0.2925 (11)	0.3826 (4)	5.2 (11)
C20	1.1960(21)	0.2151 (11)	0.3841 (5)	3.8 (8)
C21	1.242 (3)	0.1736 (10)	0.3533 (7)	6.1 (12)
C22	1.2815(24)	0.2134 (11)	0.3228 (5)	4.4 (9)
C23	1.156 (3)	0.1724 (12)	0.4177 (6)	5.6 (11)

[a]B_{eq} is the mean of the principal axes of the thermal ellipsoid.

TABLE 3. Selected interatomic distances and angles in **2b**[a] and **5a**[b]

Atoms	Distance	Atoms	Angle
		2b	
S_1---N_1	1.657(11)	S_1—N_1—S_2	104.0(5)
S_1---N_3	1.648(11)	N_1—S_1—N_3	109.3(6)
S_1---C_2	1.839(13)	N_1—S_1—C_2	99.5(5)
S_2---N_1	1.622(11)	N_3—S_1—C_2	101.5(6)
S_2---N_2	1.638(11)	N_1—S_2—N_2	109.4(6)
S_2---C_3	1.824(12)	N_1—S_2—C_3	99.3(5)
N_2---C_1	1.346(16)	N_2—S_2—C_3	101.5(6)
N_3---C_1	1.317(15)	C_1—N_2—S_2	117.6(9)
C_2---C_3	1.557(14)	C_1—N_3—S_1	115.9(10)
C_2---C_7	1.534(16)	N_2—C_1—N_3	131.8(13)
C_3---C_4	1.492(17)	S_1—C_2—C_7	113.5(9)
C_4---C_5	1.545(18)	S_2—C_3—C_4	116.6(9)
C_4---C_8	1.529(15)	C_4—C_8—C_7	94.1(9)
C_5---C_6	1.558(16)	C_3—C_4—C_5	107.7(10)
C_7---C_8	1.525(16)	C_2—C_7—C_6	104.2(11)
		5a	
S_1---N_1	1.666(13)	S_1—N_3—S_2	105.4(5)
S_1---N_3	1.634(13)	N_1—S_1—N_3	108.2(7)
S_1---C_{10}	1.839(14)	N_1—S_1—C_{10}	100.1(6)
S_2---N_2	1.635(13)	N_3—S_1—C_{10}	99.4(6)
S_2---N_3	1.648(13)	N_2—S_2—N_3	108.0(7)
S_2---C_9	1.807(14)	N_2—S_2—C_9	101.4(7)
N_1---C_8	1.328(19)	N_3—S_2—C_9	97.4(6)
N_2---C_8	1.324(22)	S_1—N_1—C_8	117.3(11)
S_3---N_4	1.631(13)	S_2—N_2—C_8	119.4(11)
S_3---N_6	1.664(13)	N_1—C_8—N_2	130.2(15)
S_3---C_{15}	1.850(14)	S_3—N_6—S_4	104.7(7)
S_4---N_5	1.681(12)	N_4—S_3—N_6	108.2(7)
S_4---N_6	1.631(13)	N_4—S_3—C_{15}	100.8(7)
S_4---C_{14}	1.827(16)	N_6—S_3—C_{15}	99.1(6)
S_4---C_{16}	1.333(20)	N_5—S_4—C_6	109.3(6)
N_5---C_{16}	1.333(19)	N_5—S_4—C_{14}	100.2(6)
N_9---C_{10}	1.541(19)	N_6—S_4—C_{14}	98.8(6)
C_9---C_{13}	1.558(20)	S_3—N_4—C_{16}	118.3(10)
C_{10}---C_{11}	1.515(20)	S_3—N_4—C_{16}	118.3(10)
C_{11}---C_{12}	1.524(21)	N_4—C_{16}—N_5	129.7(14)
C_{11}---C_{15}	1.554(21)	S_3—C_{15}—C_{11}	111.1(9)
C_{13}---C_{12}	1.528(20)	S_4—C_{14}—C_{13}	115.8(10)
C_{13}---C_{14}	1.533(20)	S_2—C_9—C_{13}	119.1(9)
C_{14}---C_{15}	1.564(19)	S_1—C_{10}—C_{11}	118.3(10)

[a]Atomic numbering scheme as defined in Fig. 1.
[b]Atomic numbering scheme as defined in Fig. 3.

syn-exo geometry of norbornene derivatives of dithiatriazines, at least in $CDCl_3$ solution.

The results of MNDO calculations on the four possible geometries of addition of a model HCN_3S_2 to NBE are presented in Table 7. The *syn-exo* isomer has a significantly lower calculated energy than the other three possibilities. These data are consistent with the known fact that 1,3-dipolar cycloadditions to NBE *always go exo* (14).

Structure of NBD adducts

Tables 4 and 6 list the solution NMR spectral data for $CF_3C_6H_4CN_3S_2{\cdot}C_7H_8$, **4**. These are highly similar to those observed for a range of dithiatriazine NBD adducts, so that discussion of a single example is entirely sufficient. The presence of two distinct isomers is evident from both the ^{13}C and the ^1H NMR spectra. Intensity differences due to different isomer populations resulting from different preparations have been an aid

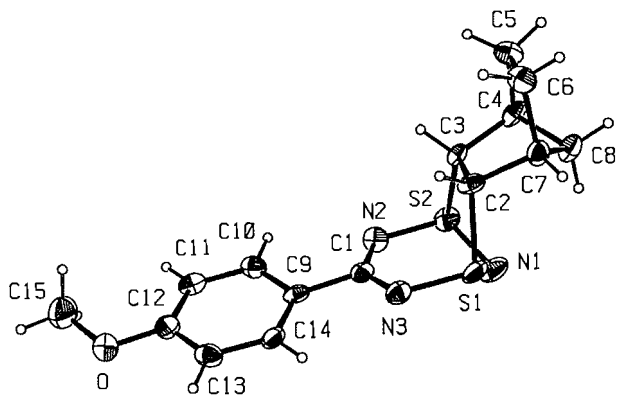

FIG. 1. ORTEP diagram of **2***b* showing the atom numbering scheme and the *syn-exo* orientation of the norbornene unit, as well as the way in which N_1 tips below the CNNSS plane.

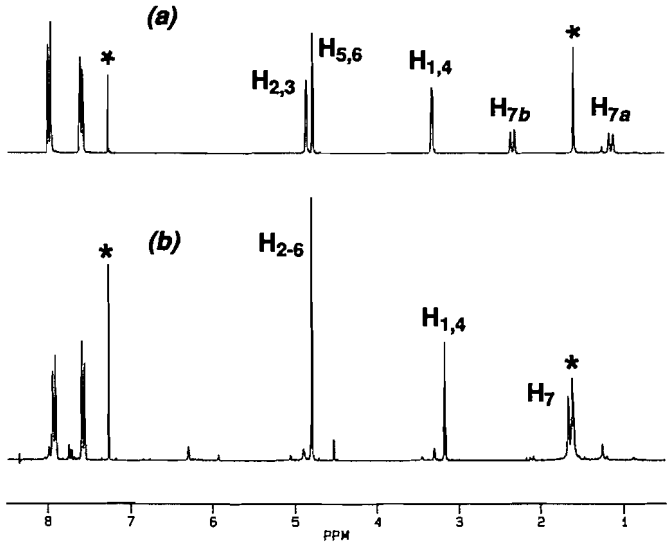

FIG. 2. ^{1}H NMR spectra of solutions of (*a*) **5***a* and (*b*) **5***b* in $CDCl_3$. Asterisks mark solvent impurities. Small peaks in (*b*) are due to the presence of a little **4***a* and **4***b*.

in assigning the peaks. In ^{1}H spectra (Table 4), the aromatic signals for the two isomers are not differentiated, while in the ^{13}C spectra (Table 6) only the signals of $C_{11,12,13}$ are not differentiated (i.e. those of the nuclei furthest from the point of attachment to NBD). In the ^{1}H spectrum, the total NBD region integrates to 8 H, and the aromatic region to 4 H. Since the NMR data for free dithiatriazines are known (16), and are quite different in the $CF_3C_6H_4$ region from those reported here, we are also not dealing with an association–dissociation equilibrium. Moreover, although we experienced a fair degree of variation in the relative abundances of the two isomers, it appears that these are established during synthesis, and we were not able to alter the ratio of any particular sample of adduct. The relative populations were not affected by heating the sample within the NMR tube, nor by the addition of excess NBD. We were also not able to effect a separation of these components, or even a noticeable enrichment of one component through frequent attempts at fractional crystallization.

There is a very strong similarity among the chemical shifts of comparable protons and carbons of **4***a* and **2** (Tables 4 and 6), as well as with the reported values of $PhCN_3S_2$·NBD which has the *syn-exo* geometry in the solid state (2, 24). We thus assign **4***a* to this *syn-exo* geometry in solution. It is characterized by the parameter $\Delta\delta = 0.92$ ppm. We further suggest that **4***b* has one of the other three possible geometries (listed in Scheme 2) which are consistent with S addition and a plane of symmetry in the molecule. Addition to any other atoms in the ring would either lead to a lower symmetry product, or alter the electronic environment sufficiently that the aromatic protons would no longer be shift-equivalent in the two isomers. The data in Table 7 show the MNDO calculated heats of formation for model derivatives of the four possible structures. In fact, the lowest energy belongs to the *syn-endo* geometry, although the difference with the *syn-exo* geometry is very small. On the other hand, the two *anti* structures are calculated to have considerably higher energy (23–26 kJ mol^{-1} more). The *syn-endo* geometry has H_{7b} far removed from the dithiatriazine ring, and in a similar environment to H_{7a}. Consistently, $\Delta\delta = 0.09$ ppm for this isomer in solution, very close to that of the free diene, for which of course $\Delta\delta = 0$.

The difference in ^{1}H chemical shifts are mirrored in the ^{13}C spectra of the two isomers (Table 6). Thus the resonance due to C_7 shifts from 50.76 ppm in **4***b* about 10 ppm upfield to 40.87 ppm in **4***a*. This supports the idea of a through-space deshielding of H_{7b}, since it is well known that under such conditions the attached carbon atom becomes more shielded as the substituent is deshielded.

These conclusions are further supported by the NMR param-

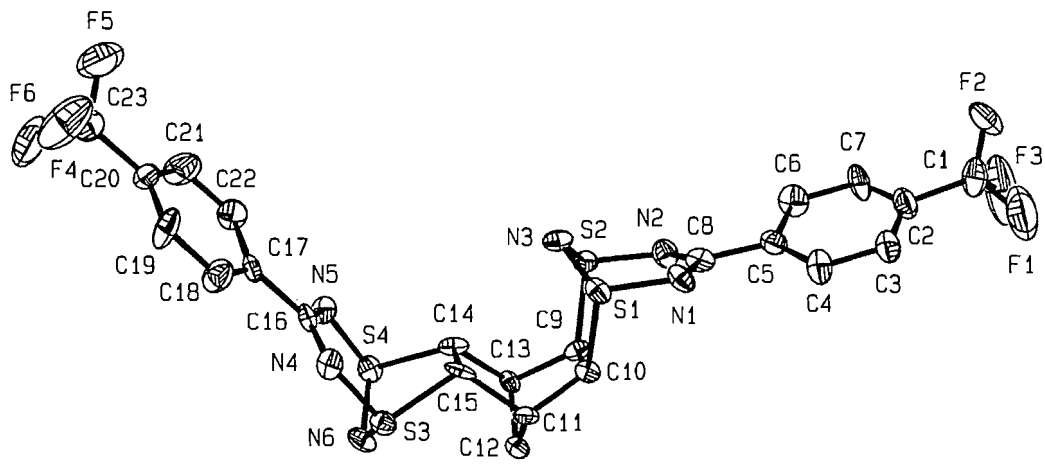

FIG. 3. ORTEP diagram of **5***a* showing the atom numbering scheme and the *exo* (at the left) and *endo* (at right) modes of addition to the diene.

Can. J. Chem. Downloaded from www.nrcresearchpress.com by EESC ESCOLA DE ENGENHARIA on 09/08/12
For personal use only.

TABLE 4. ^{1}H NMR data of alkene adducts

(*a*) Norbornene adducts

Molecule	Reference	$H_{5,6}$	$H_{1,4}$	$H_{2b,3b}$	$H_{2a,3a}$	H_{7b}	H_{7a}	Δ_{AB}[b]
$NBD_{(CDCl3)}$		5.98	2.84	1.60	0.95	1.07	1.32	0.25
4*a*	16	4.67	2.66	1.60	1.40	1.90	0.97	0.93
2*b*	16	4.62	2.62	1.58	1.36	1.87	0.94	0.93
$NBE_{(SO2)}$		7.28	4.15	2.92	2.23	2.39	2.57	0.18
3	12	7.06	4.38	3.14	2.97	2.84	2.68	0.16

(*b*) Norbornadiene adducts

Molecule	Reference	$H_{2,3}$	$H_{5,6}$	$H_{1,4}$	H_{7b}	H_{7a}	Δ_{AB}[b]
$NBC_{(CDCl3)}$		6.73	—	3.55	1.97	—	0
4*a* (65%)		6.28	4.52	3.29	2.13	1.21	0.92
4*b* (35%)		5.92	5.06	3.43	1.54	1.45	0.09
$PhCN_3S_2$.NBD	2	6.24	4.48	3.24	2.08	1.16	0.92
$Me_2NCN_3S_2$.NBD	3	6.21	4.18	3.13	2.00	1.06	0.94
$Et_2NCN_3S_2$.NBD	3	6.24	4.19	3.12	2.05	1.08	0.97
$^iPr_2NCN_3S_2$.NBD	3	6.23	4.16	3.13	2.03	1.04	0.99
$Ph_2PN_3S_2$.NBD[a]	4	6.23	4.13	3.21	1.84	1.18	0.66
$(PhO)_2PN_3S_2$.NBD[a]	4	6.12	3.93	3.08	1.68	1.09	0.59
$Me_2PN_3S_2$.NBD[a]	4	6.39	4.31	3.26	1.80	1.20	0.60
$(CF_3)_2PN_3S_2$.NBD[a]	5	6.45	4.71	3.3	1.67	1.33	0.34
$(C_2F_5)_2PN_3S_2$.NBD[a]	5	6.52	4.75	3.38	1.68	1.37	0.31
$S_3N_3O_2^-$.NBD	6	6.19	5.10	3.00	1.91	0.97	0.94
$Ph_3PNS_3N_3$.NBD	7	6.43	5.39	3.19	1.90	1.19	0.71
$C_6H_4S_2N_2$.NBD	8	6.29, 6.19	4.45, 4.05	3.31	2.17	1.22	1.05
S_4N_4.2NBD	9	6.29	4.38	3.40	1.64	1.45	0.19
$(S_3N)_2$.NBD	10	6.44	4.24	3.36	1.99	1.79	0.20
S_4N_2.NBD	11	6.46, 6.33	2.81, 2.54	3.36, 3.22	1.82	1.69	0.13

(*c*) *bis*-Norbornadiene adducts

Molecule	$H_{2,3}$	$H_{5,6}$	$H_{1,4}$	H_{7b}	H_{7a}	Δ_{AB}[b]
5*a*	4.90	4.81	3.36	2.37	1.17	1.20
5*b*	4.80	—	3.18	1.69	—	0

[a]Assignment altered from original citation.
[b]$\Delta_{AB} = \delta(H_{7b}) - \delta(H_{7a})$.

eters recently reported for *cis*- and *trans*-2-butene adducts of $CF_3CN_3S_2$ (13). These workers demonstrated by combined crystallographic and solution NMR studies that protons attached to the fused C—C bond have characteristic chemical shifts in $CDCl_3$ or CD_3CN solution depending on whether they are *syn* or *anti*. For a number of strained and unstrained olefin adducts H_{syn} are found in the range 4.4 to 5.2 ppm, while H_{anti} are 2.8 to 3.9 ppm. Presumably this is due to *antiaromatic* shielding from the dithiatriazine ring. These protons correspond to $H_{5,6}$ in NBD and NBE adducts of dithiatriazines, which in *all* cases fall within the range 4.16–5.06 ppm.

In conclusion the MNDO calculations as well as the chemical shifts of $H_{5,6}$ rule out the formation of *anti* adducts. This geometry has considerably higher energy attributable to strong steric interactions. Thus the NBD and NBE adducts have *syn* geometry, and so **4***b* must have *syn-endo* geometry as shown in Scheme 1. This mode of addition has never been demonstrated before for any thiazene or heterothiazene NBD adduct. Precedents for such isomerism exist, however, for 1,3-dipolar cycloadditions to NBD (14, 27). Taniguchi et al. conclude "1,3-dipoles cannot undergo cycloadditions from the *endo* side of norbornene. This is probably because of the steric hindrance of the *endo*-5,6-hydrogens. On the other hand, in the case of norbornadiene, it is possible that 1,3-dipoles attack the carbon–carbon double bond from the *endo* side because of the absence of such steric hindrance" (27). These workers suggest that homoconjugation on the *endo* side of NBD serves to balance the π-electron distribution on the two non-identical faces of the double bond.

Structures of bis adducts of dithiatriazines with NBD

Isomer formation in alkene adducts of cyclic thiazenes was not reported before ref. 13. Such isomerism may not be observed for weakly bound thiazene–alkene adducts, for which rapid equilibria are established leading to only the most thermodynamically stable species being formed (8). If, as we believe, the adducts with dithiatriazines are relatively stable,[4] we speculated that it may be possible to add a single NBD molecule to two dithiatriazine rings. Thus we have reacted **1** with exactly 0.5 equivalents of NBD in refluxing acetonitrile for several hours. The resulting brown solutions contained a small amount of colourless precipitate, which was removed in a hot filtration. This proved to be **5***a*. On cooling to room temperature, colour-

[4]One indication for this stability is the presence of small parent ion peaks in the mass spectra of all the dithiatriazine NBD adducts reported in this work.

Can. J. Chem. Downloaded from www.nrcresearchpress.com by EESC ESCOLA DE ENGENHARIA on 09/08/12
For personal use only.

Can. J. Chem. Downloaded from www.nrcresearchpress.com by EESC ESCOLA DE ENGENHARIA on 09/08/12
For personal use only.

less microcrystalline **5***b* precipitates, and more of this could be won from the mother liquor. Considerable care must be taken with solvent volumes and reaction conditions in order to avoid contamination of the products by both **1** and **4**. Taking the mother liquor to dryness always leads to some **4**. **5***a* and **5***b* correspond to two isomeric forms of the *bis* adducts.

The NMR parameters of these *bis* adducts are also presented in Table 4, as well as in Fig. 2. Their spectra are extremely simple; **5***a* is the less abundant species and is also the less symmetric; **5***b* is the more symmetrical isomer. The spectrum of **5***b* can only be interpreted in terms of identical addition geometry at both double bonds in NBD. We only consider the *syn* mode of addition; *anti* addition can be ruled out both on steric grounds and by the chemical shifts of $H_{5,6}$ (identical to $H_{2,3}$ in **5***a*). MNDO calculations on model compounds of these adducts with H atoms on the dithiatriazine ring in place of the $CF_3C_6H_4$ groups showed that only two structures are reasonable, one which we label *exo-exo*, the other *exo-endo*. The energy of these two isomers is calculated to be only 8 kJ mol^{-1} apart, and the *exo-endo* is the higher of these two, in full accord with the proportion of **5***a* and **5***b* obtained from our reactions. On the other hand, the *endo-endo* geometry lies a full 71 kJ mol^{-1} higher than the *exo-endo*, and is thus a much less likely structure. Our confidence in the assignment of the *exo-exo* geometry to **5***b* is increased by the dominance of *exo* addition in all known mono adducts of NBD and NBE. In fact the formation of **5***a* and **5***b* can be explained by a second *exo* addition occurring to a typical mixture of **4***a* and **4***b* in solution.

The only geometry for **5***a* consistent with the spectra is *exo-endo*, which establishes it as only the second species in which *endo* addition of a thiazene to NBD has been identified. This geometry has been confirmed by a single crystal X-ray structure (Fig. 3). Very thin, long plates of **5***a* were grown by slow diffusion of hexanes into CH_2Cl_2 solutions of the adduct at room temperature. Care had to be taken not to heat the adduct or leave its solutions exposed to sunlight for long periods, otherwise the crystal formed contained orange zones which appear to be intergrown crystals of dithiatriazine. The thinness of the crystals has limited the amount of X-ray data available, leading to structural parameters less accurate than normal. However, the structure is entirely conclusive regarding the geometry of addition.

Finally, we comment on the other ^1H NMR parameters of these species. As mentioned above, $H_{2,3}$ and $H_{5,6}$ fall within the expected range for *syn* addition. $H_{1,4}$ for all NBD adducts fall within the same narrow range. The chemical shifts of the bridge methylene protons are the most interesting. First of all, the $\Delta\delta$ parameter in **5***a* is the largest of any thiazene adduct reported at 1.20 ppm. Consistently, in the MNDO calculated structures of the model adducts, the through-space contact between the H_{7b} and the apical N atom is 2.579 Å in the *exo-endo bis* adduct (2.450 Å in the X-ray crystal structure using the *calculated* hydrogen atom position), whereas in the MNDO calculated *syn-exo mono* adduct this distance is larger at 2.680 Å. These distances are all less than the sum of the accepted van der Waals radii for H and N of 2.75 Å (28).

Structure of 1-heptene adducts

To demonstrate the utility of the combined data from our work and from that of ref. 13, we have prepared and characterized by NMR the 1-heptene adduct of **1**. An indication of the strength of the adduct bond is the observation of a small parent-ion peak in the mass spectrum of **6**. The NMR spectra of **6** also show the presence of isomers (Tables 5 and 6 and Fig. 4).

TABLE 5. ^1H NMR data of 1-heptene adducts

	6*a*	**6***b*
H_{1syn}	4.49 d.d. (12.4, 7.1)	3.83 d.d. (11.6, 5.7)
H_{1anti}	2.83 d.d. (12.4, 4.0)	3.44 d.d. (11.6, 9.9)
H_{2syn}	4.91 m	—
H_{2anti}	—	3.71 m
H_3	~1.3 m + ~1.6 m	2.28 m
H_4	1.49 m	1.60 m
H_5	~1.3 m	~1.3 m
H_6	~1.3 m	~1.3 m
H_7	0.90 m	0.90 m
H_{10}[a]	7.97 d (8.6)	8.02 d(8.6)
H_{11}[a]	7.57 d (8.6)	7.59 d (8.6)

[a]Aromatic protons; see Table 6 for attached carbon labeling scheme.

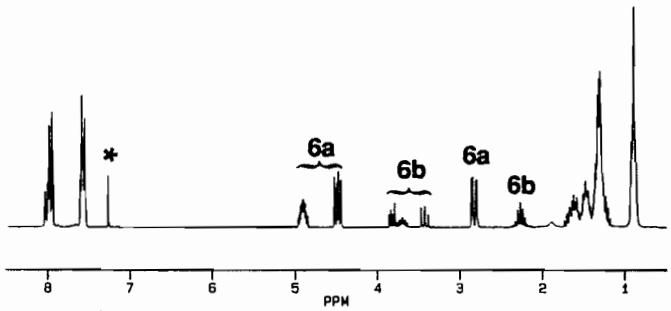

FIG. 4. ^1H NMR spectrum of a mixture of two isomers of **6***a* and **6***b* in $CDCl_3$ solution. An asterisk marks solvent impurity.

Different samples from different preparations of **6** show different amounts of these two isomers which we label as **6***a* and **6***b*. The main features of the spectrum are readily interpreted from the 2-D correlation spectra. We also see clear evidence that the *anti* protons are at much higher field than the *syn* protons (13). Deshielding of the latter by proximity to the antiaromatic dithiatriazine ring is invoked to explain these large differences ranging between 0.5 and 1.7 ppm. The deshielding of the CH_2 group of C_3 is also marked, at 2.3 ppm compared to the average of H_3 for the anti isomer of 1.4 ppm. The ^{13}C spectra have undifferentiated signals for C_6 and C_7 in the olefin, and the CF_3 carbon atom on the aryl ring. All other signals are differentiated in the two isomers.

We have not attempted to separate these isomers, although recrystallization from pentane significantly altered the isomer population. Our main interest in synthesizing this adduct was to demonstrate the ability to assign alkene adduct structures of dithiatriazines with confidence based on the NMR parameters alone, and to determine whether aryl dithiatriazines form stable adducts with unactivated alkenes. In this vein we have also attempted to prepare an ethene adduct. The reaction of dithiatriazine with ethene does lead to the formation of a fine white solid. However, this solid proved to be extremely insoluble and we therefore concentrated on longer-chain alkenes which greatly enhanced solubility of the adducts.

Solution structures of alkene adducts of thiazenes

Over the years numerous alkene adducts, mostly with norbornadiene, have been reported for a wide variety of cyclic and acyclic thiazenes (1–11). The data for NBD adducts are collected together in Table 4. Erroneous assignments in the literature have been corrected; corrected entries have been marked.

TABLE 6. ^{13}C NMR data of alkene adducts[a]

Atom	$NBE_{(CDCl_3)}$	**2***a*	$NBE_{(SO_2)}$	**3**[b]	**4***a*	**4***b*
C_1	41.76	38.09	43.15	41.71	43.98	46.15
C_2	24.60	27.94	25.88	28.71	138.71	130.98
C_5	135.31	87.92	137.69	94.07	83.98	82.99
C_7	48.52	33.04	49.76	35.51	40.87	50.76
C_8		158.19			158.72	159.21
C_9		141.92			142.03	142.37
C_{10}		127.10			127.00	126.93
C_{11}[c]		124.70(4)			124.66(4)[f]	124.66(4)[f]
C_{12}[d]		132.35(32)			132.28(32)[f]	132.28(32)[f]
C_{13}[e]		123.96(272)			123.91(273)[f]	123.91(273)[f]

Atom	NBD	**5***a*	**5***b*	**6***a*	**6***b*
C_1	50.27	42.07	40.03	68.95	66.98
C_2	143.42	82.22	85.16	83.64	84.76
C_3				33.00	28.89
C_4				28.22	30.63
C_5		85.46		31.09	31.46
C_6				22.20	22.20
C_7	75.33	34.85	28.4	13.79	13.79
C_8		159.52, 157.90	158.4	158.58	159.85
C_9		141.18, 140.81	140.93	141.56	141.47
C_{10}		127.45, 127.10	127.23	127.17	127.30
C_{11}		124.88(4), 124.82(4)	124.9(4)	124.75(4)[f]	124.75(4)[f]
C_{12}		133.03(32), 132.95(32)	133.00(32)	132.49(32.4)[f]	132.53(32.4)[f]
C_{13}		123.88(272), 123.84(272)	123.84(273)	123.92(272.5)[f]	123.92(272.5)[f]

[a]Numbering scheme in rings: symmetry-related entries have been entered only for the first nucleus of the set.

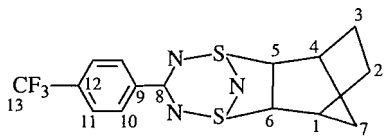

[b]Reference 12.
[c]Quartet, $^3J(^{19}F—^{13}C)$.
[d]Quartet, $^2J(^{19}F—^{13}C)$.
[e]Quartet, $^1J(^{19}F—^{13}C)$.
[f]Signals undifferentiated in isomers.

TABLE 7. MNDO calculated heats of formation (kJ mol^{-1})

Adduct	Isomer	NBE adduct	NBD adduct	1-Heptene adduct
Mono-adducts	*Syn-exo*	514	663	—
	Syn-endo	522	662	—
	Anti-endo	560	684	—
	Anti-exo	536	687	—
	Syn	—	—	373
	Anti	—	—	376
Bis-adducts	*Exo-exo*	—	1088	—
	Exo-endo	—	1096	—
	Endo-endo	—	1167	—

We focus discussion on our calculated parameter $\Delta\delta$ for $H_{7a,b}$ in these compounds. Very small values occur for the acyclic adducts of S_3N (10) and S_4N_2 (11), which lack an apical nitrogen atom. The largest values are found for the dithiatriazine derivatives (0.92–0.99 ppm) and the fused-ring analogue $C_6H_4S_2N_2$ (1.05 ppm) (8). Smaller values are found for adducts of phosphadithiatriazines, ranging from 0.3–0.6 ppm (4, 5). The smallest value for a cyclic system is the *bis* NBD adduct of S_4N_4 (9), which has been the subject of much controversy. Essentially the value of $\Delta\delta$ decreases with increasing ring size and ring floppiness. We believe that the trend emerging from all this data is that the smaller the thiazene ring that the olefin is attached to, the

Can. J. Chem. Downloaded from www.nrcresearchpress.com by EESC ESCOLA DE ENGENHARIA on 09/08/12
For personal use only.

Can. J. Chem. Downloaded from www.nrcresearchpress.com by EESC ESCOLA DE ENGENHARIA on 09/08/12
For personal use only.

more distinct the environments of $H_{7a,b}$ becomes in the dominant *syn-exo* mode of addition. Thus these NMR parameters are most reliable in the structure assignment of small ring systems.

^1H NMR spectrum of 3

Recently Chivers et al. reported the synthesis, crystal structure, and ^{13}C NMR spectra of $S_3N_3{\cdot}C_7H_{10}$, **3** (12). This adduct is isoelectronic to the dithiatriazine adducts **2**. However, the ^1H NMR spectrum was not reported. 2-D NMR techniques are readily extended to the assignment of this proton spectrum. The results are reported in Table 1. This compound is only soluble in SO_2. We found that acceptable spectra, including COSY-45 and HETCORR sequences, could be obtained in an automated **5** mm dual ^1H–^{13}C probe by using a 4 mm Pyrex tube insert which contained the SO_2 solution, sealed under vacuum, within a standard 5 mm NMR tube. The remaining coaxial space was filled with deuterated benzene for a lock signal.

We found very large solvent effects on the ^1H chemical shifts for both NBE and the adduct in liquid SO_2. However, the relative positions of the protons is unaltered from those in $CDCl_3$. Assignment is again straightforward using standard Karplus and W-coupling reasoning. The surprising fact is the small value of $\Delta\delta$ for the adduct, which by crystallography has the *syn-exo* geometry in the solid state (12). $\Delta\delta$ is hardly different from that in the free alkene in the same solvent. The spectra are consistent with only one solution species, and since this is an NBE adduct, isomerism is not expected; the solution species must be a *syn-exo* adduct. We feel that strong solvent interactions between SO_2 and $H_{7a,b}$ are overriding the through-space interaction with the apical nitrogen atom in this compound. Thus while 2-D NMR techniques can easily be applied in this exotic solvent using a modern FT-NMR spectrometer, the structural parameters developed above for standard NMR solvents such as $CDCl_3$ cannot be used.

Conclusions

The application of 2D-NMR techniques to the interpretation of the NMR spectra of alkene adducts of thiazenes is essential in order to reduce the risk of wrong spectral assignments. The parameters identified in this paper allow reliable structure determination using NMR for both chain- and cyclic-alkene thiazene adducts in conventional NMR solvents such as $CDCl_3$ or CD_3CN. The reliability of this method is greater for addition to small ring thiazenes for which more rigid adducts are expected in solution.

We have presented conclusive NMR evidence for the presence of a second, *endo*, mode of addition of thiazenes to NBD. The presence of such species may have been overlooked in the past as "impurity" signals in NMR spectra of the adducts. The strongly anti-aromatic electronic structure of dithiatriazines make this ring system an excellent candidate for observing potential isomerism. We have discovered the first example of *bis* addition of thiazenes to a single NBD molecule, and the first crystallographic confirmation of *endo* addition.

Acknowledgements

We thank the Natural Sciences and Engineering Research Council of Canada for support in the form of an operating grant (R.T.B.) and an equipment grant for the Infrared spectrometer, as well as the University of Lethbridge for the purchase of the NMR spectrometer. K.P. was supported through the University of Lethbridge Research Fund. C.D.B. acknowledges a DOE/ASTA Traineeship.

1. R.T. Boeré, A.W. Cordes, and R.T. Oakley. J. Chem. Soc. Chem. Commun. 929 (1985).
2. R.T. Boeré, C.L. French, R.T. Oakley, A.W. Cordes, J.A.J. Privett, S.L. Craig, and J.B. Graham. J. Am. Chem. Soc. **107**, 7710 (1985).
3. T. Chivers, F. Edelmann, J.F. Richardson, N.R.M. Smith, O. Treu Jr., and M. Trsic. Inorg. Chem. **25**, 2119 (1986).
4. N. Burford, T. Chivers, A.W. Cordes, W.G. Laidlaw, M.C. Noble, R.T. Oakley, P.N. Swepston. J. Am. Chem. Soc. **104**, 1282 (1982).
5. H.W. Roesky, J. Lucas, M. Noltemeyer, and G.M. Sheldrick. Chem. Ber. **117**, 1583 (1984).
6. R.T. Oakley and M. Shevalier. Private communication.
7. S.W. Liblong, R.T. Oakley, A.W. Cordes, and M.C. Noble. Can. J. Chem. **61**, 2062 (1983).
8. A.W. Cordes, M. Hojo, H. Koenig, M.C. Noble, R.T. Oakley, and W.T. Pennington. Inorg. Chem. **25**, 1137 (1986).
9. M.R. Brinkman and C.W. Allen. J. Am. Chem. Soc. **94**, 1550 (1972).
10. A.W. Cordes, H. Koenig, M.C. Noble, and R.T. Oakley. Inorg. Chem. **22**, 3375 (1983).
11. H. Koenig, R.T. Oakley, A.W. Cordes, and M.C. Noble. Can. J. Chem. **61**, 1185 (1983).
12. A. Apblett, T. Chivers, A.W. Cordes, and R. Vollmerhaus. Inorg. Chem. **30**, 1393 (1991); **30**, 5052 (1991).
13. R. Maggiulli, R. Mews, M. Noltemeyer, W. Offermann, R. Paape, and W.D. Stohrer. Chem. Ber. **124**, 39 (1991).
14. G. Bianchi, C. de Micheli, and R. Gandolphi. *In* The chemistry of functional groups. Supplement A, Part 1. *Edited by* S. Patai. Wiley, New York, NY. 1977. pp. 369–532.
15. R.E. Hoffmeyer, W.T. Chan, J.D. Goddard, and R.T. Oakley. Can. J. Chem. **66**, 2279 (1988).
16. R.T. Boeré, J. Fait, K. Larsen, and J. Yip. Inorg. Chem. **31**, 1417 (1992).
17. D.T. Cromer and J.B. Mann. Acta Crystallogr. A**24**, 321 (1968).
18. R.F. Stewart, E.R. Davidson, and W.T. Simpson. J. Chem. Phys. **42**, 3175 (1965).
19. D.T. Cromer and D. Liberman. J. Chem. Phys. **53**, 1891 (1970).
20. G.M. Sheldrick. SHELX-76. A program for crystal structure determination, University of Cambridge, Cambridge, U.K. 1976.
21. C.K. Johnson. ORTEP II. Report ORNL-5138. Oak Ridge National Laboratory, TN, U.S.A., 1976.
22. E.J. Gabe, Y. LePage, J.P. Charland, F.L. Lee, and P.S. White. J. Appl. Cryst. **22**, 383(1989).
23. HyperChem Release 3 for Windows. Autodesk, Inc., 2320 Marinship Way, Sausalito, CA 94965, U.S.A., 1993.
24. J.A. James, S.L. Craig, A.W. Cordes, R.T. Oakley, and R.T. Boeré. Acta Crystallogr. C**42**, 508 (1986).
25. A.L. Ternay. Contemporary organic chemistry. Saunders, Philadelphia. 1976. pp. 205, 212.
26. A.P. Marchand. Stereochemical applications of NMR studies in rigid bicyclic systems. VCH Publishers, Deerfield Beach, FL. 1982.
27. H. Taniguchi, T. Ikeda, Y. Yoshida, and E. Imoto. Bull. Chem. Soc. Jpn. **50**, 2694 (1977).
28. A. Bondi. J. Phys. Chem. **68**, 441 (1964).

1993 R.U. Lemieux Award Lecture
Organometallic-type reactions in aqueous media — a new challenge in organic synthesis[1]

T.H. CHAN,[1] C.J. LI, M.C. LEE, AND Z.Y. WEI
Department of Chemistry, McGill University, Montreal, QC H3A 2K6, Canada

Received July 5, 1993

T.H. CHAN, C.J. LI, M.C. LEE, and Z.Y. WEI. Can. J. Chem. **72**, 1181 (1994).

The development of organometallic-type reactions in aqueous media is reviewed. Coupling reactions of allyl halides with carbonyl compounds mediated by zinc, or tin, or indium in aqueous media to give homoallylic alcohols are discussed. The stereochemical outcome is compared with similar reactions in organic solvents. A concise synthesis of (+)-muscarine is used to illustrate the usefulness of aqueous organometallic-type reactions in organic synthesis. The procedure to protect–deprotect hydroxy functional groups may not be necessary in these reactions. An application in the carbohydrate area is demonstrated with the synthesis of (+)-3-deoxy-D-*glycero*-D-*galacto*-nonulosonic acid (KDN). The mechanistic possibilities of organometallic-type reactions in aqueous media are outlined.

T.H. CHAN, C.J. LI, M.C. LEE et Z.Y. WEI. Can. J. Chem. **72**, 1181 (1994).

On passe en revue le développement de réactions de type organométalliques dans des milieux aqueux. On discute des réactions de couplage des halogénures allyliques et des composés carbonylés, catalysées par le zinc, l'étain ou l'indium en solutions aqueuses et conduisant à des alcools homoallyliques. On compare le résultat stéréochimique de ces réactions avec ceux de réactions semblables dans des solvants organiques. On a utilisé une synthèse concise de la (+)-muscarine pour illustrer l'utilité des réactions de type organométallique, en solutions aqueuses, en synthèse organique. Dans ces réactions, il n'est pas toujours nécessaire de protéger, puis déprotéger, les groupes hydroxyles fonctionnels. On a démontré son utilité dans le domaine des carbohydrates en procédant à la synthèse de l'acide (+)-3-désoxy-D-*glycéro*-D-*galacto*-nonulosonique. On décrit brièvement les possibilités mécanistiques des réactions du type organométallique en solutions aqueuses.

[Traduit par la Rédaction]

Introduction

The importance of organometallic reactions in organic synthesis is well recognized. Organometallic reactions using Grignard reagents or organolithium compounds are the cornerstone of organic synthesis. In their most general form, these reagents are used to construct new carbon–carbon bonds, leading to compounds of greater complexity. A cardinal restriction in the use of many organometallic reagents is the strict exclusion of moisture. Thus, we accept, without question, the limitations imposed by these restrictions, namely, that the reactions cannot be carried out in aqueous media, and that these reagents cannot coexist with a trace of water, or with reactive hydroxy or acidic hydrogens. These inherent limitations profoundly govern our thinking about organic synthesis. We accept, first of all, that anhydrous organic solvents are required for these reactions. Furthermore, reactive hydroxy or acidic groups must be protected, and indeed, extensive protection–deprotection chemistry has been developed for that purpose. As well, we accept that compounds such as carbohydrates, insoluble in organic solvents, will have to be derivatized so that they become soluble. This has evolved to become part of the accepted way of doing synthesis in the carbohydrate field. Finally, many stereochemical formulations, e.g., Cram's rule (1) and its modifications, are based generally on conclusions reached from reactions carried out in organic solvents.

If one can perform organometallic-type reactions in aqueous media just as generally and easily as in organic solvents, such reactions may offer considerable advantages: (*i*) There is the practical convenience of not having to handle inflammable and anhydrous organic solvents. (*ii*) The tedious task of protection–deprotection chemistry for certain functional groups often encountered in organic synthesis may not be required. (*iii*) Water-soluble compounds can be reacted directly without the need of derivatization. This is a point of particular interest in carbohydrate chemistry. (*iv*) The stereochemical outcomes of organometallic reactions may well change from organic to aqueous media and thus offer new opportunities in synthesis. Several years ago, we began a program to study organometallic-type reactions in aqueous media with a view to exploring the above-mentioned possibilities.

It may be useful to examine the factors that may lead to choosing appropriate organometallic reagents for aqueous media. It is generally known that the less reactive organometalloid reagents, such as organosilicon compounds, do not react with water (2). Can they be used for organometallic-type reactions in aqueous media? The answer is negative. Precisely because silicon is less reactive, the preparation of organosilanes directly from silicon and organic halides is not as easy as the Grignard reagents or organolithiums. Furthermore, formation of a C—C bond using organosilicon reagents requires strongly acidic conditions (3). Organosilanes are not likely to be candidates.

What about the somewhat more reactive organotin compounds? It was known as early as 1961 that tin reacts with benzyl chloride directly to form the corresponding organotin compounds **1** and **2** (Scheme 1) (4). What is interesting, and was little exploited at that time, is the fact that the reaction could be carried out in a number of solvents, including water. It was reported that the yield of tribenzyltin chloride (**2**) was quite respectable when the reaction was carried out in aqueous medium. Even though the tin–chlorine bond was partially hydrolysed, the tin–carbon bond survived in water to a large extent in spite of the fairly high temperature. It was in the 70s, and then increasingly so in the 80s, that the use of tin, and zinc as well, to mediate the allylation of aldehydes and ketones in water to give the corresponding homoallylic alcohols (**3**) (Scheme 2) was reported, first by Wolinsky and co-workers in

[1]This work was presented by Professor Chan as the Lemieux Award Lecture at the 76th Annual Conference of the Canadian Society for Chemistry, Sherbrooke, Québec, June 1, 1993.

Can. J. Chem. Downloaded from www.nrcresearchpress.com by EESC ESCOLA DE ENGENHARIA on 09/08/12
For personal use only.

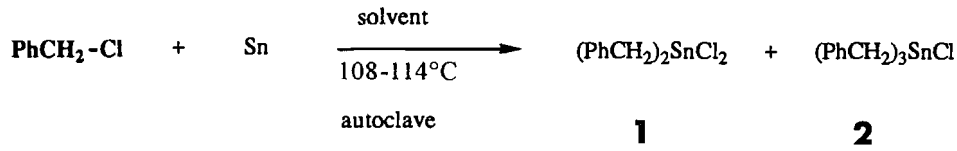

SCHEME 1

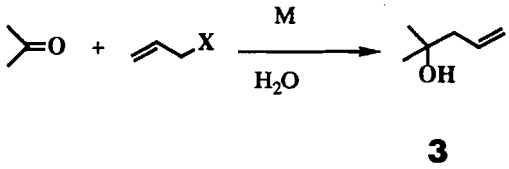

SCHEME 2

1977 (5), then by Nokami et al. in 1983 (6), later on more systematically by Luche and co-workers in France (7), and more recently by Wilson and Guazzaroni in the U.S. (8). The metal used can be either Sn or Zn, and the solvent used can be water, with or without organic cosolvents. The yields are in general good to excellent. But there is always an induction period of indefinite time, and the use of catalyst, ammonium chloride or hydrobromic acid, appears to promote the reaction. The use of heat or ultrasound radiation has also been found to facilitate the reaction. The side products most often reported are the reduced carbonyl compounds, the alcohols **4**, and (or) the pinacols **5**

4

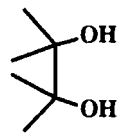

5

from the reductive coupling of the precursor carbonyl compounds.

Results and discussion

When we began our work in this area, the first question we posed was a very simple one: can one extend the known reactions to synthesize compounds other than homoallylic alcohols? Indeed, we found (9) that aldehydes and ketones could be converted to 1,3-butadienes **6** or vinylepoxides **7** by reaction with 1-chloro-3-iodopropene (**8**). Powdered zinc metal was used (Scheme 3). The intermediate chlorohydrin **9** could be isolated, which on further reaction with zinc in water gave the diene **6** in good to excellent yields. Alternatively, treatment of the chlorohydrin with base gave the vinylepoxide **7**. The results of this reaction are summarized in Table 1. The following features of the reaction are noteworthy. The carbonyl compound can contain an unprotected hydroxy group, and the reaction proceeds equally well. While this is not surprising in view of the fact that the reaction is carried out in water, one can hardly expect an hydroxy group to prevent the reaction if water is present everywhere. This is nevertheless quite contrary to conventional organometallic reactions: namely, the hydroxy group would first have to be protected, and then deprotected after the reaction. Secondly, the reaction seems to proceed in a 1,2-addition fashion. With cinnamaldehyde, the corresponding triene is obtained. Thirdly, the butadienes **6** are formed stereoselectively and, in the case of aldehydes, exclusively as the *E* isomers. On the other hand, the vinylepoxides **7** are formed as a mixture of *cis/trans* diastereomers, and the ratio is in agreement with the diastereomeric ratio of the precursor chlorohydrins **9**. This suggests that the reduction of **9** to give **6** under the experimental conditions is non-stereospecific but selective in giving the thermodynamically more stable *E* isomer. This is contrary to the usual *trans* elimination under metal/dihalide reduction conditions (10).

Another simple modification is to use 2-chloromethyl-3-iodopropene (**10**) as the allylic halide. This provides a synthesis of methylenetetrahydrofurans **11** from the carbonyl precursors in good to excellent yields (Scheme 4) (11). The reaction can be looked upon as providing a trimethylenemethane equivalent **12**, the 1,3-dipolar species. The conventional trimethylenemethane

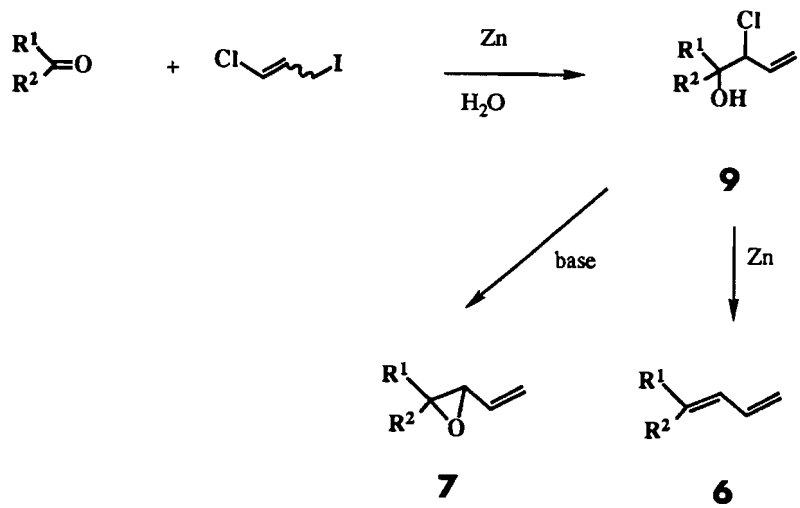

SCHEME 3

Can. J. Chem. Downloaded from www.nrcresearchpress.com by EESC ESCOLA DE ENGENHARIA on 09/08/12
For personal use only.

TABLE 1. Syntheses of 1,3-dienes (6) and vinylepoxides (7)

Entry	Aldehyde	Halide	Product	% Yield (method)[a]	*trans:cis*
1	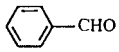	ClCH=CHCH$_2$Cl	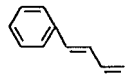	53 (A)	>98
2		ClCH=CHCH$_2$I		95 (B)	>98
3		ClCH=CHCH$_2$I	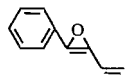	95 (C)	36:64
4	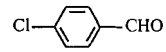	ClCH=CHCH$_2$I	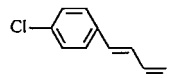	97 (B)	>98
5		ClCH=CHCH$_2$I	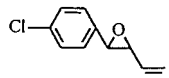	95 (C)	36:64
6	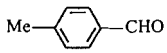	ClCH=CHCH$_2$I	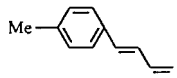	95 (B)	>98
7		ClCH=CHCH$_2$I	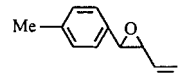	93 (C)	36:64
8	$CH_3(CH_3)_3CHO$	ClCH=CHCH$_2$Cl	$CH_3(CH_2)_3CH{=}CH{-}CH{=}CH_2$	53 (A)	95:5
9		ClCH=CHCH$_2$I		92 (B)	95:5
10		ClCH=CHCH$_2$I	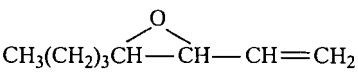	92 (C)	48:52
11	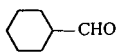	ClCH=CHCH$_2$Cl	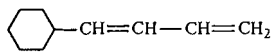	48 (A)	>98
12		ClCH=CHCH$_2$I		93 (B)	>98
13	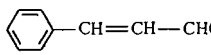	ClCH=CHCH$_2$Cl	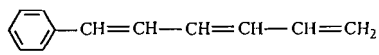	38 (A)	>98
14		ClCH=CHCH$_2$I		86 (B)	>98
15		ClCH=CHCH$_2$Cl	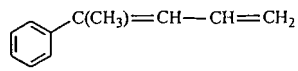	53 (A)	85:15
16		ClCH=CHCH$_2$I		80 (B)	85:15
17	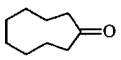	ClCH=CHCH$_2$Cl	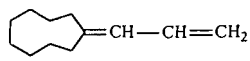	36 (A)	
18	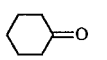	ClCH=CHCH$_2$I	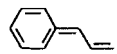	95 (B)	
19		ClCH=CHCH$_2$I		93 (C)	
20	$CH_3(CH_2)_3CO(CH_2)_3CH_3$	ClCH=CHCH$_2$Cl	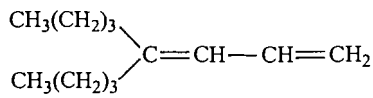	20 (A)	
21	$CH_3(CH_2)_3COCH_3$	ClCH=CHCH$_2$Cl	$CH_3(CH_2)_3C(CH_3){=}CH{-}CH{=}CH_2$	33 (A)	70:30
22		ClCH=CHCH$_2$I		75 (B)	68:32
23	$HO(CH_2)_4CHO$	ClCH=CHCH$_2$Cl	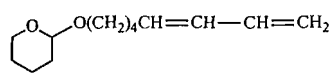	42 (A)	88:12
24	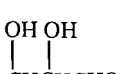	ClCH=CHCH$_2$Cl		33 (A)	>98

[a]Method: (A) A mixture of the carbonyl compound (1 mmol), 1,3-dichloropropene (1 mmol), and zinc powder (2 mmol) in 10 mL of water was heated to 35°C with vigorous stirring for 3–4 h. The reaction mixture was cooled and quenched with ether. The organic product was isolated from the ether phase and purified by flash column chromatography. (B) A mixture of the carbonyl compound (1 mmol), 1-chloro-3-iodopropene (1.5 mmol), and zinc powder (1.5 mmol) in 10 mL of water was stirred at room temperature until the zinc almost disappeared (in cases where the reaction did not start properly, 2–3 drops of hydrobromic acid or saturated ammonium hydrochloride solution could be added to initiate the reaction). To the reaction mixture was then added 2 mL of hydrobromic acid (48%) and zinc powder (10 mmol) over a period of 5 h. The reaction mixture was then extracted with ether to give, after purification by flash column chromatography, the diene. (C) The reaction was interrupted after the first stage of method (B) by extraction with ether. The intermediate chlorohydrin was isolated, and treated in ethanolic NaOH (0.4 g/10 mL) to give the vinylepoxide in quantitative yield.

Can. J. Chem. Downloaded from www.nrcresearchpress.com by EESC ESCOLA DE ENGENHARIA on 09/08/12
For personal use only.

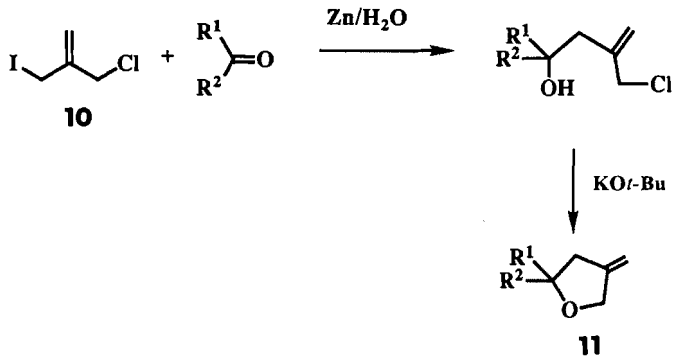

SCHEME 4

equivalents usually require balanced reactive ends, for example, compound **13** with a less reactive silyl or stannyl nucleophilic end, but a more reactive acetate electrophilic end (12), or compound **14** with a more reactive zinc or magnesium halide end

12

13 M=Si or Sn

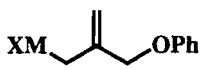

14 MX=ZnBr or MgCl

together with a less reactive phenoxy end (13). Such a balance in reactivity of the two polar centers is required to prevent self-cyclization, or di- and polymerization. In the case of the present reaction, what is the possible mechanism? Is a true organozinc intermediate actually formed, in the presence of water, with a reactive allylic halide as the other polar center?

At this point, it might be profitable to speculate on the possible mechanism of this kind of organometallic-type reaction in aqueous media. In the case where metallic zinc is used, the actual formation of the allylzinc intermediate is considered unlikely, because such organozincs are known to react instantaneously with water (14). The involvement of the less reactive allyltin intermediate may also be unlikely, while it has been known that allylic bromide does react with tin in organic solvents to give the corresponding diallyltin dibromide (**15**). In water, the same reaction gives propene, presumably because the allyltin intermediate reacts with water under the reaction conditions (Scheme 5) (15). One possible mechanism is that the metal reacts with the carbonyl compound by a single electron transfer (SET) process to give the radical anion intermediate **16**. The ketyl radical anion couples with the allylic halide to give the alkoxy radical, which on further reduction by the metal in another single electron transfer step gives the alkoxide anion, which is then protonated by water to the homoallylic alcohol product (Scheme 6). This mechanism can account not only for the product, but also for the side product of the reaction, namely, the pinacol **5**, because of the coupling of the ketyl radical anion.

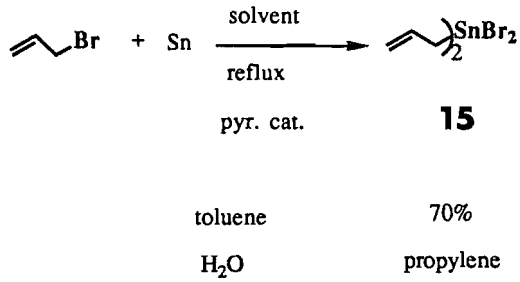

SCHEME 5

Another equally likely mechanism is the following: it is the allylic halide that reacts with the metal in an SET step to give the radical anion **17**. The radical anion then couples with the carbonyl compound to give the alkoxy radical species, which on further reduction by the metal gives the product (Scheme 7). In support of this mechanism, the self-coupling product **18** of the allylic halide **10** can also be found in the reaction mixture as a side product.

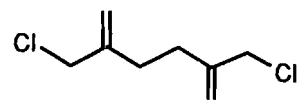

18

Irrespective of the real mechanism (a question that may take a long time to resolve), if a single electron transfer step is indeed involved, one may ask: can other metals perform the same function equally well or even better? This led us to search for other possibilities. If one looks at what is required of this metal, one

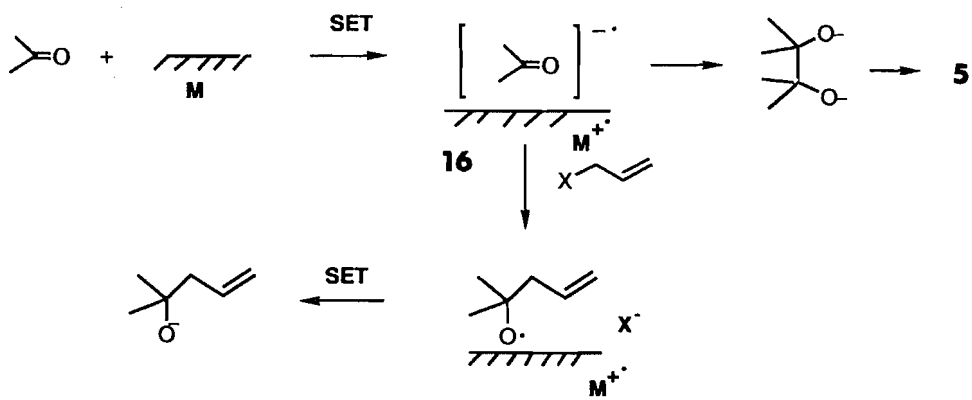

SCHEME 6

Can. J. Chem. Downloaded from www.nrcresearchpress.com by EESC ESCOLA DE ENGENHARIA on 09/08/12
For personal use only.

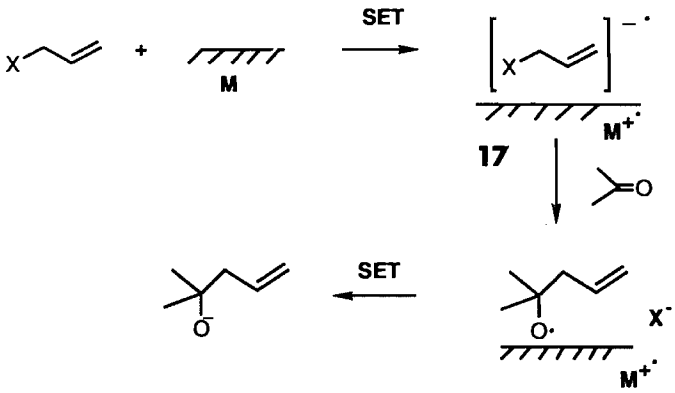

SCHEME 7

TABLE 2. First to fourth ionization potential of some metals

Metal	Ionization potential (eV)			
	I	II	III	IV
Indium	5.785	18.86	28.03	54.4
Aluminum	5.984	18.82	28.44	119.96
Magnesium	7.646	15.035	80.143	109.29
Zinc	9.39	17.96	39.7	
Tin	7.34	14.63	30.49	40.72

realizes that the metal itself must not react with water. This removes from consideration metals such as sodium, potassium, cesium, magnesium, etc., or similarly reactive metals. Furthermore, the metal must not react in air to form water-insoluble oxides. This eliminates metals such as titanium or aluminium whose oxides are water insoluble. Another consideration is that the metal must be somewhat more reactive than silicon and germanium, or perhaps even tin.

In this connection, indium metal offers some intriguing possibilities. Compared to other metals, indium has not been much explored in organometallic reactions (16). It is only recently that indium has been used in Reformatsky reactions (17), allylations (18), and cyclopropanations (19) of carbonyl compounds. While these results are interesting, the use of indium in organic solvents offers no obvious advantages over other conventional organometallic reactions. On the other hand, it is known that indium is unaffected by boiling water! It does not readily form oxide in air. Most interestingly, its first ionization potential is much lower than zinc. In Table 2, we compare the ionization potentials of five metallic elements. Indium has the lowest first ionization potential among them, but it has the highest second ionization potential. If the mechanism of the aqueous

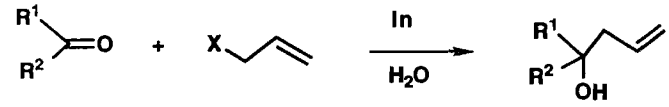

SCHEME 8

organometallic reactions is indeed initiated by a single electron transfer step and not a two-electron transfer reaction, then indium should be a reasonable candidate.

Sure enough, when allylic halide and carbonyl compounds are stirred with indium in aqueous media, the reaction proceeds very well to give the corresponding homoallylic alcohols (Scheme 8) (20). The yields are usually good to excellent (Table 3). There are few side products of alcohols or pinacols. In contrast to the zinc- and tin-mediated reactions, where some acidic initiators are usually required, the indium reaction can be applied to carbonyl compounds with acid-labile groups. An example is found by comparing the three metals in the same reaction with the substrate **19** where there is a labile acetal group. With zinc as the metal, the reaction fails with destruction of the starting materials. Using tin, the yield is very poor, but with indium the reaction proceeds normally to give the desired product in 70% yield (Scheme 9).

A useful variation on the same theme is to use the allylic halide **20** with the ester functional group. The reaction can be mediated by indium in water to give the coupled product in very good yield. This can serve, of course, as a facile route to α-methylene-γ-lactones **21** (Scheme 10).

In 1990, we reported on crossed aldol-type condensation reactions in aqueous media. Aldehydes and α-halo-carbonyl compounds condense in water with zinc or tin to give the crossed aldol-type products **22** (Scheme 11) in reasonably good yields (21). The distinctive feature of this reaction is that there does not appear to be the normal complication of crossed aldol reaction in organic solvents in that there are few elimination products, poly-aldol condensations, or self-aldol products. The major side products appear to be owing to the reduction of the α-halo-carbonyl compounds, as well as the reductive coupled products, for example, the 1,4-diketone **23** from the bromoketone **24**. The diastereoselectivity of the reaction is between

24 **23**

1:1 and 2:1, not much different from the normal diastereoselectivity of this type of reaction performed in organic solvents.

When the same crossed aldol-type reaction is carried out

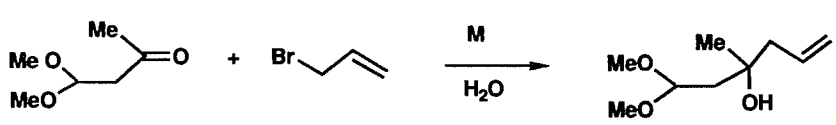

19

M	Yield, %
Zn	0 and destruction of starting materials
Sn	10
In	70

SCHEME 9

Can. J. Chem. Downloaded from www.nrcresearchpress.com by EESC ESCOLA DE ENGENHARIA on 09/08/12
For personal use only.

TABLE 3. Allylation of aldehydes and ketones mediated by indium in aqueous media

Entry	R^1	R^2	X	Metal	A/allylX/M	Time (h)	Yield	*syn:anti*
1	Ph	H	Br	In	1/1.5/1	3	97	
2	Ph	H	I	In	1/1.5/1	3	95	
3	Ph	H	Cl	In	1/1.5/1	5	60	
4	Ph	H	Cl	Sn	1/1.5/1	5	0[a,b]	
5	ClPh	H	Br	In	1/1.5/1	1	94	
6	CH_3CHOH	H	Br	In	1/1.5/1	3	85	67:33
7	$CH_3CH(ODCB)$	H	Br	In	1/1.5/1	3	75	24:76
8	$CH_3(CH_2)_2CH(OBn)$	H	Br	In	1/1.5/1	3	80	24:76
9	$PhCH(CH_3)$	H	Br	In	1/1.5/1	3	90	78:22
10	Ph	CH_3	Br	In	1/1.5/1	5	72	
11	Ph	CH_3	Br	Zn	1/1.5/1	5	18[c]	
12	Ph	CH_3	Br	Sn	1/1.5/1	3	0[a]	
13	$-(CH_2)_5-$		Br	In	1/1.5/1	6	68	
14	$-(CH_2)_5-$		Br	Sn	1/1.5/1	6	0[a]	
15	$HOCH_2C(CH_3)_2$	H	Br	In	1/1.5/1	3	85	
16	$HO(CH_2)_4$	H	Br	In	1/1.5/1	3	95	
17	$(CH_3O)_2CHCH_2$	CH_3	Br	In	1/2/1.5	6	70	
18	$(CH_3O)_2CHCH_2$	CH_3	Br	Zn	1/2/2	6	0	
19	$(CH_3O)_2CHCH_2$	CH_3	Br	Sn	1/2/2	6	10[d]	

All the reactions were performed at 1 mmol scale at room temperature in water by stirring the reaction mixture for the proper time, unless otherwise mentioned.
[a]Mediated by tin at 80°C.
[b]Promoted by sonication.
[c]Mediated by zinc with sonication.
[d]By ^1H nmr.

TABLE 4. Crossed aldol reactions mediated by indium in water

Entry	RCHO	Halide	RCHO/halide/In	Time (h)	*erythro:threo*	Yield
1	PhCHO	$BrC(CH_3)_2COPh$	1/1.5/1	3		88
2	PhCHO	$BrCH(CH_3)COPh$	1/1.5/1	3	12:1	85
3	PhCHO	$BrCH(CH_3)COPh$	1/1/1	3	12:1	56[a]
4	*p*-MePhCHO	$BrCH(CH_3)COPh$	1/1/1	5	12:1	72
5	$CH_3(CH_2)_7CHO$	$BrCH(CH_3)COPh$	1/1/1	5	4:1	64
6	PhCHO	$BrCH_2COPh$	1/1/1	5		15
7	PhCHO	$BrCH(CH_3)COCH_3$	1/1/1	5	3:1	48

[a]In methanol/water 1:1; All reactions were performed at 1 mmol scale in water by stirring the reaction mixture for the corresponding time.

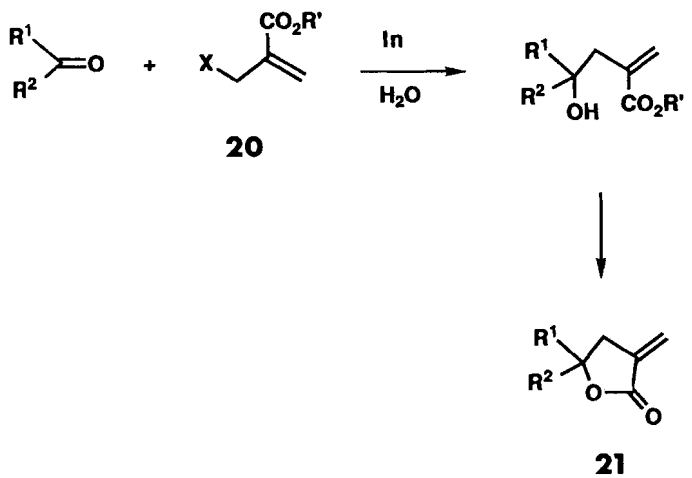

SCHEME 10

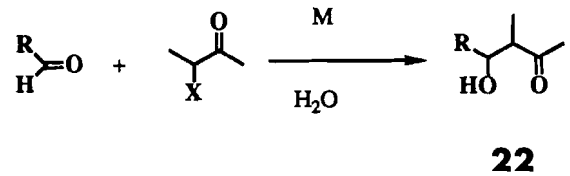

SCHEME 11

with indium instead of zinc or tin in aqueous media, the yield of the reaction is slightly improved (Table 4) (22). But the most interesting change is that the diastereoselectivity appears to have improved to between 2:1 and 12:1. Using the specific example of benzaldehyde reacting with α-bromopropiophenone (**25**), when the reaction is carried out in water with zinc as the metal, the yield is 82% with the ratio of the two diastereomeric products **26**, *erythro* to *threo*, being 2.5 to 1. Using tin as the metal for the same reaction, the yield is slightly poorer, and the ratio of the two diastereomers, *erythro* to *threo*, becomes 1 to 1.1. But when the same reaction is carried out with indium in water, the yield is good at 85% but, more dramatically, the ratio of the two diastereomers is now 12 to 1 in favour of the *erythro* compound (Scheme 12). While one cannot give a logical explanation at this time for the stereochemical differences, the improved diastereoselectivity renders the indium-mediated crossed aldol condensation reactions synthetically useful.

Not surprisingly, Reformatsky-type condensation reactions can also be carried out with indium in water. α-Haloesters (**27**)

Can. J. Chem. Downloaded from www.nrcresearchpress.com by EESC ESCOLA DE ENGENHARIA on 09/08/12
For personal use only.

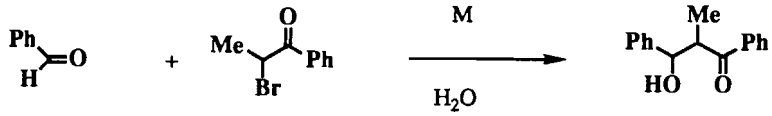

M used	Yield of **26**, %	**26**, *erythro*:*threo*
Zn	82	2.5:1
Sn	67	1:1.1
In	85	12:1

SCHEME 12

TABLE 5. Reformatsky reactions mediated by indium in water[a]

Entry	α-Halocarbonyl (equiv.)	Aldehyde (equiv.)	In (equiv.)	*erythro*:*threo*[b]	% yield
1	$BrCMe_2CO_2Et$ (1.0)	PhCHO (1.0)	1.0		52
2	$BrCHMeCO_2Et$ (1.0)	PhCHO (1.0)	1.0	2.2:1	35
3	$PhCHBrCO_2Me$ (1.5)	PhCHO (1.0)	1.0		0
4	$MeCHBrCO_2H$ (1.5)	PhCHO (1.0)	1.5	2.2:1	40
5	$MeCHBrCO_2Na$ (1.5)	PhCHO (1.0)	1.5	2.2:1	35
6	nBuCHBrCO_2H (1.5)	PhCHO (1.0)	1.5	2.2:1	5
7	$PhCHBrCO_2H$ (1.5)	PhCHO (1.0)	1.5	1.7:1	37
8	(−)-$MeCHBrCO_2H$ (1.5)	PhCHO (1.0)	1.5	2.2:1	37
9	$PhCHBrCO_2Na$ (1.5)	C_3H_7CHO (1.0)	1.0		0

[a]Reaction time = 6 h.
[b]Analyzed by ^1H nmr.

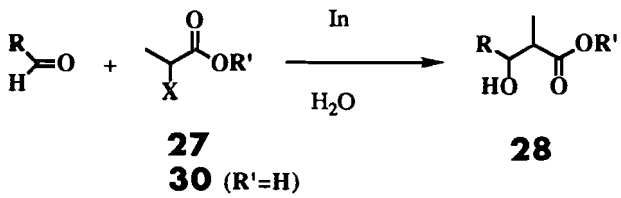

27
30 (R'=H)

28

SCHEME 13

react with carbonyl compounds to give the corresponding β-hydroxyesters (**28**) in moderate yields (Scheme 13). The reaction appears to be chemoselective in that only aromatic aldehydes participate in this kind of reaction. Aliphatic aldehydes are recovered unchanged under identical reaction conditions (Table 5). The major products obtained in these situations are the reduced esters **29**. The diastereoselectivity observed is unexceptional, in the range of 2 to 1.

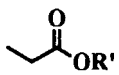

29
31 (R'=H)

Somewhat surprising is the observation that the free α-haloacids **30** can also undergo the same Reformatsky-type condensation reactions with aromatic aldehydes in water in more or less the same modest yields (Scheme 13). Again, the side product is the reduced acid **31** and the diastereoselectivity is uneventful (Table 5). An interesting aspect of the experimental result is that when optically active (*S*)-(−)-bromopropionic acid (88% ee) is reacted with benzaldehyde and

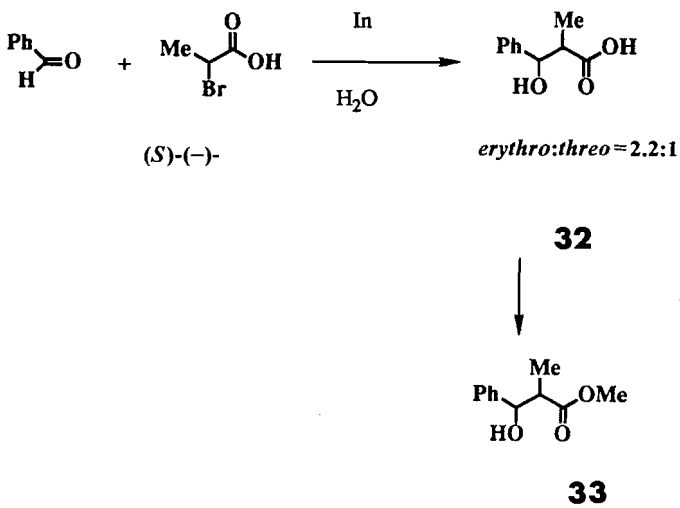

(*S*)-(−)-

erythro:*threo* = 2.2:1

32

33

SCHEME 14

indium in water, the condensation product **32** is obtained in about 50% yield. Two diastereomers are formed, in the ratio of 2.2 to 1 in favour of the *erythro* isomer. The two diastereomers have been separated as the methyl esters **33**, and both are found to be optically inactive (Scheme 14). This allows us to draw some limited conclusions about the possible mechanism of this reaction. If the reaction proceeds by first forming a radical anion with the carbonyl compound (path a), then the lack of optical activity in **33** would rule out a direct displacement of the halide by the radical anion in an S_N2-type process because this would have given an optically active **33**. On the other hand, if the reaction proceeds by first forming a radical anion with the α-haloacid (path b), the result of the

Can. J. Chem. Downloaded from www.nrcresearchpress.com by EESC ESCOLA DE ENGENHARIA on 09/08/12
For personal use only.

optical activity would imply that the carbon–halogen bond must have dissociated sufficiently, leading to racemization prior to reaction with the carbonyl compound (Scheme 15). A similar dissociation of the carbon–halogen bond on a magnesium metal surface, leading to racemization, was recently advanced to account for the stereochemical observations of Grignard reactions (23).

One can take advantage, in synthesis, of the change in stereoselectivity in organometallic-type reactions in aqueous media. We recently reported a concise synthesis of (+)-muscarine (**34**) by using the zinc-mediated allylation reaction (24). Normally, the stereoselectivity observed in the addition of C-nucleophiles such as organometallic reagents to chiral α-alkoxyaldehydes (and ketones) is opposite to Cram's rule. The anti-Cram stereoselectivity has been rationalized on the basis of chelation control. The carbonyl compound **35** forms the chelate **36** as shown in Scheme 16. The C-nucleophile (R–) attacks from the less hindered side as indicated by the arrow, giving the chelation-controlled product **37** in preference to the non-chelation product **38** (25). One would expect the formation of the chelate **36** in aqueous media to be much diminished or even disrupted. In Table 6, the allylation of a number of α-alkoxyaldehydes with allylmagnesium bromide in ether is compared with the reaction with allyl bromide/zinc in water. In all cases where the reaction is conducted in organic solvent, the *syn* isomer is obtained as the major isomer, in agreement with the chelation model. But in cases where the reaction is conducted in water, a reversal of stereoselectivity is observed, now with the *anti* isomer as the major product. While it is possible that the observed stereoselectivity in aqueous organometallic-type reactions may be due to factors associated with the metal surface in such heterogeneous reactions, it is interesting to note that in the case of

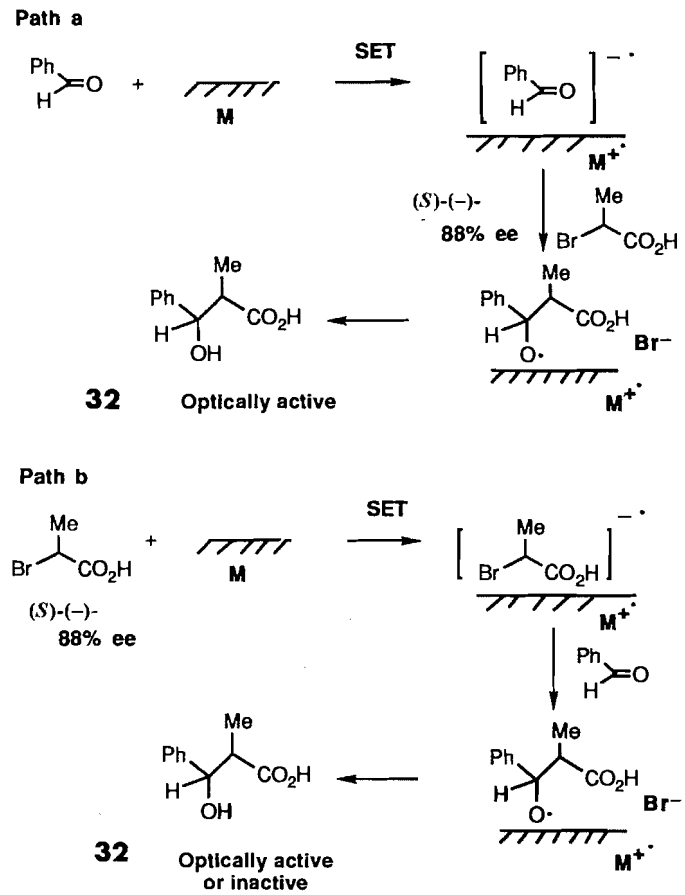

SCHEME 15

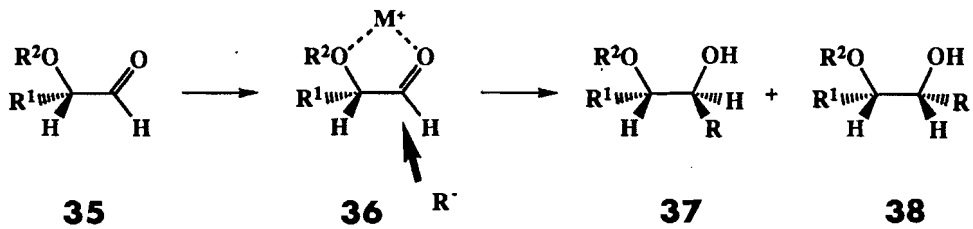

SCHEME 16

TABLE 6. Stereoselective allylation of α-substituted aldehydes

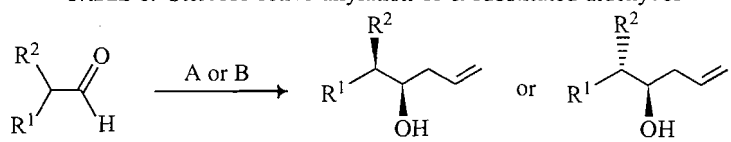

Entry	R^1	R^2	Method (M)	Yield (%)	*syn*:*anti*[a]
1	Me	ODCB	A(Zn)	85	29:71
2	Me	ODCB	B(Mg)	45	60:40
3	Me	OBn	A(Zn)	85	35:65
4	Me	OBn	B(Mg)	50	65:35
5	Bu	OBn	A(Zn)	80	24:76
6	Bu	OBn	B(Mg)	60	60:40
7	Ph	OBn	A(Zn)	58	43:57
8	Ph	OBn	B(Mg)	75	67:33
9	Ph	Me	A(Zn)	85	68:32
10	Ph	Me	B(Mg)	90	60:40

A: Aqueous medium, Zn, RT, catalyzed by NH_4Cl; B: allylmagnesium bromide, ether, −78°C.
[a]Determined by ^1H nmr.

Can. J. Chem. Downloaded from www.nrcresearchpress.com by EESC ESCOLA DE ENGENHARIA on 09/08/12
For personal use only.

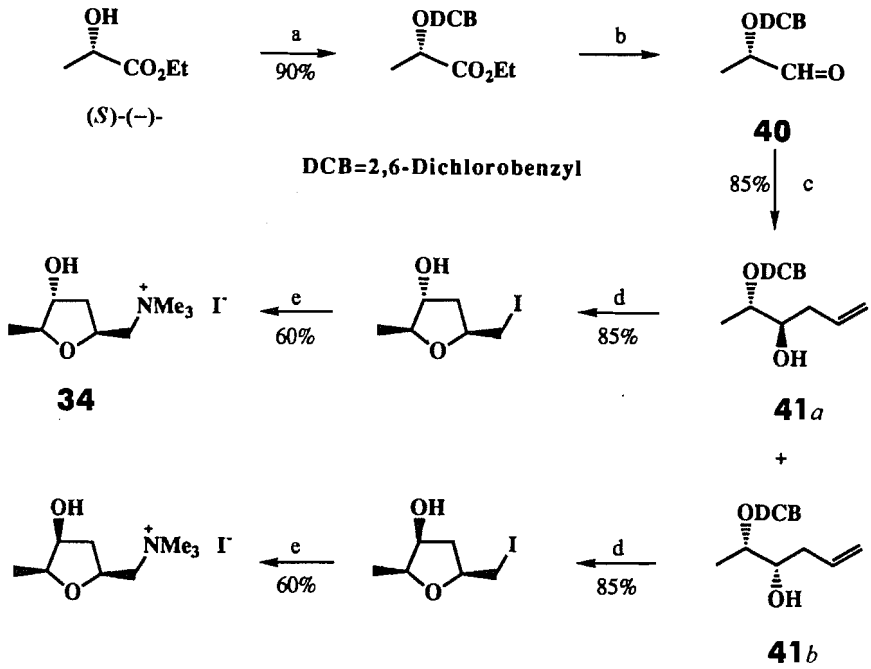

(a) DCBBr/Ag_2O/Et_2O/reflux/6 h; (b) DIBAL-H/Et_2O/−78°C/2 h; (c) CH_2=$CHCH_2Br$/Zn/H_2O/NH_4Cl/3 h; (d) I_2/CH_3CN/0°C/3 h; (e) NMe_3/EtOH/80°C/4 h

SCHEME 17

α-methylphenylacetaldehyde (**39**), where there is no possibility of chelation, there is no significant difference in the diastereoselectivity between allylations in organic or aqueous media.

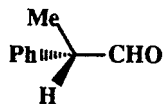

39

(+)-Muscarine is synthesized from (*S*)-(−)-ethyl lactate in five steps with the application of the zinc-mediated allylation reaction in aqueous media (Scheme 17). In the critical step in which compound **40** is transformed into the two diastereomers **41***a* and **41***b*, the aqueous reaction gives the desired diastereomer **41***a* as the major product whereas the same reaction with allylmagnesium bromide in ether gives **41***b* as the major product.

Finally, organometallic-type reactions in aqueous media may offer a unique opportunity in carbohydrate chemistry. We have demonstrated this with the syntheses of the two carbohydrate molecules, KDO (**42**), an eight-carbon sugar, with a carboxylic acid end, and KDN (**43**), a nine-carbon compound of similar structure. They belong to a family of compounds called sialic acids, which are now known to play some critical role in many cell-surface glycoproteins (26). Chemical syntheses of these two compounds have been reported in the literature (27), very often involving the protective group chemistry that is standard in carbohydrate chemistry.

Using the indium-mediated reaction, D-mannose can be coupled in water with allyic halide **20** bearing a methyl ester group to give the two diastereomers **44** and **45** in a ratio of 6:1. The major isomer **44** can be conveniently crystallized out. Ozonolysis of the double bond (in methanol) gives the ketone **46**, which spontaneously cyclizes to the methyl ester **47** of KDN (28). Saponification with KOH in aqueous methanol according to literature procedure (29) gives KDN (Scheme 18). This synthesis is concise, and offers the distinct advantage that the mannose does not need to be derivatized, but is used directly in water.

The same approach can be carried out starting with D-arabinose (Scheme 19). Coupling with **20** by indium in water gives the two diastereomers **48** and **49**, in a ratio of 1 to 5 with the wrong isomer **49** predominating. The major epimer **49** can be acetylated and ozonolyzed to give the unsaturated keto-ester **50**, which was converted to KDO (**42**) (30).

It is perhaps instructive to compare these syntheses with the enzymic syntheses of both KDN and KDO recently reported by Wong and co-workers (31). With the sialic acid aldolase from *Escherichia coli* as the enzyme, D-mannose couples with pyruvate in water to give D-KDN (Scheme 20). However, when L-mannose is used as the substrate, L-KDN is obtained as the product. This represents a reversal of stereoselectivity at the new stereogenic center, a situation that is normally not the case for enzymic reactions. Similarly, when D-arabinose is used as a substrate (which is not a natural substrate of the enzyme), D-KDO and the 4-epimer (**51**) are obtained in a ratio of between 1:2.6 and 1:1.5, also with the wrong epimer predominating (Scheme 21). What is interesting is that in both the enzymic reactions, and in the chemical synthesis using indium in aqueous media, the same *syn* selectivity (anti-Cram) is observed in the critical C—C bond formation step. Normally, anti-Cram selectivity in the reaction of α-hydroxyaldehydes with nucleophiles in organic solvents is explained by chelation control. Since both the enzymic and the chemical coupling are carried out in aqueous solution, the chelation control explanation may be invalid, as we have demonstrated for the zinc-mediated allylation of α-alkoxyaldehydes in water. At present, we explain the *syn* selectivity for α-hydroxyaldehydes by the Felkin model (32), which predicts the *syn* stereochemical outcome if the hydroxy group is considered to be of medium size.

Can. J. Chem. Downloaded from www.nrcresearchpress.com by EESC ESCOLA DE ENGENHARIA on 09/08/12
For personal use only.

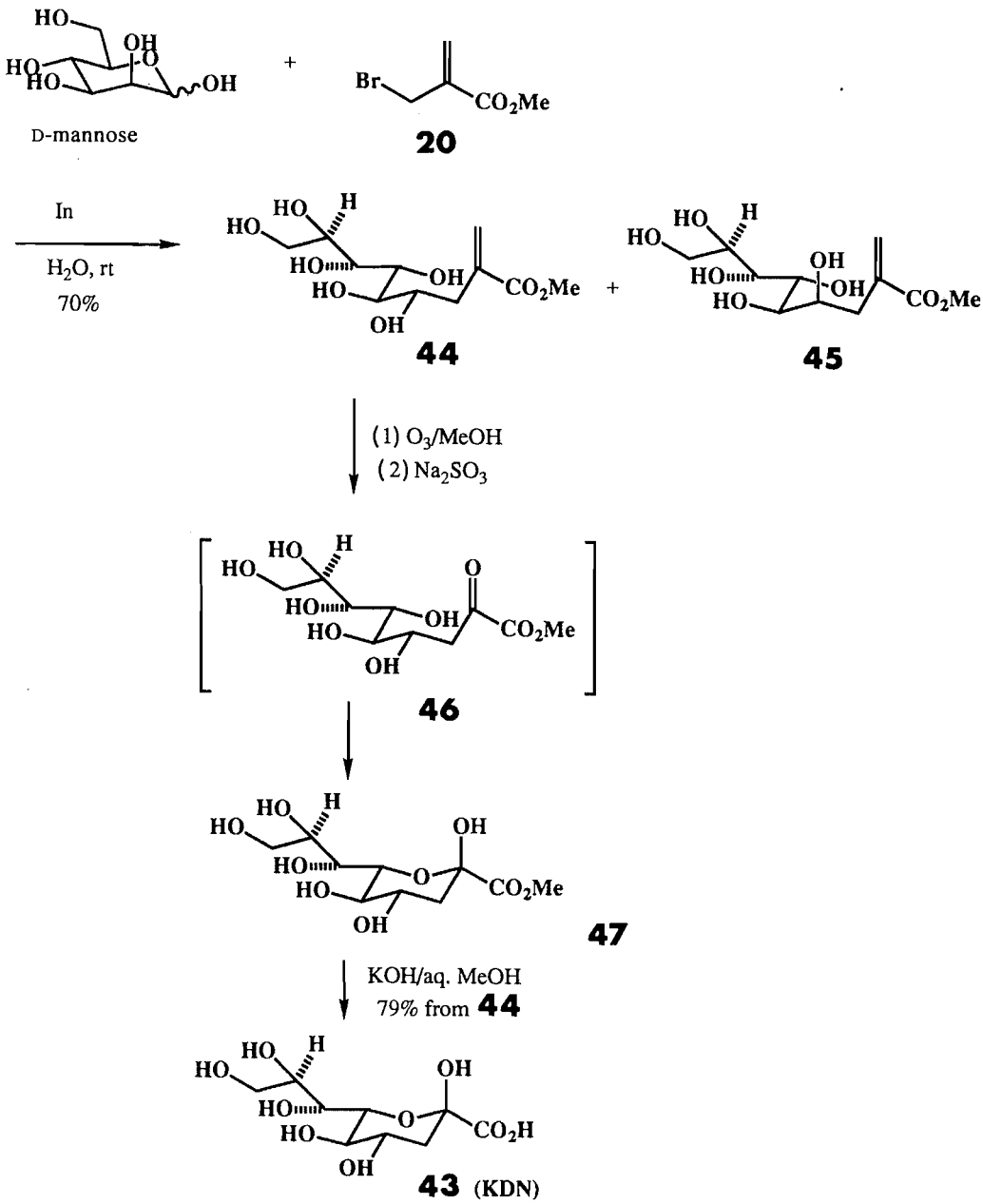

SCHEME 18

Can. J. Chem. Downloaded from www.nrcresearchpress.com by EESC ESCOLA DE ENGENHARIA on 09/08/12
For personal use only.

Can. J. Chem. Downloaded from www.nrcresearchpress.com by EESC ESCOLA DE ENGENHARIA on 09/08/12
For personal use only.

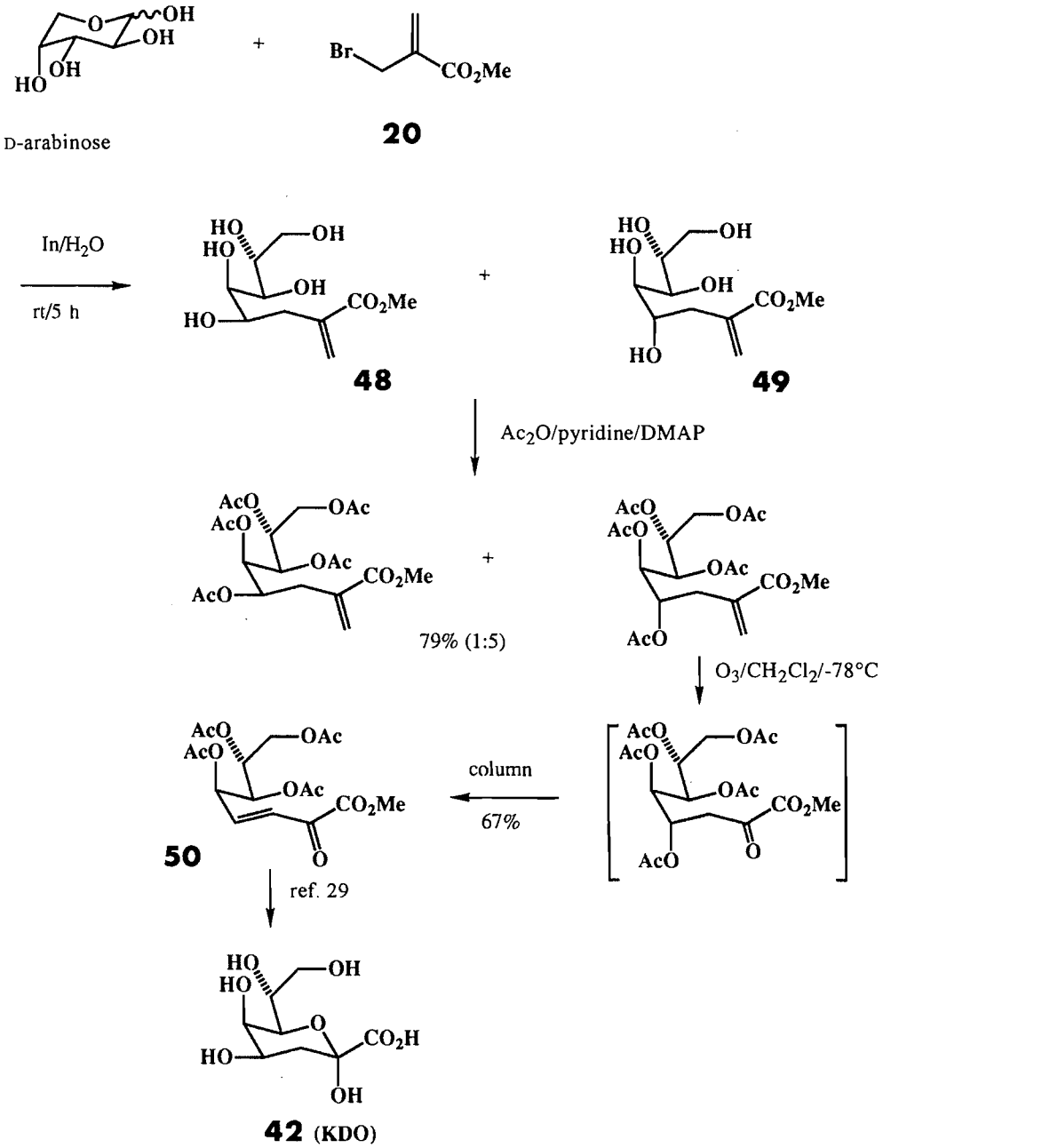

SCHEME 19

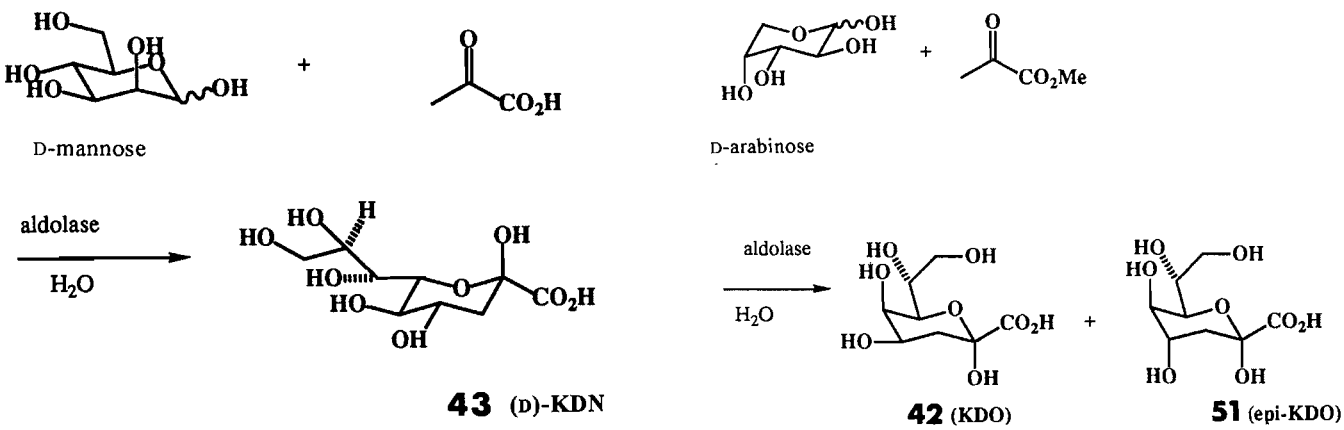

SCHEME 20

SCHEME 21

Conclusion

We have demonstrated that certain organometallic-type reactions can be carried out in aqueous media. The reactions offer the following advantages. Anhydrous organic solvents are no longer needed. We have shown that reactive hydroxy or acidic groups need not be protected, and therefore much of the protection–deprotection chemistry in synthesis may become unnecessary. In some cases there are different stereochemical outcomes from reactions in organic solvents. These can be exploited in organic synthesis. Finally, as demonstrated in the synthesis of KDN, water-soluble compounds can be used as such without the need to be derivatized. There remain many challenges. The types of reactions for forming the carbon–carbon bond are still quite limited, and one would like to extend the scope of aqueous organometallic-type reactions. The mechanism of the reactions is far from having been established. Nevertheless, there is no doubt that organometallic-type reactions in aqueous media can play a useful role in organic synthesis.

Acknowledgement

We are grateful to the Natural Sciences and Engineering Research Council of Canada (NSERC) and le Fonds pour la formation des chercheurs et l'aide à la recherche (FCAR) for their financial support.

1. D.J. Cram and F.A. Abd Elhafez. J. Am. Chem. Soc. **74**, 5828 (1952); N.T. Anh. Top. Curr. Chem. **88**, 145 (1980).
2. E. Colvin. Silicon reagents in organic synthesis. Academic Press, New York. 1988.
3. T.H. Chan and I. Fleming. Synthesis, 761 (1979); G. Majetich. *In* Organic synthesis, theory and applications. *Edited by* T. Hudlicky. Jai Press, Greenwich, Conn. 1989. pp. 173–240.
4. K. Sisido, Y. Takeda, and Z. Kinngawa. J. Am. Chem. Soc. **83**, 538 (1961).
5. T.A. Killinger, N.A. Boughton, T.A. Runge, and J. Wolinsky. J. Organomet. Chem. **124**, 131 (1977).
6. J. Nakomi, J. Otera, T. Sudo, and R. Okawara. Organometallics, **2**, 191 (1983); T. Mandai, J. Nokami, T. Yano, Y. Yoshinaga, and J. Otera. J. Org. Chem. **49**, 172 (1984); J. Nokami, T. Tamaoka, H. Ogawa, and S. Wakabayashi. Chem. Lett. 541 (1986).
7. C. Petrier, J. Einhorn, and J.L. Luche. Tetrahedron Lett. **26**, 1449 (1985); C. Petrier and J.L. Luche. J. Org. Chem. **50**, 910 (1985); C. Einhorn and J.L. Luche. J. Organomet. Chem. **322**, 177 (1987).
8. S.R. Wilson and M.E. Guazzaroni. J. Org. Chem. **54**, 3087 (1989).
9. T.H. Chan and C.J. Li. Organometallics, **9**, 2649 (1990).
10. W.M. Schubert, B.S. Rabinovitch, N.R. Larson, and V.A. Sims. J. Am. Chem. Soc. **74**, 182 (1952).
11. C.J. Li and T.H. Chan. Organometallics, **10**, 2548 (1991).
12. B.M. Trost and S.A. King. J. Am. Chem. Soc. **112**, 408 (1990).
13. J. van der Louw, J.L. van der Baan, H. Stichter, C.J.J. Out, F. Bickelhaupt, and G.W. Klump. Tetrahedron Lett. **29**, 3579 (1988); J. van der Louw, C.J.J. Out, J.L. van der Baan, F. de Kanter, F. Bickelhaupt, and G.W. Klump. Tetrahedron Lett. **30**, 4863 (1989).
14. R.J. Herold, S.L. Aggarwal, and V. Neff. Can. J. Chem. **41**, 1368 (1963).
15. K. Sisido and Y. Takeda. J. Org. Chem. **26**, 2301 (1961).
16. D.G. Tuck. *In* Comprehensive organometallic chemistry. Vol. 1. *Edited by* G. Wilkinson, F.G.A. Stone, and E.W. Abel. Pergamon Press, Oxford. 1982. pp. 683–723.
17. L.C. Chao and R.D. Rieke. J. Org. Chem. **40**, 2253, (1975); S. Araki, H. Ito, and Y. Butsugan. Synth. Commun. **18**, 453 (1989).
18. S. Araki and Y. Butsugan. J. Chem. Soc. Chem. Commun. 1286 (1989).
19. S. Araki, N. Katsumura, H. Ito, and Y. Butsugan. Tetrahedron Lett. **30**, 1581 (1989).
20. C.J. Li and T.H. Chan. Tetrahedron Lett. **32**, 7017 (1991).
21. T.H. Chan, C.J. Li, and Z.Y. Wei. J. Chem. Soc. Chem. Commun. 505 (1990).
22. C.J. Li, M.C. Lee, and T.H. Chan. To be published.
23. H.M. Walborsky and C. Hamdouchi. J. Am. Chem. Soc. **115**, 6406 (1993).
24. T.H. Chan and C.J. Li. Can. J. Chem. **70**, 2726 (1992).
25. D.J. Cram and K.R. Kopecky. J. Am. Chem. Soc. **81**, 2748 (1959); M.T. Reetz. Angew. Chem. Int. Ed. Engl. **23**, 556 (1984); C.H. Heathcock, S.I. Kiyooka, and T.A. Blumenkopf. J. Org. Chem. **49**, 4214 (1984); M.M. Midland and R.W. Koops. J. Org. Chem. **55**, 5058 (1990).
26. R. Schauer. Adv. Carbohydr. Chem. Biochem. **40**, 131 (1982); M.L. Philips, E. Nudelman, F.C. Gaeta, M. Perez, A.K. Singhal, S. Hakomori, and J.C. Paulson. Science, **63**, 475 (1990).
27. D. Nadano, M. Iwasaki, S. Endo, K. Kitajima, S. Inoue, and Y. Inoue. J. Biol. Chem. **261**, 11550 (1986); R. Shirai, M. Nakamura, S. Hara, H. Takayanagi, and H. Ogura. Tetrahedron Lett. **29**, 4449 (1988); B. Giese, T. Linker, and R. Muhn. Tetrahedron, **45**, 935 (1989); S.J. Danishefski, W.H. Pearson, and B.E. Segmuller. J. Am. Chem. Soc. **107**, 1280 (1985); B.P. Brauchand and M.S. Meier. J. Org. Chem. **54**, 1320 (1989); S.F. Martin and P.W. Zinke. J. Org. Chem. **56**, 6600 (1991).
28. T.H. Chan and C.J. Li. J. Chem. Soc. Chem. Commun. 747 (1992).
29. A. Dondoni, P. Merino, and J. Orduna. Tetrahedron Lett. **32**, 3247 (1991).
30. C.J. Li. Ph.D. Thesis, McGill University, Montreal. 1992; S. Abel, T. Linker, and B. Giese. Synlett, 171 (1991).
31. C.H. Lin, T. Sugai, R.L. Halcomb, Y. Ichikawa, and C.H. Wong. J. Am. Chem. Soc. **114**, 10138 (1992); C.G.-L. Narvor, Y. Ichikawa, and C.H. Wong. J. Am. Chem. Soc. **113**, 7816 (1991).
32. M. Cherest, H. Felkin, and N. Prudent. Tetrahedron Lett. 2199 (1968).

Can. J. Chem. Downloaded from www.nrcresearchpress.com by EESC ESCOLA DE ENGENHARIA on 09/08/12
For personal use only.

Facial selective Diels–Alder reactions of (1*R*,5*R*)-(+)-3-carbomethoxy-6,6-dimethylbicyclo[3.1.1]hept-3-en2-one. Unusual ketalization–fragmentation reaction of adducts

HSING-JANG LIU, SEW YEU CHEW,[1] ERIC N.C. BROWNE,[2] AND JEUNG BEA KIM
Department of Chemistry, The University of Alberta, Edmonton, AB T6G 2G2, Canada

Received June 17, 1993

HSING-JANG LIU, SEW YEU CHEW, ERIC N.C. BROWNE, and JEUNG BEA KIM. Can. J. Chem. **72**, 1193 (1994).

The stereofacially differentiated enone ester **5** has been used to study the effects of steric influence on the Diels–Alder reaction. In general, under Lewis acid catalysis, **5** adds to dienes at low to ambient temperatures in a reasonable rate. Yields of predictable chiral adducts are moderate with the unexpected exception of zinc chloride catalyzed reactions, which provide good to high yields. In all cases only products of addition to the *Si* face of general type **21** were observed. The regiochemistry of the adducts is exclusively that predicted by the *ortho* and *para* rules. The stereochemistry shows a high selectivity in favor of ester-*endo* transition state products. Rationales for the observed stereoselectivities are discussed. The fragmentation of adducts of **5**, in particular keto ester **9**, has been briefly examined. Olefins **30** and **46** derived from **9** have been converted to ring-opened cadinane skeletons **31** and **47**, respectively, by conditions we have previously reported. In an entirely new and unexpected reaction, simultaneous ketalization and fragmentation of the cyclobutane ring of ketones derived from **9** gave ring-opened ketals **34** + **35** (from **29**), **36** + **37** (from **9**), **39** (from **38**) and **42** + **43** (from **40**).

HSING-JANG LIU, SEW YEU CHEW, ERIC N.C. BROWNE et JEUNG BEA KIM. Can. J. Chem. **72**, 1193 (1994).

On a utilisé l'énone ester **5** stéréofacialement différencié pour étudier les effets stériques sur la réaction de Diels–Alder. En général, dans des conditions de catalyse acide de Lewis, le composé **5** s'additionne aux dièmes à des vitesses raisonnables, à des températures ne dépassant pas la température ambiante. Les rendements des adduits chiraux attendus sont modérés, à l'exception notable des réactions catalysées par le chlorure de zinc qui donnent des rendements allant de bons à excellents. Dans tous les cas, on n'observe que les produits d'addition sur la face *Si*, de type général **21**. La régiochimie des produits est exclusivement celle que l'on peut prédire sur la base des règles *ortho* et *para*. La stéréochimie présente une grande sélectivité pour les produits formés par le biais de l'état de transition *endo* de l'ester. On a examiné brièvement la fragmentation des adduits du produit **5**, en particulier le céto ester **9**. Utilisant des conditions rapportées antérieurement, on a transformé les oléfines **30** et **46**, provenant du produit **9**, en squelettes des cadinanes à cycle ouvert **31** et **47** respectivement. Par une réaction aussi nouvelle qu'inattendue, une cétalisation et une fragmentation simultanée du noyau cyclobutane des cétones dérivés du produit **9** ont fourni les cétals à cycles ouverts **34** + **35** (à partir de **29**), **36** + **37** (à partir de **9**), **39** (à partir de **38**) et **42** + **43** (à partir de **40**).

[Traduit par la Rédaction]

Introduction

Lewis acids such as aluminum chloride, boron trifluoride, and stannic chloride produce large increases in the rate of Diels–Alder reactions (1). Furthermore, catalysis by Lewis acids also influences the regio- and stereoselectivity of Diels–Alder reactions so that the *ortho* (2–4) and *para* selectivity (5–7) of the addition as well as the *endo* selectivity (8–11) are greatly increased. On the other hand, Valenta and co-workers (12) reported a reversal of regioselectivity of Diels–Alder reactions of quinones catalyzed by Lewis acids. Previously it was assumed that in a Diels–Alder reaction Lewis acids that increase the regioselectivity would promote formation of the major thermal regioisomer. It now appears that this is not the case and the orientation of the product may depend on the specific Lewis acid used (13, 14).

Recently, extensive efforts have been made to induce asymmetry in carbon–carbon bond-forming reactions (15, 16). Among these, the asymmetric Diels–Alder reaction pioneered by Walborsky et al. (17, 18) has been established as an important method. In this pericyclic reaction as many as four chiral centers can be created simultaneously. Hypothetically, 16 stereoisomers can be produced at four new chiral centers, but high stereoselection can be attained with the aid of the elements that govern the stereochemical course of the reaction such as *cis* addition, *endo* addition, and diastereofacial selectivities. The majority of the work on asymmetric Diels–Alder reactions deals with optically active dienophiles[3] or dienes[4] that carry a removable chiral auxiliary group. Such intermediates typically undergo Diels–Alder reactions in the presence of a Lewis acid catalyst with diastereoselection exceeding 90% (for example, see ref. 25). They are devised in such a way that the chiral auxiliary group effectively blocks the *Re* face of the dienophile or diene and this induces high diastereofacial selectivity. But compared to the use of a covalently attached chiral auxiliary group, the use of a chiral catalyst is a potentially more attractive method to achieve asymmetric Diels–Alder reactions of prochiral dienes and dienophiles because two synthetic steps, attachment and removal of the chiral auxiliary, are avoided. Unfortunately, the attempted use of chiral Lewis acids (26–31) has given variable results. Only chiral titanium reagents (30, 31) give greater than 90% asymmetric induction.

In principle, the addition of substituted cyclohexenones to a substituted 1,3-butadiene is a versatile approach to decalin systems. However, the thermal cycloaddition of dienes to cyclohexenones requires drastic conditions and produces low yields of the adduct (32). In recent years greater understanding of the steric and electronic effects governing this reaction and the use of Lewis acid catalysts has led to the use of specifically functionalized dienes and dienophiles to produce previously unat-

[1]Taken in part from the Ph.D. thesis of S.Y. Chew, The University of Alberta, 1991.

[2]Present address: Wyeth–Ayerst Research Inc., 1025 Laurentian Blvd., St. Laurent, QC H4R 1J6, Canada.

[3]For selected examples see refs. 19–22.

[4]For selected examples see refs. 23–25.

Can. J. Chem. Downloaded from www.nrcresearchpress.com by EESC ESCOLA DE ENGENHARIA on 09/08/12
For personal use only.

tainable substitution patterns regio- and stereoselectively.[5] Wenkert and co-workers[6] have made an extensive study of the Diels–Alder reaction of cyclohexenones using aluminum chloride as a catalyst. Our group (14, 35–38) has carried out an intensive study of the Diels–Alder reactions of the 4,4-dimethyl-2-cyclohexen-1-ones **1–4**. These studies have shown that structural features in the dienophile, such as the presence of a cross-conjugated carbalkoxy group or additional double bond, and the nature of the Lewis acid strongly influence the regio- and stereoselectivity of the reaction. The results have been rationalized on the basis of steric and electronic effects on the relative stabilities of keto–*endo* and ester–*endo* transition states.

After examining the steric and electronic effects influencing the regiochemistry of Diels–Alder reactions of enone esters **1–4** we were interested in further investigating the steric influence on the diastereofacial selectivity of Diels–Alder reactions of enones. The stereofacially differentiated chiral dienophile **5** was chosen for this study. A series of Diels–Alder reactions of **5** and various dienes using different Lewis acid catalysts under different reaction conditions is described in the first part of this report.[7] This study shows that dienophile **5** can be a useful chiral reagent for Diels–Alder based synthetic schemes. In the second part of this report we briefly describe our initial examination of the fragmentation chemistry of adducts of **5** with the goal of generating the cadinane skeleton. The synthetic potential of dienophile **5** has been demonstrated by strategic application to the synthesis of chiral cadinane sesquiterpenes.[8]

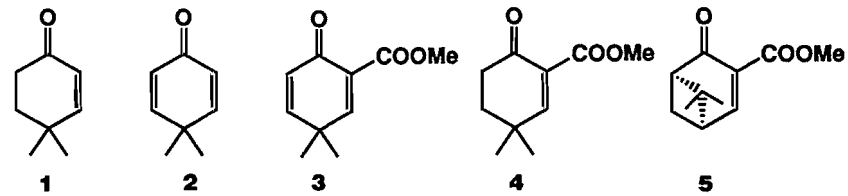

1 2 3 4 5

[1]

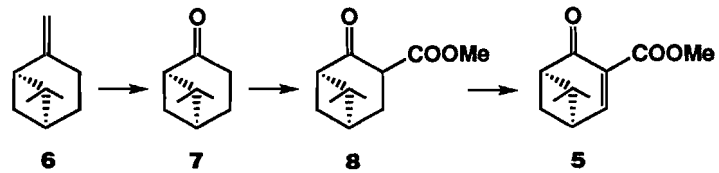

6 7 8 5

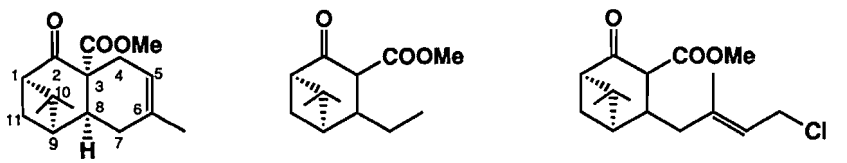

9 10 11

Results and discussion

1. Diels–Alder reactions of enone ester 5

As this study was beginning, a single example of a Diels–Alder addition of a symmetrical diene to the corresponding ethyl ester of **5** was reported (40). However, that report did not explore the use of Lewis acid catalysis nor the influence of stereochemical and electronic factors on the addition. Enone ester **5** could be prepared in high yield from (−)-β-pinene (**6**)[9] in three steps (eq. [1]). (−)-β-Pinene has been used as an inexpensive chiral starting material for a number of chiral syntheses and for the preparation of chiral reagents (41–46). The preparation of (+)-nopinone (**7**) by ozonolysis of (−)-β-pinene has been frequently reported.[10] In our hands ozonolysis of (−)-β-pinene in a 1:1 mixture of dichloromethane–methanol followed by reduction of the products of ozonolysis with dimethyl sulfide gave (+)-nopinone (**7**)[11] in 78% yield. The carbomethoxy group was introduced by treating (+)-nopinone (**7**) with sodium hydride and dimethyl carbonate. Keto ester **8** identical to that previously reported (45) was obtained in 94% yield. The dehydrogenation

[5]For a recent review of Diels–Alder reactions of cycloalkenones see ref. 33.

[6]For the most recent paper in the series see ref. 34.

[7]Some of this work has been reported in a preliminary communication (39).

[8]The full synthetic application of dienophile **5** to natural product targets will be reported in a separate publication.

[9]Commercial (−)-β-pinene, which was obtained from the Aldrich Chemical Co., had an optical purity of 92%.

[10]For examples of ozonolysis of (−)-β-pinene see refs. 40, 43, 47, and 48.

[11]Problems in the synthesis of (+)-nopinone have been reported. In one case the attempted purification of (+)-nopinone by vacuum distillation resulted in an explosion (49). Similarly, allowing the concentrated reduction mixture to warm up from 0°C to room temperature also resulted in a violent explosion (50). Because of the risk of explosion we recommend that researchers exercise appropriate caution when attempting this synthesis. The conversion of **6** to **7** by an alternate method would be advantageous. A recent report accomplishes the conversion in reasonable yield by osmate dihydroxylation followed by oxidative cleavage (51, 52).

Can. J. Chem. Downloaded from www.nrcresearchpress.com by EESC ESCOLA DE ENGENHARIA on 09/08/12
For personal use only.

TABLE 1. Lewis acid catalyzed Diels–Alder addition of isoprene to enone ester **5**[a]

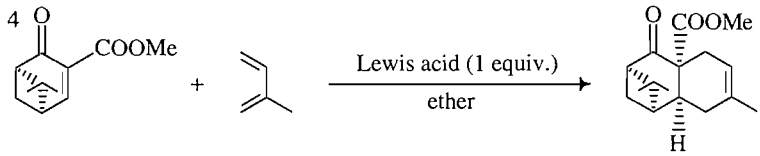

5 (20 equiv.) **9**

Lewis acid	Temp (°C)	Time (h)	Yield (%)
$BF_3{\cdot}OEt_2$	−10	12	29
$FeCl_3$	−20	2.75	34
$SnCl_4$	20	2	52
$SnCl_4$	−20	3	55
Et_2AlCl	−20	3	7[a]
$ZnCl_2$	−20	21	95

[a]The major identified products of this reaction were **10** and **11**.

of keto ester **8** was carried out by the routine selenenylation/oxidative elimination method first developed by Reich et al. (53). Keto ester **8** was treated with phenylselenenyl chloride pyridine complex (54) in dichloromethane. The resulting selenide was oxidized with aqueous hydrogen peroxide to give the required enone ester **5** in 88% yield (65% overall from β-pinene).

A variety of conditions and Lewis acids, particularly boron trifluoride etherate, stannic chloride, and ferric chloride, were examined for the Diels–Alder reactions of enone ester **5**. These particular Lewis acids were chosen because we had previously observed that they were suitable as catalysts for related dienophiles (14, 38, 55, 56). However, it was found that in the present case these Lewis acids gave poor to moderate yields of Diels–Alder adducts (Table 1). In addition, the reaction of enone ester **5** with *trans*-piperylene catalyzed by stannic chloride and boron trifluoride etherate gave no Diels–Alder adduct and no starting material was recovered. To examine the cause of these poor yields, the stability of **5** and the adduct **9** under the various reaction conditions was examined. The adduct **9** in ether was treated with stannic chloride at room temperature and was found to remain intact even after 26 h. On the other hand, a mixture of **5** and stannic chloride in ether at room temperature rapidly decomposed. At −20°C, however, decomposition of the enone ester was not observed. Because of the demonstrated sensitivity of the dienophile to stannic chloride, the Diels–Alder reaction of **5** with isoprene using zinc chloride, a weaker Lewis acid, was investigated. Although the reaction was slower, a very high yield (95%) of adduct **9** was obtained. Consequently, in further investigations of the scope of Diels–Alder reactions of **5**, zinc chloride was used as the Lewis acid catalyst and good to high yields of adducts were obtained.[12] The results of this study are summarized in Table 2. Although it has been successfully used in Diels–Alder reactions (57–64), the striking superiority of zinc chloride as a catalyst in this series was unexpected. The yields of Diels–Alder adduct **9** formed with various Lewis acids were in the order of $Et_2AlCl < BF_3{\cdot}OEt_2 < FeCl_3 < SnCl_4 < ZnCl_2$, which was almost exactly opposite to the general order of Lewis acidity: $BX_3 > AlX_3 > FeX_3 > SbX_5 > SnX_4 > ZnX_2$ (65). This could be the result of greater stability of the strained ring system in the reactant and products to the relatively mild acid condition of zinc chloride catalysis than to the stronger Lewis acids examined.

In principle, Diels–Alder addition to enone ester **5** could occur from either the sterically more hindered *Re* face or the less hindered *Si* face to give stereochemically distinct products. However, only products of addition to the *Si* face of general type **21** were obtained (eq. [2]), as indicated by the stereochemistry of the ring junction of all the adducts. As expected, the *gem*-dimethyl group in **5** served to direct the Diels–Alder addition exclusively to the less hindered *Si* face. The structures of the adducts were established by spectroscopic methods including ^1H nmr, ^1H decoupling, and NOE experiments. The results of the NOE experiments are summarized in Table 3.

A. Addition to isoprene

The reaction of enone ester **5** with isoprene in ether under zinc chloride catalysis proceeded smoothly to give a single adduct in 95% yield. The spectral data of the adduct suggested that structure **9** could be assigned. However, orientational reversal in violation of the *para* rule in the Diels–Alder addition of isoprene has been observed (14, 36, 37). To rule out the possibility that the addition of isoprene to enone ester **5** could produce the regioisomeric keto ester **22**, extensive proton decoupling experiments were carried out and all the protons of the adduct were assigned. The signal due to the peri-deshielded

[12]The experimental procedure for zinc chloride catalyzed reactions was slightly different from the typical method for stannic chloride, ferric chloride, and boron trifluoride etherate. Zinc chloride is only slightly soluble in ether and requires a comparatively large amount of ether to dissolve it completely. To keep the initial concentration of **5** in the reaction mixture the same for all catalysts studied, the zinc chloride solution was introduced before the diene whereas for stannic chloride, ferric chloride, and boron trifluoride etherate catalyzed reactions the Lewis acid was introduced after the diene. The zinc chloride used in the Diels–Alder reactions was dried either by a flame or under vacuum before dissolving it in ether to make a clear solution. This ethereal zinc chloride solution was added to a solution of enone ester **5** at the stated temperature followed by the diene. When the zinc chloride solution was added, a thick white precipitate formed and the progress of the reaction was monitored by the disappearance of this precipitate. The formation of this precipitate was probably due to the formation of a complex between zinc chloride and **5**. Attempts to recrystallize this white precipitate were unsuccessful as it decomposed at room temperature or when it was exposed to air.

Can. J. Chem. Downloaded from www.nrcresearchpress.com by EESC ESCOLA DE ENGENHARIA on 09/08/12
For personal use only.

TABLE 2. Zinc chloride catalyzed Diels–Alder addition of dienes to enone ester **5**[a]

Entry	Diene (equiv.)	Temp (°C)	Time (h)	Product(s)	(ratio)	Yield (%)
1		–20	1.5	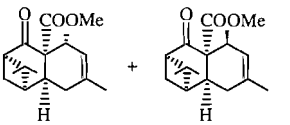 **12** + **13**	(88:12)	59
2	(10)	–40	24		(91:9)	100
3		–20	109	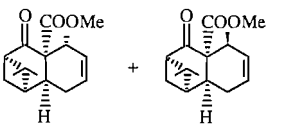 **14** + **15**	(86:14)	77
4[b]	(10)	–20	55		(100:0)	58
5	(20)	–20	41	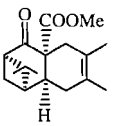 **16**		93
6	(20)	–20	88	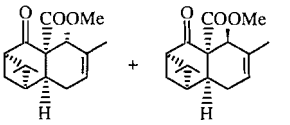 **17** + **18**	(81:19)	84[d]
7	(20)	–20	61	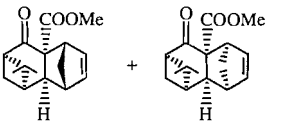 **19** + **20**	(89:11)	53

[a]Unless otherwise specified, reactions were carried out in ether using 1 equiv. of zinc chloride.
[b]Two equivalents of zinc chloride were used.
[c]A 3:7 mixture of *cis*- and *trans*-3-methyl-1,3-pentadiene was used.
[d]Based on 76% consumption of starting enone ester **5**.

allylic C-4 equatorial methine proton (δ 3.05) was coupled to the C-5 vinylic proton (δ 5.48) with a normal vicinal coupling pattern (6 Hz). The regioisomeric adduct **22** would be expected to show a much smaller allylic coupling of the C-4 equatorial proton to the vinylic C-6 proton. Clearly, the observed coupling was consistent only with structure **9**.

The stereochemistry of the ring junction was determined by NOE experiments. Irradiation of the methyl singlet at δ 0.97 resulted in enhancements of the ring junction C-8 proton (δ 3.20, 4.9%) and the methyl at δ 1.34 (3.1%), respectively. When the methyl at δ 1.34 was irradiated, NOE enhancements of the bridgehead C-1 proton (δ 2.66, 3.9%), bridge C-11$_{exo}$ proton (δ 2.47, 3.4%), bridgehead C-9 proton (δ 2.15, 3.2%), and the methyl at δ 0.97 (2.9%) were observed. This implied that the ring junction C-8 proton was on the same face as the *gem*-dimethyl group and therefore the addition of isoprene was to the *Si* face of **5**, giving adduct **9** with the C-8 proton in the α orientation. On the basis of the *cis* principle the adduct would be expected to have an α-carbomethoxy group. The regiochemistry and stereochemistry of adduct **9** has been further confirmed by its successful conversion to various cadinane sesquiterpenes.[8]

The Diels–Alder reaction of enone ester **5** with isoprene catalyzed by diethylaluminum chloride produced three identifiable compounds. The first two eluted were isolated as an inseparable 1:5 mixture. The minor component of this mixture was identical by ^{1}H nmr to **9**. The major component was readily identified as the 1,4-ethyl addition product **10**. The third product eluted was identified as chloro compound **11**. Compounds **10** and **11** were apparently formed by preferential 1,4-addition of an ethyl anion equivalent and isoprene, respectively, to the enone ester. Diethylaluminum chloride has been used as a catalyst in both Diels–Alder (22, 66, 67) and ene reactions (68, 69). In ene reactions the alkly group of diethylaluminum chloride can act as a nucleophile and add to aldehydes to give secondary alcohols (68). Thus the ethyl equivalent from the catalyst could add to enone ester **5** in a Michael fashion to give compound **10**. Evans et al. reported (22) that the influence exerted by diethylaluminum chloride is most likely attributed to the formation of a bidentate complex (such as **5***a*) with β-dicarbonyl groups. During the formation of this complex, free chloride would be liberated and the chloride could then trap the intermediate from the Friedel–Crafts type addition of isoprene to **5** to give **11**.

B. Addition to trans*-2-methyl-1,3-pentadiene*

The zinc chloride catalyzed Diels–Alder reaction of enone ester **5** with *trans*-2-methyl-1,3-pentadiene proceeded smoothly at −20°C to give a mixture of two separable adducts

Can. J. Chem. Downloaded from www.nrcresearchpress.com by EESC ESCOLA DE ENGENHARIA on 09/08/12
For personal use only.

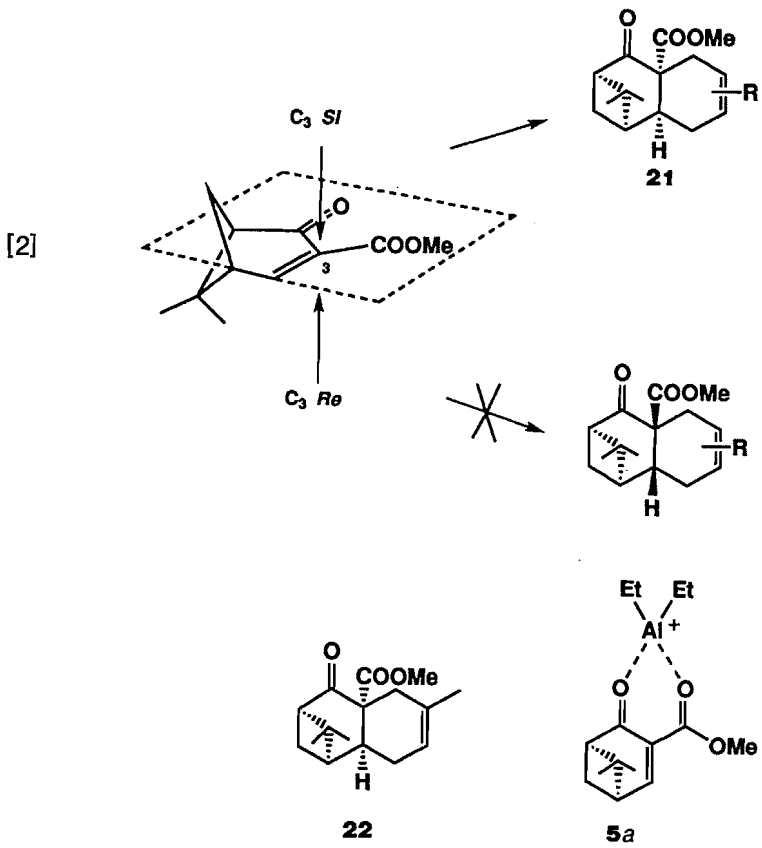

(88:12) in 59% combined yield. If the Diels–Alder reaction obeyed the normal *ortho* and *para* rules, then structures **12** and **13** could be tentatively assigned to the two adducts on the basis of their spectral data. To conclusively determine the regiochemistry of the adducts, extensive proton decoupling experiments were carried out on the major isomer and a complete spectral assignment was made.

The ring junction C-8 proton (δ 2.94), which appeared as a dddd, was coupled to C-7_{ax} (7.5 Hz), C-7_{eq} (7.5 Hz), C-9 (2 Hz), and C-11_{exo} (W-coupling, 2 Hz) protons. This coupling pattern indicated that two hydrogens were attached to C-7, a feature which was also observed in adduct **9** in which there was no substituent at C-7. Consequently the methyl substituent could only be located at C-4. The regiochemistry of the minor isomer was assigned in the same manner on the basis of its ^{1}H nmr spectrum, which also showed a dddd (6, 6, 1.5, 1.5 Hz) for the C-8 proton (δ 3.25).

The relative stereochemistry of adducts **12** and **13** remained to be determined. The two adducts could be epimers as a result of diastereoselective addition to **5** by both the keto-*endo* and ester-*endo* routes. On the other hand, they could be diastereomers resulting from the nonspecific addition of the diene to the *Re* and *Si* face of the enone ester. The conclusive assignment of stereochemistry was determined by NOE experiments. Irradiation of the *endo* methyl (δ 0.89) of the minor isomer resulted in enhancement of the C-8 proton (δ 3.25, 5.6%). Similarly saturation of the *endo* methyl (δ 0.90) of the major isomer gave enhancement of the C-8 proton (6.8%). This indicated that both isomers had the same relative stereochemistry of the bridge and ring junction. The addition of *trans*-2-methyl-1,3-pentadiene must have occurred exclusively from the *Si* face, and adducts **12** and **13** were therefore epimeric at C-4. Irradiation of the C-4 methyl doublet (δ 1.26) of the major isomer resulted in enhancement of C-5 (δ 5.19, 4.6%) and C-4 (δ 2.46, 3.6%) protons while saturation of the C-4 methyl doublet (δ 1.04) of the minor isomer gave enhancement of C-4 (δ 3.16, 8.5%) and C-11_{endo} (δ 1.87, 4.6%) protons, respectively. This experiment showed that the C-4 methyl of the minor isomer was on the same face as the bridge methylene group and so the minor isomer must have structure **13**. As well, the stereochemistry of the major adduct must be that depicted by structure **12**.

When the zinc chloride catalyzed reaction of **5** and *trans*-2-methyl-1,3-pentadiene was carried out at −40°C a slight increase in stereoselectivity in favor of **13** was observed and the combined yield of isolated adducts improved dramatically from 59% to 100%.

C. Addition of trans-*piperylene*

When an ether solution of enone ester **5** was reacted with *trans*-piperylene at −20°C using zinc chloride catalysis two separable adducts in a ratio of 86:14 were obtained in 77% combined yield. If the Diels–Alder reaction obeyed the normal *ortho* rule then the structures of the adducts could tentatively be assigned as **14** and **15**. Previous examples in this series indicated that the multiplicity and coupling pattern of the ring junction C-8 proton could be used to determine the regiochemistry of the Diels–Alder adducts of the 1-substituted dienes. Detailed proton decoupling experiments on the major isomer showed that irradiation of the C-8 proton dddd (δ 2.90) led to simplification of the signals for protons at C-11_{exo} (δ 2.46), C-7_{eq} (2.40), C-9 (2.11), and C-7_{ax} (1.92). When the signal for the C-9 proton (δ 2.11) was irradiated the multiplicity of the signal for the C-8 proton (δ 2.90) changed from dddd to ddd. Also irradiation of the C-7_{ax} proton (δ 1.92) resulted in simplification of

Can. J. Chem. Downloaded from www.nrcresearchpress.com by EESC ESCOLA DE ENGENHARIA on 09/08/12
For personal use only.

TABLE 3. NOE data for Diels–Alder adducts

Compound	Irradiation	(δ ppm)	% Enhancement (H)
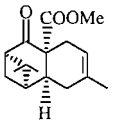 **9**	*endo* CH_3	(0.97)	4.9 (H-8), 3.1 (*exo* CH_3)
	exo CH_3	(1.34)	3.9 (H-1), 3.4 (H-11_{exo}) 3.2 (H-9), 2.9 (*endo* CH_3)
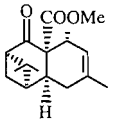 **12**	*endo* CH_3	(0.90)	6.8 (H-8)
	C-4-CH_3	(1.26)	4.6 (H-5), 3.6 (H-4)
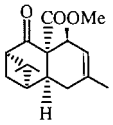 **13**	*endo* CH_3	(0.89)	5.6 (H-8)
	exo CH_3	(1.32)	4.3 (H-1), 3.7 (H-11_{exo})
	C-4-CH_3	(1.04)	8.5 (H-4), 4.6 (H-11_{endo})
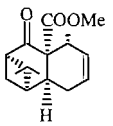 **14**	*endo* CH_3	(0.94)	5.7 (H-8)
	C-4-CH_3	(1.30)	4.7 (H-4), 4.7 (H-5)
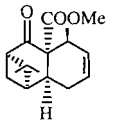 **15**	*endo* CH_3	(0.90)	5.3 (H-8)
	C-4-CH_3	(1.06)	8.7 (H-4), 4.0 (H-11_{endo})
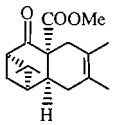 **16**	*endo* CH_3	(0.96)	8.7 (H-8), 3.7 (*exo* CH_3)
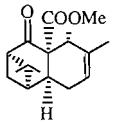 **17**	*endo* CH_3	(0.93)	5.9 (H-8)
	exo CH_3	(1.33)	4.7 (H-1), 2.6 (H-9)
	C-4-CH_3	(1.23)	6.0 (H-4)
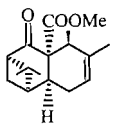 **18**	*endo* CH_3	(0.82)	4.0 (H-8)
	exo CH_3	(1.34)	4.1 (H-1), 3.2 (H-11_{exo})
	C-4-CH_3	(1.00)	8.4 (H-4), 3.8 (H-11_{endo})
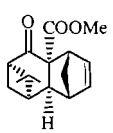 **19**	*endo* CH_3	(0.92)	3.0 (H-8)

the signal for the proton at C-8 (δ 2.90). Similarly, ^{1}H nmr of the minor isomer also showed the proton at C-8 (δ 3.25) as a dddd (6.5, 6.5, 1.5, 1.5 Hz). As with the previous examples, this coupling pattern indicated that two hydrogens were attached at C-7 and consequently the methyl substituent had to be at C-4. This confirmed the regiochemistry of the Diels–Alder adducts shown by structures **14** and **15**.

To determine the stereochemistry of the ring junction and the C-4 methyl, NOE experiments were carried out. When the *endo* methyl (δ 0.94) of the major isomer was irradiated, enhancement of the signal for the C-8 proton (δ 2.90, 5.7%) was observed. Similarly, irradiation of the *endo* methyl (δ 0.90) of the minor isomer resulted in enhancement of the C-8 proton (δ 3.25, 5.3%). This indicated that the C-8 proton of both isomers was on the same face as the *gem*-dimethyl group and therefore addition of diene occurred at the *Si* face of enone ester **5** and the two isomers were epimers. The carbomethoxy group was assigned in accordance with the *cis* principle. When the C-4 methyl signal (δ 1.06) of the minor isomer was irradiated, NOE enhancements on protons at C-4 (δ 3.22, 8.7%) and C-11_{endo} (δ 1.86, 4.0%) were observed. On the other hand, saturation of the C-4 methyl signal (δ 1.30) of the major isomer resulted in enhancements on protons at C-4 (δ 2.46, 4.7%) and C-5 (δ 5.56, 4.7%). This evidence unambiguously fixed the stereochemistry of the substituents of the major isomer as specified by structure **14** and of the minor isomer as **15**.

When two equivalents of zinc chloride were used in the Diels–Alder reaction of enone ester **5** and *trans*-piperylene, only adduct **14** was obtained in a shorter time but in lower yield of 58%.

D. Addition to 2,3-dimethylbutadiene

Enone ester **5** reacted with 2,3-dimethylbutadiene using zinc chloride as a catalyst to give a single adduct in 93% yield. The spectral data were consistent with the expected product **16**. As in the preceding cases the stereochemistry was determined on the basis of the *cis* principle and by an NOE experiment. Irradiation of the *endo* methyl (δ 0.96) resulted in NOE enhancement of the proton at C-8 (δ 3.18, 8.7%) and the *exo* methyl (δ 1.34, 3.7%). This confirmed the assignment of the stereochemistry of **16** as shown.

E. Addition to 3-methyl-1,3-pentadiene

The zinc chloride catalyzed addition of a commercial 7:3 mixture of isomers of 3-methyl-1,3-pentadiene[13] to enone ester **5** gave a mixture (81:19) of two separable isomeric adducts in 84% combined yield (based on 76% conversion). If the Diels–Alder reaction followed the normal *ortho* rule then the structures of the adducts could be tentatively assigned as keto esters **17** and **18**. The regiochemistry of both adducts was confirmed after examination of the ^{1}H nmr spectra and extensive proton decoupling experiments on the minor isomer. The signal at δ 3.28 due to the C-8 proton of the minor isomer appeared as a dddd (11, 7.5, 2, 2 Hz), which was coupled to protons at C-7_{ax} (11 Hz), C-7_{eq} (7 Hz), C-9 (2 Hz), and C-11_{exo} (W-coupling, 2 Hz). The C-8 proton (δ 3.06) of the major isomer also showed a dddd splitting (8, 6, 1.5, and 1.5 Hz). In addition the C-4 proton (δ 3.04) of the minor adduct appeared as a quartet (7.5 Hz) while the C-4 proton (δ 2.73) of the major adduct appeared as a broad quartet (7 Hz). In each case this indicated the presence of two protons at C-7. The methyl substituent must then be at C-4 and the vinylic methyl substituent must be at C-5.

[13]The diene used in this study was obtained from Aldrich Chemical Co. as a mixture of *trans* and *cis* isomers. The ratio of this mixture was determined by ^{1}H nmr to be 7:3. Comparison of the ^{1}H nmr spectrum of this mixture to those of *trans*-piperylene and *cis*-piperylene clearly showed that the major isomer was *trans*-3-methyl-1,3-pentadiene.

Can. J. Chem. Downloaded from www.nrcresearchpress.com by EESC ESCOLA DE ENGENHARIA on 09/08/12
For personal use only.

Can. J. Chem. Downloaded from www.nrcresearchpress.com by EESC ESCOLA DE ENGENHARIA on 09/08/12
For personal use only.

Evidence of the ring junction and C-4 stereochemistry of both adducts was obtained from NOE experiments. Irradiation of the *endo* methyl (δ 0.93) of the major adduct resulted in enhancement of the C-8 proton (δ 3.06, 5.9%) and saturation of the C-4 methyl (δ 1.23) gave enhancement of the C-4 proton (δ 2.73, 6%). When the *endo* methyl (δ 0.82) of the minor isomer was irradiated, enhancement was observed on the proton at C-8 (δ 3.23, 4.0%) and when the C-4 methyl (δ 1.00) was saturated, enhancements on proton at C-4 (δ 3.04, 8.4%) and C-11_{endo} (δ 2.43, 3.8%) were observed. On the basis of the *cis* principle and these NOE experiments, the stereochemistry of the major and minor adducts was established as that of structures **17** and **18**, respectively. Again this indicated that complete diastereofacial selectivity was achieved and the addition of diene was to the *Si* face of enone ester **5**.

F. Addition of cyclopentadiene

The zinc chloride catalyzed addition of cyclopentadiene to enone ester **5** produced an inseparable mixture of two adducts (89:11 ratio) in 53% yield. Preliminary analysis of the spectra indicated that the adducts obtained were **19** and **20**. Extensive proton decoupling experiments on the major isomer led to assignment of all its protons. Irradiation of the protons at C-7 (δ 2.76) and C-9 (δ 2.42) led to a small change in the multiplicity of the ring junction C-8 signal (δ 2.61). When the *endo* methyl (δ 0.92) of the major isomer was irradiated in an NOE experiment the C-8 proton signal (δ 2.61, 3.0%) was enhanced. On the basis of the *cis* principle and this observation, the major isomer was assigned with the C-8 proton and the carbomethoxy group in the α orientation. Previous observations indicated that the addition of dienes to enone ester **5** occurred exclusively from the *Si* face of **5** and it was expected that exclusive addition to the *Si* face of **5** would also occur for cyclopentadiene. If so, the minor isomer would also contain the same stereochemistry for the C-8 proton and the carbomethoxy group. The stereochemistry of the methylene bridge on the bicyclo[2.2.1]heptene ring system was determined by comparing the difference in chemical shift between the two vinylic protons with the known compounds **23** and **24**.[14] Since the major isomer exhibited a larger difference in chemical shift between the two vinylic protons (Δδ 0.48) than the minor isomer (Δδ 0.17), it was assigned structure **19** while the minor isomer was assigned structure **20**.

G. endo *Selectivities of the addition*

The results summarized in Table 2 show that the addition of dienes to enone ester **5** occurred in moderate to very high diastereomeric excess (62–100%). As we have described for other related dienophiles (14, 55, 56), there are in fact two dienophilic components in enone ester **5**: the unsaturated ketone (**5***b*) and the unsaturated ester (**5***c*) moieties. Normally it would not be necessary to distinguish between these two moieties except in certain cases where the diene substituents at C-1 or C-4 are not identical. In those cases *endo* addition to the enone or to the unsaturated ester moiety of **5** would give stereochemically distinguishable products. The factors determining which dienophilic moiety would dominate the reaction pathway are expected to be a function of the most effective secondary orbital overlap with the diene. We found that addition of 1-substituted dienes (Table 2, Entries 1–4, 6, and 7) to enone ester **5** occurs predominantly with secondary overlap of the ester group (ester-*endo* transition state **25**) rather than of the ketone carbonyl (keto-*endo* transition state **26**). This stereoselectivity in favor of the ester-*endo* transition state may be due to combined electronic and steric effects.

Comparison of the two transiton states indicates that addition via transition state **26** should encounter significant steric interaction between the diene and the methylene bridge of the dienophile. For example, keto ester **13** would be the result of addition via transition state **26***a* while keto ester **12** would result from addition via transition state **25***a*. The preferential formation of adduct **12** can be attributed at least in part to the destabilization of transition state **26***a* by a steric interaction of the diene with the methylene bridge of the dienophile. On the other hand, addition via transition state **25***a*, allowing preferential secondary orbital interaction with the ester carbonyl, would eliminate this steric interaction. Similarly, addition of the other C-1 substituted dienes in this study also must have occurred preferentially by transition states of type **25**.

H. Optical purity

The (−)-β-pinene used to prepare enone ester **5** was 92% optically pure. After having demonstrated the Diels–Alder reaction of enone ester **5**, the optical purity of the Diels–Alder adducts was examined. Optically active nmr shift reagents such as $Eu(hfc)_3$ have been used to evaluate the optical yield of reactions (70, 71). The direct application of $Eu(hfc)_3$ to adduct **9** showed separation of the signals for the methoxy group (δ 3.75) and the vinylic methyl (δ 1.72). The chemical shift difference (Δδ) increased with an increase in the amount of the shift reagent $Eu(hfc)_3$ added. In all experiments the integral of the split signals was consistently in the ratio of 96:4. Thus the optical purity of the starting material (92%) was retained in the Diels–Alder adducts. The enantiomeric set of adducts that would be obtained from the relatively unavailable enantiomeric (+)-β-pinene can nevertheless be prepared relatively easily using the conversion of (+)-α-pinene to (−)-nopinone reported by Lavallee and Bouthillier (72). The (−)-nopinone so obtained would provide the (−)-enantiomer of **5** by the method we have described.

2. Cyclobutane ring fragmentation reactions

Having successfully generated various Diels–Alder adducts of enone ester **5**, we wished to demonstrate its utility in the synthesis of natural products. The carbon skeleton of cadinane sesquiterpenes can be readily obtained from adduct **9** by cleavage of the cyclobutane ring system (eq. [3]). The first requirement of such a plan would be to selectively open the cyclobutane ring. The results of our preliminary investigation of these ring opening reactions are summarized in Scheme 1. A number of methods have been reported for fragmentation of the cyclobutane ring system of pinene derivatives (40, 44, 73, 74). Our group (75) has reported the fragmentation of pinenes to limonene derivatives using dimethyl sulfoxide activated by phenyl dichlorophosphate. To apply this method, the transformation of **9** to **27** by a Wittig reaction was attempted. Unfortunately the starting material was recovered unchanged. The failure of the Wittig reaction is probably due to steric hindrance at the ketone carbonyl by the neighbouring groups. Removal of the carbomethoxy group prior to the Wittig reaction could reduce any such hindrance.

Thus treatment of **9** with lithium iodide monohydrate in 2,4,6-collidine under reflux for 2.3 h gave two chromatographically separable products (1:9 ratio, 97% combined yield). The

[14]H.J. Liu and S.Y. Chew. Unpublished results.

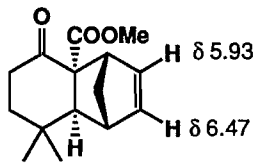

23

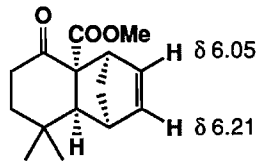

24

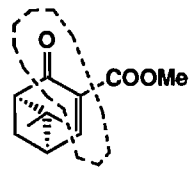

5b

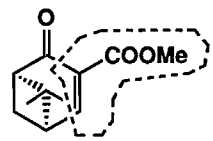

5c

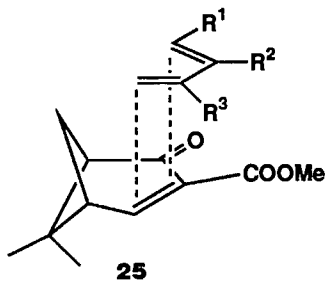

25

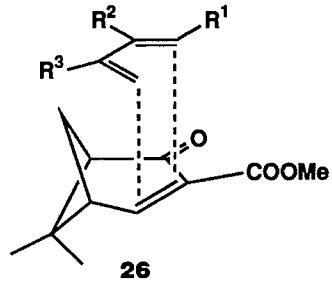

26

25*a* $R^1 = R^3 = CH_3$, $R^2 = H$

26*a* $R^1 = R^3 = CH_3$, $R^2 = H$

isomers were easily identified by their spectral data as the epimeric pair of ketones **28** and **29**. Conclusive assignment of the ring junction stereochemistry in each isomer was determined from NOE and proton decoupling experiments. Extensive proton decoupling of the less polar minor isomer resulted in the assignment of all protons. The ring junction C-8 proton (δ 2.30) appeared as a multiplet that was simplified when the C-11_{exo} (δ 2.47), C-9 (δ 2.06), and C-7 (δ 1.99) protons were irradiated individually. Irradiation of the C-1 (δ 2.58) and C-4_{ax} (δ 1.82) protons led to changes of the C-3 proton signal (δ 2.36) indicating a long-range W-coupling between the C-1 and C-3 protons. In an NOE experiment, irradiation of the *endo* methyl (δ 0.91) resulted in enhancement of the C-3 (5.5%) and C-8 (5.5%) protons. The simultaneous NOE enhancement of those protons indicated that the minor isomer has *cis*-fused structure **28**. Thus the major isomer was assigned *trans*-fused structure **29**. In final confirmation of the stereochemistry at C-3, the minor isomer **28** was epimerized with sodium hydroxide in aqueous methanol. A 1:9 mixture of **28** and **29** was obtained in 92% yield.

Transformation of *trans*-fused ketone **29** to *exo*-methylene derivative **30** was accomplished by a modification of the Wittig reaction developed by Corey and co-workers (76). Treatment of **29** with methylenetriphenylphosphorane at room temperature for 20 h gave **30** in 99% yield. Compound **30** was added to a mixture of dimethyl sulfoxide and phenyl dichlorophosphate at −40°C and stirred for 1 h. The mixture was warmed to 10°C and, after distillation,[15] a pale yellow solid with a melting point of 40–41°C was obtained in 56% yield. The spectral data indicated structure **31** for the product. The stereochemistry was presumed to have remained unchanged as no epimer was isolated. We have rationalized the formation of **31** as outlined in eq. [4]. Complex **32** (77), which results from the interaction of dimethyl sulfoxide and phenyl dichlorophosphate, would serve as an electrophile. Selective electrophilic attack on the exocyclic double bond would induce cleavage of the cyclobutane ring and deprotonation. The resulting allylic sulfonium ion would then be readily displaced by chloride to give the product **31**.

The easy rearrangement of **30** to **31** provides a useful route to the cadinane sesquiterpenes. However, since **31** contains three double bonds, this might contribute to problems in selectively functionalizing a particular double bond in later stages of a planned synthetic sequence. Thus in an attempt to reduce the trisubstituted double bond **29** was reacted with excess borane in tetrahydrofuran followed by the addition of hydrogen peroxide. A mixture of two isomeric alcohols identified as **33** (1:2 ratio, quantitative yield) was obtained in which both the double bond and the ketone carbonyl were attacked.

To prevent the undesired over-reduction, the ketone clearly required protection prior to hydroboration. Routine ketalization of **29** with *p*-toluenesulfonic acid and ethylene glycol in refluxing benzene (Dean–Stark apparatus) surprisingly gave an inseparable mixture of two fragmentation products **34** and **35** (2:1 ratio) in 81% yield. The stereochemistry of the ring junction was presumed to be the usually thermodynamically more stable *trans* configuration. Epimerization at C-7 was not expected since migration of the double bond was not observed. Migration of the endocyclic double bond during ketalization of a decalin system is not unprecedented (78) and so the products were tentatively assigned structures **34** and **35**. It has been reported (79)

[15]Purification by distillation gave more product than the yield obtained using flash chromatography (36%).

Can. J. Chem. Downloaded from www.nrcresearchpress.com by EESC ESCOLA DE ENGENHARIA on 09/08/12
For personal use only.

Can. J. Chem. Downloaded from www.nrcresearchpress.com by EESC ESCOLA DE ENGENHARIA on 09/08/12
For personal use only.

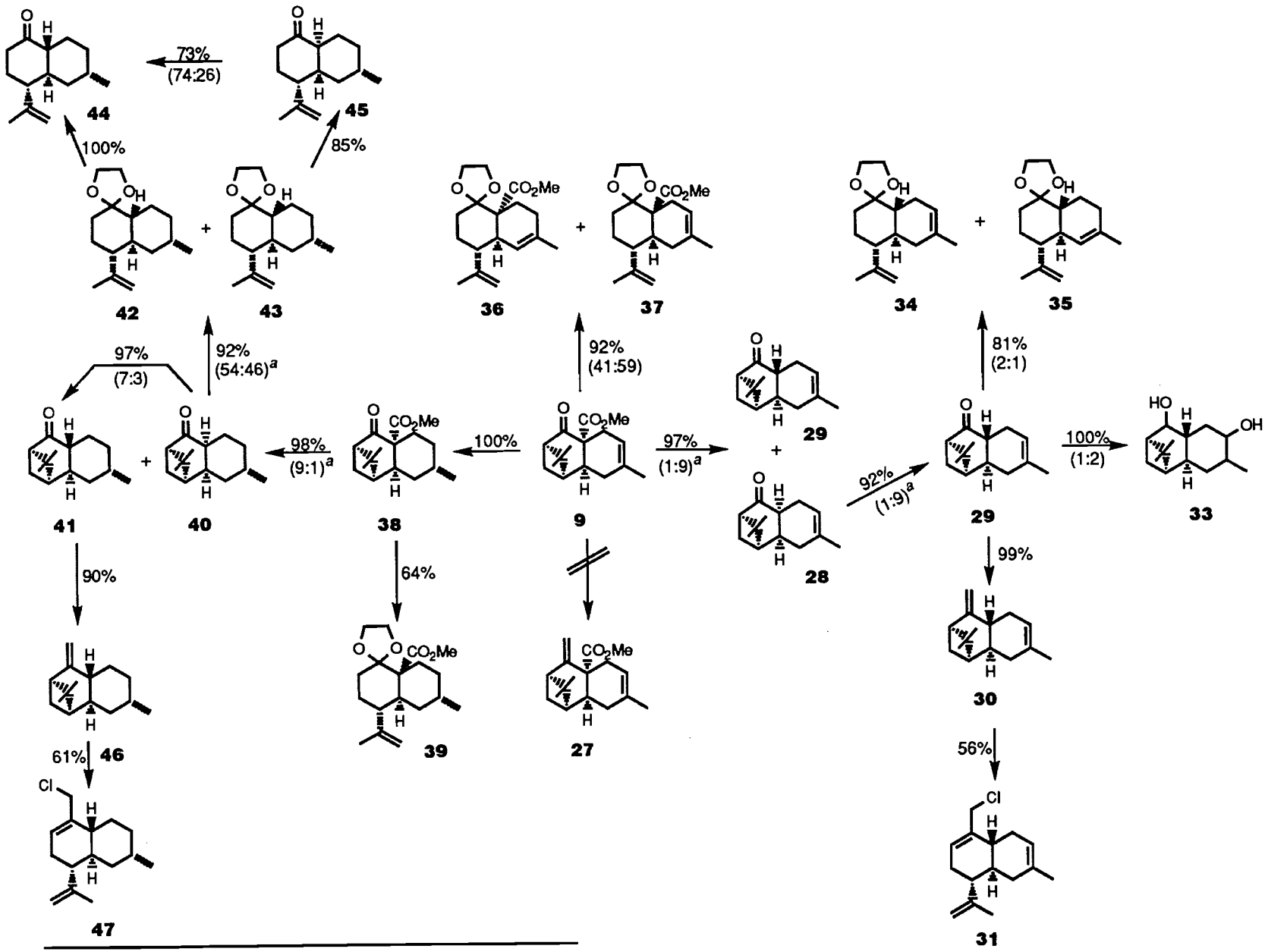

SCHEME 1. Cyclobutane ring fragmentation reactions.

[3]

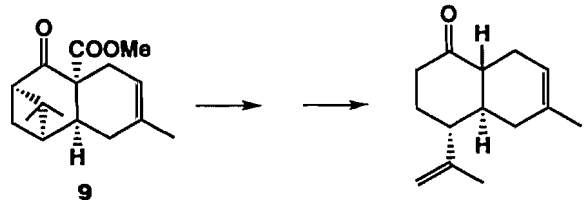

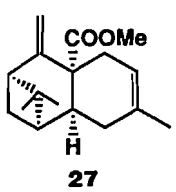

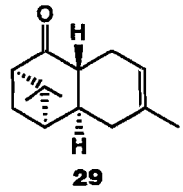

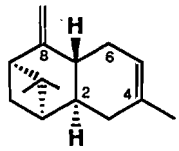

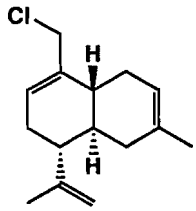

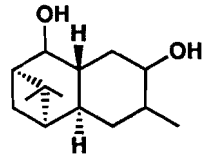

[4]

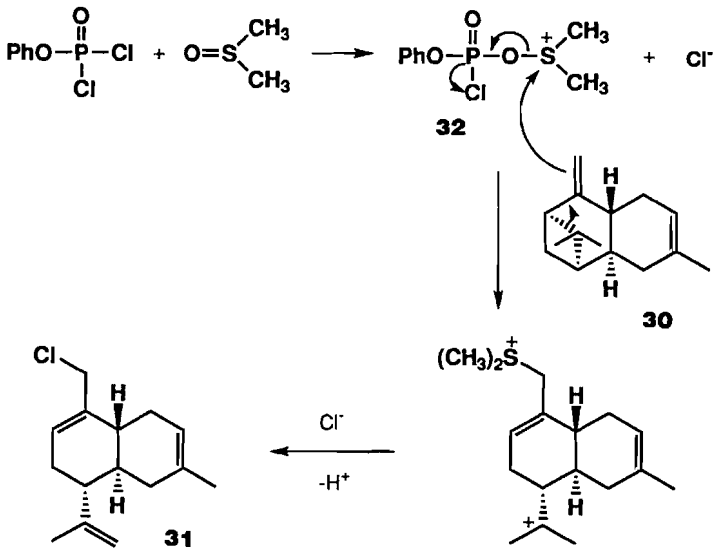

that ^{1}H nmr data can be used to differentiate between the *cis* and *trans*-fused pairs of $\Delta^{4,5}$-cadinenes. In the *cis*-fused compounds there is a significant coupling between the olefinic proton and the ring junction C-6 proton whereas in the *trans* isomers there is little or no coupling between these two protons. The only coupling constant of 1.5 Hz (q) observed for the C-5 proton of **35** is most likely due to long-range coupling with the vinylic methyl group since the dihedral angle between C-5 and C-6 protons is about 90°. This further supports our assignment of a *trans* ring junction to **35** and, by inference, to **34**.

Having discovered this somewhat unexpected ring-opening reaction we undertook an investigation of the reaction with various other substrates. Ketalization–fragmentation of **9** gave the inseparable double bond isomeric ring cleavage products **36** and **37** (41:59 ratio, 92% yield based on 46% consumed starting material). The reaction was slow due to the more sterically hindered ketone carbonyl.

To obtain a clean product of the ring cleavage reactin for unambiguous identification without the complication caused by isomeric mixtures of products from migration of the double bond, the trisubstituted double bond of **9** was hydrogenated on platinum oxide. After filtration and concentration a quantitative yield of **38** was obtained. Extensive ^{1}H decoupling on **38** allowed all the protons to be assigned. Most of the signals for protons in the cyclohexane ring were close together, which unfortunately obscured the results of NOE experiments. We

Can. J. Chem. Downloaded from www.nrcresearchpress.com by EESC ESCOLA DE ENGENHARIA on 09/08/12
For personal use only.

[5]

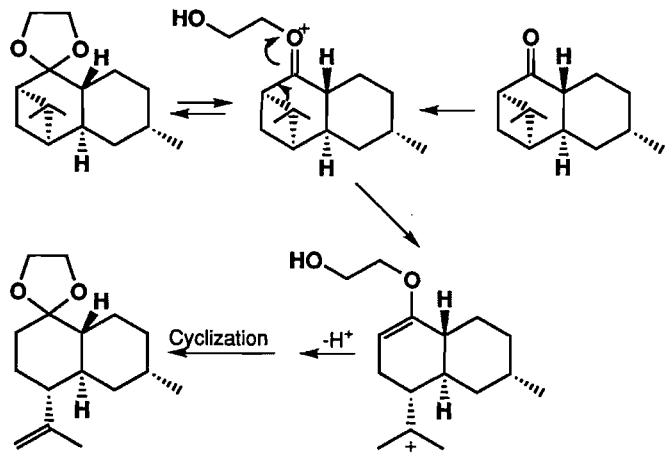

have presumed, after examination of a molecular model of **9**, that the addition of hydrogen would occur from the less hindered face opposite to the carbomethoxy group. In this case **38** would then have an α-methyl on C-6.

Using the same ring ketalization–fragmentation conditions used on **29** and **9**, keto ester **38** was converted to a single compound **39** (64% yield based on 30% consumed starting material). The ketalization–fragmentation of **38** proceeded very slowly (100 h) with only 30% conversion of starting material, probably due to steric hindrance at the ketone carbonyl by the carbomethoxy group. To facilitate the fragmentation, the hindering carbomethoxy group was removed. Treatment of **38** with lithium iodide monohydrate in refluxing 2,4,6-collidine gave two chromatographically separable ketones (1:9) in virtually quantitative yield. From the spectral data the two decarbomethoxylated compounds were assigned structures **40** and **41**. The ring junction stereochemistry was confirmed by epimerization. The minor isomer was treated with sodium hydroxide in aqueous methanol to give an equilibrium 3:7 mixture of the minor and major isomers in 97% yield. Thus the minor and major isomers could be assigned structures **40** and **41**, respectively.

Ketone **40** was then subjected to the ketalization–fragmentation reaction to give chromatographically separable ketals **42** and **43** (54:46) in 92% yield. The spectral data confirmed the assignment of structures **42** and **43** to the ketals. To prove the ring junction stereochemistry, both ketals were hydrolyzed. Treatment of **42** with *p*-toluenesulfonic acid in refluxing aqueous acetone gave ketone **44** in quantitative yield. When ketal **43** was similarly treated, ketone **45** was obtained in 85% yield. Extensive ^{1}H decoupling experiments on ketone **45** allowed assignment of all the cyclohexanone protons. The ring junction C-1 proton at δ 2.40 had a W-coupling of 1 Hz to the C-3 equatorial proton at δ 2.28. Examination of a molecular model shows that ketone **45** would have conformation **45***a* in which a long-range W-coupling between the C-1 and C-3$_{eq}$ protons would be expected in the ^{1}H nmr spectrum. On the other hand, such a W-coupling would not be expected in **44***a*. To fully confirm the ring junction stereochemistry, ketone **45** was epimerized with sodium hydroxide in aqueous methanol to give an equilibrium mixture (74:26) of **44** and **45** in 73% yield. Thus C-1 of ketal **42** was assigned with a β-oriented hydrogen and the C-1 hydrogen of **43** was α-oriented.

This new fragmentation reaction employing *p*-toluenesulfonic acid and ethylene glycol gave clean products in high yields. Significantly, under this mild reaction condition no epimerization of the C-5 stereogenic center was observed. We were interested in determining a possible mechanism for this reaction. An investigation was made to determine if fragmentation occurred without the presence of ethylene glycol. Treatment of **40** with *p*-toluenesulfonic acid in refluxing benzene for 41 h resulted in the formation of a complex mixture. Six spots, including the starting material, were observed by thin-layer chromatography. This indicated that ethylene glycol was essential for the fragmentation to occur cleanly. Based on this, a plausible mechanism for the fragmentation reaction is shown in eq. [5].

Since the fragmentation reaction of **30** with phenyl dichlorophosphate and dimethyl sulfoxide gave only a moderate (56%) yield of the fragmentation product **31**, this fragmentation was also applied to **46** to see if the yield would be improved. Wittig reaction of ketone **41** with methylenetriphenylphosphorane gave **46** in 90% yield. Compound **46** was then treated with phenyl dichlorophosphate and dimethyl sulfoxide. After purification, compound **47** was obtained in 61% yield. Since **30** and **46** gave almost the same yield of fragmentation products it seems likely that the trisubsituted double bond in **30** does not affect the yield of the fragmentation reaction.

Conclusion

The Diels–Alder reactions of enone ester **5** with various dienes provided good to high yields of chiral adducts with complete diastereofacial selectivity in 62–100% diastereomeric excess. The observed regiochemistry was as predicted by the *ortho* and *para* rules. We have shown that enone ester **5** is a new versatile intermediate and, in addition, that it is a useful chiral synthon for synthetic chemists. The new and established fragmentation reactions described provide useful access to cadinane and related skeletons. We will report on wider use of these adducts and fragmentations and their application to the synthesis of natural products in a future publication.[8]

Experimental

General

All melting points were determined on a Kofler hot stage apparatus and are uncorrected. Elemental analyses were performed by the microanalytical laboratory of this department. Infrared spectra (ir) were recorded on a Perkin–Elmer model 457 or Nicolet 7-119 FT-IR spectrometer and were obtained in chloroform cast unless otherwise stated. High-resolution mass spectra (ms) were obtained using a Kra-

Can. J. Chem. Downloaded from www.nrcresearchpress.com by EESC ESCOLA DE ENGENHARIA on 09/08/12
For personal use only.

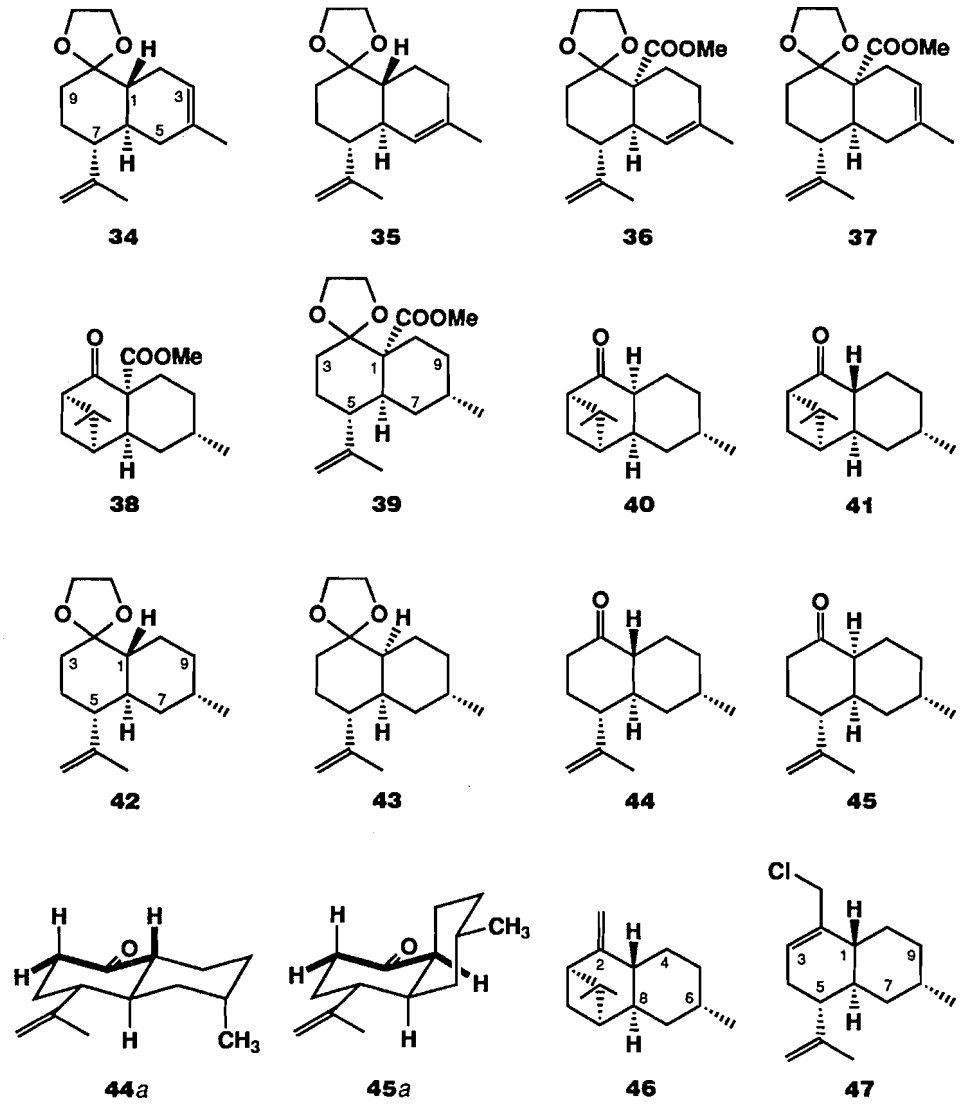

tos AEI MS-50 high-resolution mass spectrometer. Chemical ionization mass spectra (cims) were obtained using an AEI MS-12 mass spectrometer with ammonia as the reagent gas. Proton nuclear magnetic resonance spectra (^{1}H nmr) were recorded on Bruker AM-300 (300 MHz) or AM-400 (400 MHz) spectrometers and were obtained from solutions in deuteriochloroform using tetramethylsilane (TMS) as an internal reference. Coupling constants are reported to within ±0.5 Hz. Chemical shift measurements are reported in ppm downfield from TMS in delta (δ) units. The following abbreviations were used: s = singlet, d = doublet, t = triplet, q = quartet, m = multiplet, ax = axial, eq = equatorial. Carbon-13 nuclear magnetic resonance spectra (^{13}C nmr) were recorded on a Bruker AM-300 (75 MHz) spectrometer from solutions in deuteriochloroform. Carbon-13 multiplicities were derived from off-resonance or the APT (Attached Proton Test) experiment. Methyl and methine groups were shown as signals possessing opposite phase (a) with respect to the deuteriochloroform signal whereas methylene groups, quaternary carbon atoms, and carbonyl groups appeared in phase (p) with it. Nuclear Overhauser Enhancement (NOE) experiments were determined in the difference mode in which a control spectrum was computer-subtracted from the irradiated spectrum after Fourier transformation. Positive enhancements were defined as signals possessing antiphase with respect to the irradiated signal. Samples for NOE measurements were deoxygenated with argon gas for 5–10 min. Optical rotations were determined in a Perkin–Elmer 241 polarimeter. Specific rotation ($[\alpha]_D$) was reported in degrees at the specified temperature and concentration (*c*) was given in g/100 mL in the specified solvent.

All reactions were carried out under a slight positive pressure of argon gas. Argon was passed through a column of 4A molecular sieves and self-indicating silica gel. All reactions were monitored by analytical thin-layer chromatography (tlc) on silica gel. Visualization of the chromatograms was completed either by dipping in an ethanol solution of vanillin (5% w/v) or an aqueous solution of phosphomolybdic acid (3% w/v). Solvents were removed under reduced pressure on a rotary evaporator. Purification and separation of product mixtures were carried out using flash chromatography (80) on silica gel (230–400 mesh).

Materials

The anhydrous solvents used were distilled under an argon atmosphere. Diethyl ether, tetrahydrofuran (THF), and 1,2-dimethoxyethane (DME) were dried with sodium and benzophenone. Dichloromethane, pyridine, and dimethyl sulfoxide (DMSO) were distilled from calcium hydride. Benzene was distilled from lithium aluminium hydride. Anhydrous zinc chloride was fused or vacuum dried before use. Unless otherwise stated, anhydrous magnesium sulfate was used for drying organic solutions.

(1R,5S)-(+)-6,6-Dimethylbicyclo[3.1.1]heptan-2-one ((+)-nopinone) (7)

WARNING: *See footnote 11.* At −78°C ozone was passed through

Can. J. Chem. Downloaded from www.nrcresearchpress.com by EESC ESCOLA DE ENGENHARIA on 09/08/12
For personal use only.

Can. J. Chem. Downloaded from www.nrcresearchpress.com by EESC ESCOLA DE ENGENHARIA on 09/08/12
For personal use only.

a solution of (1*S*,5*S*)-(−)-β-pinene (**6**) (39.17 g, 0.288 mol) in methylene chloride – methanol (1:1, 386 mL). After 6 h a persistent blue color appeared and the reaction was stopped. Excess ozone was purged with oxygen for 10 min and dimethyl sulfide (25.3 mL) was added to the reaction mixture at −78°C. The mixture was stirred overnight at room temperature and the solvent was removed under reduced pressure on a rotary evaporator. Flash chromatography of the residue eluting with 0–10% ether in petroleum ether gave pure **7** (24.294 g) as a colorless oil and also impure **7** (ca. 10 g). The impure product was chromatographed again to give additional **7** (6.608 g, total yield 30.902 g, 0.244 mol, 78% yield): $[\alpha]_D^{23}$ +16.5 (neat);[16] ir: 1715 (C=O) cm^{-1}; ^1H nmr (300 MHz) δ: 2.48–2.66 (complex, 3H), 2.34 (ddd, 1H, *J* = 19, 9, 2.5 Hz, C-3 *H*α), 2.24 (m, 1H), 1.88–2.12 (complex, 2H), 1.59 (d, 1H, *J* = 10 Hz), 1.33 (s, 3H, *exo* CH_3), 0.85 (s, 3H, *endo* CH_3); ^{13}C nmr δ: 214.9 (C=O), 58.0 (*C*HC=O), 41.2 (*C*Me$_2$), 40.4 (*C*HCMe$_2$), 32.8 (*C*H$_2$C=O), 25.9 (*exo* CH_3), 25.2 (CH_2), 22.1 (*endo* CH_3), 21.4 (CH_2); ms M^+: 138.1046 (calcd. for $C_9H_{14}O$: 138.1045).

*(1R,5R)-3-Carbomethoxy-6,6-dimethylbicyclo[3.1.1]heptan-2-one (**8**)*

Sodium hydride (80% dispersion in oil, 4.038 g, 0.168 mol, washed with petroleum ether and DME) was suspended in DME (60 mL) under argon. Dimethyl carbonate (30.280 g, 0.336 mol) was added and the suspension was heated under reflux while stirring with a mechanical stirrer. A solution of (+)-nopinone (**7**) (9.293 g, 0.0673 mol) in DME (22 mL) was added dropwise. Heating was continued for 6 h and the mixture was then cooled to 0°C. An aqueous 10% solution of acetic acid was then added with stirring until the solution was acidic. The mixture was extracted with ether (3 × 70 mL). The extracts were washed with water, saturated aqueous sodium bicarbonate, water, and saturated aqueous sodium chloride, and then were dried, filtered, and concentrated. Flash chromatography of the residue eluting with 0–4% ether in petroleum ether gave keto ester **8** (12.410 g, 0.063 mol, 94% yield) as a light yellow liquid that crystallized on standing. This compound existed as a 1:1:2 mixture of enol and epimeric β-keto esters: ir: 1739 (ester, C=O), 1704 (ketone, C=O) cm^{-1}; ^1H nmr (300 MHz) δ: 11.94 (br s, C=CO*H*, enol), 3.77, 3.76, 3.61 (each s, OCH_3), 1.35, 1.33 (each s, *exo* CH_3), 0.95, 0.88, 0.87 (each s, *endo* CH_3); ms M^+: 196.1105 (calcd. for $C_{11}H_{16}O_3$: 196.1100). Anal. calcd. for $C_{11}H_{16}O_3$: C 67.31, H 8.22; found: C 67.48, H 8.12.

*(1R,5R)-(+)-3-Carbomethoxy-6,6-dimethylbicyclo[3.1.1]hept-3-en-2-one (**5**)*

Pyridine (1.39 mL, 0.0172 mol) was added to a solution of phenylselenenyl chloride (3.70 g, 0.0193 mol) in dichloromethane (99.7 mL) at 0°C under argon. After stirring for 10 min keto ester **8** (3.07 g, 0.0157 mol) in dichloromethane (15.5 mL) was added. After 4 h the reaction mixture was washed with aqueous 1 M hydrochloric acid (2 × 50 mL). The organic solution was cooled to 0°C and aqueous 30% hydrogen peroxide solution (1.7 mL) was added. After stirring for 10 min additional aqueous 30% hydrogen peroxide (1.7 mL) was added. After 1 h aqueous sodium bisulfite solution (50 mL) was added and the layers were separated. The organic layer was washed with saturated aqueous sodium bicarbonate, dried, filtered, and concentrated. Flash chromatography of the residue eluting with 2–30% ether in petroleum ether gave **5** (2.680 g, 0.0138 mol, 88% yield) as a colorless oil: $[\alpha]_D^{23}$ +229.83 (*c* 1.15, $CHCl_3$); ir: 1747, 1714, 1698 (C=O) cm^{-1}; ^1H nmr (300 MHz) δ: 8.40 (dd, *J* = 6, 1.5 Hz, 1H, =C*H*), 3.84 (s, 3H, OCH_3), 2.77–2.93 (complex, 3H), 2.14 (d, 1H, *J* = 9 Hz, O=CCHC*H*$_{endo}$), 1.54 (s, 3H, *exo* CH_3), 1.04 (s, 3H, *endo* CH_3); ^{13}C nmr δ: 197.8 (C=O), 165.6 (=CH), 164.1 (OC=O), 127.9 (=C), 58.8 (CH), 54.8 (C), 51.9 (OCH_3), 44.2 (CH), 40.2 (CH_2), 26.5 (CH_3), 22.3 (CH_3); ms M^+: 194.0946 (calcd. for $C_{11}H_{14}O_3$: 194.0943). Anal. calcd. for $C_{11}H_{14}O_3$: C 68.01, H 7.27; found: C 67.91, H 7.37.

[16]The specific rotation reported for the product as a neat liquid ranges from +17.4 to +18.9 (45, 47, 48). The specific rotation reported for solutions in methanol ranges from +35.3 to +38.8 (40, 43, 48).

General Diels–Alder reactions

The Diels–Alder reactions were carried out using the general procedures illustrated below with isoprene for boron trifluoride etherate, stannic chloride, ferric chloride, and diethylaluminum chloride catalyzed reactions and *trans*-2-methyl-1,3-pentadiene for zinc chloride catalyzed reactions. Temperatures and times of the reactions as well as the quantities of dienes and Lewis acids are shown in Tables 1 and 2.

$BF_3{\cdot}OEt_2$, $SnCl_4$, and $FeCl_3$ catalyzed reactions

*(1R,3R,8S,9R)-(+)-3-Carbomethoxy-6,10,10-trimethyltricyclo[7.1.1.0^{3,8}]undec-5-en-2-one (**9**).* To a solution of **5** (104.3 mg, 0.538 mmol) and isoprene (1.08 mL, 10.8 mmol) in ether (3.90 mL) at −20°C was added stannic chloride (63 μL) under argon. After stirring for 3 h a saturated aqueous sodium bicarbonate solution (3 mL) was added. The mixture was extracted with ether and the extracts were washed with water, dried, filtered, and concentrated. Flash chromatography eluting with 2–3% ether in petroleum ether gave **9** (77.6 mg, 0.296 mmol, 55% yield) as a colorless oil: $[\alpha]_D^{23}$ +54.20 (*c* 1.12, $CHCl_3$); ir: 1741, 1726 (C=O, ester), 1710 (C=O, ketone) cm^{-1}; ^1H nmr (300 MHz) δ: 5.48 (m, 1H, C=C*H*), 3.75 (s, 3H, OCH_3), 3.20 (dddd, 1H, *J* = 8, 8, 1.5, 1.5 Hz, C-8*H*), 3.05 (dd, 1H, *J* = 15.5, 6 Hz, =CHC*H*$_{eq}$H), 2.66 (dd, 1H, *J* = 5.5, 5.5 Hz, O=CC*H*), 2.47 (dddd, 1H, *J* = 11, 7, 5.5, 1.5 Hz, O=CCHCH*H*$_{exo}$), 2.15 (complex, 3H, C(CH$_3$)$_2$C*H*, =CHCH*H*$_{ax}$, C*H*$_{eq}$HC(CH$_3$)=), 1.95 (d, 1H, *J* = 11 Hz, O=CCHCH*H*$_{endo}$), 1.87 (m, 1H, CH*H*$_{ax}$C(CH$_3$)=), 1.72 (br s, 3H, =CC*H*$_3$), 1.34 (s, 3H, *exo* CH_3), 0.97 (s, 3H, *endo* CH_3); ^{13}C nmr δ: 209.8 (C=O), 172.5 (OC=O), 136.8 (C=), 118.8 (CH=), 58.8 (C), 57.9 (CH), 52.9 (OCH_3), 48.6 (CH), 42.4 (C), 34.4 (CH_2), 33.5 (CH), 32.7 (CH_2), 26.7 (CH_3), 25.1 (CH_2), 23.3 (CH_3), 21.7 (CH_3); ms M^+: 262.1561 (calcd. for $C_{16}H_{22}O_3$: 262.1570). Anal. calcd. for $C_{16}H_{22}O_3$: C 73.24, H 8.46; found: C 73.54, H 8.61.

Et_2AlCl catalyzed reaction

*3-Carbomethoxy-4-ethyl-6,6-dimethylbicyclo[3.1.1]heptan-2-one (**10**) and 3-carbomethoxy-4-(4-chloro-2-methyl-2-butenyl)-6,6-dimethylbicyclo[3.1.1]heptan-2-one (**11**).* Enone ester **5** (90.9 mg, 0.468 mmol) was dissolved in ether (3.4 mL) and cooled to −20°C. Then diethylaluminum chloride (0.26 mL of 1.8 M solution) and isoprene (0.94 mL, 9.37 mmol) were added under argon. After stirring for 3 h saturated aqueous sodium bicarbonate (3.0 mL) was added. The reaction mixture was extracted with ether and the extracts were washed with water, dried, filtered, and concentrated. Flash chromatography of the residue eluting with 1–5% ether in petroleum ether gave an inseparable mixture of **9** and **10** (47 mg, 1:5 ratio by ^1H nmr integration). The following is the spectroscopic data attributed to **10**: ir: 1744 (C=O, ester), 1712 (C=O, ketone) cm^{-1}; ^1H nmr (300 MHz) δ: 3.81 (s, 3H, OCH_3), 3.24 (d, 1H, *J* = 8 Hz, C*H*COOCH$_3$), 2.64 (dd, 1H, *J* = 5, 5 Hz, O=CC*H*), 2.45 (complex, 2H, CHC*H*H, C*H*Et), 2.16 (m, 1H, C(CH$_3$)$_2$C*H*), 1.64 (d, 1H, *J* = 11 Hz, CHCH*H*), 1.48 (m, 2H, C*H*$_2$CH$_3$), 1.36 (s, 3H, *exo* CH_3), 0.97 (s, 3H, *endo* CH_3), 0.92 (t, 3H, *J* = 7.5 Hz, CH$_2$C*H*$_3$); ms M^+: 224.1412 (calcd. for $C_{13}H_{20}O_3$: 224.1413). Further elution gave a mixture of unidentified compounds (8.2 mg) followed by **11** (9.3 mg, 0.031 mmol, 7% yield) as an oil: ir: 1740 (C=O, ester), 1711 (C=O, ketone) cm^{-1}; ^1H nmr (300 MHz) δ: 5.48 (ddq, 1H, *J* = 7.5, 7.5, 1 Hz, CH$_3$C=C*H*), 4.05 (d, 1H, *J* = 7.5 Hz, C*H*HCl), 4.04 (d, 1H, *J* = 7.5 Hz, CH*H*Cl), 3.77 (s, 3H, OCH_3), 3.24 (d, 1H, *J* = 8 Hz, C*H*COOCH$_3$), 2.80 (m, 1H, C*H*CHCOOCH$_3$), 2.65 (dd, 1H, *J* = 5, 5 Hz, O=CC*H*), 2.46 (m, 1H, CHC*H*H), 2.16 (d, 2H, *J* = 7.5 Hz, CHC*H*$_2$C=), 2.09 (m, 1H, C(CH$_3$)$_2$C*H*), 1.72 (d, 3H, *J* = 1 Hz, C*H*$_3$C=CH), 1.65 (d, 1H, *J* = 11 Hz, CHCH*H*), 1.36 (s, 3H, *exo* CH_3), 0.96 (s, 3H, *endo* CH_3); ^{13}C nmr δ: 207.7 (p), 170.6 (p), 139.4 (p), 123.7 (a), 57.5 (a), 57.2 (a), 52.4 (a), 44.8 (p), 44.8 (a), 43.4 (p), 40.4 (p), 34.0 (a), 26.7 (a), 23.0 (p), 21.2 (a), 15.9 (a); ms M^+: 298.1344, 300.1306 (calcd. for $C_{16}H_{23}O_3Cl$: 298.1336, 300.1306).

$ZnCl_2$ catalyzed reactions

*(1R,3R,4R,8S,9R)-(+)-3-Carbomethoxy-4,6,10,10-tetramethyltricyclo[7.1.1.0^{3,8}]undec-5-en-2-one (**12**) and (1R,3R,4S,8S,9R)-(+)-3-carbomethoxy-4,6,10,10-tetramethyltricyclo[7.1.1.0^{3,8}]undec-5-en-*

Can. J. Chem. Downloaded from www.nrcresearchpress.com by EESC ESCOLA DE ENGENHARIA on 09/08/12
For personal use only.

*2-one(**13**)*. Enone ester **5** (97.3 mg, 0.501 mmol) was dissolved in ether (1.23 mL) and cooled to −40°C. Zinc chloride solution[12] (68.3 mg, 0.501 mmol in 2.42 mL ether) and *trans*-2-methyl-1,3- pentadiene (0.57 mL, 5.01 mmol) were added under argon. The mixture was stirred for 24 h and saturated aqueous sodium bicarbonate solution (3 mL) was added. The mixture was then extracted with ether and the extracts were washed with water, dried, filtered, and concentrated. Flash chromatography of the residue eluting with 2–5% ether in petroleum ether gave impure **13**. Further elution with 5% ether in petroleum ether gave pure **12** (126.1 mg, 0.459 mmol, 91% yield) as a colorless oil: $[\alpha]_D^{23}$ +27.4 (*c* 1.05, $CHCl_3$); ir: 1746 (C═O, ester), 1711 (C═O, ketone) cm^{-1}; ^1H nmr (300 MHz) δ: 5.19 (m, 1H, ═C*H*), 3.69 (s, 3H, OCH_3), 2.94 (dddd, 1H, *J* = 7.5, 7.5, 2, 2 Hz, C-8*H*),2.66 (dd, 1H, *J* = 5.5, 5.5 Hz, O═CC*H*), 2.46 (complex, 2H, CHCHH_{exo}, ═CHC*H*CH_3), 2.27 (dd, 1H, *J* = 16, 8 Hz, C*H*HC═), 2.09 (ddd, 1H, *J* = 5.5, 5.5, 2 Hz, C$(CH_3)_2$C*H*), 1.91 (m, 1H, CH*H*C═), 1.82 (d, 1H, *J* = 11 Hz, CHCHH_{endo}), 1.76 (br s, 3H, ═CCH_3), 1.32 (s, 3H, *exo* CH_3), 1.26 (d, 3H, *J* = 7 Hz, CHCH_3), 0.90 (s, 3H, *endo* CH_3); ^{13}C nmr δ: 208.5 (C═O), 171.9 (OC═O), 135.2 (C═), 125.6 (CH═), 60.6 (C), 58.4 (CH), 51.8 (OCH_3), 48.9 (CH), 41.4 (C), 38.7 (CH), 36.6 (CH), 33.6 (CH_2), 26.5 (CH_3), 24.9 (CH_2), 23.0 (CH_3), 21.6 (CH_3), 17.6 (CH_3); ms M^+: 276.1723 (calcd. for $C_{17}H_{24}O_3$: 276.1726). Anal. calcd. for $C_{17}H_{24}O_3$: C 73.87, H 8.76; found: C 73.80, H 8.71. Flash chromatography again of the impure **13** eluting with 2–4% ether in petroleum ether gave **13** (12.5 mg, 0.045 mmol, 9%) as a colorless oil: $[\alpha]_D^{23}$ +145.34 (*c* 0.869, $CHCl_3$); ir: 1724 (C═O, ester), 1708 (C═O, ketone) cm^{-1}; ^1H nmr (300 MHz) δ: 5.42 (m, 1H, ═C*H*), 3.76 (s, 3H, OCH_3), 3.25 (dddd, 1H, *J* = 6, 6, 1.5, 1.5 Hz, C-8*H*), 3.16 (m, 1H, ═CHC$H_{eq}CH_3$), 2.55 (dd, 1H, *J* = 5.5, 5.5 Hz, O═CC*H*), 2.44 (dddd, 1H, *J* = 11, 5.5, 5.5, 1.5 Hz, CHCHH_{exo}), 2.15 (m, 1H, CH_{eq}HC═), 1.96 (complex, 2H, C$(CH_3)_2$C*H*, CHH_{ax}C═), 1.87 (d, 1H, *J* = 11 Hz, CHCHH_{endo}), 1.77 (br s, 3H, ═CCH_3), 1.32 (s, 3H, *exo* CH_3), 1.04 (d, 3H, *J* = 7.5 Hz, CHCH_3), 0.89 (s, 3H, *endo* CH_3); ^{13}C nmr δ: 209.8 (C═O), 174.0 (OC═O), 135.1 (═C), 125.9 (═CH), 61.4 (C), 58.5 (CH), 53.0 (OCH_3), 47.6 (CH), 42.6 (C), 37.0 (CH), 35.7 (CH), 33.3 (CH_2), 26.7 (CH_3), 24.9 (CH_2), 23.9 (CH_3), 21.6 (CH_3), 18.4 (CH_3); ms M^+: 276.1719 (calcd. for $C_{17}H_{24}O_3$: 276.1726).

*Analytical data for Diels–Alder adducts **14–20***

*(1R,3R,4R,8S,9R)-(+)-3-Carbomethoxy-4,10,10-trimethyltricyclo-[7.1.1.0^{3,8}]undec-5-en-2-one (**14**) and (1R,3R,4S,8S,9R)-(+)-3- carbomethoxy-4,10,10-trimethyltricyclo[7.1.1.0^{3,8}]undec-5-en-2-one (**15**)*

14 (a colorless oil): $[\alpha]_D^{23}$ +44.9 (*c* 1.50, $CHCl_3$); ir: 1744, 1722 (C═O, ester), 1709 (C═O, ketone) cm^{-1}; ^1H nmr (400 MHz) δ: 5.92 (ddd, 1H, *J* = 9.5, 6, 3 Hz, CH_2C*H*═), 5.56 (ddd, 1H, *J* = 9.5, 3, 3 Hz, CHC*H*═), 3.72 (s, 3H, OCH_3), 2.90 (dddd, 1H, *J* = 7.5, 7.5, 1.5, 1.5 Hz, C-8*H*), 2.62 (dd, 1H, *J* = 5.5, 5.5 Hz, O═CC*H*), 2.46 (complex, 3H, C*H*CH_3, CHCH_{exo}H, CH_{eq}HCH═), 2.11 (ddd, 1H, *J* = 6, 6, 2 Hz, C$(CH_3)_2$C*H*), 1.92 (m, 1H, CHH_{ax}CH═), 1.86 (d, 1H, *J* = 11 Hz, CHCHH_{endo}), 1.34 (s, 3H, *exo* CH_3), 1.30 (d, 3H, *J* = 7 Hz, CHCH_3), 0.94 (s, 3H, *endo* CH_3); ^{13}C nmr δ: 208.4 (C═O), 171.9 (OC═O), 132.5 (CH═), 126.9 (CH═), 60.8 (C), 58.2 (CH), 51.8 (OCH_3), 48.9 (CH), 41.5 (C), 37.8 (CH), 36.2 (CH), 28.2 (CH_2), 26.5 (CH_3), 24.7 (CH_2), 21.5 (CH_3), 17.2 (CH_3); ms M^+: 262.1568 (calcd. for $C_{16}H_{22}O_3$: 262.1570). Anal. calcd. for $C_{16}H_{22}O_3$: C 73.24, H 8.46; found: C 73.02, H 8.43.

15 (a colorless oil): $[\alpha]_D^{23}$ +153 (*c* 1.66, $CHCl_3$); ir: 1724 (C═O, ester), 1710 (C═O, ketone) cm^{-1}; ^1H nmr (300 MHz) δ: 5.97 (dddd, 1H, *J* = 10, 5, 5, 1.5 Hz, CH_2C*H*═), 5.80 (dddd, 1H, *J* = 10, 5, 1.5, 1.5 Hz, CHC*H*═), 3.77 (s, 3H, OCH_3), 3.25 (dddd, 1H, *J* = 6.5, 6.5, 1.5, 1.5 Hz, C-8*H*), 3.22 (m, 1H, C*H*CH_3), 2.58 (dd, 1H, *J* = 5.5, 5.5 Hz, O═CC*H*), 2.48 (dddd, 1H, *J* = 11, 6, 6, 1.5 Hz, CHCHH_{exo}), 2.21 (m, 1H, CH_{eq}HCH═), 2.01 (complex, 2H, C$(CH_3)_2$C*H*, CHH_{ax}CH═), 1.86 (d, 1H, *J* = 11 Hz, CHCHH_{endo}), 1.33 (s, 3H, *exo* CH_3), 1.06 (d, 3H, *J* = 7.5 Hz, CHCH_3), 0.90 (s, 3H, *endo* CH_3); ^{13}C nmr δ: 209.8 (C═O), 174.0 (OC═O), 133.1 (CH═), 127.0 (CH═), 61.8 (C), 58.4 (CH), 53.1 (OCH_3), 47.6 (CH), 42.4 (C), 36.5 (CH), 35.2 (CH), 27.8 (CH_2), 26.7 (CH_3), 25.2 (CH_2), 21.6 (CH_3), 18.2 (CH_3); ms M^+: 262.1569 (calcd. for $C_{16}H_{22}O_3$: 262.1570).

*(1R,3R,8S,9R)-(+)-3-Carbomethoxy-5,6,10,10-tetramethyltricyclo-[7.1.1.0^{3,8}]undec-5-en-2-one (**16**)*

16 (a colorless oil purified by gravity chromatography on neutral alumina): $[\alpha]_D^{23}$ +68.97 (*c* 1.07, $CHCl_3$); ir: 1727 (C═O, ester), 1710 (C═O, ketone) cm^{-1}; ^1H nmr (400 MHz) δ: 3.76 (s, 3H, OCH_3), 3.18 (dddd, 1H, *J* = 9, 7.5, 1.5, 1.5 Hz, C-8*H*), 2.87 (d, 1H, *J* = 14.5 Hz, C-4H_{eq}), 2.66 (dd, 1H, *J* = 5.5, 5.5 Hz, O═CC*H*), 2.47 (m, 1H, CHCH_{exo}H), 2.27 (br d, 1H, *J* = 14.5 Hz, C-4H_{ax}), 2.11 (m, 2H, C$(CH_3)_2$C*H*, C-7H_{eq}), 1.93 (complex, 2H, CHCHH_{endo}, C-7H_{ax}), 1.68 (br s, 3H, ═CCH_3), 1.65 (br s, 3H, ═CCH_3), 1.34 (s, 3H, *exo* CH_3), 0.96 (s, 3H, *endo* CH_3); ^{13}C nmr δ: 210.1 (C═O), 172.2 (OC═O), 128.2 (C═), 125.6 (C═), 60.2 (C), 58.0 (CH), 52.7 (OCH_3), 48.1 (CH), 42.0 (C), 41.0 (CH_2), 34.6 (CH_2), 33.8 (CH), 26.7 (CH_3), 24.9 (CH_2), 21.8 (CH_3), 19.0 (CH_3), 18.4 (CH_3); ms M^+: 276.1725 (calcd. for $C_{17}H_{24}O_3$: 276.1726). Anal. calcd. for $C_{17}H_{24}O_3$: C 73.87, H 8.76; found: C 73.92, H 8.77.

*(1R,3R,4R,8S,9R)-(+)-3-Carbomethoxy-4,5,10,10-tetramethyltricyclo[7.1.1.0^{3,8}]undec-5-en-2-one (**17**) and (1R,3R,4S,8S,9R)-(+)-3- carbomethoxy-4,5,10,10-tetramethyltricyclo[7.1.1.0^{3,8}]-undec-5-en-2-one (**18**)*

The reaction of **5** with 3-methyl-1,3-pentadiene did not go to completion; 24% of **5** was recovered.

17 (a white solid): $[\alpha]_D^{23}$ +99.65 (*c* 2.56, $CHCl_3$); mp 66–68°C; ir: 1723 (C═O, ester), 1702 (C═O, ketone) cm^{-1}; ^1H nmr (300 MHz) δ: 5.60 (m, 1H, C*H*═), 3.72 (s, 3H, OCH_3), 3.06 (dddd, 1H, *J* = 8, 6, 1.5, 1.5 Hz, C-8*H*), 2.73 (br q, 1H, *J* = 7 Hz, C*H*CH_3), 2.64 (dd, 1H, *J* = 5.5, 5.5 Hz, O═CC*H*), 2.43 (complex, 2H, CHCHH_{exo}, CH_{eq}HCH═), 2.10 (ddd, 1H, *J* = 6, 6, 2 Hz, C$(CH_3)_2$C*H*), 1.97 (d, 1H, *J* = 11 Hz, CHCHH_{endo}), 1.87 (m, 1H, CHH_{ax}CH═), 1.70 (br s, 3H, ═CCH_3), 1.33 (s, 3H, *exo* CH_3), 1.23 (d, 3H, *J* = 7 Hz, CHCH_3), 0.93 (s, 3H, *endo* CH_3); ^{13}C nmr δ: 208.7 (C═O), 172.0 (OC═O), 138.8 (C═), 122.1 (CH═), 63.1 (C), 58.3 (CH), 52.0 (OCH_3), 49.3 (CH), 42.5 (C), 41.1 (CH), 35.7 (CH), 28.1 (CH_2), 26.7 (CH_3), 24.5 (CH_2), 21.7 (CH_3), 20.2 (CH_3), 14.1 (CH_3); ms M^+: 276.1727 (calcd. for $C_{17}H_{24}O_3$: 276.1726). Anal. calcd. for $C_{17}H_{24}O_3$: C 73.87, H 8.76; found: C 73.83, H 8.88.

18 (an oil): $[\alpha]_D^{23}$ +84.58 (*c* 2.32, $CHCl_3$); ir 1742 (C═O, ester), 1713 (C═O, ketone) cm^{-1}; ^1H nmr (300 MHz) δ: 5.64 (br d, 1H, *J* = 7.5 Hz, C*H*═), 3.71 (s, 3H, OCH_3), 3.28 (dddd, 1H, *J* = 11, 7.5, 2, 2 Hz, C-8*H*), 3.04 (q, 1H, *J* = 7.5 Hz, C*H*CH_3), 2.65 (dd, 1H, *J* = 5.5, 5.5 Hz, O═CC*H*), 2.51 (dddd, 1H, *J* = 11, 6, 6, 2 Hz, CHCHH_{exo}), 2.18 (ddd, 1H, *J* = 15, 7, 7 Hz, CH_{eq}HCH═), 2.03 (ddd, 1H, *J* = 6, 6, 2.5 Hz, C$(CH_3)_2$C*H*), 1.88 (m, 1H, CHH_{ax}CH═), 1.77 (d, 1H, *J* = 11 Hz, CHCHH_{endo}), 1.68 (dd, 3H, *J* = 2.5, 1.5 Hz, ═CCH_3), 1.34 (s, 3H, *exo* CH_3), 1.00 (d, 3H, *J* = 7.5 Hz, CHCH_3), 0.82 (s, 3H, *endo* CH_3); ^{13}C nmr δ: 209.4 (C═O), 173.5 (OC═O), 139.8 (C═), 121.4 (CH═), 61.6 (C), 58.9 (CH), 53.2 (OCH_3), 46.0 (CH), 44.0 (CH), 40.3 (C), 36.3 (CH), 27.4 (CH_2), 26.7 (CH_3), 24.5 (CH_2), 22.2 (CH_3), 22.0 (CH_3), 16.5 (CH_3); ms M^+: 276.1727 (calcd. for $C_{17}H_{24}O_3$: 276.1726).

*(1R,3R,4S,7R,8S,9R)-3-Carbomethoxy-10,10-dimethyltetracyclo-[7.1.1.1^{4,7}.0^{3,8}]dodec-5-en-2-one (**19**) and (1R,3R,4R,7S,8S,9R)-3-carbomethoxy-10,10-dimethyltetracyclo[7.1.1.1^{4,7}.0^{3,8}]dodec-5-en-2-one (**20**)*

After the reaction was completed, flash chromatography of the residue with 4% ether in petroleum ether gave a mixture of impure **19** and **20**. Bulb-to-bulb distillation (64°C/1–1.5 Torr: 1 Torr = 133.3 Pa) gave a mixture of pure **19** and **20** (89:11 ratio by ^1H nmr integration): ir: 1731 (C═O, ester), 1709 (C═O, ketone) cm^{-1}; ms M^+: 260.1415 (calcd. for $C_{16}H_{20}O_3$: 260.1413). ^1H nmr (300 MHz) showed two sets of signals. The major set for **19**: δ: 6.46 (dd, 1H, *J* = 5.5, 3 Hz, C*H*═CH), 5.98 (dd, 1H, *J* = 5.5, 3 Hz, CH═C*H*), 3.67 (s, 3H, OCH_3), 3.50 (m, 1H, ═CHC*H*), 2.76 (m, 1H, C*H*CH═), 2.70 (dd, 1H, *J* = 6, 6 Hz, O═CC*H*), 2.63 (m, 1H, CHCHH_{exo}), 2.61 (m, 1H, C-8*H*), 2.42 (m, 1H, C$(CH_3)_2$C*H*), 2.02 (d, 1H, *J* = 12 Hz, CHCHH_{endo}), 1.98 (br d, 1H, *J* = 10.5 Hz, CHCH*H*CH), 1.40 (s, 3H, *exo* CH_3), 1.34 (m, 1H,

Can. J. Chem. Downloaded from www.nrcresearchpress.com by EESC ESCOLA DE ENGENHARIA on 09/08/12
For personal use only.

CHC*H*HCH), 0.92 (s, 3H, *endo* CH_3). The minor set for **20**: δ: 6.30 (dd, 1H, J = 5.5, 3 Hz, CH=C*H*), 6.13 (dd, 1H, J = 5.5, 3H, C*H*=CH), 3.76 (s, 3H, OCH_3), 3.37 (m, 1H), 3.31 (m, 1H), 2.97 (m, 1H), 2.28 (m, 2H), 2.17 (m, 1H), 1.33 (s, 3H, *exo* CH_3), 0.92 (s, 3H, *endo* CH_3).

*(1R,3S,8S,9R)-(+)-6,10,10-Trimethyltricyclo[7.1.1.0^{3,8}]undec-5-en-2-one (**28**) and (1R,3R,8S,9R)-(−)-6,10,10-trimethyltricyclo[7.1.1.0^{3,8}]undec-5-en-2-one (**29**)*

Keto ester **9** (4.632 g, 17.7 mmol) was dissolved in 2,4,6-collidine (30 mL) under argon. Anhydrous lithium iodide (18.94 g, 142 mmol) and then water (2.54 mL, 142 mmol) were introduced to the stirred solution. The mixture was heated under reflux for 2.3 h, then cooled to room temperature, poured into ice-cold aqueous 5% hydrochloric acid, and extracted with ether. The extracts were washed with ice-cold 5% aqueous hydrochloric acid and water and then were dried, filtered, and concentrated. Flash chromatography eluting with 4% ether in petroleum ether gave **28** as a solid (0.222 g, 1.1 mmol, 6% yield): $[\alpha]_D^{23}$ +107.3 (*c* 2.07, $CHCl_3$); mp 52–54°C; ir 1705 (C=O) cm^{-1}; ^1H nmr (300 MHz) δ: 5.67 (dm, 1H, J = 6 Hz, =C*H*), 2.63 (dd, 1H, J = 14, 7 Hz, =CHC*H*H), 2.58 (dd, 1H, J = 5.5, 5.5 Hz, C-1*H*), 2.47 (m, 1H, C*H*$_{exo}$CH), 2.36 (m, 1H, C-3*H*), 2.30 (m, 1H, C-8*H*), 2.06 (ddd, 1H, J = 5.5, 5.5, 2 Hz, $C(CH_3)_2CH$), 1.99 (dd, 1H, J = 15, 6 Hz, C-7*H*), 1.93 (m, 1H, C-7*H*), 1.82 (m, 1H, =CHCH*H*), 1.78 (br s, 3H, =CCH_3), 1.65 (d, 1H, J = 11 Hz, CH*H*$_{endo}$CH), 1.34 (s, 3H, *exo* CH_3), 0.91 (s, 3H, *endo* CH_3); ^{13}C nmr δ: 216.3 (C=O), 137.8 (=C), 121.4 (=CH), 57.5 (CH), 47.7 (CH), 44.2 (CH), 40.4 (C), 33.0 (CH_2), 32.0 (CH), 29.0 (CH_2), 25.8 (CH_3), 23.6 (CH_2), 23.2 (CH_3), 21.8 (CH_3); ms M^+: 204.1512 (calcd. for $C_{14}H_{20}O$: 204.1514). Continued elution gave a mixture of **28** and **29** (0.393 g, 1.9 mmol, 11% yield, 1:2 ratio by ^1H nmr integration). Further elution gave pure **29** (2.899 g, 14.2 mmol, 80% yield: $[\alpha]_D^{23}$ −47.8 (*c* 2.286, $CHCl_3$); ir: 1714 (C=O) cm^{-1}; ^1H nmr (300 MHz) δ: 5.48 (br s, 1H, =C*H*), 2.60 (dd, 1H, J = 5, 5 Hz, C-1*H*), 2.30–2.50 (complex, 3H), 1.83–2.22 (complex, 6H), 1.70 (br s, 3H, =CCH_3), 1.38 (s, 3H, *exo* CH_3), 0.78 (s, 3H, *endo* CH_3); ^{13}C nmr δ: 214.7 (C=O), 135.6 (=C), 121.2 (=CH), 58.5 (CH), 46.4 (CH), 45.0 (CH), 44.7 (C), 36.6 (CH_2), 36.5 (CH), 26.8(CH_3), 25.0 (CH_2), 24.0 (CH_2), 23.7 (CH_3), 21.9 (CH_3); ms M^+: 204.1516 (calcd. for $C_{14}H_{20}O$: 204.1514). Anal. calcd. for $C_{14}H_{20}O$: C 82.29, H 9.87; found: C 82.59, H 9.78.

*Epimerization of **28** to **29***

Ketone **28** (21 mg, 0.103 mmol) was dissolved in methanol (5 mL), and aqueous 3 M sodium hydroxide solution (1 mL) was added. After refluxing for 24 h water was added and the mixture was extracted with ether. The extracts were washed with saturated aqueous sodium chloride solution, dried, filtered, and concentrated. The crude product (19.4 mg, 92% yield) was a mixture of **28** and **29** (1:9 ratio by 300 MHz ^1H nmr integration).

*(1R,2S,7R,9R)-(−)-4,10,10-Trimethyl-8-methylenetricyclo-[7.1.1.0^{2,7}]undec-4-ene (**30**)*

Potassium hydride (1.44 g, 35% by weight) was washed three times with dry benzene under argon. DMSO (6 mL) was introduced by syringe and the mixture was stirred at room temperature until evolution of hydrogen stopped (ca. 25 min). Methyltriphenylphosphonium bromide (4.30 g, 12 mmol) in DMSO (11 mL) was then added to the light greenish yellow solution. The resulting bright yellowish green solution was stirred at room temperature for 10 min. Ketone **29** (1.176 g, 5.77 mmol) in benzene (4 mL) was added to the above solution of methylenetriphenylphosphorane. The resulting dark red solution was stirred at room temperature for 20 h. Water was added and the mixture was extracted with petroleum ether. The combined extracts were washed with water, dried, filtered, and concentrated. The crude product was passed through a layer of silica gel in a sintered glass funnel and the silica gel was washed with 1–2% ether in petroleum ether. The filtrate was concentrated to give **30** (1.1585 g, 5.74 mmol, 99% yield) as a colorless liquid: $[\alpha]_D^{23}$ −84.67 (*c* 2.10, $CHCl_3$); ir: 1643 (C=C) cm^{-1}; ^1H nmr (300 MHz) δ: 5.47 (br m, 1H, =C*H*), 4.66 (dd, 1H, J = 2, 2 Hz, =C*H*H), 4.60 (dd, 1H, J = 2, 2 Hz, =CH*H*), 2.53 (dd, 1H, J = 5.5, 5.5 Hz, C-9*H*), 2.18–2.40 (complex, 3H), 1.98 (complex, 2H), 1.79 (complex, 3H), 1.70 (complex, 4H, =CCH_3, CHCHH_{endo}), 1.29 (s, 3H, *exo* CH_3), 0.66 (s, 3H, *endo* CH_3); ^{13}C nmr δ: 153.7 (C=), 135.6 (=C), 121.5 (=CH), 103.85 (=CH_2), 52.9 (CH), 45.4 (CH), 42.8 (C), 38.2 (CH), 37.5 (CH), 37.3 (CH_2), 28.4 (CH_2), 26.8 (CH_3), 24.2 (CH_2), 23.8 (CH_3), 21.4 (CH_3); ms M^+: 202.1722 (calcd. for $C_{15}H_{22}$: 202.1723).

*(1R,5R,6S)-(−)-2-Chloromethyl-8-methyl-5-(1-methylethenyl)-bicyclo[4.4.0]deca-2,8-diene (**31**)*

Phenyl dichlorophosphate (73 μL, 0.491 mmol) and DMSO (63 μL, 0.892 mmol) were added to dry dichloromethane (0.5 mL) at −40°C. A colorless solution formed. Compound **30** (90.1 mg, 0.446 mmol) in dichloromethane (1 mL) was then added. After stirring at −40°C for 1 h and then at −20°C to 10°C for 45 min, water (50 μL) was added. The mixture was filtered through a layer of silica gel in a sintered glass funnel and washed with 40% ether in petroleum ether. The filtrate was concentrated and the residue was distilled (bulb-to-bulb at 66–68°C/1.5–2 Torr) to give **31** (58.8 mg, 0.248 mmol, 56% yield) as a solid: $[\alpha]_D^{26}$ −193.9 (*c* 2.33, $CHCl_3$); mp 40–41°C; ir: 1643 (C=C) cm^{-1}; ^1H nmr (300 MHz) δ: 5.86 (br d, 1H, J = 5 Hz, $ClCH_2C$=C*H*), 5.49 (br d, 1H, J = 5 Hz, CH_3C=C*H*), 4.78 (m, 2H, CH_3C=CH_2), 4.20 (dm, 1H, J = 11 Hz, C*H*HCl), 3.95 (d, 1H, J = 11 Hz, CH*H*Cl), 1.50–2.50 (complex, 9H), 1.67 (br s, 6H, CH_3C=CH_2, CH_3C=CH); ^{13}C nmr δ: 146.9 (C=), 136.4 (C=), 134.4 (=C), 127.8 (=CH), 120.2 (=CH), 112.2 (=CH_2), 47.9 (CH_2Cl), 47.5 (CH), 38.2 (CH), 37.3 (CH), 35.6 (CH_2), 31.0 (CH_2), 29.8 (CH_2), 23.5 (CH_3), 18.2 (CH_3); ms M^+: 238.1305, 236.1331 (calcd. for $C_{15}H_{21}Cl$: 238.1303, 236.1333).

*6,10,10-Trimethyltricyclo[7.1.1.0^{3,8}]undecane-2,5-diol (**33**)*

To a solution of **29** (119.7 mg, 0.587 mmol) in THF (0.60 mL) cooled to 0°C, 1 M borane–THF solution (1.50 mL) was added dropwise under argon. The reaction mixture was stirred at 0°C for 1 h and for a further 2 h at room temperature. Excess borane was decomposed by dropwise addition of water (0.6 mL). Aqueous 3 M sodium hydroxide solution (0.6 mL) was introduced followed by dropwise addition of aqueous 30% hydrogen peroxide solution (0.6 mL). The reaction mixture was stirred for 1 h at room temperature and potassium carbonate (1.25 g) was then added. The mixture was extracted with ether (3 × 5 mL) and the combined organic layers were washed with water, dried, filtered, and concentrated to give **33** (177.5 mg as a 1:2 mixture, 135% crude yield): ir: 3362 (OH) cm^{-1}; ^1H nmr (300 MHz) δ: 4.21 (m, 0.67H), 3.92 (m, 0.33H), 3.65 (t, 0.67H, J = 6.5 Hz), 3.31 (m, 0.33H), 0.9–2.26 (complex, 22H); ms $M^+ - H_2O$: 206.1669 (calcd. for $C_{14}H_{22}O$: 206.1672); $M^+ - 2H_2O$: 188.1562 (calcd. for $C_{14}H_{20}$: 188.1566).

*(1R,6S,7R)-10,10-Ethylenedioxy-4-methyl-7-(1-methylethenyl)-bicyclo[4.4.0]dec-3-ene (**34**) and (1S,6R,10R)-7,7-ethylenedioxy-3-methyl-10-(1-methylethenyl)bicyclo[4.4.0]dec-2-ene (**35**)*

Ethylene glycol (43.1 mg, 0.69 mmol) and *p*-toluenesulfonic acid (13.9 mg, 0.073 mmol) were added to a solution of **29** (65.2 mg, 0.32 mmol) in benzene (8 mL). The mixture was heated under reflux with removal of water by a Dean–Stark apparatus for 20 h. The benzene layer was washed twice each with aqueous 1 M sodium hydroxide solution and saturated aqueous sodium chloride solution and then was dried, filtered, and concentrated. Flash chromatography of the residue eluting with 4% ether in petroleum ether gave a mixture of **34** and **35** (64.0 mg, 81% yield, 2:1 ratio): ir: 1644 (C=C) cm^{-1}; ^1H nmr (300 MHz) δ: 5.27 (br s, 0.67H, =C*H*), 5.15 (q, 0.33H, J = 1.5 Hz, CHC*H*=), 4.81 (m, 0.33H, C=C*H*H), 4.65 (m, 1.67H, C=CH*H*, C=CH_2), 3.95 (complex, 4H, OCH_2CH_2O), 1.30–2.15 (complex, 17H); ms M^+: 248.1774 (calcd. for $C_{16}H_{24}O_2$: 248.1777).

*(1S,6R,10R)-6-Carbomethoxy-7,7-ethylenedioxy-3-methyl-10-(1-methylethenyl)bicyclo[4.4.0]dec-2-ene (**36**) and (1R,6S,7R)-1-carbomethoxy-10,10-ethylenedioxy-4-methyl-7-(1-methylethenyl)bicyclo[4.4.0]dec-3-ene (**37**)*

To a solution of keto ester **9** (88.6 mg, 0.338 mmol) were added eth-

Can. J. Chem. Downloaded from www.nrcresearchpress.com by EESC ESCOLA DE ENGENHARIA on 09/08/12
For personal use only.

ylene glycol (50.5 mg, 0.813 mmol) and *p*-toluenesulfonic acid (16.6 mg, 0.086 mmol). The mixture was refluxed with removal of water by a Dean–Stark apparatus for 48 h. The benzene layer was washed with aqueous 1 M sodium hydroxide solution and saturated aqueous sodium chloride solution and then was dried, filtered, and concentrated. Flash chromatography eluting with 6–20% ether in petroleum ether gave recovered starting material **9** (48.0 mg, 54% recovery). Continuing elution gave a mixture of **36** and **37** (41.9 mg, 92% yield based on consumed starting material, 41:59 ratio): ir: 1729 (C=O, ester), 1643 (C=C) cm^{-1}; ^1H nmr (300 MHz) δ: 5.37 (dq, 0.41H, J = 5, 1.5 Hz, C*H*=CCH$_3$), 5.30 (br s, 0.59H, CH$_3$C=C*H*), 4.75 (m, 2H, C=C*H*$_2$), 3.79–4.00 (m, 4H, OC*H*$_2$C*H*$_2$O), 3.70, 3.67 (each s, 3H, OC*H*$_3$), 2.90, 2.84 (each m, 1H), 2.22–2.50 (complex, 2H), 1.46–2.16 (complex, 13H); ms M$^+$: 306.1830 (calcd. for $C_{18}H_{26}O_4$: 306.1832).

*(1R,3R,6S,8S,9R)-(+)-3-Carbomethoxy-6,10,10-trimethyltricyclo-[7.1.1.0^{3,8}]undecan-2-one (**38**)*

Keto ester **9** (48 mg, 0.183 mmol) in a solution of ethanol (10 mL), containing glacial acetic acid (0.5 mL) and platinum oxide (12 mg) was hydrogenated at 35 psi (1 psi = 6.89 kPa) for 24 h. The reaction mixture was then filtered through a layer of Celite in a sintered glass funnel and concentrated to give compound **38** (49 mg, 0.184 mmol, 100% yield): $[\alpha]_D^{26}$ +122.62 (*c* 1.70, $CHCl_3$); ir: 1737 (C=O, ester), 1707 (C=O, ketone) cm^{-1}; ^1H nmr (300 MHz) δ: 3.80 (s, 3H, OC*H*$_3$), 3.02 (br d, 1H, J = 7 Hz, C-8*H*), 2.62 (dd, 1H, J = 5.5, 5.5 Hz, O=CC*H*), 2.56 (m, 2H, CHCH*H*$_{exo}$, C-4*H*), 2.18 (d, 1H, J = 11 Hz, CHCH*H*$_{endo}$), 2.11 (ddd, 1H, J = 5.5, 5.5, 1 Hz, C(CH$_3$)$_2$C*H*), 1.86 (ddd, 1H, J = 14.5, 13.5, 4.5 Hz, CH$_2$CH*H*), 1.72 (m, 1H, CH$_3$CHC*H*H), 1.60 (complex, 2H, C*H*CH$_3$, C*H*HCHCH$_3$), 1.37 (s, 3H, *exo* C*H*$_3$), 1.32 (m, 1H, CH*H*CHCH$_3$), 1.01 (complex, 4H, *endo* C*H*$_3$, CH$_3$CHC*H*H), 0.86 (d, 3H, J = 6.5 Hz, CHC*H*$_3$); ^{13}C nmr δ: 210.3 (p), 172.6 (p), 58.0 (a), 57.4 (p), 52.7 (a), 49.3 (a), 44.9 (p), 38.6 (p), 33.9 (a), 32.6 (p), 31.9 (p), 27.3 (p), 27.1 (a), 26.9 (a), 23.1 (a), 21.6 (a); ms M$^+$: 264.1724 (calcd. for $C_{16}H_{24}O_3$: 264.1726).

*(1R,5R,6S,8S)-1-Carbomethoxy-2,2-ethylenedioxy-8-methyl-5-(1-methylethenyl)bicyclo[4.4.0]decane (**39**)*

Ethylene glycol (19.6 mg, 0.316 mmol) and *p*-toluenesulfonic acid (6.3 mg, 0.033 mmol) were added to a solution of **38** (27.8 mg, 0.105 mmol) in benzene (8 mL). The mixture was heated under reflux with removal of water by a Dean–Stark apparatus for 100 h. The benzene layer was washed with aqueous 1 M sodium hydroxide solution and saturated sodium chloride solution and then was dried, filtered, and concentrated. Flash chromatography eluting with 3–10% ether in petroleum ether gave recovered starting material **38** (19.6 mg, 0.074 mmol, 70% recovery). Continued elution gave **39** (6.1 mg, 0.02 mmol, 64% yield based on 30% consumed starting material): ir: 1728 (C=O) cm^{-1}; ^1H nmr (300 MHz) δ: 4.76 (br s, 1H, C=C*H*H), 4.73 (m, 1H, C=CH*H*), 3.85 (m, 4H, OC*H*$_2$C*H*$_2$O), 3.73 (s, 3H, OC*H*$_3$), 2.36 (complex, 3H), 1.44–1.78 (complex, 11H), 0.80–1.08 (complex, 2H), 0.75 (d, 3H, J = 6.5 Hz, CHC*H*$_3$); ms M$^+$: 308.1992 (calcd. for $C_{18}H_{28}O_4$: 308.1988).

*(1R,3S,6S,8S,9R)-(+)-6,10,10-Trimethyltricyclo[7.1.1.0^{3,8}]-undecan-2-one (**40**) and (1R,3R,6S,8S,9R) (+)- 6,10,10-trimethyltricyclo[7.1.1.0^{3,8}]undecan-2-one (**41**)*

Keto ester **38** (59.2 mg, 0.224 mmol) was dissolved in 2,4,6-collidine (1.40 mL) under argon. Anhydrous lithium iodide (239.7 mg, 1.8 mmol) and then water (30 μL, 1.8 mmol) were added to the stirred solution. The mixture was heated under reflux for 3.5 h, then cooled to room temperature, poured into ice-cold aqueous 1 M hydrochloric acid, and extracted with ether. The extract was washed with ice-cold aqueous 1 M hydrochloric acid and water and then was dried, filtered, and concentrated. Flash chromatography eluting with 4% ether in petroleum ether gave **40** (4 mg, 0.019 mmol, 8% yield) as a white solid: $[\alpha]_D^{26}$ +96.13 (c 0.766, $CHCl_3$); mp 32–33°C; ir: 1707 (C=O) cm^{-1}; ^1H nmr (300 MHz) δ: 2.55 (dd, 1H, J = 5, 5 Hz, C-1*H*), 2.47 (dddd, 1H, J = 10, 8, 6, 1 Hz, CHCH*H*$_{exo}$), 2.37 (complex, 2H), 1.99 (complex, 4H), 1.66 (complex, 2H), 1.42 (m, 1H), 1.34 (s, 3H, *exo* C*H*$_3$), 1.20 (m, 1H), 0.98 (d, 3H, J = 7 Hz, CHC*H*$_3$), 0.90 (s, 3H, *endo* C*H*$_3$); ^{13}C nmr δ: 216.7 (p), 58.2 (a), 48.1 (a), 44.9 (a), 41.0 (p), 33.2 (p), 31.2 (p), 28.4 (a), 27.6 (p), 26.0 (a), 25.7 (a), 24.3 (p), 23.2 (a), 21.8 (a); ms M$^+$: 206.1665 (calcd. for $C_{14}H_{22}O$: 206.1672). Anal. calcd. for $C_{14}H_{22}O$: C 81.49, H 10.75; found: C 81.29, H 10.52. Continued elution gave a mixture of **40** and **41** (1:14, 8.4 mg, 0.041 mmol, 18% yield) and pure **41** (33.2 mg, 0.161 mmol, 72% yield): $[\alpha]_D^{26}$ +66.71 (c 1.67, $CHCl_3$); ir: 1712 (C=O) cm^{-1}; ^1H nmr (300 MHz) δ: 2.54 (dd, 1H, J = 5, 5 Hz, C-1*H*), 2.40 (ddd, 1H, J = 10, 7, 5 Hz, CHCH*H*$_{exo}$), 2.17 (complex, 2H), 1.93 (complex, 3H), 1.85 (d, 1H, J = 10 Hz, CHCH*H*$_{endo}$), 1.50–1.72 (complex, 3H), 1.42 (complex, 2H), 1.36 (s, 3H, *exo* C*H*$_3$), 1.05 (d, 3H, J = 7.5 Hz, CHC*H*$_3$), 0.80 (s, 3H, *endo* C*H*$_3$); ^{13}C nmr δ: 214.9 (p), 58.4 (a), 50.9 (a), 46.0 (a), 45.1 (p), 37.8 (p), 33.7 (a), 32.1 (p), 28.3 (a), 26.9 (a), 24.5 (p), 22.0 (a), 19.7 (p), 19.4 (a); ms M$^+$: 206.1666 (calcd. for $C_{14}H_{22}O$: 206.1672).

*Epimerization of **40** to **41***

Ketone **40** (14.6 mg, 0.071 mmol) was dissolved in methanol (3.5 mL) and an aqueous 3 M sodium hydroxide solution (0.7 mL) was added. The mixture was refluxed for 24 h, then cooled to room temperature, and extracted with ether. The ether extracts were washed with water, dried, filtered, and concentrated to give a mixture of **40** and **41** (14.2 mg, 97% yield, 3:7 ratio by ^1H nmr integration).

*(1R,5R,6S,8S)-(−)-2,2-Ethylenedioxy-8-methyl-5-(1-methylethenyl)bicyclo[4.4.0]decane (**42**) and (1S,5R,6S,8S)-(+)-2,2-ethylenedioxy-8-methyl-5-(1-methylethenyl)bicyclo[4.4.0]-decane (**43**)*

Ethylene glycol (60 μL, 1.1 mmol) and *p*-toluenesulfonic acid (15.5 mg, 0.081 mmol) were added to a solution of **40** (25.5 mg, 0.125 mmol) in benzene (6 mL). The mixture was heated under reflux with removal of water by a Dean–Stark apparatus for 48 h. The benzene layer was washed with aqueous 1 M sodium hydroxide solution and saturated aqueous sodium chloride solution and then was dried, filtered, and concentrated. Flash chromatography eluting with 3% ether in petroleum ether gave **42** (15.0 mg, 0.06 mmol, 48% yield) as a white solid: $[\alpha]_D^{26}$ −13.9 (*c* 1.50, $CHCl_3$); mp 39–41°C; ir: 1646 (C=C) cm^{-1}; ^1H nmr (300 MHz) δ: 4.69 (br s, 2H, C=C*H*$_2$), 3.93 (m, 4H, OC*H*$_2$C*H*$_2$O), 1.95 (m, 1H), 1.25–1.86 (complex, 15H), 1.04 (m, 1H), 0.96 (d, 3H, J = 7.5 Hz, CHC*H*$_3$); ^{13}C nmr δ: 148.4 (=C), 111.1 (=CH$_2$), 110.0 (O-C-O), 65.3 (CH$_2$), 65.0 (CH$_2$), 52.0 (CH), 50.0 (CH), 37.4 (CH$_2$), 35.3 (CH$_2$), 35.0 (CH), 31.2 (CH$_2$), 29.2 (CH$_2$), 27.3 (CH), 18.6 (CH$_3$), 18.5 (CH$_2$), 17.9 (CH$_3$); ms M$^+$: 250.1931 (calcd. for $C_{16}H_{26}O_2$: 250.1934). Continued elution gave a mixture of **42** and **43** (2.1 mg, 0.008 mmol, 7% yield, 22:78 ratio by ^1H nmr integration) and pure **43** (11.5 mg, 0.046 mmol, 37% yield) as a white solid: $[\alpha]_D^{26}$ +27.7 (*c* 1.15, $CHCl_3$); mp 60–61°C (ether – petroleum ether); ir: 1644 (C=C) cm^{-1}; ^1H nmr (300 MHz) δ: 4.73 (br s, 2H, C=C*H*$_2$), 3.94 (br s, 4H, OC*H*$_2$C*H*$_2$O), 2.36 (m, 1H), 1.92 (m, 1H), 1.40–1.79 (complex, 13H), 0.85 (complex, 2H), 0.80 (d, 3H, J = 6.5 Hz, CHC*H*$_3$); ^{13}C nmr δ: 148.2 (=C), 111.3 (=CH$_2$), 111.1 (O-C-O), 64.2 (CH$_2$), 64.1 (CH$_2$), 44.8 (CH), 42.4 (CH), 37.2 (CH$_2$), 36.3 (CH), 35.1 (CH$_2$), 30.4 (CH$_2$), 29.4 (CH$_2$), 26.4 (CH), 23.5 (CH$_2$), 22.9 (CH$_3$), 18.2 (CH$_3$); ms M$^+$: 250.1930 (calcd. for $C_{16}H_{26}O_2$: 250.1934). Anal. calcd. for $C_{16}H_{26}O_2$: C 76.70, H 10.47; found: C 76.59, H 10.52.

*(1R,5R,6S,8S)-(−)-8-Methyl-5-(1-methylethenyl)bicyclo[4.4.0]-decan-2-one (**44**)*

A solution of acetal **42** (9.3 mg, 0.037 mmol) in acetone–water (10:1, 1 mL) containing *p*-toluenesulfonic acid (2.3 mg, 0.012 mmol) was refluxed for 3 h. Excess solvent was then removed under reduced pressure. The residue was diluted with ether and the ethereal solution was washed with aqueous 1 M sodium hydroxide solution and saturated sodium chloride solution and then was dried, filtered, and concentrated to give **44** (7.6 mg, 0.037 mmol, 100% yield) as a white solid: $[\alpha]_D^{26}$ −11.12 (*c* 0.8, $CHCl_3$); mp 71–73°C; ir: 1712 (C=O), 1640 (C=C) cm^{-1}; ^1H nmr (300 MHz) δ: 4.78 (m, 2H, C=C*H*$_2$), 2.42

Can. J. Chem. Downloaded from www.nrcresearchpress.com by EESC ESCOLA DE ENGENHARIA on 09/08/12
For personal use only.

(complex, 2H), 2.20 (ddd, 1H, J = 12, 11, 4 Hz), 1.44–2.05 (complex, 13H), 1.24 (ddd, 1H, J = 13, 11, 4 Hz), 0.92 (d, 3H, J = 7.5 Hz, $CHCH_3$); ^{13}C nmr δ: 212.3 (C=O), 146.6 (=C), 112.3 (=CH_2), 54.4 (CH), 51.6 (CH), 41.4 (CH_2), 39.9 (CH), 37.9 (CH_2), 32.5 (CH_2), 30.5 (CH_2), 27.0 (CH), 19.6 (CH_2), 18.5 (CH_3), 17.6 (CH_3); ms M^+:206.1674 (calcd. for $C_{14}H_{22}O$: 206.1672).

(1S,5R,6S,8S)-(+)-8-Methyl-5-(1-methylethenyl)bicyclo[4.4.0]-decan-2-one (45)

A solution of acetal **43** (26.5 mg, 0.106 mmol) in acetone–water (10:1, 1.5 mL) containing *p*-toluenesulfonic acid (6.6 mg, 0.035 mmol) was refluxed for 3.5 h. Excess solvent was then removed by a rotary evaporator. The residue was diluted with ether and the ethereal solution was washed with aqueous 1 M sodium hydroxide solution and saturated sodium chloride solution and then was dried, filtered, and concentrated. Flash chromatography eluting with 2–3% ether in petroleum ether gave **45** (18.6 mg, 0.09 mmol, 85% yield) as an oil: $[\alpha]_D^{26}$ +106.75 (*c* 1.17, $CHCl_3$); ir: 1710 (C=O), 1640 (C=C) cm^{-1}; ^1H nmr (300 MHz) δ: 4.72 (m, 2H, C=CH_2), 2.72 (ddd, 1H, J = 12, 12, 3.5 Hz, CHC=), 2.56 (ddd, 1H, J = 15, 13.5, 6 Hz, O=CCHH_{ax}), 2.40 (dddd, 1H, J = 12, 4.5, 4, 1 Hz, CHC=O), 2.28 (dddd, 1H, J = 15, 4, 2, 1 Hz, O=CCH_{eq}H), 2.00 (m, 1H, C-6*H*), 1.90 (m, 1H, O=CCH_2CHH), 1.48–1.82 (complex, 6H), 1.64 (dd, 3H, J = 1, 1 Hz, CH_3C=), 0.91 (complex, 2H), 0.84 (d, 3H, J = 6 Hz, $CHCH_3$); ^{13}C nmr δ: 215.2 (C=O), 146.6 (=C), 112.4 (=CH_2), 52.6 (CH), 42.5 (CH), 39.0 (CH), 38.0 (CH_2), 36.2 (CH_2), 34.4 (CH_2), 31.6 (CH_2), 26.1 (CH), 26.1 (CH_2), 22.8 (CH_3), 18.2 (CH_3); ms M^+: 206.1659 (calcd. for $C_{14}H_{22}O$: 206.1672).

Epimerization of 45 to 44

Ketone **45** (11.0 mg, 0.053 mmol) was dissolved in methanol (2.0 mL) and aqueous 3 M sodium hydroxide solution (0.35 mL) was added to this solution. The mixture was refluxed for 22 h, cooled to room temperature, and extracted with ether. The ether extracts were washed with water, dried, filtered, and concentrated to give a mixture of **44** and **45** (8.0 mg, 73% yield, 74:26 ratio by ^1H nmr integration).

(1R,3R,6S,8S,9R)-(+)-6,10,10-Trimethyl-2-methylenetricyclo-[7.1.1.0^{3,8}]undecane (46)

Potassium hydride (291 mg, 35% by weight, 2.55 mmol) was washed three times with dry benzene under argon. DMSO (1.5 mL) was introduced by syringe and the mixture was stirred at room temperature until the evolution of hydrogen ceased. Methyltriphenylphosphonium bromide (903.9 mg, 2.53 mmol) in DMSO (1.5 mL) was added to the light greenish yellow solution. The resulting bright yellowish green solution was stirred at room temperature for 10 min. Ketone **41** (122.7 mg, 0.6 mmol) in benzene (2 mL) was added to the above solution of methylenetriphenylphosphorane. The resulting dark red solution was stirred at room temperature for 21 h. Water was then added and the mixture was extracted with petroleum ether. The extracts were washed with water, dried, filtered, and concentrated. The crude product was then passed through a layer of silica gel in a sintered glass funnel and the silica gel was washed with petroleum ether. The filtrate was concentrated to give **46** (109.1 mg, 0.535 mmol, 90% yield) as an oil: $[\alpha]_D^{26}$ +28.83 (*c* 0.822, $CHCl_3$); ir: 1640 (C=C) cm^{-1}; ^1H nmr (300 MHz) δ: 4.67 (dd, 1H, J = 2, 2 Hz, C=C*H*H), 4.55 (dd, 1H, J = 2, 2 Hz, C=CH*H*), 2.49 (dd, 1H, J = 5.5, 5.5 Hz, C-1*H*), 1.97–2.22 (complex, 3H), 1.48–1.86 (complex, 8H), 1.36 (m, 1H), 1.28 (s, 3H, *exo* CH_3), 1.02 (d, 3H, J = 7 Hz, $CHCH_3$), 0.68 (s, 3H, *endo* CH_3); ^{13}C nmr δ: 154.1 (=C), 103.0 (=CH_2), 52.9 (CH), 46.4 (CH), 43.4 (C), 43.0 (CH), 38.5 (CH_2), 34.3 (CH), 32.6 (CH_2), 28.5 (CH), 27.0 (CH_3), 24.5 (CH_2), 22.6 (CH_2), 21.4 (CH_3), 19.5 (CH_3); ms M^+: 204.1888 (calcd. for $C_{15}H_{24}$: 204.1879).

(1R,5R,6S,8S)-(−)-2-Chloromethyl-8-methyl-5-(1-methylethenyl)-bicyclo[4.4.0]dec-2-ene (47)

Dimethyl sulfoxide (33 μL, 0.46 mmol) was added to a solution of phenyl dichlorophosphate (41 μL, 0.276 mmol) in dichloromethane (0.5 mL) at −50°C under argon. Compound **46** (37.5 mg, 0.184 mmol) in dichloromethane (0.5 mL) was then added. The reaction mixture was stirred at −50°C to −45°C for 24 h. Then sodium bicarbonate (23.7 mg, 0.282 mmol) in water (0.5 mL) was added and the reaction mixture was stirred at 0°C for 3 h. The mixture was extracted with ether and the extracts were washed with water, dried, filtered, and concentrated. The crude product was filtered through a layer of silica gel in a sintered glass funnel and the silica gel was washed with petroleum ether. After concentration compound **47** (26.7 mg, 0.113 mmol, 61% yield) was obtained as a white solid: $[\alpha]_D^{26}$ −34.21 (*c* 0.95, $CHCl_3$); mp 73–75°C; ir: 1658, 1644 (C=C) cm^{-1}; ^1H nmr (300 MHz) δ: 5.81 (m, 1H, $ClCH_2C$=C*H*), 4.73 (m, 2H, C=CH_2), 4.22 (br d, 1H, J = 11 Hz, C*H*HCl), 3.93 (d, 1H, J = 11 Hz, CH*H*Cl), 1.62 (s, 3H, =CCCH_3), 0.98 (d, 3H, J = 7.5 Hz, $CHCH_3$); ^{13}C nmr δ: 147.3 (=C), 136.8 (=C), 127.9 (=CH), 112.2 (=CH_2), 48.0 (CH_2Cl), 47.6 (CH), 42.2 (CH), 36.3 (CH_2), 35.4 (CH), 32.0 (CH_2), 31.2 (CH_2), 27.5 (CH), 23.9 (CH_2), 18.4 (CH_3), 17.8 (CH_3); ms M^+: 240.1465, 238.1490 (calcd. for $C_{15}H_{23}Cl$: 240.1460, 238.1487). Anal. calcd. for $C_{15}H_{23}Cl$: C 75.43, H 9.71; found: C 75.40, H 9.82.

Acknowledgements

We are grateful to the Natural Sciences and Engineering Research Council of Canada and the University of Alberta for financial support.

1. P. Yates and P. Eaton. J. Am. Chem. Soc. **82**, 4436 (1960).
2. T. Inukai and T. Kojima. J. Chem. Soc. Chem. Commun. 1334 (1969).
3. T. Inukai and T. Kojima. J. Org. Chem. **35**, 1342 (1970).
4. T. Inukai and T. Kojima. J. Org. Chem. **36**, 924 (1971).
5. J.N. Marx and L.R. Norman. J. Org. Chem. **40**, 1602 (1975).
6. T. Inukai and T. Kojima. J. Org. Chem. **31**, 1121 (1966).
7. E.F. Lutz and G.M. Bailey. J. Am. Chem. Soc. **86**, 3899 (1964).
8. T. Inukai and T. Kojima. J. Org. Chem. **31**, 2032 (1966).
9. T. Inukai and T. Kojima. J. Org. Chem. **32**, 872 (1967).
10. J. Sauer and J. Kredel. Tetrahedron Lett. 731 (1966).
11. K.L. Williamson and Y.F.L. Hsu. J. Am. Chem. Soc. **92**, 7385 (1970).
12. Z. Stojanac, R. Dickenson, N. Stojanac, R. Woznow, and Z. Valenta. Can. J. Chem. **53**, 616 (1975).
13. J.S. Tou and W. Reusch. J. Org. Chem. **45**, 5012 (1980).
14. H.J. Liu and E.N.C. Browne. Can. J. Chem. **65**, 1262 (1987).
15. A.I. Meyers (*Editor*). Synthesis of chiral racemic compounds. Tetrahedron Symposia in Print no. 15. Tetrahedron, **40**, 1213 (1984).
16. J.D. Morrison. Asymmetric synthesis. Academic Press, New York. 1984.
17. H.M. Walborsky, L. Barash, and T.C. Davis. Tetrahedron, **19**, 2333 (1963).
18. H.M. Walborsky, L. Barash, and T.C. Davis. J. Org. Chem. **26**, 4778 (1961).
19. W. Oppolzer, D. Dupuis, G. Poli, T.M. Raynham, and S. Bernardinelli. Tetrahedron Lett. **29**, 5885 (1988).
20. L.A. Reed, J. Davis, W. Choy, and S. Masamune. J. Org. Chem. **48**, 4441 (1983).
21. W.R. Roush, H.R. Gillis, and A.I. Ko. J. Am. Chem. Soc. **104**, 2269 (1982).
22. D.A. Evans, K.T. Chapman, and J. Bisaha. J. Am. Chem. Soc. **110**, 1238 (1988).
23. A.P. Kozikowski, T.R. Nieduzak, and J.P. Springer. Tetrahedron Lett. **27**, 819 (1986).
24. R.F. Menezes, C.A. Zezza, J. Sheu, and M.B. Smith. Tetrahedron Lett. **30**, 3295 (1989).
25. B.M. Trost, D. O'Krongly, and J. Belletire. J. Am. Chem. Soc. **102**, 7595 (1980).
26. S. Hashimoto, N. Komeshima, and K. Koga. J. Chem. Soc. Chem. Commun. 437 (1979).
27. H. Takemura, N. Komeshima, I. Takahashi, S. Hashimoto, N. Ikota, K. Tomioka, and K. Koga. Tetrahedron Lett. **28**, 5687 (1987).

28. M. Bednarski, C. Maring, and S. Danishefsky. Tetrahedron Lett. **24**, 3451 (1983).
29. K. Furuta, Y. Miwa, K. Iwanaga, and H. Yamamoto. J. Am. Chem. Soc. **110**, 6254 (1988).
30. K. Narasaka, M. Inoue, and T. Yamada. Chem. Lett. 1967 (1986).
31. K. Narasaka, M. Inoue, and N. Okada. Chem. Lett. 1109 (1986).
32. P.D. Bartlett and G.F. Woods. J. Am. Chem. Soc. **62**, 2933 (1940).
33. F. Fringuelli, A. Taticchi, and E. Wenkert. Org. Prep. Proced. Int. **22**, 131 (1990).
34. L. Minuti, R. Selvaggia, A. Taticchi, M. Guo, and E. Wenkert. Can. J. Chem. **70**, 1481 (1992).
35. H.J. Liu and E.N.C. Browne. Tetrahedron Lett. 2929 (1977).
36. H.J. Liu and E.N.C. Browne. Can. J. Chem. **57**, 377 (1979).
37. H.J. Liu and E.N.C. Browne. Can. J. Chem. **59**, 601 (1981).
38. H.J. Liu, E.N.C. Browne, and S.Y. Chew. Can. J. Chem. **66**, 2345 (1988).
39. H.J. Liu, S.Y. Chew, and E.N.C. Browne. Tetrahedron Lett. **32**, 2005 (1991).
40. D.L. Boger, M.D. Mullican, M.R. Hellberg, and M. Patel. J. Org. Chem. **50**, 1904 (1985).
41. G. Zweifel and H.C. Brown. J. Am. Chem. Soc. **86**, 393 (1964).
42. L. Moore, D. Gooding, and J. Wolinski. J. Org. Chem. **48**, 3750 (1983).
43. J.P. Konopelski and C. Djerassi. J. Org. Chem. **45**, 2297 (1980).
44. J.P. Konopelski, P. Sundararaman, G. Barth, and C. Djerassi. J. Am. Chem. Soc. **102**, 2737 (1980).
45. T. Inokuchi, G. Asanuma, and S. Torii. J. Org. Chem. **47**, 4622 (1982).
46. T. Hosokawa, S. Miyagi, S.I. Murahashi, and A. Sonoda. J. Chem. Soc. Chem. Commun. 687 (1978).
47. T. Hirata. Bull. Chem. Soc. Jpn. 45, 3458 (1972).
48. J. Grimshaw, J.T. Grimshaw, and H.R. Juneja. J. Chem. Soc. Perkin Trans. 1, 50 (1972).
49. P.M. Gordon. Chem. Eng. News, **68** (no. 32), 2 (1990).
50. J.T.B. Ferreira. Chem. Eng. News, **68** (no. 50), 4 (1990).
51. S. Weissman. Chem. Eng. News, **69** (no. 4), 4 (1991).
52. H.C. Brown, S.A. Weissman, P.T. Perumal, and U.P. Dhokte. J. Org. Chem. **55**, 1220 (1990).
53. H.J. Reich, J.M. Renga, and I.L. Reich. J. Am. Chem. Soc. **97**, 5434 (1975).
54. D. Liotta, C. Barnum, R. Puleo, G. Zima, C. Bayer, and H.S. Kezar. J. Org. Chem. **46**, 2970 (1981).
55. H.J. Liu, E.N.C. Browne, and P.R. Pednekar. Can. J. Chem. **60**, 921 (1982).
56. H.J. Liu, T.K. Ngooi, and E.N.C. Browne. Can. J. Chem. **66**, 3143 (1988).
57. A.I. Meyers and C.A. Busacca. Tetrahedron Lett. **30**, 6977 (1989).
58. A.I. Meyers and C.A. Busacca. Tetrahedron Lett. **30**, 6973 (1989).
59. A.P. Kozikowski, K. Sugiyama, and E. Huie. Tetrahedron Lett. **22**, 3381 (1981).
60. J.F. Kervin and S. Danishefsky. Tetrahedron Lett. **23**, 3739 (1982).
61. S.S.P. Chou and D.J. Sun. J. Chem. Soc. Chem. Commun. 1176 (1988).
62. S. Danishefsky, E.R. Larson, and D. Askin. J. Am. Chem. Soc. **104**, 6457 (1982).
63. J. Proteau and P.B. Hopkins. J. Org. Chem. **50**, 141 (1985).
64. T. Sano, J. Toda, and Y. Tsuda. Chem. Pharm. Bull. **31**, 356 (1983).
65. D.P.N. Satchell and R.S. Satchell. Chem. Rev. **69**, 251 (1969).
66. C.Y. Chen and D.J. Hart. J. Org. Chem. **55**, 6236 (1990).
67. M.J. Taschner and P.T. Cyr. Tetrahedron Lett. **31**, 5297 (1990).
68. B.B. Snider. Acc. Chem. Res. **13**, 426 (1980).
69. B.B. Snider and D.J. Rodini. Tetrahedron Lett. **21**, 1815 (1980).
70. T.C. Morrill. Lanthanide shift reagents in stereochemical analysis. VCH, Deerfield Beach, Fla. 1986.
71. T.J. Wenzel. NMR shift reagents. CRC Press, Boca Raton, Fla. 1987.
72. P. Lavallee and G. Bouthillier. J. Org. Chem. **51**, 1362 (1985).
73. A. Van der Gen, L.M. Van der Linde, and J.G. Witteveen. Recl. Trav. Chim. Pays-Bas, **90**, 1034 (1971).
74. N. Bluthe, J. Ecoto, M. Fetizon, and S. Lazare. J. Chem. Soc. Perkin Trans. 1, 1747 (1980).
75. H.J. Liu and J.M. Nyangulu. Tetrahedron Lett. **30**, 5097 (1989).
76. R. Greenwald, M. Chaykovsky, and E.J. Corey. J. Org. Chem. **28**, 1128 (1963).
77. H.J. Liu and J.M. Nyangulu. Tetrahedron Lett. **29**, 5467 (1988).
78. J.E. McMurry. J. Am. Chem. Soc. **90**, 6821 (1968).
79. A.K. Borg-Karlson and T. Norin. Tetrahedron, **37**, 425 (1981).
80. C.W. Still, M. Kahn, and A. Mitra. J. Org. Chem. **43**, 2923 (1978).

Can. J. Chem. Downloaded from www.nrcresearchpress.com by EESC ESCOLA DE ENGENHARIA on 09/08/12
For personal use only.

Single crystal polarized spectra in the near-infrared region: a local-mode analysis of the spectra of $CsMnCl_3 \cdot 2X_2O$ (X = H, D)

IAN M. WALKER[1]
Department of Chemistry, York University, Downsview, ON M3J 1P3, Canada

AND

PAUL J. MCCARTHY
Department of Chemistry, Canisius College, Buffalo, NY 14208, U.S.A.

Received June 16, 1993

IAN M. WALKER and PAUL J. MCCARTHY. Can. J. Chem. **72**, 1211 (1994).

Polarized near-infrared spectra of single crystals of $CsMnCl_3 \cdot 2X_2O$ (X = H, D) were recorded at 10 K. Those bands which could be assigned to O—H or O—D stretch overtones were analyzed using local-mode theory specifically adapted for systems having less than C_{2v} symmetry. Both O—H oscillators form nearly linear hydrogen bonds to neighboring chloride ions at different distances. As a result, the local-mode harmonic frequency and anharmonicity parameters show characteristic shifts from their gas-phase values. The parameter values cover an unusually narrow range in this crystal, considering the spread in hydrogen-bond distances. Assignment of stretch overtone bands to specific oscillators in the crystal was made by using the polarization behavior expected of local modes in the oriented gas model. Several of the overtone bands show combinations with lattice modes or low-energy hydrogen-bond modes in unusual detail.

IAN M. WALKER et PAUL J. MCCARTHY. Can. J. Chem. **72**, 1211 (1994).

Opérant à 10 K, on a déterminé les spectres polarisés du proche infrarouge de cristaux uniques de $CsMnCl_3 \cdot 2X_2O$ (X = H, D). Utilisant la théorie du mode local adaptée spécifiquement pour les systèmes ayant une symétrie inférieure à C_{2v}, on a analysé les bandes qui peuvent être attribuées aux harmoniques des élongations O—H et O—D. Les deux oscillateurs O—H forment des liaisons hydrogènes pratiquement linéaires avec les ions chlorures voisins, à des distances diverses. Il en résulte que la fréquence harmonique du mode local et les paramètres d'inharmonicité présentent des déplacements caractéristiques par rapport à leurs valeurs en phase gazeuse. Considérant la plage des distances des liaisons hydrogènes dans ce cristal, les valeurs des paramètres ne couvrent qu'un champ inhabituellement restreint. On a fait l'attribution des harmoniques des bandes d'élongation à des oscillateurs spécifiques du cristal en se basant sur le comportement de polarisation attendu des modes locaux dans le modèle gazeux orienté. Plusieurs bandes harmoniques présentent, avec un détail inusité, des combinaisons avec les modes du réseau ou les modes des liaisons hydrogènes de basse énergie.

[Traduit par la Rédaction]

Introduction

In a series of recent articles we have applied local-mode theory to the analysis of the fundamental and overtone vibrational spectra of water (1–3) and $-NH_2$ (4) in crystals. Our purpose has been to correlate the local-mode parameters with the length and strength of the hydrogen bonds formed by O—H and N—H oscillators with adjacent electronegative atoms in the crystal. Here we are extending our study to $CsMnCl_3 \cdot 2H_2O$ and its deuterated analog.

$CsMnCl_3 \cdot 2H_2O$ belongs to the orthorhombic space group, *Pcca* (D_{2h}^8, no. 54) (5). The unit cell has the following dimensions: $a = 9.060$ Å, $b = 7.285$ Å, and $c = 11.455$ Å, with $Z = 4$. The basic structure consists of chains of *cis*[-Cl(MnO_2Cl_2)-] propagating along the *a* axis with the cesium ions lying between the chains in the *ab* plane. Because of this the material has a layered structure with [001] cleavage planes. The X-ray study (5) has reported the positions of all atoms except hydrogen (Table 1). The fractional coordinates of the hydrogen atoms have been estimated by El Saffar (6) using Baur's method (7), in which the electrostatic energy is minimized as a function of proton position. De Jonge et al. (8) determined the hydrogen coordinates using two methods based on nuclear quadrupole resonance spectroscopy. One of these used the principal axes of the electric field gradient tensor at the deuterium sites in $CsMnCl_3 \cdot 2D_2O$, and the other used the observed dipole–dipole splitting of the proton resonances of $CsMnCl_3 \cdot 2H_2O$ in a field of 1350 Oe. The latter authors also calculated the positions using Baur's method. The four parameter sets differ little from each other, and we have used the average in Table 1, since it is not clear which might be most accurate. Refinement of the hydrogen positions must await a full neutron diffraction study.

TABLE 1. Fractional coordinates of the atoms in $CsMnCl_3 \cdot 2H_2O$[a]

Atom[b]	*x/a*	*y/b*	*z/c*
Cs	0.250	0.000	0.146
Mn	0.000	0.467	0.250
Cl_I	0.250	0.500	0.146
Cl_{II}	0.085	0.228	0.391
O	0.080	0.669	0.361
H_A	0.028_5	0.693	0.434
H_B	0.184	0.695	0.373

[a]Non-hydrogen values from ref. 5; hydrogen values are averages from data in refs. 6 and 8 (see text).

[b]Atom designations follow refs. 5 and 10, Cl_I is bridging, Cl_{II} is non-bridging.

The water molecules lie largely in the *ac* plane (Fig. 1), and the Raman spectrum of the bending mode shows that all water molecules are equivalent (9). (In the following the atom designations are those of refs. 5 and 10.) Hydrogen bonding to non-bridging chlorines (Cl_{II}) is a significant feature of the structure. O—H_A forms a hydrogen bond to Cl_{II} on a chain lying adjacent in the *ac* plane (O···Cl = 3.297 Å), and O—H_B forms one to Cl_{II} in the same chain (O···Cl = 3.145 Å). Both O—H···Cl angles are

[1]Author to whom correspondence may be addressed. Telephone: (905) 877-9162.

Can. J. Chem. Downloaded from www.nrcresearchpress.com by ESC ESCOLA DE ENGENHARIA on 09/08/12
For personal use only.

Can. J. Chem. Downloaded from www.nrcresearchpress.com by EESC ESCOLA DE ENGENHARIA on 09/08/12
For personal use only.

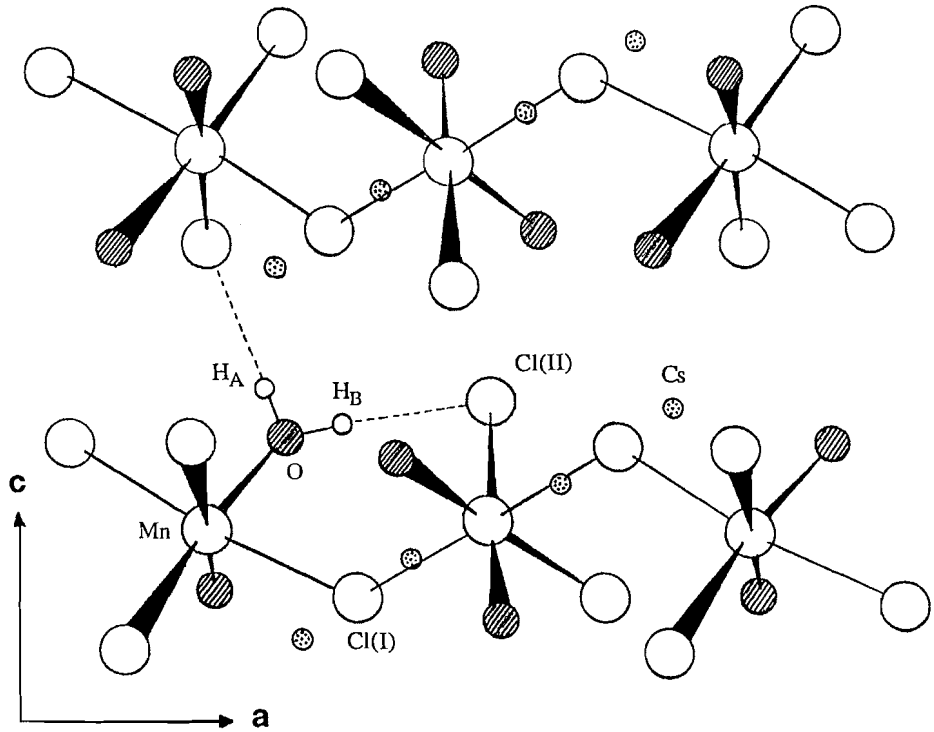

FIG. 1. Structure of $CsMnCl_3 \cdot 2H_2O$ in the *ac* projection. Only one set of hydrogens and hydrogen bonds are shown; adapted from refs. 5 and 10.

calculated to be 175°. Since the oxygen atom also lies 3.155 Å from a bridging chlorine (Cl_I), Jia et al. (9) have suggested that the O—H_B forms a bifurcated hydrogen bond. While the two O···Cl distances in this bifurcated hydrogen bond are quite similar, the interaction with Cl_I should be quite weak, since the $H_B \cdots Cl_I$ distance and O—$H_B \cdots Cl_I$ angle are calculated to be 3.023 Å and 89°. The fact that the two O···Cl_{II} distances are not equal suggests that the O—H bonds of water form hydrogen bonds of slightly different energy, and that the local-mode parameters of the two O—H bonds might be somewhat different. As will be seen below, this is *not* very clearly borne out by our results.

Since this crystal is orthorhombic, a rather strong correlation between known polarizations and relative intensities of the overtone–combination bands should be observed. This is indeed borne out by the experimental evidence.

The spectra are especially interesting in that the principal bands have considerable associated fine structure, which may be due to lattice modes or, more specifically, hydrogen-bond modes (see below).

Local-mode theory has proven itself to be especially well suited to the analysis of the overtone spectra of gas- and liquid-phase molecules containing C—H, N—H, and O—H bonds (11). The literature in the area has been reviewed (11*a*, 11*b*), and several treatments of the theory for HOH and other small molecules are available (11*c*, 11*d*, 11*e*). Our adaptation of the theory to water molecules on general sites in crystals has been presented in detail elsewhere (2, 3).

Briefly, following Mills and Robiette (11*d*), we write the vibrational basis functions as products of harmonic oscillator eigenfunctions along local coordinates, each being described by a local-mode quantum number v_i. So for a water molecule the basis ket could be written $|v_1 v_2\rangle$, or in the present case $|v_A v_B\rangle$. The diagonal elements of the secular determinant may be calculated from the relation:

$$[1] \quad \langle v_i, v_j|\mathrm{H}|v_i, v_j\rangle = \Sigma\omega_k(v_k + 1/2) + \Sigma X_k(v_k + 1/2)^2$$

where ω_k are the harmonic frequencies of the O—H bonds and X_k are the anharmonicity parameters, and index k runs over oscillators A and B. Allowance for coupling between stretching local modes that are close in energy is made by including off-diagonal elements of the form:

$$[2] \quad \langle v_i + 1, v_j - 1|\mathrm{H}|v_i v_j\rangle = \lambda[(v_i + 1)v_j]^{1/2}$$

The X terms are usually negative; thus, in first order, states such as $|1, 1\rangle$, which represents a stretch–stretch combination, occur at higher energy than the corresponding pure overtones, $|20\rangle$ and $|02\rangle$. In the case of the D_2O molecule, the eigenstates are roughly equal mixtures of the local-mode basis functions. We have adopted the literature convention (11) of designating the symmetric and antisymmetric combinations $|v0\rangle_+$ and $|v0\rangle_-$, respectively, even though such terminology does not rigorously apply in the present case. All other symbols have their conventional meanings (2, 3).

Experimental

Well-formed crystals of $CsMnCl_3 \cdot 2H_2O$ suitable for spectroscopy were grown from water by slow evaporation of a solution containing equimolar amounts of CsCl and $MnCl_2 \cdot 4H_2O$. Moderately deuterated crystals were obtained from the same starting materials by slow evaporation of a D_2O solution over concentrated H_2SO_4 in a desiccator. More highly deuterated crystals were obtained by using anhydrous $MnCl_2$; water of hydration is removed by heating at about 120°C for a few hours. $CsMnCl_3 \cdot 2H_2O$ grows as large rectangular plates showing the [001] face.

The crystals were mounted in a Displex cryogenic refrigerator and the near-infrared (near-ir) spectra were recorded at 10 K using a Varian-2300 spectrophotometer. Polarized light was obtained by a pair of Glan–Thompson prisms. Spectra were taken with the electric vector of the light parallel to each of the three orthogonal crystal axes of

TABLE 2. Squares of direction cosines of vibrations along the crystal axes in $CsMnCl_3 \cdot 2H_2O$

	Molecular frame			Local frame	
Polarization	A_1	B_1	B_2	O-H_A	O-H_B
E‖*a*	0.17	0.80	0.02	0.23	0.94
E‖*b*	0.10	0.00	0.90	0.03	0.04
E‖*c*	0.73	0.20	0.08	0.74	0.02

$CsMnCl_3 \cdot 2H_2O$ and its deutero analog. The orientations were confirmed by comparison of the spectra in the visible region with those reported by Day and Dubicki (12).

The ir and Raman spectra of $CsMnCl_3 \cdot 2X_2O$ (X = H, D) below 350 cm^{-1} have been reported (13), as well as the complete Raman spectra to 3600 cm^{-1} (9). In addition, we recorded the ir spectra (4000–600 cm^{-1}) in Fluorolube and Nujol mulls at room temperature using a Nicolet 5DX FTIR spectrophotometer. The band energies we observed are for the most part the same as those reported by Jia et al. (9), but the various ν(OH) values they report are too close in energy to be resolved in our spectra. The fact that the ir and Raman values are identical or nearly so indicates that factor-group splitting is of relatively little importance in these spectra, a fact that has been previously noted (9, 13).

Results and discussion

Since the waters in $CsMnCl_3 \cdot 2H_2O$ lie on general sites, a fundamental problem in interpreting the intensities of the vibrational bands lies in relating the directions of the vibrational modes to the crystal axes. There are two situations that are likely to arise in the present instance. In the first situation some vibrations, including bends and librations, are expected to be polarized parallel or perpendicular to the HOH bisector of the water molecule (11*e*). In this situation it is useful to describe the orientation of the water molecule in the crystal by means of a molecular reference frame. It is convenient to label the axes of this frame with the symmetry species appropriate to gas-phase water (point group C_{2v}). Thus we place A_1, B_1, and B_2 axes along the HOH bisector, the H–H vector, and the normal to the plane of the water molecule, respectively. The values of the squares of the direction cosines of these vectors with respect to the crystal axes can be found in the first three columns of Table 2. Of the six fundamental vibrations for bound water, we expect the symmetric stretch (ν_s) and the bend (δ) to be A_1 polarized, while the antisymmetric stretch (ν_a) and the rock (ρ_r) would be B_1 polarized, and the wag (ρ_w) B_2. The twist (ρ_t) is inactive in high-symmetry environments, but may show up in crystals where the site symmetry is low (2, 3).

The symmetry of each combination will be the direct product of the symmetries of the fundamentals, and combination bands would be expected to behave as dipoles along the coordinates of the molecular frame. Coupled overtone states would also be expected to be polarized along the coordinates of the molecular frame (11*e*).

In the other situation where the upper states are localized primarily on one oscillator, the spectral bands are expected to be polarized along the individual OH (or OD) bond directions (14). Using the coordinates listed in Table 1, the squares of the direction cosines of the O—H bonds along the crystal axes can be calculated. They are listed in the last two columns of Table 2.

Spectra of $CsMnCl_3 \cdot 2H_2O$

For many parts of the near-ir spectra only general group assignments can be made. We will confine quantitative analysis to the O—H stretches, both fundamentals and first and second overtones.

Since the water molecules lie largely in the *ac* plane, electric dipole selection rules predict that the A_1 and B_1 bands will be found principally in the E‖*a* and E‖*c* spectra. The B_2 features, which represent out-of-plane vibrations of water, are expected to appear mainly in the E‖*b* spectrum. This latter spectrum in fact contains only two bands of notable intensity (3906 and 4074 cm^{-1}); these can reasonably be assigned to $\nu_a + \rho_t$ and $\nu_s + \rho_w$, although the order is not certain. The strong band at 4013 cm^{-1} in the other two polarizations could be $\nu_s + \rho_r$ and /or $\nu_a + \rho_r$, since both features can occur with some intensity in either the E‖*a* or E‖*c* spectrum. This analysis has the librations increase in energy in the order: $\rho_t < \rho_r < \rho_w$. This differs from the order, $\rho_w < \rho_t < \rho_r$, proposed by Jia et al. (9). Polarized near-ir spectra of combination bands have been of use in identifying in-plane and out-of-plane librations also in other systems (15).

Broad, rather weak, bands in the 4170–4830 cm^{-1} region most probably represent $\nu + 2\rho$ combinations, while a sharp spike at 4786 cm^{-1} may be assigned to 3δ.

The very strong band in E‖*a* and E‖*c* polarizations around 5000 cm^{-1} can be seen in a very thin crystal as a poorly resolved multiplet with principal components 4965, 4984, and 5015 cm^{-1}. These are readily assigned to $\nu + \delta$, and the polarization behavior is that expected for water lying mainly in the *ac* plane. Weaker features lying between 5350 and 5750 cm^{-1} are probably due to $\nu + \rho + \delta$. None of the bands mentioned thus far are shown in the figures.

The first overtone bands appear as an intense doublet at 6438 and 6454 cm^{-1} (Fig. 2). A study of the intensities of the C—H stretch overtones of the methyl groups of durene in several polarizations shows very good agreement with the predictions of the oriented gas model, and indicates that the dipole moment has components along the C—H local modes (14). We therefore feel justified in using the direction cosines of the local O—H oscillators as a guide in assigning the transitions. The band at 6438 cm^{-1} is strongly *a* polarized, which is expected for the O—H_B oscillator (Table 2). The band at 6454 cm^{-1} has a strong *c* and weaker *a* component, behaviour expected for the O—H_A oscillator. The bands are assigned accordingly in Table 3. As expected, neither band has a significant *b* component.

The $|11\rangle$ local mode is expected to be A_1 polarized (11*e*), and so to be strongest in E‖*c* and weakest in E‖*b* polarization. The band whose average position is 6746 cm^{-1} corresponds quite well to these expectations. The $|11\rangle$ band is broader than the $|20\rangle$ or $|02\rangle$ bands. Since the Raman spectra of $CsMnCl_3 \cdot 2H_2O$ show three intense and three very weak features in the ν(OH) region (9), the $|11\rangle$ band may be composed of various combinations of the fundamentals in which oscillators on adjacent waters of the same chain are excited. All these combinations are expected to be close in energy and so may appear as an unresolved, broad multiplet. Since a different combination may be predominant in each polarization, it is not surprising that this band shows somewhat different maxima in the three polarizations. The $\nu + 2\delta$ bands are expected to be in this same region, and the weak bands at 6576 and 6657 cm^{-1} may be these. These weak features are, however, more probably lattice modes, and their nature will be discussed below.

A group of bands between 7800 and 8500 cm^{-1} (not shown in the figures) is due to $2\nu + \delta$. The assignment is strengthened by a comparison with the spectra of the partially deuterated crystal discussed below.

Can. J. Chem. Downloaded from www.nrcresearchpress.com by EESC ESCOLA DE ENGENHARIA on 09/08/12
For personal use only.

Can. J. Chem. Downloaded from www.nrcresearchpress.com by EESC ESCOLA DE ENGENHARIA on 09/08/12
For personal use only.

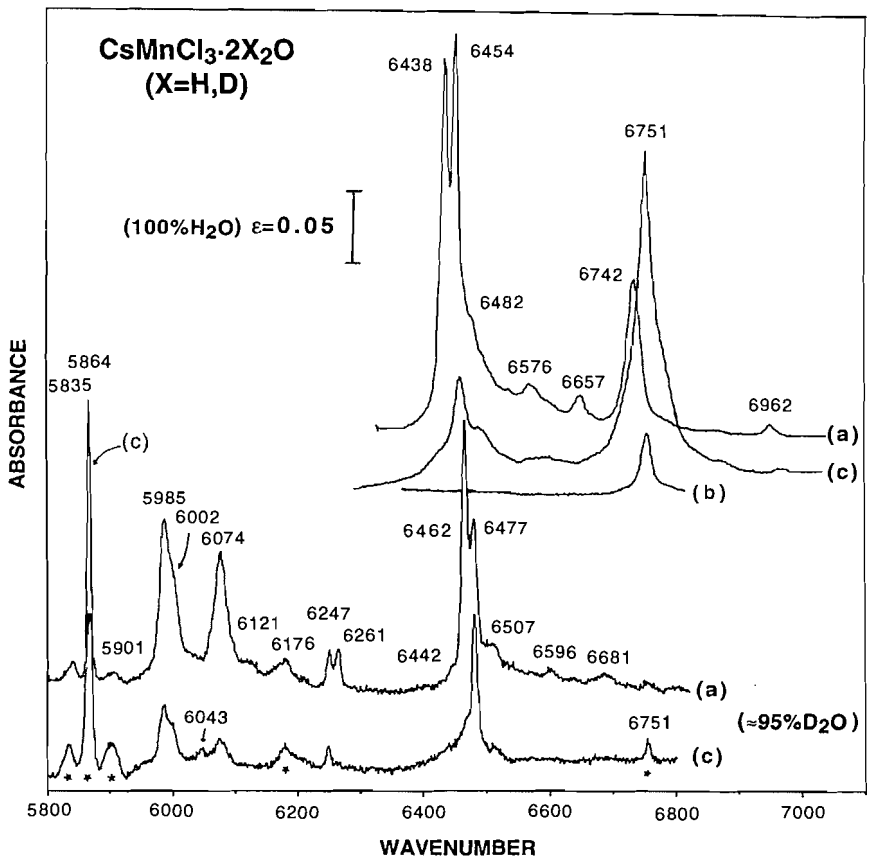

FIG. 2. Polarized crystal spectra (5800–7000 cm^{-1}) of $CsMnCl_3 \cdot 2X_2O$ (X = H, D) at 10 K. The spectra were recorded with the electric vector of the light parallel to the *a*, *b*, and *c* crystal axes. In the mixed crystal in *b* polarization only the bands marked with an asterisk appear weakly.

The second overtones are assigned to the doublet at 9189 and 9218 cm^{-1} (Fig. 3). The lower energy band is, like the $|02\rangle$ band, largely *a* polarized, so is assigned to the excitation of the O—H_B oscillator. The band at 9218 cm^{-1} is strongest in polarization *c*, but has a significant *a* component, like the corresponding $|20\rangle$ band.

The $|21\rangle$ and $|12\rangle$ bands should be very similar in energy, and they are seen as a rather broad, unresolved band at 9808 cm^{-1}.

Spectra of $CsMnCl_3 \cdot 2HOD$ and $CsMnCl_3 \cdot 2D_2O$

Since the deuterated crystals that we prepared contained residual H_2O, the spectra are quite complex. Bands due to H_2O, D_2O, and HOD are all present, and indeed are often found together in the same region of the spectrum. Crystals with two different degrees of deuteration were studied, and this allows us to make some rather firm band assignments. Because of uncertainty about the exact amout of H_2O present in the deuterated crystals, extinction coefficients for bands in these crystals could only be roughly estimated. The deuterated spectra appear to be more intense than the protiated spectra, but by less than a factor of two.

The region 3850–4760 cm^{-1} contains many rather weak features of varying intensity as well as two strong bands at 3909 and 4010 cm^{-1}. These two bands increase in intensity as the amount of H_2O increases and could be due to ν(OD) + δ(HOD) or to $\nu + \rho$ of residual H_2O. The remaining bands could be due to any of the three species of water present. Since the region contains no bands that pertain directly to this report, we have made no attempt to characterize them further.

In terms only of binary combinations, the region 4700–5100 cm^{-1} (Fig. 4) contains $\nu + \delta$ of H_2O, ν(OH) + δ of HOD, and 2ν(OD) of both HOD and D_2O. The strong bands at 4781 and 4799 cm^{-1} increase in intensity with addition of H_2O. They can be assigned to ν(OH) + δ(HOD), since they lie about 1427 cm^{-1} above ν(OH); δ(HOD) in the ir is found at 1431 cm^{-1}. The complex band centered around 4850 cm^{-1} contains a lower energy doublet (4830, 4842 cm^{-1}) that decreases in intensity as D_2O concentration decreases. These bands are accordingly assigned to $|20\rangle_+$ and $|02\rangle_-$ of D_2O. The 4830 cm^{-1} band is the weaker of the pair, and this mirrors the 2ν region of the protiated species. As expected, these bands are very weak in E$\|b$ polarization. The higher energy part (4857 cm^{-1}) of this complex band increases in intensity as D_2O concentration decreases. It is most probably one of the 2ν(OD) bands of HOD. (It can be noted in Fig. 2 that 2ν(OH) in HOD also lies higher in energy than the analogous band in H_2O.) The multiplet around 5000 cm^{-1}also has a complex dependence on H_2O concentration, and it is likely that the component centered around 5012 cm^{-1} is the $|11\rangle$ band of D_2O. The position of the band maximum varies with polarization, as was also found for the $|11\rangle$ band of the protiated species. The rest of this band seems to be principally $\nu + \delta$ of H_2O. The other features in this region cannot be assigned at present.

The region 5100–5700 cm^{-1} contains a few weak features that could be any of the ternary bands, $\nu + \delta + \rho(H_2O)$, ν(OH) + 2δ(HOD), or $2\nu + \rho(D_2O)$.

In the region 5800–6850 cm^{-1} (Fig. 2) the band at 5864 cm^{-1} is due to ν(OH) + ν(OD) of HOD. Since only a single band is seen, the two possible combinations must lie within 11 cm^{-1},

TABLE 3. Calculated and observed energies for $CsMnCl_3 \cdot 2X_2O$ (X = H, D)

Band	Energy, cm^{-1} Obsd[b]	Calcd.	Assignment[a]
1	2468	2476	$\|10\rangle_+$ (DOD)
2	2498	2497	$\|01\rangle$ (HOD)
3	2504	2505	$\|10\rangle$ (HOD)
4	2525	2525	$\|10\rangle_-$ (DOD)
5	3358	3365	$\|01\rangle$ (HOH)
6	3371	3375	$\|10\rangle$ (HOH)
7	4830	4818	$\|20\rangle_+$ (DOD)
8	4842	4833	$\|20\rangle_-$ (DOD)
9	5012	5014	$\|11\rangle$ (DOD)
10	5864	5870	$\|01\rangle$(OH) + $\|10\rangle$(OD)
11	5864	5872	$\|10\rangle$(OH) + $\|01\rangle$(OD)
12	6438	6429	$\|02\rangle$ (HOH)
13	6454	6448	$\|20\rangle$ (HOH)
14	6746	6740	$\|11\rangle$ (HOH)
15	6984	6987	$\|30\rangle_+$ (DOD)
16	6984	6989	$\|30\rangle_-$ (DOD)
17	9189	9192	$\|03\rangle$ (HOH)
18	9218	9220	$\|30\rangle$ (HOH)
19	9808	9804	$\|12\rangle$ (HOH)
20	9808	9813	$\|21\rangle$ (HOH)

Root-mean-square deviation = 5.92 cm^{-1}

Parameters used in best fit[c]

O—H	O—D	Ratio (O—D/O—H)[d]
ω_A = 3677 (9)	2679 (10)	0.729
ω_B = 3666 (9)	2662 (10)	0.726
X_A = −151 (3)	−87 (3)	0.577
X_B = −151 (3)	−83 (3)	0.550
λ = 0	−24	

[a]The numbers in the kets refer to oscillators A and B, respectively. States $|v0\rangle_+$ and $|v0\rangle_-$ refer to symmetric and antisymmetric combinations of the $|v0\rangle$ and $|0v\rangle$ states, respectively. The mixtures are in general somewhat unequal.

[b]Data below 4000 cm^{-1} from ref. 9.

[c]Standard deviations in parentheses; all data in cm^{-1}.

[d]Theoretical ratios are 0.728 and 0.529.

which is the width of the band at half-height in E||*c*. This band is strongest in *c* polarization, just as is the $|11\rangle$ band of H_2O.

The band at 5985 cm^{-1} with shoulder at 6002 cm^{-1} as well as the band at 6074 cm^{-1} decrease in intensity as D_2O content decreases. The first pair lies ca. 1158 cm^{-1} above the 2ν(OD) bands and can be assigned to be $|20\rangle_+ + \delta$ and $|20\rangle_- + \delta$ of D_2O; $\delta(D_2O)$ is observed at 1196 cm^{-1} in the ir spectrum. The band at 6176 cm^{-1} gains some intensity as H_2O increases. Since it lies about 1385 cm^{-1} above the 4781, 4799 cm^{-1} multiplet, it may represent ν(OH) + 2δ(HOD).

The 6247, 6261 cm^{-1} pair is most probably $|02\rangle$(OD) + δ and $|20\rangle$(OD) + δ of HOD, since it increases in size as H_2O is added and lies ca. 1418 cm^{-1} above 2ν(OD). The higher energy band is almost absent from the *c* spectrum. This is reminiscent of the $|02\rangle$ and $|20\rangle$ bands of H_2O, but in this case it is the lower energy band which is absent.

The next set of bands can be assigned with more assurance. In polarization *a* the principal bands at 6462 and 6477 cm^{-1} are the $|02\rangle + |20\rangle$ of OH in HOD. These lie about 24 cm^{-1} higher in energy than the corresponding bands in the nondeuterated crystal. In polarization *c* only the higher energy band is seen, as was

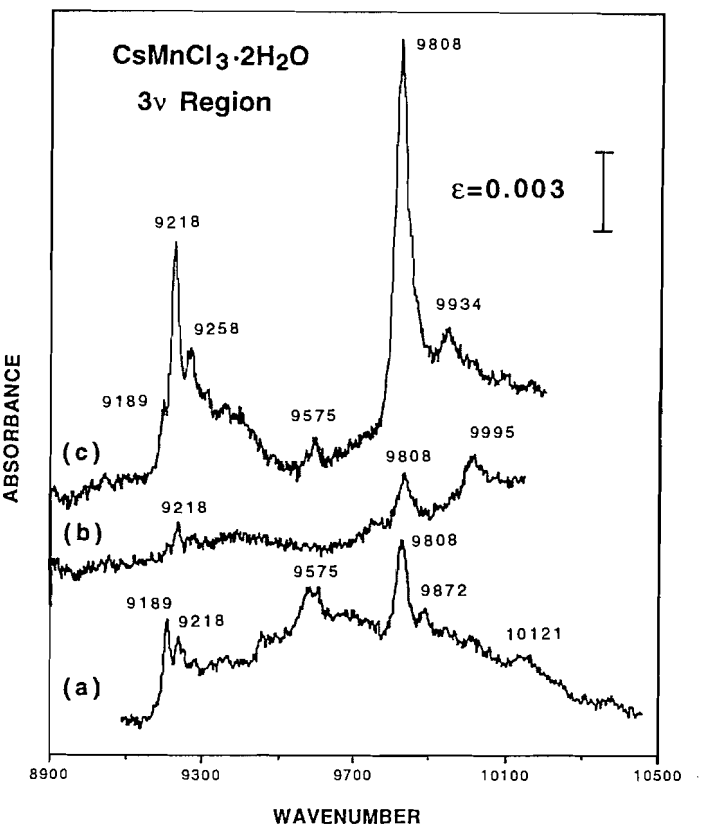

FIG. 3. Polarized crystal spectra (8900–10 500 cm^{-1}) of $CsMnCl_3 \cdot 2H_2O$ at 10 K.

found also in the nondeuterated crystal. The weak satellite at 6442 cm^{-1} is very sensitive to the amount of H_2O present and appears to be $|02\rangle$ of H_2O; the $|20\rangle$ band would lie under the strong band at 6462 cm^{-1}. The weak $|11\rangle$ band of H_2O is at 6751 cm^{-1}. It is strongest in *c* polarization, as it is in the nondeuterated crystal, and its intensity matches that expected for the amount of H_2O present. In the more highly deuterated crystal only the bands due to $|02\rangle$ and $|20\rangle$ of OH in HOD are observed, since there is too little H_2O present for its bands to be seen. It seems possible that the lower values in the protiated crystal are due to Fermi resonance between 2ν and ν + 2δ. This would be lacking in the highly deuterated crystals, since almost all OH would be in HOD and δ(HOD) lies about 200 cm^{-1} lower in energy than $\delta(H_2O)$. No assignments can be made at present for the other features shown in the spectra in Fig. 2.

In the region 6850–7350 cm^{-1} some very weak bands are probably due to 3ν of D_2O and HOD. Studies in this region are hindered by the presence of background absorption due to water vapour in the sample beam. A band at 6984 cm^{-1} found in both *a* and *c* polarizations is a reasonable choice for the second overtones of D_2O.

The region 7350–8330 cm^{-1} (not shown here) contains a band group with principal peak at 7884 cm^{-1}; the group lies about 1415 cm^{-1} above the 6462, 6477 cm^{-1} doublet. These peaks can therefore be assigned to 2ν(OH) + δ(HOD). The peak at 7884 cm^{-1} has a width of 26 cm^{-1} at half-height and so the expected two components are not seen. These bands increase in intensity as the H_2O/D_2O ratio increases. A similar band group was found in $CsMnCl_3 \cdot 2H_2O$ with principal peak at 8014 cm^{-1}, which lies about 1568 cm^{-1} (approximately $\delta(H_2O)$) above the

Can. J. Chem. Downloaded from www.nrcresearchpress.com by EESC ESCOLA DE ENGENHARIA on 09/08/12
For personal use only.

Can. J. Chem. Downloaded from www.nrcresearchpress.com by EESC ESCOLA DE ENGENHARIA on 09/08/12
For personal use only.

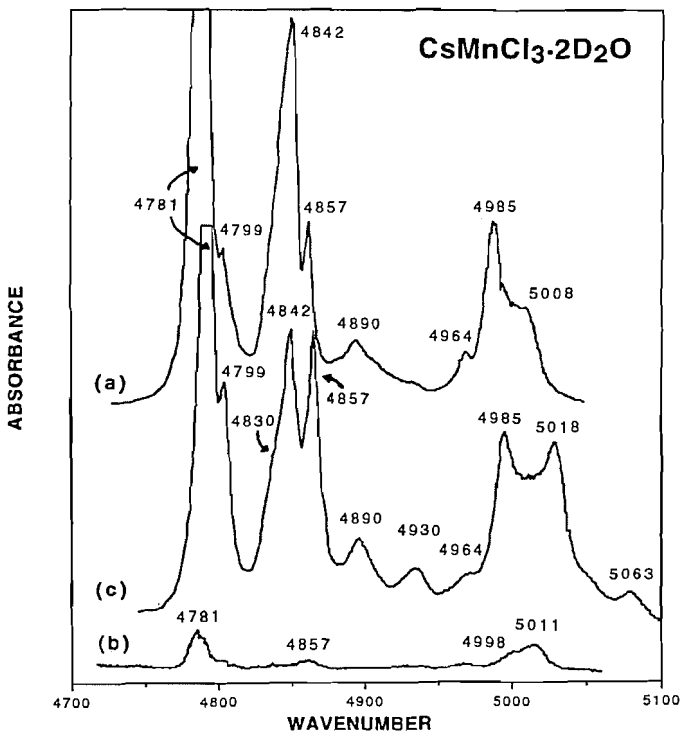

FIG. 4. Polarized crystal spectra (4700–5100 cm^{-1}) of $CsMnCl_3 \cdot 2D_2O$. The *a* spectrum is in reality 3 times as strong as shown here.

doublet at 6438, 6454 cm^{-1}. Since the peak has a width of 42 cm^{-1} at half-height, the expected two components are again not seen.

Fine structure

On the high-energy side of several bands are one or more weak shoulders or discrete bands. The best example we found is the E||*c* spectrum of a thick crystal of $CsMnCl_3 \cdot 2H_2O$. In this spectrum 11 bands lie 32–246 cm^{-1} above the $|20\rangle$ band at 6454 cm^{-1}, the bands at 137 and 220 cm^{-1} being especially prominent. These satellite bands are most probably lattice vibrations coupled to the principal mode. Their frequencies closely match those of the lattice modes found in the Raman spectra of this compound (9, 13). Similar, but less extensive, structure is found above the $|11\rangle$ band, especially notable being a band at 222 cm^{-1}. Likewise, five bands lie between 41 and 365 cm^{-1} above $|30\rangle$, and at least one weak band lies 127 cm^{-1} above $|12\rangle + |21\rangle$. There are also bands associated with the $\nu + \delta$ doublet, as well as with the principal $2\nu + \delta$ peak at 8014 cm^{-1}. Coupling of ν(OH) and ν(OD) with lattice modes has also been observed in the fundamental Raman spectrum (9).

A slightly different view would interpret some of these features as specific hydrogen-bond modes that are excited along with the stretch overtone or stretch plus bend combination band. It was pointed out by Sandorfy (16) that the coupling by hydrogen bonding of two nonlinear species results in the conversion of six rotational and translational degrees of freedom into six hydrogen-bond modes. For an O—H···O hydrogen bond these are: (1) the oxygen–oxygen stretch; (2) the O—H···O deformation; (3) the O—H···O wag; and (4) the torsional motion. (2) and (3) are doubly degenerate, but the degeneracy will be lifted if the symmetry is less than C_3. For weak or moderately strong hydrogen bonds (1) is often about 100–200 cm^{-1}, (2) about 500–700 cm^{-1}, and (3) less than 100 cm^{-1} (16). Similar values might be expected for O—H···Cl groups.

Local-mode results

The vibrational energies were calculated by diagonalization of the appropriate matrices (2). Because of the inequivalence of the O—H or O—D bonds in the compound, the matrices for each species contain five parameters: ω and X for each O—H or O—D oscillator, and λ, the coupling constant between the two oscillators. An initial set of 10 parameters was chosen and the vibrational energies were calculated. An iterative process adjusted all parameters to minimize the sum of the squares of the differences between calculated and observed energies. The parameters that gave the most reasonable fit are listed in Table 3 along with the observed and calculated energies. As we found in earlier studies (2, 3), numerous local minima in the RMS function can be obtained by quite small variations in the initial input parameters.

The standard deviations of the parameters were calculated by the method outlined by Cowan (17). This, however, seems to depend mainly on the steepness of the approach to the minimum and assumes no uncertainty in the band positions. We have calculated that, if the latter uncertainties are included, the standard deviations will be about 2–4% greater than those listed in Table 3.

The energies of the fundamentals used in the fitting were taken from the Raman spectra of Jia et al. (9). Of the eight ν(OD) features found near 2500 cm^{-1}, we have reassigned some of the more prominent ones (Table 3).

The ν(OH) fundamentals appear to have the same energies in H_2O and HOD (9), suggesting an initial choice of λ close to zero in H_2O. This choice is strengthened by noting that the splitting of the first O—H overtone states of H_2O and HOD are very nearly the same.

On the basis of the observed X-ray data and the calculated hydrogen positions, the two O—H···Cl hydrogen bonds in this compound are expected to be of quite different strengths. The overtone spectra in the 2ν and 3ν regions indicate that they are, however, not very different at all, and the local-mode parameters of the two O—H and O—D bonds are the same to within one standard deviation. On the other hand, similar data for $M_2MnCl_4 \cdot 2H_2O$ (M = Rb, Cs)[2] indicate that the two hydrogen bonds should be rather similar in strength. Yet the 2ν region shows a large splitting between the $|20\rangle$ and $|02\rangle$ bands and the local-mode parameters are quite different. One may conclude that the dependence of local-mode parameters on the details of hydrogen-bond interactions is more complex than the simple model would suggest, and (or) that the theoretical apparatus used to determine the proton positions in these compounds does not give very reliable results.

The λ coupling in the D_2O crystal is considerably reduced compared to the value found in gas-phase D_2O (−58.3 cm^{-1}). The reduction in λ that we found here is greater than was observed in $BaCl_2 \cdot 2D_2O$ (3). The diminution in λ seems to be especially pronounced for H_2O as well; the value of λ is considerably smaller than in $BaCl_2 \cdot 2H_2O$ and in gas-phase water (−49.5 cm^{-1}). These effects are undoubtedly a consequence of hydrogen bonding, but are imperfectly understood at present.

[2]I.M. Walker and P.J. McCarthy. Unpublished data.

Conclusions

Several salient points emerge from this study. First, this solid affords the best opportunity to date to apply the oriented gas model to the study of the overtones of a hydrogen-bonded system containing only one kind of water molecule. Modes that involve only stretch overtones obey the predictions of the first-order theory in that they are polarized almost exclusively in the plane of the water molecule. We have presented evidence that the dipole moment operator has components along the individual O—H bonds, and we have assigned the spectra with this in mind. Certain families of combination bands involving stretch and bend features have a pronounced out-of-plane component in addition to the normal in-plane component. This behaviour is not expected for the dipole moment of water in the gas phase, and it may be attributed to a breakdown in the selection rules that accompanies the loss of C_{2v} symmetry (18).

Second, it is of interest to compare the local-mode results in the present case with those obtained in our study of $BaCl_2 \cdot 2H_2O$. In both crystals the water molecules lie on general positions. Three of the O—H oscillators in $BaCl_2 \cdot 2H_2O$ form normal hydrogen bonds, having O···Cl distances and hydrogen-bond angles that are comparable to those found in $CsMnCl_3 \cdot 2H_2O$. The average value of the X parameter for these three oscillators is $-162.5\ cm^{-1}$, with a spread of $11\ cm^{-1}$ between the values. The corresponding variation in the O···Cl distance is 0.05 Å, the mean value being 3.16 Å. The mean of the anharmonicity constants in $CsMnCl_3 \cdot 2H_2O$ is slightly smaller than that in $BaCl_2 \cdot 2H_2O$; this may reflect the longer O···Cl distances found in the latter case. It is surprising, however, that the X values are virtually identical in $CsMnCl_3 \cdot 2H_2O$, while the range in O···Cl distances is three times as great as in $BaCl_2 \cdot 2H_2O$. It is worth noting then that the difference in energy between the $|02\rangle$ and $|20\rangle$ and between the $|03\rangle$ and $|30\rangle$ bands of $CsMnCl_3 \cdot 2H_2O$ should be attributed principally to differences in ω for the two oscillators. We may conclude that O—H anharmonicities in similar salts are sensitive to the whole of the crystalline environment. Therefore, attempts to correlate anharmonicities with hydrogen-bond strengths must be carried out with great caution. On the whole, the most reliable guide to assigning overtone bands to specific oscillators is the polarization of the bands in crystals of known structure.

Finally, $CsMnCl_3 \cdot 2H_2O$ is unusual in that it is possible to observe under high resolution numerous combinations of stretch overtones with low-frequency crystal and (or) hydrogen-bond modes. While there is some evidence for such bands in several of the other crystals we have studied, only in the present case is there sufficient resolution to allow us to observe and catalogue the individual bands.

Acknowledgments

I.M.W. thanks the Natural Sciences and Engineering Research Council of Canada for financial assistance. P.J.M. thanks the Research Corporation for a grant to purchase the cryogenic refrigerator.

1. I.M. Walker and P.J. McCarthy. J. Phys. Chem. **93**, 2230 (1989).
2. P.J. McCarthy and I.M. Walker. Inorg. Chem. **29**, 820 (1990).
3. P.J. McCarthy and I.M. Walker. Inorg. Chem. **30**, 2772 (1991).
4. I.M. Walker and P.J. McCarthy. Inorg. Chem. **31**, 4122 (1992).
5. S.J. Jensen, P. Andersen, and S.E. Rasmussen. Acta Chem. Scand. **16**, 1890 (1962).
6. Z.M. El Saffar. J. Chem. Phys. **52**, 4097 (1970).
7. W.H. Baur. Acta Crystallogr. **19**, 909 (1965).
8. W.J.M. de Jonge, J.P.A.M. Hijmans, and E.C.A. Gevers. Physica, **52**, 129 (1971).
9. W. Jia, E. Strauss, W.M. Yen, K. Xia, and M. Zhao. Phys. Rev. B, **39**, 12853 (1989).
10. R.D. Spence, W.J.M. de Jonge, and K.V.S. Rama Rao. J. Chem. Phys. **51**, 4694 (1969).
11. (*a*) B.R. Henry. J. Phys. Chem. **80**, 2160 (1976); (*b*) M.S. Child. Acc. Chem. Res. **18**, 45 (1985); (*c*) M.S. Child and L. Halonen. Adv. Chem. Phys. **57**, 1 (1984); (*d*) I.M. Mills and A.G. Robiette. Mol. Phys. **56**, 743 (1985); (*e*) P.R. Stannard, M.L. Elert, and W.M. Gelbart. J. Chem. Phys. **74**, 6050 (1981).
12. P. Day and L. Dubicki. Faraday Soc. Trans. 2, 363 (1973).
13. D.M. Adams and D.C. Newton. J. Chem. Soc. (A), 3499 (1971).
14. J.W. Perry and A.H. Zewail. J. Phys. Chem. **86**, 5197 (1982).
15. I.M. Walker and P.J. McCarthy. Can. J. Chem. **64**, 1012 (1986).
16. C. Sandorfy. Top. Curr. Chem. **120**, 41 (1984).
17. R.D. Cowan. The theory of atomic structure and spectra. University of California Press, Berkeley, Calif. 1981. pp. 468ff.
18. F.A. Cotton. Chemical applications of group theory. 3rd ed. John Wiley, New York. 1990. pp. 341–346.

Can. J. Chem. Downloaded from www.nrcresearchpress.com by EESC ESCOLA DE ENGENHARIA on 09/08/12
For personal use only.

Solid state and solution stereochemistry of crown ethers and models. *ortho*-Dimethoxydiphenyl ether and related dibenzo-15-crown-5 and tetrabenzo-30-crown-10 ethers as studied by X-ray crystallography and ^{1}H and ^{13}C NMR spectroscopy

G.W. BUCHANAN,[1] A. RODRIGUE, AND K. BOURQUE

Ottawa–Carleton Chemistry Institute, Department of Chemistry, Carleton University, Ottawa, ON K1S 5B6, Canada

AND

A.C. CHIVERTON, I.R. CASTLEDEN, AND S. FORTIER

Department of Chemistry, Queen's University, Kingston, ON K7L 3N6, Canada

Received March 23, 1993[2]

G.W. BUCHANAN, A RODRIGUE, K. BOURQUE, A.C. CHIVERTON, I.R. CASTLEDEN, and S. FORTIER. Can. J. Chem. **72**, 1218 (1994).

Solid phase 45.3 MHz ^{13}C NMR spectra of *ortho*-dimethoxydiphenyl ether, **1**, dibenzo[*b*,*e*]-15-crown-5- ether, **2**, and tetrabenzo[*b*,*e*,*q*,*t*]-30-crown-10 ether, **3**, have been obtained. Chemical shift trends are discussed in terms of the asymmetric units and structural features available from X-ray crystallographic data. Comparison with solution ^{13}C spectra are made. The crystal structures of **1** and **3** were determined by X-ray diffraction at room temperature. **1** crystallizes in space group $P2_1/a$ with a = 13.366(1), b = 8.230(1), c = 12.303(1) Å, β = 116.63(1)°, Z = 4. **3** crystallizes in space group $P2_1/c$ with a = 7.903(1), b = 26.337(2), c = 7.852(1) Å, β = 97.28(1)°, Z = 2. The structures were solved by direct methods and refined by full-matrix least squares to residuals of 0.055 using 1727 reflections for **1** and of 0.042 using 2590 reflections for **3**.

G.W. BUCHANAN, A RODRIGUE, K. BOURQUE, A.C. CHIVERTON, I.R. CASTLEDEN et S. FORTIER. Can. J. Chem. **72**, 1218 (1994).

On a déterminé les spectres RMN du ^{13}C en phase solide, à 45,3 MHz, des éthers *ortho*-diméthoxydiphénylique, **1**, dibenzo[*b*,*e*]-15-couronne-5, **2**, et tétrabenzo[*b*,*e*,*q*,*t*]-30-couronne-10, **3**. On discute des tendances dans les déplacements chimiques en fonction des unités asymétriques et des caractéristiques structurales disponibles à partir de données de diffraction des rayons X. Une comparaison est faite avec les spectres RMN du ^{13}C obtenus en solution. On a déterminé les structures cristallines des composés **1** et **3** par diffraction des rayons X à la température ambiante. Le composé **1** cristallise dans le groupe d'espace $P2_1/a$, avec a = 13,366(1), b = 8,230(1) et c = 12,303(1) Å, β = 116,53(1)° et Z = 4. Le composé **3** cristallise dans le groupe d'espace $P2_1/c$, avec a = 7,903(1), b = 26,337(2) et c = 7,852(1) Å, β = 97,28(1)° et Z = 2. On a résolu les structures par des méthodes directes et on les a affinées par la méthode des moindres carrés jusqu'à des valeurs résiduelles de 0,055 pour 1727 réflexions pour le composé **1** et 0,042 pour 2590 réflexions pour le composé **3**.

[Traduit par la Rédaction]

Introduction

Following the early work of Truter and co-workers (1), a number of recent publications (2–6) have dealt with correlations between solid state ^{13}C NMR behaviour and X-ray crystallographic structures of benz-annelated crown ethers with a variety of structures. This has included the benzo- and dibenzo-15-crown-5 systems depicted below (1, 5).

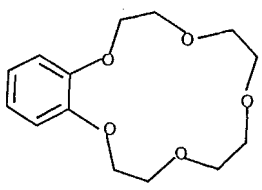

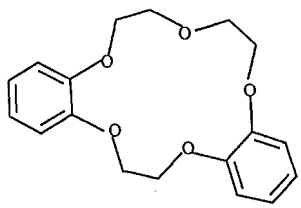

With the exception of some solution complexation studies (7), no work has yet been reported concerning crown ethers derived formally from diphenyl ether. Herein we present solid phase ^{13}C NMR results for the dibenzo-15-crown- 5 ether system (below) and its tetrabenzo-30-crown-10 dimer formally derived from such a precursor. As a simpler model, the *ortho*-dimethoxydiphenyl ether molecule has been studied in detail and correlations of sterically induced chemical shift trends with X-ray derived structural features are presented. Solution ^{13}C chemical shift assignments are made on the basis of NOESY and HETCOR results.

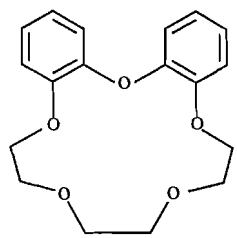

Results and discussion

Structures and numbering schemes for the three compounds examined are shown in Fig. 1. In Figs. 2 and 3, respectively, are the ORTEP diagrams resulting from the X-ray crystallographic studies of **1** and **3**. Solid phase ^{13}C spectra are illustrated in Fig. 4. Table 1 lists non-hydrogen atomic coordinates and equivalent isotropic displacement parameters. In Table 2 are presented the bond lengths and angles while selected torsional angles are listed in Table 3. Crystallographic data are in Table 4 and ^{13}C NMR chemical shifts are in Table 5.

Solution NMR assignments

For **1** the starting point for assignment of the ^{1}H spectrum is the NOESY correlation observed between the OCH_3 proton res-

[1]Author to whom correspondence may be addressed.

[2]Revision received November 22, 1993.

Can. J. Chem. Downloaded from www.nrcresearchpress.com by ESC ESCOLA DE ENGENHARIA on 09/08/12
For personal use only.

Can. J. Chem. Downloaded from www.nrcresearchpress.com by EESC ESCOLA DE ENGENHARIA on 09/08/12
For personal use only.

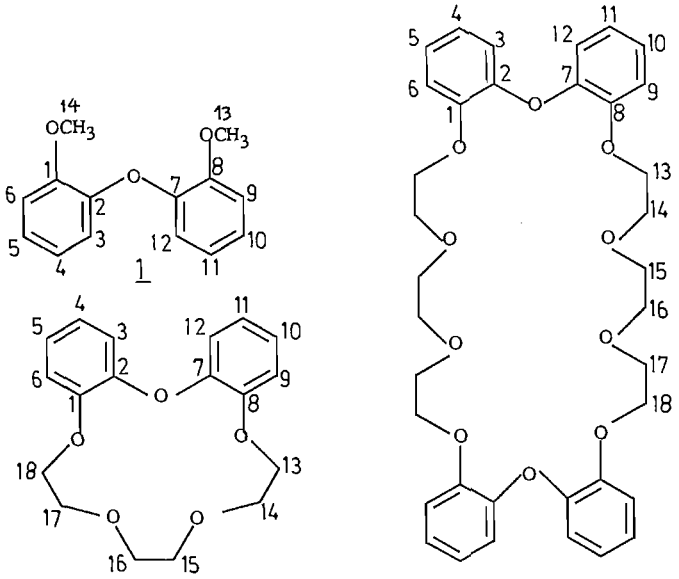

FIG. 1. Structures and numbering schemes.

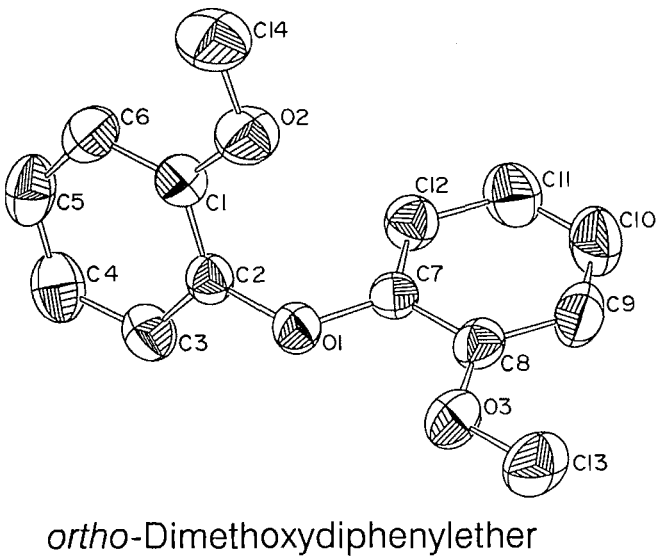

FIG. 2. ORTEP plot for **1**.

onance and the *ortho* aromatic protons on C-6,9. Subsequent ^1H–^1H COSY and ^1H–^{13}C HETCOR (direct and long range) furnished the solution ^{13}C assignments shown in Table 4. These values are also consistent with predicted shieldings based on additivity employing the early published findings for anisole (8) and diphenyl ether (9). For the dibenzo-15-crown-5 system **2**, similar 2D experiments were used to obtain unambiguous ^{13}C chemical shifts in solution, with the key observation being the NOESY observed between the aromatic proton at 6.95 ppm and the CH_2O resonance at 4.15 ppm. This leads to clear assignment of the C6,9 and C13,18 sites. With these assignments as a starting point, the remainder followed via COSY and HETCOR. For the aromatic carbons, the results are all within 1 ppm of those found for corresponding sites of **1**, with the exception of C6, which is deshielded by ca. 3 ppm in **2**. This difference is most likely due to conformational effects involving the C6-C1-O-C18 unit. Unfortunately, X-ray crystallographic data for **2**

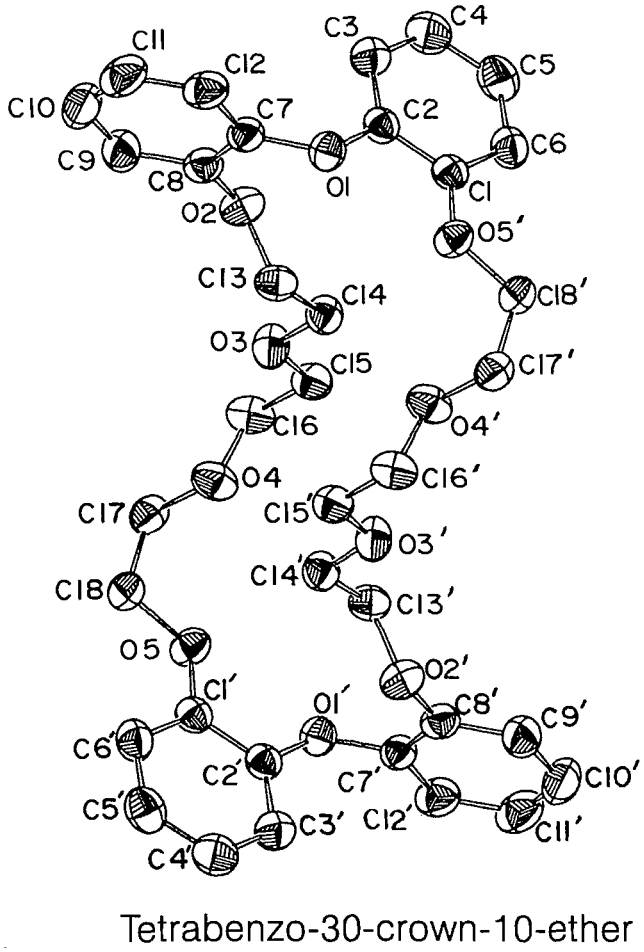

FIG. 3. ORTEP plot for **3**.

could not be obtained. The existence of nine ^{13}C resonances for **2** at temperatures between 300 and 173 K indicates rapid conformational interconversion on the NMR timescale over this range of temperatures, although substantial (up to 3 ppm) temperature-dependent chemical shifts were noted for some resonances. The solution ^{13}C spectrum for the tetrabenzo-30-crown-10 system **3** is remarkably similar to that of **2**, with the largest chemical shift difference between corresponding sites being 0.3 ppm. The spectrum of **3** is essentially temperature independent from ambient temperature to 173 K in CD_2Cl_2 solution, with the existence of nine lines indicating rapid conformational interconversion on the NMR timescale.

Solid phase ^{13}C spectra

As is clear from Fig. 4, the 45.3 MHz ^{13}C CPMAS spectrum of **1** suggests the existence of an asymmetric conformation in the solid, although crystal packing phenomena could also lead to additional resonances over those found in solution (1). In the event of an asymmetric conformation, a total of 14 lines should be observed. Experimentally, one finds a total of 12 lines with the aromatic CH at 111.9 ppm being of triple intensity. The X-ray crystallographic structure (Fig. 2) indeed shows the presence of such an asymmetric geometry. Unfortunately, 2D HETCOR NMR methods for unambiguous assignment of solid phase ^{13}C spectra are limited by the inherently low resolution of solid phase ^1H spectra even under the most optimal conditions. Hence one can make very few definite attributions of solid

Can. J. Chem. Downloaded from www.nrcresearchpress.com by EESC ESCOLA DE ENGENHARIA on 09/08/12
For personal use only.

TABLE 1. Selected atomic positional and equivalent isotropic displacement parameters

	x/a	*y/b*	*z/c*	*U*(eq)[a]
		1		
O1	0.46457(9)	0.5475(1)	0.6700(1)	0.0497(5)
O2	0.5607(1)	0.6371(2)	0.9049(1)	0.0655(7)
O3	0.2691(1)	0.4173(2)	0.5839(1)	0.0591(6)
C1	0.6173(1)	0.6756(2)	0.8390(2)	0.0453(7)
C2	0.5679(1)	0.6247(2)	0.7187(1)	0.0420(6)
C3	0.6157(2)	0.6586(2)	0.6425(2)	0.0526(8)
C4	0.7156(2)	0.7431(2)	0.6866(2)	0.063(1)
C5	0.7663(2)	0.7913(2)	0.8053(2)	0.063(1)
C6	0.7186(2)	0.7580(2)	0.8827(2)	0.0564(8)
C7	0.4616(1)	0.3868(2)	0.7010(1)	0.0418(6)
C8	0.3548(1)	0.3179(2)	0.6547(2)	0.0470(7)
C9	0.3456(2)	0.1572(2)	0.6822(2)	0.064(1)
C10	0.4387(2)	0.0668(3)	0.7518(2)	0.071(1)
C11	0.5429(2)	0.1349(3)	0.7953(2)	0.067(1)
C12	0.5544(2)	0.2957(2)	0.7699(2)	0.0518(8)
C13	0.1577(2)	0.3584(3)	0.5443(2)	0.074(1)
C14	0.6015(2)	0.7033(3)	1.0229(2)	0.082(1)
		3		
O1	0.5010(1)	0.62995(4)	0.3816(1)	0.0410(3)
O2	0.2733(1)	0.63917(4)	0.0721(1)	0.0472(3)
O3	−0.0238(1)	0.57644(4)	−0.0689(1)	0.0479(4)
O4	−0.2161(1)	0.52367(4)	−0.3457(1)	0.0497(3)
O5	0.3194(1)	0.56556(4)	0.5302(1)	0.0433(3)
C1	0.2681(2)	0.61503(5)	0.5354(2)	0.0374(4)
C2	0.3624(2)	0.64972(5)	0.4513(2)	0.0381(4)
C3	0.3217(2)	0.70039(6)	0.4459(2)	0.0508(5)
C4	0.1861(2)	0.71781(7)	0.5267(2)	0.0589(6)
C5	0.0940(2)	0.68396(7)	0.6125(2)	0.0557(6)
C6	0.1346(2)	0.63255(6)	0.6181(2)	0.0465(5)
C7	0.5494(2)	0.65329(5)	0.2368(2)	0.0390(4)
C8	0.4403(2)	0.65512(5)	0.0832(2)	0.0415(4)
C9	0.4977(2)	0.67656(6)	−0.0597(2)	0.0525(5)
C10	0.6618(3)	0.69542(7)	−0.0502(3)	0.0638(7)
C11	0.7703(2)	0.69294(7)	0.1020(3)	0.0646(7)
C12	0.7140(2)	0.67180(6)	0.2461(2)	0.0508(5)
C13	0.2501(2)	0.58546(6)	0.0928(2)	0.0428(4)
C14	0.0643(2)	0.57504(6)	0.0994(2)	0.0431(4)
C15	−0.1990(2)	0.56447(6)	−0.0758(2)	0.0437(5)
C16	−0.2780(2)	0.56561(6)	−0.2599(2)	0.0479(5)
C17	−0.2676(2)	0.52276(6)	−0.5249(2)	0.0440(4)
C18	0.2146(2)	0.52729(6)	0.5914(2)	0.0460(5)

[a] $U(\text{eq}) = 1/3\Sigma_i\Sigma_j U_{ij} a_i^* a_j^* \mathbf{a}_i \mathbf{a}_j$.

phase ^{13}C resonances. In many cases, however, the solution spectral data serve as a valuable point of reference and many of the assignments in Table 4 have been made on this basis. It is of interest to speculate on the origin of the triple intensity aromatic CH at 111.9 ppm and also the relatively shielded quaternary carbon resonance at 142.0 ppm. Based on the solution spectrum, two of the carbons contributing to the triple intensity 111.9 resonance will be C6 and C9. For the other carbon, the expectation is that it must be either C3 or C12 (8, 9).

Examination of the torsional angles obtained from the X-ray crystal structure (Table 2) reveals one important difference in the environments of C3 vs. C12. Specifically, for the C2-O1-C7-C12 network, the torsional angle is −4.5°, while that for the corresponding C7-O1-C2-C3 network is 108.0°. Recent *ab initio* theoretical calculations of shieldings for

TABLE 2. Selected bond lengths and angles with esd's in parentheses

Bond	Length Å	Bond	Length Å
1		**3**	
O1—C2	1.389(2)	O1—C2	1.387(2)
O1—C7	1.382(2)	O1—C7	1.388(2)
O2—C1	1.371(3)	O2—C8	1.377(2)
O2—C14	1.411(3)	O2—C13	1.438(2)
O3—C8	1.359(2)	O3—C14	1.414(2)
O3—C13	1.427(3)	O3—C15	1.414(2)
C1—C2	1.387(2)	O4—C16	1.413(2)
C1—C6	1.390(3)	O4—C17	1.414(2)
C2—C3	1.378(3)	O5—C1	1.367(2)
C3—C4	1.383(3)	O5—C18	1.426(2)
C4—C5	1.364(3)	C1—C2	1.396(2)
C5—C6	1.390(4)	C1—C6	1.386(2)
C7—C8	1.398(2)	C2—C3	1.372(2)
C7—C12	1.369(2)	C3—C4	1.391(3)
C8—C9	1.384(3)	C4—C5	1.379(3)
C9—C10	1.371(3)	C5—C6	1.391(2)
C10—C11	1.368(3)	C7—C8	1.391(2)
C11—C12	1.384(3)	C7—C12	1.383(2)
		C8—C9	1.383(2)
		C9—C10	1.382(3)
		C11—C12	1.384(3)
		C13—C14	1.502(2)
		C15—C16	1.500(2)
		C17—C18	1.497(2)

Bonds	Angle (deg)	Bonds	Angle (deg)
1		**3**	
C2—O1—C7	117.7(1)	C2—O1—C7	118.1(1)
C1—O2—C14	117.2(2)	C8—O2—C13	115.3(1)
C8—O3—C13	117.7(2)	C14—O3—C15	113.2(1)
O2—C1—C2	115.9(2)	C16—O4—C17	114.5(1)
O2—C1—C6	125.7(2)	C1—O5—C18	118.5(1)
C2—C1—C6	118.4(2)	O5—C1—C2	115.6(1)
O1—C2—C1	120.2(2)	O5—C1—C6	125.3(1)
O1—C2—C3	118.3(1)	C2—C1—C6	119.1(1)
C1—C2—C3	121.4(2)	O1—C2—C1	115.9(1)
C2—C3—C4	119.7(2)	O1—C2—C3	123.1(1)
C3—C4—C5	119.7(3)	C1—C2—C3	120.9(1)
C4—C5—C6	121.1(2)	C2—C3—C4	119.9(2)
C1—C6—C5	119.8(2)	C3—C4—C5	119.6(2)
O1—C7—C8	115.2(1)	C4—C5—C6	120.7(2)
O1—C7—C12	124.4(2)	C1—C6—C5	119.7(1)
C8—C7—C12	120.4(2)	O1—C7—C8	121.3(1)
O3—C8—C7	115.5(2)	O1—C7—C12	117.9(1)
O3—C8—C9	126.1(2)	C8—C7—C12	120.6(1)
C7—C8—C9	118.3(2)	O2—C8—C7	121.9(1)
C8—C9—C10	121.0(2)	O2—C8—C9	118.9(1)
C9—C10—C11	120.1(2)	C7—C8—C9	119.1(1)
C10—C11—C12	120.0(2)	C8—C9—C10	120.3(2)
C7—C12—C11	120.1(2)	C9—C10—C11	120.3(2)
		C10—C11—C12	119.9(2)
		C7—C12—C11	119.7(2)
		O2—C13—C14	108.8(1)
		O3—C14—C13	109.3(1)
		O3—C15—C16	108.6(1)
		O4—C16—C15	108.5(1)
		O4—C17—C18	107.7(1)
		O5—C18—C17	107.8(1)

Can. J. Chem. Downloaded from www.nrcresearchpress.com by EESC ESCOLA DE ENGENHARIA on 09/08/12
For personal use only.

TABLE 3. Selected torsion angles with esd's in parentheses

Bonds	Angle (deg)	Bonds	Angle (deg)
1		**3**	
C7-O1-C2-C1	−76.3(2)	C7-O1-C2-C1	150.4(1)
C7-O1-C2-C3	108.0(2)	C7-O1-C2-C3	−32.2(2)
C2-O1-C7-C8	176.7(2)	C2-O1-C7-C8	−62.4(2)
C2-O1-C7-C12	−4.5(3)	C2-O1-C7-C12	121.9(1)
C14-O2-C1-C2	−172.7(2)	C13-O2-C8-C7	−68.3(2)
C14-O2-C1-C6	8.1(3)	C13-O2-C8-C9	116.0(1)
C13-O3-C8-C7	−173.9(2)	C8-O2-C13-C14	173.0(1)
C13-O3-C8-C9	7.4(3)	C15-O3-C14-C13	177.0(1)
O2-C1-C2-O1	3.2(2)	C14-O3-C15-C16	−178.3(1)
O2-C1-C2-C3	178.8(2)	C17-O4-C16-C15	−174.2(1)
C6-C1-C2-O1	−177.5(2)	C16-O4-C17-C18	−171.5(1)
C6-C1-C2-C3	−1.9(3)	C18-O5-C1-C2	−171.1(1)
O2-C1-C6-C5	−179.0(2)	C18-O5-C1-C6	9.8(2)
C2-C1-C6-C5	1.8(3)	C1-O5-C18-C17	163.3(1)
O1-C2-C3-C4	176.5(2)	O5-C1-C2-O1	−3.4(2)
C1-C2-C3-C4	0.9(3)	O5-C1-C2-C3	179.2(1)
C2-C3-C4-C5	0.4(3)	C6-C1-C2-O1	175.8(1)
C3-C4-C5-C6	−0.6(3)	C6-C1-C2-C3	−1.7(2)
C4-C5-C6-C1	−0.6(3)	O5-C1-C6-C5	−179.4(1)
O1-C7-C8-O3	1.2(3)	C2-C1-C6-C5	1.6(2)
O1-C7-C8-C9	−180.0(2)	O1-C2-C3-C4	−176.6(1)
C12-C7-C8-O3	−177.6(2)	C1-C2-C3-C4	0.7(2)
C12-C7-C8-C9	1.2(3)	C2-C3-C4-C5	0.3(2)
O1-C7-C12-C11	−179.5(2)	C3-C4-C5-C6	−0.4(3)
C8-C7-C12-C11	−0.8(3)	C4-C5-C6-C1	−0.5(2)
O3-C8-C9-C10	177.9(2)	O1-C7-C8-O2	7.5(2)
C7-C8-C9-C10	−0.8(4)	O1-C7-C8-C9	−176.8(1)
C8-C9-C10-C11	0.0(4)	C12-C7-C8-O2	−176.9(1)
C9-C10-C11-C12	0.4(4)	C12-C7-C8-C9	−1.1(2)
C10-C11-C12-C7	−0.0(4)	O1-C7-C12-C11	176.6(1)
		C8-C7-C12-C11	0.8(2)
		O2-C8-C9-C10	176.5(1)
		C7-C8-C9-C10	0.6(2)
		C8-C9-C10-C11	0.2(3)
		C9-C10-C11-C12	−0.5(3)
		C10-C11-C12-C7	−0.0(3)
		O2-C13-C14-O3	78.1(1)
		O3-C15-C16-O4	70.1(1)
		O4-C17-C18-O5	76.3(1)

C-O-C-C networks as a function of dihedral angle (6, 10) as well as earlier experimental results (11) indicate that the terminal carbons of such four-atom networks will be substantially shielded (ca. 5 ppm) in the *cisoid* geometry relative to cases where the terminal atoms are nearly perpendicular. Hence we assign C12 as the third contributing carbon to the triple intensity resonance at 111.9 ppm. Via a similar argument, the highly shielded (δ_C = 142.0) quaternary carbon in the solid phase ^{13}C spectrum of **1** is attributed to C2, with its counterpart C7 being ca. 6 ppm deshielded.

The solid phase ^{13}C spectrum of **2** indicates that, in the crystalline state, the molecule lacks any symmetry elements. Unfortunately, the X-ray crystal structure is not available so that detailed discussion of shielding differences in terms of known structural features is not possible.

In the case of **3**, the X-ray crystal structure indicates that the molecule possesses a centre of symmetry and the ^{13}C CPMAS spectrum is consistent with this structural feature. Based on a consideration of torsional angles, one can make some predictions of relative shielding for many of the nonequivalent sites of **3** in the solid phase ^{13}C spectrum. For C3 vs. C12, for example, the torsional angles for the C3-C2-O1-C7 and C12-C7-O1-C2 networks are −32.2° and 121.9°, respectively. Based on a consideration of the calculated absolute ^{13}C isotropic shielding as a function of torsional angle for a *C-C-O-C network (10), one would predict that C3 should be ca. 2 ppm more shielded than C12. The experimental difference for **3** is 2.4 ppm.

In the case of the aliphatic carbons of **3**, solution nOe and HETCOR results (vide supra) show that the C13, C18 pair are most shielded. In the solid phase C13 and C18 are not averaged by conformational motion and thus give separate resonances in the ^{13}C CPMAS spectrum. In the crystal structure there is a large difference in the C18-O5-C1-C6 angle (9.8°), relative to that for the corresponding network containing C13, i.e., C13-O2-C8-C9, which is 116.0°. Based on our earlier calculations of shielding for a *C-O-C-C network as a function of dihedral angle (10), C18 is assigned as the most shielded aliphatic carbon, appearing at 67.9 ppm. The C13 position is deemed to be the next most shielded at 69.2 ppm. The geometry for the O3C15-C16-O4 network (70.1°) is close to that found for the O4-C17-C18-O5 unit (76.3°). Hence the triple intensity line at 70.4 ppm is attributed to C15, C16, and C17. The remaining solid phase ^{13}C resonance at 72.4 ppm is assigned to C14. The basis for this lies with the torsional angle of 78.1° found for the O2-C13-C14-O3 unit. Expansion of an O-C-C-O angle from 70 to ca. 78° is expected to lead to deshielding of ca. 1 ppm in the isotropic ^{13}C shift as calculated employing ethylene glycol as a model (10).

X-ray crystallographic structures

With respect to the torsional angles in the 30-membered ring of **3**, the O-C-C-O angles in the areas of the molecule not restricted by the geometry of the aromatic ring are *gauche*, in accord with that expected (12). There is, however, some expansion of the angles to 70°–78°, and noted previously. For the C-C-O-C units, the normal (11) crown ether geometry is *transoid*. In **3**, the C17-C18-O5-C1 angle is contracted to 163.3°, while the angles for the C13-C14-O3-C15 and C14-C13-O2-C8 moieties are 177.0° and 173.0°, respectively.

In the case of **1**, the molecule adopts a conformation that minimizes the steric interaction between the *ortho* methyl groups as well as between the two aromatic rings. The key torsional angles here are C2-O1-C7-C12, which is −4.5°, and C1-C2-O1-C7, which is −76.3°. The resulting angle between the planes of the two aromatic rings is ca. 72°. Previous studies of X-ray structures of *ortho*-substituted diphenyl ethers (13) have shown that a perpendicular conformation (interplanar angle of 90°) is adopted only in cases where at least three *ortho* substituents are present.

To conclude, these studies again show the complementarity between solid phase ^{13}C NMR and X-ray crystallography for solid state stereochemical studies. For systems such as **1**, it is hoped that the next step will be single crystal ^{13}C studies, so that details of the ^{13}C chemical shift anisotropies, as were recently published for 1,4-dimethoxybenzene (14), may be available.

Experimental

Materials

Compound **1** was prepared via condensation of the sodium salt of guaiacol (2-methoxyphenol) with *o*-bromoanisole according to the published method (15) using CuCl. Subsequently, didemethylation of **1** was carried out to give 2,2′-oxydiphenol using chlorotrimethylsilane and sodium iodide in dry acetonitrile as previously reported (16). A

Can. J. Chem. Downloaded from www.nrcresearchpress.com by EESC ESCOLA DE ENGENHARIA on 09/08/12
For personal use only.

TABLE 4. Crystallographic data

Parameter	Crystal data	
Compound	**1**	**3**
Molecular formula	$C_{14}O_3H_{14}$	$C_{36}O_{10}H_{40}$
Molecular weight	230.25	632.68
Space group, Z	$P2_1/a$, 4	$P2_1/c$, 2
a, Å	13.366(1)	7.903(1)
b, Å	8.230(1)	26.337(2)
c, Å	12.303(1)	7.852(1)
β, degrees	116.63(1)	97.28(1)
V, Å^3; T	1209.8; 292 K	1621.1; 292 K
Density (calcd.), g cm^{-3}	1.264	1.296
Number of reflections used for unit cell determination, 2θ range	25, 24–47	25, 25–44
Number of measured reflections	2056	3076
Number of observed reflections with $I \geq 3\sigma$	1727	2590
2θ range scanned, deg	8.04–129.82	6.72–139.90
μ, cm^{-1}	7.3	7.9
Crystal dimensions, mm	0.37 × 0.25 × 0.20	0.35 × 0.30 × 0.25
Final R, Rw	0.055, 0.066	0.042, 0.056
Largest shift/error in final least-squares cycle	0.0048	0.0046
Maximum and minimum residual eρ in final difference Fourier map, e Å^{-3}	0.221, −0.448	0.149, −0.244
Goodness of fit	1.061	1.080

TABLE 5. ^{13}C chemical shifts (ppm from TMS ± 0.1)

	1 (sol'n)[a]	**1** (solid)	**2** (sol'n)[a]	**2** (solid)	**3** (sol'n)[a]	**3** (solid)
C1	150.6	(148.8)[b]	149.6	(152.8)[e]	149.7	150.4
C2	146.0	142.0	146.9	(141.8)[f]	146.9	(148.2)[k]
C3	118.8	119.1	119.1	(123.3)[g]	119.2	120.9
C4	120.9	(122.3)[c]	121.3	(125.7)[h]	121.6	(124.8)[l]
C5	123.8	(125.2)[d]	123.7	(126.1)[h]	123.7	(124.8)[l]
C6	112.6	111.9	115.3	(114.9)[i]	115.5	115.7
C7		(147.9)[b]		(147.4)[f]		(147.2)[k]
C8		152.1		(151.9)[e]		(148.2)[k]
C9		111.9		(114.1)[i]		117.9
C10		(127.2)[d]		(128.6)[h]		(126.2)[l]
C11		(123.2)[c]		(124.9)[h]		(124.8)[l]
C12		111.9		(121.6)[g]		123.3
C13			69.2	(68.2)[j]	69.5	69.2
C14			69.6	(69.1)[j]	69.7	72.4
C15			70.7	71.2	70.9	70.4
C16				71.2		70.4
C17				(69.1)[j]		70.4
C18				(68.2)[j]		67.9
OCH_3	55.9	53.8 54.8				

[a]0.1 M in $CDCl_3$.
[b–l]Parentheses indicate possible interchange of assignments.

mixture of **2** and **3** was obtained upon condensation of 2,2′- oxydiphenol with the ditosylate of triethylene glycol according to the following procedure.

To NaH (0.96 g, 0.04 mol), as a dispersion in dry THF (250 mL), was added 2,2′-oxydiphenol (3.13 g, 0.015 mol) and the mixture was stirred at room temperature for 2 h to allow complete salt formation. To this was added the ditosylate of triethylene glycol (9.20 g, 0.02 mol) in 100 mL of dry THF over a period of 30 min. This mixture was then heated at reflux and stirred for 2 days. After cooling the reaction vessel, the excess NaH was slowly destroyed with water (100 mL) and the organic compounds were extracted with CH_2Cl_2 and dried over anhydrous $MgSO_4$. After solvent removal, the crude oily product was purified by flash chromatography using silica gel and 1:1 ethyl acetate: 30–60 petroleum ether. The first material eluted was unreacted ditosylate and crude solid **2** (2.32 g). Later fractions contained a lower melting solid. Final purification was accomplished via recrystallization from ethyl acetate – petroleum ether to give **2** (yield 23%), mp 116–118°C (lit. (7) mp 114–115°C), and **3** (yield 20%), mp 93–94°C.

Spectra

Solid phase ^{13}C NMR spectra were recorded at 45.3 MHz on a Bruker CXP-180 spectrometer using techniques described previously (2). Solution ^{1}H and ^{13}C spectra were obtained using a Bruker AMX-400 system. In the NOESY experiments, the mixing times were selected to be consistent with the $1/T_1$ criterion (17), and for these molecules the time was set at 0.3 s. For the ^1J HETCOR experiments, delays were set to correspond to an average $^1J_{CH}$ value of 140 Hz.

Can. J. Chem. Downloaded from www.nrcresearchpress.com by EESC ESCOLA DE ENGENHARIA on 09/08/12
For personal use only.

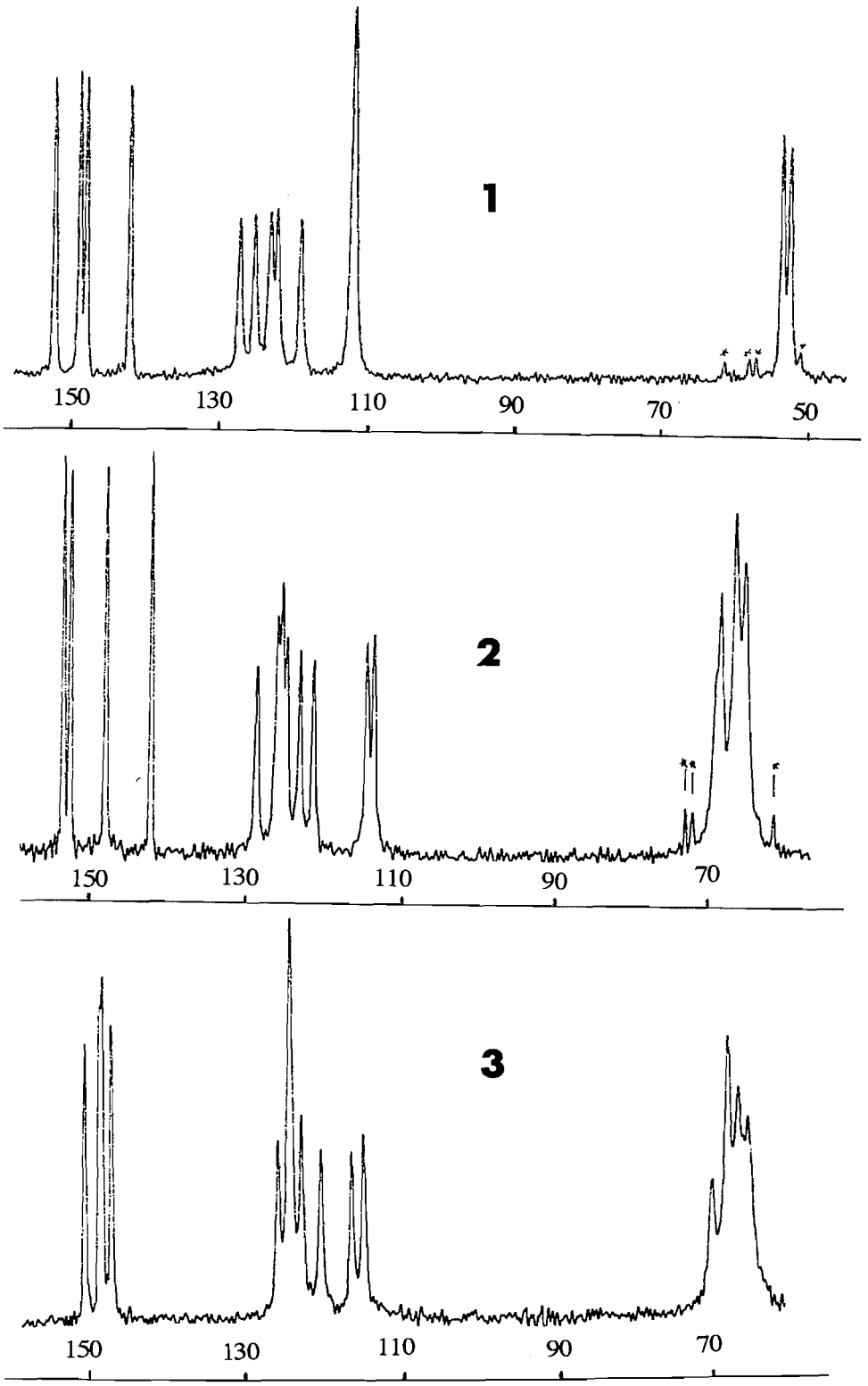

FIG. 4. 45.3 MHz ^{13}C CPMAS NMR spectra.

Cry*stallographic measurements and structure solution*

Pertinent data about the crytals use and the measurement of diffraction intensities are summarized in Table 4. The crystals of **1** and **3** were mounted at the end of glass fibres. The intensity data were collected on an Enraf–Nonius CAD-4 diffractometer using graphite-monochromated radiation, CuKα (λ = 1.5418 Å). The intensities were collected using the ω–2θ scanning procedure and three reflections were measured after every 7200 s of exposure time to check on the stability of the crystal. The maximum variation in the intensity of the standard reflections was 2.4% for **1** and 4.4% for **3**. The data were rescaled to take into account these variations, and were corrected for Lorentz and polarization effects. The two structures were solved by direct methods using the XTAL program package (18). For **1**, all of the hydrogen positions were found in the difference Fourier map. For **3**, all of the hydro-

gen atom positions, except the methyl hydrogens, were found in the difference Fourier map. The positions of the methyl hydrogens were calculated. The structures were refined by full-matrix least squares. The function minimized was $\Sigma w\|F_o - F_c\|^2$, where $w = 1/[\sigma_{Fo}{}^2 + eF_o{}^2]$, with $e = 0.0002$ for **1** and $e = 0.0004$ for **3**. All reflections with $I \geq 3\sigma I$ were used. Anisotropic temperature factors were used for the non-hydrogen atoms. Isotropic temperature factors equal in magnitude to the equivalent isotropic values of their parent atoms were assigned to the hydrogens. The hydrogen atoms were included in the calculations, but neither their positions nor their temperature factors were refined.[3] The scattering factors were taken from Cromer and Waber (19). Anomalous dispersion coefficients were taken from Cromer (20). All calculations were done on a Sparc station 1+ using the XTAL program package (18). The program ORTEP (21) was used for the preparation of the illustrations.

1. P.S. Belton, S.F. Tanner, K.M. Wright, M.P. Payne, M.R. Truter, and J.N. Wingfield. J. Chem. Soc. Perkin Trans. 2, 1307 (1985).
2. G.W. Buchanan, R.A. Kirby, and J.P. Charland. J. Am. Chem. Soc. **110**, 2477 (1988).
3. G.W. Buchanan, R.A. Kirby, and J.P. Charland. Can. J. Chem. **68**, 49 (1990).
4. G.W. Buchanan, R.A. Kirby, J.P. Charland, and C.I. Ratcliffe. J. Org. Chem. **56**, 203 (1991).

[3]Tables of structure amplitudes, thermal parameters, and H-atom coordinates can be purchased from: The Depository of Unpublished Data, Document Delivery, CISTI, National Research Council Canada, Ottawa, ON K1A 0S2, Canada.

Tables of atomic coordinates have also been deposited with the Cambridge Crystallographic Data Centre, and can be obtained on request from The Director, Cambridge Crystallographic Data Centre, University Chemical Laboratory, 12 Union Road, Cambridge, CB2 1EZ, U.K.

5. G.W. Buchanan, S. Mathias, Y. Lear, and C. Bensimon. Can. J. Chem. **69**, 404 (1991).
6. G.W. Buchanan and D.J. Landry. Magn. Reson. Chem. **29**, 127 (1991).
7. K. Torizuka and T. Sato. Org. Magn. Reson. **12**, 190 (1979).
8. K.S. Dhami and J.B. Stothers. Can. J. Chem. **44**, 2855 (1966).
9. G.W. Buchanan, G. Montaudo, and P. Finocchiaro. Can. J. Chem. **52**, 767 (1974).
10. G.W. Buchanan, C. Morat, R.A. Kirby, and J.S. Tse. Can. J. Chem. **69**, 1964 (1991).
11. N.K. Wilson and J.B. Stothers. Top. Stereochem. **8**, 1 (1973).
12. A.C. Coxon, D.A. Laidler, R.B. Pettman, and J.F. Stoddart. J. Am. Chem. Soc. **100**, 8260 (1978).
13. E.A.H. Griffith, W.D. Chandler, and B.E. Robertson. Can. J. Chem. **50**, 2963 (1972); **50**, 2972 (1972).
14. C.M. Carter, J.C. Facelli, D.W. Alderman, D.M. Grant, N.K. Dalley, and B.E. Wilson. J. Chem. Soc. Faraday Trans. **84**, 3673 (1988).
15. D.E. Kime and J.K. Norymberski. J. Chem. Soc. Perkin Trans. 1, 1048 (1977).
16. G.A. Olah, S.C. Narang, B.V.B. Gupta, and R. Malhotra. J. Org. Chem. **44**, 1247 (1979).
17. A.E. Derome. Modern NMR techniques for chemistry research. Pergamon Press, Oxford. 1987.
18. S.R. Hall and J.M. Stewart. XTAL 3.0 reference manual. Lamb: Perth, Universities of Western Australia and Maryland (1990).
19. D.T. Cromer and J.T. Waber. International tables for X-ray crystallography. Vol. IV. Kynoch Press, Birmingham. Present Distributor: Kluwer Academic Publishers, Dordrecht. 1974.
20. D.T. Cromer. International tables for X-ray crystallography. Vol. IV. Kynoch Press, Birmingham. Present Distributor: Kluwer Academic Publishers, Dordecht. 1974.
21. C.K. Johnson. ORTEP. Oak Ridge National Laboratory, Oak Ridge, Tenn. Report ORNL-3794. 1976.

Can. J. Chem. Downloaded from www.nrcresearchpress.com by EESC ESCOLA DE ENGENHARIA on 09/08/12
For personal use only.

Synthesis of tridentate amine Pt(II) complexes and study of their reactions with purine and pyrimidine bases

FERNANDE D. ROCHON AND GUYLAINE LAPERRIÈRE

Département de chimie, Université du Québec à Montréal, C.P. 8888, Succ. A, Montréal, QC H3C 3P8, Canada

Received September 2, 1993

FERNANDE D. ROCHON and GUYLAINE LAPERRIÈRE. Can. J. Chem. **72**, 1225 (1994).

Complexes of the type [Pt(L)X] where L is a tridentate N ligand and X = Cl or I, were synthesized and characterized. Three of the ligands are N-derivatives of diethylenetriamine, (2-aminoethyl)(*N*-dimethyl-2-aminoethyl)amine, (2-aminoethyl)(*N*-diethyl-2-aminoethyl)amine, and (2-aminoethyl)(*N*-methyl-2-aminoethyl)*N*-methylamine. The other two ligands are di(3-aminopropyl)amine and (2-aminoethyl)(3-aminopropyl)amine. A new method for the synthesis of the chloro complexes from the direct reaction of the amine with $K_2[PtCl_4]$ was developed. The reactions of these five compounds with several purine and pyrimidine bases were studied by NMR techniques. The Pt(II) complexes containing two five-membered chelates were shown to be more reactive than the one containing two six-membered rings, while the complex containing one five- and one six-membered chelates showed intermediate reactivity. For the diethylenetriamine derivatives, the complexes containing ligands with two alkyl groups on the same terminal N atom were more reactive than the one containing one methyl group on a terminal N atom and one methyl group on a non-terminal N atom.

FERNANDE D. ROCHON et GUYLAINE LAPERRIÈRE. Can. J. Chem. **72**, 1225 (1994).

Des complexes de type [Pt(L)X]X où L est un ligand tridentate azoté et X = Cl or I, ont été synthétisés et caractérisés. Trois des ligands sont des dérivés du diéthylènetriamine, (2-aminoéthyl)(*N*-diméthyl-2-aminoéthyl)amine, (2-aminoéthyl)(*N*-diéthyl-2-aminoéthyl)amine et (2-aminoéthyl)(*N*-méthyl-2-aminoéthyl)*N*-méthylamine. Les deux autres ligands sont di(3-aminopropyl)amine et (2-aminoéthyl)(3-aminopropyl)amine. Une nouvelle méthode de synthèse des complexes chloro par une réaction directe de l'amine avec $K_2[PtCl_4]$ a été mise au point. Les réactions des cinq complexes avec quelques bases purines et pyrimidines ont été étudiées par rmn protonique. Les composés de platine contenant deux chélates à cinq membres sont plus réactifs que celui contenant deux chélates de six atomes, tandis que complexe contenant un cycle à cinq et un cycle à six atomes, a montré une réactivité intermédiaire. Pour les dérivés de l'éthylènediamine, les deux complexes contenant des ligands avec deux groupements alkyles sur le même atome N terminal ont montré une réactivité supérieure à celui contenant un groupement méthyl sur un N terminal et un autre méthyl sur le N non-terminal.

Introduction

[M(dien)Cl]Cl (dien = diethylenetriamine and M = Pt and Pd) has often been used to study substitution reactions of square-planar metal complexes (1). The reactions are usually simple since it contains only one leaving group. In particular, it has proved to be a very useful model for the first binding step of the antitumor compound *cisplatin* (*cis*-$Pt(NH_3)_2Cl_2$) to DNA (2–8).

Kinetic studies of the substitution reactions of [Pt(dien)X]X with pyridine have shown that these reactions are three times faster for X = Cl than for the iodo complex (9). This parallels the order of the increasing bond strength. With a more bulky ligand like *N,N,N,N*-tetraethyldiethylenetriamine (Et_4dien), the complex [Pt(Et_4dien)I]I is much less reactive than the *dien* complex. The greater stability of the latter was assumed to be due to the presence of two bulky ethyl groups on each side of the platinum plane, which severely blocks the access of the entering ligand towards the metal center (1). The crystal structure of [Pt(Et_4dien)I]I was reported in 1980 (10). The results have shown that the terminal methyl groups are oriented away from platinum, slightly reducing the steric hindrance around the metal center.

The synthetic procedure to prepare the complexes [Pt(dien)X]X, where X = Br and I, has been known since 1934 (11). The same method for X = Cl was later shown by Watt and Cude (12) to produce a dichloro-bridged dimer containing bidentate *dien* ligands. These authors suggested a new method to synthesize the iodo complex from the reaction of the ligand with $PtI_2 \cdot H_2O$. The chloro complex could then be obtained by adding HCl, after removing the iodide ligand with a silver salt. A different method was published more recently (13). The product of the reaction of $PtCl_2$ with HCl was treated with dien.3HCl, the pH adjusted to 3 with LiOH and the mixture refluxed for 3 days. [Pt(dien)Cl]Cl·HCl was then isolated and treated with LiOH at 80°C at pH 10. [Pt(dien)Cl]Cl was eventually obtained after adjusting the pH to 4. These authors have also synthesized [Pt(Me_4dien)Cl]PF_6 and [Pt(Et_4dien)Cl]PF_6·HCl by similar methods.

We have found that these published methods are not adequate to prepare [Pt(L)Cl]Cl for L other than *dien* derivatives. We have therefore decided to try to develop a new simple method which would be more general for tridentate N ligands. We have chosen three alkyl derivatives of *dien*, two of which have dialkyl groups of one of the terminal N atom, *N,N*-dimethyldiethylenetriamine (Me_2dien) and *N,N*-diethyldiethylenetriamine (Et_2dien), while the third ligand has one methyl group of a terminal N and a second methyl group on the non-terminal N (MeMedien). We have also chosen one tridentate ligand, containing three methylene groups between the N atoms (NH_2—$(CH_2)_3$—NH—$(CH_2)_3$—NH_2, dipn) and finally a fifth ligand containing two and three methylene groups between the N atoms (NH_2—$(CH_2)_2$—NH—$(CH_2)_3$—NH_2, enpn).

The reactions of the five synthesized complexes [Pt(L)Cl]Cl with several purine and pyrimidine derivatives were studied by ^{1}H NMR. The results of these studies are described below.

Experimental section

The decomposition points were measured on a Fisher-Johns instrument. The conductivity measurements were done on a Radiometer ohmmeter CDM2e with a Radiometer electrode CDC 114 RF. The IR spectra were recorded in the solid state (Nujol mull, CsI plates) on a Perkin-Elmer 783 spectrometer. The ^{1}H NMR spectra were measured on a Varian EM 360L instrument, equipped with a signal averager

Can. J. Chem. Downloaded from www.nrcresearchpress.com by EESC ESCOLA DE ENGENHARIA on 09/08/12
For personal use only.

Can. J. Chem. Downloaded from www.nrcresearchpress.com by EESC ESCOLA DE ENGENHARIA on 09/08/12
For personal use only.

Varian V2048 for accumulation purposes. Sodium-2,2-dimethyl-2-silapentane-5-sulfonate was used as an internal reference. The concentration of the solutions varied from 0.1 to 0.2 M. K_2PtCl_4 was bought from Johnson Matthey Inc. and was purified by crystallization from water before use.

$PtI_2 \cdot H_2O$

This was synthesized from K_2PtCl_4 as previously described (12).

[Pt(L)I]I

The three 5-membered chelates where L = Me_2dien, Et_2dien, and MeMedien were synthesized by the method described by Watt and Cude (12). The yields are 57, 45, and 35% respectively. The conductivities in water are Λ_{mol} = 127, 122, and 131 10^{-4} S m^2 mol^{-1}. Anal. calcd. for [Pt(Et_2dien)I]I: C 15.9, H 3.5; found: C 16.1, H 3.8.

[Pt(L)Cl]Cl

Method 1: The two complexes with L = Me_2dien and Et_2dien were synthesized by the method reported by Watt and Cude (12). Yields: 10 and 12% respectively; dec. pt: 200 and 190°C; Λ_{mol} = 125 and 121 10^{-4} S m^2 mol^{-1}.

Method 2a: [Pt(Me_2dien)Cl]Cl, [Pt(Et_2dien)Cl]Cl, and [Pt(MeMedien)Cl]Cl: Two mmoles of purified K_2PtCl_4 were dissolved in 10 mL of water. A 5 mL aqueous solution containing 2.5 mmol of ligand was added dropwise to the Pt solution. The mixture was stirred during 48 h and heated twice at 60°C for 8 h (not heated overnight). The mixture was then filtered and the yellow filtrate evaporated to dryness at room temperature. The residue was washed with cold acetone. The product was dissolved in 8 mL of ethanol to remove KCl. The filtrate was evaporated to dryness and the residue dissolved in 4 mL of ethanol. The mixture was filtered and the filtrate again evaporated to dryness. The residue was washed several times with acetone and then with ether and finally dried with a vacuum pump for at least 24 h. [Pt(Me_2dien)Cl]Cl: yield: 78%, dec. pt. 200°C, $\Lambda_{mol} = 123 \times 10^{-4}$ S m^{-2} mol^{-1}; anal. calcd.: C 18.1, H 4.3, Cl 17.8; found: C 18.8, H 4.9, Cl 17.0; IR (cm^{-1}): 3412s, 1600m, 1080s, 1042s, 785s, 726s, ν(Pt—Cl) 335s; ^{1}H NMR (ppm) in D_2O, ($\Delta\delta$ from ligand): CH_3, 2.91 (0.72) and CH_2, 3.04 (0.55). [Pt(Et_2dien)Cl]Cl: yield: 75%, dec. pt. 192°C, $\Lambda_{mol} = 120 \times 10^{-4}$ S m^2 mol^{-1}; anal. calcd.: C 22.6, H 5.0, Cl 16.7; C 23.2, H 5.6, Cl 16.0; IR (cm^{-1}): 3400s, 1600m, 1073s, 1028s, 755s, 725s, ν(Pt—Cl) 335s; ^{1}H NMR (ppm) in D_2O, ($\Delta\delta$ from ligand): CH_3, 1.57 (0.58) and CH_2, 3.06 (0.48). [Pt(MeMedien)Cl]Cl: yield: 68%, dec. pt. 195°C, $\Lambda_{mol} = 118 \times 10^{-4}$ S m^2 mol^{-1}; anal. calcd.: C 18.1, H 4.3, Cl 17.8; C 18.4, H 5.0, Cl 16.8; IR (cm^{-1}): 3405s, 1600m, 1042s, 1017m, 775m, 725s, ν(Pt—Cl) 333s; ^{1}H NMR (ppm) in D_2O, ($\Delta\delta$ from ligand): CH_3, 2.75 (ligand 2.20, 2.28) and CH_2, ~3.2 (~0.6).

Method 2b: [Pt(dipn)Cl]Cl and [Pt(enpn)Cl]Cl: Two mmoles of purified K_2PtCl_4 were dissolved in 10 mL of water. A 6 mL aqueous solution containing 3.0 mmol of ligand was added dropwise to the Pt solution. The mixture was stirred for 72 h and heated at 60°C for three periods of 8 h (not heated overnight). The mixture was then treated as described above. [Pt(dipn)Cl]Cl: yield: 65%, dec. pt. 198°C, $\Lambda_{mol} = 123 \times 10^{-4}$ S m^2 mol^{-1}; anal. calcd.: C 18.1, H 4.3, Cl 17.8; C 18.4, H 5.2, Cl 16.8; IR (cm^{-1}): 3395s, 1600s, 1080m, 1047s, 726s, ν(Pt—Cl) 332m; ^{1}H NMR (ppm) in D_2O, ($\Delta\delta$ from ligand): N—CH_2—C 3.13 (0.5) and C—CH_2—C, 2.07 (0.48). [Pt(enpn)Cl]Cl: yield: 62%, dec. pt. 189°C, $\Lambda_{mol} = 130 \times 10^{-4}$ S m^2 mol^{-1}; anal. calcd.: C 15.7, H 4.0, Cl 18.5; C 16.2, H 4.8, Cl 17.2; IR (cm^{-1}): 3392s, 1595s, 1061s, 1043m, 724s, ν(Pt—Cl) 335m ^{1}H NMR (ppm) in D_2O, ($\Delta\delta$ from ligand): N—CH_2—C ~2.95 (~0.35) and C—CH_2—C, 2.02 (0.43).

Reactions of [Pt(L)Cl]Cl with purine and pyrimidine bases

Two methods were used. The first procedure was used only with pyrimidine. [Pt(L)Cl]Cl (0.1 M) was dissolved in 0.5 mL of D_2O directly in the NMR tube. An equivalent amount of pyrimidine was added. The solution was then heated at 40°C (8 h per day) until equilibrium was reached (about 3–4 days). The second method was used for all the other reactions. The purine or pyrimidine bases were added in a 1:1 ratio to the 6 mL 0.1 M [Pt(L)Cl]Cl aqueous (H_2O) solution. The mixture was mixed and heated (~8 per day) to 70°C until equilibrium has been reached (for 2 to 6 days). The solution was then evaporated to dryness and the residue dissolved in D_2O for the NMR spectra.

Results and discussion

Complexes [Pt(L)Cl]Cl

Five complexes of the type [Pt(L)Cl]Cl where L is a tridentate N ligand, were synthesized and characterized mainly by elemental analysis, conductivity measurements, NMR and IR spectroscopy. Three of the complexes contain N-methyl derivatives of diethylenetriamine, (2-aminoethyl)(*N*-dimethyl-2-aminoethyl)amine (*Me_2dien*), (2-aminoethyl)(*N*-diethyl-2-aminoethyl)amine (*Et_2dien*) and (2-aminoethyl)(*N*-methyl-2-aminoethyl)*N*-methylamine (*MeMedien*). The fourth complex contains a ligand with three methylene groups between the N atoms, di(3-aminopropyl)amine (*dipn*) which allows the formation of two 6-membered rings chelates. The last compound will form one 6-membered and one 5-membered chelate (2-aminoethyl)(3-aminopropyl)amine (*enpn*).

Two different methods were used for the preparation of the Pt(II) complexes. The first method is based on the method reported by Watt and Cude (12). The iodo complex is synthesized from $PtI_2.H_2O$. This method has a few advantages over the use of K_2PtX_4 as starting material. The purification steps are greatly reduced since there are no by-products to remove (KX) and $PtI_2.H_2O$ is very insoluble in water which makes it easy to remove by filtration. A second step is necessary to obtain the chloro complexes. The iodo atoms are precipitated by a silver salt in the dark in the presence of HCl. This method gives a good yield for L = diethylenetriamine. We have attempted to prepare the iodo complexes with our five tridentate ligands using this method. The three N-derivatives of *dien* gave the complex [Pt(L)I]I but the yields were lower than the one reported for *dien*, 57% for L = *Me_2dien*, 45% for *Et_2dien*, and 35% for *MeMedien*. The other two ligands, *dipn* and *enpn* did not produce any significant amount of [Pt(L)I]I and a decomposition of the reacting mixtures was observed. From the three iodo complexes, attempts were made to prepare the corresponding chloro compounds following mainly the method described by Watt and Cude (12). Only two complexes were obtained and with very low yields, [Pt(Me_2dien)Cl]Cl 10% [Pt(Et_2dien)Cl]Cl 12%. The compound [Pt(MeMedien)Cl]Cl could not be isolated, even after prolonged periods of reaction time.

From these reactions, it can be seen that the substitution of the iodo ligand by the chloro ligand is more difficult for the N-substituted ligands than for *dien*. Furthermore, the iodo complex with the ligand *MeMedien* containing one methyl group on a terminal N atom and one on the non-terminal N atom, seems more stable than the iodo complexes containing the ligands with two methyl or two ethyl groups on a terminal N atom, which in turn are more stable than [Pt(dien)I]I. Molecular models have shown that steric reasons are an important factor for the difference between *dien* and the other ligands, but the different reactivities of the N-substituted complexes cannot be due only to steric factors. The two complexes with *Me_2dien* and *Et_2dien* have one alkyl group on each side of the platinum plane which severely limits access of the entering ligand towards the metal center. For the *MeMedien* complex, there are theoretically two isomers: the two methyl groups can be on the same side or on opposite sides of the platinum plane. The formation of the latter isomer should be predominant. Therefore the steric hindrance is not larger for *MeMedien* than for the *Me_2dien and Et_2dien* complexes. The rate of formation of the trigonal bypyramid in the

Can. J. Chem. Downloaded from www.nrcresearchpress.com by EESC ESCOLA DE ENGENHARIA on 09/08/12
For personal use only.

transition state might explain the lower reactivity of [Pt(MeMedien)I]I compared to the complexes with two alkyl groups on one terminal N atom. In the transition state, the two terminal N atoms are located in the apical positions, while the third N atom is located in the plane along with the entering and leaving ligands. For the terminal N-dialkyl complexes, the entering ligand might approach the complex almost in a position *trans* to the N-substituted atom. Therefore, the transition state might be of lower energy than the one of the complex containing *MeMedien*, with a methyl group on a terminal N atom and one methyl group on the non-terminal N atom.

Following these results (no formation of [Pt(dipn)I]I and [Pt(enpn)I]I and the low yields of [Pt(L)Cl]Cl), we decided to develop a new and more general method for the synthesis of the chloro complexes. We have tried several methods without success. The use of K_2PtCl_4 in water brings purification problems, since all the products are soluble in water. We have tried the reaction of K_2PtCl_4 in DMF, since KCl is not soluble in DMF. At room temperature no reaction was observed after three weeks. When the solution was heated to 60°C, insoluble brown compounds were observed. When the solution was heated over 60°C, decomposition occurred rapidly. We have tried using $PtCl_2$ as starting material in water or in a mixture of water–ethanol. Results similar to those with DMF were obtained. We therefore decided to come back to the use of K_2PtCl_4 in water and try the use of different organic solvents in the purification process.

Prolonged heating at ~60°C of K_2PtCl_4 in aqueous solution with the five ligands under study produced the complexes [Pt(L)Cl]Cl. An excess of ligand was required for the reaction to proceed. Acetone was used to remove the excess ligand while ethanol was used to remove KCl (solubility of KCl in ethanol is 0.03 g/100 mL at 20°C). The reaction is faster for the alkyl derivatives of *dien* (*Me_2dien*, *Et_2dien*, and *MeMedien*) and slower for the ligand containing more C atoms between the N atoms (*enpn* and *dipn*). The first syntheses indicated a high % of C and H and a low % of Cl. Further washings with acetone to remove the excess ligand, gave reasonably good elemental analyses (see Experimental section). The complexes must be thoroughly dried under vacuum for at least 24 h. Special care must be taken for handling some of the complexes, since they are quite hygroscopic.

The conductivities of the complexes were measured in water. The results on fresh solutions showed values ranging from 118 to 130×10^{-4} S m^2 mol^{-1}. The conductivities were again measured after 48 h. The results were identical suggesting that the complexes do not hydrolyze easily.

The IR spectra of the synthesized compounds [Pt(L)Cl]Cl were measured in the solid state in Nujol. The main bands are shown in the Experimental section. The stretching —NH_2 and N—H vibrations were observed around 3400 cm^{-1} while the bending modes were found at 1600 cm^{-1}. Two stretching C—N bands were observed between 1017 and 1080 cm^{-1}. Two bands for the complexes containing the dialkyl derivatives of *dien* were observed for $\rho(NH_2)$ at 725 and ~770 cm^{-1}, while only one band was observed at 725 cm^{-1} for the *dipn* and *enpn* complexes. One band around 334 cm^{-1} was observed for the stretching ν(Pt—Cl). These assignments are based on those reported for similar complexes (12–15).

The ^{1}H NMR spectra of the complexes were measured in D_2O. All the peaks were observed at lower fields than those of the free ligands measured in the same solvent. The results are shown in the Experimental section. As expected, the protons located closer to Pt were more deshielded than those located further away. Most of the peaks overlapped and it was not possible to detect ^{195}Pt couplings with certainty. No free ligands could be detected in the aqueous solutions of the complexes.

Reactions with purine and pyrimidine bases

The reaction of [Pt(L)Cl]Cl with several purine and pyrimidine bases were studied in aqueous solution by ^{1}H NMR spectroscopy. The binding site of the bases can be determined by the chemical shift of the protons of the ligand in the complex and by the coupling of the protons in the close environment of Pt with ^{195}Pt (~34% natural abundance).

Two types of reactions were performed. A few reactions were done directly in the NMR tube in D_2O solution at room temperature. The spectra were recorded several times until equilibrium had been obtained. The intensity of the peaks of the complexed ligands (purine or pyrimidine) was compared to those of the free ligands. The extent of reaction was very small. Furthermore, since the reactions are very slow, some deuteration was noted after a few days on some of the protons. Therefore, most of the reactions were studied according to the following method. The reactants were dissolved in H_2O and the solution heated to 70°C 8 h per day, for 3–6 days. The solution was then evaporated to dryness under reduced pressure and the residue dissolved in D_2O. This method has the advantage of increasing the extent of reaction and also eliminates the problems due to deuteration of some of the protons. The results reported below correspond to equilibrium concentrations. Only the study with pyrimidine was done by the first method, because it has a low boiling point and the second method would eliminate some of the ligand in the evaporating process.

The reactions of the five complexes [Pt(L)Cl]Cl with inosine (ino) in a 1:1 ratio produced the complexes [Pt(L)(ino)]Cl_2. The binding site of inosine is N(7) as expected. The ^{1}H NMR spectra showed that the proton H(8) is deshielded by 0.54–0.74 ppm upon coordination, compared to 0.10–0.14 ppm for H(2) and 0.07–0.11 ppm for H(1′). Furthermore, a coupling with ^{195}Pt was observed for H(8) with $^3J(^{195}\text{Pt}—^1\text{H}(8)) = 22$ –24 Hz. The amount of coordinated inosine was 50% for *Me_2dien* and *Et_2dien*, 30% for *MeMedien*, 10% for *enpn*, and <5% for *dipn*. It seems that for the *dien* derivatives, [Pt(MeMedien)Cl]Cl is less reactive towards inosine than [Pt(Me_2dien or Et_2dien)Cl]Cl. The complex containing two six-membered chelate (L = *dipn*) is very stable and hardly reacts with inosine, while [Pt(enpn)Cl]Cl is slightly more reactive.

Similar reactions with guanosine were slightly more difficult to study, since guanosine is not very soluble in water. The NMR solutions were more dilute. The binding site is again N(7). The proton H(8) was deshielded by 0.34 to 0.47 ppm and H(1′) by 0.04–0.10 ppm upon coordination. The amount of coordinated guanosine was 90% for the *Me_2dien* and *Et_2dien* complexes, ~40% for *MeMedien*, ~20% for *enpn*, and ~10% for *dipn*. For the three latter complexes, free solid guanosine was observed. It was removed by filtration and weighed in order to determine the extent of the reactions. The order of reactivity of the complexes towards guanosine is similar to the results obtained with inosine.

Since the complexes containing six-membered chelates were not very reactive towards purine bases, similar reactions were done with smaller molecules, cytosine and pyrimidine. The reactions with cytosine were done at 70°C for 3 days. The

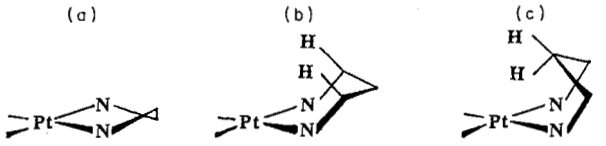

FIG. 1. Conformation of a Pt-chelate for (a) a five-membered ring, (*b*) a six-membered ring: chair (*c*) a six-membered ring: boat.

results have shown that the binding site of cytosine is N(3). The protons H(5) and H(6) are doublets with coupling constants of 7 Hz (free and bonded cytosine). The deshielding of H(5) in bonded cytosine is slightly larger (0.11–0.13 ppm) than of H(6) (0.07–0.09 ppm). No coupling $^4J(^1H(5)—^{195}Pt)$ could be measured. The amount of coordinated cytosine was 50% (*Me_2dien*), 40% (*Et_2dien*), 30% (*MeMedien*), 20% (*enpn*), and 15% (*dipn*). When the solutions were heated for another 6 days at 40°C, the amount of bonded cytosine was increased to 70% for *Me_2dien* and 65% for *Et_2dien*, but not for the other ligands. One side of the coupling $^4J(^1H(5)—^{195}Pt)$ could then be observed (~12 Hz for *Me_2dien* and ~15 Hz for *Et_2dien*).

Pyrimidine is a small simple molecule with two equivalent N atoms. By convention, N(1) is the binding site. These studies were done only in the NMR tubes. The reactions were first done in a mole-to-mole ratio. For the three ligands *MeMedien*, *enpn*, and *dipn* whose spectra indicated a great quantity of unreacted pyrimidine, the reactions were repeated in a Pt:pyrimidine ratio of 2:1 in order to reduce the intensity of the peaks caused by free pyrimidine. The spectra were measured 3 days after mixing the complexes with pyrimidine. The spectrum of free pyrimidine in D_2O solution, showed couplings ^3J(H(6 or 4)—H(5)) of 6 Hz, and ^5J(H(5)—H(2)) of 1.5 Hz. Binding of Pt at N(1) destroys the symmetry of pyrimidine and the number of peaks observed is increased. The deshielding of H(2) upon coordination varies from 0.40 to 0.52 ppm, H(6) 0.35 to 0.47 ppm, H(4) 0.16 to 0.20 ppm, and H(5) 0.15 to 0.21 ppm. ^{195}Pt couplings were observed with H(2) (^3J(Pt—H(2)) = 22–24 Hz) and with H(6) (^3J(Pt—H(2)) = 25–26 Hz). No such coupling was detected for H(4), indicating that pyrimidine does not bind as a bidentate ligand. H(6) is observed as a doublet of doublets of doublets with $^3J = 6$ Hz, $^4J = 2$ and 1 Hz. H(5) is observed as a doublet of triplets with $^3J = 5.4$ Hz and $^5J \sim 1.5$ Hz. H(2) is observed as a triplet (plus the satellites caused by coupling with ^{195}Pt) with $^4J = 2.1$ Hz. The amount of coordinated pyrimidine for the 1:1 ratio reactions were ~85% for *Me_2dien*, ~80% for *Et_2dien*, ~30% for *MeMedien*, and ~20% for *enpn* and *dipn*.

A few reactions with guanosine-5′ monophosphate were performed on three of the complexes. This ligand is interesting, since it is very soluble in water (in contrast to guanosine). The results have shown that for *Me_2dien* and *MeMedien*, the reactions were complete since no free guanosine-5′-monophosphate was observed. With [Pt(dipn)Cl]Cl, the amount of coordinated nucleoside at equilibrium was ~40%. The binding site is N(7). The proton H(8) was deshielded upon coordination by 0.44–0.55 ppm and coupled with ^{195}Pt with $^3J = 22$–24 Hz and H(1′) (doublet with $J \sim 5$ Hz) was deshielded by 0.12–0.15 Hz.

This study clearly shows that the complexes [Pt(L)Cl]Cl, where L is a diethylenetriamine derivative with two 5-membered chelate rings, are more reactive than the complex containing two 6-membered chelates (dipn). The complex [Pt(enpn)Cl]Cl containing one 5-membered chelate and one 6-membered chelate showed intermediate behavior. For the *dien* derivatives, the complexes containing two alkyl groups on a terminal N atom (*Me_2dien* and *Et_2dien*) are more reactive than [Pt(MeMedien)Cl]Cl which contains a ligand with one alkyl group on a terminal N and one alkyl group on a non-terminal N atom. The extent of reaction of the two complexes [Pt(Me_2dien)Cl]Cl and [Pt(Et_2dien)Cl]Cl are very similar. This is in agreement with the results obtained from the crystal structure of [Pt(Et_4dien)I]I (9). The authors have found that the terminal —CH_3 are located away from the Pt atom. Therefore the access to the metal center is not too different for the two ligands.

The addition of one more C atom in the chelate ring seems to play an important role in the kinetics of the reactions. The crystal structures of several [Pt(dien)X]X (10, 16–20) have shown that the C atoms of the *dien* ligand are close to the platinum coordination plane (Fig. 1*a*). For the 6-membered ring chelate, molecular models have shown that the three C atoms are considerably out of the plane (21). Two types of conformation (chair and boat) are possible for the 6-membered chelate with trimethylenediamine (Fig. 1).

In solution, the two forms probably exist, but the chair conformation should predominate. The approach of the entering ligand towards the metal will be much more difficult with the complex containing the 6-membered chelate compared to the 5-membered chelate. Furthermore, the presence of two 6-membered chelates where the three C atoms of each chelate could be located on different sides of the platinum plane, would severely block the access of the entering ligand towards the platinum center. In a different project, we have studied the reaction of [Pt(bis(aminopropyl)phenylphosphine)Cl]Cl (which contains two 6-membered chelates) with pyridine, inosine, guanosine, cytosine, and pyrimidine. No reaction was observed.

The results obtained with diethylenetriamine derivatives might seem surprising, but are similar to the substitution reactions of [Pt(L)I]I for chloride ligands, described earlier in this publication. The complex [Pt(MeMedien)Cl]Cl which contains one methyl group on a terminal N atom and one on a non-terminal N atom is much more stable than the two complexes containing two methyl or ethyl groups on a terminal N atom. If we examine the molecular models, the two substituents on the same terminal N atom are much closer to the leaving group than a methyl group on a non-terminal N atom. Therefore we must assume a S_N2 substitution reaction. The rate of formation of the trigonal bypyramid in the transition state might explain the lower reactivity of [Pt(MeMedien)Cl]Cl compared to the complexes with two alkyl groups on one terminal N atom. In the transition state, the two terminal N atoms are located in the apical positions, while the third N atom is located in the plane along with the entering and leaving ligands. For the terminal *N,N*-dialkyl complexes, the entering ligand might approach the complex almost in a position *trans* to the N-substituted atom. Therefore, the transition state might be of lower energy than the one of the complex containing *MeMedien*, with a methyl group on a terminal N atom and one methyl group on the non-terminal N atom.

Acknowledgment

The authors are grateful to the Natural Sciences and Engineering Research Council of Canada for financial support of the project.

1. F. Basolo and R.G. Pearson. Mechanisms of inorganic reactions. John Wiley and Sons, New York, NY. 1967.

Can. J. Chem. Downloaded from www.nrcresearchpress.com by EESC ESCOLA DE ENGENHARIA on 09/08/12
For personal use only.

2. P.C. Kong and T. Theophanides. Inorg. Chem. **13**, 1981 (1974).
3. N.P. Johnson, J.P. Macquet, J.L. Wiebers, and B. Monsurrat. Nucleic Acids Res. **10**, 5255 (1982).
4. M.I. Djuran, E.L.M. Lempers, and J. Reedijk. Inorg. Chem. **30**, 2648 (1991).
5. J.P. Macquet, J.L. Butour, and N.P. Johnson. Platinum, gold and other metal chemotherapeutic agents. *Edited by* S.J. Lippard. Am. Chem. Soc. Symp. Ser. 209, Washington, DC. 1983.
6. C.J. Van Garderen, L.P.A. Van Houte, H. Van Den Elst, J.H. Van Boom, and J. Reedijk. J. Am. Chem. Soc. **111**, 4123 (1989).
7. G. Raudaschl-Sieber, H. Schollhorn, U. Thewalt, and B. Lippert. J. Am. Chem. Soc. **107**, 3591 (1985).
8. E.L.M. Lempers, K. Inagaki, and J. Reedijk. Inorg. Chim. Acta, **152**, 201 (1988).
9. F. Basolo, H.B. Gray, and R.G. Pearson. J. Am. Chem. Soc. 4200 (1960).
10. R.C.E. Durley, W.L. Waltz, and B.E. Robertson. Can. J. Chem. **58**, 664 (1980).
11. F.G. Mann. J. Chem. Soc. 466 (1934).
12. G.W. Watt and W.A. Cude. Inorg. Chem. **7**, 335 (1968).
13. R.M. Alcock, F.R. Hartley, and D.E. Rogers. J. Chem. Soc. Dalton, 1070 (1973).
14. G.W. Watt and D.S. Klett. Spectrochim. Acta, **20**, 1053 (1964).
15. T.G. Appleton and J.R. Hall. Inorg. Chem. **9**, 1800 (1970).
16. R. Melanson, J. Hubert, and F.D. Rochon. Can. J. Chem. **53**, 1139 (1975).
17. R. Melanson and F.D. Rochon. Acta Crystallogr. Sect. B, **34**, 3594 (1978).
18. J.F. Britten, C.J.L. Lock, and W.N.C. Pratt. Acta Crystallogr. Sect. B, **38**, 2148 (1982).
19. R. Melanson, F.D. Rochon and J. Hubert. Acta Crystallogr. Sect B, **35**, 736 (1979).
20. R. Melanson and F.D. Rochon. Can. J. Chem. **57**, 57 (1979).
21. T.G. Appleton and J.R. Hall. Inorg. Chem. **10**, 1717 (1971).

Can. J. Chem. Downloaded from www.nrcresearchpress.com by EESC ESCOLA DE ENGENHARIA on 09/08/12
For personal use only.

Ab initio study of C—H bond breaking in olefins. II. GVB computations on propene ↔ H + *cis*- or *trans*-propen-1-yl

GEORGE R. DE MARÉ

Laboratoire de Chimie Physique Moléculaire, Faculté des Sciences, CP.160/09, Université Libre de Bruxelles, 50 av. F.D. Roosevelt, B-1050 Brussels, Belgium

EARL M. EVLETH

Dynamique des Interactions Moléculaires, E.R. 271, Tour 22, Université Pierre et Marie Curie, 4 Place Jussieu, 75230 Paris, France

RAYMOND A. POIRIER

Department of Chemistry, Memorial University of Newfoundland, Saint John's, NF A1B 3X7, Canada

AND

GUY J. COLLIN

Département des Sciences Fondamentales, Université du Québec à Chicoutimi, Chicoutimi, QC G7H 2B1, Canada

Received August 25, 1993

GEORGE R. DE MARÉ, EARL M. EVLETH, RAYMOND A. POIRIER, and GUY J. COLLIN. Can. J. Chem. **72**, 1230 (1994).

The Generalized-Valence-Bond-Perfect-Pairing (GVB-PP) method has been used to investigate the structural behaviour, energy, and dipole moment along the reaction coordinates for propene ↔ H + *cis*- or *trans*-propen-1-yl. Geometry optimizations were carried out at the GVB(9)/STO-3G level (complete valence shell) for the minimum energy propene structure (complete optimization) and for numerous structures up to r(C—H) = 10 Å (only the elongated C—H distance kept fixed). The dissociation curves are smooth, without a maximum, and yield predicted dissociation energies of propene to H + *cis*-propen-1-yl and H + *trans*-propen-1-yl of 555.8 and 554.8 kJ mol^{-1}, respectively. These values are within several percent of those obtained for C—H bond rupture in ethylene using GVB and MCSCF methods with the same basis set. They are obviously too high but they confirm that removal of a hydrogen atom from the CH_2 moiety in propene requires about the same energy as removal of a hydrogen atom from ethylene. GVB(7)/6-31G//GVB(9)/STO-3G computations lower the predicted dissociation energies of propene → H + *cis*-propen-1-yl and H + *trans*-propen-1-yl to 448.2 and 448.6 kJ mol^{-1}, respectively.

The reduced energy concept ($E_R = (E_\infty - E_r)/D_e$) is applied to the reaction coordinates. Linear behaviour for ln E_R versus bond length is observed at long bond distances. At r(C—H) = 3 Å, the values of the slopes, d(ln E_R)/dr(C—H), which are related to the effective Morse constant B are –3.73 and –3.74 (GVB(9)/STO-3G) and –2.75 and –2.81 (GVB(7)/6-31G//GVB(9)/STO-3G) for the H + *cis*- and H + *trans*-propen-1-yl reaction coordinates, respectively.

GEORGE R. DE MARÉ, EARL M. EVLETH, RAYMOND A. POIRIER et GUY J. COLLIN. Can. J. Chem. **72**, 1230 (1994).

On a utilisé la méthode de l'appariement parfait de la liaison de valence généralisée (GVB-PP) pour étudier le comportement structurel, l'énergie et le moment dipolaire le long des coordonnées de la réaction propène ↔ H + *cis*- ou *trans*-propén-1-yle. On a effectué les optimisations de géométrie au niveau GVB(9)/STO-3G (couche de valence complète) pour la structure du propène à énergie minimale (optimisation complète) et pour de nombreuses structures jusqu'à r(C—H) = 10 Å (seule la distance C—H allongée est maintenue constante). Les courbes de dissociation sont lisses, sans un maximum, et elles conduisent à prédire des énergies de dissociation pour les réactions du propène en H + *cis*-propén-1-yle et en H + *trans*-propén-1-yle de 555,8 et 554,8 kJ/mol respectivement. Ces valeurs sont à l'intérieur des limites de quelques pour-cent de celles obtenues pour la rupture de la liaison C—H dans l'éthylène lorsque des calculs ont été effectuées par les méthodes GVB et MCSCF, avec le même ensemble de base. Ces valeurs sont évidemment trop élevées, mais elles confirment que l'enlèvement d'un atome d'hydrogène à partir de la portion CH_2 du propène nécessite approximativement la même énergie que l'enlèvement d'un atome d'hydrogène à partir de l'éthylène. Des calculs au niveau GVB(7)/6-31G//GVB(9)/STO-3G abaissent les valeurs des énergies de dissociation des réactions du propène en H + *cis*-propén-1-yle et en H + *trans*-propén-1-yle à 448,2 et 448,6 kJ/mol respectivement.

On a appliqué le concept de l'énergie réduite ($E_R = E_\infty - E_r)/D_e$) aux coordonnées de la réaction. Pour des longueurs de liaison élevées, on observe un comportement linéaire de ln E_R en fonction de la longueur de liaison. À r(C—H) = 3 Å, les valeurs des pentes d(ln E_R)/dr(C—H), qui sont reliées à la constante de Morse efficace, B, sont respectivement de –3,73 et –3,74 (GVB(9)/STO-3G) et de –2,75 et –2,81 (GVB(7)/6-31G//GVB(9)/STO-3G) pour les coordonnées des réactions H + *cis*- et H + *trans*-propén-1-yle.

[Traduit par la Rédaction]

1. Introduction

Propene (**1**) has been the object of many investigations of its thermal (1–8) and photochemical reactions (9–19), but the overall reaction mechanisms are still not fully elucidated. An important reason is the large number of products at lower pyrolysis temperatures: for instance Kallend et al. (8) identified 26 products, many of which are more reactive than **1**. Another reason is the low relative importance of the three α-CH bond cleavages compared to cleavage of the β-CH and α-CC bonds. The primary unimolecular processes involving cleavage of only one formal single bond in **1** are shown in Fig. 1. In this paper we examine the reaction coordinates for **1** ↔ H + C_3H_5 where C_3H_5 corresponds to either the *cis*-propen-1-yl or the *trans*-propen-1-yl radical (structures **2** and **3** in Fig. 1, respectively), using the Generalized-Valence-Bond-Perfect-Pairing (GVB-PP) method (20). Radicals **2** and **3** are formed in the direct photolysis of **1**.[1] They are also formed in the addition of methyl radicals to acetylene (21) and in the direct photolysis of both *trans*-

[1]G.J. Collin and H. Deslauriers. Unpublished results.

Can. J. Chem. Downloaded from www.nrcresearchpress.com by EESC ESCOLA DE ENGENHARIA on 09/08/12
For personal use only.

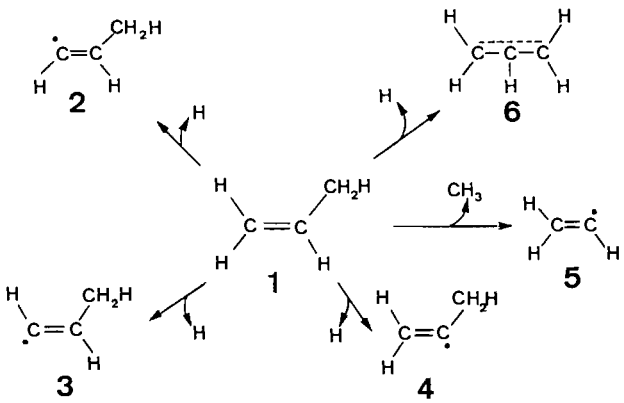

FIG. 1. Unimolecular dissociation processes in propene (**1**) involving the rupture of only one bond.

and *cis*-2-butene (9, 22, 23) and of larger olefins with the double bond in the 2-position (24). It is therefore of interest to obtain information on their structures, relative energies, etc.

Recently we reported an *ab initio* study of the reaction coordinate for ethylene ↔ H + vinyl(**5**), corresponding to C—H bond-breaking in ethylene or to hydrogen atom capture by **5** (25). As expected the single configuration Self-Consistent-Field (SCF) computations predicted an energy plateau at large C—H separations but this plateau is much too high energetically. The dipole moment increased with increasing C—H separation, indicating that the separated species constitute an ionic pair (25). This behaviour was expected: it is the result of the methodology employed in generating the wave function and is independent of the composition of the basis. However, if a correct methodology is employed, the computed bond energy will be dependent on the basis set composition. Both GVB-PP and Multi-Configuration-SCF (MCSCF) methods were used: the single configuration SCF method is inadequate except (*a*) at equilibrium geometries or (*b*) at long internuclear distances with an open-shell methodology. The minimal levels necessary for the GVB-PP and MCSCF calculations to obtain satisfactory results were determined, not only for the C—H reaction coordinate in ethylene, but also for H—X reaction coordinates where X = CH_3, OH, and F (25).

Thermal reactions of 1

At low temperatures and moderate to high pressures the thermal reactions of **1** are initiated mainly by the bimolecular disproportionation reaction [1] (6)

[1] $2\,\mathbf{1} \rightarrow$ allyl(**6**) + isopropyl

whereas at higher temperatures and low concentrations of **1** the decomposition processes [2]–[5] are necessary to explain the results (see ref. 1 and references therein).

[2] $\mathbf{1} \rightarrow H + \mathbf{6}$

[3] $\mathbf{1} \rightarrow \dot{C}H_3 + \mathbf{5}$

[4] $\mathbf{1} \rightarrow CH_4 + C_2H_2$

[5] $\mathbf{1} \rightarrow H_2 + C_3H_4$

The relative importance of the primary steps

[6] $\mathbf{1} \rightarrow H + \mathbf{2}$

and

[7] $\mathbf{1} \rightarrow H + \mathbf{3}$

in the thermal reactions of **1** have not yet been determined experimentally but the participation of $H\dot{C}{=}CH{-}CH_3$ radicals of undefined geometry in its shock tube pyrolysis has been proposed by Hidaka et al. (1).

Photochemical reactions of 1

Because processes [2] and [3] require less energy than the cleavage of any of the three vinylic α-CH bonds, the equivalent bond ruptures are quite important in the triplet mercury photosensitization of **1** at low pressures (13, 26) and also in its direct photolysis (17, footnote 1). Process [2] is very interesting because, on the time scale for photon absorption, the in-plane C—H bond of the methyl group differs from the two out-of-plane ones (27).

Avrahami and Kebarle (19) were the first to show that isomerization to cyclopropane occurs in the triplet mercury photosensitization, presumably via the trimethylene biradical

[8] $\mathbf{1} \rightarrow$ cyclopropane

formed by a 1,2-H atom migration in triplet **1**. Product analysis led them to conclude that processes [2], [3], and [8] occur in the ratio 89:11:0.2 at a total pressure of ca. 10 torr. Placzek and Rabinovitch (28) found that the relative cyclopropane yield increased to a maximum of about 1.4% at 70 torr pressure, its precursor(s) being deactivated by collisional quenching. It is interesting to note that the formation of the trimethylene biradical requires a 1,2 H-atom shift and that if it were followed by a second 1,2 shift in the biradical to yield **1**, H-atom scrambling in the "unreacted" parent compound should be observed. Thus starting with the 1,3,3,3,-**1**-d_4 isotopomer, one would expect the formation of the 1,1,3,3-**1**-d_4, 1,1,2,3-**1**-d_4 and 1,2,3,3-**1**-d_4 isotopomers. However, Hirokami and Sato (13) reported that the ratio of the *cis*- to *trans*-1,3,3,3-**1**-d_4 isomers after prolonged photosensitization with Hg $6(^3P_1)$, Cd $(^3P_1)$, or benzene was unity. No other isotopomers were reported. Furthermore they searched specifically for 2,3,3,3-**1**-d_4 and found no evidence for its formation. This is even more remarkable when one considers the facile H-atom scrambling observed in the triplet photosensitizations of ethylene-d_2 by mercury (29, 30), cadmium (31), and organic compounds (32). This underlines the remarkable effect of the CH_3 moiety on the processes following energy transfer to **1**. Note also that *trans*-cyclopropane-d_2 isomerizes to **1**-d_2 (33). A possible explanation, put forward by Bernardi et al. (34) is that "It is conceivable that the structural isomerization proceeds by a path not involving trimethylene, and hence may not be pertinent to the [1,2] shift transition state." Clearly more experimental work is needed on this problem which we are currently investigating by theoretical methods.

To our knowledge, the importance of the 1,3-H atom shift corresponding to the reaction ↔ no-reaction sequence $H{-}CH_2CH{=}CH_2 \leftrightarrow CH_2{=}CHCH_2{-}H$ (the products of which would be indistinguishable from those from two consecutive 1,2-H atoms shifts in the same direction) has not been determined experimentally. However, *ab initio* computations on the relative energy of the transition state (barrier) for this isomerization indicate that it may be in competition with process (2) (33–35) in the vibrationally excited ground state.

Can. J. Chem. Downloaded from www.nrcresearchpress.com by EESC ESCOLA DE ENGENHARIA on 09/08/12
For personal use only.

TABLE 1. Full valence GVB(9)/STO-3G optimizations on **1** → H + **2** and on **1** → H + **3** (internuclear distances are in Å, angles in deg, dipole moments (μ) in debyes, and relative energies (ΔE) in kJ mol^{-1}; see Fig. 2 for atom numbering)

			1 → H + **2**				**1** → H + **3**			
Parameter	Expt. (43)	[a]	A	B	C	[b]	A	B	C	[c]
r(H1—C1)	1.091 ± 0.003	1.1001	1.5	3.0	10.0	—	1.1009	1.0994	1.0993	1.0993
r(H2—C1)	1.081 ± 0.003	1.0999	1.1007	1.0991	1.0990	1.0990	1.5	3.0	10.0	—
r(H3—C2)	1.090 ± 0.003	1.1032	1.1033	1.1033	1.1033	1.1033	1.1024	1.1030	1.1030	1.1030
r(H4—C3)	1.085 ± 0.004	1.1064	1.1063	1.1064	1.1065	1.1065	1.1065	1.1067	1.1067	1.1067
r(H(5,6)—C3)	1.098 ± 0.014	1.0956	1.0956	1.0956	1.0956	1.0956	1.0956	1.0957	1.0957	1.0957
r(C1—C2)	1.336 ± 0.004	1.3484	1.3460	1.3389	1.3388	1.3388	1.3462	1.3388	1.3386	1.3386
r(C2—C3)	1.501 ± 0.004	1.5427	1.5421	1.5443	1.5444	1.5454	1.5437	1.5449	1.5449	1.5448
∠C1C2C3	124.3 ± 0.3	124.40	125.03	124.08	123.96	123.94	123.79	124.38	124.44	124.50
∠H1C1C2	120.5 ± 0.3	121.98	120.73	119.19	121.97	—	125.27	130.99	131.08	131.13
∠H2C1C2	121.5 ± 0.3	121.80	125.16	130.96	131.04	131.07	120.65	119.61	121.79	—
∠H3C2C1	119.0 ± 0.3	119.90	119.23	120.13	120.22	120.24	120.34	119.84	119.79	119.75
∠H4C3C2	111.2 ± 0.3	110.76	110.68	110.79	110.79	110.80	110.80	110.86	110.86	110.87
∠H(5,6)C3C2	109.2[d]	110.65	110.60	110.63	110.64	110.63	110.62	110.60	110.60	110.58
∠H(5,6)C3C2C1	120.5[d]	±120.48	±120.49	±120.47	±120.46	±120.46	±120.47	±120.46	±120.46	±120.47
μ	0.364 ± 0.003(44)	0.168	0.215	0.261	0.244	0.244	0.281	0.389	0.373	0.373
ΔE	—	0.0	169.7	550.9	555.8	[e]	170.1	550.0	554.8	[f]

[a]Completely optimized GVB(9)/STO-3G structure of **1**.
[b]ROHF-GVB(8)/STO-3G optimized structure of **2**, i.e. H1 removed.
[c]ROHF-GVB(8)/STO-3G optimized structure of **3**, i.e. H2 removed.
[d]Computed using the experimental geometry given in ref. 43.
[e,f]The sum of the energies from a SCF/STO-3G computation on an isolation H atom (E = −0.466582 hartree) and for the ROHF-GVB(8)/STO-3G optimized structure of **2** (E = −115.119237 hartree) or for the ROHF-GVB(8)/STO-3G optimized structure of **3** (E = −115.119652 hartree) are equal to that of the GVB(9)/STO-3G optimized C_3H_6 structures with r(H1—C1) or r(H2—C1) ≥ 4 Å (E = −115.585819 and −115.586234 hartree, respectively).

In our previous work it was shown that inexpensive GVB and MCSCF computations could yield reasonable potential energy curves and total dissociation energies that are within 20% of the best experimental values (25). This paper is the first of several that will be devoted to the chemistry of **1**, including new experimental results on its direct photolysis[1] and theoretical studies on decomposition/isomerization processes in its ground and first triplet electronic states. Here we report surfaces for **1** ↔ H + **2** and **1** ↔ H + **3** which can be treated by GVB methods. Later work will deal with the methodologically difficult surface **1** ↔ H + **4**. The eventual goal is to use the information in theoretically modeling the photochemistry (and thermal reactions) of **1**.

2. Method

The computations were performed with the MONSTERGAUSS *ab initio* program package (37) with the STO-3G (38) and 6-31G (39) basis sets. The optimally conditioned (OC) variable-metric gradient minimization technique (40)[2] was used for all geometry optimizations. The molecular orbitals generated by a complete SCF (single configuration) geometry optimization of **1** were used to identify the valence-virtual orbital pairs for use in the GVB-PP computations. The computations designated by GVB(N) indicate that N correlated valence – virtual orbital pairs were used. Thus GVB(9)/STO-3G included all nine valence orbitals in the correlated valence – virtual pairs. Complete geometry optimization was performed at the minimum energy structure of **1**. Along the reaction coordinate only the C—H internuclear distance corresponding to the bond being broken was kept rigorously fixed. No symmetry restrictions were imposed during the optimizations. However, if one starts the optimization with a slightly deformed structure, the minimum energy structure was found to have C_s symmetry.

Single computations, with the extended 6-31G basis set and including seven correlated pairs were performed at the STO-3G optimized geometries. These are designated by GVB(7)/6-31G//GVB(9)/STO-3G throughout the text. The number of correlated pairs had to be reduced because of memory limitations in the program. The seven valence – virtual orbital pairs chosen for the correlations represent the three σ(C—H) bonds, the two σ(C—C) bonds, the π(C1—C2) bond, and the π-bond involving the methyl group and localized on the C3, H5, and H6 atoms. The two valence orbitals excluded in the excitations were essentially localized on the methyl group and this should not influence the relative energetics to any appreciable extent (25, 41, 42).

3. Results and discussion

3.1. GVB(9)/STO-3G optimizations on 1 ↔ H + cis-propen-1-yl

The results of the GVB(9)/STO-3G optimizations at four points (including the minimum energy structure) along the reaction coordinate for process (6) (or the inverse process, capture of an H atom by **2**) are presented in Table 1. The experimental r_s (substitution) structure, determined from the microwave spectra of seven isotopomers of **1** (43), is also given for comparison. As expected, the GVB(9)/STO-3G optimized bond lengths are all longer than those obtained in a complete RHF/STO-3G optimization of **1**. They are shown in Fig. 2 along with the atom numbering used throughout the text. The consistency of the GVB(9)/STO-3G results at long H1—C1

[2]The routine is described in ref. 40*a*.

Can. J. Chem. Downloaded from www.nrcresearchpress.com by EESC ESCOLA DE ENGENHARIA on 09/08/12
For personal use only.

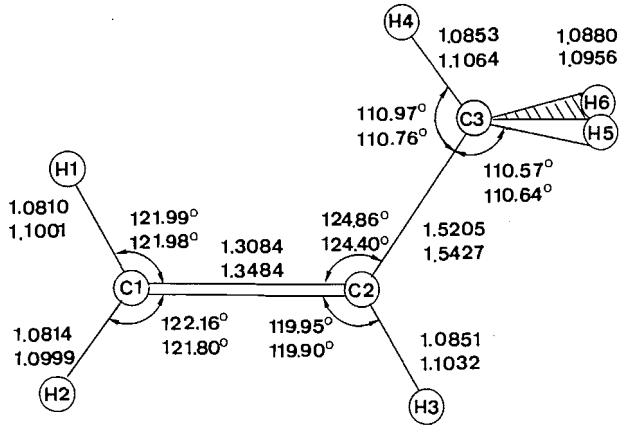

FIG. 2. Atom numbering used throughout the text. The top and bottom values of the geometrical parameters are those obtained by complete SCF/STO-3G and GVB(9)/STO-3G optimizations, respectively.

internuclear distances was tested by carrying out a ROHF-GVB(8)/STO-3G optimization on the radical **2**. The results are juxtaposed in Table 1 next to those for **1** with r(H1—C1) = 10 Å. Only minor differences are observed between the corresponding geometrical parameters for the radical and structures of **1** with r(H1—C1) ≥ 3 Å. (Indeed all parameters are predicted to be essentially independent of r(H1—C1) for internuclear distances greater than about 3.0 Å.) Especially, as noted in Table 1, the GVB(9)/STO-3G energy of **1** at large H1—C1 internuclear distances is equal to the sum of the STO-3G energy of an isolated H atom and the ROHF-GVB(8)/STO-3G energy of **2**. Also the computed dipole moments for the radical and the complex are the same.

The geometrical parameters which undergo the largest variations as the H1—C1 bond is elongated from the optimized equilibrium position (r(H1—C1) = 1.1001 Å) are the two C—C bonds and the angles H1C1C2 and H2C1C2. The behaviour of these four geometrical parameters along the reaction coordinate is shown in Fig. 3 for a large number of optimizations. It is interesting to note that H1 is predicted to move towards the space above the C—C bond. This may reflect the attraction of the π electrons or alternatively it may be due to the role of a lower energy singlet propylidene on the hypersurface of this reaction. H2, which is on the radical center, moves towards the free electron. Similar behaviour was observed for the corresponding H atoms along the ethylene ↔ H + **5** reaction coordinate (25). It is probably a common feature for α-CH bond cleavage in olefins.

For the optimized minimum energy structures, the H2—C1 bond length is predicted to be shorter in **2** than in **1** by about 0.001 Å while the remaining C—H bond lengths remain essentially unchanged (see Table 1). This is in contrast to the GVB(2)/STO-3G results on ethylene which predicted that the C—H bond lengths in **5** are longer than in the parent compound by 0.001 to 0.003 Å (25). The difference between these results for **2** and **5** appears to be an artifact of including all or only part of the valence shell orbitals in the correlated pairs. Indeed, including the full valence shell in the correlated pairs in a series of optimizations (GVB(6)/STO-3G) along the ethylene ↔ H + **5** reaction coordinate results in a shortening of the C—H bond on the radical center whereas those on the CH_2 moiety remain essentially unchanged.[3] Note also that Wu and Carter (42) performed a full valence GVB-PP optimization on **5**, using a VDZP (valence double-ζ with polarization) basis set, and found that the C—H bond on the radical center was predicted to be shorter than those on the CH_2 moiety.

The strange behaviour of ∠H1C1C2 for r(H1—C1) in the range 2.5–3.5 Å merits attention. Is it an artifact of the computations or is it real? Note that similar behaviour is observed for the corresponding angle in ethylene.[3] At first glance one might impute the behaviour to computational (integral-space) accuracy.

As the H1—C1 bond is elongated, the relative energy rises smoothly to a plateau lying 555.8 kJ mol^{-1} above the minimum (Fig. 4). Thus there is no predicted activation energy for the reverse step, capture of an H atom by **2**. This appears to be a general feature for the GVB-PP potential energy curves for these reactions, even if the correlated pairs include only part of the valence shell (25).

3.2. *GVB(9)/STO-3G optimizations on* **1** ↔ *H + trans-propen-1-yl*

Some results of the optimizations are given in Table 1 (at r(H2—H1) = 1.5, 3.0, and 10.0 Å) and in Figs. 5 and 6. As expected the two C—C bonds and the angles H1C1C2 and H2C1C2 undergo the largest variations as H2 is drawn away from the equilibrium position at r(H2—C1) = 1.0999 Å. The dissociation energy is predicted to be 554.8 kJ mol^{-1}, thus only 1 kJ mol^{-1} less than for the removal of H1 from **1**. It is not expected that zero-point energies will make a big difference in this result. It is therefore concluded that the important difference in the ratio for α-CC/β-CH bond cleavage observed in the photolysis of the 2-butenes (α-CC/β-CH = 0.95 and 1.34 for *cis*- and *trans*-2-butene, respectively (22)) does not originate in the energies of formation of the radicals **2** and **3**.

The terminal α-CH bond dissociation energies in **1** are expected to be near that for the C—H bond dissociation energy in ethylene, $D_e(CH_2CH—H)$. Using various geometries and GVB-PP and MCSCF treatments with the same basis set, we previously found $D_e(CH_2CH—H)$ values in the range 543–549 kJ mol^{-1} (25) or about 1 to 2% less than those found here for the terminal α-CH bond cleavages in **1**. These values are obviously too high but they confirm that removal of a hydrogen atom from the CH_2 moiety in **1** requires about the same energy as removal of a hydrogen atom from ethylene. Note that the scatter in the experimental data for the C—H dissociation in ethylene is important, as exemplified by recent literature values of $D_0(CH_2CH—H)$ = 459.0 ± 3.3 kJ mol^{-1} (45) and 488.3 ± 5.0 kJ mol^{-1} (46).

Using various GVB and CI methods, Wu and Carter (42) obtained theoretical $D_e(CH_2CH—H)$ from 436.0 to 490.3 kJ mol^{-1}, thus covering the experimental range of values. They used a much higher level of theory and computing enough points along the reaction coordinate would be expensive in computational time. It is suggested that as a first approximation the GVB(9)/STO-3G curves for **1** could be simply multiplied by a factor of 460/555 = 0.83 to obtain realistic reaction coordinates. Alternatively, considering that the highest value obtained by Wu and Carter (42) was obtained at the highest level of theory, a scaling factor of 490/555 = 0.88 may be more appropriate.

The effect on the reaction coordinates of using a split-valence basis-set in the computations has been investigated by carrying out complete series of GVB(7)/6-31G//GVB(9)/STO-3G computations (see below).

[3]G.R. De Maré. Unpublished results.

Can. J. Chem. Downloaded from www.nrcresearchpress.com by EESC ESCOLA DE ENGENHARIA on 09/08/12
For personal use only.

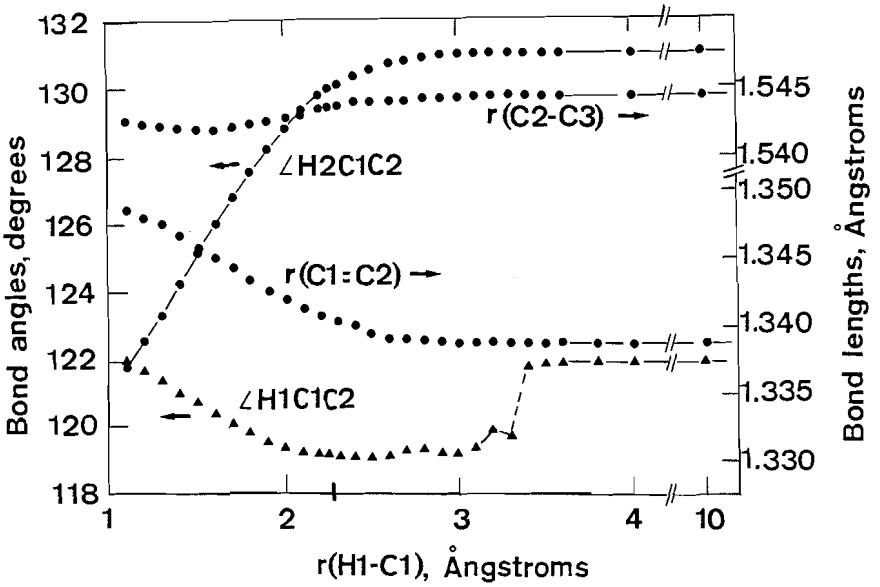

FIG. 3. The GVB(9)/STO-3G optimized values of r(C1—C2), r(C2—C3), ∠H1C1C2, and ∠H2C1C2 as a function of the H1—C1 internuclear distance in **1**. For r(H1—C1) greater than 3.2 Å, ∠H1C2C1 remains essentially equal to the input value.

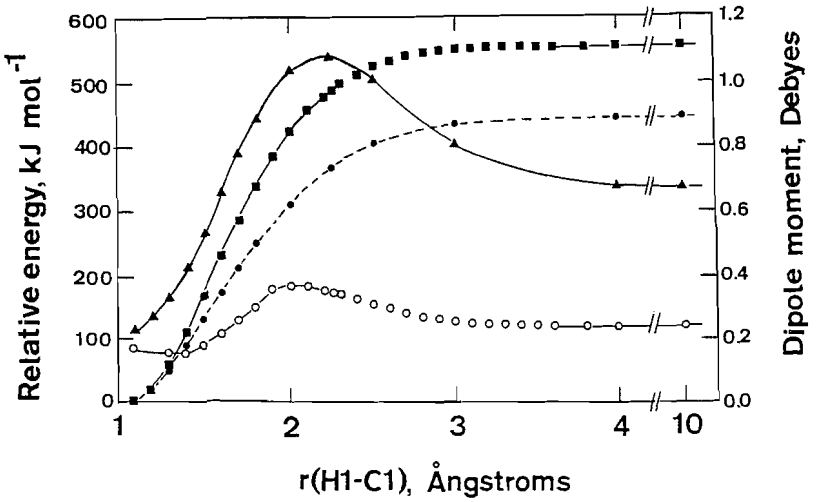

FIG. 4. The GVB(9)/STO-3G relative energies (■) and dipole moments (○) and the GVB(7)/6-31G//GVB(9)/STO-3G relative energies (●) and dipole moments (▲) as a function of the H1—C1 internuclear distance in **1**.

3.3. GVB(7)/6-31G//GVB(9)/STO-3G computations

The relative energies from the GVB(7)/6-31G//GVB(9)/STO-3G computations are represented in Figs. 4 and 6 for comparison with the GVB(9)/STO-3G results. Whereas the form of the curves for the GVB(7)/6-31G//GVB(9)/STO-3G relative energies are similar to those from the GVB(9)/STO-3G optimizations, the predicted dissociation energies are now much closer to the expected values (see above) being lowered by about 100 kJ mol^{-1} to 448.2 and 448.6 kJ mol^{-1} for the formation of **2** and **3**, respectively. The order of the relative energies of **2** and **3** is reversed but complete geometry optimizations of the radical structures at the GVB(7)/6-31G level could change this. Any effect on the total energy due to the methyl group being *cis* or *trans* to the free electron is predicted to be very small.

3.4. Reduced energy surfaces for propene

Plots of the reduced energy E_R (see below) and of ln E_R versus the H1—C1 and H2—C1 internuclear distances in **1** for the series of GVB(9)/STO-3G optimizations and GVB(7)/6-31G//GVB(9)/STO-3G computations are given in Fig. 7.

We have previously shown (25, 47) that computed surface forms obtained with various molecular orbital generating methodologies and different basis sets can be compared by using a reduced energy (E_R) expression, $E_R = 1 - E(r)/D_e$, where $E(r)$ is the computed relative energy at interatomic distance r and D_e is the total computed dissociation energy. ($E(r) = 0$ at r_e, the equilibrium bond distance.) It was also shown that ln E_R is linear with distance at long bond distances. This also occurs when one employs the Morse equation, $E_R = 2 \exp(-B(r - r_e)) - \exp(-2B(r - r_e))$. At long bond distances the slope, d(ln E_R)/dr, approaches a value of $-B$. Note that $B = (k/2D_e)^{1/2}$ where k is the force constant. The resulting linearity can be used as a criterion of whether the computational results are valid. It should be noted that various molecular dynamic modeling schemes have assumed exponential linearities in the long bond distance region (e.g. see refs. 48, 49). Such linearity is expected for sim-

Can. J. Chem. Downloaded from www.nrcresearchpress.com by EESC ESCOLA DE ENGENHARIA on 09/08/12
For personal use only.

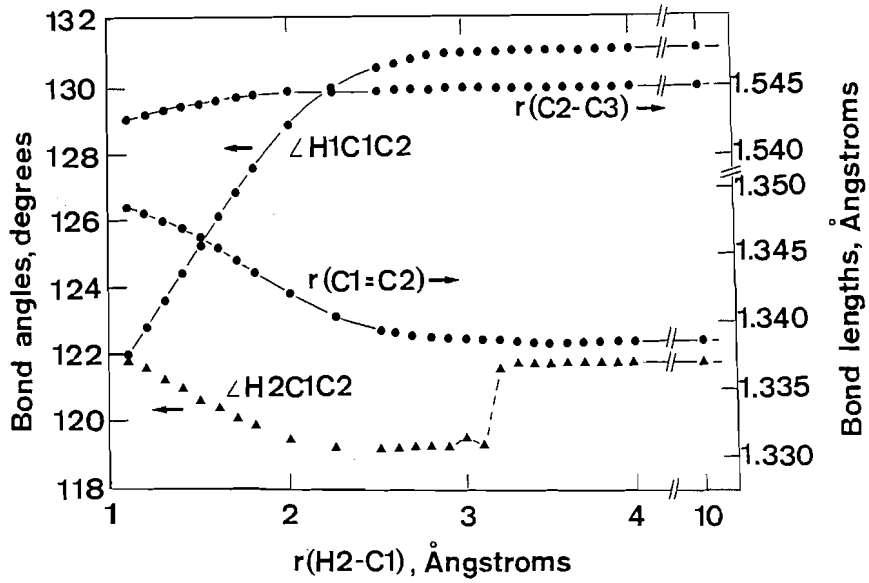

FIG. 5. The GVB(9)/STO-3G optimized values of r(C1—C2), r(C2—C3), ∠H1C1C2, and ∠H2C1C2 as a function of the H2—C1 internuclear distance in **1**. For r(H2—C1) greater than 3.2 Å, ∠H2C2C1 remains essentially equal to the input value.

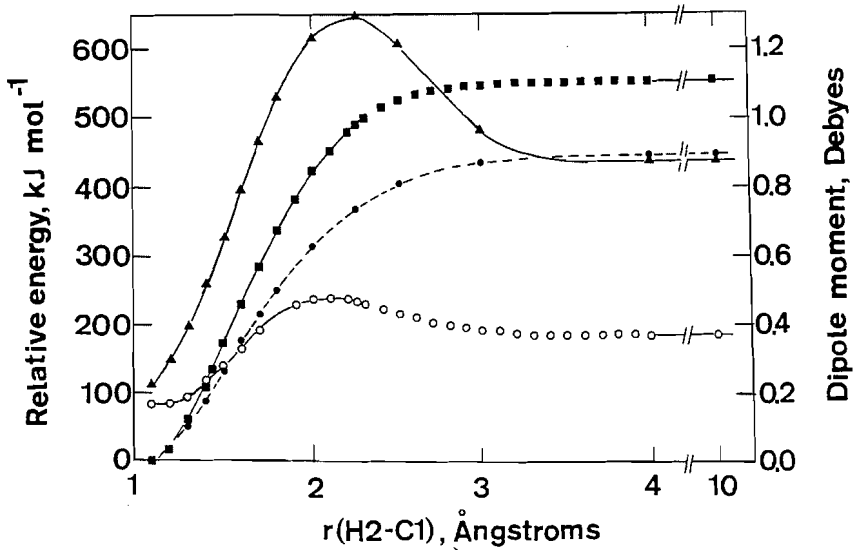

FIG. 6. The GVB(9)/STO-3G relative energies (■) and dipole moments (○) and the GVB(7)/6-31G//GVB(9)/STO-3G relative energies (●) and dipole moments (▲) as a function of the H2—C1 internuclear distance in **1**.

ple two electron bond ruptures because various integral forms that are involved in calculating the interaction energies at longer distances contain exponential terms.[4] Since linearity is expected, one of the goals of this paper is to verify if this situation exists along the computed primary α-CH bond rupture surfaces of **1**, as has been observed for its homolog, ethylene (25). Nevertheless we point out that in other work[5] one of us has found that both the large MCSCF treated OO rupture in HOOH and the H—O rupture in the HOO radical have non-linear ln E_R behaviour in the region where one finds linearity in the other systems discussed in ref. 25.

Although it may be fortuitous, the E_R and ln E_R curves from the GVB(9)/STO-3G optimizations for steps [6] and [7] are superimposable. Moreover, they can also be superimposed on the corresponding curves from the GVB(2)/STO-3G optimizations on ethylene ↔ H + **5**. The differences in the curves are less than the diameters of the points in Fig. 7. There are nearly linear regions in the plots of ln E_R versus the H1—C1 and the H2—C2 internuclear distances in the range r(C—H) = 2.5 to 3.5 Å. It is at these internuclear distances that the interaction energy becomes greater than kT and radical-H capture is becoming dynamically important. As noted above and in ref. 25, the optimized geometries of the radical moieties are essentially independent of the distance to the departing (or approaching) H atom for r(H—C) ≥ 3 Å.

As for the d(ln E_R)/dr(C—H) slopes, which are related to the effective Morse constant B discussed above, the corresponding values at 3 Å for the GVB(9)/STO-3G curves are both 3.7 Å^{-1}. These slopes are thus the same as those found for all the GVB and MCSCF calculations carried out in the study on ethylene (25). Although this value is much larger than normal Morse B

[4]Reference 50. For example, see formulae 11.29, 11.32, and 11.33. This rationalization is highly simplistic but it was the guiding one in first examining the possibility of this relationship.

[5]E.M. Evleth. Unpublished results.

Can. J. Chem. Downloaded from www.nrcresearchpress.com by EESC ESCOLA DE ENGENHARIA on 09/08/12
For personal use only.

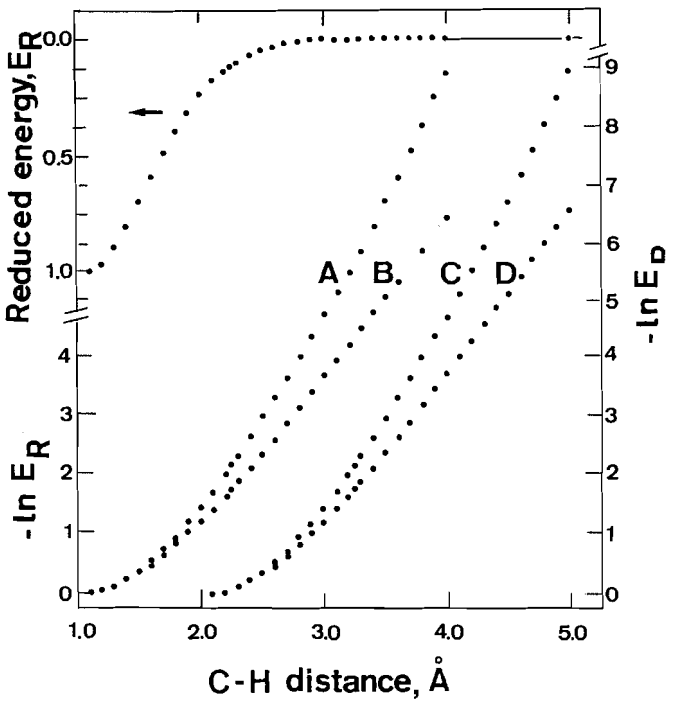

FIG. 7. Plots of the reduced energies (E_R) (upper curve) and of –ln E_R as a function of the internuclear distance along the reaction coordinates for **1** — H + **2** (plots A and B) and **1** — H + **3** (plots C and D). On the scale used the plots of E_R are superimposed. Plots A and C: GVB(9)/STO-3G; plots B and D: GVB(7)/6-31G//GVB(9)/STO-3G. Plots C and D have been displaced by 1 Å to the right.

constants (1.8–1.9 $Å^{-1}$ (48)), it is in the same range as those found for other STO-3G calculations (47). It was speculated that the slopes might be reduced by using a larger basis set (25). This is in fact the case for the GVB(7)/6-31G//GVB(9)/STO-3G results: the $d(\ln E_R)/dr$(C—H) slopes at 3 Å are lowered to 2.75 and 2.81 $Å^{-1}$ for the reaction coordinates of steps [6] and [7], respectively.

The essential fact is that for a given basis set, E_R is nearly insensitive to the GVB or MCSCF level of treatment within a range capable of providing gradient optimizations and frequency calculations of the interacting system.

3.5. Dipole moments

One of the salient conclusions made in ref. 25 for the GVB and MCSCF computations is that the dipole moment behaviour can be used as a criterion to predict whether the computations are valid and also to predict the distance at which effective interaction between dissimilar (or polar) species begins or ends. The same conclusion can be made for the present results (see Figs. 4 and 6).

4. Conclusions

The main result of the study presented here is that the behaviour of the potential energy surfaces for primary α-CH bond rupture in **1** are similar to hydrogen bond ruptures in ethylene, methane, water, and HF. The behaviour of the reduced energy curves, E_R is very similar to that found for ethylene, where it was found to be independent of geometry optimization. This behaviour will allow for a simple modeling of the dynamics of unimolecular decomposition via primary α-C—H bond dissociation in olefins. These channels are identical to those for H-atom capture by the corresponding radicals.

Another important conclusion is that the bond dissociation energies (and therefore the energies of formation of the radicals) are nearly equal for both the primary α-CH bonds in **1**. Thus the energies of formation of the radicals can not explain the difference in the ratios for α-CC/β-CH cleavage in the direct photolysis of the 2-butenes (α-CC/β-CH = 0.95 and 1.34 for *cis*- and *trans*-2-butene, respectively (22)).

Although the energy is still increasing, the remaining structural parameters become essentially independent of the *r*(C—H) distance somewhere between 2.75 Å and 3.0 Å. It is interesting to note that, as in the case of ethylene, the departing H atom is predicted to move towards the space above the formal C—C double bond, probably reflecting the attraction of the π electrons.

5. Acknowledgements

We wish to thank the Department of Scientific Affairs of NATO for financial support (CRG.920599). R.A.P. also gratefully acknowledges the continued financial support of the Natural Sciences and Engineering Council of Canada (NSERC).

1. Y. Hidaka, T. Nakamura, H. Tanaka, A. Jinno, H. Kawano, and T. Higashihara. Int. J. Chem. Kinet. **24**, 761 (1992).
2. W. Tsang. J. Phys. Chem. Ref. Data, **20**, 221 (1991).
3. V.S. Rao and G.B. Skinner. J. Phys. Chem. **93**, 1869 (1989).
4. J.H. Kiefer, M.Z. Al-Alami, and K.A. Budach. J. Phys. Chem. **86**, 808 (1982).
5. A. Burcat. Fuel, **54**, 87 (1975).
6. M. Simon and M.H. Back. Can. J. Chem. **48**, 317 (1970).
7. G.A. Chappell and H. Shaw. J. Phys. Chem. **72**, 4672 (1968).
8. A.S. Kallend, J.H. Purnell, and B.C. Gowenlock. Proc. R. Soc. A **300**, 120 (1967).
9. G.J. Collin. Adv. Photochem. **14**, 135 (1988).
10. H. Deslauriers and G.J. Collin. J. Chim. Phys. **82**, 1033 (1985).
11. J. Niedzielski, W. Makulski, and J. Gawlowski. J. Photochem. **19**, 123 (1982).
12. P. Borrell, A. Cervenka, and J.W. Turner. J. Chem. Soc. B, 2293 (1971).
13. S. Hirokami and S. Sato. Bull. Chem. Soc. Jpn. **43**, 2389 (1970).
14. E. Tsuikow-Roux. J. Phys. Chem. **71**, 870 (1967).
15. S. Arai, S. Shida, and T. Hishikawa. Bull. Chem. Soc. Jpn. **39**, 2548 (1966).
16. R. Gorden, Jr., R.D. Doepker, and P. Ausloos. J. Chem. Phys. **44**, 3733 (1966).
17. D.A. Becker, H. Okabe, and J.R. McNesby. J. Phys. Chem. **69**, 538 (1965).
18. A. Heller and A.S. Gordon. J. Chem. Phys. **42**, 1262 (1965).
19. M. Avrahami and P. Kebarle. J. Phys. Chem. **67**, 354 (1963).
20. F.W. Bobrowicz and W.A. Goddard, III. *In* Methods of electronic structure theory. Vol. 3. *Edited by* H.F. Schaefer III. Plenum Press, New York, NY. 1977. pp. 79–127.
21. T. Ibuki, T. Murata, and Y. Takezaki. J. Phys. Chem. **78**, 2543 (1974).
22. H. Deslauriers, W. Makulski, and G.J. Collin. Can. J. Chem. **65**, 1631 (1987).
23. A. Wieckowski and G.J. Collin. J. Phys. Chem. **81**, 2592 (1977).
24. G.J. Collin. Rev. Chem. Intermediates, **2**, 377 (1988).
25. G.R. De Maré and E.M. Evleth. J. Mol. Struct. Theochem. **259**, 273 (1992).
26. F.P. Lossing, D.G.H. Marsden, and J.B. Farmer. Can. J. Chem. **34**, 791 (1956).
27. D.C. McKean. Int. J. Chem. Kinet. **21**, 445 (1989).
28. D.W. Placzek and B.S. Rabinovitch. Can. J. Chem. **43**, 820 (1965).
29. A.B. Callear and R.J. Cvetanovic. J. Chem. Phys. **24**, 873 (1956).
30. D.W. Setser, B.S. Rabinovitch, and D.W. Placzek. J. Am. Chem. Soc. **85**, 862 (1963).
31. S. Tsunashima, S-I. Hirokami, and S. Sato. Can. J. Chem. **46**, 995 (1968).

Can. J. Chem. Downloaded from www.nrcresearchpress.com by EESC ESCOLA DE ENGENHARIA on 09/08/12
For personal use only.

32. S. Sato. Pure Appl. Chem. **16**, 87 (1968).
33. E.V. Waage and B.S. Rabinovitch. J. Phys. Chem. **76**, 1695 (1972).
34. F. Bernardi, M.A. Robb, H.B. Schlegel, and G. Tonachini. J. Am. Chem. Soc. **106**, 1198 (1984).
35. R.A. Poirier, D. Majlessi, and Th.J. Zielinski. J. Comput. Chem. **7**, 464 (1986).
36. W.R. Rodwell, W.J. Bouma, and L. Radom. Int. J. Quant. Chem. **18**, 107 (1980).
37. M.R. Peterson and R.A. Poirier. MONSTERGAUSS. 1986.
38. W.J. Hehre, R.F. Stewart, and J.A. Pople. J. Chem. Phys. **51**, 2657 (1969).
39. W.J. Hehre, R. Ditchfield, and J.A. Pople. J. Chem. Phys. **56**, 2257 (1972).
40. W.C. Davidon. (*a*) W.C. Davidon and L. Nazareth. Technical memos 303 and 306, Applied Mathematics Division, Argonne National Laboratory, Argonne, Il 60430; (*b*) W.C. Davidon Math. Prog. **9**, 69 (1975).
41. C.J. Wu and E.A. Carter. J. Am. Chem. Soc. **112**, 5893 (1990).
42. C.J. Wu and E.A. Carter. J. Phys. Chem. **95**, 8352 (1991).
43. D.R. Lide, Jr., and D. Christensen. J. Chem. Phys. **35**, 1374 (1961).
44. David R. Lide, Jr., and D.E. Mann. J. Chem. Phys. **27**, 868 (1957).
45. K.M. Ervin, S. Gronert, S.E. Barlow, M.K. Gillis, A.G. Harrison, V.M. Bierbaum, C.H. Depuy, W.C. Lineberger, and G.B. Ellison. J. Am. Chem. Soc. **112**, 5750 (1990).
46. H. Shiromaru, Y. Achiba, K. Kimura, and Y.T. Lee. J. Phys. Chem. **91**, 17 (1987).
47. E.M. Evleth and E. Kassab. Chem. Phys. Lett. **131**, 475 (1986).
48. C.J. Cobos and J. Troe. J. Chem. Phys. **83**, 1010 (1985).
49. S.C. King, J.F. LeBlanc, and P.D. Pacey. Chem. Phys. **123**, 329 (1988).
50. H. Eyring, J. Walter, and G.E. Kimball. Quantum chemistry. Wiley, New York. 1944.

Can. J. Chem. Downloaded from www.nrcresearchpress.com by EESC ESCOLA DE ENGENHARIA on 09/08/12
For personal use only.

Contribution à l'étude du polymorphisme de quelques métallothionéines par chromatographie liquide de haute performance

GUY BORDIN,[1] FERNANDO CORDEIRO RAPOSO ET ADELA-ROSA RODRIGUEZ

Commission des Communautés Européennes, Centre Commun de Recherche, Institut des Matériaux et Mesures de Référence, Retieseweg, B-2440 Geel, Belgique

Reçu le 19 octobre 1992

GUY BORDIN, FERNANDO CORDEIRO RAPOSO et ADELA-ROSA RODRIGUEZ. Can. J. Chem. **72**, 1238 (1994).

Quatre métallothionéines commerciales extraites de foie de lapin (RL, RL I, RL II) et de rein de cheval (HK) ont été étudiées par chromatographie d'exclusion stérique et sur phase non-polaire, afin de caractériser leur polymorphisme. Les isoformes sont détectées en UV à 250 nm. Les séparations par exclusion stérique montrent que les métallothionéines sont partiellement dimérisées, avec des proportions molaires de dimères variant de 5% pour HK à 15% pour RL II. Par chromatographie sur phase non-polaire, on montre que RL est composée de quatre isoformes dominantes, RL I de deux, RL II de trois et HK de deux. Pour la série RL, RL I et RL II, une attribution des pics est proposée. Les résultats des deux méthodes convergent pour estimer que RL est constituée de 20 à 30% de RL I et de 70 à 80% de RL II.

GUY BORDIN, FERNANDO CORDEIRO RAPOSO, and ADELA-ROSA RODRIGUEZ. Can. J. Chem. **72**, 1238 (1994).

Four commercially available metallothioneins from rabbit liver (RL, RL I, RL II) and from horse kidney (HK) have been studied by size exclusion chromatography and by reverse-phase chromatography, to characterize their polymorphism. The isoforms are detected by UV at 250 nm. Separations by size exclusion show that the metallothioneins are partially dimerized, with molar rates of dimer ranging from 5% for HK to 15% for RL II. The four chromatograms obtained by reverse phase exhibit a different morphology: RL separates in four main isoforms, RL I into two, RL II into three, and HK into two. An attribution of the various peaks for the RL, RL I, and RL II series is proposed. The comparable results obtained by the two methods allow us to estimate that RL is composed of 20–30% RL I and 70–80% of RL II.

Introduction

Les métallothionéines (MT) constituent une famille de métalloprotéines originales. Un poids moléculaire relativement bas, une proportion élevée de cystéine (≈30%), l'absence d'acides aminés aromatiques et la présence permanente de cations métalliques complexés (essentiellement cadmium, zinc et (ou) cuivre selon l'origine des MT) dont la teneur totale varie peu sont les éléments structuraux qui caractérisent ces protéines atypiques (1). La distribution des 20 résidus cystéinyles sur les 61 acides aminés que compte une chaîne métallothionéinique est invariante quelle que soit l'origine des MT, au moins chez les mammifères (2), avec 7 séquences Cys-X-Cys, où X est un amino-acide autre que la cystéine. Les caractéristiques optiques traduisent parfaitement l'existence de liaisons entre les atomes de soufre des cystéines et les cations métalliques (de 6 à 7 atomes par gramme de métal par mole de MT). Les 20 thiolates participent ainsi à la chélation des cations dans un rapport global soufre/métal de 3/1 environ (3, 4). Découvertes en 1957 par Margoshes et Vallee (5) dans le cortex rénal du cheval, des MT ont été identifiées depuis cette époque chez de très nombreuses espèces animales dont l'homme (6) et la moule *Mytilus edulis* (7), chez divers microorganismes comme l'ascomycète *Neurospora crassa* (8) et même chez certaines plantes dont la tomate (9). Il est donc acceptable d'envisager une présence ubiquiste des métallothionéines dans le monde vivant.

Au cours des 15 dernières années, les connaissances sur la structure chimique et sur les fonctions biochimiques des MT ont fortement progressé. On a par exemple pu mettre en évidence le fait que certaines MT existent sous plusieurs isoformes (isométallothionéines, isoMT), ce polymorphisme provenant d'une variation de structure primaire par substitution de 1 à 15 acides aminés survenue au cours de l'évolution des espèces (10). Le nombre d'isoformes d'une MT pourra donc tout naturellement dépendre de l'espèce considérée. Kojima et al. (11) parlent d'au moins quatre isoMT chez le cheval (foie et rein), Klauser et al. (12) également d'au moins quatre chez le lapin (foie), alors que Hunziker et Kägi (13) identifient cinq isoformes humaines (foie) et Richards et Steele (14) en dénombrent trois chez le porc (foie et rein) et deux chez le rat (foie).

Cependant, au-delà de cette variabilité «naturelle» parfois importante du nombre d'isométallothionéines, des écarts d'ordre méthodologique divisent toujours les auteurs. Les méthodes classiquement employées pour séparer les isoMT sont celles basées sur les différences de charges électriques induites par les variations de structure primaire : électrophorèse, chromatographie d'échange d'ions (15). Mais une substitution de quelques amino-acides n'induira pas toujours une différence de charges électriques telle qu'elle puisse permettre une séparation efficace des isoformes (10). Cette limitation semble toutefois pouvoir être levée par l'utilisation d'une autre technique chromatographique, la chromatographie liquide sur phase non-polaire. Elle conduit généralement à de bien meilleures résolutions et permet de montrer la présence d'isoformes supplémentaires non détectées par les méthodes «classiques» (12, 16). Par exemple, Richards et Steele (14) identifient deux isoMT dans le cytosol de foie de porc par échange d'ions (DEAE-Séphadex A 25), mais en isolent trois sur une colonne de phase non-polaire (RP C_{18}). Enfin, l'emploi d'une même méthode de séparation ne constitue pas encore à ce jour une garantie de similitude de résultats. Bien qu'ils utilisent des méthodologies très voisines (même type de colonne, mêmes solvants d'élution) pour étudier la MT extraite du rein de cheval, Richards et Steele (14) et van Beek et Baars (17) n'aboutissent à des résultats que difficilement comparables. Au-delà du nombre de pics observés (respectivement sept et trois), les chromatogrammes présentent des morphologies fort différentes. Les conclusions ne peuvent donc qu'être partielles.

Les divergences sur l'existence voire sur la possibilité d'existence de formes dimères et (ou) polymères de MT sont également importantes. En réalité, fort peu de travaux font men-

[1]Auteur à qui adresser toute correspondance. Téléphone : 32-14-571211. Télécopieur : 32-14584273. Télex : 33589 EURAT B.

Can. J. Chem. Downloaded from www.nrcresearchpress.com by EESC ESCOLA DE ENGENHARIA on 09/08/12
For personal use only.

Can. J. Chem. Downloaded from www.nrcresearchpress.com by EESC ESCOLA DE ENGENHARIA on 09/08/12
For personal use only.

TABLEAU 1. Concentrations en cadmium et en zinc de chaque métallothionéine

MT	Cd (10^{-2}) (mol g^{-1})	Zn (10^{-2}) (mol g^{-1})	Cd + Zn (10^{-2}) (mol g^{-1})
RL – M 7641 lot 20H9650	74,01	20,34	94,35
RL I – M 5267 lot 90H9600	62,72	17,44	80,16
RL II – M 5392 lot 79F9510	64,14	15,30	79,44
HK – M 4766 lot 41H9505	44,12	26,00	70,12

tion de MT dimérisées et encore moins de formes polymérisées. En 1977, Webb et Etienne (18) observent dans des MT extraites de foie de rat et de lapin qu'une petite proportion du cadmium apparaît associée à des composés protéiniques de poids moléculaires supérieurs — non déterminés — à ceux des MT. Ils pensent que ces composés sont des polymères de MT, formés par des liaisons S—S intermoléculaires. Suzuki et Yamamura (19) suggèrent également la présence dans le foie de lapin de dimères de MT dont les liaisons S—S peuvent être rompues sous l'action d'un agent réducteur. Cet important travail ne présente cependant aucun aspect quantitatif. Langston et Zhou (20) identifient chez le bivalve marin *Littorina littorea* deux métalloprotéines Cd-BP_I et Cd-BP_{II} aux caractéristiques semblables à celles des MT et dont les poids moléculaires (PM) sont d'un rapport 2. Ils envisagent ainsi la possibilité que l'un des composés (PM = 20 000 D) soit la forme dimère de l'autre (PM = 10 000 D), mais n'avancent aucun argument. On pourra encore citer Suzuki et al. (16) qui, en 1983, font mention, sans plus de précision, de la présence de MT dimérisées dans le foie de caille du Japon et de la grenouille *Xenopus laevis* mais de leur absence chez le rat (foie et rein).

Considérant tous ces résultats parfois contradictoires, il nous a paru nécessaire d'entreprendre une étude chromatographique systématique des seules MT actuellement disponibles, celles commercialisées par Sigma et que certains auteurs utilisent déjà comme «références» sans que toutes leurs caractéristiques soient encore bien connues. Pour ce travail, deux types de séparation ont été utilisés, la chromatographie d'exclusion stérique et celle sur phase non-polaire. De nouvelles caractéristiques de ces MT sont ainsi révélées : proportion de forme dimère, nombre d'isoformes dominantes.

Matériel et méthodes

Echantillons et réactifs

Les quatre MT étudiées proviennent de la firme Sigma (Saint Louis, EUA) et sont extraites soit de foie de lapin (RL lot 20H9650, RL I lot 90H9600 et RL II lot 79F9515) soit de rein de cheval (HK lot 41H9505). RL I et RL II sont les isoformes de RL obtenues par séparation «classique» (échange anionique). Leurs concentrations métalliques (Cd et Zn) figurent dans le tableau 1. Les solutions mères de MT (1000 mg L^{-1}) sont préparées dans des solutions tampon de phosphate de sodium (voir ci-dessous) et conservées à 4°C. Eau (Alltech) et acétonitrile (Merck) sont de qualité chromatographique, les sels minéraux étant «pro analisi».

Appareillage et mode opératoire

Le système chromatographique (Kontron, Zürich, Suisse) se compose d'une pompe HPLC 420, d'un mélangeur de solvants GF 425, d'un injecteur automatique HPLC 360 avec une boucle d'injection de 100 μL et d'un détecteur UV 430 à double longueur d'onde. L'ensemble des opérations, ainsi que le traitement des données (intégration des pics) sont contrôlés par le système informatique Data System 450-MT.

Exclusion stérique : élution isocratique sur une colonne Bio-Sil SEC 125 (300 × 7,8 mm, Bio-Rad) avec une solution tampon de phosphate (Na_2HPO_4 0,15 M, NaH_2PO_4 0,04 M, NaCl 0,15 M, pH = 7,15) à un débit de 0,5 mL min^{-1}.

Phase non-polaire : élution sur une colonne Bio-Sil C_{18} HL 90-5S (150 × 4,6 mm, silice à greffes octadécyle C_{18}, Bio-Rad) en mode binaire linéaire A–B (A : tampon phosphate Na_2HPO_4 0,01 M, pH = 7,0; B : acétonitrile), 3–20% B en 30 min à un débit de 1,3 mL min^{-1}.

Les phases mobiles sont filtrées sur des membranes Millipore de 0,22 μm et continuellement dégazées à l'hélium. Les pics sont détectés à 250 nm (absorbance due aux thiolates métalliques Cd-S et Zn-S) et à 280 nm (détection «négative» : absorbance faible due à l'absence d'acides aminés aromatiques). Sauf spécification, les résultats exposés ci-dessous se rapportent à la détection à 250 nm. Toutes les expériences décrites sont réalisées à température ambiente (≈20°C).

Les concentrations métalliques sont déterminées par spectrométrie d'absorption atomique sur un Perkin Elmer 5000, muni d'un four de graphite HGA-400 et d'un échantillonneur automatique AS-40.

Résultats et discussion

Chromatographie d'exclusion stérique

Afin de déterminer le poids moléculaire (PM) de chaque MT, la colonne a d'abord été calibrée au moyen d'un mélange standard (Bio-Rad) contenant les protéines suivantes : thyroglobuline (PM = 670 000 D, t_R = 11,28 min), IgG (PM = 158 000 D, t_R = 12,62 min), ovalbumine (PM = 44 000 D, t_R = 14,63 min), myoglobuline (PM = 17 000 D, t_R = 16,98 min) et cyanocobalamine (PM = 1350 D, t_R = 21,54 min). La répétabilité de la séparation a été vérifiée en injectant cinq fois de suite le mélange de protéines. Pour chacun des temps de rétention, le coéfficient de variation (c.v.) est inférieur à 1,5%. La résolution (R) de chaque pic est excellente ($1,2 < R < 3,3$). On a obtenu la droite de calibration suivante :

$$\ln PM = 19{,}48 - 0{,}58 t_R \quad (r = -0{,}991)$$

où t_R est le temps de rétention en minutes, pour un intervalle d'application en PM s'étendant de 1000 à 700 000 D. Chaque métallothionéine a ensuite été chromatographiée cinq fois. Les chromatogrammes obtenus sont montrés sur la figure 1. Leur morphologie est semblable avec un pic dominant élué vers 17,60 min précédé d'un pic d'absorbance beaucoup plus faible élué vers 16,40 min (c.v. < 1%). Le tableau 2 rassemble les temps de rétention des deux pics et les poids moléculaires correspondants pour chacune des MT. Les pics 1 et 2 (pic principal) correspondent respectivement à l'élution de molécules de PM de 21 000 à 22 000 D et 11 000 D (c.v. < 6%).

Ce poids moléculaire moyen de MT d'environ 11 000 D s'accorde parfaitement aux valeurs classiquement déterminées par cette technique chromatographique, l'écart avec la valeur obtenue à partir de la structure primaire (6000–7000 D) étant attribué à la forme non globulaire de cette métalloprotéine (21). Le petit pic, PM double de celui des MT, pourrait donc provenir de l'élution des dimères des MT formés par des liaisons S—S intermoléculaires. Ces produits étant purifiés, cette hypothèse seule paraît envisageable.

L'échange thiol–disulfure est un mécanisme chimique ayant une fonction fondamentale au niveau biologique (22) :

Can. J. Chem. Downloaded from www.nrcresearchpress.com by EESC ESCOLA DE ENGENHARIA on 09/08/12
For personal use only.

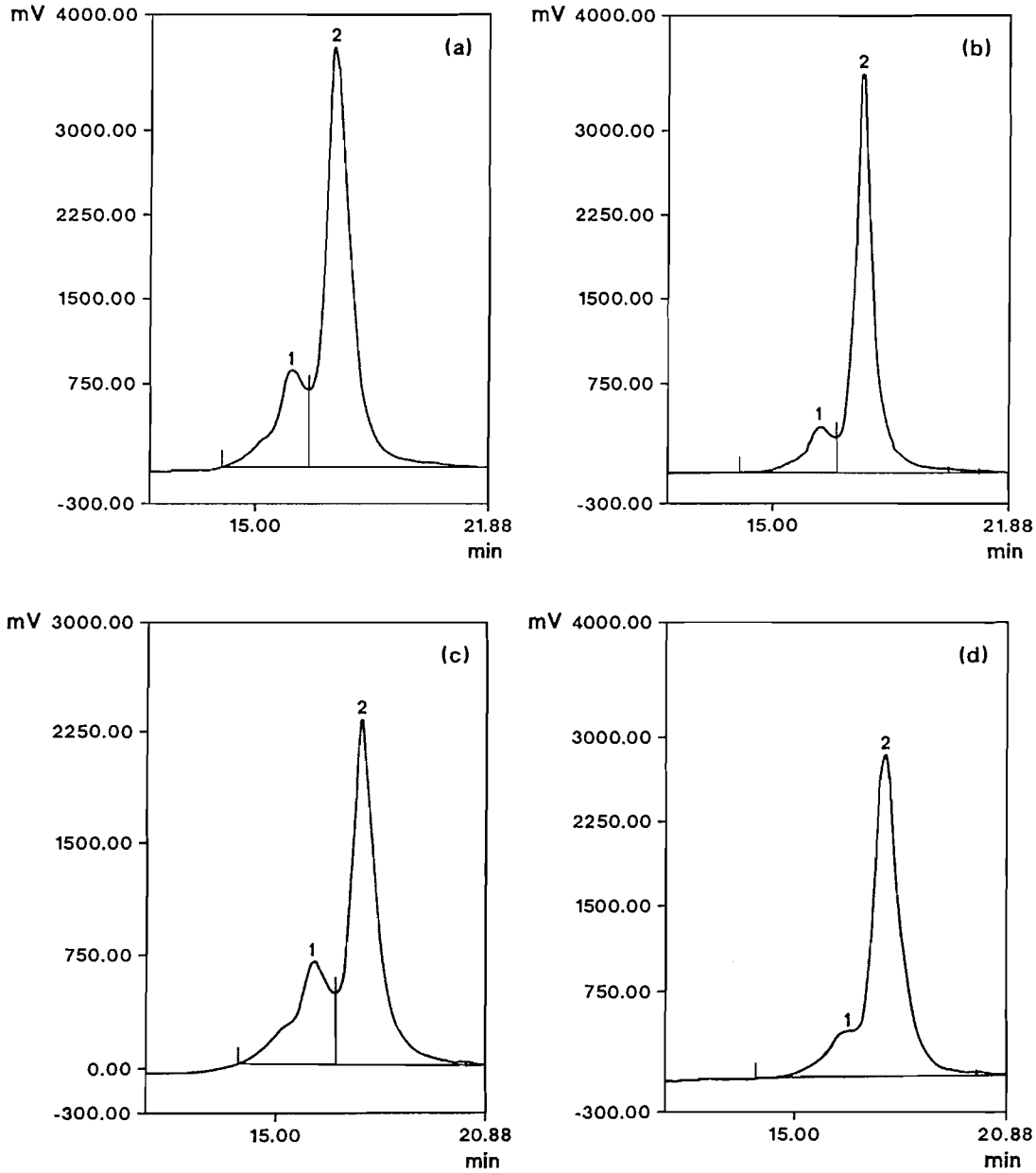

FIG. 1. Profils d'élution des métallothionéines en exclusion stérique. Détection UV à 250 nm (conditions expérimentales dans le texte). (*a*) RL $C_{MT} = 200$ mg L^{-1} ($1{,}83 \times 10^{-5}$ M); (*b*) RL I $C_{MT} = 150$ mg L^{-1} ($1{,}39 \times 10^{-5}$ M); (*c*) RL II $C_{MT} = 150$ mg L^{-1} ($1{,}33 \times 10^{-5}$ M); (*d*) HK $C_{MT} = 150$ mg L^{-1} ($1{,}40 \times 10^{-5}$ M). Unité en ordonnée : 1000 mV sur l'enregistreur correspondent à 0,005 unités d'absorbance pleine échelle.

$$RSH + XSSX \rightarrow RSSX + XSH$$

$$RSH + RSSX \rightarrow RSSR + XSH$$

Cette réaction est ainsi classiquement utilisée pour réduire les liaisons S—S protéiniques. Les dimères de MT devraient donc être réduits par un thiol tel que le 2-mercaptoéthanol. La figure 2 montre le chromatogramme de RL avant (2*a*) et après (2*b*) l'addition de mercaptoéthanol (0,5% v/v, 80°C pendant 10 min). On observe effectivement une quasi-disparition du premier pic parallèlement à une augmentation du pic principal. Un résultat identique est obtenu pour les trois autres MT. Le taux moyen de récupération (aire du pic après réduction/somme des aires des deux pics avant réduction) est de 102% (±4%, n = 13), pour l'ensemble des quatre MT. Il y a donc une réponse spectrophotométrique identique des deux espèces. L'excès de réducteur (PM = 78,13) est logiquement élué quelques minutes après la MT.

Chaque MT a été chromatographiée une dizaine de fois à des concentrations (C_{MT}) comprises entre 10 et 200 mg L^{-1} afin d'étudier d'une part, la linéarité entre le signal UV et la concentration et d'autre part, l'évolution du rapport entre les deux pics. Pour chaque MT, on a étudié la linéarité de l'aire du premier pic (S_1) et de celle du second pic (S_2) en fonction de C_{MT} en mg L^{-1}. Les droites ainsi obtenues ($r > 0{,}996$) sont caractérisées par les pentes rassemblées dans le tableau 3. Deux importantes conclusions peuvent déjà être tirées. Premièrement, pour chaque MT, l'excellence des corrélations de S_1 et $S_2 = f(C_{MT})$ montrent que le taux de dimères est indépendant de la concentration totale en MT. Deuxièmement, les différences qui existent entre

TABLEAU 2. Temps de rétention (t_R) et poids moléculaires (PM) des deux espèces correspondant aux deux pics obtenus par chromatographie d'exclusion stérique des MT

	Pic 1		Pic 2	
MT	t_R (min)	PM (D)	t_R (min)	PM (D)
RL	16,40 ± 0,05	21 380 ± 700	17,55 ± 0,02	10 940 ± 400
RL I	16,41 ± 0,02	21 160 ± 700	17,57 ± 0,02	10 830 ± 400
RL II	16,33 ± 0,50	22 250 ± 1100	17,50 ± 0,05	11 270 ± 700
HK	16,41 ± 0,02	21 160 ± 500	17,59 ± 0,04	10 700 ± 300

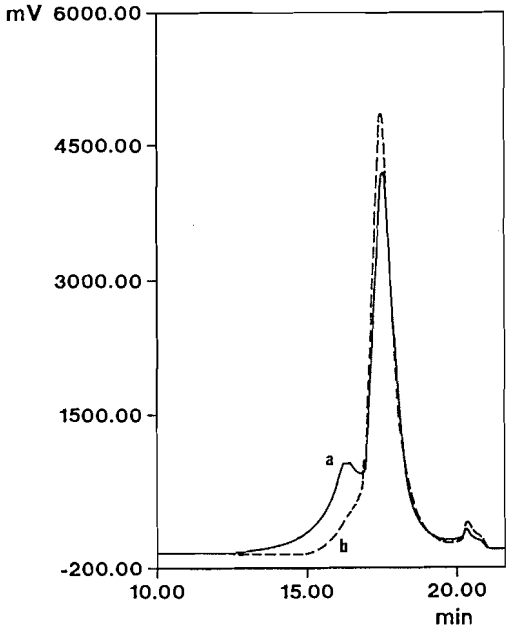

FIG. 2. Chromatogramme de RL en exclusion stérique avant (*a* : —) et après (*b* : ---) addition de 2-mercaptoéthanol. C_{MT} = 200 mg L^{-1} (1,83 × 10^{-5} M). Unité d'ordonnée : cf. figure 1.

les rapports de pentes ($S_2 = f(C_{MT})/S_1 = f(C_{MT})$) indiquent clairement que le taux de dimères varie d'une MT à l'autre : plus ce rapport sera élevé, plus le taux de dimérisation de la MT considérée sera faible. On peut donc déjà établir la séquence décroissante suivante pour les taux de dimères : RL II > RL > RL I > HK.

Estimation du pourcentage molaire de dimères : la formation du dimère (D) à partir du monomère (M) de chaque MT résulte de la réaction (simplifiée) 2M ⇌ D. Pour une concentration molaire totale en MT, nous avons $C_{MT} = C_M + 2C_D$, où C_M est la concentration molaire en monomères et C_D celle en dimères. Pour chaque chromatogramme, on peut exprimer l'aire des pics comme suit : $S_1 = a_D \cdot C_D$ et $S_2 = a_M \cdot C_M$, où a_D et a_M sont les adsorptivités molaires respectives du dimère et du monomère. Par ailleurs, on peut poser $a_D = 2a_M$, pour tenir compte du fait que la réponse du détecteur est la même pour le monomère et pour le dimère. De toutes ces équations, on tire $C_M = 2C_D(S_2/S_1)$. À titre d'exemple, le tableau 4 rassemble les détails de calcul de S_2/S_1, de C_D, de C_M et du pourcentage de dimères pour la métallothionéine RL. On constate une très bonne reproductibilité du rapport S_2/S_1 et de la proportion de dimères (c.v. = 3,5%).

Le tableau 5 regroupe les valeurs moyennes des pourcentages molaires de dimères de chaque MT. On constate bien que, d'une MT à l'autre, la proportion molaire de protéine dimérisée est variable, allant de 5% pour HK à environ 15% pour RL II. On

TABLEAU 3. Pentes des droites «aire du premier pic S_1» et «aire du second pic S_2» en fonction des concentrations totales en MT (en mg L^{-1})

	Pentes (mV min mg^{-1} L)		
MT	$S_1 = f(C_{MT})$	$S_2 = f(C_{MT})$	Rp[a]
RL	4,84 ± 0,52	16,88 ± 0,69	3,49
RL I	2,56 ± 0,18	14,78 ± 2,56	5,77
RL II	4,64 ± 0,50	13,50 ± 1,39	2,91
HK	2,44 ± 0,89	17,32 ± 1,65	7,10

[a]Rp est le rapport des pentes $S_2 = f(C_{MT})/S_1 = f(C_{MT})$.

notera également que RL II a un taux de dimères double de celui de RL I, RL étant dans une situation intermédiaire. La nature (structure primaire) d'une MT intervient donc dans son degré de dimérisation.

De ce modèle, il découle également que la pente de la droite $S_1 = f(C_D)$ devrait être double de celle de $S_2 = f(C_M)$. Les pentes de ces droites ($r > 0,997$) sont rassemblées dans le tableau 6. Pour chaque MT, le rapport des pentes évoqué est bien égal à 2, confirmant ainsi le modèle proposé.

L'examen des absorbances à 280 nm renforce ces conclusions. Dans cette zone, contrairement aux disulfures (22), les thiolates n'absorbent pratiquement plus. Dans notre cas, bien que faible, cette absorbance reste mesurable pour chaque pic. Le tableau 7 regroupe les rapports S_2/S_1 à 250 et à 280 nm des quatre MT. Celles ayant les plus faibles taux de dimères (RL I et HK) montrent la plus grande diminution de ce rapport. On en déduit que la réduction d'absorbance entre 250 et 280 nm affecte beaucoup plus le second pic (monomère) que le premier (dimère). La présence de liaison(s) S—S explique donc probablement cette absorbance relativement plus grande du premier pic à 280 nm.

Tous ces éléments militent donc pour la thèse de la dimérisation partielle des MT étudiées.

Étant donné que l'absorbance à 250 nm est due aux thiolates métalliques Cd-S et Zn-S, il nous a semblé intéressant de considérer également S_1 et S_2 en fonction de (Cd + Zn). Les pentes correspondantes sont rassemblées dans le tableau 8. Il existe un écart non négligeable entre les pentes de la série RL, RL I, RL II d'un côté et celle de HK de l'autre, ceci étant probablement explicable par les caractéristiques métalliques différentes de HK. Par rapport aux trois MT RL, elle a en effet une concentration totale en métal plus faible tout en ayant une proportion de Zn assez supérieure (tableau 1). Tout ceci s'accorde bien avec les résultats des études spectrophotométriques menées sur ces mêmes MT (23).

Nous avons déjà mentionné que la RL (13,1% de dimères) est en réalité un «mélange» des deux formes RL I (7,5% de dimères)

Can. J. Chem. Downloaded from www.nrcresearchpress.com by ESC ESCOLA DE ENGENHARIA on 09/08/12
For personal use only.

Can. J. Chem. Downloaded from www.nrcresearchpress.com by EESC ESCOLA DE ENGENHARIA on 09/08/12
For personal use only.

TABLEAU 4. Rapport des aires des deux pics (S_2/S_1) à 250 nm, concentrations en dimères (C_D) et en monomères (C_M) et pourcentage molaire de dimères correspondants, calculés pour différentes concentrations totales de RL

C_{MT} (10^{-5} M)	S_2/S_1	C_D (10^{-6} M)	C_M (10^{-5} M)	Dimère (% molaire)
1,833	3,46	2,055	1,422	12,6
1,833	3,41	2,078	1,417	12,8
1,833	3,10	2,235	1,386	13,9
1,833	3,21	2,177	1,398	13,4
1,371	3,38	1,565	1,058	12,8
0,914	3,34	1,053	0,703	13,0
0,731	3,32	0,846	0,562	13,1
0,640	3,01	0,798	0,480	14,2
0,457	3,38	0,522	0,353	12,9
0,183	2,93	0,233	0,136	14,6
0,137	3,69	0,146	0,108	11,9
0,091	3,52	0,101	0,071	12,4
0,091	3,44	0,103	0,071	12,7
Moyenne	3,32 ± 0,17			13,1 ± 0,4

TABLEAU 5. Pourcentage molaire de dimères de chaque MT

MT	% de dimère	*n*
RL	13,1 ± 0,4	13
RL I	7,5 ± 0,5	8
RL II	15,3 ± 0,8	12
HK	5,1 ± 0,6	8

TABLEAU 6. Pentes des droites «aire du premier pic S_1» en fonction de la concentration en dimères, «aire du second pic S_2» en fonction de la concentration en monomères et rapports de pentes (dimères/monomères) correspondants

	Pentes de $S = f(C)$ ($\times 10^8$) (mV min M^{-1})		
MT	$S_1 = f(C_D)$	$S_2 = f(C_M)$	Rp[a]
RL	4,75 ± 0,33	2,37 ± 0,13	2,00
RL I	3,73 ± 0,38	1,87 ± 0,21	1,99
RL II	4,07 ± 0,42	2,02 ± 0,25	2,01
HK	4,26 ± 0,35	2,12 ± 0,22	2,01

[a]Rp est le rapport de pentes $S_1 = f(C_D)/S_2 = f(C_M)$.

TABLEAU 7. Variation (δ) de rapport des aires des deux pics (S_2/S_1) de 250 à 280 nm pour chaque MT

MT	S_2/S_1 (250 nm)	S_2/S_1 (280 nm)	δ (%)	*n*
RL	3,32 ± 0,17	1,90 ± 0,50	−43	13
RL I	6,24 ± 0,44	2,55 ± 3,35	−59	8
RL II	2,77 ± 0,20	1,39 ± 0,11	−50	12
HK	8,93 ± 1,35	2,76 ± 0,31	−69	8

et RL II (15,3% de dimères). Les taux moyens de dimères que nous venons de déterminer doivent donc permettre de calculer la proportion respective de chacune des deux isoformes (x% de RL I et y% de RL II) de RL à l'aide du système suivant :

$$x \cdot 7{,}5 + y \cdot 15{,}3 = 13{,}1$$

$$x + y = 1$$

TABLEAU 8. Pentes des droites «aire du premier pic S_1» et «aire du second pic S_2» en fonction de la somme des concentrations métalliques de chaque MT

	Pentes (mV min M^{-1}) ($\times 10^6$)	
MT	$S_1 = f(\text{Cd} + \text{Zn})$	$S_2 = f(\text{Cd} + \text{Zn})$
RL	5,11 ± 0,55	17,86 ± 0,72
RL I	3,19 ± 0,21	18,42 ± 2,28
RL II	5,83 ± 0,38	17,00 ± 1,14
HK	3,47 ± 1,33	24,64 ± 2,49

On obtient ainsi $x = 28\%$ (±4%) de RL I et $y = 72\%$ (±11%) de RL II.

En 1982, Geller et Winge (24), sur la base des travaux de Kägi et Vallee (3, 4) et de Tsunoo et al. (25) entre autres, écrivaient que les métallothionéines ne contenant pas de cuivre, c'est-à-dire celles induites par Cd^{2+} ou Zn^{2+}, ne contenaient que des cystéines réduites (sous forme de thiolates de cadmium et (ou) de zinc). Nos résultats semblent donc devoir infirmer cette assertion. Il a effectivement bien été montré que la présence de cuivre, in vivo ou in vitro, conduisait à la formation de liaisons S—S intramoléculaires (16, 26). Cependant, Webb et Etienne (18) expliquent la présence de MT (extraites de foie de lapin et de rat) polymérisées par la perte partielle de Zn^{2+}, moins fortement complexé que Cd^{2+} (3), suivie de la formation de liaisons S—S intermoléculaires. Des auteurs comme Minkel et al. (27) considèrent que la polymérisation des MT ne serait que le résultat de l'oxydation des MT survenue au cours de leur extraction. Or, plusieurs auteurs travaillant sur les MT extraites de mollusques marins comme l'huître *Crassostrea virginica* (28, 29) ont pu montrer que l'origine écologique (écosystème) avait une influence sur la présence ou non de forme dimère : les huîtres de Caroline du Nord (EUA) possèdent les deux formes MT 10 et MT 20 (nomenclature faisant référence aux poids moléculaires respectifs de 10 et 20 kD), celles provenant de la Baie de Chesapeake ou de zones plus nordiques d'Amérique du Nord, soumises au même procédé d'extraction, ne possédant que la forme monomère MT 10. La forme dimère n'est donc assurément pas le résultat du mode opératoire utilisé pour l'extraction des MT.

Can. J. Chem. Downloaded from www.nrcresearchpress.com by EESC ESCOLA DE ENGENHARIA on 09/08/12
For personal use only.

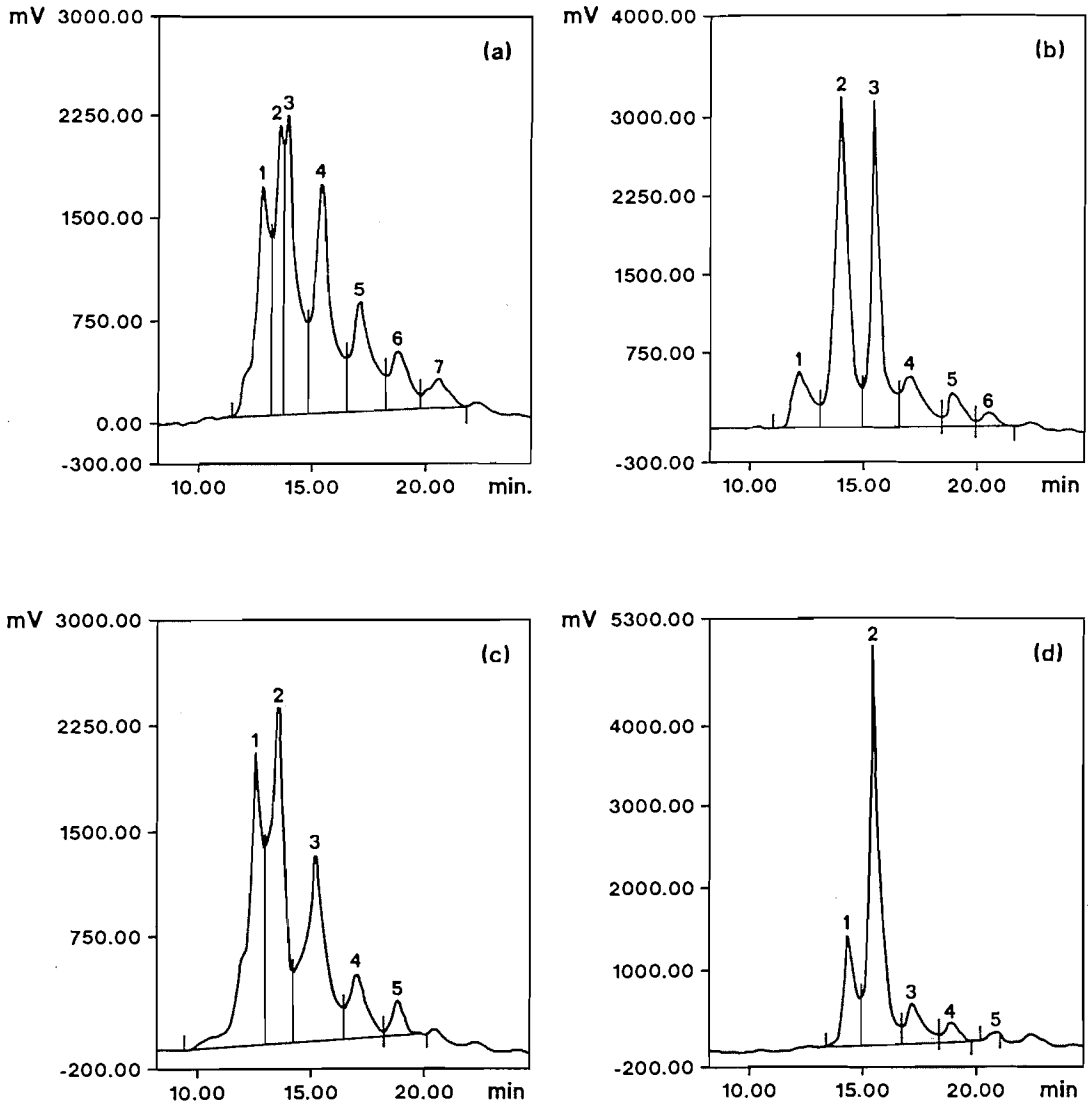

FIG. 3. Profils d'élution des métallothionéines en chromatographie sur phase non-polaire. Détection UV à 250 nm (conditions expérimentales dans le texte). (*a*) RL C_{MT} = 130 mg L^{-1} (1,19 × 10^{-5} M); (*b*) RL I C_{MT} = 100 mg L^{-1} (9,23 × 10^{-6} M); (*c*) RL II C_{MT} = 100 mg L^{-1} (8,87 × 10^{-6} M); (*d*) HK C_{MT} = 100 mg L^{-1} (9,35 × 10^{-6} M). Unité d'ordonnée : cf. figure 1.

Chromatographie sur phase non-polaire

Les chromatogrammes-types obtenus pour chaque MT sont représentés sur la figure 3. Bien que les morphologies soient différentes, on peut néanmoins dégager plusieurs caractéristiques communes : (*i*) tous les pics sont élués entre 12 et 21 min, soit par une phase mobile contenant entre 10 et 15% d'acétonitrile; (*ii*) les pics sont toujours très bien séparés ($R > 1$, sauf pour les pics 2 et 3 de RL où $R \approx 0,7$, figure 3*a*); (*iii*) la reproductibilité des temps de rétention de chaque pic est excellente (c.v. < 1% pour 10–15 séparations à différentes concentrations entre 50 et 180 mg L^{-1}), de même que celle du signal UV (somme des aires des pics ΣS) (c.v. compris entre 1 et 7%).

Considérons à présent chaque chromatogramme séparément. La RL se sépare en sept pics, dont quatre dominants et trois de moindre importance. La morphologie de RL I est très différente et relativement simple : deux pics largement dominants entourés de trois à quatre petits pics. RL II se compose de trois isoformes principales et de deux à trois autres formes de moindre importance quantitative. Enfin, la HK montre un pic prépondérant (pic n°2 de la figure 3*d*), un pic secondaire (pic n°1) et deux à trois pics mineurs.

Livrons-nous à une étude comparative des quatre chromatogrammes. Le tableau 9 rassemble les temps de rétention des principaux pics de chaque MT. On peut en tirer les conclusions suivantes : (*i*) un seul pic est «commun» aux quatre MT, celui élué à 15,30 minutes, soit par une phase mobile contenant 11,7% d'acétonitrile; (*ii*) le pic secondaire de HK (à 14,30 min) est propre à cette molécule : on ne le retrouve pas dans la série RL; (*iii*) la superposition des chromatogrammes de RL I et de RL II conduit, en termes de nombre de pics et de temps de rétention, à un nouveau chromatogramme qualitativement semblable à celui de RL (figure 4). Il semble donc probable que les deux premiers pics de RL soient attribuables à RL II, que le troisième le soit à RL I et que le quatrième provienne d'une double contribution.

L'ordre d'élution (valeurs des facteurs de capacité k') des différentes isoformes dépend de leur composition en acides aminés. Le caractère plus ou moins hydrophobe de chaque amino-acide détermine son facteur de capacité sur une colonne de phase non-polaire (30). Nos résultats montrent une élution plus rapide de RL II que de RL I, celle-ci devant donc être plus hydrophobe. En 1979, Kimura et al. (31) déterminaient la struc-

TABLEAU 9. Temps de rétention des principaux pics de chaque MT chromatographiée sur phase non-polaire. La structure du tableau schématise la position relative des différents pics de chaque MT

MT	t_R des principaux pics (min)				
RL	12,85	13,59	13,91		15,36
RL I			13,74		15,28
RL II	12,82	13,47			15,28
HK				14,30	15,30

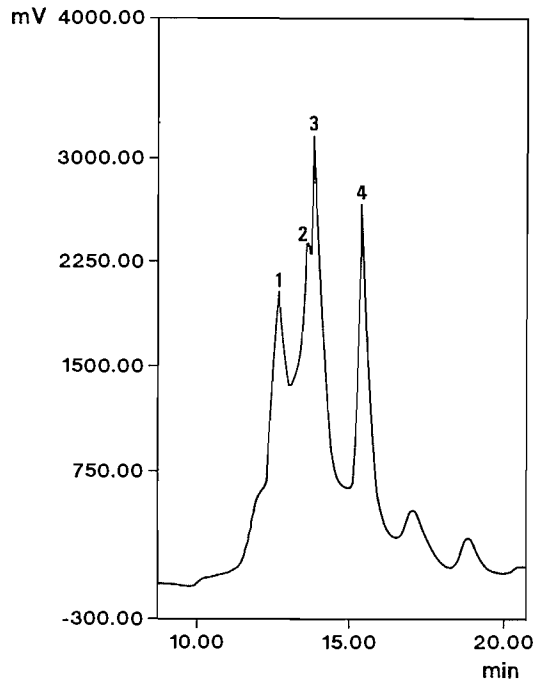

FIG. 4. Superposition des chromatogrammes en phase non-polaire de RL I et de RL II (C_{MT} = 100 mg L^{-1}). A comparer *qualitativement* à la figure 3*a*. Unité d'ordonnée : cf figure 1.

ture primaire des formes I et II de la RL. La principale différence réside en la présence dans RL I d'arginine et parfois de leucine, deux acides aminés plus hydrophobes que leurs substituts dans RL II comme la sérine. La RL I est séparée en deux pics principaux (figure 3*b*). Or, toujours selon les mêmes auteurs, il existerait une variante de cette MT dans laquelle une sérine serait substituée par une leucine, ce qui devrait induire une différence notable de comportement chromatographique. Il a déjà été montré (32, 33) que les facteurs de capacité de peptides contenant jusqu'à une vingtaine d'acides aminés, pouvaient se calculer en additionnant les facteurs de capacité des acides aminés constitutifs. Au-delà de 20 amino-acides, ce calcul devient plus spéculatif, le comportement chromatographique des longues chaînes peptidiques dépendant également de leurs structures secondaires et tertiaires. Il peut néanmoins fournir une bonne approximation. Pour tout ce qui suit, nous insistons sur le fait que nous ne procédons qu'à des estimations de l'hydrophobicité relative des différentes isoformes, sachant pertinemment que les échelles d'hydrophobicité d'acides aminés dont nous disposons ont été établies sur des phases non-polaires et avec des phases mobiles différentes des notres.

Par rapport à la structure primaire de RL II, celle de RL I varie de la manière suivante, +1 Glu, +1 Arg, −1 Ser et −1 Ala. Cette variation devrait provoquer, selon les k' d'acides aminés publiés par Grushka et al. (30), ou selon les paramètres d'hydrophobicité déterminés par Parker et al. (34), une augmentation du caractère hydrophobe de RL I, donc de son temps de rétention. C'est bien ce que l'on observe, avec $t_{R\,RL\,I} > t_{R\,RL\,II}$. Si on substitue dans RL I une sérine supplémentaire par une leucine ($t_{R\,Leu} \gg t_{R\,Ser}$), on devrait assister à une nouvelle augmentation du caractère hydrophobe et avoir $t_{R\,RL\,I(Leu)} > t_{R\,RL\,I(Ser)} > t_{R\,RL\,II}$. Sur le chromatogramme de RL I, le premier pic (t_R = 13,74 min) pourrait donc correspondre à la forme «sérine» et le second (t_R = 15,28 min) à la forme «leucine». Cette hypothèse reste naturellement à vérifier. Pour RL II, seule la structure primaire globale est connue. La séparation de RL conduit donc à l'ordre suivant (selon les t_R indiqués dans le tableau 9) : RL II (2 isoformes non identifiées) – RL I_{Ser} – RL I_{Leu}.

Kojima et al. (11) ont publié en 1976 la structure primaire de HK-A et de HK-B, les deux isoMT obtenues par séparation anionique classique de HK. Les compositions moyennes montrent que HK-A auraient deux variantes sérine/leucine. Par rapport à RL I_{Leu}, et en se basant sur les échelles d'hydrophobicité déjà citées (30, 32–34), l'isoforme HK-A_{Leu} (+1 Pro, +3 Gly, +1 Val, +1 Arg, −1 Asp, −2 Ala, −1 Ile, −2 Lys) ne devrait voir son caractère hydrophobe que fort peu varier, ce qui équivaudrait à des temps de rétention très proches. Nos chromatogrammes montrent que le pic principal de HK et celui de RL I_{Leu} ont le même t_R = 15,3 min. On estime également de la même manière que la variante sérine HK-A_{Ser} serait moins hydrophobe que RL I_{Leu} et aurait donc un temps de rétention plus faible que celui de RL I_{Leu} et de HK-A_{Leu}. Cette isoforme HK-A_{Ser} doit donc correspondre au premier pic de HK à 14,3 min. Enfin, on peut également estimer le caractère hydrophobe de HK-B (−1 Pro, +2 Val, +2 Thr, +2 Ala, −2 Gly, +1 Gln, −1 Arg, +1 Lys) comme étant plus faible que celui de HK-A_{Ser}. On devrait alors avoir $t_{R\,HK\text{-}B} < t_{R\,HK\text{-}ASer}$. Soit un pic qui devrait sortir à un t_R < 14,3 min, mais qui est absent de notre chromatogramme. Le lot de HK étudié dans ce travail semble donc correspondre à l'isoforme pure HK-A.

La linéarité de la réponse UV en fonction des concentrations en MT et en métal a été étudiée pour le signal total (ΣS) et pour celui du pic «commun», pic toujours le mieux résolu (S_c, aire du pic commun). Les pentes des droites obtenues (r > 0,991) sont rassemblées dans le tableau 10. Compte tenu des incertitudes et suite au traitement statistique classique effectué, on peut estimer que les pentes «totales» ne diffèrent pas significativement les unes des autres, à l'exception de celle de HK calculée par rapport à la concentration en MT, notablement plus faible. Cette dernière apparaît bien différente des trois RL. Les pentes du pic «commun» $S_c = f(C_{MT})$ et $S_c = f(Cd + Zn)$ varient assez fortement, reflétant la contribution relative de cette isoforme à chacune des MT. HK montre ainsi des pentes nettement plus élevées que celles de la série RL. Ces valeurs de pentes permettent alors de calculer, par rapport aux pentes totales, que les isoformes éluées à 15,30 minutes représentent 70,0% de la HK (c'est à dire 70% de variante «leucine»), 21,1% de la RL, 29,5% de la RL I et 18,8% de la RL II.

Concernant la série MT RL, on déduit de ces chiffres une participation inégale des formes RL I et RL II à la RL globale. Si x et y sont respectivement les proportions de RL I et de RL II dans RL, on peut alors écrire :

$$x \cdot 29{,}5 + y \cdot 18{,}8 = 21{,}1$$

$$x + y = 1$$

Can. J. Chem. Downloaded from www.nrcresearchpress.com by EESC ESCOLA DE ENGENHARIA on 09/08/12
For personal use only.

TABLEAU 10. Pentes des droites «somme des aires des pics ΣS» et «aire du pic commun S_c» de chaque MT séparée sur phase non-polaire, en fonction des concentrations en MT et en métaux

	Pentes (mV min M^{-1}) ($\times 10^7$)			
MT	$\Sigma S = f(C_{MT})$	$S_c = f(C_{MT})$	$\Sigma S = f(Cd + Zn)$	$S_c = f(Cd + Zn)$
RL	38,57 ± 8,25	8,12 ± 1,30	6,28 ± 1,34	1,32 ± 0,21
RL I	40,45 ± 1,95	11,95 ± 0,65	7,78 ± 0,39	2,29 ± 0,13
RL II	43,96 ± 10,91	8,25 ± 1,04	8,52 ± 2,46	1,60 ± 0,21
HK	25,78 ± 6,04	18,31 ± 5,00	5,66 ± 1,33	4,02 ± 1,10

On aboutit ainsi à 21% (±5%) de RL I et à 79% (±14%) de RL II. Ces résultats confirment ceux obtenus précédemment à partir des pourcentages de dimères, À notre connaissance, aucun travail quantitatif de cet ordre n'avait encore, à ce jour, été publié. En 1987, Richards et Steele (14) ne faisaient que mentionner que l'isoforme la plus abondante de la RL était une sous-espèce de la RL II. Plus globalement, travaillant, entre autres, sur les MT-RL et MT-HK, ces mêmes auteurs obtenaient des chromatogrammes fort semblables pour ces deux molécules : deux pics dominants et quatre à cinq pics mineurs. Notre travail montre ainsi que le polymorphisme de la métallothionéine extraite de foie de lapin (RL) est en fait nettement plus complexe. Pour la HK, nos résultats s'apparentent davantage.

Conclusion

L'utilisation de la chromatographie d'exclusion stérique et de la chromatographie sur phase non-polaire avec détection UV nous a permis de mieux caractériser les quatre métallothionéines RL, RL I, RL II extraites du foie de lapin et HK, extraites du rein de cheval. On a ainsi pu montrer que : (*i*) les quatre MT sont partiellement dimérisées (pourcentage molaire de forme dimère : 5–15%); (*ii*) la RL, composée de RL I et RL II séparables par échange d'ions, apparaît constituée de quatre isoformes dominantes, alors que la HK ne se sépare qu'en deux isoformes; (*iii*) RL I et RL II se subdivisent également en deux et trois sous-espèces respectivement; les deux pics de RL I correspondent essentiellement à une substitution sérine/leucine; (*iv*) globalement, RL I et RL II contribuent respectivement pour 20–30% et 70–80% de RL; (*v*) le lot de HK ne semble contenir que la forme HK-A, dont environ 70% de sous-espèce contenant de la leucine.

1. J.H.R. Kägi et M. Nordberg (*Éditeurs*). Metallothionein. Birkhäuser Verlag, Basel. 1979.
2. Y. Kojima et J.H.R. Kägi. Trends Biochem. Sci. **3**, 90 (1978).
3. J.H.R. Kägi et B.L. Vallee. J. Biol. Chem. **235**, 3460 (1960).
4. J.H.R. Kägi et B.L. Vallee. J. Biol. Chem. **236**, 2435 (1961).
5. M. Margoshes et B.L. Vallee. J. Am. Chem. Soc. **79**, 4813 (1957).
6. P. Pulido, J.H.R. Kägi et B.L. Vallee. Biochemistry, **5**, 1768 (1966).
7. F. Noël-Lambot. Experientia, **32**, 324 (1976).
8. K. Lerch. *Dans* Metallothionein. *Édité par* J.H.R. Kägi et M. Nordberg. Birkhäuser Verlag, Basel. 1979. p. 173.
9. M. Bartlof, E. Brennan et C.A. Price. Plant Physiol. **66**, 438 (1980).
10. J.H.R. Kägi, M. Vasák, K. Lerch, D.E.O. Gilg, P. Hunziker, W.R. Berhard et M. Good. Environ. Health Perspect. **54**, 93 (1984).
11. Y. Kojima, C. Berger et J.H.R. Kägi. *Dans* Metallothionein. *Édité par* J.H.R. Kägi et M. Nordberg. Birkhäuser Verlag, Basel. 1979. p. 153.
12. S. Klauser, J.H.R. Kägi et K.J. Wilson. Biochem. J. **209**, 71 (1983).
13. P. Hunziker et J.H.R. Kägi. 15th Meeting of the Federation of European Societies, Bruxelles, Abstracts, 1983. p. 217.
14. M.P. Richards et N.C. Steele. J. Chromatogr. **402**, 243 (1987).
15. M. Nordberg et Y. Kojima. *Dans* Metallothionein. *Édité par* J.H.R. Kägi et M. Nordberg. Birkhäuser Verlag, Basel. 1979. p. 41.
16. K.T. Suzuki, H. Sunaga, Y. Aoki et M. Yamamura. J. Chromatogr. **281**, 159 (1983).
17. H. van Beek et A.J. Baars. At. Spectrosc. **11**, 70 (1990).
18. M. Webb et T. Etienne. Biochem. Pharmacol. **26**, 25 (1977).
19. K.T. Suzuki et M. Yamamura. Biochem. Pharmacol. **29**, 689 (1980).
20. W.J. Langston et M. Zhou. Mar. Biol. **92**, 505 (1986).
21. J.H.R. Kägi, S.R. Himmelhoch, P.D. Whanger, J.L. Bethune et B.L. Vallee. J. Biol. Chem. **249**, 3537 (1974).
22. P.C. Jocelyn. Biochemistry of the SH group. Academic Press, London, 1972.
23. A. Muñoz Piñeiro. Thèse de doctorat, Universidad Complutense de Madrid, 1992.
24. B.L. Geller et D.R. Winge. Arch. Biochem. Biophys. **218**, 109 (1982).
25. H. Tsunoo, K. Kino, H. Nakajima, A. Hata, I.Y. Huang et A. Yoshida. J. Biol. Chem. **253**, 4172 (1978).
26. K.T. Suzuki et T. Maitani. Biochem. J. **199**, 289 (1981).
27. D.T. Minkel, K. Poulsen, S. Wielgus, C.F. Shaw et D.H. Petering. Biochem. J. **191**, 475 (1980).
28. D.W. Engel et M. Brouwer. *Dans* Physiological mechanisms of marine pollutant toxicity. *Édité par* W.B. Vernberg, A. Calabrese, F.P. Thurberg et F.J. Vernberg. Academic Press, New York. 1982. p. 89.
29. G. Roesijadi, S.L. Kielland et P. Klerks. Arch. Biochem. Biophys. **273**, 403 (1989).
30. E. Grushka, S. Levin et C. Gilon. J. Chromatogr. **235**, 401 (1982).
31. M. Kimura, N. Otaki et M. Imano. *Dans* Metallothionein. *Édité par* J.H.R. Kägi et M. Nordberg. Birkhäuser Verlag, Basel. 1979. p. 163.
32. I. Molnár et C. Horváth. J. Chromatogr. **142**, 623 (1977).
33. B. Grego, F. Lambrou et M.T.W. Hearn. J. Chromatogr. **266**, 89 (1983).
34. J.M.R. Parker, D. Guo et R.S. Hodges. Biochemistry, **25**, 5425 (1986).

Can. J. Chem. Downloaded from www.nrcresearchpress.com by ESC ESCOLA DE ENGENHARIA on 09/08/12
For personal use only.

Photoionophores derived from crown ether polycarboxylic acids: synthesis, ion binding, and spectroscopic characterization

THOMAS M. FYLES[1] AND VALIA VEETTIL SURESH

Department of Chemistry, University of Victoria, Box 3055, Victoria, BC V8W 3P6, Canada

Received November 1, 1993

THOMAS M. FYLES and VALIA VEETTIL SURESH. Can. J. Chem. **72**, 1246 (1994).

Three types of potential photoionophores based on polycarboxylic acid crown ethers were prepared, and their cation complexation behaviours and spectroscopic properties were surveyed. The first type were neutral macropolycyclic hosts prepared by capping across the faces of the crown ether with aromatic diamine chromophores. The second were bis-crown ether carboxylates bearing a bridging aromatic chromophore. The third type appended an additional chromophore-donor site on the crown ether carboxylic acid framework. Cation complexation was examined by potentiometric titration. The neutral ligands were rather poor hosts for alkali metal cations. The other two types of crown ether carboxylates showed a combination of size selectivity and electrostatic stabilization, leading to significant and selective ion binding in water. Ligands of the third type also exhibited cation-dependent absorption spectra in neutral and basic aqueous solution. No significant alkali metal or alkaline earth cation-induced perturbation of the emission spectra was uncovered, but a sodium- and cesium-dependent long wavelength emission enhancement was observed in one of the neutral ligand systems.

THOMAS M. FYLES et VALIA VEETTIL SURESH. Can. J. Chem. **72**, 1246 (1994).

On a préparé trois types de photoionophores potentiels basés sur des éthers couronnes portant des acides polycarboxyliques et on a étudié leurs comportements dans la complexation de cations ainsi que leurs propriétés spectroscopiques. Le premier type comprend des hôtes macropolycycliques neutres dont les faces de l'éther couronne sont recouvertes de chromophores diaminés aromatiques. Le second comporte des carboxylates de bis(éther couronne) portant un chromophore aromatique agissant comme pont. Dans le troisième type, l'éther couronne d'acide carboxylique porte un site additionnel de chromophore donneur. On a étudié la complexation des cations par titrage potentiométrique. Les coordinats neutres sont des hôtes relativement mauvais pour les cations des métaux alcalins. Les deux autres types de carboxylates d'éthers couronnes présentent une combinaison de sélectivité selon la grosseur et de stabilisation électrostatique qui conduit, dans l'eau, à des liaisons sélectives et importantes avec les ions. En solutions aqueuses neutres ou basiques, les coordinats du troisième type présentent aussi des spectres d'absorption qui varient avec la nature du cation. On n'a mis en évidence aucune autre perturbation importante des spectres d'émission qui aurait pu être induite par des métaux alcalins ou alcalinoterreux; toutefois, dans un des systèmes de coordinats neutres, on a observé que le sodium et le césium provoquent une augmentation d'une émission à une grande longueur d'onde.

[Traduit par la Rédaction]

Photoionophores are selective complexing agents for specific ionic species in which the complexed guest species induces a perturbation in the electronic state of the host molecule. Perturbations can be detected by absorption or emission spectroscopy to define chromoionophores (1, 2) or fluoroionophores (2), respectively. In principle, ion-selective complexing agents could be modified by addition of a suitable chromophore to yield a functional photoionophore with the selectivity of the unmodified ion-binding host. For alkali metal and alkaline earth cations several examples of this strategy are reported for crown ether (2–12), cryptand (13, 14), hemispherand (15), calixarene (16, 17), and cyclophane hosts (18). Phenols (1, 4, 12), polycyclic aromatic (3, 13, 18), and heteroaromatic chromophores (5, 8, 9, 11) have all been exploited. Despite the successes, there is still a need for photoionophores for alkali metal cations that could be used in aqueous solution over a range of pH values (10). The majority of the known photoionophores are either insoluble in water, insensitive to alkali metal cations, or pH sensitive.

This paper evaluates several potential photoionophores derived from crown ether polycarboxylic acids based on *R,R*-(+)-tartaric acid. The parent crown ether offers a conformationally controlled framework and an array of carboxylate donors that provide electrostatic stabilization of bound guests (19). These features could promote favourable ion–chromophore organization (20), together with favourable ion binding in water (21). Figure 1 summarizes the geometries of the photoionophores investigated. Each case builds on the tendency of the carboxylic acid groups to occupy axial positions on the macrocyclic periphery (22). In case of type A this would lead to capping across the face of the macrocycle; hence, this type is referred to as captand. The additional arms above and below the macrocyclic plane place the chromophore in proximity to a bound cation and define a three-dimensional cavity (23, 24). Type B is akin to other bis-crown ethers (25), with the additional feature that the chromophore lies between the rings. The crown ethers are expected to act as independent carboxylate crown ethers. Type C unites several themes in crown ether chemistry: lariat ether structure (26), phenol ionization to provide a cation-sensitive chromophore (1), and axial orientation to place the additional donor site above the crown ether plane.

The goals of this survey were to establish synthetic procedures with simple chromophores, to evaluate cation binding by potentiometric methods, and to examine the optical properties of the photoionophores produced. This would provide essential information for the design of more sensitive photoionophores incorporating more sophisticated chromophores.

Results and discussion

Synthesis

The synthesis of captands (24) (Fig. 1, type A) was achieved by coupling the known tetraacid chloride **1** with appropriate diamines (Scheme 1). Precedent literature discouraged the use of flexible diamines (23), so rigid aromatic spacers of approximately complementary span to the known transannular dimensions of the crown ether tetraacid were chosen. High dilution coupling of **1** with excess *m*-xylylene, *p*-xylylene, or 2,2′-

[1]Author to whom correspondence may be addressed. bitnet: fyles@uvvm.uvic.ca.

Can. J. Chem. Downloaded from www.nrcresearchpress.com by EESC ESCOLA DE ENGENHARIA on 09/08/12
For personal use only.

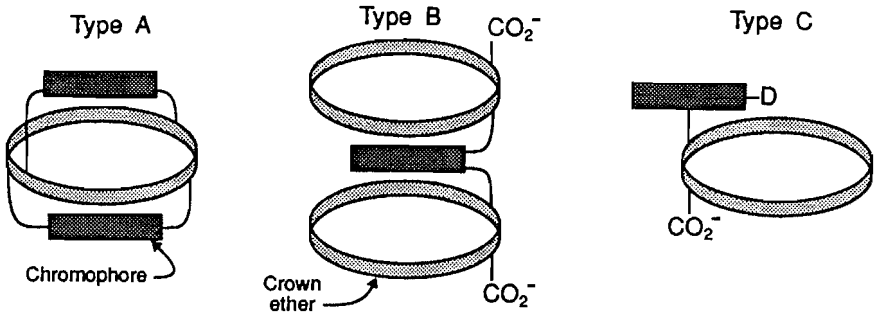

FIG. 1. Schematic diagrams of photoionophores prepared.

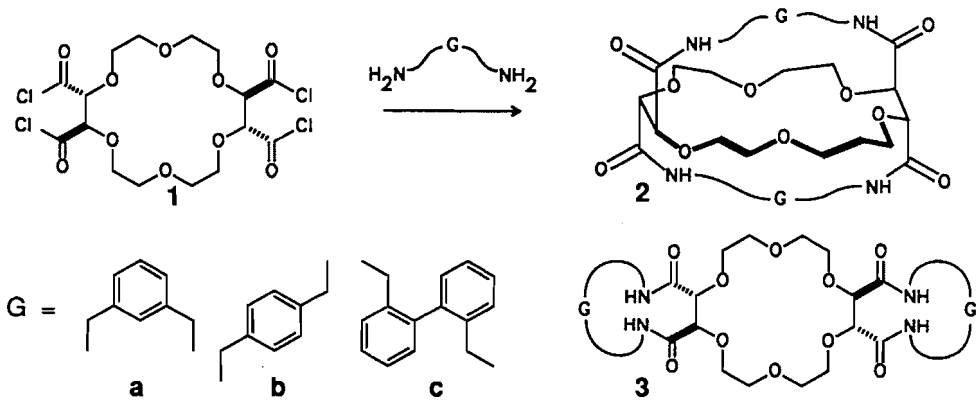

SCHEME 1

bis(aminomethyl)biphenyl gave the captands **2***a*, **2***b*, and **2***c* in yields of 95, 40, and 85%, respectively (Scheme 1). The characterization of **2***a* and **2***b* by NMR and crystal structure determination has been discussed previously.

Compound **2***c* offers an interesting candidate to explore the effect of rotational freedom of diamines on the capping reaction. Rotation around the central bond between the two benzene rings is partly hindered and the two amino groups have a constrained but variable span. This diamine could potentially cap across the faces of the crown ether ring (*syn*-capping, between the acid groups of two different tartaric acid units, **2**) or along the edges (*ortho*-capping, between the acid groups of the same tartaric acid unit, **3**). *Anti*-capping (between the two different tartaric acid units spanning the two faces of the crown ether) is very unlikely from the analysis of CPK models and simple molecular mechanics explorations.[2] The ^{13}C NMR spectrum of the compound showed four signals for each major subunit (carbonyl, crown ether methine, $ArCH_2$) and two equal groups of crown ether ring signals. The spectra suggested either a mixture (approximately 1:1) of *syn*- (**2***c*) and *ortho*-capped (**3**) isomers, each undergoing rapid motion about the Ar—Ar bond, or two slowly interconverting *syn*-capped isomers differing in the biphenyl chirality. The latter possibility was more likely, as no evidence for a mixture could be obtained from careful chromatographic examinations of the product (normal and reverse-phase TLC, high performance size exclusion chromatography). Variable temperature NMR showed apparently homogeneous broadening, suggesting a single conformational process of a single compound. The molecular ion observed in the mass spectrum and the elemental analysis indicate that if a mixture was present, it was a mixture of isomers.

The synthesis of bis-crown ethers (Fig. 1, type B) derived from tartaric acid crown ethers is a straightforward extension of previous synthetic work with the crown ether anhydride **4**, which reacts readily with amines to give crown ether amide–acids (27). Thus *m*-xylylene diamine cleanly quenched 2 equiv. of **4** in excess triethylamine to give the expected product **5***a* (Scheme 2) in 89% yield, full characterized by ^1H NMR, ^{13}C NMR, mass spectrometry, and elemental analysis.

A potentially more useful chromophore was incorporated via 9,10-bis(aminomethyl)anthracene. Unfortunately this diamine was only sparingly soluble in organic solvents, which precluded its use in the high dilution capping process of Scheme 1. It was sufficiently soluble in tetrahydrofuran (THF) containing triethylamine, so that the reaction of solid diamine with a solution of **4** eventually gave the bis-crown ether **5***d* in reasonable yield (76%). The product **5***d* was quite soluble and characterized by ^1H NMR, ^{13}C NMR, mass spectrometry, and elemental analysis. Over a period of 2 months, **5***d* decomposed in diffuse daylight, so subsequent samples were kept in brown vials covered with aluminium foil.

Lariat ethers (Fig. 1, type C) derived from tartaric acid crown ethers were simply prepared by quenching the known crown ether acid anhydrides **4** or **7** with 2-aminophenol (Scheme 3). This was expected to place an additional ionizable donor in an axial position, potentially adjacent to a cation bound in the crown ether ring. The monophenol adduct **6** was isolated in 84% yield and characterized by ^1H NMR, ^{13}C NMR, mass spectrometry, and elemental analysis.

The bisphenol crown ether **8** could be formed as either the *syn*- or *anti*-**8** isomer, or more likely as a mixture of the two. Excess triethylamine with stoichiometric aromatic amines is known to favour the formation of the *syn* isomers in many other cases (28). The product, isolated in 85% yield, was predominantly (75–85%) one isomer as judged by ^1H NMR and ^{13}C NMR. The isomeric nature of the product was confirmed by

[2]PC Model, Serena Software, Bloomington, Ind.

Can. J. Chem. Downloaded from www.nrcresearchpress.com by EESC ESCOLA DE ENGENHARIA on 09/08/12
For personal use only.

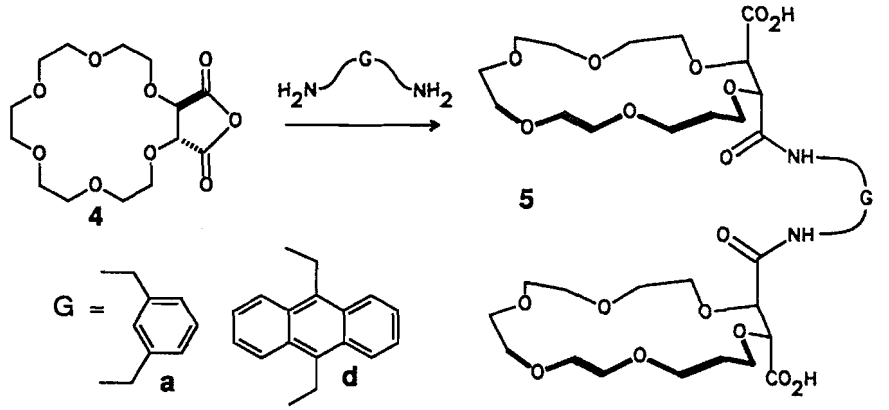

SCHEME 2

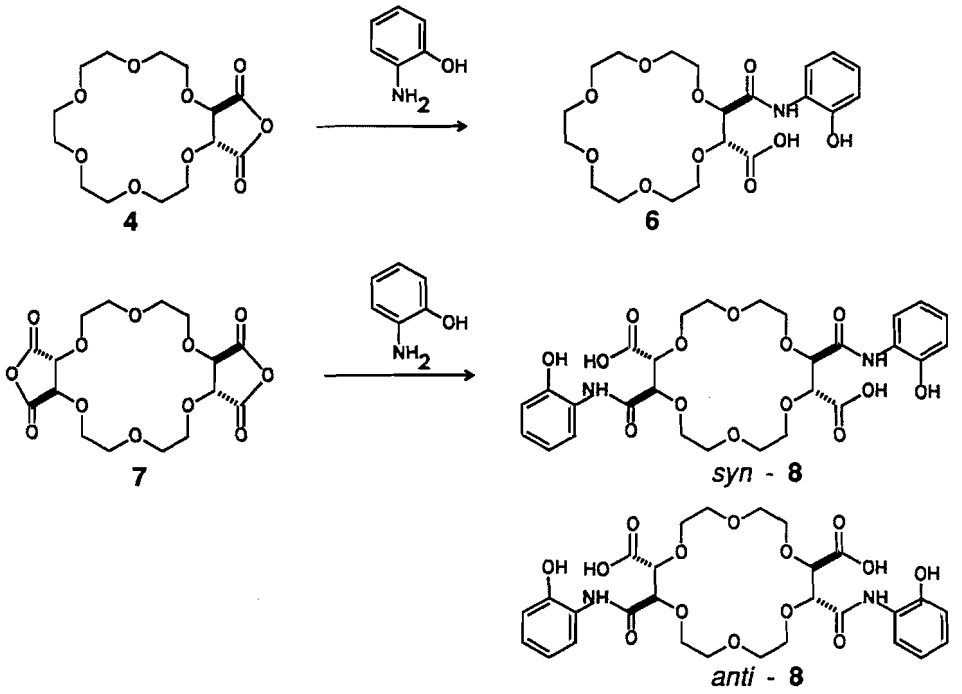

SCHEME 3

mass spectrometry (single molecular ion), elemental analysis, and equivalent weight determination by acid–base titration. That the major isomer was *syn* rests on similarity with excellent synthetic precedent (28). Like all acidic crown ethers, **8** was strongly bound to chromatographic media and separation by chromatography was fruitless. Fractional crystallization was not productive, the hydrodynamic radii of *syn*- and *anti*-**8** were too similar to permit separation by size-exclusion chromatography, and the chemoselectivity of the reaction could not be improved by variation in reaction time, solvent, or temperature. Consequently, all studies were done with a mixture of isomers, assumed to be predominantly *syn*-**8**. The composition of this mixture (78% *syn*) was established by integration of the carbonyl carbon signals of a ^{13}C NMR spectrum with an acquisition delay of 10 s to permit full relaxation between pulses.

Stability constants for complexation of cations

The stability constants for K^+ complex formation by the neutral captands **2***a*–**2***c* were determined in 50% aqueous methanol by potentiometric titration using a potassium-selective electrode. The values of log $K_s \pm 0.3$ (M^{-1}) were found to be 2.8 for **2***a*, 3.0 for **2***b*, and 3.6 for **2***c*. These stability constants are comparable to neutral crown ethers, but considerably smaller than cryptands in similar solvents (29). The values increased as the length and flexibility of the aromatic cap increased, suggesting that the captand cavity was too small or too rigid for optimal cation–donor interactions.

The stability constants for ion binding by ionizable crown ethers **5***a*, **5***d*, and **6** and the *syn*-**8**–*anti*-**8** mixture were determined by pH-metric titration (30). Table 1 summarizes the results in comparison with the parent di- and tetra-carboxylate crown ethers (Di and Tet). As previously, the reported values are cumulative association constants defined by equilibria between l ligands of charge z^-, m cations of charge y^+, and h protons:

$$[1]\quad lL + mM^{yx+} + hH^+ \rightleftharpoons l\mathrm{L}^{z-}m\mathrm{M}^{y+}h\mathrm{H}^+$$

$$[2]\quad \beta_{lmh} = \frac{[l\mathrm{L}^{z-}m\mathrm{M}^{y+}h\mathrm{H}^+]}{[\mathrm{L}^{z-}]^l[\mathrm{M}^{y+}]^m[\mathrm{H}^+]^h}$$

Can. J. Chem. Downloaded from www.nrcresearchpress.com by EESC ESCOLA DE ENGENHARIA on 09/08/12
For personal use only.

TABLE 1. Logarithm of cumulative stability constants for complex formation[a]

Cation	Stoich. *lmh*	Compound					
		5a	***5c***	**6**	***syn*-8**	Di (21)	Tet (21)
H^{+b}	101	4.08	4.42	10.24	11.0	4.37	4.88
	102	7.78(3.70)	8.09(3.67)	14.0(3.76)	20.39 (9.29)	7.0 (2.72)	9.17 (4.29)
	103				24.16 (3.77)		12.01 (2.84)
	104				27.61 (3.45)		14.14 (2.13)
Li^+	110	—	2.3	3.1	3.6	—	—
	111		*	12.7 (2.5)	*		
	120		*	*	*		
Na^+	110	—	2.7	3.4	4.6	3.3	4.5
	111		*	12.0 (1.8)	14.1 (3.0)	6.7 (2.4)	9.0 (4.1)
	120		*	*	*	*	*
K^+	110	2.8	3.6	4.1	5.3	4.2	4.8
	111	*	*	12.7 (2.5)	14.7 (3.6)	7.6 (3.2)	9.6 (4.7)
	120	6.3	*	*	*	*	
Rb^+	110	1.9	3.6	3.1	3.9	—	—
	111	*	*	12.2 (2.0)	14.8 (3.7)		
	120	*	*	*	*		
Cs^+	110	2.4	3.3	3.1	3.5	—	—
	111	*	*	11.8 (1.6)	14.4 (3.3)		
	120	*	*	*	*		
Ca^{2+}	110	3.0	3.7	4.28	6.1	5.6	8.6
	111	*	*	12.7 (2.5)	14.7 (3.6)	*	11.9 (7.0)
	120	*	*	*	*	*	*
Sr^{2+}	110	4.1	4.4	5.5	6.5	5.9	8.0
	111	*	*	13.8 (3.5)	14.6 (3.5)	8.9 (4.2)	10.9 (6.1)
	120	7.5	*	*	*	*	*
Ba^{2+}	110	4.1	5.2	5.5	5.7	6.5	7.2
	111	*	*	14.0 (3.7)	14.3 (3.2)	*	11.06 (6.2)
	120	7.2	*	*	*	*	*

[a]Determined at 25°C, I = 0.1 M with Me_4NNO_3 in water. The values in parentheses are calculated for 1:1 association of M^{n+} and the protonated ligand. The asterisk indicates the complex of the given stoichiometry was not detected. The dash indicates that the system was not examined. Uncertainty: acidity constants, log $\beta_{l0h} \pm 0.1$; association constants, log $\beta_{lmh} \pm 0.2$.

[b]The logarithm of dissociation constants follows the conventions of pK_a.

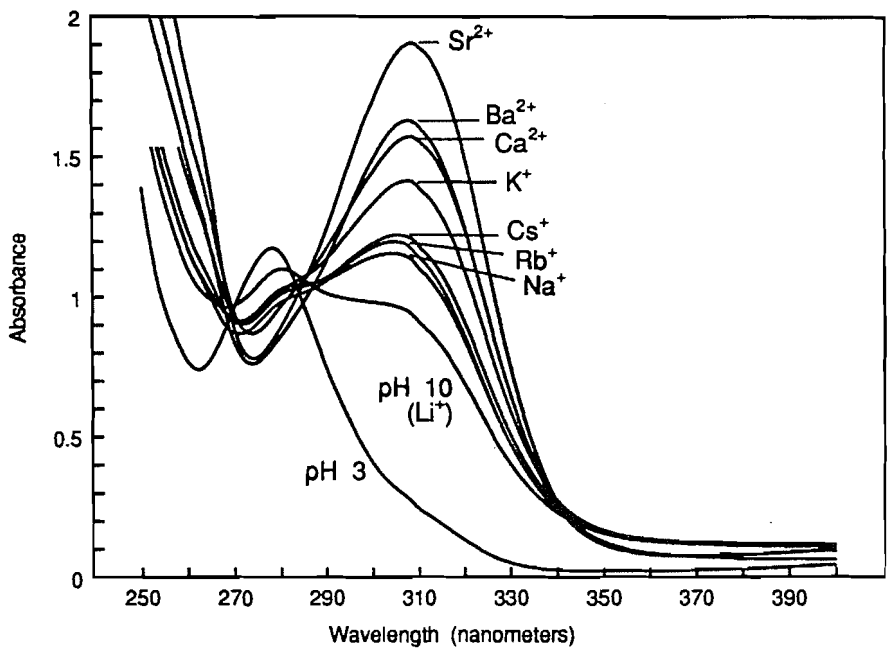

FIG. 2. Cation-dependent UV–visible spectra of **6**. [L] = 1×10^{-4} M, [M^{n+}] = 0.01 M, pH 10 (aqueous lithium phosphate buffer).

Can. J. Chem. Downloaded from www.nrcresearchpress.com by EESC ESCOLA DE ENGENHARIA on 09/08/12
For personal use only.

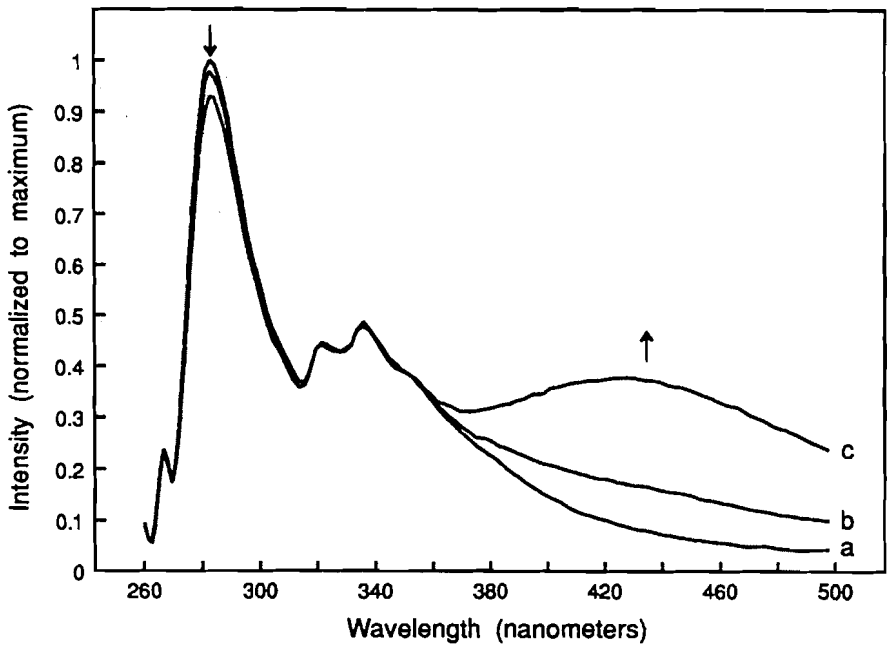

FIG. 3. Effect of Cs^+ on the emission spectrum of **2***c* [L] = 8×10^{-6} M in 0.03% methanol in water; excitation wavelength = 250 nm. (*a*) No cation added. (*b*) [Cs^+] = 4×10^{-3} M. (*c*) [Cs^+] = 2×10^{-2} M.

where β_{lmh} is the cumulative association constant and the integers *l*, *m*, and *h* represent the number of ligands, number of metal ions, and the number of protons. For comparison between complexes formed at different levels of ligand protonation, stepwise association constants could be calculated by correcting for the pK_a values imbedded in the cumulative constants.

The mixture of *syn*- and *anti*-**8** was treated as a mixture of two ligands in a 78:22 ratio. The differences between the phenolic pK_as could not be distinguished, but significant differences in the carboxylate pK_as were evident in the unprocessed titration curves. Nonlinear fitting of the titration curve gave values of 5.85 for pK_3 and 4.36 for pK_4 of *anti*-**8**. The metal ion complexes of the *syn* and *anti* isomers were insignificantly different at the ligand and cation concentrations used, so the data reported in Table 1 reflect a weighted average value for the mixture.

The complexation data are completely consistent with previous studies of the parent crown ethers Di and Tet (19, 21). Cation recognition is controlled by two factors: a crown ether recognition factor that reflects host–guest size complementarity effects and an electrostatic enhancement factor involving additional coordination in favourable instances. The cation size effect is evident in the optimal binding of potassium ion from among the alkali metal cations. The electrostatic factor is evident in the preferential association with divalent alkaline earth cations over alkali metal cations and in the general destabilization provoked by ligand protonation in all cases. Comparison of **6** and Di, or **8** and Tet, shows that a phenolic donor is inferior to a carboxylate donor at constant ligand charge. This is consistent with a proximity effect, suggesting that direct phenolate–cation chelate interaction is not a major stabilizing factor.

Chromoionophore survey

The UV–visible absorption spectra of compounds **5***a*, **5***d*, **6**, and **8** were examined in the presence of alkali metal and alkaline earth cation chlorides in water and basic buffer solution. Compounds **5***a* and **5***d* showed no significant changes of any type. Both compounds **6** and **8** showed bathochromic shifts on deprotonation (275–308 nm), but only **6** showed significant influence of cation type and concentration. Figure 2 shows the cation-dependent intensity changes provoked by addition of 0.01 M salt to a 10^{-4} M solution of **6**. The pH 10 phosphate buffer solution contained 0.01 M Li^+ in all cases, underscoring the cation selectivity of the changes. The changes were salt concentration dependent in the range $5 \times 10^{-4} - 5 \times 10^{-3}$ M; Fig. 2 illustrates the limiting spectra for all cations.

The ordering of the intensity changes ($Sr^{2+} > Ba^{2+} > Ca^{2+} > K^+$ etc.) paralleled the order of the stability constants reported in Table 1. The preferred cation was Sr^{2+}, as this guest had both good size complementarity with an 18-crown-6 cavity and a favourable charge density for electrostatic stabilization by phenolate and carboxylate groups. The destabilization on ligand protonation, represented by the difference in the stepwise association constants for the 110 and 111 complexes, also followed the same series. It is tempting to speculate that the absorption spectrum is reporting the extent of direct phenolate–cation chelation in the different complexes. This is likely to be modest, even in a favourable case such as Sr^{2+}, since the potential for chelation did not play a major role in complex stabilization based on the evidence discussed above.

Fluoroionophore survey

The quenching of fluorescence of the three captands and two bis-crown ethers with alkali metal cations (Li^+, Na^+, K^+, Rb^+, and Cs^+), alkaline earth metal cations (Ca^{2+}, Ba^{2+}, and Sr^{2+}), and heavy metal cations (Cu^{2+}, Hg^{2+}, and Cd^{2+}) was examined (Table 2). The emission spectra were recorded and the change in emission intensity at the emission maximum provoked by a change in the concentration of metal ion was considered as a quenching efficiency.

A cursory examination of Table 2 indicates no significant (higher than 20%) quenching of the fluorescence by alkali

Can. J. Chem. Downloaded from www.nrcresearchpress.com by EESC ESCOLA DE ENGENHARIA on 09/08/12
For personal use only.

TABLE 2. Quenching of photoionophore fluorescence by cation salts[a]

Metal ion	Compounds				
	2a[b]	**2b**[b]	**2c**[b]	**5c**[c]	**5f**
Li^+	−4	−13	17	0	—
Na^+	−6	−9	11	−3	4
K^+	−2	−5	10	−1	1
Rb^+	−6	−13	13	2	—
Cs^+	−6	−8	7	−8	−8
Mg^{2+}	−3	−15	9	−5	—
Ca^{2+}	−2	0	15	6	—
Sr^{2+}	−6	−5	11	3	20
Ba^{2+}	−5	−12	12	4	25
Cu^{2+}	97[d]	99[e]	99[f]	57	86[i]
Hg^{2+}	92	90[g]	94[h]	88	93[j]
Cd^{2+}	−3	−6	12	—	—

[a]Expressed as a percentage change of the original intensity at the emission maximum: +, decrease in intensity; −, increrase in intensity. Ionophore concentration = 10^{-6} M; cation concentration = 0.01 M; all measurements were done in 0.3% methanol–water.
[b]Excitation, 250 nm; emission, 283–285 nm.
[c]Excitation, 360 nm; emission, 401–403 nm.
[d]$[Cu^{2+}] = 1.0 \times 10^{-3}$ M.
[e]$[Cu^{2+}] = 1.6 \times 10^{-3}$ M.
[f]$[Cu^{2+}] = 2.0 \times 10^{-3}$ M.
[g]$[Hg^{2+}] = 1.6 \times 10^{-2}$ M.
[h]$[Hg^{2+}] = 2.4 \times 10^{-2}$ M.
[i]$[Cu^{2+}] = 6.0 \times 10^{-3}$ M.
[j]$[Hg^{2+}] = 1.4 \times 10^{-2}$ M.

metal ions in any case. Significant quenching by heavy metal cations was noted. A preliminary study of the Cu^{2+} and Hg^{2+} quenching suggested that the quenching involves both simple diffusional quenching and a complexation induced static quenching (31). Owing to the weak fluorescence exhibited by these fluorophores, a more detailed study appeared to be unwarranted at this stage.

One significant feature was noted in the emission spectrum of the biphenyl captand **2c**: the appearance of a new emission band at long wavelength region (455 nm) in the presence of increasing concentrations of Cs^+ or Na^+. Other alkali metal cations did not give a significant long wavelength enhancement. All the emission maxima in Fig. 3 originated from a single species, as established by comparison of the excitation spectra for different emission maxima. One possible explanation might be based on excimer formation of the biphenyl capped crown ether with the metal ion, provided that the excimer emitted much more intensely than the parent captand molecule. The slight decrease in intensity of the emission at 288 nm would be due to the depletion of the population of either the ground or excited state of the free ligand to form an excimer. Since the intensity of emission was proportional to the concentration of metal ion, the excimer, if present, was potentially an inclusion complex of metal ion and the captand molecule. This interesting observation warrants more detailed investigation, particularly as it relates to the development of a sodium-sensitive fluoroionophore.

Summary

This survey demonstrates that modification of known ion-binding ligands, particularly by appending additional donors, can result in a combination of satisfactory levels of ion complexation in water and significant spectroscopic changes. The survey data, combined with literature reports, suggest that useful photoionophores might be assembled as lariat ethers (type C) with betaine phenolate donors (ref. 12; chromoionophore) or coumarin donors (ref. 11; fluoroionophore).

Experimental

Melting points were taken on a Riechardt hot-stage microscope and are uncorrected. ^1H NMR spectra were recorded with a Perkin-Elmer R32 (90 MHz, CW) or Bruker AMX 360 (360.14 MHz, FT) spectrometer using $CDCl_3$, CD_2Cl_2, or CD_3OD as solvent. The 90-MHz spectra were referenced to Me_4Si as internal standard. The 360-MHz spectra were referenced with the central solvent line as standard (7.24 δ for $CDCl_3$, 5.32 δ for CD_2Cl_2 and 3.30 δ for CD_3OD, all relative to Me_4Si). ^{14}C NMR spectra were recorded with a Bruker WM250 (62.89 MHz) or Bruker AMX360 (90.57 MHz) spectrometer, with the central solvent line as standard (77.0 ppm for $CDCl_3$, 53.8 for CD_2Cl_2, and 49.0 for CD_3OD, all relative to Me_4Si). Mass spectra were recorded on a Finnegan 3300 GC–MS instrument, with methane chemical ionization (CH_4 CI), or a Kratos Concept IH32 operating in LSIMS mode (Cs^+ ion bombardment, cooled thiogycerol matrix). Elemental analyses were performed by Canadian Microanalytical Services, New Westminster, B.C., and are quoted as percentages. Absorption spectra were recorded using a Cary 14 UV–visible spectrometer. Fluorescence spectra were recorded using a Perkin-Elmer 3300 spectrofluorimeter.

The crown ether diacid (Di) and tetraacid (Tet) were synthesized as previously described (19, 27). The known diamine 2,2′-bis(aminomethyl)biphenyl (32) was prepared from the dibromide by a Gabriel synthesis. Thus 2,2′-bis(bromomethyl)biphenyl (2 g, 5.8 mmol; mp 88–90°C (lit. (32) mp 90°C)) was dissolved in dimethylacetamide (DMA; 250 mL), along with freshly prepared potassium phthalimide (3 g, 16 mmol) containing two drops of diethylamine catalyst. The mixture was stirred at 50°C for 5 h and the solvent was removed under reduced pressure. The resulting yellow paste was dissolved in water and extracted with dichloromethane; the organic layer was washed with water, dried with anhydrous sodium sulphate, and evaporated to dryness under reduced pressure to yield a white solid. The solid was dissolved in ethanol (200 mL) and hydrazine (10 mL, excess) was added. The mixture was stirred for 5 h at 50°C. The resulting white solid was filtered and washed twice with ethanol (50-mL portions). The ethanol filtrate was evaporated to dryness and dichloromethane (50 mL) was added. The resulting white precipitate was filtered and washed twice with small portions of dichloromethane. The filtrate was dried over anhydrous sulphate and evaporated to dryness to yield 1.5 g (85%) of a colourless oil. ^1H NMR ($CDCl_3$) δ: 7.54 (d, 2H), 7.25–7.48 (m, 4H), 7.11 (d, 2H), 3.55 (dd, 4H), 3.0 (br s, 4H); ^{13}C NMR ($CDCl_3$) δ: 141.2, 136.8, 128.8, 127.9, 127.8, 127.6, 48.8; MS *m/z*: 213 $(M + 1)^+$.

The known diamine 9,10-bis(aminomethyl)anthracene (33) was similarly prepared from 9,10-bis(chloromethyl)anthracene (34) in an initial yield of 84%, mp 221–229°C (lit (34) mp 222–228°C for the same initial product). MS (CH_3 CI) *m/z*: 237 $(M + 1)^+$. This crude diamine was used without further purification for subsequent reactions.

The known tetraacid chloride (**1**) (ref. 35) was prepared from the crown ether tetraacid (0.6 g, 1.4 mmol) dissolved in $POCl_3$ (25 mL) and freshly sublimed PCl_5 (1.14 g, 5.5 mmol) was added with continuous stirring. The mixture was stirred at 45°C for 12 h and the solvent was removed under reduced pressure. The excess PCl_5 was removed by sublimation under high vacuum. The crude white solid product was dissolved in dry toluene (10 mL) and used without further purification.

m-Xylylene capped crown ether (2a)

Dry toluene (500 mL) was placed in a 3-L four-neck flask equipped with two precision dropping funnels and a mechanical stirrer. A toluene solution of acid chloride **1** (0.63 g, 1.4 mmol, 100 mL) was placed in one of the funnels and a toluene solution of 1,3-bis(aminomethyl)benzene (0.59 g, 4 mmol, 100 mL) was placed in the other funnel.

Can. J. Chem. Downloaded from www.nrcresearchpress.com by EESC ESCOLA DE ENGENHARIA on 09/08/12
For personal use only.

Can. J. Chem. Downloaded from www.nrcresearchpress.com by EESC ESCOLA DE ENGENHARIA on 09/08/12
For personal use only.

The solutions were added dropwise at equal rates to the reaction flask with continuous and vigorous stirring over 48 h at room temperature. After completion of the addition, the mixture was stirred for another 12 h and the solvent was removed under reduced pressure. The resulting pale yellow solid was dissolved in water (200 mL) and extracted twice with petroleum ether, diethyl ether, dichloromethane, and chloroform (100-mL portions) in that order. The chlorocarbon extracts were mixed and evaporated to dryness to give a 95% yield of **2***a* (mp > 275°C). The product was further purified by recrystallization from acetonitrile. ^{1}H NMR ($CDCl_3$) δ: 7.6 (d, 4H), 7.2 (s, 8H), 5.0 (dd, 2H), 4.3 (s, 4H), 3.6 (d, 2H), 3.6–3.3 (m, 16H); ^{13}C NMR ($CDCl_3$) δ: 169.3, 138.8, 128.5, 127.1, 125.0, 80.9, 70.4, 69.4, 42.4; MS (CH_4 CI) *m/z*: 641 $(M + 1)^+$. Anal. calcd. for $C_{32}H_{40}O_{10}N_4 + H_2O$: C 58.34, H 6.42, N 8.50; found: 58.34, H 6.31, N 8.31.

p-*Xylylene capped crown ether (***2**b*)*

As described above for **2***a*, 1,4-bis(aminomethyl)benzene (0.85 g, 6.2 mmol) and acid chloride **1** (0.63 g, 1.4 mmol) gave **2***b* as a white solid (0.35 g, 40%). ^{1}H NMR ($CDCl_3$) δ: 7.1 (s, 8H), 6.7 (d, 4H), 4.9 (t, 2H), 4.4 (s, 4H), 3.7 (d, 2H), 3.6–3.5 (m, 6H), 3.3–3.2 (m, 16H); ^{13}C NMR ($CDCl_3$) δ: 169.2, 139.2, 128.5, 78.1, 70.4, 70.3, 43.4; MS (CH_4 CI) *m/z*: 641 $(M + 1)^+$; mp > 275°C. Anal. calcd. for $C_{32}H_{40}O_{10}N_4 + H_2O$: C 58.34, H 6.42, N 8.50; found: C 58.07, H 6.25, N 8.23.

*Biphenyl capped crown ether (***2**d*)*

As described for **2***a* acid chloride **1** (0.6 g, 1.14 mmol) and 2,2′-bis(aminomethyl)biphenyl (0.65 g, 3.1 mmol) gave **2***d* as a pale yellow solid (0.76 g, 85%). ^{1}H NMR ($CDCl_3$) δ: 7.6–6.9 (m, 12H), 4.8 (m, 2H), 4.7–4.6 (m, 4H), 4.2–3.6 (m, 2H), 3.5–3.1 (m, 16H); ^{13}C NMR ($CDCl_3$) δ: 170.3, 170.1, 169.5, 169.4, 139.5, 139.2, 138.7, 138.4, 135.9, 135.5, 135.0, 134.7, 130.5, 130.0, 129.6, 129.5, 129.4, 129.0, 128.6, 128.5, 128.4, 128.0, 127.9, 127.6, 127.2, 126.7, 83.0, 82.4, 81.9, 81.3, 77.3, 71.6, 71.3, 71.2, 70.7, 68.5, 68.2, 67.9, 67.4, 42.5, 42.2, 41.6 (2 peaks); MS (CH_4 CI) *m/z*: 793 $(M + 1)^+$. Anal. calcd. for $C_{44}H_{48}O_{14}N_4 + 2.5\ H_2O$: C 63.07, H 6.37, N 6.68; found: C 63.25, H 6.18, N 6.46.

*1,3-Bis(*R,R-*1′,4′,7′,10′,13′,16′-hexaoxacyclooctadecan-2-carboxyl-3-carboxamidomethyl)benzene (***5**a*)*

A solution of anhydride **4** (ref. 27, 0.95 g, 2.8 mmol) in THF (150 mL) was mixed with 1,3-bis(aminomethyl)benzene (0.2 g, 1.4 mmol), followed by the addition of dry triethylamine (2 mL). The mixture was stirred for 7 h at room temperature under an inert atmosphere. The excess solvent was removed under reduced pressure to give a glassy solid. The product was dissolved in water and extracted twice with dichloromethane (20 mL) to remove neutral impurities. The water solution was passed through a cation-exchange resin to remove triethylammonium chloride. The acidic fractions (< pH 3) were collected and the water was removed under reduced pressure to give **5***a* as a colourless solid (1.02 g, 89%). ^{1}H NMR ($CDCl_3$) δ: 7.5 (t, 1H), 7.4–7.2 (m, 3H), 4.9 (m, 2H), 4.5 (dd, 4H), 3.9–3.8 (m, 2H), 3.6–3.4 (m, 40H); ^{13}C NMR ($CDCl_3$) δ: 171.7, 168.4, 138.7, 128.5, 127.0, 126.2, 81.3, 80.5, 71.2, 70.5, 70.2, 69.9, 69.8, 69.7, 69.6, 42.8; MS (CH_4 CI) *m/z*: 805 $(M + 1)^+$; MS (LSIMS) *m/z*: 805 $(M + H)^+$, 827 $(M + Na)^+$. Anal. calcd. for $C_{36}H_{56}O_{18}N_2 + 2\ H_2O$: C 51.42, H 7.19, N, 3.33; found: C 51.31, H 7.29, N 3.47.

*9,10-Bis(*R,R-*1′,4′,7′,10′,13′,16′-hexaoxacyclooctadecan-2-carboxyl-3-carboxamidomethyl)anthracene (***5**c*)*

A solution of anhydride **4** (ref. 27; 0.9 g, 2.6 mmol) in THF (300 mL) was stirred with solid 9,10-bis(aminomethyl)anthracene (0.5 g, 2 mmol) for 14 h in presence of triethylamine (2 mL) at room temperature. The solvent was removed under reduced pressure. The resulting yellow pasty solid was dissolved in water and extracted with dichloromethane. The chlorocarbon layer was washed with water and evaporated to dryness to yield 0.9 g (76%) of **5***c* as yellow powder. ^{1}H NMR ($CDCl_3$) δ: 8.4 and 7.5 (AA′XX′, 4H), 5.6 (dd, 2H), 5.4 (dd, 2H), 4.3 (dd, 4H), 3.6–2.9 (m, 40H); ^{13}C NMR ($CDCl_3$) δ: 171.5, 168.8, 130.3, 130.2, 130.1, 126.3, 126.2, 124.9, 124.6, 81.3, 80.7, 71.4, 71.2, 70.5, 70.0, 69.9, 69.8, 69.5, 69.3, 35.6; MS (LSIMS) *m/z*: 906 $(M + H)^+$. Anal. calcd. for $C_{44}H_{60}O_{18}N_2 + 2\ H_2O$: C 56.16, H 6.85, N 2.97; found: C 56.04, H 6.91, N 3.01.

R,R-N-*(2-Hydroxyphenyl)-1,4,7,10,13,16-hexaoxacylcooctadecan-2-carboamido-3-carboxylic acid (***6**)*

2-Aminophenol (0.3 g, 3.7 mmol) and the crown ether anhydride **4** (ref. 27; 0.93 g, 2.7 mmol) were dissolved in dry THF (150 mL), followed by triethylamine (1 mL). The mixture was stirred for 6 h at room temperature, the solvent was removed under reduced pressure, and the resulting brown solid was dissolved in water (150 mL) and extracted twice with dichloromethane (50-mL portions). The combined extracts were washed twice with water (100 mL) and evaporated. The brown residue was dissolved in water and passed through a cation-exchange column. Acidic fractions were combined and evaporated to dryness to give a pale yellow solid (1.0 g, 84%). ^{1}H NMR ($CDCl_3$) δ: 9.4 (b, 1H), 7.3 (d, 1H), 7.1 (t, 1H), 7.0 (d, 1H), 6.8 (t, 1H), 4.4 (d, 2H), 3.8–3.4 (m, 20H); ^{13}C NMR ($CDCl_3$) δ: 171.2, 169.1, 149.2, 127.3, 125.2, 123.4, 120.3, 119.3, 80.9, 80.7, 71.2, 71.0, 70.5, 70.4, 70.1, 69.9, 69.6, 69.4; MS (LSIMS) *m/z*: 466 $(M + Na)^+$, 445 $(M + H)^+$. Anal. calcd. for $C_{20}H_{29}O_{10}N + H_2O$: C 52.05, H 6.77, N 3.03; found: C 52.50, H 6.45, N 3.19.

syn- *and* anti-R,R-N,N′-*Bis(2-hydroxyphenyl)-1,4,7,10,13,16-hexaoxacyclooctadecan-2,11(12)-dicarboxamido-3,12(11)-dicarboxylic acid (***8**)*

Crown ether bisanhydride **7** (ref. 35; 0.92 g, 2.2 mmol) and triethylamine (1 mL) were dissolved in dry THF (150 mL) and a solution of 2-aminophenol (0.5 g, 4.5 mmol) in dry THF (50 mL) was added dropwise within 4 h with constant stirring at room temperature. The solvent was removed under reduced pressure, and the brown residue was dissolved in water and extracted with two portions of dichloromethane (100 mL). The organic extract was washed twice with water (50 mL), and the solvent was evaporated to give 1.41 g of tan solid. The solid was dissolved in water and passed through a cation-exchange column. Acidic fractions were combined and evaporated to a viscous oil which solidified on evacuation under high vacuum (1.3 g, 91%). ^{1}H NMR ($CDCl_3$) δ: 8.7 (b, 2H), 7.3 (d, 2H), 7.0 (d, 2H), 6.9 (t, 2H), 6.8 (t, 2H), 4.3 (d, 4H), 3.9–3.5 (m, 16H); ^{13}C NMR ($CDCl_3$) δ: 171.7, 169.2, 148.8, 127.4, 124.8, 123.6, 120.4, 118.7, 81.2, 79.9, 71.0, 70.5, 69.2, 68.8; MS (LSIMS) *m/z*: 623 $(M + H)^+$. Anal. calcd. for $C_{28}H_{34}O_{14}N_2 + 2\ H_2O$: C 51.06, H 5.81, N 4.25; found: C 51.14, H 5.65, N 4.17.

Stability constant determinations

Stability constants for ionizable ligands were determined by pH titration using procedures previously described (30). Stability constants for the neutral ligands (captands) were determined using an ion selective electrode. The cell assembly comprised calomel‖0.1 M tetramethylammonium nitrate (TMAN)‖sample solution|potassium selective glass electrode (Phillips G515K). The potassium electrode was preconditioned in 1:1 v/v methanol–water mixture and titrated with a 0.1 M KCl solution. The titrations were repeated to get a concordant values of slope and intercept. The titrant was taken in an automatic burette (Metrohm 655 Dosimat) and added to the cell in aliquots scaled to give concentration corresponding to increase of 0.2 pK^+. Ten millilitres of 1:1 v/v methanol–water solution was placed in a temperature controlled cell and the ionic strength was maintained constant using 0.1 M TMAN. In a typical titration, 20 μL of the ligand solution was introduced into the cell and titrated against the standard KCl solution. The added volume of the titrant was stored along with the response of the electrode. The collected data was then analyzed by using the slope and intercept from the electrode calibration titrations to derive $[M^+]_{free}$ values at each point in the titration. A 1:1 complexation stoichiometry was assumed, to give via the mass balance relationships the expression for

$$K_s = \frac{[M^+]_{tot} - [M^+]_{free}}{[M^+]_{free}([L]_{tot} - [M^+]_{tot} + [M^+]_{free}}$$

Values of K_s were calculated at each point and averaged over the range of $0.2 < [M^+]_{free}/([M^+]_{tot} - [M^+]_{free}) < 0.8$.

Fluorescence studies

In the case of neutral ligands, the ligands were dissolved in 50% methanol–water and 0.02 mL of the stock solution was diluted to 3 mL with water and the required amount of metal ion solution. All metal ion solutions (0.1 M) were prepared by dissolving the chloride salts in deionized water. The appropriate concentration of the metal ions for individual fluorescence spectrum was obtained by diluting the stock solution with water. The excitation wavelength was determined from the absorption spectrum, taking the absorption maximum as the excitation wavelength. The emission wavelength was scanned from 10 nm higher than the excitation wavelength. The purity and absorption of all metal ion solutions and the solvent were recorded separately and subtracted from the emission spectrum of the compound wherever necessary. Emission and Raman scattering were differentiated by changing the excitation wavelength. All fluorescence spectra were recorded with excitation slits and emission slits set to 5 nm and uncorrected spectra were recorded.

In the case of ionizable ligands, a lithium–phosphate buffer of pH 10 was used. A few microlitres of the stock solution of the ligand was added to the cell containing buffer solution. The emission of the buffer was recorded and subtracted from the emission of the ligands. The metal ion effect was monitored using different volumes of 0.1 M metal chloride stock solution added to the cell. The solutions were prepared individually with the ligand solution, metal chloride solution, and made up to 3 mL with a pH 10 buffer solution.

Acknowledgements

The ongoing support of the Natural Sciences and Engineering Research Council of Canada is gratefully acknowledged.

1. M. Takagi and K. Ueno. Top. Curr. Chem. **121**, 39 (1984).
2. H.-G. Löhr and F. Vögtle. Acc. Chem. Res. **18**, 65 (1985).
3. A.P. de Silva and S.A. de Silva. J. Chem. Soc. Chem. Commun. 1709 (1986).
4. J. van Gent, E.J.R. Sudhölter, P.V. Lambeck, T.J.A. Popma, G.J. Gerritsma, and D.N. Reinhoudt. J. Chem. Soc. Chem. Commun. 893 (1988).
5. S. Fery-Forgues, M.-T. Le Bris, J.-P. Guetté, and B. Valeur. J. Phys. Chem. **92**, 6233 (1988).
6. J. Bourson and B. Valeur. J. Phys. Chem. **93**, 3871 (1989).
7. H. Forrest and G.E. Pacey. Talanta, **36**, 335 (1989).
8. S.M.S. Al-Amir, D.C. Ashworth, R. Narayanaswamy, and R.E. Moss. Talanta, **36**, 645 (1989).
9. S. Fery-Forgues, J. Bourson, L. Dallery, and B. Valeur. New J. Chem. **14**, 617 (1990).
10. J. Bourson, M.-N. Borrel, and B. Valeur. Anal. Chim. Acta, **257**, 189 (1992).
11. J. Bourson, J. Pouget, and B. Valeur. J. Phys. Chem. **97**, 4552 (1993).
12. C. Reichardt, S. Asharin-Fard, and G. Schäfer. Liebigs. Ann. Chem. 23 (1993).
13. F. Fages, J.P. Desvergne, H. Bouas-Laurent, P. Marsau, J.-M. Lehn, F. Kotzyba-Hibert, A.-M. Albrecht-Gary, and M. Al-Joubbeh. J. Am. Chem. Soc. **111**, 8672 (1989).
14. R.A. Bartsch, D.A. Babb, B.P. Czech, D.H. Desai, E. Chapoteau, C.R. Gebauer, W. Zazulak, and A. Kumar. J. Inclusion Phenom. Mol. Recognit. Chem. **9**, 113 (1990).
15. R.C. Helgeson, B.P. Czech, E. Chapoteau, C.R. Gebauer, A. Kumar, and D.J. Cram. J. Am. Chem. Soc. **111**, 6339 (1989).
16. I. Aoki, T. Sasaki, S. Tsutsui, and S. Shinkai. Tetrahedron Lett. **33**, 89 (1992).
17. K. Iwamoto, K. Araki, H. Fujishima, and S. Shinkai. J. Chem. Soc. Perkin Trans. 1, 1885 (1992).
18. M. Dhaenens, J.-M. Lehn, and J.-P. Vigneron, J. Chem. Soc. Perkin Trans. 2, 1379 (1993).
19. P.J. Dutton, T.M. Fyles, and S.J. McDermid. Can. J. Chem. **66**, 1097 (1988), and references therein.
20. H.S. Brown, C.P. Muenchausen, and L.R. Sousa. J. Org. Chem. **45**, 1682 (1980).
21. T.M. Fyles. *In* Cation binding by macrocycles. *Edited by* Y. Inoue and G.W. Gokel. Marcel Dekker, New York. 1990. pp. 253–310.
22. P.J. Dutton, F.R. Fronczek, T.M. Fyles, R.D. Gandour, and V.V. Suresh. Can. J. Chem. **71**, 239 (1993), and references therein.
23. J.-P. Behr, C.J. Burrows, R. Heng, and J.-M. Lehn. Tetrahedron Lett. **26**, 215 (1985).
24. T.M. Fyles, V.V. Suresh, F.R. Fronczek, and R.D. Gandour. Tetrahedron Lett. **31**, 1101 (1990).
25. K. Kimura and T. Shono. *In* Cation binding by macrocycles. *Edited by* Y. Inoue and G.W. Gokel. Marcel Dekker, New York. 1990. pp 429–463.
26. G.W. Gokel and J.E. Trafton. *In* Cation binding by macrocycles. *Edited by* Y. Inoue and G.W. Gokel. Marcel Dekker, New York. 1990. pp. 211–251.
27. L.A. Frederich, T.M. Fyles, N.P. Gurprasad, and D.M. Whitfield. Can. J. Chem. **59**, 1724 (1981).
28. J. Desroches, H. Dugas, M. Bouclair, T.M. Fyles, and G.D. Robertson. Can. J. Chem. **65**, 1513 (1987), and references therein.
29. R.M. Izatt, K. Pawlak, J.S. Bradshaw, and R.L. Breuning. Chem. Rev. **91**, 1721 (1991).
30. A. Anantanarayan and T.M. Fyles. Can. J. Chem. **68**, 1338 (1990).
31. V.V. Suresh. Ph.D. thesis, University of Victoria, Victoria. 1992.
32. R.R. Hiatt, M.J. Shiao, and F. Georges. J. Org. Chem. **44**, 3265 (1979).
33. M.W. Miller, R.W. Amidon, and P.O. Tawney. J. Am. Chem. Soc. **77**, 2845 (1955).
34. J.H. Golden. J. Chem. Soc. 3741 (1961).
35. J.-P. Behr, J.-M. Girodeau, R.C. Hayward, J.-M. Lehn, and J.-P. Sauvage. Helv. Chim. Acta, **63**, 2096 (1980).

Can. J. Chem. Downloaded from www.nrcresearchpress.com by EESC ESCOLA DE ENGENHARIA on 09/08/12
For personal use only.

The photochemistry of 1-naphthylmethyl carbonates and carbamates

T. PARMAN, J.A. PINCOCK,[1] AND P.J. WEDGE
Department of Chemistry, Dalhousie University, Halifax, NS B3H 4J3, Canada

Received August 16, 1993

T. PARMAN, J.A. PINCOCK, and P.J. WEDGE. Can. J. Chem. **72**, 1254 (1994).

The photochemistry in methanol of 1-naphthylmethyl phenyl carbonate (**3**) and 1-naphthylmethyl benzyl carbonate (**4**) has been studied. Products resulting from both the 1-naphthylmethyl cation and the 1-naphthylmethyl radical are obtained for **3**, but only from the cation for **4**. Similar results were obtained for the corresponding 1-naphthylmethyl derivatives **5** and **6** of *N*-phenyl and *N*-benzyl carbamic acids. The product yields for all four compounds can be explained by a mechanism of initial homolytic cleavage of the 1-naphthylmethyl carbon–oxygen bond from the excited singlet state. The radical pair generated then partitions between the two pathways: electron transfer to form the ion pair or decarboxylation. For PhO-CO-O˙ and PhNH-CO-O˙, decarboxylation is rapid and competitive with electron transfer. For $PhCH_2O$-CO-O˙ and $PhCH_2NH$-CO-O˙, decarboxylation is slower, electron transfer dominates, and only products from the ion pair are obtained.

T. PARMAN, J.A. PINCOCK et P.J. WEDGE. Can. J. Chem. **72**, 1254 (1994).

On a étudié la photochimie du carbonate de 1-naphtylméthyle phényle (**3**) et du carbonate de 1-naphtylméthyle phényle (**4**) dans le méthanol. Avec le composé **3**, on obtient les deux produits provenant du cation et du radical 1-naphtylméthyle; toutefois, avec le composé **4**, on n'obtient que le composé provenant du cation. On a obtenu des résultats semblables avec les dérivés 1-naphtylméthyles correspondants **5** et **6** des acides *N*-phényl- et *N*-benzylcarbamiques. On peut expliquer les rendements obtenus pour les quatre produits en se basant sur un mécanisme impliquant un clivage initial homolytique de la liaison oxygène–carbone du 1-naphtylméthyle à partir de l'état singulet excité. La paire de radicaux qui est générée conduit à deux voies réactionnelles, une décarboxylation ou la formation d'une paire d'ions après un transfert d'électron. Pour les PhOCOO˙ et PhNHCOO˙, la décarboxylation est rapide et est en compétition avec le transfert d'électron. Pour le $PhCH_2OCOO$˙ et le $PhCH_2NHCOO$˙, la décarboxylation est plus lente, le transfert d'électron domine et on obtient seulement des produits provenant de la paire d'ions.

[Traduit par la Rédaction]

Introduction

The solution photochemistry of esters of carboxylic acids (R^1-CO-OR^2) has been extensively studied and the fundamental excited state processes are well understood (1, 2). Esters with saturated alkyl groups have only a weakly absorbing n,π^* transition around 215 nm, which is outside the range of the standard Hg arc light sources. Therefore, most results have been obtained for compounds that have chromophores such as aromatic rings (i.e., R^2 = Ar or $ArCH_2$) conjugated to the ester functional

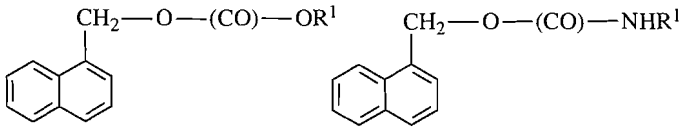

3 R^1 = Ph
4 R^1 = $PhCH_2$

5 R^1 = Ph
6 R^1 = $PhCH_2$

group. For the former (R^2 = Ar), carbonyl carbon–oxygen bond cleavage in the excited state is usually the dominant process often leading to photo-Fries products (3–5). For the latter (R^2 = $ArCH_2$), arylmethyl carbon–oxygen bond cleavage is facile and products characteristic of arylmethyl cations and radicals result (vide infra).

Much less is known about the photochemistry of carbonates (R^1O-CO-OR^2) and carbamates (R^1NH-CO-OR^2), and again, most of the information available deals with compounds having chromophores conjugated to the functional group. In agreement with the observations for esters, when R^1 is aryl in carbonates and carbamates and R^2 is methyl or ethyl, carbonyl carbon–oxygen (ArO-CO) or carbonyl carbon–nitrogen (ArNH-CO) bond

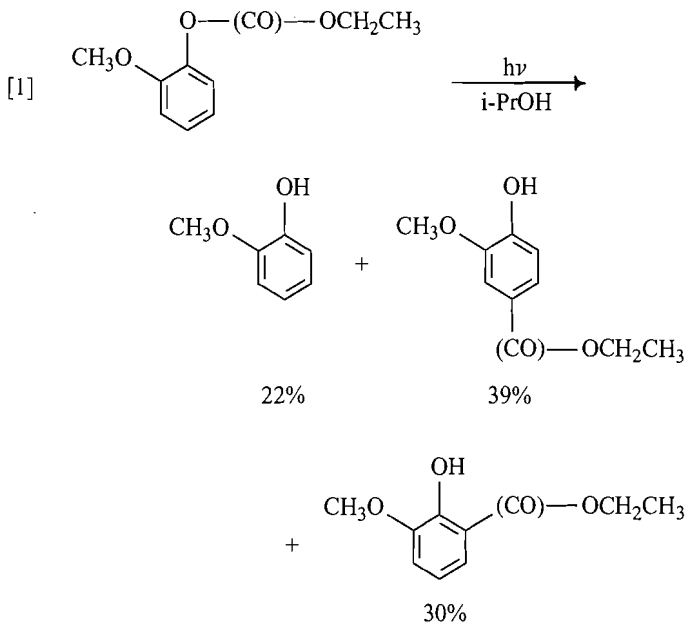

cleavage, respectively, dominate and photo-Fries products result. Two examples are given in eqs. [1] (6) and [2] (7).

More recently, there has been interest in the photochemistry of carbamates as a method for the generation of amines in solution. An efficient procedure has been developed using σ-nitrobenzyl carbamates (eq. [3], ref. 8), although the photochemistry involved is that of the nitrobenzyl functional group and not of the carbamate directly. The amine is released by ground state fragmentation of the α-hydroxy carbamate **1**. More relevant to carbamate photochemistry is the irradiation of the 3,5-dimethoxybenzyl derivatives (**2**) (eq. [4], ref. 9). This particular substitution pattern was chosen to enhance the efficiency

[1]Author to whom correspondence may be addressed. Telephone: (902) 494-3324. Fax: (902) 494-1310.

Can. J. Chem. Downloaded from www.nrcresearchpress.com by EESC ESCOLA DE ENGENHARIA on 09/08/12
For personal use only.

Can. J. Chem. Downloaded from www.nrcresearchpress.com by EESC ESCOLA DE ENGENHARIA on 09/08/12
For personal use only.

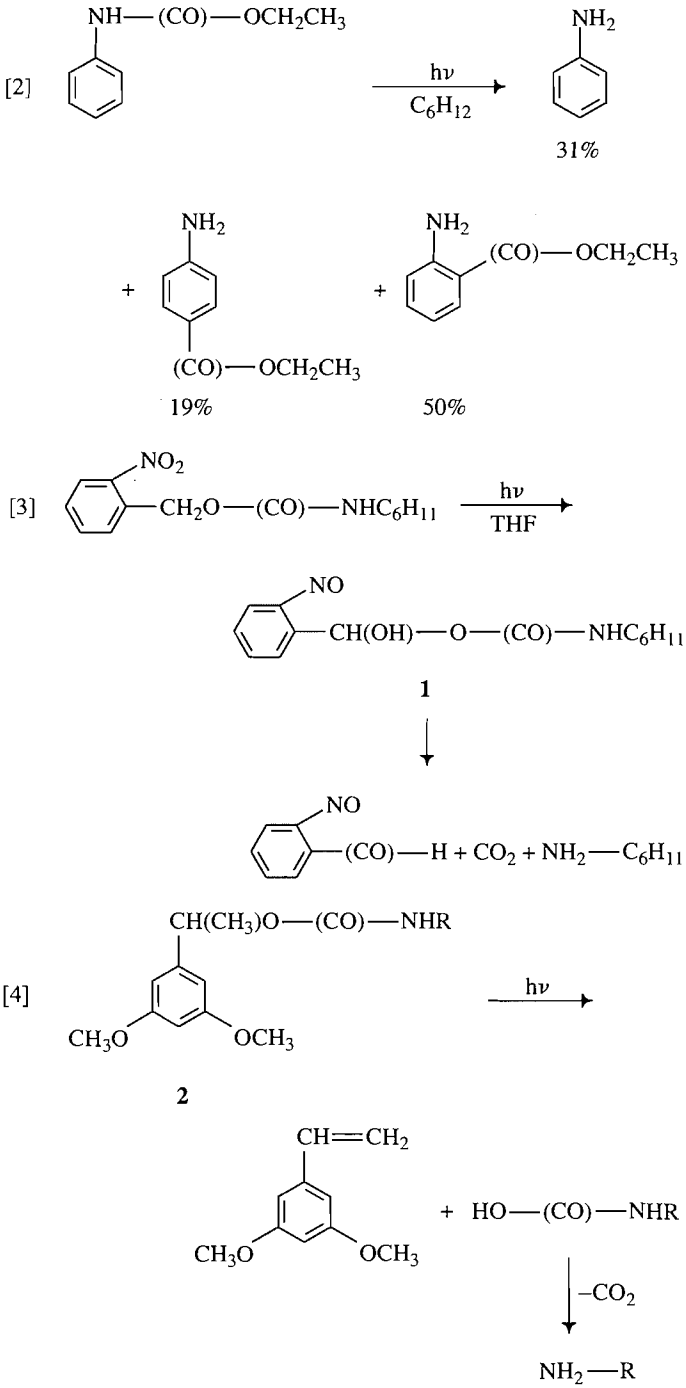

of heterolytic cleavage of the benzylic carbon–oxygen bond according to "*meta* effect" arguments (10).

According to the *meta* effect, substituents on the aromatic ring in photochemical cleavage reactions of arylmethyl substrates with leaving groups operate by controlling the competition between homolytic (k_R^X, R for radical) and heterolytic (k_I^X, I for ionic) cleavage of the arylmethyl carbon–oxygen bond in the excited singlet state (Scheme 1). The idea was founded on the observation (10), for substituted benzylic acetates, that the *meta*-methoxy isomer gave higher yields of the product derived from the intermediate cation than did the isomeric *para* compound. The effect was rationalized by electron density changes upon excitation giving enhanced rates of heterolytic cleavage for the *meta* isomer, electron donation favouring the pathway

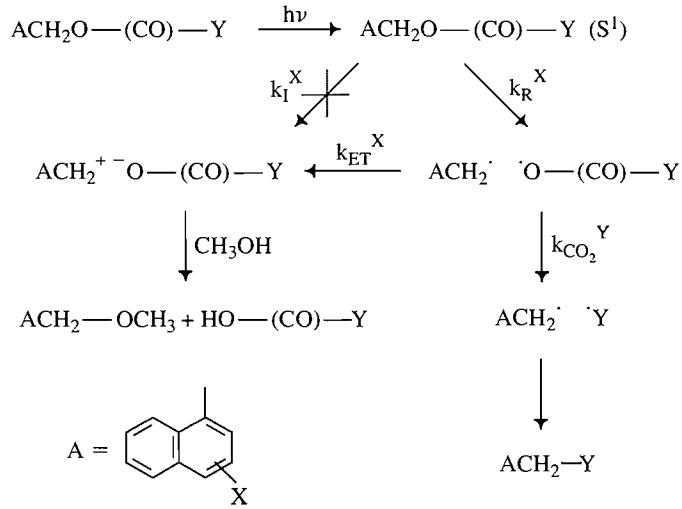

SCHEME 1. General mechanism for the photolysis in methanol of 1-naphthylmethyl compounds of carboxylic acid derivatives. For esters, Y = R; for carbonates, Y = OR; and for carbamates, Y = NHR.

for the formation of the arylmethyl cation. This observation, which is contrary to ground state expectations, was called the photochemical *meta* effect (10).

Recently, we have reported (11–13) on the photochemistry of 1-naphthylmethyl esters of carboxylic acids in the solvent methanol. As expected (14), for an arylmethyl substrate with a leaving group, the products obtained resulted from both the intermediate arylmethyl radical and the arylmethyl cation. On the basis of the variation in product yields as a function of substituents (X) on the naphthalene ring (11, 12) and of the structure (Y = alkyl) of the carboxylic acid (13), a mechanism was formulated as outlined in Scheme 1.

After excitation, homolytic carbon–oxygen bond cleavage forming the radical pair (k_R^X) occurs from the excited singlet state. Although intersystem crossing is reasonably efficient for naphthalene derivatives, the triplet state is unreactive because the excitation energy (~250 kJ/mol) is lower than the bond dissociation energy (~270 kJ/mol). The two critical steps that control product distribution follow the formation of the radical pair: electron transfer that converts the radical pair to the ion pair (k_{ET}^X) and decarboxylation of the acyloxy radical ($k_{CO_2}^Y$) to give a new radical pair. The ether and carboxylic acid products result from reaction of the ion pair with the solvent methanol and the hydrocarbon product results from in-cage coupling of the radical pair. The competition between these two reaction pathways can be systematically varied by changing the structure of the ester. Thus, variation of the alkyl group Y from methyl to *t*-butyl in the acyloxy radical changes $k_{CO_2}^Y$ from 1×10^9 to 11×10^9 s^{-1}, in agreement with the expectation that this process should be faster for the more stable alkyl radical. Variation in substituents (X) on the naphthalene ring varies the oxidation potential of the 1-naphthylmethyl radical and, thus, the rate of electron transfer. These oxidation potentials were shown to correlate with σ^+ ($\rho^+ = -8.4$) (15). The rates of electron transfer agreed very well with Marcus theory in both the normal and inverted regions (11, 12). For electron-withdrawing groups, the rates were slow (6.9×10^8 s^{-1} for X = 4-CN), passed through a maximum (6.0×10^{10} s^{-1} for X = 4-CH_3), and then decreased for strong electron-donating groups (3.3×10^9 s^{-1} for X = 4,7-$(OCH_3)_2$). The calculated reorganization energy was 0.52 eV. The important feature of Scheme 1 is that only homolytic cleavage of the excited state is

TABLE 1. Photophysical data for the carbonates and carbamates

Compounds[a]	ϕ_f[b]	τ_s, ns	$E_{0,0}$, kcal/mol (kJ/mol)	λ_{max}, nm (ε)
NM phenyl carbonate	0.11	31.0	93 (389)	276 (7054)
NM benzyl carbonate (**4**)	0.14	36.0	92 (385)	276 (6815)
NM phenyl carbamate (**5**)	0.12	38.5	93 (389)	276 (7327)
NM benzyl carbamate (**6**)	0.14	38.5	93 (389)	276 (5977)
NM phenyl acetate	0.14	49.0	92 (385)	275 (7400)
Naphthalene	0.20	90.0	92 (385)	270 (4918)

[a]NM, 1-naphthylmethyl.
[b]ϕ_f were determined by comparing the emission spectrum of the compound to the emission spectrum of naphthalene.

required to explain the product yields. No heterolytic cleavage to form ion pairs is included, i.e., $k_R^X \gg k_I^X$.

Based on these ideas, the photochemistry of 1-naphthylmethyl carbonates and carbamates is of obvious interest. The acyloxy radicals generated (R-O-CO-O· and R-NH-CO-O·, respectively) should have very different reactivity than those generated in ester photochemistry (R-CO-O·). If rates of electron transfer and decarboxylation are the dominant factors controlling product distribution, major changes in yield should be observed. Moreover, the study of the carbamates will provide the information necessary to design photolabile amine protecting groups.

In this paper, we report on the synthesis and photochemistry in methanol of the compounds **3–6**. The results are consistent with the mechanism outlined in Scheme 1.

Results and discussion

Synthesis of carbonates and carbamates

The carbonates were prepared by reaction in benzene with pyridine of 1-naphthylmethanol with phenyl chloroformate for **3** and benzyl chloroformate for **4**. The carbamates were prepared by reaction of 1-naphthylmethanol with phenyl isocyanate for **5** and benzyl isocyanate for **6**. Details and data for characterization are in the Experimental section.

*Excited state properties of carbonates **3** and **4** and carbamates **5** and **6***

To understand the excited state properties of the substrates, absorption and fluorescence measurements were taken. Values for the singlet energy, fluorescence quantum yield, and singlet lifetime are reported in Table 1, along with the corresponding values for 1-naphthylmethyl phenylacetate and naphthalene for comparison. The similarity in the values for the ester, carbonates, and carbamates indicates that inclusion of the oxygen or nitrogen into the functional group has little effect on the excited state behaviour. Therefore, the excitation energy is still localized on the naphthalene ring and the excited state should react by the normal arylmethyl carbon–oxygen bond cleavage. The decrease in fluorescence quantum yield and lifetime by going from naphthalene to the functionalized derivatives is a reflection of the efficiency of this bond cleavage process.

*Photolysis of carbonates **3** and **4***

A solution of the carbonate in methanol (nitrogen purged) was photolyzed in an immersion well with a 200-W, Pyrex-filtered medium-pressure Hanovia mercury lamp. Conversion of 1.3 g of starting material took 6 h. Progress of the reaction was monitored by HPLC. The products obtained and their yields (in parentheses) by calibrated HPLC are shown in eq. [5] for **3** and eq. [6] for **4** (A equals 1-naphthyl). The mass balance is

[5] $ACH_2O{-}(CO){-}OPh \xrightarrow[CH_3OH]{h\nu} ACH_2OCH_3$ **7** (43%)

3

+ PhOH + ACH_2OPh + 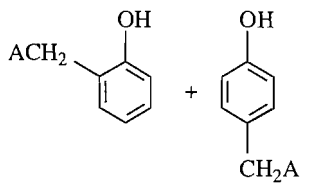 +

8 (43%) **9** (2%) **10** (31%) **11** (24%)

[6] $ACH_2O{-}(CO){-}OCH_2Ph \xrightarrow[CH_3OH]{h\nu}$

4

ACH_2OCH_3 + $HO{-}CH_2Ph$

7 (93%) **12** (97%)

clearly excellent. Determining that the structure of **11** was *para* was simply based on the coupling pattern of the aromatic H's in the ^1H NMR and the carbon count in the ^{13}C NMR. The assignment of **10** as *ortho* was based on the observation that the hydrogen *para* to the OH at δ 6.80 (calcd. (16), 6.76) showed two *ortho* couplings. The *meta* isomer, which was not detected, would have had a hydrogen *para* to the OH at δ 6.68 (calcd.) with only one *ortho* coupling.

The first observation to discuss is that none of the products derived from the carbonates **3** and **4** contained CO_2. In Scheme 1, for esters, the carboxylic acids (Y = alkyl) are stable and isolable. For carbonates (Y = OR), this is not so. The ground state

Can. J. Chem. Downloaded from www.nrcresearchpress.com by ESC ESCOLA DE ENGENHARIA on 09/08/12
For personal use only.

Can. J. Chem. Downloaded from www.nrcresearchpress.com by EESC ESCOLA DE ENGENHARIA on 09/08/12
For personal use only.

decomposition by loss of carbon dioxide of alkyl monocarbonates in aqueous solution has been studied (17). Not surprisingly, the reaction is base catalyzed and the rate levels off at high pH where the carbonate is completely ionized (eq. [7]). Based on

[7] $RO—(CO)—OH \rightleftharpoons RO—(CO)—O^- + H^+ \longrightarrow RO^-$

the pK_a of the alcohol and a Bronsted plot, rate constants for decomposition in water of about 10^{-3} s^{-1} for $PhCH_2OCO_2^-$ and about 10^3 s^{-1} for $PhOCO_2^-$ can be estimated. The values in methanol should not be much different. Since these alkyl carbonates are also reasonably strong acids ($pK_a^R \leq 0$) (17), they will be greater than 50% ionized in neutral solvents, so that the rate of loss of CO_2 will be fast relative to the photolysis times. Thus, the phenolic products **8**, **10**, and **11** in [5] and the alcohol **12** in [6] could be formed by thermal decomposition of the corresponding monocarbonates. In fact for the benzyl carbonate **4**, the essentially equivalent and quantitative yields of the ether **7** and the alcohol **12** suggest that both products are derived from the ion pair in Scheme 1. If the general mechanism in the scheme is correct, this means $k_{ET}^X \gg k_{CO_2}^Y$ (Y = OCH_2Ph) for this substrate. A value for the rate constant of decarboxylation of acyloxy radicals of this type (RO-CO-O·) has been estimated by laser flash photolysis studies (18) to be less than 10^6 s^{-1}. Since electron transfer rates in these radical pairs can be expected to be greater than 10^9 s^{-1} (vide supra), the mechanism is reasonable.

The situation is not so clear for the phenyl carbonate **3** (eq. [5]). The phenolic products **10** and **11** could be derived from the ion pair by a Friedel–Crafts type reaction of the 1-naphthylmethyl cation with the monocarbonate anion $PhOCO_2^-$. The oxygen, of course, would be *ortho–para* directing. Thermal loss of carbon dioxide would then give **10** and **11**. This possibility was tested by studying the ground state solvolysis of **3**. Thus, reaction of **3** in CH_3OH at 50°C (40% conversion after 35 h) resulted in conversion to only the ether **7** and the phenol **8**. No **10** and **11** were observed. Thus, **10** and **11** are not derived from the ion pair; neither is **9**, which could have been formed from the ion pair by coupling of the 1-naphthylmethyl cation with the phenoxide anion. This possibility is unlikely anyway, since the estimated rate constant of $\sim 10^3$ s^{-1} for thermal decarboxylation of $PhOCO_2^-$ is too small to compete with the expected very rapid trapping ($>10^9$ s^{-1}) of the ion pair in methanol.

A referee has raised the point that the above conclusions are based on the assumption that the ground state solvolysis of **3** in methanol occurs by the S_N1 mechanism. This is a valid comment, since the solvolysis of benzyl systems represents one of the classic cases of curved Hammett plots, as the mechanism changes from an ion pair S_N1 mechanism for stable cations to a solvent-assisted S_N2 mechanism for less stable cations. A detailed study of substituent effects on solvolysis rates in 80% acetone – water for benzyl tosylates (19) indicates that the change occurs near $\sigma^+ = 0$ for the unsubstituted case with $\rho^+ = -5.8$, indicating an S_N1 mechanism, for better electron-donating groups. A similar conclusion was reached from results on the rates of solvolysis of benzyl tosylates as a function of both substituents and solvents (20), including methanol. Fitting solvolysis rates to the Grunwald–Winstein equation indicated that the sensitivity to solvent nucleophilicity (L) dropped and the sensitivity to solvent ionizing power (*m*) exceeded unity as the substituent changed from H to 4-CH_3. To our knowledge, there is no available literature on the solvolysis of arylmethyl carbonates. However, based on the similarity of the pK_a of carbonic (17) and sulfonic (21) acids, they should be comparable as leaving groups. As well, changing from phenyl to 1-naphthyl is known to increase the rate of solvolysis of arylmethyl derivatives by a factor of about 20 (22). This is similar to the rate increase observed for changing a substituent from H to 4-CH_3 in benzyl systems (19). By analogy then, the solvolysis of 1-naphthylmethyl carbonates in methanol probably proceeds by a rate-determining S_N1 ionization to the very short-lived ion pair.

The conclusion drawn from this section is that photolysis of these carbonates again follows the general mechanism shown in Scheme 1 for ester photochemistry. Compounds **3** and **4** have very similar excited state properties. Therefore, the logical expectation is that the partitioning between k_R^X and k_I^X should be the same for both. However, the ratio of the yields of products derived from the ion pair versus the radical pair is 43:57 for **3** and >20:1 for **4**. Again, processes occurring after the excited state step must be of major importance.

One question still left to discuss is at what stage does decarboxylation occur in the pathway for formation of the radical coupled products **9–11**. Product **9** would have to be formed by coupling of the radical pair after decarboxylation. Products **10** and **11** could be formed either before or after decarboxylation. The rate constant for this decarboxylation process (eq. [8]) is

[8] $ACH_2^{\cdot}\ {}^{\cdot}O—(CO)—OPh \xrightarrow{-CO_2} ACH_2^{\cdot}\ {}^{\cdot}OPh$

unknown but, because of the stability of the phenoxy radical, will certainly be much greater than the case of RO-CO-O· ($<10^6$ s^{-1}) (18) where R is alkyl. However, coupling of the radical pairs after decarboxylation to form the products cannot be the explanation because the product distribution between **9**, **10**, and **11** should reflect the spin density in the phenoxy radical. Estimates of these values, from ESR measurements (23), are approximately 20% at oxygen, 40% at the *para* carbon, and 20% at each of the two *ortho* carbons. The yield of **9** (2%), therefore, seems lower than expected.

A resolution of this problem was prompted by a literature observation (24) on the photoreactivity of benzyl phenyl ether, which gave phenolic products analogous to **10** and **11** (eq. [9]).

[9] $PhCH_2—OPh$ (**13**) $\xrightarrow[CH_3CH_2OH]{h\nu}$

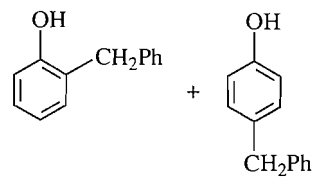

18% 14%

In agreement with this report, photolysis of **9** in methanol resulted in rapid conversion (0.72 g in 3.5 h) to **10** and **11**. The product ratio of **10**:**11** was 47:53. Therefore, the conversion of **9** and **10** to **11** is more efficient than the formation of **9** from the carbonate **3**. Since the chromophores of **3** and **9** are the same, no buildup of **9** in the reaction mixtures would be expected and none was observed. Thus, although most of the phenols **10** and **11** probably result from coupling after decarboxylation of the acyloxy radical (eq. [8]), some probably result from secondary photolysis of **9**.

As mentioned above, another possibility is that coupling occurs before decarboxylation as shown in eq. [10] for the for-

Can. J. Chem. Downloaded from www.nrcresearchpress.com by ESC ESCOLA DE ENGENHARIA on 09/08/12
For personal use only.

[10] $ACH_2^{\cdot}$ $^{\cdot}O-(CO)-Ph \longrightarrow$

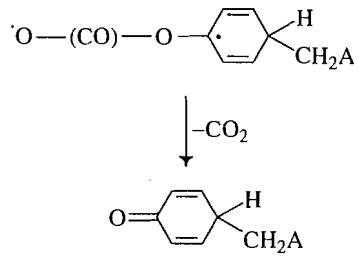

mation of **11**. The intermediate should rapidly lose CO_2 and the resulting ketone would then tautomerize to the phenol **11**. The choice between these various possibilities can only be made if a rate constant for decarboxylation of PhO-CO-O$^{\cdot}$ can be determined by laser flash photolysis.

No matter what the mechanism for decarboxylation, the conclusion reached is that for the photolysis of the phenyl carbonate **3**, the products **9–11** come from the initially formed radical pair. The general mechanism in Scheme 1 rationalizes all the results for both carbonates without including k_1^X. For the benzyl carbonate **4**, decarboxylation of the acyloxy radical is slow ($<10^6$ s^{-1}) and, therefore, electron transfer to form the ion pair dominates. For the phenyl carbonate **3**, decarboxylation is much faster and competes with electron transfer so that products from both the radical pair and the ion pair are observed.

*Photolysis of carbamates **5** and **6***

Products and their yields for these two photolyses are shown in eqs. [11] and [12]. These reactions were not as clean as the

[11] $ACH_2O-(CO)-NHPh \xrightarrow[CH_3OH]{h\nu} ACH_2OCH_3$

5 **7** (23%)

$+ NH_2Ph + ACH_2NHPh +$ 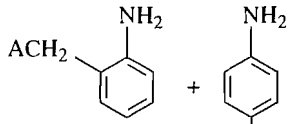 $+$

14 **15** (26%) **16** (7%) **17** (8%)

[12] $ACH_2O-(CO)-NHCH_2Ph \xrightarrow[CH_3OH]{h\nu}$

6

$ACH_2OCH_3 + NH_2CH_2Ph$

7 (73%) **18**

carbonate cases and the solutions turned murky as the reaction proceeded. Moreover, the mass balances are clearly lower (~70%). However, the products obtained show the same general trend as for the carbonates. For the phenyl carbamate **5**, the ether **7** (from the ion pair intermediate) and the radical coupling products **15–17** are formed in competition with each other, whereas for the benzyl carbamate **6**, only the ion pair derived products, the ether and amine, were detected.

Once again there is information (25, 26) about the ground state stability of the potential carbamic acid products **19** (eq. [13]). Now at high pH, decarboxylation is slow because the

[13] $R-NH_2^+-(CO)-O^- \rightleftharpoons R-NH-(CO)-OH$ (**19**)

$R-NH_2 + CO_2$

$R-NH-(CO)-O^-$

$R-NH^- + CO_2$

instability of R-NH– makes it a poor leaving group. At lower pH, the rate constant for decarboxylation through the zwitterion has been estimated at 10^8–10^{10} s^{-1} depending on the amine. Therefore, these products will not survive the photolysis reaction times.

As far as the radicals are concerned, nothing is known about the rate constants for decarboxylation of RNH-CO-O$^{\cdot}$ species, although unsuccessful attempts to measure them have been reported (18).

Finally, the possibility that the coupling products **16** and **17** result from secondary photolysis of **15** was investigated. Surprisingly, in contrast to the ether **9**, irradiation of **15** in methanol gave no reaction. Therefore, the products shown in eq. [11] are all primary photoproducts. The fact that the ether **9** is photoreactive, but the structurally analogous amine **15** is not, may be a result of a stronger bond in the amine. Bond strengths of 277 kJ/mol for CH_3-OPh versus 298 kJ/mol for CH_3-HPh have been reported (27).

The conclusion to be reached from the carbamate photochemistry is essentially the same as that for the carbonates. Again the general mechanism shown in Scheme 1 rationalizes all the results without including heterolytic cleavage of the excited state. Homolytic cleavage gives the radical pair. For carbamate **5**, the decarboxylation of the radical PhNH-CO-O$^{\cdot}$ competes with electron tranfer and products derived from both the ion pair and the radical pair are observed. For **6**, on the other hand, decarboxylation of $PhCH_2NH$-CO-O$^{\cdot}$ is slower, electron transfer dominates, and only products from the ion pair are detected.

Experimental

General experimental

^1H and ^{13}C NMR spectra were obtained in $CDCl_3$ on a Bruker AC 250F NMR spectrometer in automation mode. Chemical shifts are reported in parts per million (δ) relative to tetramethylsilane (0.00) as an internal standard. Multiplicities are abbreviated as follows: s = singlet, d = doublet, t = triplet, q = quartet, m = multiplet. IR spectra were obtained on a Nicolet 205 FT-IR spectrometer and the frequencies are reported in wave numbers (cm^{-1}). C, H, and N analyses were done by Canadian Microanalytical Services Ltd, Delta, BC V4G 1G7, Canada. GC–MS analyses were done on a Hewlett Packard 5890A GC 5970 with a mass selective detector, using a Hewlett Packard 9816 microcomputer. The column used was a 25 m × 0.2 mm 5% phenyl methyl silcone on fused silica with a film thickness of 0.25 μm. Masses are reported in units of mass over charge (*m/z*). Intensities are reported as a percent of the base peak intensity. The molecular ion is indicated by $M^{+\cdot}$. GC–FID analyses were performed using a Hewlett Packard 5890A gas chromatograph and a Hewlett Packard 7673 automatic injector, with a Hewlett Packard 7673A controller and a Hewlett Packard 3396A integrator. A 1-m glass column was used with 10% Fluorad FC-431 and 1% H_3PO_4 on Chromosorb W HP 80/100 mesh. The detector used was a flame ionization detector. HPLC analyses were obtained with a Waters 6000 solvent delivery system and a Waters U6K injector under isocratic conditions with a flow rate of 2 mL/min, using a Brownlee Lab Spheri-10 10-μL reverse-phase column (25 × 0.46 cm) with a Waters model 450 variable wavelength detector. UV

Can. J. Chem. Downloaded from www.nrcresearchpress.com by EESC ESCOLA DE ENGENHARIA on 09/08/12
For personal use only.

detection for monitoring the reaction was 280 nm. Absorption spectra were obtained using a Varian Cary 219 spectrophotometer. Silica gel T-6145 plates from Sigma were used for TLC. Silica gel 60 Å (70–230 mesh) was used for normal column chromatography.

*Synthesis of the 1-naphthylmethyl carbonates (**3**, **4**)*

The appropriate chloroformate (0.044 mol, 5.5 mL) in 40 mL of benzene was slowly added to a well-stirred solution of 6.33 g (0.04 mol) of 1-naphthylmethanol and 4 mL of pyridine in 150 mL of benzene. The reaction mixture was stirred for 6 h and then poured into 50 mL of water, and the organic layer was separated. This layer was washed with 80 mL of 10% HCl, 80 mL of 5% NaOH, and 80 mL of water, dried with $MgSO_4$, and evaporated to give an oil.

*1-Naphthylmethyl phenyl carbonate (**3**)*

The crude oil was distilled under vacuum to give a solid product. The solid was recrystallized from hexane. mp 56–57°C; IR (Nujol) ν_{max}: 1745 (C═O), 1580, 1440, 1240 (C—O), 1200, 1050 (C—O), 730, 790, 675 cm^{-1}; ^1H NMR δ: 8.09 (d, 1H, J = 8.4 Hz), 7.88 (d, 2H, J = 8.4 Hz), 7.63–7.33 (m, 6H), 7.24–7.15 (m, 3H), 5.74 (s, 2H); ^{13}C NMR δ: 153.8 (C═O), 151.3 (C), 133.7 (C), 131.5 (C), 130.2 (C), 129.7 (CH), 129.3 (CH), 128.7 (CH), 128.0 (CH), 126.7 (CH), 126.0 (CH), 125.9 (CH), 125.1 (CH), 123.3 (CH), 120.9 (CH), 68.5 (CH_2); GC–MS *m/z*: 278 (3, $M^{+\cdot}$), 142 (12), 141 (100), 140 (3), 139 (6), 115 (15). Anal. calcd. for $C_{18}H_{14}O_3$: C 77.68, H 5.07; found: C 77.45, H 5.12.

*1-Naphthylmethyl benzyl carbonate (**4**)*

The crude oil was purified by column chromatography using 400 g of silica gel and eluting with 25% ethyl acetate – 75% hexane. Fractions were collected every 30 mL. Fractions 18–30 were combined and the solvent was removed to give 8.83 g (80% yield) of the purified carbonate. For the quantitative photolysis and spectroscopy, the carbonate was further purified by bulb-to-bulb distillation. bp 99°C/0.15 Torr (1 Torr = 133.3 Pa); IR (neat) ν_{max}: 3063, 2961, 1744 (C═O), 1600, 1513, 1498, 1456, 1391, 1258 (C—O), 1245 (C—O), 952, 936, 909, 801, 792, 777 cm^{-1}; ^1H NMR δ: 7.98 (d, 1H, J = 7.6 Hz), 7.78 (m, 2H), 7.52–7.26 (m, 9H), 5.59 (s, 2H), 5.13 (s, 2H); ^{13}C NMR δ: 155.1 (C═O), 135.2 (C), 133.7 (C), 131.5 (C), 130.7 (C), 129.5 (CH), 128.7 (CH), 128.53 (CH), 128.47 (CH), 128.3 (CH), 127.6 (CH), 126.7 (CH), 125.9 (CH), 125.2 (CH), 123.5 (CH), 69.7 (CH_2), 67.2 (CH_2); GC–MS *m/z*: 292 (38, $M^{+\cdot}$), 201 (51), 141 (62), 129 (100), 128 (25), 127 (27), 115 (32), 91 (66), 77 (17), 65 (17), 51 (13). Anal. calcd. for $C_{19}H_{16}O_3$: C 78.06, H 5.52; found: C 78.11, H 5.52.

*Synthesis of the 1-naphthylmethyl carbamates (**5**, **6**)*

The appropriate isocyanate (2.5 mL, 0.023 mol) was slowly added to 3.0 g (0.019 mol) of 1-naphthylmethanol. The reaction mixture was heated with stirring on a hot water bath for 10 min. The viscous liquid solidified upon cooling to give the crude carbamate.

*1-Naphthylmethyl N-phenyl carbamate (**5**)*

The crude carbamate was purified by chromatography on silica gel eluting with 70% dichloromethane – 30% hexane. It was purified further by recrystallization from hexane to constant melting point. mp 89–90°C; IR (Nujol) ν_{max}: 3330 (NH), 1680 (C═O), 1585, 1520, 1300, 1230 (C—O), 1050, 790, 755, 730 cm^{-1}; ^1H NMR δ: 8.09 (d, 1H, J = 7.9 Hz), 7.89 (t, 2H, J = 7.7 Hz), 7.61–7.26 (m, 8H), 7.06 (t, 1H, J = 7.2 Hz), 6.65 (br s, 1H), 5.67 (s, 2H); ^{13}C NMR δ: 148.0 (C═O), 136.2 (C), 133.3 (C), 131.7 (C), 130.6 (C), 129.5 (CH), 129.1 (CH), 128.8 (CH), 127.8 (CH), 126.7 (CH), 126.0 (CH), 125.3 (CH), 124.7 (CH), 123.6 (CH), 123.5 (CH), 118.6 (C), 65.4 (CH_2); GC–MS *m/z*: 277 (12, $M^{+\cdot}$), 141 (100), 116 (10). Exact mass calcd. for $C_{18}H_{15}NO_2$: 277.1103; found: 277.1095.

*1-Naphthylmethyl N-benzyl carbamate (**6**)*

The crude carbamate was purified by column chromatography using silica gel and eluting with dichloromethane. The carbamate was further purified by recrystallization from hexane–dichloromethane to constant melting point. mp 118–119°C; IR (Nujol) ν_{max}: 3310 (NH), 2953, 2854, 1680 (C═O), 1545, 1456, 1264, 777, 700 cm^{-1}; ^1H NMR δ: 8.06 (d, 1H, J = 7.8 Hz), 7.86 (m, 2H), 7.47 (m, 4H), 7.29 (s, 5H), 5.61 (s, 2H), 5.05 (br s, 1H), 4.40 (d, 2H, J = 5.8 Hz); ^{13}C NMR δ: 156.4 (C═O), 138.4 (C), 133.6 (C), 131.9 (C), 131.6 (C), 129.1 (CH), 128.6 (CH), 128.5 (CH), 127.4 (CH), 127.3 (CH), 126.4 (CH), 125.8 (CH), 125.2 (CH), 123.6 (CH), 65.0 (CH_2), 45.0 (CH_2); GC–MS 291 ($M^{+\cdot}$, 29), 158 (76), 150 (19), 142 (14), 141 (100), 140 (18), 139 (18), 129 (37), 128 (14), 127 (13), 115 (37), 106 (11), 91 (19), 77 (14), 51 (14). Exact mass calcd. for $C_{19}H_{17}NO_2$: 291.1259; found: 291.1256.

Fluorescence measurements

A Perkin-Elmer MPF 66 fluorescence spectrometer was used for the fluorescence studies. The samples were degassed by three freeze–pump–thaw cycles. Fluorescence quantum yields were determined by comparison with a fluorescence quantum yield of 0.24 (28) for naphthalene in methanol. Singlet state energies were determined by the position of the 0,0 band using the overlap between the excitation and emission spectra. Fluorescence lifetimes were measured using a Photochemical Research Associates single photon counting apparatus, using a H_2 lamp with a pulse width of about 1 ns.

Preparative photolysis

A solution of ~1 g of the 1-naphthylmethyl carbonate or carbamate in 420 mL of distilled methanol was placed in an immersion well and degassed with nitrogen for 15 min before irradiation; degassing was continued during the irradiation. The light source was a Pyrex-filtered 200-W medium-pressure Hanovia mercury lamp. Irradiation was continued until the starting material was greater than 90% consumed. The photolysis solution was concentrated under vacuum to give an oil. The products were separated on a column packed with silica gel. The products isolated in this manner were further purified if necessary.

Characterization of the photoproducts

Phenol (**8**), benzyl alcohol (**12**), aniline (**14**), and benzyl amine (**15**) were purchased from the Aldrich Chemical Company and purified if necessary. Product **7**, 1-naphthylmethyl methyl ether, was available in the laboratory and has been previously characterized (13).

*1-Naphthylmethyl phenyl ether (**9**)*

An insufficient quantity of pure compound was isolated from the photolysis mixture of the carbonate for the study of its photochemistry. This compound was synthesized using the following procedure. Sodium phenoxide was prepared by adding 1.02 g (0.044 mol) of sodium to 30 mL of methanol, followed by the addition of 4.02 g (0.043 mol) of phenol. The sodium phenoxide solution was slowly added to 4.6 mL (0.031 mol) of 1-(chloromethyl)naphthalene in 20 mL of methanol. The reaction mixture was stirred overnight and then concentrated by rotary evaporation to 10 mL. Water (40 mL) was added and the water layer was washed with dichloromethane (3 × 20 mL). The organic layers were combined and dried over $MgSO_4$. The crude product was recrystallized from ethanol. mp 68–68.5°C (lit. (29) mp 66–67°C); ^1H NMR δ: 8.05 (m, 1H), 7.90 (d, 1H, J = 5.7 Hz), 7.85 (d, 1H, J = 9.3 Hz), 7.60 (1H, d, J = 5.9 Hz), 7.55–7.43 (m, 3H), 7.32 (t, 2H, J = 7.3 Hz), 7.07 (d, 2H, J = 7.8 Hz), 6.99 (t, 1H, J = 7.3 Hz), 5.49 (s, 2H); ^{13}C NMR δ: 158.9 (C),133.8 (C), 132.4 (C), 131.6 (C), 129.6 (CH), 129.0 (CH), 128.7 (CH), 126.6 (CH), 126.5 (CH), 125.9 (CH), 125.4 (CH), 123.7 (CH), 121.1 (CH), 114.9 (CH), 68.6 (CH_2); GC–MS *m/z*: 234 (5, $M^{+\cdot}$), 142 (12), 141 (100), 115 (37), 65 (11).

*2-(1-Naphthylmethyl)phenol (**10**)*

IR (neat) ν_{max}: 3400 (br), 3025, 2950, 2900, 1580, 1500, 1455, 1260, 760 cm^{-1}; ^1H NMR δ: 8.03 (m, 1H), 7.85 (m, 1H), 7.75 (d, 1H, J = 8.4 Hz), 7.49–7.36 (m, 4H), 7.11 (t, 1H, J = 7.7 Hz), 6.95 (d, 1H, J = 6.3 Hz), 6.80 (m, 2H), 4.44 (s, 2H); ^{13}C NMR δ: 153.6 (C), 135.6 (C), 133.9 (C), 132.8 (C), 132.2 (C), 130.8 (CH), 128.7 (CH), 127.7 (C), 127.3 (CH), 126.6 (CH), 126.1 (CH), 125.7 (CH), 125.6 (CH), 124.1 (CH), 121.0 (CH), 115.5 (CH), 32.8 (CH_2); GC–MS *m/z*: 234 (51, $M^{+\cdot}$), 215 (13), 202 (10), 128 (100).

Can. J. Chem. Downloaded from www.nrcresearchpress.com by EESC ESCOLA DE ENGENHARIA on 09/08/12
For personal use only.

4-(1-Naphthylmethyl)phenol (11)

IR (neat) ν_{max}: 3380 (br), 3075, 2990, 2924, 1620, 1511, 1440, 1260, 792 cm^{-1}; ^1H NMR δ: 7.97 (m, 1H), 7.84 (m, 1H), 7.73 (d, 2H, J = 8.4 Hz), 7.48–7.30 (m, 4H), 7.03 (d, 2H, J = 8.2 Hz), 6.71 (d, 2H, J = 8.4 Hz), 4.36 (s, 2H); ^{13}C NMR δ: 153.2 (C), 140.6 (C), 133.9 (C), 131.3 (C), 129.8 (CH), 128.6 (CH), 127.1 (CH), 127.0 (CH), 125.9 (CH), 125.6 (CH), 125.5 (CH), 124.2 (CH), 115.2 (CH), 38.2 (CH_2); GC–MS *m/z*: 234 (100, $M^{+\cdot}$), 233 (44), 217 (16), 215 (32), 203 (11), 202 (20), 189 (9), 141 (16), 128 (32), 107 (14), 77 (11).

N-*(1-Naphthylmethyl)aniline (15)*

This compound was isolated from the photolysis mixture and also synthesized because more compound was needed for further analyses. Aniline (2.2 mL, 0.024 mol) was added to a solution of 3.75 g (0.024 mol) of 1-naphthaldehyde in 80 mL of methanol. The solution was refluxed overnight. After cooling, the solvent was removed to give the crude imine. The crude imine was purified by column chromatography using 250 g of silica gel and eluting with 90% hexane – 10% ethyl acetate. Fractions were collected every 20 mL and fractions 9–19 were found to contain the imine. The fractions were combined and the solvent was removed to give 3.9 g (0.017 mol) of the imine (yield 79%). The imine was dissolved in 200 mL of methanol and 0.63 g (0.017 mol) of sodium borohydride was added slowly. The solution was refluxed for 20 min and then cooled. Excess sodium borohydride was added to ensure that all of the imine had been reduced (as indicated by the disappearance of the yellow color). The amine was liberated by addition of an equal amount of water to the flask. The amine was precipitated and collected. It was purified by recrystallization from methanol–water to give 0.60 g of the amine (15% yield), which was identical by spectroscopy to that isolated from the photolysis mixture of carbamate **5**. mp 63.4–64°C (lit. (30) mp 64°C); ^1H NMR δ: 7.89–7.77 (m, 4H), 7.51–7.40 (m, 2H), 6.77–6.65 (m, 4H), 4.70 (s, 2H), 3.97 (br s, 1H); ^{13}C NMR δ: 148.2 (C), 134.3 (C), 133.8 (C), 131.5 (C), 129.3 (CH), 128.7 (CH), 128.2 (CH), 126.3 (CH), 126.0 (CH), 125.8 (CH), 125.5 (CH), 123.6 (CH), 117.5 (CH), 112.7 (CH), 47.2 (CH_2); GC–MS *m/z*: 233 ($M^{+\cdot}$, 31), 142 (40), 141 (100), 115 (29), 77 (12), 65 (19).

2-(1-Naphthylmethyl)aniline (16)

^1H NMR δ: 8.08 (m, 1H), 7.88 (m, 1H), 7.76 (d, 1H, J = 8.2 Hz), 7.52–7.48 (m, 2H), 7.37 (t, 1H, J = 8.2 Hz), 7.15–7.08 (m, 2H), 6.92 (d, 1H, J = 7.5 Hz), 6.76–6.70 (m, 2H), 4.31 (s, 2H), 3.57 (br s, 2H); ^{13}C NMR δ: 144.6 (C), 134.7 (C), 133.8 (C), 132.2 (C), 130.7 (CH), 128.8 (CH), 127.6 (CH), 127.2 (CH), 126.1 (CH), 125.9 (CH), 125.7 (CH), 125.68 (CH), 124.3 (C), 123.8 (CH), 118.9 (CH), 115.7 (CH), 34.5 (CH_2); GC–MS *m/z*: 233 ($M^{+\cdot}$, 100), 232 (57), 215 (28), 128 (13), 115 (14), 106 (11).

4-(1-Naphthylmethyl)aniline (17)

^1H NMR δ: 7.99 (m, 1H), 7.84 (m, 1H), 7.73 (d, 1H, J = 8.1 Hz), 7.46–7.37 (m, 3H), 7.26 (d, 1H, J = 6.6 Hz), 7.00 (d, 2H, J = 8.1 Hz), 6.66 (d, 2H, J = 8.1 Hz), 4.36 (s, 2H), 3.60 (br s, 2H); ^{13}C NMR δ: 143.0 (C), 137.2 (C), 133.9 (C), 132.1 (C), 129.6 (C), 128.6 (CH), 127.1 (CH), 127.0 (CH), 125.9 (CH), 125.53 (CH), 125.50 (CH), 124.3 (CH), 116.0 (CH), 38.2 (CH_2); GC–MS *m/z*: 233 ($M^{+\cdot}$, 100), 232 (59), 217 (13), 215 (17), 115 (11), 106 (25).

Quantitative photolysis

Compounds **3–6** were irradiated in the same manner as was described under the preparative photolysis section, but in this case only 100 mg of the substrate was used. Analyses were done with less than 50% of the starting material consumed. The product yields were calculated at various percent conversions and no change in product ratio as a function of time was indicated. Dark reactions were found to be negligibly slow. Standard solutions were prepared which contained a known amount of the photoproducts. These standards were used to determine the yields of photoproducts for the photolysis by HPLC. The peak heights of the products in the sample were measured and compared with the peak heights of a standard solution of the corresponding product.

Photolysis of 1-naphthylmethyl phenyl ether (9)

A solution of 173 mg of the ether in 300 mL of methanol was irradiated until >90% of the ether had reacted. There were two photoproducts formed from this reaction. They were separated on a 30 × 2.2 cm column packed with 25 g of silica gel. One 100-mL fraction was collected, followed by ten 10-mL fractions and then ten 30-mL fractions. The fractions were analyzed by HPLC. Fractions 9–13 were combined. The solvent was removed giving 47 mg of photoproduct. This product was identified as 2-(1-naphthylmethyl)phenol (**10**) by comparison with previously recorded spectra. Fractions 17–19 were combined and the solvent was removed to give 18 mg of photoproduct. By comparison with previously recorded spectra this photoproduct was identified as 4-(1-naphthylmethyl)phenol (**11**).

Photolysis of N-*(1-naphthylmethyl)aniline (15)*

This compound was photolysed in a manner analogous to that described above. After 48 h of irradiation, no product formation was detected.

Acknowledgements

This research was supported by a grant from the Natural Sciences and Engineering Research Council of Canada. P.J.W. thanks Dalhousie University Faculty of Graduate Studies for a graduate fellowship and both NSERC of Canada and the I.W. Killam Fund for graduate scholarships.

1. R.S. Givens and N. Nevi. The chemistry of functional groups. Suppl. B. *In* The chemistry of acid derivatives. *Edited by* S. Patai. Wiley, Chichester. 1979. p. 641.
2. J.A. Pincock. Ester photochemistry. *In* Handbook of organic photochemistry. *Edited by* W. Horspool. CRC Press, Inc., Boca Raton. 1994. In press.
3. R. Martin. Org. Prep. Proced. Int. **24**, 369 (1992).
4. D. Bellus. Adv. Photochem. **8**, 109 (1971).
5. G. Kaupp. Angew. Chem. Int. Ed. Engl. **19**, 243 (1980).
6. E.A. Caress and I.E. Rosenberg. J. Org. Chem. **37**, 3160 (1972).
7. J.E. Herweh and C.E. Hoyle. J. Org. Chem. **45**, 2195 (1980).
8. J.F. Cameron and J.M.J. Fréchet. J. Am. Chem. Soc. **113**, 4303 (1991).
9. J.F. Cameron and J.M.J. Fréchet. J. Org. Chem. **55**, 5919 (1990).
10. H.E. Zimmermen and V.R. Sandel. J. Am. Chem. Soc. **85**, 915 (1963).
11. D.P. DeCosta and J.A. Pincock. J. Am. Chem. Soc. **111**, 8948 (1989).
12. J.W. Hilborn and J.A. Pincock. J. Am. Chem. Soc. **113**, 2683 (1991).
13. D.P. DeCosta and J.A. Pincock. J. Am. Chem. Soc. **115**, 2180 (1993).
14. S.J. Cristol and T.H. Bindel. Org. Photochem. **6**, 327 (1983).
15. P.H. Milne, D.D.M. Wayner, D.P. DeCosta, and J.A. Pincock. Can. J. Chem. **70**, 121 (1992).
16. D.H. Williams and I. Fleming. Spectroscopic methods in organic chemistry. 4th ed. McGraw-Hill, London. 1987. p. 139.
17. C.K. Sauers, W.P. Jencks, and S. Groh. J. Am. Chem. Soc. **97**, 5546 (1975).
18. J. Chateauneuf, J. Lusztyk, B. Maillard, and K.U. Ingold. J. Am. Chem. Soc. **110**, 6727 (1988).
19. M. Fujio, M. Goto, T. Susuki, I. Akasaka, M. Mishima, and Y. Tsuno. Bull. Chem. Soc. Jpn. **63**, 1146 (1990).
20. D. Kevill and H. Ren. J. Org. Chem. **54**, 5654 (1989).
21. F. Bordwell. Acc. Chem. Res. **21**, 456 (1988).
22. Y. Tsuno, M. Sawada, T. Fujii, and Y. Yukawa. Bull. Chem. Soc. Jpn. **48**, 3347 (1975).
23. T.J. Stone and W.A. Waters. J. Chem. Soc. 213 (1964).
24. D.P. Kelly, J.T. Pinhey, and R.D.G. Rigby. Aust. J. Chem. **22**, 977 (1969).
25. S.L. Johnson and D.L. Morrison. J. Am. Chem. Soc. **94**, 1323 (1972).

26. M. Caplow. J. Am. Chem. Soc. **90**, 6795 (1968).
27. D.F. McMillen and D.M. Golden. Annu. Rev. Phys. Chem. **33**, 493 (1982).
28. B. Arnold, L. Donald, A. Jurgens, and J.A. Pincock. Can. J. Chem. **63**, 3140 (1985).
29. T. Nakaya, T. Tomomoto, and M. Imoto. Bull. Chem. Soc. Jpn. **40**, 691 (1967).
30. N. Chapman and J. James. J. Chem. Soc. 1865 (1953).

Can. J. Chem. Downloaded from www.nrcresearchpress.com by EESC ESCOLA DE ENGENHARIA on 09/08/12
For personal use only.

The preparation of *C*-aryl glucals via palladium-catalyzed cross-coupling methods

RICHARD W. FRIESEN,[1] RICHARD W. LOO, AND CLAUDIO F. STURINO

Lash Miller Chemical Laboratories, Department of Chemistry, University of Toronto, Toronto, ON M5S 1A1, Canada

Received September 27, 1993

RICHARD W. FRIESEN, RICHARD W. LOO, and CLAUDIO F. STURINO. Can. J. Chem. **72**, 1262 (1994).

The *C*-aryl glucals **17–31** have been prepared by the palladium-catalyzed cross coupling of 1-tributylstannyl-3,4,6-tri-*O*-(*tert*-butyldimethylsilyl)-D-glucal (**11**) and aryl bromides. The major by-product in all of these reactions is the dimer **33**, the product of homocoupling of **11**. Alternatively, the *C*-aryl glucals **34–40** can be obtained from the palladium-catalyzed coupling of 1-iodo-3,4,6-tri-*O*-(triisopropylsilyl)-D-glucal (**16**) and a variety of metalated aromatics, including ArZnCl, $ArB(OH)_2$, and $ArB(OMe)_2$. The advantages of the latter procedure include superior coupling yields under milder reaction conditions and the high yielding preparation of **16** directly from 3,4,6-tri-*O*-(triisopropylsilyl)-D-glucal (**12**) by a metalation–iodination sequence.

RICHARD W. FRIESEN, RICHARD W. LOO et CLAUDIO F. STURINO. Can. J. Chem. **72**, 1262 (1994).

On a préparé les *C*-aryl glucals **17–31** par un couplage croisé catalysé par le palladium du 1-tributylstannyl-3,4,6-tri-*O*-(*tert*-butyldiméthylsilyl)-D-glucal (**11**) et des bromures d'aryle. Le sous-produit principal de toutes ces réactions est le dimère **33**, le produit d'homocouplage du produit **11**. On peut aussi obtenir les *C*-aryl glucals **34–40** par un couplage catalysé par le palladium du 1-iodo-3,4,6-tri-*O*-(triisopropylsilyl)-D-glucal (**16**) avec une variété de produits aromatiques métallés comportant le ArZnCl, le $ArB(OH)_2$ et $ArB(OMe)_2$. Les avantages de la dernière méthode incluent des rendements supérieurs de couplage dans des conditions plus douces et la préparation avec un rendement élevé du composé **16** directement à partir du 3,4,6-tri-*O*-(triisopropylsilyl)-D-glucal (**12**) par une séquence de métallation et d'iodation.

[Traduit par la Rédaction]

Introduction

The class of natural products known as the *C*-aryl glycosides (1, 2) has recently received a great deal of attention in the synthetic community since many of these compounds exhibit unique antibiotic and (or) antitumor activity. Although the key structural unit that identifies these compounds is the novel carbon–carbon bond that unites the carbohydrate and aromatic fragments, a further subclassification can be made based upon the type of substitution at C1 and C2 of the carbohydrate moiety. Three broad groupings of naturally occurring *C*-aryl glycosides made on this basis can be illustrated in general terms by **1–3** with representative examples including vineomycinone B2 methyl ester (3), chaetiacandin (4, 5), and papulacandin D (6, 7), respectively. Synthetic strategies directed toward the preparation of any of these classes must address not only the method of creating the key carbon–carbon bond with a large array of substituted aromatics, but also must be concerned with its stereoselective formation with respect to the various substituents at C1–C5 on the carbohydrate framework. Previously reported strategies directed toward the synthesis of *C*-aryl glycosides[2] address, for the most part, the preparation of only one of the three main *C*-aryl glycoside subclasses (8).

We became interested in developing a rapid, facile, and general route to *C*-aryl glycosides that would be relatively flexible with respect to aromatic substitution pattern and type and with respect to the availability of the range of *C*-aryl glycoside subclasses as described above (9–12). The fundamental difference between our anticipated route to *C*-aryl glycosides and previous results is that the functionalization of C1 and C2, and the determination of the anomeric carbon stereogenicity, would occur subsequent to the key C—C bond-forming reaction by the regio- and stereoselective functionalization of the enol ether double bond in a *C*-aryl glucal **8**. The general strategy that we

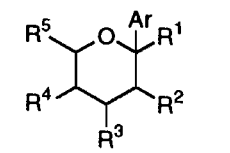

1 $R^1 = R^2 = H$
2 $R^1 = H$, R^2 = alkoxy
3 $R^1 = R^2$ = alkoxy

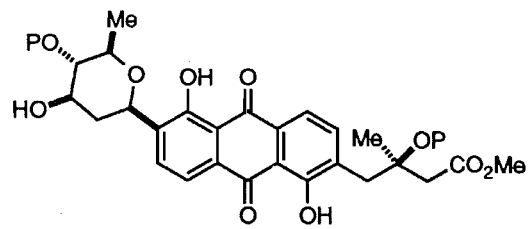

Vineomycinone B2 methyl ester
(P = carbohydrate)

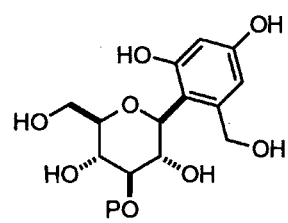

Chaetiacandin
(P = 6-O-acyl-galactopyranosyl)

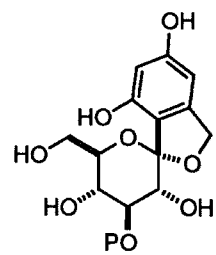

Papulacandin D (P = acyl)

[1]Author to whom correspondence may be addressed. Present address: Merck Frosst Centre for Therapeutic Research, P.O. Box 1005, Pointe Claire-Dorval, Quebec, Canada H9R 4P8. Telephone: (514) 428-3164. Fax: (514) 695-0693.

[2]An excellent review of recent methods for *C*-glycoside formation, including *C*-aryl glycosides, is found in ref. 8. For alternative methods for preparing *C*-aryl glycosides, see ref. 8 as well as the extensive summaries of references found in refs. 9, 20, and 21.

Can. J. Chem. Downloaded from www.nrcresearchpress.com by EESC ESCOLA DE ENGENHARIA on 09/08/12
For personal use only.

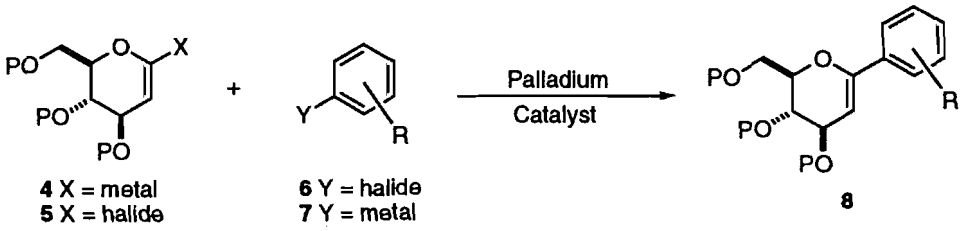

SCHEME 1

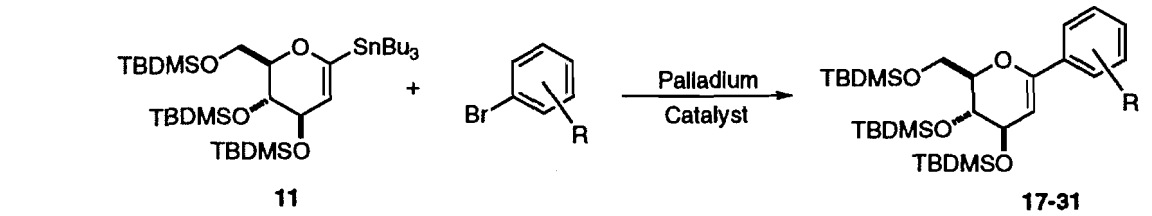

SCHEME 2

envisaged for the preparation of **8** was the palladium-catalyzed reaction (13, 14) of suitably derivatized organometallic and organic halide coupling partners (**4** + **6** → **8** or **5** + **7** → **8**) (see Scheme 1). Herein, we deail the results of our investigations that have led to the facile and efficient preparation of *C*-aryl glucals **8**, the key intermediates with respect to a general entry into the synthesis of *C*-aryl glycosides.[3]

Results and discussion

*(a) Palladium-catalyzed coupling reactions of 1-tributylstannyl-3,4,6-tri-O-(tert-butyldimethylsilyl)-D-glucal (**11**) and 1-tributylstannyl-3,4,6-tri-O-(triisopropylsilyl)-D-glucal (**14**)*

At the time we began this study, there was some indication in the literature that simple metalated enol ethers related to those illustrated by **4** (X = tin, zinc) would undergo palladium- catalyzed coupling reactions with aryl halides (22, 23). In addition, the preparation of stynnylated glucal **4** (X = *n*-Bu_3Sn) had been described by several groups (24–26). Therefore, it was the strategy illustrated by **4** + **6** → **8** (Scheme 1) that received our initial attention.

Previous reports from this laboratory have detailed the preparation of 1-tributylstannyl-3,4,6-tri-*O*-(*tert*-butyldimethylsilyl)-D-glucal (**11**) and 1-tributylstannyl-3,4,6-tri-*O*-(triisopropylsilyl)-D-glucal (**14**) (27). These compounds were prepared from the corresponding C1-unsubstituted silylated glucals **9** (TDMS = *tert*-butyldimethylsilyl) and **12** (TIPS = triisopropylsilyl), respectively, via metalation (*t*-BuLi, ether, 0°C) and trapping of the derived vinyl anions **10** and **13** with *n*-Bu_3SnCl. The problems that we have encountered in the preparation of **11**, due to competing metalation α to silicon on one or more of the *tert*-butyldimethylsilyl (TBDMS) protecting groups, have been documented (27).[4] As a result, the optimum yield in the preparation of **11** via this method is 30%. Conversely, the C1-metalation of **12** proceeds cleanly and **14** is readily obtained in 70–90% yield (27).

We now report the full details of a study involving the palladium-catalyzed coupling reactions of 1-tributylstannyl-

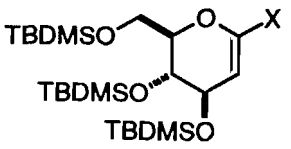

9 X = H
10 X = Li
11 X = *n*-Bu_3Sn

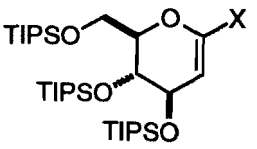

12 X = H
13 X = Li
14 X = *n*-Bu_3Sn
15 X = ZnCl
16 X = I

3,4,6-tri-*O*-(*tert*-butyldimethylsilyl)-D-glucal (**11**) with aryl bromides (Scheme 2, Table 1).[5] The initial investigation was concerned with the coupling of the simplest substrate, bromobenzene, and involved systematic variation of the typical palladium catalysts (14, 22, 23), solvent, and temperature. A representative sampling of the results is found in Table 1, entries 1–7. The optimum reaction conditions for the preparation of the *C*-phenyl glycal **17** (R = H) by the coupling of glucal **11** and bromobenzene were realized in refluxing THF (0.06 M in **11**), using $Pd(Ph_3P)_4$ as catalyst (Table 1, entry 3). Employing these conditions, **17** was produced very cleanly along with a small amount (ca. 10%) of a single by-product (vide infra).

While the coupling of bromobenzene proceeded readily under these "standard" conditions, similar reactions of glucal **11** with substituted bromobenzenes (1-bromo-4-nitrobenzene and 4-bromoanisole) were not reproducible and often failed completely under apparently identical reaction conditions. Similarly, attempts at using aryl iodides or aryl triflates (31, 32) in these coupling reactions gave poor and irreproducible results. After a great deal of experimentation, it was found that concentration, temperature, and catalyst all play an important role in the success or failure of the coupling reaction of **11** with substituted aryl bromides. The reaction conditions that appear to be

[3]Similar palladium-catalyzed coupling strategies (15–18) and alternative strategies (19–21) have been directed toward the preparation of *C*-aryl glycals.

[4]There have been other reports describing the problems associated with the vinylic deprotonation of a variety of highly substituted cyclic vinyl ethers containing silyl protecting groups (28–30). For example, Crich and Ritchie isolated a phenylthio derivative of **9** that had been formed upon metalation of **9** followed by trapping with $(PhS)_2$. They proposed that the phenylthio moiety had been introduced into the TBDMS group at C6 although no evidence in support of this proposal was given (30).

[5]For a prelminary account of this work, see ref. 9.

Can. J. Chem. Downloaded from www.nrcresearchpress.com by EESC ESCOLA DE ENGENHARIA on 09/08/12
For personal use only.

TABLE 1. Palladium-catalyzed coupling of the stannylated glucal **11** and aryl bromides[a]

Entry	ArX (1.1–2 equiv.)	Reaction conditions (catalyst/solvent/time)	Coupled product yield, % (dimer)[b]
1	PhBr	$Pd(Ph_3P)_4$/PhH/15 h	**17** 50[c]
2	PhBr	$Pd(Ph_3P)_4$/DMF[d]/15 h	**17** 34[c]
3	PhBr	$Pd(Ph_3P)_4$/THF/15 h	**17** 70[c]
4	PhBr	$Pd(Ph_3P)_4$/MeCN/15 h	**17** NR
5	PhBr	$Pd(Ph_3P)_2Cl_2$/PhH/15 h	**17** 52[c]
6	PhBr	$Pd(OAc)_2$/PhH/15 h	**17** Trace[c]
7	PhBr	$Pd(PhCN)_2Cl_2$/PhH/15 h	**17** Trace[c]
8	4-$NO_2C_6H_4Br$	$Pd(Ph_3P)_2Cl_2$/PhMe/30 min	**18** 78 (4)
9	4-CNC_6H_4Br	$Pd(Pd_3P)_2Cl_2$/PhMe/20 min	**19** 81 (8)
10	1-Bromonaphthalene	$Pd(Ph_3P)_2Cl_2$PhMe[d]/2 h	**20** 59 (15)[e]
11	4-$MeO_2CC_6H_4Br$	$Pd(Ph_3P)_2Cl_2$/PhMe/15 h	**21** 56 (8)
12	2-$MeO_2CC_6H_4Br$	$Pd(Ph_3P)_2Cl_2$/PhMe/15 h	**22** 48 (5)
13	4-ClC_6H_4Br	$Pd(Ph_3P)_2Cl_2$/PhMe/45 min	**23** 49 (8)
14	2-MeC_6H_4Br	$Pd(Ph_3P)_2Cl_2$/PhMe/2 h	**24** 49 (11)
15	2-$AcOCH_2C_6H_4Br$	$Pd(Ph_3P)_2Cl_2$/PhMe/2 h	**25** 46 (15)
16	PhBr	$Pd(Ph_3P)_2Cl_2$/PhMe/30 min	**17** 41 (12)
17	2-$AcOC_6H_4Br$	$Pd(Ph_3P)_2Cl_2$/PhMe/1 h	**26** 40 (11)
18	2-$BnOC_6H_4Br$	$Pd(Ph_3P)_2Cl_2$/PhMe/1 h	**27** 44 (4)
19	4-$MeOC_6H_4Br$	$Pd(Ph_3P)_2Cl_2$/PhMe[d]/2 h	**28** 30 (13)
20	2,5-$(MeO)_2C_6H_3Br$	$Pd(Ph_3P)_2Cl_2$/PhMe[d]/1 h	**29** 65 (9)
21	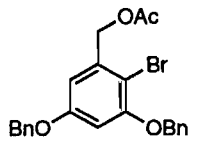	$Pd(Ph_3P)_2Cl_2$/PhMe/15 h	**30** 36 (18)
22		$Pd(Ph_3P)_2Cl_2$/mesitylene/1 h	**30** 51[c]
23		$Pd(Ph_3P)_2Cl_2$/PhH/15 h	**30** 85[c,f]
24	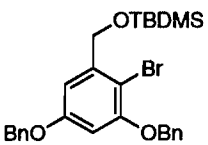	$Pd(Ph_3P)_2Cl_2$/PhMe/15 h	**31** 56 (13)
25	4-CNC_6H_4Br	$Pd(Ph_3P)_4$/mesitylene/30 min	**32** 66[c]

[a]See Scheme 2; 5 mol% catalyst. Approximate concentration **11** in refluxing solvent unless stated otherwise: 0.05 M for entries 1–7 and 0.2–1 M for entries 8–25.

[b]Yields of isolated, chromatographically pure products. Numbers in parentheses refer to the isolated yield of dimer **33**. Note that a 10% yield of dimer **33** involves the consumption of 20% of **11**.

[c]Dimer yield not measured.

[d]Reaction done at 100°C.

[e]The yield is based on an ^1H NMR integrated ratio of a chromatographically pure mixture of **20** and **33**. A small amount of pure **20** was isolated and characterized.

[f]Four equivalents of **11** used with respect to aryl bromide.

[g]Reaction carried out with glucal **14**.

universally successful involve refluxing toluene solutions of the stannyl glucal **11**, at concentrations of 0.2–1.0 M in **11**, in the presence of $Pd(Ph_3P)_2Cl_2$ (5 mol%) and the aryl bromide (1.1–2 equiv.).

Employing the revised "standard" reaction conditions, a wide variety of substituted aryl bromides were coupled successfully (Table 1, entries 8–24). Included in this list are aryl bromides containing electron-withdrawing and -donating substituents along with several highly substituted aromatics (see Table 1, entries 21–24). In all cases, the crude reaction mixtures were quite clean, providing the expected *C*-aryl glucals **17–31** in moderate to good yields. Several trends and additional points of interest regarding this coupling reaction are worth noting.

Firstly, the conditions of choice for the preparations of the unsubstituted *C*-phenyl glucal **17** are the original "standard" reaction conditions (compare Table 1, entries 3 and 16). For reasons that we cannot explain, bromobenzene is the sole example in which satisfactory coupling reactions take place under conditions of $Pd(Ph_3P)_4$ catalysis in THF. Secondly, the isolated yields of the *C*-aryl glucals reflect, at least qualitatively, an ordering based on the electronic properties of the aromatic substituent. In most cases, electron-poor aryl bromides (X = CN, NO_2, CO_2R) provide higher yields of coupled products than those aryl bromides with electron-donating substituents (X = alkyl, OR).[6] In addition, a general trend towards greater forma-

[6]A similar ordering, based on electron-withdrawing properties, has been observed in the palladium-catalyzed rate (not yield) of reaction of organostannanes with substituted aryl bromides (33) and terminal acetylenes (34, 35).

Can. J. Chem. Downloaded from www.nrcresearchpress.com by EESC ESCOLA DE ENGENHARIA on 09/08/12
For personal use only.

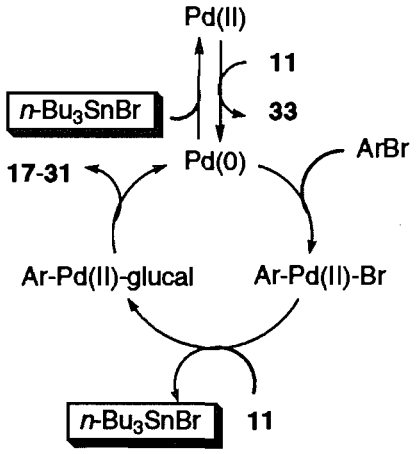

SCHEME 3

tion of the by-products (vide infra) is observed with electron-rich aryl bromides. Thirdly, more efficient coupling reactions could be effected in some cases by using an excess (with respect to the aryl bromide) of the stannyl glucal **11** and considering the aryl bromide as the limiting reagent (compare Table 1, entries 21 and 23).[7] However, due to the difficulties associated with obtaining significant quantities of **11** (vide supra), we have generally used **11** as the limiting reagent in our coupling reactions. The entries in Table 1 result from an optimization of the reaction conditions in light of this limitation. Finally, the major by-product that is produced in all of the reactions that we have performed results from the homocoupling of **11** (36). This dimer **33** accounts for the consumption of up to

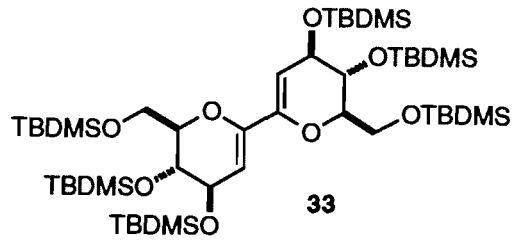

36% of the starting material **11** (Table 1, entry 21) and in many cases proved to be extremely difficult to separate from the desired *C*-aryl glucal. A variety of reaction modifications were considered in order to decrease the production of this dimer. None of these attempts, including employing nickel catalysts or using the vinyl zinc glucal derived from **10**, met with success.

Several established synthetic procedures for the preparation of 1,3-dienes involve the Pd(II) mediated homocoupling of vinylsilanes (37) or vinylstannanes (38). The mechanism that has been postulated to account for the dimerization reaction in the presence of Pd(II) suggests that dimerization of the organometallic reagent should proceed to an extent equal to the amount of Pd(II) used (Scheme 3).[8] Indeed, when stannylated glucal **11** is treated solely with $Pd(Ph_3P)_2Cl_2$ in refluxing toluene, dimer formation is observed, while repeating the same reaction using $Pd(Ph_3P)_4$ as catalyst produces no dimer. Thus, it is the presence of Pd(II) that is responsible for dimer formation. In our work, this dimerization mechanism would limit the yield of dimer **33** to a maximum of 5%. However, from Table 1 we see that many of the cited reactions result in the production of more dimer than would be expected based on the use of 5 mol% of Pd(II) catalyst. A possible explanation for these results involves the oxidation of the catalytically active Pd(0) species back to Pd(II) by one of two processes. Either advantitious molecular oxygen is responsible or, alternatively, the oxidation of Pd(0) to a Pd(II) is being mediated by Bu_3SnBr, the by-product that is formed in the catalytic cross-coupling cycle.[9] Support for the latter hypothesis can be found by treating stannylated glucal **11** solely with $Pd(Ph_3P)_4$ and *n*-Bu_3SnCl in the absence of aryl bromide. The formation of dimer **33** takes place after several hours. Regardless of which mechanism is operative, the additional Pd(II) that is produced can lead to excessive dimer formation. Furthermore, the latter experiment suggests that dimerization of **11** is unavoidable under the conditions that we are using.

Although the preparation of *C*-aryl glucals **17–31** via this method is fairly efficient and broad in scope, there are several problems that are evident. The first is the limited availability of the stannylated glucal **11** via vinylic metalation/stannylation methods (27). This problem is especially evident if one is considering using **11** in excess with respect to the aryl bromide, a set of conditions that is desirable when the aryl bromide is the more difficult reaction partner to obtain.[7] In addition, we are faced with poor yields in the coupling reactions of **11** with electron-rich aromatic bromides as well as the consumption of the stannylated glucal **11** by an apparently unavoidable dimerization process.

The first of these problems has been overcome by the facile and high-yielding formation of 1-tributylstannyl-3,4,6-tri-*O*-(triisopropylsilyl)-D-glucal (**14**) (27). Therefore, it was imperative that we demonstrate that this stannylated glucal could be utilized in the key palladium-catalyzed cross-coupling reaction with aryl bromides.

It soon became evident that the apparently simple change from TBDMS to TIPS protecting groups on the stannylated glucal was in fact a major and detrimental modification. Whereas the *C*-aryl glucal **19** was efficiently prepared (81% yield) by the coupling of **11** and 4-bromobenzonitrile (Table 1, entry 9), the best yield that we could achieve in the coupling of **14** and 4-bromobenzonitrile was 67% (Table 1, entry 25). Results with other substituted aryl bromides including 4-bromo anisole and methyl 2-bromobenzoate were similarly discouraging, in many cases providing no coupled material.

The mechanism that has been proposed for the Stille reaction (see Scheme 3) (40) involves a rapid oxidative addition of Pd(0) to the organic halide (here ArBr), followed by a slow transmetalation step with the organometallic partner to provide a diorgano-Pd(II) species.[10] We attributed the disappointing results that were observed in the attempted coupling reactions of

[7]We have used this observation to our advantage in the synthesis of the tricyclic spiroketal core of the papulacandins, a synthesis that involves the intermediacy of glucal **30** (10).

[8]For those cases in which the diene was the desired product, an added oxidant such as Cu(II) or *t*-BuOOH was used to reoxidize the Pd(0) that was produced in the reaction back to Pd(II) to make the reactions catalytic in Pd(II). In our reactions, it is this dimerization process that produces Pd(0), the species that is catalytically active in the desired cross-coupling process.

[9]In a subsequent but related study, Tius et al. noted that the rigorous exclusion of oxygen minimized the dimerization of a zinc glucal during palladium-mediated coupling reactions with aryl bromides (17). In addition, the oxidative addition of Pd(0) to a Six—X bonds has been reported (39).

[10]Detailed mechanistic investigations into the related reactions with platinum have been described (41, 42).

Can. J. Chem. Downloaded from www.nrcresearchpress.com by EESC ESCOLA DE ENGENHARIA on 09/08/12
For personal use only.

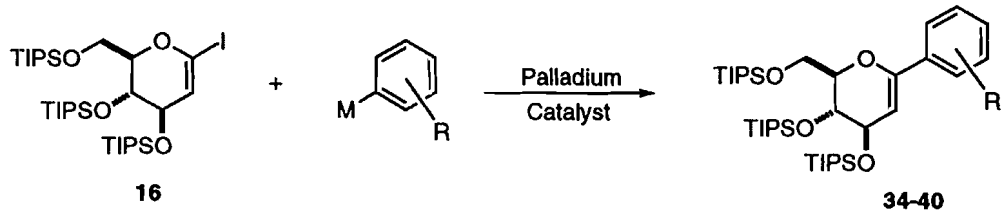

SCHEME 4

stannylated glucal **14** and aryl bromides to a decrease in the rate of an already slow transmetalation step. Although not initially obvious, but clearly seen from molecular models, the protecting group change from TBDMS to TIPS dramatically increases the steric bulk around the C1 position of the glucal. We believe that it is this protecting group change from TBDMS to TIPS that manifests itself in decreasing the rate of the slow transmetalation step, leading to inferior results in the cross-coupling reaction. Therefore, we reasoned that if we could reverse the sense of the coupling reaction by making the carbohydrate moiety the more reactive organic halide partner, we might be able to overcome this steric bias. The initial rapid oxidation addition of Pd(0) to a 1-haloglucal would be much less susceptible to steric factors (14) and the slow transmetalation step would then take place on the metal centre of a glucal-Pd(II)-halide, remote from the sterically encumbered C1 position of the glucal.

*(b) Preparation and palladium-catalyzed coupling of 3,4,6-tri-O-(triisopropylsilyl)-1-iodo-D-glucal (**16**) with metalated aromatics*

The readily available stannylated glucal **14** was converted into the iodo glucal **16**[11] (89–100% yield) by treatment of a CH_2Cl_2 solution of **14** with I_2 in CH_2Cl_2 (43–45). Based on the success of the coupling reaction of the iodo glucal **16** with metalated aromatics (vide infra), we sought a more direct pre-paration of **16** that would bypass the intermediacy of **14** and the use of toxic tributyltin chloride that is required in this method.

Reaction of the easily generated vinyl lithium intermediate **13** (27) with *N*-iodosuccinimide (NIS) met with limited success. The optimum conditions provided **16** in 30% yield along with 25% of recovered **12**. The preparation of other organometallic species from **13** (vinyl copper, vinyl silane, vinyl Grignard) followed by the attempted trapping of these intermediates with an iodonium source (I_2 or NIS) were similarly unsuccessful. However, metalation of **12** with *t*-BuLi (27) followed by transmetalation of the derived lithio derivative **13** with $ZnCl_2$ (approximately 4 equiv., ether solution) and subsequent quenching of the reaction mixture with either NIS (4.4 equiv.) or I_2 (3.7 equiv.), provided the iodo glucal **16** in yields of 67 and 81%, respectively, along with recoverable starting material (27 and 6%, respectively). It was imperative in this preparation of **16** that an excess of $ZnCl_2$ (with respect to the amount of *t*-BuLi that was used initially to metalate **12**) be used to generate **15** from **13**, presumably to convert the excess *t*-BuLi into the less reactive *t*-BuZnCl. In the event that less $ZnCl_2$ was used, the *t*-BuLi remaining in the reaction mixture would simply react (metal–halogen exchange) with the iodo glucal **16** that was produced.

Although a variety of metalated aromatics (such as zinc halides (46, 47) and boronic acids (48, 49)) have been demonstrated to undergo palladium-catalyzed cross-coupling reactions with organic halides, the use of 1-alkoxy-1-iodo alkenes as the organic halide partner in a Stille coupling reaction with organometallics had not been documented prior to our initial report (12). To test the utility of the iodo glucal **16** in the coupling reaction, **16** and a variety of metalated benzenes were treated with a palladium catalyst under appropriate reaction conditions (Scheme 4; Table 2, entries 1–13).[12] The optimum isolated yields of the *C*-phenyl glucal **34** (R = H) were obtained using phenylboronic acid (81%), dimethyl phenylboronate[13] (87–90%), and phenylzinc chloride (90%) as coupling partners. Inferior results were observed with PhLi, *n*-Bu_3SnPh, and PhMgBr (Table 2, entries 1–3). The coupling reactions in the former cases were extremely clean. The only by-product that was observed was biphenyl, arising from the now expected dimerization of the metalated benzene. The palladium catalyst is necessary in these reactions since, in its absence, no cross coupling is observed (Table 2, entry 10). A noteworthy exception is the reaction of **16** with the higher-order mixed cuprate reagent $Ph_2Cu(CN)Li_2$ (Table 2, entry 5) that produced **34** in low yield in the absence of palladium (51). While the reaction with phenylzinc chloride proceeds quickly and cleanly at room temperature in THF with $Pd(Ph_3P)_2Cl_2$ as catalyst, the reaction occurs much more slowly and in lower yield using $Pd(Ph_3P)_4$ (compare Table 2, entries 12 and 13). It appears that 4 equivalents of PhZnCl, with respect to the iodo glucal **16**, is the ratio required for an optimum coupling reaction. When 2 equivalents of PhZnCl were utilized, there was incomplete consumption of **16** after 24 h (compare Table 2, entries 11 and 13). Similarly, 2–4 equivalents of $PhB(OH)_2$ or $PhB(OMe)_2$ are required for high-yielding coupling reactions. The ability to use the boronate esters in the coupling reaction[13] under a variety of reaction conditions (see Table 2, entries 6–9) is noteworthy since the (sometimes) problematic isolation of the boronic acids (derived from the esters by hydrolysis) can now be avoided.

The coupling reaction using iodo glucal **16** can be extended to include substituted arylboronic acids, dimethyl arylboronates, and arylzinc chlorides as well (Table 2, entries 14–21). The isolated yields of the *C*-aryl glucals **35–40** obtained under these mild reaction conditions are superior to those that we had observed for every analogous example in the coupling of tin glucal **11** and aryl bromides (compare Table 1, entries 3, 9, 10, 14, and 19 with Table 2, entries 9, 14, 20, 21, and 15, respectively). For example, the poorest substrates in the coupling

[11]An iodo glucal analogous to **16** was obtained as an unexpected product (75%) in the attempted cross coupling of a C-1 stannylated glucal with 3-iodo-2-propyn-1-ol (16). The isolable vinyl iodide **16** is stable for several months when stored under vacuum in the dark. We have only stored the iodide **16** for this length of time although it may be stable for longer storage periods since no decomposition was noted under these conditions. However, if **16** is stored in the presence of light, or even under argon in the dark, decomposition to a dark red mixture of unidentified compounds is rapid.

[12]For a preliminary account of this work, see ref. 12.

[13]Boronate esters can be used in the coupling reaction without prior hydrolysis to, or isolation of, the boronic acids (50).

Can. J. Chem. Downloaded from www.nrcresearchpress.com by EESC ESCOLA DE ENGENHARIA on 09/08/12
For personal use only.

TABLE 2. Palladium-catalyzed coupling of iodo glucal **16** and metalated aromatics[a]

Entry	ArM[b] (equiv.)	Reaction conditions (solvent/temp/time)	Coupled product (yield, %)[c]
1	PhLi (4)	THF/rt[d]	NR
2	$PhSnBu_3$ (4)	THF/reflux/24 h[d]	**34** 20
3	PhMgBr (4)	PhMe/reflux/10 h[e]	**34** 25
4	$PhB(OH)_2$ (4)	THF – aq.Na_2CO_3/75°C/1.5 h[d]	**34** 81
5	$Ph_2Cu(CN)Li_2$ (3)	THF/–20°C/15 h[f]	**34** 25
6	$PhB(OMe)_2$ (2)	THF – aq.Na_2CO_3/70°C/4 h	**34** 84
7	$PhB(OMe)_2$ (2)	THF – aq.Na_2CO_3/rt/72 h[d]	**34** 80
8	$PhB(OMe)_2$ (4)	THF – aq.Na_2CO_3/rt/72 h[g]	**34** 87
9	$PhB(OMe)_2$ (4)	THF – aq.Na_2CO_3/rt/15 h[d]	**34** 90
10	PhZnCl (4)	THF/rt/24 h[f]	NR
11	PhZnCl (2)	THF/rt/24 h[d]	INC
12	PhZnCl (4)	THF/rt/16 h[e]	**34** 74
13	PhZnCl (4)	THF/rt/30 min[d]	**34** 90
14	$4\text{-}NCC_6H_4B(OMe)_2$ (2)	THF – aq.Na_2CO_3/70°C/15 h	**35** 90
15	$4\text{-}MeOC_6H_4B(OH)_2$ (2)	THF – aq.Na_2CO_3/75°C/40 min[d]	**36** 81
16	$4\text{-}MeOC_6H_4ZnCl$ (4)	THF/rt/15 min	**36** 73
17	2-FurylZnCl (4)	THF/rt/30 min	**37** 79
18	2-FurylB(OMe)_2 (2)	THF – aq.Na_2CO_3/60°C/40 min	**37** 78
19	$2,5\text{-}Cl_2C_6H_3B(OH)_2$ (2)	THF – aq.Na_2CO_3/75°C/15 min[d]	**38** 79
20	1-NaphthylB$(OH)_2$ (2)	THF – aq.Na_2CO_3/75°C/90 min[d]	**39** 75
21	$2\text{-}MeC_6H_4ZnCl$ (4)	THF/rt/15 min	**40** 68
22	$CH_2CHB(OMe)_2$ (4)	THF – aq.Na_2CO_3/65°C/5.5 h	**41** 60
23	$(CH_2CH)_4Sn$ (2)	THF/reflux/8 h[d]	**41** 67

[a]See Scheme 4. $Pd(Ph_3P)_2Cl_2$ catalyst (5 mol%) unless stated otherwise. Reactions of $ArB(OH)_2$ and $ArB(OMe)_2$ use 2 equivalents of 2 M Na_2CO_3 per mole of ArM.

[b]The metalated aromatics were commercially available or were prepared according to literature procedures from the corresponding aryl bromides (see Experimental). Numbers in parentheses refer to the number of equivalents of ArM used with respect to **16**.

[c]Yield of chromatographically purified product. NR indicates no reaction. INC indicates incomplete reaction.

[d]$Pd(Ph_3P)_2Cl_2$ catalyst (10 mol%).

[e]$Pd(Ph_3P)_4$ catalyst (10 mol%).

[f]No Pd catalyst.

[g]$Pd(Ph_3P)_2Cl_2$ catalyst (2 mol%).

reaction with the tin glucal **11** are electron-rich aromatic bromides. Thus, the improved yield in the preparation of the anisole derivative **36** (Table 2, entries 15 and 16 (73–81%)) compared with the yield for the preparation of **28** (Table 1, entry 19 (30%)) was gratifying since many of the naturally occurring *C*-aryl glycosides are oxygen-substituted aromatics (1, 2). As expected, there was no evidence for the production of the glucal dimer that previously had been the major by-product (up to 18%) in all of our coupling reactions with stannyl glucal **11**. Furthermore, purification of the glucals **34–40** is more easily accomplished than in the original procedure since the presence of the dimer **33** had, in some cases, hampered chromatographic isolation (see Table 1, entry 10). Finally, the reaction is not limited to the coupling of metalated benzenes but can be extended to include metalated heteroaromatics such as furan (Table 2, entries 17 and 18) as well as metalated olefins such as tetravinyltin or dimethyl vinylboronate (Table 2, entries 19 and 20). Each of the resulting *C*-glucal products **37** and **41**, respectively, have the potential for further synthetic manipulation. For example, *C*-furyl glucals such as **37** have been demonstrated to be useful synthetic equivalents for the preparation of C1-carboxyl glycosides (52) while dienes related to **41** undergo stereoselective Diels–Alder reactions (53).

Summary

A wide range of novel *C*-aryl glucals have been prepared by two complementary and operationally simple two-step procedures. The first process involves the vinylic metalation/stannylation of a suitably protected glucal followed by a palladium-catalyzed coupling of the resulting stannylated glucal with an aryl bromide (Scheme 2), while the second process calls for the initial preparation of an iodo glucal followed by coupling with a metalated aromatic (Scheme 4). This latter procedure is noteworthy since it does not require the use of stannylated intermediates and provides *C*-aryl glucals in an efficient three-step procedure from D-glucal (protection, metalation/iodination, coupling). We feel that the wide range of substituted aromatic moieties that can be appended onto the carbohydrate nucleus, creating the unique carbon–carbon bond present in the *C*-aryl glycosides, makes this an attractive method for the preparation of this class of compounds. The preliminary investigations that have been reported from our laboratories (10, 11) and from other groups (15, 17, 19–21) addressing the synthetic capabilities of the remaining enol ether double bond in the *C*-aryl glucals are encouraging. Indeed, several stereoselective procedures have been developed, resulting in an important and general method for the preparation of *C*-aryl glycosides.

Experimental

General information

^1H NMR spectra were recorded at 200 MHz in $CDCl_3$ unless stated otherwise. Broad band proton-decoupled ^{13}C NMR spectra were recorded at 50 MHz in $CDCl_3$ unless stated otherwise. IR spectra were recorded on neat samples unless stated otherwise. Work-up procedures involving the drying of organics was done with $MgSO_4$. The prepara-

Can. J. Chem. Downloaded from www.nrcresearchpress.com by EESC ESCOLA DE ENGENHARIA on 09/08/12
For personal use only.

Can. J. Chem. Downloaded from www.nrcresearchpress.com by EESC ESCOLA DE ENGENHARIA on 09/08/12
For personal use only.

tion of 1-tributylstannyl-3,4,6-tri-*O*-(*tert*-butyldimethylsilyl)-D-glucal (**11**), 3,4,6-tri-*O*-(triisopropylsilyl)-D-glucal (**12**), 1-tributylstannyl-3,4,6-tri-*O*-(triisopropylsilyl)-D-glucal (**14**), and other general experimental procedures have been described elsewhere (27). **Note:** Compounds for which high-resolution mass measurements are given exhibited one spot by TLC analysis.

*General procedure A: coupling of 1-tributylstannyl-3,4,6-tri-*O-(tert-*butyldimethylsilyl)-D-glucal (**11**) and aryl bromides*

A flame-dried 5 mL round-bottom flask was charged with the stannylglucal **11**, the appropriate aryl bromide (1.1–2 equiv.) and the reaction solvent (0.2–1 M in **11**). The palladium catalyst (5 mol%) was added and the reaction mixture was heated at the temperature and for the times indicated in Table 1. When TLC analysis indicated the disappearance of **11**, the reaction mixture was cooled to room temperature and the solvent was removed in vacuo. The crude reaction mixture was subjected to flash column chromatography on silica gel to provide the corresponding aryl *C*-glucal and the dimer **33**.

*1-C-Phenyl-3,4,6-tri-*O-(tert-*butyldimethylsilyl)-D-glucal (**17**)*

Following general procedure A, **11** (84.2 mg, 0.108 mmol) was reacted with bromobenzene (0.054 mL). After chromatography (elution with 50:1 hexanes:Et_2O v/v), **17** (42.4 mg, 70%) was obtained as a colorless oil; $[\alpha]_D^{25}$ −20.5 (*c* 1.2); IR: 2956, 2856, 2803, 1652, 1483, 1153, 813, 669 cm^{-1}; ^1H NMR (400 MHz) δ: 0.00 (s, 3H), 0.03 (s, 3H), 0.10 (s, 6H), 0.11 (s, 6H), 0.868 (s, 9H), 0.873 (s, 9H), 0.89 (s, 9H), 3.84 (m, 2H), 3.96 (dd, 1H, J = 4.3, 6.9 Hz), 4.14 (m, 2H), 5.23 (dd, 1H, J = 0.9, 4.2 Hz), 7.30 (m, 3H), 7.60 (m, 2H); ^{13}C NMR δ: −5.6, −5.5, −4.9, −4.4, −4.3, −4.2, 18.0, 18.2, 25.7, 25.8, 25.9, 61.6, 69.0, 70.3, 80.4, 98.1, 125.4, 128.2, 128.5, 135.7, 150.8. Exact Mass calcd. for $C_{29}H_{53}O_4Si_3$ $(M - CH_3)^+$: 549.3251; found: 549.3245.

*1-C-(4-Nitrophenyl)-3,4,6-tri-*O-(tert-*butyldimethylsilyl)-D-glucal (**18**)*

Following general procedure A, **11** (93.2 mg, 0.12 mmol) was reacted with 1-bromo-4-nitrobenzene (24 mg). After chromatography (elution with 50:1 hexanes:Et_2O v/v), **18** (56.8 mg, 78%) was obtained as a yellow solid (mp 50–52°C); $[\alpha]_D^{25}$ −17.1 (*c* 0.40); IR ($CHCl_3$): 2956, 2930, 2893, 1651, 1344, 1257, 765, 750 cm^{-1}; ^1H NMR (400 MHz) δ: −0.01 (s, 3H), 0.01 (s, 3H), 0.10 (s, 6H), 0.12 (s, 6H), 0.86 (s, 18H), 0.90 (s, 9H), 3.79 (m, 1H), 3.87 (t, 1H, J = 3.2 Hz), 3.98 (dd, 1H, J = 7.6, 11.2 Hz), 4.11 (t, 1H, J = 3.2 Hz), 4.21 (m, 1H), 5.43 (d, 1H, J = 4.4 Hz), 7.75 (d, 2H, J = 8.8 Hz), 8.17 (d, 2H, J = 8.8 Hz). Exact Mass calcd. for $C_{26}H_{46}NO_6Si_3$ $(M - C_4H_9)^+$: 552.2633; found: 552.2630. Anal. calcd. for $C_{30}H_{55}NO_6Si_3$: C 59.07, H 9.09; found: C 59.24, H 9.06.

*1-C-(4-Cyanophenyl)-3,4,6-tri-*O-(tert-*butyldimethylsilyl)-D-glucal (**19**)*

Following general procedure A, **11** (148.5 mg, 0.19 mmol) was reacted with 4-bromobenzonitrile (35 mg). After chromatography (elution with 50:1 hexanes:Et_2O v/v), **19** (90.7 mg, 81%) was obtained as a yellow oil; $[\alpha]_D^{25}$ −20.2 (*c* 0.60); IR: 2954, 2929, 2886, 2228, 1650, 1471, 1250, 777, 672 cm^{-1}; ^1H NMR (400 MHz) δ: −0.02 (s, 3H), 0.00 (s, 3H), 0.10 (s, 6H), 0.11 (s, 6H), 0.86 (s, 18H), 0.89 (s, 9H), 3.78 (dd, 1H, J = 3.7, 11.4 Hz), 3.86 (m, 1H), 3.96 (dd, 1H, J = 7.4, 11.4 Hz), 4.09 (m, 1H), 4.19 (m, 1H), 5.37 (dd, 1H, J = 1.0, 4.6 Hz), 7.61 (m, 2H), 7.69 (m, 2H). Exact Mass calcd. for $C_{27}H_{46}NO_4Si_3$ $(M - C_4H_9)^+$: 532.2734; found: 532.2726.

*1-C-(1-Naphthyl)-3,4,6-tri-*O-(tert-*butyldimethylsilyl)-D-glucal (**20**)*

Following general procedure A, **11** (50.3 mg, 0.065 mmol) was reacted with 1-bromonaphthalene (20 mg). After chromatography (elution with 50:1 hexanes:Et_2O v/v), a mixture of **20** and **33** was obtained. Integration of the ^1H NMR spectrum of the mixture indicated a 59% yield of **20** and a 15% yield of **33**. A small amount of pure **20** was isolated by drip column chromatography (elution with 100:1 hexanes:Et_2O v/v) as a colorless oil; $[\alpha]_D^{25}$ −15.7 (*c* 0.80); IR: 2954, 2929, 2886, 1662, 1472, 1463, 1256, 775, 667 cm^{-1}; ^1H NMR (400 MHz) δ: 0.00 (s, 3H), 0.02 (s, 3H), 0.099 (s, 3H), 0.103 (s, 3H), 0.146 (s, 3H), 0.150 (s, 3H), 0.86 (s, 9H), 0.91 (s, 9H), 0.94 (s, 9H), 3.93 (dd, 1H, J = 2.4, 11.3 Hz), 3.97 (m, 1H), 4.08 (dd, 1H, J = 7.3, 11.2 Hz), 4.15 (m, 1H), 4.26 (m, 1H), 5.01 (dd, 1H, J = 1.1, 4.8 Hz), 7.43 (m, 4H), 7.80 (m, 2H), 8.30 (m, 1H). Exact Mass calcd. for $C_{33}H_{55}O_4Si_3$ $(M - CH_3)^+$: 599.3408; found: 599.3394.

*1-C-(4-Carbomethoxyphenyl)-3,4,6-tri-*O-(tert-*butyldimethylsilyl)-D-glucal (**21**)*

Following general procedure A, **11** (129.1 mg, 0.166 mmol) was reacted with methyl 4-bromobenzoate (39 mg). After chromatography (elution with 30:1 hexanes:Et_2O v/v), **21** (57.8 mg, 56%) was obtained as a colorless oil; $[\alpha]_D^{25}$ −17.5 (*c* 2.1); IR: 2954, 2930, 2857, 1728, 1651, 1472, 1463, 1277, 1256 cm^{-1}; ^1H NMR (400 MHz) δ: −0.02 (s, 3H), 0.01 (s, 3H), 0.10 (s, 6H), 0.11 (s, 3H), 0.12 (s, 3H), 0.86 (s, 18H), 0.89 (s, 9H), 3.81 (dd, 1H, J = 3.6, 11.4 Hz), 3.87 (m, 1H), 3.90 (s, 3H), 3.98 (dd, 1H, J = 7.2, 11.3 Hz), 4.12 (m, 1H), 4.17 (m, 1H), 5.36 (d, 1H, J = 4.4 Hz), 7.66 (m, 2H), 7.98 (m, 2H); ^{13}C NMR δ: −5.6, −5.5, −4.9, −4.5, −4.4, −4.3, 17.9, 18.2, 25.6, 25.7, 52.0, 61.4, 68.5, 70.1, 80.6, 100.0, 125.2, 129.5, 129.9, 140.0, 149.8, 167.2. Exact Mass calcd. for $C_{31}H_{55}O_6Si_3$ $(M - CH_3)^+$: 607.3306; found: 607.3293.

*1-C-(2-Carbomethoxyphenyl)-3,4,6-tri-*O-(tert-*butyldimethylsilyl)-D-glucal (**22**)*

Following general procedure A, **11** (124.0 mg, 0.159 mmol) was reacted with methyl 2-bromobenzoate (42 mg). After chromatography (elution with 30:1 hexanes: Et_2O v/v), **22** (47.3 mg, 48%) was obtained as a colorless oil; $[\alpha]_D^{25}$ −43.8 (*c* 0.021); IR: 2954, 2929, 2857, 1735, 1665 cm^{-1}; ^1H NMR (400 MHz) δ: −0.05 (s, 3H), −0.02 (s, 3H), 0.11 (s, 6H), 0.115 (s, 3H), 0.121 (s, 3H), 0.83, 0.89, 0.91 (s each, 9H each), 3.83 (s, 3H), 3.83–3.96 (m, 4H), 4.27 (m, 1H), 4.94 (d, 1H, J = 3.7 Hz), 7.34 (m, 1H), 7.41 (m, 2H), 7.62 (m, 1H). Exact Mass calcd. for $C_{31}H_{55}O_6Si_3$ $(M - CH_3)^+$: 607.3306; found: 607.3315.

*1-C-(4-Chlorophenyl)-3,4,6-tri-*O-(tert-*butyldimethylsilyl)-D-glucal (**23**)*

Following general procedure A, **11** (142.1 mg, 0.183 mmol) was reacted with 4-chlorobromobenzene (40.7 mg). After chromatography (elution with 150:1 hexanes: Et_2O v/v), **23** (52.6 mg, 49%) was obtained as a colorless oil; $[\alpha]_D^{25}$ −17.7 (*c* 1.3); IR ($CHCl_3$): 2955, 2929, 2857, 1654, 1472, 1463, 1255 cm^{-1}; ^1H NMR (400 MHz) δ: −0.01 (s, 3H), 0.02 (s, 3H), 0.10 (s, 6H), 0.11 (s, 6H), 0.869 (s, 9H), 0.873 (s, 9H), 0.89 (s, 9H), 3.79 (m, 2H), 3.97 (dd, 1H, J = 7.2, 11.4 Hz), 4.15 (m, 2H), 5.23 (dd, 1H, J = 1.0, 4.5 Hz), 7.27 (m, 2H), 7.53 (m, 2H). Exact Mass calcd. for $C_{29}H_{52}ClO_4Si_3$ $(M - CH_3)^+$: 583.2862; found: 583.2861.

*1-C-(2-Methylphenyl)-3,4,6-tri-*O-(tert-*butyldimethylsilyl)-D-glucal (**24**)*

Following general procedure A, **11** (113.0 mg, 0.145 mmol) was reacted with 2-bromotoluene (30 μL). After chromatography (elution with 50:1 hexanes: Et_2O v/v), **24** (40.3 mg, 48%) was obtained as a colorless oil; $[\alpha]_D^{25}$ −23.5 (*c* 0.80); IR: 2955, 2929, 2857, 1663, 1463, 1360, 1346, 777, 760 cm^{-1}; ^1H NMR (400 MHz) δ: 0.00 (s, 3H), 0.04 (s, 3H), 0.08 (s, 3H), 0.09 (s, 3H), 0.10 (s, 3H), 0.11 (s, 3H), 0.86 (s, 9H), 0.89 (s, 9H), 0.90 (s, 9H), 2.37 (s, 3H), 3.88 (m, 2H), 3.97 (dd, 1H, J = 7.2, 11.1 Hz), 4.08 (m, 1H), 4.79 (dd, 1H, J = 0.9, 4.6 Hz), 7.19 (m, 4H). Exact Mass calcd. for $C_{27}H_{49}O_4Si_3$ $(M - C_4H_9)^+$: 521.2938; found: 521.2940.

*1-C-(2-Acetyloxymethylphenyl)-3,4,6-tri-*O-(tert-*butyldimethylsilyl)-D-glucal (**25**)*

Following general procedure A, **11** (104.6 mg, 0.134 mmol) was reacted with 2-acetoxymethylbromobenzene (38 mg). After chromatography (elution with 50:1 hexanes: Et_2O v/v), **25** (38.7 mg, 46%) was obtained as a colorless oil; $[\alpha]_D^{25}$ −20.4 (*c* 0.50); IR: 3068, 3030, 2929, 1747, 1661, 1472, 1463, 1253 cm^{-1}; ^1H NMR (400 MHz) δ: 0.00 (s, 6H), 0.088 (s, 3H), 0.093 (s, 3H), 0.10 (s, 3H), 0.11 (s, 3H), 0.86 (s, 9H), 0.88 (s, 9H), 0.89 (s, 9H), 2.07 (s, 3H), 3.87 (m, 2H), 3.97 (dd, 1H,

Can. J. Chem. Downloaded from www.nrcresearchpress.com by EESC ESCOLA DE ENGENHARIA on 09/08/12
For personal use only.

J = 7.1, 11.2 Hz), 4.08 (m, 1H), 4.15 (m, 1H), 4.90 (dd, 1H, J = 1.0, 4.6 Hz), 5.24 (d, 1H, J = 12.9 Hz), 5.28 (d, 1H, J = 12.9 Hz), 7.31 (m, 4H); ^{13}C NMR δ: −5.7, −4.9, −4.5, −4.4, 17.8, 18.1, 20.9, 25.6, 25.8, 61.6, 64.1, 67.9, 69.5, 80.9, 101.6, 127.9, 128.7, 129.3, 134.6, 136.3, 151.7, 170.9. Exact Mass calcd. for $C_{29}H_{51}O_6Si_3$ $(M - C_4H_9)^+$: 579.2993; found: 579.2974.

*1-C-(2-Acetyloxyphenyl)-3,4,6-tri-O-(*tert*-butyldimethylsilyl)-D-glucal (**26**)*

Following general procedure A, **11** (92.5 mg, 0.119 mmol) was reacted with 2-bromophenyl acetate (31.4 mg). After chromatography (elution with 30:1 hexanes: Et_2O v/v), **26** (29.6 mg, 40%) was obtained as a colorless oil; $[\alpha]_D^{25}$ −21.3 (*c* 0.70); IR: 2954, 2923, 2857, 1772, 1660, 1488, 1212, 1190 cm^{-1}; ^{1}H NMR (400 MHz) δ: −0.01 (s, 3H), 0.01 (s, 3H), 0.08 (s, 3H), 0.09 (s, 3H), 0.10 (s, 6H), 0.86 (s, 9H), 0.88 (s, 9H), 0.89 (s, 9H), 2.25 (s, 3H), 3.89 (m, 3H), 4.05 (m, 1H), 4.11 (m, 1H), 5.02 (dd, 1H, J = 1.0, 4.5 Hz), 7.01 (dd, 1H, J = 1.2, 8.0 Hz), 7.25 (m, 2H), 7.49 (dd, 1H, J = 1.8, 7.7 Hz). Exact Mass calcd. for $C_{31}H_{55}O_6Si_3$ $(M - CH_3)^+$: 607.3306; found: 607.3296.

*1-C-(2-Benzyloxyphenyl)-3,4,6-tri-O-(*tert*-butyldimethylsilyl)-D-glucal (**27**)*

Following general procedure A, **11** (97.4 mg, 0.125 mmol) was reacted with 2-benzyloxybromobenzene (36 mg). After chromatography (elution with 30:1 hexanes: Et_2O v/v), **27** (36.9 mg, 44%) was obtained as a colorless oil; $[\alpha]_D^{25}$ −3.1 (*c* 1.1); IR: 2953, 2856, 1648, 1254, 1222, 1158 cm^{-1}; ^{1}H NMR (400 MHz) δ: −0.02 (s, 3H), −0.01 (s, 3H), 0.00 (s, 3H), 0.03 (s, 3H), 0.10 (s, 6H), 0.84 (s, 9H), 0.86 (s, 9H), 0.87 (s, 9H), 3.90 (m, 3H), 4.12 (m, 2H), 5.10 (s, 2H), 5.23 (dd, 1H, J = 0.8, 4.3 Hz), 6.91 (m, 2H), 7.18 (m, 1H), 7.31 (m, 3H), 7.40 (m, 2H), 7.63 (dd, 1H, J = 1.8, 7.8 Hz); ^{13}C NMR δ: −5.5, −4.9, −4.5, −4.5, 17.9, 18.2, 25.8, 61.5, 69.0, 70.2, 70.6, 80.3, 103.1, 113.4, 120.8, 125.6, 127.4, 127.8, 128.6, 129.2, 129.5, 137.4, 147.7, 156.4. Exact Mass calcd. for $C_{33}H_{53}O_5Si_3$ $(M - C_4H_9)^+$: 613.3200; found: 613.3205.

*1-C-(4-Methoxyphenyl)-3,4,6-tri-O-(*tert*-butyldimethylsilyl)-D-glucal (**28**)*

Following general procedure A, **11** (122.1 mg, 0.157 mmol) was reacted with 4-bromoanisole (32 mg). After chromatography (elution with 50:1 hexanes: Et_2O v/v), **28** (26.5 mg, 30%) was obtained as a colorless oil; $[\alpha]_D^{25}$ −19.9 (*c* 0.70); IR: 2954, 2929, 2885, 1653, 1252, 1175, 1104 cm^{-1}; ^{1}H NMR (400 MHz) δ: 0.00 (s, 3H), 0.03 (s, 3H), 0.09 (s, 3H), 0.10 (s, 3H), 0.11 (s, 6H), 0.87 (s, 9H), 0.88 (s, 9H), 0.89 (s, 9H), 3.79 (s, 3H), 3.85 (m, 2H), 3.96 (dd, 1H, J = 6.7, 11.3 Hz), 4.12 (m, 2H), 5.12 (d, 1H, J = 4.0 Hz), 6.84 (m, 2H), 7.53 (m, 2H). Exact Mass calcd. for $C_{30}H_{55}O_5Si_3$ $(M - CH_3)^+$: 579.3357; found: 579.3324.

*1-C-(2,5-Dimethoxyphenyl)-3,4,6-tri-O-(*tert*-butyldimethylsilyl)-D-glucal (**29**)*

Following general procedure A, **11** (101.8 mg, 0.131 mmol) was reacted with 2,5-dimethoxybromobenzene (33 mg). After chromatography (elution with 50:1 hexane:Et_2O v/v), **29** (52.4 mg, 65%) was obtained as a colorless oil; $[\alpha]_D^{25}$ −5.0 (*c* 0.70); IR ($CHCl_3$): 2993, 2953, 2886, 1650, 1500, 1471, 812, 778 cm^{-1}; ^{1}H NMR (400 MHz) δ: 0.02 (s, 3H), 0.04 (s, 3H), 0.106 (s, 3H), 0.111 (s, 3H), 0.12 (s, 6H), 0.87 (s, 9H), 0.90 (s, 9H), 0.91 (s, 9H), 3.75 (s, 3H), 3.77 (s, 3H), 3.87 (m, 1H), 3.92 (s, 1H), 3.93 (d, 1H, J = 0.8 Hz), 4.03 (m, 1H), 4.23 (m, 1H), 5.62 (d, 1H, J = 3.5 Hz), 6.79 (m, 2H), 7.20 (d, 1H, J = 3.0 Hz); ^{13}C NMR δ: −5.5, −4.9, −4.2, 17.9, 18.1, 18.2, 25.8, 25.9, 55.7, 56.3, 61.9, 70.2, 70.4, 80.4, 103.8, 113.3, 114.0, 114.7, 125.4, 147.6, 151.7, 153.6. Exact Mass calcd. for $C_{28}H_{51}O_6Si_3$ $(M - C_4H_9)^+$: 567.2993; found: 567.2973.

*1-C-(6-Acetyloxymethyl-2,4-dibenzyloxyphenyl)-3,4,6-tri-O-(*tert*-butyldimethylsilyl)-D-glucal (**30**)*

Following general procedure A, **11** (139.2 mg, 0.179 mmol) was reacted with 1-acetyloxymethyl-2-bromo-3,5-dibenzyloxybenzene (7) (86.8 mg) in mesitylene. After chromatography (elution with 9:1 hexanes: EtOAc v/v), **30** (72.2 mg, 51%) was obtained as a colorless oil; $[\alpha]_D^{25}$ −23.8 (*c* 1.45); IR: 2953, 2930, 2885, 1743, 1671 cm^{-1}; ^{1}H NMR (400 MHz) δ: −0.059, −0.056, 0.05, 0.08, 0.10, 0.11 (s each, 3H each), 0.83, 0.87, 0.89 (s each, 9H each), 2.07 (s, 3H), 3.73 (dd, 1H, J = 5.6, 10.3 Hz), 4.00–4.09 (m, 4H), 4.81 (dd, 1H, J = 1.1, 4.7 Hz), 4.99 (s, 2H), 5.00 (s, 2H), 5.13 (d, 1H, J = 12.9 Hz), 5.19 (d, 1H, J = 12.9 Hz), 6.48 (d, 1H, J = 2.3 Hz), 6.57 (d, 1H, J = 2.3 Hz), 7.34–7.37 (m, 10H); ^{13}C NMR δ: −5.63, −5.58, −5.0, −4.7, −4.5, 17.8, 17.9, 18.0, 20.8, 25.6, 25.7, 61.1, 63.6, 67.7, 69.3, 70.0, 80.4, 100.6, 103.0, 105.8, 119.2, 127.1, 127.6, 127.7, 128.1, 128.5, 128.7, 136.8, 137.1, 137.9, 146.8, 157.9, 170.7. Exact Mass calcd. for $C_{47}H_{72}O_8Si_3$ (M^+): 848.4534; found: 848.4573. Anal. calcd. for $C_{47}H_{72}NO_8Si_3$: C 66.46, H 8.54; found: C 66.31, H 8.53.

*1-C-(6-*tert*-Butyldimethylsiloxymethyl-2,4-dibenzyloxyphenyl)-3,4,6-tri-O-(*tert*-butyldimethylsilyl)-D-glucal (**31**)*

Following general procedure A, **11** (135.6 mg, 0.174 mmol) was reacted with 1-*tert*-butyldimethylsilyloxymethyl-2-bromo-3,5-dibenzyloxybenzene (107 mg). After chromatography (elution with 10:1 hexanes: EtOAc v/v), **31** (89.9 mg, 56%) was obtained as a colorless oil; $[\alpha]_D^{25}$ −17.1 (*c* 1.38); IR: 2959, 2931, 2854, 1680, 1602, 1469, 1258, 1159, 1061, 836 cm^{-1}; ^{1}H NMR (400 MHz) δ: −0.08, −0.07, 0.03, 0.04, 0.05, 0.06, 0.09 (s, each, 3H each), 0.82, 0.86, 0.89, 0.91 (s each, 9H each), 3.69 (m, 1H), 4.02–4.10 (m, 4H), 4.70–4.81 (m, 3H), 4.96–5.04 (m, 4H), 6.41 (d, 1H, J = 2.4 Hz), 6.82 (d, 1H, J = 2.4 Hz), 7.22–7.39 (m, 10H); ^{13}C NMR δ: −5.6, −5.5, −5.4, −4.9, −4.6, −4.5, −4.4, 17.90, 17.96, 18.02, 18.1, 25.7, 25.8, 61.1, 62.1, 68.1, 69.5, 69.9, 70.4, 80.1, 99.8, 102.6, 103.6, 117.0, 127.2, 127.6, 127.7, 128.0, 128.5, 128.7, 137.2, 137.5, 143.4, 147.1, 157.6, 160.0. Exact Mass calcd. for $C_{51}H_{85}O_7Si_4$ $(M + H)^+$: 920.5294; found: 920.5303.

*Dimer **33***

The isolated yields of **33** from each individual experiment can be found in Table 1. Colorless oil; $[\alpha]_D^{25}$ −35.4 (*c* 0.50); IR: 2954, 2936, 1623, 1251, 1105 cm^{-1}; ^{1}H NMR (400 MHz) δ: 0.01 (s, 6H), 0.03 (s, 6H), 0.06 (s, 18H), 0.07 (s, 6H), 0.84 (s, 18H), 0.86 (s, 18H), 0.87 (s, 18H), 3.71 (dd, 2H, J = 3.7, 11.3 Hz), 3.8 (m, 2H), 3.86 (dd, 2H, J = 7.0, 11.4 Hz), 3.98 (m, 2H), 4.03 (m, 2H), 5.80 (dd, 2H, J = 1.5, 4.8 Hz); ^{13}C NMR δ: −5.7, −5.4, −4.9, −4.6, −4.6, −4.4, 17.8, 18.2, 25.6, 25.7, 25.8, 61.5, 67.7, 70.2, 80.5, 98.6, 145.8. Exact Mass calcd. for $C_{48}H_{102}O_8Si_6$ (M^+): 974.6190; found: 974.6194.

*Preparation of 1-iodo-3,4,6-tri-O-(triisopropylsilyl)-D-glucal (**16**) from **14***

Tin glucal **14** (15) (2.0 g, 2.3 mmol) was dissolved in CH_2Cl_2 (10 mmol) under an argon atmosphere. To this colorless mixture was added a solution of iodine (0.5 g) in CH_2Cl_2 (10 mL) dropwise until a persistent red color, indicating an excess of iodine, remained. The complete consumption of **14** was confirmed by TLC and saturated aqueous $Na_2S_2O_3$ was then added. The mixture was subsequently extracted with CH_2Cl_2, and the combined organic phases were dried and concentrated. Column chromatography of the residual oil on silica gel (5% ether in hexanes or 10% CH_2Cl_2 in hexanes) yielded **16** (1.5 g, 89%) as a colorless oil; $[\alpha]_D^{25}$ −23.6 (*c* 0.30); IR: 1463, 1624, 2866-2958 cm^{-1}; ^{1}H NMR δ: 1.03–1.05 (m, 63H), 3.82–3.91 (m, 2H), 4.06–4.15 (m, 2H), 4.30–4.37 (m, 1H), 5.38 (dd, 1H, J = 1.5, 5.5 Hz); ^{13}C NMR δ: 12.2, 12.5, 12.6, 18.2, 61.9, 68.2, 69.7, 86.2, 107.8, 111.9. Exact Mass calcd. for $C_{30}H_{62}O_4Si_3I$ $(M - C_3H_7)^+$: 697.3001; found: 697.3013.

*Preparation of 1-iodo-3,4,6-tri-O-(triisopropylsilyl)-D-glucal (**16**) from **12***

To a solution of **12** (15) (1.8595 g, 3.0 mmol) in THF (9 mL, 0.35 M) at −78°C was added *t*-BuLi (7.2 mL of a 1.7 M solution in pentane, 12.0 mmol) dropwise. The mixture was stirred for 1.25 h at 0°C and then $ZnCl_2$ (15.1 mL of a 1.0 M solution in Et_2O, 15.0 mmol) was added and the mixture was stirred at room temperature for 40 min. I_2 (1.4 g, 11.1 mmol) was added as a solid and the resulting solution was stirred for 2 h at room temperature. Work-up and chromatography as above provided **16** (1.8238 g, 81%) and the starting material **12** (0.1085 g, 6%).

Can. J. Chem. Downloaded from www.nrcresearchpress.com by ESC ESCOLA DE ENGENHARIA on 09/08/12
For personal use only.

*General procedure B: preparation and coupling of arylzinc chlorides with 1-iodo-3,4,6-tri-*O*-(triisopropylsilyl)-*D*-glucal (**16**)*

A solution of 4-bromoanisole (0.41 mL, 3.3 mmol) in THF (1 mL) at −78°C was treated dropwise with *n*-BuLi (2.0 mL of a 1.6 M solution in hexane) and the resulting white mixture was stirred for 1 h at −78°C. $ZnCl_2$ (3.2 mL of a 1.0 M solution in ether) was then slowly added, and the mixture was warmed to room temperature and stirred for a further 30 min. The ensuing two-phase mixture was concentrated in vacuo and the viscous residue containing 4-methoxyphenylzinc chloride was then dissolved in 1 mL THF to yield a 1.4 M solution of the arylzinc chloride.

4-Methoxyphenylzinc chloride (0.67 mL of a 1.4 M solution in THF) was added dropwise to a solution of **16** (162.1 mg, 0.21 mmol) and $Pd(PPh_3)_2Cl_2$ (7.7 mg, 0.01 mmol) in THF (0.5 mL). The light yellow mixture was stirred at room temperature until the color of the solution changed to dark red (15 min). The consumption of **16** was then confirmed by TLC analysis and the solvent was removed on the rotovap. The crude reaction mixture was purified by column chromatography on silica gel (4:1 hexanes:benzene) to yield 1-*C*-(4-methoxy)phenyl-3,4,6-tri-*O*-(triisopropylsilyl)-*D*-glucal (**36**) (115.3 mg, 73%, Table 2, entry 16) as a colorless oil. This material exhibited: $[\alpha]_D^{25}$ −0.8 (*c* 0.99); IR: 1651, 2866-2945 cm^{-1}; ^1H NMR δ: 1.01–1.06 (m, 63H), 3.79–3.91 (m, 4H), 4.08–4.18 (m, 3H), 4.39–4.44 (m, 1H), 5.22 (dd, 1H, *J* = 1.4, 5.4 Hz) 6.81–6.87 (m, 2H), 7.52–7.59 (m, 2H); ^{13}C NMR δ: 12.2, 12.6, 12.7, 18.2, 18.3, 18.4, 55.6, 62.3, 67.2, 70.5, 81.6, 95.6, 113.7, 127.2, 129.6, 150.6, 160.3. Exact Mass calcd. for $C_{40}H_{76}O_5Si_3$ (M^+): 720.5001; found: 720.4988.

*1-C-Phenyl-3,4,6-tri-*O*-(triisopropylsilyl)-1-*D*-glucal (**34**)*

Following general procedure B, **16** (108.4 mg, 0.15 mmol) was reacted with phenylzinc chloride (Table 2, entry 13). After chromatography (elution with 0.5% EtOAc in hexanes), **34** (91.3 mg, 90%) was obtained as a colorless oil: $[\alpha]_D^{25}$ −8.2 (*c* 0.77); IR: 1463, 1495, 1650, 2866–2964 cm^{-1}; ^1H NMR δ: 1.02–1.08 (m, 63H), 3.90 (dd, 1H, *J* = 4.3, 11.1 Hz), 4.06–4.20 (m, 3H), 4.43–4.48 (m, 1H), 5.35 (dd, 1H, *J* = 1.5, 5.3 Hz); ^{13}C NMR δ: 12.2, 12.6, 12.7, 18.2, 18.3, 18.4, 62.3, 67.1, 70.4, 81.7, 97.1, 125.9, 128.4, 128.7, 136.9, 150.9. Exact Mass calcd. for $C_{39}H_{74}O_4Si_3$ (M^+): 690.4895; found: 690.4885. Anal. calcd. for $C_{39}H_{74}O_4Si_3$: C 67.76, H 10.79; found: C 67.43, H 11.00.

*1-O-(2-Furyl)3,4,6-tri-*O*-(triisopropylsilyl)-*D*-glucal (**37**)*

Following general procedure B, **16** (91.5 mg, 0.12 mmol) was reacted with 2-furylzinc chloride (Table 2, entry 17). After chromatography (elution with 20% benzene in hexanes), **37** (66.2 mg, 79%) was obtained as a colorless oil; $[\alpha]_D^{25}$ −8.3 (*c* 0.41); IR: 1463, 1492, 1667, 2868–2963 cm^{-1}; ^1H NMR δ: 1.02–1.06 (m, 63H), 3.88 (dd, 1H, *J* = 4.4, 11.2 Hz), 4.02–4.19 (m, 4H), 4.35–4.40 (m, 1H), 5.39 (dd, 1H, *J* = 1.5, 5.3 Hz), 6.37 (dd, 1H, *J* = 1.8, 3.4 Hz), 6.50 (d, 1H, *J* = 3.4 Hz), 7.33 (s, 1H); ^{13}C NMR δ: 12.2, 12.6, 12.7, 18.2, 18.3, 18.4, 62.3, 66.4, 70.6, 81.6, 95.9, 107.4, 111.4, 142.5, 143.6, 150.8. Exact Mass calcd. for $C_{37}H_{72}O_5Si_3$ (M^+): 680.4688; found: 680.4700. Anal. calcd. for $C_{37}H_{72}O_5Si_3$: C 65.24, H 10.65; found: C 64.79, H 10.55.

*1-C-(2-Methylphenyl)-3,4,6-tri-*O*-(triisopropylsilyl)-*D*-glucal (**40**)*

Following general procedure B, **16** (101.8 mg, 0.14 mmol) was reacted with 2-methylphenylzinc chloride (Table 2, entry 21). After chromatography (elution with 10% benzene in hexanes), **40** (66.2 mg, 68%) was obtained as a colorless oil; $[\alpha]_D^{25}$ −24.9 (*c* 0.33); IR: 681, 1463, 1658, 2866–2958 cm^{-1}; ^1H NMR δ: 1.00–1.06 (m, 63H), 2.39 (s, 3H), 3.97 (dd, 1H, *J* = 4.8, 11 Hz), 4.10–4.19 (m, 3H), 4.36–4.40 (m, 1H), 4.89 (dd, 1H, *J* = 2.2, 4.8 Hz), 7.11–7.27 (m, 4H); ^{13}C NMR δ: 12.2, 12.6, 18.2, 18.3, 20.1, 62.4, 66.7, 69.8, 82.0, 99.8, 125.8, 128.8, 129.6, 130.6, 137.4, 137.7, 153.4. Exact Mass calcd. for $C_{40}H_{76}O_4Si_3$ (M^+): 704.5051; found: 704.5048.

*General procedure C: preparation and coupling of arylboronate esters with 1-iodo-3,4,6-tri-*O*(triisopropylsilyl)-*D*-glucal (**16**)*

A solution of distilled bromobenzene (60 μL, 0.5 mmol) in THF (0.5 mL) at −78°C was treated with *n*-BuLi (0.2 mL of a 2.5 M solution in hexanes, 0.5 mmol) and the resulting solution was stirred for 1.25 h. Trimethylborate (60 μL, 0.5 mmol) was then added dropwise and the resulting milky white solution was warmed to room temperature and stirred a further 30 min. Iodo glucal **16** (185.1 mg, 0.25 mmol) dissolved in THF (2 mL), Na_2CO_3 (0.5 mL of a 2.0 M aqueous solution), and $PdCl_2(PPh_3)_2$ (7.8 mg, 0.0125 mmol) were added to the solution. The reaction temperature was then raised to 70°C and stirring was continued for another 4 h. The crude mixture was concentrated and the residual material was subjected to column chromatography (eluting with 5% benzene in hexanes) to afford 1-*C*-phenyl-3,4,6-tri-*O*-(triisopropylsilyl)-*D*-glucal (**34**) (145.6 mg, 84%, Table 2, entry 6) as a colorless oil.

*1-C-(4-Cyanophenyl)-3,4,6-tri-*O*-(triisopropylsilyl)-1-*D*-glucal (**35**)*

Following general procedure C, **16** (187.8 mg, 0.25 mmol) was reacted with the boronate ester generated from 4-bromobenzonitrile (Table 2, entry 14). After chromatography (elution with 20% benzene in hexanes), **35** (162.4 mg, 90%) was obtained as a colorless oil; $[\alpha]_D^{25}$ −8.2 (c 0.27); IR: 1646, 1650, 2229, 2866–2959 cm^{-1}; ^1H NMR δ: 1.03–1.05 (m, 63H), 3.84 (dd, 1H, *J* = 3.8, 11.4 Hz), 4.07–4.20 (m, 3H), 4.47–4.53 (m, 1H), 5.49 (dd, 1H, *J* = 1.4, 5.4 Hz), 7.68 (dd, 4H, *J* = 8.7, 25.6 Hz); ^{13}C NMR δ: 11.8, 12.2, 12.3, 17.8, 17.9, 18.0, 61.7, 66.3, 69.8, 81.7, 99.6, 111.7, 119.1, 125.9, 132.0, 140.6, 148.7. Exact Mass calcd. for $C_{40}H_{73}O_4Si_3N$ (M^+): 715.4847; found: 715.4808. Anal. calcd. for $C_{40}H_{73}O_4Si_3N$: C 67.07, H 10.27; found: C 67.12, H 10.19.

*1-C-(2-Furyl)-3,4,6-tri-*O*-(triisopropylsilyl)-*D*-glucal (**37**)*

Following general procedure C, **16** (134.9 mg, 0.18 mmol) was reacted with the boronate ester generated from furan (Table 2, entry 18). After chromatography (elution with 5% benzene in hexanes), **37** (96.1 mg, 78%) was obtained as a colorless oil.

*1-C-Ethenyl-3,4,6-tri-*O*-(triisopropylsilyl)-*D*-glucal (**41**)*

Following general procedure C, **16** (119.1 mg, 0.16 mmol) was reacted with the boronate ester generated from vinyl magnesium bromide (Table 2, entry 22). After chromatography (elution with 5% benzene in hexanes), **41** (61.1 mg, 60%) was obtained as a colorless oil; $[\alpha]_D^{25}$ −34.2 (*c* 0.64); IR: 1600, 1658, 2866–2958 cm^{-1}; ^1H NMR δ: 1.03 (s, 63H), 3.81 (dd, 1H, *J* = 3.7, 11.3 Hz), 3.95–4.04 (m, 3H), 4.30–4.34 (m, 1H), 4.81 (t, 1H, *J* = 3.2 Hz), 5.08 (d, 1H, *J* = 10.8 Hz), 5.62 (dd, 1H, *J* = 1.6, 17.2), 6.03 (dd, 1H, *J* = 10.7, 17.5); ^{13}C NMR δ: 12.2, 12.5, 12.7, 18.2, 18.3, 62.4, 66.9, 70.5, 81.2, 101.6, 115.2, 133.2, 149.6. Exact Mass calcd. for $C_{35}H_{72}O_4Si_3$ (M^+): 640.4738; found: 640.4747. Anal. calcd. for $C_{35}H_{72}O_4Si_3$: C 65.56, H 11.32; found: C 65.96, H 11.57.

*General procedure D: preparation and coupling of arylboronic acids with 1-iodo-3,4,6-tri-*O*-(triisopropylsilyl)-*D*-glucal (**16**)*

A solution of the Grignard reagent derived from the reaction of 1-bromonaphthalene (0.7 mL, 5 mmol) and magnesium turnings (136.4 mg, 5.5 mmol) in ether (5 mL) was added over 45 min to a solution of trimethylborate in ether (15 mL) at −78°C. The reaction mixture was stirred at this temperature overnight and then treated with 10% H_2SO_4 (10 mL). The mixture was extracted with ether and then the ether extract was acidified with concentrated H_2SO_4. The ether phase was washed with saturated brine and water and was then concentrated to provide 1-naphthylboronic acid, which was used as such.

To a solution of 1-naphthylboronic acid (25.8 mg, 0.15 mmol), **16** (54.3 mg, 0.073 mmol), and $Pd(PPh_3)_2Cl_2$ (5 mg, 0.007 mmol) in THF (0.5 mL) was added Na_2CO_3 (0.15 mL, 2 M aqueous solution) and the resulting two-phase mixture was stirred at 75°C for 90 min. The consumption of **16** was confirmed by TLC analysis, the mixture was cooled to room temperature, and water was added. The crude mixture was extracted with ether, and the combined organic phases were dried and concentrated. Column chromatography of the residual oil on silica gel (1% EtOAc in hexanes) yielded 1-*C*-(1-naphthyl)-3,4,6-tri-*O*-(triisopropylsilyl)-*D*-glucal (**39**) (40.7 mg, 75%, Table 2, entry 20) as a

Can. J. Chem. Downloaded from www.nrcresearchpress.com by EESC ESCOLA DE ENGENHARIA on 09/08/12
For personal use only.

colorless oil; $[\alpha]_D^{25}$ −8.8 (*c* 0.16); IR: 1666, 2867–2945 cm^{-1}; ^1H NMR δ: 1.02–1.11 (s, 63H), 4.06 (dd, 1H, *J* = 4.8, 11 Hz), 4.20–4.29 (m, 3H), 4.47–4.51 (m, 1H), 5.10 (t, 1H, *J* = 3.4 Hz), 7.36–7.47 (m, 4H), 7.77–7.82 (m, 2H), 8.34–8.39 (m, 1H); ^{13}C NMR δ: 12.2, 12.6, 12.7, 18.2, 18.4, 62.5, 66.8, 69.8, 82.2, 101.1, 125.5, 126.2, 126.3, 126.4, 126.9, 127.0, 128.3, 129.2, 132.1, 134.0, 152.8. Exact Mass calcd. for $C_{43}H_{76}O_4Si_3$ (M^+): 740.5051; found: 740.5007.

1-C-Phenyl-3,4,6-tri-O-(triisopropylsilyl)-1-D-glucal (34)

Following general procedure D, **16** (98.4 mg, 0.13 mmol) was reacted with phenylboronic acid (Table 2, entry 4). After chromatography (elution with 1% EtOAc in hexanes), **34** (72.8 mg, 81%) was obtained as a colorless oil.

1-C-(4-Methoxyphenyl)-3,4,6-tri-O-(triisopropylsilyl)-1-D-glucal (36)

Following general procedure D, **16** (29 mg, 0.04 mmol) was reacted with 4-methoxyphenylboronic acid (Table 2, entry 15). After chromatography (elution with 1% EtOAc in hexanes), **36** (22.9 mg, 81%) was obtained as a colorless oil.

1-C-(2,4-Dichlorophenyl)-3,4,6-tri-O-(triisopropylsilyl)-1-D-glucal (38)

Following general procedure D, **16** (58.9 mg, 0.08 mmol) was reacted with 2,5-dichlorophenylboronic acid (Table 2, entry 19). After chromatography (elution with 1% EtOAc in hexanes), **38** (49.8 mg, 79%) was obtained as a colorless oil; $[\alpha]_D^{25}$ −18.9 (*c* 0.35); IR: 1463, 1492, 1662, 1666, 2867–2945 cm^{-1}; ^1H NMR δ: 1.02–1.06 (m, 63H), 3.96 (dd, 1H, *J* = 4.7, 11.1 Hz), 4.10–4.19 (m, 3H), 4.37–4.41 (, 1H), 5.11 (dd, 1H, *J* = 2.5, 4.3 Hz), 7.18 (dd, 1H, *J* = 1.9, 8.3 Hz), 7.35 (d, 1H, *J* = 1.9 Hz) 7.36 (d, 1H, *J* = 8.3 Hz); ^{13}C NMR δ: 12.2, 12.5, 12.6, 18.2, 18.3, 62.1, 66.5, 69.8, 82.2, 102.2, 127.2, 130.2, 132.1, 134.0, 134.9, 135.0, 149.0. Exact Mass calcd. for $C_{36}H_{65}O_4Si_3Cl_2$ $(M-C_3H_7)^+$: 715.3568; found: 715.3560.

1-C-Phenyl-3,4,6-tri-O-(triisopropylsilyl)-1-D-glucal (34) from higher order mixed cuprate and 1-iodo-3,4,6-tri-O-(triisopropylsilyl)-D-glucal (16)

To a slurry of CuCN (90.2 mg, 1.0 mmol) in THF (2 mL) at −78°C was added phenyllithium (5.8 mL of a 0.35 M solution in ether) and the resulting mixture was warmed to −20°C for 5 min. After recooling to −78°C, a solution of **16** (241.5 mg, 0.33 mmol) in THF (2 mL) was added and the resulting mixture was stirred at −20°C for 15 h. Saturated NH_4Cl was added and the mixture extracted with ether. The ether phase was washed with water and saturated brine, dried, and concentrated. Flash chromatography as described above provided **34** (55.3 mg, 25%, Table 2, entry 5) as a colorless oil together with 109.7 mg of recovered **16**.

1-C-Ethenyl-3,4,6-tri-O-(triisopropylsilyl)-D-glucal (41) from tetravinyltin *and 1-iodo-3,4,6-tri-O-(triisopropylsilyl)-D-glucal (16)*

A mixture of tetravinyltin (0.024 mL, 0.13 mmol), **16** (45 mg, 0.061 mmol), and $Pd(PPh_3)_2Cl_2$ (4.3 mg, 0.006 mmol) in THF (0.5 mL) was refluxed for 8 h. The mixture was concentrated and column chromatography of the residual oil on silica gel (5% CH_2Cl_2 in hexanes) yielded **41** (26.1 mg, 67%, Table 2, entry 23) as a colorless oil.

Acknowledgements

We would like to thank Dr. Thomas Keller (University of Toronto) for a generous gift of the boronic acids found in Table 2, entries 15 and 19, and Professor Brian Keay (University of Calgary) for helpful discussions regarding the boronate ester coupling reactions. Financial support from the Natural Sciences and Engineering Research Council (NSERC) of Canada is gratefully acknowledged.

1. G.D. Daves, Jr. Acc. Chem. Res. **23**, 201 (1990).
2. U. Hacksell and G.D. Daves, Jr. Prog. Med. Chem. **22**, 1 (1985).
3. S. Omura, H. Tanaka, R. Oiwa, J. Awaya, R. Masuma, and K. Tanaka. J. Antibiot. **30**, 908 (1977).
4. T. Komori, M. Yamashita, Y. Tsurumi, and M. Kohsaka. J. Antibiot. **38**, 455 (1985).
5. T. Komori and Y. Itoh. J. Antibiot. **38**, 544 (1985).
6. P. Traxler, J. Gruner, and J.A.L. Auden. J. Antibiot. **30**, 289 (1977).
7. P. Traxler, W. Tosch, and O. Zak. J. Antibiot. **40**, 1146 (1987).
8. M.H.D. Postema. Tetrahedron, **48**, 8545 (1992).
9. R.W. Friesen and C.F. Sturino. J. Org. Chem. **55**, 2572 (1990).
10. R.W. Friesen and C.F. Sturino. J. Org. Chem. **55**, 5808 (1990).
11. R.W. Friesen and A.K. Daljeet. Tetrahedron Lett. **31**, 6133 (1990).
12. R.W. Friesen and R.W. Loo. J. Org. Chem. **56**, 4821 (1991).
13. J. Tsuji. *In* Organic synthesis with palladium compounds. Springer-Verlag, New York. 1980. Chap. IV-7.
14. J.K. Stille. Angew. Chem. Int. Ed. Engl. **25**, 508 (1986).
15. E. Dubois and J.-M. Beau. Tetrahedron Lett. **31**, 5165 (1990).
16. E. Dubois and J.-M. Beau. J. Chem. Soc. Chem. Commun. 1191 (1990).
17. M.A. Tius, J. Gomez-Galeno, X. Gu, and J.H. Zaidi. J. Am. Chem. Soc. **113**, 5775 (1991).
18. H.-C. Zhang, M. Brakta, and G.D. Daves, Jr. Tetrahedron Lett. **34**, 1571 (1993).
19. S.J. Danishefsky, G. Phillips, and M. Ciufolini. Carbohydr. Res. **171**, 317 (1987).
20. V.A. Boyd, B.E. Drake, and G.A. Sulikowski. J. Org. Chem. **58**, 3191 (1993).
21. K.A. Parker and C.A. Coburn. J. Am. Chem. Soc. **113**, 8516 (1991).
22. C.E. Russell and L.S. Hegedus. J. Am. Chem. Soc. **105**, 943 (1983).
23. M. Kosugi, T. Sumiya, Y. Obara, M. Suzuki, H. Sano, and T. Migita. Bull. Chem. Soc. Jpn. **60**, 767 (1986).
24. K.C. Nicolaou, C.-K. Hwang, and M.E. Duggan. J. Chem. Soc. Chem. Commun. 925 (1986).
25. S. Hanessian, M. Martin, and R.C. Desai. J. Chem. Soc. Chem. Commun. 926 (1986).
26. P. Lesimple, J.-M. Beau, G. Jaurand, and P. Sinaÿ. Tetrahedron Lett. **27**, 6201 (1986).
27. R.W. Friesen, C.F. Sturino, A.K. Daljeet, and A.E. Kolaczewska. J. Org. Chem. **56**, 1944 (1991).
28. R.K. Boeckman, Jr., A.B. Charette, T. Asberom, and B.H. Johnston. J. Am. Chem. Soc. **109**, 7553 (1987).
29. L.A. Paquette and J.A. Oplinger. Tetrahedron, **45**, 107 (1989).
30. D. Crich and T.J. Ritchie. Tetrahedron, **44**, 2319 (1989).
31. A.M. Echavarren and J.K. Stille. J. Am. Chem. Soc. **109**, 5478 (1987).
32. W.J. Scott and J.E. McMurry. Acc. Chem. Res. **21**, 47 (1988).
33. D. Milstein and J.K. Stille. J. Am. Chem. Soc. **101**, 4992 (1979).
34. R. Singh and G. Just. J. Org. Chem. **54**, 4453 (1989).
35. P. Fitton and A.E. Rick. J. Organomet. Chem. **28**, 287 (1971).
36. J.K. Stille and B.L. Groh. J. Am. Chem. Soc. **109**, 813 (1987).
37. W.P. Weber, R.A. Felix, A.K. Willard, and K.E. Koenig. Tetrahedron Lett. 4701 (1971).
38. S. Kanemoto, S. Matsubara, and K. Oshima. Chem. Lett. 5 (1987).
39. N. Chatani, N. Amishiro, and S. Murai. J. Am. Chem. Soc. **113**, 7778 (1991).
40. J.K. Stille. Pure Appl. Chem. **57**, 1771 (1985).
41. P.J. Stang, M.H. Kowalski, M.D. Schiavelli, and D.J. Longford. J. Am. Chem. Soc. **111**, 3347 (1989).
42. P.J. Stang and M.H. Kowalski. J. Am. Chem. Soc. **111**, 3356 (1989).
43. D. Seyferth. J. Am. Chem. Soc. **79**, 2133 (1957).
44. S.D. Rosenberg, A.J. Gibbons, and H.E. Ramsden. J. Am. Chem. Soc. **79**, 2137 (1957).
45. P. Bakelmans, M. Gielen, P. Malfroid, and J. Nasielski. Bull. Soc. Chim. Belg. **77**, 85 (1968).
46. E. Negishi, A.O. King, and N. Okukado. J. Org. Chem. **42**, 1821 (1977).

47. E. Negishi, T. Takahashi, S. Baba, D.E. Van Horn, and N. Okukado. J. Am. Chem. Soc. **109**, 2393 (1987).
48. N. Miyaura, T. Yanagi, and A. Suzuki. Synth. Commun. **11**, 513 (1981).
49. N. Miyaura, K. Yamada, H. Suginome, and A. Suzuki. J. Am. Chem. Soc. **107**, 972 (1985).
50. W.A. Cristofoli and B.A. Keay. Tetrahedron Lett. **32**, 5881 (1991).
51. G.H. Posner. Org. React. **22**, 253 (1975).
52. S.J. Danishefsky, M.P. DeNinno, and S. Chen. J. Am. Chem. Soc. **110**, 3929 (1988).
53. R.M. Giuliano, A.D. Jordan, Jr., A.D. Gauthier, and K. Hoogsteen. J. Org. Chem. **58**, 4979 (1993).

Can. J. Chem. Downloaded from www.nrcresearchpress.com by EESC ESCOLA DE ENGENHARIA on 09/08/12
For personal use only.

Crystal chemistry of tetraradial species. Part 4. Hydrogen bonding to aromatic π systems: crystal structures of fifteen tetraphenylborates with organic ammonium cations[1,2]

PRADIP K. BAKSHI,[3] ANTONY LINDEN,[4] BEVERLY R. VINCENT,[5] STEPHEN P. ROE, D. ADHIKESAVALU,[6] T. STANLEY CAMERON, AND OSVALD KNOP[7]

Department of Chemistry, Dalhousie University, Halifax, NS B3H 4J3, Canada

Received September 28, 1993

PRADIP K. BAKSHI, ANTONY LINDEN, BEVERLY R. VINCENT, STEPHEN P. ROE, D. ADHIKESAVALU, T. STANLEY CAMERON, and OSVALD KNOP. Can. J. Chem. **72**, 1273 (1994).

The aim of this investigation is to provide a classification and examples of N—H...π (and also O—H...π) bonds to the aromatic π systems in organic ammonium tetraphenylborates that would serve as reference for X—H...π(arene) bonds in general. To this end the crystal structures of the tetraphenylborates of the following cations have been determined: Me_3NH^+, Et_3NH^+, quinuclidinium, DabcoH$^+$, Et(*iso*-Pr)$_2$NH$^+$ (monohydrate), $(Ph_3B)NH[—(CH_2)_2—]_2NHMe^+$ (Me_2CO solvate), $Me_2NH_2^+$ (MeCN and Et_2CO solvates), $Et_2NH_2^+$, (*iso*-Pr)$_2NH_2^+$, azoniacycloheptane, guanidinium (monohydrate), $MeNH_3^+$, $EtNH_3^+$, and 1-adamantammonium (monohydrate). These structures contain a variety of normal, bifurcated, and trifurcated N—H...π bonds as well as normal O—H...π bonds to the phenyl groups of the anion. The X—H...π bonds will form whenever opportunity arises, even though the result may be unfavourable bonding geometry. Branched bonds and orientational disorder represent compromise solutions in situations where the H(X) hydrogens are presented with competing phenyl acceptors or where the general organization of the crystal structure offers unfavourable bonding conditions to these hydrogens. The distributions of the distances from X or H(X) to the centre of the phenyl-ring skeleton are analyzed in detail, as are also those of the mean X...C and H(X)...C distances to the ring carbons.

PRADIP K. BAKSHI, ANTONY LINDEN, BEVERLY R. VINCENT, STEPHEN P. ROE, D. ADHIKESAVALU, T. STANLEY CAMERON et OSVALD KNOP. Can. J. Chem. **72**, 1273 (1994).

Le but du présent travail est de fournir une classification et des exemples de liaisons N—H...π (ainsi qui O—H...π) impliquant des systèmes π aromatiques dans des tétraphénylborates d'ammonium organiques qui pourrait servir de référence pour des liaisons X—H...π(arène) en général. À cette fin, on a déterminé les structures cristallines des tétraphénylborates des cations suivants: Me_3NH^+, Et_3NH^+, quinuclidinium, DabcoH$^+$, Et(*iso*-Pr)$_2$NH$^+$ (monohydraté), $(PhB)_3NH[—(CH_2)_2—]_2NHMe^+$ (solvaté par du Me_2CO), $Me_2NH_2^+$ (solvaté par du MeCN ou par du Et_2CO), azoniacycloheptane, guanidinum (monohydraté), $MeNH_3^+$, $EtNH_3^+$ et 1-adamantammonium (monohydraté). Ces structures comportent diverses liaisons N—H...π normales, bifurquées et trifurquées ainsi que des liaisons O—H...π normales vers les groupes phényles de l'anion. Les liaisons X—H...π se forment chaque fois que la possibilité existe, même si la géométrie qui en résulte n'est pas toujours favorable. Les liaisons formant des branches et le désordre orientationnel représentent des solutions de compromis pour des situations dans lesquelles les hydrogènes H(X) se voient offrir des différents accepteurs phényles ou dans lesquelles l'organisation générale de la structure cristalline offre des conditions de liaison non favorables à ces hydrogènes. On a analysé en détail les répartitions des distances allant de X ou H(X) au centre du noyau phényle du squelette ainsi que les distances moyennes X...C et H(X)...C avec les atomes de carbone du cycle.

[Traduit par la Rédaction]

In this paper we present the results of what we believe is the first systematic, goal-oriented experimental investigation of hydrogen bonding to aromatic π systems is crystals, a subject of sustained and growing interest. The investigation was undertaken to lay a more secure foundation for a better understanding of this type of bonding interaction, in particular as regards its geometric aspects.

The possibility of formation of an X—H...acc hydrogen bond in which the acceptor is a delocalized π system was recognized as early as the 1940s. Since then numerous spectroscopic investigations (3–27) have furnished evidence for the existence of such bonding interactions, mostly in solution. There has also been some theoretical work (27–37). In contrast, crystallographic studies, which would provide direct rather than stereochemically circumstantial evidence of such interactions in solids, have been sporadic and often serendipitous, and those involving *aromatic* π systems have been even fewer (38–50). Moreover, at times a crystal-structure determination actually may have uncovered an X—H...π bond, but this feature went unnoticed by the authors because of lack of attention to hydrogen bonding, or was noticed but not reported because the authors may not have been comfortable with the idea of an X—H...π interaction (see below).

Historically, the first demonstration of the existence of an X—H...π bond *in a crystal* appears to come from a calorimetric-cum-crystallographic study of NH_4BPh_4 (38). This was also the first reported demonstration of such an interaction (later confirmed and elaborated in ref. 43) involving specifically an aromatic π system, albeit one between weakly charged[8] rather than neutral species. On ir evidence this interaction is very weak and is associated with an estimated activation energy for NH_4^+ reorientation of the order of only 0.5 kcal/mol (cf. also refs. 24 and 26); its effect on the spectral features is not easy to assess and interpret (16, 43).

[1]For Part 3, see ref. 1.

[2]Erratum for Part 2 (2): the *b* value of $Ph_4Br.H_2O$ in Table 1 (p. 3060) should read 10.659(2) Å, not 10.65(2) Å.

[3]Holder of a graduate scholarship, Canadian Commonwealth Scholarship and Fellowship Plan, and a Killam Graduate Scholarship.

[4]Present address: Organisch-Chemisches Institut, Universität Zürich, CH-8057 Zürich, Switzerland.

[5]Present address: Molecular Structure Corporation, The Woodlands, TX 77381-4238.

[6]Present address: Muthurangam Government Arts College, Vellore, India 632 002.

[7]To whom correspondence may be addressed (telephone (902) 494-3317 or (902) 494-3305; facsimile, (902) 494-1310).

[8]See Appendix for the net charges on the atoms in NH_4^+, CH_4, H_2O, BPh_4^-, and CPh_4.

Can. J. Chem. Downloaded from www.nrcresearchpress.com by EESC ESCOLA DE ENGENHARIA on 09/08/12
For personal use only.

Can. J. Chem. Downloaded from www.nrcresearchpress.com by EESC ESCOLA DE ENGENHARIA on 09/08/12
For personal use only.

TABLE 1. Crystal structures discussed in this work[a]

Compound	Abbreviation	Reference
This investigation		
1 $Me_3NH^+TB^-$	3MTB	Table 2
2 $Et_3NH^+TB^-$	3ETB	Table 2
3 Quinuclidinium TB^-	QTB	Table 2
4 $DabcoH^+TB^-$[b]	DaHTB	Table 2
5 Et(*iso*-Pr)$_2$NH$^+$TB$^-$.H_2O	E2PiTBw	Table 2
6 $(Ph_3B)NH[(CH_2)_2]_2NHMe^+TB^-.Me_2CO$[c]	1MPzBTB.Me_2CO	Table 2
7 $Me_2NH_2^+TB^-.MeCN$	2MTB.MeCN	Table 3
8 $Me_2NH_2^+TB^-.Et_2CO$	2MTB.Et_2CO	Table 3
9 $Et_2NH_2^+TB^-$	2ETB	Table 3
10 (*iso*-Pr)$_2NH_2^+TB^-$	2PiTB	Table 3
11 Azoniacycloheptane TB^-	AC7TB	Table 3
12 $[C(NH_2)_3]^+TB^-.H_2O$[d]	GTBw	Table 3
13 $MeNH_3^+TB^-$	1MTB	Table 4
14 $EtNH_3^+TB^-$	1ETB	Table 4
15 1-Adamantammonium $TB^-.H_2O$	AdTBw	Table 4
Cited from the literature		
16 $NH_4^+TB^-$	ATB	33, 43
17 $Me_4N^+TB^-$	4MTB	51
18 *n*-$Bu_3NH^+TB^-.H_2O$	3BnTBw	42
19 $[Me_2C{=}NHMe]^+TB^-$	ImA	1
20 $[Me_2C{=}NHEt]^+TB^-$	ImC	1
21 $[MeEtC{=}NHMe]^+TB^-$	ImD	1
22 $[Me_2C{=}NH(-CH_2CH_2Ph)]^+TB^-.H_2O$	ImEw	1
23 $C_{25}H_{36}O_2$[e]		41
24 $C_{24}H_{24}N_3O_5I.EtOH$[f]		39, 40
25 Na_4[calix[4]arene sulfonate]·13.5H_2O		47
26 1,1-C_6H_{10}(—C_6H_2-3,4-Me_2-4-NH_2)$_2$		50
27 $BC_{14}H_{16}NO$[g]		52
Tetraphenylborates of cations without H(N)		
28 $[Me_2C{=}NMe_2]^+TB^-$	ImB	1
29 $Et_4N^+TB^-$ ($P3_121$)	4ETB	Unpublished
30 *n*-$Pr_4N^+TB^-$ ($C2/m$)	4PnTB	Unpublished
31 *n*-$Bu_4N^+TB^-$ ($P\bar{1}$)	4BnTB	Unpublished
32 C[—$(CH_2)_3$—]$_3N^+TB^-$[h] ($P2_1/n$)	AzPpTB	Unpublished

[a] TB^- = tetraphenylborate anion.
[b] $DabcoH^+$ = N(—CH_2CH_2—)$_3NH^+$, 1-aza-4-azoniabicyclo[2.2.2]octane (singly protonated Dabco cation).
[c] *N*-Triphenylboro-*N'*-Me-piperazinium TB.
[d] Guanidinium TB.
[e] 2,2-Bis-(2-OH-5-Me-3-*t*-Bu phenyl)propane.
[f] *aci-p*-Iodobenzoylamino-cyclol, ethanol solvate.
[g] *B,B*-Ph_2-boroxazolidine, 2-aminoethyl diphenylborinate.
[h] 1-Azoniapropellane TB.

In the following we shall be concerned mostly with interionic N—H^+...π^- interactions in crystalline tetraphenylborates (TB) of organic ammonium cations (Table 1). The fifteen title compounds **1–15** plus the previously reported (1) iminium TBs **19–22**, ATB (**16**), and 3BnTBw (**18**) now provide a sufficient variety of H...π bonding interactions on which to base a classification of bond types and geometries.

Types of X—H...π bonds (X = N, O)

In the crystal structures of the TBs in Table 1 the N atom may be bonded to 1–4 atoms; some of the structures (**12**, **14**, **15**) contain more than one cation nitrogen; and in yet others (**5**, **12**, **15**, **18**, **22**) the H(N) atom is bonded to a phenyl ring indirectly, via a water molecule. These structures thus provide examples of normal N—H...π bonds (types **A–D**, Fig. 1), bifurcated N—H...2π bonds (**E**, **F**) as well as of trifurcated N—H...3π bonds (**H**, **J**). In addition to these homodesmic geometries there are also heterodesmic bifurcation (**G**) and normal N—H...O(—H...π)$_2$ bonds (**L**), the latter of course corresponding to O—H...π rather than N—H...π interactions.

In the **L** type situation the oxygen of the water molecule is 3-coordinate, i.e. the N—H(N) vector approximately bisects the H—O—H angle and thus also the angle between the two lone electron pairs on the O atom. An extension to tetrahedrally 4-coordinate oxygen, in which *two* N—H(N) vectors point at the O atom (each H(N) engages a lone pair on the oxygen; type **L'**, not shown in Fig. 1), has also been observed (see below under GTBw).

Can. J. Chem. Downloaded from www.nrcresearchpress.com by EESC ESCOLA DE ENGENHARIA on 09/08/12
For personal use only.

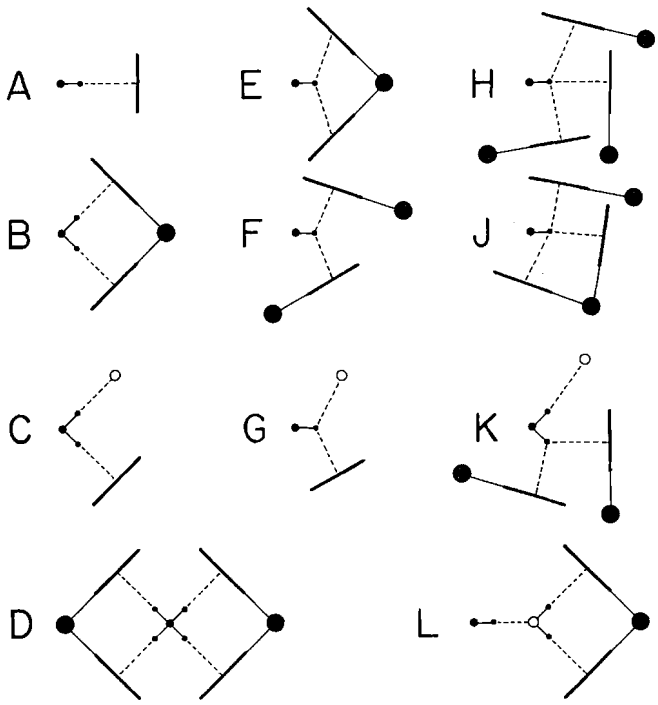

FIG. 1. Schematic synopsis of N—H(N)...π and N—H(N)...O—H-(O)...π bonding geometries in the tetraphenylborates **1–16**, **18–22**, and in **27** (Table 1). Full circles: large, B; medium, N; small, H. Open circles: X = N or O. Heavy lines represent phenyl rings projected on edge. For occurrence of types **A–L** see footnote 9.

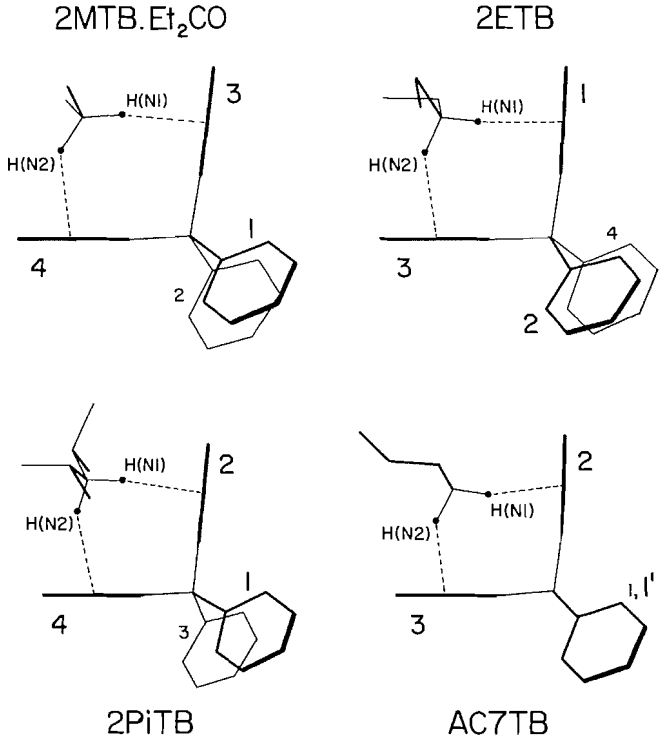

FIG. 3. Normal N—H...π bonds in tetraphenylborates in which the cation nitrogen carries two H(N) atoms, both engaged in H bonds. The projection plane is approximately the N,H(N),H(N)′ plane. Type **B**: 2MTB.Et_2CO, 2ETB, 2PiTB, AC7TB.

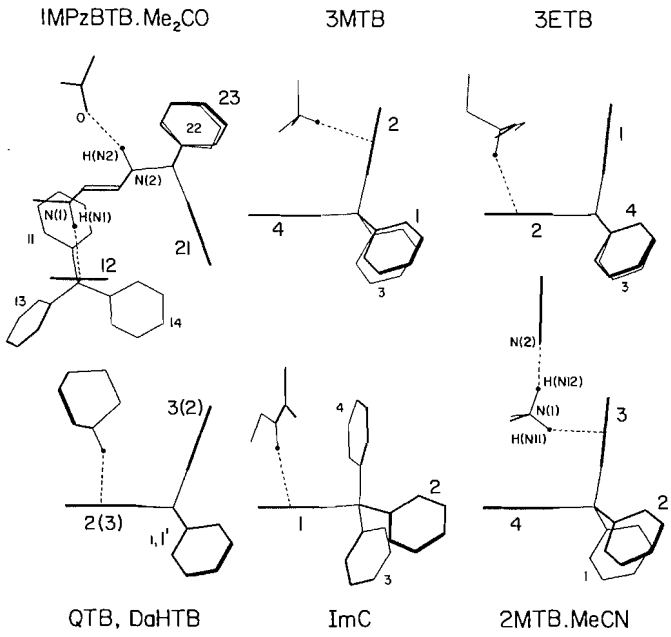

FIG. 2. Normal hydrogen bonds in tetraphenylborates in which the cation is engaged in one N—H(N)...π bond. The black dot represents H(N). Ring numbers in parentheses refer to DaHTB. Broken lines connect H(N) with the centre π_c of the associated ring. Type **A**: 3MTB, 3ETB, QTB, DaHTB, ImC, IMPzBTB.Me_2CO. Type **C**: 2MTB.MeCN.

Some of the structures contain more than one type of hydrogen bond.[9] The actual H-bonding situations are presented in Figs. 2–8.

Directionality and length of the X—H(X)...π bond: general considerations and 1:1 complexes

In a normal X—H...acc hydrogen bond where the acceptor is an atom or, more properly, an electron lone pair localized on an atom, description of the bond geometry presents no problem. The X...acc and H...acc distances ideally are distances between atomic nuclei, and their accuracy and that of the X—H—acc angle in the crystal will depend primarily on the confidence and accuracy with which the H atom has been located, but in principle there is no fundamental difficulty with characterizing the dimensional properties of the bond. This is not so with H bonds to delocalized π systems, especially where the delocalization extends over several atoms. Here the nature and position of the acceptor are ill defined: in general, one cannot single out the acceptor nucleus at which the X—H vector would preferentially point and which would constitute the terminal point of the H...acc segment, i.e. define the H...acc bond length.

For the purposes of the present, purely qualitative considerations we shall regard the H bonding as an essentially electrostatic interaction between the charge on the poorly shielded proton and the electron density in the phenyl

[9]The bond types are distributed among the structures of Table 1 as follows: **A**, **1–4**, **6**, **7**, **12–15**, **20**; **B**, **8–11**; **C**, **7**; **D**, **16**; **E** symmetric, **19**; **E** asymmetric, **13**, **14**, **21**; **F**, **12**, **14**; **G**, **12**; **H**, **12**; **J**, **13**, **14**; **K**, **27**; **L** symmetric, **5**; **L** asymmetric, **15**, **18**, **22**; **L′**, **12**.

Can. J. Chem. Downloaded from www.nrcresearchpress.com by EESC ESCOLA DE ENGENHARIA on 09/08/12
For personal use only.

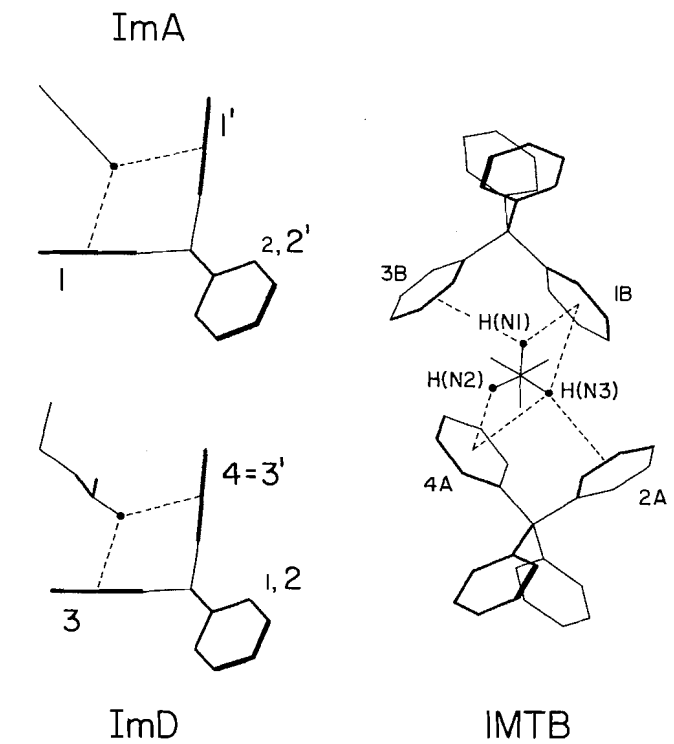

FIG. 4. Bifurcated and trifurcated N—H...π bonds in tetraphenylborates (see also Figs. 6 and 7). Type **E**: ImA, ImD, 1MTB. Type **J**: 1MTB. The projection plane for ImA and ImD is the N,π_c,π_c' plane, for 1MTB the H(N1),H(N2),H(N3) plane.

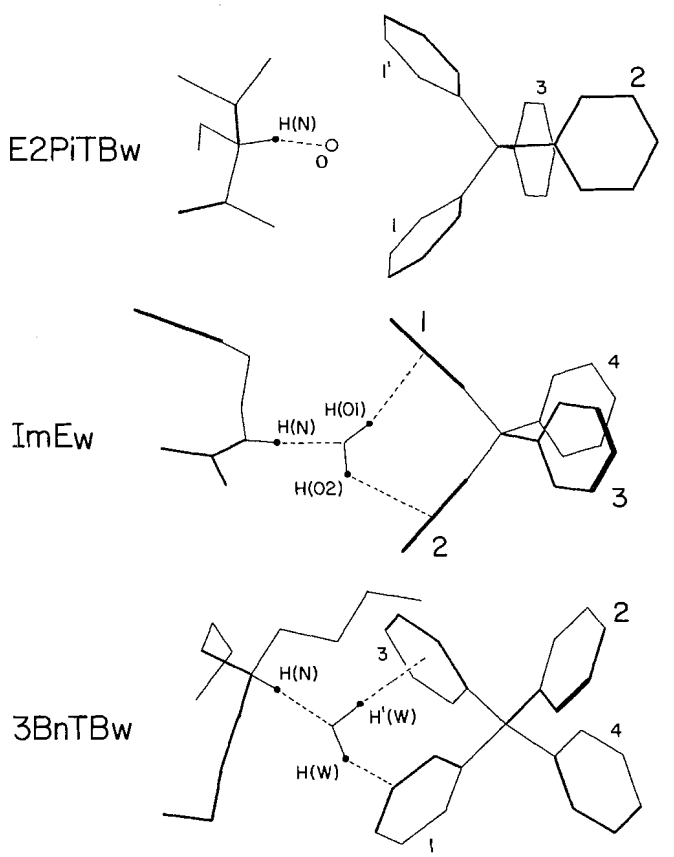

FIG. 5. N—H(N)...O[—H(O)...π]$_2$ bonds in tetraphenylborates. Projection on the N,H(N),O plane. Type **L**: symmetric, E2PiTBw; asymmetric, 3BnTBw, ImEw (see also Figs. 6 and 8).

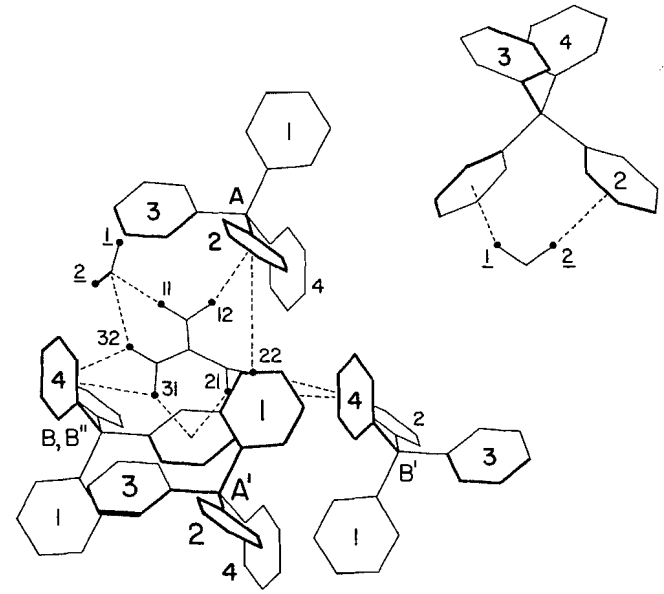

FIG. 6. Hydrogen bonding in GTBw (**12**). Projection on the cation-skeleton plane. Broken lines, H bonds drawn to the centres of the associated rings. Numbering: 32 = H(N32) etc.; 1, 2 = H(O1), H(O2). Upper right-hand corner: H bonding of the H_2O molecule.

ring.[10] The salient features of this simple model will not be obscured if we examine the electron-density distribution in the *benzene molecule* instead of the more specific (though more complicated and currently unavailable) distribution in the C_6H_5—B group itself.

Inspection of the calculated electron-density distribution in C_6H_6 (Figs. 9 and 10) shows that the outer contours above and below the C_6 ring skeleton (in planes *B–D* perpendicular to the molecular plane σ_h) are relatively flat. This is certainly true for *C*, the plane passing through neighbouring carbon nuclei, up to ~0.4 au = 2.7 e/Å^3 (about 0.5 Å above σ_h) for the total density, and up to ~0.04 au = 0.3 e/Å^3 (about 1 Å above σ_h) even for the π density. In planes *B* and *D*, which pass through the centre π_c of the molecule, significant indentation above π_c is observed for the >0.008 au contours (at ~1 Å above σ_h), but the shapes of these higher-density contours are such that the region of low electron density (i.e. unfavourable for electrostatic interaction) toward the centre is relatively narrow and thus not extensively exclusionary.

If it is assumed that the interaction between the H(X) atom and the electron cloud is strongest in regions of high electron density, then the features of the density distribution in Figs. 9 and 10 will not lead to expectation of high directional selectivity of the X—H(X)...π bond. This has also been concluded from *ab initio* model studies of isolated H_2O–C_6H_6 (25, 27, 30, 31, 34–37), NH_3–C_6H_6 (30, 31, 34, 36), HF–C_6H_6 (31, 33, 36) and other such pairs as well as from the limited number of experimental studies of such pairs (22, 23, 25, 27). While the results differ in the details, the consensus for the H_2O–C_6H_6 complex, which has received the most attention, appears to be that the

[10]The conclusion from an *ab initio* (MP2) study of the isolated HF–C_6H_6 complex (33) was that roughly half of the bonding is electrostatic (induced dipole – permanent dipole interaction) and the other half is due to charge-transfer H-bond formation. In the present case of *interionic* H-bond formation the Coulombic component may be expected to be at least half the total interaction and probably significantly higher.

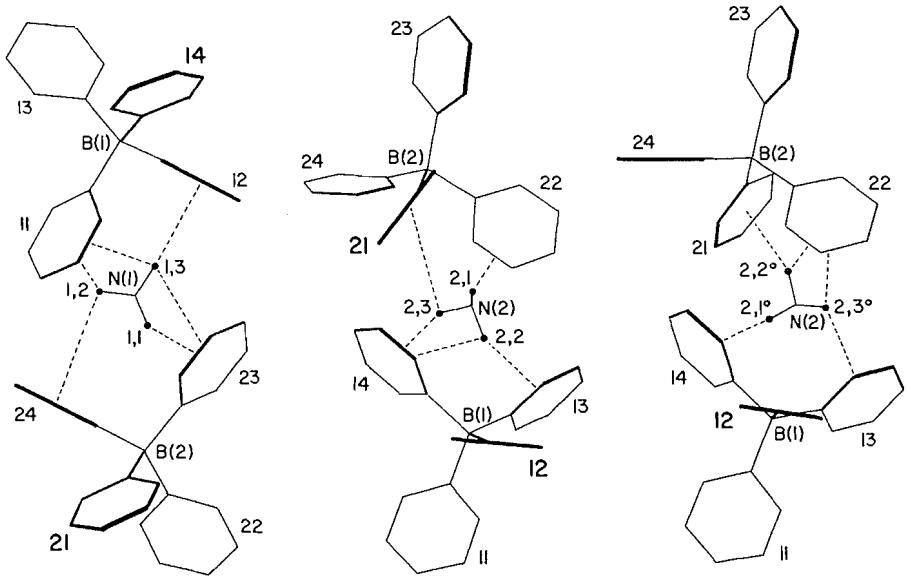

FIG. 7. Hydrogen bonding in 1ETB (**14**). For clarity the N(1) system and the two orientations of the N(2) system (resolved twofold disorder) are presented separately. Projections approximately on the plane of the respective H(N) atom triplets with avoidance of overlap. Broken lines, H bonds drawn to the centres of the associated rings. Numbering: 1,1 = H(N1,1) etc.; 2,3 = H(N2,3) etc.; 2,3° = H(N2,3*) etc.

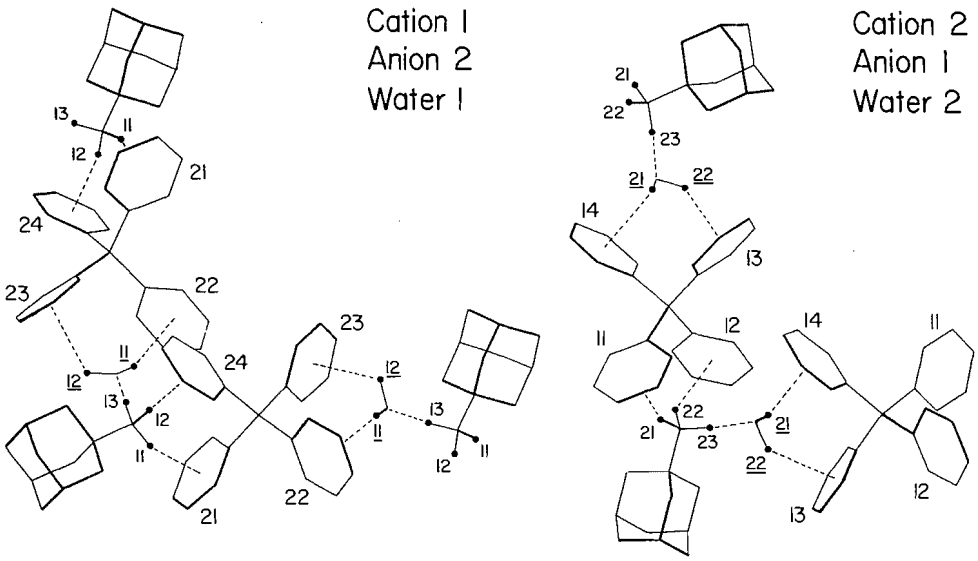

FIG. 8. Hydrogen bonding in AdTBw (**15**). For clarity the two H-bonding systems are presented separately. Broken lines, H bonds. Numbering: large type, rings; small type, 12 = H(N12) etc.; small type underlined, 22 = H(O22) etc.

H_2O molecule is situated above the C_6 ring skeleton, with the oxygen atom on or somewhat off (statically or dynamically) the C_6 axis and with the O—H vectors pointing simultaneously (?) and probably asymmetrically at the annular electron cloud above the ring skeleton. The potential surface for the movement of the H_2O molecule relative to the C_6H_6 molecule is very flat, permitting the H_2O molecule to rotate nearly freely with respect to the C_6 axis. These findings are consistent with the above expectation from the electron-density distribution in Figs. 9 and 10 concerning the lack of strong directional preference of the H bond. The estimates of the O...π_c distance in the complex range from 3.2 to 3.4 Å,[11] which is in good agreement with the corresponding distances observed in crystals (see below).

[11]In some of the studies the distance specified is that between the centres of mass of the two molecules, i.e. between π_c and a point ~0.07 Å from the oxygen atom on the C_2 axis of the H_2O molecule.

The conclusions for the NH_3–C_6H_6 complex are less compelling.

Directionality and length of the X—H(X)...π bond: crystals

In crystals the conditions for the formation of X—H(X)...π bonds are quite different. In the isolated donor–acceptor pairs of the preceding section there are no external constraints on the component molecules and the direction of the bond is the outcome of the two molecules being free to assume a relative orientation that corresponds to the minimum energy of the system. By contrast, in crystals the donor–acceptor pair is not isolated and constraints arise from packing and from multiple choices: the environment and relative orientation in a crystal are largely determined by packing efficiency (and Coulombic energy in ionic crystals), and there may be more than one π system available for bond formation. Thus an H_2O molecule in the TBs is

Can. J. Chem. Downloaded from www.nrcresearchpress.com by EESC ESCOLA DE ENGENHARIA on 09/08/12
For personal use only.

Can. J. Chem. Downloaded from www.nrcresearchpress.com by EESC ESCOLA DE ENGENHARIA on 09/08/12
For personal use only.

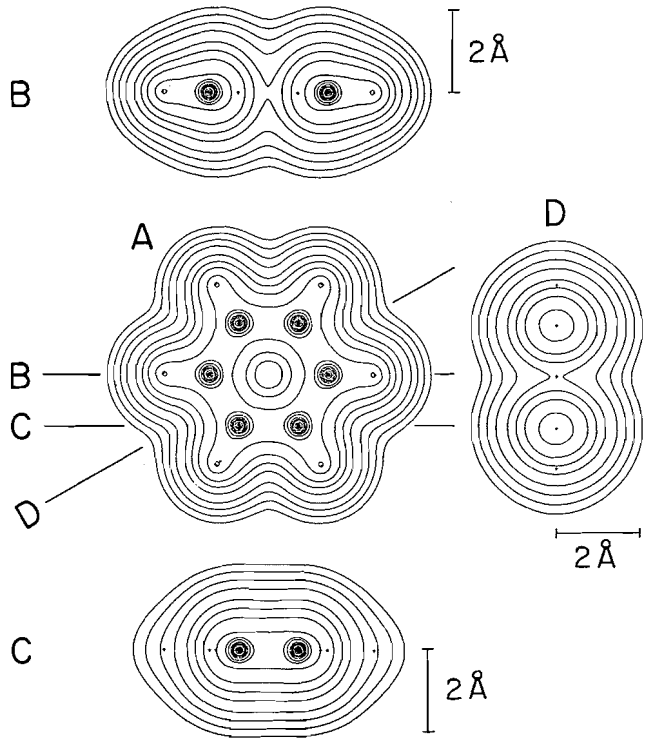

FIG. 9. Distribution of the calculated total electron density in the benzene molecule (6-31G**). *A*, distribution in the molecular plane; *B–D*, distributions in planes perpendicular to the molecular plane, as indicated. The outermost contour represents 0.002 au and is followed by the 0.004, 0.008, 0.02, 0.04, 0.08 au etc. contours (1 au = 6.749 e/Å^3).

found to be H-bonded simultaneously to *two* phenyl rings (types **L** and **L′**, Fig. 1); in **23** and **24** the direction of the —O—H vector is determined by the conformational limits of the molecule. The actual direction of the bond with respect to the ring cannot therefore be predicted with confidence and a reliable crystal-structure determination is required.

In the TBs that contain cations in which a nitrogen carries at most two N(H) atoms the positions of these hydrogens (and hence the orientations of the corresponding N—H vectors) are known with reasonable confidence, either from a difference map or from geometrical considerations (cf. Experimental).[12] In a normal bond the N—H vector is seen to be directed at some point in the general area of the electron cloud of the associated ring. The angle $\phi \leq 90°$ which this vector makes with the ring plane varies considerably from situation to situation and is undoubtedly strongly affected by accidents of packing. Furthermore, since the N—H vector can approach the ring from a variety of directions, the angle ψ formed by the projection of the N—H vector onto the ring plane and the (approximate) B—C(α)—C(δ) line (Fig. 11) should be examined in conjunction with ϕ. In a crystal, both ϕ and ψ are likely to be governed less by "chemical" forces than by the particulars of packing, and although the distribution of ϕ values and the possibility of a correlation between these two angles must not be left uninvestigated, it is not certain that ϕ is the quantity best suited to serve as a principal parameter in formulating general norms of N—H...π bonding from empirical data. It seems more profitable at this, the fact-finding stage to concentrate instead on examining interatomic *distances*. Similar considerations apply to the O—H vector in the water of hydration.

Since the length of the X—H(X)...π bond cannot be properly defined, a suitable device must be substituted if bonds are to be compared. Any such device must be capable of being uniquely specified from the parameters of the crystal structure. Two quantities that are known with considerable accuracy and that will be used in the following are the mean distance $\bar{d}$(X...C) of the X atom to the ring carbons and the distance d(X...π_c) from X to the centre π_c of the associated ring. The two companion distances $\bar{d}$[H(X)...C] and d[H(X)...π_c], in the absence of neutron-diffraction results, are not as reliable, but their lower accuracy does not render them less informative. Basing a discussion of the X—H(X)...π bonding on distances from the ring centre when the X—H vector in reality points elsewhere is of course artificial (see below). Yet this artifice provides us with a simple and generally applicable scheme which is useful for classification and statistics without obscuring the essential features of the bonding.

The $\bar{d}$(X...C), d(X...π_c), $\bar{d}$[H(X)...C], and d[H(X)...π_c] distances for the compounds of Table 1 are detailed in Table 5. The standard deviations of $\bar{d}$(X...C) and $\bar{d}$[H(X)...C] in fact give indirect information about ϕ, and the X—H(X)—π_c = ω "bond" angle is obtained directly from d[X—H(X)] ~ 1 Å, d(X...π_c), and d[H(X)...π_c].

Within the accuracy of a standard X-ray structure determination the uncorrected X—H bond length may be taken as constant. For collinear X,H(X), π_c triplets (ω = 180°) the difference d(X...π_c) − d[H(X)...π_c] would thus also be constant, and the corresponding points in a d[H(X)...π_c] vs. d(X...π_c) plot for normal (i.e. not branched) X—H(X)...π bonds would fall on a 45° line. This is seen to be the case for a number of X = N points in Fig. 12 which also shows the range and distribution of the H(N)...π_c and N...π_c distances in the compounds of Table 1. For bonds that can be identified visually and from distances to the ring as normal the ω angles for X = N fall between 180° and 120°, with a sample mean $\bar{\omega}$ = 156(16)°. However, a more detailed analysis (Table 6) reveals that $\bar{\omega}$ for cations with a single H atom on the nitrogen is 163(13)°, whereas where there are competing H(N) donors on the nitrogen, $\bar{\omega}$ for the normal bonds is 144(12)°.[13]

For type **B** bonds, with two H(N) on the cation nitrogen and two normal bonds to phenyl rings of the same anion, one bond angle is consistently and significantly larger than the other: $\bar{\omega}_1$ = 178(4)°, $\bar{\omega}_2$ = 149(5)°, i.e. one N—H vector points at the centre of the associated ring (ϕ ~ 90°), while the other points at the electron cloud in the general vicinity of C(δ) of *its* associated ring (Fig. 3). This appears to be the consequence of the constraint of the H(1)—N—H(2) angle at the nitrogen to approximately tetrahedral: one of the H(N) atoms makes a "better" bond than the other, although the H(1)—N—H(2) triplet probably undergoes a significant quasi-librational motion which would tend to compensate, dynamically, for the disparity. In the extreme case of ATB (**16**) the four N—H...π bonds are equivalent by symmetry and ω = 141° (43).

The means of the 26 N...π_c and H(N)...π_c distances in the normal-bonds sample are 3.25(18) and 2.34(19) Å, respectively. The corresponding means for particular subsets of the

[12]Where the nitrogen carries three H atoms, as in **13–15**, the positions of these hydrogens are known with less certainty, but they are still adequate for describing the geometry of the bonds (see below).

[13]One abnormally high value is not included in the mean.

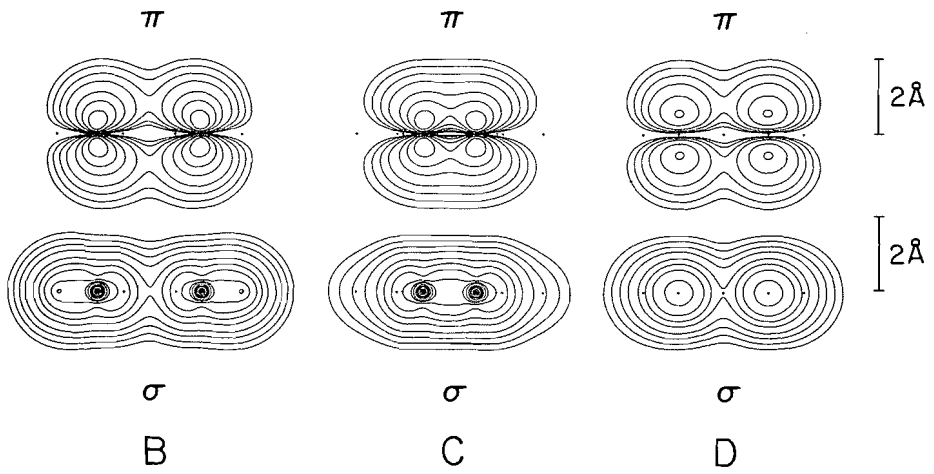

FIG. 10. Electron-density distribution in the σ and π systems of the benzene molecule (6-31G**) in planes *B–D* of Fig. 9.

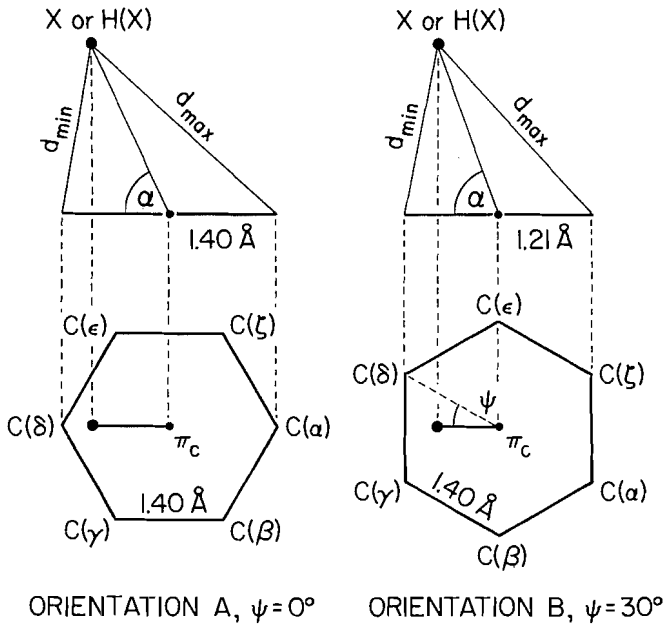

FIG. 11. Orientation of the X—π_c or H(X)—π_c vector relative to the benzene ring plane. Only orientations in planes perpendicular to the ring plane are considered; the ring is taken to contain C_6 symmetry; the C(α) may or may not be attached to the B atom of the TB anion, i.e. $0 < |\alpha| \leq 90°$.

normal-bonds sample (Table 6) are statistically indistinguishable from the overall means. The distributions of the distances are strongly skewed toward low values, $0.9 \leq \gamma_1 < 1.3$.[14]

The distribution of the points in the companion plot, $\bar{d}$[H(N)...C] vs. $\bar{d}$(N...C) (Fig. 12), resembles that of the d[H(N)...π_c] vs. d(N...π_c) plot, in that it too is skewed toward low values. The points cluster about the $\bar{d}$(N...C),$\bar{d}$[H(N)...C] means of 3.54(16),2.72(16) Å for the normal bonds and 3.59(20),2.73(18) Å for the type **A** bonds only. In comparing $\bar{d}$(X...C) with d(X...π_c) etc. the following should be realized: d(X...π_c) is a distance between an atom and π_c, which is a point not occupied by an atom but well defined by the C atoms of the phenyl ring, and ω represents the angle defined by X,H(X),π_c. By contrast, $\bar{d}$(X...C), although a length, does not represent the distance from X to any uniquely defined and physically significant point in the crystal structure; it should be regarded as exactly what it stands for, an arithmetic mean, i.e. a number. The angle ω calculated from $\bar{d}$(X...C) and $\bar{d}$[H(X)...C] is therefore a *fictitious* angle, the value of which should not be compared with the ω obtained from d(X...π_c) and d[H(X)...π_c]. Nevertheless, its *distribution* is qualitatively similar to that for the latter distances and thus corroborative.

Linear regressions of $\bar{d}$(X...C) on d(X...π_c) for X = N, X = O, and X = N + O show that, statistically, there is no difference between N and O in our sample. The combined regression yields $\bar{d}$(X...C) = 0.64(1) + 0.89(1)d(X...π_c) (n = 70, r^2 = 0.99, σ = 0.02 Å ~ 2% of range) and $\bar{d}$[H(X)...C] = 0.68(1) + 0.87(1)d[H(X)...π_c] (n = 67, r^2 = 1.00, σ = 0.03 Å ~ 2% of range). Converting regression equations to differences one obtains $\delta_X = \bar{d}$(X...C) − d(X...π_c) = 0.64(1) − 0.11(1)d(X...π_c) and $\delta_H = \bar{d}$[H(X)...C] − d[H(X)...π_c] = 0.68(1) − 0.13(1)d-[H(X)...π_c], i.e. the differences are not constant. Their mean values are 0.28(5) Å for δ_X and 0.36(6) Å for δ_H in the normal bonds, and 0.25(4) and 0.28(6) Å, respectively, in the branched bonds.

Reference to Fig. 11 will show that for X (or H(X)) situated on the C_6 axis of the C_6H_6 molecule, $\delta_{bz} = \{[d(X...\pi_c)]^2 + 1.96\}^{1/2} - d(X...\pi_c)$. This expression is nonlinear, but it turns out that $\delta_X - \delta_{bz} = -0.001$, −0.015, and −0.038 Å, respectively, for d(X...C) = 3.0, 3.5, and 4.0 Å; and $\delta_H - \delta_{bz} = -0.021$, −0.010, and −0.021 Å, respectively, for $\bar{d}$[H(X)...C] = 2.0, 2.5, and 3.0 Å. If one keeps in mind that $\bar{d}$ in addition responds to pivoting of the phenyl ring about π_c, the linear expressions for δ_X and δ_H obtained from the regressions will be seen to represent the differences between $\bar{d}$(X...C) and d(X...π_c), and between $\bar{d}$[H(X)...C] and d[H(X)...π_c], over the observed ranges reasonably well.

The ranges and distributions of the bond distances and ω for X = O are qualitatively very similar to those for X = N (Tables 5 and 6), especially when allowance is made for the greater uncertainty in the location of the H(O) atoms of the H_2O molecules. The means for $\bar{d}$(O...C) and d(O...π_c) are 3.64(14) and 3.34(17) Å, respectively, which is in agreement with the O...π_c distances of 3.2–3.4 Å estimated from investigations of the H_2O–C_6H_6 complex. The two H(O) hydrogens of a water molecule form asymmetric bonds, $\bar{\omega}_1$ = 145(10)°, $\bar{\omega}_2$ = 126(8)°,

[14] γ_1 and γ_2 are the moment coefficients of skewness and kurtosis, respectively.

Can. J. Chem. Downloaded from www.nrcresearchpress.com by EESC ESCOLA DE ENGENHARIA on 09/08/12
For personal use only.

Can. J. Chem. Downloaded from www.nrcresearchpress.com by EESC ESCOLA DE ENGENHARIA on 09/08/12
For personal use only.

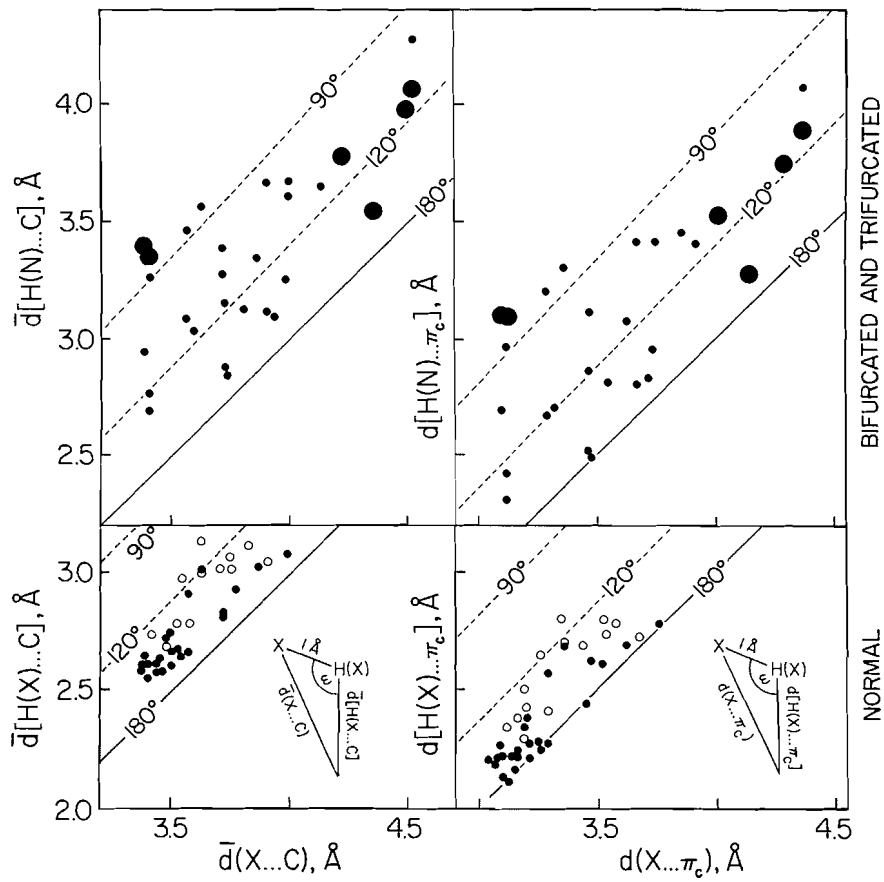

FIG. 12. The mean H(X)...C distances plotted against the mean X...C distances, and the H(X)...π_c distances against the X...π_c distances (Table 5). Full circles: small, X = N, normal or bifurcated bonds; large, X = N, trifurcated bonds. Open circles: X = O, normal bonds. The angle ω describes the angularity of the X—H...π_c bond as described in the figure.

but this is not reflected in the d(O...π_c) and d[H(O)...π_c] means.

Branched X—H(X)...π bonds

We now turn to the branched (bifurcated and trifurcated) N—H(N)...π bonds (no example of a branched O—H(O)...π bond appears to have been reported to date). All the branched bonds in Table 5 except that in **19** are asymmetric.

Bifurcation (and *a fortiori* trifurcation) is the result of compromise in the choice of acceptor. The N—H vector now cannot be said to point at the electron cloud of the phenyl ring in a particular direction, so the notion of bond angle becomes diffuse: in type **E** bonds the vector points more or less at the boron atom, and there appears to be no clear way of dealing with lateral H-bonding interaction. However, the angle ω = N—H(N)—π_c retains its validity and in fact is the only "bond" angle that in the circumstances can be uniquely defined. This angle in general is significantly smaller than for the normal bonds, and its distribution is considerably broader (Fig. 12). The overall mean $\bar{\omega}$ is 119(22)° (n = 24, γ_1 = 0.47, γ_2 = 2.65); the mean for the smaller of the two ω angles in the bifurcated bonds is 103(11)° (n = 12, γ_1 = 0.02, γ_2 = 2.02) and that for the larger angle is 136(16)° (n = 12, γ_1 = 0.66, γ_2 = 2.32), i.e. the skewness of the ω distribution comes from the larger angle.

The three means for d(N...π_c) in bifurcated bonds (Table 6) are numerically different, as are those for d[H(N)...π_c] and again for $\bar{\omega}$. However, the sample of Table 1 is too small for definite statistical inferences to be drawn, even though the means for the larger ω and for the smaller ω are probably genuinely different. The frequency of occurrence of significant asymmetry in bifurcated bonds will have to be investigated further.[15]

Only two examples of trifurcated bonds are available at present, those in **12** and **13**, so any discussion of such bonds would be of necessity incomplete. Of the two, the bond in **12** is the more symmetric, the three component N...π_c distances being quite similar, and likewise for the three H(N)...π_c distances and for the three ω angles.

Although the statistics leave something to be desired, there is a clear increase in the numerical value of the means for N...π_c and H(N)...π_c from the normal to the trifurcated bonds and a decrease for $\bar{\omega}$ (Table 6). This trend would be expected: if bifurcation represents a compromise, trifurcation represents an even greater compromise. The difficulty that sometimes arises with multibranched H bonds involves the ambiguity in recognizing which and how many acceptors should legitimately be included in the H-bonded environment of the donor hydrogen. Correlations like those of Fig. 12 may be helpful in verifying visual assignment of acceptors, but on occasion it may be difficult to

[15]This matter for ordinary H bonds (i.e. bonds not to delocalized π acceptors) and the question of whether bifurcated H bonds are stronger than normal H bonds in situations that warrant comparison have been discussed, on ir and crystallographic evidence, by Knop, Falk et al. in a series of papers on the ammonium and alkylammonium ions published between 1979 and 1985 in Can. J. Chem. and J. Chem. Soc. Faraday Trans. 2.

Can. J. Chem. Downloaded from www.nrcresearchpress.com by EESC ESCOLA DE ENGENHARIA on 09/08/12
For personal use only.

know whether or not bifurcated bonds with one ω close to 180° or below 90°, and with large N...π_c and H(N)...π_c separations, should be reassigned as normal bonds (or vice versa), and trifurcated bonds with such characteristics as bifurcated bonds. These are problems for further empirical analysis as additional data accumulate.

Minimum and maximum X...C and H(X)...C distances

As mentioned above, information about ϕ can be obtained indirectly from the esd's of the $\bar{d}$(X...C) and $\bar{d}$[H(X)...C] values. For an X atom situated on the C_6 axis of the benzene molecule the X...C distances would be equal and the esd of $\bar{d}$(X...C) would be zero, while for an X atom in the molecular plane and 3.5 Å from π_c the esd of $\bar{d}$(X...C) would be approximately equal to 1 Å. The *observed* esd range for $\bar{d}$(N...C) is 0.03–0.39 Å for the normal bonds (mean, 0.14(6) Å; $\gamma_1 = 2.55$, $\gamma_2 = 13.4$), 0.13–0.91 Å for the bifurcated bonds (mean, 0.28(22) Å; $\gamma_1 = 1.46$, $\gamma_2 = 4.34$), and 0.13–0.67 Å for the trifurcated bonds (Table 5). The corresponding esd ranges for $\bar{d}$[H(N)...C] are 0.04–0.50 Å (mean, 0.18(12) Å; $\gamma_1 = 1.04$, $\gamma_2 = 3.40$), 0.14–0.96 Å, and 0.21–0.59 Å, respectively. For $\bar{d}$(O...C) and $\bar{d}$[H(O)...C] the esd ranges are 0.06–0.59 and 0.12–0.59 Å, respectively. Thus even when allowance is made for the distortion of the ring in the TBs, the range of ϕ is seen to be wide. However, the distributions of the esd's are strongly skewed toward low values, indicating preference for large ϕ.

Another way of assessing the inclination of the X—H vector to the ring skeleton plane is to examine the difference Δ(X...C) between the longest, d_{max}(X...C), and the shortest, d_{min}(X...C) distance from X to the ring carbons, and the corresponding differences Δ[H(X)...C] between d_{max}[H(X)...C] and d_{min}[H(X)...C] (Table 7). The lower bound of Δ is zero, which for an undistorted benzene ring would correspond to an X—H vector coincident with the C_6 axis. For the normal X—H(X)...π bonds in the TBs, Δ(N...C) ranges from 0.04 to 1.0 Å, Δ[H(N)...C] from 0.04 to ~1.3 Å, Δ(O...C) from 0.04 to 1.14 Å, and Δ[H(O)...C] from ~0.3 to ~1.0 Å. The difference $\Delta\Delta_N = \Delta$(N...C) − Δ[H(N)...C] for these bonds ranges from −0.32 to 0.44 Å (mean, 0.13(20) Å; $n = 20$, $\gamma_1 = -0.34$, $\gamma_2 = 2.53$), and $\Delta\Delta_O = \Delta$(O...C) − Δ[H(O)...C] from −0.46 to 0.49 Å (mean, 0.14(28); $n = 12$, $\gamma_1 = -0.65$, $\gamma_2 = 2.52$). The differences $\Delta\Delta_N$ and $\Delta\Delta_O$ reflect not only the inclination of the X—H(X) vector to the ring plane but also the proximity of the X and H(X) atoms to the quasi-C_6 axis of the phenyl ring.

The difference Δ, for the geometry referred to the undistorted benzene molecule (Fig. 11), is related to the angle α_X formed by the X—π_c vector with the ring plane (the plane X,H(X), $\pi_c \perp$ ring plane) by $\Delta = d_{max}(X...C) - d_{min}(X...C) = (K + k\cos\alpha_X)^{1/2} - (K - k\cos\alpha_X)^{1/2}$, where X = N, O, or H(X), $K = [d(X...\pi_c)]^2 + b^2$, $k = 2bd(X...\pi_c)$, $K \pm k = [d(X...\pi_c) \pm k]^2$, and $b = d$(C—C) = 1.40 Å for orientation A and d(C—C) cos 30° = 1.21 Å for orientation B in Fig. 11. Then for $\alpha_X = 90°$, Δ = 0; for $\alpha_X = 0°$, $\Delta = (K + k)^{1/2} - (K - k)^{1/2}$, with $0 < \Delta < 2.80$ Å for orientation A and $0 < \Delta < 2.42$ Å for orientation B. In Fig. 13 the loci of equal α_X calculated for this model are represented by solid contour lines for orientation A and by broken contour lines for orientation B. Further, $\phi = \omega + \alpha_H - 180°$, provided the X,H(X),$\pi_c$ plane remains perpendicular to the ring plane.

The distribution of the Δ values (Fig. 13), especially for X = O, is erratic, but this may merely reflect the relative smallness of the sample. For the normal bonds there appears to exist a weak correlation between Δ(X...C) and d(X...π_c), and between

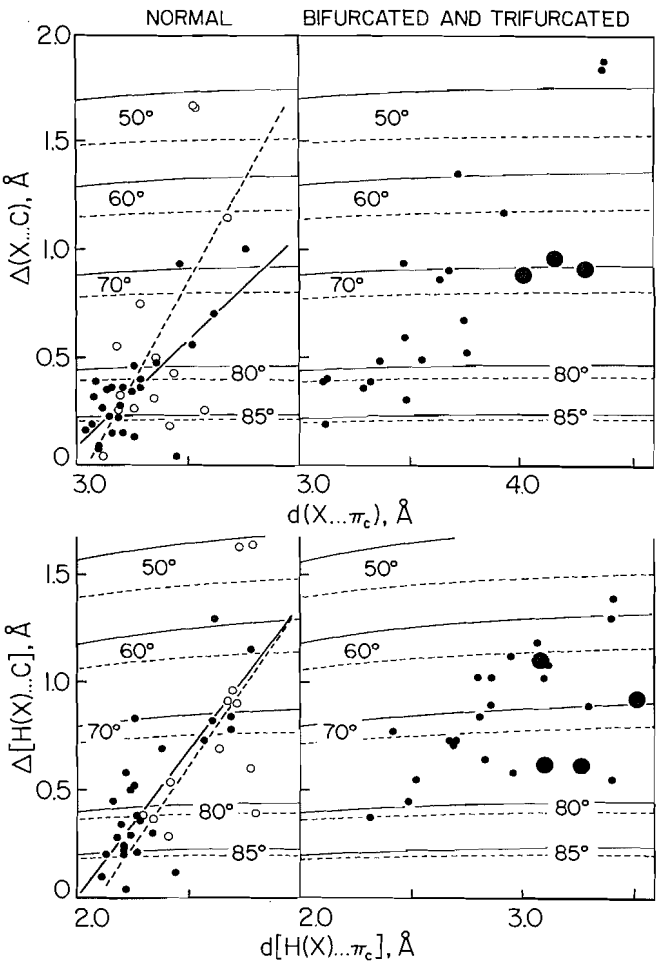

FIG. 13. The difference Δ(X...C) between the maximum and minimum X...C distances plotted against the X...π_c distances, and the differences Δ[H(X)...C] between the maximum and minimum H(X)...C distances plotted against the H(X)...π_c distances (Tables 5 and 7). For circle symbols see caption of Fig. 12. Regression lines Δ(X...C) on d(X...π_c): solid, X = N, $r^2 = 0.56$; broken, X = O, $r^2 = 0.36$. Regression lines Δ[H(X)...C] on d[H(X)...π_c]: solid, X = N, $r^2 = 0.64$; broken, X = O. $r^2 = 0.37$. Constant-α lines: solid, orientation A; broken, orientation B of Fig. 11.

Δ[H(X)...C] and d[H(X)...π_c]. For X = N, the approximate means of d(N...π_c), Δ(N...C), and α_N in the Δ(N...C) vs. d(N...π_c) plot of Fig. 13 are 3.27 Å, 0.35 Å, and 82°, respectively. Recognizable trends also exist for the branched bonds. The more distant X or H(X) is from the ring plane, the larger Δ and the smaller α; for H(X) specifically, the smaller α_H in straight X—H(X)—π_c bonds, the smaller ϕ.

Individual crystal structures

The crystal data of compounds **1–15** (Table 1; all new structure determinations) are listed in Tables 2–4. Tables of other crystallographic parameters and derived quantities have been deposited.[16] The contents of the deposited tables are as follows:

[16]This material may be purchased from the Depository of Unpublished Data, Document Delivery, CISTI, National Research Council of Canada, Ottawa ON, Canada K1A 0S2.

Tables A, B, C have also been deposited with the Cambridge Crystallographic Data Centre, and can be obtained on request from The Director, Cambridge Crystallographic Data Centre, University Chemical Laboratory, 12 Union Road, Cambridge, CB2 1EZ, U.K.

TABLE 2. Crystal data of tetraphenylborates: one hydrogen atom on the cation nitrogen[a]

Parameter	3MTB[b]	3ETB[b]	QTB[c]	DaHTB[d]	E2PiTBw[d]	1MPzBTB.Me_2CO[d]
Formula	$BC_{27}H_{30}N$	$BC_{30}H_{36}N$	$BC_{31}H_{34}N$	$BC_{30}H_{33}N_2$	$BC_{32}H_{42}NO$	$B_2C_{50}H_{54}N_2O$
f.w.	379.4	421.4	431.4	432.4	467.5	720.6
Crystal size, mm^3	0.3 × 0.3 × 0.4	0.4 × 0.7 × 0.7	0.05 × 0.2 × 0.4	0.2 × 0.2 × 0.15	0.27 × 0.33 × 0.45	0.25 × 0.15 × 0.1
μ, cm^{-1}	0.59	0.59	4.62	0.63	0.59	0.62
θ-range, deg[e]	2–23/25	2–23/25	3–60/25	2–25/24	2–25/21	2–25/19
Max/min[f]	1.08/0.71	1.30/0.86	1.61/0.59	1.00/0.95	1.00/0.87	1.00/0.96
a, Å	9.856(4)	9.684(1)	18.426(5)	18.208(3)	20.047(2)	9.819(3)
b, Å	12.683(3)	14.470(4)	13.334(1)	13.303(3)	14.167(2)	17.709(3)
c, Å	9.435(3)	9.383(1)	9.994(7)	9.987(2)	10.067(2)	24.223(3)
β, deg	107.80(4)	109.92(1)	90	90	90	95.46(2)
V, $Å^3$	1123(1)	1234(1)	2455(3)	2419(1)	2859(1)	4193(3)
Z	2	2	4	4	4	4
ρ_c, g/cm^3	1.122(1)	1.135(1)	1.167(2)	1.187(1)	1.086(1)	1.142(1)
Space group	$P2_1$ (no. 4)	$P2_1$ (no. 4)	*Pnma* (no. 62)	*Pnma* (no. 62)	*Pnma* (no. 62)	$P2_1/n$ (no. 14)
F(000), e	408	456	928	928	1016	1544
Reflections:						
total measured	3626	3054	2062	2448	2626	7505
unique total	1703	1833	2062	2448	2626	7031
unique used[g]	1259	1793	799	1061	833	1882
$100R_{merg}$	1.9	5.0	—	—	—	7.1
d/p	4.8[h]	6.3[h]	5.2[h]	6.5[h]	5.0[h]	3.8[h]
$100R$; $100R_w$	6.6; 6.7	6.3; 6.3	4.9; 5.1	3.9; 3.6	7.8; 7.8	4.6; 4.6
G.O.F.	0.69	0.76	2.58	2.08	2.10	1.76
Residual e.d.[j]	−0.15/0.19	−0.26/0.34	−0.17/0.16	−0.16/0.14	−0.37/0.47	−0.17/0.33

[a]For details of weighting schemes and other information see Experimental. $T \sim 18°C$. The footnotes apply also to Tables 3 and 4.
[b]CAD-4; Mo *K*α, λ = 0.70926 Å (graphite monochromator).
[c]Modified Picker diffractometer; Cu *K*α, λ = 1.54178 Å (graphite monochromator).
[d]Rigaku AFC5R; Mo *K*α, λ = 0.71069 Å (graphite monochromator).
[e]$\theta_{min} < \theta < \theta_{max}/n$. The lattice parameters and orientation matrices were obtained by least squares from the setting angles θ of suitable *n* reflections.
[f]Max/min empirical absorption corrections from DIFABS (53) or transmission factors from ψ-scans (DaHTB, E2PiTBw, 2PiTB).
[g]$I > 3\sigma(I)$ unless stated otherwise.
[h]H(C) atoms placed geometrically (C—H, 1.08 Å, $U_{iso}(H) = 1.2B_{eq}(C)$) and not refined.
[i]H(C) atoms placed geometrically (C—H, 1.08 Å) and refined isotropically.
[j]Minimum and maximum residual electron density ($e/Å^3$) in final difference map.

TABLE 3. Crystal data of tetraphenylborates: two hydrogen atoms on the cation nitrogen[a]

Parameter	2MTB.MeCN[b]	2MTB.Et_2CO[b]	2ETB[b]	2PiTB[d]	AC7TB[d]	GTBw[b]
Formula	$BC_{28}H_{31}N_2$	$BC_{31}H_{38}NO$	$BC_{28}H_{32}N$	$BC_{30}H_{36}N$	$BC_{30}H_{34}N$	$BC_{25}H_{28}N_3O$
f.w.	406.4	451.5	393.4	421.4	419.4	397.3
Crystal size, mm^3	0.3 × 0.3 × 0.4	0.3 × 0.4 × 0.5	0.6 × 0.35 × 0.25	0.3 × 0.4 × 0.4	0.25 × 0.3 × 0.35	0.3 × 0.4 × 0.5
μ, cm^{-1}	0.59	0.59	0.58	0.58	0.60	0.68
θ-range, deg[e]	2–23/25	2–23/25	2–23/25	2–25/20	2–30/25	2–23/25
Max/min[f]	1.18/0.60	1.19/0.60	1.09/0.68	1.00/0.95	1.24/0.50	1.12/0.85
a, Å	13.481(3)	11.623(3)	9.452(3)	12.889(6)	9.549(2)	10.411(4)
b, Å	13.478(4)	16.469(3)	15.406(7)	13.405(5)	13.905(3)	9.524(3)
c, Å	14.428(2)	14.573(3)	16.165(5)	14.912(8)	10.023(2)	23.102(7)
β, deg	109.75(1)	94.67(3)	90	98.81(4)	112.45(2)	103.50(3)
V, $Å^3$	2467(2)	2780(2)	2354(3)	2546(4)	1230(1)	2227(3)
Z	4	4	4	4	2	4
ρ_c, g/cm^3	1.094(1)	1.079(1)	1.110(1)	1.099(2)	1.132(1)	1.185(2)
Space group	$P2_1/a$ (no. 14)	$P2_1/n$ (no. 14)	$P2_12_12_1$ (no. 19)	$P2_1/n$ (no. 14)	$P2_1/m$ (no. 11)	$P2_1/c$ (no. 14)
F(000), e	872	976	848	912	452	848
Reflections:						
total measured	4225	3322	2332	4224	3929	3873
unique total	3402	2500	1906	4006	3731	3329
unique used[g]	1655[k]	1586	1115[k]	978	1261	1268[m]
$100R_{merg}$	1.7	2.5	3.2	7.2	3.7	2.7
d/p	5.2[i]	5.0[i]	4.1[h]	3.4[h]	7.3[h]	4.7[h]
$100R$; $100R_w$	5.7; 5.7	6.9; 6.9	4.9; 4.9	4.3; 4.3	5.7; 6.3	3.5; 3.5
G.O.F.	1.16	1.44	1.13	2.11	3.02	1.45
Residual e.d.[j]	−0.17/0.14	−0.18/0.27	−0.16/0.17	−0.15/0.16	−0.16/0.13	−0.14/0.10

[a]For details of weighting schemes and other information see Experimental. $T \sim 18°C$. For footnotes *b–j* see Table 2.
[k]$I > 2\sigma(I)$.
[m]$I > 1.5\sigma(I)$.

Can. J. Chem. Downloaded from www.nrcresearchpress.com by EESC ESCOLA DE ENGENHARIA on 09/08/12
For personal use only.

TABLE 4. Crystal data of tetraphenylborates: three hydrogen atoms on the cation nitrogen[a]

Parameter	1MTB[b]	1ETB[b]	AdTBw[d]
Formula	$BC_{25}H_{26}N$	$BC_{26}H_{28}N$	$BC_{34}H_{40}NO$
f.w.	351.3	365.3	489.5
Crystal size, mm^3	0.4 × 0.5 × 0.7	0.5 × 0.6 × 0.8	0.8 × 0.65 × 0.5
μ, cm^{-1}	0.60	0.59	0.60
θ-range, deg[e]	2–23/25	2–23/25	2–30/21
Max/min[f]	1.16/0.86	1.21/0.83	1.40/0.48
a, Å	14.799(6)	14.865(2)	13.686(6)
b, Å	15.526(5)	9.756(2)	15.568(6)
c, Å	8.971(2)	29.934(6)	14.177(5)
β, deg	90	92.38(1)	100.69(3)
V, $Å^3$	2061(2)	4337(3)	2968(4)
Z	4	8	4
ρ_c, g/cm^3	1.133(1)	1.119(1)	1.095(1)
Space group	$Pna2_1$ (no. 33)	$P2/c$ (no. 13)	$P2_1$ (no. 4)
F(000), e	752	1568	1056
Reflections:			
total measured	2130	6565	6735
unique total	1674	6441	6401
unique used[g]	1232	4004	2372
$100R_{merg}$	6.8	1.8	5.0
d/p	5.1[h]	6.7[i]	4.1[h]
$100R$; $100R_w$	4.4; 4.2	6.5; 7.8	6.3; 7.0
G.O.F.	1.85	1.17	3.28
Residual e.d.[j]	−0.14/0.14	−0.45/0.41	−0.21/0.36

[a]For details of weighting schemes and other information see Experimental. $T \sim 18°C$. For footnotes *b–m* see Tables 2 and 3.

TABLE 5. X—H...π (X = N, O) bonding: mean distances (Å) $\bar{d}$(X...C) and $\bar{d}$[H(X)...C], and the distances *d*(X...π_c) and *d*[H(X)...π_c] from X to the centre of the associated phenyl ring R (*d*(N—H), 1.02; *d*(O—H), 1.00 Å)[a]

Compound	H(X)...R bond	$\bar{d}$(X...C)	*d*(X...π_c)	$\bar{d}$[H(X)...C]	*d*[H(X)...π_c]
		N—H(N)...π bonds			
1	H(N)...R2	3.53(12)	3.25	2.67(14)	2.28
2	H(N)...R2	3.77(20)	3.52	2.93(32)	2.61
3	H(N)...R2	3.50(5)	3.21	2.66(8)	2.27
4	H(N)...R3	3.46(9)	3.12	2.57(4)	2.11
6	H(N1)...R12	3.50(14)	3.21	2.60(9)	2.21
19	H(N)[b]...R(2, 4)	3.60(13)	3.32	3.03(27)	2.70
20	H(N)...R1	3.99(39)	3.76	3.08(44)	2.78
21	H(N)[c] ...R3	3.39(15)	3.10	2.94(27)	2.69
	...R4	3.81(18)	3.55	3.12(31)	2.81
7	H(N11)...R3	3.38(12)	3.08	2.61(7)	2.21
8	H(N1)...R3	3.54(16)	3.26	2.65(19)	2.26
	H(N2)...R4	3.48(9)	3.19	2.72(11)	2.34
9	H(N1)...R1	3.54(20)	3.26	2.64(18)	2.24
	H(N2)...R3	3.45(5)	3.16	2.63(10)	2.24
10	H(N1)...R2	3.72(13)	3.45	2.81(4)	2.44
	H(N2)...R4	3.87(27)	3.62	3.02(31)	2.69
11	H(N1)...R2	3.44(9)	3.15	2.57(16)	2.16
	H(N2)...R3	3.37(8)	3.07	2.58(10)	2.18
12	H(N12)...R2A	3.57(15)	3.29	2.91(26)	2.57
	H(N21)[c] ...R3B	3.94(77)	3.72	3.09(57)	2.83
	...R4B′	4.53(67)	4.37	4.26(52)	4.06
	H(N22)[d] ...R1A′	4.23(33)	4.01	3.77(35)	3.52
	...R2A	4.50(35)	4.29	3.96(49)	3.74
	...R4B′	4.53(67)	4.37	4.05(80)	3.88
	H(N31)[c] ...R3B	3.74(11)	3.48	2.84(17)	2.49
	...R4B″	3.63(17)	3.36	3.56(33)	3.30
	H(N32)[e]...R4B″	3.63(17)	3.36	3.01(28)	2.69
13	H(N1)[c] ...R1B	3.41(15)	3.12	2.69(14)	2.31
	...R3B	4.14(42)	3.92	3.64(48)	3.40

Can. J. Chem. Downloaded from www.nrcresearchpress.com by EESC ESCOLA DE ENGENHARIA on 09/08/12
For personal use only.

TABLE 5. (*Concluded*)

Compound	H(X)...R bond	$\bar{d}$(X...C)	d(X...π_c)	$\bar{d}$[H(X)...C]	d[H(X)...π_c]
	H(N2)...R4A	3.39(13)	3.09	2.64(30)	2.26
	H(N3)[d] ...R1B	3.41(15)	3.12	3.35(40)	3.08
	H(N3)[d] ...R4A	3.39(13)	3.09	3.39(21)	3.10
	H(N3)[d] ...R2A	4.36(34)	4.15	3.54(22)	3.27
14	H(N1,1)...R23B	3.40(3)	3.10	2.61(15)	2.22
	H(N1,2)[c] ...R11A	3.41(7)	3.12	2.76(28)	2.42
	H(N1,2)[c] ...R24B	4.00(19)	3.75	3.67(22)	3.41
	H(N1,3)[c] ...R11A	3.41(7)	3.12	3.26(23)	2.96
	H(N1,3)[c] ...R12A	3.99(24)	3.74	3.25(39)	2.95
	H(N2,1)...R22	3.72(37)	3.47	2.92(50)	2.62
	H(N2,2)[c] ...R13	3.73(21)	3.47	2.87(22)	2.52
	H(N2,2)[c] ...R14	3.57(14)	3.29	3.46(40)	3.20
	H(N2,3)[c] ...R14	3.57(14)	3.29	3.08(27)	2.67
	H(N2,3)[c] ...R21	3.91(37)	3.67	3.65(54)	3.41
	H(N2,1)*...R14	3.57(14)	3.29	2.66(15)	2.27
	H(N2,2)*[c] ...R21	3.91(37)	3.67	3.11(36)	2.80
	H(N2,2)*[c] ...R22	3.72(37)	3.47	3.27(37)	2.86
	H(N2,3)*[c] ...R13	3.73(21)	3.47	3.15(36)	2.86
	H(N2,3)*[c] ...R22	3.72(37)	3.47	3.38(39)	3.11
15	H(N11)...R21	3.40(4)	3.10	2.55(8)	2.13
	H(N12)...R24	3.45(13)	3.16	2.62(2)	2.22
	H(N21)...R11	3.44(13)	3.14	2.61(9)	2.21
	H(N22)...R12	3.49(12)	3.20	2.74(25)	2.38
16	H(N)...R1 (LT)	3.34(6)	3.04	2.60(12)	2.20
	H(N)...R1 (RT)	3.35(6)	3.05	[f]	
27	H(1)[c] ...R1[g]	3.87(34)	3.63	3.34(41)	3.07
	H(1)[c] ...R2[h]	4.00(91)	3.86	3.60(76)	3.45
		O—H(O)...π bonds			
5	H(O)...R1 2×	3.70(6)	3.42	[f]	
12	H(O1)...R1	3.63(19)	3.36	3.01(39)	2.70
	H(O2)...R2	3.91(43)	3.68	3.04(34)	2.72
15	H(O11)...R22	3.58(12)	3.20	2.78(20)	2.42
	H(O12)...R23	3.63(12)	3.35	3.13(14)	2.80
	H(O21)...R14	3.83(26)	3.58	3.11(12)	2.78
	H(O22)...R13	3.53(9)	3.29	2.78(22)	2.41
18	H(W)...R1	3.42(2)	3.12	2.73(14)	2.34
	H′(W)...R3	3.48(9)	3.19	2.68(14)	2.29
22	H(O1)...R1	3.71(15)	3.44	3.01(32)	2.68
	H(O2)...R2	3.55(10)	3.26	2.97(24)	2.64
23	H(14)...R5	3.75(59)	3.53	3.06(59)	2.79
	H(145)...R1	3.76(59)	3.54	3.01(59)	2.73
24		3.47(21)	3.19		
25	H(O)...R1		3.16		2.38
	H(O)...R2		3.19		2.50

[a]For compound identification see Table 1. Numbers in parentheses: standard deviations of mean for the six X...C and H(X)...C distances to the ring carbons, respectively. R1, phenyl ring 1 etc., as in the original description (Tables A and C for **1–15**).
[b]Symmetrically bifurcated.
[c]Asymmetrically bifurcated.
[d]Asymmetrically trifurcated.
[e]Bifurcated to O_w.
[f]Hydrogen not located.
[g]Intermolecular contact; N—H(1)—$\pi_c(1)$ = 116°.
[h]Intramolecular contact; N—H(1)—$\pi_c(2)$ = 106°.

Tables A (Positional and anisotropic thermal parameters of nonhydrogen atoms), B (Positional parameters and isotropic temperature factors of hydrogen atoms), C (Interatomic distances and bond angles), and D (Deviations $\bar{d}$(C) and δ(B) from and angles between best planes through the phenyl-rings skeletons of the anions). Tables E–U (Observed and calculated structure factors for **1–15**) (150 pages) are available from the Editorial Office.

3MTB and 3ETB

The unit cells of these two structures ($P2_1$) are quite similar and the ion packing in both is of a distorted zincblende type. The N—H...π bonding is of type **A** (Fig. 2).

The reorientational behaviour of the cation in the 3MTB crystal between 185 and 348 K has been studied by ^{2}H nmr spectroscopy (26). The authors concluded that the cation undergoes a complicated composite motion: the complete ion jumps about its N—H axis (E_a = 20.1(20) kJ/mol), the CH_3 groups jump about their respective C_3 axes, and the N—H axis undergoes large-amplitude librations. A TLS analysis of our results for 3MTB indicates that while the anisotropic thermal parameters of the nonhydrogen atoms in the cation are relatively large

Can. J. Chem. Downloaded from www.nrcresearchpress.com by EESC ESCOLA DE ENGENHARIA on 09/08/12
For personal use only.

TABLE 6. Mean values of the X...π_c and H(X)...π_c distances (Å) and "bond" angles ω (deg) in compounds of Table 1

Sample[a]	⟨d(X...π_c)⟩	⟨d[H(X)...π_c]⟩	$\bar{\omega}$
Normal bonds, X = N			
All	3.25(18)	2.34(19)	156(16)
A	3.31(23)	2.35(23)	163(13)
B, large ω	3.28(11)	2.28(10)	178(4)
B, small ω	3.26(21)	2.36(20)	149(5)
Competing	3.22(12)	2.36(19)	144(12)[b]
16[c]	3.04	2.20	141
Normal bonds, X = O			
All	3.34(17)	2.58(18)	135(12)
H_2O, all	3.35(17)	2.58(18)	135(13)
H_2O, large ω	3.36(18)	2.50(17)	145(10)
H_2O, small ω	3.33(15)	2.65(17)	126(8)
Bifurcated bonds, X = N			
All	3.51(29)	2.92(40)	119(22)
Large ω[d]	3.47(21)	2.70(22)	136(16)
Small ω[d]	3.61(33)	3.21(37)	103(11)
Trifurcated bonds, X = N			
12 + **13**	3.84(53)	3.43(31)	109(23)
12 only	4.22(15)	3.71(15)	114(2)

[a]All = all appropriate values in Table 5; competing = bonds to a single acceptor ring under constraint in cations with multiple H-bond engagements (**12–15**); **A** = type **A** bonds in **1–4**, **6**, **7**, **20**; **B** = type **B** bonds in **8–11**. d(N—H) = 1.02 Å; d(O—H) = 1.00 Å.

[b]An ω value of 180° (**14**) excluded; if included, $\bar{\omega}$ = 148(16)°.

[c]Low-temperature structure determination.

[d]The corresponding means for the *shorter distances* (instead of large ω) are 3.33(20) and 2.69(12) Å, and for the longer distances (instead of small ω), 3.69(26) and 3.22(36) Å, respectively.

(0.06 Å^2 < U_{ii} < 1.14 Å^2, Table A), they are quite satisfactorily accounted for as arising from a rigid-body motion (RBM) of the cation: $R(U_{ij})$ = 5.1%, rms(U_{ij}) = 0.0037, rms[esd(U_{ij})] = 0.0020. The translation component of the RBM is practically isotropic, the mean principal displacements being ~0.25 Å. The mean amplitudes about the principal axes L_1, L_2, L_3 of libration are 6.2°, 10.1°, and 10.8°, respectively (Fig. 14). The component with the largest amplitude, about L_3, corresponds to a pivoting motion of the N—H vector about N between the C(α) and the C(δ) atoms of the associated ring; the librations about L_2 and L_1 pivot the N—H vector along a path approximately perpendicular to the N,C(α),C(δ) plane, also by significant amounts. In addition, the H(N) atom would ride on the N atom, which would extend the displacement range of the N—H vector even further. The conformity of the librational behaviour to the RBM model seems to indicate that the drag which the H bond would be expected to exert on the motion of the cation is either not appreciable or absorbed by the U_{ij} of the N atom or both. The combined effect of the three librational components thus confirms the one conclusion from the nmr study that can be verified by crystallography, viz. the N—H axis undergoes large-amplitude librations.

QTB and DaHTB

Stereochemically the two cations, HC(—CH_2CH_2—)$_3NH^+$ and N(—CH_2CH_2—)$_3NH^+$, differ only in minor respects, so it is not surprising to find that QTB and DaHTB are isostructural. The anions are of symmetry C_s, and the ion packing is of a distorted NaCl type. The H(N)...π bonding is of type **A** (Figs. 1 and 2).

The thermal motion of the cation is reasonably consistent with the RBM model (first number, QTB; second number, DaHTB): $R(U_{ij})$ = 10.1% (5.1%); rms (U_{ij}) = 0.0061 (0.0025); rms[esd(U_{ij})] = 0.0044 (0.0021); mean librational amplitude about L_1, 4.0° (5.0°); about L_2, 6.2° (6.2°); about L_3, 8.3° (8.0°)

TABLE 7. Minimum and maximum distances (Å) of X and H(X) atoms from phenyl ring carbons in X—H(X)...π groupings (N—H, 1.02 Å; O—H, 1.00 Å)[a]

	d(X...C)			d[H(X)...C]		
Compound	Minimum	Maximum	100Δ	Minimum	Maximum	100Δ
N—H(N)...π bonding						
1	(24) 3.38	(21) 3.72	34	(23) 2.51	(21) 2.87	36
2	(24) 3.51	(21) 4.07	56	(24) 2.48	(21) 3.40	82
3	(24) 3.45	(21) 3.60	15	(21) 2.58	(24) 2.79	21
4	(34) 3.36	(31) 3.63	27	(33) 2.55	(31) 2.65	10
6	(125) 3.31	(122) 3.67	36	(125) 2.48	(122) 2.70	22
19[b]	(22) 3.40	(25) 3.78	38	(21) 2.66	(24) 3.39	73
20	(16) 3.47	(13) 4.47	100	(16) 2.47	(13) 3.62	115
21[c]	(33) 3.18	(35) 3.57	39	(31) 2.58	(34) 3.29	71
	(42) 3.57	(45) 4.06	49	(41) 2.69	(44) 3.53	84
7	(34) 3.24	(31) 3.56	32	(32) 2.52	(34) 2.72	20
8	(32) 3.30	(35) 3.76	46	(32) 2.37	(35) 2.89	52
	(41) 3.38	(44) 3.60	22	(44) 2.59	(41) 2.89	30
9	(12) 3.67	(15) 3.80	13	(12) 2.38	(15) 2.88	50
	(36) 3.39	(34) 3.54	15	(33) 2.49	(31) 2.78	29
10	(25) 3.70	(21) 3.74	4	(25) 2.76	(21) 2.88	12
	(46) 3.50	(43) 4.20	70	(45) 2.57	(42) 3.41	84
11	(21) 3.34	(24) 3.57	23	(21) 2.35	(24) 2.80	45
	(31) 3.29	(34) 3.48	19	(34) 2.46	(31) 2.74	28
12	(25) 3.37	(22) 3.77	40	(24) 2.55	(21) 3.28	73
	(34) 3.27	(31) 4.62	135	(34) 3.25	(31) 3.89	64
	(44) 3.59	(41) 5.43	189	(44) 3.60	(41) 4.92	132

Can. J. Chem. Downloaded from www.nrcresearchpress.com by EESC ESCOLA DE ENGENHARIA on 09/08/12
For personal use only.

TABLE 7. (*Concluded*)

Compound	*d*(X...C) Minimum	*d*(X...C) Maximum	100Δ	*d*[H(X)...C] Minimum	*d*[H(X)...C] Maximum	100Δ
	(15) 3.77	(12) 4.65	88	(15) 3.29	(12) 4.21	92
	(22) 4.04	(25) 4.95	91	(24) 2.55	(21) 3.28	73
	(44) 3.59	(41) 5.43	184	(44) 2.86	(41) 5.12	226
	(31) 3.61	(34) 3.91	30	(31) 2.64	(34) 3.09	45
	(46) 3.37	(43) 3.85	48	(41) 3.11	(44) 4.00	89
	(46) 3.37	(43) 3.85	48	(45) 2.60	(42) 3.38	78
	(15) 3.20	(12) 3.60	40	(16) 2.49	(14) 2.86	37
13	(32) 3.52	(35) 4.69	117	(32) 2.95	(35) 4.25	130
	(44) 3.22	(41) 3.61	39	(44) 2.24	(41) 3.07	83
	(15) 3.20	(12) 3.60	40	(14) 2.81	(11) 3.91	110
	(44) 3.22	(41) 3.61	39	(46) 3.06	(43) 3.68	62
	(22) 3.86	(25) 4.82	96	(22) 3.22	(25) 3.83	61
14	(235) 3.36	(231) 3.45	9	(236) 2.43	(234) 2.84	41
	(113) 3.31	(111) 3.50	19	(113) 2.35	(116) 3.12	77
	(241) 3.76	(244) 4.28	52	(246) 3.38	(243) 3.93	55
	(113) 3.31	(111) 3.50	19	(116) 2.98	(114) 3.56	58
	(126) 3.64	(123) 4.31	67	(126) 2.66	(123) 3.78	112
	(222) 3.23	(225) 4.16	93	(222) 2.24	(225) 3.53	129
	(136) 3.42	(122) 4.01	59	(131) 2.60	(134) 3.15	55
	(142) 3.38	(144) 3.74	36	(141) 2.96	(144) 3.98	102
	(142) 3.38	(144) 3.74	36	(143) 2.69	(146) 3.42	73
	(212) 3.39	(215) 4.39	100	(213) 2.91	(216) 4.30	139
	(142) 3.38	(144) 3.74	36	(142) 2.49	(144) 2.87	38
	(212) 3.39	(215) 4.39	100	(212) 2.58	(215) 3.60	102
	(222) 3.23	(225) 4.16	93	(222) 2.74	(225) 3.76	102
	(136) 3.42	(133) 4.01	59	(136) 2.69	(133) 3.58	89
	(222) 3.23	(225) 4.16	93	(223) 2.81	(226) 3.89	108
15	(212) 3.37	(214) 3.45	8	(215) 2.45	(212) 2.65	20
	(242) 3.27	(245) 3.63	36	(244) 2.60	(241) 2.64	4
	(112) 3.26	(115) 3.61	35	(113) 2.49	(116) 2.73	24
	(126) 3.35	(123) 3.63	28	(126) 2.39	(123) 3.08	69
16 LT	(1) 3.26	(4) 3.42	16	(1) 2.44	(4) 2.78	34
27[c]	(3) 3.44	(6) 4.30	86	(4) 2.72	(7) 3.90	118
	(9) 2.62	(12) 5.17	255	(9) 2.49	(12) 4.63	214
	O—H(O)...π bonding					
5	(14) 3.62	(11) 3.80	18	—	—	—
12	(16) 3.37	(13) 3.87	50	(15) 2.50	(12) 3.46	96
	(26) 3.32	(23) 4.46	114	(26) 2.57	(23) 3.47	90
15	(226) 3.42	(223) 3.74	32	(225) 2.51	(222) 3.04	53
	(236) 3.47	(233) 3.78	31	(233) 2.93	(236) 3.32	39
	(136) 3.40	(133) 3.65	25	(131) 2.47	(134) 3.07	60
	(142) 3.45	(145) 4.19	74	(142) 2.97	(145) 3.25	28
18	(16) 3.40	(11) 3.44	4	(13) 2.55	(11) 2.91	36
	(26) 3.35	(23) 3.60	25	(26) 2.49	(23) 2.87	38
22	(12) 3.49	(15) 3.91	42	(12) 2.53	(15) 3.44	91
	(23) 3.41	(26) 3.67	26	(24) 2.64	(21) 3.33	69
23	(1) 2.88	(4) 4.54	166	(1) 2.13	(4) 3.76	163
	(15) 2.87	(45) 4.52	165	(15) 2.19	(45) 3.81	162
24	(18) 3.20	(21) 3.75	55			

[a] $\Delta = d_{max} - d_{min}$. Numbers in parentheses identify the carbon atoms in the original papers. For compound identification see Table 1.
[b] Symmetric bifurcation.
[c] Asymmetric bifurcation; also in **12–14**; asymmetric trifurcation in **12** and **13**.

(Fig. 15). The poorer fit for QTB probably stems from the lower-quality data for that crystal and not from a basic difference between the two cations.

It is noteworthy that DaHTB was obtained by recrystallization of a precipitate that had formed on adding a solution of $NaBPh_4$ to a solution of the amine neutralized by HCl to yield the *doubly protonated* $DabcoH_2^{2+}$ cation, in the expectation that the 1:2 tetraphenylborate might result (cf. Experimental). However, the final product was the TB of the *singly* protonated cation, $DabcoH^+$.

E2PiTBw

The $Et(iso\text{-}Pr)_2NH^+$ cation (Hünig's base) is of interest in that the packing of the alkyl groups round the N atom

Can. J. Chem. Downloaded from www.nrcresearchpress.com by EESC ESCOLA DE ENGENHARIA on 09/08/12
For personal use only.

Can. J. Chem. Downloaded from www.nrcresearchpress.com by EESC ESCOLA DE ENGENHARIA on 09/08/12
For personal use only.

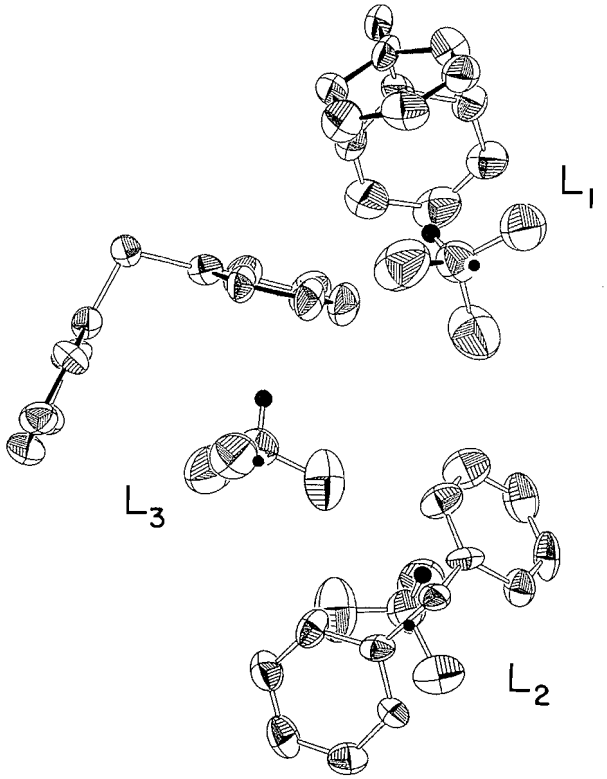

FIG. 14. Rigid-body libration of the cation in 3MTB. Projections down the principal axes of libration L_1, L_2, L_3. Large black circles, H(N); small black circles, points of intersection of the librational axes with the projection plane.

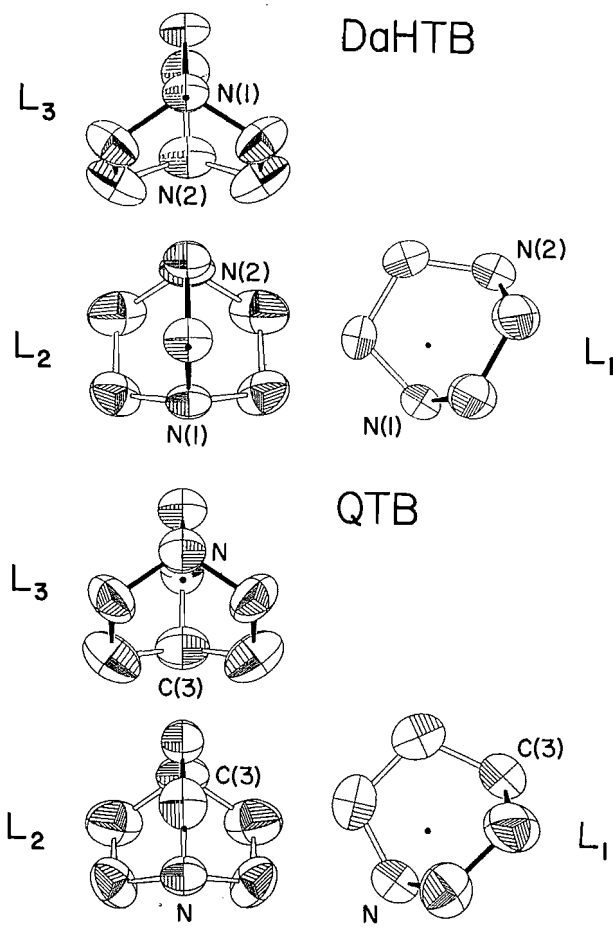

FIG. 15. Rigid-body libration of the cation in QTB and DaHTB (see caption of Fig. 14).

approaches the limit of sterical crowding in alkylammonium ions.

The arrangement of the B and N atoms in this orthorhombic structure can be related in a simple way to the NaCl-type packing. The unit-cell dimension a is, within $\frac{1}{2}$%, double the c dimension. Furthermore, the ratio $(\frac{1}{2}a\sqrt{2}):b:c\sqrt{2}$ is 0.999:0.998:1.003 when normalized to the mean, 14.193 Å. The positions of the B and N atoms are then found to be close to those that would be occupied by the ions in a fcc cells of a NaCl-type structure with $a \sim 14.19$ Å. This cell is bounded by planes parallel to (201), (20$\bar{1}$), and (010). The TB ions are bisected by 040 planes and approximately also by planes parallel to (201) or (20$\bar{1}$), i.e. the anion is of symmetry C_s but close to C_{2v}. Since the B and N atoms are the approximate centroids of the anions and of Et(*iso*-Pr)$_2$NH...OH$_2$ units, respectively, the ion packing may be formulated as an assembly of [cat...OH$_2$]$^+$[TB]$^-$ pairs with a NaCl arrangement.

The H bonding in E2PiTBw is of the symmetrically bifurcated **L** type (Fig. 5), with d(N...O) = 2.765(1) Å, $\bar{d}$(O...C) = 3.70(6) Å, and d(O...π_c) = 3.42 Å. The H(N) atom was placed geometrically; the hydrogens of the H$_2$O molecule could not be located.

The refinement of the cation required considerable care because of the disorder in the positions of some of the C atoms. This disorder is reminiscent of that encountered previously (1) in [Me$_2$C=NHMe]TB (**19**) and [Me$_2$C=NMe$_2$]TB (**28**) but is more complicated (Fig. 16). The N atom and three of the peripheral C atoms (C(2), C(6), C(6)′) are well fixed in the structure but the three C(α) atoms are disordered. The N atom and C(2), the C(β) atom of the ethyl group, are located on the mirror plane, but the C(α) of the ethyl group is clearly displaced well away (~0.7 Å) from the plane. Since C(6), a C(β) atom of the *iso*-propyl group, is well fixed in the structure and related to C(6)′ by the mirror, there must also be two alternative positions for the C(α) *iso*-propyl C atoms. This also requires two different positions for the second C(β) of the *iso*-propyl group attached to C(6).

1MPzBTB.Me$_2$CO

As explained in Experimental, the intended product was *N*-Me-piperazinium(2+) tetraphenylborate, [MeHN(—CH$_2$-CH$_2$—)$_2$NH$_2$]$^{2+}$[TB$^-$]$_2$. Unexpectedly, abstraction of a phenyl group from a TB cation resulted in a singly-charged cation containing a N—B bond, and ultimately in the above solvated salt (Fig. 2).

The length of the N—B bond, 1.683(8) Å, is in the general range of N—B bond lengths: the corresponding bond lengths in Ph$_3$B—NH$_2$Me and Ph$_3$B—NHMe$_2$ (both crystals $P2_1/c$; unpublished results) are 1.670(7) and 1.675(8) Å, respectively.

The simultaneous presence of the quasi-neutral Ph$_3$B—N group and of Ph$_4$B$^-$ in the structure affords us a comparison of their stereochemistries:

	Ph$_3$B—N (**6**)	Ph$_4$B$^-$ (**6**)	Ph$_4$B$^-$ (overall)
$\bar{d}$(B—C), Å	1.618(11)	1.653(9)	1.646(18)
⟨C—B—C⟩, $\bar{\alpha}$	112.3(33)°	111.7(1)°	104.4(17)°
⟨C—B—C⟩, $\bar{\alpha}'$	112.3(33)°	108.4(8)°	112.1(12)°
⟨C—B—N(2)⟩	106.5(8)°	—	—
⟨C(2)—C(1)—C(6)⟩	114.9(3)°	114.6(9)°	

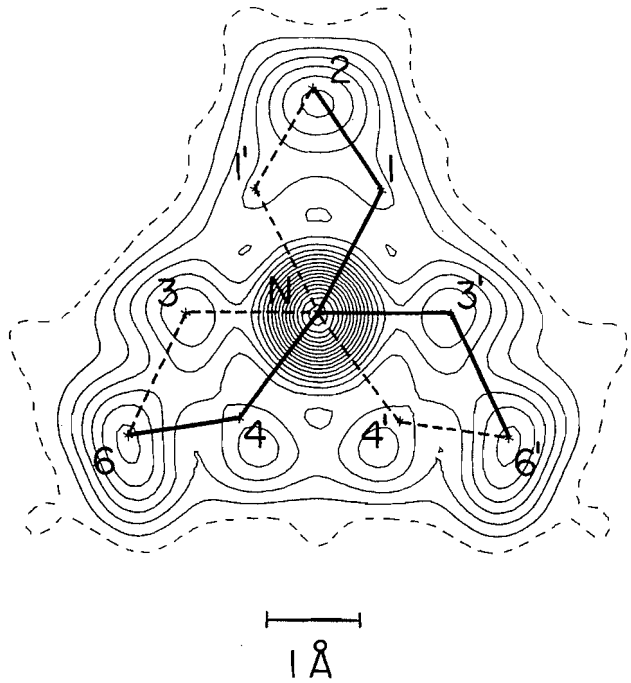

FIG. 16. Electron-density map of the cation in E2PiTBw (**5**) in the plane defined by the atoms 1 = C(1), 3 = C(3), and 3′ = C(3)′. The alternative orientations of the disordered cation are shown. Contour intervals, 0.25 e/Å^3.

(for the meaning of α and α′ and for the overall means in the anion see below). The shortening of the B—C bond in the cation is significant. It is curious that in the anion of **6** the mean C—B—C valence angle $\bar{\alpha}$ is larger than the mean conjugate angle $\bar{\alpha}'$. The opposite is observed in all the other quasi-D_{2d} TB anions discussed in the relevant section below.

The N(1)—H(N1)...π_c(12) bond is of type **A**. The second *N*-hydrogen of the cation is engaged in a weak normal H bond to the O atom of the acetone molecule, N(2)—H(N2)...O: *d*[N(2)...O] = 3.09 Å, *d*[H(N2)...O] = 2.11 Å.

2MTB.MeCN and 2MTB.Et$_2$CO

The TB precipitates that form on combining the requisite reagent solutions are microcrystalline and must be recrystallized to obtain crystals suitable for X-ray diffraction. In this 2MTB is no exception. The products of recrystallization from both MeCN and Et_2CO were solvated, which would suggest that the initial precipitate (from H_2O or EtOH/H_2O solution) also was solvated, and that unsolvated 2MTB, if it does form, does not do so readily. Attempts to prepare the unsolvated salt have therefore been abandoned, at least for the present.

The crystal packing in 2MTB.MeCN may be described, probably not very usefully, as of a highly distorted NaCl type. The hydrogen bonding of the cation is of type **C** (Fig. 1): one H(N) is involved in a bond to a phenyl ring, N(1)—H(N11)...π_c(3), while the other forms a bond to the N atom of the MeCN molecule (N(1)—H(N12)...N(2), *d*[N(1)...N(2)] = 2.89(1) Å, *d*[H(N12)...N(2)] = 1.90 Å, N(1)—H(N12)—N(2) ~ 161°, Fig. 2).

In contrast to 2MTB.MeCN, the solvent molecule in 2MTB.Et_2CO is not involved in H bonding. Each H(N) is bonded to a phenyl ring of the same anion (type **B**, Fig. 1), though not symmetrically (Fig. 3).

A recent ^{2}H nmr study (26) of the precipitate from aqueous (D_2O) solutions of Me_2ND_2Cl and $NaBPh_4$ indicated that between 215 and 245 K the Me groups undergo rapid C_3 jumps about their respective C—N axes. Between 250–300 K the detailed reorientational behaviour of the cation could not be clearly determined, but above 320 K the complete cation exerts also rapid C_2 jumps about its C_2 axis. The latter behaviour would be consistent with a type **B** situation, but in view of what is said above the exact composition of the precipitate and hence the nature of the cation environment cannot be regarded as known, so the structural interpretation of the C_2 cation reorientation in that material must await further clarification.

2ETB, 2PiTB, and AC7TB

The ion packing in AC7TB ($P2_1/m \subset Cmcm$) is of a distorted NaCl type; in 2ETB and 2PiTB the packing could be regarded as of a highly distorted zincblende type, although it is probably better described as a transition type between ZnS and NaCl.

The hydrogen bonding in all three crystals is of type **B** (Fig. 3): 2ETB, N—H(N1)...π_c(1), N—H(N2)...π_c(3); 2PiTB, N—H(N1)...π_c(2), N—H(N2)...π_c(4); AC7TB, N—H(N1)...π_c(2), N—H(N2)...π_c(3).

While the mean conformation of the 7-membered ring cation in AC7TB is of C_s symmetry, the large U_{ii} values of the C atoms more distant from the N atom indicated the presence of disorder. Treating the C(2) and C(3) atoms as if in twofold orientational disorder with respect to the crystallographic mirror plane significantly reduced the U_{ii} of these atoms, even though some of them still remain large (Table A).

GTBw

This is the most interesting structure of the fifteen in the context of this investigation. The presence of three pairs of H(N) hydrogens in the trigonal, essentially planar $C(NH_2)_3^+$ cation plus the water molecule of hydration (all atoms in general positions) would lead us to expect a variety of hydrogen-bond types, especially since the NH_2 groups are geometrically fixed relative to one another. Faced with the multiple bonding choices, the cation must thus find a compromise situation in which its tendency to formation of hydrogen bonds to the anions and to the water molecule is, on the average, only imperfectly satisfied. Thus while *all* the H(N) and H(O) atoms are found to be engaged in hydrogen bonding, with the exception of N—H(N11)...O, N—H(N12)...π_c(2), O—H(O1)...π_c(1), and O—H(O2)...π_c(2) all the H bonds are branched, with presumed trifurcation in N—H(N22)...3π (Fig. 6, Tables 5 and 7). Beside some of the types illustrated in Fig. 1 the structure contains an example of type **L′** bond, in which the water oxygen is approximately tetrahedrally coordinated by four hydrogens (H(O1), H(O2), H(N11), and H(N32); Fig. 17). The H(N32) atom is involved in a bifurcated bond to ring 4 (cf. Fig. 6). The H—O—H angles in this coordination range from ~92° to ~147°, with a mean of 111(2)°.

The skeleton planes of the disc-like guanidinium cations, the B atoms, and the O atoms are all arranged in planes ||(100) (at $z \sim \pm\frac{1}{4}$), which accounts for the length of the *c* dimension of the unit cell. These planar slabs also contain the H bonds, although some cross-linking occurs through branched components of a few of the bonds.

The cation skeletons are planar (mean deviation $\bar{d}$(C, N) from the best plane, 0.005 Å; Table D) and rigid. A TLS analysis of the thermal motion of the cation reveals a surprising degree of compliance with the RBM model and a considerable librational freedom in spite of the H bonding: $R(U_{ij})$ = 2.6%,

Can. J. Chem. Downloaded from www.nrcresearchpress.com by EESC ESCOLA DE ENGENHARIA on 09/08/12
For personal use only.

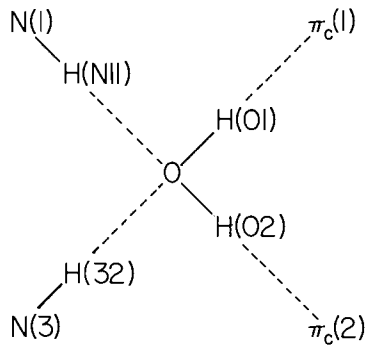

Distances in Å:	
O...N(I)	3.84
O...N(3)	3.69
O...π_c(I)	3.36
O...π_c(2)	3.68
O...H(NII)	1.84
O...H(N32)	3.02 *
π_c(I)...H(OI)	2.70
π_c(2)...H(02)	2.72

* bifurcated

FIG. 17. Schematic representation of type **L′** hydrogen bonding in GTBw (**12**).

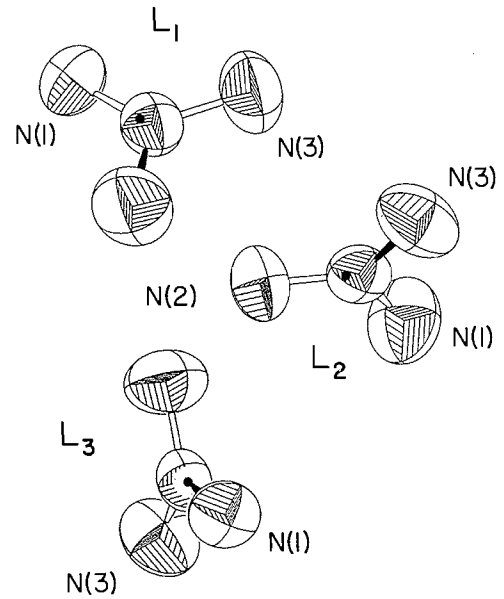

FIG. 18. Rigid-body libration of the cation in GTBw (**12**) (see caption of Fig. 14).

rms(U_{ij}) = 0.0025, rms[esd(U_{ij})] = 0.0039; mean amplitudes about the three principal axes of libration, 8.3° about L_1, 10.4° about L_2, and 12.2° about L_3 (Fig. 18). The translation motion is essentially isotropic, with mean principal displacements of ~0.25 Å.

1MTB and 1ETB

In these crystals the cation is situated between two pairs of phenyl rings, each pair from a different anion (Figs. 4 and 7). This arrangement is reminiscent of ImC (Fig. 5 of ref. 1).

The cation is H-bonded to all four rings by bonds of different types. In 1MTB the H(N2) atom is involved in a type **A** bond to ring 4A; H(N1) forms a bifurcated bond to rings 1B and 3B; and the bonding of H(N3) is probably best described as trifurcated, to rings 1B, 2A, and 4A (cf. Tables 5, 7, and C for interatomic distances). The boron atoms and the ethane-like cations are arranged in sheets ||(100) in such a way that strings of H-bonded ...an...cat...an...cat... sequences run parallel to (011) in the sheets at $z \sim \frac{1}{4}$ and parallel to (0$\bar{1}$1) in the sheets at $z \sim \frac{3}{4}$ (Fig. 19). These sheets are separated by the van der Waals surfaces of the phenyl rings, so that the whole arrangement can be regarded as a

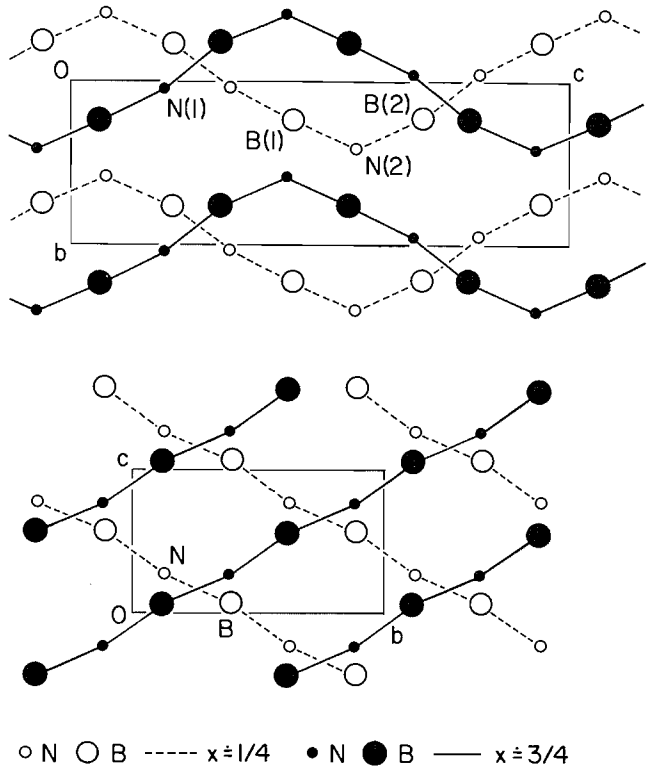

FIG. 19. Organization of H-bonded ...an...cat...an...cat... sequences in sheets ||(100) in 1MTB (bottom) and 1ETB (top). Drawing schematic but to scale. Labelled circles, atoms with coordinates as listed (Table A). Note the nonequivalent N and B atoms in 1ETB.

molecular crystal consisting of stacks of electroneutral infinite cation–anion sheets in the direction perpendicular to (100).

The organization of the H-bonded cations and anions in 1ETB is similar, but instead of essentially straight ...an...cat...an...cat... strings the ions in a sheet are arranged in zigzag chains with a period |cat(2)...an(1)...cat(1)...an(2)| (Fig. 19). As a consequence the cations now have two types of H-bond environment, at N(1) and N(2). Furthermore, cat(2), which is at the turning point in the zigzag chain, is subject to twofold orientational disorder, with the result that N(2) can engage in either of the two alternative sets of H bonds (Fig. 7). At N(1) there are three N—H(N)...π bonds, one each of types **A**, **F**, and **J**; at N(2) there are two alternative sets of such bonds, one each of types **A**, **E**, and **F**.

The relationship of the arrangements of the B and N atoms in 1MTB and 1ETB is seen when the upper half ($\frac{1}{2} \leq c \leq 1$) of the 1ETB cells is reflected in the (020) plane and the two halves are joined along (002) after the cation–anion strings have been brought into smooth continuation by suitable translation and scaling adjustments. The resulting arrangement corresponds to the 1MTB cell doubled along its *b* axis. This relationship is reflected in the dimensions of the two unit cells: *a*(1ETB) ~ *a*(1MTB), *b*(1ETB) ~ *c*(1MTB), *c*(1ETB) ~ 2*b*(1MTB). The difference V_1(1ETB) − V_1(1MTB) between the volumes per fomula unit of the two compounds is ~27 Å^3, consistent with the average volume increment per CH_2 (see below).

The conclusion from a variable-temperature ^{2}H nmr study of 1MTB (26) is that in the experimental temperature interval 158–298 K the ND_3 and CD_3 groups undergo rapid C_3 jumps about the C—N axis. At the upper end of this interval the correlation times τ are in the ps range, and the activation energy E_a

Can. J. Chem. Downloaded from www.nrcresearchpress.com by EESC ESCOLA DE ENGENHARIA on 09/08/12
For personal use only.

Can. J. Chem. Downloaded from www.nrcresearchpress.com by EESC ESCOLA DE ENGENHARIA on 09/08/12
For personal use only.

for the C_3 reorientation of the ND_3 group is 4.1(5) kJ/mol, comparable to that in $MeNH_3ClO_4$. Motion of the C—N axis appears to be restricted to large-amplitude librations. This last conclusion is consistent with the large U_{ii} values of the N and C atoms in the cation (Table A). The low E_a value for the C_3 reorientation of the ND_3 group is somewhat surprising in view of the N and H(N2) to ring 4A distances, which are short compared to the total distribution of distances in our sample (Tables 5 and 7, Figs. 12 and 13), i.e. correspond to a H-bond energy at the high end of the N—H...π sample. In fact, points for the H(N2)...π_c(4A) and H(N1)...π_c(1B) appear to lie outside the main body of the sample distribution, so that the obliqueness of the N—H...π_c angle may play a role.

AdTBw

This compound, like 1ETB, contains two sets of cations and two sets of anions (Fig. 8). The structure ($P2_1/m \subset Cmcm$) may be viewed as having a very obliquely distorted zincblende-type packing. Each of the two N atoms is engaged in two normal (type **A**) bonds and a type **L** bond, so that an N atom is involved both in normal N—H(N)...π and normal N—H(N)...O bonding.

Although adamantane is a cage-like entity, the cations conform poorly to the RBM model, regardless of whether the N atom is excluded from or included in the TLS analysis:

	$R(U_{ij})$	rms(U_{ij})	L_1	L_2	L_3	T
cat(1) (ex N)	14.0%	0.0095	3.0°	5.3°	7.1°	0.2 Å
(in N)	13.8%	0.0092	3.5°	5.1°	7.1°	0.2 Å
cat(2) (ex N)	10.4%	0.0063	3.5°	3.7°	8.8°	0.25 Å
(in N)	10.7%	0.0063	3.4°	3.8°	8.8°	0.25 Å

(L_1 stands for the mean librational amplitude about the principal libration axis L_1 etc.; T, mean translational displacement).[17]

Comments and conclusions

Tetraphenylborate anion

The fifteen crystal structures of Tables 2–4 contain 17 distinct TB anions, of which four (**3–5**, **11**) are of symmetry C_s and 13 of symmetry C_1. However, most of these anions retain conformations close to D_{2d} or C_{2v} in spite of the chemical and geometric diversity of the counter cations. Notably, the two C—B—C valence angles α, which in the D_{2d} conformation are bisected by the S_4 axis (resulting in α_1 and α_2 in C_{2v}) and which are defined by two pairs of C(α) atoms with non-repeating labels (e.g. C(1)—B—C(3) for α_1 and C(2)—B—C(4) for α_2), persist as the two smallest C—B—C angles of the six in the anion. The mean of the difference between α_1 and α_2 is only 2.1°. The conjugate C—B—C valence angle α′ is significantly larger than α.

The means (uncorrected for thermal motion) for the B—C bond length, α, α′, and the endocyclic C—C—C angle at the C(α) carbon[18] in **1–15** *plus* the iminium TBs **19–22** and **28** *plus* 4MTB (**17**) are $\overline{d}$(B—C) = 1.646(18) Å (n = 88, γ_1 = 0.81, γ_2 = 4.49), $\overline{\alpha}$ = 104.4(17)° (n = 47, γ_1 = 1.05, γ_2 = 4.55), $\overline{\alpha'}$ = 112.1(12)° (n = 92, γ_1 = −0.47, γ_2 = 5.60), ⟨C(2)—C(1)—C(6)⟩ = 115.0(9)° (n = 83, γ_1 = −0.06, γ_2 = 5.87). These values compare with the respective means for **17**, **19–22**, and **28** (1), 1.640(20) Å, 104.0(10)°, 112.8(13)°, and 114.7(6)°, i.e. the two sets of data are statistically indistinguishable.

The planarity of the 60 phenyl ring skeletons in **1–14** is satisfactory. The mean deviation $\overline{d}$(C) of the C atoms from the best planes through the ring skeletons is 0.007(4) Å, i.e. comparable to that for the five iminium salts (1). The deviations δ(B) of the boron atoms from their respective ring planes are listed in Table D, which also contains the interplane angles.

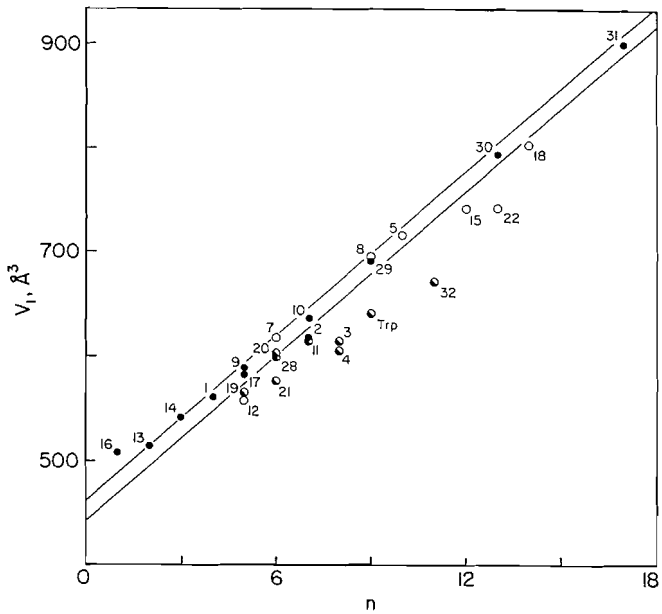

FIG. 20. Volume per formula unit V_1 plotted against the number n of nonhydrogen atoms (C, N, O, but excluding the anion atoms) per formula for compounds of Table 1 (for Trp see footnote 20). Full circles, alkyl cations, unsolvated compounds; half-full circles, cations deficient in hydrogen, unsolvated compounds; open circles, solvated compounds (see text). Only points **12** and **29–31** are included in the regression of V_1 on n. Vertical width of the regression band, 6σ of regression.

Volume relationships and solvation

When the volume V_1 per formula unit for the unsolvated tetra-*n*-alkylammonium TBs 4MTB (**17**), 4ETB (**29**), 4PnTB (**30**), and 4BnTB (**31**)[19] is regressed on the number n of C+N atoms in the cation, an excellent straight line results (Fig. 20): $V_1 = 452(4) + 26.4(3)n$, $r^2 = 1.000$, σ = 3 Å ~ 1% of V_1 range. The intercept of this line (n = 0) may be taken as an estimate of the effective volume of the TB^- anion in *n*-alkylammonium TB crystals. Points for most of the other unsolvated *n*-alkyl $R_nNH_{4-n}^+$ ($n \neq 4$) TBs of Table 1 fall within the ±3σ limits of the regression line. The exceptions are 3ETB (**2**), which is significantly outside these limits, and ATB (**16**), which for its n is overhydrogenated, as are 1MTB and 1ETB, though to a lesser extent. The number of H(N) atoms thus seems to be a factor, i.e. H bonding plays a role.

[17]Compare ref. 54 for a discussion of the analysis of segmented RBM.

[18]In **15** the rings were constrained to regular hexagons, see Experimental.

[19]The crystal data (unpublished) for compounds **29–32** are as follows: 4ETB, a = 9.930(3) Å, c = 24.308(8) Å, V = 2076(4) Å^3, Z = 3; 4PnTB, a = 20.199(4) Å, b = 16.391(2) Å, c = 11.810(3) Å, β = 125.77(2)°, V = 3173(2) Å^3, Z = 4; 4BnTB, a = 10.202(5) Å, b = 18.710(8) Å, c = 20.756(10) Å, α = 69.26(4)°, β = 86.21(4)°, γ = 76.45(4)°, V = 3601(6) Å^3, Z = 4; AzPpTB, a = 9.903(2) Å, b = 19.897(2) Å, c = 13.630(2) Å, β = 92.33(1)°, V = 2684(2) Å^3, Z = 4.

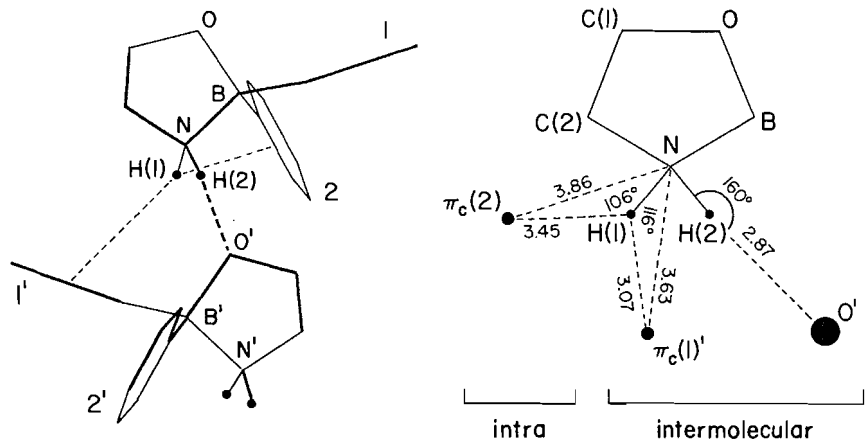

FIG. 21. Hydrogen bonding in *B,B*-Ph_2boroxazolidine (**27**). H(1) and H(2) are H(N) and H(N'), respectively, of ref. 52; rings 1 and 2 are defined, respectively, by carbon atoms C(3)—C(8) and C(9)—C(14) of that reference.

Points for the remaining unsolvated TBs all fall below the regression line, most of them considerably below the -3σ limit. The cations in these TBs contain either a double bond (**19–21**, **28**), a ring (**11**), or a cage (**3**, **4**, **32**; also tropanium TB),[20] i.e. they are all deficient in hydrogen relative to the *n*-alkyl compounds with the same *n* value. The deviations of these points from the regression line are roughly proportional to the H deficit. This leaves the monohydrates E2PiTBw (**5**), GTBw (**12**), AdTBw (**15**), 3BnTBw (**18**), ImEw (**22**), and the monosolvated **7** and **8**, as well as the question, can a criterion of the tendency to solvation of the TBs be formulated?

Of the cations in the five monohydrates only those in **5** and **18** are *n*-alkylammonium ions; the cation in **22** contains a double bond *and* a phenyl ring, that in **15** contains a cage, and the $C(NH_2)_3^+$ ion in **12** is H-deficient, disc-like and rigidly compact. If allowance is made for these features and *n* is increased to *n* + 1 to take account of the H_2O oxygen, the point for **5** in Fig. 20 falls on the regression line, the point for **18** is slightly below the -3σ limit, and the points for **12**, **15**, and **22** are now significantly below the -3σ limit, in accordance with the expectation for H-deficient cations. Furthermore, the points for the two nonaqueous solvates of 2MTB, **7** and **8**, fall within the $\pm 3\sigma$ regression band when their *n* are adjusted to include the nonhydrogen atoms of the two solvent molecules, MeCN and Et_2CO, respectively.

These observations suggest that whatever the specific reason for solvation (awkward cation shape, inefficient packing), the V_1/n(C+N+O) ratio in a particular solvate structure remains constant and equal to ~26 Å^3 per nonhydrogen atom outside the BPh_4^- anion, i.e. the same as the slope of the above regression line. However, in TBs with a reduced H-atom complement V_1 is decreased, on the average, by ~12 Å^3 per "missing" H atom in the cation (unsolvated structures) and by about 5 Å^3 per "missing" H atom in the cation *and* solvent units (solvated structures).

Unrecognized or unreported X—H...π bonds

As pointed out in the introductory section, the presence of a H bond to an aromatic π system may not always have been noticed, even though the published crystal-structure determination contains, implicitly, evidence of such a bond. This situation in fact appears to occur more frequently than might be supposed (cf. ref. 55). Since this paper is not intended to be an enchiridion of N—H...π bonds, we have not attempted (with the exception of TBs) a systematic literature search for such unrecognized or unreported bonds, especially since an exhaustive search of the Cambridge Structural Data Base for N—H...π and possibly other X—H...π bonds already is underway (55). However, we should like to draw attention to a particularly interesting but less than obvious example, that of a heterodesmic bifurcated N—H...2π bond in *B,B*-Ph_2-boroxazolidine (**27**). Determination of the crystal structure of this compound was undertaken for other chemical reasons, namely to demonstrate the existence of a 5-membered heteroatomic ring in this molecule (52). Besides succeeding in this demonstration, the authors noted that one of the two H(N) atoms is involved in an intermolecular N—H(N)...O bond of moderate strength. However, it appears that the second H(N) also is engaged in a H bond. The interesting feature of this bifurcated N—H(N)...2π bond is that it involves an intermolecular *and* an intramolecular interaction (Fig. 21), at N...π_c and H(N)...π_c distances that may seem marginal (Tables 5 and 7). Referring to this situation as H bonding would probably have appeared contentious at the time; even today one might hesitate to regard the N,H(N),Ph grouping as H-bonded if it were not for the suggestive geometry and for having the benefit of the general N—H(N)...π scheme such as is now available in Figs. 1, 12, and 13.

Conclusions

The crystal structures of the TBs **1–15** (Table 1) contain a variety of normal and branched N—H...π bonds as well as of normal O—H...π bonds. These bonds are classified in Figs. 1 and 17. Together with the bonds in the other structures of Table 1 they constitute a sample which is sufficiently large and homogeneous to permit a number of general observations on the characteristics of X—H...π(arene) bonds in crystals.

An N—H...π bond in the TBs is established whenever opportunity arises. Only strongly competing interactions (e.g. N—H...OH_2, N—H...N≡C—, N—H...Cl^-) or exceptionally unfavourable packing will engender other bonding engagements. Where the overall organization of the crystal structure offers to the H(N) atom more than one choice of phenyl accep-

[20]Tropanium TB = 8-Me-8-azoniabicyclo[3.2.1]octane TB, $C_8H_{16}N^+TB^-$, *C2/m*, *a* = 15.866(4) Å, *b* = 11.873(4) Å, *b* = 13.625(4) Å, β = 92.58(3)°, *V* = 2564(2) Å^3, *Z* = 4 (unpublished result).

Can. J. Chem. Downloaded from www.nrcresearchpress.com by EESC ESCOLA DE ENGENHARIA on 09/08/12
For personal use only.

Can. J. Chem. Downloaded from www.nrcresearchpress.com by EESC ESCOLA DE ENGENHARIA on 09/08/12
For personal use only.

tor, orientational disorder may occur between two equivalent or near-equivalent H-bonding situations. An alternative to disorder is the formation of a bifurcated (occasionally trifurcated) H bond, which provides a (partially dynamic) compromise between orientations that otherwise would constitute the components of a disorder. Temperature lowering may resolve the compromise solutions, bifurcation and dynamic disorder, into unambiguous normal bond arrangements, possibly with simultaneous occurrence of a crystallographic transition.[15]

The presence of a solvent molecule in a TB structure may result in the formation of a heterodesmic H bond, such as in types **C**, **G**, and **K** (Fig. 1), or in the formation of a type **L** or **L′** bond (Figs. 1 and 17), in which a H(N) hydrogen is bonded to a phenyl ring via an H_2O molecule. In the last-named situation the relation of the H_2O molecule to the ring is quite different from that considered in studies of the isolated H_2O–C_6H_6 complex: in a crystal the direction of the O—H(O) vector(s) is constrained by packing and the overall organization of the crystal structure, so that the geometry of the O—H(O)...ring grouping is determined not solely by the energy-minimization requirement of this grouping alone, as it would be in the isolated H_2O–C_6H_6 pair. However, the distances O...π_c to the centre of the phenyl ring in the crystal are in the same range as the O...π_c distances estimated for the H_O–C_6H_6 complex; in the present sample statistically meaningful distinction cannot be made between the distances implicit in the O—H(O)...π_c and N—H(N)...π_c bonds.

The means of the N...π_c and H(N)...π_c distances in the normal N—H(N)...π bonds of the TBs are 3.25(18) and 2.34(19) Å, respectively. The distributions of the distances in the normal and the branched bonds have been analyzed in detail.

The individual crystal structures exhibit many interesting features in their own right. The ion packing in the unsolvated TBs is either of a distorted NaCl or a distorted zincblende type. A structure of particular interest is that of the guanidinium TB hydrate: all six H(N) atoms of the cation participate in H bonding to the phenyl groups or to the water molecule (Fig. 6). The guanidinium skeleton in GTBw offers a textbook example of a unit conforming to the rigid-body-motion model, in spite of the extensive involvement of the cation in hydrogen bonding.

Experimental

Preparation

The title compounds were prepared by combining an aqueous solution of $NaBPh_4$ with an aqueous or ethanolic solution of the requisite organic ammonium halide at room temperature. The resulting precipitate of the tetraphenylborate was filtered, washed, and recrystallized from a suitable solvent (water/acetone, Et_2CO, MeCN, MeOH) by evaporation at room temperature. The recrystallized salt was unsolvated (**1–4**, **9–11**, **13**, **14**) or monosolvated (**5–8**, **12**, **15**).

The formation of DaHTB and 1MPzBTB.Me_2CO calls for special comment. Since the original intention was to see if it was possible to obtain crystalline $DabcoH_2^{2+}(TB^-)_2$, an aqueous solution of Dabco = $N(—CH_2CH_2—)_3N$ was neutralized with HCl to $HN(—CH_2CH_2—)_3NH^{2+}$ and aqueous $NaBPh_4$ was added to give a $DabcoH_2^{2+}$:TB^- ratio of 1:2. In spite of this solution stoichiometry the precipitate that formed was $DabcoH^+TB^-$, not $DaH_2^{2+}(TB^-)_2$. The circumstances of this process as a means of controlling stoichiometry are being investigated, with a view to practical application.

In the case of 1MPzBTB.Me_2CO, the intended product was $[MeHN(—CH_2CH_2—)_2NH_2]^{2+}(TB^-)_2$. Considering the reluctance of Dabco to form the diprotonated 1:2 salt, one would not have been surprised to obtain an analogous result with *N*-Me-piperazine, i.e. a 1:1 instead of the 1:2 salt. However, either in the initial precipitation or on recrystallizing by evaporation from water/acetone solution *at room temperature*, elimination of a phenyl ring from a TB^- anion as benzene must have taken place, resulting in the formation of the solvated 1MPzBTB.Me_2CO salt. While it is known that the TB^- anion in alkylammonium salts, when heated in solution or on pyrolysis, can lose a phenyl ring and form a B—N bond, it is unexpected to find that this process should occur under room-temperature conditions.

Structure determination

The general details of the structure determinations will be found in ref. 1; particulars are listed in Tables 2–4 and under the individual crystal structures, otherwise as below.

We wish to reiterate that in general organic ammonium tetraphenylborate crystals are weak and fickle scatterers. As pointed out previously (1), significant reflections were seldom observed above a $(\sin\theta)/\lambda$ limit of 0.48 $Å^{-1}$ ($\theta = 20°$ for Mo radiation). Since in this laboratory X-ray data collection routinely extends to a limit of 0.55 $Å^{-1}$ ($\theta = 23°$), the ratios of observed reflections to total measured unique reflections never exceeded 50%. When attempts were made to collect the data at lower temperatures they produced little if any improvement in these ratios. However, a worthwhile improvement in the volume and quality of usable reflections was obtained for QTB by substituting Cu for Mo radiation.[21] Low-angle reflections were examined for possible second-order intensity leakage from their respective *2h2k2l* homologues.

Tables of structure factors are available from the Editorial Office (Tables E–U).[16]

Systematic absences. Pnma (**3–5**): 0*kl*, *k+l* odd; *hk*0, *h* odd; *h*00, *h* odd; 0*k*0, *k* odd; 00*l*, *l* odd. $Pna2_1$ (**13**): 0*kl*, *k+l* odd; *h*0*l*, *h* odd; *h*00, *h* odd; 0*k*0, *k* odd; 00*l*, *l* odd. $P2_12_12_1$ (**9**): *h*00, *h* odd; 0*k*0, *k* odd; 00*l*, *l* odd. *P2/c* (**14**): *h*0*l*, *l* odd; 00*l*, *l* odd. $P2_1/m$ (**11**), $P2_1$ (**1**, **2**, **15**): 0*k*0, *k* odd. $P2_1/c$ (**12**): *h*0*l*, *l* odd; 0*k*0, *k* odd; 00*l*, *l* odd. $P2_1/a$ (**7**): *h*0*l*, *h* odd; 0*k*0, *k* odd; *h*00, *h* odd. $P2_1/n$ (**6**, **8**, **10**): *h*0*l*, *h+l* odd; 0*k*0, *k* odd; *h*00, *h* odd; 00*l*, *l* odd.

Weighting schemes. Unit weights: **1**, **2**, **4–9**, **12**, **13**. SHELX weights, $w = p/[\sigma^2(F) + qF^2]$: **11** ($p = 2.360$, $q = 0.000485$), **14** ($p = 1.506$, $q = 0.0100$), **15** ($p = 3.024$, $q = 0.00103$). Sigma weights (see under compound **C** of ref. 1): **3**, **10**.

Location of hydrogen atoms. The H(C) atoms were placed geometrically and refined isotropically or not refined (Tables 2–4). Similar procedure was followed for H(N) in cations containing one or two hydrogen atoms on the nitrogen; in some cases evidence of the H(N) atom was seen in the difference map. In 1MTB, 1ETB, and AdTBw, in which there are three H atoms on the nitrogen, at least one H(N) was located from a difference map and the others were generated geometrically. The N—H distances were then constrained to 1.02 Å and kept fixed during the refinement. The hydrogens of the water molecules were located from the difference map, the O—H distances were then constrained to 1.0 Å and kept fixed in the refinement.

Other comments. The problem of cation disorder in E2PiTBw has been dealt with above (cf. Fig. 16). In the refinement of the AdTBw structure the phenyl-ring skeletons were constrained to regular hexagons, hence all the endocyclic C—C—C angles were fixed at 120°.

Acknowledgments

We thank Mr. Pierre Losier and Professor Neil Burford for the crystal of 2PiTB; Dr. Witold Kwiatkowski for calculating the net charges; and Professor R.J. Boyd and Mr. Jian Wang for supplying us with the graphs of the electron-density distribution in the benzene molecule. This investigation was supported by grants from the Natural Sciences and Engineering Research Council of Canada to the two last-named authors.

1. O. Knop, T.S. Cameron, P.K. Bakshi, W. Kwiatkowski, S.C. Choi, and D. Adhikesavalu. Can. J. Chem. **71**, 1495 (1993).
2. B.R. Vincent, O. Knop, A. Linden, T.S. Cameron, and K.N. Robertson. Can. J. Chem. **66**, 3060 (1988).

[21] An in-house modified Picker single-crystal diffractometer is used as a dedicated instrument for data acquisition with Cu radiation.

Can. J. Chem. Downloaded from www.nrcresearchpress.com by EESC ESCOLA DE ENGENHARIA on 09/08/12
For personal use only.

3. R.E. Richards and H.W. Thompson. J. Chem. Soc. 1260 (1947).
4. L.H. Jones and R.M. Badger. J. Am. Chem. Soc. **73**, 3132 (1951).
5. G.C. Pimentel and A.L. McClellan. The hydrogen bond. Freeman, San Francisco. 1960.
6. W. Beckering. J. Phys. Chem. **65**, 206 (1961).
7. R. West. J. Am. Chem. Soc. **81**, 1614 (1959).
8. R. West and C.S. Kraihanzel. J. Am. Chem. Soc. **83**, 765 (1961).
9. C. Aulin-Erdtman and R. Sandén. Acta Chem. Scand. **17**, 1991 (1963).
10. T. Cairns and G. Eglinton. J. Chem. Soc. 5906 (1963).
11. M.R. Basila, E.L. Saier, and L.R. Cousins. J. Am. Chem. Soc. **87**, 1665 (1965).
12. Z. Yoshida and E. Osawa. J. Am. Chem. Soc. **87**, 1467 (1965).
13. Z. Yoshida and E. Osawa. J. Am. Chem. Soc. **88**, 4019 (1966).
14. D.A. Dows. Spectrochim. Acta, **22**, 1479 (1966).
15. M.D. Joesten and L.J. Schaad. Hydrogen bonding. Dekker, New York. 1974.
16. O. Knop, I.A. Oxton, and M. Falk. Can. J. Chem. **57**, 404 (1979); (errata) **57**, 2003 (1979).
17. S.A. McDonald, G.L. Johnson, B.W. Keelan, and L. Andrews. J. Am. Chem. Soc. **102**, 2892 (1980).
18. S. Yamazaki, S.-I. Ikawa, and M. Kimura. J. Quant. Spectrosc. Radiat. Transfer, **24**, 421 (1980).
19. L. Andrews, G.L. Johnson, and B.J. Kelsall. J. Chem. Phys. **76**, 5767 (1982).
20. L. Andrews, G.L. Johnson, and S.R. Davis. J. Phys. Chem. **89**, 1706 (1985).
21. A.D. Nikolić, S.D. Petrović, N. Perišić-Janjić, and N.L. Kobilarov. J. Mol. Struct. **143**, 329 (1986).
22. A. Engdahl and B. Nelander. J. Phys. Chem. **89**, 2860 (1985).
23. A. Engdahl and B. Nelander. J. Phys. Chem. **91**, 2253 (1987).
24. M.P. Roberts and H.L. Strauss. J. Phys. Chem. **91**, 4241 (1987).
25. A.J. Gotch and T.S. Zwier. J. Chem. Phys. **96**, 3388 (1992).
26. M.H.L. Gruwel and R.E. Wasylishen. Z. Naturforsch. **45***a*, 55 (1990).
27. S. Suzuki, P.G. Green, R.E. Bumgarner, S. Dasgupta, W.A. Goddard III, and G.A. Blake. Science, **257**, 942 (1992).
28. D. Bonchev and P. Cremaschi. Gazz. Chim. Ital. **104**, 1195 (1974).
29. G. Karlström, P. Linse, A. Wallqvist, and B. Jönsson. J. Am. Chem. Soc. **105**, 3777 (1983).
30. J.A. Menapace and E.R. Bernstein. J. Phys. Chem. **91**, 2533 (1987).
31. B.V. Cheney, M.W. Schulz, J. Cheney, and W.G. Richards. J. Am. Chem. Soc. **110**, 4195 (1988).
32. P. Linse. J. Comput. Chem. **9**, 505 (1988).
33. J.L. Brédas and G.B. Street. J. Am. Chem. Soc. **110**, 7001 (1988).
34. J.L. Brédas and G.B. Street. J. Chem. Phys. **90**, 7291 (1989).
35. W.L. Jorgensen and D.L. Severance. J. Am. Chem. Soc. **112**, 4768 (1990).
36. B.V. Cheney and M.W. Schulz. J. Phys. Chem. **94**, 6268 (1990).
37. J.D. Augspurger, C.E. Dykstra, and T.S. Zwier. J. Phys. Chem. **96**, 7252 (1992).
38. T. Davies and L.A.K. Staveley. Trans. Faraday Soc. **53**, 19 (1957).
39. A.T. McPhail and G.A. Sim. J. Chem. Soc. Chem. Commun. 124 (1965).
40. A.T. McPhail, G.A. Sim, A.J. Frey, and H. Ott. J. Chem. Soc. B, 377 (1966).
41. A.D.U. Hardy and D.D. McNicol. J. Chem. Soc. Perkin 2, 1140 (1976).
42. A. Aubry, J. Protas, E. Moreno-Gonzalez, and M. Marraud. Acta Crystallogr. **B33**, 2572 (1977).
43. W.J. Westerhaus, O. Knop, and M. Falk. Can. J. Chem. **58**, 1355 (1980).
44. B.R. Vincent. Doctoral thesis. Dalhousie University, Halifax, NS. 1987.
45. A. Linden, T.S. Cameron, and O. Knop. Abstract ING-50-F2. Book of abstracts. 70th Canadian Chemical Conference, Quebec, PQ, June 7–11, 1987.
46. Yu. E. Ovchinnikov, V.E. Shklover, Yu. T. Struchkov, V.V. Dement'ev, T.M. Frunze, and B.A. Antipova. J. Organomet. Chem. **335**, 157 (1987).
47. J.L. Atwood, F. Hamada, K.D. Robinson, G.W. Orr, and R.L. Vincent. Nature (London), **349**, 683 (1991).
48. H.S. Rzepa, M.L. Webb, A.M.Z. Slavin, and D.J. Williams. J. Chem. Soc. Chem. Commun. 765 (1991).
49. J.L. Atwood, S.G. Bott, C. Jones, and C.L. Raston. J. Chem. Soc. Chem. Commun. 1349 (1992).
50. L.R. Hanton, C.A. Hunter, and D.H. Purvis. J. Chem. Soc. Chem. Commun. 1134 (1992).
51. K. Hoffmann and E. Weiss. J. Organomet. Chem. **67**, 221 (1974).
52. S.J. Rettig and J. Trotter. Can. J. Chem. **51**, 1288 (1973).
53. N. Walker and D. Stuart. Acta Crystallogr. **A39**, 158 (1983).
54. X.-M. He and B.M. Craven. Acta Crystallogr. **A49**, 10 (1993).
55. R.S. Rowland. Abstract C006. Book of abstracts. Annual Meeting, American Crystallographic Association, Albuquerque, NM, May 23–28 (1993).
56. S.C. Choi, R.J. Boyd, and O. Knop. Can. J. Chem. **66**, 2465 (1988).

Appendix

The Mulliken net charges in the 6-31G* optimized NH_4^+ ion are $\epsilon_M(N) = -0.951$ e and $\epsilon_M(H) = 0.488$ e, and in CH_4, $\epsilon_M(C) = -0.660$ e and $\epsilon_M(H) = 0.165$ e (56). The corresponding Löwdin net charges ϵ_L are -0.489 and 0.372 e in NH_4^+, and -0.630 and 0.158 e in CH_4. In H_2O the charges are $\epsilon_M(O) = -0.869$ e and $\epsilon_M(H) = 0.434$ e.

The MNDO net charges in BPh_4^- (in the S_4 conformation corresponding to the global energy minimum) are -0.233 e on B, 0.048 e on C(α), -0.085 e on the other C atoms (mean), and 0.037 e on the H atoms (mean); in CPh_4 they are 0.149 e on the central carbon, -0.066 e on C(α), -0.054 e on the other carbons (mean), and 0.060 e on the H atoms (mean). The corresponding AM1 net charges in BPh_4^- are 0.054, -0.040, -0.155, and 0.110 e, respectively; in CPh_4 they are 0.114, -0.064, -0.128, and 0.135 e, respectively.[22] Thus the difference in the net charges on the corresponding C and H atoms (other than C(α)) in the charged species BPh_4^- and the neutral species CPh_4 are relatively small and justify qualitative comparisons of hydrogen bonding to phenyl rings carrying an ionic charge (BPh_4^-) with that to phenyl rings in molecular crystals.

[22]W. Kwiatkowski and O. Knop. Unpublished results.

Characterization and nonrigid behaviour of a carboxylate-bridged rhodium dimer

WILLIAM R. CULLEN AND STEVEN J. RETTIG
Department of Chemistry, University of British Columbia, 2036 Main Mall, Vancouver, BC V6T 1Y6, Canada

AND

EUGENE B. WICKENHEISER
Department of Chemistry, Augustana University College, Camrose, AB T4V 2R3, Canada

Received June 17, 1993

WILLIAM R. CULLEN, STEVEN J. RETTIG, and EUGENE B. WICKENHEISER. Can. J. Chem. **72**, 1294 (1994).

Bis(μ-*t*-butylacetato)bis(norbornadiene)dirhodium(I) **1** is prepared by a reaction between pivaloyl camphor and (norbornadiene)rhodium(I) chloride dimer. A molecular rearrangement takes place in which the pivaloyl groups of the pivaloyl camphor starting material are incorporated into the end product as bridging *t*-butylcarboxylate ligands. A variable temperature ^{1}H NMR study and corresponding dynamic computer fit of the NMR data, and crystal structure are reported for the structurally nonrigid dimer. Crystals of **1** are triclinic, $a = 10.454(1)$, $b = 10.817(1)$, $c = 12.424(1)$ Å, $\alpha = 64.904(7)$, $\beta = 100.320(7)$, $\gamma = 109.382(8)°$, $Z = 2$, space group $P\bar{1}$. The structure was solved by heavy atom methods and was refined by full-matrix least-squares procedures to $R = 0.070$ and $R_w = 0.081$ for 3093 reflections with $I \geq 3\sigma(I)$.

WILLIAM R. CULLEN, STEVEN J. RETTIG et EUGENE B. WICKENHEISER. Can. J. Chem. **72**, 1294 (1994).

On a préparé le bis(μ-*tert*-butylacétato)bis(norbornadiène)dirhodium(I), **1**, par réaction du pivaloyl camphre avec le chlorure de (norbornadiène)rhodium(I) à l'état dimère. Il se produit un réarrangement moléculaire au cours duquel les groupes pivaloyles du pivaloyl camphre s'incorporent dans le produit final sous la forme de coordinats *tert*-butylcarboxylates agissant comme ponts. On rapporte les résultats d'une étude rmn du ^{1}H et de l'ajustement dynamique des données rmn correspondantes ainsi que la structure cristalline du dimère de structure non rigide. Les cristaux du composé **1** sont tricliniques, $a = 10{,}454(1)$, $b = 10{,}817(1)$, $c = 12{,}424(1)$ Å, $\alpha = 64{,}904(7)$, $\beta = 100{,}320(7)$, $\gamma = 109{,}382(8)°$, $Z = 2$ et groupe d'espace $P\bar{1}$. On a résolu la structure par la méthode aux atomes lourds et on l'a affinée par la méthode des moindres carrés jusqu'à des valeurs de $R = 0{,}070$ et $R_w = 0{,}081$ pour 3093 réflexions avec $I \geq 3\sigma(I)$.

[Traduit par la rédaction]

Introduction

There are several reasons for the ongoing interest in binuclear transition metal complexes, ranging from theoretical studies of metal–metal interactions, and spectroscopic, magnetic, and structural modelling of biological molecules, to their involvement in catalytic processes (1–14). Complexes in which two metal centres are closely situated may exhibit the cooperative catalytic effects of two metals in the activation and reaction of the substrate molecule (15–21). The catalytic activity can also reflect the reactivity of metal cluster compounds, a bimetallic complex being the smallest imaginable cluster. Complexes of carboxylate ligands are usually found as bridged dimers and as such lend themselves to the preparation of bimetallic compounds. The bridging mode is common for the transition metal carboxylates; the preferred conformation is the hinged form (22) in which the two metals are brought into close proximity, allowing metal–metal interactions in the case of $Rh_2(O_2CR)_4$ compounds (1–3, 23, 24). Transition metal dimers with carboxylate ligands are a reasonably stable class of molecules with potential for catalytic activity, and thus have been studied as catalyst precursors and as synthetic precursors for other classes of molecules (6, 25–31).

Of the bridged-carboxylate complexes that have been prepared, some have been observed to be sterically nonrigid, or evidence exists suggesting this property (4, 32, 33). Studying the associated molecular motion can yield insight into the nature of the species and the interactions between the atoms making up the molecule. The focus of this paper is the characterization and quantification of the nonrigid behaviour of a dirhodium complex, bis(μ-*t*-butylacetato)bis(norbornadiene)-dirhodium(I), **1**, manifest in its temperature-dependent ^{1}H NMR spectrum.

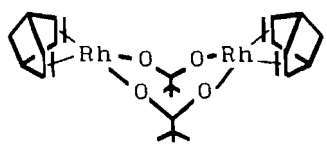

1

Experimental

The preparation of the dimer was carried out under a nitrogen atmosphere, using standard Schlenk and vacuum line techniques. Ether and hexane were distilled from calcium hydride prior to their use in the reactions. The (norbornadiene)rhodium(I) chloride dimer and pivaloyl-(+)-camphor were prepared by literature methods (34, 35).

Preparation of bis(μ-t-butylacetato)bis(norbornadiene)dirhodium, ***1***

A suspension of the (norbornadiene)rhodium(I) chloride dimer (100 mg, 217 μmol) and pivaloyl-(+)-camphor (110 mg, 493 μmol) in 20 mL of diethyl ether, was prepared, cooled to −78°C, and a solution of potassium hydroxide (120 mg, 2.1 mmol), in 2 mL of water, was added dropwise. The mixture was stirred at −78°C for 2 h, allowed to warm to room temperature, and was stirred for an additional 1 h. The product was extracted from the aqueous layer with several portions of ether, the extracts combined, and the solvent removed at reduced pressure. The red powder thus obtained was recrystallized from ether/hexane giving 167 mg of deep red crystals (65% yield) which were identified as **1**. Anal. calcd. for $C_{24}H_{34}O_4Rh_2$: C 48.66, H 5.78; found: C 48.24, H 5.79. ^{1}H NMR (toluene-d_8, ambient temperature): d 1.01 (s, 4H, C(14)H_2 and C(7)H_2), 1.09 (s, 18H, C(16)$(CH_3)_3$ and C(21)$(CH_3)_3$), 3.62 (broad unresolved peak, 4H, C(1)H, C(4)H, C(8)H, and C(12)H), 3.85 (broad s, 8H, C(2)H, C(3)H, C(5)H, C(6)H, C(9)H, C(10)H, C(12)H, and C(13)H). The electron ionization (70 eV) mass spectrum showed the presence of the parent molecular ion (592 *m/z*) and fragmentation peaks corresponding to the presence of the mono-

Can. J. Chem. Downloaded from www.nrcresearchpress.com by EESC ESCOLA DE ENGENHARIA on 09/08/12
For personal use only.

Can. J. Chem. Downloaded from www.nrcresearchpress.com by EESC ESCOLA DE ENGENHARIA on 09/08/12
For personal use only.

mer (296 *m/z*) and the NBDRh$^+$ ion (195 *m/z*). The base peak is due to the presence of the $CH(CH_3)_3^+$ ion (57 *m/z*).

The ^{1}H NMR spectrum was recorded on a Varian XL-300 spectrometer, and the mass spectrum on a Kratos AES M50 spectrometer.

X-ray crystallographic analysis of $[(CH_3)_3CCO_2]_2Rh_2(C_7H_8)_2$

A crystal ca. 0.12 × 0.25 × 0.45 mm in size was mounted on a glass fibre. Unit-cell parameters were refined by least-squares on setting angles for 25 reflections (2θ = 60.0–76.8°) measured on a diffractometer with Cu-K_α radiation ($\lambda_{K\alpha1}$ = 1.54056, $\lambda_{K\alpha2}$ = 1.54439 Å). Crystal data at 21°C are as follows:

$C_{24}H_{34}O_4Rh_2$ fw = 592.35

Triclinic, a = 10.454(1), b = 10.817(1), c = 12.424(1) Å, α = 64.904(7), β = 100.320(7), γ = 109.382(8)°, Z = 2, ρ_c = 1.641 Mg m^{-3}, $F(000)$ = 600, μ(Cu-K_α) = 116.03 cm^{-1}. Absent reflections: none, space group $P\bar{1}$ (No. 2, reduced cell) from structure analysis.

Intensities were measured with graphite-monochromated Cu-K_α radiation on an Enraf-Nonius CAD4-F diffractometer. An ω–2θ scan at 1.1–10.0° min^{-1} over a range of (1.00 + 0.14 tan θ)° in ω (scan extended by 25% on each side for background measurement) was employed. Data were measured to 2θ = 150°. The intensities of three check reflections, measured every hour of X-ray exposure time throughout the data collection, showed only small random variations. The data were processed[1] and corrected for Lorentz and polarization effects, and absorption (analytical, transmission factors 0.055–0.343). Of the 4903 independent reflections measured, 3093 (63.1%) had intensities greater than or equal to 3σ(I) above background where $\sigma^2(I) = [C + 2B + (0.040(C - B))^2]$ with C = scan count, B = normalized total background count.

The structure was solved by heavy atom methods, the coordinates of the rhodium atoms being determined from the Patterson function and those of the remaining non-hydrogen atoms from a subsequent difference Fourier synthesis. The non-hydrogen atoms were refined with anisotropic thermal parameters, the hydrogen atoms associated with the metal-bound carbon atoms of the norbornadiene ligands were refined with isotropic thermal parameters, and the remaining hydrogen atoms were fixed in idealized positions (C—H = 0.98 Å, U_H = 1.2 $U_{\text{bonded atom}}$). Scattering factors for all atoms and anomalous dispersion corrections for the non-hydrogen atoms were taken from ref. 36. An isotropic type I extinction correction was applied, the final value of g being 0.29(4) × 10^4. The weighting scheme $w = 1/\sigma^2(F)$ gave uniform average values of $w(|F_o| - |F_c|)^2$ over ranges of both $|F_o|$ and sin θ/λ and was employed in the final stages of full-matrix least-squares refinement of 304 variables. Reflections with $I < 3\sigma(I)$ were not included in the refinement. Convergence was reached at R = 0.070 and R_w = 0.081 for 3093 reflections with $I \geq 3\sigma(I)$. The function minimized was $\Sigma w(|F_o| - |F_c|)^2$, $R = \Sigma||F_o| - |F_c||/\Sigma|F_o|$, $R_w = (\Sigma w(|F_o| - |F_c|)^2/\Sigma w|F_o|^2)^{1/2}$. On the final cycle of refinement the maximum parameter shift corresponded to 0.22σ. The mean error in an observation of unit weight was 1.71. The final difference map showed maximum fluctuations of −3.1 and +2.1 e Å^{-3} (both near Rh atoms). The relatively high values of R and R_w are due to poor crystal quality. A data set collected earlier with molybdenum radiation was of even lower quality, with only about 25% of the reflections out to 2θ = 45° having significant intensity.

The final positional and (equivalent) isotropic thermal parameters for the non-hydrogen atoms appear in Table 1. Bond lengths and angles are given in Tables 2 and 3, respectively. Hydrogen atom parameters, anisotropic thermal parameters, torsion angles, and structure factors have been deposited.[2]

TABLE 1. Final positional (fractional × 10^4, Rh × 10^5, H × 10^3) and isotropic thermal parameters (U × 10^3 Å^2) with estimated standard deviations in parentheses

Atom	x	y	z	U_{eq}/U_{iso}
Rh(1)	37953(11)	8785(11)	32849(10)	43
Rh(2)	17169(12)	9322(11)	11491(9)	45
O(1)	778(11)	−832(11)	2619(9)	55
O(2)	1960(9)	−397(11)	4111(9)	51
O(3)	3927(12)	−745(10)	2864(9)	53
O(4)	2894(11)	−230(10)	1020(9)	52
C(1)	5910(18)	2564(16)	4146(14)	56
C(2)	4422(17)	2099(15)	4326(14)	48
C(3)	3782(19)	2822(16)	3245(15)	48
C(4)	4983(16)	3749(15)	2405(15)	56
C(5)	5361(17)	2604(18)	2239(16)	59
C(6)	5894(19)	1834(18)	3338(15)	56
C(7)	6142(16)	4121(16)	3285(16)	60
C(8)	1826(19)	3742(17)	320(16)	63
C(9)	933(18)	2384(18)	1244(15)	53
C(10)	16(17)	1676(17)	575(15)	52
C(11)	378(18)	2551(17)	−734(15)	60
C(12)	1728(19)	2278(17)	−663(13)	59
C(13)	2613(20)	3048(15)	−39(17)	69
C(14)	815(20)	4070(17)	−765(15)	65
C(15)	929(14)	−1090(13)	3686(13)	40
C(16)	−177(16)	−2225(16)	4488(13)	52
C(17)	293(21)	−2756(23)	5780(16)	90
C(18)	−709(25)	−3459(21)	4113(20)	105
C(19)	−1313(22)	−1597(29)	4329(22)	108
C(20)	3549(16)	−945(14)	1916(14)	46
C(21)	3917(16)	−2169(15)	1838(14)	49
C(22)	3610(20)	−2168(20)	582(17)	70
C(23)	3078(24)	−3536(17)	2744(18)	85
C(24)	5402(20)	−2004(21)	2153(19)	78
H(2)	398(19)	190(20)	498(16)	97(69)
H(3)	305(15)	269(16)	330(14)	58(52)
H(5)	527(21)	254(21)	133(18)	113(72)
H(6)	618(13)	126(12)	342(11)	22(33)
H(9)	53(20)	229(21)	184(18)	102(72)
H(10)	−81(15)	102(15)	67(13)	52(44)
H(12)	199(15)	156(16)	−102(13)	64(46)
H(13)	371(11)	345(11)	5(9)	16(26)

Dynamic NMR computer modelling

The computer modelling of the nonrigid behaviour of **1** was done using the dynamic computer fitting program DNMR4. The modified version used here works on an AT-compatible personal computer equipped with a math coprocessor. The low-temperature-limit spectrum was collected at a temperature of −44°C and T_2 values were calculated by half-height line widths ($w_{1/2}$) from this spectrum ($T_2 = 1/\pi w_{1/2}$ = 0.090 s). The coupling constants employed were as follows: $J_{\text{aliph H, adjacent olefin H}}$ = 3.3 Hz, $J_{\text{aliph H, distant olefin H}}$ = 0 Hz, $J_{\text{aliph H, bridgehead H}}$ = 1.7 Hz, $J_{\text{cis olefin H's}}$ = 3.3 Hz. Because of the size of the spin system, the aliphatic exchange and the olefinic exchange was modelled sepa-

[1]Computer programs used include locally written programs for data processing and locally modified versions of the following: MULTAN80, multisolution program by P. Main, S.J. Fiske, S.E. Hull, L. Lessinger, G. Germain, J.P. Declercq, and M.M. Woolfson; ORFLS, full-matrix least-squares, and ORFFE, function and errors, by W.R. Busing, K.O. Martin, and H.A. Levy; FORDAP, Patterson and Fourier syntheses, by A. Zalkin; ORTEP II, illustrations, by C.K. Johnson.

[2]Supplementary material mentioned in the text may be purchased from the Depository of Unpublished Data, Document Delivery, CISTI, National Research Council of Canada, Ottawa, ON K1A 0S2, Canada.

Tables of hydrogen atom coordinates, bond lengths and bond angles have also been deposited with the Cambridge Crystallographic Data Centre, and can be obtained on request from The Director, Cambridge Crystallographic Data Centre, University Chemical Laboratory, 12 Union Road, Cambridge, CB2 1EZ, U.K.

TABLE 2. Bond lengths (Å) with estimated standard deviations in parentheses

Bond	Length (Å)	Bond	Length (Å)
Rh(1)—O(2)	2.094(9)	C(1)—C(7)	1.53(2)
Rh(1)—O(3)	2.084(8)	C(2)—C(3)	1.41(2)
Rh(1)—C(2)	2.102(13)	C(3)—C(4)	1.55(2)
Rh(1)—C(3)	2.086(14)	C(4)—C(5)	1.52(2)
Rh(1)—C(5)	2.128(15)	C(4)—C(7)	1.55(2)
Rh(1)—C(6)	2.09(2)	C(5)—C(6)	1.39(2)
Rh(1)—M(1)	1.971(13)	C(8)—C(9)	1.55(2)
Rh(1)—M(2)	1.993(14)	C(8)—C(13)	1.51(2)
Rh(2)—O(1)	2.094(10)	C(8)—C(14)	1.55(2)
Rh(2)—O(4)	2.095(9)	C(9)—C(10)	1.40(2)
Rh(2)—C(9)	2.05(2)	C(10)—C(11)	1.54(2)
Rh(2)—C(10)	2.08(2)	C(11)—C(12)	1.52(2)
Rh(2)—C(12)	2.099(14)	C(11)—C(14)	1.54(2)
Rh(2)—C(13)	2.122(14)	C(12)—C(13)	1.39(2)
Rh(2)—M(3)	1.942(14)	C(15)—C(16)	1.51(2)
Rh(2)—M(4)	1.993(12)	C(16)—C(17)	1.51(2)
O(1)—C(15)	1.23(2)	C(16)—C(18)	1.50(2)
O(2)—C(15)	1.26(2)	C(16)—C(19)	1.50(3)
O(3)—C(20)	1.26(2)	C(20)—C(21)	1.54(2)
O(4)—C(20)	1.29(2)	C(21)—C(22)	1.54(2)
C(1)—C(2)	1.49(2)	C(21)—C(23)	1.52(2)
C(1)—C(6)	1.51(2)	C(21)—C(24)	1.50(2)

rately. The displayed plots were obtained by the addition of the two individual spectra obtained from the DNMR program.

^{1}H NMR data were collected on a Varian XL-300 (300 MHz) equipped with variable temperature apparatus. The toluene-d_8 employed as solvent for the variable temperature study was run through an alumina column and degassed by three freeze–pump–thaw cycles prior to its use.

Results and discussion

Compound **1** was obtained during the attempted synthesis of a (nbd)rhodium β-diketonate complex. The formation of **1** may have occurred by the initial formation of the target complex (**2**)

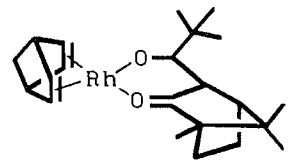

2

followed by a rearrangement. It is conceivable that the pivaloyl camphor underwent a base hydrolysis reaction, possibly catalyzed in the presence of rhodium, to give camphor and *t*-butyl acetic acid. The *t*-butyl acetic acid could then have reacted with the rhodium moiety to give the observed product. The high yield indicates that the operative reaction path is favourable. It is interesting to note that the preparation of several rhodium(I) β-diketonates with adjacent phenyl groups have been carried out successfully under the same conditions (37). Rhodium diketonates of this type are hydrogenation and hydrosilylation catalysts, and the phenyl analogue of the target complex, bis(ethene)(3-benzoyl-(+)-camphorato-*O*,*O*′)rhodium(I), **3**, is among this group of catalysts (37, 38). Compound **1** was tested for its ability to act as a hydrogenation catalyst using the same conditions as the rhodium diketonates (1 atm H_2; 25°C, methanol as solvent; 1-octene as substrate) and no reaction was observed.

The acetato analogue of **1**, bis(μ-acetato)bis(norbornadiene)dirhodium(I), **4**, has previously been prepared and stud-

TABLE 3. Bond angles (deg) with estimated standard deviations in parentheses

Bonds	Angle (deg)	Bonds	Angle (deg)
O(2)—Rh(1)—O(3)	91.3(4)	C(9)—C(8)—C(14)	101.6(14)
O(2)—Rh(1)—M(1)	97.9(5)	C(13)—C(8)—C(14)	100.3(14)
O(2)—Rh(1)—M(2)	167.8(5)	C(8)—C(9)—C(10)	105.1(14)
O(3)—Rh(1)—M(1)	167.2(5)	C(9)—C(10)—C(11)	107.1(14)
O(3)—Rh(1)—M(2)	98.0(5)	C(10)—C(11)—C(12)	98.6(13)
M(1)—Rh(1)—M(2)	71.8(6)	C(10)—C(11)—C(14)	100.4(12)
O(1)—Rh(2)—O(4)	90.1(4)	C(12)—C(11)—C(14)	102.4(14)
O(1)—Rh(2)—M(3)	96.2(5)	C(11)—C(12)—C(13)	105.2(14)
O(1)—Rh(2)—M(4)	166.5(6)	C(8)—C(13)—C(12)	108(2)
O(4)—Rh(2)—M(3)	167.0(5)	C(8)—C(14)—C(11)	94.1(12)
O(4)—Rh(2)—M(4)	100.3(5)	O(1)—C(15)—O(2)	121.5(12)
M(3)—Rh(2)—M(4)	72.0(6)	O(1)—C(15)—C(16)	118.3(13)
Rh(2)—O(1)—C(15)	131.5(9)	O(2)—C(15)—C(16)	120.1(13)
Rh(1)—O(2)—C(15)	126.9(9)	C(15)—C(16)—C(17)	112.9(14)
Rh(1)—O(3)—C(20)	128.7(9)	C(15)—C(16)—C(18)	109.7(13)
Rh(2)—O(4)—C(20)	123.1(9)	C(15)—C(16)—C(19)	107.5(14)
C(2)—C(1)—C(6)	99.0(14)	C(17)—C(16)—C(18)	109.1(15)
C(2)—C(1)—C(7)	102.0(13)	C(17)—C(16)—C(19)	110(2)
C(6)—C(1)—C(7)	102.6(13)	C(18)—C(16)—C(19)	108(2)
C(1)—C(2)—C(3)	108.0(14)	O(3)—C(20)—O(4)	126.3(12)
C(2)—C(3)—C(4)	103.2(15)	O(3)—C(20)—C(21)	115.9(13)
C(3)—C(4)—C(5)	100.6(11)	O(4)—C(20)—C(21)	117.8(13)
C(3)—C(4)—C(7)	101.5(13)	C(20)—C(21)—C(22)	111.4(12)
C(5)—C(4)—C(7)	100.8(13)	C(20)—C(21)—C(23)	106.2(12)
C(4)—C(5)—C(6)	106.2(14)	C(20)—C(21)—C(24)	109.1(13)
C(1)—C(6)—C(5)	105.9(14)	C(22)—C(21)—C(23)	111.0(15)
C(1)—C(7)—C(4)	93.0(12)	C(22)—C(21)—C(24)	109.0(14)
C(9)—C(8)—C(13)	98.4(12)	C(23)—C(21)—C(24)	110(2)

Can. J. Chem. Downloaded from www.nrcresearchpress.com by EESC ESCOLA DE ENGENHARIA on 09/08/12
For personal use only.

Can. J. Chem. Downloaded from www.nrcresearchpress.com by ESC ESCOLA DE ENGENHARIA on 09/08/12
For personal use only.

ied by X-ray crystallography (39). The major structural differences between **1** and **4** arise from the steric constraints of the *t*-butyl group, thus a significant difference is present in the angle between the acetate ligand planes (97.7° for the *t*-butyl carboxylate and 82.49° for the acetate bridges) and in the Rh—O—C bonds. The rhodium atoms are displaced further from their coordination planes in **1** owing to the repulsion of the *t*-butyl ligands; the Rh(1) and Rh(2) atoms are displaced 0.165(1) and 0.138(1) Å, respectively, from the mean planes of their substituents (two O atoms, two midpoints of C=C bonds) corresponding to 0.1574(2) and 0.0985(2) Å in **4**.

The crowding effect of the *t*-butyl group is not otherwise apparent. The bond lengths between the rhodium atoms and the olefins, as well as those between the rhodium atoms and the oxygens of the carboxylate groups, do not show significant differences in **1** and **4**. The dihedral angle between the normals to the mean coordination planes of the two Rh atoms (calculated with the midpoints of the coordinated C=C bonds) is 50.5° in **1**, coinciding with an angle of 50.1° in **4**. Furthermore, the angles of the bonds surrounding the rhodium atoms show like deviations from the square planar model with M—Rh—M bond angles being 71.8(6)° for Rh(1) (corresponding to 72.7(1)° in **4**); for Rh(2): 72.0(6)° (72.7(1)° in **4**); the O—Rh—M angles being 97.9(5)° and 98.0(5)° in Rh(1) (96.6(1)° and 97.4(1)° in **4**); for Rh(2): 96.2(5)° and 100.3(5)° (95.8(1)° and 99.6(1)° in **4**); the O—Rh—O angles being 91.3(4)° for Rh(1) and 90.1(4)° for Rh(2) (91.9(1)° and 91.6(1)° in **4**).

The ^{1}H NMR at ambient temperature contains a sharp singlet (1.09 ppm), assigned to the methyl-group protons of the bridging carboxylate ligands, and two broad resonances (3.62 and 3.85 ppm), the shapes of which are temperature dependent, suggesting that **1** is structurally nonrigid. From chemical shift and integral intensity these resonances can be assigned to the protons of the norbornadiene ligands as follows: the resonance at 3.62 ppm is due to the aliphatic hydrogen atoms attached to C(1), C(4), C(8), and C(11), and the resonance at 3.85 ppm is due to the olefinic hydrogen atoms attached to C(2), C(3), C(5), C(6), C(9), C(10), C(12), and C(13) (Fig. 1). In the low-temperature-limit spectrum, where lowering the temperature no longer effects resonance resolution, the broad resonances resolve into two resonances for the aliphatic protons and two resonances for the olefinic protons. The areas of these peaks are consistent with the assignments.

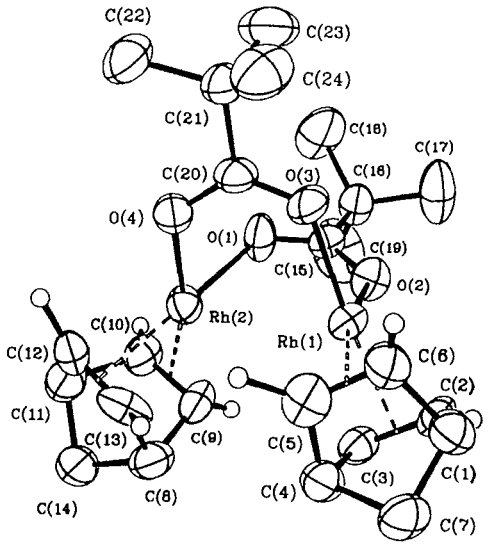

FIG. 1. Crystal structure of **1**.

The ^{1}H NMR spectrum can be understood by observing the crystal structure of **1** (Fig. 1; stereoview in Fig. 2). Two mirror planes exist in the symmetry of **1**, giving rise to, in the static (or solid state) structure, two sets of aliphatic protons (one set inside and one set outside the hinged form of **1**) and, similarly, two sets of olefinic protons. It does appear that the hinged form of **1** is the most stable conformation in solution as this form explains the low temperature limit. It is possible to envision another form of the molecule in solution in which one carboxylic unit is above the plane defined by the oxygen atoms and the other unit is below the plane. This chair form (with reference to the position of the carboxylate groups relative to the internal plane of the carboxylate oxygens) would make the aliphatic protons chemically equivalent and give rise to a single resonance. The olefinic protons in this form would be in two separate groups, depending on the protons' relative proximity to the

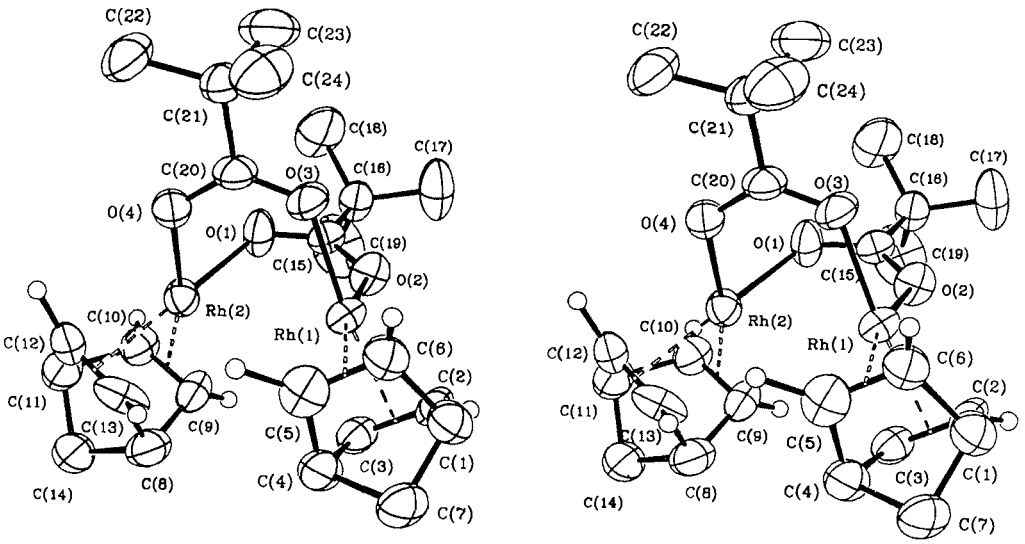

FIG. 2. Stereoview of the bis(μ-*t*-butylcarboxylato)-bis[(η^4-norbornadiene)rhodium(I)] molecule; 50% probability thermal ellipsoids are shown for the non-hydrogen atoms.

Can. J. Chem. Downloaded from www.nrcresearchpress.com by EESC ESCOLA DE ENGENHARIA on 09/08/12
For personal use only.

t-butyl groups on the bridging carboxylate ligands. Although the observed ^1H NMR spectra do not support the presence of this structure, it may play a part in the motion the complex undergoes.

Several mechanisms have been proposed to explain the observed nonrigid behaviour of related carboxylate-bridged transition metal complexes; these are discussed here. One possible explanation for the exchange process is the rotation of the nbd ligand about an axis through the bridgehead carbon and the rhodium on each side of the dimer. A motion of this type would explain the exchange of the olefinic and aliphatic protons in **1**, and has been used to explain the observed olefin ligand exchange in bis(olefin)(acac)Rh species (40–42), as well as the exchange of the protons of the nbd ligand observed in the $^{13}C^1H$ NMR spectrum of the acetate complex **4** (6). The activation energies associated with this type of exchange are significantly higher than those associated with the motion studied here, ranging from 58.2 to 63.6 kJ/mol in the bis(olefin)(acac)Rh complexes (42).

Another way to account for the exchange is by the dissociation of one rhodium–oxygen bond followed by rotation and reassociation to give the inverted dimer. This process has been shown to occur in the palladium carboxylate dimers of the type bis(μ-acetato)dihalobis(dimethylphosphine)dipalladium(II). In the presence of coordinating solvents the rate of exchange is increased; in the absence of a coordinating solvent, the rate of exchange is not significant and any motion is then attributable to other possible modes (33).

A third model employed to explain the behaviour in carboxylate-bridged palladium complexes involves an inversion of the eight-membered ring including the metals and the carboxylate bridges. This motion best fits the present observations and is further explored below.

To calculate the exchange rate for the observed process, the NMR data were fitted using the computer fitting program DNMR4. The exchange between the olefinic protons was calculated separately from the exchange of the aliphatic protons due to the size limitations of the program; each whole computer generated spectrum was obtained by the addition of the two independently generated spectra. A comparison between the experimental and calculated spectra is shown in Fig. 3. The rate constants obtained from the computer fits are listed in Table 4.

Having obtained the rate constants for the exchange (Table 4), the activation parameters were calculated from the slope and intercept of the plot of ln k versus $1/T$ (Fig. 4; Tables 5 and 6). The data in Table 5 represent the treatment of the data as though the two sets of protons are independent and the corresponding activation parameters are listed in Table 7. Assuming that the exchange of the olefinic and aliphatic protons are fixed to occur at the same rate, the combined data gives rise to the following activation parameters: $\Delta H^{\ddagger}$ = 73.68 kJ/mol; $\Delta S^{\ddagger}$ = 100.3 J/mol·K; $\Delta G^{\ddagger}$ = 44.43 kJ/mol. The standard deviations calculated for the activation parameters have been obtained statistically and are a reflection of the goodness of the fit of the plot to a straight line. The correspondingly lower standard deviation of $\Delta G^{\ddagger}$ is due to the covariance of $\Delta H^{\ddagger}$ and $\Delta S^{\ddagger}$ (43). The rigid nature of the nbd ligand ensures that the rate constants are the same for both groups of protons, therefore the calculation of the activation parameters can be done by treating the data as one group. In combining the rate constants, the associated error in the activation parameters decreases as there are more data points. This treatment of data is contained in Table 6; a summary of the activation parameters can be found in Table 7.

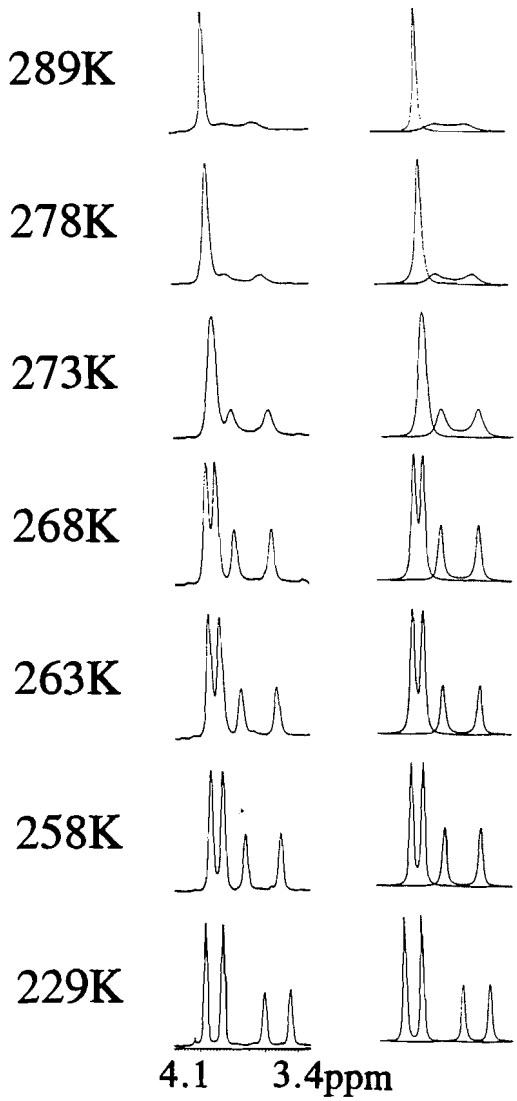

FIG. 3. Observed variable-temperature ^1H NMR spectra of the aliphatic and olefinic resonances in **1** (left) and the DNMR4-generated spectra (right).

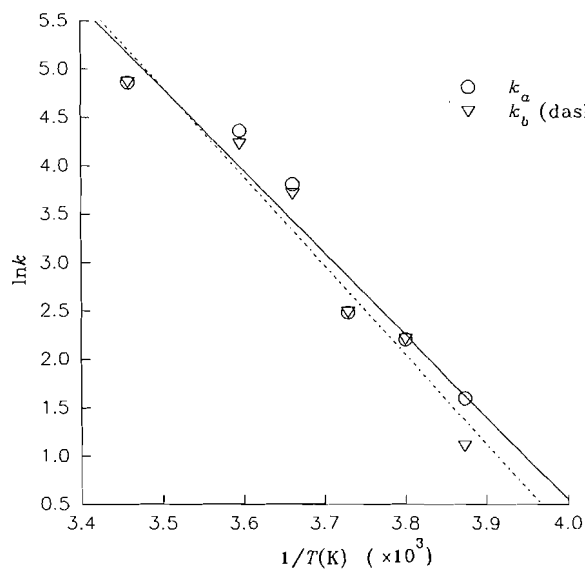

FIG. 4. Plot of ln k versus $1/T$ (K) for the rate constants generated by DNMR4.

Can. J. Chem. Downloaded from www.nrcresearchpress.com by EESC ESCOLA DE ENGENHARIA on 09/08/12
For personal use only.

TABLE 4. Rate constants for the exchange of aliphatic protons (k_A) and olefinic protons (k_B)

Temperature $(K)^{-1} \times 10^3$	k_A (s^{-1})	ln k_A	k_B (s^{-1})	ln k_B
3.874	5	1.6	3	1.1
3.800	9	2.2	9	2.2
3.729	12	2.48	12	2.48
3.661	45	3.81	41	3.71
3.595	78	4.36	68	4.22
3.458	129	4.86	131	4.86

TABLE 5. Statistical analysis[a]

$T(K)^{-1}$ $(\times 10^3)$	ln k_A	$\hat{Y}$	$(Y - \hat{Y})^2$	ln k_B	$\hat{Y}$	$(Y - \hat{Y})^2$
3.874	1.6	1.62	0.00	1.1	1.36	0.07
3.800	2.2	2.25	0.00	2.2	2.05	0.02
3.729	2.48	2.85	0.14	2.48	2.70	0.048
3.661	3.81	3.43	0.14	3.71	3.33	0.14
3.595	4.36	3.99	0.137	4.22	3.94	0.0784
3.458	4.86	5.16	0.0900	4.86	5.20	0.116
Σ			0.51			0.48

Parameter	Aliphatic	Olefinic
r	−0.97	−0.98
a	34.58	37.07
b	-8.508×10^3	-9.216×10^3
S_Y	1.3	1.4
S_X	1.5×10^{-4}	1.5×10^{-4}
σ_Y	1.2	1.3
σ_X	1.4×10^{-4}	1.4×10^{-4}
$\bar{X}$	3.69×10^{-3}	3.69×10^{-3}
$S_{Y\|X}$	0.36	0.35
$S^2_{Y\|X}$	0.13	0.12
σ_a	4.0	3.8
σ_b	1.1×10^3	1.0×10^3

[a] $S^2_{Y|X} = 1/(n-2) \cdot \Sigma(Y - \hat{Y})^2$; $\sigma_a = S_{Y|X} \cdot \sqrt{[(1/n) + \bar{X}^2/((n-1) \cdot S_X^2)]}$; $\sigma_b = S_{Y|X}/(S_X \cdot \sqrt{(n-1)})$.

The magnitude of the activation parameters is indicative of a ring inversion process giving rise to the exchange. The spectra of **1** were collected in the non-coordinating solvent toluene-d_8, the dissociation–rotation–association mode of exchange is thus expected to be insignificant. Free carboxylate ligand is not detectable in the NMR spectrum at any of the temperatures employed in the DNMR study, neither is a broadening of the resonance of the *t*-butyl protons which is also expected in this type of exchange. If, on the other hand, the nbd rotation occurs as previously suggested for **4**, then the activation parameters for the motion should be very close for **1** and **4** since the crystal structures are very similar and suggest the same nbd–rhodium and carboxylate–rhodium interactions (bond distances and angles are within experimental error for the Rh–nbd data of **1** and **4**). An activation energy of ~30 kJ/mol ($CDCl_3$, $^{13}C^1H$ NMR, $T_{coal} = -12°C$) was reported for **4**. The effects of the *t*-butyl group can account for the difference in the activation parameters for a ring inversion mechanism but not for a nbd rotation mechanism. The above therefore demonstrates that, in the case of rhodium carboxylate dimers, the exchange is due to a ring inversion. Sufficient evidence has not yet been presented to indicate the presence of nondissociative rotational motion

TABLE 6. Statistical analysis of the data set as combined[a]

$T(K)^{-1}$ $(\times 10^3)$	ln k_A	ln k_B	$\hat{Y}$	$(Y - \hat{Y})^2$ k_A	$(Y - \hat{Y})^2$ k_B
3.874	1.6	1.1	1.49	0.01	0.2
3.800	2.2	2.2	2.15	0.003	0.003
3.729	2.48	2.48	2.78	0.088	0.088
3.661	3.81	3.71	3.38	0.18	0.11
3.595	4.36	4.22	3.97	0.156	0.0650
3.458	4.86	4.86	5.18	0.102	0.102
Σ				1.1	

Parameter	Combined exchange
r	−0.97
a	35.82
b	-8.862×10^3
S_Y	1.3
S_X	1.4×10^{-4}
σ_Y	1.2
σ_X	1.4×10^{-4}
$\bar{X}$	3.69×10^{-3}
$S_{Y\|X}$	0.33
$S^2_{Y\|X}$	0.11
σ_a	2.6
σ_b	6.9×10^2

[a] See footnote 2 for depository material.

occurring between a square-planar rhodium atom and a chelating ligand (44).

The fluxionality of the carboxylate-bridged rhodium dimer can be compared to that of six-membered rings; its eight- membered ring may imply that a cyclooctane-like molecule or one of its unsaturated derivatives would be comparable; however, present knowledge points towards the boat–chair conformation of cyclooctane as the dominant form, unlike the hinged form which explains the solution and solid phase of **1**. The use of the unsaturated hydrocarbon cyclooctatetraene as a model for the nonrigidity of **1** is inappropriate on two counts: the paths to ring inversion are not accessible to the dimer and the energy requirements for the paths are much higher than those observed here. One path is that of bond rehybridization (57.3 kJ/mol) (45), and the other proceeds by way of a planar intermediate (≈65.7 kJ/mol), requiring highly strained bond angles in the intermediate. Furthermore, it appears that any possible form of unsaturated cyclooctane would not contain a reasonable facsimile of the fixed carboxylate units present in **1**. It is the rigid nature of the carboxylate group and the stable boat conformation then that beg comparison with a six-membered ring.

Heterocyclic six-membered rings with varying degrees of saturation and substitution have energy barriers to inversion in the range of ~21–46 kJ/mol (46). The acetate complex **4** has an activation barrier in the middle of this range, and the free energy of activation for **1** lies at the high end of this region. Three major factors contribute to the moderate to relatively high inversion barriers. Firstly the carboxylate bridges are not the equivalent of a single bond between the two oxygen atoms in that rotation of the connection between the oxygen atoms is not possible. The rotation must then occur elsewhere in the ring, decreasing the number of different molecular motions that can lead to the inversion. Secondly, oxygen atoms may hinder the rotation of the O—Rh bond by an interaction of the oxygen's *p*-

TABLE 7. Calculated activation parameters with estimated standard deviations in parentheses[a]

	$\Delta H^{\ddagger}$ (kJ/mol)		$\Delta S^{\ddagger}$ (J/mol)		$\Delta G^{\ddagger}$ (kJ/mol)[b]	
	Aliphatic	Olefinic	Aliphatic	Olefinic	Aliphatic	Olefinic
Individual plots	70.8(8.9)	76.6(8.6)	90.0(33.0)	110.6(32.0)	44.5(0.68)	44.4(0.65)
Combined plots	73.7(5.8)	73.7(5.8)	100.3(21.0)	100.3(21.0)	44.4(0.44)	44.4(0.44)

[a]Standard deviations are calculated as follows: (*a*) $\sigma_{\Delta H^{\ddagger}} = \sigma_b \cdot 1.987 \times 10^{-3}$ kJ/mol; (*b*) $\sigma_{\Delta S^{\ddagger}} = \sigma_a \cdot 1.987 \times 10^{-3}$ kJ/mol; (*c*) $\sigma_{\Delta G^{\ddagger}}$: $(\sigma_{\Delta G^{\ddagger}})^2 = (\sigma_{\Delta H^{\ddagger}})^2 + (T \cdot \sigma_{\Delta S^{\ddagger}})^2 - (2T \cdot \sigma_{\Delta H^{\ddagger}} \cdot \sigma_{\Delta S^{\ddagger}})$.
[b]Calculated at 291.8 K.

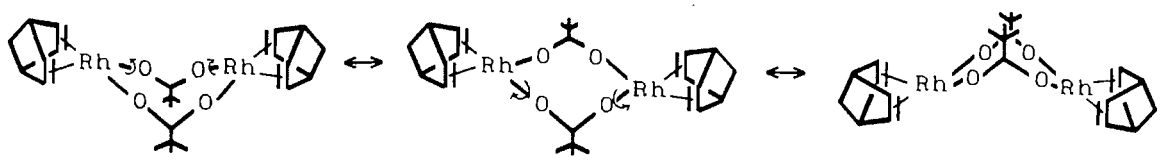

FIG. 5. Proposed mechanism for the exchange of aliphatic and olefinic nbd protons in **1**.

and unoccupied rhodium d_{xz} orbitals; motion through a conformation of this sort would require additional energy to disengage these interactions. Finally, the presence of the bulky *t*-butyl groups force the inversion to take place with the accompanying strain and bond angle deformation expected in the motion of a sterically crowded molecule. The presence of a rhodium–rhodium bond would further increase the barrier; however, the existence of such an interaction is not justifiable from the crystal-structure data.

The predicted transition state is similar to that of the twist-boat form of cyclohexane (47), since we expect the inversion to occur by a sequential progression of the rigid carboxylates from one side of the ring to the other. The transition state here is equivalent to the "chair" form of **1** described as a possible solution structure. If the inversion does not happen sequentially, the transition state would be planar and the energy barrier similar to that of cyclooctatetraene; the difference in activation energies between that of the motion observed here (44.4 kJ/mol) and the planar mechanism of cyclooctatetraene (65.7 kJ/mol) favours the postulated intermediate. It is difficult, if not impossible, to prove the structure of the transition state; however, the form described here does account for the difference in the energy barrier in **1** and **4** as being due to the steric restriction of the motion due to the presence of the *t*-butyl groups; on the other hand, a planar transition state should be relatively unaffected by the bulky groups. (The steric crowding caused by these groups is evidenced in the crystal structures mentioned earlier.) The implied, and most feasible, mechanism for the ring inversion of rhodium–carboxylate dimers can thus be represented by the sequence shown in Fig. 5.

Acknowledgements

We wish to thank the Natural Sciences and Engineering Research Council of Canada and Augustana University College for financial support. We also thank John Stevens for his help in the adaptation of the DNMR4 program.

1. F.A. Cotton, T.R. Felthouse, and S. Klein. Inorg. Chem. **20**, 3037 (1981).
2. B.E. Burnsten and F.A. Cotton. Inorg. Chem. **20**, 3042 (1981).
3. H. Nakatsuji, Y. Onishi, J. Ushio, and T. Yonezawa. Inorg. Chem. **22**, 1623 (1983).
4. R.H. Beer, W.B. Tolman, S.G. Bott, and S.J. Lippard. Inorg. Chem. **30**, 2082 (1991).
5. L. Que Jr. and A.E. True. Prog. Inorg. Chem. **38**, 97 (1990).
6. M.J. Chen and H.M. Feder. Inorg. Chem. **18**, 1864 (1979).
7. F.A. Cotton, F. Barcelo, P. Lahuerta, R. Llusar, J. Paya, and M.A. Ubeda. Inorg. Chem. **27**, 1010 (1988).
8. F.A. Cotton, K.R. Dunbar, and C.T. Eagle. Inorg. Chem. **26**, 4127 (1987).
9. P. Lahuerta, J. Paya, X. Solans, and M.A. Ubeda. Inorg. Chem. **31**, 385 (1992).
10. P. Lahuerta, J. Paya, and A. Bianchi. Inorg. Chem. **31**, 5336 (1992).
11. P. Lahuerta, J. Paya, A. Aguirre, S. Garcia-Granda, and F. Gomez-Beltran. Inorg. Chim. Acta, **192**, 43 (1992).
12. P. Lahuerta, R. Martinez-Manez, J. Paya, E. Peris, and W. Diaz. Inorg. Chim. Acta, **173**, 99 (1990).
13. T.A. Ryan. Coord. Chem. Rev. **57**, 117 (1984).
14. L. Cassar and J. Halpern. Chem. Commun. 1082 (1970).
15. T.G. Shenk, J.M. Downes, C.R.C. Milne, P.B. Mackenzie, H. Boucher, J. Whelan, and B. Bosnich. Inorg. Chem. **24**, 2334 (1985).
16. T.G. Shenk, C.R.C. Milne, J.F. Sawyer, and B. Bosnich. Inorg. Chem. **24**, 2338 (1985).
17. B.R. Sutherland and M. Cowie. Organometallics, **4**, 1637 (1985).
18. B.R. Sutherland and M. Cowie. Organometallics, **4**, 1801 (1985).
19. A.L. Balch. Homogeneous catalysis with metal phosphine complexes. *Edited by* L.H. Pignolet. Plenum Press, New York. 1983. pp. 167–213.
20. E.L. Meutterties, T.N. Rhodin, E. Band, C. Bruker, and W. Pretzer. Chem. Rev. **79**, 91 (1979).
21. C.P. Kubiak and R. Eisenberg. J. Am. Chem. Soc. **99**, 6129 (1977).
22. J.J. Bonnet, P. Kalck, and R. Poilblanc. Inorg. Chem. **16**, 1514 (1977).
23. M.C. Baird. Prog. Inorg. Chem. **9**, 1 (1968).
24. T. Kawamura, K. Fukanachi, T. Sowa, S. Hayashida, and T. Yonezawa. J. Am. Chem. Soc. **103**, 364 (1981).
25. C. Oldham. Prog. Inorg. Chem. **10**, 223 (1968).
26. R.S. Lifsey, X.Q. Lin, M.Y. Chavan, M.Q. Ahsan, K.M. Ashan, and J.L. Bear. Inorg. Chem. **26**, 830 (1987).
27. M.Y. Chavan, T.P. Zhu, X.Q. Lin, M. Ahsan, J.L. Bear, and K.M. Kadish. Inorg. Chem. **23**, 4538 (1984).
28. T.R. Felthouse. Prog. Inorg. Chem. **29**, 73 (1982).
29. M.Q. Ahsan, I. Bernal, and J.L. Bear. Inorg. Chem. **25**, 260 (1986).
30. F.A. Cotton and T.R. Felthouse. Inorg. Chem. **20**, 584 (1981).
31. J. Duncan, T. Malinski, T.P. Zhu, Z.S. Hu, K.M. Kadish, and J.L. Bear. J. Am. Chem. Soc. **104**, 5507 (1982).

Can. J. Chem. Downloaded from www.nrcresearchpress.com by EESC ESCOLA DE ENGENHARIA on 09/08/12
For personal use only.

32. R.G. Brown, R.V. Raghunath, and J.M. Davidson. J. Chem. Soc. Dalton, 176 (1977).
33. J. Powell and T. Jack. Inorg. Chem. **11**, 1039 (1972).
34. E.W. Abel, M.A. Bennett, and G. Wilkinson. J. Chem. Soc. 3178 (1959).
35. G.M. Whitesides and D.W. Lewis. J. Am. Chem. Soc. **92**, 6979 (1970).
36. International tables for X-ray crystallography, Kynoch Press, Birmingham, U.K. (present distributor Kluwer Academic Publishers: Dordrecht, The Netherlands), 1974; Vol. IV. pp. 99–102, 149.
37. W.R. Cullen and E.B. Wickenheiser. J. Organomet. Chem. **370**, 141 (1989).
38. W.R. Cullen, S.J. Rettig, and E.B. Wickenheiser. J. Mol. Catal. **66**, 251 (1991).
39. A.H. Reis Jr., C. Willi, S. Siegel, and B. Tani. Inorg. Chem. **18**, 1859 (1979).
40. M. Herberholt, C.G. Kreiter, and G.O. Wiedersatz. J. Organomet. Chem. **120**, 103 (1976).
41. M. Cocivera, G. Ferguson, F.J. Lalor, and P. Szczencinski. Organometallics, **1**, 1139 (1982).
42. A. Maisonant and R. Poilblanc. Inorg. Chem. Acta, **29**, 203 (1978).
43. J. Sandstrom. Dynamic NMR Spectroscopy. Academic Press, New York. 1982.
44. E.B. Wickenheiser and W.R. Cullen. Inorg. Chem. **29**, 4671 (1990).
45. F.A.L. Anet. J. Am. Chem. Soc. **84**, 671 (1962).
46. J.B. Lambert, H.F. Shurvell, L. Verbit, R.G. Cooks, and G.H. Stout. *In* Organic structural analysis. Macmillan Publishing Co., New York. 1976.
47. F.A.L. Anet and R. Anet. *In* Dynamic nuclear magnetic resonance spectroscopy. *Edited by* L.M. Jackman and F.A. Cotton. Academic Press, New York. 1975.

Can. J. Chem. Downloaded from www.nrcresearchpress.com by EESC ESCOLA DE ENGENHARIA on 09/08/12
For personal use only.

Electron ionization mass spectrometry of aryl- and fluoroalkyl-substituted palladium(II) β-diketonates and monothio-β-diketonates

MARK L.J. REIMER[1] AND JOHN B. WESTMORE[2]

Department of Chemistry, University of Manitoba, Winnipeg, MB R3T 2N2, Canada

AND

MANORANJAN DAS[3]

School of Chemistry, University of New South Wales, P.O. Box 1, Kensington, N.S.W. 2033, Australia

Received August 24, 1993

MARK L.J. REIMER, JOHN B. WESTMORE, and MANORANJAN DAS. Can. J. Chem. **72**, 1302 (1994).

Positive ion electron ionization mass spectra are presented for palladium(II) β-diketonates and monothio-β-diketonates of the general form $Pd^{II}[RC(X)CHC(O)R']_2$, where R = phenyl, 4-methoxyphenyl, 2-thienyl, or 2-naphthyl; R′ = trifluoromethyl, pentafluoroethyl, or *n*-heptafluoropropyl; and X = O or S. The mass spectral behavior is in sharp contrast to that of metals of the first transition series. The spectra of the β-diketonates are dominated by metal-containing ions that arise by migration of the R group from the ligand (L) to palladium, but there is no evidence for fluorine-to-metal transfer. These findings are consistent with HSAB theory. The strong tendency of palladium to form bonds with unsaturated carbon also leads to remarkably abundant metal-containing ions that arise by losses of CO or aryloxy radicals from $[PdRL]^{+\cdot}$ ions. In contrast, in decompositions of ions in the spectra of the monothio-β-diketonates, migration of the R group is suppressed; competition for palladium $d\pi$ electrons by the sulfur donor makes palladium a poorer aryl group acceptor.

MARK L.J. REIMER, JOHN B. WESTMORE et MANORANJAN DAS. Can. J. Chem. **72**, 1302 (1994).

On rapporte les spectres de masse des ions positifs obtenus par ionisation électronique des β-dicétonates et des monothio-β-dicétonates de palladium(II) de formule générale $Pd^{II}[RC(X)CHC(O)R']_2$, dans laquelle R = phényle, 4-méthoxyphényle, 2-thiényle ou 2-naphtyle, R′ = trifluorométhyle, pentafluoroéthyle ou *n*-heptafluoropropyle et X = O ou S. Les spectres de masse font contraste avec ceux des dérivés de la première série de métaux de transition. Les spectres des β-dicétonates sont dominés par les ions contenant des métaux qui se forment par la migration du groupe R du ligand (L) vers le palladium; on n'a pas de données suggérant un transfert de fluor vers le métal. Ces observations sont en accord avec la théorie HSAB. La forte tendance du palladium à former des liaisons avec des carbones insaturés conduit aussi à une quantité importante d'ions contenant un métal qui provient d'une perte de CO ou des radicaux aryloxy par les ions $[PdRL]^{+\cdot}$. Par ailleurs, les spectres de décomposition des ions des monothio-β-dicétonates montrent que la migration du groupe R est supprimée; la compétition du soufre donneur pour les électrons $d\pi$ palladium fait de ce dernier un piètre accepteur du groupe aryle.

[Traduit par la Rédaction]

Introduction

Our recent efforts in characterizing the mass spectral behavior of volatile transition metal chelates under electron ionization (EI) conditions have included the examination of fluorinated β-diketonates and monothio-β-diketonates of cobalt(III) (1) and nickel(II) (2). The mass spectra of these complexes showed interesting differences, which could be attributed to the relative stabilities of the +3, +2, and +1 oxidation states of the metals, and also to the relative acid hardness of the metals in these oxidaion states, according to the Hard and Soft Acid and Base (HSAB) principle (3–6). As well, the HSAB concept can be used to rationalize ion decompositions involving metal–fluorine bond formation on the basis of the specific oxidation state of the metal, and whether it is bound to oxygen or sulfur. Other authors had earlier suggested the usefulness of these approaches (7). Thus, the mass spectra of metal complexes can often be used to draw conclusions about the condensed phase chemistry of the metals. In addition, an understanding of such spectra is useful for characterization of synthesized complexes, and for development of analytical methods.

The chemistry of palladium is significantly different from that of cobalt or nickel, or any other first transition series metal. A number of its features of importance to this paper, drawn from authoritative texts (8, 9), are now summarized. The +2 oxidation state is the most common, though the zero oxidation state is also well known. The +4 state is also well known but is less easily formed. The +1 and +3 states are both very rare. The reluctance of palladium to assume an odd-oxidation state is attributed to the instability associated with an unpaired electron in an outer orbital. This is typical for second and third transition series elements, where even-electron configurations are generally more stable than odd-electron ones (10). In the +2 oxidation state, or lower, palladium is classified as a class "b" metal (11), i.e., as a soft acid (HSAB), so that it forms stronger bonds to sulfur than to oxygen or fluorine. The strong binding preference of palladium(II) for sulfur (and other heavy-atom donors) is due in large part to metal–ligand π-bond overlap of filled metal *d* orbitals with empty *d* orbitals of the heavy atom (ref. 8, p. 165, and ref. 12). Palladium(II) also readily forms σ and π bonds to a wide variety of carbon compounds, especially to alkenes and alkynes (ref. 9, p. 871). We shall show that these characteristics account for some novel features in the mass spectra of the title compounds. Although the mass spectra of several of the palladium(II) β-diketonates have appeared in an earlier communication (13), this study provides the first opportunity for direct comparisons with those of the corresponding palladium(II) monothio-β-diketonates generated under comparable ionizing conditions. We correlate the features of the spectra to the rela-

[1]Present address: Phoenix International Life Sciences Inc., 2330 Cohen Street, Saint-Laurent (Montreal), QC H4R 2N6, Canada

[2]Author to whom correspondence may be addressed. Telephone: (204) 474-9761. Fax: (204) 275-0905. E-mail: westmor@cc.umanitoba.ca

[3]Present address: 9 Golmuri Market, Jamshedpur-3, Bihar, India 831003.

Can. J. Chem. Downloaded from www.nrcresearchpress.com by EESC ESCOLA DE ENGENHARIA on 09/08/12
For personal use only.

Can. J. Chem. Downloaded from www.nrcresearchpress.com by EESC ESCOLA DE ENGENHARIA on 09/08/12
For personal use only.

TABLE 1. The palladium chelates examined and their molar masses

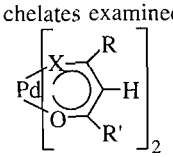

Complex	X	R	R′	M_r (^{106}Pd)
1*a*	O	C_6H_5	CF_3	536
1*b*	S	C_6H_5	CF_3	568
2*a*	O	2-C_4H_3S	CF_3	548
2*b*	S	2-C_4H_3S	CF_3	580
3*b*	S	*p*-$CH_3OC_6H_4$	CF_3	628
4*a*	O	C_6H_5	C_2F_5	636
4*b*	S	C_6H_5	C_2F_5	668
5*a*	O	2-C_4H_3S	C_2F_5	648
5*b*	S	2-C_4H_3S	C_2F_5	680
6*b*	S	2-$C_{10}H_7$	C_2F_5	768
7*a*	O	C_6H_5	*n*-C_3F_7	736
7*b*	S	C_6H_5	*n*-C_3F_7	768
8*a*	O	2-C_4H_3S	*n*-C_3F_7	748
8*b*	S	2-C_4H_3S	*n*-C_3F_7	780
9*b*	S	2-$C_{10}H_7$	*n*-C_3F_7	868

tive stabilities of the metl oxidation states, to the HSAB concept, and to the electronic properties of the ligand donor atoms and of the R and R′ substituents.

The electron ionization (EI) positive ion mass spectra of organic compounds often show an abundant molecular ion ($M^{+\cdot}$), which initially eliminates an odd-electron ($OE^{\cdot}$) neutral species; generally, the resulting ion then loses one or more even-electron (EE^0) neutral species. (An explanation of the symbolism used has been given previously (1).) In the case of transition metal compounds the odd- ($OE^{+\cdot}$) or even-electron (EE^+) character of the metal-containing ion can be altered by a formal change of the oxidation state of the metal (14, 15). For example, we may depict the molecular ion, $[NiL_2]^+$, of a nickel complex either as $[Ni^{II}L_2]^{+\cdot}$ or $[Ni^{III}L_2]^+$ by formal movement of an electron between nickel and the ligand, L. This is a reasonable approach for nickel because, although its +2 state is the usual one, its +3 state is also known (ref. 9, p. 753). In view of the discussion above, in this paper we represent the molecular ion of the palladium complexes as $[PdL_2]^{+\cdot}$ without specifying whether the unpaired electron resides in a molecular orbital based mainly on the metal or on the ligand, even though all of the present ligands contain substituents capable of delocalizing the positive charge and unpaired electron so that it is not therefore necessary to propose a formal +3 state for palladium. Similarly, we represent fragment radical ions without specifying a particular formal oxidation state for palladium, leaving the radical nature of the ion to alert the reader to the considerations discussed here. In the case of even-electron ions that are reasonably d^8 it seems appropriate to represent palladium as Pd^{II}. In the tables we write ion formulae without specifying their odd- or even-electron character, or the oxidation state of the metal.

Table 1 lists the palladium complexes for which the positive ion EI mass spectra were obtained. These are fluorinated β-diketonates and monothio-β-diketonates having the general formula $Pd^{II}(RCXCHCOR')_2$, where R = phenyl, 4-methoxyphenyl, 2-thienyl, or 2-naphthyl; R′ = trifluoromethyl, pentafluoroethyl, or *n*-heptafluoropropyl; and X = O or S. Decompositions of selected collisionally activated ions were studied with the aid of product ion and constant neutral loss spectra acquired under linked scanning conditions.

Experimental

Mass spectrometry

For these studies a VG 7070E-HF double-focusing (EB geometry) mass spectrometer (VG Analytical Ltd., Manchester, England) equipped with a data system based on a DEC PDP-11/73 microcomputer (Digital Equipment Corp., Maynard, Mass.) was used. Samples were admitted to the ion source on a direct insertion probe. In many cases ambient heating from the ion source was sufficient to obtain steady evaporation and reproducible EI mass spectra; in other cases the probe temperature was raised but it never exceeded 100°C. The mass spectra were recorded under the following conditions: ion accelerating voltage, 6 kV; ionizing energy, 70 eV; trap current, 200 μA; source temperature 200°C; scan rate, 1.0 s/decade; resolving power, 1400 (10% valley definition). Ion decomposition mass spectra of selected ions in the spectra of **2***a* and **3***b* were recorded by linked scanning, at a scan rate of 5.0 s/decade, as follows: (*a*) product ion scans at a constant magnetic field/electric field ratio (i.e., *B*/*E* constant with accelerating voltage (*V*) fixed), and (*b*) constant neutral loss scans such that $B[1-(E/E_0)]^{1/2}/E$ was constant, with *V* fixed. Precursor ions were collisionally activated in the first field-free region of the instrument by adjusting the helium pressure in the collision cell to achieve approximately 50% attenuation of the parent ion signal.

Ligand syntheses

The fluorinated β-diketones used in the syntheses of complexes **1***a* and **2***a* were purchased from Aldrich Chemical Co. (Milwaukee, Wis.). The remaining β-diketones were synthesized by a Claisen condensation of the appropriate methyl ketone ($RCOCH_3$) with the fluorinated ethyl ester ($R'COOC_2H_5$), as previously described (16). The fluorinated monothio-β-diketones were synthesized from their corresponding β-diketones (17–20).

Syntheses of palladium chelates

(a) β-Diketonates

A filtered solution of potassium tetrachloropalladate(II) (4.9 mmol; Aldrich) in 50 mL of water was added to a solution of the ligand (9.8 mmol) in ethanol (50 mL). The mixture was digested on a steam bath for 15 min and then cooled in ice water for 1 h. The desired product, obtained as a yellow-green precipitate, was filtered off under suction, washed with water and then with ice-cold absolute alcohol, and air dried (21).

(b) Monothio-β-diketonates

Potassium tetrachloropalladate(II) (4.9 mmol) in water (50 mL) was added to a solution of the ligand (9.8 mmol) in acetone (50 mL). The resulting red/orange precipitate was filtered off under suction and recrystallized from acetone (20, 22, 23).

Results and discussion

Relative abundances of ions in the EI mass spectra (Tables 2 and 4) are quoted for specific *m/z* values; for palladium-containing ions the *m/z* value is listed for the biggest peak within a given group of isotopic peaks observed for a given ion type, and corresponds to those containing ^{106}Pd (natural abundance 27.1%). Thus, the listed abundances of palladium-free ions should be multiplied by 0.271 to find their abundances relative to palladium-containing ions.

Mass spectra of β-diketonates

Table 2 lists the EI mass spectra of the six palladium(II) β-diketonates, while, as representative plots, Figs. 1(*a*) and 1(*b*) show the spectra of **1***a* and **2***a*. All of the spectra show many palladium-containing ions, to which the discussion in this section will be largely confined. Although the base peak corre-

TABLE 2. EI mass spectra, *m/z* (%RA), of β-diketonates of palladium(II)[a]

	Ion/R,R′					
	1*a* C_6H_5, CF_3	**2***a* C_4H_3S, CF_3	**4***a* C_6H_5, C_2F_5	**5***a* C_4H_3S, C_2F_5	**7***a* C_6H_5, C_3F_7	**8***a* C_4H_3S, C_3F_7
$[PdL_2]^+$	536 (68)	548 (42)	636 (51)	648 (44)	736 (42)	748 (33)
$[PdL(L - F)^+$	517 (1.3)					
$[PdL(L - CF_2)]^+$			586 (4.0)	598 (1.4)	686 (1.5)	698 (0.9)
$[PdL(L - R')]^+$	467 (4.3)	479 (2.6)	517 (7.6)	529 (4.9)	567 (6.7)	579 (6.0)
$[PdRL]^+$	398 (9.9)	410 (9.8)	448 (7.3)	460 (8.2)	498 (5.3)	510 (5.5)
$[PdR(L - CO)]^+$	370 (20)	382 (1.4)	420 (12)	432 (1.4)	470 (7.1)	482 (1.2)
$[PdR(L - R')]^+$	329 (2.9)	341 (2.6)	329 (7.3)	341 (6.6)	329 (6.6)	341 (7.4)
$[PdL]^+$	321 (3.0)	327 (1.7)	371 (2.8)	377 (2.7)	421 (2.0)	427 (2.5)
$[Pd(L - H)]^+$	320 (2.8)	326 (2.4)	370 (2.5)	376 (3.1)	420 (1.7)	426 (2.8)
$[Pd(L - O)]^+$	305 (3.2)	311 (34)	355 (1.9)	361 (35)	405 (1.3)	411 (28)
$[Pd(L - CO)]^+$	293 (5.3)	299 (1.9)	343 (4.3)	349 (2.2)	393 (3.6)	399 (2.0)
$[PdR(HCCR')]^+$				333 (5.1)		383 (4.2)
$[PdR(CHR)]^+$	273 (33)	285 (12)	273 (25)	285 (7.2)	273 (19)	285 (5.7)
$[PdL_2]^{2+}$	268 (2.8)	274 (8.6)	318 (4.6)	324 (3.1)	368 (2.0)	374 (2.5)
$[PdR(L - R'CO)]^+$			301 (3.0)	313 (3.1)	301 (3.0)	313 (2.6)
$[PdR_2]^+$		272 (5.5)		272 (7.5)[b]		272 (7.3)
$[Pd(L - H - R')]^+$	251 (9.6)	257 (1.7)	251 (17)	257 (3.2)	251 (18)	257 (3.6)
$[PdRC_2O]^+$	223 (3.4)		223 (5.8)		223 (5.4)	229 (2.0)
$[PdRCO]^+$	211 (3.1)		211 (2.2)		211 (1.9)	
$[Pd(CHR)]^+$	196 (7.5)	202 (4.7)	196 (8.9)	202 (7.8)	196 (10)	202 (7.8)
$[PdRC]^+$	195 (11)	201 (6.1)	195 (13)	201 (9.2)	195 (13)	201 (8.8)
$[PdR]^+$	183 (65)	189 (28)	183 (55)	189 (34)	183 (55)	189 (32)
$[PdCOCH]^+$		147 (4.1)		147 (5.5)		147 (4.5)
$^{108}Pd^{+c}$	108 (6.9)	108 (4.0)	108 (4.8)	108 (4.1)	108 (4.2)	108 (3.2)
HL^+	216 (33)	222 (50)	266 (20)	272 (19)	316 (9.9)	322 (23)
L^+	215 (10)	221 (2.0)	265 (6.7)	271 (1.1)	315 (5.1)	321 (1.7)
$[L - S]^+$				239 (9.4)		289 (8.4)
$[R_2CH]^+$	167 (25)	179 (27)	167 (19)	179 (31)	167 (15)	179 (26)
$[R_2]^+$		166 (15)		166 (15)		166 (12)
$[HL - R']^+$	147 (37)	153 (45)	147 (48)	153 (37)	147 (45)	153 (51)
$[RC_3O]^+$		135 (2.9)		135 (4.0)		135 (3.5)
$[RCOCH]^+$			118 (3.7)		118 (7.3)	124 (5.5)
$[RCO]^+$	105 (100)	111 (100)	105 (100)	111 (100)	105 (100)	111 (100)
$[RCH]^+$	90 (8.9)	96 (4.5)	90 (8.8)	96 (6.9)	90 (10)	96 (7.5)
$[RC]^+$	89 (16)	95 (2.5)	89 (14)		89 (13)	
R^+	77 (90)	83 (24)	77 (79)	83 (20)	77 (70)	83 (17)
$[HL - R']^{2+}$	73.5 (3.5)	76.5 (4.9)	73.5 (3.6)	76.5 (3.5)	73.5 (2.9)	76.5 (4.2)
CF_3^+	69 (60)	69 (77)	69 (67)	69 (56)	69 (57)	69 (65)
Base peak as $\%\Sigma_{50}$	15	19	16	20	18	20

[a]Based on ^{106}Pd for palladium-containing ions.
[b]Estimated from *m/z* 274 peak height (^{108}Pd, 26.7% natural abundance).
[c]Quoted because isotopic contribution from $C_6H_5CO^+$ ion interferes with abundance of ^{106}Pd.

ponds to a palladium-free ion, when isotopic abundances are taken into account the molecular ion, $[PdL_2]^{+\cdot}$, is actually the most abundant ion in each spectrum. Collisionally activated decompositions (CAD) of selected ions generated from **1***a* and **2***a* are summarized in Table 3.

Chart 1 shows proposed fragmentation pathways. Initially, we will limit our discussion to features of the spectra that appear to be peculiar to the present complexes. Many of the more prominent fragment ions are formed by reactions involving migration of the phenyl or 2-thienyl group (R) to Pd. The $[PdRL]^{+\cdot}$ ion, formed from $[PdL_2]^{+\cdot}$ by migration of the R group with elimination of the remainder of the ligand, is a confirmed precursor of the $[PdR(L - CO)]^{+\cdot}$, $[Pd^{II}(L - O)]^+$, $[Pd^{II}R(CHR)]^+$, $[PdR_2]^{+\cdot}$, and $[Pd^{II}R]^+$ ions, and a probable precursor of the $[Pd^{II}R(L - R')]^+$ ion. The formation of $[PdRL]^{+\cdot}$ from $[PdL_2]^{+\cdot}$ parallels the formation of $[Met^{III}RL]^+$ from $[Met^{III}L_2]^+$ (Met = Co or Ni, R = aryl, R′ = CF_3 (1, 2)). However, its subsequent decompositions exhibit a number of new features.

The $[PdRL]^{+\cdot}$ ion eliminates CO (confirmed for **1***a* and **2***a* by linked-scanning results) to give a fragment ion that is much more prominent in the spectra of phenyl-containing complexes (**1***a*, **4***a*, **7***a*) than of 2-thienyl-containing complexes (**2***a*, **5***a*, **8***a*), an observation to which we shall return. A similar elimination of CO is observed in the fragmentation $[Pd^{II}L]^+ \rightarrow [Pd^{II}(L - CO)]^+$. This unusually prominent decomposition, which is not a significant feature of the corresponding complexes of cobalt or nickel, is, presumably, a feature of the electronic properties of palladium(II). Bearing this in mind, a number of competing fragmentation mechanisms can be proposed. Three possibilities, shown in Scheme 1, are based on the following guidelines: (*a*) according to the HSAB principle,

Can. J. Chem. Downloaded from www.nrcresearchpress.com by EESC ESCOLA DE ENGENHARIA on 09/08/12
For personal use only.

Can. J. Chem. Downloaded from www.nrcresearchpress.com by EESC ESCOLA DE ENGENHARIA on 09/08/12
For personal use only.

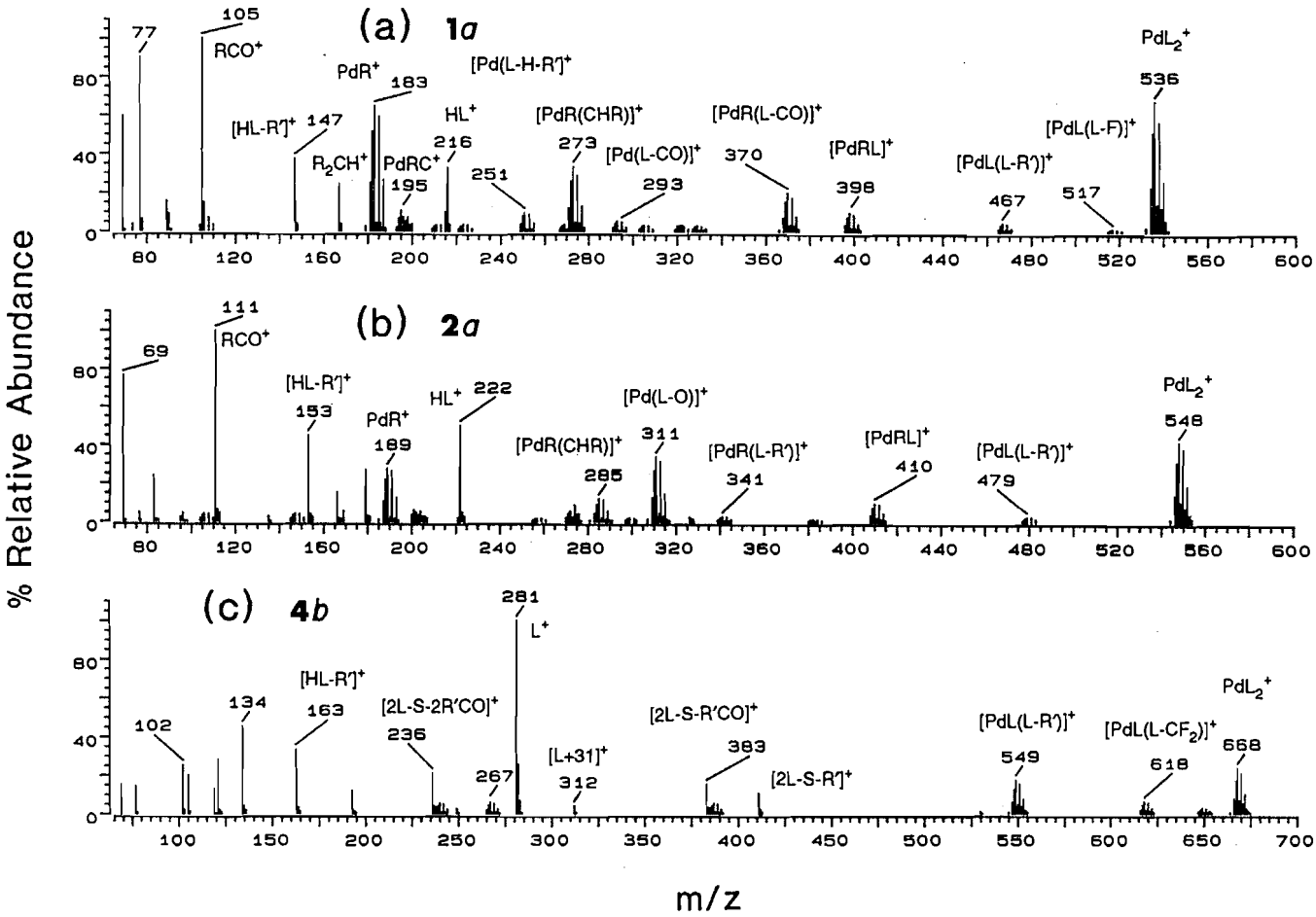

FIG. 1. EI mass spectra of (a) bis(1,1,1-trifluoro-4-phenyl-2,4-butanedionato)palladium(II), **1***a*; (b) bis(1,1,1-trifluoro-4-(2-thienyl)- 2,4-butanedionato)palladium(II), **2***a*; (c) bis(1,1,1,2,2-pentafluoro-5- mercapto-5-phenyl-pent-4-en-3-onato)palladium(II), **4***b*.

TABLE 3. Collisionally activated ion decompositions

(*a*) Product ion spectra

Parent ion (*m/z*)		Product ions (*m/z*)
1*a*	398	370, 305, 273, 195, 183, 167
	370	273, 195, 183, 167
	321	293, 215, 183
2*a*	548	479, 410, 341, 327, 326, 311, 257, 179, 166, 111
	410	382, 311, 285, 272, 189, 179, 166, 111
	327	299
3*b*	628	559, 367, 261
	367	270, 213, 164

(*b*) Constant neutral loss spectrum

Neutral lost		Parent ion (*m/z*)
3*b*	97 u	490, 393, 367

migration of hard F to soft Pd^{II} is not expected, even though Pd—F bonds are known in the chemistry of palladium(II) (supporting this, the mass spectra show no evidence of fragment ions that *must* contain Pt—F bonds), and (*b*) the known tendency of palladium to form bonds to carbon, especially to unsaturated carbon (ref. 9, p. 871), as illustrated by the presence of ions such as $[PdR_2]^{+\cdot}$, $[Pd^{II}R]^+$, and $[Pd^{II}R(CHR)]^+$ in the mass spectra. Since the mass spectra contain no evidence regarding which CO group is eliminated, mechanisms in which either CO group can be lost are presented. In mechanism (a), the perfluoroalkyl substituent migrates to the central carbon atom, accompanied by extrusion of the included CO group. The resulting ion, by migration of the phenyl group to palladium, would readily eliminate a substituted ketene to give $[PdR_2]^{+\cdot}$, as shown. However, CAD/linked-scanning for **1***a* did not provide support for the latter step; the only confirmed precursor of $[PdR_2]^{+\cdot}$ is $[PdRL]^{+\cdot}$. Hence, while mechanism (a) cannot be excluded, its occurrence remains in doubt. Therefore, we make alternative proposals, in which the phenyl group migrates to the central carbon atom, accompanied by elimination of CO, either preceding (mechanism (b)) or following (mechanism (c)) formation of a bond between palladium and the central carbon atom. The resulting ion, by elimination of R'CO$^{\cdot}$, supported for **1***a* by CAD/linked-scanning, gives rise to $[Pd^{II}R(CHR)]^+$, a major ion species, especially for phenyl-substituted complexes. While the details of mechanisms (b) and (c) are uncertain, the formation of a tropylium ion structure for the product ion is attractive. The tropylium ion structure might also be present in $[Pd(CHR)]^{+\cdot}$, a further fragment ion observed for all complexes.

Table 2 shows that, among the phenyl-containing complexes, the relative abundances of the $[PdR(L - CO)]^{+\cdot}$ ions vary con-

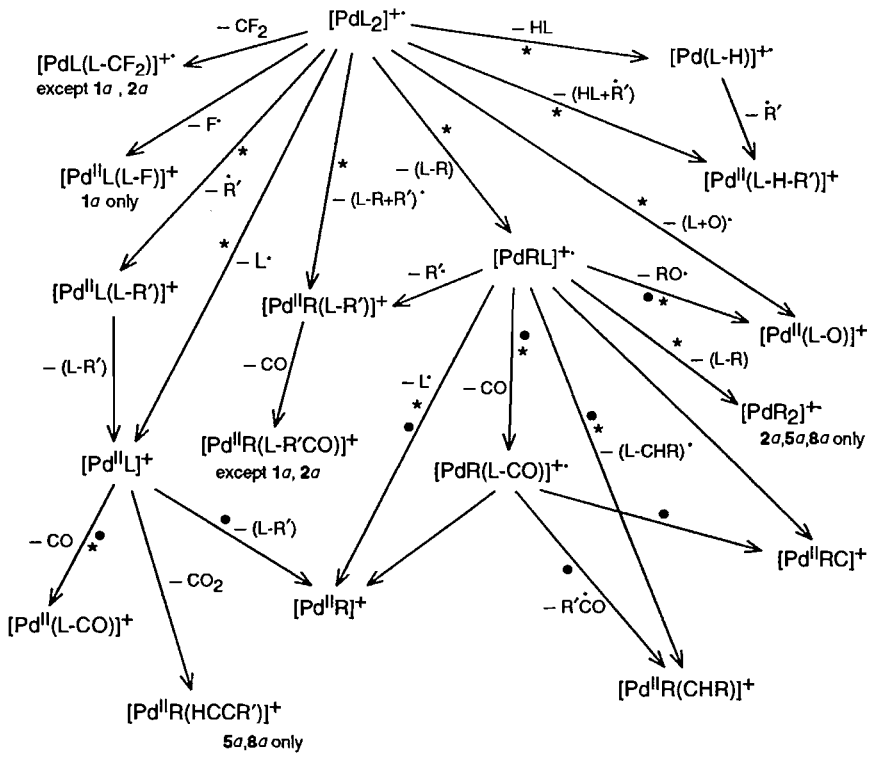

CHART 1. Fragmentation pathways proposed for β-diketonates. Fragment ions are common to all complexes, except where noted.

siderably, decreasing in the order **1***a* > **4***a* > **7***a*. This trend is consistent with the mechanisms of Scheme 1 since conformational/steric factors would become increasingly restrictive with increasing bulk of the perfluoroalkyl group.

The low abundances of the $[PdR(L - CO)]^{+\cdot}$ and $[Pd^{II}R(CHR)]^{+}$ ions for 2-thienyl-substituted complexes suggest that other decomposition channels are favored for these complexes; suitable candidates are those leading to formation of the $[PdR_2]^{+\cdot}$ and $[Pd^{II}(L - O)]^{+}$ ions, which are strongly favored for 2-thienyl-substituted over phenyl-substituted complexes. Rationales for these channels now follow.

The $[PdR_2]^{+\cdot}$ ion is observed only when R = 2-thienyl; recalling the introductory discussion, we can represent this ion by the canonical forms $[Pd^{II}R_2]^{+\cdot}$ and $[Pd^{III}R_2]^{+}$. The latter presumably makes a minor contribution because it is evident that the 2-thienyl group is better able to stabilize the $OE^{+\cdot}$ ion, perhaps as illustrated in Scheme 2. Of the many canonical forms that can be written when R is 2-thienyl, those involving Pd^{II} would be reponsible for the high stability of this species. On the other hand, the $[Pd^{II}R]^{+}$ ion is prominent in the mass spectra of all phenyl- and 2-thienyl-containing β-diketonates, to give an EE^{+} ion with palladium in its natural +2 oxidation state.

The EI mass spectra of all complexes exhibit ions that can only be assigned as $[Pd^{II}(L - O)]^{+}$. These ions are prominent for β-diketonates with a 2-thienyl substituent (**2***a*, **5***a*, and **8***a*) but are also observed, at lower abundance, when R = phenyl. The CAD/product ion spectra of ions generated from **2***a* (Table 3) indicate that both $[PdRL]^{+\cdot}$ and $[PdL_2]^{+\cdot}$ are precursors of this ion. Since the latter may be an indirect precursor, we propose a decomposition of $[PdRL]^{+\cdot}$ by a fragmentation mechanism involving elimination of RO· and leading to a stable product ion (shown in Scheme 3 for R = 2-thienyl). The extraordinary abundance of this species for the 2-thienyl-substituted complexes may be attributed to the resonance stabilization afforded by the lone pair of electrons on the sulfur of the 2-thienyl group. Similarly, the appearance of an abundant "$[PdL - 16]^{+\cdot}$" ion in the mass spectrum of bis(1,1,1-trifluoro-4-(2-furyl)-2,4-butanedionato)Pd(II) (13) reinforces the importance of a substituent-based, heteroatom lone pair in the formation of $Pd^{II}(L - O)]^{+}$.

The formation of $[Pd(L - H)]^{+\cdot}$ from $[PdL_2]^{+\cdot}$ involves the intramolecular transfer of hydrogen into the eliminated ligand, resulting in the expulsion of the neutral product HL. Earlier (2), we discussed mechanisms for this decomposition in which the transferred hydrogen originates either from the central carbon of the ligand or from the aryl substituent. In the present spectra, two pieces of evidence suggest that hydrogen is transferred from the central position: (*a*) by analogy with the earlier work, transfer from the aryl group would be favored by an increase in palladium oxidation state to +3; this does not readily occur, and (*b*) the observation of prominant $[Pd^{II}(L - H - R')]^{+}$ ions suggests that $[Pd(L - H)]^{+\cdot}$ readily eliminates the (OE˙) neutral species R′˙. These observations are consistent with the mechanisms shown in Scheme 4.

Low abundance, but mechanistically significant, ions are observed for loss of CF_2 from $[PdL_2]^{+\cdot}$ when R′ = C_2F_5 or *n*-C_3F_7. For fluorinated β-diketonate complexes of many metals this loss has been attributed to decompositions resembling mechanism (a) in Scheme 5. Support for migration of fluorine to the metal in such cases was given by the observation of fragment ions, and eliminated neutral species, that *had* to contain metal–fluorine bonds (1, 2, 24, 25). This mechanism probably

Can. J. Chem. Downloaded from www.nrcresearchpress.com by EESC ESCOLA DE ENGENHARIA on 09/08/12
For personal use only.

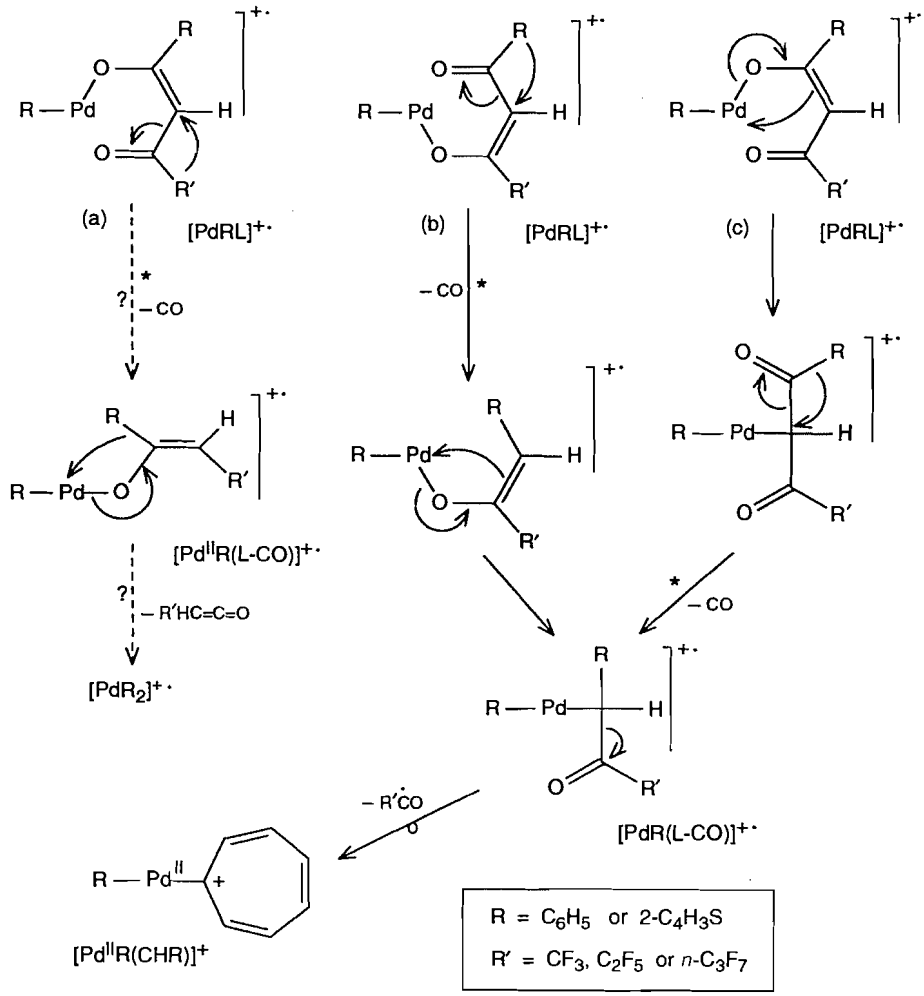

SCHEME 1

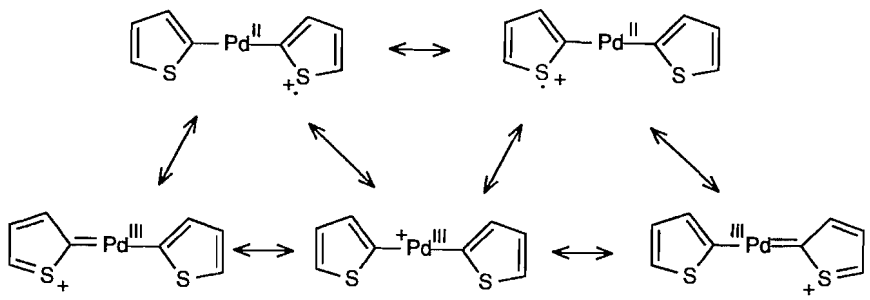

SCHEME 2

does not operate for the current complexes for we have noted above that palladium is reluctant to form bonds to fluorine, and to adopt the +3 oxidation state. Also, experimentally, we find no evidence for formation of Pd—F bonds. We therefore propose mechanism (b) in Scheme 5 as an alternative to mechanism (a), in which F (when R′ = C_2F_5) or CF_3 (when R′ = *n*-C_3F_7) migrates to the central carbon atom. (If CF_3 migration does not occur then more extensive fluorine rearrangement is required.)

The $[Pd^{II}R(HCCR')]^+$ ions formed when R = C_4H_3S (**5***a* and **8***a* only) could occur by elimination of CO_2 from $[Pd^{II}L]^+$, as shown in mechanism (a) of Scheme 6. After initial migration of the 2-thienyl substituent to palladium, to yield an acylium ion, the bond rearrangements shown lead to formation of a bond between palladium and unsaturated carbon, and elimination of CO_2. This mechanism is very similar to that proposed (26, 27) for elimination of CO_2 from the $[MetL(L - CF_3)]^+$ acylium ion in the mass spectra of aryl-substituted trifluoro-β-diketonates of iron and cobalt (mechanism (b)) but differs in the way by which the product ion is stabilized. For the iron and cobalt complexes it was suggested that stabilization of the vinyl cation by the aromatic group was necessary to explain the non-occurrence of such ions in the absence of the aromatic group. In the case of palladium we propose that migration of the 2-thienyl substituent to palladium (for which the spectra provide ample support) leads to the required acylium ion intermediate and that the driving force for the decomposition is formation of the bond between palladium and unsaturated carbon. The resulting ion would be stabilized by back-bonding from

Can. J. Chem. Downloaded from www.nrcresearchpress.com by EESC ESCOLA DE ENGENHARIA on 09/08/12
For personal use only.

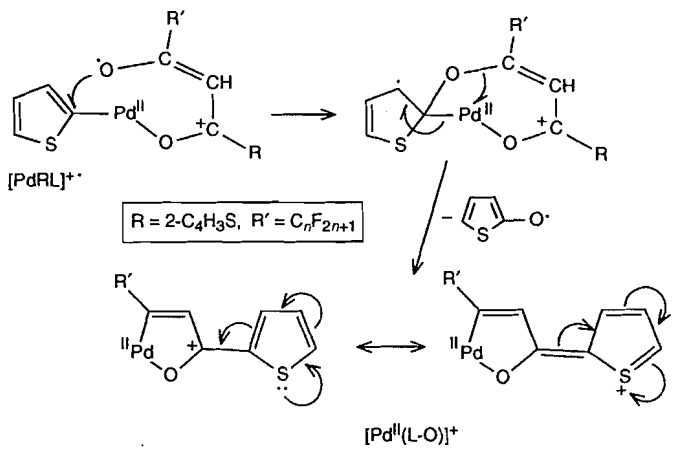

SCHEME 3

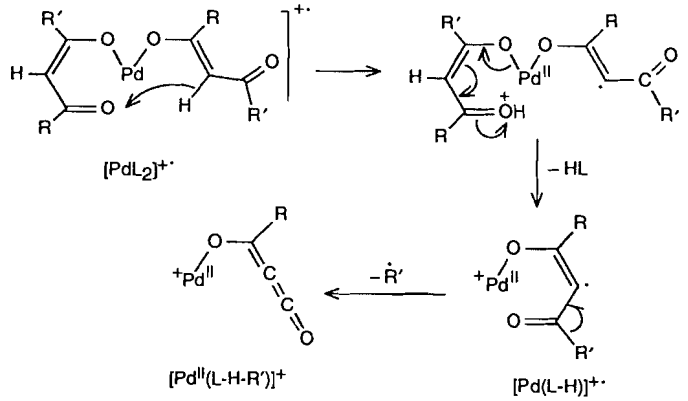

SCHEME 4

occupied palladium d/π orbitals into vacant π^* orbitals on the unsaturated group.

Many of the remaining fragment ions in the spectra can be accounted for by straightforward eliminations of the OE· species F·, R′·, and L· from $[PdL_2]^{+\cdot}$ to yield $[Pd^{II}L(L - F)]^+$, $[Pd^{II}L(L - R')]^+$, and $[Pd^{II}L]^+$, respectively, and by loss of R′CO· (or a two-step loss of R′· and CO) from $[PdRL]^{+\cdot}$ to give $[Pd^{II}R(L - R'CO)]^+$. There are also a number of lighter fragment ions, of uncertain origin, containing Pd—C bonds.

Finally, Table 2 shows data supporting formation of L^+ from

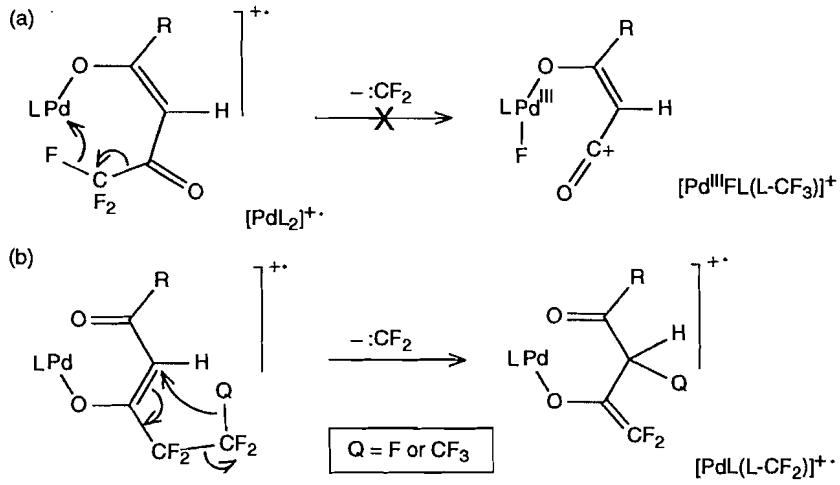

SCHEME 5

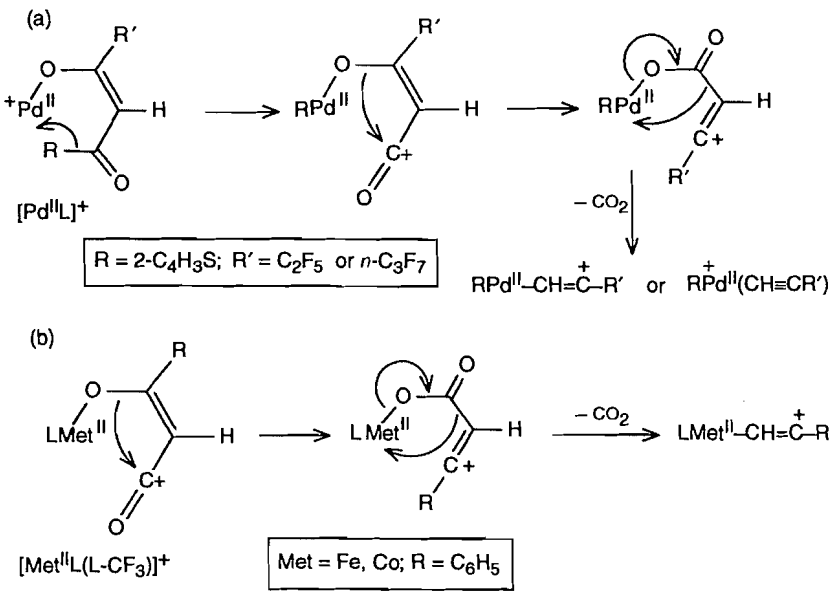

SCHEME 6

Can. J. Chem. Downloaded from www.nrcresearchpress.com by EESC ESCOLA DE ENGENHARIA on 09/08/12
For personal use only.

TABLE 4. EI mass spectra, *m/z* (%RA), of monothio-β-diketonates of palladium(II)

	Ion/R,R′								
	1*b* C_6H_5, CF_3	**2***b* C_4H_3S, CF_3	**3***b* $CH_3OC_6H_4$, CF_3	**4***b* C_6H_5, C_2F_5	**5***b* C_4H_3S, C_2F_5	**6***b* $C_{10}H_7$, C_2F_5	**7***b* C_6H_5, C_3F_7	**8***b* C_4H_3S, C_3F_7	**9***b* $C_{10}H_7$, C_3H_7
$[PdL_2]^+$	568 (20)	580 (14)	628 (17)	668 (24)	680 (27)	768 (13)	768 (23)	780 (8.9)	868 (23)
$[PdL(L - F)]^+$				649 (2.8)	661 (1.2)	749 (1.5)	749 (1.6)	761 (2.6)	849 (0.6)
$[PdL(L - S)]^+$							736 (0.9)	748 (1.1)	
$[PdL(L - CF_2)]^+$				618 (6.3)	630 (3.5)	718 (2.6)	718 (1.2)	730 (1.1)	818 (1.6)
$[PdL(L - C_2F_4)]^+$					580 (1.2)				
$[PdL(L - R')]^+$	499 (4.6)	511 (4.5)	559 (2.2)	549 (18)	561 (12)	649 (6.2)	599 (11)	611 (8.1)	699 (11)
$[PdL]^+$	337 (3.2)	343 (2.4)	367 (3.8)	387 (5.4)	393 (3.5)	437 (4.3)	437 (5.1)	443 (3.8)	487 (4.8)
$[Pd(L - S)]^+$							405 (2.9)	411 (1.1)	
$[Pd(L - H - R')]^+$	267 (3.8)	273 (2.1)	297 (3.5)	267 (5.8)	273 (3.5)	317 (3.5)	267 (8.7)	273 (4.9)	317 (4.2)
$[PdSC(R)CH]^+$	240 (4.1)	246 (3.3)	270 (2.5)	240 (5.4)	246 (5.2)	290 (4.1)	240 (7.3)	246 (7.0)	290 (4.3)
$[Pd(HCCR)]^+$	208 (1.4)	214 (1.7)			214 (2.4)	258 (2.4)	208 (2.7)	214 (4.1)	258 (2.6)
$[PdR]^+$	183 (2.0)		213 (0.8)						
$[2L - S]^+$		442 (1.6)	490 (2.8)	530 (1.3)	542 (6.0)	630 (9.0)	630 (1.2)	642 (9.8)	730 (7.5)
$[2L - S - R']^+$				411 (11)	423 (2.3)	511 (2.7)	461 (4.9)	473 (2.2)	561 (3.2)
$[2L - S - R'CO]^+$		345 (4.5)	393 (6.5)	383 (15)	395 (14)	483 (17)	433 (8.0)	445 (15)	533 (17)
$[L + 31]^+$				312 (3.9)	318 (6.4)	362 (2.7)	362 (2.2)	368 (9.1)	412 (1.2)
$[2L - S - 2R'CO]^+$		248 (8.3)	296 (17)	236 (21)	248 (39)	336 (40)			336 (41)
HL^+	232 (18)	238 (22)	262 (36)	282 (26)	288 (9.3)	332 (24)	332 (23)	338 (13)	382 (42)
L^+	231 (100)	237 (58)	261 (100)	281 (100)	287 (68)	331 (100)	331 (100)	337 (58)	381 (100)
$[L - S]^+$		205 (100)	229 (12)	249 (2.6)	255 (100)	299 (12)	299 (1.7)	305 (100)	349 (12)
$[R + 116]^+$				193 (12)	199 (15)	243 (5.8)	193 (6.1)	199 (20)	243 (3.3)
$[HL - R']^+$	163 (6.0)	169 (11)	193 (18)	163 (34)	169 (24)	213 (33)	163 (18)	169 (32)	213 (32)
$[L - S - CF_2]^+$	149 (5.5)	155 (13)	179 (21)						
$[R(C_2S)H]^+$	134 (30)	140 (23)	164 (28)	134 (45)	140 (36)	184 (72)	134 (53)	140 (45)	184 (67)
$[RC_3O]^+$	129 (4.1)	135 (3.9)	159 (6.0)						179 (10)
$[RCS]^+$	121 (8.0)	127 (16)	151 (19)	121 (28)	127 (27)	171 (27)	121 (18)	127 (27)	171 (26)
$[RCO]^+$	105 (4.7)	111 (4.6)	135 (7.5)	105 (20)	111 (8.6)	155 (16)	105 (12)	111 (6.9)	155 (11)
$[RCCH]^+$	102 (5.2)	108 (18)	132 (22)	102 (26)	108 (42)	152 (96)	102 (14)	108 (37)	152 (82)
$[RCH_2]^+$	91 (3.2)	97 (6.3)	121 (8.8)	91 (4.2)	97 (8.8)	141 (3.3)	91 (2.5)	97 (6.8)	141 (6.0)
$[RCH]^+$	90 (2.3)	96 (6.7)		90 (2.5)	96 (5.4)	140 (2.9)	90 (4.3)	96 (7.0)	140 (3.6)
R^+	77 (5.8)	83 (6.8)		77 (14)	83 (15)	127 (14)	77 (7.5)	83 (4.7)	127 (9.7)
R'^+	69 (4.1)	69 (22)	69 (7.5)	119 (13)	119 (10)	119 (3.1)			
CF_3^+				69 (15)	69 (27)	69 (9.9)	69 (11)	69 (24)	69 (10)
Base peak as $\%\Sigma_{50}$	42	28	29	22	19	19	28	22	19

$[Pd^{II}L]^+$ and $[PdRL]^{+\cdot}$ precursors (not shown in Chart 1), indicating that thermal decomposition, while it cannot be ruled out to a minor extent, is probably not a significant feature of the spectra. Also not shown in Chart 1 are decompositions of $[PdRL]^{+\cdot}$ and $[PdR(L - CO)]^{+\cdot}$ to the prominent palladium-free ion $[R_2CH]^+$. While the formation mechanisms involved are obscure, the prominence of the latter ion suggests that it has a tropylium ion structure, [R—trop]$^+$.

Pd(II) monothio-β-diketonates

Table 4 lists EI mass spectra of the nine monothio-β-diketonates, while, as a representative plot, Fig. 1(*c*) shows the mass spectrum of **4***b*. Compared to the mass spectra of the corresponding β-diketonates, there are fewer palladium-containing ions and their relative abundances are lower. Notably absent are ions resulting by migration of the aryl substituent to palladium. Table 3 gives CAD/linked-scanning results for selected ions generated from **3***b*. Chart 3 shows proposed fragmentation pathways. In the following paragraphs, attention is drawn mainly to contrasts between the palladium-containing ion sin the spectra of the monothio-β-diketonates and β-diketonates, but we also discuss the formation of some unusual palladium-free ions.

Palladium-containing ions

The minor loss of elemental sulfur, observed in the cases of **7***b* and **8***b* (R′ = *n*-C_3F_7) in the decomposition $[PdL_2]^{+\cdot} \rightarrow [PdL(L - S)]^{+\cdot}$ and (possibly) $[Pd^{II}L]^+ \rightarrow [Pd^{II}(L - S)]^+$, is noteworthy. This shows that, although Pd—O bond scission would be expected to occur more readily, Pd—S scission does occur to a limited extent; subsequent elimination of a sulfur atom may be promoted by Pd—C bond formation.

The $[Pd^{II}R]^+$ ion appears as a minor species in the spectra of **1***b* and **3***b*, in marked contrast to its predominance in the β-diketonate spectra. In fact, this ion is the only evidence given by the spectra for aryl group migration to Pd. Thus, the sulfur atoms reduce the ability of palladium to act as an aryl group acceptor. Above, we have noted the tendency of palladium(II) to back-bond to sulfur. Consequently, the ability of palladium to back-bond to an aryl group would be decreased when it is already engaged in back-bonding to sulfur. Only when the Pd—S bonds are not longer present does bond formation between palladium and an aryl group occur.

The $[PdSC(R)CH]^{+\cdot}$ ion would be formed most readily from $[Pd^{II}L]^+$ by loss of R′CO$^{\cdot}$. Its analogue is also observed in the mass spectra of cobalt(III) and nickel(II) monothio-β-dike-

Can. J. Chem. Downloaded from www.nrcresearchpress.com by EESC ESCOLA DE ENGENHARIA on 09/08/12
For personal use only.

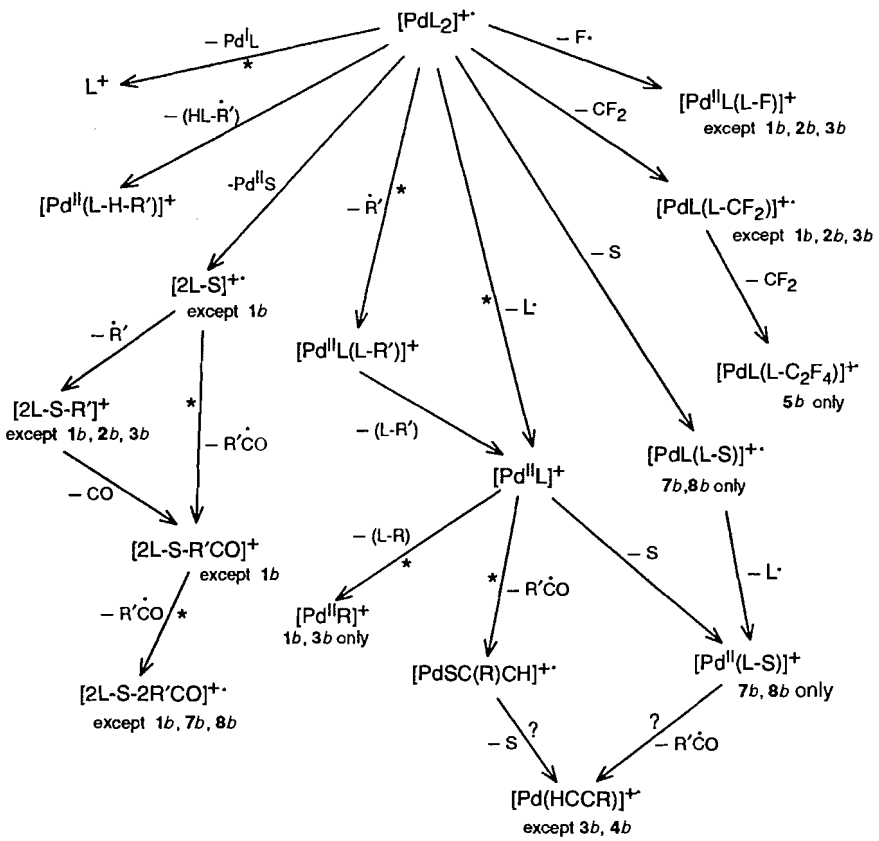

* decomposition supported by CAD/linked scanning for **3***b*

CHART 2. Fragmentation pathways proposed for monothio-β-diketonates. Fragment ions are common to all complexes, except where noted.

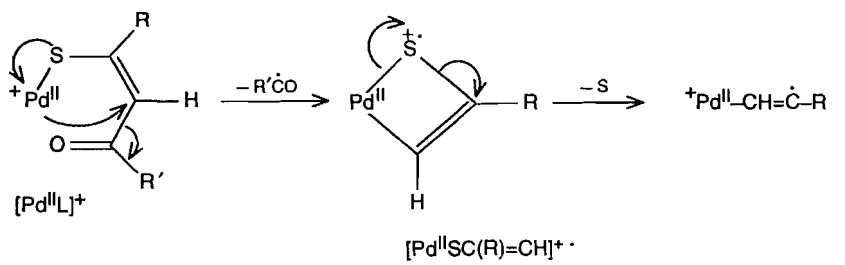

SCHEME 7

tonates (1, 2). For such complexes the decomposition would result in a formal reduction of the metal to its +1 oxidation state. Since this oxidation state is not favored in palladium complexes, we propose the alternative mechanism shown in Scheme 7 for this decomposition. Because elimination of the $OE^{+\cdot}$ fragment R′CO· from the EE^+ ion $[Pd^{II}L]^+$ should not be a favored process, the decomposition may be assisted by Pd—C bond formation, as shown. The sequence of bond reorganizations differs from a similar mechanism proposed earlier for decomposition of analogous platinum complexes (23). By loss of S the $[PdSC(R)CH]^{+\cdot}$ ion would yield $[PdCHCR]^{+\cdot}$.

The $[Pd^{II}(L - H - R')]^+$ ion, here observed for all monothio-β-diketonates, was also observed in the mass spectrum of bis(1,1,1-trifluoro-4-mercapto-4-(2-naphthyl)-but-3-en-2-onato)Pt(II) (28), but was not reported for the analogous palladium(II) complexes (23, 28). For its formation we propose the mechanism already shown in Scheme 4.

Palladium-free ions

With the exception of **1***b*, all of the monothio-β-diketonates exhibit metal-free ions at *m/z* values greater than $[L]^+$. Initially, loss of $Pd^{II}S$ from $[PdL_2]^{+\cdot}$ forms $[2L - S]^{+\cdot}$, which then loses R′·, CO, and R′CO· to form $[2L - S - R']^+$, $[2L - S - R'CO]^+$, and $[2L - S - 2R'CO]^{+\cdot}$. Except for minor details, the mechanisms shown in Scheme 8 are similar to those described for corresponding decompositions observed for chelates of 1,1,1-trifluoro-4-mercapto-4-(2-naphthyl)-but-3-en-2-one formed with Ni, Pd, Pt, Fe, Ru, Co, and Rh metal ions (28).

Conclusions

There are significant differences between the mass spectra of the β-diketonates and monothio-β-diketonates. The mass spectra of the former are dominated by ion decompositions in which the aryl or thienyl group migrates to palladium. In the mass spectra of the latter, migration of such groups is suppressed

Can. J. Chem. Downloaded from www.nrcresearchpress.com by EESC ESCOLA DE ENGENHARIA on 09/08/12
For personal use only.

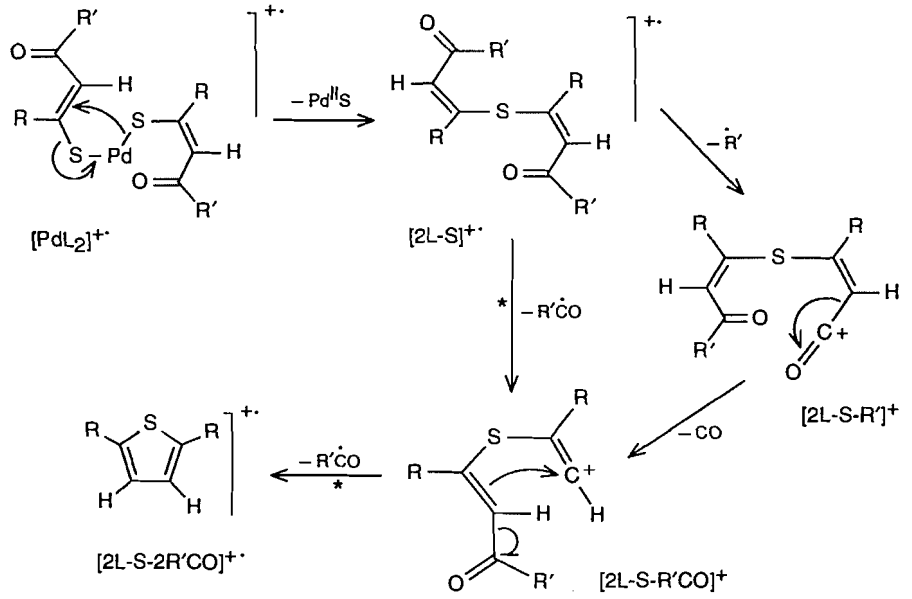

SCHEME 8

because competition for $d\pi$ electrons by sulfur makes palladium a poorer aryl group acceptor. The reluctance of palladium(II) to undergo valency changes, together with the characteristic electronic properties, as discussed, gives rise to some remarkably prominent ions, thus leading to mass spectra that differ considerably from those of the corresponding complexes of first transition series metals.

Acknowledgements

We thank Mr. Wayne Buchannon for his assistance in the operation and maintenance of the mass spectrometer and the Natural Sciences and Engineering Research Council of Canada (NSERC) for financial support. We also thank NSERC and the University of Manitoba for grants to purchase the mass spectrometer.

1. M.L.J. Reimer, J.B. Westmore, and M. Das. Can. J. Chem. **70**, 952 (1992).
2. M.L.J. Reimer, J.B. Westmore, and M. Das. Can. J. Chem. **71**, 1450 (1993).
3. R.G. Pearson. J. Am. Chem. Soc. **85**, 3533 (1963).
4. R.G. Pearson. Science, **151**, 172 (1966).
5. R.G. Pearson. Chem. Br. **3**, 103 (1967).
6. R.G. Pearson. J. Chem. Educ. **45**, 581 (1968).
7. J.M. Miller and G.L. Wilson. Adv. Inorg. Chem. Radiochem. **18**, 229 (1976).
8. F.R. Hartley. The chemistry of platinum and palladium. Applied Science Publishers Ltd., Barking, England. 1965. pp. 13–21.
9. F.A. Cotton and G. Wilkinson. Advanced inorganic chemistry. 5th ed. Wiley, New York. 1988. pp. 917–932.
10. C.S.G. Phillips and R.J.P. Williams. Inorganic chemistry. Vol. 2. Oxford, England. 1966. p. 294.
11. S. Ahrland, J. Chatt, and N.R. Davies. Q. Rev. **12**, 265 (1958).
12. F.A. Cotton and G. Wilkinson. Advanced inorganic chemistry. 4th ed. Wiley, New York. 1980. p. 950.
13. M. Das. Inorg. Chim. Acta, **76**, L111 (1983).
14. J.S. Shannon and J.M. Swan. Chem. Commun. 33 (1965).
15. M.J. Lacey and J.S. Shannon. Org. Mass Spectrom. **6**, 931 (1972).
16. M. Das. Transition Met. Chem. (London), **5**, 17 (1980).
17. M. Das and S.E. Livingstone. Org. Mass Spectrom. **9**, 781 (1974).
18. R.K.Y. Ho and S.E. Livingstone. Aust. J. Chem. **21**, 1781 (1968).
19. M. Das. Inorg. Chim. Acta, **36**, 79 (1979).
20. M. Das. Inorg. Chim. Acta, **48**, 33 (1981).
21. D.T. Haworth, M.R. Pitluck, B.D. Pollard, and M. Das. Synth. React. Inorg. Met.-Org. Chem. **13**, 601 (1983).
22. M. Das and S.E. Livingstone. J. Chem. Soc. Dalton Trans. 662 (1977).
23. M. Das and S.E. Livingstone. Aust. J. Chem. **27**, 749 (1974).
24. A.L. Clobes, M.L. Morris, and R.D. Koob. J. Am. Chem. Soc. **91**, 3087 (1969).
25. C. Reichert, G.M. Bancroft, and J.B. Westmore. Can. J. Chem. **48**, 1362 (1970).
26. A.L. Clobes, M.L. Morris, and R.D. Koob. Org. Mass Spectrom. **5**, 633 (1971).
27. A.L. Clobes, M.L. Morris, and R.D. Koob. Org. Mass Spectrom. **3**, 1255 (1970).
28. S.E. Livingstone and D.S. Moore. Aust. J. Chem. **29**, 283 (1976).

Can. J. Chem. Downloaded from www.nrcresearchpress.com by EESC ESCOLA DE ENGENHARIA on 09/08/12
For personal use only.

Total asymmetric syntheses of (1*S*,2*S*)-norcoronamic acid, and of (1*R*,2*R*)- and (1*S*,2*S*)-coronamic acids from the diastereoselective cyclization of 2-(*N*-benzylideneamino)-4-chlorobutyronitriles[1]

ANNE GAUCHER, JEAN OLLIVIER, JACQUELINE MARGUERITE, RENÉE PAUGAM, AND JACQUES SALAÜN[2]

Laboratoire des carbocycles (associé un Centre national de la recherche scientifique), Institut de chimie moléculaire d'Orsay, Bât. 420, Université de Paris-Sud, 91405 Orsay, France

Received July 19, 1993

ANNE GAUCHER, JEAN OLLIVIER, JACQUELINE MARGUERITE, RENÉE PAUGAM, and JACQUES SALAÜN. Can. J. Chem. **72**, 1312 (1994).

(3*R*)-2-(*N*-Benzylideneamino)-4-chloro-3-methylbutyronitrile **3**, prepared from the commercially available methyl (2*S*)-3-hydroxy-2-methyl propionate **5** (96% ee), readily underwent potassium carbonate induced cyclization to provide, after acid hydrolysis (6 N HCl) and chromatography, the (1*S*,2*S*)-norcoronamic acid **1***a* with 88% diastereoselectivity and >95% enantiomeric excess. From (2*R*)-2-(hydroxymethyl)butyl acetate **23** (>88% ee) obtained by enzymatic enantioselective hydrolysis with lipase PS, was prepared the (3*S*)-2-(*N*-benzylideneamino)-3-(chloromethyl)valeronitrile **29**, which after base-induced cyclization (K_2CO_3) and acid (6 N HCl) or basic (0.8 N NaOH) hydrolysis led to the non-natural (1*R*,2*R*)-coronamic acid **18** (>88% ee). Also from this same acetate (2*R*)-**23** was prepared the (3*R*)-3-(chloromethyl)-2-[(diphenylmethylene)amino]pentanenitrile **37**, which provided the (1*S*,2*S*)-coronamic acid **17** (>88% ee) after base-induced cyclization (K_2CO_3 or LDA) and acid hydrolysis (6 N HCl). It is noteworthy that these short synthetic sequences, which do not require any expensive chiral auxiliary or optically active precursors, do not alter the enantiomeric purity of the stereogenic centers of these 2,3-methanoamino acids. However, the *E* diastereoselectivity of these cyclizations was not improved by using bulky *N*-(diphenylmethylene)amino substituent, contrary to results of some molecular mechanic calculations (MAD).

ANNE GAUCHER, JEAN OLLIVIER, JACQUELINE MARGUERITE, RENÉE PAUGAM et JACQUES SALAÜN. Can. J. Chem. **72**, 1312 (1994).

Le (3*R*)-2-(*N*-benzylidèneamino)-4-chloro-3-méthylbutyronitrile **3**, préparé à partir du (2*S*)-3-hydroxy-2-méthylpropionate de méthyle **5** (96% ee) commercial, est facilement cyclisé par le carbonate de potassium, pour fournir après hydrolyse acide (HCl, 6 N) et chromatographie l'acide (1*S*,2*S*)-norcoronamique **1***a* avec 88% de diastéréosélectivité et >95% d'excès énantiomérique. À partir de l'acétate de 2-(hydroxyméthyl)butyle (2*R*)-**23** (>88% ee), obtenu par hydrolyse enzymatique énantiosélective avec la lipase PS, a été préparé le (3*S*)-2-(*N*-benzylidèneamino)-3-(chlorométhyl)pentanenitrile **29**, lequel après cyclisation en milieu basique (K_2CO_3) et hydrolyse acide (HCl, 6 N) ou basique (NaOH 0,8 N) conduit à l'acide (1*R*,2*R*)-coronamique-**18** non naturel (>88% ee). À partir du même acétate (2*R*)-**23**, a été préparé le (3*R*)-3-(chlorométhyl)-2-[diphénylméthylèneamino]pentanenitrile **37**, lequel après cyclisation en milieu basique (K_2CO_3 ou LDA) et hydrolyse acide (HCl, 6 N) fournit l'acide (1*S*,2*S*)-coronamique **17** (>88% ee). Il est remarquable que ces courtes séquences de synthèse, ne nécessitant pas d'auxiliaire chiral ou de précurseurs optiquement actifs coûteux, n'altèrent pas la pureté énantiomérique des centres asymétriques de ces 2,3-méthanoaminoacides. Cependant, la diastéréosélectivité *E* de la cyclisation n'est pas améliorée par l'utilisation de substituant *N*-(diphénylméthylène)amino stériquement encombrant, contrairement aux résultats indiqués par les calculs de la mécanique moléculaire (MAD).

1-Amino-1-cyclopropanecarboxylic acid (ACC) and its derivatives are currently attracting special attention because of their outstanding biological activities and potential use in conformationally restricted peptides providing biosynthetic and mechanistic probes (2–4). As a matter of fact, they constitute a unique form of constrained amino acids, naturally occurring either unbound or simply linked as dipeptides (5). However, the structure of BZR-cotoxin, the major component of BZR-toxin, which causes leaf spot disease in corn and induced high pathogenicity in rice plant, has been recently determined to be a cyclic nonadepsipeptide involving the ACC moiety (6).

Asymmetric syntheses of 1-aminocyclopropanecarboxylic acid derivatives have recently been reported from the cycloaddition of diazomethane to a dehydro amino acid derivative using (1*R*,2*R*,5*R*)-2-hydroxy-3-pinanone as chiral auxiliary (7), from the cyclopropanation of optically active 3-alkylidene-1,4-oxazin-2-ones with (diethylamino)phenyloxosulfonium methylide (8), or from the stepwise dialkylation of the bislactim ethers of cyclo(L-Val-Gly-) and (L-*tert*-Leu-Gly-) with a large excess of *trans*-1,4-dichloro-2-butene (9). (For other stereocontrolled approaches to differentially substituted ACC derivatives see ref. 10*a*–*g*).

We have recently reported a new preparation of ACC based on the quantitative base-induced cyclization of a 2-imino-4-chlorobutyronitrile readily available from acrolein; this synthesis is suitable for large-scale preparations (11). We report herein an adaptation of this route to the general construction of the *E* 2-alkyl ACC frameworks that permits us to prepare these 2,3-methanoamino acids, in either *d* or *l* enantiomeric forms, in high optical purity, and which do not require any chiral auxiliary or cyclopropanating reagents.

Synthesis of (1*S*,2*S*)-norcoronamic acid 1*a*

(1*S*,2*S*)-2-Methyl-1-aminocyclopropanecarboxylic acid **1***a* (norcoronamic acid) was isolated from norcoronatine, a component of the phytotoxic fraction of *Pseudomonas syringae* pv *glycinea* (12). *N*-Methyl (1*S*,2*S*)-norcoronamic acid **1***b*, isolated from streptomyces *braegensis* subsp. *japonicus*, has been found to be a constituent of the cyclic peptide portion of the recently discovered DNA-intercalating antibiotics of the quinomycin family (13).

Taking into account our synthesis of ACC from acrolein (11), a suitable precursor of the amino acid (1*S*,2*S*)-**1***a* could be a 1-(benzylideneamino)cyclopropylcarbonitrile such as (1*S*,2*S*)-**2**, arising from the diastereoselective base-induced cyclization of the (3*R*)-4-chloro-2-(benzylideneamino)-3-methylbutane-

[1]Parts of this work were presented orally by J.S. to the IUPAC 9th International Conference on Organic Synthesis (ICOS-92), see ref. 1.

[2]Author to whom correspondence may be addressed. Telephone: (33) 1 69 41 78 60. Fax: (33) 1 69 41 62 78.

Can. J. Chem. Downloaded from www.nrcresearchpress.com by EESC ESCOLA DE ENGENHARIA on 09/08/12
For personal use only.

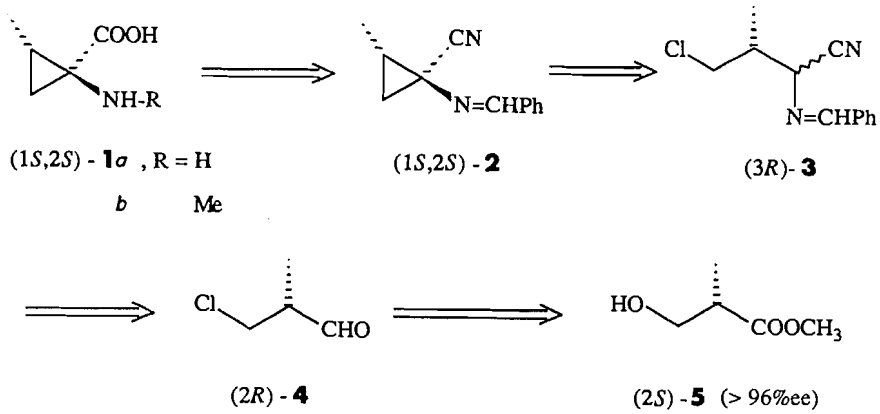

SCHEME 1

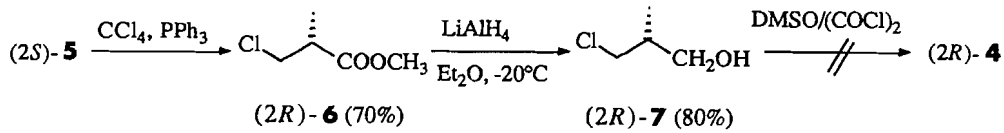

SCHEME 2

nitrile **3**. A convenient Strecker synthesis (14) would provide this Schiff base **3** from the 3-chloroisobutyraldehyde (2*R*)-**4** prepared by chlorination and controlled reduction of the commercially available methyl 3-hydroxy-2-methyl propionate (2*S*)- **5**,[3] as shown on the retrosynthetic scheme (Scheme 1).

Chlorination of the hydroxyester (2*S*)-**5** by triphenylphosphine in carbon tetrachloride (16) at 80°C for 11 h gave the expected methyl (2*R*)-3-chloro-2-methylpropionate **6** in 70% yield. Then, addition of a 1 M lithium aluminum hydride solution in diethyl ether (2 equiv.) at –20°C, to avoid any further reduction of the chlorine atom (17), provided the (2*R*)-3-chloro-2-methylpropan-1-ol (2*R*)-**7** in 80% yield. However, Swern oxidation (DMSO, $(COCl)_2$, NEt_3) (18) of (2*R*)-**7** did not provide the expected β-chloroisobutyraldehyde (2*R*)-**4**, but led exclusively to 2-methyl acrolein, likely arising from base-induced (NEt_3) dehydrochlorination (Scheme 2).

To overcome this problem, the leaving group, i.e., the chlorine atom, should be introduced at a further step of this sequence. Effectively silylation of (2*S*)-**5** by *tert*-butyldimethylsilyl chloride[4] in DMF in the presence of 2.5 equivalents of imidazole (20) gave the (2*S*)-methyl 3-*tert*-butyldimethylsiloxy-2-methylpropionate **8** in 93% yield. Controlled reduction of the ester **8** by 2 equivalents of diisobutylaluminum hydride (DIBAH) in dichloromethane at –78°C gave the (2*S*)-3-*tert*-butyldimethylsiloxy-2-methyl propanal **9** in 80% yield, as well as 20% of the corresponding alcohol. Alternatively, complete stepwise reduction of **8** by DIBAH (5 equiv.) followed by a Swern oxidation (DMSO, $(COCl)_2$, NEt_3) (18) led exclusively to the expected aldehyde (2*S*)-**9** in 86% yield (21). To avoid any racemization, the crude aldehyde (2*S*)-**9**[5] was treated directly by an excess of trimethylsilylcyanide (TMSCN) in the presence of a catalytic amount of zinc iodide at 0°C. When complete disappearance of the carbonyl stretching of **9** was observed by IR ($\nu_{C=O}$ 1730 cm^{-1}), addition of methanol and 1.1 equivalents of benzylamine led, after heating at 40°C for 2 h, to a 1:1 diastereomeric mixture of the (2*R*,3*R*)- and (2*S*,3*R*)-2-(*N*-benzylamino)-4-*tert*-butyldimethylsiloxy-3-methylbutyronitriles (3*R*)-**10**, in 60% overall yield from the siloxy ester (2*S*)-**8**. Although these diastereoisomers are easily separable by simple liquid chromatography, due to the formation of a planar carbanion at the C-2 carbon of the nitrile **10** in the further cyclization step (vide infra), such a separation appeared in fact not necessary.

Deprotection of **10** with tetra-*n*-butylammonium fluoride (20) in THF at room temperature for 30 min gave the (3*R*)-2-(*N*-benzylamino)-4-hydroxy-3-methylbutyronitrile **11***a* (X = OH) in 94% yield. Treatment of aminoalcohol **11***a* with tosyl chloride in pyridine at 0°C following the classical conditions of tosylation was ineffective, while reaction with tosyl chloride and pyridine in chloroform (23) provided a 32:42:26 mixture of O-tosyl, *N*-tosyl, and *N*,*O*-ditosyl derivatives; on the other hand, use of tosyl chloride in triethylamine containing a catalytic amount of *N*,*N*-dimethylaminopyridine (DMAP) (24) in dichloromethane led in 91% yield, exclusively, to the (3*R*)-2-(*N*-benzylamino)-3-methyl-4-*p*-tosyloxybutyronitrile **11***b* (X = OTs). Thus, as reported, the chemoselectivity of the O- or N-tosylation appeared highly dependent on the basicity of the amine used for the dehydrochlorination (25). Reaction of the *O*-tosylate **11***b* with lithium chloride in *N*-methyl pyrrolidine (NMP) at room temperature[6] for 2 h gave a 1:1 diastereomeric mixture of (3*R*)-2(*N*-benzylamino)-4-chloro-3-methyl butyronitriles **11***c* in 81% yield (Scheme 3).

ACC is biosynthesized from (*S*)-adenosylmethionine under the catalytic influence of a pyridoxal 5′-phosphate-linked enzyme (ACC synthase) (27) obtained, for instance, from ripe tomatoes (28). Base-induced cyclizations of *N*-protected

[3]The (*R*)- and (*S*)-methyl 3-hydroxy-2-methylpropionate, resulting from the enantioselective hydroxylation of methyl isobutyrate by microorganisms, are convenient bifunctional building blocks for the synthesis of a wide variety of optically active molecules, see ref. 15.

[4]This protecting group is stable to the Swern oxidation conditions, see T.T. Tidwell (19).

[5]Silica gel chromatography of aldehyde (2*S*)-**9** entailed partial isomerization, see ref. 22.

[6]Use of dimethylformamide (DMF) for the nucleophilic substitution of tosylate by lithium chloride generally required heating at 85°C, while use of *N*-methylpyrrolidone (NMP) activates and achieves the reaction at room temperature (26).

Can. J. Chem. Downloaded from www.nrcresearchpress.com by ESC ESCOLA DE ENGENHARIA on 09/08/12
For personal use only.

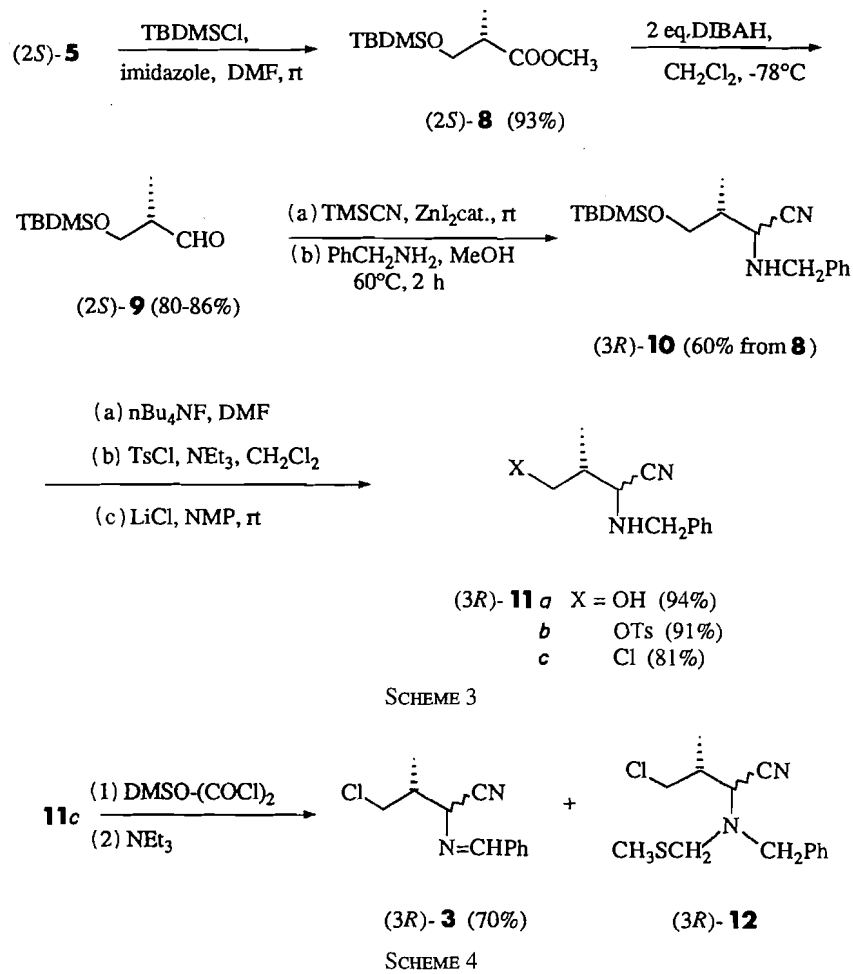

SCHEME 3

SCHEME 4

2-aminobutyrates substituted in γ by a leaving group (i.e., bromide (29–31) dimethylsulfonium (32), trimethylammonium (33), and 4-bromo-2-azidobutyrates (34)) have been reported to provide ACC in high yields. However, although the nitrile and carboxylate groups have comparable ability to stabilize an adjacent carbanion,[7] the cyclization of 2-*N*-benzyl-4-chlorobutyronitrile (36, 37) and of (3*R*)-**11***c* were unfortunately not achieved under a variety of basic conditions (i.e., K_2CO_3 and Cs_2CO_3 in DMF at 80°C, KOH in DMSO, K-*t*-BuO in THF, *n*-BuLi, NaH in THF, ...) (37). As we had previously reported the quantitative ready cyclization of a 4-chloro-2-iminobutyronitrile under smooth basic conditions (i.e., K_2CO_3 in DMF at room temperature, for instance (11, 36)), we undertook the transformation of the benzylamine **11***c* into the corresponding imine. First of all, we tried to cleave the *N*-benzyl protecting group; curiously, in spite of many attempts under various hydrogenolysis conditions (i.e., either with 5–10% Pd/C catalysis under 1–53 psi (1 psi = 6.9 kPa) hydrogen pressure (38), with a stoechiometric amount of Pd/C and ammonium formiate as hydrogen source (39), or with 20% of the Pearlman catalyst (40) ($Pd(OH)_2$) under 1–53 psi hydrogen pressure), the amine deprotection of **11***c* and of its chlorohydrate derivative, prepared by bubbling gaseous HCl through an etheral solution of **11***c*, failed. So, formation of the corresponding imine by transimination with benzophenone imine (41), which was successfully achieved from the parent 2-amino-4-chlorobutyronitrile (11), was not obtained from **11***c* by this way.

Swern oxidation is currently used to prepare carbonyl compounds from primary or secondary alcohols (18), but only a few reports concern the oxidation of amines into imines by the DMSO($(COCl)_2$/NEt_3 reagent (42); effectively, treatment of the *N*-benzylamine **11***c* under Swern oxidation conditions (18, 43) led to the expected imine, i.e., the (3*R*)-2-(phenylmethyleneamino)-4-chloro-3-methylbutyronitrile **3**, in 70% yield, as well as 5% of methylthiomethylamine **12** as by-product (44) (Scheme 4).

Indeed, formation of the imine moiety activates the proton in α of the nitrile function since the Schiff base (3*R*)-**3** underwent cyclization even upon simple treatment with potassium carbonate in DMF at room temperature for 30 min to provide, in 80% yield, a 84:16 diastereomeric mixture of (1*S*,2*S*)-**2** and (1*R*,2*S*)-1-(phenylmethyleneamino)-2-methylcyclopropanenitrile **13**. Simple chromatography on silica gel allowed us to obtain a mixture containing 94% of the diastereomer (1*S*,2*S*)-**2**. This ratio was determined by ^{1}H NMR spectroscopy, from the integration of the benzylic proton of the imines (1*S*,2*S*)-**2** and (1*R*,2*S*)-**13** recorded at δ 8.60 and 8.65 ppm, respectively.

The diastereoselectivity observed in the cyclization of (3*R*)-**3**, i.e., major formation of the *E* diastereomer (1*S*,2*S*)-**2**, likely arises from an *s-trans* conformation of the intermediate iminonitrile carbanion **15** (10*f*, 45) where the methyl and nitrile groups would have a *syn* relationship, to minimize the steric

[7]Effectively, the pK_a of phenylacetonitrile and ethylphenylacetate in DMSO (K as counterion) are 21.9 and 22.6, respectively; see F.G. Bordwell (35).

Can. J. Chem. Downloaded from www.nrcresearchpress.com by EESC ESCOLA DE ENGENHARIA on 09/08/12
For personal use only.

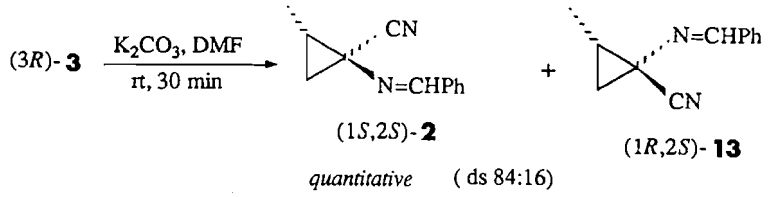

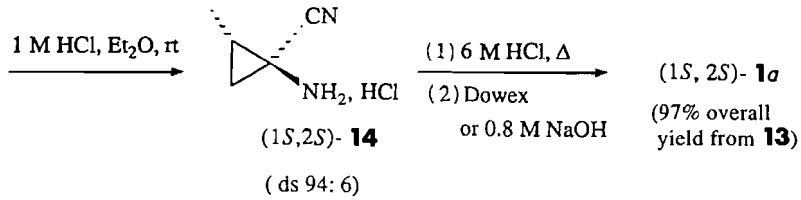

SCHEME 5

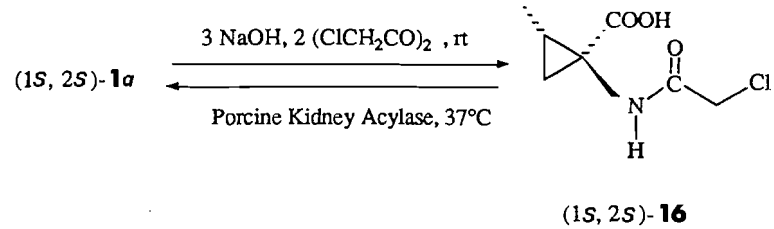

SCHEME 6

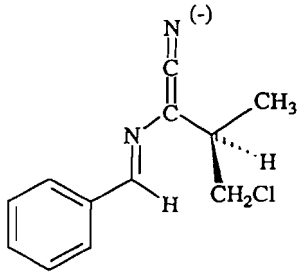

15

FIG. 1

interactions as confirmed by molecular mechanic calculations MAD (Molecular Advanced Design) (Fig. 1).[8]

Then, acid hydrolysis of (1*S*,2*S*)-**2** (ds 94:6) with 1 M HCl at room temperature for 15 h (11) gave the (1*S*,2*S*)-1-amino-2-methylcyclopropanecarbonitrile hydrochloride **14** containing 6% of its (1*R*,2*S*) stereoisomer, as evidenced from ^{1}H NMR spectroscopy by the occurrence of two doublets at δ 1.19 and 1.29 ppm (ratio 94:6, J = 6.7 and 6.27 Hz, respectively). Finally, 6 M HCl hydrolysis of (1*S*,2*S*)-**14** at reflux for 11 h (11) followed by ion-exchange chromatography (Dowex 50 × 8-100) furnished, quantitatively (97% overall yield from (1*S*,2*S*)-**2**), the (1*S*,2*S*)-norcoronamic acid **1***a*, as well as one-pot 6 M HCl hydrolysis of the iminonitrile (1*S*,2*S*)-**2**. Alternatively, basic hydrolysis of the iminonitrile (1*S*,2*S*)-**2** by 0.8 M sodium hydroxide at reflux for 24 h (11) also gave, after neutralization to pH 7 by concentrated HCl and reverse-phase liquid chromatography, (1*S*,2*S*)-**1***a*, quantitatively (Scheme 5).

It must be emphasized that the competitive formation of any products arising from three-membered ring opening has not been observed under these conditions, contrary to recent reports concerning the syntheses of 2,2-dialkyl-ACC derivatives (46).

The 94:6 diastereomeric excess of this norcoronamic acid **1***a* was easily determined from its ^{1}H NMR spectra: effectively, the (1*R*,2*S*) stereoisomer is characterized by a multiplet at δ 0.75 attributed to the proton at C-2 of the cyclopropane ring, while the methyl of (1*S*,2*S*)-**1***a* is clearly characterized by a doublet at δ 1.03 ppm (3H, J = 6 Hz) (47). To determine its enantiomeric excess, (1*S*,2*S*)-**1***a* was treated with 4 N sodium hydroxide and chloroacetic anhydride to provide the (1*S*,2*S*)-1-(*N*-chloroacetyl)-2-methylcyclopropanecarboxylic acid **16**. It had previously been reported that only the (1*S*,2*S*) diastereomer of this aminochloroacetamide is a substrate for the Porcine Kidney Acylase (48); effectively, (1*S*,2*S*)-**16** underwent total hydrolysis upon treatment with this enzyme to give back the free amino acid (1*S*,2*S*)-**1***a* as shown in ^{1}H NMR spectroscopy by the total disappearance of the chloroacetylmethylene signal at δ 3.88 ppm (Scheme 6).

In conclusion, in nine steps from commercially available (2*S*)-methyl 3-hydroxy-2-methylpropionate **5** we have prepared in 22% overall yield the (1*S*,2*S*)-norcoronamic acid **1***a* with 94:6 diastereoselectivity and >95% enantiomeric excess. This scheme did not alter the optical purity of the stereogenic center of the asymmetric precursor **5**, and the availability of both its enantiomers allows for the unambiguous preparation of either the *d* or *l* forms of this 2,3-methano amino acid.

Synthesis of non-natural (1*R*,2*R*)-coronamic acid 18

The coronamic acid, i.e, the (1*S*,2*S*)-2-ethyl-1-aminocyclopropanecarboxylic acid **17**, was isolated from the hydrolysis of coronatine, produced by *Pseudomonas caronafacience* var. *atropupurea* (49, 50). This plant toxin induces chlorosis in Italian ryegrass or soya (50, 51), hypertrophy of potato cells, and inhibition of corn root grown (52). Its (1*S*,2*R*) non-natural

[8]MAD version 2.0 is available from Oxford Molecular, École Polytechnique, Palaiseau, France.

Can. J. Chem. Downloaded from www.nrcresearchpress.com by EESC ESCOLA DE ENGENHARIA on 09/08/12
For personal use only.

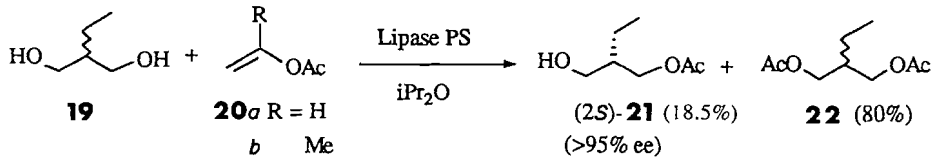

SCHEME 7

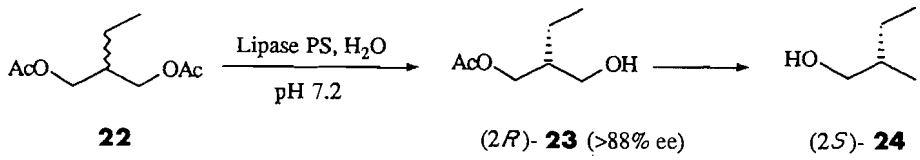

SCHEME 8

diastereoisomer known as *allo* coronamic acid is converted into 1-butene by plant tissues (53).

Synthesis of coronamic acid following the scheme used for the preparation of (1*S*,2*S*)-norcoronamic acid **1***a* (see Scheme 1) required (2*S*)-methyl 2-(hydroxymethyl)butyrate; unfortunately in contrast to (2*S*)-**5**, this chiral ester was not available. Condensation of 2-ethylmalonic acid with (–)-menthol in the presence of dicyclohexylcarbodiimide and 4-*N*,*N*-dimethylaminopyridine (DMAP) was reported to furnish the corresponding (2*R*)-monomenthyl acid ester with 99% diastereoselectivity (54); following this procedure, we in fact obtained, after recrystallization, a 1:1 diastereomeric mixture of these half-esters. To readily obtain a suitable precursor of the 2-methanoamino acid **17** we first investigated the enzymatic monoacetylation of 2-ethyl-1,3-propanediol **19**, by the lipase PS extracted from the microorganism *Pseudomonas cepacia* (55). After many attempts, it appeared that vinyl acetate **20***a* (R = H) (2 equiv.) was more effective than 2-propenyl acetate **20***b* (R = Me) as enantioselective acetylation agent and that diisopropyl ether must be preferred to chloroform or vinyl acetate as solvent. Higher enantiomeric excesses (>95%) were obtained when the reaction of the 1,3-diol **19** was complete (as monitored by TLC) but, under these conditions, the 1,3-diacetate **22** was formed in 80% yield and the expected (2*S*)-2-(hydroxymethyl)butyl acetate **21** ($[\alpha]_D^{20}$ –13.8, *c* = 1, $CDCl_3$) was isolated after silica gel chromatography in only 18.5% yield (Scheme 7).

Otherwise, hydrolysis of 2-(acetoxymethyl)butyl acetate **22**, readily available from the 1,3-diol **19** (acetic anhydride, DMAP in ether at 0°C) by lipase PS led in 65% yield, after silica gel chromatography, to the monoacetate (2*R*)-**23** ($[\alpha]_D^{20}$ + 12.1, *c* = 1, $CDCl_3$) with 88% enantiomeric excess, as determined from its ^{1}H NMR spectra recorded in the presence of 0.5 equivalent of a chiral shift reagent ($Eu(hfc)_3$), by relative integration of the methylene signals at δ 10.2 and 12.6 ppm, compared to the racemic monoacetate. It must be emphasized that the diacetate **22** underwent ready hydrolysis into racemic monoacetate in the lack of lipase PS; thus **22** must be added to an aqueous solution of lipase PS buffered at pH 7.2 by 0.1 M potassium phosphate. Higher enantiomeric excesses were obtained when the reaction was stopped after 69% hydrolysis. Enzymatic hydrolysis of homologous esters, i.e., 3-butyryloxy-2-ethylpropyl butyrate, did not improve the enantiomeric excess.

The (2*R*) absolute configuration of **23** was established by its transformation into the known (2*S*)-2-methylbutan-1-ol **24**,[9] by tosylation (TsCl, pyridine, DMAP) and reduction ($LiAlH_4$); therefore the (2*S*) absolute configuration of the monoacetate **21** was also confirmed (Scheme 8).

First of all, we performed the total synthesis of the non-natural (1*R*,2*R*)-coronamic acid **18** from the monoacetate (2*R*)-**23** (>88% ee). Silylation by *tert*-butyldimethylsilyl choride (DMF, 2.5 equiv. of imidazole, cat. DMAP) (19, 20) followed by deacetylation with potassium carbonate in methanol provided the (2*S*)-2-(*tert*-butyldimethylsiloxymethyl)-butanol **25** in 84% overall yield. Swern oxidation (DMSO, $(COCl)_2$, Et-iPr_2N) (18)[10] gave the corresponding aldehyde (2*R*)-**26**, which was directly treated with an excess of TMSCN in the presence of zinc iodide in diethyl ether at 0°C. After complete reaction of the aldehyde monitored by gas chromatography, addition of a solution of 1.1 equivalents of benzylamine in methanol led, upon heating at 60°C for 4 h, to a 1:1 diastereomeric mixture of (2*R*,3*S*)- and (2*S*,3*S*)-2-(*N*-benzylamino)-3-(*tert*-butyldimethylsiloxymethyl) pentanenitrile **27**, in 66% overall yield from the butanol (2*S*)-**25**.

Desilylation of (3*S*)-**27** (nBu_4NF, THF) (20), chemoselective tosylation (TsCl, 1 equiv. NEt_3, DMAP, CH_2Cl_2) (24), and chlorination (LiCl, NMP) (26), analogous to the transformation of (3*R*)-**10** into the 4-chlorobutyronitrile (3*R*)-**11***c* (vide supra, Scheme 3) gave a 1:1 diastereomeric mixture of (2*R*,3*S*)- and (2*S*,3*S*)-2-(*N*-benzylamino)-3-(chloromethyl)valeronitriles **28** in 76% overall yield from (2*S*)-**25** (Scheme 9).

Contrary to (3*R*)-**11***c*, the 2-(*N*-benzylamino)-3-(chloromethyl)valeronitrile **28** underwent Swern oxidation (42) into the imine **29** with only 30% yield; use of an excess of DMSO and $(COCl)_2$ reagents did not improve the yield but entailed mainly formation of methylthiomethylamine derivative (3*S*)-**30** (18, 19, 44). Use of *N*,*N*-diisopropylethylamine, known to limit, by steric hindrance, formation of methylthiomethyl ether (44) in the Swern oxidation of alcohol, totally inhibited the reaction of (3*S*)-**28**. Manganese dioxide in refluxing toluene was ineffective (58*a*),[11] as was also pyridinium dichromate (59) in dichloromethane (3% of oxidation). On the other hand, use of *tert*-butyl hydroperoxide (8 equiv., TBHP) (60) and a catalytic amount of ruthenium dichloride – triphenylphosphine (5% $RuCl_2$–$(PPh_3)_2$) (61) in the presence of molecular sieves (4 Å) to trap *tert*-butanol and water formed as by-products, at room temperature, gave the expected imine (3*S*)-**29** in 60% yield (Scheme 10).

[9](S)-2-Methyl-1-butanol ($[\alpha]_D^{20}$ –6.3 ± 0.3, c = 1, ethanol) is used as chiral building block: see ref. 56.

[10]Hindered amine, i.e., iPr_2EtN, and work-up with buffered water at pH 7 were used to avoid any racemization of the aldehyde. See ref. 57.

[11]For a review of manganese dioxide oxidation see ref. 58*b*.

Can. J. Chem. Downloaded from www.nrcresearchpress.com by EESC ESCOLA DE ENGENHARIA on 09/08/12
For personal use only.

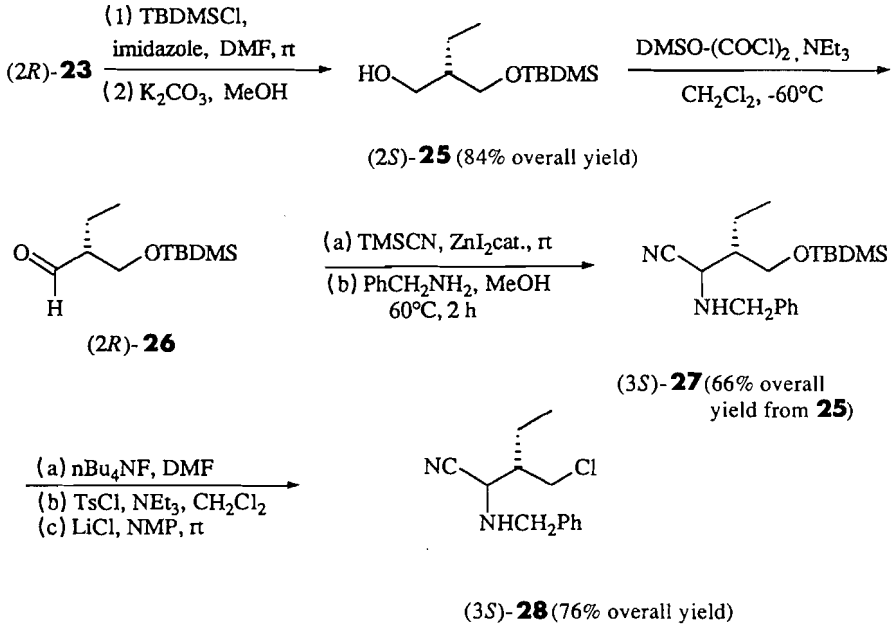

SCHEME 9

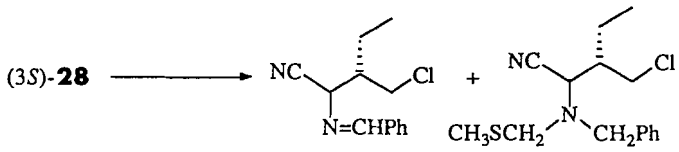

	(3S)-29 %	(3S)-30 %
$(COCl)_2$/DMSO		
1.1 equiv./2.2 equiv.	30	-
2 equiv./3 equiv.	-	100
MnO_2, toluene	-	-
PDC, rt	3	-
$RuCl_2$, $(PPh_3)_3$/TBHP	60	-

SCHEME 10

Upon treatment with potassium carbonate in DMF at room temperature for 30 min the chloroimine (3*S*)-**29** underwent cyclization to provide, in 70% yield, a 80:20 mixture of (1*R*,2*R*)-**31** and (1*S*,2*R*)-1-(*N*-phenylmethyleneamino)-2-ethyl cyclopropanecarbonitrile **32**, as shown by ^{1}H NMR spectroscopy from the simple integration of the benzylic proton of these *N*-benzyl cyclopropylimines at δ 8.55 and 8.60 ppm, respectively. Acid hydrolysis of (1*R*,2*R*)-**31** (containing 20% of (1*S*,2*R*)-**32**)[12] with 1 M HCl at room temperature for 15 h gave the (1*R*,2*R*)-1-amino-2-ethylcyclopropanecarbonitrile hydrochloride (1*R*,2*R*)-**33** in 80% yield. Addition of 6 M hydrochloric acid to (1*R*,2*R*)-**33** led, on heating at reflux for 15 h, to a 80:20 mixture of (1*R*,2*R*)- and (1*S*,2*R*)-coronamic acid hydrochlorides, in 70% yield.

Otherwise, treatment of the aminonitrile hydrochloride (1*R*,2*R*)-**33** with an 0.8 M sodium hydroxide solution at reflux for 24 h led, quantitatively, after neutralization (conc. HCl) and reverse-phase liquid chromatography, to the (1*R*,2*R*)-coronamic acid **18** (Scheme 11).

The absolute stereochemistry was determined from ^{1}H NMR spectroscopy by the occurrence of two triplets at δ 0.72 and 0.84 ppm corresponding to the (1*R*,2*R*)-coronamic acid **18** and (1*S*,2*R*)-*allo* coronamic acid, respectively, with the diastereomeric ratio 80:20. As reported, the corresponding methyl esters, prepared upon treatment with an esterifying medium (MeOH–$SOCl_2$) (45), were readily separable by flash liquid chromatography on silica gel (9); then, acidic hydrolysis (HCl, propylene oxide) allowed us to isolate diastereomerically pure (1*R*,2*R*)-coronamic acid **18**. The enantiomeric excess of (1*R*,2*R*)-**18** determined by examination of the ^{19}F NMR of its Mosher amide derivative (8) (obtained upon treatment with the (*S*)-2-methoxy-2-trifluoromethylphenyl acetyl chloride) (62), was 88%; thus, this sequence also did not alter the optical purity of the stereogenic center of the asymmetric precursor, i.e., the monoacetate (2*R*)-**23**.

In nine steps from (2*R*)-2-(hydroxymethyl)but-1-yl acetate **23**, readily prepared by enantioselective hydrolysis of 2-(acetoxymethyl)but-1-yl acetate **22** catalysed by lipase PS, we have prepared in 18% overall yield the non-natural (1*R*,2*R*)-coronamic acid **18** with 88% enantiomeric excess.

Synthesis of (1*S*,2*S*)-coronamic acid 17

To improve the *E* diastereoselectivity of the cyclization of the 2-(*N*-benzylideneamino)-4-chlorobutyronitriles, and taking into account the results of some molecular mechanic calculations (MAD)[8] indicating that a bulky *N*-benzylideneamino substituent should favor formation of the *E* 1-amino-2-ethylcyclopropanecarboxylic acid, we prepared the suitable benzophenone imine (3*R*)-**37**.

Thus, treatment of the (2*S*)-2-(acetoxymethyl) butanal **34**, prepared by Swern oxidation (18) of the butanol (2*R*)-**23** by 1.25 equivalents of TMSCN and 5% of ZnI_2 at room temperature for 1 h, was followed by the addition of 1.1 equivalents of aminodiphenylmethane in methanol. The mixture was heated at reflux for 8 h. After cooling to room temperature, 2 equivalents

[12]In spite of many attempts, and in contrast to (1*S*,2*S*)-**18**, the iminonitrile **36** was not separated from its stereomer (1*S*,2*R*)-**37** by simple liquid chromatography on silica gel.

Can. J. Chem. Downloaded from www.nrcresearchpress.com by ESC ESCOLA DE ENGENHARIA on 09/08/12
For personal use only.

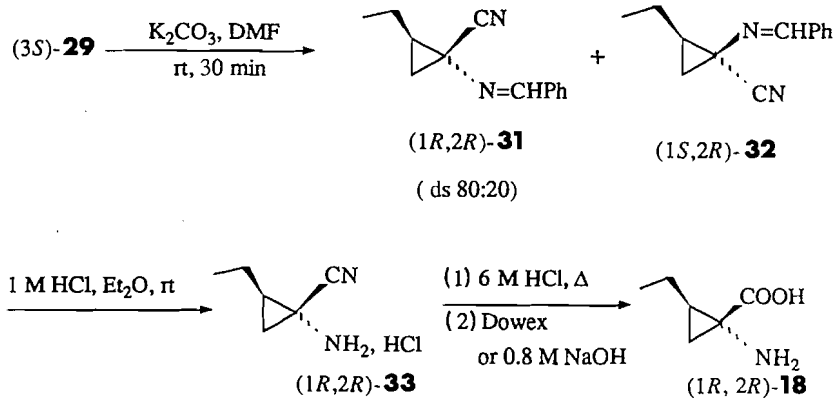

SCHEME 11

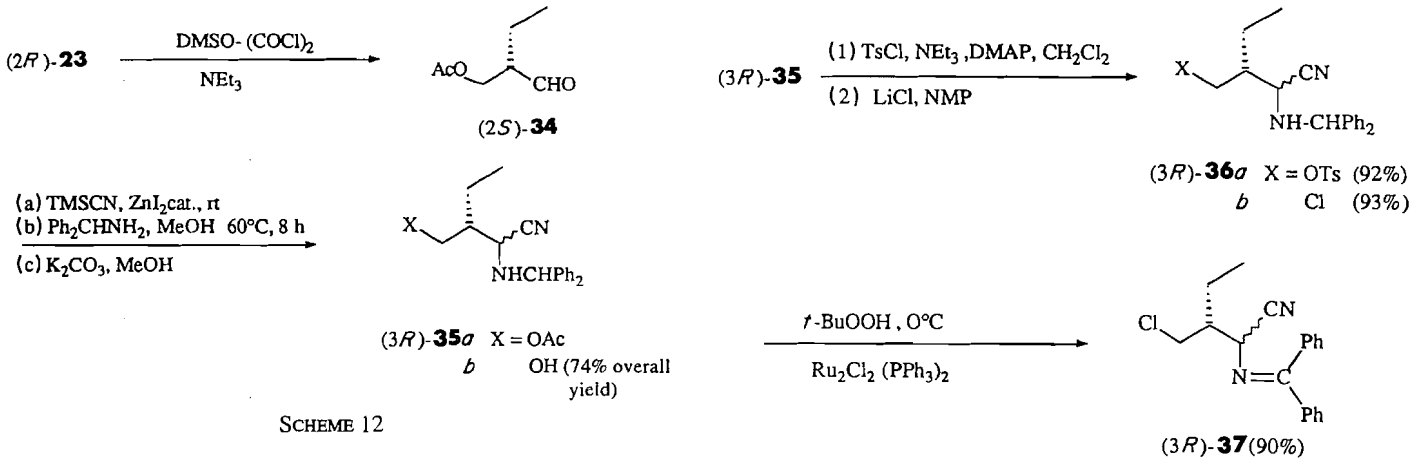

SCHEME 12

SCHEME 13

of potassium carbonate were added to the acetate **35***a* to give directly a 55:45 diastereomeric mixture of (2*R*,3*R*)- and (2*S*,3*R*)-2-[N-(diphenyl)methylamino]-3-(hydroxymethyl)-valeronitrile **35***b* in 74% overall yield from (2*R*)-**23** (Scheme 12).

Chemoselective tosylation (TsCl, NEt_3, DMAP, CH_2Cl_2) (24) gave the tosylate (3*R*)-**36***a* (92%), and chlorination (LiCl, NMP) (26) gave the (3*R*)-2-[*N*-(diphenyl)methylamino)-3-(chloromethyl)valeronitrile **36***b* in 93% yield. Oxidation of this chloroamine **36***b* with a 3 M solution of *tert*-butylperoxide in isooctane in the presence of $RuCl_2$–$(PPh_3)_2$ at 0°C for 15 h gave the expected (3*R*)-3-(chloromethyl)-2-[diphenylmethyleneamino)valeronitrile **37** in 90% yield (Scheme 13).

Upon treatment with 1.1 equivalents of potassium carbonate in DMF at room temperature for 3 h, the chloroimine (3*R*)-**37** underwent cyclization to provide, in 92% yield a 65:35 diastereomeric mixture of (1*S*,2*S*)-**38** and (1*R*,2*S*)-1-(*N*-diphenylmethyleneamino)-2-ethyl cyclopropanecarbonitrile **39** (Scheme 14). Unfortunately, contrary to the forecast of the molecular mechanic calculations (MAD),[8] the diastereoselectivity of the cyclization (3*R*)-**37** → (1*S*,2*S*)-**38** was only slightly improved by the presence of a diphenylmethyleneamino substituent. The cyclization was performed under various basic conditions, and the diastereoselectivity was improved to 76:24 by using lithium diisopropylamide at –90°C; however, addition of HMPA has no effect on the diastereoselectivity.

Flash chromatography eluted with dichloromethane allowed us to readily isolate the diastereomerically pure cyclopropylcarbonitrile (1*S*,2*S*)-**38** in 72% yield, and its diastereomer (1*R*,2*S*)-**39** in 23% yield (Scheme 14). Finally, addition of 1 N HCl in diethyl ether to (1*S*,2*S*)-**38** provided the (1*S*,2*S*)-1-amino-2-ethylcyclopropane carbonitrile hydrochloride **40**, while addition of 6 M hydrochloric acid provided, after heating at reflux for 15 h, the expected amino acid hydrochloride, which by chromatography through a Dowex 50 × 8-100 ion-exchange column led in 97% yield to the (1*S*,2*S*)-coronamic acid **17** with 88% enantiomeric excess, determined by ^{19}F NMR analysis of the corresponding Mosher amide (Scheme 15).

Analogously, the cyclopropylcarbonitrile (1*R*,2*S*)-**39** was hydrolyzed by 6 N HCl at reflux into the (1*R*,2*S*)-*allo*-coronamic **17′** (88% ee).

In seven steps from the butanol (2*R*)-**23** and in 30% overall yield we have performed the total synthesis of the (1*S*,2*S*)-coronamic acid **17**. Again, the enantiomeric purity of this 2,3-methano amino acid depends only on the optical purity of its precursor, i.e., the 2-(hydroxymethyl)but-1-yl acetate (2*R*)-**23**. It is noteworthy that these sequences did not alter at all the enantiomeric purity of the stereogenic centers.

Experimental section

Methyl (2R)-3-chloro-2-methylpropionate ***6***

To a solution of 16.7 g (63.3 mmol) of triphenylphosphine in 90 mL of carbon tetrachloride was added dropwise, under argon at room temperature, 4.7 mL (42.19 mmol) of (2*S*)-methyl- 3-hydroxy-2-methyl-propionate **5**. The mixture was stirred for 11 h at 80°C; then carbon

Can. J. Chem. Downloaded from www.nrcresearchpress.com by EESC ESCOLA DE ENGENHARIA on 09/08/12
For personal use only.

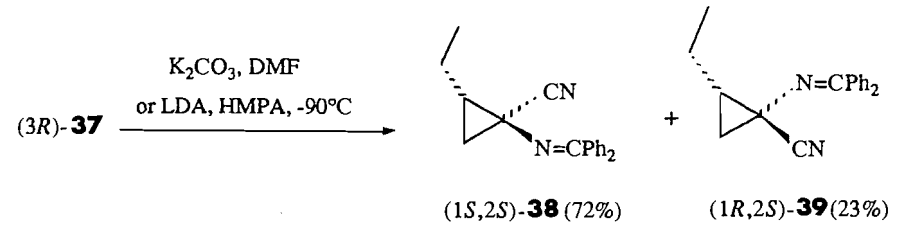

SCHEME 14

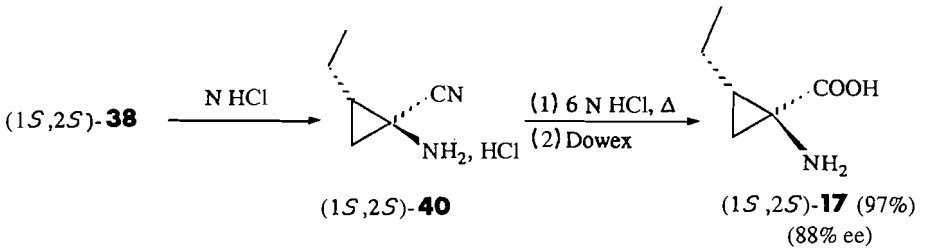

SCHEME 15

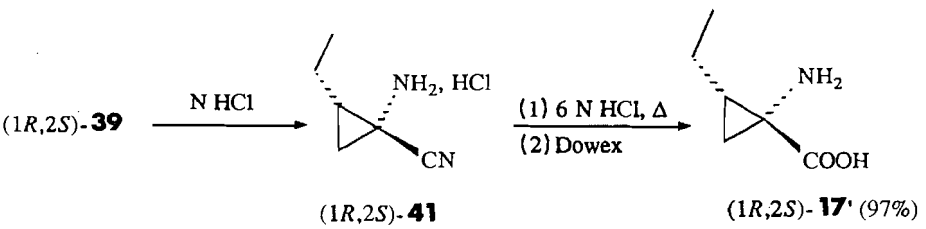

SCHEME 16

tetrachloride and chloroform (formed as by-product) were removed under reduced pressure. The residue was treated with 80 mL of pentane and the triphenylphosphine oxide was eliminated by filtration. The solvent was removed under reduced pressure and the residue was distilled to yield 4.6 g (80%) of pure methyl (2*R*)-3-chloro-2-methylpropionate **6**: bp 70°C/27 Torr (1 Torr = 133.3 Pa); $[\alpha]_D^{20}$ +10.4 (*c* = 1, CCl_4); IR (CCl_4): 2960–2660 (CH alkyl), 1750 ($\nu_{C=O}$), 1170 (ν_{C-O}) cm^{-1}; ^1H NMR (250 MHz, $CDCl_3$) δ: 1.29 (s, 3H, *J* = 7.06 Hz), 2.85 (m, 1H), 3.68 (dd, 1H, *J* = 18.58 and 5.96 Hz), 3.76 (dd, 1H, *J* = 18.56 and 8.49 Hz), 3.75 (s, 3H); ^{13}C NMR (250 MHz, $CDCl_3$) δ: 15.01 (CH_3), 42.10 (C-H), 45.87 (CH_2Cl), 51.97 (CH_3O), 173.5 (C=O); MS (70 eV) *m/z* (%): 136 (0.2) [M^+], 121 (2.3), 103 (47), 101 (2).

(2R)-3-Chloro-2-methylpropan-1-ol 7

To a solution of 400 mg (2.9 mmol) of (2*R*)-methyl 3-chloro-2-methylpropionate **6** in 4 mL of anhydrous diethyl ether, under argon at –20°C, was added dropwise 2.9 mL (2.9 mmol) of 1 M lithium aluminum hydride solution in ether. The mixture was stirred at –20°C for 30 min, then hydrolyzed by portionwise addition of wet sodium sulfate. After filtration on Celite, the ethereal solution was dried (Na_2SO_4); evaporation of the solvent afforded 231 mg (75%) of (2*R*)-3-chloro-2-methylpropan-1-ol **7**: IR (CCl_4): 3600, 3060, 2880, 1050 (C—O) cm^{-1}; ^1H NMR (250 MHz, $CDCl_3$) δ: 1.05 (d, 3H, *J* = 6.85 Hz), 1.65 (s, 1H, OH), 2.05 (m, 1H, CH), 3.63 (m, 4H, CH_2Cl and CH_2OH); ^{13}C NMR (250 MHz, $CDCl_3$) δ: 14.40 (CH_3), 37.74 (CH), 47.62 (CH_2Cl), 64.58 (CH_2OH); MS (70 eV) *m/z* (%): 110 (0.1) [M^+], 109 (0.4), 109 (0.1) [M^+], 107 (0.2), 93 (0.33), 92 (0.21), 90 (0.6), 57 (12.25), 42 (100).

Swern oxidation of 7

To a solution of 140 μL of oxalyl chloride in 4 mL of dichloromethane was added dropwise at –60°C a solution of 250 μL of dimethyl sulfoxide in 0.5 mL of dichloromethane. The solution was stirred for 5 min, then was added a solution of 158 mg (1.46 mmol) of (2*R*)-3-chloro-2-methylpropan-1-ol **7** in 2 mL of dichloromethane within 5 min, maintaining the temperature of the mixture below –55°C. The mixture was stirred at –50°C for 20 min, after which it was cooled to –70°C to add dropwise 1 mL of triethylamine. Then the mixture was allowed to reach room temperature. After addition of 3.5 mL of water, the mixture was stirred for 1 h and extracted twice with 10 mL of dichloromethane. The organic was washed with saturated NaCl and dried over Na_2SO_4. Evaporation of solvent left a volatile residue identified by ^1H NMR as 2-methyl acrolein.

*Methyl (2S)-3-(*tert*-butyldimethylsiloxy)-2-methylpropionate 8*

To a solution of 7.2 g (105.9 mmol) of imidazole and 7.6 g (5.8 mmol) of *tert*-butyldimethylsilyl chloride in 7.5 mL of dimethylformamide (DMF) was added dropwise, under argon, a solution of 5 g (42 mmol) of (2*S*)-methyl 3-hydroxy-2-methylpropionate **5** in 7.5 mL of DMF. The mixture was stirred for 12 h at room temperature and 120 mL of ether and 12 mL of water were added. The organic layer was then washed with water (3 × 12 mL), and dried over anhydrous sodium sulfate. Evaporation of the solvent afforded 9.3 g of an oil, which was purified by chromatography on silica gel (hexane:ether, 95:5) to give 9.1 g (93%) of methyl (2*S*)-3-(*tert*-butyldimethylsiloxy)-2-methylpropionate **8**: $[\alpha]_D^{20}$ +20.7 (*c* = 1, CCl_4); IR (neat): 2960, 2860, 1750 ($\nu_{C=O}$), 1255 (ν_{C-Si}) cm^{-1}; ^1H NMR (250 MHz, $CDCl_3$) δ: 0.03 (s, 6H, $Si(CH_3)_2$), 0.9 (s, 9H, Si-$C(CH_3)_3$), 1.14 (d, 3H, *J* = 7 Hz), CH_3), 2.67 (m, 1H, CH), 3.68 (s, 3H, CH_3O), 3.64 (dd, 1H, *J* = 14.56 and 5.97 Hz), 3.75 (dd, 1H, *J* = 14.56 and 7.06 Hz); ^{13}C NMR (50 MHz, $CDCl_3$) δ: –5.55 (CH_3-Si), 13.40 (CH_3), 18.15, 25.72, 42.47, 51.44 (CH_3-O), 65.19 (CH_3-O), 175.39 (C=O). Anal. calcd. for $C_{11}H_{24}O_3Si$ (232.4): C 56.85, H 10.41; found: C 56.61, H 10.62.

*(2S)-3-(*tert*-Butylidimethylsiloxy)-2-methylpropanal 9*

To a solution of 5 g (21.5 mmol) of (2*S*)-methyl-3-*tert*-butyldimethylsiloxy-2-methylpropionate in 125 mL of dichloromethane at –78°C, under argon, was added dropwise 45.5 mL (45.5 mmol) of a 1 M solution of diisobutylaluminum hydride in toluene. As shown by thin-layer chromatography, the reaction was instantaneous; then 6.3 mL of methanol was added, the mixture was allowed to reach room

Can. J. Chem. Downloaded from www.nrcresearchpress.com by EESC ESCOLA DE ENGENHARIA on 09/08/12
For personal use only.

Can. J. Chem. Downloaded from www.nrcresearchpress.com by EESC ESCOLA DE ENGENHARIA on 09/08/12
For personal use only.

temperature, and 55 mL of a saturated sodium and potassium tartrate solution was added followed by 350 mL of ethyl acetate. The organic phase was decanted, dried on anhydrous sodium sulfate, and the solvent removed under reduced pressure to give 4.36 g of an oil containing the (2*S*)-3-(*tert*)butyldimethylsiloxy)-2-methylpropanal (80%), as well as 20% of (2*R*)-3-(*tert*-butyldimethylsiloxy)-2-methyl propanol. To avoid any racemization, the crude aldehyde was not isolated for the further steps: however, 100 mg of this mixture was purified by chromatography on silica gel (ether:hexane, 25:75) to furnish the pure aldehyde (2*S*)-**9**: $[\alpha]_D^{20}$ +25.4 (*c* = 1, CCl_4); IR (neat): 2960, 2860, 2720, 1730 ($\nu_{C=O}$), 1255 (ν_{C-Si}) cm^{-1}; ^1H NMR (200 MHz, $CDCl_3$) δ: 0.03 (s, 6H, CH_3Si), 0.85 (s, 9H, $SiC(CH_3)_3$), 1.09 (d, 3H, *J* = 6.95 Hz, CH_3), 2.53 (m, 1H), 3.80 (dd, 1H, *J* = 10.1 and 6.2 Hz), 3.84 (dd, 1H, *J* = 10.1 and 5.3 Hz), 9.75 (d, 1H, *J* = 1.52 Hz, CHO); ^{13}C NMR (250 MHz, $CDCl_3$) δ: –5.57 (CH_3Si), 10.23 (CH_3), 18.17, 25.73, 48.75, 63.38 (CH_2O), 204.65 (C=O); MS (CI) *m/z* (%): 220 (M + 18, 8.7), 203 (M + 1, 100), 202 (M^+, 13.64), 147 (43.64).

(2R,3R)- and (2S,3R)-2-(N-Benzylamino)-4-(tert-butyldimethylsiloxy)-3-methylbutyronitrile ***10***

To a mixture of 4.36 g (21.5 mmol) of (2*S*)-3-*tert*-butyldimethylsiloxy-2-methylpropanal **9** (containing 20% of the corresponding alcohol) and 40 mg (0.11 mmol) of zinc iodide, kept under argon, was added 3.6 mL (26.8 mmol) of trimethylsilylcyanide ($CNSiMe_3$). The reaction was monitored by IR; after 1 h at room temperature the carbonyl stretching ($\nu_{C=O}$ = 1730 cm^{-1}) disappeared completely. A sample (~100 mg) was purified by chromatography on silica gel (ether:hexane, 5:95) to give a 1:1 diastereomeric mixture of (3*S*)-3-methyl-2-trimethylsiloxy-4-(*tert*-butyldimethylsiloxy)butyronitrile: IR (neat): 2960–2860, 1260 (C-Si), 1100 (CH_2OSi), 870 and 840 (C—Si) cm^{-1}; ^1H NMR (200 MHz, $CDCl_3$) δ: 0.08 (s, 12H), 0.22 (s, 18H, $SiCH_3)_3$), 0.9 (s, 18H, C-$(CH_3)_3$), 1.06 (d, 3H, *J* = 6.89 Hz), 1.09 (d, 3H, *J* = 6.89 Hz), 2.0 (m, 2H), 3.55 (m, 4H, CH_2O), 4.63 (d, 1H, *J* = 6.3 Hz), 4.67 (d, 1H, *J* = 4.86 Hz); ^{13}C NMR (50 MHz, $CDCl_3$) δ: –5.56 (CH_3Si), –5.15 (CH_3Si), 10.89, 11.63, 18.17, 25.80, 41.32, 61.50, 62.84, 63.08, 63.28, 119.24 (C≡N).

To this 2,4-disiloxybutyronitrile was added 34 mL of methanol and the mixture was stirred at room temperature for 5 min. Then 2.3 mL (19 mmol, 1.1 equiv.) of benzylamine was added dropwise, and the mixture was stirred at 40°C for 2 h. The solvent was removed under reduced pressure and the residue treated with 30 mL of ether. The precipitate was eliminated by filtration through Celite and the organic phase concentrated under reduced pressure. The residue was purified by chromatography on silica gel (ether:pentane, 20:80) to give 4.13 g (60% overall yield from (2*S*)-**8**) of a 1:1 diastereomeric mixture of (2*R*,3*R*)- and (2*S*,3*R*)-2-*N*(benzylamino)-4-(*tert*-butyldimethylsiloxy)-3-methylbutyronitrile **10**, which were separated, although not necessary for the following steps, by a second chromatography on silica gel (ether:hexane, 5:95).

*First diastereomer (2R,3R)- or (2S,3R)-**10***: R_f: 0.46 (ether:pentane, 25:75), colourless oil; $[\alpha]_D^{20}$ +84 (*c* = 1, CCl_4): IR (CCl_4): 3340 (NH), 3040, 2960–2860, 2210 ($\nu_{C=O}$), 1260 (C—Si) 1100 (CH_2OSi) cm^{-1}; ^1H NMR (200 MHz, $CDCl_3$) δ: 0.05 (s, 6H, CH_3Si), 0.85 (s, 9H, $C(CH_3)_3$), 1.15 (d, 3H, *J* = 7 Hz, CH_3), 2.15 (m, 2H), 3.50–3.70 (m, 3H), 3.85 (d, 1H, *J* = 12.78 Hz), 4.05 (d, 1H, *J* = 12.78 Hz), 7.45 (m, 5H); ^{13}C NMR (50 MHz, $CDCl_3$) δ: –5.64 (CH_3Si), 13.20, 18.08, 25.74, 38.39, 51.89, 53.30, 65.07, 119.45 (C≡N), 127.36, 128.38, 128.44, and 138.45 (arom. C). Anal. calcd. for $C_{18}H_{30}N_2OSi$ (318.54): C 67.88, H 9.49; found: C 67.63, H 9.46.

*Second diastereomer (2S,3R)- or (2R,3R)-**10***: R_f: 0.40 (ether:pentane, 25:75), colourless oil; $[\alpha]_D^{20}$ –59 (*c* = 1, CCl_4); IR (CCl_4): 2210 ($\nu_{C=O}$) cm^{-1}; ^1H NMR (250 MHz, $CDCl_3$) δ: 0.05 (s, 6H, $Si(CH_3)_2$), 0.85 (s, 9H, $C(CH_3)_3$), 1.07 (d, 3H, *J* = 6.9 Hz, CH_3), 1.88 (br s, 1H, NH), 2.05 (m, 1H, CH_3), 3.55–3.75 (m, 3H), 3.82 (d, 1H, *J* = 12.9 Hz), 4.14 (d, 1H, *J* = 12.9 Hz), 7.45 (m, 5H, arom. H); ^{13}C NMR (50 MHz, $CDCl_3$) δ: –5.61 (CH_3Si), 12.65, 18.08, 25.72, 38.83, 50.69, 51.96, 64.30, 119.25 (C≡N), 127.41, 128.31, 128.47, and 138.32 (arom. C). Anal. calcd. for $C_{18}H_{30}N_2OSi$ (318.54): C 67.88, H 949; found: C 67.92, H 9.52.

(3R)-2-(N-Benzylamino)-4-hydroxy-3-methylbutyronitrile ***11***a

To a solution of 330 mg (1.04 mmol) of the 1:1 stereoisomeric mixture of (3*R*)-2-(*N*-benzylamino)-4-*tert*-butyldimethylsiloxy-3-methylbutyronitrile **10** in 4 mL of anhydrous THF, under argon, was added at room temperature 2.7 mL (2.7 mmol) of a 1 M solution of *N*-tetrabutylammonium fluoride in THF. The mixture was stirred at room temperature for 30 min. The solvent was removed under reduced pressure and the residue treated with 20 mL of ether. The organic phase was washed with 2 mL of half-saturated sodium chloride, dried on sodium sulfate, filtered, and concentrated under reduced pressure, to produce a brown oil that was purified by chromatography on silica gel (ether:hexane, 90:10) to offer 200 mg (94%) of a 1:1 stereoisomeric mixture of (2*R*,3*R*)- and (2*S*,3*R*)-2-(*N*-benzylamino)-4-hydroxy-3-methylbutyronitrile **11***a*: IR (neat): 3700–3140 ($\nu_{OH,NH}$), 2210 (ν_{C-O}), cm^{-1}; ^1H NMR (200 MHz, $CDCl_3$) δ: 1.05 (d, 3H, *J* = 7.16 Hz, CH_3), 1.09 (d, 3H, *J* = 7.52 Hz, CH_3), 2.15 (m, 4H), 2.50 (nr s, 2H, OH), 3.52 (m, 2H), 3.70 (m, 4H), 3.80 (d, 1H, *J* = 12.9 Hz), 4.09 (d, 1H, *J* = 12.9 Hz), 3.84 (d, 1H, *J* = 12.7 Hz), 4.1 (d, 1H, *J* = 12.7 Hz), 7.30 (m, 10H, arom. H); ^{13}C NMR (50 MHz, $CDCl_3$) δ: 12.61, 13.82, 38.39, 37.79, 51.91, 53.37, 54.67, 65.44, 68.88, 118.74 (C≡N), 127.70, 127.84, 128.39, 128.68, 128.74, and 137.47 (arom. H). Anal. calcd. for $C_{12}H_{16}N_2O$ (204.27): C 70.56, H 7.89; found: C 70.50, H 8.08.

(3R)-2-(N-Benzylamino)-4-(p-tolylsulfonyloxy)-3-methylbutyronitrile ***11***b

(a) Tosylation by tosyl chloride in pyridine

To a solution of 347 mg (1.7 mmol) of (3*R*)-2-(*N*-benzylamino)-4-hydroxy-3-methylbutyronitrile **11***a* in 8.5 mL of freshly distilled pyridine was added portionwise at 0°C under argon 356 mg (1.9 mmol) of tosyl chloride. The mixture was kept at 0°C for 48 h. After addition of 10 mL of water, the aqueous phase was extracted by 2 × 20 mL of ether; then the gathered organic phases were washed twice with 5 mL of a 0.1 M hydrochloric acid solution and with 5 mL of a saturated solution of sodium bicarbonate, dried on anhydrous sodium sulfate, filtered, and concentrated under reduced pressure to give a residue identical with the alcohol **11***a*.

(b) Tosylation by tosyl chloride and pyridine in chloroform

To a solution of 300 mg (1.5 mmol) of (3*R*)-**11***a* and 243 μL (3 mmol, 2 equiv.) of pyridine in 2 mL of chloroform freshly purified by chromatography through basic alumina (to remove stabilizing ethanol) was added, at 0°C under argon, 430 mg (2.25 mmol, 1.5 equiv.) of tosyl chloride in 500 μL of chloroform. The mixture was kept at 0°C for 48 h. After work-up (see above), ^1H NMR of the crude residue showed the formation of a 2.6:4.2:3.2 mixture of *N,O*-ditosyloxy, *N*-tosyloxy, and *O*-tosyloxy derivatives of **11***a*.

(c) Tosylation by tosyl chloride, triethylamine, and 4-N,N-dimethylaminopyridine in dichloromethane

To a solution of 1 g (4.9 mmol) of benzylaminoalcohol **11***a* in 20 mL of dichloromethane were added 750 μL (5.39 mmol, 1.1 equiv.) of triethylamine and 30 mg (5%) of 4-*N,N*-dimethylaminopyridine (DMAP). The mixture was cooled to 0°C, then a solution of 1.03 g (5.39 mmol, 1.1 equiv.) of tosyl chloride in 10 mL of dichloromethane was added dropwise. The mixture was stirred at 0°C for 4 h and added to 100 mL of dichloromethane. After the usual work-up (see above) the residue was purified by chromatography on silica gel to offer 1.6 g (91%) of a 1:1 diastereomeric mixture of (3*R*)-2-(*N*-benzylamino)-3-methyl-4-(*para*-tolylsulfonyloxy)butyronitrile **11***b* as a colourless oil: IR (neat): 3340–3220 (ν_{NH}), 2220 ($\nu_{C\equiv N}$), 1600 ($\nu_{C=C}$) cm^{-1}; ^1H NMR (200 MHz, $CDCl_3$) δ: 1.07 (d, 3H, *J* = 7.2 Hz, CH_3), 1.09 (d, 3H, *J* = 7.2 Hz), 1.51 (br s, 2H, NH), 2.25 (m, 2H), 2.44 (s, 6H), 3.4–4.2 (m, 10H), and 7.29–7.80 (m, 18H, arom. H); ^{13}C NMR (50 MHz, $CDCl_3$) δ: 11.73, 12.86, 21.04, 35.69, 50.44, 50.97, 51.29, 70.06, 118.11 (C≡N), 118.40 (C≡N), 127, 127.33, 127.70, 128.01, 129.52, 132.09, 137.76, and 144.63 (arom. C).

(3R)-2-(N-Benzylamino)-4-chloro-3-methylbutyronitrile ***11***c

To 16 mL of *N*-methylpyrrolidone (NMP) under argon was added

Can. J. Chem. Downloaded from www.nrcresearchpress.com by EESC ESCOLA DE ENGENHARIA on 09/08/12
For personal use only.

528 mg (12.5 mmol, 3 equiv.) of lithium chloride. The mixture was stirred at room temperature until complete dissolution of LiCl. Then, a solution of 1.5 g (4.19 mmol) of (3*R*)-2-(*N*-benzylamino)-3-methyl-4-*p*-tolylsulfonyloxybutyronitrile **11***b* in 3 mL of NMP was added dropwise. The mixture was stirred at room temperature for 2 h, filtered through silica gel (ether:hexane, 25:75), and concentrated under reduced pressure to give 754 mg (81%) of a 1:1 diastereomeric mixture of (3*R*)-2-(*N*-benzylamino)-4-chloro-3-methylbutyronitrile **11***c* which was separated by chromatography on silica gel (ether:pentane, 25:75).

*First diastereomer (2*R*,3*R*) or (2*S*,3*R*)-**11**c*: R_f: 0.54 (ether:pentane, 50:50); colourless oil; $[\alpha]_D^{20}$ + 104.3 (*c* = 1, CCl_4); IR (CCl_4): 3380–3320 (ν_{NH}), 1600 (ν arom.$_{C=C}$) cm^{-1}; ^1H NMR (200 MHz, $CDCl_3$) δ: 1.20 (d, 3H, *J* = 6.78 Hz), 1.57 (br s, 1H, NH), 2.25 (m, 1H), 3.3–3.75 (m, 3H), 3.82 (d, 1H, *J* = 12.84 Hz), 4.08 (d, 1H, *J* = 12.84 Hz), 7.35 (m, 5H, arom. H); ^{13}C NMR (50 MHz, $CDCl_3$) δ: 13.83, 38.96, 46.18, 51.56, 51.86, 119.12 (C≡N), 127.54, 128.26, 128.47, and 138.05. Anal. calcd. for $C_{12}H_{15}ClN_2$ (222.77): C 64.71, H 7.02, Cl 15.94; found: C 64.49, H 6.78, Cl 15.92.

*Second diastereomer (2*S*,3*R*)- or (2*R*,3*R*) **11**c*: R_f: 0.5 (ether:pentane, 50:50); colourless oil; $[\alpha]_D^{20}$ −104.7 (*c* = 1, CCl_4); IR (CCl_4): 3400–3000 (ν_{NH}), 2210 ($\nu_{C\equiv N}$), 1610 (ν arom.$_{C=C}$) cm^{-1}; ^1H NMR (200 MHz, $CDCl_3$) δ: 1.21 (d, 3H, *J* = 6.78 Hz), 1.57 (br s, 1H, NH), 2.21 (m, 1H), 3.43–3.81 (m, 3H), 3.86 (d, 1H, *J* = 12.86 Hz), 4.15 (d, 1H, *J* = 12.86 Hz), 7.35 (m, 5H, arom. H); ^{13}C NMR (50 MHz, $CDCl_3$) δ: 14.54, 38.50, 46.59, 51.79, 52.31, 118.35 (C≡N), 127.61, 128.31, 128.54, and 137.97. Anal. calcd. for $C_{12}H_{15}ClN_2$ (222.77): C 64.71, H 7.02, Cl 15.94; found: C 64.96, H 6.78, Cl 16.17.

*(3*R*)-2-(*N*-Benzylideneamino)-4-chloro-3-methylbutyronitrile 3*

To a solution of 35.74 mg (0.59 mmol, 1.1 equiv.) of oxalyl chloride in 1.3 mL of dichloromethane, under argon at –60°C, was added dropwise a solution of 76.30 mg (1.2 mmol, 2.2 equiv.) in 140 μL of dichloromethane. The mixture was stirred for 5 min at –60°C and a solution of 120 mg (0.54 mmol) of (3*R*)-2-(*N*-benzylamino)-4-chloro-3-methylamine in 675 μL of dichloromethane was added within 5 min. The mixture was stirred at –60°C for 20 min, then cooled to –78°C to add 450 μL (2.7 mmol, 5 equiv.) of triethylamine. The mixture was allowed to reach room temperature and 1.1 mL of water was added. After separation, the aqueous phase was extracted by 2 × 10 mL of dichloromethane. The gathered organic phases were washed by 2 mL of saturated NaCl, and concentrated under reduced pressure to eliminate dichloromethane. The residue was dissolved with 15 mL of ether, dried on anhydrous sodium sulfate, and after filtration the solvent was removed under reduced pressure to give a yellow oil that was purified by chromatography on silica gel (ether:hexane, 20:80, containing 1% of triethylamine) to give 84 mg (70%) of a 1:1 mixture of (2*R*,3*R*)- and (2*S*,3*R*)-2-(*N*-benzylideneamino)-4-chloro-3-methylbutyronitriles **3** as a pale yellow oil: IR (CCl_4): 2215 ($\nu_{C\equiv N}$), 1665 ($\nu_{C=C}$), 1600 ($\nu_{C=C}$) cm^{-1}; ^1H NMR (250 MHz, $CDCl_3$) δ (diastereomeric mixture): 1.18 (d, 3H, *J* = 6.78 Hz), 1.22 (d, 3H, *J* = 6.72 Hz), 2.50 (m, 2H), 3.67 (m, 4H), 4.88 (dd, 1H, *J* = 6.65 and 1.6 Hz), 4.97 (dd, 1H, *J* = 4.52 and 1.60 Hz), 7.50 (m, 6H), 7.8 (m, 4H), 8.57 (d, 2H, *J* = 1.6 Hz); ^{13}C NMR (50 MHz, $CDCl_3$) δ: 13.89, 14.17, 39.96, 40.29, 46.06, 46.51, 59.57, 60.79, 116.34 (C≡N), 128.78, 131.89 and 134.79 (arom. C), 163.86 (C=N), 164.09 (C≡N); MS (CI, NH_3) (*m/z*): 221 (100), 200 (M^+, 1.71), 199 (M – 1, 2.44).

*(1*S*,2*S*)-1-(*N*-Benzylideneamino)-2-methylcyclopropanecarbonitrile 2*

To a solution of 110 mg (0.5 mmol) of (3*R*)-2-(*N*-benzylideneamino)-4-chloro-3-methylbutyronitrile in 2 mL of dimethylformamide (DMF) was added, portionwise, 76 mg (0.55 mmol, 1.1 equiv.) of potassium carbonate. The mixture was stirred at room temperature for 30 min, then 40 mL of ether and 4 mL of water were added. After separation, the organic phase was washed by 2 × 4 mL of water, dried on anhydrous magnesium sulfate, filtered, and concentrated under reduced pressure to give a brown oil that, after chromatography on alumina (ether:pentane, 20:80), gave 75 mg (80%) of a 84:16 mixture of (1*S*,2*S*)- and (1*R*,2*S*)-cyclopropanecarbonitriles **2** and **13**. A second chromatography on silica gel (ether:hexane, 10:90 containing 1% of triethylamine) provided a 94:6 diastereomeric mixture containing as major product the (1*S*,2*S*)-1-(*N*-benzylideneamino)-2- methylcyclopropanecarbonitrile **2** as a pale yellow oil: IR (CCl_4): 2215 ($\nu_{C\equiv N}$) and 1650 ($\nu_{C=N}$) cm^{-1}; 1H NMR (200 MHz, $CDCl_3$) δ (94:6 diastereomeric mixture): 1.42 (d, 3H, *J* = 6.09 Hz, CH_3), 1.45–1.68 (m, 2H), 1.78 (m, 1H), 7.45 (m, 3H), 7.70 (m, 2H), 8.6 (s, 1H, CH=N, major diastereomer **2**), 8.65 (s, 1H, CH=N, minor diastereomer **13**); ^{13}C NMR (50 MHz, $CDCl_3$) δ (94:6 diastereomeric mixture): 12.29, 14.94, 25.14, 25.65, 26.26, 29.64, 42.70, 117.06 (C≡N), 128.05, 128.63, 130.99, 135.31, 158.99 (CH=N), 160.07 (CH=N); MS (70 ev) (*m/z*) ((1*S*,2*S*)-**2**): 184 (M^+, 60.58), 169 (87.89), 142 (99.60), 115 (69.29), 104 (79.70), 89 (100), 77 (50.02); ((1*R*,2*S*)-**13**): 184 (M^+, 58.20), 169 (72.60), 142 (100), 115 (75.61), 104 (71.04), 89 (98.57), 77 (43.79).

*(1*S*,2*S*)-1-Amino-2-methylcyclopropanecarbonitrile hydrochloride **14***

To a solution of 70 mg (0.38 mmol) of (1*S*,2S)-1-(*N*-benzylideneamino)-2-methylcyclopropanecarbonitrile **2** in 2.4 mL of ether was added dropwise 4.8 mL (4.8 mmol) of a 1 M hydrochloric acid solution. The mixture was stirred at room temperature for 15 h. After separation, the aqueous phase was extracted by 2 × 0.5 mL of ether, and concentrated under reduced pressure to give 50 mg (100%) of a 94:6 diastereomeric mixture of (1*S*,2*S*)-**14** and (1*R*,2*S*)-1-amino-2-methylcyclopropanecarbonitrile hydrochloride as a white solid: ^1H NMR (200 MHz, DMSO-d_6) δ (94:6 diastereomeric mixture) **14**: 1.19 (d, 3H, *J* = 6.7 Hz, CH_3, major diastereomer), 1.29 (d, 3H, *J* = 6.27 Hz, CH_3, minor diastereomer), 1.35 (dd, 2H, *J* = 7.40 and 6.40 Hz), 1.58–1.90 (m, 2H); ^{13}C NMR (50 MHz, DMSO-d_6) δ (94:6 diastereomeric mixture): 14.09, 19.02, 19.85, 26.57, 118.51 (C≡N).

*(1*S*,2*S*)-Norcoronamic acid **1**a*

(a) Acid hydrolysis

A solution of 16 mg (0.12 mmol) of (1*S*,2*S*)-1-amino-2-methylcyclopropanecarbonitrile hydrochloride **14** (containing 6% of its (1*R*,2*S*) diastereomer) in 2 mL (12 mmol) of 6 M hydrochloric acid was refluxed for 11 h. Removal of water and HCl under reduced pressure left 18 mg (100%) of a 94:6 mixture of (1*S*,2*S*)- and (1*R*,2*S*)-norcoronamic acid hydrochloride as a white solid: ^1H NMR (200 MHz, D_2O) δ (94:6 diastereomeric mixture): 0.93 (d, 3H, *J* = 7.45 Hz, CH_3, minor diastereomer), 1.04 (d, *J* = 6.10 Hz, CH_3, major diastereomer), 1.20–1.41 (m, 2H), 1.44–1.70 (m, 1H); ^{13}C NMR (50 MHz, D_2O, dioxane as internal reference) δ: 11.92, 20.78, 23.45, 47.81, 172.5 (COOH). Finally, ion exchange chromatography through Dowex resin (50 × 8-100) with water until the eluent was neutral gave 11 mg (97%) of (1*S*,2*S*)-norcoronamic acid **1***a*.

(b) Basic hydrolysis

To a solution of 12 mg (0.09 mmol) of 1-amino-2-methyl cyclopropanecarbonitrile hydrochloride **14** in 500 μL of water was added 16 mg (0.4 mmol, 4.5 equiv.) of sodium hydroxide and the mixture was refluxed for 24 h. After cooling to 0°C, concentrated hydrochloric acid was added until the solution was neutral. Reverse-phase liquid chromatography through octadecyl-functionalized silica gel gave 8 mg (100%) of a 94:6 mixture of (1*S*,2*S*)- and (1*R*,2*S*)-norcoronamic acid **1***a* as a white solid: ^1H NMR (250 MHz, D_2O) δ (94:6 diastereomeric mixture): 0.75 (m, 1H, minor diastereomer), 1.03 (d, 3H, *J* = 6 Hz, CH_3, major diastereomer), 1.08–1.22 (m, 2H), 1.30–1.48 (m, 1H) in accordance with the literature (47).

*Determination of the enantiomeric excess of (1*S*,2*S*)-norcoronamic acid **1**a*

To a solution of 38 mg (0.33 mmol) of norcoronamic acid in 83 μL of 4 N sodium hydroxide aqueous solution was added 113 mg of chloroacetic acid anhydride and 167 μL of 4 N sodium hydroxide aqueous solution. The mixture was stirred at room temperature for 4 h and the aqueous phase extracted by 12 × 5 mL of ethyl acetate. The gathered organic phases were dried on anhydrous sodium sulfate and, after filtration, concentrated under reduced pressure. The residue was dis-

Can. J. Chem. Downloaded from www.nrcresearchpress.com by EESC ESCOLA DE ENGENHARIA on 09/08/12
For personal use only.

solved in methanol. Reverse-phase chromatography (octadecyl-functionalized silica gel) eluted by methanol:water (90:10) provided 10 mg (16%) of (1*S*,2*S*)-*N*-chloroacetyl norcoronamic acid **16** as a yellow oil: ^{1}H NMR (250 MHz, D_2O) δ (94:6 diastereomeric mixture): 1.01 (d, 3H, J = 6.16 Hz, CH_3, major diastereomer), 1.07 (dd, 1H, J = 9.67 and 5.20 Hz), 1.22–1.28 (m, 1H), 1.38–1.46 (m, 1H), 1.67 (br s, 1H), 3.88 (s, 2H, CH_2Cl, major diastereomer), 3.92 (s, 2H, CH_2Cl, minor diastereomer); ^{13}C NMR (250 MHz, D_2O, dioxane as internal reference) δ (94:6 diastereomeric mixture): 12.44, 24.88, 26.42, 39.19, 43.11, 171.90, and 175.69 (C=O).

To a solution of 6.30 mg (0.033 mmol) of (1*S*,2*S*)-*N*-chloroacetyl norcoronamic acid **16** in 2 mL of 0.1 M potassium phosphate in water was added 1.5 mg of porcine Kidney Acylase. The mixture was stirred at 37°C for 15 h. After filtration and removal of water under reduced pressure, the residue was dried under high vacuum (0.05 Torr) to give 4 mg of crude (1*S*,2*S*)-norcoronamic acid; ^{1}H NMR spectroscopy exhibited complete disappearance of the *N*-chloroacetyl signal at δ 3.88 ppm.

*2-(Hydroxymethyl)butanol **19***

To a solution of 6 g (159.6 mmol) of lithium aluminum hydride in 150 mL of anhydrous diethyl ether under argon was added dropwise a solution of 20 g (106.4 mmol) of ethyl 2-ethylmalonate in 150 mL of ether. The mixture was stirred at room temperature for 1.5 h, then cooled to 0°C and hydrolyzed by portionwise addition of wet sodium sulfate until a clear solution was obtained. After filtration through a sintered glass funnel, the organic phase was dried on anhydrous sodium sulfate and concentrated on a rotary evaporator to give an oil that was distilled to yield 8.86 g (80%) of pure 2-(hydroxymethyl)butanol **19**: bp 128°C/12 Torr; IR (neat): 3700–3020 (ν_{OH}), 2960–2860 cm^{-1}; ^{1}H NMR (250 MHz, $CDCl_3$) δ: 0.95 (3H, t, J = 7.4 Hz), 1.31 (2H, dq, J = 7.4 and 5.1 Hz), 1.70 (1H, m), 2.35 (2H, t, J = 4.2 Hz), 3.58–3.84 (4H); ^{13}C NMR (50 MHz, $CDCl_3$) δ: 11.4 (CH_3), 20.39 (CH_2), 43.62 (CH), 64.26 (CH_2O); MS (70 eV) (*m/z*) (%): 86 (M – 18, 2), 68 (7.2), 57 (30), 56 (100), 41 (27.50).

*(2S)-2-(Hydroxymethyl)butyl acetate **21***

To a solution of 3 g (29 mmol) of 2-(hydroxymethyl)butanol **19** in 58 mL of diisopropyl ether containing 1.6 g of lipase PS (*Pseudomonas cepacia* (55) was added dropwise 5.4 mL (58 mmol, 2 equiv.) of vinylacetate. The mixture was stirred at room temperature for 1 h, until complete disappearance of the 1,3-diol as monitored by TLC, then filtered through a sintered glass funnel, and concentrated by removal of the solvent on a rotary evaporator. The residue was purified by chromatography on silica gel (ether:pentane, 50:50) to yield 760 mg (18.5%) of (2*S*)-2-(hydroxymethyl)butyl acetate **21** as a colourless oil: $[\alpha]_D^{20}$ –13.8 (*c* 1, $CHCl_3$); IR (neat): 3700–3100 (ν_{OH}), 1745 ($\nu_{C=O}$) cm^{-1}; ^{1}H NMR (250 MHz, $CDCl_3$) δ: 0.97 (3H, t, J = 7.45 Hz), 1.37 (2H, m), 1.91 (1H, br s), 2.1 (3H, s), 3.47–3.68 (2H, m), 4.11 (1H, dd, J = 11.26 and 6.38 Hz), 4.24 (1H, dd, J_{AB} = 11.26 and 4.42 Hz); ^{13}C NMR (250 MHz, $CDCl_3$) δ: 11.27 (CH_3), 20.55 (CH_2), 20.77 (CH_3CO), 41.90 (CH), 62.12 (CH_2O), 64.30 (CH_2O), 171.64 (C=O); MS (CI/NH_3) (*m/z*) (%): 147 (M – H$^+$, 0.14), 129 (0.12), 103 (M$^+$ – CH_3CO, 2.45), 61 (29), 57 (23), 56 (70), 43 (100). Anal. calcd. for $C_7H_{14}O_3$ (146.19): C 57.51, H 9.65; found: C 56.37, H 9.63.

The >95% enantiomeric excess of (2*S*)-**21** was determined from its ^{1}H NMR spectra, recorded in the presence of Eu(hfc)$_3$, in comparison with the corresponding racemic monoacetate.

*2-(Acetoxymethyl)butyl acetate **22***

To a solution of 5 g (48 mmol) of 2-(hydroxymethyl)butan-1-ol **24** in 48 mL of diethyl ether containing 12.9 g (105.6 mmol) of 4-*N*,*N*-dimethylaminopyridine was added dropwise 10 mL (105.6 mmol) of acetic anhydride. The mixture was stirred for 1.5 h, then filtered through a sintered glass funnel. Removal of the solvent on a rotary evaporator left an oil that was purified by chromatography on silica gel (ether:pentane, 20:80) to give 8.7 g (98%) of diacetate **22**; bp 108°C/15 Torr; IR (neat): 1745 ($\nu_{C=O}$) cm^{-1}; ^{1}H NMR (200 MHz, $CDCl_3$) δ: 0.95 (3H, t, J = 7.43 Hz), 1.41 (2H, d, J = 7.3 Hz), 1.91 (1H, m), 2.05 (6H, s, CH_3-CO), 4.02 (2H, dd, J = 11.10 and 6.08 Hz), 4.09 (2H, dd, J = 11.10 and 5.38 Hz); ^{13}C NMR (50 MHz, $CDCl_3$) δ: 11.91 (CH_3), 20.85 (CH_2), 20.98 (CH_3-CO), 38.71 (CH), 64.30 (CH_2O), 171.09 (C=O); MS (CI/NH_3) (*m/z*) (%): 206 (M$^+$ + 18, 100), 189 (M$^+$ + 1, 6), 188 (M$^+$, 0.1).

*(2R)-2-(Hydroxymethyl)butyl acetate **23***

In a 200 mL Erlenmeyer fitted with an automatic burette and a pH-meter was stirred at room temperature a suspension of 2 g of lipase PS (*Pseudomonas cepacia*) in 100 mL of a buffered (pH 7.2) aqueous 0.1 M phosphate solution (KH_2PO_4). Then 2 g (10.6 mmol) of 1,3-diacetate **22** was added dropwise. The pH was maintained at 7.2 by the automatic addition of 2 M NaOH. When 3.62 mL of NaOH was consumed (69% of hydrolysis), the mixture was filtered through Celite and extracted by 5 × 200 mL of ether. The organic phase was dried over anhydrous sodium sulfate and concentrated on a rotary evaporator to leave an oil that was purified by chromatography on silica gel (ether:pentane, 50:50) yielding 1 g (65%) of (2*R*)-2- (hydroxymethyl)butyl acetate **23** as a colourless oil: $[\alpha]_D^{20}$ +12.1 (*c* 1, $CHCl_3$), ee >88% determined by ^{1}H NMR in the presence of Eu(hfc)$_3$, as compared to the racemic monoacetate **23**. IR (neat): 3700–3100 (ν_{OH}), 1745 ($\nu_{C=O}$) cm^{-1}; ^{1}H NMR (200 MHz, $CDCl_3$) δ: 0.89 (3H, t, J = 7.33 Hz), 1.28 (2H, m), 1.67 (1H, m), 2.01 (3H, s), 2.66 (1H, br s), 3.44 (1H, dd, J = 13.14 and 5.60 Hz), 3.54 (1H, dd, J = 13.14 and 4.29 Hz), 4.04 (1H, dd, J = 14.44 and 6.56 Hz), 4.24 (1H, dd, J = 14.44 and 4.48 Hz); ^{13}C NMR (62.5 MHz, $CDCl_3$) δ: 11.22 (CH_3), 20.55 (CH_2), 20.73 (CH_3CO), 41.83 (CH), 62.00 (CH_2O), 64.28 (CH_2O), 171.59 (C=O); MS (70 eV) (*m/z*) (%): 146 (M$^+$, 0.03), 128 (M – 18, 0.12), 117 (M – 29, 0.17), 103 (M – 43, 6.37), 61 (42), 57 (33), 56 (76), 43 (100). Anal. calcd. for $C_7H_{14}O_3$ (146.19): C 57.51, H 9.65; found: C 56.53, H 9.58.

*(2S)-2-Methylbutan-1-ol **24***

To a solution of 200 mg (1.4 mmol) of acetate (2*R*)-**23** in 7 mL of dichloromethane containing 250 mg (2.1 mmol) of 4-*N*,*N*-dimethylaminopyridine was added 530 mg (2.8 mmol) of tosyl chloride. The mixture was stirred at room temperature for 48 h, and then 35 mL of dichloromethane was added. The organic phase was washed by 5 mL of saturated sodium chloride solution, dried over anhydrous sodium sulfate, and concentrated on a rotary evaporator. The residue was purified by chromatography on silica gel to yield 252 mg (60%) of (2*S*)-3-(*p*-tolylsulfonyloxy)-2-ethylprop-1-yl acetate: IR (neat): 1750 ($\nu_{C=O}$) and 1600 ($\nu_{C=C}$) cm^{-1}; ^{1}H NMR (200 MHz, $CDCl_3$) δ: 0.85 (3H, t, J = 7.45 Hz), 1.23–1.41 (2H, m), 1.81–2.04 (1H, m), 1.92 (3H, s), 2.42 (3H, s), 3.85–4.08 (4H, m), 7.33 (2H, d, J = 8.1 Hz), 7.76 (2H, d, J = 8.1 Hz); ^{13}C NMR (50 MHz, $CDCl_3$) δ: 10.88 (CH_3), 20.31 (CH_2), 20.55, 21.49, 38.88 (CH), 62.93 and 69.25 (CH_2O), 127.79, 129.73, 132.57 and 144.75 (arom. C), 170.60 (C=O).

To a solution of 50 mg (1.33 mmol) of lithium aluminum hydride in 7 mL of ether was added dropwise a solution of 120 mg (0.4 mmol) of (2*S*)-2-(*p*-tolylsulfonyloxy-2-ethylprop-1-yl acetate in 3 mL of ether. The mixture was stirred at room temperature for 1 h and hydrolyzed by portionwise addition of wet sodium sulfate to get a clear solution. After filtration through a sintered glass funnel the organic phase was dried on anhydrous sodium sulfate and concentrated on a rotary evaporator. The residue was purified by chromatography on silica gel (ether:hexane, 50:50) to yield 31.7 mg (90%) of (2*S*)-2-methylbutanol **29** as a colourless oil:$[\alpha]_D^{20}$ –6.7, *c* 1, ethanol (56).

*(2S)-2-(*tert*-Butyldimethylsiloxymethyl)butanol **25***

To a solution of 1.75 g (25.7 mmol) of imidazole and 1.86 g (12.3 mmol) of *tert*-butyldimethylsilyl chloride in 12.5 mL of DMF containing 50 mg (0.4 mmol) of *N*,*N*-dimethylaminopyridine was added 1.5 g (10.3 mmol) of (2*R*)-2-(hydroxymethyl)butyl acetate **23**. The mixture was stirred for 2 h at room temperature, then 500 mL of ether and 50 mL of water were added. The organic phase was separated and washed by 3 × 50 mL of water, dried on anhydrous sodium sulfate, and concentrated on a rotary evaporator to give an oil that was purified by chromatography on silica gel (pentane:ether, 90:10) to yield 2.52 g (94%) of 2*S*)-2-(*tert*-butyldimethylsiloxymethyl)butanol **25**: ($[\alpha]_D^{20}$ –2.3, *c* 1,

Can. J. Chem. Downloaded from www.nrcresearchpress.com by EESC ESCOLA DE ENGENHARIA on 09/08/12
For personal use only.

$CDCl_3$); IR (neat): 1750 ($\nu_{C=O}$), 1250 (ν_{C-Si}) cm^{-1}; ^1H NMR (200 MHz, $CDCl_3$) δ: 0.04 (6H, s) 0.89 (9H, s), 0.93 (3H, t, J = 7.41 Hz), 1.36 (2H, m), 1.72 (1H, m), 2.06 (3H, s), 3.55 (1H, dd, J = 10.05 and 5.84 Hz), 3.61 (1H, dd, J = 10.05 and 4.97 Hz), 4.07 (2H, d, J = 5.8 Hz); ^{13}C NMR (250 MHz, $CDCl_3$) δ: –5.67, 11.31, 18.16, 20.61, 20.78, 25.76, 41.77, 62.15, 64.29, 170.94. Anal. calcd. for $C_{13}H_{28}O_3Si$ (260.45): C 59.96, H 10.85; found: C 60.25, H 10.72.

To a solution of 1.5 g (5.75 mmol) of this acetate in 45 mL of methanol was added 2.6 g (18.5 mmol) of potassium carbonate and the mixture was stirred for 2 h. Then, 250 mL of ether and 30 mL of saturated ammonium chloride solution were added. The mixture was stirred, the organic phase separated and dried on anhydrous sodium sulfate, and concentrated on a rotary evaporator. The residue was purified by chromatography on silica gel to yield 1.12 g (89%) of (2*S*)-2-(*tert*-butyldimethylsiloxymethyl)butanol **25** as a colourless oil: $[\alpha]_D^{20}$ –8.6, *c* 0.8, $CHCl_3$); IR (neat): 3700–3100 (ν_{OH}) cm^{-1}; ^1H NMR (250 MHz, $CDCl_3$) δ: 0.08 (6H, s), 0.9 (9H, s), 0.93 (3H, t, J = 7.39 Hz), 1.15–1.35 (2H, m), 1.55–1.75 (1H, m), 2.95 (1H, dd, J = 6.5 and 4.8 Hz), 3.47–3.86 (4H, m); ^{13}C NMR (50 MHz, $CDCl_3$) δ: –5.64 (CH_3-Si), 11.74 (CH_3), 18.12 (C), 20.55, 25.82, 43.57, 66.45 and 67.22 (CH_2-O); MS (EI) (*m/z*): 161 (M – 57, 5.64), 105 (29), 75 (100), 74 (47), 69 (39); MS (CI, NH_3) (*m/e*): 220 (M^+ + 2, 27), 219 (M^+ + 1, 100). Anal. calcd. for $C_{11}H_{26}O_2Si$ (218.41): C 60.49, H 11.20; found: C 60.54, H 11.78.

*(2*R*)-2-(*tert*-Butyldimethylsiloxymethyl)butanal **26***

To a solution of 0.87 mL (9.9 mmol) of oxalyl chloride in 23 mL of dichloromethane at –60°C was added dropwise within 5 min a solution of 0.82 mL (11.6 mmol) of DMSO in 1.8 mL of dichloromethane. The mixture was stirred for 5 min and a solution of 1.8 g (8.25 mmol) of (2*S*)-**25** in 16 mL of dichloromethane was added dropwise. The mixture was stirred at –60°C for 20 min, cooled to –78°C, and 8.34 mL (48 mmol) of *N,N*-diisopropylethylamine was added. The mixture was allowed to reach 0°C and poured into 50 mL of ice-water. The aqueous phase was extracted by 2 × 50 mL of dichloromethane. The collected organic phases were successively washed by 2 × 20 mL of 1 M HCl solution and 20 mL of a buffered 0.1 M phosphate solution (pH 7). Removal of dichloromethane on a rotary evaporator left a residue that was dissolved in 50 mL of ether. The ethereal solution was dried on anhydrous sodium sulfate, filtered, and concentrated on a rotary evaporator to give the crude aldehyde **26**, which was directly used for the next step.

However, a 50 mg sample was purified by chromatography on silica gel (ether:pentane, 25:75) to give the pure aldehyde. IR (neat): 1730 ($\nu_{C=O}$), 1250 (ν_{C-Si}) cm^{-1}; ^1H NMR (250 MHz, $CDCl_3$) δ: 0.05 (6H, s), 0.87 (9H, s), 0.96 (3H, t, J = 7.40 Hz), 1.49–1.75 (2H, m), 2.35 (1H, m), 3.86 (2H, d, J = 5.65 Hz), 9.7 (1H, d, J = 2.42 Hz); ^{13}C NMR (250 MHz, $CDCl_3$) δ: –5.57 (CH_3-Si), 11.42 (CH_3-CH_2-), 18.54 (CH_2-CH_3), 18.17 (C), 25.75 (C-CH_3), 55.75 (CH), 61.56 (CH_2-O), 204.97 (C=O); MS (CI, NH_3) (*m/z*): 234 (M^+ + 18, 16), 217 (M^+ + 1, 100), 216 (M^+, 17).

*(3*S*)-2-(*N*-Benzylamino)-3-(*tert*-butyldimethylsiloxymethyl)valeronitrile **27***

To a solution of 1.8 g (7 mmol) of aldehyde (2*R*)-**26** in 14 mL of anhydrous diethyl ether containing 12 mg (0.03 mmol) of zinc iodide was added dropwise 1.71 mL (8.8 mmol) of trimethysilyl cyanide. The mixture was stirred at room temperature; after 1 h the aldehyde was totally consumed, as monitored by gas chromatography. The crude (3*S*)-2-(*N*-benzylamino)-3-(*tert*-butyldimethylsiloxymethyl)valeronitrile **27** was directly used for the next step. However, 50 mg were purified by chromatography on silica gel (ether:hexane, 10:90). IR (neat): 2080, 2960, 1260, and 1100 cm^{-1}; ^1H NMR (200 MHz, $CDCl_3$) δ: 0.06 (6H, s), 0.07 (6H, s), 0.21 (18H), 0.90 (18H, s), 0.97 (3H, t, J = 7.44 Hz), 0.98 (3H, t, J = 7.32 Hz), 1.2–1.8 (6H, m), 3.48–3.75 (4H, m), 4.63 (1H, d, J = 6.17 Hz), 4.65 (1H, d, J = 4.56 Hz); ^{13}C NMR (6.25 MHz, $CDCl_3$) δ: –5.51 and –0.47 (CH_3-Si), 11.70 (CH_3), 11.81 (CH_3), 18.98 (CH_2), 20.96 (C), 25.80 (CH_3-C), 47.89, 48.04, 60.12, 60,41, 61.43, 62.66, 119.56, and 120.25 (C≡N); MS (EI) (*m/z*): 287 (M^+, 0.21), 258 (M – 29, 15), 230 (M – 57, 0.78), 159 (100).

To a solution of 7 mmol of this nitrile in 21 mL of methanol at 0°C was added dropwise 0.84 mL (7.7 mmol) of benzylamine. The mixture was stirred at 60°C for 4 h; then, methanol was removed on a rotary evaporator and the residue was dissolved in 25 mL of anhydrous diethyl ether. After filtration of Celite and removal of ether in vacuo, the residue was purified by chromatography on silica gel (ether:pentane, 40:60) to yield 1.8 g (66% overall yield from (2*S*)-**25**) of a 1:1 diastereomeric mixture of (2*S*,3*S*)- and (2*R*,3*S*)-2-(*N*-benzylamino)-3-(*tert*-butyldimethylsiloxymethyl)pentanenitrile **27** as a colourless oil. IR (CCl_4): 3340 (ν_{N-H}), 2220 ($\nu_{C\equiv N}$) cm^{-1}; ^1H NMR (250 MHz, $CDCl_3$) δ: 0.057 (6H, s), 0.068 (6H, s), 0.84 (9H, s), 0.85 (9H, s), 0.94 (3H, t, J = 7.27 Hz), 0.95 (3H, t, J = 7.39 Hz), 1.10–2.0 (8H, m), 3.56–3.94 (6H, m), 3.78 (1H, d, J = 12.74 Hz), 3.79 (1H, d, J = 12.91 Hz), 4.07 (1H, d, J = 12.74 Hz), 4.09 (1H, d, J = 12.91 Hz), 7.34 (10H, m); ^{13}C NMR (50 MHz, $CDCl_3$) δ: –5.66 (CH_3-Si), 11.60, 11.80, 18.1, 20.44, 20.99, 25.75, 45, 45.11, 51.40, 51.93, 52.75, 61.65 and 63.46 (CH_2-O), 119.35 and 119.84 (C≡N), 127.40, 128.40, 128.47, and 138.50 (arom. C); MS (EI) (*m/z*): 261 (2.12), 245 (1.82), 244 (1.42), 219 (26), 218 (33), 217 (100), 216 (21).

*(3*S*)-2-(*N*-Benzylamino)-3-(chloromethyl)pentanenitrile **28***

To a solution of 1.7 g (5 mmol) of siloxyvaleronitrile (3*S*)-**27** in 18 mL of anhydrous THF was added, at room temperature, 11.3 mL (11.3 mmol) of a 1 M solution of *N*-tetrabutylammonium fluoride in THF. The mixture was stirred at room temperature for 30 min; then, THF was removed on a rotary evaporator and the residue was dissolved in 100 mL of ether and washed with 10 mL of half-saturated sodium chloride. The organic phase was dried over anhydrous sodium sulfate, filtered, and concentrated in vacuo. The residue was purified by chromatography on silica gel (ether:hexane, 75:25) to yield 1 g (92%) of a 1:1 diastereomeric mixture of (2*R*,3*S*)- and (2*S*,3*S*)-2-(*N*- benzylamino)-3-(hydroxymethyl)valeronitrile as a white paste. IR (neat): 3680–3140 ($\nu_{OH\ and\ NH}$), 2220 ($\nu_{C\equiv N}$), 1610 (arom. C=C) cm^{-1}; ^1H NMR (250 MHz, $CDCl_3$) δ: 0.87 (3H, t, J = 7.47 Hz), 0.90 (3H, t, J = 7.47 Hz), 1.20–1.85 (6H, m), 2.20–2.80 (4H, m), 3.52–3.78 (6H, m), 3.73 (1H, d, J = 12.85 Hz), 3.75 (1H, d, J = 11.88 Hz), 4.01 (1H, d, J = 12.85 Hz), 4.03 (1H, d, J = 11.88 Hz), 7.31 (10H, m); ^{13}C NMR (50 MHz, $CDCl_3$) δ: 11.24, 11.71, 20.06, 21.36, 44.30, 44.51, 51.83, 51.97, 53.13, 53.44, 63.23, 63.88, 118.84 and 119.05 (C≡N), 127.64, 127.75, 128.33, 128.62, 128.68 (arom. CH), 137.56 and 137.78 (arom. C); MS (EI) (*m/z*): 174 (1.15), 173 (5.56), 172 (5.52), 92 (18.68), 91 (100), 77 (1.43); MS (CI, NH_3) (*m/e*): 175 (33), 174 (100). Anal. calcd. for $C_{13}H_{18}N_2O$ (218.3): C 71.53, H 8.31; found: C 71.38, H 8.27.

To a solution of 900 mg (4.1 mmol) of this hydroxyvaleronitrile in 15 mL of dichloromethane containing 50 mg (0.1 equiv.) of 4-*N,N*-dimethylaminopyridine and 0.75 mL (4.5 mmol) of triethylamine was added, dropwise at 0°C under argon, a solution of 0.86 g (4.5 mmol) of tosyl chloride in 8 mL of dichloromethane. The mixture was stirred at 0°C for 4 h and added to 100 mL of dichloromethane. The organic phase was washed with 10 mL of a saturated sodium chloride solution, dried on anhydrous sodium sulfate, and concentrated on a rotary evaporator. The residue was purified by chromatography on silica gel (ether:pentane, 50:50) to yield 1.5 g (98%) of a 1:1 diastereomeric mixture of (2*R*,3*S*)- and (2*S*,3*S*)-2-(*N*-benzylamino)-3-(*p*-tosylsulfonyloxymethyl)valeronitrile as a pale yellow oil. IR (neat): 3340–3220 (ν_{NH}), 2220 ($\nu_{C\equiv N}$), and 1600 (arom. C=C) cm^{-1}; ^1H NMR (200 MHz, $CDCl_3$) δ: 0.88 (3H, t, J = 7.41 Hz), 0.97 (3H, t, J = 7.38 Hz), 1.21–2.05 (8H, m), 2.44 (6H, s), 3.51–4.37 (10H, m), 7.29–7.80 (18H, m); ^{13}C NMR (50 MHz, $CDCl_3$) δ: 10.89, 11.40, 20.19, 20.45., 21.57, 42.85, 43, 50.64, 50.87, 51.68, 52, 67.45 and 68.49 (CH_2-O), 118.8 (C≡N), 127, 127.60, 127.90, 128.25, 128.54, 129.91, 132.70, 137.98, and 145.03 (arom. C).

To a solution of 255 mg (6 mmol) of lithium chloride in 8 mL of *N*-methylpyrrolidone was added dropwise a solution of 1.5 g (4 mmol) of this tosylate. The mixture was stirred at room temperature for 2 h; after evaporation of the solvent on a rotary evaporator the residue was purified by chromatography on silica gel (ether:hexane, 25:75) to yield 800 mg (84%) of a 1:1 diastereomeric mixture of (2*R*,3*S*)-

Can. J. Chem. Downloaded from www.nrcresearchpress.com by ESC ESCOLA DE ENGENHARIA on 09/08/12
For personal use only.

and (2*S*,3*S*)-2(*N*-benzylamino)-3-(chloromethyl)valeronitrile **28** as a colourless oil. IR (CCl_4): 3360–3320 (ν_{NH}), 2220 ($\nu_{C\equiv N}$), 1610 (arom. C=C) cm^{-1}; ^1H NMR (200 MHz, $CDCl_3$) δ: 0.99 (3H, t, J = 7.37 Hz), 1.01 (3H, t, J = 7.40 Hz), 1.19–2.01 (8H, m), 3.62–4.02 (6H, m), 3.83 (1H, d, J = 12.87 Hz), 4.09 (1H, d, J = 12.87 Hz), 7.35 (10H, m); ^{13}C NMR (50 MHz, $CDCl_3$) δ: 11.01, 11.57, 21.20, 43.47, 43.94, 44.65 and 45.55 (CH_2Cl), 51.15 and 51.52 (CH_2Ph), 51.80 and 52.03 (CH-C≡N), 119.32 (C≡N), 127.67, 128.40, 128.58, and 138.06 (arom. C); MS (CI, NH_3) (*m/z*): 239 (M^+ +1, 18), 238 (M^+ +1, 11), 237 (M^+, 71) and 236 (M^+, 4.63), 235 (M – 1, 4), 212 (M – C≡N), 181, 210 (M – C≡N, 100), and 174 (78). Anal. calcd. for $C_{13}H_{17}ClN_2$ (236.75): C 65.95, H 7.24; found: C 65.83, H 7.40.

*(3S)-2-(N-Benzylideneamino)-3-(chloromethyl)valeronitrile **29***

To a mixture of 22 mg of ruthenium dichloride – bis(triphenylphosphine) ($RuCl_2$–$(PPh_3)_2$) and 345 mg of 4 Å molecular sieves was added dropwise at room temperature a solution of 470 mg (2 mmol) of (3*S*)-2-(*N*-benzylamino)-3-(chloromethyl)pentanenitrile **28** in 6.5 mL of freshly distilled benzene. The mixture was stirred at room temperature for 5 min; then, 10 mL of a 1.6 M solution of *tert*-butylperoxide in benzene (8 equiv.) was added dropwise. The mixture was stirred at room temperature for 30 h, and 20 mL of 10% sodium hydrogen sulfite was added to destroy the excess peroxide. After addition of 200 mL of ether, the organic phase was separated, washed by 2 × 20 mL of saturated sodium chloride solution, dried on anhydrous sodium sulfate, and concentrated on a rotary evaporator. The residue was purified by chromatography on silica gel previously treated by a solution of ether and pentane (15:85) containing 1% of NEt_3 to yield 281 mg (60%) of a 1:1 mixture of the imine (2*R*,3*S*)- and (2*S*,3*S*)-**29** as a pale yellow oil. IR (neat): 2220 ($\nu_{C\equiv N}$), 1660 ($\nu_{C=N}$), 1610 (arom. C=C) cm^{-1}; ^1H NMR (200 MHz, $CDCl_3$) δ: 0.99 (3H, t, J = 7.4 Hz), 1.01 (3H, t, J = 7.4 Hz), 1.48–1.94 (4H, m), 2.15–2.42 (2H, m), 3.80 (4H, m), 4.85 (1H, d, J = 7.26 and 1.2 Hz), 4.98 (1H, dd, J = 5.92 and 1.2 Hz), 7.40 (6H, m), 7.82 (4H, m), 8.53 (2H, d, J = 1.2 Hz); ^{13}C NMR (62.50 MHz, $CDCl_3$) δ: 11.12, 21.05, 43.74, 46.49, 58.92, 59.98, 116.87 (C≡N), 124, 128.05, 128.77, 129.5, 131.89, 132.36 and 134.72 (arom. C), 163.81 and 163.99 (CH=N); MS (CI, NH_3) (*m/z*): 237 (M^+ + 1, 38), 236 (M^+, 22), 235 (100), 234 (M^+, 4.20).

*(1R,2R)-1-(N-Benzylideneamino)-2-ethylcyclopropanecarbonitrile **31***

To a solution of 560 mg (2.4 mmol) of the imine (3*S*)-**29** in 9.6 mL of anhydrous DMF was added portionwise 360 mg (2.6 mmol) of potassium carbonate. The mixture was stirred at room temperature for 1.5 h; then, 200 mL of ether containing 20 mL of water was added. The organic phase was separated, washed by 2 × 20 mL of water, and dried on a rotary evaporator. The residue was purified by chromatography on silica gel (ether:pentane containing 1% of NEt_3, 5:95) to yield 332 mg (70%) of a 80:20 diastereomeric mixture of 1-(*N*-benzylideneamino)-2-ethylcyclopropanecarbonitrile (1*R*,2*R*)-**31** and (1*S*,2*R*)-**32**, as a colourless oil. IR (CCl_4): 2220 ($\nu_{C\equiv N}$), 1640 ($\nu_{C=N}$), 1600 (arom. C=C) cm^{-1}; ^1H NMR (200 MHz, $CDCl_3$) δ: 0.98 (3H, t, J = 7.37 Hz), 1.1 (3H, t, J = 7.37 Hz), 1.55–1.90 (10H, m), 7.45 (6H, m), 7.70 (4H, m), 8.55 (1H, s, CH=N), 8.60 (1H, s, CH=N). The 80:20 diastereomeric ratio was determined from the relative integration of these imine proton signals at δ 8.55 and 8.6, respectively.) ^{13}C NMR (6.25 MHz, $CDCl_3$) δ: 10.13, 12.85, 23.89, 25.35, 26.56, 32.44, 42.19, 117.29 (C≡N), 128.13, 127.7, 131.04 and 132.35 (arom. C), 158.95 (CH=N); MS (CI, NH_3) (*m/z*): 199 (M^+ + 1, 100), 198 (M^+, 14), 197 (M^+ – 1, 1).

*(1R,2R)-1-Amino-2-ethylcyclopropanecarbonitrile hydrochloride **33***

To a solution of 265 mg (1.35 mmol) of the 80:20 mixture of cyclopropanecarbonitrile (1*R*,2*R*)-**31** and (1*S*,2*R*)-**32** in 9.5 mL of ether was added dropwise 19 mL (19 mmol, 12.6 equiv.) of a 1 M solution of HCl. The mixture was stirred at room temperature for 15 h. The aqueous phase, separated, was washed by 2 × 1 mL of ether and concentrated on a rotary evaporator. The residue was dried in vacuo (0.05 Torr) to yield 158 mg (80%) of the 80:20 mixture of hydrochlorides (1*R*,2*R*)- and (1*S*,2*R*)-**33** as a white solid. ^1H NMR (250 MHz, D_2O) δ: 0.85 (3H, t, J = 7.3 Hz), 1.21–1.32 (2H, m), 1.37–1.49 (2H, m), 1.51–1.63 (1H, m); ^{13}C NMR (250 MHz, D_2O, dioxane as internal reference) δ: 12.86, 20.61, 24.04, 28.16, 35.62, 117.64 (C≡N).

*(1R,2R)-Coronamic acid **18***

(a) Acid hydrolysis

A solution of 20 mg (0.14 mmol) of 1-amino-2-ethyl cyclopropanecarbonitrile hydrochloride (1*R*,2*R*)-**33** (containing 20% of its (1*S*,2*R*) diastereomer) in 2 mL of 6 M HCl was heated at reflux for 11 h. Removal of water and HCl under vacuum, on a rotary evaporator, yielded 200 mg (70%) of (1*R*,2*R*)-1-amino-2-ethylcyclopropanecarboxylic acid hydrochloride (containing 20% of its (1*S*,2*R*) diastereomer) as a white solid. ^1H NMR (250 MHz, D_2O) δ: 0.70 (3H, 5, J = 7.1 Hz), 1.24 (2H, d, J = 8.15 Hz), 1.29–1.60 (3H, m); ^{13}C NMR (62.5 MHz, D_2O, dioxane as internal reference) δ: 14.97, 21.57, 22.06, 27.44, 32.34, 40.31, 174.29.

(b) Basic hydrolysis

To a solution of 110 mg (0.75 mmol) of hydrochloride (1*R*,2*R*)-**33** (containing 20% of its (1*S*,2*R*) diastereomer) in 5.1 mL of freshly distilled water was added 160 mg (4.13 mmol) of sodium hydroxide and the mixture was heated as reflux for 24 h.

After cooling to 0°C, concentrated HCl was added until the solution was neutral (pH 7). Reverse-phase liquid chromatography through octadecyl-functionalized silica gel provided 96 mg (100%) of a 80:20 mixture of (1*R*,2*R*)- and (1*S*,2*R*)-coronamic acid **18** as a white solid. ^1H NMR (250 MHz, D_2O) δ: 0.72 (3H, t, J = 7.04 Hz, major (1*R*,2*R*) diastereomer), 0.84 (3H, t, J = 7.04 Hz, minor (1*S*,2*R*) diasteromer), 1.08 (2H, d, J = 7.91 Hz), 1.18–1.48 (3H, m) (^1H NMR data according to the literature (47)); ^{13}C NMR (50 MHz, D_2O, dioxane as internal reference at 67.6 MHz) δ: 13.81, 13.94, 18.17, 18.86, 20.92, 21.66, 26.80, 28.69, 40.69, 44.18, 175.28, and 177.09 (C=O).

Following reported procedures, the methyl esters of (1*R*,2*R*)- and (1*S*,2*R*)-coronamic acid **18** (45) were readily isolated by flash liquid chromatography (9).

*Procedure for the preparation of the Mosher amide of (1R,2R)-coronamic acid **18***

To a mixture of 10 mg (0.077 mmol) of coronamic acid **23** in 2 mL of THF was added a solution of 22 mg (0.08 mmol) of (*R*)-2-methoxy-2-trifluoromethylphenyl acetic acid chloride (62) in 24 mL (0.33 mmol) of propylene oxide. The mixture was heated to reflux for 0.5 h, cooled to room temperature, and concentrated on a rotary evaporator. ^{19}F NMR spectroscopy of the resulting Mosher amide showed two singlets at δ –92.98 and –92.85 ppm, ratio 94.25:5.75, respectively; which compared to provided data,[13] allowed us to determine the 88% ee of (1*R*,2*R*)-**18**.

*(2S)-2-(Acetoxymethyl) butanal **34***

To a solution of 2.03 mL (23.35 mmol, 1.1 equiv.) of oxalyl chloride in 31 mL of dichloromethane at –60°C were added dropwise 3.3 mL (46.71 mmol, 2.2 equiv.) of DMSO. The mixture was stirred for 5 min; a solution of 3.1 g (21.23 mmol) of (2*R*)-2-(acetoxymethyl) butanol **23** in 16 mL of dichloromethane was added dropwise. The mixture was stirred at –60°C for 20 min and cooled to –78°C. Then 21.5 mL (123 mmol, 5.8 equiv.) of diisopropylethylamine was added. The mixture was allowed to reach 0°C and was poured into 50 mL of water containing 15 g of ice. The aqueous phase was extracted by 2 × 100 mL of dichloromethane. The organic phase were washed by 2 × 20 mL of 1 M HCl and by a 0.1 M buffered phosphate solution at pH 7. The dichloromethane was removed on a rotary evaporator and the residue added to 100 mL of diethyl ether. The organic phase was dried on anhydrous Na_2SO_4 and concentrated under vacuum. The crude aldehyde (2*S*)-**34** was used directly for the next step. However, 50 mg of the residue was purified by chromatography on silica gel (Et_2O:pentane, 25:75) to give the pure (2*S*)-2-(acetoxymethyl)butanal **34**. IR (neat): 2985, 2880,

[13]We are grateful for spectroscopic data on the Mosher amide of amino acid **23**, kindly provided by Professor R.M. Williams.

Can. J. Chem. Downloaded from www.nrcresearchpress.com by EESC ESCOLA DE ENGENHARIA on 09/08/12
For personal use only.

2730, 1745–1730 ($\nu_{C=O}$) cm^{-1}; ^1H NMR (250 MHz, $CDCl_3$) δ: 1.0 (3H, t, J = 7.45 Hz), 1.48–1.90 (2H, m, CH_2), 2.10 (3H, s), 2.58 (1H, m), 4.28 (1H, dd, J = 12.5 and 5 Hz), 4.36 (1H, dd, J = 12.5 and 6.25 Hz), 9.70 (1H, d, J = 1.5 Hz); ^{13}C NMR (50 MHz, $CDCl_3$) δ: 10.88, 18.59, 20.35, 52.08, 61.55, 170.49 (C=O), 202.07 (CHO); MS (CI, NH_3) (*m/z*): 162 (M + 18, 100), 145 (M + 1, 58), 144 (M^+, 25), 143 (M − 1, 0.26).

(3R)-3-(Acetoxymethyl)-2-[N-(diphenyl)methylamino]valeronitrile ***35****a*

To 900 mg (6.25 mmol) of the neat aldehyde (2*S*)-**34** was added, under argon, at room temperature 1.04 mL (7.8 mmol, 1.25 equiv.) of trimethylsilylcyanide. After stirring for 1 h, an NMR sample of the mixture confirmed the total disappearance of the aldehyde. To the crude mixture was then added a solution of 1.18 mL (6.87 mmol, 1.1 equiv.) of aminodiphenylmethane in MeOH (30 mL). After refluxing for 8 h, the reaction was allowed to warm to room temperature. A sample extracted for structural analysis provided, after the usual work-up, the expected nitrile: (3*R*)-3-(acetoxymethyl)-2-[*N*-(diphenyl)methylamino]valeronitrile **35***a*. IR (neat): 3340, 3080, 3040, 2980, 2950, 2890, 2230, 1745, 1610 cm^{-1}; ^1H NMR (250 MHz, $CDCl_3$) δ: 0.95 (3H, t, J = 7.45 Hz), 1.01 (3H, t, 7.44 Hz), 1.42–1.54 (2H, m), 1.62–1.77 (2H, m), 1.93 (3H, s), 1.98 (3H, s), 2.01–2.14 (2H, m), 3.45–3.53 (2H, m), 3.59 (1H, d, J = 4.2 Hz), 3.64 (1H, d, J = 4.2 Hz), 4.20–4.46 (4H, m), 5.14 (1H, s), 5.16 (1H, s), 7.23–7.49 (20H, m); ^{13}C NMR (50 MHz, $CDCl_3$) δ: 11.18, 11.62, 20.38, 20.79, 42.36, 42.59, 49.18, 49.31, 61.75, 62.66, 65.30, 119.18, 119.31, 126.74, 127.32, 127.48, 127.62, 128.60, 140.94, 142.94, 170.59; MS (CI, NH_3) (*m/z*) (%): 336 (M^+), 252 (7), 251 (19), 250 (100), 167 (16). Anal. calcd. for $C_{21}H_{24}N_2O_2$ (336.44): C 74.97, H 7.19, N 8.33; found: C 74.47, H 7.20, N 8.19.

(3R)-2-[N-(Diphenyl)methylamino]-3-(hydroxymethyl)valeronitrile ***35****b*

To this crude aminoacetate **35***a* was added at room temperature 860 mg (2 equiv.) of potassium carbonate. The mixture was stirred for 2 h, the solvent was removed on a rotary evaporator, and the residue was added to CH_2Cl_2; the organic phase was filtered on Celite, dried on Na_2SO_4, filtered, and concentrated on a rotary evaporator. Chromatography on silica gel (CH_2Cl_2:ether, 24:1) provided 992 mg (54%) of a 55:45 diastereomeric mixture of the aminoalcohol **35***b*. IR ($CDCl_3$): 3640, 3350, 3100, 3080, 3040, 2980, 2945, 2890, 2220, 1610 cm^{-1}; ^1H NMR (250 MHz, $CDCl_3$) δ: 0.96 (3H, t, J = 7.36 Hz), 0.98 (3H, t, 7.26 Hz), 1.23–1.91 (6H, m), 2.10–2.50 (2H, m), 2.90–3.10 (2H, m), 3.48–3.96 (6H, m), 5.08 (1H, s), 5.13 (1H, s), 7.22–7.56 (20H, m); ^{13}C NMR (50 MHz, $CDCl_3$) δ: 11.21, 11.52, 20.15, 20.87, 44.42, 44.70, 51.32, 62.62, 62.82, 65.33, 65.50, 118.95, 119.20, 126.72, 127.21, 127.36, 127.45, 127.58, 127.68, 128.56, 128.74, 140.67, 140.85, 142.68, 142.85; MS (CI, NH_3) (*m/z*): 294 (M^+, abs), 221 (6), 220 (30), 206 (17), 205 (100), 177 (10), 145 (12), 81 (12), 57 (22).

*(3R)-2-[N-(Diphenyl)methylamino]-3-(*p*-tosyloxymethyl)valeronitrile* ***36****a*

To a solution of 1 g (3.4 mmol) of the alcohol **35***b* in CH_2Cl_2 (12 ml) at 0°C were added NEt_3 (0.52 mL, 3.74 mmol, 1.1 equiv.) and 2,4-dimethylaminopyridine (DMAP, 0.1 equiv.). To the mixture was added dropwise a solution of tosylchloride (3.74 mmol, 1.1 equiv.) in CH_2Cl_2 (5 mL). After stirring for 4 h at 0°C, the mixture was poured into a mixture of CH_2Cl_2 (70 mL) and brine (10 mL). The organic fraction was separated, dried on $MgSO_4$, filtered, and concentrated. Purification by chromatography on silica gel (CH_2Cl_2:Et_2O, 98.5:1.5) provided 1.4 g (92%) of a white crystalline 55:45 diastereomeric mixture of the expected tosylate **36***a*. IR (CCl_4): 3340, 3220, 3090, 3030, 2980, 2880, 2220, 1600 cm^{-1}; ^1H NMR (200 MHz, $CDCl_3$) δ: 0.82 (3H, t, J = 7.4 Hz), 0.91 (3H, t, J = 7.4 Hz), 1.10–1.96 (8H, m), 2.44 (3H, s), 2.46 (3H, s), 3.38–3.58 (2H, m), 4.06–4.48 (4H, m), 5.04 (1H, s), 5.08 (1H, s), 7.20–7.77 (28H, m); ^{13}C NMR (50 MHz, $CDCl_3$) δ: 10.77, 11.35, 20.14, 29.39, 21.52, 42.79, 42.89, 49.26, 49.45, 67.02, 68.20, 118.69, 126.81, 127.22, 127.54, 127.74, 127.74, 128.60, 128.81, 129.80, 132.29 (a and b), 140.47, 142.84 (a and b), 145.00 (a and b); MS (CI, NH_3) (*m/z*) (%): 449 (M + 1) (76). Anal. calcd. for $C_{26}H_{28}N_2SO_3$ (448.58): C 69.62, H 6.29, N 6.24; found: C 69.45, H 6.33, N 5.95.

(3R)-3-(Chloromethyl)-2-[N-(diphenyl)methylamino]valeronitrile ***36****b*

To a solution of 1 g (2.23 mmol) of the tosylate **36***a* in *N*-methylpyrrolidone (2.5 mL) was added dropwise at room temperature 142 mg (3.34 mmol, 1.5 equiv.) of LiCl. After stirring for one night, ether (70 mL) and water (5 mL) were added. The organic phase was separated and washed with water (3 × 10 mL), dried on $MgSO_4$, filtered, and concentrated. Purification by silica gel chromatography (hexane:ether, 17:3) provided 650 mg (93%) of a white crystalline (55:45) diastereomeric mixture of the chloride **36***b*. IR (neat): 3330, 3100–2840, 2220, 1620 cm^{-1}; ^1H NMR (250 MHz, $CDCl_3$) δ: 0.99 (3H, t, J = 7.5 Hz), 1.02 (3H, t, J = 7.5 Hz), 1.4–2.1 (8H, m), 3.45–4.15 (6H, m), 5.17 (1H, s), 5.20 (1H, s), 7.10–7.60 (20H, m); ^{13}C NMR (50 MHz, $CDCl_3$) δ: 10.89, 11.52, 21.17, 43.28, 43.67, 44.90, 45.67, 49.75, 50.20, 65.47, 126.93, 127.42, 127.62, 127.79, 128.72, 140.50, 143.03; MS (CI, NH_3) (*m/z*) (%): 315 (M + 1) (6), 313 (M + 1) (13), 314 (71), 311 (8), 252 (16), 251 (26), 250 (40), 167 (100). Anal. calcd. for $C_{19}H_{21}ClN_2$ (312.84): C 72.95, H 6.77, N 8.95; found: C 72.95, H 6.74, N 8.65.

(3R)-3-(Chloromethyl)-2-[diphenylmethyleneamino]pentanenitrile ***37***

To a mixture of 30 mg (1%) of $RuCl_2(PPh_3)_2$ and 560 mg of 4 Å powdered molecular sieves in C_6H_6 (5 mL) was added, under argon, 1 g (3.2 mmol) of the chloroamine **36***b*. After stirring for 5 min, the solution was cooled to 0°C and 8.5 mL (8 equiv.) of a 3 M solution of *tert*- butylperoxide in isooctane was added. After additional stirring for 15 h at 0°C, dimethyl sulfide (1.8 mL) was added and the mixture was allowed to warm to room temperature. After concentration on a rotary evaporator, the crude product was dissolved in a minimum amount of CH_2Cl_2 and purified by flash chromatography on silica gel eluted with CH_2Cl_2 to provide 900 mg (90%) of the expected imine (3*R*)-**37**. IR (neat): 1678, 1638, 1610, 1588 cm^{-1}; ^1H NMR (250 MHz, $CDCl_3$) δ: 0.95 (3H, t, J = 7.5 Hz), 0.98 (3H, t, 7.5 Hz), 1.2–1.86 (2H, m), 2.08–2.18 (1H, m), 2.29–2.36 (1H, m), 3.66–3.80 (6H, m), 4.26 (1H, d, J = 8.25 Hz), 4.48 (1H, d, J = 5.25 Hz), 7.23–7.83 (20 H, m); ^{13}C NMR (50 MHz, $CDCl_3$) δ: 10.99, 11.14, 20.54, 21.25, 43.42, 43.90, 46.17, 46.60, 53.60, 54.09, 119.49, 126.81, 127.13, 127.23, 127.47, 127.65, 128.07, 128.69, 128.80, 129.25, 129.83, 131.19, 132.22, 134.80, 138.10, 174.55; MS (CI, NH_3) (*m/z*) (%): 312 (M + 1) (10), 310 (M + 1) (16), 313 (8), 311 (15), 263 (12), 262 (77), 220 (45), 219 (31), 117 (14), 116 (100), 115 (18), 104 (18), 55 (16), 51 (35). Anal. calcd. for $C_{19}H_{19}ClN_2$ (310.82): C 73.42, H 6.16; found: C 73.29, H 6.34.

(1S,2S)-1-(Diphenylmethyleneamino)-2-ethyl cyclopropanecarbonitrile ***38***

(a) Cyclization by potassium carbonate

To a solution of the chloroimine (3*R*)-**37** (200 mg, 0.64 mmol) in DMF (10 mL) was added K_2CO_3 (100 mg, 1.1 equiv.). After stirring for 3 h, ether (50 mL) and water (10 mL) were added. The organic fraction was washed with H_2O (2 × 10 mL), dried on $MgSO_4$, filtered, and concentrated on a rotary evaporator. Purification by flash silica gel chromatography eluted with CH_2Cl_2 gave 113 mg (65%) of the (1*S*,2*S*)-cyclopropylcarbonitrile **38** and 48 mg (27%) of the (1*R*,2*S*)-cyclopropylcarbonitrile **39**.

(b) Cyclization by lithium diisopropylamide

A solution of 200 mg (0.64 mmol) of the chloroimine (3*R*)-**37** in 10 mL of THF was added dropwise within 30 min to a solution of lithium diisopropylamide (prepared from 2.5 mL of 1.6 M *n*-BuLi and 0.54 mL of diisopropylamine) in 20 mL of THF at –90°C. After stirring for 3 h at –90°C the reaction mixture was quenched by 10 mL of saturated NH_4Cl solution. Addition of 100 mL of diethyl ether and the usual work-up gave, after flash chromatography on silica gel (CH_2Cl_2), 127 mg (72%) of (1*S*,2*S*)-**38** and 40 mg (23%) of (1*R*,2*S*)-**39**.

Can. J. Chem. Downloaded from www.nrcresearchpress.com by EESC ESCOLA DE ENGENHARIA on 09/08/12
For personal use only.

(c) Cyclization of lithium diisopropylamide in the presence of HMPA

A solution of 200 mg (0.64 mmol) of the chloroimine (3*R*)-**37** in 10 mL of THF was added dropwise to a stirred solution of 1.36 mmol of lithium diisopropylamide (prepared from 0.85 mL of 1.6 M *n*-BuLi and 0.19 mL of diisopropylamine) in 5 mL of THF containing 0.25 mL (1.45 mmol) of HMPA at –90°C. Work-up as previously described provided 160 mg (91%) of a 75:25 diastereomeric mixture of (1*S*,2*S*)-**38** and (1*R*,2*S*)-**39**, readily separated by flash chromatography on silica gel (CH_2Cl_2).

(1S,2S)-1-(Diphenylmethyleneamino)-2-ethylcyclopropanecarbonitrile ***38***: $[\alpha]_D^{20}$ -1.20 (*c* 1.085, CH_2Cl_2); IR (neat): 3330, 3100–2880, 2230, 1670, 1620, 1580 cm^{-1}; ^1H NMR (250 MHz, $CDCl_3$) δ: 1.07 (3H, t, *J* = 7.25 Hz), 1.26–1.33 (1H, m), 1.40–1.73 (4H, m), 7.31–7.80 (10H, m); ^{13}C NMR (50 MHz, $CDCl_3$) δ: 12.76, 23.60, 27.11, 33.36, 37.37, 118.21, 128.08, 128.44, 128.56, 129.66, 130.00, 130.64, 136.06, 139.32, 171.56; MS (CI, NH_3) (*m/z*) (%): 274 (M + 1) (15), 218 (59), 206 (32), 166 (39), 165 (100), 115 (46), 77 (40). Anal. calcd. for $C_{19}H_{18}N_2$ (274.36): C 83.18, H 6.61; found: C 83.45, H 6.39.

(1R,2S)-1-(Diphenylmethyleneamino)-2-ethylcyclopropanecarbonitrile ***39***: $[\alpha]_D^{20}$ – 24.2 (*c* 0.95, CH_2Cl_2); IR (CH_2Cl_2): 3330, 3150–2880, 2230, 1668, 1610, 1585 cm^{-1}; ^1H NMR (250 MHz, $CDCl_3$) δ: 1.13 (3H, t, *J* = 7 Hz), 1.26–1.29 (1H, m), 1.70–1.84 (4H, m), 7.31–7.83 (10H, m); ^{13}C NMR (50 MHz, $CDCl_3$) δ: 13.24, 21.21, 26.15, 34.17, 120.21, 128.04, 128.19, 128.42, 128.53, 129.66, 130.55, 132.34, 135.98, 137.50, 139.50, 171.38; MS (CI, NH_3) (*m/z*) (%): 274 (M^+) (20), 218 (80), 206 (43), 166 (41), 165 (100), 77 (37). Anal. calcd. for $C_{19}H_{18}N_2$ (274.36): C 83.18, H 6.61; found: C 83.56, H 6.12.

(1S,2S)-1-Amino-2-ethylcyclopropanecarbonitrile hydrochloride ***40***

To a solution of 144 mg (0.42 mmol) of the imine **38** in 8 mL of diethyl ether was added 8 mL (15 equiv.) of 1 N HCl. The solution was stirred for 15 h (monitored by TLC), then extracted with ether (2 × 5 mL). The aqueous phase was concentrated on a rotary evaporator to provide 75 mg (97%) of the hydrochloride (1*S*,2*S*)-**40**. $[\alpha]_D^{20}$ –14.5 (*c* 0.7, H_2O); 1H NMR (200 MHz, $CDCl_3$) δ: 0.85 (3H, t, *J* = 7.3 Hz), 1.23–1.64 (5H, m); ^{13}C NMR (50 MHz, $CDCl_3$) δ: 12.76, 20.54, 23.93, 27.32, 28.08, 117.53.

(1R,2S)-1-Amino-2-ethylcyclopropanecarbonitrile hydrochloride ***41***

To a solution of 120 mg (0.43 mmol) of the imine **39** in 7 mL of diethyl ether was added 7 mL (15 equiv.) of 1 N HCl. The mixture was stirred for 15 h (monitored by TLC). Work-up as for (1*S*,2*S*)-**40** led to 62 mg (98%) of the hydrochloride (1*S*,2*S*)-**41**. $[\alpha]_D^{20}$ +29.8 (*c* 1.2, H_2O). ^1H NMR (200 MHz, $CDCl_3$) δ: 0.85 (3H, t, *J* = 7.3 Hz), 1–1.8 (5H, m); ^{13}C NMR (50 MHz, $CDCl_3$) δ: 14.67, 21.12, 22.13, 27.44, 30.05, 120.62.

(1S,2S)-1-Amino-2-ethylcyclopropanecarboxylic acid: coronamic acid ***17***

A solution of 37 mg (0.25 mmol) of the nitrile hydrochloride (1*S*,2*S*)-**40** in 10 mL of 6 N HCl was heated at reflux for 15 h. After cooling, removal of HCl and H_2O under vacuum provided 39 mg (95%) of a white solid hydrochloride. ^1H NMR (250 MHz, D_2O) δ: 0.69 (3H, 5, *J* = 7.2 Hz), 1.24 (2H, d, *J* = 8 Hz), 1.27–1.52 (3H, m); ^{13}C NMR (50 MHz, $CDCl_3$) δ: 14.97, 21.57, 22.06, 27.44, 32.34, 40.31, 174.29.

The residue was dissolved in 2 mL of distilled H_2O and purified by chromatography through an ion exchange resin (Dowex 50 × 8-100) to give 14 mg (97%) of (1*S*,2*S*)-coronamic acid **17**. $[\alpha]_D^{20}$ +28 (*c* 0.5, H_2O) (lit. (9) $[\alpha]_D^{20}$ +30.8 (*c* 0.51, H_2O)), ^1H NMR (200 MHz, D_2O) δ: 0.66 (3H, t, *J* = 7.2 Hz), 1.03 (2H, d, *J* = 8.3 Hz), 1.15–1.45 (3H, m); ^{13}C NMR (50 MHz, D_2O, $CDCl_3$ as external reference) δ: 15.16 19.43, 22.36, 30.04, 42.12, 176.68.

Mosher amide synthesis of coronamic acid ***17***

To a suspension of 4 mg (0.03 mmol) of the coronamic acid (1*S*,2*S*)-**17** in 1 mL of THF was added 8 mg (0.031 mmol) of the (*S*) Mosher acid chloride (62) and 0.5 mL of propylene oxide. The mixture was heated at reflux for 30 min, cooled to room temperature, and evaporated to leave an oil. The enantiomeric excess was determined by ^{19}F NMR analysis of the resulting amide: ^{19}F NMR (δ CF_3CH_2OH as reference –80 ppm): –71.93 (94%) for (1*S*,2*S*)-coronamic acid, –71.81 (6%) for (1*R*,2*R*)-coronamic acid[13] compared to data kindly provided by Prof. R.M. Williams (ref. 8 and footnote 13).

1. J. Salaün. IUPAC 9th Int. Conf. Organic Synthesis (ICOS-92), Montreal, Quebec, June 1992.
2. C.H. Stammer. Tetrahedron, **46**, 2231 (1990).
3. R.M. Williams. *In* Synthesis of optically active α-amino acids. Vol. 7. *Edited by* J.E. Baldwin and P.D. Magnus. Organic Chemistry Series. Pergamon Press, Oxford. 1989. pp. 30, 59, 113.
4. A. Alami, M. Calmes, J. Daunis, and R. Jacquier. Bull. Soc. Chim. Fr. **130**, 5 (1993).
5. L. Fowden, P.J. Lea, and E.A. Bell. *In* The nonprotein aminoacids of plants. Advances in enzymology. *Edited* by A. Meister. Wiley, New York. 1979. pp. 117–175.
6. K. Ueda, J.-Z. Xia, N. Doke, and S. Nakatsuka. Tetrahedron Lett. **33**, 5377 (1992).
7. A. Alami, M. Calmes, J. Daunis, F. Escale, R. Jacquier, M.-L. Roumestant, and P. Viallefont. Tetrahedron: Asymmetry, **2**, 175 (1991).
8. R.M. Williams and G.J. Fegley. J. Am. Chem. Soc. **113**, 8797 (1991).
9. U. Groth, W. Halfbrodt, and V. Schöllkopf. Liebigs Ann. Chem. 351 (1992).
10. (*a*) R.K. Hill, S.R. Prakash, R. Wiesendanger, W. Angst. B. Martinoni, D. Arigoni, H.W. Liu, and C.T. Walsh. J. Am. Chem. Soc. **106**, 795 (1984); (*b*) M.C. Pirrung and G.M. McGeehan. J. Org. Chem. **51**, 2103 (1986); (*c*) R.W. Woodward and P.K. Subramanian. J. Org. Chem. **52**, 15 (1987); (*d*) J.L. Marco. Heterocycles, **26**, 2579 (1987); (*e*) M. Bernabe, D. Fernandez, P. de Frutos, and E. Fernandez-Alvarez. Tetrahedron Lett. **30**, 3101 (1989); (*f*) D.J. Aitken, J. Royer, and H.P. Husson. J. Org. Chem. **55**, 2184 (1990); (*g*) C. Alcaraz, A. Herrero, J.L. Marco, E. Fernandez-Alvarez, and M. Bernabé. Tetrahedron Lett. **33**, 5605 (1992).
11. J. Salaün, J. Marguerite, and B. Karkour. J. Org. Chem. **55**, 4276 (1990); J. Salaün and S. Tondu. Fr. Patent 89 12086 (1989).
12. R.E. Mitchell. Phytochemistry, **24**, 1485 (1985); Mitchell, M.C. Pirrung, and G.M. McGeehan. Phytochemistry, **26**, 2595 (1987).
13. M.J. Rance, J.C. Ruddock, M.S. Pacey, W.P. Cullen, L.H. Huang, M.T. Jefferson, E.B. Whipple, H. Maeda, and J. Tone. J. Antibiot. **42**, 206 (1989); K.R. Fox. J. Antibiot. **43**, 1307 (1990).
14. A. Strecker. Ann. Chem. Pharm. **75**, 27 (1850); F. Tiemann. Ber. Dtsch. Chem. Ges. **13**, 382 (1880); F. Tiemann, L. Friendlander, and K. Prist. Ber. Dtsch. Chem. Ges. **14**, 1967 (1881); **14**, 1982 (1881); **15**, 2029 (1882); K. Mai and G. Patil. Tetrahedron Lett. **25**, 4583 (1984); Synth. Commun. **15**, 157 (1985).
15. Aldrichimica Acta, **17**, 42 (1984); see refs. cited therein.
16. J.B. Lee and I.W. Downie. Tetrahedron, 359 (1967); J.B. Lee and T.J. Nolan. Can. J. Chem. **44**, 1331 (1966).
17. S. Krishnamurthy. J. Org. Chem. **45**, 2550 (1980).
18. A.J. Mancuso and D. Swern. Synthesis, 165 (1981).
19. T.T. Tidwell. Synthesis, 857 (1990).
20. E.J. Corey and R. Venkateswarlu. J. Am. Chem. Soc. **94**, 6190 (1972).
21. J.A. Marshall and B.E. Blough. J. Org. Chem. **55**, 1540 (1990); D.A. Evans, R.L. Dow, T.L. Shih, J.M. Takaes, and R. Zahler. J. Am. Chem. Soc. **122**, 5290 (1990).
22. W.R. Roush, A.D. Palkowitz, and K. Ando. J. Am. Chem. Soc. **122**, 6348 (1990).
23. G.W. Kabalka, M. Warma, and R.S. Warma. J. Org. Chem. **51**, 2386 (1986).
24. D.P. Curran and T.A. Heffner. J. Org. Chem. **55**, 4585 (1990); L.N. Jugheinm and S.K. Sigmund. J. Org. Chem. **52**, 4007 (1987).
25. K. Kurrita. Chem. Ind. 345 (1974).
26. H.B. Heubest and W.R. Jackson. J. Chem. Soc. 954 (1962); M.A.

Tius, X. Gu, J.W. Truesdell, S. Savariar, and P.P. Crooker. Synthesis, 36 (1988).
27. A.T. Kunishi, M. Lieberman, L.W. Mapson, and D.A. Wardale. Plant. Physiol. **41**, 376 (1966); T. Boller, R.C. Herner, and H. Kende. Planta, **145**, 293 (1979).
28. R. Wiesendanger, B. Martinoni, T. Boller, and D. Arigoni. J. Chem. Soc. Chem. Commun. 238 (1986).
29. P. Stazewski and C. Tamm. Synthesis, 298 (1987).
30. E.W. Logush. Tetrahedron Lett. **27**, 5935 (1986).
31. Z. Procházka, M. Budisinsky, J. Smoliková, P. Trska, and K. Jost. Collect. Czech. Chem. Commun. **47**, 2291 (1982).
32. D.H. Rich and J.P. Tam. Synthesis, 46 (1978).
33. H. Ruderknecht and C. Niemann. J. Am. Chem. Soc. **73**, 4259 (1951).
34. M.C. Pirrung and G.M. McGeehan. J. Org. Chem. **48**, 5144 (1983); G.E. Dubois, G.A. Crosby, C.V. McGarrangh, S.Y.W. Ng, R.A. Stephenson, P.C. Wang, and R.E. Wingard, Jr. J. Org. Chem. **47**, 1319 (1982).
35. F.G. Bordwell. Acc. Chem. Res. **21**, 456 (1988).
36. A. Gaucher, J. Ollivier, and J. Salaün. Synlett, 151 (1991).
37. A. Gaucher. Ph. D. Thesis, University of Paris-Sud, Orsay (France), December 1992.
38. M.P. Georgiadis and S.A. Haroutonnian. Synthesis, 615 (1989).
39. S. Barn and L.D. Spicer. Synth. Commun. 17 (1987); S. Rarn and R.E. Ehrenkaufer. Synthesis, 133 (1986).
40. W.M. Pearlman. Tetrahedron Lett. 1663 (1967); Y. Yamamoto, W. Iko, and K. Maruyama. J. Chem. Soc. Chem. Commun. 1131 (1985).
41. M.J. O'Donnell and R.L. Polt. J. Org. Chem. **47**, 2663 (1982).
42. D. Keirs and K. Overton. J. Chem. Soc. Chem. Commun. 1660 (1987); M. Dufour, J.C. Gramain, H.P. Husson, M.E. Sirribaldi, and Y. Train. J. Org. Chem. **55**, 5483 (1990).
43. T.T. Tidwell. Synthesis, 857 (1990); Org. React. **39**, 297 (1990).
44. K. Omura and D. Swern. Tetrahedron, **34**, 1651 (1978).
45. J. Bland, A. Shah, A. Bortolussi, and C.H. Stammer. J. Org. Chem. **53**, 992 (1988).
46. N. de Kimpe, P. Sulmon, P. Brunet, F. Lambein, and N. Schamp. Tetrahedron Lett. **30**, 1863 (1989); N. de Kimpe, P. Sulmon, and N. Schamp. Tetrahedron Lett. **30**, 5029 (1989); N. de Kimpe, P. Sulmon, and P. Brunet. J. Org. Chem. **55**, 5777 (1990).
47. J.E. Baldwin, R.M. Adlington, and B.J. Rawlings. Tetrahedron Lett. **26**, 481 (1985).
48. J.E. Baldwin, R.M. Adlington, B.J. Rawlings, and R.M. Jones. Tetrahedron Lett. **26**, 485 (1985).
49. A. Ichihara, K. Shiraishi, H. Sato, S. Sakamura, K. Nishiyama, R. Sakai, A. Furnsaki, and T. Matsumoto. J. Am. Chem. Soc. **99**, 636 (1977).
50. R.E. Mitchell. Physiol. Plant Pathol. **20**, 83 (1982).
51. R.E. Mitchell and H. Young. Phytochemistry, **17**, 2028 (1978).
52. R. Sakai. Proc. 11th Pesticide Sci. Symp. Sapporo, Japan. 1978. p. 21; K. Shiraishi, K. Konama, H. Sato, A. Ichihara, S. Sakamura, K. Nishiyama, and R. Sakai. Agric. Biol. Chem. **43**, 1753 (1979).
53. M. Guy and H. Kende. Planta, **160**, 281 (1984).
54. M. Ihara, M. Takahashi, N. Taniguchi, N. Fukumoto, and T. Kametani. J. Chem. Soc. Chem. Commun. 619 (1987).
55. K. Tsuji, Y. Terao, and K. Achiwa. Tetrahedron Lett. **30**, 6189 (1989).
56. R.W. Hoffmann. Chem. Ber. **115**, 2357 (1982); P.E. Sonnet. J. Chromatogr. **292**, 295 (1984); M. Hjalmarsson, H.E. Hoegberg, Acta Chem. Scand. Ser. B: **B39**, 793 (1985); H. Bruner. Organometallics, **5**, 2212 (1986); H.J. Bestmann. Angew. Chem. **99**, 784 (1987).
57. D.M. Walba, W.N. Thurnes, and R.C. Haltiwanger. J. Org. Chem. **53**, 1046 (1988).
58. (*a*) J.S. Sandhu, S. Mohan, and R.L. Kapoor. Chem. Ind. 152 (1971); (*b*) J. Fatiadi. Synthesis, 65 (1976), 133 (1976).
59. E.J. Corey and G. Smith. Tetrahedron Lett. 399 (1979).
60. K.B. Sharpless and T. Verhoeven. Aldrichimica Acta, **12**, 63 (1979).
61. S.I. Murahashi, T. Nasta, and H. Taki. J. Chem. Soc. Chem. Commun. 613 (1985); F.R. Keene, M.J. Ridd, and M.R. Snow. J. Am. Chem. Soc. **105**, 7075 (1983); S.I. Murahashi, N. Yoshimura, T. Tsumiyama, and T. Kojima. J. Am. Chem. Soc. **105**, 5002 (1983).
62. H.S. Mosher, J.A. Dale, and D.L. Dull. J. Org. Chem. **34**, 2543 (1969).

Can. J. Chem. Downloaded from www.nrcresearchpress.com by EESC ESCOLA DE ENGENHARIA on 09/08/12
For personal use only.

Synthesis, spectroscopic, and structural studies of dimethyltellurium(IV) alkylene and diphenyl dithiophosphates. Crystal structures of $Me_2Te[S_2POCMe_2CMe_2O]_2$ and $Me_2Te[S_2POCH_2CEt_2CH_2O]_2$

JOHN E. DRAKE,[1] LAYLA N. KHASROU, ANIL G. MISLANKAR, AND RAJU RATNANI[2]
Department of Chemistry and Biochemistry, University of Windsor, Windsor, ON N9B 3P4, Canada
Received September 20, 1993

JOHN E. DRAKE, LAYLA N. KHASROU, ANIL G. MISLANKAR, and RAJU RATNANI. Can. J. Chem. **72**, 1328 (1994).

Dimethyltellurium alkylene dithiophosphates of the type $Me_2Te[S_2POGO]_2$, where G = —CMe_2CMe_2—, —CHMeCHMe—, —$CH_2CMe_2CH_2$—, and —$CH_2CEt_2CH_2$—, have been synthesized in 80–90% yields by reaction of the corresponding sodium or ammonium salts of the appropriate dithiophosphoric acids with dimethyltellurium dichloride in toluene. $Me_2Te[S_2P(OPh)_2]_2$ was also prepared in a similar fashion. The compounds have been characterised by elemental analyses and ^1H, ^{13}C, ^{31}P, and ^{125}Te NMR, infrared and Raman spectroscopy. The crystal structures of $Me_2Te[S_2POCMe_2CMe_2O]_2$ and $Me_2Te[S_2POCH_2CEt_2CH_2O]_2$ were determined. $Me_2Te[S_2POCMe_2CMe_2O]_2$, **1**, crystallizes in space group $P2_1/c$ (No. 14) with the cell parameters a = 12.707(3) Å, b = 11.482(2) Å, c = 16.782(2) Å, β = 98.00(1)°, V = 2424(1) Å^3, Z = 4, R = 0.0399, R_w = 0.0343. $Me_2Te[S_2POCH_2CEt_2CH_2O]_2$, **4**, crystallizes in space group $P\bar{1}$ (No. 2) with the cell parameters a = 12.580(3) Å, b = 13.313(3) Å, c = 8.206(1) Å, α = 91.28(2)°, β = 104.94(2)°, γ = 78.52(2)°, V = 1301(1) Å^3, Z = 2, R = 0.0364, R_w = 0.0295. The immediate environment about tellurium in both molecules is that of the saw-horse structure typical of tellurium(IV) compounds with the two methyl groups equatorial and one sulfur atom from each dithiophosphate group occupying the axial positions. The consideration of the second sulfur atom as part of the coordinating sphere is discussed in terms of a modification of Pauling's approach to partial bond orders. The ^1H NMR spectra suggest that these dithiophosphates may be fluxional in solution and/or that there is rapid exchange of the sulfur atoms.

JOHN E. DRAKE, LAYLA N. KHASROU, ANIL G. MISLANKAR et RAJU RATNANI. Can. J. Chem. **72**, 1328 (1994).

On a synthétisé les dithiophosphates d'alkylidène du diméthyltellure, $Me_2Te[S_2POGO]_2$ dans lesquels G = —CMe_2CMe_2—, —CHMeCHMe—, —$CH_2CMe_2CH_2$— et —$CH_2CEt_2CH_2$—, avec des rendements allant de 80 à 90% par réaction des sels correspondants de sodium ou d'ammonium des acides dithiophosphoriques appropriés avec le dichlorure de diméthyltellure dans le toluène. On a aussi préparé le $Me_2Te[S_2P(OPh)_2]_2$ de la même manière. On a caractérisé les composés par des analyses élémentaires, par rmn du ^1H, du ^{13}C, du ^{31}P et du ^{125}Te et par spectroscopies infrarouge et Raman. On a déterminé les structures cristallines des composés $Me_2Te[S_2POCMe_2CMe_2O]_2$ et $Me_2Te[S_2POCH_2CEt_2O]_2$. Le produit $Me_2Te[S_2POCMe_2CMe_2O]_2$, **1**, cristallise dans le groupe d'espace $P2_1/c$ (No. 14) avec a = 12,707(3), b = 11,482(2) et c = 16,782(2) Å, β = 98,00(1)°, V = 2424(1) Å^3, Z = 4, R = 0,0399, R_w = 0,0343. Le produit $Me_2Te[S_2POCH_2CEt_2O]_2$, **4**, cristallise dans le groupe d'espace $P\bar{1}$ (No. 2) avec a = 12,580(3), b = 13,313(3) et c = 8,2061(1) Å, α = 91,28(2), β = 104,94(2) et γ = 78,52(2)°, V = 1301(1) Å^3, Z = 2, R = 0,0364, R_w = 0,0295. Dans chacune de ces molécules, l'environnement immédiat du tellure est une structure typique des composés du tellure(IV) avec deux groupes méthyles équatoriaux et une atome de soufre de chaque groupe dithiophosphate se trouvant dans les positions axiales. On discute de la considération due deuxième atome de soufre comme une partie de la sphère de coordination en fonction d'une modification de l'approche de Pauling auz ordres des liaisons partielles. Les spectres de RMN du ^1H suggèrent que ces dithiophosphates peuvent être en fluxion en solution et/ou qu'il existe un échange rapide des atomes de soufre.

[Traduit par la Rédaction]

Introduction

Tetrakis compounds of tellurium(IV) containing the dithiocarbamate entity such as $Te(S_2CNR_2)_4$ have been reported in the literature (1–4), whereas the analogous xanthates and dithiophosphates are unknown. This presumably reflects a greater tendency in the xanthates and dithiophosphates to undergo reductive-elimination to tellurium(II) and the corresponding disulfide. Related tellurium(IV) compounds can be stabilized by the introduction of organic substituents on tellurium. In general, the stability of compounds of the general type $R_2Te[S—S]_2$ increases in the order for changing R of Ph < MeOPh < Me and within each series in the order for changing the nature of the [S—S] group of xanthate < dithiophosphate < dithiocarbamate. Thus a variety of stable compounds of organotellurium(IV) with 1,1-dithio ligands such as *N*,*N*-dialkyl dithiocarbamates (5–14), *O*-alkyl dithiocarbonates (xanthates) (11, 12, 15–17) and *O*,*O*-dialkyl dithiophosphates (11–14, 17–22) have been described in the literature. However, related cyclic dithiophosphate derivatives of tellurium(IV) that contain glycolic units have received much less attention despite the fact that they may be less susceptible to reductive elimination to tellurium(II) than their alkyl counterparts. Thus only a few derivatives of the type $R_2Te[S_2POGO]_2$ (23) and $RTe[S_2POCH_2CMe_2CH_2O]_3$ (21) where (R = Ph, or MeOPh) have been reported in the literature.

We report on the synthesis and characterization of dimethyltellurium(IV) alkylene dithiophosphates of the type $Me_2Te[S_2POGO]_2$, where G = —CMe_2CMe_2—, —CHMe-CHMe—, —$CH_2CMe_2CH_2$—, and —$CH_2CEt_2CH_2$—, as well as $Me_2Te[S_2P(OPh)_2]_2$. X-Ray crystal structures are reported for $Me_2Te[S_2POCMe_2CMe_2O]_2$, **1**, which contains a five-membered ring

[1]Author to whom correspondence should be addressed; (519)-253-4232 (Ext 3551); Fax No. (519)-973-7098; E-mail ak4@uwindsor.ca.
[2]Present address: Department of Chemistry, Dayanand College, Ajmer 305001, India.

Can. J. Chem. Downloaded from www.nrcresearchpress.com by EESC ESCOLA DE ENGENHARIA on 09/08/12
For personal use only.

Can. J. Chem. Downloaded from www.nrcresearchpress.com by EESC ESCOLA DE ENGENHARIA on 09/08/12
For personal use only.

including phosphorus, and $Me_2Te[S_2POCH_2CEt_2CH_2O]_2$, **4**, which contains a six-membered ring.

Experimental

Materials

$TeCl_4$ and Me_4Sn were obtained from Aldrich. Me_2TeCl_2 was prepared by the reaction of $TeCl_4$ and Me_4Sn in toluene at 60°C under reflux for 4 h based on a procedure previously reported for the preparation of Ph_2TeCl_2 (24). Sodium/ammonium salts of alkylene (25) and diphenyl (26) dithiophosphates were prepared by literature methods. The reactions were carried out under anhydrous conditions.

*Synthesis of the dimethyltellurium(IV) alkylene dithiophosphate compounds, $Me_2Te[S_2POCMe_2CMe_2O]_2$, **1**, $Me_2Te[S_2POCHMeCHMeO]_2$, **2**, $Me_2Te[S_2POCH_2CMe_2CH_2O]_2$, **3**, and $Me_2Te[S_2POCH_2CEt_2CH_2O]_2$, **4***

Typically, the sodium salt of *O,O*-2,3-dimethylbutylene dithiophosphate (0.316 g, 1.35 mmol) was added to a solution of dimethyltellurium dichloride (0.154 g, 0.67 mmol) in dried toluene (15 mL). The mixture was stirred and refluxed at 30°C for 2 h. The reaction mixture was filtered to remove NaCl and any unreacted materials. The solvent was reduced to 5 mL under vacuum. Then *n*-hexane (approximately 5 mL) was added and the solution was left overnight in the refrigerator at –6°C. Crystals of $Me_2Te[S_2POCMe_2CMe_2O]_2$, **1**, were formed, washed with *n*-hexane, and dried under vacuum (white crystals; decomp. 153–155°C; 0.320 g; yield 82%; Anal. calcd. for $C_{14}H_{30}O_4P_2S_4Te$: C 29.98, H 5.21; found: C 30.42, H 5.42; IR 1137 (s), 954 (s), and 910 (vs) compared with 1138 (s), 955 (s), and 902 (s) in the starting salt). Similarly were formed crystals of the follow ing compounds. $Me_2Te[S_2POCHMeCHMeO]_2$, **2**, pale brown crystals; mp 109–110°C; yield 81%; IR 1065 (m), 1018 (m), and 931 (vs) compared with 1068 (m), 1020 (m), and 926(vs) in the starting salt. $Me_2Te[S_2POCH_2CMe_2CH_2O]_2$, **3**, pale brown crystals, decomp. 159–161°C; yield 88%; IR 1047 (s) and 994 (vs) compared with 1051 (s) and 1001 (s) in the starting salt. $Me_2Te[S_2POCH_2CEt_2CH_2O]_2$, **4**, white crystals; mp 136°C; yield 83%; IR 1067 (s), 1016 (s), 991 (vs), and 935 (s) compared with 1070 (s), 1019 (s), 993 (vs), and 933 (s) in the starting salt.

*Synthesis of dimethyltellurium(IV) diphenyl dithiophosphate, $Me_2Te[S_2P(OPh)_2]_2$, **5***

The ammonium salt of diphenyl dithiophosphate (0.348 g, 1.16 mmol) was added to a solution of dimethyltellurium dichloride (0.133 g, 0.58 mmol) in toluene (15 mL). The reaction solution was refluxed at 30°C with stirring for 2 h. The product solution was filtered to remove NH_4Cl and any unreacted materials and the solvent removed under reduced pressure. $Me_2Te[S_2P(OPh)_2]_2$, **5**, was obtained as a pale yellow viscous oil (0.385 g; 92% yield; IR 1186 (vs), 1024 (m), 867 (vs) compared with 1192 (vs), 1025 (m), and 867 (vs) in the starting salt). Attempts to bring about crystallization were not successful.

*Alternative synthesis of $Me_2Te[S_2POCH_2CMe_2CH_2O]_2$, **4***

A solution of neopentylene dithiophosphoric acid (0.252 g, 1.27 mmol) in toluene (10 mL) was added to a solution of dimethyltellurium dichloride (0.145 g, 0.63 mmol) in toluene (15 mL). The reaction mixture was refluxed at 60°C for 3 h. Then *n*-hexane (approximately 5 mL) was added and the solution was left in the refrigerator overnight at –6°C. Crystals of $Me_2Te[S_2POCH_2CMe_2CH_2O]_2$ were obtained, washed with *n*-hexane and dried under vacuum (pale brown crystals; decomp. 159–161°C; 0.28 g; yield 80%).

Physical measurements

All solvents were dried and distilled prior to use. The elemental analysis was performed at Guelph Laboratories. Density measurements were performed by the flotation method. The infrared spectra were recorded on a Nicolet 5DX FT spectrometer as CsI pellets and far infrared spectra on a Bomem IR Spectrometer between polyethylene films. The Raman spectra were recorded on a Spectra-Physics 164 spectrometer using the 5145-Å exciting line of an argon ion laser with samples sealed in capillary tubes. The ^1H and ^{13}C NMR spectra were recorded on a Bruker 300 FT/NMR spectrometer in $CDCl_3/C_6D_6$ using Me_4Si as internal standard. The ^{31}P and ^{125}Te NMR spectra were recorded on a Bruker 200 FT/NMR spectrometer in $CDCl_3/C_6D_6$ using H_3PO_4 and Me_2Te as external standards as appropriate. The melting points were determined on a Fisher-Johns apparatus.

X-ray crystallographic analysis

White block crystals of $Me_2Te[S_2POCMe_2CMe_2O]_2$ (**1**) and $Me_2Te[S_2POCH_2CEt_2CH_2O]_2$ (**4**) were sealed in thin-walled glass capillaries and mounted on a Rigaku AFC6S diffractometer, with graphite-monochromated Mo Kα radiation.

Cell constants and an orientation matrix for data collection, obtained from a least-squares refinement using the setting angles of 25 carefully centered reflections in the range $20.24° < 2\theta < 25.53°$ corresponded to monoclinic (for **1**) and triclinic (for **4**) cells whose dimensions are given in Table 1. For **1**, the systematic absences ($h0l$, $l = 2n + 1$; $0k0$, $k = 2n + 1$) are observed. Based on packing considerations, statistical analyses of intensity distributions, and the successful solution and refinement of the structures, the space groups were determined to be $P2_1/c$ (No. 14) for **1** and $P\bar{1}$ (No. 2) for **4**.

The data were collected at a temperature of 23 ± 1°C using the ω-2θ scan technique to a maximum 2θ value of 50.0°. The ω scans of several intense reflections, made prior to data collection, had an average width at half-height of 0.38° for **1** and 0.42° for **4** with a takeoff angle of 6.0°. Scans of $(1.31 + 0.30 \tan\theta)°$ for **1** and $(1.68 + 0.30 \tan\theta)°$ for **4** were made at a speed of 8.0°/min (in ω). The weak reflections ($I < 10.0\sigma(I)$) were rescanned (maximum of 2 rescans) and the counts were accumulated to assure good counting statistics. Stationary background counts were recorded on each side of the reflection. The ratio of peak counting time to background counting time was 2:1. The diameter of the incident beam collimator was 0.5 mm, and the crystal to detector distance was 285.0 mm.

Of the 4720 (for **1**) or 4840 (for **4**) reflections which were collected, 4507 (for **1**) or 4573 (for **4**) were unique (R_{int} = 0.072 and 0.055). The intensities of three representative reflections which were measured after every 150 reflections remained constant throughout data collection indicating crystal and electronic stability (no decay correction was applied).

The linear absorption coefficient for Mo Kα is 17.05 cm^{-1} (for **1**) and 15.93 cm^{-1} (for **4**). An empirical absorption correction, based on azimuthal scans of several reflections, was applied which resulted in transmission factors ranging from 0.76 to 1.00 (for **1**) and 0.85 to 1.00 (for **4**). The data were corrected for Lorentz and polarization effects.

The structures were solved by direct methods.[3] The non-hydrogen atoms were refined anisotropically and the hydrogen atoms were included in their idealised positions with C—H set at 0.95 Å and with isotropic thermal parameters set at 1.2 times that of the carbon atom to which they were attached. The final cycle of full-matrix least-squares refinement[4] was based on 2326 (for **1**) and 2283 (for **4**) observed reflections ($I > 3.00\sigma(I)$) and 226 (for **1**) and 244 (for **4**) variable parameters and converged (largest parameter shift was 0.001 times its esd) with unweighted and weighted agreement factors of $R = \Sigma||F_o| - |F_c||/\Sigma|F_o| = 0.0399$ (for **1**) and 0.0364 (for **4**) and $R_w = [(\Sigma w(|F_o| - |F_c|)^2/\Sigma wF_o^2)]^{1/2} = 0.0343$ (for **1**) and 0.0295 (for **4**).

[3]For structure solution methods, see ref. 27(*a*); for DIRDIF: direct methods for difference structures — an automatic procedure for phase extension and refinement of difference structure factors, see ref. 27(*b*).

[4]Least-squares: Function minimized: $\Sigma w(|F_o| - |F_c|)^2$, where $w = 4F_o^2(F_o^2)$, $\sigma^2(F_o^2) = [S^2(C + R^2B) + (pF_o^2)^2]/(Lp)^2$, S = scan rate, C = total integrated peak count, R = ratio of scan time to background counting time, Lp = Lorentz-polarization factor, and p = p factor.

TABLE 1. Summary of crystal data, intensity collection, and structural refinement for $Me_2Te[S_2\overline{POCMe_2CMe_2O}]_2$ and, $Me_2Te[S_2\overline{POCH_2CEt_2CH_2O}]_2$, **4**

Parameter	$Me_2Te[S_2\overline{POCMe_2CMe_2O}]_2$, **1**	$Me_2Te[S_2\overline{POCH_2CEt_2CH_2O}]_2$, **4**
Cell constants		
a (Å)	12.707 (3)	12.580 (3)
b (Å)	11.482 (2)	13.313 (3)
c (Å)	16.782 (2)	8.206 (1)
α (deg)	90.00	91.28 (2)
β (deg)	98.00 (1)	104.94 (2)
γ (deg)	90.00	78.52 (2)
Cell volume (Å^3)	2424 (1)	1301 (1)
Crystal system	Monoclinic	Triclinic
Space group	$P2_1/c$	$P\bar{1}$
Mol. wt. (g mol^{-1})	580.18	608.23
Z	4	2
Crystal dimensions, mm	0.54 × 0.35 × 0.27	0.77 × 0.31 × 0.15
Absorption coefficient μ (cm^{-1})	17.05	15.93
Transmission factors	0.76–1.00	0.85–1.00
Temperature, °C	23	23
Radiation	MoKα 0.71069 Å	
Monochromator	Highly oriented graphite	
Total reflections measured	4720	4804
Unique data used	2326	2283
No. of parameters (NP)	226	244
$R = \Sigma\|\|F_o\| - \|F_c\|\|/\Sigma\|F_o\|$	0.0399	0.0364
$R_w = [(\Sigma w(\|F_o\| - \|F_c\|)^2/\Sigma w F_o^2)]^{1/2}$	0.0343	0.0295
Goodness-of-fit (GOF)	1.52	1.28
Largest shift/esd, final cycle	0.0003	0.0002
Largest residual electron density (e Å^{-3})	0.54	0.49
Atom associated with residual density	Te	Te

The standard deviation of an observation of unit weight[5] was 1.50. The weighting scheme was based on counting statistics and included a factor (p = 0.03) to downweight the intense reflections. Plots of $\Sigma w(|F_o| - |F_c|)^2$ versus $|F_o|$, reflection order in data collection, sin θ/λ, and various classes of indices showed no unusual trends. The maximum and minimum peaks on the final difference Fourier map corresponded to 0.54 and –0.75 e/Å^3, respectively for **1** and 0.49 and –0.38 e/Å^3, respectively for **4**.

Neutral-atom scattering factors were taken from Cromer and Waber (28*a*). Anomalous dispersion effects were included in F_c (29); the values for $\Delta f'$ and $\Delta f''$ were those of Cromer and Waber (28*b*). All calculations were performed using the TEXSAN (30) crystallographic software package of Molecular Structure Corp.

The final atomic coordinates and equivalent isotropic thermal parameters (Tables 2 and 3) are given, respectively, for **1** and **4** for the non-hydrogen atoms and important distances and bond angles in Tables 4 and 5. The molecular structures of the two compounds are displayed as ORTEP diagrams in Figs. 1 and 2. Tables of final thermal parameters of non-hydrogen atoms, final fractional coordinates, and thermal parameters of hydrogen atoms as well as tables of observed and calculated structure factors have been deposited.[6]

Calculation of Pauling bond order

The formula proposed by Pauling (31) for calculating the bond orders of partial bonds is given by $d_n - d = -0.60 \log n$, where d_n is the bond length for bond number, n, and d is the length of the single bond of the same type. Based on the C—C single bond of 1.54 Å, Pauling's formula gives a bond length of 1.36 Å for n = 2; 1.72 Å for n = 0.5; and 1.90 Å for n = 0.25. These give percentage increases in bond length for the partial bonds of approximately 12 and 23% respectively for n = 0.5 and 0.25. It is reasonable to assume that similar relationships relating bond order to interatomic distances for the much longer secondary interactions or partial bonds involving Te and S should utilize percentage differences "normalized" to 1.54 as follows rather than absolute differences. Pauling's relationship, which can be written as $n = 10^X$, where $X = (d - d_n)/0.6$, can be modified to allow for percentage differences "normalized" to 1.54 to give $X = [1.54(d - d_n)/d]/0.6$ or $X = 2.5(d - d_n)/d$. Based on a Te—S single bond length of 2.63 Å, typical calculated values of the lengths of partial bonds for various values of n are as follows: 2.63 Å (n = 1.0), 2.76 (0.75), 2.95 (0.50), 3.26 (0.25) and 3.68 Å (n = 0.10). This scale appears to be compatible with the sum of the van der Waals radii of 3.86 Å for Te and S (32).

Results and discussion

A variety of dimethyltellurium(IV) alkylene and diphenyl dithiophosphate compounds are prepared in 80–90% yields by the reaction of dimethyltellurium dichloride with the ammonium or sodium salts of the appropriate dithiophosphoric acids in toluene at 30°C.

$$Me_2TeCl_2 + 2MS_2\overline{POGO} \rightarrow Me_2Te[S_2\overline{POGO}]_2 + 2MCl$$

M = NH_4 or Na; G = —CMe_2CMe_2—, —CHMeCHMe—, $CH_2CMe_2CH_2$—, —$CH_2CEt_2CH_2$—

$$Me_2TeCl_2 + 2NH_4S_2P(OPh)_2 \rightarrow Me_2Te[S_2P(OPh)_2]_2 + 2NH_4Cl$$

Alternatively, these compounds can be prepared in similar yields by the reaction of Me_2TeCl_2 and the corresponding

[5]Standard deviation of an observation of unit weight: $[\Sigma w(|F_o| - |F_c|)^2/(N_o - N_v)]^{1/2}$, where N_o = number of observations and N_v = number of variables.

[6]A complete set of data may be purchased from: The Depository of Unpublished Data, CISTI, National Research Council Canada, Ottawa, ON K1A 0S2, Canada.

Tables of hydrogen atom fractional coordinates have also been deposited with the Cambridge Crystallographic Data Centre, and can be obtained on request from The Director, Cambridge Crystallographic Data Centre, University Chemical Laboratory, 12 Union Road, Cambridge, CB2 1EZ, U.K.

Can. J. Chem. Downloaded from www.nrcresearchpress.com by EESC ESCOLA DE ENGENHARIA on 09/08/12
For personal use only.

Can. J. Chem. Downloaded from www.nrcresearchpress.com by EESC ESCOLA DE ENGENHARIA on 09/08/12
For personal use only.

TABLE 2. Final fractional coordinates and B(eq) for $Me_2Te[S_2\overline{POCMe_2CMe_2O}]_2$, **1**[a]

Atom	x	y	z	B(eq)
Te(1)	0.36641(4)	0.02693(4)	0.18211(3)	2.68(2)
S(1)	0.3512(2)	0.1764(2)	0.2967(1)	3.8(1)
S(2)	0.1491(2)	0.1944(2)	0.1471(2)	5.1(1)
S(3)	0.4046(2)	−0.1155(2)	0.0643(1)	3.5(1)
S(4)	0.3160(2)	−0.2527(2)	0.2168(1)	4.0(1)
P(1)	0.2059(2)	0.2460(2)	0.2545(1)	2.9(1)
P(2)	0.3257(2)	−0.2549(2)	0.1023(1)	2.7(1)
O(1)	0.2156(4)	0.3850(4)	0.2636(3)	3.6(3)
O(2)	0.1325(4)	0.2254(4)	0.3233(3)	3.4(2)
O(3)	0.3792(4)	−0.3714(4)	0.0734(3)	3.0(2)
O(4)	0.2153(4)	−0.2660(4)	0.0440(3)	3.4(3)
C(1)	0.4359(7)	0.1582(7)	0.1168(5)	4.2(5)
C(2)	0.5098(6)	−0.0281(7)	0.2514(5)	3.7(4)
C(3)	0.1676(8)	0.4274(8)	0.3321(6)	4.7(5)
C(4)	0.0880(8)	0.3348(8)	0.3482(6)	4.7(5)
C(5)	0.138(1)	0.5497(8)	0.3212(9)	9.9(8)
C(6)	0.259(1)	0.422(1)	0.4062(8)	11(1)
C(7)	0.054(1)	0.324(1)	0.4275(7)	8.0(7)
C(8)	−0.015(1)	0.357(1)	0.2862(8)	11(1)
C(9)	0.3135(7)	−0.4249(8)	0.0031(5)	3.8(4)
C(10)	0.1998(7)	−0.3844(7)	0.0104(5)	3.6(4)
C(11)	0.3526(7)	−0.3716(9)	−0.0716(6)	5.1(5)
C(12)	0.3300(8)	−0.5541(7)	0.0057(6)	5.1(5)
C(13)	0.1504(7)	−0.4585(8)	0.0725(6)	5.3(5)
C(14)	0.1243(8)	−0.3786(9)	−0.0651(6)	5.8(6)

[a]Standard deviations in parentheses.

TABLE 3. Final fractional coordinates and B(eq) for $Me_2Te[S_2\overline{POCM_2CEt_2CH_2O}]_2$, **4**[a]

Atom	x	y	z	B(eq)
Te(1)	0.02484(5)	0.77172(4)	0.47218(7)	3.54(3)
S(1)	0.0945(2)	0.9086(2)	0.6810(3)	4.6(1)
S(2)	0.3155(2)	0.7524(2)	0.5850(3)	6.5(2)
S(3	−0.0688(2)	0.6270(2)	0.2969(2)	4.4(1)
S(4)	−0.0487(2)	0.8087(2)	0.0312(3)	4.6(1)
P(1)	0.2622(2)	0.8399(2)	0.7479(3)	4.1(1)
P(2)	−0.1161(2)	0.6953(2)	0.0606(2)	3.3(1)
O(1)	0.3258(4)	0.9315(4)	0.7979(6)	4.3(3)
O(2)	0.2848(4)	0.7783(4)	0.9201(6)	4.1(3)
O(3)	−0.0908(3)	0.6053(3)	−0.0632(5)	3.2(2)
O(4)	−0.2502(4)	0.7269(4)	0.0094(6)	3.9(3)
C(1)	0.0655(7)	0.6631(6)	0.6737(9)	5.0(5)
C(2)	−0.1366(6)	0.8417(6)	0.501(1)	5.5(5)
C(3)	0.3106(6)	0.9881(6)	0.948(1)	4.6(5)
C(4)	0.3429(6)	0.9168(6)	1.105(1)	3.6(4)
C(5)	0.2701(6)	0.8372(6)	1.068(1)	4.1(4)
C(6)	0.4695(7)	0.8668(6)	1.143(1)	4.9(5)
C(7)	0.5141(7)	0.7872(7)	1.285(1)	6.8(6)
C(8)	0.3137(7)	0.9790(7)	1.255(1)	5.2(5)
C(9)	0.3755(7)	1.0670(7)	1.311(1)	6.8(6)
C(10)	−0.1564(6)	0.5254(5)	−0.0784(9)	3.6(4)
C(11)	−0.2820(6)	0.5679(5)	−0.1437(9)	3.1(4)
C(12)	−0.3157(6)	0.6462(6)	−0.019(1)	4.3(5)
C(13)	−0.3410(7)	0.4775(6)	−0.141(1)	5.0(5)
C(14)	−0.4684(8)	0.5035(7)	−0.212(1)	7.5(7)
C(15)	−0.3079(6)	0.6179(6)	−0.321(1)	4.3(4)
C(16)	−0.2711(7)	0.5495(7)	−0.453(1)	5.9(5)

[a]Standard deviations in parentheses.

TABLE 4. Interatomic distances (Å) in compounds **1** and **4**[a,b]

$Me_2Te[S_2\overline{POCMe_2CMe_2O}]_2$ (**1**)		$Me_2Te[S_2\overline{POCH_2CEt_2CH_2O}]_2$ (**4**)	
Atoms	Distance	Atoms	Distance
Te(1)—S(1)	2.604(2)	Te(1)—S(1)	2.597(2)
Te(1)—S(3)	2.661(2)	Te(1)—S(3)	2.660(2)
Te(1)—C(1)	2.127(8)	Te(1)—C(1)	2.113(7)
Te(1)—C(2)	2.117(8)	Te(1)—C(2)	2.128(7)
S(1)—P(1)	2.045(3)	S(1)—P(1)	2.060(3)
S(2)—P(1)	1.939(3)	S(2)—P(1)	1.917(3)
S(3)—P(2)	2.038(3)	S(3)—P(2)	2.052(3)
S(4)—P(2)	1.944(3)	S(4)—P(2)	1.920(3)
P(1)—O(1)	1.607(5)	P(1)—O(1)	1.580(5)
P(1)—O(2)	1.600(5)	P(1)—O(2)	1.582(5)
P(2)—O(3)	1.605(5)	P(2)—O(3)	1.590(4)
P(2)—O(4)	1.599(5)	P(2)—O(4)	1.601(5)
O(1)—C(3)	1.459(9)	O(1)—C(3)	1.466(8)
O(2)—C(4)	1.46(1)	O(2)—C(5)	1.461(6)
O(3)—C(9)	1.480(9)	O(3)—C(10)	1.455(8)
O(4)—C(10)	1.475(9)	O(4)—C(12)	1.458(8)
C(3)—C(4)	1.52(1)	C(3)—C(4)	1.53(1)
C(3)—C(5)	1.46(1)	C(4)—C(5)	1.51(1)
C(3)—C(6)	1.58(2)	C(4)—C(6)	1.552(9)
C(4)—C(7)	1.46(1)	C(6)—C(7)	1.51(1)
C(4)—C(8)	1.58(1)	C(4)—C(8)	1.55(1)
C(9)—C(10)	1.54(1)	C(8)—C(9)	1.53(1)
C(9)—C(11)	1.54(1)	C(10)—C(11)	1.525(9)
C(9)—C(12)	1.50(1)	C(11)—C(12)	1.523(9)
C(10)—C(13)	1.54(1)	C(11)—C(13)	1.54(1)
C(10)—C(14)	1.48(1)	C(13)—C(14)	1.53(1)
		C(11)—C(15)	1.540(9)
		C(15)—C(16)	1.51(1)
Te(1)—S(2)	3.349(3)	Te(1)—S(2)	3.490(3)
Te(1)—S(4)	3.341(2)	Te(1)—S(4)	3.516(2)
Te(1)—S(4)′	4.864(3)	Te(1)—S(1)″	4.321(3)
		Te(1)—S(4)‴	4.904(2)

[a]Symmetry equivalent position $(1 - x, 0.5 + y, 0.5 - z)$ is denoted by a prime, $(-x, 2 - y, 1 - z)$ by a double prime, and $(x, y, 1 + z)$ by a triple prime.
[b]Numbers in parentheses refer to estimated standard deviations in the least significant digits.

dithiophosphoric acids in toluene by refluxing at 60°C.

$$Me_2TeCl_2 + 2HS_2\overline{POGO} \rightarrow Me_2Te[S_2\overline{POGO}]_2 + 2HCl$$

In contrast with other organotellurium compounds of the type Ph_2TeL_2, where L = dithiocarbamate, dithiocarbonate, or *O,O*-dialkyl dithiophosphate, which were found to undergo complete reductive elimination in solution within a matter of days, these Me_2TeL_2 derivatives are stable in common organic solvents such as C_6H_6, CS_2, CCl_4, and $CHCl_3$ for several weeks. The cyclic derivatives, which are crystalline solids, are less soluble than the open chain $Me_2Te[S_2P(OPh)_2]_2$ derivative, which is a pale yellow viscous liquid.

The crystal structures of $Me_2Te[S_2\overline{POCMe_2CMe_2O}]_2$, ***1***, *and* $Me_2Te[S_2\overline{POCH_2CEt_2CH_2O}]_2$, ***4***

Dimethylbis(*O,O*-2,3-dimethylbutylene dithiophosphato)tellurium(IV), **1**, crystallizes in the space group $P2_1/c$ and dimethylbis (*O,O*-2,2-diethylpropylene dithiophosphato)tellurium(IV), **4**, in the space group $P\bar{1}$. The ORTEP diagrams (Figs. 1 and 2) illustrate that for both molecules the immediate environment about tellurium is that of the saw-horse structure typical of tellurium(IV) compounds in which the lone-pair is assumed to

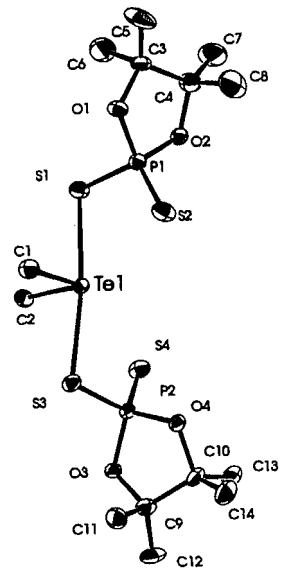

FIG. 1. ORTEP plot of the molecule $Me_2Te[S_2\overline{POCMe_2CMe_2O}]_2$ (**1**). The atoms are drawn with 25% probability ellipsoids. Hydrogen atoms are omitted for clarity.

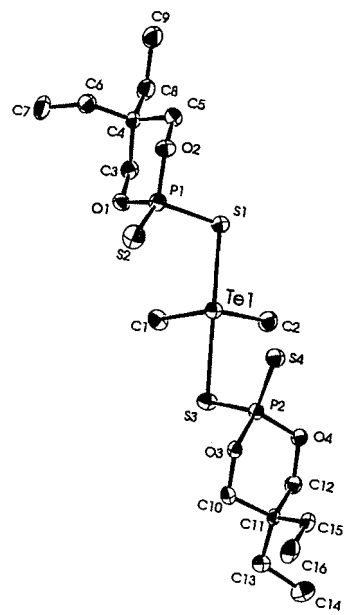

FIG. 2. ORTEP plot of the molecule $Me_2Te[S_2\overline{POCH_2CEt_2CH_2O}]_2$ (**4**). The atoms are drawn with 25% probability ellipsoids. Hydrogen atoms are omitted for clarity.

be stereochemically active and occupying an equatorial position in a distorted trigonal bipyramid. The two methyl groups occupy the other two equatorial positions with the axial positions being occupied by one sulfur atom from each of the dithiophosphate groups. The Te—C bond lengths, 2.127(8) and 2.117(8) Å in **1** and 2.128(7) and 2.113(7) Å in **4**, are similar to those reported for the related species $Me_2Te[S_2CNMe_2]_2$ (10) and $Me_2Te[S_2COMe]_2$ (15). In both **1** and **4**, one of the Te—S bonds is significantly longer than the other, 2.604(2) and 2.661(2) Å in **1** and 2.597(2) and 2.660(2) Å in **4**. These bond lengths bracket those reported for the non-cyclic dithiophosphate derivatives, $Ph_2Te[S_2P(OMe)_2]_2$ (18) and $Ph_2Te[S_2P(OEt)_2]_2$ (13) in which both Te—S bonds are of

Can. J. Chem. Downloaded from www.nrcresearchpress.com by EESC ESCOLA DE ENGENHARIA on 09/08/12
For personal use only.

TABLE 5. Bond angles (deg) in compounds **1** and **4** with standard deviations in parentheses

$Me_2Te[S_2POCMe_2CMe_2O]_2$ (**1**)		$Me_2Te[S_2POCH_2CEt_2CH_2O]_2$ (**4**)	
Bonds	Angle	Bonds	Angle
S(1)—Te(1)—S(3)	173.26(7)	S(1)—Te(1)—S(3)	169.52(7)
S(1)—Te(1)—C(1)	89.6(2)	S(1)—Te(1)—C(1)	90.9(2)
S(1)—Te(1)—C(2)	86.4(2)	S(1)—Te(1)—C(2)	84.3(2)
S(3)—Te(1)—C(1)	85.5(2)	S(3)—Te(1)—C(1)	83.2(2)
S(3)—Te(1)—C(2)	89.6(2)	S(3)—Te(1)—C(2)	88.2(2)
C(1)—Te(1)—C(2)	96.2(3)	C(1)—Te(1)—C(2)	96.6(3)
Te(1)—S(1)—P(1)	99.1(1)	Te(1)—S(1)—P(1)	97.4(3)
Te(1)—S(3)—P(2)	95.9(1)	Te(1)—S(3)—P(2)	99.4(1)
S(1)—P(1)—S(2)	113.8(1)	S(1)—P(1)—S(2)	116.4(1)
S(1)—P(1)—O(1)	107.6(2)	S(1)—P(1)—O(1)	104.7(2)
S(1)—P(1)—O(2)	106.4(2)	S(1)—P(1)—O(2)	107.2(2)
S(2)—P(1)—O(1)	113.9(2)	S(2)—P(1)—O(1)	113.4(2)
S(2)—P(1)—O(2)	116.5(3)	S(2)—P(1)—O(2)	110.3(2)
O(1)—P(1)—O(2)	97.1(3)	O(1)—P(1)—O(2)	104.1(3)
S(3)—P(2)—S(4)	113.6(1)	S(3)—P(2)—S(4)	116.7(1)
S(3)—P(2)—O(3)	108.2(2)	S(3)—P(2)—O(3)	105.3(2)
S(3)—P(2)—O(4)	107.4(2)	S(3)—P(2)—O(4)	107.1(2)
S(4)—P(2)—O(3)	113.4(2)	S(4)—P(2)—O(3)	111.8(2)
S(4)—P(2)—O(4)	115.8(2)	S(4)—P(2)—O(4)	111.5(2)
O(3)—P(2)—O(4)	97.0(3)	O(3)—P(2)—O(4)	103.5(3)
P(1)—O(1)—C(3)	111.8(5)	P(1)—O(1)—C(3)	117.5(4)
P(1)—O(2)—C(4)	111.6(5)	P(1)—O(2)—C(5)	117.5(4)
P(2)—O(3)—C(9)	111.7(5)	P(2)—O(3)—C(10)	116.6(4)
P(2)—O(4)—C(10)	111.5(5)	P(2)—O(4)—C(12)	118.9(4)
O(1)—C(3)—C(4)	105.6(7)	O(1)—C(3)—C(4)	111.6(6)
O(2)—C(4)—C(3)	104.9(7)	O(2)—C(5)—C(4)	112.0(6)
		C(3)—C(4)—C(5)	107.6(6)
O(3)—C(9)—C(10)	104.1(6)	O(3)—C(10)—C(11)	112.1(6)
O(4)—C(10)—C(9)	103.4(6)	O(4)—C(12)—C(11)	113.0(6)
		C(10)—C(11)—C(12)	107.3(6)
S(1)—Te(1)—S(2)	66.86(7)	S(1)—Te(1)—S(2)	65.56(7)
S(3)—Te(1)—S(4)	66.31(6)	S(3)—Te(1)—S(4)	64.66(6)

similar length and average 2.622(3) and 2.615(6) Å, respectively. By contrast, in $Me_2Te[S_2COMe]_2$ the two Te—S bonds again differ in length, 2.566(1) and 2.280(1) Å, and the sulfur atom of the longer Te—S bond is 3.755(1) Å from the tellurium atom of an adjacent molecule. This is the only such contact less than the sum of the van der Waals radii of 3.86 Å (32) and it has been proposed that it constitutes a secondary intermolecular interaction (15). A similar phenomenon was noted for R_2TeCl_2 where one Te—Cl bond was much longer than the other and it too appeared to be the only one involved in any intermolecular association (33). However, neither of the longer Te—S bonds in **1** and **4** is associated with an intermolecular contact under 5.0 Å.

As was found for non-cyclic dithiophosphates (11, 13, 18), the terminal sulfur atoms are oriented toward the tellurium atom at distances, 3.341(2) and 3.349(3) Å in **1** and 3.490(3) and 3.516(2) Å in **4**, well within the sum of the van der Waals radii. The nature and importance of these secondary interactions is not clear so we introduce a more quantitative approach than hitherto attempted by estimating bond orders for these partial bonds based on proposals made recently in calculating a bond order for an unusually long Si—Si bond in a disilane derivative (34). The calculation was based on that devised by Pauling for partial bonds primarily involving hydrogen and first-row elements (31). We allow for the involvement of heavier elements and estimate that intramolecular Te--S interactions ranging from 3.345(4) to 3.50(1) Å, as in **1** and **4**, correspond to partial Pauling bond orders of 0.20 to 0.14. This suggests that the second sulfur atom of these anisobidentate ligands could be included in the coordination sphere around tellurium. This was the approach taken for $Me_2Te[S_2COMe]_2$ (15) and $Ph_2Te[S_2P(OEt)_2]_2$ (13) in which the two Te--S intramolecular secondary interactions, 3.303(1) and 3.352(1) Å in the former and 3.367(2) and 3.353(3) Å in the latter, were included and the structures were described as a pseudo-pentagonal bipyramid and a bi-capped trigonal bipyramid, respectively, rather than as the pseudo-trigonal bipyramid formed by the closest atoms. The same trigonal bipyramidal arrangement occurs in $C_8H_8Te[S_2P(OEt)_2]_2$ (10) but it was described as an eight coordinate linear polymer because in addition to the two Te--S intramolecular contacts at approximately 3.47 Å, there is an intermolecular contact at 3.729(4) Å. The immediate environments around tellurium are identical in $Ph_2Te[S_2P(OEt)_2]_2$ and $C_8H_8Te[S_2P(OEt)_2]_2$, but the relative orientations of the dithiophosphate ligands differ, presumably as a result of the additional intermolecular link in the latter (13).

The structures of **1** and **4** more closely resemble that of $C_8H_8Te[S_2P(OEt)_2]_2$ than that of $Ph_2Te[S_2P(OEt)_2]_2$ although neither have the intramolecular Te--S link observed in the former. If the dithiophosphates are considered to be mono-

Can. J. Chem. Downloaded from www.nrcresearchpress.com by EESC ESCOLA DE ENGENHARIA on 09/08/12
For personal use only.

Can. J. Chem. Downloaded from www.nrcresearchpress.com by EESC ESCOLA DE ENGENHARIA on 09/08/12
For personal use only.

dentate and only linked through the one sulfur atom then tellurium is at the centre of a distorted pseudo trigonal bipyramid with a stereochemically active lone pair occupying the third trigonal planar position. On the other hand, if the dithiophosphate groups are considered to be anisobidentate with the second sulfur atoms forming part of the coordination sphere, then the environment is a distorted octahedron with each of the anisobonding sulfur atoms taking up positions approximately *trans* to one of the methyl groups attached to tellurium. Thus, the methyl carbon atom C(2), Te(1), S(1), and S(2) are essentially coplanar (mean deviation from plane is 0.002 Å in **1** and .023 Å in **4**) with the second methyl carbon atom C(1) out of the plane by 2.11(1) Å in **1** and 2.10(1) Å in **4**. Similarly, C(1), Te(1), S(3), and S(4) are approximately coplanar (mean deviations of 0.07 and 0.13 Å, respectively, for **1** and **4**) with the C(2) methyl group out of the plane by 2.07(1) and 2.14(1) Å, respectively, for **1** and **4**. The dihedral angle between the plane Te(1), S(1), and S(2) and the plane Te(1), S(3), and S(4) in **4** is 94.0(2)°, indicating minimal distortion from the arrangement that would exist if the linkages were bidentate, with the anisobonded atoms *cis* to one another. The deviation from 90° is somewhat larger in **1**, where the corresponding dihedral angle is 77.0(2)°.

It has been proposed that dithiocarbamates have stronger chelating ability than xanthates because the secondary Te--S bonds in $C_8H_8Te[S_2CNEt_2]_2$ are slightly shorter than those of the corresponding xanthate, and conversely that dithiophosphates have lesser chelating ability because the corresponding distances in $C_8H_8Te[S_2P(OEt)_2]_2$ are longer. The average Te--S secondary interactions in $Ph_2Te[S_2P(OMe)_2]_2$ and $Ph_2Te[S_2P(OEt)_2]_2$, 3.37(1) and 3.360(7) Å, respectively, are shorter than those in **1** and **4** suggesting that the cyclic dithiophosphates are weaker chelating agents than non-cyclic dithiophosphates and both are weaker than dithiocarbamates and xanthates.

The S—Te—S angles in **1** and **4** are 173.26(7) and 169.52(7)°, respectively, so that deviation from 180° is slightly less than in the dimethyltellurium xanthate and dithiocarbamate derivatives $Me_2Te[S_2COMe]_2$ (15) and $Me_2Te[S_2CNMe_2]_2$ (10), where the angles are 165.90(3) and 166.5(1)°, respectively. The C—Te—C bond angles of 96.2(3) and 96.6(3)°, respectively, in **1** and **4** are the same as in $Me_2Te[S_2COMe]_2$, and larger than the values of 93.9(2) and 95.5(3)° for $Me_2Te[S_2CNMe_2]_2$. The bite angles of 66.31(6) and 66.86(7)° in **1** and 64.66(6) and 65.56(7)° in **4** are comparable to those reported for non-cyclic dithiophosphate derivatives such as $Ph_2Te[S_2P(OMe)_2]_2$ (18) and $Ph_2Te[S_2P(OEt)_2]_2$ (13) which range from 66.3(1) to 66.88(6)°.

The TeS—P bonds, which average 2.042(3) Å in **1** and 2.056(4) Å in **4**, are longer than the terminal or anisobonded P=S bonds, which average 1.942(3) Å in **1** and 1.919(2) Å in **4**. These distances are comparable to those reported for the related non-cyclic derivatives. The S—P—S bond angles average 113.7(1)° in **1** and 116.5(2)° in **4**. The comparable angles in $Ph_2Te[S_2P(OMe)_2]_2$ (18) and $Ph_2Te[S_2P(OEt)_2]_2$ (13) range from 114.4(1) to 116.3(1)° so the values in **1** and **4** bracket those reported for non-cyclic derivatives. The O—P—O bond angles average 97.05(5)° in **1** and 103.8(3)° in **4**. The comparable angles in the two derivatives containing the non-cyclic dimethoxy and diethoxy dithiophosphates (18, 13) range from 93.6(5) to 96.2(5)°, which indicates that the larger O—P—O angle is related to the constraints imposed by the ring systems and particularly by the six-membered ring in **4**. The bond lengths and angles within the ring systems are as expected.

In **1**, a view down a C—C bond, either C(3)—C(4) or C(9)—C(10), shows that the four methyl groups attached to the carbon atoms of the ring are in the staggered configuration expected for the more stable arrangement of the ring. As a result, two methyl groups are oriented above and below the approximate plane of the distorted five-membered ring at an average distance of 3.23(3) Å from P. The second pair of methyl groups, at an average distance of 3.80(1) Å, are oriented away from phosphorus. The twist in the ring is demonstrated by the fact that C(3) is 0.15 Å below and C(4) 0.31 Å above the plane formed by P(1), O(1), and O(2). The distortion is slightly greater in the second five-membered ring.

In **4**, the six-membered rings take up the chair conformation expected for an "inorganic hexane ring." Thus P(2) is 0.63 Å above the plane containing O(3), O(4), C(10), and C(12) and C(11) is 0.71 Å below it. The second ring is similar, with the corresponding distances for P(1) and C(4) being 0.62 and 0.72 Å. The orientation within the rings results in one of the ethyl groups being oriented away from phosphorus and the other towards it to give two very different distances; 3.661(8) and 3.691(8) Å for P(1)—C(6) and P(2)—C(15), respectively, and 4.460(9) and 4.448(8) Å for P(1)—C(8) and P(2)—C(13). The staggered configuration around the ring also gives non-equivalent hydrogen positions for the CH_2 groups of the two rings.

Infrared and Raman spectra

Characteristic features of the infrared and Raman spectra involving bonding to tellurium are summarized in Table 6 for compounds **1**–**5**. The infrared spectra, particularly in the region around 1000 cm^{-1}, provide useful fingerprint identifications because all of the compounds have distinctive strong bands which are similar, but not identical, to those of the starting salts. This is exemplified in the cyclic derivatives, **1**–**4**, by the bands of strong intensity in the region 994–908 cm^{-1}, which are attributable to ring vibrations that are probably coupled with C—C stretching vibrations (35, 36). The similarity of these outstanding features suggests that either the bonding within the dithiophosphate groups is essentially unchanged or that the vibrational spectra are unlikely to provide definitive evidence as to the mode of attachment of the dithiophosphate.

There are three dominant peaks in the Raman spectra of $Me_2Te[S_2POCMe_2CMe_2O]_2$, **1**, and $Me_2Te[S_2POCH_2CEt_2CH_2O]_2$, **4**, at 525 (70), 313 (100), and 270 (45) cm^{-1} for **1** and 525 (75), 344 (60), and 257 (100) cm^{-1} for **4**. None of these peaks are present in the starting salts and so, by analogy with the Me_2TeX_2 series, X = Cl, Br, I (37), these can be assigned to the symmetric Te—C and two Te—S stretching vibrations. The relative intensities of the bands differ in the two compounds as they do in the infrared spectra. This lack of consistency, which is also a common feature in the spectra of the Me_2TeX_2 derivatives, is not related to structural changes, because the crystal structures show similar Te—C and Te—S environments in **1** and **4**. As is the case in the infrared spectrum of Me_2TeI_2 (37), there is no strong feature in the 525 cm^{-1} region, but a weak peak at 526 cm^{-1} can be assigned to the asymmetric Te—C stretch. The observation of near accidental degeneracy of the two Te—C stretches is consistent with the observation of C—Te—C angles of 96.2(3) and 96.6(3)°, respectively for **1** and **4**, as found for the Me_2TeX_2 species (38), while the considerable separation between the two Te—S stretching vibrations in both molecules is to be expected for two bonds at nearly 180° to one another. Finally, the features in the spectra of compounds **2**, **3**, and **5** are sufficiently

TABLE 6. Selected features in the vibrational spectra (cm^{-1}) of compounds **1** to **5**[a,b]

Compound	$\nu(Te—C)_{asym}$		$\nu(Te—C)_{sym}$		$\nu(Te—S)_{asym}$ and $\nu(Te—S)_{sym}$[c]			
	IR[d]	Raman[e]	IR[d]	Raman[e]	IR[d]	Raman[e]	IR[d]	Raman[e]
$Me_2Te[S_2POCMe_2CMe_2O]_2$, **1**	526 w	530 (sh)	526 w	525 (70)	313 m	313 (100)	274 ms	270 (45)
$Me_2Te[S_2POCHMeCHMeO]_2$, **2**	525 w, sh	525 (50)	525 w, sh	525 (50)	322 ms	322 (65)	286 ms	288 (100)
$Me_2Te[S_2POCH_2CMe_2CH_2O]_2$, **3**	522 m, br	529 (95)	522 m, br	521 (80)	336 m	344 (50)	245 mw	245 (100)
$Me_2Te[S_2POCH_2CEt_2CH_2O]_2$, **4**	514 s, br	525 (35)	514 s, br	525 (75)	337 m	344 (60)	255 w	257 (100)
$Me_2Te[S_2P(OPh)_2]_2$, **5**	523 ms	530 (30)	523 ms	525 (95)	313 w	313 (100)	274 w	270 (60)

[a]Parentheses denote relative intensities in the Raman effect.
[b]s = strong, m = medium, w = weak, v =very, sh = shoulder.
[c]There is ambiguity as to the correct order of assignments — see text.
[d]Run as KBr pellets to 400 cm^{-1} and as Nujol mulls below 450 cm^{-1}.
[e]Run as a solid in a glass capillary.

TABLE 7. ^1H, ^{13}C, ^{31}P, and ^{125}Te NMR chemical shifts for compounds **1–5**[a,b,c,d,e]

Compounds **1–5**	Te—CH_3 [Te—CH_3]	OC—CH_3/CH_2 [OC—CH_3/CH_2]	OCH_n/OC_6H_5 [OCH_n/OC_6H_5]	[OC—*C*—CO]	^{31}P {^{125}Te}
$Me_2Te[S_2POCMe_2CMe_2O]_2$, **1**	2.68s (6H) [19.15s]	1.44s (24H) [24.36d; J^{PC}, 4.1]	 [90.02s]		105.0 {572.3}
$Me_2Te[S_2POCHMeCHMeO]_2$, **2**	2.72s (6H) [19.11s]	1.34d (12H; *J*, 7.5) [15.82d; J^{PC}, 5.0]	4.68dq (4H; J^{PH}, 15.6; *J*, 7.5) [78.60s]		109.2 {574.9}
$Me_2Te[S_2POCH_2CMe_2CH_2O]_2$, **3**	2.79s (6H) [19.34s] [18.79s][f]	1.05s (12H) [21.66s] [21.19s][f]	4.03d (4H; J^{PH}, 15.6) [76.17s][f]	 [32.54s] [32.15s][f]	92.0 {576.9}
$Me_2Te[S_2POCH_2CEt_2CH_2O]_2$, **4**[g]	2.78s (6H) [19.47s]	1.45q (8H; *J*, 7.5) [23.09s]	4.12d (8H; *J*, 15.8) [73.98d; J^{PC}, 8.7]	 [37.47d; J^{PC}, 5.0]	92.5 {579.0}
$Me_2Te[S_2P(OPh)_2]_2$, **5**	2.40s (6H) [18.19s]		7.35–7.20m (20H) [150.72d; J^{PC}, 9.6: 129.46s: 125.54s: 121.90d; J^{PC}, 4.1]		91.3 {590.0}

[a]^{13}C NMR chemical shifts given in [ ], and ^{125}Te NMR chemical shifts in { }.
[b]The spectra were recorded in $CDCl_3$ and reported in ppm from Me_4Si for ^1H and ^{13}C, from H_3PO_4 for ^{31}P and from Me_2Te for ^{125}Te.
[c]s = singlet; d = doublet; t = triplet; q = quartet; dq = doublet of quartet; m = multiplet.
[d]For ^1H NMR spectra, the number of protons are given in parentheses, along with the values of the J^{HH} coupling constants.
[e]Values of J^{HH}, written as *J*, J^{PH}, and J^{PC} coupling constants given in Hz.
[f]Also recorded in C_6D_6.
[g]CH_2CH_3 at 0.84t (12H; *J*, 7.5) and CH_2CH_3 at [7.17s].

similar to those of **1** and **4** to suggest that the dithiophosphate groups are bonded in similar fashion in all five derivatives.

Nuclear magnetic resonance spectra

The ^1H NMR spectra data for compounds **1–5** are presented in Table 7. The methyl group directly attached to tellurium experiences an upfield shift of approximately 0.35 ppm in all four cyclic derivatives, **1–4**, relative to the sharp singlet observed for Me_2TeCl_2 at 3.13 ppm, and close to the shift observed for monosubstituted dithiocarbamate derivatives, $Me_2TeCl[S_2CNR_2]$ (10). The shift for compound **5** is slightly larger with the result that its chemical shift is essentially the same as those of the analogous bis substituted dithiocarbamates, $Me_2Te[S_2CNR_2]_2$ (10). Changes in the chemical shifts of methyl groups have been related to changes in the electronegativity of the groups attached to the central atom so the effective electronegativity of the non-cyclic dithiophosphate is, not unexpectedly, of a similar order of magnitude to that of the dithiocarbamate group, which in $Me_2Te[S_2CNMe_2]_2$ is also bonded in an anisobidentate manner (10). The effective electronegativity of the cyclic dithiophosphates is slightly larger but still less than that of chlorine as expected. The similarity of the chemical shift is consistent with all of the compounds having identical links between tellurium and the sulfur atoms of the dithiophosphate groups.

The values of the chemical shifts within the dithiophosphate groups are found to be similar to those of the salts from which they were prepared so that, as with the vibrational spectra, there are no significant changes as a result of being linked to tellurium. Despite the fact that the solid state structure of **1**

Can. J. Chem. Downloaded from www.nrcresearchpress.com by EESC ESCOLA DE ENGENHARIA on 09/08/12
For personal use only.

Can. J. Chem. Downloaded from www.nrcresearchpress.com by EESC ESCOLA DE ENGENHARIA on 09/08/12
For personal use only.

shows non-equivalent methyl groups substituted on the five-membered ring, only a single peak is observed at 1.44 ppm. The corresponding peak in the salt is also a singlet at 1.46 ppm, so in neither case is the non-equivalence maintained in solution. The same is true for the hydrogen atoms of the CH_2 groups in the six-membered ring, which are also non-equivalent in the solid state structure of **4** but only show single peaks at 4.12 ppm, compared to 4.13 ppm in the ammonium salt. However, in both **4** and its starting salt, these hydrogen atoms attached to the α-carbon atoms of the glycoxy groups show coupling with phosphorus to give doublets, with very similar values for $J(PCCH)$ close to 15 Hz. This is equally true for **2** and **3** and their starting salts and, in general, the chemical shifts and coupling constants for **1–4** are very similar to those reported for other metal complexes in which the linkage of the dithiophosphate groups was assumed to be bidentate (39–45).

The $^{13}C\{H\}$ NMR spectra data for compounds **1–5** are presented in Table 8. The peaks attributable to CH_3—Te fall between 19.11 and 19.47 ppm for the cyclic dithiophosphates, **1–4**, and at 18.19 ppm for $Me_2Te[S_2P(OPh)_2]_2$, which are bracketed by those of the related mono- and bis-substituted dithiocarbamates $Me_2TeCl[S_2CNMe_2]$ and $Me_2Te[S_2CNMe_2]_2$ of 20.5 and 16.6 ppm, respectively (10); all of the values being shifted slightly when compared with the value for Me_2TeCl_2 of 26.9 ppm. However, the signals attributable to all of the carbon atoms of the cyclic dithiophosphate groups are hardly shifted at all relative to the positions of the corresponding salts. In general, the values of the coupling constants, $J(P^2C)$ and $J(P^3C)$, which are included in Table 8, are typical of such groups in a variety of environments, as is the fact that these couplings are not observed in a consistent manner (40, 41, 44, 46).

The ^{125}Te NMR chemical shifts for compounds **1–5**, which are displayed in Table 8 along with those of the ^1H and ^{31}P NMR spectra, fall in the range of 559–590 ppm; a shift towards Me_2TeCl_2, 727.7 ppm, relative to the related dithiocarbamate derivatives, $Me_2Te[S_2CNMe_2]_2$ and $Me_2Te[S_2CNEt_2]_2$, 475 and 463 ppm, respectively (10).

The $^{31}P\{H\}$ NMR spectral data, which are presented in Table 7 along with the ^1H NMR data, show the presence of a single peak in all compounds **1–5**. This indicates the presence of only one species and also that the two dithiophosphate groups are in identical environments. It has been proposed that the difference in the phosphorus chemical shift between that of the appropriate free acid and the derivative is a strong indicator of the mode of binding (47). Downfield shifts in the range 8–15 ppm were claimed to be consistent with the presence of bidentate ligands while negligible shifts or even upfields shifts were associated with monodentate linkages. In compounds **1–5** the downfield shifts range from 11 to 16 ppm, which is consistent with the presence of bidentate ligands in solution rather than anisobidentate as found in the solid state structures. This is indicative of rapid interchange between the two sulfur atoms in a similar process found in phosphorus compounds containing four-membered rings (48). It could also account for the fact that, as with other bidentate dithiophosphate complexes, there was no sign of the non-equivalence of substituents on the carbon atoms in the ring in either the ^1H or ^{13}C NMR spectra; a fact confirmed by recording spectra down to –90°C. In this connection it should be noted that in general tin dithiophosphates are bidentate and the ^1H and ^{13}C NMR spectra of $Me_2Sn[S_2POCH_2CMe_2CH_2O]_2$ and related species show no signs of non-equivalence even though the solid state structures show anisobidentate linkages (49, 50). In discussing the orientation of the groups about tellurium, we pointed out that if the anisobonded sulfur atoms were included in the coordination sphere, then the implications were for an inactive lone pair of electrons. This could be a contributing factor in allowing rapid exchange to take place.

Acknowledgements

We thank the Natural Sciences and Engineering Research Council of Canada and the University of Windsor for financial support. One of us (L.N.K.) thanks the former for an NSERC Research Reorientation Associateship and one of us (R.R.) thanks Dayanand College, Ajmer, India, for granting a leave of absence.

1. M.A.K. Ahmed, W.R. McWhinnie, and P. Granger. Polyhedron, **5**, 859 (1986).
2. N. Zumbulyadis and H.J. Gysling. Inorg. Chem. **21**, 564 (1982).
3. M.A.K. Ahmed, A.E. McCarthy, W.R. McWhinnie, and F.J. Berry. J. Chem. Soc. Dalton Trans. 771 (1986).
4. A.M. Bond, D. Dakternieks, R. Di Giacomo, and A.F. Hollenkamp. Inorg. Chem. **28**, 1510 (1989).
5. J.H.E. Bailey, J.E. Drake, A.B. Sarkar, and M.L.Y. Wong. Can. J. Chem. **67**, 1735 (1989).
6. J.H.E. Bailey, J.E. Drake, and M.L.Y. Wong. Can. J. Chem. **69**, 1948 (1991).
7. J.E. Drake and M.L.Y. Wong. J. Organomet. Chem. **377**, 43 (1989).
8. S. Husebye, K. Maartmann-Moe, and W. Steffensen. Acta Chem. Scand. **44**, 139 (1990).
9. S. Husebye, K. Maartmann-Moe, and W. Steffensen. Acta Chem. Scand. **44**, 579 (1990).
10. J.H.E. Bailey and J.E. Drake. Can. J. Chem. **71**, 42 (1993).
11. D. Dakternieks, R. DiGiacomo, R.W. Gable, and B.F. Hoskins. J. Am. Chem. Soc. **110**, 6753 (1988).
12. A.K. Singh and J.K. Basumatary. J. Organomet. Chem. **364**, 73 (1989).
13. D. Dakternieks, R. Di Giacomo, R.W. Gable, and B.F. Hoskins. J. Organomet. Chem. **349**, 305 (1988).
14. D. Dakternieks, R. DiGiacomo, R.W. Gable, and B.F. Hoskins. J. Am. Chem. Soc. **110**, 6762 (1988).
15. M. Wieber, E. Schmidt, and C. Burschka. Z. Anorg. Allg. Chem. **525**, 127 (1985).
16. A.K. Singh, J.K. Basumatary, T.P. Singh, and B. Padmanabhan. J. Organomet. Chem. **424**, 33 (1992).
17. S. Husebye, K. Maartmann-Moe, and O. Mikalsen. Acta Chem. Scand. **44**, 464 (1990).
18. R.K. Chadha, J.E. Drake, N.T. McManus, B.A. Quinlan, and A.B. Sarkar. Organometallics, **6**, 813 (1987).
19. D. Dakternieks, R. Di Giacomo, R.W. Gable, and B.F. Hoskins. J. Am. Chem. Soc. **110**, 6541 (1988).
20. S. Husebye, K. Maartmann-Moe, and O. Mikalsen. Acta Chem. Scand. **43**, 868 (1989).
21. T.N. Srivastava, J.D. Singh, and S.K. Srivastava. Synth. React. Inorg. Metal. Org. Chem. **20**, 503 (1990).
22. T.N. Srivastava, J.D. Singh, and S.K. Srivastava. Phosphorus Sulfur Silicon Relat. Elem. **55**, 117 (1991).
23. T.N. Srivastava, J.D. Singh, and S.K. Srivastava. Polyhedron, **9**, 943 (1990).
24. R.C. Paul, K.K. Bhasin, and R.K. Chadha. J. Inorg. Nucl. Chem. **37**, 2337 (1975).
25. H.P.S. Chauhan, C.P. Bhasin, G. Srivastava, and R.C. Mehrotra. Phosphorus Sulfur, **15**, 99 (1983).
26. J.H. Fletcher, J.H. Hamilton, I. Hechenbleikner, E.I. Hoegberg, B.J. Sertl, and J.T. Cassaday. J. Am. Chem. Soc. **72**, 2461 (1950).

27. (*a*) J.C. Calbrese. Ph.D. Thesis, University of Wisconsin, Madison, WI. 1972; (*b*) P.T. Beurskens. Technical Report 1984/1; Crystallography Laboratory: Toernooiveld, 6525 Ed Nijmegen, Netherlands.
28. D.T. Cromer and J.T. Waber. International tables for X-ray crystallography. Vol. IV. The Kynoch Press, Birmingham, England. 1974. Table 2.2 A; (*b*) Table 2.3.1.
29. J.A. Ibers and W.C. Hamilton. Acta Crystallogr. **17**, 781 (1964).
30. TEXSAN-TEXRAY Structures Analysis Package; Molecular Structure Corp.: Woodlands, TX, 1985.
31. L. Pauling. J. Am. Chem. Soc. **69**, 542 (1947); The nature of the chemical bond. 3rd ed. Cornell University Press, Ithaca, NY. 1960. p. 255.
32. A.J. Bondi. Phys. Chem. **68**, 441 (1964).
33. R.K. Chadha, J.E. Drake, and J.L. Hencher. Can. J. Chem. **61**, 1222 (1983).
34. H. Bock, K. Ruppert, C. Nather, Z. Havlas, H-F. Herrmann, C. Arad, I. Gobel, A. John, J. Meuret, S. Nick, A. Rauschenbach, W. Seitz, T. Vaupel, and B. Solouki. Angew. Chem. Int. Ed. Engl. **31**, 550 (1992).
35. J. Cason, W.N. Baxter, and W. DeAcetis. J. Org. Chem. **24**, 247 (1959).
36. R.A.Y. Jones and A.R. Katritzky. J. Chem. Soc. 4376 (1960).
37. G.C. Hayward and P.J. Hendra. J. Chem. Soc. (A), 1760 (1969).
38. G.D. Christofferson, R.A. Sparks, and J.D. McCullough. Acta Crystallogr. **11**, 782 (1958).
39. R. Ratnani, G. Srivastava, and R.C. Mehrotra. Transition Met. Chem. **17**, 137 (1992).
40. S. Pandey, G. Srivastava, and R.C. Mehrotra. Transition Met. Chem. **16**, 252 (1991).
41. R. Ratnani, G. Srivastava, and R.C. Mehrotra. Transition Met. Chem. **16**, 204 (1991).
42. R. Ratnani, G. Srivastava, and R.C. Mehrotra. Phosphorus, Sulfur, and Silicon, **48**, 245 (1990).
43. R. Ahmad, G. Srivastava, and R.C. Mehrotra. Inorg. Chim. Acta, **89**, 41 (1984).
44. R. Ratnani, G. Srivastava, and R.C. Mehrotra. Inorg. Chim. Acta, **161**, 253 (1989).
45. J.S. Yadav, R.C. Mehrotra, G. Srivastava, and R.K. Mehrotra. Phosphorus, Sulfur, and Silicon, **62**, 169 (1991).
46. R.J. Rao, G. Srivastava, R.C. Mehrotra, B.S. Saraswat, and J. Mason. Polyhedron, **3**, 485 (1984).
47. C. Glidewell. Inorg. Chim. Acta, **25**, 159 (1977).
48. D.T. Kennepohl, A.A. Pinkerton, Y.F. Lee, and R.G. Cavell. Inorg. Chem. **29**, 5086 (1990).
49. H. Preut, V-D. Ngo, and F. Huber. Acta Crystallogr. C**42**, 809 (1986).
50. H. Preut, V-D. Ngo, and F. Huber. Acta Crystallogr. C**43**, 164 (1987).

Can. J. Chem. Downloaded from www.nrcresearchpress.com by EESC ESCOLA DE ENGENHARIA on 09/08/12
For personal use only.

Ab initio study on the thermal decarboxylation of but-3-enoic acid and its derivatives

YOULIANG WANG AND RAYMOND A. POIRIER[1]

Department of Chemistry, Memorial University of Newfoundland, St. John's, NF A1B 3X7, Canada

Received September 2, 1993

YOULIANG WANG and RAYMOND A. POIRIER. Can. J. Chem. **72**, 1338 (1994).

The mechanism for thermal decarboxylation of but-3-enoic acid and its derivatives HXC=CYCH$_2$COOH (X, Y = H, F, CH$_3$, C$_2$H$_5$, and Cl) leading to carbon dioxide and olefins has been studied from the theoretical point of view by *ab initio* MO calculations. The transition states obtained by our *ab initio* calculations are completely consistent with the experimental data, and support the "synchronous" mechanism for thermal decarboxylation of but-3-enoic acid and its derivatives via a "twisted chair" six-membered cyclic transition state. The effects of β- and γ-substituents on the activation energy (E_a) can be explained in terms of electronic charge distribution. β-Substitution decreases the activation energy, while γ-substitution increases it. Changes in the activation energy are related to changes in the charges at C_γ(C1) and C_β(C2) as the substituents are varied. The activation energy decreases with an increase of negative charge at C_γ, while it increases with an increase of negative charge at C_β. The best estimate of 156.8 kJ/mol for the activation energy with MP2/6-31G*//HF/3-21G$^{(*)}$ is in reasonable agreement with the available experimental values of 164 ± 7 kJ/mol and 160 kJ/mol for decarboxylation of but-3-enoic acid. The calculated primary k_H/k_D, 2.86, and k_{12C}/k_{14C}, 1.03, for the decarboxylation of but-3-enoic acid, are also in excellent agreement with the available experimental values of 2.7 and 1.035, respectively, supporting the transition state structure obtained.

YOULIANG WANG et RAYMOND A. POIRIER. Can. J. Chem. **72**, 1338 (1994).

Faisant appel à des calculs d'OM *ab initio*, on a étudié d'un point de vue théorique le mécanisme de la décarboxylation thermique de l'acide but-3-énoïque et de ses dérivés HXC=CYCH$_2$COOH (X, Y = H, F, CH$_3$, C$_2$H$_5$ et Cl) qui conduit au dioxyde de carbone et à des olléfines. Les états de transition obtenus par nos calculs *ab initio* sont en parfait accord avec les données expérimentales et ils supportent le mécanisme "synchrone" pour la décarboxylation de l'acide but-3-énoïque et de ses dérivés qui se produirait par le biais d'un état de transition cyclique à six chaînons possédant une conformation chaise déformée. On peut expliquer les effets des substituants en β et en γ sur l'énergie d'activation (E_a) en fonction d'une distribution de la charge électronique. Une substitution en β diminue l'énergie d'activation alors qu'une substitution en γ l'augmente. Les changements dans les énergie d'activation sont reliés aux changements dans les charges sur les C_γ(C1) et C_β(C2) qui accompagnent les variations de substituants. L'énergie d'activation diminue avec une augmentation de la charge négative sur C_γ alors qu'elle augmente avec une augmentation de charge négative sur le C_β. La meilleure évaluation de l'énergie d'activation (156,8 kJ/mol) déterminée avec l'ensemble MP2/6-31G*//HF/3-21G$^{(*)}$ est en bon accord avec les valeurs expérimentales disponibles (164 ± 7 et 160 kJ/mol) pour la décarboxylation de l'acide but-3-énoïque. Les valeurs calculées de k_H/k_D (2,86) et de k_{12C}/k_{14C} (1,03) pour la décarboxylation de l'acide but-3-énoïque sont aussi en bon accord avec les valeurs expérimentales disponibles (2,7 et 1,035 respectivement); ces résultats supportent la structure proposée pour l'état de transition.

[Traduit par la Rédaction]

I. Introduction

A great deal of effort has and is being made to further our understanding of the relationship between structure and reactivity (1–3). In the past the attention focused on the electronic properties of the reactants or on the electronic properties of an assumed transition state structure. With quantum mechanical calculations it is now possible to look at structure reactivity relationships in terms of what occurs in "the transition state," giving us better insight into what factors control reactivity (3). In this paper we investigate the factors which control the reactivity of the decarboxylation reaction in but-3-enoic acids. Decarboxylation is an important organic reaction in many fields, e.g., organic synthesis, molecular biochemistry in which many life processes in both plants and animals are related to decarboxylation (4), and mechanistic studies (1–3). Because of its importance, the mechanism for the decarboxylation of acids has been studied since the 60's (5) and is still of great interest both experimentally and theoretically (3*b*–3*d*, 6, 7). For instance, the thermal decarboxylation of formic acid has been the object of recent high level experimental and theoretical work (3*b*).

As a β,γ-unsaturated acid, but-3-enoic acid decomposes to propene and eliminates carbon dioxide (1, 2, 5, 6).

$$CH_2{=}CHCH_2COOH \rightarrow CH_3CH{=}CH_2 + CO_2$$

[1]To whom correspondence may be addressed.

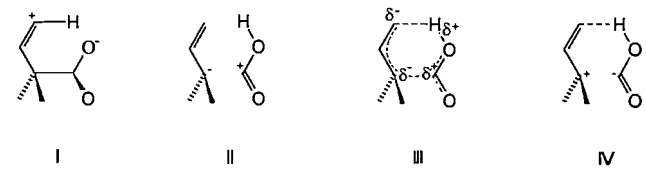

I II III IV

FIG. 1. Transition states considered for thermal decarboxylation of but-3-enoic acid.

The kinetics of this vapor-phase thermal decarboxylation process were first studied several years ago (5). Most of the mechanistic studies, owing largely to Bigley and co-workers (5, 6), were directed towards understanding the nature of the transition state. Several possible transition state structures were considered, which are illustrated in Fig. 1.

Experimental energies of activation and relative rates of decarboxylation for but-3-enoic acid and some substituted but-3-enoic acids are listed in Table 1. The experimental evidence indicates that substituents at C_α, C_β, and C_γ all affect the reaction rate (5), for example, methyl substitution at the partially positive C_β increases reaction rates but substitution at C_γ causes an appreciable decrease in the reaction rate. This gas-phase thermal decomposition reaction shows sizable primary kinetic isotope effects (5*c*), e.g., k_H/k_D = 2.81 ± 0.18 at 543 K and k_{12C}/k_{14C} = 1.035 ± 0.01 at 551 K for 2,2-dimethyl-4-phenyl but-3-enoic acid. The results of these studies are consistent with a synchronous reaction via a six-membered cyclic transition state (cf. structure **III** in Fig.

Can. J. Chem. Downloaded from www.nrcresearchpress.com by EESC ESCOLA DE ENGENHARIA on 09/08/12
For personal use only.

TABLE 1. The experimental activation energies and relative rates of reaction (5*d*) for the decarboxylation of several substituted but-3-enoic acids (at 500 K)

Reactants	E_a (kJ/mol)	Relative rate
$H_2C{=}CHCH_2COOH$	168	1
	164 ± 7 (ref. 5*a*)	
	160 (ref 6)	
$H_2C{=}CHC(CH_3)_2COOH$	153	5.6
$H_2C{=}C(CH_3)C(CH_3)_2COOH$	138	168
$H(CH_3)C{=}CHC(CH_3)_2COOH$	168	0.84
$H(CH_3)C{=}C(C_2H_5)C(CH_3)_2COOH$	150	54.1
$C_6H_5CH{=}CHC(CH_3)_2COOH$	162 (ref. 1)	—
$H_2C{=}C(C_6H_5)C(CH_3)_2COOH$	128 (ref 1)	—

1). The experimental results also suggest that the reaction is homogeneous, first order, has a negative entropy of activation, proceeds at the same rate in the gas as in the liquid phase.

To date, no *ab initio* calculations have been reported on the decarboxylation of but-3-enoic acid and no quantum mechanical calculations have been reported on the decarboxylation of substituted but-3-enoic acids. The only calculated results available for $H_2C{=}CHCH_2COOH$ are from MINDO/3 calculations carried out by Dewar and Ford (8). Dewar and Ford predicted a "flattened boat" six-membered cyclic transition state structure with an activation enthalpy (ΔH^*) of 194 kJ/mol and a primary kinetic isotope effect of $k_H/k_D = 2.1$. The MINDO/3 results are consistent with the known experimental data. In this paper the results of *ab initio* calculations on the decarboxylation of a series of substituted but-3-enoic acids have been reported in order to further our understanding of how different substituents stabilize or destabilize the transition state.

II. Computational details

Ab initio calculations were carried out for some selected β-, γ-substituted but-3-enoic acids $HXC{=}CYCH_2COOH$ (X, Y = H, F, CH_3, C_2H_5, and Cl). These are typical substituents (experimentally) that represent both electron donation and electron withdrawing types of groups. The compounds calculated are $CH_2{=}CHCH_2COOH$ (**1**), $HFC{=}CHCH_2COOH$ (**2**), $CH_2{=}CFCH_2COOH$ (**3**), $CH_3CH{=}CHCH_2COOH$ (**4**), $CH_2{=}C(CH_3)CH_2COOH$ (**5**), $CH_3CH_2CH{=}CHCH_2COOH$ (**6**), $CH_2{=}C(CH_2CH_3)CH_2COOH$ (**7**), $HClC{=}CHCH_2COOH$ (**8**), $HFC{=}CFCH_2COOH$ (**9**), and $CH_2{=}CClCH_2COOH$ (**10**). All minima were fully optimized with the OC method (9) and the transition states were fully optimized using the minimization of sum of squares gradient technique VA05AD (10). The transition structures were characterized to ensure that the symmetrized force constant matrix had only one negative eigenvalue, i.e., only one imaginary frequency.

All geometry optimizations and single-point SCF calculations were carried out with MUNGAUSS (11). The structures were optimized with the 3-21G(*) basis set and single-point calculations performed with the 6-31G* basis set (HF/6-31G*//HF/3-21G(*)). For but-3-enoic acid, the MP2/6-31G//HF/3-21G(*) calculations were performed with GAUSSIAN 86 (12). The additivity rule (13) was used to obtain MP2/6-31G*//HF/3-21G(*) estimates of the activation energy E_a, where, E_a(MP2/6-31G*) = E_a(MP2/6-31G) + E_a(HF/6-31G*) − E_a(HF/6-31G). The normal-mode vibrational frequencies for but-3-enoic acid were calculated at the HF/6-31G//HF/3-21G(*) level. These frequencies were used to compute the zero-point energy (ZPE) corrections and primary kinetic isotope effects (k_H/k_D and k_{12C}/k_{14C}) using a modified version of BEBOVIB (14).

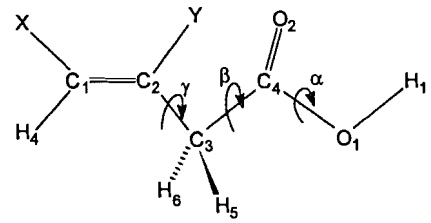

FIG. 2. The structural parameters of but-3-enoic acids. The different conformations calculated in Table 2 are defined by the torsion angles α, β, γ, and all have C_s symmetry. α = 0, β = 0, γ = 0 for conformer **a**.

III. Results and discussion

III.1. Electronic structure and properties of reactants

Conformational change and stability

The structural parameters for the equilibrium geometries of but-3-enoic acids are illustrated in Fig. 2. Because of the free rotation about the C—O and C—C single bonds, there are many possible conformations. The different conformations are defined by the three torsion angles, α, β, and γ (cf. Fig. 2), which correspond to rotation (clockwise) about the C4—O1, C3—C4, and C2—C3 single bonds respectively. Conformers **a** to **h** in Table 2, defined by α, β, and γ, are constrained to have C_s symmetry. Breaking of the C_s symmetry leads to other four structures (**i**, **j**, **k**, and **l**) of which three are transition states and one is a minimum (**l**). The relative energies of these eight conformers are given in Table 2, along with the corresponding HF/3-21G(*) total energies. Conformer **a** with α, β, γ = 0° is the lowest energy conformation, while conformer **h** with α, β, γ = 180° is the highest energy conformation. The conformational energy hypersurface illustrated in Fig. 3, indicates that the rotational barriers connecting these conformers (**a**, **b**, **d**) are relatively low and that their interconversion essentially involves free rotation about the C2—C3, C3—C4, or C4—O1 single bonds.

Equilibrium geometries

For all the substituted but-3-enoic acids conformer **a** (cf. Fig. 2) was assumed to be the lowest energy conformation. The HF/3-21G(*) optimized structural parameters for all of the reactants $HXC{=}CYCH_2COOH$ (X, Y = H, F, Cl, CH_3, C_2H_5), are listed in Table 3. These results indicate that β- and γ-substitution primarily affects the C1—C2 double-bond (1.304–1.320 Å) and C2—C3 single-bond (1.502–1.528 Å) lengths. The influence of

Can. J. Chem. Downloaded from www.nrcresearchpress.com by EESC ESCOLA DE ENGENHARIA on 09/08/12
For personal use only.

TABLE 2. The total energies (in Hartrees) and relative energies (in kJ/mol) calculated at HF/3-21G(*) for different conformers of but-3-enoic acid

Conformer	α	β	γ	Total energies	ΔE (kJ/mol)
a	0	0	0	−302.98464	0.00
b	0	0	180	−302.98309	4.07
c	0	180	0	−302.98039	11.2
d	0	180	180	−302.97641	21.6
e	180	0	0	−302.97152	34.4
f	180	0	180	−302.96967	39.3
g	180	180	0	−302.96207	59.3
h	180	180	180	−302.95649	73.9
l	184	−133	164	−302.97111	35.5

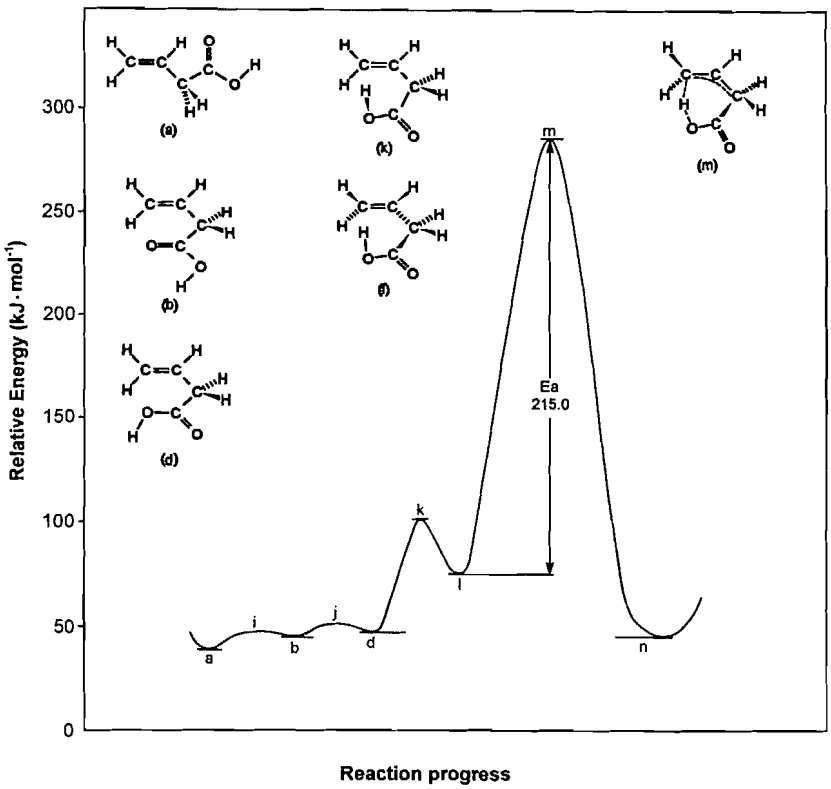

FIG. 3. HF/3-21G(*) relative energies (in kJ/mol) of the stationary points examined on the $H_2C{=}CHCH_2COOH$ potential energy surface.

substituents on the geometries is related to their electronic properties. CH_3 and C_2H_5 increase the C1—C2 and C2—C3 bond lengths, while F and Cl decrease the C1—C2 and C2—C3 bond lengths. For instance, both the C1—C2 and C2—C3 bond lengths are longer (by 0.005 and 0.019 Å, respectively) in the β-CH_3 and β-C_2H_5 cases, while in the β-F and β-Cl cases, these bond lengths are shorter (by −0.007 and −0.004 Å, respectively). For γ-CH_3 and γ-C_2H_5 the C1—C2 and C2—C3 bond lengths increase slightly, while for γ-F and γ-Cl, and C1—C2 and C2—C3 bond lengths decrease, significantly in the case of the C1—C2 bond (by −0.011 Å). Since in going from the reactant to the product, the C1—C2 double-bond becomes a single-bond and the C2—C3 single-bond becomes a double-bond, longer C1—C2 bond and shorter C2—C3 bond in the reactant are expected to facilitate the decarboxylation reaction.

III.2. Electronic structure and properties of the transition state

Barrier heights, relative energies and activation energies

The relative energies for the different stationary points on the $H_2C{=}CHCH_2COOH$ potential energy surface are illustrated in Fig. 3. It shows the energy change for the process of thermal decarboxylation of $H_2C{=}CHCH_2COOH$ starting with the most stable conformer (**a**), going through intermediates, the transition state (**m**) and finally to product (**n**) $H_3CCH{=}CH_2$ and CO_2. The geometries corresponding to stationary points **a**, **b**, **d**, and **l** are different conformers of but-3-enoic acid and **i**, **j**, **k** are characterized to be the saddle points, interconnecting these conformers, respectively. The **d** to **l** conformational change, which involves rotation about the C4—O1 single- bond, has the highest rotational barrier (40.6 kJ/mol) but much lower than the activation energy (215.0 kJ/mol). The geometry corresponding

Can. J. Chem. Downloaded from www.nrcresearchpress.com by EESC ESCOLA DE ENGENHARIA on 09/08/12
For personal use only.

TABLE 3. The HF/3-21G(*) optimized geometries for HXC═CYCH$_2$COOH (conformation **a**)

X	H	F	H	CH_3	H	C_2H_5	H	Cl	F	H
Y	H	H	F	H	CH_3	H	C_2H_5	H	F	Cl
				Bond length (Å)						
C1—C2	1.3145	1.3039	1.3074	1.3151	1.3192	1.3152	1.3196	1.3037	1.3044	1.3081
C2—C3	1.5091	1.5045	1.5048	1.5097	1.5277	1.5097	1.5276	1.5082	1.5019	1.5080
C3—C4	1.5023	1.5033	1.5047	1.5024	1.5034	1.5024	1.5023	1.5041	1.5059	1.5056
C4—O1	1.3560	1.3541	1.3637	1.3568	1.3621	1.3566	1.3614	1.3521	1.3617	1.3641
C4—O2	1.2025	1.2015	1.1963	1.2026	1.2023	1.2026	1.2029	1.2017	1.1955	1.1957
O1—H1	0.9685	0.9686	0.9684	0.9685	0.9685	0.9687	0.9686	0.9687	0.9685	0.9684
C1—X	1.0728	1.3646	1.0696	1.5143	1.0733	1.5095	1.0732	1.8265	1.3593	1.0697
C2—Y	1.0726	1.0709	1.3587	1.0736	1.5220	1.0735	1.5198	1.0715	1.3545	1.8262
H4—C1	1.0751	1.0690	1.0700	1.0773	1.0751	1.0787	1.0752	1.0666	1.0656	1.0738
H5—C3	1.0849	1.0847	1.0840	1.0851	1.0848	1.0851	1.0849	1.0842	1.0840	1.0843
H6—C3	1.0849	1.0847	1.0840	1.0851	1.0848	1.0851	1.0849	1.0842	1.0840	1.0843
				Bond angle (deg)						
C3—C2—C1	124.23	123.47	124.51	124.22	117.65	124.25	117.66	123.18	122.43	123.00
C4—C3—C2	111.90	111.13	117.62	111.83	119.78	111.86	119.62	111.07	116.79	120.88
O1—C4—C3	110.61	110.35	107.30	110.58	108.20	110.58	108.39	110.39	107.20	106.71
O2—C4—C3	127.09	126.98	130.71	127.22	130.67	127.23	130.43	126.70	130.43	131.33
H1—O1—C4	111.93	112.16	111.70	111.87	111.67	111.92	111.72	112.31	111.90	111.78
X—C1—C2	121.26	121.84	120.56	124.06	121.47	124.54	121.44	120.85	122.44	122.10
Y—C1—C2	120.76	119.80	119.75	120.73	120.50	120.63	120.44	120.87	120.03	116.77
H4—C1—C2	122.47	122.38	120.98	119.88	122.31	120.13	122.38	127.32	123.12	120.50
H5—C3—C2	111.60	112.15	109.89	111.81	105.62	111.80	105.69	111.72	110.54	108.74
H6—C3—C2	111.60	112.15	109.89	111.81	105.62	111.80	105.69	111.72	110.54	108.74
				Torsion angle (deg)						
H5—C3—C2—C1	59.65	60.13	58.22	59.77	55.60	59.76	56.00	59.94	58.73	57.67
H6—C3—C2—C1	−59.65	−60.13	−58.22	−59.77	−55.60	−59.76	−56.00	−59.94	−58.73	−57.67

TABLE 4. Activation energies (E_a in kJ/mol) for thermal decarboxylation of HXC═CYCH$_2$COOH

X	Y	HF/3-21G(*)	HF/6-31G*//HF/3-21G(*)	MP2/6-31G*//HF/3-21G(*)[a]
H	H	215.0	231.9	156.8 (164 ± 7)[b] (160)[c] (199)[d] (140.7)[e]
F	H	245.2	257.8	182.7
H	F	202.0	214.2	139.1
CH_3	H	230.0	247.0	171.9
H	CH_3	197.6	211.3	136.2
C_2H_5	H	238.7	257.0	181.9
H	C_2H_5	194.8	209.8	134.7
Cl	H	227.8	248.2	173.1
F	F	223.9	232.5	157.4
H	Cl	217.3	230.5	155.4

[a]MP2/6-31G* results were estimated on those of MP2/6-31G for H$_2$C═CHCH$_2$COOH, and the same correlation energy was used to estimate for the substituted cases.
[b]Smith and Blau's experimental result (5*a*).
[c]Bigley and Clarke's experimental result (6).
[d]Dewar's MINDO/3 result (8).
[e]After ZPE correction.

to stationary point **l** is taken as the reacting conformer. The activation energy (E_a) is defined as the energy difference between stationary points **m** and **l** which should correspond to the rate-determining step of reaction.

For but-3-enoic acid, the *ab initio* activation energies (E_a) are compared with Dewar's MINDO/3 result (8) and the available experimental values (5, 6). The results are listed in Table 4. Dewar's MINDO/3 activation energy of 199 kJ/mol is close to our HF/3-21G(*) result (215.0 kJ/mol). The MP2/6.31G//HF/321G(*) single point calculation (E_a = 161.2 kJ/mol), compared with HF/6-31G//HF/3-21G(*) result (E_a = 237.4 kJ/mol), shows the importance of electron correlation (−76.2 kJ/mol) in this decarboxylation reaction. The MP2/6-31G*//HF/3-21G(*) E_a is 156.8 kJ/mol, which is in reasonable agreement with the experimental values of 164 ± 7 kJ/mol (5*a*) and 160 kJ/mol (6). This agreement supports the reliability of the transition state structure obtained from our *ab initio* calculations. The normal mode vibrational frequencies were also calculated (scaled by 0.9) to

Can. J. Chem. Downloaded from www.nrcresearchpress.com by EESC ESCOLA DE ENGENHARIA on 09/08/12
For personal use only.

TABLE 5. The HF/3-21G(*) optimized geometries for HXC=CYCH$_2$COOH at stationary point (**I**)

X	H	F	H	CH_3	H	C_2H_5	H	Cl	F	H
Y	H	H	F	H	CH_3	H	C_2H_5	H	F	Cl
					Bond length (Å)					
C1—C2	1.3175	1.3079	1.3077	1.3186	1.3194	1.3189	1.3196	1.3117	1.3054	1.3119
C2—C3	1.5157	1.5111	1.4999	1.5163	1.5215	1.5092	1.5235	1.5140	1.4964	1.5103
C3—C4	1.5170	1.5184	1.5152	1.5178	1.5156	1.5240	1.5164	1.5175	1.5172	1.5177
C4—O1	1.3602	1.3614	1.3578	1.3599	1.3603	1.3562	1.3595	1.3609	1.3585	1.3597
C4—O2	1.1963	1.1952	1.1949	1.1967	1.1965	1.1972	1.1968	1.1951	1.1940	1.1949
O1—H1	0.9642	0.9645	0.9643	0.9643	0.9643	0.9651	0.9643	0.9644	0.9645	0.9644
C1—X	1.0725	1.3614	1.0698	1.5093	1.0730	1.5090	1.0708	1.7458	1.3562	1.0705
C2—Y	1.0746	1.0722	1.3659	1.0753	1.5142	1.0764	1.5200	1.0732	1.3612	1.7600
H4—C1	1.0731	1.0672	1.0685	1.0757	1.0722	1.0785	1.0724	1.0678	1.0641	1.0712
H5—C3	1.0876	1.0870	1.0866	1.0877	1.0881	1.0805	1.0881	1.0874	1.0866	1.0862
H6—C3	1.0815	1.0809	1.0810	1.0815	1.0816	1.0864	1.0816	1.0812	1.0808	1.0806
					Bond angle (deg)					
C3—C2—C1	126.28	125.39	128.98	126.10	124.06	124.34	123.22	125.35	126.87	127.79
C4—C3—C2	115.17	114.97	115.07	115.24	115.91	112.25	116.17	115.27	115.24	114.48
O1—C4—C3	115.19	115.18	115.71	115.20	115.20	114.89	115.37	115.30	115.71	115.45
O2—C4—C3	124.41	124.39	123.69	124.42	124.44	124.25	124.25	124.29	123.60	124.04
H1—O1—C4	114.41	114.80	115.26	114.12	114.36	113.82	114.28	115.03	115.56	115.06
X—C1—C2	120.99	121.28	120.29	124.17	121.05	124.98	121.86	121.78	122.08	121.50
Y—C1—C2	119.35	118.03	120.30	119.29	122.37	119.86	124.13	119.28	120.51	119.95
H4—C1—C2	122.65	125.96	121.10	120.18	122.70	119.53	122.15	124.73	123.17	120.94
H5—C3—C2	109.06	108.84	107.65	109.06	108.74	111.64	108.80	108.79	107.27	108.82
H6—C3—C2	110.20	110.48	110.22	110.60	109.74	110.10	109.80	109.89	110.59	109.68
					Torsion angle (deg)					
C4—C3—C2—C1	16.14	16.84	17.24	20.99	14.22	115.62	18.21	12.55	19.69	12.51
O1—C4—C3—C2	49.85	48.28	47.35	47.20	51.12	−40.37	48.48	50.66	45.81	51.12
O2—C4—C3—C2	−132.55	−132.90	−134.94	−135.28	−131.73	−218.51	−134.61	−130.70	−135.58	−130.74
H1—O1—C4—C3	−4.02	3.93	−0.83	−3.98	−5.52	4.78	−6.02	3.00	5.61	2.49
H2—C1—C2—C3	177.70	177.89	177.92	177.15	177.71	180.28	177.28	177.79	178.14	177.42
H3—C2—C1—C3	182.62	183.24	182.01	183.29	182.93	180.64	183.22	182.63	182.58	183.00
H4—C1—C2—C3	−2.12	−3.20	−1.70	−2.85	−1.85	0.30	−2.30	−2.54	−2.90	−2.73
H5—C3—C2—C1	137.34	137.92	138.59	141.78	135.53	235.49	139.36	134.16	140.84	133.99
H6—C3—C2—C1	−104.98	−104.27	−104.49	−100.39	−107.11	−4.39	−103.30	−108.36	−102.22	−108.24

correct for ZPE at HF/6-31G//HF/3-21G(*). The ZPE contribution to E_a is −16.1 kJ/mol and therefore the cyclic transition state has a smaller ZPE than the reacting conformer.

The HF/3-21G(*) optimized geometries for the reacting conformers (**I**) and transition states (**m**) are given in Tables 5 and 6, respectively. The HF/6-31*//HF/3-21G(*) single point calculations were carried out on these optimized geometries to obtain E_a. The HF/6-31G*//HF/3-21G(*) E_a for the cases studied are all within 210~260 kJ/mol and are higher than HF/3-21G(*) values. For the substituted but-3-enoic acids the activation energy is estimated as E_a (MP2/6-31G*) = E_a (HF/6-31G*) + ΔE_0, where ΔE_0 is the correlation contributions for but-3-enoic acid (−76.2 kJ/mol). Since all the HXC=CYCH$_2$COOH geometries for **l** and **m** are very similar (cf. Tables 5 and 6) the correlation energy contribution to E_a is expected to be approximately constant.

The results of activation energies for all the substituted but-3-enoic acids at HF/3-21G(*), HF/631G*//HF/3-21G(*), and MP2/6-31G*//HF/3-21G(*) levels, are listed in Table 4. Comparison of the activation energies of γ- and β-substitution at the three levels considered indicates that β-substitution leads to a decrease in E_a and that γ-substitution leads to an increase in E_a. These results (e.g., for CH_3, and C_2H_5-substituted cases) are consistent with the experimental observation (5*d*) (cf. Table 1).

It is interesting to note that for HFC=CFCH$_2$COOH, the substitution effect is almost balanced, resulting in an activation energy of 157.4 kJ/mol with MP2/6-31G*//HF/3-21G(*) essentially equal to that of but-3-enoic acid (156.8 kJ/mol). For β-substitution, E_a decreases in the order, H > Cl > F > CH_3 > C_2H_5. For γ-substitution, E_a increases in the order, H < CH_3 < Cl < C_2H_5 < F. The effect of these substituents on the activation energies can be explained in terms of their electronic properties. For instance, substitution at the γ position decreases the negative charge at C1, making the hydrogen (H1) transfer from O1 to C1 less favourable, and thus resulting in a higher activation energy. Substitution at the β-position increases the positive charge at C2 stabilizing the allyl-like anion (involving C1—C2—C3) in the transition state, resulting in a lower activation energy. The relationship between the activation energy and the charge distribution is presented in Fig. 5, and will be discussed in detail in the following section.

Transition state geometries

The structural parameters for optimized transition states at HF/3-21G(*) are listed in Table 6. All transition states have similar cyclic structures as illustrated in Fig. 4.

The transition states obtained by our *ab initio* calculations are consistent with the experimental data and resemble struc-

Can. J. Chem. Downloaded from www.nrcresearchpress.com by EESC ESCOLA DE ENGENHARIA on 09/08/12
For personal use only.

TABLE 6. The HF/3-21G(*) optimized transition state geometries (**m**) of HXC=CYCH$_2$COOH

X	H	F	H	CH_3	H	C_2H_5	H	Cl	F	H
Y	H	H	F	H	CH_3	H	C_2H_5	H	F	Cl
					Bond length (Å)					
C1—C2	1.3976	1.3910	1.3917	1.3982	1.4043	1.3949	1.4052	1.3965	1.3965	1.3981
C2—C3	1.4111	1.4070	1.4102	1.4127	1.4278	1.4118	1.4306	1.4051	1.4062	1.4122
C3—C4	1.8107	1.8202	1.7855	1.8062	1.7533	1.8115	1.7392	1.8405	1.7897	1.8014
H1-C1	1.3056	1.3149	1.3054	1.2850	1.2866	1.2800	1.2922	1.3178	1.3208	1.3034
O1—H1	1.3736	1.3513	1.3690	1.4035	1.3940	1.4174	1.3903	1.3318	1.3379	1.3679
C4—O1	1.2459	1.2454	1.2496	1.2447	1.2524	1.2433	1.2542	1.2449	1.2504	1.2468
C4—O2	1.1982	1.1950	1.1976	1.1993	1.2035	1.1992	1.2054	1.1928	1.1947	1.1973
C1—X	1.0740	1.3860	1.0732	1.5310	1.0753	1.5333	1.0757	1.7699	1.3810	1.0729
C2—Y	1.0758	1.0745	1.3334	1.0771	1.5023	1.0772	1.5079	1.0749	1.3259	1.7205
H4—C1	1.0808	1.0775	1.0781	1.0821	1.0802	1.0834	1.0800	1.0767	1.0764	1.0803
H5—C3	1.0813	1.0817	1.0790	1.0813	1.0817	1.0810	1.0814	1.0811	1.0799	1.0809
H6—C3	1.0724	1.0719	1.0726	1.0726	1.0731	1.0725	1.0706	1.0722	1.0727	1.0717
					Bond angle (deg)					
H1—C1—C2	90.41	91.07	91.46	88.91	90.58	88.52	90.62	91.49	92.22	91.10
O1—H1—C1	153.22	153.62	152.23	154.62	152.78	154.95	153.03	153.65	152.71	152.87
C4—O1—H1	109.50	109.71	110.43	108.56	108.56	108.42	107.79	110.23	110.51	109.92
C3—C4—O1	112.03	110.97	112.26	111.87	112.91	111.75	112.67	110.94	111.34	112.11
O2—C4—O1	137.10	137.90	136.67	137.19	135.23	137.45	134.81	138.33	137.16	137.18
H4—C1—C2	117.02	119.25	115.60	115.12	116.73	114.48	116.71	118.58	116.31	115.56
Y—C2—C1	119.11	117.76	118.59	118.67	120.14	118.65	119.86	118.87	118.88	119.20
X—C1—C2	118.72	116.21	117.54	120.92	118.43	124.54	118.41	118.32	115.85	118.62
H5—C3—C4	98.71	97.69	99.44	98.73	100.55	98.87	101.86	97.54	98.85	99.00
H6—C3—C4	103.52	103.76	105.14	103.68	104.37	103.45	104.22	103.55	105.18	104.22
					Torsion angle (deg)					
O1—H1—C1—C2	33.79	36.76	32.44	38.06	34.22	36.98	30.85	33.41	34.38	34.03
C4—O1—H1—C1	−15.18	−19.63	−13.15	−19.66	−12.37	−18.08	−12.43	−15.58	−16.21	−14.42
C3—C4—O1—C1	7.36	7.99	4.80	6.81	5.77	6.56	11.11	8.16	5.93	5.63
O2—C4—O1—H1	187.18	188.07	184.15	187.31	185.55	186.79	192.30	187.59	185.32	185.05
H4—C1—C2—C3	41.46	46.58	45.15	39.33	41.66	38.22	42.48	45.41	49.50	43.30
Y—C2—C1—H1	104.38	106.82	107.21	104.81	103.68	104.49	106.04	105.90	109.36	105.60
X—C1—C2—C3	−173.82	−173.78	−172.54	−173.85	−174.95	−173.74	−174.15	−173.10	−173.61	−173.59
H5—C3—C4—O1	84.34	84.27	87.82	85.46	84.53	85.78	77.05	83.60	86.30	85.56
H6—C3—C4—O1	−158.48	−159.04	−153.95	−157.52	−158.21	−157.13	−165.13	−159.31	−156.00	−156.70

ture **III** proposed by Bigley (1) (shown in Fig. 1). Several features may be noted with respect to the "synchronicity" of thermal decarboxylation. In going from reactant to transition state the C1—C2 bond increases from ~1.31 Å (double bond) to ~1.40 Å. The C2—C3 bond decreases from 1.51~1.53 Å (single bond) to 1.40~1.43 Å. Therefore, in the transition state the C1—C2 and C2—C3 bonds are almost equal. Both C3—C4 and H1—O1 bonds which are breaking in the transition state have increased significantly. The C3—C4 bond increases from ~1.50 Å to ~1.80 Å and the H1—O1 bond increases from ~0.97 Å to ~1.35 Å. The hydrogen atom (H1) being transferred is approximately midway between C1 and O1 (C1—H1 ~1.25 Å), and the O1—C4—O2 bond angle (~139°) is intermediate between that in the reactant (~120°) and the CO_2 molecule. The *ab initio* transition state structure is not a "flattened boat" as obtained by Dewar's MINDO/3 calculations, but a "twisted chair" six-membered cyclic transition state (cf. Fig. 4). For both Dewar's and our *ab initio* transition states, C1—C2 and C2—C3 bonds are almost equal (exactly equal in Dewar's case, 1.420 Å). *Ab initio* H1—C1 bond is longer (1.306 vs. Dewar's 1.218 Å), and *ab initio* H1—O1 is shorter (1.374 vs. Dewar's 1.419 Å). The largest discrepancy between the *ab initio* and the MINDO/3 result occurs in the C3—C4 bond, 1.81 Å compared to Dewar's 1.68 Å respectively. These results show that *ab initio* transition state is looser than Dewar's.

All the *ab initio* transition state structures are quite similar (cf. Tables 6). β-, γ-Substituents only result in minor changes in bond angles and torsion angles. For all substituted transition states, only H1—O1, H1—C1, C2—C1, C3—C4, and C2—C3 bond lengths change slightly with the different substituents. The C3—C4 and H1—C1 bonds are longer in the case of γ-substituted than in the case of β-substituted acids, which have a tighter transition state. For example, H1—C1 in β-F and β-Cl cases (~1.305 Å) are shorter than the corresponding γ-substitution cases (1.315 ~ 1.320 Å) and the unsubstituted one (1.306 Å). H1—C1 in all $CH_3$and C_2H_5 substituted cases (1.28 ~ 1.29 Å) are shorter and close to that in the corresponding product.

The relative energies ($(E_\gamma - E_\beta)_{ts}$) between γ- and the corresponding β-substituted transition state (**m**) at HF/3-21G(*) and HF/6-31G*//HF/3-21G(*) are given in Table 7, along with the relative energies ($(E_\gamma - E_\beta)_{re}$) between γ- and the corresponding β-substituted reacting conformers (**l**). These results clearly show that the values of $(E_\gamma - E_\beta)_{re}$ are much smaller than the corresponding $(E_\gamma - E_\beta)_{ts}$, while all β-substituted transition states are more stable than the corresponding γ-substituted

Can. J. Chem. Downloaded from www.nrcresearchpress.com by EESC ESCOLA DE ENGENHARIA on 09/08/12
For personal use only.

Can. J. Chem. Downloaded from www.nrcresearchpress.com by EESC ESCOLA DE ENGENHARIA on 09/08/12
For personal use only.

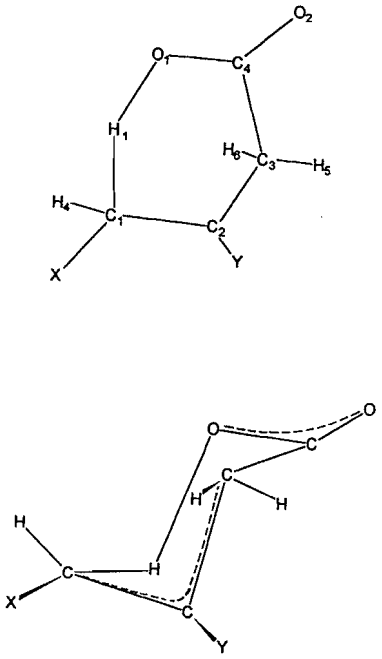

FIG. 4. Geometry of the decarboxylation transition state.

ones. Therefore it is the stability of β-substituted transition states that result in lower activation energies than the γ-substituted ones.

Electronic structure

The effect of substituents on the activation energies is consistent with the electronic structure. The net atomic charge (Q) calculated from Mulliken population analysis at HF/6-31G*//HF/3-21G$^{(*)}$ are tabulated in Table 8 for all the transition states considered. Since we are only interested in trends in atomic charges to obtain a "qualitative" understanding of the relationship between activation energy and electronic structure, simple Mulliken population analysis (MPA) is suitable for our purpose. All the results show that there is a high degree of delocalization in the transition state as predicted in structure **III** of Fig. 1. Mulliken charges are consistent with the expected charge distribution (cf. Fig. 1). There is a sizable positive charge at C2 and C4 (except for γ-F substituted case), and negative charge at C1 and C3. The charges at C1(Q_{C1}) and C2(Q_{C2}) play a dominant role in affecting the stability of the transition state. The activation energy is related to the trends in the charges at C1 and C2 as the substituents are varied. The relationship between E_a and Q_{C1}, and between E_a and Q_{C2} are presented in Fig. 5. The correlation coefficients (+0.555 for Q_{C1} and −0.596 for Q_{C2}, respectively) are obtained with the assumption that all data points are linearly related. The analysis of the data in Table 8 illustrates that the charge distribution for the three F-substituted cases is different from the others because of its high electronegativity. For instance, the β-F case has a large positive charge at C2 (0.65 vs. ~0.03 for theothers), and the γ-F case has a small negative charge at C1 (−0.03 vs. ~−0.60 for the others). In Fig. 5(*a*) (E_a vs. Q_{C1}), the two points involving γ-F do not correlate with the others and in Fig. 5(*b*) (E_a vs. Q_{C2}), the two points involving β-F do not correlate with the others. Excluding the three F-substituted cases, the correlation coefficients of E_a vs. Q_{C1} and E_a vs. Q_{C2} become +0.866 and −0.907, respectively. Such a good correlation indicates that the activation energy decreases

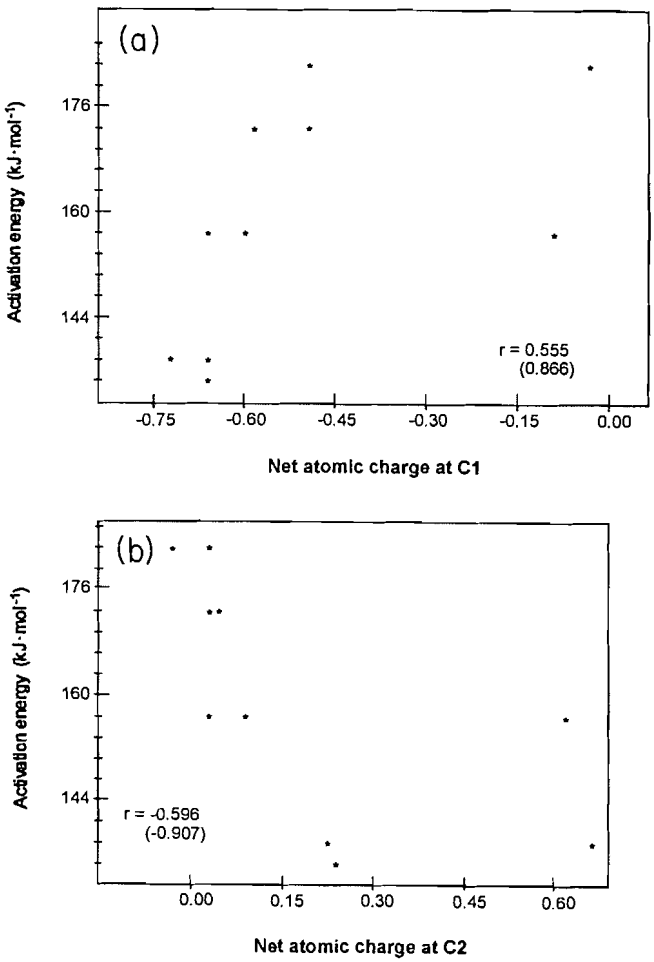

FIG. 5. Relationships between E_a and the atomic charges at C1 and C2, respectively. The values of r are the correlation coefficients, and in parentheses are the correlation coefficients excluding the three F-substituted cases. (*a*) E_a vs. Q_{C1}; (*b*) E_a vs. Q_{C2}.

with an increase of negative charge at C1, while it increases with an increase of negative charge at C2. Therefore, the atomic charges at C1 and C2 are important factors in controlling the activation energy. For example, in β-Cl substituted cases, the charge at C1 is −0.65 and the charge at C2 is 0.09, very close to the unsubstituted case for which Q_{C1} and Q_{C2} are −0.66 and 0.04, respectively, and thus leading to only a small change in activation energy. The MP2/6-31G*//HF/3-21G$^{(*)}$ E_a is 155.4 kJ/mol for β-Cl substituted case, compared with 156.8 kJ/mol for the unsubstituted case. In general, β-substitution affects the charge at the β-carbon, with only small variations at the γ-carbon, and similarly for γ-substitution. For the three F-substituted cases, both Q_{C1} and Q_{C2} change significantly and therefore the two factors combine. For example, in the γ-F substituted case, Q_{C1} is −0.03, demonstrating the most positive charge at C1, and Q_{C2} is −0.03, demonstrating the most negative charge at C2. Both of these factors increase the activation energy so that for this case, it is the highest among all cases considered (MP2/6-31G*//HF/321G$^{(*)}$ E_a, in this case, is 182.7 kJ/mol). Therefore, for highly electron-withdrawing substituents, such as F, the activation energy depends on both Q_{C1} and Q_{C2}.

In general, for all β-substituted cases, Q_{C1} is negative and Q_{C2} is positive, resulting in tighter or more reactant-like transi-

TABLE 7. The relative stabilities (in kJ/mol) between β- and the corresponding γ-substituted reacting conformers and transition states

		F	CH_3	C_2H_5	Cl
$(E_\gamma - E_\beta)_{re}$					
	HF/3-21G(*)	14.9	0.3	−11.1	4.6
	HF/6-31G*//HF/3-21G(*)	15.1	−1.5	−14.8	2.2
$(E_\gamma - E_\beta)_{ts}$					
	HF/3-21G(*)	58.0	32.7	32.8	15.1
	HF/6-31G*//HF/3-21G(*)	58.7	34.1	32.6	19.9

TABLE 8. Net atomic charges for the $HXC{=}CYCH_2COOH$ transition states at the HF/6-31G*//HF/3-21G(*) level

X	H	F	H	CH_3	H	C_2H_5	H	Cl	F	H
Y	H	H	F	H	CH_3	H	C_2H_5	H	F	Cl
C1	−0.6590	−0.0267	−0.7223	−0.4947	−0.6584	−0.4996	−0.6625	−0.5784	−0.0853	−0.6509
C2	0.0350	−0.0253	0.6549	0.0316	0.2289	0.0325	0.2391	0.0469	0.6105	0.0912
H1	0.4389	0.4302	0.4541	0.4423	0.4362	0.4398	0.4367	0.4804	0.4470	0.4484
O1	−0.6746	−0.6713	−0.6894	−0.6748	−0.6958	−0.6743	−0.6969	−0.6670	−0.6876	−0.6786
C3	−0.5633	−0.5818	−0.6281	−0.5655	−0.5624	−0.5675	−0.5593	−0.5741	−0.6481	−0.5641
C4	0.8211	0.8271	0.8379	0.8200	0.8215	0.8199	0.8154	0.8285	0.8422	0.8359
O2	−0.5640	−0.5516	−0.5662	−0.5702	−0.5847	−0.5709	−0.5897	−0.5429	−0.5536	−0.5582
H4	0.2348	0.2345	0.2482	0.2393	0.2325	0.2365	0.2292	0.2750	0.2426	0.2466
X	0.2119	−0.3977	0.2352	−0.4889	0.2068	−0.3064	0.2029	−0.0314	−0.3807	0.2323
Y	0.2453	0.2700	−0.3345	0.2411	−0.5380	0.2404	−0.3768	0.2704	−0.3157	0.0900
H5	0.2354	0.2434	0.2499	0.2344	0.2337	0.2336	0.2321	0.2437	0.2577	0.2492
H6	0.2385	0.2493	0.2599	0.2364	0.2326	0.2363	0.2411	0.2489	0.2712	0.2583

TABLE 9. The calculated and experimental results of KIEs for the decarboxylation of but-3-enoic acid at 650 K

	Obsd (ref. 15)	MINDO/3 (8)	HF/6-31G//HF/3-21G(*)
k_H/k_D	2.7	2.1	2.45[a] 2.86[b]
k_{12C}/k_{14C}	1.035 ± 0.010[c]	1.031	1.02[a] 1.03[b]

[a]Using Wigner's equation to calculate quantum tunneling effect (14*a*).
[b]Using Bell's equation to calculate quantum tunneling effect (14*a*).
[c]Data is for $C_6H_5{-}CH{=}CHC(CH_3)_2COOH$ at 550 K (5*b*).

tion state structures. On the other hand, in the γ-substituted cases, Q_{C1} is less negative and Q_{C2} is only slightly positive (negative for γ-F substituted case), leading to looser or more product-like transition state structures. Therefore β-substitution decreases the activation energy, while γ-substitution increases the activation energy. The relation of charge distribution to the activation energy indicates that the "ideal" transition state is one which can be characterized as the interaction between an allyl-like anion (C1—C2—C3) and a protonated CO_2 molecule, both of which involve charge delocalization.

III.3. Kinetic isotope effects

The primary kinetic isotope effects (KIEs) k_H/k_D (at H1) and k_{12C}/k_{14C} (at C4) for thermal decarboxylation of $H_2O{=}CHCH_2COOH$ were calculated using a modified BEBOVIB program (14). The KIEs are calculated at the HF/3-21G(*) optimized geometry using HF/6-31G normal-mode vibrational frequencies scaled by a factor of 0.9. The calculated and available experimental KIE results are listed in Table 9. The sizable primary k_H/k_D (2.86) at H1 and k_{12C}/k_{14C} (1.03) at C4 are obtained for but-3-enoic acid at 650 K, which are in excellent agreement with the available experimental values of 2.7 (15) and 1.035 (5*b*), respectively, and with Dewar's MINDO/3 results of 2.1 and 1.031, respectively (8), supporting the "twisted chair" sixmembered cyclic transition state structure.

IV. Conclusions

In summarizing our results the following conclusions can be drawn:

(*a*) The transition states obtained by our *ab initio* calculations are consistent with the experimental data, and support the "synchronous" mechanism for thermal decarboxylation of but-3-enoic acid and its derivatives via a six-membered cyclic transition state.

(*b*) The calculated results are also similar to Dewar's MINDO/3 result, but there are some improvements. The geometry of transition state is a "twisted chair" rather than Dewar's "flattened boat."

(*c*) The effects of β- and γ-substituents on the activation energy can be explained in terms of the electronic charge distribution. The atomic charges at C1 and C2 are important factors in controlling the activation energy. The "ideal" transition state is characterized as the interaction between an allyl-like anion (C1—C2—C3) and a protonated CO_2 molecule, both of which involve charge delocalization. β-Substitution decreases E_a, while γ-substitution increases E_a. This conclusion is also consistent with experimental observations.

(*d*) The result of E_a (156.8 kJ/mol) for thermal decarboxylation of $H_2C{=}CHCH_2{-}COOH$ with MP2/6-31G*///HF/3-21G(*) is in good agreement with the available experimental values of 164 ± 7 kJ/mol and 160 kJ/mol.

(*e*) Our calculated results of primary k_H/k_D (2.86) and k_{12C}/k_{14C} (1.03) is also in excellent agreement with the available experimental values (2.7 and 1.035, respectively) for but-3-enoic acid, supporting the transition state structure obtained.

Can. J. Chem. Downloaded from www.nrcresearchpress.com by EESC ESCOLA DE ENGENHARIA on 09/08/12
For personal use only.

Acknowledgements

We would like to thank the Newfoundland and Labrador Computer Services (NLCS) and MemorialUniversity of Newfoundland Computer Services for their generous allocation of computer time. The continuing support of the Natural Sciences and Engineering Research Council (NSERC) is acknowledged by R.A.P.

1. W.H. Richardson and H.E. O'Neal. *In* Comprehensive chemical kinetics. Vol. 5. *Edited by* C.H. Banford and C.F.H. Tipper. Elsevier, Amsterdam. 1972. pp. 447–456.
2. G.G. Smith and F.W. Kelly. *In* Progress in Physical Organic Chemistry. Vol. 8. *Edited by* A. Streitwieser, Jr. and R.W. Taft. Wiley-Interscience, New York. 1971. pp. 150–153.
3. (*a*) V.I. Minkin, B. Ya. Smikin, and R.M. Minyaev. Quantum chemistry of organic compounds (mechanisms of reactions). Springer-Verlag, Berlin. 1990; (*b*) J.D. Goddard, Y. Yamaguchi, and H.F. Schacefer, III. J. Chem. Phys. **96**, 1158 (1992); (*c*) J.M. Ugalde. THEOCHEM, **258**, 167 (1992); (*d*) K. Kamiya and K. Morokuma. J. Chem. Phys. **94**, 7278 (1991).
4. (*a*) E.M. Kosower. Molecular biochemistry. McGraw-Hill, New York. 1962. p. 77; (*b*) L.L. Ingraham. Biochemical mechanisms. John Wiley and Sons, New York. 1962. p. 58.
5. (*a*) G.G. Smith and S.F. Blau. J. Phys. Chem. **68**, 1231 (1964); (*b*) D.B. Bigley and J.C. Thurman. J. Chem. Soc. B, 941 (1967); (*c*) D.B. Bigley and J.C. Thurman. J. Chem. Soc. 6202 (1965); (*d*) D.B. Bigley and R.W. May. J. Chem. Soc. B. 557 (1967).
6. D.B. Bigley and M.J. Clarke. J. Chem. Soc. Perkin Trans. II, 1 (1982).
7. (*a*) D.B. Bigley, C.L. Fetter, and M.J. Clarke. J. Chem. Soc. Perkin Trans. II, 553 (1980); (*b*) A. al-Borno and D.B. Bigley. J. Chem. Soc. Perkin Trans. II, 1311 (1983); (*c*) J.A. van Doorn and N. Meijboom. J. Chem. Soc. Perkin Trans. II, 1309 (1989); (*d*) J.H. Hurley and S.J. Remington. J. Am. Chem. Soc. **114**, 4769 (1992).
8. M.J.S. Dewar and G.P. Ford. J. Am. Chem. Soc. **99**, 8343 (1977).
9. W.C. Davidon. Math. Prog. **9**, 1 (1975).
10. M.J.D. Powell. Subroutine VAO5AD, AERE Subroutine Library, Harwell, Didcot, Berkshire, U.K.
11. R.A. Poirier, M.R. Peterson, and A. Yadav. MUNGAUSS. Chemistry Department, Memorial University of Newfoundland, St. John's, Newfoundland, Canada. 1989.
12. M.J. Frisch, J.S. Binkley, H.B. Schlegel, K. Raghavachari, C.F. Melius, R.L. Martin, J.J.P. Stewart, F.W. Bobrowicz, C.M. Rohlfing, L.R. Kahn, D.J. Defrees, R. Seeger, R.A. Whiteside, D.J. Fox, E.M. Fleuder, and J.A. Pople. Carnegie-Mellon Quantum Chemistry Publishing Unit, Pittsburgh, PA. 1984.
13. W.J. Hehre, L. Radom, P.v.R. Schleyer, and J.A. Pople. *Ab initio* molecular orbital theory. Wiley, New York, NY. 1986.
14. (*a*) L.B. Sims and D.E. Lewis. *In* Isotopes in organic chemistry. *Edited by* E. Buncel and C.C. Lee. Vol. 6. Elsevier Science, Amsterdam. 1984. pp. 161–259; (*b*) R.A. Poirier, Y. Wang, and K.C. Westaway. 76th Canadian Chemistry Conference, May 30 – June 4, Sherbrooke, Quebec. Abstr. No. 240. (1993).
15. H. Kwart and M.C. Latimore. J. Am. Chem. Soc. **93**, 3770 (1970).

Can. J. Chem. Downloaded from www.nrcresearchpress.com by EESC ESCOLA DE ENGENHARIA on 09/08/12
For personal use only.

Synthesis of enantiomeric β-amino ketones via 1,3-dipolar cycloaddition and chromatographic resolution

CHANTAL LOUIS, SIBEL MILL, VINCENT MANCUSO, AND CLAUDE HOOTELÉ[1]

Organic Chemistry Department, Faculty of Sciences, University of Brussels, B-1050 Brussels, Belgium

Received August 19, 1993

CHANTAL LOUIS, SIBEL MILL, VINCENT MANCUSO, and CLAUDE HOOTELÉ. Can. J. Chem. **72**, 1347 (1994).

The cycloaddition reactions of 3,4,5,6-tetrahydropyridine 1-oxide **1** with the homochiral alkynyl sulfoxides **6***a–e* proceed in high yield to afford, with low asymmetric induction, mixtures of diastereomeric isoxazolines that are readily separated by column chromatography. The resolved isoxazolines can be subsequently converted, by hydrogenolysis, to enantiomeric β-amino ketones.

CHANTAL LOUIS, SIBEL MILL, VINCENT MANCUSO et CLAUDE HOOTELÉ. Can. J. Chem. **72**, 1347 (1994).

Les réactions de cycloaddition entre la 3,4,5,6-tétrahydropyridine 1-oxyde **1** et les sulfoxydes acétyléniques homochiraux **6***a–e* conduisent avec de bons rendements et une induction asymétrique faible à des mélanges d'isoxazolines diastéréoisomères facilement séparables par chromatographie sur colonne. Les isoxazolines résolues peuvent être converties, par hydrogénolyse, en β-aminocétones énantiomères.

[Traduit par la Rédaction]

Introduction

β-Amino ketones constitute an important class of compounds for which the synthesis deserves interest. In this regard, we previously reported a new efficient synthesis based on the observation that 4-isoxazolines **3** can be viewed as masked β-amino ketones, which could be released by hydrogenolysis of the N—O bond (1) (Scheme 1). Although 4-isoxazolines have proven to be thermally labile heterocycles and display an array of rearrangements (2, 3), we established that under carefully controlled conditions they can be prepared in good yield by nitrone–alkyne cycloaddition. Hydrogenolysis of the N—O bond can be performed by hydrogen in the presence of Pd/C. Application of this procedure to the synthesis of 2-phenacylpiperidine, for example (**4**, R = C_6H_5), proceeds from nitrone **1** and phenylacetylene with 70% overall yield. In the present study we report the extension of our method for the synthesis of the two enantiomers of β-amino ketones.

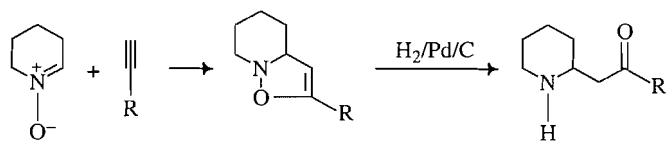

1 **2** **3** **4**

SCHEME 1

Asymmetric nitrone–alkene 1,3-dipolar cycloadditions involving either chiral nitrones or chiral alkenes have received attention: high asymmetric induction has been observed, for example, in the condensation of nitrones with alkenyl sulfoxides (4) or, very recently, with chiral allyl ethers (5). On the other hand, to the best of our knowledge, no attention has been paid to nitrone–alkyne cycloadditions in the chiral mode. Hence we undertook a study of the cycloaddition of the prochiral nitrone **1** onto several chiral alkynyl sulfoxides as dipolarophiles.

Results and discussion

(+)-1-Alkynyl *p*-tolyl sulfoxides **6***a–e* were prepared by the Andersen synthesis using the reaction of alkynylmagnesium bromides **5***a–e* with *l*-menthyl (−)-*S*-*p*-toluenesulfinate in toluene (6) (Scheme 2). Based on the fact that Grignard reactions with chiral sulfinate esters proceed stereospecifically with inversion of configuration at the sulfur atom (7), the acetylenic sulfoxides **6***a–e* are assigned the *S* configuration; the optical purity and the absolute configuration of **6***c–e* were previously confirmed by their conversion into the corresponding alkenyl derivatives (6).[2]

The reaction of nitrone **1** with the alkynyl sulfoxides **6***a–e* gave mixtures of the diastereomeric isoxazolines **7***a–e* and **8***a–e* (Scheme 3); the large differences in the R_fs allowed the complete separation of the individual diastereomers of each pair by flash chromatography on silica gel. Typical results are presented in Table 1 and deserve some comments.

All the cycloadditions proceed with excellent yields. It appears that the electron-poor alkynyl sulfoxides possess a higher reactivity than the corresponding terminal alkynes: whereas the condensation of **1** with pentyne or heptyne requires refluxing toluene or 1,1,1-trichloroethane (1), these new cycloadditions are performed in chloroform at room temperature (with a 1:1 alkyne: nitrone ratio). On the other hand, the cycloadditions are highly regioselective, the electron-withdrawing group occupying the 3-position of the isoxazolines (as demonstrated by their subsequent conversion). The enhanced reactivity and the observed regioselectivity are in agreement with previous observations and theoretical predictions (2, 8). According to Houk's perturbation treatment of 1,3-dipolar cycloadditions, the preferred regioisomer will arise from the transition state in which the atoms with the largest orbital coefficients interact, i.e., the transition state in which the carbon of the nitrone moiety becomes bonded to the carbon of the dipolarophile bearing the sulfoxide group. Furthermore, lowering of the LUMO level of the dipolarophile is responsible for the observed increased reactivity of the alkynyl sulfoxides.

The asymmetric induction is low in all the cycloadditions. In the case of **6***e*, experiments were also carried out in other solvents: 1,4-dioxane, benzene, acetonitrile, and chloroform:ethanol (4:1); apart from a substantial acceleration relative to chloroform in the first two solvents, the results were essentially identical. In the same way, replacement of the *p*-tolyl group of

[1]Author to whom correspondence may be addressed.

[2]The specific rotation values measured for the sulfoxides **6***c–e* agree within the limits of experimental errors with those published in the literature (6) (see experimental section).

Can. J. Chem. Downloaded from www.nrcresearchpress.com by EESC ESCOLA DE ENGENHARIA on 09/08/12
For personal use only.

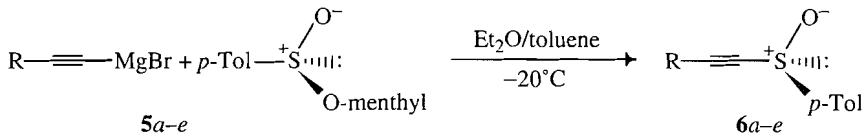

5a–e 6a–e

SCHEME 2

TABLE 1. Nitrone cycloaddition to alkynyl sulfoxides

			Isoxazoline **7**		Isoxazoline **8**	
Entry	Sulfoxide	R	Yield[a], %	$[\alpha]_D$[b] (*c*)	Yield[a], %	$[\alpha]_D$[b] (*c*)
1	**6***a*	C_6H_5	42	−45 (0.2)	46	−217 (0.6)
2	**6***b*	CH_3	47	+240 (1.5)	44	−33 (2.1)
3	**6***c*	*n*-C_3H_7	44	+191 (1.7)	52	−51 (1.0)
4	**6***d*	*n*-C_4H_9	42	+158 (1.2)	51	−57 (1.8)
5	**6***e*	*n*-C_5H_{11}	43	+162 (1.6)	50	−60 (1.6)

[a]Isolated yield by flash column chromatography on silica gel (AcOEt).
[b]Measured for solution in MeOH at 22°C.

6*e* by a methyl, a *tert*-butyl, or an α-naphthyl group brought no new prospect.

The results described above indicate a very low level of asymmetric induction, but the quantitative chromatographic diastereomeric resolution of the isoxazolines **7** and **8** opened a new route to optically active β-amino ketones. Hydrogenolysis of the separated isoxazolines furnished, after filtration through alumina, the expected enantiomeric β-amino ketones in good yield. The best results were achieved when the hydrogenolysis (H_2/Pt) was carried out in methanol in the presence of citric acid; this acid was intially introduced to slower racemization of the β-amino ketones;[3] its presence was found to improve the yield. Typical results obtained from **7***b–e* and **8***b–e* are presented in Table 2.

Control experiments allowed us to establish that in the conditions described above, the ketones **4** suffered no loss of optical activity (9). It appears therefore that the β-amino ketones obtained by this method should be of high optical purity. Indeed a sample of resolved (−)-pelletierine **4***b*, liberated from pure (*R*)-pelletierine hydrogen (*R*)-6,6′ dinitrobiphenyl-2,2′-dicarboxylate[4] ($[\alpha]_D^{22}$ +156 (pyridine, *c* 3)) showed an optical rotation $[\alpha]_D^{22}$ −26 ($CHCl_3$, *c* 1.6) comparable with the value reported in Table 2. Moreover, (−)-**4***c* was transformed[5] into (−)-halosaline **9**, indentical with the natural compound (11, 12) of which the optical purity is known to be higher than 90%.[6]

The levorotatory ketones **4***b* and **4***c* were previously assigned

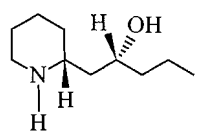

9

[3]We have observed that the optically active compounds **4** epimerize more slowly (in methanol at room temperature) than the corresponding N-Me derivatives. This difference was already pointed out in the case of pelletierine **4***b* and N-methylpelletierine: see ref. 9.

[4]Racemic pelletierine has been resolved with 6,6′-dinitrobiphenyl-2,2′-dicarboxylic acid, see refs. 9 and 14.

[5]S. Mill and C. Hootelé; to be published.

[6]In ref. 11, an optical purity of 90% was determined for a sample of **4***c* prepared from natural halosaline; the specific rotation value quoted ($[\alpha]_D^{22}$ −11.4 (chloroform, *c* 1)) is, however, clearly in error.

TABLE 2. Reduction of isoxazolines **7** and **8** to β-amino ketones

Entry	Isoxazoline	β-Amino ketone	Yield, %	$[\alpha]_D$[a] (*c*)
1	**7***b*	(+)-(*S*) **4***b*	82	+25 (1.4)
2	**8***b*	(−)-(*R*) **4***b*	74	−22 (0.9)
3	**7***c*	(+)-(*S*) **4***c*	95	+21 (2.5)
4	**8***c*	(−)-(*R*) **4***c*	94	−21 (1.8)
5	**7***d*	(+)-(*S*) **4***d*	85	+20 (1.9)
6	**8***d*	(−)-(*R*) **4***d*	89	−20 (2.1)
7	**7***e*	(+)-(*S*) **4***e*	88	+15 (1.8) +22 (2.3)[b]
8	**8***e*	(−)-(*R*) **4***e*	79	−15 (1.1) −23 (1.1)[b]

[a]Measured for solutions in $CHCl_3$ at 22°C unless otherwise stated.
[b]Measured for solutions in MeOH at 22°C.

R configurations, inter alia through correlation with pipecolic acid (10, 11, 13). We assign the homologous levorotatory ketones **4***d* and **4***e* the same *R* absolute configuration from the sign of the rotation and from the similar chromatographic behaviour of the diastereomer isoxazolines throughout the series.

The methodology described here represents an alternative to the classical resolution with a chiral acid (14); it gives access to both enantiomeric forms and should be applicable to a wide range of β-amino ketones.

Experimental

Mass spectra were obtained on a Micromass 7070 spectrometer with electron impact inonization. ^1H and ^{13}C NMR spectra were recorded on a Bruker WM 250 apparatus, in $CDCl_3$, with TMS as internal standard unless otherwise stated. Optical rotations were measured on a Perkin–Elmer 141 polarimeter. Analytical thin-layer chromatography was performed on Polygram Sil G/UV254 plates. Visualization was accomplished with UV light and ethanolic phosphomolybdic acid solution followed by heating.

General procedure for the synthesis of 1-alkynyl p*-tolyl sulfoxides*

(+)-1-Alkynyl *p*-tolyl sulfoxides were prepared according to the procedure described in the literature (6) for **6***c–e*. The following specific rotation values ($[\alpha]_D^{22}$, (*c*)) were measured in chloroform: **6***a*: +76 (2.5); **6***b*: +122 (2.8); **6***c*: +89 (1.4); **6***d*: +84 (2.2); **6***e*: +77 (2.5). For **6***a*: ^1H NMR (60 MHz), δ: 7.9–7 (9H, m), 2.3 (3H, s); for **6***b*: ^1H NMR, δ: 7.67 (2H, d, J = 8 Hz), 7.33 (2H, d, J = 8 Hz), 2.42 (3H, s), 2.06 (3H, s); ^{13}C NMR, δ: 142.5, 141.4, 130.4, 125.3, 102.0, 78.0, 21.6, 5.1.

Can. J. Chem. Downloaded from www.nrcresearchpress.com by ESC ESCOLA DE ENGENHARIA on 09/08/12
For personal use only.

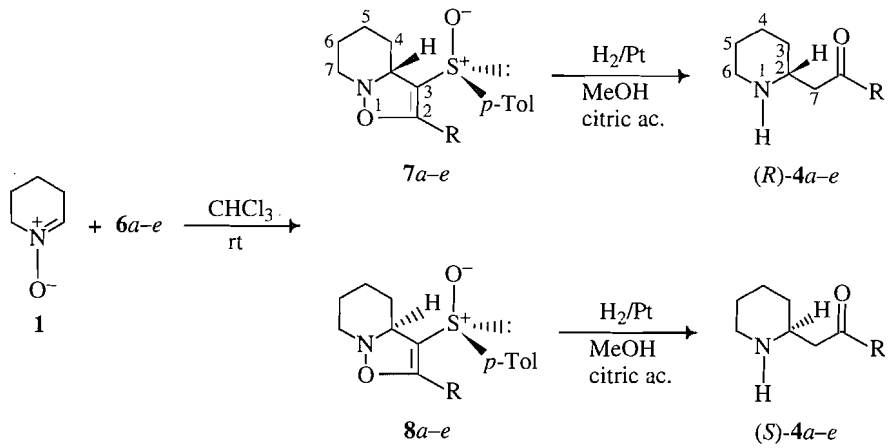

SCHEME 3

Sulfoxide **6***a* is somewhat unstable and proved difficult to obtain in a pure state.

General procedure for the cycloaddition reactions

To a well-stirred solution of *N*-hydroxypiperidine (3.06 mmol; 1 equiv.) in chloroform (free of ethanol and freshly distilled, 20 mL) at 0°C was added yellow mercury(II) oxide (6.14 mmol; 2 equiv.). The mixture was then allowed to come to room temperature and the reaction was checked by TLC (alumina, AcOEt). After 10 min, the slurry was filtered through Celite (chloroform, 10 mL). Half of the solvent was then removed under reduced pressure and the alkynyl sulfoxide (3.06 mmol; 1 equiv.) was added to the solution. The mixture was left at room temperature for 24 h and the reaction followed by TLC (silica, AcOEt). The solvent was removed under reduced pressure and the recovered oil was flash chromatographed over silica (AcOEt) to give the isoxazolines **7** and **8**.

Isoxazoline 7a. ^{1}H NMR, δ ppm: 7.83–7.79 (m, 2H, aromatic), 7.54–7.43 (m, 5H), 7.32 (d, 2H, aromatic, J = 8 Hz), 4.26 (m, 1H, H3a), 3.26 (m, 2H, H7), 2.41 (s, 3H, $ArCH_3$), 2.09–2.0 (m, 1H), 1.77–1.64 (m, 3H), 1.55–1.40 (m, 2H); ^{13}C NMR, δ ppm: 163.5 (C2), 140.5, 139.1, 131.4, 130.0, 129.6, 128.9, 128.7, 127.2, 124.6, 113.5 (C3), 65.3 (C3a), 51.7 (C7), 26.6, 22.5, 21.3 ($ArCH_3$), 19.9; MS *m/z*: 321 ($M^{+\cdot}$ − H_2O, 14%), 320 (13), 246 (69), 226 (1), 200 (13), 139 (10), 124 (20), 123 (68), 105 (100), 91 (31); R_f: 0.51 (AcOEt:hexane 9:1).

Isoxazoline 8a. ^{1}H NMR, δ ppm: 7.89–7.26 (m, 9H, aromatic), 4.77 (m, 1H, H3a), 3.36–2.89 (m, 2H, H7), 2.40 (s, 3H, $ArCH_3$), 2.0–1.49 (m, 5H), 1.06–0.97 (m, 1H); ^{13}C NMR, δ ppm: 161.8 (C2), 140.6, 140.4, 131.1, 130.0, 129.8, 128.8, 128.6, 124.6, 124.3, 113.0 (C3), 64.8 (C3a), 52.3 (C7), 25.6, 22.9, 21.3 ($ArCH_3$), 19.9; MS *m/z*: 339 ($M^{+\cdot}$, <1%), 278 (5), 258 (7), 246 (19), 226 (13), 200 (13), 139 (56), 123 (30), 105 (100), 91 (32); R_f: 0.38 (AcOEt:hexane 9:1).

Isoxazoline 7b. ^{1}H NMR, δ ppm: 7.43 (d, 2H, J = 8 Hz, aromatic), 7.30 (d, 2H, J = 8 Hz, aromatic), 4.06 (m, 1H, H3a), 3.17 (m, 1H, eq. H7), 3.06 (dt, 1H, J = 3 and 12 Hz, ax. H7), 2.41 (s, 3H, $ArCH_3$), 2.24 (d, 3H, J = 1.5 Hz, CH_3), 1.96 (m, 1H), 1.69–1.61 (m, 3H), 1.46–1.39 (m, 2H); ^{13}C NMR, δ ppm: 164.9 (C2), 141.0, 139.5, 130.6, 125.0, 113.3 (C3), 64.7 (C3a), 52.4 (C7), 26.7, 23.0, 21.9 ($ArCH_3$), 20.1, 12.2 (CH_3); MS *m/z*: 277 ($M^{+\cdot}$, 11%), 276 (10), 260 (34), 229 (41), 217 (34), 214 (34), 186 (26), 173 (31), 154 (34), 139 (54), 124 (100), 123 (47), 91 (85); R_f: 0.50 (AcOEt).

Isoxazoline 8b. ^{1}H NMR, δ ppm: 7.45 (d, 2H, J = 8 Hz, aromatic), 7.30 (d, 2H, J = 8 Hz, aromatic), 4.58 (m, 1H, H3a), 3.07 (m, 1H, eq. H7), 2.79 (m, 1H, ax. H7), 2.41 (s, 3H, $ArCH_3$), 2.22 (d, 3H, J = 1.5 Hz, CH_3), 1.63–1.23 (m, 5H), 0.98 (m, 1H); ^{13}C NMR, δ ppm: 163.1 (C2), 140.5, 129.7, 128.7, 124.6, 112.0 (C3), 64.5 (C3a), 52.3 (C7), 25.2, 23.1, 21.3 ($ArCH_3$), 21.1, 11.6 (CH_3); MS *m/z*: 277 ($M^{+\cdot}$, 9%), 276 (6), 260 (27), 246 (31), 229 (40), 217 (26), 214 (26), 186 (22), 173 (23), 154 (32), 139 (63), 124 (100), 123 (67), 96 (35), 91 (85); R_f: 0.37 (AcOEt).

Isoxazoline 7c. ^{1}H NMR, δ ppm: 7.43 (d, 2H, J = 8 Hz, aromatic), 7.30 (d, 2H, J = 8 Hz, aromatic), 4.06 (m, 1H, H3a), 3.18 (m, 1H, eq. H7), 3.03 (br dt, 1H, J = 3 and 11 Hz, ax. H7), 2.68–2.50 (m, 2H, allylic CH_2), 2.41 (s, 3H, $ArCH_3$), 1.99–1.39 (m, 8H), 1.06 (t, 3H, J = 7.5 Hz, CH_3); ^{13}C NMR, δ ppm: 168.4 (C2), 140.9, 139.6, 130.5, 125.1, 113.0 (C3), 64.6 (C3a), 52.3 (C7), 28.3 (allylic CH_2), 26.7, 23.0, 21.9 ($ArCH_3$), 21.2, 20.1, 14.6 (CH_3); R_f: 0.54 (AcOEt).

Isoxazoline 8c. ^{1}H NMR, δ ppm: 7.52 (d, 2H, J = 8 Hz, aromatic), 7.31 (d, 2H, J = 8 Hz, aromatic), 4.62 (m, 1H, H3a), 3.07 (m, 1H, H7), 2.88–2.48 (m, 3H, H7 + allylic CH_2), 2.41 (s, 3H, $ArCH_3$), 1.80–1.28 (m, 7H), 1.06 (t, 3H, J = 7.5 Hz, CH_3), 1.01–0.85 (m, 1H); ^{13}C NMR, δ ppm: 166.8 (C2), 140.4, 129.6, 124.6, 111.7 (C3), 64.1 (C3a), 52.2 (C7), 27.6 (allylic CH_2), 25.1, 23.0, 21.3 ($ArCH_3$), 20.8, 19.8, 13.9 (CH_3); R_f: 0.38 (AcOEt).

Isoxazoline 7d. ^{1}H NMR, δ ppm: 7.42 (d, 2H, J = 8 Hz, aromatic), 7.30 (d, 2H, J = 8 Hz, aromatic), 4.06 (m, 1H, H3a), 3.16 (m, 1H, H7), 3.03 (dt, 1H, J = 3 and 12 Hz, ax. H7), 2.62 (m, 2H, allylic CH_2), 2.40 (s, 3H, $ArCH_3$), 2.0–1.4 (m, 10H), 0.97 (t, 3H, J = 7 Hz); ^{13}C NMR, δ ppm: 168.3 (C2), 140.7, 139.4, 130.5, 125.0, 112.6 (C3), 64.4 (C3a), 52.2 (C7), 29.7 (allylic CH_2), 26.5, 25.9, 22.9, 21.7 ($ArCH_3$), 19.9, 14.1 (CH_3); MS *m/z*: 319 ($M^{+\cdot}$, 8), 318 (6), 302 (15), 278 (11), 271 (6), 246 (100), 234 (15), 218 (13), 217 (13), 208 (50), 196 (69), 180 (42), 140 (31), 139 (81); R_f: 0.52 (AcOEt).

Isoxazoline 8d. ^{1}H NMR, δ ppm: 7.51 (d, 2H, J = 8 Hz, aromatic H), 7.30 (d, 2H, J = 8 Hz, aromatic), 4.61 (m, 1H, H3a), 3.07 (m, 1H, eq. H7), 2.75–2.50 (m, 3H, ax. H7 + allylic CH_2), 2.41 (s, 3H, $ArCH_3$), 1.75–1.40 (m, 8H), 0.97 (t, 3H, J = 7 Hz), 0.97–0.2 (2H); ^{13}C NMR, δ ppm: 167.3 (C2), 140.8, 130.0, 124.9, 111.9 (C3), 64.0 (C3a), 52.5 (C7), 29.7 (allylic CH_2), 25.8, 25.5, 23.3, 22.8, 21.6 (CH_3), 20.1, 14.0 (CH_3); MS *m/z*: 319 ($M^{+\cdot}$, 11%), 318 (7), 302 (31), 271 (15), 246 (69), 234 (24), 229 (18), 217 (53), 208 (63), 196 (95), 180 (68), 140 (100); R_f: 0.40 (AcOEt).

Isoxazoline 7e. ^{1}H NMR, δ ppm: 7.43 (d, 2H, J = 8 Hz, aromatic), 7.30 (d, 2H, J = 8 Hz, aromatic), 4.06 (m, 1H, H3a), 3.15 (m, 1H, eq. H7), 3.05 (m, 1H, ax. H7), 2.64 (m, 2H, allylic CH_2), 2.41 (s, 3H, $ArCH_3$), 1.94 (m, 1H), 1.66 (m, 5H), 1.40 (m, 6H), 0.93 (t, 3H, J = 7 Hz, CH_3); ^{13}C NMR, δ ppm: 168.1 (C2), 140.3, 139.0, 130.0, 124.5, 112.2 (C3), 64.0 (C3a), 51.7 (C7), 31.5 (allylic CH_2), 26.9, 26.1, 25.8, 22.4, 22.3, 21.3 ($ArCH_3$), 19.5, 13.9 (CH_3); MS *m/z*: 333 ($M^{+\cdot}$, 12%), 332 (11), 317 (9), 316 (10), 278 (10), 260 (12), 246 (84), 234 (10), 222 (27), 210 (33), 194 (10), 139 (50), 124 (100); R_f: 0.52 (AcOEt:hexane 9:1).

Isoxazoline 8e. ^{1}H NMR, δ ppm: 7.52 (d, 2H, J = 8 Hz, aromatic), 7.31 (d, 2H, J = 8 Hz, aromatic), 4.63 (m, 1H, H3a), 3.07 (m, 1H, eq. H7), 2.75–2.49 (m, 3H, H7 + allylic CH_2), 2.41 (s, 3H, $ArCH_3$), 1.78–1.19 (m, 11H), 1.01–0.84 (m, 2H), 0.94 (t, 3H, J = 7 Hz, CH_3); ^{13}C NMR, δ ppm: 167.0 (C2), 140.4, 129.7, 124.6, 111.5 (C3), 63.9 (C3a), 52.2 (C7), 31.5 (allylic CH_2), 27.0, 25.7, 25.2, 23.0, 22.3, 21.3 ($ArCH_3$), 19.7, 13.9 (CH_3); MS *m/z*: 333 ($M^{+\cdot}$, 16%), 332 (9), 317 (34), 316 (30), 278 (11), 260 (13), 246 (32), 234 (26), 222 (41), 210

Can. J. Chem. Downloaded from www.nrcresearchpress.com by EESC ESCOLA DE ENGENHARIA on 09/08/12
For personal use only.

(50), 194 (44), 140 (34), 139 (100), 124 (100), 123 (98); R_f: 0.35 (AcOEt:hexane 9:1).

General procedure for the hydrogenolysis of isoxazolines 7 and 8

The isoxazoline (7.7×10^{-4} mol; 1 equiv.) was dissolved in a methanolic solution (15 mL) of citric acid (566 mg; 2.68 mmol; 3.5 equiv.). The mixture was hydrogenated over PtO_2 (25 mg; 5 wt.%) at room temperature and atmospheric pressure. After 3 equivalents of H_2 were absorbed, the slurry was filtered through Celite. After removal of the solvent under reduced pressure, chloroform (30 mL) was added to the residue. The solution was extracted with 0.2 M aqueous HCl (3 × 30 mL). The aqueous solution was basified with 15 M aqueous ammonia and extracted with chloroform (3 × 30 mL). Removal of the solvent under reduced pressure followed by filtration through a short column of alumina gave the pure β-amino ketone **4**.

(−)4b. ^{1}H NMR, δ ppm: 3.03–2.90 (m, 2H), 2.65 (dt, 1H, J = 3 and 12 Hz), 2.49 (d, 2H, J = 6 Hz), 2.27 (br signal, 1H), 2.13 (s, 3H), 1.8–1.1 (m, 6H); MS *m/z*: 141 ($M^{+\cdot}$, 11%), 98 (18), 84 (100).

(−)4c. ^{1}H NMR, δ ppm: 3.04–2.90 (m, 2H), 2.66 (dt, 1H, J = 3 and 12 Hz), 2.47 (d, 2H, J = 6 Hz), 2.36 (t, 2H, J = 7 Hz), 2.18 (br signal, 1H), 1.8–1.1 (m, 8H), 0.90 (t, 3H, J = 7 Hz); MS *m/z*: 169 ($M^{+\cdot}$, 6%), 140 (4), 126 (3), 98 (13), 84 (100).

(−)4d. ^{1}H NMR, δ ppm: 3.03–2.89 (m, 2H), 2.66 (dt, 1H, J = 3 and 12 Hz), 2.47 (d, 2H, J = 6 Hz), 2.38 (t, 2H, J = 7 Hz), 2.5 (br signal, 1H), 1.8–1.1 (m, 10H), 0.90 (t, 3H, J = 7 Hz); MS *m/z*: 183 ($M^{+\cdot}$, 39%), 154 (6), 140 (52), 126 (48), 98 (100), 84 (100).

(−)4e. ^{1}H NMR, δ ppm: 3.04–2.90 (m, 2H), 2.66 (dt, 1H, J = 3 and 12 Hz), 2.47 (d, 2H, J = 6 Hz), 2.37 (t, 2H, J = 7 Hz), 2.28 (br signal, 1H), 1.8–1.1 (m, 12H), 0.88 (t, 3H, J = 7 Hz); MS *m/z*: 197 ($M^{+\cdot}$, 17%), 196 (5), 140 (20), 126 (27), 99 (10), 98 (51), 84 (100).

Acknowledgments

S.M. and V.M. wish to thank the Institut pour l'Encouragement de la Recherche Scientifique dans l'Industrie et l'Agriculture (IRSIA, Belgium), and C.L. (Research Assistant) thanks the National Fund for Scientific Research (FNRS, Belgium) for fellowships. C.H. is a Research Associate of the FNRS.

1. V. Mancuso and C. Hootelé. Tetrahedron Lett. **29**, 5917 (1988).
2. J.J. Tufariello. *In* 1,3-Dipolar cycloaddition chemistry. Vol. 2. *Edited by* A. Padwa. Wiley–Interscience, New York. 1984. Chap. 9, pp. 122–127.
3. J.P. Freeman. Chem. Rev. **83**, 241 (1983).
4. (*a*) T. Koizumi, H. Hirai, E. Yoshii. J. Org. Chem. **47**, 4004 (1982); (*b*) T. Takahashi, A. Fujii, J. Sugita, T. Hagi, K. Kitano, Y. Arai, T. Koizumi. Tetrahedron: Asymmetry **2**, 1379 (1991).
5. M. Ito, M. Maeda, C. Bayashi. Tetrahedron Lett. **33**, 3765 (1992).
6. H. Kosugi, M. Kitaoka, K. Tagami, A. Takahashi, and H. Uda. J. Org. Chem. **52**, 1078 (1987).
7. (*a*) K.K. Andersen. Tetrahedron Lett. 93 (1962); (*b*) M. Axelrod, P. Bickart, J. Jacobus, M. Green, and K. Mislow. J. Am. Chem. Soc. **90**, 4835 (1968); (*c*) K.K. Andersen. *In* The chemistry of sulfones and sulfoxides. *Edited by* S. Patai, Z. Rappoport, and C. Stirling. John Wiley & Sons, New York. 1988. Chap. 3, pp. 55–94; (*d*) G.H. Posner. *In* The chemistry of sulfones and sulfoxides. *Edited by* S. Patai, Z. Rappoport, and C. Stirling. John Wiley & Sons, New York. 1988. Chap. 16, pp. 823–849; (*e*) A. Nudelman. *In* The chemistry of sulfinic acids, esters and their derivatives. *Edited by* S. Patai. John Wiley & Sons, New York. 1990. Chap. 3, pp. 35–85.
8. (*a*) R. Sustmann. Pure Appl. Chem. **40**, 569 (1974); (*b*) K.N. Houk, J. Sims, R.E. Duke, R.W. Strozier, and J.K. George. J. Am. Chem. Soc. **95**, 7287 (1973); (*c*) K.N. Houk, J. Sims, C.R. Watts, and L.J. Luskus. J. Am. Chem. Soc. **95**, 7301 (1973).
9. F. Galinovsky, G. Bianchetti, and O. Vogl. Monatsh. Chem. **84**, 1221 (1953); F. Galinovsky and R. Höllinger. Monatsch. Chem. **85**, 1012 (1954).
10. H.C. Beyerman, L. Maat, A. Van Veen, A. Zweistra, and W. Von Philipsborn. Recl. Trav. Chim. Pays-Bas, **84**, 1367 (1965).
11. K-H. Michel, F. Sandberg, F. Haglid, and T. Norin. Acta Pharma. Suec. **4**, 97 (1967).
12. M. Hanaoka, M. Kohzu, and S. Yasuda. Chem. Pharm. Bull. **36**, 4248 (1988).
13. J.C. Craig, C. Lee, W.E. Pereira, H.C. Beyerman, and L. Maat. Tetrahedron, **34**, 501 (1978).
14. H.C. Beyerman and L. Maat. Recl. Trav. Chim. Pays-Bas, **84**, 385 (1965).

Can. J. Chem. Downloaded from www.nrcresearchpress.com by EESC ESCOLA DE ENGENHARIA on 09/08/12
For personal use only.

The oxidation of *ortho*-anisidine in alkaline medium. A product characterization and an EPR study

ADELE BOLOGNESE,[1] MARINA BUONANNO, AND ANTONIO CANTILENA
Dipartimento di Chimica Organica e Biologica, Università di Napoli Federico II, Via Mezzocannone 16, I-80134 Naples, Italy

GIOVANNI MUSCI
Centro di Biologia Molecolare del CNR, Dipartimento di Scienze Biomediche, Università di Roma La Sapienza, Piazzale Aldo Moro 5, I-00185 Rome, Italy

AND

ANGELO ALBERTI[1]
I.Co.C.E.A.-CNR, Via della Chimica 8, I-40064 Ozzano Emilia, Italy

Received August 3, 1993

ADELE BOLOGNESE, MARINA BUONANNO, ANTONIO CANTILENA, GIOVANNI MUSCI, and ANGELO ALBERTI. Can. J. Chem. **72**, 1351 (1994).

Alkaline oxidation of *ortho*-anisidine by potassium ferricyanide in alkaline aqueous solution was examined. Azo compounds, a diamine, and *para*-iminoquinones were isolated from the highly coloured reaction mixture. The reaction was also carried out within the cavity of an EPR spectrometer and two radical species have been detected. Following these product results and EPR studies, a radical mechanism is proposed for the process.

ADELE BOLOGNESE, MARINA BUONANNO, ANTONIO CANTILENA, GIOVANNI MUSCI et ANGELO ALBERTI. Can. J. Chem. **72**, 1351 (1994).

On a examiné l'oxydation alcaline de l'*ortho*-anisidine par le ferricyanure de potassium, en solution aqueuse alcaline. On a isolé des composés azo, une diamine et des *para*-iminoquinones du milieu réactionnel très coloré. On a aussi réalisé la réaction à l'intérieur de la cavité d'un spectromètre de RPE et on a détecté deux espèces radicalaires. Sur la base de la nature des produits observés et des études de RPE, on propose un mécanisme radicalaire pour ce processus.

[Traduit par la Rédaction]

Introduction

The oxidations of phenols, catechols, and *o*-aminophenols have particular interest in relation to the biosynthesis of ommochromes, cinnabarines, actinomycins, and melanins (1, 2). Since, in striking contrast with the well-known behaviour of phenols and catechols, no carbon–carbon dimer formation has ever been reported in the oxidation of *o*-aminophenols, the possibility of the occurrence of a radical process has never been taken into account and an ionic mechanism has usually been credited (3–5).

On the other hand, some of us recently proposed that the first step in the formation of the phenoxazine-3-one system present in ommochrome pigments might be a radical–radical coupling of the *o*-aminophenol residue of the 3-hydroxykynurenine, this hypothesis being supported by EPR investigations carried out on the oxidation mixture of the latter compound and potassium ferricyanide (6, 7). It is actually possible that the reactivity of *o*-aminophenols is more akin to that of aromatic amines than to that of phenols, and as a consequence a radical pathway cannot be excluded on the basis of the absence of carbon–carbon dimeric products. To further check this point we have investigated the potassium ferricyanide oxidation of *o*-anisidine by combining conventional product studies with EPR spectroscopy.

Results

Product studies

When *o*-anisidine **1** (10 mmol in 20 mL of water–methanol 1:1 vv) was treated with an excess of alkaline potassium ferricyanide (40 mmol in 20 mL of water, pH 9) at room temperature for 1 h a deep red mixture was obtained from which five coloured products **2**, **2′**, **3**, **4**, and **5** were chromatographically isolated and then characterized. No trace of **1** was left in the reaction mixture.

The structures of compounds **2** and **2′**, whose colour shifted from yellow to pink by mineral acid treatment, were determined on the basis of the following mass and NMR spectroscopic data. Both compounds showed the molecular ion peak at *m/e* 242 along with a strong peak at *m/e* 107 due to the anisyl residue. The ^{1}H NMR of **2** exhibited two doublets (2H, δ 8.74 and 2H, δ 7.06) and two triplets (2H, δ 6.99 and 2H, δ 7.40) for the eight aromatic protons and a singlet (6H, δ 4.00) for the two equivalent methoxy groups. On the other hand **2′** exhibited two doublets (2H, δ 6.82 and 2H, δ 6.57) and two triplets (2H, δ 7.12 and 2H, δ 6.73) for the eight aromatic protons and a singlet (6H, δ 3.76) for the two methoxy groups. The actual assignment of the two isomers was based on the assumption that in the *syn* isomer the N=N double bond would shield the aromatic ring(s) more than in the *anti* isomer.

Similarly, the very polar brown compound **3**, with a molecular ion signal at *m/e* 244, was identified as 2-methoxy-4-(2-methoxyphenylamino)aniline. It exhibited signals from the four protons of the disubstituted ring (δ 7.10, 7.01, 7.16, 6.84), the three protons of the trisubstituted ring (δ 6.59, 6.81, and 5.80), and the signals from the two different methoxy groups (δ 3.83 and 3.81) along with signals from NH (δ 6.82, D_2O changeable) and NH_2 protons (δ 4.82, D_2O changeable). Treatment of a chloroform solution of **3** with aqueous ferricyanide afforded **4**. The mass spectrum of this latter compound, identified as the 2-methoxy-4-(2methoxyphenylimino)cyclohexa-2,5-dien-1-one, showed, along with the molecular ion peak at *m/e* 243, the characteristic peak at M + 2, i.e., *m*/2 245, typical of a

[1]Authors to whom correspondence may be addressed.

Can. J. Chem. Downloaded from www.nrcresearchpress.com by EESC ESCOLA DE ENGENHARIA on 09/08/12
For personal use only.

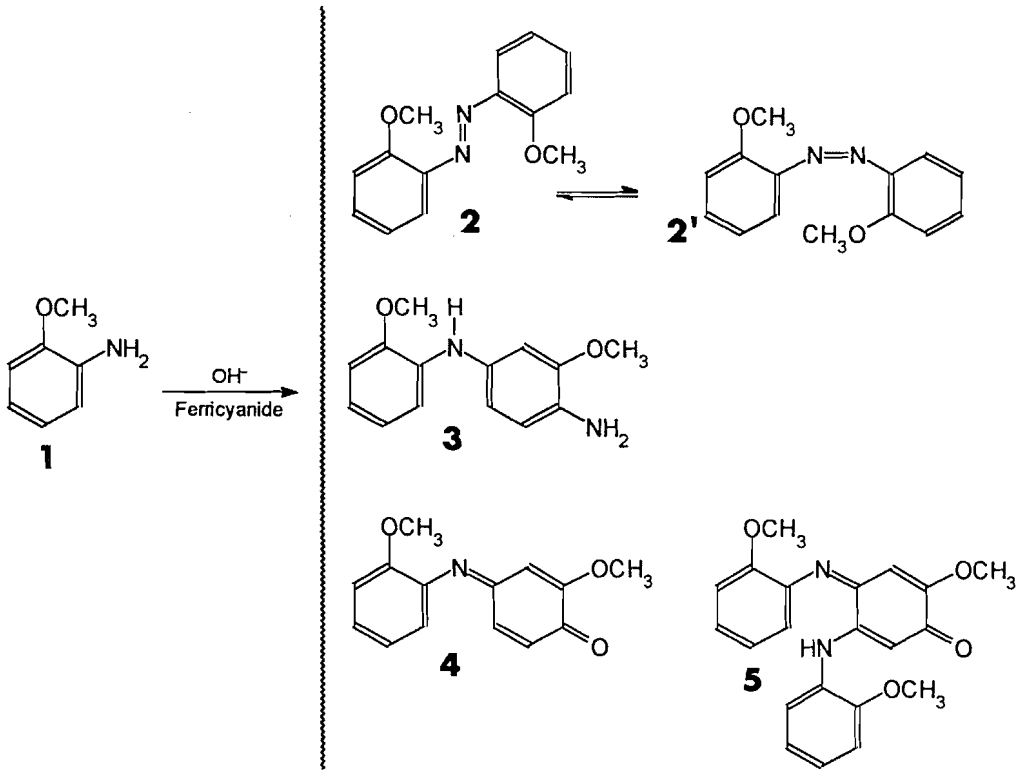

high-potential *p*-quinoneimine (8). The ^{1}H NMR signals at δ 6.11, 7.33, and 6.69 were assigned to the three protons of the quinonic ring, while the four protons of the aryliminic group were assigned the signals at δ 6.96, 7.21, 6.95, and 6.75, and the signals at δ 3.65 and 3.85 were attributed to the quinonic and aryliminic methoxy groups, respectively.

Also the mass spectrum of compound **5**, identified as the 2-methoxy-4-(2-methoxyphenylimino)-5-(2′-methoxyphenyl)-aminocyclohexa-2,5-dien-1-one, showed, beside the molecular ion peak at *m/e* 364, a peak at M + 2 (reduction peak), while the NMR spectrum exhibited signals for the two protons of the quinoneiminic ring (δ 6.23 and 5.76), the four protons of the arylimic ring (δ 7.46, 6.95, 7.89, and 7.00), the four protons of the arylaminic ring (δ 7.02, 7.20, 7.00, and 6.87), the three different methoxy groups (δ 3.62, 3.86, and 3.83), and a broad D_2O changeable singlet at δ 8.65 due to the NH group.

EPR studies

When the reaction between *o*-anisidine and potassium ferricyanide in alkaline water (pH 9) was carried out in a flat flow-cell inside the cavity of an EPR spectrometer and the spectra recorded within 500 ms of mixing, the broad signal shown in Fig. 1 was obtained. A well-fitting computer simulation of the signal, which was characterized by a *g*-factor of 2.0035, was obtained by assuming coupling of the unpaired electron with five different hydrogens and a nitrogen atom (a_H 1.5, a_H 2.5, a_H 6.2, a_H 8.2, a_H 12.8, a_N 7.8 gauss). On the basis of these spectral parameters, and by analogy with data available in the literature for the *ortho*-fluoro (9) and *ortho*-carbossiphenyl aminyl (10), the spectrum was attributed to the *o*-anisyl aminyl radical **A**.

When the flow of the reaction mixture through the flat cell inside the EPR cavity was interrupted, a rather persistent and very broad three-line spectrum (coupling with a single nitrogen, a_N 12.8 G, *g* 2.0059) appeared after ca. 5 min. This very simple signal must be due to a nitroxide originating in situ from oxidation of a reaction product (Fig. 2).

In an attempt to obtain aminyl **A** by a different method, a degassed benzene solution of amine **1** was continuously photolysed in the presence of di-*tert*-butyl peroxide. This resulted in the observation of a much better resolved spectrum than the one observed in aqueous alkaline solution, exhibiting a much

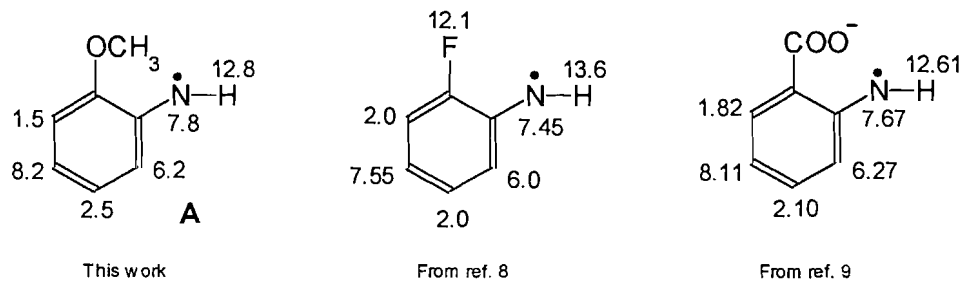

Hyperfine coupling constants for some arylaminyl radicals

Can. J. Chem. Downloaded from www.nrcresearchpress.com by EESC ESCOLA DE ENGENHARIA on 09/08/12
For personal use only.

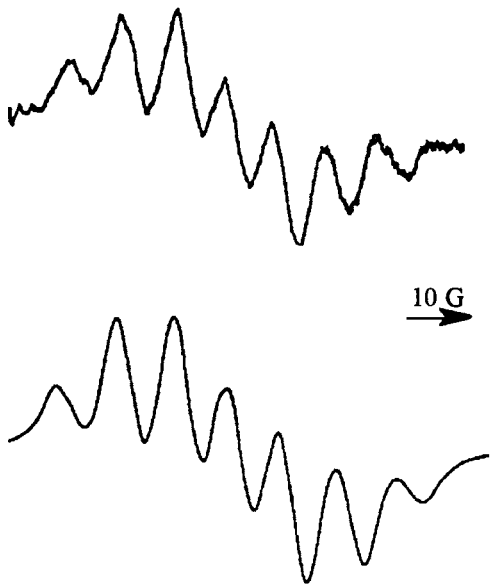

FIG. 1. Experimental and simulated EPR spectrum observed within 500 min from mixing of *o*-anisidine and ferricyanide in alkaline aqueous solution.

smaller overall splitting. Simulation of the spectrum indicated coupling of the unpaired electron with a set of two equivalent protons, in addition to two unequivalent protons and a nitrogen (a_{2H} 1.47, a_H 4.9, a_H 5.35, a_N 10.36 gauss). The spectrum cannot be due to the expected aminyl because the number of interacting nuclei, the values of the couplings, as well as the value of the measured *g*-factor (2.0043_9) are in agreement with an aryl(oxy)aminyl radical of type Ar(RO)N˙(11), and we therefore assign the observed spectrum to the *tert*-butoxy(2-methoxyphenyl)aminyl **B**.

The oxidation of *o*-anisidine also led to the observation of radical species, but again their spectra were not found indicative of an aminyl structure. Addition of a small amount of *meta*-chloroperbenzoic acid to a degassed benzene solution of compound **1** afforded a strong EPR signal due to a single radical species, which was identified as the *o*-anisyl nitroxide **C** on the basis of its spectral parameters, i.e., a_{2H} 0.95, a_{2H} 3.47, a_N 9.62, a_H 12.46, *g* 2.0060_0. A very similar spectrum still assigned to **C**, i.e., a_{2H} 1.01, a_H 3.6, a_H 3.7, a_N 10.32, a_H 13.03 G, *g* 2.0059_1, was obtained by reacting *o*-anisidine with hydrogen peroxide in acetic acid solution.

Treatment of compound **3** with *m*-chloroperbenzoic acid in benzene afforded a partially resolved EPR spectrum characterized by a *g*-factor of 2.0056 and by the following couplings: a_{3H} 0.22, a_{2H} 0.73, a_N 0.73, a_H 0.94, a_H 2.2, a_H 2.93, and a_H 10.78 G, which was attributed to radical **D**.

Discussion

In comprehensive studies of the oxidation of aromatic amines, Haynes and Hewgill (12, 13) reported that, contrary to the oxidation of phenols, no products arising from carbon–carbon coupling have ever been isolated. Indeeed, also in the present study on the oxidation of *o*-anisidine by ferricyanide, all the isolated products arise from nitrogen–nitrogen or nitrogen–carbon couplings whereas no occurrence of carbon–carbon coupling could be established.

Consistent with the formation of nitrogen-centred radicals in the oxidation of aniline with one-electron oxidizing agents in basic solutions (14), we propose the reaction sequence shown in Scheme 1 to account for the formation of the products isolated, **2–5**. Accordingly, oxidation of **1** would result in the initial formation of the aminyl radical **A**, which undergoes rapid nitrogen–nitrogen or nitrogen–carbon dimerization within the cage. The former process leads to the formation of hydrazo(2,2′-dimethoxy)benzene, which readily undergoes further oxidation to the isomeric *anti*, **2**, and *syn*, **2′**, 2,2′-dimethoxyazobenzenes representing the major reaction products. The *anti* isomer, by far the most abundant, could be partially converted to the *syn* by heating at 60°C in chloroform solution (*anti/syn* = 80/20 after 30 min, as determined by NMR); **2** ⇌ **2′** isomerization also took place under visible light irradiation either in chloroform solution or on silica gel plate. Nitrogen–carbon dimerization, on the other hand, takes place at the positions of higher spin density, resulting in the formation of 2-methoxy-4-(2-methoxyphenylamino)aniline **3**. While bielectronic oxidation of this compound, followed by hydrolysis of the resulting quinonediimine (not observed), may account for the formation of the quinoneimine **4**, monoelectronic oxidation would result in the diarylaminyl radical **D** whose coupling with aminyl **A** followed by bielectronic oxidation and hydrolysis would eventually afford compound **5**.

Although the mechanism outlined in the scheme accounts for the isolated products, it should be substantiated by additional evidence, such as the detection and identification of some of the intermediates. Indeed, the first, very short-lived radical observed in EPR experiments within 500 ms from the mixing of the reactant solutions can be assigned to the hypothesized aminyl on the basis of its spectral parameters. The observed spectrum was, however, characterized by a very large linewidth (see Fig. 2), and the values of the two *meta* couplings were obtained by computer simulation. As no EPR parameters are available for this radical in the literature, we tried to generate aminyl **A** through abstraction of an aminic hydrogen from *o*-anisidine by means of in situ photolytically generated *tert*-butoxyl radicals to gain further support for the assignment. The spectrum observed in this case was characterized by a higher *g* and by the absence of the α-hydrogen splitting and could be assigned to

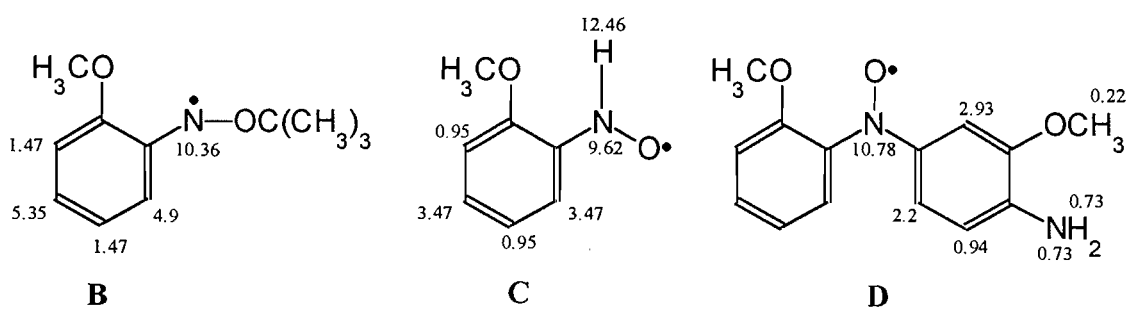

Can. J. Chem. Downloaded from www.nrcresearchpress.com by EESC ESCOLA DE ENGENHARIA on 09/08/12
For personal use only.

Can. J. Chem. Downloaded from www.nrcresearchpress.com by EESC ESCOLA DE ENGENHARIA on 09/08/12
For personal use only.

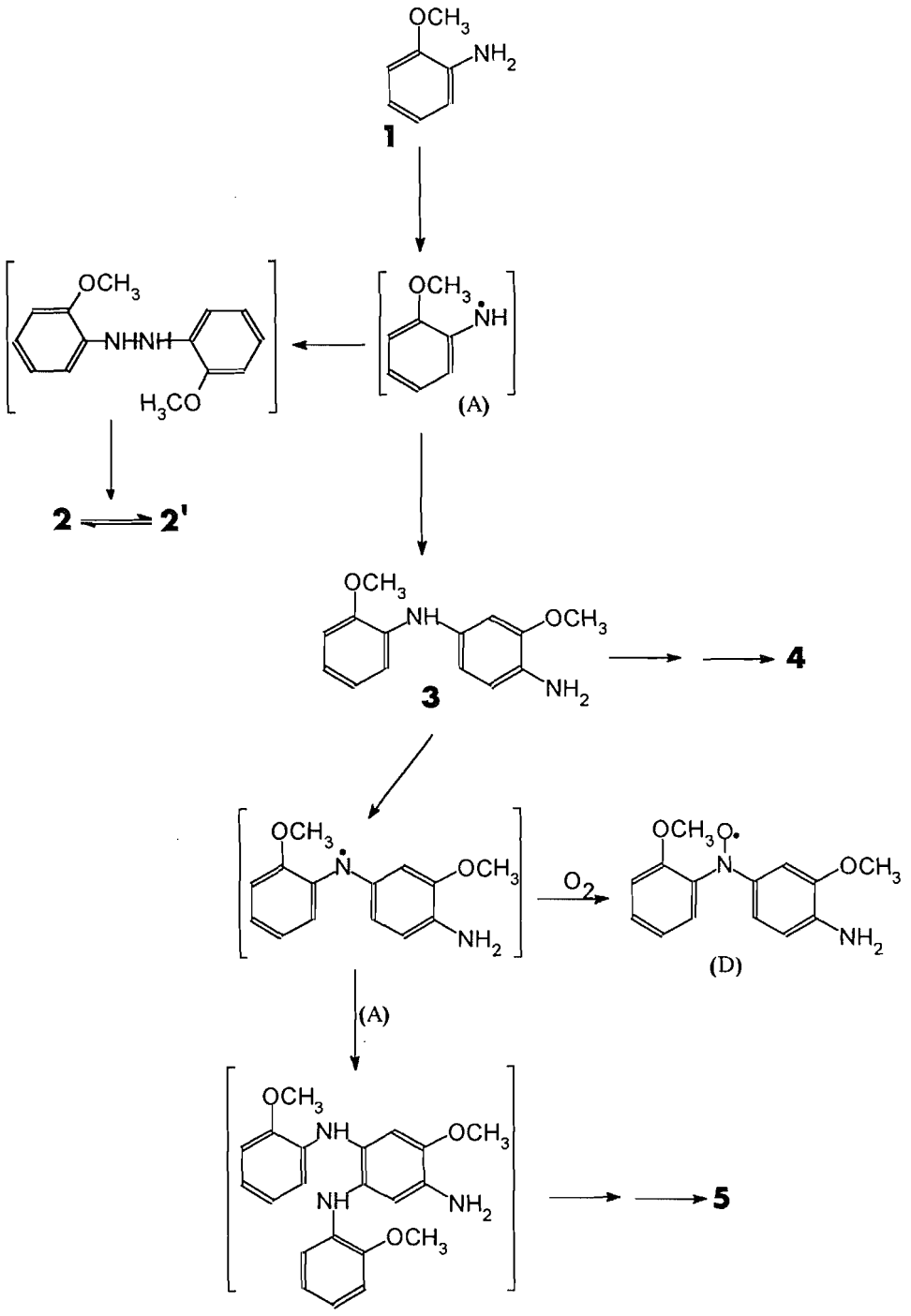

SCHEME 1

the *tert*-butoxyl aminyl **B**. The formation of this species can be explained by proposing hydrogen abstraction by $^tBuO^{\cdot}$ radicals with formation of the aminyl, which immediately couples with another *tert*-butoxy radical giving an intermediate compound that by further hydrogen abstraction produces **B**. Compound **1** did not react with PbO_2, while the anisylnitroxide **C** was formed with other oxidizing agents such as H_2O_2 or *m*-Cl-C_6H_4-CO_3H.

To find out whether the nitroxide reponsible for the broad three-line spectrum observed in the anisidine/ferricyanide system under static conditions could be originate from oxidation of **3**, we treated this compound with *meta*-chloroperbenzoic acid in benzene and obtained the spectrum shown in Fig. 3 together with its computer simulation.

The spectrum parameters indicate that the species responsible for this spectrum is a nitroxide; although it is also evident that the unpaired electron is delocalized onto just one aromatic ring, it is believed that the nitroxide can be identified as radical **D**: couplings with the two hydrogens and the nitrogen of an amino group and with the three hydrogens of a methoxy group are actually observed, whereas the lack of delocalization with the ring on the left might be explained in terms of steric hindrance that might force the anisyl moiety into a plane orthogo-

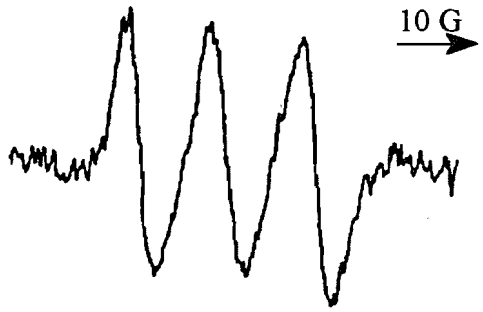

FIG. 2. EPR spectrum observed after 5 min from mixing *o*-anisidine and ferricyanide.

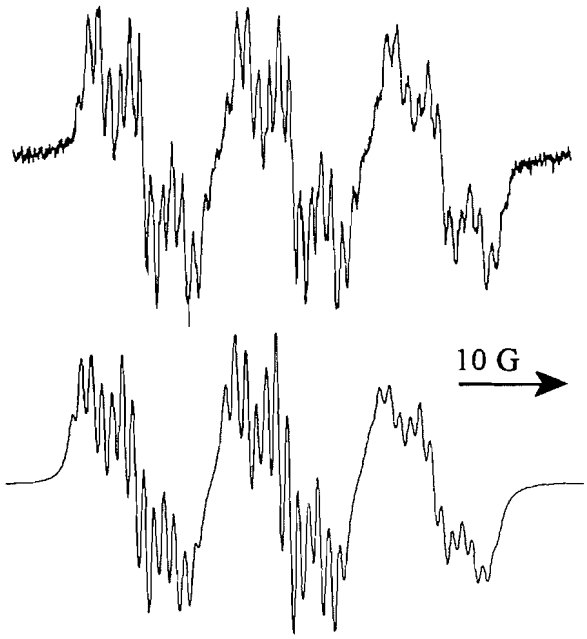

FIG. 3. Experimental and simulated spectra of nitroxide (D).

nal to that of the rest of the molecule, thus making spin delocalization impossible. It is hard to say whether nitroxide **D** is also responsible for the three-line spectrum mentioned above.

The *g*-values are the same in both cases, and the complex spectral pattern observed for **D** might explain the broad unresolved lines observed in the aqueous solution where dissolved oxygen is present. However, the nitroxyl nitrogen splitting is rather different in the two spectra, being markedly smaller in the "authentic" **D**. It should, however, be borne in mind that the nitrogen splitting in nitroxides is extremely sensitive to solvent (15), being larger in water, owing to hydrogen-bonding stabilization of structures characterized by large spin density on the nitrogen, than in apolar solvents such as benzene. Although it is not unambiguously proved that radical **D** is actually responsible for the broad spectrum observed in the oxidation of *o*-anisidine with ferricyanide in alkaline water under static conditions, we believe that our results do not contradict this possibility.

Conclusions

Oxidation of *ortho*-anisidine with potassium ferricyanide in alkaline water affords mainly *anti*-2,2′-dimethoxyazobenzene, together with a smaller amount of the *syn* isomer. No traces of carbon–carbon coupling compounds could be detected, other minor products being 2-methoxy-4-(2-methoxyphenylamino)aniline, 2-methoxy-4-(2-methoxyphenylimimo)-cyclohexan-2,5-dien-1-one, and 2-methoxy-4-(2-methoxyphenilimino)-5-(2′-methoxyphenyl)aminocyclohexa-2,5-dien-1-one. The nature of the observed products as well as EPR studies suggest a radical nature for the process. The *o*-anisyl aminyl is the first radical formed.

Experimental

Materials and product studies

ortho-Anisidine, potassium ferricyanide, di-*tert*-butyl peroxide, and *meta*-chloroperbenzoic acid were commercial chemicals.

The IR spectra were taken on a Perkin–Elmer IFT 1760-X spectrometer in chloroform. The ^{1}H NMR spectra, in deuterochloroform (reported in δ), were recorded on a Bruker 270 MHz spectrometer with Me_4Si as internal reference. Mass spectra were obtained with a VG ZAB 2F mass spectrometer (electron energy 70 eV, ion source temperature 250°C). UV spectra, in chloroform, were recorded with a Perkin–Elmer Lambda 7 spectrophotometer. Melting points were determined with a Kofler apparatus and are uncorrected. The purity of the compounds was checked by ascending TLC on Merck's precoated silica gel F-254 plates (0.25 mm) with fluorescent backing and the reported R_f are measured using chloroform as eluent.

Oxidation of o*-anisidine in alkaline medium*

To a solution of *o*-anisidine (**1**) 10 mmol in 20 mL of a water–methanol mixture (1:1, vv) an excess of a solution of potassium ferricyanide (40 mmol in 20 mL of water at pH 9) was added dropwise. After 2 h stirring, the mixture was extracted with chloroform. The organic layer was washed, dried, and analyzed chromatographically on silica gel plates (0.500 mm) using chloroform as eluent. Four fractions were isolated showing R_f 0.8, 0.7, 0.5, and 0.3, identified with compounds **2** (240 mg), **2′** (8 mg), **3** (9 mg), and **4** (162 mg), respectively.

anti *2,2′-Dimethoxyazobenzene (2)*

The compound was obtained as yellow crystals with mp 152–153°C; UV, λ_{max} (log ε): 312 (3.50), 368 (3.57), 460s; IR: 1615, 1250 cm^{-1}; ^{1}H NMR: 7.67 (2H, d, J_m = 1.6 Hz, J_o = 8.2 Hz), 7.40 (2H, t, J_m = 1.6 Hz, J_o = 8.2 Hz), 7.06 (2H, d, J_m = 1.6 Hz, J_o = 8.2 Hz), 6.99 (2H, t, J_m = 1.6 Hz, J_o = 8.2 Hz), 4.00 (6H, s); MS: 242 (M^+), 107. Anal. calcd. for $C_{14}H_{14}N_2O_2$: C 69.40, H 5.83, N 11.56; found: C 69.43, H 5.81, N 11.58.

syn *2,2′-Dimethoxyazobenzene (2′)*

The compound was obtained as pale-yellow crystals with mp 153–155°C; UV, λ_{max} (log ε): 312 (3.45), 360 (3.75); IR: 1615, 1250 cm^{-1}; ^{1}H NMR: 7.12 (2H, t, J_m = 1.5 Hz, J_o = 8.1 Hz), 6.83 (2H, d, J_m = 1.5 Hz, J_o = 8.1 Hz), 6.73 (2H, t, J_m = 1.5 Hz, J_o = 8.1 Hz), 6.57 (2H, d, J_m = 1.5 Hz, J_o = 8.1 Hz), 3.76 (6H, s); MS: 242 (M^+), 107. Anal. calcd. for $C_{14}H_{14}N_2O_2$: C 69.40, H 5.83, N 11.56; found: C 69.40, H 5.80, N 11.57.

2-Methoxy-4-(2-methoxyphenylimino)cyclohexa-2,5-dien-1-one (3)

The compound **3** was isolated as orange crystals with mp >250°C; UV, λ_{max} (log ε): 348 (3.47), 479 (3.45) nm; IR: 1680, 1245 cm^{-1}; ^{1}H NMR: 7.33 (1H, d, J_m = 2.3 Hz, J_o = 8.7 Hz), 7.21 (1H, t), 6.96 (1H, d), 6.95 (1H, t), 6.75 (1H, d), 6.69 (1H, d, J_o = 8.7), 6.11 (1H, s, J_m = 2.3 Hz); MS: 243 (M^+), 245 (M + 2). Anal. calcd. for $C_{14}H_{13}NO_3$: C 69.12, H 5.39, N 5.76; found: C 69.09, H 5.40, N 5.74.

2-Methoxy-4-(2-methoxyphenylimino)-5-(2′-methoxyphenyl)-aminocyclohexa-2,5-dien-1-one (4)

The compound was isolated as purple crystals with mp 101–102°C; UV, λ_{max} (log ε): 458 (3.81) nm; IR: 3300, 1680, 1245 cm^{-1}; ^{1}H NMR: 8.65 (1H, bs), 7.89 (1H, t), 7.46 (1H, d), 7.20 (1H, t), 7.02 (1H, d), 7.00 (2H, d + t), 6.95 (1H, t), 6.87 (1H, d), 6.23 (1H, s), 5.76 (1H, s), 3.86 (3H, s), 3.83 (3H, s), 3.62 (3H, s); MS: 364 (M^+), 366 (M + 2). Anal. calcd. for $C_{21}H_{20}N_2O_4$: C 69.22, H 5.53, N 7.68; found: C 69.29, H 5.51, N 5.70.

EPR studies

Can. J. Chem. Downloaded from www.nrcresearchpress.com by EESC ESCOLA DE ENGENHARIA on 09/08/12
For personal use only.

EPR studies

EPR spectra were recorded at room temperature either on a Varian E-9 spectrometer equipped with a Stelar Prometheus data system for acquisition and handling of the data, or on a Bruker ER 200 D spectrometer equipped with a Bruker 3220 data system, an NMR gaussmeter for field calibration, and a Systron Donner frequency counter for the determination of g-factors. The latter were calibrated with respect to that of the perylene radical cation in concentrated sulphuric acid. Where necessary, the EPR cavity was irradiated with the light from a high-pressure 1-kW mercury lamp.

Rapid flow experiments were carried out by allowing two pump-driven solutions to mix immediately before the flat section of the EPR cell. The mixture reached the central part of the cell in 50–500 ms.

Acknowledgment

We are grateful to Dr. C. Chatgilialoglu for the helpful discussions. We also thank the Centro di Metodologie Chimico Fisiche of the University of Naples for the NMR spectra and M.U.R.S.T. (Rome) for financial support.

1. A. Butenandt and W. Schäfer. *In* Recent progress in the chemistry of natural and synthetic matters and related fields. Academic Press, New York. 1962. p. 25.
2. W. Schäfer. Prog. Org. Chem. **6**, 135 (1964).
3. K.T. Finley. *In* The chemistry of quinonoid compounds. Part II. *Edited by* S. Patai. J. Wiley, New York. 1974.
4. J.F. Corbett. J. Chem. Soc. (B), 1418 (1970).
5. J.F. Corbett. J. Chem. Soc. (B), 827 (1969).
6. A. Bolognese, R. Bonomo, R. Chillemi, and S. Sciuto. J. Heterocycl. Chem. **27**, 2207 (1990).
7. A. Bolognese and G. Musci. Gazz. Chim. Ital. **121**, 241 (1991).
8. K.P. Zeller and R. Muller. *In* The chemistry of quinonoid compounds. Part 1. *Edited by* S. Patai. J. Wiley and Sons, New York. 1988.
9. M.L. Kaplan, M.L. Maniona, and H.D. Roth. J. Phys. Chem. **78**, 1837 (1974).
10. P. Neta and R.W. Fessenden. J. Phys. Chem. **78**, 523 (1974).
11. F.A. Neugebauer. *In* Landolt-Bornstein, New Series. Vol. 9. Part c1. *Edited by* K.-H. Hellweg. Springer Verlag, Berlin. 1979, and references therein.
12. R.K. Haynes and F.R. Hewgill. J. Chem. Soc. Perkin Trans. 1, 396 (1972).
13. R.K. Haynes and F.R. Hewgill. J. Chem. Soc. Perkin Trans. 1, 813 (1972).
14. D.H. Roseblatt and E.P. Burrow. The chemistry of amino, nitroso and nitro compounds. Part II. Supp. F. *Edited by* S. Patai. J. Wiley, New York. 1982.
15. A.R. Forrester. *In* Landolt-Bornstein, New Series. Vol 9. Part c1. *Edited by* K.-H. Hellweg. Springer Verlag, Berlin. 1979, and references therein.

Can. J. Chem. Downloaded from www.nrcresearchpress.com by EESC ESCOLA DE ENGENHARIA on 09/08/12
For personal use only.

Synthèses de diallylamines et triallylamines à partir des 3-acetoxy-3-aryl-2-méthylène propionitriles et des 3-acétoxy-3-aryl-2-méthylène propionates de méthyle

MOHAMED AKSSIRA ET FARID EL GUEMMOUT
Faculté des Sciences de Tetouan, Maroc

ET

PATRICK BAUCHAT ET ANDRÉ FOUCAUD[1]
Groupe de physicochimie structurale associé au Centre national de la recherche scientifique, Université de Rennes, Campus de Beaulieu, 35042 Rennes, France

Reçu le 3 juin 1993

MOHAMED AKSSIRA, FARID EL GUEMMOUT, PATRICK BAUCHAT et ANDRÉ FOUCAUD. Can. J. Chem. **72**, 1357 (1994).

Les réactions des 3-acétoxy-3-aryl-2-méthylène propionitriles **1** avec l'ammoniac donnent les diallylamines **3***ZZ* correspondantes. La réaction de **1** avec une allylamine primaire ou avec l'éthylène diamine donne la diallylamine **11** ou **13***ZZ*. Le traitement des 3-acétoxy-3-aryl-2-méthylène propionate de méthyle **2** avec l'isopropylamine ou l'éthylène diamine donne les allylamines **6***EE*, **14** ou **15**, mais la réaction de **2** avec l'ammoniac donne seulement les triallylamines **4***EEE* avec de bons rendements.

MOHAMED AKSSIRA, FARID EL GUEMMOUT, PATRICK BAUCHAT, and ANDRÉ FOUCAUD. Can. J. Chem. **72**, 1357 (1994).

The reactions of 3-acetoxy-3-aryl-2-methylene propionitriles **1** with ammonia yielded the corresponding diallylamines **3***ZZ*. The reaction of **1** with a primary allylamine or with ethylene diamine gave the diallylamine **11** or **13***ZZ*. The treatment of methyl 3-acetoxy-3-aryl-2-methylene propionates **2** with isopropylamine or ethylene diamine gave the allylamines **6***EE* or **14** and **15**, but the reaction of **2** with ammonia gave only the triallylamines **4***EEE* in good yields.

Introduction

Les groupements aminoallyliques existent dans de nombreux composés naturels (1) et les allylamines sont des composés biologiquement importants (2–4). Diverses méthodes de synthèses des allylamines ont été développées (5–7) mais les voies d'accès aux diallylamines restent limitées (8–10). Nous avons décrit la préparation de monoallylamines primaires ou secondaires à partir des 3-acyloxy 2-méthylène propionates de méthyle **2** (11). Nous rapportons dans ce mémoire la synthèse stéréosélective de diallylamines et triallylamines qui présentent, en β de l'atome d'azote, un groupement nitrile ou ester.

Résultats et discussion

Les matériaux de départ **1** et **2** sont aisément obtenus par la réaction, en présence de diazabicyclooctane, d'un aldéhyde avec l'acrylonitrile pour **1**, ou avec l'acrylate de méthyle pour **2** (réaction de Baylis–Hillman (12)) suivie de l'acétylation par le chlorure d'acétyle de l'alcool obtenu (11).

La réaction d'un excès d'ammoniaque, en solution aqueuse, avec les nitriles **1***a–c* dans le méthanol, à la température ambiante, donne les diallylamines **3***a–c* (schéma 1). Dans les mêmes conditions, les esters **2** donnent uniquement les amines tertiaires **4** (schéma 2). Les diallylamines intermédiaires **5** ne sont pas obtenues, même lorsque la température reste voisine de 0°C.

Ces résultats suggèrent que l'état de transition dans la réaction d'addition de l'amine **5** sur l'ester **2** est bien solvaté par chélation des carbonyles des groupements esters avec le groupement NH (liaison H à trois centres) (13). Il en résulte que la vitesse d'addition de **5** sur **2** pour donner **4** devient plus grande que la vitesse de formation de **5** (14). Cet intermédiaire **5** ne peut donc pas être isolé.

Les diallylamines tertiaires **6** sont obtenues en traitant 2 équivalents d'esters **2** avec 3 équivalents d'isopropylamine

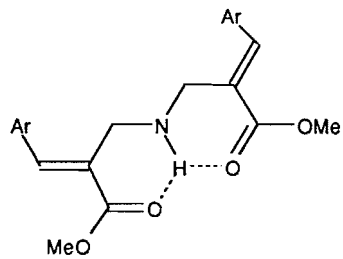

5

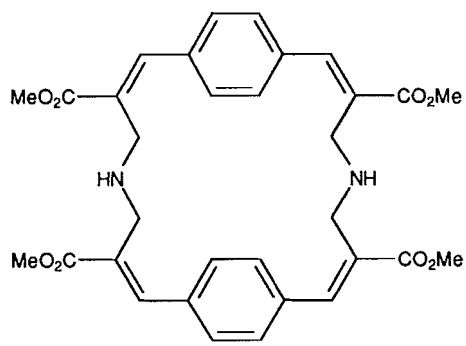

8

dans le tetrahydrofurane (l'amine en excès neutralise l'acide acétique formé). La réaction des esters **2** avec un excès d'isopropylamine conduit aux allylamines **7** (11). La chélation entre le groupement NH et le carbonyle de l'ester est observée dans le spectre infrarouge des composés **7** (ν_{NH} = 3340 cm^{-1}, fréquence indépendante de la concentration de **7** dans le tétrachlorure de carbone) (schéma 2). Le paracyclophane **8**, qui a été isolé (15), comprend des motifs analogues à **5**, dont l'encombrement

1. Auteur à qui adresser toute correspondance. Tél. : 99 28 62 72. Télécopie : 99 28 67 38.

Can. J. Chem. Downloaded from www.nrcresearchpress.com by EESC ESCOLA DE ENGENHARIA on 09/08/12
For personal use only.

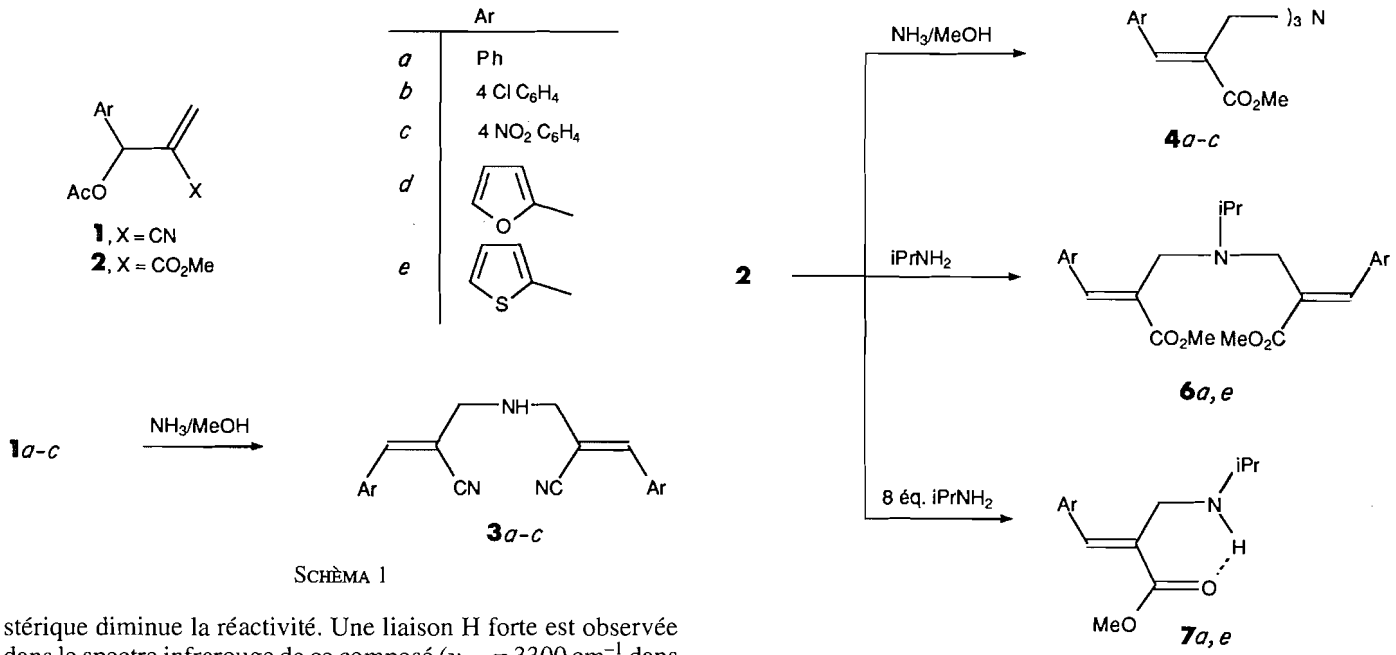

SCHÈMA 1

SCHÈMA 2

stérique diminue la réactivité. Une liaison H forte est observée dans le spectre infrarouge de ce composé (ν_{NH} = 3300 cm^{-1} dans $CHCl_3$), ce qui est en faveur de l'existence de liaison H dans **5**.

Cette réactivité particulière des amines intermédiaires **5** peut être mise à profit pour préparer les triallylamines dissymétriques **9** et **10** par la réaction des amines primaires **12** (11) avec les esters **2** (schéma 3). Lorsque **12***d* est traité par **1***a*, la diallylamine **11** est effectivement obtenue. Contrairement à la diallylamine **5**, ce composé **11** ne réagit pas sur **2***a* dans les conditions utilisées. Ce résultat confirme l'importance de la présence de deux groupements esters pour accélérer la réaction de **5** avec les esters **2**.

La réaction d'un équivalent d'éthylènediamine dans le THF avec un équivalent de nitrile **1** ou d'ester **2** conduit aux allylamines **13** ou **14**. En utilisant deux équivalents d'ester **2**, le composé **15** est obtenu (schéma 4).

Les structures des composés sont établies à partir des données de RMN. En particulier les spectres de RMN ^{13}C montrent une constante de couplage à longue distance entre le carbone du groupement nitrile et le proton vinylique de ^3J = 14,5 Hz pour les composés **3**, **11** et **13**, ce qui est en accord avec une configuration *Z* de la double liaison (16).

Les spectres de RMN ^1H des composés **4**, **6**, **9**, **10**, **14** et **15** montrent un signal du proton vinylique, déblindé par le groupement ester voisin en position *cis*, vers δ = 7,40–8,05, en accord avec la littérature (17–20). Deux isomères *EE* et *EZ* du composé **6***a* sont obtenus dans le rapport *EE* : *EZ* = 68 : 32. Le proton vinylique en *trans* du groupement ester pour **6***a EZ* est à δ = 6,62 et les protons vinyliques en *cis* du groupement ester dans **6***a EE* et **6***a EZ* sont à δ = 7,67–7,74.

Ainsi les nitriles **1** conduisent, en général de façon exclusive ou très prépondérante, aux allylamines *Z*, alors que les esters **2**

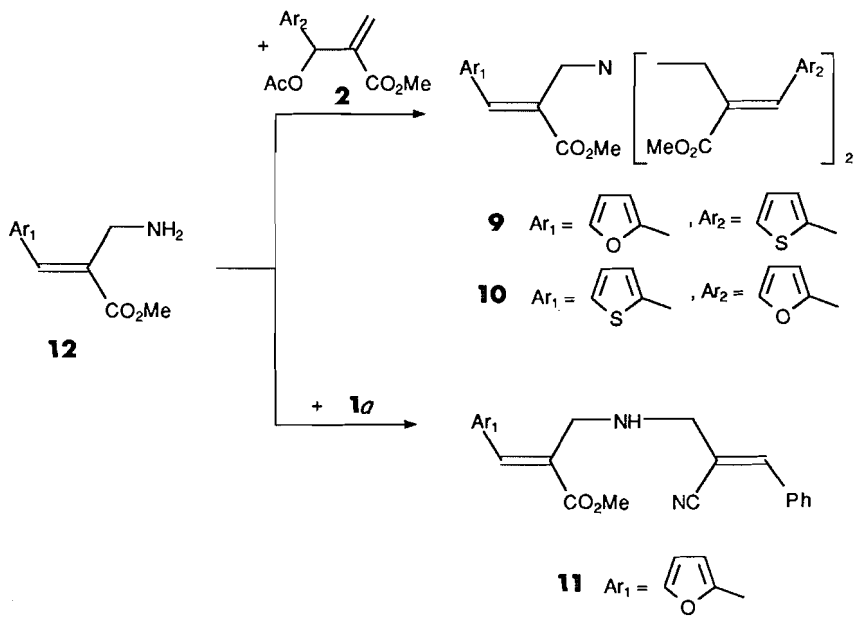

SCHÈMA 3

Can. J. Chem. Downloaded from www.nrcresearchpress.com by EESC ESCOLA DE ENGENHARIA on 09/08/12
For personal use only.

Can. J. Chem. Downloaded from www.nrcresearchpress.com by EESC ESCOLA DE ENGENHARIA on 09/08/12
For personal use only.

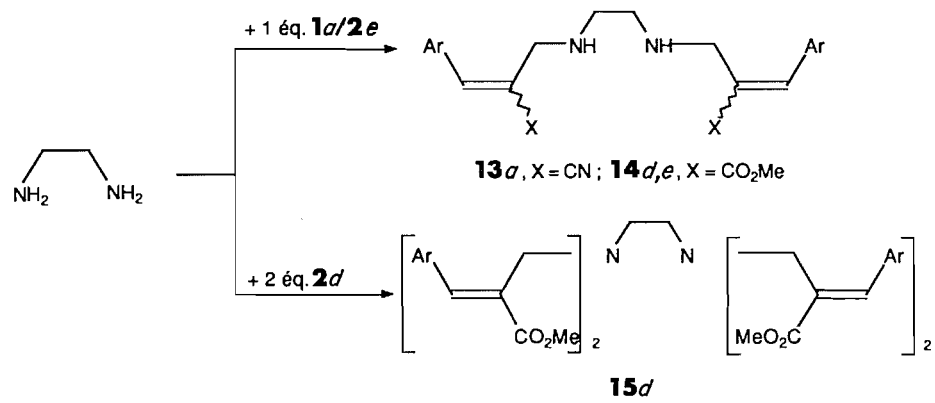

SCHÈMA 4

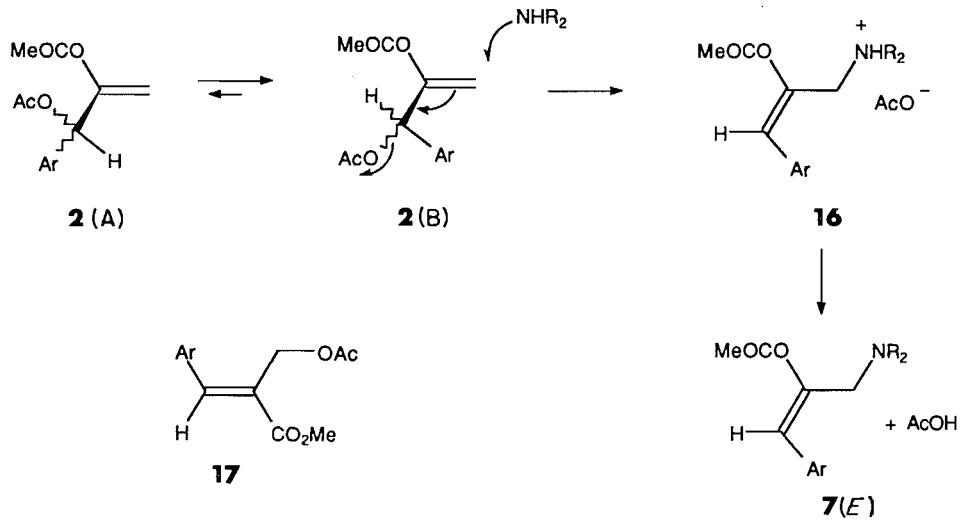

SCHÈMA 5

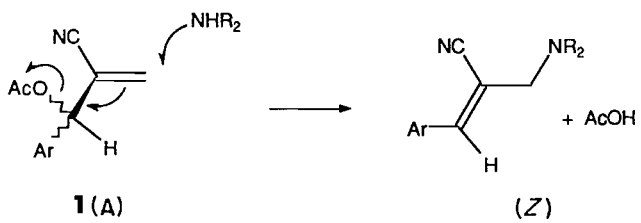

SCHÈMA 6

donnent les isomères *E* (sauf pour **6***a* où les isomères *EE* et *EZ* sont obtenus). Cette stéréochimie pourrait s'expliquer par les mécanismes présentés dans les schémas 5 et 6.

L'ester **2** possède une conformation privilégiée **2** (B) (schéma 5), qui conduira, par un état de transition où les intéractions stériques entre les groupements CO_2Me et Ar sont faibles, au sel **16** qui est déprotoné pour donner **7***E*. Un sel analogue à **16** a été proposé comme intermédiaire lors de l'isomérisation des esters **2** en acétate **17** catalysée par le diazabicyclo octane (11). La déprotonation de **16** est un processus plus rapide que la transformation de **16** en acétate **17**. L'acétate **17** n'est donc probablement pas un intermédiaire dans la formation de **7**. Les exigences stériques du groupement nitrile étant faibles, **1** (A) représente une conformation privilégiée qui conduira à l'isomère *Z* (schéma 6).

En conclusion, nous avons précisé les limites d'utilisation d'une méthode simple de synthèse de diallylamines qui comportent un groupement électroattracteur en β du groupement amino. À partir des nitriles **1**, on obtient les diallylamines secondaires *Z,Z*. À partir des esters **2**, il n'est pas possible d'isoler les diallylamines secondaires, leur réactivité vis à vis des esters **2** étant trop importante. On peut cependant préparer, à partir de **2**, les diallylamines tertiaires *E,E* ou les triallylamines, *E,E,E*.

Partie expérimentale

Les spectres RMN ont été enregistrés à 300 MHz (^{1}H) et 75,4 MHz (^{13}C) avec un spectromètre Bruker AC 300 (solvant $CDCl_3$). Les spectres de masse sont obtenus avec un spectromètre Varian MAT 311 à 70 eV et les spectres infrarouge sont enregistrés avec un spectromètre Perkin Elmer 1420. Les analyses élémentaires ont été effectuées au Laboratoire Central de Microanalyse du CNRS (Lyon). Les points de fusion sont pris à l'aide d'un banc chauffant Kofler.

Diallylamines 3 and triallylamines 4

À une solution de **1** ou **2** (5 mmol) dans le méthanol (10 mL) est ajouté goutte à goutte, sous agitation et à la température ambiante, un mélange d'une solution aqueuse de NH_3 à 28% (1 mL) et de méthanol (5 mL). Après agitation à la température ambiante pendant 10 h, le méthanol est évaporé. Le résidu est dissous dans le chloroforme (50 mL) et extrait à l'eau (2 × 20 mL). La phase organique est séchée (Na_2SO_4) et évaporée. Les produits **3** ou **4** cristallisent.

Di-(2-cyano-3-phényl-2-propényl) amine **3**a Z. *F* = 73°C ($CHCl_3$), 50%. IR (Nujol) ν : 2210, 3320 cm^{-1}. RMN ^{1}H, δ : 1,85 (s, 1H), 3,60 (s, 4H); 7,12 (s, 2H), 7,3–7,5 (m, 6H), 7,6 – 7,9 (m, 4H). RMN ^{13}C, δ : 52,02, 109,51 (C-2), 118,38 (dt, *J* = 14,6, 4,3 Hz, C≡N), 128,95,

Can. J. Chem. Downloaded from www.nrcresearchpress.com by EESC ESCOLA DE ENGENHARIA on 09/08/12
For personal use only.

128,98, 130,60, 133,12, 144,16 (C-3). SMHR trouvé : 299,1431; calc. pour $C_{20}H_{17}N_3$: 299,1424. Anal. calc. pour $C_{20}H_{17}N_3$: C 80,27, H 5,69, N 14,04; trouvé : C 80,31, H 5,51, N 14,26.

Di(2-cyano-3-(4′-chlorophényl)-2-propénylamine ***3***b Z. F = 69°C (CCl_4), 61%. IR (Nujol) ν : 2210, 3318 cm^{-1}. RMN ^1H, δ : 2,00 (s, 1H) : 3,70 (s, 4H), 7,36 (s, 2H), 7,36–7,82 (m, 8H). RMN ^{13}C, δ : 51,56, 111,20 (C-2); 118,32 (dt, J = 14,6, 4,7 Hz, C≡N), 128,86, 130,09, 132,20, 134,60, 142,41 (C-3). SMHR trouvé : 367,0607; calc. pour $C_{20}H_{15}N_3{}^{35}Cl_2$: 367,0643. Anal. calc. pour $C_{20}H_{15}N_3Cl_2$: C 65,24, H 4,10, N 11,41; trouvé : C 65,34, H 4,17, N 11,46.

Di(2-cyano-3-(4′-nitrophényl)-2-propénylamine ***3***c Z. F = 132°C ($CHCl_3$), 80%. IR (Nujol) ν : 2215, 3360 cm^{-1}. RMN ^1H, δ : 1,80 (s, 1H), 3,70 (s, 4H), 7,32 (s, 2H), 7,27–7.90 (m, 8H). RMN ^{13}C, δ : 51,60, 114,96 (C-2), 117,93 (dt, ^3J = 14,5, 4,6 Hz, C≡N), 123,98, 129,56, 139,82, 141,94 (C-3), 143,62. SMHR trouvé : 389,1160; calc. pour $C_{20}H_{15}N_5O_4$: 389,1123. Anal. calc. pour $C_{20}H_{15}N_5O_4$: C 61,69, H 3,88, N 17,98; trouvé : C 61,49, H 3,97, N 17,93.

Tri(2-methoxycarbonyl-3-phenyl-2-propényl) amine ***4***a E. F = 160°C (MeOH), 95%. RMN ^1H, δ : 3,57 (s, 6H), 3,67 (s, 9H), 7,18 (m, 9H), 7,61 (m, 6H), 7,90 (s, 3H). RMN ^{13}C, δ : 50,69, 52,13, 128,44, 128,99 (C-2), 129,33, 130,77, 134,82, 143,73 (C-3), 169,17 (C=O). Anal. calc. pour $C_{33}H_{33}NO_6$: C 73,47, H 6,12; trouvé : C 73,29, H 6.23.

Tri(2-méthoxycarbonyl-3-(4′-chlorophényl)-2-propényl) amine ***4***b E. F = 152°C (MeCN), 90%. RMN ^1H, δ : 3,45 (s, 6H), 3,63 (s, 9H), 7,07–7,50 (m, 12H), 7,80 (s, 3H). RMN ^{13}C, δ : 50,67, 52,28, 128,76, 129,44 (C-2), 129,45, 133,12, 135,53, 142,33 (C-3), 168,77 (C=O). Anal. calc. pour $C_{33}H_{30}NO_6Cl_3$: C 61,63, H 4,67; trouvé : C 61,50, H 4,72.

Tri(2-méthoxycarbonyl-3-(4′-nitrophényl)-2-propényl) amine ***4***c E. F = 180°C (MeOH), 90%. RMN ^1H, δ : 3,56 (s, 6H), 3,86 (s, 9H), 7,66–8,22 (m, 15H). Anal. calc. pour $C_{33}H_{30}N_4O_{12}$: C 58,75, H 4,45; trouvé : C 58,81, H 4,32.

Diallylamines ***6***

À une solution de **2** (5 mmol) dans le THF (15 mL), on ajoute l'isopropylamine (0,59 g, 10 mmol). La solution est agitée à la température ambiante pendant 30 min. Le solvant est évaporé sous vide. Le résidu est dissous dans l'éther éthylique (50 mL). Cette solution est lavée à l'eau (2 × 30 mL); la phase organique est séchée (Na_2SO_4) puis évaporée. Les amines **6** sont purifiées par cristallisation ou distillation.

Isopropyl di(2-methoxycarbonyl-3-phenyl-2-propényl) amine ***6***a

$Eb_{0,02}$ = 220°C, 40% : mélange d'isomères *EE* et *EZ* dans le rapport 67 : 33. L'isomère ***6****a EE* cristallise.

6*aEE* : 114°C. RMN ^1H, δ : 0,90 (d, 6H, J = 6 Hz), 2,90 (m, 1H), 3,42 (s, 4H), 3,70 (s, 6H), 7,30 (m, 10H), 7,67 (s, 2H). SMHR trouvé : 407,2075; calc. pour $C_{25}H_{29}NO_4$: 407,2096.

6*aEZ* (isomère non purifié) : RMN ^1H, δ : 1,02 (d, 6H, J = 6Hz), 2,90 (m, 1H), 3,31 (d, 2H, J = 1 Hz), 3,52 (s, 3H), 3,60 (s, 2H), 3,77 (s, 3H), 6,62 (t, 1H, J = 1 Hz), 7,47 (m, 10H), 7,74 (s, 1H).

Isopropyl di(3-(2′-furyl)-2-methoxycarbonyl-2-propényl) amine ***6***dEE. F = 92°C (hexane), 93%. RMN ^1H, δ : 1,05 (d, 6H, J = 7 Hz), 2,90 (m, 1H), 3,67 (s, 10H, OCH_3, CH_2), 6,27 (m, 2H), 6,65 (m, 2H), 7,35 (s, 2H), 7,48 (m, 2H). RMN ^{13}C, δ : 17,81, 46,39, 49,98, 51,67, 111,93, 116,21, 127,11 (C-3), 127,90 (C-2), 144,12, 151,28, 169,23. SMHR trouvé : 387,1669; calc. pour $C_{21}H_{25}NO_6$: 287,1681. Anal. calc. pour $C_{21}H_{25}NO_6$: C 65,12, H 6,46; trouvé : C 65,20, H 6,70.

Isopropyl di(2-methoxycarbonyl-3-(2′-thienyl)-2-propényl) amine ***6***eEE. F = 129°C (MeCN), 73%. RMN ^1H, δ : 1,05 (d, 6H, J = 7 Hz), 2,97 (m, 1H), 3,61 (s, 6H), 3,64 (s, 4H), 7,00 (m, 2H), 7,32 (m, 4H), 7,75 (s, 2H). RMN ^{13}C, δ : 17,96, 46,05, 50,49, 51,68, 127,17, 128,23 (C-2), 129,26, 133,27 (C-3), 133,28, 137,93, 169,13. Anal. calc. pour $C_{21}H_{25}O_4NS_2$: C 60,11, H 6,00, N 3,34, S, 15,28; trouvé : C 60,10, H 6,03, N 3,41, S 15,18.

Allylamines ***9****,* ***10*** *et* ***11***

À une solution d'amine **12** (11) (5 mmol) dans le THF (20 mL), on ajoute une solution d'ester **2** ou de nitrile **1***a* (2,5 mmol), dans le THF (10 mL).

Le mélange est porté à reflux sous agitation pendant 1 h (cas de la réaction avec **2**) ou agité 4 h à la température ambiante (cas du nitrile **1***a*). Le solvant est évaporé sous pression réduite. Les composés **9**, **10** ou **11** cristallisent.

Di[2-methoxycarbonyl-3-(2′-thienyl)-2-propényl] [3-(2′-furyl)-2-methoxycarbonyl-2-propényl] amine ***9***. F = 122°C ($CHCl_3$–CCl_4), 76%. RMN ^1H, δ : 3,58 (s, 10H), 3,70 (s, 3H), 3,78 (s, 2H), 6,37 (m, 1H), 6,70 (m, 1H), 6,95 (m, 1H), 7,37–7,52 (m, 7H), 7,93 (s, 2H). RMN ^{13}C, δ : 49,77, 50,10, 51,57, 51,58, 112,31, 118,14, 125,35, 124,63, 127,52, 127,98, 130,88, 134,32, 134,92, 136,85, 145,87, 150,28, 167,96, 167,97. Anal. calc. pour $C_{27}H_{27}NO_7S_2$ + 1/2 CCl_4 : C 53,40, H 4,37, N 2,27, S 10,36; trouvé : C 53,44, H 4,48, N 2,37, S 10,34. Lors de la cristallisation, une mole de CCl_4 est piégée par deux moles de **9**.

Di[3-(2′-furyl)-2-methoxycarbonyl-2-propényl] [2-methoxycarbonyl-3-(2′-thienyl)-2-propényl] amine ***10***. F = 152°C (CCl_4–$CHCl_3$), 75%. RMN ^1H, δ : 3,56 (s, 6H), 3,63 (s, 3H), 3,67 (s, 2H), 3,75 (s, 4H), 6,39 (dd, 2H, J = 3 et 2 Hz), 6,70 (d, 2H, J = 3 Hz), 6,92 (d, 1H, J = 2 Hz), 7,39 (m, 2H), 7,51 (d, 2H, J = 2 Hz), 7,54 (s, 2H), 7,93 (s, 1H). RMN ^{13}C, δ : 50,36, 50,71, 51,80, 51,84, 111,89, 116,97, 126,10, 126,90, 126,66, 127,32, 128,47, 129,53, 134,67, 137,89, 144,73, 151,19, 169,17, 169,18. Anal. calc. pour $C_{27}H_{27}NO_8S$ + 1/2 CCl_4 : C 54,81, H 4,49, N 2,36, S 5,32; trouvé : C 54,78, H 4,56, N 2,37, S 5,22. Comme pour le composé **9**, une mole de CCl_4 est piégée par deux moles de **10** à l'état cristallisé.

[2-Cyano-3-phenyl-2Z-propényl] [3-(2′-furyl)-2-methoxycarbonyl-2E-propényl] amine ***11***. F = 77°C (CCl_4), 60%. IR, ν : 1685, 2220 cm^{-1}. RMN ^1H, δ : 2,28 (s, 1H), 3,59 (d, 2H, J = 1 Hz), 3,80 (s, 3H), 3,95 (s, 2H), 6,46 (dd, 1H, J = 2 Hz et 3 Hz), 6,68 (d, 1H, J = 3 Hz), 7,09 (s, 1H), 7,40 (m, 3H), 7,46 (d, 1H, J = 2 Hz), 7,50 (s, 1H), 7,72 (m, 2H). RMN ^{13}C, δ : 44,25, 52,20, 52,82, 110,30, 112,30, 117,52, 118,58 (dt, ^3J = 15 Hz; 4,5 Hz, C≡N), 125,82, 127,80, 128,80, 128,81, 130,21, 133,45, 143,93, 145,33, 150,78, 168,43. SMHR trouvé : 322,1334; calc. pour $C_{19}H_{18}N_2O_3$: 322,1317. Anal. calc. pour $C_{19}H_{18}N_2O_3$: C 70,79, H 5,62, N 8,69; trouvé : C 70,63, H 5,67, N 8,80.

Réactions du nitrile ***1*** *et des esters* ***2*** *avec l'éthylène diamine*

À une solution de **1** ou **2** (5 mmol) dans le THF (10 mL), est ajoutée sous agitation, goutte à goutte, une solution d'éthylène diamine (5 mmol, 0,3 g pour préparer **13** et **14**; 2,5 mmol, 0,15 g, pour préparer **15**) dans le THF (5 mL). Le mélange est agité 1 h à la température ambiante puis traité comme précédemment.

N,N′-Di(2-cyano-3-phenyl-2-propényl) éthylène diamine ***13***a. 58%. Mélange de deux isomères ***13****aZZ* et ***13****aEE*, non séparés, dans le rapport ***13****aZZ* : ***13****aEE* = 5,4 : 1.

13*aZZ*. RMN ^1H, δ : 2,50 (s, 2H), 2,77 (s, 4H), 3,39 (s, 4H), 7,35 (s, 2H), 7,49 (s, 6H), 7,73 (s, 4H). RMN ^{13}C, δ : 47,67, 53,84, 110,27 (C-2), 118,48 (dt, ^3J = 14,5 Hz, 5 Hz, C≡N), 128,45, 128,79, 130,11, 133,33, 143,55 (C-3). ***13****aEE*. RMN ^1H, δ : 2,52 (s, 2H), 2,50 (s, 4H), 3,51 (s, 4H), 7,35 (s, 2H), 7,49 (s, 6H), 7,77 (s, 4H), RMN ^{13}C, δ : 47,35, 52,64, 110,79 (C-2), 118,83 (dt, ^3J = 7 Hz, 5 Hz, C≡N), 128,80, 128,39, 130,01, 133,43, 143,48 (C-3). SMHR trouvé : 342,1844; calc. pour $C_{22}H_{22}N_4$: 342,1853. Anal. calc. pour $C_{22}H_{22}N_4$: C 77,19, H 6,43; trouvé C 77,00, H 6,55.

N,N′-Di(3-(2′-furyl)-2-méthoxycarbonyl-2E-propényl) éthylène diamine ***14***d. F = 116°C (MeCN), 60%. IR (Nujol) ν : 1615, 1688, 3310 cm^{-1}. RMN ^1H, δ : 1,72 (s, 2H), 2,70 (s, 4H), 3,72 (s, 6H), 3,95 (s, 4H), 6,45 (dd, 2H, J = 2 Hz), 6,65 (d, 2H, J = 2 Hz), 7,43 (s, 2H), 7,45 (d, 2H, J = 2 Hz). SMHR trouvé : 388,1628; calc. pour $C_{20}H_{24}N_2O_6$: 338,1634. Anal. calc. pour $C_{20}H_{24}N_2O_6$: C 61,84, H 6,22, N 7,22; trouvé : C 61,68, H 6,21, N 7,45.

N,N′-Di(2-méthoxycarbonyl-3-(2′-thiényl)-2E-propényl) éthylène diamine ***14***e. F = 129°C (MeCN), 58%. IR (Nujol) ν : 1612, 1690, 3300 cm^{-1}. RMN ^1H, δ : 1,63 (s, 2H), 2,77 (s, 4H), 3,72 (s, 6H), 3,76 (s, 4H), 7,00–7,43 (m, 6H), 7,86 (s, 2H). RMN ^{13}C, δ : 43,44, 43,48, 52,01, 117,37 (C-2), 128,10, 132,25, 135,30, 136,04, 138,01 (C-3), 166,35. SMHR trouvé : 420,1170; calc. pour $C_{20}H_{24}N_2O_4S_2$: 420,1177. Anal. calc. pour $C_{20}H_{24}N_2O_4S_2$: C 57,11, H 5,75, N 6,67, S 15,24; trouvé : C 57,13, H 5,77, N 7,03, S 15,06.

N,N,N′,N′-Tetra(3-(2′-furyl)-2-méthoxycarbonyl-2E-propényl) éth-

ylène diamine ***15***d. F = 140°C (MeOH), 64%. IR ν : 1635, 1705 cm^{-1}. RMN ^1H, δ : 2,68 (s, 4H), 3,60 (s, 8H), 3,64 (s, 12H), 6,40 (dd, 4H, J = 3,40 Hz, 1,8 Hz), 6,70 (d, 4H, J = 3,4 Hz), 7,41 (s, 4H), 7,49 (s, 4H, J = 1,8 Hz). RMN ^{13}C, δ : 50,78, 51,77, 52,40, 111,96, 116,47, 127,06 (C-2), 127,89 (C-3), 144,33, 151,14, 169,06. Anal. calc. pour $C_{38}H_{40}N_2O_2$: C 63,68, H 5,63, N 3,91; trouvé : C 63,47, H 5,67, N 3,91.

1. R.R. Rando et F. Bangerter. J. Am Chem. Soc. **98**, 6762 (1976); C.Y.P. Teng et B. Ganem. Tetrahedron Lett. **23**, 313 (1982).
2. T. Kondo, H. Nakai et T. Goto. Tetrahedron, **29**, 1801 (1973).
3. A Stütz. Angew. Chem. Int. Ed. Engl. **26**, 320 (1987).
4. J.E. Bäckvall, R.E. Nordberg, J.E. Nyström, T. Högberg et B. Ulff. J. Org. Chem. **46**, 3479 (1981).
5. R. Ben Cheikh, R. Chaabouni, A. Laurent, P. Mison et A. Nafti. Synthesis, 685 (1983); S-I. Murahashi, Y. Taniguchi, Y. Imada et Y. Tanigawa. J. Org. Chem. **54**, 3292 (1989) et références citées.
6. L. Capella, A. Degl'Innocenti, A. Mordini, G. Reginato, A. Ricci et G. Seconi. Synthesis, 1201 (1991); N. De Kimpe, E. Stanoeva, R. Verhé et N. Schamp. Synthesis, 587 (1988), et références citées; E. Doomes, U. Clarke et J.J. Neitzel. J. Org. Chem. **52**, 1540 (1987); J.B. Baruah et A.G. Samuelson. Tetrahedron, **47**, 9449 (1991).
7. I. Shimizu et J. Tsuji. Chem. Lett. 233 (1984).
8. N.X. Hu, Y. Aso, T. Otsubo et F. Ogura. Tetrahedron Lett. **29**, 4949 (1988).
9. J. Barluenga, J. Perez-Prieto et G. Asensio. Tetrahedron, **46**, 2453 (1980); J. Barluenga, R. Gonzalez et F.J. Fananas. Tetrahedron Lett. **33**, 831 (1992).
10. B.M. Trost et E. Keinan. J. Org. Chem. **44**, 3451 (1979).
11. A. Foucaud et F. El Guemmout. Bull. Soc. Chim. Fr. 403 (1989).
12. A.B. Baylis et M.E. Hillman. German Patent 2155113 (1972); H.M.R. Hoffmann et J. Rabe. Angew. Chem. Int. Ed. Engl. **22**, 795 (1983); H. Amri et J. Villieras. Tetrahedron Lett. **27**, 4307 (1986).
13. M.C. Etter. Acc. Chem. Res. **23**, 120 (1990).
14. A.J. Parker. Chem. Rev. **69**, 1 (1969).
15. P. Bauchat et A. Foucaud. Tetrahedron Lett. **30**, 6337 (1989).
16. R.E. Bilbo et D.W. Boykin. J. Chem. Res. (S), 332 (1980).
17. C. Pascual, J. Meier et W. Simon. Helv. Chim. Acta, **49**, 164 (1966).
18. U.E. Matter, C. Pascual, E. Pretsch, A. Pross, W. Simon et S. Sternhell. Tetrahedron, **25**, 691 (1969); **25**, 2023 (1969).
19. S.W. Tobey. J. Org. Chem. **34**, 1281 (1969).
20. W.R. Schoen et W.H. Parsons. Tetrahedron Lett. **29**, 5201 (1988).

Can. J. Chem. Downloaded from www.nrcresearchpress.com by EESC ESCOLA DE ENGENHARIA on 09/08/12
For personal use only.

Preparation of 2- and 4-substituted 3-hydroxy-5-methylfurans and the aluminum and gallium complexes of 3-hydroxy-5-methyl-2-(*N*-methylformamido)furan[1]

T.G. Lutz, D.J. Clevette, H.R. Hoveyda, and V. Karunaratne
Department of Chemistry, University of British Columbia, 2036 Main Mall, Vancouver, BC V6T 1Z1, Canada

A. Nordin and S. Sjöberg[2]
Department of Inorganic Chemistry, University of Umeå, S-901 87 Umedå, Sweden

and

M. Winter and C. Orvig[2]
Department of Chemistry, University of British Columbia, 2036 Main Mall, Vancouver, BC V6T 1Z1, Canada

Received October 8, 1993

T.G. Lutz, D.J. Clevette, H.R. Hoveyda, V. Karunaratne, A. Nordin, S. Sjöberg, M. Winter, and C. Orvig. Can. J. Chem. **72**, 1362 (1994).

In model studies designed to study the synthesis of potentially hexadentate chelates based on the linkage of three furan rings to a triamine via amide linkages, new 2- and 4-substituted 3-hydroxy-5-methylfurans have been prepared. Particularly, 3-hydroxy-5-methyl-(*N*-methylformamido)furan (Hahm) and its Al and Ga complexes ($M(ahm)_3$) have been prepared and thoroughly characterized by a variety of techniques, in the solid state and in solution. Solution equilibrium studies ($\mu = 0.6$ M NaCl, 25°C) uncovered a complicated set of equilibria in the Al^{3+}/Hahm system; the solution potentiometric data were best explained by the presence of mixed ligand (HL = Hahm, $L^- = ahm^-$) hydroxo species $[Al_3(OH)_4L_3]^{2+}$ and $[Al(OH)_2L_2]^-$, in addition to the expected $[AlL_n]^{(3-n)+}$ ($n = 1, 2, 3$) species. Further solution studies at HL:M ratios of 3:1 ($\mu = 0.15$ M NaCl, 25°C) showed that Hahm is a relatively weak complexing agent for both Al and Ga, forming tris-ligand species with overall formation constants of $10^{19.5}$ and $10^{20.6}$, respectively.

T.G. Lutz, D.J. Clevette, H.R. Hoveyda, V. Karunaratne, A. Nordin, S. Sjöberg, M. Winter et C. Orvig. Can. J. Chem. **72**, 1362 (1994).

Dans le cadre de travaux orientés vers l'étude de la synthèse de chélates hexacoordinés potentiels basés sur la liaison de trois noyaux furaniques à une triamine par le biais de liaisons amides, on a synthétisé de nouveaux 3-hydroxy-5-méthylfuranes substitués en positions 2 et 4. On a préparé en particulier le 3-hydroxy-5-méthyl-2-(*N*-méthylformamido)furane (Hahm) ainsi que ses complexes avec de l'aluminium et du gallium ($M(ahm)_3$) et on les a caractérisés à fond par diverses techniques, tant à l'état solide qu'en solution. Les études d'équilibre en solution ($\mu = 0{,}6$ M NaCl, 25°C) ont permis de mettre en évidence l'existence d'un ensemble d'équilibres compliqués dans le système Al^{3+}/Hahm; pour bien expliquer les données potentiométriques en solution, on doit suggérer l'existence d'espèces hydroxo $[Al_3(OH)_4L_3]^{3+}$ et $[Al(OH)_2L_2]^-$ à coordinats mixtes (HL = Hahm, $L^- = ahm^-$), en plus des espèces $[AlL_n]^{(3-n)+}$ ($n = 1$, 2 et 3) attendues. Des études ultérieures en solution, à des rapports HL:M des 3:1 ($\mu = 0{,}15$ M NaCl, 25°C) montrent que le Hahm est un agent complexant relativement faible tant pour l'aluminium que pour le gallium, formant des espèces tricoordinées avec des constantes de formation globales respectives de $10^{19,5}$ et $10^{20,6}$.

[Traduit par la Rédaction]

Introduction

A number of low molecular weight complexes of aluminum, gallium, and indium have been prepared and investigated in these laboratories in recent years; their properties have recommended them for *in vivo* examination (2, 3). These complexes are tris(bidentate ligand)metal(III) species, and incorporate as ligands various pyrones (e.g. maltol, **1**) (4, 5), *N*-substituted-3-hydroxy-4-pyridinones (**2**) (6–8) and isomaltol (**3**) (9). The

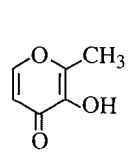

1

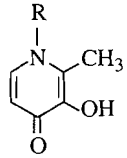

2

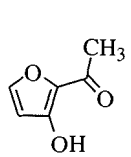

3

properties of interest are hydrolytic stability, water solubility, neutral charge, and lipophilicity, all occurring simultaneously. Some of these ligands had very high affinities for the group IIIA (or 13) ions (8) and certain of the complexes formed unusual solid state hydrogen bonding arrays (6, 7).

In efforts to extend the coexistence of these four properties into hexadentate analogs of these binding moieties, we have undertaken model studies involving the preparation of some new ligands for the group 13 ions. The hydrolytic instability (10) of aluminum, gallium, and indium is an important factor in the aqueous chemistry of their trivalent ions and must be compensated for in the design of their chelates.

Initial model studies designed to study the synthesis of potentially hexadentate chelates were based on the functionalization of maltol (**1**) with triamines to form hexadentate tris(3-hydroxy-4-pyridinone) analogs of **2** similar to the bis(pyridinones) already reported (11); however, in both the bis and tris cases the 1 position of the maltol ring (where R—N is substituted for O) is far removed from the α-hydroxyketone chelating moiety and the resulting ligands form polymeric complexes by bridging metal ions. The ketone carbonyl of isomaltol (**3**) does not undergo Schiff base condensation with amines to form imines, rather isomaltol undergoes a ring opening, dehydration, and ring closing sequence of reactions to produce *N*-substituted-3-hydroxy-2-methyl-4-pyridinones (**2**) (12). The failure to form imines with isomaltol initiated a search for a ligand that had a

[1]Equilibrium and structural studies of silicon(IV) and aluminum(III) in aqueous solution. 32. The previous paper in this series is ref. 1.

[2]Authors to whom correspondence should be addressed.

Can. J. Chem. Downloaded from www.nrcresearchpress.com by EESC ESCOLA DE ENGENHARIA on 09/08/12
For personal use only.

Can. J. Chem. Downloaded from www.nrcresearchpress.com by EESC ESCOLA DE ENGENHARIA on 09/08/12
For personal use only.

bulkier substituent at the 5 position to inhibit the ring opening reaction. An attractive candidate was found, 2-ethoxycarbonyl-3-hydroxy-5-methylfuran (Hehm, see Scheme 1), which not only had a methyl group at the 5 position, but also had an ester group at the 2 position, allowing for a route to modify the ligand by the formation of various amides. Little work has been done on such highly substituted furans, especially those containing a butanedionyl moiety, but a short communication by Takei et al. described the synthesis of furan derivatives (including the desired Hehm) by reacting diketene with various sulfur ylides in benzene (13).

The possibility of linking three isomaltol analogs together to a tripodal backbone such as tris(2-aminoethyl)amine (tren) via the replacement of the 2-acyl group with an amide linkage was envisaged. We report herein on model studies toward the objective of linking three furan rings to a triamine via amide linkages; new 2- and 4-substituted 3-hydroxy-5-methylfurans have been prepared, and their chemistry has been studied both in the presence and absence of the group 13 ions. 3-Hydroxy-5-methyl-2-(*N*-methylformamido)furan (Hahm) and its Al and Ga complexes ($M(ahm)_3$) have been prepared and thoroughly characterized by a variety of techniques in the solid state and in solution.

Experimental

Materials and methods

These were mostly as previously described (4, 6, 8, 9). Dimethylsulfide (Aldrich), ethyl bromoacetate (Aldrich), methylamine (40% in H_2O — Fisher), and $Al(NO_3)_3{\cdot}9H_2O$ (Mallinckrodt) were used as supplied. Ga ingots (Alfa) were dissolved in concentrated HCl; this solution was standarized and used as the starting material for the synthesis of Ga complexes. Diketene and benzene were freshly distilled before use. Carbethoxymethyldimethylsulfonium bromide was synthesized according to the method of Payne (14).

NMR spectra are reported δ downfield from TMS (^{13}C, ^1H, APT, SINEPT) and were recorded on Bruker AC-200E, Varian XL 300, and Varian XL 400 spectrometers. IR spectra were recorded as KBr disks with a PE 783 spectrophotometer and are referenced to polystyrene film. Mass spectra were obtained with either a Kratos MS 50 (electron-impact ionization, EI) or an AE MS-9 (fast-atom-bombardment ionization, FAB) instrument. Melting points were measured on a Mel-Temp apparatus and are uncorrected. Analyses for C, H, N were performed by Mr. Peter Borda in this department.

Ethyl (dimethylsulfuranylidene)acetate (EDSA)

This was prepared from dimethylsulfide and ethyl bromoacetate via carbethoxymethyldimethylsulfonium bromide according to Payne (14), with some modification. The carbethoxymethyldimethylsulfonium bromide solution was stirred vigorously using an overhead stirrer, and was cooled for 15 min in an ice bath. After the additions of the saturated K_2CO_3 and 12.5 M NaOH solutions, the ice bath was removed and the mixture was left to stir for an additional 25 min. The light yellow ylide was stored at 5°C under N_2.

2-Ethoxycarbonyl-3-hydroxy-5-methylfuran (Hehm) (13)

EDSA (12 g, 75 mmol) was stirred in 40 mL of benzene. To this, freshly distilled diketene (4.8 g, 57 mmol) was added, and the mixture was refluxed for 15 h. Most of the benzene was removed by rotary evaporation; the remaining solution was cooled and a precipitate formed. The precipitate was removed by filtration and recrystallized from methanol to give 6.9 g (75%) of an off-white crystalline product (mp 50–51°C). It was soluble in methanol, ethanol, chloroform, ether, ethyl acetate, benzene, and water. Anal. calcd. for $C_8H_{10}O_4$: C 56.47, H 5.92; found: C 56.40, H 5.80. ^1H NMR ($CDCl_3$): 7.6 (br, OH), 5.9 (q, J = 1 Hz, 1H, ring H), 4.3 (q, J = 6 Hz, 2H, CH_2), 2.25 (s, 3H, ring CH_3), 1.35 (t, J = 6 Hz, 3H, CH_3). ^{13}C NMR ($CDCl_3$): 160.4 (*C*=O), 156.2 (*C*C=O), 155.9 (*C*CH_3), 124.4 (*C*OH), 100.9 (*C*H), 59.7 (CH_2CH_3), 13.6 (C*C*H_3), 13.5 (CH_2CH_3). EIMS *m/z*: 170 (M^+), 142, 124. IR (cm^{-1}): 3240 (br); 1670, 1630, 1555 ($\nu_{C=O}$, $\nu_{C=C}$, mixed); 1260, 1180, 1080.

4-(1′,3′-Butanedionyl)-2-ethoxycarbonyl-3-hydroxy-5-methylfuran (Hehbm)

A preparation similar to that for Hehm using a 2:1 ratio of diketene to EDSA afforded a pale yellow solid. Anal. calcd. for $C_{12}H_{14}O_6$: C 56.69, H 5.55; found: C 56.59, H 5.80. ^1H NMR ($CDCl_3$): 8.45 (s, ~1H, OH), 6.23 (s, 1H, ring H), 4.41 (q, J = 6 Hz, 2H, ethyl CH_2), 2.67 (s, 3H, acetyl CH_3), 2.19 (s, 3H, ring methyl), 1.43 (t, J = 6 Hz, 3H, ethyl CH_3). ^{13}C NMR ($CDCl_3$): 191.4 (CH_3CO), 179.4 (exocyclic *C*OH), 160.8 (ring *C*C=O), 160.5 (ring *C*=O), 153.6 (*C*CH_3), 124.7 (ring *C*OH), 111.1 (ring *C*=CCH_3), 99.1 (methine C), 60.7 (CH_2CH_3), 24.7 (CO*C*H_3), 15.4 (C*C*H_3), 14.1 (CH_2CH_3). EIMS: *m/z*: 254 (M^+), 239, 197, 166, 151, 124. IR (cm^{-1}): 3320 (br); 1680, 1630 ($\nu_{C=O}$, $\nu_{C=C}$, mixed).

3-Hydroxy-5-methyl-2-(N-methylformamido)furan (Hahm)

Hehm (4.67 g, 27 mmol) was dissolved in 110 mL ethanol and methylamine (40% in H_2O) (2.12 g, 27 mmol) was added. The resulting solution was refluxed for 20 h. The volume was then reduced by rotary evaporation to give 3.3 g (77%) of an off-white powder which was recrystallized from ethanol. It was soluble in methanol, ethanol, chloroform, water, and benzene. Anal. calcd. for $C_7H_9NO_3$: C 54.20, H 5.85, N 9.03; found: C 53.94, H 5.82, N 8.79. ^1H NMR (CD_3OD): 5.94 (q, J = 1 Hz, 1H, ring H), 3.47 (s, 3H, amide CH_3), 2.27 (d, J = 1 Hz, 3H, ring methyl). EIMS: *m/z*: 155 (M^+), 140, 126. IR (cm^{-1}): 3390 (s, ν_{NH}); 3400–2800 (br, ν_{OH}); 1665, 1610, 1575, 1485, 1445 (amide bands, $\nu_{C=O}$, $\nu_{C=C}$, all mixed).

$Al(ahm)_3{\cdot}3H_2O$

Hahm (0.475 g, 3.1 mmol) was dissolved in 40 mL H_2O and the pH was raised to 9 (2 M NaOH). $AlCl_3{\cdot}6H_2O$ (0.246 g, 1.0 mmol) was then added and the pH was adjusted to 7.3. A white precipitate formed (0.36 g, 72%) which was recrystallized from methanol. $Al(ahm)_3$ was soluble in methanol, acetone, and water (3.1 mM). Anal. calcd. for $C_{21}H_{24}AlN_3O_9{\cdot}3H_2O$: C 46.16, H 5.53, N 7.72; found: C 45.94, H 5.27, N 7.66. ^1H NMR (CD_3OD): 6.11 (s, 1H, ring H), 3.56 (s, 3H, amide CH_3), 2.28 (s, 3H, ring methyl). FABMS *m/z*: 824 ($M_2L_5^+$); 490 (HML_3^+); 355 (ML_2^+). IR (cm^{-1}): 3700–2800 (br, ν_{NH}, ν_{OH}); 1645, 1590, 1530, 1475, 1450 (amide bands, $\nu_{C=O}$, $\nu_{C=C}$, all mixed).

$Ga(ahm)_3$

Hahm (0.528 g, 3.4 mmol) was dissolved in 60 mL H_2O and the pH was raised to 9. A solution of 0.445 M $GaCl_3$ in excess HCl (2.5 mL, 1.1 mmol) was added. Adjustment of the pH to 7.0 with 2 M NaOH resulted in an off-white powder (0.45 g, 75%) which was recrystallized from pyridine. It was soluble in pyridine, methanol, water (1.6 mM), and slightly soluble in acetone. Anal. calcd. for $C_{21}H_{24}GaN_3O_9$: C 47.39, H 4.55, N 7.93; found: C 47.15, H 4.70; N 7.99. ^1H NMR (pyridine-d_5): 6.38 (s, 1H, ring H), 3.03 (s, 3H, amide CH_3), 1.86 (s, 3H, ring methyl). FABMS *m/z*: 532 (HML_3^+); 377 (ML_2^+). IR (cm^{-1}): 3700–2500 (br, ν_{NH}, ν_{OH}); 1630, 1580, 1530, 1470, 1440 (amide bands, $\nu_{C=O}$, $\nu_{C=C}$, all mixed).

Potentiometric equilibrium measurements

Potentiometric measurements (at μ = 0.6 or 0.15 M NaCl for the Al/Hahm system; at μ = 0.15 M NaCl for the Ga/Hahm system) of the ligand in the absence, and presence, of metal ions were performed as described previously (9, 15). The temperature was maintained at 25.0 ± 0.1°C throughout. Stock solutions of Hahm were prepared by dissolving it in slightly acidified solutions ($-\log [H^+] \approx 2.5$, μ = 0.6 or 0.15 M NaCl). The total ligand concentration was determined potentiometrically using the Gran extrapolation method (16). The titrated amount was found to be within ± 0.2% of the value expected from weighing. Stock solutions of NaCl, $AlCl_3$, and dilute HCl were prepared and standarized as described previously (15). Metal containing

Can. J. Chem. Downloaded from www.nrcresearchpress.com by EESC ESCOLA DE ENGENHARIA on 09/08/12
For personal use only.

solutions were also prepared from appropriate dilution of atomic absorption standard solutions of Al or Ga (Sigma or Aldrich). The exact amount of excess acid present in the metal ion solutions was determined by a Gran's plot (17). The reproducibility and reversibility of Al/Hahm equilibria (μ = 0.6 M NaCl) were tested by performing both forward titrations (increasing – log [H^+] by coulometrically generated OH^-) and backward titrations (decreasing – log [H^+] by the addition of H^+).

The deprotonation of Hahm in 0.6 M NaCl was studied in separate experiments within the range $2.5 \leq -\log [H^+] \leq 9$. The three component titrations (μ = 0.6 M NaCl) were performed at constant ratios of the total concentrations of Hahm (B) and Al (C). The B/C ratios 1, 2, 3, 6, and 8 were studied with $0.001 \leq B \leq 0.008$ M and $0.001 \leq C \leq 0.007$ M. The upper – log [H^+] limits in these titrations were set by the appearance of sluggish equilibria, probably due to the formation of polynuclear hydrolysis products, viz. $[Al_{13}O_4(OH)_{24}]^{7+}$, at low B/C ratios; and $-\log [H^+] \geq 4$. At B/C high ratios with $-\log [H^+] \geq 7$ the formation of a precipitate was frequently observed.

A limited number of potentiometric titrations in μ = 0.15 M NaCl were then undertaken at 3:1 HL:M ratios to compare the overall formation constants of the 3:1 Hahm complexes with aluminum and gallium. For the determination of the formation constants, titrations were done with $B \sim 0.002$ M in the range $2 \leq -\log [H^+] \leq 4$ because the formation of mixed hydroxo species can be neglected in this range.

Data treatment

The equilibria can be divided into three groups:

(*i*) the binary Hahm equilibrium:

$$[1] \quad HL \rightleftharpoons H^+ + L^- \qquad \beta_{-110}$$

(*ii*) the hydrolytic equilibria for the metal ions:

$$[2] \quad pH^+ + rM^{3+} \rightleftharpoons [H_pM_r]^{(p+3r)+} \qquad \beta_{p0r}$$

incorporating the hydrolysis species for Al: $[Al(OH)_n]^{(3-n)+}$ (n = 1, 2, 3, 4), $[Al_3(OH)_4]^{5+}$, and $[Al_{13}O_4(OH)_{24}]^{7+}$ with appropriate formation constants (18–20)

(*iii*) three component equilibria of the general form:

$$[3] \quad pH^+ + q\text{Hahm} + rM^{3+} \rightleftharpoons [H_p(\text{Hahm})_qM_r]^{(p+3r)+} \qquad \beta_{pqr}$$

In the evaluation of the experimental μ = 0.6 M data, the least-squares computer program LETAGROPVRID (21) (version ETITR (22)) was used. Triplets of pqr, and corresponding equilibrium constants that best fit the experimental data were determined by minimizing the error squares sum $U = \Sigma(H_{calc} - H_{exp})^2$. The LETAGROP calculations also give standard deviations $\sigma(H)$ and $3\sigma(\log \beta_{pqr})$ defined according to Sillén (23, 24). Here H denotes the total proton concentration calculated over the zero level H_2O, HL, and Al^{3+}.

The analysis of the μ = 0.6 M experimental data was started by calculating Z values for each point in a titration using the relation

$$[4] \quad Z = ([H^+] - H - k_w[H^+]^{-1})/B$$

This is the average number of OH^- reacted per B. The experiments thus provide sets of data Z vs. – log [H^+] which are presented in Fig. 1; the Al complexation clearly starts at low $-\log [H^+] < 2$. Furthermore, at B/C ratios of 1, Z clearly exceeds 1. This is direct evidence that hydroxo and/or mixed ligand hydroxo-complexes of Al were formed. To discover whether specified ranges existed where the formation of binary Al^{3+}/L^- complexes prevail, $\bar{n}$ vs. – log [L^-] (L^- = ahm$^-$) curves were plotted (Fig. 2). The quantity $\bar{n}$ is the average number of L^- coordinated per Al^{3+} (25). Coincident $\bar{n}$ curves are obtained if predominantly mononuclear AlL_n complexes are formed. A limited curve with $\bar{n} \leq 2.5$ was found; however, deviations from this curve are clearly seen at C/B ratios 1 and 2, as well as at high ratios with $\bar{n} > 2.5$. Data from the "mononuclear wall" were used to evaluate the stability of the different

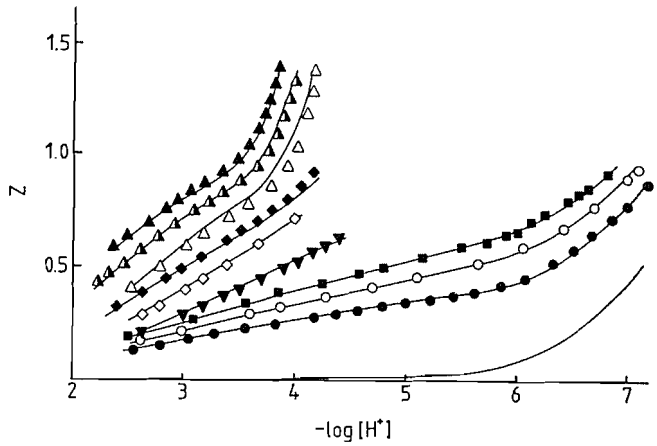

FIG. 1. A part of the experimental data (25°C, μ = 0.6 M NaCl) plotted as curves of Z vs. –log [H^+]. The full curves were calculated using the set of proposed constants in Table 1. The bottom curve represents the ligand in the absence of Al^{3+}. The different symbols denote starting concentrations B, C: ▲ 7.29, 7.00; Δ 3.79, 3.75; △ 1.89, 1.88; ◆ 4.67, 2.30; ◇ 2.35, 1.18; ▼ 5.04, 1.67; ■ 5.76, 1.15; ○ 6.32, 1.05; ● 7.28, 0.91.

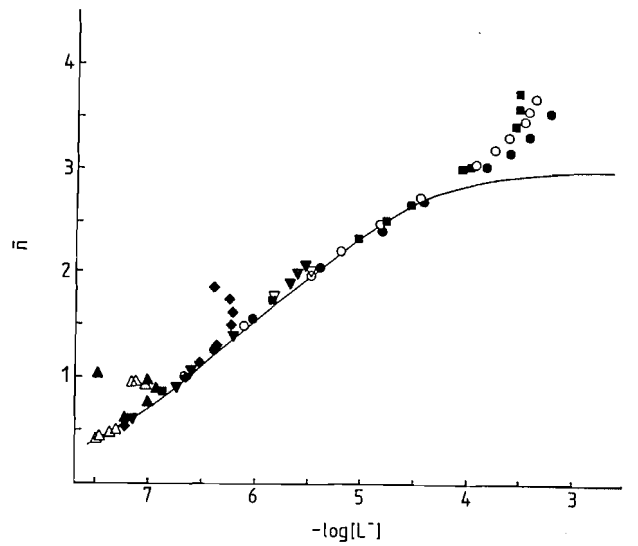

FIG. 2. Experimental data (25°C, μ = 0.6 M NaCl) plotted as curves of $\bar{n}$ vs. –log [L^-] (L^- = ahm$^-$). The symbols are the same as in Fig. 1. The full curve was calculated using log $\beta_{-n,n,1}$ values (n = 1, 2, 3) from Table 1.

$Al(ahm)_n$ species (n = 1, 2, 3). The results of this calculation are presented in Table 1.

In the search for composition (pqr) and stability (β_{pqr}) of any additional complexes (necessary to explain the deviations from the mononuclear $\bar{n}$ curve), pqr analysis using the LETAGROPVRID program was undertaken. The principle behind this method is that complexes of different pqr compositions are tested successively, one by one, and the complex that gives the lowest error square sum is considered to give the best fit. If there are still systematic deviations between calculated and experimental values of H, additional complexes must be included and combinations of two or more pqr sets must be tested. In this work, two data sets were defined; one with $B/C \geq 3$ (set 1) and one with B/C = 1 and 2 (set 2). The result of the analysis on set 1 is presented in Fig. 3, and shows that the lowest value in U was obtained for the complex $[H_{-4}(HL)_2Al]^-$; log β_{-421} = –12.08 (5) and $\sigma(H)$ = 0.05 mM indicate a good fit to experimental data, and no systematic deviations were

TABLE 1. Binary and ternary complexes in the H^+–Hahm–Al^{3+} system determined potentiometrically at 25°C, μ = 0.6 M NaCl[a]

No. of titr./ No. points	p	q	r	Tentative structure	log β_{pqr}	Reference
3/98	−1	1	0	L^-	−7.090 (2)	This work
	−1	0	1	$[Al(OH)]^{2+}$	−5.52	18
	−2	0	1	$[Al(OH)_2]^+$	−11.3	20
	−3	0	1	$Al(OH)_3$	−17.3	20
	−4	0	1	$[Al(OH)_4]^-$	−23.46	19
	−4	0	3	$[Al_3(OH)_4]^{5+}$	−13.57	18
	−32	0	13	$[Al_{13}O_4(OH)_{24}]^{7+}$	−109.2	18
14/552	−1	1	1	$[AlL]^{2+}$	0.19 (1)	This work
	−2	2	1	$[AlL_2]^+$	−0.76 (2)	This work
	−3	3	1	AlL_3	−3.02 (3)	This work
	−7	3	3	$[Al_3(OH)_4L_3]^{2+}$	−10.43 (5)	This work
	−4	2	1	$[Al(OH)_2L_2]^-$	−12.08 (5)	This work

[a]The formation constants are defined according to the reaction: $pH^+ + qHL + rM^3 \rightleftharpoons [H_pM_r]^{(p+3r)+}$ where HL = Hahm. Numbers in parentheses represent errors corresponding to $3\sigma(\log \beta_{pqr})$.

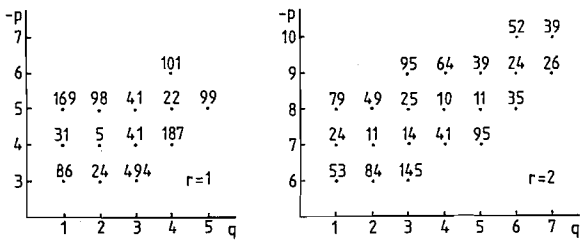

FIG. 3. Results of the *pqr* analysis on data with $B/C > 3$. The figure gives $U_H(p, r)_q$ assuming one ternary complex.

observed. Similar calculations were performed on set 2. The high Z values ($Z \leq 1.5$) that were observed with $-\log [H^+] \approx 4$, indicate the formation of ternary hydroxo species; furthermore, the high buffer capacity of the system in this range also implied that polynuclear Al complexes were likely. The *pqr* search clearly showed that polynuclear complexes were formed, the best fit being obtained with p,q,r −7,3,3. No attempts were made to include additional complexes as the remaining residuals were too small to justify this ($\sigma(H)$ = 0.07 mM). The results of the final calculation where the different formation constants were refined on the whole data set are given in Table 1. In order to visualize the amounts of different species, the program SOLGASWATER (26) was used and calculated distribution diagrams are presented in Fig. 4.

In the μ = 0.15 NaCl HL:M 3:1 studies, the computations allowed for the presence of hydrolytic species of Al and Ga with formation constants for these various metal species taken from ref. 10. The stability constants for the main species ML^{2+}, ML_2^+, and ML_3 were determined by using the Fortran computer program BEST (27). Because of the presence of mixed hydroxo/ligand/aluminum complexes noted from the μ = 0.6 M data, these 3:1 results are noted in the results and discussion section only for comparison between the two metal ions.

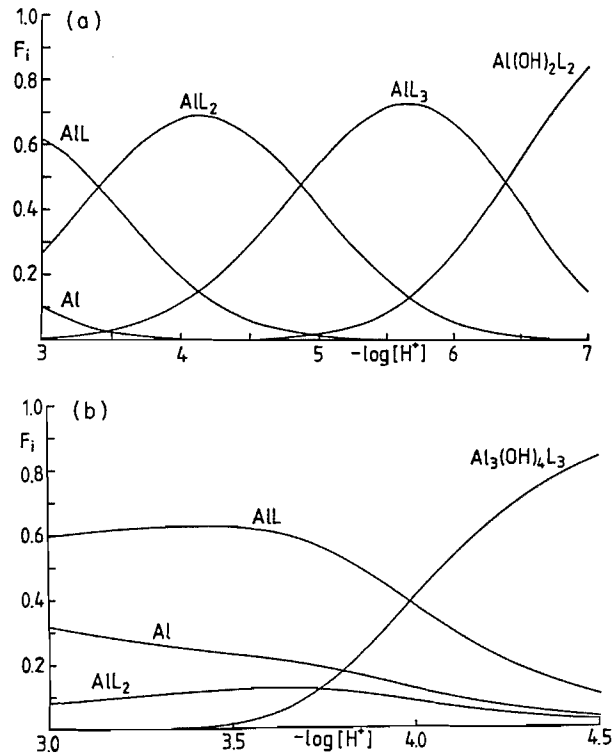

FIG. 4. Distribution diagrams F_i vs. $-\log [H^+]$, where F_i is defined as the ratio between Al^{3+} in a species and total Al^{3+}. The total ligand and Al^{3+} concentrations (mM): (*a*) 5 and 1, respectively, and (*b*) 5 and 5, respectively.

Results and discussion

Hehm

The yield of Hehm was improved significantly by increasing the ratio of EDSA to diketene to 1.3:1 from 1:1 (13) and by refluxing for 6 h (Scheme 1). Any impurities in the starting materials or benzene solvent resulted in a red oil, shown by thin layer chromatography to consist of at least eight products. Hexanes extraction of the oil gave rise to Hehm and another product (Hehbm) that was separable from Hehm by fractional crystallization. For this reason, both the benzene and the diketene were distilled before use, and the EDSA was checked for impurities by ^1H NMR. Using pure starting materials in the appropriate stoichiometry resulted in a 75% yield of Hehm, which was then recrystallized from ethanol.

A short communication characterized Hehm only by elemental analysis and mp (13). In our work, the IR spectrum of Hehm showed a broad OH stretch at 3240 cm^{-1} indicative of a hydrogen bonded, rather than a free, OH group. Hehm also has two strong bands occurring at 1670 and 1630 cm^{-1} corresponding to C=O and C=C stretches, respectively (28). The C=O stretch occurs at a lower energy than in saturated esters due to exten-

Can. J. Chem. Downloaded from www.nrcresearchpress.com by EESC ESCOLA DE ENGENHARIA on 09/08/12
For personal use only.

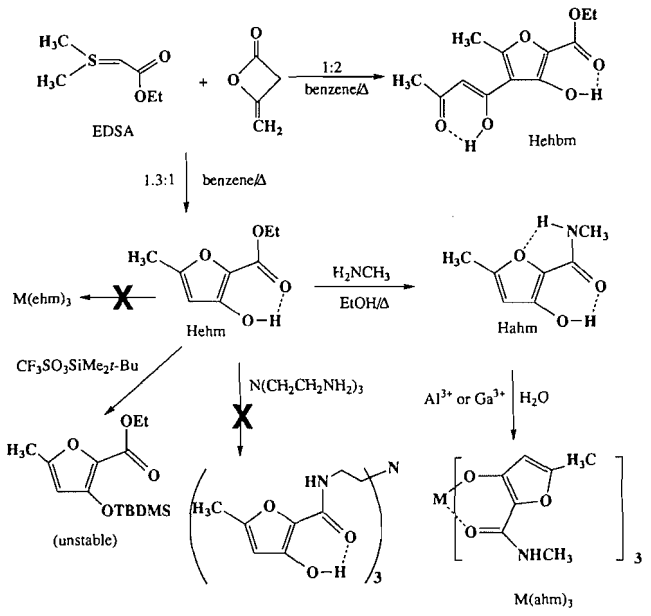

SCHEME 1

sive conjugation and hydrogen bonding with the hydroxyl hydrogen, analogous to that seen with isomaltol (9). There are three bands in the C—O stretch region at 1260, 1180, and 1080 cm^{-1}, but it is not possible to assign any one band due to ring vibrations and C—H bending modes occurring in the same region. The ^1H NMR spectrum showed the presence of an ethyl group with chemical shifts diagnostic of esters. The long range coupling between the ring methyl hydrogens and the adjacent ring hydrogen is also consistent with the Hehm structure. A broad OH peak was also seen further downfield at δ 8.45 in $CDCl_3$. The EI mass spectrum of Hehm showed a parent peak at *m/z* 170, a peak at *m/z* 142 from loss of ethanol, and a base peak at *m/z* 124 from fragmentation typical of β-hydroxy esters by means of the McLafferty rearrangement (29).

Functionalization of Hehm

Hehm did react with methylamine to form the amide Hahm, but did not react completely with triamines such as tren to form potentially hexadentate chelating ligands (Scheme 1). With tren (dioxane, 24 h, 65°C) there was evidence that two of the three amines had reacted to form a difunctionalized compound with the third arm unreacted. There was, however, ample evidence that Hehm would not lend itself to a variety of transformations. Its reaction with di(isobutyl)aluminumhydride gave starting material; even functionalization of the 3-OH was elusive as reactions with benzyl chloride, or KH/benzyl bromide, yielded no reaction. The only successful reaction, the protection of the 3-hydroxy group as a *t*-butyldimethylsilyl ether, worked satisfactorily (Scheme 1); however, the protected compound underwent basic hydrolysis (NaOH/THF) to yield the starting material. A considerable number of attempts were made to make Hehm analogs in which the ester functionality was more active in order to complete the target hexadentate molecule; these were all unsuccessful.

Metal complexes of Hehm

Metal complexes of Hehm were prepared by a 3:1 stoichiometric addition of ligand to metal in a 3:2 water:ethanol solution due to the low water solubility of Hehm. The pH was initially raised to 9, and upon slow addition of the metal salt, the pH dropped to ~ 2. The pH was then raised again to 6.5 with 2 M NaOH resulting in an off-white precipitate. ^1H NMR, IR and MS evidence was found for the Al and Ga complexes $M(ehm)_3$, but isolation of analytically pure samples was impossible, and the spectra always contained features attributable to Hehm. Hehm reversibly hydrolyzes under the acidic synthetic conditions, so that as the pH was increased from 2 to 7, only low yields of the complexes were found. The isolated products usually contained ~ 20% Hehm. Any attempts to purify the complexes resulted in decomposition to starting materials. The IR spectra showed the expected bathochromic shifts in $\nu_{C=O}$, but there was also a peak at 1670 cm^{-1} from Hehm. The DCI (negative ion detection) mass spectrum of the gallium complex of Hehm showed two parent ion peaks corresponding to $[ML_3 - H]^-$ at *m/z* 575 and 577 (^{69}Ga, ^{71}Ga). The base peaks were *m/z* 547 and 549 ($[M(ehm)_3 - CH_2CH_3]^-$) suggesting that a gallium complex incorporating one hydrolyzed Hehm ligand may be formed.

Hehbm

If the reaction of EDSA and diketene was carried out using an excess of diketene, rather than an excess of EDSA, the side product in the synthesis of Hehm became the predominant product (Scheme 1). This product (Hehbm-4-(1′,3′-butanedionyl)-2-ethoxycarbonyl-3-hydroxy-5-methylfuran) was characterized by IR, NMR, MS, and elemental analyses. If two equivalents of diketene react instead of one, the extra diketene unit is attached at the 4 position of the ring. Hehbm has potential as a ligand in its own right, and has not been reported in the literature. The mass spectrum of Hehbm showed a parent peak at *m/z* 254, loss of a methyl group (*m/z* 239), loss of CH_3CO and a methyl (*m/z* 197), and loss of ethanol from the 197 peak (*m/z* 151). The base peak at *m/z* 124 is from the loss of CO from the *m/z* 151 fragment peak. The ^1H NMR spectrum in deuterated chloroform confirmed the structure shown (Scheme 1) by comparison with the spectrum of Hehm. There was no long range coupling between the methine hydrogen and the furan ring methyl hydrogens (as seen in Hehm), thus providing evidence that the methine hydrogen is not directly attached to the C-4 ring carbon. Only one peak due to the OH hydrogen on the side chain at the 4-position is seen at 8.45 ppm, suggesting that strong hydrogen bonding is occurring in the enol form in solution. Further evidence to support this structure was found in the ^{13}C NMR spectrum ($CDCl_3$). An attached proton test (APT) showed twelve carbons present, three of which were methyl, one methylene, one methine, and six quaternary. The extra C_4 unit attached to the 4-position of the ring showed ^{13}C NMR chemical shifts of 179.4, 99.1, 191.4, and 24.7 ppm, analogous to a similar β-diketone compound (30).

The positions of the various ring substituents were confirmed by using the NMR technique SINEPT. Irradiation of the methine hydrogen on the side chain on the ring 4-position resulted in the enhancement of ^{13}C signals at 99.1 ppm (one bond coupling), 191.4 and 179.4 ppm (two bond coupling), and at 111.1 ppm (three bond coupling). No enhancement was seen at the methyl carbon on the C_4 side chain. The pulse sequence requires a known $^3J_{CH}$ value for three bond coupling (in this case 4 Hz), or an approximation if not known, such that enhancement of the ^{13}C signal will be selective to coupled carbons that are three bonds away. However, some enhancement breakthrough can occur at carbons that are coupled through

Can. J. Chem. Downloaded from www.nrcresearchpress.com by EESC ESCOLA DE ENGENHARIA on 09/08/12
For personal use only.

Can. J. Chem. Downloaded from www.nrcresearchpress.com by ESC ESCOLA DE ENGENHARIA on 09/08/12
For personal use only.

only one or two bonds if the coupling constants through one and/or two bonds are multiples of the chosen $^3J_{CH}$ value; the ^{13}C enhancements at 99.1, 191.4, and 179.4 ppm are all due to breakthrough. The lack of enhancement expected at the methyl carbon on the C_4 side chain and at the ring 4 carbon may be because the time involved in the refocussing sequence is longer than the hydrogen relaxation time, a factor commonly found when trying to enhance carbon signals through three bonds. This results in the hydrogens relaxing to their normal Boltzmann distribution of populations before the ^{13}C spectrum is acquired. However, the enhancement breakthroughs as well as the expected enhancement, confirm the presence of the predicted side chain, which is bonded to the 4-position of the ring. Irradiation of the methyl at the 5 position resulted in enhancement of the carbon signals at 160.8, 15.4 ppm, as well as 191.4, 99.1, and 24.7 ppm. The 15.4 and 160.8 ppm enhancements occur through two and three bond couplings, respectively. The other three enhancements are actually due to the irradiation of the methyl group on the C_4 side chain, also showing enhancements due to one (24.7 ppm), two (191.4 ppm), and three (99.1 ppm) bond coupling. Simultaneous irradiation of both methyl groups was seen because the irradiation was not selective enough to distinguish between the two methyl groups. This SINEPT experiment shows that the ring 5-methyl is bonded to a carbon having a chemical shift of 160.8 ppm, and therefore must be bonded to the carbon next to the ring oxygen. This experiment also reinforces the structure of the C_4 side chain. Due to the presence of two metal binding sites on Hehbm, its use as a ligand was not pursued in this work but should be of interest.

Hahm

Hahm (3-hydroxy-5-methyl-2-(*N*-methylformamido)furan) is a new potentially bidentate amide ligand which has not been previously reported, to our knowledge. Hahm was prepared in high yield by refluxing overnight equimolar quantities of Hehm and methylamine (40% in H_2O) in ethanol. Reactions of isomaltol (**3**) with methylamine, or other primary amines, resulted in 6-membered-ring pyridinone insertion products (**2**) obviating the formation of furan-based Schiff base chelating agents (31); however, the fact that Hehm contains a bulkier methyl group at the 5 position on Hehm rather than a hydrogen, favored the formation of an amide, and no pyridinones were detected. Two intramolecular hydrogen bonds probably provide a very stable structure for Hahm (Scheme 1). In the solid state, Hahm is a stable off-white powder; however, in water, it undergoes a slow decomposition which is time-, concentration-, and pH-dependent. Unusual aqueous solution behavior was first observed during the potentiometric titrations; as a result compound preparation (*vide infra*) and solution studies in water were undertaken with freshly prepared solutions.

The infrared spectrum of Hahm, in the solid form, showed an N—H stretch at 3390 cm^{-1}, suggesting that a conjugate structure predisposed to chelation may be formed (Scheme 1). The O—H stretching vibration results, due to hydrogen bonding, in a broad band centered around 3100 cm^{-1}. Due to solubility limitations in non-protic solvents, solution studies to investigate the hydrogen bonding in Hahm, although desirable, were not undertaken. A band characteristic of all amides is the strongly absorbing $\nu_{C=O}$ (amide I band) which occurs at 1665 cm^{-1} in Hahm. There is considerable mixing of the C=O and the C=C vibrations such that the bands at 1665 and 1610 cm^{-1} are most likely combination bands, being primarily due to $\nu_{C=O}$ and $\nu_{C=C}$, respectively. The broad band at 1575 cm^{-1} (amide II band) is a combination band primarily due to a δ_{NH} coupled to a ν_{CN}. The C—N stretch (amide III band) region occurs between 1305 and 1220 cm^{-1}, but because of the presence of many other bands in this region, a definite assignment was not possible.

The ^1H NMR spectra of Hahm were obtained in D_2O, CD_3OD, and DMSO-d_6. In all solvents, the spectra of the ring substituents were consistent with the proposed structure (three peaks in a 3:3:1 ratio). A small long range coupling (1 Hz) between the ring hydrogen at the 4-position and the methyl group at the 5-position was also observed. The EI mass spectrum of Hahm showed the parent peak at *m/z* 155; loss of a methyl group resulted in a peak at *m/z* 140 and loss of N—CH_3 gave rise to a peak at *m/z* 126.

Hahm complexes

Synthesis of the metal complexes of Hahm in high yield were carried out in water, but required that the pH be raised to 9 initially due to the lower water solubility of Hahm. The nitrate salt of the desired metal was then added to a freshly prepared Hahm solution, giving a 3:1 Hahm-to-metal ratio; the pH was readjusted to ~7. The aluminum and gallium complexes were obtained in 72 and 75% yields, respectively.

Upon coordination to the metal, the N—H and O—H stretches in the IR spectrum broadened to cover the ~3500 to 2800 cm^{-1} region, with maximum absorbance at 3400 cm^{-1}. Notably, the carbonyl stretch shifted 20 to 40 cm^{-1} lower in the complexes, consistent with complexation, and there was one very strong amide band at 1530 cm^{-1}, with weaker shoulder bands at higher wavenumbers. The two bands at 1610 and 1575 cm^{-1} in the spectrum of Hahm shifted into one overlapped band at 1530 cm^{-1}.

The ^1H NMR spectra of the Hahm complexes were consistent with the formulations; they showed that the environment at the 5-methyl was scarcely affected by chelation to the metal and the 1 Hz coupling constant between the ring 4-hydrogen and 5-methyl group, which was small for the ligand, was unresolvable for the metal complexes. The ring hydrogen and the amide methyl underwent significant shifts, since they are closer to the binding site. $Ga(ahm)_3$ decomposed in methanol, showing a broad shoulder or additional peaks from the free ligand. A spectrum consistent with the proposed structure was obtained in pyridine-d_5. In an effort to detect the amide hydrogen, DMSO-d_6 was used, but both the aluminum and gallium complexes decomposed becoming solvolyzed in this solvent.

The metal complexes decomposed under electron impact ionization conditions, so their mass spectra were obtained by fast atom bombardment ionization. Peaks from HML_3^+, ML_2^+, and ML^+ were present for both complexes. For the aluminum complex, the base peak was that from ML_2^+, while a weak $M_2L_5^+$ peak was observed at *m/z* 824, typical of neutral tris(bidentate) chelate complexes (4). The mass spectrum of the gallium complex showed many peaks due to the matrix (thioglycerol), but the most intense metal–ligand fragment was ML_2^+. Peaks due to HML_3^+ and $M_2L_5^+$ were observed with the appropriate isotopic ratios, the former being more intense.

Stability constants for $M(ahm)_3$

Solution potentiometry at $\mu = 0.6$ M demonstrated that Hahm is a weak acid ($K_a = 10^{-7.09}$) and that the ahm^- anion is not an outstanding binding group for aluminum (Table 1). The ahm^-

Can. J. Chem. Downloaded from www.nrcresearchpress.com by EESC ESCOLA DE ENGENHARIA on 09/08/12
For personal use only.

anion, however, may have potential as the metal binding component of higher dentate chelating agents. Table 1 lists the formation constants β_{pqr} at μ = 0.6 M as defined in the experimental section. The speciation was characterized by a series of $AlL_n^{(3-n)+}$ complexes (n = 1, 2, 3). These had the following stepwise constants: log K_1 = 7.28, log K_2 = 6.14, log K_3 = 4.83 as calculated from the data in Table 1 and defined by:

$$[5] \quad K_n = \frac{[ML_n^{\{3-n\}+}]}{[ML_{n-1}^{\{4-n\}+}][L^-]}$$

(for an overall stability constant for the $Al(ahm)_3$ complex of $10^{18.25}$). The formation constants are less than those for the group 13 M^{3+} complexes of the 2,4-pentanedionato (acac) anion where log K_1 is ~ 8.7, log K_2 ~ 7.8, and log K_3 ~ 6.5 (32).

In neutral solutions with excess ligand ($B/C > 3$), a deprotonation of the AlL_3 complex was observed with elimination of the ligand. Whether the resulting –4,2,1 complex was a mixed hydroxo complex, $[Al(OH)_2L_2]^-$, or a species where the amide N is deprotonated cannot be predicted from the pH measurements; however, it seems reasonable to assume this species to be a mixed hydroxo complex. Similar anions have been found in other Al^{3+} systems with ligands forming complexes of high and intermediate stability, such as polycarboxylates like oxalate (33) and citrate (20), polyphenols like gallate (15), catecholate (34), and 1,2-dihydroxynaphthalene-4-sulfonate (35), as well as aromatic *o*-carboxylic phenols like salicylate (36). All these complexes are formed in neutral or slightly alkaline solutions and can be regarded as precursors to the $[Al(OH)_4]^-$ ion. In acidic solutions (– log $[H^+] \approx 4$) with $B/C < 3$ a cationic trinuclear complex is formed (cf. Fig. 4*b*). A possible structure of this complex is $[Al_3(OH)_4L_3]^{2+}$, consistent with the connection between the binary hydrolysis (cf. $[Al_3(OH)_4]^{5+}$) and mixed ligand/hydroxo complexes formed. Mixed complexes of this type have been reported in several Al^{3+} systems and seem to be formed more as a rule than as an exception (37).

For purposes of rough comparison, the pK_a of Hahm and the logarithms of the overall formation constants for the 3:1 aluminum and gallium complexes were determined from the 0.15 M data to be 7.15, 19.5, and 20.5, respectively. Determination of the protonation constant of Hahm actually showed two inflection points, one corresponding to the deprotonation of the hydroxyl proton, and one that might be due to the deprotonation of the amide nitrogen (– log $K \approx 12.4$); however, the ionic strength was no longer constant at – log $[H^+] > 12$. Although the overall values are higher than those of isomaltol (9), at millimolar concentration, the predominant species was still due to undesirable hydrolysis, at pH greater than 7 for gallium and at pH greater than 8.5 for aluminum. The onset of hydrolysis was delayed until a higher pH compared to isomaltol, but still occurred to a significant extent. At higher ratios of Hahm:M, the ligand easily competes with hydrolysis, such that the ML_3 species predominate in the intermediate pH regime.

Concluding remarks

The synthesis of Hehm can be carried out cleanly and in high yield if the starting materials are pure and an excess of EDSA is used. A close analogue of Hehm, Hehbm, was formed as an impurity if the ratio was inappropriate and as a major product if a 1:1 ratio of EDSA:diketene was used. Attempts to prepare potentially hexadentate ligands based on the amidation of Hehm failed and Hehm did not undergo reactions typical of an ester; however, Hahm was produced in high yield from Hehm and methylamine. Aluminum and gallium complexes of Hahm have been prepared and thoroughly characterized; they have higher formation constants than their isomaltol analogs, likely as a result of the amide carbonyl being a harder donor by resonance than a ketone carbonyl. The Al system has been shown by extensive potentiometric study to contain mixed ahm⁻/hydroxo $[Al(OH)_2L_2]^-$ and $[Al_3(OH)_4L_3]^{2+}$ complexes, in addition to the simple $AlL_n^{(3-n)+}$ species (n = 1, 2, 3).

Acknowledgements

Acknowledgement is made to the British Columbia Health Research Foundation, NSERC of Canada, the U.S. Public Health Service (CA 48964), and the Swedish Natural Science Research Council for support of this work, to Drs. Ray Andersen and Nick Burlinson for most helpful discussions, and to Dr. Lars-Olaf Öhman for assistance.

1. I. Fattahpour Sedeh, S. Sjöberg, and L.-O. Öhman. J. Inorg. Biochem. **50**, 119 (1993).
2. D.J. Clevette, D.M. Lyster, W.O. Nelson, T. Rihela, G.A. Webb, and C. Orvig. Inorg. Chem. **29**, 667 (1990).
3. Z. Zhang, D.M. Lyster, G.A. Webb, and C. Orvig. Nucl. Med. Biol. **19**, 327 (1992).
4. M.M. Finnegan, T.G. Lutz, W.O. Nelson, A. Smith, and C. Orvig. Inorg. Chem. **26**, 2171(1987).
5. T. Hedlund and L.-O. Öhman. Acta Chem. Scand. **A42**, 702 (1988).
6. W.O. Nelson, T.B. Karpishin, S.J. Rettig, and C. Orvig. Inorg. Chem. **27**, 1045 (1988); W.O. Nelson, S.J. Rettig, and C. Orvig. Inorg. Chem. **28**, 3153 (1989).
7. C.A. Matsuba, W.O. Nelson, S.J. Rettig, and C. Orvig. Inorg. Chem. **27**, 3935 (1988).
8. D.J. Clevette, W.O. Nelson, A. Nordin, C. Orvig, and S. Sjöberg. Inorg. Chem. **28**, 2079 (1989).
9. T.G. Lutz, D.J. Clevette, S.J. Rettig, and C. Orvig. Inorg. Chem. **28**, 715 (1989).
10. C.F. Baes, Jr. and R.E. Mesmer. The hydrolysis of cations. 2nd. ed. Wiley, New York. 1976.
11. W.O. Nelson, T.B. Karpishin, S.J. Rettig, and C. Orvig. Can. J. Chem. **66**, 123 (1988).
12. R.L.N. Harris. Aust. J. Chem. **29**, 1329 (1976); Th. Severin and A. Loidl. Z. Lebensm. Unters.-Forsch. **161**, 119 (1976).
13. H. Takei, M. Higo, K. Saito, and T. Mukaiyama. Bull. Chem. Soc. Jpn. **41**, 1738 (1968).
14. G.B. Payne. J. Org. Chem. **32**, 3351 (1967).
15. L.-O. Öhman and S. Sjöberg. Acta Chem. Scand. Ser. A, **A35**, 201 (1981).
16. G. Gran. Acta Chem. Scand. **4**, 559 (1950).
17. G. Gran. The Analyst, **77**, 661 (1952); Anal. Chim. Acta, **206**, 111 (1988).
18. L.-O. Öhman and W. Forsling. Acta Chem. Scand. Ser. A, **A35**, 795 (1981).
19. L.-O. Öhman, S. Sjöberg, and N. Ingri. Acta Chem. Scand. Ser. A **A37**, 561 (1983).
20. L.-O. Öhman. Inorg. Chem. **27**, 2565 (1988).
21. N. Ingri and L.G. Sillén. Ark. Kemi, **23**, 97 (1964).
22. N. Arnek, L.G. Sillén, and O. Wahlberg. Ark. Kemi, **31**, 353 (1969); P. Brauner, L.G. Sillén, and R. Whiteker. Ark. Kemi, **31**, 365 (1969).
23. L.G. Sillén. Acta Chem. Scand. **16**, 159 (1962).
24. L.G. Sillén and B. Warnqvist. Ark. Kemi, **31**, 341 (1969).
25. H. Rossotti. The study of ionic equilibria. Longman, London. 1978. p. 76.
26. G. Eriksson. Anal. Chim. Acta, **112**, 375 (1979).
27. R.J. Motekaitis and A.E. Martell. Can. J. Chem. **60**, 2403 (1982).

28. L.J. Bellamy. Infrared spectra of complex molecules. Vol. 2. Chapman and Hall, New York. 1980. p. 210.
29. R. Grigg, M.V. Sargent, D.H. Williams, and J.A. Knight. Tetrahedron, **21**, 3441 (1965).
30. R.J. Andersen, M.J. Le Blanc, and F.W. Sum. J. Org. Chem. **45**, 1169 (1980).
31. T.G. Lutz. M.Sc. thesis, University of British Columbia, Vancouver, BC. 1988.
32. A.E. Martell and R.M. Smith. Critical stability constants. Vol. 3. Plenum, New York. 1977. p. 246.
33. L.-O. Öhman and S. Sjöberg. J. Chem. Soc. Dalton Trans. 2665 (1985).
34. L.-O. Öhman and S. Sjöberg. Polyhedron, **2**, 1329 (1983).
35. L.-O. Öhman, S. Sjöberg, and N. Ingri. Acta Chem. Scand. Ser. A, **A37**, 561 (1983).
36. L.-O. Öhman and S. Sjöberg. Acta Chem. Scand., Ser. A, **A37**, 875 (1983).
37. L.-O. Öhman and S. Sjöberg. *In* Metal speciation: theory, analysis and application. *Edited by* J.R. Kramer, H.E. Allen. Lewis Publishers, Chelsea, MI. 1988. p. 1.

Can. J. Chem. Downloaded from www.nrcresearchpress.com by EESC ESCOLA DE ENGENHARIA on 09/08/12
For personal use only.

Solubility and solvation of pyronato and pyridinato complexes of aluminum, gallium, and indium in alcohol–water mixtures

EMMA BEATTY, JOHN BURGESS,[1] AND MARTTAND S. PATEL
Department of Chemistry, University of Leicester, Leicester LE1 7RH, U.K.

Received April 20, 1993[2]

EMMA BEATTY, JOHN BURGESS, and MARTTAND S. PATEL. Can. J. Chem. **72**, 1370 (1994).

Solubilities are reported for aluminum, gallium, and indium tris-ligand complexes of the pyrones maltol and ethylmaltol and of a number of 4-pyridinones in water–methanol and water – *tert*-butyl alcohol solvent mixtures, at 298.2 K. Trends and patterns in transfer chemical potentials derived from these solubilities are discussed in terms of the dependence of solvation on the nature of the ligand, the metal, and the cosolvent.

EMMA BEATTY, JOHN BURGESS et MARTTAND S. PATEL. Can. J. Chem. **72**, 1370 (1994).

Opérant à 298,2 K, dans des mélanges d'eau–méthanol et d'eau – alcool *tert*-butylique, on a mesuré les solubilités des complexes tricoordinés de l'aluminium, du gallium et de l'indium avec les pyrones maltol et éthylmaltol et un certain nombre de 4-pyridones. On discute des tendances et des patrons observés dans les potentiels chimiques de transfert dérivés de ces solubilités en fonction de la dépendance de la solvatation sur la nature du coordinat, du métal et du cosolvant.

[Traduit par la Rédaction]

Introduction

Extensive series of ligands of the 4-pyrone (maltol), **1**, and 4-pyridinone, **2**, type have been developed for the control of

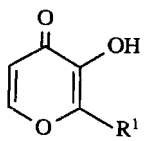

1

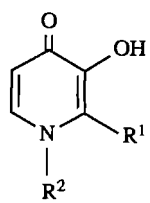

2

iron levels in the body, either for administering iron to anaemic patients or for the removal of excessive body burdens, as in haemochromatosis or thalassemia (1, 2). In view of the similarities between iron(III) and aluminum(III) complexes, it seems possible that ligands of this type might be useful in lowering aluminum levels in the body (3), perhaps thereby slowing the progress of at least some types of dementia. These ligands and their metal(III) complexes are able to penetrate various body membranes, hence the possibilities of the control of iron and aluminum levels. Complementarily, these species may afford a convenient way of administering elements, particular those with a stable 3+ oxidation state, of diagnostic or therapeutic value into the body (2). Such elements include, for example, gallium (^{67}Ga, ^{68}Ga) (4–7) and indium (^{111}In) (4, 5, 8) for diagnosis, yttrium (^{90}Y for radiotherapy of tumours (5, 9)), and gadolinium (for magnetic resonance imaging, MRI (10)). These tris-ligand–metal(III) complexes are moderately water-soluble, and also reasonably soluble in a number of organic solvents. Their favorable pharmacokinetic characteristics (11) may derive from the balance between hydrophilic and lipophilic regions. In the present paper we report the results of our measurements of solubilities of some aluminum(III), gallium(III), and indium(III) complexes of ligands of type **1** and **2** in methanol–water and in *tert*-butyl alcohol – water solvent mixtures. It is especially interesting that the pyrone complexes are more soluble in alcohol–water mixtures than in water or the alcohol alone. This suggests particularly favorable solvation when the water component can solvate the hydrophilic areas, the alcohol the lipophilic areas, of the complex. Such solvation characteristics may stabilize this type of complex at fat–water interfaces, e.g., at the surfaces of membranes. They may thus be important in connection with transport through membranes and barriers, for adsorption at the interface is a necessary prerequisite to passage through the membrane (12).

Experimental

Maltol was obtained from Aldrich, ethylmaltol from Pfizer; the pyridinones were prepared from these by published methods (13). Yields were between 45 and 70%; products were characterized by their melting points and ^{1}H NMR spectra. The aluminum, gallium, and indium complexes were also prepared by established methods (7) in yields of 80–90%. The complexes were characterized by melting points, ^{1}H NMR, and ultraviolet–visible spectra (where known).

Saturated solutions were obtained by equilibrating a generous excess of solid complex with the appropriate solvent medium for several days, with occasional agitation, in a thermostatted bath (298.2 K). Aliquots of supernatant saturated solution were removed and diluted as appropriate. Absorbances were measured at the wavelengths given in Table 1, and solubilities thence calculated from the dilutions used and the respective molar extinction coefficients (Table 1) (13).

Results

Absorbances and solubilities for all the complexes studied are collected in Table 1. This table also includes transfer chemical potentials calculated from these experimental results (cf. Discussion below). The absorbances in Table 1, and the solubilities calculated from them, are reported to a higher precision than warranted by the experimental procedure to avoid the introduction of any rounding-off uncertainties. The transfer chemical potentials are quoted to one decimal place; uncertainties in these values may be taken to be between 5 and 10%.

Discussion

The maltol and ethylmaltol complexes show solubility maxima in methanol–water mixtures. The solubility plot for tris-maltolato–indium(III), In(memal)$_3$, is shown in Fig. 1, which indicates particularly favorable solvation in 60–80% methanol. This is compatible with the greater solubility of this complex in methanol than in water. Presumably the higher sol-

[1]Author to whom correspondence may be addressed. Telephone: [UK] + 533 522089. Fax: [UK] + 533 523789.

[2]Revision received November 24, 1993.

Can. J. Chem. Downloaded from www.nrcresearchpress.com by EESC ESCOLA DE ENGENHARIA on 09/08/12
For personal use only.

TABLE 1. Solubilities and transfer chemical potentials for tris-ligand complexes of aluminum, gallium, and indium in alcohol–water mixtures at 298.2 K

		Volume % ROH						
		0	20	40	60	80	90	100
		Al(memal)$_3$ (ε_{305} = 18 000)						
t-BuOH:	ASS[a]	560	820	1500	1880	970	330	
	10^2 soly[b]	3.1	4.6	8.3	10.4	5.4	1.8	
	Δ[c]		−1.0	−2.4	−3.0	−1.4	+1.3	
		Al(etmal)$_3$ (ε_{304} = 23 000)						
MeOH:	ASS	29.4	38.7	73	235	530		410
	10^4 soly	12.8	16.8	32	102	230		180
	Δ		−0.7	−2.3	−5.2	−7.2		−6.6
t-BuOH:	ASS	29.4	34.6	71.8	106	76.2	41.3	
	10^4 soly	12.8	15.0	31	46	33	18	
	Δ		−0.4	−2.2	−3.2	−2.4	−0.8	
		Al(mpp)$_3$ (ε_{303} = 21 400)						
t-BuOH:	ASS	920	640	300	104	21.9	8.8	
	10^4 soly	430	298	142	49	10.2	4.1	
	Δ		+0.9	+2.7	+5.4	+9.3	+11.5	
		Al(dmpp)$_3$ (ε_{303} = 30 000)						
t-BuOH:	ASS	106	223	360	148	36.3	18.0	
	10^4 soly	25	74	120	49	12	0.60	
	Δ		−1.9	−3.1	−0.8	+2.7	+4.4	
		Al(empp)$_3$ (ε_{293} = 21 000)						
MeOH:	ASS	2110	3830	7100	9950	19000		10200
	soly	0.10	0.18	0.38	0.47	0.90		0.49
	Δ		−1.5	−3.0	−3.8	−5.4		−3.9
t-BuOH:	ASS	2110	3520	4700	3390	610	215	
	soly	0.10	0.167	0.223	0.161	0.029	0.010	
	Δ		−1.3	−2.0	−1.2	+3.1	+5.7	
		Al(depp)$_3$ (ε_{292} = 19 000)						
MeOH:	ASS	3450	5370	6950	11400	16400		21100
	soly	0.18	0.28	0.37	0.60	0.86		1.11
	Δ		−1.1	−1.7	−3.0	−3.9		−4.5
t-BuOH:	ASS	3450	8300	13100	8740	3320	480	
	soly	0.181	0.44	0.69	0.46	0.175	0.026	
	Δ		−2.2	−3.2	−2.3	+0.1	+4.9	
		Ga(memal)$_3$ (ε_{305} = 20 130)						
MeOH:	ASS	46	67	135	240	400		275
	10^4 soly	23	33	67	119	198		136
	Δ		−0.9	−2.7	−4.1	−5.4		−4.5
		In(memal)$_3$ (ε_{275} = 20 000)						
MeOH:	ASS	43	52	123	1120	1130		720
	10^4 soly	21	26	62	560	560		360
	Δ		−0.5	−2.6	−8.1	−8.1		−7.0
		In(etmal)$_3$ (ε_{303} = 19 940)						
MeOH:	ASS	2.3	4.4	19.6	80	169		114
	10^4 soly	1.1	2.2	9.8	40	85		57
	Δ		−1.6	−5.3	−8.8	−10.7		−9.7
		In(empp)$_3$ (ε_{294} = 27 030)						
MeOH:	ASS	59	129	360	920	1610		630
	10^4 soly	22	48	132	340	620		230
	Δ		−1.9	−4.5	−6.8	−8.2		−5.9
		In(depp)$_3$ (ε_{293} = 27 500)						
MeOH:	ASS	20	38	108	350	720		1410
	10^4 soly	7.4	13.9	39	125	260		510
	Δ		−1.6	−4.1	−7.0	−8.8		−10.5

[a]ASS = absorbance of saturated solution, i.e., measured absorbance time dilution.
[b]Abbreviation: soly = solubility, in mol dm^{-3}.
[c]Δ = transfer chemical potential, i.e., $\delta_m\mu^0$ (complex), cf. equations in text.

Can. J. Chem. Downloaded from www.nrcresearchpress.com by EESC ESCOLA DE ENGENHARIA on 09/08/12
For personal use only.

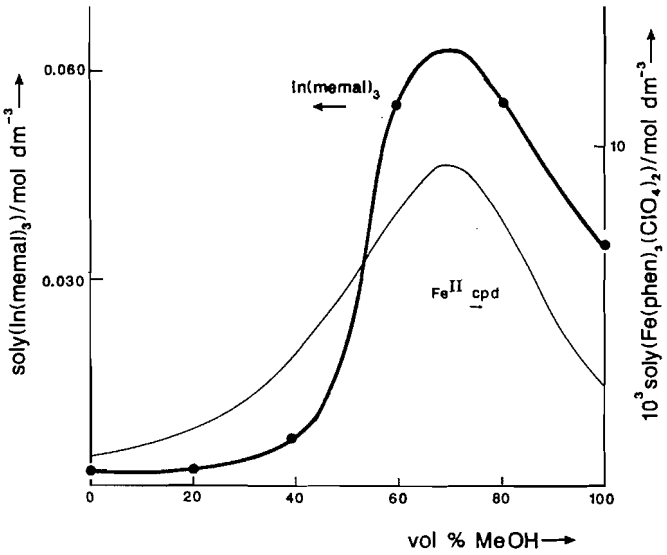

FIG. 1. Dependence of the solubilities of tris-maltolato–indium(III) and of tris-1,10-phenanthrolineiron(II) perchlorate on solvent composition in methanol–water mixtures, at 298.2 K.

ubility in the binary aqueous mixtures than in either water or methanol alone can be attributed to favorable interactions between ligand oxygens and water, and favorable interactions at lipophilic parts of the periphery of the complex with the methanol. It is interesting to compare this behavior for [In(memal)$_3$] with that of a salt, e.g., [Fe(phen)$_3$](ClO$_4$)$_2$, consisting of a hydrophobic cation well solvated by methanol and a hydrophilic anion well solvated by water. The solubility patterns of the indium complex and of the perchlorate of the [Fe(phen)$_3$]$^{2+}$ cation (14) are compared in Fig. 1, which shows a remarkably similar pattern for these two compounds.

The solubility results of Fig. 1 and in Table 1 can be converted into transfer chemical potentials using the formulae

$$\delta_m\mu^0 = -RT \ln\{(\text{soly in mixed solvent})/(\text{soly in water})\}$$

for an uncharged solute,

$$\delta_m\mu^0 = -nRT \ln\{(K_{sp} \text{ in mixed solvent})/(K_{sp} \text{ in water})\}$$

for an electrolyte with $z_+ + z_- = n$ (K_{sp} = solubility product). Relative solubilities can thence be discussed in energy-related terms. The consequent minima in transfer chemical potentials are shown in Fig. 2. This figure also shows analogous plots, derived from published solubilities (15), for a number of other compounds that have both hydrophilic and lipophilic areas on their surfaces. Thus eicosanoic acid (arachidic acid, Me(CH$_2$)$_{18}$CO$_2$H) has a long hydrocarbon chain balanced to a modest extent by the hydrophilic carboxylic acid group; the sulfa drug sulfathiazole, **3**, and the amino acid tryptophan, **4**, are other examples of compounds with similarly balanced peripheries. These compounds can be linked to the salt [Fe(phen)$_3$](ClO$_4$)$_2$ mentioned above through ternary complexes such as [Fe(CN)$_2$(bipy)$_2$], where hydrophilic cyanide and hydrophobic 2,2′-bipyridyl ligands are now both bonded to the iron(II) center. [Fe(CN)$_2$(bipy)$_2$] also exhibits solubility maxima, and thus transfer chemical potential minima, in alcohol–water mixtures (16).

Figure 3 compares our new results for the tris-maltolato com-

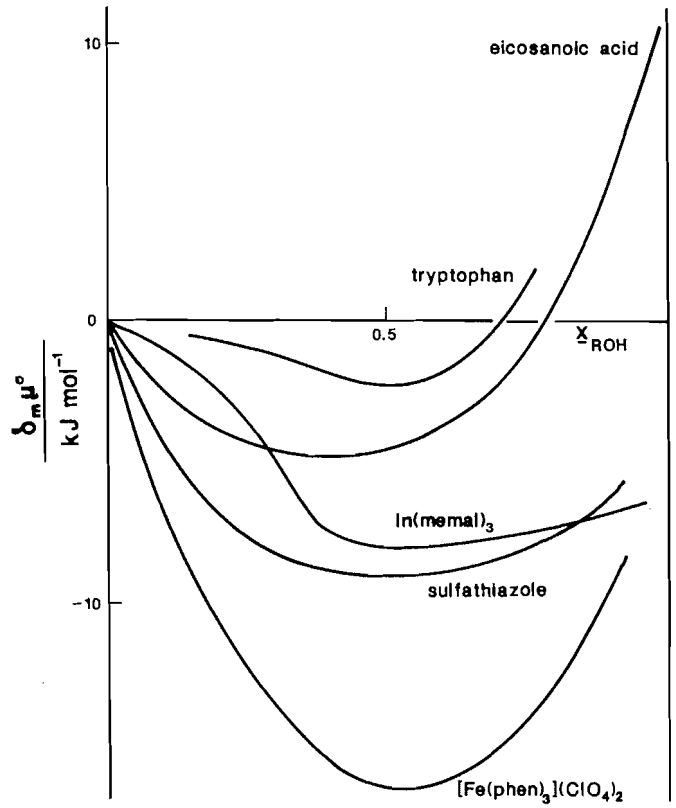

FIG. 2. Dependence of transfer chemical potentials (molar scale) on solvent composition for the compounds indicated, for methanol–water mixtures at 298.2 K.

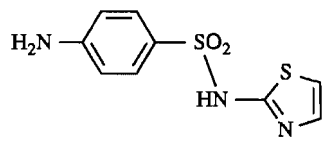

3

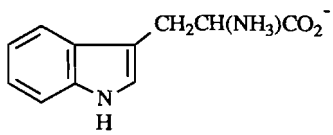

4

plexes of indium and of gallium with published data for analogous complexes of iron and of aluminum (17). In all cases there is a minimum at about 2:1 methanol:water. The indium complex shows a bigger minimum than the gallium, aluminum, and iron complexes. This comparison also applies to transfer chemical potentials from water to methanol. Thus complexes of the largest metal ion, viz., indium, show greatest sensitivity to solvation environment. This behavior is not unique to the present group of ligands, for similar behavior has been established for tris(8-hydroxyquinolinato)–aluminum(III) and –indium(III) (18), and in comparisons of the acetylacetonate (2,4-pentanedionate) complex UO$_2$(acac)$_2$ with VO(acac)$_2$ and with first-row transition metal(II) complexes M(acac)$_2$ (19), though in these latter comparisons the presence of different numbers of oxide ligands rather complicates the discussion. It seems likely that the

Can. J. Chem. Downloaded from www.nrcresearchpress.com by EESC ESCOLA DE ENGENHARIA on 09/08/12
For personal use only.

Can. J. Chem. Downloaded from www.nrcresearchpress.com by EESC ESCOLA DE ENGENHARIA on 09/08/12
For personal use only.

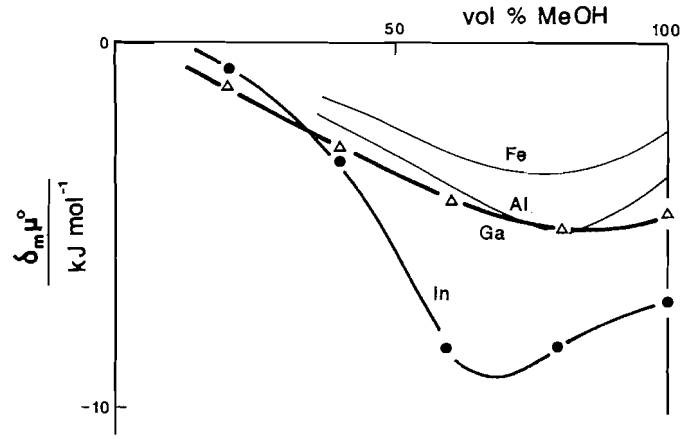

FIG. 3. Transfer chemical potentials for tris-maltolato complexes to methanol – water mixtures, at 298.2 K.

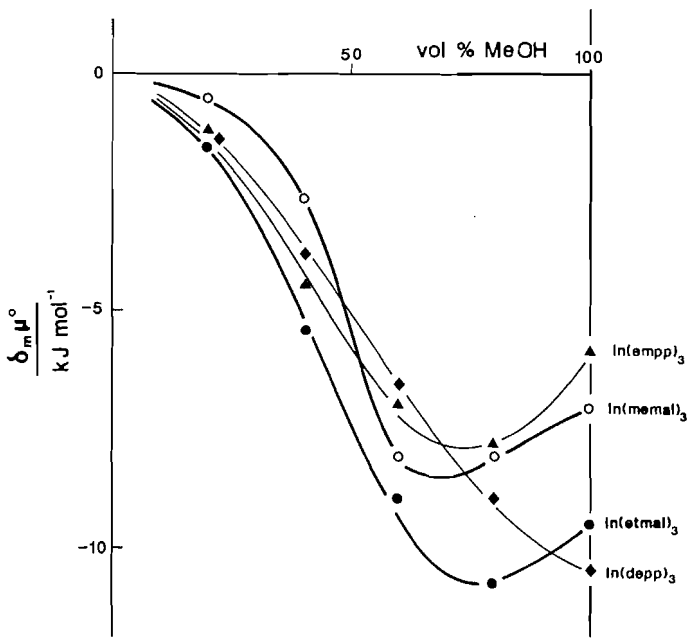

FIG. 4. Transfer chemical potentials for indium complexes to methanol–water mixtures, at 298.2 K.

observed size effects can be attributed to sterically controlled differences in hydrogen-bonding interactions between solvent components and coordinated oxygen atoms in the respective complexes. The importance of such hydrogen bonding in complexes of this type seems to have been first suggested to explain effects of dissolved β-diketonate complexes of a variety of metals on the infrared spectra of chloroform and of methanol (20). This evidence was later considerably strengthened by the results of water–alkane partition experiments on beryllium β-diketonates (21) and on tris-acetylacetonate and tris-monothioacetylacetonate complexes of cobalt(III) (22). X-ray diffraction studies have indicated significant hydrogen bonding between waters of crystallization in, for example, *fac*-[M(dmpp)$_3$], M = Al or Ga, and the coordinated oxygens of the dimethylpyridinone ligands (23).

Figure 4 shows transfer chemical potential trends for a range of indium complexes. Tris-ethylmaltolato–indium(III), In(etmal)$_3$ (ethylmaltol = **1** with R = Et), exhibits a solubility

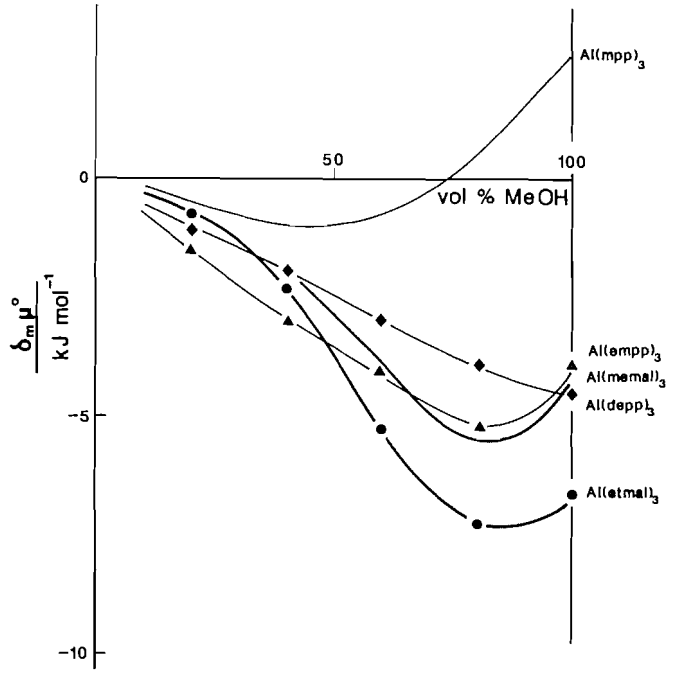

FIG. 5. Transfer chemical potentials for aluminum complexes to methanol–water mixtures, at 298.2 K.

maximum, and a transfer chemical potential minimum, at a mixed solvent composition similar to that of the parent complex tris-maltolato–indium(III). The less hydrophilic ethyl-substituted derivative is, as expected, markedly more soluble in methanol in comparison with water than is its parent. The ethyl methyl derivative In(empp)$_3$, empp = **2** with R^1 = Et, R^2 = Me, also shows a marked transfer chemical potential minimum. On going to significantly more hydrophobic species, such as the tris-diethylpyridinone (**2** with R^1 = R^2 = Et) complex of indium(III), In(depp)$_3$, the transfer chemical potential minimum disappears. Such complexes are continuously more favorably solvated by the methanol as its proportion increases.

Figures 5 and 6 show transfer chemical potential trends for a range of aluminum complexes, with methanol and *tert*-butyl alcohol as cosolvents, respectively. As expected, the pattern for transfer to methanol–water mixtures is similar to that for the analogous indium complexes (Fig. 4), though for aluminum the published (17) trend for Al(mpp)$_3$, mpp = **2** with R^1 = Me, R^2 = H, provides a comparison with a particularly hydrophilic pyridinone complex. Figure 5 has been drawn to the same scale as Fig. 4 to facilitate comparison, as indeed has Fig. 6. This last figure's main feature is that it shows all the complexes, except Al(mpp)$_3$, to have positive transfer quantities to *tert*-butyl alcohol-rich mixtures. Thus in general *tert*-butyl alcohol solvates not just less well than methanol but also less well even than water. All complexes, again with the exception of the particularly hydrophilic Al(mpp)$_3$, show a minimum. In other words, addition of up to 40–60% *tert*-butyl alcohol increases solvation, but then further decreasing the proportion of water leads to a fairly rapid rise in potential, with the pyridinone complexes having more positive transfer chemical potentials than the pyrone complexes. The tris-pyridinone complexes of aluminum thus become relatively less favorably solvated than the tris-pyrone complexes on transfer from water into 90% *tert*-butyl alcohol. This comparison, and the greater stabilization of aluminum tris-pyridinone complexes on addition of

Can. J. Chem. Downloaded from www.nrcresearchpress.com by EESC ESCOLA DE ENGENHARIA on 09/08/12
For personal use only.

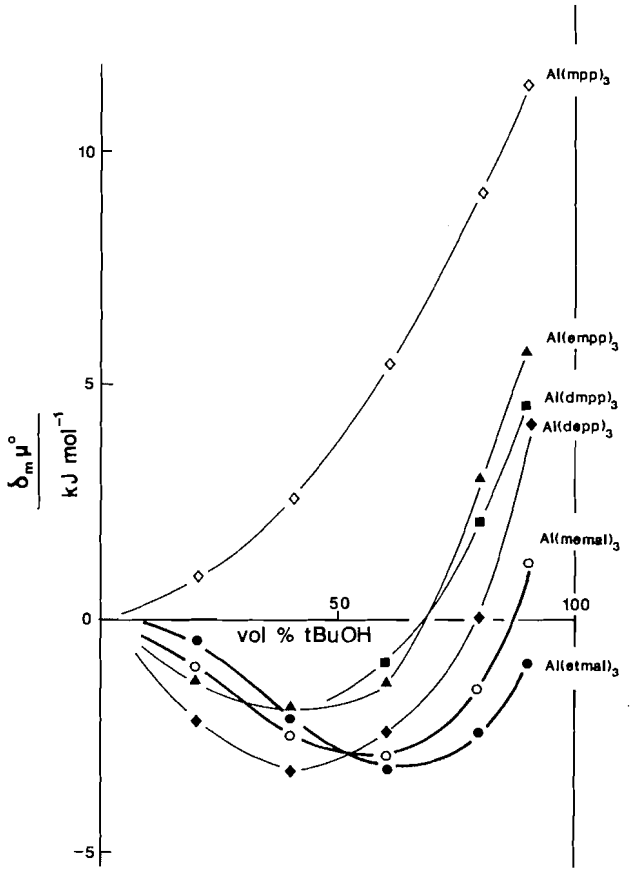

FIG. 6. Transfer chemical potentials for aluminum complexes to *tert*-butyl alcohol – water mixtures, at 298.2 K.

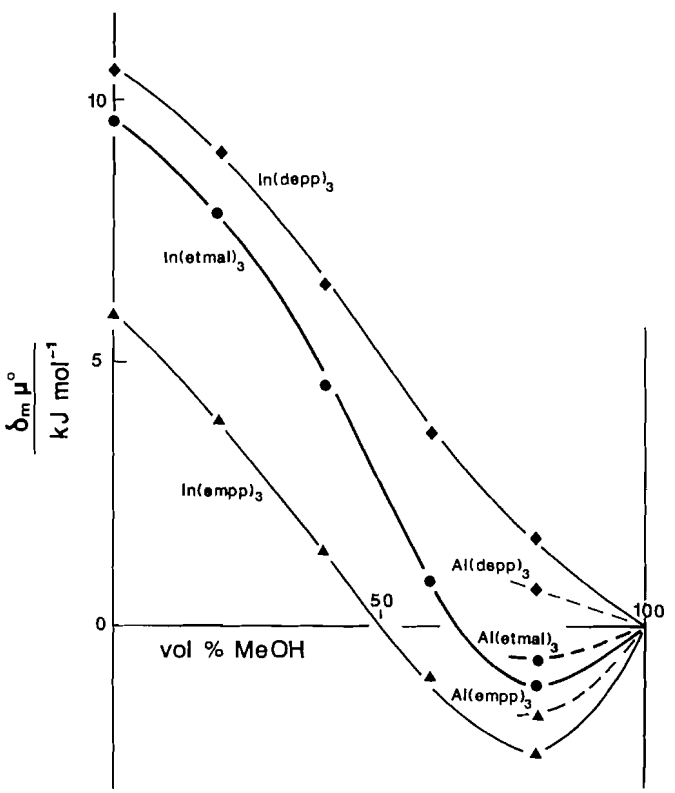

FIG. 7. Transfer chemical potentials for indium and aluminum complexes from methanol to methanol–water mixtures, at 298.2 K.

water to 90% *tert*-butyl alcohol, both suggest that the pyridinone complexes are the more hydrophilic. Greater hydration of pyridinone than of pyrone complexes is also supported by partial molar volumes, which are 264 cm^3 mol^{-1} for $Al(memal)_3$, 238 cm^3 mol^{-1} for the slightly larger complex $Al(dmpp)_3$ {memal = **1** with R^1 = Me; dmpp = **2** with $R^1 = R^2$ = Me}.[3] This comparison strongly suggests more electrostrictive hydration around the latter.

Most of the above discussion has been based on water as the reference solvent. The complementary point of view takes methanol or *tert*-butyl alcohol as the reference medium. The addition of water to the latter causes marked stabilization of *all* the aluminum complexes (Fig. 6), showing the importance of hydration at the 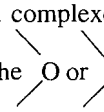 sites in the heterocyclic rings and at coordinating oxygens. The consideration of methanol as reference solvent leads to greater discrimination (Fig. 7). Now the addition of water destabilizes the most hydrophobic complexes, viz., the diethyl derivatives $Al(depp)_3$ and $In(depp)_3$, stabilizes the memal and etmal complexes moderately, and the empp complexes a little more.

The well-established intermolecular associations in alcohol–water mixtures (24) may have an influence on solubility trends through their effects on solvent–solute interactions. Thus the increased hydrogen-bonding structure of alcohol–water mixtures may make both components less available for solvating a solute. If solvent–solvent interactions play a dominant rôle, then extrema in the solubility and transfer chemical potential trends at solvent compositions corresponding to regions of maximum structuredness would be expected, i.e., at around mole fractions of 0.23 (40% by volume) methanol and of 0.04 (17% by volume) *tert*-butyl alcohol (24). This is not the case, as is apparent from several of the figures, and indeed the marked dependence of transfer chemical potential minima on the nature of the solute in *tert*-butyl alcohol – water mixtures (Fig. 6) shows that solute–solvent interactions dominate over solvent–solvent. The situation is analogous to that reported earlier for the tris(3-hydroxy-1,2-dimethylpyridin-4-ato)aluminum(III)–water–methanol system (25).

The success and potential value of these complexes in a pharmacological context is due in considerable measure to their solvation characteristics, which enable them to cross various biological barriers and membranes. Significant solubility both in water and in alcohols (e.g., Table 1) is important both in relation to significant solvation in aqueous and lipoid environments and in relation to distribution between these two types of environment. The synergic solvation reported for several systems in the present paper may prove advantageous in stabilizing the respective ligands or complexes at interfaces and thus positioning them favorably for trans-membrane transport, as mentioned in the Introduction. However, if the solute is particularly well stabilized at an interface, then it may be reluctant to move on. The ideal properties in the present context are probably a combination of appreciable and similar solubilities in water and in alcohols, and a small degree of synergic solvation in alcohol–water mixtures (26).

Acknowledgements

We are grateful to Professor R.C. Hider and Dr. P.S. Dobbin for advice on the preparation of the pyridinone ligands, and to

[3] J. Burgess and P. Guardado. Unpublished results.

Professor J. Narbutt and Professor R.C. Hider for helpful discussions on solvation of complexes in hydrogen-bonding media and in biological membranes, respectively.

1. (*a*) J.B. Porter, E.R. Huehns, and R.C. Hider. Baillière's Clin. Haematol. **2**, 257 (1989); (*b*) P.S. Dobbin and R.C. Hider. Chem. Br. 565 (1990); (*c*) N.F. Olivieri, D.M. Templeton, G. Koren, D. Chung, C. Hermann, M.H. Freedman, and R.A. McClelland. Ann. N.Y. Acad. Sci. **612**, 369 (1990).
2. R.C. Hider and A.D. Hall. Prog. Med. Chem. **28**, 41 (1991).
3. (*a*) G.J. Kontoghiorghes and J. Barr. First Int. Symp. on Chelation, London. 1989. p. 19; (*b*) R.A. Yokel, A.K. Datta, and E.G. Jackton. J. Pharmacol. Exp. Ther. **257**, 100 (1991).
4. (*a*) A.E. Martell and M.J. Welch. Recl. Trav. Chim. Pays-Bas, **106**, 386 (1987); (*b*) C.J. Mathias, Y. Sun, M.J. Welch, M.A. Green, J.A. Thomas, K.R. Wade, and A.E. Martell. Nucl. Med. Biol. **15**, 69 (1988); (*c*) D.J. Clevette, D.M. Lyster, W.O. Nelson, T. Rihela, G.A. Webb, and C. Orvig. Inorg. Chem. **29**, 667 (1990).
5. C.J. Broan, J.P.L. Cox, A.S. Craig, R. Kataky, D. Parker, A. Harrison, A.M. Randall, and G. Ferguson. J. Chem. Soc. Perkin Trans. 2, 87 (1991).
6. M.-F. Tsan and U. Scheffel. J. Nucl. Med. **27**, 1215 (1986).
7. M.M. Finnegan, T.G. Lutz, W.O. Nelson, A. Smith, and C. Orvig. Inorg. Chem. **26**, 2171 (1987).
8. (*a*) D.C. Costa, D. Lui, and P.J. Ell. Nucl. Med. Commun. **9**, 725 (1988); (*b*) D.C. Berridge, J.J. Earnshaw, M. Frier, A.C. Perkins, M.L. Wastie, B.R. Hopkinson, and G.S. Makin. Br. J. Surg. **76**, 41 (1989); (*c*) C. Thiemermann, G.R. May, C.P. Page, and J.R. Vane. Br. J. Pharmacol. **99**, 303 (1990).
9. (*a*) J.L. Humm. J. Nucl. Med. **27**, 1490 (1986); (*b*) J.P.L. Cox, K.J. Jankowski, R. Kataky, D. Parker, N.R.A. Beeley, B.A. Boyce, M.A.W. Eaton, K. Millar, A.T. Millica, A. Harrison, and C. Walker. J. Chem. Soc. Chem. Commun. 797 (1989); (*c*) C. Mottahennessy, R.M. Sharkey, and D.M. Goldenberg. Appl. Radiat. Isot. **42**, 421 (1991).
10. (*a*) R.B. Lauffer. Chem. Rev. **87**, 901 (1987); (*b*) M.J. Kendrick, M.T. May, M.J. Plishka, and K.D. Robinson. Metals in biological systems. Ellis Horwood, Chichester. 1992; (*c*) D.W. Chakeres and P. Schmalbrock. Fundamentals of magnetic resonance imaging. Williams and Wilkins, Baltimore, Md. 1992.
11. D.J. Clevette and C. Orvig. Polyhedron, **9**, 151 (1990).
12. W.D. Stein. Transport and diffusion across cell membranes. Academic Press, New York. 1986.
13. (*a*) W.O. Nelson, T.B. Karpishin, S.J. Rettig, and C. Orvig. Can. J. Chem. **66**, 123 (1988); (*b*) G.J. Kontoghiorges and L. Sheppard. Inorg. Chim. Acta, **136**, L11 (1988); (*c*) G.J. Kontoghiorges, L. Sheppard, and J. Barr. Inorg. Chim. Acta, **152**, 195 (1988).
14. F.M. van Meter and H.M. Neumann. J. Am. Chem. Soc. **98**, 1382 (1976).
15. (*a*) A.I. Shkadova. Farm. Zh. (Kiev), **24**, 39 (1969); (*b*) A.S. Kertes (*Editor*). Solubility data series. Vol. 35. Pergamon Press, Oxford. 1988; (*c*) Y. Nozaki and C. Tanford. J. Biol. Chem. **246**, 2211 (1971).
16. J. Burgess, S. Radulović, and F. Sanchez. Transition Met. Chem. (London), **12**, 529 (1987).
17. J. Burgess and M.S. Patel. Inorg. Chim. Acta, **170**, 241 (1990).
18. J. Burgess, D.N. Drasdo, and M.S. Patel. J. Pharm. Sci. **83**, 54 (1994).
19. A. Al-Alousy and J. Burgess. Polyhedron, **11**, 531 (1992).
20. T.S. Davis and J.P. Fackler. Inorg. Chem. **5**, 242 (1966).
21. J. Narbutt. J. Inorg. Nucl. Chem. **43**, 3343 (1981).
22. J. Narbutt. J. Phys. Chem. **95**, 3432 (1991).
23. W.O. Nelson, T.B. Karpishin, S.J. Rettig, and C. Orvig. Inorg. Chem. **27**, 1045 (1988).
24. F. Franks and D.J.G. Ives. Q. Rev. Chem. Soc. **20**, 1 (1966).
25. J. Burgess and M.S. Patel. J. Chem. Soc., Dalton Trans. 2647 (1992).
26. J. Burgess, M.S. Patel, and R.C. Hider. J. Pharm. Pharmacol. In press.

Can. J. Chem. Downloaded from www.nrcresearchpress.com by ESC ESCOLA DE ENGENHARIA on 09/08/12
For personal use only.

Smith-degradative studies on the polysaccharide portion of A-band lipopolysaccharide from a mutant (AK1401) of *Pseudomonas aeruginosa* strain PAO1

TODD L. ARSENAULT AND DAVID B. MACLEAN[1]
Department of Chemistry, McMaster University, Hamilton, ON L8S 4M1, Canada

AND

WEI ZOU AND WALTER A. SZAREK[1]
Department of Chemistry, Queen's University, Kingston, ON K7L 3N6, Canada

Received October 7, 1993

TODD L. ARSENAULT, DAVID B. MACLEAN, WEI ZOU, AND WALTER A. SZAREK. Can. J. Chem. **72**, 1376 (1994).

Hepta-*O*-acetyl-*O*-α-D-Rha*p*-(1→3)-*O*-α-D-Rha*p*-(1→2)-glycerol (**5**) was the major component derived by way of Smith degradation of A-band polysaccharide (a D-rhamnan isolated from a mutant, AK1401, of *Pseudomonas aeruginosa* strain PAO1). The structure has been verified by an unambiguous synthesis of **5**. Based on mass spectrometric evidence, hepta-*O*-acetyl-*O*-Rib*p*-(1→3)-*O*-α-D-Rha*p*-(1→2)-glycerol is considered to be one of the minor components. The Smith degradation of A-band polysaccharide and the synthesis of **5** are reported.

TODD L. ARSENAULT, DAVID B. MACLEAN, WEI ZOU ET WALTER A. SZAREK. Can. J. Chem. **72**, 1376 (1994).

L'hepta-*O*-acétyl-*O*-α-D-Rha*p*-(1→3)-*O*-α-D-Rha*p*-(1→2)-glycérol (**5**) est le produit majeur obtenu par une dégradation de Smith du polysaccharide de la bande A (un D-rhamnane isolé d'un mutant, le AK1401, de la lignée PAO1 de la *Pseudomonas aeruginosa*). On a vérifié la structure par un synthèse non ambiguë du composé **5**. Sur la base des données de la spectrométrie de masse, on considère que l'hepta-*O*-acétyl-*O*-Rib*p*-(1→3)-*O*-α-D-Rha*p*-(1→2)-glycérol est un des produits mineurs. On rapporte la dégradation de Smith du polysaccharide de la bande A ainsi que la synthèse du composé **5**.

[Traduit par la Rédaction]

Introduction

AK1401 is a mutant of *Pseudomonas aeruginosa* strain PAO1 (serotype O5) that does not express O-antigen, but does express A-band lipopolysaccharide (LPS) (1, 2). The polysaccharide portion of the A-band LPS (A-PS) from AK1401 was found (2) to consist mainly of D-rhamnose, with smaller amounts of 3-*O*-methylrhamnose, ribose, mannose, glucose, and a 3-*O*-methylhexose. ^{1}H NMR spectra of the intact A-PS indicated that the main structural feature was a repeating trisaccharide of α-D-rhamnose, namely [→2)-*O*-α-D-Rha*p*-(1→3)-*O*-α-D-Rha*p*-(1→3)-*O*-α-D-Rha*p*-(1→]$_n$ (see **1**, Scheme 1). Here we report a Smith degradation (3) of A-PS, which was undertaken to test the validity of the deductions, from NMR analysis, of the structural features. The degradation of A-PS was expected to follow the course outlined in Scheme 1. Thus the polymer **2**, resulting from periodate oxidation – sodium borohydride reduction, would afford, after hydrolysis, the disaccharide **3** and 1,2-propanediol (**4**). Compound **5** would be formed upon reduction of **3** followed by acetylation. Also, we report the synthesis of **5**.

Results and discussion

The A-PS was subjected to the degradation procedure outlined in Scheme 1 and the acetylated product was examined by TLC on silica ($CHCl_3$–MeOH, 19:1 v/v). The chromatogram showed a major component (oblong spot, $R_f = 0.5$) and at least two minor components (sharp spots, $R_f = 0.31$ and 0.26) contained within a streak from the origin to the top spot. The product mixture was resolved into two fractions by column chromatography, one containing the major component and the other containing both of the minor components. HPLC analysis was not helpful in resolving the mixture.

A GC examination of the fraction containing the major component isolated by column chromatography and of the whole

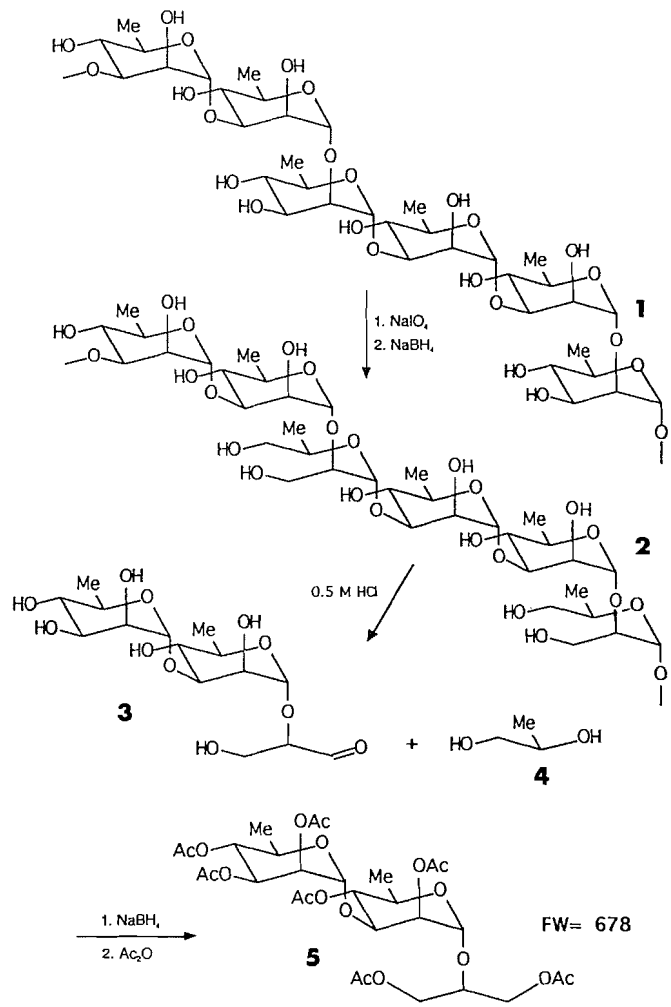

SCHEME 1

[1]Authors to whom correspondence may be addressed.

Can. J. Chem. Downloaded from www.nrcresearchpress.com by EESC ESCOLA DE ENGENHARIA on 09/08/12
For personal use only.

Can. J. Chem. Downloaded from www.nrcresearchpress.com by EESC ESCOLA DE ENGENHARIA on 09/08/12
For personal use only.

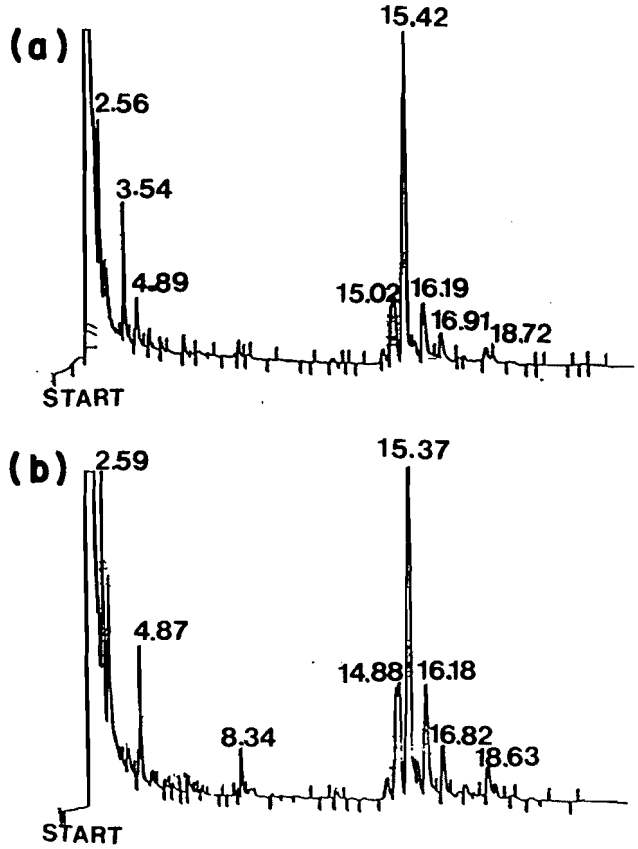

FIG. 1. Gas chromatography of oligosaccharide acetates resulting from Smith degradation of the AK1401 A-PS. (*a*) Total mixture. (*b*) Fraction isolated by column chromatography ($R_f = 0.5$ in TLC).

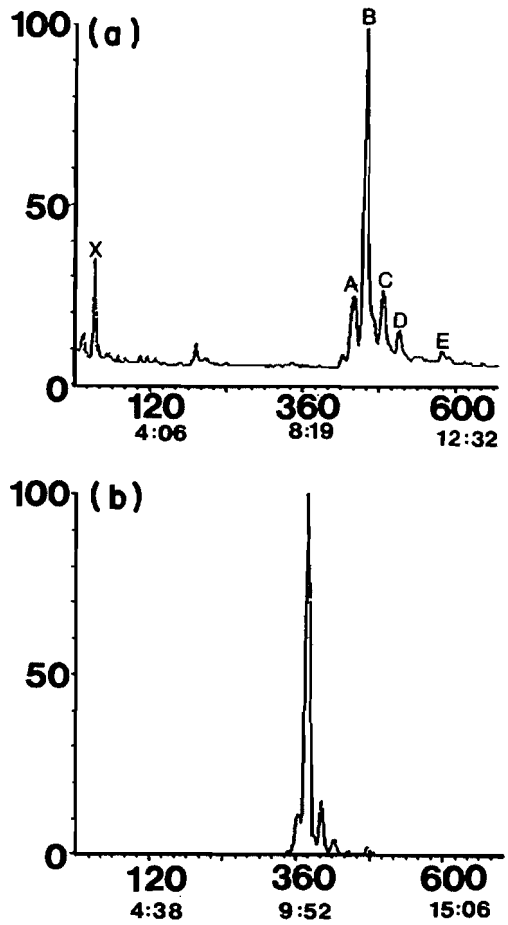

FIG. 2. Total ion-current chromatograms of oligosaccharide acetates from Smith-degraded AK1401 A-PS. (*a*) Electron impact. (*b*) Ammonia chemical ionization.

mixture gave the same chromatogram (Fig. 1), suggesting that the higher polarity components were involatile. (Mass spectrometric examination has shown that the involatile compounds are oligomers; their structures are under investigation.) Moreover, the chromatograms clearly show that the mixture was much more complex than TLC or column chromatography had indicated. GC–MS under EI conditions of the whole mixture gave the chromatogram shown in Fig. 2*a*; that obtained using GC–MS under NH_3-CI conditions is shown in Fig. 2*b*. In the latter case, the chromatographic resolution was not as good as it was in the EI experiment, because the column had to be overloaded to overcome the relative insensitivity of the CI experiment. The relative abundances of the volatile components of the mixture, namely X:A:B:C:D:E = 0.053:0.163:0.584:0.114:0.042:0.044, were derived from the integrated areas of the peaks in Fig. 1*b*.

Interpretation of the mass spectra of the components is not straightforward because literature spectra do not exist (based on a search of probable compositions in the Chemical Abstracts Formula index and the EPA/NIH mass spectral data base). However, the principal component seen in the GC (peak B in Fig. 2*a*) shows an intense ion at *m/z* 696 $(M + NH_4)^+$ in the NH_3-CIMS experiment, which corresponds in mass to the composition expected for the major degradation product derived from the rhamnan, namely *O*-α-D-Rha*p*-(1→3)-*O*-α-D-Rha*p*-(1→2)-Gly-ol$(OAc)_7$ (**5**) (see Scheme 1).

In the course of an investigation of a rhamnan isolated from *P. aeruginosa* IID 1008 (ATCC 27584), Yokota et al. (4) reported on its Smith degradation. They isolated a compound containing two D-rhamnose units and one glycerol, to which they assigned the structure of **5**; their structural assignment was based upon the structure of the rhamnan from which it was derived.

Interpretation of the spectrum of **5** was facilitated by the presence of a related compound of lower molecular weight (peak X, Fig. 2*a*). The NH_3-CI spectrum of peak X shows an ion at *m/z* 466 $(M + NH_4)^+$, suggesting that the formula weight is 448. The EI spectrum of peak X, shown in Fig. 3, is interpreted in Scheme 2. The structures assigned to the ions are based on analogous fragmentations proposed for monosaccharide peracetates (5). Therefore, peak X is attributed to *O*-α-D-Rha*p*-(1→2)-Gly-ol$(OAc)_5$ (**6**) (see Table 1), which can result from overhydrolysis of the Smith-degraded A-PS or be derived from the nonreducing terminus of the A-PS if the end sequence was *O*-α-D-Rha*p*-(1→3)-*O*-α-D-Rha*p*-(1→2)-*O*-α-D-Rha*p*-(1→. In this sequence the nonreducing, terminal unit would be oxidized and lost, the central unit would survive intact, and the third rhamnose unit would be converted into the glycerol portion.

The EI spectrum of peak B is shown in Fig. 4 and is interpreted in Scheme 3. The ion at *m/z* 273 is prominent in the case of this component, as are its daughter ions, thus indicating that rhamnose is the monosaccharide at the nonreducing terminus; the ion at *m/z* 159 is again indicative of the presence of the glycerol portion. The presence of an ion at *m/z* 503 shows that this compound contains a rhamnose–rhamnose disaccharide moiety coupled with the glycerol unit. The ion at *m/z* 259 is assigned by analogy to a corresponding fragment ion described by Peltier et

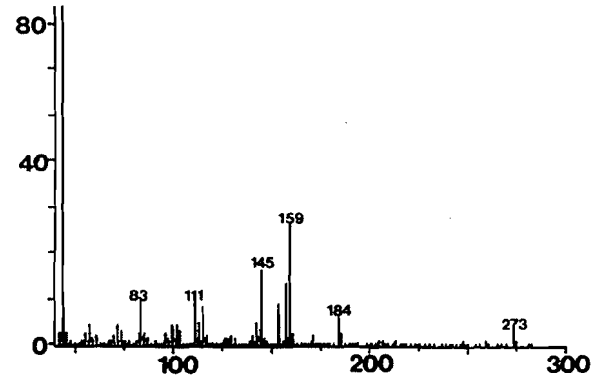

FIG. 3. EI mass spectrum of peak X (molecular weight = 448), i.e., *O*-α-D-Rha*p*-(1→2)-Gly-ol(OAc)$_5$.

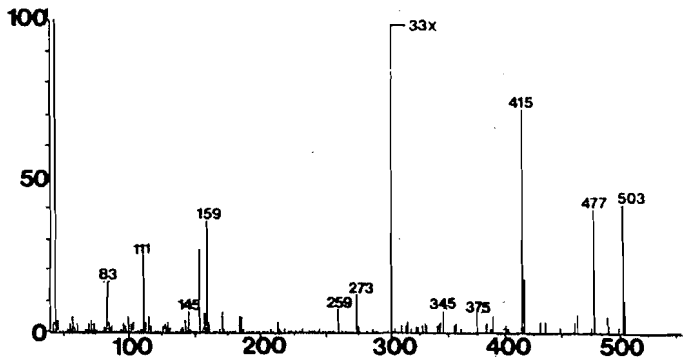

FIG. 4. EI mass spectrum of peak B (molecular weight = 678), i.e., *O*-α-D-Rha*p*-(1→3)-*O*-α-D-Rha*p*-(1→2)-Gly-ol(OAc)$_7$.

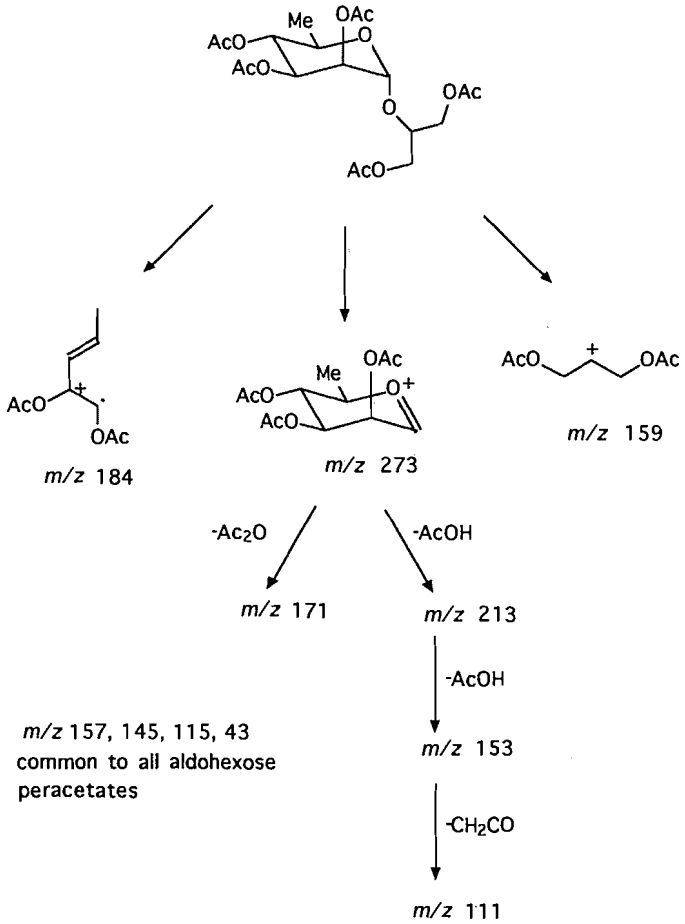

SCHEME 2

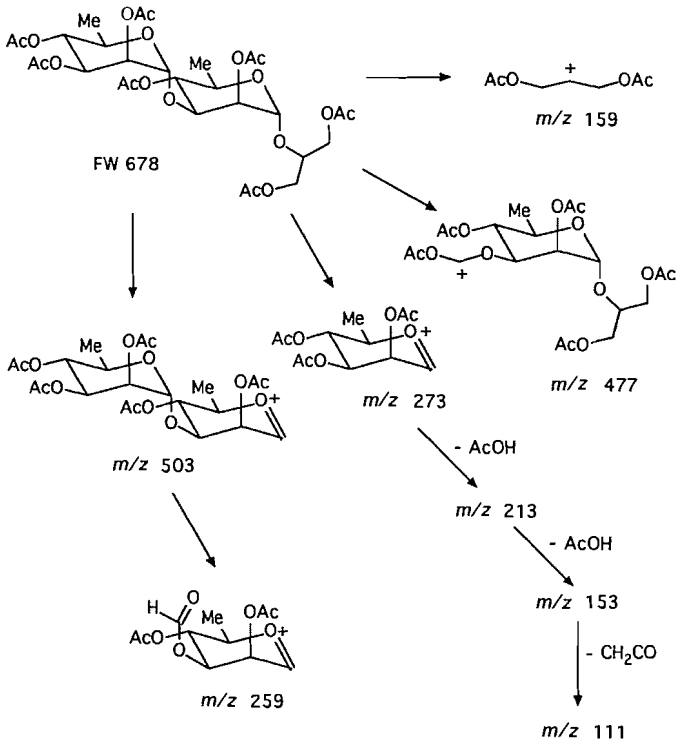

SCHEME 3

al. (6). The ion at *m/z* 477 is analogous to an ion in the spectrum of *N*-arylglycosylamine disaccharide peracetates (7), disaccharide peracetates (8, 9), and permethylated disaccharides (10, 11). The ion at *m/z* 415 could not be assigned with certainty. The ions at *m/z* 259 and 477 resulted from decomposition of the ring at the nonreducing terminus. The masses of the ions illustrated in Scheme 3 were measured by high-resolution mass spectrometry and agree with calculated values within ±0.005 Da.

Only the spectra of D and E of the remaining peaks of Fig. 2*a* were amenable to interpretation. The more straightforward was the spectrum of D (see Fig. 5), which has an ion at *m/z* 159 derived from a glycerol moiety and an intense ion at *m/z* 259, but none at *m/z* 273. These data suggest that the nonreducing terminal unit is not rhamnose and the ion at *m/z* 259 arises from a route different from, or additional to, that proposed for an ion of the same mass in the major component. A pentose in the nonreducing terminal position would be expected to form an ion at *m/z* 259; thus the terminal sugar in compound D may be ribose, a minor component of A-PS (2). Moreover, the disaccharide – oxonium ion is shifted from *m/z* 503 in the spectrum of B to *m/z* 489 in the spectrum of D. Also, the ion at *m/z* 415 in peak B is absent, but is replaced by an ion at *m/z* 401, a change that corresponds to replacement of a rhamnose unit by ribose and which indicates that the nonreducing terminal unit is a component of this ionic species. The mass of the disaccharide – oxonium ion (*m/z* 489) suggests that the other monosaccharide is rhamnose, an indication that is confirmed by the presence of ions at *m/z* 477 and 259. The former was observed in the spectrum of the major component and may be assigned the same structure in this spectrum; the latter ion signal is more intense than that in the spectrum of the major component and probably is derived from two ions, that shown in Scheme 3 and the oxonium ion

Can. J. Chem. Downloaded from www.nrcresearchpress.com by EESC ESCOLA DE ENGENHARIA on 09/08/12
For personal use only.

TABLE 1. Products of Smith degradation

Component	FW	Structure
X	448	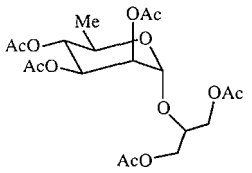 **6**
B	678	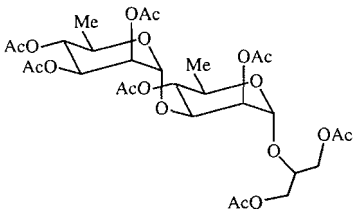 **5**
D	664	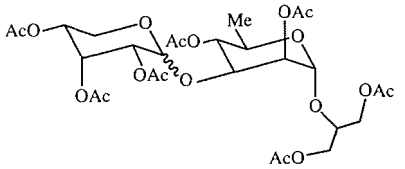 **7**
E	692	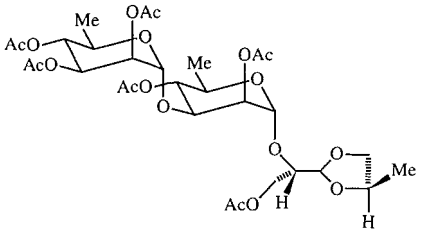 **8**

arising from the ribose unit. The EI data suggest the composition of component D is Rib-Rha-Gly-ol$(OAc)_7$ (FW = 664), an assignment corroborated by the observation of the ion at *m/z* 682 $(M + 18)^+$ in the NH_3-CI spectrum.

A more specific structure can be assigned to component D if one considers the possibility of different ring sizes. If the ribose were present as the furanoside, one would expect fragmentation at C-4–C-5 of the molecular ion of the pentofuranoside to give *m/z* 591 $(M - CH_2OAc)^+$ and 73 $(CH_2OAc)^+$. Since neither of these fragments is present, component D probably contains a ribopyranose unit. From an analysis of possible linkages, a ribopyranoside would survive Smith degradation only if it were linked at C-3 or occupied a branching position in A-PS; similarly, the rhamnose residue in this component must be linked at C-3. Thus, the structure of component D can be defined as *O*-Rib*p*-(1→3)-*O*-α-D-Rha*p*-(1→2)-Gly-ol$(OAc)_7$ (**7**). Only the absolute configuration of the ribose unit and the stereochemistry of the ribose–rhamnose linkage are uncertain.[2] This proposed structure is consistent with the EI and CI mass spectra of this component; however, the structure could be verified only by an examination by GC and GC–MS of the corresponding synthetic standard.

Peak E, although the least abundant component of the mixture, is interesting; by NH_3-CI, its formula weight is 692 (14 amu more than for component B). The EI spectrum (Fig. 6) does not have an ion at *m/z* 159 (glycerol moiety) and contains ions indicative of a rhamnose–rhamnose disaccharide moiety (*m/z* 503, 415, 273, 259, 153, 111). Therefore, the aglycone would have the extra 14 amu; this deduction cannot beverified by the EI spectrum because the aglycone-containing ion (*m/z* 477 in component B) is absent (no *m/z* 477 nor 491).However, there is an abundant ion at *m/z* 87. An ion of this mass might be expected from a compound having the structure of **8**, a compound derived from that which might form intramolecularly in the course of the acid hydrolysis of **2**. A recent example of a similar intramolecular acetalation has been observed by Aspinall et al. (12).

Compound **5** has been synthesized by an unambiguous

[2]The D configuration for the ribose unit is shown arbitrarily in the structural formula given for **7**.

Can. J. Chem. Downloaded from www.nrcresearchpress.com by EESC ESCOLA DE ENGENHARIA on 09/08/12
For personal use only.

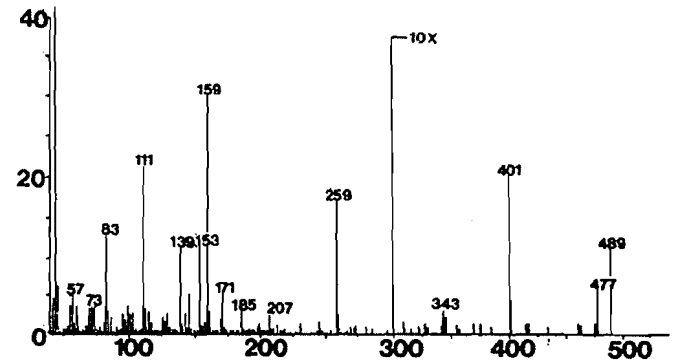

FIG. 5. EI mass spectrum of peak D (molecular weight = 664), i.e., *O*-Rib*p*-(1→3)-*O*-α-D-Rha*p*-(1→2)-Gly-ol(OAc)$_7$.

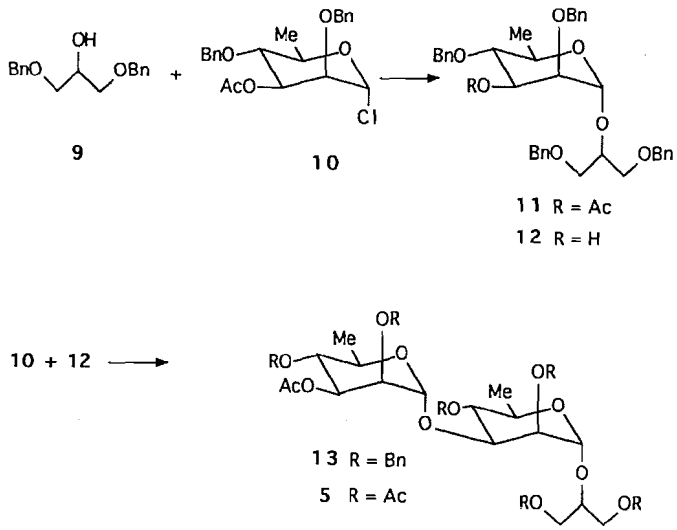

SCHEME 4

method (see below) and the properties of the synthetic and naturally derived materials have been compared. Their EI spectra are virtually identical and their GC retention times are identical. Thus, peak B of Fig. 2*a* may be attributed to the presence of compound **5** and one may conclude that the repeating unit of the rhamnan present in A-PS has the structure deduced from the NMR analysis (2). Unfortunately, the relationship of the minor sugars to the overall structure was not clarified in the present work.

*Synthesis of hepta-*O*-acetyl-*O*-α-D-Rha*p*-(1→3)-*O*-α-D-Rha*p*-(1→2)-glycerol (5)*

The synthesis of an authentic sample of compound **5** is shown in Scheme 4. The reaction of 1,3-di-*O*-benzylglycerol (**9**) (13) with 3-*O*-acetyl-2,4-di-*O*-benzyl-α-D-rhamnopyranosyl chloride (**10**) (14) was performed in the presence of silver triflate and powdered, 4 Å molecular sieves at −10°C to afford the rhamnopyranoside **11** in 50% yield. *O*-Deacetylation of **11** with 0.5% sodium methoxide in methanol at room temperature for 4 h gave *O*-(2′,4′-di-*O*-benzyl-α-D-rhamnopyranosyl)-(1′→2)-1,3-di-*O*-benzylglycerol (**12**), a glycosyl acceptor, that was in turn glycosylated with **10**, again by use of silver triflate and powdered, 4 Å molecular sieves, to give the disaccharide–glycerol conjugate **13**. *O*-Debenzylation of **13** by catalytic hydrogenolysis over 10% Pd–C in methanol, followed by treatment of the product with acetic anhydride–pyridine, afforded the title compound **5**.

Experimental

Methods and materials

Optical rotations were measured with a Perkin-Elmer model 241 polarimeter for solutions in a 0.1-dm cell at room temperature. NMR spectra were recorded on a Bruker AC-F200 spectrometer; $CDCl_3$ was the solvent and Me_4Si was used as the internal standard. Chemical shifts (δ) are given in ppm downfield from the signal of Me_4Si.

Gas chromatography was performed on a Hewlett-Packard 5890 instrument equipped with an on-column injector, a flame ionization detector, and an HP3990A integrator. The columns used were all wide-bore (0.32 mm inside diameter), bonded-phase (0.25 μm film thickness), fused-silica capillary columns (J&W Scientific). The carrier gas was helium, which was passed through an oxygen trap and a water trap (Chromatographic Specialities). Nitrogen at a pressure of 30 psig (1 psi = 6.895 kPa) was used as a makeup gas. GC–MS was performed on a VG MassLab TRIO-2 instrument using the same column and oven temperature. The helium pressure was 2 psig, the transfer line was maintained at 280°C, and the ion-source temperature was 200°C. The sample was analyzed by electron impact and chemical ionization (NH_3) in separate experiments.

The mixture of oligosaccharide acetates resulting from the Smith degradation of the AK1401 A-PS was analyzed by TLC on silica (developed in CH_2Cl_2–MeOH (19:1 v/v) and visualized by spraying with 1% orcinol in 50% sulfuric acid). Analytical HPLC was performed using a Supelco LC-Sil silica column, an eluting solvent of CH_2Cl_2–MeOH (99:1 v/v), and differential refractive-index detection. Preparative column chromatography was performed on a 20 × 2 cm diameter column packed with Merck Kieselgel 60 (230–400 mesh). Elution was performed initially with CH_2Cl_2–MeOH (99:1 v/v) and

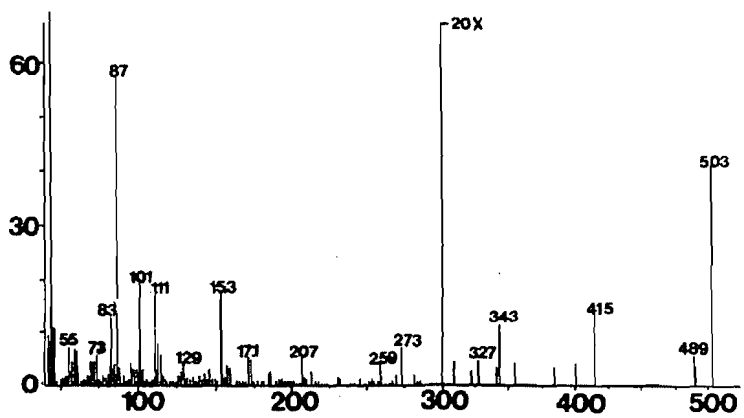

FIG. 6. EI mass spectrum of peak E (molecular weight = 692).

Can. J. Chem. Downloaded from www.nrcresearchpress.com by EESC ESCOLA DE ENGENHARIA on 09/08/12
For personal use only.

Can. J. Chem. Downloaded from www.nrcresearchpress.com by EESC ESCOLA DE ENGENHARIA on 09/08/12
For personal use only.

then with CH_2Cl_2–MeOH (97:3 v/v). Fractions were monitored by TLC as described.

In the synthetic sequence TLC was performed using glass plates precoated with E. Merck Silica Gel 60 F-254. The developed plates were dried, sprayed with a solution of cerium(IV) sulfate (1%) and molybdic acid (1.5%) in 10% aqueous sulfuric acid, and heated at 150°C. Column chromatography was performed using E. Merck No. 9385-5 Silica Gel 60 (230–400 mesh).

The isolation of A-PS from *P. aeruginosa* has been described elsewhere (2).

Smith degradation

A solution of AK1401 A-PS (26 mg) in distilled water (25 mL) was cooled to 4°C and treated with sodium periodate (268 mg, 0.00125 mol). The mixture was kept in the dark at 4°C for 75 h, after which the excess of sodium periodate was destroyed with ethylene glycol. The resulting solution, at ambient temperature, was treated with sodium borohydride (40 mg, 0.001 mol) and stirred for 0.5 h. More sodium borohydride (40 mg) was then added and the mixture was stirred an additional 1.5 h. The reaction was quenched by the addition of 2 M HCl and the pH was adjusted to neutral with 5% sodium hydrogen carbonate. The sample was concentrated to ≈1 mL and transferred to dialysis bags (12 000 – 14 000 molecular weight cutoff). The bags were dialyzed against two 4-L portions of distilled water (first portion, 6 h; second portion, 10 h) and then their contents were freeze-dried to yield a white solid (21 mg).

The bulk of the polymer so obtained was hydrolyzed by dissolving it in aqueous HCl (10 mL, 0.5 M) and allowing the solution to stand at ambient temperature for 52 h with occasional shaking (these very mild conditions allow the selective hydrolysis of the glycosidic linkages of the oxidized residues). The reaction mixture was neutralized with 5% sodium hydrogen carbonate, sodium borohydride (50 mg) was added, and the mixture was stirred at ambient temperature for 18 h. The reaction was quenched by the addition of 5% acetic acid in methanol and the boric acid was removed by distillation. The residue was dried under vacuum (0.005 Torr, 1 Torr = 133.3 Pa) and treated with acetic anhydride (5 mL); the mixture was stirred in an oil bath at 115°C for 2 h. The reaction mixture was quenched by the addition of a saturated aqueous solution (20 mL) of sodium hydrogen carbonate and stirred for 1 h. The solution was extracted with $CHCl_3$ (3 × 20 mL), and the combined extracts were washed with a saturated aqueous solution of sodium hydrogen carbonate (2 × 50 mL) and then with water (2 × 25 mL). The extract was dried over anhydrous sodium sulfate, filtered, and evaporated to yield a yellow oil (20 mg).

*Synthesis of hepta-*O*-acetyl-*O*-α-D-Rha*p*-(1→3)-*O*-α-D-Rha*p*-(1→2)-glycerol (**5**)*

*1,3-Di-*O*-benzylglycerol (**9**)*

This compound was prepared by the method of Fairbourne et al. (13).

*3-*O*-Acetyl-2,4-di-*O*-benzyl-α-D-rhamnopyranosyl chloride (**10**)*

This compound was prepared in several steps from methyl α-D-mannopyranoside as described previously (14).

*O-(3′-*O*-Acetyl-2′,4′-di-*O*-benzyl-α-D-rhamnopyranosyl)-(1′→2)-1,3-di-*O*-benzylglycerol (**11**)*

To a solution of **9** (131 mg) and silver triflate (200 mg) in dichloromethane (3 mL) in the presence of powdered, 4 Å molecular sieves (200 mg) was added **10** (140 mg) in dichloromethane (2 mL) at −10°C under nitrogen. The mixture was stirred at that temperature for 1 h and then at room temperature for 12 h. The mixture was filtered, the filtrate was concentrated, and the residue was purified by chromatography on silica gel (hexane – ethyl acetate, 3:1 v/v) to give **11** as a syrup (111 mg, 50%). ^{13}C NMR (50.32 MHz, $CDCl_3$) δ: 18.00 (C-6′), 21.12 (*C*H_3CO), 67.85 (C-5′), 70.33, 70.82 (C-1, C-3), 73.67, 75.01, 76.56, 79.37 (C-2′, C-3′, C-4′, C-2), 72.89, 73.42, 74.80 (4 *C*H_2Ph), 97.44 (C-1′), 127.55, 127.65, 127.70, 127.74, 127.86, 128.06, 128.35, 128.40, 128.43, 128.52, 137.69, 138.23, 138.84 (4 Ph), 170.03 (C=O).

*O-(2′,4′-Di-*O*-benzyl-α-D-rhamnopyranosyl)-(1′→2)-1,3-di-*O*-benzylglycerol (**12**)*

Compound **11** (111 mg) was dissolved in a solution (4 mL) of 0.5% sodium methoxide in methanol, and the reaction mixture was kept at room temperature for 4 h when it was shown by TLC that the deacetylation was complete. The solution was passed through a column of Amberlite IR-120 (H^+ form) ion-exchange resin and the column was washed with methanol. Evaporation of the solvent gave **12** (100 mg, 96%). ^{13}C NMR (50.32 MHz, $CDCl_3$) δ: 18.00 (C-6′), 67.38 (C-5′), 70.26, 70.65 (C-1, C-3), 71.54, 74.73, 78.86, 82.45 (C-2′, C-3′, C-4′, C-2), 72.84, 73.49, 74.96 (4 *C*H_2Ph), 96.61 (C-1′), 127.61, 127.69, 127.96, 128.40, 128.53, 137.81, 137.92, 138.23, 138.56 (4 Ph); ^{1}H NMR (200 MHz, $CDCl_3$) δ: 1.24 (3H, d, $J_{5',6'}$ = 6.2 Hz, 6′-CH_3), 2.26 (1H, d, J = 9.2 Hz, 3-OH), 3.29 (1H, t, $J_{3',4'} = J_{4',5'}$ = 9.35 Hz, H-4′), 3.46–4.04 (8H, m, H-1(2), H-2, H-3(2), H-2′, H-3′, H-5′), 4.40–4.92 (8H, m, 4 *C*H_2Ph), 5.11 (1H, d, $J_{1',2'}$ = 1.35 Hz, H-1′), 7.23–7.45 (20H, m, 4 Ph).

*O-(3″-*O*-Acetyl-2″,4″-di-*O*-benzyl-α-D-rhamnopyranosyl)-(1″→3′)-*O*-(2′,4′-di-*O*-benzyl-α-D-rhamnopyranosyl)-(1′→2)-1,3-di-*O*-benzylglycerol (**13**)*

To a solution of **12** (100 mg) and silver triflate (120 mg) in dichloromethane (3 mL) in the presence of powdered, 4 Å molecular sieves (200 mg) was added **10** (150 mg) in dichloromethane (2 mL) at −10°C under nitrogen. The mixture was stirred at that temperature for 1 h and then at room temperature overnight. The mixture was filtered, the filtrate was concentrated, and the residue was subjected to chromatography on silica gel (hexane – ethyl acetate, 3:1 v/v) to give **13** (ca. 100 mg). ^{13}C NMR (50.32 MHz, $CDCl_3$) δ: 17.97, 18.19 (C-6″, C-6′), 21.13 (*C*H_3CO), 67.88, 68.35 (C-5″, C-5′), 70.40, 70.59 (C-1, C-3), 72.73, 72.93, 73.42, 74.72 (6 *C*H_2Ph), 73.69, 76.55, 77.19, 78.29, 78.41, 79.21, 80.94 (C-2″, C-3″, C-4″, C-2′, C-3′, C-4′, C-2), 97.32, 98.65 (C-1″, C-1′), 127.10, 127.53, 127.59, 127.65, 127.70, 127.90, 128.31, 128.39, 128.45, 128.60, 138.17, 138.88 (6 Ph), 170.16 (C=O).

*O-(2″,3″,4″-Tri-*O*-acetyl-α-D-rhamnopyranosyl)-(1″→3′)-O-(2′,4′-di-*O*-acetyl-α-D-rhamnopyranosyl)-(1′→2)-1,3-di-*O*-acetylglycerol (**5**) (hepta-*O*-acetyl-*O*-α-D-Rha*p*-(1→3)-*O*-α-D-Rha*p*-(1→2)-glycerol)*

To a solution of **13** (100 mg) in methanol (3 mL) was added 10% Pd–C (ca. 100 mg). The mixture was subjected to a hydrogen pressure (50 psig) at room temperature for 10 h and then filtered to remove the catalyst. The filtrate was concentrated to a residue which was treated with acetic anhydride – pyridine (2 mL, 1:1 v/v) at room temperature for 2 h. Toluene was added and the solution was evaporated. Chromatography of the residue on silica gel (ethyl acetate – hexane, 2:1 v/v) gave compound **5** (55 mg) as an amorphous, low-melting solid. $[\alpha]_D$ 36 (*c* 1.2, MeOH); ^{13}C NMR (50.32 MHz, $CDCl_3$) δ: 17.22, 17.31 (C-6″, C-6′), 20.59, 20.66, 20.89 (7 *C*H_3CO), 63.02, 63.54 (C-1, C-3), 67.08, 67.20 (C-5″, C-5′), 68.50, 70.13, 70.73, 76.16, 72.07, 73.46, 74.89 (C-2″, C-3″, C-4″, C-2′, C-3′, C-4′, C-2), 97.03, 98.73 (C-1″, C-1′), 169.57, 170.01, 170.26 (7 C=O); ^{1}H NMR (200 MHz, $CDCl_3$) δ: 1.17 (3H, d, $J_{5'',6''}$ = 6.3 Hz, 6″-CH_3), 1.19 (3H, d, $J_{5',6'}$ = 6.3 Hz, 6′-CH_3), 1.96–2.19 (21H, 7s's, 7 CH_3CO), 3.87 (1H, dq, $J_{5'',6''}$ = 6.3 Hz, $J_{4'',5''}$ = 9.4 Hz, H-5″), 3.91 (1H, dq, $J_{5',6'}$ = 6.3 Hz, $J_{4',5'}$ = 9.4 Hz, H-5′), 4.02–4.20 (6H, m, H-3′, H-1(2), H-2, H-3(2)), 4.89 (1H, d, $J_{1'',2''}$ = 1.60 Hz, H-1″), 4.93 (1H, d, $J_{1',2'}$ = 1.65 Hz, H-1′), 5.04–5.19 (5H, m, H-4″, H-3″, H-2″, H-4′, H-2′).

Acknowledgements

This work was supported by grants from the Canadian Cystic Fibrosis Foundation (CCFF) and the Natural Sciences and Engineering Research Council of Canada. T.L.A. gratefully acknowledges the receipt of Ontario Graduate Scholarships 1986–1987 and 1988–1989 and a CCFF studentship 1989–1991. We thank Dr. A.M. Kropinski for the sample of A-PS.

1. D. Berry and A.M. Kropinski. Can. J. Microbiol. **32**, 436 (1986).

2. T.L. Arsenault, D.W. Hughes, D.B. MacLean, W.A. Szarek, A.M.B. Kropinski, and J.S. Lam. Can. J. Chem. **69**, 1273 (1991).
3. I.J. Goldstein, G.W. Hay, B.A. Lewis, and F. Smith. *In* Methods in carbohydrate chemistry. Vol. V. *Edited by* R.L. Whistler. Academic Press, New York, N.Y. 1965. pp. 361–370.
4. S.-I. Yokota, S. Kaya, S. Sawada, T. Kawamura, Y. Araki, and E. Ito. Eur. J. Biochem. **167**, 203 (1987).
5. K. Biemann, D.C. DeJongh, and H.K. Schnoes. J. Am. Chem. Soc. **85**, 1763 (1963).
6. J.M. Peltier, D.B. MacLean, and W.A. Szarek. Rapid Commun. Mass Spectrom. **5**, 446 (1991).
7. O.S. Chizhov, N.K. Kochetkov, N.N. Malysheva, A.I. Shiyonok, and V.L. Chashchin. Org. Mass Spectrom. **5**, 1157 (1971).
8. K.G. Das and B. Thayumanavan. Org. Mass Spectrom. **10**, 455 (1975).
9. C. Bosso, F. Taravel, J. Ulrich, and M. Vignon. Org. Mass Spectrom. **13**, 477 (1978).
10. O.S. Chizhov, L.A. Polyakova, and N.K. Kochetkov. Dokl. Akad. Nauk SSSR, Ser. Khim. **158**, 685 (1964).
11. T. Radford and D.C. DeJongh. *In* Biochemical applications of mass spectrometry. *Edited by* G.R. Waller. Wiley–Interscience, New York, N.Y. 1972. pp. 331–350.
12. G.O. Aspinall, A.G. McDonald, and H. Pang. Carbohydr. Res. **231**, 13 (1992).
13. A. Fairbourne, G.P. Gibson, and D.W. Stephens. J. Chem. Soc. 445 (1931).
14. W. Zou, A.K. Sen, W.A. Szarek, and D.B. MacLean. Can. J. Chem. **71**, 2194 (1993).

Can. J. Chem. Downloaded from www.nrcresearchpress.com by EESC ESCOLA DE ENGENHARIA on 09/08/12
For personal use only.

Reaction of unsaturated azlactones with sulfur nucleophiles: some observations

ARYA K. MUKERJEE,[1] LAXMI RAO, SEYED SAIED HOMAMI, AND KIRAN JOSEPH
Chemistry Department, Faculty of Science, Banaras Hindu University, Varanasi-221005, India

Received April 15, 1993

ARYA K. MUKERJEE, LAXMI RAO, SEYED SAIED HOMAMI, and KIRAN JOSEPH. Can. J. Chem. **72**, 1383 (1994).

Unsaturated azlactones undergo thiolysis with toluene-α-thiol, but 2-substituted (*Z*)-4-*o*-acetoxybenzylidene-4,5-dihydrooxazol-5-ones form 3-acylaminocoumarins in the presence of triethylamine. Sodium sulfide in ethanol brings about ethanolysis of the 1,5 bond and deacetylation of an acetoxy group. (*Z*)-4-Benzylidene-4,5-dihydrooxazol-5-one reacts with potassium thiocyanate to give (*E*)-4(5)-benzylidene-2-thiohydantoin.

ARYA K. MUKERJEE, LAXMI RAO, SEYED SAIED HOMAMI et KIRAN JOSEPH. Can. J. Chem. **72**, 1383 (1994).

Sous l'influence du toluène-α-thiol, les azlactones insaturées subissent une thiolyse; toutefois, les (*Z*)-4-*o*-acétoxybenzylidène-4,5-dihydrooxazol-5-ones substituées en position 2, mises en présences de triéthylamine, conduisent à des 3-acylaminocoumarines. Le sulfite de sodium dans l'éthanol provoque une éthanolyse de la liaison 1,5 et une désacylation du groupe acétoxyle. La (*Z*)-4-benzylidène-4,5-dihydrooxazol-5-one réagit avec le thiocyanate de potassium pour conduire à la (*E*)-4(5)-benzylidène-2-thiohydantoïne.

[Traduit par la Rédaction]

Can. J. Chem. Downloaded from www.nrcresearchpress.com by EESC ESCOLA DE ENGENHARIA on 09/08/12
For personal use only.

The reaction of thiols with unsaturated azlactones, for example, **1***a*, *d* (1, and, for the synthesis of penicillamine, ref. 2) and α,β-unsaturated acid derivatives (3), was reported to form adducts, but these additions do not seem to have been properly investigated. Compounds **1***a–g* can behave as bielectrophiles, undergoing cleavage of the 1,5 bond and (or) involvement of the olefinic centre. To probe regioselectivity of the reaction and stereochemistry of the products, the present work using sulfur nucleophiles was undertaken (see ref. 4 for a preliminary communication, and ref. 5).

The required substrates **1***a*, *c*, *d*, *e* were prepared by known methods (for a recent review on azlactones, see ref. 6). The condensation of hippuric acid with triethyl orthoformate and benzaldehyde by the Erlenmeyer procedure (1, 7) afforded 4-ethoxymethlene- and 4-benzylidene-2-phenyl-4,5-dihydrooxazol-5-ones (**1***a*) and (**1***d*), respectively, the (*Z*) isomer being the major product (6). The similar acetic anhydride-mediated condensation of hippuric acid with salicylaldehyde produced (8) 3-benzoylaminocoumarin (**2***a*) and (*Z*)-4-*o*-acetoxybenzylidene-2-phenyl-4,5-dihydrooxazol-5-one (**1***e*). The separation was not only tedious but gave low yields of contaminated compounds. Pure **1***e* was therefore prepared by the acetic anhydride-mediated cyclodehydration of (*Z*)-2-benzoylamino-*o*-hydroxycinnamic acid **4***a*. The condensation of aniline with **1***a* furnished 4-anilinomethylene-2- phenyl-4,5-dihydrooxazol-5-one (**1***c*) (1).

Toluene-α-thiol reacted with **1***a* in pyridine or benzene containing triethylamine to give a mixture from which *S*-benzylthio 2-benzoylamino-3-(*S*-benzylthio)-acrylate (**6**) was separated in pure form by preparative tlc (Scheme 1). The conversion of **1***a* to **6** could proceed by initial thiolysis of the 1,5 bond, followed by conjugate addition of toluene-α-thiol and subsequent elimination of ethanol. Alternatively, it could involve substitution of the ethoxy group by the thiol moiety to form **1***b*, which in turn would undergo thiolysis, affording **6**. The latter pathway would be favored because of the following reasons. Compound **1***a* reacted with aniline to give only the 4-anilinomethylene derivative **1***c*, the 1,5 bond remaining unaffected. This indicated the greater vulnerability of the 4-ethoxymethylene group towards nucleophiles. The ir absorption band near 1790 cm^{-1}, characteristic of the azlactone carbonyl, and the absence of signals due to the ethoxy group in the ^1H nmr spectrum of the crude mixture clearly indicated the presence of **1***b*. Also, two doublets due to the CH-CH group in the ^1H nmr spectrum of the crude mixture could be assigned to structure **7**. As already mentioned, only compound **6** could be separated in pure form. It is noteworthy that the condensation of toluene-α-thiol with **1***c* in boiling eth-

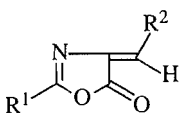

1

a: R^1 = Ph, R^2 = EtO
b: R^1 = Ph, R^2 = $PhCH_2S$
c: R^1 = Ph, R^2 = PhNH
d: R^1 = R^2 = Ph
e: R^1 = Ph, R^2 = 2-$AcOC_6H_4$
f: R^1 = Ph, R^2 = 2,3-$(AcO)_2C_6H_3$
g: R^1 = BzNH—C(=CHPh)—, R^2 = 2-$AcOC_6H_4$

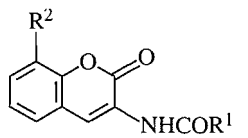

2

a: R^1 = Ph, R^2 = H
b: R^1 = Ph, R^2 = OAc
c: R^1 = Ph, R^2 = OH
d: R^1 = BzNH—C(=CHPh)—, R^2 = H

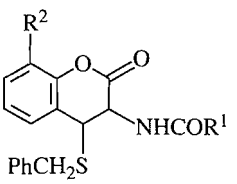

3

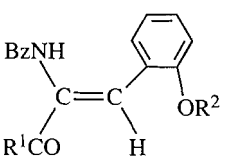

4

a: R^1 = OH, R^2 = H
b: R^1 = $PhCH_2S$, R^2 = Ac
c: R^1 = EtO, R^2 = Ac
d: R^1 = EtO, R^2 = H

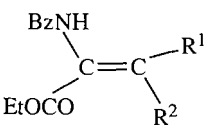

5

a: R^1 = Ph, R^2 = H
b: R^1 = H, R^2 = Ph

[1]Author to whom correspondence may be addressed.

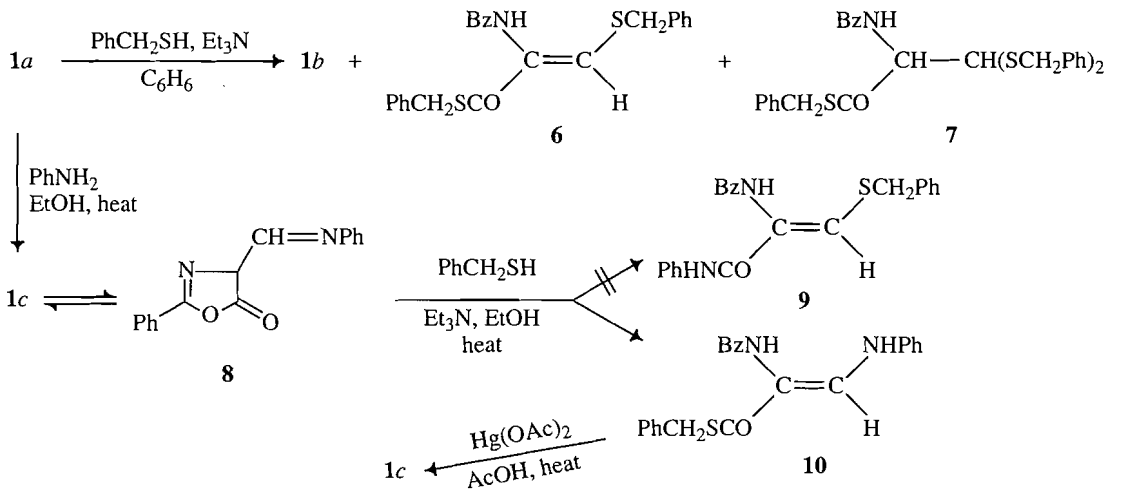

SCHEME 1

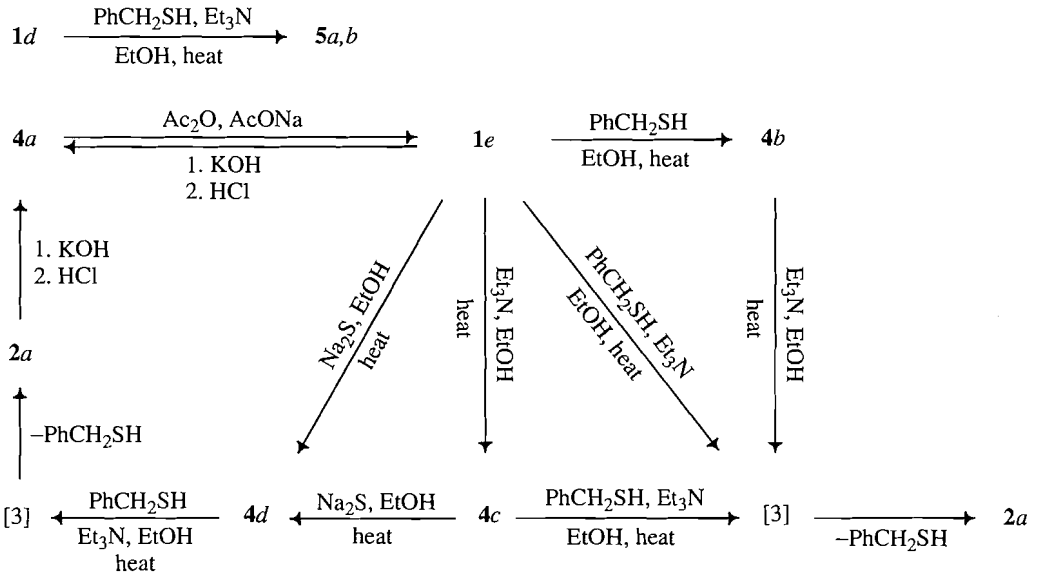

SCHEME 2

anol containing triethylamine led to the formation of *S*-benzylthio 2-benzoylamino-3-anilinoacrylate (**10**), which was also obtained by the triethylamine-mediated reaction of toluene-α-thiol with **1***a* in the presence of aniline. Unlike the ethoxy group of **1***a*, the 4-anilino moiety of **1***c* remained unaffected in this reaction. Dethionation of **10** led to the formation of **1***c*, which lent support to the proposed structure. It should be emphasized that the similar reaction of the alternative isomeric structure **9** would not form **1***c*.

Triethylamine-mediated reaction of toluene-α-thiol with **1***d* in boiling ethanol afforded a sulfur-free product that has been characterized as an (*E*)–(*Z*) mixture of ethyl 2-benzoylaminocinnamate (**5***a*, *b*). The same mixture **5***a*, *b* was also obtained when pure ethyl (*Z*)-2-benzoylaminocinnamate (**5***a*), known in the literature (9), was subjected to the described reaction conditions. These isomers, characterized on the basis of ^{1}H nmr data, could not be separated. The conversion of **1***d* to **5***a*, *b* would be possible by addition of thiol to the double bond of **5***a*, generated in situ, followed by β-elimination.

To probe the mechanism, the reaction of **1***e* with toluene-α-thiol was carried out under different reaction conditions. When the reactants were heated in ethanol alone, a sulfur-containing product was isolated that has been characterized as *S*-benzylthio (*Z*)-2-benzoylamino-*o*-acetoxycinnamate (**4***b*); it recyclized to **1***e* on passage through a silica gel column, but it was stable in neutral solutions. The use of triethylamine in this reaction furnished 3-benzoylaminocoumarin (**2***a*) in good yields. It is noteworthy that **1***e* underwent ethanolysis of the 1,5 bond, when heated in ethanol containing triethylamine, to give (*Z*)-2-benzoylamino-*o*-acetoxycinnamate (**4***c*), which afforded the coumarin **2***a* on reaction with toluene-α-thiol in ethanol in the presence of triethylamine. On the other hand, the thiolester **4***b* furnished **2***a* on heating in ethanol containing triethylamine.

The reaction of **1***e* with sodium sulfide gave ethyl (*Z*)-2-benzoylamino-*o*-hydroxycinnamate (**4***d*). Similarly, the acetyl derivative **4***c* when heated with sodium sulfide in ethanol gave **4***d*, which in the presence of triethylamine underwent thiol-aided cyclization to the coumarin **2***a* (Scheme 2).

These results indicate that the conversion of **1***e* into **2***a* involves, first, thiolysis of the 1,5 bond to give the thiolester **4***b*, which upon transesterification with ethanol under the basic conditions liberates the thiol moiety, which, in turn, leads to

Can. J. Chem. Downloaded from www.nrcresearchpress.com by EESC ESCOLA DE ENGENHARIA on 09/08/12
For personal use only.

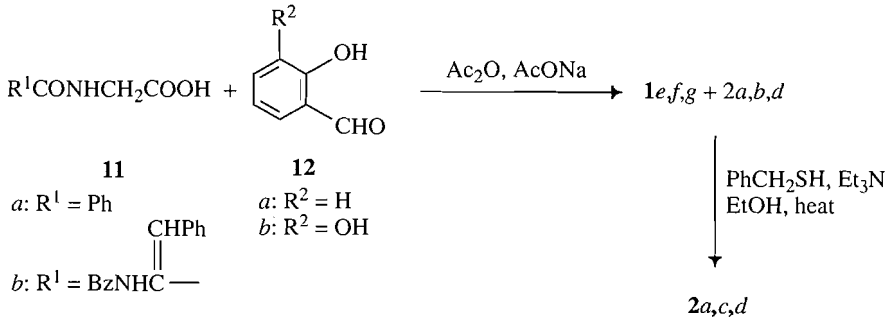

SCHEME 3

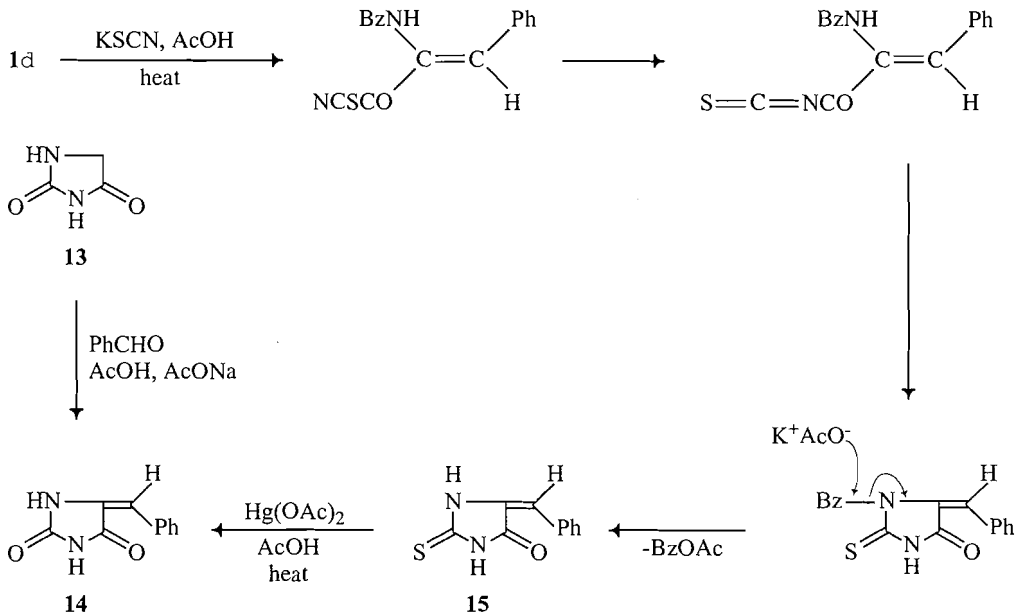

SCHEME 4

deacetylation of **4***c*. *S*-Benzylthio acetate, generated in the medium, subsequently undergoes ethanolysis to liberate the free thiol, which, once again, reacts with the ethyl ester **4***d*, acting as a Michael acceptor, to give 3-benzoylamino-4-benzylthio-3,4-dihydrocoumarin (**3**); this then undergoes β-elimination to afford **2***a*.

In the light of the observation that the thiol–triethylamine combination brings about a useful isomerization, the mixture of **1***e*, *f*, *g* and **2***a*, *b*, *d*, obtained by the Erlenmeyer procedure was subjected, without separation, to the reaction conditions described to give 3-acylaminocoumarins **2***a*, *c*, *d* exclusively (Scheme 3). It would be mentioned that **2***d* was isolated in somewhat lower yields, as it underwent partial deacylation.

Compounds **1***a*, *c*, *e* when heated with potassium thiocyanate failed to give any tangible results, but **1***d* furnished (*E*)-4(5)-benzylidene-2-thiohydantoin (**15**) on prolonged heating with potassium thiocyanate in glacial acetic acid (Scheme 4). The stereochemistry of **15** was assigned on the basis of its ^{1}H nmr spectrum in which the olefinic proton was shielded. Dethionation of **15** with mercury(II) acetate in boiling glacial acetic acid afforded (*E*)-4(5)-benzylidenehydantoin (**14**), which was characterized by comparison with an authentic sample and with its (*Z*) isomer, already known in the literature (9).

The role of sulfur nucleophiles in the isomerization process is quite apparent. Some of the present reactions resemble ordered biochemical transformations and are potentially important. In view of the speed and simple work-up, the reported findings may have synthetic utility.

The products reported were characterized on the basis of spectral data, elemental analyses, and (or) by comparison with authentic samples.

Experimental

Melting points were determined on a Toshniwal melting point apparatus and are uncorrected. The ir and ^{1}H nmr spectra using TMS as an internal reference were recorded on Perkin–Elmer 720 or 783 and Jeol FX-90Q spectrometers, respectively. The mass spectra were recorded on a VG micromass 70-70H and (or) Finnigan-Mat 1020 instrument, using the direct inlet system at 70 eV.

Compound ***1****e*

An equimolar mixture of the cinnamic acid derivative **4***a* (10) and freshly fused sodium acetate, in acetic anhydride (5.0 mol), was heated over a steam bath for 20 min, cooled, and poured into crushed ice to give a solid that was collected, washed with distilled water, and recrystallized from ethanol–benzene to afford yellow crystals; yield, 79%; mp 160°C (lit. (11) mp 162°C); ν_{max} (Nujol): 1790, 1770, 1640 cm^{-1}; δ ($CDCl_3$): 2.35 (s, 3H, $COCH_3$), 6.97–8.97 (m, 10H, =CH and ArH) ppm.

Compound **2**a

Method A

A mixture of **1***e*, toluene-α-thiol, and triethylamine, in the molar

Can. J. Chem. Downloaded from www.nrcresearchpress.com by EESC ESCOLA DE ENGENHARIA on 09/08/12
For personal use only.

Can. J. Chem. Downloaded from www.nrcresearchpress.com by EESC ESCOLA DE ENGENHARIA on 09/08/12
For personal use only.

ratio of 1:1:2, was heated under reflux in ethanol (30 mL g^{-1} of **1***e*) for 2 h. The mixture was concentrated to dryness under reduced pressure, triturated with ethanol, filtered under suction, and the crude product recrystallized from ethanol–benzene to give colourless crystals; yield, 69%; mp 175°C (lit. (8) mp 173°C).

Method B

A mixture of the ethyl ester **4***c* or **4***d*, toluene-α-thiol, and triethylamine, in the molar ratio of 1:1:2, was heated under reflux in ethanol (30 mL g^{-1} of **4***c*) for 2–5 h and worked up as before; yield, 48%.

The similar heating of a mixture of the thiol ester **4***b* and triethylamine, in the molar ratio of 1:2, in ethanol (30 mL g^{-1} of **4***b*) for 2 h, followed by the usual work-up, afforded **2***a* in 79% yield; mp 175°C (lit. (8) mp 173°C); ν_{max} (Nujol): 3360, 1710, 1665, 1625 cm^{-1}; δ ($CDCl_3$): 7.39–8.13 (m, 9H, ArH), 9.04 (s, 2H, one exchangeable with D_2O, 4-CH and NH) ppm.

*3-Acylaminocoumarins (***2**a, c, d*); general procedure*

An equimolar mixture of 3-acylglycine (**11***a*), salicylaldehyde and freshly fused sodium acetate, and acetic anhydride (2.5 mol) in glacial acetic acid (10 mL g^{-1} of **11***a*) was heated over a steam bath for 3 h. On using **11***b*, the mixture was stirred for 8 h at room temperature. The mixture was poured into cold water to give yellowish crystals, which were filtered, washed, dried, and subjected to the reaction conditions described above under compound **2***a*. For the physical constants of **2***a*, see above.

Compound **2**c

Yield, 90%; mp 221°C (lit. (12) mp 224°C). ν_{max} (Nujol): 3350, 3260, 1710, 1650, 1620 cm^{-1}; δ (DMSO-d_6): 7.05–8.0 (m, 8H, ArH), 8.56 (s, 1H, 4-CH), 9.64 (s, 1H, exchangeable with D_2O, NH), 10.25 (s, 1H, exchangeable with D_2O, OH) ppm. Anal. calcd. for $C_{16}H_{11}NO_4 \cdot \frac{1}{2}H_2O$: C 66.20, H 4.14, N 4.82%; found: C 66.09, H 4.32, N 4.64%.

Compound **2**d

Yield, 40%; mp 207°C. ν_{max} (KBr): 3400, 3200, 1710, 1680, 1645 cm^{-1}; δ ($CDCl_3$): 7.17–7.92 (m, 16H, one exchangeable with D_2O, =CH, ArH, and NH), 8.70 (s, 1H, 4-CH), 8.79 (brs, 1H, exchangeable with D_2O, NH), ppm; M^+: 410; Anal. calcd. for $C_{25}H_{18}N_2O_4 \cdot \frac{1}{3}H_2O$: C 72.11, H 4.48, N 6.82%; found: C 71.95, H 4.30, N 6.54%.

Compound **4**b

A mixture of **1***e* and toluene-α-thiol, in the molar ratio of 1:2, was heated under reflux in ethanol (50 mL g^{-1} of **1***e*) for 22 h. The solvent was removed under reduced pressure, and the residue triturated with cold ethanol to give a colorless undefined solid that was collected and recrystallized from benzene; yield, 69%; mp 155°C. ν_{max} (Nujol): 3200, 1770, 1660, 1620 cm^{-1}; δ ($CDCl_3$): 2.35 (s, 3H, CH_3CO), 4.35 (s, 2H, PhCH_2S), 7.22 (d, 1H, J = 4.0 Hz, ArH), 7.30 (s, 1H, =CH), 7.39–8.04 (m, 14H, one exchangeable with D_2O, ArH and NH) ppm; *m/z* (%): 308(4) (M^+ − $PhCH_2S$), 307 (6) (M^+ − $PhCH_2SH$). Anal. calcd. for $C_{25}H_{21}NO_4S$: C 69.60, H 4.87, N 3.24%; found: C 69.96, H 4.81, N 3.23%.

Compound **4**c

An equimolar mixture of **1***e* and triethylamine was heated under reflux in ethanol (50 mL g^{-1} of **1***e*) for 1.5 h and worked up as before. The crude product was recrystallized from ethanol to give a colorless undefined solid; yield, 98%; mp 165°C. ν_{max} (Nujol): 3240, 1760, 1715, 1660, 1645 cm^{-1}; δ ($CDCl_3$): 1.26 (t, 3H, J = 7.0 Hz, CH_3CH_2), 2.13 (s, 3H, CH_3CO), 4.33 (q, 2H, J = 7.0 Hz, CH_3CH_2), 7.19 (s, 1H, =CH), 7.39–8.39 (m, 10H, one exchangeable with D_2O, ArH and NH) ppm; Anal. calcd. for $C_{20}H_{19}NO_5 \cdot \frac{1}{3}H_2O$: C 66.85, H 5.47, N 3.89%; found: C 66.98, H 5.47, N 4.07%.

Compound **4**d

An equimolar mixture of **1***e* or **4***c* and sodium sulfide was heated under reflux in ethanol (50 mL g^{-1} of **1***e*) for 2 h. The solvent was removed under reduced pressure to give a pasty mass, which was washed with cold benzene. The residue was treated with water and left at room temperature for 24 h in an open container. A solid separated out that was filtered and recrystallized from benzene; yield, 40%; mp 169°C. ν_{max} (KBr): 3400, 3240, 1730, 1690, 1645, 1635 cm^{-1}; δ ($CDCl_3$): 1.35 (t, 3H, J = 7.0 Hz, CH_3CH_2), 4.37 (q, 2H, J = 7.0 Hz, CH_3CH_2), 6.83–8.0 (m, 11H, one exchangeable with D_2O, =CH, ArH, and OH), 8.88 (s, 1H, exchangeable with D_2O, NH) ppm; M^+: 311.

It was characterized as its *O*-acetyl derivative **4***c*. Thus, acetylation of **4***d* with acetic anhydride and fused sodium acetate afforded **4***c* in quantitative yields. For the physical constants of **4***c*, see above.

Compound **6**

An equimolar mixture of **1***a* and toluene-α-thiol was heated under reflux in benzene containing triethylamine (2 mol mol^{-1} of **1***a*) for 3 h. It was concentrated to dryness under reduced pressure, treated with hexane, filtered, and washed with aqueous ethanol. The crude product was subjected to tlc (silica gel/benzene), when pure **6** was obtained. The same colorless product was also obtained on storing a mixture of **1***a* and toluene-α-thiol in dry pyridine for 24 h at room temperature, followed by work-up as before; yield, 27%; mp 152–154°C. ν_{max} (Nujol): 3220, 1640 cm^{-1}; δ ($CDCl_3$): 4.09 (s, 2H, PhCH_2S), 4.19 (s, 2H, PhCH_2S), 7.07–8.0 (m, 17H, one exchangeable with D_2O, =CH, ArH, and NH) ppm; *m/z* (%): 419 (1) (M^+), 328 (3) (M^+ − $PhCH_2$), 296 (23) (M^+ − $PhCH_2S$), 295 (10) (M^+ − $PhCH_2SH$). Anal. calcd. for $C_{24}H_{21}NO_2S_2 \cdot \frac{1}{3}H_2O$: C 67.76, H 5.09, N 3.29, S 15.05%; found: C 67.93, H 5.13, N 3.36, S 14.86%.

Compound ***10***

A mixture of **1***c*, toluene-α-thiol, and triethylamine, in the molar ratio of 1:1.1:1.2, was heated under reflux in ethanol (75 mL g^{-1} of **1***c*) for 30 min. It was concentrated and the curdy white solid was filtered. The crude product was recrystallized from ethanol or benzene. Compound **10** was also obtained when a mixture of **1***a*, aniline, and toluene-α-thiol was heated under reflux in triethylamine-containing ethanol and worked up as before; yield, 98%; mp 222–224°C. ν_{max} (Nujol): 3340, 3250, 1670, 1640 cm^{-1}; δ (DMSO-d_6): 4.07 (s, 2H, CH_2), 6.97–8.04 (m, 16H, =CH and ArH), 9.30 (d, 1H, J = 12.8 Hz, exchangeable with D_2O, =CH-N*H*), 9.38 (s, 1H, exchangeable with D_2O, CONH) ppm; *m/z* (%): 388 (19) (M^+), 310 (25) (M^+ − C_6H_6), 265 (9) (M^+ − $PhCH_2S$), 264 (100) (M^+ − $PhCH_2SH$). Anal. calcd. for $C_{23}H_{20}N_2O_2S$: C 71.13, H 5.15, N 7.21%; found: C 71.28, H 5.40, N 6.97%.

Compound ***15***

An equimolar mixture of **1***d* and potassium thiocyanate was heated under reflux in glacial acetic acid (12 mL g^{-1} of **1***d*) for 10 h. It was concentrated to dryness over a steam bath, washed with water, and dried. The pasty residue was triturated with benzene and filtered. The benzene-insoluble material was recrystallized from ethanol to give yellow crystals of **15**. This compound was identical to the product obtained by a known method; yield, 51%; mp 257–258°C (lit. (13*a*)[2] mp 257–258°C); ν_{max} (Nujol): 3220, 1720, 1640 cm^{-1}; δ[H_2] (Me_2CO): 6.44 (s, 1H, =CH), 7.20–7.60 (m, 6H, one exchangeable with D_2O, ArH and NH), 10.65 (s, 1H, exchangeable with D_2O, NH) ppm.

Dethionation (14) of ***10*** *and* ***15****; formation of* **1**c and ***14***

A mixture of **10/15** and mercury(II) acetate, in the molar ratio of 1:1.2, in glacial acetic acid (50 mL g^{-1} of **10**), was heated under reflux for 3 h. A blackish precipitate separated that was filtered off and the filtrate concentrated to dryness over a steam bath. The residue was treated with water, filtered, and recrystallized from ethanol to give yellow crystals of **1***c*/**14**.

Compound **1**c

Yield, 77%; mp 155–156°C (lit. (1) mp 156–157°C); ν_{max} (Nujol):

[2]This compound was reported to be formed on using ammonium thiocyanate, carrying out the condensation for several hours in a sealed tube. The stereochemistry, however, was not discussed. See: ref. 13*b*.

3270, 3210, 1780, 1740, 1720, 1660, 1630 cm^{-1}; δ ($CDCl_3$): 7.17–8.17 (m, 11H, =CH and ArH), 9.46 (d, 1H, J = 12.0 Hz, exchangeable with D_2O, =CHN*H*) ppm.

Compound ***14***

Yield, 42%; mp 219–222°C (lit. (15) mp 220°C); ν_{max} (Nujol): 3200, 3150, 1760, 1720, 1645 cm^{-1}; δ[H_2] (Me_2CO): 6.39 (s, 1H, =CH), 7.16–7.51 (m, 6H, one exchangeable with D_2O, NH and ArH), 9.48 (brs, 1H, exchangeable with D_2O, NH) ppm.

Acknowledgement

We thank the Council of Scientific and Industrial Research, New Delhi, for the award of a SeniorResearch Fellowship to one of us (L.R.).

1. J.W. Cornforth. *In* The chemistry of penicillin. *Edited by* H.T. Clarke, J.R. Johnson, and R. Robinson. Princeton University Press, Princeton, N.J. 1949. p. 730.
2. H.M. Crooks, Jr. *In* The chemistry of penicillin. *Edited by* H.T. Clarke, J.R. Johnson, and R. Robinson. Princeton University Press, Princeton, N.J. 1949. p. 455, and references cited therein.
3. A.M. Islam, A.M.S. El-Sharief, I.M. Ismail, and A.A. Harb. Egypt. J. Chem. **26**, 221 (1983); Chem. Abstr. **101**, 191751 (1984).
4. A.K. Mukerjee, K. Joseph, and L. Rao. J. Chem. Soc. Perkin Trans. 1, 2611 (1991).
5. S.S. Homami and A.K. Mukerjee. Indian J. Chem. **31B**, 411 (1992).
6. Y.S. Rao and R. Filler. *In* The chemistry of heterocyclic compounds. Vol. 45. *Edited by* I. Truchi. John Wiley and Sons, New York. 1986. p. 361.
7. H.E. Carter. Org. React. **3**, 198 (1946).
8. E. Erlenmeyer and W. Stadlin. Liebigs Ann. Chem. **337**, 283 (1904).
9. A.M. Tikdari, P.K. Tripathy, and A.K. Mukerjee. J. Chem. Soc. Perkin Trans. 1, 1659 (1988).
10. P.K. Tripathy and A.K. Mukerjee. Indian J. Chem. **26B**, 61 (1987).
11. Sir J. Cornforth and Du Ming-hui. J. Chem. Soc. Perkin Trans. 1, 2183 (1991).
12. A. Jain and A.K. Mukerjee. J. Prakt. Chem. **331**, 493 (1989).
13. (*a*) V.G. Zubenko. Trudy L'vov. Med. Inst. **12**, 83 (1957); Chem. Abstr. **54**, 21059 (1960); (*b*) J.M. Swan. Australian J. Sci. Res. **A5**, 711 (1952).
14. S.S. Homami. Indian J. Heterocycl. Chem. **1**, 125 (1991).
15. G. Billek. Monatsh. Chem. **92**, 352 (1961).

Can. J. Chem. Downloaded from www.nrcresearchpress.com by EESC ESCOLA DE ENGENHARIA on 09/08/12
For personal use only.

Electronic structure analysis of compounds of interest in drug design: mono- and dicarboxylated pyridines

KENNETH E. EDGECOMBE
Department of Chemistry, Queen's University, Kingston, ON K7L 3N6, Canada

DONALD F. WEAVER
Departments of Chemistry and Medicine, Queen's University, Kingston, ON K7L 3N6, Canada

AND

VEDENE H. SMITH, JR.
Department of Chemistry, Queen's University, Kingston, ON K7L 3N6, Canada

Received May 26, 1993

KENNETH E. EDGECOMBE, DONALD F. WEAVER, and VEDENE H. SMITH, JR. Can. J. Chem. **72**, 1388 (1994).

The search for efficacious drug molecules involves, amongst other considerations, identifying compounds that will have activity in the receptor microenvironment through some highly specific microscopic pathway that is governed by molecular interactions. Widespread in the search for compounds with biological activity is the use of quantum pharmacologic structure-activity calculations. In this study, we identify the topological features of *ab initio* charge densities for a series of carboxylated pyridines. As well, results from conformational and geometric analysis obtained with semi-empirical AM1 and *ab initio* level geometries are compared. Carboxylated pyridines such as quinolinic and dipicolinic acids, both known to be neuroactive compounds, are logical candidates for a systematic study investigating the suitability of relating topological properties calculated in this manner to biological activity. Future reports will detail the correlation of these properties to biological activity.

KENNETH E. EDGECOMBE, DONALD F. WEAVER et VEDENE H. SMITH, JR. Can. J. Chem. **72**, 1388 (1994).

La recherche de molécules efficaces comme drogues implique, entre autres considérations, l'identification de composés qui auront une activité dans le microenvironement du récepteur par le biais de voies microscopiques hautement spécifiques dirigées par des interactions moléculaires. Dans cette recherche de composés possédant une activité biologique, on fait grand usage de calculs quantiques de l'activité pharmacologique en fonction de la structure. Dans le présent travail, on a identifié les caractéristiques topologiques des densités de charge *ab initio* d'une série de d'acides pyridinecarboxyliques. De plus, on compare les résultats d'analyses conformationnelles et géométriques obtenues avec des géométries de niveau semi-empirique AM1 et *ab initio*. Les acides pyridinecarboxyliques comme les acides quinolinique et dipicolinique, qui sont tous les deux reconnus comme des composés neuroactifs, sont des candidats logiques pour une étude systématique visant à déterminer la possibilité d'établir une corrélation entre les propriétés topologiques calculées de cette manière et l'activité biologique. Des travaux ultérieurs donneront les détails de la corrélation entre ces propriétés et l'activité biologique.

[Traduit par la Rédaction]

1. Introduction

Drug discovery has traditionally relied on the time-honored methods of serendipity and massive screening programs which are inefficient, both in time and economics. Clearly, there is a need for rational drug design in which fundamental insights concerning the molecular properties of the disease are exploited to permit the intelligent design of new drugs. Recent advances in quantum chemistry are permitting computer-assisted rational drug design to emerge as a forceful new drug design strategy. In the past decade, advances in computer technology and the development of efficient computational packages have allowed quantum pharmacology to enjoy a leap forward not only in the size of the pharmacological problem to be investigated but also in the range of theoretical models and methods to be used.

Quantum pharmacology has been (and continues to be) dominated by empirical force field (molecular mechanics) calculations. Such calculations emphasize the importance of conformational, geometric, and other steric considerations in directing the drug-receptor interaction while inadequately treating electronic properties. However, as Birley et al. (1) have observed: "...the electron distribution in the ring is of importance for activity and the three-dimensional structure is not the only criterion." This statement emphasizes that the electron density is likewise of fundamental importance when modeling the interaction of a drug with its receptor. Molecular mechanics, employing a simple Coulomb potential within the force field energy function, fails to treat electrons explicitly and fails to provide an adequate evaluation of subtle electronic effects key to drug reactivity. The need for an improved theoretical treatment of electronic effects in bioactive molecules is thus a quantum pharmacologic priority. In this study we examine the topological properties of the electron density and its associated fields ($\nabla\rho$, the gradient, and $\nabla^2\rho$, the Laplacian) in a series of neuroactive molecules. Examining the electron density in this manner reveals elements of molecular structure within the theory of molecular structure proposed by Bader et al. (2).

This approach uses the topological properties of the charge density to define atoms in molecules. By using zero-flux surfaces which satisfy the condition

$$\nabla\rho(\boldsymbol{r})\cdot\boldsymbol{n} = 0$$

for every point on the surface of the subsystem, where $\boldsymbol{n}$ is a unit vector normal to the surface, a molecule may be partitioned into atoms. Points on these surfaces where $\nabla\rho(\boldsymbol{r}) = 0$ are critical points. Should a critical point fall on the path between bonded atoms along which the electron density is a maximum with respect to lateral displacement, it is known as a bond critical point. As well, critical points in the density may be characterized by the eigenvalues of the second derivatives of the electron density (the Hessian) at the critical point with its rank equal to the number of nonzero eigenvalues and its signature equal to the sum of the signs of the eigenvalues. There are four possible sig-

Can. J. Chem. Downloaded from www.nrcresearchpress.com by EESC ESCOLA DE ENGENHARIA on 09/08/12
For personal use only.

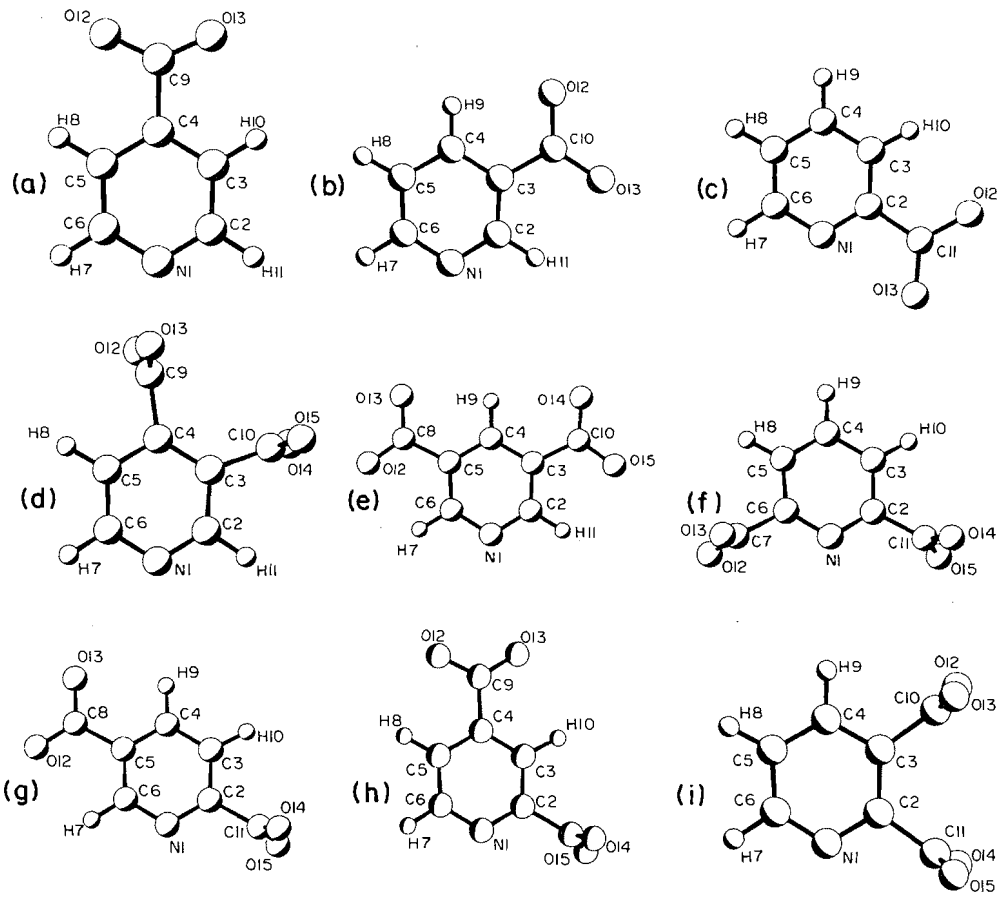

Fig. 1. Structures of the mono- and dicarboxylated pyridines: (*a*) isonicotinate, (*b*) nicotinate, (*c*) picolinate, (*d*) cinchomeronate, (*e*) dinicotinate, (*f*) dipicolinate, (*g*) isocinchomeronate, (*h*) lutidinate, (*i*) quinolinate.

natures of critical points of rank three and these are denoted as (rank,signature). These critical points correspond to a local maximum in $\rho(\boldsymbol{r})$, a peak, (3,–3); a saddle point in $\rho(\boldsymbol{r})$ which is a maximum in the surface it defines, a pass, (3,–1); a saddle point in $\rho(\boldsymbol{r})$ which is a minimum in the surface it defines, a pale, (3,+1); and a local minimum in $\rho(\boldsymbol{r})$, a pit, (3,+3).

Bader et al. (2) have shown that by examining the Laplacian of the charge density, the Lewis model of localized electron pairs and the VSEPR model of molecular geometry may be recovered. Where the Laplacian of the charge density is negative ($\nabla^2\rho(\boldsymbol{r}) < 0$) charge is locally concentrated and where it is positive ($\nabla^2\rho(\boldsymbol{r}) > 0$) it is locally depleted. Thus, by examining the field $\nabla(-\nabla^2\rho(\boldsymbol{r}))$ for critical points in the same manner as examining the field $\nabla\rho(\boldsymbol{r})$, it is possible to recover the VSEPR model of lone and bonding pairs of electrons. That is, if

$$\nabla(-\nabla^2\rho(\boldsymbol{r})) = 0$$

$\boldsymbol{r}$ is a critical point in that field and may be classified in much the same manner as the critical points in $\nabla\rho(\boldsymbol{r})$. A (3,–3) critical point is a local maximum in $-\nabla^2\rho(\boldsymbol{r})$ and this feature may be used to locate the electron pairs of the VSEPR model. It must be noted, however, that these regions of negative Laplacian values are not localized electron pairs.

This report, part of an extensive systematic study of possible neuroactive drug candidates, focuses on the mono- and dicarboxylated pyridines. Of these, quinolinic acid is an endogenous excitatory amino acid and is active at the *N*-methyl-*D*-aspartate (NMDA) receptor. As well, dipicolinic acid behaves as a partial agonist on NMDA receptors (1). This behavior makes the carboxylated pyridines an ideal series for investigations into drug design targeted at the NMDA receptor. The suitability of using the topological properties of the electron density to correlate with biological activity will be examined in a later report.

2. Method

The geometries of each of the pyridine mono- and dicarboxylates have been energy optimized at the semi-empirical AM1 (3) and *ab initio* molecular orbital levels of theory. AM1 calculations were performed using MOPAC 5.01 (4) utilizing the keywords PRECISE, PULAY, and SHIFT=10. *Ab initio* calculations used the HONDO 8 (5) and GAUSSIAN 92 (6) series of programs. The *ab initio* calculations utilized the STO-3G (7), 3-21G (8), and 3-21+G (9) basis sets. After AM1 optimizations, single point *ab initio* calculations at the STO-3G and 3-21G levels were performed to obtain the appropriate wavefunctions for the electron density analysis. The topological analysis of the electron density was facilitated by use of the AIMPAC series of programs (10). All calculations were carried out on an IBM RISC 6000 Model 520 computer.

The nine species examined in this report are displayed in Fig. 1 along with their common names. The geometries displayed are those calculated at the 3-31+G basis set level. Note that the basis set level and geometry used will be indicated by the nota-

Can. J. Chem. Downloaded from www.nrcresearchpress.com by EESC ESCOLA DE ENGENHARIA on 09/08/12
For personal use only.

TABLE 1. AM1 heats of formation and *ab initio* total energies for the pyridine mono- and dicarboxylates[a,b]

Molecule	ΔH_f	E_T STO-3G	E_T 3-21G	E_T 3-21+g[c]
Picolinate	−76.2276	−427.98226	−431.29167	−431.38982
Isonicotinate	−80.9123	−427.99475	−431.30745	−431.40566
Nicotinate	−80.7484	−427.99232	−431.30580	−431.40436
Cinchomeronate				
(⊥⊥)	−118.0903	−612.20962	−617.15923	−617.34337
(_⊥)		−612.20960	−617.15574	
(⊥_)		−612.20961	−617.15430	
(_ _)		−612.19980	−617.15189	
Dinicotinate				
(_ _)	−138.2241	−612.24209	−617.20704	−617.38836
(_⊥)		−612.23880	−617.18441	
(⊥⊥)			−617.16112	
Dipicolinate				
(⊥⊥)	−129.0365	−612.21898	−617.14661	
(_ _)				−617.35893
Isocinchomeronate				
(⊥_)	−137.7636	−612.23676	−617.18386	
(_ _)				−617.38083
Lutidinate				
(⊥_)	−133.9108	−612.23346	−617.17856	
(_ _)				−617.37348
Quinolinate				
(⊥⊥)	−113.1725	−612.19882	−617.12583	
(⊥_)		−612.19888	−617.14448	−617.33257

[a]Heat of formation in kcal/mol and total energies in Hartree atomic units.
[b]All monocarboxylates have $—CO_2^-$ groups planar with the ring while the orientation in the dicarboxylates is indicated by ⊥ for perpendicular and _ for planar with the ring.
[c]The optimizations at this level used GAUSSIAN 92. Cinchomeronate displays distortions from planarity in the ring and the CO_2^- groups are twisted well out of the plane.

tion "basis set"//"geometry", where "geometry" will be the level of calculation or basis set used in the optimization.

3. Results

3.1. Conformational analysis

The heats of formation and total energies for the mono- and dicarboxylated pyridines are listed in Table 1. Symmetry was not used in any of the optimizations. The carboxylate groups are co-planar to the ring in the monocarboxylated pyridines, however, the results vary in the dicarboxylates. At the AM1 level, although there may be several possible stationary points on the potential surface, only one geometry is found for each of the dicarboxylates. Using the HONDO 8 program, at the STO-3G and 3-21G levels, depending on the species, there may be up to four stationary points involving rotation of the carboxylate groups. In fact, at the STO-3G level, three points are essentially equivalent (to five places after the decimal) for cinchomeronate while a fourth is slightly higher in energy. Proceeding to the 3-21G level, however, leads to differentiation resulting in the conformation with both carboxylate groups perpendicular to the plane of the ring being the lower in energy, in agreement with the AM1 result. Similarly, with dinicotinate, the AM1 conformation is found to be the lowest energy at both the STO-3G and 3-21G levels. The AM1 conformation for quinolinate is not the lowest energy at the STO-3G or 3-21G levels. Improving the basis set by adding diffuse functions to the 3-21G basis sets for heavy atoms (3-21+G) yields conformations different from those obtained at the AM1 level except in two cases, cinchomeronate and dinicotinate. At the 3-21+G level, the pyridine ring in cinchomeronate is slightly distorted and no longer planar and the carboxylate groups are neither planar with the ring nor perpendicular to it either.

3.2. Topological analysis

3.2.1. Topological analysis on AM1 optimized geometries

At this point, the topological properties of wavefunctions found using AM1 optimized geometries are presented. This separates the effects of geometry and basis set from each other as here wavefunctions at the STO-3G//AM1 and 3-21G//AM1 levels are presented, whereas the results of STO-3G//STO-3G, 3-21G//3-21G, and 3-21+G//3-21+G level analysis will be discussed later.

(i) Positions of bond critical points

Tables 2 and 3 contain the distance from the bond critical point to each atom along the bond paths in the pyridine mono- and dicarboxylates, respectively. The distance from each atom involved in the bond is given for the STO-3G//AM1 and 3-21G//AM1 level densities. Only the distance from one atom involved in the bond is discussed as the other undergoes the reverse trend as the geometry is fixed.

There is a significant change in the distance from N to the

Can. J. Chem. Downloaded from www.nrcresearchpress.com by EESC ESCOLA DE ENGENHARIA on 09/08/12
For personal use only.

Can. J. Chem. Downloaded from www.nrcresearchpress.com by EESC ESCOLA DE ENGENHARIA on 09/08/12
For personal use only.

TABLE 2. Distance from the bond critical point to each atom along the bond path in the pyridine monocarboxylates[a]

	STO-3G//AM1		3-21G//AM1	
	r_A	r_B	r_A	r_B
Isonicotinate				
N1—C2	1.7020	0.8483	1.5879	0.9619
N1—C6	1.7019	0.8483	1.5879	0.9618
C2—C3	1.4593	1.1949	1.3889	1.2652
C3—C4	1.4764	1.1688	1.3429	1.3023
C4—C5	1.1686	1.4765	1.3023	1.3428
C5—C6	1.1948	1.4592	1.2652	1.3888
C6—H7	1.2033	0.8808	1.3288	0.7554
C5—H8	1.2261	0.8513	1.3494	0.7280
C4—C9	1.7379	1.1388	1.5695	1.3072
C3—H10	1.2260	0.8513	1.3494	0.7280
C2—H11	1.2034	0.8809	1.3288	0.7554
Nicotinate				
N1—C2	1.7106	0.8366	1.5966	0.9501
N1—C6	1.7011	0.8498	1.5773	0.9731
C2—C3	1.4811	1.1862	1.3953	1.2721
C3—C4	1.1229	1.5176	1.2576	1.3828
C4—C5	1.1852	1.4553	1.2965	1.3438
C5—C6	1.3225	1.3313	1.2906	1.3631
C6—H7	1.1999	0.8837	1.3273	0.7564
C5—H8	1.1869	0.8842	1.3106	0.7605
C4—H9	1.2298	0.8510	1.3533	0.7275
C3—C10	1.7385	1.1311	1.5652	1.3044
C2—H11	1.2432	0.8479	1.3682	0.7229
Picolinate				
N1—C2	1.7099	0.8439	1.5882	0.9626
N1—C6	1.6863	0.8661	1.5670	0.9847
C2—C3	1.1968	1.4853	1.3335	1.3484
C3—C4	1.1134	1.5123	1.2474	1.3781
C4—C5	1.3614	1.2834	1.3448	1.2998
C5—C6	1.3158	1.3341	1.2978	1.3520
C6—H7	1.2067	0.8787	1.3318	0.7536
C5—H8	1.1816	0.8876	1.3074	0.7619
C4—H9	1.1922	0.8834	1.3158	0.7598
C3—H10	1.2058	0.8677	1.3281	0.7455
C2—C11	1.7612	1.1599	1.6203	1.3007

[a]Distances in atomic units.

TABLE 3. Distance from the bond critical point to each atom along the bond path in the pyridine dicarboxylates[a]

	STO-3G//AM1		3-21G//AM1	
	r_A	r_B	r_A	r_B
Cinchomeronate				
N1—C2	1.7078	0.8373	1.5949	0.9500
N1—C6	1.7002	0.8506	1.5827	0.9679
C2—C3	1.5499	1.1280	1.4145	1.2634
C3—C4	1.3040	1.3468	1.3048	1.3459
C4—C5	1.0988	1.5619	1.2878	1.3729
C5—C6	1.1981	1.4466	1.2663	1.3783
C6—H7	1.1699	0.9119	1.3091	0.7728
C5—H8	1.1808	0.8929	1.3148	0.7588
C4—C9	1.7169	1.1620	1.5700	1.3089
C3—C10	1.7165	1.1582	1.5657	1.3090
C2—H11	1.1964	0.8901	1.3328	0.7536

TABLE 3 (*concluded*)

	STO-3G//AM1		3-21G//AM1	
	r_A	r_B	r_A	r_B
Dinicotinate				
N1—C2	1.7093	0.8395	1.5903	0.9583
N1—C6	1.7093	0.8395	1.5903	0.9583
C2—C3	1.4771	1.1877	1.4036	1.2612
C3—C4	1.2664	1.3810	1.2984	1.3490
C4—C5	1.3811	1.2663	1.3491	1.2983
C5—C6	1.1875	1.4771	1.2611	1.4035
C6—H7	1.2128	0.8750	1.3516	0.7361
C5—C8	1.6880	1.1661	1.5171	1.3370
C4—H9	1.2276	0.8543	1.3623	0.7196
C3—C10	1.6879	1.1661	1.5170	1.3370
C2—H11	1.2128	0.8750	1.3516	0.7361
Dipicolinate				
N1—C2	1.7009	0.8595	1.5752	0.9832
N1—C6	1.7009	0.8595	1.5752	0.9832
C2—C3	1.2024	1.4718	1.3350	1.3390
C3—C4	1.1161	1.5149	1.2502	1.3805
C4—C5	1.5149	1.1160	1.3805	1.2501
C5—C6	1.4718	1.2027	1.3391	1.3352
C6—C7	1.7111	1.1915	1.5734	1.3291
C5—H8	1.1725	0.8979	1.3084	0.7620
C4—H9	1.1645	0.9110	1.3000	0.7755
C3—H10	1.1725	0.8979	1.3084	0.7621
C2—C11	1.7112	1.1915	1.5735	1.3291
Isocinchomeronate				
N1—C2	1.7108	0.8477	1.5820	0.9746
N1—C6	1.6997	0.8511	1.5831	0.9674
C2—C3	1.2088	1.4653	1.3491	1.3250
C3—C4	1.2777	1.3545	1.2925	1.3395
C4—C5	1.5184	1.1269	1.3850	1.2603
C5—C6	1.1881	1.4733	1.2682	1.3933
C6—H7	1.2136	0.8743	1.3507	0.7372
C5—C8	1.6850	1.1637	1.5127	1.3360
C4—H9	1.2014	0.8769	1.3364	0.7419
C3—H10	1.1763	0.8953	1.3100	0.7616
C2—C11	1.7070	1.1916	1.5678	1.3307
Lutidinate				
N1—C2	1.7117	0.8446	1.5928	0.9615
N1—C6	1.6883	0.8655	1.5752	0.9783
C2—C3	1.3147	1.3650	1.3701	1.3096
C3—C4	1.3192	1.3185	1.2976	1.3402
C4—C5	1.1823	1.4708	1.3071	1.3461
C5—C6	1.1948	1.4490	1.2601	1.3835
C6—H7	1.1759	0.9082	1.3130	0.7711
C5—H8	1.1955	0.8782	1.3321	0.7416
C4—C9	1.6888	1.1734	1.5241	1.3380
C3—H10	1.2089	0.8674	1.3429	0.7335
C2—C11	1.7114	1.1910	1.3715	1.3309
Quinolinate				
N1—C2	1.7245	0.8411	1.6044	0.9585
N1—C6	1.6838	0.8625	1.5680	0.9779
C2—C3	1.3173	1.3753	1.3550	1.3374
C3—C4	1.0540	1.5915	1.2437	1.4016
C4—C5	1.1807	1.4596	1.2949	1.3450
C5—C6	1.3335	1.3104	1.3001	1.3435
C6—H7	1.1725	0.9109	1.3111	0.7723
C5—H8	1.1534	0.9153	1.2913	0.7774
C4—H9	1.1838	0.8934	1.3180	0.7591
C3—C10	1.7173	1.1602	1.5677	1.3098
C2—C11	1.7330	1.1904	1.6043	1.3191

[a]Distances in atomic units.

Can. J. Chem. Downloaded from www.nrcresearchpress.com by ESC ESCOLA DE ENGENHARIA on 09/08/12
For personal use only.

TABLE 4. Charge density at the bond critical points in the pyridine monocarboxylates at the AM1 geometries[a,b]

	2		**3**		**4**	
Bond	STO-3G	3-21G	STO-3G	3-21G	STO-3G	3-21G
1—2	0.2907	0.3026	0.2915	0.3024	0.2963	0.3030
1—6	0.3025	0.3064	0.2967	0.3051	0.2963	0.3030
2—3	0.2820	0.2828	0.2851	0.2872	0.2867	0.2894
3—4	0.2930	0.2966	0.2910	0.2940	0.2905	0.2929
4—5	0.2903	0.2908	0.2904	0.2926	0.2906	0.2929
5—6	0.2885	0.2902	0.2877	0.2892	0.2867	0.2894
6—7	0.2546	0.2563	0.2544	0.2562	0.2546	0.2562
5—8	0.2559	0.2553	0.2561	0.2555	0.2573	0.2577
4—9	0.2557	0.2559	0.2570	0.2583	0.2302	0.2333
3—10	0.2570	0.2570	0.2311	0.2342	0.2573	0.2577
2—11	0.2215	0.2241	0.2556	0.2585	0.2546	0.2562

[a]Values in atomic units.
[b]**2**, **3**, and **4** represent picolinate, nicotinate, and isonicotinate, respectively.

TABLE 5. Charge density at the bond critical points in the pyridine dicarboxylates at the AM1 geometries[a,b]

	2,3		2,4		2,5	
Bond	STO-3G	3-21G	STO-3G	3-21G	STO-3G	3-21G
1—2	0.2839	0.2959	0.2905	0.3006	0.2910	0.3022
1—6	0.3037	0.3076	0.3018	0.3044	0.2972	0.3041
2—3	0.2787	0.2785	0.2829	0.2831	0.2836	0.2845
3—4	0.2876	0.2912	0.2927	0.2946	0.2928	0.2950
4—5	0.2906	0.2921	0.2889	0.2901	0.2897	0.2920
5—6	0.2898	0.2916	0.2889	0.2919	0.2862	0.2882
6—7	0.2500	0.2538	0.2523	0.2541	0.2546	0.2580
5—8	0.2536	0.2534	0.2560	0.2569	0.2389	0.2402
4—9	0.2549	0.2559	0.2368	0.2380	0.2557	0.2575
3—10	0.2317	0.2329	0.2565	0.2579	0.2553	0.2555
2—11	0.2236	0.2239	0.2293	0.2303	0.2301	0.2313
	2,6		3,4		3,5	
Bond	STO-3G	3-21G	STO-3G	3-21G	STO-3G	3-21G
1—2	0.2953	0.3027	0.2931	0.3030	0.2926	0.3035
1—6	0.2953	0.3027	0.2974	0.3036	0.2926	0.3035
2—3	0.2836	0.2843	0.2811	0.2829	0.2857	0.2875
3—4	0.2918	0.2945	0.2874	0.2886	0.2902	0.2919
4—5	0.2918	0.2945	0.2852	0.2872	0.2902	0.2919
5—6	0.2836	0.2843	0.2890	0.2916	0.2857	0.2875
6—7	0.2292	0.2302	0.2522	0.2541	0.2544	0.2581
5—8	0.2551	0.2554	0.2553	0.2555	0.2380	0.2392
4—9	0.2533	0.2539	0.2319	0.2336	0.2566	0.2592
3—10	0.2551	0.2554	0.2323	0.2336	0.2380	0.2392
2—11	0.2292	0.2302	0.2538	0.2564	0.2544	0.2581

[a]Values in atomic units.
[b]The column numbers are substitution positions.

bond critical points with this distance decreasing in each species by about 0.12 au going from the STO-3G to 3-21G results. The distance from C2 to the bond critical point in the C2—C3 bond decreases unless a carboxylate group is directly attached to C2. The exception to this trend is quinolinate. The distance from C3 to the bond critical point in the C3—C4 bond increases except in lutidinate and isonicotinate. The distance from C4 to the bond critical point in the C4—C5 bond also increases but the exceptions are now picolinate, dipicolinate, and isocinchomeronate. In all cases, the distance from the ring carbon to the bond critical point in the C—H bond increases. However, the distance from the ring carbon to the bond critical point in the C—CO_2^- bond decreases.

(ii) Charge density at bond critical points

The value of the charge density at the bond critical points for the mono- and dicarboxylated pyridines are listed in Tables 4 and 5, respectively. The values found at the STO-3G//AM1 and

TABLE 6. Laplacian of the charge density at the bond critical points in the pyridine monocarboxylates at the AM1 geometries[a,b]

	2		**3**		**4**	
Bond	STO-3G	3-21G	STO-3G	3-21G	STO-3G	3-21G
1—2	−0.0159	−0.6431	0.0752	−0.6318	−0.0816	−0.6417
1—6	−0.2787	−0.6813	−0.0886	−0.6634	−0.0814	−0.6418
2—3	−0.7497	−0.8227	−0.7553	−0.8349	−0.7518	−0.8447
3—4	−0.7718	−0.8805	−0.7806	−0.8716	−0.7926	−0.8762
4—4	−0.7955	−0.8643	−0.7835	−0.8754	−0.7927	−0.8764
5—6	−0.7708	−0.8500	−0.7696	−0.8452	−0.7519	−0.8450
6—7	−0.6180	−0.7548	−0.6108	−0.7536	−0.6158	−0.7532
5—8	−0.6099	−0.7388	−0.6165	−0.7409	−0.6351	−0.7529
4—9	−0.6196	−0.7508	−0.6371	−0.7610	−0.4478	−0.5817
3—10	−0.6275	−0.7487	−0.4500	−0.5847	−0.6352	−0.7530
2—11	−0.4064	−0.5269	−0.6336	−0.7634	−0.6158	−0.7531

[a]Values in atomic units.
[b]**2**, **3**, and **4** represent picolinate, nicotinate, and isonicotinate while STO-3G and 3-21G represent the basis set used for the single point *ab initio* calculation.

TABLE 7. Laplacian of the charge density at the bond critical points in the pyridine dicarboxylates at the AM1 geometries[a,b]

	2,3		2,4		2,5	
Bond	STO-3G	3-21G	STO-3G	3-21G	STO-3G	3-21G
1—2	0.0862	−0.5940	−0.0084	−0.6221	−0.0360	−0.6452
1—6	−0.2411	−0.6782	−0.2586	−0.6631	−0.1088	−0.6596
2—3	−0.7435	−0.7997	−0.7542	−0.8213	−0.7497	−0.8263
3—4	−0.7173	−0.8431	−0.8012	−0.8797	−0.7945	−0.8823
4—5	−0.7823	−0.8693	−0.7840	−0.8609	−0.7680	−0.8600
5—6	−0.7718	−0.8554	−0.7536	−0.8518	−0.7500	−0.8339
6—7	−0.5880	−0.7424	−0.5936	−0.7445	−0.6155	−0.7619
5—8	−0.5867	−0.7300	−0.6110	−0.7466	−0.5153	−0.6285
4—9	−0.6074	−0.7484	−0.5061	−0.6189	−0.6181	−0.7575
3—10	−0.4767	−0.5853	−0.6221	−0.7538	−0.6047	−0.7398
2—11	−0.4374	−0.5350	−0.4708	−0.5753	−0.4752	−0.5809
	2,6		3,4		3,5	
Bond	STO-3G	3-21G	STO-3G	3-21G	STO-3G	3-21G
1—2	−0.1816	−0.6562	0.0605	−0.6308	0.0505	−0.6465
1—6	−0.1818	−0.6562	−0.0931	−0.6473	0.0505	−0.6464
2—3	−0.7496	−0.8241	−0.7100	−0.8011	−0.7509	−0.8281
3—4	−0.7621	−0.8694	−0.7867	−0.8504	−0.7921	−0.8691
4—5	−0.7622	−0.8696	−0.7369	−0.8401	−0.7921	−0.8692
5—6	−0.7494	−0.8238	−0.7595	−0.8512	−0.7510	−0.8284
6—7	−0.4696	−0.5741	−0.5879	−0.7432	−0.6109	−0.7611
5—8	−0.5993	−0.7383	−0.6065	−0.7410	−0.5109	−0.6229
4—9	−0.5964	−0.7414	−0.4781	−0.5905	−0.6317	−0.7678
3—10	−0.5992	−0.7383	−0.4794	−0.5894	−0.5109	−0.6230
2—11	−0.4695	−0.5741	−0.6063	−0.7531	−0.6109	−0.7611

[a]Values in atomic units.
[b]The column numbers indicate the substitution position while STO-3G and 3-21G indicate the basis set used.

3-21G//AM1 levels are listed. The value of $\rho(\boldsymbol{r})$ at the critical point, $\rho(\boldsymbol{r}_c)$, is dependent on bond length as well as on the basis set used and the position of the substituents on the ring. However, some trends are apparent upon proceeding from the STO-3G to 3-21G basis set. The value of $\rho(\boldsymbol{r}_c)$ for the N—C bonds increases. The change is unevenly distributed but depends on the separation distance of the carboxylate substituents. The results for the C—C bonds also vary but the overall change is slight. Similarly, the change in $\rho(\boldsymbol{r}_c)$ for the C—H bonds is small and varies. Surprisingly, the value of $\rho(\boldsymbol{r}_c)$ in the C—CO_2^- bonds also changes very little but as the value of $\rho(\boldsymbol{r}_c)$ is the lowest here for each basis set, the lack of change and the low value of the density could be due to the long bond.

(iii) Laplacian of the charge density at $\mathbf{r}_c$

The value of the Laplacian of the charge density at the bond

Can. J. Chem. Downloaded from www.nrcresearchpress.com by EESC ESCOLA DE ENGENHARIA on 09/08/12
For personal use only.

TABLE 8. Distance from the nitrogen to the maximum in $-\nabla^2\rho$ associated with the lone pair of electrons on N in the pyridine ring and the values of the charge density and the Laplacian at that point[a]

	STO-3G//AM1			3-21G//AM1		
Compound	r'	ρ	$\nabla^2\rho$	r'	ρ	$\nabla^2\rho$
Pico.	0.6932	0.7253	−4.6592	0.7248	0.6237	−3.0289
Nico.	0.6923	0.7277	−4.6888	0.7261	0.6200	−2.9850
Ison.	0.7016	0.7244	−4.6272	0.7264	0.6189	−2.9737
Quin.	0.6921	0.7295	−4.6150	0.7259	0.6209	−2.9932
Lut.	0.6940	0.7248	−4.6140	0.7265	0.6188	−2.9685
Isoc.	0.6927	0.7277	−4.6667	0.7263	0.6196	−2.9743
Dipic.	0.6934	0.7256	−4.6470	0.7248	0.6238	−3.0265
Cinc.	0.6939	0.7248	−4.6078	0.7286	0.6118	−2.8901
Dinic.	0.6923	0.7290	−4.6753	0.7279	0.6149	−2.9205

[a]Values in atomic units.

critical points, $\nabla^2\rho(r_c)$, are listed in Tables 6 and 7 for the mono- and dicarboxylated pyridines. The values found with STO-3G//AM1 and 3-21G//AM1 level calculations are listed. Overall, there is a large decrease in the value of $\nabla^2\rho(r_c)$ to more negative values. Also, the value of the Laplacian at the bond critical point has been shown to indicate the type of bonding taking place between two atoms (2). That is, when $\nabla^2\rho(r_c) < 0$, charge is locally concentrated and the electronic charge in the bonding region is shared, indicating covalent or polar interactions. When $\nabla^2\rho(r_c)$ is positive, $\rho(r_c)$ is usually low in value and the bond is more closed-shell in nature or rather, ionic for the present circumstances. Thus, it is surprising to observe that $\nabla^2\rho(r_c)$ is positive (although small in value) or near zero at the STO-3G//AM1 level in several of the N—C bonds. Upon proceeding to the 3-21G//AM1 level, however, all $\nabla^2\rho(r_c)$ values are negative although slightly smaller in magnitude than in most other bonds in the ring of the species examined. No other bonds display this behavior and although they do become more negative, the change is substantially less than for the N—C bonds.

(iv) Maximum in $-\nabla^2\rho(\mathbf{r})$

Topological features of the Laplacian of the charge density, $\nabla^2\rho(r_c)$, recover the VSEPR model of lone and bonding pairs of electrons. Just as by examining the topological features of the charge density, locating and characterizing the critical points allows insight into the ebb and flow of bonding electrons around the ring, the lone pair of electrons on the nitrogen can be located and characterized using the Laplacian of the charge density. That is, the (3,–3) critical points in the field $\nabla(-\nabla^2\rho(r))$ can be located and properties at these points can be calculated.

Table 8 contains the distance of this (3,–3) critical point in $-\nabla^2\rho(r)$, associated with the lone pair on the pyridine nitrogen, r', from the nitrogen as a function of compound and basis set. As well, the charge and $\nabla^2\rho$ at that point are tabulated. Examining the values of r' going from the STO-3G to 3-21G basis set, there is a reorganization amongst the compounds in terms of the shortest to the longest r'. There is a definite increase in r' and a decrease in the range, from 0.6921 to 0.7016 au at the STO-3G level, to 0.7248 to 0.7286 au at the 3-21G level. Although there is reorganization of the ranking of the compounds with regards to the smallest to the largest in terms of $\rho(r)$ at this (3,–3) critical point in $-\nabla^2\rho(r)$, the variation in the value of $\rho(r)$ is now greater at the 3-21G level. Of interest is that this reorganization at the 3-21G level gives the inverse ordering to that of r' (smallest to largest), because the closer the critical point to N, the larger $\rho(r)$ is at the point. Similarly, examining the values listed for the Laplacian shows that there is again reorganization; now the trend at the 3-21G level is the same as that found for r', that is, from the smallest (most negative) to the largest (most positive). Also, although the value of $\nabla^2\rho$ is larger in magnitude at the STO-3G level, the range of this rapidly changing function is smaller, changing 0.08 au from the smallest to the largest as opposed to 0.13 au for the 3-21G basis set.

3.2.2. Topological analysis of ab initio *optimized geometries*

(i) Positions of bond critical points

The earlier discussion of results in Tables 2 and 3 focused on the change in the position of the bond critical point as a function of basis set with the geometries constant. Tables 9 and 10 contain the distance from the bond critical point to each atom along a bond path in the pyridine mono- and dicarboxylates, respectively, at the STO-3G//STO-3G, 3-21G//3-21G, and 3-21+G//3-21+G levels. With the geometries changing as well as the basis set, comparison of the distances of nuclei to bond critical points is made more difficult. For example, at the STO-3G level, the C—CO_2^- bond length in isonicotinate is 3.0972 au while at the 3-21+G level it is 2.9114 au. This bond shortening should be reflected in distances from the bond critical point to the nuclei if basis set effects on the density were minimal. However, at the STO-3G level the critical point is 1.3032 au from the carboxylate carbon and this distance increases to 1.3618 au at the 3-21+G level despite the decreased bond length. Since these bond critical points are points on the surface of the topologically defined atom in a molecule, the change in basis set may give rise to a change in the size of the atoms (or distortions), resulting in changes in the distances to the critical points and the bond lengths. Earlier, a change in basis set at fixed geometry would change the placement of the internuclear surface, thus distorting the "shape" of the atom. By allowing the geometry to change, the interatomic surfaces assume positions to lower the total energy. As observed by Boyd and Edgecombe (11), for a homonuclear diatomic molecule, by symmetry the bond critical point is required to be at the bond midpoint. Thus, lengthening the bond by amount x will result in a change of the distance between the bond critical point to a nucleus by $x/2$. There is no restriction in the present systems and so changes in bond lengths from the AM1 values may not give rise to symmetric or systematic changes in distances to the bond critical point.

Can. J. Chem. Downloaded from www.nrcresearchpress.com by ESC ESCOLA DE ENGENHARIA on 09/08/12
For personal use only.

TABLE 9. Distance from the bond critical point to each atom along the bond path in the pyridine monocarboxylates[a,b]

	STO-3G		3-21G		3-21+G	
	r_A	r_B	r_A	r_B	r_A	r_B
Isonicotinate						
N1—C2	1.7046	0.8570	1.5860	0.9373	1.5919	0.9382
N1—C6	1.7051	0.8576	1.5857	0.9368	1.5918	0.9382
C2—C3	1.4820	1.1334	1.3673	1.2412	1.3709	1.2443
C3—C4	1.5401	1.0923	1.3287	1.2808	1.3148	1.3053
C4—C5	1.0902	1.5422	1.2807	1.3292	1.3052	1.3148
C5—C6	1.1368	1.4805	1.2416	1.3669	1.2443	1.3709
C6—H7	1.1738	0.8822	1.2762	0.7520	1.2848	0.7413
C5—H8	1.1872	0.8595	1.2964	0.7245	1.3058	0.7178
C4—C9	1.7940	1.3032	1.6011	1.3226	1.5496	1.3618
C3—H10	1.1897	0.8570	1.2964	0.7237	1.3058	0.7177
C2—H11	1.1739	0.8821	1.2753	0.7518	1.2848	0.7413
Nicotinate						
N1—C2	1.7185	0.8454	1.5962	0.9292	1.5983	0.9350
N1—C6	1.7021	0.8565	1.5752	0.9445	1.5811	0.9472
C2—C3	1.5484	1.0861	1.3674	1.2408	1.3690	1.2527
C3—C4	1.0472	1.5814	1.2354	1.3707	1.2548	1.3604
C4—C5	1.1439	1.4717	1.2799	1.3374	1.2965	1.3279
C5—C6	1.2952	1.3240	1.2739	1.3389	1.2633	1.3505
C6—H7	1.1671	0.8851	1.2743	0.7531	1.2843	0.7424
C5—H8	1.1596	0.8851	1.2671	0.7596	1.2767	0.7520
C4—H9	1.1932	0.8553	1.3014	0.7213	1.3103	0.7149
C3—C10	1.7914	1.3001	1.5926	1.3126	1.5381	1.3585
C2—H11	1.1992	0.8550	1.3022	0.7178	1.3109	0.7081
Picolinate						
N1—C2	1.7316	0.8492	1.5957	0.9189	1.5941	0.9247
N1—C6	1.6872	0.8771	1.5683	0.9519	1.5783	0.9489
C2—C3	1.1117	1.5384	1.2926	1.3338	1.3228	1.3127
C3—C4	1.0718	1.5323	1.2263	1.3755	1.2404	1.3686
C4—C5	1.3272	1.2980	1.3125	1.3124	1.3153	1.3116
C5—C6	1.3202	1.2933	1.2961	1.3108	1.2934	1.3182
C6—H7	1.1748	0.8813	1.2774	0.7506	1.2870	0.7403
C5—H8	1.1542	0.8886	1.2665	0.7605	1.2757	0.7531
C4—H9	1.1642	0.8843	1.2707	0.7586	1.2792	0.7513
C3—H10	1.1965	0.8483	1.3040	0.7124	1.3100	0.7102
C2—C11	1.7984	1.3122	1.6210	1.3192	1.5728	1.3503

[a]Distances in atomic units.
[b]Calculations at the STO-3G//STO-3G, 3-21G//3-21G or 3-21+G//3-21+G levels.

TABLE 10. Distance from the bond critical point to each atom along the bond path in the pyridine dicarboxylates[a,b]

	STO-3G		3-21G		3-21+G	
	r_A	r_B	r_A	r_B	r_A	r_B
Cinchomeronate						
N1—C2	1.7254	0.8546	1.5966	0.9241	1.5976	0.9329
N1—C6	1.6912	0.8490	1.5786	0.9466	1.5835	0.9494
C2—C3	1.5953	1.0282	1.3937	1.2346	1.3861	1.2473
C3—C4	1.3158	1.3691	1.2886	1.3433	1.2744	1.3604
C4—C5	1.0283	1.5974	1.2688	1.3654	1.3077	1.3345
C5—C6	1.1492	1.4772	1.2254	1.3702	1.2295	1.3707
C6—H7	1.1413	0.9152	1.2622	0.7722	1.2742	0.7562
C5—H8	1.1436	0.9026	1.2858	0.7340	1.2875	0.7381
C4—C9	1.7685	1.3217	1.6075	1.3462	1.5524	1.3597
C3—C10	1.7662	1.3222	1.5932	1.3443	1.5311	1.3744
C2—H11	1.1566	0.8996	1.2953	0.7249	1.3027	0.7169

Can. J. Chem. Downloaded from www.nrcresearchpress.com by EESC ESCOLA DE ENGENHARIA on 09/08/12
For personal use only.

TABLE 10 (*concluded*)

	STO-3G		3-21G		3-21+G	
	r_A	r_B	r_A	r_B	r_A	r_B
Dinicotinate						
N1—C2	1.7141	0.8476	1.5895	0.9375	1.5919	0.9427
C2—C6	1.7136	0.8476	1.5895	0.9375	1.5921	0.9432
C2—C3	1.5351	1.0958	1.3762	1.2338	1.3782	1.2406
C3—C4	1.2015	1.4315	1.2811	1.3356	1.2926	1.3348
C4—C5	1.4311	1.2018	1.3356	1.2811	1.3350	1.2929
C5—C6	1.0955	1.5350	1.2338	1.3762	1.2403	1.3779
C6—H7	1.1711	0.8823	1.2905	0.7313	1.3009	0.7189
C5—C8	1.7417	1.3157	1.5483	1.3514	1.4919	1.3967
C4—H9	1.1872	0.8618	1.3051	0.7161	1.3208	0.7020
C3—C10	1.7418	1.3157	1.5483	1.3514	1.4919	1.3967
C2—H11	1.1718	0.8825	1.2904	0.7313	1.3009	0.7189
Dipicolinate						
N1—C2	1.7009	0.8595	1.5774	0.9560	1.5906	0.9368
N1—C6	1.7009	0.8595	1.5774	0.9560	1.5907	0.9370
C2—C3	1.2024	1.4718	1.3001	1.3253	1.3077	1.3204
C3—C4	1.1161	1.5149	1.2350	1.3723	1.2641	1.3491
C4—C5	1.5149	1.1160	1.3723	1.2350	1.3492	1.2642
C5—C6	1.4718	1.2027	1.3253	1.3001	1.3202	1.3076
C6—C7	1.7111	1.1915	1.6004	1.3360	1.5291	1.3909
C5—H8	1.1725	0.8979	1.2627	0.7631	1.2991	0.7212
C4—H9	1.1645	0.9110	1.2602	0.7746	1.2689	0.7655
C3—H10	1.1725	0.8979	1.2627	0.7631	1.2991	0.7212
C2—C11	1.7112	1.1915	1.6004	1.3360	1.5291	1.3909
Isocinchomeronate						
N1—C2	1.7236	0.8555	1.5834	0.9451	1.5888	0.9351
N1—C6	1.7054	0.8649	1.5830	0.9474	1.5910	0.9436
C2—C3	1.1435	1.5000	1.3195	1.3133	1.3419	1.2875
C3—C4	1.2691	1.3431	1.2823	1.3238	1.2799	1.3354
C4—C5	1.5694	1.0598	1.3742	1.2395	1.3395	1.2830
C5—C6	1.1035	1.5210	1.2399	1.3630	1.2715	1.3470
C6—H7	1.1763	0.8812	1.2905	0.7331	1.3007	0.7206
C5—C8	1.7370	1.3098	1.5419	1.3487	1.4884	1.3974
C4—H9	1.1674	0.8824	1.2881	0.7374	1.2976	0.7285
C3—H10	1.1434	0.9019	1.2636	0.7631	1.2972	0.7238
C2—C11	1.7558	1.3217	1.5944	1.3368	1.5263	1.3901
Lutidinate						
N1—C2	1.7277	0.8550	1.5939	0.9342	1.5980	0.9245
N1—C6	1.6873	0.8777	1.5725	0.9530	1.5848	0.9436
C2—C3	1.2737	1.3769	1.3463	1.2895	1.3551	1.2849
C3—C4	1.3696	1.2537	1.2830	1.3210	1.2794	1.3395
C4—C5	1.1147	1.5229	1.2893	1.3314	1.2912	1.3347
C5—C6	1.1479	1.4585	1.2365	1.3593	1.2591	1.3487
C6—H7	1.1475	0.9116	1.2657	0.7689	1.2767	0.7544
C5—H8	1.1576	0.8860	1.2815	0.7384	1.2956	0.7280
C4—C9	1.7451	1.3179	1.5613	1.3567	1.5050	1.4008
C3—H10	1.1690	0.8769	1.2886	0.7326	1.3188	0.6995
C2—C11	1.7593	1.3197	1.5953	1.3344	1.5307	1.3856
Quinolinate						
N1—C2	1.7373	0.8489	1.6092	0.9431	1.6031	0.9486
N1—C6	1.6825	0.8835	1.5576	0.9489	1.5681	0.9452
C2—C3	1.3751	1.3165	1.3635	1.2796	1.3913	1.2629
C3—C4	0.9824	1.6281	1.2120	1.3989	1.2399	1.3816
C4—C5	1.1460	1.4811	1.2740	1.3403	1.2907	1.3297
C5—C6	1.2860	1.3139	1.2643	1.3406	1.2578	1.3501
C6—H7	1.1424	0.9149	1.2656	0.7701	1.2779	0.7546
C5—H8	1.1258	0.9192	1.2515	0.7793	1.2645	0.7674
C4—H9	1.1830	0.8655	1.3007	0.7207	1.3085	0.7155
C3—C10	1.7504	1.3305	1.5748	1.3546	1.5290	1.3836
C2—C11	1.7818	1.3189	1.6386	1.3102	1.5828	1.3295
H9···O12					1.7747	2.5509

[a]Distances in atomic units.
[b]Calculated at the STO-3G//STO-3G, 3-21G//3-21G, nd 3-21+G//3-21+G levels.

Can. J. Chem. Downloaded from www.nrcresearchpress.com by EESC ESCOLA DE ENGENHARIA on 09/08/12
For personal use only.

Can. J. Chem. Downloaded from www.nrcresearchpress.com by EESC ESCOLA DE ENGENHARIA on 09/08/12
For personal use only.

Examination of Table 9 reveals that while the N—C bond length for isonicotinate decreases proceeding from the STO-3G to 3-21G levels, the distance from the bond critical point to the carbon increases and the distance to N decreases. The addition of diffuse functions leads to a slight increase in the N—C bond but now the distance to the N nucleus increases but that to C remains relatively unchanged. The underlying question is which basis set describes the species best.

The position of the carboxylate groups on the ring has a definite effect on the position of the bond critical points between the ring atoms. For example, examining the 3-21+G results in Table 9, the distance of the critical point from C2 in the N1—C2 bond changes from 0.9382 to 0.9350 to 0.9247 au as the position of substitution on the ring changes from 4 to 3 to 2. Similarly, the C6—N1 bond undergoes change but in the opposite direction with the C6 to critical point distance changing from 0.9382 to 0.9472 to 0.9489 au for the same process. As the distance from N1 to the critical point in the N1—C6 bond decreases, it appears that there is a distortion of the density around N1. In the N1—C2 bond this distance increases but then decreases slightly.

Examination of the 3-21+G results listed in Table 10 and specifically the series with 2,3, 2,4, 2,5, and 2,6 substitution, reveals that the distance from N1 to the bond critical point increases as the second carboxylate group is moved from 3 to 4 to 5 to 6. In the N1—C2 bond this distance decreases as the group is moved 3 to 4 to 5 but then increases slightly when the group is moved to 6. Similarly, examining this distance in the 2,3, 3,4, and 3,5 series, in the N1—C6 bond the distance increases while in the N1—C2 bond it decreases.

There are some trends found amongst the changes resulting from the changes in basis set level. The distance from N1 to bond critical points in all species decreases going from the STO-3G to 3-21G level and then increases slightly upon proceeding to the 3-21+G level. The distance from H to the bond critical point in the C—H bonds decreases for the same process with the exception of one bond in cinchomeronate which increases slightly upon proceeding to the 3-21+G//3-21+G level. The shortest distance from H to the bond critical point at the 3-21+G level is in lutidinate where the hydrogen is located between two carboxylate groups. In the other example of a hydrogen between two carboxylate groups, dinicotinate, the distance is also short.

The distance from the ring carbon to the critical point in the C—CO_2^- bond is decreased when the basis set is expanded.

TABLE 11. Charge density at the bond critical points in the pyridine monocarboxylates at the STO-3G//STO-3G level[a,b]

Bond	2	3	4
1—2	0.2821	0.2891	0.2961
1—6	0.3013	0.2971	0.2959
2—3	0.2884	0.2906	0.2954
3—4	0.2978	0.2922	0.2924
4—5	0.2956	0.2962	0.2921
5—6	0.2975	0.2963	0.2950
6—7	0.2609	0.2611	0.2607
5—8	0.2618	0.2619	0.2638
4—9	0.2614	0.2641	0.1892
3—10	0.2654	0.1901	0.2641
2—11	0.1875	0.2636	0.2608

[a]Values in atomic units.
[b]**2**, **3**, and **4** represent picolinate, nicotinate, and isonicotinate, respectively.

This shortening ranges from 0.2 to 0.11 au proceeding from the STO-3G to 3-21G results and from 0.06 to 0.05 au proceeding from the 3-21G to 3-21+G results.

Examining Tables 9 and 10 for trends in the distance from a ring carbon to a ring bond critical point it is apparent that the N—C bonds have the shortest values at all levels. Thereafter, the results are mixed, depending on the basis set level used and species examined. At the STO-3G level it is usually the carbon bonded to a carboxylate group that displays the shortest distance to the critical point. Proceeding to the 3-21G and then the 3-21+G levels does reveal a clear trend. At the 3-21+G level, disregarding the N—C bonds, the shortest critical point to ring carbon distance occurs at C3 and C5. While at the STO-3G level this distance may be very short at C4 in, for example, isonicotinate, with a value of 1.09 au, but upon proceeding to the 3-21+G level there is an increase of 0.21 au.

An intramolecular hydrogen bond was characterized in quinolinate between H9 and O12. The resulting distances from the H and O nuclei are listed in Table 10. This was the only intramolecular hydrogen bond that could be identified in this study.

(ii) Charge density at bond critical points $\rho(\mathbf{r}_c)$

The value of $\rho(\mathbf{r}_c)$ has been shown to vary monotonically with bond length in main group diatomic (11) and binary hydrides (12). Thus care must be taken when comparing charge densities at bond critical points of different length bonds. For example, in Tables 11 and 12, the charge density at bond critical points in the mono- and dicarboxylated pyridines calculated at

TABLE 12. Charge density at the bond critical points in the pyridine dicarboxylates at the STO-3G//STO-3G level[a,b]

Bond	2,3	2,4	2,5	2,6	3,4	3,5
1—2	0.2790	0.2843	0.2860	0.2953	0.2869	0.2916
1—6	0.3025	0.3015	0.2945	0.2953	0.3023	0.2918
2—3	0.2783	0.2884	0.2895	0.2836	0.2907	0.2919
3—4	0.2945	0.2955	0.2976	0.2918	0.2796	0.2929
4—5	0.2934	0.2916	0.2924	0.2918	0.2914	0.2929
5—6	0.3006	0.2977	0.2933	0.2836	0.2934	0.2920
6—7	0.2572	0.2574	0.2609	0.2292	0.2574	0.2615
5—8	0.2583	0.2621	0.2016	0.2551	0.2606	0.1999
4—9	0.2639	0.1990	0.2616	0.2533	0.1932	0.2637
3—10	0.1953	0.2629	0.2606	0.2551	0.1934	0.1998
2—11	0.1913	0.1967	0.1969	0.2292	0.2597	0.2613

[a]Values in atomic units.
[b]The column headers are the substitution positions.

TABLE 13. Laplacian of the charge density at the bond critical points in the pyridine monocarboxylates at the STO-3G//STO-3G level[a,b]

Bond	2	3	4
1—2	0.0077	0.0179	−0.1495
1—6	−0.3311	−0.1422	−0.1528
2—3	−0.7685	−0.7578	−0.7816
3—4	−0.7799	−0.7550	−0.7870
4—5	−0.8214	−0.8048	−0.7845
5—6	−0.8126	−0.8101	−0.7803
6—7	−0.6422	−0.6382	−0.6414
5—8	−0.6328	−0.6388	−0.6574
4—9	−0.6423	−0.6649	−0.2695
3—10	−0.6697	−0.2734	−0.6594
2—11	−0.2596	−0.6646	−0.6415

[a]Values in atomic units.
[b]**2**, **3**, and **4** represent picolinate, nicotinate, and isonicotinate, respectively.

TABLE 15. Charge density at the bond critical points in the pyridine monocarboxylates at the 3-21G//3-21G level[a,b]

Bond	2	3	4
1—2	0.3122	0.3085	0.3112
1—6	0.3155	0.3148	0.3115
2—3	0.3016	0.3067	0.3046
3—4	0.3045	0.3055	0.3047
4—5	0.2975	0.3000	0.3045
5—6	0.3049	0.3030	0.3045
6—7	0.2730	0.2727	0.2727
5—8	0.2679	0.2683	0.2747
4—9	0.2692	0.2760	0.2235
3—10	0.2779	0.2262	0.2751
2—11	0.2200	0.2802	0.2730

[a]Values in atomic units.
[b]**2**, **3**, and **4** represent picolinate, nicotinate, and isonicotinate, respectively.

the STO-3G//STO-3G level are given. Examination reveals that the density is lowest at the C—CO_2^- bond critical point.However, at the STO-3G level, the C—CO_2^- bond is the longest at about 3.09 au as opposed to other heavy atom to heavy atom bonds which are 2.65 au or less. There have been attempts to link $\rho(\boldsymbol{r}_c)$ with bond order (13), however, there will be no attempt to do so in this report.

Tables 15 and 16 contain listings of $\rho(\boldsymbol{r}_c)$ for the mono- and dicarboxylated pyridines at the 3-21G//3-21G level. Tables 19 and 20 contain the corresponding values calculated at the 3-21+G//3-21+G level. As expected from the shortening of bonds, proceeding from the STO-3G to 3-21G level results in an increase in $\rho(\boldsymbol{r}_c)$. Proceeding further to the 3-21+G level gives rise to changes that appear to be related to the minor changes in bond length, increasing or decreasing slightly with the slight changes in bond length.

Examining the 3-21+G results, there is a trend of the N1—C6 bond $\rho(\boldsymbol{r}_c)$ being greater than or equal to that for N1—C2. There is one exception to this, isocinchomeronate. Here the N1—C2 value is greater, again reflecting differences in bond length. Note that this did not appear at the STO-3G level where these values could be considered equal.

The effect of the position of the substituents on the ring can be observed by comparing $\rho(\boldsymbol{r}_c)$ values of the C—C bonds from opposite sides of the ring. Although the differences at the STO-3G level are larger, they are still pronounced at the 3-21G and 3-21+G levels. For example, at the 3-21+G level, the series with substituents at the 2,3, 2,4, 2,5, and 2,6 positions, the value of $\rho(\boldsymbol{r}_c)$ in the C2—C3 bond increases as the second carboxylate group moves around the ring. On the opposite side of the ring in the C5—C6 bond, $\rho(\boldsymbol{r}_c)$ (which is larger) starts to increase but then decreases until it is the same with substituents at 2,6. At the STO-3G level, the same trend in $\rho(\boldsymbol{r}_c)$ for the C2—C3 bond is not followed when the carboxylate group moves from C5 to C6, i.e. 2,5 to 2,6. On the other hand, $\rho(\boldsymbol{r}_c)$ for the C5—C6 bond (larger than in the C2—C3 bond) decreases regularly until equal to that in the C2—C3 bond.

Although this analysis has emphasized that the change in the density at the bond critical points can be related to the change in bond length, from the previous analysis of changes in basis set at fixed geometries there are also changes arising from the selection of the basis set. However, the change in $\rho(\boldsymbol{r}_c)$ due to the change from the STO-3G to 3-21G basis set was small except in the N—C bonds. This trend was fairly constant. Also, the changes in geometries and $\rho(\boldsymbol{r}_c)$ are small between the 3-21G and 3-21+G results leading to the conclusion that the differences in $\rho(\boldsymbol{r}_c)$ are mainly due to geometric differences.

As indicated in the topological analysis of distances from the nuclei to the bond critical point, a hydrogen bond was characterized between H9 and O12 in quinolinate. The value of $\rho(\boldsymbol{r}_c)$ for that bond was found to be 0.0205 au. This may appear to be small, but it is a reasonable value given the bond length, 4.3256 au, and the weak nature of the interaction.

(iii) Laplacian of the charge density

Tables 13 and 14 contain values of $\nabla^2\rho(\boldsymbol{r}_c)$ for the mono- and

TABLE 14. Laplacian of the charge density at the bond critical points in the pyridine dicarboxylates at the STO-3G//STO-3G level[a,b]

Bond	2,3	2,4	2,5	2,6	3,4	3,5
1—2	0.0501	−0.0517	−0.0622	−0.1816	−0.0402	−0.0088
1—6	−0.3658	−0.3312	−0.1857	−0.1818	−0.1151	−0.0066
2—3	−0.7419	−0.7765	−0.7713	−0.7496	−0.7063	−0.7601
3—4	−0.6731	−0.8124	−0.8146	−0.7621	−0.7583	−0.7974
4—5	−0.7921	−0.7856	−0.7540	−0.7622	−0.7272	−0.7975
5—6	−0.8176	−0.7875	−0.7660	−0.7494	−0.7756	−0.7608
6—7	−0.6071	−0.6121	−0.6380	−0.4696	−0.6068	−0.6364
5—8	−0.5992	−0.6301	−0.3458	−0.5993	−0.6191	−0.3377
4—9	−0.6509	−0.3332	−0.6394	−0.5964	−0.3060	−0.6567
3—10	−0.3150	−0.6410	−0.6207	−0.5992	−0.3078	−0.3374
2—11	−0.2959	−0.3244	−0.3261	−0.4695	−0.6248	−0.6354

[a]Values in atomic units.
[b]The column headers are the substitution positions.

Can. J. Chem. Downloaded from www.nrcresearchpress.com by EESC ESCOLA DE ENGENHARIA on 09/08/12
For personal use only.

TABLE 16. Charge density at the bond critical points in the pyridine dicarboxylates at the 3-21G//3-21G level[a,b]

Bond	2,3	2,4	2,5	2,6	3,4	3,5
1—2	0.2981	0.3081	0.3104	0.3098	0.3097	0.3099
1—6	0.3218	0.3134	0.3100	0.3098	0.3126	0.3099
2—3	0.2944	0.2968	0.2977	0.3000	0.2997	0.3056
3—4	0.3033	0.3056	0.3033	0.3021	0.2958	0.3019
4—5	0.3002	0.3007	0.3025	0.3021	0.2965	0.3019
5—6	0.3049	0.3079	0.3076	0.3000	0.3079	0.3056
6—7	0.2678	0.2683	0.2773	0.2234	0.2675	0.2779
5—8	0.2635	0.2729	0.2318	0.2680	0.2743	0.2298
4—9	0.2767	0.2262	0.2733	0.2653	0.2165	0.2778
3—10	0.2221	0.2743	0.2682	0.2680	0.2196	0.2298
2—11	0.2185	0.2248	0.2245	0.2234	0.2795	0.2779

[a]Values in atomic units.
[b]The column headers are the substitution positions.

TABLE 17. Laplacian of the charge density at the bond critical points in the pyridine monocarboxylates at the 3-21G//3-21G level[a,b]

Bond	**2**	**3**	**4**
1—2	−0.6374	−0.6310	−0.6589
1—6	−0.7052	−0.6918	−0.6600
2—3	−0.9232	−0.9381	−0.9249
3—4	−0.9225	−0.9315	−0.9390
4—5	−0.9008	−0.9139	−0.9379
5—6	−0.9308	−0.9201	−0.9249
6—7	−0.8332	−0.8320	−0.8319
5—8	−0.7976	−0.7995	−0.8352
4—9	−0.8109	−0.8480	−0.5229
3—10	−0.8526	−0.5361	−0.8369
2—11	−0.4982	−0.8726	−0.8334

[a]Values in atomic units.
[b]**2**, **3**, and **4** represent picolinate, nicotinate, and isonicotinate, respectively.

dicarboxylated pyridines, respectively, at the STO-3G//STO-3G level. As with the STO-3G//AM1 results, there are several values of $\nabla^2\rho(\boldsymbol{r}_c)$ in the N—C bonds that are positive or near zero. Tables 17 and 18 contain values of $\nabla^2\rho(\boldsymbol{r}_c)$ for the carboxylated pyridines calculated at the 3-21G//3-21G level. Again, as with the 3-21G//AM1 results, the $\nabla^2\rho(\boldsymbol{r}_c)$ values for the N—C bonds have become very negative. Tables 21 and 22 contain the $\nabla^2\rho(\boldsymbol{r}_c)$ values calculated at the 3-21+G//3-21+G level. The 3-21G and 3-21+G results are quite similar.

Examining the series with substitution in the 2,3, 2,5, 2,4, and 2,6 positions reveals a trend observed at all three levels in the N1—C2 bond. That is, $\nabla^2\rho(\boldsymbol{r}_c)$ in the N1—C2 bond becomes more negative as the second carboxylate group is moved around the ring.A similar trend but with $\nabla^2\rho(\boldsymbol{r}_c)$ becoming more positive is observed in the N1—C6 bond for the same movement. There is one exception to the latter trend at the 3-21G level at the last step (2,5 to 2,6) with $\nabla^2\rho(\boldsymbol{r}_c)$ becoming more negative. There is also a similar trend in the C2—C3 bond at the 3-21G and 3-21+G levels, that is, $\nabla^2\rho(\boldsymbol{r}_c)$ becomes more negative as the carboxylate group moves from C3 to C6. This trend is not evident at the STO-3G level. Table 22 contains an extra entry for quinolinate due to the characterization of a hydrogen bond between H9 and O12. As expected, $\nabla^2\rho(\boldsymbol{r}_c)$ is positive, although small in magnitude, indicating a closed shell interaction that is characteristic of hydrogen bonds.

(iv) Maximum in $-\nabla^2\rho(\mathbf{r})$

The distance of the (3,−3) critical point in the negative of the Laplacian to the nitrogen nucleus, r', the value of the charge density, $\rho(\boldsymbol{r}')$, and the value of the Laplacian at that point are listed in Table 23 for the carboxylated pyridines at the STO-3G//STO-3G, 3-21G//3-21G, and 3-21+G//3-21+G levels. At the STO-3G level, substitution at position 4 gives the largest r' value while substitution at 2 the smallest in the monocarboxylates. This holds for the dicarboxylates as well, so that 2,6 substitution gives the smallest value with those with 2,3 and 2,5 substitution following closely. 3,4 substitution gives the largest value of r'.

At the STO-3G level, substitution at position 2 gives the largest value of $\rho(\boldsymbol{r}')$ with that for substitution at 4 giving the lowest

TABLE 18. Laplacian of the charge density at the bond critical points in the pyridine dicarboxylates at the 3-21G//3-21G level[a,b]

Bond	2,3	2,4	2,5	2,6	3,4	3,5
1—2	−0.5933	−0.6334	−0.6659	−0.6783	−0.6266	−0.6523
1—6	−0.7414	−0.6934	−0.6694	−0.6783	−0.6774	−0.6523
2—3	−0.8814	−0.8949	−0.8976	−0.9081	−0.8910	−0.9243
3—4	−0.9027	−0.9370	−0.9254	−0.9075	−0.8897	−0.9220
4—5	−0.9125	−0.9173	−0.9146	−0.9075	−0.8900	−0.9220
5—6	−0.9253	−0.9362	−0.9369	−0.9080	−0.9342	−0.9243
6—7	−0.8081	−0.8102	−0.8562	−0.5310	−0.8052	−0.8579
5—8	−0.7723	−0.8209	−0.5780	−0.7947	−0.8278	−0.5676
4—9	−0.8482	−0.5490	−0.8325	−0.7929	−0.4925	−0.8599
3—10	−0.5228	−0.8316	−0.7972	−0.7947	−0.5083	−0.5676
2—11	−0.4970	−0.5403	−0.5388	−0.5310	−0.8645	−0.8579

[a]Values in atomic units.
[b]The column headers are the substitution positions.

Can. J. Chem. Downloaded from www.nrcresearchpress.com by EESC ESCOLA DE ENGENHARIA on 09/08/12
For personal use only.

Can. J. Chem. Downloaded from www.nrcresearchpress.com by EESC ESCOLA DE ENGENHARIA on 09/08/12
For personal use only.

TABLE 19. Charge density at the bond critical points in the pyridine monocarboxylates at the 3-21+G//3-21+G level[a,b]

Bond	2	3	4
1—2	0.3118	0.3064	0.3088
1—6	0.3121	0.3118	0.3088
2—3	0.2992	0.3032	0.3035
3—4	0.3036	0.3034	0.3021
4—5	0.2981	0.2991	0.3021
5—6	0.3047	0.3038	0.3035
6—7	0.2746	0.2746	0.2749
5—8	0.2684	0.2686	0.2748
4—9	0.2698	0.2761	0.2294
3—10	0.2770	0.2322	0.2748
2—11	0.2275	0.2820	0.2749

[a]Values in atomic units.
[b]**2**, **3**, and **4** represent picolinate, nicotinate, and isonicotinate, respectively.

TABLE 21. Laplacian of the charge density at the bond critical points in the pyridine monocarboxylates at the 3-21+G//3-21+G level[a,b]

Bond	2	3	4
1—2	−0.6375	−0.6272	−0.6408
1—6	−0.6757	−0.6739	−0.6409
2—3	−0.9134	−0.9241	−0.9250
3—4	−0.9260	−0.9267	−0.9289
4—5	−0.9088	−0.9159	−0.9290
5—6	−0.9354	−0.9275	−0.9249
6—7	−0.8440	−0.8444	−0.8453
5—8	−0.8026	−0.8030	−0.8392
4—9	−0.8159	−0.8528	−0.5684
3—10	−0.8517	−0.5826	−0.8392
2—11	−0.5525	−0.8873	−0.8453

[a]Values in atomic units.
[b]**2**, **3**, and **4** represent picolinate, nicotinate, and isonicotinate, respectively.

value. In the dicarboxylated species this trend appears to hold with the 2,6-and 2,3-substituted species having the largest values while the lowest value is found with 3,4 substitution.

Substitution at the two position gives rise to the most negative value of the Laplacian at the critical point at the STO-3G level and the least negative is found with substitution at position 4. This trend appears to hold for the dicarboxylates with the most negative values found for the 2,3- and 2,6-substituted species. The least negative value was found for the 3,4-disubstituted species.

The results calculated at the 3-21G level can expect to be influenced by the change in geometric parameters, that is, the bond shortening found upon proceeding to the 3-21G level from the STO-3G level can be expected to influence the density around the position of the lone pair on nitrogen. Surprisingly, although r' increases slightly, $\rho(\boldsymbol{r}')$ decreases dramatically and $\nabla^2\rho(\boldsymbol{r}')$ becomes much less negative. At the STO-3G level, substitution at the 3 position resulted in values of $\boldsymbol{r}'$, r, and $\nabla^2\rho$ close to those found with substitution at position 2. At the 3-21G level these values are now closer to those found with substitution at position 4. Overall, in the mono- and dicarboxylated pyridines, those substituted in the 2 and 2,6 positions have the smallest r', largest ρ, and most negative $\nabla^2\rho$. As well, those substituted at the 3 and/or 4 positions have the largest r', smallest ρ, and least negative $\nabla^2\rho$. The difference between the smallest and largest value at each level has become larger. At the STO-3G level, r', ρ, and $\nabla^2\rho$ varied by 0.0029, 0.0073, and 0.1194 au, respectively. These differences become larger at the 3-21G level, having values of 0.0054, 0.0169, and 0.1631 au for differences in r', ρ, and $\nabla^2\rho$, respectively.

As with the 3-21G calculations, it should be expected that values calculated at the 3-21+G level would be affected by changes in geometries due to basis set level. The monocarboxylated series has the shortest r' value with picolinate and as with the 3-21G results, nicotinate and isonicotinate are almost equivalent. The effect of substitution in the 2 position can be seen in the dicarboxylates as well with dipicolinate having the lowest r' value of the species studied. The series of shortest to longest r' continues with 2,4, 2,5, 2,3, 3,5, and 3,4 substitution. The values of $\rho(\boldsymbol{r}')$ give rise to a series that follows the same trend going from highest to lowest $\rho(\boldsymbol{r}')$. Dipicolinate has the highest value of $\rho(\boldsymbol{r}')$ while cinchomeronate the lowest. The same pattern is followed when examining $\nabla^2\rho(\boldsymbol{r}')$ going from most negative to most positive. Note that the range of values has expanded again from those calculated at the 3-21G level. r', $\rho(\boldsymbol{r}')$, and $\nabla^2\rho(\boldsymbol{r}')$ now vary by 0.097, 0.0341, and 0.3608 au, respectively, roughly double the variation at the 3-21G level.

3.3. Geometric analysis: bond lengths

The calculated bond lengths at all levels of theory used in this study can be recovered using the critical point data listed in Tables 2 and 9 for the monocarboxylates, and in Tables 3 and 10 for the dicarboxylates. Using this technique trends are apparent when changes in bond lengths are considered in relation to the changes in method or basis set level.

TABLE 20. Charge density at the bond critical points in the pyridine dicarboxylates at the 3-21+G//3-21+G level[a,b]

Bond	2,3	2,4	2,5	2,6	3,4	3,5
1—2	0.3003	0.3100	0.3120	0.3100	0.3073	0.3078
1—6	0.3183	0.3107	0.3074	0.3099	0.3100	0.3076
2—3	0.2911	0.2972	0.3005	0.3012	0.2989	0.3038
3—4	0.3011	0.3019	0.3019	0.3024	0.2955	0.2994
4—5	0.3000	0.3002	0.3011	0.3023	0.2947	0.2993
5—6	0.3055	0.3058	0.3040	0.3013	0.3077	0.3040
6—7	0.2711	0.2713	0.2797	0.2291	0.2713	0.2806
5—8	0.2649	0.2735	0.2353	0.2757	0.2719	0.2346
4—9	0.2767	0.2313	0.2743	0.2643	0.2302	0.2790
3—10	0.2285	0.2795	0.2752	0.2757	0.2305	0.2346
2—11	0.2324	0.2299	0.2300	0.2291	0.2810	0.2806
9···12	0.0205					

[a]Values in atomic units.
[b]The column headers are the substitution positions.

TABLE 22. Laplacian of the charge density at the bond critical points in the pyridine dicarboxylates at the 3-21+G//3-21+G level[a,b]

Bond	2,3	2,4	2,5	2,6	3,4	3,5
1—2	−0.6087	−0.6184	−0.6538	−0.6400	−0.6272	−0.6476
1—6	−0.7125	−0.6561	−0.6425	−0.6396	−0.6641	−0.6468
2—3	−0.8590	−0.8996	−0.9145	−0.9188	−0.8935	−0.9196
3—4	−0.9040	−0.9243	−0.9272	−0.9263	−0.8852	−0.9134
4—5	−0.9194	−0.9174	−0.9196	−0.9259	−0.8889	−0.9128
5—6	−0.9343	−0.9386	−0.9290	−0.9192	−0.9390	−0.9204
6—7	−0.8270	−0.8254	−0.8722	−0.5706	−0.8267	−0.8775
5—8	−0.7823	−0.8308	−0.6070	−0.8422	−0.8191	−0.6025
4—9	−0.8532	−0.5866	−0.8402	−0.7978	−0.5773	−0.8728
3—10	−0.5663	−0.8698	−0.8382	−0.8421	−0.5781	−0.6026
2—11	−0.5855	−0.5753	−0.5767	−0.5706	−0.8780	−0.8775
9···12	+0.0983					

[a]Values in atomic units.
[b]The column headers are the substitution positions.

TABLE 23. Distance from the nitrogen at the maximum in $-\nabla^2\rho$ associated with the lone pair of electrons on N in the pyridine ring and values of the charge density and Laplacian at that point[a]

	STO-3G//STO-3G		
Compound	r'	ρ	$\nabla^2\rho$
Picolinate	0.6937	0.7230	−4.6465
Nicotinate	0.6942	0.7223	−4.6273
Isonicotinate	0.6960	0.7183	−4.5540
Quinolinate	0.6938	0.7256	−4.6330
Lutidinate	0.6955	0.7210	−4.5659
Isocinchomeronate	0.6939	0.7246	−4.6282
Dipicolinate	0.6934	0.7256	−4.6470
Cinchomeronate	0.6963	0.7183	−4.5276
Dinicotinate	0.6945	0.7228	−4.6007
	3-21G//3-21G		
Picolinate	0.7236	0.6301	−3.0686
Nicotinate	0.7265	0.6213	−2.9716
Isonicotinate	0.7269	0.6200	−2.9560
Quinolinate	0.7267	0.6212	−2.9614
Lutidinate	0.7271	0.6199	−2.9490
Isocinchomeronate	0.7268	0.6207	−2.9596
Dipicolinate	0.7253	0.6255	−3.0111
Cinchomeronate	0.7290	0.6132	−2.8800
Dinicotinate	0.7284	0.6155	−2.9055
	3-21+G//3-21+G		
Picolinate	0.7250	0.6172	−2.9286
Nicotinate	0.7294	0.6015	−2.7645
Isonicotinate	0.7297	0.6006	−2.7572
Quinolinate	0.7289	0.6040	−2.7788
Lutidinate	0.7265	0.6115	−2.8674
Isocinchomeronate	0.7267	0.6109	−2.8577
Dipicolinate	0.7227	0.6247	−3.0084
Cinchomeronate	0.7324	0.5905	−2.6476
Dinicotinate	0.7316	0.5935	−2.6779

[a]Values in atomic units.

(i) AM1 to STO-3G

With the exception of one N—C bond in cinchomeronate, all N—C bonds lengthen upon proceeding to the STO-3G level. In general, there is a decrease in the ring C—C and the C—H bond lengths but a significant increase in the C—CO_2^- bond lengths. The change in the C—O bond lengths vary but in a number of cases, considering the changes in the C—CO_2^- bonds, the variation is in the fourth place after the decimal.

(ii) STO-3G to 3-21G

For this process, all the N—C bonds shorten and, in general, all the C—C bonds shorten. The C—H and C—O bonds shorten, with the shortening in the area of about 0.02 au.The C—CO_2^- bonds decrease by as much as 0.15 to 0.17 au. The N—C2 bond in quinolinate does not shorten as much as in other compounds.

(iii) 3-21G to 3-21+G

The addition of diffuse functions to the heavy atoms should help in the description of the extra density in the anions. However, rather than having clear trends, the results are mixed. There is N—C bond lengthening in the monocarboxylates, but in the dicarboxylates there is a mixture of lengthening and shortening. In cinchomeronate and dinicotinate, the N—C bonds lengthen but in dipicolinate they shorten. The N—C bonds in the remaining dicarboxylates shorten if a carboxylate group is attached to C2 or lengthen if not. Thus, whether the N—C bond lengthens or shortens depends entirely, in the dicarboxylates, on the location of the carboxylate groups. The one compound that does not appear to follow this trend is quinolinate where the N—C2 bond shortening is minimal. All the ring C—C bonds lengthen. Interestingly, throughout the series, changes in the C—H bond lengths do not display systematic trends other than when *ortho* to the N position. Here the C—H bonds shorten slightly. There is definite shortening in all the C—CO_2^- bonds.

4. Discussion

4.1. Geometric, conformational, and topological analysis

The present results suggest that the AM1 method does not reproduce geometries and conformations correctly for the species studied. The method did not locate many of the stationary points on the energy surface and, in particular, gave the conformations that have been found to be the lowest in energy at the 3-21+G level in only two cases out of the nine examined. As well, in many cases the trends observed with the 3-21+G optimized bond lengths are not reproduced by the AM1 method; however, this may be a function of differing conformations. As would be expected (14), due to its small size, the STO-3G basis set is

Can. J. Chem. Downloaded from www.nrcresearchpress.com by EESC ESCOLA DE ENGENHARIA on 09/08/12
For personal use only.

Can. J. Chem. Downloaded from www.nrcresearchpress.com by EESC ESCOLA DE ENGENHARIA on 09/08/12
For personal use only.

incapable of adequately describing the C—CO_2^- bond, resulting in extremely long C—CO_2^- bond lengths.

Comparisons of the results from the topological analysis of the charge density calculated at the AM1 and *ab initio* geometries is broken down into three sections: (*1*) comparison of distances of passes from atoms involved in the bond, (*2*) values of the charge density and its Laplacian at the critical points, and (*3*) values associated with the critical point in the Laplacian associated with the ring nitrogen lone pair.

Detailed direct comparison between the topological properties found using wavefunctions calculated at the STO-3G//AM1 and 3-21G//AM1 levels and those found using wavefunctions at the STO-3G//STO-3G, 3-21G//3-21G, and 3-21+G//3-21+G levels are difficult to undertake due to the changes in conformation and geometry. However, given the linear relationships found by Boyd and Edgecombe (11) between bond lengths and the position of bond critical points, passes, it is possible to correlate trends observed at these different geometries with the basis sets used. This permits the identification of the minimum level at which a certain degree of confidence can be placed in calculated trends. The approach used is to examine the ratio $r_A/(r_A + r_B)$, where r_A is the distance from atom A to the critical point in the bond to atom B which is a distance r_B from the critical point. The results found at the 3-21+G//3-21+G level will be used as the benchmark for comparison. The r_A and r_B values tabulated in Tables 4, 5, 11, and 12 are used to calculate this ratio.

Examining this ratio for the N1—C2 bond at the STO-3G//AM1 and STO-3G//STO-3G levels and comparing to the benchmark shows that the results at this level are approximately 0.04 too large. At the 3-21G//AM1 level the ratio is 0.01 or less too small while moving to the 3-21G//3-21G results gives differences that range from –0.006 to 0.002, that is, at this level the ratios are very close to the benchmark. Moving along the ring to the C2—C3 bond, the range of differences are ±0.06 and ±0.07, respectively, at the STO-3G//AM1 and STO-3G//STO-3G levels. With the 3-21G basis set these values fall with one fairly large difference, 0.02, at the AM1 geometry and a range of –0.009 to 0.004 at the 3-21G geometry. Similarly, in the C3—C4 bond the differences for this ratio have the ranges –0.08 to 0.06, ±0.08, ±0.008, and ±0.01, respectively, for the STO-3G//AM1, STO-3G//STO-3G, 3-21G//AM1, and 3-21G//3-21G calculations. Very similar results are found for the C4—C5 bond, that is, –0.05 to 0.08, –0.01 to 0.08, ±0.01, and ±0.01, respectively, for the ratio differences at the STO-3G//AM1, STO-3G//STO-3G, 3-21G//AM1, and 3-21G//3-21G levels. The corresponding ratio differences in the C5—C6 bond are in the ±0.04, ±0.04, ±0.009, and ±0.009 ranges, respectively. Lastly, the corresponding ratio differences for the N1—C6 bond are very much like those found for the N1—C2 bond, overestimated by approximately 0.04 at the STO-3G//AM1 and STO-3G//STO-3G levels, underestimated by approximately 0.01 at the 3-21G//AM1 level and having a range of –0.007 to 0.002 at the 3-21G//3-21G level.

Although none of the four levels compared with the 3-21+G//3-21+G ratio results reproduced those results completely, comparing the ratios with a view to overall changes from one species to another, the 3-21G//3-21G results are the best of the four. As well, the 3-21G//AM1 results appear to display the same trends with some minor exceptions. The ratio values found with the split-valence basis sets are also quite close to those found at the benchmark level.

The geometric changes that occur upon changing method or basis set preclude a direct comparison with $\rho(r_c)$ or $\nabla^2\rho(r_c)$. As pointed out by Boyd and Edgecombe (11), there is a linear correlation of $\rho(r_c)$ and $\nabla^2\rho(r_c)$ with bond length and examination of $\rho(r_c)$ for particular bonds throughout a series shows this to be true unless influenced by the ring substituents. Note that although the 3-21G//3-21G results are, on average, quite close to those found at the 3-21+G//3-21+G level, the 3-21G//AM1 results are not. This appears to be the result of geometric and conformational differences.

Values of r', ρ, and $\nabla^2\rho$ at the maximum in $-\nabla^2\rho$ associated with the lone pair of electrons on nitrogen in the pyridine ring found at the 3-21G//3-21G level appear to be quite well reproduced at the 3-21G//AM1 level. Both give values close to those found at the 3-21+G//3-21+G level. This indicates that the position and values associated with this maximum in $-\nabla^2\rho$ is not as sensitive to geometric change, but rather is very dependent on the basis set used. The STO-3G results are quite different.

4.2. Applicability of results to quantum pharmacology calculations

Quinolinic acid, an endogenous neurotoxin active at the NMDA receptor site, plays a role in epilepsy and neurodegenerative disease. Accordingly, quinolinic acid and its mono- and dicarboxylated pyridine analogues are important target molecules in the rational design of neuroactive drug molecules. Exploitation of these structures in drug design demands an exacting understanding of the geometric, conformational, and topological properties of this analogue series. These features are necessary for a comprehensive understanding of both drug molecule structure and drug–receptor interactions through such non-bonded interactions as ion–ion, ion–dipole, dipole–dipole, and hydrogen bonding.

Although molecular mechanics is the most widely cited methodology in quantum pharmacology, it fails to adequately consider electronic properties. These properties must be examined through molecular orbital calculations. Since there are a variety of molecular orbital methods ranging from semi-empirical to *ab initio*, it is also necessary to clarify the quality and interchangeability of results obtained using these methodologies.

As demonstrated in this study, AM1, STO-3G, and 3-21G calculations do not provide equivalent treatments of geometric, conformational, and topological properties. Split-valence basis sets yield answers significantly different from those obtained from semi-empirical parameterizations. Furthermore, the utility of the theory of molecular structure calculations in representing molecular topology and electron distribution properties (both essential in conceptualizing drug–receptor interactions) has been demonstrated.

Acknowledgements

The authors gratefully acknowledge the financial support of NSERC and the National Center of Excellence in Neural Regeneration and Functional Recovery. D.F.W. is an Ontario Ministry of Health Career Scientist. Useful conversations with K. Jhamandas and R. Boegman, Department of Pharmacology, Queen's University are gratefully acknowledged.

1. S. Birley, J.F. Collins, M.N. Perkins, and T.W. Stone. Br. J. Pharmacol. **77**, 7 (1982).
2. R.F.W. Bader. Atoms in molecules: a quantum theory. Oxford University Press, Oxford. 1990; and references therein.

3. M.J.S. Dewar, E.G. Zoebisch, E.F. Healy, and J.J.P. Stewart. J. Am. Chem. Soc. **107**, 3902 (1985).
4. J.J.P. Stewart. Quantum Chem. Prog. Exchange Bull. **9**, 99 (1989), QCPE Program No. 581.
5. M. Dupuis, A. Farazdel, S.P. Karna, and S.A. Maluendes. *In* MOTECC: modern techniques in computational chemistry. *Edited by* E. Clementi. ESCOM, Leiden, The Netherlands. 1990.
6. M.J. Frisch, G.W. Trucks, M. Head-Gordon, P.M.W. Gill, M.W. Wong, J.B. Foresman, B.G. Johnson, H.B. Schlegel, M.A. Robb, E.S. Replogle, R. Gomperts, J.L. Andres, K. Raghavachari, J.S. Binkley, C. Gonzalez, R.L. Martin, D.J. Fox, D.J. Defrees, J. Baker, J.J.P. Stewart, and J.A. Pople. GAUSSIAN 92, Revision A. Gaussian, Inc., Pittsburgh PA, 1992.
7. W.J. Hehre, R.F. Stewart, and J.A. Pople. J. Chem. Phys. **51**, 2657 (1969).
8. J.S. Binkley, J.A. Pople, and W.J. Hehre. J. Am. Chem. Soc. **102**, 939 (1980).
9. T. Clark, J. Chandrasekhar, G.W. Spitznagel, and P.v.R. Schleyer. J. Comput. Chem. **4**, 294 (1983).
10. F.W. Biegler-König, R.F.W. Bader, and T. Tang. J. Comput. Chem. **3**, 317 (1982) and updates; R.F.W. Bader. Department of Chemistry. McMaster University, 1280 Main St. West, Hamilton, ON L8S 4M1.
11. R.J. Boyd and K.E. Edgecombe. J. Comput. Chem. **8**, 489 (1987).
12. K.E. Edgecombe. Ph.D. Thesis. Dalhousie University, Halifax. 1987.
13. R.F.W. Bader, T.S. Slee, D. Cremer, and E. Kraka. J. Am. Chem. Soc. **105**, 5061 (1983); D. Cremer and E. Kraka. Croatica Chem. Acta, **57**, 1259 (1984); R.J. Boyd, O. Knop, and S.C. Choi. J. Am. Chem. Soc. **110**, 7299 (1988).
14. K.E. Edgecombe and R.J. Boyd. Can. J. Chem. **62**, 2881 (1984).

Can. J. Chem. Downloaded from www.nrcresearchpress.com by EESC ESCOLA DE ENGENHARIA on 09/08/12
For personal use only.

Metal ion complexes of 1,4,7-triazacyclononane and their aminoalkyl derivatives. Analysis of chelate rings fusion and molecular mechanics study

IGOR V. PLETNEV

Department of Chemistry, Moscow State University, Moscow 119899 GSP-3, Russia

Received December 24, 1992[1]

IGOR V. PLETNEV. Can. J. Chem. **72**, 1404 (1994).

Stereochemistry of metal ion complexes of 1,4,7-triazacyclononane, their *N,N′,N″*-tris(aminoethyl), tris(aminopropyl), and their *N,N′*-(4,7-diazadecylene) derivatives is described in terms of the fusion of chelate rings at metal–nitrogen coordination bonds. Molecular mechanics calculations and analysis of the X-ray data confirm that the semi-quantitative analysis is valid and that fusion plays a critical role in the structure of the complexes. Molecular mechanics study of puckering of the ethylenediamine chelate ring, an essential part in this study, is also presented.

IGOR V. PLETNEV. Can. J. Chem. **72**, 1404 (1994).

On décrit la stéréochimie des complexes d'ions métalliques du 1,4,7-triazacyclononane et de ses dérivés *N,N′,N″*-tris(aminoéthyl)-, tris(aminopropyl)- et *N,N′*-(4,7-diazadécylène)- en fonctions de la fusion de noyaux chélates au niveau des liaisons de coordination métal–azote. Des calculs de mécanique moléculaire ainsi que des données de diffraction des rayons X confirment la validité d'une analyse semi-quantitative et prouvent le rôle critique que la fusion joue dans la structure des complexes. On présente aussi une étude de mécanique moléculaire du plissement du cycle chélaté de l'éthylènediamine qui est essentiel dans cette hypothèse.

[Traduit par la Rédaction]

Introduction

1,4,7-Triazacyclononane (tacn) and its derivatives are known as versatile ligands. They are useful in the selective complexation and sequestering of metal ions, the stabilization of unusual oxidation states, magnetic resonance imaging, biomimicricy, etc. (for a review, see ref. 1; for some representative examples, see refs. 2–6). Stereochemistry of complexation plays a key role in all applications. Much is known about the stereochemistry from both experimental (1) and theoretical studies (e.g., molecular mechanics, MM calculations (7)).

However, to understand the factors governing the stereochemical patterns, we believe one should focus on the fusion of the chelate rings in these complexes. Simple semi-quantitative analysis of how the conformation of one ring influence the conformation of the other and therefore the whole structure appears helpful in rationalizing the stereochemistry observed (8) and the molecular design (9).

In this paper we attempt to apply this approach to conceptualise the stereochemical configurations in tacn complexes and their aminoalkyl derivatives (Fig. 1). MM calculations are used to investigate the puckering of an ethylenediamine chelate ring, which is a key subject in the consideration, and to refine the conformations predicted in polychelate systems.

Computations

All MM calculations were performed on a PC AT clone equipped with 80286/287 processor using the program MMPC (Molecular Mechanics for Personal Computing; C language) written by the author (available upon request).

The program minimizes the energy of the molecule in the Cartesian atomic coordinates space, taking into account contributions to total energy, E, from: (*i*) bond lengths stretching, E_b; (*ii*) bond angles bending, E_a; (*iii*) torsional strain, E_t, and (*iv*) nonbonded interactions, E_{nb}. Fletcher–Reeves and Davidson–Fletcher–Powell gradient minimization algorithms (10) are implemented in conjunction with analytical first derivatives given by Boyd (11).

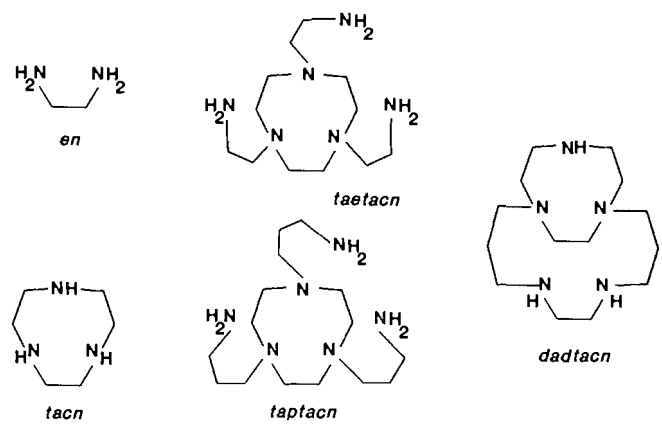

FIG. 1. Ligands discussed in this paper.

Test calculation of αα-[Co(tetraethylenepentaamine)Cl_2]$^+$, which has been subjected to an MM study earlier (12), is in excellent agreement with published data. The structures presented below are compatible with X-ray data; this proves that the software is reliable.

All calculations were performed using the force field developed by Hancock (13). This force field is one of the most extensively tested to date and the most reliable. Initially all nonbonded interactions in molecule(s) of interest were considered. However, it was found that the force field (13) demanded strongly that long-range interactions (i.e., those at distance greater than 1.20 times the sum of van der Waals atomic radii (14)) be excluded when computing the energy. Certain difficulties caused by the oscillations of the energy gradient were eliminated by multiplying all nonbonded energies by a smoothing function.

Typically, the initial geometry of the molecules under study (i.e., the starting point for MM optimization) was constructed using reasonable bond lengths, bond angles and torsional angles, the last set of parameters being derived from semi-quantitative fusion analysis. Minimization was considered complete when the root-mean-squared gradient decreased to 0.005 kcal mol^{-1} Å^{-1}. The puckering of the *en* ring was studied using the "torsional angle drive" method (15).

[1]Revision received August 26, 1993.

Can. J. Chem. Downloaded from www.nrcresearchpress.com by EESC ESCOLA DE ENGENHARIA on 09/08/12
For personal use only.

Can. J. Chem. Downloaded from www.nrcresearchpress.com by EESC ESCOLA DE ENGENHARIA on 09/08/12
For personal use only.

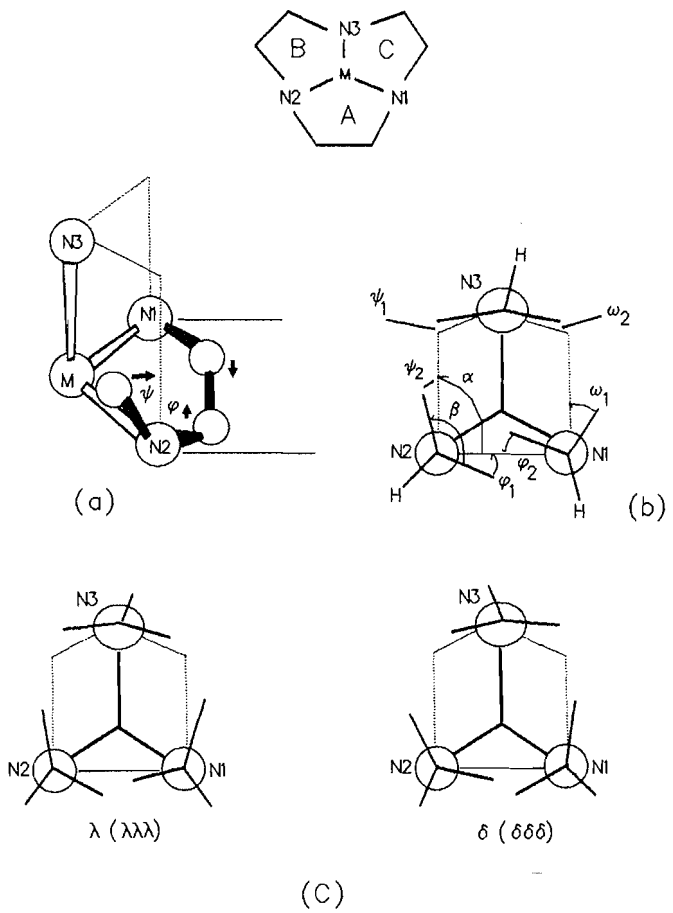

FIG. 2. Fusion of chelate rings in a complex of *fac*-coordinated tacn ligand.

Results and discussion

Theoretical basis

Stereochemistry of metal ion complexes can be most naturally described by the conformations of the chelate rings. Evidently, the conformations are not independent and they do influence each other. A very simple formalism is useful to describe such interrelations.

Let us consider a *fac*-coordinated tacn ligand in an octahedral complex (the usual mode of coordination). This moiety comprises three fused ethylenediamine (*en*) chelate rings, A–C in Fig. 2. Let us assume that the first ring, A, adopts some fixed conformation, e.g., the optimal (16) symmetrical *gauche*, *sym-gauche*. It means (see Fig. 2*a*) that one carbon atom, say, one adjacent to N_1, is above the coordination plane N_1MN_2, while another carbon lies below the plane (the placement could be inverted, resulting in an opposite chirality of puckered *en* ring). Fixing the conformation of ring A influences the conformation of ring B: the carbon adjacent to N_2, ring B, is forced — by the tetrahedral structure of the coordinated nitrogen — to appear in front of the plane N_2MN_3. This, in turn, induces positioning of another carbon in B to lie behind that plane (if *sym-gauche* form of the *en* ring is still to be maintained). Now, positions of *both* carbon atoms in ring C have been predefined by the structure of both rings A and B.

This qualitative consideration can easily turn semi-quantitative. The convenient way is to refer to the angles of rotation around the M—N coordination bond, needed to place carbon atoms into the respective coordination plane NMN of the *en* ring (see Newman projection, Fig. 2*b*). There are two such *principal* angles in each ring (Fig. 2*b*, angles φ_1, φ_2; ψ_1, ψ_2; ω_1, ω_2).

Clearly, the fusion of two chelate rings (say, A and B) means that the principal angles at the common coordination bond (φ_1 and ψ_2, rotation around M—N_2) are related to each other. The relationship is dictated by the directionality of bonds inherent to both ligating donor atom (N_2, sp^3-nitrogen; angle β of 120° on Fig. 2*b*) and the metal ion center (octahedral, angle α of 90°); that is, $\psi_2 = \varphi_1 + 30°$.[2] Apparently, such a relationship could be drawn for any pair of fused chelate rings; for example, $\omega_1 = \varphi_2 - 30°$.

For a *syn-gauche* conformation of the *en* ring, the principal angles, torsional angles NMNC, are near 15° (16).[3] Therefore, a value of −15° for φ_1, ring A, leads to $\psi_2 = 15°$, ring B; and a value of −15° for φ_2 leads to $\omega_1 = -45°$, ring C. Now $\omega_1 = -45°$ does not match the *sym-gauche* conformation. Therefore optimal conformations for neighboring *en* rings are untenable in a *fac*-coordinated tacn. To answer the question what ring conformations are possible and in what combination, we need a more detailed description of the way in which principal angles may vary in any ring, i.e., *en* ring puckering.

Puckering of the ethylenediamine chelate ring

It is well known that ethylenediamine chelate ring adopts various asymmetric conformations of the *gauche* type that have somewhat higher energy than the *sym* form (17). However, both the energy and the geometry of distorted conformations need further scrutiny (earlier works, e.g., (17–19), have used only rough computational models; a more recent paper (20) did not specifically consider the puckering of the ring). Therefore, a study of an isolated *en* ring with "state-of-the-art" MM parametrization (13) was carried out.

Calculations were made with different strain-free M—N bond lengths — 1.9, 2.10, and 2.30 Å, to include different-sized metals. Other force-field parameters were the same as those for high-spin nickel(II). Thus the results obtained at r^0(M—N) 2.10 Å are applicable directly to Ni complex, while results for r^0(M—N) = 1.9 Å and r^0(M—N) = 2.30 Å may serve as good approximations (an approach developed earlier (13)).

Full optimization of the *en* ring structure converged to the *sym-gauche* form despite variations in the starting conformation. The principal torsional angles (M—N rotation) are (φ_1, φ_2) = (−14.9°, −14.9°) (high-spin nickel; puckered *en* ring is chiral and the above values are only for the λ-enantiomer). The structural parameters are very close to those reported earlier, e.g., in ref. 16.

In order to obtain asymmetric conformations, one of two principal angles was fixed at some predefined value, allowing all other parameters to change. This technique was used earlier (19) and, evidently, simulates a situation in polychelate complexes, where the rings are fused. With such a constraint, a vari-

[2]Note, that for *quantitative* description one should consider all the rotation angles as having definite sign (from here on positive is clockwise) and fixed rotation axis (here MN_2). Thus (consult Fig. 2*b*), the angle φ_1, i.e., torsional angle N_1MN_2C, is < 0; ψ_2, angle N_3MN_2C is > 0; $\alpha > 0$; and $\beta > 0$. Note that one could change diastereotopic configuration of nitrogen center, i.e., exchange H and $C_{ring\ B}$ on Fig. 2*b*. In that case, β would be $< 0 = -120°$, resulting in $\psi_2 = \varphi_1 - 210° = \varphi_1 + 150°$.

[3]Accounting for the signs of rotation angles and enantiomeric duality, (15°, 15°) and (−15°, −15°).

Can. J. Chem. Downloaded from www.nrcresearchpress.com by EESC ESCOLA DE ENGENHARIA on 09/08/12
For personal use only.

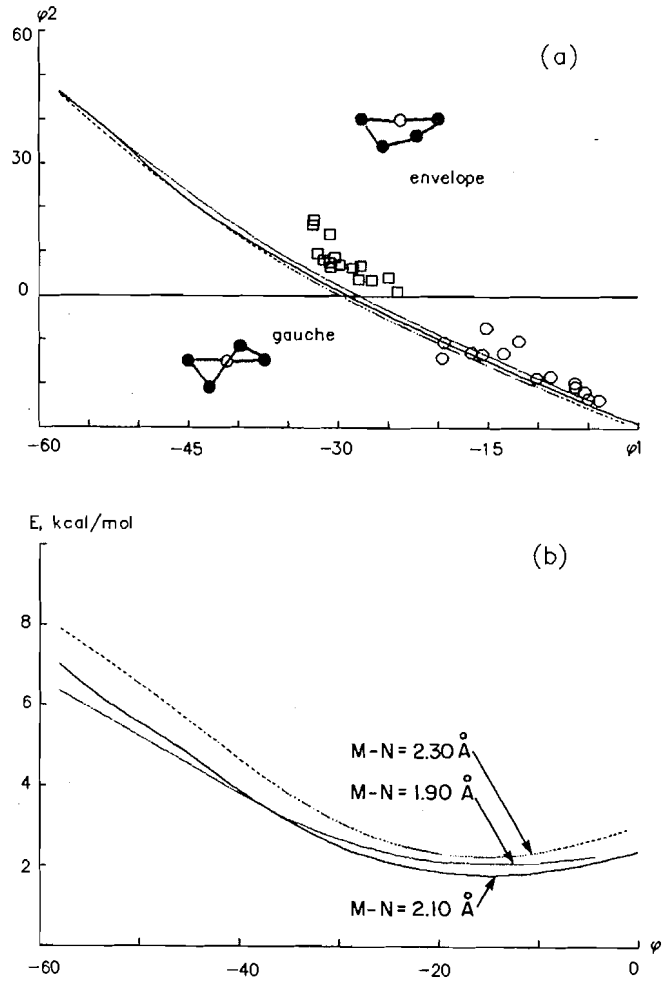

FIG. 3. (*a*) Interdependence between the two principal angles describing a puckering of *en* ring (λ-form). Experimental data: squares (*en* ring in tacn complexes) and circles. (*b*) Strain energy of puckered *en* ring vs. principal angle φ_1 (or φ_2). Calculated at ideal M—N bond lengths of 1.90 (···), 2.10 (--) and 2.30 Å (- -).

ety of asymmetric conformations were obtained. A pair of principal angles (φ_1, φ_2) uniquely described each of them. The curve that relates φ_1 with φ_2 (or vice versa) and, in a sense, represents the path of pseudorotation of the ring, is shown in Fig. 3*a*. The curve in Fig. 3*b* reflects the accompanying change of energy. (For simplicity, the curves are drawn for λ-enantiomer only.) Some experimental (X-ray (21–35)) points, also placed on Fig. 3*a*, confirm the validity of the calculated values.

The curves in Fig. 3 illustrate some features of *en* ring puckering. When starting from the *sym-gauche* point (−14.9°, −14.9°), one of the *en* ring carbon atoms progressively deviates below the coordination plane (φ_1 becomes more negative), the other carbon follows it, approaching the plane from the other-side (φ_2 becomes less negative). Finally, the second atom crosses over the plane ($\varphi_2 = 0°$) and appears on the same side as the first carbon (thus producing an *envelope* conformation). As Fig. 3*b* shows, this move costs energy, primarily because of an increase in torsional and bending strain. For example, moving from the *sym-gauche* point to the border-line point (−30°, 0°) requires ca. 0.7 kcal/mol, and further puckering to $\varphi_1 = -45°$ costs approximately 2.4 kcal/mol.

It should be mentioned that above values are only for "concerted" movement along the curve in Fig. 3*a*. Any deviation from this "least-energy" path requires additional energy. Indeed, any point on the curve is a local energy minimum obtained at fixed value of one principal angle, with the other principal angle being free to change. Thus, the puckering of *en* ring in polychelate "fused" systems must proceed along this path unless additional severe restrictions are present. Therefore, if two *en* rings are fused and one ring has a fixed conformation, e.g., (ψ_1, ψ_2), one principal angle in the neighboring ring, φ_1, is then fixed and one can deduce from Fig. 3*a* what should be the angle φ_2 and the conformation of the second ring (φ_1, φ_2). Moreover, with the curve in Fig. 3*b*, it is possible to conclude the energy of certain combinations of conformations. Consequently, it is also possible to find an optimal combination. (Naturally, chiral duality of puckered *en* ring must be taken into account. Thus, $\varphi_1 = -15°$ induces $\varphi_2 = -15°$ and *sym-gauche* conformation, if one assumes λ chirality; assuming δ chirality, $\varphi_2 = 40°$ and highly asymmetrical conformation will be obtained.)

Fusion of chelate rings in fac*-coordinated tacn*

The stereochemcial possibilities in tacn complexes may now be considered using an extremely simple mechanistic model. As it was stated above, principal angles of fused rings are related to each other: $\psi_2 = \varphi_1 + 30°$; $\omega_1 = \varphi_2 - 30°$; $\psi_1 = \omega_2 - 30°$.

Moreover, two principal angles in any ring are related, through the "least-energy" curve in Fig. 3 (least-squares approximation: $X_2 = (-33.3 \pm 2.6) + (-1.25 \pm 0.09)X_1$, $X = \varphi$, ψ, ω; λ-configuration; $X_2 = 33.3 - 1.25X_1$, δ-configuration). Thus, any of six principal angles in M(tacn) may be expressed as an explicit function of any other principal angles through a chain of relationships. Furthermore, owing to the cyclic nature of the ligand there are two such chains for any pair of principal angles. For examples, ψ_1 may be related to φ_1 through the chains φ_1–φ_2–ω_1–ω_2–ψ_1 and φ_1–ψ_2–ψ_1 (see Fig. 2). Apparently, the values produced either way must be equal. Solving this equality in conjunction with the above functions, one may estimate the values of the principal angles accounting for (*a*) macroring closure, (*b*) proper directionality of bonds around donor and metal centers, and (*c*) least steric strain in chelate rings.

Omitting computational details, two distinctly different sets of principal angles (φ_1, φ_2, ω_1, ω_2, ψ_1, ψ_2) were obtained this way: (*i*) (−30.8°, 5.2°, −24.8°, −2.3°, −32.3°, −0.8°) and (*ii*) (−54.5°, 34.8°, 4.8°, 27.3°, −2.7°, −24.5°). These values are dictated by geometric requirements. For energetic reasons, the first set seems to be preferable (first *en* ring in case (*ii*) is in a very strained conformation of a highly puckered *envelope*, cf. Fig. 3*b*). The values in selected set (*i*) should be averaged for all *en* rings due to the evident symmetry of the problem. This results in the following principal angles for the *en* rings in M(tacn): (−29.3°, 0.7°). They represent the *envelope* conformation which is practically on border-line *gauche/envelope* (see Fig. 3).[4]

As Table 1 shows, the values obtained with this simplest model are in surprisingly good agreement with the experimen-

[4]As for an isolated *en* ring, there are possible two enantiomers for *fac*-M(tacn), λ(λ, λ, λ) and δ(δ, δ, δ), as shown on Fig. 2*c*. For δ-form the values should be (−0.7, 29.3).

TABLE 1. Principal torsional angles in *en* rings of *fac*-coordinated tacn moiety, deg[a]

Structure	φ_1	φ_2	ψ_1	ψ_2	ω_1	ω_2	Reference
Ni(II)–tacn	−30.9	7.4	−30.4	8.6	−31.5	8.1	28
	−29.5	6.6	−29.5	6.6	−29.5	6.6	[b]
Ni(III)–tacn	−32.1	9.4	−28.6	6.2	−30.8	6.4	29
Cr(III)–tacn	−31.1	8.3	−31.6	11.4		7.4	30
Cu(II)–tacn	−31.4	10.7	−29.5	5.0	−31.3	9.7	31
Pb(II)–tacn	−30.9	14.0	−32.6	16.0	−32.5	17.0	32
Ni(II)–tdacn	−25.3	8.8					33
Ni(II)–taptacn	−26.7	3.3	−28.0	3.5	−27.8	6.7	34
	−26.9	4.4	−26.9	4.4	−26.9	4.4	[b]
Co(III)–taetacn	−26.9	4.9	−26.9	4.9	−26.9	4.9	[b]
Ni(II)–tdadtacn	−25.0	4.0					35
Cu(II)–tdadtacn	−29.9	7.0					35
Ni(II)–dadtacn	−29.2	5.8	−27.4	4.6	−26.7	4.1	[b]
Average	−28.9	5.7	−29.1	7.1	−26.4	7.5	

[a]Torsional angles NMNC, positive clockwise; in some cases chirality of published structures was inverted for convenience. Ligands: tdacn = 1-tia-4,7-diazacyclononane, dadtdacn = *N,N'*-(4,7-diazadecylene) derivative of tdacn, tdadtacn = thia-substituted dadtacn.
[b]MM calculated, this work.

TABLE 2. Selected structural parameters for Ni(II) bis(tacn) complex

Parameter	X-ray[a]	Calcd.[b]	Calcd.[c]
M—N, Å	2.10	2.09	2.09
N—Ni—N, deg	82.6	84.1	84.5
Ni—N—C, deg	104.8	103.7	103.7
	110.0	109.8	109.8

[a]Reference 28.
[b]This work.
[c]Reference 36.

tal data. In all cases the three chelate rings of complex are in an *envelope* form with the same chirality.

However, calculations seem to have underestimated one of two principal angles, 0.7 vs. 5.7–7.5°, Table 1 (see also Fig. 3*a*). The main reason is likely in the assumption of ideal 90° interplanar angles α in the coordination octahedron. In practice, as X-ray data and molecular mechanics calculations show, each *en* ring tends to compress the angle at the metal ion, resulting in a decrease of the octahedral interplanar angles. Taking this effect into account, one could obtain more precise agreement. It should be noted that since we neglect inter-ring diatomic interactions in fusions, such omissions may lead to some discrepancies.

Nevertheless, the above simple analysis still provides a reasonable semi-quantitative description. This proves that the conformation of a coordinated tacn is rigidly dictated by the interior structure of the *en* rings and fusing them together "around an octahedral center" yields strained *envelope* conformations. MM calculations naturally produce better refined structural results (see Tables 1 and 2, where the data for $[Ni(tacn)_2]^{2+}$ complex are compared with the experimental values). But semi-quantitative analysis rationalizes the observed/calculated stereochemistry, and, more importantly, gives a good starting point for MM optimization of the complex structure. (A common choice of X-ray geometry as a starting one is, apparently, of little use if calculations were made *prior* to experiment, e.g., in a molecular design).

Complexes of tris (N-pendant) tacn

Attachment of complexing arms to tacn nitrogens means formation of extra chelate rings in complexes, and rigid structure of M(tacn) moiety strongly affects the conformation and orientation of the pendant arms.

Let us consider an octahedral complex of tris(N-functionalized) tacn. There are two *cis* positions available for coordination by pendant functionality at each tacn nitrogen (coordination in *trans* position is unlikely). Therefore, there are two enantiomeric ways to occupy these positions, relating to the Δ and Λ chirality of metal center (Fig. 4). Combining with the chirality of M(tacn) moiety, this gives rise to two clearly distinct isomers, A and B (diastereomeric configurations Δλ ≡ Λδ and Δδ ≡ Λδ, respectively). As it is seen from Fig. 4, where λ-M(tacn) is presented, the isomers differ greatly in the conformational possibilities of the "pendant chelate rings". Given the values of the principal angles in tacn rings ca. −30° and 0° and considering a fusion, the principal angle θ in pendant rings could be approximately 30° for isomer A and −60° for isomer B. Thus, isomer A favors ring conformations, which deviate much less from planarity.

The fusion requirements expressed through θ allow consideration for complexing arms of different types.

Aminoethyl pendant arms (taetacn)

The ligand taetacn is a best example since the pendant chelate rings are ethylenediamine. Isomer A is, undoubtedly, preferable because of the more reasonable principal angle θ of ca. 30°, just like *en* rings of M(tacn) itself. This should be combined with the counter-part angle θ′ of ca. 0°, resulting in a relatively stable *asym-gauche* (or close to *envelope*) conformation.

Note that the values correspond to δ chirality and the overall configuration of the complex cation should be described as Δλδ ≡ Λδλ (chiralities are given in the order metal – tacn rings – pendant rings). Inversion of pendant rings chirality, Δλλ ≡ Λδδ, forces them to adopt a highly strained *envelope* conformation (see Fig. 3, the region near (30°, −50°)). Therefore, the last configuration is unfavorable.

Isomer B of M(taetacn) is not favorable at all. An angle of θ ~ −60° requires too large a deviation of the carbon atom (adjacent to tacn nitrogen) from the pendant ring coordination plane NMN (cf. Fig. 3). Nevertheless, if a structure of B type existed, it should have pendant chelate rings in an envelope conforma-

Can. J. Chem. Downloaded from www.nrcresearchpress.com by EESC ESCOLA DE ENGENHARIA on 09/08/12
For personal use only.

Can. J. Chem. Downloaded from www.nrcresearchpress.com by ESC ESCOLA DE ENGENHARIA on 09/08/12
For personal use only.

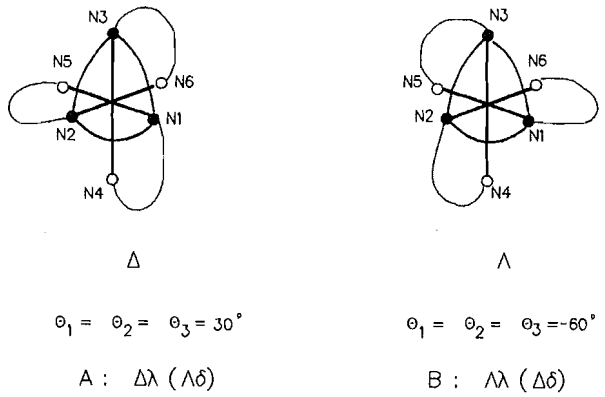

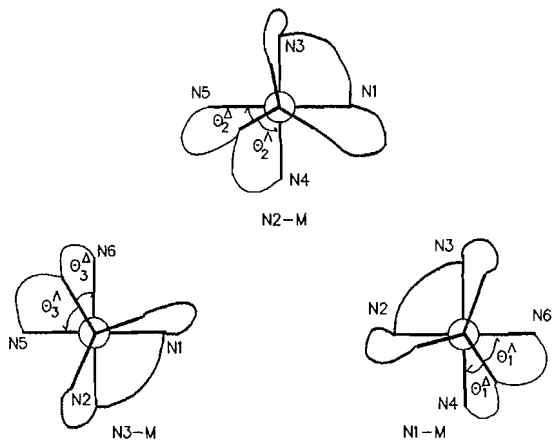

FIG. 4. Fusion of chelate rings in complexes of *N,N',N''*-tris(pendant arm) tacn. Tacn moiety is *fac*-coordinated and in λ-chirality.

tion, where both carbons are on the same side of NMN, and one primary nitrogen lies closer to the plane. It requires a λ chirality of rings and an overall configuration of ΛλΛ ≡ Δδδ. Configuration ΛλδΛ ≡ ΔδλΔ requires the latter carbon to deviate even further from NMN than the former, which seems to be a forbidden case.

Thus, isomer A, ΔλδΔ, should be the realistic choice for M(taetacn) octahedral complex. A corresponding trial structure (for Co(III) as central ion) was generated from the standard bond lengths, bond angles, and the above principal (torsional) angles, and was subjected to MM optimization. This results in the structure presented in Fig. 5*a* and Table 3. Table 3 shows that the calculated parameters are in agreement with those obtained in the X-ray study of $[Co(taetacn)]^{3+}$ (37). It should be emphasized that the starting point for MM minimization originated from semi-quantitative fusion analysis, and no X-ray data were used in the starting geometry.[5]

Molecular mechanics calculations provide further insight into the steric demands of the ligand. Figure 6 represents the strain energy of M(taetacn) as a function of "ideal" M—N bond

[5]The authors of ref. 37 have also performed MM analysis (Table 3). Extensive calculations were made for all four of possible diastereomers, and the result was exactly the same as ours. The ΔλδΔ form (isomer A), which is found in crystal structure, appeared to be the least-strained, while for the ΔδλΔ configuration, minimization proved impossible (i.e., the structure is not viable).

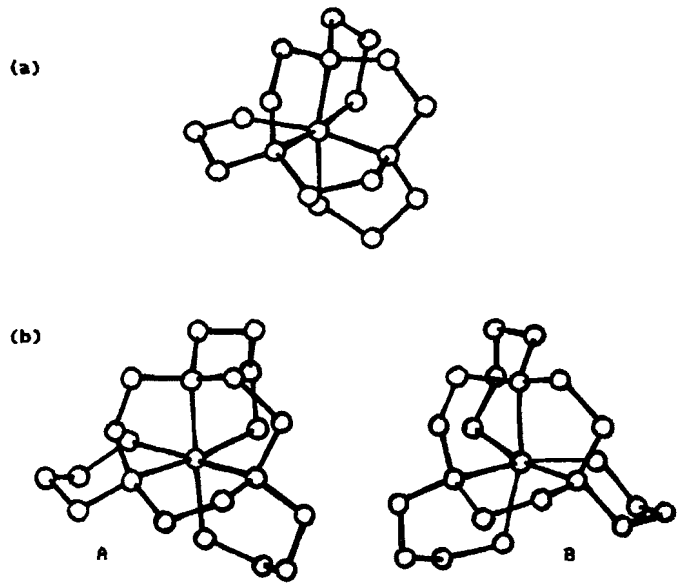

FIG. 5. Calculated structures of nickel(II) complexes of taetacn (*a*) and taptacn (*b*).

TABLE 3. Selected structural parameters for Co(III) taetacn complex[a]

Parameter	X-ray[b]	Calcd.[c]	Calcd.[d]
Bond lengths, Å			
$Co—N_c$	1.96	1.95	1.97
$Co—N_p$	2.01	1.97	1.98
Bond angles, deg			
$N_c—Co—N_c$	87.3	88.0	87.5
$N_c—Co—N_p$	84.9	85.3	84.5
$N_p—Co—N_p$	90.9	89.6	88.7
$Co—N_c—C_c$	107.2	106.4	105.3
	109.2	109.4	109.3
$Co—N_p—C_p$	111.2	111.8	112.4
$C_c—N_c—C_c$	110.3	110.9	111.5
$C_c—N_c—C_p$	111.8	111.6	111.0
	110.4	110.7	112.0
$N_c—C_c—C_c$	107.8	108.6	109.3
	110.0	110.6	110.5
$N_c—C_p—C_p$	108.3	108.1	107.2
	108.4	108.6	108.2
Torsional angles, deg			
$N_c—C_c—C_c—N_c$	−42.6	−40.8	−42.5
$N_c—C_p—C_p—N_p$	44.2	42.4	45.9
$Co—N_c—C_c—C_c$	19.8	18.6	19.1
	44.8	43.1	44.5
$Co—N_p—C_p—C_p$	−22.5	−20.5	−24.6
$Co—N_c—C_p—C_p$	−45.9	−45.4	−46.5
$C_p—N_c—C_c—C_c$	−98.5	−100.0	−99.7
	162.7	160.3	160.4
$C_c—N_c—C_c—C_c$	−74.0	−75.8	−73.9
	137.5	135.6	135.1
$C_c—N_c—C_p—C_p$	73.4	74.2	73.5
	−163.4	−161.8	−161.1

[a]Lowercase subscript "c" designates atoms in (triaza)cyclononane moiety, "p" indicates atoms in pendant arms.
[b]Reference 37.
[c]This work, isomer A.
[d]Reference 37.

Can. J. Chem. Downloaded from www.nrcresearchpress.com by EESC ESCOLA DE ENGENHARIA on 09/08/12
For personal use only.

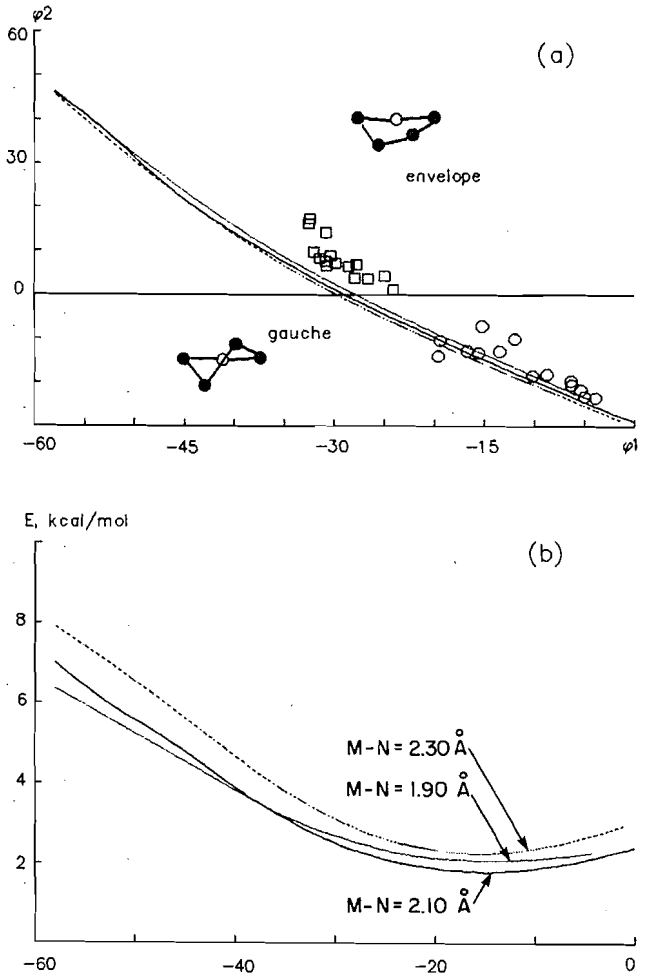

FIG. 6. Strain energy of metal ion complexes as a function of ideal strain-free M—N bond length.

length, that is, a function of the metal ion size. Ideal length was varied, while other metal-dependent force field parameters were kept constant and equal to those of high-spin Ni(II). For convenience, a curve for the bis(tacn) system is also presented in Fig. 6 (the curve is practically identical to that obtained earlier (36), best-fit M—N length 2.07 Å vs. 2.08 Å (36)).

It is clear that the size-selectivity profile of taetacn is essentially the same as that for bis(tacn); the best-fit M—N bond length, 2.08 Å, is only slightly shifted towards larger metal ions. Thus, the metal–nitrogen bond lengths in taetacn complexes should be identical or slightly longer than those in the bis(tacn) system (and the similarity should spread onto other size-dependent properties, e.g., redox potentials). This is in good agreement with crystal data for Co(III) complexes. The average Co—N bond length in $Co(taetacn)^{3+}$, 1.986 Å (37), is slightly longer than that in $Co(2\text{-methyl tacn})_2^{3+}$, 1.97 Å (38).

Interestingly, due to the analogous steric properties of sp^3 nitrogen and oxygen atoms, the above consideration of fusion (but not of size selectivity!) should be valid for tacn functionalized with hydroxyethyl arms as well. The data recently appeared (39) on Co and Mn complexes of tris(2-hydroxypropyl) tacn, thptacn, do confirm that conclusion. For example, complex cation $[Mn(thptacn)]^{2+}$ is of type A, configuration $\Delta\lambda\delta$, with the following principal angles (calculated from X-ray data (39)): $(\varphi_1, \varphi_2) = (-31.4°, 7.8°)$; $(\psi_1, \psi_2) = (-31.1°, 9.1°)$; $(\omega_1, \omega_2) = (-30.9°, 8.8°)$; $(\theta, \theta') = (24.9°, 1.3°)$ (averaged).

Aminopropyl pendant arms (taptacn)

The ligand taptacn forms trimethylenediamine (*tn*) pendant rings, and here a choice between A and B structural types is not evident. Indeed, though *tn* ring may adopt different conformations, the most widely occurred is the least strained *chair*, with principal angles of ±45° (16); this is exactly a mid-way position between 30° and −60° for isomers A and B.

Therefore, both A and B trial structures were constructed and subjected to MM optimization (metal = high-spin nickel). The following figures were obtained (kcal/mol):

	E_{total}	E_b	E_{nb}	E_a	E_t
Isomer A	28.02	1.92	7.46	9.45	9.20
Isomer B	32.87	2.24	9.54	13.88	7.22

Structure A (Fig. 5) is ca. 5 kcal/mol more stable, and this isomer was also found in the crystal form (34). Again, structural parameters, which were calculated through semi-quantitative analysis followed by MM refinement, are in very good agreement with those obtained in X-ray diffraction study (see Table 4). The work (34) provides an unusual possibility of comparison between two independent structures of the same complex cation. Though a "great similarity" (34) was present, the following figures come from crystallographic data: root-mean-squared difference in bond lengths 0.046 Å (27 bonds); in M—N bond lengths, 0.019 Å (six bonds); in bond angles, 2.5° (51 angles); in dihedral angles, 4.5° (87 torsions). When the MM-minimized structure is compared with one of those crystals, r.m.s. differences in the same order are as follows: 0.028 Å; 0.017 Å; 1.4°; 2.2°. Therefore the match "MM/crystal" is even more precise than the "crystal/crystal".

It should be mentioned that calculations, in agreement with X-ray data (34), predict considerable elongation of (average) coordination bond lengths in $Ni(taptacn)^{2+}$, 2.14 Å, comparing with the ideal value of 2.10 Å. This is indicative of a size-selectivity profile, which is completely different from those of taetacn and bis(tacn). Indeed, as Fig. 6 shows, the presence of aminopropyl pendant arms results in a ligand preference towards large metal ions, with a predicted best-fit M—N bond length of 2.18 Å. Interestingly, this value nicely fits the size of high-spin Co(II) also (ideal Co—N, 2.17 Å (13)). Therefore, taptacn ligand should stabilize this oxidation state much more than bis(tacn). In fact, the redox potential is −0.010 V (vs. NHE) for $Co(taptacn)^{3+/2+}$ and −0.41 V for $Co(tacn)_2^{3+/2+}$ (34, 40). Thus, the calculated size-selectivity curve confirms (34) that this may be attributable to sterical demands of taptacn.

N,N′-*Bridged tacn (dadtacn)*

The ligand dadtacn (Fig. 1) is a macrobicycle comprising "fused" tacn and cyclam moieties. Complexes of dadtacn itself, to our knowledge, have not yet been described, though some data on dadtacn synthetic precursors and analogues appeared recently (35). It is therefore possible to first study the topic theoretically and then verify the results with experiments.

The discussed ligand may be considered a tacn ring functionalized with two aminopropyl pendant arms that are linked together. Therefore, one could analyze the stereochemistry of its complexes, starting from that of taptacn and study the possibility of connecting the pendant nitrogens through the ethylene bridge.

Aminopropyl side arms may be oriented as in isomer A or

TABLE 4. Selected structural parameters for Ni(II) taptacn complex[a]

Parameter	X-ray[b]	Calcd.[c]
Bond lengths, Å		
Ni—N_c	2.14	2.13
Ni—N_p	2.14	2.14
Bond angles, deg		
N_c—Ni—N_c	83.3	85.0
N_c—Ni—N_p	92.4	91.0
	95.5	95.3
	175.8	175.5
N_p—Ni—N_p	88.8	89.2
Ni—N_c—C_c	104.4	102.5
	109.1	108.1
N—N_c—C_p	115.8	116.7
Ni—N_p—C_p	117.4	117.4
C_c—N_c—C_c	109.8	110.4
C_c—N_c—C_p	106.8	108.0
	110.8	110.8
N_c—C_c—C_c	110.5	111.8
	112.7	112.8
N_c—C_p—C_p	114.6	114.5
C_p—C_p—C_p	113.2	112.0
C_p—C_p—N_p	110.8	112.0
Torsional angles, deg		
5-Membered rings		
N_c—C_c—C_c—N_c	45.9	47.1
Ni—N_c—C_c—C_c	−19.5	−20.2
	−46.3	−46.8
N_c—Ni—N_c—C_c	27.5	26.9
	−4.5	−4.4
6-Membered rings		
N_p—C_p—C_p—C_p	72.8	73.8
C_p—C_p—C_p—N_c	−72.2	−72.8
Ni—N_p—C_p—C_p	−58.7	−59.7
Ni—N_c—C_p—C_p	54.5	56.2
N_c—Ni—N_p—C_p	37.8	37.5
N_p—Ni—N_c—C_p	−35.0	−35.0

[a]Designations as in Table 3.
[b]Reference 34; bond lengths and bond angles are averaged on two similar structures presented in crystallographic unit, while torsional angles are calculated from coordinates published for one of them.
[c]This work.

isomer B. Since dadtacn only has two such arms, a third isomer with "inhomogeneous" orientation is possible. This isomer has type A conformation for one arm and type B conformation for the other.

Let us consider the fusion of chelate rings in the latter case, AB (Fig. 7, which illustrates the structure, may be easily compared with that in Fig. 4). Principal angles in pendant rings of taptacn were considered: they are $\theta_1 = -60°$ for B-type and $\theta_2 = 30°$ for A-type ring (see Fig. 4). If these *tn* rings are in symmetrical *chair* conformations, the counterpart principal angles will be $\theta_1' = 60°$ and $\theta_2' = -30°$. The values of θ_1', θ_2' may now be used to estimate the principal angles in *en* ring, which "bridges" pendant nitrogens, N_5 and N_6 in Fig. 7: $\gamma = 0°$, $\gamma' = 30°$. Thus, the AB orientation of the aminopropyl arms leads to quite reasonable principal angles, and, therefore, to relatively unstrained geometry of the bridging *en* ring. (Note that this consideration was made for λ-tacn, while the resulting values for bridging ring represents opposite chirality, δ.)

"Homogeneous" orientation of dadtacn aminopropyl arms, A

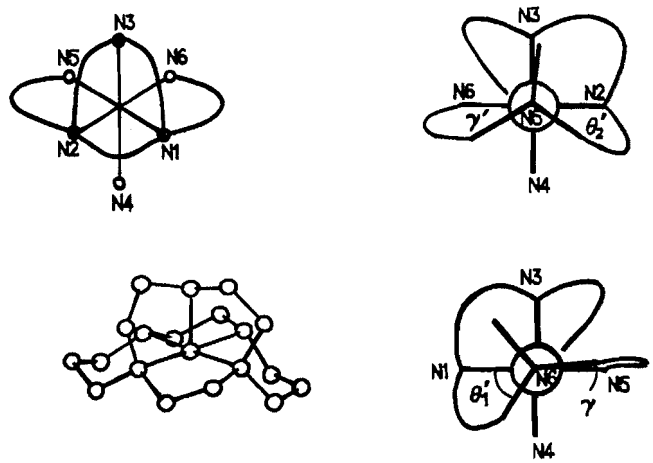

FIG. 7. Fusion of chelate rings (*a*) and calculated structure (*b*) of nickel(II) complex of dadtacn.

or B, leads to a very different picture. A simplified calculation yielded principal angles γ and γ′ to be (30°, −60°) and (0°, 90°), respectively. This gives rise to a very strained and practically impossible structure of the bridging *en* ring and makes these isomers unlikely.

Using the principal values above, a trial geometry for AB isomer of Ni(dadtacn)X was constructed and refined with MM (bare nitrogen atom was "introduced" to represent axial ligand X completing an octahedral environment). The following is a brief outline of the resulting structure.

All five coordination bonds formed by the ligand are shorter than the ideal Ni—N, average is 2.08 Å. This may be compared with an average Ni—N value of 2.07 Å, which was observed in crystal structure (35) of nickel complex of thia-substituted dadtacn (15-thia-1,5,8,12-tetraazabicyclo[10.5.2]nona decane). Average N—Ni—N bond angle in five-membered rings is 85.9°, and in six-membered ring the angle is 92.2°.

Ethylenediamine rings of tacn do have identical chirality, while cyclam's (or *N,N′*-bridging) *en* ring is in the opposite configuration. Average torsional angle around C—C bond in *en* rings is 48° (absolute value). One of the *tn* rings has a relatively flattened *chair* form, with principal angles (36°, −37°), and the other being much more puckered, (60°, −56°), thus giving rise to a nearly optimal conformation of the bridging *en* ring. This feature, predicted by fusion analysis, was also observed in Ni(thia-dadtacn), where the principal angles calculated from X-ray data (35) are (26°, −26°) and (54°, −48°).

Size selectivity profile of dadtacn as revealed from MM study is presented in Fig. 6. Best-fit M—N bond length is 2.07 Å, the same as that for bis(tacn) and taetacn, but much different from that for taptacn. It should be mentioned that cyclam itself (in *trans-I* conformation, which is identical to that of cyclam moiety in the dadtacn complex considered) has a best-fit value of 2.01 Å (41). Thus, the steric requirements of the more rigid tacn moiety override those of cyclam.

Acknowledgments

I am grateful to Professor R.D. Hancock for making available some useful information. Thanks are also due to Professor Yu. A. Zolotov, who generously provided the necessary computer facilities.

1. P. Chaudhuri and K. Wieghardt. Prog. Inorg. Chem. **35**, 329 (1987).

Can. J. Chem. Downloaded from www.nrcresearchpress.com by EESC ESCOLA DE ENGENHARIA on 09/08/12
For personal use only.

2. R. Delgado and J.J.R. Frausto da Silva. Talanta, **29**, 815 (1982).
3. A.E. Martell, R.J. Motekaitis, and M.J. Welch. J. Chem. Soc. Chem. Commun. 1748 (1990).
4. M.J. van der Merwe, J.C.A. Boeyens, and R.D. Hancock. Inorg. Chem. **22**, 3489 (1983).
5. W.P. Cacheris, S.K. Nickle, and A.D. Sherry. Inorg. Chem. **26**, 958 (1987).
6. L. Christiansen et al. Inorg. Chem. **25**, 2813 (1986).
7. R.D. Hancock and A.E. Martell. Chem. Rev. **89**, 1875 (1989).
8. I.V. Pletnev, Yu.A. Zolotov, L.A. Gribov, and M.M. Raihstat. Russ. J. Coord. Chem. **12**, 128 (1986).
9. I.V. Pletnev and Yu.A. Zolotov. Fresenius Zeitschr. Anal. Chem. **331**, 245 (1988).
10. B.D. Bunday. Basic optimization methods. Edward Arnold, London. 1984.
11. R.H. Boyd. J. Chem. Phys. **49**, 2574 (1968).
12. M.R. Snow. J. Am. Chem. Soc. **92**, 3610 (1970).
13. R.D. Hancock. Prog. Inorg. Chem. **37**, 187 (1989).
14. G.J. McDougall, R.D. Hancock, and J.C.A. Boeyens. J. Chem. Soc. Dalton Trans. 1438 (1978).
15. K.B. Wiberg and R.H. Boyd. J. Am. Chem. Soc. **94**, 8426 (1972).
16. L.J. DeHayes and D.H. Busch. Inorg. Chem. **12**, 1505 (1973).
17. C.J. Hawkins. Absolute configuration of metal complexes. Wiley–Interscience, New York, NY. 1971.
18. J.R. Gollogly and C.J. Hawkins. Inorg. Chem. **9**, 576 (1970).
19. I.V. Plethev. Vestnik Mosk. Univ. Ser. 2. Khim. (Russ.) **28**, 399 (1987).
20. R.D. Hancock et al. Inorg. Chem. **29**, 1968 (1990).
21. N.F. Curtis, D.A. Swann, and T.N. Waters. J. Chem. Soc. Dalton Trans. 1963 (1973).
22. P.O. Whimp, M.F. Bailey, and N.F. Curtis. J. Chem. Soc. A, 1956 (1970).
23. J.N. Waters and K.R. Whittie. J. Inorg. Nucl. Chem. **34**, 155 (1972).
24. B.W. Brown and E.C. Lingafelter. Acta Crystallogr. **16**, 753 (1963).
25. Y. Komiyama and E.C. Lingafelter. Acta Crystallogr. **17**, 1145 (1964).
26. B.W. Brown and E.C. Lingafelter. Acta Crystallogr. **17**, 254 (1964).
27. E.-I. Ochiai, S.J. Rettig, and J. Trotter. Can. J. Chem. **56**, 267 (1976).
28. T.N. Margulis and L.J. Zompa. Inorg. Chim. Acta, **28**, L157 (1978).
29. K. Wieghardt, W. Walz, B. Nuber, J. Weiss, A. Ozarowski, H. Stratemeyer, and D. Reiner. Inorg. Chem. **25**, 1650 (1986).
30. K. Wieghardt et al. Inorg. Chem. **19**, 2922 (1980).
31. R.D. Bereman, M.R. Churchill, P.M. Schaber, and M.E. Winkler. Inorg. Chem. **18**, 3122 (1979).
32. K. Wieghardt et al. Inorg. Chem. **25**, 1647 (1986).
33. J.C.A. Boeyens, S.M. Dobson, and R.D. Hancock. Inorg. Chem. **24**, 3073 (1985).
34. G.W. Bushnell, D.G. Fortier, and A. McAuley. Inorg. Chem. **27**, 2626 (1988).
35. D.G. Fortier and A. McAuley. Inorg. Chem. **28**, 655 (1989).
36. V.J. Thom, G.J. McDougall, J.C.A. Boeyens, and R.D. Hancock. J. Am. Chem. Soc. **106**, 3198 (1984).
37. S.G. Taylor, M.R. Snow, and T.W. Hambley. Aust. J. Chem. **36**, 2359 (1983).
38. M. Mikami, R. Kuroda, M. Konno, and Y. Saito. Acta Crystallogr. Sect. B, **B33**, 1485 (1977).
39. A.A. Belal et al. Inorg. Chem. **30**, 4397 (1991).
40. H.-J. Kuppers et al. Inorg. Chem. **25**, 2400 (1986).
41. P.J. Connolly and E.J. Billo. Inorg. Chem. **26**, 3224 (1987).

Can. J. Chem. Downloaded from www.nrcresearchpress.com by EESC ESCOLA DE ENGENHARIA on 09/08/12
For personal use only.

Comparison of heteroatom-bridged analogues of methylenebisphenols for antioxidant activities

T. NISHIYAMA, T. KAGIMASA, AND F. YAMADA

Department of Applied Chemistry, Faculty of Engineering, Kansai University, Senriyama Suita, Osaka 564, Japan

Received September 2, 1993

T. NISHIYAMA, T. KAGIMASA, and F. YAMADA. Can. J. Chem. **72**, 1412 (1994).

A series of methylenebisphenols, thiobisphenols, oxybisphenols, and iminobisphenols were evaluated as antioxidants for tetralin at 60°C by means of an oxygen-obsorption method. It was found that replacement of the bridged methylene group of methylenebisphenols by a nitrogen atom showed considerably better antioxidant effects. The antioxidant effects of these compounds were influenced by the positions of the phenolic hydroxyl groups in their molecules.

T. NISHIYAMA, T. KAGIMASA et F. YAMADA. Can. J. Chem. **72**, 1412 (1994).

Faisant appel à une méthode d'absorption d'oxygène, on a évalué une série de méthylènebisphénols, thiobisphénols, oxybisphénols et iminobisphénols comme antioxydants pour la tétraline, à 60°C. On a trouvé que le remplacement du groupe méthylène ponté des méthylènebisphénols par un atome d'azote générait des produits à effets antioxydants nettement supérieurs. Les effets antioxydants de ces composés sont influencés par les positions des groupes hydroxyles phénoliques présents dans ces molécules.

[Traduit par la Rédaction]

Introduction

In chemical industries, antioxidants have commonly been used to prevent deterioration due to the oxidation of organic substrates such as rubbers, plastics, and lubricating oils. The major pathway of the oxidation of organic materials involves a radical chain mechanism. It is well known that phenolic and amino compounds act as inhibitors for radical chain reactions of autoxidation of such organic substrates and sulfuric compounds act as decomposers for hydroperoxides (1). During the course of our studies of phenol derivatives as antioxidants, compounds containing a diarylmethyl group with a phenolic hydroxyl group showed high activities as antioxidants for paraffin wax (2), lard (3), mineral oils (4), and greases (4). In a recent study of benzylphenols (5, 6), we found that the introduction of a benzyl group to the *para* and (or) *ortho* positions on the phenols improved the antioxidant activities of phenols. The present study was initiated to compare the antioxidant activities of thiobisphenols, oxybisphenols, and iminobisphenols, in which the bridged methylene group of methylenebisphenols was replaced by a sulfur, oxygen, or nitrogen atom.

Experimental

Materials

The phenol derivatives studied in this work were as follows: 2,2′-methylenebisphenol (**1***a*), 4,4′–methylenebisphenol (**1***b*), 4,4′-methylenebis(2-methylphenol) (**1***c*), 2,2′-thiobisphenol (**2***a*), 4,4′-thiobisphenol (**2***b*), 4,4′-thiobis(2-methylphenol) (**2***c*), 2,2′-oxybisphenol (**3***a*), 4,4′-oxybisphenol (**3***b*), 2,2′-iminobisphenol (**4***a*), 4,4′-iminobisphenol (**4***b*), and 4,4′-iminobis(2-methylphenol) (**4***c*). Tetralin used for the test was washed with concentrated sulfuric acid, aqueous sodium bicarbonate, and water, dried over anhydrous sodium sulfate, and distilled under nitrogen before use. The oxidations were initiated with 2,2′-azobisisobutyronitrile (AIBN), which was recrystallized from methanol.

Determination of antioxidant activity

The volume of oxygen absorbed was determined as a function of time under 760 Torr (1 Torr = 133.3 Pa) of O_2 using 50 mL of tetralin containing an antioxidant (0.05 mmol) and AIBN as the initiator (0.5 mmol) (5). The oxidation temperature was kept at 60 ± 0.1°C. The induction period (IP) was determined graphically (7, 8) on the plot of oxygen consumption versus time as the point of intersection of a line of the rate of oxygen uptake after the inhibitor was consumed and a line tangent to the curve with a slope equal to half of the slope of the line after the inhibitor was consumed.

Results and discussion

Figure 1 shows the results of the oxidation of tetralin initiated by AIBN in the presence of bisphenols **1–4** and 2,6-di-*tert*-butyl-4-methylphenol (BHT) as antioxidants, along with a control test in the absence of an antioxidant. The oxidation proceeded smoothly in the absence of antioxidant without a noticeable IP, and a constant rate of oxygen uptake was observed, but in its presence the oxidation was found to be suppressed. Values of IP for compounds **1–4** along with BHT, are shown in Table 1. It was found that the compounds **1***c*, **2***b*, **2***c*, **3***b*, and **4** showed excellent antioxidant effects which were superior to BHT, whereas **1***a*, **1***b*, **2***a*, and **3***a* showed lower IP values compared with BHT.

In the case of methylenebis-, thiobis-, and iminobis-phenols, the compounds having two methyl substituents at *ortho* positions of the OH groups had longer IPs than that of the compounds having no methyl substituents at *ortho* positions. The effect of alkyl groups at *ortho* positions of the OH groups on its antioxidant activity has been studied by many authors. For example, Howard and Ingold (9) have reported the antioxidant activity of alkyl phenols depends on the position of substituents. They also reported that the steric effects due to *ortho* alkyl substituents are important.

Iminobisphenols **4** showed the highest antioxidant activity among **1–4**. Since diphenylamine has antioxidant ability, the increased activity of iminobisphenols (**4**) is ascribed to the synergistic effect of both bridged amino and phenolic hydroxyl groups.

When the IP values for 2,2′- and 4,4′-derivatives were compared, 4,4′-dihydroxy derivatives of **2–4** showed higher antioxidant effects than those of 2,2′-dihydroxy derivatives, whereas 2,2′-methylenebisphenol (**1***a*) exhibited higher antioxidant activities than **1***b*. From the fact that 2,2′-derivatives of **2–4** exhibited lower antioxidant activities, it can be assumed that an intramolecular hydrogen bonded *ortho*-hydroxyl groups to the

Can. J. Chem. Downloaded from www.nrcresearchpress.com by EESC ESCOLA DE ENGENHARIA on 09/08/12
For personal use only.

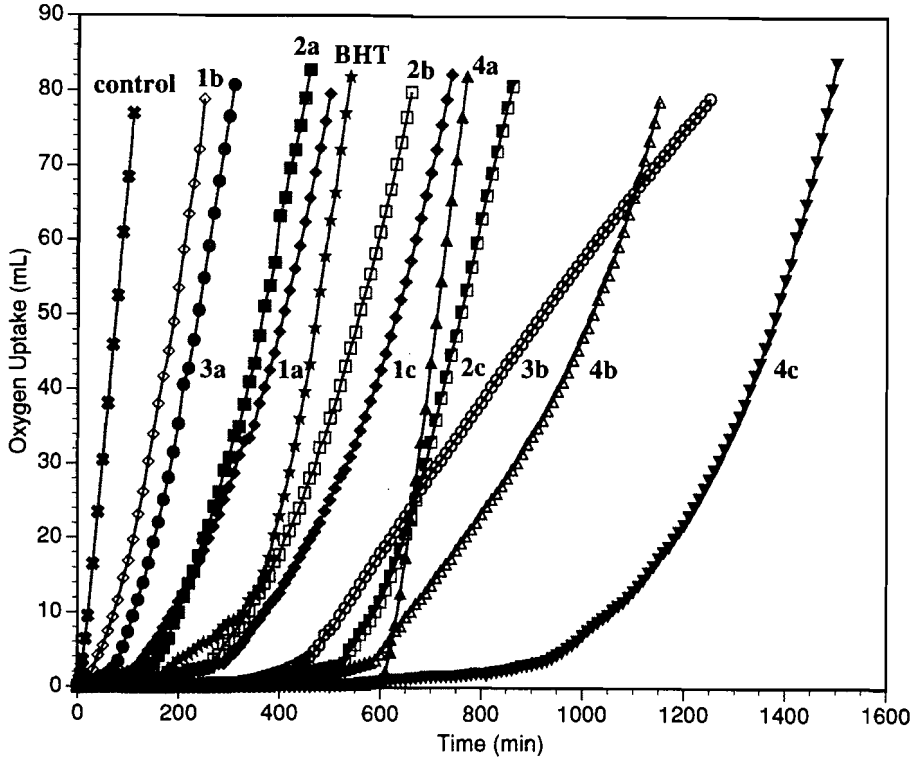

FIG. 1. Rate of oxygen uptake in the oxidation of tetralin in the absence (control) and presence of antioxidant.

TABLE 1. Antioxidant activities of bisphenols and related compounds

Antioxidant	Rates of oxygen consumption (mL/min)[a]		IP (min)
	I × 10^{-2}	II × 10^{-1}	
2,2′-Methylenebisphenol (**1***a*)	2.2	3.5	290
4,4′-Methylenebisphenol (**1***b*)	2.0	4.9	103
4,4′-Methylenebis(2-methylphenol) (**1***c*)	1.7	3.3	508
2,2′-Thiobisphenol (**2***a*)	3.2	3.3	289
4,4′-Thiobisphenol (**2***b*)	1.7	3.2	451
4,4′-Thiobis(2-methylphenol) (**2***c*)	1.5	3.0	603
2,2′-Oxybisphenol (**3***a*)	4.0	4.3	133
4,4′-Oxybisphenol (**3***b*)	3.1	0.8	458
2,2′-Iminobisphenol (**4***a*)	0.1	5.4	620
4,4′-Iminobisphenol (**4***b*)	1.9	2.5	869
4,4′-Iminobis(2-methylphenol) (**4***c*)	0.1	3.2	1241
Diphenylamine	5.0	5.3	93
BHT	5.0	4.8	376
Control	—	5.6	22

[a]The rates of oxygen consumption: I, for an inhibited autoxidation during IP; II, for an uninhibited oxidation after IP.

bridged hetero atom and reduced its ability of the reaction with peroxyl radicals. Pospisil and co-workers (10) have reported the infrared spectra of the hydroxyl groups of 2,2′-thiobisphenols; the OH groups of 2,2′-thiobisphenols existed in the form of intramolecular OH···S hydrogen bond (10). Likewise, Binder and co-workers (11) proposed the same OH···S hydrogen-bonded hydroxyl groups.

Table 1 also shows the rate of oxygen consumption. When all ArO• radicals are consumed, the rate of autoxidation should be equal to that of the control test. In fact, the rate of oxygen consumption after IP of BHT was close to the control (see II in Table 1). On the other hand, its rates of compounds **3***b* and **4***b* showed a much lower value. This means that the retardation persists, even after IP is over, owing to transformation products of the antioxidant.

In conclusion, we have compared the antioxidant activity of heteroatom-bridged analogues of methylenebisphenols. Among these compounds, iminobisphenols (**4**) exhibited significant antioxidant effect.

1. J. Pospisil. Degradation and stabilization of polymers. Vol. 1. Elsevier, Amsterdam. 1983. p. 214.

Can. J. Chem. Downloaded from www.nrcresearchpress.com by EESC ESCOLA DE ENGENHARIA on 09/08/12
For personal use only.

2. S. Matsuda and F. Yamada. Kogyo Kagaku Zasshi, **60**, 566 (1957).
3. F. Yamada and S. Matsuda. Kogyo Kagaku Zasshi, **61**, 1257 (1958).
4. F. Yamada and S. Matsuda. Kogyo Kagaku Zasshi, **61**, 1478 (1958).
5. F. Yamada, T. Nishiyama, Y. Suzuura, and T. Yamamura. Bull. Chem. Soc. Jpn. **58**, 115 (1985).
6. F. Yamada, T. Nishiyama, M. Yamamoto, and K. Tanaka. Bull. Chem. Soc. Jpn. **62**, 3603 (1989).
7. G.W. Burton and K.U. Ingold. J. Am. Chem. Soc. **103**, 6472 (1981).
8. A.A. Kharitonova, Z.G. Kozlova, V.F. Tsepalow, and G.P. Gladyshev. Kinet. Catal. (Engl. Transl.), **20**, 593 (1979).
9. J.A. Howard and K.U. Ingold. Can. J. Chem. **41**, 2800 (1963).
10. H. Pivcova, L. Jirackova, and J. Pospisil. J. Polym. Sci. Polym. Symp. **40**, 283 (1973).
11. J.L. Binder, J.C. Ambelang, and J. Webb. J. Am. Chem. Soc. **81**, 3608 (1959).

Can. J. Chem. Downloaded from www.nrcresearchpress.com by EESC ESCOLA DE ENGENHARIA on 09/08/12
For personal use only.

Youla S. Tsantrizos, Xiao-Jin Xu, Françoise Sauriol, and Rosemary C. Hynes. Novel quinazolinones and enniatins from *Fusarium lateritium* Nees. Can. J. Chem. **71**, 1362 (1993).

In this paper we stated that the *F. lateritium* metabolites 2-acetyl- and (*R*)-2-(1-hydroxyethyl)-4(3*H*)quinazolinones were new members of the quinazoline family of natural products. It has been brought to our attention that we overlooked three earlier references (1) to these compounds, one of which describes the isolation and structure elucidation of the *S* enantiomer of 2-(1-hydroxyethyl)-4(3*H*)quinazolinone (1*c*). We deeply regret our unfortunate and unintentional failure to acknowledge earlier work on these compounds and offer our apologies to the authors.

1. (*a*) H. Hikino, S. Nabetani, and T. Takemoto. J. Pharm. Soc. Jpn. **93**, 619 (1973); (*b*) M.M. Blight and J.F. Grove. J. Chem. Soc. Perkin Trans. 1, 1691 (1974); (*c*) D. Niederer, C. Tamm, and W. Zurcher. Tetrahedron Lett. **33**, 3997 (1992).

Can. J. Chem. Downloaded from www.nrcresearchpress.com by EESC ESCOLA DE ENGENHARIA on 09/08/12
For personal use only.

Double diastéréosélectivité de la cycloaddition dipolaire-1,3 d'ylures d'azométhine cycliques substitués

TAHAR LAKHLIFI
Département de chimie, Faculté des sciences, BP 4010, Université de Meknes, Maroc

AHMED SEDQUI
Département de chimie, Faculté des sciences, BP 2121, Université de Tetouan, Maroc

TOUFIK FATHI ET BERNARD LAUDE[1]
Laboratoire de chimie organique, Université de Franche-Comté, 16 Route de Gray, 25030 Besancon, France

ET

JEAN-FRANÇOIS ROBERT
Laboratoire de chimie thérapeutique, Université de Franche-Comté, Place Saint-Jacques, 25030 Besancon, France

Reçu le 27 juillet 1993

TAHAR LAKHLIFI, AHMED SEDQUI, TOUFIK FATHI, BERNARD LAUDE et JEAN-FRANÇOIS ROBERT. Can. J. Chem. **72**, 1417 (1994).

La synthèse de sept 5-phényl-3,4-dihydro-2*H*-pyrrole-2-carboxylates de méthyle précurseurs d'ylures d'azométhine cycliques pentagonaux **1** est décrite. Ces produits à caractère dipolaire réagissent avec les *N*-méthyl et *N*-phénylmaléimides de façon diastéréospécifique. L'approche des réactants se fait sur la face la moins encombrée du dipôle-1,3 et en *endo* pour donner le cycloadduit thermodynamiquement le plus stable de structure *exo*. De plus, l'oxydation de ces composés **1** permet d'accéder aux pyrroles substitués correspondants.

TAHAR LAKHLIFI, AHMED SEDQUI, TOUFIK FATHI, BERNARD LAUDE, and JEAN-FRANÇOIS ROBERT. Can. J. Chem. **72**, 1417 (1994).

Seven derivatives of methyl 5-phenyl-3,4-dihydro-2*H*-pyrrole-2-carboxylates **1** were synthetized. These compounds are precursors of pentagonal cyclic azomethine ylids, the two sides of which are diastereotopic. The 1,3-dipolar species react with *N*-methyl and *N*-phenylmaleimides diastereospecifically. The approach of the reactant species occurs from the less hindered side of the 1,3-dipole and in *endo* to lead the thermodynamically stable *exo* cycloadduct. Moreover, oxidation of the compounds **1** gives the corresponding substituted pyrroles.

Introduction

L'étude de la diastéréochimie de l'approche dipôle–dipolarophile en cycloaddition dipolaire-1,3 a déjà fait l'objet de nombreux travaux dans notre laboratoire (1–10). Ces derniers ont consisté à examiner la diastéréosélectivité de l'approche d'un dipôle-1,3 sur un dipolarophile cyclique dont les deux faces sont diastéréotopiques par suite d'un encombrement dû à la présence d'un substituant. Selon la taille et la nature de celui-ci d'une part et sa position par rapport au site dipolarophilique d'autre part, on peut observer des approches totalement ou partiellement diastéréosélectives.

Dans le présent travail, nous nous sommes intéressés au cas où l'induction asymétrique est dû à la présence d'un substituant porté par un dipôle-1,3 totalement inséré dans un cycle.

La littérature décrit quelques dipôles-1,3 de ce type et les plus connus sont des dérivés cycliques mésoioniques du type «münchnones» ou «sydnones» (11). On peut aussi signaler des dipôles-1,3 dont deux sommets font partie d'un cycle, comme certaines nitrones étudiées par Tufariello (12) ou des ylures d'azométhine décrits par Harwood et coll. (13).

Récemment, Mkhairi et Hamelin (14) ont examiné la réactivité d'imines cycliques **1** et **2** qui, activées en α de l'azote, sont des précurseurs d'ylures d'azométhine dont la partie dipolaire est totalement insérée dans un cycle pentagonal ou hexagonal (figure 1). À leur suite, nous avons étudié les réactions de précurseurs d'ylures d'azométhine **3** dérivés de l'isoquinoléine (15).

Il nous a semblé intéressant de profiter de cette expérience pour envisager la synthèse d'imines cycliques **1** diversement substituées en position 3 et 4 en vue d'étudier leur activité en tant que précurseurs de dipôles-1,3 et la diastéréosélectivité que peuvent apporter les substituants R^3 et R^4 (figure 2).

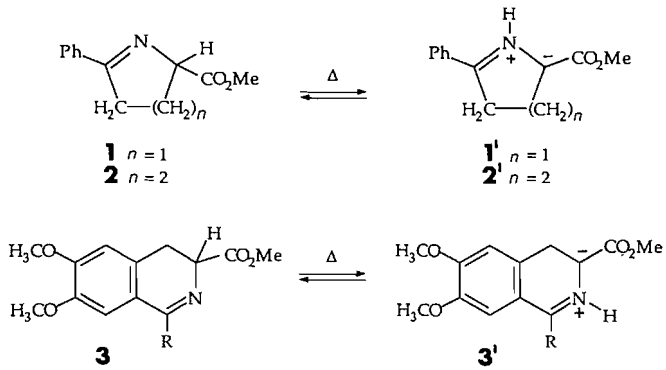

FIG. 1

Synthèse des précurseurs d'ylures d'azométhine cycliques 1 dérivés du 5-phényl-3,4-dihydro-2*H*-pyrrole-2-carboxylate de méthyle

Pour accéder à ces composés **1**, nous avions d'abord envisagé de nous inspirer de la stratégie mise en oeuvre par Mkhairi et Hamelin (14) dans le cas de **1***a* ($R^3 = R^4 = H$). Mais un examen de la littérature nous a conduit à choisir d'autres méthodes de synthèse comportant un nombre d'étapes plus réduit. En effet, les acides pyrrole-2-carboxyliques et leurs dérivés présentent un intérêt tant du point de vue de la chimie des substances naturelles que de celui de leur utilisation pharmacologique. Aussi n'est-il pas surprenant de trouver les travaux de nombreuses équipes ayant mis au point leurs propres méthodes de

1. Auteur correspondant. Téléphone : 81 66 62 70; FAX : 81 66 62 30.

Can. J. Chem. Downloaded from www.nrcresearchpress.com by ESC ESCOLA DE ENGENHARIA on 09/08/12
For personal use only.

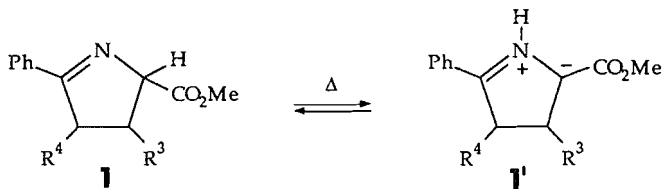

FIG. 2

synthèses en fonction de la structure particulière des dérivés recherchés. Les principales voies d'accès aux 2-carboxypyrrolines et pyrrolidines sont (*i*) les cycloadditions dipolaires [3+2] d'ylures d'azométhine sur des oléfines déficientes en électrons (16–18), (*ii*) la thermolyse de 2-azido-2,4-diénoates d'alkyle (19), (*iii*) et plus fréquemment les additions de Michaël de dérivés de la glycine et de l'acide aminomalonique aux alcènes activés (20–24).

C'est cette dernière voie que nous avons retenue en utilisant l'acétamidomalonate de diéthyle pour préparer les composés **1***a–e* et le chlorhydrate de l'aminomalonate de diéthyle pour obtenir les composés **1***f* et **1***g* (figure 3).

La synthèse des diesters acycliques **4** dérivés de l'acétamidomalonate de diéthyle a été menée à bien en adaptant un mode opératoire décrit par Leonard (22) et en améliorant certaines des réactions décrites par cet auteur. Ainsi le composé **4***a* ($R^3 = R^4 =$ H) est obtenu avec un rendement de 86% à partir de 3-bromopropiophénone au lieu de 68% à partir de la base de Mannich correspondante (22).

Pour obtenir les diesters cycliques **5***f* et **5***g*, nous avons utilisé la méthode de Koch et collaborateurs (21) qui consiste à chauffer le mélange des deux réactifs sans solvant (cf. partie expérimentale).

Les réactions successives d'hydrolyse acide par HCl 6 N puis d'estérification avaient déjà été décrites par Léonard (22) dans le cas du diester **4***a*. Nous les avons étendues aux cas de tous les composés **4** et **5** et obtenu les diverses pyrrolines **1***a–g* présentées sur la figure 3.

L'examen des valeurs de températures de fusion ou d'ébullition des composés **1** montre à l'évidence une grande disparité. Alors que le produit **1***f* fond à 220°C, on peut noter que le produit **1***c* fond à 60°C et que trois produits **1** sont restés huileux. Ceci n'est pas étonnant dans la mesure où la présence de deux et parfois trois centres de chiralité entraîne la possibilité d'existence de plusieurs diastéréoisomères pour ces composés (sauf **1***a*). Deux d'entre eux (**1***f* et **1***g*) ont été obtenus sous forme d'un seul diastéréoisomère (*trans* pour les groupes R^3 et R^4) et les autres (**1***b* à **1***e*) sous forme d'un mélange de deux diastéréoisomères.

Une étude configurationnelle et conformationnelle de ces diastéréoisomères est en cours.

En tout état de cause, l'existence des composés **1***b–e* sous forme d'un mélange de diastéréoisomères ne pose aucun

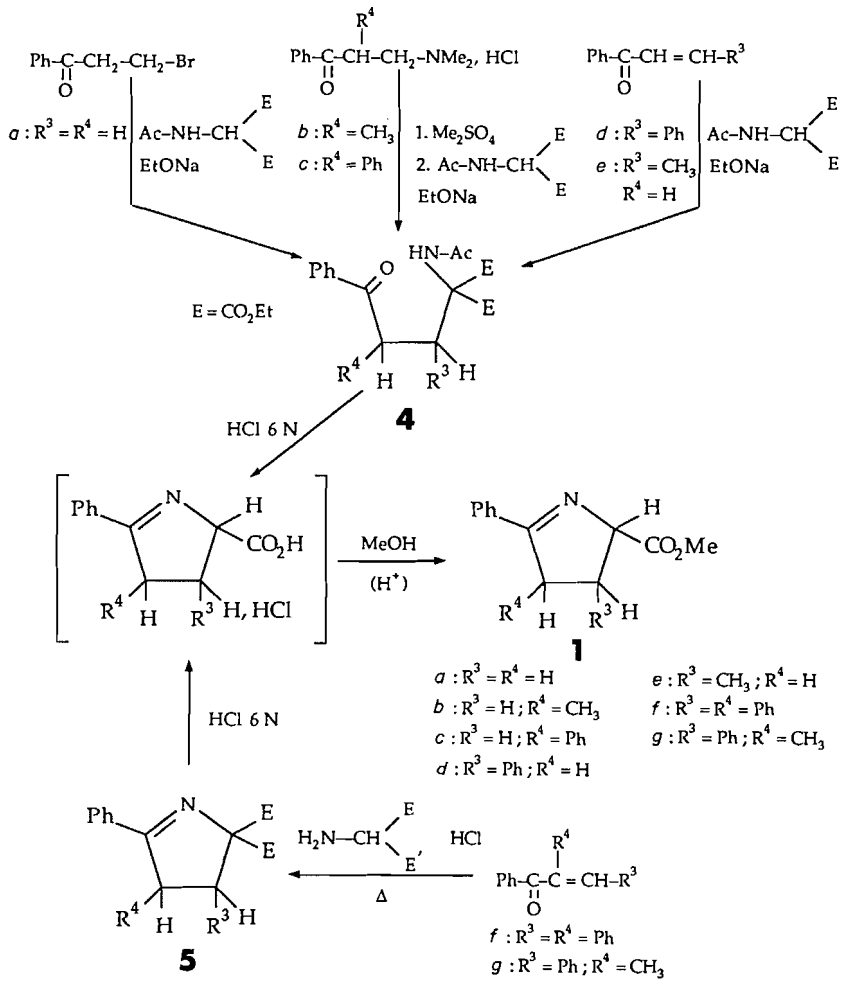

FIG. 3

Can. J. Chem. Downloaded from www.nrcresearchpress.com by EESC ESCOLA DE ENGENHARIA on 09/08/12
For personal use only.

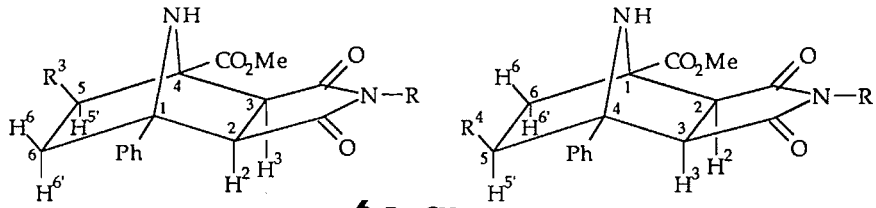

6 R = CH_3
7 R = Ph

FIG. 4

problème pour l'étude diastéréochimique de la cycloaddition dipolaire puisqu'au cours de la réaction l'ylure d'azométhine **1′** ne présentera plus qu'un seul centre de chiralité.

Cycloaddition dipolaire-1,3 des ylures d'azométhine dérivés du 5-phényl-3,4-dihydro-2*H*-pyrrole-2-carboxylate de méthyle sur les *N*-méthyl et *N*-phénylmaléimides

Les imines dérivées d'α-aminoesters sont des précurseurs d'ylures d'azométhine dont la réactivité dipolaire-1,3 a été mise en évidence simultanément par Grigg et al. (25) et Joucla et Hamelin (26). Par la suite Mkhairi et Hamelin et Grigg et al. ont étudié ces motifs insérés dans une structure cyclique (14, 27).

Sur la base de ces travaux antérieurs, nous avons donc engagé les différentes imines **1** décrites ci-dessus avec divers dipolarophiles : acétylène dicarboxylate de diméthyle, fumarate et maléate de diéthyle, *N*-méthyl et *N*-phényl maléimide. Seuls ces deux derniers ont permis d'isoler un cycloadduit. La réaction est effectuée en tube scellé dans le toluène. Les rendements observés varient entre 55 et 79%. Nous avons ainsi obtenu 10 cycloadduits **6** et **7** dérivés du 1,4-imino-*exo*-2,3- dicarboximidocyclohexane.

Selon les cas, la numérotation du 7-aza-bicyclo[2,2,1]heptane débutera par le carbone tête de pont portant le reste phényle (R^4 = H, $R^3 \neq$ H) ou celui portant le groupe méthoxycarbonyl (R^3 = H, $R^4 \neq$ H) (figure 4).

Il faut noter que les ylures d'azométhine issus des imines **1***f* et **1***g* doublement substituées par les groupes R^3 et R^4 ne manifestent aucune réactivité en cycloaddition dipolaire-1,3. Dans ce cas les deux faces du dipôle portent un substituant et l'encombrement sur chacune des faces ne permet donc pas aux deux réactifs de s'approcher suffisamment près pour donner lieu à la réaction de cycloaddition. Cette observation constitue une preuve de la disposition *trans* des groupes R^3 et R^4 dans les imines **1***f* et **1***g*. Ceci laisse bien sûr augurer qu'avec les autres ylures d'azométhine **1** ne comportant qu'un seul substituant (R^3 ou R^4 = H) la réaction interviendra sur la face du dipôle la moins encombrée puisque dans chaque cas on n'obtient qu'un seul cycloadduit.

La réaction est donc doublement diastéréospécifique. La stéréochimie de la cycloaddition est élucidée par une étude radiocristallographique de la structure du composé **7***d* (28) représentée sur la figure 5. La stéréochimie est bien du type *exo* pour tous les substituants fixés sur les atomes de carbone 2, 3 et 5 de l'enchaînement 7-aza-bicyclo[2,2,1]heptane. L'approche du dipolarophile s'effectue à la fois dans le demi-espace le moins encombré du dipôle cyclique et de façon à conduire à une disposition *exo* pour le reste maléimido.

Ce dernier résultat est conforme à ce qui avait été observée par Mkhairi et Hamelin (14) d'une part et Grigg et al. (27) d'autre part dans le cas d'ylures d'azométhine cycliques non substitués. Il justifie en particulier les valuers des constantes de

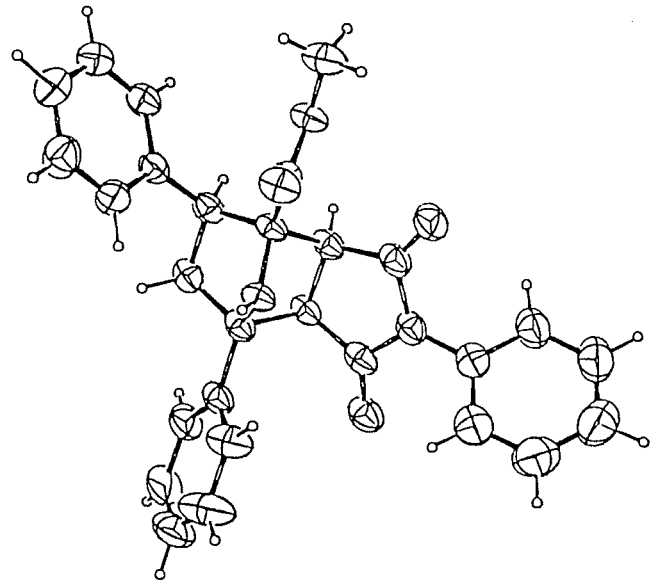

FIG. 5. Diagramne ORTEP du cycloadduit **7***d* (28).

couplage $^3J_{H2-H3}$ toutes comprises entre 6,9 et 7,1 Hz ce qui est en accord avec ce qui est généralement observé dans les systèmes du type norbornane (29) où $^3J_{Hexo-Hexo}$ = 9–10 Hz et $^3J_{Hendo-Hendo}$ = 6–9 Hz. De la même façon, on peut noter que pour tous les cycloadduits les constantes de couplages $J_{H5'-H6'}$ sont inférieures à 9 Hz ce qui implique que le substituant R^3 ou R^4 est en *exo*.

La disposition *exo* du reste maléimido est obtenue ici de façon spécifique alors que dans le cas d'autres ylures d'azométhine cycliques où l'ensemble dipolaire n'est pas complètement inséré dans le cycle on obtient un mélange résultant des deux approches *exo* et *endo*, cette dernière étant majoritaire (13, 30).

Cette apparente différence de comportement peut s'expliquer en examinant le mode d'approche des deux espèces réactantes, les dipolarophiles étant ici de configuration *Z* bloquée. On sait que les réactions de cycloaddition suivent la règle «*endo*» également appelée la règle de l'accumulation maximale de l'insaturation (31) de façon que les interactions entre les orbitales π du dipôle et du dipolarophile soient maximisées.

Lorsque l'entité dipolaire n'est pas complètement insérée dans le cycle comme c'est le cas dans l'étude présentée par Hamelin et coll. (30), l'approche des deux espèces s'effectue majoritairement de façon *endo* (figure 6) en conduisant au mélange des deux cycloadduits bien que le produit *exo* soit thermodynamiquement le plus stable.

Dans le cas de la présente étude, l'entité dipolaire est totalement insérée dans le cycle, et l'état de transition correspondant

Can. J. Chem. Downloaded from www.nrcresearchpress.com by EESC ESCOLA DE ENGENHARIA on 09/08/12
For personal use only.

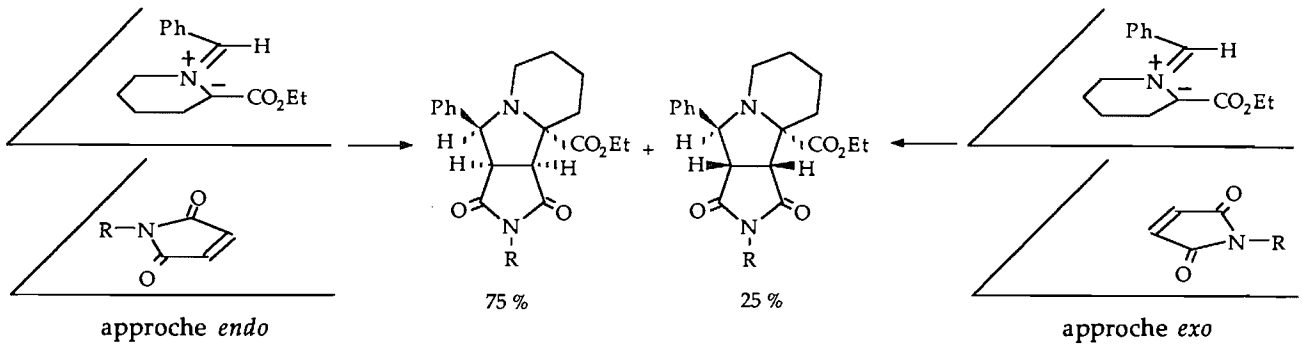

FIG. 6. Résultats décrits dans la référence 30.

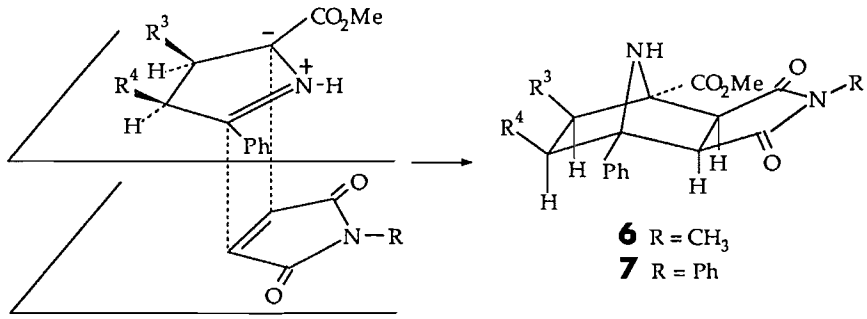

FIG. 7

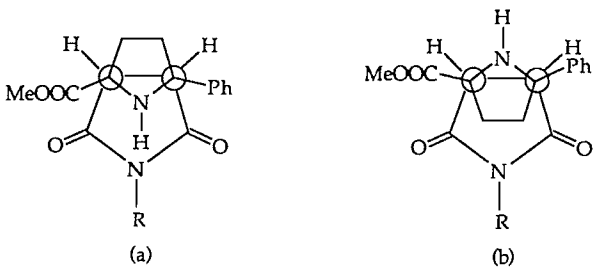

FIG. 8

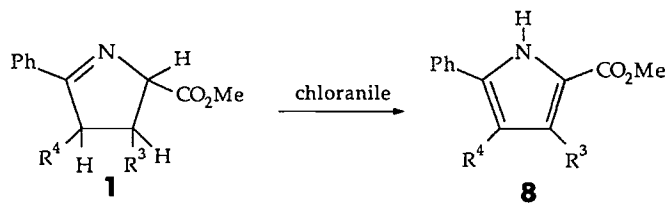

FIG. 9

à l'approche dite «*endo*» (figure 7) conduit au cycloadduit de stéréochimie *exo* puisque le reste maléimido se trouve du même côté que le pont 1,4-imino. C'est en même temps le produit thermodynamique.

Ce résultat peut aussi être expliqué en examinant les interactions stériques comme l'ont proposé Tsugé et al. (32). Les deux modes d'approche (a) et (b) dessinés sur la figure 8 représentent les deux états de transition possibles pour les réactions étudiées dans le présent travail (nous n'avons pas représenté les groupes R^3 ou R^4).

Dans le cas de (b) il existe quatre dispositions de type quasi-éclipsées autour des deux nouvelles liaisons qui se forment. Dans le cas de (a), par contre, la seule gêne stérique qui puisse intervenir est l'éventuelle répulsion entre le groupe N-H du dipôle et le groupe N-R du dipolarophile. Cette autre représentation met également en évidence, dans le cas de l'approche (a), la possibilité d'une stabilisation par interactions secondaires au niveau des orbitales frontières entre d'une part le phényle de l'ylure et l'un des groupes carbonyle du dipolarophile et d'autre part entre le groupe ester du dipôle et l'autre carbonyle du maléimide.

Il n'est donc pas étonnant d'obtenir diastéréospécifiquement le seul cycloadduit où le reste maléimido se trouve en position *exo*.

Synthèse de dérivés du 2-méthoxycarbonyl-5-phénylpyrrole

Disposant de sept composés dérivés du 5-phényl-3,4-dihydro-2*H*-pyrrole-2-carboxylate de méthyle nous avons complété cette étude en les transformant en dérivés du pyrrole par action du chloranile (figure 9).

Bien que les rendements restent très moyens, nous disposons donc d'une méthode permettant d'accéder à ces dérivés du 5-phénylpyrrole-2-carboxylate de méthyle diversement substitués sans qu'il soit nécessaire de séparer les divers diastéréoisomères des composés **1** lorsqu'on a affaire à un mélange.

Partie expérimentale

Les points de fusion déterminés sur banc Kofler ne sont pas corrigés. Les spectres d'absorption ir ont été obtenus avec un spectrophotomètre Beckman IR 33, les produits étant pastillés dans KBr. Les spectres de rmn ^1H ont été obtenus avec un spectromètre Bruker Spectrospin AC 200, les échantillons étant dissous dans $CDCl_3$ ou DMSO-d_6 avec le tétraméthylsilane comme référence interne. Les microanalyses ont été assurées par le Service d'Analyses du Centre national de la recherche scientifique à Vernaison.

1. Synthèse des diesters **4**

1.1. Synthèse de la 4-acétamido-4,4-diéthoxycarbonyl-1-phénybutan-1-one **4**a *($R^3 = R^4 = H$)*

Dans un Erlenmeyer de 100 mL, on dissout 1,36 g (0,02 mol) d'éthylate de sodium dans 25 mL d'éthanol anhydre. On ajoute alors 4,34 g

Can. J. Chem. Downloaded from www.nrcresearchpress.com by EESC ESCOLA DE ENGENHARIA on 09/08/12
For personal use only.

Can. J. Chem. Downloaded from www.nrcresearchpress.com by EESC ESCOLA DE ENGENHARIA on 09/08/12
For personal use only.

(0,02 mol) d'acétamidomalonate de diéthyle. Sous agitation magnétique, on additionne en 15 min 4,26 g (0,02 mol) de 3-bromopropiophénone. Le mélange est porté à reflux durant 18 h. Après refroidissement, la suspension obtenue est versée dans 100 mL d'eau glacée. Le solide est filtré et recristallisé dans l'isopropanol. Rdt. 86%, F = 119–120°C (litt. (22) F 119°C).

1.2. Synthèse de la 4-acétamido-4,4-diéthoxycarbonyl-2-méthyl-1-phénylbutan-1-one **4**b *(R^3 = H, R^4 = CH_3)*

Le chlorhydrate de 2-méthyl-3-diméthylaminopropiophénone est préparé selon un mode opératoire décrit dans la littérature (33, 34) avec un rendement de 81%. À une suspension de 0,05 mol de ce chlorhydrate dans 25 mL d'éthanol absolu, on additionne goutte à goutte, à température ambiante et en 30 min, 0,06 mol de sulfate de diméthyle. Une solution contenant 0.04 mol (8,68 g) d'acétamidomalonate de diéthyle et 0,08 mol (5,44 g) d'éthylate de sodium dans 30 mL d'éthanol absolu est rapidement ajoutée à la solution précédente. Le mélange est porté à reflux durant 5 h. Après retour à la température ambiante, la solution laiteuse obtenue est versée sur de la glace. On extrait à l'éther, lave la phase éthérée à l'eau, sèche sur sulfate de sodium et chasse l'éther. Le produit est purifié par distillation sous pression réduite. Rdt. 65%; Eb : 180–184°C (0,5 Torr; 1 Torr = 133,3 Pa); n_D^{20} = 1,5109; ir : ν(CO) = 1680 cm^{-1}, ν(NH) = 3360 cm^{-1}; rmn ^{1}H ($CDCl_3$) : 1,15 (d, 3H, J = 7,1), 1,20 (t, 3H, J = 7,0), 1,25 (t, 3H, J = 7,0), 1,80 (3H, s, CH_3-CO), 2,60 (dd, 1H, ^2J = 14,7, ^3J = 3,2), 3,00 (dd, 1H, ^2J = 14,7, ^3J = 9,7), 3,62 (ddq, 1H, ^3J = 9,7, ^3J = 3,2, ^3J = 7,1), 4,20 (m, 4H), 6,70 (sl, 1H, NH), 7,40–8,10 (m, 5H). Anal. calc. pour $C_{19}H_{25}NO_6$: C 62,79, H 6,93, N 3,85; tr. : C 63,01, H 6,78, N 3,73%.

1.3. Synthèse de la 4-acétamido-4,4-diéthoxycarbonyl-1,2-diphénylbutan-1-one **4**c *R^3 = H, R^4 = Ph)*

Le chlorhydrate de la 2-phényl-3-diméthylaminopropiophénone est préparé selon un mode opératoire adapté de ceux décrits dans la littérature (33, 34). Rdt. 55%; F = 204–206°C; ir : ν(CO) = 1675 cm^{-1}, ν(NH) = 3352 cm^{-1}; rmn ^{1}H ($CDCl_3$) : 2,70 (s, 3H), 2,80 (s, 3H), 3,10–4,45 (m, 3H), 5,80–6,10 (m, 1H), 7,20–8,30 (m, 10H).

Ce chlorhydrate est traité par l'acétamidomalonate de diéthyle selon le même protocole opératoire que celui décrit pour la préparation de **4***b*. Le traitement du brut réactionnel par de l'eau glacée permet d'obtenir un précipité qui est recristallisé dans l'isopropanol. Rdt. 68%; F = 104–106°C; ir : ν(CO) = 1678 cm^{-1}; rmn ^{1}H ($CDCl_3$) : 1,10 (t, 3H, J = 7,0); 1,25 (t, 3H, J = 7,0), 1,90 (s, 3H, CH_3-CO), 2,94 (dd, 1H, ^2J = 14,7, ^3J = 5), 3,27 (dd, 1H, ^2J = 14,7, ^3J = 8,2), 4,00–4,30 (m, 4H), 4,78 (dd, 1H, ^3J = 8,2, ^3J = 5), 6,70 (sl, 1H, NH), 7,15–7,95 (m, 10H). Anal. calc. pour $C_{23}H_{27}NO_6$: C 66,81, H 6,58, N 3,39; tr. : C 67,05, H 6,37, N 3,42%.

1.4. Synthèse de la 4-acétamido-4,4-diéthoxycarbonyl-1,3-diphénylbutan-1-one **4**d *(R^3 = Ph, R^4 = H)*

On dissout 0,002 mol (0,136 g) d'éthylate de sodium dans 50 mL d'éthanol absolu et ajoute 0,05 mol (10,85 g) d'acétamidomalonate de diéthyle. À la suspension obtenue, on additionne goutte à goutte à température ambiante et sous agitation magnétique une solution de 0,05 mol (10,5 g) de chalcone. Le mélange est agité à température ambiante durant 18 h puis neutralisé par 0,5 mL d'acide acétique glacial. Le solvant est éliminé, puis repris par du chloroforme, lavé à l'eau et séché sur sulfate de sodium. Après filtration et départ du solvant, le résidu est recristallisé dans l'isopropanol. Rdt. 78%; F = 102–104°C; ir : ν(CO) = 1675 cm^{-1}, ν(NH) = 3340 cm^{-1}; rmn ^{1}H ($CDCl_3$) : 1,20 (t, 3H, J = 7,0), 1,25 (t, 3H, J = 7,0), 2,10 (s, 3H, CH_3-CO), 3,40 (dd, 1H, ^2J = 17,4, ^3J = 11,5), 4,25 (dd, 1H, ^2J = 17,4, ^3J = 2,4), 4,00–4,30 (m, 4H), 4,53 (dd, 1H, ^3J = 11,5, ^3J = 2,4), 6,70 (sl, 1H, NH), 7,20–7,95 (m, 10H). Anal. calc. pour $C_{23}H_{27}NO_6$: C 66,81, H 6,58, N 3,39; tr. : C 66,98, H 6,45, N 3,47%.

1.5. Synthèse de la 4-acétamido-4,4-diéthoxycarbonyl-3-méthyl-1-phénylbutan-1-one **4**e *(R^3 = CH_3, R^4 = H)*

L'énone mise en oeuvre est la 1-phénylbut-2-èn-1-one obtenue selon le mode opératoire décrit par Fuson et al. (35). Celle-ci est mise en oeuvre selon le même protocole opératoire que celui décrit pour **4***d* et conduit à l'obtention de **4***e* avec un rendement de 74% après cristallisation de l'isopropanol. F = 118–120°C; ir : ν(CO) = 1670 cm^{-1}, ν(NH) = 3365 cm^{-1}; rmn ^{1}H ($CDCl_3$) : 0,90 (d, 3H, J = 6,7), 1,24 (t, 3H, J = 7,1), 1,28 (t, 3H, J = 7,1), 2,10 (s, 3H, CH_3-CO), 2,55 (dd, 1H, ^2J = 16,7, ^3J = 10,7), 3,30 (ddq, 1H, J = 6,7, ^3J = 10,7, ^3J = 2,2), 3,94 (dd, 1H, ^2J = 16,7, ^3J = 2,2), 4,15–4,36 (m, 4H), 6,75 (sl, 1H, NH), 7,40–8,10 (m, 5H). Anal. calc. pour $C_{19}H_{25}NO_6$: C 62,79, H 6,93, N 3,85; tr. : C 62,93, H 6,85, N 3,92%.

2. Synthèse des diesters **5**

Nous avons utilisé la méthode de Koch et coll. (21).

On mélange soigneusement 0,015 mol d'énone et 0,021 mol de chlorhydrate d'aminomalonate de diéthyle dans un Erlenmeyer de 100 mL. On porte à 170–180°C dans un bain d'huile paraffinique. On observe un dégagement de vapeurs de gaz chlorhydrique. Peu à peu le mélange se liquéfie, devient jaune soufre puis jaune clair. La réaction est terminée lorsque les vapeurs disparaissent. Après retour à la température ambiante, on ajoute 150 mL d'eau et 150 mL de benzène. La phase organique est séparée, lavée à l'eau salée, filtrée sur charbon actif et séchée sur sulfate de sodium. Après évaporation du solvant, le résidu est chromatographié sur gel de silice avec le benzène comme éluant.

*2.1. 3,4,5-Triphényl-3,4-dihydro-2*H*-pyrrole-2,2-dicarboxylate de diéthyle* **5**f *(R^3 = R^4 = Ph)*

L'énone de départ est l'α-phénylchalcone obtenue selon Dornow (36). Rdt. 39%; F = 132–134°C (méthanol); ir : ν(CO) = 1720 et 1740 cm^{-1}; rmn ^{1}H ($CDCl_3$) : 0,80 (d, 3H, J = 7,0), 1,35 (t, 3H, J = 7,0), 3,7 (AB d'un ABX_3, 2H, $^2J_{AB}$ = 10,6, J = 7,0), 4,40 (AB d'un ABX_3, 2H, $^2J_{AB}$ = 11,0, J = 7,0), 4,47 (d, 1H, J = 8,2), 5,00 (d, 1H, J = 8,2), 7,00–7,80 (m, 15H). Anal. calc. pour $C_{28}H_{27}NO_4$: C 76,16, H 6,16, N 3,17; tr. : C 76,29, H 6,05, N 3,22%.

*2.2. 3,5-Diphényl-4-méthyl-2*H*-pyrrole-2,2-dicarboxylate de diéthyle* **5**g *(R^3 = Ph, R^4 = CH_3)*

L'énone de départ est l'α-méthylchalcone obtenue selon Kohler (37). Rdt. 56%, F = 116–118°C (méthanol); ir : ν(CO) = 1730 et 1750 cm^{-1}; rmn ^{1}H ($CDCl_3$) : 0,80 (d, 3H, J = 7,0), 1,25 (t, 3H, J = 7,0), 1,30 (d, 3H, J = 7,0), 3,65 (AB d'un ABX_3, 2H, $^2J_{AB}$ = 10,6, J = 7,0), 3,80 (dq, 1H, J = 7,0, J = 5,6), 4,10 (d, 1H, J = 5,6), 4,32 (AB d'un ABX_3, 2H, $^2J_{AB}$ = 11,0, J = 7,0), 7,20–7,90 (m, 10H). Anal. calc. pour $C_{23}H_{25}NO_4$: C 72,80, H 6,64, N 3,69; tr. : C 72,95, H 6,53, N 3,57%.

3. Synthèse des dérivés du 5-phényl-3,4-dihydro-2H-pyrrole-2-carboxylate de méthyle **1**

La transformation des diesters **4** ou **5** en imines cycliques **1** a été effectuée selon un mode opératoire adapté de celui de Léonard (22).

Un mélange de 0,05 mol de diester **4** ou **5** et de 400 mL d'acide chlorhydrique 6 N est porté à reflux pendant 18 h. Après refroidissement, la solution est lavée à l'éther puis distillée sous pression réduite à l'évaporateur rotatif. L'huile résiduelle est reprise plusieurs fois par 50 mL de benzène qui est évaporé pour éliminer les traces d'eau. Le chlorhydrate de l'imino-acide brut est dissout dans 130 mL de méthanol absolu. On ajoute une quantité catalytique d'acide sulfurique concentré (3 mL) et porte à reflux pendant 3 h. Après retour à la température ambiante, on élimine le méthanol sous pression réduite. Le résidu est repris par l'eau puis porté à pH 8 par addition de carbonate de sodium solide. On extrait à l'éther ou au chloroforme. Les extraits organiques sont rassemblés, lavés et séchés sur sulfate de sodium. Après filtration et évaporation du solvant, on recristallise dans le cas des solides et distille sous pression réduite dans le cas des liquides.

*3.1. 5-Phényl-3,4-dihydro-2*H*-pyrrole-2-carboxylate de méthyle* **1**a *(R^3 = R^4 = H).* Rdt. 82%, F = 50°C (iPrOH) (litt. (22) F = 50°C); ir : ν(CO) = 1730 cm^{-1}; rmn ^{1}H ($CDCl_3$) : 2,20–2,40 (m, 2H), 3,00–3,20 (m, 2H), 3,80 (s, 3H, OCH_3), 4,95 (dddd, 1H, J = 8,0, J = 6,4, J = 1,9, J = 1,9, H^2), 7,35–7,95 (m, 5H).

*3.2. 4-Méthyl-5-phényl-3,4-dihydro-2*H*-pyrrole-2-carboxylate de*

Can. J. Chem. Downloaded from www.nrcresearchpress.com by EESC ESCOLA DE ENGENHARIA on 09/08/12
For personal use only.

méthyle **1**b ($R^3 = H$, $R^4 = CH_3$). Rdt. 45%, Eb = 91–92°C (0,01 Torr) mélange des deux diastéréoisomères *cis* et *trans* (50 : 50).

*3.3. 4,5-Diphényl-3,4-dihydro-2*H*-pyrrole-2-carboxylate de méthyle* **1**c ($R^3 = H$, $R^4 = Ph$). Rdt. 75%, F = 60°C (iPrOH) mélange des deux diastéréoisomères *cis* et *trans* (50 : 50).

*3.4. 3,5-Diphényl-3,4-dihydro-2*H*-pyrrole-2-carboxylate de méthyle* **1**d ($R^3 = Ph$, $R^4 = H$). Rdt. 55%, Eb = 188–190°C (0,6 Torr) mélange des deux diastéréoisomères *cis* et *trans* (30 : 70); rmn ^{1}H ($CDCl_3$) de l'isomère majoritaire : 3,12 (ddd, 1H, J = 17,5, J = 6,5, J = 1,7, H4), 3,61 (ddd, 1H, J = 17,5, J = 9,5, J = 1,8, H4), 3,75 (s, 3H, OCH_3), 3,87 (ddd, 1H, J = 7,9, J = 9,5, J = 6,5, H3), 4,93 (ddd, 1H, J = 7,9, J = 1,8, J = 1,7, H2), 7,15–8,00 (m, 10H). Anal. calc. pour $C_{18}H_{17}NO_2$: C 77,42, H 6,09, N 5,02; tr. : C 77,18, H 6,17, N 4,93%.

*3.5. 3-Méthyl-5-phényl-3,4-dihydro-2*H*-pyrrole-2-carboxylate de méthyle* **1**e ($R^3 = CH_3$, $R^4 = H$). Rdt. 77%, Eb = 142°C (0,8 Torr) mélange des deux diastéréoisomères *cis* et *trans* (50 : 50). Anal. calc. pour $C_{13}H_{15}NO_2$: C 71,89, H 6,91, N 6,45; tr. : C 71,70, H 7,07, N 6,43%.

*3.6. 3*c*,4*t*,5-Triphényl-3,4-dihydro-2*H*-pyrrole-2*r*-carboxylate de méthyle* **1**f ($R^3 = R^4 = Ph$). Rdt. 30%, F = 220°C (iPrOH); ir : ν(CO) = 1732 cm^{-1}; rmn ^{1}H (DMSO-d_6) : 3,38 (s, 1H, H4), 3,67 (s, 3H, OCH_3), 4,19 (d, 1H, J = 10,3, H3), 4,95 (d, 1H, J = 10,3, H2), 6,85–7,95 (m, 15H). Anal. calc. pour $C_{24}H_{21}NO_2$: C 81,10, H 5,96, N 3,94; tr. : C 81,32, H 5,79, N 3,87%.

*3.7. 4*c*-Méthyl-3*t*,5-diphényl-3,4-dihydro-2*H*-pyrrole-2*r*-carboxylate de méthyle* **1**g ($R^3 = Ph$, $R^4 = CH_3$). Rdt. 30%, F = 98–100°C (iPrOH); ir : ν(CO) = 1730 cm^{-1}; rmn ^{1}H ($CDCl_3$) : 1,35 (d, 3H, J = 7,1, CH_3), 3,38 (dd, 1H, J = 5,5, J = 5,5, H3), 3,54 (ddq, 1H, J = 7,1, J = 5,5, J = 1,2, H4), 3,70 (s, 3H, OCH_3), 4,92 (dd, 1H, J = 5,5, J = 1,2, H2), 7,15–7,90 (m, 10H). Anal. calc. pour $C_{19}H_{19}NO_2$: C 77,79, H 6,53, N 4,77; tr. : C 77,93, H 6,42, N 4,72%.

4. Réactions de cycloaddition des composés **1**a–**1**e *avec les* N*-méthyl et* N*-phénylmaléimides*

Mode opératoire général : 4 mmol de précurseur du dipôle **1** et 6 mmol de dipolarophile sont dissouts dans 5 mL de toluène. Le mélange réactionnel est introduit dans un tube à essai en Pyrex préalablement effilé au chalumeau, scellé et porté à 130°C pendant 48 h. Après refroidissement, le tube est ouvert et le solvant chassé à l'évaporateur rotatif. Le résidu est repris par un solvant approprié puis essoré après cristallisation.

*4.1.1,4-Imino-1-méthoxycarbonyl-*exo*-2,3-(*N*-méthyldicarboximido)-4-phénylcyclohexane* **6**a ($R = CH_3$, $R^3 = R^4 = H$). Rdt. 60%, F = 146°C (iPrOH); ir : ν(CO) ester = 1745 cm^{-1}, ν(CO) imido = 1680 cm^{-1}, ν(NH) = 3320 cm^{-1}; rmn ^{1}H ($CDCl_3$) : 1,75–2,45 (m, 4H, CH_2-CH_2 en 5 et 6), 2,25 (s, 1H, NH), 3,05 (d, 1H, J_{H3-H2} = 7,0, H3), 3,25 (d, 1H, J_{H2-H3} = 7,0, H2), 2,90 (s, 3H, N-CH_3), 3,90 (s, 3H, OCH_3), 7,30–7,50 (m, 5H). Anal. calc. pour $C_{17}H_{18}N_2O_4$: C 64,95, H 5,77, N 8,91; tr. : C 65,12, H 5,63, N 8,82%.

*4.2. 1,4-Imino-1-méthoxycarbonyl-*exo*-5-méthyl-*exo*-2,3-(*N*-méthyldicarboximido)-4-phénylcyclohexane* **6**b ($R = R^4 = CH_3$, $R^3 = H$). Rdt. 61%, F = 148°C (hexane–éther); ir : ν(CO) ester = 1745 cm^{-1}, ν(CO) imido = 1680 cm^{-1}, ν(NH) = 3325 cm^{-1}; rmn ^{1}H ($CDCl_3$) : 0,62 (d, 3H, J = 6,7, CH_3 en 6), 1,53 (m, H5′), 2,35–2,55 (m, 2H, CH_2 en -6), 2,50 (s, 1H, NH), 2,85 (s, 3H, N-CH_3), 3,15 (d, 1H, J = 7,0, H2), 3,27 (d, 1H, J = 7,0, H3), 3,90 (s, 3H, OCH_3), 7,20–7,55 (m, 5H). Anal. calc. pour $C_{18}H_{20}N_2O_4$: C 65,84, H 6,14, N 8,53; tr. : C 66,02, H 6,07, N 8,67%.

*4.3. 1,4-Imino-1-méthoxycarbonyl-*exo*-2,3-(*N*-méthyldicarboximido)-4-phényl-exo-5-phénylcyclohexane* **6**c ($R = CH_3$, $R^3 = H$, $R^4 = Ph$). Rdt. 55%, F = 270°C (toluène); ir : ν(CO) ester = 1743 cm^{-1}, ν(CO) imido = 1680 cm^{-1}, ν(NH) = 3320 cm^{-1}; rmn ^{1}H ($CDCl_3$) : 2,34 (dd, 1H, ^2J = 13,3, ^3J = 5,15, H6), 2,72 (dd, 1H, ^2J = 13,3, ^3J = 8,8, H6′), 2,75 (s, 1H, NH), 2,86 (s, 3H, N-CH_3), 3,48 (dd, 1H, J = 5,15, J = 8,8, H5′), 3,45 (système AB centré à 3,45 pour H2 et H3, J = 7,0), 3,95 (s, 3H, OCH_3), 6,90–7,20 (m, 10H). Anal. calc. pour $C_{23}H_{22}N_2O_4$: C 70,75, H 5,68, N 7,18; tr. : C 70,87, H 5,53, N 7,27%.

*4.4. 1,4-Imino-4-méthoxycarbonyl-*exo*-2,3-(*N*-méthyldicarboximido)-1-phényl-exo-5-phénylcyclohexane* **6**d ($R = CH_3$, $R^3 = Ph$, $R^4 = H$). Rdt. 58%, F = 260°C (toluène); ir : ν(CO) ester = 1740 cm^{-1}, ν(CO) imido = 1680 cm^{-1}, ν(NH) = 3320 cm^{-1}; rmn ^{1}H ($CDCl_3$) : 2,15 (dd, 1H, ^2J = 13,2, ^3J = 5,7, H6), 2,70 (dd, 1H, NH), 2,85 (dd, 1H, ^2J = 13,2, ^3J = 8,6, H6′), 2,90 (s, 3H, N-CH_3), 3,19 (d, 1H, J = 7,0, H2), 3,45 (d, 1H, J = 7,0, H3), 3,50 (s, 3H, OCH_3), 3,55 (dd, 1H, J = 8,6, J = 5,7, H5′), 7,15–7,55 (m, 10H). Anal. calc. pour $C_{23}H_{22}N_2O_4$: C 70,75, H 5,68, N 7,18; tr. : C 70,85, H 5,62, N 7,18%.

*4.5. 1,4-Imino-4-méthoxycarbonyl-*exo*-2,3-(*N*-méthyldicarboximido)-exo-5-méthyl-1-phénylcyclohexane* **6**e ($R = R^3 = CH_3$, $R^4 = H$). Rdt. 57%, F = 198°C (toluène); ir : ν(CO) ester = 1742 cm^{-1}; ν(CO) imido = 1680 cm^{-1}, ν(NH) = 3320 cm^{-1}; rmn ^{1}H ($CDCl_3$) : 0,23 (d, 3H, J = 6,8, CH_3 en 5), 1,36 (dd, 1H, ^2J = 12,1, ^3J = 4,4, H6), 2,48 (ddq centré à 2,48, H5′), 2,50 (s, 1H, NH), 2,61 (dd, 1H, ^2J = 12,1, ^3J = 8,0, H6′), 2,91 (s, 3H, N-CH_3), 2,97 (d, 1H, J = 7,0, H2), 3,23 (d, 1H, J = 7,0, H3), 3,90 (s, 3H, OCH_3), 7,30–7,40 (m, 5H). Anal. calc. pour $C_{18}H_{20}N_2O_4$: C 65,84, H 6,14, N 8,53; tr. : C 66,07, H 6,01, N 8,42%.

*4.6. 1,4-Imino-1-méthoxycarbonyl-*exo*-2,3-(*N*-phényldicarboximido)-4-phénylcyclohexane* **7**a ($R = Ph$, $R^3 = R^4 = H$). Rdt. 64%, F = 192°C (iPrOH); ir : ν(CO) ester = 1745 cm^{-1}, ν(CO) imido = 1675 cm^{-1}, ν(NH) = 3320 cm^{-1}; rmn ^{1}H ($CDCl_3$) : 1,60–2,60 (m, 4H, CH_2-CH_2 en 5 et 6), 3,27 (d, 1H, J = 7,0, H3), 3,40 (s, 1H, NH), 3,47 (d, 1H, J = 7,0, H2), 3,75 (s, 3H, OCH_3), 7,10–7,55 (m, 10H). Anal. calc. pour $C_{22}H_{20}N_2O_4$: C 70,20, H 5,36, N 7,44; tr. : C 70,34, H 5,27, N 7,52%.

*4.7. 1,4-Imino-1-méthoxycarbonyl-*exo*-5-méthyl-*exo*-2,3-(*N*-phényldicarboximido)-4-phénylcyclohexane* **7**b ($R = Ph$, $R^3 = H$, $R^4 = CH_3$). Rdt. 57%, F = 230°C (iPrOH); ir : ν(CO) ester = 1745 cm^{-1}, ν(CO) imido = 1680 cm^{-1}, ν(NH) = 3320 cm^{-1}; rmn ^{1}H ($CDCl_3$) : 0,72 (d, 1H, J = 6,8, CH_3 en 5), 1,52 (ddq, H5′), 2,35–2,55 (m, 2H, CH_2 en 6), 3,40 (s, 1H, NH), 3,25 (d, 1H, J = 7,0, H2), 3,57 (d, 1H, J = 7,0, H3), 3,90 (s, 3H, OCH_3), 7,10–7,50 (m, 10H). Anal. calc. pour $C_{23}H_{22}N_2O_4$: C 70,75, H 5,68, N 7,18; tr. : C 70,97, H 5,52, N 7,23%.

*4.8. 1,4-Imino-1-méthoxycarbonyl-*exo*-2,3-(N-phényldicarboxmido)-*exo*-5-phényl-4-phénylcyclohexane* **7**c ($R = R^4 = Ph$, $R^3 = H$). Rdt. 79%, F = 232°C (EtOH); ir : ν(CO) ester = 1740 cm^{-1}, ν(CO) imido = 1680 cm^{-1}, ν(NH) = 3320 cm^{-1}; rmn ^{1}H ($CDCl_3$) : 2,05 (dd, 1H, ^2J = 13,4, ^3J = 5,2, H6), 2,75 (dd, 1H, ^2J = 13,4, ^3J = 8,8, H6′), 3,70 (m, 3H, H5′, H2 et H3), 3,80 (s, 3H, OCH_3), 3,90 (s, 1H, NH), 6,75–7,45 (m, 15H). Anal. calc. pour $C_{28}H_{24}N_2O_4$: C 74,34, H 5,31, N 6,19; tr. : C 74,13, H 5,30, N 6,19%.

*4.9. 1,4-Imino-4-méthoxycarbonyl-*exo*-2,3-(*N*-phényldicarboximido)-*exo*-5-phényl-1-phénylcyclohexane* **7**d ($R = R^3 = Ph$, $R^4 = H$). Rdt. 68%, F = 270°C (acétone–éthanol, 1 : 1); ir : ν(CO) ester = 1740 cm^{-1}, ν(CO) imido = 1680 cm^{-1}, ν(NH) = 3320 cm^{-1}; rmn ^{1}H ($CDCl_3$) : 1,78 (dd, 1H, ^2J = 12,2, ^3J = 6,2, H6), 3,05 (dd, 1H, ^2J = 12,2, ^3J = 8,5, H6), 3,30 (s, 3H, OCH_3), 3,46 (d, 1H, J = 6,9, H2), 3,55 (dd, 1H, J = 6,2, J = 8,5, H5), 3,76 (d, 1H, J = 6,9, H3), 3,93 (s, 1H, NH), 7,10–7,60 (m, 15H). Anal. calc. pour $C_{28}H_{24}N_2O_4$: C 74,34, H 5,31, N 6,19; tr. : C 74,47, H 5,22, N 6,27%.

*4.10. 1,4-Imino-4-méthoxycarbonyl-*exo*-5-méthyl-*exo*-2,3-(*N*-phényldicarboximido)-1-phénylcyclohexane* **7**e ($R = Ph$, $R^3 = CH_3$, $R^4 = H$). Rdt. 56%, F = 245°C (toluène); ir : ν(CO) ester = 1740 cm^{-1}, ν(CO) imido = 1680 cm^{-1}, ν(NH) = 3320 cm^{-1}; rmn ^{1}H ($CDCl_3$) : 0,97 (d, 3H, J = 6,8, CH_3 en 5), 1,45 (dd, 1H, ^2J = 12,0, ^3J = 4,5, H6), 2,55 (ddq, 1H, J_{CH-CH_3} = 6,8, J = 4,5, J = 8,2, H5′), 2,70 (dd, 1H, ^2J = 12,0, ^3J = 8,2, H6′), 3,11 (d, 1H, J = 7,1, H2), 3,42 (d, 1H, J = 7,1, H3), 3,90 (s, 3H, OCH_3), 3,93 (s, 1H, NH), 7,10–7,50 (m, 10H). Anal. calc. pour $C_{23}H_{22}N_2O_4$: C 70,75, H 5,68, N 7,28; tr. : C 70,83, H 5,73, N 7,07%.

5. Oxydation des dérivés **1** *en pyrroles* **8**

Mode opératoire général

À une solution de 5 mmol de composé **1** dans 20 mL de xylène (mélange des isomères) on ajoute 5,5 mmol de parachloranile. Le mélange est porté à reflux pendant 16 h. Après refroidissement, on dilue avec 50 mL d'éther et verse sous agitation magnétique dans 100 mL d'une solution aqueuse de carbonate de sodium à 5%. Les deux phases sont séparées et la phase organique est lavée à l'eau jusqu'à neutralité, filtrée sur charbon actif puis séchée sur sulfate de sodium. Après filtra-

Can. J. Chem. Downloaded from www.nrcresearchpress.com by EESC ESCOLA DE ENGENHARIA on 09/08/12
For personal use only.

tion et évaporation des solvants, le résidu obtenu est repris par du méthanol et cristallisé.

5.1. 5-Phénylpyrrole-2-carboxylate de méthyle 8a *(R^3 = R^4 = H).* Rdt. 51%, F = 146–148°C; ir : ν(CO) = 1680 cm^{-1}, ν(NH) = 3300 cm^{-1}; rmn ^1H ($CDCl_3$) : 3,78 (s, 3H, OCH_3), 6,46 (dd, 1H, J = 3,0, J = 4,6, H3), 6,90 (dd, 1H, J = 3,0, J = 4,6, H4), 7,10–7,71 (m, 5H), 9,93 (sl, 1H, NH). Anal. calc. pour $C_{12}H_{11}NO_2$: C 71,62, H 5,51, N 6,96; tr. : C 71,51, H 5,72, N 6,82%.

5.2. 4-Méthyl-5-phénylpyrrole-2-carboxylate de méthyle 8b *(R^3 = H, R^4 = CH_3).* Rdt. 44%, F = 121°C; ir : ν(CO) = 1695 cm^{-1}, ν(NH) = 3310 cm^{-1}; rmn ^1H ($CDCl_3$) : 2,18 (s, 3H, CH_3 en 4), 3,73 (s, 3H, OCH_3), 7,03 (d, 1H, J = 3,0, H3), 7,10–7,23 (m, 5H), 9,71 (sl, 1H, NH). Anal. calc. pour $C_{13}H_{13}NO_2$: C 72,54, H 6,08, N 6,51; tr. : C 72,73, H 5,95, N 6,47%.

5.3. 4,5-Diphénylpyrrole-2-carboxylate de méthyle 8c *(R^3 = H, R^4 = Ph).* Rdt. 66%, F = 165°C; ir : ν(CO) = 1675 cm^{-1}, ν(NH) = 3260 cm^{-1}; rmn ^1H ($CDCl_3$) : 3,77 (s, 3H, OCH_3), 5,96 (d, 1H, J = 3,0, H3), 7,13–7,47 (m, 10H), 9,40 (sl, 1H, NH). Anal. calc. pour $C_{18}H_{15}NO_2$: C 77,96, H 5,45, N 5,05; tr. : C 77,87, H 5,52, N 5,17%.

5.4. 3,5-Diphénylpyrrole-2-carboxylate de méthyle 8d *(R^3 = Ph, R^4 = H).* Rdt. 58%, F = 177°C; ir : ν(CO) = 1665 cm^{-1}, ν(NH) = 3315 cm^{-1}; rmn ^1H ($CDCl_3$) : 3,76 (s, 3H, OCH_3), 6,63 (d, 1H, J = 4,0, H4), 7,21–7,78 (m, 10H), 9,74 (sl, 1H, NH). Anal. calc. pour $C_{18}H_{15}NO_2$: C 77,96, H 5,45, N 5,05; tr. : C 78,11, H 5,32, N 5,12%.

5.5. 3-Méthyl-5-phénylpyrrole-2-carboxylate de méthyle 8e *(R^3 = CH_3, R^4 = H).* Rdt. 55%, F = 131°C; ir : ν(CO) = 1690 cm^{-1}, ν(NH) = 3320 cm^{-1}; rmn ^1H ($CDCl_3$) : 2,23 (s, 3H, CH_3 en 3), 3,78 (s, 3H, OCH_3), 6,30 (d, 1H, J = 3,0, H4), 7,10–7,61 (m, 5H), 9,74 (sl, 1H, NH). Anal. calc. pour $C_{13}H_{13}NO_2$: C 72,54, H 6,08, N 6,51; tr. : C 72,47, H 6,13, N 6,42%.

5.6. 3,4,5-Triphénylpyrrole-2-carboxylate de méthyle 8f *(R^3 = R^4 = Ph).* Rdt. 53%, F = 220°C; ir : ν(CO) = 1680 cm^{-1}, ν(NH) = 3300 cm^{-1}; rmn ^1H ($CDCl_3$) : 3,75 (s, 3H, OCH_3), 6,90–7,31 (m, 15H), 9,30 (sl, 1H, NH). Anal. calc. pour $C_{24}H_{19}NO_2$: C 81,56, H 5,42, N 3,96; tr. : C 81,67, H 5,27, N 3,87%.

5.7. 4-Méthyl-3,5-diphénylpyrrole-2-carboxylate de méthyle 8g *(R^3 = Ph, R^4 = CH_3).* Rdt. 62%, F = 137°C; ir : ν(CO) = 1680 cm^{-1}, ν(NH) = 3300 cm^{-1}; rmn ^1H ($CDCl_3$) : 2,05 (s, 3H, CH_3 en 4), 3,60 (s, 3H, OCH_3), 7,06–7,60 (m, 10H), 9,75 (sl, 1H, NH). Anal. calc. pour $C_{19}H_{17}NO_2$: C 78,32, H 5,88, N 4,81; tr. : C 78,46, H 5,76, N 4,78%.

6. Structure cristallographique du cycloadduit 7d *(résumé)*

Cette étude est décrite complètement dans la référence 28.

$C_{28}H_{24}N_2O_4$ M_r = 452,5

Groupe spatial $P2_1/c$ (monoclinique). a = 13,321(3) Å; b = 14,566(2) Å; c = 11,625(2) Å; β = 92,18(2)°; V = 2254(1) $Å^3$ Z = 4; D_x = 1,383 Mg m^{-3}; λ(MoKα) = 0,7107 Å; μ = 84 m^{-1}; F(000) = 952 électrons T = 290 K; R final = 0,037 pour 2420 réflexions indépendantes.

Des monocristaux du composé 7*d* ont été obtenus par cristallisation dans le toluène. Le cristal choisi avait la forme d'un parallelepipède dont les dimensions approximatives étaient 0,27 × 0,30 × 0,50 mm. Les mesures des intensités des taches de diffraction ont été réalisées sur un diffractomètre automatique 4 cercles Enraf–Nonius de l'Université de Paris-Sud. De l'ensemble des paramètres (28) on peut extraire les valeurs des angles de torsion significatifs :

H3-C3-C4-N7 = 159,8°; H2-C2-C1-N7 = 154,7°;

H5-C5-C4-N7 = 147,9°

Ces valeurs indiquent que le substituant R^3 = Ph et le reste maléimido sont en disposition *exo* (figure 5).

1. S. Kitane, K. Tshiamala, J. Vebrel et B. Laude. Tetrahedron Lett. **22**, 1717 (1981).
2. K. Tshiamala, J. Vebrel et B. Laude. Spectrochim. Acta, Part A: **41A**, 499 (1985).
3. A. Sedqui, J. Vebrel et B. Laude. Chemistry Lett. 965 (1984).
4. S. Kitane, K. Tshiamala, B. Laude, J. Vebrel et E. Cerutti. Tetrahedron, **41**, 3737 (1985).
5. K. Tshiamala, S. Kitane, J. Vebrel et B. Laude. Bull. Soc. Chim. Belg. **95**, 1083 (1986).
6. A. Kerbal, K. Tshiamala, J. Vebrel et B. Laude. Bull. Soc. Chim. Belg. **97**, 149 (1988).
7. K. Moustaïd, Nguyen Dinh An, B. Laude, J. Vebrel, B. Daou et M. Soufiaoui. C.R. Acad. Sci. Paris, **312**, 1129 (1991).
8. A. Sedqui, T. Lakhlifi, B. Laude et J. Amaudrut. Bull. Soc. Chim. Belg. **98**, 865 (1989).
9. A. Sedqui, J. Vebrel, B. Laude, N. Rodier et F. Théobald. J. Chem. Res. (S), 156 (1992); (M), 1159 (1992).
10. K. Moustaïd, Nguyen Dinh An, B. Laude, M.F. Mercier et A. Sedqui. Can. J. Chem. **70**, 802 (1992).
11. K.T. Potts. Mesoionic ring systems in 1,3-dipolar cycloaddition chemistry. Tome 2. *Éditeur* : A. Padwa. J. Wiley and Sons, New York. 1984. pp. 7–82, et références citées.
12. J.T. Tufariello. Nitrones in 1,3-dipolar cycloaddition chemistry. Tome 2. *Éditeur* : A. Padwa. J. Wiley and Sons, New York. 1984. pp. 83–168, et références citées.
13. A.S. Anslow, L.M. Harwood, H. Phillips, D. Watkins et L.F. Wong. Tetrahedron: Asymmetry, **2**, 1343 (1991).
14. A. Mkhairi et J. Hamelin. Tetrahedron Lett. **28**, 1397 (1987).
15. T. Lakhlifi, A. Sedqui, B. Laude, Nguyen Dinh An et J. Vebrel. Can. J. Chem. **69**, 1156 (1991).
16. J.M. Lown. *Dans* 1,3-Dipolar cycloaddition chemistry. Tome 1. *Éditeur* : A. Padwa. J. Wiley and Sons, New York. 1984. Chap. 6 et références citées.
17. N. Imai, Y. Terao et K. Achiwa. Heterocycles, 1107 (1985).
18. P. De Shong, D.A. Kell et D.R. Sidler. J. Org. Chem. **50**, 2309 (1985).
19. J. Blake, C.D. Willson et H.J. Rapoport. J. Am. Chem. Soc. **86**, 5293 (1964).
20. R.A. Daignault et E.L. Eliel. Org. Synth. Collect. Vol. V, 303 (1973).
21. J. Koch, J.F. Robert et J.J. Panouse. C.R. Acad. Sci. Paris, Sér. C, **286**, 95 (1978); J.F. Robert, J. Koch et J.J. Panouse. Spectrochim. Acta, Part A: **35A**, 131 (1979).
22. F. Leonard. U.S. Patents 3, 164, 597 et 3, 185, 705. 1965. Geigy Chemical Corp.
23. M.P. Sammes, M.W.L. Chung et A.R. Katritzky. J. Chem. Soc. Perkin Trans. 1, 1773 (1985); M.W.L. Chung et M.P. Sammes. J. Chem. Res. (S), 258 (1987).
24. G.B. Itona et J.Y. Laronze. Synthesis, 353 (1987).
25. R. Grigg, J. Kemp, G. Sheldrick et J. Trotter. J. Chem. Soc. Chem. Commun. 109 (1978).
26. M. Joucla et J. Hamelin. Tetrahedron Lett. 2885 (1978); M. Joucla, B. Fouchet et J. Hamelin. Tetrahedron, **41**, 2707 (1985).
27. R. Grigg, L.D. Basanagouclar, D.A. Kennedy, J.F. Malone et S. Thianpatanagul. Tetrahedron Lett. 2803 (1982).
28. F. Theobald, N. Rodier, T. Lakhlifi, A. Sedqui et B. Laude. Acta Crystallogr. Sect. C: Cryst. Struct. Commun. **C46**, 1074 (1990).
29. A. Gaudemer. *Dans* Stereochemistry: fundamentals and methods. Spectrometric methods. Vol. 1. *Éditeur* : H. Kagan. Georg Thieme, Stuttgart. 1977. p. 109.
30. M. Joucla, J. Mortier, J. Hamelin et L. Toupet. Bull. Soc. Chim. Fr. 143 (1988).
31. F.A. Carey et R.J. Sundberg. Advanced organic chemistry. Vol. A. Plenum Press, New York. 1984. p. 558.
32. O. Tsugé, S. Kanemasa, M. Oke, K. Yorosu, S. Tanekana et K. Ueno. Bull. Chem. Soc. Jpn. **60**, 4067 (1987).
33. J.J. Denton, R.J. Turner, W.B. Neier, V.A. Lawson et H.P. Schedl. J. Am. Chem. Soc. **71**, 2045 (1949).
34. H.O. House, D.J. Reif et L. Wasson. J. Am. Chem. Soc. **79**, 2490 (1957).
35. R.C. Fuson, R.E. Christ et G.M. Whitman. J. Am. Chem. Soc. **58**, 2450 (1936).
36. A. Dornow. Ann. Chem. **578**, 112 (1952).
37. E.P. Kohler. Ann. Chem. **31**, 656 (1904).

Comportement particulier d'arylidènebenzothiazinonedioxydes dans les cycloadditions [3+2]. Compétition entre sites dipolarophiliques. Évolution des cycloadduits

TOUFIK FATHI, KABULA CIAMALA, NGUYEN DINH AN[1] ET JOËL VEBREL

Laboratoire de chimie organique, Université de Franche-Comté, 16 Route de Gray, 25030 Besancon, France

Reçu le 21 juillet 1993

TOUFIK FATHI, KABULA CIAMALA, NGUYEN DINH AN et JOËL VEBREL. Can. J. Chem. **72**, 1424 (1994).

La réaction de la diphénylnitrilimine sur quelques arylidènebenzothiazinonedioxydes conduit à un mélange de deux produits séparables par chromatographie. Les données spectroscopiques (infrarouge, résonance magnétique nucléaire) et une étude radiocristallographique permet de démontrer une compétition des deux sites dipolarophiliques au cours des cycloadditions dipolaires.

TOUFIK FATHI, KABULA CIAMALA, NGUYEN DINH AN, and JOËL VEBREL. Can. J. Chem. **72**, 1424 (1994).

The reaction of diphenylnitrilimine with some arylidenebenzothiazinone dioxides leads to a mixture of two products that were isolated by chromatography. Spectroscopic data (infrared, nuclear magnetic resonance) and a radiocrystallographic study illustrate a competition between the two dipolarophilic sites in dipolar cycloaddition.

Introduction

La synthèse des (2*H*)-1,2-benzothiazine-4(3*H*)-1,1-dioxydes a été largement développée ces dernières années compte tenu des propriétés anti-inflammatoires potentielles (1, 2). Par ailleurs, certains de ces dérivés présentent des aptitudes dipolarophiliques au cours des réactions de cycloaddition dipolaire (3, 4).

La cycloaddition dipolaire-1,3 des diarylnitrilimines sur plusieurs 2-arylidènetétraline-1-ones, 3-arylidènechroman-4-ones, 3-arylidèneisochroman-4-ones, 3-arylidènethiochroman-4-ones et 3-arylidèneisothiochroman-4-ones a été réalisée récemment au sein de notre équipe de recherche. L'influence des facteurs conformationnels sur la diastéréochimie de la réaction a été mise en évidence grâce à la rmn ^1H et du ^{13}C (5). La structure des 3-arylidène-2*H*-1,2-benzothiazine- 4(3*H*)- one-1,1-dioxydes **1** (figure 1) étant proche des dipolarophiles antérieurement utilisés, nous nous sommes proposés d'étudier leurs comportements dipolarophiliques vis-à-vis de la diphénylnitrilimine afin de préciser la régiochimie de la réaction ainsi que le comportement des cycloadduits en milieu acide.

Réactions de cycloaddition de la diphénylnitrilimine sur les 3-arylidène-2*H*-1,2-benzothiazine-4(3*H*)-one-1,1 dioxydes 1

La réaction de cycloaddition dipolaire-1,3 conduit à des dérivés de la spiro(1,3,4-triaryl Δ-2pyrazoline-5;2′ benzothiazine-1′-one) **2** (cycloadduit attendu compte tenu de nos précédents résultats (5)) ainsi qu'aux produits **3** inattendus qui ne seraient ni régioisomère, ni diastéréoisomère de **2** au vu des résultats spectroscopiques (ir, rmn ^1H et ^{13}C, masse) (figure 1).

Pour tous les termes de la série, les spectres de rmn protonique des bruts réactionnels permettent d'observer les signaux correspondants aux produits **2** et **3** dont les proportions sont accessibles par examen des courbes d'intégration. Les composés **2** et **3** sont aisément séparés par chromatographie en phase liquide sur silice.

Mode d'approche dipole–dipolarophile au cours de la cycloaddition

Les paramètres de rmn protonique des dipolarophiles **1** (en solution soit dans $CDCl_3$, soit dans C_6D_6) ne permettent pas à priori de déterminer la stéréochimie de la double liaison éthylénique juxtacyclique. En effet, une première observation montre que dans tous les cas, on n'observe pas un effet de solvant ASIS marquant pour le proton éthylénique. Toutefois, le fait que ce proton soit fortement déblindé (8,2–8,3 ppm) indiquerait tout de même qu'il est en *cis* par rapport au groupe carbonyle et que les composés **1** seraient donc les isomères de structure *E* par rapport à la double liaison éthylénique juxtacyclique. Nous avons déjà observé cette isomérie géométrique *E* pour les dérivés des 2-arylidènetétraline-1-ones (5).

Les valeurs des fréquences d'absorption infrarouge de la vibration ν(C=O) de 1660–1670 cm^{-1} pour les dipolarophiles **1** indiquent que le groupe carbonyle et le noyau benzènique condensé sont conjugués et donc coplanaires. La conformation privilégiée du cycle cétonique serait donc la conformation diplanaire-1,3 dite «sofa» (figure 1) où les sommets 2, 1, 8a, 4a, 4 sont dans un même plan et l'atome d'azote 3 est au-dessus de ce plan; le groupe méthyle porté par l'azote adopterait une position axiale car il est suffisamment encombrant pour ne pas pouvoir adopter une position équatoriale. Une telle conformation du groupement-NCH_3 laisse prévoir une approche *anti* du dipôle (côté opposé du groupement -NCH_3).

Analyses spectroscopiques des cycloadduits 2

L'existence d'un singulet à 5,4 ppm en rmn ^1H pour le proton H4, et celle des protons aromatiques entre 6,7 et 8 ppm, la fréquence de la bande d'absorption ir à 1700 cm^{-1} de la fonction cétone conjuguée indiquent que les produits **2** sont bien des cycloadduits. Ce sont des spiropyrazolines dont le sommet commun est l'atome 5 de la pyrazoline et l'atome 2′ de la benzothiazinone. Cette régiochimie est prouvée par l'examen des paramètres de rmn ^{13}C puisque la forte valeur du déplacement chimique du carbone quaternaire de jonction spirannique C-5:2′ comprise entre 94,5 et 94,7 ppm est en accord avec un carbone lié d'une part à l'atome d'azote 3′ et d'autre part à l'extrémité azotée du dipôle. On observe aussi un pic à 190 ppm caractéristique d'une fonction cétone (C-1′ de **2**). La régiochimie ainsi définie est conforme à nos observations antérieures : au cours de la cycloaddition des diarylnitrilimines avec divers dipolarophiles, l'extrémité azotée du dipôle se fixe toujours sur l'atome de carbone du dipolarophile porteur d'un groupe électroattracteur (6–11).

En spectrométrie de masse, l'ion moléculaire $2^{+\cdot}$ se réarrange avec perte de 169 unités de masse pour conduire à l'ion radical **2′** (figure 2).

1. Auteur correspondant. Téléphone : 33 81 66 62 73; FAX : 33 81 66 62 30.

Can. J. Chem. Downloaded from www.nrcresearchpress.com by ESC ESCOLA DE ENGENHARIA on 09/08/12
For personal use only.

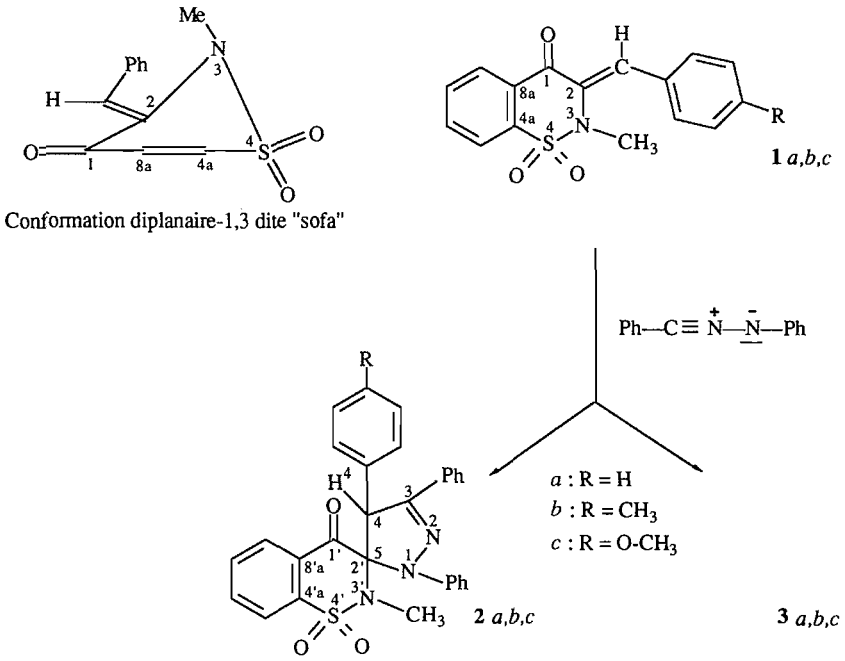

FIG. 1

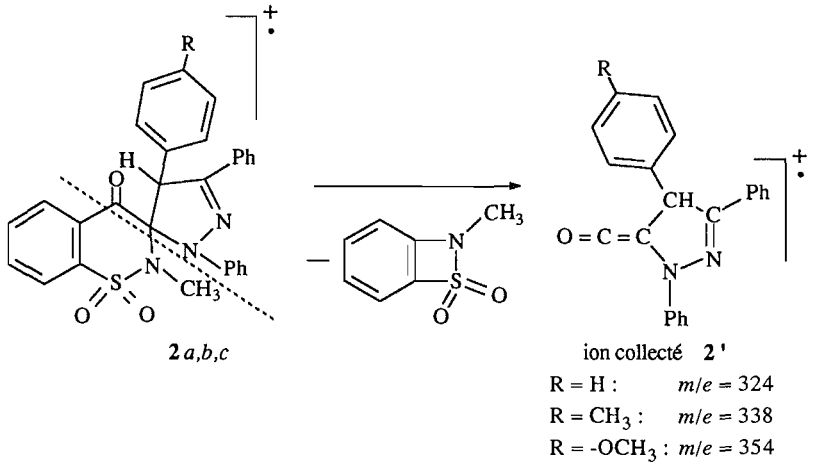

FIG. 2

Analyses spectroscopiques des produits 3

Compte tenu des observations faites pour des cycloadditions réalisées avec des produits comparables à **1** (6–11), il serait plausible de penser que les produits **3** pourraient être les régioisomères de **2** c'est-à-dire des dérivés de la spiro (1,3,5-triaryl-Δ-2-pyrazoline-4:2′-benzothiazine-1′-one).

Les données spectroscopiques ne permettent pas de retenir cette hypothèse. En effet, l'absence en rmn ^{13}C du signal vers 80 ppm pour le carbone de jonction spirannique tendrait à prouver que le produit **3** n'est pas le régioisomère de **2** mais peut être un produit d'évolution. On observe d'autre part en ir deux bandes d'absorption entre 1610 et 1660 cm^{-1} attribuables respectivement aux groupements C=C et C=O d'une fonction amide. On remarque par ailleurs pour les produits **3** un signal à 66 ppm pour un carbone tertiaire au lieu de 58 ppm dans le cas des composés **2**. Cette valeur de 66 ppm suggère une liaison entre l'atome de carbone tertiaire et un atome d'azote. L'existence d'un signal à 173 ppm est plutôt en faveur d'une fonction amide dans les composés **3** (au lieu de 190 ppm pour la fonction cétone des composés **2**). En spectrométrie de masse, on note une perte de 105 unités de masse caractéristique de l'ion benzoyle Ph-C≡O$^+$.

Une étude radiocristallographique (12) de **3***c* nous a permis d'accéder à la structure des composés **3** (figure 3). L'examen de cette structure démontre que la cycloaddition de la diphénylnitrilimine sur les dipolarophiles **1** s'effectue compétitivement sur la double liaison C=O et sur la double liaison C=C juxtacyclique. L'intermédiaire **A** obtenu lors de la réaction de la diphénylnitrilimine sur le site dipolarophilique C=O subit ensuite un réarrangement conduisant aux dérivés **3** (figure 4).

Pour confirmer cette hypothèse, nous avons effectué la cycloaddition d'une diarylnitrilimine sur un dipolarophile de même type que **1** mais ne comportant que le site dipolarophilique C=O (composé **4**) (figure 5). Nous avons pu ainsi observer une cycloaddition suivie d'un réarrangement conduisant au composé **5** (figure 5). Nous confirmons par la même

Can. J. Chem. Downloaded from www.nrcresearchpress.com by EESC ESCOLA DE ENGENHARIA on 09/08/12
For personal use only.

Can. J. Chem. Downloaded from www.nrcresearchpress.com by EESC ESCOLA DE ENGENHARIA on 09/08/12
For personal use only.

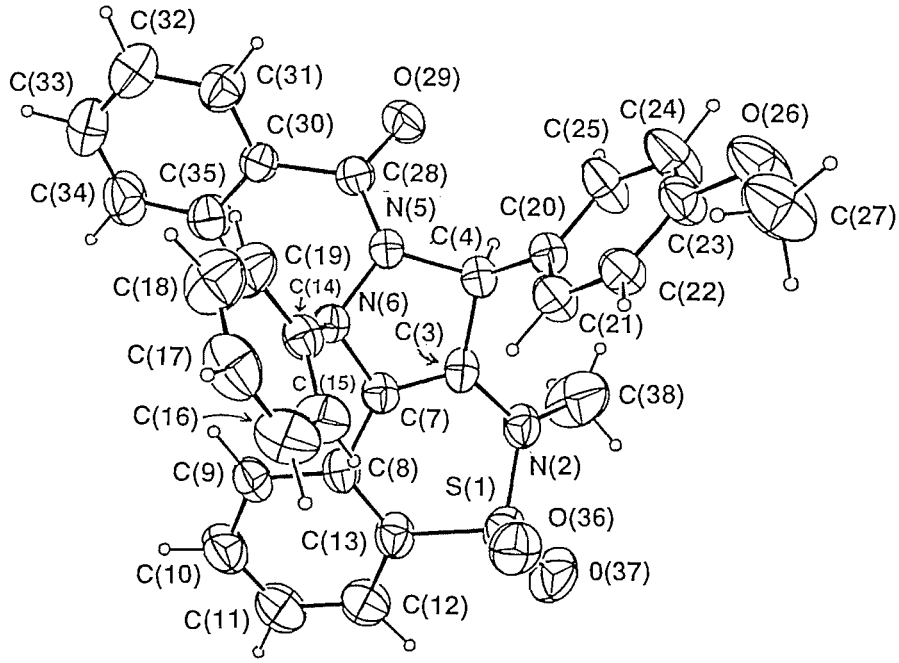

FIG. 3

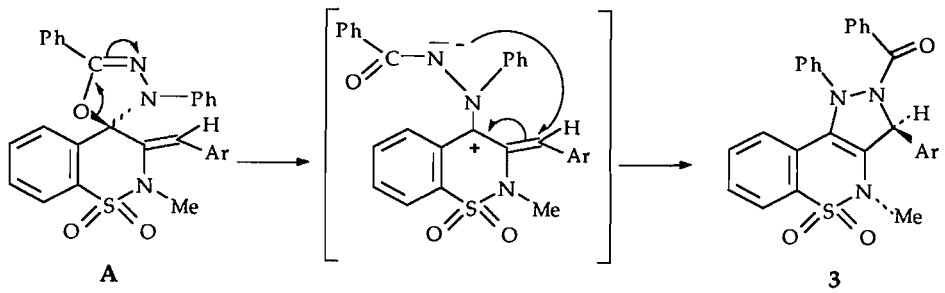

FIG. 4

occasion une compétition des deux sites dipolarophiliques des composés **1** au cours de la réaction de cycloaddition dipolaire.

La comparaison de l'aptitude réactionnelle des deux sites dipolarophiliques des composés **1** vis-à-vis des diarylnitrilimines avec celle conduisant à l'unique cycloadduit lors de la cycloaddition des mêmes dipôles sur les dérivés des arylidènetétraline-1-ones, chroman-4-ones, thiochroman-4-ones, isochroman-4-ones et isothiochroman-4-ones citées en introduction (5) nous permet de dire que le groupement SO_2 des dipolarophiles **1** active la fonction carbonyle. Par ailleurs, il n'y aurait pas d'activation par le groupement donneur $-NCH_3$ en position 3. Ceci est confirmé par les résultats obtenus avec les arylidèneisochroman-4-ones et isothiochroman-4-ones qui possèdent un groupement donneur en position 3 et qui ne présentent pas d'activité dipolarophilique au niveau du groupement carbonyle.

Étude du comportement des cycloadduits 2*a* et 2*b* en milieu acide

Les observations qui suivent se limitent au traitement acide des cycloadduits **2***a* et **2***b* car les transformations des autres produits **2***c* et **3***a*, *b*, *c* se sont révélées hasardeuses par suite de la formation de mélanges difficilement séparables.

Dans les deux cas, l'attaque par un acide fort (acide trifluoro-

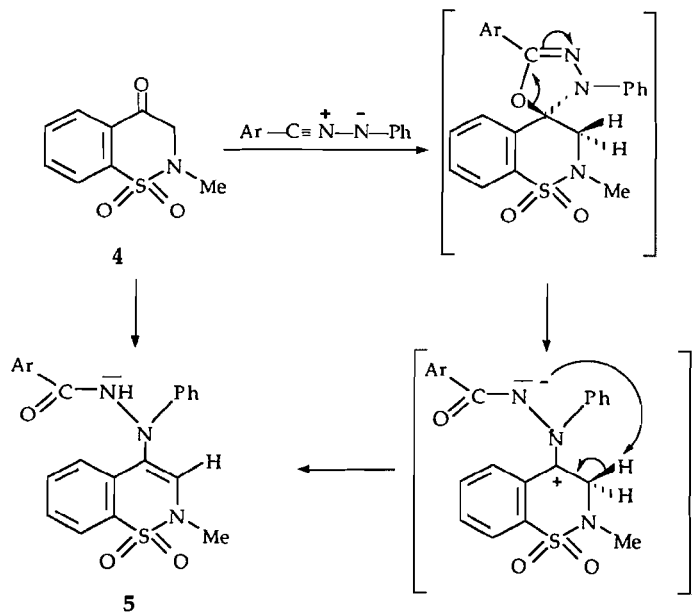

FIG. 5

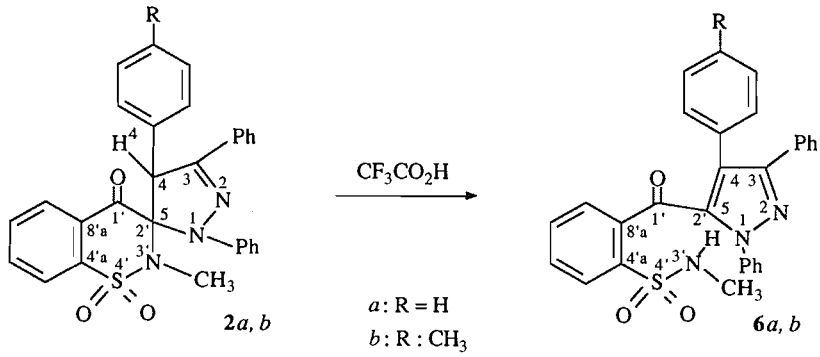

FIG. 6

acétique) aboutit à un sulfonamide **6** résultant de l'ouverture du cycle intermédiaire à la jonction spirannique entre l'atome de carbone C-5:2′ et l'atome d'azote en position 3′ (figure 6). En infrarouge, les composés **6** présentent une bande d'absorption à 1660 cm^{-1} caractéristique d'une fonction cétone fortement conjuguée. En rmn ^1H, on observe un signal fortement déblindé à 15,1 ppm attribuable au proton porté par l'atome d'azote du groupe sulfonamide. Le groupement méthyle porté par ce même atome d'azote apparaît sous la forme d'un doublet vers 3,1 ppm. La disparition du signal singulet à 15,1 ppm par addition de D_2O prouve qu'il s'agit d'un proton mobile. L'irradiation de ce proton simplifie le signal du -NCH_3 en singulet : ce proton et le groupe méthyle sont couplés entre eux et donc portés par l'atome d'azote en position 3′. En rmn ^{13}C, l'absence des signaux correspondant au carbone quaternaire de jonction spirannique et au carbone tertiaire C-4 confirme bien la structure **6**.

Conclusion

La cycloaddition de la diphénylnitrilimine sur des arylidènebenzothiazinonedioxydes a été étudiée. L'obtention de deux produits n'est pas à relier aux problèmes habituels de régio- ou de diastéréochimie. Elle résulte de la compétition entre les deux sites dipolarophiliques, la double liaison C=C arylidènique et le carbonyl cétonique. Dans le premier cas une pyrazoline est isolée et caractérisée. Dans le second cas, l'adduit subit un réarrangement inattendu conduisant à un produit d'évolution caractérisé sur la base des données spectroscopiques et d'une analyse radiocristallographique.

Partie expérimentale

Les points de fusion déterminés sur banc Kofler ne sont pas corrigés. Les spectres d'absorption ir ont été obtenus avec un spectrophotomètre Beckman IR 33, les produits étant pastillés dans KBr. Les spectres de rmn ont été obtenus avec un spectromètre Bruker Spectrospin AC 200 (200 MHz pour le proton et 50 MHz pour le ^{13}C), les échantillons étant dissous dans $CDCl_3$ (sauf indication contraire) avec le tétraméthylsilane comme référence interne. Les spectres de masse ont été enregistrés sur un spectromètre Hewlett-Packard MS Engine sous impact électronique (70 eV). Les ions moléculaires sont confirmés par l'observation de $(M + 1)^{+\cdot}$ en mode d'ionisation chimique avec le méthane comme gaz réactant. Les microanalyses ont été assurées par le Service d'Analyses du CNRS à Vernaison.

Les précurseurs de la diphénylnitrilimine et des diarylnitrilimines sont préparés selon la méthode de Huisgen et al. (13).

3-Arylidène-2H-1,2-benzothiazine-4(3H)-one-1,1-dioxydes ***1***

Ces produits ont été préparés suivant les modes opératoires décrits par Zinnes et al. (14). Les produits **1** sont cristallisés dans l'acétonitrile et chacun d'eux est décrit ci-après.

3-Benzylidène-2H-1,2-benzothiazine-4(3H)-one-1,1-dioxyde (***1***a). Rdt. 77%, *F* 163°C; ir, ν_{max} : 1670 (cétone); rmn ^1H, δ : 3,00 (s, 3H, N-CH_3), 7,50–8,20 (m, 10H).

3-p-Méthylbenzylidène-2H-1,2-benzothiazine-4(3H)-one-1,1-dioxyde (***1***b). Rdt. 76%, *F* 194°C; ir, ν_{max} : 1660 (cétone); rmn ^1H, δ : 2,40 (s, 3H, -CH_3), 3,00 (s, 3H, -N-CH_3), 7,30–8,20 (m, 9H).

3-p-Méthoxybenzylidène-2H-1,2-benzothiazine-4(3H)-one-1,1-dioxyde (***1***c). Rdt. 76%, F 171°C; ir, ν_{max} : 1665 (cétone); rmn ^1H, δ : 3,00 (s, 3H, -N-CH_3), 3,90 (s, 3H, -OCH_3), 7,00–8,20 (m, 9H).

Réactions de cycloadditions

Dans un Erlenmeyer bicol de 100 mL, on introduit 10 mmol du dipolarophile **1** et 10 mmol de l'α-chlorobenzylidènephénylhydrazone précurseur du dipôle dans 30 mL de benzène anhydre. On chauffe ce mélange à reflux sous agitation magnétique en additionnant en 15 min 2 mL de triéthylamine. Le reflux est maintenu durant 12 h. Après retour à la température ordinaire, on ajoute 20 mL de benzène, filtre le chlorhydrate de triéthylamine et élimine le solvant à l'évaporateur rotatif. Le résidu est séparé par chromatographie en phase liquide avec le chloroforme comme éluant sur la silice comme phase stationnaire. Les cycloadduits **2** et **3** ainsi séparés sont recristallisés dans l'éthanol.

*Spiro(1,3,4-triphényl-*Δ*-2-pyrazoline-5;2′-benzothiazine-1′-one)* (**2**a). Rdt. 25%, *F* 212°C; ir, ν_{max} : 1700 (cétone); rmn ^1H, δ : 2,60 (s, 3H, -NCH_3), 5,50 (s, 1H, H-4), 6,80–7,80 (m, 19H); rmn ^{13}C, δ : 31,40 (NCH_3), 59,00 (C-4), 94,70 (C-5;2′), 120,00–145,00 (C arom.), 155,20 (C-3), 190,00 (C-1′); sm *m/e* : $M^{+\cdot}$ 493 (7,9%), 388 (2%), 324 (36%), 296 (3%), 221 (3%), 195 (7,9%), 178 (14%), 104 (15,8%), 69 (100%). Anal. calc. pour $C_{29}H_{23}N_3O_3S$: C 70,55, H 4,69, N 8,51, S 6,50; tr. : C 70,67, H 4,51, N 8,42, S 6,61.

*Spiro(1,3-diphényl-4-*p*-tolyl-*Δ*-2-pyrazoline-5;2′-benzothiazine-1′-one)* (**2**b). Rdt. 30%, *F* 242°C; ir, ν_{max} : 1700 (cétone); rmn ^1H, δ : 2,35 (s, 3H, CH_3), 2,65 (s, 3H, -NCH_3), 5,45 (s, 1H, H-4), 6,75–7,80 (m, 18H); rmn ^{13}C, δ : 21,00 (CH_3), 31,50 (-NCH_3), 58,80 (C-4), 94,60 (C-5;2′), 121,00–144,50 (C arom.), 155,10 (C-3), 189,90 (C-1′); sm *m/e* : $M^{+\cdot}$ 507 (4%), 338 (23%), 310 (3%), 235 (2%), 207 (6,25%), 104 (13,8%), 69 (100%). Anal. calc. pour $C_{30}H_{25}N_3O_3S$: C 70,96, H 4,96, N 8,28, S 6,32; tr. : C 70,85, H 5,01, N 8,39, S 6,19.

*Spiro(1,3-diphényl-4-*p*-anisyl-*Δ*-2-pyrazoline-4;2′-benzothiazine-1′-one)* (**2**c). Rdt. 42%, *F* 238°C; ir, ν_{max} : 1700 (cétone); rmn ^1H, δ : 2,65 (s, 3H, -NCH_3), 3,80 (s, 3H, -OCH_3), 5,45 (s, 1H, H-4), 6,70–7,80 (m, 18H); rmn ^{13}C, δ : 31,40 (-NCH_3), 55,10 (-OCH_3), 58,60 (C-4), 94,50 (C-5;2′), 120,50–145,30 (C. arom.), 155,30 (C-3), 190,00 (C-1′); sm *m/e* : $M^{+\cdot}$ 523 (10%), 418 (2%), 388 (6%), 354 (44%), 250 (4,6%), 208 (14,5%), 149 (17,8%), 77 (90%), 69 (100%). Anal. calc. pour $C_{30}H_{25}N_3O_4S$: C 68,79, H 4,81, N 8,03, S 6,12; tr. : C 69,01, H 4,75, N 8,25, S 6,33.

1,3-Diphényl-2-benzoyl-2,3-dihydro(4H)pyrazolo[4,5-c]benzothiazine-5,5-dioxyde (***3***a). Rdt. 35%, *F* 228°C; ir, ν_{max} : 1625 (C=C), 1660 (C=O amide); rmn ^1H, δ : 3,20 (s, 3H, -NCH_3), 6,40 (s, 1H, H-3), 6,70–8,00 (m, 19H); rmn ^{13}C, δ : 33,00 (N-CH_3), 66,50 (C-3), 119,50–149,50 (C arom.), 173,00 (C amide); sm *m/e* : $M^{+\cdot}$ 493 (9,2%), 388 (15,8%), 352 (2,6%), 324 (4%), 219 (13%), 193 (19,8%), 105 (55,3%),

Can. J. Chem. Downloaded from www.nrcresearchpress.com by EESC ESCOLA DE ENGENHARIA on 09/08/12
For personal use only.

77 (100%). Anal. calc. pour $C_{29}H_{23}N_3O_3S$: C 70,55, H 4,69, N 8,51, S 6,50; tr. : C 70,65, H 4,71, N 8,52, S 6,55.

*1-Phényl-2-benzoyl-3-*p*-tolyl-2,3-dihydro(4*H*)pyrazolo[4,5-c]-benzothiazine-5,5-dioxyde (**3**b).* Rdt. 39%, *F* 230°C; ir, ν_{max} : 1625 (C═C), 1660 (C═O amide); rmn ^{1}H, δ : 2,25 (s, 3H, -CH_3), 3,25 (s, 3H, NCH_3), 6,40 (s, 1H, H-3), 6,80–8,00 (m, 18H); rmn ^{13}C, δ : 21,00 (CH_3), 32,90 (-N-CH_3), 66,20 (C-3), 120,00–149,40 (C arom.), 172,50 (C amide); sm *m/e* : $M^{+\cdot}$ 507 (7,2%), 442 (3%), 402 (14%), 338 (4,2%), 323 (3%), 219 (10%), 207 (14,8%), 105 (44%), 109 (100%). Anal. calc. pour $C_{30}H_{25}N_3O_3S$: C 70,96, H 4,96, N 8,28, S 6,32; tr. : C 71,15, H 5,17, N 8,12, S 6,41.

*1-Phényl-2-benzoyl-3-*p*-anisyl-2,3-dihydro(4*H*)pyrazolo[4,5-c]ben zothiazine-5,5-dioxyde (**3**c).* Rdt. 23%, *F* 215°C; ir, ν_{max} : 1610 (C═C), 1635 (C═O amide); rmn ^{1}H, δ : 3,20 (s, 3H, -NCH_3), 3,70 (s, 3H, OCH_3), 6,40 (s, 1H, H-3), 6,70–8,00 (m, 18H); rmn ^{13}C, δ : 32,90 (-NCH_3), 55,00 (-OCH_3), 66,20 (C-3), 120,10–149,30 (C arom.), 172,60 (C amide); sm *m/e* : $M^{+\cdot}$ 523 (6%), 458 (2%), 418 (14,1%), 354 (3,2%), 285 (2%), 219 (9,2%), 169 (10,5%), 105 (38,8%), 69 (100%). Anal. calc. pour $C_{30}H_{25}N_3O_4S$: C 68,79, H 4,81, N 8,03, S 6,12; tr. : C 68,97, H 4,64, N 8,12, S 6,25.

*Traitement acide des cycloadduits **2**a, **2**b*

Dans un ballon de 50 mL, on introduit 1,5 mmol de cycloadduits **2** et 20 mL d'acide trifluoracétique. La solution obtenue est chauffée à 50°C pendant 1 h puis versée dans un mélange eau-glace. On extrait ensuite au chloroforme, lave avec une solution d'hydrogénocarbonate de sodium puis à l'eau. Le séchage sur sulfate de sodium suivi de l'évaporation du solvant conduit à un résidu qui sera cristallisé dans l'éthanol. On obtient ainsi les dérivés du 1,3-diphényl-4- aryl-5- (2-*N*-méthylsulfonylbenzoyl)-pyrazole (composés **6**).

*1,3,4-Triphényl-5-(2-*N*-méthylsulfonylbenzoyl)-pyrazole (**6**a).* Rdt. 38%, *F* > 250°C; ir, ν_{max} : 1665 (cétone); rmn ^{1}H, δ : 3,11 (d, 3H, -NCH_3, $^3J_{NH-CH_3}$ = 4,88 Hz), 7,10–8,20 (m, 19H), 15,20 (s élargi, 1H, NH); rmn ^{13}C, δ : 37,60 (-NCH_3), 123,70–151,20 (C arom.), 169,20 (C═O). Anal. calc. pour $C_{29}H_{23}N_3O_3S$: C 70,55, H 4,69, N 8,51, S 6,50; tr. : C 70,69, H 4,72, N 8,55, S 6,63.

*1,3-Diphényl-4-*p*-tolyl-5-(2-*N*-méthylsulfonylbenzoyl)-pyrazole (**6**b).* Rdt. 36%, *F* > 250°C; ir, ν_{max} : 1660 (cétone); rmn ^{1}H, δ : 2,38 (s, 3H, CH_3), 3,12 (d, 3H, -NCH_3, $^3J_{NH-CH_3}$ = 4,97 Hz), 7,00–8,25 (m, 18H), 15,10 (s élargi, 1H, NH); rmn ^{13}C, δ : 21,20 (CH_3), 37,60 (-NCH_3), 123,50–152,10 (C arom.), 169,51 (C═O). Anal. calc. pour $C_{30}H_{25}N_3O_3S$: C 70,96, H 4,96, N 8,28, S 6,32; tr. : C 71,19, H 5,10, N 8,15, S 6,39.

*2-Méthyl-2H-1,2-benzothiazine-4-(3H)-one-1,1-dioxyde (**4**)*

Ce produit est préparé suivant le mode opératoire décrit par P. Dalla Croce et al. (4). Rdt. 87%, *F* 107°C; ir, ν_{max} : 1695 (cétone); rmn ^{1}H, δ : 2,95 (s, 3H, N-CH_3), 4,40 (s, 2H, CH_2), 7,83–8,20 (m, 4H); rmn ^{13}C, δ : 38,25 (-NCH_3), 60,75 (CH_2), 189,71 (C═O).

*4-(N-Phényl-*N*-p-méthylbenzamido)-2-méthyl-2H-1,2-benzo-thiazine-1,1-dioxyde (**5**)*

La réaction du dipolarophile **4** avec la *C-para-* anisyl- *N-* phénylnitrilimine est effectuée suivant le mode opératoire général des réactions de cycloadditions. Rdt. 66%, *F* 248°C; ir, ν_{max} : 1610 (C═C), 1652 (C═O amide); rmn ^{1}H, δ : 2,38 (s, 3H, CH_3), 3,26 (s, 3H, N-CH_3), 6,70–8,00 (m, 14H), 8,63 (s, 1H, N-H); rmn ^{13}C, δ : 21,37 (CH_3), 34,25 (N-CH_3), 113,30–146,97 (C arom.), 166,96 (C═O). Anal. calc. pour $C_{23}H_{21}N_3O_3S$: C 65,83, H 5,04, N 10,02, S 7,64; tr. : C 65,93, H 5,11, N 9,95, S 7,71.

1. J. Lombardino, E. Wiseman et W. Mc Lamore. J. Med. Chem. **14**, 1171 (1971).
2. R. Abramovitch, K. More, I. Shinkai et P. Srinivasan. J. Chem. Soc. Chem. Commun. 771 (1976).
3. P. Dalla Croce, D. Del Monaco et C. La Rosa. J. Chem. Soc. Perkin Trans. 1, 299 (1986).
4. P. Dalla Croce et R. Ferraccioli. J. Heterocycl. Chem. **27**, 427 (1990).
5. A. Kerbal, K. Tshiamala, J. Vebrel, B. Laude et M.F. Mercier. Bull. Soc. Chim. Belg. **100**, 159 (1991); A. Kerbal. Thèse Doctorat Sciences Physiques, Université de Besançon, 1988.
6. S. Kitane, K. Tshiamala, B. Laude, J. Vebrel et E. Cerutti. Tetrahedron, **41**, 3737 (1985).
7. S. Kitane, K. Sebban, J. Vebrel et B. Laude. Bull. Soc. Chim. Belg. **98**, 105 (1989).
8. K. Tshiamala, A. Kerbal, J. Vebrel et B. Laude. J. Chem. Res. (S), 106 (1988).
9. T. Fathi, Nguyen Dinh An, G. Schmitt, E. Cerutti et B. Laude. Tetrahedron, **44**, 4527 (1988).
10. K. Moustaid, Nguyen Dinh An, J. Vebrel, B. Laude, B. Daou et M. Soufiaoui. C.R. Acad. Sci. Paris, Ser. 2, **312**, 1129 (1991).
11. K. Moustaid, Nguyen Dinh An, B. Laude, M.F. Mercier et A. Sedqui. Can. J. Chem. **70**, 802 (1992).
12. F. Théobald, N. Rodier, C. Aubry, K. Ciamala et Nguyen Dinh An. Acta Crystallogr. Sous presse.
13. R. Huisgen, M. Seidel, G. Wallbillich et H. Knupfer. Tetrahedron, **17**, 3 (1962).
14. H. Zinnes, R. Cosnes et J. Shavel, Jr. J. Org. Chem. **29**, 2068 (1964), **30**, 2241 (1965); **31**, 162 (1966).

Can. J. Chem. Downloaded from www.nrcresearchpress.com by EESC ESCOLA DE ENGENHARIA on 09/08/12
For personal use only.

Asymmetric synthesis using reactions with modest group selectivity

DALE E. WARD,[1] YADONG LIU, AND CHUNG K. RHEE
Department of Chemistry, University of Saskatchewan, SK S7N 0W0, Canada
Received October 5, 1993

DALE E. WARD, YADONG LIU, and CHUNG K. RHEE. Can. J. Chem. **72**, 1429 (1994).

The isomeric purity of products from certain group-selective reactions can be significantly amplified when reactions can occur sequentially. The theoretical basis for a strategy that exploits reactions with modest enantiotopic group selectivity for asymmetric synthesis is described. The relationships between conversion, yield, and isomeric purity for such a process are calculated using a simple kinetic model. A simple method for selecting candidate group-selective reactions from known face-selective reactions is presented. Application of the strategy is illustrated with the reduction of D-glucose and D-galactose derived dialdehydes with *B*-isopinocampheyl-9-borabicyclo[3.3.1]nonane (Alpine-Borane®).

DALE E. WARD, YADONG LIU et CHUNG K. RHEE. Can. J. Chem. **72**, 1429 (1994).

On peut grandement améliorer la pureté isomérique des produits de certaines réactions sélectives pour des groupes si l'on effectue ces réactions d'une façon séquentielle. On décrit les bases théoriques d'une stratégie qui exploite des réactions possédant de modestes sélectivités énantiotopiques pour des groupes à des fins de synthèses asymétriques. Faisant appel à un modèle cinétique simple, on peut calculer facilement les relations entre la conversion, le rendement et la pureté isomérique de tels processus. On présente une méthode simple permettant de choisir les réactions plausibles pour leur sélectivité pour des groupes à partir de réactions connues pour leur sélectivité pour les faces. On illustre l'application de la stratégie à la réduction des dialdéhydes dérivés du D-glucose et du D-galactose par le *B*-isopinocamphéyl-9-borabicyclo[3.3.1]nonane (Alpine-Borane®).

[Traduit par la Rédaction]

Introduction

The development of methods for the synthesis of enantiomerically pure compounds has attracted considerable attention from synthetic organic chemists in recent years (1–3). In particular, significant advances have been achieved in the enantioselective conversion of achiral substrates into chiral products (1–3). Such transformations require a process where enantiotopic (4) faces or groups in the substrate are differentiated (5). This type of differentiation is possible since enantiotopic relationships become diastereotopic in the dissymmetric environment provided by a chiral reagent, auxiliary, solvent, additive, or catalyst (including enzymes (6) and abzymes (7)). While many methods that achieve high levels of enantiotopic face selectivity have been developed (1–3), nonenzymatic[2] examples of efficient enantiotopic group selectivity are less common (8).

An interesting feature of certain processes where enantiotopic groups can react sequentially is the coupling of an asymmetric synthesis with a kinetic resolution (9) to produce products with enhanced levels of enantiomeric purity.[3] Sih and co-workers (10*a*, *b*) explicitly demonstrated the viability of this approach in the enzyme-catalyzed hydrolysis of *meso* diacetates. Bosnich and co-workers (11) pointed out that enhanced enantiomeric purity by kinetic resolution with be general for this class of enantiotopic group-selective reactions. The synthetic potential of this type of process was brilliantly exploited by Schreiber et al. (12) who used the Sharpless epoxidation reaction to effect terminus differentiation after two-directional chain synthesis. While other nonenzymatic examples have appeared (13), no general synthetic methods that are designed to take advantage of the enhanced stereoselectivity from these reactions have been reported. We became interested in exploring the potential of this type of process to enhance the enantiomeric purity of products from reactions with innately poor enantioselectivity. In this paper we describe the theoretical basis for such a strategy and demonstrate a simple application involving the group-selective reduction of dialdehydes (14).[4]

Background and theory

Strategies for differentiating between enantiotopic faces or groups are readily illustrated by the use of two-dimensionally chiral (3, 15) objects (Fig. 1).[5] The objects **A** and **T** represent an achiral substrate with a pair of enantiotopic "reaction sites" and an achiral reagent with a single "reaction site," respectively. Interaction of **A** with **T** can occur in two different ways. Since these interactions (i.e., **p** and **q**) are enantiomorphic they should be isoenergetic and occur with equal probability. The interaction of **A** with **R**, representing a chiral reagent[6] with a

[1]Author to whom correspondence may be addressed. Telephone: (306) 966-4656. FAX: (306) 966-4730. Internet: wardd@sask.usask.ca.

[2]For reference to recent examples of enzymatic enantiotopic group selective reactions, see ref. 6*c*.

[3]Although not generally appreciated, analogous enhancement of selectivity will also occur with chemoselective reactions (or diastereotopic group-selective reactions (41*a*)) where the groups can react sequentially. Thus it is possible to obtain much higher levels of selectivity (albeit with lower yields) than would be indicated by the relative reactivity of the groups. For example, in the chemoselective reduction of a dione (e.g., 4-androsten- 3, 17-dione) the isomeric purity of the hydroxyketone fraction will increase with increasing coversion (cf. ref. 48).

[4]Preliminary results have been reported (14).

[5]In two dimensions, an object is chiral if it cannot be superimposed onto its mirror image by any in-plane translation and (or) rotation; otherwise the object is achiral. Molecules are depicted by objects with the edges representing "reaction sites". Interactions (i.e., transition states) between molecules (i.e., substrates and reagents) are indicated by the juxtaposing of objects with the appropriate edge-to-edge contact. For convenience, the object depicting the "reagent" represents the reagent and the environment (i.e., solvent, catalyst, additive, etc.); thus, if the environment is chiral, then the object that depicts the reagent is also chiral.

[6]This can be an achiral reagent in a chiral environment or a chiral reagent in an achiral or chiral environment (see footnote 7).

Can. J. Chem. Downloaded from www.nrcresearchpress.com by EESC ESCOLA DE ENGENHARIA on 09/08/12
For personal use only.

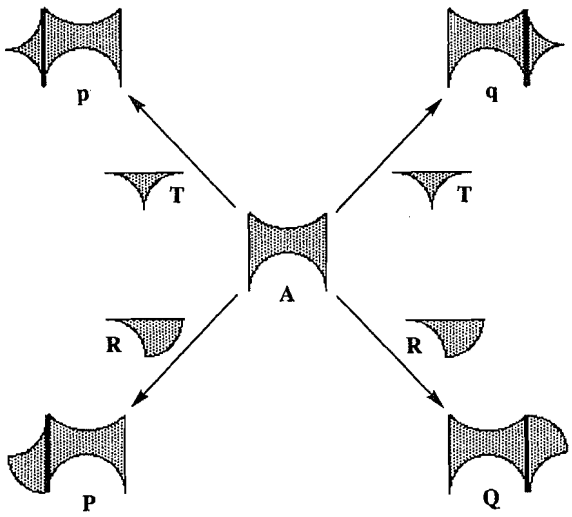

FIG. 1. Differentiation of enantiotopic faces or groups illustrated with two-dimensionally chiral objects.

single "reaction site," can also occur in two different ways. In this case, however, the interactions are heteromorphic (i.e., **P** and **Q**) and, in principle, will be of different energy and occur with unequal probability.[7]

A kinetically controlled reaction involving the differentiation of enantiotopic faces[8] or enantiotopic groups where sequential reaction is prevented[9] (e.g., eq. [1]) can be analyzed as a pair of mutually dependent parallel reactions (16). The ratio of products **P** and **Q** (i.e., the selectivity) is equal to the ratio of rate constants k_1 and k_2 at any point in the reaction.[10]

$$[1] \qquad \mathbf{P} \xleftarrow[\text{fast}]{k_1} \mathbf{A} + \mathbf{R} \xrightarrow[\text{slow}]{k_2} \mathbf{Q}$$

$$[2] \qquad \mathbf{P} + \mathbf{R} \xrightarrow[\text{slow}]{k_3} \mathbf{B} \xleftarrow[\text{fast}]{k_4} \mathbf{Q} + \mathbf{R}$$

The situation is fundamentally different when enantiotopic groups (or in certain cases[8] enantiotopic faces) can react sequentially (10–13). The initial products (**P** and **Q**) of the reaction of **A** with **R** still retain a "reaction site." Further reaction of **P** or **Q** with **R** produces **B**[11] in a pair of independent parallel reactions (16) (eq. [2]). In a process represented by eqs. [1] and [2], the ratio of **P** and **Q** (i.e., the selectivity) will be dependent on conversion and in favorable circumstances can become arbitrarily high. To determine the nature of the relationship between selectivity and conversion, expressions for the concentrations of **P** and **Q** as a function of the concentration of **A** are derived[12] (eqs. [3] and [4]).

Assuming: $[\mathbf{R}]_{\text{init}} \geq 2[\mathbf{A}]_{\text{init}}$; $[\mathbf{P}]_{\text{init}} = [\mathbf{Q}]_{\text{init}} = 0$

$$[3] \qquad [\mathbf{P}] = \frac{k_1[\mathbf{A}]_{\text{init}}}{k_1 + k_2 - k_3}\left[\left(\frac{[\mathbf{A}]}{[\mathbf{A}]_{\text{init}}}\right)^{\frac{k_3}{k_1+k_2}} - \frac{[\mathbf{A}]}{[\mathbf{A}]_{\text{init}}}\right]$$

$$[4] \qquad [\mathbf{Q}] = \frac{k_2[\mathbf{A}]_{\text{init}}}{k_1 + k_2 - k_4}\left[\left(\frac{[\mathbf{A}]}{[\mathbf{A}]_{\text{init}}}\right)^{\frac{k_4}{k_1+k_2}} - \frac{[\mathbf{A}]}{[\mathbf{A}]_{\text{init}}}\right]$$

The analysis is simplified by assuming that the reactivity of a particular group is independent of the state of the other group (i.e., $k_1 = k_4$ and $k_2 = k_3$).[13] Under this assumption, the ratio of **P** and **Q** as a function of the concentration of **A** is expressed by eq. [5]. Inspection of eq. [5] reveals that during the early part of the process (i.e., as $[\mathbf{A}]/[\mathbf{A}]_{\text{init}} \rightarrow 1$) the ratio of the initial products is approximately equal to the ratio of rate constants (i.e., $[\mathbf{P}]/[\mathbf{Q}] \rightarrow k_1/k_2$); however, at high conversion (i.e., as $[\mathbf{A}]/[\mathbf{A}]_{\text{init}} \rightarrow 0$) the ratio of these products becomes arbitrarily large (i.e., $[\mathbf{P}]/[\mathbf{Q}] \rightarrow \infty$) if k_1 is greater than k_2.

Assuming: $k_1 = k_4$ and $k_2 = k_3$

$$[5] \qquad \frac{[\mathbf{P}]}{[\mathbf{Q}]} = \frac{\left(\frac{[\mathbf{A}]}{[\mathbf{A}]_{\text{init}}}\right)^{\frac{-k_1}{k_1+k_2}} - 1}{\left(\frac{[\mathbf{A}]}{[\mathbf{A}]_{\text{init}}}\right)^{\frac{-k_2}{k_1+k_2}} - 1}$$

Figure 2 illustrates the calculated[14] results for a hypothetical process where the enantiotopic group selectivity ($E = k_1/k_2$) is 3. The yield of the initial products (**P** + **Q**) rises to a maximum, then decreases towards 0, while the stereoisomer excess (se)[15] and the yield of **B** continue to increase towards 1. In principle, any high level of se can be reached with an appropriate sacrifice in yield.

In considering how this type of process might be exploited

[7]In reactions involving the differentiation of enantiotopic groups or faces, it is useful to distinguish between those that produce unequal amounts of enantiomers and those that produce unequal amounts of diastereomers. In general (but not always), the first case involves differentiation by an achiral reagent in a chiral environment (i.e., in the presence of a chiral ligand, catalyst, additive, solvent, etc.) while the second case involves differentiation by a chiral reagent in an achiral or chiral environment. Differentiation requires the intervention of a chiral "entity." In reactions involving a chiral reagent, it is also useful to distinguish the reagents produced by the temporary attachment of a chiral "auxiliary" to an otherwise achiral substance from the others. In this way, the chiral auxiliary can be thought of as a special type of chiral environment that interacts with an achiral reagent via covalent bonding rather than some weaker form of association.

[8]Reaction at one face of a trigonal atom prevents reaction at the other face. Sequential reaction can occur (10*c*) at both faces of a diagonal atom (4*b*).

[9]The majority of examples of enantiotopic group selectivity in ref. 8 do not involve sequential reaction of the groups.

[10]Assuming that the kinetic order with respect to both substrate and reagent is the same for both reactions.

[11]The assumption that both **P** and **Q** react to give the same product (i.e., **B**) is convenient but not necessary for the analysis.

[12]See experimental for details. For an analogous derivation see refs. 10*a*, *b*.

[13]This is reasonable if the groups are relatively remote. For a similar analysis based on this assumption see ref. 12*a*. For a related analysis without this restriction see refs. 10*a*, *b* and 11. For an indication of the sensitivity of the analysis to this assumption see Table 1.

[14]Calculated according to eqs. [3] and [4] assuming that $k_1 = k_4$ and $k_2 = k_3$; see experimental section for details.

[15]Stereoisomer excess (se) is expressed in a way which is equivalent to ee if **P** and **Q** are enantiomers, or to de if **P** and **Q** are diastereomers.

Can. J. Chem. Downloaded from www.nrcresearchpress.com by EESC ESCOLA DE ENGENHARIA on 09/08/12
For personal use only.

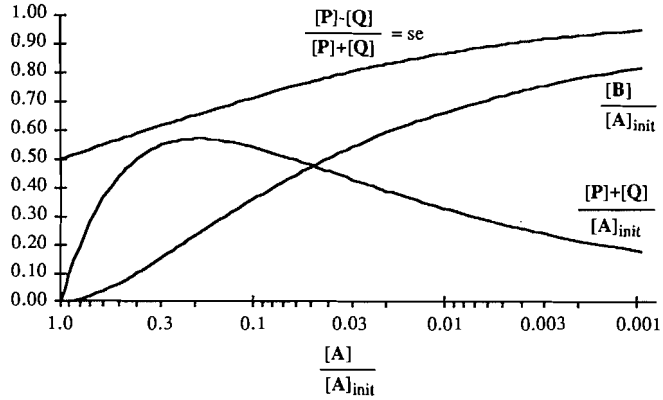

FIG. 2. Calculated evolution of stereoisomeric excess and mole fractions of products as a function of conversion for a group-selective process (i.e., eqs. [1] and [2]) assuming: $k_1 = k_4$; $k_2 = k_3$; $k_1/k_2 = 3$.

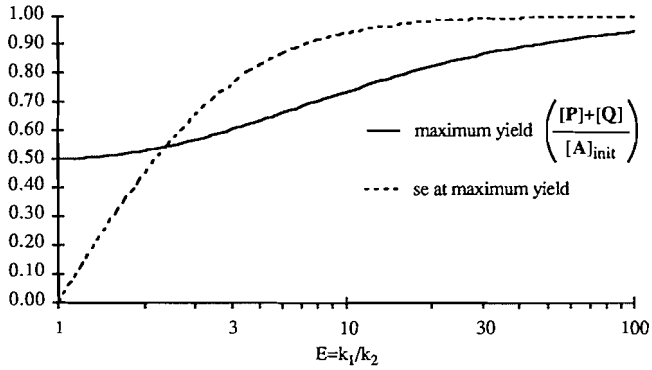

FIG. 3. Calculated maximum yield of initial products ($\mathbf{P} + \mathbf{Q}$) and stereoisomeric excess at the maximum yield as a function of the selectivity for a group-selective process (i.e., eqs. [1] and [2]) assuming: $k_1 = k_4$; $k_2 = k_3$.

in the preparation of enantiomerically pure compounds we were interested in the relationship between the group selectivity (E) of a reaction and the potential yield and stereoisomeric purity of the product. The maximum yield of the initial products ($\mathbf{P} + \mathbf{Q}$) and the se at the maximum yield as a function of the selectivity (E) were calculated.[14] The results are plotted in Fig. 3. Interestingly, the se rises much more sharply than does the maximum yield with increasing enantiotopic group selectivity. For example, it requires a calculated $E = 45$ to obtain a 90% yield of products (se = 99.6%); however, a process with $E = 7.1$ is predicted to give products with 90% se (yield = 69%).[14] Reactions (even enzyme-mediated ones (6)) with high enantiotopic group selectivity are extremely rare. However, processes with only modest selectivity can, in principle, be utilized to give modest yields of products with high se.

Figure 4 presents a plot of the maximum yield of initial products of a specific minimum se as a function of the selectivity.[14] Significantly, processes with selectivities of 3.2, 4.3, 5.3, and 6.6 are calculated to give a 50% yield of products with an se of 80%, 90%, 95%, and 98%, respectively.[16] The potential of this type of process to enhance the stereoisomeric purity of the products from reactions with innately poor selectivity is evident.[17]

[16]These cases approach the result from a hypothetical nonstereoselective reaction (100% yield) followed by separation of the stereoisomeric products. By contrast, these cases would require the separation of nonisomeric compounds (i.e., **P** and **B**).

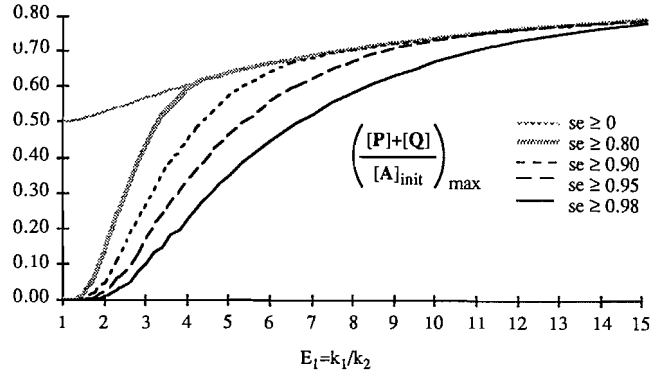

FIG. 4. Calculated maximum yield of initial products ($\mathbf{P} + \mathbf{Q}$) with a specified stereoisomeric excess as a function of the selectivity for a group-selective process (i.e., eqs. [1] and [2]) assuming: $k_1 = k_4$; $k_2 = k_3$.

To assess the sensitivity of the above conclusions to our simplifying assumptions (i.e., $k_1 = k_4$ and $k_2 = k_3$) we repeated the calculations according to eqs. [3] and [4] for various values of k_{1-4}. The enantiotopic group selectivity for the first reaction (k_1/k_2) was held constant while the selectivity (k_4/k_3) and the relative reactivity ($(k_1 + k_2)/(k_3 + k_4)$) for the "kinetic resolution" step were varied. The results are presented in Table 1. For a process with enantiotopic group selectivity of 5, variation in the relative reactivity ($(k_1 + k_2)/(k_3 + k_4)$) and (or) the relative selectivity ($(k_1/k_2)/(k_4/k_3)$) by a factor of 0.75–1.5 does not change the general prediction that obtention of a 50–60% yield of product with ≥90% se is possible. On the other hand, low selectivity ($k_4/k_3 < 2.5$) or high reactivity ($(k_1 + k_2)/(k_3 + k_4) < 0.25$) in the second (i.e., kinetic resolution) step reduces the potential yield of reasonably pure (se ≥90%) product to impractical levels (<40%).

Figure 5 shows the calculated[14] results for a hypothetical process ($E = 4.3$) indicating the possibility of obtaining a 50% yield of $\mathbf{P} + \mathbf{Q}$ with a se of 90%. This "optimal" result occurs when 2.5% of $[\mathbf{A}]_{init}$ remains. Importantly, at this point in the reaction, the yield of $\mathbf{P} + \mathbf{Q}$ is relatively insensitive to changes in the amount of remaining **A**. Thus, in practice, this point could be missed by as much as one half-life either way without seriously affecting the outcome.[18]

In principle, any reaction with an enantiotopic group selectivity of >4 might serve as the basis for a process that would provide a ≥50% yield of a product with ≥90% se. Candidate reactions can be evaluated if one knows or can estimate the relative reactivity of the two enantiomers of a chiral group with one enantiomer of a chiral reagent (or vice versa). There are numerous reports of diastereotopic face selectivity in reactions of chiral nonracemic (scalemic) (17) groups with

[17]If $k_3 = k_4 = 0$, reactions with $E = 6.6$, 5.3, 4.3, and 3.2 would produce products with se = 74%, 68%, 62%, and 54%, respectively. In general, this level of stereoselectivity is not synthetically useful.

[18]With 5% of $[\mathbf{A}]_{init}$ remaining, the calculated yield of $\mathbf{P} + \mathbf{Q}$ is 56% (se = 86%); with 1.25% of $[\mathbf{A}]_{init}$ remaining, the calculated yield is 44% (se = 93%). With initial conditions $[\mathbf{R}] = 3[\mathbf{A}]$ and $[\mathbf{P}] = [\mathbf{Q}] = 0$, if $[\mathbf{A}] = 0.025[\mathbf{A}]_{init}$ at $t = 10$ (arbitrary units) then $[\mathbf{A}] = 0.05[\mathbf{A}]_{init}$ at $t = 7.7$ and $[\mathbf{A}] = 0.0125[\mathbf{A}]_{init}$ at $t = 12.5$. Control of the reaction time to within one half-life ($t = 10 \pm 2.4$ in this case) should be straightforward.

Can. J. Chem. Downloaded from www.nrcresearchpress.com by EESC ESCOLA DE ENGENHARIA on 09/08/12
For personal use only.

Can. J. Chem. Downloaded from www.nrcresearchpress.com by EESC ESCOLA DE ENGENHARIA on 09/08/12
For personal use only.

TABLE 1. Sensitivity of simplified calculations to variations in selectivity and (or) reactivity

Entry	$\frac{k_1}{k_2}$	$\frac{k_4}{k_3}$	$\frac{k_1 + k_2}{k_3 + k_4}$	Maximum yield (% (**P** + **Q**))	% se at maximum yield	Maximum % (**P** + **Q**) with ≥90% se
1.	5.0	2.5	0.50	44	79	25
2.	5.0	2.5	0.75	52	78	29
3.	5.0	2.5	1.0	57	76	32
4.	5.0	2.5	1.5	64	75	36
5.	5.0	3.75	0.5	48	83	42
6.	5.0	3.75	0.75	56	82	47
7.	5.0	3.75	1.0	61	80	49
8.	5.0	3.75	1.5	67	78	51
9.	5.0	5.0	0.25	39	89	39
10.	5.0	5.0	0.50	52	86	50
11.	5.0	5.0	0.75	59	84	55
12.	5.0	5.0	1.0	64	83	58
13.	5.0	5.0	1.5	70	80	60
14.	5.0	7.5	0.50	56	90	56
15.	5.0	7.5	0.75	63	88	62
16.	5.0	7.5	1.0	67	86	66
17.	5.0	7.5	1.5	73	83	68
18.	3.75	5.0	0.75	57	79	48
19.	3.75	5.0	1.0	62	77	51
20.	3.75	5.0	1.5	68	74	52

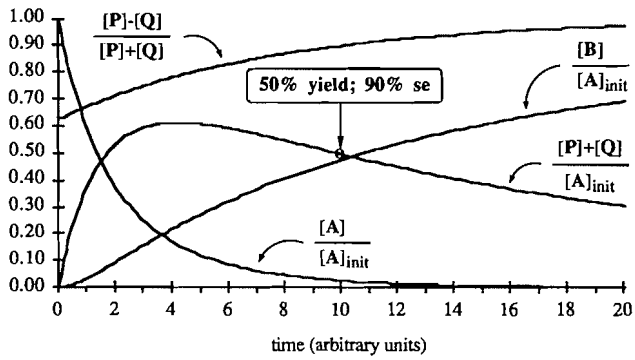

FIG. 5. Calculated evolution of stereoisomeric excess and mole fractions of components as a function of time for a group-selective process (i.e., eqs. [1] and [2]) assuming: $k_1 = k_4$; $k_2 = k_3$; $k_1/k_2 = 4.3$.

scalemic reagents (reagent and substrate selectivity or "double diastereoselectivity") (18). Unfortunately, although the diastereoselectivity for both the "matched" and "mismatched" cases is typically reported, the relative reactivity is usually not determined. The desired relative reactivity could be determined (19) from the diastereoselectivity observed in reactions of racemic groups with racemic reagents (mutual kinetic resolution) (9, 20); however, these data are rarely available (9).

Alternatively, the relative reactivity of enantiotopic groups containing diastereotopic faces towards addition of a chiral reagent can be crudely estimated from a knowledge of the individual substrate and reagent selectivities. There are numerous reports of enantiotopic face selectivity in reactions of achiral groups with chiral reagents (reagent selectivity, ***r***) and of diastereotopic face selectivity in reactions of chiral groups with achiral reagents (diastereoselectivity or substrate selectivity, ***s***) (1–3). The enantiotopic group selectivity (E) can be estimated from eq. [6] (20).[19]

$$[6] \qquad E = \frac{(r)(s) + 1}{r + s}$$

The value of E is limited by the lower of ***r*** and ***s***; high values of E require high values of both ***r*** and ***s***. Relatively few reactions[20] have been developed to date that might be predicted to have $E > 20$; however, several candidate reactions should be available with $E = 5$–10.[21,22]

The above analysis indicates how enantiotopic group-selective reactions can be identified and exploited in a strategy for asymmetric synthesis. Since processes with modest selectivity will produce only modest yields of products, we

[19]The face selectivity for one group will be (***r***)(***s***):1 (i.e., "matched"); total reactivity is (***r***):(***s***) + 1. The face selectivity for the enantiomeric group will be (***r***):(***s***) (i.e. "mismatched"); total reactivity is (***r***) + (***s***). The accuracy of this estimation depends on the suitability of the models used for the determination of ***r*** and ***s***. For a detailed discussion of the derivation, assumptions, and sources of error in the above multiplicitivity rule see ref. 18.

[20]For example, the Sharpless epoxidation reaction is the only generally used nonenzymatic method of kinetic resolution (9).

[21]Under ideal conditions, a reaction with $E = 20$ is calculated to give >80% yield of product with >98% se and according to eq. 6 would require $r,s \approx 40$. Similarly, a reaction with $E = 5$–10 would produce a 57–74% yield of product with >90% se and would require $r,s \approx 10$–20.

[22]For example, several examples of enantioselective addition of chiral nucleophiles (e.g., $LiAlH_4$ in the presence of a scalemic alcohol) to achiral carbonyl compounds together with corresponding examples of diastereoselective addition of related achiral nucleophiles (e.g., $LiAlH_4$) to related chiral carbonyl compounds with selectivities in the range of 10–20 are known (ref. 1, Vol. 2; ref. 3, Chap. 3).

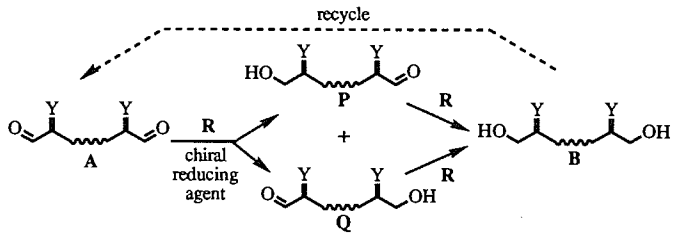

FIG. 6. Asymmetric synthesis by enantiotopic group selective reduction of *meso* dialdehydes.

focussed on the use of reactions that would allow for efficient recycling of the undesired product (**B**). The process might be further simplified if the candidate reaction did not create any new elements of stereogenicity. Therefore, as an initial test of the feasibility of the strategy (14) we decided to examine the reduction of *meso* dialdehydes with chiral reducing agents (see Fig. 6).[4] Our objective was to demonstrate that, since only modest group selectivity is required, processes that provide useful yields of products with useful levels of stereoisomeric purity can be simply and rationally designed.

Results and discussion

Dialdehydes derived from hexoses were chosen for initial study since: (*i*) they should be readily available in stereochemically pure form; (*ii*) the product hydroxyaldehydes are known hexoses; (*iii*) a variety of hexoses are available that can provide dials both with enantiotopic -CHO groups (i.e., from galactose or allose) or with diastereotopic -CHO groups in which the local symmetry is enantiotopic (i.e., from glucose). It was of interest to determine if such "pseudo-enantiotopic" -CHO groups could be differentiated in the same manner as enantiotopic -CHO groups (vide infra).

The first task was to identify possible reagents and reaction conditions to effect enantiotopic group-selective reduction of a hexose-derived *meso* dialdehyde. Group selectivity should result from the matching and mismatching of substrate diastereotopic face selectivity with reagent enantiotopic face selectivity (eq. [6]). Although few studies on the stereoselectivity of reduction of α-alkoxy aldehydes have appeared (21), the addition of various nucleophiles to these aldehydes proceeds with modest to excellent diastereotopic face selectivity (22). Both the magnitude and the sense (i.e., chelation or Cram–Felkin) of the selectivity are highly dependent on the nucleophile and the reaction conditions (22). Several chiral reagents for enantiotopic face-selective reduction of carbonyl groups (23), including aldehydes (24), have been developed in recent years. Three of the best reagents on the basis of selectivity, availability, and (or) ease of preparation are Corey's oxazaborolidine catalysts (25) used with diborane or catechol borane as the reducing agent; binaphthol-modified lithium aluminum hydride (BINAL-H) (26); and *B*-isopinocampheyl-9-borabicyclo[3.3.1]nonane (Alpine-Borane®) (27). All of these reagents can reduce acetophenone to give 1-phenylethanol with an ee of >95%. The enantiotopic group selectivity of these reagents towards the model compound (±)-2,3-dimethoxypropanal (**1**) was examined. The intention was to reduce excess racemic **1** under a variety of conditions and measure the enantiomeric purity of the product **2**. If the conversion of **1** into **2** was kept to less than 25%, then the ratio of the enantiomers of **2** would be a reasonable approximation[23] of the ratio of the rate constants for the reaction of the individual enantiomers of **1** with the reagent (i.e., the enantiotopic group selectivity). The ratio of the enantiomers of **2** could be determined by ^{13}C NMR[24] of the derived Mosher's esters **3** (28).

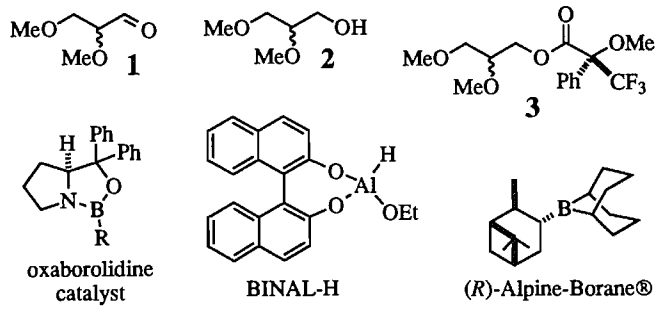

The oxazaborolidine catalysts (R = Me and R = Bu) were prepared from (*S*)-proline according to the reported procedure (29). Reduction of **1** with 0.25 equivalent of catechol borane in THF at −78°C in the presence of either of these catalysts (0.1–0.25 equiv.) gave, in each case, the alcohol **2** with an ee of less than 10%.[25] Similar results were obtained in reductions of **1** with BINAL-H (0.25 equiv.; prepared (27) from (+)-1,1′-bi-2-naphthol) in THF at −78°C.[25] Reduction of **1** with commercially available (*R*)-Alpine-Borane® (Aldrich; 0.5 M in THF; 0.25 equiv.)[25] in THF at −78°C gave the alcohol **2** as a 2.3:1 mixture of enantiomers.[26] A similar experiment conducted at −100°C produced **2** as a 4:1 ratio of enantiomers.

The initial plan was to subject *galacto*-2,3,4,5-tetramethoxyhexan-1,6-dial (**4**) to reduction by (*S*)- or (*R*)-Alpine-Borane® to produce a mixture of D- and L-2,3,4,5-tetra-*O*-methylgalactose (D-**5** and L-**5**, respectively) and 2,3,4,5-tetra-*O*-methylgalactitol (**6**) (see Scheme 1). Reaction conditions would be refined to maximize both the yield and the ratio of D-**5** and L-**5**. A method for determining the relative amounts of **4**, **5**, and **6** as well as the ratio of D-**5** and L-**5** in the reaction mixture was required. As a prelude to the development an analytical

[23]An accurate determination requires knowledge of the conversion since the ratio of enantiomers of both **1** and **2** changes with time (9). We were unable to efficiently recover **1** or monitor its disappearance at low temperature. At 20% conversion, this "initial rate" method underestimates the ratio of rate constants by 10–20% if the observed ratio of enantiomers is 2–10.

[24]Resonances in both the ^{19}H NMR and the ^{1}H NMR spectra of the mixture of esters **3** were too congested to allow quantitative determination of the ratio of diastereomers; in the ^{13}C NMR spectrum the signals due to C-1 in the diastereomeric esters were well separated (δ 64.7 and δ 65.2) and the ratio of diastereomers was determined by the ratio of the intensity of these signals.

[25]The quality of our reagent was checked by reduction of acetophenone according to the literature procedure to give 1-phenylethanol with an ee of >90%

[26]Although not established unequivocally, the major enantiomer should have the (*S*) configuration. Since (*R*)-Alpine-Borane® reduces carbonyl groups with *re* face selectivity (24*b*) and, assuming Cram–Felkin diastereoselectivity, addition of nucleophiles to the carbonyl in (*S*)-**1** should be *re* face selective (23), the reaction of (*R*)-Alpine-Borane® with (*S*)-**1** should represent the matched pair and thus the faster reaction. This assumption is consistent with the observation that reaction of **4** with (*R*)-Alpine-Borane® gives predominantly the D-galactose derivative D-**5** (vide infra).

Can. J. Chem. Downloaded from www.nrcresearchpress.com by EESC ESCOLA DE ENGENHARIA on 09/08/12
For personal use only.

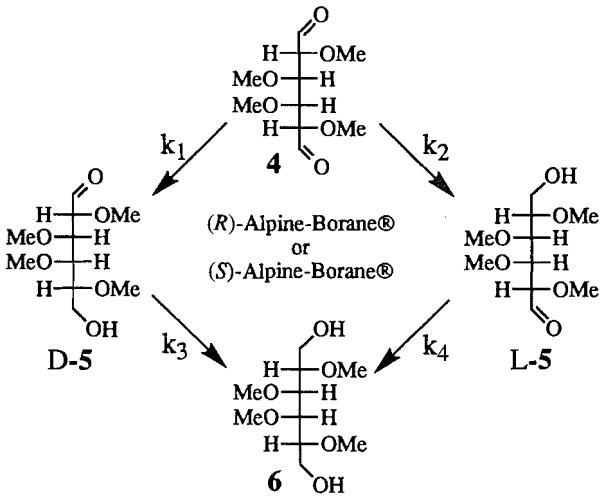

SCHEME 1

method, the independent synthesis of **4**, D-**5**, L-**5**, (±)-**5**, and **6**, was undertaken.

The diol **6** was readily prepared from galacitol in 67% yield via **7** and **8**. The diol **6** was oxidized under carefully controlled conditions using the Swern (30) protocol to give the crystalline dialdehyde **4**. The C_s symmetry of the structures of **4** and **6**–**8** was readily apparent from their ^1H and ^{13}C NMR spectra, which showed the expected simplicity. Partial hydrolysis of **8** gave (±)-**9**, which was oxidized (31) to the corresponding aldehyde (±)-**10** with tetrapropylammonium perruthenate (TPAP) and *N*-methylmorpholine *N*-oxide (NMO). Treatment of **10** with aqueous acid led to hydrolysis of the trityl group to give (±)-**5**. The ^1H NMR spectrum of **5** revealed it to be exclusively in the septanose (32) form as a 4:1 mixture of α and β anomers, as reported in the literature (33).

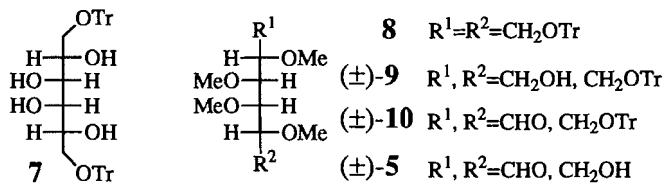

The preparation of D-**5** and L-**5** required a more circuitous route. The really available (34) 2,3,4-tri-*O*-methyl-D-galactose (**11**) was reduced (35) with sodium borohydride in ethanol to produce the known (36, 37) triol **12**. Treatment of a pyridine solution of **12** with trityl chloride (1.2 equiv.) in the presence of 4-(dimethylamino)pyridine (DMAP) gave a separable 2:1 mixture of trityldiols **13** and **14**, respectively, in 60% yield along with recovered **12** (20%). The structures of **13** and **14** were confirmed by conversion (Ac_2O, pyridine) to the corresponding diacetates **15** and **16**; the vicinal relationship between the C*H*-OAc and the CH_2-OAc protons in **16** was revealed by ^1H NMR through homonuclear decoupling experiments.

Reaction of **13** with TBDMSCl and imidazole selectively produced the primary silyl ether **17**, which was methylated (NaH, MeI) to give D-**18**. The silyl ether in D-**18** was selectively hydrolyzed by reaction with $HF_{(aq)}$ to give the alcohol D-**9** (64%) along with the diol **6** (33%). The preparation of D-**5** from D-**9** proceeded as described above for the racemic series. Alternatively, L-**18** was prepared by methylation of **19**, which was produced by reaction of **14** with TBDMSCl. Using the protocol established for the D series, L-**18** was converted into

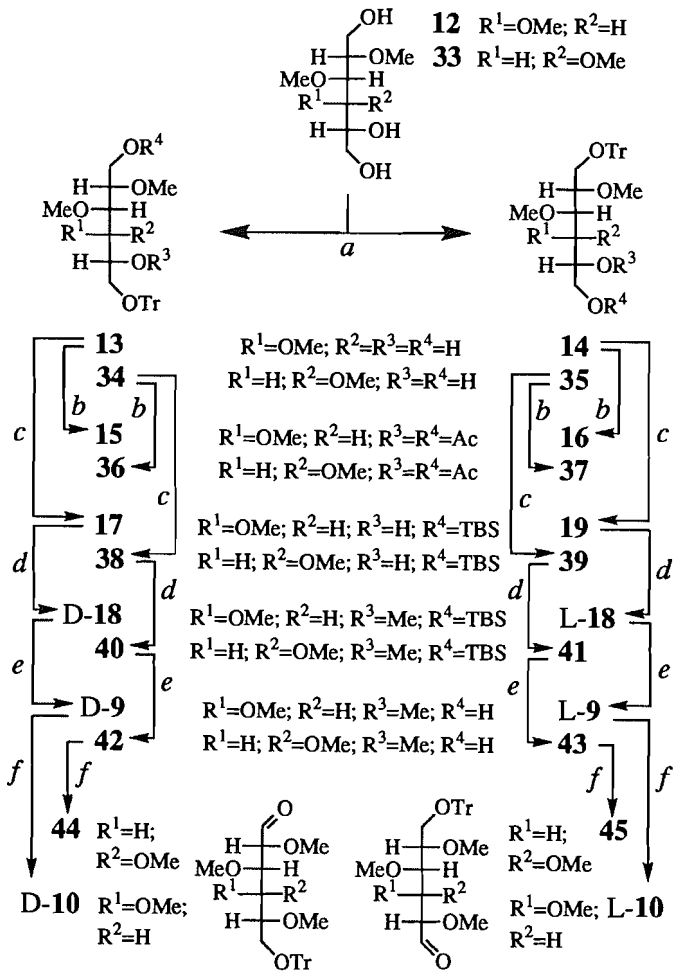

SCHEME 2. (*a*) TrCl, pyridine, DMAP. (*b*) Ac_2O, pyridine, CH_2Cl_2. (*c*) TBDMSCl, imidazole, CH_2Cl_2. (*d*) NaH, MeI, THF. (*e*) $HF_{(aq)}$, CH_3CN *or* Bu_4NF, THF. (*f*) TPAP, NMO, CH_2Cl_2.

L-**5**. As expected for compounds **5**, **9**, **10**, and **18**, spectral data for D, L, and racemic samples were indistinguishable.

The measurement of the enantiomeric ratio of **5** was problematic due to the presence of an anomeric mixture of septanose forms (32). After considerable experimentation, we found that reaction of D-**5** with 2,4-dinitrophenylhydrazine (DNPH) led to a separable 4:1 mixture of hydrazones D-**20** and D-**21**, respectively (38).[27] Treatment of D-**20** with (*S*)-MTPACl (39)[28] gave the Mosher's ester D-**22**. Similar treatment of L-**5** with DNPH gave a mixture of hydrazones L-**20** and L-**21**, which had spectral properties indistinguishable from D-**20** and D-**21**, respectively. The major (*E*)-hydrazone D-**20** was converted into the Mosher's ester L-**22**. Significantly, the Mosher's esters D-**22** and L-**22** were distinguishable by ^1H NMR; the geminal protons at C-6 for D-**22** appeared at δ 4.66 (dd, J = 6, 11 Hz) and 4.46 (dd, J = 6, 11 Hz) while those for L-**22** were at δ 4.61

[27]The stereochemistry of the major isomer was assigned as *E* on the basis of: (*i*) expected greater stability; (*ii*) H-1 of the major isomer (δ 7.58, d, J = 6.5 Hz) is shifted downfield relative to the minor isomer (δ 7.00, d, J = 4 Hz) while H-2 of the major isomer is shifted upfield (δ 4.18, brd, J = 7 Hz) relative to the minor isomer (δ 4.29, dd, J = 3.5, 4 Hz). This is consistent with the deshielding effect of the dinitrophenyl group (38).

[28](*S*)-α-Methoxy-α-(trifluoromethyl)phenylacetic acid chloride ((*S*)-MTPACl) was prepared (39) from the corresponding (*R*)-acid ((*R*)-MTPA).

Can. J. Chem. Downloaded from www.nrcresearchpress.com by EESC ESCOLA DE ENGENHARIA on 09/08/12
For personal use only.

Can. J. Chem. Downloaded from www.nrcresearchpress.com by EESC ESCOLA DE ENGENHARIA on 09/08/12
For personal use only.

(dd, J = 6, 11 Hz) and 4.48 (dd, J = 6, 11 Hz). Integration of the signals for the C-6 protons in the ^{1}H NMR spectrum of the mixture of Mosher's esters produced by treatment of (±)-**5** as above indicated the presence of a 1:1 (±5%) mixture of D-**22** and L-**22**.

The next objective was to define reaction conditions for the reduction of **4** with Alpine-Borane® that would give high selectivity and facilitate control of the conversion. Initially, reduction under the conditions that proved successful for reduction of **1** was examined. (*R*)-Alpine-Borane® (0.5 M in THF; 3 equiv.) was added to a solution of **4** (0.05 M in THF) at −78°C. After stirring at −78°C for various times (0.1–4 h), acetaldehyde was added to quench the excess reagent and the reaction mixture was concentrated to dryness. The ^{1}H NMR spectrum of the crude product was complex and we could not determine the relative proportions of **4**, **5**, and **6**[29] present. Both **5** and **6** could be isolated by preparative thin-layer chromatography (PTLC); however, we were unable to recover **4** efficiently. Alternatively, treatment of the crude product with DNPH followed by chromatography (PTLC) gave **20** and **6**. The hydrazone **20** obtained after reduction of **4** with (*R*)-Alpine-Borane® was always enriched[30] with the D isomer (D:L = 3-20:1) while that obtained after reduction with (*S*)-Alpine-Borane® was enriched[30] with the L isomer (L:D = 3–20:1).

We required a method to determine the reaction conversion directly. Reaction of **4** with methyl orthoformate in methanolic HCl solution gave the bisacetal **23** in quantitative yield. Reaction of (±)-**10** (or (±)-**5**) under the same conditions gave (±)-**24**. In the ^{1}H NMR spectra of **23** and **24** the acetal protons appeared at distinct chemical shifts. Thus, the ratio of **4** and **5** in the crude reduction product could be conveniently determined by ^{1}H NMR after treatment with methyl orthoformate as above. The use of an internal standard allowed the amount of **4** and **5** in the reaction mixture to be estimated; the amount of **6** was determined by isolation.

We examined the ^{1}H NMR spectra of (±)-**24** in the presence of (+)-Eu(hfc)$_3$ with the hope of finding a more convenient method (cf. **22**) to determine the ratio of enantiomers of **5** (40). Although the signal due to the anomeric OCH_3 group was split, accurate integration was not possible due to spectral congestion in this region. On the basis of this observation, (±)-**10** was treated with trifluoroethanol in the presence of *p*-TsOH to obtain (±)-**25** as a 2:1 mixture of β and α anomers, respectively. The proton-decoupled ^{19}F NMR spectrum of (±)-**25** showed two signals, each of which was split in the presence of (+)-Eu(hfc)$_3$. The signals due to the α anomer could be accurately integrated, allowing for the determination of the enantiomeric ratio of **25** and thus of the precursor **10** (or **5**). Septanoside **25** could be readily isolated after treatment of the crude reduction product, obtained as described above, with trifluoroethanol and *p*-TsOH. The same result (±10%) was obtained when the enantiomeric ratio of **5** in the crude reduction product was determined both via **25** and via **20**.

With suitable analytical methods established, we examined the reduction of dialdehyde **4** under a variety of conditions (time, temperature, concentration, stoichiometry) with the aim of optimizing both the yield and the enantiomeric purity of the hydroxyaldehyde product **5**. After considerable

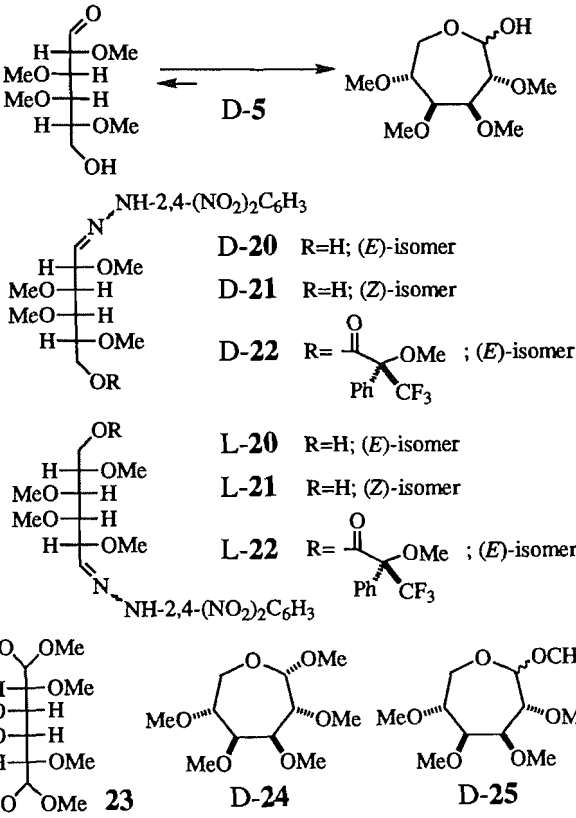

experimentation,[31] we found that addition of Alpine-Borane® (0.5 M in THF; 3 equiv.) to a solution of **4** in CH_2Cl_2 (0.12 M) at −78°C gave reproducible results and convenient reaction times (see Table 2). Analysis[31] of the crude product obtained after 2.0 h under these conditions consistently indicated the presence of **4**, **5**, and **6** in a ratio of <1:10:10; the ratio of D-**5** to L-**5** was found to be 7:1 (reduction with (*R*)-Alpine-Borane®). Reaction with (*R*)-Alpine-Borane® under the same conditions but on larger scale allowed the isolation of **5** (43%; 7:1, D:L) and **6** (46%). To demonstrate that the stereoselectivity was dependent on the conversion, the same reaction was repeated with reactions times of 1 h and 4 h. The results are presented in Table 2. As expected, reaction with (*S*)-Alpine-Borane® gave analogous results, with L-**5** being produced in excess. Reduction of **4** (0.12 M in CH_2Cl_2) with (*R*)-Alpine-Borane® at −95°C was investigated. At this temperature, a reaction time of 4 h was required to reach 95% conversion (**4**:**5**:**6** ca. <1:10:10). Again, the stereoselectivity was clearly shown to be dependent on the conversion.

To determine whether our results were consistent with the simple mathematical model represented in eqs. [3]–[5] we plotted the results against those calculated[14] assuming various values of k_1/k_2. As indicated in Figs. 7 and 8, the results observed for reduction of **4** at −78°C are reasonably predicted by the model assuming $k_1/k_2 \approx 2.9$ while reduction at −95°C can be modeled assuming $k_1/k_2 \approx 3.7$. The selectivity (i.e., k_1/k_2) for the reduction of **1** at −78°C was 2.3. It is possible to model (Fig. 7) the results observed for reduction for **4** at −78°C assuming $k_1/k_2 = 2.3$ by incorporating greater selectivity in the second step ($k_4/k_3 = 3.5$; $(k_1+k_2)/(k_3+k_4) = 0.9$). By contrast, the reduction at −95°C is not well modeled with the assumption of increased selectivity in the second step (i.e., eqs. [3] and [4]; $k_1/k_2 = 2.5$–4.0; $k_4/k_3 = (1.2–1.5) \times k_1/k_2$).

[29]Under these conditions, **5** and **6** would presumably be present as the corresponding 9-BBN borinate esters.

[30]Measured by ^{1}H NMR on the derived Mosher's esters **22**.

[31]See experimental section for details on procedures.

TABLE 2. Reduction of **4** (0.012 M in CH_2Cl_2) with Alpine-Borane® (3 equiv.)

Reagent	Temp (°C)	Time (h)	Ratio[a] **4**:**5**:**6**	% Yield[b] (**6**)	% Yield[a,c] (**5**)	Selectivity[d] D-**5**:L-**5** (%ee)
(*S*)	−78	1	4:16:10	31	50	1:3.7 (57)
(*S*)	−78	2	1:10:10	46	44	1:7 (75)
(*R*)	−78	1	3:17:10	32	52	3.5:1 (55)
(*R*)	−78	2	1:10:10	46	48 (43)[b]	7:1 (75)
(*R*)	−78	3	0.5:6:10	59	36	10:1 (82)
(*R*)	−78	4	0.2:4:10	70	23	13:1 (86)
(*R*)	−95	3	2:12:10	43	46	12:1 (85)
(*R*)	−95	4	1:9:10	50	45 (42)[b]	15:1 (87)
(*R*)	−95	5	0.5:6:10	59	34	18:1 (89)

[a]Determined by ^{1}H NMR after treatment with acidic methanol. All reactions were performed at least twice; the relative error in determining the ratio of the components was typically ±10%.
[b]Isolated yield.
[c]Because **5** was difficult to purify, isolation was only attempted in larger scale reactions.
[d]%ee = |(D-**5**) − (L-**5**)| × 100/[(D-**5**) + (L-**5**)] and was measured by ^{19}F NMR in the presence (+)-Eu(hfc)$_3$ after conversion into **25**.

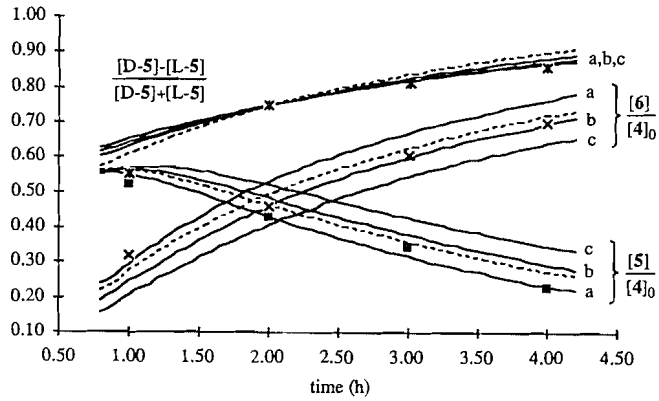

FIG. 7. Calculated and observed results for reduction of **4** with Alpine-Borane® at −78°C. Observed: ✕, ee of **5**; X, yield of **6**; ■, yield of **5**. Calculated: (a) $k_1/k_2 = k_4/k_3 = 2.7$; (b) $k_1/k_2 = k_4/k_3 = 2.9$; (c) $k_1/k_2 = k_4/k_3 = 3.1$; (- - -) $k_1/k_2 = 2.3$, $k_4/k_3 = 3.5$.

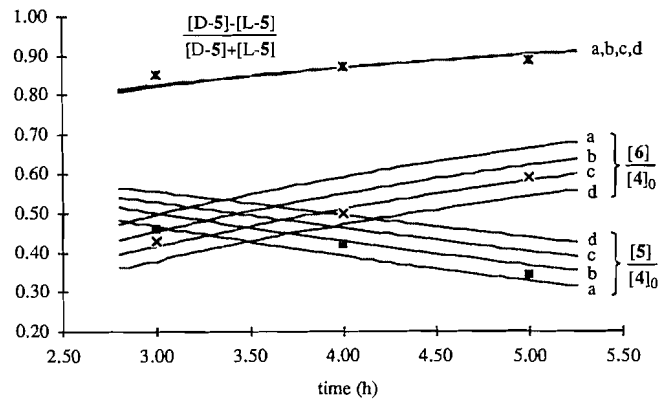

FIG. 8. Calculated and observed results for reduction of **4** with Alpine-Borane® at −95°C. Observed: ✕, ee of **5**; X, yield of **6**; ■, yield of **5**. Calculated: (a) $k_1/k_2 = k_4/k_3 = 3.3$; (b) $k_1/k_2 = k_4/k_3 = 3.5$; (c) $k_1/k_2 = k_4/k_3 = 3.7$; (d) $k_1/k_2 = k_4/k_3 = 3.9$.

It was of interest to determine if the same strategy could also be applied to differentiate diastereotopic groups with a similar amplification of stereoselectivity. Examples of this type of stereoselective process are rare (41*a*).[32] We reasoned that if the diastereotopic groups had "enantiotopic" local symmetry, then predictable group selectivity might result from the matching and mismatching of substrate and reagent face selectivity as above. The configuration of the α-alkoxy group should govern the substrate diastereotopic face selectivity for addition to hexose-derived dials. Thus, a dial derived from glucose (or gulose) would have -CHO groups with the appropriate "pseudo-enantiotopic" relationship. We investigated the reduction of **26** with Alpine-Borane® (see Scheme 3).

Dial **26** was prepared by oxidation of diol **29**, which, in turn was readily available from D-glucitol (D-sorbitol) via **30** and **31**. Authentic samples of the D-glucose derivative **27** and the L-gulose derivative **28** were prepared from 2,3,4-tri-*O*-methyl-D-glucose (**32**) (42) in analogy with the chemistry developed in the galactose series. Thus, reduction of **32** with sodium borohydride (35) gave the known (37) triol **33**, which, in turn, gave a separable 1.7:1 mixture of **34** and **35** upon treatment with trityl chloride in pyridine. The structures of **34** and **35** were confirmed by ^{1}H NMR of the corresponding diacetates **36** and **37**. The synthesis of **27** from **34** and of **28** from **35** followed the sequence silylation (**38**, **39**), methylation (**40**, **41**), desilylation (**42**, **43**), oxidation (**44**, **45**), and hydrolysis as described

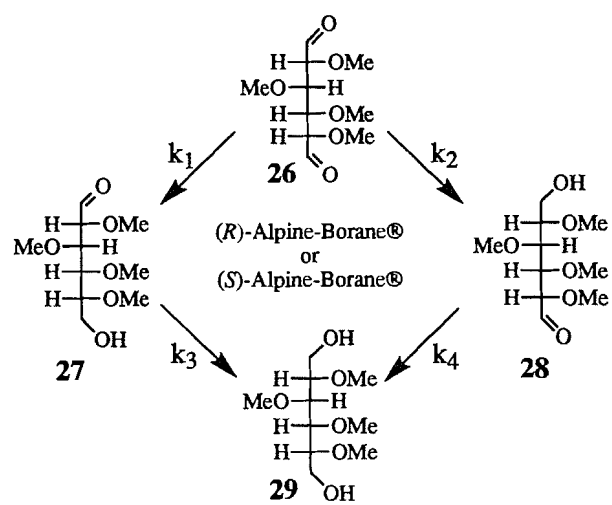

SCHEME 3

[32]For examples without kinetic enhancement of selectivity, see refs. 41 *b–f*.

Can. J. Chem. Downloaded from www.nrcresearchpress.com by EESC ESCOLA DE ENGENHARIA on 09/08/12
For personal use only.

TABLE 3. Reduction of **26** with Alpine-Borane® (3 equiv.) at −78°C

Reagent	Time (h)	Ratio[a] **26**:(**27** + **28**):**29**	% Yield[b] (**29**)	% Yield[a,c] (**27** + **28**)	Selectivity[d] **27**:**28** (%de)
(*R*)[e]	0.5	8:13:10	30	38	1:1.3 (13)
(*R*)[e]	1	3:8:10	45	36 (35)[b]	1:1.2 (9)
(*R*)[e]	2	1:3:10	68	23	1.2:1 (9)
(*R*)[e]	4	0.1:0.8:10	88	9	2.2:1 (38)
(*S*)[f]	2	4:14:10	34	48	1:5 (67)
(*S*)[f]	4	1:9:10	52	46 (44)[b]	1:11 (83)
(*S*)[f]	8	trace: 3:10	75	22 (20)[b]	<1:19 (>90)

[a]Determined by ^{1}H NMR after treatment with acidic methanol. All reactions were performed at least twice; the relative error in determining the ratio of the components was typically ±10%.
[b]Isolated yield.
[c]Because the hydroxyaldehyde fraction (**27** + **28**) was difficult to purify, isolation was only attempted in larger scale reactions.
[d]%de = |(**27** − **28**)| × 100/(**27** + **28**) and was measured by ^{1}H NMR after treatment with acidic methanol and (or) after treatment with DNPH.
[e]The initial concentration of **26** was 0.012 M in CH_2Cl_2.
[f]The initial concentration of **26** was 0.025 M in CH_2Cl_2.

above. The ^{1}H NMR spectrum of **27** revealed it to be about a 1.5–2:1 mixture of the hydroxyaldehyde and β-septanose tautomers, respectively (43); similarly, **28** was shown to exist primarily in the β-septanose form. The diastereoisomeric relationship between **27** and **28** was confirmed by reduction with sodium borohydride to give, in each case, the diol **29**.

We anticipated that ring–chain tautomerism would make mixtures of **27** and **28** difficult to analyze directly by ^{1}H NMR. Individual reaction of **27** and **28** with DNPH gave the hydrazones **46** (4–6:1 mixture of *E* and *Z* isomers (38)) and **47** (3–4:1 mixture of *E* and *Z* isomers (38)), respectively. The hydrazones **46** and **47** were readily distinguishable by ^{1}H NMR. Methods for analysis of the products from reduction of **26** were developed in analogy to those in the galactose series. Treatment of **26** with methyl orthoformate in methanolic HCl solution gave the bisacetal **48** in near quantitative yield. Reaction of **44** under these conditions gave variable mixtures (depending on reaction time) of the septanoiside **49** and dimethyl acetal **50**; similar reaction of **45** gave **51** and **52**. The acetal protons in compounds **48–52** were readily distinguished by ^{1}H NMR.

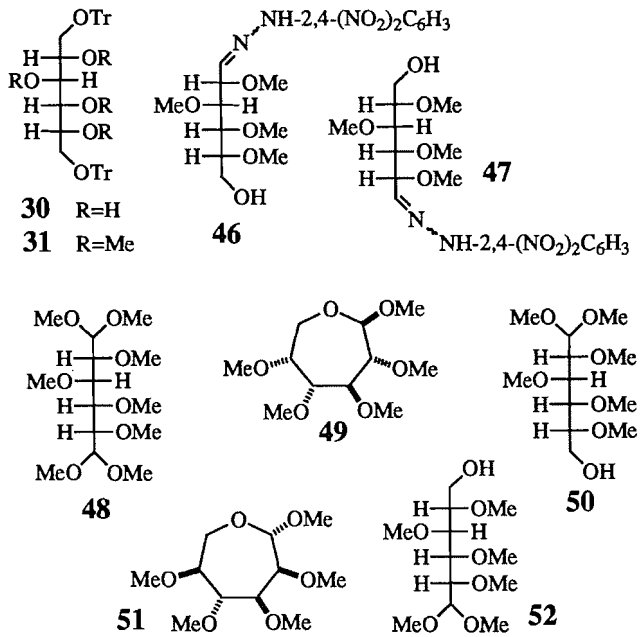

We investigated the reduction of dialdehyde **26** with Alpine-Borane® under a variety of conditions. In each case, the relative amount of **26**, **27**, and **28** present in the crude reaction product was determined by ^{1}H NMR after treatment with methyl orthoformate. The amount of **29** present could be estimated from the above spectrum and was determined by isolation. Alternatively, treatment of the crude reaction product with DNPH gave **29** and a mixture of **46** and **47**. The ratios of **26** and **27** present in the crude reaction mixture when determined after treatment with methyl orthoformate and after treatment with DNPH agreed closely (±10%).

The results for reduction of **26** under the conditions previously described for reduction of **4** are summarized in Table 3. Qualitatively similar results were obtained under other reaction conditions (concentration, stoichiometry). The reaction of (*R*)-Alpine-Borane® with **26** was considerably faster than with **4**. Analysis[31] of the crude product (after treatment with methyl orthoformate) indicated that the ratio of **26**:**27**:**28**:**29** present was ca. 14:17:21:48 after reaction for 1 h. The selective formation of **28** was surprising as we expected that (*R*)-Alpine-Borane® would preferentially reduce the C-6 aldehyde group of **26** in analogy to reactions with **4**. The selectivity in favor of **28** was slightly higher at shorter reaction times; however, at longer reaction times the hydroxyaldehyde fraction was enriched in isomer **27**. These results indicated that **28** both is formed *and* reacts faster than **27** (i.e., Scheme 3; $k_1 < k_2$ and $k_3 < k_4$) and suggest the possibility of a "mismatched" pair (18) due to substrate diastereotopic group selectivity.

The substrate diastereotopic group selectivity for reduction of **26** was assessed by reaction with 9-BBN (1 equiv., 22°C). At low conversion (i.e., <15% of **29**) the hydroxyaldehyde product was a 1.6:1 mixture of **28** and **27**, respectively. The origin of this substrate selectivity in favor of reduction of the C-1 aldehyde group in **26** is uncertain. The results observed for reduction of **26** with (*R*)-Alpine-Borane® can be rationalized assuming that the substrate (*s*) and reagent (*r*) group selectivities are approximately equal in magnitude but mismatched, resulting in low selectivity for reduction of the C-1 aldehyde group and formation of **28** (i.e., $s > r$). In the second step, selectivities are again mismatched but with a slight selectivity in favor of reduction of a C-6 aldehyde group and reaction of **28** (i.e., $s < r$). As indicated in Fig. 9, the observed results can be crudely modelled by eqs. [3] and [4] by assuming that

Can. J. Chem. Downloaded from www.nrcresearchpress.com by ESC ESCOLA DE ENGENHARIA on 09/08/12
For personal use only.

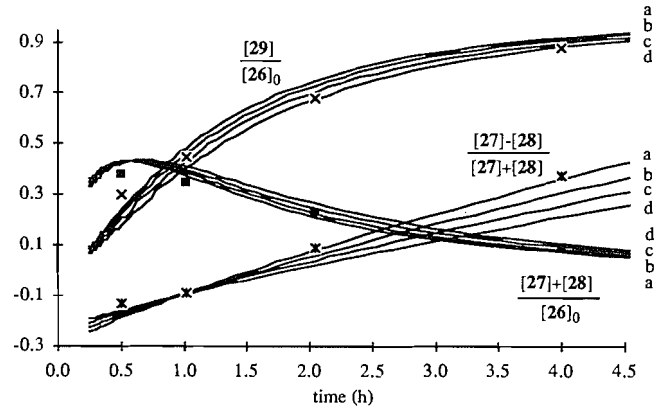

FIG. 9. Calculated and observed results for reduction of **26** with (*R*)-Alpine-Borane® at −78°C. Observed: ✕, de of (**27**, **28**); X, yield of **29**; ■, yield of (**27** + **28**). Calculated with $(k_1+k_2)/(k_3+k_4) = 0.75$: (a) $k_2/k_1 = k_4/k_3 = 1.85$; (b) $k_2/k_1 = k_4/k_3 = 1.75$; (c) $k_2/k_1 = k_4/k_3 = 1.67$; (d) $k_2/k_1 = k_4/k_3 = 1.6$.

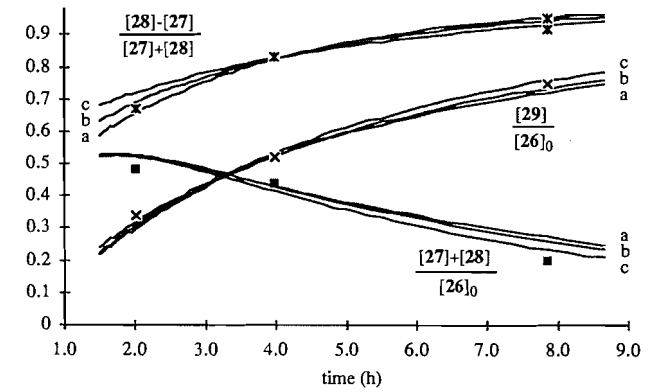

FIG. 10. Calculated and observed results for reduction of **26** with (*S*)-Alpine-Borane® at −78°C. Observed: ✕, de of (**27**, **28**); X, yield of **29**; ■, yield of (**27** + **28**). Calculated with $(k_1+k_2)/(k_3+k_4) = 0.75$: (a) $k_2/k_1 = 1.9$, $k_3/k_4 = 5.4$; (b) $k_2/k_1 = 2.4$, $k_3/k_4 = 4.3$; (c) $k_2/k_1 = k_3/k_4 = 3.2$.

the selectivities for the two steps are modest and mismatched (i.e., $k_2/k_1 \approx k_4/k_3 \approx 1.7$).

We examined the reduction of **26** with (*S*)-Alpine-Borane®, expecting the increase in selectivity associated with a matched pair. The results are presented in Table 3. Surprisingly, this reaction was considerably slower than the others and was conducted at higher concentration to achieve convenient reaction times. The selectivity observed was much higher than with (*R*)-Alpine-Borane® and is consistent with a reinforcing of reagent and substrate group selectivity. Initially, we attempted to model the results using eqs. [3] and [4] with the assumption that $k_2/k_1 = k_3/k_4$ (Scheme 3, Fig. 10). Although a reasonable approximation of the evolution of the yields with respect to time could be obtained under this assumption, the evolution of the se could be reasonably reproduced only by assuming that k_2/k_1 was considerably smaller than k_3/k_4.[33]

Considering the above, the results from reduction of **26** with Alpine-Borane® can be rationalized by assigning a small substrate diastereotopic group selectivity ($s \approx 1.8$) in favor of reduction of the C-1 carbonyl group and assuming that the reagent group selectivity is similar to that observed with **4** in the second step (i.e., $r_2 = k_4/k_3 \approx 3$) but highly attenuated in the first step (i.e., $r_1 = k_1/k_2 \approx 1.1$). Thus, in analogy to eq. [6], the selectivities for the matched case would be $k_1/k_2 = r_1 s \approx 2$ and $k_4/k_3 = r_2 s \approx 5.4$; and for the mismatched case $k_1/k_2 = r_1/s \approx 0.6$ and $k_4/k_3 = r_2/s \approx 1.7$ Possible origins for a reduced group selectivity in the first step are unclear.

Conclusion

In conclusion, theory suggests that enantiotopic group-selective reactions, even when the selectivity is modest, can be usefully exploited in asymmetric synthesis. The potential scope of such a strategy was revealed by a simple kinetic analysis. A method was presented for selecting candidate group-selective reactions that are likely to show appropriate selectivity in such processes. The strategy was illustrated by effecting the reduction of hexose-derived dialdehydes and showed that, despite low group selectivity (ca. 3–4:1), useful amounts of hydroxyaldehyde products (40–50% yield) with useful levels of stereoisomeric purity (7–15:1) could be obtained by this approach. The major by-product was the diol resulting from reduction of both aldehyde groups. The diol could be recycled by oxidation to the dialdehyde, increasing the efficiency of the overall process. The observed results were reasonably approximated by calculation using a simple mathematical model. We are actively investigating the application of this strategy to various synthetic problems. Results will be reported in due course.

Experimental

Calculations

Equations [3] and [4] are derived as follows (10*a*, *b*). Assuming that each of the reactions (eqs. [1] and [2]) is first order with respect to substrate and reagent leads to rate eqs. [7]–[9].

$$[7] \qquad \frac{d[\mathbf{A}]}{dt} = -(k_1 + k_2)[\mathbf{A}][\mathbf{R}]$$

$$[8] \qquad \frac{d[\mathbf{P}]}{dt} = k_1[\mathbf{A}][\mathbf{R}] - k_3[\mathbf{P}][\mathbf{R}]$$

$$[9] \qquad \frac{d[\mathbf{Q}]}{dt} = k_2[\mathbf{A}][\mathbf{R}] - k_4[\mathbf{Q}][\mathbf{R}]$$

Dividing eq. [8] by eq. [7] gives eq. [10] (first-order linear differential equation), which is readily solved (integrating factor method) to give eq. [3]. Equation [4] is obtained similarly. The stoichiometry of eqs. [1] and [2] dictates the relationships in eqs. [11] and [12]. Reaction time (t) is calculated by numerical integration of eq. [7] according to eq. [13] (Runge–Kutta, second order).

$$[10] \qquad \frac{d[\mathbf{P}]}{d[\mathbf{A}]} = \frac{k_3[\mathbf{P}]}{(k_1 + k_2)[\mathbf{A}]} - \frac{k_1}{(k_1 + k_2)}$$

$$[11] \qquad [\mathbf{R}]_n = [\mathbf{R}]_{\text{init}} - 2[\mathbf{A}]_{\text{init}} + 2[\mathbf{A}]_n + [\mathbf{P}]_n + [\mathbf{Q}]_n$$

$$[12] \qquad [\mathbf{B}]_n = [\mathbf{A}]_0 - [\mathbf{A}]_n - [\mathbf{P}]_n - [\mathbf{Q}]_n$$

$$[13] \qquad t_n = t_{n-1} + \frac{[\mathbf{A}]_{n-1} - [\mathbf{A}]_n}{2(k_1 + k_2)}\left[\frac{1}{[\mathbf{A}]_n[\mathbf{R}]_n} + \frac{1}{[\mathbf{A}]_{n-1}[\mathbf{R}]_{n-1}}\right]$$

All calculations were performed in a spreadsheet environment using Microsoft® Excel (v.2.2a) running on a Macintosh IIsi computer. In each case, specific values for k_1/k_2, k_4/k_3, and $(k_1+k_2)/(k_3+k_4)$ were assigned and k_{1-4} were calculated[34] with $k_1 = 1$ (arbi-

[33]Experimentally, the se is determined much more accurately than the yields (isolation). Note that keeping the product of the selectivities constant (i.e., $(k_2/k_1)(k_3/k_4) = (3.2)^2$) strongly attenuates the effect of different selectivities on the calculated evolution of the yields.

Can. J. Chem. Downloaded from www.nrcresearchpress.com by EESC ESCOLA DE ENGENHARIA on 09/08/12
For personal use only.

Can. J. Chem. Downloaded from www.nrcresearchpress.com by ESC ESCOLA DE ENGENHARIA on 09/08/12
For personal use only.

trary units). Values for $[P]_n/[A]_0$, $[Q]_n/[A]_0$, $([P]_n + [Q]_n)/[A]_0$, $([P]_n - [Q]_n)/([P]_n + [Q]_n)$, $[B]_n/[A]_0$, $[R]_n$, and reaction time (t_n) were determined for each of a series of 200 values of $[A]/[A]_0$ ranging from 1 to 0.0003. The series was set such that the nth value was equal to 96% of the $(n - 1)$th value. Initial conditions were $[A]_0 = 1$; $[R]_0 = 3$; $[P]_0 = [Q]_0 = [B]_0 = 0$ (arbitrary units). The values for $[P]_n$ and $[Q]_n$ were calculated according to eqs. [3] and [4] and $[R]_n$ was determined according to eq. [11]. Equations [12] and [13] were used to calculate values for $[B]_n$ and t_n, respectively. The maximum value of $([P]_n + [Q]_n)/[A]_0$ and the corresponding se [i.e., $([P]_n - [Q]_n)/([P]_n + [Q]_n)$] at that point were determined by inspection. Similarly, the maximum values of $([P]_n + [Q]_n)/[A]_0$ with corresponding se ≥ 0.80, 0.90, 0.95, and 0.98 were identified. Specific values of k_1/k_2 required to produce a given result were determined by calculations using successive approximations of k_1/k_2.

The data for Figs. 3 and 4 were obtained from calculations as above using a series of 100 values of k_1/k_2 ranging from 1 to 100. The series was set such that the nth value was equal to 105% of the $(n - 1)$th value. For cases where $k_1/k_2 < 3.4$, calculations using values of $[A]/[A]_0 < 0.0003$ were required to reach the desired se level. In these cases, additional $[A]/[A]_0$ data points were calculated until the desired se was reached or until $([P]_n + [Q]_n)/[A]_0 < 0.005$.

For Figures 7–10, the calculated data for each value of k_1/k_2 (and k_4/k_3) were "normalized" by adjusting the value of k_1 so that the observed se value was calculated to occur at the observed time (i.e., for Fig. 7, se = 0.75 when $t = 2$; for Fig. 8, se = 0.87 when $t = 4$; for Fig. 9, se = 0.09 when $t = 1$; for Fig. 10, se = 0.83 when $t = 4$).

Materials and methods

General experimental procedures have recently been described (44). Dimethyl sulfoxide (DMSO) was distilled from CaH_2 under reduced pressure (10 mbar; 1 bar = 100 kPa) and stored over 3Å molecular sieves. Acetaldehyde was freshly distilled. Racemine glyceraldehyde was obtained by oxidation of an equimolar mixture of D-fructose and L-sorbose with lead tetraacetate (45) and was, in turn, converted into **1** according to the known procedure (46). (*S*)-α-Methoxy-α-(trifluoromethyl)phenylacetic acid chloride ((*S*)-MTPACl) was prepared (39) from the corresponding (*R*) acid ((*R*)-MTPA). Galactitol was obtained by reduction (35) of D-galactose. 2,3,4-Tri-*O*-methyl-D-galactose (**11**) (34) and 2,3,4-tri-*O*-methyl-D-glucose (**32**) (42) were prepared from D-galactose and D-glucose, respectively. Unless otherwise noted, other reagents were commercially available and were used as received, and reactions were carried out under an atmosphere of argon and reaction temperatures refer to the bath. Low-temperature baths were $CO_{2(s)}$/acetone (−78°C), $N_{2(l)}/CH_2Cl_2$ (−95°C), and $N_{2(l)}$/EtOH (−100°C). Unless otherwise noted, all reported compounds were homogeneous by thin-layer chromatography (TLC) and by NMR. Flash column chromatography (FCC) was performed according to Still et al. (47).

*2,3-Dimethoxypropanol (**2**)*

Reduction with $NaBH_4$: $NaBH_4$ (27 mg, 0.71 mmol) was add to a solution of **1** (42 mg, 0.36 mmol) in MeOH (5 mL). After stirring for 5 min, acetaldehyde (0.1 mL) was added and the reaction mixture was concentrated under reduced pressure, and fractionated by FCC (EtOAc:hexane, 1:1) to give **2** as a colorless oil (36 mg, 84%); IR: 3409, 2970, 1378, 1101 cm^{-1}; ^1H NMR δ: 3.76 (1H, dd, $J = 4$, 11.5 Hz, H-1), 3.64 (1H, dd, $J = 5$, 11.5 Hz, H-1), 3.52 (2H, d, $J = 5$ Hz, H-3), 3.50–3.43 (1H, m, H-2), 3.46 (3H, s, OCH_3), 3.39 (3H, s, OCH_3); ^{13}C NMR δ: 80.0 (d, C-2), 72.3 (t, C-3), 62.3 (t, C-1), 59.4 (q, OCH_3), 57.7 (q, OCH_3).

Reduciton with Alpine-Borane®: A solution of the aldehyde **1** (ca. 50 mg, 0.4 mmol) in THF (4 mL) was cooled to the desired temperature and Alpine-Borane® (0.5 M in THF, 0.2 mL, 0.1 mmol) was added. After stirring for 1–3 h, acetaldehyde (ca. 0.05 mL, excess) was added. The reaction mixture was allowed to warm to room temperature and then concentrated under reduced pressure. The residual pinene was removed at 50°C under high vacuum. The residue was dissolved in ether (2 mL) and ethanolamine (7 mg, 0.11 mmol) was added to the ice-cold solution. After stirring for 15 min the cloudy mixture was filtered, concentrated, and fractionated by FCC (EtOAc:hexane, 1:1, and then MeOH:CH_2Cl_2, 1:9) to give the alcohol **2** as a colorless oil (10–12 mg, >80% based on Alpine-Borane®).

(2R)-2,3-Dimethoxypropyl (2R)-2-methoxy-2-(trifluoromethyl)phenylacetate (**3**)*

A solution of (*S*)-MTPACl (0.06 mmol) in CH_2Cl_2 (1 mL) was added to a solution of the alcohol **2** (5 mg, 0.04 mmol), Et_3N (0.02 mL), and DMAP (ca. 1 mg) in CH_2Cl_2 (1 mL). After stirring for 1 h, the reaction mixture was concentrated under reduced pressure. ^1H NMR of the crude product indicated complete conversion to the diastereomeric Mosher's esters **3**; the ratio of diastereomers could be determined by ^{13}C NMR.[24] Fractionation by preparative TLC (EtOAc:hexane, 1:1) gave a pure sample of **3**. The Mosher's esters prepared from "racemic" alcohol **2** (i.e., from $NaBH_4$ reduction of **1**) indicated a 5% de in favor of the 2*S*,2′*R* isomer[35] and showed the following spectral properties: ^1H NMR δ (2*S*,2*R* diastereomer): 7.55 (2H, m, Ph), 7.41 (3H, m, Ph), 4.51 (1H, dd, $J = 3.5$, 11.5 Hz, H-1), 4.35 (1H, dd, $J = 6.5$, 11.5 Hz, H-1), 3.58 (3H, m, C-2 OCH_3), 3.48–3.38 (3H, m, H-2, 3), 3.39 (3H, s, OCH_3), 3.34 (1.5H, s, OCH_3); (2*R*,2*R* disatereomer): 7.55 (2H, m, Ph), 7.41 (3H, m, Ph), 4.52 (1H, dd, $J = 4$, 11.5 Hz, H-1), 4.35 (1H, dd, $J = 5$, 11.5 Hz, H-1), 3.58 (3H, m, C-2 OCH_3), 3.48–3.38 (3H, m, H-2, 3) 3.39 (3H, s, OCH_3), 3.32 (3H, s, OCH_3); ^{13}C NMR (partial data; data for 2*R*,2*R* diastereomer in parentheses) δ: 77.6 (77.5) (d, C-2), 71.2 (71.2) (t, C-3), 65.2 (64.7) (t, C-1), 59.3 (59.3) (q, OCH_3), 57.9 (57.8) (q, OCH_3), 55.4 (55.4) (q, C-2′ OCH_3 (br, coupled to F)); ^{19}F NMR ([H]) δ (TFA): −72.17 (2*R*,2*R*), −72.15 (2*S*,2*R*).

galacto-*2,3,4,5-Tetramethoxyhexanedial (**4**)*

DMSO (2 M in CH_2Cl_2, 3.5 mL, 7 mmol) was added via syringe to a solution of $(COCl)_2$ (0.3 mL, 2 mmol) in CH_2Cl_2 (5 mL) at −78°C. The mixture was stirred at −78°C for 30 min. and a solution of **6** (200 mg, 0.84 mmol) in CH_2Cl_2 (3 mL) was added via syringe. The reaction mixture was allowed to warm to −50 to −55°C (internal) over 10 min and stirred at that temperature for a further 40 min. Et_3N (1.5 mL, excess) was added and, after stirring for 10 min, the reaction mixture was allowed to warm to room temperature and then was concentrated, and fractionated by FCC (MeOH:CH_2Cl_2, 1:19), yielding **4** as a white solid (mp 138–139°C; 152 mg, 76%); IR: 2938, 2842, 1728, 1106 cm^{-1}; ^1H NMR δ: 9.87 (2H, s, H-1, 6), 3.83 (4H, br s, H-2, 3, 4, 5), 3.54 (6H, s, OCH_3), 3.18 (6H, s, OCH_3); ^{13}C NMR δ: 202.7 (d, C-1, 6), 85.4 (d, C-2, 5), 79.4 (d, C-3, 4), 60.1 (q, OCH_3), 58.9 (q, OCH_3); MS (CI, NH_3), m/z (relative intensity): 252 ($[M + 18]^+$, 100), 235 ($[M + 1]^+$, 49), 146 (15), 101 (41).

*General procedure for reduction of **4** with Alpine-Borane®*

Alpine-Borane® (0.5 M in THF, 3 equiv.) was added via syringe to a cooled (−78 or −95°C) solution of **4** (10–50 mg, 0.04–0.2 mmol; 0.012 M in CH_2Cl_2). After stirring at the indicated temperature for the indicated time, acetaldehyde (excess, ca. 0.1–0.2 mL) was added and the mixture stirred for a further 0.5 h. The reaction mixture was allowed to warm to room temperature and concentrated. The resulting crude product (or aliquots) was processed in one (or more) of the following ways:

*For isolation of **5** and **6***: The crude product was dissolved in ether

[34] An absolute value for the rate constants is required for calculation of reaction time. All other variables can be determined by the ratio of the rate constants.

[35] Assignment is based on the fact that the major diastereomer present corresponds to the major diasteromer derived from **2** obtained by reduction of **1** with (*R*)-Alpine-Borane®. This indicates that the major enantiomer of our sample of **1** is also the most reactive with (*R*)-Alpine-Borane®. Since reduction of **4** with (*R*)-Alpine-Borane® gives predominantly D-**5**, it is concluded that the major enantiomer of **1** should be the (*S*) isomer (i.e., excess of L-glyceraldehyde).

Can. J. Chem. Downloaded from www.nrcresearchpress.com by ESC ESCOLA DE ENGENHARIA on 09/08/12
For personal use only.

and silica gel was added. The suspension was stirred at ambient temperature for 40 min and filtered.[36] The combined filtrate and washings were concentrated and fractionated by FCC (EtOAc:hexane, 1:4, and then MeOH:CH_2Cl_2, 1:9) to give hydroxyaldehyde fraction and a diol fraction. The hydroxyaldehyde fraction was further purified by FCC (EtOAc:hexane, 1:1) to give **5**. The diol fraction was further purified by FCC (MeOH:CH_2Cl_2, 1:9) to give **6**.

For measurement of conversion: The crude product was dissolved in methanol (ca. 1 mL) and $(CH_3O)_3CH$ (0.1 mL) and HCl (5% in methanol, a few drops) were added. After stirring overnight at room temperature, the reaction mixture was quenched by addition of $NaHCO_{3(s)}$, filtered, and concentrated. The ratio of **23** to **24** was determined by ^1H NMR. Fractionation by preparative TLC (EtOAc:hexane, 1:1, and then MeOH:CH_2Cl_2, 1:9) gave a mixture of **23** and **24** and pure **6**.

For measurement of the ratio of D-**5** *and* L-**5**: The crude product was dissolved in CH_2Cl_2 (ca. 0.5 mL) and DNPH (ca. 5 mg) was added. After 24 h, the reaction mixture was concentrated, and fractionated by preparative TLC (EtOAc:hexane, 1:1) to give **20**. The hydrazone **20** was dissolved in CH_2Cl_2 and treated with (*S*)-MTPACl in the presence of Et_3N and DMAP (39). After ca. 1 h, the reaction mixture was concentrated and fractionated by preparative TLC (EtOAc:hexane, 1:1) to give **22**. The ratio of D-**22** and L-**22** was determined by ^1H NMR.

Alternatively, the crude product was dissolved in trifluoroethanol (0.5 mL) and *p*-TsOH (ca. 3 mg) was added. After stirring 24 h at room temperature, $NaHCO_{3(s)}$ was added and the reaction mixture was filtered, concentrated, and fractionated by FCC (EtOAc:hexane, 1:3) to give **25**. The ratio of D-**25** and L-**25** was determined by ^{19}F NMR [H] in the presence of (+)-Eu(hfc)$_3$.

*(±)-2,3,4,5-Tetra-*O*-methylgalactose ((±)-***5***)*

To a solution of (±)-**10** (26 mg, 0.054 mmol) in acetonitrile (2 mL) was added 5% $HF_{(aq)}$ (a few drops). After stirring for 6 h at room temperature, the reaction mixture was quenched by addition of $NaHCO_{3(s)}$, and filtered. The resulting filtrate was concentrated, and fractionated by FCC (EtOAc:hexane, 1:1) yielding (±)-**5** as a colorless oil (ca. a 4:1 mixture of α and β septanose anomers; 12.5 mg, 100%); IR: 3496, 2974, 2933, 2827, 1102 cm^{-1}; ^1H NMR δ (α anomer): 4.86 (1H, d, J = 3.5, Hz, H-1), 4.13 (1H, d, J = 14 Hz, H-6), 3.78–3.65 (3H, m), 3.59 (3H, s, CH_3O), 3.53–3.45 (1H, m), 3.49 (3H, s, CH_3O), 3.46 (3H, s, CH_3O), 3.40 (3H, s, CH_3O), 3.35 (1H, m); δ (α anomer): 4.96 (1H, d, J = 3.5, Hz, H-1), 4.05 (1H, dd, J = 2, 14 Hz, H-6), 3.53 (3H, s, CH_3O), 3.51 (3H, s, CH_3O), 3.50 (3H, s, CH_3O), 3.44 (3H, s, CH_3O); ^{13}C NMR δ (α anomer): 97.4 (d, C-1), 83.4 (d), 82.5 (d), 81.2 (d), 79.4 (d), 67.7 (t, C-6), 60.7 (q, CH_3O), 59.3 (q, CH_3O), 58.3 (q, CH_3O), 56.9 (q, CH_3O); MS (CI, NH_3), m/z (relative intensity): 254 ([M + 18]$^+$, 24), 236 (41), 219 (100).

*2,3,4,5-Tetra-*O*-methyl-*D*-galactose (*D*-***5***)*

Hydrolysis of D-**10** as described above for (±)-**10** gave D-**5** (spectral data indistinguishable from (±)-**5**).

*2,3,4,5-Tetra-*O*-methyl-*L*-galactose (*L*-***5***)*

Hydrolysis of L-**10** as described above for (±)-**10** gave L-**5** (spectral data indistinguishable from (±)-**5**).

*2,3,4,5-Tetra-*O*-methylgalacitol (***6***)*

To a solution of **8** (290 mg, 0.40 mmol) in CH_3CN (20 mL) was added 5% $HF_{(aq)}$ (1 mL) at room temperature. After stirring overnight at room temperature, $NaHCO_{3(s)}$ (ca. 1 g) was added. The mixture was filtered, concentrated, and fractionated by FCC (MeOH:CH_2Cl_2, 1:19, and then 1:9) yielding **6** as a light yellow oil (96 mg, quantitative); IR: 3435, 2929, 1119 cm^{-1}; ^1H NMR δ: 3.88 (2H, dd, J = 5, 12 Hz, H-1, 6), 3.80 (2H, dd, J = 4, 12 Hz, H-1, 6), 3.55–3.45 (4H, m, H-2, 3, 4, 5), 3.49 (6H, s, OCH_3), 3.48 (6H, s, OCH_3); ^{13}C NMR δ: 81.2 (d, C-2,5), 80.2 (d, C-3, 4), 60.9 (t, C-1, 6), 60.3 (q, OCH_3), 57.9 (q, OCH_3); MS (CI, NH_3), m/z (relative intensity): 239 ([M + 1]$^+$, 100), 207 (11).

*1,6-Di-*O*-tritylgalacitol (***7***)*

To a solution of Ph_3CCl (6.4 g, 23 mmol) and DMAP (0.75 g, 6.1 mmol) in pyridine (40 mL) was added galacitol (2.4 g, 13 mmol). After stirring 48 h at room temperature, the reaction mixture was quenched by addition of $NH_4Cl_{(aq)}$ (30 mL), and extracted with EtOAc (3 × 50 mL). The combined organic layers was washed sequentially with water and brine, and concentrated under reduced pressure. The resulting solid was fractionated by FCC (EtOAc:hexane, 1:1, and then MeOH:CH_2Cl_2, 1:4) yielding **7** as a colorless solid (6.1 g, 69%; mp 156–157°C (EtOH)); IR: 3377, 3031, 2936, 1606, 1075 cm^{-1}; ^1H NMR δ: 7.45–7.20 (30H, m, Ph), 4.02 (2H, m, H-2, 5), 3.58 (2H, br s, OH), 3.42 (2H, dd, J = 4, 10 Hz, H-1, 6), 3.26 (2H, dd, J = 5.5, 10 Hz, H-1, 6), 2.82 (2H, br s, OH), 2.67 (2H, d, J = 6 Hz, H-3, 4); ^{13}C NMR δ: 143.5 (s, Ph), 128.6 (d, Ph), 128.0 (d, Ph), 127.3 (d, Ph), 87.1 (s, CPh_3), 72.0 (d), 69.2 (d), 66.7 (t, C-1, 6); MS: molecular ion not detected.

*2,3,4,5-Tetra-*O*-methyl-1,6-Di-*O*-tritylgalacitol (***8***)*

To a suspension of NaH (60% in oil, 2.6 g, 65 mmol) in THF (60 mL) was added a solution of **7** (4.5 g, 6.8 mmol) in THF (5 mL). After stirring for 10 min, iodomethane (3.7 mL, 59 mmol) was added and the reaction mixture was stirred overnight at room temperature. The reaction was quenched by addition of $NH_4Cl_{(aq)}$ (**CAUTION**: H_2 evolution) and extracted with EtOAc (3 × 50 mL). The combined organic layers was washed sequentially with water and brine, dried over Na_2SO_4, and concentrated. The resulting oil was fractionated by FCC (EtOAc:hexane, 1:9) yielding **8** as a colorless solid (4.8 g, 98%; mp 163–164°C ($CHCl_3$)); IR: 3085, 3050, 2939, 2829, 1596, 1090 cm^{-1}; ^1H NMR δ: 7.45–7.20 (30H, m, Ph), 3.60–3.45 (6H, m), 3.41 (6H, s, CH_3O), 3.27–3.19 (2H, m), 3.22 (6H, s, CH_3O); ^{13}C NMR δ: 144.1 (s, Ph), 128.7 (d, Ph), 127.8 (d, Ph), 127.0, (d, Ph), 87.3 (s, CPh_3), 79.3 (d), 79.1 (d), 62.7 (t, C-1, 6), 60.7 (q, CH_3O), 58.5 (q, CH_3O); MS: molecular ion not detected.

*(±)-2,3,4,5-Tetra-*O*-methyl-6-*O*-tritylgalacitol ((±)-***9***)*

To a solution of **8** (105 mg, 0.15 mmol) in MeOH (5 mL) and $CHCl_3$ (25 mL) was added trifluoroacetic acid (TFA; 0.5 mL) at room temperature. After stirring overnight at room temperature $NaHCO_{3(s)}$ (ca. 1 g) was added. The mixture was filtered, concentrated, and fractionated by FCC (MeOH:CH_2Cl_2, 1:9) to give (±)-**9** as a light yellow oil (49 mg, 70%); IR: 3463, 3051, 2963, 1095 cm^{-1}; ^1H NMR δ: 7.55–7.20 (15H, m, Ph), 3.89 (1H, dd, J = 5, 11.5 Hz), 3.81 (1H, dd, J = 4, 11.5 Hz), 3.61 (1H, dd, J = 2, 8 Hz), 3.57–3.40 (5H, m), 3.46 (3H, s, OCH_3), 3.42 (3H, s, OCH_3), 3.39 (3H, s, OCH_3), 3.22 (3H, s, OCH_3), 3.22–3.18 (1H, m); ^{13}C NMR δ: 143.9 (s, Ph), 128.7 (d, Ph), 127.8 (d, Ph), 127.1 (d, Ph), 87.1 (s, CPh_3), 80.6 (d), 79.9 (d), 79.7 (d), 79.3 (d), 62.2 (t), 61.4 (t), 60.8 (q, OCH_3), 60.2 (q, OCH_3), 58.3 (q, OCH_3), 57.6 (q, OCH_3); MS (CI, NH_3), m/z (relative intensity): 498 ([M + 18]$^+$, 3), 243 (100); and recovered **8** (23 mg, 22%).

*2,3,4,5-Tetra-*O*-methyl-6-*O*-trityl-*D*-galacitol (*D*-***9***)*

5% $HF_{(aq)}$ (5 drops) was added to a solution of D-**18** (15 mg, 0.025 mmol) in CH_3CN (5 mL) and the resulting solution was stirred for 5 min. The reaction mixture was diluted with $NaHCO_{3(aq)}$ (5 mL), extracted with CH_2Cl_2 (2 × 20 mL), and the combined organic layers dried over $Na_2SO_{4(s)}$, filtered, and concentrated under reduced pressure. The residue was fractionated by preparative TLC (EtOAc:hexane, 1:1) yielding alcohol D-**9** as a colorless oil (7.8 mg, 64%; spectral data indistinguishable from (±)-**9**) and diol **4** as a colorless oil (2 mg, 33%).

*2,3,4,5-Tetra-*O*-methyl-6-*O*-trityl-*L*-galacitol (*L*-***9***)*

Hydrolysis of L-**18** (15 mg) as described above gave L-**9** (7 mg, 58%; spectral data indistinguishable from (±)-**9**) and diol **4** (2 mg, 33%).

*(±)-2,3,4,5-Tetra-*O*-methyl-6-*O*-tritylgalactose ((±)-***10***)*

NMO (7 mg, 0.06 mmol) was added to a suspension of alcohol (±)-**9** (14 mg, 0.03 mmol) and powdered 4 Å molecular sieves (30

[36]This treatment facilitated the hydrolysis of the presumed 9-BBN borinate esters.

Can. J. Chem. Downloaded from www.nrcresearchpress.com by EESC ESCOLA DE ENGENHARIA on 09/08/12
For personal use only.

mg) in CH_2Cl_2 (4 mL). After stirring for 10 min, TPAP (ca. 1 mg) was added and, after stirring for a further 30 min, the reaction mixture was directly fractioned by FCC (EtOAc:hexane, 1:3) to give aldehyde (±)-**10** as a colorless oil (12 mg, 84%); IR: 3059, 2933, 1448, 1098 cm^{-1}; ^1H NMR δ: 9.85 (1H, d, J = 1 Hz, H-1), 7.50–7.20 (15H, m, Ph), 3.82–3.74 (2H, m), 3.60–3.37 (3H, m), 3.50 (3H, s, OCH_3), 3.38 (3H, s, OCH_3), 3.33 (3H, s, OCH_3), 3.25–3.20 (1H, m), 3.21 (3H, s, OCH_3); ^{13}C NMR δ: 202.6 (d, C-1), 143.9 (s, Ph), 128.7 (d, Ph), 127.8 (d, Ph), 127.1 (d, Ph), 87.1 (s, CPh_3), 86.0 (d, C-2), 79.7 (d), 79.3 (d), 78.8 (d), 62.0 (t, C-6), 60.6 (q, OCH_3), 60.6 (q, OCH_3), 58.6 (q(x2), OCH_3); MS (CI, NH_3), m/z (relative intensity): 496 ([M + 18]$^+$, 14), 428 (100), 411 (35), 366 (14).

*2,3,4,5-Tetra-*O*-methyl-6-*O*-trityl-*D*-galactose (*D*-**10**)*

Oxidation of D-**9** as described above for (±)-**9** gave D-**10** (spectral data indistinguishable from (±)-**10**).

*2,3,4,5-Tetra-*O*-methyl-6-*O*-trityl-*D*-galactose (*L*-**10**)*

Oxidation of L-**9** as described above for (±)-**9** gave L-**10** (spectral data indistinguishable from (±)-**10**).

*2,3,4-Tri-*O*-methyl-*D*-galacitol (**12**)*

$NaBH_4$ (150 mg, 3.9 mmol) was added to a solution of **11** (1.5 g, 6.8 mmol) in EtOH (10 mL) and the mixture was stirred overnight. TFA (2 mL) was slowly added (**CAUTION**: H_2 evolution) to the mixture and, after stirring for 10 min, the solution was diluted with toluene and concentrated under reduced pressure. Fractionation of the residue by FCC (EtOAc:hexane, 1:1, and then MeOH:CH_2Cl_2, 1:9) gave triol **12** (36, 37) as a colorless oil (1.2 g, 80%); IR: 3417, 2925, 1459, 1091 cm^{-1}; ^1H NMR (D_2O) δ: 3.65 (2H, m), 3.55 (2H, m), 3.40–3.20 (4H, m), 3.29 (3H, s, OCH_3), 3.16 (6H, s, OCH_3); MS (CI, NH_3), m/z (relative intensity): 242 ([M + 18]$^+$, 8), 225 ([M + 1]$^+$, 100), 111 (23), 101 (22), 87 (15).

*2,3,4-Tri-*O*-methyl-6-*O*-trityl-*D*-galacitol (**13**) and 2,3,4-tri-*O*-methyl-1-*O*-trityl-*D*-galacitol (**14**)*

Trityl chloride (61 mg, 0.21 mmol) was added to a solution of triol **5** (40.1 mg, 0.18 mmol) and DMAP (11 mg, 0.09 mmol) in pyridine (5 mL). After stirring for 24 h at room temperature, the mixture was diluted with toluene, concentrated under reduced pressure, and the residue fractionated by FCC (EtOAc:hexane, 1:1, and then MeOH:CH_2Cl_2, 1:9) yielding a 2:1 mixture (^1H NMR) of diols **13** and **14** as a yellow oil (50 mg, 60%) and recovered triol **5** as a yellow oil (8 mg, 20%). The mixture of diols was refractionated by preparative TLC (EtOAc:hexane, 1:1; multiple elution) to give diol **13** as a yellow oil (31 mg, 37%); IR: 3434, 3056, 2933, 1680, 1184, 1129 cm^{-1}; ^1H NMR δ: 7.50–7.15 (1.5H, m, Ph), 3.95 (1H, br t, J = 6 Hz, H-5), 3.87 (1H, dd, J = 5, 11.5 Hz, H-1), 3.78 (1H, dd, J = 4, 11.5 Hz, H-1), 3.60 (1H, dd, J = 1.5, 6.5 Hz, H-4), 3.52 (3H, s, OCH_3), 3.50 (1H, m, H-3), 3.47 (3H, s, OCH_3), 3.41 (1H, dt, J = 4, 4.5 Hz, H-2), 3.34 (1H, dd, J = 6, 9 Hz, H-6), 3.26 (3H, s, OCH_3), 3.13 (1H, dd, J = 7, 9 Hz, H-6); ^{13}C NMR δ: 143.9 (s, Ph), 128.7 (d, Ph), 127.9 (d, Ph), 127.1 (d, Ph), 86.8 (s, CPh_3), 81.5 (d), 80.2 (d), 79.1 (d), 69.8 (d, C-5), 64.5 (t, C-6), 60.9 (t, C-1), 60.5 (q, OCH_3), 60.1 (q, OCH_3), 58.0 (q, OCH_3); MS (CI, NH_3), m/z (relative intensity): 484 ([M + 18]$^+$, 1) 403 (2), 243 (100); and diol **14** as a yellow oil (15 mg, 18%); IR: 3456, 3054, 2935, 1093 cm^{-1}; ^1H NMR δ: 7.52–7.21 (15H, m, Ph), 3.76 (1H, m), 3.70–3.50 (3H, m), 3.48 (1H, m), 3.40 (6H, s, OCH_3), 3.37 (3H, s, OCH_3), 3.48–3.23 (5H, m); ^{13}C NMR δ: 143.8 (s, Ph), 128.7 (d, Ph), 127.9 (d, Ph), 127.2 (d, Ph), 87.1 (s, CPh_3), 80.5 (d), 79.9 (d), 79.3 (d), 71.4 (d, C-5), 64.7 (t, C-6), 61.9 (t, C-1), 61.2 (q, OCH_3), 59.7 (q, OCH_3), 58.4 (q, OCH_3); MS (Cl, NH_3), m/z (relative intensity): 484 ([M + 18]$^+$, 11), 403 (14), 263 (16), 262 (66), 260 (17), 243 (100).

*1,5-Di-*O*-acetyl-2,3,4-tri-*O*-methyl-6-*O*-trityl-*D*-galacitol (**15**)*

Acetic anhydride (4 drops) was added to a solution of diol **13** (5 mg) and pyridine (8 drops) in CH_2Cl_2 (1 mL) and the mixture was stirred overnight. The reaction mixture was diluted with toluene, concentrated under reduced pressure, and the residue fractionated by FCC (EtOAc:hexane, 1:1) yielding **15** as yellowish oil (5 mg); IR: 3058, 2929, 1741, 1234, 1093 cm^{-1}; ^1H NMR δ: 7.50–7.05 (15H, m, Ph), 5.34 (1H, dt, J = 2, 6.5 Hz, H-5), 4.41 (1H, dd, J = 6, 11.5 Hz, H-1), 4.21 (1H, dd, J = 6.5, 11.5 Hz, H-1), 3.73 (1H, dd, J = 2, 9 Hz, H-6), 3.59 (1H, dt, J = 2, 6.5 Hz, H-2), 3.50 (1H, m, H-4), 3.45 (3H, s, OCH_3), 3.38 (3H, s, OCH_3), 3.26 (3H, s, OCH_3), 3.22 (1H, dd, J = 2, 8.5 Hz, H-3), 3.15 (1H, dd, J = 7, 9 Hz, H-6), 2.09 (3H, s, CH_3CO), 2.07 (3H, s, CH_3CO); ^{13}C NMR δ: 170.7 (s, C=O), 170.2 (s, C=O, 143.7 (s, Ph), 128.6 (d, Ph), 127.9 (d, Ph), 127.1 (d, Ph), 87.1 (s, CPh_3), 79.8 (d), 78.1 (d), 77.8 (d), 72.1 (d, C-5), 62.9 (t), 61.6 (t), 60.8 (q, OCH_3), 60.8 (q, OCH_3), 58.3 (q, OCH_3), 21.1 (q, CH_3CO), 20.9 (q, CH_3CO); MS (Cl, NH_3), m/z (relative intensity): 568 ([M + 18]$^+$, 3), 244 (26), 243 (100).

*5,6-Di-*O*-acetyl-2,3,4-tri-*O*-methyl-1-*O*-trityle-*D*-galacitol (**16**)*

Acetylation of diol **14** (5 mg) as decribed above gave **16** as yellowish oil (5 mg); IR: 3054, 2933, 1743, 1221, 1093 cm^{-1}; ^1H NMR δ: 7.50–7.20 (15H, m, Ph), 5.30 (1H, dt, J = 1.5, 7.5 Hz, H-5), 4.27 (2H, m, H-6), 3.60–3.42 (4H, m), 3.47 (3H, s, OCH_3), 3.36 (3H, s, OCH_3), 3.22 (1H, m), 3.17 (3H, s, OCH_3), 2.14 (3H, s, CH_3CO), 2.05 (3H, s, CH_3CO); ^{13}C NMR δ: 170.6 (s, C=O), 170.2 (s, C=O), 143.9 (s, Ph), 128.6 (d, Ph), 127.9 (d, Ph), 127.2 (d, Ph), 87.2 (s, CPh_3), 79.3 (d), 78.7 (d), 78.2 (d), 70.9 (d, C-5), 62.7 (t, C-6), 61.6 (t, C-1), 61.0 (q, OCH_3), 60.8 (q, OCH_3), 58.2 (q, OCH_3), 21.0 (q, CH_3CO), 20.8 (q, CH_3CO); MS (CI, NH_3), m/z (relative intensity): 568 ([M + 18]$^+$, 2), 326 (19), 309 (14), 262 (13), 244 (31), 243 (100).

*1-*O*-(tert-Butyldimethylsilyl)-2,3,4-tri-*O*-methyl-6-*O*-trityl-*D*-galacitol (**17**)*

TBDMSCl (10 mg, 0.07 mmol) was added to a solution of diol **13** (27 mg, 0.06 mmol) and imidazole (7 mg, 0.11 mmol) in CH_2Cl_2 (4 mL), and the mixture was stirred overnight. The reaction mixture was diluted with $NH_4Cl_{(aq)}$ (4 mL), extracted with CH_2Cl_2 (3 × 10 mL), and the combined organic layers was dried over $Na_2SO_{4(s)}$, concentrated, and fractionated by preparative TLC (EtOAc:hexane, 1:1) to give **17** as a pale yellow oil (26 mg, 77%); IR: 3465, 3058, 2951, 1091 cm^{-1}; ^1H NMR δ: 7.50–7.20 (15H, m, Ph), 4.02 (1H, m), 3.88 (1H, dd, J = 5.5, 10 Hz), 3.76 (1H, dd, J = 6.5, 10 Hz), 3.53 (2H, br s), 3.51 (3H, s, OCH_3), 3.47 (3H, s, OCH_3), 3.47–3.30 (2H, m), 3.24 (3H, s, OCH_3), 3.13 (1H, dd, J = 7, 9 Hz), 0.91 (9H, s, $SiC(CH_3)_3$), 0.10 (6H, s, $SiCH_3$); ^{13}C NMR δ: 144.0 (s, Ph), 128.7 (d, Ph), 127.8 (d, Ph), 127.0 (d, Ph), 86.7 (s, CPh_3), 81.1 (d), 79.2 (d), 78.8 (d), 69.9 (d, C-5), 64.8 (t, C-6), 61.4 (t, C-1), 61.0 (q, OCH_3), 59.9 (q, OCH_3), 58.6 (q, OCH_3), 25.9 (q, $SiC(CH_3)_3$), 18.2 (s, $SiC(CH_3)_3$); MS (CI, NH_3), m/z (relative intensity): 598 ([M + 18]$^+$, 5), 395 (22), 354 (14), 340 (100); and the recovered diol **13** (2 mg, 11%).

*1-*O*-(tert-Butyldimethylsilyl)-2,3,4,5-tetra-*O*-methyl-6-*O*-trityl-*D*-galacitol (D-**18**)*

NaH (50% in oil, 10 mg, 0.21 mmol) was added to a solution of alcohol **17** (21 mg, 0.04 mmol) in THF (5 mL). After stirring for 10 min, CH_3I (0.014 mL, 0.23 mmol) was added to the suspension, and the mixture was stirred at room temperature overnight and then concentrated. The residue was triturated with $CHCl_3$ (3 × 5 mL) and the combined filtrates concentrated and fractionated by preparative TLC (EtOAc:hexane, 1:3) to give D-**18** as a colorless oil (20 mg, 93%); IR: 3054, 2923, 1447, 1097 cm^{-1}; ^1H NMR δ: 7.50–7.20 (15H, m, Ph), 3.92 (1H, dd, J = 6, 10 Hz), 3.73 (1H, dd, J = 7.5, 10 Hz), 3.60–3.40 (5H, m), 3.47 (3H, s, OCH_3), 3.46 (3H, s, OCH_3), 3.41 (3H, s, OCH_3), 3.30–3.20 (1H, m), 3.21 (3H, s, OCH_3), 0.89 (9H, s, $SiC(CH_3)_3$), 0.08 (6H, s, $SiCH_3$); ^{13}C NMR δ: 144.0 (s, Ph), 128.7 (d, Ph), 127.8 (d, Ph), 127.0 (d, Ph), 87.1 (s, CPh_3), 80.5 (d), 79.3 (d), 79.1 (d), 78.4 (d), 62.6 (t), 61.5 (t), 60.7 (q, OCH_3), 60.6 (q, OCH_3), 58.4 (q, OCH_3), 58.3 (q, OCH_3), 25.9 (q, $SiC(CH_3)_3$), 18.2 (s, $SiC(CH_3)_3$); MS (Cl, NH_3), m/z (relative intensity): 612 ([M + 18]$^+$, 23), 537 (100), 535 (17), 430 (20), 428 (43).

*1-*O*-(tert-Butyldimethylsilyl)-2,3,4,5-tetra-*O*-methyl-6-*O*-trityl-*L*-galacitol (L-**18**)*

NaH (50% oil, 7 mg, 0.15 mmol) was added to a solution of alcohol **19** (10 mg, 0.02 mmol) in THF (5 mL). After stirring for 10 min, CH_3I (0.01 mL, 0.16 mmol) was added to a suspension, and

Can. J. Chem. Downloaded from www.nrcresearchpress.com by EESC ESCOLA DE ENGENHARIA on 09/08/12
For personal use only.

the mixture was stirred at room temperature overnight and concentrated. The residue was triturated with $CHCl_3$ (3 × 5 mL) and the combined filtrates concentrated and fractionated by preparative TLC (EtOAc:hexane, 1:3) to give L-**18** as a colorless oil (9 mg, 88%; spectral data indistinguishable from D-**18**).

*1-O-(tert-Butyldimethylsilyl)-3,4,5-tri-O-methyl-6-O-trityl-L-galacitol (**19**)*

TBDMSCl (32 mg, 0.21 mmol) was added to a solution of diol **14** (81 mg, 0.17 mmol) and imidazole (29 mg, 0.42 mmol) in CH_2Cl_2 (4 mL), and the mixture was stirred overnight. The reaction mixture was diluted with $NH_4Cl_{(aq)}$ (4 mL), extracted with CH_2Cl_2 (3 × 10 mL), and the combined organic layers was dried over $Na_2SO_{4(s)}$, concentrated, and fractionated by preparative TLC (EtOAc:hexane, 1:1) to give alcohol **19** as a pale yellow oil (79 mg, 78%); IR: 3474, 3058, 2950, 1093 cm^{-1}; ^1H NMR δ: 7.50–7.20 (15H, m, Ph), 4.02 (1H, m), 3.82–3.70 (2H, m), 3.69–3.61 (1H, m), 3.50–3.45 (2H, m), 3.45–3.38 (2H, m), 3.44 (3H, s, OCH_3), 3.40 (3H, s, OCH_3), 3.30 (3H, s, OCH_3), 0.88 (9H, s, $SiC(CH_3)_3$), 0.08 (6H, s, $SiCH_3$); ^{13}C NMR δ: 144.0 (s, Ph), 128.7 (d, Ph), 127.8 (d, Ph), 127.1 (d, Ph), 87.2 (s, CPh_3), 79.6 (d), 79.2 (d), 78.4 (d), 71.1 (d, C-5), 64.4 (t, C-6), 62.3 (t, C-1), 60.8 (q, OCH_3), 60.2 (q, OCH_3), 58.5 (q, OCH_3), 25.9 (q, $SiC(CH_3)_3$), 18.2 (s, $SiC(CH_3)_3$); MS (Cl, NH_3), m/z (relative intensity): 598 ($[M + 18]^+$, 2), 353 (6), 339 (100), 330 (18); and the recovered diol **14** (5 mg, 6%).

*(E)-2,3,4,5-Tetra-O-methyl-D-galactose 2,4-dinitrophenylhydrazone (D-**20**) and (Z)-2,3,4,5-tetra-O-methyl-D-galactose 2,4-dinitro phenylhydrazone (D-**21**)*

DNPH (ca. 5 mg) was added to a stirred solution of D-**5** (3 mg) in CH_2Cl_2 (0.5 mL). After 24 h, the reaction mixture was diluted with $NaHCO_{3(aq)}$ (5 mL) and extracted with CH_2Cl_2 (10 mL). The CH_2Cl_2 layer was dried over $Na_2SO_{4(s)}$ and concentrated under reduced pressure. ^1H NMR of the crude product indicated the presence a 4:1 mixture of (*E*) and (*Z*) hydrazones.[27] Fractionation of the residue by preparative TLC (EtOAc:hexane, 1:1) gave D-**20** (4 mg, 75%); ^1H NMR δ: 9.15 (1H, d, J = 2.5 Hz, Ph), 8.35 (1H, dd, J = 2.5, 9.5 Hz, Ph), 8.00 (1H, d, J = 9.5 Hz, Ph), 7.58 (1H, d, J = 6.5 Hz, H-1), 4.18 (1H, br d, J = 7 Hz, H-2), 4.00–3.85 (2H, m), 3.61 (2H, br s), 3.58–3.50 (1H, m), 3.54 (3H, s, OCH_3), 3.51 (3H, s, OCH_3), 3.48 (3H, s, OCH_3), 3.45 (3H, s, OCH_3); and D-**21** (1 mg, 19%); ^1H NMR δ: 9.15 (1H, d, J = 2.5 Hz, Ph), 8.32 (1H, dd, J = 2.5, 9.5 Hz, Ph), 7.97 (1H, d, J = 9.5 Hz, Ph), 7.00 (1H, d, J = 4 Hz, H-1), 4.29 (1H, dd, J = 3.5, 4 Hz, H-2), 4.00–3.85 (2H, m), 3.72–3.62 (2H, m), 3.58–3.50 (1H, m), 3.54 (3H, s, OCH_3) 3.49 (3H, s, OCH_3), 3.46 (3H, s, OCH_3), 3.41 (3H, s, OCH_3).

*(E)-2,3,4,5-Tetra-O-methyl-L-galactose 2,4-dinitrophenylhydrazone (L-**20**) and (Z)-2,3,4,5-tetra-O-methyl-L-galactose 2,4-dinitro phenylhydrazone (L-**21**)*

Analogous treatment of L-**5** with DNPH as above provided L-**20** and L-**21** (^1H NMR indistinguishable from D-**20** and D-**21**, respectively).

*6-O-[(2R)-2-Methoxy-2-(trifluoromethyl)-2-phenylacetyl]-2,3,4,5-tetra-O-methyl-D-galactose 2,4-dinitrophenylhydrazone (D-**22**)*

A solution of (*S*)-MTPACl (2 mg, 0.007 mmol)[28] in CH_2Cl_2 (0.2 mL) was added to a solution of alcohol D-**20** (1.7 mg, 0.004 mmol), Et_3N (0.002 mL, 0.014 mmol), and DMAP (ca. 0.5 mg) in CH_2Cl_2 (0.3 mL). After stirring for 1 h, the reaction mixture was diluted with toluene and concentrated under reduced pressure. Fractionation of the residue by preparative TLC (EtOAc:hexane, 1:1) gave D-**22** as a yellow oil (2 mg); ^1H NMR δ: 9.14 (1H, d, J = 2.5 Hz, NPh), 8.35 (1H, dd, J = 2.5, 9.5 Hz, NPh), 7.98 (1H, d, J = 9.5 Hz, NPh), 7.60–7.50 (3H, m, Ph), 7.45–7.40 (3H, m, H-1, Ph), 4.66 (1H, dd, J = 6, 11 Hz, H-6), 4.46 (1H, dd, J = 6, 11 Hz, H-6), 4.13 (1H, dd, J = 2.5, 6 Hz, H-2), 3.73 (1H, dt, J = 2, 6 Hz, H-5), 3.58 (1H, dd, J = 2.5, 8.5 Hz, H-3), 3.56 (3H, br s, C-2′ OCH_3), 3.47 (1H, dd, J = 2, 8.5 Hz, H-4), 3.43 (3H, s, OCH_3), 3.42 (3H, s, OCH_3), 3.40 (3H, s, OCH_3), 3.39 (3H, s, OCH_3); MS (electron capture; negative ion: ECNI) (CI, NH_3), m/z (relative intensity): 632 ($[M]^-$, 5), 233 (6), 202 (8), 200 (10), 189 (10), 182 (100).

*6-O-[(2R)-2-Methoxy-2-(trifluoromethyl)-2-phenylacetyl]-2,3,4,5-tetra-O-methyl-L-galactose 2,4-dinitrophenylhydrazone (L-**22**)*

Treatment of L-**20** (1.8 mg) with (*S*)-MTPACl as above gave ester L-**22** as a yellow oil (2 mg); ^1H NMR δ: 9.14 (1H, d, J = 2.5 Hz, NPh), 8.35 (1H, dd, J = 2.5, 9.5 Hz, NPh), 7.98 (1H, d, J = 9.5 Hz, NPh), 7.60–7.50 (3H, m, Ph), 7.45–7.40 (3H, m, H-1, Ph), 4.61 (1H, dd, J = 6, 11 Hz, H-6), 4.48 (1H, dd, J = 6, 11 Hz, H-6), 4.13 (1H, dd, J = 2.5, 6.5 Hz, H-2), 3.80–3.70 (1H, m), 3.65–3.55 (1H, m), 3.57 (3H, s, OCH_3), 3.55–3.40 (2H, m), 3.48 (3H, s, OCH_3), 3.42 (6H, s, OCH_3), 3.36 (3H, s, OCH_3); MS (ECNI; CI, NH_3), m/z (relative intensity): 632 ($[M]^-$, 4), 182 (100).

*(galacto)-1,1,2,3,4,5,6,6-Octamethoxyhexane (**23**)*

To a solution of **4** (10 mg, 0.043 mmol) in methanol (1 mL) were added $(CH_3O)_3CH$ (0.1 mL) and HCl (5% in methanol, a few drops). After stirring overnight at room temperature, the reaction mixture was quenched by addition of $NaHCO_{3(s)}$, filtered, and concentrated. The resulting residue was fractionated by FCC (EtOAc:hexane, 1:1) yielded **23** as a colorless oil (14 mg, 100%); IR: 2937, 2832, 1100 cm^{-1}; ^1H NMR δ: 4.54 (2H, d, J = 7.5 Hz, H-1, 6), 3.57 (6H, s, CH_3O), 3.53–3.43 (4H, m, H-2, 3, 4, 5), 3.51 (6H, s, CH_3O), 3.45 (6H, s, CH_3O), 3.36 (6H, s, CH_3O); ^{13}C NMR δ: 105.2 (d, C-1, 6), 79.4 (d), 79.2 (d), 60.4 (q, CH_3O), 59.9 (q, CH_3O), 55.6 (q, CH_3O), 52.5 (q, CH_3O); MS (CI, NH_3), m/z (relative intensity): 295 ($[M - OCH_3]^+$, 100), 224 (23), 207 (43), 101 (73), 75 (100).

*Methyl (±)-2,3,4,5-tetramethoxy-α-galactoseptanoside ((±-**24**)*

To a solution of (±)-**10** (15 mg, 0.031 mmol) in methanol (1 mL) were added $(CH_3O)_3CH$ (0.1 mL) and HCl (5% in methanol, a few drops). After stirring overnight at room temperature, the reaction mixture was quenched by addition of $NaHCO_{3(s)}$, and filtered. The resulting filtrate was concentrated, and fractionated by FCC (EtOAc:hexane, 1:1) yielding (±)-**24** as a colorless oil (7 mg, 89%); IR: 2931, 2903, 2823, 1192 cm^{-1}; ^1H NMR δ: 4.50 (1H, d, J = 2.5 Hz, H-1), 4.11 (1H, dd, J = 2.5, 13.5 Hz, H-6), 3.80–3.75 (2H, m, H-3, 4), 3.69 (1H, dd, J = 3.5, 13.5 Hz, H-6), 3.57–3.50 (2H, m, H-2, 5), 3.54 (3H, s, CH_3O), 3.50 (3H, s, CH_3O), 3.48 (3H, s, CH_3O), 3.43 (3H, s, CH_3O), 3.40 (3H, s, CH_3O); ^{13}C NMR δ: 105.7 (d, C-1), 81.8 (d), 81.3 (d), 80.7 (d), 80.6 (d), 67.9 (t, C-6), 60.3 (q, CH_3O), 59.3 (q, CH_3O), 59.0 (q, CH_3O), 57.1 (q, CH_3O), 56.0 (q, CH_3O); MS (CI, NH_3), m/z (relative intensity): 268 ($[M + 18]^+$, 48), 236 (64), 219 (100).

Reaction of (±)-**5** under the same conditions produced (±)-**24** in analogous yield. Samples of D- and L-**24** (spectral data indistinguishable from (±)-**24**) were similarly available from D- and L-**10**, respectively.

*2,2,2-Trifluoroethyl (±)-2,3,4,5-tetra-O-methylgalactoseptanoside ((±)-**25**)*

To a solution of (±)-**10** (20 mg, 0.042 mmol) in trifluoroethanol (0.5 mL) was added TsOH (ca. 3 mg). After stirring 24 h at room temperature, the reaction mixture was quenched by addition of $NaHCO_{3(s)}$, and filtered. The resulting filtrate was concentrated, and fractionated by FCC (EtOAc:hexane, 1:3) yielding (±)-**25** as a colorless oil (ca. a 1:2 mixture of α and β amomers; 13.5 mg, 100%); IR: 2935, 2828, 1280, 1110 cm^{-1}; ^1H NMR δ (β anomer): 4.58 (1H, d, J = 6 Hz, H-1), 4.16–3.55 (5H, m), 3.54 (3H, s, CH_3O), 3.50 (6H, s, CH_3O), 3.46 (3H, s, CH_3O), 3.22 (1H, dd, J = 3.5, 3.5 Hz); δ (α anomer): 4.76 (1H, d, J = 2 Hz, H-1), 3.56 (3H, s, CH_3O), 3.50 (3H, s, CH_3O), 3.48 (3H, s, CH_3O), 3.40 (3H, s, CH_3O); ^{13}C NMR δ: 123.9 (s (q, $^1J_{CF}$ = 278 Hz), CF_3), 104.4 (d, C-1), 80.6 (d), 80.6 (d), 80.1 (d), 79.3 (d), 77.4 (d), 64.6 (t (q, $^2J_{CF}$ = 35 Hz), CH_2CF_3), 60.4 (q, CH_3O), 60.0 (q, (H_3O), 59.2 (q, CH_3O), 58.6 (t, C-6), 57.2 (q, CH_3O); δ (α anomer): 124.0 (s(q, $^1J_{CF}$ = 278 Hz), CF_3), 104.4 (d, C-1), 82.0 (d), 81.3 (d), 80.8 (d), 80.3 (d), 68.0 (t, C-6), 61.0 (q, CH_3O), 59.6 (q, CH_3O), 59.0 (q, CH_3O), 57.3 (q, CH_3O); ^{19}F NMR [H], δ (TFA): −74.63 (α anomer), −74.67 (β anomer); in the presence of (+)-Eu(hfc)$_3$ the signals for the enantiomers of the α anomer are cleanly separated. The high-field signal is due to the D-enantiomer; MS (CI, NH_3), m/z (relative intensity): 336 ($[M + 18]^+$, 51), 236 (59), 219 (100).

Can. J. Chem. Downloaded from www.nrcresearchpress.com by EESC ESCOLA DE ENGENHARIA on 09/08/12
For personal use only.

*(D-gluco-2,3,4,5-Tetramethoxyhexanedial (**26**)*

DMSO (1.0 M in CH_2Cl_2, 0.88 mL, 0.88 mmol) was added dropwise via syringe to a solution of $(COCl)_2$ (48 mg, 0.38 mmol) in CH_2Cl_2 (1 mL) at −78°C. The reaction mixture was stirred at −78°C for 30 min and a solution of diol **29** (30 mg, 0.12 mmol) in CH_2Cl_2 (1 mL) was added dropwise via syringe. The resulting mixture was allowed to warm to −55 to −50°C (internal) in 10 min and stirred at that temperature for a further 50 min. Et_3N (0.17 mL, 1.3 mmol) was added and, after stirring at −55°C for 10 min, the mixture was allowed to warm to room temperature, and then was concentrated and fractionated by FCC (EtOAc:hexane, 1:1) yielding **26** as a colorless oil (27 mg, 93%); IR: 2987, 2833, 1729, 1093 cm^{-1}; ^1H NMR δ: 9.72 (1H, s), 9.71 (1H, d, J = 2 Hz), 3.86 (1H, d, J = 5 Hz), 3.83 (1H, dd, J = 2, 5 Hz), 3.76 (1H, dd, J = 4, 5 Hz), 3.69 (1H, dd, J = 4, 5 Hz), 3.50 (3H, s, CH_3O), 3.48 (3H, s, CH_3O), 3.44 (3H, s, CH_3O), 3.31 (3H, s, CH_3O); ^{13}C NMR δ: 200.7 (d), 199.6 (d), 85.6 (d), 83.2 (d), 81.7 (d), 80.3 (d), 59.9 (q, CH_3O), 59.7 (q, CH_3O), 59.0 (q, CH_3O), 58.8 (q, CH_3O); MS (CI, NH_3), m/z (relative intensity): 252 ([M + 18]$^+$, 100), 235 ([M + 1]$^+$, 50), 101 (66).

*General procedure for reduction of **26** with Alpine-Borane®*

Alpine-Borane® (0.5 M in THF, 3 equiv.) was added via syringe to a solution of **26** in CH_2Cl_2 (10–50 mg, 0.04–0.2 mmol; 0.012 M for (*R*)-Alpine-Borane®; 0.025 M for (*S*)-Alpine-Borane®) at −78°C. After stirring for the indicated time, acetaldehyde (excess, ca. 0.1–0.2 mL) was added and the mixture stirred for a further 0.5 h. The reaction mixture was allowed to warm to room temperature and concentrated. The resulting crude product (or aliquots) was processed in one (or more) of the following ways:

*For isolation of **27**, **28**, and **29***: The crude product was dissolved in ether and silica gel was added. The suspension was stirred at ambient temperature for 40 min and filtered.[36] The combined filtrate and washings was concentrated and fractionated by FCC (EtOAc:hexane, 1:4, and then MeOH:CH_2Cl_2, 1:9) to give a hydroxyaldehyde fraction and a diol fraction. The hydroxyaldehyde fraction was further purified by FCC (EtOAc:hexane, 1:1) to give a mixture of **26** and **27**. The diol fraction was further purified by FCC (MeOH:CH_2Cl_2, 1:9) to give **29**.

*For measurement of conversion and ratio of **27** and **28***: The crude product was dissolved in methanol (ca. 1 mL) and $(CH_3O)_3CH$ (0.1 mL) and HCl (5% in methanol, a few drops) were added. After stirring for 1.5 h at room temperature, the reaction mixture was quenched by addition of $NaHCO_{3(s)}$, filtered, and concentrated. The relative amounts of **48–52** present were determined by ^1H NMR.[37] Fractionation by preparative TLC (EtOAc:hexane, 1:1, and then MeOH:CH_2Cl_2, 1:9) gave a mixture of **48–52** and pure **29**.

*For measurement of the ratio of **27** to **28***: The crude product was dissolved in CH_2Cl_2 (ca. 0.5 mL) and DNPH (ca. 5 mg) was added. After 24 h, the reaction mixture was concentrated, and fractionated by preparative TLC (EtOAc:hexane, 1:1) to give a mixture of **46** and **47**. The ratio of **46** and **47** was determined by ^1H NMR.

*2,3,4,5-Tetra-O-methyl-D-glucose (**27**)*

To a solution of **44** (30 mg, 0.063 mmol) in acetonitrile (3 mL) was added 5% $HF_{(aq)}$ (2 drops). After stirring for 3 h at room temperature, $NaHCO_{3(s)}$ was added and the reaction mixture was filtered, concentrated, and fractionated by FCC (EtOAc:hexane, 1:1) yielding **27** as colorless oil (13 mg, 87%); IR: 3420, 2930, 2827, 1727 (weak), 1096 cm^{-1}; ^1H NMR δ (hydroxyaldehyde tautomer; partial data): 9.74 (1H, s, H-1), 3.58 (3H, s, OCH_3), 3.53 (3H, s, OCH_3), 3.42 (3H, s, OCH_3), 3.30 (3H, s, OCH_3); δ (β-septanose tautomer; partial data): 4.64 (1H, d, J = 7.5 Hz, H-1), 3.55 (3H, s, OCH_3), 3.51 (3H, s, OCH_3), 3.50 (3H, s, OCH_3), 3.40 (3H, s, OCH_3); ^{13}C NMR δ: 81.3 (d), 81.2 (d), 81.1 (d), 79.0 (d), 61.6 (t), 60.5 (t), 60.3 (q, OCH_3), 59.6 (q, OCH_3), 58.7 (q, OCH_3), 57.3 (q, OCH_3); MS (CI, NH_3), m/z (relative intensity): 254 ([M + 18]$^+$, 6), 237 ([M + 1]$^+$, 5), 236 (6), 220 (100), 143 (37), 101 (53), 61 (62).

[37]Under these conditions, the major products from **27** and **28** were **50** and **52**, respectively.

*2,3,4,5-Tetra-O-methyl-L-gulose (**28**)*

To a solution of **45** (10 mg, 0.021 mmol) in acetonitrile (1 mL) was added 5% $HF_{(aq)}$ (1 drop). After stirring for 1 h at room temperature, $NaHCO_{3(s)}$ was added and then the reaction mixture was filtered, concentrated, and fractionated by preparative TLC (EtOAc:hexane, 1:1) yielding **27** as colorless oil (4 mg, 81%); IR: 3422, 2929, 2824, 1725 (weak), 1100 cm^{-1}; ^1H NMR δ: 5.09 (1H, d, J = 6 Hz, H-1), 3.85 (1H, dd, J = 2, 13.5 Hz), 3.77–3.50 (4H, m), 3.51 (3H, s, OCH_3), 3.50 (3H, s, OCH_3), 3.48 (3H, s, OCH_3), 3.43 (3H, s, OCH_3), 3.26 (1H, m); MS (CI, NH_3), m/z (relative intensity): 237 ([M + 1]$^+$, 62), 220 (100), 187 (53), 143 (26), 101 (88).

*2,3,4,5-Tetra-O-methyl-D-glucitol (**29**)*

To a solution of **31** (178 mg, 0.26 mmol) in $CHCl_3$ (5 mL) and MeOH (2 mL) was added TFA (0.1 mL). After stirring 14 h at room temperature $NaHCO_{3(s)}$ (ca. 1 g) was added and the resulting mixture was filtered, concentrated, and fractionated by FCC (MeOH:CH_2Cl_2, 1:9) to give **29** as a colorless oil (60 mg, quantitative); IR: 3434, 2930, 1111 cm^{-1}; ^1H NMR δ: 3.90 (1H, dd, J = 3.5, 12 Hz), 3.86 (1H, dd, J = 4, 11.5 Hz), 3.71 (1H, dd, J = 3.5, 12 Hz), 3.67 (1H, dd, J = 5, 11.5 Hz), 3.58–3.48 (3H, m), 3.54 (3H, s, OCH_3), 3.51 (3H, s, OCH_3), 3.50 (3H, s, OCH_3), 3.43 (3H, s, OCH_3), 3.42–3.37 (1H, m), 1.88 (2H, br s, OH); ^{13}C NMR δ: 81.3 (d), 81.2 (d), 81.1 (d), 79.0 (d), 61.6 (t), 60.5 (t), 60.3 (q, OCH_3), 59.6 (q, OCH_3), 58.7 (q, OCH_3), 57.3 (q, OCH_3); MS (CI, NH_3), m/z (relative intensity): 239 ([M + 1]$^+$, 100), 207 (25), 101 (26), 87 (15), 71 (19).

*1,6-Di-O-trityl-D-glucitol (**30**)*

To a solution of Ph_3CCl (3.1 g, 11.2 mmol) and DMAP (0.32 g, 2.6 mmol) in pyridine (25 mL) was added D-glucitol (1.0 g, 5.56 mmol). After stirring for 48 h at room temperature, the reaction mixture was diluted with EtOAc (70 mL) and $NH_4Cl_{(aq)}$ (30 mL). The organic layer was washed sequentially with water and brine, and concentrated under reduced pressure. The resulting solid was fractionated by FCC (EtOAc/hexane, 1:1, then MeOH/CH_2Cl_2, 1:4) yielding **30** as a colorless solid (3.7 g, 100%; mp 75.5–77°C [$EtOH_{(aq)}$]); IR: 3424, 3058, 1596, 1075 cm^{-1}; ^1H NMR δ: 7.45–7.20 (30H, m, Ph), 3.88 (2H, br s), 3.80 (1H, br s), 3.63 (1H, br t, J = 5.5 Hz), 3.37–3.30 (3H, m), 3.22 (1H, dd, J = 6, 10 Hz), 3.11 (1H, d, J = 5.5 Hz, OH), 3.01 (1H, br s, OH), 2.99 (1H, d, J = 5.5 Hz, OH), 2.78 (1H, d, J = 6 Hz, OH); ^{13}C NMR δ: 143.6 (s, Ph), 128.6 (d, Ph), 128.0 (d, Ph), 127.2 (d, Ph), 87.1 (s, CPh_3), 73.7 (d), 73.1 (d), 71.6 (d), 70.0 (d), 65.1 (t, C-1 or C-6), 64.9 (t, C-1 or C-6); MS: molecular ion not detected.

*2,3,4,5-Tetra-O-methyl-1,6-di-O-trityl-D-glucitol (**31**)*

To a suspension of NaH (60% in oil; 90 mg, 2.3 mmol) in THF (5 mL) was added a solution of **30** (210 mg, 0.31 mmol) in THF (1 mL) and then iodomethane (0.15 mL, 2.3 mmol). After stirring for 14 h, the reaction mixture was quenched by addition of $NH_4Cl_{(aq)}$ (**CAUTION**: H_2 evolution) and extracted with EtOAc (3 × 15 mL). The combined organic layers were washed sequentially with water and brine, dried over Na_2SO_4, and concentrated. The resulting liquid was fractionated by FCC (EtOAc:hexane, 1:3) yielding **31** as a colorless solid (mp 71–72°C; 310 mg, 72%); IR: 3085, 3051, 2925, 1598, 1093 cm^{-1}; ^1H NMR δ: 7.45–7.20 (30H, m, Ph), 3.67–3.56 (3H, m), 3.56 (3H, s, CH_3O), 3.54 (3H, s, CH_3O), 3.48 (3H, s, CH_3O), 3.43 (2H, m), 3.34 (1H, dd, J = 2.5, 7 Hz), 3.18–3.09 (2H, m), 2.90 (3H, s, CH_3O); ^{13}C NMR δ: 144.2 (s, Ph), 128.9 (d, Ph), 127.8 (d, Ph), 127.0 (d, Ph), 86.7 (s, CPh_3), 86.6 (s, CPh_3), 81.7 (d), 81.1 (d), 80.6 (d), 79.9 (d), 63.5 (t, C-1 or C-6), 62.7 (t, C-1 or C-6), 60.5 (q, CH_3O), 59.9 (q, CH_3O), 59.1 (q, CH_3O), 58.5 (q, CH_3O); MS: molecular ion not detected.

*2,3,4-Tri-O-methyl-D-glucitol (**33**)*

$NaBH_4$ (100 mg, 2.6 mmol) was added to a solution of **32** (1.3 g, 5.9 mmol) in EtOH (20 mL) and the mixture was stirred overnight. TFA (1 mL) was added slowly (**CAUTION**: H_2 evolution) to the mixture and, after stirring for 10 min, the solution was diluted with toluene and concentrated under reduced pressure. Fractionation of the residue by FCC (EtOAc:hexane, 1:1, and then MeOH:CH_2Cl_2, 1:9)

Can. J. Chem. Downloaded from www.nrcresearchpress.com by EESC ESCOLA DE ENGENHARIA on 09/08/12
For personal use only.

gave triol **33** (37) as a colorless oil (1.2 g, 87%); IR: 3394, 2934, 2831, 1085 cm^{-1}; ^1H NMR δ: 3.91–3.76 (2H, m), 3.75–3.68 (2H, m), 3.67–3.58 (1H, m), 3.58–3.40 (3H, m), 3.55 (3H, s, OCH_3), 3.48 (3H, s, OCH_3), 3.45 (3H, s, OCH_3); ^{13}C NMR δ: 81.2 (d), 80.9 (d), 78.8 (d), 71.5 (d), 63.6 (t, C-6), 61.2 (t, C-1), 60.0 (q, OCH_3), 59.3 (q, OCH_3), 58.4 (q, OCH_3); MS (CI, NH_3), m/z (relative intensity): 242 ($[M + 18]^+$, 17), 225 ($[M + 1]^+$, 100), 207 (13), 101 (27).

*2,3,4-Tri-*O*-methyl-6-*O*-trityl-*D*-glucitol* (**34**) *and 2,3,4-tri-*O*-methyl-1-*O*-trityl-*D*-glucitol* (**35**)

Trityl chloride (403 mg, 1.4 mmol) was added to a solution of triol **33** (270 mg, 1.2 mmol) in pyridine (20 mL), and the mixture was stirred at room temperature for 24 h. The mixture was diluted with toluene and concentrated, and fractionated by FCC (EtOAc:hexane, 1:1, and then MeOH:CH_2Cl_2, 1:9) yielding a 1.7:1 mixture (^1H NMR) of diols **34** and **35** as a yellow oil (314 mg, 56%) and recovered triol **33** as a yellowish oil (46 mg, 17%). The mixture of diols was refractionated by FCC (EtOAc:hexane, 1:1) to give diol **34** as a yellow oil (184 mg, 32%); IR: 3448, 2932, 1448, 1090 cm^{-1}; ^1H NMR δ: 7.60–7.20 (15H, m, Ph), 4.05 (1H, q, J = 5.5 Hz), 3.79 (1H, m), 3.60 (1H, m), 3.57–3.47 (3H, m), 3.44 (3H, s, OCH_3), 3.41 (3H, s, OCH_3), 3.35 (1H, dd, J = 6, 9.5 Hz), 3.33–3.27 (1H, m) 3.30 (3H, s, OCH_3); ^{13}C NMR δ: 143.8 (s, Ph), 128.7 (d, Ph), 127.9 (d, Ph), 127.2 (d, Ph), 86.8 (s, CPh_3), 81.4 (d), 81.0 (d), 79.1 (d), 70.2 (d, C-5), 64.7 (t, C-6), 61.5 (t, C-1), 59.9 (q, OCH_3), 58.7 (q, OCH_3), 58.7 (q, OCH_3); MS (CI, NH_3), m/z (relative intensity): 484 ($[M + 18]^+$, 1), 243 (100), 225 (13); and diol **35** as a yellow oil (102 mg, 18%); IR: 3437, 2935, 1448, 1092 cm^{-1}; ^1H NMR δ: 7.50–7.20 (15H, m, Ph), 3.78–3.62 (3H, m), 3.60–3.45 (3H, m), 3.43 (3H, s, OCH_3), 3.40 (3H, s, OCH_3), 3.37–3.32 (2H, m), 3.28 (3H, s, OCH_3), 3.24 (1H, dd, J = 5, 10 Hz); ^{13}C NMR δ: 143.9 (s, Ph), 128.6 (d, Ph), 127.9 (d, Ph), 127.1 (d, Ph), 86.9 (s, CPh_3), 80.4 (d), 79.8 (d), 78.5 (d), 71.6 (d, C-5), 63.9 (t, C-6), 61.7 (t, C-1), 59.9 (q, OCH_3), 58.7 (q, OCH_3), 58.3 (q, OCH_3); MS (CI, NH_3), m/z (relative intensity): 484 ($[M + 18]^+$, 3), 243 (100), 225 (12), 101 (14).

*1,5-Di-*O*-acetyl-2,3,4-tri-*O*-methyl-6-*O*-trityl-*D*-glucitol* (**36**)

Acetic anhydride (4 drops) was added to a solution of diol **34** (5 mg) and pyridine (8 drops) in CH_2Cl_2 (1 mL) and the mixture was stirred overnight. The reaction mixture was diluted with toluene, concentrated under reduced pressure, and the residue fractionated by FCC (EtOAc:hexane, 1:1) yielding **34** as yellowish oil (5 mg, 85%); IR: 3085, 3063, 3027, 2932, 2830, 1740, 1234, 1094 cm^{-1}; ^1H NMR δ: 7.50–7.15 (15H, m, Ph), 5.22 (1H, ddd, J = 3, 5.5, 5.5 Hz, H-5), 4.31 (1H, dd, J = 3.5, 12 Hz, H-1), 4.16 (1H, dd, J = 6.5, 12 Hz, H-1), 3.66 (1H, dd, J = 3.5, 5.5 Hz, H-4), 3.58 (1H, ddd, J = 3.5, 5.5, 6.5 Hz, H-2), 3.55–3.35 (3H, m, H-3, 6), 3.46 (3H, s, OCH_3), 3.38 (3H, s, OCH_3), 3.31 (3H, s, OCH_3), 2.17 (3H, s, CH_3CO), 2.08 (3H, s, CH_3CO); ^{13}C NMR δ: 170.8 (s, C=O), 170.0 (s, C=O), 143.8 (s, Ph), 128.7 (d, Ph), 127.8 (d, Ph), 127.1 (d, Ph), 86.6 (s, CPh_3), 80.4 (d), 79.3 (d), 79.3 (d), 73.1 (d), 64.1 (t), 62.0 (t), 60.6 (q, OCH_3), 60.2 (q, OCH_3), 59.0 (q, OCH_3), 21.2 (q, CH_3CO), 20.9 (q, CH_3CO); MS: molecular ion not detected.

*5,6-Di-*O*-acetyl-2,3,4-tri-*O*-methyl-1-*O*-trityl-*D*-glucitol* (**37**)

Acetylation of diol **35** (5 mg) as above gave **37** as yellowish oil (5 mg, 85%); IR: 2923, 1745, 1242, 1093, 706 cm^{-1}; ^1H NMR δ: 7.50–7.20 (15H, m, Ph), 5.20 (1H, m, H-5), 4.53 (1H, dd, J = 2.5, 12 Hz, H-6), 4.08 (1H, dd, J = 6.5, 12 Hz, H-6), 3.63–3.46 (3H, m), 3.47 (6H, s, OCH_3), 3.38 (1H, m), 3.13 (3H, s, OCH_3), 3.07 (1H, dd, J = 4.5, 10 Hz, H-1), 2.07 (3H, s, CH_3CO), 2.00 (3H, s, CH_3CO); ^{13}C NMR δ: 170.7 (s, C=O), 169.9 (s, C=O), 143.9 (s, Ph), 128.7 (d, Ph), 127.8 (d, Ph), 127.1 (d, Ph), 86.7 (s, CPh_3), 81.3 (d), 81.0 (d), 80.1 (d), 71.8 (d), 62.6 (t), 62.3 (t), 61.0 (q, OCH_3), 60.2 (q, OCH_3), 58.7 (q, OCH_3), 21.1 (q, CH_3CO), 20.8 (q, CH_3CO); MS: molecular ion not detected.

*1-*O*-(*tert*-Butyldimethylsilyl)-2,3,4-tri-*O*-methyl-6-*O*-trityl-*D*-glucitol* (**38**)

TBDMSCl (33 mg, 0.22 mmol) was added to a solution of diol **34** (85 mg, 0.18 mmol) and imidazole (30 mg, 0.44 mmol) in CH_2Cl_2 (5 mL). After stirring for 24 h, the reaction mixture was diluted with $NH_4Cl_{(aq)}$ (5 mL) and extracted with CH_2Cl_2 (2 × 10 mL). The combined organic layers were dried over $Na_2SO_{4(s)}$, concentrated, and fractionated by FCC (EtOAc:hexane, 1:1) to give alcohol **38** as a pale yellow oil (91 mg, 85%); IR: 3500, 2930, 1090 cm^{-1}; ^1H NMR δ: 7.60–7.20 (15H, m, Ph), 3.96 (1H, m) 3.78 (1H, dd, J = 5, 10.5 Hz), 3.69 (1H, dd, J = 5, 10.5 Hz), 3.55 (1H, dd, J = 3, 6.5 Hz), 3.50–3.40 (2H, m), 3.44 (3H, s, OCH_3), 3.43 (3H, s, OCH_3), 3.35–3.25 (2H, m), 3.28 (3H, s, OCH_3), 3.16 (1H, d, J = 5 Hz, OH); ^{13}C NMR δ: 143.9 (s, Ph), 128.8 (d, Ph), 127.6 (d, Ph), 127.1 (d, Ph), 86.7 (s, CPh_3), 81.6 (d), 80.1 (d), 78.6 (d), 70.9 (d, C-5), 64.7 (t, C-6), 62.3 (t, C-1), 59.6 (q, OCH_3), 58.9 (q, OCH_3), 58.8 (q, OCH_3), 25.9 (q, $SiC(CH_3)_3$), 18.5 (s, $SiC(CH_3)_3$); MS (CI, NH_3), m/z (relative intensity): 598 ($[M + 18]^+$, 1), 563 (10), 339 (8), 243 (100).

*6-*O*-(*tert*-Butyldimethylsilyl)-2,3,4-tri-*O*-methyl-1-*O*-trityl-*D*-glucitol* (**39**)

Silylation of diol **35** (30 mg, 0.06 mmol) as above gave **39** as a pale yellow oil (27 mg, 71%); IR: 3428, 2933, 1092 cm^{-1}; ^1H NMR δ: 7.60–7.20 (15H, m, Ph), 3.98 (1H, dd, J = 2, 11.5 Hz), 3.95 (1H, m), 3.71 (1H, dd, J = 4, 11.5 Hz), 3.57 (1H, dd, J = 1.5, 8 Hz), 3.50 (1H, dd, J = 1.5, 8 Hz), 3.47–3.42 (1H, m), 3.42 (3H, s, OCH_3), 3.40 (3H, s, OCH_3), 3.33–3.26 (2H, m), 3.24 (3H, s, OCH_3), 2.67 (1H, d, J = 6 Hz, OH), 0.91 (9H, s, $SiC(CH_3)_3$), 0.11 (6H, s, $SiCH_3$); ^{13}C NMR δ: 144.1 (s, Ph), 128.7 (d, Ph), 127.8 (d, Ph), 127.0 (d, Ph), 86.7 (s, CPh_3), 81.3 (d), 81.0 (d), 79.3 (d), 71.6 (d, C-5), 64.0 (t, C-6), 63.0 (t, C-1), 60.4 (q, OCH_3), 59.1 (q, OCH_3), 58.8 (q, OCH_3), 25.9 (q, $SiC(CH_3)_3$), 18.5 (s, $SiC(CH_3)_3$); MS (CI, NH_3), m/z (relative intensity): 598 ($[M + 18]^+$, 1), 243 (100); and recovered diol **35** (3 mg, 10%).

*1-*O*-(*tert*-Butyldimethylsilyl)-2,3,4,5-tetra-*O*-methyl-6-*O*-trityl-*D*-glucitol* (**40**)

NaH (50% oil, 20 mg, 0.42 mmol) was added to a solution of alcohol **38** (35 mg, 0.06 mmol) in THF (5 mL). After stirring for 10 min, CH_3I (0.025 mL, 0.42 mmol) was added to the suspension, and the mixture was stirred at room temperature overnight and concentrated. The residue was triturated with $CHCl_3$ (3 × 5 mL) and the combined filtrates concentrated and fractionated by preparative TLC (EtOAc:hexane, 1:3) to give **40** as a colorless oil (30 mg, 83%); IR: 2928, 1448, 1095 cm^{-1}; ^1H NMR δ: 7.50–7.20 (15H, m, Ph), 3.86 (1H, m), 3.70 (1H, m), 3.56 (1H, m), 3.48 (3H, s, OCH_3), 3.47 (6H, s, OCH_3), 3.47–3.40 (4H, m), 3.24 (3H, s, OCH_3), 3.15 (1H, m), 0.91 (9H, s, $SiC(CH_3)_3$), 0.09 (6H, s, $SiCH_3$); ^{13}C NMR δ: 145.1 (s, Ph), 129.6 (d, Ph), 128.6 (d, Ph), 127.7 (d, Ph), 87.2 (s, CPh_3), 83.1 (d), 81.6 (d), 80.9 (d), 80.5 (d), 63.6 (t), 62.9 (t), 60.9 (q, OCH_3), 60.5 (q, OCH_3), 59.6 (q, OCH_3), 58.8 (q, OCH_3), 26.2 (q, $SiC(CH_3)_3$), 18.4 (s, $SiC(CH_3)_3$); MS (CI, NH_3), m/z (relative intensity): 612 ($[M + 18]^+$, 6), 537 (55), 353 (100), 321 (20); and recovered **38** as a colorless oil (3.4 mg, 9%).

*6-*O*-(*tert*-Butyldimethylsilyl)-2,3,4,5-tetra-*O*-methyl-1-*O*-trityl-*D*-glucitol* (**41**)

Methylation of alcohol **39** (47 mg, 0.08 mmol) as above gave **41** as a colorless oil (47 mg, 96%); IR: 2928, 1448, 1098 cm^{-1}; ^1H NMR δ: 7.50–7.20 (15H, m, Ph), 3.87 (1H, dd, J = 2.5, 11 Hz), 3.70–3.60 (2H, m), 3.54 (3H, s, OCH_3), 3.52 (1H, dd, J = 3, 11 Hz), 3.47 (3H, s, OCH_3), 3.38 (1H, dd, J = 3, 10 Hz), 3.40 (3H, s, OCH_3), 3.33–3.23 (2H, m), 3.16 (1H, dd, J = 6, 10 Hz), 3.14 (3H, s, OCH_3), 0.89 (9H, s, $SiC(CH_3)_3$), 0.09 (6H, s, $SiCH_3$); ^{13}C NMR δ: 144.1 (s, Ph), 128.8 (d, Ph), 127.8 (d, Ph), 127.0 (d, Ph), 87.2 (s, CPh_3), 82.3 (d), 81.6 (d), 81.1 (d), 79.7 (d), 63.6 (t), 61.6 (t), 60.6 (q, OCH_3), 60.0 (q, OCH_3), 59.2 (q, OCH_3), 57.9 (q, OCH_3), 26.0 (q, $SiC(CH_3)_3$), 18.3 (s, $SiC(CH_3)_3$): MS (CI, NH_3), m/z (relative intensity): 598 ($[M + 18]^+$, 2), 563 (9), 243 (100).

*2,3,4,5-Tetra-*O*-methyl-6-*O*-trityl-*D*-glucitol* (**42**)

To a solution of **40** (40 mg, 0.067 mmol) in THF (3 mL) was added Bu_4NF (50 mg, 0.19 mmol). After stirring at room temperature overnight, the reaction mixture was concentrated, and fractionated by FCC (EtOAc:hexane, gradient elution from 1:4 to 1:1) yielding **42** as a colorless oil (30 mg, 93%); IR: 3460, 2930, 1093 cm^{-1}; ^1H NMR δ: 7.50–7.20 (15H, m, Ph), 3.82 (1H, dd, J = 3.5, 12 Hz), 3.63 (1H,

Can. J. Chem. Downloaded from www.nrcresearchpress.com by EESC ESCOLA DE ENGENHARIA on 09/08/12
For personal use only.

dd, J = 5.5, 12 Hz), 3.58–3.43 (5H, m), 3.50 (3H, s, OCH_3), 3.49 (3H, s, OCH_3), 3.48 (3H, s, OCH_3), 3.24 (3H, s, OCH_3), 3.14 (1H, dd, J = 4.5, 10 Hz); ^{13}C NMR δ: 144.0 (s, Ph), 128.8 (d, Ph), 127.8 (d, Ph), 127.0 (d, Ph), 86.7 (s, CPh_3), 81.3 (d), 81.0 (d), 80.5 (d), 79.5 (d), 62.2 (t), 62.0 (t), 60.4 (q, OCH_3), 60.0 (q, OCH_3), 58.8 (q, OCH_3), 58.3 (q, OCH_3); MS (CI, NH_3), m/z (relative intensity): 498 ($[M + 18]^+$, 1), 463 (10), 243 (100).

2,3,4,5-Tetra-O-methyl-1-O-trityl-D-glucitol (**43**)

Hydrolysis of **41** (56 mg, 0.094 mmol) as above gave **43** as a colorless oil (40 mg, 89%); IR: 3462, 2931, 1448, 1092 cm^{-1}; ^1H NMR δ: 7.50–7.20 (15H, m, Ph), 3.81 (1H, dd, J = 4, 12 Hz), 3.64 (1H, dd, J = 4, 12 Hz), 3.58–3.42 (3H, m), 3.51 (3H, s, OCH_3), 3.47 (3H, s, OCH_3), 3.39 (3H, s, OCH_3), 3.30–3.22 (2H, m), 3.18 (3H, s, OCH_3), 3.17–3.10 (1H, m); ^{13}C NMR δ: 143.9 (s, Ph), 128.7 (d, Ph), 127.8 (d, Ph), 127.0 (d, Ph), 86.7 (s, CPh_3), 81.5 (d), 81.3 (d), 81.2 (d), 79.6 (d), 62.7 (t), 60.7 (t), 60.2 (q, OCH_3), 60.0 (q, OCH_3), 58.8 (q, OCH_3), 57.3 (q, OCH_3); MS: molecular ion could not be detected; and diol **29** as a colorless oil (2.6 mg, 40%).

2,3,4,5-Tetra-O-methyl-6-O-trityl-D-glucitol (**44**)

To a suspension of **42** (44 mg, 0.092 mmol), 4 Å molecular sieves (200 mg), and NMO (40 mg, 0.34 mmol) in CH_2Cl_2 (5 mL) was added TPAP (8 mg). After stirring at room temperature for 40 min, the reaction mixture was directly fractionated by FCC (EtOAc:hexane, 1:2) yielding **44** as a colorless oil (41 mg, 94%); IR: 2931, 2829, 1727, 1448, 1093 cm^{-1}; ^1H NMR δ: 9.69 (1H, s, H-1), 7.50–7.20 (15H, m, Ph), 3.93 (1H, dd, J = 2, 5.5 Hz, H-3), 3.84 (1H, d, J = 5.5 Hz, H-2), 3.58 (1H, dd, J = 2, 8.5 Hz, H-4), 3.54 (1H, dd, J = 2.5, 10.5 Hz H-6), 3.54 (3H, s, OCH_3), 3.53 (3H, s, OCH_3), 3.50–3.42 (1H, m, H-5), 3.47 (3H, s, OCH_3), 3.05 (1H, dd, J = 4, 10.5 Hz, H-6), 2.97 (3H, s, OCH_3); ^{13}C NMR δ: 199.6 (d, C-1), 143.9 (s, Ph), 128.8 (d, Ph), 127.8 (d, Ph), 127.0 (d, Ph), 86.6 (s, CPh_3), 82.5 (d), 81.6 (d), 79.7 (d), 78.1 (d), 61.6 (t, C-6), 59.6 (q, OCH_3), 59.5 (q, OCH_3), 59.3 (q, OCH_3), 58.3 (q, OCH_3); MS (CI, NH_3), m/z (relative intensity): 496 ($[M + 18]^+$, 100), 372 (21), 262 (53).

2,3,4,5-Tetra-O-methyl-6-O-trityl-L-gulose (**45**)

Oxidation of alcohol **43** (40 mg, 0.083 mmol) as above gave **45** as a colorless oil (38 mg, 95%); IR: 2912, 2829, 1731, 1448, 1091 cm^{-1}; ^1H NMR δ: 9.65 (1H, s, H-1), 7.50–7.20 (15H, m, Ph), 3.74 (1H, dd, J = 2, 3.5 Hz, H-2), 3.58–3.35 (4H, m), 3.46 (3H, s, OCH_3), 3.41 (3H, s, OCH_3), 3.40 (3H, s, OCH_3), 3.18 (3H, s, OCH_3), 3.18–3.04 (2H, m); ^{13}C NMR δ: 200.7 (d, C-1), 143.9 (s, Ph), 128.7 (d, Ph), 127.9 (d, Ph), 127.1 (d, Ph), 86.8 (s, CPh_3), 86.6 (d), 81.8 (d), 81.2 (d), 80.7 (d), 62.1 (t, C-6), 60.8 (q, OCH_3), 59.9 (q, OCH_3), 58.6 (q, OCH_3) 58.3 (q, OCH_3); MS (CI, NH_3), m/z (relative intensity): 496 ($[M + 18]^+$, 3), 243 (100), 165 (10).

2,3,4,5-Tetra-O-methyl-D-glucose 2,4-dinitrophenylhydrazone (**46**)

DNPH (ca. 10 mg) was added to a solution of **27** (3 mg) in CH_2Cl_2 (1 mL). After stirring overnight, the reaction mixture was concentrated, and fractionated by preparative TLC (EtOAc:hexane, 1:1) to give the hydrazone **46** as a yellow oil (7:1 mixture of E:Z isomers; 5 mg); ^1H NMR δ: for (E) isomer (partial data): 9.14 (1H, d, J = 2.5 Hz, Ph), 8.33 (1H, dd, J = 2.5, 9.5 Hz, Ph), 7.97 (1H, d, J = 9.5 Hz, Ph), 7.54 (1H, d, J = 7 Hz, H-1), 4.27 (1H, dd, J = 6.5, 7 Hz, H-2), 3.96 (1H, dd, J = 3.5, 12 Hz, H-6), 3.75–3.65 (2H, m), 3.55 (3H, s, OCH_3), 3.49 (6H, s, OCH_3), 3.44 (3H, s, OCH_3); δ for (Z) isomer (partial data): 7.07 (1H, d, J = 3.5 Hz, H-1), 4.43 (dd, dd, J = 3.5, 6.5 Hz, H-2).

2,3,4,5-Tetra-O-methyl-L-gulose 2,4-dinitrophenylhydrazone (**47**)

Treatment of **28** (3 mg) with DNPH as above gave the hydrazone **47** as a yellow oil (ca. 4:1 mixture of E:Z isomers; 5 mg); ^1H NMR δ for E isomer (partial data): 9.14 (1H, d, J = 2.5 Hz, Ph), 8.34 (1H, dd, J = 2.5, 9.5 Hz, Ph), 7.99 (1H, d, J = 9.5 Hz, Ph), 7.54 (1H, d, J = 7 Hz, H-1), 4.04 (1H, dd, J = 7, 4 Hz, H-2) 3.87 (1H, dd, J = 3.5, 11.5 Hz, H-6), 3.72–3.58 (2H, m), 353 (3H, s, OCH_3), 351 (3H, s, OCH_3), 347 (3H, s, OCH_3), 340 (3H, s, OCH_3); δ for Z isomer (partial data): 7.97 (1H, d, J = 9.5 Hz, Ph), 6.97 (1H, d, J = 2 Hz, H-1), 4.36 (1H, dd, J = 5.5, 4 Hz, H-2).

(D-gluco)-1,1,2,3,4,5,6,6-Octamethoxyhexane (**48**)

To a solution of **26** (24 mg, 0.1 mmol) in MeOH (1 mL) was added $(CH_3O)_3CH$ (0.1 mL) and HCl (5% in methanol, few drops). After stirring overnight, the reaction mixture was quenched by addition of $NaHCO_{3(s)}$, and then filtered, concentrated, and fractionated by FCC (EtOAc:hexane, 1:1) yielding **48** as a colorless oil (32 mg, 94%); IR: 2932, 2829, 1095 cm^{-1}; ^1H NMR δ: 4.49 (1H, d, J = 5 Hz), 4.47 (1H, d, J = 3 Hz), 3.66 (1H, dd, J = 3.5, 7 Hz), 3.53 (3H, s, CH_3O), 3.53 (3H, s, CH_3O), 3.52 (3H, s, CH_3O), 3.49 (3H, s, CH_3O), 3.49–3.42 (1H, m), 3.47 (3H, s, CH_3O), 3.45 (3H, s, CH_3O), 3.42 (3H, s, CH_3O), 3.37 (3H, s, CH_3O), 3.34 (1H, dd, J = 3.0, 7.0 Hz), 3.21 (1H, dd, J = 3.5, 6 Hz); ^{13}C NMR δ: 105.4 (d), 104.6 (d), 82.2 (d), 82.0 (d), 81.7 (d), 80.4 (d), 61.0 (q, CH_3O), 60.9 (q, CH_3O), 60.1 (q, CH_3O), 59.0 (q, CH_3O), 55.9 (q, CH_3O), 55.8 (q, CH_3O), 54.7 (q, CH_3O), 53.2 (q, CH_3O); MS (CI, NH_3), m/z (relative intensity): 295 ($[M - OCH_3]^+$, 15), 224 (13), 207 (42), 101 (75), 75 (100).

Methyl 2,3,4,5-tetra-O-methyl-β-D-glucoseptanoside (**49**)

Reaction of **44** (30 mg, 0.063 mmol) with $(CH_3O)_3CH$ (0.1 mL) and HCl for 48 h as described above gave **49** as a colorless oil (13 mg, 81%); IR: 2931, 2825, 1464, 1097 cm^{-1}; ^1H NMR δ: 4.55 (1H, d, J = 7.5 Hz, H-1), 3.97 (1H, dd, J = 4, 10.5 Hz, H-6), 3.75–3.60 (4H, m), 3.51 (6H, s, CH_3O), 3.49 (3H, s, CH_3O), 3.42 (3H, s, CH_3O), 3.41 (3H, s, CH_3O), 3.15 (1H, dd, J = 3.5, 7.5 Hz, H-2); ^{13}C NMR δ: 106.4 (d, C-1), 86.0 (d), 81.4 (d), 81.2 (d), 78.2 (d), 65.6 (t, C-6), 59.5 (q, CH_3O), 59.4 (q, CH_3O), 58.8 (q, CH_3O), 58.0 (q, CH_3O), 55.5 (q, CH_3O); MS (CI, NH_3), m/z (relative intensity): 268 ($[M + 18]^+$, 10), 251 ($[M + 1]^+$, 7), 236 (11), 219 (100).

2,3,4,5-Tetra-O-methyl-D-glucose dimethyl acetal (**50**)

Reaction of **44** (40 mg, 0.084 mmol) with $(CH_3O)_3CH$ and HCl as above for 1.5 h gave, after fractionation by FCC (EtOAc:hexane, 1:1), **50** as a colorless oil (20 mg, 83%); IR: 3481, 2934, 2829, 1447, 1095 cm^{-1}; ^1H NMR δ: 4.43 (1H, d, J = 6 Hz, H-1), 3.76 (1H, dd, J = 4.5, 6.5 Hz), 3.64 (1H, dd, J = 5, 6.5 Hz), 3.54 (3H, s, CH_3O), 3.53 (3H, c, CH_3O), 3.53 (3H, s, CH_3O), 3.50 (3H, s, CH_3O), 3.46–3.38 (2H, m), 3.42 (6H, s, CH_3O), 3.29–3.24 (2H, m); ^{13}C NMR δ: 105.8 (d, C-1), 81.8 (d), 81.6 (d), 81.3 (d), 81.1 (d), 61.2 (q, CH_3O), 60.9 (q, CH_3O), 60.5 (t, C-6), 60.3 (q, CH_3O), 57.2 (q, CH_3O), 56.2 (q, CH_3O), 54.9 (q, CH_3O); MS (CI, NH_3), m/z (relative intensity): 300 ($[M + 18]^+$, 2), 265 (13), 219 (100).

Methyl 2,3,4,5-tetra-O-methyl-β-L-guloseptanoside (**51**) *and 2,3,4,5-tetra-O-methyl-L-gulose dimethyl acetal* (**52**)

Aldehyde **45** (35 mg, 0.074 mmol) was treated with $(CH_3O)_3CH$ and HCl as above for 1.5 h. Fraction of the crude product by FCC (EtOAc:hexane, 1:1) gave **52** as a colorless oil (15 mg, 72%); IR: 3474, 2933, 2829, 1096 cm^{-1}; ^1H NMR δ: 4.40 (1H, d, J = 4.5 Hz, H-1), 3.85 (1H, dd, J = 4, 12 Hz, H-6), 3.67 (1H, m, J = 5, 12 Hz, H-6), 3.55 (3H, s, CH_3O), 3.53 (3H, s, CH_3O), 3.55–3.35 (4H, m), 3.48 (3H, s, CH_3O), 3.47 (3H, s, CH_3O), 3.46 (3H, s, CH_3O), 3.45 (3H, s, CH_3O); ^{13}C NMR δ: 105.1 (d, C-6), 81.8 (d), 80.6 (d), 80.5 (d × 2), 61.8 (t, C-1), 60.3 (q, CH_3O), 59.8 (q × 2, CH_3O), 58.2 (q, CH_3O), 56.3 (q, CH_3O), 55.1 (q, CH_3O); MS (CI, NH_3), m/z (relative intensity): 300 ($[M + 18]^+$, 2), 265 (15), 236 (40), 219 (67), 101 (100); and **51** as a colorless oil (3 mg, 16%); IR: 2931, 2826, 1464, 1098 cm^{-1}; ^1H NMR δ: 4.63 (1H, d, J = 6 Hz, H-1), 3.82 (1H, dd, J = 2, 13.5 Hz, H-6), 3.76–3.68 (2H, m, H-3, 6), 3.64–3.61 (1H, dd, J = 2.5, 4 Hz, H-4), 3.51 (3H, s, CH_3O), 3.51–3.47 (1H, m, H-2), 3.47 (3H, s, CH_3O), 3.45 (6H, s, CH_3O), 3.42 (3H, s, CH_3O), 3.27–3.24 (1H, m, H-4); ^{13}C NMR δ: 102.5 (d, C-1), 81.6 (d × 2), 80.5 (d), 78.7 (d), 59.6 (q, CH_3O), 58.9 (q, CH_3O), 58.8 (t, C-6), 58.5 (q, CH_3O), 57.6 (q, CH_3O), 55.3 (q, CH_3O); MS (CI, NH_3), m/z (relative intensity): 268 ($[M + 18]^+$, 30), 251 ($[M + 1]^+$, 16), 236 (76), 219 (49), 101 (100).

The proportion of **51** in the reaction mixture increased with increasing reaction time.

Acknowledgement

Financial support from the Natural Sciences and Engi-

neering Research Council of Canada and the University of Saskatchewan is gratefully acknowledged.

1. J.D. Morrison (*Editor*). Asymmetric synthesis. Vols. 1–5. Academic Press, New York. 1983–1985.
2. D. Seebach. Angew. Chem. Int. Ed. Engl. **29**, 1320 (1990).
3. M. Nógrádi. *In* Stereoselective synthesis. Weinheim, New York. 1988.
4. (*a*) K. Mislow and M. Raban. Top. Stereochem. **1**, 1 (1969); (*b*) S.A. Kaloustian and M.K. Kaloustian. J. Chem. Educ. **52**, 56 (1975); (*c*) E.L. Eliel. J. Chem. Educ. **57**, 52 (1980).
5. Y. Izumi and T. Akira. *In* Stereodifferentiating reactions. Academic Press, New York. 1977.
6. (*a*) H.G. Davies, R.H. Green, D.B. Kelly, and S.M. Roberts. *In* Biotransformations in preparative organic chemistry: the use of isolated enzymes and whole cell preparations in synthesis. Academic Press, London. 1989; (*b*) M. Ohno and M. Otsuka. Org. React. **37**, 1 (1989); (*c*) C.A. Sih and W. Shih-Hsiung. Top. Stereochem. **19**, 63 (1989); (*d*) P.G. Hultin, F.-J. Mueseler, and J.B. Jones. J. Org. Chem. **56**, 5375 (1991).
7. S. Ikeda, M.I. Weinhouse, K.D. Janda, R.A. Lerner, and S.J. Danishefsky. J. Am. Chem. Soc. **113**, 7763 (1991).
8. R.S. Ward. Chem. Soc. Rev. **19**, 1 (1990).
9. H.B. Kagan and J.C. Fiaud. Top. Stereochem. **18**, 249 (1988).
10. (*a*) Y.F. Wang, C.S. Chen, G. Girdaukaus, and C.J. Sih. J. Am. Chem. Soc. **106**, 3695 (1984); (*b*) *In* Enzymes in organic synthesis. Ciba Found. Symp. 111. *Edited by* R. Porter and S. Clark. Pitman, London. 1985; (*c*) T. Sugimoto, T. Kobuto, J. Miyazaki, S. Tanimoto, and M. Okano. Bioorg. Chem. **10**, 311 (1981).
11. (*a*) Z. Dokuzokic, N.K. Roberts, J.F. Sawyer, J. Whelan, and B. Bosnich. J. Am. Chem. Soc. **108**, 2034 (1986); (*b*) S. Bergens and B. Bosnich. Comments Inorg. Chem. **6**, 85 (1987).
12. (*a*) S.L. Schreiber, T.S. Schreiber, and D.B. Smith. J. Am. Chem. Soc. **109**, 1525 (1987); (*b*) S.L. Schreiber, M.T. Goulet, and G. Schulte. J. Am. Chem. Soc. **109**, 4718 (1987); (*c*) S.L. Schreiber and M.T. Goulet. J. Am. Chem. Soc. **109**, 8120 (1987); (*d*) S.L. Schreiber. Chem. Scr. **27**, 563 (1987); (*e*) D.B. Smith, Z. Wang, and S.L. Schreiber. Tetrahedron, **46**, 4793 (1990).
13. (*a*) J.J. Partidge, N.K. Chada, and M.R. Uskoković. J. Am. Chem. Soc. **95**, 532 (1973); (*b*) J. Am. Chem. Soc. **95**, 7171 (1973); (*c*) J.K. Whitesell and D.E. Allen. J. Org. Chem. **50**, 3025 (1985); (*d*) W.R. Roush and J.C. Park. Tetrahedron Lett. **31**, 4707 (1990); (*e*) J.M. Chong and K.K. Sokoll. Tetrahedron Lett. **33**, 879 (1992); (*f*) T. Harada, Y. Kagamihara, S. Tanaka, K. Sakamoto, and A. Oku. J. Org. Chem. **57**, 1637 (1992); (*g*) P. Breuilles, T. Schmittberger, and D. Uguen. Tetrahedron Lett. **34**, 4205 (1993); (*h*) N. Kann and T. Rein. J. Org. Chem. **58**, 3802 (1993).
14. D.E. Ward, Y.-D. Liu, and C.K. Rhee. Synlett, 561 (1993).
15. (*a*) V. Prelog. Science, **193**, 17 (1976); (*b*) V. Prelog and G. Helmchen. Angew. Chem. Int. Ed. Engl. **21**, 567 (1982); (*c*) C.E. Wintner. J. Chem. Educ. **60**, 550 (1983).
16. J. Brandt, C. Jochum, I. Ugi, and P. Jochum. Tetrahedron, **33**, 1353 (1977).
17. C.H. Heathcock. Aldrichimica Acta, **23**, 99 (1990).
18. (*a*) S. Masamune, W. Choy, J.S. Petersen, and L.R. Sita. Angew. Chem. Int. Ed. Engl. **24**, 1 (1985); (*b*) K. Nakayama. J. Chem. Educ. **67**, 20 (1990); (*c*) W.R. Roush, L.H. Hoong, M.A.J. Palmer, J.A. Straub, and A.D. Palkowitz. J. Org. Chem. **55**, 4117 (1990).
19. A. Horeau. Tetrahedron, **31**, 1307 (1975).
20. C.H. Heathcock, M.C. Pirrung, J. Lampe, C.T. Buse, and S.D. Young. J. Org. Chem. **46**, 2290 (1981).
21. R.U. Lemieux and J.H. Howard. Can. J. Chem. **41**, 308 (1963).
22. (*a*) E.L. Eliel. *In* Asymmetric synthesis. Vol. 2. *Edited by* J.D. Morrison. Academic Press, New York. 1983. Chap. 5; (*b*) B.M. Trost and I. Fleming (*Editors*). Comprehensive organic synthesis Vols. 1, 2. Pergamon, New York. 1991.
23. (*a*) M. Nishizawa and R. Noyori. *In* Comprehensive organic synthesis. Vol. 8. *Edited by* B.M. Trost and I. Fleming. Pergamon, New York. 1991. Chap. 1.7; (*b*) M.M. Midland. *In* Asymmetric synthesis. Vol. 2. *Edited by* J.D. Morrison. Academic Press, New York. 1983. Chap. 2.
24. (*a*) M.M. Midland, S. Greer, A. Tramontano, and S.D. Szeric. J. Am. Chem. Soc. **101**, 2352 (1979); (*b*) J.M. Fernandez, K. Emerson, R.H. Larsen, and J.A. Gladsz. J. Am. Chem. Soc. **108**, 8268 (1979); (*c*) E.J. Corey and J.O. Link. Tetrahedron Lett. **30**, 6275 (1989); (*d*) R. Noyori, Y. Tanimoto, and M. Nishizawa. J. Am. Chem. Soc. **106**, 6717 (1984).
25. E.J. Corey, R.K. Bushi, and S. Shibata. J. Am. Chem. Soc. **109**, 5551 (1987).
26. R. Noyori, I. Tomino, Y. Tanimoto, and M. Nishizawa. J. Am. Chem. Soc. **106**, 6709 (1984).
27. (*a*) M.M. Midland, A. Tramontano, and S.A. Zderic. J. Am. Chem. Soc. **99**, 5211 (1977); (*b*) H.C. Brown and G.G. Pai. J. Org. Chem. **47**, 1608 (1982).
28. (*a*) J.A. Dale, D.L. Dull, and H.S. Mosher. J. Org. Chem. **34**, 2543 (1969); (*b*) J.A. Dale and H.S. Mosher. J. Am. Chem. Soc. **95**, 512 (1973).
29. D.J. Mathre, T.K. Jones, L.C. Xavier, T.J. Blacklock, R.A. Reamer, J.J. Mohan, E.T.T. Jones, K. Hoogsteen, M.W. Baum, and E.J.J. Grabowski. J. Org. Chem. **56**, 751 (1991).
30. A.J. Mancuso, S.-L. Hung, and D. Swern. J. Org. Chem. **44**, 2480 (1978).
31. W.P. Griffith, S.W. Ley, G.P. Whitcomb, and A.P. White. J. Chem. Soc. Chem. Commun. 1625 (1987).
32. J.D. Stevens. Aust. J. Chem. **28**, 525 (1975).
33. S.J. Angyal. Adv. Carbohydr. Chem. Biochem. **42**, 15 (1984).
34. F. Smith. J. Chem. Soc. 1724 (1939).
35. M.L. Wolfram and A. Thompson. Methods Carbohydr. Chem. **2**, 65 (1963).
36. E.B. Rathbone, A.M. Stephen, and K.G.R. Pachler. Carbohydr. Res. **21**, 83 (1972).
37. J.N. Bemiller. Methods Carbohydr. Chem. **5**, 298 (1965).
38. C.G. McCarty. *In* The chemistry of the carbon–nitrogen double bond. *Edited by* S. Patai. Wiley, New York. 1970. p. 343.
39. D.E. Ward and C.K. Rhee. Tetrahedron Lett. **32**, 7165 (1991).
40. (*a*) D. Parker. Chem. Rev. **91**, 1441 (1991); (*b*) T.J. Wenzel. *In* NMR shift reagents. CRC Press, Boca Raton, Fla. 1987.
41. (*a*) K. Burgess and I. Henderson. Tetrahedron Lett. **32**, 5701 (1991); (*b*) T.R. Hoye, D.R. Peck, and T.A. Swanson. J. Am. Chem. Soc. **106**, 2738 (1984); (*c*) S.L. Schreiber and Z. Wang. J. Am. Chem. Soc. **107**, 5303 (1985); (*d*) S.L. Schreiber, Z. Wang, and G. Schulte. Tetrahedron Lett. **29**, 4085 (1988); (*e*) S.L. Schreiber, T. Sammakia, and D.E. Uehling. J. Org. Chem. **54**, 15 (1989); (*f*) Z. Wang and D. Deschênes. J. Am. Chem. Soc. **114**, 1090 (1992).
42. E.J. Bourne and S. Peat. Adv. Carbohydr. Chem. **5**, 145 (1950).
43. E.F.L.J. Anet. Carbohydr. Res. **8**, 164 (1968).
44. D.E. Ward, Y. Gai, and W.M. Zoghaib. Can. J. Chem. **69**, 1487 (1991).
45. A.S. Perin. Can. J. Chem. **33**, 1218 (1955).
46. M. Petrusova and M. Fedoroko. Chem. Zvesti, **36**, 837 (1982).
47. W.C. Still, M. Kahn, and A. Mitra. J. Org. Chem. **43**, 2923 (1978).
48. D.E. Ward and C.K. Rhee. Can. J. Chem. **67**, 1206 (1989), and cited references.

Can. J. Chem. Downloaded from www.nrcresearchpress.com by EESC ESCOLA DE ENGENHARIA on 09/08/12
For personal use only.

The synthesis of β-mannopyranosides by intramolecular aglycon delivery: scope and limitations of the existing methodology

FRANK BARRESI AND OLE HINDSGAUL[1]

Department of Chemistry, University of Alberta, Edmonton, Alberta T6G 2G2, Canada

Received August 3, 1993

FRANK BARRESI and OLE HINDSGAUL. Can. J. Chem. **72**, 1447 (1994).

The synthesis of β-mannopyranosides by intramolecular aglycon delivery is shown to proceed with complete stereoselectivity in six separate cases. This strategy has been successfully applied to the synthesis of several disaccharides, including octyl 3,6-di-*O*-benzyl-4-*O*-(3,4,6-tri-*O*-benzyl-β-D-mannopyranosyl)-2-deoxy-2-phthalimido-β-D-glucopyranoside, a precursor of the naturally occurring β-D-Man-(1→4)-β-D-GlcNAc linkage, present in all N-linked glycoproteins. Exclusive formation of the β-mannosidic linkage has been confirmed in all six cases, since independently synthesized α-linked mannopyranoside standards were shown to be absent from the reaction products. The intramolecular stereocontrolled reaction proceeds even in the presence of competing methanol. The extension of this strategy to the synthesis of the core pentasaccharide of N-linked glycoproteins has revealed limitations to the methodology, especially when a block synthesis approach is investigated.

FRANK BARRESI et OLE HINDSGAUL. Can. J. Chem. **72**, 1447 (1994).

On montre que la synthèse des β-mannopyranosides par transfert intramoléculaire d'un aglycone se produit avec une stéréosélectivité complète dans six cas séparés. On a appliqué cette stratégie avec succès à la synthèse de plusieurs disaccharides, dont le 3,6-di-*O*-benzyl-4-*O*-(3,4,6-tri-*O*-benzyl-β-D-mannopyranosyl)-2-désoxy-2-phtalimido-β-D-glucopyranoside d'octyle, un précurseur du lien β-D-Man-(1→4)-β-D-GlcNAc que l'on retrouve naturellement présent dans toutes les glycoprotéines liées par l'azote. On a confirmé la formation exclusive de la liaison β-mannosidique dans les six cas puisque les mannopyranosides de référence avec liaisons α qui ont été synthétisés d'une façon indépendante sont tous absents des produits de réactions. La réaction intramoléculaire avec contrôle stéréochimique se produit même en présence de méthanol qui peut agir comme compétiteur. L'extension de cette stratégie à la synthèse du pentasaccharide central des glycoprotéines liées par l'azote a révélé les limitations de la méthodologie, spécialement lorsqu'on examine une approche à la synthèse d'un bloc.

[Traduit par la Rédaction]

Introduction

The field of glycobiology is enjoying an explosion in growth as the biological significance of oligosaccharides are becoming increasingly evident (1). The role of these structures are diverse, ranging from structural or stabilization molecules (2) to fertilization (3), viral and bacterial adhesion (4), protein trafficking (5), and intercellular recognition (i.e., P-selectins (6), L-selectins (7), E-selectins (8). To explore the functions of oligosaccharides, reliable methods of synthesizing sufficient amounts of high purity carbohydrates is necessary. Despite the great ingenuity applied in recent years to the development of new synthetic methods for stereospecific glycoside formation (9), problems in obtaining consistent high-yielding steps remain.

One of the most difficult glycosidic linkages to synthesize is found in 1,2-*cis*-β-D-mannopyranosides. This linkage is present in all N-linked oligosaccharides as part of the core pentasaccharide (Fig. 1).

Great effort has been expended in developing new methods for β-mannoside synthesis (10), with the most direct method being the insoluble silver silicate (10*a*) or silver zeolite (10*b*) procedures. The existing problems with these type of syntheses are the lack of reproducibility and the formation of the α-mannoside as a side product (often in significant quantity) which makes for difficult separation of anomers.

The ability to construct a completely stereocontrolled glycosidic linkage is of great importance in carbohydrate chemistry. More importantly, if available, such methods might permit the development of solid-phase synthesis of oligosaccharides. Experiments from this laboratory have shown that a stereocontrolled method for the synthesis of β-mannopyranosides can be accomplished (11) and was termed intramolecular aglycon

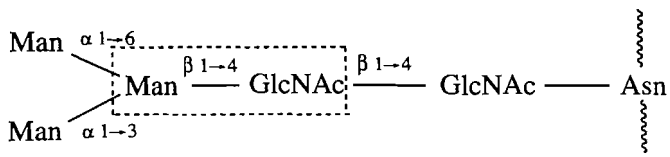

FIG. 1. Core pentasaccharide of N-linked glycoproteins.

delivery (IAD). The general strategy (Scheme 1, X = C, Y = SEt) involves covalent attachment of the aglycon alcohol **A** to a group on O-2 of a latent glycosyl donor **B**. Activation of the anomeric group in the adduct **C** leads to stereocontrolled intramolecular delivery of the aglycon to give the intermediate **D**. Quenching of **D** with water gives the β-mannoside **E**. Stork and Kim (12) have investigated a similar strategy using a temporary silicon connection (X = Si, Y = SOPh) that has been efficient for the transfer of primary carbohydrate alcohols, but not secondary carbohydrate alcohols (footnote 2) in the formation of β-mannosides. In addition, Bols has recently employed a similar approach where a silicon connection was used for the stereocontrolled synthesis of α-glucosides (13) which has been applicable to secondary carbohydrate alcohols.

The application of IAD using a carbon linker has so far produced the best results with the highly hindered and unreactive secondary carbohydrate alcohols. In this paper, the development of this strategy for the synthesis of disaccharides is described. In addition, this procedure is extended toward the synthesis of the core pentasaccharide. In applying IAD with an acetonide linker to the complex natural system, the scope and limitations of intramolecular aglycon delivery have become apparent.

Results and discussion

Our specific protocol for IAD, using an acetonide linker,

[1]Author to whom correspondence may be addressed.

[2]G. Stork, personal communication.

Can. J. Chem. Downloaded from www.nrcresearchpress.com by EESC ESCOLA DE ENGENHARIA on 09/08/12
For personal use only.

Can. J. Chem. Downloaded from www.nrcresearchpress.com by EESC ESCOLA DE ENGENHARIA on 09/08/12
For personal use only.

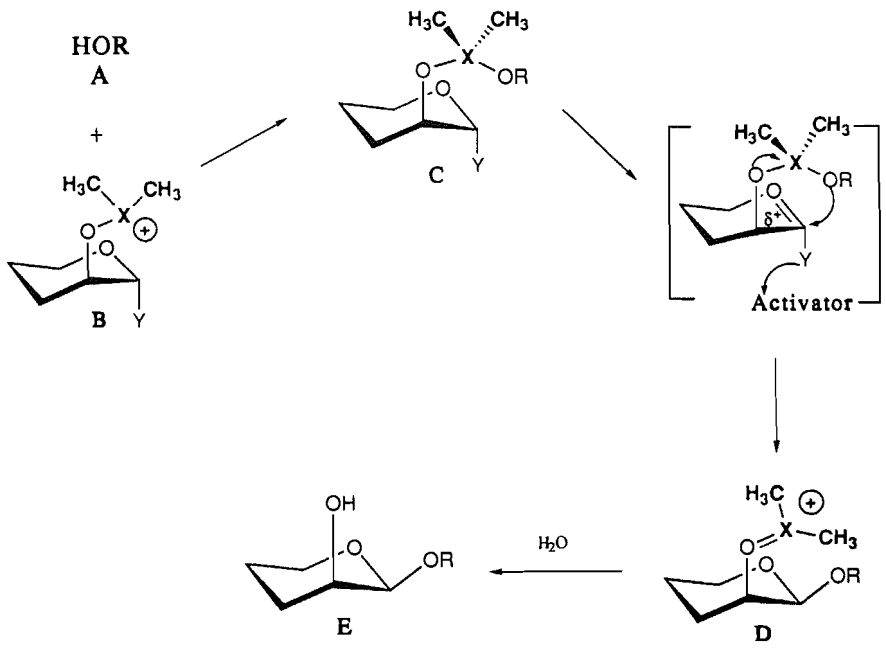

SCHEME 1

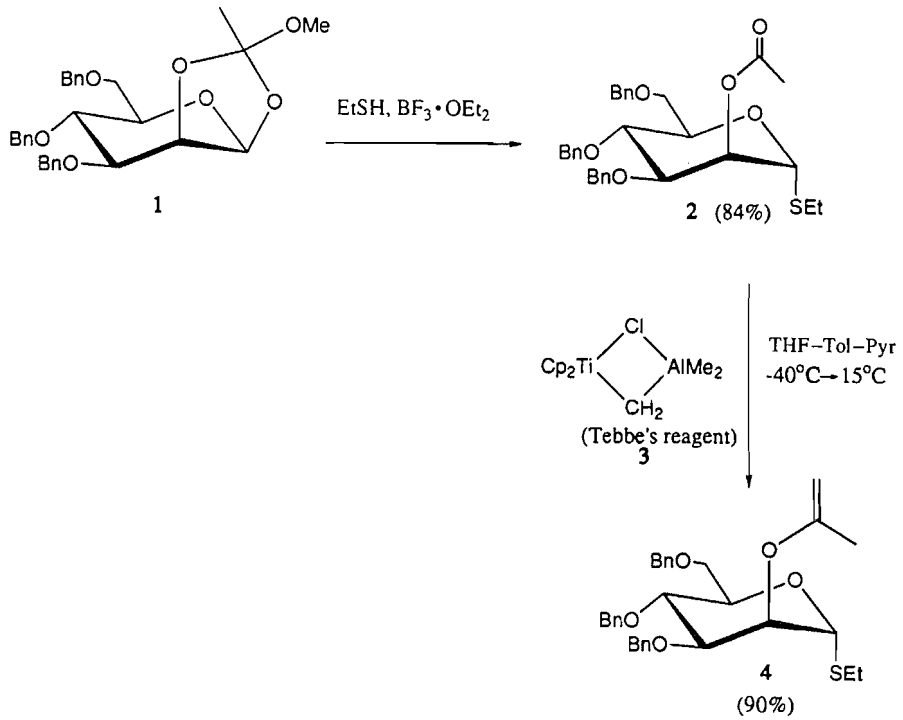

SCHEME 2

involves the synthesis of the 2-propenyl ether **4** (Scheme 2), which can be prepared from the 2-*O*-acetate **2** in good yield using a methylene transfer reagent such as Tebbe's reagent (**3**) (14). By choosing a thioglycoside, the freedom to manipulate the 2-position of the molecule was possible without affecting the anomeric centre. Furthermore, a wide variety of methods were available to activate the anomeric sulfur once the 2-position has been appropriately derivatized. The acetate **2** was prepared in 84% yield by treatment of the known ortho ester **1** (15) with boron trifluoride etherate in ethanethiol. The conversion to the vinyl ether **4** proceeds well when a solution of Tebbe's reagent is used and gave yields as high as 90%, but more consistently near 70%.

With the vinyl ether in hand, the key step was to link the alcohols **11** (16), **12**, and **13** (17) to the vinyl ether (Table 1). A variety of electrophilic agents were tried including *N*-iodosuccinimide (NIS), iodine, iodonium dicollidine perchlorate (IDCP), *N*-bromosuccinimide (NBS), mercuric acetate, mercuric sulfate, and mercuric triflate. NIS gave the best results of these reagents; however, this reagent could only couple primary carbohydrate alcohols. NIS-promoted coupling of secondary carbohydrate alcohols gave very poor yields (data not shown).

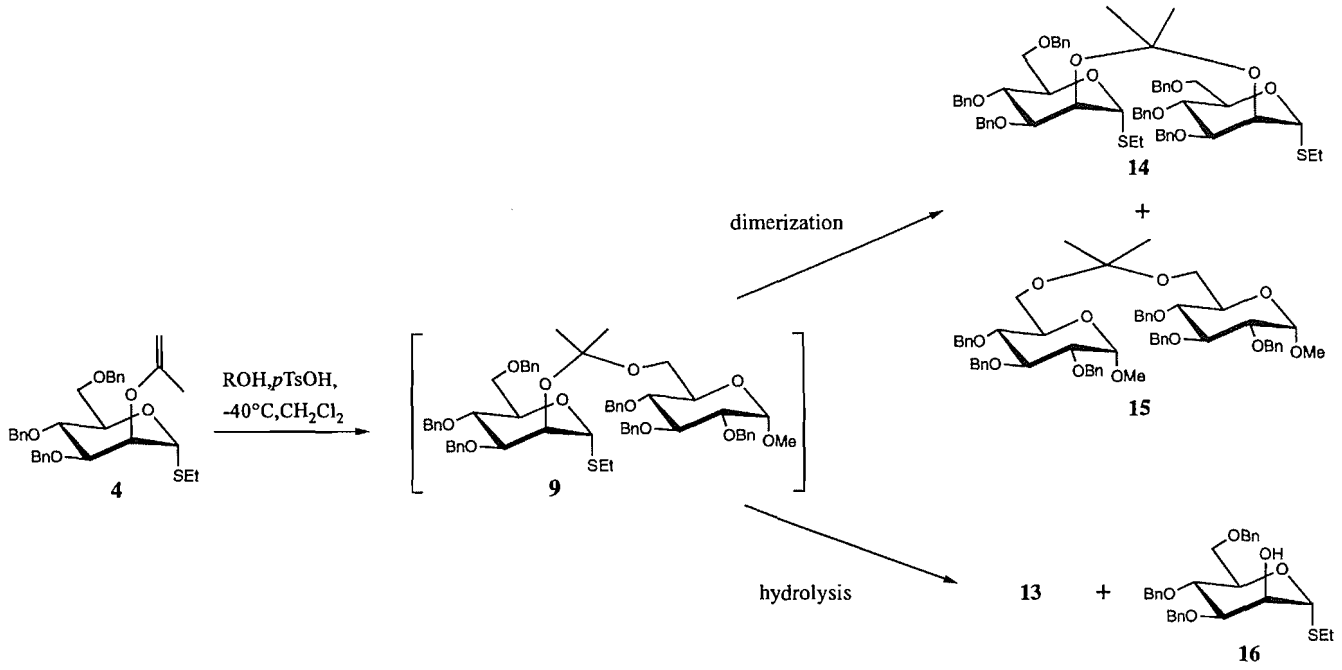

SCHEME 3. Side reactions observed during mixed acetal formation.

TABLE 1. Optimized results (11) for the synthesis of disaccharide β-mannoside

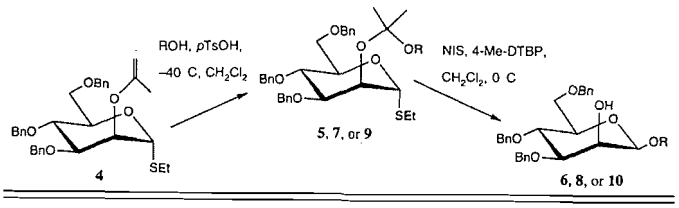

R	Mixed acetal (% yield)	β-Glycoside (% yield)
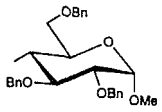 **11**	**5** (57)	**6** (77)
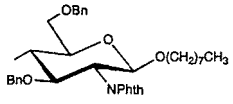 **12**	**7** (55)	**8** (51)
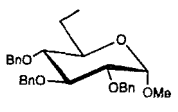 **13**	**9** (74)	**10** (61)

A variety of acid catalysts were also tried such as hydrochloric acid, hydrobromic acid, triflic acid, pyridinium *p*-toluenesulfonate, amberlite IRC-120 (H^+) resin, *p*-toluenesulfonic acid, and camphorsulfonic acid, of which the last two acids gave satisfactory results. For example, for the formation of **9**, the coupling reaction was initiated by adding catalytic toluenesulfonic acid (0.02 equiv.) to a cooled (–40°C) solution of equimolar amounts of the vinyl ether **4** and the alcohol **13** in dry dichloromethane. The resulting reaction must be quenched by addition of a base (e.g., triethylamine) after about 10 min as the mixed isopropylidene acetal **5** can form symmetrical dimerization products such as **14** and **15**, and simultaneously alcohols **13** and **16** (Scheme 3). Optimum couplings are, therefore, very sensitive to structure and require great care to reproduce. However, consistent yields of mixed acetals ranged from 55% for **7** to 74% for **9**. The secondary alcohols **11** and **12** were more difficult to couple to the vinyl ether as indicated by their lower yields (Table 1). Furthermore, acetals **5** and **7** were less stable than **9** and could only be stored under basic conditions.

A satisfactory method was thus developed that permitted the synthesis of mixed acetals in quantities sufficient to examine the second key step involving transfer of the aglycon to the anomeric centre. Initial reaction conditions were optimized for the conversion of **5** to **6**. A variety of anomeric activators were examined including dimethyl(methylthio)sulfonium triflate (DMTST), IDCP, phenyl selenyl triflate, methyl triflate, NBS, and NIS. With the exception of methyl triflate, all the activators gave varying yields of β-mannosides; however, the best results were again obtained with NIS. Other parameters such as temperature, solvent, and equivalents of activator were examined, with the best results obtained using 5 equiv. of NIS in dichloromethane, starting the reaction at 0°C, and allowing the reaction to warm to room temperature overnight. The addition of a hindered base such as 4-methyl-di-*t*-butyl pyridine (4-Me-DTBP) (5 equiv.) importantly enhanced reaction yields, presumably by preventing any mixed acetal decomposition prior to transfer to the anomeric centre. For instance, the yield of **6** from **5** increased from 42 to 77% with added 4-Me-DTBP and for the conversion of **7** to **8** yields increased from 27 to 51% with added base (Table 1). Other bases such as collidine, diisopropylethyl amine (Hunigs base), or bis(dimethylamino)napthalene (proton sponge) were not stable to the reaction conditions.

To demonstrate the stereocontrolled nature of the reaction,

Can. J. Chem. Downloaded from www.nrcresearchpress.com by EESC ESCOLA DE ENGENHARIA on 09/08/12
For personal use only.

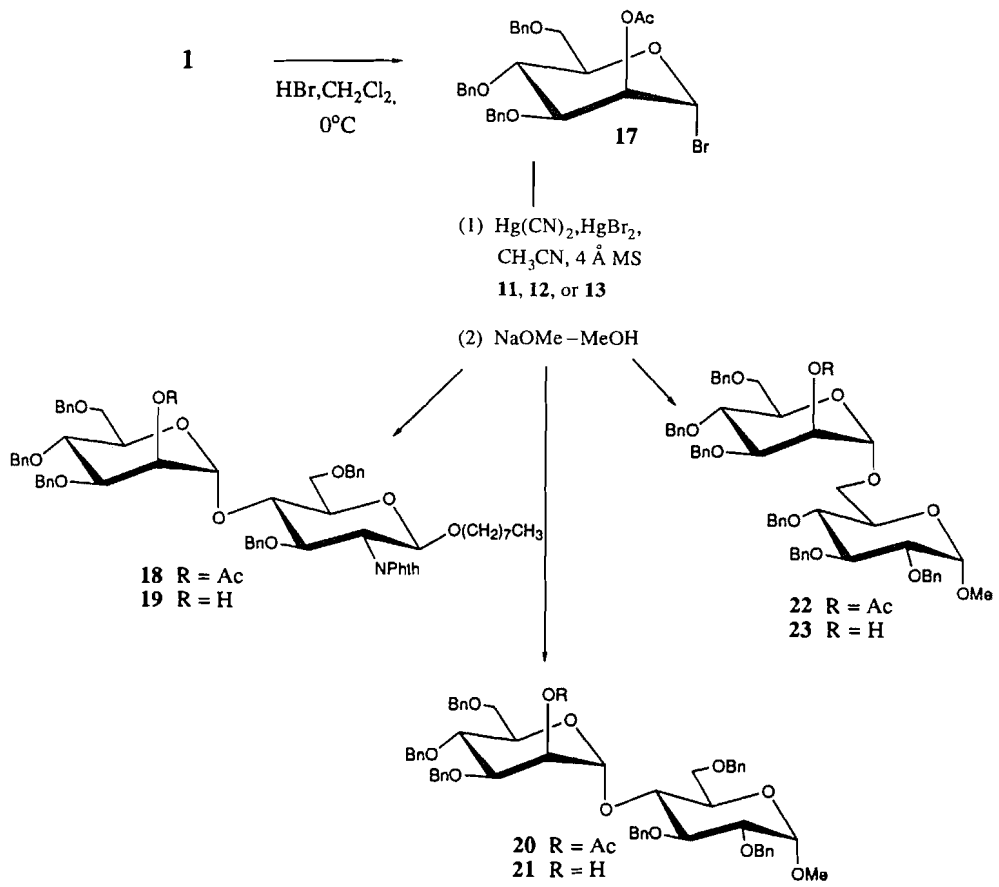

SCHEME 4

TABLE 2. NMR and chromatographic comparison for α- and β-linked disaccharide mannopyranosides

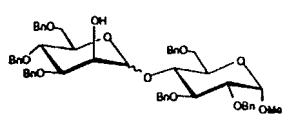
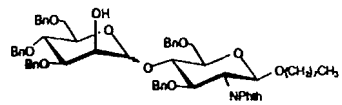
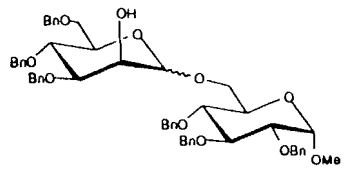

Analysis	β6	α21	β8	α19	β10	α23
δ H-1 (300 MHz)						
$J_{H\text{-}1',H\text{-}2'}$	4.58 <1 Hz	5.31 1.8 Hz	4.67 <1 Hz	5.34 1.8 Hz	4.69 <1 Hz	4.89 1.2 Hz
δ ^{13}C, C-1′ (75 MHz)	101.6	100.0	100.5	101.2	100.0	99.6
^{13}C $J_{C\text{-}1',H\text{-}1'}$ (Hz)	157	171	158	172	155	171
R_f data, EtOAc–hexane (1:2)	0.14	0.40	0.36	0.38	0.20	0.17

several approaches were taken. First of all, the stereochemistry of the anomeric linkage was confirmed by the gated ^{13}C NMR spectra of the β-mannosides **6**, **8**, and **10** where the $J_{C\text{-}1,H\text{-}1}$ couplings of the β-linkage were found to be less than 160 Hz, typical for this type of linkage (18). In addition, the α-mannosides **19**, **21**, and **23** were synthesized separately via Helferich (19) coupling of the acceptors **11**, **12**, and **13** with the bromide **17** (20), followed by de-*O*-acetylation of the 2-position (Scheme 4). ^{13}C NMR spectra of the α-anomers showed the typical α-mannoside coupling constants of >170Hz (Table 2).

With the α-mannosides synthesized, IAD reactions were monitored by TLC where the α-anomers could not be detected. Furthermore, all fractions that showed charring by TLC were isolated and NMR analysis of these fractions did not show any α-glycoside. It is important to note that in all cases, the major product was the β-mannosides and impurities isolated consisted

Can. J. Chem. Downloaded from www.nrcresearchpress.com by EESC ESCOLA DE ENGENHARIA on 09/08/12
For personal use only.

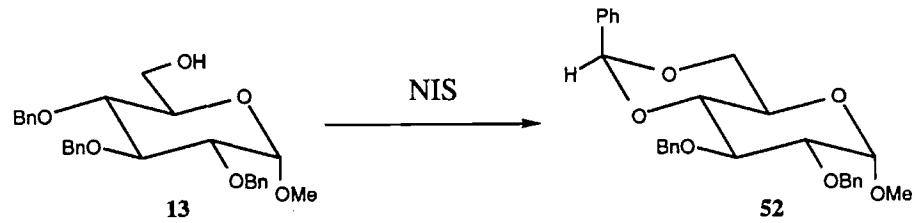

FIG. 2. Benzylidene acetal side product formed under IAD reaction conditions.

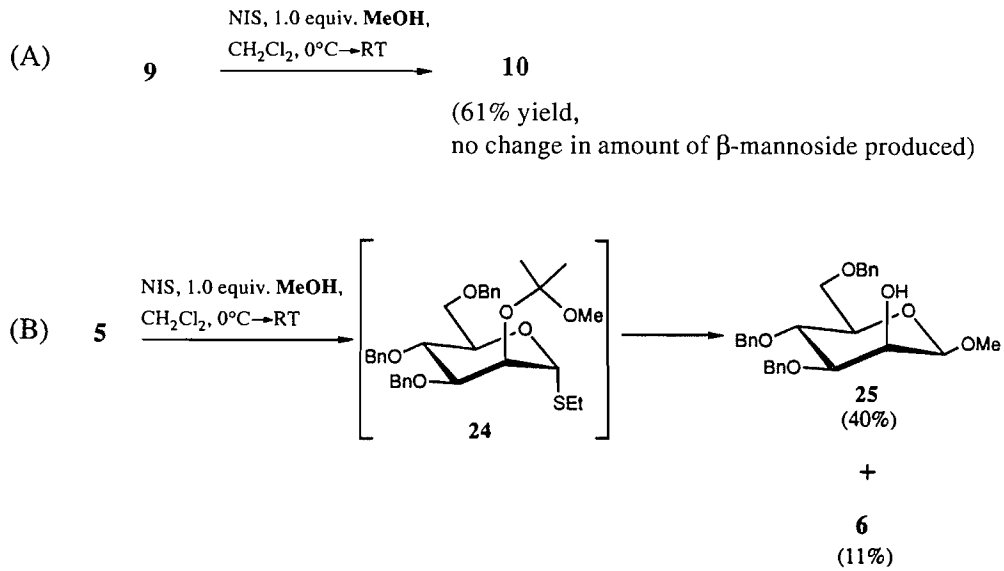

SCHEME 5. Intramolecular aglycon delivery in the presence of methanol.

of several minor compounds. In many cases small amounts of the aglycon alcohols, such as **11**, as well as the benzylidene acetal **52** (Fig. 2) could be identified. The formation of this acetal indicates that competing free radical side reactions of the benzyl groups are occurring.

A convincing experiment showing the intramolecular nature of this reaction was carried out by activation of the mixed acetals **5** and **9** in the presence of methanol. When the acetal **9** was activated with NIS in the presence of 1.0 equiv. of methanol, the yield of the β-mannoside **10** was not affected (Scheme 5*a*). This indicated that the intramolecular process was occurring faster than the competing intermolecular reaction, even with the very reactive methanol. If there were any acetal decomposition prior to activation of the anomeric group, the more reactive methanol would certainly have formed a mixture of methyl α,β-mannosides. This observation therefore supports a concerted reaction mechanism as outlined in Scheme 1. When the same reaction was carried out for the conversion of **5** to **6**, the yield of disaccharide **6** decreased to 11%, reflecting the well-known lower reactivity of secondary carbohydrate alcohols (Scheme 5B). In addition, 40% of the methyl β-mannoside **25** was obtained, presumably by *trans*-acetalization to form **24**, followed by intramolecular transfer of methoxide to give **25**. The fact that no corresponding methyl α-mannoside was observed in this reaction again supports that a free anomeric carbocation is not formed during IAD.

Further evidence for the trapping of the postulated carbocation intermediate (Scheme 1, **D**, X = C) was obtained from initial experiments using *N*-bromosuccinimide as the activator. When the mixed acetal **24** was reacted in the presence of NBS, 17% of the β-methyl glycoside **25** was isolated along with 43% of **26** (Scheme 6). The trapping of the carbocation with succinimide was observed during the formation of the disaccharide **10** as well (data not shown).

With sufficient evidence of the stereocontrolled nature of the reaction, and similar reported strategies (Refs. 12 and 13, footnote 2) supporting this concept, application of this procedure to more complex systems, namely the core pentasaccharide, was attempted. The trisaccharide **27**, containing the required 2-propenyl ether, was synthesized in 13 steps (5% overall yield) from D-mannose (21). When this vinyl ether was treated under acid-catalyzed conditions with the alcohols **11** or **13**, the mixed acetal could not be obtained. Only slow hydrolysis to alcohol **28** was observed (Scheme 7). An attempt to identify the reason for the failure of the coupling reaction was then made by synthesizing the α(1 → 6)-linked disaccharide **33** and examining its behaviour in the formation of mixed acetals.

Known disaccharide **29** (22) was converted to the ortho ester **30** (Scheme 8) via the glycosyl bromide. Zemplen deacetylation, followed by benzylation, gave the ortho ester **31** in 41% overall yield from **29**. Treatment of the ortho ester with boron trifluoride etherate in ethanethiol at 0°C gave the thioglycoside **32** (81%), which was converted to the vinyl ether with Tebbe's reagent in 69% yield.

When the disaccharide vinyl ether **33** was treated under acid-catalyzed conditions (camphorsulfonic acid, –40°C) in the presence of **12**, the mixed acetal **34** was isolated in 25% yield (61% based on recovered **12**, Scheme 8). This compound showed high instability unless stabilized by a base such as triethylamine or pyridine. Activation of its thioglycoside using

Can. J. Chem. Downloaded from www.nrcresearchpress.com by EESC ESCOLA DE ENGENHARIA on 09/08/12
For personal use only.

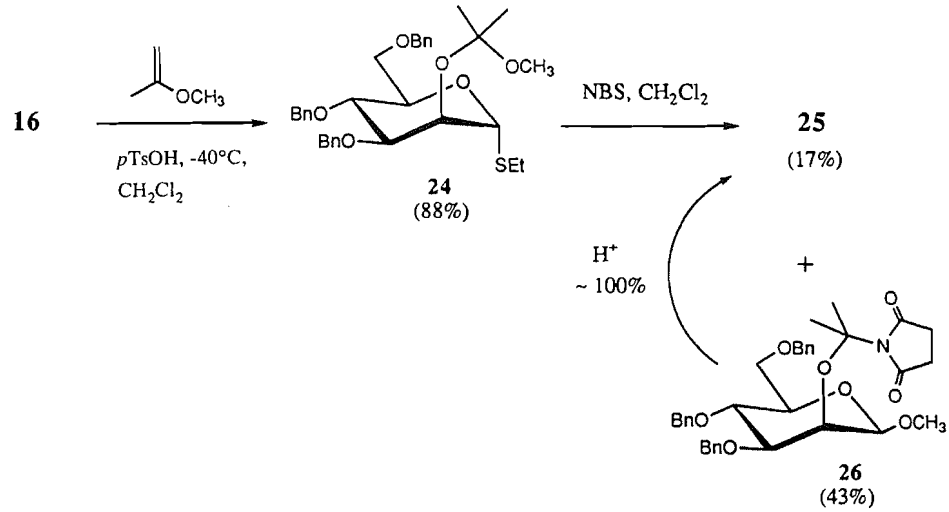

SCHEME 6

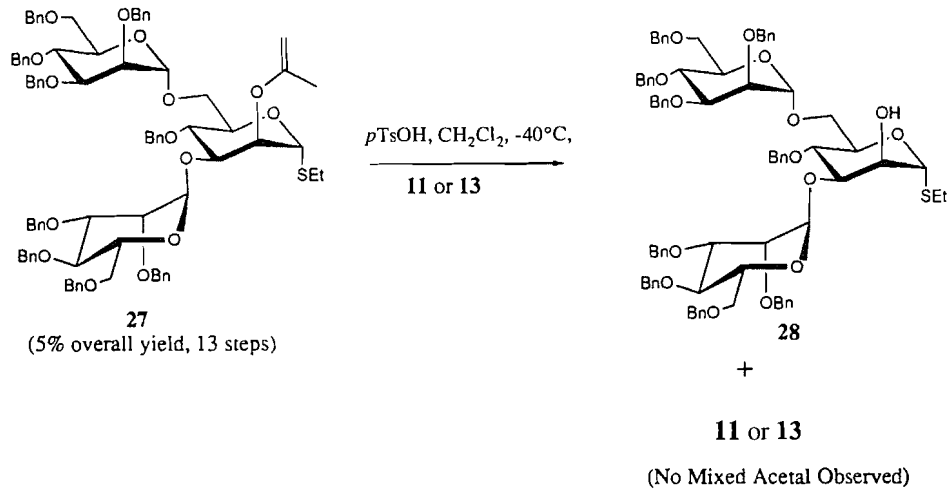

SCHEME 7. Unsuccessful attempt at mixed acetal formation using a trimannoside 2-propenyl ether.

the NIS–4-Me-DTBP procedure was sluggish, requiring extra NIS (10 equiv. total) and a reaction time of 70 h at room temperature for **34** to disappear. The reaction mixture was very complex by TLC with the β-mannoside **35** isolated as the major product in 28% yield. The corresponding α-anomer **36** was independently synthesized via a different procedure (Scheme 9) and confirmed to be absent from the reaction products (Table 3). Despite the sluggish reaction and low yield of β-mannoside **35**, glycosidic bond formation nevertheless proceeded in a completely stereocontrolled manner.

Coupling of the vinyl ether **33** with the chitobiose precursor **47** was attempted to see if the procedure could make the tetrasaccharide portion of the core pentasaccharide. Compound **47** was synthesized according to Scheme 10, by reaction of 1,3,4,6-tetra-*O*-acetyl-2-deoxy-2-phthalimido-β-D-glucopyranoside **37** (23) with octanol in a stannic chloride catalyzed reaction. De-*O*-acetylation gave the octyl glycoside **39** in 81% yield from **37**. Benzylidenation (78%) followed by benzylation of the 3-position gave **41** in 73% yield. Sodium cyanoborohydride ring opening (24) gave the alcohol **12** in 83% yield. The phthalimido chloride **45** was prepared from allyl glycoside **42** (25) by acetylation (90%), followed by isomerization and hydrolysis of the allyl group. Reducing sugar **44** was thus obtained in 75% yield from **43**. Treatment of the reducing sugar with dimethylformamide and oxalyl chloride (26) gave the glycosyl chloride **45** as a bright yellow solid, which was used directly in a silver triflate catalyzed glycosylation with the acceptor **12** (67%). The disaccharide **46** was de-*O*-acetylated to give the chitobiose precursor **47**.

Coupling of **33** and **47** was attempted, but proved to be extremely difficult. The only condition which yielded detectable product was a camphorsulfonic acid catalyzed reaction in the presence of calcium sulfate (–40°C), yielding the desired mixed acetal product **48** in only 8% yield (Scheme 11). The balance of the reaction products consisted of unreacted vinyl ether **33** and alcohol **47** as well as hydrolyzed vinyl ether. Insufficient material was obtained to attempt the activation of this mixed acetal.

With the chitobiose precursor **47** in hand, the effect of increasing the complexity of the alcohol, compared with **12**, was investigated by reacting **47** with the monosaccharide vinyl ether **4**. Acid-catalyzed conditions (camphorsulfonic acid, –40°C) yielded the trisaccharide acetal **49** in 38% isolated yield (Scheme 12); however, the reaction was virtually quantitative

Can. J. Chem. Downloaded from www.nrcresearchpress.com by EESC ESCOLA DE ENGENHARIA on 09/08/12
For personal use only.

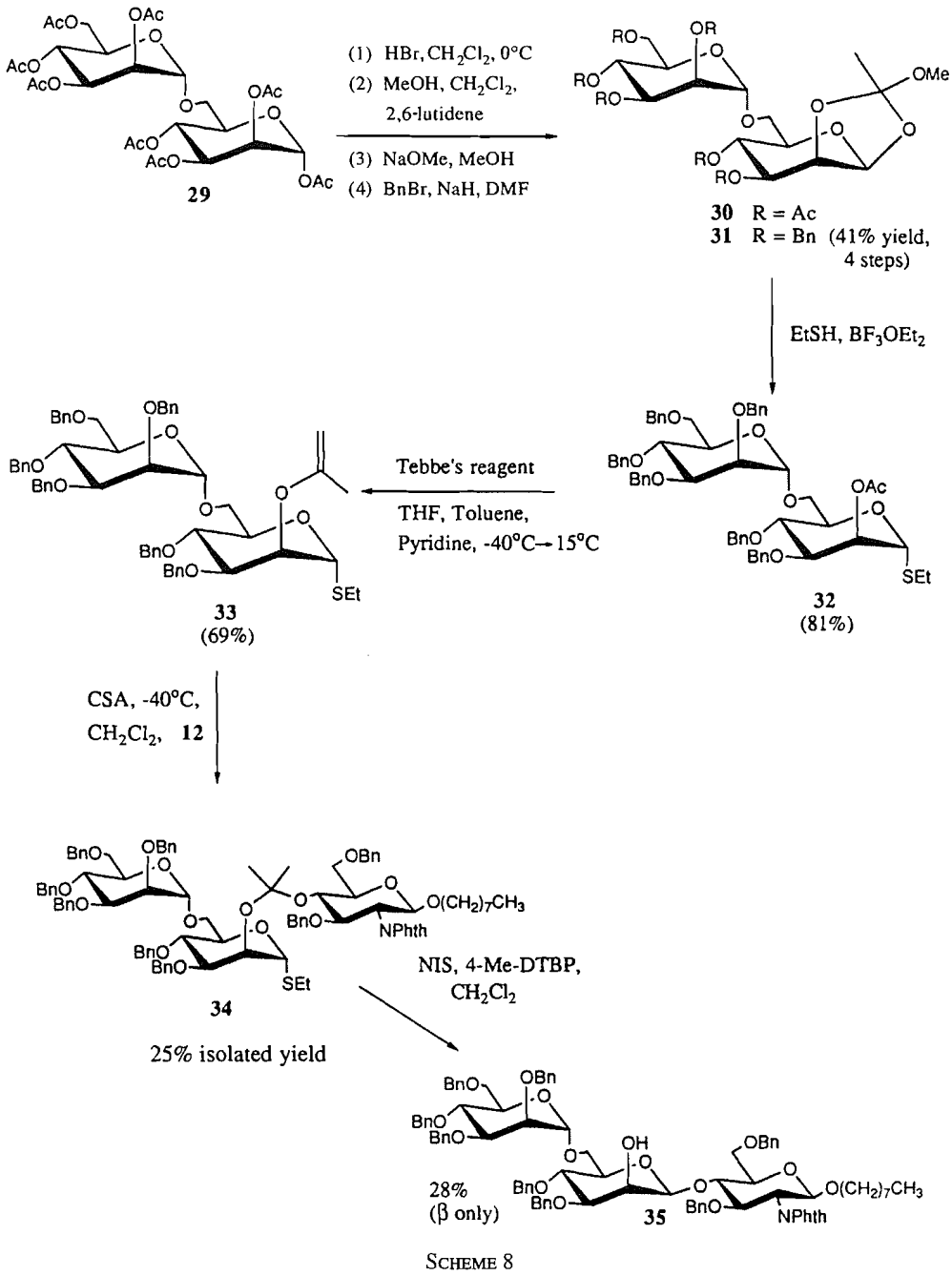

SCHEME 8

based on recovered starting materials. Activation of the acetal required 42 h and a modest yield (27%) of β-mannoside **50** was isolated as the major product along with a number of minor impurities, one of them being a benzylidene acetal, formed as in the synthesis of **6** by free radical side reactions. Again comparison with authentic α-mannoside standard **51** (Scheme 13) showed no α-linked products formed from this transfer reaction (Table 3).

The dramatic drop in coupling yields as the complexity of the carbohydrate structures increase reveal severe limitations to the existing methodology. It is clear that when comparing the vinyl ethers **4**, **27**, and **33**, acid-catalyzed coupling to form the isopropylidene acetals is extremely sensitive to the size of the vinyl ether (Table 4). The size of the alcohol is also important, although the effect is not as dramatic as with the vinyl ethers. One reason to explain these observations is that the acetal acid sensitivity increases with increased complexity of the structure, as is supported by the stabilities on storage of these particular structures when not stabilized by base. Mixed acetals such as **9** or **24** were stable and did not need to be stored in basic solutions, as was the case with the acetals such as **5** or **7** which would decompose if left at room temperature overnight. Structures such as **34**, **48**, and **49** showed extreme instability, decomposing in several hours if stored without added base. This indicates that during the acid-catalyzed reaction conditions, some of the less stable acetals may be decomposing prior to isolation or do not form in appreciable amounts in the reaction vessel before decomposition occurs.

The transfer yields for the formation of the β-mannosides also decreases with increased molecular complexity (Table 5,

Can. J. Chem. Downloaded from www.nrcresearchpress.com by EESC ESCOLA DE ENGENHARIA on 09/08/12
For personal use only.

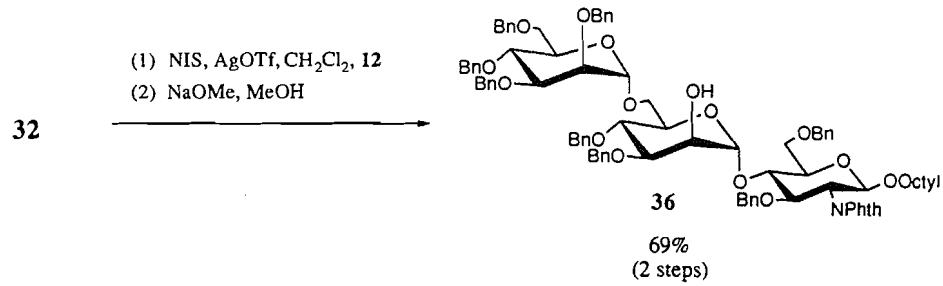

SCHEME 9

TABLE 3. NMR and chromatographic comparison for α- and β-linked trisaccharide mannopyranosides

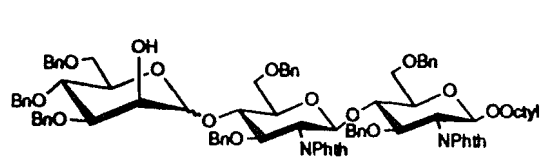
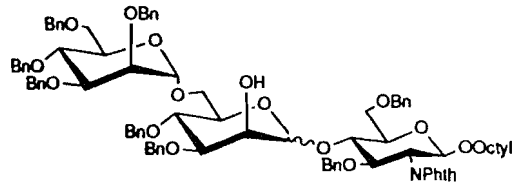

Analysis	β50	α51	β35	α36
δ H-1 (500 MHz)				
$J_{H\text{-}1',H\text{-}2'}$	4.92 <1 Hz	5.36 1.3 Hz	4.68 <1 Hz	5.27 1.2 Hz
δ ^{13}C, C-1′ (125 MHz)	100.3	100.9	101.0	101.1
^{13}C $J_{C\text{-}1',H\text{-}1'}$ (Hz)	157	170	159	173
R_f data, EtOAc–hexane (1:2)	0.27	0.27	0.34	0.50

TABLE 4. Yield comparisons for isopropylidene acetals

Vinyl ether	Alcohol	Mixed acetal	% yield
413	974		
411	557		
4	12	7	55
4	47	49	38
33	12	34	25
33	47	48	8
27	11	—	0
27	13	—	0

TABLE 5. Yield and reaction time comparisons for the formation of β-mannosides

Mixed acetal	β-Mannoside	% yield	Time (h)
24	25	60	2
9	10	61	2
5	6	77	18
7	8	51	18
49	50	27	42
34	35	28	70

with the exception of compound **6**, in which extensive optimization was performed). Analysis of the reaction times involved for the formation of the β-mannosides may explain the reduced yields. Less hindered mixed acetals such as **9** and **24** gave good yields of β-mannosides (>60% for **10** and **25**) with short reaction times (2 h). With the mixed acetals of more hindered secondary carbohydrate alcohols such as **5** and **7**, the activation of the thioglycoside is slower (18 h), which may reflect increased steric repulsion impeding the transfer step. Extremely hindered structures such as **34** and **48** have even longer thioglycoside activation times (70 and 42 h respectively). Longer reaction times allow for competing side reactions to occur, such as the free radical formation of the benzylidene structure (**52**, Fig. 2), which causes a decrease in yield.

Conclusions

In summary, the synthesis of β-mannopyranosides has been shown to occur in a completely stereocontrolled fashion by IAD. The stereochemical nature of the β-mannopyranosidic linkage has been confirmed by comparison with independently synthesized α-mannopyranoside standards and the stereocontrolled reaction was shown to proceed even in the presence of added methanol. The extension of this strategy to the core pentasaccharide of *N*-linked glycoproteins has revealed severe limitations to the methodology as currently implemented. Application of this strategy to the formation of β-mannosides in structures as complex as disaccharides occurs in acceptable yields; however, extending this process to trisaccharides causes a dramatic decrease in yield. Different linkers and activation procedures are currently being examined in an attempt to overcome these limitations.

Experimental

General methods

Optical rotations were measured with a Perkin-Elmer 241 polarim-

Can. J. Chem. Downloaded from www.nrcresearchpress.com by EESC ESCOLA DE ENGENHARIA on 09/08/12
For personal use only.

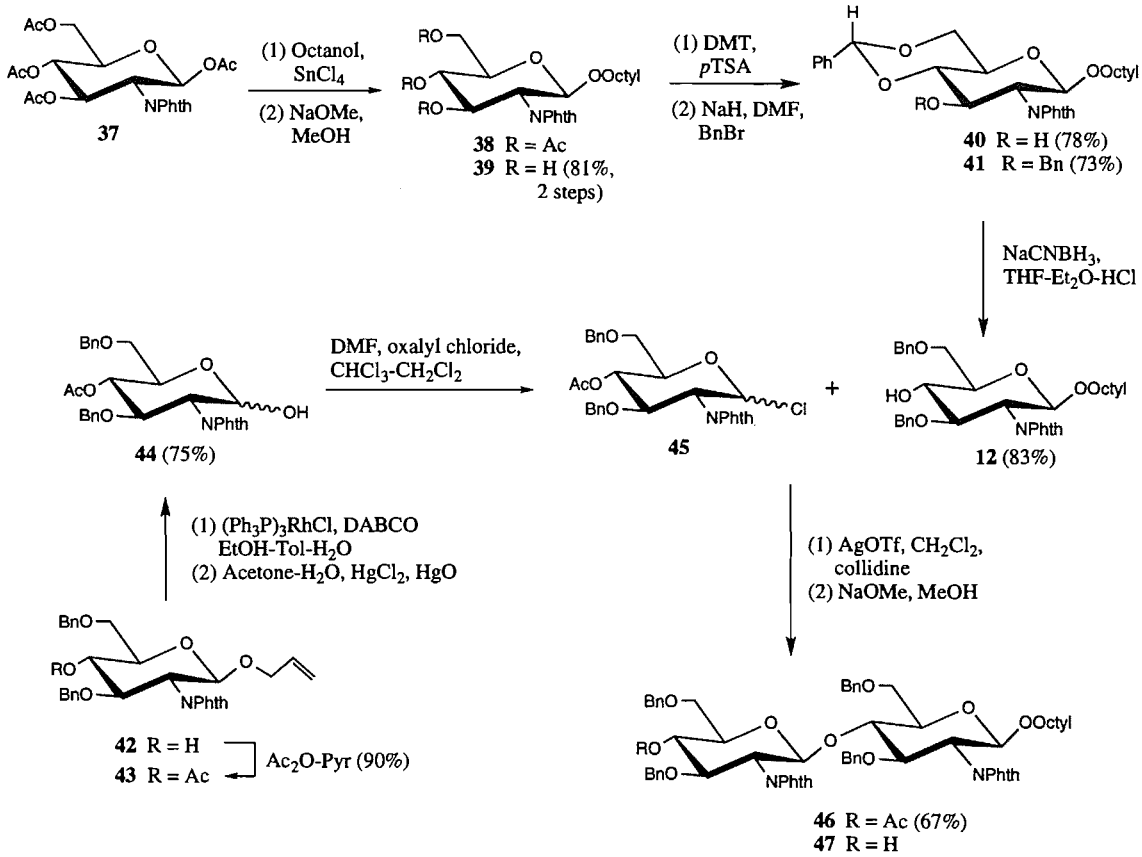

37

38 R = Ac
39 R = H (81%, 2 steps)

40 R = H (78%)
41 R = Bn (73%)

44 (75%)

45

12 (83%)

42 R = H
43 R = Ac

46 R = Ac (67%)
47 R = H

SCHEME 10

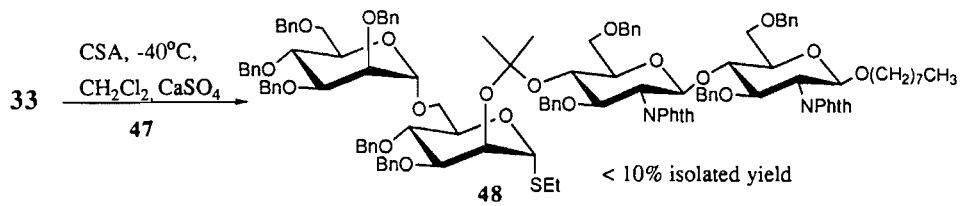

33

48

< 10% isolated yield

SCHEME 11

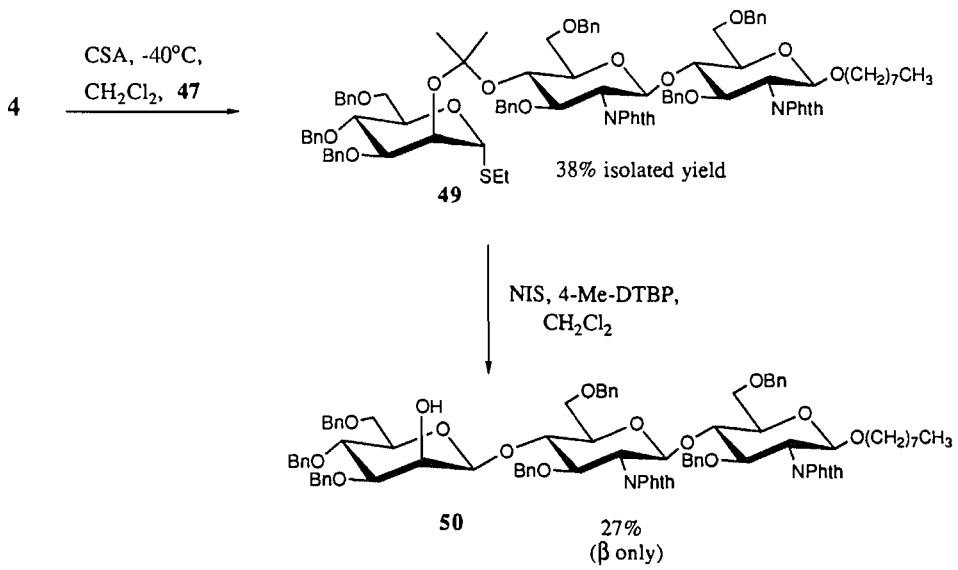

4

49

38% isolated yield

50

27%
(β only)

SCHEME 12

Can. J. Chem. Downloaded from www.nrcresearchpress.com by EESC ESCOLA DE ENGENHARIA on 09/08/12
For personal use only.

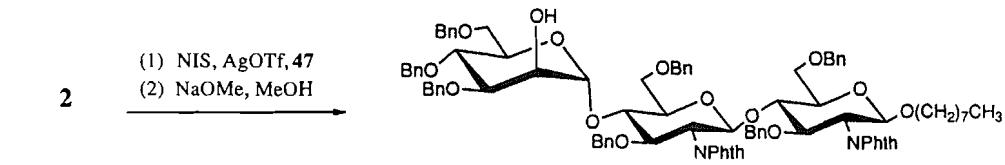

51

SCHEME 13

eter at 22 ± 2°C. Analytical TLC was performed on silica gel 60-F_{254} (Merck) with detection by quenching of fluorescence and (or) by charring with sulfuric acid. All commercial reagents were used as supplied and chromatography solvents were distilled prior to use. Column chromatography was performed on silica gel 60 (Merck, 40–60 μM). Iatrobead refers to a beaded silica gel 6RS-8060 manufactured by Iatron Laboratories (Tokyo). ^{1}H NMR spectra were recorded at 360 MHz (Bruker WM-360), 300 MHz (Bruker AM-300), or 500 MHz (Varian Unity-500) with internal $(CH_3)_4Si$ (δ 0, $CDCl_3$, CD_3OD, or D-5 pyridine). COSY spectra were obtained at 360 MHz (Bruker WM-360). ^{13}C NMR spectra were recorded at 75.5 MHz (Bruker Am-300) or 125.7 MHz (Varian Unity-500) with internal $(CH_3)_4Si$ (δ 0, $CDCl_3$ CD_3OD, or D-5 pyridine). Only partial NMR data are reported; the other data were in accord with the proposed structures. The chemical shifts and coupling constants (as observed splittings) for ^{1}H resonances are reported as though they were first order. The assignments of ^{13}C resonances, when applicable, are tentative. Organic solutions were concentrated under vacuum at ≤40°C (bath) and 12 Torr (1 Torr = 133.3 Pa). All anhydrous reactions were carried out under argon using dry solvents and phosphorous pentoxide (P_2O_5) dried starting materials (high vacuum ≅ 50 μm). Anhydrous transfers were done with standard syringe techniques; all glassware was predried overnight at 160°C. Microanalyses were carried out by the analytical services at this department and all samples submitted for elemental analysis were dried overnight under high vacuum over P_2O_5 at 56°C (refluxing acetone).

General procedure for the preparation of Tebbe's reagent (14c)

Titanocene dichloride (0.50 g, 2 mmol, 1.0 equiv.) was charged to a round-bottom flask and argon purged. Trimethylaluminum, (2.01 mL, 4 mmol, 2 equiv., 2.0 M solution in toluene) was carefully syringed into the flask. The mixture was stirred under argon atmosphere for 60 prior to use. The solution colour is a deep red, which blackens as it decomposes. When used, any exposure to air gives off white fumes.

Ethyl 2-O-acetyl-3,4,6-tri-O-benzyl-1-thia-α-D-mannopyranoside (2)

The ortho ester **1** (ref. 15; 5.0 g, 9.9 mmol) was charged to a round-bottom flask and argon purged. Ethanethiol (30 mL) was added and the solution was cooled to 0°C. Boron trifluoride etherate (1.22 mL, 9.9 mmol) was syringed into the stirred mixture and the reaction was quenched after 15 min by adding 5 mL of distilled water (dH_2O). The ethanethiol was removed in the fumehood by blowing air over the mixture for 3 h. Dichloromethane (200 mL) was added and the solution was washed with 2 × 200 mL of dH_2O. The organic layer was dried ($MgSO_4$), filtered, and concentrated to give a pale yellow syrup. Column chromatography using 18% ethyl acetate in hexane as eluent yielded 4.46 g (84%) of a colourless syrup (**2**). $[\alpha]_D$ + 86.8 (*c* 0.95, Ch_2Cl_2); R_f 0.53 in ethyl acetate – hexane (1:3); ^{1}H NMR (300 MHz, $CDCl_3$) δ: 7.30, 7.15 (m, 15H, Ph), 5.43 (dd, 1H, $J_{1,2}$ = 1.5 Hz, $J_{2,3}$ = 3.0 Hz, H-2), 5.32 (d, 1H, $J_{1,2}$ = 1.5 Hz, H-1, 4.85, 4.47 (2 × d, 2H, J_{gem} = 10.8 Hz, (CH_2Ph), 4.69, 4.48 (2 × d, 2H, J_{gem} = 12.2 Hz, OCH_2Ph), 4.68, 4.52 (2 × d, 2H, J_{gem} = 11.1 Hz, OCH_2Ph), 4.16 (m, 1H, H-5), 3.94 (dd, 1H, $J_{3,4}$ = 9.5 Hz, $J_{4,5}$ = 9.5 Hz, H-4), 3.90 (dd, 1H, $J_{2,3}$ = 3.0 Hz, $J_{3,4}$ = 9.5 Hz, H-3), 3.84 (dd, 1H, $J_{5,6}$ = 4.04 Hz, $J_{6,6'}$ = 11.0 Hz, H-6), 3.68 (dd, 1H, $J_{5,6'}$ = 1.8 Hz, $J_{6,6'}$ = 11.0 Hz, H-6′), 2.62 (m, 2H, S$CH_2$$CH_3$), 2.15 (s, 3H, CH_3, acetate), 1.28 (t, 3H, J_{vic} = 7.5 Hz, SCH_2CH_3); ^{13}C NMR (75.5 MHz, $CDCl_3$) δ: 170.4 (*C*OCH_3), 138.4, 138.2, 137.8, 129.1–127.6 (aromatic), 82.5 (C-1), 78.6 (C-2), 76.4, 71.9, 70.6 (C-3, C-4, and C-5), 75.2, 73.4, 71.9 (3 × OCH_2Ph), 68.9 (C-6) 25.5 (SCH_2CH_3), 21.2 (COCH_3), 14.9 (SCH$_2$*C*H$_3$). Anal. calcd. for $C_{31}H_{36}O_6S$: C 69.38, H 6.76, S 5.97; found: C 68.79, H 6.82, S 6.12.

Ethyl 3,4,6-tri-O-benzyl-2-O-(2-propenyl)-1-thia-α-D-mannopyranoside (4)

The 2-*O*-acetylated thioglycoside **2** (1.3 g, 2.42 mmol) was dissolved in 12 mL toluene, 4 mL tetrahydrofuran, and 0.2 mL pyridine (all solvents anhydrous) under argon atmosphere. The solution was cooled to –40°C and Tebbe's reagent (**3**) (4.8 mL, 1 mM in toluene, 4.8 mmol, 2 equiv.) was slowly added, turning the solution deep red. After 1 h, another 4.8 mL of Tebbe's reagent was added (2 equiv.) and the reaction was gradually warmed to –10°C. After 3 h, the reaction was quenched by adding 0.2 mL of 1 N NaOH at –10°C and waiting for the vigorous bubbling to cease (≅5 min) before warming the mixture to room temperature and adding a further 0.8 mL of 1 N NaOH. The solution was then filtered through a celite pad, washed with ether until the filtrate was colourless, and concentrated. Column chromatography of the deep red oil using 8% ethyl acetate in hexane as eluent yielded 1.16 g (90%) of a pale yellow syrup (**4**). $[\alpha]_D$ + 95.6 (*c* 0.98, CH_2Cl_2); R_f 0.71 in ethyl acetate – hexane, (1:3); ^{1}H NMR (300 MHz, $CDCl_3$) δ: 7.32, 7.20 (m, 15H, aromatic), 5.53 (d, 1H, $J_{1,2}$ < 1.0 Hz, H-1), 4.89, 4.50 (2 × d, J_{gem} = 10.8 Hz, OCH_2Ph), 4.67, 4.49 (2 × d, 2H, J_{gem} = 12.1 Hz, OCH_2Ph), 4.64, 4.59 (2 × d, 2H, J_{gem} = 11.5 Hz, OCH_2Ph), 4.40 (dd, 1H, $J_{1,2}$ < 1 Hz, $J_{2,3}$ = 3,4 Hz, H-2), 4.13 (ddd, 1H $J_{4,5}$ = 9.2 Hz, $J_{5,6}$ = 4.4 Hz, $J_{5,6'}$ = 1.7 Hz, H-5), 4.02 (dd, 1H, $J_{3,4}$ = 9.2 Hz, $J_{4,5}$ = 9.2 Hz, H-4), 3.98, 3.75 (2 × d, 2H, J_{gem} = 2.0 Hz, C=CH_2), 3.88 (dd, 1H, $J_{2,3}$ = 3.4 Hz, $J_{3,4}$ = 9.2 Hz, H-3), 3.83 (dd, 1H, $J_{5,6}$ = 4.4 Hz, $J_{6,6'}$ = 10.7 Hz, H-6), 3.70 (dd, 1H, $J_{5,6'}$ = 1.7 Hz, $J_{6,6'}$ = 10.7 Hz, H-6′), 2.60 (m, 2H, SCH_2CH_3), 1.59 (s, 3H, CH_2=CCH_3, vinyl ether), 1.26 (t, 3H, J_{vic} = 7.6 Hz, SCH$_2$*C*H$_3$); ^{13}C NMR δ: 158.6 (*C*=CH_2), 138.7, 138.5, 138.2, 128.5–127.5 (aromatic), 82.7 (C=*C*H$_2$), 80.4, 79.2 (C-1 and C-2), 74.8, 73.8, 71.8 (C-3, C-4, and C-5), 75.2, 73.4, 71.8 (3 × OCH_2Ph), 69.2 (C-6), 25.4 (SCH_2CH_3), 21.3 (CH_2=CCH_3), 15.1 (s, SCH_2CH_3). Anal. calcd. for $C_{32}H_{38}O_5S$: C 71.88, H 7.16, S 6.00; found: C 71.88, H 7.19, S 5.83.

Methyl 2,3,6-tri-O-benzyl-α-D-glucopyranoside-ethyl 3′,4′,6′-tri-O-benzyl-1′-thio-α-D-mannopyranoside-2′,4-isopropylidene acetal (5)

The vinyl ether **4** (374 mg, 0.699 mmol) and the alcohol **11** (ref. 16; 325 mg, 0.699 mmol) were argon purged and dissolved in 15 mL of dry dichloromethane. The mixture was cooled to –40°C and *p*-toluenesulfonic acid monohydrate (5 mg, 0.04 equiv.) was added to the mixture. The reaction was carefully monitored by TLC for the formation of the mixed acetal product **5** and quenched when the product spot was major (10 min) by adding 0.1 mL of triethylamine. Prolonged reaction times (>20 min) caused a drastic reduction in reaction yields. The mixture was concentrated and chromatographed using 18% ethyl acetate in hexane with 0.1% added triethylamine as eluent. The product **5** (397 mg, 57%) was obtained as a colourless syrup. The product was unstable after prolonged periods (>24 h) unless stabilized in an organic solution (dichloromethane or ethyl acetate – hexane) with 0.5% triethylamine (shelf life >2 months). R_f 0.46 in ethyl acetate – hexane (1:3); ^{1}H NMR (360 MHz, $CDCl_3$) δ: 5.44 (d, 1H, $J_{1,2}$ = 1 Hz, H-1′), 4.61 (d, 1H, $J_{1,2}$ = 2.5 Hz, H-1), 4.16 (dd, 1H, $J_{1,2}$ = 1 Hz, $J_{2,3}$ = 3.5 Hz, $J_{3,4}$ = 9.2 Hz, H-3′), 3.38 (s, 3H, OCH_3), 2.60 (m, 2H, SCH_2CH_3), 1.41 (s, 3H, CH_3CCH_3′), 1.37 (s, 3H, 1.37, CH_3CCH_3′), 1.28 (t, 3H,

Can. J. Chem. Downloaded from www.nrcresearchpress.com by EESC ESCOLA DE ENGENHARIA on 09/08/12
For personal use only.

Can. J. Chem. Downloaded from www.nrcresearchpress.com by EESC ESCOLA DE ENGENHARIA on 09/08/12
For personal use only.

SCH_2CH_3); ^{13}C NMR (75.5 MHz, D-5 pyridine) δ: 105.09 (CH_3CCH_3), 97.71 (C-1), 85.07 (C-1′), 81.64, 81.57, 80.59, 75.82, 72.68, 72.42, 71.95, 71.89 (C-2, C-3, C-4, C-5, C-2′, C-3′, C-4′, and C-5′), 75.29, 75.12, 73.46, 73.40, 72.70, 72.49 (6 × OCH_2Ph), 70.40, 70.27 (C-6 and C-6′), 54.93 (OCH_3), 26.57, 25.39 (CH_3CCH_3′), 25.39 (SCH_2CH_3), 15.35 (SCH_2CH_3).

*Methyl 2,3,6-tri-*O*-benzyl-4-*O*-(3,4,6-tri-*O*-benzyl-*β*-D-manno-pyranosyl)-*α*-D-glucopyranoside (6)*

The mixed acetal **5** (55 mg, 0.055 mmol) was charged to a round-bottom flask and argon purged. Dry dichloromethane (5 mL), as well as 56 mg (0.0275 mmol, 5 equiv.) of 2,6-di-*tert*-butyl-4-methylpyridine, was added and the mixture was cooled to 0°C. *N*-Iodosuccinimide (62 mg, 5 equiv.) was added to the mixture all at once and stirred overnight, allowing to warm to room temperature. After 18 h, the red solution was quenched by adding 3 mL of 0.5 M sodium thiosulphate solution, which caused the solution to go colourless. Dichloromethane (10 mL) was added and the mixture was washed with 2 × 10 mL of dH_2O. The organic layer was dried ($MgSO_4$), filtered, and concentrated to give a cloudy viscous syrup that was purified on silica gel using 40% ethyl acetate in hexane as eluent. The product **6** (38 mg, 77%), was isolated a clear syrup. In some instances, the kinetic benzylidene acetal **52** could be isolated from the reaction products in small (<20%) quantities.

Product **6**: $[\alpha]_D$ + 26.3 (*c* 0.80, CH_2Cl_2); R_f 0.14 in ethyl acetate – hexane (1:2); ^1H NMR (360 MHz, $CDCl_3$) δ: 7.40–7.16 (m, 30H, aromatic), 4.58 (d, 1H, $J_{1,2}$ = 3.7 Hz, H-1), 4.44 (d, 1H, $J_{1,2}$ < 1 Hz, H-1′), 4.00 (dd, 1H, $J_{2,3}$ = 9.2 Hz, $J_{3,4}$ = 9.2 Hz, H-3), 3.94 (dd, 1H, $J_{3,4}$ = 9.2 Hz, $J_{4,5}$ = 9.2 Hz, H-4), 3.94 (dd, 1H, $J_{2,3}$ = 3.0 Hz, $J_{1,2}$ < 1 Hz, H-2′), 3.83 (dd, 1H, $J_{3,4}$ = 9.5 Hz, $J_{4,5}$ = 9.5 Hz, H-4′), 3.76 (ddd, 1H, $J_{4,5}$ = 9.2 Hz, $J_{5,6}$ = 3.1 Hz, $J_{5,6'}$ = 2 Hz, H-5), 3.73 (dd, 1H, $J_{5,6}$ = 3.1 Hz, $J_{6,6'}$ = 10.8 Hz, H-6a), 3.66 (dd, 1H, $J_{5,6'}$ = 2 Hz, $J_{6,6'}$ = 10.8 Hz, H-6b), 3.64 (dd, 1H, $J_{5,6}$ = 1.8 Hz, $J_{6,6'}$ = 10.7 Hz, H-6′a), 3.58 (dd, 1H, $J_{5,6'}$ = 4.6 Hz, $J_{6,6'}$ = 10.7 Hz, H-6′b), 3.51 (dd, 1H, $J_{2,3}$ = 3.7 Hz, $J_{3,4}$ = 9.2 Hz, H-2), 3.37 (s, 3H, OCH_3), 3.32 (dd, 1H, $J_{2,3}$ = 3.0 Hz, *J3,4* = 9.5 Hz, H-3′), 3.24 (ddd, 1H, $J_{5,6}$ = 1.8 Hz, $J_{5,6}$ = 4.6 Hz, $J_{4,5}$ = 9.5 Hz, H-5′), 2.53 (d, 1H, J = 3.0 Hz, OH); ^{13}C NMR (75.5 MHz, $CDCl_3$) δ: 139.1–137.9, 128.5–127.4 (aromatic), 99.97 (d, $J_{C\text{-}1,H\text{-}1}$ = 157 Hz, C-1′), 98.26 (C-1), 81.64, 80.75, 79.66, 75.85, 75.73, 74.04, 69.63, 67.92 (C-2, C-3, C-4, C-5, C-2′, C-3′, C-4′, and C-5′), 75.58, 75.16, 73.54, 73.47, 73.47, 71.15 (6 × OCH_2Ph), 69.11, 68.84 (C-6 and C-6′), 55.27 (OCH_3). Anal. calcd. for $C_{55}H_{60}O_{11}$: C 73.64, H 6.74; found: C 74.06, H 6.81.

Product **52**: R_f 0.59 in ethyl acetate – hexane (1:2); ^1H NMR (360 MHz, $CDCl_3$) δ: 6.06 (s, 1H, PhC*H*), 5.81 (d, $J_{1,2}$ = 3.8 Hz, H-1), 4.13 (dd, 1H, $J_{3,4}$ = 9.0 Hz, $J_{2,3}$ = 9.0 Hz, H-3), 4.03 (m, 1H, H-5), 3.83 (dd, 1H, $J_{2,3}$ = 3.8 Hz, $J_{3,4}$ = 9.0 Hz, H-2), 3.77 (dd, 1H, $J_{5,6}$ = 2.5 Hz, $J_{6,6'}$ = 11.0 Hz, H-6), 3.62 (dd, 1H, $J_{5,6'}$ = 5.7 Hz, $J_{5,6'}$ = 11.0 Hz, H-6′), 3.42 (s, 3H, OCH_3), 3.41 (dd, 1H, $J_{3,4}$ = 9.0 Hz, $J_{4,5}$ = 9.0 Hz, H-4). The structure of this compound was confirmed by treating it with catalytic *p*-toluenesulfonic acid in dichloromethane at room temperature for 1 h, converting the kinetic benzylidene to the known thermodynamic benzylidene (27).

Activation of mixed acetal (5) in the presence of methanol

The acetal **5** (75 mg, 0.075 mmol) was added to a round-bottom flask and argon purged. Dry dichloromethane (5 mL), followed by 0.12 mL of a freshly prepared 0.62 M solution of dry methanol in dichloromethane (0.075 mmol), was added to the reaction vessel. The mixture was cooled to 0°C and NIS (84 mg, 5 equiv.) was added and the reaction was stirred overnight. The reaction was quenched at 17 h and worked up as above. Chromatographic isolation yielded 7.5 mg (11%) of **6** as well as 14 mg (40%) of the methyl glycoside **25** (see characterization under heading for the preparation of **25**).

*Octyl 3,6-di-*O*-benzyl-2-deoxy-2-phthalimido-β-D-glucopyranoside-ethyl 3′,4′,6′-tri-*O*-benzyl-1′-thio-α-D-mannopyranoside-2′,4-isopropylidene acetal (7)*

The vinyl ether **4** (150 mg, 0.28 mmol) and the alcohol **12** (169 mg, 0.28 mmol) were charged to a round-bottom flask and argon purged. Dry dichloromethane (7 mL) was syringed into the flask and the mixture was cooled to –40°C. Toluenesulfonic acid monohydrate (3 mg, 0.06 equiv.) was added and the reaction was treated as for the formation of **5**. Column chromatography using 14% ethyl acetate in hexane (0.1% added triethylamine) yielded the product **7** (175 mg, 55%). The product was unstable (<12 h) unless stored in an organic solution (dichloromethane or ethyl acetate – hexane) in 0.5% triethylamine. R_f 0.47 in ethyl acetate – hexane (1:3); ^1H NMR (300 MHz, D-5 pyridine) δ: 5.82 (d, 1H, $J_{1,2}$ = 1.0 Hz, H-1′), 5.62 (d, 1H, $J_{1,2}$ = 8.0 Hz, H-1), 3.93, 3.50 (2 × m, 2H, OCH_2, octyl), 2.72 (m, 2H, SCH_2CH_3), 1.64 (s, 3H, CH_3CCH_3′), 1.62 (s, 3H, CH_3CCH_3′), 1.33 (t, 3H SCH_2CH_3); ^{13}C NMR (75.5 MHz, D-5 pyridine) δ: 105.07 (CH_3CCH_3′), 98.74 (C-1), 85.01 (C-1′), 81.08, 80.38, 77.01, 75.84, 73.97, 72.88, 72.47 (C-2′, C-3′, C-4′, C-5′, C-3, C-4, and C-5), 75.84, 75.14, 73.42, 73.42, 72.63 (5 × OCH_2Ph), 70.30, 69.58 (C-6 and C-6′), 31.82, 29.70, 29.34, 26.15, 25.56, 22.79 (6 × CH_2, octyl, SCH_2CH_3), 27.19, 25.86 (CH_3CCH_3), 15.41 (SCH_2CH_3), 14.18 (CH_3, octyl).

*Octyl 3,6-di-*O*-benzyl-4-*O*-(3,4,6-tri-*O*-benzyl-*β*-D-manno-pyranosyl)-2-deoxy-2-phthalimido-β-D-glucopyranoside (8)*

The mixed acetal **7** (58 mg, 0.051 mmol) was dissolved, under argon atmosphere, in 5 mL of dry dichloromethane. Di-*tert*-butyl-4-methylpyridine (52 mg, 0.255 mmol, 5 equiv.) was added to the solution and cooled to 0°C. *N*-Iodosuccinimide (57 mg, 0.255 mmol, 5 equiv.) was added to the mixture and allowed to warm to room temperature overnight. The reaction was quenched after 16 h by adding 3 mL of NaS_2O_3 solution (0.5 M) and worked up as in the synthesis of **6**. Purification using 40% ethyl acetate in hexane as eluent gave 27 mg (51%) of the desired product **8** $[\alpha]_D$ + 27.6 (*c* 1.60, CH_2Cl_2); R_f 0.36 in ethyl acetate – hexane (1:2); ^1H NMR (360 MHz, $CDCl_3$) δ: 7.8–7.55 (m, 4H, phthalimido), 7.4–6.7 (m, 25H, benzyl aromatic), 5.09 (d, 1H, $J_{1,2}$ = 8.4 Hz, H-1), 4.67 (d, 1H, $J_{1,2}$ < Hz, H-1′), 4.38 (dd, 1H, $J_{2,3}$ = 10.6 Hz, $J_{3,4}$ = 8,7 Hz, H-3), 4.16 (dd, 1H, $J_{1,2}$ = 8.4 Hz, $J_{2,3}$ = 10.6 Hz, H-2), 4.07 (dd, 1H, $J_{3,4}$ = 8.7 Hz, $J_{4,5}$ = 8.7 Hz, H4), 4.02 (m, 1H, H-2′), 3.85 (dd, 1H, $J_{3,4}$ = 9.0 Hz, $J_{4,5}$ = 9.0 Hz, H-4′), 3.40 (dd, 1H, $J_{3,4}$ = 9.0 Hz, $J_{2,3}$ = 3.0 Hz, H-3′), 2.49 (d, 1H, $J_{H,OH}$ = 2.7 Hz, OH), 1.4–0.7 (m, 15H, octyl); ^{13}C NMR (75.5 MHz, $CDCl_3$) δ: 167.8 (*C*=O, phthalimido), 100.48 (d, $J_{C\text{-}1,H\text{-}1}$ = 158 Hz, C-1′), 98.48 (C-1), 81.76, 78.48, 78.21, 75.53, 74.58, 74.05, 68.06 (C-2′, C-3′, C-4′, C-5′, C-3, C-4, and C-5), 75.11, 74.80, 73.59, 73.39, 71.35 (5 × OCH_2Ph), 69.65, 69.05 (C-6 and C-6′), 68.87 (OCH_2, octyl), 55.90 (C-2), 31.67, 29.31, 29.12, 25.84, 22.60 (6 × CH_2, octyl), 14.06 (CH_3, octyl). Anal. calcd. for $C_{63}H_{71}O_{12}N$: C 73.16, H 6.92, N 1.35; found: C 72.92, H 6.99, N 1.43.

*Methyl 2,3,4,-tri-*O*-benzyl-α-D-glucopyranoside-ethyl 3′,4′,6′-tri-*O*-benzyl-1′-thio-α-D-mannopyranoside-2′,6-isopropylidene acetal (9)*

The vinyl ether **4** (100 mg, 0.187 mmol) and the alcohol **13** (ref. 17; 87 mg, 0.187 mmol) were charged to a flask and argon purged. Dry dichloromethane (5 mL) was added and the mixture was cooled to –40°C. Toluenesulfonic acid monohydrate (2 mg, ≅0.06 equiv.) was added to the flask and the reaction was treated as in the formation of **5**. Concentration of the reaction mixture, followed by column chromatography (14% ethyl acetate in hexane plus 0.1% triethylamine as eluent) yielded the mixture acetal **9** (138 mg, 74%) as a colourless syrup. The product was sufficiently stable (>24 h); however, storage for long periods (>2 months) was in an organic solution (dichloromethane or ethyl acetate – hexane) with 0.5% triethylamine. Prolonged reaction times increased the yields of vinyl ether hydrolysis products **13** and **16** (28), as well as symmetrical acetals **14** and **15**. Product **9**: R_f 0.50 in ethyl acetate – hexane (1:3); ^1H NMR (360 MHz, $CDCl_3$) δ: 7.4–7.1 (m, 30H, aromatic), 5.48 (d, 1H, $J_{1,2}$ = 1.2 Hz, H-1′), 4.63 (d, 1H, $J_{1,2}$ = 3 Hz, H-1), 4.21 (dd, 1H, $J_{1,2}$ = 1.2 Hz, $J_{2,3}$ = 3.5 Hz, H-2′), 4.11 (m, 1H, H-5′), 4.00 (dd, 1H, $J_{3,4}$ = 9.2 Hz, $J_{4,5}$ = 9.2 Hz, H-4), 3.92 (dd, 1H, $J_{3,4}$ = 9.5 Hz, $J_{4,5}$ = 9.5 Hz, H-4′), 3.86 (dd, 1H, $J_{2,3}$ = 3 Hz, $J_{3,4}$ = 9.2 Hz, H02), 3.48 (dd, 1H, $J_{2,3}$ = 3.5 Hz, $J_{3,4}$ = 9.5 Hz, H-3′), 3.32 (s, 3H, OCH_3), 2.47 (q, 2H, J_{vic} = 7.2 Hz, SCH_2CH_3), 1.38 (s, 3H, CH_3CCH_3′), 1.36 (s, 3H, CH_3CCH_3′), 1.16 (t, 3H, J_{vic} = 7.2 Hz, SCH_2CH_3); ^{13}C

Can. J. Chem. Downloaded from www.nrcresearchpress.com by ESC ESCOLA DE ENGENHARIA on 09/08/12
For personal use only.

NMR (75.5 MHz, $CDCl_3$) δ: 104.08 (CH_3CCH_3), 97.92 (C-1), 84.92 (C-1′), 82.64, 80.56, 80.00, 78.92, 75.48, 72.40, 70.56 (C-2, C-3, C-4, C-5, C-2′, C-3′, C-4′, and C-5′), 76.00, 75.12, 75.10, 73.60, 73.36, 72.56 (6 × OCH_2Ph), 69.64, 61.68 (C-6 and C-6′), 55.24 (OCH_3), 26.16, 25.80 (CH_3CCH_3), 25.56 (SCH_2CH_3), 15.00 (SCH_2CH_3). Anal. calcd. for $C_{60}H_{70}O_{11}S$: C 72.12, H 7.06, S 3.21; found: C 71.80, H 7.33, S 3.53.

Product **14**: R_f 0.57 in ethyl acetate – hexane (1:3); ^1H NMR (360 MHz, $CDCl_3$) δ: 5.50 (d, 2H, $J_{1,2}$ = 1 Hz, H-1 × 2), 4.20 (dd, 2H, $J_{1,2}$ = 1 Hz, $J_{2,3}$ = 3 Hz, H-2 × 2), 4.14 (m, 2H, H-5 × 2), 3.90 (dd, 2H, $J_{3,4}$ = 9.4 Hz, $J_{4,5}$ = 9.4 Hz, H-4 × 2), 3.82 (dd, 2H, $J_{5,6}$ = 5.0 Hz, $J_{6,6'}$ = 10.8 Hz, H-6 × 2), 3.78 (dd, 2H, $J_{3,4}$ = 9.4 Hz, $J_{2,3}$ = 3.0 Hz, H-3 × 2), 3.72 (dd, 2H, $J_{5,6'}$ = 1.0 Hz, $J_{6,6'}$ = 10.8 Hz, H-6′ × 2), 2.60 (m, 4H, SCH_2CH_3 × 2), 1.38 (s, 6H, CH_3, acetal), 1.22 (t, 6H, SCH_2CH_3 × 2).

Product **15**: R_f 0.33 in ethyl acetate – hexane (1:3); ^1H NMR (360 MHz, $CDCl_3$) δ: 4.56 (d, 2H, $J_{1,2}$ = 3.5 Hz, H-1 × 2), 3.95 (dd, 2H, $J_{3,4}$ = 9.0 Hz, $J_{4,5}$ = 9.0 Hz, H-4 × 2), 3.72 (m, 4H, H-6, H-5 × 2), 3.46 (m, 6H, H-2, H-3, and H-6′ × 2), 3.32 (s, 6H, OCH_3 × 2), 1.30 (s, 6H, CH_3, acetal × 2); ^{13}C NMR (75.5 MHz, $CDCl_3$) δ: 100.01 (CH_3CCH_3), 97.74 (C-1 × 2), 82.30, 80.17, 78.08, 69.79 (C-2, C-3, C-4, and C-5 × 2), 59.92 (C-6 × 2), 54.81 (OCH_3 × 2), 24.89 (CH_3 acetal × 2). The structures of **14** and **15** were further confirmed by treatment of these acetals with *p*-toluenesulfonic acid for 60 min at room temperature in dichloromethane. The structures were converted to their respective alcohols **13** and **16** upon this treatment.

Product **16**: R_f 0.45 in ethyl acetate – hexane, (1:2); ^1H NMR (300 MHz, $CDCl_3$) δ: 5.42 (d, 1H, $J_{1,2}$ = 1.2 Hz, H-1), 4.19 (m, 1H, H-5), 4.11 (dd, 1H, $J_{1,2}$ = 1.2 Hz, $J_{2,3}$ = 3.2 Hz, H-2), 3.90 (dd, 1H, $J_{3,4}$ = 9.0 Hz, $J_{4,5}$ = 9.0 Hz, H-4), 3.86 (dd, 1H, $J_{2,3}$ = 3.2 Hz, $J_{3,4}$ = 9.0 Hz, H-3), 3.82 (dd, 1H, $J_{5,6}$ = 4.5 Hz, $J_{6,6'}$ = 10.8 Hz, H-6), 3.70 (dd, 1H, $J_{5,6'}$ = 2.0 Hz, $J_{6,6'}$ = 10.8 Hz, H-6′), 2.64 (m, 2H, SCH_2CH_3), 1.30 (t, 3H, SCH_2CH_3); ^{13}C NMR (75.5 MHz, $CDCl_3$) δ: 83.43 (C-1), 80.50, 74.62, 71.52, 69.94 (C-2, C-3, C-4, and C-5), 69.96 (C-6), 24.90 (SCH_2CH_3), 14.85 (SCH_2CH_3).

*Methyl 2,3,4,-tri-*O*-benzyl-6-*O*-(3,4,6-tri-*O*-benzyl-*β*-D-manno-pyranosyl)-*α*-D-glucopyranoside (**10**)*

The mixed acetal **9** (63 mg, 0.0631 mmol) was charged to a round-bottom flask and argon purged. Dry dichloromethane (4 mL) was syringed into the flask and the mixture was cooled to 0°C before 70.9 mg (0.315 mmol, 5 equiv.) of *N*-iodosuccinimide was added all at once. The reaction was stirred for 2 h and 45 min, quenched by adding 3 mL of sodium thiosulfate (0.5 M), and worked up as in the synthesis of **6**. Silica gel chromatography using ethyl acetate in hexane (1:2) as eluent gave 34 mg (60%) of a white solid **10**. When this reaction was carried out in the presence of 1.0 equiv of methanol as described for the activation of **5**, the yield of **10** was unchanged. $[\alpha]_D$ +35.2 (*c* 0.40, CH_2Cl_2), R_f 0.20 in ethyl acetate –hexane. (1:2); ^1H NMR (360 MHz, $CDCl_3$) δ: 7.35–7.15 (m, 30H, aromatic), 4.51 (d, 1H, $J_{1,2}$ = 3.5 Hz, H-1), 4.10 (d, 1H, $J_{1,2}$ < 0.5 Hz, H-1′), 4.09 (dd, 1H, $J_{5,6}$ = 1.5 Hz, $J_{6,6'}$ = 10.8 Hz, H-6a′), 4.00 (dd, 1H, $J_{3,4}$ = 9.5 Hz, $J_{4,5}$ = 9.5 Hz, H-4′), 3.91 (br s, 1H, H-2′), 3.82 (dd, 1H, $J_{3,4}$ = 9.5 Hz, $J_{4,5}$ = 9.5 Hz, H-4), 3.76 (ddd, 1H, $J_{4,5}$ = 9.5 Hz, $J_{5,6}$ = 1.5 Hz, $J_{5,6'}$ = 5.5 Hz, H-5′), 3.73 (dd, 1H, $J_{5,6}$ = 2.0 Hz, $J_{6,6'}$ = 10.2 Hz, H-6a), 3.66 (dd, 1H, $J_{5,6'}$ = 5.0 Hz, $J_{6,6'}$ = 10.2 Hz, H-6b), 3.56 (dd, 1H, $J_{5,6'}$ = 5.5 Hz, $J_{6,6'}$ = 10.8 Hz, H-6b′), 3.50 (dd, 1H, $J_{3,4}$ = 9.5 Hz, $J_{2,3}$ = 3.5 Hz, H-3′), 3.32 (m, 1H, H-5), 3.32 (s, 3H, OCH_3), 2.37 (br s, 1H, OH); ^{13}C NMR (75.5 MHz, $CDCl_3$) δ: 138.8–138.0, 128.5–127.6 (aromatic), 100.00 (d, $J_{C\text{-}1,H\text{-}1}$ = 155 Hz, C-1′), 97.94 (C-1), 82.22, 81.37, 79.95, 77.65, 75.45, 74.34, 69.87, 68.33 (C-2, C-3, C-4, C-5, C-2′, C-3′, C-4′, and C-5′), 75.76, 75.22, 74.78, 73.54, 73.41, 71.42 (6 × OCH_2Ph), 69.35, 68.18 (C-6, and C-6′), 55.20 (OCH_3). Anal. calcd. for $C_{55}H_{60}O_{11}$: C 73.64, H 6.74; found: C 73.40, H 6.79.

*Octyl 4-*O*-(2-*O*-acetyl-3,4,6-tri-*O*-benzyl-*α*-D-mannopyranosyl)-3,6-di-*O*-benzyl-2-deoxy-2-phthalimido-*β*-D-glucopyranoside (**18**)*

The acceptor **12** (91 mg, 0.166 mmol), crushed 4 Å molecular sieves, mercuric cyanide (50 mg, 0.20 mmol, 1.2 equiv.), and mercuric bromide (72 mg, 0.20 mmol, 1.2 equiv.) were charged to a flask and argon purged. Dry acetonitrile (5 mL) was syringed into the mixture and stirred for 30 min. Freshly prepared bromide **17** (ref. 20, 138 mg, 0.25 mmol, 1.5 equiv.), was dissolved in 2 × 1 mL acetonitrile and dropwise added to the reaction mixture. The mixture was stirred for 2 h, filtered through a celite pad, washed with dichloromethane (30 mL), and concentrated. Fresh dichloromethane (25 mL), was added and washed with 2 × 25 mL of saturated potassium iodide and 1 × 25 mL of distilled water. The organic layer was dried ($MgSO_4$), filtered, and concentrated. The concentrate was purified using 15% ethyl acetate in hexane as eluent to give the product **18** (71 mg, 40%), with 37 mg (40%) of recovered acceptor. R_f 0.62 in ethyl acetate – hexane, (1:3); ^1H NMR (360 MHz, $CDCl_3$) δ: 5.54 (m, 1H, H-2′), 5.42 (d, 1H, $J_{1,2}$ = 1.6 Hz, H-1′), 5.10 (d, 1H, $J_{1,2}$ = 8.4 Hz, H-1), 4.22 (dd, 1H, $J_{1,2}$ = 8.4 Hz, $J_{2,3}$ = 10.6 Hz, H-2), 3.66, 3.38 (2 × m, 2H, OCH_2, octyl), 2.04 (s, 3H, $COCH_3$).

*Octyl 3-6-di-*O*-benzyl-4-0-(3,4,6-tri-*O*-benzyl-*α*-D-mannopyranosyl)-2-deoxy-2-phthalimido-*β*-D-glucopyranoside (**19**)*

The 2-*O*-acetate **18** (65 mg, 0.0604 mmol) was dissolved in 5 mL of dry methanol and 3 mg of sodium methoxide was added. The reaction was stirred for 14 h and then neutralized by adding amberlite IRC-120 (H^+) resin until neutral, filtered, and concentrated. The syrup was purified using 20% ethyl acetate in hexane as eluent to give 55 mg (88%) of the desired product **19**. $[\alpha]_D$ + 44.6 (*c* 105, CH_2Cl_2); R_f 0.38 in ethyl acetate – hexane (1:2); ^1H NMR (360 MHz, $CDCl_3$) δ: 7.8–7.6 (m, 4H, phthalimido), 7.4–7.1, 7.05–6.67 (m, 25H, benzyl aromatics), 5.34 (d, 1H, $J_{1,2}$ = 1.8 Hz, H-1′), 5.08 (d, 1H, $J_{1,2}$ = 8.5 Hz, H-1), 4.19 (dd, 1H, $J_{1,2}$ = 8.5 Hz, $J_{2,3}$ = 10.7 Hz, H-2), 3.96 (m, 1H, H-2′), 3.7 3.35 (2 × m, 2H, OCH_2, octyl), 2.20 (d, 1H, $J_{H,OH}$ = 2.8 Hz, OH), 1.4–0.7 (m, 15H, octyl); ^{13}C (75.5 MHz, $CDCl_3$) δ: 101.23 (d, $J_{C\text{-}1,H\text{-}1}$ = 172 Hz, C-1′), 98.10 (C-1), 80.94, 79.89, 78.11, 74.90, 74.21, 72.35, 69.02 (C-2′, C-3′, C-4′, C-5′, C-3, C-4, and C-5), 75.07, 74.62, 73.50, 73.38, 72.11 (5 × OCH_2Ph), 69.60, 69.60 (C-6 and C-6′), 68.90 (OCH_2, octyl), 55.81 (C-2), 31.66, 29.29, 29.13, 25.84, 22.60 (6 × CH_2, octyl), 14.06 (CH_3, octyl). Anal. calcd. for $C_{63}H_{71}O_{12}N$: C 73.16, H 6.92, N 1.35; found: C 72.80, H 6.92, N 1.40.

*Methyl 4-*O*-(2-*O*-acetyl-3,4,6-tri-*O*-benzyl-*α*-D-mannopyranosyl)-2,3,6-tri-*O*-benzyl-*α*-D-glucopyranoside (**20**)*

The alcohol **11** (76 mg, 0.164 mmol), crushed 4 Å molecular sieves, mercuric cyanide (50 mg, 0.197 mmol, 1.2 equiv.), and mercuric bromide (71 mg, 0.197 mmol, 1.2 equiv.) were added to a reaction flask and argon purged. Dry acetonitrile (5 mL), was syringed into the mixture, which was stirred for 30 min. In a separate flask, freshly prepared bromide **17** (20) was argon purged, dissolved in 2 × 1.5 mL of dry acetonitrile, and dropwise added to the acceptor. After 3 h, the reaction was treated as in the preparation of **18**. Chromatography (15% ethyl acetate in hexane as eluent) yielded the desired product **20** (63 mg, 41%) with 35 mg (46%) of recovered acceptor. R_f 0.59 in ethyl acetate – hexane (1:2); ^1H NMR (360 MHz, $CDCl_3$) δ: 5.43 (dd, 1H, $J_{1,2}$ = 1 Hz, $J_{2,3}$ = 3.6 Hz, H-2′), 5.41 (d, 1H, $J_{1,2}$ = 1.5 Hz, H-1′), 4.58 (d, 1H, H-2), 3.54 (dd, 1H, $J_{2,3}$ = 3.6 Hz, $J_{3,4}$ = 9.8 Hz, H-3′), 3.38 (s, 3H, OCH_3), 1.99 (s, 3H, $COCH_3$).

*Methyl 2,3,6-tri-*O*-benzyl-4-*O*-(3,4,6-tri-*O*-benzyl-*α*-D-manno-pyranosyl)-*α*-D-glucopyranoside (**21**)*

The 2-*O*-acetate **20** (60 mg, 0.0639 mmol) was de-*O*-acetylated using the same procedure as for the preparation of **19**. Purification was performed using 18% ethyl acetate in hexane solvent system to give the product **21** (51 mg, 89%) as a colourless syrup. $[\alpha]_D$ + 61.7 (*c* 1.10, CH_2Cl_2); R_f 0.40 in ethyl acetate – hexane (1:2); ^1H NMR (360 MHz, $CDCl_3$) δ: 7.45–7.15 (m, 30H, aromatic), 5.31 (d, 1H, $J_{1,2}$ = 1.8 Hz, H-1′), 4.60 (d, 1H, $J_{1,2}$ = 3.8 Hz, H-1), 3.88–3.66 (m, 12H), 3.60 (dd, 1H, $J_{5,6}$ = 3.8 Hz, $J_{6,6'}$ = 10.5 Hz, H-6a′), 3.53 (dd, 1H, $J_{1,2}$ = 3.8 Hz, $J_{2,3}$ = 9.5 Hz, H-2), 3.49 (dd, 1H, $J_{5,6'}$ = 1.5 Hz, $J_{6,6'}$ = 10.5 Hz, H-6b′), 3.38 (s, 3H, OCH_3), 2.08 (br s, 1H, OH); ^{13}C NMR (75.5 MHz, $CDCl_3$) δ: 138.6–138.0, 128.5–127.5 (aromatic), 101.6 (d, $J_{C\text{-}1,H\text{-}1}$ = 171 Hz,

Can. J. Chem. Downloaded from www.nrcresearchpress.com by EESC ESCOLA DE ENGENHARIA on 09/08/12
For personal use only.

C-1′), 97.8 (C-1), 81.8, 80.02, 79.9, 77.4, 74.2, 72.3, 69.8, 68.8 (C-2, C-3, C-4, C-5, C-2′, C-3′, C-4′, and C-5′), 75.5, 75.0, 73.5, 73.3, 71.9 (6 × OCH_2Ph), 69.4, 69.0 (C-6 and C-6′), 55.3 (OCH_3). Anal. calcd. for $C_{55}H_{60}O_{11}$: C 73.64, H 6.74; found: C 72.97, H 6.76.

Methyl 6-O-(2-O-acetyl-3,4,6-tri-O-benzyl-α-D-mannopyranosyl)-2,3,4,-tri-O-benzyl-α-D-glucopyranoside (22)

The alcohol **13** (76 mg, 0.164 mmol), crushed 4 Å molecular sieves, mercuric cyanide (50 mg, 0.197 mmol, 1.2 equiv.), and mercuric bromide (71 mg, 0.197 mmol, 1.2 equiv.) were added to a reaction flask and argon purged. Dry acetonitrile (5 mL) was syringed into the mixture, which was stirred for 30 min. In a separate flask, freshly prepared bromide **17** (ref. 20; 137 mg, 0.25 mmol, 1.5 equiv.) was dissolved in 2 × 1.5 mL of acetonitrile and dropwise added to the acceptor. After 45 min, the reaction was worked up as in the synthesis of **18**. Column chromatography using 12% ethyl acetate in hexane as eluent yielded the desired product **22** (120 mg, 78%). R_f 0.65 in ethyl acetate – toluene (1:2); ^{1}H NMR (360 MHz, $CDCl_3$) δ: 5.38 (dd, 1H, $J_{1,2}$ = 1.8 Hz, $J_{2,3}$ = 3.0 Hz, H-2′), 4.89 (d, 1H, $J_{1,2}$ = 1.8 Hz, H-1′), 4.58 (d, 1H, $J_{1,2}$ = 3.2 Hz, H-1), 3.98 (dd, 1H, $J_{2,3}$ = 9.0 Hz, $J_{3,4}$ = 9.0 Hz, H-3), 3.91 (dd, 1H, $J_{2,3}$ = 3.0 Hz, $J_{3,4}$ = 9.2 Hz, H-3′), 3.86 (dd, 1H, $J_{3,4}$ = 9.2 Hz, $J_{4,5}$ = 9.2 Hz, H-4′), 3.44 (dd, 1H, $J_{1,2}$ = 3.2 Hz, $J_{2,3}$ = 9.0 Hz, H-2), 3.42 (dd, 1H, $J_{3,4}$ = 9.0 Hz, $J_{4,5}$ = 9.0 Hz, H-4), 3.32 (s, 3H, OCH_3), 2.15 (s, 3H, $COCH_3$).

Methyl 2,3,4,-tri-O-benzyl-6-O-(3,4,6-tri-O-benzyl-α-D-mannopyranosyl)-α-D-glucopyranoside (23)

The 2-O-acetate **22** (115 mg, 0.12 mmol) was de-*O*-acetylated as in the synthesis of **19**. Purification using 30% ethyl acetate in hexane as eluent yielded the product **23** (83 mg, 76%), along with 2 mg (2%) of the accompanying β-isomer. $[\alpha]_D$ + 74.4 (*c* 2.55, CH_2Cl_2); R_f 0.17 in ethyl acetate – hexane (1:2); ^{1}H NMR (360 MHz, $CDCl_3$) δ: 7.40 – 7.10 (m, 30H, aromatic), 5.02–4.40 (m, 12H, 6 × OCH_2Ph), 4.96 (d, 1H, $J_{1,2}$ = 1.5 Hz, H-1′), 4.60 (d, 1H, $J_{1,2}$ = 3.7 Hz, H-1), 4.03 (dd, 1H, $J_{1,2}$ = 15 Hz, $J_{2,3}$ = 3 Hz, H-2′), 3.99 (dd, 1H, $J_{3,4}$ = 9.4 Hz, $J_{4,5}$ = 9.4 Hz, H-3), 3.85 (dd, 1H, $J_{5,6}$ = 4.5 Hz, $J_{6,6'}$ = 10 Hz, H-6a), 3.83 (m, 1H, H-3′), 3.82 (dd, 1H, $J_{5,6'}$ = 3.5 Hz, $J_{6,6'}$ = 10 Hz, H-6b), 3.70 (m, 3H, H-5, H-4′, and H-5′), 3.62 (dd, 1H, $J_{5,6}$ = 4.0 Hz, $J_{6,6'}$ = 11.0 Hz, H-6a′), 3.55 (dd, 1H, $J_{5,6'}$ = 2.0 Hz, $J_{6,6'}$ = 11.0 Hz, H-6b′), 3.50 (dd, 1H, $J_{2,3}$ = 3.7 Hz, $J_{3,4}$ = 9.8 Hz, H-2), 3.45 (dd, 1H, $J_{4,5}$ = 9.4 Hz, $J_{3,4}$ = 9.4 Hz, H-4), 3.33 (s, 3H, OCH_3), 2.40 (br s, 1H, OH); ^{13}C NMR (75.5 MHz, $CDCl_3$) δ: 138.85–137.85, 128.55–127.58 (aromatic), 99.57 (d, $J_{C\text{-}1,H\text{-}1}$ = 175 Hz, C-1′), 97.88 (C-1), 82.17, 80.09, 79.74, 77.74, 74.22, 71.21, 69.84, 68.26 (C-2, C-3, C-4, C-5, C-2′, C-3′, C-4′, and C-5′), 75.82, 75.05, 74.96, 73.41, 73.29, 71.92 (6 × OCH_2Ph), 69.84, 65.92 (C-6 and C-6′), 55.14 (OCH_3). Anal. calcd. for $C_{55}H_{60}O_{11}$: C 73.64, H 6.74; found: C 73.57, H 6.82.

Ethyl 3,4,6-tri-O-benzyl-2-O-(methoxy isopropylidene)-1-thio-α-D-mannopyranoside (24)

The alcohol **16** (200 mg, 0.405 mmol) was charged to a round-bottom flask and argon purged. Dichloromethane (10 mL) was added followed by 0.047 mL (1.2 equiv.) of dimethoxy propene. The reaction was cooled to –40°C and catalytic *p*-toluenesulfonic acid was added. After 7 min, the reaction was quenched by adding triethylamine, concentrated and purified using a 10% ethyl acetate in hexane solvent system containing 0.1% triethylamine. The product **24** (201 mg, 88%) was isolated as a sticky whole solid. R_f 0.57 in ethyl acetate – hexane (1:3); ^{1}H NMR (360 MHz, $CDCl_3$) δ: 5.35 (d, 1H, $J_{1,2}$ = 1.5 Hz, H-1), 4.22 (dd, 1H, $J_{1,2}$ = 1.5 Hz, $J_{2,3}$ = 3.0 Hz, H-2), 4.11 (m, 1H, H-5), 3.98 (dd, 1H, $J_{3,4}$ = 9.4 Hz, $J_{4,5}$ = 9.4 Hz, H-4), 3.84 (dd, 1H, $J_{5,6}$ = 4.8 Hz, $J_{6,6'}$ = 11.0 Hz, H-6), 3.80 (dd, 1H, $J_{3,4}$ = 9.4 Hz, $J_{2,3}$ = 3.0 Hz, H-3), 3.71 (dd, 1H, $J_{5,6'}$ = 1.9 Hz, $J_{6,6'}$ = 11.0 Hz, H-6′), 3.28 (s, 3H, OCH_3), 2.60 (m, 2H, SCH_2CH_3), 1.41, 1.38 (2 × s, 6H, CH_3CCH_3), 1.26 (t, 3H, SCH_2CH_3); ^{13}C NMR (75.5 MHz, $CDCl_3$) δ: 101.46 (CH_3CCH_3), 84.39 (C-1), 80.05, 75.00, 72.18, 70.24 (C-2, C-3, C-4, and C-5), 69.42 (C-6), 49.62 (OCH_3), 25.0 (SCH_2CH_3), 24.94 (CH_3CCH_3), 15.17 (SCH_2CH_3). Anal. calcd. for $C_{33}H_{42}O_6S$: C 69.93, H 7.47, S 5.66; found: C 70.04, H 7.45, S 5.94.

Methyl 3,4,6-tri-O-benzyl-β-D-mannopyranoside (25)

The acetal **24** (50 mg, 0.0883 mmol) was charged to a round-bottom flask and argon purged. Dichloromethane (3 mL) was added and the reaction was cooled to –40°C. *N*-Bromosuccinimide (47.2 mg, 3 equiv.) was added and the reaction was stirred for 1 h. The reaction was quenched by adding 1 mL of 0.5 M NaS_2O_3 solution and worked up as in the synthesis of **6**. Chromatographic purification using 35% ethyl acetate in hexane yielded 6 mg (15%) of the β-mannopyranoside **25**, as well as 20 mg of the succinimide adduct **26** (37%). Treatment of **26** with catalytic *p*-toluenesulfonic acid converted **26** to **25** in quantitative yield.

Product **25**: R_f 0.38 in ethyl acetate – hexane (1:1); ^{1}H NMR (360 MHz, $CDCl_3$) δ: 4.34 (d, 1H, $J_{1,2}$ < 1Hz, H-1), 4.20 (dd, 1H, $J_{1,2}$ < 1Hz, $J_{2,3}$ = 3.2 Hz, H-2), 3.88 (dd, 1H, $J_{3,4}$ = 9.0 Hz, $J_{4,5}$ = 9.0 Hz, H-4), 3.81 (dd, 1H, $J_{5,6}$ = 2.1 Hz, $J_{6,6'}$ = 11.0 Hz, H-6′), 3.58 (dd, 1H, $J_{2,3}$ = 3.2 Hz, $J_{3,4}$ = 9.0 Hz, H-3), 3.57 (s, 3H, OCH_3), 2.39 (d, 1H, $J_{H,OH}$ = 2.4 Hz, OH).

Product **26**: R_f 0.26 in ethyl acetate – hexane (1:2); ^{1}H NMR (360 MHz, $CDCl_3$) δ: 4.36 (dd, 1H, $J_{1,2}$ < 1Hz, $J_{2,3}$ = 2.5 Hz, H-2), 4.22 (d, 1H, $J_{1,2}$ < 1 Hz, H-1), 3.94 (dd, 1H, $J_{3,4}$ = 9.2 Hz, $J_{4,5}$ = 9.2 Hz, H-4), 3.78 (d, 2H, $J_{5,6}$ = 3.8 Hz, H-6′s), 3.47 (s, 3H, OCH_3), 3.45 (m, 2H, H-3 and H-5), 3.31 (m, 4H, CH_2CH_2, succinimide), 1.94, 1.92 (2 × s, 6H, CH_3CCH_3); ^{13}C NMR (75.5 MHz, $CDCl_3$) δ: 178.29 (CO), 101.43 (C-1), 89.90 (OCN), 82.17, 76.42, 75.05, 71.22 (C-2, C-3, C-4, and C-5), 69.59 (C-6), 57.09 (OCH_3), 28.56 (CH_2CH_2, succinimide), 27.49, 27.33 (CH_3CCH_3).

Attempted acetalization of the trisaccharide **27**

The vinyl ether **27** ref 21; 182 mg (0.13 mmol), and the alcohol **11** (72.5 mg, 1.2 equiv.) were charged to a round-bottom flask and argon purged. Calcium sulfate (1 g) was added and the flask was argon purged. Dichloromethane was added and the reaction was stirred and cooled to –40°C. After stirring for 30 min, camphorsulfonic acid (0.08 equiv.) was added. The reaction was stirred at –40°C for 4 h and quenched by adding triethylamine. The vinyl ether **27** (84 mg) was recovered (46%), as well as 62 mg of recovered **11** and 78 mg of recovered hydrolyzed vinyl ether **28**.

Product **27**: The synthesis of **27** will be published elsewhere. For characterization purposes: R_f 0.72 in ethyl acetate – hexane (1:2); ^{1}H NMR (360 MHz, $CDCl_3$) δ: 5.46 (d, $J_{1,2}$ = 1Hz, H-1), 5.13 (d, $J_{1,2}$ = 1.8 Hz, H-1′), 5.01 (d, 1H, $J_{1,2}$ = 1.6 Hz, H-1″), 2.50 (m, 2H, SCH_2CH_3), 1.76 (s, 3H, $CH_2{=}CCH_3$), 1.18 (t, 3H, SCH_2CH_3); ^{13}C NMR (75.5 MHz, $CDCl_3$ + 10% D-5 pyridine) δ: 157.23 ($C{=}CH_2$), 100.28, 97.82 (C-1′ and C-1″), 83.28 ($C{=}CH_2$), 80.55 (C-1), 79.76, 79.37, 79.37, 75.79, 75.04, 74.50, 74.30, 73.91, 72.60, 71.00 (C-2, C-3, C-4, C-5, C-2′, C-3′, C-4′, C-5′, C-2″, C-3″, C-4″, and C-5″), 68.88, 68.61, 65.72 (C-6, C-6′, and C-6″), 24.91 (SCH_2CH_3), 20.97 ($CH_3C{=}CH_2$), 14.72 (SCH_2CH_3).

Product **28**: R_f 0.59 in ethyl acetate – hexane (1:2); ^{1}H NMR (360 MHz, $CDCl_3$) δ: 5.05, 5.00, 4.96 (H-1, H-1′, and H-1″), 3.36 (s, 1H, OH), 2.50 (m, 2H, SCH_2CH_3); ^{13}C NMR (75.5 MHz, $CDCl_3$) δ: 99.50, 98.13 (C-1′ and C-1″), 84.67 (C-1), 83.31, 79.94, 79.68, 75.51, 75.41, 74.65, 73.82, 72.21, 71.78, 71.44, 70.75 (C-2, C-3, C-4, C-5, C-2′, C-3′, C-4′, C-5′, C-2″, C-3″, C-4″, and C-5″), 69.93, 69.24, 66.23 (C-6, C-6′, and C-6″), 25.05 (SCH_2CH_3), 14.99 (SCH_2CH_3).

3,4-di-O-acetyl-6-O-(2,3,4,6-tetra-O-acetyl-α-D-mannopyranosyl)-1,2-methoxyethylidene)-β-D-mannopyranoside (30)

The peracetate **29** (ref. 22; 4.0 g, 5.9 mmol) was dissolved in dichloromethane and cooled to 0°C. Hydrobromic acid gas was passed through a $CaSO_4$ drying tube and bubbled through the dichloromethane solution for 30 min. The solution was then concentrated in vacuo, coevaporated twice with toluene, and dried under high vacuum for 2 h to give a golden foam. The foam was dissolved in dichloromethane (150 mL) and 2,6-lutidene (1.8 mL 14.7 mmol, 2.5 equiv.) was syringed into the mixture. Methanol (0.6 mL, 14.7 mmol, 2.5 equiv.) was added and the reaction was stirred for 60 h. Another 100 mL of CH_2Cl_2 was added and the mixture was washed with 250 mL of saturated sodium bicarbonate solution and 3 × 250 mL of dH_2O. The organic layer was dried ($MgSO_4$), filtered, and concentrated to

Can. J. Chem. Downloaded from www.nrcresearchpress.com by EESC ESCOLA DE ENGENHARIA on 09/08/12
For personal use only.

give 4.0 g of a crude foam (≅100%). A portion of this foam was purified for characterization using ethyl acetate in hexane (1:1) as eluent, giving a white solid product **30** $[\alpha]_D$ + 47.8 (*c* 0.80, CH_2Cl_2); R_f 0.52 in ethyl acetate – hexane (7:3); ^1H NMR (360 MHz, $CDCl_3$) δ: 5.52 (d, 1H, $J_{1,2}$ = 2.8 Hz, H-1), 5.30 (m, 2H, H-2′, and H-4′), 5.24 (m, 1H, H-3′), 5.23 (dd, 1H, $J_{4,5}$ = 9 Hz, $J_{3,4}$ = 9.8 Hz, H-4), 5.15 (dd, 1H, $J_{3,4}$ = 9.8 Hz, $J_{2,3}$ = 3.8 Hz, H-3), 4.80 (d, 1H, $J_{1,2}$ = 1.7 Hz, H-1′), 4.62 (dd, 1H, $J_{1,2}$ = 2.8 Hz, $J_{2,3}$ = 3.8 Hz, H-2), 4.33 (dd, 1H, $J_{5,6}$ = 5.0 Hz, $J_{6,6'}$ = 12.6 Hz, H-6b), 4.06 (m, 2H, H-5′ and H-6b′), 3.79 (dd, 1H, $J_{5,6}$ = 5.8 Hz, $J_{6,6'}$ = 10.2 Hz, H-6a), 3.69 (ddd, 1H, $J_{5,6}$ = 5.8 Hz, $J_{5,6'}$ = 3.0 Hz, $J_{4,5}$ = 9 Hz, H-5), 3.60 (dd, 1H, $J_{5,6'}$ = 3.0 Hz, $J_{6,6'}$ = 10.2 Hz, H-6b), 3.28 (s, 3H, OCH_3), 2.15, 2.13, 2.10, 2.08, 2.06, 1.99 (6 × s, 18H, $COCH_3$), 1.72 (s, 3H, CH_3COCH_3, ortho ester); ^{13}C NMR (75.5 MHz, $CDCl_3$) δ: 170.66, 170.37, 169.98, 169.76, 169.69 (6 × $COCH_3$), 124.34 (CH_3COCH_3, ortho ester), 97.78 (C-1), 97.46 (C-1′), 76.32, 72.22, 70.51, 69.35, 69.09, 68.63, 66.41, 65.94 (C-2, C-3, C-4, C-5, C-2′, C3′, C-4′, and C-5′), 67.60 (C-6′), 62.30 (C-6), 50.05 (OCH_3), 24.17 (CH_3COCH_3, ortho ester), 20.88–20.68 ($COCH_3$). Anal. calcd. for $C_{27}H_{38}O_{18}$: C 49.85, H 5.89; found: C 49.58, H 5.85.

*3,4-Di-*O*-benzyl-6-*O*-(2,3,4,6-tetra-*O*-benzyl-α-D-mannopyranosyl)-1,2-(methoxyethylidene)-α-D-mannopyranoside (**31**)*

The crude peracetylated ortho ester **30** (4.0 g, 5.9 mmol) was dissolved in 150 mL of dry methanol, 30 mg of sodium methoxide was added, and the reaction was stirred overnight. The mixture was concentrated in vacuo and dried under high vacuum to give 2.6 g (≅100) of a white foam. A portion of this foam (2.0 g, 4.5 mmol) was dissolved in 80 mL of dry dimethyl formamide (DMF) and charged to a dropping funnel. In a separate flask, 3.0 g (75 mmol) of sodium hydride, 60% dispersion in oil was mixed with 120 mL DMF and stirred for 30 min, cooling to 0°C. The ortho ester was dropwise added to the DMF–NaH solution over a 15min period and stirred at 0°C for 30 min forming a thick gelatinous mixture. Benzyl bromide (8.9 mL, 75 mmol) was diluted in 20 mL of DMF and dropwise added to the mixture over a 10-min period. The solution became less viscous and allowed to warm to room temperature overnight. The reaction was quenched by adding 50 mL methanol and concentrating under reduced pressure to a total volume of 150 mL, and then 150 mL dichloromethane was added. This solution was washed with 2 × 300 mL of dH_2O and then 300 mL of a saturated solution of sodium chloride. The organic layer was dried ($MgSO_4$), filtered, concentrated, and purified (28% ethyl acetate in hexane with 0.1% added triethylamine as eluent) to give 2.26 g (41% from **29**) of a colourless syrup **31**. $[\alpha]_D$ + 24.4 (*c* 0.95, CH_2Cl_2); R_f 0.30 in ethyl acetate – hexane (2:3); ^1H NMR (360 MHz, $CDCl_3$) δ: 7.45–7.12 (m, 30H, aromatic), 5.33 (d, 1H, $J_{1,2}$ = 2.4 Hz, H-1), 5.00 (d, 1H, $J_{1,2}$ = 1.8 Hz, H-1′), 4.92, 4.49 (2 × d, 2H, J_{gem} = 11.0 Hz, OCH_2Ph), 4.89, 4.55 (2 × d, 2H, J_{gem} = 11.2 Hz, OCH_2Ph), 4.79 (s, 2H, OCH_2Ph), 4.72 (s, 2H, OCH_2Ph), 4.62, 4.43 (2 × d, 2H, J_{gem} = 12.2 Hz, OCH_2Ph), 4.62, 4.61 (2 × d, 2H, J_{gem} = 11.5 Hz, OCH_2Ph), 4.40 (dd, 1H, $J_{1,2}$ = 2.4 Hz, $J_{2,3}$ = 3.8 Hz, H-2), 4.02 (dd, 1H, $J_{3,4}$ = 9.2 Hz, $J_{4,5}$ = 9.2 Hz, H-4′), 3.95 (dd, 1H, $J_{5,6}$ = 4.0 Hz, $J_{6,6'}$ = 11.4 Hz, H-6a′), 3.89 (dd, 1H, $J_{2,3}$ = 3.0 Hz, $J_{3,4}$ = 9.4 Hz, H-3′), 3.83 (dd, 1H, $J_{3,4}$ = 9.2 Hz, $J_{4,5}$ = 9.2 Hz, H-4), 3.82 (dd, 1H, $J_{1,2}$ = 1.8 Hz, $J_{2,3}$ = 3.0 Hz, H-2′), 3.73 (dd, 1H, $J_{2,3}$ = 3.8 Hz, $J_{3,4}$ = 9.2 Hz, H-3), 3.73 (m, 1H, H-5), 3.68 (m, 2H, H-6a, and H-6′b), 3.61 (dd, 1H, $J_{5,6}$ = 1.6 Hz, $J_{6,6'}$ = 10.8 Hz, H-6a′), 3.35 (m, 1H, H-5′), 3.28 (s, 3H, OCH_3), 1.69 (s, 3H, CH_3COCH_3); ^{13}C NMR (75.5 MHz, $CDCl_3$) δ: 138.7–137.8, 128.9–127.4 (aromatics), 123.95 (CH_3COCH_3, ortho ester), 98.61 (C-1), 97.53 (C-1′), 79.88, 79.37, 77.14, 74.81, 74.68, 73.90, 73.35, 72.21 (6 × OCH_2Ph, C-6, and C-6′), 75.19, 74.98, 73.31, 72.62, 72.28, 71.95, 69.19, 66.34 (C-2, C-3, C-4, C-5, C-2′, C-3′, C-4′, and C-5′), 49.73 (OCH_3), 24.71 (CH_3COCH_3, ortho ester). Anal. calcd. for $C_{57}H_{62}O_{12}$: C 79.90, H 6.65; found: C 73.17, H 6.79.

*Ethyl 2-*O*-acetyl-3,4-di-*O*-benzyl-6-*O*-(2,3,4,6-tetra-*O*-benzyl-α-D-mannopyranosyl)-1-thio-α-Dmannopyranoside (**32**)*

The ortho ester **31** (1.26 g, 1.34 mmol) was charged to a round-bottom flask and argon purged. Ethanethiol (15 mL) was added and the solution was cooled to 0°C. Boron trifluoride etherate (0.17 mL, 1.34 mmol) was syringed into the mixture and the reaction was quenched after 10 min by adding 10 mL of dH_2O. The reaction was then worked up as in the preparation of **2**. Chromatography using 15% ethyl acetate in hexane yielded 1.06 g (81%) of a colourless syrup **32**. $[\alpha]_D$ + 64.9 (*c* 1.50, CH_2Cl_2); R_f 0.59 in ethyl acetate – hexane (1:2); ^1H NMR (300 MHz, $CDCl_3$) δ: 7.40–7.10 (m, 30H, aromatics), 5.42 (dd, 1H, $J_{1,2}$ = 1.5 Hz, $J_{2,3}$ = 3.2 Hz, H-2), 5.22 (d, 1H, $J_{1,2}$ = 1.3 Hz, H-1′), 5.03 (d, 1H, $J_{1,2}$ = 1.5 Hz, H-1), 4.86, 4.45 (2 × d, 2H, J_{gem} = 12 Hz, OCH_2Ph), 4.86, 4.47 (2 × d, 2H, J_{gem} = 11.0 Hz, OCH_2Ph), 4.76, 4.71 (2 × d, 2H, J_{gem} = 12 Hz, OCH_2Ph), 4.66, 4.49 (2 × d, 2H, J_{gem} = 10.8 Hz, OCH_2Ph), 4.63, 4.56 (2 × d, 2H, J_{gem} = 12.2 Hz, OCH_2Ph), 4.63, 4.44 (2 × d, 2H, J_{gem} = 10.4 Hz, OCH_2Ph), 4.13 (m, 1H, H-5), 4.01 (dd, 1H, $J_{3,4}$ = 9.5 Hz, $J_{4,5}$ = 9.5 Hz, H-4), 3.91 (dd, 1H, $J_{5,6}$ = 4.8 Hz, $J_{6,6'}$ = 11.0 Hz, H-6a′), 3.89 (m, 4H, H-2, H-3, H-2′, and H-3′), 3.75 (dd, 1H, $J_{4,5}$ = 9.2 Hz, $J_{3,4}$ = 9.2 Hz, H-4′), 3.74 (m, 1H, H-5′), 3.68 (dd, 1H, $J_{5,6}$ = 4.8 Hz, $J_{6,6'}$ = 10.8 Hz, H-6a), 3.66 (dd, 1H, $J_{5,6'}$ = 1.7 Hz, $J_{6,6'}$ = 11.0 Hz, H-6b′), 3.60 (dd, 1H, $J_{5,6'}$ = 1.7 Hz, $J_{6,6'}$ = 10.8 Hz, H-6b), 2.55 (m, 2H, J_{vic} = 7.8 Hz, SCH_2CH_3), 2.06 (s, 3H, $COCH_3$), 1.21 (t, 3H, J_{vic} = 7.5 Hz, SCH_2CH_3); ^{13}C NMR (75.5 MHz, $CDCl_3$) δ: 138.73–137.66, 128.44–127.45 (aromatic), 98.09 (C-1′), 82.28 (C-1), 79.85, 78.74, 74.89, 74.89, 74.55, 71.98, 71.46, 70.48 (C-2, C-3, C-4, C-5, C-2′, C-3′, C-4′, and C-5′), 75.06, 75.06, 73.30, 72.55, 71.88, 71.88 (6 × OCH_2Ph), 69.20, 66.13 (C-6 and C-6′), 25.41 (SCH_2CH_3), 21.10 ($COCH_3$), 14.94 (SCH_2CH_3). Anal. calcd. for $C_{58}H_{64}O_{11}S$: C 71.88, H 6.66, S 3.31; found: C 71.90, H 6.69, S. 3.23.

*Ethyl 3,4-di-*O*-benzyl-6-*O*-(2,3,4,6-tetra-*O*-benzyl-α-D-mannopyranosyl)-2-*O*-(2-propenyl)-1-thio-α-D-mannopyranoside (**33**)*

The thioglycoside **32** (583 mg, 0.60 mmol) was charged to a round-bottom flask and argon purged. Dry toluene (9 mL), tetrahydrofuran (3 mL), and pyridine (0.1 mL) were consecutively syringed into the flask and the mixture was cooled to –40°C. Tebbe's reagent (1.20 mL, 1.2 mmol, 2.0 equiv.) was slowly syringed into the mixture with some fuming. The reaction colour became a deep red. The solution was allowed to slowly warm to –10°C, and after 2.5 h, was quenched by carefully adding 0.1 mL of 1 M NaOH (vigorous methane evolution) at –10°C. After the gas evolution subsided, the mixture was warmed to room temperature and a further 0.5 mL of 1 M NaOH was added. The deep red mixture was filtered as for the preparation of **4** and then concentrated under reduced pressure and purified using column chromatography with 15% ethyl acetate in hexane with 0.1% added triethylamine as eluent. A clear syrup (402 mg, 69%) was obtained **33**. R_f 0.57 in ethyl acetate – hexane (1:3); ^1H NMR (300 MHz, $CDCl_3$) + 2% D-5 pyridine) δ: 7.40–7.10 (m, 30H, aromatic), 5.46 (d, 1H, $J_{1,2}$ = 1 Hz, H-1′), 5.05 (d, 1H, $J_{1,2}$ = 1 Hz, H-1), 4.89, 4.47 (2 × d, 2H, J_{gem} = 10.8 Hz, OCH_2Ph), 4.87 4.45 (2 × d, 2H, J_{gem} = 11.0 Hz, OCH_2Ph), 4.75, 4.70 (2 × d, 2H, J_{gem} = 12.0 Hz, OCH_2Ph), 4.63, 4.56 (2 × d, 2H, J_{gem} = 12 Hz, OCH_2Ph), 4.63, 4.44 (2 × d, 2H, J_{gem} = 11.5 Hz, OCH_2Ph), 4.40 (d, 1H, J_{gem} = 2.0 Hz, C=C*H*H′), 4.09 (m, 1H, H-5), 4.01 (d, $J_{4,5}$ = 9.0 Hz, $J_{3,4}$ = 9.0 Hz, H-4), 3.76 (d, 1H, J_{gem} = 2.0 Hz, C=CH*H*′), 3.74 (m, 1H, H-5′), 2.53 (m, 2H, SCH_2CH_3), 2.31 (s, 3H, $CH_3C{=}CH_2$), 1.20 (t, 3H, SCH_2CH_3); ^{13}C NMR (75.5 MHz, D-5 pyridine) δ: 158.73 ($C{=}CH_2$), 1.39.58–138.84, 129.27–127.69 (aromatics), 98.44 (C-1′), 83.37 ($C{=}CH_2$), 80.84 (C-1), 80.26, 75.93, 75.45, 75.31, 74.34, 72.62, 72.01 (C-2, C-3, C-4, C-5, C-2′, C-3′, C-4′, and C-5′), 75.31, 75.18, 73.38, 73.02, 71.69, 71.58 (6 × OCH_2Ph), 69.94, 66.75 (C-6 and C-6′), 25.39 (SCH_2CH_3), 21.31 ($CH_3C{=}CH_2$), 15.18 (SCH_2CH_3).

*Octyl 3,6-di-*O*-benzyl-2-deoxy-2-phthalimido-β-D-glucopyranoside-ethyl 3′,4′-di-*O*-benzyl-6′-*O*-(2″,3″,4″,6″-tetra-*O*-benzyl-α-D-mannopyranosyl)-1′-thio-α-D-mannopyranoside-2′,4-isopropylidene acetal (**34**)*

The vinyl ether **33** (88 mg, 0.091 mmol) was charged to a round-bottom flask and the alcohol **12** (66 mg, 0.109 mmol, 1.2 equiv.) was added under argon atmosphere. Dry dichloromethane (7 mL), was added to the mixture and cooled to –40°C. A 0.05 mM solution of camphorsulfonic acid was prepared by dissolving 23.3 mg of acid in 2 mL

Can. J. Chem. Downloaded from www.nrcresearchpress.com by EESC ESCOLA DE ENGENHARIA on 09/08/12
For personal use only.

of dry dichloromethane over molecular sieves under argon atmosphere. A 0.18-mL aliquot of the acid mixture (0.009 mmol, 0.1 equiv.) was syringed into the solution. The reaction was carefully monitored by TLC for product formation (60 min) and quenched by adding 0.05 mL of triethylamine. The mixture was concentrated and purified on silica gel using 17% ethyl acetate in hexane as eluent with added 0.1% triethylamine. The mixed acetal **34** (35 mg, 25%) was obtained as a colourless viscous syrup, as well as 28 mg recovered as vinyl ether **33** and 44 mg recovered as alcohol **12**. The product was unstable (<12 h at room temperature) unless stored in an organic solution with 0.5% added triethylamine. R_f 0.72 in ethyl acetate – hexane (1:2); ^{1}H NMR (360 MHz, $CDCl_3$ + 2% D-5 pyridine) δ: 5.35 (d, 1H, $J_{1,2}$ = 1 Hz, H-1_M), 5.10 (d, 1H, $J_{1,2}$ = 7.4 Hz, H-1_{Gn}), 5.03 (d, 1H $J_{1,2}$ = 1 Hz, H-$1'_M$), 2.56 (m, 2H, SCH_2CH$_3$), 1.42 (s, 3H, CH_3CCH$_{3'}$), 1.37 (s, 3H, CH$_3$CC$H_{3'}$), 1.30 (t, 3H, J_{vic} = 7.0 Hz, SCH$_2$CH_3), 1.3–0.75 (m, 15H, octyl); ^{13}C NMR (75.5 MHz, $CDCl_3$ + 2% D-5 pyridine) δ: 104.79 (OCO, acetal), 98.08, 97.76 (C-1_{Gn}, C-$1'_M$), 84.67 (C-1_M), 79.84, 79.83, 76.20, 75.06, 75.04, 74.92, 74.64, 73.14, 71.91, 71.61, 71.41 (C-2_M, C-3_M, C-4_M, C-5_M, C-$2'_M$, C-$3'_M$, C-$4'_M$, C-5_M, C-3_{Gn}, C-4_{Gn}, and C-5_{Gn}), 75.15, 74.85, 74.76, 74.72, 73.17, 73.01, 72.62, 72.49, 72.62, 72.49, 71.61, 69.43, 69.01 (8 × OCH_2Ph, C-6_M, C-$6'_M$, C-6_{Gn}, and OCH$_2$ octyl), 56.49 (C-2_{Gn}), 31.55, 29.23, 29.04, 29.00, 25.74, 25.22, 22.48 (6 × CH$_2$, octyl, SCH_2CH$_3$), 26.36, 25.81 (2 × CH$_3$, acetal), 15.21 (SCH$_2$CH_3), 13.94 (CH$_3$, octyl).

Octyl 3,6-di-O-benzyl-4-O-[3,4-di-O-benzyl-6-O-(2,3,4,6-tetra-O-benzyl-α-D-mannopyranosyl)-β-D-mannopyranosyl]-2-deoxy-2-phthalimido-β-D-glucopyranoside (35)

The mixed acetal **34** (35 mg, 0.0223 mmol) was argon purged in a round-bottom flask. Dry dichloromethane (6 mL) was syringed into the flask followed by 1.1 mL of a 0.10 mM solution of 4-Me-DTBP (0.112 mmol, 5.0 equiv.), prepared as for compound **49**. *N*-Iodosuccinimide (25 mg, 0.112 mmol, 5.0 equiv.) was added to the reaction and stirred overnight. After 18 h, the reaction was not completed, so another 25 mg (10 equiv. total) of NIS was added and the reaction was stirred an additional 52 h (70 h total) before quenching the reaction by adding 2 mL of 0.5 M sodium thiosulfate. Dichloromethane (10 mL) was then added and the solution was washed with 2 × 10 mL of dH_2O, dried ($MgSO_4$), filtered, and concentrated. Purification using 25% ethyl acetate in hexane yielded the trisaccharide **35** (9 mg, 28%) as a viscous syrup. R_f 0.37 in ethyl acetate – hexane (1:2); ^{1}H NMR (360 MHz, $CDCl_3$) δ: 7.7–7.5 (m, 4H, phthalimido), 6.95, 6.70 (m, 40H, benzyl aromatics), 5.07 (d, $J_{1,2}$ = 8.3 Hz, H-1), 4.96 (d, 1H, $J_{1,2}$ = 1.5 Hz, H-1″), 4.68 (d, 1H, $J_{1,2}$ < 1Hz, H-1′), 4.30 (m, 2H, H-3, H-3′), 4.12 (dd, $J_{1,2}$ = 8.5 Hz, $J_{2,3}$ = 10.5 Hz, H-2), 4.05 (m, 1H, H-2′), 3.70 (m, 1H, H-2″), 3.39 (dd, 1H, $J_{2,3}$ = 3.2 Hz, $J_{3,4}$ = 9.0 Hz, H-3′), 3.36 (m, 1H, OC*H*H′, octyl), 2.48 (d, 1H, $J_{H,OH}$ = 2.5 Hz, OH), 1.4–0.75 (m, 15H, octyl); ^{13}C NMR (125.7 MHz, $CDCl_3$) δ: 100.99 (d, $J_{C\text{-}1,H\text{-}1}$ = 159 Hz, C-1′), 98.44, 98.42 (C-1, C-1″), 81.82, 79.68, 78.69, 78.27, 74.88, 74.85, 74.71, 74.48, 73.54, 72.15, 67.64 (C-3, C-4, C-5, C-2′, C-3′, C-4′, C-5′, C-2″, C-3″, C-4″ and C-5″), 76.19, 75.03, 74.78, 74.73, 73.62, 73.28, 72.46, 71.59, 71.25, 69.69, 69.20, 68.87 (8 × OCH_2Ph, C-6, C-6′, C-6″, and OCH$_2$, octyl), 55.90 (C-2), 31.68, 29.31, 29.16, 29.13, 25.85, 22.62 (6 × CH$_2$, octyl), 14.08 (CH$_3$, octyl).

Octyl 3,6-di-O-benzyl-4-O-[3,4-di-O-benzyl-6-O-(2,3,4,6-tetra-O-benzyl-α-D-mannopyranosyl)-α-D-mannopyranosyl]-2-deoxy-2-phthalimido-β-D-glucopyranoside (36)

The thioglycoside **32** (58 mg, 0.0599 mmol) and the acceptor **12** (54 mg, 0.0898 mmol, 1.5 equiv.) were charged to a round-bottom flask, followed by crushed 4 Å molecular sieves (400 mg) under argon atmosphere. Dry dichloromethane (8 mL) was added and stirred for 30 min, cooling to 0°C. *N*-Iodosuccinimide (15 mg, 0.0659 mmol, 1.1 equiv.) was added to the cooled solution, followed by a catalytic amount of silver triflate (2 mg, 0.1 equiv.). After about 2 min, a deep red colour was observed in the solution and the reaction was complete by t = 4 min. The mixture was filtered and 10 mL of dichloromethane was added. The solution was washed with 10 mL of 0.5 M NaS_2O_3 solution and 10 mL of saturated sodium bicarbonate. The organic layer was dried ($MgSO_4$), filtered, concentrated, and redissolved in 10 mL of dry methanol. Sodium methoxide (3 mg) was added to the solution and stirred overnight. The reaction was neutralized with amberlite IRC-120 (H^+) resin, filtered, concentrated, and purified on Iatrobeads using 8% ethyl acetate in toluene as a solvent system. The desired trisaccharide (61 mg, 69%) was obtained as a colourless syrup. $[\alpha]_D$ + 39.9 (*c* 1.55, CH_2Cl_2); R_f 0.50 in ethyl acetate – hexane (1:2); ^{1}H NMR (500 MHz, $CDCl_3$) δ: 5.26 (d, 1H, $J_{1,2}$ = 1.5 Hz, H-1′), 5.07 (d, 1H, $J_{1,2}$ = 8.7 Hz, H-1), 5.02 (d, 1H, $J_{1,2}$ = 1Hz, H-1″), 4.36 (dd, 1H, $J_{2,3}$ = 10.7 Hz, $J_{3,4}$ = 8.9 Hz, H-3), 4.20 (dd, 1H, $J_{1,2}$ = 8.7 Hz, $J_{2,3}$ = 10.7 Hz, H-2), 3.96 (m, 1H, H-2′), 3.75 (m, 1H, H-2″), 3.34 (dt, 1H, J_{vic} = 7.0 Hz, J_{gem} = 9.8 Hz, OCHH′, octyl), 2.08 (s, 1H, OH), 1.4–0.8 (m, 15H, octyl); ^{13}C NMR (125.7 MHz, $CDCl_3$) δ: 101.08 (d, $J_{C\text{-}1,H\text{-}1}$ = 173 Hz, C-1′), 98.95 (C-1″), 98.07 (C-1), 80.82, 79.89, 79.46, 78.01, 74.86, 74.77, 74.70, 73.66, 72.12, 72.01, 68.81 (C-3, C-4, C-5, C-2′, C-3′, C-4′, C-5′, C-2″, C-3″, C-4″, and C-5″), 74.99, 74.99, 74.62, 73.39, 73.29, 72.35, 72.05, 71.72 (8 × OCH$_2$Ph), 69.55, 69.38, 69.22 (C-6, C-6′, and C-6″), 66.11 (OCH$_2$, octyl), 55.76 (C-2), 31.61, 29.24, 29.08, 25.78, 22.61, 22.55 (6 × CH$_2$, octyl), 14.03 (CH$_3$, octyl).

Octyl 3,4,6-tri-O-acetyl-2-deoxy-2-phthalimido-β-D-glucopyranoside (38)

Under argon atmosphere the anomeric acetate **37** (ref. 23; 5.0 g, 10.5 mmol) was dissolved in 50 mL of dry dichloromethane and cooled to 0°C. 1-Octanol (5.0 mL, 31.5 mmol, 3.0 equiv.) was syringed into the mixture, followed by 2.45 mL of tin tetrachloride (21 mmol, 2.0 equiv.). The mixture was allowed to warm to room temperature and quenched after 5 h by adding 100 mL of dH_2O and 50 mL of CH_2Cl_2. The organic layer was washed by another portion (100 mL) of water, dried ($MgSO_4$), filtered, and concentrated to give a tan-coloured syrup. A portion of this syrup was purified on silica gel (25% ethyl acetate in hexane as eluent) for characterization and the balance was used as crude material. $[\alpha]_D$ + 21.2 (*c 1.85, CH_2Cl_2*); R_f 0.69 in ethyl acetate – hexane (1:1); ^{1}H NMR (300 MHz, $CDCl_3$) δ: 7.90–7.70 (m, 4H, aromatic), 5.80 (dd, 1H, $J_{2,3}$ = 10.8 Hz, $J_{3,4}$ = 8.8 Hz, H-3), 5.36 (d, 1H, $J_{1,2}$ = 8.5 Hz, H-1), 5.18 (dd, 1H, $J_{3,4}$ = 8.8 Hz, $J_{4,5}$ = 10.0 Hz, H-4), 4.34 (dd, 1H, $J_{6,6'}$ = 12.2 Hz, $J_{5,6}$ = 4.6 Hz, H-6), 4.31 (dd, 1H, $J_{2,3}$ = 10.8 Hz, $J_{1,2}$ = 8.5 Hz, H-2), 4.17 (dd, 1H, $J_{6,6'}$ = 12.2 Hz, $J_{5,6'}$ = 2.3 Hz, H-6′), 3.85 (m, 2H, H-5, and OC*H*H′, octyl), 3.43 (m, 1H, OCH*H*′, octyl); ^{13}C NMR (75.5 MHz, $CDCl_3$) δ: 170.8, 170.2, 169.5 (3 × *C*OCH$_3$, acetates), 134.3, 131.5, 123.6 (aromatic), 98.3 (C-1), 71.9, 70.9, 69.2 (C-3, C-4, and C-5), 70.3 (C-6), 62.2 (O*C*H$_2$, octyl), 54.8 (C-2), 31.7, 29.3, 29.1, 25.8, 22.6 (6 × *C*H$_2$, octyl), 20.8, 20.7, 20.5 (3 × CH$_3$, acetates), 14.1 (*C*H$_3$, octyl). Anal. calcd. for $C_{38}H_{37}O_{10}N$: C 61.41, H 6.81, N 2.56; found: C 61.51, H 6.69, N 2.58.

Octyl 2-deoxy-2-phthalimido-β-D-glucopyranoside (39)

Crude **38** (10.5 mmol) was de-O-acetylated using the same procedure as in the formation of **19**. The white solid was purified by column chromatography using 7% methanol in dichloromethane as eluent. The product **39** was obtained as a white solid (3.6 g, 81% from **37**) $[\alpha]_D$ – 55.0 (*c* 0.20, CH_3OH); R_f 0.52 in methanol–dichloromethane (1:9); ^{1}H NMR (300 MHz, CD_3OD) δ: 7.92–7.75 (m, 4H, aromatic), 5.14 (d, 1H, $J_{1,2}$ = 8.5 Hz, H-1), 4.25 (dd, 1H, $J_{1,2}$ = 8.5 Hz, $J_{2,3}$ = 10.7 Hz, H-2), 3.96 (dd, 1H, $J_{2,3}$ = 10.7 Hz, $J_{3,4}$ = 8.4 Hz, H-3), 3.95–3.70, 3.60–3.46 (m, 6H, H-4, H-5, H-6, H-6′, OCH$_2$, octyl), 1.42–0.78 (m, 15H, octyl); ^{13}C NMR (75.5 MHz, CD_3OD) δ: 169.7 (CO, phthalimido), 135.5, 133.1, 124.1 (aromatic), 99.7 (C-1), 78.2, 72.6 (C-3, C-4, and C-5), 70.4 (C-6), 62.7 (O*C*H$_2$, octyl), 58.6 (C-2), 32.8, 30.3, 30.3, 30.2, 27.1, 23.6 (6 × *C*H$_2$, octyl), 14.4 (*C*H$_3$, octyl). Anal. calcd. for $C_{22}H_{31}O_7N$: C 62.69, H 7.41, N 3.32; found: C 62.02, H 7.46, N 3.27.

Octyl 4,6-O-benzylidene-2-deoxy-2-phthalimido-β-D-glucopyranoside (40)

The octyl glycoside **39** (3.6 g, 8.54 mmol) was dissolved in 140 mL of dichloromethane and 40 mL of dimethyl formamide. Dimethoxy toluene (1.54 mL, 10.3 mmol, 1.2 equiv.) and *p*-toluenesulfonic acid monohydrate (30 mg, 0.02 equiv.) were added to the mixture. The mixture was then fitted with a dropping funnel containing 4 Å molecular

Can. J. Chem. Downloaded from www.nrcresearchpress.com by EESC ESCOLA DE ENGENHARIA on 09/08/12
For personal use only.

sieves and a condenser above the dropping funnel. The solution was refluxed overnight (16 h) and neutralized by adding amberlite IR-410 (OH^-) resin until neutral. The mixture was concentrated and purified on silica gel using ethyl acetate – hexane (1:2) as eluent. The product **40** (3.4 g, 78%) was isolated as a white foam. Further elution with 7% methanol in dichloromethane recovered 0.7 g (19%) of the starting material $[\alpha]_D$ –30.4 (*c* 1.0, CH_2Cl_2); R_f 0.44 in ethyl acetate – hexane (1:2); ^{1}H NMR (300 MHz, $CDCl_3$) δ: 7.90–7.70 (m, 4H, phthalimido), 7.55–7.35 (m, 5H, phenyl), 5.58 (s, 1H, CH benzylidene), 5.27 (d, 1H, $J_{1,2}$ = 8.6 Hz, H-1), 4.64 (ddd, 1H, $J_{2,3}$ = 10.5 Hz, $J_{3,4}$ = 8.8 Hz, $J_{3,OH}$ = 3.6 Hz, H3), 4.40 (dd, 1H, $J_{6,6'}$ = 10.5 Hz, $J_{5,6}$ = 4.5 Hz, H-6), 4.24 (dd, 1H, $J_{6,6'}$ = 10.5 Hz, $J_{5,6'}$ = 8.5 Hz, H-6′), 3.89–3.78, 3.70–3.57 (m, 4H, H-2, H-4, H-5, and OC*H*H′, octyl), 3.42 (m, 1H, OCH*H*′, octyl), 2.44 (d, 1H, $J_{3,OH}$ = 3.6 Hz, OH), 1.50–0.98 (m, 12H, octyl), 0.81 (5, 3H, J_{vic} = 7.5 Hz, CH_3, octyl); ^{13}C NMR (75.5 MHz, $CDCl_3$) δ: 137.1, 134.1, 131.8, 129.4, 128.4, 126.4, 123.5 (aromatic), 102.0 (CH, benzylidene), 99.0 (C-1), 82.4 (C-3), 68.8, 66.2 (C-4, C-5), 70.2 (C-6), 68.8 (OCH_2, octyl), 56.7 (C-2), 31.7, 29.3, 29.1, 25.8, 22.6 (6 × CH_2, octyl), 14.1 (CH_3, octyl). Anal. calcd. for $C_{29}H_{35}O_7N$: C 68.35, H 6.92, N 2.75; found: C 68.31, H 7.08, N 2.78.

*Octyl 4,6-*O*-benzylidene-3-*O*-benzyl-2-deoxy-2-phthalimido-*β*-*D*-glucopyranoside (**41**)*

The alcohol **40** (3.3 g, 6.5 mmol) was dissolved in 50 mL of dry dimethyl formamide and sodium hydride (0.52 g, 13 mmol, 2.0 equiv. 60% dispersion in oil) was added. The solution was stirred at 15°C for 30 min and 1.5 mL (13 mmol, 2.0 equiv.) of benzyl bromide was added all at once. The reaction was stirred overnight at ambient temperature, quenched by adding 10 mL methanol, concentrated to dryness, and then chromatographed using 10% ethyl acetate in hexane as eluent. A pale yellow syrup **41** (2.86 g, 73%) was obtained. $[\alpha]_D$ + 23.9 (*c* 0.98, CH_2Cl_2); R_f 0.59 in ethyl acetate – hexane (1:3); ^{1}H NMR (300 MHz, $CDCl_3$) δ: 7.90–7.60 (m, 4H, phthalimido), 7.55–7.30 (m, 5H, benzylidene), 7.05–6.80 (m, 5H, benzyl), 5.63 (s, 1H, CH, benzylidene), 5.19 (d, 1H, $J_{1,2}$ = 8.4 Hz, H-1), 4.80, 4.51 (2 × d, 2H, J_{gem} = 12.2 Hz, OCH_2Ph), 4.43 (dd, 1H, $J_{5,6}$ = 8.5 Hz, $J_{6,6'}$ = 10.4 Hz, H-6), 4.41 (dd, 1H, $J_{5,6'}$ = 4.5 Hz, $J_{6,6'}$ = 10.4 Hz, H-6′), 4.21 (dd, 1H, $J_{2,3}$ = 10.4 Hz, $J_{1,2}$ = 8.4 Hz, H-2), 3.86 (dd, 1H, $J_{2,3}$ = 10.4 Hz, $J_{3,4}$ = 10 Hz, H-3), 3.81 (dd, 1H, $J_{3,4}$ = 10 Hz, $J_{4,5}$ = 9.8 Hz, H-4), 3.77 (dt, 1H, J_{gem} = 9.9 Hz, J_{vie} = 6.8 Hz, OC*H*H′, octyl), 3.64 (ddd, 1H, $J_{5,6'}$ = 4.5 Hz, $J_{5,6}$ = 8.5 Hz, $J_{4,5}$ = 9.8 Hz, H-5), 3.37 (dt, 1H, J_{gem} = 9.9 Hz, J_{vic} = 6.8 Hz, OCH*H*′, octyl), 1.43–0.84 (m, 12H, 6 × CH_2, octyl), 0.80 (t, 3H, J_{vic} = 7.5 Hz, CH_3 octyl); ^{13}C NMR (75.5 MHz, $CDCl_3$) δ: 138.0, 137.4, 133.8, 131.7, 129.0, 128.3, 128.1, 127.4, 126.1, 123.3 (aromatic), 101.4 (CH, benzylidene), 99.0 (C-1), 83.2, 77.5, 66.2 (C-3, C-4, and C-5), 77.1 (OCH_2Ph), 70.1 (C-6), 66.9 (OCH_2, octyl), 55.9 (C-2), 31.7, 29.3, 29.1, 25.8, 22.6 (6 × CH_2, octyl), 14.1 (CH_3, octyl). Anal. calcd. for $C_{36}H_{41}O_7N$: C 72.10, H 6.89, N 2.34; found: C 72.28, H 6.91, N 2.35.

*Octyl 4,6-di-*O*-benzyl-2-deoxy-2-phthalimido-*β*-*D*-glucopyranoside (**12**)*

In a three-neck, round-bottom flask, the benzylidene acetal **41** (285 mg, 4.75 mmol) was added and dissolved in 75 mL of tetrahydrofuran. Molecular sieves (3 Å), trace methyl orange (2 mg), and sodium cyanoborohydride (2.98 g, 47.5 mmol, 10 equiv.) were added and the mixture was cooled to 0°C. In a separate flask, 15 mL of ethyl ether was saturated with hydrochloric acid by bubbling HCl gas through the ethyl ether at 0°C for 20 min. The HCl–Et_2O solution was then transferred to a dropping funnel and dropwise added to the benzylidene acetal mixture until a strong pink colour persisted. The reaction was complete after 55 min and the mixture was filtered and poured into 250 mL of cold water (5°C). The solution was extracted with 2 × 200 mL of dichloromethane, and the organic layers were combined and washed with 250 mL of saturated sodium bicarbonate solution. The organic layer was then dried ($MgSO_4$), filtered, and concentrated. Purification on silica gel using 22% ethyl acetate in hexane as eluent gave the product **12** (2.37 g, 83%) as a colourless syrup. $[\alpha]_D$ + 14.4 (*c* 0.95, CH_2Cl_2); R_f 0.27 in ethyl acetate – hexane (1:3); ^{1}H NMR (360 MHz, $CDCl_3$) δ: 7.70, 7.35, 7.10, 6.95 (m, 14H, aromatics), 5.13 (d, 1H, $J_{1,2}$ = 8.3 Hz, H-1), 4.75, 4.54 (2 × d, 2H, J_{gem} = 12.1 Hz, OCH_2Ph), 4.66, 4.58 (2 × d, 2H, J_{gem} = 11.9 Hz, OCH_2Ph), 4.23 (dd, 1H, $J_{5,6}$ = 8.0 Hz, $J_{6,6'}$ = 10.5 Hz, H-6), 4.14 (dd, 1H, $J_{5,6'}$ = 8.0 Hz, $J_{6,6'}$ = 10.5 Hz, H-6′), 3.9–3.7 (m, 4H, H-2, H-3, H-4, H-5), 3.65, 3.35 (2 × m, 2H, OCHH′, octyl), 2.93 (d, 1H, $J_{4,OH}$ = 2.3 Hz, OH), 1.4–0.8 (m, 15H, octyl); ^{13}C NMR (75.5 MHz, $CDCl_3$) δ: 138.3, 137.7, 133.8, 131.8, 128.6, 128.2, 127.9, 127.9, 127.4, 123.3 (aromatics), 98.4 (C-1), 78.8, 74.7, 73.5 (C-3, C-4, and C-5), 74.3, 73.9, 71.0, 69.7 (2 × OCH_2Ph, C-6, OCH_2, octyl), 55.5 (C-2), 31.7, 29.3, 29.2, 29.1, 25.6, 22.6 (6 × CH_2, octyl), 14.1 (CH_3, octyl). Anal. calcd. for $C_{36}H_{43}O_7N$: C 71.86, H 7.20, N 2.33; found C 71.78, H 7.12, N 2.38.

*Allyl 4-*O*-acetyl-3,6-di-*O*-benzyl-2-deoxy-2-phthalimido-*β*-*D*-glucopyranoside (**43**)*

The alcohol **42** (ref. 25; 1.65 g, 3.12 mmol) was dissolved in 50 mL of pyridine. Acetic anhydride (10 mL) was added and the reaction was stirred overnight at ambient temperature. Dichloromethane (200 mL) was added, and the organic layer was washed with 2 × 200 mL of saturated sodium bicarbonate solution and 1 × 200 mL saturated sodium chloride solution. The organic layer was then dried ($MgSO_4$) filtered, and concentrated to give 1.61 g (90%) of the product **43** as a white solid after chromatography using 25% ethyl acetate in hexane as eluent $[\alpha]_D$ + 66.3 (*c* 0.80, CH_2Cl_2); R_f 0.46 in ethyl acetate – hexane (1:2); ^{1}H NMR (300 MHz, $CDCl_3$) δ: 7.80–7.60 (m, 4H, phthalimido), 7.40–7.25, 7.05–6.85 (m, 10H, benzyl), 5.68 (dddd, 1H, J_{trans} = 17.3 Hz, J_{cis} = 10.6 Hz, J_{vic} = 6.4 Hz, $J_{vic'}$ = 5.2 Hz, OCH$_2$C*H*=CH$_2$), 5.19 (d, 1H, $J_{1,2}$ = 8.5 Hz, H-1), 5.12 (dd, 1H, $J_{3,4}$ = 9.0 Hz, $J_{4,5}$ = 9.2 Hz, H-4), 5.10, 5.01 (2 × dddd, 2H, OCH$_2$CH=C*HH*′), 4.60, 4.32 (2 × d, 2H, J_{gem} = 12.0 Hz, OCH_2Ph), 4.56 (s, 2H, OCH_2Ph), 4.44 (dd, 1H, $J_{2,3}$ = 10.6 Hz, $J_{3,4}$ = 9.0 Hz, H-3), 4.31 (dd, 1H, $J_{2,3}$ = 10.6 Hz, $J_{1,2}$ = 8.5 Hz, H-2), 4.25, 4.01 (dddd, 2H, OCH_2CH=CH$_2$), 3.75 (dt, 1H, $J_{4,5}$ = 9.2 Hz, $J_{5,6}$ = 4.6 Hz, H-5), 3.62 (d, 2H, $J_{5,6}$ = 4.6 Hz, H-6), 1.96 (s, 3H, COCH_3); ^{13}C NMR (75.5 MHz, $CDCl_3$) δ: 169.68 (*C*OCH$_3$), 138.01, 137.76, 128.4–127.5 (benzyl aromatic), 133.7, 131.68, 123.37 (phthalimido), 133.58 (OCH$_2$*C*H=CH$_2$), 117.49 (OCH$_2$CH=*C*H$_2$), 97.32 (C-1), 77.06, 73.56, 72.63 (C-3, C-4, and C-5), 55.50 (C-2), 73.82, 73.67 (2 × OCH_2Ph), 69.84 (C-6, and OCH_2, octyl), 20.93 (COCH_3). Anal. calcd. for $C_{33}H_{33}O_8N$: C 69.34, H 5.82, H 2.45; found: C 68.88, H 5.95, N 2.49.

*4-*O*-Acetyl-3,6-di-*O*-benzyl-2-deoxy-2-phthalimido-α,β-*D*-glucopyranose (**44**)*

The allyl glycoside **43** (1.61 g, 2.82 mmol) was dissolved in 110 mL of a 7:3:1 mixture of ethanol–toluene–water. 1,4-Diazabicyclo[2.2.2]-octane (DABCO) (142 mg, 1.27 mmol, 0.45 equiv.) was added, followed by 391 mg of tris(triphenylphosphine)rhodium(I) chloride (Wilkinson's catalyst; 0.42 mmol, 0.15 equiv.). The mixture was refluxed for 44 h, cooled, and concentrated to a blackish solution, which was then dissolved in 50 mL of acetone. Mercuric oxide (15 mg, 0.005 equiv.) was added, followed by 50 mL of a 9:1 mixture of acetone–water containing 3.8 g (14.1 mmol, 5 equiv.) of dissolved mercuric chloride. The mixture was stirred for 12 h and then 200 mL of dichloromethane was added. The organic layer was washed with 3 × 200 mL of a saturated potassium iodide solution and 2 × 200 mL dH_2O. The organic layer was then dried ($MgSO_4$), filtered, and concentrated. Purification on silica gel using ethyl acetate – hexane (1:2) as eluent yielded 1.12 g (75%) of the product **44** as a 85:15 mixture of β:α-anomers. R_f 0.14 in ethyl acetate – hexane (1:2); ^{1}H NMR, β-anomer only (360 MHz, $CDCl_3$) δ: 7.80 – 7.60 (m, 4H, phthalimido), 7.40–7.25, 7.05–6.90 (m, 10H, benzyl aromatic), 5.38 (dd, 1H, $J_{1,2}$ = 8.2 Hz, $J_{1,OH}$ = 6 Hz, H-1β), 5.17 (dd, 1H, $J_{3,4}$ = 9.0 Hz, $J_{4,5}$ = 9.8 Hz, H-4), 4.63, 4.36 (2 × d, 2H, J_{gem} = 12.3 Hz, OCH_2Ph), 4.58 (s, 2H, OCH_2Ph), 4.52 (dd, 1H, $J_{1,2}$ = 8.2 Hz, $J_{2,3}$ = 10.6 Hz, H-2), 4.20 (dd, 1H, $J_{2,3}$ = 10.6 Hz, $J_{3,4}$ = 9.0 Hz, H-3), 3.82 (m, 1H, H-5), 3.60 (m, 2H, H-6), 2.92 (d, 1H, $J_{H,OH}$ = 6 Hz, OH), 1.93 (s, 3H, CH_3, acetate); ^{13}C NMR, β anomer only (75.5 MHz, $CDCl_3$) δ: 169.65 (CO, acetate), 133.95, 131.62, 123.42 (phthalimido), 137.72, 128.4–127.3 (benzyl aromatics), 92.94 (C-1), 76.78, 73.57, 72.28 (C-3, C-4, and C-5), 57.18 (C-2), 73.90, 73.69 (2 × OCH_2Ph), 69.38 (C-6). Anal. calcd. for $C_{30}H_{29}O_8N$: C 67.79, H 5.50, N 2.64; found: C 67.54, H 5.64, N 2.51.

Can. J. Chem. Downloaded from www.nrcresearchpress.com by EESC ESCOLA DE ENGENHARIA on 09/08/12
For personal use only.

4-O-Acetyl-3,6-di-O-benzyl-2-deoxy-2-phthalimido-α,β-D-gluco-pyranosyl chloride (45)

The reducing sugar **44** (600 mg, 1.13 mmol) was dissolved in dry dichloromethane (10 mL) under argon atmosphere. In a separate flask, Vilsmeier reagent was prepared by adding 0.84 mL (10.8 mmol) of dimethyl formamide (DMF) to 8.2 mL of chloroform. Oxalyl chloride (0.94 mL, 10.8 mmol) was syringed into the DMF–chloroform solution forming a deep yellow colour. The Vilsmeier reagent concentration was 1.08 mmol/mL. After stirring for 15 min, 5.2 mL (5.6 mmol, 5 equiv.) of the Vilsmeier solution was added to the reducing sugar and stirred for 20 min. The reaction was quenched by pouring the reaction mixture into 100 mL of cold water (5°C). Another 100 mL of dichloromethane was added and the organic layer was washed with 2 × 100 mL of dH_2O. The organic layer was dried ($MgSO_4$), filtered, and concentrated to give 620 mg of a bright yellow solid **45**. R_{fs} 0.55 (α) and 0.45 (β) in ethyl acetate – hexane (1:2); ^{1}H NMR (360 MHz, $CDCl_3$) δ: 6.22 (d, 0.45H, $J_{1,2}$ = 3.8 Hz, H-1α), 5.99 (m, 0.55H, $J_{1,2}$ = 9.2 Hz, H-1β), 5.43 (dd, 0.45H, $J_{2,3}$ = 11.0 Hz, $J_{3,4}$ = 9.0 Hz, H-3α), 5.31 (dd, 0.45H, $J_{3,4}$ = 9.0 Hz, $J_{4,5}$ = 9.0 Hz, H-4α), 5.21 (m, 0.55H, H4β), 4.64 (dd, 0.45H, $J_{1,2}$ = 3.8 Hz, $J_{2,3}$ = 11.0 Hz, H-2α), 4.43 (m, 1.1H, H-3β), 4.33 (m, 0.45H, H-5α), 3.85 (m, 0.55H, H-5β), 3.62 (m, 2H, H-6α, H-6β, H-6′α, and H-6′β), 1.94 (s, 1.65H, $COCH_3$, β), 1.90 (s, 1.35H, $COCH_3$, α); ^{13}C NMR, α only (75.5 MHz, $CDCl_3$) δ: 169.74 ($COCH_3$), 92.76 (C-1), 74.20, 73.90 (2 × OCH_2Ph), 73.86, 72.67, 72.16 (C-3, C-4, and C-5), 57.54 (C-2), 68.49 (C-6), 21.06 ($COCH_3$).

Octyl 4-O-(4-O-acetyl-3,6-di-O-benzyl-2-deoxy-2-phthalimido-β-D-glucopyranosyl)-3,6-di-O-benzyl-2-deoxy-2-phthalimido-β-D-glucopyranoside (46)

The octyl glucoside acceptor **12** (340 mg, 0.565 mmol), 4 Å molecular sieves, and 363 mg of silver triflate (1.41 mmol, 2.5 equiv.) were charged to a round-bottom flask and argon purged. Dry dichloromethane (6 mL) and *sym*-collidine (0.1 mL, 0.85 mmol, 1.5 equiv.) were added and the reaction was stirred for 30 min, cooling to –15°C. The chloride **45** (620 mg, 1.13 mmol, 2 equiv.) was dissolved in 2 × 2 mL of dichloromethane and dropwise added to the acceptor. A white colour was observed during the chloride addition (AgCl). The reaction was stirred at room temperature for 60 h and then diluted with 75 mL of dichloromethane. The organic layer was filtered and washed with 75 mL of dH_2O, 75 mL of 1 *N* HCl, 75 mL of saturated sodium bicarbonate, and then 75 mL of brine. The organic layer was then dried ($MgSO_4$), filtered, and concentrated. Purification using 17% ethyl acetate in toluene as eluent gave 423 mg (67%) of the disaccharide **46** and 70 mg (21%) of recovered acceptor **12**. R_f 0.63 in ethyl acetate – toluene (1:3); ^{1}H NMR (500 MHz, $CDCl_3$) δ: 5.33 (d, 1H, $J_{1,2}$ = 8.4 Hz, H-1′), 5.15 (dd, 1H, $J_{3,4}$ = 9.0 Hz, $J_{4,5}$ = 9.0 Hz, H-4′), 4.93 (d, 1H, $J_{1,2}$ = 8.1 Hz, H-1), 1.91 (s, 3H, $COCH_3$); ^{13}C NMR (75.5 MHz, $CDCl_3$) δ: 169.67 ($COCH_3$,), 98.18, 97.21 (C-1, and C-1′), 76.93, 76.93, 76.40, 74.61, 73.45, 72.74 (C-3, C-4, C-5, C-3′, C-4′, and C-5′), 74.43, 73.92, 73.60, 72.74 (4 × OCH_2Ph), 69.49, 69.40 (C-6 and C-6′), 68.23 (OCH_2, octyl), 56.32, 55.79 (C-2 and C-2′), 31.64, 29.24, 29.12, 25.80, 22.58 (6 × CH_2, octyl), 20.93 ($COCH_3$), 14.04 (CH_3, octyl).

Octyl 3,6-di-O-benzyl-4-O-(3,6-di-O-benzyl-2-deoxy-2-phthalimido-β-D-glucopyranosyl)-2-deoxy-2-phthalimido-β-D-glucopyranoside (47)

The disaccharide **46** (423 mg, 0.38 mmol) was dissolved in 10 mL of dry methanol and 5 mg of sodium methoxide was added. The reaction was stirred overnight, quenched by neutralizing with amberlite IRC-120 (H^+) resin, filtered, concentrated, and chromatographed using 15% ethyl acetate in toluene as eluent. The desired product **47** (282 mg) was obtained as a colourless syrup (69%). $[\alpha]_D$ –12.6 (*c* 0.70, CH_2Cl_2); R_f 0.50 in ethyl acetate – toluene (1:3); ^{1}H NMR (360 MHz, $CDCl_3$) δ: 7.9–7.5 (m, 8H, 2 × phthalimido), 7.4–6.8 (m, 20H, benzyl aromatics), 5.30 (d, 1H, $J_{1,2}$ = 8.1 Hz, H-1′), 4.92 (d, 1H, $J_{1,2}$ = 7.8 Hz, H-1), 4.25 (dd, 1H, $J_{2,3}$ = 10.5 Hz, $J_{3,4}$ = 8.5 Hz, H-3′), 4.2 (m, 4H, H-2, H-3, H-4, and H-2′), 3.82 (ddd, IH, $J_{3,4}$ = 8.5 Hz, $J_{4,5}$ = 8.5 Hz, $J_{H,OH}$ = 1.9 Hz, H-4′), 3.65, 3.23 (2 × m, 2H, OCHH′, octyl), 3.09 (d, 1H, $J_{H,OH}$ = 1.9 Hz, OH), 2.3–0.7 (m, 15H, octyl); ^{13}C NMR (75.5 MHz, $CDCl_3$) δ: 167.72 (C=O, phthalimido), 98.18, 97.08 (C-1 and C-1′), 78.41, 76.88, 75.94, 75.52, 74.65, 72.85 (C-3, C-4, C-5, C-3′, C-4′, and C-5′), 74.37, 74.22, 73.76, 72.73 (4 × OCH_2Ph), 71.06, 69.42 (C-6 and C-6′), 68.31 (OCH_2, octyl), 56.18, 55.78 (C-2 and C-2′), 31.65, 29.24, 29.11, 25.81, 22.59 (6 × CH_2, octyl), 14.05 (CH_3, octyl). Anal. calcd. for $C_{64}H_{68}O_{13}N_2$: C 71.61, H 6.39, N 2.62; found: C 71.68, H 6.32, N 2.56.

Octyl 3,6-di-O-benzyl-4-O-(3′,6′-di-O-benzyl-2′-deoxy-2′-phthalimido-β-D-glucopyranosyl)-2-deoxy-2-phthalimido-β-D-glucopyranoside-ethyl 3″,4″-di-O-benzyl-6″-O-(2‴,3‴,4‴6‴-tetra-O-benzyl-α-D-mannopyranosyl)-α-D-mannopyranoside-2″,4′-isopropylidene acetal (48)

The vinyl ether **33** (100 mg, 0.103 mmol, 1.2 equiv.), the alcohol **47** (90 mg, 0.0842 mmol, 1.0 equiv.), and 500 mg of crushed $CaSO_4$ were added to a round-bottom flask and argon purged. Dry dichloromethane (7 mL) was added and the mixture was stirred for 30 min before cooling to –40°C. A 0.05 mM solution of camphorsulfonic acid was prepared by adding 2 mL of dry dichloromethane to 23.3 mg of acid under argon. A 0.2-mL aliquot of this acidic solution (0.01 mmol, 0.11 equiv.) was syringed into the cooled solution containing vinyl ether and alcohol. A further 2 × 0.2 mL (total equiv. of acid added = 0.33) of acid was added to the reaction mixture to maximize the amount of mixed acetal as observed by TLC. The reaction was quenched after 2 h by adding 0.1 mL of triethylamine, warmed to room temperature, and filtered. The solution was then concentrated and chromatographed using 17% ethyl acetate in hexane with 0.1% added triethylamine as eluent. The mixed acetal product **48** (18 mg, 8%) was obtained, as well as 32 mg of recovered vinyl ether **13** and 53 mg of recovered alcohol **47**. The product **48** was unstable stored in a solution with 0.5% added triethylamine. R_f 0.50 in ethyl acetate – hexane (1:2); ^{1}H NMR (360 MHz, $CDCl_3$ + 2% D-5 pyridine) δ: 5.40 (d, 1H, $J_{1,2}$ = 1 Hz, H-1_M), 5.32 (d, 1H, $J_{1,2}$ = 7.5 Hz, H-1_{Gn}), 5.08 (d, 1H, $J_{1,2}$ = 1 Hz, H-$1_{M'}$, 4.92 (d, 1H, $J_{1,2}$ = 7.8 Hz, H-$1_{Gn'}$), 2.58 (m, 2H, SCH_2CH3), 1.43 (s, 3H, $CH_3CCH_{3'}$, acetal), 1.40 (s, 3H, $CH_3CCH_{3'}$, acetal), 1.26 (t, 3H, SCH_3CH_3), 1.1–0.7 (m, 15H, octyl); ^{13}C NMR (125.7 MHz, $CDCl_3$ + 2% D-5 pyridine) δ: 105.16 (OCO, acetal), 98.11, 97.72, 96.94 (C-$1'_M$, C-1_{Gn},), 84.85 (C-1_M), 80.55, 79.94, 79.87, 76.98, 76.29, 76.25, 75.15, 75.06, 74.78, 74.67, 73.03, 71.99, 71.58, 71.45 (C-2_M, C-3_M, C-4_M, C-5_M, C-$2'_M$, C-$3'_n$, C-$4'_M$, C-$5'_M$, C-3_{Gn}, C-4_{Gn}, C-5_{Gn}, C-$3'_{Gn}$, C-$4'_{Gn}$, and C-$5'_{Gn}$), 75.21, 75.00, 74.82, 74.45, 73.32, 73.30, 73.07, 72.71, 72.56, 71.76 (10 × OCH_2Ph), 69.37, 69.13, 68.51, 68.32 (C-6_{Gn}, C-$6'_{Gn}$, C-6_M, and C-$6'_M$), 66.41, (OCH_2, octyl), 57.27, 55.78 (C-2_{Gn} and C-$2'_{Gn}$), 31.66, 29.25, 29.10, 25.81, 22.60 (6 × CH_2, octyl), 25.33 (SCH_2CH_3), 26.44, 25.9 (2 × CH_3, acetal), 15.38 (SCH_2CH_3), 14.06 (CH_3 octyl).

Octyl 3,6-di-O-benzyl-4-(3′,6′-di-O-benzyl-2′-deoxy-2′-phthalimido-β-D-glucopyranosyl)-2-deoxy-2-phthalimido-β-D-glucopyranoside-ethyl 3″,4″,6″-tri-O-benzyl-1″-thio-α-D-mannopyranoside-2″,4′-isopropylidene acetal (49)

The vinyl ether **4** (137 mg, 0.256 mmol, 2.0 equiv.) and the alcohol **47** (138 mg, 0.129 mmol, 1.0 equiv.) were charged to a round-bottom flask and argon purged. Dry dichloromethane (8 mL) was syringed into the mixture and cooled to –40°C. A 0.05 mmol solution of camphorsulfonic acid in dichloromethane was prepared and 0.25 mL of this solution (0.1 equiv.) was syringed into the cooled mixture containing the vinyl ether and the alcohol. The reaction was carefully monitored by TLC for product formation and quenched after 60 min by adding several drops of triethylamine. Prolonged reaction times caused a reduction in product yield. The mixture was concentrated, and purified on silica gel using 17% ethyl acetate in hexane as eluent with 0.1% added triethylamine. The desired product **49** (78 mg, 38% was obtained, as well as 93 mg of recovered vinyl ether **4** and 82 mg of recovered alcohol **47**. The mixed acetal was unstable unless stored under basic conditions such as in a dichloromethane solution with 0.5% added triethylamine. R_f 0.53 in ethyl acetate–hexane (1:2); ^{1}H NMR (500 MHz, $CDCl_3$ + 2% D-5 pyridine) δ: 5.43 (s, 1H, $J_{1,2}$ = 1.0 Hz, H-1M), 5.32 (d, 1H, $J_{1,2}$ = 7.8 Hz, H-$1_{Gn'}$), 4.90 (d, 1H, $J_{1,2}$ = 7.8 Hz, H-1_{Gn}), 3.63, 3.21 (2 × dt, 2H, J_{vic} = 9.8 Hz, J_{gem} = 6.8 Hz, OCHH′,

Can. J. Chem. Downloaded from www.nrcresearchpress.com by EESC ESCOLA DE ENGENHARIA on 09/08/12
For personal use only.

octyl), 2.66 (m, 2H, SCH_2CH_3), 1.46 (s, 3H, $CH_3CCH_{3'}$), 1.42 (s, 3H, $CH_3CCH_{3'}$), 1.29 (t, 3H, SCH_2CH_3), 1.15–0.84 (m, 15H, octyl); ^{13}C NMR (125.7 MHz, $CDCl_3$ + 2% D-5 pyridine) δ: 104.76 (OCO, acetal), 98.05, 96.94 (C-1_{Gn}, and C-$1'_{Gn}$), 84.54 (C-1_M), 80.34, 79.73, 76.34, 76.31, 75.28, 74.65, 73.30, 72.12, 71.72 (C-3_{Gn}, C-4_{Gn}, C-5_{Gn}, C-$3'_{Gn}$, C-$4'_{Gn}$, C-$5'_{Gn}$, C-2_M, C-3_M, C-4_M, and C-5_M), 75.31, 74.89, 74.39, 73.20, 73.01, 72.66, 72.43 (7 × OCH_2Ph), 69.50, 69.26, 68.82, 68.29 (C-6_{Gn}, C-$6'_{Gn}$, C-6_M, and OCH_2, octyl), 57.15, 55.73 (C-2_{Gn}, C-$2'_{Gn}$).

*Octyl 3,6-di-*O*-benzyl-4-*O*-[3,6-di-O-benzyl-4-*O*-(3,4,6-tri-*O*-benzyl-β-D-mannopyranosyl)-2-deoxy-2-phthalimido-β-D-glucopyranosyl]-2-deoxy-2-phthalimido-β-D-glucopyranoside (50)*

The mixed acetal **49** (24 mg, 0.015 mmol) was charged to a flask and argon purged. Dry dichloromethane (3 mL) was syringed into the flask, followed by 1.5 mL of a 0.05 mM solution of 2,6-di-*tert*-butyl-4-methyl-pyridine (4-Me-DTBP, 0.075 mmol, 5 equiv.) prepared by dissolving 51 mg of 4-MeDTBP in 5 mL of dry dichloromethane under argon atmosphere over 4 Å molecular sieves). *N*- Iodosuccinimide (17 mg, 0.075 mmol, 5 equiv.) was added to the reaction and stirred overnight (42 h). The reaction was quenched by adding 2 mL of 0.5 M sodium thiosulfate solution, which caused the deep red reaction colour to become colourless. Dichloromethane, (10 mL) was added and the organic layer was washed with 2 × 10 mL of dH_2O, dried ($MgSO_4$), filtered, and concentrated. Purification using silica gel with 25% ethyl acetate in hexane as eluent gave the trisaccharide **50** (6 mg) as a viscous syrup. R_f 0.27 in ethyl acetate – hexane (1:2); ^1H NMR (500 MHz, $CDCl_3$) δ: 7.9–7.5 (m, 8H, phthalimido), 7.35–7.1, 7.0–6.9, 6.85–6.70 (m, 35H, benzyl aromatics), 5.27 (d, 1H, $J_{1,2}$ = 8.4 Hz, H-1′), 4.92 (d, 1H, $J_{1,2}$ = 8.6 Hz, H-1), 4.65 (d, 1H, $J_{1,2}$ < 0.5 Hz, H-1′), 4.40 (dd, 1H, $J_{2,3}$ = 10.8 Hz, $J_{3,4}$ = 8.6 Hz, H-3′), 4.22 (dd, 1H, $J_{1,2}$ = 8.4 Hz, $J_{2,3}$ = 10.8 Hz, H-2′), 4.10 (m, 2H, H-2, and H-4′), 4.00 (dd, 1H, $J_{1,2}$ < 0.5 Hz, $J_{2,3}$ = 3.0 Hz, H-2″), 3.84 (dd, 1H, $J_{3,4}$ = 9.4 Hz, $J_{4,5}$ = 9.4 Hz, H-4), 3.60 (dd, 1H, $J_{3,4}$ = 9.0 Hz, $J_{4,5}$ = 9.0 Hz, H-4″), 3.39 (dd, 1H, $J_{2,3}$ = 3.0 Hz, $J_{3,4}$ = 9.0 Hz, H-3″), 3.36 (dt, 1H, J_{gem} = 9.9 Hz, J_{vic} = 6.3 Hz, OC*H*H′, octyl), 3.22 (dt, 1H, J_{gem} = 9.9 Hz, J_{vic} = 6.3 Hz, OCH*H*′, octyl), 2.43 (br s, 1H, OH), 1.35–0.75 (m, 15H, octyl); ^{13}C NMR (125.7 MHz, $CDCl_3$) δ: 100.35 (d, $J_{C-1,H-1}$ = 157 Hz, C-1″), 98.12, 97.00 (C-1 and C-1′), 81.75, 78.51, 77.91, 75.72, 75.41, 74.52, 74.48, 74.01, 68.10 (C-3, C-4, C-5, C-3′, C-4′, C-5′, C-2″, C-3″, C-4″, and C-5″), 75.06, 74.83, 74.29, 73.33, 73.24, 72.59, 71.35 (7 × OCH_2Ph), 69.34, 68.90, 68.10, 68.01 (C-6, C-6′, C-6″, and OCH_2, octyl), 56.47, 55.75 (C-2 and C-2′), 31.59, 29.15, 29.12, 29.06, 25.74, 22.53 (6 × CH_2, octyl), 14.05 (CH_3, octyl).

Octyl 3,6-di-O-benzyl-4-O-[3,6-di-O-benzyl-4-O-(3,4,6-tri-O-benzyl-α-D-mannopyranosyl)-2-deoxy-2-phthalimido-β-D-glucopyranosyl]-2-deoxy-2-phthalimido-β-D-glucopyranoside (51)

The thioglycoside **2** (58 mg, 0.108 mmol, 2.0 equiv.) acceptor **47** (58 mg, 0.054 mmol), and crushed 4 Å molecular sieves were charged to a round-bottom flask and argon purged. Dry dichloromethane (7 mL) was added and stirred for 30 min, cooling the mixture to 0°C. *N*-Iodosuccinimide (24 mg, 0.108 mmol, 2.0 equiv.) and then catalytic silver triflate (0.011 mmol, 02. equiv.) were added and a characteristic burst of red colour was observed within 2 min of the addition of the silver triflate. The reaction was then worked up and de-*O*-acetylated according to the protocol for the preparation of **36**. Purification with Iatrobeads using 20% ethyl acetate in hexane as eluent gave the product **51** (40 mg, 49%), as well as some unreacted acetylated compound (13 mg, 16%). $[\alpha]_D$ + 24.8 (*c* 1.20, CH_2Cl_2); R_f 0.49 in ethyl acetate – toluene (1:3); ^1H NMR (500 MHz, $CDCl_3$) δ: 7.8–7.5 (m, 8H, phthalimido), 7.35–7.05, 7.0–6.7 (m, 35H, benzyl aromatics), 5.35 (d, 1H, $J_{1,2}$ = 1.3 Hz, H-1″), 5.26 (d, 1H, $J_{1,2}$ = 8.4 Hz, H-1′), 4.91 (d, 1H, $J_{1,2}$ = 8.2 Hz, H-1), 4.38 (dd, 1H, $J_{2,3}$ = 10.6 Hz, $J_{3,4}$ = 8.5 Hz, H-3′), 4.23 (dd, 1H, $J_{2,3}$ = 10.6 Hz, $J_{1,2}$ = 8.4 Hz, H-2′), 4.20–4.08 (m, 3H, H-2, H-3, H-4), 3.98 (dd, 1H, $J_{1,2}$ = 1.3 Hz, $J_{2,3}$ = 3.0 Hz, H-2″), 3.96 (dd, $J_{3,4}$ = 8.5 Hz, $J_{4,5}$ = 9 Hz, H-4′), 3.90 (d, 1H, $J_{3,4}$ = 9.0 Hz, $J_{4,5}$ = 9.0 Hz, H-4″), 3.81 (dd, $J_{3,4}$ = 9.0 Hz, $J_{2,3}$ = 3.0 Hz, H-3″), 3.81 (m, 1H, H-5″), 3.74 (dd, 1H, $J_{5,6}$ = 1.5 Hz, $J_{6,6'}$ = 11.0 Hz, H-6′a), 3.69 (dd, 1H, $J_{5,6}$ = 3.6 Hz, $J_{6,6'}$ = 10.8 Hz, H-6″a), 3.64 (dd, 1H, $J_{5,6'}$ = 3.5 Hz, $J_{6,6'}$ = 11.0 Hz, H-6′b), 3.64 (dt, 1H, J_{vic} = 6.6 Hz, J_{gem} = 9.8 Hz, OC*H*H′, octyl), 3.56 (dd, 1H, $J_{5,6}$ = 1.2 Hz, $J_{6,6'}$ = 10.8 Hz, H-6″b), 3.52 (dd, $J_{5,6}$ = 1.0 Hz, $J_{6,6'}$ = 11.0 Hz, H-6a), 3.41 (dd, 1H, $J_{5,6'}$ = 3.8 Hz, $J_{6,6'}$ = 11.0 Hz, H-6b), 3.32 (m, 1H, H-5′), 3.28 (m, 1H, H-5), 3.22 (dt, 1H, J_{vic} = 9.8 Hz, J_{gem} = 6.6 Hz, OCH*H*′, octyl), 2.21 (br s, 1H, OH), 1.4–0.7 (m, 15H, octyl); ^{13}C NMR (125.7 MHz, $CDCl_3$) δ: 100.01 (d, $J_{C-1,H-1}$ = 170 Hz, C-1″), 98.16, 96.81 (C-1, C-1′), 80.76, 79.91, 77.36, 75.92, 74.94, 74.60, 74.19, 72.20, 69.03 (C-3, C-4, C-5, C-3′, C-4′, C-5′, C-2″, C-3″, C-4″, and C-5″), 56.50, 55.76 (C-2 and C-2′), 75.10, 74.65, 74.35, 73.51, 73.17, 72.72, 72.07 (7 × OCH_2Ph), 69.36, 68.80, 68.29 (C-6, C-6′, and C-6″), 68.54 (OCH_2, octyl), 31.63, 29.21, 29.11, 29.08, 25.78, 22.57 (6 × CH_2, octyl), 14.04 (CH_3, octyl). Anal. calcd. for $C_{91}H_{96}O_{18}N_2$: C 72.58, H 6.43, N 1.87; found: C 72.28, H 6.45, N 1.84.

Acknowledgements

The authors acknowledge the support of the Alberta Heritage Foundation for Medical Research for a scholarship (F.B.) and the Natural Sciences and Engineering Research Council of Canada for ongoing research support.

1. (*a*) A. Varki. Glycobiology, **3**, 97 (1993); (*b*) H. Schachter. Curr. Opin. Struct. Biol. **1**, 755 (1991); (*c*) B.K. Brandley, S.J. Swiedler and P.W. Robbins. Cell, **63**, 861 (1990); (*d*) D.A. Cumming. Glycobiology **1**, 115 (1991); (*e*) B.K. Brandley. Cell Biol. **2**, 281 (1991); (*f*) T. Feizi. Trends Biochem. Sci. **16**, 84 (1991); (*g*) A. Kobata. Glycobiology **1**, 5 (1990); (*h*) J.C. Paulson. Trends Biochem. Sci. **14**, 272 (1989); (*i*) S. Hakomori. Adv. Cancer Res. **52**, 257 (1989).
2. (*a*) T.E. Hardingham and A.J. Fosang. FASEB J. **6**, 861 (1992); (*b*) E. Ruoslahti and Y. Yamaguchi. Cell, **64**, 867 (1991); (*c*) E. Ruoslahti. J. Biol. Chem. **264**, 13 369 (1989).
3. (*a*) B.D. Shur. Biochim, Biophys. Acta, **988**, 389 (1989); (*b*) D.J. Miller, M.B. Macek, and B.D. Shur. Nature (London), **357**, 589 (1992); (*c*) R.A. Kinloch, S. Mortillo, C.L. Stewart, and P.M. Wassarman. J. Cell Biol. **115**, 655 (1991).
4. (*a*) S. Sabesan, J. Duus, S. Neira, P. Domaille, S. Kelm, J.C. Paulson, and K. Bock. J. Am. Chem. Soc. **114**, 8363 (1992); (*b*) N.K. Sauter, J.E. Hanson, G.D. Glick, J.H. Brown, R.L. Crowther, S.J. Park, J.J. Skehel, and D.C. Wiley. Biochemistry, **31**, 9609 (1992); (*c*) A. Varki. Glycobiology, **2**, 25 (1992); (*d*) N. Sharon and H. Lis. Science (Washington, D.C.), **246**, 227 (1989).
5. (*a*) P.D. Stahl. Curr. Opin. Immunol. **4**, 49 (1992); (*b*) S. Kornfeld. Annu. Rev. Biochem. **61**, 307 (1992).
6. (*a*) T. Palabrica, R. Lobb, B.C. Furie, M. Aronovitz, C. Benjamin, Y.M. Hsu, S.A. Sajer, and B. Furie, Nature (London), **359**, 848 (1992); (*b*) K.L. Moore, A. Varki, and R.P. McEver. J. Cell Biol. **112**, 491 (1991).
7. (*a*) L.A. Lasky, M.S. Singer, D. Dowbenko, Y. Imai, W.J. Henzel, C. Grimley, C. Fennie, N. Gillet, S.R. Watson, and S.D. Rosen. Cell, **69**, 927 (1992); (*b*) Y. Imai, M.S. Singer, C. Fennie, L.A. Lasky, and S.D. Rosen. J. Cell Biol. **113**, 1213 (1991).
8. (*a*) M.L. Phillips, E. Nuderlman, F.C.A. Gaeta, M. Perez, A.K. Singhal, S. Hakomori, and J.C. Paulson. Science (Washington, D.C.), **250**, 1130 (1990); (*b*) G. Walz, A. Aruffo, W. Kolanus, M. Bevilacqua, and B. Seed. Science (Washington, D.C.), **250**, 1132 (1990).
9. (*a*) O. Kanie and O. Hindsgaul. Curr. Opin. Struct. Biol. **2**, 674 (1992); (*b*) B. Fraser-Reid, U.E. Udodong, Z. Wu, H. Ottosson, J.R. Merritt, C.S. Rao, C. Roberts, and R. Madsen. Synlett, 927 (1992); (*c*) P.J. Garegg. Acc. Chem. Res. **25**, 575 (1992); (*d*) K.C. Nicolaou, J. Caulfield, and R.D. Groneberg. Pure Appl. Chem. **63**, 555 (1991); (*e*) H. Paulsen. Angew. Chem. Int. Ed. Engl. **29**, 823 (1990); (*f*) R.R. Schmidt. Angew. Chem. Int. Ed. Engl. **25**, 212 (1986); (*g*) R.U. Lemieux. Chem. Soc. Rev. **7**, 423 (1978); (*h*) M. Sugimoto, K. Fujikura, S. Nunomura, Y. Ito, and T. Ogawa, Tetra-

hedron Lett. **31**, 1435 (1990); (*i*) D. Kahne, S. Walker, Y. Cheng, and D. Van Engen. J. Am. Chem. Soc. **111**, 6881 (1989); (*j*) R.L. Halcomb and S.J. Danishefsky. J. Am Chem. Soc. **111**, 6661 (1989); (*k*) R.W. Friesen and S.J. Danishefsky. J. Am Chem. Soc. **111**, 6656 (1989); (*l*) S. Sato, Y. Ito, T. Nukada, Y. Nakahara, and T. Ogawa. Carbohydr. Res. **167**, 197 (1987).

10. (*a*) H. Paulsen, R. Lebuhn, and O. Lockhoff. Carbohydr. Res. **103**, C7 (1983); (*b*) P.J. Garegg and P. Ossowski. Acta Chem. Scand. Ser. B, **37**, 249 (1983); (*c*) T. Ogawa, T. Kitajima, and T. Nukada. Carbohydr. Res. **123**, C5 (1983); (*d*) P.J. Garegg and C. Hallgren. J. Carbohydr. Chem. **11**, 425 (1992); (*e*) S. David, A. Malleron, and C. Dini. Carbohydr. Res. **188**, 193 (1989); (*f*) W. Gunther and H. Kunz. Carbohydr. Res. **228**, 21 (1992); (*g*) C. Auge, C.D. Warren, and R. W. Jeanloz. Carbohydr. Res. **82**, 85 (1980); (*h*) G. Ekborg, B. Lindberg, and J. Lonngren. Acta. Chem. Scand. **26**, 3287 (1972); (*i*) E.M. Klimov, A.V. Demchenko, N.N. Malysheva, and N. Kochetkov. Bioorg. Khim. **17**, 1660 (1991).
11. (*a*) F. Barresi and O. Hindsgaul. J. Am. Chem. Soc. **113**, 9376 (1991); (*b*) Synlett, 759 (1992).
12. G. Stork and G. Kim. J. Am. Chem. Soc. **114**, 1087 (1992).
13. (*a*) M. Bols. Chem. Commun. 791 (1993); (*b*) J. Chem. Soc. Chem. Commun. 913 (1992); (*c*) Acta Chem. Scand. **47**, 829 (1993).
14. (*a*) F.N. Tebbe, G.W. Parshall, and G.S. Reddy. J. Am. Chem. Soc. **100**, 3611 (1978); (*b*) M.H. Ali, P.M. Collins, and W.G. Overend. Carbohydr. Res. **205**, 428 (1990); (*c*) L.F. Cannizzo and R.H. Grubbs. J. Org. Chem. **50**, 2386 (1985).
15. P.J. Garegg and L. Maron. Acta Chem. Scand Ser B, **33**, 39 (1979).
16. P.J. Garegg, T. Iversen, and S. Oscarsson. Carbohydr. Res. **50**, C12 (1976).
17. A. Liptak, I. Jodal and P. Nanasi, Carbohydr. Res. **44**, 1 (1975).
18. K. Bock and C. Pedersen, Adv. Carbohydr. Chem. Biochem. **41**, 27 (1983).
19. (*a*) B. Helferich and K. Weis. Chem. Ber. **89**, 314 (1956); (*b*) B. Helferich and K-F. Wedemeyer. Justus Liebigs Ann. Chem. **563**, 139 (1949).
20. S.H. Tahir and O. Hindsgaul. Can. J. Chem. **64**, 1771 (1986).
21. F. Barresi. Ph.D. Dissertation, University of Alberta, Edmonton, Alberta. 1994.
22. P. Durette and T.Y. Shen. Carbohydr. Res. **69**, 316 (1979).
23. O. Kanie, S.C. Crawley, M.M. Palcic, and O. Hindsgaul. Carbohydr. Res. **243**, 139 (1993).
24. P.J. Garegg and H. Hultberg. Carbohydr. Res. **93**, C10 (1981).
25. Vandana, O. Hindsgaul, and J.U. Baenziger. Can. J. Chem. **65**, 1645 (1987).
26. T. Iversen and D. Bundle. Carbohydr. Res. **103**, 29 (1982).
27. N. Bagget, J.M. Duxbury, A.B. Foster, and J.M. Webber. Carbohydr. Res. **1**, 22 (1965).
28. H. Paulsen, M. Heume, and H. Nurnberger. Carbohydr. Res. **200**, 127 (1990).

Can. J. Chem. Downloaded from www.nrcresearchpress.com by EESC ESCOLA DE ENGENHARIA on 09/08/12
For personal use only.

Structural elucidation of the backbone oligosaccharide from the lipopolysaccharide of *Moraxella catarrhalis* serotype A[1,2]

HUSSEIN MASOUD, MALCOLM B. PERRY, JEAN-ROBERT BRISSON, DUŠAN UHRÍN,[3] AND JAMES C. RICHARDS[4]

Institute for Biological Sciences, National Research Council of Canada, Ottawa, ON K1A 0R6, Canada

Received December 17, 1993

HUSSEIN MASOUD, MALCOLM B. PERRY, JEAN-ROBERT BRISSON, DUŠAN UHRÍN, and JAMES C. RICHARDS. Can. J. Chem. **72**, 1466 (1994).

The cell-surface lipopolysaccharide produced by *Moraxella catarrhalis* serotype A is composed of a hydrophobic lipid A moiety and an oligosaccharide, but lacks high-molecular-weight O-polysaccharide chains. The oligosaccharide component is composed of D-glucose, D-galactose, D-glucosamine, and 3-deoxy-D-*manno*-octulosonic acid. The carbohydrate backbone was obtained from the lipopolysaccharide by employing a reaction sequence involving deacylation, dephosphorylation, and reduction of the reducing D-glucosamine terminus of the lipid A moiety. Structural analysis of the backbone oligosaccharide employed a combination of microanalytical methods and nuclear magnetic resonance spectroscopy. Homo- and hetero-nuclear chemical shift correlation techniques and nuclear Overhauser enhancement (NOE) experiments led to the unambiguous assignment of the ^{1}H and ^{13}C resonances associated with each of the component glycosyl residues and established their sequence within the backbone oligosaccharide as shown,

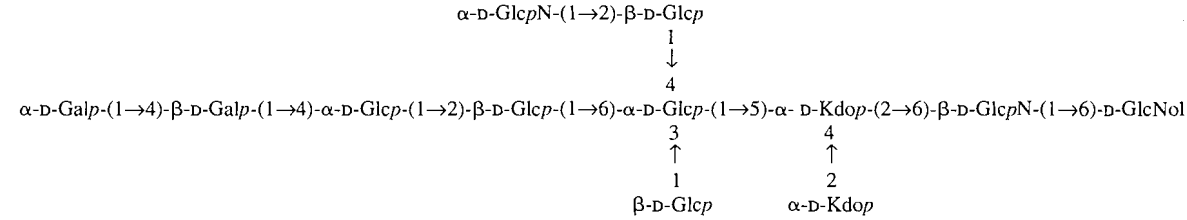

This lipopolysaccharide was found to consist of a highly branched, D-glucose-containing inner-core region which possesses a unique and unusual solution conformation. This was established by measurement of transglycosidic NOEs and three-bond ^{1}H–^{13}C coupling constants, in conjunction with molecular modeling. A D-galactose-containing disaccharide identified as a terminal group of the lipopolysaccharide was structurally identical to antigenic epitopes expressed by certain mammalian epithelial cells and may be related to the virulence potential of this human pathogen.

HUSSEIN MASOUD, MALCOLM B. PERRY, JEAN-ROBERT BRISSON, DUŠAN UHRÍN et JAMES C. RICHARDS. Can. J. Chem. **72**, 1466 (1994).

Le lipopolysaccharide de le surface cellulaire produit par le sérotype A du *Moraxella catarrhalis* est formé d'un lipide hydrophobe A et d'un oligosaccharide, mais il ne comporte pas de chaînes O-polysaccharides de poids moléculaire élevé. L'oligosaccharide comprend du D-glucose, du D-galactose, de la D-glucosamine et de l'acide 3-désoxy-D-*manno*-octulosonique. On a obtenu le squelette de l'hydrate de carbone à partir du lipopolysaccharide en faisant appel à une série de réactions impliquant une désacylation, une déphosphorylation et la réduction de la D-glucosamine réductrice terminale de la portion du lipide A. Une analyse structurale du squelette du oligosaccharide a fait appel à une combinaison de méthodes microanalytiques et de résonance magnétique nucléaire. Les techniques de corrélation des déplacements chimiques homo- et hétéronucléaires et se expériences d'effet Overhauser nucléaire ont conduit à une attribution non ambiguë des résonances du ^{1}H et ^{13}C associées à chacun des résidus glycosyles et ont permis d'établir que leur séquence dans le squelette de l'oligosaccharides est la suivante;

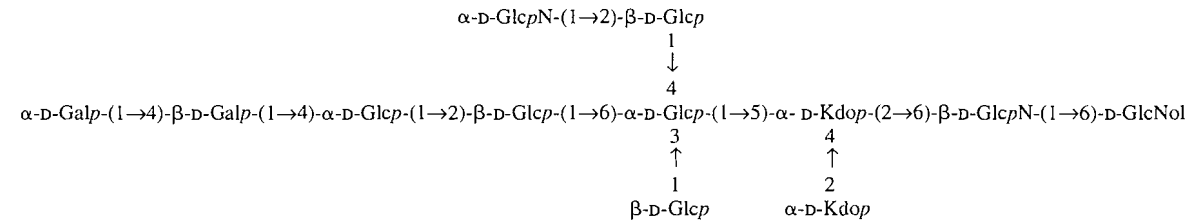

On a trouvé que ce lipopolysaccharide est formé d'une région intérieure fortement ramifiéé contenant un D-glucose, laquelle posséde une conformation unique et inhabituelle en solution. On a déterminé cette propriété par des mesures d'eOn transglycosidiques et de constantes de couplages ^{1}H–^{13}C à travers trois liaisons faites de concert avec un modelage moléculaire. Un un disaccharide contenant D-galactose identifié comme un groupe terminal du lipopolysaccharide est identique d'un point de vue structrual avec les épitipoes antigéniques fournis par des cellules épithéliales de mammaires et on peut le relier au potentiel de virulence de ce pathogène humain.

[Traduit par la Rédaction]

[1]Presented in part at the Cambridge Healthtech Institute Glycotechnology Meeting, San Francisco, Calif., May 17–19, 1993.
[2]NRCC No. 37387.
[3]Permanent address: Institute of Chemistry, Slovak Academy of Sciences, Bratislava, Slovakia.
[4]Author to whom correspondence may be addressed. Telephone: (613) 990-0854. FAX: (613) 941-1327.

Can. J. Chem. Downloaded from www.nrcresearchpress.com by EESC ESCOLA DE ENGENHARIA on 09/08/12
For personal use only.

Can. J. Chem. Downloaded from www.nrcresearchpress.com by EESC ESCOLA DE ENGENHARIA on 09/08/12
For personal use only.

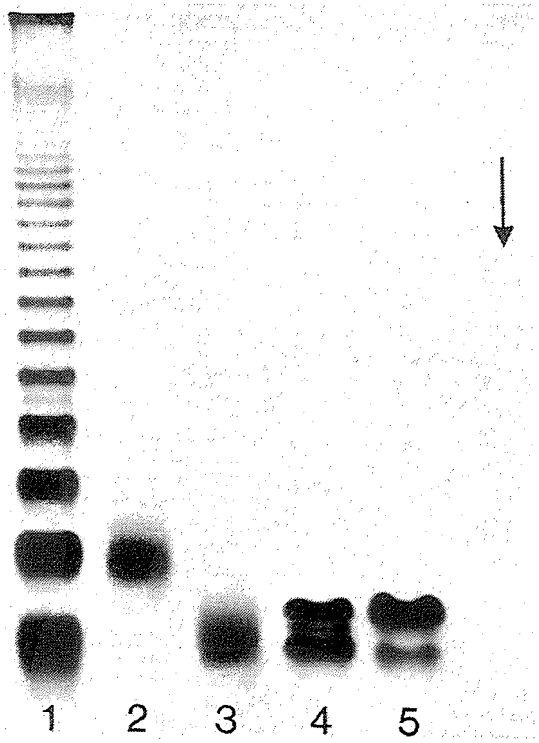

FIG. 1. DOC–PAGE patterns of LPS from *Salmonella* strains and *Moraxella catarrhalis*. Lane 1, *S. milwaukee* (S-type LPS, 10 μg); lane 2, *S. typhimurium* (SR-mutant, 5 μg); lane 3, *S. minnesota* R 60 (Ra-mutant, 2 μg); lane 4, *M. catarrhalis* serotype A (clinical isolate 0798, 3 μg); lane 5, *M. catarrhalis* serotype A (ATCC 25238, 3 μg). The vertical arrow indicates the direction of migration.

Introduction

Moraxella catarrhalis is a gram-negative diplococcus which has been reported with increasing frequency to be a significant human pathogen (1). It is currently the third most common cause of acute and chronic otitis media and it has been implicated in upper and lower respiratory tract infections, and in sporadic cases of meningitis and septicemia.

Lipopolysaccharides (LPSs, endotoxins) are biologically active components of gram-negative bacteria; they are virulence factors involved in pathogenesis of bacterial infections (2). The O-polysaccharide and core oligosaccharide moieties of LPS are immunogenic, giving rise to antibodies having specific serological properties that are involved in protective mechanisms and that also can be of diagnostic importance. The analysis of the LPS produced by strains of *M. catarrhalis* was undertaken to provide a molecular level understanding of its structural relationship with biological properties.

Very little structural information exists on the LPS of *M. catarrhalis*. Serological typing (3) and comparative immunochemical studies (4, 5) suggest that the LPS components are of the rough type (R-type) being composed of a core oligosaccharide glycosidically linked to lipid A and they lack an O-polysaccharide characteristic of smooth (S-type) LPS. A previous study of cellular and free LPS of *M. catarrhalis* ATCC 8176 and 25238 strains showed that they were identical and of the R-type in which the core oligosaccharide moieties were composed of D-glucose, D-galactose, 2-acetamido-2-deoxy-D-glucose, and 3-deoxy-D-*manno*-octulosonic acid. L-glycero-D-*manno*-Heptose and phosphate, common LPS core constituents, were noticeably absent. Our laboratory has recently reported the structure of the lipid A region of *M. catarrhalis* LPS by employing a combination of NMR- and MS-based techniques (6). In the present investigation, we describe the application of NMR techniques for the structural elucidation of the LPS core oligosaccharide of the *M. catarrhalis* serotype A reference strain (ATCC 25238) and relate the structure of the LPS to other clinical strains, suggesting the possible basis for the development of a common vaccine and a specific diagnostic antibody reagent.

Results and discussion

Extraction of fermentor-grown cells of *M. catarrhalis* serotype A by using the hot phenol – water extraction method (7), followed by ultracentrifugation of the dialyzed and concentrated separated aqueous phase, afforded a precipitated LPS gel in 2% yield based on dry cell weight. Deoxycholate–PAGE analysis of the LPS revealed two distinct bands that exhibited electrophoretic mobilities similar to that of reference Ra-type *Salmonella* LPS (Fig. 1, lanes 3–5) and showed that the preparations did not contain S-type LPS in which O-polysaccharide components would have been present. The R-type nature of the LPS is consistent with results of earlier investigations (4, 5).

Partial hydrolysis of the LPS with hot 1% (v/v) acetic acid (100°C, 2.5 h) afforded an insoluble lipid A (26%) and Bio-Gel P-2 gel filtration chromatography of the concentrated water-soluble products gave core oligosaccharide (OS) (K_{av} 0.2–0.3, 36%), and a fraction containing 3-deoxy-D-*manno*-octulosonic acid (Kdo) (K_{av} 0.98). The OS had $[\alpha]_D$ +85° (*c* 0.80, H_2O) and, on total acid hydrolysis followed by GLC–MS analyses, was found to be composed of D-glucose (D-Glc), D-galactose (D-Gal), and 2-amino-2-deoxy-D-glucose (D-GlcN) in the approximate molar ratios 5:2:1, in agreement with previous studies (4). The presence of Kdo in the core OS was confirmed by colorimetric assay (8).

Structural studies were made on *N*- and *O*-deacylated, dephosphorylated and terminal reduced LPS (Scheme 1, backbone OS). Methylation analysis of the backbone OS by the GLC–MS alditol acetate method (9) led to the identification of the *O*-acetyl derivatives from 2,3,4,6-tetra-*O*-methyl-D-glucitol-1-*d* (T_{GM} 1.0), 2,3,4,6-tetra-*O*-methyl-D-galactitol-1-*d* (T_{GM} 1.07), 3,4,6-tri-*O*-methyl-D-glucitol-1-*d* (T_{GM} 1.26), 2,3,6-tri-*O*-methyl-D-galactitol-1-*d* (T_{GM} 1.31), 2,3,6-tri-*O*-methyl-D-glucitol-1-*d* (T_{GM} 1.33), 2-*O*-methyl-D-glucitol-1-*d* (T_{GM} 1.88), 2-deoxy-3,4,6-tri-*O*-methyl-2-(*N*-methylacetamido)-D-glucitol-1-*d* (T_{GM} 2.00), 2-deoxy-1,3,4,5-tetra-*O*-methyl-2-(*N*-methylacetamido)-D-glucitol (T_{GM} 2.01), and 2-deoxy-3,4-di-*O*-methyl-2-(*N*-methylacetamido)-D-glucitol-1-*d* (T_{GM} 2.37), the latter two aminodeoxyglycitol derivatives arising from the disaccharide residue of the lipid A component. The methylation results indicated that the OS has a highly branched structure containing a D-Glc*p* residue glycosidically substituted at *O*-3, *O*-4, and *O*-6; D-Glc*p* residues monosubstituted at *O*-2 and *O*-4; a D-Gal*p* residue substituted at *O*-4; and nonreducing D-Glc*p*, D-Gal*p*, and D-Glc*p*N endgroups.

The linkages of the Kdo residues were determined from analysis of the hydrolysis products of the carboxyl-reduced methyl ester (superdeuteride) of a methylated sample of *O*-deacylated LPS (Scheme 1, LPS-OH). The *O*-methyl-reduced Kdo derivatives and accompanying *O*-methyl aldoses were sequentially hydrolyzed, reduced ($NaBD_4$), acetylated, and subjected to GLC–MS analysis. In addition to the abovementioned *O*-methyl aldose derivatives, the *O*-acetyl derivatives of 1,1,2-d_3-substituted 3-deoxy-1,4,5,7,8-penta-*O*-methyl- (T_{GM} 1.66 and 1.69) and 3-deoxy-1,7,8-tri-*O*-methyl-octitols (T_{GM}

Can. J. Chem. Downloaded from www.nrcresearchpress.com by ESC ESCOLA DE ENGENHARIA on 09/08/12
For personal use only.

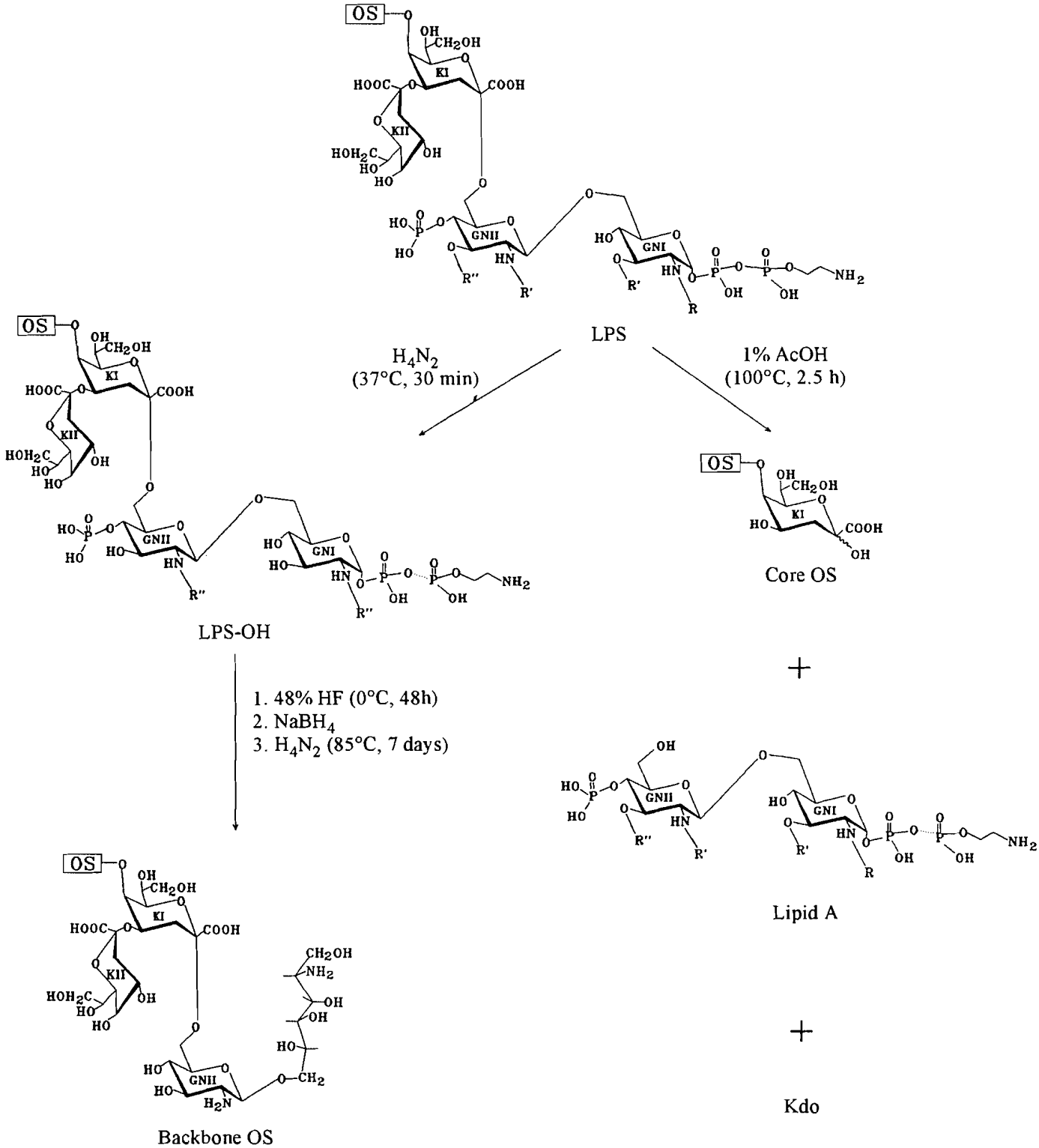

SCHEME 1. General procedure for preparation of oligosaccharides components from LPS.

~2.15) were detected. This indicated that the LPS contained one nonreducing Kdo end group and a second branched Kdo residue glycosidically substituted at positions *O*-4 and *O*-5 (Scheme 2).

The ^{1}H NMR spectrum of the backbone OS (Fig. 2) showed resonances of approximately equal signal area in the low-field region (5.5–4.5 ppm), corresponding to the anomeric protons from nine aldose residues. Correspondingly, nine major anomeric ^{13}C resonances were identified in the low-field region (90–110 ppm) of the 2D heteronuclear ^{13}C–^{1}H correlation (HMQC) spectrum (Fig. 3). In addition to these major resonances, minor anomeric resonances were observed at 4.46 (*d*, $J_{1,2}$ = 7.6 Hz, ca. 0.15 H) and 102.8 ppm (GAI′) in the ^{1}H and ^{13}C spectra, respectively (Figs. 2 and 3), which were subse-

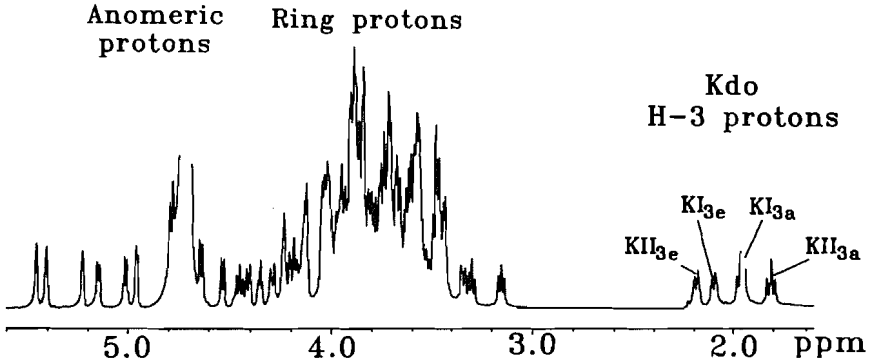

FIG. 2. ^{1}H spectrum of the LPS backbone OS from *M. catarrhalis* serotype A recorded at 600 MHz in D_2O at 32°C. The equatorial and axial protons from H-3 of the Kdo residues are indicated. The H-3a triplet of KI is partially overlapping with the methyl resonance from an acetate-containing impurity, but is fully resolved in the COSY.

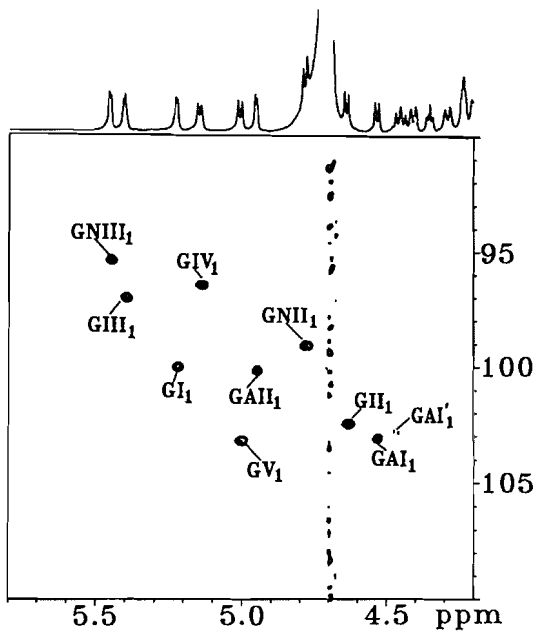

FIG. 3. Heteronuclear 2D ^{13}C–^{1}H chemical shift correlation map of the anomeric region for the backbone OS.

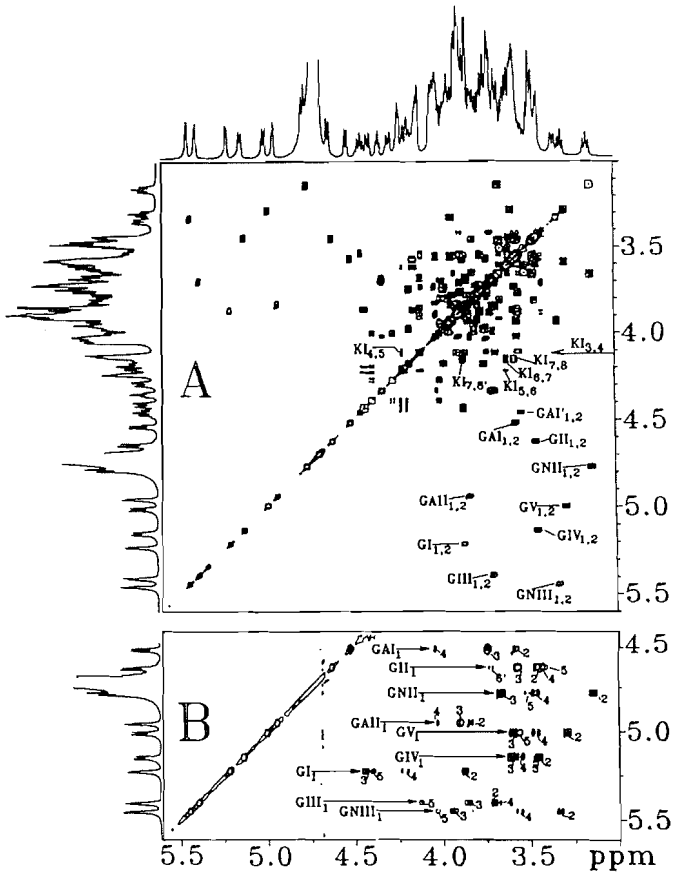

FIG. 4. Partial 2D COSY (A) and TOCSY (B) spectra of the LPS backbone OS. Cross-peaks relating anomeric and ring protons are indicated.

quently attributed to the presence of a minor OS component (ca. 15%) containing one less glycose residue. Four resonances in the high-field region (1.5–2.5 ppm) of the 1D ^{1}H NMR spectrum (Fig. 2) could be attributed to the equatorial and axial methylene protons (H-3e and H-3a, respectively) of two Kdo residues; the doublet of doublet patterns at 2.071 (J = 4.0, 12.3 Hz) and 2.161 ppm (J = 4.8, 13.0 Hz) were characteristic of equatorial H-3 protons, while the triplets at 1.937 (J = 12.0, 12.3 Hz) and 1.785 ppm (J = 12.1, 13.0 Hz) were indicative of the axial H-3 protons. The chemical shifts of the methylene proton resonances from the two Kdo residues indicated that both are in the pyranose ring form and have the α-D-configuration (10–12). As expected, cross-peaks having ^{13}C coordinates of 34.1 and 34.6 ppm in the 2D HMQC experiment could be attributed to the methylene carbons from the two Kdo residues.

^{1}H NMR resonances of the backbone OS were fully assigned from homonuclear proton correlation spectroscopy (COSY) and total correlated spectroscopy (TOCSY) (Fig. 4). From the ^{1}H chemical shifts and vicinal proton coupling constants, subspectra corresponding to all of the glycosyl residues (Fig. 5) were identified (Table 1) (13). Assignment of the ^{13}C resonances was made by direct correlation with the ^{1}H resonances by using the HMQC experiment, and by comparison with recorded ^{13}C-resonance chemical shift data (Table 2) (14, 15).

Seven ^{1}H subspectra were attributed to hexopyranosyl residues having the *gluco* configuration (labelled GI–GV; GNII and GNIII) on the basis of the observed large $J_{2,3}$ and $J_{3,4}$ couplings (~10 Hz). From the magnitude of the $J_{1,2}$ couplings, three of these residues were identified as having the α-D-configuration ($J_{1,2}$ ~4 Hz), while the other four residues were assigned the β-D-configuration ($J_{1,2}$ ~8 Hz) (Table 1). The residues labelled GNII and GNIII were identified as Glc*p*N residues on the basis of their C-2 ^{13}C chemical shifts. The H-2 resonances from these

Can. J. Chem. Downloaded from www.nrcresearchpress.com by EESC ESCOLA DE ENGENHARIA on 09/08/12
For personal use only.

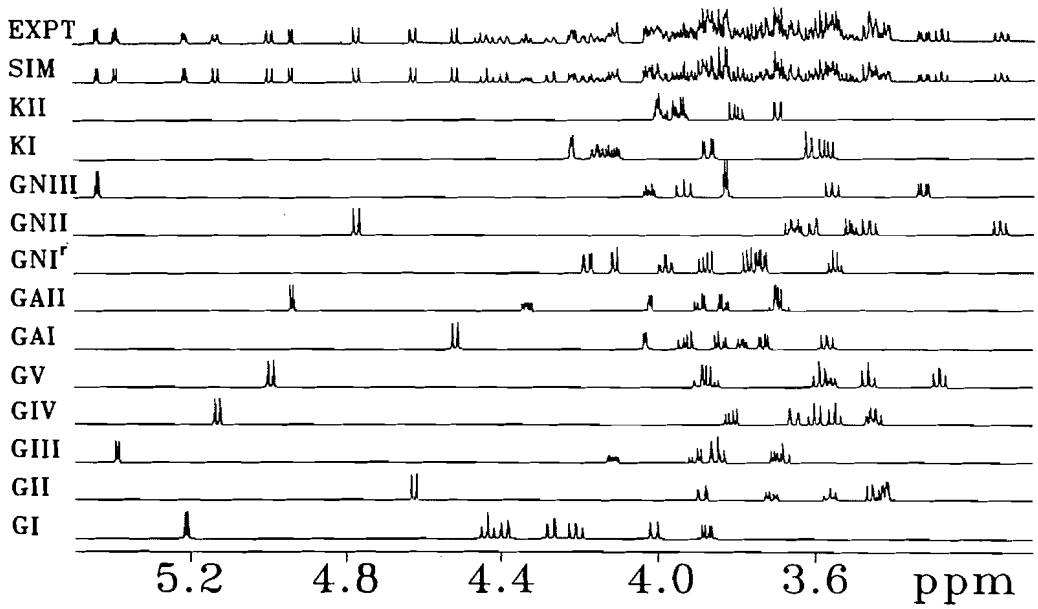

FIG. 5. Simulated (SIM) and experimental (EXPT) ^{1}H NMR spectra of the backbone OS. Subspectra of individual residues are shown separately.

TABLE 1. Proton chemical shifts (ppm) and coupling constants (Hz) for the backbone OS from *M. catarrhalis* LPS[a]

Residue	Glycose unit	H-1 ($J_{1,2}$)	H-2 ($J_{2,3}$)	H-3e[b] ($J_{3e,4}$, $J_{3e,3a}$)	H-3a[b] ($J_{3a,4}$)	H-4 ($J_{4,5}$)	H-5	H-6 ($J_{5,6}$)	H-6′ ($J_{5,6'}$, $J_{6,6'}$)	H-7 ($J_{6,7}$)	H-8 ($J_{7,8}$)	H-8′ ($J_{7,8'}$, $J_{8,8'}$)
	↓ 4											
GI	→6)-α-D-Glc*p*-(1→ 3 ↑	5.203 (4.1)	3.866 (9.8)		4.427 (9.5)	4.202 (10.5)	4.383	4.265 (1.0)	4.001 (1.0, 11.5)			
GII	→2)-β-D-Glc*p*-(1→	4.616 (8.1)	3.443 (9.5)		3.552 (9.5)	3.416 (9.5)	3.406	3.877 (1.7)	3.702 (6.1, 12.3)			
GIII	→4)-α-D-Glc*p*-(1→	5.382 (4.1)	3.691 (9.8)		3.837 (9.5)	3.674 (9.5)	4.107	3.847 (3.0)	3.894 (4.0, 12.3)			
GIV	→2)-β-D-Glc*p*-(1→	5.124 (8.1)	3.437 (9.2)		3.591 (9.4)	3.540 (9.4)	3.447	3.645 (1.7)	3.804 (6.1, 12.3)			
GV	β-D-Glc*p*-(1→	4.986 (8.1)	3.275 (9.2)		3.580 (9.4)	3.455 (9.4)	3.553	3.884 (1.7)	3.856 (6.1, 12.3)			
GAI[c]	→4)-β-D-Gal*p*-(1→	4.510 (8.0)	3.561 (10.0)		3.724 (3.8)	4.023 (1.0)	3.777	3.832 (4.5)	3.920 (7.5, 12.3)			
GAII	α-D-Gal*p*-(1→	4.931 (3.8)	3.827 (10.0)		3.883 (3.8)	4.011 (1.0)	4.326	3.697 (4.0)	3.681 (8.0, 12.3)			
GNI′	→6)-D-GlcNol	3.760[d] (6.2)	3.541 (6.5)		4.101 (1.0)	3.725 (9.0)	3.971	4.171 (2.5)	3.739 (9.0, 11.0)			
GNII	→6)-β-D-Glc*p*N-(1→	4.762 (8.5)	3.126 (10.5)		3.652 (9.0)	3.454 (10.3)	3.642	3.597 (1.5)	3.502 (6.5, 10.5)			
GNIII	α-D-Glc*p*N-(1→	5.430 (3.6)	3.319 (10.5)		3.925 (9.8)	3.549 (9.0)	4.014	3.820 (2.0)	3.820 (5.0, 12.3)			
KI	→5)-α-D-Kdo*p*-(2→ 4 ↑			2.071 (4.0, 12.3)	1.937 (12.0)	4.106 (3.1)	4.211	3.610 (1.0)		4.145 (9.0)	3.865 (2.5)	3.564 (7.0, 12.5)
KII	α-D-Kdo*p*-(2→			2.161 (4.8, 13.0)	1.785 (12.1)	3.935 (3.1)	3.992	3.688 (1.0)		3.984 (9.0)	3.939 (3.5)	3.795 (7.0, 12.5)

[a]Measured at 32°C in D_2O (pH ~6). Data is refined by spectral simulation.
[b]e and a designations indicate respective equitorial and axial H-3's of Kdo's.
[c]Partial assignments for terminal β-D-Gal*p* residue (GAI′) in truncated backbone OS: H-1, 4.46 ppm ($J_{1,2}$ = 7.6 Hz); H-2, 3.54 ppm ($J_{2,3}$ = 9.4 Hz); H-3, 3.65 ppm ($J_{3,4}$ = ~4.0 Hz); H-4, 3.91 ppm ($J_{4,5}$ = ~1 Hz); H-5, 3.61 ppm.
[d]Proton chemical shift for H-1′ = 3.869 ppm and coupling constants $J_{1,1'}$ = 12.5 Hz and $J_{1',2}$ = 6.8 Hz.

Can. J. Chem. Downloaded from www.nrcresearchpress.com by ESC ESCOLA DE ENGENHARIA on 09/08/12
For personal use only.

TABLE 2. ^{13}C chemical shifts (ppm) for the backbone OS from *M. catarrhalis* LPS[a]

Residue	Glycose unit	C-1	C-2	C-3	C-4	C-5	C-6	C-7	C-8
GI	↓ 4 →6)-α-D-Glc*p*-(1→ 3 ↑	100.0	73.8	76.9	72.5	69.8	67.3		
GII	→2)-β-D-Glc*p*-(1→	102.4	77.0	74.4	69.5	75.6	60.5		
GIII	→4)-α-D-Glc*p*-(1→	97.1	72.0	71.7	78.5	70.3	59.4		
GIV	→2)-β-D-Glc*p*-(1→	96.5	79.2	74.3	69.0	75.2	60.2		
GV	β-D-Glc*p*-(1→	103.2	73.7	75.6	68.8[b]	75.7	59.5		
GAI	→4)-β-D-Gal*p*-(1→	103.1	70.9	70.9[c]	77.3	75.3	60.3		
GAII	α-D-Gal*p*-(1→	100.2	68.4	69.0	68.8	70.7	60.5		
GNI[r]	→6)-D-GlcNol	58.8	55.3	65.8	72.0[c]	69.4	72.0		
GNII	→6)-β-D-Glc*p*N-(1→	99.1	55.7	72.0	69.9[b]	74.7	61.5		
GNIII	α-D-Glc*p*N-(1→	95.4	54.1	69.1	69.0	72.1	59.6		
KI	→5)-α-D-Kdo*p*-(2→ 4 ↑	—	—	34.1	70.3	76.3	72.6	69.0	63.1
KII	α-D-Kdo*p*-(2→	—	—	34.6	65.8	66.7	70.9	70.0	62.8

[a]Measured at 32°C in D_2O (pH ~6).
[b,c]Assignments may be reversed.

residues (3.126 and 3.319 ppm) were correlated in the HMQC experiment to ^{13}C resonances at 55.7 and 54.1 ppm, respectively, the chemical shifts of which were diagnostic of amino-substituted carbons (14). A third ^{13}C resonance in this region of the spectrum (55.3 ppm) showed a correlation to H-2 of the glucosamintol end group (GNI[r]). Two subspectra having ^1H spin systems typical of α- and β-D-*galacto*-pyranosyl residues were also identified (labelled GAI and GAII) from their vicinal ring proton coupling constant values: $J_{1,2}$ (3.8 and 8.0 Hz, respectively), $J_{2,3}$ (~10 Hz), $J_{3,4}$ (~4 Hz), and $J_{4,5}$ (1 Hz). Subspectra corresponding to the two Kdo residues were identified from connectivity pathways that were accessed through the high-field H-3 resonances (Fig. 2, Table 1). Cross-peaks relating H-3e, H-3a, and H-4 in a full-scale COSY spectrum indicated that the resonances at 2.071 (H-3e) and 1.937 (H-3a) ppm belong to the same Kdo unit (KI), while the two resonances at 2.161 (H-3e) and 1.785 (H-3a) ppm belong to the second Kdo unit (KII). The ^{13}C resonances of C-4 and C-5 of KI showed significant downfield shifts of 4.5 and 9.6 ppm, respectively, compared with that of KII (Table 2), indicative of KI being substituted at the *O*-4 and *O*-5 positions (14, 15), a conclusion consistent with the methylation analysis.

A nuclear Overhauser effect spectroscopy (NOESY) experiment confirmed the anomeric configuration of the glycopyranosyl residues through the observed NOEs relating the anomeric proton resonances to protons within the same pyranose ring systems (Fig. 6). The observed intraresidue NOE effect between the H-1 and H-2 resonances provided evidence of α-D-glycopyranose linkages (GI, GIII, GAII, and GNIII), while the NOE effects between the H-1, H-3, and H-5 resonances indicated the β-D-glycopyranose linkages (GII, GIV, GV, GAI, and GNII).

The sequence of the glycosyl residues within the carbohydrate backbone of the LPS was mainly determined from interresidue ^1H–^1H NOE measurements between anomeric and aglyconic protons on adjacent glycosyl residues (Fig. 6). Thus, the occurrence of an interresidue NOE between H-1 of GAII and H-4 of GAI established the partial sequence α-D-Gal*p*-(1→4)-β-D-Gal*p*-(1→. In addition, interresidue NOE effects were observed between H-1 of GAI and H-4 of GIII, H-1 of GIII and H-2 of GII, H-1 of GII and H-6/H-6′ of GI, and H-1 of GI and H-5 of KI. Hence, the linear partial sequence of the backbone portion of the OS was established as α-D-Gal*p*-(1→4)-β-D-Gal*p*-(1→4)-α-D-Glc*p*-(1→2)-β-D-Glc*p*-(1→6)-α-D-Glc*p*-(1→5)-α-D-Kdo*p*-(2→.

An interresidue NOE effect between H-1 of GNIII and H-2 of GIV points to the disaccharide sequence α-D-Glc*p*N-(1→2)-β-D-Glc*p*, which forms part of a side chain. However, the anomeric protons of both GIV and GV showed strong interresidue NOEs to H-3 of GI (Fig. 6), precluding assignment of the substitution pattern at GI. Results from methylation analyses suggested that the branching glycosyl residue (i.e., GI) is substituted at *O*-3, *O*-4, and *O*-6 positions. Since NOE evidence clearly indicated that GII is linked to the *O*-6 position of GI, then GIV and GV must be linked at the *O*-3 and *O*-4 positions. The precise linkage positions at GIV and GV were determined from a heteronuclear multiple bond connectivity (HMBC) experiment. Since three-bond connectivities were observed between C-1 of GIV and H-4 of GI and between C-1 of GV and H-3 of GI, this unambiguously established that the branching D-Glc*p* residue (GI) is substituted at the *O*-4 and *O*-3 positions by the respective glycose units (Fig. 7).

In the inner-core region, the branching 4,5-di-*O*-substituted Kdo residue (KI) provides the bridge between the core OS and the lipid A backbone (cf. Scheme 1). The NOE evidence indicates that the branching D-Glc*p* (GI) is attached to the *O*-5 position of KI, while the methylation analysis data is consistent with substitution at the *O*-4 position of KI by the terminal nonreducing Kdo residue (KII). This latter assignment was confirmed from the HMBC experiment in which a *trans*-glycosidic con-

Can. J. Chem. Downloaded from www.nrcresearchpress.com by EESC ESCOLA DE ENGENHARIA on 09/08/12
For personal use only.

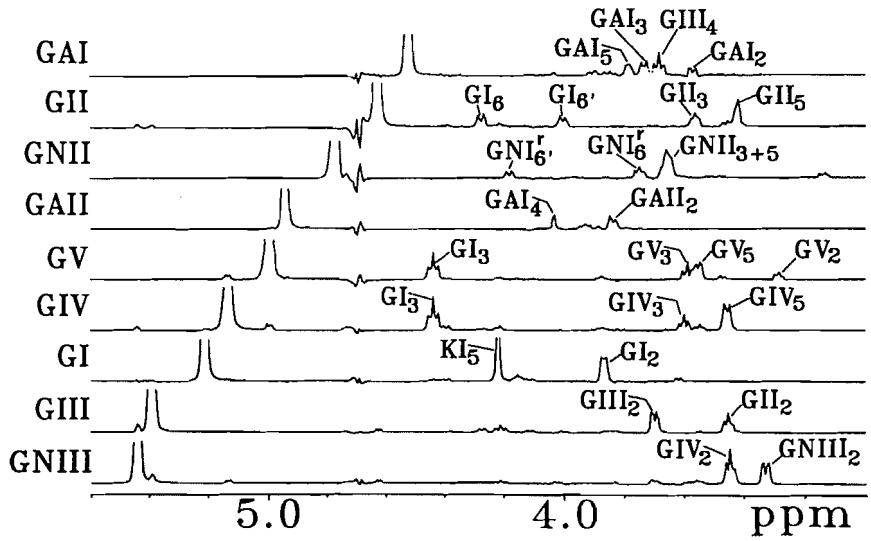

FIG. 6. Cross-sections through the anomeric resonances observed in the 2D NOESY spectrum of the backbone OS showing NOE connectivities from anomeric protons of nine glycosyl residues.

nectivity between C-2 of KII and H-4 of KI was observed. An interresidue NOE was observed between H-1 of GNII and the H-6/H-6′ pair of GNI, establishing the connectivity of the →6)-β-D-Glc*p*N-(1→6)-D-GlcNol unit derived from the lipid A region of the molecule (6). The observed rapid liberation of the lipid A from the LPS on treatment with dilute acid (Scheme 1) is in accord with the core OS being attached via a Kdo unit to the →6)-β-D-Glc*p*N-(1→ residue (GNII) and this was confirmed by tandem electrospray mass spectrometry (16). The connectivities and the linkage positions of the glycosyl residues of the backbone OS deduced from the NOE effects and $^3J_{C,H}$ couplings are illustrated in Fig. 7.

The relative deshielding of the carbon resonances observed for the ring carbons C-3 and C-4 of GI, C-2 of GII, C-4 of GIII, C-2 of GIV, C-4 of GAI, and C-4 and C-5 of KI and the resonances of the methylene carbons (C-6) of GI and GNI^r, when compared with resonances in unsubstituted residues (15), is in line with the established glycosylation at the respective linkage sites (Table 2). It is interesting to note that a similar deshielding effect was not see for ^{13}C resonance of the methylene carbon C-6 of the GNII residue, which is substituted by a Kdo unit. A similar observation has been previously reported (17). The ^{13}C chemical shifts are consistent with GAII, GNIII, and GV being the terminal nonreducing end groups, as also identified by methylation analysis.

Based on the combined NMR spectroscopic and methylation data, the structure of the major backbone OS from *M. catarrhalis* serotype A LPS can be assigned as follows:

α-D-Glc*p*N-(1→2)-β-D-Glc*p*
1
↓
4
α-D-Gal*p*-(1→4)-β-D-Gal*p*-(1→4)-α-D-Glc*p*-(1→2)-β-D-Glc*p*-(1→6)-α-D-Glc*p*-(1→5)-α-D-Kdo*p*-(2→6)-β-D-Glc*p*N-(1→6)-D-GlcNol
3 4
↑ ↑
1 2
β-D-Glc*p* α-D-Kdo*p*

The minor oligosaccharide component detected by NMR analysis (ca. 15% of backbone OS sample) was found to be a truncated form of the backbone OS that lacks the α-D-Gal*p* end group (GAII). The ^{1}H spin system (cf. Table 1) corresponding to a terminal β-D-Gal*p*-residue (labelled GAI′) was identified in the COSY spectrum from the connectivity pathway associated with the minor anomeric proton resonance at 4.46 ppm. An interresidue NOE was observed between H-1 of this residue and H-4 of GIII. In addition, the C-4 chemical shift of GAI′ (68.4 ppm) was typical of that from an unsubstituted β-D-Gal*p* residue, suggesting that the main chain of this minor OS terminates in β-D-Gal*p* and lacks the terminal α-D-Gal*p* present in the major backbone OS. As expected, treatment of the backbone OS with α-D-galactosidase afforded the truncated OS.[5]

The conformation about the glycosidic bond is to a large extent governed by the *exo*-anomeric effect (18), leading to the positioning of anomeric and aglyconic protons on contiguous residues within the expected range for the occurrence of an

[5]The backbone OS was treated with a commercial β-D-glucosidase preparation (Sigma) in an attempt to remove the terminal β-D-Glc*p* residue (GV) in the branched region of the molecule. Instead, the terminal α-D-Gal*p* residue (GAII) was quantitatively removed. The commercial preparation of β-D-glucosidase was known to contain minor amounts of α-D-galactosidase activity and this was confirmed by assaying the enzyme preparation with *p*-nitrophenyl-α-D-galactopyranoside.

Can. J. Chem. Downloaded from www.nrcresearchpress.com by EESC ESCOLA DE ENGENHARIA on 09/08/12
For personal use only.

Can. J. Chem. Downloaded from www.nrcresearchpress.com by EESC ESCOLA DE ENGENHARIA on 09/08/12
For personal use only.

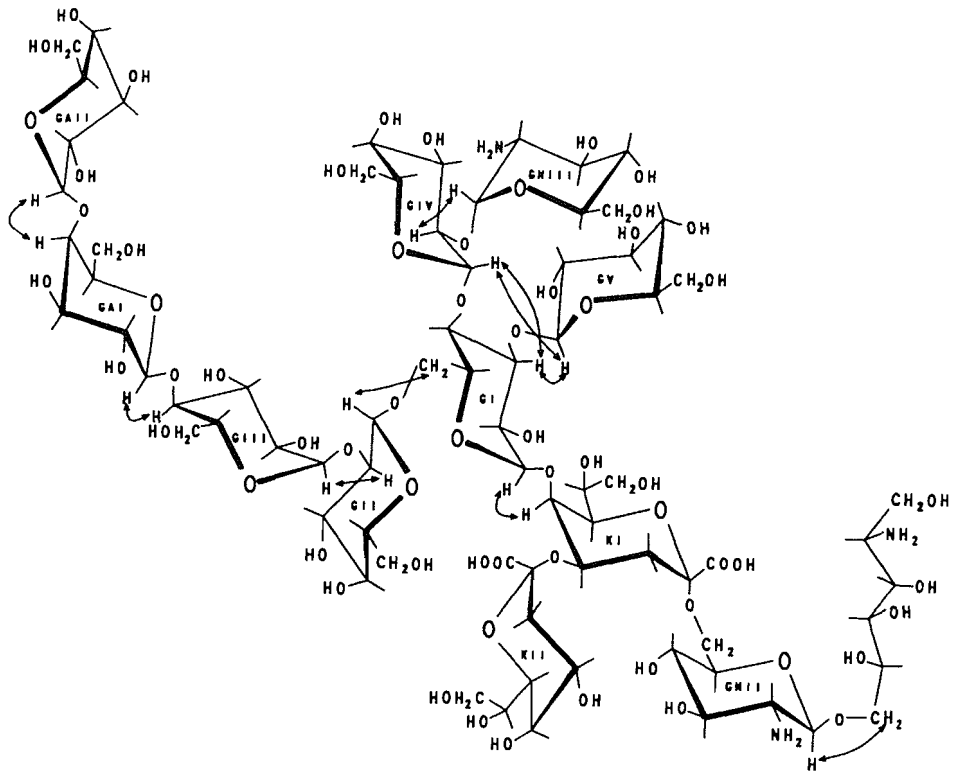

FIG. 7. Structure of the backbone OS from *M. catarrhalis* serotype A illustrating the network of observed interresidue NOE connectivities used to establish the sequence of the glycosyl residues.

interresidue NOE (i.e., interproton distance of less than ca. 3 Å) (19). This provides the basis for the successful application of NOE measurements in determining the sequence of an oligosaccharide. Thus, the observation of a strong transglycosidic NOE between H-1 of GIV and H-3 of GI, but not at H-4 of GI (Fig. 6), within the β-1,4-linked D-Glc*p*-containing disaccharide fragment (Fig. 7) suggested an unusual solution conformation in the highly branched inner core region of the molecule. The chemical shifts of H-1 (5.124 ppm) and C-1 (96.5 ppm) of GIV, which are significantly shifted from those expected for β-linked glycoses (20), also point to an unusual conformation in the →1)-β-D-Glc*p*-(1→4)-α-D-Glc*p*-(1→ disaccharide. To probe the conformation about this linkage, the $^3J_{C,H}$ value between C-1 of GIV and H-4 of GI was measured in a ^{1}H-detected 1D experiment (21). The interglycosidic proton–carbon coupling constant determined[6] from an antiphase multiplet was found to be 7.4 Hz (Fig. 8). Using a Karplus curve optimized for the COCH fragment in saccharides (22), the observed large $^3J_{C,H}$ value indicates that a C-1–O-1–C-4–H-4 conformation in which C-1 of GIV and H-4 of GI have a *trans* orientation is heavily populated. Such a conformation would position H-1 of GIV and H-3 of GI within the range expected for the occurrence of a NOE (Fig. 9). To the best of our knowledge, this is the first example of a D-Glc-containing disaccharide fragment hav-

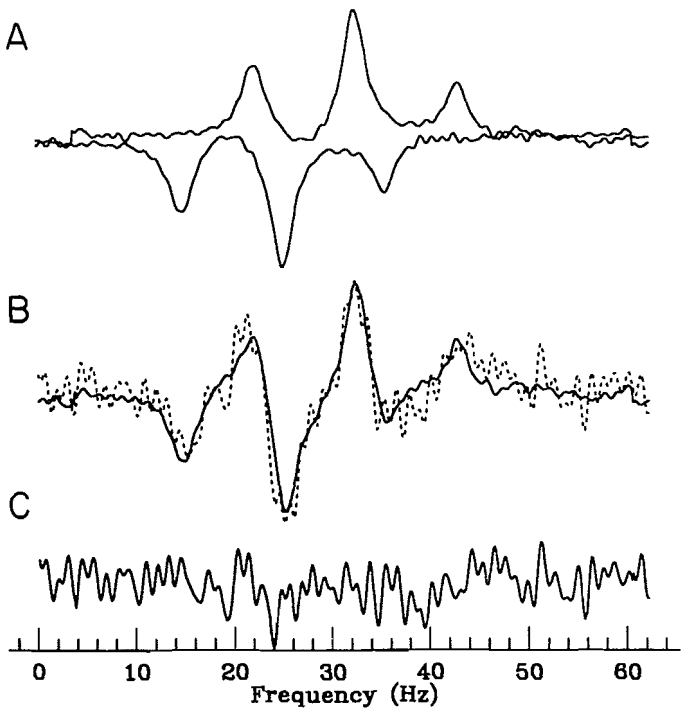

FIG. 8. Reconstruction of the antiphase proton multiplet H-4 of GI (dotted line, B) obtained in a ^{1}H-detected long-range proton–carbon correlated experiment (21). The inphase GI H-4 multiplet (A) was acquired in a z-filtered 1D TOCSY experiment (40, 41) and used to generate the theoretical antiphase multiplet (solid line, B). The difference of the two multiplets in B is shown in C.

[6]Two inphase multiplets of H-4 (GI) were shifted with respect to their chemical shifts and subtracted from each other to yield a theoretical antiphase multiplet. Their displacement and the intensity was varied and the sum of the square of the differences between the constructed and the experimental antiphase multiplets was minimized where the heteronuclear coupling constant is equal to twice the value of the displacement.

Can. J. Chem. Downloaded from www.nrcresearchpress.com by ESC ESCOLA DE ENGENHARIA on 09/08/12
For personal use only.

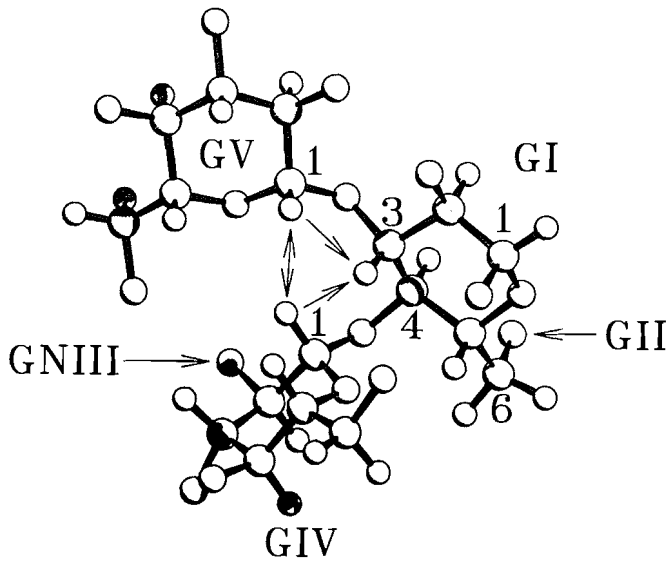

FIG. 9. Minimum energy structure of the branched region of the backbone OS showing the proximity of H-1 of GV, H-3 of GI, and H-1 of GIV to each other, and the *trans* orientation of C-1–O-1–C-4–H-4 for the GIV–GI glycosidic linkage ($\Psi_H = 208°$). This conformation is in accord with the interresidue NOEs observed between GIV H-1/GI H-3, GV H-1/GI H-3, and GIV H-1/GV H-1; and the large J (GIV C-1, GI H-4) coupling constant.

ing this conformation. Moreover, potential energy calculations predict a minor local energy minimum representative of this conformation in the highly branched core.

The structure of *M. catarrhalis* lipid A has been determined in detail (6), which permits the complete structure of the R-type LPS to be proposed as shown in Fig. 10.[7] The α-D-Gal*p*-(1→4)-β-D-Gal*p*-(→ terminal structure present in the *M. catarrhalis* LPS is also found as a component of the globo series of glycolipids associated with human epithilial cells (23). This form of molecular mimicry exhibited by *M. catarrhalis* may provide the pathogen with an advantage for evading host defence mechanisms. This structural feature also occurs in LPS of pathogenic strains of *Haemophilus influenzae* (24, 25) and *Neisseria* spp. (25) and it has been implicated in virulence potential (26). Concurrent studies on the LPS produced by clinical isolates of *M. catarrhalis* indicate that the OS structure deduced in the present investigation is common to LPS produced by these strains. A preliminary observation that mouse and rabbit antibody raised to the apparent common OS antigen shows strong cross-serological reactivity among the *M. catarrhalis* strains is being explored as the basis for a diagnostic reagent and a protective conjugate vaccine.

Experimental

Bacterial growth and LPS preparation

Moraxella catarrhalis serotype A (ATCC 25238) was grown and harvested as previously described (6). The cell pellets obtained by centrifugation were washed successively, once with ethanol, twice with acetone, and twice with petroleum ether (35–60°C), and the LPS was extracted by the hot phenol – water extraction procedure (7).

[7]The ^{1}H NMR spectrum of the *O*-deacylated LPS (Scheme 1, LPS-OH) was recently assigned (H. Masoud, M.B. Perry, and J.C. Richards, unpublished results) in which a singlet at 2.25 ppm (relative area, 3H) was attributed to the methyl protons of the acetamido substituent associated with the terminal nonreducing GlcN residue (GNIII).

Isolation and purification of core OS

Core OS was obtained by heating the LPS with 1% aqueous acetic acid (100°C, 2.5 h), followed by centrifugation (5000 rpm, 30 min) to remove insoluble lipid A. The OS was purified on a Bio-Gel P-2 (Bio-Rad) gel filtration system (2.6 × 140 cm), eluted with pyridinium acetate (0.05 M, pH 4.5). The column eluant was continuously monitored for changes in refractive index by using a Waters R403 differential refractometer. Collected fractions (4.5 mL) were assayed colourimetrically for neutral glycoses using the phenol – sulfuric acid method (27). Glycose-containing fractions were collected and lyophilized.

Preparation of LPS backbone OS

Deacylated, dephosphorylated, and reduced LPS (backbone OS) was prepared according to a modified method of that reported by Holst et al. (17). LPS samples (400 mg) were treated with anhydrous hydrazine (20 mL) with stirring at 37°C for 30 min. The reaction mixture was cooled (0°C), cold acetone (–70°C, 60 mL) was added gradually to destroy excess hydrazine, and precipitated *O*-deacylated LPS was obtained by centrifugation. The pellet was washed three times with acetone, dissolved in water, reprecipitated by addition of acetone, and lyophilized. *O*-Deacylated LPS was dephosphorylated by treatment with 48% aqueous hydrogen fluoride (20 mL) at 0°C for 48 h. The product was dried under a stream of nitrogen, dissolved in water, and dialyzed against water. The lyophilized *O*-deacylated and dephosphorylated LPS sample was treated with $NaBH_4$ (100 mg) in water (10 mL) at 22°C for 1 h, excess $NaBH_4$ was consumed by addition of acetic acid, and the solution was taken to dryness under a stream of nitrogen. The residue was successively evaporated from 10% acetic acid in methanol and then methanol, dialyzed, and lyophilized. *O*-Deacylated, dephosphorylated, and reduced LPS was dried over phosphorus pentoxide and treated with anhydrous hydrazine (15 mL, 85°C, 7 days) to remove amide-linked fatty acids. After removal of hydrazine in vacuo over sulfuric acid, the backbone OS was passed through a column (2 × 8 cm) of polyethylenimine cellulose anion-exchange resin (medium mesh, 1.06 mequiv./g, Sigma) and eluted with water (75 mL). The lyophilized product was purified on the Bio-Gel P-2 column as described above (yield, ~50 mg).

For NMR analysis the backbone OS was further purified by high-performance anion-exchange chromatography (HPAEC) on a Dionex Bio-LC system fitted with a CarboPac PA 1 pellicular anion-exchange column (9 × 250 mm) and a CarboPac PA 1 guard column (10 × 32 mm), using a flow rate of 2 mL/min. Prior to injection, the column was equilibrated with 95% of eluant A (150 mM NaOH) and 5% of eluant B (1 M sodium acetate in eluant A). Oligosaccharide samples (3 mg) in 50 μL of distilled water were eluted with the equilibration mixture of eluents A and B (0.95:0.05) for 5 min, followed by an increase in eluant B at a rate of 0.42%/min over 60 min. The column eluants were monitored with pulsed-amperometric detection (PAD) and fractions were collected, neutralized directly using aqueous acetic acid (10%), and lyophilized. Salt was removed by eluting the material on the Bio-Gel P-2 column as described above.

Analytical methods

Glycoses were determined by GLC as their alditol acetate derivatives. Samples (0.2–0.5 mg) containing *myo*-inositol (30 μg) as an internal standard were hydrolyzed with 2 M trifluoroacetic acid for 90 min at 125°C and evaporated to dryness under a stream of nitrogen. The liberated glycoses were reduced ($NaBH_4$) and acetylated (Ac_2O) as previously described (28). GLC analysis was performed with a Hewlett-Packard model 5710A gas chromatograph fitted with a hydrogen-flame ionization detector, using a fused-silica capillary column (0.3 mm × 25 m) containing 3% OV 17; an initial column temperature of 180°C was held for 2 min, followed by an increase to 240°C at 4°C/min.

Methylation analysis

Backbone OS (5 mg) was methylated with iodomethane (2 mL) in dimethyl sulfoxide (1 mL) containing an excess of potassium methylsulfinylmethanide (9). Excess iodomethane was evaporated under a

Can. J. Chem. Downloaded from www.nrcresearchpress.com by EESC ESCOLA DE ENGENHARIA on 09/08/12
For personal use only.

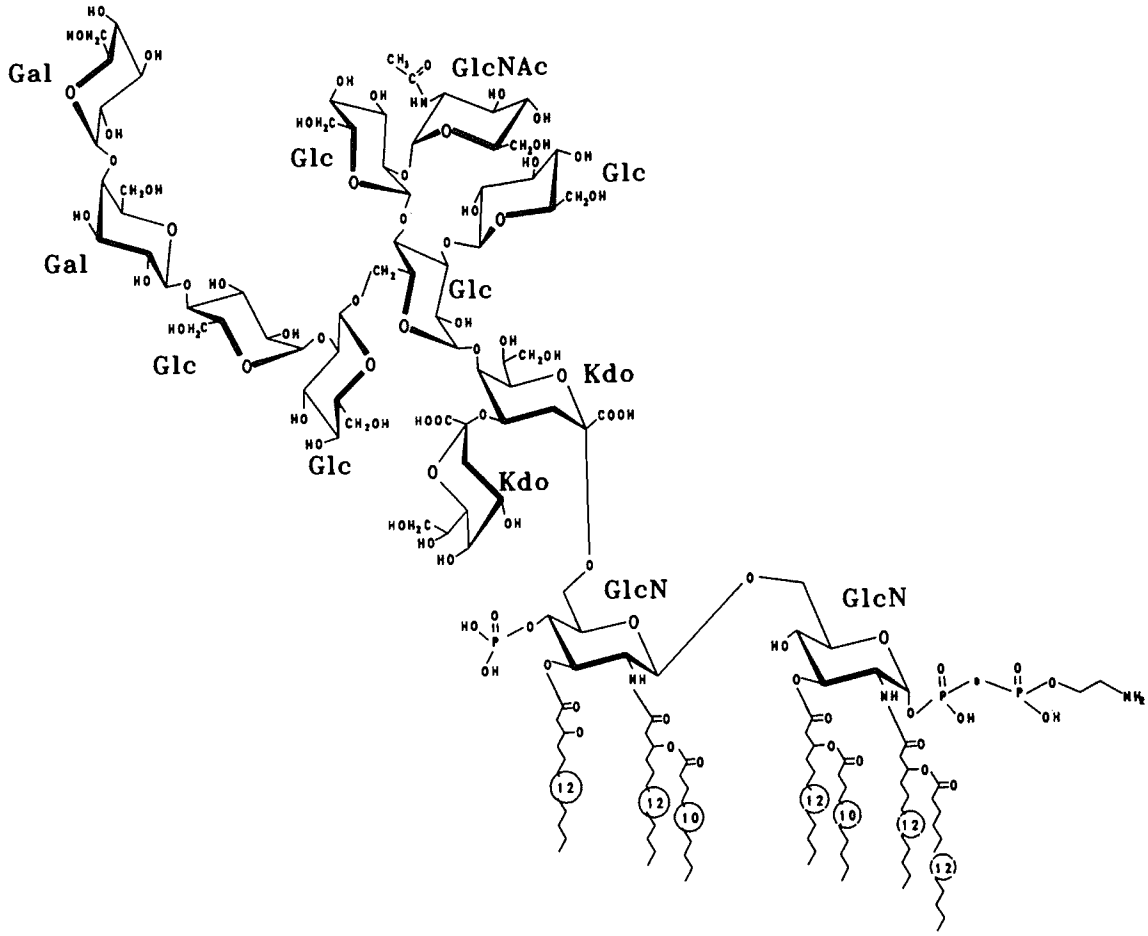

FIG. 10. Proposed chemical structure of the LPS from *M. catarrhalis* serotype A.

stream of nitrogen, water (3 mL) was added, and the methylated oligosaccharide was extracted into chloroform (2 × 5 mL) and purified on a Sep-Pak C-18 cartridge as previously described (29).

To identify 3-deoxyoctulosonic acid residues, *O*-deacetylated LPS (10 mg) was methylated and purified as described above, followed by reduction of the methylated octulosonate carboxy methyl ester groups with 1 M lithium triethylborodeuteride (0.5 mL) in tetrahydrofuran for 2 h at 22°C. The reaction mixture was acidified with glacial acetic acid, dried under a stream of nitrogen, and then evaporated from 10% acetic acid in methanol and then methanol. The residue was desalted using Dowex 50 (H^+ form) ion-exchange resin eluated with water–methanol (1:1). The methylated-reduced material was remethylated (Scheme 2) and purified as described above. Purified methylated oligosaccharides were hydrolyzed (either with 2 M trifluoroacetic acid, 100°C, 1 h, or with 0.25 M sulfuric acid in 95% acetic acid at 85°C, overnight), reduced ($NaBD_4$), acetylated according to the procedure of Stellner et al. (30), and finally analyzed using GLC–MS. Partially methylated alditol acetates were identified by EI–MS on a Hewlett-Packard 595B GLC–MS system fitted with a DB-17 fused silica capillary column (0.25 mm × 25 m), utilizing an ionization potential of 70 eV and a temperature program of 180°C for 2 min, followed by an increase to 320°C at 5°C/min.

Deoxycholate – polyacrylamide gel electrophoresis (DOC–PAGE)

PAGE was performed using the buffer system of Laemmli and Favre (31) as modified by Komuro and Galanos (32) with DOC as the detergent. LPS bands were stained and visualized by silver staining as described by Tsai and Frasch (33).

NMR spectroscopy

NMR spectra were obtained with a Bruker AMX 600 spectrometer using standard Bruker software. Measurements were made at 32°C on 2 mg of material dissolved in 0.5 mL D_2O subsequent to several lyophilizations with D_2O.

^1H NMR spectra (600 MHz) were measured using a spectral width of 4.8 kHz and a 90° pulse. Acetone was used as an internal standard. Chemical shifts were referenced to the methyl resonance (δ_H, 2.225 ppm; δ_C, 31.07 ppm). Two-dimensional COSY experiments (34) were measured over a spectral width of 2.0 kHz, using data sets (t_1, t_2) of 512 × 2048 points, and 64 scans were acquired. Spectra were processed in the magnitude mode and symmetrized about the diagonal. Two-dimensional TOCSY (35) and NOESY (36) experiments were performed in a phase-sensitive manner for a spectral width of 3.6 kHz using data sets of 512 × 2048 points and 64 scans for each t_1 value. Mixing times of 400 and 78.3 ms were employed for the NOESY and TOCSY experiments, respectively. ^1H chemical shifts and coupling constants were refined by spectral simulation using LACOONS 5 with the FT–NMR program. A full-scale COSY was carried out on a Bruker AMX 500 spectrometer for a spectral width of 2.0 kHz, by using a data set of 256 × 2048 points and 32 scans for each t_1 value.

Heteronuclear 2D ^{13}C–^1H chemical shift correlations were measured in the ^1H-detected mode via multiple quantum coherence (HMQC) with proton decoupling in the ^{13}C domain (37), using data sets of 1024 × 2048 points and spectral widths of 18.9 and 4.8 kHz for ^{13}C and ^1H domains, respectively. Thirty-two scans were acquired for each t_1 value.

The 2D heteronuclear multiple bond correlated experiment (HMBC) was carried out in the ^1H-detected mode using the pulse sequence described by Bax and Summers (38). The three-bond heteronuclear coupling constant ^3J (GIV C-1, GI H-4) was determined using a basic ^1H-detected, constant time, ^{13}C chemical shift selective filter experiment (21). The ^{13}C carrier frequency was set to the frequency of C-1 of

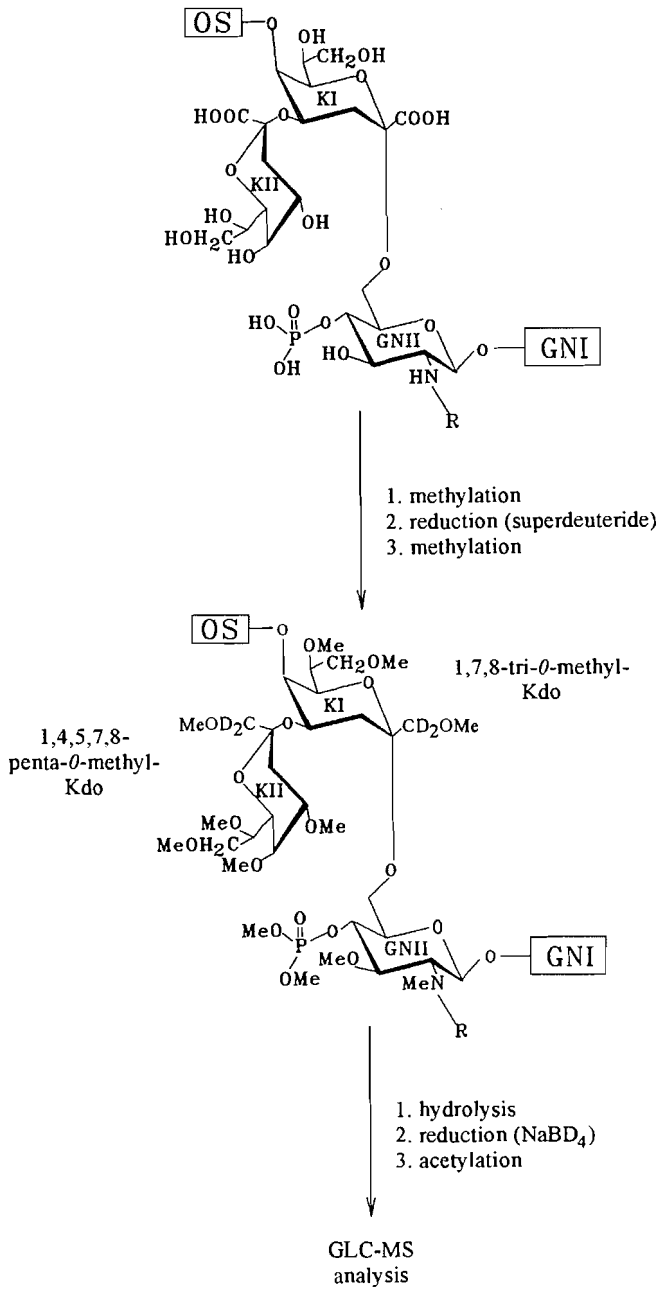

SCHEME 2. Reaction sequence for methylation analyses of Kdo residues present in LPS-OH.

GIV and the long-range evolution interval was 51.81 ms. An increment of 1.5 ms was used and 27 520 scans were acquired for each of eight experiments. The acquisition time was 1 s and the BIRD pulse (39) was applied 0.4 s before the start of the pulse sequence to suppress the ^{1}H resonances attached to ^{12}C. Total experimental time was 90 h. The inphase multiplet of H-4 of GI was acquired in a 1D TOCSY experiment (40) with a z-filter (41). A half-Gaussian pulse (42) of 53 ms was used to excite the GI H-1 proton and a mixing time of 150 ms was employed. The filter was incremented 24 times in 0.5-ms steps and 64 scans were acquired per spectrum.

Calculations

The conformational analysis was evaluated using the PFOS approach (43). The low-energy conformer which had a *trans* orientation for C-1–O-1–C-4–H-4 of the GIV–GI glycosidic linkage was further minimized by using the MM3 software (QCPE) (44).

Acknowledgements

We thank A. Martin for her technical assistance, F. Cooper for the GLC–MS analyses, D. Griffith for the large-scale production of cells, and D. Hare for providing us with FT–NMR.

1. G.V. Doern. Diagn. Microbiol. Infect. Dis. **4**, 191 (1986).
2. L.D. Cope, R. Yogev, J. Mertsola, J.C. Argyle, G.H. McCracken, Jr., and E.J. Hansen. Infect. Immun. **58**, 2343 (1990).
3. M. Vaneechoutte, G. Verschraegen, G. Claeys, and A.-M. Van Den Abeele. J. Clin. Microbiol. **28**, 182 (1990).
4. K.G. Johnson, I.J. McDonald, and M.B. Perry. Can. J. Microbiol. **22**, 460 (1976).
5. J.S. Fomsgaard, A. Fomsgaard, N. Hoiby, B. Bruun, and C. Galanos. Infect. Immun. **59**, 3346 (1991).
6. H. Masoud, M.B. Perry, and J.C. Richards. Eur. J. Biochem. **220**, 209 (1994).
7. O. Westphal, O. Lüderitz, and F. Bister. Z. Naturforsch. **7B**, 148 (1952).
8. D. Aminoff. Biochem. J. **81**, 384 (1961).
9. H.I. Hakomori. J. Biochem. (Tokyo), **66**, 205 (1964).
10. R.W. Carlson, R.L. Hollingsworth, and F.B. Dazzo. Carbohydr. Res. **176**, 127 (1988).
11. F.M. Unger. Adv. Carbohydr. Chem. Biochem. **38**, 323 (1981).
12. W.S. York, A.G. Darvill, M. McNeil, and P. Albersheim. Carbohydr. Res. **138**, 109 (1985).
13. C. Altona and C.A.G. Haasnoot. Org. Magn. Reson. **13**, 417 (1980).
14. K. Bock and C. Pedersen. Adv. Carbohydr. Chem. Biochem. **41**, 27 (1983).
15. K. Bock, C. Pedersen, and H. Pedersen. Adv. Carbohydr. Chem. Biochem. **42**, 193 (1984).
16. J.F. Kelly, P. Thibault, H. Masoud, M.B. Perry, and J.C. Richards. 41st ASMS Conference on Mass Spectrometry and Allied Topics, San Francisco, Calif., May 30 – June 4 (1993).
17. O. Holst, L. Brade, P. Kosma, and H. Brade. J. Bacteriol. **173**, 1862 (1991).
18. H. Thøgersen, R.U. Lemieux, K. Bock, and B. Meyer. Can. J. Chem. **60**, 44 (1982).
19. R.U. Lemieux, K. Bock, L.T.J. Delbaere, S. Koto, and V.S. Rao. Can. J. Chem. **58**, 631 (1981).
20. K. Bock and H. Thøgersen. Annu. Rep. NMR Spectrosc. **13**, 1 (1982).
21. D. Uhrín, A. Mele, K.E. Kővér, J. Boyd, and R.A. Dwek. J. Magn. Reson. In press.
22. I. Tvaroška, M. Hricovíni, and E. Petráková. Carbohydr. Res. **189**, 359 (1989).
23. R.E. Mandrell, J.M. Griffiss, and B.A. Macher. J. Exp. Med. **168**, 107 (1988).
24. M. Virji, J.N. Weiser, A.A. Lindberg, and E.R. Moxon. Microbial Pathogenesis **9**, 441 (1990).
25. A.A. Campagnari, S.M. Spinola, A.J. Lesse, Y.A. Kwaik, R.E. Mandrell, and M.A. Apicella. Microb. Pathog. **8**, 353 (1990).
26. E.R. Moxon and D.J. Maskell. *In* Molecular biology of bacterial infection: current status and future perspectives. Vol. 49. *Edited by* C. Hormaeche, C.W. Penn, and C.J. Smyth. SGM Symposium 1992. pp. 75–96.
27. M. Dubois, K.A. Gilles, J.K. Hamilton, P.A. Rebers, and F. Smith. Anal. Chem. **28**, 350 (1956).
28. W.S. York, A.G. Darvill, M. McNeil, T.T. Stevenson, and P. Albersheim. Methods Enzymol. **118**, 3 (1985).
29. A.J. Mort, S. Parker, and M.-S. Kuo. Anal. Biochem. **133**, 380 (1983).
30. K. Stellner, H. Saito, and S.I. Hakomori. Arch. Biochem. Biophys. **155**, 464 (1973).
31. U.K. Laemmli and M. Favre. J. Mol. Biol. **80**, 575 (1973).
32. T. Komuro and C. Galanos. J. Chromatogr. **450**, 381 (1988).
33. C. Tsai and C.E. Frasch. Anal. Biochem. **119**, 115 (1982).

Can. J. Chem. Downloaded from www.nrcresearchpress.com by EESC ESCOLA DE ENGENHARIA on 09/08/12
For personal use only.

34. A. Bax, R. Freeman, and G.A. Morris. J. Magn. Reson. **42**, 164 (1981).
35. S. Subramanian and A. Bax. J. Magn. Reson. **71**, 325 (1987).
36. A. Kumar, R.R. Ernst, and K. Wűthrich. Biochem. Biophys. Res. Commun. **95**, 1 (1980).
37. A. Bax, R.H. Griffey, and B.L. Hawkins. J. Magn. Reson. **55**, 301 (1983).
38. A. Bax and M.F. Summers. J. Am. Chem. Soc. **108**, 2093 (1986).
39. A. Bax and S. Subramanian. J. Magn. Reson. **67**, 565 (1986).
40. H. Kessler, U. Anders, G. Gemmecker, and S. Steuernagel. J. Magn. Reson. **85**, 1 (1989).
41. O.W. Sørensen, M. Rance, and R.R. Ernst. J. Magn. Reson. **56**, 527 (1984).
42. J. Friedrich, S. Davies, and R. Freeman. J. Magn. Reson. **75**, 390 (1987).
43. I. Tvaroška and S. Perèz. Carbohydr. Res. **149**, 389 (1986).
44. U. Burket and N.L. Allinger. Molecular Mechanics. ACS Monograph 177. American Chemical Society, Washington, D.C. 1982.

Can. J. Chem. Downloaded from www.nrcresearchpress.com by EESC ESCOLA DE ENGENHARIA on 09/08/12
For personal use only.

Antioxidant activities of tetrakis(4-hydroxyphenyl)pentanes and tetrakis(4-hydroxyphenyl)-*p*-xylenes

T. NISHIYAMA,[1] H. SHIOI, K. KORENAGA, R. TUJI, AND F. YAMADA

Department of Applied Chemistry, Faculty of Engineering, Kansai University, Senriyama, Suita, Osaka 564, Japan

Received August 17, 1993

T. NISHIYAMA, H. SHIOI, K. KORENAGA, R. TUJI, and F. YAMADA. Can. J. Chem. **72**, 1478 (1994).

A series of tetrakis(4-hydroxyphenyl)pentanes and tetrakis(4-hydroxyphenyl)-*p*-xylenes having relatively high molecular weights (550–810) were prepared and evaluated as antioxidants for tetralin at 60°C by means of an oxygen-absorption method. Introduction of alkyl groups to the *ortho* positions of the phenolic hydroxyl group was shown to improve antioxidant activities for both series of compounds.

T. NISHIYAMA, H. SHIOI, K. KORENAGA, R. TUJI et F. YAMADA. Can. J. Chem. **72**, 1478 (1994).

On a préparé une série de tétrakis(4-hydroxyphényl)pentanes et de tétrakis(4-hydroxyphényl)-*p*-xylènes de poids moléculaires relativement élevés (550–810) et on les a évalués comme antioxydants pour le tétraline, à 60°C, par une méthode d'absorption de l'oxygène. On a démontré que l'introduction de groupes alkyles en positions *ortho* du groupe hydroxyle du phénol améliore les activités antioxydantes dans les deux séries de composés.

[Traduit par la Rédaction]

Introduction

In chemical industries, antioxidants have commonly been used to prevent deterioration due to the oxidation of organic materials, for example, petroleum hydrocarbons, lubricating oils, rubbers, polymers, and foodstuffs (1). The oxidation upon storage at room temperature or during various processes at high temperature have been well recognized as radical chain reactions. Antioxidants such as 2,6-di-*tert*-butyl-4-methylphenol (BHT) and *tert*-butylated hydroxyanisole (BHA) react as chain-breaking inhibitors of the peroxyl radical. BHT and BHA are, however, relatively volatile and, consequently, of somewhat limited use at higher temperatures owing to their loss through vaporization. The development of antioxidants having high molecular weights (2) and the fixation of antioxidants to polymer chains (3, 4) are well-established methods to reduce the volatility of antioxidants.

During the course of our studies on phenol derivatives as antioxidants (5, 6), we have found that the introduction of the benzyl group at *ortho*- and (or) *para*-positions of the phenolic hydroxyl group improved the antioxidant activities. Furthermore, benzylphenols containing alkyl groups at both *ortho* positions for the phenolic hydroxyl group showed high activities as antioxidants.

On this basis, we expected that 1,1,5,5,-tetrakis(4-hydroxyphenyl)pentanes (**1–5**) and α,α,α′,α′-tetrakis(4-hydroxyphenyl)-*p*-xylenes (**6–11**) would act as better antioxidants compared with BHT or BHA, since they have four active phenolic moieties and alkyl or benzyl groups at the *ortho*- and or *para*-positions of the phenol skeleton. Herein, we wish to report the preparation of compounds **1–11** (Fig. 1) and their antioxidant activities evaluated by means of an oxygen-absorption method.

Results and discussion

Figure 2 shows the results of the autoxidation of tetralin initiated by 2,2′-azo-bis(isobutyronitrile) AIBN), in the presence of tetrakisphenols **1–11** and BHT as antioxidants, along with a control test in the absence of an antioxidant. The control curve was observed without any appreciable induction period (IP). On the contrary, the rates of oxygen uptake in the presence of tetrakisphenols were remarkably suppressed.

[1]Author to whom correspondence may be addressed.

First, the antioxidant activities of the tetrakis(4-hydroxyphenyl)pentanes and tetrakis(4-hydroxyphenyl)-*p*-xylenes were compared. In comparison with **1** and **6** having 2,5-dimethyl substituents on phenol rings, the IP value of **1** showed a slightly higher value (see IP values in Table 1). However, the IP values of **2** and **7**, **3** and **8**, and **5** and **10** showed almost the same values.

Next, the positions of the alkyl substituents on the phenol rings on their antioxidant effect were compared. The relative antioxidant potency of the tetrakis(4-hydroxyphenyl)pentanes was observed in the order **3** > **2** > **4**,**5** > **1**. Similarly, the IP values of the tetrakis(4-hydroxyphenyl)-*p*-xylenes decreased in the order **8**,**11** > **7** > **10** > **9** > **6**. In particular, for compounds **2**, **3**, **7**, **8**, and **11** having two alkyl substituents at *ortho* positions of OH groups, the IP values were 2.5–3.0 times larger than that for BHT. These results indicated that the factors which enhance the peroxyl radical trapping ability of tetrakisphenols are greatly dependent on the position of the ring substituents of the phenol nuclei. These factors are, first, alkyl substitution at both *ortho* positions and, second, a bulky substitution at the *ortho* position.

The stoichiometric factors (n) for all the antioxidants examined are listed in Table 1. Compounds **2**, **3**, **7**, **8**, and **11** exhibited much higher stoichiometric factors (5.2–6.0) in comparison with those of other compounds. This means that these four compounds react with five to six pieces of peroxyl radicals, respectively.

Table 1 also shows the rates of oxygen consumption after IP. As can be seen from Table 1, relatively lower rates were observed for all classes of tetrakisphenols in comparison with BHT. When all ArO· radicals are consumed, the rate of autoxidation should be equal to that of the control test. In fact, the rate of oxygen consumption after IP of BHT was close to the control value. On the other hand, the rates of oxygen consumption of compounds **1–11** were not close to the control value, but much lower. This means that the retardation ability persists, even after IP is over, owing to some transformation products of the antioxidant.

In conclusion, we have synthesized a series of tetrakisphenols. Among these compounds, the compounds having two alkyl substituents at *ortho* positions of OH groups, such as **2**, **3**, **7**, **8**, and **11**, exhibited significant antioxidant effect. However, no influence of the structure between tetrakis(4-hydroxyphenyl)pentanes and tetrakis(4-hydroxyphenyl)-*p*-xylenes on their antioxidant effect was observed.

Can. J. Chem. Downloaded from www.nrcresearchpress.com by EESC ESCOLA DE ENGENHARIA on 09/08/12
For personal use only.

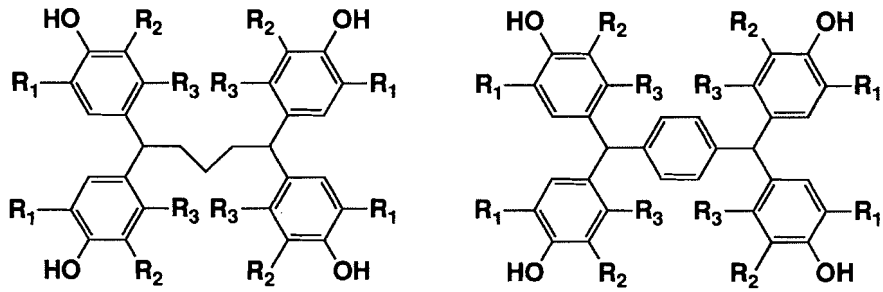

1, $R_1=R_3=CH_3$, $R_2=H$
2, $R_1=R_2=CH_3$, $R_3=H$
3, $R_1=R_2=R_3=CH_3$
4, $R_1=CH(CH_3)_2$, $R_2=H$, $R_3=CH_3$
5, $R_1=C(CH_3)_3$, $R_2=H$, $R_3=CH_3$

6, $R_1=R_3=CH_3$, $R_2=H$
7, $R_1=R_2=CH_3$, $R_3=H$
8, $R_1=R_2=R_3=CH_3$
9, $R_1=CH(CH_3)_2$, $R_2=H$, $R_3=CH_3$
10, $R_1=C(CH_3)_3$, $R_2=H$, $R_3=CH_3$
11, $R_1=R_2=CH(CH_3)_2$, $R_3=H$

FIG. 1. 1,1,5,5-Tetrakis(4-hydroxyphenyl)pentanes (**1–5**) and α,α,α′,α′-tetrakis(4-hydroxyphenyl)-*p*-xylenes (**6–11**).

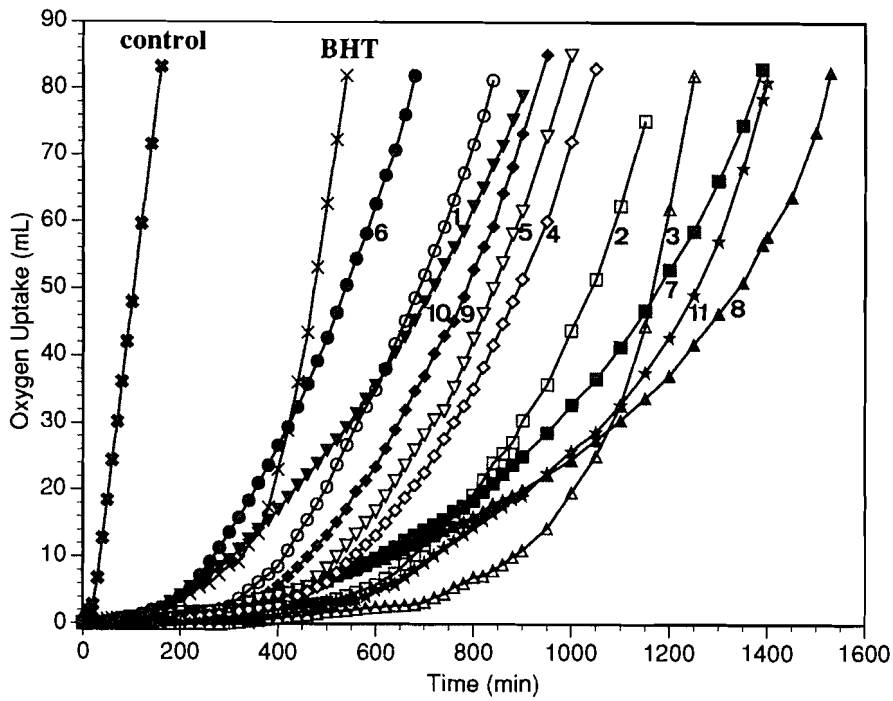

FIG. 2. Rate of oxygen uptake in the oxidation of tetralin in the absence and presence of antioxidant.

We are planning to test the toxicity of **1–11** and the antioxidant activities for other substrates.

Experimental

General

Melting points were measured on a Yanaco MP-J3 micro melting apparatus and uncorrected. Infrared spectra were determined with a Perkin-Elmer model 1600 grating infrared spectrophotometer using a potassium bromide pellet. Nuclear magnetic resonance spectra were recorded with a Jeol GSX-400 spectrometer operating at 400 MHz for ^1H and 100.6 MHz for ^{13}C. Unless otherwise noted, the solvent was $(CD_3)_2CO$ and chemical shifts are given with respect to TMS.

Determination of antioxidant activities

The volume of oxygen consumption was determined as a function of time under 760 Torr (1 Torr = 133.3 Pa) of O_2 (5). The oxidation temperature was kept at 60 ± 0.1°C. The IP was determined graphically (7, 8) on the plot of oxygen consumption versus time as the point of intersection of a line of the rate of oxygen uptake after the inhibitor was consumed and a line tangent to the curve with a slope equal to half of the slope of the line after the inhibitor was consumed. Stoichiometric factors (n) were determined at 60°C by the IP method (9, 10).

Materials

Tetralin was washed with concentrated sulfuric acid, aqueous sodium bicarbonate, and water, dried over anhydrous sodium sulfate, and distilled under nitrogen before use. AIBN was recrystallized from methanol.

The tetrakis(4-hydroxyphenyl)pentanes **1–5** and tetrakis(4-hydroxyphenyl)-*p*-xylenes **6–11** were prepared by the condensation reaction of glutaraldehyde or terephthalaldehyde with the corresponding phenols in the molecular ratio of one to four in the presence of an acidic catalyst (11, 12). A typical experimental procedure is described for the synthesis of **1**. To the solution of 2,5-dimethylphenol (12.2 g, 0.1 mmol) and glutaraldehyde (2.5 g, 25 mmol) in nitromethane (30 mL), concentrated HCl (1.5 mL) was added dropwise at room temperature.

Can. J. Chem. Downloaded from www.nrcresearchpress.com by EESC ESCOLA DE ENGENHARIA on 09/08/12
For personal use only.

Can. J. Chem. Downloaded from www.nrcresearchpress.com by EESC ESCOLA DE ENGENHARIA on 09/08/12
For personal use only.

TABLE 1. Antioxidant activities of tetrakisphenols **1–11**

Compound	mp (°C)	IP (min)	*n*	Rates of oxygen consumption (mL/min)
1	226.2–227.0	493	3.07	0.21
2	206.0–206.5	938	5.16	0.32
3	228.0–229.0	1038	5.56	0.36
4	179.9–181.2	678	4.01	0.25
5	198.8–199.1	672	3.98	0.25
6	>300	384	2.47	0.25
7	248.2–250.0	973	5.31	0.19
8	263.1–263.8	1167	6.04	0.20
9	285.2–285.9	487	3.04	0.18
10	>300	601	3.63	0.22
11	145.1–146.2	1126	5.89	0.26
BHT		376	2.67	0.48
Control		22	—	0.56

After being stirred for 24 h, the mixture was poured into water and extracted with ethyl acetate. The organic layer was washed with water, dried over anhydrous Na_2SO_4, and concentrated. The residue was chromatographed on silica gel with 10% ethyl acetate in hexane as eluants. The first fraction contained 2,5-dimethylphenol. The second fraction was evaporated in vacuo to leave a solid. Recrystallization of the solid from acetone gave 2.8 g (20%) of **1**. The yield, spectral, and analytical data are as follows.

1,1,5,5-Tetrakis(2,5-dimethyl-4-hydroxyphenyl)pentane (1)
^{1}H nmr δ: 1.81–1.88 (m, 6H), 2.04 (s, 12H), 2.06 (s, 12H), 2.89 (br s, 4H), 3.95 (t, J = 7.3 Hz, 2H), 6.52 (s, 4H), 6.77 (s, 4H); ^{13}C nmr δ: 16.1, 19.3, 32.3, 37.0, 42.0, 117.3, 121.7, 130.2, 134.9, 153.7; ir: 3484 cm^{-1} (s, br). Anal. calcd. for $C_{37}H_{44}O_4$: C 80.39, H 8.02; found: C, 79.99, H, 8.10.

1,1,5,5-Tetrakis(3,5-dimethyl-4-hydroxyphenyl)pentane (2)
Yield: 10%; ^{1}H nmr δ: 1.81–1.88 (m, 6H), 2.02 (s, 24H), 2.75 (br s, 4H), 3.44 (t, J = 7.7 Hz, 2H), 6.67 (s, 8H); ^{13}C nmr δ: 16.7, 27.3, 36.8, 50.5, 124.2, 128.4, 138.1, 152.0; ir: 3500 cm^{-1} (s, br). Anal. calcd. for $C_{37}H_{44}O_4$: C 80.39, H 8.02; found: C 80.01, H 7.98.

1,1,5,5,-Tetrakis(2,3,5-trimethyl-4-hydroxyphenyl)pentane (3)
Yield: 11%; ^{1}H nmr δ: 2.03–2.06 (m, 6H), 2.09 (s, 24H), 2.12 (s, 12H), 2.81 (br s, 4H), 3.65 (t, J = 7.7 Hz, 2H), 6.47 (s, 4H); ^{13}C nmr δ: 12.9, 15.3, 16.9, 32.3, 37.2, 43.1, 121.1, 123.5, 127.5, 133.5, 135.3, 151.5; ir: 3480 cm^{-1} (s, br). Anal. calcd. for $C_{41}H_{52}O_4$: C 80.49, H 8.78; found: C 80.20, H 8.48.

1,1,5,5-Tetrakis(2-methyl-5-isopropyl-4-hydroxyphenyl)pentane (4)
Yield: 42%; ^{1}H nmr δ: 1.12 (d, J = 6.8 Hz, 12H), 1.17 (d, J = 6.8 Hz, 12H), 1.85–1.91 (m, 6H), 2.11 (s, 6H), 2.18 (s, 6H), 3.06–3.13 (m, 4H), 4.00 (t, J = 7.0 Hz, 2H), 4.66 (br s, 4H), 6.48 (s, 4H), 6.91 (s, 4H); ^{13}C nmr δ: 19.2, 23.1, 27.4, 27.8, 37.5, 42.4, 117.6, 125.7, 132.2, 134.3, 134.9, 152.5; ir: 3479 cm^{-1} (s, br). Anal. calcd. for $C_{45}H_{60}O_4$: C 81.28, H 9.09; found: C 79.89, H 9.01.

*1,1,5,5-Tetrakis(2-methyl-5-*tert*-butyl-4-hydroxyphenyl)pentane (5)*
Yield: 18%; ^{1}H nmr δ: 0.90 (s, 36H), 1.44–1.51 (m, 6H), 1.69 (s, 12H), 2.42 (br s, 4H), 3.65 (t, J = 7.6 Hz, 2H), 6.13 (s, 4H), 6.64 (s, 4H); ^{13}C nmr δ: 19.0, 27.6, 30.9, 35.0, 37.8, 42.3, 118.8, 126.3, 133.3, 134.4, 134.5, 153.9; ir: 3494 cm^{-1} (s, br). Anal. calcd. for $C_{49}H_{68}O_4$: C 81.62, H 9.51; found: C 81.43, H 9.31.

α,α,α′,α′-*Tetrakis(2,5-dimethyl-4-hydroxyphenyl)*-p-*xylene (6)*
Yield: 15%; ^{1}H nmr (DMSO-d_6) δ: 1.93 (s, 12H), 1.96 (s, 12H), 2.08 (s, 4H), 5.38 (s, 2H), 6.27 (s, 4H), 6.56 (s, 4H), 6.86 (s, 4H); ^{13}C nmr (DMSO-d_6) δ: 15.9, 18.9, 30.7, 48.0, 116.7, 120.0, 129.0, 130.8, 132.6, 133.9, 141.3, 153.2; ir: 3485 cm^{-1} (s, br). Anal. calcd. for $C_{40}H_{42}O_4$: C 81.88, H 7.21; found: C, 81.57, H 7.24.

α,α,α′,α′-*Tetrakis(3,5-dimethyl-4-hydroxyphenyl)*-p-*xylene (7)*
Yield: 22%; ^{1}H nmr δ: 2.13 (s, 24H), 2.85 (s, 2H), 2.88 (s, 2H), 5.23 (s, 2H), 6.99 (s, 4H), 7.01 (s, 4H), 7.33 (s, 4H); ^{13}C nmr δ: 16.7, 55.9, 124.2, 129.1, 129.7, 130.1, 136.6, 143.7, 152.2; ir: 3475 cm^{-1} (m, br). Anal. calcd. for $C_{40}H_{42}O_4$: C 81.88, H 7.21; found: C 81.68, H 7.19.

α,α,α′,α′-Tetrakis(2,3,5-trimethyl-4-hydroxyphenyl)-p-*xylene (8)*
Yield: 29%; ^{1}H nmr δ: 2.06 (s, 12H), 2.08 (s, 12H), 2.17 (s, 12H), 2.87 (br s, 4H), 5.66 (s, 2H), 6.91 (s, 2H), 6.97 (s, 2H), 7.35 (s, 4H); ^{13}C nmr δ: 13.0, 15.8, 17.1, 51.2, 121.0, 124.0, 129.3, 129.9, 134.2, 135.1, 143.4, 152.2; ir: 3510 cm^{-1} (s, br). Anal. calcd. for $C_{44}H_{50}O_4$: C 82.20, H 7.84; found: C 81.87, H 7.79.

α,α,α′,α′-*Tetrakis(2-methyl-5-isopropyl-4-hydroxyphenyl)*-p-*xylene (9)*
Yield: 33%; ^{1}H nmr δ: 1.03 (d, J = 6.6 Hz, 24H), 2.05 (s, 12H), 2.91 (s, 2H), 2.94 (s, 2H), 3.12–3.22 (m, 4H), 5.55 (s, 2H), 6.60 (s, 4H), 6.63 (s, 4H), 6.94 (s, 4H); ^{13}C nmr δ: 19.4, 23.1, 27.6, 49.9, 117.8, 128.1, 130.2, 132.1, 134.5, 135.1, 142.9, 153.1; ir: 3493 cm^{-1} (s, br). Anal. calcd. for $C_{48}H_{58}O_4$: C 82.48, H 8.36; found: C 82.21, H 8.12.

α,α,α′,α′-Tetrakis(2-methyl-5-tert-*butyl-4-hydroxyphenyl)*-p-*xylene (10)*
Yield: 31%; ^{1}H nmr δ: 1.25 (s, 36H), 2.11 (s, 12H), 2.93 (br s, 4H), 5.60 (s, 2H), 6.65 (s, 4H), 6.74 (s, 4H), 6.97 (s, 4H); ^{13}C nmr δ: 19.1, 35.1, 49.8, 118.9, 128.8, 130.2, 133.2, 133.9, 135.3, 143.1, 154.4; ir: 3481 cm^{-1} (s, br). Anal. calcd. for $C_{52}H_{66}O_4$: C 82.71, H 8.81; found: C 82.80, H 8.80.

α,α,α′,α′-Tetrakis(3,5-diisopropyl-4-hydroxyphenyl)-p-*xylene (11)*
Yield: 11%; ^{1}H nmr δ: 1.07 (d, J = 6.6 Hz, 48H), 2.75 (s, 2H), 2.79 (s, 2H), 3.22–3.28 (m, 8H), 5.31 (s, 2H), 6.81 (s, 8H), 6.99 (s, 4H); ^{13}C nmr δ: 23.5, 27.6, 57.1, 125.1, 129.8, 135.3, 137.3, 144.4, 149.7; ir: 3495 cm^{-1} (s, br). Anal. calcd. for $C_{56}H_{74}O_4$: C 82.92, H 9.19; found: C 82.61, H 9.08.

1. W.O. Lundberg. Autoxidation and antioxidants. Vol. I and II. Interscience, New York. 1961; G. Scott. Atmospheric oxidation and antioxidants. Elsevier, Amsterdam. 1965.
2. Shell Oil Company. U.S. Pat. 3,116,305 (1963).
3. J. Pospisil. Degradation and stabilization of polymers. Vol. 1. Elsevier, Amsterdam. 1983. p. 214.
4. B.K. Hunter, K.E. Russell, and A.K. Zaghloul. Can. J. Chem. **61**, 124 (1983).
5. F. Yamada, T. Nishiyama, Y. Suzuura, and T. Yamamura. Bull. Chem. Soc. Jpn. **58**, 115 (1985).
6. F. Yamada, T. Nishiyama, M. Yamamoto, and K. Tanaka. Bull. Chem. Soc. Jpn. **62**, 3603 (1989).
7. G.W. Burton and K.U. Ingold. J. Am. Chem. Soc. **103**, 6472 (1981).
8. A.A. Kharitonova, Z.G. Kozlova, V.F. Tsepalow, and G.P. Gladyshev. Kinet. Catal. (Engl. Transl.), **20**, 593 (1979).
9. M. Prusikova, L. Jirackova, and J. Pospisil. Collect. Czech. Chem. Commun. **37**, 3788 (1972).
10. E.C. Horswill, J.A. Howard, and K.U. Ingold. Can. J. Chem. **44**, 985 (1966).
11. A. Chwala and W. Bartek. Monatsh. Chem. **82**, 652 (1951).
12. H. Suzuki. Tetrahedron Lett. **33**, 6319 (1992).

An X-ray and conformational study of the α-chloro derivatives of 5,7-dihydro-1,11-dimethyl-6*H*-dibenzo[*a*,*c*]cyclohepten-6-one

ROBERT R. FRASER,[1] CORINNE BENSIMON, NEIL C. FAIBISH, AND FANZUO KONG[2]
Department of Chemistry, University of Ottawa, Ottawa, ON K1N 6N5, Canada

Received June 30, 1993[3]

ROBERT R. FRASER, CORINNE BENSIMON, NEIL C. FAIBISH, and FANZUO KONG. Can. J. Chem. **72**, 1481 (1994).

The crystal structures for four α-chloro derivatives **2–5** of the titled ketone **1** have been determined, confirming their earlier assignments of stereochemistry. Variations in the conformations of **2–5** suggested some flexibility in the central seven-membered ring. Molecular mechanics calculations of the changes in energy as a function of the internal torsional angles at the carbonyl of these chloro derivatives indicated the ring flexibility to be comparable to that of cyclohexanone. In the three compounds containing an axial chlorine the distance between the chlorine atom and two of the carbon atoms of the more remote benzene ring was 3.2 ± 0.1 Å, suggesting the value for the thickness of a benzene ring may be significantly smaller than the accepted value when it is interacting with a single atom.

ROBERT R. FRASER, CORINNE BENSIMON, NEIL C. FAIBISH et FANZUO KONG. Can. J. Chem. **72**, 1481 (1994).

On a déterminé les structures cristallines des quatre dérivés α-chlorés **2–5** de la cétone **1** mentionnée dans le titre et on a ainsi confirmé les attributions de stéréochimie faites antérieurement. Les variations dans les structures des composés **2–5** suggèrent l'existence d'une certaine flexibilité dans le cycle central à sept chaînons. Des calculs de mécanique moléculaire des changements d'énergie en fonctions des angles de torsion internes au niveau du carbonyle de ces dérivés chlorés indiquent que la flexibilité du cycle est comparable à celle de la cyclohexanone. Dans les trois composés contenant un atome de chlore axial, la distance entre l'atome de chlore et deux des atomes de carbone du noyau benzénique le plus éloigné est de 3,2 ± 0,1 Å; ceci suggère que la valeur pour l'épaisseur d'un noyau benzénique interagissant avec un seul atome est peut-être beaucoup plus faible que la valeur généralement acceptée.

[Traduit par la Rédaction]

The bridged biaryl ketone, 5.7-dihydro-1, 11-dimethyl-6*H*-dibenzo[*a*,*c*]cycloheptene-6-one,[4] **1**, first reported by Mislow et al. (1), is a chiral derivative of biphenyl. A C_2 axis passes through its central ring giving rise to two possible orientations α to the carbonyl, either "axial" or "equatorial" on the basis of their similarity to the geometry at the α positions of cyclohexanone (see Fig. 1). The ring was considered by Mislow to possess a single rigid conformation as indicated by molecular models and supported by its proton nmr spectra (2). We have used this ketone in a variety of studies involving the effects of stereochemistry on reactivity since it offered certain advantages over cyclohexanone as a model. One example involves a study of the hydrogen–deuterium exchange reaction for the axial and equatorial protons α to the carbonyl (3). In another, measurement of the variation in rates of addition of nucleophiles to **1** as a function of the stereochemistry of its α methyl and chloro derivatives provided evidence for the primary importance of torsional interactions as contributors to the antiperiplanar effect (4). The validity of the assumption of rigidity of **1**, and thus its ability as a model to provide derivatives of known fixed stereochemistry, was examined for **1** and its methyl derivatives using X-ray crystallography complemented by molecular mechanics calculations (5). In the solid state, these compounds showed a C_2 symmetric structure except for the axial monomethyl derivative in which the torsional angles changed by 23° at the C—C bonds α to the carbonyl. Molecular mechanics calculations using the MMX program[5] provided conformations whose dihedral angles matched each of those observed to within 2° and energies matched to within 0.5 kcal/mol. Calculated energy differences between diastereoisomers similarly agreed with data obtained by equilibration experiments. The X-ray data for hydrocarbon derivatives of **1** not only verified their stereochemistry but provided a sucessful test of the performance of MMX as well as quantitative information on their rigidity. In this paper we describe the same combination of X-ray crystallographic analysis with information from MMX calculations in elucidating the conformational properties of the α chloro derivatives **2–5**.

X-ray crystallographic analysis

Table 1 presents a summary of the crystal data for the following derivatives of **1**: equatorial monochloroketone **2**, diaxial dichloroketone **3**, diequatorial dichloroketone **4**, and the geminal dichloroketone **5**. The X-ray data confirm the structural and stereochemical assignments made earlier (4) for compounds **2–5**. Each of the equatorial chlorines are oriented in eclipsed or nearly eclipsed conformations, the dihedral angles between the C—Cl and the adjacent C—O bond being 6° and 5° (or 14°) in **2** and **4**, respectively. The axial chlorines in **3** are found to be antiperiplanar (to the more remote π lobe of the carbonyl) as proposed (4*b*), having dihedral angles of 90° ± 10°.

The most descriptive information with respect to the conformation of these compounds is provided by the torsional or dihedral angles given in Table 2. For comparison, that previously reported for **1** appears in the first column. For the equatorial monochloroketone **2** two symmetry-independent molecules **2***a* and **2***b*, having very similar conformations, were found in one unit cell. The ORTEP plots for **2***a* and **2***b* along with those for **3***a*, **3***b*, **4**, and **5** appear in Fig. 2. In contrast to **1**, the seven-membered ring in this structure differs from the symmetric from primarily through a 15° rotation about C1—C2 and C1—C15, which is accompanied by much smaller changes at the C2—C3 and C15—C14 bonds. Again, for the diaxial α,α′-dichloroketone **3** two symmetry-independent molecules were found in

[1]Author to whom correspondence may be addressed.

[2]Permanent address: Research Center for Eco-Environmental Sciences, Academia Sinica, P.O. Box 2871, Beijing, China.

[3]Revision received January 17, 1994.

[4]The IUPAC system for numbering the atoms of **1** as shown in the structure on the left in Fig. 1 has been replaced by that shown on the right to avoid the use of subscripts for naming quaternary atoms.

[5]P.C. Model Molecular Modeling Program, Serena Software, P.O. Box 3076, Bloomington, IN 47402-3076, U.S.A.

Can. J. Chem. Downloaded from www.nrcresearchpress.com by EESC ESCOLA DE ENGENHARIA on 09/08/12
For personal use only.

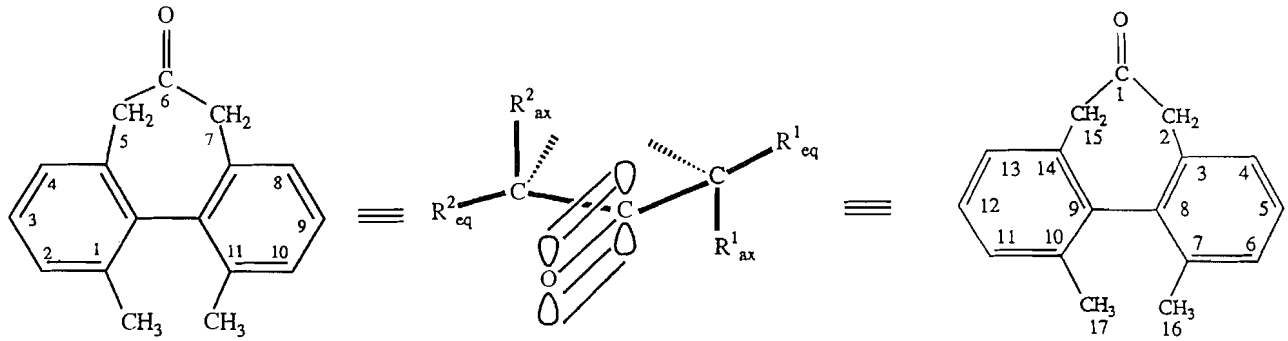

FIG. 1. The structure and three-dimensional representation for **1** and its chloro derivatives. For **2**, R_{eq} = Cl; for **3**, R_{ax} = R'_{ax} = Cl; for **4**, R_{eq} = R'_{eq} = Cl; for **5**, R_{eq} = R_{ax} = Cl; for **6**, R_{ax} = Cl and all unspecified R = H.

TABLE 1. X-ray crystal data for compounds **2–5**

	2	**3**	**4**	**5**
Empirical formula	$C_{17}H_{15}ClO$	$C_{17}H_{14}Cl_2O$	$C_{17}H_{14}Cl_2O$	$C_{17}H_{14}Cl_2O$
F.W.	270.75	305.20	305.20	305.20
Crystal dimensions (mm)	0.20 × 0.20 × 0.20	0.30 × 0.30 × 0.40	0.20 × 0.20 × 0.20	0.40 × 0.40 × 0.50
Space group	Monoclinic $P2_1/n$	Triclinic $P\bar{1}$	Monoclinic $C2/c$	Monoclinic Aa
Lattice parameters a (Å)	14.6176 (24)	8.0621 (12)	24.378 (5)	7.062 (3)
b (Å)	9.2072 (12)	14.0147 (9)	7.6691 (19)	26.884 (2)
c (Å)	21.323 (6)	14.3391 (15)	17.009 (4)	8.167 (3)
α (Å)		74.969 (7)		
β (Å)	105.354 (14)	75.190 (10)	115.287 (15)	106.83 (3)
γ (Å)		88.997 (9)		
V (Å^3)	2767.4 (8)	1510.7 (3)	2875.2 (11)	1484.0 (8)
Z	8	4	8	4
D_c (g/cm^3)	1.300	1.342	1.410	1.366
Maximum 2θ	45	45	50	45
No. of reflections measured	4178	4853	2587	2125
No. of unique reflections	3591	3931	2524	1928
No. of reflections with $I_{net} > 2.5\ \sigma(I_{net})$	1804	3446	1810	1762
Range for h	−15 to +15	−8 to +8	−28 to +26	−7 to +7
Range for k	0 to 19	0 to 14	0 to 9	0 to 28
Range for l	0 to 22	−14 to +15	0 to 20	0 to 8
For significant reflections R_f	0.072	0.0341	0.064	0.043
R_w	0.070	0.0274	0.075	0.032
For all reflections R_f	0.138	0.0405	0.100	0.047
R_w	0.111	0.0275	0.076	0.032
F(000)	567.94	631.94	1266.46	631.94
In the last D-map				
the deepest hole (e/Å^3)	−0.320	−0.170	−0.760	−0.160
the highest peak (e/Å^3)	0.290	0.200	1.510	0.150
S	0.82	6.62	3.08	4.3

one unit cell. Both molecules possess conformations that deviate by less than 3° from C_2 symmetry. The diequatorial α,α′-dichloroketone **4** shows the presence of an asymmetrically distorted central ring that places the two equatorial chlorines in very different conformations with respect to the carbonyl group. An unusually low value for the C1-C15-C14-C13 torsional angle of **4** is also seen. These distortions likely arise from the intermolecular forces between the proximate pairs of C—Cl bonds in the unit cell. Geminal dichloro derivative **5** deviates only slightly more from C_2 symmetry than does **3**. The above variations in conformation, like those found previously for the methyl derivatives of **1**, indicate some flexibility in the central ring.

Bond lengths and nonbonded distances

Table 3 describes some bond lengths and nonbonded distances, selected for their representation of unusual spatial effects. The most notable variations in bond lengths are the longer C—Cl bonds for the axial chlorines of **3** and **5** compared with those equatorially oriented in **2**, **4**, and **5**, whose averages were 1.805 and 1.785 Å, respectively. This type of correlation was recently noted by Laube and Ha (6) in a survey of X-ray data for several types of α-substituted ketones. From the observation of a maximum length for conformations in which the X-C-C-O dihedral angle is 90° and ab initio calculations in support thereof, they attributed the stereochemical correlation to a hyperconjugative interaction. The constancy in length of the C1—C2 bond (see Table 3) in the α haloketones **2**, **3**, and **5** provides no evidence for or against this interpretation. Alternatively, the longer C—Cl bond length for the axial C—Cl bonds may be attributed to the same factors responsible for the longer axial bonds in cyclohexanes and six-membered

Can. J. Chem. Downloaded from www.nrcresearchpress.com by EESC ESCOLA DE ENGENHARIA on 09/08/12
For personal use only.

TABLE 2. Torsional angles[a] (deg) obtained from the X-ray study

Bonds	1[b]	2*a*	2*b*	3*a*	3*b*	4	5
O-C1-C2-R_e	−12.3 (14)[c]	5.3 (3)	−6.3 (3)	17.8 (15)	−15.7 (15)	14.2 (2)	−16.0 (3)
O-C1-C2-R_a	97.4 (14)	121.3 (36)	−123.0 (36)	−90.5 (3)	92.1 (3)	−100.6 (5)	95.3 (6)
O-C1-C15-R'_e	−12.3 (14)	−34.0 (10)	33.1 (10)	21.2 (16)	−22.9 (15)	2.1 (2)	−13.0 (3)
O-C1-C15-R'_a	97.4 (14)	76.3 (42)	−75.4 (42)	−89.6 (3)	88.5 (3)	−113.3 (5)	101.4 (8)
O-C1-C2-C3	−138.8 (3)	−120.9 (8)	118.6 (8)	141.5 (4)	−140.5 (4)	141.1 (5)	−141.2 (8)
O-C1-C15-C14	−138.8 (3)	−153.5 (10)	156.1 (9)	142.9 (4)	−144.3 (4)	128.2 (5)	−137.3 (9)
C2-C1-C15-C14	41.2 (3)	27.7 (4)	−27.2 (4)	−38.2 (2)	37.8 (2)	−51.0 (3)	47.0 (5)
C3-C2-C1-C15	41.2 (3)	57.9 (5)	−58.5 (5)	−37.5 (2)	38.0 (2)	−39.7 (3)	34.5 (4)
C1-C2-C3-C4	109.9 (3)	98.8 (7)	−100.4 (7)	−114.9 (3)	114.7 (4)	−104.6 (4)	112.1 (7)
C1-C15-C14-C13	109.9 (3)	112.1 (8)	−112.3 (7)	−115.1 (4)	116.2 (3)	−96.7 (4)	108.5 (8)
C3-C8-C9-C14	56.8 (3)	57.4 (5)	−59.4 (5)	−58.4 (2)	57.5 (2)	−56.5 (3)	60.0 (5)
C7-C8-C9-C10	59.7 (4)	63.4 (6)	−64.4 (5)	−62.4 (3)	61.4 (2)	−65.2 (4)	62.3 (5)

[a]The relative sign is important with respect to the data for an individual structure.
[b]Taken from the symmetric crystalline form.
[c]Standard deviations appear in parentheses.

TABLE 3. Selected bond lengths (Å) and nonbonded distances

Bond	2*a*	2*b*	3*a*	3*b*	4	5
C1—O1	1.204 (10)[a]	1.195 (9)	1.199 (3)	1.199 (3)	1.186 (6)	1.195 (10)
C1—C2	1.514 (10)	1.519 (11)	1.522 (4)	1.517 (4)	1.547 (7)	1.522 (13)
C2—C3	1.514 (11)	1.524 (11)	1.493 (4)	1.498 (4)	1.518 (7)	1.513 (10)
C1—C15	1.490 (12)	1.500 (10)	1.518 (4)	1.524 (4)	1.546 (7)	1.511 (11)
C15—C14	1.499 (12)	1.508 (10)	1.482 (4)	1.501 (3)	1.518 (8)	1.517 (11)
C2—R_a	0.98 (7)	1.00 (7)	1.800 (3)	1.810 (3)	1.138 (5)	1.807 (6)
C2—R_e	1.778 (7)	1.781 (7)	0.91 (2)	0.92 (2)	1.782 (4)	1.792 (6)
C15—R'_a	0.96 (7)	1.00 (5)	1.810 (3)	1.802 (3)	1.117 (5)	1.117 (7)
C15—R'_e	0.92 (8)	1.01 (9)	0.95 (2)	0.98 (2)	1.776 (5)	1.108 (7)
C8—C9	1.482 (10)	1.503 (10)	1.493 (3)	1.493 (3)	1.500 (7)	1.478 (10)
C7—C16	1.480 (12)	1.498 (11)	1.498 (5)	1.513 (6)	1.515 (7)	1.510 (10)
C10—C17	1.539 (13)	1.507 (11)	1.510 (6)	1.510 (4)	1.497 (8)	1.484 (15)
C16---C17	3.28 (3.30)[b]	3.28	3.28 (3.30)[b]	3.24	3.23 (3.30)[b]	3.28 (3.30)[b]

[a]Standard deviations appear in parentheses.
[b]Calculated value by MMX.

heterocycles (7) (as revealed by their smaller onebond ^{13}C–H coupling constants). The origin of this correlation remains uncertain (7).

The last entry in Table 3 shows the distance between the two carbon atoms of the *ortho* methyl groups of the biphenyl moiety, which is consistently at 3.26 Å, a value considerably less than the distance normally seen between neighboring methyls. At this separation considerable strain is clearly created, resulting in distortions elsewhere in the hydrocarbon framework. Notably, the dihedral angle between the two aromatic rings has a value of 58°–62°, about 10° higher than in the biaryl ketone lacking these methyls (5). In addition, each of the two aromatic rings is forced to be nonplanar by the prevention of further increase in dihedral angle by the three-carbon bridge at the other *ortho* positions. This can be seen in Table 2 where the dihedral angles C7-C8-C9-C10 are consistently larger than the C3-C8-C9-C14 angles.

The van der Waals thickness of a benzene ring

In those compounds possessing an axial chlorine, the distance between the chlorine and the carbon atoms of the distal benzene is provded by the crystal data. In Table 4, it is seen that the chlorine is found as close as 3.05 Å from C-8 or C-9. For the axial chlorines the average observed distance of closest approach[6] of 3.14 Å is significantly less than the sum (3.65 Å) of the van der Waals' distances for a chlorine atom (1.8 Å) and an aromatic ring (half thickness 1.85 Å) (8). In this instance, in which a chlorine atom is compressed against the benzene ring, its estimated thickness seems too large.[7] This appears to be true in situations involving other single atoms. There is recent theoretical (9) and experimental (footnote 5 and ref. 10) evidence that a hydrogen atom also attains a very close approach.

Molecular mechanics calculations using MMX

MMX is a new program recently made available[5] for performing molecular mechanics calculations on an IBM 386 or equivalent, and a detailed description of its method of operation has appeared (12). This program, based on the MM2 force field of

[6]This distance is normally considered to be the most reliable estimate for the sum of the van der Waals' radii for two contiguous atoms. Any example of distance less than the accepted minimum is then considered as evidence for the presence of a bonding interaction (8). Allinger and Burkert have pointed out that, in certain situations, this distance may require adjustments that include contributions from attractive intramolecular interactions (11).

[7]A referee has suggested the alternative view that this be referred to as a case of spatial overcrowding.

Can. J. Chem. Downloaded from www.nrcresearchpress.com by EESC ESCOLA DE ENGENHARIA on 09/08/12
For personal use only.

Can. J. Chem. Downloaded from www.nrcresearchpress.com by EESC ESCOLA DE ENGENHARIA on 09/08/12
For personal use only.

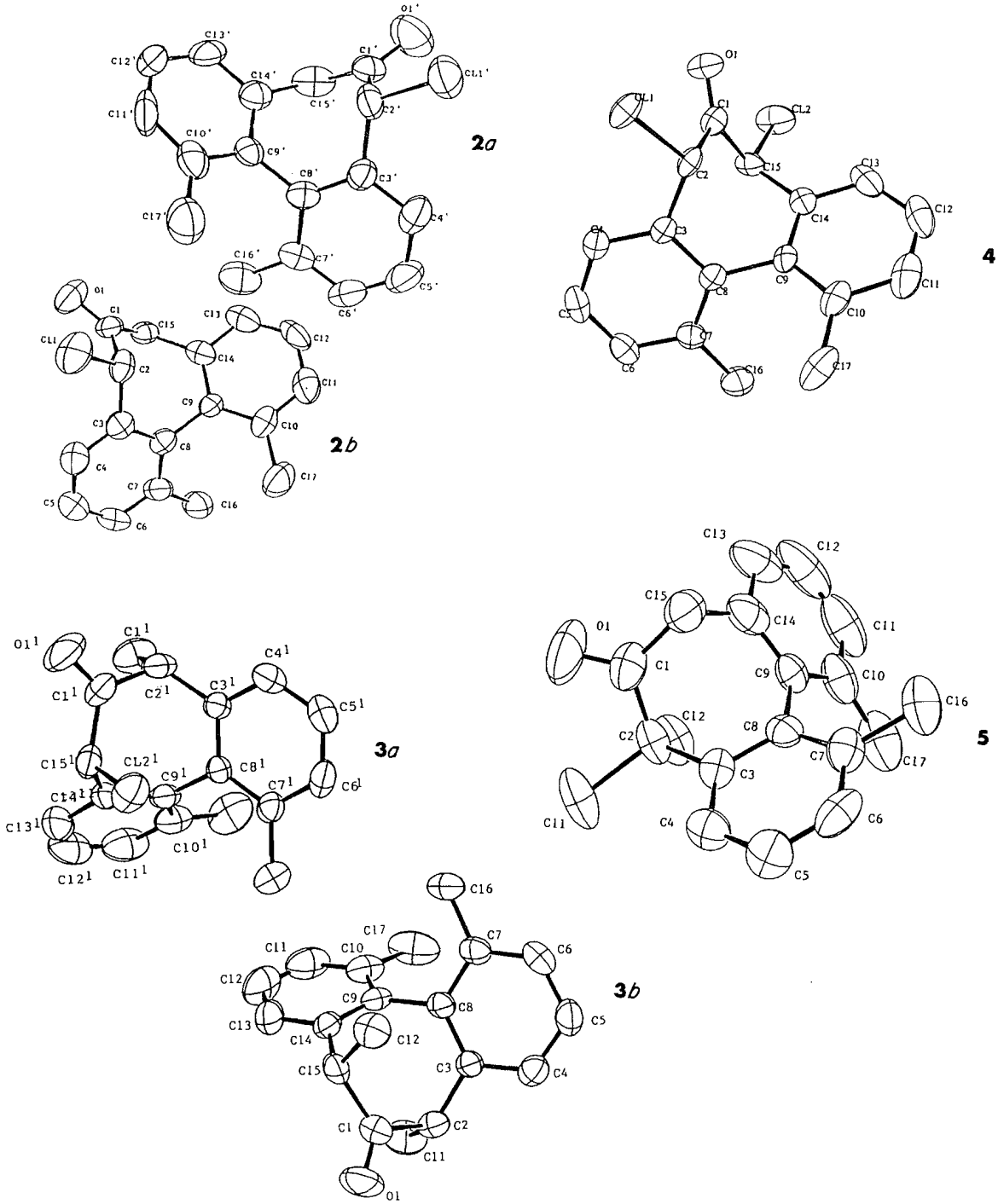

FIG. 2. The ORTEP plot for the crystal structures for **2–5**.

Allinger, has already gained considerable acceptance (13). As pointed out by Lipkowitz (14), any modifications of established programs such as MM2 should be adopted with some caution. Previously, we found that the conformational properties of **1** and its methyl derivatives as observed in the solid state could be reproduced satisfactorily using MMX. To further probe the reliability of MMX, we have used it to calculate the most stable conformations for the chloroketones **2–6**. The axial isomer **6**, though not attainable in crystalline form, was included for comparison. The resultant energies and torsional angles for the central ring are listed in Table 5. For **3** the torsional angles agree

TABLE 4. Selected chlorine–carbon distances (Å) obtained from crystal structures and calculated by MMX (in parentheses)

3a		**5**	
Cl(C2)...C9	3.21 (3.14)	Cl(C2)...C9	3.05 (3.00)
...C14	3.36 (3.35)	...C14	3.23 (3.19)
...C10	3.75 (3.64)	...C10	3.56 (3.45)
Cl(C15)...C8	3.17 (3.14)		
...C3	3.34 (3.35)		
...C7	3.69 (3.64)		

Can. J. Chem. Downloaded from www.nrcresearchpress.com by EESC ESCOLA DE ENGENHARIA on 09/08/12
For personal use only.

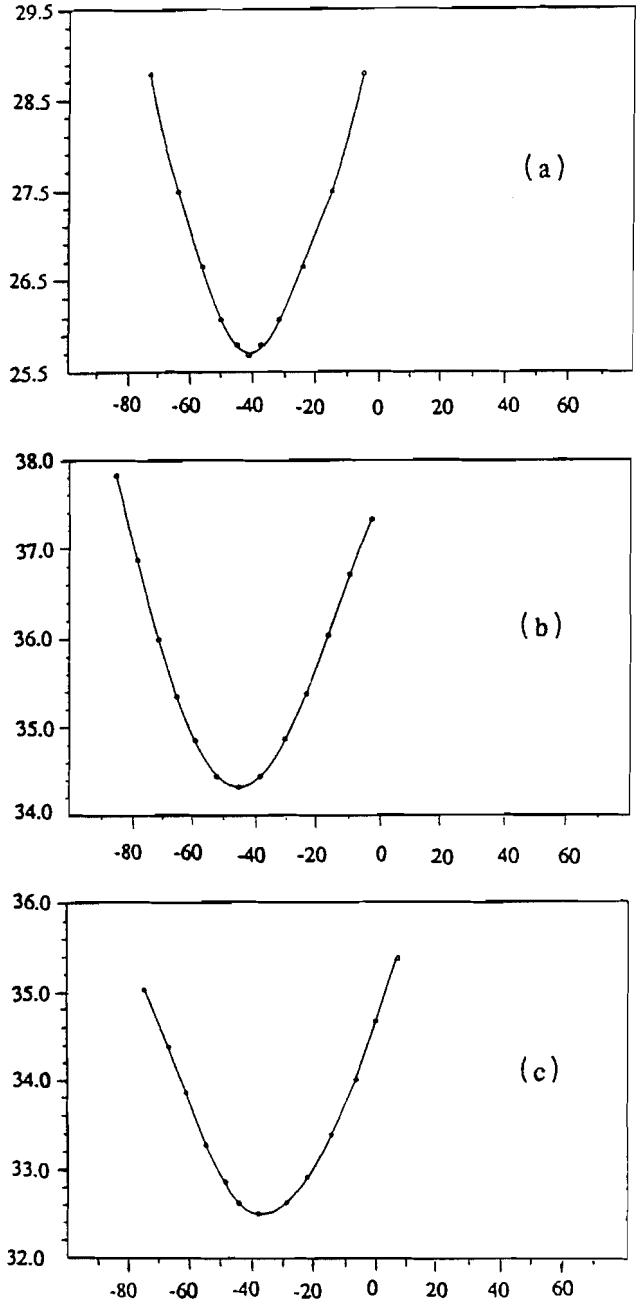

FIG. 3. A plot of energy (kcal/mol) versus the torsional angle (deg) at C1—C2 for **1**, **2**, and **6** (*a*)–(*c*).

well with those observed for its crystal structure. For **2**, **4**, and **5** we also calculated that conformation most closely corresponding to an observed crystal form. Table 5 gives their energies and torsional angles with the differences from the solid state values appearing in parentheses. The differences are generally small, less than 2°, except for several angles involving a C—H bond. The value for the energy of each structure calculated to match the X-ray structure differs by less than 0.5 kcal/mol from the calculated global minimum although the dihedral angle at C1—C2 changed by up to 12° in order to do so.

In addition to providing conformations compatible with those observed in the solid state, these calculations revealed considerable flexibility in the central ring. To compare the conformational mobility of the chloroketones **2–5** with the parent ketone **1**, we calculated their variation in energy over an 80° change in

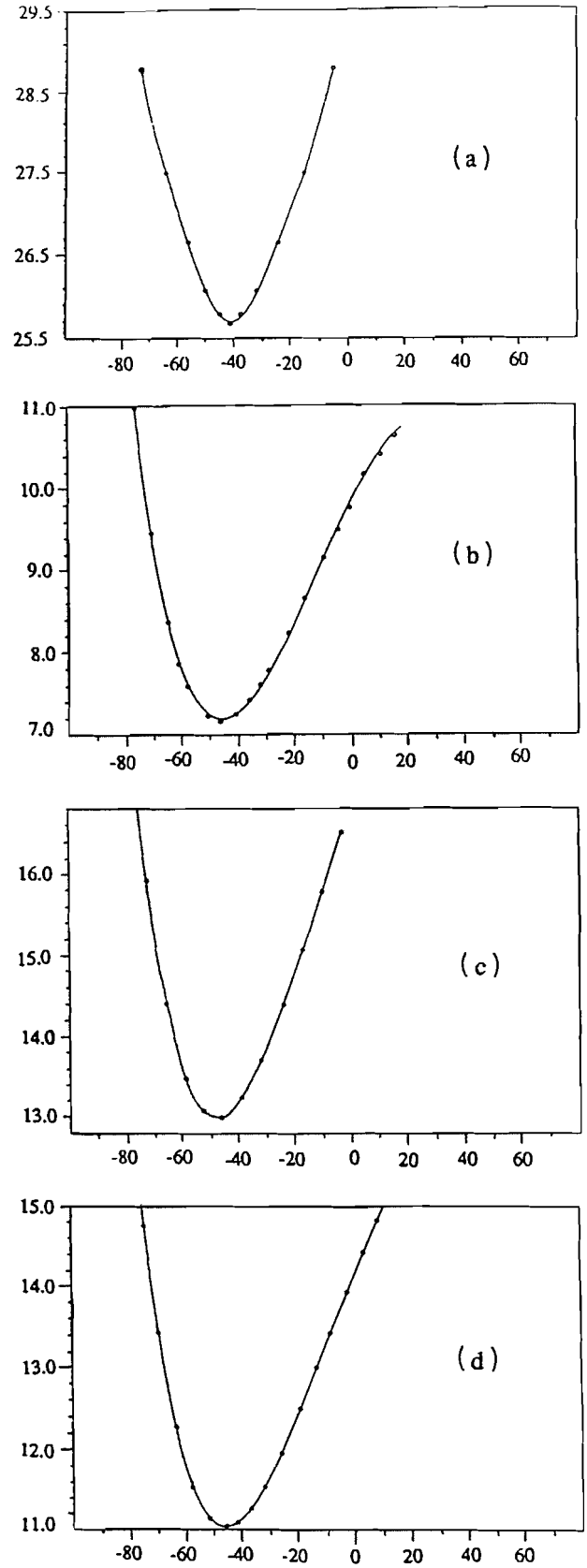

FIG. 4. A plot of energy (kcal/mol) versus the torsional angle (deg) for **1** (*a*), cyclohexanone (*b*), axial 2-chlorocyclohexanone, dielectric constant = 1.5 (*c*), axial 2-chlorocyclohexanone, dielectric constant = 6.0 (*d*).

TABLE 5. Calculated dihedral angles[a] (deg) for compounds **2–6**

	2	**2′**	**3**	**4**	**4′**	**5**	**5′**	**6**
Energy (kcal/mol)	34.29	34.77	39.63	43.79	44.20	43.80	44.18	32.49
O-C1-C2-R_c	5.5	−3.2 (2.1)[b]	19.4 (1.6)[c]	6.7	11.5 (2.7)[d]	27.3	18.4 (2.4)[e]	22.9
O-C1-C2-R_a	−107	−116.9 (4.4)	−93.7 (3.2)	−105.5	−100.3 (0.3)	−88.6	−97.6 (2.3)	−90.3
O-C1-C15-R'_e	17.0	27.6 (6.4)	21.0 (0.2)	6.8	3.0 (0.9)	4.9	13.5 (0.5)	12.8
O-C1-C15-R'_a	−99.2	−87 (10.7)	−92.1 (2.5)	−105.4	−110.2 (3.1)	−111.8	−102.6 (1.2)	−103.3
O-C1-C2-C3	135.2	123.4 (2.5)	139.8 (1.7)	136.5	142.0 (0.9)	151.6	142.7 (1.5)	143.3
O-C1-C15-C14	139.6	151.2 (2.2)	141.4 (1.5)	136.7	130.2 (2.0)	126.3	135.9 (1.4)	135.4
C2-C1-C15-C14	−40.6	−28.5 (0.8)	−38.7 (0.5)	−43.3	−50.0 (1.0)	−53.8	−47.2 (0.2)	−45.9
C3-C2-C1-C15	−44.6	−56.9 (1.0)	−40.1 (2.6)	−43.5	−37.9 (1.8)	−28.2	−34.1 (0.4)	−35.5
C1-C2-C3-C4	−107.9	−99.1 (0.3)	−115.8 (0.7)	−107.9	−109.1 (4.5)	−118.8	−116.8 (4.5)	−116.1
C1-C15-C14-C13	−111.6	−116.4 (4.3)	−115.8 (0.9)	−107.7	−97.2 (0.5)	−108.8	−111.1 (2.6)	−111.1
C3-C8-C9-C14	−58.4	−57.7 (0.3)	−58.2 (0.2)	−58.4	−57.5 (1.0)	−59.5	−59.2 (0.8)	−58.2
C7-C8-C9-C10	−62.7	−63 (0.4)	−62.3 (0.1)	−63.4	−63.4 (1.2)	−63.7	−63.5 (1.2)	−62.4

[a]These data represent the minimum energy conformations for **2–6**. The data for **2′**, **4′**, and **5′** were calculated to reproduce the conformations observed for **2**, **4**, and **5**, respectively.
[b]Difference with respect to crystal structure **2***a*.
[c]Difference with respect to crystal structure **3***a*.
[d]Difference with respect to crystal structure **4**.
[e]Difference with respect to crystal structure **5**.

the C3-C2-C1-C15 dihedral angle from the most stable conformation. In contrast to the parent 1,3-cycloheptadiene (15), only one conformation could be found for **1** or any of its derivatives, undoubtedly due to the aforementioned effect of the *ortho* methyl groups in maintaining the 60° dihedral angle between the rings of the biphenyl moiety. The flexibility of **1** is shown in Fig. 3(*a*), which depicts its variation in energy with change in dihedral angle, as previously reported (5). This curve shows the presence of a shallow energy well, allowing deviation from the minimum energy conformation by about 15° for a 1 kcal/mol change in energy. The energy dependence of equatorial monochloroketone **2** versus dihedral angle is plotted in Fig. 3(*b*). This curve shows a slightly less energetic dependence on dihedral angle (i.e., greater flexibility than **1**) as does that for the axial isomer **6** shown in Fig. 3(*c*). Curves calculated for the disubstituted derivatives **3** and **4** showed comparable shapes. Thus all chloro derivatives exhibit greater flexibility than **1**, just as we had found previously for its α methyl derivatives. One other comparison is noteworthy. The axial and diaxial isomers have greater calculated stabilities than the mono and diequatorial derivatives of **1**. The calculated difference between axial **6** and equatorial **2** is 1.7 kcal/mol, which agrees well with that recently calculated for the two rotamers of 2-chloropropionaldehyde, which have almost identical stereochemistry (16). The difference in stability was attributed mainly to a difference in the dipolar interactions as previously seen for 2-chlorocyclohexanone (17). The close correspondence of these results obtained for **6** and **2** with those for 2-chloropropionaldehyde (by ab initio methods) provides support for the MMX method as applied by us.

For comparison with **1** we also calculated the energy profiles versus dihedral angle at C1—C2 for cyclohexanone and its axial and equatorial conformational isomers. Figure 4 shows the results for **1** (curve *a*), cyclohexanone (curve *b*), and axial 2-chlorocyclohexanone (curve *c*). The curve for the equatorial conformer is not shown as it is very similar to that in (*c*). In fact all the curves have comparable profiles. In the MMX calculations, a value of 1.5 was used for the dielectric constant, *D*, of the medium. Selection of the appropriate value for this constant in any calculation of polar interactions has been a longstanding problem.[8] As a simple[9] check on the importance of the choice of dielectric constant on the plot of energy versus dihedral angle, we repeated the calculations on axial 2-chlorocyclohexanone us-ing a value of 6 for *D*. The resultant curve in Fig. 4(*d*) shows that the position of the minimum in energy is unaltered while the rigidity is diminished slightly with the increase in dielectric constant.

Summary

X-ray crystallography has confirmed the conformational and configurational properties in the α chloroketones **2–5**. The degree of rigidity in **1–5** has been estimated by calculation of the variation in the strain energy as a function of the dihedral angle at C1—C2. The parent ketone has the advantage[10] over cyclohexanone as a model system possessing slighter greater rigidity. Its chloro derivatives, like those of cyclohexanone, exhibit slightly reduced rigidity. At the same time it is important to bear in mind that none of these carbonyl compounds merits the description "rigid" in the strict sense of the word.

Experimental

The synthesis of compounds **2–5** has been reported previously (4*b*). Recrystallization of each of these from methylene chloride – hexanes gave suitable single crystals for X-ray determination.

A summary of the crystal data for compounds **2–5** is given in Table 1. The diffraction intensities were collected on a Nonius diffractometer at 295 K (except for **4** collected on a Rigaku diffractometer at 143 K) with MoKα radiation (λ = 0.7093 Å) using the θ/2θ scan technique with profile analysis (20). A graphite monochromator was used to achieve the monochromatic radiation. All the data were collected at a speed of 4° in ω/min. The standards were measured after every 150 reflections, no crystal decay was noticed. The space group is determined by systematic absence. Cell dimensions were obtained from 24

[8]The Kirkwood–Westheimer approach to the solution of this problem is reviewed by Hine (18).

[9]The work of Wiberg and Wong (19) illustrates the approximate nature of quantitative evaluation of solvent effect even in using ab initio calculations with the reaction field model.

[10]A major advantage for **1** is its single energy minimum. In contrast, cyclohexanone is in equilibrium with a boat conformation only 3–4 kcal/mol higher in energy.

Can. J. Chem. Downloaded from www.nrcresearchpress.com by EESC ESCOLA DE ENGENHARIA on 09/08/12
For personal use only.

TABLE 6. Coordinates of non-hydrogen atoms

Atom	x	y	z	B_{eq}
		Compound **2**		
Cl1	0.91677(16)	0.99887(24)	0.09629(11)	5.25(11)
Cl1′	0.40712(17)	0.2321 (3)	0.08011(13)	6.18(12)
O1	0.9304 (5)	0.9869 (8)	0.2328 (3)	7.0 (3)
O1′	0.4207 (5)	0.2157 (7)	0.2170 (3)	6.8 (3)
C1	0.8826 (5)	0.8867 (9)	0.2063 (4)	4.1 (4)
C2	0.8581 (5)	0.8680 (8)	0.1332 (4)	3.8 (3)
C3	0.7510 (5)	0.8699 (8)	0.1087 (3)	3.6 (3)
C4	0.7041 (6)	0.9957 (8)	0.0827 (4)	4.5 (4)
C5	0.6044 (6)	0.9961 (9)	0.0690 (4)	5.2 (4)
C6	0.5572 (5)	0.8791 (10)	0.0833 (4)	5.1 (4)
C7	0.6031 (5)	0.7507 (9)	0.1071 (3)	3.8 (3)
C8	0.7034 (5)	0.7465 (8)	0.1201 (3)	3.6 (3)
C9	0.7566 (5)	0.6147 (8)	0.1484 (3)	3.4 (3)
C10	0.7514 (5)	0.4805 (8)	0.1157 (4)	4.4 (4)
C11	0.8091 (6)	0.3690 (8)	0.1460 (5)	6.2 (6)
C12	0.8702 (6)	0.3800 (9)	0.2072 (5)	5.6 (4)
C13	0.8783 (5)	0.5106 (10)	0.2377 (4)	4.9 (4)
C14	0.8243 (5)	0.6300 (9)	0.2097 (4)	4.0 (4)
C15	0.8422 (5)	0.7755 (11)	0.2421 (4)	5.2 (4)
C16	0.5461 (6)	0.6284 (11)	0.1214 (4)	5.7 (5)
C17	0.6861 (8)	0.4655 (10)	0.0464 (5)	6.6 (5)
C1′	0.3779 (5)	0.3227 (8)	0.1949 (4)	4.0 (3)
C2′	0.3530 (5)	0.3587 (8)	0.1228 (4)	4.2 (4)
C3′	0.2452 (5)	0.3638 (8)	0.0985 (3)	3.8 (3)
C4′	0.1948 (5)	0.2468 (9)	0.0651 (4)	4.3 (4)
C5′	0.0975 (6)	0.2496 (10)	0.0510 (4)	5.3 (4)
C6′	0.0506 (5)	0.3640 (10)	0.0708 (4)	4.8 (4)
C7′	0.0995 (5)	0.4833 (9)	0.1026 (3)	4.0 (3)
C8′	0.1991 (5)	0.4851 (8)	0.1157 (3)	3.2 (3)
C9′	0.2586 (5)	0.6093 (7)	0.1498 (3)	3.1 (3)
C10′	0.2532 (5)	0.7495 (8)	0.1230 (4)	4.2 (4)
C11′	0.3107 (6)	0.8591 (9)	0.1578 (5)	5.2 (4)
C12′	0.3727 (5)	0.8318 (9)	0.2172 (4)	5.3 (4)
C13′	0.3809 (5)	0.6933 (10)	0.2425 (4)	4.9 (4)
C14′	0.3247 (5)	0.5795 (8)	0.2099 (3)	3.6 (3)
C15′	0.3401 (4)	0.4267 (8)	0.2361 (3)	3.5 (3)
C16′	0.0449 (6)	0.6024 (10)	0.1241 (4)	5.1 (4)
C17′	0.1876 (7)	0.7845 (10)	0.0574 (4)	6.0 (5)
		Compound **3**		
Cl1	0.22571(10)	1.12359(5)	0.15950(5)	5.80(4)
Cl2	−0.10386(9)	0.84627(5)	0.42794(5)	4.87(4)
Cl1′	0.40567(8)	0.43651(5)	0.42764(5)	4.24(3)
Cl2′	0.72621(10)	0.29311(5)	0.15839(5)	5.33(4)
O1	−0.13116(24)	1.08824(13)	0.34618(16)	7.51(13)
O1′	0.37938(21)	0.23450(12)	0.34788(14)	6.02(11)
C1	−0.0281 (3)	1.03277(16)	0.31706(18)	4.16(13)
C2	0.1636 (3)	1.05933(15)	0.29032(17)	3.76(14)
C3	0.2716 (3)	0.97493(15)	0.31984(16)	2.95(12)
C4	0.3565 (3)	0.97876(17)	0.39150(18)	4.17(14)
C5	0.4414 (3)	0.89953(18)	0.43122(18)	4.56(15)
C6	0.4380 (3)	0.81470(17)	0.40152(18)	4.16(13)
C7	0.3542 (3)	0.80691(16)	0.32994(17)	3.32(12)
C8	0.2750 (3)	0.89002(15)	0.28579(15)	2.72(12)
C9	0.1887 (3)	0.88704(15)	0.20599(16)	3.24(12)
C19	0.2838 (3)	0.87146(17)	0.11552(18)	4.53(15)
C11	0.1983 (4)	0.86527(20)	0.04454(19)	6.53(19)
C12	0.0257 (4)	0.87529(19)	0.06077(20)	7.12(21)
C13	−0.0677 (4)	0.89507(18)	0.14747(21)	5.68(17)
C14	0.0133 (3)	0.90228(15)	0.22129(17)	3.60(13)
C15	−0.0891 (3)	0.93431(17)	0.30846(19)	4.04(13)
C16	0.3411 (3)	0.70814(17)	0.30948(20)	5.11(16)

TABLE 6. (*concluded*)

Atom	x	y	z	B_{eq}
C17	0.4772 (4)	0.86798(21)	0.08962(21)	6.99(18)
C1′	0.4781 (3)	0.30544(16)	0.31817(17)	3.50(12)
C2′	0.4115 (3)	0.40829(16)	0.31063(17)	3.53(13)
C3′	0.5052 (3)	0.48624(15)	0.21994(16)	3.34(12)
C4′	0.4153 (3)	0.52968(18)	0.15061(20)	5.18(17)
C5′	0.4972 (4)	0.59395(19)	0.06134(20)	6.78(20)
C6′	0.6698 (4)	0.61355(18)	0.03971(19)	6.23(19)
C7′	0.7651 (3)	0.57196(16)	0.10727(17)	4.42(15)
C8′	0.6808 (3)	0.50983(14)	0.19970(15)	3.03(12)
C9′	0.7759 (3)	0.46644(15)	0.27616(15)	2.76(11)
C10′	0.8587 (3)	0.52835(16)	0.31534(16)	3.32(12)
C11′	0.9502 (3)	0.48481(17)	0.38434(17)	3.92(13)
C12′	0.9587 (3)	0.38466(17)	0.41631(18)	4.06(14)
C13′	0.8716 (3)	0.32399(16)	0.38167(17)	3.51(12)
C14′	0.7788 (3)	0.36394(15)	0.31279(15)	2.80(12)
C15′	0.6709 (3)	0.29222(15)	0.28856(16)	3.34(12)
C16′	0.9581 (4)	0.59132(20)	0.07558(20)	6.76(18)
C17′	0.8423 (3)	0.63898(17)	0.29158(19)	4.95(16)
		Compound **4**		
Cl1	0.19931(5)	0.22635(18)	0.20402(9)	3.11(6)
Cl2	0.42755(6)	0.3695 (3)	0.44458(8)	4.38(8)
O1	0.29693(16)	0.3100 (5)	0.37124(22)	3.49(19)
C1	0.31628(21)	0.2735 (7)	0.3202 (3)	2.49(24)
C2	0.27752(19)	0.1980 (6)	0.2287 (3)	2.26(23)
C3	0.29555(19)	0.2721 (6)	0.1603 (3)	2.11(20)
C4	0.26082(21)	0.3965 (7)	0.1006 (3)	2.66(23)
C5	0.28090(24)	0.4669 (7)	0.0419 (3)	3.2 (3)
C6	0.33592(24)	0.4151 (7)	0.0439 (3)	3.1 (3)
C7	0.37232(22)	0.2938 (7)	0.1049 (3)	2.67(25)
C8	0.35125(20)	0.2156 (6)	0.1614 (3)	2.13(21)
C9	0.38760(19)	0.0820 (6)	0.2277 (3)	2.18(23)
C10	0.40109(21)	−0.0820 (7)	0.2034 (4)	3.0 (3)
C11	0.43280(23)	−0.2009 (7)	0.2696 (4)	4.2 (3)
C12	0.44926(23)	−0.1610 (8)	0.3562 (4)	4.4 (3)
C13	0.43521(22)	−0.0016 (8)	0.3799 (4)	3.8 (3)
C14	0.40452(20)	0.1202 (7)	0.3161 (3)	2.65(23)
C15	0.38358(21)	0.2930 (7)	0.3372 (3)	2.70(25)
C16	0.43451(25)	0.2540 (8)	0.1095 (4)	3.7 (3)
C17	0.3808 (3)	−0.1358 (8)	0.1106 (4)	4.4 (3)
		Compound **5**		
Cl1	−0.28904	−0.04879	−0.05134	7.42(13)
Cl2	−0.1802 (3)	−0.14898(6)	−0.0856 (4)	6.01(11)
O	−0.1147 (9)	−0.04960(25)	−0.3167 (8)	9.8 (4)
C1	−0.0100 (11)	−0.0729 (3)	−0.2008 (11)	5.4 (4)
C2	0.1995 (11)	−0.0861 (3)	−0.1963 (10)	5.3 (4)
C3	0.2543 (10)	−0.1392 (3)	−0.1390 (12)	5.2 (4)
C4	0.2762 (12)	−0.1744 (4)	−0.2560 (11)	7.7 (6)
C5	0.3076 (17)	−0.2229 (5)	−0.2074 (19)	9.5 (8)
C6	0.3195 (13)	−0.2362 (3)	−0.0426 (19)	8.0 (7)
C7	0.2978 (11)	−0.2027 (3)	0.0791 (13)	5.3 (5)
C8	0.2701 (9)	−0.1524 (3)	0.0290 (10)	3.8 (3)
C9	0.2551 (10)	−0.11304(23)	0.1509 (9)	3.5 (3)
C10	0.4145 (9)	−0.10353(24)	0.2954 (10)	4.1 (3)
C11	0.3946 (11)	−0.0665 (3)	0.4089 (9)	4.9 (4)
C12	0.2266 (13)	−0.03931(25)	0.3840 (10)	5.2 (4)
C13	0.0695 (10)	−0.04685(23)	0.2396 (9)	4.5 (4)
C14	0.0820 (9)	−0.08345(22)	0.1215 (9)	3.7 (3)
C15	−0.0793 (9)	−0.08687(23)	−0.0469 (11)	4.5 (4)
C16	0.2901 (11)	−0.2206 (3)	0.2491 (13)	7.3 (6)
C17	0.6122 (10)	−0.1290 (3)	0.3267 (11)	6.0 (4)

Can. J. Chem. Downloaded from www.nrcresearchpress.com by EESC ESCOLA DE ENGENHARIA on 09/08/12
For personal use only.

reflections with 2θ in the range 30°–40° for **2**, and in the range 40°–45° for **3**; and from 25 reflections in the range 40°–50° for **4**, and from 21 reflections in the range 40°–45° for **5**. Lorentz and polarization factors were applied but no corrections were made for absorption.

The structures were solved by the direct method. All the atoms were refined anisotropically except for the hydrogen atoms, which were found by Fourier map for compounds **2** and **3**. For compounds **4** and **5**, the positions of the hydrogens were calculated. All the calculations were performed with the NRCVAX Crystal Structure Package (21). The refined atomic parameters are listed in Table 6.[11]

The calculation of steric energies for the compounds in this paper was carried out using PCMODEL, V4.0, and the MMX program contained therein.[5] In deriving the conformation of lowest energy we used the C_2 symmetric form as starting point. To obtain the variation in energy as a function of dihedral angle at the C1—C2 bond, this bond was fixed at each new value (using 4° intervals) and the energy for this specifically constrained conformation minimized. Energy values for changes in dihedral angle over twice the range plotted in Fig. 3 revealed no other conformational minimum. Each calculated total energy included stretching, bending, stretching–bending, torsional, van der Waals, and electostatic contributions. Except where noted, a value of 1.5 was used for the dielectric constant.

Acknowledgment

We wish to thank the Natural Sciences and Engineering Research Council of Canada for their financial support.

1. K. Mislow, M.A.W. Glass, R.E. O'Brien, P. Rutkin, D.H. Steinberg, J. Weiss, and C. Djerassi. J. Am. Chem. Soc. **84**, 1455 (1962).

[11]Tables of all bond lengths, bond angles, atomic coordinates, mean plane data, anisotropic parameters, and structure factors for **2**, **3**, **4**, and **5** can be purchased from: The Depository of Unpublished Data, Document Delivery, CISTI, National Research Council Canada, Ottawa, ON K1A 0S2, Canada.

Tables of bond lengths and angles and atomic coordinates have also been deposited with the Cambridge Crystallographic Data Centre, and can be obtained on request from The Director, Cambridge Crystallographic Data Centre, University Chemical Laboratory, 12 Union Road, Cambridge, CB2 1EZ, U.K.

2. K. Mislow and A.J. Gordon. J. Am. Chem. Soc. **85**, 3521 (1963).
3. R.R. Fraser and P.J. Champagne. Can. J. Chem. **54**, 3809 (1976).
4. (*a*) R.R. Fraser and M. Stanciulescu. J. Am. Chem. Soc. **109**, 1580 (1987); (*b*) R.R. Fraser, F. Kong, M. Stanciulescu, Y.-D. Wu, and K.N. Houk. J. Org. Chem. **58**, 4431 (1993).
5. R.R. Fraser, C. Bensimon, F. Kong, and X. Wu. Can. J. Chem. **71**, 685 (1993).
6. T. Laube and T.K. Ha. J. Am. Chem. Soc. **110**, 5511 (1988).
7. S. Wolfe and C.-K. Kim. Can. J. Chem. **69**, 1408 (1991).
8. J.D. Dunitz. X-ray analysis and the structure of organic molecules. Cornell University Press, Ithaca, N.Y. 1979. p. 339. Although the exact source of the quoted value was not given, it likely represented contributions from "stacked" aromatic rings.
9. (*a*) P. Linse. J. Am. Chem. Soc. **114**, 4366 (1992); (*b*) W.L. Jorgenson and D.L. Severance. J. Am. Chem. Soc. **112**, 4768 (1990).
10. J.E. Cochran, T.J. Parrott, B.J. Whitlock, and H.W. Whitlock. J. Am. Chem. Soc. **114**, 2270 (1992).
11. U. Burkert and N.L. Allinger. Molecular mechanics. ACS Monogr. 177, 1982.
12. J.J. Gajewski, K.E. Gilbert, and J. McKelvey. Adv. Mol. Model. **2**, 65 (1990).
13. (*a*) W.-N. Chou, J.B. White, and W.B. Smith. J. Am. Chem. Soc. **114**, 4658 (1992); (*b*) T.G. Lease and K.J. Shea. J. Am. Chem. Soc. **115**, 2248 (1993); (*c*) D.A. Forsythe and S.M. Johnson. J. Am. Chem. Soc. **115**, 3364 (1993).
14. K.B. Lipkowitz. *In* The conformational analysis of cyclohexenes, cyclohexadienes and related aromatic compounds. *Edited by* P.W. Rabideau. VCH Publishers, New York. 1987. Chap. 5.
15. (*a*) G. Favini, A. Maggi, and R. Todeschini. J. Mol. Struct. **105**, 17 (1983); (*b*) S. Saebo and J.E. Boggs. J. Mol. Struct. **87**, 365 (1982).
16. S. Frenking, K.F. Kohler, and M.T. Reetz. Tetrahedron, **47**, 8991 (1991).
17. L. Dosen-Micovic and N.L. Allinger. Tetrahedron, **34**, 3885 (1978).
18. J. Hine. Structural effects on equilibria in organic chemistry. John Wiley and Sons, Inc., New York. 1975. p. 35.
19. K.B. Wiberg and M.W. Wong. J. Am. Chem. Soc. **115**, 1078 (1993).
20. D.F. Grant and E.J. Gabe. J. Appl. Crystallogr. **11**, 114 (1978).
21. E.J. Gabe, F.L. Lee, and Y. Lepage. J. Appl. Crystallogr. **22**, 284 (1989).

Can. J. Chem. Downloaded from www.nrcresearchpress.com by EESC ESCOLA DE ENGENHARIA on 09/08/12
For personal use only.

The volumetric and thermochemical properties of aqueous solutions of L-valine, L-leucine, and L-isoleucine at 288.15, 298.15, 313.15, and 328.15 K

MICHELLE M. DUKE, ANDREW W. HAKIN,[1] ROBERT M. MCKAY, AND KATHRYN E. PREUSS
Department of Chemistry, University of Lethbridge, 4401 University Drive, Lethbridge, AB T1K 3M4, Canada

Received September 22, 1993

MICHELLE M. DUKE, ANDREW W. HAKIN, ROBERT M. MCKAY, and KATHRYN E. PREUSS. Can. J. Chem. **72**, 1489 (1994).

Densities and volumetric heat capacities have been measured for aqueous solutions of L-valine, L-leucine, and L-isoleucine at 288.15, 298.15, 313.15, and 328.15 K. These data have been used to calculate apparent molar volumes, $V_{2,\phi}$, and apparent molar heat capacities, $C_{p,2,\phi}$, which in turn have been used to obtain standard state volumes, $\bar{V}_2^0$, and standard state heat capacities, $\bar{C}_{p,2}^0$, for each aqueous amino acid system. Helgeson, Kirkham, and Flowers equations, for neutral organics in water, have been used to model the calculated standard state volumes and heat capacities of the amino acids as a function of temperature at constant pressure. The results of our fitting procedures may be used to predict the behaviour of $\bar{V}_2^0$ and $\bar{C}_{p,2}^0$ for the selected amino acid systems outside of the temperature range utilised in this investigation.

MICHELLE M. DUKE, ANDREW W. HAKIN, ROBERT M. MCKAY, et KATHRYN E. PREUSS. Can. J. Chem. **72**, 1489 (1994).

On a mesuré les densités et la capacités calorifiques volumétriques de solutions aqueuses de L-valine, de L-leucine, et de L-isoleucine, à 288,15, 298,15, 313,15, et 328,15 K. On a utilisé ces données pour calculer les volumes molaires apparents, $V_{2,\phi}$, ainsi que les capacités calorifiques molaires apparentes, $C_{p,2,\phi}$, qui ont été utilisées à leur tour pour déterminer les volumes de l'état de référence, $\bar{V}_2^0$, ainsi que les capacités calorifiques de l'état de référence, $\bar{V}_{p,2}^0$, de chaque système aquence d'acide aminé. On a utilisé les équations de Helgeson, Kirkham et Flowers, développées pour les composés organiques neutres dans l'eau, comme modèle des volumes et des capacités calorifiques calculés de l'état de référence des acides aminés en fonction de la température, à pression constante. On peut utiliser les résultats de nos procédures d'ajustement pour prédire le comportement des valeurs de $V_{2,\phi}^0$ et $C_{p,2,\phi}$ de systèmes d'acides aminés choisis à des températures à l'extérieur de la plage utilisée dans notre étude.

[Traduit par la Rédaction]

Introduction

The thermodynamic properties of aqueous amino acid systems have been investigated by several authors (1–7). Many previous investigators restricted their attention to ambient temperature and pressure conditions, 298.15 K and 1 atm. However, currently there is considerable interest in extending the temperature and pressure range of thermodynamic data for amino acid systems (7–10). Shock has recently applied semi-empirical modelling procedures to aqueous amino acid systems to yield estimates of thermodynamic properties up to 1000°C and 5 kbar (1 bar = 1000 000 Pa). These data are some of the essential building blocks that must be used in order to comprehend the documented existence of high temperature and pressure life forms (8).

Many of the Helgeson, Kirkham, and Flowers (HKF) equations for estimating standard state volumes and heat capacities of neutral organic species in aqueous solution are constructed using thermodynamic data collected at 298.15 K and 1 atm. To increase the accuracy and utility of these models we have collected density and volumetric heat capacity data for L-valine, L-leucine, and L-isoleucine in water at 288.15, 298.15, 313.15, and 328.15 K. These data have been used to calculate apparent molar volumes and heat capacities, which in turn have been used to calculate standard state volumes and heat capacities for each aqueous amino acid system as a function of temperature. The temperature dependencies of the standard state properties have been modelled using constant pressure variants of revised HKF equations for neutral organic species in water.

Experimental

L-Valine (99 + %), and L-leucine (99 + %), and L-isoleucine (99 + %), were obtained from Sigma Chemicals Limited. The acids were purified by repeated recrystallisation from water and were dried and stored over phosphorus pentoxide in a vacuum oven set at 50°C. The NMR spectra of the amino acids were obtained on a Brüker 250 MHz instrument using D_2O as an internal standard. The recorded spectra were in excellent agreement with the reference spectra (11).

All solutions were prepared by weight on the molality concentration scale using bi-distilled, degassed water. Solutions were stored in sealable 125 mL Nalgene bottles.

Densities were measured relative to water with a Sodev O2D vibrating tube, flow densitometer (12). This experimental apparatus routinely measures densities with part per million precision. Volumetric heat capacities were measured relative to water using a Picker flow microcalorimeter (13).

Details of the densitometer, the flow microcalorimeter, and the procedures used in their calibrations have been described previously (7, 14).

Results and discussion

Densities at 288.15, 298.15, 313.15, and 328.15 K for solutions of L-valine, L-leucine, and L-isoleucine in water are reported in Tables 1, 2, and 3, respectively. Apparent molar volumes, $V_{2,\phi}$, were calculated from these data using the equation:

$$[1] \qquad V_{2,\phi} = \left[\frac{M}{\rho}\right] - \left[\frac{\rho - \rho_1^0}{m\rho\rho_1^0}\right]$$

were m is the molality of the solution, M is the molecular weight of the solute, ρ_1^0 is the density of pure water at the temperature of interest (15), and ρ is the density of the solution under study. Calculated apparent molar volumes are reported for L-valine, L-leucine, and L-isoleucine in Tables 1, 2, and 3, respectively.

Specific heat capacity data for L-valine, L-leucine, and L-isoleucine in water were calculated from volumetric heat ca-

[1]Author to whom correspondence should be addressed.

Can. J. Chem. Downloaded from www.nrcresearchpress.com by EESC ESCOLA DE ENGENHARIA on 09/08/12
For personal use only.

Can. J. Chem. Downloaded from www.nrcresearchpress.com by EESC ESCOLA DE ENGENHARIA on 09/08/12
For personal use only.

TABLE 1. Densities, ρ, apparent molar volumes, $V_{2,\phi}$, and apparent molar heat capacities, $C_{p,2,\phi}$, of aqueous solutions of L-valine at 288.15, 298.15, 313.15, and 328.15 K[a]

m (mol kg^{-1})	ρ (g cm^{-3})	$V_{2,\phi}$ (cm^3 mol^{-1})	$C_{p,2,\phi}$ (J K^{-1} mol^{-1})
		288.15 K	
0.3422	1.008073	90.13 (0.01)	249.9 (0.2)
0.2835	1.006575	90.12 (0.02)	295.9 (0.3)
0.1933	1.004243	90.10 (0.03)	295.0 (0.4)
0.1119	1.002096	90.12 (0.05)	293.1 (0.6)
0.0845	1.001371	90.08 (0.06)	294.6 (0.8)
0.0612	1.000749	90.07 (0.08)	293.9 (1.2)
0.0401	1.000185	90.01 (0.13)	291.9 (1.8)
0.2499	1.005703	90.15 (0.02)	294.7 (0.3)
0.1670	1.003550	90.12 (0.03)	296.2 (0.4)
0.0766	1.001160	90.09 (0.07)	293.7 (0.9)
0.0336	1.000008	90.09 (0.15)	292.1 (2.1)
0.0188	0.999621	89.50 (0.27)	274.1 (3.7)
0.0237	0.999744	89.94 (0.21)	289.1 (3.0)
0.2499	1.005709	90.12 (0.02)	295.5 (0.3)
0.1670	1.003551	90.11 (0.03)	295.5 (0.4)
0.0766	1.001160	90.09 (0.07)	295.1 (0.9)
		298.15 K	
0.3422	1.005827	90.84 (0.02)	307.5 (0.2)
0.2835	1.004365	90.82 (0.02)	305.7 (0.3)
0.1933	1.002080	90.81 (0.03)	307.8 (0.4)
0.1119	0.999979	90.81 (0.05)	306.4 (0.6)
0.0845	0.999265	90.84 (0.06)	306.0 (0.8)
0.0612	0.998659	90.81 (0.08)	306.1 (1.2)
0.0401	0.998115	90.54 (0.13)	299.5 (1.8)
0.2499	1.003504	90.87 (0.02)	305.9 (0.3)
0.1670	1.001401	90.83 (0.03)	307.6 (0.4)
0.0766	0.999062	90.80 (0.07)	304.8 (0.9)
0.0336	0.997934	90.81 (0.15)	308.4 (2.1)
0.0188	0.997551	90.49 (0.27)	304.1 (3.7)
0.0237	0.997674	90.73 (0.21)	305.4 (3.0)
0.2499	1.003504	90.86 (0.02)	306.1 (0.3)
0.1670	1.001400	90.83 (0.03)	306.3 (0.4)
0.0336	0.997934	90.81 (0.15)	311.4 (2.1)
0.2499	1.003506	90.86 (0.02)	305.1 (0.3)
0.1670	1.001402	90.82 (0.03)	305.7 (0.4)
0.0766	0.999062	90.80 (0.07)	307.9 (0.9)
0.0336	0.997939	90.66 (0.15)	306.0 (2.1)
		313.15 K	
0.2499	0.998518	91.83 (0.02)	317.0 (0.3)
0.1670	0.996468	91.78 (0.03)	320.8 (0.4)
0.0766	0.994192	91.67 (0.07)	316.9 (0.9)
0.0336	0.993088	91.67 (0.15)	314.4 (2.1)
0.0188	0.992706	91.71 (0.27)	321.0 (3.7)
0.0237	0.992831	91.70 (0.22)	309.1 (3.0)
0.2499	0.998552	91.69 (0.02)	317.7 (0.3)
0.1670	0.996472	91.76 (0.03)	318.2 (0.4)
0.3422	1.000775	91.83 (0.02)	318.1 (0.2)
0.2835	0.999349	91.81 (0.02)	318.2 (0.3)
0.1933	0.997132	91.75 (0.03)	318.6 (0.4)
0.1119	0.995087	91.71 (0.05)	314.2 (0.6)
0.0845	0.994388	91.73 (0.06)	313.6 (0.8)
0.0612	0.993797	91.68 (0.08)	309.3 (1.2)
0.0401	0.993253	91.72 (0.13)	316.8 (1.8)

TABLE 1. *(concluded)*

m (mol kg^{-1})	ρ (g cm^{-3})	$V_{2,\phi}$ (cm^3 mol^{-1})	$C_{p,2,\phi}$ (J K^{-1} mol^{-1})
		328.15 K	
0.2499	0.991890	92.70 (0.02)	327.6 (0.3)
0.1670	0.989884	92.59 (0.03)	324.7 (0.4)
0.0766	0.987637	95.52 (0.07)	321.7 (0.9)
0.0336	0.986543	92.75 (0.15)	323.6 (2.1)
0.0188	0.986172	92.65 (0.27)	314.3 (3.7)
0.0237	0.986294	92.66 (0.22)	327.5 (3.0)
0.3422	0.994106	92.71 (0.02)	328.1 (0.2)
0.2835	0.992706	92.69 (0.02)	327.7 (0.3)
0.1933	0.990526	92.63 (0.03)	328.5 (0.4)
0.1119	0.988514	92.60 (0.05)	326.9 (0.6)
0.0845	0.987823	92.67 (0.06)	323.8 (0.8)
0.0612	0.987242	92.63 (0.08)	330.9 (1.2)
0.0401	0.986712	92.58 (0.13)	333.4 (1.8)
0.3422	0.994117	92.68 (0.02)	—

[a]Estimated uncertainties for $V_{2,\phi}$ and $C_{p,2,\phi}$ in parentheses.

pacity data at each temperature investigated. Apparent molar heat capacities, $C_{p,2,\phi}$, were calculated from specific heat data using eq. [2]:

$$[2] \qquad C_{p,2,\phi} = Mc_p + \frac{(c_p - c^0_{p,1})}{m}$$

were c_p is the specific heat capacity of the solution, and $c^0_{p,1}$ is the specific heat capacity of pure water at the temperature of interest (16). Apparent molar heat capacity data as a function of temperature are also contained in Tables 1, 2, and 3.

Procedures for estimating the uncertainties in apparent molar volumes, $\delta V_{2,\phi}$, and apparent molar heat capacities, $\delta C_{p,2,\phi}$, have been described previously (7, 17).

The apparent molar properties of the aqueous amino acid systems were found to be well represented by the linear equation:

$$[3] \qquad Y_{2,\phi} = \bar{Y}^0_2 + S_Y m$$

where Y represents the extensive thermodynamic property of interest, Y^0_2 is the value of $Y_{2,\phi}$ at infinite dilution, m is the molality of the solution, and S_Y is the experimental slope. The appropriate form of eq. [3] was fitted to our calculated $V_{2,\phi}$, and $C_{p,2,\phi}$ data using weighted linear least-squares regression analyses. Weights used in these analyses were calculated as the reciprocals of the square in the uncertainties in the apparent molar volumes and heat capacities.

Calculated standard state (infinite dilution) volumes, $\bar{V}^0_2$, and heat capacities, $\bar{C}^0_{p,2}$, are reported and compared to available literature data in Table 4. A review of this table indicates that our calculated standard state volume and heat capacity data are in very good agreement with those available in the literature. Unfortunately, we were unable to locate literature standard state data for the investigated amino acid systems at temperatures removed from 298.15 K.

Side chain contributions of amino acids to standard state volumes and heat capacities (1) can be calculated using the relationship:

$$[4] \qquad \bar{Y}^0_2(\text{R}) = \bar{Y}^0_2(\text{amino acid}) - \bar{Y}^0_2(\text{glycine})$$

Can. J. Chem. Downloaded from www.nrcresearchpress.com by EESC ESCOLA DE ENGENHARIA on 09/08/12
For personal use only.

TABLE 2. Densities, ρ, apparent molar volumes, $V_{2,\phi}$, and apparent molar heat capacities, $C_{p,2,\phi}$, of aqueous solutions of L-leucine at 288.15, 298.15, 313.15, and 328.15 K[a]

m (mol kg^{-1})	ρ (g cm^{-3})	$V_{2,\phi}$ (cm^3 mol^{-1})	$C_{p,2,\phi}$ (J K^{-1} mol^{-1})
		288.15 K	
0.1739	1.003304	106.66 (0.03)	388.9 (0.4)
0.1461	1.002634	106.72 (0.03)	389.1 (0.5)
0.1185	1.001974	106.72 (0.04)	389.7 (0.6)
0.1042	1.001625	106.78 (0.05)	388.9 (0.7)
0.0872	1.001221	106.73 (0.06)	388.3 (0.8)
0.0545	1.000433	106.69 (0.09)	387.6 (1.3)
0.0309	0.998543	106.79 (0.16)	387.0 (2.3)
0.0209	0.996133	106.67 (0.24)	386.3 (3.4)
		298.15 K	
0.1739	1.001102	107.69 (0.03)	398.1 (0.4)
0.1461	1.000463	107.70 (0.03)	398.0 (0.5)
0.1185	0.999825	107.70 (0.04)	398.3 (0.6)
0.1042	0.999492	107.72 (0.05)	397.7 (0.7)
0.0872	0.999098	107.70 (0.06)	396.6 (0.8)
0.0545	0.998331	107.74 (0.09)	398.4 (1.3)
0.0309	0.997778	107.68 (0.16)	398.3 (2.3)
0.0209	0.997542	107.67 (0.24)	399.7 (3.4)
		313.15 K	
0.1739	0.996116	109.06 (0.03)	406.0 (0.4)
0.1461	0.995502	109.05 (0.04)	404.8 (0.5)
0.1185	0.994891	109.06 (0.04)	407.1 (0.6)
0.1042	0.994573	109.03 (0.05)	405.1 (0.7)
0.0872	0.994190	109.04 (0.06)	406.2 (0.8)
0.0545	0.993456	109.04 (0.09)	407.4 (1.3)
0.0309	0.992923	108.99 (0.16)	407.7 (2.3)
0.0209	0.992698	108.84 (0.24)	405.4 (3.4)
		328.15 K	
0.1739	0.989461	110.39 (0.03)	413.2 (0.4)
0.1461	0.988883	110.29 (0.04)	411.0 (0.5)
0.1185	0.988291	110.26 (0.04)	412.3 (0.6)
0.1042	0.987978	110.30 (0.05)	413.2 (0.7)
0.0872	0.987612	110.25 (0.06)	414.2 (0.8)
0.0545	0.986890	110.41 (0.09)	409.5 (1.3)

[a]Estimated uncertainties for $V_{2,\phi}$ and $C_{p,2,\phi}$ in parentheses.

TABLE 3. Densities, ρ, apparent molar volumes, $V_{2,\phi}$, and apparent molar heat capacities, $C_{p,2,\phi}$, of aqueous solutions of L-isoleucine at 288.15, 298.15, 313.15, and 328.15 K[a]

m (mol kg^{-1})	ρ (g cm^{-3})	$V_{2,\phi}$ (cm^3 mol^{-1})	$C_{p,2,\phi}$ (J K^{-1} mol^{-1})
		288.15 K	
0.2416	1.005302	104.95 (0.02)	373.7 (0.3)
0.1057	1.001852	104.95 (0.05)	374.1 (0.7)
0.0738	1.001025	105.00 (0.07)	373.0 (1.0)
0.0467	1.000321	105.00 (0.11)	370.6 (1.5)
0.0362	1.000045	105.03 (0.14)	371.8 (1.9)
0.0483	1.003650	104.97 (0.10)	371.7 (1.5)
0.2474	1.005458	104.91 (0.02)	374.2 (0.3)
0.2038	1.004364	104.89 (0.02)	374.2 (0.4)
0.1768	1.003684	104.87 (0.03)	374.0 (0.4)
0.1637	1.003348	104.88 (0.03)	373.5 (0.4)
0.1232	1.002309	104.89 (0.04)	374.0 (0.6)
0.2416	1.005298	104.97 (0.02)	—
		298.15 K	
0.2416	1.003073	105.86 (0.02)	384.6 (0.3)
0.1057	0.999725	105.82 (0.05)	384.2 (0.7)
0.0738	0.998924	105.81 (0.07)	384.2 (1.0)
0.0467	0.998236	105.83 (0.11)	385.0 (1.5)
0.0362	0.997972	105.71 (0.14)	386.7 (1.9)
0.0483	0.998277	105.85 (0.10)	383.4 (1.5)
0.2474	1.003228	105.80 (0.02)	384.7 (0.3)
0.2038	1.002163	105.79 (0.03)	384.4 (0.4)
0.1768	1.001501	105.78 (0.03)	384.1 (0.4)
0.1637	1.001176	105.78 (0.03)	384.0 (0.4)
0.1232	1.000167	105.78 (0.04)	384.3 (0.6)
		313.15 K	
0.2416	0.998043	107.11 (0.02)	394.2 (0.3)
0.1057	0.994800	107.15 (0.05)	392.7 (0.7)
0.0738	0.994034	107.05 (0.07)	393.3 (1.0)
0.0467	0.993368	107.09 (0.11)	392.3 (1.5)
0.0361	0.993110	107.08 (0.14)	394.9 (1.9)
0.0483	0.993410	107.06 (0.11)	395.8 (1.5)
0.2474	0.998184	107.09 (0.02)	394.4 (0.3)
0.2038	0.997161	107.06 (0.03)	393.9 (0.4)
0.1768	0.996522	107.05 (0.03)	393.7 (0.4)
0.1637	0.996207	107.05 (0.03)	393.9 (0.4)
0.1232	0.995235	107.03 (0.04)	393.3 (0.6)
0.1057	0.994807	107.08 (0.05)	—
		328.15 K	
0.2416	0.991379	108.26 (0.02)	400.4 (0.3)
0.1057	0.988227	108.18 (0.05)	400.5 (0.7)
0.0738	0.987468	108.18 (0.07)	401.4 (1.0)
0.0467	0.986813	108.32 (0.11)	406.6 (1.5)
0.0483	0.986860	108.16 (0.11)	399.1 (1.5)
0.2474	0.991499	108.32 (0.02)	401.2 (0.3)
0.2038	0.990521	108.20 (0.03)	399.3 (0.3)
0.1768	0.989895	108.19 (0.03)	399.9 (0.4)
0.1637	0.989591	108.18 (0.03)	399.6 (0.4)
0.1232	0.988636	108.21 (0.04)	398.9 (0.6)

[a]Estimated uncertainties for $V_{2,\phi}$ and $C_{p,2,\phi}$ in parentheses.

where $\bar{Y}_2^0$ (R) defines the side chain contribution of the amino acid relative to the C—H group of glycine. Combining standard state data from this investigation with those we have published previously (7) allows us to look at the temperature dependence of side chain contributions for L-alanine, L-serine, L-threonine, L-valine, L-leucine, and L-isoleucine. Standard state volume and heat capacity side chain contributions are shown as functions of temperature in Figs. 1 and 2, respectively.

Looking first at Fig. 2, it is clear that at any given temperature the magnitude of $\bar{C}_{p,2}^0$ (R) increases with increasing alkyl chain length (1). The interaction of alkyl groups with water is hydrophobic in nature i.e., the alkyl side chains have a structure promoting effect on the solvent, water. With increasing temperature, we observe decreasing $\bar{C}_{p,2}^0$ (R) values for L-alanine, L-valine, L-leucine, and L-isoleucine. This observation is expected, for as the temperature increases the extent of hydrogen bonding within the solvent decreases. In other words, the degree of ordering within the solvent decreases which has the effect of reducing the capacity of the structuring effect caused by the hydrophobic hydration of the alkyl groups of the amino acid side chains. L-Serine and L-threonine are distinct from the other aliphatic amino acids. An increase in $\bar{C}_{p,2}^0$ (R) as a function of temperature for these compounds appears

TABLE 4. Comparison of calculated $\bar{V}_2^0$ and $\bar{C}_{p,2}^0$ values with lieterature data

T (K)	$\bar{V}_2^0$ ($cm^3\ mol^{-1}$)		$\bar{C}_{p,2}^0$ ($J\ K^{-1}\ mol^{-1}$)	
		L-Valine		
288.15	90.08		294.4	
298.15	90.80	(90.79,[a] 90.91,[b] 90.65,[c] 90.78[f])	305.8	(301.9,[a] 307.5[d])
313.15	91.67		316.3	
328.15	92.57		325.2	
		L-Leucine		
288.15	106.81		388.1	
298.15	107.73	(107.57,[a] 107.74,[b] 107.83,[c] 107.75,[e] 107.74[f])	397.5	(397.7,[a] 402.4,[d] 399.0[e])
313.15	109.00		406.8	
328.15	110.18		411.9	
		L-Isoleucine		
288.15	104.90		372.9	
298.15	105.76	(105.45,[a] 105.80[c])	383.8	(383.3[a])
313.15	107.04		392.8	
328.15	108.09		399.5	

[a]Reference 1.
[b]Reference 2.
[c]Reference 3.
[d]Reference 4.
[e]Reference 5.
[f]Reference 6.

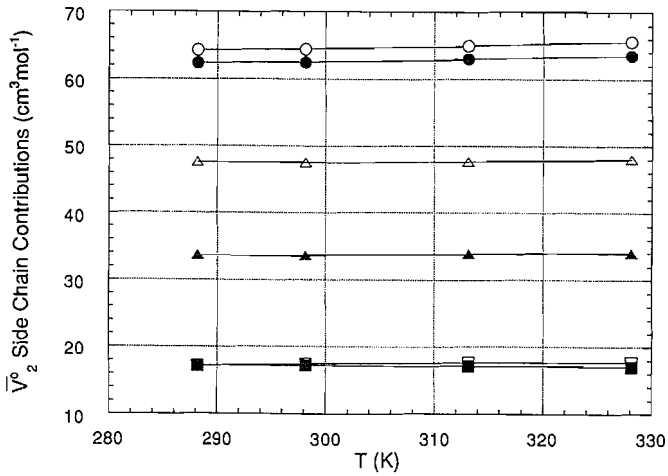

FIG. 1. The temperature dependence of side chain standard state volume contributions, relative to C—H, for aqueous amino acid systems. ○ L-Leucine, ● L-isoleucine, △ L-valine, ▲ L-threonine, □ L-serine, ■ L-alanine.

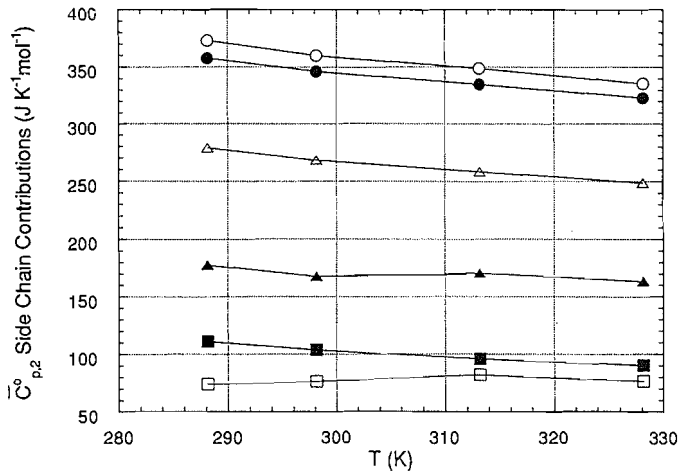

FIG. 2. The temperature dependence of side chain standard state heat capacity contributions, relative to C—H, for aqueous amino acid systems. ○ L-Leucine, ● L-isoleucine, △ L-valine, ▲ L-threonine, □ L-serine, ■ L-alanine.

to indicate that hydrophilic hydration may play a role in their overall solution behaviour. For L-serine the increase in $\bar{C}_{p,2}^0$ (R) up to approximately 313.15 K indicates that hydrophilic hydration may be dominant for this particular side chain in water. For L-threonine, although the polar —OH group is expected to affect neighbouring water molecules, it is envisaged that the overall solution behaviour of the species will be determined predominantly by the interaction of the alkyl groups within the side chain with water.

Turning to Fig. 1, we observe increasing values for $\bar{V}_2^0$ (R) with increasing temperature. This observation reinforces our interpretation of the trends shown in Fig. 2, i.e., as the temperature increases the hydrophobic character of the alkyl groups on the amino acid side chains decreases. A more detailed look at $\bar{V}_2^0$ (R) values for L-alanine reveals that they are approximately independent of temperature. We are unable to explain this trend. However, we note the comments of previous authors (1) who have stated that the interpretation of standard state volumes in terms of solution structure is a more difficult proposition that the interpretation of standard state heat capac-

Can. J. Chem. Downloaded from www.nrcresearchpress.com by EESC ESCOLA DE ENGENHARIA on 09/08/12
For personal use only.

Can. J. Chem. Downloaded from www.nrcresearchpress.com by EESC ESCOLA DE ENGENHARIA on 09/08/12
For personal use only.

ity data. This is because a strict interpretation of standard state volume data demands that one considers the contributions of several components (21–23).

To obtain information on the stability of aqueous amino acid systems at elevated temperatures and pressures, one requires values of apparent standard molar Gibbs free energies. These data can be calculated for a given amino acid system, at the temperature and pressure of interest, provided one has suitable equations of state for the temperature and pressure dependencies of the standard state volume and heat capacity of the system. These equations of state are well represented by the revised HKF equations for neutral organics in water reported by Shock and Helgeson (10). The equations are defined by:

$$[5] \qquad \bar{V}_2^0 = a_1 + \frac{a_2}{\Psi + P} + \left(a_3 + \frac{a_4}{\Psi + P}\right)\left(\frac{1}{T - \theta}\right) - \omega_e Q$$

$$[6] \qquad \bar{C}_{p,2}^0 = c_1 + \frac{c_2}{(T-\theta)^2} - \left(\frac{2T}{(T-\theta)^3}\right)\left[a_3(P - P_r) + a_4 \ln\left(\frac{\Psi + P}{\Psi + P_r}\right)\right] + \omega_e T X$$

where a_1, a_2, a_3, a_4, c_1, and c_2 are species-dependent parameters; θ and Ψ represent solvent-dependent parameters. T, P, and P_r represent the temperature and pressure of interest and the reference pressure (1 bar), respectively. ω_e defines the effective Born coefficient for the neutral organic aqueous species of interest. This coefficient is assumed to be independent of temperature and pressure.

The revised HKF equations are comprised of two components; the solvation contributions defined by $-\omega_e Q$ and $\omega_e TX$, respectively, and the structural contributions represented by the remainder of the base equations. The Q and X parameters of the solvation contributions are defined using the temperature and pressure dependencies of the dielectric constant of water (8, 20).

At constant pressure, eq. [5] may be reduced to:

$$[7] \qquad \bar{V}_2^0 = \sigma + \frac{\xi}{T - \theta} - \omega_e Q$$

were σ and ξ are fitting parameters.

In a similar manner eq. [6] is simplified, under the constant pressure condition of $P = P_r$, to the form:

$$[8] \qquad \bar{C}_{p,2}^0 = c_1 + \frac{c_2}{(T-\theta)^2} + \omega_e T X$$

Regression analyses have been used to fit eqs. [7] and [8] to calculated standard state volumes and heat capacities for each amino acid system. Values for Q and X at the reference pressure, P_r, were calculated from a BASIC computer program that was constructed using the procedures outlined by Helgeson and Kirkham (18, 19). Values for the effective Born coefficients of the amino acids were obtained from the compilations reported in ref. 10. To remain consistent with the Shock and Helgeson analyses, the solvent parameter θ was given a value of 228 K in all of our fitting procedures. Calculated values for σ, ξ, c_1, and c_2 are reported in Table 5.

Figures 3 and 4 compare the temperature dependencies of calculated structural contributions to standard state volumes

TABLE 5. Calculated parameters to eqs. [7] and [8] for aqueous solutions of L-valine, L-leucine, and L-isoleucine

Amino acid	σ (cm^3 mol^{-1})	ξ (cm^3 K mol^{-1})	$\omega_e \times 10^{-5}$ [a] (J mol^{-1})
L-Valine	94.89	−343.02	−1.27653
L-Leucine	113.27	−466.46	−1.84054
L-Isoleucine	110.90	−442.07	−1.92297

Amino acid	c_1 (J K^{-1} mol^{-1})	c_2 (J K mol^{-1})	$\omega_e \times 10^{-5}$ [a] (J mol^{-1})
L-Valine	327.17	-1.6216×10^5	−1.27653
L-Leucine	405.30	-1.2270×10^5	−1.84054
L-Isoleucine	392.93	-1.3525×10^5	−1.92297

[a]Data obtained from ref. 10.

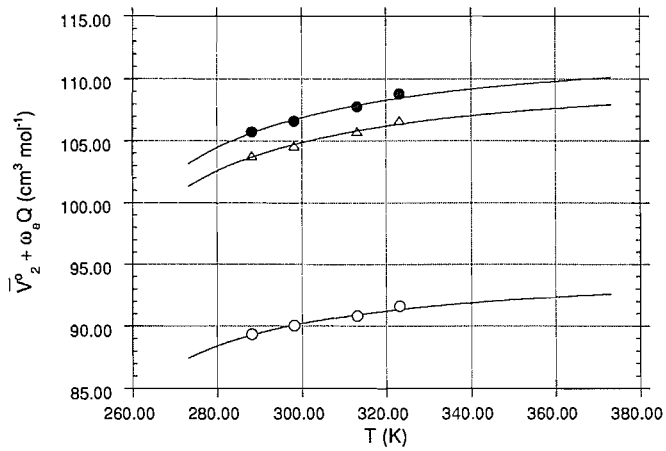

FIG. 3. Structural contributions to standard state volumes versus temperature for ○ L-valine, ● L-leucine, △ L-isoleucine in water. The solid curves represent fits of the revised HKF constant pressure equation, eq. [7], to the calculated structural contributions of the standard state volumes.

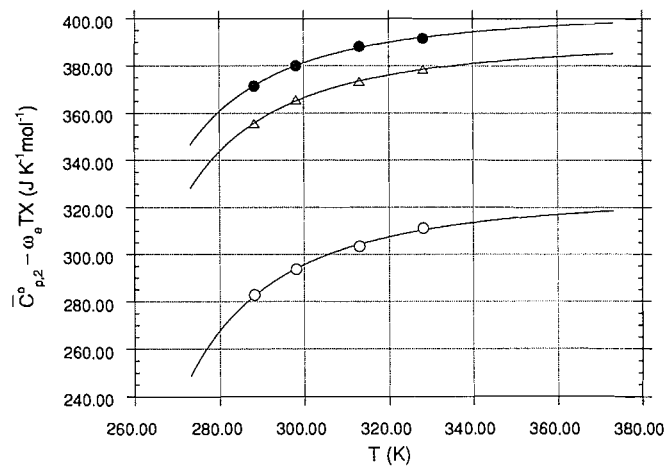

FIG. 4. Structural contributions to standard state heat capacities versus temperature for ○ L-valine, ● L-leucine, △ L-isoleucine in water. The solid curves represent fits of the revised HKF constant pressure equation, eq. [8], to the calculated structural contributions of the standard state heat capacities.

and heat capacities to those which can be estimated using the revised HKF constant pressure equations. The data calculated using the HKF equations are denoted using solid curves. Inspection of Figs. 3 and 4 indicates that the standard state volume and heat capacity data for the amino acids have characteristic profiles. Because these profiles define the structural contributions to the standard state properties one should be able to analyse these data using a group additivity type analysis. The limited information which one can obtain from side chain group analyses, of the type presented in this paper, clearly indicates the requirement for a detailed group additivity scheme.

Our aim is to use group contributions to standard state volumes and heat capacities of amino acids as a function of temperature to predict the temperature dependencies of standard state volumes and heat capacities of various aqueous peptide systems. Only very limited data are available in the literature for such systems. At present we have not analysed sufficient amino acid systems to amass the volumetric and thermochemical data sets required to perform such analyses, however this work is in progress.

Acknowledgements

AWH is grateful to the Natural Sciences and Engineering Research Council of Canada (NSERC) for operating support and to the University of Lethbridge for equipment funding. K.E.P. is grateful to NSERC for the award of an Undergraduate Student Research Award.

1. C. Jolicoeur, B. Riedl, D. Desrochers, L.L. Lemelin, R. Zamojska, and O. Onea. J. Solution Chem. **15**, 109 (1986).
2. S. Cabani, G. Conti, E. Matteoli, and M.R. Tiné. J. Chem. Soc. Faraday Trans. I, **77**, 2377 (1981).
3. A.K. Mishra and J.C. Ahluwalia. J. Phys. Chem. **88**, 86 (1984).
4. G. DiPaolo and B. Belleau. Can. J. Chem. **56**, 1827 (1978).
5. J.C. Ahluwalia, C. Ostiguy, G. Perron, and J.E. Desnoyers. Can. J. Chem. **55**, 3364 (1977).
6. F.J. Millero, A. Lo Surdo, and C. Shin. J. Phys. Chem. **82**, 784 (1978).
7. A.W. Hakin, M.M. Duke, S.A. Klassen, R.M. McKay, and K.E. Preuss. Can. J. Chem. **72**, 362 (1994).
8. E.L. Shock. Geochim. Cosmochim. Acta, **56**, 3481 (1992).
9. E.L. Shock. Geochim. Cosmochim. Acta, **54**, 1185 (1990).
10. E.L. Shock and H.C. Helgeson. Geochim. Cosmochim. Acta, **54**, 915 (1990).
11. C.J. Pouchert and J.R. Campbell. The Aldrich Library of NMR Spectra. Vol. III. 1974.
12. P. Picker, E. Tremblay, and C. Jolicoeur. J. Solution Chem. **3**, 377 (1974).
13. P. Picker, P.-A. Leduc, P.R. Philip, and J.E. Desnoyers. J. Chem. Thermodyn. **3**, 631 (1971).
14. A.W. Hakin, S.A.M. Mudrack, and C.I. Beswick. Can. J. Chem. **71**, 925 (1993).
15. G.S. Kell. J. Chem. Eng. Data, **12**, 66 (1967).
16. G.S. Kell. *In* Water — A comprehensive treatise. Vol. I. *Edited by* F. Franks. Plenum Press, New York. 1972. pp. 363–412.
17. G.R. Hedwig. J. Solution Chem. **17**, 383 (1988).
18. H.C. Helgeson and D.H. Kirkham. Am. J. Sci. **274**, 1089 (1974).
19. H.C. Helgeson and D.H. Kirkham. Am. J. Sci. **276**, 97 (1976).
20. J.W. Johnson and D. Norton. Am. J. Sci. **291**, 541 (1991).
21. D.P. Kharakoz. Biophys. Chem. **34**, 115 (1989).
22. R.A. Pierotti. J. Phys. Chem. **69**, 281 (1965).
23. S. Terasawa, H. Itsuki, and S.A. Arakawa, J. Phys. Chem. **79**, 2345 (1975).

Can. J. Chem. Downloaded from www.nrcresearchpress.com by EESC ESCOLA DE ENGENHARIA on 09/08/12
For personal use only.

The structure of the rodent and porcine neuropeptide galanin and antagonists as determined by FTIR and CD spectroscopy[1,2]

ANDERS B.A. WENNERBERG
Department of Medical Biochemistry and Biophysics, Karolinska Institutet, S-171 77 Stockholm, Sweden

MICHAEL JACKSON
Institute for Biodiagnostics, National Research Council Canada, Winnipeg, MB R3B 1Y6, Canada

ANDERS ÖHMAN AND ASTRID GRÄSLUND
Department of Medical Biochemistry and Biophysics, University of Umeå, S-901 87 Umeå, Sweden

ÜLO LANGEL AND TAMAS BARTFAI
Department of Neurochemistry and Neurotoxicology, University of Stockholm, S-106 91 Stockholm, Sweden

RUDOLF RIGLER
Department of Medical Biochemistry and Biophysics, Karolinska Institutet, S-171 77 Stockholm, Sweden

AND

HENRY H. MANTSCH[3]
Institute for Biodiagnostics, National Research Council Canada, Winnipeg, MB R3B 1Y6, Canada

Received November 9, 1993

ANDERS B.A. WENNERBERG, MICHAEL JACKSON, ANDERS ÖHMAN, ASTRID GRÄSLUND, ÜLO LANGEL, TAMAS BARTFAI, RUDOLF RIGLER, and HENRY H. MANTSCH. Can. J. Chem. **72**, 1495 (1994).

FT-IR spectroscopy was used to study the conformation of the porcine neuropeptide galanin, fragments 1–16 of the porcine and human peptides and the antagonists M15 and M35. All peptides were shown to be structureless in aqueous solution. Upon addition to SDS micelles, only porcine galanin and the fragment consisting of amino acids 1–16 showed any evidence of interaction, adopting a helical structure. No interaction could be demonstrated with zwitterionic lipids for any peptide except M15 which formed a thermally unstable helical conformation which unfolded promoting aggregation at around 45°C.

Additional studies on rat galanin in various solvent systems were made by using circular dichroism spectroscopy. The results obtained support the observations made by FT-IR spectroscopy.

ANDERS B.A. WENNERBERG, MICHAEL JACKSON, ANDERS ÖHMAN, ASTRID GRÄSLUND, ÜLO LANGEL, TAMAS BARTFAI, RUDOLF RIGLER et HENRY H. MANTSCH. Can. J. Chem. **72**, 1495 (1994).

On a utilisé la spectroscopie IR par FT pour étudier la conformation du neuropeptide de porc, galanine, des fragments 1–16 des peptides humain et de proc et les antagonistes M15 et M35. On a montré que, en solutions aqueuses, tous les peptides sont sans structure. Par addition de micelles SDS, seule la galanine de porc et le fragment comportant les acides aminés 1–16 ont présenté des signes d'interaction en adoptant une structure hélicoïdale. Aucun des lipides zwitterioniques, à l'exception du M15 que donne une conformation hélicoïdale thermiquement instable et qui se défait avec une promotion de l'agrégation autour de 45°C, ne démontre d'interaction.

Faisant appel au dichroïsme circulaire, on a fait des études supplémentaires sur la galanine de rat dans divers systèmes. Les résultats obtenus confirment les observations faible à l'aide de l'IR par FT.

[Traduit par la rédaction]

Introduction

Galanin is a 29 amino acid neuropeptide initially isolated from the small intestine of the pig (1) and since located in various parts of the central and peripheral nervous system (2), including neurons in the respiratory, gastrointestinal and urogenital tracts, adrenal medulla and pancreas. The amino acid sequences of rat, pig, and human galanin (1) have been determined (Table 1). The first 15 residues are absolutely conserved in all species and receptor affinity has been correlated with this sequence. In particular, tryptophan in position 2 is crucial for receptor binding (3). All galanins, with the exception of the human isoform, are secreted as C-terminal amides. As the sequences bear no homology to any other family of neuropeptides, it appears that galanin is the first member of a new family of neuropeptides.

The physiological effects of galanin are diverse and vary with species. Depending upon species, galanin may modulate the physiological effects of growth hormone, insulin, glucagon, prolactin, somatostatin, and dopamine (4). Evidence exists that galanin functions as a neurotransmitter in the pancreas in some animals, with a possible role in the neural regulation of islet function as part of the metabolic response to stress (5). There are indications that the inhibitory effect of galanin on insulin secretion results from an action of the peptide on K^+ channels and indirectly, on Ca^{2+} channels within the β-cells (6). In addition, galanin is an effective inhibitor of substance P. Biochemical characterization of the galanin receptor shows that it is a glycoprotein of 54 kDa belonging to the G-protein coupled class of receptors (7). The involvement of a G-protein in galanin-mediated insulin suppression has been suggested (8).

[1]NRCC No. 34717.

[2]Abbreviations used: FT-IR, Fourier transform infrared; CD, circular dichroism; DHPC, dihexadecylphosphatidylcholine; DOPC, 1,2-dioleoyl-sn-glycero-3-phosphocholine; DOPG, 1,2-dioleoyl-sn-glycero-3-phosphoglycerol; HFP, 1,1,1,3,3,3-hexafluoro-2-propanol; TFE, trifluoroethanol; SDS, sodium dodecyl sulphate.

[3]Author to whom correspondence should be addressed.

Can. J. Chem. Downloaded from www.nrcresearchpress.com by EESC ESCOLA DE ENGENHARIA on 09/08/12
For personal use only.

TABLE 1. Amino acid sequences of porcine, rat, and human galanin and of the antagonists M15 and M35

	1				5					10					15
Porcine	Gly	Trp	Thr	Leu	Asn	Ser	Ala	Gly	Tyr	Leu	Leu	Gly	Pro	His	Ala
Human	Gly	Trp	Thr	Leu	Asn	Ser	Ala	Gly	Tyr	Leu	Leu	Gly	Pro	His	Ala
Rodent	Gly	Trp	Thr	Leu	Asn	Ser	Ala	Gly	Tyr	Leu	Leu	Gly	Pro	His	Ala
M15	Gly	Trp	Thr	Leu	Asn	Ser	Ala	Gly	Tyr	Leu	Leu	Gly	Pro	**Gln**	**Gln**
M35	Gly	Trp	Thr	Leu	Asn	Ser	Ala	Gly	Tyr	Leu	Leu	Gly	Pro	**Pro**	**Pro**

	16				20					25					30	
Porcine	Ile	Asp	Asn	His	Arg	Ser	Phe	His	Asp	Lys	Tyr	Gly	Leu	Ala		NH_2
Human	**Val**	**Gly**	Asn	His	Arg	Ser	Phe	**Ser**	Asp	Lys	**Asn**	Gly	Leu	**Thr**	**Ser**	COOH
Rodent	Ile	Asp	Asn	His	Arg	Ser	Phe	**Ser**	Asp	Lys	**His**	Gly	Leu	**Thr**		NH_2
M15	**Phe**	**Phe**	**Gly**	**Leu**	**Met**											NH_2
M35	**Gly**	**Phe**	**Ser**	**Pro**	**Phe**	**Arg**										NH_2

The widespread physiological effects of galanin have stimulated interest in the preparation of pharmacologically useful derivatives, particularly given its possible use in pain modulation due to its antagonism of substance P (3). Such an undertaking will be greatly facilitated by an understanding of the relationship between galanin structure and function. Infrared and circular dichroism spectroscopy are valuable tools for obtaining semi-quantitative information concerning the secondary structure of proteins and peptides in solution. We have used these techniques to assess the conformation of rat and porcine galanin, the first 16 amino acids of porcine and human galanin as C-terminal acids as well as that of analogues composed of the first 13 amino acids of galanin and either the final 7 amino acids from the substance P sequence (M15) or the final 8 amino acids from the bradykinin sequence (M35) as C-terminal amides in aqueous solution. The amphipathic nature of galanin suggests the possibility of interaction with membranes. In addition, we have therefore studied the interaction of galanin with model membrane systems to assess the nature of any conformational changes induced upon interaction with membranes.

Experimental

Materials

Galanin and its analogues (see Table 1) were synthesized by solid phase synthesis or purchased from Sigma (St. Louis, MO). The purity of synthetic peptides was determined by HPLC chromatography and the amino acid sequence confirmed. Sodium dodecyl sulfate (SDS) was purchased from BDH Ltd (Poole, England), 2,2,2-Trifluoroethanol (TFE) from E. Merck (Darmstadt, Germany), and 1,1,1,3,3,3-hexafluoro-2-propanol (HFP) from Sigma. The lipids 1,2-dioleoyl-sn-glycero-3-phosphocholine (DOPC) and 1,2-dioleoyl-sn-glycero-3-phosphoglycerol (DOPG) were obtained either from Sigma or Avanti Polar Lipids (Pelham, AL).

Methods

FT-IR studies. Peptide samples in aqueous solution were prepared by dissolution of the peptide in TRIS buffered saline (50 mM TRIS, 150 mM NaCl, pD 7.6: TBS) to a final concentration of 10 mg/mL. Liposomes were prepared by sonication of lipids in the appropriate buffer and liposome suspensions added to the required amount of peptide to yield a lipid-to-protein ratio of 50:1 and a final peptide concentration of 10 mg/mL. Spectra were recorded on a Digilab FTS-60 Fourier transform infrared spectrometer equipped with a liquid-nitrogen cooled mercury–cadmium–telluride detector and continuously purged with dry nitrogen. Approximately 3 μL of sample was placed between a pair of CaF_2 windows separated by a 50 μm Mylar spacer and mounted in a Harrick demountable cell. Temperature was maintained by a circulating water bath. For each sample 100 interferograms were recorded, co-added, and Fourier transformed to generate a spectrum of resolution 2 cm^{-1}. Buffer spectra were recorded under identical conditions and interactively subtracted from sample spectra. Residual water vapour was interactively subtracted. All spectra were subjected to Fourier self-deconvolution performed as described previously (9) using a half width of 13.5 cm^{-1} and a resolution enhancement factor $k = 1.7$.

CD-studies. Rat galanin solutions with a concentration of approximately 25 μM were titrated with SDS and phospholipid vesicle solutions prepared from DOPC and DOPG. In the titration with SDS a 10 mM phosphate buffer (pH = 7.0) was used, in all other cases water was used. CD-spectra of the peptide were recorded in solvents with 0, 1, 2, 5, 10, and 20 mM SDS and with 0, 0.025, 0.05, 0.1, 0.2, 0.5, 1.0, and 2.0 mg/mL of vesicle solution. CD-spectra of the peptide in 100% TFE and 100% HFP were also recorded. CD-spectra were recorded using a Jasco-720 spectropolarimeter with 2 mm Hellma quartz cuvettes at a temperature of 25°C. A resolution of 0.5 nm and a scan speed of 10 nm per min were used. The acquired spectra were the average of three continuous scans, usually measured between 185 and 250 nm, and corrected with respect to baseline and for dilution. Quantitative evaluation of CD spectra is dependent upon a knowledge of the extinction coefficient of the peptide. This parameter was determined for galanin, dissolved in water, by quantitation of the peptide using amino acid analysis and light absorption spectroscopy and yielded a value of $\epsilon_{278} = 6620\ M^{-1}\ cm^{-1}$.

Results and discussion

The FT-IR spectrum of porcine galanin in TBS buffer (pD 7.6) is shown in Fig. 1. The amide I mode, predominantly (80%) a C=O stretching vibration, gives rise to a broad band centered at 1646 cm^{-1}. Such a position is characteristic of proteins and peptides which have little or no repetitive secondary structure, generally referred to as a "random" conformation (assignments

Can. J. Chem. Downloaded from www.nrcresearchpress.com by EESC ESCOLA DE ENGENHARIA on 09/08/12
For personal use only.

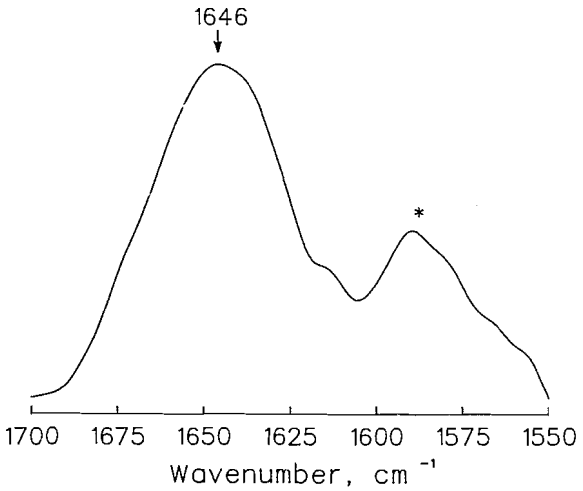

FIG. 1. Infrared spectrum of porcine galanin in TBS buffer, pD 7.6 in the spectral region 1550–1700 cm^{-1}.

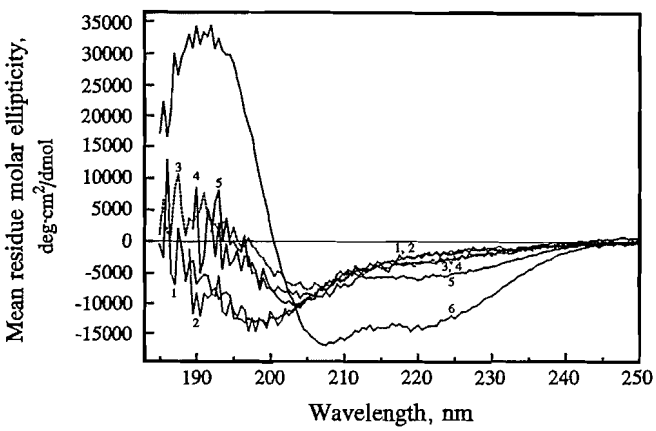

FIG. 2. Circular dichroism spectra of rat galanin at 25°C in pure water (*1*), in water containing 0.1 mg/mL DOPC (*2*), 10 mM SDS and 10 mM phosphate (*3*), 0.1 mg/mL DOPG (*4*), and in 100% HFP (*5*), or 100% TFE (*6*).

in this work are based on refs. 10–12). Useful structural information can also be obtained from the amide II mode, predominantly attributed to N—H bending vibrations, which gives rise to absorptions in the frequency range 1520 to 1560 cm^{-1}. The amide II mode is highly sensitive to the strength of hydrogen bonds involving the amide N—H groups, strong hydrogen bonds restricting the bending vibration and increasing the amide II frequency. In addition, upon dissolution in ^2H_2O, exchange of amide protons for solvent deuterons shifts the amide II band lower in frequency by approximately 100 cm^{-1}. The disappearance rate of the amide II band can therefore be a useful indicator of the degree of solvent exposure and the strength of any hydrogen bonds present, a high degree of solvent exposure and weak hydrogen bonds facilitating exchange. When galanin is dissolved in deuterated buffer the amide II band completely disappears, suggesting little if any hydrogen bonding involving the amide groups and a high degree of solvent exposure. Thus, analysis of both the amide I and the amide II bands suggests that galanin is unordered in aqueous solution. Circular dichroism spectra (Fig. 2) of rat galanin in aqueous solution are also indicative of a peptide with little or no long range order. The apparent lack of long range order in galanin is not surprising considering the high number of positive charges

TABLE 2. Percentages of α-helical structure of rat galanin as evaluated from CD spectra in pure water, in water containing 0.1 mg/mL DOPC, 0.1 mg/mL DOPG or 10 mM SDS as well as in pure hexafuropropanol and pure trifluoroethanol

Medium	% α-helix
H_2O	12
DOPC	13
DOPG	17
SDS	16
HFP	22
TFE	41

carried by the peptide, charge repulsion preventing folding into a more compact and energetically favorable conformation.

The spectral features in the frequency range 1560–1620 cm^{-1} arise from amino acid side chain vibrations (tyrosine, tryptophan, arginine, and aspartate). The absorption at 1590 cm^{-1} from arginine (marked with an asterisk) is particularly prominent.

Similar results were obtained from fragments 1–16 of human and porcine galanin as well as from the two analogues M15 and M35 (spectra not shown).

While the structure of a biological peptide in solution is important, it does not necessarily reflect the active conformation of the peptide. It is possible that unstructured peptides must in fact be induced to adopt an active, folded conformation. This may be achieved by structural rearrangements upon interaction with a recognition site. This recognition site may be part of an integral membrane protein (receptor) or the lipid bilayer of the cell membrane. To assess any conformational changes which may occur in the presence of membranes we recorded CD and IR spectra in a range of membrane mimetic environments.

Organic solvents are often used as membrane mimetic agents, usually to avoid the problems inherent in studying membrane suspensions with such techniques as NMR spectroscopy. The most commonly used organic solvent for such purposes is trifluoroethanol. It has been suggested that TFE provides a "helix-stabilizing" medium, stabilizing helical structures in polypeptide strands which have helix-forming propensity (13).

It has been shown by NMR spectroscopy (14) that rat galanin adopts a helical structure in TFE solution but not in aqueous solution. In agreement with this finding CD spectra (Fig. 2) of rat galanin in TFE are indicative of the presence of significant proportions of α-helical secondary structure. If we assume that the peptide chain contains only unordered and α-helical secondary structures (there is no evidence from CD or NMR spectra to suggest the presence of β-sheet structures) the amplitude at 222 nm can be used to determine the relative fraction of either (15, 16). From the spectra in Fig. 2 the percentages of α-helical structure in a variety of environments could be calculated (see Table 2). The highest proportion of helical secondary structure was found in TFE, followed by hexafluoropropanol. Only minor differences in ellipticity at 222 nm are seen between spectra in pure H_2O and those measured in the presence of SDS, DOPG, and DOPC.

The FT-IR spectrum of porcine galanin in TFE is shown in Fig. 3. Following deconvolution the amide I maximum is observed at 1658 cm^{-1}, a position indicative of the adoption of helical structure. The other analogues of galanin studied here

Can. J. Chem. Downloaded from www.nrcresearchpress.com by EESC ESCOLA DE ENGENHARIA on 09/08/12
For personal use only.

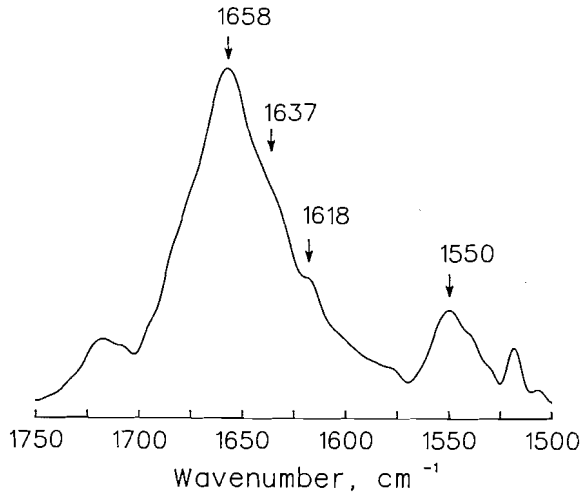

FIG. 3. Infrared spectrum of porcine galanin dissolved in TFE in the 1500–1750 cm^{-1} region.

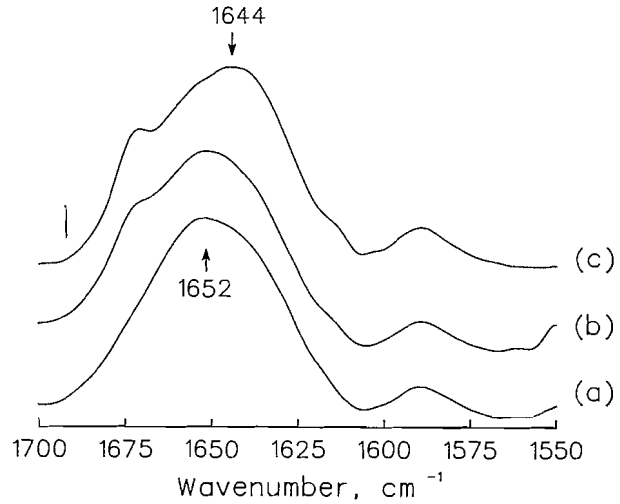

FIG. 4. Comparison of the infrared spectrum of porcine galanin (*a*) with porcine galanin fragment 1-16 (*b*) and human galanin fragment 1-16 (*c*), all in TBS buffer, pD 7.6 containing 5% SDS.

also adopted helical structures in TFE solution (spectra not shown). The frequency and small halfwidth of the amide I band suggest that helical structures are present in significant proportions (>75%). In addition, the position of the amide II band at 1550 cm^{-1} is also suggestive of significant helical structure. This result conflicts with the quantitative determination of the percentage of helices in galanin in TFE obtained from the CD data. This discrepancy may be related to the fact that in the CD calculations extinction coefficients obtained for helical and unordered polypeptide chains in aqueous solution were used for data obtained in organic solvents.

The presence of significant proportions of helical structures in peptides in TFE is often taken to indicate that the peptide is capable of adopting a helical secondary structure within the hydrophobic core of lipid membranes, i.e., is a reliable measure of its propensity to form helical secondary structures. However, we recently undertook a FT-IR spectroscopic examination of the effects of halogenated alcohols on the secondary structure of a variety of proteins and polypeptides (17). Each protein studied, whether it be predominantly helical, β-sheet or structureless in aqueous solution exhibited an amide I maximum at 1657 cm^{-1}. The adoption of helical secondary structures by peptide chains in TFE solution appears therefore to be the result of properties of TFE rather than any intrinsic properties of the polypeptide chain. Results obtained from studies of peptide conformation in halogenated alcohols should be treated with caution.

The weak absorption at 1618 cm^{-1} arises from tyrosine side chain vibrations. The additional feature in Fig. 3, at 1637 cm^{-1}, may have four possible origins. Firstly, it may be attributed to β-sheet structures. This is, however, unlikely, as preliminary NMR spectroscopic data show no resonances attributable to β-sheet in TFE solution (18). Secondly, a weak feature at 1637 cm^{-1} may be attributed to bound water present in the hygroscopic TFE (unpublished observations, M.J. H.M.). Thirdly, this feature may reflect hydrogen bonding of TFE to amide C=O groups. Finally, it may reflect the presence of β-turns. At present it is not possible to distinguish between the last three possibilities.

Another feature is apparent in spectra of galanin at around 1720 cm^{-1} in TFE solution (Fig. 3). This may be attributed to absorptions arising from the protonated COOH groups of aspartic acid residues present in galanin. The appearance of infrared bands arising from the protonated form of carboxylic acid side chains is a feature which we have consistently noted in spectra of proteins in TFE solution, which can be related to the acidic nature of this solvent. The relatively low frequency of the carbonyl absorption suggests that they are involved in hydrogen bonds, presumably with TFE. Protonation of and hydrogen bonding to side chains by TFE may be expected to have important structural consequences. Again, this illustrates the care with which data obtained for peptides in TFE solution should be treated.

More realistic attempts to study the interactions of peptides with membranes require the use of liposome or micellar systems. As galanin carries a net positive charge, any interaction would be expected to be specific for negatively charged liposomes or micelles. The spectrum of porcine galanin in the presence of 5% SDS is shown in Fig. 4*a*. The amide I maximum under these conditions is seen at 1652 cm^{-1}. Such an absorption in deuterated buffers is characteristic of peptides which have a helical structure. However, significant disorder in peptide chains is still present as evidenced by the large halfwidth of the amide I band (indicating a high degree of motional freedom of amide C=O groups) and the occurrence of a shoulder on the amide I band at 1644 cm^{-1}. This small increase in helical content agrees well with our CD results. The adoption of a partial α-helical structure is presumably the result of the neutralization of the positive charge on the peptide chain by the negatively charged sulphate headgroups. Porcine fragment 1–16 could also be shown to interact with SDS in a similar manner, resulting in the formation of a similar proportion of helical secondary structures (Fig. 4*b*). Rather surprisingly, the human galanin fragment 1–16 showed no interaction with SDS. This difference between the human and porcine fragments is difficult to rationalise considering the minor differences in sequence between the two peptides (porcine Ile16 to human Val16). The additional feature at 1672 cm^{-1} arises from the trifluoroacetate counterion commonly bound to synthetic peptides. In the presence of SDS, M35 and M15 exhibited spectra similar to those seen in aqueous solution.

Addition of porcine galanin, human or porcine fragments 1–16 and M35 to suspensions of the zwitterionic lipid DHPC

Can. J. Chem. Downloaded from www.nrcresearchpress.com by EESC ESCOLA DE ENGENHARIA on 09/08/12
For personal use only.

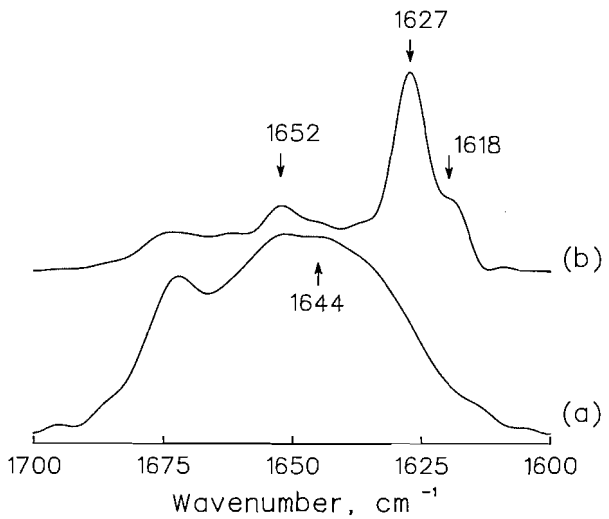

FIG. 5. FT-IR spectra in the amide I region of M15 in the presence at DHPC at 20°C (*a*) and 45°C (*b*).

resulted in spectra identical to those seen in aqueous solution, in agreement with our CD results obtained for rat galanin in the presence of DOPC. An amide I maximum centered at 1646 cm^{-1} (similar to that seen in Fig. 1) indicated that no interaction had occurred between the peptide and the lipid bilayer. On the other hand, the galanin antagonist M15 exhibited a weak band at 1652 cm^{-1} (in addition to the major band at 1644 cm^{-1}) in the presence of DHPC, indicative of the appearance of some helical structure (Fig. 5*a*). This may be attributed to the high content of hydrophobic amino acids in the sequence, which will favour penetration of the peptide into the hydrophobic bilayer core. Again, the band at 1672 cm^{-1} arises from trifluoroacetate contamination. Elevation of the temperature to 45°C (Fig. 5*b*) resulted in the appearance of a new band at 1627 cm^{-1}. This strong feature, typical of proteins which are aggregated following thermal or solvent denaturation (18), arises from the formation of intermolecular hydrogen bonds between amide C═O and N—H groups of peptide chains. Thermal denaturation of the peptide at the relatively low temperature of 45°C suggests that the membrane induced α-helix is unstable. In addition to the intense amide I band at 1627 cm^{-1} a weaker feature at 1618 cm^{-1} is apparent, a position similar to that seen for the side chain vibrations of tyrosine. However, the intensity of this absorption is greater than would be expected for a peptide of this size containing a single tyrosine residue. The additional intensity may be attributed to absorptions arising from a second class of intermolecular hydrogen bonds formed between peptide chains. The much lower frequency associated with this class of intermolecular hydrogen bonds indicates that it is extremely strong, suggesting close alignment of aggregated chains. The presence of two amide I bands indicative of aggregation is not unusual, and has been demonstrated for other biologically active peptides including magainins (19) and substance P (20).

In conclusion, studies such as that presented here highlight the utility of spectroscopic techniques in comparing the structural properties of biological peptides and their analogues, possibly as a first step in general screening for the design of novel therapeutic agents.

Acknowledgments

Amino acid analysis was performed by A. Tousi (University of Umeå). This study was supported by grants from the Karolinska Institutet, The Technical Science Research Board, The Swedish Natural Science Research Council, The Magn. Bergwall Foundation, and The Ivor Bendixson Foundation.

1. K. Tatemoto, A. Rökaeus, H. Jörnvall, T.J. McDonald, and V. Mutt. FEBS Lett. **164**, 124 (1983).
2. T. Melander, T. Hökfelt, and A. Rökaeus. J. Comp. Neurol. **248**, 475 (1986).
3. Z. Wiesenfeld-Hallin, X.-J. Xu, U. Langel, K. Bedecs. T. Hökfelt, and T. Bartfai. Proc. Natl. Acad. Sci. USA, **89**, 3334 (1992).
4. F.E. Bauer, L. Ginsberg, M. Venetikou, D.J. MacKay, J.M. Burrin, and S.R. Bloom. Lancet, **ii**, 192 (1986).
5. B.E. Dunning and G.J. Taborsky. Am. J. Physiol. **256**, E191 (1989).
6. J. de Weille, H. Schmid-Antomarchi, M. Fosset, and M. Lazdunski. Proc. Natl. Acad. Sci. USA, **85**, 1312 (1988).
7. B. Amiranoff, A.-M. Lorinet, and M. Laburthe. J. Biol. Chem. **264**, 20714 (1989).
8. B. Amiranoff, A.-M. Lorinet, I. Lagny-Pourmir, and M. Laburthe. Eur. J. Biochem. **177**, 147 (1988).
9. J.K. Kauppinnen, D.J. Moffatt, H.H. Mantsch, and D.G. Cameron. Appl. Spectrosc. **35**, 271 (1981).
10. H. Susi and D.M. Byler. Methods Enzymol. **130**, 290 (1986).
11. W.K. Surewicz and H.H. Mantsch. Biochim. Biophys. Acta, **952**, 115 (1988).
12. M. Jackson, P.I. Haris, and D. Chapman. J. Mol. Struct. **214**, 329 (1989).
13. F.D. Sönnichsen, J.E. Van Eyk, R.S. Hodges, and B.D. Sykes. Biochemistry, **31**, 8790 (1992).
14. A.B.A. Wennerberg, R.M. Cooke, M. Carlquist, R. Rigler, and I. Campbell. Biochem. Biophys. Res. Commun. **166**, 1102 (1990).
15. N. Greenfield and G.D. Fasman. Biochemistry, **8**, 4108 (1969).
16. I.D. Campbell and R.A. Dwek. *In* Biological spectroscopy. The Benjamin Cummings Publishing Company, Inc., Menlo Park, CA. 1984.
17. M. Jackson and H.H. Mantsch. Biochim. Biophys. Acta, **1118**, 139 (1992).
18. A.H. Clark, D.P.H.P. Saunderson, and A. Suggett. Int. J. Pept. Protein Res. **17**, 353 (1981).
19. M. Jackson, M.H. Mantsch, and J.H. Spencer. Biochemistry, **31**, 7289 (1992).
20. L.-P. Choo, M. Jackson, and H.H. Mantsch. Biochem. J. In press.

Can. J. Chem. Downloaded from www.nrcresearchpress.com by EESC ESCOLA DE ENGENHARIA on 09/08/12
For personal use only.

Design and synthesis of analogues of ionomycin

THOMAS Q. HU AND LARRY WEILER[1]

Department of Chemistry, University of British Columbia, 2036 Main Mall, Vancouver, BC V6T 1Z1 Canada

Received June 30, 1993[2]

THOMAS Q. HU and LARRY WEILER. Can. J. Chem. **72**, 1500 (1994).

Based on the analysis of the crystal structure of the Ca^{2+} salt of ionomycin and the chemical and physical data on ionomycin, a number of ionomycin analogues have been synthesized to study the structural features affecting the Ca^{2+} binding and transport. Compounds **2**, **3**, and **4** were synthesized to study the effect of additional intramolecular oxygen coordination sites on Ca^{2+} transport. Compounds ***5a–5d*** were prepared to study the effect of lipid solubility on Ca^{2+} binding and transport. Compounds ***6a–6c*** were prepared to study the effect of the distance between the β-diketone and the carboxyl group on Ca^{2+} transport. A general synthetic route to these compounds has been developed. The key reactions in this route are the consecutive regioselective alkylations of the dianion of 2,4-pentanedione with the appropriate bromides.

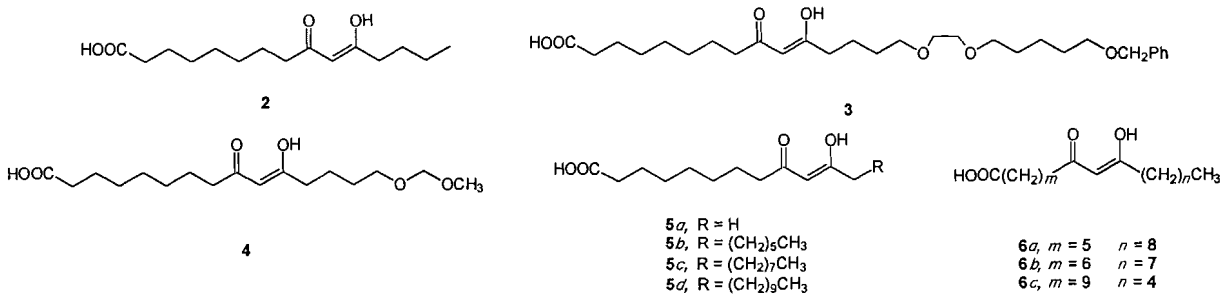

2 **3** **4**

5a, R = H
5b, R = $(CH_2)_5CH_3$
5c, R = $(CH_2)_7CH_3$
5d, R = $(CH_2)_9CH_3$

6a, *m* = 5 *n* = 8
6b, *m* = 6 *n* = 7
6c, *m* = 9 *n* = 4

THOMAS Q. HU et LARRY WEILER. Can. J. Chem. **72**, 1500 (1994).

En se basant sur une analyse de la structure cristalline du sel de Ca^{2+} de l'ionomycine et sur les données chimiques et physiques de l'ionomycine, on a synthétisé une série d'analogues de l'ionomycine dans le but d'étudier leurs caractéristiques structurales affectant leur liaison au Ca^{2+} et son transport. On a synthétisé les composés **2**, **3** et **4** pour étudier l'effet d'une augmentation des sites intramoléculaires de coordination de l'oxygène sur le transport du Ca^{2+}. On a préparé les composés ***5a–5d*** pour étudier l'effet de la solubilité lipidique sur la liaison avec le Ca^{2+} et sur son transport. On a préparé les composés ***6a–6c*** pour étudier l'effet de la distance entre la β-dicétone et le groupe carboxyle sur le transport du Ca^{2+}. On a mis au point une méthode générale de synthèse de ces composés. Les réactions clés de cette voie sont les alcoylations régiosélectives consécutives du dianion de la pentane-2,4-dione avec les bromures appropriés.

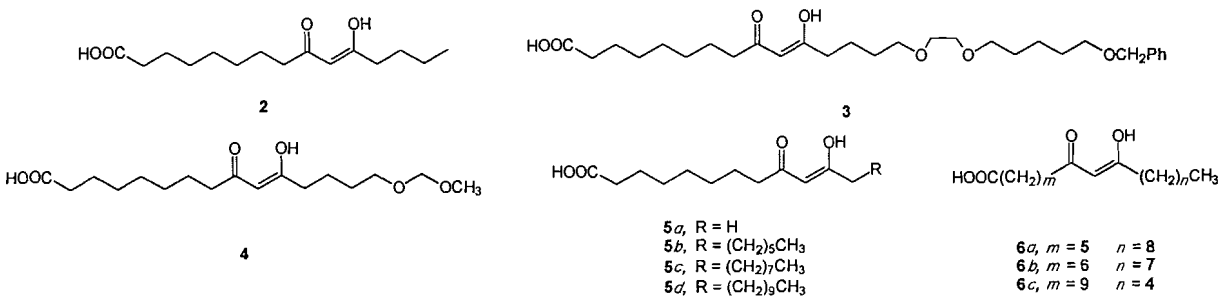

2 **3** **4**

5a, R = H
5b, R = $(CH_2)_5CH_3$
5c, R = $(CH_2)_7CH_3$
5d, R = $(CH_2)_9CH_3$

6a, *m* = 5 *n* = 8
6b, *m* = 6 *n* = 7
6c, *m* = 9 *n* = 4

[Traduit par la Rédaction]

Introduction

Ionomycin (**1**) is a polyether calcium ionophore isolated from a strain of *Streptomyces conglobatus* (1). Its molecular structure was determined by Toeplitz et al. using ^1H NMR spectroscopy, mass spectrometry, and X-ray crystallographic analysis of three crystalline forms of its cadmium and calcium salts (2).

Like other polyether Ca^{2+} ionophores, ionomycin has been found to be a potent antimicrobial agent. It is active against Gram-positive bacteria with no demonstrable effect against Gram-negative bacteria. However, ionomycin was found to have unusual physical, chemical and biological properties. It possesses a β-diketo group that, together with the carboxyl group, confers dibasic character to the ionophore. It has a very high affinity for Ca^{2+} and other divalent cations. In fact, the calcium salt of ionomycin was extracted from an aqueous solution of pH 12 that had been made alkaline with sodium hydroxide (3).

Ionomycin is unique among the polyether ionophores in that it forms a neutral 1:1 Ca^{2+} salt (2). As shown in the crystal structure of this Ca^{2+} salt of ionomycin (Fig. 1), the carboxylate group, the enolate of the β-diketone, two hydroxyl groups, and a tetrahydrofuranyl oxygen form an octahedral complex around the Ca^{2+}. The ligand wraps around the Ca^{2+} ion with the oxygen atoms directed towards the inside of the sphere. The alkyl groups, on the other hand, protrude from the shell, providing the Ca^{2+} salt with its lipophilic properties.

Liu and Hermann investigated the extraction of Ca^{2+} ions

[1]Author to whom correspondence may be addressed.

[2]Revision received January 4, 1994.

Can. J. Chem. Downloaded from www.nrcresearchpress.com by EESC ESCOLA DE ENGENHARIA on 09/08/12
For personal use only.

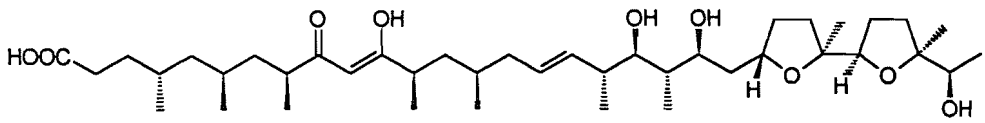

1

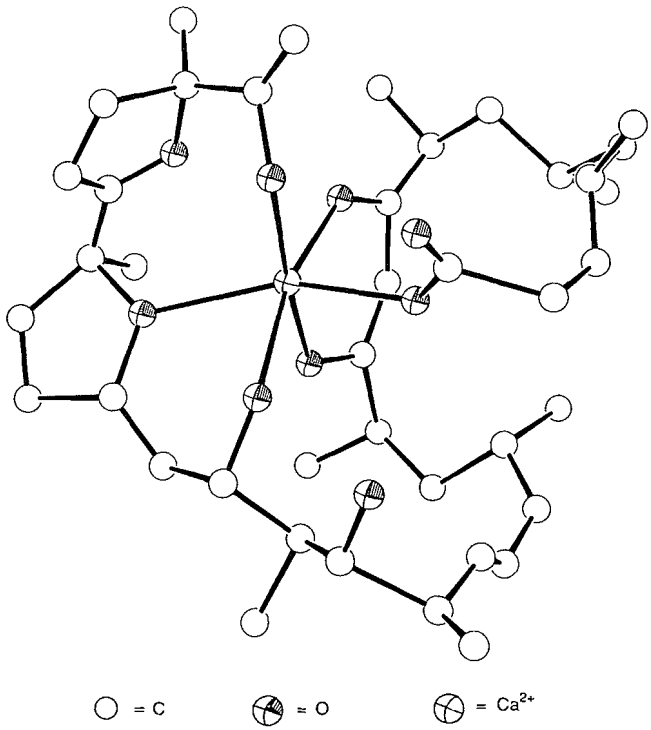

FIG. 1. Crystal structure of the calcium salt of ionomycin (2).

from an aqueous phase into an organic phase and the transport of Ca^{2+} across an organic barrier by ionomycin (4). The selectivity of ionomycin for divalent cations was shown to be $Ca^{2+} > Mg^{2+} \gg Sr^{2+} = Ba^{2+}$. No complexation or transport of monovalent cations by ionomycin could be detected.

Owing to its ability to selectively bind and transport Ca^{2+} across an organic barrier, ionomycin has been widely used as a tool to investigate the role of calcium ion as a second messenger in biological systems. In studies of rat liver mitochondria, it was shown that ionomycin efficiently catalyzed the exchange of two protons for one Ca^{2+} across the cell membrane (5, 6). Ionomycin has been found to stimulate the release of histamine from mast cells and catecholamine from pheochromocytoma cells by transporting Ca^{2+} across the cell membranes (7). It has also been linked to the activation of human blood platelets by facilitating the transport of Ca^{2+} across the membrane and mobilizing Ca^{2+} stored in organelles (8).

Although the ability of ionomycin to mimic the effects of many physiological cell stimuli has been demonstrated, little is known about the structural features controlling Ca^{2+} binding and transport by ionomycin. This prompted us to design and synthesize a series of simple ionomycin analogues to study the role of the functional groups of ionomycin in Ca^{2+} binding and transport and to study the effect of other structural features, such as lipophilicity and oxygen coordination sites, on Ca^{2+} transport.

Results and discussion

The design of ionomycin analogues was based on the literature data on the mode of action of ionomycin itself. The functional groups thought to be vital to the function of ionomycin would be retained in the synthetic analogues while the numerous stereochemical centers found along the carbon backbone of ionomycin would be omitted to simplify the synthesis of these model compounds. The chemical and physical data on ionomycin suggest that the β-diketone and carboxyl groups are crucial to its ionophoric properties. The crystal structure of the Ca^{2+} salt of ionomycin (Fig. 1) shows that both these groups are ionized and coordinated to the metal cation in the formation of the 1:1 Ca^{2+} salt. It was considered important to retain these two functional groups in the model compounds.

In the natural product, there is a seven-carbon chain separating the β-diketone and the carboxyl groups. The presence of this seven-carbon chain could certainly contribute to the high lipid solubility of the ionophore–Ca^{2+} complex. The distance between these two functional groups is such that a 12-membered ring is formed on chelation of a calcium ion by the carboxylate oxygen and the first oxygen of the β-diketone enolate as shown in **A**. Thus a seven-methylene unit was chosen as the linker for these two functional groups in the initial model compounds.

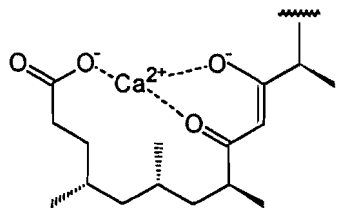

A

High lipophilicity of the model compounds may be needed for suitable membrane solubility. One of the simplest analogues fulfilling these requirements would be a 9,11-dioxocarboxylic acid such as 9,11-dioxopentadecanoic acid (**2**), which was chosen as one of the first target molecules.

Since one tetrahydrofuranyl and two hydroxyl oxygens of ionomycin are involved in coordination to the Ca^{2+} (Fig. 1), we speculated that it might be necessary to incorporate a side chain that contained appropriately placed oxygen atoms to retain the six Ca^{2+} binding sites found in ionomycin. A side chain that contains an ethylene glycol and an ether function five methylene units away was chosen to mimic the Ca^{2+} coordination sites in ionomycin. An ether function, such as a benzyl ether, could compensate for the decrease of lipophilicity created by the introduction of three oxygen atoms in such a molecule. Therefore, a benzyloxypentyloxyethoxyl unit was incorporated into analogue **2** to give another target analogue, 15-[2-(5-benzyloxy)-pentyloxy]-ethoxy-9,11-dioxopentadecanoic acid (**3**).

The presence of six oxygen coordination sites may not be necessary for binding and transport of Ca^{2+}. A molecule of water from the aqueous medium could occupy a Ca^{2+} coordina-

Can. J. Chem. Downloaded from www.nrcresearchpress.com by EESC ESCOLA DE ENGENHARIA on 09/08/12
For personal use only.

Can. J. Chem. Downloaded from www.nrcresearchpress.com by EESC ESCOLA DE ENGENHARIA on 09/08/12
For personal use only.

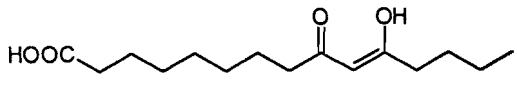

2

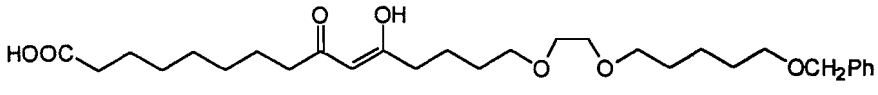

3

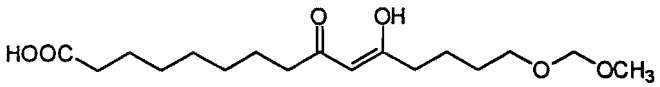

4

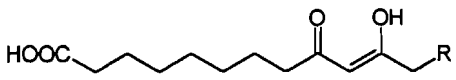

5*a*, R = H
5*b*, R = $(CH_2)_5CH_3$
5*c*, R = $(CH_2)_7CH_3$
5*d*, R = $(CH_2)_9CH_3$

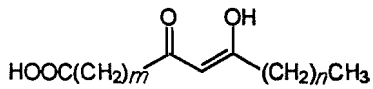

6*a*, *m* = 5 *n* = 8
6*b*, *m* = 6 *n* = 7
6*c*, *m* = 9 *n* = 4

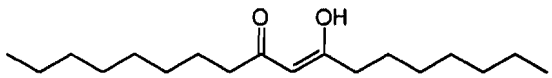

7

tion site as is often observed in the binding of Ca^{2+} with proteins and other ionophores such as lasalocid A (9, 10). Thus, it may be sufficient to incorporate a side chain that contains only one or two oxygen atoms as potential Ca^{2+} coordination sites. With this in mind we added a methoxymethoxyl unit to analogue **2** to give the target molecule, 15-methoxymethoxy-9,11-dioxopentadecanoic acid (**4**).

In addition to these three analogues, compounds **5***a*–**5***d* were synthesized as models to study the effect of lipid solubility on Ca^{2+} binding and transport. On the other hand, compounds **6***a*–**6***c*, which should have the same lipid solubility as **5***b* but have a different number of methylene units separating the β-diketone and the carboxyl group, were synthesized to study the effect of the distance between the β-diketone and carboxyl groups on Ca^{2+} binding and transport. Compound **7** possesses only the β-diketo group and was chosen as the final target.

Retrosynthetically, the carboxyl function of each proposed analogue could be made by oxidation of a hydroxyl group. The ether units in analogues **3** and **4** could be prepared using known chemistry (11). Thus the crucial part in the synthesis of the analogues was the introduction of the β-diketone and the construction of the carbon framework. A β-diketone could be prepared by oxidation of a β-hydroxyl ketone, which in turn could be generated by an aldol condensation between a methyl ketone and an aldehyde (eq. [1]). This route was used for the synthesis of the β-diketone in ionomycin (12).

Alternatively, the β-diketone could be generated by alkylation of the anion of a dithiane with an epoxide, followed by oxidation of the hydroxyl group and hydrolysis of the dithiane (eq. [2]). This method was employed in the synthesis of an ionomycin fragment (13).

Either of these two methods could be applied to the synthesis

[1] 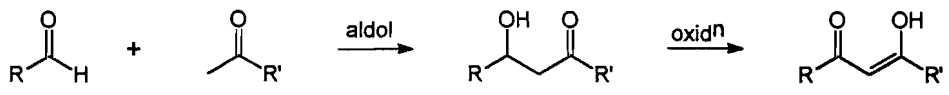

Can. J. Chem. Downloaded from www.nrcresearchpress.com by EESC ESCOLA DE ENGENHARIA on 09/08/12
For personal use only.

[2] 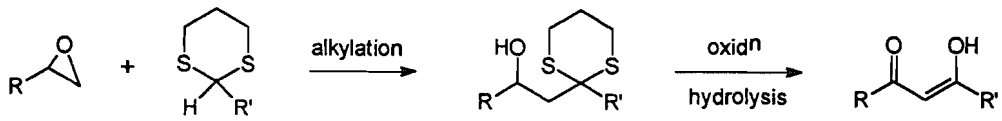

[3] 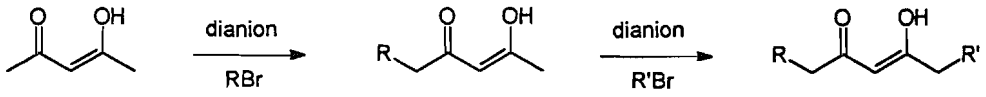

[4] 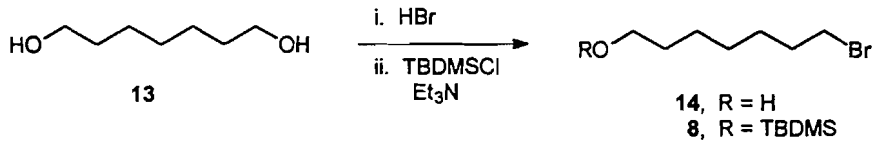

13

14, R = H
8, R = TBDMS

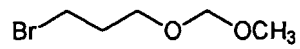

11

of the proposed analogues of ionomycin. However, neither route appeared to be very efficient for the synthesis of simple, unsubstituted compounds. A logical precursor of a β-diketone appeared to be the simplest β-diketone, the commercially available 2,4-pentanedione. Consecutive alkylation of 2,4-pentanedione at the methyl carbons could be achieved using the dianion chemistry (eq. [3]) (14). Thus we require bromides **8–12** for the synthesis of analogues **2–5**.

The synthesis of bromide **8**, a common intermediate in the preparation of many of the analogues, is illustrated in eq. [4]. Monobromination of 1,7-heptanediol (**13**) was achieved in 72% yield by continuously extracting a mixture of diol **13** and aqueous hydrobromic acid with heptane (15). The hydroxyl group of bromide **14** was protected as its *tert*-butyldimethylsilyl ether (16) to give bromide **8** in 82% yield. Bromide **11** was prepared in good yield by treatment of 3-bromo-1-propanol with phosphorus pentoxide and dimethoxymethane (17).

The synthesis of bromide **10** is outlined in Scheme 1. It started with the monobenzylation of 1,5-pentanediol (**15**) (18). The resulting mono alcohol **16** was subjected to the modified Williamson ether synthesis (19), which involved the vigorous mixing of a two-phase system containing **16**, 1-bromo-2-tetrahydropyranyloxylethane, and aqueous sodium hydroxide in the presence of a phase transfer catalyst, tetrabutylammonium hydrogen sulfate. The reaction gave the desired ether **17** in 83% yield. In contrast, only a small amount of alcohol **16** could be converted to ether **17** when the reaction was carried out using sodium hydride as a base in polar aprotic solvents such as dimethylformamide. The tetrahydropyranyl ether protecting group in **17** was cleaved to give alcohol **18** (20). The alcohol **18** was subjected to a second modified Williamson ether synthesis using 1-bromo-3-*tert*-butyldimethylsilyloxylpropane to give the ether **19**. Deprotection of the TBDMS ether (21) gave alcohol **20**, which was converted to bromide **10** (22) in good yield.

Next we proceeded to carry out the dianion alkylation reactions on 2,4-pentanedione as shown in Scheme 2 for the synthesis of analogue **2**. The dianion of 2,4-pentanedione was reacted with bromide **8** to give the monoalkylated β-diketone **21** in 81% yield.

The structure of the monoalkylated β-diketone **21** was confirmed by ^{1}H NMR spectroscopy, which exhibited a triplet at δ 2.51 that integrated to 0.4 proton and a triplet at δ 2.27 that integrated to 1.6 protons ascribable to the methylene protons at C-8 of the keto and enol forms of the β-diketone, respectively. A 0.6-proton singlet at δ 2.24 and a 2.4-proton singlet at δ 2.06 were assigned to the methyl protons at C-12 of the keto and enol forms, respectively. A 0.8-proton singlet at δ 15.50, a 0.8-proton singlet at δ 5.49, and a 0.4-proton singlet at δ 3.58 were assigned to the enol hydroxyl proton, the vinyl proton, and the methylene proton at C-10, respectively (Fig. 2).

The second dianion alkylation reaction was achieved by treat-

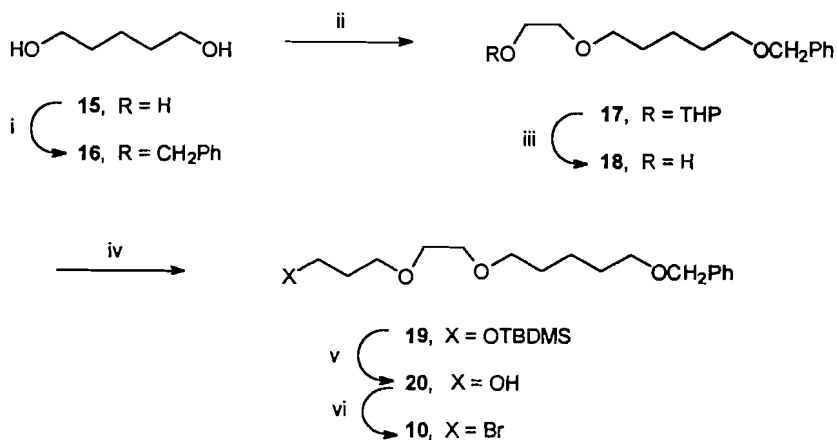

SCHEME 1.

i. NaH, $PhCH_2Br$, 54%; ii. NaOH, Bu_4NHSO_4, $THPO(CH_2)_2Br$, 83%; iii. PPTs, 83%; iv. NaOH, Bu_4NHSO_4, $TBDMSO(CH_2)_3Br$, 83%; v. Bu_4NF, 89%, vi. Ph_3P, CBr_4, 91%

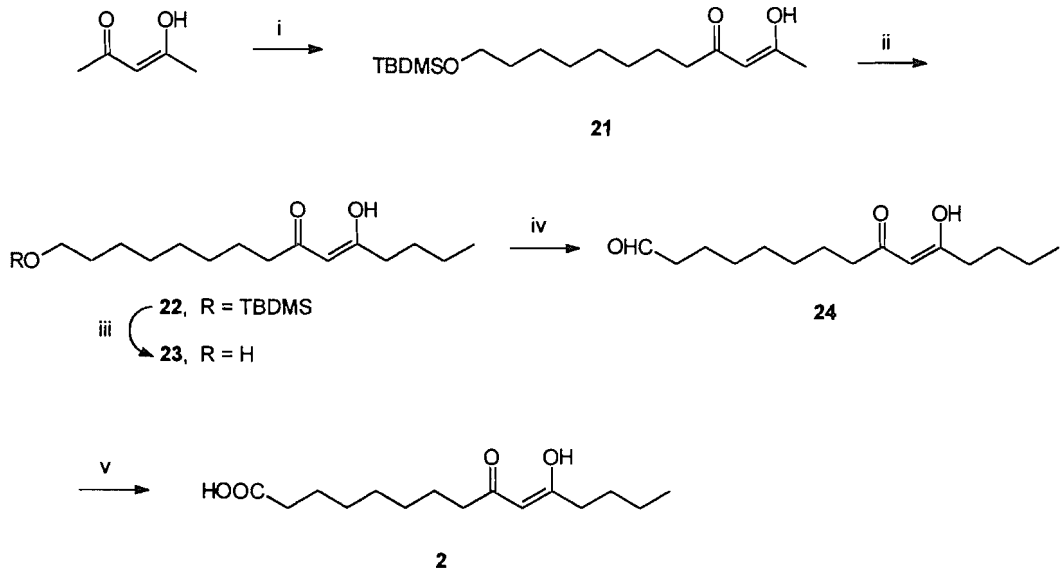

SCHEME 2.

i. NaH, *n*-BuLi, TBDMSO$(CH_2)_7$Br (**8**), 81%; ii. 2.0 LDA, $CH_3(CH_2)_2$Br, 81%; iii. Bu_4NF, 91%; iv. DMSO, DCC, Cl_2CHCO_2H; v. $AgNO_3$, NaOH, 69%

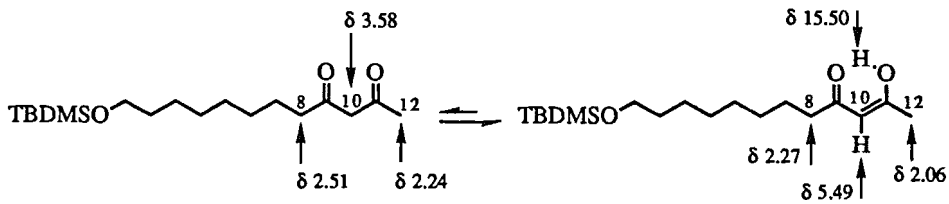

FIG. 2. Partial ^{1}H NMR assignments to the keto and enol forms of **21**.

ing the β-diketone **21** with two equivalents of lithium diisopropylamide to regioselectively generate the primary dianion that subsequently was reacted with one equivalent of 1-bromopropane (**9**) to produce the β-diketone **22** in 81% yield. The regioselectivity in this alkylation was confirmed by ^{1}H NMR and mass spectroscopy. The ^{1}H NMR spectrum of compound **22** showed four triplets at δ 2.50, 2.48, 2.28, and 2.26 integrating to a total of four protons ascribable to the methylene protons at C-8 and C-12 of the keto and enol forms of **22**. In addition, three singlets at δ 15.51, 5.48, and 3.54 integrating to a total of two protons were assigned to the enol hydroxyl proton, the vinyl proton, and the methylene proton at C-10. The mass spectrum of compound **22** showed peaks at *m/z* 313 and 127 corresponding to fragmentation α to the β-diketone group of **22**.

To complete the synthesis of analogue **2**, the silyl ether protecting group of compound **22** was cleaved to give alcohol **23**, which was oxidized to aldehyde **24** under Moffatt conditions (23). Treatment of **24** with silver oxide (24) produced the acid **2** in 69% yield for the two steps.

The synthesis of analogues **3**, **4**, and **5***a*–**5***d* started with the β-diketone **21** and followed a similar path with comparable yields as for **2** (Scheme 3). The syntheses of analogues **6***a*–**6***c* were accomplished in similar yields to those of analogue **5***b* (Scheme 4) and the synthesis of compound **7** was achieved by two consecutive dianion alkylations.

In conclusion, a series of analogues of ionomycin were designed to study the structural features affecting the ability of Ca^{2+} binding and transport by ionomycin. The syntheses of these analogues were achieved by consecutive regioselective alkylation of the dianion of 2,4-pentanedione with the appropriate bromides and subsequent oxidation of the β-diketone ω-alcohols. The results of the studies on the Ca^{2+} binding and transport properties of these ionomycin analogues and their potential as Ca^{2+} ionophores are reported in the following paper in this series (25).

Experimental section

General procedures

Melting points were determined on a Mel-Temp II melting point apparatus and were not corrected. Infrared spectra were recorded on a Bomem Michelson 100 FT-IR spectrophotometer using internal calibration. Liquid samples were applied directly between two 3-mm NaCl plates, and solid samples were dissolved in chloroform. Proton nuclear magnetic resonance spectra were recorded at 400 MHz on a Bruker WH-400 spectrometer or at 300 MHz on a Varian XL-300 spectrometer. Chemical shifts are reported on the δ scale, with deuterochloroform as solvent and tetramethylsilane as an internal standard. The multiplicity, coupling constants (if observable), and integrated peak area are indicated in parentheses after each signal. High-resolution mass spectra were determined on a Kratos-AEI model MS 50 spectrometer at 70 eV. Elemental analyses were performed by Mr. Peter Borda, Microanalysis Laboratory, University of British Columbia, Vancouver, B.C.

All reactions were monitored by thin-layer chromatography (TLC). Analytical TLC was performed on aluminum backed, precoated silica (SiO_2) gel plates (E. Merck, type 5554). The plates were visualized by ultraviolet fluorescence or by heating the plates after spraying them with a mixture of methanol, acetic acid, sulfuric acid, and anisaldehyde (90:10:5:1 by volume). Silica gel $PF_{254+366}$ supplied by E. Merck was used for both analytical and preparative thin-layer chromatography.

Can. J. Chem. Downloaded from www.nrcresearchpress.com by EESC ESCOLA DE ENGENHARIA on 09/08/12
For personal use only.

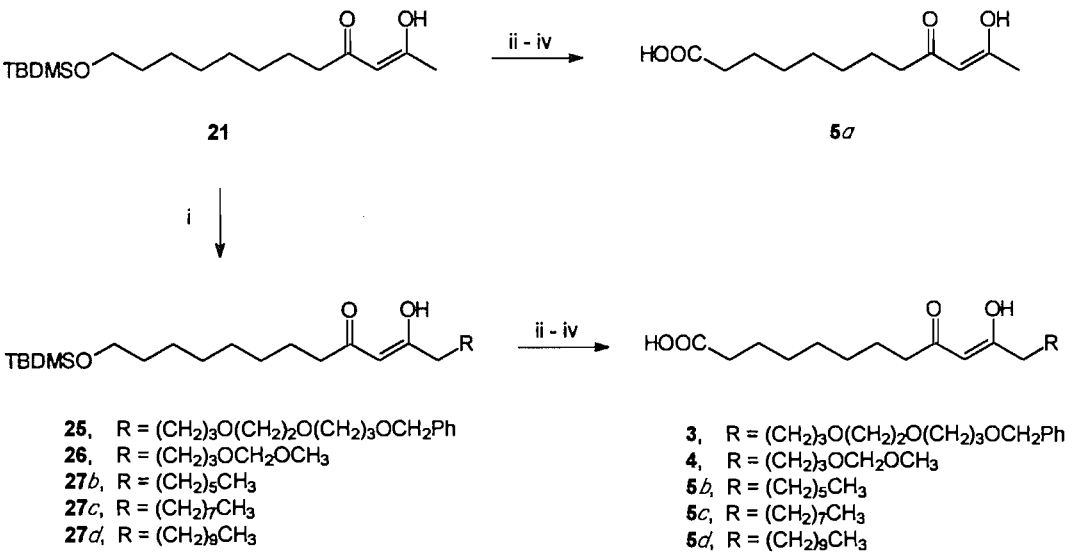

SCHEME 3.

i. 2.0 LDA, RBr; ii. Bu_4NF; iii. DMSO, DCC, Cl_2CHCO_2H; iv. $AgNO_3$, NaOH

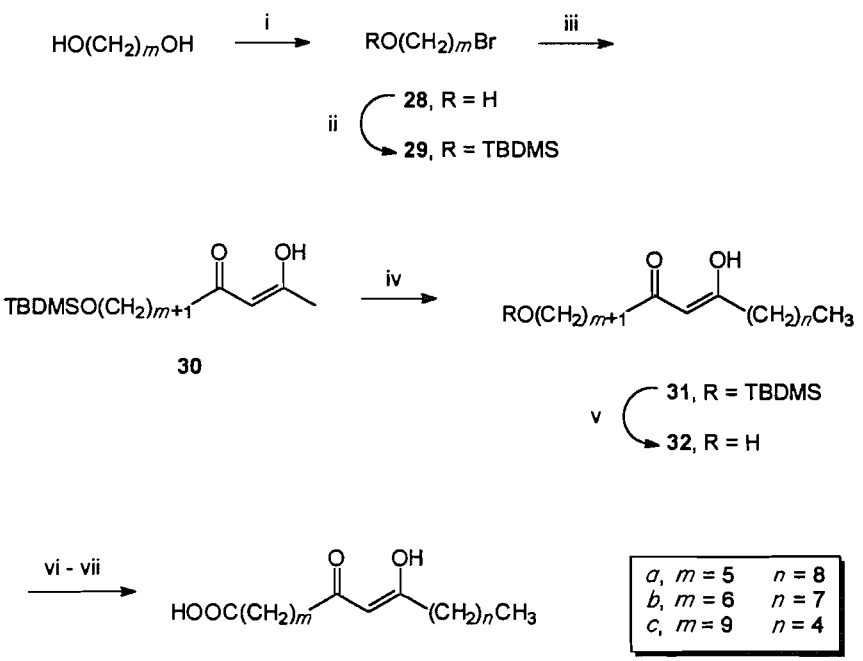

SCHEME 4.

i. HBr; ii. Et_3N, DMAP, TBDMSCl; iii. dianion from 2,4-pentanedione; iv. 2.0 LDA, $CH_3(CH_2)_{n-1}Br$; v. Bu_4NF: vi. DMSO, DCC, Cl_2CHCO_2H; vii. $AgNO_3$, NaOH

Flash chromatography (26) was performed using Silica Gel 60, 230–400 mesh ASTM, supplied by E. Merck. All solvent systems are expressed in ratios by volume (v/v).

Materials

The petroleum ether used was of boiling range 30–60°C. Dry solvents and reagents were prepared as follows: diethyl ether and tetrahydrofuran by distillation from sodium benzophenone; dichloromethane by distillation from calcium hydride and methanol by distillation from magnesium methoxide. *n*-Butyllithium (in hexane) was obtained from the Aldrich Chemical Company and was standardized by titration against 2,2-diphenylacetic acid in THF at room temperature to the appearance of a faint yellow colour (27). All other reagents and solvents were either of reagent grade and used directly, or purified according to literature procedures (28). All reactions were run under a dry nitrogen atmosphere. Organic extracts were dried over anhydrous magnesium sulfate.

A. General procedure for the preparation of (1, n) bromo alcohols from (1, n)-diols

A suspension of the diol in 48% HBr was prepared in a 1-L liquid–liquid continuous extractor. The suspension was heated in an oil bath while being continuously extracted with 300 mL of heptane at 90°C for 72 h. The extract was cooled and the organic layer separated, washed

Can. J. Chem. Downloaded from www.nrcresearchpress.com by EESC ESCOLA DE ENGENHARIA on 09/08/12
For personal use only.

Can. J. Chem. Downloaded from www.nrcresearchpress.com by EESC ESCOLA DE ENGENHARIA on 09/08/12
For personal use only.

with saturated $NaHCO_3$, brine, and dried over $MgSO_4$. Removal of the solvent under reduced pressure gave the crude bromo alcohol, which was further purified by column chromatography.

*7-Bromo-1-heptanol (**14**)*

This compound was prepared according to procedure A using 1,7-heptanediol (**13**) (5.8 g, 44 mmol) and 48% HBr (7.5 mL, 66 mmol). The crude oil was purified by column chromatography using petroleum ether:ethyl acetate (6:1) as eluent to give 6.2 g (72%) of **14** as a colourless liquid: R_f 0.54 (1:1 petroleum ether:ethyl acetate eluent); IR ν_{max}: 3347, 2930, 2858, 1452, 1254, 1054, and 726 cm^{-1}; ^1H NMR (300 MHz) δ: 3.66 (t, J = 6 Hz, 2H), 3.42 (t, J = 6 Hz, 2H), 1.87 (qn, J = 6 Hz, 2H), 1.57 (m, 2H), and 1.52–1.25 (m, 7H). Exact Mass calcd. for $C_7H_{15}BrO$–H: 195.0204, 193.0224; found: 195.0213, 193.0228.

B. General procedure for the preparation of tert-*butyldimethylsilyl ethers from alcohols*

Freshly distilled triethylamine (2.0 equiv.) was added into a solution of the alcohol (1.0 equiv.) in 100 mL of CH_2Cl_2 at room temperature. A catalytic amount of 4-dimethylaminopyridine and *tert*-butyldimethylsilyl chloride (1.5 equiv.) was added. The reaction was stirred at room temperature for 24 h. The mixture was then quenched with 1 N HCl and extracted with ether three times. The combined organic layers were washed twice with saturated $NaHCO_3$ and once with brine. The organic phase was dried over $MgSO_4$ and concentrated under reduced pressure. The crude product was purified by column chromatography.

*1-Bromo-7-(*tert-*butyldimethylsilyloxy)-heptane (**8**)*

This compound was prepared according to procedure B, using the alcohol **13** (1.17 g, 6.0 mmol). Purification of the crude product by column chromatography using petroleum ether:ethyl acetate (15:1) as eluent gave 1.50 g (82%) of **8** as a colourless oil: R_f 0.83 (6:1 petroleum ether:ethyl acetate eluent); IR ν_{max}: 2937, 2858, 1466, 1388, 1361, 1254, 1101, 938, 838, and 776 cm^{-1}; ^1H NMR (400 MHz) δ: 3.64 (t, J = 6 Hz, 2H), 3.44 (t, J = 6 Hz, 2H), 1.86 (qn, J = 6 Hz, 2H), 1.53–1.31 (m, 8H), 0.89 (s, 9H), and 0.05 (s, 6H). Exact Mass calcd. for $C_{13}H_{29}SiBrO - C_4H_9$: 253.0438, 251.0458; found: 253.0450, 251.0460.

*1-Bromo-3-methoxymethoxypropane (**11**)*

To a solution of 3-bromo-1-propanol (3.08 g, 22.1 mmol) in 35 mL of CH_2Cl_2 was added dimethoxymethane (30.3 g, 399 mmol). The solution was cooled to 0°C and phosphorus pentoxide (approximately 1.0 g at a time) was added every 10 min until the reaction was completed as shown by TLC. The mixture was poured into 200 mL of an ice-cooled saturated $NaHCO_3$ and the gummy residue remaining in the reaction flask carefully quenched with saturated $NaHCO_3$. The aqueous layer from the combined work-up solutions was extracted with ether. The combined organic layers were washed with brine, dried over $MgSO_4$, and concentrated under reduced pressure. Vacuum distillation of the crude product gave 3.67 g (91%) of **11** as a colourless liquid: bp 85°C/32 Torr (1 Torr = 133.3 Pa); IR ν_{max}: 2931, 2886, 1476, 1449, 1383, 1284, 1258, 1216, 1144, 1045, 919, 880, and 766 cm^{-1}; ^1H NMR (400 MHz) δ: 4.63 (s, 2H), 3.67 (t, J = 6 Hz, 2H), 3.54 (t, J = 6 Hz, 2h), 3.38 (s, 3H), and 2.14 (qn, J = 6 Hz, 2H). Exact Mass calcd. for $C_5H_{11}BrO_2$–H: 182.9841; found: 182.9847.

*5-Benzyloxy-1-pentanol (**16**)*

Sodium hydride (4.58 g, 80% in oil, 153 mmol) was added to a 500-mL, two-neck, round-bottom flask and washed twice with 20 mL of THF. A solution of 1,5-pentanediol (**15**) (7.95 g, 76.4 mmol) in 20 mL of THF and 200 mL of THF was then added. The mixture was stirred at room temperature for 30 min. Benzyl bromide (9.1 mL, 77 mmol) was slowly added and the mixture was refluxed overnight. The reaction mixture was quenched with H_2O. The organic layer was washed once with 1 N HCl and twice with brine, dried over $MgSO_4$, and concentrated under reduced pressure. The crude product was chromatographed on a silica gel column using petroleum ether:ethyl acetate (3:1) as eluent to give 7.98 g (54%) of **16** as a colourless oil: R_f 0.38 (1:1 petroleum ether:ethyl acetate eluent); IR ν_{max}: 3372, 3090, 3063, 3030, 2897, 2850, 1496, 1454, 1363, 1206, and 1077 cm^{-1}; ^1H NMR (400 MHz) δ: 7.40–7.24 (m, 5H), 4.52 (s, 2H), 3.65 (t, J = 6 Hz, 2H), 3.52 (t, J = 6 Hz, 2H), and 1.70–1.40 (m, 7H). Exact Mass calcd. for $C_{12}H_{18}O_2$: 194.1302; found: 194.1304.

*5-Benzyloxy-1-(2-tetrahydropyranyloxy)-ethoxypentane (**17**)*

A 25-mL, three-neck round-bottom flask was charged with 50% sodium hydroxide (4.0 mL, 50 mmol), 1-bromo-2-tetrahydropyranyloxyethane (4.18 g, 20.0 mmol), and the alcohol **16** (0.97 g, 5.0 mmol). Tetrabutylammonium hydrogen sulfate (0.15 g, 0.44 mmol) was added. The two-phase mixture was stirred vigorously and heated to 65°C for 72 h. The reaction mixture was cooled to room temperature and taken up into 100 mL of ether. The organic layer was washed with H_2O, brine, dried over $MgSO_4$, and concentrated under reduced pressure. Purification of the crude product by column chromatography using petroleum ether:ethyl acetate (6:1) as eluent gave 1.34 g (83%) of **17** as a light yellow oil: R_f 0.16 (6:1 petroleum ether:ethyl acetate eluent); IR ν_{max}: 3086, 3060, 3029, 2935, 2861, 1495, 1453, 1359, 1269, 1201, 1184, 1106, 1032, 988, 929, 906, 872, 814, and 739 cm^{-1}; ^1H NMR (300 MHz) δ: 7.40–7.24 (m, 5H), 4.64 (t, J = 4 Hz, 1H), 4.50 (s, 2H), 3.94–3.80 (m, 2H), 3.62–3.55 (m, 2H), 3.50–3.46 (m, 6H), and 1.90–1.40 (m, 12H). Exact Mass calcd. for $C_{19}H_{30}O_4$: 322.2136; found: 322.2152.

*2-(5-Benzyloxy)-pentyloxy-1-ethanol (**18**)*

Pyridinium *p*-toluenesulfonate (42 mg, 0.16 mmol) was added to a solution of the tetrahydropyranyl ether **17** (550 mg, 1.60 mmol) in 15 mL of MeOH. The mixture was stirred at room temperature for 12 h. The solvent was removed under reduced pressure and the residue was taken up in ether, washed with saturated $NaHCO_3$ and brine, dried over $MgSO_4$, and concentrated under reduced pressure. The crude oil was chromatographed on a silica gel column using petroleum ether:ethyl acetate (6:1) as eluent to give 368 mg (91%) of **18** as a light yellow oil: R_f 0.30 (1:1 petroleum ether:ethyl acetate eluent); IR ν_{max}: 3414, 3082, 3063, 3030, 2932, 2862, 1495, 1454, 1362, 1207, 1086, 893, and 740 cm^{-1}; ^1H NMR (300 MHz) δ: 7.40–7.24 (m, 5H), 4.52 (s, 2H), 3.72 (m, 2H), 3.56–3.44 (m, 2H), 3.44 (t, J = 5 Hz, 4H), 2.04 (t, J = 5 Hz, 1H), and 1.69–1.53 (m, 4H), 1.50–1.40 (m, 2H). Exact Mass calcd. for $C_{14}H_{22}O_3$: 238.1563; found: 238.1559.

*5-Benzyloxy-1-[2-(3-*tert-*butyldimethylsilyloxy)propyloxy]-ethoxypentane (**19**)*

Following the procedure for the preparation of 5-benzyloxy-1-(2-tetrahydropyranyloxy)-ethoxypentane (**17**), the alcohol **18** (300 mg, 1.26 mmol) was reacted with 1-bromo-3-*tert*-butyldimethylsilyloxypropane (1.28 g, 5.04 mmol) to give the ether **19**. The crude product was purified by column chromatography using petroleum ether:ethyl acetate (6:1) as eluent to give 1.34 g (83%) of **19** as a light yellow oil: R_f 0.20 (6:1 petroleum ether:ethyl acetate eluent); IR ν_{max}: 3087, 3064, 3030, 2934, 2862, 1463, 1360, 1253, 1108, 1015, 841, 777, and 737 cm^{-1}; ^1H NMR (300 MHz) δ: 7.36–7.24 (m, 5H), 4.50 (s, 2H), 3.70 (t, J = 6 Hz, 2H), 3.58–3.51 (m, 6H), 3.50–3.42 (m, 4H), 1.79 (qn, J = 6 Hz, 2H), 1.69–1.58 (m, 4H), 1.49–1.40 (m, 2H), 0.89 (s, 9H), and 0.04 (6H, s). Exact Mass calcd. for $C_{23}H_{42}SiO_4$: 410.2841; found: 410.2861.

C. General procedure for the cleavage of tert-*butyldimethylsilyl ethers*

To a solution of the silyl ether (1.0 equiv.) in 40 mL of THF was added a solution of tetrabutylammonium fluoride in THF (2.0 equiv.). The solution was stirred at room temperature for 12 h. The solvent was removed under reduced pressure and the residue was taken up in ether. The organic layer was washed twice with brine, dried over $MgSO_4$, and concentrated under reduced pressure. The crude product was purified by column chromatography.

*3-[2-(5-Benzyloxy)-pentyloxy]-ethoxy-1-propanol (**20**)*

This compound was prepared according to procedure C using the silyl ether **19** (430 mg, 1.05 mmol) and a solution of tetrabutylammo-

Can. J. Chem. Downloaded from www.nrcresearchpress.com by EESC ESCOLA DE ENGENHARIA on 09/08/12
For personal use only.

nium fluoride in THF (1.0 M, 2.10 mL, 2.1 mmol). Purification of the crude product by column chromatography using petroleum ether:ethyl acetate (3:1) as eluent gave 275 mg (89%) of **20** as a colourless oil: R_f 0.20 (1:1 petroleum ether:ethyl acetate eluent); IR ν_{max}: 3426, 3085, 3063, 3030, 2932, 2863, 1495, 1454, 1361, 1296, 1204, 1091, and 740 cm^{-1}; ^1H NMR (400 MHz) δ: 7.38–7.26 (m, 5H), 4.50 (s, 2H), 3.78 (bt, J = 6 Hz, 2H), 3.69 (t, J = 6 Hz, 2H), 3.62–3.58 (m, 2H), 3.57–3.55 (m, 2H), 3.47 (t, J = Hz, 2H), 3.45 (t, J = 6 Hz, 2H), 2.48 (bs, 1H), 1.83 (qn, J = Hz, 2H), 1.69–1.56 (m, 4H), and 1.49–1.40 (m, 2H). Exact Mass calcd. for $C_{17}H_{28}O_4 - C_3H_8O$: 236.1407; found: 236.1400.

*5-Benzyloxy-1-[2-(3-bromo)-propyloxy]-ethoxyheptane (**10**)*

A 25-mL round-bottom flask was charged with the alcohol **21** (296 mg, 1.00 mmol) in 12 mL of CH_2Cl_2. The solution was cooled to 0°C. Freshly recrystallized triphenylphosphine (340 mg, 1.30 mmol) and carbon tetrabromide (415 mg, 1.25 mmol) were added. The mixture was stirred at 0°C for 30 min, allowed to warm up to room temperature, and then diluted with ether. The organic layer was washed with H_2O, brine, dried over $MgSO_4$, and concentrated under reduced pressure. The crude product was purified by column chromatography using petroleum ether:ethyl acetate (9:1) as eluent to give 315 mg (88%) of **10** as a colourless oil: R_f 0.14 (9:1 petroleum ether:ethyl acetate eluent); IR ν_{max}: 3080, 3063, 3030, 2930, 2862, 1495, 1454, 1360, 1256, 1209, and 1110 cm^{-1}; ^1H NMR (400 MHz) δ: 7.38–7.25 (m, 5H), 4.50 (s, 2H), 3.66–3.36 (m, 6H), 3.54–3.44 (m, 6H), 2.12 (qn, J = 6 Hz, 2H), 1.69–1.56 (m, 4H), and 1.49–1.40 (m, 2H). Exact Mass calcd. for $C_{17}H_{27}BrO_3$: 360.1116, 358.1136; found: 360.1109, 358.1139.

D. General procedure for the alkylation of the dianion from 2,4-pentanedione

Sodium hydride (1.2 equiv.) was added to a 100-mL, two-neck round-bottom flask and washed twice with 20 mL of THF. Then 20 mL of THF was added and the resulting suspension was cooled to 0°C. A solution of 2,4-pentanedione (1.2 equiv.) in 15 mL of THF was added through an addition funnel. The resulting white suspension was stirred for 30 min and treated with *n*-BuLi (1.2 equiv.). The orange solution was stirred for 20 min. A solution of the bromide (1.0 equiv.) in 10 mL of THF was slowly added through the addition funnel and the mixture was stirred at 0°C for 1 h and at room temperature for 20 min. The mixture was quenched with saturated NH_4Cl, acidified with 1 N HCl, and extracted with ether three times. The combined organic layers were washed twice with saturated $NaHCO_3$ and once with brine, dried over $MgSO_4$, and concentrated under reduced pressure. The crude product was purified by column chromatography.

*12-(tert-Butyldimethylsilyloxy)-2,4-dodecanedione (**21**)*

This compound was prepared according to procedure D using sodium hydride (610 mg, 50% in oil, 12.7 mmol), 2,4-pentanedione (1.36 mL, 12.7 mmol), *n*-BuLi (7.84 mL, 1.62 M, 12.7 mmol), and the bromide **8** (3.26 g, 10.6 mmol). Purification of the crude product by column chromatography using a mixture of petroleum ether and ethyl acetate (15:1) as eluent gave 2.20 g of **21** and 700 mg of **8**. The yield, based on the recovered bromide, was 81%: R_f 0.61 (6:1 petroleum ether:ethyl acetate eluent); IR ν_{max}: 2934, 2857, 1709, 1614, 1465, 1253, 1100, 1006, 939, 838, and 776 cm^{-1}; ^1H NMR (400 MHz) δ: 15.50 (bs, 0.8 H), 5.49 (s, 0.8 H), 3.61 (t, J = 7 Hz, 2H), 3.58 (s, 0.4 H), 2.51 (t, J = 8 Hz, 0.4 H), 2.27 (t, J = 8 Hz, 1.6 H), 2.24 (s, 0.6 H), 2.06 (s, 2.4 H), 1.65–1.46 (m, 6H), 1.36–1.26 (m, 6H), 0.89 (s, 9H), and 0.04 (s, 6H). Exact Mass calcd. for $C_{18}H_{36}SiO_3 - CH_3$: 313.2190; found: 313.2208.

E. General procedure for the regioselective alkylation of β-diketone dianions

Lithium diisopropylamide (2.0 equiv.) was prepared at –78°C by addition of *n*-BuLi (2.0 equiv.) to a solution of diisopropylamine (2.0 equiv.) in 20 mL of THF and stirring of the mixture for 30 min. It was then cannulated into an addition funnel and added to a solution of the β-diketone (1.0 equiv.) in 20 mL of THF at –78°C over a period of 1 h. The mixture was stirred at –78°C for 24 h and allowed to warm up to 0°C. The bromide (1.0 equiv.) in 10 mL of THF was slowly added and the mixture was stirred at 0°C for 12 h. The mixture was then quenched with saturated NH_4Cl, acidified with 1 N HCl, and extracted with ether three times. The combined organic phases were washed with saturated $NaHCO_3$, brine, dried over $MgSO_4$, and concentrated under reduced pressure. The crude product was purified by column chromatography.

*15-(tert-Butyldimethylsilyloxy)-5,7-pentadecanedione (**22**)*

This compound was prepared according to procedure E using *n*-Buli (1.70 mL, 1.53 M, 2.60 mmol), diisopropylamine (0.36 mL, 2.6 mmol), the β-diketone **21** (426 mg, 1.30 mmol), and 1-bromopropane (**9**) (160 mg, 1.30 mmol). Purification of the crude product by column chromatography using petroleum ether:ethyl acetate (20:1) gave 294 mg of **22** and 294 mg of the starting β-diketone **21**. The yield, based on the recovered β-diketone **21**, was 81%: R_f 0.74 (6:1 petroleum ether:ethyl acetate eluent); IR ν_{max}: 2936, 2858, 1707, 1611, 1463, 1253, 1100, 949, 838, 776, and 704 cm^{-1}; ^1H NMR (400 MHz) δ: 15.50 (bs, 0.8H), 5.48 (s, 0.8H), 3.61 (t, J = 7 Hz, 2H), 3.54 (s, 0.4H), 2.50 (t, J = 8 Hz, 0.4H), 2.48 (t, J = 8 Hz, 0.4H), 2.28 (t, J = 8 Hz, 1.6H), 2.26 (t, J = 8 Hz, 1.6H), 1.66–1.48 (m, 6H), 1.40–1.24 (m, 10H), 0.93 (t, J = 7 Hz, 3H), 0.90 (s, 9H), 0.06 (s, 6H). Exact Mass calcd. for $C_{21}H_{42}SiO_3 - CH_3$: 355.2658; found: 355.2662.

*15-Hydroxy-5,7-pentadecanedione (**23**)*

This compound was prepared according to procedure C using the silyl ether **22** (444 mg, 1.20 mmol) and tetrabutylammonium fluoride in THF (2.40 mL, 1.0 M, 2.4 mmol). Purification of the crude product by column chromatography using petroleum ether:ethyl acetate (6:1) as eluent gave 277 mg of **23** as a colourless solid: R_f 0.58 (1:1 petroleum ether:ethyl acetate eluent); mp 41.5°C; IR ν_{max}: 3621, 3462, 2934, 2859, 1723, 1700, 1605, 1460, 1355, 1307, 1149, 1098, 1005, 957, and 916 cm^{-1}; ^1H NMR (400 MHz) δ: 15.50 (bs, 0.7H), 5.48 (s, 0.7H), 3.65 (t, J = 7 Hz, 2H), 3.53 (s, 0.6H), 2.51 (t, J = 8 Hz, 0.6H), 2.50 (t, J = 8 Hz, 0.6 H), 2.28 (5, J = 8 Hz, 1.4 H), 2.27 (t, J = 8 Hz, 1.4H), 1.67–1.50 (m, 8H), 1.40–1.12 (m, 9H), and 0.93 (5, J = 7 Hz, 3H). Exact Mass calcd. for $C_{15}H_{28}O_3$: 256.2031, found: 256.2031.

F. General procedure for the oxidation of alcohols to acids

To the alcohol (1.0 equiv.) in 15 mL of CH_2Cl_2 and 15 mL of dimethyl sulfoxide was added 1,3-dicyclohexylcarbodiimide (6.0 equiv.) and dichloroacetic acid (0.5 equiv.). This mixture was stirred for 2 h, diluted with ethyl acetate, and treated with oxalic acid (6.0 equiv.). The mixture was poured into brine, filtered to remove the urea precipitate, and extracted with ethyl acetate. The organic layer was concentrated under reduced pressure. The resulting oil was dissolved in 24 mL 50% THF–H_2O. Silver nitrate (8.0 equiv.) and NaOH (16 equiv.) were added and the mixture was stirred for 4 h. The precipitate was filtered and washed with ethyl acetate and water. The aqueous layer was acidified with 1 N HCl and was then extracted with ethyl acetate. The organic extract was washed with brine, dried over $MgSO_4$, and concentrated under reduced pressure. The crude product was purified by recrystallization from hexanes or by column chromatography.

*9,11-Dioxopentadecanoic acid (**2**)*

This compound was prepared according to F using the alcohol **23** (384 mg, 1.34 mmol), 1,3-dicyclohexylcarbodiimide (1.67 g, 7.95 mmol), and dichloroacetic acid (53 mL, 0.69 mmol). The crude aldehyde **24** was subsequently treated with silver nitrate (1.85 g, 10.8 mmol) and NaOH (0.86 g, 22 mmol). The crude product was purified by recrystallization from hexanes to give 270 mg (69%) of **2** as colourless crystals: R_f 0.54 (5% HOAc in 3:1 petroleum ether:ethyl acetate eluent); mp 43.0°C; IR ν_{max}: 3346-2480, 2937, 2861, 1713, 1601, 1459, 1286, 1116, 968, and 903 cm^{-1}; ^1H NMR (300 MHz) δ: 15.50 (bs, 0.7H), 5.48 (s, 0.7H), 3.53 (s, 0.6H), 2.51 (t, J = 8 Hz, 0.6H), 2.50 (t, J = 8Hz, 0.6H), 2.33 (t, J = 7 Hz, 2H), 2.28 (t, J = 8 Hz, 1.4H), 2.27 (t, J = 8 Hz, 1.4H), 1.70–1.56 (m, 7H), 1.40–1.27 (m, 8H), and 0.93 (t, J = 7 Hz, 3H). Exact Mass calcd. for $C_{15}H_{26}O_4$: 270.1824; found: 270.1828. Anal. calcd. for $C_{15}H_{26}O_4$: C 66.67, H 9.63; found: C 66.60, H 9.65.

Can. J. Chem. Downloaded from www.nrcresearchpress.com by EESC ESCOLA DE ENGENHARIA on 09/08/12
For personal use only.

*1-[2-(5-Benzyloxy)pentyloxy]-ethoxy-15-(*tert*-butyldimethylsilyloxy)-5,7-pentadecanedione (**25**)*

This compound was prepared according to E using the β-diketone **21** (426 mg, 1.30 mmol) and the bromide **10** (359 mg, 1.00 mmol). The crude product was purified by column chromatography using silica gel and petroleum ether:ethyl acetate (9:1) to give 270 mg of **25** and 104 mg of **10**. The yield, based on the recovered bromide, was 85%: R_f 0.12 (9:1 petroleum ether:ethyl acetate eluent); IR ν_{max}: 3080, 3060, 3026, 1710, 1703, 1609, 1460, 1360, 1252, 1110, and 840 cm^{-1}; ^1H NMR (400 MHz) δ: 15.48 (bs, 0.8H), 7.38–7.26 (m, 5H), 5.47 (s, 0.8H), 4.51 (s, 2H), 3.65–3.53 (m, 6.4H), 3.50–3.44 (m, 6H), 2.53 (t, J = 8 Hz, 0.4H), 2.48 (t, J = 8 Hz, 0.4H), 2.30 (t, J = 8 Hz, 1.6H), 2.26 (t, J = 8 Hz, 1.6H), 1.72–1.38 (m, 14H), 1.36–1.25 (m, 8H), 0.90 (s, 9H), and 0.50 (s, 6H). Exact Mass calcd. for $C_{35}H_{62}SiO_6$: 606.4299; found: 606.4313.

1-[2-(5-Benzyloxy)pentyloxy]-ethoxy-15-hydroxy-5,7-pentadecanedione

This compound was prepared according to procedure C using the silyl ether **25** (1.40 g, 2.58 mmol). The crude product was purified by column chromatography using petroleum ether:ethyl (6:1) as eluent to give 993 mg (87%) of the desired alcohol from **25** as a colourless oil: R_f 0.30 (1:1 petroleum ether:ethyl acetate eluent); IR ν_{max}: 3437, 3080, 3060, 3030, 2930, 2863, 1710, 1702, 1606, 1453, 1361, 1096, and 739 cm^{-1}; ^1H NMR (400 MHz) δ: 15.50 (bs, 0.8H), 7.38–7.24 (m, 5H), 5.48 (s, 0.8H), 4.50 (s, 2H), 3.64 (t, J = 7 Hz, 2H), 3.57 (s, 2H), 3.56 (s, 2H), 3.53 (s, 0.4H), 3.50–3.43 (m, 6H), 2.53 (t, J = 8Hz, 0.4H), 2.49 (t, J = 8 Hz, 0.4H), 2.30 (t, J = 8 Hz, 1.6H), 2.26 (t, J = 8Hz, 1.6H), 1.72–1.50 (m, 13H), 1.46–1.38 (m, 2H), and 1.38–1.25 (m, 8H). Exact Mass calcd. for $C_{29}H_{48}O_6$: 492.3438; found: 492.3445.

*15-[2-(5-Benzyloxy)-pentyloxy)-ethoxy-9,11-dioxopentadecanoic acid (**3**)*

This compound was prepared according to procedure F using the above alcohol (2.11 g, 4.29 mmol). The crude product was purified by column chromatography using petroleum ether:ethyl acetate (6:1) that also contained 5% acetic acid as eluent to give 1.58 g (74%) of **3** as a colourless oil: R_f 0.30 (5% HOAc in 3:1 petroleum ether:ethyl acetate eluent); IR ν_{max}: 3120, 3080, 3060, 3028, 2933, 2859, 1726, 1604, 1455, 1360, 1246, 1105, 928, and 738 cm^{-1}; ^1H NMR (400 MHz) δ: 15.50 (bs, 0.8H), 7.38–7.24 (m, 5H), 5.47 (s, 0.8H), 4.50 (s, 2H), 3.60–3.55 (m, 4H), 3.53 (s, 0.4H), 3.50–3.42 (m, 6H), 2.53 (t, J = 8 Hz, 0.4H), 2.48 (t, J = 8 Hz, 0.4H), 2.34 (t, J = 8 Hz, 2H), 2.30 (t, J = 8 Hz, 1.6H), 2.26 (t, J = 8 Hz, 1.6H), 1.72–1.52 (m, 13H), 1.46–1.38 (m, 2H), and 1.38–1.25 (m, 8H). Exact Mass calcd. for $C_{29}H_{46}O_7$: 506.3231; found: 506.3237.

*1-Methoxymethoxy-15-(*tert*-butyldimethylsilyloxy)-5,7-pentadecanedione (**26**)*

This compound was prepared according to procedure E using the β-diketone **21** (2.16 g, 6.59 mmol) and the bromide **11** (1.08 g, 5.93 mmol). The crude product was purified by column chromatography using petroleum ether:ethyl acetate (15:1) as eluent to give 1.56 g (73%) of **26** as a colourless oil: R_f 0.24 (6:1 petroleum ether:ethyl acetate eluent); IR ν_{max}: 2936, 2858, 1708, 1611, 1463, 1387, 1253, 1148, 1103, 1044, and 924 cm^{-1}; ^1H NMR (400 MHz) δ: 15.50 (bs, 0.8H), 5.48 (s, 0.8H), 4.62 (s, 1.6H), 4.61 (s, 0.4H), 3.61 (t, J = 7 Hz, 2H), 3.57 (s, 0.4H), 3.56 (t, J = 7 Hz, 2H), 3.38 (s, 3H), 2.56 (t, J = 8 Hz, 0.4H), 2.51 (t, J = 8 Hz, 0.4H), 2.32 (t, J = 8 Hz, 1.6H), 2.26 (t, J = 8 Hz, 1.6H), 1.78–1.45 (m, 8H), 1.38–1.25 (m, 8H), 0.90 (s, 9H), and 0.50 (s, 6H). Exact Mass calcd. for $C_{23}H_{46}SiO_5 - CH_3$: 415.2868; found: 415.2875.

1-Methoxymethoxy-15-hydroxy-5,7-pentadecanedione

This compound was prepared according to procedure C using the silyl ether **26** (215 mg, 0.50 mmol). The crude product was purified by column chromatography using petroleum ether:ethyl acetate (6:1) as eluent to give 136 mg (86%) of the desired alcohol from **26** as a white solid: R_f 0.36 (1:1 petroleum ether:ethyl acetate eluent); mp 42.0°C; IR ν_{max}: 3635, 3458, 2932, 2860, 1704, 1610, 1452, 1217, 1148, 1112, 1039, and 923 cm^{-1}; ^1H NMR (400 MHz) δ: 15.50 (bs, 0.8H), 5.48 (s, 0.8H), 4.62 (s, 1.6H), 4.61 (s, 0.4H), 3.65 (t, J = 7 Hz, 2H), 3.56 (s, 0.4H), 3.55 (t, J = 7 Hz, 2H), 3.37 (s, 3H), 2.57 (t, J = 8 Hz, 0.4H), 2.50 (t, J = 8 Hz, 0.4H), 2.32 (t, J = 8 Hz, 1.6H), 2.27 (t, J = 8 Hz, 1.6H), 1.77–1.50 (m, 9H), and 1.42–1.25 (m, 8H). Exact Mass calcd. for $C_{17}H_{32}O_5$: 316.2241; found: 316.2247.

*15-Methoxymethoxy-9,11-dioxopentadecanoic acid (**4**)*

This compound was prepared according to procedure F using the above alcohol (128 mg, 0.40 mmol). The crude product was purified by recrystallization from hexanes to give 94 mg (73%) of **4** as a white solid R_f 0.34 (5% HOAc in 3:1 petroleum ether:ethyl acetate eluent); mp 43.0°C; IR ν_{max}: 3116, 2932, 2860, 1717, 1611, 1461, 1416, 1221, 1148, 1111, 1039, and 923 cm^{-1}; ^1H NMR (300 MHz) δ: 15.50 (bs, 0.8H), 5.49 (s, 0.8H), 4.63 (s, 1.6H), 4.62 (s, 0.4H), 3.57–3.52 (m, 2.4H), 3.38 (s, 2.4H), 3.37 (s, 0.6H), 2.56 (t, J = 8 Hz, 0.4H), 2.50 (t, J = 8 Hz, 0.4H), 2.35 (t, J = 8 Hz, 2H), 2.32 (t, J = 8 Hz, 1.6H), 2.27 (t, J = 8 Hz, 1.6H), 1.77–1.52 (m, 8H), and 1.42–1.25 (m, 6H). Exact Mass calcd. for $C_{17}H_{30}O_6$: 330.2034; found: 330.2036. Anal. calcd. for $C_{17}H_{30}O_6$: C 61.78, H 9.09; found: C 61.72, H 9.08.

12-Hydroxy-2,4-dodecanedione

This compound was prepared according to procedure C using the silyl ether **21** (2.01 g, 6.13 mmol). The crude product was purified by column chromatography using petroleum ether:ethyl acetate (6:1) as eluent to give 1.23 g (94%) of the desired alcohol from **21** as a white solid: R_f 0.50 (1:1 petroleum ether:ethyl acetate eluent); mp 40.5°C; IR ν_{max}: 3621, 3460, 2932, 2858, 1720, 1702, 1610, 1440, 1362, 1304, 1157, 1074, 1011, 956, and 915 cm^{-1}; ^1H NMR (400 MHz) δ: 15.48 (bs, 0.8H), 5.48 (s, 0.8H), 3.65 (t, J = 7 Hz, 2H), 3.57 (s, 0.4H), 2.50 (t, J = 8 Hz, 0.4H), 2.27 (t, J = 8 Hz, 1.6H), 2.22 (s, 0.6H), 2.05 (s, 2.4H), 1.66–1.52 (m, 5H), and 1.42–1.28 (m, 8H). Exact Mass calcd. for $C_{12}H_{22}O_3$: 214.1563; found: 214.1569.

*9,11-Dioxododecanoic acid (**5a**)*

This compound was prepared according to procedure F using the above alcohol (750 mg, 3.50 mmol). The crude product was purified by recrystallization from hexanes to give 480 mg (60%) of **5a** as a white solid: R_f 0.48 (5% HOAc in 3:1 petroleum ether:ethyl acetate eluent); mp 41.5°C; IR ν_{max}: 3340–2500, 2935, 2860, 1712, 1607, 1460, 1410, 1364, 1290, 1135, 1097, 954, and 915 cm^{-1}; ^1H NMR (400 MHz) δ: 15.48 (bs, 0.8H), 5.48 (s, 0.8H), 3.57 (s, 0.4H), 2.48 (t, J = 8 Hz, 0.4H), 2.39 (t, J = 7 Hz, 0.8H), 2.32 (t, J = 8 Hz, 2H), 2.23 (t, J = 8 Hz, 0.8H), 2.21 (s, 0.6H), 2.11 (s, 1.2H), 2.03 (s, 1.2H), 1.66–1.50 (m, 4H), and 1.40–1.22 (m, 6H). Exact Mass calcd. for $C_{12}H_{20}O_4$: 228.1356; found: 228.1362.

*18-(*tert*-Butyldimethylsilyloxy)-8,10-octadecanedione (**27**b)*

This compound was prepared according to procedure E using the β-diketone **21** (4.00 g, 12.2 mmol) and 1-bromohexane (1.81 g, 11.0 mmol). The crude product was purified by column chromatography using petroleum ether: ethyl acetate (20:1) as eluent to give 3.50 g (85%) of **27***b* as a colourless oil: R_f 0.76 (6:1 petroleum ether:ethyl acetate eluent); IR ν_{max}: 2931, 2857, 1711, 1612, 1463, 1392, 1365, 1252, 1101, 837, and 776 cm^{-1}; ^1H NMR (400 MHz) δ: 15.50 (bs, 0.8H) 5.48 (s, 0.8H), 3.61 (t, J = 7 Hz, 2H), 3.53 (s, 0.4H), 2.50 (t, J = 8 Hz, 0.8H), 2.27 (t, J = 8 Hz, 3.2H), 1.66–1.46 (m, 8H), 1.38–1.22 (m, 14H), 0.90 (s, 9H), 0.88 (t, J = 7 Hz, 3H), and 0.06 (s, 6H). Exact Mass calcd. for $C_{24}H_{48}SiO_3 - CH_3$: 397.3126; found: 397.3137.

18-Hydroxy-8,10-octadecanedione

This compound was prepared according to procedure C using the silyl ether **27***b* (2.66 g, 6.46 mmol). The crude product was purified by recrystallization from hexanes to give 1.68 g (87%) of the desired alcohol from **27***b* as a white solid: R_f 0.62 (1:1 petroleum ether:ethyl acetate eluent); mp 56.0°C; IR ν_{max}: 3623, 3460, 2932, 2857, 1724, 1708, 1604, 1460, 1372, 1294, 1146, 1112, and 917 cm^{-1}; ^1H NMR (400 MHz) δ: 15.50 (bs, 0.8H), 5.48 (s, 0.8H), 3.66 (t, J = 7 Hz, 2H), 3.53 (s, 0.4H), 2.51 (t, J = 8 Hz, 0.8H), 2.27 (t, J = 8 Hz, 3.2H), 1.66–1.50 (m, 9H), 1.42–1.20 (m, 14H), and 0.88 (t, J = 7 Hz, 3H). Exact Mass calcd. for $C_{18}H_{34}O_3$: 298.2499; found: 298.2499.

Can. J. Chem. Downloaded from www.nrcresearchpress.com by ESC ESCOLA DE ENGENHARIA on 09/08/12
For personal use only.

9,11-Dioxooctadecanoic acid (5b)

This compound was prepared according to procedure F using the above alcohol (850 mg, 2.85 mmol). The crude product was purified by recrystallization from hexanes to give 500 mg (56%) of **5*b*** as a white solid: R_f 0.55 (5% HOAc in 3:1 petroleum ether:ethyl acetate eluent); mp 57.0°C; IR ν_{max}: 3310–2480, 2932, 2859, 1707, 1609, 14,66, 1407, 1290, 1132, 951, and 916 cm^{-1}; IR (KBr) ν_{max}: 3543, 3483, 2931, 2849, 1719, 1688, 1642, 1461, 1440, 1421, 1310, 1237, 1188, 1138, and 903 cm^{-1}; ^1H NMR (300 MHz) δ: 15.50 (bs, 0.8H), 5.48 (s, 0.8H), 3.53 (s, 0.4H), 2.50 (t, J = 8 Hz, 0.8H), 2.36 (t, J = 7 Hz, 2H), 2.28 (t, J = 8 Hz, 3.2 H), 1.70–1.50 (m, 8H), 1.40–1.24 (m, 12H), and 0.90 (t, J = 7 Hz, 3H). Exact Mass calcd. for $C_{18}H_{32}O_4$: 312.2292; found: 312.2293. Anal. calcd. for $C_{18}H_{32}O_4$: C 69.23, H 10.33; found: C 69.22, H 10.33.

*1-(*tert*-Butyldimethylsilyloxy)-9,11-eicosanedione (27c)*

This compound was prepared according to procedure E using the β-diketone **21** (1.97 g, 6.0 mmol) and 1-bromooctane (1.04 g, 5.4 mmol). The crude product was purified by column chromatography using petroleum ether:ethyl acetate (20:1) as eluent to give 1.52 g (73%) of **27*c*** as a colourless oil: R_f 0.78 (6:1 petroleum ether:ethyl acetate eluent); IR ν_{max}: 2930, 2856, 1707, 1611, 1463, 1366, 1253, 1100, 1044, 943, 837, and 776 cm^{-1}; ^1H NMR (400 MHz) δ: 15.50 (bs, 0.8H), 5.48 (s, 0.8H), 3.61 (t, J = 7 Hz, 2H), 3.54 (s, 0.4H), 2.50 (t, J = 8 Hz, 0.8H), 2.27 (t, J = 8 Hz, 3.2H), 1.66–1.48 (m, 8H), 1.36–1.24 (m, 18H), 0.90 (s, 9H), 0.88 (t, J = 7 Hz, 3H), and 0.07 (s, 6H). Exact Mass calcd. for $C_{26}H_{52}SiO_3$: 440.3672; found: 440.3654.

1-Hydroxy-9,11-eicosanedione

This compound was prepared according to procedure C using the silyl ether **27*c*** (1.40 g, 3.2 mmol). The crude product was purified by recrystallization from hexanes to give 940 mg (91%) of the desired alcohol from **27*c*** as a white solid: R_f 0.65 (1:1 petroleum ether:ethyl acetate eluent); mp 65.5°C; IR ν_{max}: 3622, 2930, 2857, 1724, 1700, 1608, 1460, 1364, 1308, 1047, and 905 cm^{-1}; ^1H NMR (400 MHz) δ: 15.50 (bs, 0.8H), 5.48 (s, 0.8H), 3.66 (t, J = 7 Hz, 2H), 3.54 (s, 0.4H), 2.50 (t, J = 8 Hz, 0.8H), 2.27 (t, J = 8 Hz, 3.2H), 1.64–1.50 (m, 11H), 1.49–1.22 (m, 16H), and 0.88 (t, J = 7 Hz, 3H). Exact Mass calcd. for $C_{20}H_{38}O_3$: 326.2811; found: 326.2814.

9,11-Dioxoeicosanoic acid (5c)

This compound was prepared according to procedure F using the above alcohol (630 mg, 2.11 mmol). The crude product was purified by recrystallization from hexanes to give 520 mg (79%) of **5*c*** as a white solid: R_f 0.56 (5% HOAc in 3:1 petroleum ether:ethyl acetate eluent); mp 64.0°C; IR ν_{max}: 3355–2490, 2931, 2858, 1708, 1606, 1459, 1413, 1292, 1134, 1104, and 953 cm^{-1}; ^1H NMR (300 MHz) δ: 15.50 (bs, 0.8H), 5.48 (s, 0.8H), 3.53 (s, 0.4H), 2.49 (t, J = 8 Hz, 0.8H), 2.36 (t, J = 7 Hz, 2H), 2.28 (t, J = 8 Hz, 3.2H), 1.70–1.50 (m, 8H), 1.40–1.22 (m, 16H), and 0.90 (t, J = 7 Hz, 3H). Exact Mass calcd. for $C_{20}H_{36}O_4$: 340.2604; found: 340.2620. Anal. calcd. for $C_{20}H_{36}O_4$: C 70.59, H 10.58; found: C 70.32, H 10.66.

*1-(*tert*-Butyldimethylsilyloxy)-9,11-doeicosanedione (27d)*

This compound was prepared according to procedure E using the β-diketone **21** (1.67 g, 5.1 mmol) and 1-bromodecane (1.12 g, 5.1 mmol). The crude product was purified by column chromatography using petroleum ether:ethyl acetate (20:1) as eluent to give 0.95 g (70%) of **27*d*** as a colourless oil: R_f 0.80 (6:1 petroleum ether:ethyl acetate eluent); IR ν_{max}: 2928, 2856, 1711, 1611, 1463, 1390, 1365, 1252, 1101, 1011, 944, and 837 cm^{-1}; ^1H NMR (400 MHz) δ: 15.50 (bs, 0.8H), 5.48 (s, 0.8H), 3.60 (t, J = 7 Hz, 2H), 3.54 (s, 0.4H), 2.50 (t, J = 8 Hz, 0.8H), 2.27 (t, J = 8 Hz, 3.2H), 1.66–1.46 (m, 8H), 1.36–1.22 (m, 22H), 0.90 (s, 9H), 0.89 (t, J = 7 Hz, 3H), and 0.07 (s, 6H). Exact Mass calcd. for $C_{28}H_{56}SiO_3$: 467.3906; found: 467.3960.

1-Hydroxy-9,11-doeicosanedione

This compound was prepared according to procedure C using the silyl ether **27*d*** (870 mg, 1.86 mmol). The crude product was purified by recrystallization from hexanes to give 560 mg (85%) of the desired alcohol from **27*d*** as a white solid: R_f 0.68 (1:1 petroleum ether:ethyl acetate eluent); mp 70.5°C; IR ν_{max}: 3623, 3458, 2929, 2857, 1607, 1459, 1380, 1285, 1148, 1053, 947, and 898 cm^{-1}; ^1H NMR (400 MHz) δ: 15.50 (bs, 0.8H), 5.47 (s, 0.8H), 3.64 (t, J = 7 Hz, 2H), 3.54 (s, 0.4H), 2.50 (t, J = 8 Hz, 0.8H), 2.24 (t, J = 8 Hz, 3.2H), 1.64–1.50 (m, 11H), 1.42–1.22 (m, 20H), and 0.89 (t, J = 7 Hz, 3H). Exact Mass calcd. for $C_{22}H_{42}O_3$: 354.3123; found: 354.3132.

9,11-Dioxodoeicosanoic acid (5d)

This compound was prepared according to procedure F using the above alcohol (450 mg, 1.27 mmol). The crude product was purified by recrystallization from hexanes to give 140 mg (34%) of **5*d*** as a white solid: R_f 0.57 (5% HOAc in 3:1 petroleum ether:ethyl acetate eluent); mp 69.5°C; IR ν_{max}: 3370–2510, 2929, 2857, 1718, 1607, 1460, 1408, 1292, 1135, 1090, and 952 cm^{-1}; ^1H NMR (300 MHz) δ: 15.50 (bs, 0.8H), 5.48 (s, 0.8H), 3.54 (s, 0.4H), 2.50 (t, J = 8 Hz, 0.8H), 2.36 (t, J = 7 Hz, 2H), 2.26 (t, J = 8 Hz, 3.2 H), 1.72–1.52 (m, 8H), 1.42–1.22 (m, 20H), and 0.89 (t, J = 7 Hz, 3H). Exact Mass calcd. for $C_{22}H_{40}O_4$: 368.2916; found: 368.2935. Anal. calcd. for $C_{22}H_{40}O_4$: C 71.74, H 10.87; found: C 71.20, H 10.94.

5-Bromo-1-pentanol (28a)

This compound was prepared according to procedure A using 1,5-pentanediol (15.0 g, 140 mmol) and 48% HBr (24 mL, 211 mmol). The crude product was purified by column chromatography using petroleum ether:ethyl acetate (6:1) as eluent to give 12.4 g (52%) of **28*a*** as a colourless liquid: R_f 0.46 (1:1 petroleum ether:ethyl acetate); IR ν_{max}: 3346, 2936, 2865, 1456, 1434, 1274, 1238, 1137, 1061, 1014, 984, 950, and 734 cm^{-1}; ^1H NMR (400 MHz) δ: 3.70 (t, J = 8 Hz, 2H), 3.42 (t, J = 8 Hz, 2H), 1.92 (qn, J = 8 Hz, 2H), 1.72 (s, 1H), and 1.64–1.48 (m, 4H). Exact Mass calcd. for $C_5H_{11}BrO$ – H: 166.9892, 164.9912; found: 166.9902, 164.9911.

*1-Bromo-5-(*tert*-butyldimethylsilyloxy)-pentane (29a)*

This compound was prepared according to procedure B using the alcohol **28*a*** (2.90 g, 17.4 mmol). The crude product was purified by column chromatography using petroleum ether:ethyl acetate (15:1) as eluent to give 3.81 g (81%) of **29*a*** as a colourless oil: R_f 0.80 (6:1 petroleum ether:ethyl acetate); IR ν_{max}: 2950, 2940, 2890, 2858, 1467, 1388, 1361, 1254, 1102, 1006, 835, and 775 cm^{-1}; ^1H NMR (400 MHz) δ: 3.61 (t, J = 8 Hz, 2H), 3.41 (t, J = 8 Hz, 2H), 1.88 (qn, J = 8 Hz, 2H), 1.58–1.45 (m, 4H), 0.90 (s, 9H), and 0.07 (s, 6H). Exact Mass calcd. for $C_{11}H_{25}SiBrO$ – H: 281.0753, 279.0771; found: 281.0527, 2879.0772.

*10-(*tert*-Butyldimethylsilyloxy)-2,4-decanedione (30a)*

Following procedure D, the β-diketone **30*a*** was prepared using 2,4-pentanedione (1.72 g, 17.2 mmol) and bromide **29*a*** (4.83 g, 17.2 mmol). The crude product was purified by column chromatography using petroleum ether:ethyl acetate (15:1) as eluent to give 2.12 g (60%) of **30*a*** as a colourless oil: R_f 0.56 (6:1 petroleum ether:ethyl acetate); IR ν_{max}: 2936, 2858, 1716, 1614, 1465, 1361, 1252, 1100, 1005, 936, 837, and 775 cm^{-1}; ^1H NMR (400 MHz) δ: 15.50 (bs, 0.8 H), 5.49 (s, 0.8 H), 3.60 (t, J = 8 Hz, 2H), 3.59 (s, 0.4 H), 2.52 (t, J = 8 Hz, 0.4 H), 2.26 (t, J = 8 Hz, 1.6 H), 2.24 (s, 0.6 H), 2.07 (s, 2.4 H), 1.68–1.56 (m, 2H), 1.55–1.46 (m, 2H), 1.38–1.25 (m, 4H), 0.90 (s, 9H), and 0.06 (s, 6H). Exact Mass calcd. for $C_{16}H_{32}SiO_3$ – CH_3: 285.1879; found: 285.1884.

*1-(*tert*-Butyldimethylsilyloxy)-7,9-octadecanedione (31a)*

This compound was prepared according to procedure E using the β-diketone **30**a (1.2 g, 4.2 mmol) and 1-bromooctane (**12*b***) (0.77 g, 4.0 mmol). The crude product was purified by column chromatography using petroleum ether:ethyl acetate (20:1) as eluent to give 0.77 g (75%) of **31*a*** as a colourless oil: R_f 0.74 (6:1 petroleum ether:ethyl acetate); IR ν_{max}: 2930, 2856, 1722, 1707, 1611, 1463, 1387, 1360, 1252, 1101, 1006, 937, 836, 812, and 775 cm^{-1}; ^1H NMR (400 MHz) δ: 15.50 (bs, 0.8H), 5.48 (s, 0.8H), 3.61 (t, J = 8 Hz, 2H), 3.53 (s, 0.4H), 2.51 (t, J = 8 Hz, 0.4H), 2.50 (t, J = 8 Hz, 0.4H), 2.28 (t, J = 8 Hz, 1.6H), 2.27

Can. J. Chem. Downloaded from www.nrcresearchpress.com by EESC ESCOLA DE ENGENHARIA on 09/08/12
For personal use only.

(t, J = 8 Hz, 1.6H), 1.66–1.48 (m, 8H), 1.38–1.22 (m, 14H), 0.90 (s, 9H), 0.89 (t, J = 8 Hz, 3H), and 0.06 (s, 6H). Exact Mass calcd. for $C_{24}H_{48}SiO_3$: 412.3360; found: 412.3367.

*1-Hydroxy-7,9-octadecanedione (**32**a)*

This compound was prepared according to procedure C using the silyl ether **31***a* (640 mg, 1.55 mmol). The crude product was purified by recrystallization from hexanes to give 410 mg (89%) of **32***a* as a white solid: R_f 0.56 (1:1 petroleum ether:ethyl acetate); mp 57.5°C; IR ν_{max}: 3623, 2930, 2858, 1607, 1459, 1329, 1141, 1052, 965, and 904 cm^{-1}; ^1H NMR (400 MHz) δ: 15.50 (bs, 0.8H), 5.48 (s, 0.8H), 3.64 (t, J = 8 Hz, 2H), 3.55 (s, 0.4H), 2.52 (t, J = 8 Hz, 0.4H), 2.50 (t, J = 8 Hz, 0.4H), 2.29 (t, J = 8 Hz, 1.6H), 2.27 (t, J = 8 Hz, 1.6H), 1.70–1.50 (m, 9H), 1.42–1.18 (m, 14H), and 0.89 (t, J = 7 Hz, 3H). Exact Mass calcd. for $C_{18}H_{34}O_3$: 298.2499; found: 298.2505.

*7,9-Dioxooctadecanoic acid (**6**a)*

This compound was prepared according to procedure F using the alcohol 32*a* (298 mg, 1.00 mmol). The crude product was purified by recrystallization from hexanes to give 210 mg (67%) of **6***a* as a solid: R_f 0.52 (5% HOAc in 3:1 petroleum ether:ethyl acetate); mp 58.0°C; IR ν_{max}: 3340–2490, 2930, 2858, 1709, 1607, 1460, 1409, 1291, 1131, 950, and 907 cm^{-1}; ^1H NMR (300 MHz) δ: 15.50 (bs, 0.8H), 5.49 (s, 0.8H), 3.53 (s, 0.4H), 2.53 (t, J = 8 Hz, 0.4H), 2.49 (t, J = 8 Hz, 0.4H), 2.36 (t, J = 7 Hz, 2H), 2.30 (t, J = 8 Hz, 1.6H), 2.27 (t, J = 8 Hz, 1.6H), 1.72–1.52 (m, 6H), 1.46–1.22 (m, 14H), and 0.90 (t, J = 7 Hz, 3H). Exact Mass calcd. for $C_{18}H_{32}O_4$: 312.2292; found: 312.2291. Anal. calcd. for $C_{18}H_{32}O_4$: C 69.23, H 10.33; found: C 69.24, H 10.33.

*6-Bromo-1-hexanol (**28**b)*

This compound was prepared according to procedure A using 1,6-hexanediol (5.9 g, 50 mmol) and 48% HBr (8.2 mL, 73 mmol). The crude product was purified by column chromatography using petroleum ether:ethyl acetate (6:1) as eluent to give 4.2 g (46%) of **28***b* as a colourless liquid: R_f 0.48 (1:1 petroleum ether:ethyl acetate); IR ν_{max}: 3335, 2932, 2860, 1447, 1260, and 1055 cm^{-1}; ^1H NMR (400 MHz) δ: 3.68 (t, J = 8 Hz, 2H), 3.43 (t, J = 8 Hz, 2H), 1.88 (qn, J = 8 Hz, 2H), 1.62 (m, 2H), and 1.52–1.34 (m, 5H). Exact Mass calcd. for $C_6H_{13}BrO$ – H: 181.0048, 179.0068; found: 181.0043, 179.0063.

*1-Bromo-6-(*tert*-butyldimethylsilyloxy)-hexane (**29**b)*

This compound was prepared according to procedure B using the alcohol **28***b* (2.86 g, 15.8 mmol). The crude product was purified by column chromatography using petroleum ether:ethyl acetate (15:1) as eluent to give 4.12 g (88%) of **29***b* as a colourless oil: R_f 0.82 (6:1 petroleum ether:ethyl acetate); IR ν_{max}: 2936, 2858, 1466, 1253, 1101, 837, and 775 cm^{-1}; ^1H NMR (400 MHz) δ: 3.61 (t, J = 8 Hz, 2H), 3.41 (t, J = 8 Hz, 2H), 1.87 (qn, J = 8 Hz, 2H), 1.58–1.50 (m, 2H), 1.48–1.41 (m, 2H), 1.40–1.33 (m, 2H), 0.90 (s, 9H), and 0.06 (s, 6H). Exact Mass calcd. for $C_{12}H_{27}SiBrO$ – H: 295.2000, 293.2020; found: 295.0917, 293.0928.

2,4-Dodecanedione

Following procedure D, this β-diketone was prepared from 2,4-pentanedione (3.00 g, 30.0 mmol) and 1-bromoheptane (5.37 g, 30.0 mmol). The crude product was purified by column chromatography using petroleum ether:ethyl acetate (15:1) as eluent to give 2.70 g (63%) of 2,4-dodecanedione as a colourless oil: R_f 0.64 (6:1 petroleum ether:ethyl acetate); IR ν_{max}: 2931, 2856, 1713, 1614, 1449, 1363, 1241, 946, and 777 cm^{-1}; ^1H NMR (400 MHz) δ: 15.50 (bs, 0.8H), 5.49 (s, 0.8H), 3.58 (s, 0.4H), 2.50 (t, J = 8 Hz, 0.4H), 2.27 (t, J = 8 Hz, 1.6H), 2.24 (s, 0.6H), 2.07 (s, 2.4H), 1.68–1.52 (m, 2H), 1.40–1.20 (m, 10H), and 0.89 (t, J = 7 Hz, 3H). Exact Mass calcd. for $C_{12}H_{22}O_2$: 198.1614; found: 198.1626.

*1-(*tert*-Butyldimethylsilyloxy)-8,10-octadecanedione (**31**b)*

This compound was prepared according to procedure E using 2,4-dodecanedione (2.50 g, 12.6 mmol) and the bromide **29***b* (3.10 g, 10.5 mmol). The crude product was purified by column chromatography using petroleum ether:ethyl acetate (20:1) as eluent to give 2.30 g (75%) of **31***b* as a colourless oil: R_f 0.76 (6:1 petroleum ether:ethyl acetate); IR ν_{max}: 2909, 2856, 1704, 1615, 1459, 1360, 1251, 1100, 945, 838, and 775 cm^{-1}; ^1H NMR (400 MHz) δ: 15.50 (bs, 0.8H), 5.48 (s, 0.8H), 3.61 (t, J = 8 Hz, 2H), 3.53 (s, 0.4H), 2.50 (t, J = 8 Hz, 0.8H), 2.27 (t, J = 8 Hz, 3.2H), 1.66–1.42 (m, 8H), 1.40–1.22 (m, 14H), 0.90 (s, 9H), 0.89 (t, J = 7 Hz, 3H), and 0.06 (s, 6H). Exact Mass calcd. for $C_{24}H_{48}SiO_3$: 412.3360; found: 412.3377.

*1-Hydroxy-8,10-octadecanedione (**32**b)*

This compound was prepared according to procedure C using the silyl ether **31***b* (2.00 g, 4.85 mmol). The crude product was purified by recrystallization from hexanes to give 1.26 g (87%) of **32***b* as a white solid: R_f 0.64 (1:1 petroleum ether:ethyl acetate); mp 57.0°C; IR ν_{max}: 3622, 3460, 2931, 2857, 1703, 1607, 1458, 1335, 1051, and 902 cm^{-1}; ^1H NMR (400 MHz) δ: 15.50 (bs, 0.8H), 5.48 (s, 0.8H), 3.64 (t, J = 8 Hz, 2H), 3.54 (s, 0.4H), 2.51 (t, J = 8 Hz, 0.4H), 250 (t, J = 8 Hz, 0.4H), 2.26 (t, J = 8 Hz, 1.6H), 2.25 (t, J = 8 Hz, 1.6H), 1.70–1.20 (m, 23H), and 0.89 (t, J = 7 Hz, 3H). Exact Mass calcd. for $C_{18}H_{34}O_3$: 298.2499; found: 298.2514.

*8,10-Dioxooctadecanoic acid (**6**b)*

This compound was prepared according to procedure F using the alcohol **32***b* (596 mg, 2.00 mmol). The crude product was purified by recrystallization from hexanes to give 306 mg (50%) of **6***b* as a white solid: R_f 0.53 (5% HOAc in 3:1 petroleum ether:ethyl acetate); mp 58.5°C; IR ν_{max}: 3340–2480, 2931, 2858, 1708, 1608, 1459, 1300, and 1127 cm^{-1}; ^1H NMR (400 MHz) δ: 15.50 (bs, 0.8H), 5.49 (s, 0.8H), 3.54 (s, 0.4H), 2.51 (t, J = 8 Hz, 0.4H), 2.50 (t, J = 8 Hz, 0.4H), 2.36 (t, J = 8 Hz, 2H), 2.27 (t, J = 8 Hz, 1.6H), 2.26 (t, J = 8 Hz, 1.6H), 1.72–1.50 (m, 6H), 1.48–1.20 (m, 14H), and 0.90 (t, J = 7 Hz, 3H). Exact Mass calcd. for $C_{18}H_{32}O_4$: 312.2292; found: 312.2307. Anal. calcd. for $C_{18}H_{32}O_4$: C 69.23, H 10.33; found: C 68.94, H 10.38.

*9-Bromo-1-nonanol (**28**c)*

This compound was prepared according to procedure A using 1,9-nonanediol (10.0 g, 62.5 mmol) and 48% HBr (10.5 mL, 93.8 mmol). The crude product was purified by column chromatography using petroleum ether:ethyl acetate (6:1) as eluent to give 9.78 g (70%) of **28***c* as a white solid: R_f 0.58 (1:1 petroleum ether:ethyl acetate); mp 34.0°C; IR ν_{max}: 3622, 3460, 2929, 2857, 1459, 1386, 1352, 1274, 1111, 1044, and 889 cm^{-1}; ^1H NMR (400 MHz) δ: 3.64 (t, J = 7 Hz, 2H), 3.42 (t, J = 7 Hz, 2H), 1.83 (qn, J = 8 Hz, 2H), 1.58 (m, 2H), and 1.48–1.30 (m, 11H). Exact Mass calcd. for $C_9H_{19}BrO$ – H_2O: 206.0489, 204.0514; found: 206.0494, 204.0509.

*1-Bromo-9-(*tert*-butyldimethylsilyloxy)-nonane (**29**c)*

This compound was prepared according to procedure B using the alcohol **28***c* (2.66 g, 11.9 mmol). The crude product was purified by column chromatography using petroleum ether:ethyl acetate (15:1) as eluent to give 3.60 g (90%) of **29***c* (3.60 g, 90%) as a colourless oil: R_f 0.84 (6:1 petroleum ether:ethyl); IR ν_{max}: 2933, 2856, 1466, 1387, 1360, 1252, 1101, 1006, 839, 775, and 717 cm^{-1}; ^1H NMR (400 MHz) δ: 3.60 (t, J = 7 Hz, 2H), 3.41 (t, J = 7 Hz, 2H), 1.86 (qn, J = 7 Hz, 2H), 1.54–1.48 (m, 2H), 1.46–1.37 (m, 2H), 1.35–1.26 (m, 8H), 0.89 (s, 9H), and 0.05 (s, 6H). Exact Mass calcd. for $C_{15}H_{33}SiBrO$ – C_4H_9: 281.0173, 279.0193; found: 281.0748, 279.0786.

*14-(*tert*-Butyldimethylsilyloxy)-2,4-tetradecanedione (**30**c)*

Following procedure D, the β-diketone **30***c* was prepared from 2,4-pentanedione (0.98 g, 9.4 mmol) and bromide **29***c*. The crude product was purified by column chromatography using petroleum ether:ethyl acetate (15:1) as eluent to give 2.12 g (79%) of **30***c* as a colourless oil: R_f 0.66 (6:1 petroleum ether:ethyl acetate); IR ν_{max}: 2932, 2856, 1709, 1616, 1465, 1387, 1361, 1251, 1100, 1006, 940, 838, 813, and 776 cm^{-1}; ^1H NMR (400 MHz) δ: 15.50 (bs, 0.8H), 5.49 (s, 0.8H), 3.59 (t, J = 7 Hz, 2H), 3.57 (s, 0.4H), 2.49 (t, J = 8 Hz, 0.4H), 2.27 (t, J = 8 Hz, 1.6H), 2.24 (s, 0.6H), 2.06 (s, 2.4H), 1.65–1.46 (m, 6H), 1.40–1.24 (m, 10H), 0.89 (s, 9H), and 0.06 (s, 6H). Exact Mass calcd. for $C_{20}H_{40}SiO_3$ – H: 355.2658; found: 355.2676.

Can. J. Chem. Downloaded from www.nrcresearchpress.com by EESC ESCOLA DE ENGENHARIA on 09/08/12
For personal use only.

*18-(*tert*-Butyldimethylsilyloxy)-6,8-octadecanedione (**31**c)*

This compound was prepared according to procedure E using the β-diketone **30***c* (1.2 g, 3.2 mmol) and 1-bromobutane (0.60 g, 3.2 mmol). The crude product was purified by column chromatography using petroleum ether:ethyl acetate (20:1) as eluent to give 0.65 g (77%) of **31***c* as a colourless oil: R_f 0.77 (6:1 petroleum ether:ethyl acetate); IR ν_{max}: 2934, 2856, 1730, 1707, 1612, 1463, 1386, 1361, 1252, 1100, 1006, 940, and 838 cm^{-1}; ^1H NMR (400 MHz) δ: 15.66 (bs, 0.1H), 15.54 (bs, 0.7H), 5.48 (s, 0.7H), 5.47 (s, 0.1H), 3.61 (t, J = 7 Hz, 2H), 3.54 (s, 0.4H), 2.49 (t, J = 8 Hz, 0.8H), 2.27 (m, 3.2H), 1.66–1.46 (m, 8H), 1.38–1.22 (m, 14H), 0.90 (s, 12H), and 0.06 (s, 6H). Exact Mass calcd. for $C_{24}H_{48}SiO_3$ – H: 411.3282; found: 411.3287.

*18-Hydroxy-6,8-octadecanedione (**32**c)*

This compound was prepared according to procedure C using the silyl ether **31***c* (360 mg, 0.87 mmol). The crude product was purified by recrystallization from hexanes to give 250 mg (96%) of **32***c* as a white solid: R_f 0.66 (1:1 petroleum ether:ethyl acetate); mp 56.0°C; IR ν_{max}: 3621, 3456, 2974, 2931, 1700, 1608, 1455, 1390, and 1047 cm^{-1}; ^1H NMR (400 MHz) δ: 15.50 (bs, 0.8H), 5.48 (s, 0.8H), 3.64 (t, J = 7 Hz, 2H), 3.53 (s, 0.4H), 2.51 (t, J = 8 Hz, 0.8H), 2.27 (t, J = 8 Hz, 3.2H), 1.64–1.50 (m, 9H), 1.42–1.22 (m, 14H), and 0.92–0.86 (m, 3H). Exact Mass calcd. for $C_{18}H_{34}O_3$: 298.2499; found: 298.2504.

*11,13-Dioxooctadecanoic acid (**6**c)*

This compound was prepared according to procedure F using the alcohol **32***c* (200 mg, 0.67 mmol). The crude product was purified by recrystallization from hexanes to give 130 mg (64%) of **6***c* as a white solid: R_f 0.56 (5% HOAc in 3:1 petroleum ether:ethyl acetate); mp 56.5°C; IR ν_{max}: 3350–2500, 2933, 2859, 1710, 1605, 1458, 1395, 1281, 1138, 1047, 951, and 879 cm^{-1}; ^1H NMR (300 MHz) δ: 15.50 (bs, 0.8H), 5.48 (s, 0.8H), 3.55 (s, 0.4H), 2.50 (t, J = 8 Hz, 0.8H), 2.35 (t, J = 7 Hz, 2H), 2.27 (t, J = 8 Hz, 3.2H), 1.70–1.52 (m, 6H), 1.40–1.22 (m, 14H), and 0.94–0.86 (m, 3H). Exact Mass calcd. for $C_{18}H_{32}O_4$: 312.2292; found: 312.2294. Anal. calcd. for $C_{18}H_{32}O_4$: C 69.23, H 10.33; found: C68.94, H 10.25.

*2,4-Undecanedione (**33**)*

This compound was prepared according to procedure D using 1-bromohexane (**12***a*) (4.50 mL, 32.0 mmol) and 2,4-pentanedione (4.10 mL, 40.0 mmol). Distillation of the crude product under reduced pressure (155°C/50 Torr) gave 3.70 g (63%) of **33** as a colourless oil: R_f 0.60 (6:1 petroleum ether:ethyl acetate eluent); IR ν_{max}: 2930, 2858, 1711, 1613, 1446, 1364, 1254, and 947 cm^{-1}; ^1H NMR (400 MHz) δ: 15.50 (bs, 0.8H), 5.49 (s, 0.8H), 3.58 (s, 0.4H), 2.51 (t, J = 8 Hz, 0.4H), 2.27 (t, J = 8 Hz, 1.6H), 2.25 (s, 0.6H), 2.06 (s, 2.4H), 1.65–1.52 (m, 2H), 1.38–1.22 (m, 8H), and 0.89 (t, J = 7 Hz, 3H). Exact Mass calcd. for $C_{11}H_{20}O_2$: 184.1458; found: 184.1459.

*8,10-Octadecanedione (**7**)*

This compound was prepared according to procedure E using the β-diketone **33** (756 mg, 4.11 mmol) and 1-bromoheptane (660 mg, 3.69 mmol). Purification of the crude product by column chromatography using petroleum ether:ethyl acetate (20:1) gave 803 mg (77%) of **7** as a colourless oil: R_f 0.78 (6:1 petroleum ether:ethyl acetate eluent); IR ν_{max}: 2934, 2857, 1704, 1613, 1455, 1276, 1142, 1102, and 942 cm^{-1}; ^1H NMR (400 MHz) δ: 15.50 (bs, 0.8H), 5.48 (s, 0.8H), 3.53 (s, 0.4H), 2.50 (t, J = 8 Hz, 0.8H), 2.26 (t, J = 8 Hz, 3.2H), 1.64–1.50 (m, 4H), 1.48–1.22 (m, 18H), and 0.89 (t, J = 7 Hz, 6H). Exact Mass calcd. for $C_{18}H_{34}O_2$: 282.2550; found: 282.2565. Anal. calcd. for $C_{18}H_{34}O_2$: C 76.52, H 12.14; found: C 76.80, H 12.16.

Acknowledgements

We are grateful to the Natural Sciences and Engineering Research Council of Canada and Merck Frosst Canada for financial support of this work.

1. E. Meyers, D.S. Slusarchyk, and W.C. Liu. U.S. Patent 3 873 693 (1975); Chem. Abstr. **83**, 41512a (1975).
2. B.K. Toeplitz, A.I. Cohen, R.T. Funke, W.L. Parker, and J.Z. Gougoutas. J. Am. Chem. Soc. **101**, 3344 (1979).
3. E. Meyers, D.S. Slusarchyk, W.C. Liu, G. Astle, W.H. Trejo, and W.E. Brown. J. Antibiot. **31**, 815 (1978).
4. C.M. Liu and T.E. Hermann. J. Biol. Chem. **253**, 5892 (1978).
5. R.F. Kauffman, R.W. Taylor, and D.R. Pfeiffer. J. Biol. Chem. **253**, 5892 (1978).
6. R.F. Kauffman, R.W. Taylor, and D.R. Pfeiffer. J. Biol. Chem. **255**, 2735 (1980).
7. J.P. Bennett, S. Cockcroft, and B.D. Gomperts. Nature, **282**, 851 (1979).
8. S.E. Rittenhouse and W.C. Horne. Biochem. Biophys. Res. Commun. **123**, 393 (1984).
9. (*a*) B.W. Dijkstra, K.H. Kalk, W.G.J. Hol, and J. Drenth. J. Mol. Biol. **147**, 97 (1981); (*b*) R.H. Kretsinger. Annu. Rev. Biochem. **45**, 239 (1976); (*c*) R.H. Kretsinger. Crit. Rev. Biochem. 114 (1980).
10. S.M. Johnson, J. Jerrin. S.J. Liu, and I.C. Paul. J. Am. Chem. Soc. **92**, 4428 (1970).
11. (*a*) A.F. Gallaugher and H. Hibbert. J. Am Chem. Soc. **58**, 813 (1936); (*b*) C.G. Krespan. J. Org. Chem. **39**, 2351 (1974); (*c*) M. Newcomb, S.S. Moore, and D.J. Cram. J. Am Chem. Soc. **99**, 6405 (1977).
12. (*a*) S. Hanessian, N.G. Cooke, B. Dehoff, and Y. Sakito. J. Am. Chem. Soc. **112**, 5276 (1990); (*b*) D.A. Evans, R.L. Dow, T.L. Shih, J.M. Takacs, and R. Zahler. J. Am. Chem. Soc. **112**, 5290 (1990).
13. L. Weiler and K. Shelly. Can. J. Chem. **66**, 1359 (1988).
14. (*a*) A.H. Alberts and D.J. Cram. J. Am. Chem. Soc. **101**, 3545 (1979); (*b*) C.M. Thompson and D.L.C. Green, Tetrahedron, **47**, 4223 (1991).
15. C.A. Hendrich. Tetrahedron, **33**, 1845 (1977).
16. S.K. Chandhary and O. Hernandez. Tetrahedron Lett. 99 (1979).
17. K. Fuji, S. Nakano, and E. Fujita. Synthesis, 276 (1975).
18. T. Gibson. J. Org. Chem. **45**, 1095 (1980).
19. H.H. Freedman and R.A. Dubois. Tetrahedron Lett. **38**, 3251 (1975).
20. E.J. Corey, H. Niwa, and J. Knolle. J. Am. Chem. Soc. **100**, 1942 (1978).
21. E.J. Corey, and B.B. Snider. J. Am. Chem. Soc. **94**, 2549 (1972).
22. R. Appel. Angew. Chem. Int. Ed. Engl. **14**, 801 (1975).
23. J.G. Moffatt. J. Org. Chem. **36**, 1909 (1971).
24. E.J. Corey and J.J. Das. J. Am. Chem. Soc. **104**, 5551 (1982).
25. T.Q. Hu and L. Weiler. Can. J. Chem. **72**, 1512 (1994).
26. W.C. Still, M. Kahn, and A. Mitra. J. Org. Chem. **43**, 2923 (1978).
27. M.F. Lipton, C.M. Sorensen, A.C. Saddler, and R.H. Shapiro. J. Organomet. Chem. **186**, 155 (1980).
28. D.D. Perrin, W.L.F. Armarego, and D.R. Perrin. *In* Purification of laboratory chemicals. Pergamon Press, Oxford. 1966.

Binding and transport of calcium ions by synthetic analogues of ionomycin

THOMAS Q. HU AND LARRY WEILER[1]

Department of Chemistry, University of British Columbia, 2036 Main Mall, Vancouver, BC V6T 1Z1, Canada

Received June 30, 1993[2]

THOMAS Q. HU and LARRY WEILER. Can. J. Chem. **72**, 1512 (1994).

The transport of calcium ions across an organic barrier by a series of synthetic analogues of ionomycin was measured in a cylindrical glass cell using chloroform as the artificial membrane. The presence of a β-diketone and carboxyl group in the same molecule and a sufficient lipid solubility of the compounds were shown to be necessary and sufficient conditions for Ca^{2+} transport. Small and no transport of Ca^{2+} were found for analogues **5** and **6**, respectively, due to the low lipid solubility of these compounds. The Ca^{2+} transport rate for analogues **8** and **13–15** followed the order of **8** > **13** > **14** > **15**, which demonstrated that optimal Ca^{2+} transport was achieved when the β-diketone was separated from the carboxyl group by seven methylene units, identical to that found in ionomycin. Analogues **8–10** were comparable to ionomycin and calcimycin in terms of Ca^{2+} transport. Ca^{2+} transport by the analogues was found to be a saturable process that obeyed Michaelis-Menten kinetics. It was dependent on the pH in the aqueous source phase and independent of the pH in the receiving phase. Both the carboxyl and the β-diketo groups were ionized in the transport of Ca^{2+}, indicating that the stoichiometry of Ca^{2+} complex in transport was 1:1. The pK_a of the β-diketone of the analogues was determined to be in the range of 10.90–11.16 in 80% MeOH–H_2O. The pK_a values were related to the lipid solubility of the compounds and the hydrocarbon chain length between the β-diketone and the carboxyl group. The binding constants of the analogues with Ca^{2+} and Mg^{2+} in 80% MeOH–H_2O were determined to be in the order of 10^2 M^{-1} and 10^3 M^{-1}, respectively, using the pK_a method. The stoichiometry of Mg^{2+} binding was found to be 1:1 by the mole ratio method. The selectivity in binding and in transport followed the same order, being $Mg^{2+} > Ca^{2+} \gg Na^+, K^+$.

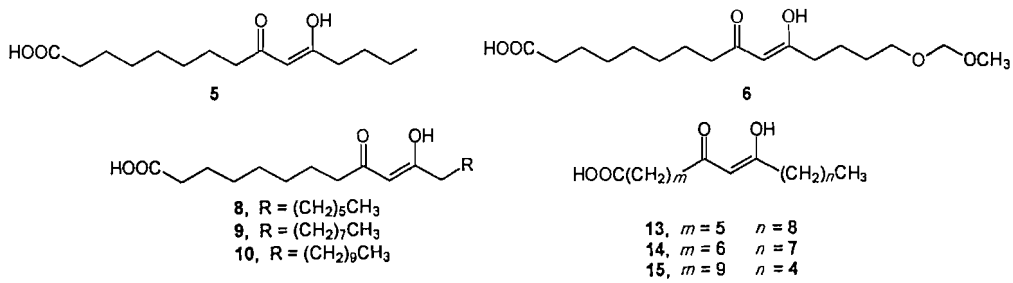

THOMAS Q. HU et LARRY WEILER. Can. J. Chem. **72**, 1512 (1994).

Opérant dans une cellule de verre cylindrique et utilisant du chloroforme comme membrane artificielle, on a mesuré le transport d'ions calcium à travers une barrière organique par une série d'analogues de l'ionomycine. On a montré que la présence d'une β-dicétone et d'un groupe carboxyle dans la même molécule et une solubilité lipidique suffisante des composés sont des conditions nécessaires et suffisantes pour le transport du Ca^{2+}. À cause de faible solubilité lipidique de ces composés, on n'a observé aucun ou que de faibles transports avec les analogues **5** et **6** respectivement. Les vitesses de transport du Ca^{2+} des composés **8** et **13–15** sont dans l'ordre décroissant suivant : **8**, **13**, **14** et **15** qui démontre que le transport optimal du Ca^{2+} se fait lorsque la β-dicétone est séparée du groupe carboxyle par sept groupes méthylènes, comme dans l'ionomycine. En terme de transport du Ca^{2+}, les analogues **8–10** se comparent à l'ionomycine et à la calcimycine. On a trouvé que le transport du Ca^{2+} par les analogues est un processus qui peut être saturé et qui obéit à la cinétique de Michaelis–Menten. Il est dépendant du pH de la phase aqueuse agissant comme source et il est indépendant du pH de la phase qui les reçoit. Les groupes carboxyle et β-dicétonique sont tous les deux ionisés au cours du transport du Ca^{2+}; ceci indique que la stoechiométrie du complexe de transport du Ca^{2+} est 1 : 1. On a déterminé que, dans un mélange 80% de MeOH–H_2O, les pK_a des β-dicétones des analogues sont de l'ordre de 10,90–11,16. On a relié les valeurs de pK_a avec la solubilité lipidique des composés et la longueur de la chaîne carbonée entre la β-dicétone et le groupe carboxyle. Utilisant la méthode des pK_a, on a déterminé que, dans un mélange 80% de MeOH–H_2O, les constantes de liaison des analogues avec le Ca^{2+} et le Mg^{2+} sont respectivement de l'ordre de 10^2 et 10^3 M^{-1}. Utilisant la méthode des rapports molaires, on a déterminé que la stoechiométrie de liaison du Mg^{2+} est 1 : 1. On a observé que la sélectivité de liaison et de transport suit toujours l'ordre décroissant suivant : Mg^{2+}, Ca^{2+}, Na^+ et K^+.

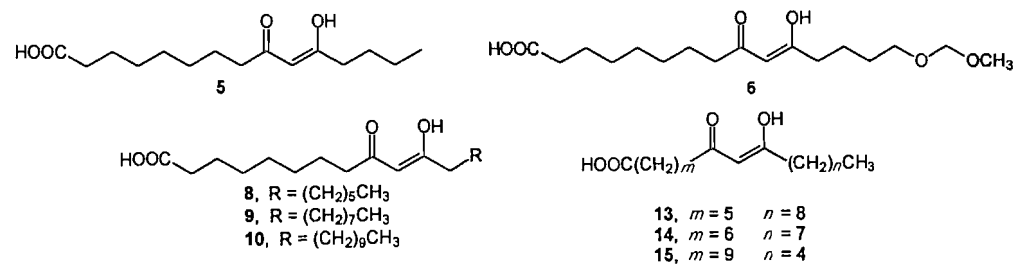

[Traduit par la Rédaction]

[1]Author to whom correspondence may be addressed.

[2]Revision received January 4, 1994.

Can. J. Chem. Downloaded from www.nrcresearchpress.com by EESC ESCOLA DE ENGENHARIA on 09/08/12
For personal use only.

Can. J. Chem. Downloaded from www.nrcresearchpress.com by EESC ESCOLA DE ENGENHARIA on 09/08/12
For personal use only.

Introduction

Although the importance of calcium ions in the skeletal structures of living organisms has been recognized for more than a century, only recently have other biological roles for Ca^{2+}, particularly its function as an intracellular messenger, been demonstrated (1). A minute flow of calcium ions across cell membranes has been found to trigger such diverse processes as the regulation of muscle contraction, the secretion of hormones, the transport of salt and water across the intestinal lining, and the control of glycogen metabolism in the liver (2). For a substance to serve as an intracellular messenger, a target protein must be able to bind it tightly and with high specificity. The size and charge of calcium ions are such that the negatively charged oxygens found on the side chains of aspartate and glutamate residues as well as uncharged oxygens from the carbonyls of a protein backbone can bind calcium ions more strongly and specifically than other common biological ions such as potassium, sodium, and magnesium ions (3).

The ability of the cell membrane to effect a large increase in Ca^{2+} concentration inside the cell is a key in the role of Ca^{2+} as an intracellular messenger (4). The intracellular concentration of free Ca^{2+} is very low, on the order of 10^{-7} M in virtually all animal cells (5). On the other hand, the concentration of free Ca^{2+} in the extracellular medium is high, on the order of 10^{-3} M in vertebrates and higher in marine invertebrates (4). This Ca^{2+} concentration gradient, together with a membrane potential of −40 to −90 mV, allows for a rapid entry of Ca^{2+} into the cell upon the activation of calcium-selective channels by appropriate electrical or chemical signals (4).

Because of the important role of Ca^{2+} in the cell, it is essential to regulate intracellular Ca^{2+} levels to be able to effectively control many cellular processes. Two typical ways of altering intracellular Ca^{2+} concentrations are to inject a calcium salt or a Ca^{2+} chelating agent such as ethylenediaminetetraacetic acid (EDTA) into the cell, or to add a substance to the extracellular fluid that will alter the concentration of intracellular Ca^{2+}.

The first approach was adopted by Heilbrunn and Wiercinski who injected calcium salts into frog muscle to stimulate contraction (6). This approach is simple, but it has several difficulties. First, the micropipette can cause irreversible damage to the cell. Second, the quantity of calcium salts that must be injected to significantly raise the concentration of Ca^{2+} in the cytoplasm, and yet be low enough to avoid irreparable damage, is often unknown. Finally, since calcium ion buffering systems exist within cells, an elevated free Ca^{2+} concentration in the cytoplasm is difficult to maintain for more than a few seconds by the injection method.

An alternative approach is to introduce a substance that affects either the Ca^{2+} permeability of the cell membrane or the intracellular Ca^{2+} reservoirs. Since the extracellular Ca^{2+} concentration is 10^3–10^6 higher than the intracellular Ca^{2+} concentration, Ca^{2+} may be transported across the cell membrane down its concentration gradient by lipophilic compounds known as Ca^{2+} ionophores (7). Such ionophores have proven useful in altering intracellular Ca^{2+} levels. Three such ionophores are lasalocid A (**1**) (formerly known as X-537A), calcimycin (**2**) (formerly known as A23187), and ionomycin (**3**) (8–12). The transport of Ca^{2+} from one aqueous phase to another by these ionophores is due to their ability to form lipid soluble ionophore–Ca^{2+} complexes (13) and to the favorable Ca^{2+} complexation and decomplexation kinetics involved in the transport cycle (14).

Efforts to develop synthetic Ca^{2+} ionophores based on the analysis of the structures of lasalocid A and calcimycin have met with certain success (15–17). Two diglycolamic acids prepared by Umen and Scarpa were shown to transport Ca^{2+} across an artificial membrane comparable to lasalocid A and calcimycin (15). The use of lipophilic acyclic polyether dicarboxylic acids as mobile carriers to transport Ca^{2+}, Mg^{2+}, and Ba^{2+} across an artificial membrane was reported by Hiratani et al. (16). Fyles and co-workers have shown that crown ether dicarboxylic acids selectively transported alkaline earth cations across an organic barrier as a 1:1 complex (17).

An artificial membrane such as bulk liquid membrane was used by the above authors and others as a simple method to study ionophore-catalyzed cation transport (18, 19). Chloroform is usually employed in these transport studies because its dielectric constant ($\epsilon = 4.8$) is similar to the dielectric constant of the interior of a phospholipid membrane ($\epsilon = 2$–4) (20).

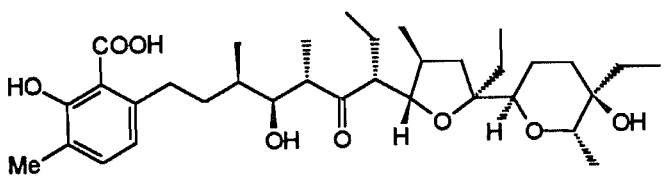

1

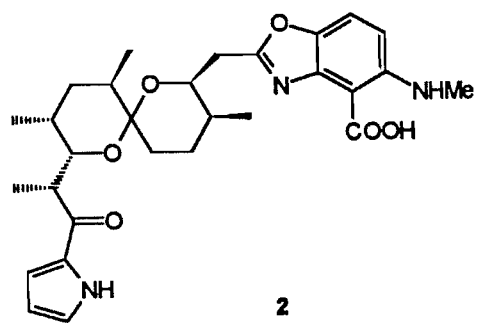

2

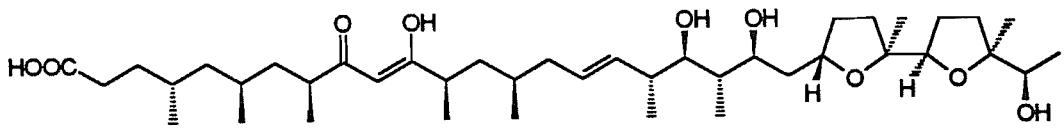

3

TABLE 1. Amount of Ca^{2+} in the receiving phase as a function of time using analogue **4** as the carrier

Time (h)	0	12	16	20	24	36	42	48	60
Ca^{2+} (mmol)	0	5.8	7.8	10	12	17	19	22	25

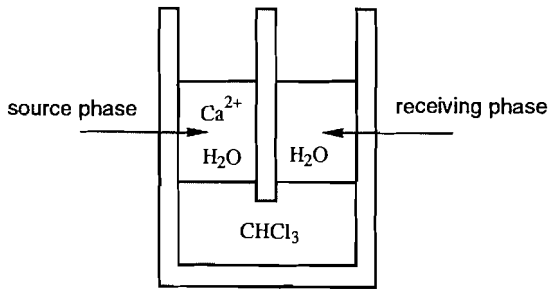

FIG. 1. Cylindrical glass cell for the studies of Ca^{2+} transport.

Among the known naturally occurring polyether Ca^{2+} ionophores, ionomycin is unique in that it forms a 1:1 Ca^{2+} salt and it has a high selectivity for Ca^{2+} in binding and transport (11, 12). Ionomycin has been widely used as a tool to investigate the role of Ca^{2+} as a second messenger in biological system (21, 22). However, no attempt has been made to understand the structural features controlling the Ca^{2+} binding and transport by ionomycin or to develop simple compounds that will mimic the action of ionomycin. We recently reported the design and synthesis of some simple analogues of ionomycin (23). Herein we describe the results of our studies on the Ca^{2+} binding and transport properties of these ionomycin analogues and their potential as Ca^{2+} ionophores.

Results and discussion

Transport experiments were carried out using a cylindrical glass cell system (Fig. 1) containing a source phase (10 mL), a chloroform phase (40 mL), and a receiving phase (10 mL). The volume of the chloroform solution was such that two separate compartments were created above the organic solution (Fig. 1). The chloroform solution was stirred continuously and samples (0.2 mL) were withdrawn from the receiving phase at different times and analyzed by calcium atomic absorption spectrophotometry.

Table 1 lists the amount of Ca^{2+} in the receiving phase at different times using analogue **4** as the carrier. Each value in the table is the average of three independent experiments with a standard error of less than 10%. The data in Table 1 illustrates that the amount of Ca^{2+} in the receiving phase increases linearly up to 24 h. At this time approximately 0.5% of the Ca^{2+} of the source phase has been transported into the receiving phase. A plot of Ca^{2+} transported versus time within this linear range (Fig. 2) gives a slope 0.50. The initial transport rate, J, expressed as the moles of Ca^{2+} transported per square centimeter of the chloroform per hour was $(7.3 \pm 0.7) \times 10^{-8}$ mol cm^{-2} h^{-1}. We observed this linear relationship between the initial Ca^{2+} transport and time in all our transport experiments and consequently we have used the initial transport rate J to compare the Ca^{2+} transport efficiency of the various analogues.

To insure that the above Ca^{2+} transport was not due to the leakage of Ca^{2+} across the chloroform layer (blank transport of Ca^{2+}), we carried out the transport experiment in the absence of analogue **4** in the chloroform phase. Analysis of the samples withdrawn from the receiving phase showed no detectable Ca^{2+}. This established the carrier role of analogue **4** in the transport of Ca^{2+} across an organic barrier. We next carried out the transport experiments on analogues **5** and **6** to examine the effect of oxygen donor sites on Ca^{2+} transport.

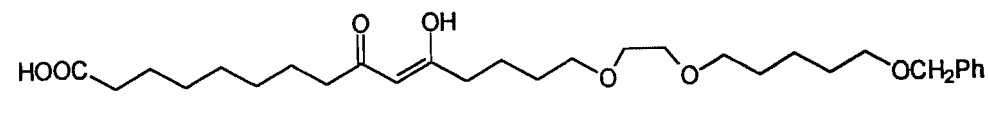

4

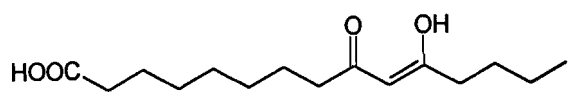

5

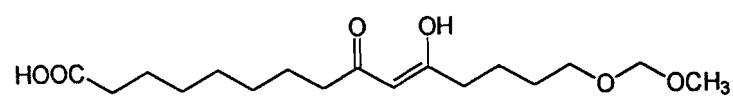

6

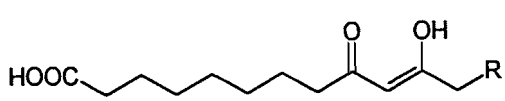

8, R = $(CH_2)_5CH_3$
9, R = $(CH_2)_7CH_3$
10, R = $(CH_2)_9CH_3$

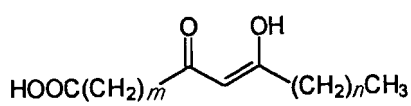

13, $m = 5$ $n = 8$
14, $m = 6$ $n = 7$
15, $m = 9$ $n = 4$

Can. J. Chem. Downloaded from www.nrcresearchpress.com by EESC ESCOLA DE ENGENHARIA on 09/08/12
For personal use only.

TABLE 2. Ca^{2+} transport rates (J) for analogues **4–10** and **13–15**, calcimycin (**2**), and ionomycin (**3**)

Analogues	$J(10^{-8}$ mol cm^{-2} h$^{-1})$
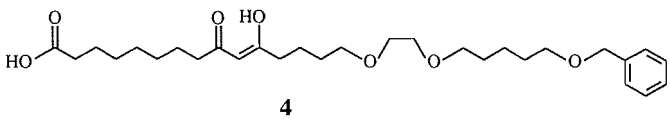 **4**	7.3 ± 0.7
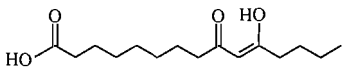 **5**	0.3 ± 0.1
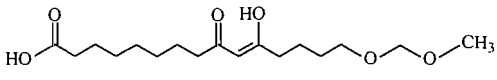 **6**	<0.1[a]
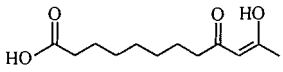 **7**	<0.1[a]
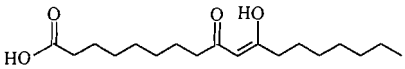 **8**	15 ± 2
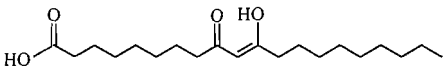 **9**	15 ± 2
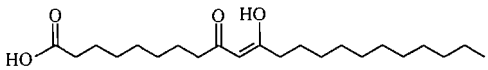 **10**	13 ± 1
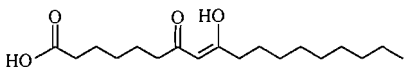 **13**	3.5 ± 0.4
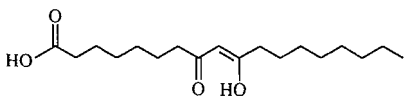 **14**	9.5 ± 0.9
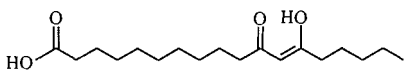 **15**	0.9 ± 0.1
Calcimycin (**2**)	12 ± 1
Ionomycin (**3**)	21 ± 2

[a]No detectable Ca^{2+} transport.

Table 2 summarizes the transport results on analogues **4**, **5**, and **6**.

Compound **4** was the most efficient carrier for the transport of Ca^{2+} of these three analogues. This could be due to the effect of the three oxygen atoms on the side chain of **4** on coordination of Ca^{2+}. However, no detectable transport of Ca^{2+} was observed for analogue **6**, which has two additional oxygen atoms compared to analogue **5**. We anticipated that the additional oxygen atoms should facilitate Ca^{2+} transport (24). However, it appeared that the additional oxygen atoms on the side chain of **6** actually were detrimental to Ca^{2+} transport.

Besides providing potential Ca^{2+} coordination sites, additional oxygen atoms on the side chain of analogues **4** and **6** could change the lipophilicity of these molecules, which may affect the Ca^{2+} transport of the compounds. To investigate the effect of carrier lipophilicity on Ca^{2+} transport we car-

Can. J. Chem. Downloaded from www.nrcresearchpress.com by EESC ESCOLA DE ENGENHARIA on 09/08/12
For personal use only.

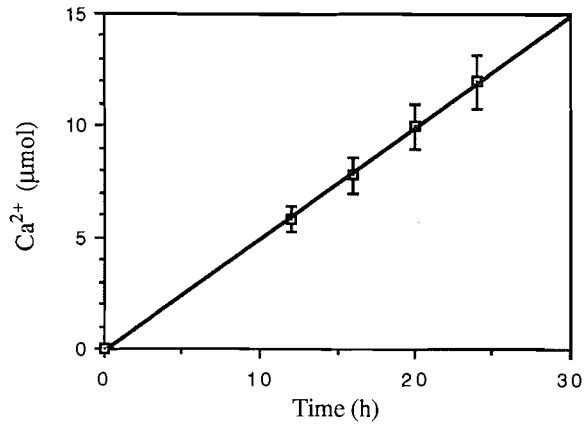

FIG. 2. Transport of Ca^{2+} by **4**.

ried out the transport experiments on analogues **7–10**, which have different hydrocarbon side chains (Table 2). These results demonstrate that the lipophilicity of the carrier does play an important role in the transport of Ca^{2+}. Analogue **7** with no methylene units on the hydrocarbon side chain did not transport Ca^{2+} across the chloroform phase. Analogue **5** with three methylene units on the side chain was able to transport Ca^{2+}. The addition of more methylene units in compounds **8**, **9**, and **10** resulted in a significant increase of Ca^{2+} transport. In fact, analogues **8–10** are more efficient Ca^{2+} carriers than analogue **4**.

Additional evidence pointing to the importance of lipid solubility of the carrier in Ca^{2+} transport was obtained when the concentration of the analogues **7–10** in the chloroform phase was monitored during the transport experiments. A small volume (1 mL) of the chloroform solution was withdrawn at different times, the solvent was evaporated, and the residue was dissolved in methanol. The magnitude of the UV absorption of the methanol solution at 276 nm was used to determine the carrier concentration in the organic phase. The concentration of analogues **8**, **9**, and **10** in the chloroform phase was found to remain constant throughout the transport experiments. In contrast, the concentration of analogue **7** in the chloroform phase steadily decreased. Using UV spectroscopy the lost carrier was found to be in the aqueous source phase. Thus, analogues **8**, **9**, and **10** are efficient Ca^{2+} carriers because they and their Ca^{2+} complexes had sufficient lipid solubility to remain in the chloroform phase. Analogue **7** did not transport Ca^{2+} across the chloroform layer because it was extracted into the aqueous source phase due to its higher hydrophilicity.

Interestingly, the transport rate of analogue **10** was only comparable to analogues **8** and **9** even though it had more methylene units on the side chain. This may be due to the low solubility of **10** in the high dielectric constant interface of the chloroform and aqueous source phase where Ca^{2+} transport is initiated (18*a*). If this rationale is correct, the transport of Ca^{2+} will depend upon the concentration of interfacial carrier. A good carrier must be neither too hydrophobic nor too hydrophilic. Analogues **8** and **9** appear to have the optimal lipid solubility for Ca^{2+} transport.

The above results not only illustrate the importance of lipophilicity of the carrier in Ca^{2+} transport, but also suggest that other compounds possessing the β-diketone and carboxyl group with different carbon skeletons may also be efficient Ca^{2+} carriers if their lipophilicity is similar to analogues **8–10**. The structural simplicity of analogues **5** and **7–10** allowed us to use Rekker's hydrophobic fragmental constant method (*f* method) (25) to calculate their logarithms of the partition coefficient (log *P*) between chloroform and water. Table 3 lists the calculated log *P* values and Ca^{2+} transport rates for analogues **5** and **7–10**. The *f* values are not available for the fragments of analogues **4** and **6**. The data in Table 3 suggest that the minimum value of log *P* for Ca^{2+} transport is about 4 and the optimal value of log *P* is in the range of 6–8. The future design of Ca^{2+} ionophores based on ionomycin should have a calculated or experimentally determined value of log *P* in this range.

TABLE 3. Ca^{2+} transport rates (*J*) and calculated log *P* values for analogues **5** and **7–10**

Analogue	*J* (10^{-8} mol cm^{-2} h^{-1})	log *P*
7	<0.1[a]	2.18
5	0.3 ± 0.1	4.06
8	15 ± 2	5.95
9	15 ± 2	7.20
10	13 ± 1	8.45

[a]No detectable Ca^{2+} transport.

To further understand the ability of analogues **8–10** to transport Ca^{2+} we studied the role of the β-diketone and carboxyl group in Ca^{2+} transport. Transport experiments were carried out using compounds **11** (log *P* = 9.40) and **12** (log *P* = 8.53), respectively. No detectable transport of Ca^{2+} was observed even though the lipid solubility of these two compounds was sufficiently high compared to compounds **8–10**. This indicates that both the β-diketone and carboxyl group are required for the transport of Ca^{2+}. The stronger binding of compounds containing two β-diketo groups relative to those with a single β-diketo binding site is known (26).

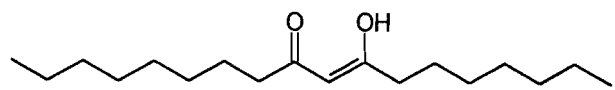

11

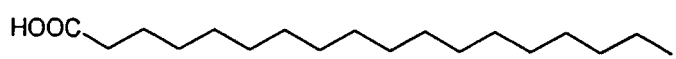

12

To determine if the presence of the two functional groups *within* the same molecule was required for Ca^{2+} transport, we performed a transport experiment with both **11** and **12** in the chloroform phase and again found no detectable presence of Ca^{2+} in the receiving phase. This demonstrates that both functional groups must be present in the same molecule for Ca^{2+} transport, and that the distance between the two functional groups may be important. The effect of the distance between these two functional groups on Ca^{2+} transport was then investigated using analogues **13–15**. These three compounds have the same lipid solubility (log *P* = 5.95) as analogue **8** but have the β-diketone and the carboxyl group closer together or further apart than in **8**. The number of methylene units (*n*) between the two functional groups and the Ca^{2+} transport rate (*J*) of these compounds is given in Table 2.

The results show that moving the β-diketone closer to or further away from the carboxyl group produces a significant decrease in the Ca^{2+} transport rate. The low Ca^{2+} transport rate of analogue **15** is likely due to the large unfavorable entropy

Can. J. Chem. Downloaded from www.nrcresearchpress.com by EESC ESCOLA DE ENGENHARIA on 09/08/12
For personal use only.

Can. J. Chem. Downloaded from www.nrcresearchpress.com by EESC ESCOLA DE ENGENHARIA on 09/08/12
For personal use only.

change associated with the formation of its Ca^{2+} complex. The first step in the ionophore-catalyzed Ca^{2+} transport is believed to be the binding of the ionophore with Ca^{2+} to form the Ca^{2+} complex (17, 18*a*, 27). As the number of methylene units between the β-diketone and the carboxyl group is increased, additional loss of entropy would be required to bind and transport Ca^{2+}, resulting in a less effective Ca^{2+} complexation and transport. This trend can be expected to continue until the β-diketone is so far removed from the carboxyl group that the two functional groups act independently, in which case no transport of Ca^{2+} would be observed.

On the other hand, as the number of methylene units between the β-diketone and the carboxyl group is reduced, the enthalpy of the Ca^{2+} complex would increase due to the increasing steric strain (bond angle strain, torsional angle strain, and transannular interactions) in the chelate rings of the complex. This unfavorable enthalpy may outweigh the more favorable entropy. It appears that the competing role of enthalpy and entropy may be minimized when seven methylene units separate the two functional groups such as in analogue **8**. It would also appear that ionomycin was biosynthesized with the optimal distance between the two functional groups for Ca^{2+} transport.

The high efficiency of analogues **8–10** as Ca^{2+} carriers was illustrated by comparison of these analogues with calcimycin and ionomycin (Table 2). As seen from these data, Ca^{2+} transport by ionomycin is about twice as fast as calcimycin at the same molar concentration. This is in agreement with the transport results obtained for these two ionophores in other transport systems (28) and is due to the difference in the molar ratio of the ionophore–Ca^{2+} complex. Ionomycin transports Ca^{2+} as a 1:1 complex while calcimycin transports Ca^{2+} as a 2:1 complex (12, 13).

Ca^{2+} transport by analogues **8–10** is faster than by calcimycin, but slower than by ionomycin. The higher Ca^{2+} transport rate of ionomycin relative to analogues **8–10** may be attributed to the smaller entropy change associated with the formation of ionomycin–Ca^{2+} complex. Although the β-diketone and carboxyl group in both ionomycin and analogues **8–10** are separated by a seven-carbon chain, there are three methyl substituents on this chain in ionomycin. These three methyl substituents, with their particular stereochemistry, may destabilize undesired rotomers of the acyclic bonds and reduce the number of conformations to those suitable for Ca^{2+} complexation (29). This would reduce the entropy loss in the formation of Ca^{2+} complex and thus could increase the Ca^{2+} transport rate for ionomycin.

Analogues **8–10** are interesting Ca^{2+} carriers because of their simple structures and high efficiency of Ca^{2+} transport. However, a useful Ca^{2+} ionophore should transport Ca^{2+} both efficiently and selectively. In particular, it should have selectivity for Ca^{2+} over Na^+ and K^+ because of the ubiquitous presence of Na^{2+} and K^+ in biological systems. Calcimycin and ionomycin both have selectivity for Ca^{2+} over Na^+ and K^+ (9, 20). Ionomycin is also selective for Ca^{2+} over Mg^{2+} (20).

To study the cation selectivity of our compounds, three transport experiments were carried out on analogue **8**. For each experiment, a solution of equimolar concentration of calcium chloride (250 mM) and the chloride of the competing cation was placed in the source phase. Samples were withdrawn from the receiving phase and analyzed for Ca^{2+} and the competing cation. No detectable transport of Na^+ or K^+ was observed in these experiments. Thus, the requirement of cation selectivity for Ca^{2+} over Na^+ and K^+ was met in analogue **8**. Unlike ionomycin, analogue **8** transported Mg^{2+} at a faster rate than Ca^{2+}.

The cation transport selectivity of **8** is likely due to the selectivity in binding (see later) which is expected to follow the order of ionic potentials of the cations $Mg^{2+} > Ca^{2+} > Na^+ > K^+$. Magnesium and calcium ions are both doubly charged and will bind to the enolate of β-diketone and the carboxylate more strongly than singly charged cations such as Na^+ and K^+. On the other hand, the smaller magnesium ion (0.65 Å) will bind to the enolate of β-diketone and the carboxylate more strongly than calcium ion (0.99 Å) (3).

The cation selectivity of ionomycin for Ca^{2+} over Mg^{2+} in transport may be due to the size-match selectivity (30). Ionomycin has a limited number of low-energy conformations in which the size of the chelating portion of the molecule matches the size of Ca^{2+}, but not the size of Mg^{2+}. The coordination of cations by the additional oxygen atoms of ionomycin could also be the source of its selectivity for Ca^{2+} over Mg^{2+}. The magnesium ion is small and its coordination with additional oxygen atoms of the ionophore would increase steric crowding of the molecule more than the coordination of a larger calcium ion. As a result, the less favourable enthalpy in the Mg^{2+} complex could lead to the reversed cation selectivity in transport by ionomycin.

Analogues **9** and **13** were found to induce Ca^{2+} transport across cultured human leukemic cells (THP-1 cells) at or greater than 1 mM.[3] Cellular Ca^{2+} transport by analogues **9** and **13** was transient and significantly smaller than that by calcimycin bromide or ionomycin. In vivo testing also showed that analogues **6** and **7** did not transport Ca^{2+} across the membrane of THP-1 cells.[3] This result is in agreement with those of the transport experiments using chloroform as the artificial membrane and is likely due to the low lipophilicity of the compounds in the cell membrane.

To gain insight into the transport mechanism of the analogues, we investigated the effect of substrate concentration and pH on Ca^{2+} transport. The first step in the transport of Ca^{2+} across the chloroform phase is the binding of the ionophore to Ca^{2+} at the interface of the chloroform and the aqueous source phase (18*a*, 27). This is followed by the diffusion of the Ca^{2+} complex across the chloroform phase and Ca^{2+} release into the aqueous receiving phase (18*a*, 27). If the binding of Ca^{2+} is reversible, the ionophore-catalyzed Ca^{2+} transport would show saturation kinetics (18*a*, 31). Equation [1] describes the process involved in an ionophore-catalyzed Ca^{2+} transport. The ionophore (L^{2-}) binds reversibly to Ca^{2+} to form an ionophore–Ca^{2+} complex (CaL) that then diffuses across the membrane and releases Ca^{2+} with the regeneration of the ionophore on protonation. If the binding of Ca^{2+} is reversible, the transport rate (J) can be related to the maximal rate (J_{max}) through the Michealis–Menten equation (eq. [2]) in which K_s and k_{-s} refer to the rate of association and dissociation at the interface of the organic phase and the source phase, and K_r refers to the dissociation at the interface of the organic phase and the receiving phase. K_M is approximately equal to the equilibrium dissociation constant of the ionophore–Ca^{2+} complex if $k_r \ll k_{-s}$ (31, 32).

$$[1] \qquad L^{2-} + Ca^{2+} \underset{k_{-s}}{\overset{k_s}{\rightleftharpoons}} CaL \xrightarrow{k_r} L^{2-} + Ca^{2+}$$

[3] C. Chan. Unpublished results (1992).

Can. J. Chem. Downloaded from www.nrcresearchpress.com by EESC ESCOLA DE ENGENHARIA on 09/08/12
For personal use only.

TABLE 4. Variation of Ca^{2+} transport rates (J) for analogue **8** with Ca^{2+} concentration in the source phase

$[Ca^{2+}]$(mM)	J (10^{-8} mol cm^{-2} h^{-1})
10	0.6 ± 0.1
50	4.4 ± 0.4
100	5.9 ± 0.6
250	13 ± 1
500	15 ± 2
1000	16 ± 2

TABLE 5. Ca^{2+} transport rates (J) for analogue **8** at various pH in the receiving phase

pH	J (10^{-8} mol cm^{-2} h^{-1})
8.0	15 ± 2
7.0	16 ± 2
6.0	16 ± 2
5.0	15 ± 2

$$[2] \qquad J = \frac{J_{max}[Ca^{2+}]}{K_M + [Ca^{2+}]} \qquad K_M = \frac{k_r + k_s}{k_s}$$

Table 4 lists the results of the transport experiments using analogue **8** and various concentrations of calcium chloride in the source phase. The data could be fitted into the Michaelis–Menten equation (eq. [2]) by nonlinear regression to give a hyperbolic curve with a standard error of less than 10% (33). Therefore, Ca^{2+} transport across the chloroform layer by analogue **8** is a saturable process that obeys the Michaelis–Menten kinetics. The values of the Michaelis–Menten constant K_M and the maximal transport rate J_{max} were determined to be K_M = 170 mM and $J_{max} = 20 \times 10^{-8}$ mol cm^{-2} h^{-1}, respectively, by the above nonlinear regression analysis. The large K_M indicates that the binding of Ca^{2+} by analogue **8** is weak ($k_{-s} \gg k_s$) and (or) the diffusion of the analogue-Ca^{2+} complex and the release of Ca^{2+} is very fast compared to the binding of Ca^{2+} ($k_r \gg k_s$). Our studies on the binding of **8** with Ca^{2+} in aqueous methanol (see later) also suggested that $k_{-s} \gg k_s$.

The exchange of Ca^{2+} from the ionophore–Ca^{2+} complex (CaL) in the chloroform layer for protons from the aqueous receiving phase is the final step of the ionophore-catalyzed transport cycle. If this process is irreversible as suggested by the Michaelis–Menten kinetics, a small change in the concentration of hydrogen ions in the receiving phase should not significantly affect the transport rate. This was found to be the case when the pH of the receiving phase was varied and the Ca^{2+} transport rate was determined (Table 5).

The presence of the carboxyl and β-diketo groups in the same molecule was shown above to be necessary for Ca^{2+} transport. However, it was not clear if ionization of the β-diketone is required for transport. The role of the enolate of the β-diketone in the transport of Ca^{2+} was investigated by varying the pH in the aqueous source phase above pH 7. No detectable transport of Ca^{2+} was found when the source phase was buffered at pH ≤ 7.0. Table 6 shows the results of the transport experiments using analogue **5** while varying the pH in the source phase.

The logarithm of Ca^{2+} transport rate (log J) was found to be linear with the pH in the source phase. Thus, transport of Ca^{2+} by analogue **5** is directly dependent on the hydroxide concentration in the source phase. The dependence of Ca^{2+} transport on the hydroxide concentration in the source phase suggests that the formation of the carboxylate and (or) the enolate of the β-diketone of analogue **5** is required for the transport of Ca^{2+}. Nonlinear regression analysis of the transport rate data versus pH using eq. [3] derived from the Henderson–Hasselbalch equation gave a typical plot (Fig. 3) for the ionization of a monoprotic acid with a pK_a of 9.6 ± 0.1.

TABLE 6. Effect of pH of the source phase on Ca^{2+} transport rates (J) for analogue **5**

pH	J (10^{-8} mol cm^{-2} h^{-1})
7.5	1.3 ± 0.1
8.0	1.5 ± 0.1
8.5	2.5 ± 0.2
9.0	4.6 ± 0.4
9.5	9.0 ± 0.9
10.0	14 ± 1

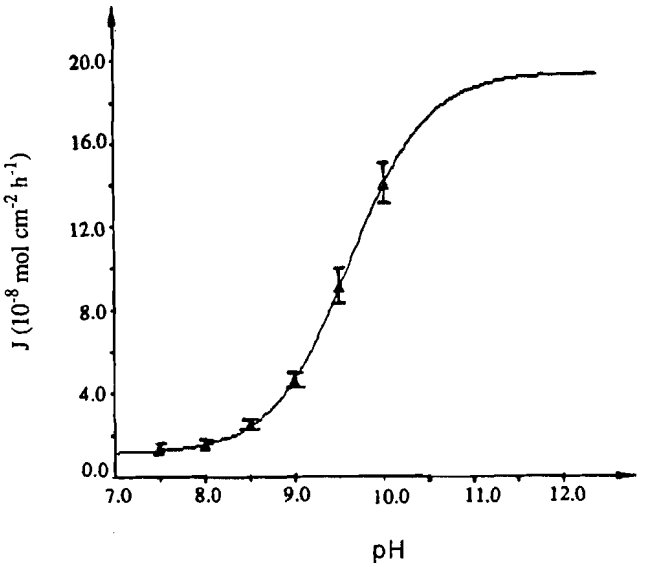

FIG. 3. Plot of the dependence of transport rates on pH of the source phase. The points represent the experimental values and the solid line is determined by nonlinear regression according to eq. [3].

$$[3] \qquad J = \frac{J_{min} + J_{max} \times 10^{pH-pK_a}}{10^{pH-pK_a} + 1}$$

In their studies of competitive alkaline-earth cations extraction from aqueous solution into chloroform by polyether dicarboxylic acids, Kang et al. demonstrated that the carboxyl groups of the alkanoic acids were completely deprotonated at the interface of the aqueous solution and chloroform at pH (pH in the aqueous phase) 6 or above and that the resulting dicarboxylates extracted divalent cations as neutral complexes into the chloroform phase (34). On the other hand, β-dicarbonyl compounds were shown to have pK_a values in the range of 8.5–10.5 (26*a*, 35). Thus we conclude that the carboxyl group in our analogues is completely ionized at the aqueous interface in all of our experiments and we assign the pK_a value of 9.6 to the ionization of the β-diketone of **5**. Such a dependence of transport rate on pH of the source phase indicates that ioniza-

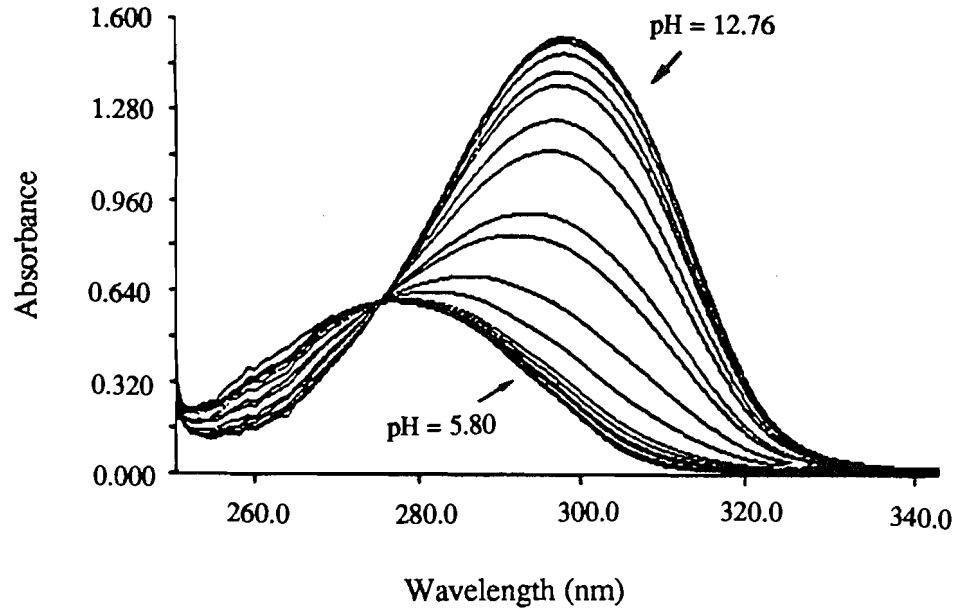

FIG. 4. UV absorption spectra of analogue **13** as a function of pH.

tion of the β-diketone at the interface of the aqueous source phase and chloroform is required for Ca^{2+} transport.

The formation of the carboxylate and the enolate of the β-diketone at the interface of the aqueous source phase and chloroform in the transport of Ca^{2+}, the requirement of both the carboxyl and β-diketone groups within the same molecule for Ca^{2+} transport, and the requirement of electrical neutrality of the Ca^{2+} complex in chloroform (34) indicate that the stoichiometry of the Ca^{2+} complex involved in transport is 1:1.

To understand the structural features controlling the Ca^{2+} specificity of ionomycin and the transport behavior of the analogues, we investigated the cation binding of analogues **5**, **8–11**, **13**, and **15** by UV spectrophotometric titrations (36). The inability of analogue **8** to transport Na^+ and K^+ suggests that the binding of the analogues with these cations may be very small. Thus neither the mole ratio method (37) nor the continuous variation method (38) appears to be applicable to the studies of Na^+ or K^+ binding. However, the binding constants of the analogues with various cations could be determined by measuring the pK_a difference of the β-diketone of an analogue in the absence and in the presence of a large excess of metal ions. For example, if HL^- represents a β-diketo ω-carboxylate, its acid dissociation constant K_a is then defined by eq. [5] and the binding constant (β) of the enolate L^{2-} with Ca^{2+} by eq. [7].

$$[4] \qquad HL^- \rightleftharpoons H^+ + L^{2-}$$

$$[5] \qquad K_a = \frac{[H^+][L^{2-}]}{[HL^-]}$$

$$[6] \qquad L^{2-} + Ca^{2+} \rightleftharpoons CaL$$

$$[7] \qquad \beta = \frac{[CaL]}{[Ca^{2+}][L^{2-}]}$$

In the presence of a large excess of Ca^{2+}, the acid dissociation constant $K_{a'}$ will be defined by eq. [9], which can be used to determine the binding constant β.

$$[8] \qquad HL^- + Ca^{2+} \rightleftharpoons H^+ + CaL$$

$$[9] \qquad K_{a'} = \frac{[H^+][CaL]}{[HL^-][Ca^{2+}]} = \frac{[CaL]}{[Ca^{2+}][L^{2-}]} \frac{[H^+][L^{2-}]}{[HL^-]}$$

$$= \beta K_a$$

Measurement of the pK_a of the β-diketone of the analogues by UV spectrophotometric titration is based on the different absorptions of the enol form of the β-diketone and its conjugated base, the enolate of the β-diketone (39, 40). For example, the UV absorbance maximum of analogue **13** in 80% MeOH–H_2O shifts to longer wavelength and increases in magnitude as the pH of the solution is raised (Fig. 4). The absorbance at 298 nm (ascribable to the enolate of the β-diketone) versus pH was fitted to a modified Henderson–Hasselbalch equation by nonlinear regression to give a pK_a value of 11.16 ± 0.02 for analogue **13** (Fig. 5) (33).

Table 7 summarizes the pK_a of the β-diketone of a number of analogues. The pK_a value of the β-diketone of ionomycin is significantly higher than that of the β-diketone of the analogues. This is likely due to the lower stability of the dianion of ionomycin in polar solvent such as 80% MeOH–H_2O. The alkyl groups on ionomycin may destabilize its dianion relative to its monoanion to a greater extent than in the case of the simple analogues. A similar hydrophobic effect is found in the series **5** and **8–10**. Namely the lipid solubilities and the pK_a values of these analogues follow the same order of **10** > **9** > **8** > **5**. The pK_a of the β-diketone also depends on the position of the β-diketone relative to the carboxylate group. The closer the β-diketone is to the carboxylate (as in analogue **13**), the higher the pK_a value, presumably due to stronger charge repulsion between the enolate anion and the carboxylate anion as they are brought closer together.

The binding constants of the analogues with Ca^{2+}, Mg^{2+}, K^+, and Na^+ were determined by measuring the pK_a values of the β-diketone in the presence of a large excess of the cation (molar ratio of cation to analogue > 200) and using eq. [9]

Can. J. Chem. Downloaded from www.nrcresearchpress.com by ESC ESCOLA DE ENGENHARIA on 09/08/12
For personal use only.

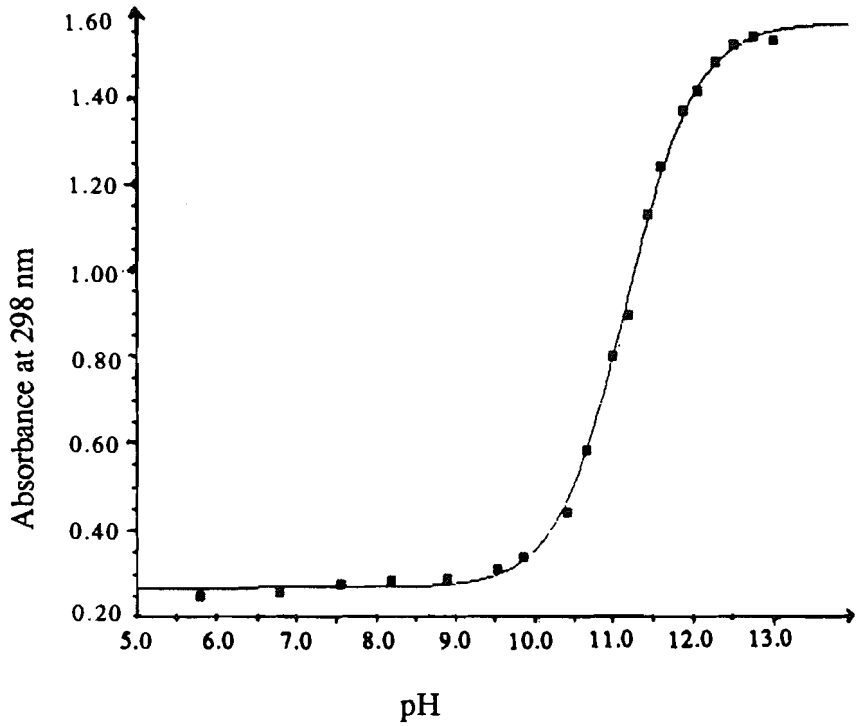

FIG. 5. Plot of absorbance at 298 nm versus pH for analogue **13**. The squares represent data points and the curve is determined by nonlinear regression.

TABLE 7. pK_a of the β-diketone of the analogues and ionomycin (**3**)

Analogue	pK_a (±0.02)
Ionomycin (**3**)[a]	11.94
5	10.92
8	11.03
9	11.04
10	11.07
11	10.86
13	11.16
15	10.90

[a]Value taken from ref. 40.

TABLE 8. Binding constants of ionomycin (**3**) and analogues with Ca^{2+} and Mg^{2+}

Analogue	Ca^{2+} β (10^2 M^{-1})	Mg^{2+} β (10^3 M^{-1})
Ionomycin (**3**)[a]	1.9×10^4	8.9×10^3
5	1.7 ± 0.1	4.4 ± 0.2
8	1.8 ± 0.1	3.4 ± 0.2
9	2.2 ± 0.2	5.6 ± 0.2
10	2.0 ± 0.1	5.7 ± 0.3
13	3.0 ± 0.2	7.6 ± 0.4
15	1.2 ± 0.1	1.9 ± 0.1

[a]Value taken from ref. 40.

TABLE 9. Binding constants of analogues with K^+ and Na^+

Analogue	K^+ β (M^{-2})	Na^+ β (M^{-2})
5	0.8 ± 0.1	1.0 ± 0.1
8	0.9 ± 0.1	1.2 ± 0.1
9	0.8 ± 0.1	1.2 ± 0.1
10	0.8 ± 0.1	1.1 ± 0.1
13	1.3 ± 0.1	1.8 ± 0.1
15	0.9 ± 0.1	0.8 ± 0.1

(Tables 8 and 9). The data shows that the selectivity in binding for the analogues is $Mg^{2+} > Ca^{2+} \gg Na^+ > K^+$. This follows the same order as the cation transport selectivity. Thus we suggest that the cation transport selectivity results from the cation binding selectivity for our analogues. The binding constants also correlate with the pK_a of the β-diketone. For example, moving the β-diketone closer to the carboxyl group in the series **15**, **8**, and **13** increases the pK_a of the β-diketone and its binding constants with cations. The binding constants of ionomycin with Ca^{2+} and Mg^{2+} are 3 to 4 orders of magnitude stronger than those of the analogues reported here. This may be due to the fact that ionomycin has a limited number of conformations available compared to the analogues and consequently the loss of entropy in binding of ionomycin is significantly less than the loss of entropy in binding of the analogues (41).

Because of the strong binding of these analogues with Mg^{2+}, the mole ratio method could be used to determine the binding constant of these analogues with Mg^{2+} and also to determine the stoichiometry of the complex on binding. At pH = 9.10 there was no significant ionization of the β-diketone of **13**, but in the presence of Mg^{2+} ionization of the β-diketone occurred at this pH (Fig. 6). From the absorbance at 298 nm in the absence of magnesium ion (A_0), the absorbance at complete complexation (A_{max}) and the absorbance at each titration point (A), the concentration of the Mg^{2+} complex at equilibrium $[Mg_xL_y]$ was calculated using eq. [10]. The concentrations of

Can. J. Chem. Downloaded from www.nrcresearchpress.com by EESC ESCOLA DE ENGENHARIA on 09/08/12
For personal use only.

TABLE 10. Absorbance, concentrations of the Mg^{2+} complex, free analogue, and Mg^{2+} at each titration point, and the binding constants based on 1:1 stoichiometry

A_{298}	$[Mg_xL_y]$ (10^{-4} M)	$[Mg^{2+}]$ (10^{-4} M)	$[L^{2-}]$ (10^{-4} M)	β (10^3 M^{-1})
0.384	—	—	0.08	—
0.608	0.17	0.33	0.62	8.3
0.741	0.27	0.71	0.52	7.3
0.853	0.35	1.12	0.43	7.2
1.032	0.48	2.20	0.30	7.2
1.132	0.56	3.32	0.22	7.7
1.246	0.63	5.65	0.14	8.0
1.302	0.68	7.97	0.09	9.4

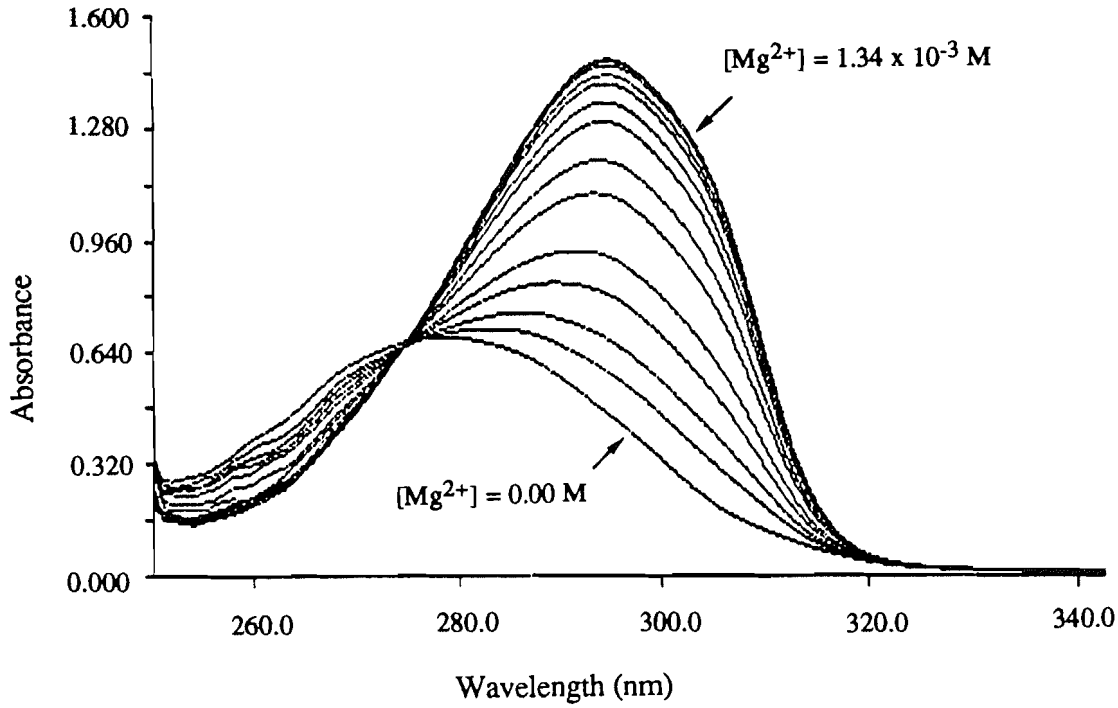

FIG. 6. UV spectrophotometric absorption spectra of analogue **13** as the concentration of $MgCl_2$ increased from 0.00 to 1.34 × 10^{-3} M.

free analogues $[L^{2-}]$ and free magnesium ion $[Mg^{2+}]$ were calculated respectively based on mass balance. Assuming a binding stoichiometry of 1:1, the binding constant calculated using eq. [11] (Table 10) was found to be β (Mg^{2+}) = (7.9 ± 0.5) × 10^3 M^{-1}. The consistency of the calculated binding constants at each titration point is additional evidence of the 1:1 stoichiometry (42). The binding constant determined using this method is in a good agreement with the binding constant of β (Mg^{2+}) = (7.6 ± 0.4) × 10^3 M^{-1} obtained using the pK_a method.

$$[10] \qquad [Mg_xL_y] = \frac{(A - A_0)[L]_t}{A_{max} - A_0}$$

$$[11] \qquad \beta(Mg^{2+}) = \frac{[MgL]}{[Mg^{2+}][L^{2-}]}$$

Alternatively, the data for the number of moles of magnesium ions $[Mg_xL_y]$ bound per mole of the analogue $[L]_t$ versus the concentration of free Mg^{2+} could be fitted to the Scatchard equation by nonlinear regression (Fig. 7) (33, 43) to give the binding constant of β (Mg^{2+}) = (7.1 ± 0.1) × 10^3 M^{-1}. The stoichiometry of binding again was found to be 1:1.

Table 11 summarizes the calculated binding constants of a number of analogues with Mg^{2+} using the pK_a method and the mole ratio method. The stoichiometry in binding for all the analogues was found to be 1:1 by the latter method. The binding constants of the analogues with Mg^{2+} determined by these two methods are consistent. Therefore, the binding constants of the analogues with Ca^{2+} determined by the pK_a method can confidently be compared with the binding constants of ionomycin and other Ca^{2+} ionophores with Ca^{2+} determined by the mole ratio method. The 1:1 stoichiometry of Mg^{2+} binding, together with the requirement of the presence of the carboxyl and β-diketone groups in the same molecule for Ca^{2+} transport, and the formation of both the carboxylate and enolate of the β-diketone in transport, suggested that the Ca^{2+} complex had a 1:1 stoichiometry in binding and transport.

In conclusion, the basic structural requirements for efficient Ca^{2+} transport are the presence of the β-diketone and the carboxyl group in the same molecule, and a simple alkyl side chain with sufficient lipid solubility. The distance between the β-diketone and the carboxyl group is important in controlling the efficiency of Ca^{2+} transport. Optimal Ca^{2+} transport is achieved when the β-diketone is separated from the carboxyl

Can. J. Chem. Downloaded from www.nrcresearchpress.com by EESC ESCOLA DE ENGENHARIA on 09/08/12
For personal use only.

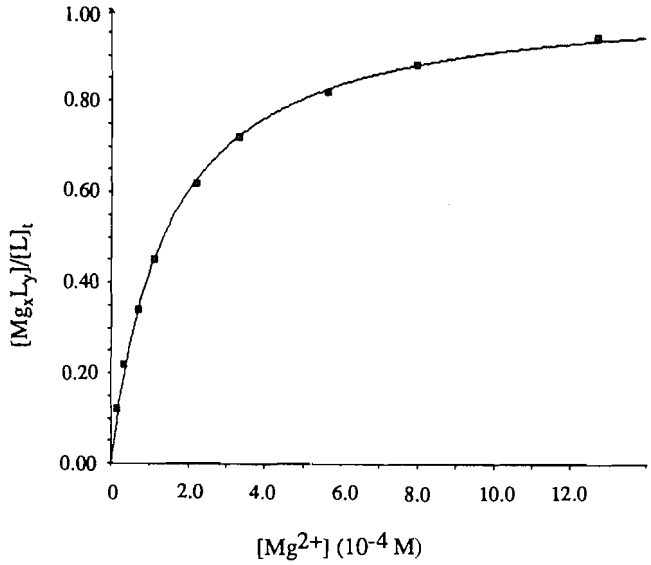

FIG. 7. Nonlinear regression plot of the number of moles of Mg^{2+} bound per mole of analogue **13** versus concentration of free Mg^{2+}.

TABLE 11. Binding constants of analogues with Mg^{2+} using the pK_a method and the mole ratio method

Analogue	β^a (10^3 M^{-1})	β^b (10^3 M^{-1})
5	4.4 ± 0.2	5.5 ± 0.1
8	3.4 ± 0.2	5.6 ± 0.1
9	5.6 ± 0.2	6.2 ± 0.1
10	5.7 ± 0.3	6.2 ± 0.1
13	7.6 ± 0.4	7.1 ± 0.1
15	1.9 ± 0.1	4.5 ± 0.1

[a]Values determined using the pK_a method.
[b]Values determined using the mole ratio method.

group by seven methylene units, identical to that found in ionomycin. It appears that additional oxygen binding sites on the side chain of the analogues do not enhance the transport of Ca^{2+}. Analogues with sufficient lipid solubility are comparable to calcimycin and ionomycin in terms of Ca^{2+} transport. Ca^{2+} transport by synthetic analogues of ionomycin is a saturable process that obeys Michaelis–Menten kinetics. Ca^{2+} transport is dependent of the pH in the aqueous source phase and independent of the pH in the receiving phase. Both the carboxyl and the β-diketone groups are ionized in the transport of Ca^{2+}, indicating that the stoichiometry of Ca^{2+} complex in transport is 1:1.

The pK_a of the β-diketone of the analogues was measured by UV spectrophotometric titration and found to be lower than that of the β-diketone in ionomycin. The pK_a values of the analogues were related to the lipid solubility of the compounds and the length of the hydrocarbon chain between the β-diketone and the carboxyl group. The binding constants of the analogues with Ca^{2+}, Mg^{2+}, K^+, and Na^+ were determined by measuring the pK_a and the β-diketone in the presence and absence of the cation. The selectivity in binding by the analogues were the same as the selectivity in transport, which was $Mg^{2+} > Ca^{2+} \gg Na^+$, K^+. The binding constants of the analogues with Ca^{2+} and Mg^{2+} were 3 to 4 orders of magnitude lower than those of ionomycin. The mole ratio method was used to determine the binding constants of the analogues with Mg^{2+} and the stoichiometry in binding. The consistency of the Mg^{2+} binding constants determined by both the pK_a and the mole ratio methods verified the utility of the pK_a method for the measurement of binding constants of the analogues with Ca^{2+}, K^+, and Na^+.

Experimental section

Determination of metal ion transport

The transport of metal ions across a chloroform liquid membrane by synthetic analogues of ionomycin was determined in a cylindrical glass cell shown in Fig. 1. To determine the Ca^{2+} transport of the various analogues, a 200 mM solution of analogue in 40 mL of glass-distilled chloroform (OmniSolv BDH Inc.) was placed at the bottom of the transport vessel. A solution of 500 mM calcium chloride and 40 mM CHES/Me_4NOH buffer in 10 mL of distilled deionized water at pH = 9.50 was placed on one side of the transport vessel as the source phase. A solution of 40 mM MOPS/Me_4NOH buffer in 10 mL of distilled deionized water at pH = 7.00 was placed on the other side of the transport vessel as the receiving phase. The chloroform solution was stirred continuously with a 10 × 3 mm microstirring bar at a constant speed of 400 ± 20 rpm as determined by a chronometric speedcounter.

An aliquot of 200 mL of the receiving phase was withdrawn at regular intervals, diluted with 4.80 mL of distilled deionized water and analyzed for Ca^{2+} by calcium atomic absorption spectrophotometry. In all the transport experiments the concentration of Ca^{2+} in the receiving phase increased linearly with time when the quantity of Ca^{2+} transported was small. Results from separate runs were reproducible within ±10%. The initial transport rate (J) is expressed as the moles of Ca^{2+} transported per square centimeter of the organic phase per hour.

Cation selectivity in transport was determined using a source phase of 10 mL of distilled deionized water containing equimolar concentration (250 mM) of calcium chloride and the chloride of the competing cation (Mg^{2+}, Na^+, and K^+ respectively), and 40 mM CHES/Me_4NOH buffer at pH = 9.50. The samples taken from the receiving phase were analyzed for the concentrations of both cations by atomic absorption spectrometry on a Perkin–Elmer model 560 atomic absorption spectrophotometer.

Buffers that had negligible affinity for Mg^{2+}, Ca^{2+}, Na^+, and K^+ were used to control the pH in the source phase and the receiving phase (44). They were prepared by mixing an aqueous solution of 10% tetramethylammonium hydroxide with an acid having a pK_a close to the desired working pH and diluting the solution with distilled deionized water to a final concentration of 40 mM.

Cation selectivity in transport

The transport experiments were carried out according to the general procedure for the determination of metal ion transport with 250 mM calcium chloride, 250 mM of the chloride of the competing cation, and 40 mM CHES/Me_4NOH buffer in 10 mL of distilled deionized water at pH = 9.5 for the source phase.

Effect of calcium concentration in the source phase on calcium transport

The transport experiments were carried out according to the general procedure for the determination of metal ion transport using a given concentration of calcium chloride and 40 mM CHES/Me_4NOH buffer in 10 mL of distilled deionized water at pH = 9.5 for the source phase.

Effect of pH in the receiving phase on calcium transport

The transport experiments were carried out according to the general procedure for the determination of metal ion transport using 40 mM of a given buffer in 10 mL of distilled deionized water at a given pH for the receiving phase.

Effect of pH in the source phase on calcium transport by analogue **4**

The transport experiments were carried out according to the general procedure for the determination of metal ion transport. The com-

Can. J. Chem. Downloaded from www.nrcresearchpress.com by EESC ESCOLA DE ENGENHARIA on 09/08/12
For personal use only.

positions of the three layers in the transport vessel were 300 mM of analogue **4** in 40 mL of chloroform for the organic phase, 40 mM MOPS/Me_4NOH buffer in 10 mL of distilled deionized water at pH = 6.5 for the receiving phase, and 500 mM calcium chloride and 40 mM of a given buffer in 10 mL of distilled deionized water at a given pH for the source phase.

Determination of the pK_a of the β-diketone of the synthetic analogues of ionomycin

The pK_a of the β-diketone of the synthetic analogues was determined in 80% MeOH–H_2O by UV spectrophotometric titration at 25°C on a Perkin–Elmer UV–visible Lambda 2 spectrometer with a thermostated sample cell. An aliquot of 1.0 mL 80% MeOH–H_2O was placed in a disposable cuvette (1.0 cm pathlength) in the sample cell and the baseline was recorded from 260 to 350 nm and stored. The solvent was then replaced by a solution of 80 mM analogue and 50 mM Et_4NClO_4 in 1.0 mL of 80% MeOH–H_2O. Small aliquots (4–20 μL) of 0.1, 0.25, 0.5, and 5.0% Me_4NOH (the titrant) in 80% MeOH–H_2O were added and the spectra were recorded. The addition of the titrant was terminated when the maximum absorption of the spectrum remained constant.

The values of pH at each titration point were determined with the same solutions on a 5-fold greater scale on a PHM82 Standard pH meter (Bach–Simpson Limited). The pH meter was standardized with pH = 7.0 and pH = 10.0 aqueous buffer solutions. No correction was made for differences in the pH readings between pure aqueous solutions and 80% MeOH–H_2O solutions.

The absorbance at 298 nm versus pH was computer-fitted to a modified Henderson–Hasselbalch equation by nonlinear regression (33) to calculate the pK_a values.

Determination of the binding constants of the analogues with various metal cations

The binding constant of the analogues with various metal cations was determined in 80% MeOH–H_2O by UV spectrophotometric titration at 25°C. The UV spectrophotometric titration of the analogues was carried out in the presence of 50 mM NaCl, 50 mM KBr, 16.7 mM $CaCl_2$, and 16.7 mM $MgCl_2$, respectively (in place of Et_4NClO_4). The absorbance at 298 nm versus pH was computer-fitted to a modified Henderson–Hasselbalch equation by nonlinear regression to calculate the pK_a of a β-diketone in the presence of the metal ion. The difference between p$K_{a'}$ and pK_a gave the logarithm of the dissociation constant of the analogue–cation complex.

The binding constant of the analogues with Mg^{2+} was also determined using the mole ratio method. A solution of 80 mM analogue and 50 mM CHES/Me_4NOH buffer in 80% MeOH–H_2O was titrated with a solution of 5, 10, 25, 50, 100, and 250 mM $MgCl_2$ in 80% MeOH–H_2O. Calculations of the number of moles of Mg^{2+} bound per mole of the analogue versus the concentration of free Mg^{2+} at each titration point were computer-fitted to the Scatchard equation by nonlinear regression to determine the binding constant (33, 43). This method also allowed the determination of the stoichiometry of the complex.

Acknowledgements

This work was supported by grants from the Natural Sciences and Engineering Research Council of Canada and Merck Frosst Canada. We are grateful to Dr. R. Young of Merck Frosst Canada for valuable discussions, and to Dr. C. Chan of Merck Frosst Canada for performing the in vivo assays.

1. A.K. Campbell. *In* Intracellular calcium, its universal role as regulator. John Wiley & Sons, Toronto. 1983.
2. (*a*) M.J. Berridge. Sci. Am. **253**, 142 (1985); (*b*) E. Carafoli and J.T. Penniston. Sci. Am. **253**, 70 (1985); (*c*) E. Ochial. J. Chem. Educ. **68**, 10 (1991).
3. B.E.C. Nordin. *In* Calcium in human biology. Springer-Verlag, Germany. 1988.
4. (*a*) S. Hagiwara and L. Byerly. Annu. Rev. Neurosci. **4**, 69 (1981); (*b*) M.P. Blaustein. *In* Calcium in biological systems. Plenum, New York. 1985.
5. (*a*) C.C. Ashley and A.K. Campbell. *In* Detection and measurement of free calcium in cells. Elservier/North-Holland, Amsterdam. 1979; (*b*) J.R. Blinks, W.G. Wier, P. Hess, and F.G. Prendergast. Prog. Biophys. Mol. Biol. 1 (1981).
6. L.V. Heilbrunn and F.J. Wiercinski. J. Cell Comp. Physiol. **29**, 15 (1947).
7. B.C. Pressman, E.J. Harris, W.S. Jagger, and J.H. Johnson. Proc. Natl. Acad. Sci. U.S.A. **58**, 1949 (1967).
8. J. Berger, A.I. Rachlin, W.E. Scott, L.H. Sternbach, and M.W. Goldberg. J. Am. Chem. Soc. **73**, 5295 (1951).
9. (*a*) P.W. Reed. Fed. Proc. **31**, 432 (1972); (*b*) P.W. Reed and H.A. Lardy. J. Biol. Chem. **247**, 6970 (1972).
10. (*a*) J.W. Westley, R.H. Evens, T. Williams, and A. Stempel. J. Chem. Soc. Chem. Commun. 71 (1970); (*b*) M.O. Chaney, P.V. Demarco, N.D. Johes, and J.L. Occolowitz. J. Am. Chem. Soc. **96**, 1932 (1974).
11. (*a*) E. Meyers, D.S. Slusarchyk, and W.C. Liu. U.S. Patent 3 873 693 (1975); Chem. Abstr. **83**, 41512a (1975); (*b*) E. Meyers, D.S. Slusarchyk, W.C. Liu, G. Astle, W.H. Trejo, and W.E. Brown. J. Antibiot. **31**, 815 (1978).
12. B.K. Toeplitz, A.I. Cohen, R.T. Funke, W.L. Parker, and J.Z. Gougoutas. J. Am. Chem. Soc. **101**, 3344 (1979).
13. E.F. Gale, E. Cundliffe, P.E. Reynolds, M.H. Richmond, and M.J. Waring. *In* The molecular basis of antibiotic action. John Wiley and Sons, Toronto. 1972.
14. J.W. Westley. *In* Polyether antibiotics — naturally occurring acid ionophores. Vol. 1. Marcel Dekker, New York. 1982.
15. M.J. Umen and A. Scarpa. J. Med. Chem **21**, 505 (1978).
16. (*a*) K. Hiratani, H. Sughara, K. Taguchi, and K. Iio. Chem. Lett. 1657 (1983); (*b*) Chem. Lett. 1457 (1984).
17. L.M. Dulyea, T.M. Fyles, and D.M. Whitfield. Can. J. Chem. **62**, 498 (1984).
18. (*a*) T.M. Fyles. *In* Inclusion aspects of membrane chemistry. Kluwer Academic, The Netherlands. 1991. pp 59–110; (*b*) B.C. Pressman. Fed. Am. Soc. Exp. Biol. **32**, 1698 (1973).
19. J. Rebek, Jr., B. Askew, D. Nemeth, and K. Parris. J. Am. Chem. Soc. **109**, 2432 (1987).
20. (*a*) D.E. Fenton. Chem. Soc. Rev. **6**, 325 (1977); (*b*) W.D. Stein. *In* Channels, carriers, and pumps. Academic Press, New York. 1990.
21. R.F. Kauffman, R.W. Taylor, and D.R. Pfeiffer. J. Biol. Chem. **253**, 5892 (1978).
22. R.F. Kauffman, R.W. Taylor, and D.R. Pfeiffer. J. Biol. Chem. **255**, 2735 (1980).
23. T.Q. Hu and L. Weiler. Can. J. Chem. **72**, 1500 (1994).
24. W. Saegner, I.H. Suh, and G. Weber. Isr. J. Chem. **18**, 253 (1979).
25. R.F. Rekker. *In* The hydrophobic fragmental constant; its derivation and application with a means of characterizing membrane systems. Elsevier, Amsterdam. 1977.
26. (*a*) A.H. Alberts and D.J. Cram. J. Am. Chem. Soc. **101**, 3545 (1979); (*b*) Y. Ito, T. Sugaya, M. Nakatsuka, and T. Suegusa. J. Am. Chem. Soc. **99**, 8366 (1977).
27. (*a*) T.M. Fyles, V.A. Malik-Diemer, and D.M. Whitfield. Can. J. Chem. **59**, 1734 (1981); (*b*) T.M. Fyles, V.A. Malik-Diemer, C.A. McGavin, and D.M. Whitfield. Can. J. Chem. **60**, 2259, (1982); (*c*) F.G. Riddell. Chem. Br. **28**, 533 (1992).
28. C.M. Liu and T.E. Hermann. J. Biol. Chem. **253**, 5892 (1978).
29. (*a*) W.C. Still, P. Hauck, and D. Kempf. Tetrahedron Lett. **28**, 2817 (1987); (*b*) S.D. Erickson, M.H.J. Ohlmeyer, and W.C. Still. Tetrahedron Lett. **33**, 5925 (1992).
30. R.D. Hancock and A.E. Martell. Chem. Rev. **89**, 1875 (1989).
31. (*a*) H.N. Christensen. *In* Biological transport. W.A.Benjamin Inc., Reading, Mass. 1975; (*b*) K.D. Neame and T.G. Richards. *In* Elementary kinetics of membrane carrier transport. Blackwell Scientific, Oxford. 1972.
32. (*a*) L. Michaelis and M.L. Menten. Biochem. J. **49**, 333 (1913);

Can. J. Chem. Downloaded from www.nrcresearchpress.com by EESC ESCOLA DE ENGENHARIA on 09/08/12
For personal use only.

(*b*) G.E. Briggs and J.B.S. Haldane. Biochem. J. **19**, 338 (1925); (*c*) A. Kotyk and K. Janacek. *In* Cell membrane transport. Plenum Press, New York. 1975.
33. R.J. Leatherbarrow. *In* Enzfitter. Elsevier, Amsterdam. 1987.
34. S.I. Kang, A. Czech, B.P. Czeck, L.E. Stewart, and R.A. Bartsch. Anal. Chem. **57**, 1713 (1985).
35. R.G. Pearson and R.L. Dillon. J. Am. Chem. Soc. **75**, 2439 (1953).
36. K.A. Connors. *In* Binding constants. John Wiley & Sons, Toronto. 1987.
37. (*a*) J.H. Yoe and A.E. Harvey. J. Am. Chem. Soc. **70**, 648 (1948); (*b*) C.D. Chriswell and A.A. Schilt. Anal. Chem. **47**, 1623 (1975).
38. (*a*) P. Job. Ann. Chim. **9**, 113 (1928); (*b*) W. Likussar and D.F. Boltz. Anal. Chem. **43**, 1265 (1971).
39. M. Seco. J. Chem. Educ. **66**, 779 (1989).
40. M.K. Stiles, M.E. Craig, S.L.N. Gunnell, D.R. Pfeiffer, and R.W. Taylor. J. Biol. Chem. **266**, 8336 (1991).
41. (*a*) W.C. Still, D. Cai, D. Lee, P. Hauck, A. Bernardi, and A. Romero. Lect. Heterocycl. Chem. **9**, 33 (1987); (*b*) W.C. Still and W. Smith. J. Am. Chem. Soc. **110**, 7917 (1988); (*c*) W.C. Still and T. Iimori. J. Am. Chem. Soc. **111**, 3439 (1989); (*d*) W.C. Still and S.D. Erickson. Tetrahedron Lett. **31**, 4253 (1990).
42. B.L. Poh, L.H. Seah, and C.S. Lia. Tetrahedron, **46**, 4379 (1990).
43. G. Scratchard. Ann. N.Y. Acad. Sci. **51**, 660 (1949).
44. D.E. Gueffroy. *In* A guide for the preparation and use of buffers in biological systems. Calbiochem, San Diego, Calif. 1981.

Can. J. Chem. Downloaded from www.nrcresearchpress.com by EESC ESCOLA DE ENGENHARIA on 09/08/12
For personal use only.

Crystal and solution structure of a pendant-armed macrocyclic complex of palladium(II)

B. CHAK, A. MCAULEY, AND T.W. WHITCOMBE
Department of Chemistry, University of Victoria, Victoria, BC V8W 3P6, Canada

Received August 17, 1993

B. CHAK, A. MCAULEY, and T.W. WHITCOMBE. Can. J. Chem. **72**, 1525 (1994).

The synthesis and X-ray crystal structure of [Pd)py_2[9]aneN_2S)]$(BF_4)_2$ (py_2[9]aneN_2S = 1-thia-4,7-bis(pyridylmethyl)diazacyclononane) ($P2_1/n$, a = 10.233(4) Å, b = 11.484(5) Å, c = 19.913(6) Å, β = 94.03(4)°, V = 2334(2) Å^3, R = 0.0705, R_w = 0.0759) are presented. The crystal structure indicates a long range interaction (2.92 Å) between the planar palladium and the apical sulphur atom. Although this distance is longer than the value for a Pd—S bond observed normally there is evidence for a net positive interaction provided by the solution structure as determined by NMR spectroscopy. Comparative analysis of the structural features exhibited by this complex with similar nine-membered chelating ligands emphasizes the presence of an axial Pd—S bond.

B. CHAK, A. MCAULEY et T.W. WHITCOMBE. Can. J. Chem. **72**, 1525 (1994).

On a réalisé la synthèse du [Pd(py_2[9]aneN_2S)]$(BF_4)_2$ (py_2[9]aneN_2S = 1-thia-4,7-bis(pyridylméthyl)-diazacyclononane) et on en a déterminé la structure par diffraction des rayons X ($P2_1/n$, a = 10,233(4), b = 11,484(5) et c = 19,913(6) Å, β = 94,03(4)°, R = 0,0705 et R_w = 0,0759). La structure cristalline indique la présence d'une interaction à longue distance (2,92 Å) entre le palladium plan et l'atome de soufre apical. Même si cette distance est plus longue que la valeur d'une liaison Pd—S observée normalement, la structure en solution, telle que déterminée par spectroscopie rmn, fournit une preuve de l'existence d'une nette interaction positive. Une analyse comparative des caractéristiques de structure de ce complexe avec ceux de coordinats chélatants à neuf chaînons semblables fait ressortir la présence d'une liaison Pd—S axiale.

[Traduit par la Rédaction]

Introduction

There has been considerable recent interest in the chemistry of metal complexes involving macrocyclic ligands with pendant arms (1). In some instances this derives from biological studies where it has been demonstrated that the complexation of functional groups that are integral parts of the structure but not fixed rigidly in place, provides a mechanism for activation of the metal site (2, 3). Examples of novel chemistry have emerged from these studies, including the demonstrated electrochemical reduction of CO_2 to CO through the use of a pendant-arm macrocyclic complex of nickel (4).

In addition, less common coordination geometries have been detected. The tris(pyridylmethyl)-1,4,7-triazacyclonane (py_3[9]aneN_3) complex of Pd(II) has been shown to contain a square pyramidal PdN_5 core, in which the metal-coordinated and -uncoordinated pyridine nitrogens interconvert within the NMR time scale (5). There are also several recent examples of fluxionality at Pd(II) detected by NMR spectroscopy involving both pendant armed and simple macrocyclic ligands (6, 7). In particular, several complexes with thia-macrocyclic ligands have been examined (8, 9).

In the present paper, the synthesis of the ligand 1-thia-4,7-bis(pyridylmethyl)diazacyclononane (py_2[9]aneN_2S) (Scheme 1) is reported together with the crystal structure of its palladium(II) complex. The metal complex provides an interesting contrast to [Pd(py_3[9]aneN_3)]$^{2+}$ in that the presence of only two arms prohibits a complete scrambling of the coordination environment but does not preclude the possibility of fluxional NMR spectroscopy.

The coordination of the [9]aneN_2S ring in a facial geometry results in the sulfur atom being positioned axially[1] such that the inter-atomic distance is borderline between a "bonding" and "non-bonding" interaction. One method of investigating such potential bonding is to compare the torsional angles within the 9-membered ring of the present complex with those for well-characterized metal-ion – N_2S ring systems in which data for axial bonds have been structurally characterized. The structural rigidity of the complex in solution may also be monitored by NMR techniques in which fluxional processes involving the axial donor of the ligand are not observed.

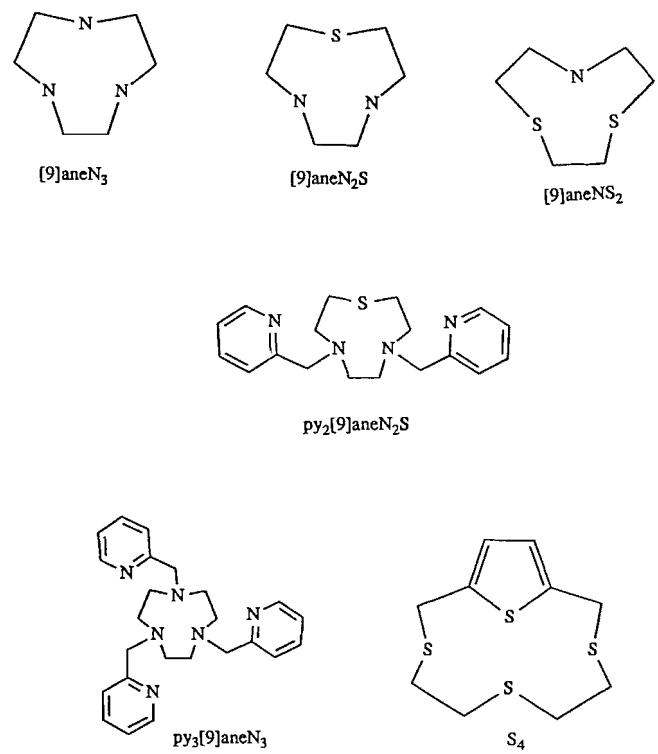

SCHEME 1

Experimental

The nine-membered macrocyclic ligand, [9]aneN_2S, was prepared by literature procedures (10, 11). All chemicals used were of reagent grade unless otherwise specified.

[1]S. Chandrasekar and A. McAuley. Unpublished work.

Can. J. Chem. Downloaded from www.nrcresearchpress.com by EESC ESCOLA DE ENGENHARIA on 09/08/12
For personal use only.

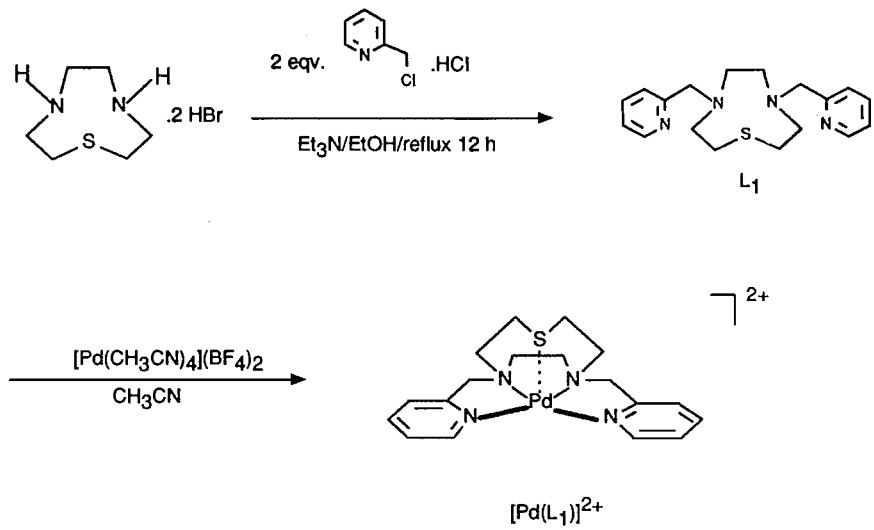

SCHEME 2

1-Thia-4,7-bis(pyridylmethyl)diazacyclononane ($py_2[9]aneN_2S$)

To a 100 mL round bottom flask equipped with a magnetic stirrer, reflux condensor, and nitrogen inlet was added a solution containing the dihydrobromide salt of [9]aneN$_2$S (0.465 g, 1.51 mmol), 2-(chloromethyl)pyridine.HCl (0.50 g, 3.05 mmol), and 9.5 equiv. of triethylamine (14.3 mmol) in absolute ethanol. The reaction mixture was refluxed for 12 h under a N_2 atmosphere and subsequently extracted with chloroform (3 × 100 mL). The chloroform extract was washed with water (5 × 100 mL) and dried over anhydrous Na_2SO_4. The solvent was removed using a rotary evaporator. The pale yellow oil obtained consisted of mainly the desired product but traces of unreacted 2-(chloromethyl)pyridine.HCl were detected. Yield: 0.3 g (≈ 60%). MS(CI): M + 1 329, M + 29 357. ^{1}H NMR ($CDCl_3$): δ 2.65 (s, 4H, NCH_2CH_2N), δ 2.95 (m, 4H, CH_2N), δ 3.05 (m, 4H, CH_2S), δ 3.82 (s, 4H, CH_2—py), δ 7.12, δ 7.51, δ 7.63, δ 8.48 (m, 8H, pyridine—H). ^{13}C NMR ($CDCl_3$): δ 32.0 (CH_2S), δ 56.0 (NCH_2CH_2N), δ 59.0 (CH_2N), δ 64.2 (CH_2—pyridine), δ 121.8, δ 123.2, δ 136.2, δ 148.9. δ 160.0 (pyridine—C). The oil was used directly in reaction with the metal ion to give the palladium(II) complex.

$[Pd(py_2[9]aneN_2S)](BF_4)_2$

To an acetonitrile solution of the ligand (0.11 g, 0.34 mmol) was added solid $[Pd(CH_3CN)_4](BF_4)_2$ (0.13 g, 0.29 mmol). The solution immediately turned orange/brown and was heated to a gentle reflux for an hour, under an atmosphere of nitrogen, to ensure complete complexation. After cooling to room temperature, the solution was taken to dryness to give an orange/brown solid. Redissolving this solid in a minimum of acetonitrile and slow diffusion of diethyl ether yielded orange/brown crystals of $[Pd(py_2[9]aneN_2S)](BF_4)_2$ of X-ray quality. Yield of crystals: 120 mg. Anal. calcd. for $C_{18}H_{24}N_4SPdB_2F_8$: C 35.53, H 3.98, N 9.21; found: C 35.74, H 3.91, N 9.29.

Crystallography

An orange/brown crystal was mounted inside a Lindemann tube using epoxy resin. An initial unit cell and space group were obtained by Weissenberg and precession photography. The crystal was transferred to a Picker Four-circle Diffractometer and the unit cell refined using 10 reflections in the 2θ range, 37° to 52°, while the choice of space group was confirmed. The data were collected using 200 steps of 0.01° in 2θ at 0.25 s per step. Background counting for 25 s was carried out before and after each reflection measurement. Three standard reflections were measured at the beginning of every 50 reflections, with no significant decay being observed.

A total of 5356 reflections were obtained of which 3790 were within the limits $I > 2\sigma(I)$. Refinement was achieved through location of the palladium atom by the direct methods package of SHELX76 (12) and subsequent structural refinement using the least-squares difference maps. The atomic scattering factors and Pd *f*-curve were taken from the usual source (13). Absorption correction was performed using a locally modified version of an existing program (14). Final values of R = 0.0705 and R_w = 0.0759 were obtained with all non-hydrogen atoms anisotropic. The hydrogen atoms were not included in the structure refinement. A final difference map gave a maximum residual electron density of 0.2 e/Å^3 and a maximum shift/e.s.d. of 0.005 for final convergence.

Spectroscopy

^{1}H and ^{13}C NMR spectra were recorded on either a Bruker WM 250 MHz or a Bruker AMX 360 MHz spectrometer, operating at the appropriate frequencies. The UVspectra were obtained with a Varian Cary 5 spectrometer. Electrochemical measurements were performed with a PAR 273 Galvanostat/Potentiostat connected to an IBM PC with the HEADSTART software package. The electrochemical cell consisted of the usual three electrode arrangement with a platinum working and counter electrode. The choice of reference electrode was solvent dependent, being Ag/AgCl in aqueous media (0.1 M $LiClO_4$) and Ag/AgNO3 in non-aqueous media (0.1 M Bu_4NPF_6). In the non-aqueous environment, the reference electrode was calibrated against the $Fc^{+/0}$ couple.

Results and discussion

Synthesis and spectroscopy

The synthesis of the ligand, $py_2[9]aneN_2S$, is outlined in Scheme 2, together with the formation of the palladium(II) complex. The formation of the dihydrobromide salt of 1,4-diaza-7-thiacyclononane (**II**) was achieved by literature procedures (10, 11) and proceeds with reasonable yields. Care must be taken during the detosylation of the amines to avoid cleavage of the C—S bonds with the ring.

The methyl pyridine moiety was added to the ring by the reaction of **II** with 2-(chloromethyl)pyridine.HCl in the presence of triethylamine in absolute ethanol. The ligand, which was isolated as a pale yellow oil in 60% yield, was found not to be stable upon exposure to air and light for periods of time, gradually darkening to a brown colored oil. Therefore, the freshly made ligand was complexed immediately with the metal ion upon isolation.

The palladium(II) complex was prepared by the reaction of equimolar quantities of the ligand and $[Pd(CH_3CN)_4](BF_4)_2$ in freshly distilled, dry acetonitrile under an atmosphere of nitrogen. The initial yellow color, arising from the palladium salt, disappeared rapidly giving an orange/brown solution. X-ray

Can. J. Chem. Downloaded from www.nrcresearchpress.com by EESC ESCOLA DE ENGENHARIA on 09/08/12
For personal use only.

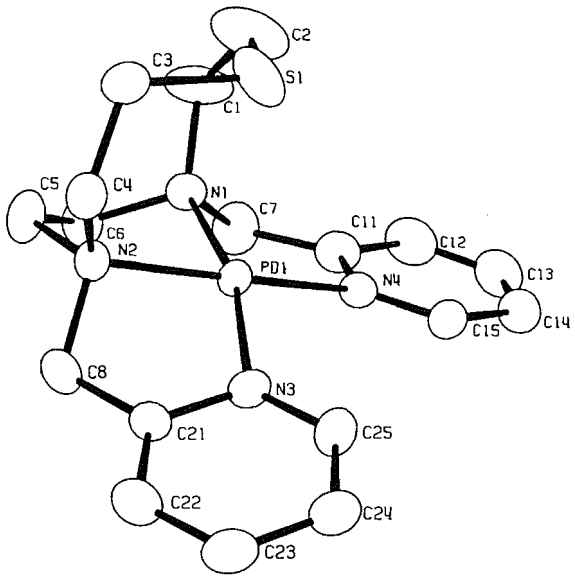

FIG. 1. ORTEP diagram of the cation $[Pd(py_2[9]aneN_2S)]^{2+}$. Bond distances, Pd...N(1) 2.044(6) Å, Pd...N(2) 2.028(6) Å, Pd...N(3) 2.041(6) Å, Pd...N(4) 2.041(6) Å, Pd...S(1) 2.915(3) Å.

quality crystals of $[Pd(py_2[9]aneN_2S)](BF_4)_2$ were obtained by slow diffusion of diethyl ether into an acetonitrile solution of the impure reaction product.

The UV/visible spectrum of the palladium complex in CH_3CN exhibits two bands at 264 and 301 nm with extinction coefficients of 6.2×10^3 and 3.5×10^3 M^{-1} cm^{-1}, respectively. No distinct absorptions were observed in the visible portion of the spectrum, even at high concentrations (≈0.01 M), suggesting that the *d–d* transitions have been shifted to higher energy and are masked by the charge transfer bands.

Electrochemical data for the palladium complex provides evidence for a single, irreversible reduction at −1.25 V in CH_3CN and no observable reactivity in aqueous media. The absence of reversible electrochemistry is suggestive of decomposition of the Pd(I) complex formed, although the observed shape and size of the reduction peak were invariant with scan speed. The lack of any observable oxidation peak is consistent with the "open-chain" structure of this macrocyclic complex and the presence of a sulphur donor atom which are known to result in an increase in the electrochemical potential for such complexes (15).

Crystallography

The ORTEP diagram of $[Pd(py_2[9]aneN_2S)](BF_4)_2$, together with the atomic labelling scheme, is provided in Fig. 1. The crystallographic parameters, fractional atomic coordinates, selected bond lengths, and bond angles are provided in Tables 1–4, respectively. All other crystallographic tables have been deposited as supplementary material (Table S1 contains experimental crystallographic data, Tables S2–S6 contain fractional coordinates, bond lengths, bond angles, interatomic distances, and anisotropic temperature parameters for the complex (11 pages), Tables S7 lists calculated and observed structure factors (16 pages), and full details of NMR simulations (9 pages)).[2]

TABLE 1. Crystallographic parameters for $[Pd(py_2[9]aneN_2S)](BF_4)_2$[a]

Formula	$C_{18}H_{24}N_4SB_2F_8Pd$
Molecular weight	608.5 g/mol
Space group	Monoclinic, $P2_1/n$ (no. 14)
Unit cell	
a	10.233(4) Å
b	11.484(5) Å
c	19.913(6) Å
β	94.03(4)°
Volume	2334(2) Å^3
Z	4
r_{calc}	1.731 g/cm^3
r_{meas}	1.721 g/cm^3
Radiation	Mo K_α, 0.71069 Å
2θ	0.1–55.0°
No. of reflections	5356
$I > 2\sigma(I)$	3790
No. of parameters	307
Residual electron density	0.68 e/Å^3
Maximum final shift/e.s.d.	0.005
R, R_w	0.0705, 0.0759

[a] $R = \Sigma(|F_o| - |F_c|)/\Sigma|F_o|$, $R_w = [\Sigma(|F_o| - |F_c|)^2/-\Sigma w(|F_o|^2]^{1/2}$.

The asymmetric unit for the compound contains the whole cation defining a static structure for the complex which does not express the time-averaged symmetry observed in the ^{13}C or ^1H NMR spectra (*vide infra*). The palladium atom is coordinated by the two tertiary nitrogens of the macrocyclic ring and the nitrogen atoms of the pyridine pendant arms, forming an approximate PdN_4 plane. The sulfur atom is disposed apically relative to this coordination plane.

The Pd—N bond distances are in the range 2.028(6) and 2.044(6) Å, with no significant structural variation. The chelating angles are, respectively, N(1)—Pd—N(2): 87.1(3)°, N—Pd—py: 82.5(3)° and 83.6(3)°, and py—Pd—py: 105.8(3)°, which are consistent with the structural constraints imposed by the five-membered chelating rings and the presence of a double bond within the pyridine ring. The angle obtained for the N(1)—Pd—N(2) chelate is close to the value of 86° obtained for the analogous $Pd(trien)^{2+}$ complex ion (trien: triethylenetetraamine) (16).

The distance to the apical sulfur atom is 2.915(3) Å, which is consistent with, but shorter than, the value of 2.952(4) Å reported (17) for $[Pd([9]aneS_3)_2](PF_6)_2$. Typically, palladium–sulfur bonds are in the range 2.2 to 2.4 Å, as observed in the equatorial plane for the $[Pd([9]aneS_3)_2](PF_6)_2$ complex (Table 5). Hence, the present distance is certainly longer than might be considered bonding. However, the coordination geometry of the palladium atom and the disposition of the macrocyclic ligand indicate some form of interaction is present. This is confirmed by the calculation of the mean plane for the four nitrogen atoms (Table 6). Although these atoms do not form a perfectly planar donor set, the calculations show that the palladium atom is distended 0.148 Å out of the mean plane described by the nitrogen atoms towards the apical sulfur atom. The basal angles, N(3)—Pd—N(1) and N(4)—Pd—N(2), are 165.3(3)° and 169.3(3)°, respectively, which are consistent with the theoretical value for a square pyramidal d^8 ion given by Hoffman et

[2]This supplementary material can be purchased from: The Depository of Unpublished Data, Document Delivery, CISTI, National Research Council Canada, Ottawa, ON K1A 0S2, Canada.

Crystallographic parameters fractional coordinates, bond lengths and bond angles for $[Pd(py_2[9]aneN_2S)](BF_4)_2$ have also been deposited with the Cambridge Crystallographic Data Centre, and can be obtained on request from The Director, Cambridge Crystallographic Data Centre, University Chemical Laboratory, 12 Union Road, Cambridge, CB2 1EZ, U.K.

Can. J. Chem. Downloaded from www.nrcresearchpress.com by EESC ESCOLA DE ENGENHARIA on 09/08/12
For personal use only.

Can. J. Chem. Downloaded from www.nrcresearchpress.com by EESC ESCOLA DE ENGENHARIA on 09/08/12
For personal use only.

TABLE 2. Fractional coordinates for $[Pd(py_2[9]aneN_2S)](BF_4)_2$[a]

Atom	x/a	y/b	z/c	U_{eq}
Pd(1)	9182(5)	24179(4)	43892(3)	440(2)
S(1)	495(3)	4914(3)	4208(1)	93(1)
N(1)	2340(5)	2927(6)	4469(4)	56(2)
N(2)	999(6)	2554(5)	3376(3)	54(2)
N(3)	−841(5)	1646(5)	4118(3)	53(2)
N(4)	1203(7)	2216(5)	5413(3)	52(2)
C(1)	3091(9)	4196(9)	4501(8)	122(6)
C(2)	2195(14)	5057(11)	4529(9)	155(8)
C(3)	534(9)	4747(7)	3314(5)	69(3)
C(4)	182(9)	3537(7)	3068(4)	63(3)
C(5)	2424(9)	2661(9)	3213(5)	76(3)
C(6)	3321(8)	2370(8)	3845(5)	74(3)
C(7)	3449(8)	2308(9)	5056(5)	81(4)
C(8)	369(8)	1422(7)	3120(4)	66(3)
C(11)	2508(9)	2321(7)	5614(5)	66(3)
C(12)	2898(12)	2364(9)	6304(6)	87(4)
C(13)	1985(13)	2260(9)	6766(6)	89(4)
C(14)	722(11)	2139(9)	6545(5)	78(4)
C(15)	353(9)	2139(7)	5865(4)	64(3)
C(21)	−828(7)	1251(6)	3473(4)	53(2)
C(22)	−1977(9)	714(8)	3156(5)	74(3)
C(23)	−3069(9)	572(8)	3511(6)	76(4)
C(24)	−3039(8)	976(8)	4186(5)	70(3)
C(25)	−1930(7)	1515(8)	4449(4)	61(3)
B(1)	6260(9)	4329(10)	3560(5)	64(3)
B(2)	1735(10)	3967(12)	1238(6)	74(4)
F(1)	6127(6)	3905(7)	4180(3)	119(3)
F(2)	7404(6)	4668(8)	3418(4)	147(4)
F(3)	5809(16)	3536(13)	3153(5)	265(9)
F(4)	5398(9)	5112(11)	3425(8)	244(8)
F(5)	1646(14)	4578(9)	1825(5)	213(7)
F(6)	2722(7)	4484(8)	961(5)	153(4)
F(7)	730(9)	4251(11)	884(8)	242(8)
F(8)	1803(16)	2869(9)	1334(10)	284(11)

[a]Estimated standard deviations are given in parentheses. Coordinates × 10^n where n = 5, 4, 4, 4, 4, 4 for Pd, S, N, C, B, F. Temperature parameters × 10^n where n = 4, 3, 3, 3, 3, 3 for Pd, S, N, C, B, F. U_{eq} is the equivalent isotropic temperature parameter: $U_{eq} = \frac{1}{3}\Sigma_i\Sigma_j U_{ij} a_i^* a_j^* (a_i \cdot a_j)$, $T = \exp -(8\pi^2 U_{iso} \sin^2 \theta/\lambda^2)$.

TABLE 3. Selected bond lengths for $[Pd(py_2[9]aneN_2S)](BF_4)_2$[a]

Atoms	Distance	Atoms	Distance
S(1)—Pd(1)	2.915(3)	N(1)—Pd(1)	2.044(6)
N(2)—Pd(1)	2.028(6)	N(3)—Pd(1)	2.041(6)
N(4)—Pd(1)	2.041(6)		
C(1)—N(1)	1.48(1)	C(2)—C(1)	1.35(2)
C(2)—S(1)	1.82(1)	C(3)—S(1)	1.79(1)
C(4)—C(3)	1.51(1)	C(4)—N(2)	1.51(1)
C(5)—N(2)	1.52(1)	C(6)—C(5)	1.54(1)
C(6)—N(1)	1.51(1)		
C(7)—N(1)	1.47(1)	C(11)—C(7)	1.52(1)
C(11)—C(12)	1.40(1)	C(12)—C(13)	1.36(2)
C(13)—C(14)	1.34(2)	C(14)—C(15)	1.38(1)
C(15)—N(4)	1.30(1)	C(11)—N(4)	1.37(1)
C(8)—N(2)	1.52(1)	C(21)—C(8)	1.47(1)
C(21)—C(22)	1.43(1)	C(22)—C(23)	1.37(1)
C(23)—C(24)	1.42(1)	C(24)—C(25)	1.36(1)
C(25)—N(3)	1.34(1)	C(21)—N(3)	1.36(1)

[a]Estimated standard deviations are given in parentheses.

TABLE 4. Selected bond angles for $[Pd(py_2[9]aneN_2S)](BF_4)_2$[a]

Atoms	Angle	Atoms	Angle
N(1)—Pd(1)—S(1)	82.1(2)	N(2)—Pd(1)—S(1)	79.5(2)
N(2)—Pd(1)—N(1)	87.1(3)	N(3)—Pd(1)—S(1)	105.9(2)
N(3)—Pd(1)—N(1)	165.3(3)	N(3)—Pd(1)—N(2)	82.5(3)
N(4)—Pd(1)—S(1)	104.1(2)	N(4)—Pd(1)—N(1)	83.6(3)
N(4)—Pd(1)—N(2)	169.3(3)	N(4)—Pd(1)—N(3)	105.8(3)

[a]Estimated standard deviations are given in parentheses.

TABLE 5. Pd—S bond lengths in various Pd(II) macrocyclic thioether complexes

Complex	Equatorial	Axial	Reference
$[Pd([9]aneS_3)_2]^{2+}$	2.322(6)	2.952(4)	17*a*
$[Pd([9]aneS_3)Br_2]$	2.266(4)	3.125(1)	17*b*
$[Pd([9]aneNS_2)_2]^{2+}$	2.322(3)	3.011(3)	23
$[Pd(py_2[9]aneN_2S)]^{2+}$	None	2.915(3)	This work
$[Pd([10]aneS_3)_2]^{2+}$	2.329(2)	3.034(1)	24, 25
$[Pd(py[14]aneNS_3)]^{2+}$[a]	2.284(6)	3.120	[e]
$[Pd(S_4)Br_2]$	2.280(7)	3.182(4)	8
$[Pd(S_4)(\eta^3\text{-allyl})]^+$	2.320(8)	2.786(4)	9
$[Pd(tp_2[14]aneN_2S_2)]^{2+}$[b]	2.298(10)	3.210	[e]
$[Pd([18]aneS_6)]^{2+}$[c]	2.309(3)	3.273(2)	26
$[Pd([18]aneS_6)]^{2+}$[d]	2.335(2)	3.015(3)	27
$[Pd([18]aneS_4N_2)]^{2+}$	2.334(6)	2.977(7)	28

[a]py[14]aneNS$_3$ = N-(2′-pyridylmethyl)-1,4,7-trithia-11-azacyclotetradecane.
[b]tp$_2$[14]aneN$_2$S$_2$ = N,N′-bis(2′thiophenemethyl)-1,7-dithia-4,11-diazacyclotetradecane.
[c]Tetraphenylborate salt.
[d]Hexaflurophosphate salt.
[e]B. Chak, A. McAuley, and T.W. Whitcombe. Unpublished results.

TABLE 6. Mean planes calculated for $[Pd(py_2[9]aneN_2S)](BF_4)_2$[a]

Atoms	X	Y	Z	P
N(1)	2.8212	3.3610	8.8763	0.0490
N(2)	0.5497	2.9332	6.7066	−0.0469
N(3)	−1.4366	1.8897	8.1805	0.0381
N(4)	0.4737	2.5452	10.7526	−0.0393
Pd(1)	0.3254	2.7767	8.7186	−0.1479
S(1)	−0.0823	5.6432	8.3583	−2.9144
C(5)	2.0312	3.0557	6.3824	0.4323
C(6)	2.8598	2.7219	7.6386	0.9566

[a]The equation for the mean plane described by the four coordinated nitrogen atoms is: $0.3821X - 0.9207Y - 0.0792Z + 2.9751 = 0$ and P is the perpendicular distance between the atom and the mean plane, given in Å.

al. (18). These angles are also consistent with the basal angles of 168.8(1)° and 163.3(2)° found (5) in $[Pd(py_3[9]aneN_3)]^{2+}$. Such results indicate that the ligand geometry around the palladium atom is consistent with a five-coordinate, square pyramidal geometry.

A further analysis of the disposition of the nine-membered N_2S ring is provided by the technique of dihedral mapping (19).

The torsion angles within the macrocyclic ligand provide a method for determining the consistency and similarity of the structure with respect to analogous compounds. This is illustrated in Fig. 2, where the complexes $[Pd(py_2[9]aneN_2S)]^{2+}$, $[Pd(py_3[9]aneN_3)]^{2+}$ (5), $[Ni([9]aneN_2S)_2]^{2+}$ (11), $[Ni(N_4S)(ClO_4)]^{2+}$ (20), $[Cu(N_4S)]^{2+}$ (20), $[Pd([9]aneN_3)_2]^{2+}$ (6), and $[Pt([9]aneN_3)_2]^{2+}$ (21) are mapped in this manner. The latter two complexes provide a distinct comparison with the other ions

Can. J. Chem. Downloaded from www.nrcresearchpress.com by EESC ESCOLA DE ENGENHARIA on 09/08/12
For personal use only.

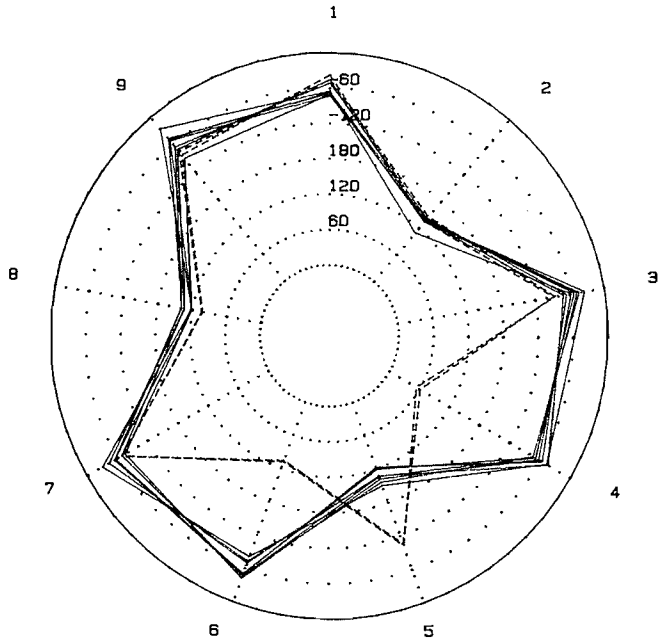

FIG. 2. Polar coordinate map of the torsion angles within the nine-membered rings of $[Pd(py_2[9]aneN_2S)]^{2+}$, $[Pd(py_3[9]aneN_3)]^{2+}$ (5), $[Ni([9]aneN_2S)_2]^{2+}$ (11*b*), $[Ni(N_4S)(ClO_4)]^{2+}$ (20), and $[Cu(N_4S)]^{2+}$ (20) (solid lines) and $[Pd([9]aneN_3)_2]^{2+}$ (6) and $[Pt([9]aneN_3)_2]^{2+}$ (21) (dotted lines).

since the apical nitrogens are not coordinated to the metal center and, as the map indicates, the [9]ane ring does not have the symmetrical shape exhibited by the octahedral and five-coordinate species. The similarity of the maps for $[Pd(py_2[9]aneN_2S)]^{2+}$, $[Pd(py_3[9]aneN_3)]^{2+}$, $[Ni([9]aneN_2S)_2]^{2+}$, $[Ni(N_4S)(ClO_4)]^{2+}$, and $[Cu(N_4S)]^{2+}$ is a result of the similar disposition of the apical atom. Also, since the latter complexes exhibit bonding to this apical donor, the observation provides confirmation for the interpretation of the apical Pd—S interaction as bonding.

Nuclear Magnetic Resonance Spectroscopy

The free ligand, $py_2[9]aneN_2S$, was characterized by ^1H and ^{13}C NMR spectroscopy. The ^{13}C NMR spectrum exhibits nine lines which is consistent with a time-averaging of the nine magnetically inequivalent carbon atom pairs in the ligand (Fig. 3). The ^1H NMR spectrum (Fig. 3) exhibits a singlet at δ2.65 which has been assigned to the methylene protons of the ethylene bridge between the two ring amines. The appearance of these protons as a singlet indicates that the molecule is undergoing rapid inversion of the nitrogen atoms at ambient temperature. If this were not the case, the chirality of the amine would impose an anisochronicity on these nuclei resulting in the appearance of an A_2B_2 or AA′BB′ sub-spectrum in the ^1H NMR spectra.

The ^1H NMR of the palladium complex contains such sub-spectra resulting from the coordination of the macrocyclic ligand. The coordination of the ligand around the metal center inhibits inversion of the nitrogens and produces a spectrum in which the magnetic equivalence of the protons has been removed. The resulting ^1H and ^{13}C spectra are consistent with the time-averaged spectrum obtained for the free ligand (Fig. 4). This is a result of vibrational motion in solution which is not observed in the solid state wherein time averaging of the structure is not possible.

The coordination of the macrocycle results in the divison of the protons into three distinct groups. The first group of protons

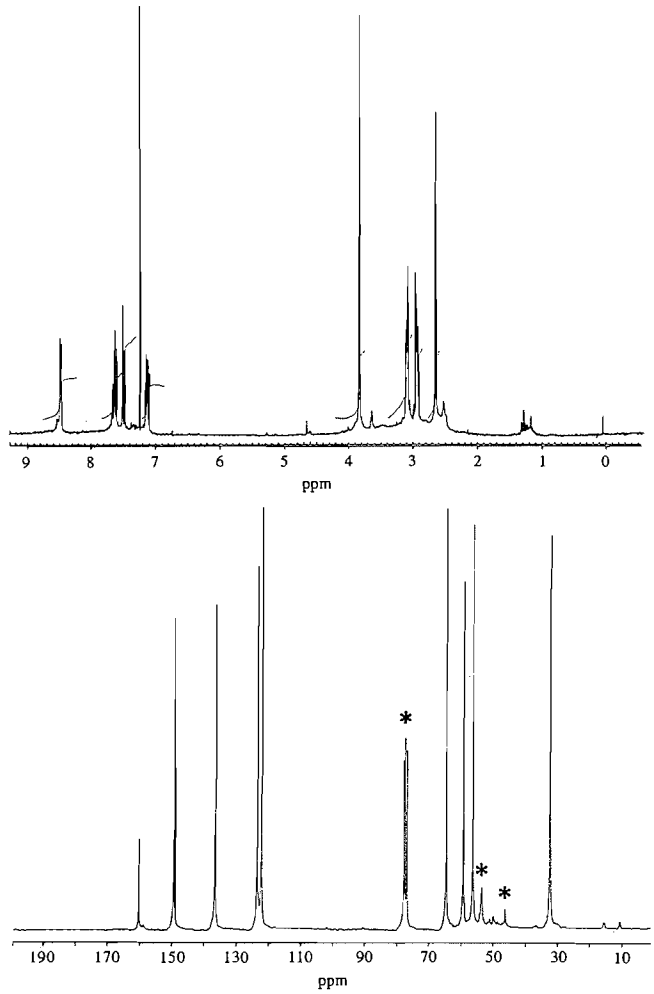

FIG. 3. ^{13}C and ^1H NMR spectra for the free ligand $py_2[9]aneN_2S$. Solvent ($CDCl_3$) and impurities are labelled with *.

are the ones on C5 and C6, the diamino chelate, which may be simulated using an AA′BB′ pattern (Table 7). The results are consistent with a time averaging of the envelope geometry observed in the solid state. In this case though, the time averaging only renders the H_a and H_a' protons equivalent and does not provide for the interconversion with the H_b and H_b' protons, as observed in the free ligand.

The thio-amino chelate results in a pattern that may be described as ABCC′. This portion of the molecule is difficult to simulate due to the overlapping resonances arising from the B and C protons and the equivalence of H_c and H_c'. The latter protons are assigned to the C2 and C3 carbon atoms, next to the apical sulphur. The remaining signals in the ^1H nmr spectrum may be assigned to the pyridylmethyl chelate which appears as an ABCDMX sub-spectrum, wherein the two protons of the methylene group are designated H_m and H_x. The H_m proton is equatorial and is coplanar with the pyridine ring resulting in coupling between this proton and the aromatic protons.

Further verification of the assigned resonances is provided by an analysis of the ^1H-^{13}C HETCORR (Fig. 4), where it is readily observed that the ^{13}C resonances at δ126.3 and δ142.5 are associated with the middle carbon positions of the pyridyl ring since they correlate with the proton triplets. However, designating an unambiguous choice for these resonances is dependent upon simulation of the proton spectrum.

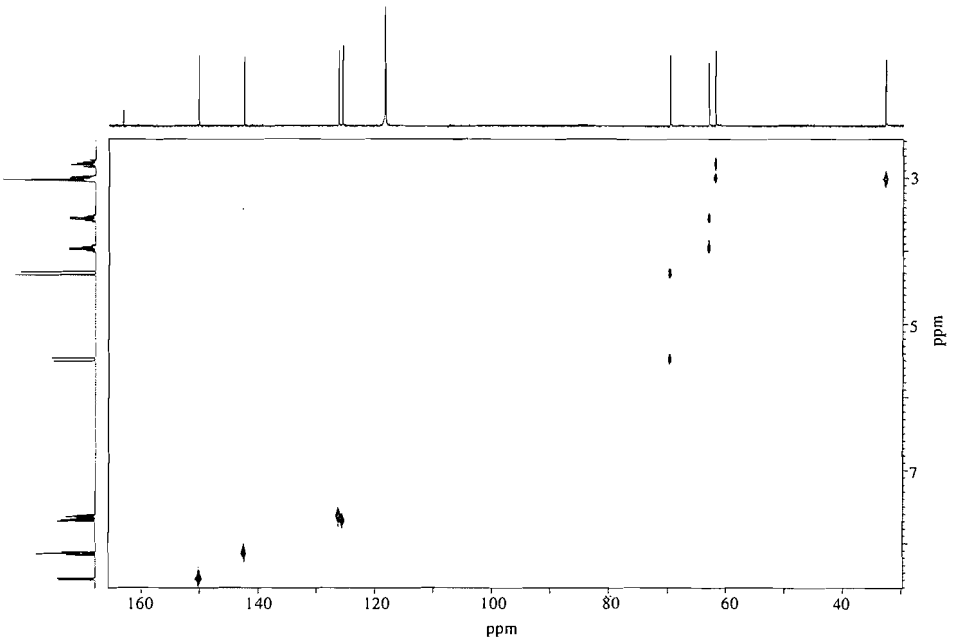

FIG. 4. HETCORR for $[Pd(py_2[9]aneN_2S)]^{2+}$ in CD_3CN. The ^1H and ^{13}C NMR spectra are displayed on the vertical and horizontal axes, respectively. The peak at 117 ppm is due to CD_3CN.

TABLE 7. Simulated ^1H NMR parameters for $[Pd(py_2[9]aneN_2S)]^{2+}$

(*a*) Diamino chelate: AA′BB′ sub-spectrum

$\delta_a = \delta_{a'} = 3.97$ ppm	$\delta_b = \delta_{b'} = 3.55$ ppm
$J_{ab} = J_{a'b'} = -14.64$ Hz	$J_{ab'} = J_{a'b} = 7.19$ Hz
$J_{aa'} = 6.55$ Hz	$J_{bb'} = 5.35$ Hz

(*b*) Thio-amino chelate: ABCC′ sub-spectrum

$\delta_a = 2.81$ ppm	$\delta_b = 3.00$ ppm	$\delta_c = \delta_{c'} = 3.03$ ppm
$J_{ab} = -10.34$ Hz	$J_{ac} = 0.73$ Hz	$J_{ac'} = 8.365$ Hz
$J_{bc'} = 6.56$ Hz	$J_{cc'} = -15.17$ Hz	$J_{bc} = 5.64$ Hz

(*c*) Pyridylmethyl chelate: ABCDMX sub-spectrum

$\delta_a = 8.49$ ppm	$\delta_b = 7.63$ ppm	$\delta_c = 8.14$ ppm	$\delta_d = 7.69$ ppm
$\delta_m = 5.48$ ppm	$\delta_x = 4.30$ ppm		
$J_{ab} = 5.67$ Hz $J_{ac} = -1.42$ Hz	$J_{ad} = 0.0$ Hz	$J_{am} = -0.70$ Hz	
$J_{bc} = 7.80$ Hz $J_{bd} = -1.219$ Hz	$J_{bm} = -0.302$ Hz		
$J_{cd} = 8.02$ Hz $J_{cm} = 0.001$ Hz	$J_{dm} = 0.002$ Hz		

Of particular interest is the AB sub-spectrum from the benzylic-like protons of the methylene group in the pendant arms. These two protons are rendered inequivalent by the chelation of the pyridine and tertiary nitrogens, resulting in an "axial" and "equatorial" disposition. Intuitively it would be expected that these two resonances display the same intensity since they integrate to the same area. However, the peak at δ5.48 is only one half of the height of the peak at δ4.30, which indicates that it is coupled to another proton. This coupling constant must be smaller than the intrinsic linewidth since the peak appears as a doublet. This is consistent with a long-range coupling of this peak with the protons of the pyridine ring.

Such a feature is accommodated structurally by considering the disposition of the equatorial proton which would be essentially co-planar with the ring, based upon "normal" bonding angles and distances for a methylene moiety. Furthermore, the presence of this coupling provides confirmatory evidence for the absence of fluxional processes within this molecule since disruption of the co-planarity of the equatorial proton with the ring would result in its elimination. Hence, the nitrogen atoms are not pivotting and it is difficult to envisage a mechanism for the displacement of the apical sulphur which does not involve a distortion of the coordinated amines. By itself, this does not necessitate that the apical sulphur is bonded to the palladium but provides evidence that the ligand is not changing its coordination environment in solution through a fluxional process.

This aspect facilitates the simulation of the resonances associated with the pyridine protons. The simulated parameters for the complete spectrum are provided in Table 7, while a comparison of simulated and experimental features is presented in Fig. 5. Such simulated parameters permit the assignment of the chemical shifts in the ^{13}C NMR spectra, with the resonance at δ142.5 arising from the carbon attached to H_c.

The remaining spectroscopic features observed in the proton spectrum have been simulated using standard iterative com-

Can. J. Chem. Downloaded from www.nrcresearchpress.com by EESC ESCOLA DE ENGENHARIA on 09/08/12
For personal use only.

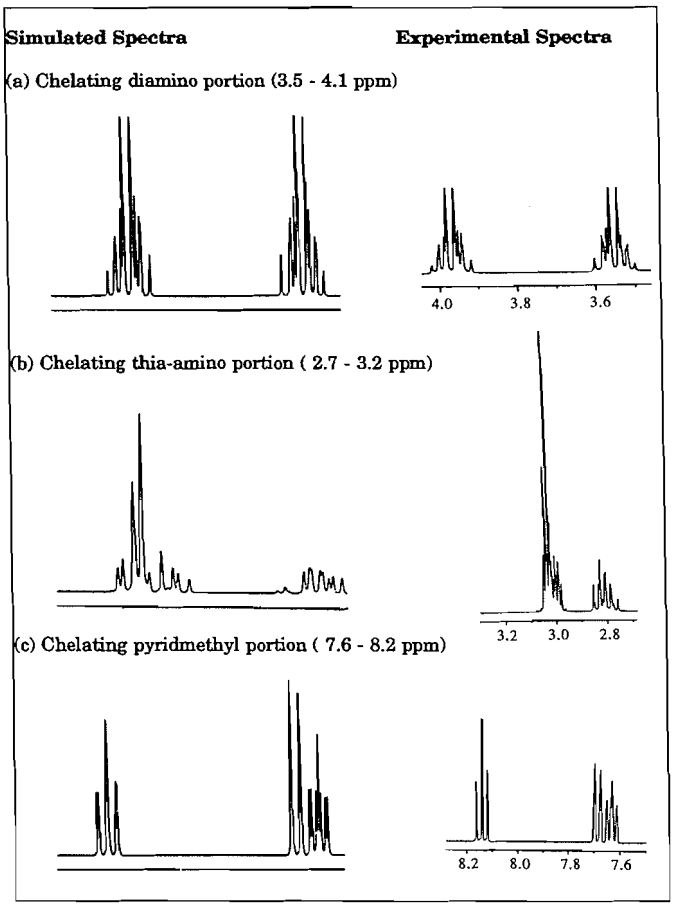

FIG. 5. Comparison of simulated and experimental ^{1}H NMR spectra for $[Pd(py_2[9]aneN_2S)]^{2+}$. Selected regions are shown.

puter techniques (22*a*, 22*b*, footnote 3). The values obtained for the chemical shifts and coupling constants are consistent with a structural model in which the molecule adopts a "static" structure. That is, the sulphur atom maintains a constant position and does not undergo any fluxional displacement. Such a fluxional process has been observed (6, 21) for the platinum and palladium complexes of 1,4,7-triazacyclononane in which the apical donor is not bound to the metal center in the solid state. This results in ^{1}H NMR spectra that may be interpreted only in terms of a "dynamic" structure in which the metal is undergoing a series of inner-sphere substitutions reactions, rotating between several equivalent configurations.

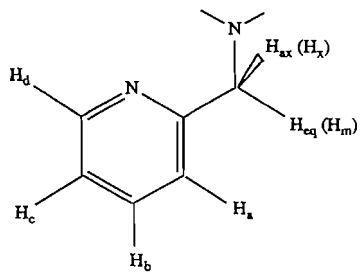

Variable temperature spectra provide further evidence for the absence of a fluxional process in this molecule, since no coalescence of any of the peaks was observed between −45°C and +80°C, in contrast to $[Pd([9]aneN_3)_2]^{2+}$ (6). It is possible, but viewed as unlikely, that the inversion of the apical sulphur is more rapid than the temperature range accessed. However, the spectroscopic implications are that in solution, the molecule is constrained to a single configuration similar to that observed in the solid state. The coupling constants and chemical shifts observed for the ^{1}H NMR are consistent with an apical disposition of the sulphur atom providing further evidence for a distal palladium–sulphur interaction. Hence, in both the solid state and solution structures, the sulphur atom appears to be bonded to the palladium atom.

[3]K.R. Dixon. Unpublished modifications.

Acknowledgements

We would like to thank Natural Sciences and Engineering Research Council Canada (NSERC) and the University of Victoria for their continued support of this research. B.C. also acknowledges the receipt of a NSERC post-graduate scholarship. The assistance of Mrs. K. Beveridge is appreciated.

1. P.V. Bernhardt and G.A. Lawrence. Coord. Chem. Rev. **104**, 297 (1990).
2. L.F. Lindoy. The chemistry of macrocyclic ligand complexes. Cambridge University Press, New York. 1989.
3. R.W. Hay. Bio-inorganic chemistry. John Wiley and Sons, New York. 1984.
4. E. Kimura, X. Bu, M. Shionoya, S. Wada, and S. Maruyama. Inorg. Chem. **31**, 4542 (1992).
5. K. Wieghardt, W. Schmidt, W. Herrmann, and H.J. Kueppers. Inorg. Chem. **24**, 1208 (1983).
6. G. Hunter, A. McAuley, and T.W. Whitcombe. Inorg. Chem. **27**, 2634 (1988).
7. E.W. Abel, P.D. Beer, I. Moss, K.G. Orrell, V. Lik, P.A. Bates, and M.B. Hursthouse. J. Organomet. Chem. **341**, 559 (1988).
8. C.R. Lucas, S. Liu, M.J. Newlands, J.-P. Charland, and E.J. Gabe. Can. J. Chem. **66**, 1506 (1988).
9. C.R. Lucas, S. Liu, M.J. Newlands, and E. Gabe. Can. J. Chem. **68**, 1357 (1990).
10. J.C.A. Boeyens, S.M. Dobson, and R.D. Hancock. Inorg. Chem. **24**, 73 (1985).
11. S.M. Hart, J.C.A. Boeyens, J.P. Michael, and R.D. Hancock. J. Chem. Soc. Dalton Trans. 1601 (1983).
12. G.M. Sheldrick. SHELX76. Cambridge University. 1976.
13. International tables of crystallography. Vol. IV. Kynoch Press, Birmingham, U.K. 1974.
14. P. Coppens, L. Lieserowitz, and D. Rabinovich. Program Bicabs: Correction of crystallographic data for absorption and secondary extinction effects. University of British Columbia 360/67 Version, Feb. 1969. Modified by G.W. Bushnell, University of Victoria.
15. R.I. Haines and A. McAuley. Coord. Chem. Rev. **33**, 77 (1981).
16. F. Hori, K. Matsumoto, S. Ooi, and H. Kuroya. Bull. Chem. Soc. Jpn. **50**, 138 (1977).
17. (*a*) A.J. Blake, A.J. Holder, T.I. Hyde, Y.V. Roberts, A.J. Lavery, and M. Schröder. J. Organomet. Chem. **323**, 261 (1987); (*b*) K. Wieghardt, H.-J. Küppers, E. Raabe, and C. Krüger. Angew. Chem. Int. Ed. Engl. **25**, 1101 (1986).
18. A.R. Rossi and R. Hoffmann. Inorg. Chem. **14**, 365 (1975).
19. J.P. Ounsworth and L. Weiler. J. Chem. Ed. **64**, 568 (1987).
20. D.G. Fortier and A. McAuley. Inorg. Chem. **28**, 655 (1989).
21. K. Wieghardt, M. Köppen, W. Swiridoff, and J. Weiss. J. Chem. Soc. Dalton Trans. 1869 (1983).
22. (*a*) R.B. Johannsen, J.A. Ferreti, and R.K. Harris. J. Magn. Reson. **3**, 84 (1970); (*b*) J.D. Swalen. Computer programs for chemistry. Vol. 1. *Edited by* D.F. Detar. W.A. Benjamin, New York. 1968.
23. A.J. Blake, R.D. Crofts, B. deGroot, and M. Schröder. J. Chem. Soc. Dalton Trans. 485 (1993).
24. S. Chandrasekhar and A. McAuley. Inorg. Chem. **31**, 2663 (1992).

Can. J. Chem. Downloaded from www.nrcresearchpress.com by EESC ESCOLA DE ENGENHARIA on 09/08/12
For personal use only.

25. G.J. Grant, K.A. Sanders, W.N. Setzer, and D.G. VanDerveer. Inorg. Chem. **30**, 4053 (1991).
26. A.J. Blake, R.O. Gould, A.J. Lavery, and M. Schröder. Angew. Chem. Int. Ed. Engl. 25, 274 (1986).
27. A.J. Blake and M. Schröder. *In* Advance in inorganic chemistry. *Edited by* A.G. Sykes. Academic Press, New York. 1990. p. 1.
28. G. Reid, A.J. Blake, T.I. Hyde, and M. Schröder. J. Chem. Soc. Chem. Commun. 1397 (1988).

Can. J. Chem. Downloaded from www.nrcresearchpress.com by EESC ESCOLA DE ENGENHARIA on 09/08/12
For personal use only.

Senegalene, une nouvelle acétogénine oléfinique mono-tétrahydrofuranique des graines d'*Annona senegalensis*[1]

SEVSER SAHPAZ, ALAIN LAURENS, REYNALD HOCQUEMILLER ET ANDRÉ CAVÉ[2]

Laboratoire de pharmacognosie, associé au Centre national de la recherche scientifique, Faculté de pharmacie, Université Paris-XI, 92290 Châtenay-Malabry, France

ET

DIEGO CORTES

Laboratoire de pharmacognosie, Faculté de médecine et pharmacie, Université de Rouen, 76800 Saint Etienne du Rouvray, France et Departamento de Farmacología, Facultad de Farmacia, Universidad de Valencia, 46100 Burjasot (Valencia), España

Reçu le 17 décembre 1993

SEVSER SAHPAZ, ALAIN LAURENS, REYNALD HOCQUEMILLER, ANDRÉ CAVÉ et DIEGO CORTES. Can. J. Chem. **72**, 1533 (1994).

Cinq acétogénines cytotoxiques ont été isolées de l'extrait méthanolique de graines d'*Annona senegalensis*. La première est nouvelle et a été dénommée sénégalène **1**. Sa structure, déterminée par étude spectroscopique (2D-NMR, SMIC, SMFAB-Li) est caractérisée par la présence d'un système diol et l'insaturation de la chaîne alkyle. Les quatre autres ont été identifiées à la molvizarine **2**, l'asimicine **3**, la rolliniastatine-2 **4** et la squamocine **5**. Une étude des relations structure–activité du sénégalène et de ses dérivés a été réalisée.

SEVSER SAHPAZ, ALAIN LAURENS, REYNALD HOCQUEMILLER, ANDRÉ CAVÉ, and DIEGO CORTES. Can. J. Chem. **72**, 1533 (1994).

Using activity-directed fractionation, the chromatography of the bioactive methanol extract of *Annona senegalensis* seeds led to isolation of a new mono-tetrahydrofuranic γ-lactone acetogenin characterized by the presence of a double bond on the alkyl chain, senegalene **1**. Its structure was elucidated on the basis of spectroscopic (2D-NMR and MS) and chemical methods. Four known acetogenins have been also isolated: molvizarin **2**, asimicin **3**, rolliniastatin-2 **4**, and squamocin **5**. Comparative structure–activity relationships were studied using senegalene **1** and its derivatives in KB and VERO cell lines in *in vitro* tests.

Introduction

Le genre *Annona* (Annonaceae) est caractérisé par la présence d'acétogénines à forte activité cytotoxique (1). Les acétogénines de sept espèces, *A. bullata*, *A. cherimolia*, *A. densicoma*, *A. montana*, *A. muricata*, *A. reticulata* et *A. squamosa* (2) ont fait pour le moment l'objet d'études approfondies. *Annona senegalensis* n'a jusqu'à présent fait l'objet d'aucune recherche dans ce domaine. Seule a été signalée, dans les feuilles et les fruits, la présence d'huile essentielle composée de mono et de sesquiterpènes (3), dans les racines, de diterpènes de type kaurane (4) et dans les écorces de tiges, d'acides aminés (5).

Dans le présent travail, nous décrivons l'isolement à partir des graines d'une nouvelle acétogénine oléfinique mono-tétrahydrofuranique (mono-THF), le sénégalène **1**, la détermination de sa structure ainsi que l'étude de son activité cytotoxique.

Résultats et discussion

L'extrait méthanolique (A) des graines d'*A. senegalensis* présente une importante cytotoxicité sur le test sur larves d'*Artemia salina* (1), CL_{50} : $2{,}5 \times 10^{-2}$ µg/mL. Le fractionnement de cet extrait a été guidé par ce test. (A), mis en solution dans du méthanol aqueux (95 : 5), est soumis successivement à une extraction liquide–liquide par l'hexane et le dichlorométhane. L'extrait chlorométhylénique (B) conserve l'activité cytotoxique de l'extrait initial (A), CL_{50} : $1{,}7 \times 10^{-2}$ µg/mL. Par chromatographie sur colonne de (B), cinq acétogénines sont isolées, une nouvelle, le sénégalène **1**, et quatre connues, caractérisées par la présence de trois hydroxyles alcooliques et par différentes configurations au niveau du système bis-THF α,α′-dihydroxylé, identifiées par comparaison à des échantillons authentiques : la molvizarine **2** (6), l'asimicine **3** (7), la rolliniastatine-2 **4** (8), et la squamocine **5** (9).

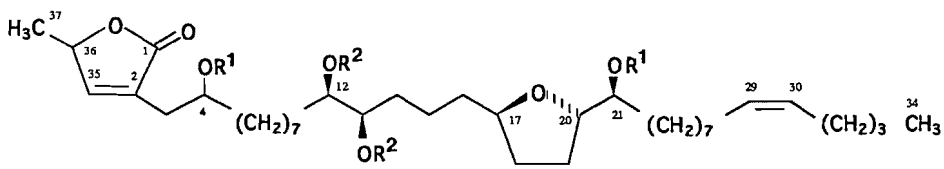

Sénégalène **1** :	$R^1 = R^2 = H$
Tétraacétyl-sénégalène **1***a* :	$R^1 = R^2 = Ac$
2-(35),29-(30)-Tétrahydro-sénégalène **1***b* :	$R^1 = R^2 = H$
2-(35),29-(30)-Tétrahydro-tétraacétyl-sénégalène **1***c* :	$R^1 = R^2 = Ac$
12,13-Acétonide-sénégalène **1***d* :	$R^1 = H$; R^2 = acétonide
29,30-Époxy-tétraacétyl-sénégalène **1***e* :	$R^1 = R^2 = Ac$

Le sénégalène **1** est un solide amorphe, $[\alpha]_D$ +16 (c = 0,21, $CHCl_3$). Il présente, sur le spectre de masse en ionisation chimique, un pic moléculaire à m/z 623 $[MH]^+$ et à m/z 640 [M +

1. Partie 25 dans la série «Acétogénines des Annonacées»; pour la partie 24, voir la référence 24.

2. Auteur à qui adresser toute correspondance.

Can. J. Chem. Downloaded from www.nrcresearchpress.com by EESC ESCOLA DE ENGENHARIA on 09/08/12
For personal use only.

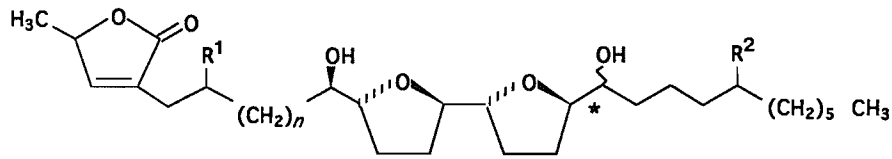

thréo - trans - thréo - trans -

Molvizarine **2** : R^1 = OH; R^2 = H; n = 8; * (*érythro*)
Asimicine **3** : R^1 = OH; R^2 = H; n = 10; * (*thréo*)
Rolliniastatine-2 **4** : R^1 = OH; R^2 = H; n = 10; * (*érythro*)
Squamocine **5** : R^1 = H; R^2 = OH; n = 10; * (*érythro*)

$NH_4]^+$ correspondant à une masse moléculaire de 622. Sa formule brute $C_{37}H_{66}O_7$, est déduite du HRSMIC, $[MH]^+$ = 623,4908 (calculé pour $C_{37}H_{67}O_7$ = 623,4887).

L'existence de quatre hydroxyles est mise en évidence par l'observation d'une bande large à 3350 cm^{-1} en IR, par les pertes successives de quatre molécules d'eau à partir de $[MH]^+$, et par la préparation du dérivé tétraacétylé **1***a*.

Le spectre IR de **1** présente une bande à 1750 cm^{-1}, caractéristique d'un carbonyle de γ-lactone α,β-insaturée. Ceci est confirmé par l'analyse des spectres 1D-RMN (^1H et ^{13}C spin echo) et 2D-RMN (^1H–^1H Cosy 45 et ^1H–^{13}C XH Corr). Le spectre RMN ^1H présente un système de trois signaux à δ 7,18 (d, 1H), δ 5,04 (dq, 1H) et δ 1,42 (d, 3H), corrélés en RMN ^{13}C avec trois carbones à δ 151,89 (C-35), δ 77,88 (C-36) et δ 18,84 (C-37), et deux autres signaux de carbones quaternaires à δ 174,57 (C-1) et δ 130,75 (C-2) caractéristiques d'une γ-lactone α,β-insaturée (voir tableau 1). De plus, la présence d'un système ABX en RMN ^1H à δ 2,50 (ddd, 1H), δ 2,36 (dd, 1H) et δ 3,81 (m, 1H), corrélé avec les résonances respectivement à δ 32,97 et δ 69,48 en RMN ^{13}C, prouve l'existence d'un OH en position 4, en β de la γ-lactone (10).

Le spectre de RMN ^{13}C montre deux autres signaux à δ 81,70 et δ 79,20 attribués aux carbones oxygénés d'un noyau mono-THF α-monohydroxylé (11). La corrélation de ceux-ci avec les multiplets à δ 3,81 et δ 3,90 en RMN ^1H confirme cette hypothèse (tableau 1).

La position du système mono-THF α-hydroxylé et celle des deux autres hydroxyles restant sur la chaîne hydrocarbonée sont déterminées par l'analyse des fragments de masse de **1**, **1***a*, **1***b* et **1***c*. Les fragmentations sur le SMIC de **1** à *m/z* 341 et 281, à *m/z* 411 et à *m/z* 441, permettent de placer le cycle THF entre les carbones 17 et 20 et le groupe OH adjacent sur le carbone 21 (voir figure 1), ce qui est confirmé par l'examen des spectres de masse des dérivés **1***a*, **1***b* et **1***c*.

L'emplacement du système diol sur les carbones 12 et 13 est mis en évidence par les fragments obtenus sur le SMIC (NH_3) de **1** (*m/z* 269 et *m/z* 353) et de **1***a* (*m/z* 353 et *m/z* 437). La préparation du dérivé acétonide **1***d* (12) et l'obtention sur le SM de **1***d* des fragments à *m/z* 339 (C-13/C-14), *m/z* 381 (C-16/C-17), *m/z* 451 (C-20/C-21) et *m/z* 481 (C-21/C-22), confirment la position du groupe diol sur la chaîne hydrocarbonée. Un système mono-THF α-hydroxylé accompagné d'un groupement α-diol a déjà été observé chez la gigantetrocine et la gigantriocine, acétogénines isolées de *Goniothalamus giganteus* (11) et la 10,13-*trans*-13,14-*érythro*-densicomacine et la 10,13-*trans*-13,14-*thréo*-densicomacine isolées d'*Annona densicoma* (13). Il semble que la 10,13-*trans*-13,14-*thréo*-densicomacine soit identique à la gigantetrocine. Mais par rapport à ces acétogénines, le sénégalène présente une grande originalité liée à la position du système diol entre le THF et la lactone.

Deux signaux en RMN ^{13}C à δ 130,36 et δ 128,91 corrélés avec un multiplet vers δ 5,35 (2H) en RMN ^1H correspondant à deux méthines sp^2, sont en faveur de la présence d'une double liaison de configuration *cis* sur la chaîne du sénégalène, ce qui est en accord avec les trois constantes de couplage mesurées lors de l'irradiation sélective des protons à δ 2,19 et δ 2,01 : J = 10,6 Hz, J' = 4,5 Hz et J'' = 6 Hz.

TABLEAU 1. Corrélation ^1H–^{13}C du sénégalène **1**

H	δ[a]	Couplage en RMN ^1H–^{13}C (multiplicités spin echo)
3a	2,36 dd	32,97 (CH_2)
3b	2,50 ddd	32,97 (CH_2)
4	3,81 m	69,48 (CH)
5	1,48 m	37,0 (CH_2)
6–10	1,25–1,45 m	29,15–29,57 (CH_2)
11	1,55 m	33,21 (CH_2)
12	3,41 m	74,06 (CH)[b]
13	3,41 m	74,20 (CH)[b]
14	1,33 m	35,27 (CH_2)
15,16	1,25–1,45 m	25,87–29,57 (CH_2)
17	3,90 m	79,20 (CH)
18,19	1,62, 1,95 m	25,87–29,57 (CH_2)
20	3,81 m	81,70 (CH)
21	3,41 m	73,54 (CH)[b]
22–26	1,25–1,45 m	29,15–29,57 (CH_2)
27	1,55 m	25,87 (CH_2)
28	2,19 m	29,57 (CH_2)
29, 30	5,35 m	130,36, 128,91 (CH)
31	2,01 m	27,06 (CH_2)
32	1,25–1,45 m	22,48 (CH_2)
33	1,25–1,45 m	31,69 (CH_2)
34	0,86 t	13,92 (CH_3)
35	7,18 d	151,89 (CH)
36	5,04 dq	77,88 (CH)
37	1,42 d	18,84 (CH_3)

[a]Constantes de couplage: J_{3a-3b} = 15 Hz; $J_{3a-4\ trans}$ = 8 Hz; $J_{3b-4\ cis}$ = 3 Hz; $J_{3a,b-35}$ = 1 Hz; J_{35-36} = 1,5 Hz; J_{36-37} = 7,5 Hz.
[b]Ces déplacements chimiques (^{13}C RMN) peuvent être inversés.

L'existence d'un système oléfinique, en plus de l'insaturation de la lactone, est confirmée par la préparation des dérivés tétrahydrogénés **1***b* et **1***c* obtenus par hydrogénation catalytique (14) du sénégalène **1** et du tétraacétyl-sénégalène **1***a*. En effet on observe, d'une part la disparition des signaux correspondants aux doubles liaisons sur les spectres RMN ^1H et ^{13}C de **1***b* et **1***c*, d'autre part l'obtention des pics moléculaires augmentés de quatre uma sur le SMIC. De plus, les fragments obtenus sur le SM FAB-Li (15, 16) du sénégalène **1** et du tétrahydro-sénégalène **1***b*, correspondant au pic moléculaire $[M + Li]^+$ (**1** : *m/z* 629; **1***b* : *m/z* 633), aux pics dus à la coupure C-3/C-4 (**1** : *m/z* 517; **1***b* : *m/z* 519) et à la coupure sur le noyau THF (**1** : *m/z* 375 et 245; **1***b* : *m/z* 377 et 247), sont en faveur d'une structure mono-THF, avec un système diol entre la γ-lactone et le THF, et

Can. J. Chem. Downloaded from www.nrcresearchpress.com by ESC ESCOLA DE ENGENHARIA on 09/08/12
For personal use only.

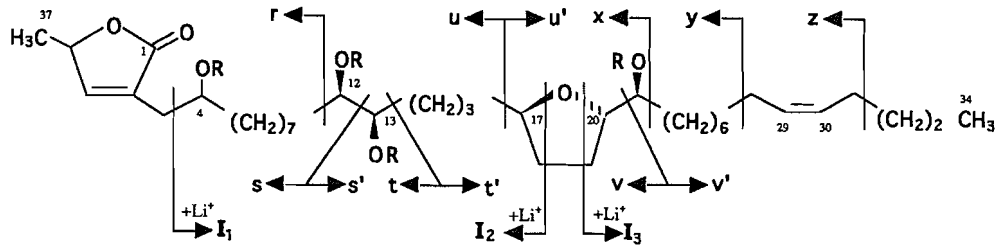

	l_1[a]	r	s–s′	t–t′	u–u′	l_2[a]	l_3[a]	v–v′	x	y	z
1	517	239	269–353	[299]–323	341–281	375	245	411–211	[441]	525	579
1*a*	—	281	353–437	425–365	467–323	—	—	537–253	609	[693]	747
1*b*	519	241	271–355	301–325	[343]–283	377	247	413–213	443	—	—
1*c*	—	283	355–439	427–367	469–325	—	—	539–255	611	—	—

[ ] : Fragments de faible intensité.
[a]SMFAB : *m*-NBA + LiCl.

FIG. 1. Fragmentations de **1**, **1***a*, **1***b* et **1***c* en spectrométrie de masse.

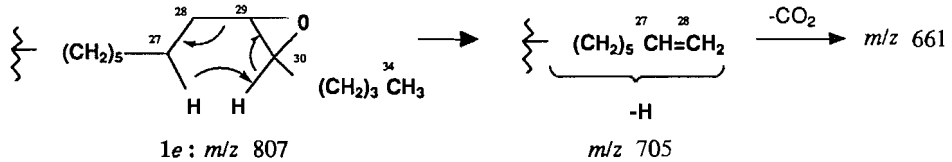

1*e* : *m/z* 807 *m/z* 705

FIG. 2. Fragments de **1***e* en SM.

un système oléfinique entre le THF et le CH_3 terminal (voir figure 1, fragments l_1, l_2 et l_3).

La position de la double liaison sur la chaîne entre le système THF (C_{17}/C_{20}) et le méthyle terminal (CH_3-34) est confirmée, sur le SM de **1***b* et **1***c*, par l'obtention des fragments lactoniques augmentés uniquement de deux uma tandis que la masse moléculaire est quant à elle augmentée de quatre. Une fragmentation entre les carbones 27 et 28 et une autre entre les carbones 31 et 32 (**1** : *m/z* 525 et *m/z* 579; **1***a* : *m/z* 693 et *m/z* 747), permettent de placer la double liaison en 29–30. Ces fragments ne sont pas observés sur les spectres de masse des dérivés tétrahydrogénés **1***b* et **1***c* (voir figure 1).

La préparation de l'époxyde du tétraacétyl-sénégalène (**1***e*) confirme la présence de la double liaison ainsi que sa position en 29–30 sur la chaîne (17). Le pic moléculaire de **1***e* est augmenté de 16 uma $[MH]^+$ *m/z* 807 sur le SMIC. Des fragments caractéristiques de coupure au niveau de l'époxyde sont observés (voir figure 2); le fragment à *m/z* 705 peut être expliqué par un mécanisme similaire à celui proposé (18, 19).

La configuration relative de **1**, au niveau du système THF α-hydroxylé (C-20/C-21 : *thréo*) et diol (C-12/C-13 : *thréo*), est proposée en fonction des déplacements chimiques en RMN ^{13}C des carbones concernés par rapport aux acétogénines mono-THF de configurations relatives connues : solamine et corossolone (10, 20, 21), gigantetrocine et gigantriocine (11) et densicomacines 1 et 2 (13).

Le sénégalène constitue donc le quatrième exemple décrit d'acétogénine possédant une double liaison sur la chaîne aliphatique. Contrairement à la giganenine (22) qui possède cette double liaison du côté lactonique, chez le sénégalène la double liaison est située entre le THF et le méthyle terminal comme dans la gigantetronenine et la gigantrionenine (23). Toutefois il diffère très largement de ces dernières par la position des différentes fonctions et surtout du groupement diol sur la chaîne entre le THF et la lactone.

TABLEAU 2. Cytotoxicité du sénégalène et de ses dérivés sur lignées cellulaires (CE_{50} μg/mL)

Produit	KB	VERO
Sénégalène **1**	$1{,}5 \times 10^{-4}$	2×10^{-1}
Tétraacétyl-sénégalène **1***a*	$3{,}5 \times 10^{-3}$	8×10^{-2}
Tétrahydro-sénégalène **1***b*	$1{,}6 \times 10^{-2}$	0,25
Époxy-tétraacétyl-sénégalène **1***e*	$1{,}4 \times 10^{-2}$	0,6
Vinblastine	10^{-3}	>3

La cytotoxicité du sénégalène et de ses dérivés, étudiée sur lignées cellulaires KB et VERO, est rapportée dans le tableau 2. Le sénégalène **1** ($CE_{50} = 1{,}5 \times 10^{-4}$ μg/mL) présente une activité importante sur cellules KB. La réduction des doubles liaisons diminue fortement cette activité ($CE_{50} = 1{,}6 \times 10^{-2}$ μg/mL). L'acétylation des hydroxyles (**1***a* : $CE_{50} = 3{,}5 \times 10^{-3}$ μg/mL) ou l'époxydation de la double liaison oléfinique (**1***e* : $CE_{50} = 1{,}4 \times 10^{-2}$ μg/mL) diminue également l'activité. La CE_{50} du sénégalène est sensiblement plus élevée sur KB que celle de la vinblastine utilisée comme témoin.

Partie expérimentale

Méthodes générales

Les pouvoirs rotatoires ont été mesurés à l'aide d'un polarimètre Schmidt–Haensch type Polartronic I. Les spectres ont été enregistrés sur les appareils suivants: UV, Unicam Sp 1800; IR, Perkin–Elmer type 257; RMN ^1H et ^{13}C, Bruker AC-200 à 200 MHz (^1H) et à 50 MHz (^{13}C); SMIC et SMIE, Nermag–Sidar; SMFAB, Kratos MS-80. Les chromatographies sur colonne ont été réalisées sur Kieselgel 60 (Merck 9385) ou 60 H (Merck 7736), les chromatographies analytiques sur couche mince (CCM) sur DC Alufolien Kieselgel 60 F 254 (Merck 5554).

Can. J. Chem. Downloaded from www.nrcresearchpress.com by EESC ESCOLA DE ENGENHARIA on 09/08/12
For personal use only.

Can. J. Chem. Downloaded from www.nrcresearchpress.com by EESC ESCOLA DE ENGENHARIA on 09/08/12
For personal use only.

Matériel végétal

Les graines d'*Annona senegalensis* ont été récoltées en Juillet 1990 en Casamance (Sénégal); un échantillon d'herbier est déposé sous la référence AL 282 à la Faculté mixte de Médecine et de Pharmacie de Dakar.

Extraction et isolement des acétogénines

L'extraction et le fractionnement des graines d'*Annona senegalensis* ont été guidés par le test sur larves de crevettes d'*Artemia salina* (Brine Shrimp). Les graines séchées et broyées (2,3 kg) sont traitées par le méthanol. Après évaporation, on obtient un résidu de 155,3 g qui a été ensuite repris par le méthanol à chaud. Le fractionnement est effectué dans un premier temps par partage liquide–liquide entre l'extrait méthanolique (A) (additionné de 5% d'eau) et l'hexane. La solution hydrométhanolique est réextraite ensuite par le dichlorométhane. La phase organique (B) (56,2 g) a été fractionnée par chromatographie flash (éluant : CH_2Cl_2/AcOEt/MeOH 10 : 9,5 : 0,5) pour donner cinq acétogénines : le sénégalène **1**, la molvizarine **2**, l'asimicine **3**, la rolliniastatine-2 **4** et la squamocine **5**.

Sénégalène ***1***. $C_{37}H_{66}O_7$; M = 622; $[\alpha]_D$ +16 (*c* 0,21, $CHCl_3$). IR, ν_{max} cm^{-1} (film): 3350, 2840, 1750, 1450, 1310, 1050, 748; HRSMIC, $[MH]^+$ = 623,4908 (calculé pour $C_{37}H_{67}O_7$ = 623,4887); SMIC (NH_3), *m/z*: 640 $[M + NH_4]^+$, 623 (100%) $[MH]^+$, 605 $[MH - H_2O]^+$, 587 $[MH - 2H_2O]^+$, 569 $[MH - 3H_2O]^+$, 551 $[MH - 4H_2O]^+$ (figure 1); RMN ^1H et ^{13}C : voir tableau 1.

Tétraacétyl-sénégalène ***1***a

Par traitement de **1** (10 mg) avec anhydride acétique – pyridine (2 : 1, température ambiante, 1 nuit), le produit **1***a* (huileux) est obtenu quantitativement. $C_{45}H_{74}O_{11}$; RMN ^1H ($CDCl_3$), δ : 0,87 (3H, t, CH_3-34), 1,17–1,70 (34H, m, H-5 à 11, H-22 à 28 et H-31 à 33), 1,40 (3H, d, CH_3-37), 1,56–1,96 (10H, 2m, H-14 à 16 et H-18, 19), 2,02 (3H, s, $OCOCH_3$-4), 2,09 (9H, s, $OCOCH_3$-12, 13, 21), 2,53 (2H, m, H-3), 3,82 et 3,95 (2H, 2m, H-17, 20), 4,82 (3H, m, H-12, 13, 21), 5,0 (1H, dq, H-36), 5,08 (1H, m, H-4), 5,32 (2H, td, H-29, 30), 7,06 (1H, d, H-35). SMFAB (NBA + EtOH), *m/z* : 790 $[M + Na]^+$, 731 $[M - AcOH]^+$, 671 $[M - 2AcOH]^+$, 611 $[M - 3AcOH]^+$, 551 $[M - 4AcOH]^+$ (figure 1).

2,35,29,30-Tétrahydro-sénégalène ***1***b

Par réduction catalytique de **1** en solution méthanolique (5 mg), par H_2 et 10% Pd/C à température ambiante et sous pression atmosphérique pendant 2 h, le produit **1***b* est obtenu quantitativement. $C_{37}H_{70}O_7$; SMIC (NH_3), *m/z* : 644 $[M + NH_4]^+$, 627 (100%) $[MH]^+$, 609 $[M - H_2O]^+$, 591 $[M - 2H_2O]^+$, 573 $[M - 3H_2O]^+$, 555 $[M - 4H_2O]^+$ (figure 1).

2,35,29,30-Tétrahydro-tétraacétyl-sénégalène ***1***c

Par réduction catalytique de **1***a* en solution méthanolique (5 mg), par H_2 et 10% Pd/C à température ambiante et sous pression atmosphérique pendant 2 h, le produit **1***c* est obtenu quantitativement. $C_{45}H_{78}O_{11}$; SMIC (NH_3), *m/z* : 812 $[M + NH_4]^+$, 795 (100%) $[MH]^+$, 735 $[M - AcOH]^+$, 675 $[M - 2AcOH]^+$, 615 $[M - 3AcOH]^+$, 555 $[M - 4AcOH]^+$ (figure 1).

12,13-Acétonide-sénégalène ***1***d

Le produit, **1** (36,2 mg), est traité avec 2,2-diméthoxypropane (9,1 mg), acide *p*-toluènesulfonique (traces) et benzène (1 mL) sous reflux pendant 1 h. Après 1 h d'agitation 0,2 mg de K_2CO_3 sont rajoutés à froid. L'agitation est prolongée pendant 4 h. Le produit de réaction, **1***d*, est ensuite réextrait par l'éther et lavé d'abord par une solution de NaCl saturée et ensuite par H_2O. Le rendement est de 80%. $C_{40}H_{70}O_7$; SMIC (NH_3), *m/z* : 680 $[M + NH_4]^+$, 663 $[MH]^+$, 644 $[M - H_2O]^+$, 626 $[M - 2H_2O]^+$, 605 $[MH - 58]^+$.

29,30-Epoxy-tétraacétyl-sénégalène ***1***e

Le produit, **1***a* (98 mg), est traité avec *m*-CPBA (73,5 mg) et chloroforme (12 mL) pendant 8 h à température ambiante. Le produit de réaction, **1***e*, est lavé d'abord par une solution de 1% de $NaHCO_3$ et ensuite par H_2O et purifié sur colonne de silice. $C_{45}H_{78}O_{12}$; SMIC (NH_3), *m/z* : 824 $[M + NH_4]^+$, 807 $[MH]^+$, 746 $[M - AcOH]^+$, 686 $[M - 2AcOH]^+$, 626 $[M - 3AcOH]^+$, 566 $[M - 4AcOH]^+$ (figure 2).

Molvizarine ***2***. $C_{37}H_{66}O_7$; M = 622; $[\alpha]_D$ +10 (*c* 0,20, $CHCl_3$). Identifiée par analyse des données spectrales, SM, ^1H et ^{13}C RMN (6), et comparaison à un échantillon authentique (*co*-CCM).

Asimicine ***3***. $C_{37}H_{66}O_7$; M = 622; $[\alpha]_D$ +11 (*c* 0,22, $CHCl_3$). Identifiée par analyse des données spectrales, SM, ^1H et ^{13}C RMN, comparaison aux données de la littérature (1) et à un échantillon authentique (*co*-CCM).

Rolliniastatine-2 ***4*** *(= bullatacine).* $C_{37}H_{66}O_7$; M = 622; $[\alpha]_D$ +15 (*c* 0,27, $CHCl_3$) (litt. (8) $[\alpha]_D$ +5,3 (*c* 0,23, $CHCl_3$)); (litt. bullatacin (1) $[\alpha]_{578}$ +14,7 (*c* 0,004, $CHCl_3$)). Identifiée par analyse des données spectrales, SM, ^1H et ^{13}C RMN, et comparaison à un échantillon authentique (*co*-CCM).

Squamocine ***5***. $C_{37}H_{66}O_7$; M = 622; $[\alpha]_D$ +14 (*c* 0,2, $CHCl_3$) (litt. (1) $[\alpha]_D$ +15 (*c* 1,7, MeOH)). Identifiée par analyse des données spectrales, SM, ^1H et ^{13}C RMN, comparaison aux données de la littérature et à un échantillon authentique (*co*-CCM).

1. J.K. Rupprecht, Y.-H. Hui et J.L. McLaughlin. J. Nat. Prod. **53**, 237 (1990).
2. X.P. Fang, M.J. Rieser, Z.M. Gu, G.X. Zhao et J.L. McLaughlin. Phytochem. Anal. **4**, 27 (1993).
3. O. Ekundayo et B.O. Oguntimein. Planta Med. **52**, 202 (1986).
4. M. Leboeuf, A. Cavé, P.K. Bhaumik, B. Mukherjee et R. Mukherjee. Phytochemistry, **21**, 2783 (1982).
5. D. Bamba, G. Balansard, C. Maillard, G. Duménil et A. Gayte-Sorbier. Plant. Med. Phytother. **18**, 36 (1984).
6. D. Cortes, S.H. Myint et R. Hocquemiller. Tetrahedron, **38**, 8195 (1991).
7. J.K. Rupprecht, C.-J. Chang, J.M. Cassady et J.L. McLaughlin. Heterocycles, **24**, 1197 (1986).
8. G.R. Pettit, R. Reissen, J.E. Leet, J. Polonsky, C.R. Smith, J.M. Schmidt, C. Dufresne, D. Schanfelberger et C. Moretti. Heterocycles, **28**, 212 (1989).
9. Y. Fujimoto, T. Eguchi, K. Kakinuma, N. Ikekawa, M. Sahai et Y.K. Gupta. Chem. Pharm. Bull. **36**, 4802 (1988).
10. D. Cortes, S.H. Myint, A. Laurens, R. Hocquemiller, M. Leboeuf et A. Cavé. Can. J. Chem. **69**, 8 (1991).
11. X.P. Fang, J.K. Rupprecht, A. Alkofahi, Y.H. Hui, Y.M. Liu, D.L. Smith, K.V. Wood et J.L. McLaughlin. Heterocycles, **36**, 11 (1991).
12. J.A. Musich et H. Rapoport. J. Am. Chem. Soc. **15**, 4865 (1978).
13. J.G. Yu, D.K. Ho, J.M. Cassady, L. Xu et C.-J. Chang. J. Org. Chem. **57**, 6198 (1992).
14. D. Cortes, S.H. Myint, J.C. Harmange, S. Sahpaz et B. Figadère. Tetrahedron Lett. **33**, 5225 (1992).
15. O. Laprévote, C. Girard, B.C. Das, T. Laugel, R. Roblot, M. Leboeuf et A. Cavé. Rapid Commun. Mass Spectrom. **6**, 352 (1992).
16. O. Laprévote, C. Girard, B.C. Das, D. Cortes et A. Cavé. Tetrahedron Lett. **33**, 5237 (1992).
17. Y. Hashidoko, S. Tahara et J. Mizutani. Phytochemistry, **30**, 3729 (1991).
18. N.J. Jensen et M.L. Gross. Mass Spectrom. Rev. **6**, 497 (1987).
19. O. Laprévote, F. Roblot, R. Hocquemiller et A. Cavé. Tetrahedron Lett. **31**, 2283 (1990).
20. S.H. Myint, D. Cortes, A. Laurens, R. Hocquemiller, M. Leboeuf, A. Cavé, J. Cotte et A.M. Quéro. Phytochemistry, **30**, 3335 (1991).
21. J.C. Harmange, B. Figadère et A. Cavé. Tetrahedron Lett. **33**, 5749 (1992).
22. X.P. Fang, J.E. Anderson, D.L. Smith, K.V. Wood et J.L. McLaughlin. Heterocycles, **34**, 1075 (1992).
23. X.P. Fang, J.E. Anderson, D.L. Smith, J.L. McLaughlin et K.V. Wood. J. Nat. Prod. **55**, 1655 (1992).
24. D. Gromek, B. Figadère, R. Hocquemiller, A. Cavé et D. Cortes. Tetrahedron, **49**, 5247 (1993).

The oscillatory Belousov–Zhabotinsky reaction with flavones in batch systems using aqueous–DMF mixed medium

G. MAYA, P.V. LALITHA, AND R. RAMASWAMY

Department of Chemistry, Indian Institute of Technology, Madras – 600 036, India

Received May 25, 1993[1]

G. MAYA, P.V. LALITHA, and R. RAMASWAMY. Can. J. Chem. **72**, 1537 (1994).

Oscillatory systems of the Belousov–Zhabotinsky type with flavones as substrates are described for the first time. Since quercetin and morin are water insoluble, a mixed medium containing DMF and water was used with one of the three catalysts Ce(III), ferroin, or Mn(II). The oscillatory behaviour of a water-soluble substrate (gallic acid) was studied in nine different aqueous–organic mixed media as well as in pure aqueous medium in the bromate–Ce(III) system. The results obtained from a catalyzed system with quercetin or morin as the substrate in an aqueous–organic mixed medium are in agreement with the accepted (FKN) mechanism for an aqueous system.

G. MAYA, P.V. LALITHA et R. RAMASWAMY. Can. J. Chem. **72**, 1537 (1994).

On décrit pour la première fois des systèmes oscillatoires du type Belousov-Zhabotinsky impliquant des flavones comme substrats. La quercétine et la morine étant insoluble dans l'eau, on a utilisé un milieu mixte contenant du DMF et de l'eau avec un des trois catalyseurs suivants: le Ce(III), la ferroïne ou le Mn(II). On a étudié le caractère oscillatoire d'un substrat soluble dans l'eau (l'acide gallique) dans neufs milieux mixtes (eau/solvants organiques) ainsi que dans de l'eau pure dans le système bromate/Ce(III). Les résultats obtenus dans le système catalysé avec la quercétine ou la morine comme substrats, dans un milieu mixte organique aqueux, sont conformes au mécanisme accepté (FKN) du système aqueux.

[Traduit par la Rédaction]

Can. J. Chem. Downloaded from www.nrcresearchpress.com by EESC ESCOLA DE ENGENHARIA on 09/08/12
For personal use only.

Introduction

The Belousov–Zhabotinsky (1, 2) oscillatory reaction has attracted the attention of researchers for many years because of their challenging chemistry and their wealth of dynamic behaviour. A number of substrates have been used in this system with different catalysts (3–9). The mechanistic aspects have been presented in detail as the Field–Koros–Noyes (FKN) mechanism (10–12). A systematic study of the aromatic bromate oscillators has been rendered difficult by the poor solubility of many organic compounds and the bromo derivatives in pure aqueous medium. This difficulty has been overcome by employing aqueous–organic mixed media, containing a small percentage of organic solvent in oscillatory systems (13–18). This paper reports on the study of oscillatory behaviour of gallic acid in the Ce(III)-catalysed system in nine different aqueous–organic mixed media. The oscillatory behaviour of two flavones, namely, quercetin and morin, is reported for the first time using three different BZ catalysts (Ce(III), Mn(II), and ferroin).

Experimental

The experimental procedure is the same as that reported elsewhere (14, 15).

Results and discussion

(A) Gallic acid as substrate

Nine different organic solvents (Table 1) in the form of aqueous–organic mixed media were tested for their suitability for the investigation using gallic acid as a substrate. The reasons for choosing gallic acid as a substrate are as follows: (*i*) It exhibits dynamic behaviour in pure aqueous medium over a wide range of concentration conditions in the B–Z systems (Mn(II), Ce(III), ferroin, and uncatalyzed) (19–21). (*ii*) Since it is water soluble, the study would enable a comparison of its dynamic behaviour in different mixed media as well as in pure aqueous medium. In fact, aqueous–organic media have been used successfully in the ferroin-catalyzed as well as the uncatalyzed bromate systems with gallic acid as substrate (15, 16).

In this study using gallic acid, the system contains 5%(v) of the organic solvent (Table 1). The oscillatory characteristics are presented in Table 1. In the following seven media, namely, water, dimethylformamide (DMF), acetonitrile (AN), tetrahydrofuran (THF), *N*-methyl 2-pyrolidone (N-mp), 1,4-dioxan, and benzene, there are initially two to three large amplitude oscillations (~400 mV) with the initial potential reaching as low as 0.25 V (vs. SCE) followed by six to seven small amplitude (~150 mV) oscillations with peak potentials close to 1.15 V (vs. SCE). The latter oscillations in the high potential region are characteristic of periodic changes in [Ce(IV)]/[Ce(III)] and the large amplitude oscillations characterize changes in $[Br_2]$/$[Br^-]$. Gallic acid exhibits similar oscillatory behaviour in seven of the media employed in the Ce(III) system as presented in Table 1. However, in the mixed media involving 5%(v) of dimethyl sulphoxide (DMSO), CCl_4, or methanol, there are no oscillations. This study shows that the mixed media involving 5%(v) DMF, AN, THF, dioxan, N-mp, or benzene are as good as the aqueous medium and this would facilitate investigations of the structurally related water insoluble substrates in the bromate–Ce(III) system.

The present work also reports for the first time the oscillatory behaviour of two flavones (quercetin and morin) in 20%(v) DMF. The structure of quercetin and morin are given below:

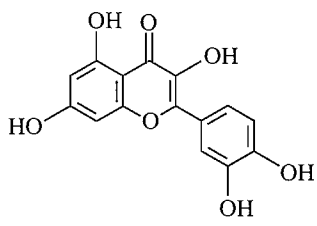

quercetin

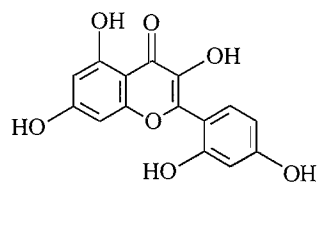

morin

The concentration ranges used and the oscillatory parameters are listed in Tables 2 and 3. The oscillatory characteristics at a typical concentration condition are also presented for comparison. These systems exhibit dynamic behaviour only over a nar-

[1]Revision received January 15, 1994.

TABLE 1. Oscillatory behaviour of the gallic acid – Ce(III) – bromate system in different media. Concentration conditions: organic solvent: 5% (v); temperature, 30°C; gallic acid: 0.026 M; H_2SO_4: 1.96 M; Ce(III): 0.005 M; $KBrO_3$: 0.06 M[a]

No.	Solvent	T_i	T_t	n	t	A	Potential range V vs. SCE
1	Water	0.8	5.3	10	0.45	335	0.77 –1.105
2	DMF	0.6	5.7	10	0.51	290	0.775–1.065
3	Acetonitrile	0.7	5.9	10	0.52	300	0.83 –1.13
4	THF	0.7	6	10	0.53	395	0.69 –1.085
5	1,4-Dioxan	0.8	4.6	9	0.42	285	0.85 –1.135
6	*N*-methyl-2-pyrolidone	0.8	3.3	7	0.36	310	0.68 –0.99
7	Benzene	0.7	5.8	10	0.51	310	0.75 –1.06
8	DMSO						
9	CCl_4	No oscillations					
10	CH_3OH						

[a]T_i: Induction time (min); T_t: total time (min); n: number of oscillations; t: time per oscillations (min); A: amplitude of oscillations (mV).

TABLE 2. Quercetin–H_2SO_4–catalyst–$KBrO_3$ system in 20% (v) DMF at 30°C

(*A*) Concentration range of constituents used

Catalyst		[Quercetin] M	[H_2SO_4] M	[Catalyst] M	[$KBrO_3$] M
Ce(III)	Concentration range	0.002–0.01	0.7–2.0	0.00033–0.0026	0.03–0.12
	Composition	0.007	1.0	0.001	0.10
Mn(II)	Concentration range	0.004–0.006	1.0–1.4	0.0033–0.01	0.08–0.12
	Composition	0.005	1.2	0.0067	0.10
Ferroin	Concentration range	0.015–0.020	0.8–1.2	0.001–0.0013	0.08–0.12
	Composition	0.017	1.0	0.012	0.10

(*B*) Oscillatory characteristics for systems in (*A*)

Catalyst	T_i	T_t	n	t	A	Potential range V vs. SCE
Ce(III)	0–1.2	12.6–4.0	24–7	0.73–0.40	225–25	0.44 –0.92
	0	8.1	16	0.51	195	0.68 –0.875
Mn(II)	0	6.5–2.3	5–8	0.81–0.38	80–45	0.86 –0.995
	0	3	6	0.50	60	0.91 –0.97
Ferroin	0	33.7–8	33–14	1.35–0.37	280–115	0.515–0.855
	0	15.1	23	0.65	280	0.565–0.845

row range of the concentrations of the constituents, presumably due to the moderate reactivity of these flavones towards bromination. This can be attributed to the fused ring structure of flavones.

B. Ce(III) system: quercetin/morin as the substrate

At high concentrations of substrate and low concentrations of H_2SO_4, Ce(III), or $KBrO_3$, the system exhibits two types of oscillations. Initially there are large amplitude oscillations indicative of Br_2/Br^- oscillations (~0.44–0.85 V) (22) followed by small amplitude oscillations in [Ce(IV)]/[Ce(III)] as evident from the potential range (~0.8–0.9 V) (17, 18). Similarly, at low substrate concentration and high concentrations of H_2SO_4, Ce(III), or $KBrO_3$, the system exhibits oscillations in [Ce(IV)]/[Ce(III)] as sensed by the platinum indicator electrode (~0.75–0.95 V). These characteristics are similar for quercetin and morin as the substrates. Typical oscillatory profiles for quercetin and morin in the Ce(III) system are shown in Fig. 1. In the case of quercetin system, the oscillations are characterized by small amplitude (0.80–0.89 V vs. SCE) indicative of Ce(IV)/Ce(III) oscillations, whereas morin exhibits high amplitude oscillations (0.66–0.90 V) initially, due to the mixed control of potential by both Br_2/Br^- and Ce(IV)/Ce(III) couples followed by small amplitude oscillations (0.81–0.93 V).

The mechanism of the catalyzed bromate system in mixed media is found to be the same as that in pure aqueous medium, even though the oscillatory characteristics are altered in the presence of an organic solvent (15). As these substrates are not water soluble, a comparison of the oscillatory behaviour in mixed medium and pure aqueous medium could not be made. In the FKN mechanism for the catalyzed bromate system, an important step is the oxidation of catalyst metal ion.

[A] $BrO_2^{\cdot} + M^{n+} + H^+ \rightleftharpoons HBrO_2 + M^{(n+1)+}$

Can. J. Chem. Downloaded from www.nrcresearchpress.com by EESC ESCOLA DE ENGENHARIA on 09/08/12
For personal use only.

TABLE 3. Morin–H_2SO_4–catalyst–$KBrO_3$ system in 20% (v) DMF at 30°C

(*A*) Concentration range of constituents used

Catalyst		[Morin] M	[H_2SO_4] M	[Catalyst] M	[$KBrO_3$] M
Ce(III)	Concentration range	0.002–0.004	0.08–1.5	0.002–0.005	0.08–0.12
	Composition	0.003	1.0	0.001	0.10
Mn(II)	Concentration range	0.003–0.009	0.8–1.6	0.003–0.008	0.08–0.13
	Composition	0.006	1.2	0.005	0.10
Ferroin	Concentration range	0.005–0.02	0.8–1.8	0.001	0.05–0.12
	Composition	0.015	1.0	0.001	0.10

(*B*) Oscillatory characteristics for systems in (*A*)

Catalyst	T_i	T_t	n	t	A	Potential range V vs. SCE
Ce(III)	0	7–0.5	16–2	0.63–0.25	365–95	0.44–1.01
	0	2.8	6	0.46	170	0.84–1.01
Mn(II)	0–4	7.3–2.4	10–5	1.24–0.3	320–60	0.59–1.02
	0	3.6	6	0.6	320	0.59–0.91
Ferroin	0–0.6	11.7–3.5	29–3	1.16–0.14	435–60	0.27–0.995
	0	11.7	23	0.51	290	0.64–0.93

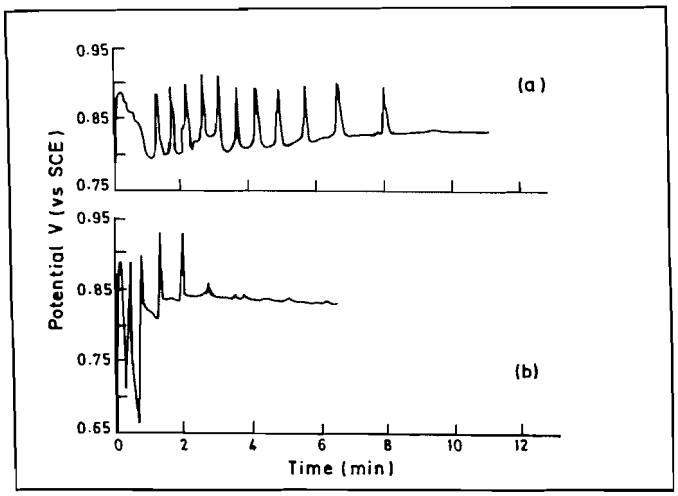

FIG. 1. Oscillatory behaviour of flavone–H_2SO_4–Ce(III)–$KBrO_3$ systems in DMF (20%v) – water mixed medium at 30 ± 0.1°C. Concentration conditions: [substrate]: 0.004 M; [H_2SO_4]: 1 M; [Ce(III)]: 0.001 M; [$KBrO_3$]: 0.1 M. (*a*) Quercetin, (*b*) morin.

The change in the concentration of the constituents alters the oscillatory parameters, as a result of which the rate of the reaction [A] is enhanced or decreased.

C. Ferroin-catalyzed system: quercetin/morin as the substrate

The B–Z system containing quercetin or morin as substrate exhibits large amplitude oscillations when the system contains a high concentration of substrate or low concentrations of H_2SO_4, ferroin, or $KBrO_3$. On the other hand, there are two types of oscillations, characterized by large amplitude (Br_2/Br^-) and small amplitude (ferrin/ferroin, in the high potential region), at low concentration of the substrate or high concentration of H_2SO_4, ferroin, or potassium bromate. The indicator electrode is responsive to the redox couple present depending on the concentrations of the redox couples and the exchange current density values. It is interesting to note that in spite of the higher exchange current density of Pt/ferrin, ferroin ($\sim 10^{-3}$ A cm^{-2}) compared to Pt/Br_2, Br^- ($\sim 10^{-5}$ A cm^{-2}), the systems are characterised by mixed control of potential (of the indicator electrode) under certain concentration conditions. The high amplitude oscillations are caused by a certain initial high concentration of bromine and substrate and a subsequent low concentration of bromine caused by fast bromination. As the reaction proceeds, the concentration of substrate and bromine decreases, now the indicator electrode responds to the $M^{(n+1)+}/M^{n+}$ potential as the [Br_2] is so low that it would no longer control the potential of the Pt electrode (17). Typical oscillatory profiles in the ferroin-catalyzed system with quercetin and morin as substrates are presented in Fig. 2. Here also, the oscillations with quercetin are predominantly ferrin/ferroin controlled, (~0.83–0.89 V) whereas with morin, they are mostly mixed controlled (~0.64–0.92 V). An increase of sustrate concentration increases the time per oscillation, whereas increase in the concentrations of H_2SO_4 or $KBrO_3$ tends to decrease the time per oscillation. The time per oscillation and induction time in quercetin–catalyst–bromate systems are higher than those in morin–catalyst–bromate systems. These observations suggest that morin is more reactive towards bromination compared to quercetin, under the conditions employed.

Conclusions

A critical examination of the oscillatory characteristics — time per oscillation (t) and the value of base and peak potentials, allow us to draw the following conclusions for a catalyzed bromate–flavone system involving one of the three metal ions (Ce(III), Mn(II), or ferroin).

The redox reaction involving metal ion catalyst is favoured by a high concentration of potassium bromate, H^+, or catalyst and a low concentration of substrate. The steps leading to bro-

Can. J. Chem. Downloaded from www.nrcresearchpress.com by EESC ESCOLA DE ENGENHARIA on 09/08/12
For personal use only.

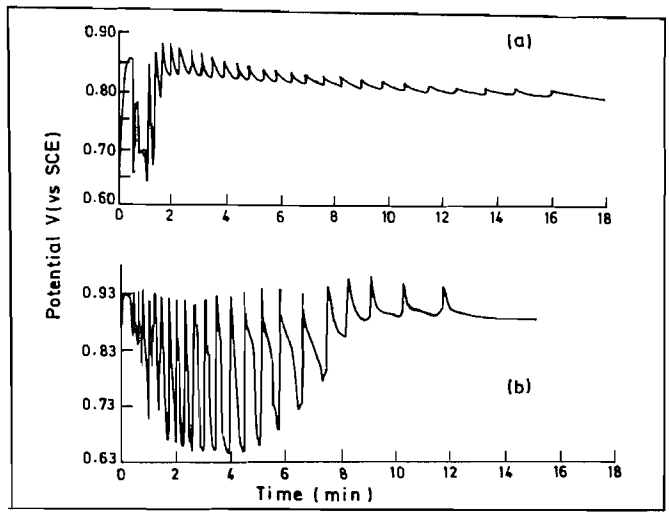

FIG. 2. Oscillatory behaviour of flavone–H_2SO_4–ferroin–$KBrO_3$ systems in DMF (20%v) – water mixed medium at 30 ± 0.1°C. Concentration conditions: [substrate]: 0.015 M; [H_2SO_4]: 1 M; [ferroin]: 0.001 M; [$KBrO_3$]: 0.1 M. (*a*) Quercetin, (*b*) morin.

mine consumption and bromine formation are favoured by a low concentration of potassium bromate, H^+, or catalyst and high concentration of the substrate. Such conclusion can be substantiated by considering the steps involved in the generally accepted (FKN) mechanism for the B–Z reaction.

[1] $BrO_3^- + HBrO_2 + H^+ \rightarrow 2\ BrO_2\cdot + H_2O$

[2] $BrO_2\cdot + M^{n+} + H^+ \rightarrow M^{(n+1)+} + HBrO_2$

[3] $BrO_2\cdot + R{-}H \rightarrow R\cdot + HBrO_2$

The common autocatalytic step [1] is favoured by a high concentration of BrO_3^-. This would be followed by either step [2] or step [3]. A high concentration of $BrO_2\cdot$ (bromate), H^+, or M^{n+} would favour the step involving the redox reaction of the metal ion. Alternatively step [3] would be favoured by a high concentration of the substrate or a low concentration of the metal ion. These observations establish the validity of the generally accepted mechanism of the oscillatory systems in aqueous media to those in aqueous organic mixed media as well.

Acknowledgements

One of the authors (P.V.L.) thanks CSIR, India, and I.I.T., Madras, for financial assistance.

1. A.M. Zhabotinsky. Dokl. Akad. Nauk, SSSR, **157**, 392 (1964).
2. R.J. Field and M. Burger (*Editors*). Oscillations and travelling waves in chemical systems. John Wiley and Sons. 1985.
3. S. Ramanathan and R. Ramaswamy. Trans. SAEST, **16**, 241 (1981).
4. M. Varga, L. Gyorgyi, and E. Koros. React. Kinet. Catal. Lett. **42**, 375 (1990).
5. M. Melichercik and L. Treindl. Collect. Czech. Chem. Commun. **55**, 1673 (1990).
6. E. Koros, M. Burger, Z. Nagy, and M. Orban. Acta Pharm. Hung. **48**, 172 (1978).
7. P.G. Bowers, K.E. Caldwell, and D.E. Prendergast. J. Phys. Chem. **76**, 2185 (1972).
8. V.J. Farage and D. Janjic. Helv. Chim. Acta, **61**, 1539 (1978).
9. R.P. Rastogi, R.D. Yadava, S. Singh, and A. Sharma. Ind. J. Chem. **A24**, 43 (1985).
10. R.J. Field, E. Koros, and R.M. Noyes. J. Am. Chem. Soc. **94**, 8649 (1972).
11. P. Sevcik and L. Adamcikova. J. Phys. Chem. **89**, 5178 (1985).
12. O. Gurel and D. Gurel. Topics in current chemistry, oscillations in chemical reactions. Springer-Verlag, Berlin. 1983. 118.
13. P.V. Lalitha and R. Ramaswamy. Collect. Czech. Chem. Commun. **57**, 2235 (1992).
14. P.V. Lalitha and R. Ramaswamy. React. Kinet. Catal. Lett. **47**, 133 (1992).
15. P.V. Lalitha and R. Ramaswamy. Int. J. Chem. Kinet, **25**, 457 (1993).
16. P.V. Lalitha and R. Ramaswamy. Proc. Ind. Acad. Sci. Chem. Sci. **104**, 619 (1992).
17. P.V. Lalitha, R. Ramaswamy, Geetha Ramakrishnan, and P. Sambasiva Rao. J. Phys. Chem. **96**, 7679 (1992).
18. P.V. Lalitha and R. Ramaswamy. React. Kinet. Catal. Lett. In press.
19. V.K. Gupta and K. Srinivasulu. React. Kinet. Catal. Lett. **18**, 45 (1981).
20. J.S. Babu, M.M. Bokadia, and K. Srinivasulu. Bull. Chem. Soc. Jpn. **49**, 2875 (1976).
21. R. Ramaswamy and M. Krishnaratnam. Ind. J. Tech. **24**, 510 (1986).
22. P.V. Lalitha and R. Ramaswamy. Ind. J. Chem. **32A**, 177 (1993).

Can. J. Chem. Downloaded from www.nrcresearchpress.com by EESC ESCOLA DE ENGENHARIA on 09/08/12
For personal use only.

Transposition en série tricyclique — synthèse et réactivité de bis-triméthylsilyl-bicyclo[*n*,1,0]2-alcène antioxydes

MARIE-CATHERINE GRELIER-MARLY ET MICHELINE GRIGNON-DUBOIS[1]

Laboratoire de chimie organique et organométallique, Université Bordeaux I, 351, Cours de la Libération, 33405 Talence-Cédex, France

Reçu le 17 juin 1993

MARIE-CATHERINE GRELIER-MARLY et MICHELINE GRIGNON-DUBOIS. Can. J. Chem. **72**, 1541 (1994).

Les bis-triméthylsilyl-bicyclo[*n*,1,0]2-alcène antioxydes ($n = 4$ et 6) ont été synthétisés en trois étapes (dichlorocyclopropanation, silylation et époxydation) à partir des cyclo-1,3-diènes correspondants. Leur isomérisation en présence de divers acides de Lewis a été étudiée et comparée aux résultats décrits en série carbonée. Contrairement au 2-carène oxyde qui conduisait exclusivement à la rupture de la liaison C2—O, nous assistons ici essentiellement à celle de la liaison C3—O. Elle s'accompagne de l'ouverture disrotatoire du cyclopropane qui procède par un mécanisme différent selon la valeur de *n*, conduisant ainsi majoritairement au 7,8-bis-triméthylsilyl-9-hydroxy-bicyclo[4,3,0]non-6-ène quand $n = 6$ et au 2,2′-bis-triméthylsilyl-cyclohex-3-ène carboxaldéhyde quand $n = 4$.

MARIE-CATHERINE GRELIER-MARLY and MICHELINE GRIGNON-DUBOIS. Can. J. Chem. **72**, 1541 (1994).

The bis-trimethylsilyl-bicyclo[*n*,1,0]2-alkene antioxides ($n = 4$ and 6) have been synthesized from their 1,3-diene precursors by a three-step process (dichlorocyclopropanation, silylation, and epoxidation). Their rearrangement in the presence of solid and liquid Lewis acids was studied, and compared with the previously described reactivity of 2-carene oxide. With these silylated epoxides, the breaking of the C3—O bond is favoured while C2—O bond breaking had previously been observed with 2-carene oxide. All the resulting products were the three-membered ring-opened ones, but the opening mechanism differs according to the value of *n*, leading mainly to 7,8-bis-trimethylsilyl-9-hydroxy-bicyclo[4,3,0]non-6-ene when $n = 6$ and 2,2′-bis-trimethylsilyl-cyclohex-3-ene carboxaldehyde when $n = 4$.

La transposition du 2,3-époxynorcarane en présence d'acides est connue pour conduire à des menthénol ou menthénones résultant de l'ouverture des deux cycles à trois chaînons sans réarrangement du cycle à 6 chaînons (1). Ayant montré par ailleurs que la substitution du cyclopropane par un ou deux groupes silyles modifie sa réactivité (2*a*), nous avons envisagé le cas du bis-triméthylsilyl-bicyclo[4,1,0]2-heptène antioxyde afin d'examiner l'influence du silicium sur le réarrangement de ces squelettes. L'étude des triméthylsilylbicyclo[*n*,1,0]alcanes et alcènes nous avait permis de mettre en évidence l'importance de la taille du grand cycle dans la réactivité électrophile de ces composés (2*b*, 2*c*). Nous avons donc également envisagé le cas du bis-triméthylsilyl-bicyclo[6,1,0]2-nonène antioxyde.

Résultats et discussion

Les bis-triméthylsilyl-bicyclo[*n*,1,0]2-alcène oxydes sont obtenus quantitativement par action de l'acide métachloroperbenzoïque (3) sur les bicyclo[*n*,1,0]alcènes siliciés **1** et **2**, dont nous avions précédemment proposé une voie de synthèse en deux étapes à partir des cyclo-1,3-diènes (2*c*) (schéma 1). Dans les deux cas, nous isolons un seul stéréoisomère. Le fait que Clark et al. (1*a*) et Coates et coll. (1*c*) n'obtenaient que l'isomère *trans* lors de l'époxydation du 2,3-carène ou des bromonorcarènes suggère qu'il en est de même en série siliciée. Cependant, l'éventualité d'une interaction $(p–d)\pi$ entre l'oxygène et le silicium (4), qui pourrait stabiliser l'isomère *cis* par rapport au *trans*, doit être envisagée. L'analyse du spectre de RMN ^{1}H (250 MHz) ne permet pas de déterminer sans ambiguïté la stéréochimie du composé **3**, les signaux des protons H1 et H2 n'étant pas différenciés. Dans le cas du composé **4**, ce couplage est nul. Une étude conformationnelle des deux isomères a été effectuée par mécanique moléculaire.[2] Les valeurs suivantes, mesurées pour l'angle dièdre H1-C-C-H2, montrent qu'il serait hasardeux de déduire la stéréochimie à partir du seul couplage $^3J(H_1, H_2)$:

3 *trans* : 26° ^3J = 6.7 Hz; **3** *cis* : 50° ^3J = 4,8 Hz

4 *trans* : 103° ^3J = 1 Hz; **4** *cis* : 78° ^3J = 0,6 Hz

Par contre, la proximité de l'oxygène et du silicium *endo* dans les isomères *cis*, devrait avoir des conséquences sur les caractéristiques RMN de ce dernier. Nous nous sommes donc tourné vers la RMN du ^{29}Si dont nous avions démontré l'intérêt dans le domaine de l'analyse structurale des dérivés organosiliciés (6). Les déplacements chimiques et les constantes de couplage ^{29}Si,^{1}H des composés **3** et **4** ont été mesurés et comparés aux valeurs précédemment rapportées pour les bicycloalcanes et alcènes correspondants (6*a*–*c*). L'utilisation de séquence SPT (6) a permis l'attribution des signaux $SiMe_3$ dans le spectre proton. Nous avons ainsi pu corréler les déplacements chimiques ^{1}H et ^{29}Si des groupes silyles de tous ces composés ainsi que les déplacements chimiques du ^{13}C, à partir des spectres COSY (^{1}H, ^{13}C). L'ensemble de ces résultats est rassemblé dans le tableau 1. La similitude des valeurs observées dans toute cette série montre qu'il n'y a pas d'interaction entre l'oxygène et le silicium *endo*, ce qui est en faveur d'une géométrie *trans*. Les effets stériques des groupes triméthylsilyles contrôlent donc la stéréochimie de la réaction.

Réactivité des époxydes 3 et 4

1. Cas du 9,9′ bis-triméthylsilyl-bicyclo[6,1,0]2-alcène antioxyde, 4

Le composé **4** a été soumis à toute une gamme d'acides solides et liquides, tous réputés conduire à l'ouverture de la fonction époxyde : BF_3/Et_2O (7), Al_2O_3 (1*c*, 7, 8), SiO_2 (7, 9), $FeCl_3/SiO_2$ (9), et ZnI_2 (10). À l'exception de SiO_2 qui laisse le composé **4** inchangé, on constate que la réaction n'est jamais univoque et conduit au mélange des dérivés **5–7** où **5** est toujours majoritaire (schéma 2; tableau 2); la meilleure sélectivité est obtenue avec ZnI_2, qui permet d'isoler **5** avec 78% de rende-

1. Auteur à qui adresser toute correspondance. Téléphone : 56846286; Fax : 56846646.

2. Macromodel, développé et distribué par Clark Still, Columbia University, New York (paramètresMM2 1987). Les couplages $^3J(^1H, ^1H)$ sont mesurés à partir des paramètres d'Altona implantés dans le programme : réf. 5.

Can. J. Chem. Downloaded from www.nrcresearchpress.com by EESC ESCOLA DE ENGENHARIA on 09/08/12
For personal use only.

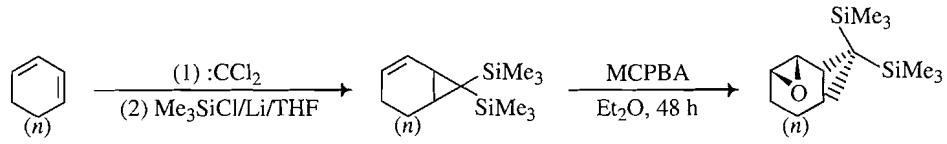

$n = 1$ **1** **3**
$n = 3$ **2** **4**

SCHÉMA 1

TABLEAU 1. Caractéristiques RMN des composés **1–4**

Produits		δ ^{29}Si	J (^{29}Si,^{1}H) (Hz) $^{2}J_{Si-CH_3}$	$^{3}J_{Si-C-CH}$	δ ^{1}H	δ ^{13}C
Cycles à 6						
SiMe$_3$ SiMe$_3$	*endo*	−0,1	6,3	3,6	0,21	3,3
	exo	5,3	6,3	7,0	0,10	−0,93
1	*endo*	−0,9	6,3	3,45	0,12	3,44
	exo	5,9	6,3	6,6	0,0	−0,92
3	*endo*	−0,3	6,4	3,4	0,0	3,59
	exo	6,5	6,4	6,95	−0,16	−0,94
Cycles à 8						
SiMe$_3$ SiMe$_3$	*endo*	0,05	6,3	4,6	0,20	3,90
	exo	5,95	6,3	7,1	0,05	−0,87
2	*endo*	0,2	6,3	4,2	0,12	3,73
	exo	5,4	6,3	7,0	−0,05	−0,74
4	*endo*	−0,27	6,3	4,4	0,11	3,69
	exo	6,39	6,3	7,2	−0,07	−0,94

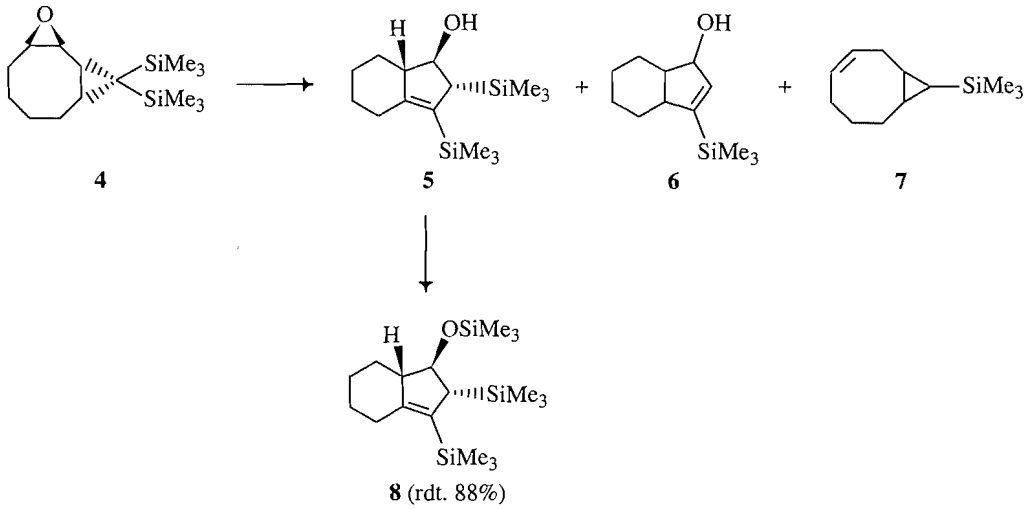

SCHÉMA 2

ment. Les spectres IR et de RMN (^{1}H et ^{13}C) montrent qu'il s'agit d'un alcool disilicié constitué d'un seul isomère; la formule brute $C_{15}H_{30}Si_2O$ a pu être confirmée par une détermination de la masse exacte (M = 282,182) en spectométrie de masse. Ces données physico-chimiques, pas plus qu'une étude de RMN 2D (COSY), ne nous ont permis de choisir parmi les trois formules **A–C**, toutes théoriquement possibles (cf. schéma 3). En effet, selon que l'ouverture de l'époxyde va s'effectuer par scission de la liaison C2—O ou C3—O, on devrait obtenir un squelette bicyclo[5,2,0]- ou [4,3,0]nonène, résultat respectivement du réarrangement du carbocation cyclopropylcarbinyle ou homocyclopropylcarbinyle. Notons cependant que les valeurs des couplages ^{1}J (^{13}C,^{1}H) des CH_2 et des CH (cf. tableau 3) seraient plutôt en faveur d'un bicycle «6+5» et donc de **B** ou de **C**, sans pour autant permettre de rejeter totalement **A**.

L'identification de **5** a été rendue possible grâce à la RMN du ^{29}Si : en effet, les déplacements chimiques du ^{29}Si observés (7,13 et −14,86 ppm) montrent que, seul, un des siliciums est en position vinylique (−14,86 ppm), ce qui nous permet de rejeter définitivement les structures **A** et **C**. Les couplages ^{29}Si,^{1}H mesurés pour ce signal (cf. partie expérimentale) sont en accord avec la structure proposée. En ce qui concerne le deuxième silicium (7,13 ppm), la complexité du spectre non découplé suggère qu'il est porté par un CH cyclique et est tout à

Can. J. Chem. Downloaded from www.nrcresearchpress.com by EESC ESCOLA DE ENGENHARIA on 09/08/12
For personal use only.

Can. J. Chem. Downloaded from www.nrcresearchpress.com by ESC ESCOLA DE ENGENHARIA on 09/08/12
For personal use only.

TABLEAU 2. Composition du mélange réactionnel obtenu par ouverture de l'époxyde **4** (pourcentages relatifs déterminés par CPG)

	Composition du mélange réactionnel (%)			
Réactifs	**4**	**5**	**6**	**7**
BF_3/Et_2O[a]	33	38	7	12
Al_2O_3	49	33	13	5
SiO_2	100	0	0	0
$FeCl_3/SiO_2$	17	60	14	9
ZnI_2	0	78	12	10

[a]On isole en outre 10% de **2**.

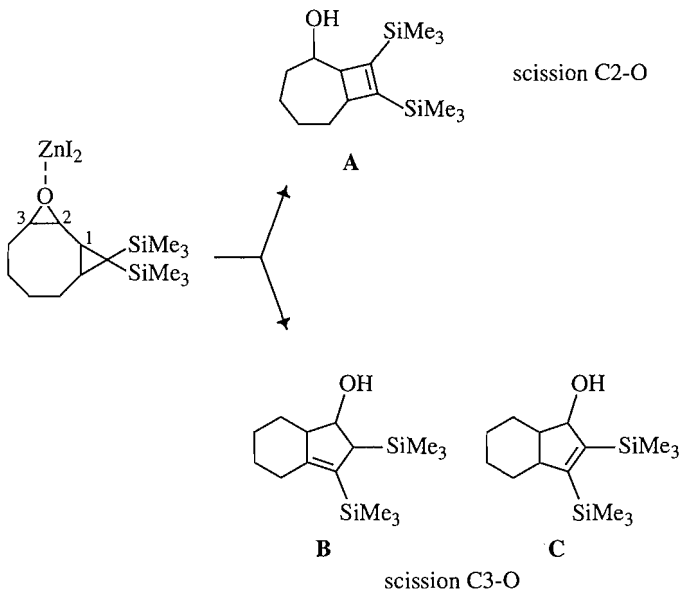

SCHÉMA 3

fait comparable à celle observée avec des structures telles que I et II :[3]

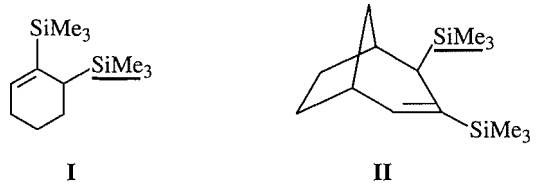

I II

Le composé **5** est constitué d'un seul isomère. La comparaison des constantes de couplage mesurées ^3J (H8, H9) ≤ 1 Hz et ^3J (H9, H1) ≤ 1 Hz aux valeurs calculées (5) pour chacun des isomères possibles (*trans* : ^3J (H8, H9) = 0,5 Hz et ^3J (H9, H1) = 1Hz; *cis* : ^3J (H8, H9) = 8 Hz et ^3J (H1, H9) = 8,7 Hz) permet de retenir pour le composé **5** la structure où les protons sont tous en *trans* avec le silicium Si-8 en axial. Ce résultat est en accord avec les données de la littérature (11) concernant la plus grande stabilité de ce type de géométrie.

L'action de l'hexaméthyldisilazane sur **5** conduit à **8** (rdt. 75%). L'examen des spectres de RMN ^1H et ^{13}C montre que l'on n'a pas modifié le squelette et il apparait dans la zone des $SiMe_3$, un signal supplémentaire dû au groupe siloxy. En RMN du ^{29}Si, les signaux des deux siliciums préexistants ne sont pas

3. M. Grignon-Dubois et M. Laguerre. Résultats à paraître.

TABLEAU 3. Corrélations $^{13}C,^1H$ pour le composé **5**

Type	δ ^{13}C (ppm)	δ ^1H (ppm)	^1J ($^{13}C,^1H$)
C=	159,9	—	—
C=	147,5	—	—
CH	69,30	3,83	144,3
CH	53,26	2,88	134,3
CH_2	38,39	1,98 et 1,34	124,8
CH	33,94	1,88	127,6
CH_2	31,59	2,19 et 2,05	124,7
CH_2	27,43	1,66 et 1,26	126,6
CH_2	24,00	1,62 et 1,33	128,7
$SiMe_3$	−0,64	−0,01	119,2
$SiMe_3$	−2,30	−0,98	119,2

modifiés par cette réaction. Le déplacement chimique et les couplages observés pour le signal supplémentaire (cf. partie expérimentale) sont tout-à-fait caractéristiques d'un groupement O-$SiMe_3$ porté par un CH cyclique.

Le mécanisme rapporté dans la figure 1 fait intervenir l'ouverture de l'époxyde par scission de la liaison C3—O avec stabilisation de la charge résultante par ouverture disrotatoire du cyclopropane. Le carbocation **A** ainsi formé est stabilisé par la présence des deux groupes triméthylsilyles en position β (12). Le composé **5** résulte de la migration de l'un d'eux, suivie de la perte du proton «tête-de-pont». Sa stéréochimie *trans* implique que c'est le groupe silyle initialement en position *endo* qui effectue cette migration (fig. 2). Le composé **6** résulterait de la stabilisation de **A** par perte du même groupe silyle. La superposition des signaux dans le spectre de RMN ^1H ne nous a pas permis de confirmer la stéréochimie de la jonction de cycle, prévue *cis* par le mécanisme proposée (fig. 2). Notons que les migrations de groupe triméthylsilyle ont été observées par ailleurs dans d'autres séries (12*c*, 13).

Quel que soit l'acide de Lewis utilisé, on isole en outre un sous-produit (rdt. 0–9%) dont les caractéristiques spectrales sont compatibles avec celles du 9-triméthylsilyl-bicyclo[6,1,0]-non-3-ène.

2. Cas du 6,6′ bis-triméthylsilyl-bicyclo[4,1,0]2-alcène antioxyde, 3

L'époxyde **3** a été mis a réagir avec ZnI_2 (réactif le plus sélectif dans le cas de **4**) et SiO_2. La réaction est totale et on isole trois produits originaux disiliciés, **9–11** (schéma 4).

(*i*) **9**, produit majoritaire de la réaction, est un liquide incolore constitué d'un seul isomère, présentant en IR les bandes d'absorption caractéristiques d'un aldéhyde non conjugué (2840 et 1720 cm^{-1}), d'une double liaison (1640 cm^{-1}) et du groupe $SiMe_3$ (1250 et 840 cm^{-1}). L'analyse des spectres de RMN ^{13}C et ^1H nous a permis de l'identifier au 2,2′-bis-triméthylsilyl-cyclo-3-hexène carboxaldéhyde.

(*ii*) La formule de **10** a été établie sur la base des données IR et RMN ^{13}C et ^1H. On note en particulier sur le spectre de RMN ^{13}C, la présence de deux CH cyclopropaniques ayant des déplacements chimiques voisins et de deux CH_2 liés à un carbone sp^2. Ces arguments permettent de rejeter l'éventualité d'un carbonyle en position 1.

(*iii*) Les données structurales relatives à **11** montrent qu'il s'agit d'une cyclohepténone non conjuguée *gem*-disiliciée. La présence dans le spectre de RMN ^1H d'un singulet d'intégration 2H, compatible avec un groupe CH_2 lié à un carbonyle, et l'analyse des couplages des protons éthyléniques, qui montre que les deux groupes silyles sont en position allylique, nous a

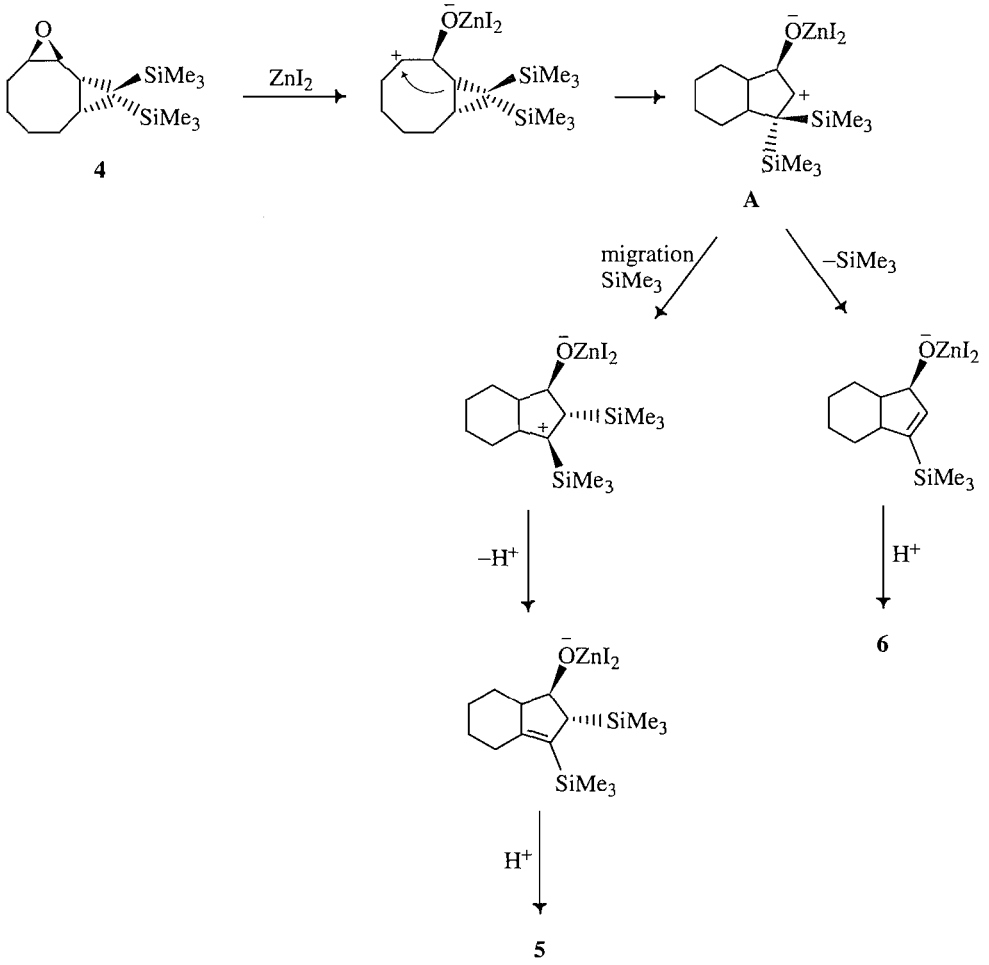

FIGURE 1

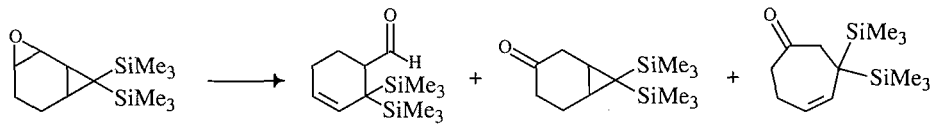

ZnI_2	rdt. :	63%	12%	18%
SiO_2	rdt. :	66%	27%	—

SCHÉMA 4

permis de l'identifier à la 1,1′-bis-triméthylsilyl-cyclohept-2-ène-6-one.

Le mécanisme décrit dans la figure 3 rend compte de ces résultats. Les composés **9** et **11**, qui constituent de 66 à 81% du mélange, résultent d'une ouverture de l'époxyde par scission de la liaison C3—O. Comme précédemment, l'ouverture disrotatoire du cyclopropane conduit à un carbocation β-disilicié (**A**), mais la régiochimie de cette ouverture est différente de celle observée avec le composé **4**, montrant l'influence de la taille du grand cycle (fig. 2). La stabilisation de **A** s'effectue par perte d'un proton. L'ouverture du cyclopropylalcoolate qui en résulte rend compte de l'obtention de **9** et **11**. La formation de bicyclo[3,2,0]hepténol, normalement attendu à partir du carbocation **B**, n'est pas observée. Notons que bien que stériquement contraint, l'obtention de ce type de squelette est envisageable, puisque il a été isolé par Coates et coll. (1*c*) par action du butyllithium sur l'*exo*-7-bromo-bicyclo[4,1,0]2-heptène antioxyde; le mécanisme faisait dans ce cas intervenir une ouverture conrotatoire de l'anion cyclopropanique via l'ouverture de l'époxyde par scission de la liaison C2—O. Seul le composé **10**, dont le rendement varie avec le réactif (tableau 2), résulte de la scission de la liaison C2—O, qui est comme précédemment défavorisée alors qu'elle intervient exclusivement à partir du 2,3-époxycarane.

Conclusion

Ce travail montre que la présence de groupes silyles sur le noyau cyclopropanique modifie la réactivité des bicyclo[*n*,1,0]alcène antioxydes. Contrairement à ce qui avait été observé avec les dérivés du norcaranes, l'ouverture de l'époxyde s'effectue majoritairement par scission de la liaison C3—O suivie d'une ouverture disrotatoire du cyclopropane, favorisée ici par la formation de carbocations β-disiliciés. La régiochimie de cette ouverture est liée à la taille du grand cycle

Can. J. Chem. Downloaded from www.nrcresearchpress.com by EESC ESCOLA DE ENGENHARIA on 09/08/12
For personal use only.

Can. J. Chem. Downloaded from www.nrcresearchpress.com by EESC ESCOLA DE ENGENHARIA on 09/08/12
For personal use only.

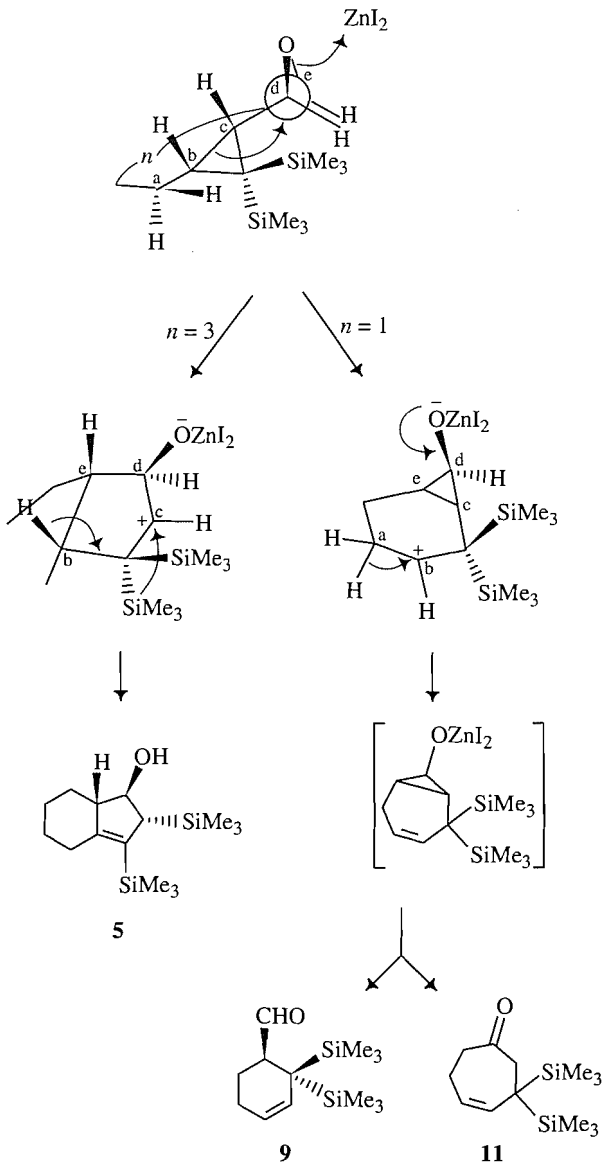

FIGURE 2

et doit traduire, tant la tension du système bicyclique formé, que la géométrie des carbocations intermédiaires dont dépend le recouvrement des orbitales impliquées dans la transposition du squelette. Ainsi, avec $n = 6$, on isole majoritairement des bicycles de type [4,3,0] plus stables que les [6,1,0] (14). Avec $n = 4$, la tension des bicycles [4,1,0] est comparable à celle des bicycles [3,2,0] (14*b*) et les facteurs géométriques doivent jouer ici un rôle important. Cependant, seule une étude conformationnelle des intermédiaires de réaction permettrait de dégager les facteurs prépondérants. Sur le plan synthétique, nous avons pu accéder à des composés originaux (alcool, aldéhyde, cétone) hautement fonctionnalisés qui pourraient constituer d'intéressants intermédiaires de synthèse.

Partie expérimentale

Caractéristiques physico-chimiques des produits obtenus

Les analyses centésimales ont été effectuées au service central d'analyse du CNRS (F-69390 Vernaison). Les spectres de masse (SM) ont été enregistrés sur un appareil VG micromass 16 F (70 eV) et les spectres IR sur un spectromètre Perkin–Elmer 1420; tous les dérivés siliciés isolés présentent en IR des bandes de très forte intensité à 1250 et 850 cm^{-1} caractéristiques des groupes $SiMe_3$ et qui peuvent masquer le reste du spectre. Les spectres de RMN ont été enregistrés sur un appareil Bruker AC 250 fonctionnant à 250 MHz dans le cas du proton et 62.9 MHz pour le ^{13}C (solvant, $CDCl_3$; C_6H_{12} ref. int. à 1,4 ppm (^1H) ou 27,08 ppm (^{13}C)) et AC 200 fonctionnant à 39,763 MHz dans le cas du ^{29}Si (spectres enregistrés dans un mélange C_6D_6/CCl_4 50 : 50). Les déplacements chimiques du silicium sont déterminés par la technique INEPT refocalisé (15). Les constantes de couplage $^{29}Si,^1H$ sont extraites des spectres SPT (16) et INEPT découplés des protons du groupe $SiMe_3$ (17) et confirmées par simulation sur un Microvax 3100 de Digital à l'aide du programme informatique précédemment décrit (6*d*).

Les composés **1–2** ont été synthétisés par addition de dichlorocarbène respectivement sur les cyclohexadiène- et cyclooctadiène-1,3 suivie d'une silylation et sont identiques aux échantillons précédemment décrits (2*c*).

Réaction d'époxydation

La réaction est conduite sous atmosphère d'argon. Dans un ballon de Grignard de 250 mL, muni d'une agitation mécanique efficace, d'une ampoule à brome et d'un réfrigérant ascendant relié à une colonne de chlorure de calcium, on ajoute goutte à goutte 0,03 mol de substrat à une solution de 150 mL d'éther anhydre et 0,035 mol (1,2 équiv.) d'acide métachloroperbenzoïque (pureté : 50–60%). L'agitation est poursuivie pendant 48 h, puis le solvant est évaporé et le résidu repris au pentane. L'acide métachlorobenzoïque formé est éliminé par filtration. Cette opération est répétée deux fois. Les traces d'acide résiduelles sont ensuite éliminées par lavage avec une solution saturée de Na_2CO_3, puis à l'eau jusqu'à neutralité. La phase organique est séchée sur sulfate de sodium et le solvant évaporé. La pureté du produit ainsi obtenu est supérieure à 99%.

7,7′-Bis-triméthylsilyl-bicyclo[4,1,0]2-heptène antioxyde (3) : 7,6 g, rdt. 99%. IR (film KBr, cm^{-1}) : 2995, 2950, 2900, 1442, 1415, 1265, 1255, 1105, 1070, 1005, 985, 965, 900, 865, 840, 785, 755, 680, 645, 620, 540, 490, 425, 350. RMN ^1H ($CDCl_3$, 250 MHz) δ ppm : −0,16 (s, 9H, $SiMe_3$), 0,0 (s, 9H, $SiMe_3$), 1,0 (m, 1H, H-6, $J_{1,6}$ 7,4 Hz), 1,1 (m, 1H, H-1, $J_{1,6}$ 7,4 Hz), 1,2 (m, 2H), 1,8 (m, 2H), 3,1 (s él, 2H, H-2 et H-3). RMN ^{13}C ($CDCl_3$, 62,86 MHz) δ ppm, $SiMe_3$: −0,94, 3,59; CH_2 : 20,0, 23,1; CH : 18,6, 18,9, 51,4, 54,2; C : 6,4. RMN ^{29}Si (cf. tableau 1). SM *m/e* (%) : 182 (2,5), 181 (18,1), 151 (6,5), 147 (18,1), 133 (7,1), 91 (11,8), 75 (13,9), 74 (14,8), 73 (100), 59 (13,5), 45 (21,1), 43 (9,1). Anal. calc. pour $C_{13}H_{26}OSi_2$: C 61,34, H 10,30, O 6,29; trouvée : C 61,61, H 10,23, O 6,32.

9,9′-Bis-triméthylsilyl-bicyclo[6,1,0]2-nonène antioxyde (4) : 8,4 g, rdt. 99%. IR (film KBr, cm^{-1}) : 3000, 2995, 2920, 2860, 1455, 1435, 1265, 1255, 1050, 980, 958, 938, 882, 872, 842, 830, 770, 758, 690, 680, 620, 482, 440, 355. RMN ^1H ($CDCl_3$, 250 MHz) δ ppm : −0,07 (s, 9H, $SiMe_3$), 0,11 (s, 9H, $SiMe_3$), 0,8 (m, 1H, H-8, $J_{8,1}$ 11,2 Hz), 1,0–1,4 (m, 5H), 1,8 (m, 2H), 2,0–2,2 (m, 2H), 2,9 (dt, 1H, H-3, $J_{3,2}$ 3,5 Hz, $J_{3,4}$ 8,5 Hz), 3,1 (dd, 1H, H-2, $J_{1,2}$ 0,5 Hz, $J_{2,3}$ 3,5 Hz). RMN ^{13}C ($CDCl_3$, 62,86 MHz) δ ppm, $SiMe_3$: −0,94, 3,69; CH_2 : 22,5 27,5, 28,5, 30,0; CH : 23,9, 27,5, 54,6, 58,4; C : 4,3. RMN ^{29}Si (cf. tableau 1). SM *m/e* (%) : 282 (0,5), 209 (8,2), 147 (10,3), 75 (14,6), 73 (100), 59 (8,4), 45 (11,2). Anal. calc. pour $C_{15}H_{30}OSi_2$: C 63,76, H 10,70, O 5,66; trouvée : C 63,21, H 10,52, O 5,38.

*Transposition des époxydes **3** et **4***

Par l'alumine activée

À une solution de 2 g d'époxyde dans 30 mL de cyclohexane séché sur tamis moléculaire (4 Å), on ajoute 25 g d'alumine neutre activée (grade I : 0% d'eau) et on agite pendant 24 h. Après filtration, l'alumine est lavée avec un mélange éther–méthanol (1 : 1; v/v). Le solvant est évaporé sous vide et le résidu est analysé par chromatographie en phase gazeuse (CPG). La purification des produits se fait par chromatographie liquide basse pression (SiO_2 : 230–400 mesh, éluant : cyclohexane–éther 8 : 2).

Par l'éthérate de trifluorure de bore

À 5 mmol d'époxyde mis en solution dans 90 mL de benzène anhy-

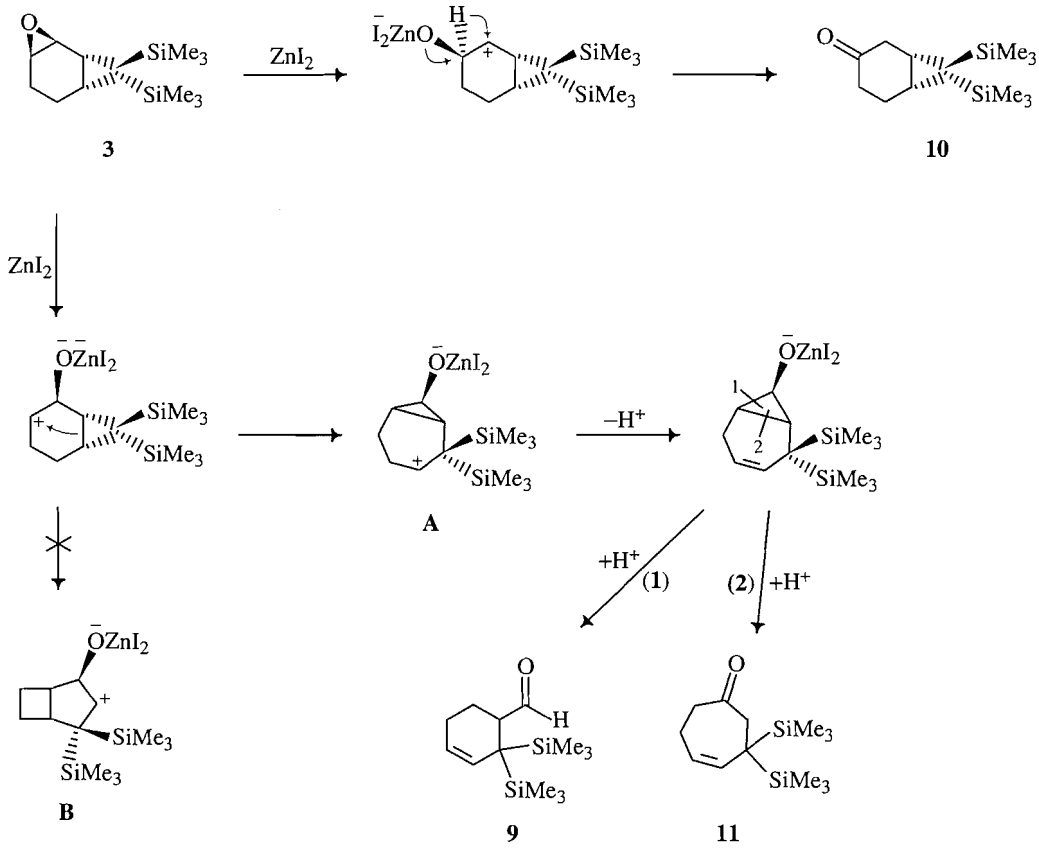

FIGURE 3

dre et maintenu à température ambiante, on ajoute 1,3 équivalents d'éthérate de trifluorure de bore (BF_3/Et_2O) fraîchement distillé sur hydrure de calcium. La manipulation s'effectue sous atmosphère inerte. L'agitation est maintenue pendant 15 min. L'hydrolyse est effectuée par addition d'eau au milieu réactionnel. Après extraction à l'éther de la phase aqueuse, la phase organique est lavée à l'eau jusqu'à neutralité et séchée sur sulfate de sodium anhydre. Après évaporation du solvant, le résidu est purifié comme précédemment.

Par le complexe $FeCl_3$–SiO_2

Le complexe $FeCl_3$–SiO_2 est préparé en mélangeant 50 g de silice (granulométrie 70–230 mesh) avec 4 g de chlorure de fer selon la référence 9. L'ensemble est vigoureusement agité pendant 24 h afin d'obtenir une adsorption homogène. On isole ainsi une poudre vert-jaune qui est utilisé sans purification. Dans un ballon de 50 mL équipé d'une agitation magnétique efficace, on place 2 mmol d'époxyde et 2,4 g de complexe $FeCl_3$ anhydre. On maintient l'agitation à température ambiante jusqu'à obtention d'une poudre brune que l'on extrait à l'éther. Le solvant évaporé, le mélange réactionnel est purifié comme précédemment.

Par l'iodure de zinc

L'iodure de zinc anhydre (2 mmol, 6,4 g) est dissout dans un minimum d'éther anhydre, puis introduit dans un Grignard à trois tubulures muni d'une agitation magnétique efficace, d'une ampoule à brome et d'un réfrigérant ascendant relié à une colonne de chlorure de calcium. On rajoute 90 mL de benzène anhydre et on distille l'éther à pression atmosphérique afin d'obtenir une suspension. Puis, on additionne goutte à goutte 5 mmol d'époxyde dilué dans 30 mL de benzène sec. Le mélange est porté à reflux pendant 8 h. L'avancement de la réaction est suivi grâce au changement de coloration du milieu réactionnel : rose avant et pendant l'addition, jaune en fin de réaction. La solution est alors filtrée, lavée à l'eau, séchée sur sulfate de sodium et le solvant est évaporé. La purification est effectuée comme précédemment.

7,8-Bis-triméthylsilyl-9-hydroxy-bicyclo[4,3,0]non-6-ène (**5**) : rdt. 71% avec ZnI_2. IR (film NaCl, cm^{-1}) : 3460, 2950, 2920, 2860, 1600, 1450, 1250, 850, 830, 750, 680. RMN ^1H ($CDCl_3$, 250 MHz) δ ppm : −0,13 (s, 9H, $SiMe_3$), −0,23 (s, 9H, $SiMe_3$), 1,3 (m, 3H, CH_2 et OH), 1,6 (m, 3H), 1,9 (s él, 1H, H-8), 2,0–2,3 (m, 3H), 2,9 (s él, 1H, H-1), 3,8 (s él, 1H, H-9). RMN ^{13}C ($CDCl_3$, 62,86 MHz) δ ppm, $SiMe_3$: −0,1, 0,0; CH_2 : 24,0, 27,4, 31,6, 38,4; CH : 33,9 (C-8), 53,3 (C-1), 69,3 (C-9); C : 147,5 (C-7), 158,9 (C-6). RMN ^{29}Si ($CDCl_3$, 39,73 MHz) δ ppm, ^nJ (^{29}Si, ^1H) Hz (nombre d'H couplés) : Si-7, −14,8 ^2J = 6,65 (9H), ^3J = 1,14 (1H), ^4J = 1,14 (1H); Si-8, 7,1 ^2J = 6,65 (9H), ^2J = 4,10 (1H), ^3J = 3 (1H). SM *m/e* (%) : 282 (1,2), 192 (5,6), 147 (15,3), 75 (18,6), 73 (100,0), 45 (8,0). Anal. calc. pour $C_{15}H_{30}OSi_2$ (%) : C 63,76, H 10,70, O 5,66, Si 19,88; trouvée : C 61,10, H 10,43, O 5,42, Si 19,60.

7-Triméthylsilyl-9-hydroxy-bicyclo[4,3,0]non-6-ène (**6**) : rdt. 10% avec ZnI_2. IR (film NaCl, cm^{-1}) : 3600. RMN ^1H ($CDCl_3$, 250 MHz) δ ppm : 0,00 (s, 9H, $SiMe_3$), 1,2–2,0 (m, 10H, H du cycle), 3,7 (m, 1H, H-9), 5,0 (m, 2H, OH et H-8). RMN ^{13}C ($CDCl_3$, 62,86 MHz) δ ppm, $SiMe_3$: −3,17; CH_2 : 20,6, 27,0, 27,1, 39,0; CH : 30,8, 46,5, 70,6, 145,3; C : 159,8.

9-Triméthylsilyl-bicyclo[6,1,0]non-3-ène (**7**) : rdt. 9% avec ZnI_2. IR (film NaCl, cm^{-1}) : 3010, 2990, 2960, 2900, 2880, 2840, 1480, 1430, 1260, 1250, 1030, 1020, 950, 850, 840, 760, 730, 690, 650. Raman : ν(C=C) 1650 cm^{-1}. RMN ^1H ($CDCl_3$, 250 MHz) δ ppm : 0,0 (s, 9H, $SiMe_3$), 1,0 (m, 1H, H-9), 1,17–1,85 (m, 10H), 5,50 (m, 2H, H-3 et 4). RMN ^{13}C ($CDCl_3$, 62,86 MHz) δ ppm, $SiMe_3$: 0,38; CH_2 : 25,58, 25,78, 30,20, 31,13; CH : 24,36, 26,16, 28,30, 126,46, 133,36.

2,2′-Bis-triméthylsilyl-3-cyclohexène carboxaldéhyde (**9**) : rdt. 63% avec ZnI_2; 66% avec SiO_2. IR (film NaCl, cm^{-1}) : 3020, 2940, 2910, 2840, 1710, 1450, 1250, 850, 660, 640. RMN ^1H ($CDCl_3$, 250 MHz) δ ppm : 0,08 (s, 9H, $SiMe_3$), 0,13 (s, 9H, $SiMe_3$), 1,5 (m, 1H, H-6), 1,9–2,2 (m, 3H, H-6′, H-5 et H-5′), 2,7 (dt, 1H, H-1, $J_{1,6}$ 11,9 Hz, $J_{1,7} = J_{1,6'}$ 2,6 Hz), 5,5 (d, 1H, H-3, $J_{3,4}$ 10,5 Hz), 5,6 (m, 1H, H-4), 9,9 (d, H-7, $J_{1,7}$ 2,4 Hz). RMN ^{13}C ($CDCl_3$, 62,86 MHz) δ ppm, $SiMe_3$: −1,14, 1,54; CH_2 : 21,5, 24,0; CH : 52,5, 122,9 128,8, 204,7; C : 10,0. SM

Can. J. Chem. Downloaded from www.nrcresearchpress.com by EESC ESCOLA DE ENGENHARIA on 09/08/12
For personal use only.

m/e (%) : 254 (M, 12), 181 (26,7), 165 (9,4), 147 (15,4), 91 (9,9), 75 (12,1), 74 (7,9), 73 (100), 45 (13,2), 43 (5,3). Anal. calc. pour $C_{13}H_{26}OSi_2$: C 61,34, H 10,30, O 6,29; trouvée : C 61,68, H 10,53, O 6,56.

7,7′-Bis-triméthylsilylbicyclo[4,1,0]heptan-3-one (10) : rdt. 12% avec ZnI_2; 27% avec SiO_2. IR (film NaCl, cm^{-1}) : 3000, 2960, 2940, 2900, 2860, 1715, 1420, 1270, 1150, 960, 880, 840, 820, 750, 680. RMN ^1H ($CDCl_3$, 250 MHz) δ ppm : −0,17 (s, 9H, $SiMe_3$), 0,0 (s, 9H, $SiMe_3$), 1,2 (m, 2H, H-1 et H-6), 1,6 (m, 1H, H-5), 2,0–2,2 (m, 3H), 2,3 (m, 1H), 2,5 (m, 1H). RMN ^{13}C ($CDCl_3$, 62,86 MHz) δ ppm, $SiMe_3$: −0,97, 3,1; CH_2 : 22,2, 38,6, 39,1; CH : 18,5, 19,5; C : 8,5. Anal. calc. pour $C_{13}H_{26}OSi_2$: C 61,34, H 10,30, O 6,29; trouvée : C 61,09, H 10,54, O 6,85.

1,1′-Bis-triméthylsilyl-cyclohept-2-ène-6-one (11) : rdt. 18%. IR (film NaCl, cm^{-1}) : 3020, 2960, 2900, 2860, 1710, 1630, 1410, 1255, 1090, 950, 880, 850, 830, 670. RMN ^1H ($CDCl_3$, 250 MHz) δ ppm : 0,06 (s, 18H, $SiMe_3$), 2,3 (m, 2H, H-4 et H-4′), 2,7 (m, 2H, H-5 et H-5′), 2,9 (s, 2H, H-2 et H-2′), 5,4 (d, 1H, H-2, $J_{2,3}$ 11,5 Hz), 5,7 (dt, 1H, H-3, $J_{2,3}$ = 11,4 Hz, $J_{3,4} = J_{3,4'}$ 6,3 Hz). RMN ^{13}C ($CDCl_3$, 62,86 MHz) δ ppm, $SiMe_3$: −1,32; CH_2 : 22,0, 42,8, 45,5; CH : 124,0, 132,0; C : 27,4, 214,2. Anal. calc. pour $C_{13}H_{26}OSi_2$: C 61,34, H 10,30, O 6,29; trouvée : C 61,76, H 10,65, O 6,82.

Silylation de 5

Dans un ballon de 50 mL, on introduit 0,3 g de substrat, 0,085 g de pyridine, 0,350 g d'hexaméthyldisilazane et 20 mL de cyclohexane. Le milieu est porté au reflux et on ajoute quelques gouttes de Me_3SiCl pour amorcer la silylation. Après 16 h d'agitation, le solvant est évaporé et le mélange réactionnel (0,37 g) est purifié par chromatographie liquide basse pression (SiO_2 : 230–400 mesh, éluant : cyclohexane).

7,8-Bis-triméthylsilyl-9-triméthylsiloxy-bicyclo[4,3,0]non-6-ène (8) : 0,33 g, rdt. 88%. IR (film NaCl, cm^{-1}) : 3460, 2950, 2915, 2860, 1590, 1450, 1250, 1080, 850, 830, 750, 680. RMN ^1H ($CDCl_3$, 250 MHz) δ ppm : −0,09 (s, 9H, $SiMe_3$), −0,01 (s, 9H, $SiMe_3$), 0,0 (s, 9H, $SiMe_3$), 1,3 (m, 3H), 1,6 (m, 3H), 1,9 (m, 1H, H-8, $J_{8,9}$ 5,2 Hz), 2,0 (m, 2H), 2,7 (m, 1H, H-1, $J_{1,2}$ 2 Hz), 3,8 (m, 1H, H-9, $J_{8,9}$ 4 Hz). RMN ^{13}C ($CDCl_3$, 62,86 MHz) δ ppm, $SiMe_3$: −2,53, −0,93, 0,00; CH_2 : 24,3, 27,9, 31,2, 38,6; CH : 32,5, 52,9, 70,4; C : 142,4, 160,4. RMN ^{29}Si ($CDCl_3$, 39,73 MHz) δ ppm, ^nJ (^{29}Si,^1H) en Hz (nombre d'H couplés) : Si-7, −14,9, ^2J 6,6 (9H), ^3J 1,14 (1H), ^4J 1,14 (2H); Si-8, −0,5, ^2J 6,6 (9H), ^2J 4,1 (1H), ^3J 3,0 (1H); OSi, 13,6, ^2J 6,6 (9H), ^3J 3,5 (1H), ^4J 0,6 (1H).

1. (*a*) B.C. Clark, Jr., T.C. Chafin, P.L. Lee et G.L.K. Hunter. J. Org. Chem. **43**, 519 (1978); (*b*) K. Arata, J.O. Bleosoe, Jr. et R. Tanabe. Tetrahedron Lett. 3861 (1976); (*c*) R.M. Coates et L.A Last. J. Am. Chem. Soc. **105**, 7322 (1983); L.A. Last, E.R. Fretz et R.M. Coates. J. Org. Chem. **47**, 3211 (1982).
2. (*a*) M. Grignon-Dubois, J. Dunogues et R. Calas. Synthesis, 737 (1976); Tetrahedron Lett. **22**, 2883 (1981); (*b*) M. Ahra, M. Grignon-Dubois et J. Dunogues. J. Organomet. Chem. **271**, 15 (1984); M. Laguerre, M. Grignon-Dubois et J. Dunogues. Tetrahedron, **37**, 1161 (1981); M. Ahra et M. Grignon-Dubois. Bull. Soc. Chim. Fr. 820 (1985); (*c*) M. Grignon-Dubois, J. Dunogues et M. Ahra. Recl. Trav. Chim. Pays-Bas, **107**, 216 (1988).
3. N. Prilezhaev. Ber. **42**, 4811 (1909); D. Swern. Chem. Rev. **45**, 16 (1949); Org. React. **7**, 378 (1953).
4. S.N. Tandura, M.G. Voronkov et N.V. Alekseev. Top. Curr. Chem. **131**, 99 (1986).
5. C.A.G. Haasnoot, A.A.M.F. De Leeuw et C. Altona. Tetrahedron, **36**, 2783 (1980).
6. (*a*) M. Grignon-Dubois et M. Laguerre. Actual. Chim. 21 décembre 1983; (*b*) M. Grignon-Dubois, M. Laguerre, B. Barbe et M. Petraud. Organometallics, **3**, 359 (1984); (*c*) M. Grignon-Dubois, M. Ahra et M. Laguerre. J. Organomet. Chem. **348**, 157 (1988); (*d*) M. Grignon-Dubois et M. Laguerre. Comput. Chem. **9**, 279 (1985).
7. F.M. Hershenson et L. Christensen. Synth. Commun. **11**, 615 (1981); M. Taran. Thèse de Doctorat d'État, Bordeaux. 1983.
8. R. Arata, J.O. Bleosoe, Jr. et R. Tanabe. J. Org. Chem. **43**, 1660 (1978); H. Suga et H. Miyake. Synthesis, 395 (1988); J.W. Apsimon et S.F. Hall. Can. J. Chem. **56**, 2156 (1978); V.S. Joshi, N.P. Damodaran et S. Dev. Tetrahedron Lett. 475 (1971); R.S. Prasad et S. Dev. Tetrahedron Lett. 1437 (1976); V.S. Joshi, N.P. Damodaran et S. Dev. Tetrahedron Lett. 5817 (1968).
9. A. Fadel et J. Salaun. Tetrahedron Lett. **41**, 413 (1985); **41**, 1267 (1985).
10. J. Cymerman Craig, S.M. Torkelson, P.R. Findell et R.I. Weiner. Eur. J. Med. Chem. **32**, 961 (1989).
11. (*a*) R.J. Unwalla, S. Profeta, Jr. et F.K. Cartledge. J. Org. Chem. **53**, 5658 (1988); (*b*) M. Grignon-Dubois, M. Fialeix et J-M. Leger. Can. J. Chem. **71**, 754 (1993).
12. (*a*) W.P. Weber. Silicon reagents for organic synthesis. Springer-Verlag, Berlin. 1983; (*b*) E.W. Colvin. Silicon in organic synthesis. Butterworths, London. 1981; (*c*) I. Fleming, J. Dunogues et R. Smithers. Org. React. **37**, 55 (1989).
13. R.L. Danheiser, D.J. Carini, D.M. Fink et A. Basak. Tetrahedron, **39**, 935 (1983); R.L. Danheiser, D.J. Carini et Kwasigroch. J. Org. Chem. **51**, 3870 (1986).
14. (*a*) P.v.R. Schleyer, J.E. Williams et K.R. Blanchard. J. Am. Chem. Soc. **102**, 2377 (1970); (*b*) J.F. Liebman et A. Greenberg. Chem. Rev. **76**, 311 (1976).
15. (*a*) D.T. Pegg, D.M. Doddrell, W.M. Brooks and M.R. Bendall. J. Magn. Reson. **44**, 32 (1981); (*b*) D.M. Doddrell and D.T. Pegg. J. Am. Chem. Soc. **102**, 6388 (1980).
16. (*a*) S.A. Linde, H.J. Jakobsen et B.S. Kimber. J. Am. Chem. Soc. **97**, 3219 (1975); (*b*) K.G.R. Pachler et P.L. Wessels. J. Magn. Reson. **12**, 337 (1973); **28**, 3219 (1975).
17. (*a*) D.M. Doddrell, D.T. Pegg et M.R. Bendall. J. Magn. Reson. **48**, 323 (1982); (*b*) D.T. Pegg, D.M. Doddrell et M.R. Bendall. J. Chem. Phys. **77**, 2745 (1982).

Can. J. Chem. Downloaded from www.nrcresearchpress.com by ESC ESCOLA DE ENGENHARIA on 09/08/12
For personal use only.

Synthesis and separation of diastereomers of *O*-(2,2,2-trifluoroethyl)-3′,5′-dinucleoside phosphates

WEIDE LUO, ELENA ATRAZHEVA, NANCY FREGEAU, WILLIAM H. GMEINER,[1] AND J. WILLIAM LOWN[2]

Department of Chemistry, University of Alberta, Edmonton, AB T6G 2G2, Canada

Received August 10, 1993

WEIDE LUO, ELENA ATRAZHEVA, NANCY FREGEAU, WILLIAM H. GMEINER, and J. WILLIAM LOWN. Can. J. Chem. **72**, 1548 (1994).

The synthesis, diastereomeric separation, and characterization are described for a series of novel *O*-(2,2,2-trifluoroethyl)-3′,5′-dinucleoside phosphates, required for incorporation into antisense probes in the magnetic resonance imaging investigation of biodistribution. Preliminary assignment of the absolute configuration of the *R*p and *S*p diastereomers is made on the basis of ^{31}P NMR spectra.

WEIDE LUO, ELENA ATRAZHEVA, NANCY FREGEAU, WILLIAM H. GMEINER et J. WILLIAM LOWN. Can. J. Chem. **72**, 1548 (1994).

On décrit la synthèse, la séparation des diastéréoisomères et la caractérisation d'une série de nouveaux phosphates de *O*-(2,2,2-trifluoroéthyl)-3′,5′-dinucléosides requis pour l'incorporation dans des sondes pour une étude MRI de biodistribution. Faisant appel à la RMN du ^{31}P, on fait une attribution préliminaire de la configuration absolue des diastéréoisomères *R*p et *S*p.
[Traduit par la Rédaction]

Introduction

Synthetic oligonucleotides that have backbone modifications are useful as model compounds for studying DNA structure and dynamics (1, 2), and as probes for elucidating specific interactions of DNA with proteins and enzymes (3–5). Phosphoric triesters have long been studied as models of these modifications. The phosphoric triester linkage in oligonucleotides can be constructed by oxidative substitution of dinucleoside H-phosphonates with an alcohol (6), transesterification of dinucleoside phosphoric triesters (7), or alkylation of dinucleoside phosphoric diesters. As an example of the latter, two *O*-alkyl-5,5′-dinucleoside phosphates have been synthesized as potential anti-AIDS reagents (8).

The phosphoric triester linkage possesses a chiral centre at the phosphorus atom. The absolute configuration can be defined in the manner of Cahn et al. (9), by inspection of the four groups about the phosphorus atom. The *R*p and *S*p isomers of dinucleoside monophosphate methyl, ethyl, or trifluoroethyl triesters, so defined, are shown in Fig. 1. The stereochemistry of alkylated DNA phosphate groups has been shown to be of biochemical significance (10, 11). Stereochemistry is also clearly important when such modified DNAs are used as probes in structural studies or for antisense applications. Because dinucleoside monophosphate alkyl triesters are almost always produced as a mixture of diastereomers by various preparative methods, the separation of the diastereomers is required. This has often proved to be difficult.

We require certain trifluoroethyl phosphate triester derivatives of nucleosides to extend our studies on the application of ^{19}F NMR in magnetic resonance imaging (MRI) determination of biodistribution of antisense probes (12). In this paper, we present the synthesis of dinucleoside monophosphate 2,2,2-trifluoroethyl triesters, including dinucleotides of TT, TC, TA, CA, AT, and AA, by the phosphite-triester method and separation of the *S*p and *R*p diastereomers. Their absolute configurations were tentatively assigned by comparison of chemical shifts of ^{31}P NMR signals between diastereomers.

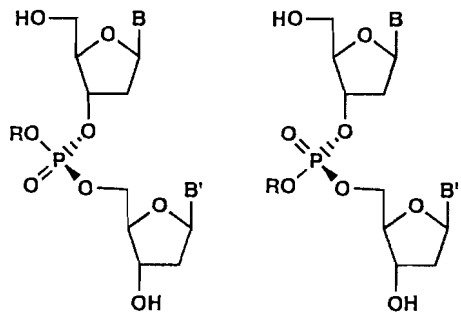

R = Me, Et *R*p *S*p
R = CH_2CF_3 *S*p *R*p

FIG. 1. Designation of *R*p and *S*p configurations of diastereomeric *O*-(2,2,2-trifluoroethyl)-3′,5′-inucleoside phosphates and the related methyl and ethyl derivatives.

Results and discussion

To avoid the difficulty of separation of diastereomeric mixtures of phosphoric triesters, we initially carried out the synthetic route as outlined in Scheme 1, in which the key intermediates, dinucleoside H-phosphonates **1**, were subjected to separation of P-diastereomers by flash chromatography on silica gel (13). The next steps to the target molecules (**4**) (sulfurization, alkylation of dinucleoside phosphothioates **2** with 2,2,2-trifluoroethyl iodide, and the oxidation of the resulting phosphoric thiotriesters **3** with *m*-chloroperbenzoic acid) were expected to be stereospecific (14). In the event, our attempts to generate *O*-(2,2,2-trifluoroethyl)dinucleoside phosphothioates **3** from compounds **2** by alkylation in the presence of bases such as pyridine, triethylamine, DABCO, and *N*,*N*-diisopropylethylamine were unsuccessful. The reason for the failure of alkylation is not clear. However, it is possible owing to the lower nucleophilicity of 2,2,2-trifluoroethyl iodide.

The synthesis of the dinucleotides by the phosphite-triester method, which has been applied in DNA solid-phase synthesis, proceeded in two steps: the preparation of deoxyribonucleoside-3′-*O*-(*N*,*N*-di-*iso*-propylamino)phosphoramidites (**5**, **6**, and **7**) and their coupling reactions with 3′-*O*-protected deoxyri-

[1]Present address: The Eppley Institute for Research in Cancer and Allied Diseases, Omaha, NE 68198-6805, U.S.A.

[2]Author to whom correspondence may be addressed.

Can. J. Chem. Downloaded from www.nrcresearchpress.com by ESC ESCOLA DE ENGENHARIA on 09/08/12
For personal use only.

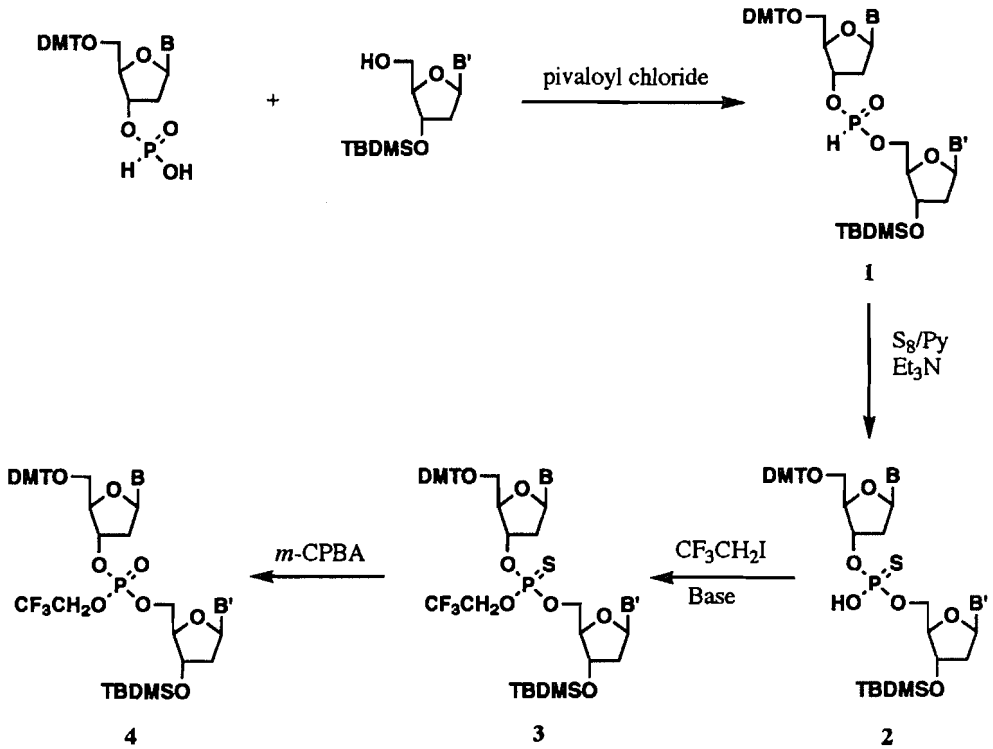

SCHEME 1. Outline of attempted synthesis of the desired *O*-(2,2,2-trifluoroethyl)-3′,5′-dinucleoside phosphates via and dinucleoside H-phosphonates.

bonucleosides under the catalysis of tetrazole followed by oxidation with iodine solution, as outlined in Scheme 2.

The phosphitylating reagent (**8**) was prepared in a similar manner as described for chloro-*N,N*-diisopropylamino methoxyphosphine (15). Phosphorus trichloride was allowed to react with 1 equivalent of 2,2,2-trifluoroethanol at low temperature for 5 h. The crude product of the reaction contained unreacted phosphorus trichloride, 2,2,2-trifluoroethyl phosphodichloridite (**9**), di-2,2,2-trifluoroethyl phosphochloridite, and tri(2,2,2-trifluoroethoxy)phosphine, which could be detected by their ^{31}P NMR signals (δ 219.0, 180.8, 166.0, and 139.3, respectively). The desired product **9** was isolated from the mixture by two successive fractional distillations in a yield of 31%. The purity of the compound obtained was proven by its ^{31}P NMR spectrum, in which only one signal at δ 180.8 was observed. The compound **8** was then prepared by the reaction of **9** with 2 equivalents of diisopropylamine in a solution of dichloromethane at low temperature in a yield of 70%. This reagent is extremely sensitive to moisture and air, but can be stored at −30°C for ex-tended periods (at least 2 months) under an argon atmosphere.

The 5′-protected nucleosides (**10**, **11**, and **12**) were prepared by reported methods (15). The syntheses of **5**, **6**, and **7** from **10**, **11**, and **12** with phosphitylating agent **8**, according to the procedure for their methyl analogues described by McBride and Caruthers (16), proceeded normally with yields of 94, 87, and 80%, respectively. Each of the products was an approximately 1:1 mixture of the *S*p and *R*p diastereomers, as indicated by ^{31}P NMR and ^{19}F NMR analyses.

Compounds **5** and **7** were initially used to couple directly to unprotected thymidine under the catalysis of tetrazole. After treatment with the oxidizing reagent *tert*-butyl hydrogen peroxide, dinucleotides **13** and **14** were obtained in yields of 42 and 31%, respectively. To improve the yield, we considered that protection on the 3′-hydroxy group in the deoxyribonucleoside might be beneficial. *tert*-Butyldimethylsilyl was the group of choice as the blocking functionality in this case. Compounds **15**, **16**, and **17** (17) were synthesized from **10**, **11**, and **12** by silylation with *tert*-butyldimethylsilyl chloride under the catalytic action of imidazole, followed by treatment with zinc bromide in dichloromethane to remove the 5′-dimethoxytrityl group (15). The coupling reaction of **5** and **17** (1:1 equiv.) with tetrazole as a catalyst was carried out at room temperature in acetonitrile for 4 h. The resulting dinucleoside phosphite triester was oxidized without isolation by a 0.1 M solution of iodine in a mixture of tetrahydrofuran, 2,6-lutidine, and water (40:10:1 by volume). The desired product **18** was obtained in 91% yield as a 1:1 mixture of diastereomers. By following a similar procedure, dinucleotides **19**, **20**, **21**, and **22** were also successfully prepared from appropriate nucleosides in good yields (85, 77, 93, and 77%, respectively). Removal of the silyl protecting group in each of the dinucleosides was achieved by treatment of the silyl ethers **18**, **19**, **20**, and **21** with tetrabutylammonium fluoride in tetrahydrofuran, affording compounds **25**, **13**, **23**, and **24**, respectively, in good yields.

The separations of the diastereomers, however, proved to be difficult. In the TLC analysis for these dinucleotides, only two of the compounds, **13** and **20**, showed detectable differences in R_f values between the diastereomers when the TLC plates were developed by a mixture of acetic acid and ethyl acetate (4:96, v/v). Therefore, the diastereomeric mixtures of **13** and **20** were separated by flash chromatography on silica gel eluted with the same solvent system to afford fast-moving diastereomers **13***a* and **20***a* and then the slowmoving **13***b* and **20***b* with good recovery yields (70–80 or 30–40% of each diastereomer). Other diastereomeric mixtures of dinucleotides, such as **14**, **19**, **22**, **24**, and **25**, were partially separated by flash chromatography on silica gel eluted with a gradually increasing proportion of methanol in chloroform solution. The optimum concentrations of

Can. J. Chem. Downloaded from www.nrcresearchpress.com by EESC ESCOLA DE ENGENHARIA on 09/08/12
For personal use only.

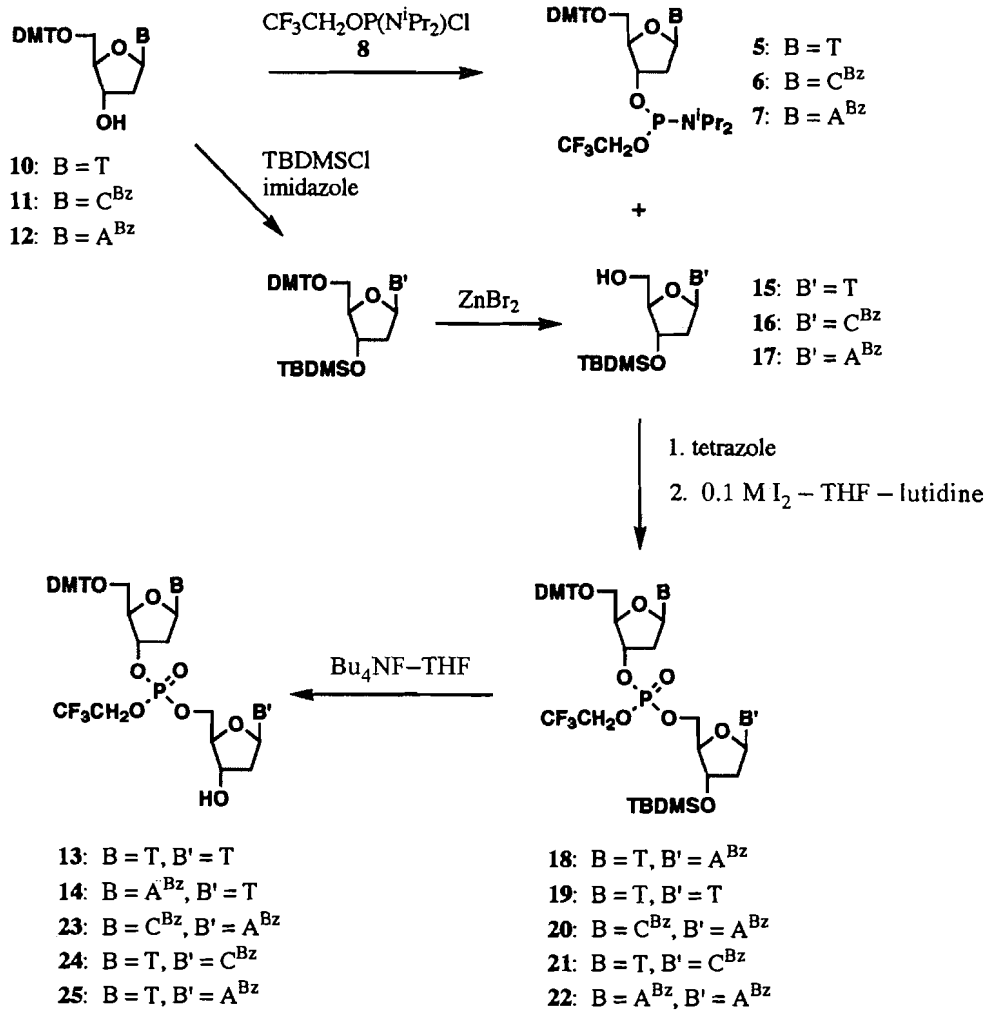

SCHEME 2. Outline of alternative and successful synthesis and separation of diastereomeric *O*-(2,2,2-trifluoroethyl)-3′,5′-dinucleoside phosphates via the 3′-*O*-(*N*,*N*-diisopropylamino)phosphoramidites.

TABLE 1. Separation and ^{31}P NMR data of the diastereomers

Dinucleotide	No.	Eluting solvent in separation	^{31}P NMR: δ of *R*p, *S*p diastereomer (fast, slow moving)	Solvent
TT	**13**	C	−1.46/−1.60	Py-d_5
AT	**14**	2–4.5% B	−2.71/−2.87	CD_3OD
TT	**19**	1–3% B	−2.26/−2.33	$CDCl_3$
CA	**20**	C	−2.28/−2.35	$CDCl_3$
AA	**22**	0.5–0.75% B	−2.20/−2.44	$CDCl_3$
TC	**24**	2–4.5% B	−1.34/−1.37	Py-d_5
TA	**25**	2–4.5% B	−1.67/−1.78	Py-d_5

NOTE: Solvent B, methanol in chloroform; solvent C, 4% acetic acid in ethyl acetate.

methanol for separation of the individual diastereomeric mixtures, as well as ^{31}P NMR data of the separated diastereomers, are listed in Table 1. The separations of each pair of diastereomers were followed by ^{31}P NMR analysis. As an example, the ^{31}P NMR spectra of separated diastereomers **22***a* and **22***b* are shown in Fig. 2. Each diastereomer in each pair showed very similar ^{1}H NMR spectra. The largest differences in chemical shift were usually observed for the base aromatic protons as shown in Fig. 3.

Potter and co-workers (18–20) have examined ^{31}P NMR spectra for a variety of dinucleoside methyl phosphotriesters of known configuration, and in all cases it was observed that the *S*p isomer resonates at lower field than the *R*p isomer. Similarly, Summers et al. (21) and Weinfeld et al. (7) found the signal from the *S*p isomer of ethylated internucleotide phosphate at a lower field than the equivalent signal from the *R*p isomer. Although dinucleoside 2,2,2-trifluoroethyl phosphotriesters have not been reported hitherto, ^{31}P NMR is our method of

Can. J. Chem. Downloaded from www.nrcresearchpress.com by EESC ESCOLA DE ENGENHARIA on 09/08/12
For personal use only.

Can. J. Chem. Downloaded from www.nrcresearchpress.com by EESC ESCOLA DE ENGENHARIA on 09/08/12
For personal use only.

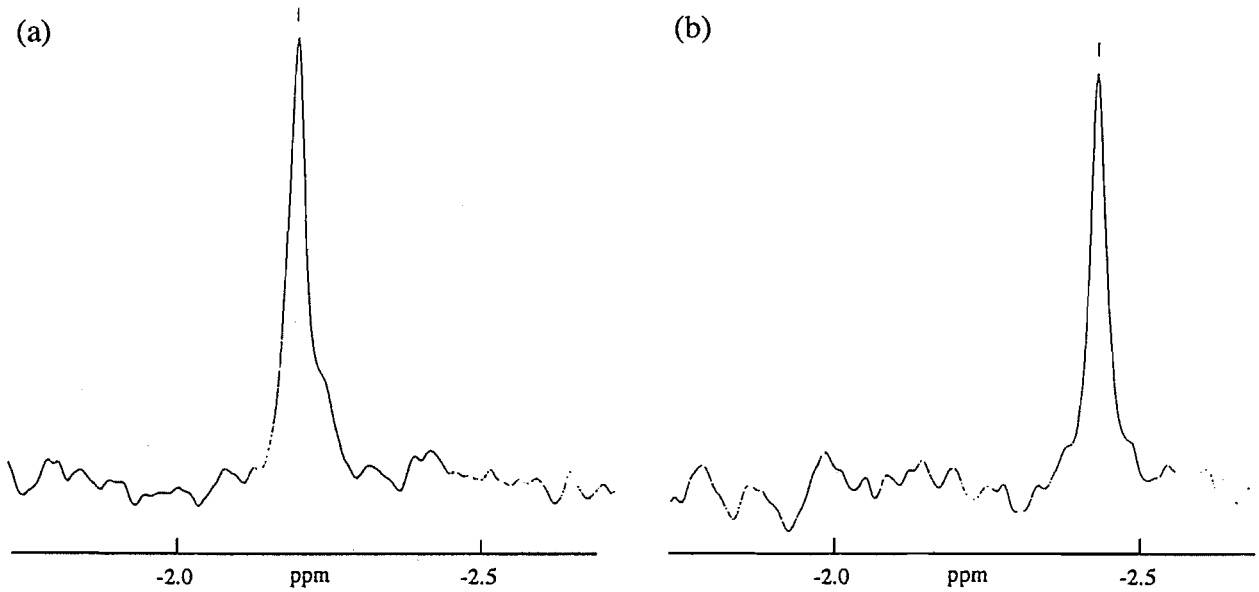

FIG. 2. ^{31}P NMR spectra of separated diastereomers **22***a* (*a*) and **22***b* (*b*).

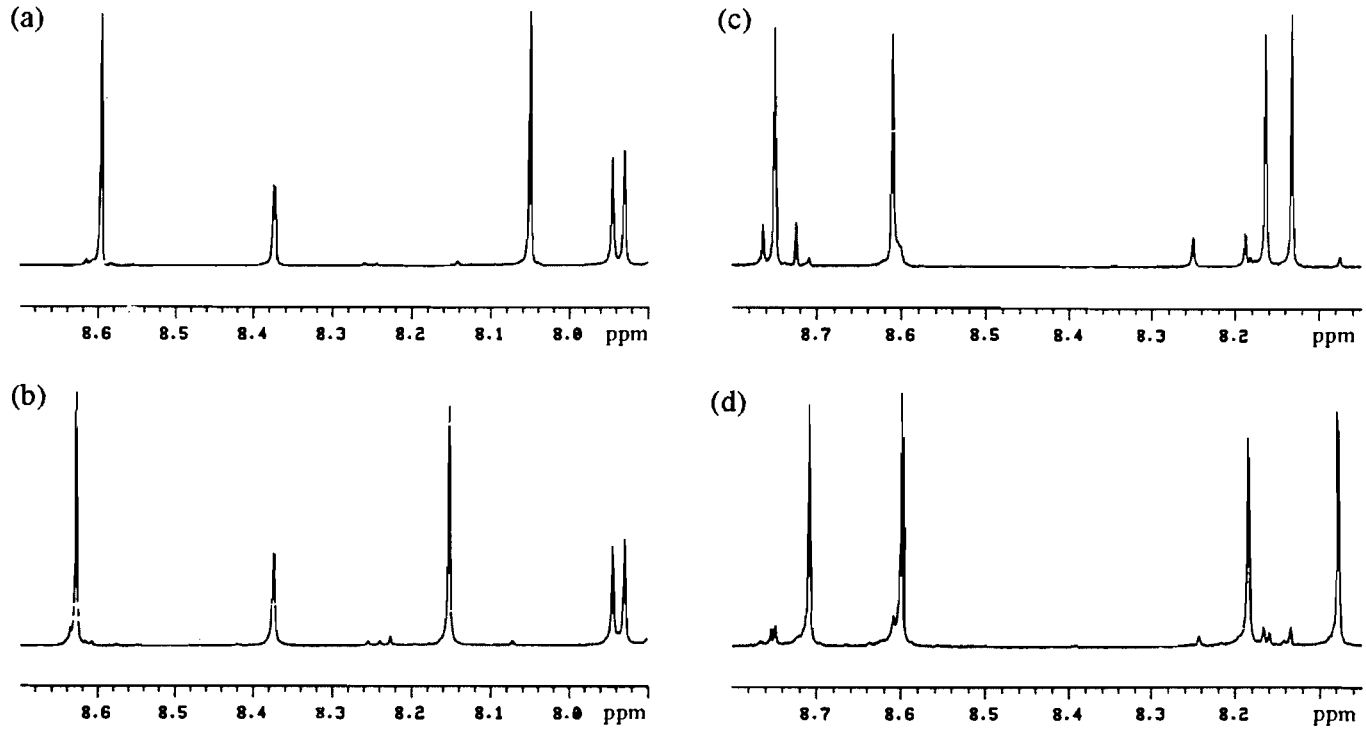

FIG. 3. Comparison of the ^1H NMR spectra of the base aromatic protons of **20***a* (*a*) and **20***b* (*b*) in $CDCl_3$–Py-d_5 (5:1), and **22***a* (*c*) and **22***b* (*d*) in $CDCl_3$.

choice for an initial examination of the absolute configuration about the phosphorus chiral centre. Considering that the weighting order of the four groups about the phosphorus atom in dinucleoside 2,2,2-trifluoroethyl phosphotriesters is different from that in the methyl or ethyl analogues, the faster moving isomers, from which the ^{31}P signal appears at lower field, are tentatively assigned as *R*p isomers and the slower moving isomers are assigned as *S*p. Studies directed towards a more definitive assignment of phosphorus configuration and towards the incorporation of diastereomeric *O*-(2,2,2-trifluoroethyl)-3′,5′-dinucleoside phosphates into specific antisense probes for MRI experiments are ongoing and will be reported in due course.

Experimental

General methods

NMR spectra were recorded on Bruker WH-200 or WH-400 spectrometers. ^1H, ^{19}F, and ^{31}P spectra were referenced to internal tetramethylsilane, external 50% trichlorofluoromethane in deuterium chloroform, and external 85% phosphoric acid in deuterium oxide, respectively. High-resolution mass spectra (HREIMS) and fast-atom bombardment mass spectra (FABMS) were recorded using A.E.I. model MS50 or MS9 mass spectrometers.

Can. J. Chem. Downloaded from www.nrcresearchpress.com by ESC ESCOLA DE ENGENHARIA on 09/08/12
For personal use only.

Acetonitrile and dichloromethane were distilled from phosphorus pentoxide, chloroform from anhydrous sodium carbonate, and pyridine from potassium hydroxide, toluene-4-sulfonyl chloride, or calcium hydride. Flash chromatography was performed with silica gel, 230–400 mesh ASTM. Merck silica gel plates (60 F_{254}) were used for analytical TLC, and the spots were examined with UV light and 1 N hydrochloric acid spray. Solvent systems for TLC development were as follows: A, Et_3N–EtOAc–CH_2Cl_2 (10:45:45); B, CH_3OH–$CHCl_3$ (1:9); C, AcOH–EtOAc (4:96). The concentrations of all solvent systems were determined by volume.

*2,2,2-Trifluoroethyl phosphodichloridite (**9**)*

2,2,2-Trifluoroethanol (97.3 g, 70 mL, 0.97 mol) contained in a pressure-equalizing dropping funnel was added dropwise over 2 h into magnetically stirred phosphorus trichloride (136.9 g, 87 mL, 1.00 mol) at −20°C, contained in a 250-mL three-necked flask vented via an air condenser equipped with a calcium chloride drying tube. During the addition, the temperature of the Dry Ice – acetone bath was maintained between −20 and −15°C. After the addition was completed, the temperature was allowed to increase to −5°C and maintained for 4 h. Then the bath was removed, and the mixture was allowed to warm up to room temperature with stirring (1 h) and set aside overnight in a fume hood to degas. The homogeneous liquid was fractionated by distillation at atmospheric pressure using a Vigreux column (300–400 mm long). The fraction boiling from 85 to 110°C was refractionated. The pure product (bp 94°C/700 Torr, 64 g, 0.30 mol) was obtained in 31% yield. ^{1}H NMR ($CDCl_3$) δ: 4.45 (dq, J = 8, 7.5 Hz); ^{31}P NMR ($CDCl_3$) δ: 180.84.

*Chloro-*N,N*-diisopropylamino-(2,2,2-trifluoroethoxy)phosphine (**8**)*

Under an argon atmosphere, a solution of diisopropylamine (17.83 g, 0.176 mol) in dichloromethane (40 mL), contained in a 100-mL addition funnel equipped with a calcium chloride drying tube, was added to a magnetically stirred solution of **9** (17.74 g, 0.088 mol) in dichloromethane (50 mL) in a 250-mL three-necked flask at −20°C. During the addition, the temperature of the Dry Ice – acetone bath was maintained between −20 and −10°C. Then the mixture was allowed to warm up slowly to room temperature over 3 h. The white precipitate of diisopropylamine hydrochloride was removed rapidly by vacuum filtration. The filtrate was concentrated by distillation at atmospheric pressure. The residue was fractionated under reduced pressure and the product (**8**, bp 73°C/11 Torr, 16.35 g, 0.0616 mol) was obtained in 70% yield. ^{1}H NMR ($CDCl_3$) δ: 4.04 (dq, 2H, J = 8, 8 Hz, CH_2), 3.74 (dh, 2H, J = 12, 7 Hz, CH), 1.5 (m, 12H, CH_3); ^{31}P NMR ($CDCl_3$) δ: 180.00; ^{19}F NMR ($CDCl_3$) δ: −75.25 (dq, J = 7, 8 Hz); HREIMS *m/e*: 267.0576, 265.0608 ($C_{H816}{}^{37}ClF_3NOP$ and $C_{H816}{}^{35}ClF_3NOP$, 5.19 and 11.41).

*General procedure for preparation of deoxyribonucleoside-3′-*O*-(*N,N*-diisopropylamino)-(2,2,2-trifluoroethyl)phosphoramidites*

Under an argon atmosphere, phosphitylating reagent **8** (1.65 mL, 1.99 g, 7.5 mmol) was injected over 10 s into a magnetically stirred solution of 5′-dimethoxytrityldeoxyribonucleoside **10**, **11**, or **12** (5.0 mmol) and diisopropylethylamine (2.58 g, 2.91 mL, 20.0 mmol) in dichloromethane (15 mL) at room temperature. The mixture was stirred for 20 min, ethanol (0.5 mL) was then added, and the mixture was stirred for 5 min to quench excess phosphitylating reagent. The reaction mixture was transferred to a 250-mL separatory funnel, diluted with a mixture of triethylamine and ethyl acetate (1:20, 100 mL), and washed with 10% aqueous sodium carbonate (2 × 60 mL) and then with saturated aqueous sodium chloride (60 mL). The organic phase was dried over anhydrous sodium sulfate, filtered, and evaporated to a foam under reduced pressure. The crude product was purified by flash chromatography using a mixture of triethylamine, ethyl acetate, dichloromethane, and petroleum ether in the ratio of 1:10:10:20 as eluent. The desired product was obtained in the yield of 80–95%.

*(R*p*,S*p*)-5′-*O*-(4,4′-Dimethoxytrityl)thymidine-3′-*O*-(*N,N*-diisopropylamino)-(2,2,2-trifluoroethyl)phosphoramidites (**5**)*

From **10** (5.0 mmol), **5** (3.64 g, 4.70 mmol) was isolated in 94% yield. TLC (silica gel, solvent A) R_f 0.80; ^{1}H NMR ($CDCl_3$) δ: 8.10 (bs, 1H, NH), 7.67 and 7.58 (s, 1H, H6), 7.4–7.2 (m, 9H, ArH), 6.83 (d, 4H, J = 8 Hz, ArH), 6.40 (m, 1H, H1′), 4.66 (m, 1H, H3′), 4.20 and 4.14 (m, 1H, H4′), 3.98 (m, 2H, CF_3CH_2), 3.80 (s, 6H, CH_3O), 3.60 (m, 2H, $CH(CH_3)_2$), 3.50 and 3.33 (m, 1H each, H5′ and H5″), 2.50 and 2.33 (m, 2H, H2′ and H2″), 1.40 and 1.42 (s, 3H, 5-CH_3), 1.20 (m, 12H, $CH(CH_3)_2$); ^{31}P NMR ($CDCl_3$) δ: 152.89 and 152.62 (1:1, q, J = 6 Hz); ^{19}F NMR ($CDCl_3$) δ: −75.10 and −75.28 (1:1, dt, J = 6, 9 Hz); FABMS *m/e*: 774 ($M + H^+$).

*(R*p*,S*p*)-N^4-Benzoyl-5′-(4,4′-dimethoxytrityl)-2′-deoxycytidine-3′-*O*-(N,N-diisopropylamino)-(2,2,2-trifluoroethyl)phosphoramidites (**6**)*

From **11** (5.0 mmol), **6** (3.75 g, 4.35 mmol) was isolated in 87% yield. TLC (silica gel, solvent A) R_f 0.75; ^{1}H NMR ($CDCl_3$) δ: 9.10 (bs, 1H, NH), 8.35 and 8.30 (d, 1H, J = 7 Hz, H6), 7.90 (d, 2H, J = 8 Hz, BzH), 7.62 (t, 1H, J = 8 Hz, BzH), 7.52 (t, 2H, J = 8 Hz, BzH), 7.42 (d, 1H, J = 7 Hz, H5), 7.3 (m, 9H, ArH), 6.88 (d, 4H, J = 8 Hz, ArH), 6.32 and 6.30 (dd, 1H, J = 6, 6 Hz, H1′), 4.66 (m, 1H, H3′), 4.28 and 4.24 (m, 1H, H4′), 3.97 and 3.87 (ddq, 1H each, J = 12, 8, 8 Hz, CF_3CH_2), 3.81 (s, 6H, CH_3O), 3.63 (m, 2H, $CH(CH_3)_2$), 3.50 and 3.43 (m, 1H each, H5′ and H5″), 2.80 and 2.33 (m, 2H, H2′ and H2″), 1.20 (m, 12H, $CH(CH_3)_2$); ^{31}P NMR ($CDCl_3$) δ: 153.07 and 152.66 (1:1, q, J = 6 Hz); ^{19}F NMR ($CDCl_3$) δ: −75.05 and −75.04 (1:1, dt, J = 6, 9 Hz); FABMS *m/e*: 863 ($M + H^+$).

*(R*p*,S*p*)-N^6-Benzoyl-5′-(4,4′-dimethoxytrityl)-2′-deoxyadenosine-3′-*O*-(N,N-diisopropylamino)-(2,2,2-trifluoroethyl)-phosphoramidites (**7**)*

From **12** (5.0 mmol), **7** (4.0 mmol) was isolated in 80% yield. TLC (silica gel, solvent A) R_f 0.80; ^{1}H NMR ($CDCl_3$) δ: 9.10 (bs, 1H, NH), 8.70 (s, 1H, H2), 8.20 and 8.15 (s, 1H, H8), 8.00 (d, 2H, J = 8 Hz, BzH), 7.65 (t, 1H, J = 8 Hz, BzH), 7.50 (t, 2H, J = 8 Hz, BzH), 7.4–7.2 (m, 9H, ArH), 6.75 (d, 4H, J = 8 Hz, ArH), 6.48 (m, 1H, H1′), 4.77 (m, 1H, H3′), 4.28 and 4.32 (m, 1H, H4′), 3.82 and 3.80 (dq, 1H each, J = 9, 9 Hz, CF_3CH_2), 3.74 (s, 6H, CH_3O), 3.60 (m, 2H, $CH(CH_3)_2$), 3.40 and 3.31 (m, 1H each, H5′ and H5″), 2.92 and 2.66 (m, 2H, H2′ and H2″), 1.20 (m, 12 H, $CH(CH_3)_2$); ^{31}P NMR ($CDCl_3$) δ: 152.90 and 152.70 (1:1, q, J = 6 Hz); ^{19}F NMR ($CDCl_3$) δ: −75.07 and −75.08 (1:1, dt, J = 6, 9 Hz); FABMS *m/e*: 909 and 807 ($M + Na^+$ and $M + H^+$).

*(R*p*,S*p*)-5′-*O*-(4,4′-Dimethoxytrityl)thymidylyl-3′,5′-N^6-benzoyl-3′-*O*-[(1,1-dimethylethyl)dimethylsilyl]-2′-deoxyadenosine (2,2,2-trifluoroethyl)phosphates (**18**)*

Under an argon atmosphere, phosphoramidite **5** (1.70 g, 2.2 mmol) and tetrazole (0.28 g, 4.06 mmol) were added to a magnetically stirred solution of **17** (0.938 g, 2.00 mmol) in acetonitrile (50 mL). The mixture was stirred at room temperature for 4 h and then 0.10 M iodine solution in a mixture of tetrahydrofuran, 2,6-lutidine, and water (40:10:1 by volume, 22 mL) was added. The mixture was stirred for 10 min and then transferred to a 250-mL separatory funnel and diluted with ethyl acetate (100 mL). The liquid was washed with saturated aqueous sodium bicarbonate (2 × 60 mL) and then with saturated aqueous sodium chloride (60 mL). The aqueous phases were extracted with ethyl acetate (2 × 50 mL). The organic phases were combined, dried over anhydrous sodium sulfate, filtered, and concentrated under reduced pressure to a foam (2.76 g). The crude residue was subjected to flash chromatography with 3% solution of methanol in chloroform as eluent, giving dinucleotides **18** as a 1:1 mixture of two diastereomers (2.11 g, 1.82 mmol, 91% yield). TLC (silica gel, solvent B) R_f 0.52; ^{1}H NMR ($CDCl_3$) δ: 9.10 (bs, 1H, NH), 8.75 and 8.44 (m, 1H each, H2 and H8), 8.22 and 8.20 (s, 1H, H6), 8.00 (m, 2H, BzH), 7.60 (m, 1H, BzH), 7.50 (m, 2H, BzH), 7.36–7.20 (m, 9H, ArH), 6.82 (m, 4H, ArH), 6.52 (dd, 0.5H, H1′), 6.45 and 6.43 (m, 1.5H, H1′), 5.12 (m, 1H, H3′), 4.70 (m, 1H, H3′), 4.4–4.1 (m, 6H, H4′, H4′, CF_3CH_2, H5′, and H5″), 3.77 (s, 6 H, CH_3O), 3.47 and 3.33 (m, 1H each, H5′ and H5″), 2.91, 2.57, 2.49, and 2.38 (m, 1H each, H2′ and H2″), 1.37 and 1.35 (s, 3H, 5-CH_3), 0.91 and 0.92 (s, 9H, $C(CH_3)_3$), 0.12 (s, 6H,

Can. J. Chem. Downloaded from www.nrcresearchpress.com by EESC ESCOLA DE ENGENHARIA on 09/08/12
For personal use only.

$Si(CH_3)_2$); ^{31}P NMR ($CDCl_3$) δ: −1.90 and −2.42 (1:1); ^{19}F NMR ($CDCl_3$) δ: −75.27 and −75.37 (1:1, t, J = 8 Hz); FABMS *m/e*: 1180 and 1158 (M + Na^+ and M + H^+).

*(Rp,Sp)-5′-O-(4,4′-Dimethoxytrityl)thymidylyl-3′,5′-N^6-benzoyl-2′-deoxyadenosine (2,2,2-trifluoroethyl)phosphates (**25***a* and **25***b*)*

To a solution of **18** (310 mg, 0.272 mmol) in tetrahydrofuran (5 mL) was added 1 M tetrabutylammonium fluoride solution in tetrahydrofuran (containing 5% water, 1 mL). The mixture was stirred at room temperature for 20 min and then concentrated under reduced pressure. The residue was subjected to flash chromatography on silica gel with 0–6% methanol in chloroform. Products **25***a* and **25***b* (260 mg, 0.249 mmol) were obtained in 92% yield as a 1:1 mixture of two diastereomers: ^{31}P NMR (Py-d_5) δ: −1.67 and −1.78; FABMS *m/e*: 1066 and 1044 (M + Na^+ and M + H^+). The isomers were partially separated by further flash chromatography on silica gel, eluted with 2–4.5% methanol in chloroform. The percentage of methanol was increased at the rate of 0.25%/200 mL. With TLC analysis, compounds **25***a* and **25***b* were distributed in 30 of 60 eluted fractions. The first 5 fractions afforded 90% pure isomer **25***a* (25 mg). TLC (silica gel, solvent B) R_f 0.30; ^1H NMR (Py-d_5) δ: 13.3 and 12.3 (bs, 1H each, NH), 8.97 and 8.89 (s, 1H each, H2 and H8), 8.54 (s, 1H, H6), 8.28 (d, 2H, BzH), 7.68 (m, 3H, BzH), 7.55–7.36 (m, 8H, ArH), 7.27 (t, 1H, J = 8 Hz, ArH), 7.00 (d, 4H, J = 8 Hz, ArH), 6.90–6.80 (m, 2H, H1′), 5.60 (m, 1H, H3′), 5.10 (m, 1H, H3′), 4.82 (m, 2H, CF_3CH_2), 4.70 (m, 2H, H5′ and H5″), 4.64 (m, 1H, H4′), 4.56 (m, 1H, H4′), 3.67 (s, 6H, CH_3O), 3.63 (m, 2H, H5′ and H5″), 3.17 (ddd, 1H, J = 13, 6.5, 6.5 Hz, H2′ or H2″), 2.87 (m, 1H, H2′ or H2″), 2.75 (m, 2H, H2′ and H2″), 1.70 (s, 3H, 5-CH_3); ^{31}P NMR (Py-d_5) δ: −1.67; ^{19}F NMR (Py-d_5) δ: −75.01 (t, J = 8 Hz). The last 5 fractions gave the other isomer (**25***b*, 92% pure, 20 mg). TLC (silica gel, solvent B) R_f 0.30; ^1H NMR (Py-d_5) δ: 13.3 and 12.3 (bs, 1H each, NH), 8.96 and 8.84 (s, 1H each, H2 and H8), 8.54 (s, 1H, H6), 8.30 (d, 2H, BzH), 7.68 (m, 3H, BzH), 7.55–7.36 (m, 8H, ArH), 7.27 (t, 1H, J = 8 Hz, ArH), 7.00 (d, 4H, J = 8 Hz, ArH), 6.90–6.80 (m, 2H, H1′), 5.60 (m, 1H, H3′), 5.10 (m, 1H, H3′), 4.79 (m, 2H, CF_3CH_2), 4.72 (m, 2H, H5′ and H5″), 4.65 (m, 1H, H4′), 4.54 (m, 1H, H4′), 3.67 (s, 6H, CH_3O), 3.63 (m, 2H, H5′ and H5″), 3.19 (ddd, 1H, J = 13, 6.5, 6.5 Hz, H2′), 2.87 (m, 1H, H2′ or H2″), 2.75 (m, 2H, H2′ or H2″), 1.70 (s, 3H, 5-CH_3); ^{31}P NMR (Py-d_5) δ: −1.78; ^{19}F NMR (Py-d_5) δ: −75.00 (t, J = 8 Hz). From other fractions, the diastereomeric mixture of **25***a* and **25***b* (182 mg) was recovered.

*(Rp,Sp)-5′-O-(4,4′-Dimethoxytrityl)thymidylyl-3′,5′-3′-O-[(1,1-dimethylethyl)dimethylsilyl]thymidine 2,2,2-trifluoroethyl)-phosphates (**19**a and **19**b)*

Using a similar procedure as for **18**, from **5** (2.38 g, 3.08 mmol) and **15** (0.98 g, 2.75 mmol), **19** (2.31 g, 2.21 mmol, 80% yield) was obtained as a 1:1 mixture of two diastereomers, which were partially separated in the manner as described for **25***a* and **25***b* with 1–3% methanol in chloroform as eluent. Compound **19***a*: TLC (silica gel, solvent B) R_f 0.50; ^1H NMR ($CDCl_3$) δ: 9.10 (bs, 2H, NH), 7.50 (m, 1H, H6), 7.40–7.10 (m, 10H, H6 and ArH), 6.83 (d, 4H, J = 8 Hz, ArH), 6.18 (m, 2H, H1′), 5.15 (m, 1H, H3′), 4.4–4.1 (m, 5H, H3′, CF_3CH_2, H5′, and H5″), 3.95 (m, 2H, H4′), 3.75 (s, 6H, CH_3O), 3.52 and 3.40 (m, 1H each, H5′ and H5″), 2.60, 2.50, 2.40 and 2.20 (m, 1H each, H2′ and H2″), 1.85 and 1.45 (d, 3H each, J = 1 Hz, 5-CH_3), 0.90 (s, 9H, $C(CH_3)_3$), 0.05 (s, 6H, $Si(CH_3)_2$); ^{31}P NMR ($CDCl_3$) δ: −2.26; ^{19}F NMR ($CDCl_3$) δ: −75.24 (t, J = 8 Hz); FABMS *m/e*: 1067 (M + Na^+). Compound **19***b*: TLC (silica gel, solvent B) R_f 0.50; ^1H NMR ($CDCl_3$) δ: 9.10 (bs, 2H, NH), 7.50 (m, 1H, H6), 7.40–7.10 (m, 10H, H6 and ArH), 6.82 (d, 4H, J = 8 Hz, ArH), 6.43 (dd, 1H, J = 9, 5 Hz, H1′), 6.16 (t, 1H, J = 7 Hz, H1′), 5.15 (m, 1H, H3′), 4.4–4.1 (m, 5H, H3′, CF_3CH_2, H5′, and H5″), 3.95 (m, 2H, H4′), 3.75 (s, 6H, CH_3O), 3.52 and 3.35 (m, 1H each, H5′ and H5″), 2.60, 2.50, 2.40, and 2.20 (m, 1H each, H2′ and H2″), 1.85 and 1.40 (d, 3H each, J = 1 Hz, 5-CH_3), 0.90 (s, 9H, $C(CH_3)_3$), 0.05 (s, 6H, $Si(CH_3)_2$); ^{31}P NMR ($CDCl_3$) δ: −2.26; ^{19}F NMR ($CDCl_3$) δ: −75.24 (t, J = 8 Hz); FABMS *m/e*: 1067 (M + Na^+).

*(Rp,Sp)-5′-O-(4,4′-Dimethoxytrityl)thymidylyl-3′,5′-thymidine (2,2,2-trifluoroethyl)phosphates (**13**a and **13**b)*

Desilylation method

Using the desilylation procedure described for **18**, **19** (0.47 g, 0.45 mmol) gave an 85% yield of a 1:1 diastereomeric mixture of **13***a* and **13***b* (0.36 g, 0.38 mmol). The mixture was separated by flash chromatography on silica gel, eluted with 4% acetic acid in ethyl acetate, giving 18% of **13***a*, 13% of diastereomeric mixture, and 20% of **13***b*. Compound **13***a*: TLC (silica gel, solvent B) R_f 0.27 and TLC (silica gel, solvent C) R_f 0.29; ^1H NMR (Py-d_5) δ: 13.25 (bs, 2H, NH), 7.75–7.24 (m, 11H, H6 and ArH), 7.02 (d, 4H, J = 9 Hz, ArH), 6.83 (m, 2H, H1′), 5.70 (m, 1H, H3′), 4.92 (p, 2H, CF_3CH_2), 4.80 (m, 1H, H3′), 4.65 (m, 3H, H4′, H5′, and H5″), 4.45 (m, 1H, H4′), 3.75 (s, 6H, CH_3O), 3.67 (m, 2H, H5′ and H5″), 2.86 and 2.54 (m, 2H each, H2′ and H2″), 2.05 and 1.70 (d, 3H each, J = 1 Hz, 5-CH_3); ^{31}P NMR (Py-d_5) δ: −1.46; ^{19}F NMR (Py-d_5) δ: −74.99 (t, J = 8 Hz); FABMS *m/e*: 953 (M + Na^+). Compound **13***b*: TLC (silica gel, solvent B) R_f 0.27 and TLC (silica gel, solvent C) R_f 0.20; ^1H NMR (Py-d_5) δ: 13.2 (bs, 2H, NH), 7.7–7.2 (m, 11H, H6 and ArH), 7.00 (d, 4H, J = 9 Hz, ArH), 6.90–6.78 (m, 2H, H1′), 5.70 (m, 1H, H3′), 4.85 (m, 3H, H3′ and CF_3CH_2), 4.70–4.45 (m, 4H, H4′, H5′, and H5″), 3.7 (s, 6H, CH_3O), 3.67 (m, 2H, H5′ and H5″), 2.91 and 2.62 (m, 2H each, H2′ and H2″), 2.05 and 1.67 (d, 3H each, J = 1 Hz, 5-CH_3); ^{31}P NMR (Py-d_5) δ: −1.60; ^{19}F NMR (Py-d_5) δ: −74.98 (t, J = 8 Hz); FABMS *m/e*: 953 (M + Na^+).

Direct method

Thymidine (245 mg, 1.00 mmol) was dried by coevaporation with acetonitrile and pyridine (5:1, 2 × 5 mL) under reduced pressure. Under an argon atmosphere, the thymidine was dissolved in pyridine (3 mL) and a solution of **5** (512 mg, 0.661 mmol) in acetonitrile (10 mL), which was saturated with tetrazole, was added by syringe. The mixture was stirred at room temperature overnight. *tert*-Butyl hydrogen peroxide solution in 2,2,4-trimethylpentane (3 M, 0.33 mL) was added. After stirring for 10 min, the mixture was poured into aqueous saturated sodium chloride (30 mL) and extracted with chloroform (2 × 40 mL). The extracts were combined, dried over anhydrous sodium sulfate, filtered, and concentrated under reduced pressure. The residue was subjected to flash chromatography on silica gel. Elution with 6% methanol in chloroform gave products **13***a* and **13***b* as a 1:1 diastereomeric mixture (258 mg, 0.278 mmol, 42% yield).

*(Rp,Sp)-N^6-Benzoyl-5′-(4,4′-dimethoxytrityl)-2′-deoxyadenoylyl-3′,5′-thymidine (2,2,2-trifluoroethyl)phosphates (**14**a and **14**b)*

Using a similar procedure as described for **13** (direct method) from **7** (886 mg, 1.0 mmol) and thymidine (290 mg, 1.2 mmol), **14** (318 mg, 0.31 mmol, 31% yield) was obtained as a 1:1 mixture of diastereomers. The mixture was partially separated in the manner as described for **25**, giving **14***a* and **14***b*. Compound **14***a*: TLC (silica gel, solvent B) R_f 0.32; ^1H NMR (CD_3OD) δ: 13.3 and 10.3 (bs, 1H each, NH), 8.57 (s, 1H, H2), 8.46 (s, 1H, H8), 8.07 (d, 2H, J = 8 Hz, BzH), 7.65 (d, 1H, J = 8 Hz, BzH), 7.55 (t, 2H, J = 8 Hz, BzH), 7.42 (q, 1H, J = 1 Hz, H6), 7.37–7.12 (m, 7H, ArH), 6.78 (d, 4H, J = 8 Hz, ArH), 6.53 and 6.21 (t, 1H each, J = 6.5 Hz, H1′), 5.48 (m, 1H, H3′), 4.63 (dq, 2H, J = 8, 8 Hz, CF_3CH_2), 4.48–4.33 (m, 4H, H3′, H5′, H5″, and H4′), 4.05 (m, 1H, H4′), 3.73 (s, 6H, CH_3O), 3.40 (m, 2H, H5′ and H5″), 2.90–2.80 and 2.28–2.23 (m, 2H each, H2′ and H2″), 1.81 (s, 3H, 5-CH_3); ^{31}P NMR (CD_3OD) δ: −2.71; ^{19}F NMR (CD_3OD) δ: −76.88 (t, J = 8 Hz); FABMS *m/e*: 1066 (M + Na^+). Compound **14***b*: TLC (silica gel, solvent B) R_f 0.32; ^1H NMR (CD_3OD) δ: 13.3 and 10.3 (bs, 1H each, NH), 8.56 (s, 1H, H2), 8.43 (s, 1H, H8), 8.07 (d, 2H, J = 8 Hz, BzH), 7.65 (d, 1H, J = 8 Hz, BzH), 7.55 (t, 2H, J = 8 Hz, BzH), 7.47 (q, 1H, J = 1 Hz, H6), 7.37–7.12 (m, 7H, ArH), 6.75 (d, 4H, J = 8 Hz, ArH), 6.52 and 6.20 (t, 1H each, J = 6.5 Hz, H1′), 5.42 (m, 1H, H3′), 4.59 (dq, 2H, J = 8, 8 Hz, CF_3CH_2), 4.48–4.33 (m, 4H, H3′, H5′, H5″, and H4′), 4.05 (m, 1H, H4′), 3.73 (s, 6H, CH_3O), 3.40 (m, 2H, H5′ and H5″), 2.90–2.80 and 2.28–2.23 (m, 2H each, H2′ and H2″), 1.80 (s, 3H, 5-CH_3); ^{31}P NMR (CD_3OD) δ: −2.87; ^{19}F NMR (CD_3OD) δ: −76.85 (t, J = 8 Hz); FABMS *m/e*: 1066 (M + Na^+).

Can. J. Chem. Downloaded from www.nrcresearchpress.com by ESC ESCOLA DE ENGENHARIA on 09/08/12
For personal use only.

*(Rp,Sp)-N^4-Benzoyl-5′-(4,4′-dimethoxytrityl)-2′-deoxycytidylyl-3′,5′-N^6-benzoyl-3′-O-[(1,1dimethylethyl)dimethylsilyl]-2′-deoxyadenosine (2,2,2-trifluoroethyl)phosphates (**20**a and **20**b)*

Using a similar procedure as described for **18**, from **6** (2.62 g, 3.04 mmol) and **17** (1.23 g, 2.62 mmol), **20** (2.52 g, 2.02 mmol, 77% yield) was obtained as a 1:1 mixture of two diastereomers. The mixture (500 mg) was separated by flash chromatography on silica gel, eluted with 4% acetic acid in ethyl acetate, giving **20***a* (180 mg, 36%) and **20***b* (216 mg, 43%). Compound **20***a*: TLC (silica gel, solvent B) R_f 0.61 and TLC (silica gel, solvent C) R_f 0.32; ^{1}H NMR ($CDCl_3$) δ: 9.25 (bs, 1H, NH), 8.67 and 8.24 (s, 1H each, H2 and H8), 8.10 (d, 1H, J = 7.5 Hz, H6), 8.05 and 7.93 (dd, 2H each, J = 8, 1 Hz, BzH), 7.55 and 7.50 (td, 1H each, J = 8, 1 Hz, BzH), 7.45 and 7.42 (t, 2H each, BzH), 7.36–7.19 (m, 10H, ArH and H5), 6.95 (dd, 4H, J = 8, 1 Hz, ArH), 6.46 and 6.31 (t, 1H each, J = 7.5 Hz, H1′), 5.11 (m, 1H, H3′), 4.71 (ddd, 1H, J = 6, 4.5, 4.5 Hz, H3′), 4.43–4.24 and 4.16 (m, 6H, H4′, CF_3CH_2, H5′, and H5″), 3.72 (s, 6H, CH_3O), 3.44 (m, 2H, H5′ and H5″), 2.99–2.91 (m, 2H, H2′ and (or) H2″), 2.46 (ddd, 1H, J = 14, 5.5, 4.5 Hz, H2′ or H2″), 2.36 (m, 1H, H2′ or H2″), 0.93 (s, 9H, $C(CH_3)_3$), 0.15 (s, 6H, $Si(CH_3)_2$); ^{31}P NMR ($CDCl_3$) δ: −2.28; ^{19}F NMR ($CDCl_3$) δ: −75.23 (t, J = 8 Hz); FABMS *m/e*: 1269 (M + Na^+). Compound **20***b*: TLC (silica gel, solvent B) R_f 0.61 and TLC (silica gel, solvent C) R_f 0.22; ^{1}H NMR ($CDCl_3$) δ: 9.25 (bs, 1H, NH), 8.78 and 8.30 (s, 1H each, H2 and H8), 8.10 (d, 1H, J = 7.5 Hz, H6), 8.00 and 7.90 (dd, 2H each, J = 8, 1 Hz, BzH), 7.50 and 7.46 (td, 1H each, J = 8, 1 Hz, BzH), 7.40 and 7.36 (t, 2H each, BzH), 7.34–7.16 (m, 10H, ArH and H5), 6.81 (dd, 4H, J = 8, 1 Hz, ArH), 6.45 and 6.28 (t, 1H each, J = 7.5 Hz, H1′), 5.13 (m, 1H, H3′), 4.73 (ddd, 1H, J = 6, 4.5, 4.5 Hz, H3′), 4.39–4.18 and 4.16 (m, 6 H, H4′, CF_3CH_2, H5′, and H5″), 3.68 (s, 6H, CH_3O), 3.42 and 5.38 (dd, 1H each, J = 11, 3.5 Hz, H5′ and H5″), 2.96 (ddd, 1H, J = 13, 6.5, 6.5 Hz, H2′ or H2″), 2.91 (ddd, 1H, J = 14, 5.5, 2.5 Hz, H2′ or H2″), 2.43 (ddd, 1H, J = 14, 5.5, 4.5 Hz, H2′ or H2″), 2.32 (m, 1H, H2′ or H2″), 0.90 (s, 9H, $C(CH_3)_3$), 0.10 (s, 6H, $Si(CH_3)_2$); ^{31}P NMR ($CDCl_3$) δ: −2.35; ^{19}F NMR ($CDCl_3$) δ: −75.29 (t, J = 8 Hz); FABMS *m/e*: 1269 (M + Na^+).

*(Rp,Sp)-N^4-Benzoyl-5′-(4,4′-dimethoxytrityl)-2′-deoxycytidylyl-3′,5′-N^6-benzoyl-2′-deoxyadenosine (2,2,2-trifluoroethyl)phosphates (**23**a and **23**b)*

Using the desilylation procedure described for **18**, **20***a* (70 mg, 0.056 mmol) gave **23***a* (30 mg, 0.027 mmol, 48% yield). TLC (silica gel, solvent B) R_f 0.30 and TLC (silica gel, solvent C) R_f 0.35; ^{1}H NMR (Py-d_5) δ: 13.5 and 12.3 (bs, 1H each, NH), 8.71 and 8.52 (s, 1H each, H2 and H8), 8.09 (d, 1H, J = 7.5 Hz, H6), 8.05 and 7.94 (dd, 2H each, J = 8, 1 Hz, BzH), 7.41–7.03 (m, 16H, ArH and H5), 6.75 (dd, 4H, J = 8, 1 Hz, ArH), 6.50 and 6.30 (t, 1H each, J = 6.5 Hz, H1′), 5.27 (m, 1H, H3′), 4.87 (m, 1H, H3′), 4.55–4.35 (m, 6H, H4′, CF_3CH_2, H5′, and H5″), 3.49 (s, 6H, CH_3O), 3.41 (m, 2H, H5′ and H5″), 2.97 (ddd, 1H, J = 14, 6.5, 6 Hz, H2′ or H2″), 2.92 (ddd, 1H, J = 14, 6.5, 2.5 Hz, H2′ or H2″), 2.53 (ddd, 1H, J = 14, 6.5, 4.5 Hz, H2′ or H2″), 2.43 (ddd, 1H, J = 14, 6.5, 7 Hz, H2′ or H2″); ^{31}P NMR (Py-d_5) δ: −1.76; ^{19}F NMR (Py-d_5) δ: −75.39 (t, J = 8 Hz); FABMS *m/e*: 1155 (M + Na^+).

Using the desilylation procedure described for **18**, **20***b* (200 mg, 0.161 mmol) gave 47% yield of **23***b* (85 mg, 0.075 mmol). TLC (silica gel, solvent B) R_f 0.30 and TLC (silica gel, solvent C) R_f 0.35; ^{1}H NMR (Py-d_5) δ: 13.5 and 12.3 (bs, 1H each, NH), 8.73 and 8.57 (s, 1H each, H2 and H8), 8.09 (d, 1H, J = 7.5 Hz, H6), 8.05 and 7.94 (dd, 2H each, J = 8, 1 Hz, BzH), 7.41–7.03 (m, 16H, ArH and H5), 6.75 (dd, 4H, J = 8, 1 Hz, ArH), 6.60 and 6.39 (t, 1H each, J = 6.5 Hz, H1′), 5.27 (m, 1H, H3′), 4.87 (m, 1 H, H3′), 4.55–4.35 (m, 6H, H4′, CF_3CH_2, H5′, and H5″), 3.49 (s, 6H, CH_3O), 3.41 (m, 2H, H5′ and H5″), 2.97 (ddd, 1H, J = 14, 6.5, 6 Hz, H2′ or H2″), 2.92 (ddd, 1H, J = 14, 6.5, 2.5 Hz, H2′ or H2″), 2.53 (ddd, 1H, J = 14, 6.5, 4.5 Hz, H2′ or H2″), 2.43 (ddd, 1H, J = 14, 6.5, 7 Hz, H2′ or H2″); ^{31}P NMR (Py-d_5) δ: −1.86; ^{19}F NMR (Py-d_5) δ: −75.36 (t, J = 8 Hz); FABMS *m/e*: 1155 (M + Na^+).

*(Rp,Sp)-5′-O-(4,4′-Dimethoxytrityl)thymidylyl-3′,5′-N^4-benzoyl-3′-O-[(1,1-dimethylethyl)-dimethylsilyl]-2′-deoxycytidine (2,2,2-trifluoroethyl)phosphates (**21**a and **21**b)*

Using a similar procedure as described for **18**, from **5** (722 mg, 0.94 mmol) and **16** (380 mg, 0.85 mmol), **21** (900 mg, 0.794 mmol, 93% yield) was obtained as a 1:1 mixture of two diastereomers. TLC (silica gel, solvent B) R_f 0.57; ^{1}H NMR ($CDCl_3$) δ: 8.75 and 8.72 (bs, 1H, NH), 8.62 (m, 2H, NH and TH6), 8.03 and 7.99 (d, 1H, J = 8 Hz, C-H6), 7.82 and 7.89 (d, 1H, J = 8 Hz, H5), 7.86 (d, 2H, J = 8 Hz, BzH), 7.70 (t, 1H, J = 8 Hz, BzH), 7.61 (t, 2H, J = 8 Hz, BzH), 7.55 (m, 3H, ArH), 7.30 (m, 6H, ArH), 6.83 (m, 4H, ArH), 6.43 and 6.41 (t, 1H, J = 5.5 Hz, H1′), 6.21 (m, 1H, H1′), 5.16 (m, 1H, H3′), 4.50–1.40 (m, 7H, H3′, H4′, CF_3CH_2, H5′, and H5″), 3.78 (s, 6H, CH_3O), 3.54 and 3.39 (m, 2H, H5′ and H5″), 2.70–2.30 and 2.19 (m, 4H, H2′ and H2″), 1.42 and 1.41 (s, 3H, 5-CH_3), 0.88 and 0.89 (s, 9H, $C(CH_3)_3$), 0.08 and 0.07 (s, 6H, $Si(CH_3)_2$); ^{31}P NMR ($CDCl_3$) δ: −1.93 and −1.97 (1:1); ^{19}F NMR ($CDCl_3$) δ: −75.18 and −75.29 (1:1, t, J = 8 Hz); FABMS *m/e*: 1156 (M + Na^+).

*(Rp,Sp)-5′-O-(4,4′-Dimethoxytrityl)thymidylyl-3′,5′-N^4-benzoyl-2′-deoxycytidine (2,2,2-trifluoroethyl)phosphates (**24**a and **24**b)*

Using the desilylation procedure described for **18**, **21** (480 mg, 0.420 mmol) gave 79% yield of a 1:1 diastereomeric mixture (**24***a* and **24***b*, 340 mg, 0.334 mmol), which was partially separated in the same manner as described for **25**, giving **24***a* and **24***b*. Compound **24***a*: TLC (silica gel, solvent B) R_f 0.33; ^{1}H NMR (Py-d_5) δ: 13.3 and 12.3 (bs, 1H each, NH), 8.40 (d, 1H, J = 8 Hz, C-H6), 8.20 (s, 1H, T-H6), 8.20 (d, 2H, J = 8 Hz, BzH), 7.78 (d, 1H, J = 8 Hz, BzH), 7.73 (t, 2H, J = 8 Hz, BzH), 7.72 (d, 1H, J = 8 Hz, H5), 7.61 (t, 2H, J = 8 Hz, BzH), 7.56–7.30 (m, 9H, ArH), 7.01 (d, 4H, J = 8 Hz, ArH), 6.90 and 6.80 (t, 1H each, J = 6 Hz, H1′), 5.72 (m, 1H, H3′), 4.98 (m, 2H, CF_3CH_2), 4.83 (m, 1H, H3′), 4.72 (m, 2H, H5′ and H5″), 4.68 and 4.60 (m, 1H each, H4′), 3.69 (s, 6H, CH_3O), 3.62 (m, 2H, H5′ and H5″), 2.98–2.80 (m, 3H, H2′ and H2″), 2.56 (ddd, 1H, J = 14, 7, 6 Hz, H2′ or H2″), 1.70 (s, 3H, 5-CH_3); ^{31}P NMR (Py-d_5) δ: −1.34; ^{19}F NMR (Py-d_5) δ: −74.87 (t, J = 8 Hz); FABMS *m/e*: 1042 (M + Na^+). Compound **24***b*: TLC (silica gel, solvent B) R_f 0.33; ^{1}H NMR (Py-d_5) δ: 13.3 and 12.3 (bs, 1H each, NH), 8.47 (d, 1H, J = 8 Hz, C-H6), 8.20 (s, 1H, T-H6), 8.20 (d, 2H, J = 8 Hz, BzH), 7.78 (d, 1H, J = 8 Hz, BzH), 7.73 (t, 2H, J = 8 Hz, BzH), 7.72 (d, 1H, J = 8 Hz, H5), 7.61 (t, 2H, J = 8 Hz, BzH), 7.56–7.30 (m, 9H, ArH), 7.01 (d, 4H, J = 8 Hz, ArH), 6.90 and 6.80 (t, 1H each, J = 6 Hz, H1′), 5.72 (m, 1H, H3′), 4.98 (m, 2H, CF_3CH_2), 4.84 (m, 1H, H3′), 4.76 (m, 2H, H5′ and H5″), 4.63 (m, 2H, H4′), 3.69 (s, 6H, CH_3O), 3.62 (m, 2H, H5′ and H5″), 2.98–2.80 (m, 3H, H2′ and H2″), 2.59 (ddd, 1H, J = 14, 7, 6 Hz, H2′ or H2″), 1.70 (s, 3H, 5-CH_3); ^{31}P NMR (Py-d_5) δ: −1.37; ^{19}F NMR (Py-d_5) δ: −74.88 (t, J = 8 Hz); FABMS *m/e*: 1042 (M + Na^+).

*(Rp,Sp)-N^6-Benzoyl-5′-(4,4′-dimethoxytrityl)-2′-deoxyadenoylyl-3′,5′-N^6-benzoyl-3′-O-[(1,1-dimethylethyl)dimethylsilyl]-2′-deoxyadenosine (2,2,2-trifluoroethyl)phosphates (**22**a and **22**b)*

Using a similar procedure as described for **18**, from **7** (443 mg, 0.50 mmol) and **17** (233 mg, 0.50 mmol), **22** (479 mg, 0.377 mmol, 77% yield) was obtained as a 1:1 mixture of two diastereomers, which was partially separated in a similar manner as used for **25** with 0.5–0.75% methanol in chloroform as eluent, giving **22***a* and **22***b*. Compound **22***a*: TLC (silica gel, solvent B) R_f 0.43; ^{1}H NMR ($CDCl_3$) δ: 13.3 and 12.3 (bs, 2H, NH), 8.73, 8.60, 8.17 and 8.13 (s, 1H each, H2 and H8), 8.00 and 7.95 (d, 2H each, J = 8 Hz, BzH), 7.68 (t, 1H, J = 8 Hz, BzH), 7.60–7.13 (m, 14H, ArH), 6.75 (d, 4H, J = 8 Hz, ArH), 6.45 (dd, 1H, J = 9, 6 Hz, H1′), 6.43 (t, 1H, J = 6.5 Hz, H1′), 5.24 (m, 1H, H3′), 4.71 (m, 1H, H3′), 4.42–4.20 and 4.17 (m, 6H, H4′, CF_3CH_2, H5′, and H5″), 3.72 (s, 6H, CH_3O), 3.40 and 3.36 (dd, 1H each, J = 10, 4 Hz, H5′ and H5″), 3.12, 2.92, 2.48, and 2.73 (m, 1H each, H2′ and H2″), 0.92 (s, 9H, $C(CH_3)_3$), 0.12 (s, 6H, $Si(CH_3)_2$); ^{31}P NMR ($CDCl_3$) δ: −2.20; ^{19}F NMR ($CDCl_3$) δ: −75.23 (t, J = 8 Hz); FABMS *m/z*: 1293 (M + Na^+). Compound **22***b*: TLC (silica gel, solvent B) R_f 0.43; ^{1}H NMR ($CDCl_3$) δ: 13.3 and 12.3 (bs, 2H, NH), 8.70, 8.59, 8.19 and 8.09 (s, 1H each, H2 and H8), 8.00 and 7.95 (d, 2H each, J = 8 Hz, BzH), 7.68 (t, 1H, J = 8 Hz, BzH), 7.60–7.13 (m, 14H, ArH), 6.75 (d, 4H, J = 8 Hz, ArH), 6.41 (dd, 1H, J = 9, 6 Hz, H1′), 6.44 (t, 1H, J = 6.5 Hz, H1′), 5.24 (m, 1H, H3′), 4.71 (m, 1H, H3′), 4.42–4.20 and 4.17 (m, 6H, H4′, CF_3CH_2, H5′, and H5″), 3.74 (s, 6H, CH_3O), 3.40 and 3.36 (dd,

1H each, J = 10, 4 Hz, H5′ and H5″), 3.06, 2.95, 2.48, and 2.48 (m, 1H each, H2′ and H2″), 0.92 (s, 9H, $C(CH_3)_3$), 0.12 (s, 6H, $Si(CH_3)_2$); ^{31}P NMR ($CDCl_3$) δ: −2.44; ^{19}F NMR ($CDCl_3$) δ: −75.29 (t, J = 8 Hz); FABMS *m/e*: 1293 ($M + Na^+$).

Acknowledgments

This work was supported by a grant (J.W.L.) from the Natural Sciences and Engineering Research Council of Canada and by the Department of Chemistry of the University of Alberta.

1. P.S. Miller, N. Dreon, S.M. Pulford, and K.B. McParland. J. Biol. Chem. **255**, 9659 (1980).
2. R. Cosstick and F. Eckstein. Biochemistry, **24**, 3630 (1985).
3. W.J. Stec, G. Zon, W. Egan, and B. Stec. J. Am. Chem. Soc. **106**, 6077 (1984).
4. B.D. Strollar, G. Zon, and R.W. Pastor. Proc. Natl. Acad. Sci. U.S.A. **83**, 4469 (1986).
5. M. Koziolkiewicz, B. Uznanski, W.J. Stec, and G. Zon. Chem. Scr. **26**, 251 (1986).
6. B.C. Froehler. Tetrahedron Lett. **27**, 5575 (1986).
7. M. Weinfeld, A.F. Drake, R. Kuroda, and D.C. Livingston. Anal. Biochem. **178**, 93 (1989).
8. C. Meier, J.-M. Neumann, F. Andre, Y. Henin, and T. Huynh-Dinh. J. Org. Chem. **57**, 7300 (1992).
9. R.S. Cahn, C. Ingold, and V. Prelog. Angew. Chem. Int. Ed. Engl. **5**, 385 (1966).
10. M.R. Hamblin and B.V.L. Potter. FEBS Lett. **189**, 315 (1985).
11. M. Weinfeld, A.F. Drake, J.F. Saunders, and M.C. Paterson. Nucleic Acids Res. **13**, 7067 (1985).
12. W.H. Gmeiner, R.T. Pon, and J.W. Lown. J. Org. Chem. **56**, 3602 (1991).
13. F. Seela and U. Kretschmer. J. Org. Chem. **56**, 3861 (1991).
14. W.J. Stec, G. Zon, K.A. Gallo, and R.A. Byrd. Tetrahedron Lett. **26**, 2191 (1985).
15. M.J. Gait. Oligonucleotide synthesis. IRL Press, Washington, D.C. 1984.
16. L.J. McBride and M.H. Caruthers. Tetrahedron Lett. **24**, 245 (1983).
17. K.K. Ogilvie. Can. J. Chem. **51**, 3799 (1973).
18. B.V.L. Potter, B.A. Connolly, and F. Eckstein. Biochemistry, **22**, 1369 (1983).
19. F. Seela, J. Ott, and B.V.L. Potter. J. Am. Chem. Soc. **105**, 5879 (1983).
20. B.V.L. Potter, F. Eckstein, and B. Uznanski. Nucleic Acids Res. **11**, 7087–7102 (1983).
21. M.F. Summers, C. Powell, W. Egan, R.A. Byrd, W.D. Wilson, and G. Zon. Nucleic Acids Res. **14**, 7421 (1986).

Can. J. Chem. Downloaded from www.nrcresearchpress.com by EESC ESCOLA DE ENGENHARIA on 09/08/12
For personal use only.

The photochemistry of 8-methyl-2,3-benzobicyclo[4.2.0]octa-2,4,7-triene

CHRISTOPHER OWEN BENDER,[1] DONALD LAVERNE BENGTSON, DOUGLAS DOLMAN, AND RYAN TODD MCKAY

Department of Chemistry, University of Lethbridge, Lethbridge, AB T1K 3M4, Canada

Received November 26, 1993

CHRISTOPHER OWEN BENDER, DONALD LAVERNE BENGTSON, DOUGLAS DOLMAN, and RYAN TODD MCKAY. Can. J. Chem. **72**, 1556 (1994).

8-Methyl-2,3-benzobicyclo[4.2.0]octa-2,4,7-triene (**20**) was prepared by Shapiro reaction from 8-methyl-2,3-benzobicyclo[4.2.0]octa-2,7-dien-4-one (**19**). Triene **20** was found to be thermally and photochemically reactive. 6-Methylbenzocyclooctatetraene (i.e., 6-methyl COT **21**) was the unique product formed when solutions of **20** were heated at 150°C for 10 h. The direct irradiation of triene **20** gave 6-methylbenzosemibullvalene (i.e., SB **22**, 46%, Φ = 0.073), 5-methyl-7,8-benzotetracyclo[3.3.0^{2,4}.0^{3,6}]oct-7-ene (**23**, 35%, Φ = 0.062), 6-methyl COT **21** (4%, Φ = 0.008), 7-methyl COT **24** (1%, Φ = 0.002), and naphthalene (3%, Φ = 0.006). Sensitized irradiations of **20** gave SB **22** (45%, Φ = 0.022), 6-methyl COT **21** (2%, Φ = 0.001), and naphthalene (4%, Φ = 0.002). Studies with deuterium-labelled triene (**20***a*) indicated that the semibullvalene **22** was produced from both S_1 and T_1 excited states of **20** by Zimmerman di-π-methane rearrangement.

CHRISTOPHER OWEN BENDER, DONALD LAVERNE BENGTSON, DOUGLAS DOLMAN et RYAN TODD MCKAY. Can. J. Chem. **72**, 1556 (1994).

On a préparé le 8-méthyl-2,3-benzobicyclo[4.2.0]octa-2,4,7-triène (**20**) par la réaction de Shapiro effectuée à l'aide de la 8-méthyl-2,3-benzobicyclo[4.2.0]octa-2,7-dièn-4-one (**19**). On a trouvé que le triène **20** est réactif tant thermiquement que photochimiquement. Le 6-méthylbenzocyclooctatétraène (soit, le 6-méthyl COT, **21**) est l'unique produit formé lorsqu'on chauffe des solutions du composé **20** à 150°C pendant 10 h. L'irradiation directe du triène **20** conduit au 6-méthylbenzosemibullvalène (soit le SB **22**, 46%, Φ = 0,073), au 5-méthyl-7,8-benzotétracyclo[3.3.0^{2,4}.0^{3,6}]oct-7-ène (**23**, 35%, Φ = 0,062), le 6-méthyl COT **21** (4%, Φ = 0,008), le 7-méthyl COT **24** (1%, Φ = 0,002) et le naphtalène (3%, Φ = 0,006). Des irradiations sensibilisées du composé **20** conduisent au composé SB **22** (45%, Φ = 0,022), au 6-méthyl COT **21** (2%, Φ = 0,001) et au naphtalène (4%, Φ = 0,002). Des études avec du triène marqué au deutérium (**20***a*) indiquent que le semibullvalène **22** se forme aussi bien à partir des états excités S_1 et T_1 du produit **20**, par le biais d'une transposition di-π-méthane de Zimmerman.

[Traduit par la Rédaction]

Introduction

The synthesis of polyquinanes continues to be an area of interest (1) due to the biological and therapeutic activity exhibited by numerous members of this class of compound. Effective routes to a variety of these cyclopentanoids have been elaborated using semibullvalene (SB) derivatives as starting materials (2), and this in turn has made the development of additional methods of SB synthesis an attractive undertaking. Recently, we (3–8) and others (9) have observed that SBs can be generated from the sensitized and (or) direct irradiation of 2,3-benzobicyclo[4.2.0]octa-2,4,7-trienes; for example, trienes **1–3** give SBs **4–6** (6–8) (Scheme 1). Intriguingly, the SBs are not produced by a single mechanistic pathway. The results of deuterium-labelling experiments have shown that at least three routes can be used to generate the SB product, and in some cases their mode of formation has been shown to be multiplicity dependent, e.g., triene **7** gives SB **9** via a 1,2-shift mechanism (route i, Scheme 2) from S_1, but utilizes a Zimmerman di-π-methane rearrangement (DPM rearrangement) to provide the same semibullvalene from T_1 (route ii, Scheme 2 (3)). The third, and least observed, route involves initial bridging between the distal carbons (i.e., C-4 and C-8) of the vinyl groups. This mechanism was invoked to explain the formation of the SB **5** from the triene **12** (route iii, Scheme 2 (5)).

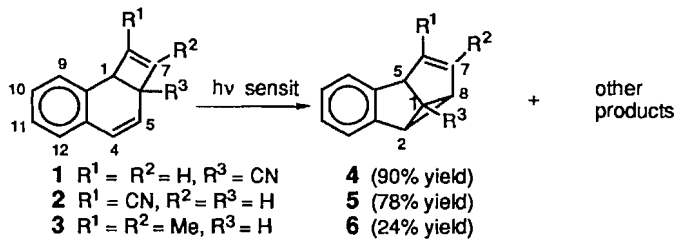

SCHEME 1

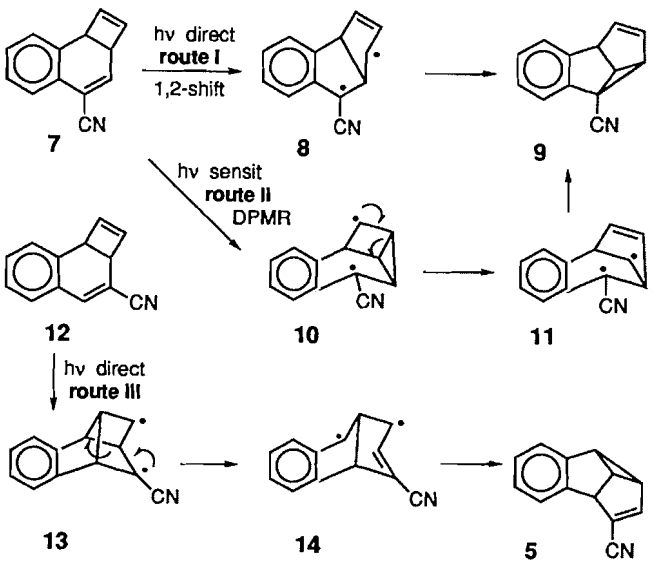

SCHEME 2

Those triene derivatives that have been examined to date contain π-conjugating groups (e.g., CN (3–7), CO_2R (9), Ph (10)), with the single exception of the 7,8-dimethyl derivative **3** (8); only SB **6** and naphthalene were detected, in meager yields, as photoproducts from the direct or sensitized irradiation of triene **3**. To explore further the factors that control the excited-state

[1]Author to whom correspondence may be addressed. Telephone: (403) 329-2307. Fax: (403) 329-2057.

Can. J. Chem. Downloaded from www.nrcresearchpress.com by EESC ESCOLA DE ENGENHARIA on 09/08/12
For personal use only.

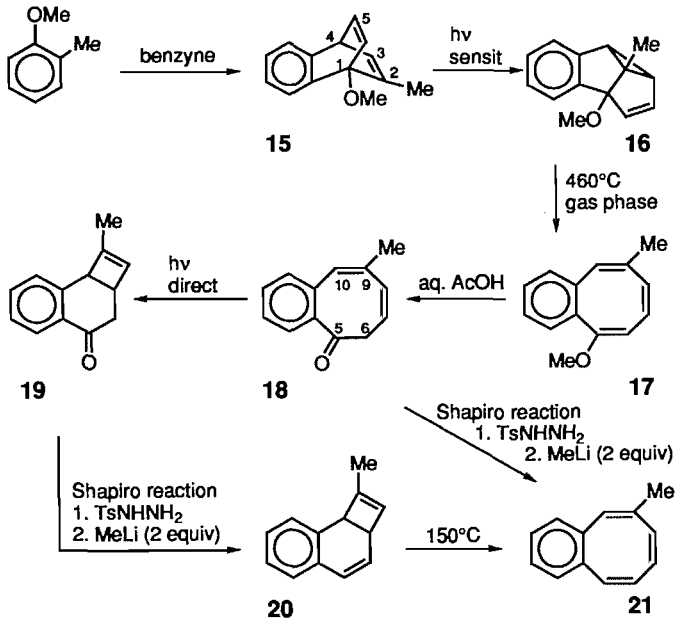

SCHEME 3

reactivity of simple alkyl-substituted trienes, we have studied, and now report on, the photochemistry of the monomethyl compound **20**.

Results

The preparation of 8-methyl-2,3-benzobicyclo[4.2.0]octa-2,4,7-triene (**20**), which starts with the addition of benzyne to *o*-methylanisole, is outlined in Scheme 3. The first four steps in the synthetic sequence follow those used in the reported preparation of the 7,8-dimethyl triene **3** (8). Although the ketone **18** could be converted to the COT **21** via the Shapiro reaction, it was found that the subsequent photo-conversion of **21** to the desired triene **20** was excessively slow (e.g., the production of ca. 1 mg of **20** per hour of irradiation). A more efficient route was to photoclose the ketone **18** to the bicyclo[4.2.0] system **19**, which was then transformed to the desired triene **20** by the Shapiro reaction. Additionally, in the photochemical step (**18** → **19**) it was found to be advantageous to carry out the irradiation in the presence of piperylene to quench the triplet-state activity of ketone **19**, and thus limit the formation of secondary products that otherwise occur.

The structural assignment of triene **20** was based on comparison of its NMR spectral data with those of the known 7,8-dimethyl analogue **3**; the chemical shifts of corresponding protons were within δ 0.15, and coupling constants between corresponding protons were identical (8). Supporting evidence for structure **20** was obtained from its thermal reactivity. Like

TABLE 1. The ^{1}H NMR data of semibullvalenes **6**, **22**, and **25**

	Description and signal positions, δ[a]		
Assignment	**22**[b]	**6**[b]	**25**[c]
Aromatics	7.01–7.33 m	6.97–7.36 m	6.80–7.33 m
H-1	3.33 q	3.18 q	3.14 q
H-2	2.96 t	2.82 t	2.96 t
H-5	3.60 d	3.54 d	3.81 dd
H-6	—	—	5.47 dd
H-7	4.86 brs	—	5.08 dd
H-8	2.58 dt	2.39 t	2.60 dt
Methyl	1.72 s	1.56 s	—

[a]Coupling constants for **22** are $J_{1,2} = J_{1,5} = J_{1,8} = J_{2,8} = 6.5$, and $J_{7,8} = 2.5$ Hz; corresponding coupling constants for **6** and **25** are within 0.5 Hz.
[b]Run in $CDCl_3$.
[c]Run in CCl_4.

many other derivatives of the triene system (3–7), **20** is smoothly converted to COT product on heating (→**21**). The arrangement is noticeable on GC columns at temperatures >110°C, and is essentially quantitative when solutions of **20** are maintained at ca. 150°C for 10 h.

The triene is also photochemically reactive, and the semibullvalene 6-methylbenzotricyclo[3.3.0.0^{2,8}]octa-3,6-diene (**22**) was formed as the major product under both direct (λ ≥ 295 nm) and sensitized (λ ≥ 320 nm; dimethylaminobenzophenone) irradiation conditions. The structures, analytical yields (based on consumed substrate; GC analysis), and quantum yields (Φ's) of all the photoproducts are given in Scheme 4.

The characterizations of the photoproducts rest on spectral data. In the case of the SB **22**, the proton NMR spectrum showed chemical shifts and coupling constants that are typical for the rigid benzosemibullvalene skeleton. Table 1 compares the proton chemical shifts of **22** with those of related SBs: the 6,7-dimethyl derivative **6** (8), and the unsubstituted parent compound (**25**, Scheme 5) (11).

For 5-methyl-7,8-benzotetracyclo[3.3.0^{2,4}.0^{3,6}]oct-7-ene (**23**), the C_s symmetry of the molecule was revealed by the ^{13}C NMR spectrum, which showed only eight lines; the chemical shifts of the aliphatic ring and methyl carbons (δ 55.2 C-1(6), δ 20.1 C-2(3), δ 26.9 C-4, δ 67.0 C-5, and δ 15.5 CH_3) correlate well with those reported (21) for the corresponding 5-methyl alkene analogue (**26**, Scheme 5) (δ 54.7 C-1(6), δ 20.3 C-2(3), δ 24.0 C-4, δ 65.2 C-5, and δ 14.3 CH_3). Additionally, in the ^{1}H NMR spectrum, the signals due to the non-aromatic ring protons (δ 3.59 H-1(6), δ 2.05 H-2(3), and δ 2.69 H-4) appear as an AA″MX′X spin system as they do in the analogue **26** (δ 3.14 H-1(6), δ 1.98 H-2(3), and δ 2.41 H-4); in both compounds, H-4 occurs as a triplet, with $J_{4,2} = J_{4,3} = 3.5$ Hz (12).

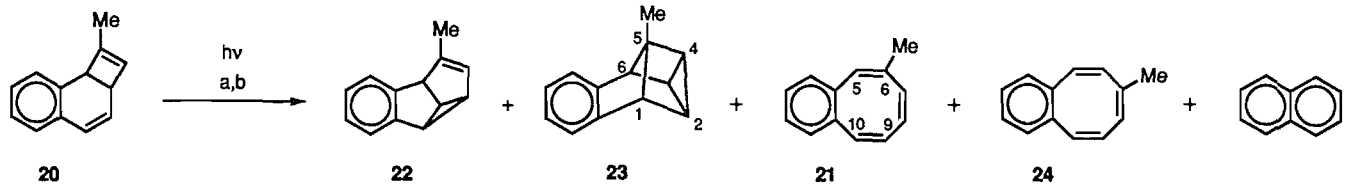

Chemical and quantum (Φ) yields					
a, Direct	46%(0.073)	35%(0.062)	4%(0.008)	1%(0.002)	3%(0.006)
b, Sensitized	45%(0.022)	-	2%(0.001)	-	4%(0.002)

SCHEME 4

Can. J. Chem. Downloaded from www.nrcresearchpress.com by EESC ESCOLA DE ENGENHARIA on 09/08/12
For personal use only.

TABLE 2. The ^{1}H NMR data of cyclooctatetraenes **21**, **24**, **27**, and **28**

Assignment	Description and signal positions, δ[a]			
	21	**27**	**24**	**28**
Aromatics	6.95–7.24 m	6.95–7.28 m	6.96–7.20 m	6.95–7.21 m
H-5	6.34 br s	7.22 s	6.49	6.75 d
H-6	—	—	5.62 d	5.95 d
H-7	5.82 m	5.76 d	—	—
H-8	5.82 m	6.08 dd	5.62 br s	6.67 d
H-9	6.04 dd	6.04 dd	5.99 br d	6.07 dd
H-10	6.57 d	6.55 d	6.49 d	6.73 d
Methyl	1.88 m	—	1.76 br s	—

[a]Run in $CDCl_3$ solvent. Coupling constants for **21** and **24**, where applicable, are $J_{5,6} = J_{9,10} = 11.5$, and $J_{8,9} = 2.5$ Hz. For **27** and **28**, $J_{9,10} = 11.5$, and $J_{8,9} = 4$ Hz.

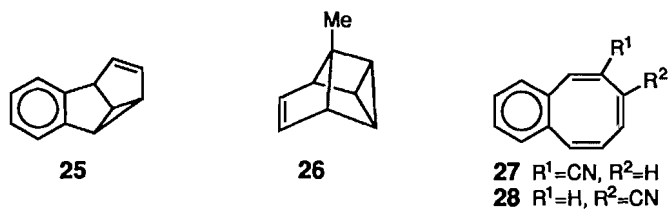

SCHEME 5

The structures given to the COTs **21** and **24** were based on comparison of their proton NMR spectra with those of the known cyano-substituted COTs **27** and **28** (Scheme 5) (13); the spectral details are displayed in Table 2. The chemical shifts and coupling constants for corresponding protons are closely similar, except for the proton *cis*-vinyl to the substituent (i.e., H-5 in **21**, and H-8 in **24**). As expected, these protons in the methyl derivatives show upfield chemical shifts (δ 0.88 for H-5 in **21**, and δ 1.05 for H-8 in **24**) that are consistent with the reported substituent constant differences of minus δ 1.04 for olefinic protons *cis* to methyl (−0.26) and cyano (+0.78) groups (14). A final point with respect to the NMR spectrum of **21** is that the signal positions for H-7 and H-8 are essentially coincidental at 400 MHz. The addition of the alkene-complexing agent AgFOD, however, permitted resolution of these signals at 250 MHz (note Experimental for details).

Subsequent to the structural assignments, control experiments were performed on the photoproducts individually to ascertain if any photo-interconversion could have occurred under the direct or sensitized conditions used during the irradiations of triene **20**. In each case the substrates proved to be very stable, and only from the direct irradiation ($\lambda \geq 295$ nm) of COT **21** was a photorearrangement noted; a trace amount of triene **20** was slowly formed, according to GC analysis.

Mechanistic considerations

As noted in the Introduction, previous studies with several of the cyano-substituted derivatives of the triene system had revealed that the semibullvalene product can be formed by three different mechanistic routes. It was therefore pertinent to investigate the situation with triene **20**, since here both the 1,2-shift mechanism and the Zimmerman DPM rearrangement could account for the production of SB **22**; the operation of the third mechanism (route iii, Scheme 2) can be ruled out since this would have led to 2-methylbenzosemibullvalene, a product not observed in this study. These two options, which are shown in Scheme 6 as route i and route ii, respectively, are skeletally different. It was therefore possible to determine the extent to which they participated in the semibullvalene formation by examination of the deuterium distributions in the SB produced from the labelled triene material **20***a*.

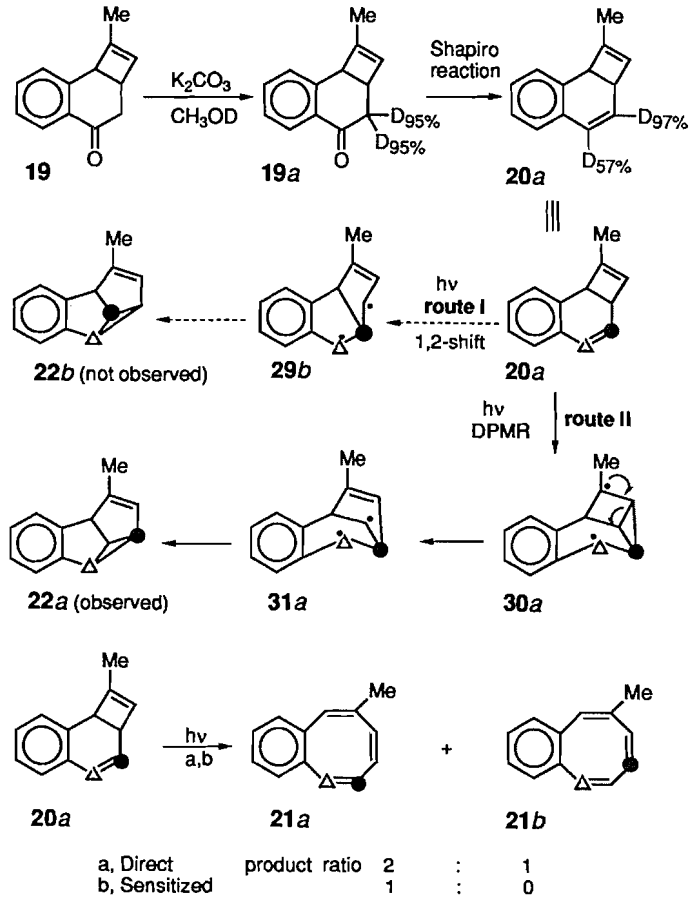

SCHEME 6

The doubly deuterated triene **20***a* (ca. 57%-d_1 at C-4, and 97%-d_1 at C-5) was prepared from the labelled ketone **19***a* via the Shapiro reaction, as outlined in Scheme 6. The occurrence of the additional deuterium at C-4 of the triene is not exceptional. Similar partial deuterium incorporations at this site (i.e., on the carbon of the original carbonyl) have been reported using the tosylhydrazone–alkyllithium procedure, and a mechanistic rationalization has been proposed by Shapiro and Hornaman (15). Importantly, the major label at C-5 in **20***a* was ideally

Can. J. Chem. Downloaded from www.nrcresearchpress.com by EESC ESCOLA DE ENGENHARIA on 09/08/12
For personal use only.

located to distinguish between the mechanisms depicted in Scheme 6 as routes i and ii. The SB product isolated from either the direct or the sensitized irradiation of triene **20***a* contained identical deuterium distributions, as determined by proton NMR analyses. In each case the labels were located at C-2 and C-8, in agreement with the structure designated as **22***a*. Thus, the 1,2-shift pathway (i.e., route i, Scheme 6) does not function in the formation of SB **22** from triene **20**.

An additional interesting result from the labelling studies was the finding that the deuterium distributions in the labelled COT **21** material isolated from the direct irradiation of **20***a* were not the same as those from sensitization (note: the deuterium distributions found in the labelled tetracycle **23** and COT **24** are unexceptional, and are given in the Experimental). The labels in the COT **21** from sensitized runs were attached to C-10 (55%) and C-9 (97%), corresponding to an electrocyclic $2\sigma_s + 2\pi_s$ ring opening of **20***a* to give COT **21***a* (Scheme 6). Those from the direct irradiation were located at C-10 (57%), at C-9 (65%), and at C-8 (36%), and accord largely with the presence of a 2:1 mixture of label isomers represented by structures **21***a* and **21***b*, respectively (note Scheme 6). Mechanistically, we are unable to account for the formation of COT **24***a* and the label isomers **21***a* and **21***b* from the direct irradiation of triene **20***a* in terms of a single mechanism (vide infra).

Discussion

The assignments of excited-state multiplicities responsible for the numerous products encountered in the photochemistry of triene **20** were straightforward. The tetracycle **23** and COT **24** were assumed to be uniquely singlet derived since they are formed only upon direct irradiations. By contrast, the remaining three compounds, viz, SB **22**, COT **21**, and naphthalene, are produced from both S_1 and T_1, depending upon the mode of excitation employed. They are T_1 derived when generated from sensitization, and are mostly (70–100%) from S_1 when direct irradiation is used. This latter conclusion follows from the observation that the quantum yields (summarized in Scheme 4) for the photoproducts from the direct irradiation of triene **20** are at least three times greater than those from the sensitized runs. Application of the bracketing expression $\Phi^{dir} - \Phi^{sens} \leq {}^1\Phi \leq \Phi^{dir}$ (16) then suggests that *at least* 70% of SB **22**, COT **21**, and naphthalene from direct irradiation must be from S_1.

This latter interpretation is reasonable only if energy transfer to T_1 of triene **20** is efficient in the sensitized irradiations. To ensure that this condition was met, sensitization experiments with different sensitizers were performed: *p*-dimethylaminobenzophenone (E_T 62 kcal/mol), thioxanthone (E_T 65.5 kcal/mol), and benzophenone (E_T 69 kcal/mol). In all cases the quantum yields were the same, within experimental error. Furthermore, in the case of benzophenone sensitization, the photoreduction of the sensitizer was effectively quenched in the presence of the triene, and thus it seems reasonable to infer that triplet energy transfer to **20** was indeed efficient.

The finding that SB **22** can be produced from both S_1 and T_1 is significant. The deuterium-labelling studies are consistent with the operation of a DPM rearrangement in each case, and although such a transformation from the triplet excited state is normal in rigid molecules, it is rare that S_1 undergoes the same major process. A further example of this uncommon situation involving a DPM rearrangement from both S_1 and T_1 was noted previously for the 8-cyano triene **2** (6). It is possible that the reaction synchronicity differs in the singlet and triplet excited states of these compounds. Interestingly, Robb and co-workers

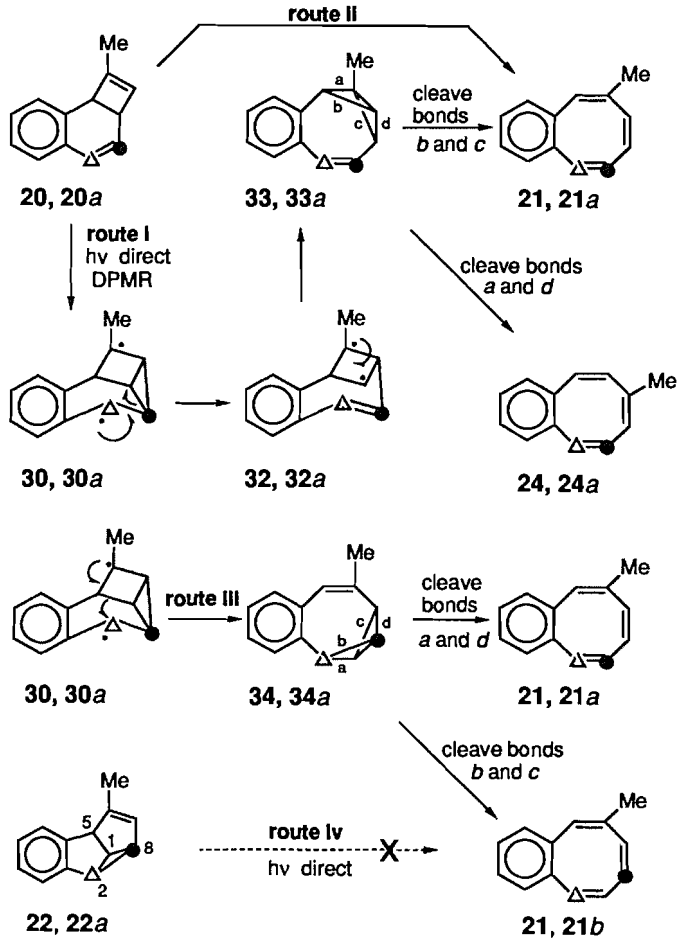

SCHEME 7

obtained results from a theoretical approach that suggest some or all the steps in the traditional Zimmerman mechanism may merge into one step for singlet DPMRs, and the reaction may become concerted (17). On the other hand, for the triplet reaction in constrained systems, Zimmerman recently reported further experimental and theoretical work in support of the stepwise mechanism (18).

We note that the formation of SB **22** is especially favorable when generated from T_1. This finding is attributed to the stabilization of the radical centres of intermediate **30** by the methyl group and aromatic ring, and falls in line with the generalization that electron-stabilizing groups at the distal carbons of the di-π-methane moiety promote the Zimmerman rearrangement (19).

Lastly with respect to the DPMR, the formation of COT **24** and part of COT **21** in the direct irradiation of triene **20** can also be interpreted in terms of a singlet-derived Zimmerman rearrangement. Here, it is suggested that the DPM mechanism involves closure to an alternative vinylcyclopropane, shown as octavalene **33** (Scheme 7, route i), which then undergoes thermal reorganization to the COTs. A similar rationale was invoked to account for the formation of the cyano-COTs **27** and **28** from the direct photolysis of triene **2** (6), and independently generated 1,3-cyclobutanediyls like the proposed intermediate **32** are reported to give bicyclobutanes by bonding at the radical centres (20). An additional route from **20** to COT **21** (but not to

Can. J. Chem. Downloaded from www.nrcresearchpress.com by EESC ESCOLA DE ENGENHARIA on 09/08/12
For personal use only.

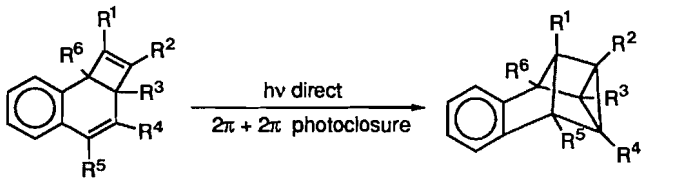

2 R^1 = CN, R^2 = R^3 = R^4 = R^5 = R^6 = H — **38** (ref. 6)
35 R^2 = CN, R^1 = R^3 = R^4 = R^5 = R^6 = H — **39** (ref. 7)
36 R^1 = R^2 = Ph, R^3 = R^4 = R^5 = R^6 = H — **40** (ref. 10)
1 R^3 = CN, R^1 = R^2 = R^4 = R^5 = R^6 = H — (ref. 1)
3 R^1 = R^2 = Me, R^3 = R^4 = R^5 = R^6 = H — (ref. 8)
7 R^5 = CN, R^1 = R^2 = R^3 = R^4 = R^6 = H — (ref. 3)
12 R^4 = CN, R^1 = R^2 = R^3 = R^5 = R^6 = H — (ref. 5)
37 R^6 = CN, R^1 = R^2 = R^3 = R^4 = R^5 = H — (ref. 4)

No photoclosure observed

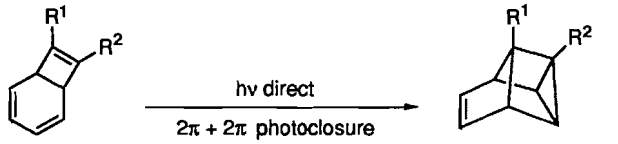

41 R^1 = CMe_3, R^2 = CO_2Me — **44** (ref. 22)
42 R^1 = Ph, R^2 = CO_2Me — **45** (ref. 23)
43 R^1 = R^2 = CMe_3 — (ref. 24)

No photoclosure observed

SCHEME 8

COT **24**) may also be via $2\sigma_s + 2\pi_s$ electrocyclic opening (21) of the cyclobutene ring of the triene (note Scheme 7, route ii). Unfortunately, the labelling pattern used in this study does not permit us to discern to what extent this pathway is used in direct irradiations. However, operation of route ii (Scheme 7), and not route i, does account for the formation of COT **21** and the absence of COT **24** from sensitization irradiation of triene **20**.

A further pathway to COT **21** must also function in the direct irradiation of triene **20**, since neither route i nor route ii (Scheme 7) can account for the label distribution observed in the deuterated product COT **21***b* (Scheme 6). One initially attractive mechanistic explanation for the low deuterium content at C-9 in the labelled COT **21**, and one that has literature precedent in analogous compounds (11, 13), was based on the secondary photochemical conversion of the primary SB **22** product to the COT, via cleavage of bonds C1—C5 and C2—C8 (Scheme 7, route iv). This possibility was discounted, however, by the finding that the semibullvalene was stable (GC showed no COT production) to the conditions used in the direct irradiation (Pyrex-filtered light) of triene **20**. A possible mechanism (route iii, Scheme 7) that can account for the formation of COT **21***b* (and in part **21***a*) is via the thermal isomerization of the octavalene intermediate **34***a* (cf. the fate of octavalene **33***a*, vide supra). In view of the low yield of COT **21**, and the fact that the involvement of intermediates has not been excluded, further speculation regarding additional pathways to COT **21** is deferred.

An unexpected product from the direct photolysis of **20** was the tetracycle **23**. Until now, intramolecular $2\pi + 2\pi$ photoclosures in bicyclo[4.2.0]octatrienes have been found only in compounds containing π-conjugating substituents at one or both sp^2 carbons of the cyclobutene ring, e.g., note compounds **2** (6), **35** (7), **36** (10), **41** (22), and **42** (23) in Scheme 8. By contrast, compounds **1** (7), **3** (8), **7** (3), **12** (5), **37** (4), and **43** (24) do not photoclose. Failure to undergo the cycloaddition was attributed to the lack of sufficient donor–acceptor interaction between the potential $2\pi + 2\pi$ partners (7). However, the present results

TABLE 3. Changes[a] in atom–atom interaction energies (eV), resulting from electronic excitation to the lowest singlet (S_1) and triplet (T_1) states of trienes **3** and **20**

	Changes in interaction energy (eV)			
	3		**20**	
Atom–atom	S_1	T_1	S_1	T_1
1–2	−0.98	−0.68	−0.03	−0.06
1–6	−0.48	−0.29	−0.45	−0.29
1–8	1.78	0.94	1.82	0.97
2–3	2.66	3.64	2.76	3.75
2–8	−0.27	−0.07	−0.22	−0.06
2–9	0.04	−0.24	−0.02	−0.26
3–4	−3.41	−3.56	−3.61	−3.63
3–7	−0.14	−0.03	−0.12	−0.03
3–12	1.42	2.49	1.48	2.52
4–8	−0.15	−0.02	−0.11	−0.03
4–5	4.28	6.31	4.49	6.38
5–6	−1.03	−1.07	−1.04	−1.09
5–7	−0.56	−0.15	−0.46	−0.12
6–7	1.86	1.21	1.75	1.22
7–8	0.13	−0.23	−0.19	−0.48
9–10	−0.20	0.46	−0.17	0.49
10–11	1.66	2.17	1.79	2.32
11–12	−1.15	−1.24	−1.24	−1.28

[a]Ground state geometries were obtained from MNDO calculations, and changes in interaction energies were calculated by the CNDO/S-CI method (31). Negative values are interpreted as attractive "forces" tending to bring atoms together, while positive values are repulsive. Calculations on the full molecules were performed; only selected values are given here.

show that this is not the feature that controls the reaction in bicyclo[4.2.0]octatrienes, since the "donor–acceptor" properties of model olefins representing the individual addends in **20** are essentially the same as those in the non-photoclosing dimethyl triene **3**. For example, in both trienes the "donor" portion is common (styrene, IP_V = 8.43 eV (25)), and the electron affinities of models for the "acceptor" vinyl groups are nearly identical (cf. EA_V = 2.27 eV (26) for the tetramethylethylene moiety in **3**, versus an EA_V = 2.24 eV (26) for the trimethylethylene moiety in **20**).

In an attempt to explain the deviation in behaviour of the two alkylated trienes, we turned to a theoretical approach that had successfully predicted the $2\pi + 2\pi$ products encountered in the photochemistry of benzobarrelene derivatives (13). However, this approach, which is based upon CNDO/2-CI calculations of the changes in atom–atom interaction energies for the lowest singlets of the trienes, did not prove useful in the present case. Inspection of Table 3 (see Experimental section: Calculations) does not reveal any significant divergence of the initial distributions of electronic excitation in **3**, compared to **20**, that would account for the observed variation in their photoclosure reactivities. In particular, the calculations predict that bonding between C-4 and C-8 and between C-5 and C-7 should be favorable in both compounds (−0.15 eV and −0.56 eV for **3**; and −0.11 eV and −0.46 eV for **20**).

Finally, we note that despite the difference in the stereoelectronic nature of a methyl substituent versus a cyano substituent, the photochemistry of triene **20** resembles that of **2** much more closely than that of the dimethyl derivative **3**. Further studies of the photochemistry of other methyl triene derivatives, as well as that of the unsubstituted parent, are in progress.

Can. J. Chem. Downloaded from www.nrcresearchpress.com by EESC ESCOLA DE ENGENHARIA on 09/08/12
For personal use only.

Can. J. Chem. Downloaded from www.nrcresearchpress.com by EESC ESCOLA DE ENGENHARIA on 09/08/12
For personal use only.

Experimental

Instrumentation and materials

The NMR spectra were recorded on either Bruker 250- or 400-MHz instruments, with TMS as internal standard. The chemical shifts are in δ units and the coupling constants (*J*) in Hz. The abbreviations br, s, d, t, q, and m refer to broad, singlet, doublet, triplet, quartet, and multiplet, respectively. The GC/MS was recorded on an HP 5890 (GC)/5970 (MS) instrument fitted with a DB-5 (J & W Scientific) fused silica capillary column, 15 m × 0.25 μm. The IR spectra were recorded on a Bomem MB 102 FT spectrometer. The UV spectra were measured on a Varian DMS 100S spectrometer; maxima are given in nm, with λ_{max} values in parentheses; sh = shoulder. Melting points are uncorrected. Elemental analyses were performed by Galbraith Labs, Inc., Knoxville, Tenn. Column chromatography was carried out on Silica Gel 60 (Merck; 230–400 mesh) mixed with Sylvania 2282 phosphor and slurry packed into quartz columns permitting monitoring by a hand UV lamp, or on Lobar columns (Merck; size B, LiChroprep Si 60), or on silica gel/$AgNO_3$ columns (10:1, by weight). The GC analyses were made on a Varian 3700 instrument (FID), coupled to a Varian CDS 111 computing integrator, and fitted with an SE-30 fused silica capillary column 30 m × 0.32 mm. Cyclohexane solvent for quantum yields was prepared by scrubbing with 20% fuming sulfuric acid, followed by washing with 10% aqueous sodium hydroxide, drying ($MgSO_4$), and finally distilling from calcium hydride. The sensitizers *p*-dimethylaminobenzophenone, thioxanthone, and benzophenone were recrystallized (after sublimation) prior to use.

General procedures for preparative photolyses

The apparatus consisted of a 450-W Hanovia medium pressure mercury arc surrounded by a water-cooled quartz immersion well. Unless otherwise stated, the light was filtered through either a cyclindrical sleeve of Pyrex or Corex glass. Three types of sample cell were used. Cell A (250-mL sample volume) consisted of a cylindrical well, which surrounded the aqueous filter jacket. Cell A was fitted with gas inlet and exit ports, and sample solutions were magnetically stirred, and purged with argon prior to, and during, irradiations. Cell B (35-mL sample volume) and Cell C (3.5 mL) were a quartz test-tube-like vessel and a quartz cuvette, respectively; sample solutions contained therein were deoxygenated by flushing with argon and sealed under a positive pressure; the solutions were magnetically stirred throughout the course of the irradiations.

*2-Methyl-1-methoxy-4-hydro-1,4-ethenonaphthalene (**15**)*

A mixture of benzene diazonium carboxylate, prepared, as previously described (13), from 10.5 g (76.8 mmol) of anthranilic acid, and 500 mL of 2-methylanisole was stirred at 45–60°C overnight, and then concentrated on a rotovap. The residue was dissolved in toluene (50 mL), diluted with 500 mL of hexane, filtered, and the filtrate concentrated. The residue was then short-path distilled (90°C/0.1 Torr; 1 Torr = 133.3 Pa) and the distillate was chromatographed on Silica Gel 60 (0.9 cm × 30 cm) with 2% ether – hexane. The main band was concentrated and the residue was rechromatographed on a Lobar silica gel column with 5% ether – hexane. Concentration of the third band gave 470.5 mg (4.5%) of colourless barrelene (**15**), mp 43–45°C (from ethanol); UV (hexane): 277 (760), 270 (780), 263 (640), 255 sh (640), and 234 sh (1160); ^{1}H NMR (250 MHz; $CDCl_3$): 7.29–7.41 (m, 1H, aromatic), 6.80–6.97 (m, 5H, 3 aromatics, H-5 and H-6), 6.27 (sym m, 1H, H-3), 4.61 (dt, 1H, H-4, $J_{4,3} = J_{4,5} = 6$, $J_{4,6} = 1.5$), 3.78 (s, 3H, methoxyl), and 1.83 (d, 3H, methyl, $J_{Me,3} = 1.5$); ^{13}C NMR (62.9 MHz; $CDCl_3$): 14.7, 47.5, 55.1, 90.8, 119.2, 121.4, 123.0, 123.5, 131.5, 137.2, 138.4, 146.2, 147.7, and 151.5. Anal. calcd. for $C_{14}H_{14}O$: C 84.81, H 7.12; found: C 84.78, H 7.09.

*Sensitized photolysis of barrelene **15***

A 250 mL solution of cyclohexane containing 986.9 mg (5.0 mmol) of barrelene **15** and 15 mL of acetone sensitizer was photolyzed with Pyrex-filtered light for 2 h. The photolysate was concentrated and the residue chromatographed on Silica Gel 60 (0.9 cm × 20 cm) with 4% ethyl acetate – hexane solvent. The main band was rechromatographed on a silica gel/$AgNO_3$ column with 1.5% ethyl acetate – hexane solvent. The first band contained 179.9 mg (18%) of 5-methoxy-6-methylbenzotricyclo[3.3.0.0^{2,8}]octa-3,6-diene as a colourless solid, mp 85–87°C; UV (hexane): 282 (760), 274 (870), 268 sh (700), and 232 (5 270); ^{1}H NMR (250 MHz; $CDCl_3$): 7.13–7.32 (m, 4H, aromatics), 4.88 (m, 1H, H-7), 3.43 (t, 1H, H-1, $J_{1,2} = J_{1,8} = 6.5$), 3.32 (s, 3H, methoxyl), 3.10 (t, 1H, H-2, $J_{2,1} = J_{2,8} = 6.5$), 2.71 (dt, 1H, H-8, $J_{8,1} = J_{8,2} = 6.5 = J_{8,7} = 2.5$), and 1.66 (d, 3H, methyl, $J_{Me,1} = 1.2$); ^{13}C NMR (62.9 MHz; $CDCl_3$): 10.6 (methyl), 37.4 (C2), 37.7 (C8), 51.2 (C1), 52.9 (methoxyl), 99.1, 117.5 (C7), 119.3, 125.2, 125.3, 127.3, 136.4, 145.2, and 147.5; assignments as determined by Hetcorr experiments. Mass spectrum showed molecular ion at *m/e* = 198.1046 (94%); $C_{14}H_{14}O$ requires 198.1045. Anal. found: C 85.20, H 7.10.

The second band gave 330.7 mg (34%) of 5-methoxy-1-methylbenzotricyclo[3.3.0.0^{2,8}]octa-3,6-diene (SB **16**) as a colourless liquid, after short-path distillation at 80°C/0.1 Torr; UV (hexane): 282.5 (820), 275 (920), 269 sh (710), and 230 (2 430); ^{1}H NMR (250 MHz; $CDCl_3$): 7.12–7.29 (m, 4H, aromatics), 5.65 (d, 1H, H-6, $J_{6,7} = 5$), 5.15 (dd, 1H, H-7, $J_{7,6} = 5$, $J_{7,8} = 2.5$), 3.50 (s, 3H, methoxyl), 3.04 (d, 1H, H-2, $J_{2,8} = 6.5$), 2.71 (dd, 1H, H-8, $J_{8,7} = 2.5$, $J_{8,2} = 6.5$), and 1.43 (s, 3H, methyl); ^{13}C NMR (62.9 MHz; $CDCl_3$): 14.3 (methyl), 44.5 (C2), 46.8 (C8), 54.8 (methoxyl), 61.2, 98.5, 120.2 (C7), 120.7, 125.1, 125.44, 127.3, 135.1 (C6), 135.9, and 148.7; assignments as determined by Hetcorr experiments. Mass spectrum showed molecular ion at *m/e* = 198.1051 (100%); $C_{14}H_{14}O$ requires 198.1045. Anal. found: C 84.63, H 7.03. The third band gave 169.3 mg (17%) of recovered barrelene.

*Gas phase thermolysis of SB **16**, and conversion of COT **17** to ketone **18***

Over a 1.5 h period 592.6 mg (3.0 mmol) of SB **16** was distilled into a Pyrex tube (2 cm × 30 cm) packed with glass beads (0.5 cm diameter) maintained at ca. 460°C. The pressure was kept at 6 Torr by the passage of argon. The thermolysis product, mostly COT **17**, collected in an ice-cooled U-trap, was not purified, but was treated directly with 8 mL of 80% aqueous acetic acid. The solution was stirred at room temperature overnight, then treated with 200 mL of 15% aqueous $KHCO_3$, and extracted with 200 mL hexane. The extract was washed (2 × 50 mL water), dried (Na_2SO_4), concentrated, and chromatographed on Silica Gel 60 (0.9 cm × 7 cm) with 5% ether – hexane solvent. The main band was rechromatographed on a Lobar column (3% ethyl acetate – hexane). The first fraction gave 292.3 mg (53%) of ketone **18**, mp 46–48°C (from hexane); IR (Nujol): 1685 (C=O) cm^{-1}; UV (hexane): 366 sh (220), 351 sh (660), 336 sh (1140), 312 sh (3080), 305 (3270), 234 (27300); ^{1}H NMR (250 MHz; $CDCl_3$): 8.35 (dd, 1H, H-4, $J = 7.7$, $J = 1.7$), 7.46–7.52 (m, 1H, aromatic), 7.26–7.34 (m, 2H, 2 aromatics), 6.71 (br s, 1H, H-10), 6.15 (d, 1H, H-8, $J_{8,7} = 10$), 5.76 (dt, 1H, H-7, $J_{7,8} = 10$, $J_{7,6} = J_{7,6'} = 8$), 3.43 (d, 2H, H-6 and H-6′, $J_{6,7} = J_{6,7'} = 8$), and 2.08 (d, 3H, methyl, $J_{Me,10} = 1.1$); ^{13}C NMR (62.9 MHz; $CDCl_3$): 24.7 (methyl), 44.3 (CH_2), 126.37 (C7), 126.40, 128.8 (C10), 130.6 (C4), 132.0, 132.9 (C8), 133.3, 136.0, 136.8, 138.1, 195.0 (C=O); assignments as determined by Hetcorr experiments. Mass spectrum showed molecular ion at *m/e* = 184.0886 (94%), 169 (100%), $C_{13}H_{12}O$ requires 184.0888. Anal. calcd. for $C_{13}H_{12}O$: C 84.75, H 6.57; found: C 84.73, H 6.74.

*Cyclohexanone **19** from irradiation of ketone **18***

A 250 mL solution of cyclohexane containing 474.4 mg (2.40 mmol) of ketone **18** and 40 mL of piperylene quencher was photolyzed with Pyrex-filtered light for 15 min in Cell A. The photolysate was concentrated and the residue chromatographed on Silica Gel 60 (0.9 cm × 10 cm) with 100 mL of 5% ethyl acetate – hexane solvent. The main band was rechromatographed on a Lobar column with 2.5% ethyl acetate – hexane solvent. The first band gave 64.5 mg (14%) of recovered ketone **18**; the second band contained 386.2 mg (81%) of colourless cyclohexanone **19**, mp 47–48°C (from hexane); IR (Njuol): 1663 (C=O) cm^{-1}; UV (cyclohexane): 328 (85), 289 (1350); ^{1}H NMR (250 MHz; $CDCl_3$): 7.87 (dd, 1H, aromatic, $J = 1.5$, $J = 7.5$), 7.52 (dt,

Can. J. Chem. Downloaded from www.nrcresearchpress.com by EESC ESCOLA DE ENGENHARIA on 09/08/12
For personal use only.

1H, aromatic, J = 1.5, J = 7.5), 7.25–7.34 (m, 2H, 2 aromatics), 5.80 (m, 1H, H-7), 3.88 (br d, 1H, H-1, $J_{1,6}$ = 4.0), 3.51 (sym m, 1H, H-6,), 2.84 (dd, 1H, H-5′, $J_{5',5}$ = 16, $J_{5',6}$ = 2.0), 2.72 (dd, 1H, H-5, $J_{5,5'}$ = 16, $J_{5,6}$ = 7.5), and 1.50 (sym m, 3H, methyl); ^{13}C NMR (62.9 MHz; $CDCl_3$): 14.0 (methyl), 35.1 (C6), 41.3 (CH_2), 46.4 (C1), 126.3, 127.4, 128.7, 130.7 (C7), 133.1, 144.1, 154.0, 196.7 (C=O), one carbon missing; assignments as determined by Hetcorr experiments. Mass spectrum showed molecular ion at *m/e* = 184.0886 (63%), 115 (100%); $C_{13}H_{12}O$ requires 184.0888. Anal. found: C 84.75, H 6.57.

*Triene **20** from cyclohexanone **19** via the Shapiro reaction (27)*

A solution of 66 mg (0.36 mmol) of cyclohexanone **19**, 66 mg (0.36 mmol) of *p*-toluenesulfonylhydrazide, and 0.1 mL of acetic acid in 1 mL of methanol was refluxed for 30 min, left to stand at room temperature overnight, and then cooled to −12°C for 12 h. The resulting crystals were filtered and dried in vacuo to give 102 mg (81%) of the tosylhydrazone as white crystals, mp 185–187°C (dec.). A solution of 0.5 mL (0.7 mmol) of 1.4 M methyllithium in ether was slowly added (2 min) to a stirred, ice-cooled slurry of 102 mg (0.29 mmol) of the tosylhydrazone in 2 mL of dry ether, under a nitrogen atmosphere. The resulting orange solution was stirred at room temperature for 1.25 h, refluxed for 10 min, cooled, and then made slightly acidic by the addition of aqueous ammonium chloride solution. The ether layer was washed with water, dried ($MgSO_4$), concentrated, and the residue chromatographed on Silica Gel 60 (0.9 cm × 10 cm) with hexane solvent. The main band gave 48.7 mg (88%) of triene **20** as a colourless oil (>99% pure by GC); UV (cyclohexane): 302 (1110), 295 sh (2300), 290 sh (2900), 282 (4750), and 271 (5120); ^{1}H NMR (400 MHz; $CDCl_3$): 7.08–7.26 (m, 2H, aromatics), 6.99–7.04 (m, 2H, aromatics), 6.22 (d, 1H, H-4, $J_{4,5}$ = 10), 5.90 (dd, 1H, H-5, $J_{5,4}$ = 10, $J_{5,6}$ = 4.5), 5.84 (br s, 1H, H-7), 3.91 (d, 1H, H-1, $J_{1,6}$ = 4.5), 3.48 (br s, 1H, H-6), and 1.65 (br s, 3H, methyl); spin decoupling experiments: irradiation of H-5 collapsed H-4 to an s; irradiation of H-7 modified the methyl signal, irradiation of H-1 modified H-6 and the methyl signal; irradiation of H-6 collapsed H-5 to a d ($J_{5,4}$ = 10) and H-1 to an s; irradiation of the methyl signal sharpened H-7 and H-1, and collapsed H-6 to a t ($J_{6,1}$ = $J_{6,5}$ = 4.5); ^{13}C NMR (62.9 MHz; $CDCl_3$): 14.3 (methyl), 39.7 (C6), 45.6(C1), 125.4 (C4), 126.5, 127.4, 127.8, 128.0, 129.5 (C5), 132.1 (C7), 134.7, 149.0, one carbon missing; assignments as determined by Hetcorr experiments. Mass spectrum showed molecular ion at *m/e* = 168.0936 (70%), 128 (100%; M^+ − propyne); $C_{13}H_{12}$ requires 168.0939. Anal. calcd. for $C_{13}H_{12}$: C 92.81, H 7.19; found: C 93.01, H 7.31.

*Thermolysis of triene **20***

A solution of 6.1 mg (0.036 mmol) of **20** in 1 mL of *n*-nonane was refluxed (ca. 150°C) for 5 h. The thermolysis product was chromatographed on Silica Gel 60 (0.9 cm × 10 cm; cyclohexane). Short-path distillation (60°C/0.1 Torr) of the main band gave 5.5 mg (90%) of COT **21**; UV (cyclohexane): 269 sh (1200) and 234 (22 500); ^{1}H NMR (400 MHz; $CDCl_3$): 7.16–7.24 (m, 2H, aromatics), 6.95–6.96 (m, 2H, aromatics), 6.57 (d, 1H, H-10, $J_{10,9}$ = 11.5), 6.34 (br s, 1H, H-5), 6.04 (dd, 1H, H-9, $J_{9,8}$ = 2.5, $J_{9,10}$ = 11.5), 5.82 (m, 2H, H-7 and H-8), and 1.88 (m, 3H, methyl); spin decoupling experiments: irradiation of the methyl signal sharpened H-5; irradiation of the H-7, H-8 multiplet collapsed H-9 to a d ($J_{9,10}$ = 11.5); irradiation of H-9 collapsed H-10 to an s, and modified the H-7, H-8 multiplet; irradiation of H-5 collapsed the methyl signal to an s; irradiation of H-10 collapsed H-9 to a br s; ^{13}C NMR (62.9 MHz; $CDCl_3$): 24.0 (methyl), 126.4, 126.9, 128.5, 129.0, 129.2, 129.6, 131.3, 133.7, 134.2, 138.0, 139.1, and 139.3; a solution containing 0.1 M **21** and 0.2 M Ag FOD (Aldrich) gave ^{1}H NMR (250 MHz; $CDCl_3$): 7.17–7.27 (m, 2H, aromatics), 6.95–7.20 (m, 2H, aromatics), 6.75 (d, 1H, H-10, $J_{10,9}$ = 11.5), 6.50 (br s, 1H, H-5), 6.24 (dd, 1H, H-9, $J_{9,8}$ = 2.5, $J_{9,10}$ = 11.5), 5.98 (d, 1H, H-7, $J_{7,8}$ = 11.5), 5.92 (dd, 1H, H-8, $J_{8,7}$ = 11.5, $J_{8,9}$ = 2.5), and 1.96 (d, 3H, methyl, $J_{Me,5}$ = 1.3). Mass spectrum showed molecular ion at *m/e* = 168.0936 (100%).

*Direct irradiation of triene **20***

A solution of 64.2 mg (0.38 mmol) of **20** and 43.2 mg of undecane (GC standard) in 250 mL of cyclohexane was irradiated (Pyrex filter) for 2.5 h in Cell A (78% conversion by GC). The photolysate composition analysed (as determined by GC peak areas calibrated (peak area versus mass) for the undecane internal standard against individual photolysate components) for 1.37 mg (2%) of naphthalene, 17.4 mg (27%) of pentacyclic **23**, 2.3 mg (3.5%) of COT **21**, ca. 0.6 mg (1%) of COT **24**, 13.9 mg (22%) of triene **20**, and 22.9 mg (36%) of SB **22**. The photolysate was concentrated and chromatographed on Silica Gel 60 (0.9 cm × 10 cm; 100 mL hexane) to remove polymeric materials. The eluate was concentrated and chromatographed on a Lobar column with hexane solvent. The first band contained a trace of naphthalene (identified by GC and TLC comparison with an authentic sample). The second band gave 15.2 mg (24%) of colourless pentacyclic **23**, after short-path distillation (60°C/0.1 Torr); UV (hexane): 274 (965), 267 (865), 265 sh (750), 261 (610), and 255 sh (410); ^{1}H NMR (400 MHz; $CDCl_3$): 7.13–7.19 (m, 2H, aromatics), 7.10–7.13 (m, 2H, aromatics), 3.59 (br s, 2H, H-1 and H-6), 2.69 (t, 1H, H-4, $J_{4,2}$ = $J_{4,3}$ = 3.5), 2.04–2.06 (m, 2H, H-2 and H-3), and 0.90 (s, 3H, methyl); spin decoupling experiments: irradiation of H-1(6) collapsed H-2(3) to a d ($J_{4,2(3)}$ = 3.5); irradiation of H-2(3) sharpened H-1(6), and collapsed H-4 to an s; irradiation of H-4 collapsed H-2(3) to an s. ^{13}C NMR (62.9 MHz; $CDCl_3$): 15.5, 20.1, 26.9, 55.2, 67.0, 122.1, 125.8, and 146.9. Mass spectrum showed molecular ion at *m/e* = 168.0934 (52%), 128 (100%); $C_{13}H_{12}$ requires 168.0939.

The third band gave 11.7 mg (18%) of recovered triene **20**. The fifth band gave 19.8 mg (31%) of SB **22**, mp 53–54.5°C, after crystallization from ethanol; UV (hexane): 283 (820), 275 (1000), and 269 sh (920); ^{1}H NMR (400 MHz; $CDCl_3$): 7.33 (d, 1H, aromatic, J = 7), 7.06–7.16 (m, 2H, aromatics), 7.01 (d, 1H, aromatic, J = 7), 4.86 (br s, 1H, H-7), 3.60 (d, 1H, H-5, $J_{5,1}$ = 6.25), 3.33 (q, 1H, H-1, $J_{1,2}$ = $J_{1,5}$ = $J_{1,8}$ = 6.5), 2.96 (t, 1H, H-2, $J_{2,1}$ = $J_{2,8}$ = 6.5), 2.58 (dt, 1H, H-8, $J_{8,1}$ = 6.5, $J_{8,7}$ = 2.5), and 1.72 (s, 3H, methyl); spin decoupling experiments: irradiation of the methyl collapsed H-7 to a d ($J_{7,8}$ = 2.5); irradiation of H-8 collapsed H-2 to a d ($J_{2,1}$ = 6.3); irradiation of H-2 collapsed H-8 to an unresolved dd, and H-1 to a t ($J_{1,5}$ = $J_{1,8}$ = 6.2); irradiation of H-1 collapsed H-8 to an unresolved d, H-2 to a d ($J_{2,8}$ = 7), and collapsed H-5 to an s; irradiation of H-5 collapsed H-1 to a t ($J_{1,2}$ = $J_{1,8}$ = 6.5); irradiation of H-7 collapsed H-8 to a t ($J_{8,1}$ = $J_{8,2}$ = 6.5) and sharpened the methyl signal. ^{13}C NMR (62.9 MHz; $CDCl_3$): 13.9, 37.3, 38.2, 49.2, 57.4, 116.7, 120.5, 125.0, 125.3, 126.1, 138.7, 146.4, and 149.9. Mass spectrum showed molecular ion at *m/e* = 168.0935 (100%); $C_{13}H_{12}$ requires 168.0939.

The fourth band contained a mixture of the COTs **21** and **24**. These were separated on a silica gel/$AgNO_3$ column with hexane solvent. The first band contained ca. 1.5 mg (2%) of COT **21** (identified by NMR and GC comparison with an authentic sample, vide supra). The second band contained ca. 0.5 mg (1%) of COT **24** of GC purity >98%; ^{1}H NMR (400 MHz; $CDCl_3$): 7.17–7.20 (m, 2H, aromatics), 6.96–6.98 (m, 2H, aromatics), 6.49 (d, 2H, H-5 and H-10, $J_{5,6}$ = $J_{10,9}$ = 11.5), 5.98–6.00 (br d, 1H, H-9, $J_{9,10}$ = 11.5), 5.96 (d, 1H, H-6, $J_{6,5}$ = 11.5), 5.62 (br s, 1H, H-8), and 1.76 (br s, 3H, methyl); mass spectrum from GC/MS showed molecular ion at *m/e* = 168.1 (75%), 153.1 (100%).

*Sensitized irradiation of triene **20***

A solution of 32.2 mg (0.19 mmol) of **20**, 10.0 mg of undecane (GC standard), and 31.2 mg (0.14 mmol) of *p*-dimethylaminobenzophenone in 40 mL of cyclohexane was irradiated for 30 min in Cell B, with light filtered through a WG 360 glass (Schott) filter (53% conversion by GC). The photolysate composition analysed (as determined by GC peak areas calibrated (peak area versus mass) for the undecane internal standard against the individual photolysate components) for ca. 0.5 mg (2%) of naphthalene, ca. 0.2 mg (0.5%) of COT **21**, 15.2 mg (47%) of triene **20**, and 7.5 mg (23%) of SB **22**. The photolysate was concentrated and chromatographed on Silica Gel 60 (0.9 cm × 10 cm; 100 mL hexane) to remove polymeric materials and sensitizer. The eluate was concentrated and chromatographed on a Lobar column with hexane solvent. The first band contained a trace of naphthalene (identified by GC and TLC comparison with an authentic sample). The second band gave a trace of COT **21** (identified by NMR and GC

Can. J. Chem. Downloaded from www.nrcresearchpress.com by EESC ESCOLA DE ENGENHARIA on 09/08/12
For personal use only.

comparison with an authentic sample). The third band gave 13.8 mg (43%) of recovered triene **20**, and the final band gave 7.3 mg (23%) of SB **22** (GC purity > 99%).

*Labelled cyclohexanone **10**a*

To a solution of 458.7 mg (2.49 mmol) of cyclohexanone **19** in 47 g of methanol-d_1 was added 20 mg of potassium carbonate. The solution was stirred at room temperature for 48 h. The solvent was removed under vacuum (oil pump) and the residue was taken up in hexane (15 mL) and washed with D_2O (2 mL). The hexane solution was concentrated and chromatographed on SG 60 (0.9 cm × 3 cm) with 5% ethyl acetate – hexane. The main band gave 445.3 (97%) of deuterated cyclohexanone **19***a* (95%-d_2 labelled at C-5), mp 47–48°C; ^{1}H NMR (250 MHz; $CDCl_3$): 7.87 (dd, 1.00H, aromatic, J = 1.5, J = 7.5), 7.52 (dt, 1.02H, aromatic, J = 1.5, J = 7.5), 7.25–7.34 (m, 2.07H, 2 aromatics and residual $CHCl_3$), 5.80 (m, 1.00H, H-7), 3.88 (br s, 1.01H, H-1), 3.51 (br s, 1.00H, H-6), 2.72 and 2.84 (m and m, 0.05H, H-5′ and H-5), and 1.50 (sym m, 3.09H, methyl).

*Labelled triene **20**a from cyclohexanone **19**a via the Shapiro reaction*

A solution of 445.3 mg (2.39 mmol) of deuterated cyclohexanone **19***a* (95%-d_2 at C-5), 457.1 mg (2.49 mmol) of *p*-toluenesulfonylhydrazide, and 0.3 mL of acetic acid-d_1 in 3 mL of methanol-d_1 was left to stand at room temperature for 18 h, and then cooled to −12°C for 12 h. The resulting crystals were filtered and dried in vacuo to give 597.5 mg (82%) of labelled tosylhydrazone as white crystals, mp 185–187°C (dec.). The procedure described above for the preparation of triene **20** was used to convert 201.9 mg (0.57 mmol) of the labelled tosylhydrazone to 115.6 mg (96%) of labelled triene **20***a* (GC purity >99%); ^{1}H NMR (250 MHz; $CDCl_3$): 6.97–7.14 (m, 2.20H, 2 aromatics and residual $CHCl_3$), 6.89–6.97 (m, 2.00H, aromatics), 6.13 (s, 0.43H, H-4), 5.81 (dd, 0.03H, H-5, $J_{5,4}$ = 10, $J_{5,6}$ = 4.5), 5.76 (br s, 1.00H, H-7), 3.82 (d, 1.00H, H-1, $J_{1,6}$ = 4.5), 3.39 (br s, 1.00H, H-6), and 1.56 (br s, 3.05H, methyl), i.e., triene **20***a* is 97%-d_1 labelled at C-5 and 57%-d_1 labelled at C-4.

*Thermolysis of labelled triene **20**a*

A solution of 8.2 mg (0.049 mmol) of **20***a* in 1 mL of *n*-nonane was refluxed (ca. 150°C) for 16 h. The thermolysis product was chromatographed on Silica Gel 60 (0.9 cm × 10 cm; hexane). Short-path distillation (60°C/0.1 Torr) of the main band gave 7.6 mg (93%) of COT **21***a*; ^{1}H NMR (250 MHz; $CDCl_3$): 7.12–7.23 (m, 2.05H, aromatics), 6.92–7.00 (m, 2.00H, aromatics), 6.57 (br s, 0.42H, H-10), 6.34 (br s, 1.00H, H-5), 6.04 (m, 0.02H, H-9), 5.82 (m, 2.02H, H-7 and H-8), and 1.88 (d, 3.14H, methyl, $J_{Me,5}$ = 1.5).

*Direct irradiation of labelled triene **20**a*

A solution of 112.0 mg (0.67 mmol) of **20***a* and 14.2 mg of undecane (GC standard) in 250 mL of cyclohexane was irradiated (Pyrex filter) for 3.3 h in Cell A (79% conversion by GC). The photolysate was worked up as in the case of the direct irradiation of unlabelled triene **20** to give ca. 1.0 mg (1%) of naphthalene, and 11.2 mg (17%) of pentacyclic **23**-$d_{1.5}$, ^{1}H NMR (250 MHz; $CDCl_3$): 7.09–7.20 (m, 4.21H, 4 aromatics + residual $CHCl_3$), 3.58 (s, 1.45H, H-6 and residual H-1), 2.67 (d, 1.00H, H-4, $J_{4,3}$ = 3.5), 2.05 (br s, 1.02H, H-2, and H-3), and 0.90 (s, 3.40H, methyl); 17.9 mg (16%) of recovered triene **20***a*, ^{1}H NMR (250 MHz; $CDCl_3$): 7.08–7.17 (m, 2.06H, 2 aromatics), 6.98–7.00 (m, 2.00H, aromatics), 6.14 (s, 0.42H, H-4), 5.90 (dd, 0.03H, H-5, $J_{5,4}$ = 10, $J_{5,6}$ = 4.5), 5.84 (br s, 0.99H, H-7), 3.91 (d, 1.00H, H-1, $J_{1,6}$ = 4.5), 3.48 (br s, 1.00H, H-6), and 1.64 (br s, 3.15H, methyl); 29.2 mg (26%) of SB **22***a*, ^{1}H NMR (250 MHz; $CDCl_3$): 7.34 (d, 1.00H, aromatic, J = 7), 7.01–7.17 (m, 3.05H, aromatics), 4.86 (br s, 0.97H, H-7), 3.60 (d, 1.00H, H-5, $J_{5,1}$ = 6.25), 3.33 (t, 0.97H, H-1, $J_{1,2} = J_{1,5}$ = 6.5), 2.96 (d, 0.45H, H-2, $J_{2,1}$ = 6.5), 2.58 (m, 0.03H, H-8), and 1.72 (s, 3.06H, methyl); 2.5 mg (2%) of labelled COT **21**; a solution containing 0.02 M COT and 0.2 M Ag FOD (Aldrich) gave ^{1}H NMR (250 MHz; $CDCl_3$): 7.15–7.27 (m, 2.92H, 2 aromatics plus residual $CHCl_3$), 6.93–7.10 (m, 2.00H, aromatics), 6.65–6.71 (m, 0.43H, H-10, $J_{10,9}$ = 11.5), 6.45 (br s, 0.97H, H-5), 6.14–6.19 (m, 0.35H, H-9), 5.92 (d, broad larger limb, 0.98H, H-7, $J_{7,8}$ = 11.5) and 5.88 (d, 0.74H, H-8, $J_{8,7}$ = 11.5), and 1.92 (d, 3H, methyl, $J_{Me,5}$ = 1.2); and 1.2 mg (1%) of COT **24***a*, ^{1}H NMR (250 MHz; $CDCl_3$): 7.18–7.22 (m, 2.11H, aromatics), 6.94–6.99 (m, 2.00H, aromatics), 6.49 (d and br s, 1.48H, H-5 and H-10, $J_{5,6}$ = 11.5), 5.92 (d, 1.02H, H-6 and residual H-9, $J_{9,10}$ = 11.5), 5.62 (br s, 1.00H, H-8), and 1.76 (s, 3.43H, methyl).

*Sensitized irradiation of triene **20**a*

A solution of 45.4 mg (0.27 mmol) of **20***a*, 13.3 mg of undecane (GC standard), and 45.4 mg (0.20 mmol) of *p*-dimethylaminobenzophenone in 40 mL of cyclohexane was irradiated for 40 min in Cell B, with light filtered through a WG 360 glass (Schott) filter (57% conversion by GC). The photolysate was worked up as in the case of the sensitized irradiation of unlabelled triene **11** to give a trace of naphthalene; 13.4 mg (30%) of recovered triene **20***a*, ^{1}H NMR (250 MHz; $CDCl_3$): 7.07–7.17 (m, 2.00H, 2 aromatics), 6.96–7.06 (m, 2.00H, aromatics), 6.22 (s, 0.42H, H-4), 5.90 (dd, 0.02H, H-5, $J_{5,4}$ = 10, $J_{5,6}$ = 4.5), 5.84 (br s, 0.97H, H-7), 3.91 (d, 0.98H, H-1, $J_{1,6}$ = 4.5), 3.48 (br s, 1.00H, H-6), and 1.64 (br s, 3.07H, methyl); a trace of COT **21***a*, ^{1}H NMR (250 MHz; $CDCl_3$): 7.14–7.21 (m, 1.96H, aromatics), 6.94–6.98 (m, 2.00H, aromatics), 6.57 (br s, 0.45H, H-10), 6.34, (br s, 0.99H, H-5), 6.04 (m, 0.03H, H-9), 5.83 (m, 1.98H, H-7 and H-8), and 1.88 (d, 3.29H, methyl, $J_{Me,5}$ = 1.5); and 7.3 mg (16%) of SB **22***a*, ^{1}H NMR (250 MHz; $CDCl_3$): 7.34 (d, 1.00H, aromatic, J = 7), 7.01–7.17 (m, 3.15H, aromatics), 4.86 (br s, 0.98H, H-7), 3.60 (d, 1.00H, H-5, $J_{5,1}$ = 6.25), 3.33 (t, 1.00H, H-1, $J_{1,2} = J_{1,5}$ = 6.5), 2.96 (d, 0.45H, H-2, $J_{2,1}$ = 6.5), 2.58 (m, 0.02H, H-8), and 1.72 (s, 3.06H, methyl).

Quantum yield determinations

Quantum yield measurements were performed on an apparatus previously described (28), which includes an optical bench arranged for beam splitting into a ferrioxalate actinometer (29). Cyclohexane solutions (3.5 mL) of reactants (ca. (4.5–6.5) × 10^{-3} M) and sensitizer, if any (*p*-dimethylaminobenzophenone, 5.0 × 10^{-3} M; benzophenone, 8.2 × 10^{-2} M; and thioxanthone, 1.2 × 10^{-3} M), were deoxygenated prior to irradiation by flushing with argon. A positive pressure of argon was maintained over the stirred solutions throughout the course of the irradiations. The quantum yields (Φ's) were obtained from several runs extrapolated to zero conversion. Product analyses were determined by GC (internal tetradecane standard). For the direct irradiation of triene **20**, light of wavelength 280 nm was used. For sensitized runs the sensitizers absorbed >95% of the incident light (366 nm) employed.

Calculations

The CNDO semi-empirical molecular orbital calculations were performed on the full molecules, as previously described (13), except that the ground state geometries were determined using the MNDO approximation (30), since optimization via the CNDO approach led to collapse of the bridgehead C5—C6—C7 angle of triene **20**. The version of MNDO used was contained in the HyperChem package of programs.[2] The vertical excitation energies were obtained by configuration interaction (60 states) with the CNDO/S parametization (31), using a modified version of the program QCPE no. 315, originally written by Del Bene and Jaffé (31, 32). The CI expansion coefficients were employed to partition the excitation energy into single atom and atom–atom interaction energies (13); the latter energies are listed in Table 3. We interpret negative values to indicate "forces" that tend to bring atoms together, while positive values cause the atoms to move further apart. Inspection of Table 3 shows that the entries for compound **3** are mostly very similar to those for **20**; only for the 1–2 atom–atom interaction energies are there significant differences between the two trienes, and for which we are unwilling to identify a mechanistic consequence.

Acknowledgements

The authors thank the Spectroscopic Services Laboratory of

[2]HyperChem Release 3 for Windows. Autodesk, Inc., 2320 (1993), Marinsjip Way, Sausalito, CA 94965, U.S.A.

the University of Alberta (U. of A.) and the Agriculture Canada Research Station at Lethbridge for the 400-MHz NMR. The U. of A. is also thanked for the precision mass spectra. Financial support from the Natural Sciences and Engineering Research Council of Canada is gratefully acknowledged.

1. (*a*) D. De Keukeleire and S.-L. He. Chem. Rev. **93**, 359 (1993); (*b*) M. Demuth. *In* Comprehensive organic synthesis. Vol. 2. *Edited by* L.E. Paquette. Pergamon Press, Oxford. 1991. p. 215; (*c*) M. Demuth. *In* Organic photochemistry. Vol. 11. *Edited by* A. Padwa. Marcel Dekker, New York. 1991. p. 37; (*d*) P.A. Wender, R. Ternansky, M. deLong, S. Singh, A. Olivero, and K. Rice. Pure Appl. Chem. **62**, 1597 (1990).
2. (*a*) M. Demuth. Mod. Synth. Methods, **4**, 89 (1986); (*b*) Pure Appl. Chem. **58**, 1233 (1986); (*c*) M. Demuth and K. Schaffner. Angew. Chem. Int. Ed. Engl. **21**, 820 (1982).
3. C.O. Bender, D. Dolman, and N. Tu. J. Org. Chem. **56**, 5015 (1991).
4. C.O. Bender, D.S. Clyne, and D. Dolman. Can. J. Chem. **69**, 70 (1991).
5. C.O. Bender and D. Dolman. Can. J. Chem. **67**, 82 (1989).
6. C.O. Bender, D. Dolman, and G.K. Murphy. Can. J. Chem. **66**, 1556 (1988).
7. C.O. Bender, D.L. Bengtson, D. Dolman, and S.F. O'Shea. Can. J. Chem. **64**, 237 (1986).
8. C.O. Bender, I.M. Cassis, D. Dolman, L.D. Heerze, and F.L. Schultz. Can. J. Chem. **62**, 2769 (1984).
9. J.R. Scheffer and M. Yap. J. Org. Chem. **54**, 2561 (1989).
10. P.J. Collin and W.H.F. Sasse. Tetrahedron Lett. 1689 (1968).
11. H.E. Zimmerman, R.S. Givens, and R.M. Pagni. J. Am. Chem. Soc. **90**, 6096 (1968).
12. J. Stapersma, J.D.C. Rood, and G.W. Klumpp. Tetrahedron, **38**, 191 (1982).
13. C.O. Bender, D.W. Brooks, W. Cheng, D. Dolman, S.F. O'Shea, and S.S. Shugarman. Can. J. Chem. **56**, 3027 (1978).
14. C. Pascual, J. Meier, and W. Simon. Helv. Chim. Acta, **49**, 164 (1966).
15. R.H. Shapiro and E.C. Hornaman. J. Org. Chem. **39**, 2302 (1974).
16. H.E. Zimmerman, J.M. Nuss, and A.W. Tantillo. J. Org. Chem. **53**, 3792 (1988).
17. M. Reguero, F. Bernardi, H. Jones, M. Olivucci, I.N. Ragzos, and M.A. Robb. J. Am. Chem. Soc. **115**, 2073 (1993).
18. H.E. Zimmerman, H.M. Sulbach, and M.B. Tollefson. J. Am. Chem. Soc. **115**, 6548 (1993).
19. (*a*) H.E. Zimmerman. *In* Rearrangements in ground and excited states. Vol. 3. *Edited by* P. de Mayo. Academic Press, New York. 1980. Essay 16, pp. 131–166; (*b*) S.S. Hixson, P.S. Mariano, and H.E. Zimmerman. Chem. Rev. **73**, 531 (1973).
20. W. Adam, M. Dörr, J. Kron, and R.J. Rosenthal. J. Am. Chem. Soc. **109**, 7074 (1987).
21. R.B. Woodward and R. Hoffmann. *In* The conservation of orbital symmetry. Verlag Chemie, Weinheim, and Academic Press, New York. 1970. p. 63.
22. Y. Hanzawa and L.A. Paquette. Synthesis, 661 (1982).
23. A.H.A. Tinnemans and D.C. Neckers. J. Am. Chem. Soc. **99**, 6459 (1977).
24. Y. Hanzawa and L.A. Paquette. J. Am. Chem. Soc. **103**, 2269 (1981).
25. M.J.S. Dewar and S.D. Worley. J. Am. Chem. Soc. **50**, 654 (1969).
26. K.D. Jordan and P.D. Burrow. Acc. Chem. Res. **11**, 341 (1978).
27. (*a*) R.H. Shapiro and M.J. Heath. J. Am. Chem. Soc. **89**, 5734 (1967); (*b*) R.M. Adlington and A.G.M. Barrett. Acc. Chem. Res. **16**, 55 (1983).
28. C.O. Bender, D.L. Bengtson, D. Dolman, C.E.L. Herle, and S.F. O'Shea. Can. J. Chem. **60**, 1942 (1982).
29. C.G. Hatchard and C.A. Parker. Proc. R. Soc. London, A: **235**, 518 (1956).
30. M.J.S. Dewar and M.L. McKee. J. Am. Chem. Soc. **99**, 5231 (1977).
31. J. Del Bene and H.H. Jaffé. J. Chem. Phys. **50**, 1126 (1969).
32. (*a*) J. Del Bene and H.H. Jaffé. J. Chem. Phys. **48**, 1807 (1968); (*b*) **48**, 4050 (1968); (*c*) **49**, 1221 (1968).

Can. J. Chem. Downloaded from www.nrcresearchpress.com by EESC ESCOLA DE ENGENHARIA on 09/08/12
For personal use only.

Laser flash photolysis study of the photoenols generated from *ortho*-benzylbenzophenone in different solvents

J.C. NETTO-FERREIRA

Departamento de Química, Universidade Federal Rural do Rio de Janeiro, Rio de Janeiro, Brazil, 23851

V. WINTGENS

Laboratoire des Matériaux Moléculaires, Centre national de la recherche scientifique, Thiais, 94320-France

AND

J.C. SCAIANO[1]

Department of Chemistry, University of Ottawa, Ottawa, ON K1N 6N5, Canada

Received October 18, 1993

J.C. NETTO-FERREIRA, V. WINTGENS, and J.C. SCAIANO. Can. J. Chem. **72**, 1565 (1994).

Irradiation of *ortho*-benzylbenzophenone leads to the formation of two (*E,E* and *Z,E*) out of the possible four photoenols. Laser flash photolysis studies show that the process involves the intermediacy of a short-lived biradical ($\tau \sim 50$ ns in methanol) that decays concurrently with the formation of the photoenols. The *Z,E* enol is very short lived and decays by an allowed 1,5-hydrogen shift to regenerate the starting material; its lifetime is <30 ns, 280 ns, 1.4 μs, and 90 ns, in benzene, acetonitrile, methanol, and trifluoroethanol, respectively. The *Z,E* enol is stabilized in hydroxylic solvents, although the acidity of trifluoroethanol seems to promote reketonization. *E,E* Enol lifetimes range from 80 μs (trifluoroethanol) to 470 μs (benzene) and its decay involves cyclization leading to 10-phenylanthrone following oxidation of the appropriate dihydroanthracene formed initially.

J.C. NETTO-FERREIRA, V. WINTGENS et J.C. SCAIANO. Can. J. Chem. **72**, 1565 (1994).

L'irradiation de l'*ortho*-benzylbenzophénone conduit à la formation de deux (*E,E* et *Z,E*) des quatre photoénols possibles. Des études de photolyse éclair au laser montrent que le processus implique un biradical de courte vie ($\tau \sim 50$ ns, dans le méthanol) comme intermédiaire qui se décomposé concurremment avec la formation de photoénols. La durée de vie de l'énol *Z,E* est très courte et il se décompose par un déplacement 1,5 d'hydrogène pour régénérer le produit de départ; son temps de vie est respectivement de <30 ns, 280 ns, 1,4 μs et 90 ns dans le benzène, l'acétonitrile, le méthanol et le trifluoroéthanol. L'énol *Z,E* est stabilisé dans les solvants hydroxylés, même si l'acidité du trifluoroéthanol semble favoriser une recétonisation. Les temps de vie de l'énol *E,E* varient de 80 μs (trifluoroéthanol) à 470 μs (benzène) et sa décomposition implique une cyclisation conduisant à la 10-phénylanthrone après une oxydation du dihydroanthracène approprié qui se forme initialement.

[Traduit par la Rédaction]

Introduction

Aromatic ketones containing alkyl substituents in the *ortho* position give upon excitation a mixture of isomeric enols showing similar spectroscopic properties but very different kinetic behaviour. Triplet excited states and a rotationally equilibrated 1,4-biradical are the precursors for these photoenols (1–4).

In most cases the photoenols decay by a thermally allowed 1,5-hydrogen shift, regenerating the starting ketone. However, there are a few examples in which photoenol decay results in product formation. For example, photolysis of 2-substituted *ortho*-ethylbenzophenones gives *ortho*-vinylbenzophenone by elimination of the 2-substituent (5). Suitably substituted aromatic ketones can form the corresponding benzocyclobutenols in fairly high quantum yields, suggesting that intramolecular [2+2] cycloaddition may be a more common process in photoenol chemistry than had been previously assumed (6–9). Other examples include chloride elimination from α-chloro acetophenones with the concomitant formation of 1-indanones (10–12), the formation of 3-phenylphthalide from the photolysis of *ortho*-benzoylbenzaldehyde (13), and, finally, the synthesis of 2-hydroxy-2-alkyl(or aryl)-1-indanones from *ortho*-alkyl substituted aromatic α-diketones (14–18).[2]

In this paper we show results obtained by laser flash photolysis and product studies on the photoenols in different solvents, generated by irradiation of *ortho*-benzylbenzophenone (**1**).

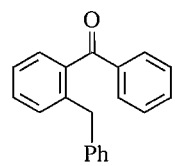

1

Previous studies on this ketone showing some of the possible intermediates involved in the dynamics of product formation from **1** have already been reported (19–21); however, a complete understanding of these processes is not yet available. Our goal was to provide such an understanding through the characterization of intermediates and products resulting from the photochemistry of *ortho*-benzylbenzophenone **1**.

Experimental part

Materials

The solvents employed were Spectrograde or Gold Label and were used as received. Dimethyl ketomalonate, dimethyl acetylenedicarboxylate, and maleic anhydride (all from Aldrich) were used as received. 1,3-Cyclohexadiene (Aldrich) was bulb-to-bulb distilled shortly before use.

ortho-Benzylbenzophenone (**1**) was synthesized in a three-step reaction. 2-Bromobenzhydrol was prepared by a Grignard reaction between phenylmagnesium bromide and 2-bromobenzaldehyde. The alcohol was then refluxed in the presence of iodine and red phosphorus

[1]Author to whom correspondence may be addressed.

[2]Also, V. Wintgens, J.C. Netto-Ferreira, and J.C. Scaiano, unpublished results.

Can. J. Chem. Downloaded from www.nrcresearchpress.com by EESC ESCOLA DE ENGENHARIA on 09/08/12
For personal use only.

using an acetic acid – water mixture as the solvent. The 2-bromodiphenylmethane obtained in this reaction was purified by fractional distillation under reduced pressure, following the same procedure described for the chlorine derivative (22). A Grignard reagent was prepared using this bromo derivative to which benzonitrile was added, with the resulting mixture being left under reflux for 8 h (a procedure similar to that described for the synthesis of 2-benzylphenyl-2-pyridylketone (23). After acid hydrolysis, **1** was extracted with ethyl ether from the crude mixture, and purified by preparative thin-layer chromatography in a Chromatotron apparatus (silica gel, 1.5% ethyl acetate – hexane), yielding pale yellow crystals, mp 50–51°C (lit. (22) mp 50–52°C).

General techniques

UV–visible spectra were recorded with a Hewlett–Packard 8451-A diode array spectrometer.

GC analyses were carried out on a Perkin–Elmer model 8320 capillary gas chromatograph employing a 12-m J&W bonded-phase vitreous silica BP1 silicone column. GC–MS analyses were performed on a Hewlett–Packard model 5995 instrument.

Melting points were determined in a Mel-Temp apparatus and were not corrected.

Product studies

Typical samples were 1 mL, containing 0.03 M of **1** in benzene or in trifluoroethanol. The samples were contained in Pyrex tubes and were deaerated by bubbling with oxygen-free nitrogen. The irradiations were carried out in a "merry-go-round" apparatus with nine RPR-3000 lamps. The products were analysed by GC and GC–MS.

Laser flash photolysis

Samples were contained in 7×7 mm^2 cells made of Suprasil quartz tubing and were deaerated by bubbling with oxygen-free nitrogen. The samples were irradiated with the pulses (308 nm, ≈5 ns, ≤20 mJ/pulse) from a Lumonics EX-510 excimer laser. Our detection system incorporates a monochromator–photomultiplier combination; the signals from the RCA-4840 photomultiplier were captured by a Tektronix 2440 transient digitizer, and were then transferred to a MacIntosh IIci computer that controlled the system and provided suitable storage and processing facilitioes through the use of a home-developed program using LabVIEW-2.2 software. Further details on similar laser systems have been reported elsewhere (24, 25).

Results

Product studies

Irradiation of *ortho*-benzylbenzophenone (**1**) in benzene at 300 nm leads to the formation of at least four products as analysed by GC–MS. The main product has a molecular weight of 270 and was attributed to 10-phenylanthrone (**2***b*), the keto form of 10-phenyl-9-anthranol (**2***a*). This product can be easily formed by an intramolecular cyclization from the corresponding *E,E* enol formed from **1** (vide infra), through the intermediacy of the properly substituted dihydroanthracene. Further oxidation of this intermediate leads to **2**.

While the irradiation was conducted with deaerated samples, they may still have contained some traces of oxygen, or be exposed to it during post-irradiation handling. Thus, oxygen

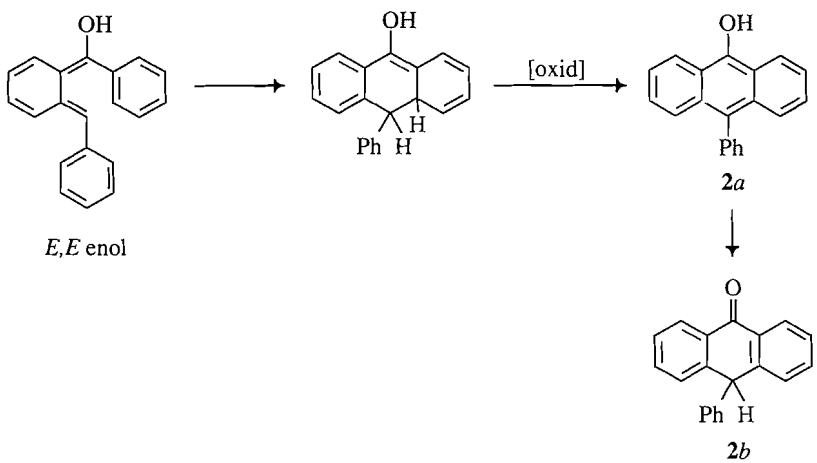

E,E enol

insertion in **2** can explain the formation of 10-hydroxy-10-phenyl-anthrone (26) (**3**), (mol. wt. 286), the other identified product obtained upon irradiation of **1**. The two other peaks present in the GC trace and accounting for ca. 20% of products could not be identified.

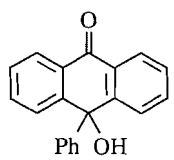

3

A mixture of the same products was obtained when **1** was photolyzed in trifluoroethanol.

Laser flash photolysis

Laser flash photolysis of *ortho*-benzylbenzophenone (**1**) in deaerated benzene leads to a transient spectrum with maxima at 340 and 440 nm (Fig. 1). The clean first-order decay associated with these two mixima (see insert in Fig. 1) leads us to conclude that it cannot be associated with a mixture of transients. The lifetime measured for this species is ca. 470 μs. Triplet quenchers such as 1,3-cyclohexadiene have no effect on this transient lifetime. On the other hand, the very efficient dienophile, dimethyl ketomalonate, quenches this transient with a rate constant of 3×10^4 M^{-1} s^{-1}. We were not able to observe any quenching by using either maleic anhydride or dimethyl acetylenedicarboxylate as quenchers. Based on these data, the transient responsible for the decay initially observed was tentatively identified as one of the four possible photoenols derived from **1**, i.e., the *E,E* enol **4** (vide infra).

The transient spectrum in deaerated acetonitrile is quite similar to that recorded in benzene. However, in this case two decay components are clearly observed. The shorter lived transient ($\tau = 280$ ns) was attributed to the *Z,E* enol **5**, with its faster deac-

Can. J. Chem. Downloaded from www.nrcresearchpress.com by EESC ESCOLA DE ENGENHARIA on 09/08/12
For personal use only.

Can. J. Chem. Downloaded from www.nrcresearchpress.com by EESC ESCOLA DE ENGENHARIA on 09/08/12
For personal use only.

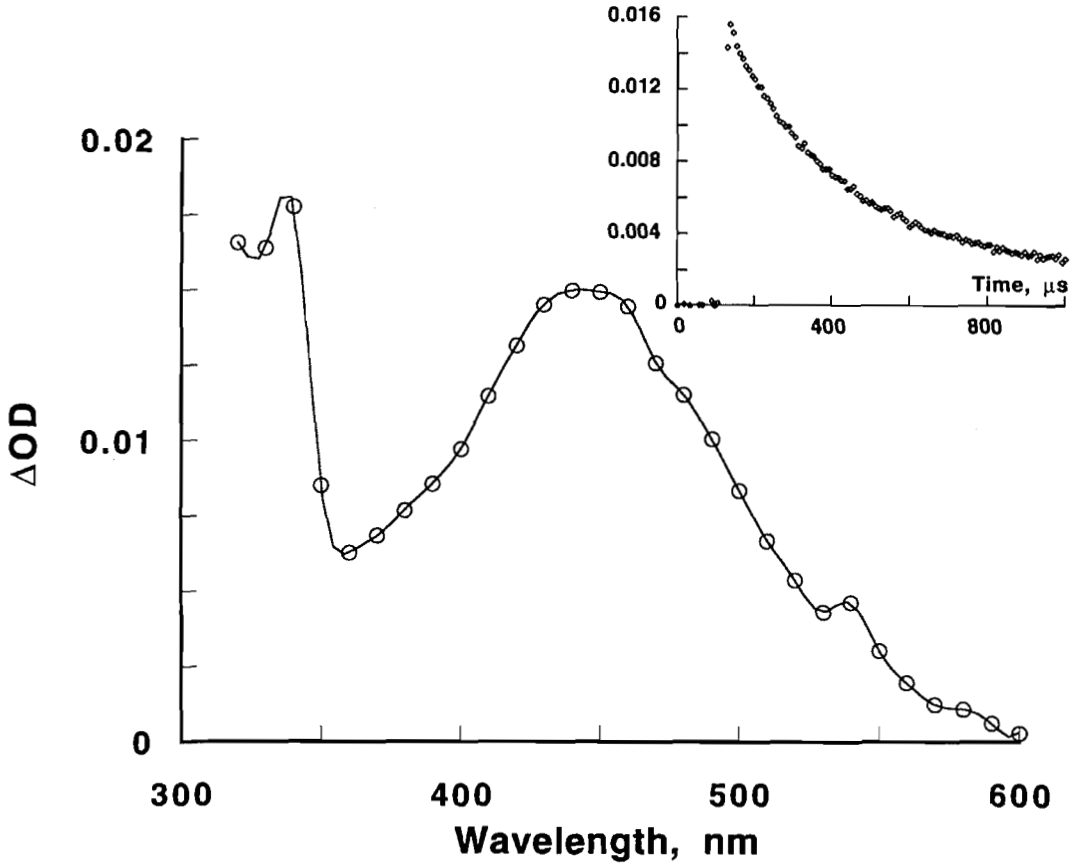

FIG. 1. Enol absorption spectrum obtained on 308 nm excitation of *ortho*-benzylbenzophenone (**1**) in benzene, and (insert) decay of the photoenol.

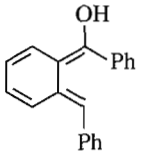

4 (*E,E* enol)

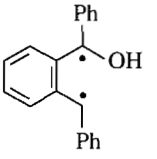

6

tivation rate constant being due to the allowed 1,5-hydrogen shift reketonization process. For the *E,E* enol we measured a lifetime of 190 μs.

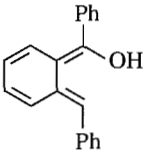

5 (*Z,E* enol)

At 330 nm we could also observe a very short-lived transient ($\tau \sim 20$ ns), readily quenched by oxygen but not by 1,3-cyclohexadiene. Concomitantly, a growth was noticed at 440 nm (the photoenol region) on the same time scale, following the same kinetics as those observed for the decay at 330 nm. This short-lived transient was attributed to biradical **6**, the expected precursor of the enols.

Just as in the case of benzene and acetonitrile, the spectrum recorded in methanol on a 50 μs time scale shows two bands with maxima at 320 and 440 nm (Fig. 2). A slight shift to the red could be observed when the spectrum was recorded 50 μs after the laser pulse, compared to the one recorded at 1 μs. The decay is clearly biexponential, from which we measured lifetimes of 1.4 and 150 μs, with both decays being insensitive to the presence of oxygen. Again, a short-lived transient was observed

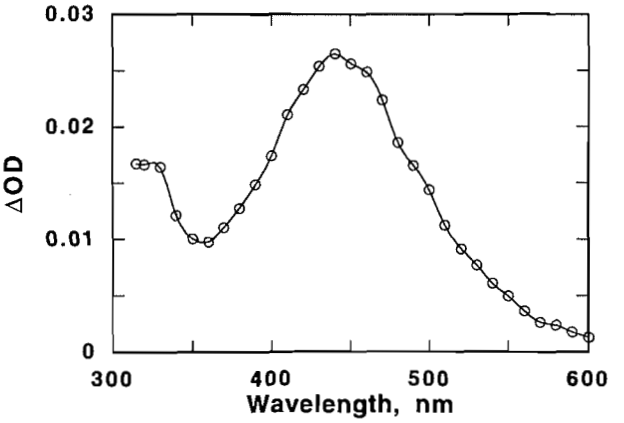

FIG. 2. Enols absorption spectra obtained on 308 nm excitation of *ortho*-benzylbenzophenone (**1**) in methanol on a 50 μs time scale.

Can. J. Chem. Downloaded from www.nrcresearchpress.com by EESC ESCOLA DE ENGENHARIA on 09/08/12
For personal use only.

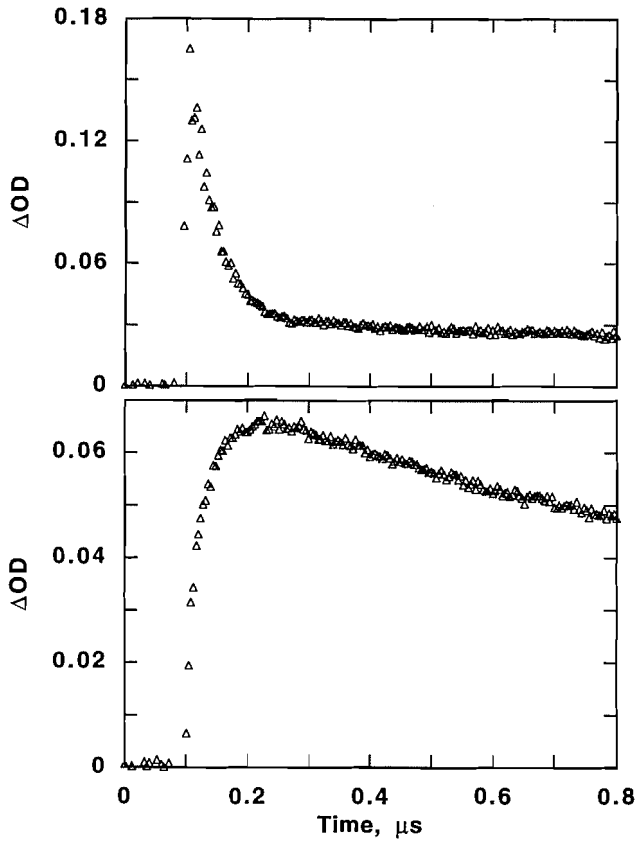

FIG. 3. Top: Decay of absorption at 330 nm due to biradical **6** generated from *ortho*-benzylbenzophenone (**1**) upon 308 nm excitation in methanol. Bottom: growth at 440 nm for the enol mixture generated as above.

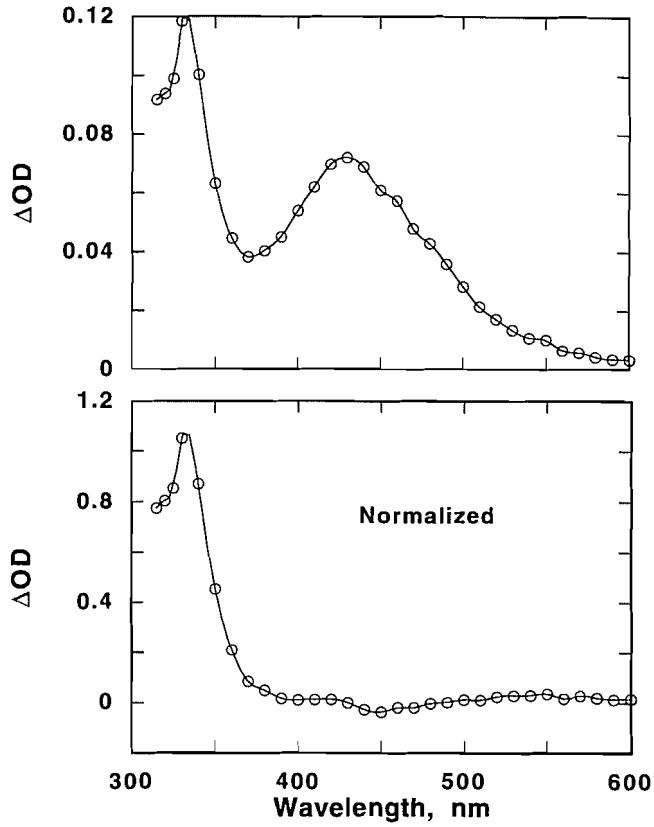

FIG. 4. Top: Enols absorption spectra obtained on excitation of *ortho*-benzylbenzophenone (**1**) in methanol on 1 μs time scale. Bottom: Difference spectrum from the subtraction of the spectrum in Fig. 2 from that in Fig. 4, top.

when the decay was monitored at 330 nm (Fig. 3, top), showing the same kinetics as the growth observed at 440 nm on the 100 ns time scale (Fig. 3, bottom).

When the spectrum in methanol was recorded on a 1 μs time scale, a very sharp and intense band with maximum absorption at 320 nm could be noticed in addition to the already reported photoenol absorptions at 320 and 440 nm (Fig. 4, top). Subtracting the spectrum at 50 μs decay (due to photoenols **4** and **5**) from the one recorded on this short time scale, corresponding to the biradical plus photoenols mixture, we obtain only one maximum at 330 nm, which can be assigned to biradical **6** (Fig. 4, bottom).

From the spectroscopic and kinetic points of view, there is great similarity between the data obtained in the previous solvents and in trifluoroethanol, the last solvent used in this work. For example, in this solvent we were able to observe the decay related to biradical **6** (τ = 30 ns, λ_{max} = 320 nm) and the enol growth at 430 nm. At this wavelength we observe a two- component decay from which we obtain lifetimes of 90 ns (*Z,E* enol) and 80 μs (*E,E* enol).

Table 1 summarizes the data obtained in these experiments.

Discussion

Upon irradiation, *ortho*-benzylbenzophenone (**1**) can give a mixture of four possible photoenols: the already mentioned **4** (*E,E* enol) and **5** (*Z,E* enol), as well as **7** (*Z,Z* enol) and **8** (*E,Z* enol).

It is clear that **7** and, in particular, **8** show considerable steric

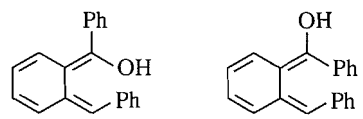

7 (*Z,Z* enol) **8** (*E,Z* enol)

congestion and, in principle, their involvement in product formation from **1** should not be expected. In fact, quenching experiments under steady-state conditions performed by Pfau et al. (21), using selected dienophiles and benzene as solvent, show conclusively that **4** was the only photoenol formed. These data are in full agreement with results obtained in this work for the same solvent. We note that **5** is probably formed in nonpolar solvents such as benzene. However, its lifetime is probably too short for **5** to be either detected spectroscopically, or trapped in preparative work.

It is well known that an increase in solvent polarity leads to an enhancement in photoenol lifetime, which is more effective in hydroxylic solvents (2–4). In these cases the hydrogen bonds formed between the hydroxylic protons of the enol and the solvent are responsible for a considerable slowdown of the reketonization process. Thus, we rationalize our results as a consequence of changes in hydrogen bonding in the various solvents employed. An inspection of Table 1 shows that there was a substantial increase in the *Z,E* enol lifetime on going from benzene to methanol. Thus, this species can become an observable transient under laser flash photolysis conditions. The shortening in the lifetime of **5** in trifluoroethanol can be easily

TABLE 1. Spectroscopic and kinetic data for the transients observed upon laser flash photolysis of **1** in several solvents

	Lifetime (μs)			Maximum absorption (nm)	
Solvent	Biradical[a]	*E,E* Enol	*Z,E* Enol	Biradical	Enols
Benzene	—	470	<0.03	—	340 and 440[b]
ACN[d]	~0.020	190	0.28	330	330 and 440[c]
Methanol	0.050	150	1.4	330	320 and 440[c]
TFE[e]	0.030	80	0.090	320	320 and 430[c]

[a]Errors estimated as ±30%.
[b]The *Z,E* enol was not observed in benzene.
[c]Both enols show the same absorption maxima in this solvent.
[d]Acetonitrile.
[e]Trifluoroethanol.

explained by assuming that either its acidity or traces of organic acids can catalyze the reversion of this photoenol to the corresponding ketone (20, 27).

Photodecomposition of *ortho*-benzylbenzophenone yields a photoenol mixture from which several products can be formed. The immediate precursor of these enols is the biradical **6**. Since it was not possible to resolve the biradical formation in any of the solvents used, it is safe to assume that its precursor, i.e., the triplet state for **1**, has a lifetime of less than 20 ns.

Acknowledgements

Work in Ottawa has been supported by an operating grant from the Natural Sciences and Engineering Research Council of Canada.

1. P.K. Das, M.V. Encinas, R.D. Small, Jr., and J.C. Scaiano. J. Am. Chem. Soc. **101**, 6965 (1979).
2. J.C. Scaiano. Acc. Chem. Res. **15**, 252 (1982).
3. L.J. Johnston and J.C. Scaiano. Chem. Rev. **89**, 521 (1989).
4. R. Haag, J. Wirz, and P.J. Wagner. Helv. Chim. Acta, **60**, 2595 (1977).
5. S.S. Teng and E.F. Ullman. J. Am. Chem. Soc. **98**, 541 (1976).
6. Y. Ito, Y. Umehara, T. Hijiya, Y. Yamada, and T. Matsuura. J. Am. Chem. Soc. **102**, 5917 (1980).
7. R.M. Wilson, K. Hannemann, K. Peters, and E.M. Peters. J. Am. Chem. Soc. **109**, 4741 (1987).
8. R.M. Wilson, K. Hannemann, W.R. Heineman, and J.R. Kirchhoff. J. Am. Chem. Soc. **109**, 4743 (1987).
9. P.J. Wagner, D. Subrahmanyam, and B.S. Park. J. Am. Chem. Soc. **113**, 709 (1991).
10. J.C. Netto-Ferreira, V. Wintgens, and J.C. Scaiano. J. Photochem. Photobiol. A: **57**, 153 (1991).
11. W.R. Bergmark. J. Chem. Soc. Chem. Commun. 61 (1978).
12. W.R. Bergmark, C. Barnes, J. Clark, S. Paparian, and S. Marynowski. J. Org. Chem. **50**, 5612 (1985).
13. J.C. Netto-Ferreira and J.C. Scaiano. Can. J. Chem. **71**, 1209 (1993).
14. R. Bishop and N.K. Hamer. J. Chem. Soc. (C), 1193 (1970).
15. N.K. Hamer and C.J. Samuel. J. Chem. Soc. Perkin Trans. 2, 1316 (1973).
16. N.K. Hamer. J. Chem. Soc. Perkin Trans. 1, 508 (1979).
17. Y. Ogata and K. Takagi. Bull. Chem. Soc. Jpn. **47**, 2255 (1974).
18. Y. Ogata and K. Takagi. J. Org. Chem. **39**, 1385 (1974).
19. E.F. Zwicker, L.I. Grossweiner, and N.C. Yang. J. Am. Chem. Soc. **85**, 2671 (1963).
20. G. Porter and M.F. Tchir. J. Chem. Soc. (A), 3772 (1971).
21. M. Pfau, S. Combrisson, J.E. Rowe, and J.a.N.D. Heindel. Tetrahedron, **34**, 3459 (1978).
22. C.K. Bradsherr. J. Am. Chem. Soc. **62**, 486 (1940).
23. F.A. Vingiello and M.M. Schlechter. J. Org. Chem. **28**, 2448 (1963).
24. J.C. Scaiano. J. Am. Chem. Soc. **102**, 7747 (1980).
25. J.C. Scaiano, M. Tanner, and D. Weir. J. Am. Chem. Soc. **107**, 4396 (1985).
26. H. Mauser and G. Gauglitz. Chem. Ber. **106**, 1985 (1973).
27. J.C. Scaiano, V. Wintgens, and J.C. Netto-Ferreira. Tetrahedron Lett. **33**, 5905 (1992).

Can. J. Chem. Downloaded from www.nrcresearchpress.com by EESC ESCOLA DE ENGENHARIA on 09/08/12
For personal use only.

The chemistry of thujone. XVII.[1] The synthesis of ambergris fragrances and related analogues

JAMES P. KUTNEY[2] AND YONG-HUANG CHEN

Department of Chemistry, University of British Columbia, 2036 Main Mall, Vancouver, BC V6T 1Z1, Canada

Received August 11, 1993

JAMES P. KUTNEY and YONG-HUANG CHEN. Can. J. Chem. **72**, 1570 (1994).

A strategy to utilize the thujone-derived enone **1** for the development of a synthetic route to ambergris fragrances is presented. Thujone (**8**) is transformed to the tricyclic enone **9**, via the Robinson annulation reaction, and the latter is then elaborated to the *cis*-fused tricyclic intermediates **10**, **11**, and **12**. Extrusion of the isopropyl side chain in **12** is achieved through an initial ozonation reaction and the resulting ketone **14** is then treated with *m*-CPBA to afford **16**. Cyclopropyl ring opening in **16** is performed via initial saponification to the alcohol **17** and the latter is then reacted with $FeCl_3$ and sodium acetate to enone **1**. The necessary elaboration of a tetrahydrofuran ring attached to ring B of **1** is achieved through reaction of **1** with vinylmagnesium bromide, alkylation, hydroboration, and final acid-catalyzed ring closure of the 1,5-diol **4**. The route affords the opportunity of synthesizing a variety of analogues within the Ambrox series.

JAMES P. KUTNEY et YONG-HUANG CHEN. Can. J. Chem. **72**, 1570 (1994).

On propose une stratégie dans le but d'utiliser l'énone **1** dérivée de la thujone pour le développement d'une voie de synthèse des essences de l'Ambregris. On transforme la thujone (**8**) en énone tricyclique **9** par le biais d'une réaction d'annélation de Robinson et, par la suite, cette dernière cétone est transformée en intermédiaires tricycliques **10**, **11** et **12** à fusion *cis*. L'extrusion de la chaîne latérale isopropyle du composé **12** est réalisée à l'aide d'une réaction d'ozonolyse initiale, suivie par la traitement de la cétone **14** qui en résulte avec de l'acide *m*-CPBA pour obtenir le produit **16**. On effectue l'ouverture du cyclopropyle du composé **16** en procédant au départ à une saponification en alcool **17** et en soumettant ensuite ce composé à une réaction avec du $FeCl_3$ et de l'acétate de sodium pour obtenir l'énone **1**. On procède à l'élaboration du noyau tétrahydrofurane attaché au cycle B du composé **1** en soumettant ce produit à une réaction avec le bromure de vinylmagnésium, puis à une alkylation, à une hydroboration et finalement à une ouverture de cycle acidocatalysée conduisant au 1,5-diol, **4**. Cette voie offre la possibilité de synthétiser une variété d'analogues de la série de l'Ambrox.

[Traduit par la Rédaction]

Ambergris and ambergris fragrances represent a most valuable family of perfumes. Their outstanding fragrances accounts for man's familiarity with this substance over many years (2, 3). One of the classics of amber chemicals, (–)-Ambrox (**2**), in a mixture with (+)-iso-Ambrox (**3**) and in the form of the base Fixateur 404 (trade name of Firmenich) has been available in the perfumery industry for more than 30 years. Extensive studies correlating structure with smell have also been described (3). (–)-Ambrox (**2**), present in trace amounts in whale secretions, is prepared commercially from sclareol, a natural product isolated from clary sage. As future requirements within the ambergris family will depend increasingly on synthetic materials, it was therefore in our interest to develop a versatile route to this family of compounds from thujone (**8**), a readily available waste by-product in the B.C. forest industry.

The retrosynthetic analysis that was considered for the possible elaboration of a versatile route to **2** and **3** and (or) their related analogues is summarized in Scheme 1. The *cis*-fused enone **1** was a promising starting material: the convex β face and the steric hindrance from the axial methyl at C4 in ring A of the major conformer (nonsteroidal) should ensure a favorable conjugate addition (e.g., by a vinyl anion equivalent) from the β face of the ring B segment thereby generating a chiral center at C9 with the same configuration as that in (–)-Ambrox (**2**). The conjugate addition might also provide an excellent opportunity to stereoselectively introduce a methyl group at C8, by trapping the enolate produced in the addition reaction with appropriate methylating reagents, for example, iodomethane. The *cis*-fused γ,δ-enone **6**, thus obtained, would subsequently be converted to its epimer, the *trans*-fused γ,δ-enone **5**.

We also envisaged that the furan ring C of (–)-Ambrox (**2**) or (+)-iso-Ambrox (**3**) may be formed by an acid-catalyzed cyclization of the *trans*-fused 1,5-diol **4**, which would be prepared by stereoselective reduction of **5** and subsequent hydroboration. Conformational analysis of **4** reveals that an axial orientation of the secondary hydroxyl group at C7, as shown, would be necessary to ensure a facile migration of the axial hydride from the vicinal tertiary carbon (C8). Alternatively, an equatorial orientation of this secondary hydroxyl group as shown in **7** would probably lead to some skeletal rearrangement.

To evaluate the feasibility of the above strategy, the synthesis of **1** became our initial consideration. The successful synthetic route from thujone (**8**) is summarized in Schemes 2 and 3. The readily available enone **9**, obtained in earlier studies (5), was catalytically reduced to the *cis*-fused ketone **10** in essentially quantitative yield, and the latter upon methylation to **11** and Wolff–Kishner removal of the carbonyl group in **11**, affords **12**.

The desired removal of the isopropyl side chain could be achieved via initial application of a previously developed ozonation reaction (6). Ozonation of **12** at low temperature provides a reaction mixture containing the tertiary alcohol **13** (42% yield) and the ketone **14** (27%). Although separation and characterization of these compounds was completed (see Experimental), the desired ketone **14** could be obtained in 62% overall yield from **12** by further manipulation of the reaction mixture obtained directly from the ozonation of **12**. Treatment of this mixture with pyridinium tosylate affords facile dehydration of **13** to the vinylcyclopropane analogue **15** and the resulting mixture is treated successively with potassium permangate and lead tetraacetate. Alternatively, the pure alcohol **13**, separated from **14**, is dehydrated to **15** (91% yield) and the latter ozonized to **14**.

[1]For Part XVI, see ref. 1.

[2]Author to whom correspondence may be addressed. Telephone (604) 822-2710.

Can. J. Chem. Downloaded from www.nrcresearchpress.com by EESC ESCOLA DE ENGENHARIA on 09/08/12
For personal use only.

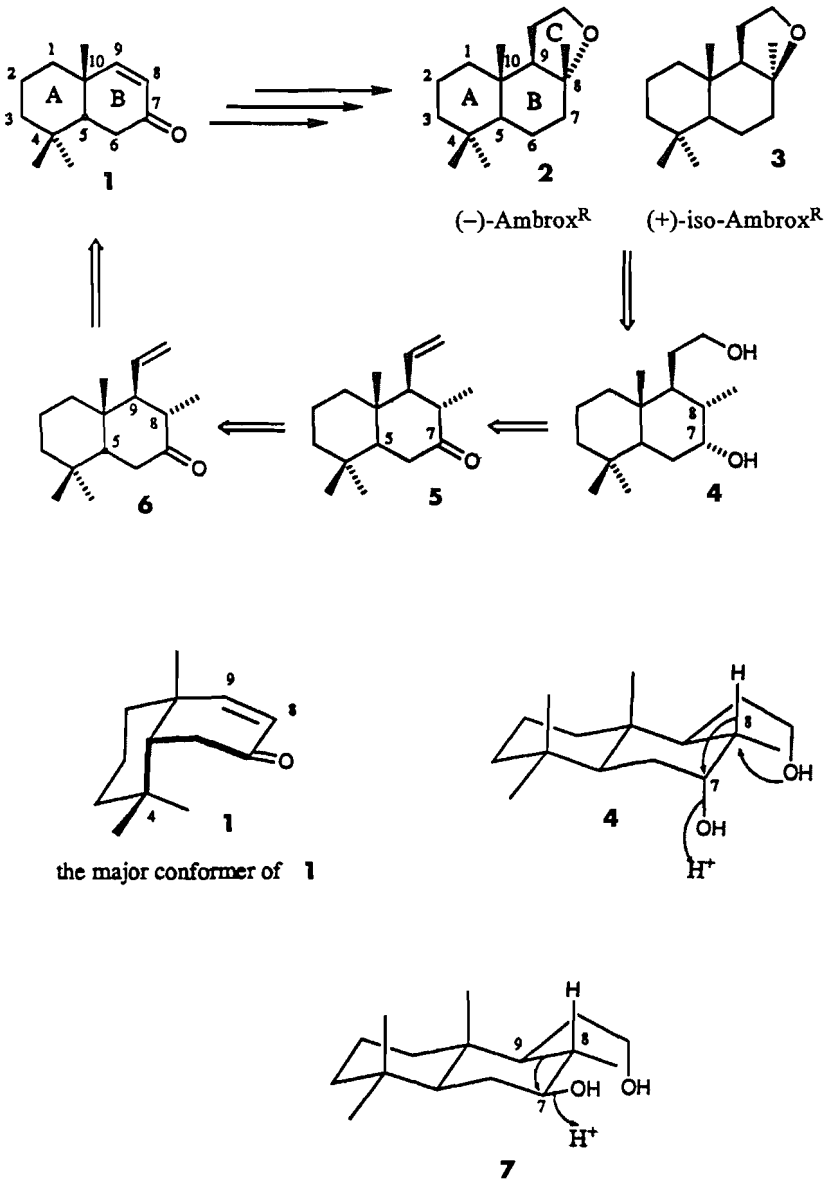

SCHEME 1. Summary of overall strategy for synthesis of ambergris fragrances from thujone-derived synthons.

It should be noted that the ketone **14** can be prepared from **9** in an overall yield of 27% by performing the sequence 9 → → → **14** without purification of intermediates.

Elaboration of **14** to the desired enone **1** followed the sequence summarized in Scheme 3. It was perceived that a Baeyer–Villiger reaction would cleave the side chain of **14** in a regioselective manner to afford **16**, in view of a previous study (7–9) involving the preferential insertion of oxygen into the cyclopropyl side chain of methyl cyclopropyl ketone. For this purpose, stirring **14** in methylene chloride with *m*-CPBA at room temperature for 2 days gave **16** in 79% yield based on the recovery of starting material (46% yield). An optimization of the reaction was carried out according to Table 1. *p*-Toluenesulfonic acid had little catalytic effect on the *m*-CPBA oxidation reaction. Under refluxing conditions, the reaction appeared to accelerate at the beginning but slowed down quickly after a few hours and started to afford some unidentified by-products. When the concentration of the substrate was increased to 0.82 M, the reaction was quite complete after refluxing in methylene chloride for 12 h and the yield of **16** was 82%. Although the use of trifluoroperacetic acid (7) improved the yield to as high as 94%, the reaction was not easily reproducible. This was probably due to the instability of trifluoroperacetic acid. Therefore, the preferred procedure for the preparation of **16** was to employ a high concentration of substance **14** with *m*-CPBA as the oxidizing agent in refluxing methylene chloride.

The mass spectrum of acetate **16** showed the molecular ion peak at *m/z* 236. The IR spectrum had a carbonyl absorption at 1735 cm^{-1} while the ^{1}H NMR spectrum displayed four methyl singlets at δ 0.80, 0.97, 1.05, and 2.10 ppm. The methyl singlet at δ 2.10 ppm was obviously due to the acetate group, which unambiguously demonstrated the insertion of oxygen into the position between the quaternary cyclopropyl carbon (C7) and the carbonyl carbon.

Regioselective ring opening of alkyl-substituted cyclopropanols by ferric chloride has been studied extensively by DePuy and van Lanen (10). From these studies it is clear that the more substituted C—C bond is preferentially cleaved.

Saponification of **16** was carried out in dilute potassium hydroxide – ethanol solution for 30 min. The rather polar **17**

Can. J. Chem. Downloaded from www.nrcresearchpress.com by EESC ESCOLA DE ENGENHARIA on 09/08/12
For personal use only.

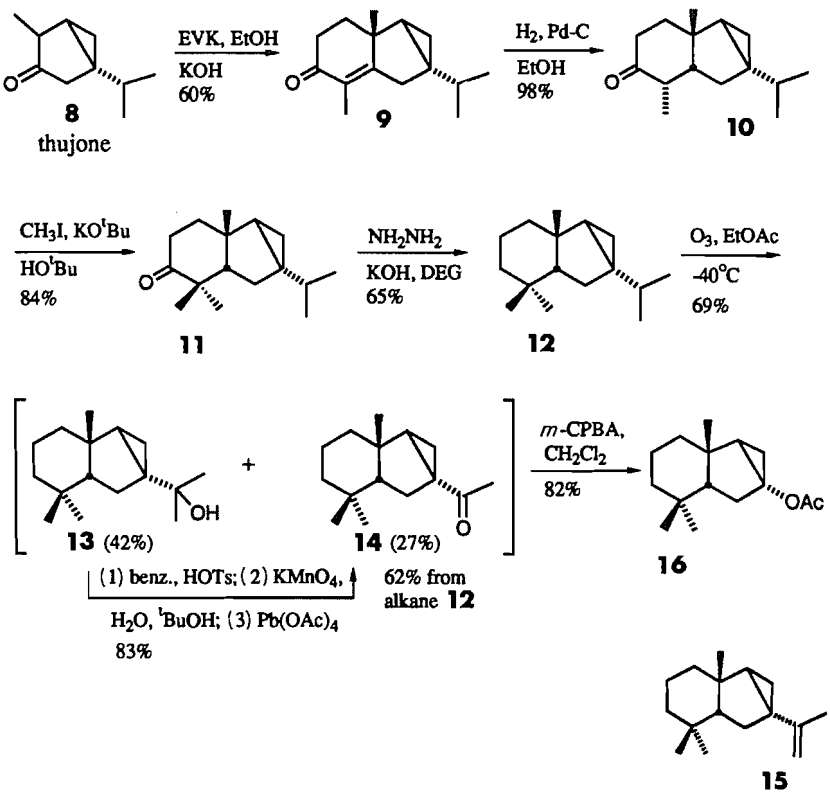

SCHEME 2. Conversion of thujone (**8**) to tricyclic acetate **16**.

TABLE 1. The optimization of Baeyer–Villiger reaction of ketone **14**

	Experiment				
	1	2	3	4	5
14	176 mg	176 mg	176 mg	93 mg	1.80 g
Peracids[a]	*m*-CPBA 346 mg (2.0 equiv.)	*m*-CPBA 346 mg (2.0 equiv.)	*m*-CPBA 346 mg (2.0 equiv.)	CF_3CO_3H 312 μL (2.7M) (2.0 equiv.)	*m*-CPBA 4.45 g (2.5 equiv.)
CH_2Cl_2	5.0 mL	5.0 mL	5.0 mL	2.0 mL	10 mL
HOTs (mg)	0	39	0	0	0
Temperature	r.t.	r.t.	Reflux	r.t.	Reflux
Time (h)	48	48	24	48	12
% Recovery of **14**	46	46	30	48	5
% Yield of **16**	79	78	60	94	82

[a]*m*-CPBA (80–85% pure) was used without further purification while CF_3CO_3H was prepared in situ according to ref. 7.

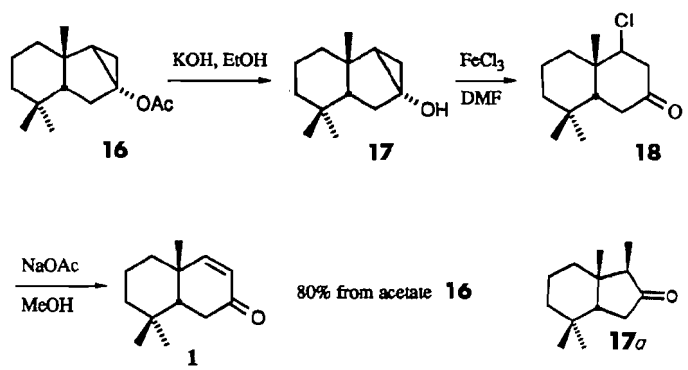

SCHEME 3. Conversion of tricyclic acetate **16** to enone **1**.

was obtained in almost quantitative yield provided the reaction mixture was worked up immediately, since **17** is unstable and undergoes facile conversion to the undesirable cyclopentanone analogue **17***a*.

The lability of cyclopropanol **17** dictated its immediate application to the next reaction. The mixture of anhydrous ferric chloride and **17** in anhydrous *N,N*-dimethylformamide was agitated under nitrogen at room temperature for 24 h. The major product **18** was isolated, in addition to a small amount of **17***a*, as evidenced from its spectral data (see Experimental).

The β-chloroketone **18** had its mass spectrum showing molecular ion peaks at *m/z* 230 (0.2%) and 228 (0.6%) corresponding to formulas $C_{13}H_{21}O^{37}Cl$ and $C_{13}H_{21}O^{35}Cl$, and other characteristic spectral data (see Experimental). The orientation of the chlorine function in **18** was uncertain.

Can. J. Chem. Downloaded from www.nrcresearchpress.com by EESC ESCOLA DE ENGENHARIA on 09/08/12
For personal use only.

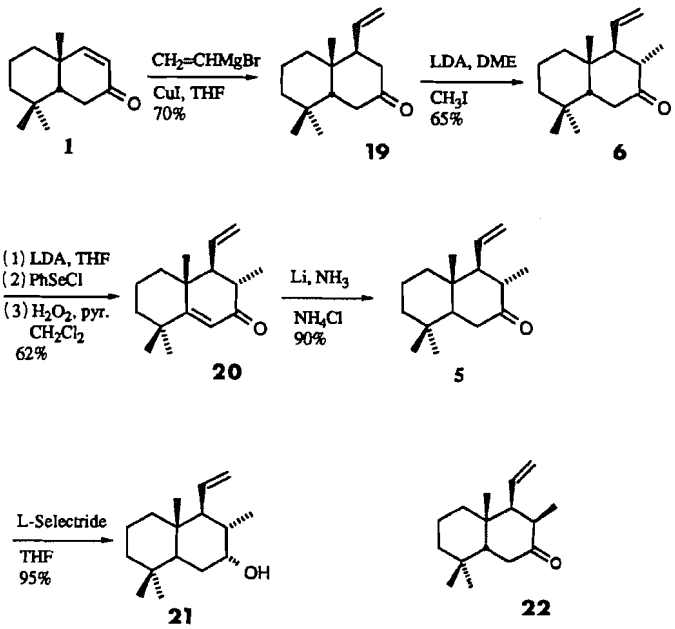

SCHEME 4. Conversion of enone **1** to bicyclic alcohol **21**.

The β-chloroketone **18** underwent elimination of hydrogen chloride to give enone **1** easily even without addition of any base. Consequently, the crude product from the above ring-cleavage reaction was treated with sodium acetate in refluxing methanol for a few hours. The overall yield of **1** from acetate **16** was 80%, equivalent to a 93% yield for each step. The ketone **1** was a white solid with mp 64–66°C (lit. (11) mp 68°C).

As noted earlier, the racemate of **1** was prepared previously by an interesting photochemical epimerization (11).

To complete the synthesis of (–)-Ambrox (**2**), as outlined in Schemes 4 and 5, a diastereoselective conjugate addition to enone **1** from the β face of the molecule was essential. Conjugate addition to enones by organocopper reagents has been widely employed in organic synthesis, as indicated in several reviews (12, 13). Diastereoselective addition is generally established with the incoming group approaching in a manner perpendicular to the enone plane in order to allow maximum orbital overlap during the progress of the reaction. This stereoelectronic requirement clearly demands a careful conformational analysis of the enone in order to determine the facial preference of the conjugate addition. Such an analysis of enone **1**, as shown in **1***a* and **1***b*, suggested that the desired conversion of **1** to **19** (Scheme 4) could be expected.

Experimentally, conjugate addition of **1** with 2.0 equivalents of vinylmagnesium bromide and a catalytic amount of cuprous iodide in dimethyl sulfide:THF (1:5, v/v) solution gave the β-face addition product **19** in 70% yield, the stereochemistry of which was confirmed by the ^{1}H NMR spectrum of the subsequent methylation product **6** (see later). The absence of dimethyl sulfide (14) or the use of cuprous bromide as catalyst led to decrease in yields, likely due to the formation of competing 1,2-addition by-products. Some polar by-products were often observed in the reaction.

The alkylation of **19** to **6** involved a detailed study, to establish optimum conditions and information about the stereochemistry of methylation.

After the enone **19** was treated with LDA in dimethoxyethane

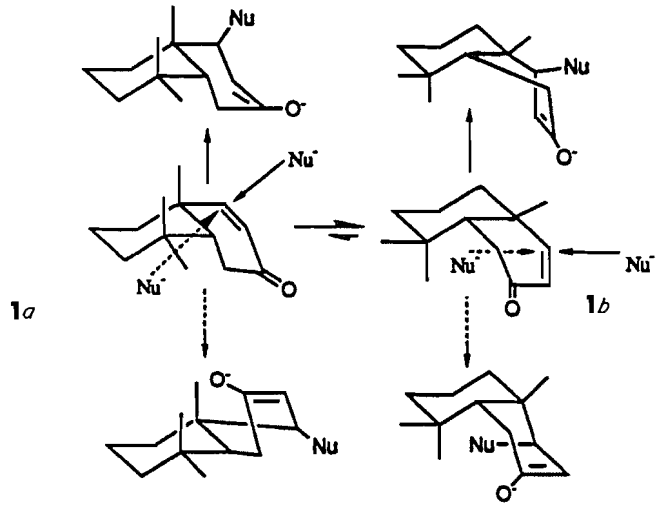

(DME) (15), initially at –78°C for 30 min, the mixture was warmed to approximately 45°C. Iodomethane (5.0 equiv.) was added rapidly to the mixture. Compound **6** together with its minor epimer **22** (6:1) was isolated in 60–70% yield. Since these two epimers were not separable, a basic treatment with potassium hydroxide in methanol was performed to convert the epimeric mixture into the more stable compound **6** (97% pure by GC). When THF was used as the solvent for the methylation reaction, a very large recovery (>60%) of starting material was observed, presumably because the sluggishness of the methylation reaction led to a quick equilibration of the initially generated enolate with the methylation products through proton exchange (16). It should be noted that the deprotonation in ring B of **19** was regioselective and the alternative deprotonation at C6 was not observed.

The mass spectrum of **6** revealed the molecular ion peak at *m/z* 234. Its IR spectrum indicated a carbonyl stretching absorption at 1700 cm^{-1}, and a carbon–carbon double bond stretching absorption at 1630 cm^{-1}. Its ^{1}H NMR spectrum, in $CDCl_3$, displayed three methyl singlets at δ 0.82, 0.94, and 1.14 ppm and one methyl doublet (J = 6 Hz) at δ 1.04 ppm. Also present was a one-proton multiplet at δ 2.30 ppm, a complex three-proton multiplet at δ 2.40–2.70 ppm, corresponding to the allylic proton at C9, and three protons α to the carbonyl group. The olefinic signal at δ 5.01 ppm appeared as a doublet of doublets of doublets (J = 17.0, 1.8, and 0.5 Hz). This signal was assigned to Hb (see **6***a*) since the resonance of Hb was expected to have a

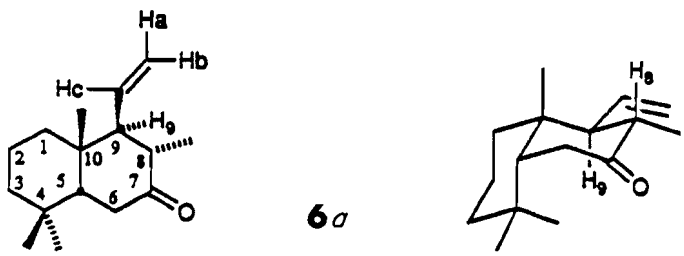

large J value (15–20 Hz), due to coupling with Hc, which was *trans* to Hb, and two small J values due to coupling with Ha and H9. Thus, the three J values were tentatively assigned as J (Hb,Hc) = 17.0 Hz, J (Ha,Hb) = 1.8 Hz, J (Hb,H9) = 0.5 Hz). The olefinic proton signal at δ 5.14 ppm appeared as a doublet of doublets (J = 10.2 and 1.8 Hz). This signal was assigned to Ha since the resonance of Ha should have a J value at 8–12 Hz, due to coupling with Hc, which was *cis* to Ha, and a small J

Can. J. Chem. Downloaded from www.nrcresearchpress.com by EESC ESCOLA DE ENGENHARIA on 09/08/12
For personal use only.

Can. J. Chem. Downloaded from www.nrcresearchpress.com by EESC ESCOLA DE ENGENHARIA on 09/08/12
For personal use only.

value of 1.8 Hz due to coupling with Hb. On this basis, J (Ha,Hc) = 10.2 Hz. The olefinic proton signal at δ 5.55 appeared as a doublet of triplets (J = 17.0 and 10.2 Hz). It was assigned to Hc since the resonance of Hc was expected to appear at lower field and should show J values of 17.0 and 10.2 Hz, thereby revealing J (Hc,H9) = J (Ha,Hc) = 10.2 Hz. The large coupling constant between Hc and H9 (J = 10.2 Hz) indicated a near coplanarity of the C9—H9 and C11—Hc bonds. In the nonsteroid-like conformer **6***a*, the vinyl side chain is drawn as shown in order to portray this situation and to indicate minimal interactions with neighboring groups, as revealed from molecular models.

The epimer **22**, generated as a minor product together with **6** during the methylation of **19**, was not characterized by spectroscopy since its separation from **6** was very difficult. However, a partially enriched sample (50% by GC) obtained from the methylation in THF was converted into **6** (97% pure by GC) by treatment of the mixture with a dilute KOH–methanol solution. The existence of **22** was then indirectly confirmed.

To confirm the stereoselectivity of the conjugate addition reaction and the regioselectivity of the methylation reaction, a detailed ^{1}H NMR spectral analysis of **6** was conducted. The ^{1}H NMR spectrum in deuterated benzene afforded a clear resolution of the four proton signals at δ 2.20–2.70 ppm previously observed in the spectrum taken in deuterated chloroform. Decoupling by irradiation at δ 5.75 ppm (Hc signal, see **6***a*) caused a one-proton triplet (J = 10.2 Hz) at δ 2.42 ppm to collapse into a doublet (J = 10.2 Hz) in addition to the collapsing of the Ha signal at δ 4.94 ppm and Hb at δ 4.82 ppm into two broad singlets. Therefore, the triplet signal at δ 2.42 ppm was clearly due to the allylic proton (H9), which apparently coupled only with Hc and one neighbouring axial proton (J = 10.2 Hz). Thus, the methylation of **19** must have taken place at C8 rather than at C6. The methylation at C6 would have produced an isomer that should have a more complex signal (doublet of doublets or triplet) for the allylic proton (H9) if irradiation at the Hc signal had occurred. The only methyl doublet signal in the $CDCl_3$ spectrum that appeared at δ 1.15 (J = 5.1 Hz) was assigned to the methyl group at C8. A one-proton multiplet, consisting of six lines of equal spacing (5.1 Hz) and an intensity ratio 1:3:4:4:3:1, appeared at δ 1.90 ppm in the C_6D_6 spectrum and at δ 2.28 ppm in $CDCl_3$, respectively. The splitting pattern of this signal was indeed a doublet of quartets with J = 10.2 Hz for the doublet coupling and J = 5.1 Hz for the quartet coupling. Thus, this signal was assigned to the α methine proton at C8.

In fact, the structure **23**, which had reverse configurations at

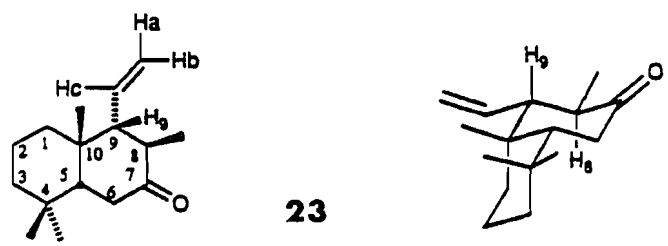

23

C8 and C9 with regard to **6**, could also account for the result of decoupling experiments, especially the large coupling constant between Hc and H1 (J (Hc,H1) = 10.2 Hz) due to the diaxial orientation of these two protons. Therefore, to eliminate further doubt about the stereochemistry of **6**, NOE difference experiments were carried out. Unfortunately, this study did not provide unambiguous evidence due to the close proximity of signals in the aliphatic proton region in both $CDCl_3$ and C_6D_6 spectra. As a result, the interpretation of NOE difference experiments was very difficult. However, important evidence was later obtained from *trans* isomer **5**, the epimer of **6** (see later).

To obtain **6** more effectively, we had tried to carry out an "one-pot" reaction by quenching the enolate generated in the conjugate addition with iodomethane. The one-pot operation would eliminate intermediate isolation and could be an efficient way to ensure the desired regioselective methylation (17, 18). However, the one-pot process proved to be very sluggish and produced mostly by-products, in addition to **6** (10%) and **19** (10%). Attempts to improve the reaction, by changing solvents (Et_2O, THF, DME), temperature, and using HMPA as additive, failed. Since the conjugate addition proceeded well to produce **19** in good yield, the methylation step must be responsible for the sluggishness of this one-pot operation. In view of the apparent sluggishness of the methylation reaction, under the experimental conditions, competitive proton exchange between the initially formed enolate from the conjugate addition reaction and the methylation product **6** could occur. The enolate of **6**, thus generated, would then be further methylated. O-Methylation of enolates might be also responsible for the lack of reasonable yields of **6**.

The stereochemical conversion of the A/B *cis* fusion in **6** to the desired A/B *trans* fusion in **5** was realized through a two-step sequence as shown in Scheme 4. Slow addition of **6**, dissolved in THF solution, to a LDA–THF solution at –78°C under nitrogen was followed by rapid injection of a phenylselenenyl chloride – THF mixture. After stirring 1 h at room temperature and removal of solvent, methylene chloride, pyridine, and hydrogen peroxide were added, and the resulting mixture was stirred overnight. Dienone **20** was then isolated in 62% yield (based on a 25% recovery of starting material). The mass spectrum of **20** indicated a molecular ion peak at m/z 232. The UV spectrum, with absorptions at 242 nm and 383 nm, and the IR spectrum, with an intense conjugated carbonyl stretching absorption at 1660 cm^{-1}, substantiated the desired enone chromophore. The ^{1}H NMR spectrum revealed a methyl doublet (J = 5.1 Hz) at δ 1.07 ppm and three methyl singlets at δ 1.17, 1.22, and 1.25 ppm. A triplet (J = 10.2 Hz) at δ 2.12 ppm and a multiplet at δ 2.40 ppm, consisting of six equally spaced (5.1 Hz) lines that had an intensity ratio 1:3:4:4:3:1, were assigned to the allylic proton at C9 and the methine proton at C8 (dq, J = 10.2 and 5.1 Hz). Four olefinic protons at δ 5.05 (dd, J = 17.0 and 1.8 Hz), 5.18 (dd, J = 10.2 and 1.8 Hz), 5.64 (dt, J = 17.0 and 10.1 Hz), and 6.00 (s) ppm were attributed to the three vinyl protons and H6, respectively.

To reduce the large recovery of starting material and improve the yield of dehydrogenation, different conditions were applied (19). One-pot elimination of the phenylselenide oxide by direct H_2O_2 (30%) addition to the phenylselenide prepared in THF or DME led to an even greater recovery of starting material (50%) and a lower yield of **20** (50% based on recovery). Another one-pot elimination of phenylselenide oxide, by transferring the phenylselenide into a sodium periodate solution in methanol–H_2O (1:1) mixture, resulted in the formation of a new compound of unknown structure (25% based on recovery) in addition to **20** (40% based on recovery) and the recovered starting material (25%).

TLC monitoring of the reaction showed that only a small quantity of starting material **6** was left after the introduction of

Can. J. Chem. Downloaded from www.nrcresearchpress.com by EESC ESCOLA DE ENGENHARIA on 09/08/12
For personal use only.

phenylselenenyl chloride, and the newly generated phenylselenides appeared as two UV-active spots (TLC) of apparently different intensities. Attempts to separate these two compounds by silica gel chromatography failed, as only the starting material **6** was isolated. Apparently, the selenides were very labile. In fact, even leaving the phenylselenides in THF–H_2O mixture overnight regenerated the starting material **6** as exclusive product.

It was expected that the phenylselenylation of **6** would produce two diastereomers resulting from the attacks on the α and β faces of the enolates of **6**. The results obtained reveal that the β attack, to afford the axial orientation of the selenyl unit, was the dominant course of the reaction.

The stereochemistry of Birch reduction of octalones has been well studied (20) and theories to rationalize the data have been put forth (21, 22). It was therefore expected that the reduction of **20** should proceed to afford **5**. Treatment of **20** in anhydrous ether:ammonia (1:2), employing a slight excess of lithium for 1 h and quenching the resulting mixture by ammonium chloride, afforded **5** in 90% yield. The mass spectrum of **5** showed its molecular ion peak at *m/z* 234 while the IR spectrum indicated the carbonyl stretching absorption at 1706 cm^{-1}. The ^1H NMR spectrum, in $CDCl_3$, displayed three methyl singlets at δ 0.88, 0.90, and 1.09 ppm, a methyl doublet (J = 6.0 Hz) at δ 0.93 ppm, a four-proton multiplet at δ 2.00–2.50 ppm, and three olefinic protons at δ 4.98 ppm (dd, J = 16.8 and 1.6 Hz), 5.12 ppm (dd, J = 10.0 and 1.6 Hz), and 5.56 ppm (dt, J = 16.8 and 10.0 Hz). As in the case of **6**, these olefinic signals were assigned to the three vinyl protons. The large coupling constant (J = 12.0 Hz) between the H9 and H8 signals were again observed from the H9 signals (δ 1.96 ppm, t, J = 12.0 Hz) in the ^1H NMR spectrum (C_6D_6), which proved beyond any doubt that the vinyl side chain and the methyl group at C8 in **5** were both oriented in an equatorial manner.

As stated earlier (Scheme 1), an axial secondary hydroxyl group at C7 in diol **4** was required for the cyclization to occur in a desired manner. To this end, enone **5** was treated with L-Selectride in THF at –78°C, and the axial alcohol **21** was isolated in nearly quantitative yield. The mass spectrum indicated the molecular ion peak at *m/z* 236 and a fragment ion at *m/z* 218 due to the loss of a water molecule. The IR spectrum showed a broad intense hydroxyl stretching absorption near 3450 cm^{-1} and a carbon–carbon double bond stretching absorption at 1630 cm^{-1}. The ^1H NMR spectrum revealed a quartet (J = 3.0 Hz) at δ 3.92 ppm corresponding to the C7 proton adjacent to the axial hydroxyl group and three one-proton multiplets at δ 4.94 (dd, J = 17.2 and 2.4 Hz), 5.02 (dd, J = 10.4 and 2.4 Hz), and 5.52 (dt, J = 17.2 and 10.4 Hz) ppm. The fact that the C7 proton appeared as a quartet at δ 3.92 ppm with a small coupling constant (J = 3.0 Hz) confirmed its equatorial orientation.

The hydroboration of **21**, with borane in THF, followed by basic hydrogen peroxide work-up, produced mainly the 1,5-diol **4** (70%) (Scheme 5) in addition to a minor 1,4-diol **24** (10%). Diol **4** had its mass spectrum showing the molecular ion peak at *m/z* 254 and two fragment ions at *m/z* 236 and 218 corresponding to loss of one and two water molecules from the parent molecular ion. The ^1H NMR spectrum revealed two overlapping methyl singlets at δ 0.82 ppm, one methyl singlet at δ 0.85 ppm, a methyl doublet at δ 0.98 (J = 6.0 Hz), a one-proton multiplet (dt, J = 7.2 and 9.6 Hz) at δ 3.50, a one-proton multiplet at δ 3.62 ppm (J = 5.6 and 9.6 Hz), and a quartet (J = 3.0 Hz) at δ 3.85 ppm corresponding to the C7 hydrogen. The two one-proton multiplets at δ 3.50 and 3.62 ppm were due to the C6 methylene group.

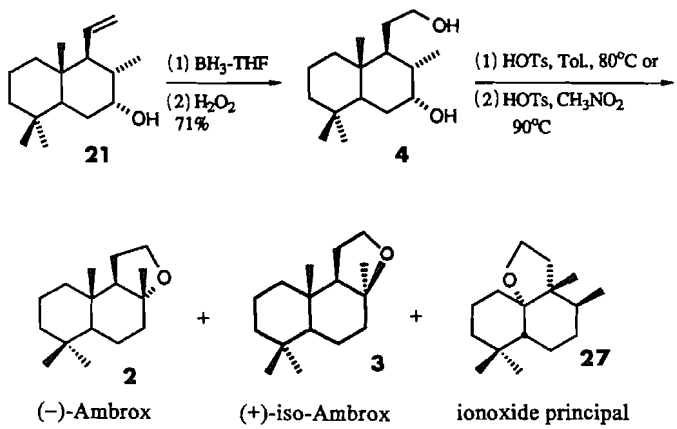

SCHEME 5. Conversion of bicyclic alcohol **21** to ambergris fragrances.

The minor product **24** appeared to be a mixture of two diastereomers with a ratio of 4:1, as indicated in the ^1H NMR spectrum. These two diastereomers were difficult to separate by column chromatography. The mass spectrum of the mixture revealed a molecular ion peak at *m/z* 254, while the IR spectrum showed an intense hydroxyl absorption at 3400 cm^{-1}. In the ^1H NMR spectrum, the minor diastereomer had a broad singlet at δ 3.77 ppm corresponding to H7 and a quartet (J = 8.0 Hz) at δ 4.12 ppm corresponding to the proton at C11 while the major isomer had a broad singlet at δ 3.87 ppm corresponding to H7 and a quartet (J = 8.0 Hz) at δ 4.21 ppm corresponding to the proton at C11 in the ^1H NMR spectrum. Further assignment of the stereochemistry at C11 to these two diastereomers was not possible based on the above obtained data.

Finally, for preparative purposes, the conversion of ketone **5** to diol **4** (Schemes 4 and 5) can be accomplished as a one-pot operation in an overall yield of 65%.

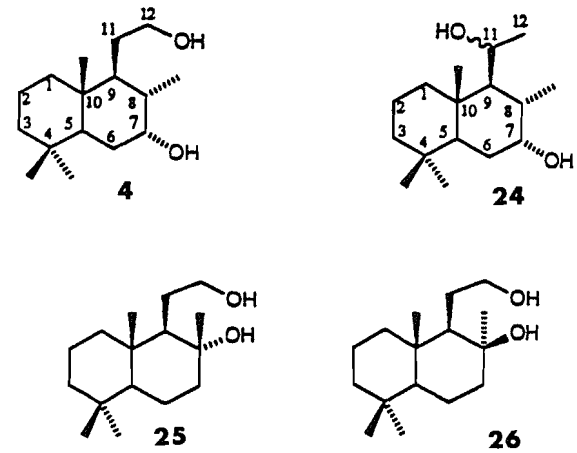

As summarized in the reviews noted earlier (2–4), most of the synthetic sequences to natural or racemic Ambrox involved a cyclization of a 1,4-difunctional (at C8 and C12) intermediate to form the tetrahydrofuran ring. Cyclizations of the 1,4-diol **25** by β-naphthalenensulfonic acid in toluene (23–26) or *p*-toluenesulfonyl chloride in pyridine (27, 28) and the epimeric 1,4-diol **26** by *p*-toluenesulfonic acid in nitromethane (29) are of more direct relevance to our designed cyclization of diol **4**.

TABLE 2. Cyclization of the 1,5-diol **4**

Conditions	Composition of dehydration products, %				
	2	**3**	**27**	**28**	Hydrocarbons
HOTs (2.0 equiv.), CH_3NO_2 80°C, 2 h	31	30	—	15	22
HOTs (2.0 equiv.), toluene 80°C, 2 h	48	10	—	15	8
HOTs (6.0 equiv.), CH_3NO_2 100°C, 0.5 h	—	19	34	—	41

It is assumed (29) that these cyclization reactions catalyzed by acids proceed through a tertiary carbocation (i) which is formed by elimination of the tertiary hydroxyl group in **25** or **26**. The α-face attack by the primary hydroxyl is kinetically preferred to the β-face attack because the latter would be subjected to steric hindrance from the angular methyl group in the transition state (iii). Thus, (–)-Ambrox (**2**) is preferentially produced through a lower energy transition state (ii). However, (+)-iso- Ambrox (**3**) resulting from the β-face attack will become the major product under prolonged treatment and can actually be obtained from **2** under the same condition (23–26).

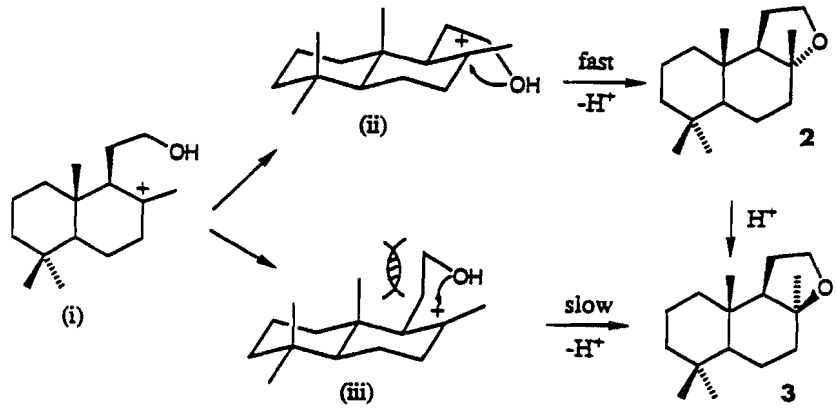

The final steps in the sequence, as summarized in the overall strategy shown in Scheme 1, involved the acid-catalyzed cyclization of the 1,5-diol **4** to afford the tetrahydrofuran ring system present in **2** and **3**. To this end, an extensive study directed at the cyclization of **4** to the target compounds was undertaken. A summary of the results is provided in Table 2.

Treatment of **4** with *p*-toluenesulfonic acid (2.0 equiv.) in nitromethane at 80°C for 2 h gave (–)-Ambrox (**2**, 31%), (+)-iso-Ambrox (**3**, 30%), a mixture of alcohols (**28**, 15%), and a mixture of hydrocarbons. The yield of **2** was improved to 48% using toluene as the solvent. All spectroscopic data of **2** and **3** were consistent with those recorded in the literature (30).

The mixture of alcohols labelled as **28** in Table 2 contained several compounds, as shown in the gas chromatogram and the complex ^{1}H NMR spectrum. This mixture could not be further purified in spite of extensive chromatographic studies. It displayed a hydroxyl stretching absorption at 3450 cm^{-1} in the IR spectrum and a molecular ion peak at *m/z* 220 in the mass spectrum. Although further characterization data were not obtained due to the difficulties associated with purification, it is assumed that the mixture represents alkenes (see **28***a* and **28***b*) in which one molecule of water had been lost from diol **4**. In view of the subsequent isolation of **27**, the principal component of "ionoxide" previously reported by Vlad et al. (31), it is speculated that such alkenes could be intermediates in a plausible mechanistic pathway from either diol **4** or (+)-iso-Ambrox (**3**) to **27** (Scheme 6). However, direct evidence for this proposal is unavailable from our studies.

The nonpolar hydrocarbon mixture, obtained in the first eluted fractions in column chromatography, contained several compounds, as revealed from the gas chromatograph. Here, again, attempts at purification failed. The IR spectrum indicated no hydroxyl stretching absorption while the mass spectrum showed an ion peak at *m/z* 218. Thus, this mixture appears to consist of a dehydrated product of diol. The ^{1}H NMR spectrum displayed poorly resolved aliphatic proton signals at δ 0.60–2.65 ppm and olefinic proton signals at δ 5.00–5.60 ppm.

In conclusion, we have succeeded in synthesizing (–)-Ambrox (**2**) from the thujone-derived enone **1** in seven steps and in an overall yield of 9.5%. Moreover, a novel synthesis of **27**, the principal component of "ionoxide," was discovered. It is claimed (31) that ionoxide possesses a very distinct musk–ambergris odor and a high rating as a perfume. The successful strategy should be applicable to the synthesis of other ambergris fragrances, and such studies are presently underway.

Two recent publications concerning the synthesis of racemic Ambrox^R are noted (32, 33).

Experimental

In general, solvents (ACS grade) were used for chromatography without further purification. Petroleum ether refers to the fraction boiling in the range 30–60°C. Anhydrous diethyl ether, tetrahydrofuran,

Can. J. Chem. Downloaded from www.nrcresearchpress.com by EESC ESCOLA DE ENGENHARIA on 09/08/12
For personal use only.

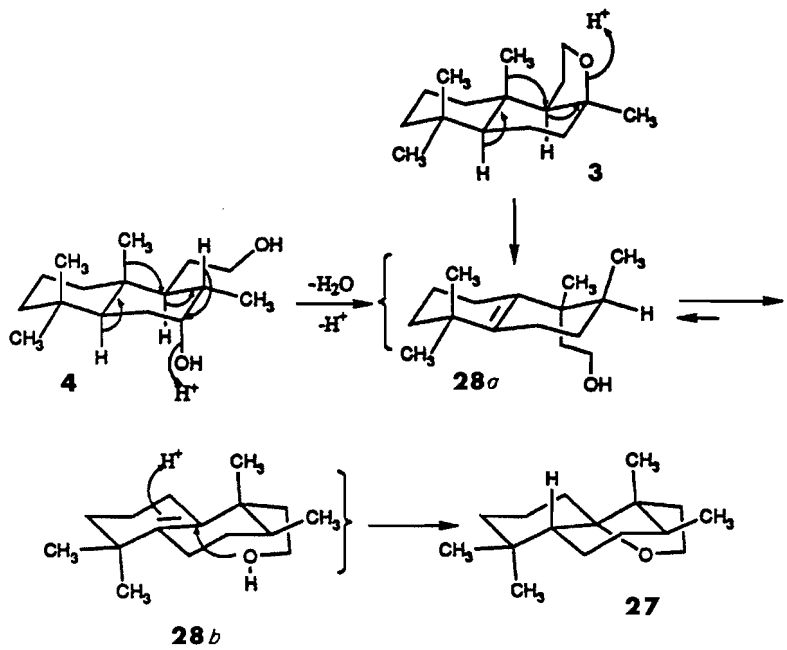

SCHEME 6. Proposed mechanism for the formation of **27** from postulated intermediates **28**.

and benzene were prepared by distillation from a mixture containing sodium and benzophenone. Anhydrous methylene chloride, chloroform, and *n*-pentane were prepared by distillation from phosphorus pentoxide. Anhydrous diisopropylamine, HMPA, DMF, and DMSO were prepared by distillation from calcium hydride and stored in the presence of molecular sieves under nitrogen. Anhydrous methanol and ethanol were distilled from magnesium. *n*-Butyllithium, LDA, and vinylmagnesium bromide solutions were standardized by titration against *sec*-butanol in benzene using 1,10-phenanthroline as indicator under nitrogen. Borane in THF and L-Selectride were standardized by measuring hydrogen released from their reaction with 1:1 glycerol:water solution. Thujone was obtained by distillation of Western red cedar leaf oil, which was generously donated by Intrinsic Research and Development Incorporated.

Unless stated otherwise, all reactions were carried out under a positive pressure of dry nitrogen. Reactions at –78, –40, –25, and 0°C were performed with Dry Ice/acetone, Dry Ice/acetonitrile, Dry Ice/carbon tetrachloride, and ice/water cooling baths respectively.

Reactions were monitored by thin-layer chromatography (TLC) and (or) gas chromatography (GC). Analytical TLC was carried out on aluminum-backed silica gel plates (Merck Silica Gel 60 F_{254}). Visualization was realized by ultraviolet light and (or) by heating after spraying with 10% ammonium molybdate in 10% sulfuric acid. Gas chromatography was performed on a Hewlett-Packard 5890A gas chromatograph, using a flame ionization detector and a 14.5 m × 0.252 mm fused silica capillary column coated with cyanopropylphenyl silicone gum (DB 1701). Unless otherwise stated, all reaction products were purified by flash chromatography using silica gel (230–400 mesh) supplied by E. Merck Co. with air pressure to obtain a suitable flow. Unless otherwise stated, the eluting solvents were ethyl acetate:hexanes mixtures. Hexanes is a commercial mixture containing predominantly *n*-hexane and methylcyclopentane.

Melting points were measured using a Kofler block melting point apparatus and are uncorrected. Optical rotations were recorded on a Perkin–Elmer 141 automatic polarimeter in chloroform solution using a quartz cell of 10 cm path length with the concentration (in g/100 mL) given in parentheses. The ultraviolet spectra were recorded on Cary 15 or Perkin–Elmer Lambda 4B UV/VIS spectrometers using quartz cells of 1 cm path length. The infrared spectra were recorded on Perkin–Elmer 710, 710B, and 1710 spectrometers in chloroform solution using NaCl cells of 0.1 mm path length or as thin film using NaCl plates. The ^{1}H NMR spectra were obtained from Bruker WH-400, AE-200, or Varian XL-300 spectrometers with deuteriochloroform as solvent and the chemical shifts are reported in the delta (δ) scale in ppm relative to tetramethylsilane. The ^{13}C spectra were taken on Bruker AE-200 or XL-300 spectrometers and chemical shifts are reported in the delta (δ) scale in ppm relative to tetramethylsilane. The low- and high-resolution mass spectra were recorded on AEI-MS 902 or Kratos-MS-50 spectrometers using the electron impact ionization method while the chemical ionization mass spectra were recorded on a Delsi Nermag R10-1 OC spectrometer using ammonia as carrier gas. CD spectra were recorded on a Jasco J-20 automatic recording spectropolarimeter. Elemental analyses were performed by Mr. P. Borda, Microanalytical Laboratory, University of British Columbia.

All compounds in the Experimental section are named in accordance with IUPAC and Chemical Abstract rules. Names for compounds of the tricyclo[4.4.0.0]decane skeleton (i.e., the cycloprop[α]indene skeleton) are also included to facilitate comparison with other similar compounds previously prepared and named by our group. However, the numbering system employed in the Discussion follows the normal conventions of terpenoid and steroid literature in order to have convenient comparison with natural products and with related analogues.

*Catalytic hydrogenation: enone **9** to ketone **10***

*[1aS-(1aα,1bβ,5α,5aβ,6aα)] 1a,1b,2,3,5,5a,6,6a-Octahydro-1b,5-dimethyl-6a-(1-methylethyl)cycloprop[α]inden-4(1H)-one (**10**) or [1R,2S,6S,7S,9R] 2,6-dimethyl-9-(1-methylethyl)tricyclo[4.4.0.0^{7,9}]decan-3-one (**10**)*

Enone **9** (62 g, 282 mmol) prepared via the previously published procedure (5) was dissolved in ethanol (500 mL), and 10% palladium–carbon catalyst (1.50 g) was added. The mixture was vigorously stirred under 1 atm (101.3 kPa) H_2 for 8 h and filtered through a thick Celite cake. Evaporation of ethanol gave **10** as a colorless oil (62 g, 99%).

The physical properties of **10** are as follows: $[\alpha]_D^{25}$ +61.5 (*c* 1.00, $CHCl_3$). IR (film) ν_{max} : 3050 (C—H stretching of the cyclopropyl group), 1710 (C=O stretching) cm^{-1}. ^{1}H NMR (400 MHz, $CDCl_3$) δ: 0.20 (1H, *J* = 4.8 and 8.0 Hz), 0.42 (1H, t, *J* = 4.8 Hz), 0.85 (3H, d, *J* = 6.8 Hz), 0.87–1.00 (7H, including 0.91 (3H, d, *J* = 6.8 Hz) and 0.94 (3H, d, *J* = 7.2 Hz)), 1.10–1.40 (5H, m, including 1.24 (3H, s)), 1.45–1.90 (4H, m), 2.15 (1H, m), 2.42 (1H, m), 2.58 (1H, m). MS *m/z*: 220

Can. J. Chem. Downloaded from www.nrcresearchpress.com by ESC ESCOLA DE ENGENHARIA on 09/08/12
For personal use only.

Can. J. Chem. Downloaded from www.nrcresearchpress.com by EESC ESCOLA DE ENGENHARIA on 09/08/12
For personal use only.

(M^+, 8%), 205 (5%), 93 (75%), 86 (100%). High-resolution mass measurement: calcd. for $C_{15}H_{24}O$: 220.1821; found: 220.1815. Anal. calcd. for $C_{15}H_{24}O$: C 81.76, H 10.98; found: C 81.67, H 11.00.

*Methylation: ketone **10** to ketone **11***

*[1aS-(1aα,1bβ,5aβ,6aα)] 1a,1b,2,3,5,5a,6,6a-Octahydro-1b,5,5-trimethyl-6a-(1-methylethyl)cycloprop[α]inden-4(1H)-one (**11**) or [1S,6R,7S,9S] 2,2,6- trimethyl-9-(1-methylethyl)tricyclo[4.4.0.0^{7,9}]decan-3-one (**11**)*

To the solution of ketone **10** (62 g, 0.282 mol) in anhydrous *tert*-butanol (700 mL), potassium *tert*butoxide (130.5 g, 1.07 mol) was added slowly under nitrogen. Iodomethane (66.6 mL, 1.07 mol) was added in a dropwise manner with stirring to ensure a gentle reflux. Upon completion of addition, refluxing was continued for 30 min. The mixture was cooled, quenched with water (700 mL), and extracted with petroleum ether (3 × 500 mL). Evaporation of solvent gave an oil, which was chromatographed to provide the methylated ketone **11** (55.1 g, 84%).

The physical properties of **11** are as follows: $[\alpha]_D^{25}$ +14.0 (*c* 1.0, $CHCl_3$). IR ν_{max} (film): 3060, 1700 cm^{-1}. ^1H NMR (400 MHz, $CDCl_3$) δ: 0.18 (1H, dd, *J* = 4.0 and 8.0 Hz), 0.40 (1H, t, *J* = 4.0 Hz), 0.80–0.88 (4H, m, including 0.85 (3H, d, *J* = 7.2 Hz)), 0.90 (3H, d, *J* = 7.2 Hz), 0.97 (3H, s), 1.22 (3H, s), 1.25–1.50 (6H, m, including 1.32 (3H, s)), 1.65–1.90 (3H, m), 215 (1H, td, *J* = 4.4 and 15.2 Hz), 2.70 (1H, m). MS *m/z*: 234 (M, 56%), 219 (14%), 201 (22%), 191 (30%), 173 (51%), 43 (100%). High-resolution mass measurement: calcd. for $C_{16}H_{26}O$: 234.1983; found: 234.1986.

*Wolff–Kishner–Huang–Minlon reaction: ketone **11** to alkane **12***

*[1aS-(1aα,1bβ,5aβ,6aα)]Decahydro-1b,5,5-trimethyl-6a-(1-methylethyl)cycloprop[α]indene (**12**), or [1R,6S,7S,9R] 9-(1-methylethyl)-2,2,6-trimethyltricyclo[4.4.0.0^{7,9}]decane (**12**)*

Ketone **11** (42.0 g, 180 mmol) in diethylene glycol (300 mL) was treated with potassium hydroxide (37 g, 528 mmol) and hydrazine monohydrate (26.8 mL, 552 mmol). The mixture was heated at 100°C for 1.5 h under nitrogen. The temperature was then raised to 220°C to remove water and excess hydrazine. Refluxing was continued at 210°C for 4 h. The mixture was cooled, diluted with water (1 L), and extracted with petroleum ether (3 × 600 mL). Evaporation of the solvent gave a brown oil, which was rapidly chromatographed using petroleum ether as eluting solvent to afford **12** as a colourless oil (24.50 g, 62%).

The physical properties of **12** are as follows: $[\alpha]_D^{25}$ +42.5 (*c* 1.00, $CHCl_3$). IR ν_{max} (film): 3060 cm^{-1}. ^1H NMR (400 MHz, $CDCl_3$) δ: 0.04 (1H, dd, *J* = 4.6 and 8.4 Hz), 0.40 (1H, t, *J* = 4.6 Hz), 0.72–0.82 (4H, including 0.78 (3H, s)), 0.82–1.65 (22H, including 0.88 (3H, d, *J* = 7.2 Hz), 0.95 (3H, d, *J* = 7.2 Hz), 0.98 (3H, s), and 1.07 (3H, s)). MS *m/z*: 220 (M^+, 3%), 205 (10%), 177 (46%), 109 (100%). High-resolution mass measurement: calcd. for $C_{16}H_{28}$: 220.2191; found: 220.2198.

*Ozonolysis: alkane **12** to alcohol **13** and ketone **14***

*[1aR](1aα,2aβ,5aβ,6aα)] Decahydro-α-hydroxy-α,α,1b,5,5-penta-methylcycloprop[α]inden-6a-methanol (**13**) or [1R,6S,7R,9S] 9-(1-hydroxyl-1-methylethyl)-2,2,6- trimethyltricyclo [4.4.0.0^{7,9}]decane (**13**) and [1aR-(1aα,2aβ,5aβ,6aα)] 6a-acetyl-decahydro-1b,5,5-trimethylcycloprop[α]indene (**14**) or [1R,6S,7R,9S] 9-acetyl-2,2,6-trimethyltricyclo[4.4.0.0^{7,9}]-decan-3-one (14)*

Compound **12** (4.50 g, 20.4 mmol) in ethyl acetate (500 mL) was cooled to –40°C. A stream of ozone in oxygen (90 V, flow rate 9.1 mL/s) was passed for 6.5 h. The oxygen flow was allowed to pass through the solution until the blue colour disappeared. Dimethyl sulfide (1.0 mL) was added and the stirred mixture was warmed slowly to room temperature. After washing with water and saturated sodium bicarbonate solution, the mixture was dried over magnesium sulfate. Solvent evaporation gave an oil, which was chromatographed to afford compounds **13** (2.01 g, 42%) and **14** (1.23 g, 27%) in a total yield of 69%.

The physical properties of **13** are as follows: $[\alpha]_D^{25}$ +49.2 (*c* 1.00, $CHCl_3$). IR ν_{max} (film): 3400 (O—H stretching), 3060 (C—H stretching) cm^{-1}. ^1H NMR (400 MHz, $CDCl_3$) δ: 0.40–0.55 (2H, m), 0.72 (3H, s), 0.80–1.90 (23H, including 0.92 (3H, s), 1.05 (3H, s), 1.10 (3H, s), and 1.19 (3H, s)). MS *m/z*: 236 (M^+, 1%), 218 (36%), 203 (27%), 178 (41%), 163 (60%), 59 (100%). High-resolution mass measurement: calcd. for $C_{16}H_{28}O$: 236.2140; found: 236.2140. Anal. calcd. for $C_{16}H_{28}O$: C 81.29, H 11.94; found: C 81.23, H 12.00.

The physical properties of **14** are as follows: $[\alpha]_D^{25}$ +82 (*c* 0.24, $CHCl_3$). IR ν_{max} (film): 1675 (C=O stretching) cm^{-1}. ^1H NMR (400 MHz, $CDCl_3$) δ: 0.83 (3H, s), 1.00 (3H, s), 1.05 (1H, m), 1.10–1.70 (12H, m, including 1.15 (3H, s)), 1.80 (1H, dd, *J* = 4.0 and 12.0 Hz), 2.00 (3H, s), 2.20 (1H, t, *J* = 12.0 Hz). MS *m/z*: 220 (M^+, 34%), 205 (16%), 177 (17%), 109 (34%), 43 (100%). High resolution mass measurement: calcd. for $C_{15}H_{24}O$: 220.1827; found: 220.1825.

*Dehydration: alcohol **13** to alkene **15***

*[1aR-(1aα,1bβ,5aβ,6aα)] Decahydro-1b,5,5-trimethyl-6a-(1-methylethenyl)cycloprop[α]indene (**15**) or [1R,6S,7R,9S] 9-(1-methylethenyl)-2,2,6-trimethyltricyclo[4.4.0.0^{7,9}]decane (**15**)*

To the alcohol **13** (171 mg, 0.724 mmol) in benzene (15.0 mL) solution, pyridinium tosylate (28 mg, 0.11 mmol, 0.15 equiv.) was added. The mixture was refluxed, utilizing a Dean–Stark apparatus, for 15 min. After the reaction mixture was washed with saturated sodium bicarbonate solution (10 mL), the organic layer was separated and concentrated in vacuo. Column chromatography by ethyl acetate:hexanes mixture (8:1, v/v) gave the vinyl cyclopropane **15** (127 mg, 91%) and the starting alcohol **13** (20.0 mg, 12%).

The physical properties of **15** are as follows: $[\alpha]_D^{25}$ +87.9 (*c* 1.09, $CHCl_3$). IR ν_{max} (film): 3075, 1650 cm^{-1}. ^1H NMR (400 MHz, $CDCl_3$) δ: 0.52 (1H, dd, *J* = 4.8 and 8.8 Hz), 0.68 (1H, t, *J* = 4.8 Hz), 0.81 (3H, s), 1.00 (3H, s), 1.02–1.58 (11H, m, including 1.13 (3H, s)), 1.65 (3H, s), 1.70–1.92 (2H, m), 4.65–4.85 (2H, 2 br s). MS *m/z*: 218 (M^+, 27%), 203 (23%), 189 (4%), 175 (21%), 147 (31%), 147 (51%), 109 (100%). High-resolution mass measurement: calcd. for $C_{16}H_{26}$: 218.2035; found: 218.2030.

*Ozonolysis: alkene **15** to ketone **14***

Method A

To a solution of the vinyl cyclopropane **15** (200 mg, 0.917 mmol) in a solvent mixture of *tert*-BuOH:water (9.0 mL, 2:1, v/v), potassium permanganate (436 mg, 2.76 mmol) was added at room temperature. The resulting dark purple solution was stirred first at room temperature for 40 min, and then at 40°C for 10 min. The mixture was then diluted with water (20 mL) and extracted with ethyl acetate (2 × 25 mL). The combined extract was washed with brine (10 mL) and concentrated in vacuo. The oil obtained above was then dissolved in methanol (10 mL) and treated with $Pb(OAc)_4$ (313 mg, 0.706 mmol) for 1 h at room temperature. After concentration in vacuo, the crude product was column chromatographed using ethyl acetate:hexanes mixture (1:8, v/v) to give the starting vinyl cyclopropane **15** (4.1 mg, 2%) and ketone **14** (180 mg, 91%, based on recovery).

Method B

A stream of ozone was passed through a solution of the vinyl cyclopropane **15** (117 mg, 0.536 mmol) in methylene chloride (5.0 mL) at –40°C for 30 min. After addition of dimethyl sulfide (2 mL), the mixture was warmed slowly and then stirred at room temperature for 2 days. Concentration of the reaction mixture in vacuo gave a crude product that was chromatographed with ethyl acetate:hexanes mixture (1:8, v/v) to provide ketone **14** (73 mg, 62%).

*Baeyer–Villiger reaction: ketone **14** to acetate **16***

*[1aR-(1aα,1bβ,5aβ,6aα)] Decahydro-1b,5,5-trimethylcycloprop[α]inden-6a-yl acetate (**16**) or [1R,6S,7R,9S) 9-acetoxy-2,2,6-trimethyltricylo[4.4.0.0^{7,9}]decane (**16**)*

To the solution of ketone **14** (1.80 g, 8.18 mmol) in methylene chloride (10 mL) was added *m*-CPBA (4.45 g, 80–85% pure, 2.1 mmol, 2.5 equiv.). The above mixture was refluxed for 12 h during which time a milky thick slurry was observed. After cooling to room temperature, methylene chloride (50 mL) was added and the mixture was washed

Can. J. Chem. Downloaded from www.nrcresearchpress.com by EESC ESCOLA DE ENGENHARIA on 09/08/12
For personal use only.

rapidly with 10% brine solution (50 mL). The organic layer was separated, washed with brine solution (20 mL), dried with magnesium sulfate, and concentrated in vacuo. Column chromatography of the crude product using ethyl acetate:hexanes mixture (1:8 v/v) gave acetate **16** (1.50 g, 82% based on starting material recovery) and starting ketone **14** (0.09 g).

The physical properties of **16** are as follows: $[\alpha]_D^{25}$ +36.7 (*c* 1.0, $CHCl_3$). IR ν_{max} (film): 3050 (C—H stretching), 1735 (C=O stretching) cm^{-1}. ^1H NMR (400 MHz, $CDCl_3$) δ: 0.70 (1H, m), 0.80 (3H, s), 0.90–1.02 (4H, m, including 0.97 (3H, s)), 1.05 (3H, s), 1.10–1.70 (8H, m), 1.90–2.10 (4H, including 2.10 (3H, s)), 2.23 (1H, dd, *J* = 8.0 and 12.0 Hz). MS *m/z*: 236 (M^+, 1%), 221 (19%), 194 (21%), 179 (22%), 109 (100%). High-resolution mass measurement: calcd. for $C_{15}H_{24}O_2$: 236.1776; found: 236.1774.

*Saponification: acetate **16** to cyclopropanol **17***

*[1aR-(1aα,1bβ,5aβ,6aα)] Decahydro-1b,5,5-trimethylcyclopro[α]inden-6a-ol (**17**) or [1R,6S,7R,9S] 2,2,6-trimethyltricyclo[4.4.0.0^{7,9}]decan-9-ol (**17**)*

Acetate **16** (589 mg, 2.50 mmol) was dissolved in ethanol (20 mL) at room temperature. To this solution was added powdered potassium hydroxide (230 mg, 3.28 mmol) under nitrogen. The resulting mixture was stirred for 30 min, diluted with water (20 mL), and extracted with methylene chloride (2 × 20 mL). The methylene chloride solution was dried over magnesium sulfate, and concentrated to provide alcohol **17** as an oil (490 mg, 100%).

The physical properties of **17** are as follows: $[\alpha]_D^{25}$ +34.5 (*c* 1.00, $CHCl_3$). IR ν_{max} (film): 3050–3650 cm^{-1}. ^1H NMR (400 MHz, $CDCl_3$) δ: 0.80 (3H, s), 0.96 (3H, s), 1.01 (3H, s), 1.98 (2H, m). MS *m/z*: 194 (M^+, 3%), 179 (5%), 124 (29%), 109 (100%), 81 (23%). High-resolution mass measurement: calcd. for $C_{13}H_{22}O$: 194.1672; found: 194.1665.

*Cyclopropane ring opening reaction by $FeCl_3$: cyclopropanol **17** to β-chloroketone **18***

*[4aS-(4aα,8aα)] 4-Chloro-3,4,4a,5,6,7,8,8a-octahydro-4a,8,8-trimethylnaphthalen-2(1H)-one (**18**)*

The alcohol **17** (490 mg, 2.53 mmol) obtained from the above reaction was dissolved in anhydrous DMF (12.5 mL) under nitrogen and cooled to 0°C. Anhydrous ferric chloride (1.03 g, 6.35 mml) was then added to this solution. After stirring for 1 h, the resulting brown mixture was warmed to room temperature and stirring continued for 24 h. Addition of 1 M hydrochloric acid (20 mL) to the mixture was followed by extraction with diethyl ether (2 × 20 mL). After drying over magnesium sulfate and solvent removal, the crude product containing **18** was subjected to dehydrochlorination without further separation.

The physical properties of **18** are as follows: IR ν_{max} (film): 1720 cm^{-1}. ^1H NMR (400 MHz, $CDCl_3$) δ: 0.76 (3H, s), 0.90 (3H, s), 1.25 (3H, s), 2.10–3.00 (4H, m), 4.70 (1H, dd, *J* = 6.0 and 12.0 Hz). MS *m/z*: 228/230 (M^+, 0.6%/0.2%), 206 (1%), 193 (8%), 43 (100%). High-resolution mass measurement: calcd. for $C_{13}H_{21}O_{37}Cl$: 230.1251; found: 230.1223; calcd. for $C_{13}H_{21}O_{35}Cl$: 228.1281; found: 228.1276.

*Dehydrochlorination: β-chloroketone **18** to enone **1***

*[4aR-(4aα,8α)] 4a,5,6,7,8,8a-Hexahydro-4a,8,8-trimethylnaphthalen-2(1H)-one (**1**)*

The above crude product containing β-chloroketone **18** was dissolved in a saturated sodium acetate – methanol solution (10 mL). This mixture was refluxed for 3 h and concentrated in vacuo. Purification by column chromatography with ethyl acetate:hexanes (2:8) gave enone **1** (384 mg, overall 80% from acetate **16**).

The physical properties of **1** are as follows: Mp 64–66°C. $[\alpha]_D^{25}$ +47.6 (*c* 1.00, $CHCl_3$). UV (MeOH, *c* 20.0 mg/L) λ_{max}:235 nm (log ε = 3.842). IR ν_{max} (film): 1664 (C=O stretching) cm^{-1}. ^1H NMR (400 MHz, $CDCl_3$) δ: 0.77 (3H, s), 0.96 (3H, s), 1.22 (3h, s), 1.22 (3H, s), 1.27–1.75 (7H, m), 2.50–2.80 (2H, m), 5.95 (1H, d, *J* = 9.6 Hz), 6.27 (1H, d, *J* = 9.6 Hz). MS *m/z*: 192 (M^+, 13%), 150 (45%), 69 (100%). High-resolution mass measurement: calcd. for $C_{13}H_{20}O$: 192.1514; found: 192.1518. Anal. calcd for $C_{13}H_{20}O$: C 81.20, H 10.50; found: C 81.13, H 10.48.

*Conjugate addition: α,β-enone **1** to cis-fused γ,δ-enone **19***

*[4R-(4aα,4aα,8aα)] 4-Ethenyl-3,4,4a,5,6,7,8,8a-octahydro-4a,8,8-trimethylnaphthalen-2(1H)-one (**19**)*

To a solution of enone **1** (718 mg, 3.74 mmol) in anhydrous THF (20 mL), cuprous iodide (112 mg, 0.59 mmol, 0.15 equiv.) and dimethyl sulfide (5 mL) were introduced under a nitrogen atmosphere. This mixture was cooled to 0°C and 0.66 M vinylmagnesium bromide in THF solution (8.2 mL, 5.41 mmol, 1.4 equiv.) was added in a dropwise manner over a period of 1 h. After the mixture was warmed to room temperature and stirred for another hour, saturated brine solution (20 mL) was introduced to quench the excess vinylmagnesium bromide. The organic layer was separated; the aqueous layer was extracted with diethyl ether (10 mL). The combined organic solution was dried over magnesium sulfate and concentrated in vacuo to give a crude oil, which was then chromatographed to provide enone **19** in 70% yield (576 mg).

The physical properties of **19** are as follows: $[\alpha]_D^{25}$ +22.2 (*c* 1.00, $CHCl_3$). IR ν_{max} (film): 1710 (C=O stretch), 1635 (C=C stretch) cm^{-1}. ^1H NMR (400 MHz, $CDCl_3$) δ: 0.80–1.70 (14H, including 0.90 (3H, s), 0.95 (3H, s), and 1.09 (3H, s)), 1.90 (1H, m), 2.25–3.10 (5H, m), 4.95–5.15 (2H, m), 5.70 (1H, m). MS *m/z*: 220 (M^+, 16%), 205 (4%), 123 (68%), 43 (100%). High-resolution mass measurement: calcd. for $C_{15}H_{24}O$: 220.1828; found: 220.1831.

*Methylation by LDA and iodomethane: cis-fused γ,δ-enone **19** to cis-fused γ,δ-enone **6***

*[3S-(3α,4β,4aβ,8aβ)] 4-Ethenyl-3,4,4a,5,6,7,8,8a-octahydro-3,4a,8,8-tetramethylnaphthalen-2(1H)-one (**6**)*

A solution of LDA in *n*-pentane (0.68 M, 2.6 mL, 1.77 mmol) was concentrated to remove *n*-pentane. The resulting white viscous mixture was cooled to –40°C, and anhydrous dimethoxyethane (1 mL) was then added under nitrogen. Enone **19** (350 mg, 1.59 mmol) in dimethoxyethane (3.5 mL) was introduced to the LDA solution in a dropwise manner over a period of 1 h. This enolate solution was warmed rapidly to 50°C and freshly distilled iodomethane (0.40 mL, 6.42 mmol) was added rapidly. The resulting turbid yellowish mixture was stirred at 50°C for 30 min and quenched with a solution of potassium hydroxide (100 mg) in methanol (10 mL). After stirring for 30 min, the reaction mixture was concentrated in vacuo to give the crude product, which was chromatographed with ethyl acetate:hexanes (1:8, v/v) to afford **6** (207 mg, 65% based on recovery of **19**) and the starting enone **19** (53 mg, 15%).

The physical properties of **6** are as follows: $[\alpha]_D^{25}$ +29.3 (*c* 1.00, $CHCl_3$). IR ν_{max} (film): 1700 (C=O stretching), 1630 (C=C stretching) cm^{-1}. ^1H NMR (400 MHz, $CDCl_3$) δ: 0.70–1.60 (18H, m, including 0.82 (3H, s), 0.94 (3H, s), and 1.04 (3H, d, *J* = 6.4 Hz), 1.14 (3H, s)), 1.90 (1H, m), 2.30 (1H, m), 2.45–2.70 (3H, m), 4.95–5.20 (2H, m), 5.55 (1H, m). MS *m/z*: 234 (M^+, 2%), 219 (1%), 167 (36%), 149 (100%).

*Dehydrogenation by $PhSeCl/H_2O_2$: cis-fused γ,δ-enone **6** to dienone **20***

*[3S-(3α,4β,4aβ,8aβ)] 4-Ethenyl-4,4a,5,6,7,8-hexahydro-3,4a,8,8-tetramethylnapthalen-2(3H)-one (**20**)*

A solution of LDA in *n*-pentane (0.50 M, 2.30 mL, 1.15 mmol) was concentrated in vacuo to remove *n*-pentane. The viscous mixture was cooled to –40°C and anhydrous THF (1 mL) was then added under nitrogen. The solution of **6** (250 mg, 1.07 mmol) in anhydrous THF (3 mL) was added in a dropwise manner with stirring over a 45 min period. The resulting mixture was warmed to room temperature and phenylselenyl chloride (212 mg, 1.10 mmol) was introduced. Stirring at room temperature was continued for 1.5 h before addition of pyridine (0.5 mL), methylene chloride (5 mL), and hydrogen peroxide (0.5 mL of 30% H_2O_2 in 3 mL of water). The two-phase mixture was stirred at room temperature for 5 h and separated. The aqueous layer was extracted with methylene chloride (5 mL). The combined organic layers were dried over magnesium sulfate and concentrated in vacuo to

Can. J. Chem. Downloaded from www.nrcresearchpress.com by ESC ESCOLA DE ENGENHARIA on 09/08/12
For personal use only.

yield a crude product. Purification by column chromatography with ethyl acetate:hexanes (1:8, v/v) afforded dienone **20** (134 mg, 62% based on recovery of starting material) and the starting material **6** (31 mg).

The physical properties of **20** are as follows: $[\alpha]_D^{25}$ –4.2 (*c* 1.00, $CHCl_3$). UV (MeOH, *c* 40.0 mg/L) λ_{max}: 242 nm ($\log \epsilon = 3.96$). IR ν_{max} (film): 1665 (C=O stretching) cm^{-1}. ^1H NMR (400 MHz, $CDCl_3$) δ: 0.80–1.90 (18H, m, including 1.07 (3H, d, J = 5.1 Hz), 1.17 (3H, s), 1.22 (3H, s), and 1.25 (3H, s)), 2.12 (1H, t, J = 10.2 Hz), 2.40 (1H, m), 5.00–5.25 (2H, m), 5.69 (1H, m), 6.00 (1H, s). MS *m/z*: 232 (M^+, 21%), 217 (17%), 189 (3%), 178 (8%), 164 (100%), 149 (49%), 121 (15%). High-resolution mass measurement: calcd. for $C_{16}H_{24}O$: 232.1827; found: 232.1829.

*Birch reduction: dienone **20** to* trans*-fused* γ,δ*-enone **5***

*[3S-(3α,4β,4aβ,8aα) 4-Ethenyl-3,4,4a,5,6,7,8,8a-octahydro-3,4a,8,8-tetramethylnaphthalen-2(1*H*)-one (**5**)*

To a solution of dienone **20** (300 mg, 1.29 mmol) in anhydrous THF (2 mL), anhydrous ammonia (4 mL) was distilled from sodium under a nitrogen atmosphere. Small pieces of lithium were added slowly over a 30 min period until a persistent dark blue color remained. After stirring for 1 h at –33°C, ammonium chloride powder was introduced to quench excess lithium. Evaporation of ammonia and THF gave a yellowish oil, which was chromatographed to afford the *trans*-fused decalone **5** (268 mg, 90%).

The physical properties of **5** are as follows: $[\alpha]_D^{25}$ –8.38 (*c* 2.40, $CHCl_3$). IR ν_{max} (film): 1706 (C=O stretching) cm^{-1}. ^1H NMR (400 MHz, $CDCl_3$) δ: 0.75–1.80 (19H, m, including 0.88 (3H, s), 0.90 (3H, s), 0.97 (3H, d, J = 6.0 Hz), and 1.09 (3H, s)), 2.00–2.50 (4H, m), 4.98 (1H, dd, J = 1.6 and 16.8 Hz), 5.12 (1H, dd, J = 1.6 and 10.0 Hz), 5.56 (1H, dt, J = 10.0 and 16.8 Hz). MS *m/z*: 234 (M^+, 34%), 219 (9%), 203 (0.3%), 137 (11%), 123 (100%), 109 (19%). High-resolution mass measurement: calcd. for $C_{16}H_{26}O$: 236.2140; found: 236.2097.

Reduction by L-Selectride: trans*-fused* γ,δ*-enone **5** to alcohol **21***

*[2R-(2α,3α,4β,4aβ,8aα)] 4-Ethenyl-decahydro-3,4a,8,8-tetramethylnapthalen-2-ol (**21**)*

The *trans*-fused ketone **5** (250 mg, 1.07 mmol) in anhydrous THF (2 mL) was added in a dropwise manner to L-Selectride (0.72 M, 3.0 mL, THF), at –78°C for 30 min. The solution was stirred for 1.5 h, warmed to 0°C, and stirred for an additional hour. Aqueous sodium hydroxide solution (3.0 mL, 3M) and aqueous 30% hydrogen peroxide (3 mL) were then introduced. The resulting mixture was stirred for 30 min, saturated with potassium carbonate, and separated. The aqueous layer was further extracted with diethyl ether (2 × 10 mL). The organic solutions were combined and concentrated in vacuo. Purification by column chromatography with ethyl acetate:hexanes (2:8, v/v) gave alcohol **21** (240 mg, 95%).

The physical properties of **21** are as follows: $[\alpha]_D^{25}$ –40.9 (c 1.00, $CHCl_3$). IR ν_{max} (film): 3450 (O—H stretching), 1630 (C=O stretching) cm^{-1}. ^1H NMR (400 MHz, $CDCl_3$) δ: 0.70–1.85 (24H, m), 3.92 (1H, q, J = 3.0 Hz), 4.94 (1H, dd, J = 2.4 and 17.2 Hz), 5.02 (1H, dd, J = 2.4 and 10.4 Hz), 5.52 (1H, td, J = 10.4 and 17.2 Hz). MS *m/z*: 236 (M^+, 2%), 218 (2%), 203 (5%), 123 (100%). High-resolution mass measurement: calcd. for $C_{16}H_{28}O$: 236.1240; found: 236.2136. Anal. calcd. for $C_{16}H_{28}O$: C 81.29, H 11.09; found: C 81.22, H 11.11.

*Hydroboration: alcohol **21** to 1.5-diol **4***

*[1S-(1α,2β,3β,4β,4aβ,8aα)] Decahydro-3-hydroxyl-2,5,5,8a-tetramethylnaphthalene-1-ethanol (**4**)*

To a cooled solution (0°C) of alcohol **21** (300 mg, 1.27 mmol) in anhydrous THF (2 mL), a solution of borane in anhydrous THF (7.0 mL, 0.56 M) was added in a dropwise manner, under nitrogen over a period of 30 min. The solution was warmed to room temperature and then stirred for 1.5 h. After water (1 mL), aqueous sodium hydroxide (3 mL, 3 M), and aqueous hydrogen peroxide (3 mL, 30%) were introduced, and the resulting mixture was stirred overnight, saturated with sodium chloride, and separated. The aqueous layer was further extracted with diethyl ether (10 mL). The organic solutions were combined, dried over magnesium sulfate, and concentrated in vacuo to give the crude product. The crude product was chromatographed with ethyl acetate:methanol:hexanes (1:2:2, v/v/v) to afford diol **4** in 71% yield (229 mg).

The physical properties of **4** are as follows: mp 128–130°C. $[\alpha]_D^{25}$ –16.9 (*c* 1.00, $CHCl_3$). IR ν_{max} (film): 3400 (O-H stretching) cm^{-1}. ^1H NMR (400 MHz, $CDCl_3$) δ: 0.70–1.80 (27H, m, including 0.82 (6H, two overlapped singlets), 0.86 (3H, s), and 0.98 (3H, d, J = 6.0 Hz)), 3.50 (1H, dt, J = 7.2 and 9.6 Hz), 3.62 (1H, dt, J = 5.6 and 9.6 Hz), 3.85 (1H, q, J = 3.0 Hz). MS *m/z*: 236 ($M^+ - H_2O$, 7%), 221 (7%), 191 (17%), 177 (6%), 167 (19%), 138 (62%), 123 (100%). High-resolution mass measurement: calcd. for $C_{16}H_{30}O_2$: 254.2236; found: 254.2241. Anal. calcd. for $C_{16}H_{30}O_2$: C 75.53, H 11.89; found: C 75.75, H 12.00.

*Cyclization: 1,5-diol **4** to **2**, **3**, and **27***

*[3aR-(3aα,5aβ,9aα,9bβ)] Dodecahydro-3a,6,6,9a-tetramethyl-1*H*-naphtho[2,1-*b*]furan (**2**). [3aS-(3aα,5aα,9aβ,9bα)] Dodecahydro-3a,6,6,9a-tetramethyl-1*H*-naphtho[2,1-*b*]furan (**3**). [3aR-(3aα,4α,6aα,10aS*)] Dodecahydro-3a,4,7,7-tetramethyl-2*H*-naphtho[8a,1-*b*]furan (**27**)*

Procedure no. 1

Diol **4** (20 mg, 0.079 mmol) in anhydrous toluene (2 mL) was treated with *p*-toluenesulfonic acid (27 mg, 0.16 mmol, 2.0 equiv.) under a nitrogen atmosphere. This solution was then heated at 80°C for 2 h. The resulting mixture was transferred by the use of diethyl ether (10 mL) to a separatory funnel, washed with saturated sodium carbonate solution, dried over magnesium sulfate, and concentrated in vacuo. Column chromatography with hexanes, ethyl acetate:hexanes (1:50, v/v), ethyl acetate:hexanes (1:20, v/v), and ethyl acetate:hexanes (1:8, v/v) consecutively gave a mixture of hydrocarbons (1.4 mg, 8%), (+)-iso-Ambrox (**3**) (1.9 mg, 10%), and (–)-Ambrox (**2**) (8.9 mg, 48%).

Procedure no. 2

Diol **4** (20 mg, 0.079 mmol) in nitromethane (2 mL) was treated with *p*-toluenesulfonic acid (81 mg, 0.47 mmol, 6.0 equiv.) under a nitrogen atmosphere. The solution was then heated at 100°C for 30 min. After a work-up similar to that in procedure no. 1, the crude product was chromatographed with hexanes and ethyl acetate:hexanes (1:50, v/v) to give a mixture of hydrocarbons (7.0 mg, 41%), the ionoxide principal **27** (6.4 mg, 34%), and (+)-iso-Ambrox (**3**) (3.5 mg, 19%).

The physical properties of **2** are as follows: mp 74–76°C. $[\alpha]_D^{25}$ –25.1 (*c* 1.00, $CHCl_3$). IR ($CHCl_3$) ν_{max}: 1450, 1385, 995, 970 cm^{-1}. ^1H NMR (400 MHz, $CDCl_3$) δ: 0.83 (3H, s), 0.84 (3H, s), 0.88 (3H, s), 1.09 (3H, s), 3.83 (1H, q, J = 8 Hz), 3.92 (1H, m). MS *m/z*: 236 (M^+, 3%), 221 (100%), 205 (7%), 177 (4%), 137 (40%), 97 (38%), 84 (24%), 81 (20%), 69 (20%), 59 (23%), 55 (19%), 43 (21%). High-resolution mass measurement: calcd. for $C_{16}H_{28}O$: 236.2140; found: 236.2139. For comparison, the reported literature values for **2** (30) are mp 77–75.5°C. $[\alpha]_D^{20}$ –24.7 (*c* 1.0, $CHCl_3$). The IR, ^1H NMR, and mass spectroscopic data are also identical with those presented above.

The physical properties of **3** are as follows: mp 57–59°C. $[\alpha]_D^{25}$ +7.4 (*c* 1.00, $CDCl_3$). IR ($CHCl_3$) ν_{max}: 1440, 1390, 1010, 980 cm^{-1}. ^1H NMR (400 MHz, $CDCl_3$) δ: 0.86 (3H, s), 0.89 (3H, s), 0.90 (3H, s), 1.06 (3H, s), 3.70 (q, J = 8 Hz), 3.80 (1H, dt, J = 3 and 8 Hz). MS *m/z*: 236 (M^+, 0.0%), 221 ($M^+ - CH_3$, 100%), 177 (2%), 137 (21%), 109 (8%), 97 (33%), 84 (32%), 69 (22%), 55 (34%), 47 (8%), 43 (50%). High-resolution mass measurement: calcd. for $C_{15}H_{25}O$ ($M^+ - CH_3$): 221.1905; found: 221.1906. Chemical ionization MS using methane as carrier gas: 251 ($M + CH_5^+$), 237 ($M + H^+$). For comparison, the reported literature values for **3** (30) are Mp 60–60.5°C. $[\alpha]_D^{25}$ +7.5 (*c* 1.00, $CHCl_3$). The IR, ^1H NMR, and mass spectroscopic data are also identical with those presented above.

The physical properties of **27** are as follows: $[\alpha]_D^{25}$ +37.1 (*c* 1.00, $CHCl_3$). IR (film) ν_{max}: 1380, 1370, 1030, 1045 cm^{-1}. ^1H NMR (400 MHz, $CDCl_3$) δ: 0.81 (3H), 0.83 (3H, d, J = 6 Hz), 0.87 (3H, s), 0.94

(3H, s), 3.70 (1H, dt, J = 2 and 9 Hz), 3.81 (1H, q, J = 9 Hz). MS m/z: 236 (M^+, 10%), 221 (5%), 194 (15%), 193 (100%). High-resolution mass measurement: calcd. for $C_{16}H_{28}O$: 236.2140; found: 236.2142.

Acknowledgements

Financial aid from the Natural Sciences and Engineering Research Council of Canada is gratefully acknowledged.

1. J.P. Kutney, P.J. Grunning, R.G. Clewley, J. Somerville, and S.J. Rettig. Can. J. Chem. **70**, 2094 (1992).
2. G. Ohloff. *In* Fragrance chemistry. The science of the sense and smell. *Edited by* E.T. Theimer. Academic Press, New York. 1982. p. 535, and references cited therein.
3. G. Frater and D. Lamparsky. *In* Perfumes, art science and technology. *Edited by* P.M. Muller and D. Lamparsky. Elsevier Applied Science, New York. 1991. p. 547, and references cited therein.
4. G. Ohloff, B. Winter, and C. Fehr. *In* Perfumes, art science and technology. *Edited by* P.M. Muller and D. Lamparsky. Elsevier Applied Science, New York. 1991. p. 289, and references cited therein.
5. J.P. Kutney, J. Balsevich, and P. Grice. Can. J. Chem. **58**, 2641 (1980).
6. J.P. Kutney, K. Piotrowska, Y.H. Chen, K.P.N. Cheng, Z. Gao, and S.J. Rettig. Can. J. Chem. **68**, 1698 (1990).
7. W.D. Emmons and G.B. Lucas. J. Am. Chem. Soc. **77**, 2287 (1955).
8. R.R. Sauers and R.W. Ubersax. J. Am. Chem. Soc. **87**, 3939 (1965).
9. G.R. Krow. Tetrahedron, **37**, 2697 (1981).
10. C.H. DePuy and R.J. van Lenen. J. Org. Chem. **39**, 3360 (1974).
11. M. Miyashita and A. Yoshikoshi. J. Am. Chem. Soc. **96**, 1917 (1974).
12. G.H. Posner. Org. React. (N.Y.), **19**, 1 (1972).
13. G.H. Posner. An introduction to synthesis using organocopper reagents. John Wiley, New York. 1980.
14. S.H. Bertz and G. Dabbagh. Tetrahedron, **45**, 425 (1989).
15. M. Gall and H.O. House. Org. Synth. **52**, 39 (1972).
16. H.O. House. Modern synthetic reactions. W.A. Benjamin, Inc. New York. 1972. p. 502.
17. R.J.K. Taylor. Synthesis, 364 (1985).
18. M.J. Chapdelaine and M. Hulce. Org. React. (N.Y.), **38**, 225 (1990).
19. H.J. Reich, S. Wollowitz, J.E. Trend, F. Chow, and D.F. Wendelborn. J. Org. Chem. **43**, 1697 (1978).
20. D. Caine. Org. React. (N.Y.), **23**, 1 (1976).
21. G. Stork and S.D. Darling. J. Am. Chem. Soc. **86**, 1761 (1964).
22. M.J.T. Robinson. Tetrahedron, **21**, 2475 (1965).
23. M. Stoll and M. Hinder. Helv. Chim. Acta, **33**, 1251 (1950).
24. M. Hinder and M. Stoll. Helv. Chim. Acta, **33**, 1308 (1950).
25. M. Stoll. U.S. Patent 3,029,255 (1962).
26. J.N. Schumacker, W.M. Henley, E. Bernasek, and C.E. Teague. U.S. Patent 3,050,532 (1962).
27. I.C. Coste-Maniera, J.P. Zahra, and B. Waegell. Tetrahedron Lett. **29**, 1017 (1988).
28. K. Mori and H. Tamura. Liebigs Ann. Chem. 361 (1990).
29. G. Buchi and H. Wuest. Helv. Chim. Acta, **72**, 996 (1989).
30. G. Ohloff, W. Giersch, W. Pickenhagen, A. Furrer, and B. Frei. Helv. Chim. Acta, **68**, 2022 (1985).
31. P.F. Vlad, M.N. Kottsa, I.P. Dragalin, L.A. Zadorozhnaya, V.E. Sibirseva, and L.M. Sitnova. Russ. Chem. Rev. **58**, 2037 (1988).
32. R.L. Snowden and S.M. Linder. Tetrahedron Lett. **32**, 4119 (1991).
33. R.L. Snowden, J.-C. Eichenberger, S.M. Linder, P. Sonnay, C. Vial, and K.H. Schulte-Elte. J. Org. Chem. **57**, 955 (1992).

Can. J. Chem. Downloaded from www.nrcresearchpress.com by ESC ESCOLA DE ENGENHARIA on 09/08/12
For personal use only.

Sulfur bonding in cyclic $P_2S_2N_4$ systems: a density functional comparison of 1,1,5,5-tetramethylbicyclo[3.3.0]-1,5-diphospha-3,7-dithia-2,4,6,8-tetrazocine with the 1,1,3,5,5-pentamethyl-1,5-diphospha-3,7-dithia-2,4,6,8-tetrazocine anion

HEIKO JACOBSEN, TOM ZIEGLER,[1] TRISTRAM CHIVERS, AND RAINER VOLLMERHAUS

Department of Chemistry, University of Calgary, 2500 University Drive N.W., Calgary, AB T2N 1N4, Canada

Received November 12, 1993

HEIKO JACOBSEN, TOM ZIEGLER, TRISTRAM CHIVERS, and RAINER VOLLMERHAUS. Can. J. Chem. **72**, 1582 (1994).

The electronic structure and the bonding of the title compounds have been investigated using density functional theory within the local density approximation, adding nonlocal corrections to exchange and correlation energy. The cross-ring sulfur–sulfur bond energy in 1,1,5,5-tetramethylbicyclo[3.3.0]-1,5-diphospha-3,7-dithia-2,4,6,8-tetrazocine was estimated to be about 133 kJ/mol. The HOMO of the 1,1,3,5,5-pentamethyl-1,5-diphospha-3,7-dithia-2,4,6,8-tetrazocine anion is mainly localized at the site of the unmethylated sulfur atom and is antibonding with respect to the sulfur–carbon bond of the methylated sulfur atom, which has a relatively weak estimated bond strength of 218 kJ/mol.

HEIKO JACOBSEN, TOM ZIEGLER, TRISTRAM CHIVERS et RAINER VOLLMERHAUS. Can. J. Chem. **72**, 1582 (1994).

Faisant appel à la théorie de la densité fonctionnelle dans le cadre de l'approximation de la densité locale, tout en ajoutant des corrections non locales pour les énergies d'échange et de corrélation, on a étudié la structure électronique et les liaisons des composés mentionnés dans le titre. On a évalué que l'énergie de la liaison soufre–soufre à travers le cycle du 1,1,5,5-tétraméthylbicyclo[3.3.0]-1,5-diphospha-3,7-dithia-2,4,6,8-tétrazocine est d'environ 133 kJ/mol. L'orbital moléculaire OH de l'anion 1,1,5,5-tétraméthylbicyclo[3.3.0]-1,5-diphospha-3,7-dithia-2,4,6,8-tétrazocine est principalement délocalisé au niveau de l'atome de soufre qui n'est pas méthylé et elle est antiliante par rapport à la liaison soufre–carbone de l'atome de soufre méthylé dont la force de liaison évaluée, 218 kJ/mol, est relativement faible.

[Traduit par la Rédaction]

Introduction

The first eight-membered $P_2S_2N_4$ system containing a sulfur–sulfur bond was described by Chivers and co-workers (1) in 1982. 1,1,5,5-Tetramethylbicyclo[3.3.0]-1,5-diphospha- 3,7-dithia-2,4,6,8-tetrazocine, 1,5-$Me_4P_2S_2N_4$ (**1***a*), possesses a puckered bicyclic structure with a short sulfur–sulfur contact of 2.55 Å (see Scheme 1). Subsequently, the structure of the tetraphenyl derivative 1,5-$Ph_4P_2S_2N_4$ (**1***b*) was reported (2). This molecule also exhibits a cradle configuration with an S—S bond length of 2.53 Å. These S—S bond lengths are comparable with the value for the parent compound S_4N_4 (d_{S-S} = 2.58 Å) (3).

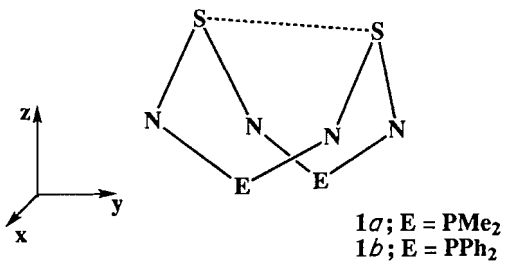

1*a*; E = PMe_2
1*b*; E = PPh_2

SCHEME 1

The bonding in cyclic 1,5-$P_2S_2N_4$ systems has been investigated by Hückel-MO theory (1, 2). It has been shown that the formation of a sulfur–sulfur σ bond is the driving and stabilizing force on going from a planar 10π-electron system to the puckered structure having two allyl-like 4π-electron systems (1). Oakley and co-workers have demonstrated that the frontier orbitals in dithiatetrazocines represent bonding and antibonding sulfur–sulfur σ and σ* orbitals for the HOMO and the LUMO, respectively (4). Although it is appealing to equate these orbitals with the σ and σ* orbitals of a disulfide linkage, the phase properties and one-electron energies of the σ/σ* orbitals in dithiatetrazocines suggest a direct isolobal analogy with the π/π* levels of an electron-deficient olefin (4). This concept can easily be transferred to the 1,5-$P_2S_2N_4$ systems; the HOMO **I***a* and the LUMO **I***b* are depicted in Scheme 2.

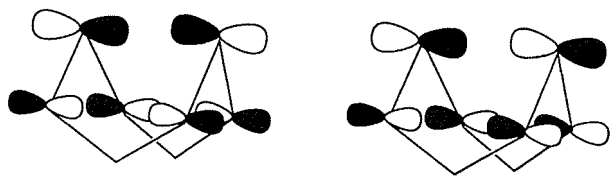

I*a* **I***b*

SCHEME 2

As a test of the analogy mentioned above, the platinum complex Pt(η^2-S,S′-1,5-$Ph_4P_2S_2N_4$)$(PPh_3)_2$ has been prepared as an analogue of the classical η^2-alkene complexes Pt(C_2R_4)-$(PPh_3)_2$ (5). A density functional analysis revealed that the heterocyclic ligand coordinated to the metal shows both donation from σ(S—S), **I***a*, as well as back-donation into σ*(S—S), **I***b*. The back-donation and the overall bond strength for the $P_2S_2N_4$ ligand falls between that of the electron-deficient alkene $C_2(CN)_4$ and that of the more electron-rich alkene C_2H_4 (5).

Recently, Chivers et al. prepared the eight-membered anionic system 1,1,3,5,5-pentaphenyl-1,5-diphospha-3,7-dithia-2,4,6,8-tetrazocine (**2***a*) as the lithium derivative (6). This system, in which one of the sulfur centers has been phenylated, adopts a boat configuration with an almost planar arrangement of the two NPN units and an S—S distance of 3.31 Å. The geometry of this ion is shown schematically in Scheme 3. The

[1]Author to whom correspondence may be addressed. Telephone: (403) 220-5368. FAX: (403) 289-9488. E-mail: ziegler@zinc.chem.ucalgary.ca

Can. J. Chem. Downloaded from www.nrcresearchpress.com by EESC ESCOLA DE ENGENHARIA on 09/08/12
For personal use only.

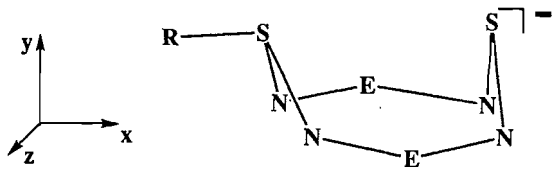

2*a*; E = PPh_2, R=Ph
2*b*; E = PMe_2, R=Me

SCHEME 3

lithium atom is bonded to two nitrogens on the opposite side of the ring from the site of nucleophilic attack (6).[2]

This finding prompted us to reinvestigate the bonding in cyclic 1,5-$P_2S_2N_4$ systems using approximate density functional theory (DFT). In particular, we wanted to determine (*a*) the fate of the σ(S—S) and σ*(S—S) orbitals under nucleophilic attack, (*b*) the charge distribution in the anionic system **2**, and (*c*) a rough estimate of the thermodynamics of this process. We also included a calculation involving a coordinated lithium cation, as found in the crystal structure analysis.

Computational details

Single point calculations were performed for 1,5-$Me_4P_2S_2N_4$ (**1***a*) and for the hypothetical structures $Me_5P_2S_2N_4^-$ (**2***b*) and Li[$Me_5P_2S_2N_4$] (**3**), utilizing the AMOL program package developed by Baerends et al. (7) and vectorized by Ravenek (8). The applied basis set was of double ζ quality, augmented by one polarization function. Electron correlation was treated at the LDA/NL level of theory. The application of DFT to molecular structures and energetics has been reviewed recently (9). We refer the reader to this work for further references and a more detailed description of the method.

The structure of **1***a* was taken from the X-ray data (1), and symmetrized according to C_{2v} symmetry. The geometries for **2***b* and **3** were also based on the X-ray data for the lithium derivative of **2***a* (6). For the sake of computational ease, phenyl groups have been replaced by methyl groups, and a C_s symmetry has been adopted. For the geometric arrangements, we refer to refs. 1 and 6.

Results and discussion

Figure 1 shows a selection of the orbital manifold for 1,5-$Me_4P_2S_2N_4$ (**1**) and $Me_5P_2S_2N_4^-$ (**2***b*). For 1,5-$Me_4P_2S_2N_4$ (**1**), the orbitals $a_1(12)$ and $b_2(8)$ represent the HOMO and LUMO of this system and correspond to the orbitals **I***a* and **I***b*, respectively, shown in Scheme 2. The HOMO–LUMO gap has been calculated to amount to 3.60 eV or 344 nm. The UV–visible spectrum of this compound (measured in CH_2Cl_2) shows one band at 265 nm (1). We note that the calculated HOMO–LUMO transition is of lower energy than the experimentally observed value. This suggests that the observed UV band might correspond to a transition into a higher excited electronic state. A possible transition, which is allowed by symmetry, is the excitation from the HOMO $a_1(12)$ to the LUMO + 1, $a_1(13)$. The $a_1(13)$ orbital lies 4.9 eV above the HOMO, which corresponds to 252 nm. DFT has been used extensively to calculate excitation energies and usually provides results in close agreement with the experimental values (9). Thus, it seems likely that the observed transition for 1,5-$Me_4P_2S_2N_4$ (**1**) is HOMO to LUMO + 1. The calculated intensities for these two different electronic transitions would be necessary for a correct assignment of the UV spectrum. Unfortunately, this feature is presently not available in the AMOL program package.

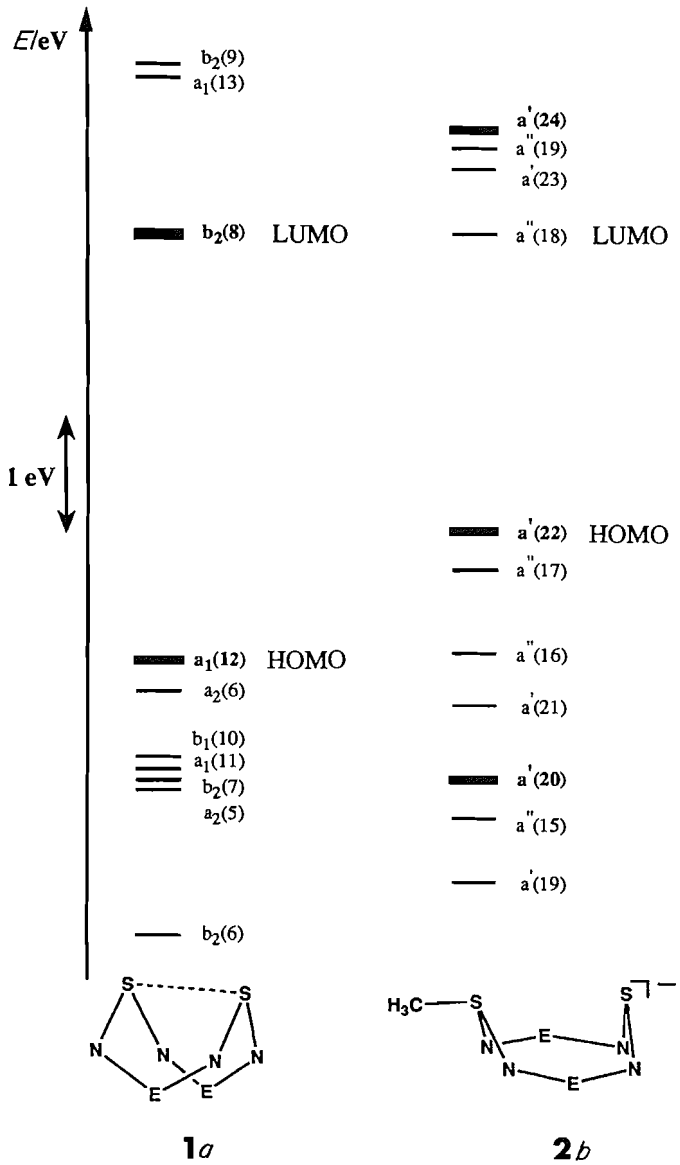

FIG. 1. Partial orbital diagram for 1,5-$Me_4P_2S_2N_4$ and $Me_5P_2S_2N_4^-$. Some important orbitals are outlined in bold.

For the anionic system $Me_5P_2S_2N_4^-$ (**3**), the HOMO–LUMO gap decreases to 2.59 eV or 479 nm. Coordination of a Li^+ cation to form Li[$Me_5P_2S_2N_4$] (**3**) increases this value to 3.08 eV or 402 nm. We thus expect the S-methylated 1,5-$P_2S_2N_4$ anion to absorb light in the blue region of the visible spectrum and to appear yellow to orange in color.

The methylation reaction can be viewed as a nucleophilic attack of a methyl anion at one of the sulfur centers of 1,5-$Me_4P_2S_2N_4$ (**1***a*). The incoming species will attack via the antibonding σ*(S—S) orbital and will induce a cleavage of the sulfur–sulfur bond. This process is shown in Scheme 4. The lone pair of the methyl anion together with the σ(S—S)/σ*(S—S) set of the ring system will form a new set of three

[2]The lithium derivative of **2***a* exists as a centrosymmetric, step-shaped dimer in which each lithium forms a bridge with the nitrogen atoms of the second $P_2S_2N_4$ ring (6).

Can. J. Chem. Downloaded from www.nrcresearchpress.com by EESC ESCOLA DE ENGENHARIA on 09/08/12
For personal use only.

Can. J. Chem. Downloaded from www.nrcresearchpress.com by EESC ESCOLA DE ENGENHARIA on 09/08/12
For personal use only.

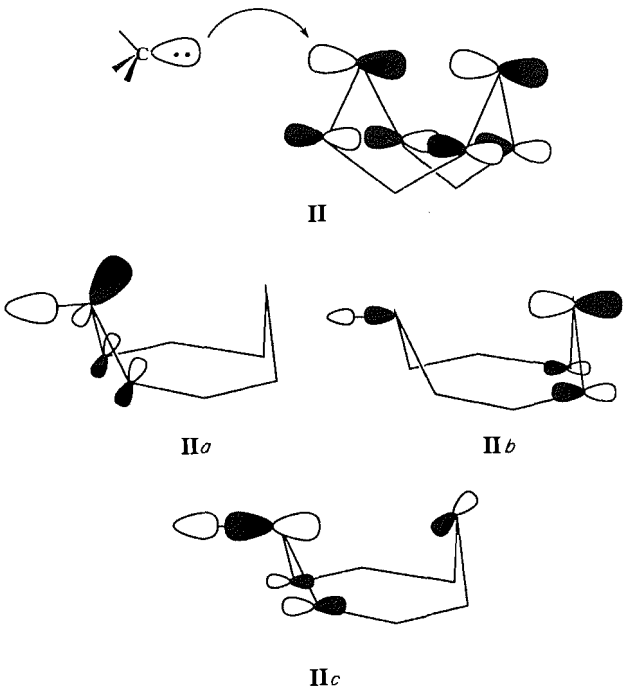

SCHEME 4

orbitals in the S-methylated structure, two of which are doubly occupied. Since all relevant orbitals are symmetric with respect to the preserved mirror plane of the molecule, they will all belong to the a' representation of the C_s point group. This new set of orbitals **II***a*, **II***b*, and **II***c* is illustrated in Scheme 4.

Of these three orbitals, **II***a* is lowest in energy. This orbital is essentially bonding with respect to the methyl group and a ring sulfur atom, and nonbonding with respect to the two-ring sulfur atoms. We can identify this orbital as $a'(20)$ of Fig. 1. The next orbital **II***b* is also an S—S nonbonding orbital, but it is slightly antibonding with respect to the C—S bond. This orbital corresponds to $a'(22)$ and thus represents the HOMO of $Me_5P_2S_2N_4^-$ (**2***b*). Whereas the bonding orbital **II***a* is mainly localized on the methylated site of the ring system, the HOMO **II***b* is mainly limited to the opposite side of the ring. Finally, there is orbital **II***c*, which is antibonding both with respect to the C—S bond as well as the S—S link. Figure 1 shows that this antibonding orbital, $a'(24)$, belongs to the set of unoccupied orbitals, lying about 1 eV in energy above the LUMO.

We now turn to a discussion of the atomic charges, which are displayed in Fig. 2. The calculations for the atomic charges were based on a Mulliken population analysis. These values are good indicators for electronic structure changes, but the absolute numbers should not be taken too seriously. The neutral structure 1,5-$Me_4P_2S_2N_4$ (**1***a*) possesses negative partial charges at the nitrogen atoms as well as positive partial charges at the phosphorus and sulfur atoms, with the charge at P being almost three times as high as the charge at S. This molecule possesses a dipole moment in the $z(y)$ direction,[3] for which the absolute value is calculated to be $\mu_{z(y)} = 5.15$D. On going to the anionic structure $Me_5P_2S_2N_4^-$ (**2***b*), we find the most dramatic

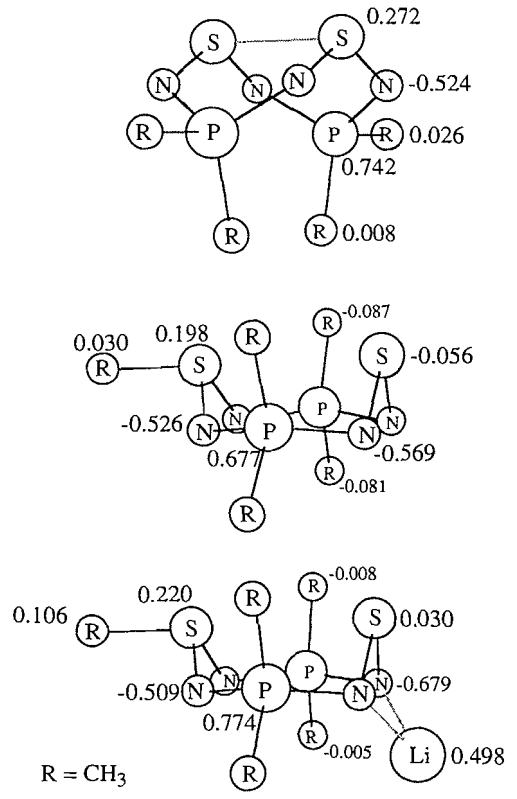

FIG. 2. Atomic charges (in au) for 1,5-$Me_4P_2S_2N_4$, $Me_5P_2S_2N_4^-$, and $Li[Me_5P_2S_2N_4]$.

increase of charge at the sulfur opposite to the site of methylation. Compared to the neutral structure, we calculate an increase of negative charge by 0.328 au. The negative charge on the two nitrogens at the methylation site is 0.043 au smaller than the charge at the N atoms bound to the second S atom. The fact that the HOMO of the anionic system is localized at the site opposite the methylation site is well reflected in the charge distribution. Furthermore, the structures of the known metal complexes of the anions $Ph_4RP_2S_2N_4^-$ (R = alkyl, aryl) are consistent both with the composition of the HOMO and the calculated atomic charges for $Me_5P_2S_2N_4^-$ (**2***b*). These anions have been shown to form η^1-S complexes with Pt(II) or Pd(II) (10) and η^2-N,S complexes with Ti, Zr, or Hf (11). In all cases the metal is attached to the side of the $P_2S_2N_4$ ring opposite to the S—R group. The anion **2***b* possesses a high charge separation in the $x(y)$ direction of the S—S vector. Since phosphorus and nitrogen atoms from almost a planar arrangement, charge separation in the $y(z)$ direction becomes less effective. The coordination of lithium to the ring system leads to a further polarization of charge. The negative charge of the coordinating N atoms increases, whereas for the second pair of N atoms it decreases. Interestingly, the coordination of the metal cation also induces an increase of the atomic charge at the S-methyl group and thus might activate the S—C bond. Consistent with this prediction, we note that S-dealkylation occurs in some reactions of the lithium derivatives $[Li[Ph_4RP_2S_2N_4]]_2$ (R = alkyl).[4]

Finally, we will comment on the thermodynamics of this process. Since we are not working with optimized structures but refer in all cases to the geometries in the crystal, we are provid-

[3]We refer to Schemes 1 and 3 for the coordinate systems. Since the point groups C_{2v} and C_s require a different set of coordinate systems, for a given C_{2v} direction, we refer in parentheses to its C_s counterpart, and vice versa.

[4]T. Chivers, R.W. Hilts, and R. Vollmerhaus. Unpublished results.

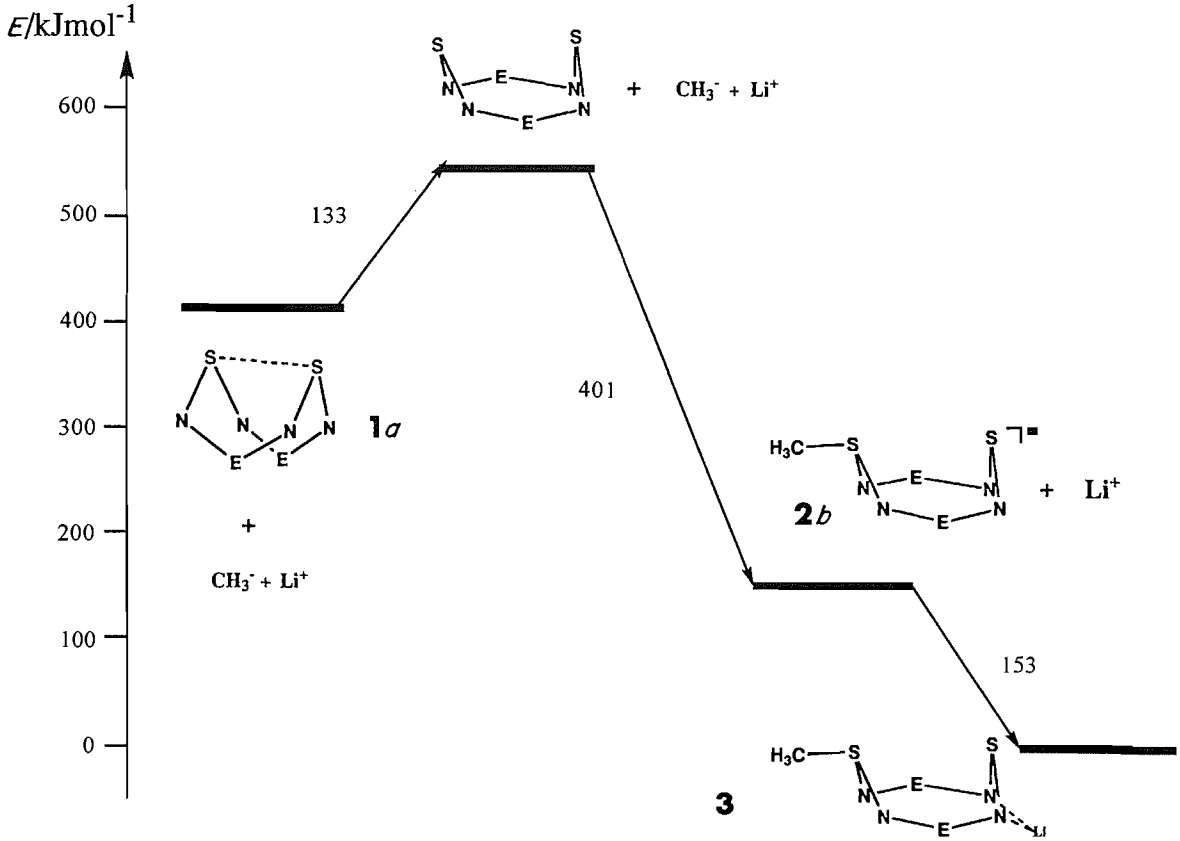

FIG. 3. Total energies for several 1,5-$P_2S_2N_4$ systems relative to $Li[Me_5P_2S_2N_4]$.

ing good estimates rather than accurate numbers for different bonding energies. However, these values provide some insight into the nature of the bonds involved. The total energies for various systems are summarized in Fig. 3. The value for $Li[Me_5P_2S_2N_4]$ (**3**) is set to zero. In the first step, we look at the change in energy when 1,5-$Me_4P_2S_2N_4$ (**1***a*) is distorted in a such a way that the ring now takes on the geometry of the methylated system. This deformation requires an energy of 133 kJ/mol, which we define as the cross-ring S—S bond energy. This energy is about half the energy for an S—S linkage in disulfide structures (HSSH: 276 ± 8 kJ/mol; CH_3SSCH_3: 272.8 ± 3.8 kJ/mol (12)). The cross-ring S—S bond distance is significantly longer than that in disulfides (d_{S-S}(HSSH): 2.058 ± 0.005 Å; $d_{S-S}(CH_3SSCH_3)$: 2.038 Å (13)), which provides one reason for a lower bonding energy. We calculated the change in S—S bonding energy for HSSH on going from the equilibrium structure to an elongated structure with d_{S-S} = 2.55 Å to be 71 kJ/mol. This accounts for only half of the energy difference between the intramolecular S—S bond and that of typical disulfide bonds. This again emphasizes that the cross-ring S—S bond is significantly different from a disulfide linkage. We should point out that our definition of the transannular S—S bond not only describes the S—S bonding interaction but also includes changes in the torsional energy of the cyclic system. We can estimate this contribution to be about 20 kJ/mol. Thus the cross-ring S—S bond strength as defined above provides a reasonable approximation to the S—S bonding interaction.

If we now look at the energy after adding a CH_3^- anion to the distorted ring to form $Me_5P_2S_2N_4^-$ (**2***b*), we gain a total of 401 kJ/mol. This energy decrease stems from two sources, namely, the formation of a C—S bond as well as the more effective stabilization of the electronic charge on the $P_2S_2N_4$ system. The last term can be obtained by the calculated difference in the vertical electron affinities of the two species involved. It amounts to 185 kJ/mol. Therefore, we can estimate the strength of the C—S bond to be about 218 kJ/mol. This value is smaller than typical values for S—C bonds (HS—CH_3: 312.5 ± 4.2 kJ/mol; CH_3S—CH_3: 307.9 ± 3.3 kJ/mol; $C_6H_5CH_2$—SCH_3: 256.9 ± 8 kJ/mol (12)). The S—C destabilizing nature of the HOMO of $Me_5P_2S_2N_4^-$ (**2***b*) is responsible for the somewhat lower S—C bond strength in the methylated ring system.

Acknowledgements

The financial assistance of the Natural Sciences and Engineering Research Council of Canada (NSERC) in the form of a postgraduate scholarship (R.V.) and operating grants (T.C. and T.Z.) is gratefully acknowledged. We thank Professor R.T. Oakley for helpful comments.

1. N. Burford, T. Chivers, P.W. Codding, and R.T. Oakley. Inorg. Chem. **21**, 982 (1982).
2. N. Burford, T. Chivers, and J.F. Richardson. Inorg. Chem. **22**, 1482 (1983).
3. N.N. Greenwood and A. Earnshaw. Chemistry of the elements. Pergamon Press, Oxford. 1984. p. 857.
4. R.T. Boeré, W. Cordes, S.C. Craig, R.T. Oakley, and R.W. Reed. J. Am. Chem. Soc. **109**, 868 (1987).
5. T. Chivers, K.S. Dhathathreyan, and T. Ziegler. J. Chem. Soc. Chem. Commun. 86 (1989).
6. T. Chivers, M. Edwards, R.W. Hilts, M. Parvez, and R. Vollmerhaus. J. Chem. Soc. Chem. Commun. 1483 (1993).
7. E.J. Baerends, D.E. Ellis, and P. Ros. Chem. Phys. **2**, 41 (1973).
8. W. Ravenek. *In* Algorithms and applications on vector and parallel

Can. J. Chem. Downloaded from www.nrcresearchpress.com by EESC ESCOLA DE ENGENHARIA on 09/08/12
For personal use only.

computers. *Edited by* H.J.J. Riele, Th.J. Dekker, and H.A. van de Vorst. Elsevier, Amsterdam. 1987.
9. T. Ziegler. Chem. Rev. **91**, 651 (1991).
10. T. Chivers, M. Edwards, R.W. Hilts, A. Meetsma, and J.C. van de Grampel. J. Chem. Soc. Dalton Trans. 3053 (1992).
11. T. Chivers, R.W. Hilts, and M. Parvez. Inorg. Chem. **33**, 997 (1994).
12. R.D. Lide (*Editor*). CRC handbook of chemistry and physics. 74th ed. Boca Raton, Fla. 1993. pp. **9**: 135–141.
13. M.D. Harmony, V.W. Laurie, R.L. Kuczkowski, R.H. Schewendemann, D.A. Ramsay, F.J. Lovas, W.J. Laffert, and A.G. Maki. J. Phys. Chem. Ref. Data, **8**, 619 (1979).

Can. J. Chem. Downloaded from www.nrcresearchpress.com by EESC ESCOLA DE ENGENHARIA on 09/08/12
For personal use only.

Photophysical behavior of oligoethylene glycols labeled with naphthalene carboxylate and phosphate esters

SAM LEE AND MITCHELL A. WINNIK[1]

Department of Chemistry and Erindale College, University of Toronto, 80 St. George St., Toronto, ON M5S 1A1, Canada

Received April 21, 1993

SAM LEE and MITCHELL A. WINNIK. Can. J. Chem. **72**, 1587 (1994).

The fluorescence spectra of tri- and tetraethylene glycol esterified with 2-(1-naphthyl)ethyl ethyl phosphate and 2-(1-naphthyl)ethyl 2-(ethoxy)ethyl phosphate were studied in dilute solutions of tetrahydrofuran (THF) and diethyl ether. They were compared with the fluorescence from tri- and tetraethylene glycol esterified with 1-naphthyl acetic acid. These compounds form intramolecular excimers. The extent of excimer formation is not extensive, but the relative amount of excimer emission from these compounds varies with the choice of solvent. Three synthetic intermediates to the phosphates, the 2-(1-naphthyl)ethyl *N*,*N*-diisopropylphosphoramidites of tri- and tetraethylene glycol and of 2-ethoxyethanol, were also examined. These compounds form intramolecular exciplexes. In THF, the relative amount of exciplex emission from the phosphoramidites follows the same trend as the carboxylate esters. In diethyl ether, the trend is different. Rates of fluorescence decay have been measured for these compounds. The results are discussed in terms of how information about the conformational and dynamic behavior of these molecules in solution can be obtained, and how the solvent can influence the relative amounts of excimer or exciplex fluorescence.

SAM LEE et MITCHELL A. WINNIK. Can. J. Chem. **72**, 1587 (1994).

Opérant en solutions diluées de tétrahydrofurane (THF) ou d'éther éthylique, on a étudié les spectres de fluorescence de tri- et tétra-éthylèneglycols estérifiés avec des phosphates de 2-(1-naphtyl)éthyléthyle ou de 2-(1-naphtyl)éthyl 2-(éthoxy)éthyle. On les a comparés avec les spectres de fluorescence de tri- et tétra-éthylèneglycols estérifiés avec de l'acide 1-naphtylacétique. Le degré de formation d'excimères n'est pas élevé, mais l'intensité relative de l'émission provenant des excimères de ces composés varie avec la nature du solvant. On a aussi étudié les trois intermédiaires de synthèse des phosphates, les 2-(1-naphtyl)éthyl *N*,*N*-diisopropylphosphoramidites des tri- et tétra-éthylèneglycols et du 2-éthoxyéthanol. Ces composés forment des excimères intramoléculaires. Dans le THF, l'intensité relative de leur émission suit la tendance observée avec les esters des acides carboxyliques. Dans l'éther éthylique, la tendance est différente. On a mesuré les vitesses de décroissance de la fluorescence de ces composés. On discute les résultats en fonction de la façon par laquelle on peut obtenir des informations relatives au comportement conformationnel et dynamique de ces molécules en solution, et comment le solvant peut influencer l'intensité relative de fluorescence de l'excimère ou de l'exciplexe.

[Traduit par la Rédaction]

Introduction

One of the fundamental aspects of polymer chemistry is the conformation and motion of linear polymer chains in solution. The shape and dynamic behavior of a polymer coil are affected by factors such as chain stiffness, excluded volume, and hydrodynamic interactions. These topics have been studied for many decades (1–3). Within this context, we have had a continuing interest in the cyclization of polymer chains.

The extent of cyclization and dynamics of cyclization can be studied in various ways (4–11). We have recently begun to explore a new approach that involves a series of reactions currently used in solid-phase oligonucleotide synthesis (12, 13). This "phosphite triester" method can, in principle, be used to generate linear polymers that contain two chromophores separated by a fixed number of monomer units and that are symmetrically positioned within the chain. This would permit the motion of the interior segments to be probed as the "backbone-to-backbone" cyclization of the linear chain.

To begin, we investigated the synthesis of model oligomers, based upon triethylene glycol and tetraethylene glycol, and naphthalene as the fluorophore label (14). This allowed us to optimize reaction conditions and to prepare well-characterized intermediates and products. We have also described briefly the steady-state fluorescence properties of these molecules. In this paper, we examine their fluorescence behavior and fluorescence decay kinetics in detail. We compare their properties with naphthalene end-labeled tri- and tetraethylene glycol where the fluorophores are attached via carboxylate ester groups. The results of the fluorescence decay kinetics measurements are, in fact, rather disappointing. The extent of naphthalene excimer formation is sufficiently small that only limited insights are possible. Thus, naphthalene is not really an adequate excimer-forming chromophore for such studies. Ironically, some of our most interesting observations derive from examination of phosphoramidite synthetic intermediates.

Results and discussion

Materials

We have synthesized the bis-phosphates **131**, **232**, **141**, and **242** using a procedure described previously (14). For polymers, pyrene is the common choice for the excimer-forming probe. For these shorter chains, we chose to label these oligomers with naphthalene. The major reason for choosing naphthalene was the ease in purifying and characterizing the reaction intermediates. **131** and **232** are oligoethylene glycols where the two naphthalene probes are separated by three oxyethylene monomer units. The ends of these two labelled glycols are flanked by one and two monomer units, respectively. **141** and **242** both have four oxyethylene monomer units separating the two chromophores. The ends of these two labelled glycols are also flanked by one and two monomer units, respectively. The phosphate **22** served as the model compound for these bis-phosphates.

In the preparation of the bis-phosphates, the bis-phospho-

[1]Author to whom correspondence may be addressed. Telephone: (416) 978-8545. Fax: (416) 978-0541.

[2]Revision received November 1, 1993.

Can. J. Chem. Downloaded from www.nrcresearchpress.com by ESC ESCOLA DE ENGENHARIA on 09/08/12
For personal use only.

Can. J. Chem. Downloaded from www.nrcresearchpress.com by EESC ESCOLA DE ENGENHARIA on 09/08/12
For personal use only.

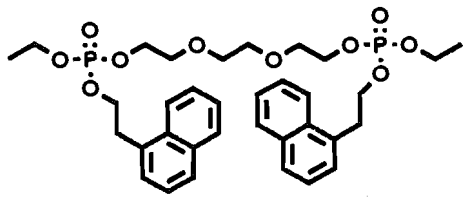

131

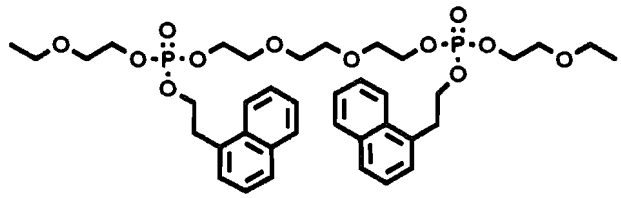

232

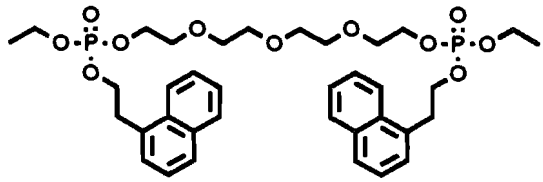

141

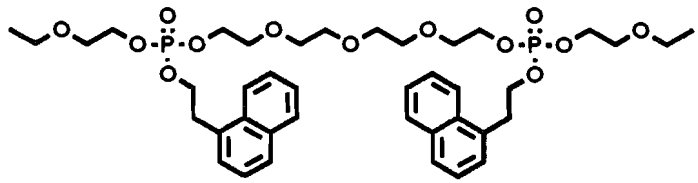

242

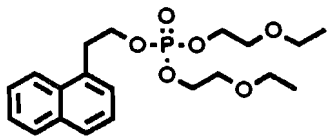

22

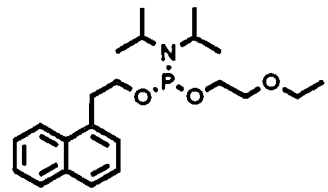

P2

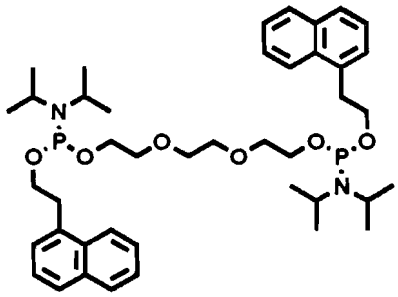

P3

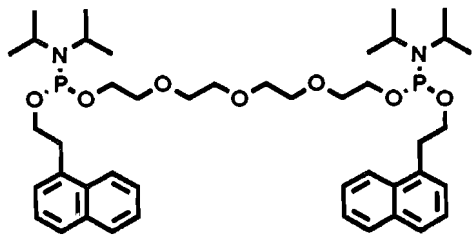

P4

ramidites **P3** and **P4** were synthetic intermediates. These compounds also exhibit fluorescence behavior that is interesting and informative on their own. As a model compound, the phosphoramidite **P2** was also synthesized.

For a comparative study, **N3N** and **N4N** were also prepared. These two diesters differ from the bis-phosphates in the type of functional group used to attach the naphthalene probe onto triethylene glycol and tetraethylene glycol. They also do not have any additional monomer units flanking the labelled ends. In this system, the ester **N2** served as the model compound.

Bis-phosphate fluorescence

Fluorescence spectra of the four bis-phosphate ester derivatives are shown in Fig. 1 along with that of the model com-

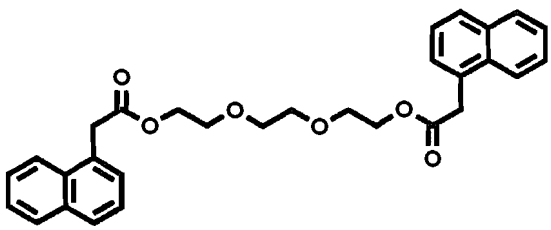

N3N

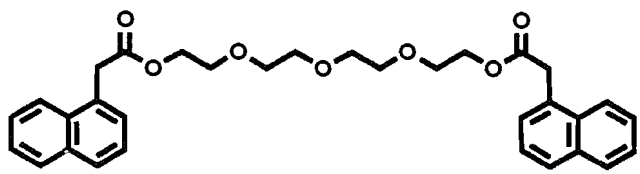

N4N

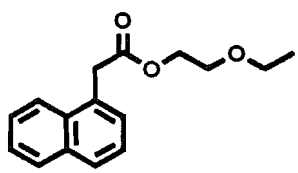

N2

Can. J. Chem. Downloaded from www.nrcresearchpress.com by EESC ESCOLA DE ENGENHARIA on 09/08/12
For personal use only.

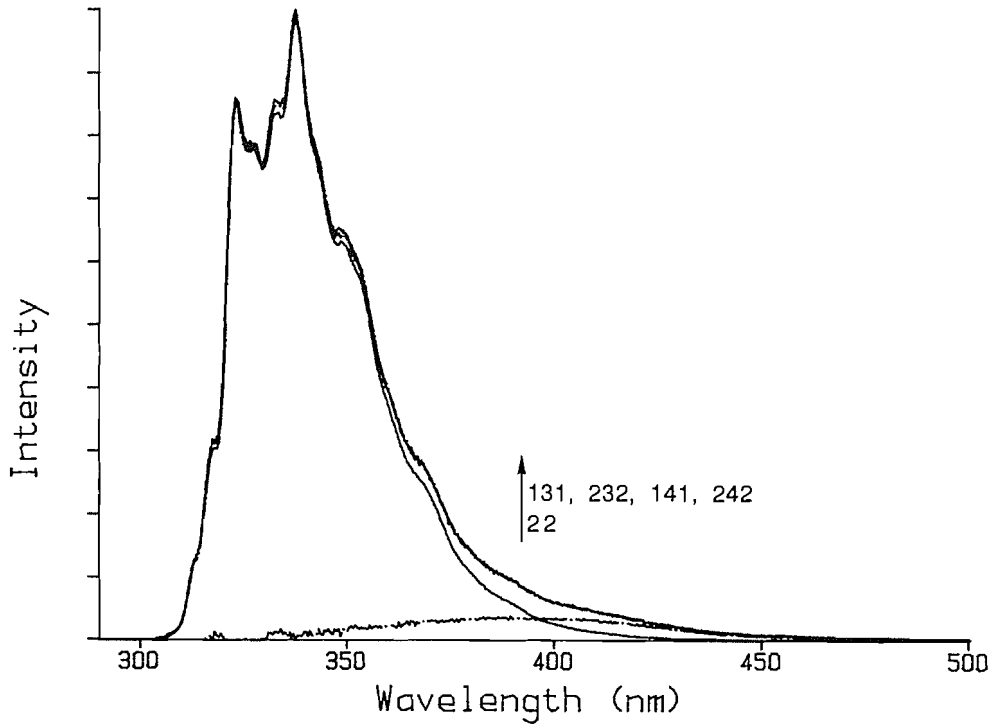

FIG. 1. Normalized fluorescence spectra of the model phosphate (**22**) and the bis-phosphates (**131**, **232**, **141**, and **242**) in diethyl ether at room temperature (labels refer to the solid lines). The excimer band (— · —) was obtained by subtraction of the fluorescence spectrum of **22** from the spectrum of **242**.

pound **22** for dilute solutions of these molecules in diethyl ether. The spectra are similar for solutions in THF (not shown). There is very little excimer emission. The absence of significant excimer emission could be due to very slow cyclization of these molecules or it may be related to the weak tendency of naphthalene to form excimers. We will come back to this point later. Fluorescence decay measurements (Table 1) indicate that the naphthalene decay times are nearly indistinguishable from that of the model compound. One interesting feature is that the bis-phosphates have slightly shorter lifetimes in diethyl ether and, in both solvents, give poorer fits to a single exponential decay profile than the model compound. This effect is so consistent that it suggests that the naphthalenes do interact in the excited state.

Diester fluorescence

Fluorescence spectra of **N3N** and **N4N** in dilute solution in THF are shown in Fig. 2 along with that of the model ester **N2**. Corresponding spectra for these molecules in diethyl ether solution are shown in Fig. 3. There is clear indication in both solvents of a new emission, observed as a long tail extending toward lower energies. When the fluorescence spectrum of the model compound is subtracted from either of the two normalized spectra, a broad, structureless band centered at 400 nm is recovered. This new fluorescence emission comes from the intramolecular excimer. At the concentrations examined ($<10^{-4}$ M), values of the excimer-to-monomer intensity ratio I_E/I_M are independent of concentration. Hence excimer formation is an intramolecular process.

Excitation spectra were examined for both molecules in both solvents. Identical spectra were obtained when the emission was monitored at 450 nm (the excimer band) and when the emission was monitored at 324 nm. If a significant fraction of the naphthalene groups were associated prior to absorption of a photon, one would expect a red shift of the excitation spectrum of the excimer relative to that of the monomer. As a consequence, we conclude that excimers observed in this system arise through diffusion together of naphthalenes subsequent to excitation.

The only surprise in these spectra is that I_E/I_M is *larger* for **N4N** than for **N3N** for samples in diethyl ether. One expects the rate and extent of cyclization to decrease with increasing chain length. We observe this for **N3N** and **N4N** in THF, but not in diethyl ether.

Excimer formation kinetics are normally described by the Birks model, Scheme 1 (15). For weakly bound excimers, of which naphthalene is an example, $k_{-1} \gg k_E$. In this so-called high-temperature limit, Scheme 1 predicts the "monomer" fluorescence intensity ($I_M(t)$) to decay exponentially following δ-pulse excitation:

$$[1] \qquad I_M(t) = a_1 \exp(-\lambda_1 t)$$

$$[2] \qquad \lambda_1 = k_M + k_q$$

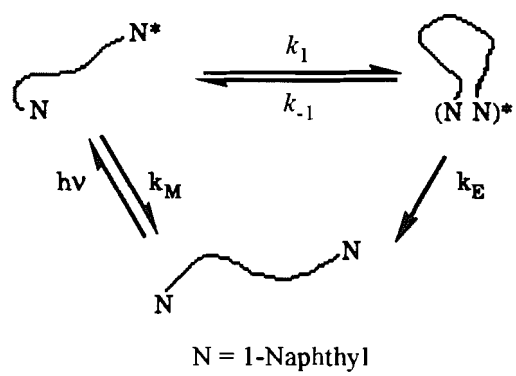

N = 1-Naphthyl

SCHEME 1

Can. J. Chem. Downloaded from www.nrcresearchpress.com by EESC ESCOLA DE ENGENHARIA on 09/08/12
For personal use only.

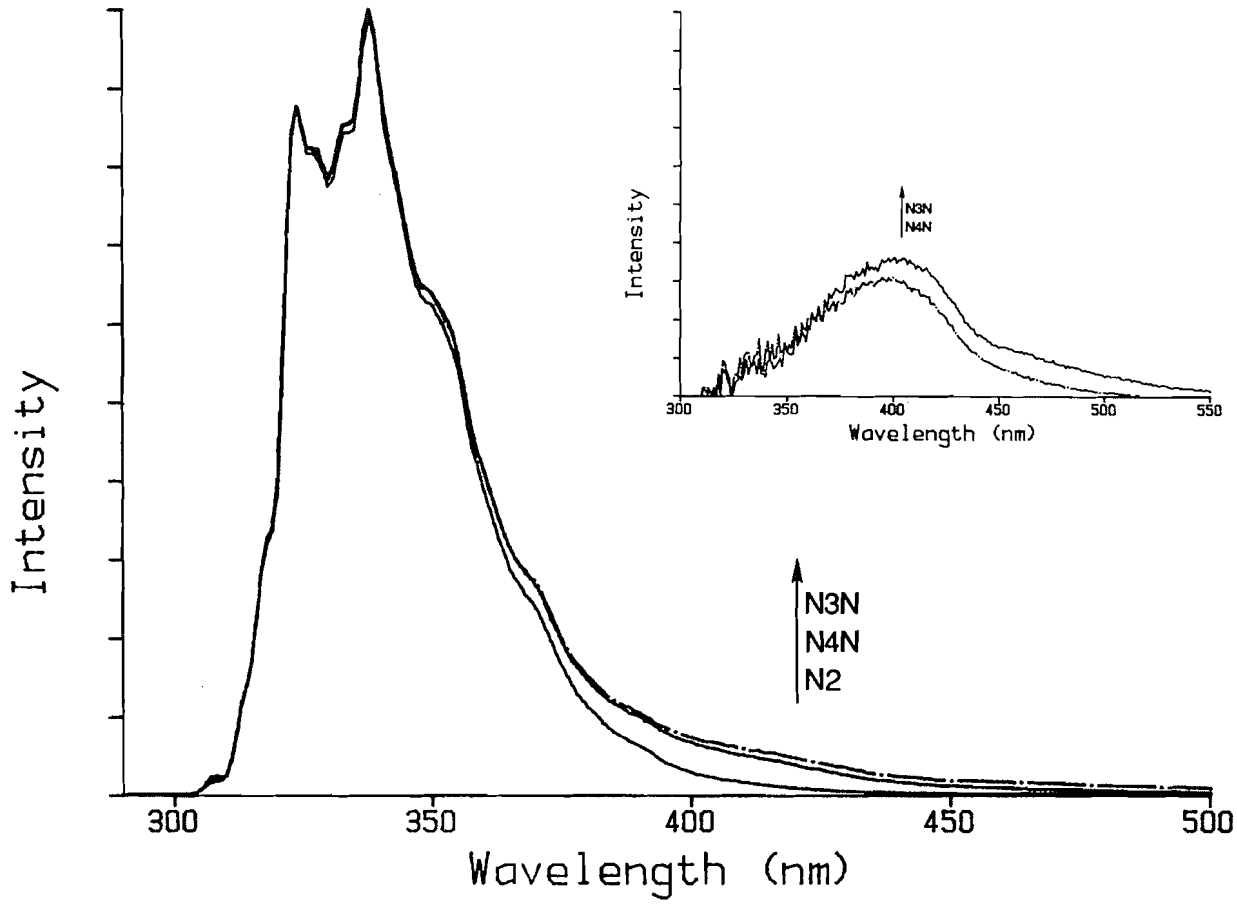

FIG. 2. Normalized fluorescence spectra of the model ester **N2** and the diesters **N3N** and **N4N** in THF at room temperature. Inset: excimer bands obtained by subtraction of the fluorescence spectrum of the model compound from the corresponding diester fluorescence spectra (expansion: ×8).

where $k_q = (k_1/k_{-1})k_E$. Under these circumstances, there is essentially a conformational preequilibrium (with $K = k_1/k_{-1}$) preceding the quenching step k_E, and k_q values can be obtained from $I_M(t)$ if the rate, k_M, is known. The value of these rate constants can be determined from $I_M(t)$ if the rate, k_M, is known. This can be found from an independent measurement using a model compound, where τ_M is its excited state lifetime in dilute solution:

$$[3] \qquad I_M(t) = a_0 \exp(-\lambda_M t); \qquad \lambda_M = k_M = {\tau_M}^{-1}$$

This analysis fails here, but for a reason that is itself quite interesting. This is related to the choice of model compounds. **N2** has a lifetime (50 ns, Table 1) that is significantly shorter than that of 1-methylnaphthalene (75 ns, THF; 80 ns, ether). Thus the ester group, or perhaps the PEO chain, causes some quenching of excited naphthalene. In retrospect, we recall the finding of Monnerie and co-workers that the ether functionality quenches anthracene fluorescence, but we did not anticipate this kind of effect here, where the solvents are also ethers (16). Comparison of the fluorescence lifetime of methylnaphthalene with that of the model phosphate **22** shows that this effect is present here as well.

Under these circumstances, we would normally assume that the quenching effect on the bis-naphthalene derivative is the same as on the model compound, and thus only affects k_M. This may not be true here since the excimer-forming diesters have the same monomer lifetime as the model compound. The one conclusion one can draw here is that the extent of excimer formation must be small.

We can still make comparisons between di-labeled pairs. The quantum efficiencies (Φ) are related to the rate constant in Scheme 1 by the expression

$$[4] \qquad \frac{\Phi_E}{\Phi_M} = \frac{k_{fE}}{k_{fM}}\left(\frac{k_1}{k_{-1} + k_E}\right) \propto \frac{I_E}{I_M}$$

where k_{fE} and k_{fM} are the respective radiative rate constants. These terms do not depend upon chain length. When cyclization does not involve ring strain, then k_{-1} is similarly independent of chain length. Thus, when one wishes to compare intramolecular excimer formation in two samples of different chain length, the expressions

$$[5] \qquad \frac{(I_E/I_M)}{(I_E/I_M)'} = \frac{k_1}{k_1'} \quad \text{or} \quad \frac{(k_1/k_{-1})}{(k_1/k_{-1})'}$$

are particularly useful. By writing (k_1/k_{-1}) we emphasize that a conformational preequilibrium precedes quenching when the system is operating in the high temperature limit. Equation [5] allows us to quantify the enhanced formation of excimer for **N4N** over **N3N** in ether, and for **N3N** over **N4N** in THF. When these esters were examined in other solvents, it became clear that the relative extent of excimer formation is also dependent on the choice of solvent (Table 2).

Can. J. Chem. Downloaded from www.nrcresearchpress.com by EESC ESCOLA DE ENGENHARIA on 09/08/12
For personal use only.

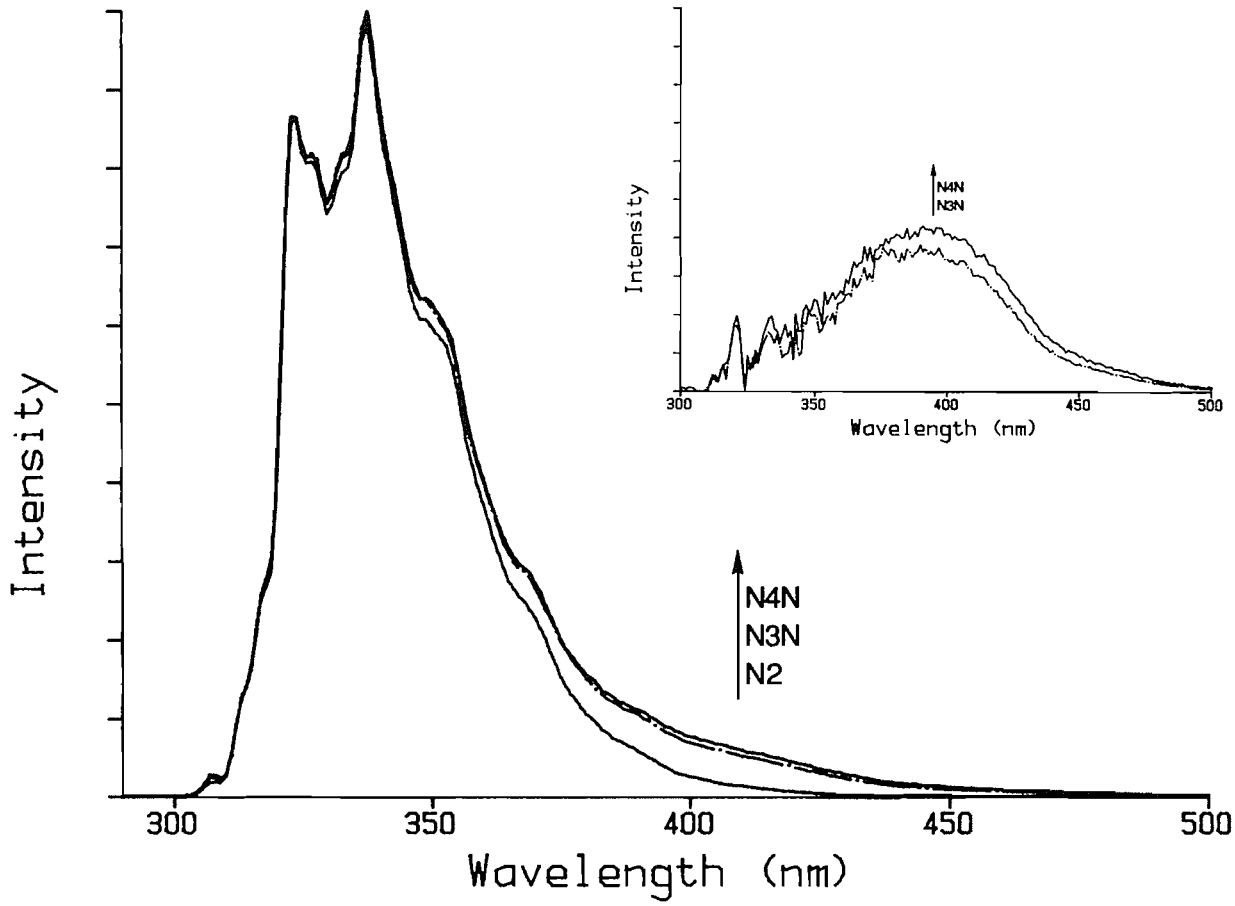

FIG. 3. Normalized fluorescence spectra of the model ester **N2** and the diesters **N3N** and **N4N** in diethyl ether at room temperature. Inset: excimer bands obtained by subtraction of the fluorescence spectrum of the model compound from the corresponding diester fluorescence spectra (expansion: ×8).

TABLE 1. Fluorescence lifetimes ($\tau = \lambda^{-1}$) of naphthalene-labeled oligoethylene glycols in THF and diethyl ether at 22°C

	Solvent	
Compound	THF τ (χ^2)[a]	Diethyl ether τ (χ^2)
1-Methyl naphthalene	75.2 (1.170)	80.5 (1.008)
N2	50.3 (1.185)	49.9 (1.164)
N3N	51.0 (1.119)	50.3 (1.224)
N4N	51.0 (1.181)	51.1 (1.399)
22	63.9 (1.106)	67.0 (1.108)
131	64.0 (1.278)	66.5 (1.154)
141	64.3 (1.254)	66.8 (1.264)
232	64.2 (1.248)	66.6 (1.113)
242	64.5 (1.491)	66.5 (2.057)

[a]τ is the lifetime determined by monitoring the decay of the monomer emission. Data were fit to a single exponential decay. χ^2 is the chi-square value evaluating goodness of fit.

TABLE 2. Ratio of excimer to monomer intensities (I_E/I_M) for **N3N** and **N4N** in different solvents at 22°C

	I_E/I_M[a]	
Solvent	**N3N**	**N4N**
Tetrahydrofuran	0.11	0.09
Acetonitrile	0.15	0.13
Benzene	0.15	0.14
Diethyl ether	0.11	0.13
Cyclohexane[b]	0.23	0.27

[a]Error in all values is less than ±0.004.
[b]Excitation spectra give no evidence of preassociation.

Bis-phosphoramidite fluorescence

The fluorescence spectra of **P2**, **P3**, and **P4** in THF are presented in Fig. 4. They are compared with the model phosphate **22** by normalizing their 0–0 fluorescence band to that of the phosphate at 323 nm. The phosphoramidites all have an additional tail extending to longer wavelengths which peaks at about 485 nm. This extra emission comes from the intramolecular exciplex formed from the interaction of the excited naphthalene moiety with the phosphoramidite group. While the amount of intramolecular exciplex emission is not extensive, the amount of fluorescence self-quenching in these molecules is substantial. When the total fluorescence intensity from the phosphate **22** is compared with that of the phosphoramidite **P2**, at equal concentrations of the chromophore, the phosphoramidite only exhibits 17% of the total fluorescence emission from **22**.

The lifetimes can be similarly compared. The quantum yield for fluorescence (Φ_f) is related to the radiative rate constant for fluorescence (k_f) and the rate constant for quenching of the excited chromophore by radiationless pathways (Σk_d):

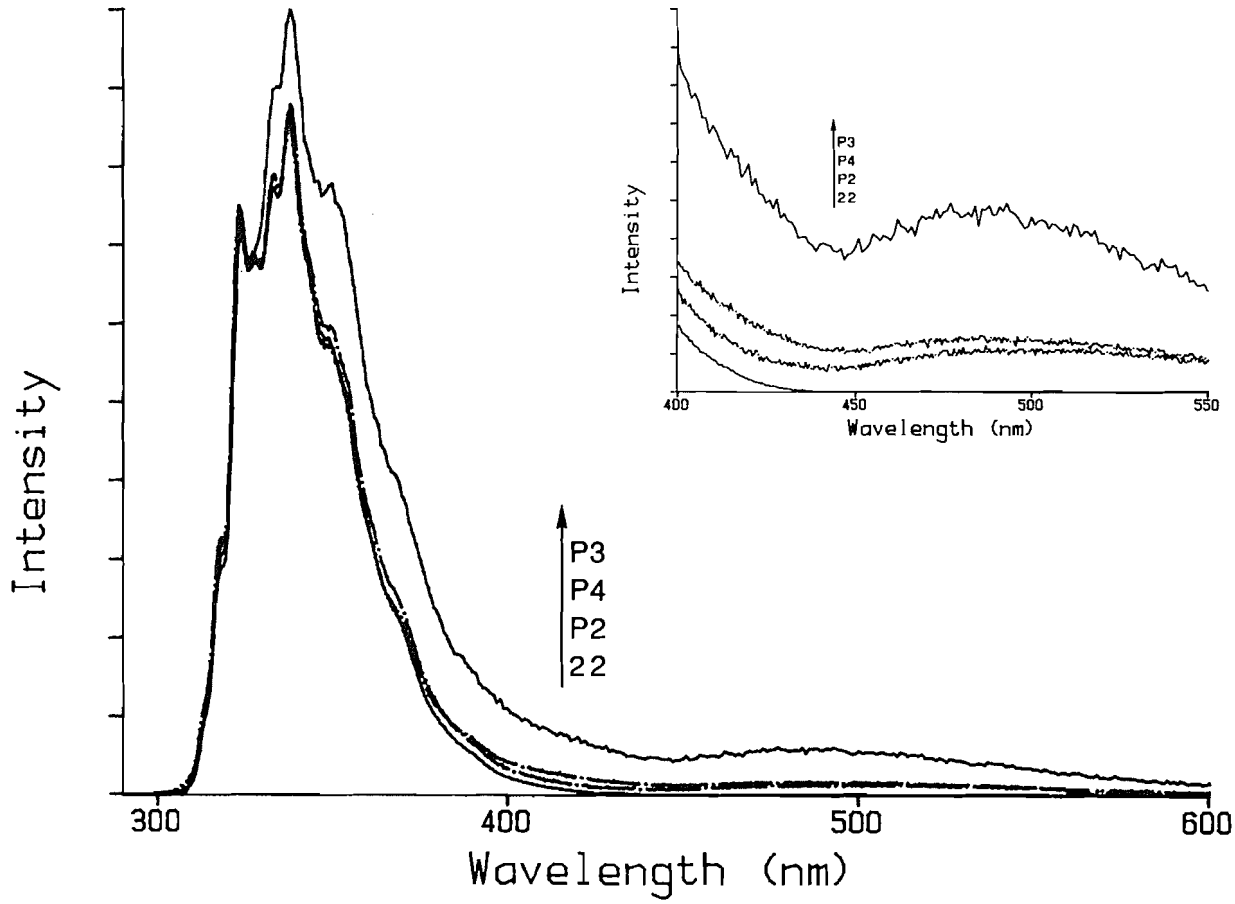

FIG. 4. Normalized fluorescence spectra of the model phosphate (**22**), model phosphoramidite (**P2**), and the bis-phosphoramidites (**P3** and **P4**) in THF at room temperature. Inset: ×8 expansion of the 400–550 nm region.

$$[6] \qquad \Phi_f = \frac{k_f}{k_f + \Sigma k_d}$$

Since the measured lifetime $\tau = 1/(k_f + \Sigma k_d)$, $\Phi_f(\mathbf{P2})/\Phi_f(\mathbf{22})$ (= 0.17) should be equal to $\tau(\mathbf{P2})/\tau(\mathbf{22})$. However, $\tau(\mathbf{P2})/\tau(\mathbf{22})$ = 0.05 (Table 3), indicating that additional mechanisms, apart from exciplex formation, are available to quench **P2** fluorescence that are not present in the model compound **22**.

The bis-phosphoramidites show more exciplex emission than the phosphoramidite **P2** because the excited chromophore can form a complex, either with the "proximal" phosphoramidite group in a way similar to that of the model phosphoramidite **P2**, or with the "distal" phosphoramidite group at the other end of the molecule. Excimer formation is also possible, but the amount is insignificant because the naphthalene excimer is more weakly bound compared with the exciplex. In the case of **P4**, where the phosphoramidite groups are separated by four monomer units, the exciplex emission is greater than in **P2** by only a small amount. The shorter bis-phosphoramidite **P3**, where the phosphoramidite groups are separated by three monomer units, exhibits substantially greater exciplex emission than either **P2** or **P4**.

The fluorescence spectra of the phosphoramidites and the model phosphate were also recorded in diethyl ether (Fig. 5). Subtracting the normalized fluorescence spectrum of the model phosphate from each of the corresponding phosphoramidites yields exciplex fluorescence bands containing two broad peaks: one centered at 360 nm and the other at 485 nm. The band centered at 360 nm might be due to a second, higher energy exciplex. The bis-phosphoramidite **P3** shows the greatest amount of exciplex fluorescence. Interestingly, the bis-phosphoramidite **P4** exhibits less exciplex emission than that of the model phosphoramidite **P2**.

TABLE 3. Fluorescence decay data for the phosphoramidite **P2** in THF and diethyl ether at 22°C

THF[a] τ_i (a_i)[c]	Diethyl ether[b] τ_i (a_i)
62.6 (0.028)	51.8 (0.004)
15.0 (0.031)	15.7 (0.028)
1.00 (0.941)	0.697 (0.968)

[a] χ^2 (chi-square) value in THF = 1.068.
[b] χ^2 (chi-square) value in diethyl ether = 1.057.
[c] Decay data were fit to a sum of three exponentials (λ). a_i is the normalized pre-exponential value for the corresponding lifetimes ($\tau = \lambda^{-1}$).

The excitation spectra of the phosphoramidites in diethyl ether, obtained by monitoring the emission at 323 nm, are identical to the spectra obtained by monitoring the emission at 485 nm. Hence, the naphthalene–phosphoramidite complex does not exist prior to excitation, and exciplex formation is a result of a dynamic process.

The fluorescence decay profile of the phosphoramidites are

Can. J. Chem. Downloaded from www.nrcresearchpress.com by EESC ESCOLA DE ENGENHARIA on 09/08/12
For personal use only.

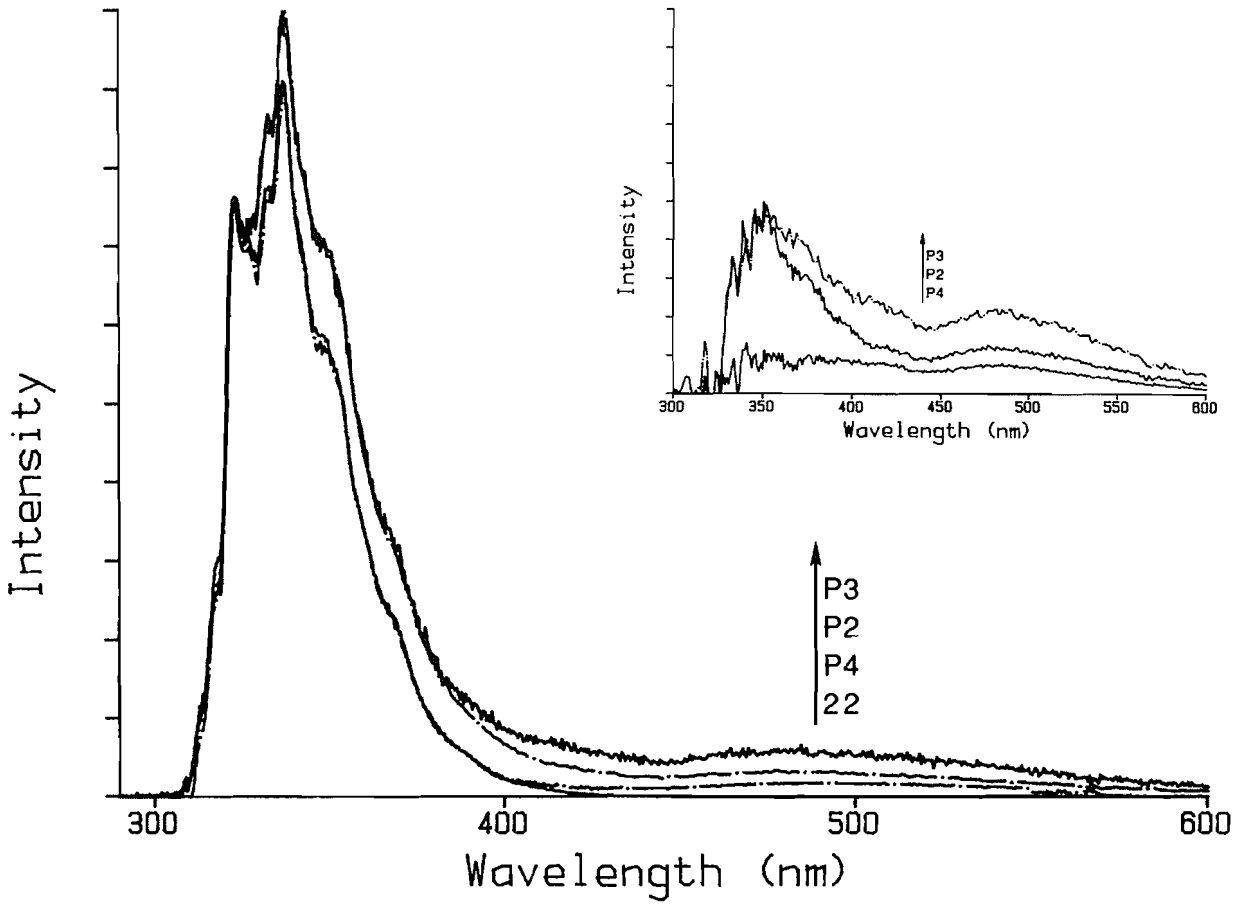

FIG. 5. Normalized fluorescence spectra of the model phosphate (**22**), model phosphoramidite (**P2**), and the bis-phosphoramidites (**P3** and **P4**) in diethyl ether at room temperature. Inset: exciplex bands obtained by subtraction of the model phosphate fluorescence spectrum from the fluorescence spectra of the corresponding phosphoramidites.

strongly nonexponential. For **P2**, three exponential terms are needed to fit the data (Table 3). The quenching kinetics are complex, but one reasonable interpretation of the decay data is that exciplex formation is much faster than exciplex decay. Calculation of the mean decay time $\langle\tau\rangle$ (eq. [7]) from the two (short time) components of the decay sets the timescale for exciplex formation. This value is 1.1 ns in diethyl ether and 1.4 ns in THF. The weak 63 ns component in THF (52 ns in ether) is due to reformation of excited naphthalene from exciplex dissociation. Even incorporating the long third component into the calculation of $\langle\tau\rangle$ increases its value only to 1.3 ns in ether and 3.1 ns in THF.

$$[7] \qquad \langle\tau\rangle = \frac{a_1\tau_1 + a_2\tau_2}{a_1 + a_2}$$

Chain conformation and dynamics

When the chain is short, structural features associated with interactions between neighboring monomer units limit the relative orientations of the chromophores and perturb the nature of their photoreaction. However, there is ample evidence to suggest that these oligomers are sufficiently long to permit all possible orientations of the terminal chromophores to occur (17–19). Our observations thus provide qualitative and semiqualitative information about chain conformation in these tri- and tetraethylene glycol derivatives. In the phosphoramidites, exciplex formation between excited state naphthalene and the proximal phosphoramidite group is very fast. In the longer bis-phosphoramidite **P4** the effect of the distal phosphoramidite group is minimal because the excited naphthalene is, on average, quenched by the proximal phosphoramidite group before it can encounter the phosphoramidite group at the other end of the chain. In the shorter bis-phosphoramidite **P3**, cyclization of the chain ends is much faster, and quenching of the excited naphthalene chromophore by the distal phosphoramidite group is now competitive with quenching by the proximal phosphoramidite group. To compete, the interaction with the distal phosphoramidite group must occur on a timescale of 1–3 ns. This result is consistent with those obtained from doubly end-labelled molecules of similar lengths. The longer pentaethylene glycol, esterified at both ends with naphthalene, has a short-lifetime component of 2 ns in isopentane (19). Bis(1-pyrenylmethyl) dodecanedicarboxylate in 2-methyltetrahydrofuran has a short lifetime component of 5 ns (20): the stiffer hydrocarbon chain and the extra drag arising from the bulky pyrene groups slows the rate of terminal cyclization.

We have discussed exciplex emission in the phosphoramidites as though exciplex formation was largely irreversible, corresponding to the low-temperature limit ($k_{-1} \ll k_E$) of Scheme 1. The major evidence for the validity of this point of view is the large extent of monomer quenching caused by the presence of the phosphoramidite group. Thus, the phosphoramidites give us some information about chain dynamics.

The esters, on the other hand, operate in the high-temperature limit, and can provide information only about the probability

Can. J. Chem. Downloaded from www.nrcresearchpress.com by EESC ESCOLA DE ENGENHARIA on 09/08/12
For personal use only.

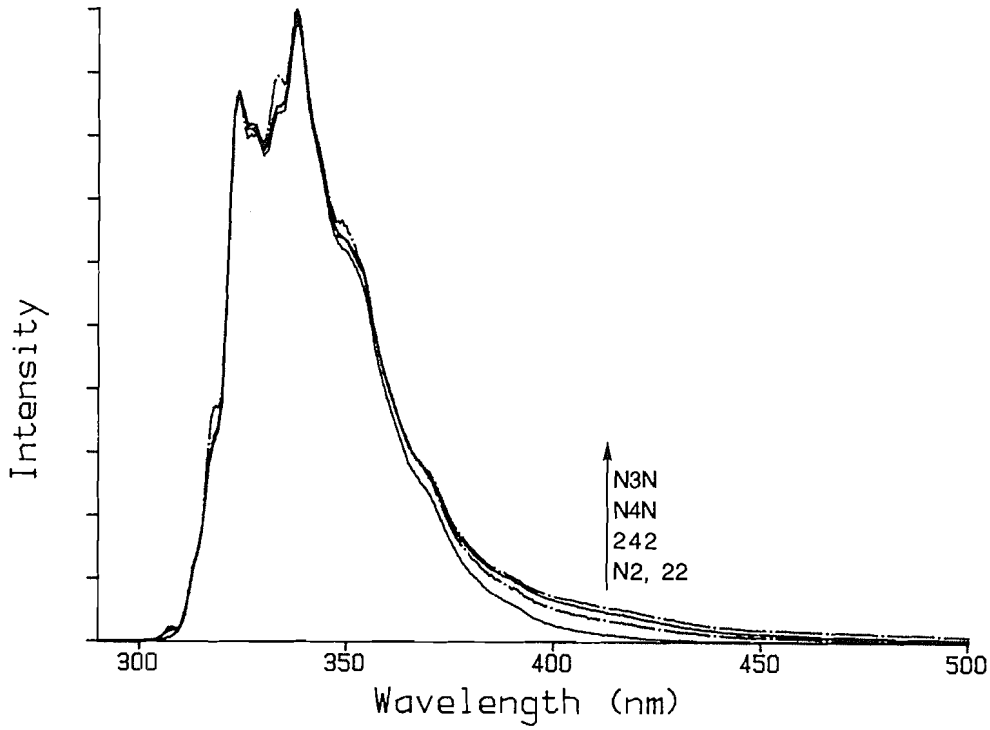

FIG. 6. Normalized fluorescence spectra of the bis-phosphates (represented by **242**), the diesters (**N3N** and **N4N**), and the model compounds (**N2** and **22**) in THF at room temperature.

of the chain ends coming together. Comparing phosphates with carboxylate esters (Fig. 6), we note significantly less excimer from the phosphates, implying the importance of steric effects when the chromophores are not situated at the chain ends. These presumably operate locally and interfere with the N* + N interaction.

Our most interesting observations were the reduced emission of **P4** relative to **P2** in diethyl ether, and the enhanced emission of **N4N** over **N3N** in diethyl ether and cyclohexane. The enhancement could be due either to an unfavourable solvent interaction with the end groups, or to an unfavourable solvent interaction with the oligomeric chain. When the interactions between the chromophores and the solvent are sufficiently unfavourable, some association of the aromatic groups could occur. One documented example of this effect involves pyrene-end-capped polyethylene oxide (PEO, $M_w = 8000$) in aqueous solution (21–24). Hydrophobic attractions between the pyrenes lead to a small proportion of the chains (ca. 6%) with their ends in contact. Another example involves bis-pyrene-1-carboxylate esters of 1,*n*-alkane diols in linear hydrocarbons (25). Excitation spectra in our systems indicate that preassociation of N-groups is unlikely to be important here.

On the other hand, diethyl ether and cyclohexane are non-solvents for PEO. Some vestige of this effect may well be operating on these tri- and tetraethylene glycol derivatives. The dimensions of high molecular weight polymers are very sensitive to solvent quality, although very poor solvents induce phase separation rather than collapse. This might also explain the reduced emission of **P4** compared to **P2** if the oligoethylene glycol chain is collapsed, raising the conformational barriers to exciplex formation. These effects become less important for shorter chains. It is very rare to encounter examples of such solvent effects on oligomers as short as those we examine here.

Experimental

Sample preparation

All solvents were of spectroscopic grade except diethyl ether (ACS). THF and diethyl ether were distilled from lithium aluminum hydride. Benzene and cyclohexane were distilled from sodium. Acetonitrile was distilled from calcium hydride. All compounds were freshly chromatographed before solutions were prepared with them. The concentration of chromophore in all solutions was of the order of 10^{-6}–10^{-5} M. Sample solutions were degassed by vigorously bubbling with argon (Union Carbide, <0.5 ppm, <3 ppm water), presaturated with the solvent, for 20 min.

Fluorescence

All fluorescence measurements were recorded at room temperature. Steady state fluorescence spectra were recorded on a SPEX Fluorolog 2 spectrometer at a right angle geometry using 1 mm excitation and emission slit widths. The excitation wavelength was 282 nm. Emission spectra were corrected for scattering and the wavelength sensitivity of the photomultiplier tube. I_E/I_M ratios were obtained by subtracting the normalized spectrum of the model compound from the diester, and integrating over the result to obtain I_E. I_M were obtained from integration of the spectrum of the model compound.

Fluorescence decay curves were obtained by the single photon counting technique (26). The excitation source was a coaxial flashlamp (Edinburgh Instruments, model 199F) filled with deuterium at a pressure of 100 Torr (1 Torr = 133.3 Pa). The excitation wavelength (282 nm) was selected by a Jobin–Yvon model H-20 monochromator, and that of the fluorescence (323 nm) by a SPEX Minimate model 1760 monochromator. The electronic signals were processed using ordinary Ortec instrumentation. The analyses of the decay curves were performed with the δ-pulse deconvolution method (27) using iterative weighted linear least-squares analysis to find the parameters of the fluorescence decay curves having the best fit. Degassed *p*-terphenyl in cyclohexane was used as the reference for the decay profiles.

Materials

All general procedures and techniques, including the synthesis of the phosphates and phosphoramidites, have been previously described

Can. J. Chem. Downloaded from www.nrcresearchpress.com by EESC ESCOLA DE ENGENHARIA on 09/08/12
For personal use only.

(14). The carboxylic acid esters were prepared by DCC coupling of the corresponding acid and alcohol.

2-Ethoxyethyl (1-naphthyl)acetate (N2)

Yield: 60% as a clear, colourless oil; R_f 0.51 (80% diethyl ether – 20% hexane); IR (neat): 780, 1050, 1125, 1170, 1265, 1385, 1450, 1510, 1600, 1735 cm^{-1}; UV (THF), λ_{max} nm (ϵ): 224 (7.09 × 10^4), 272 (5830), 282 (6860), 292 (4770), 314 (305); ^1H NMR (acetone-d_6): 1.07 (t, 3H, $^3J_{HH'}$ = 7.0 Hz, CH_3), 3.38 (q, 2H, $^3J_{HH'}$ = 7.0 Hz, CH_2CH_3), 3.56 (t, 2H, $^3J_{HH'}$ = 4.1 and 5.1 Hz, $COOCH_2CH_2$), 4.13 (s, 2H, $C_{10}H_7CH_2$), 4.19 (t, 2H, $^3J_{HH'}$ = 4.5 and 5.0 Hz, $COOCH_2$), 7.43–8.05 (m, 7H, naphthyl-*H*); ^{13}C NMR (acetone-d_6): 15.47 (CH_3), 39.28 ($C_{10}H_7CH_2$), 64.71 ($COOCH_2$), 66.76 (CH_2CH_3), 68.89 ($COOCH_2CH_2$), 124.87, 126.30, 126.53, 126.98, 128.61, 128.85, 129.41, 132.08, 133.17, 134.81 (naphthyl-*C*), 171.79 (*C*OO); mass spectrum, *m/e* (rel. intensity): 259 (M + 1)$^+$ (19), 258 M$^+$ (57), 186 (49), 168 (60), 141 (100), 115 (42).

Triethylene glycol di-(1-naphthyl)acetate (N3N)

Yield: 72% as a clear, colourless oil; R_f 0.27 (80% diethyl ether – 20% hexane); IR (neat): 780, 960, 1050, 1130, 1265, 1510, 1600, 1740 cm^{-1}; ^1H NMR (acetone-d_6): 3.43 (s, 4H, OCH_2CH_2O), 3.60 (t, 4H, $^3J_{HH'}$ = 4.7 and 4.8 Hz, $COOCH_2CH_2$), 4.12 (s, 4H, $C_{10}H_7CH_2$), 4.19 (t, 4H, $^3J_{HH'}$ = 4.7 and 4.9 Hz, $COOCH_2$), 7.42–8.04 (m, 14H, naphthyl-*H*); ^{13}C NMR (acetone-d_6): 39.27 ($C_{10}H_7CH_2$), 64.69 ($COOCH_2$), 69.59 ($COOCH_2CH_2$), 71.13 (OCH_2CH_2O), 124.89, 126.31, 126.54, 127.02, 128.60, 128.86, 129.40, 132.06, 133.15, 134.79 (naphthyl-*C*), 171.78 (*C*OO); mass spectrum, *m/e* (rel. intensity): 487 (M + 1)$^+$ (15), 486 M$^+$ (28), 213 (25), 168 (100), 141 (93), 115 (28).

Tetraethylene glycol di-(1-naphthyl)acetate (N4N)

Yield: 71% as a clear, colourless oil; R_f 0.15 (80% diethyl ether – 20% hexane); IR (neat): 780, 960, 1050, 1130, 1250, 1450, 1510, 1600, 1730 cm^{-1}; ^1H NMR ($CDCl_3$): 3.43 (m, 8H, $CH_2CH_2OCH_2CH_2$), 3.56 (t, 4H, $^3J_{HH'}$ = 4.7 and 4.8 Hz, $COOCH_2CH_2$), 4.04 (s, 4H, $C_{10}H_7CH_2$), 4.20 (t, 4H, $^3J_{HH'}$ = 4.8 Hz, $COOCH_2$), 7.35–7.97 (m, 14H, naphthyl-*H*); ^{13}C NMR ($CDCl_3$): 38.74 ($C_{10}H_7CH_2$), 63.85 ($COOCH_2$), 68.68 ($COOCH_2CH_2$), 70.17 ($COOCH_2CH_2OCH_2$), 70.20 ($COOCH_2CH_2OCH_2CH_2$) 123.57, 125.21, 125.49, 126.07, 127.75, 127.77, 128.43, 130.24, 131.82, 133.52 (naphthyl-*C*), 171.16 (*C*OO); mass spectrum, *m/e* (rel. intensity): 531 (M + 1)$^+$ (10), 530 M$^+$ (20), 362 (5), 213 (39), 168 (100), 141 (93), 115 (27).

Acknowledgements

The authors thank the Natural Sciences and Engineering Research Council of Canada for its support of this research.

1. P.J. Flory. Principles of polymer chemistry. Cornell University Press, Ithaca, N.Y. 1969.
2. P.G. deGennes. Scaling concepts in polymer physics. Cornell University Press, Ithaca, N.Y. 1979.
3. H. Fujita. Polymer solutions. Elsevier, New York. 1990.
4. J.A. Semlyen. Cyclic polymers. Elsevier, New York. 1986.
5. J.F. Brown and G.M. Slusarczark. J. Am. Chem. Soc. **87**, 931 (1965).
6. J.P. Flory and J.A. Semlyen. J. Am. Chem. Soc. **88**, 3209 (1966).
7. M. Sisido, Y. Imanishi, and T. Hagashimura. Macromolecules, **9**, 316 (1976).
8. (*a*) K. Horie and I. Mita. Macromolecules, **11**, 1175 (1978); (*b*) K. Horie, W. Schnabel, I. Mita, and H. Ushiki. Macromolecules, **14**, 1422 (1981).
9. (*a*) G.I. Closs and C.E. Doubleday. J. Am. Chem. Soc. **95**, 2735 (1973); (*b*) F.J.J. DeKanter, R. Kaptein, and R.A. Van Santen. Chem. Phys. Lett. **45**, 575 (1977); (*c*) F.J.J. DeKanter, R.J. Sagdeev, and R. Kaptein. Chem. Phys. Lett. **58**, 334 (1978); (*d*) F.J.J. DeKanter and R. Kaptein. Chem. Phys. Lett. **58**, 340 (1978).
10. M.A. Winnik. Acc. Chem. Res. **18**, 73 (1985).
11. M.A. Winnik, T. Redpath, and D.H. Richards. Macromolecules, **13**, 328 (1980).
12. T. Atkinson and M. Smith. *In* Oligoribonucleotide synthesis — A practical approach. *Edited by* M.J. Gait. IRL Press, Oxford. 1984. pp. 35–80.
13. S.A. Narang. Synthesis and applications of DNA and RNA. Academic, Orlando, Fla. 1987.
14. S. Lee and M.A. Winnik. Can. J. Chem. **71**, 1216 (1993).
15. J.B. Birks. Photophysics of aromatic molecules. Wiley, New York. 1985.
16. J.L. Halary, J.M. Ubrich, J.M. Nunzi, L. Monnerie, and R.S. Stein. Polymer, **25**, 956 (1984).
17. K. Zachariasse and W. Kühnle. Z. Phys. Chem. **101**, 267 (1976).
18. F. Mendicuti, B. Patel, and W.L. Mattice. Polymer, **31**, 453 (1990).
19. C.-H. Tung and Y.-M. Wang. J. Am. Chem. Soc. **112**, 6322 (1990).
20. D.F. Eaton and B.E. Smart. J. Am. Chem. Soc. **112**, 2821 (1990).
21. S.-T. Cheung, M.A. Winnik, and A.E.C. Redpath. Makromol. Chem. **183**, 1815 (1982).
22. H.T. Oyama, W.T. Tang, and C.W. Frank. Macromolecules, **20**, 474 (1987).
23. K. Char, C.W. Frank, A.P. Gast, and W.T. Tang. Macromolecules, **20**, 1833 (1987).
24. K. Char, C.W. Frank, and A.P. Gast. Macromolecules, **22**, 3177 (1989).
25. P. Reynders, W. Kühnle, and K.A. Zachariasse. J. Phys. Chem. **94**, 4073 (1990).
26. D.V. O'Connor and D. Phillips. Time-correlated single photon counting. Academic, London. 1984.
27. M. Zuker, A.G. Szabo, L. Bramall, D.T. Krajcarski, and B. Selinger. Rev. Sci. Instrum. **56**, 14 (1985).

Can. J. Chem. Downloaded from www.nrcresearchpress.com by EESC ESCOLA DE ENGENHARIA on 09/08/12
For personal use only.

Computational conformational analysis of neural membrane lipids: development of force field parameters for phospholipids using semi-empirical molecular orbital calculations

ALBERT Y. JIN AND LISBETH A. BENESCH
Department of Chemistry, Queen's University, Kingston, ON K7L 3N6, Canada

AND

DONALD F. WEAVER
Departments of Chemistry and Medicine, Queen's University, Kingston, ON K7L 3N6, Canada

Received December 31, 1993

ALBERT Y. JIN, LISBETH A. BENESCH, and DONALD F. WEAVER. Can. J. Chem. **72**, 1596 (1994).

MM2 force field parameters for phospholipids were developed. These parameters — MM2(Lipid) — were employed in energy-minimization calculations (using crystal structures as starting conformations) on four phospholipids: dimyristoylphosphatidylglycerol, dilauroylphosphatidyl-*N,N*-dimethylamine, 1,2-dilauroyl-*dl*-phosphatidylethanolamine, and deoxylysophosphatidylcholine. After minimization, slight conformational changes were seen in the hydrocarbon chains, while greater change was seen at the head group. The diacylglycerol backbone of the energy-minimized structures exhibited conformations corresponding to experimentally observed conformations. The energy minimization of a randomly and significantly altered geometry of 1,2-dilauroyl-*dl*-phosphatidylethanolamine resulted in a head group conformation that closely agreed with *ab initio* theoretical calculations. The utility of AM1 in molecular mechanics parameterization was demonstrated.

ALBERT Y. JIN, LISBETH A. BENESCH et DONALD F. WEAVER. Can. J. Chem. **72**, 1596 (1994).

On a mis au point des paramètres de champ de force MM2 pour les phospholipides. On a utilisé ces paramètres — MM2(Lipides) — pour faire des calculs de minimisations d'énergie (utilisant des structures cristallines comme conformations de départ) sur quatre phospholipides: dimyristoylphosphatidylglycérol, dilauroylphosphatidyl-*N,N*-diméthylamine, 1,2-dilauroyl-*dl*-phosphatidyléthanolamine et désoxylysophosphatidylcholine. Après minimisation, on a observé de faibles changements conformationnels dans les chaînes hydrocarbonées, alors que l'on a observé des changements plus importants au niveau du groupe de tête. Le squelette diacylglycérol des structures pour lesquelles on a minimisé l'énergie présente des conformations correspondant aux conformations observées expérimentalement. La minimisation énergétique d'une 1,2-dilauroyl-*dl*-phosphatidyléthanolamine dont la structure avait été modifiée d'une façon importante et au hasard a conduit à un groupe de tête qui est en bon accord avec celui obtenu par des caculs théoriques *ab initio*. On démontre l'utilité du AM1 dans la paramétrisation de la mécanique moléculaire.

[Traduit par la Rédaction]

1. Introduction

The past decade has witnessed considerable interest in applying molecular mechanics to conformational optimization calculations for large molecules of biological and pharmaceutical significance. One class of molecules which has received surprisingly little attention are the phospholipids which constitute the major components of biological membranes (1–4). Although the molecular mechanics approach has been applied extensively to peptides, nucleotides, and other biomolecules through force fields such as MM2 (5), CHARMM (6) and AMBER (7), the equivalent treatment of membrane phospholipids is decidedly lacking. Recent experimental work has strongly suggested that molecules such as peptides or drugs, undergo significant conformational changes induced by interactions with the surrounding environment, either aqueous or lipid (8, 9). Moreover, the limitations of vacuum phase conformational calculations on biological molecules further emphasize the need to develop computational simulation methods to model environmental effects in the biological milieu. Therefore, it is imperative that the influence of a phospholipid environment be considered when searching for low energy bioactive conformations of molecules such as intramembrane proteins or drugs. This is particularly relevant in neurochemistry because neurohormones, neurotransmitters, and neuroreceptors all exist in an environment dominated by brain lipids.

As a first step towards achieving realistic neurochemical simulations, the molecular properties of membrane phospholipids must be modelled accurately. Phosphatidylcholines and phosphatidylethanolamines are two lipids which are of particular interest because both are present in large quantities in brain (neuronal) membranes. As such, they constitute a significant portion of the lipid environment of various neuropeptides and drugs (10). For this reason, we have developed an MM2 force field parameterization (MM2(Lipid)) suited to the geometry optimization of phospholipids found in neuronal membranes. (The popularity of the MM2 program precipitated the effort to develop parameters suited to this force field.) These parameters were then used to calculate the energy-minimized structures of four phospholipids. The ability of these parameters to generate experimentally determined geometries was also evaluated.

2. Methods

Although MM2 has been optimized for many classes of molecules, this important force field is unable to treat neuronal phospholipids. A set of computational procedures, as outlined by Hopfinger and Pearlstein (11), in conjunction with X-ray crystallographic data, *ab initio* molecular orbital calculations and semi-empirical molecular orbital calculations were used to generate an appropriate set of atom types and parameters. New parameters pertaining to the phosphate head group are shown in Table 1.

2.1 Atom types

The basis of any force field is the allocation of atom type; that

Can. J. Chem. Downloaded from www.nrcresearchpress.com by EESC ESCOLA DE ENGENHARIA on 09/08/12
For personal use only.

TABLE 1. MM2(Lipid) parameters for lipid phosphate headgroups

(*a*) Bond stretching parameters

Bond	l_0(Å)	k_s(mdyn/Å)
6–60	1.580	2.046
47–60	1.477	7.759

(*b*) Bond angle bending parameters

Bond angle	θ_0(degrees)	k_θ(mdyn Å/rad^2)
1–6–60	118.3	0.412
6–60–6	105.0	0.315
6–60–47	116.42	0.377
47–60–47	115.58	0.384

(*c*) Torsional parameters

Torsional angle	V_1 (kcal/mol)	V_2 (kcal/mol)	V_3 (kcal/mol)
1–1–6–60	38.466	−25.305	10.630
1–6–60–47	−5.900	−1.000	0.000
1–6–60–6	5.900	−2.500	0.250
5–1–6–60	0.000	0.000	−0.500

(*d*) Van der Waals' parameters

Atom type	r(Å)	ε(kcal/mol)
47 (O)	1.68	0.050
60 (P)	2.02	0.168

(*e*) Electrostatic parameters

Bond	Bond dipole moment (Debyes)
6–60	8.91
47–60	9.42

is, the selection of atoms which are sufficiently alike in a chemical and physical sense to be treated identically in the molecular mechanical refinement. The Born–Oppenheimer approximation states that the Schrödinger equation can be separated into a part that describes the motion of electrons and a part that describes the motion of nuclei, and that these can be treated independently. In molecular mechanics, which treats electrons in a classical electrostatic manner, nuclear positioning is dominant and a wide range of atom types per element is necessary. MM2(Lipid) employs eleven atom types for its description of neuronal lipids. Although the treatment of sp^3 atom types is straightforward, a variety of sp^2 atom types are necessary to ensure geometrical precision. The number of atom types employed in MM2(Lipid) represents the minimum number required for an accurate representation, while endeavouring to avoid the problems associated with excessive (and thus cumbersome) parameterization.

The MM2 atom types that were employed are shown in the lipids illustrated in Fig. 1.

2.2 Bond length and bond angle parameters

During the solvation of peptides and drugs by membrane lipids, lipid molecules may undergo significant geometrical alteration; accordingly, bond length and bond angle parameters must be carefully selected.

For the lipid tail, the C—C and C—H bond lengths were taken from the MM2(91) parameter set. The k_s stretching force constants were taken from the molecular mechanics literature. For example, the C—C (type 1–1) stretching constant is given as 4.40, 4.40, 4.40 and 4.48 mdyn/Å by Allinger (12), Schleyer and co-workers (13), Ermer and Lifson (14), and Boyd and co-workers (15), respectively; the C—H (type 1–5) stretching constant is given as 4.60, 3.85, 4.60, 4.54 and 4.70 mdyn/Å by Allinger (12), Fitzwater and Bartell (16), Schleyer and co-workers (13), Ermer and Lifson (14), and Boyd and co-workers (15), respectively. In view of this, MM2(Lipid) uses values of 4.40 and 4.60 mdyn/Å for 1–1 and 1–5 bond types.

Vibrational spectroscopy studies demonstrate that bond angles exhibit greater variability than bond lengths and thus are of greater import for precise geometrical and conformational analysis. For the lipid tail, the C—C—C, C—C—H, and H—C—H equilibrium values were obtained from the MM2(91) parameter set. The k_θ angle bending parameters were adapted from the molecular mechanics literature. For example, the C—C—C (type 1–1–1) bending constant is given as 0.450, 0.629, 0.570, 0.647, and 0.800 mdyn/deg by Allinger (12), Fitz-

Can. J. Chem. Downloaded from www.nrcresearchpress.com by EESC ESCOLA DE ENGENHARIA on 09/08/12
For personal use only.

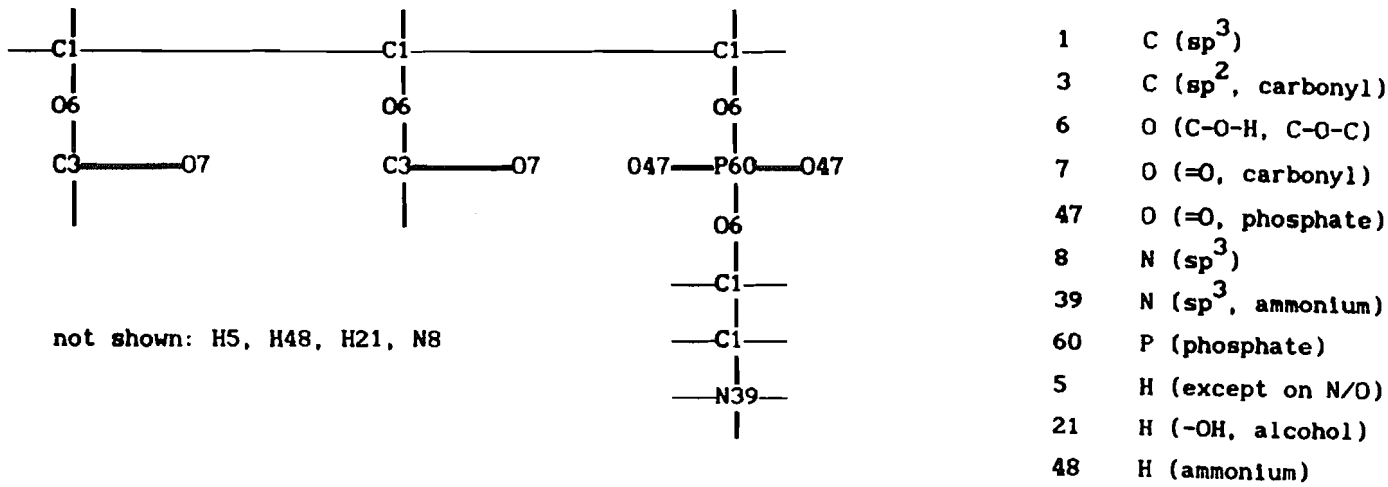

FIG. 1. MM2 (Lipid) atom types.

water and Bartell (16), Schleyer and co-workers (13), Ermer and Lifson (14), and Boyd and co-workers (15), respectively; the C—C—H (type 1–1–5) bending constant is given as 0.360, 0.322, 0.400, 0.521, and 0.608 mdyn/deg by Allinger (12), Fitzwater and Bartell (16), Schleyer and co-workers (13), Ermer and Lifson (14), and Boyd and co-workers (15), respectively; the H—C—H (type 5–1–5) bending constant is given as 0.320, 0.350, 0.330, 0.549, and 0.508 mdyn/deg by Allinger (12), Fitzwater and Bartell (16), Schleyer and co-workers (13), Ermer and Lifson (14), and Boyd and co-workers (15), respectively. Accordingly, the MM2(Lipid) parameterization uses values of 0.450, 0.360, and 0.320 mdyn/deg for the 1–1–1, 1–1–5, and 5–1–5 bond angle types.

For the phosphate head group, equilibrium values for bond lengths and bond angles were taken from *ab initio* molecular orbital calculations on dimethyl phosphonate and phosphoric acid, as reported by Van Wazer and Ewig (17, 18). In accord with Hopfinger and Pearlstein (11), the k_s and k_θ force constants were determined by calculating the energy of the model compound dimethyl phosphate at various values of a given bond length or bond angle; energies were calculated using AM1 semi-empirical molecular orbital calculations. These energies were then plotted as a function of the given structural parameter and the data was fit, using a least-squares fitting routine, to the truncated Taylor series expansion used in the MM2 force field. Taking into account the difference in force constants used in the MM2 force field and those determined through quantum chemical techniques, scaling factors, as determined by Leonard and Ashman (19), were then applied to the calculated force constants.

2.3 Torsional angle parameters

The explicit incorporation of torsional terms is necessary for the consideration of atom pairs which are separated by a chain of three bonds.

Parameters for the lipid tail (C—C—C—C, C—C—C—H, and H—C—C—H) were taken from MM2(91). Thus, for the group C—CH_2—CH_2—C, the barrier to rotation is determined by the sum of the V_1, V_2, and V_3 terms for one C—C—C—C angle, four C—C—C—H angles, and four H—C—C—H angles. For the phosphate head group, rotational barriers were determined by plotting the conformational energy (calculated using the AM1 Hamiltonian (20)) of either dimethyl phosphate or diethyl phosphate as a function of a given torsional angle. Although the positions of the maxima and minima were well-determined by AM1 (in comparison to *ab initio* values), the barrier heights were excessively large and were set to reflect values from *ab initio* molecular orbital calculations reported in the literature (17, 21, 22). For example, for the torsional angle P—O—C—H, the AM1 result indicates maxima at 60°, 180°, and 300°, with an average barrier height of 1.1 kcal/mol. The 4-31G* basis set *ab initio* molecular orbital result predicts maxima at the same locations but rotational barriers of only 0.5 kcal/mol (17). Therefore, the V_1, V_2, and V_3 terms for P—O—C—H were set to yield a rotational barrier of 0.5 kcal/mol at 60°, 180°, and 300°.

2.4 Van der Waals' parameters

The sum of the attractive and repulsive energies constitutes the van der Waals' interaction potential between a pair of non-bonded atoms. For neutral, non-polar molecules, the general forms of this interaction are the Lennard–Jones and Buckingham potentials; the Hill potential employed in MM2(Lipid) is a specific example of the Buckingham potential. Hill demonstrated that this potential energy function provides a good description for simple molecules (23). Using the Hill potential, atoms are regarded as distensible spheres of radius r_0 and "hardness" ϵ.

The van der Waals' radii for P and O (sp^2, phosphate) were initially taken from experimental values (24). However, there is a consistent difference between established molecular mechanics values and experimental values; accordingly, an empirically derived scaling factor of 1.12 was applied. Thus, the van der Waals' radius for P was 1.12×1.800 Å = 2.02 Å. Similarly, the van der Waals' radius for O (sp^2, phosphate) was 1.68 Å.

The van der Waals' parameters for the remaining atom types were adopted from the MM2(91) parameter set.

2.5 Electrostatic parameters

Since the accurate conformational analysis of large biomolecules, like lipids, requires the inclusion of non-bonded interactions, the evaluation of electrostatic interactions are of utmost importance. In classical electrostatic theory, the interaction energy between diffuse charge clouds is calculated by a series expansion. For interactions between point charges, the dipole–dipole interaction energy is the leading term and can be calcu-

Can. J. Chem. Downloaded from www.nrcresearchpress.com by EESC ESCOLA DE ENGENHARIA on 09/08/12
For personal use only.

TABLE 2. Steric energies of crystal structures and energy minimized structures

Compound	Crytal structure (kcal/mol)	Energy-minimized structure (kcal/mol)	Root-mean-square fit (Å)
Lipid1	238.14	10.63	0.264
Lipid2	71.52	19.41	0.192
Lipid3	294.22	20.28	0.335
Lipid4	250692.30[a]	89.51	0.639

[a]High steric energy reflects distortion in crystal structure.

Can. J. Chem. Downloaded from www.nrcresearchpress.com by EESC ESCOLA DE ENGENHARIA on 09/08/12
For personal use only.

lated by the Jeans' function (25). Thus there are two possible approaches for the treatment of electrostatic interactions: the point charge model, in which the charges are treated as geometric points placed at the atomic nuclei; and, the dipole model, in which bond moments are assigned to every bond in the molecule. Allinger has concluded that the two treatments are essentially equivalent (26). Since MM2(Lipid) employs the dipole model, it was necessary to assign bond moments to all possible bonds in each lipid.

For the bond types 47–60 and 6–60, bond moments, BM, were calculated from the equation:

$$BM = (2.385)l_0(Q_1 - Q_2); (Q_1 \geq Q_2)$$

where, for atoms 1 and 2, Q_1 and Q_2 are the charge densities, l_0 is the bond length, and the factor 2.385 converts BM to Debye units (when l_0 is in Å and the charge densities are in electron units) (11). The charge densities of P, O(sp^3), and O(sp^2, phosphate) were obtained from an electrostatic potential method (CHELP) (27). The bond moments for 47–60 and 6–60 are (in Debyes), 9.42 and 8.91, respectively.

2.6 Computational methods

All computational tasks were accomplished on an IBM RS/6000 550 RISC computer operating under AIX. MM2 force field calculations were performed using the MM2(91) program (5). Parameterization of the MM2(Lipid) force field was effected using both semi-empirical and *ab initio* molecular orbital calculations. Semi-empirical molecular orbital calculations were executed using the AM1 Hamiltonian (20) as implemented in the MOPAC 5.1 program. The PRECISE option was used as SCF convergence criteria. Geometry optimization was performed using the PULAY optimization procedure within MOPAC. Root-mean-square fitting to crystal structures was performed using the COMP function of the KGNGRAF graphics program distributed with the MOTECC-90 family of programs (28). DREIDING force field calculations were performed using the program BIOGRAF (version 3.0), from Biodesign, Inc. (29).

3. Results

Four lipids with known crystal structures were chosen to evaluate the MM2(Lipid) parameters: dimyristoylphosphatidylglycerol (lipid1) (30), dilauroylphosphatidyl-*N*,*N*-dimethylethanolamine (lipid2) (31), 1,2-dilauroyl-*dl*-phosphatidylethanolamine (lipid3) (32), and deoxylysophosphatidylcholine (lipid4) (33). For each lipid, the energy-minimized structure was determined using the crystal structure as the starting conformation. The conformational energy of both the crystal structures and the energy-minimized structures, as well as the root-mean-square fit, is shown in Table 2. Figure 2 shows the energy-minimized structure of lipid1. Initial and final values for the bond lengths, bond angles, and torsional angles of lipid1 are shown in Tables 3, 4, and 5. (Lipid1 atom numbering is shown in Fig. 3).

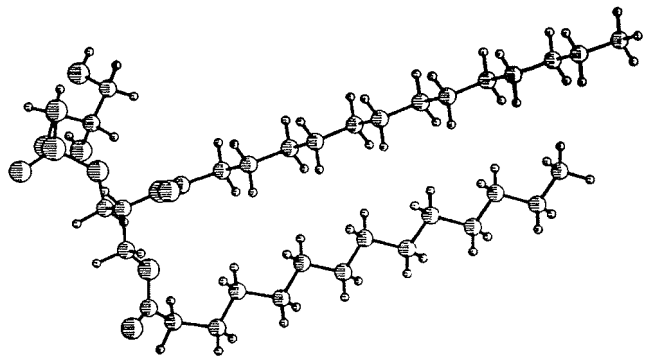

FIG. 2. Energy-minimized structure of lipid1.

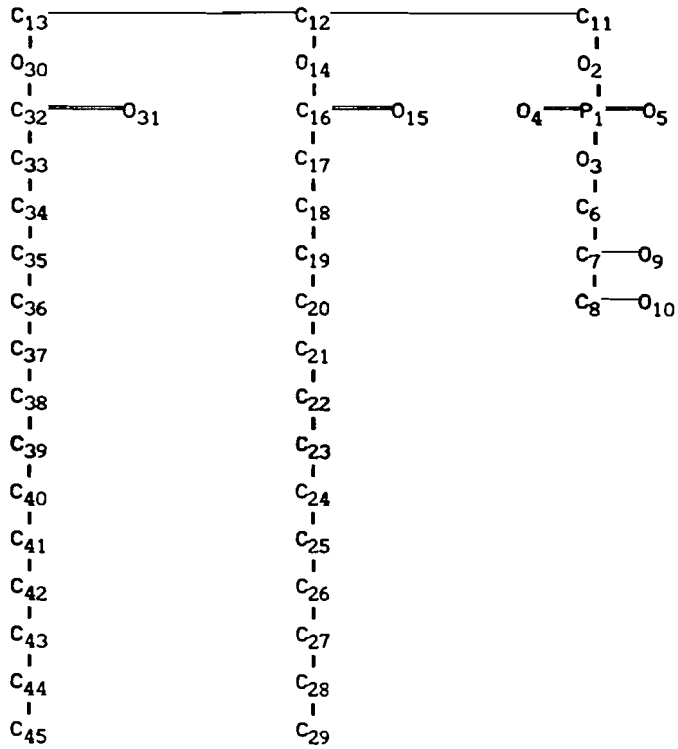

FIG. 3. Atom numbering for lipid1.

3.1 Head group conformation

After the energy minimization of each lipid, the most significant conformational changes occurred at the head group. These changes are due to the removal of hydrogen-bonding and ionic interactions that are present in the crystal lattice. For example,

Can. J. Chem. Downloaded from www.nrcresearchpress.com by EESC ESCOLA DE ENGENHARIA on 09/08/12
For personal use only.

TABLE 3. Lipid1 initial and final bond lengths

Bond	Initial length	Final length
P(1)—O(2)	1.5791	1.6885
P(1)—O(3)	1.6073	1.7811
P(1)—O(4)	1.5494	1.4853
P(1)—O(5)	1.4953	1.4870
O(2)—C(11)	1.4832	1.4114
O(3)—C(6)	1.4779	1.4066
C(6)—C(7)	1.5562	1.5163
C(7)—C(8)	1.5928	1.5144
C(7)—O(9)	1.4545	1.4282
C(8)—O(10)	1.3691	1.4271
C(11)—C(12)	1.5474	1.5285
C(12)—C(13)	1.5312	1.5301
C(12)—O(14)	1.5043	1.4155
C(13)—O(30)	1.5027	1.4085
O(14)—C(16)	1.3440	1.3465
O(15)—C(16)	1.1819	1.2005
C(16)—C(17)	1.4668	1.5206
C(17)—C(18)	1.4992	1.5379
C(18)—C(19)	1.5195	1.5389
C(19)—C(20)	1.5416	1.5387
C(20)—C(21)	1.4710	1.5375
C(21)—C(22)	1.4949	1.5387
C(22)—C(23)	1.5240	1.5374
C(23)—C(24)	1.4703	1.5382
C(24)—C(25)	1.4597	1.5380
C(25)—C(26)	1.4390	1.5375
C(26)—C(27)	1.4639	1.5383
C(27)—C(28)	1.5055	1.5371
C(28)—C(29)	1.4576	1.5347
O(30)—C(32)	1.4257	1.3417
O(31)—C(32)	1.1779	1.2006
C(32)—C(33)	1.4412	1.5169
C(33)—C(34)	1.5061	1.5363
C(34)—C(35)	1.3191	1.5385
C(35)—C(36)	1.4041	1.5371
C(36)—C(37)	1.4381	1.5378
C(37)—C(38)	1.4598	1.5375
C(38)—C(39)	1.4252	1.5370
C(39)—C(40)	1.4104	1.5377
C(40)—C(41)	1.3510	1.5371
C(41)—C(42)	1.4864	1.5378
C(42)—C(43)	1.3536	1.5373
C(43)—C(44)	1.6161	1.5374
C(44)—C(45)	1.3883	1.5344

TABLE 4. Lipid1 initial and final bond angles

Atoms	Initial angle	Final angle
O(2)—P(1)—O(3)	103.741	95.166
O(2)—P(1)—O(4)	130.791	112.629
O(2)—P(1)—O(5)	112.817	116.818
O(3)—P(1)—O(4)	112.714	113.946
O(3)—P(1)—O(5)	102.029	105.055
O(4)—P(1)—O(5)	120.741	111.930
P(1)—O(2)—C(11)	115.774	122.906
P(1)—O(3)—C(6)	119.846	121.928
O(3)—C(6)—C(7)	106.067	107.534
C(6)—C(7)—C(8)	106.842	113.237
C(6)—C(7)—O(9)	111.282	107.562
C(8)—C(7)—O(9)	108.463	107.389
C(7)—C(8)—O(10)	112.970	108.009
O(2)—C(11)—C(12)	108.649	114.076
C(11)—C(12)—C(13)	111.958	108.185
C(11)—C(12)—O(14)	109.322	108.434
C(13)—C(12)—O(14)	116.250	110.174
C(12)—C(13)—O(30)	100.976	106.941
C(12)—O(14)—C(16)	115.413	119.725
O(14)—C(16)—O(15)	126.041	125.244
O(14)—C(16)—C(17)	108.072	109.475
O(15)—C(16)—C(17)	125.825	125.267
C(16)—C(17)—C(18)	117.742	113.892
C(17)—C(18)—C(19)	117.868	112.537
C(18)—C(19)—C(20)	110.062	111.809
C(19)—C(20)—C(21)	111.318	112.627
C(20)—C(21)—C(22)	116.144	111.872
C(21)—C(22)—C(23)	118.533	112.128
C(22)—C(23)—C(24)	117.569	112.319
C(23)—C(24)—C(25)	117.537	111.698
C(24)—C(25)—C(26)	119.417	112.510
C(25)—C(26)—C(27)	123.629	111.749
C(26)—C(27)—C(28)	133.447	112.262
C(27)—C(28)—C(29)	125.808	111.861
C(13)—O(30)—C(32)	110.248	119.372
O(30)—C(32)—O(31)	121.539	125.470
O(30)—C(32)—C(33)	101.085	109.072
O(31)—C(32)—C(33)	136.976	125.452
C(32)—C(33)—C(34)	112.883	112.756
C(33)—C(34)—C(35)	123.290	113.509
C(34)—C(35)—C(36)	126.740	111.399
C(35)—C(36)—C(37)	129.024	112.679
C(36)—C(37)—C(38)	123.591	110.935
C(37)—C(38)—C(39)	122.847	112.740
C(38)—C(39)—C(40)	126.188	111.177
C(39)—C(40)—C(41)	127.038	112.426
C(40)—C(41)—C(42)	125.598	111.557
C(41)—C(42)—C(43)	130.215	112.170
C(42)—C(43)—C(44)	131.068	111.837
C(43)—C(44)—C(45)	117.978	111.881

the 60–47 (P—O) and the 60–6 (P—O) bond lengths changed by approximately 0.092 Å and 0.128 Å, respectively. Overall, changes in bond length, bond angle, and torsional angle at the phosphate head group did not result in conformations that were significantly different from the known crystal structure.

3.2 Diacylglycerol backbone conformation

The conformations of the glycerol backbone of lipid1, lipid2, and lipid3 were in agreement with two experimentally observed conformations shown in Figs. 4*a* and 4*b* (34). Both lipid1 and lipid2 achieved the conformation shown in Fig. 4*a* while lipid3 attained the conformation shown in Fig. 4*b*. It has been postulated by Hauser et al. that these conformations allow optimal van der Waals' and hydrophobic interactions between the fatty acyl chains (34).

3.3 Hydrocarbon chain conformation

For lipid1, lipid2, and lipid3 the conformation of the hydro-

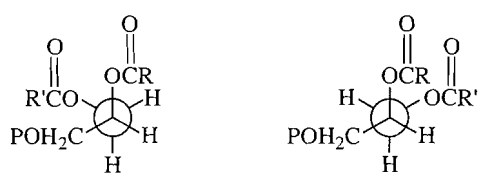

FIG. 4. Experimentally observed diacylglycerol backbone conformations (34).

Can. J. Chem. Downloaded from www.nrcresearchpress.com by EESC ESCOLA DE ENGENHARIA on 09/08/12
For personal use only.

TABLE 5. Lipid1 initial and final torsional angles

Atoms	Initial angle	Final angle
P(1) O(2) C(11) C(12)	−146.109	−95.519
P(1) O(3) C(6) C(7)	143.145	105.631
O(2) P(1) O(3) C(6)	−85.505	−95.431
O(2) C(11) C(12) C(13)	151.302	176.204
O(2) C(11) C(12) O(14)	−78.404	−64.316
O(3) P(1) O(2) C(11)	−76.052	−116.658
O(3) C(6) C(7) C(8)	179.948	−171.687
O(3) C(6) C(7) O(9)	61.721	69.821
O(4) P(1) O(2) C(11)	165.957	124.708
O(4) P(1) O(3) C(6)	26.112	22.141
O(5) P(1) O(2) C(11)	33.559	−6.907
O(5) P(1) O(3) C(6)	157.090	145.004
O(6) C(7) C(8) O(10)	−66.513	−58.571
O(9) C(7) C(8) O(10)	53.545	60.021
C(11) C(12) C(13) O(30)	64.154	57.191
C(11) C(12) O(14) C(16)	159.557	174.070
C(12) C(13) O(30) C(32)	163.814	−164.376
C(12) O(14) C(16) O(15)	−4.462	−4.231
C(12) O(14) C(16) C(17)	178.258	174.442
C(13) C(12) O(14) C(16)	−72.512	−67.705
C(13) O(30) C(32) O(31)	3.646	−2.722
C(13) O(30) C(32) C(33)	−170.251	176.429
O(14) C(12) C(13) O(30)	−62.473	−61.186
O(14) C(16) C(17) C(18)	177.703	−176.940
O(15) C(16) C(17) C(18)	.415	1.733
C(16) C(17) C(18) C(19)	−179.406	−178.247
C(17) C(18) C(19) C(20)	−178.522	179.095
C(18) C(19) C(20) C(21)	−178.983	−178.670
C(19) C(20) C(21) C(22)	177.306	179.872
C(20) C(21) C(22) C(23)	177.257	179.808
C(21) C(22) C(23) C(24)	179.916	−179.256
C(22) C(23) C(24) C(25)	−178.607	179.109
C(23) C(24) C(25) C(26)	−170.311	−179.477
C(24) C(25) C(26) C(27)	−179.035	178.689
C(25) C(26) C(27) C(28)	−176.825	179.941
C(26) C(27) C(28) C(29)	173.817	178.788
O(30) C(32) C(33) C(34)	109.610	90.639
O(31) C(32) C(33) C(34)	−62.758	−90.210
C(32) C(33) C(34) C(35)	−57.103	−59.794
C(33) C(34) C(35) C(36)	178.394	−177.077
C(34) C(35) C(36) C(37)	−179.271	−176.353
C(35) C(36) C(37) C(38)	179.534	177.753
C(36) C(37) C(38) C(39)	−179.825	−178.416
C(37) C(38) C(39) C(40)	178.174	178.402
C(38) C(39) C(40) C(41)	176.027	179.485
C(39) C(40) C(41) C(42)	177.027	−179.714
C(40) C(41) C(42) C(43)	172.356	178.968
C(41) C(42) C(43) C(44)	179.502	−178.920
C(42) C(43) C(44) C(45)	−174.179	179.885

carbon chains remained essentially unaltered after energy minimization. The larger RMS fit for lipid4, however, can be attributed to a distortion of the hydrocarbon chain at the acyl ester group in the crystal structure (33). As noted by Hauser et al., "it cannot be definitely concluded whether this irregularity reflects a statistical disorder of the chains only or is also due to some accommodation problems of the carboxyl ester group and of the methyl chain end" (33). In the energy-minimized structure, this irregularity was significantly alleviated.

3.4 Energy minimization of an unfavourable conformation

Commencing a minimization using the X-ray structure as a starting conformation does not adequately challenge the utility of a force field energy refinement process. To further evaluate the MM2(Lipid) parameters, the crystal structure geometry of lipid3 was randomly and significantly altered to yield an unfavourable conformation and then minimized. In the resulting energy minimized structure, shown in Fig. 5, the polar head group has undergone a conformational change due to an apparent interaction between the ammonium and the phosphate moieties. This interaction is similar to that observed in *ab initio* molecular orbital calculations performed on the phosphorylethanolamine group (35). The initial steric energy of the altered lipid3 geometry was 5831.2 kcal/mol and the final steric energy of the minimized structure was 26.6 kcal/mol. The root-mean-square fit between the crystal structure and the minimized structure was 0.877 Å.

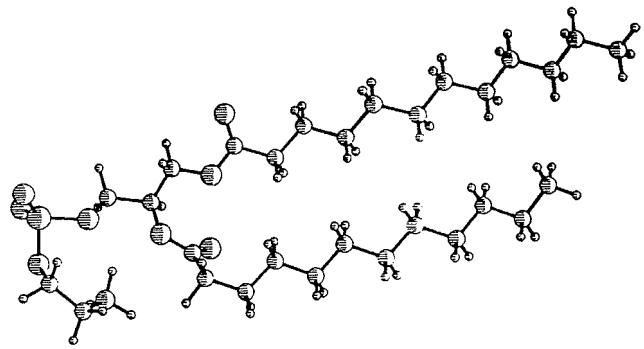

FIG. 5. Energy-minimized structure of lipid3 (from an unfavourable initial conformation).

4. Discussion

4.1 Force field parameterization

The strength of the molecular mechanics method lies in its ability to predict reasonably accurate structures and energies of a diverse range of large molecules. However, this can be realized only upon validation of both the potential energy functions and the parameters that are incorporated into these functions. Unfortunately, it is unreasonable to expect that every required parameter will be included in any given molecular mechanics program. Therefore, the user is often obliged to supply missing parameters. Regrettably, most reports of molecular mechanics parameterization are vague.

4.1.1 General approach to the parameterization process

Force field parameterization can be approached in a number of ways. Very often, the techniques that are employed will involve both logical and intuitive processes; as Allinger has described, "there is an art and a science to molecular mechanics parameterization" (26). In some cases, parameters can be obtained through the application of least-squares methods to an appropriate data set. On the other hand, it is also not uncommon to obtain parameters through what is euphemistically referred to as "judicious selection". In the final analysis, the vindication of any parameterization method lies in the validity of the subsequent calculations.

Although the current trend in force field parameterization is to employ more rigorous *ab initio* molecular orbital calculations, there is some question concerning the applicability of parameters derived by these methods. As Alemán and Orozco have observed (36), even when the *ab initio* wavefunction is evaluated at the restricted Hartree–Fock level and less rigorous low level basis sets are used, the size of the model compound

Can. J. Chem. Downloaded from www.nrcresearchpress.com by EESC ESCOLA DE ENGENHARIA on 09/08/12
For personal use only.

must still be quite small. Therefore, there is the possibility that parameters derived from such a specific molecular environment may not necessarily be applicable to large molecule problems. However, it is well within the ability of current semi-empirical molecular orbital methods to obtain force field parameters from calculations based on more reasonably sized model compounds. Hopfinger has suggested the utility of MNDO calculations during molecular mechanics parameterization (11). More recently, Alemán and Orozco have suggested that the AM1 Hamiltonian is remarkably capable of reproducing parameters that are used by a variety of force fields, particularly MM2 (36). In studies on dihydropyridines, Bikker and Weaver have also found that because of the parameterization of AM1 and the employment of up to four Gaussian functions to correct the nuclear core repulsion term, the behaviour of the atom pairs N—O, C—O, C—N, C—H, and N—H are better evaluated by AM1 than by either MNDO or PM3 (37). For the parameterization of MM2(Lipid), the AM1 Hamiltonian was well-suited to the task of generating data sets from which bond length and bond angle parameters could be determined. Also, the use of AM1 was of great value in the evaluation of the torsional angle parameters.

4.1.2 Bond length and bond angle parameters

Generally, the preferred route by which these parameters are evaluated employ *ab initio* molecular orbital methods. However, it was found that for the model compounds dimethyl phosphate and diethyl phosphate, AM1 calculations yielded bond lengths and bond angles that were similar to both experimental values and *ab initio* theoretical results reported in the literature. For example, in diethyl phosphate, the average C—O bond length obtained through AM1 was 1.42 Å. This is quite similar to the experimental C—O bond length of 1.43 ± 0.01 Å (38). Van Wazer and Ewig have also reported similar values based on calculations of methyl phosphinate, dimethyl phosphonate, and trimethyl phosphate at the STO-3G*, 3-21G*, and 4-31G* *ab initio* level (18). Bond angles from AM1 also agreed well with *ab initio* results. For example, the average H—C—O bond angle calculated by AM1 for dimethyl phosphate was 109.433°. This is similar to the average H—C—O angle calculated for dimethyl phosphonate at the STO-3G* level (110.208°) (18). Hence, it was clear that there was no compromise in accuracy in choosing the faster semi-empirical route over a more computationally intensive *ab initio* approach.

4.1.3 Torsional parameters

The development of torsional parameters is generally one of the more difficult tasks that is encountered in parameterization. Often, there is little or no experimental data available and it is not always possible to devise and execute experiments aimed at determining the full potential function. In the approach taken in the parameterization of MM2(Lipid), semi-empirical calculations were used in conjunction with *ab initio* results to determine rotational barriers. The performance of AM1 was found to be quite acceptable in this respect. As mentioned above, the locations of maxima and minima for torsional rotational barriers involving phosphorus atoms were well-determined by AM1. However, the barrier heights were significantly exaggerated using the AM1 method. Accordingly, the barrier heights in MM2(Lipid) were adjusted to agree with *ab initio* values (17, 21, 22). (Alternatively, rotational barrier heights could have been evaluated by performing *ab initio* point calculations at the extrema determined by AM1.) This approach, while retaining a high degree of accuracy, has the added benefit of being much faster than an *ab initio* calculation of the full torsional potential function. It should be noted that the indiscriminate use of other semi-empirical methods could be problematic since various Hamiltonians treat different dihedral angles with varying success. For example, both PM3 and MNDO may yield misleading representations of some torsional angles, such as those of conjugate bonds or ester functionalities (36, 37).

4.1.4 Van der Waals' parameters

In developing MM2(Lipid), the determination of accurate van der Waals' radii was to a great extent confounded by the lack of a standard definition. For example, from the crystallographic point of view, the sum of the van der Waals' radii can be considered to be the distance of closest approach between two non-bonded atoms in a solid (24). However, Allinger has pointed out that this differs substantially from the molecular mechanics definition (26), in which the sum of the van der Waals' radii is the distance at which the van der Waals' potential for two non-bonded atoms is at a minimum. The actual measurement of van der Waals' radii has also been subjected to a variety of treatments. Francl et al. have obtained atomic radii for a series of molecules by fitting calculated total electron densities using spheres of adjustable radii centered on the nuclei (39). Alternatively, Bader has proposed a method of partitioning the total molecular charge distribution between the nuclei in a molecule by using bond critical points (40). In Bader's theory of molecular structure, a reasonable approximation of a van der Waals' radius could be obtained by taking the distance from the nucleus to the 0.002-au contour (1.000 au = 6.748 e/Å^3); this distance is termed the non-bonded radius (41). A brief comparison of the different methods revealed significant differences. For example, the non-bonded radius for carbon determined via Bader's methodology was 1.65 Å (40), whereas that determined by Francl was 1.893 ± 0.050 Å (39). The experimental carbon van der Waals' radius as determined crystallographically by Bondi was 1.70 Å (24). In molecular mechanics force fields, the typical carbon van der Waals' radius is 1.90–1.94 Å; this empirically derived and significantly larger radius is necessary to ensure the adequacy of molecular mechanics in reproducing experimental conformations.

By convention, in the parameterization of molecular mechanics force fields, it is customary to use experimental van der Waals' radii with an appropriate empirical scaling factor. Accordingly, in parameterizing MM2(Lipid) for phosphorus and oxygen, the experimental radii reported by Bondi were used. Because the van der Waals' radii elucidated through crystallographic means are generally smaller than the radii used in molecular mechanics, a scaling factor of 1.12 was applied to these experimental values to obtain van der Waals' radii appropriate for the MM2 force field.

4.1.5 Electrostatic parameters

For MM2(Lipid), it was necessary to develop electrostatic parameters for non-bonded interactions. Schaumberger and Kohler have used a number of approaches to calculate charge densities for phosphorylcholine and its derivatives (27). For example, in Mulliken population analysis, charges can be derived by summing the Mulliken populations of all orbitals on each atom (42). However, because the overlap populations are distributed evenly among the overlapping orbitals in this approach, unrealistic charge distributions may result. To a cer-

Can. J. Chem. Downloaded from www.nrcresearchpress.com by EESC ESCOLA DE ENGENHARIA on 09/08/12
For personal use only.

tain extent, this problem may be overcome through natural population analysis (43, 44). Through this method, transformations are used to redistribute overlap populations into orthonormal atomic orbitals with a maximal occupation number. Alternatively, the "CHELP" (charges from electrostatic potentials) procedure, developed by Chirlian and Francl (45), offers a completely different approach. In this method, charge is distributed between the atoms in a molecule such that at several thousand points, the resulting potential is fitted to the electrostatic potential arising from the wavefunction of the molecule. For phosphorylcholine and its derivatives, the dipole moments calculated from the CHELP charges correspond closely with the dipole moments calculated from the wavefunction directly. Thus, in the parameterization of MM2(Lipid), CHELP charges were used to calculate the bond dipole moments for bond types 6–60 and 47–60.

4.2 Comparison to the DREIDING force field

The MM2(Lipid) force field parameterization represents a significant advance over current force fields in its ability to deal with phospholipids. For example, the AMBER force field in molecular modelling packages such as BIOGRAF has been parameterized for phosphorus in nucleotides but not lipids (7). In contrast, the DREIDING force field has been parameterized for a wide variety of molecules (29). However, these parameters are often too generic. For example, the harmonic bond stretching constants for the P(sp^3)—O(sp^3), P(sp^3)—O(sp^2) and P(sp^3)—OH bonds are each 700 kcal/mol. Consequently, in special situations, there may be some compromise in the validity of conformational calculations. For comparison purposes, the structure of lipid3 was energy-minimized starting from its crystal structure using the DREIDING force field. The final structure was accompanied by a decrease in steric energy from 589.2 to 81.4 kcal/mol and the root-mean-square fit to the crystal structure was 0.98 Å. Energy minimization of a distorted lipid3 geometry resulted in a structure with a steric energy of 87.0 kcal/mol and a root-mean-square fit of 1.82 Å to the crystal structure. In this conformation, the headgroup was oriented almost perpendicular to the plane of the two fatty acyl chains and consequently, a lipid bilayer would be difficult to achieve. However, the DREIDING force field predicts that this conformation is accessible as it is only slightly higher in energy than that minimized from the crystal structure. In contrast, using the MM2(Lipid) force field, this conformation had a steric energy of 49.3 kcal/mol, which is almost 30 kcal/mol higher in energy than the conformation obtained from minimization of the crystal structure using the MM2(Lipid) force field. Thus, in this case, the MM2(Lipid) force field accurately predicts that this conformation is unfavourable.

4.3 The need for molecular mechanics parameters for lipids

The biological activity of many compounds is significantly dependent upon their *in vivo* conformation. Since the biological activity of many drugs is a manifestation of an interaction with a membrane-bound receptor protein, both drug and receptor conformation are dependent on not only an aqueous environment, but also a lipid environment. For example, both lipid–peptide and lipid–protein interactions can be profoundly responsible for the efficacy of peptide antibiotics and membrane protein function. The ability of both gramicidin A and valinomycin to alter specific ion fluxes is dependent on hydrophobic interactions with lipid membranes (46). Intrinsic membrane proteins, such as rhodopsin, also rely on the presence of lipid. Dissociation of such proteins from a membrane environment inevitably results in a loss of function, as well as a loss of both secondary and tertiary structure (47). Currently, many experimental methods are available to investigate interactions with lipids: fluorescence spectroscopy, differential scanning calorimetry, electron spin resonance and nuclear magnetic resonance. The particular utility of a molecular mechanics approach lies in its ability to provide a detailed conformational and thermodynamic description of both the molecule of interest and its environment. The failure of current molecular mechanics programs to accurately model lipid molecules detracts from the significance of conformational investigations on compounds of pharmaceutical interest. The MM2(Lipid) parameters have been successfully applied in the geometry optimization of four lipids, indicating that their usage will both greatly assist in conformational investigations and enhance the validity of a simulated membrane environment.

5. Conclusions

The results of the energy minimization calculations show that the MM2(Lipid) force field accurately predicts the conformation of phospholipids. When crystal structures were used as starting points for energy minimization, only small conformational changes were observed in the hydrocarbon chains and in the phosphate head group. After minimization, the diacylglycerol backbone achieved one of two stable conformations that have been observed experimentally (34).

AM1 was well-suited to the parameterization of MM2(Lipid). As a molecular mechanics parameterization tool, AM1 is particularly useful for three reasons: it is capable of performing calculations on reasonably sized compounds; it is computationally less demanding than *ab initio* molecular orbital methods; and, most importantly, it is capable of determining molecular mechanics parameters with a high degree of precision. However, in determining torsional angle parameters, AM1 values provide excessively high barriers to rotation.

Acknowledgements

A.Y.J. acknowledges the support of an NSERC Graduate Student Scholarship. D.F.W. acknowledges an Ontario Ministry of Health Career Scientist Award. This research was funded in part by grants from the Medical Research Council of Canada and by the American Epilepsy Society. Calculations were performed at the Queen's – IBM Molecular Modelling Laboratory, supported by IBM Canada, Queen's University, and Kingston General Hospital.

1. G. Vanderkooi. Biochemistry, **30**, 10760 (1991).
2. T.R. Stouch, K.B. Ward, A. Altieri, and A.T. Hagler. J. Comp. Chem. **12**, 1033 (1991).
3. G. Vanderkooi. J. Phys. Chem. **94**, 4366 (1990).
4. G. Vanderkooi. Chem. Phys. Lipids, **55**, 253 (1990).
5. N.L. Allinger. MM2(91). Quantum Chemistry Program Exchange, Bloomington, Indiana.
6. B.R. Brooks, R.E. Bruccoleri, B.D. Olafson, D.J. States, S. Swaminathan, and M. Karplus. J. Comp. Chem. **4**, 187 (1983).
7. S.J. Weiner, P.A. Kollman, D.A. Case, U.C. Singh, C. Ghio, G. Alagona, S. Profeta Jr., and P. Weiner. J. Am. Chem. Soc. **106**, 768 (1984).
8. R.P. Hicks, D.J. Beard, and J.K. Young. Biopolymers **32**, 85 (1992).
9. F. Macquaire, F. Baleux, E. Giaccobi, T. Huynh-Dinh, J.-M. Neumann, and A. Sanson. Biochemistry, **31**, 2576 (1992).

10. B.W. Agranoff, *In* Basic neurochemistry. 4th ed. *Edited by* G.J. Siegel, B.W. Agranoff, R.W. Albers, and P.B. Molinoff. Raven Press, New York, 1989. pp. 91–107.
11. A.J. Hopfinger and R.A. Pearlstein. J. Comp. Chem. **5**, 486 (1984).
12. N.L. Allinger. J. Am. Chem. Soc. **99**, 8127 (1977).
13. E.M. Engler, J.D. Andose, and P. van R. Schleyer. J. Am. Chem. Soc. **95**, 8005 (1973).
14. O. Ermer and S. Lifson. J. Am. Chem. Soc. **95**, 4121 (1973).
15. S. Chang, D. McNally, S. Shary-Tehrany, M.J. Hickey, and R.H. Boyd. J. Am. Chem. Soc. **92**, 3109 (1970).
16. S. Fitzwater and L.S. Bartell. J. Am. Chem. Soc. **98**, 5107 (1976).
17. J.R. Van Wazer and C.S. Ewig. J. Am. Chem. Soc. **108**, 4354 (1986).
18. J.R. Van Wazer and C.S. Ewig. J. Am. Chem. Soc. **107**, 1965 (1985).
19. J.M. Leonard and W.P. Ashman. J. Comp. Chem. **11**, 952 (1990).
20. M.J.S. Dewar, E.G. Zoebisch, E.F. Healy, and J.J.P. Stewart. J. Am. Chem. Soc. **107**, 3902 (1985).
21. O. Matsuoka, C. Tosi, and E. Clementi. Biopolymers, **17**, 33 (1978).
22. C. Tosi, E. Clementi, and O. Matsuoka. Biopolymers, **17**, 51 (1978).
23. T.L. Hill. J. Chem. Phys. **16**, 399 (1948).
24. A. Bondi. J. Phys. Chem. **68**, 441 (1964).
25. U. Burkert and N.L. Allinger. Molecular mechanics, ACS Monograph 177. American Chemical Society, Washington, D.C., (1982).
26. N.L. Allinger. Reviews In computational chemistry, **2**, 81 (1990).
27. M. Schaumberger and J. Kohler. J. Comp. Chem. **13**, 318 (1992).
28. M. Dupuis, A. Farazdel, S.P. Karna, and S.A. Maluendes. *In* MOTECC-90: Modern techniques in computational chemistry. *Edited by* E. Clementi. ESCOM Science Publishers, Leiden. 1990. pp. 277–324.
29. S.L. Mayo, B.D. Olafson, and W.A. Goddard(III). J. Phys. Chem. **94**, 8897 (1990).
30. I. Pascher, S. Sundell, K. Harlos, and H. Eibl. Biochim. Biophys. Acta, **896**, 77 (1987).
31. I. Pascher and S. Sundell. Biochim. Biophys. Acta, **855**, 68 (1986).
32. P.B. Hitchcock, R. Mason, K.M. Thomas, and G.G. Shipley. Proc. Nat. Acad. Sci. U.S.A. **71**, 3036 (1974).
33. H. Hauser, I. Pascher, and S. Sundell. J. Mol. Biol. **137**, 249 (1980).
34. H. Hauser, I. Pascher, and S. Sundell. Biochemistry, **27**, 9166 (1988).
35. B. Pullman and H. Berthod. FEBS Lett. **44**, 266 (1974).
36. C. Alemán and M. Orozco. J. Compt.-Aid. Mol. Des. **6**, 331 (1992).
37. J.A. Bikker and D.F. Weaver. J. Mol. Struct. (THEOCHEM), In press.
38. R.C. Weast (*Editor*). Handbook of chemistry and physics, 68th ed. Chemical Rubber Co., Cleveland, OH. 1987.
39. M.M. Francl, R.F. Hout Jr., and W.J. Hebre. J. Am. Chem. Soc. **106**, 563 (1984).
40. R.F.W. Bader, P.M. Beddall, and P.E. Cade. J. Am. Chem. Soc. **93**, 3095 (1971).
41. R.F.W. Bader, J. Am. Chem. Soc. **109**, 7968 (1987).
42. R.S. Mulliken. J. Chem. Phys. **23**, 1833 (1955).
43. P.O. Löwdin. Phys. Rev. **97**, 1474 (1955).
44. A.E. Reed, R.B. Weinstock, and F. Weinhold. J. Chem. Phys. **83**, 735 (1985).
45. L.E. Chirlian and M.M. Francl. J. Comp. Chem. **8**, 894 (1987).
46. R.M. Epand and R.F. Epand. *In* The structure of biological membranes. *Edited by* P. Yeagle. CRC Press, Boca Raton. 1992. pp. 573–601.
47. B.S. Selinsky, *In* The structure of biological membranes. *Edited by* P. Yeagle. CRC Press, Boca Raton. 1992. pp. 603–651.

Can. J. Chem. Downloaded from www.nrcresearchpress.com by EESC ESCOLA DE ENGENHARIA on 09/08/12
For personal use only.

A binuclear bis{bis(dimethylphosphino)methane}disilver(I) complex with weakly bonded hexafluoroacetylacetonato ligands

ZHENG YUAN, NEIL H. DRYDEN, JAGADESE J. VITTAL, AND RICHARD J. PUDDEPHATT[1]

Department of Chemistry, University of Western Ontario, London, ON N6A 5B7 Canada

Received December 9, 1993

ZHENG YUAN, NEIL H. DRYDEN, JAGADESE J. VITTAL, and RICHARD J. PUDDEPHATT. Can. J. Chem. **72**, 1605 (1994).

The new complex $[Ag_2(hfac)_2(\mu\text{-dmpm})_2]$ (hfac = hexafluoroacetylacetonato, dmpm = $Me_2PCH_2PMe_2$) has been prepared and characterized both spectroscopically and by an X-ray structure determination (orthorhombic, *Pbca* (No. 61), $a = 9.960(2)$, $b = 14.694(3)$, $c = 22.548(3)$ Å, $Z = 4$, $R = 0.0495$, $R_w = 0.0532$). The data indicate that the $hfac^-$ ligands have mostly ionic character and it is suggested that this may be responsible for the low volatility of complexes $[Ag(hfac)L_n]$ compared to $[Cu(hfac)L_n]$; these complexes are of interest as precursors for chemical vapour deposition of silver.

ZHENG YUAN, NEIL H. DRYDEN, JAGADESE J. VITTAL et RICHARD J. PUDDEPHATT. Can. J. Chem. **72**, 1605 (1994).

On a préparé le nouveau complexe $[Ag_2(hfac)_2(\mu\text{-dmpm})_2]$ (hfac = hexafluoroacétylacétonato, dmpm = $Me_2PCH_2PMe_2$) et on l'a caractérisé tant par spectroscopie que par diffraction des rayons x (cristaux orthorhombiques, *Pbca* (No. 61), $a = 9{,}960(2)$, $b = 14{,}694(3)$ et $c = 22{,}548(3)$ Å, $Z = 4$, $R = 0{,}0495$, $R_w = 0{,}0532$). Les données indiquent que les coordinats $hfac^-$ possèdent principalement un caractère ionique et ils suggèrent que cette propriété peut être responsable pour la faible volatilité des complexes $[Ag(hfac)_n]$ par comparaison avec les complexes $[Cu(hfac)_n]$; ces complexes présentent de l'intérêt comme précurseurs pour le dépôt de la vapeur chimique de l'argent.

[Traduit par la rédaction]

Introduction

There has been recent interest in new methods of formation of silver films, which have potential applications as components of high-temperature superconducting materials (1), as contacts in microelectronic devices if problems of diffusion can be overcome (2), and as biocides in biomaterials used in appliances such as catheters (3). However, the formation of silver films by chemical vapour deposition (CVD) has proved to be difficult and the best precursors still have only borderline suitability for an effective CVD process (4, 5). There are excellent precursors for CVD of copper having the formula [Cu(hfac)L] or $[Cu(hfac)L_2]$ (6), hfac = 1,1,1,5,5,5-hexafluoropentanedionato, but the corresponding silver complexes are considerably less volatile and many decompose before volatilization under vacuum. For example, $[Cu(hfac)(CH_2{=}CHSiMe_3)]$ is a liquid with high volatility but the corresponding silver complex is a solid which cannot be sublimed (4, 6). It has recently been shown that [Cu(hfac)(cod)], cod = 1,5-cyclooctadiene, is a monomer **A** but that the corresponding silver complex exists as a dimer $[Ag_2(\mu\text{-hfac})_2(cod)_2]$, with the unusual structure **B** (7). Of

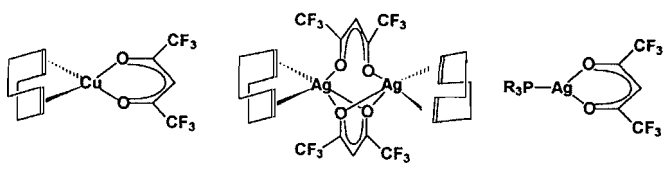

A B C

course, the lower volatility of **B** can then be rationalized. One possible reason for the different structures is that silver(I) is larger than copper(I) and so can accommodate a higher coordination number (7). Of the known complexes of empirical formula [Ag(hfac)L], the best CVD precursors so far reported are $[Ag(hfac)(PR_3)]$, **C**, where R = Me or Et (4). They are monomeric and reliably volatile and they give silver films by CVD at temperatures of 250–350°C depending on the conditions used (4). However, they are still markedly less volatile than the copper analogues (6). Since both $[Cu(hfac)(PR_3)]$ and $[Cu(hfac)(PR_3)_2]$ are good precursors for CVD of Cu (6), it appeared useful to test the four-coordinate complexes $[Ag(hfac)(PR_3)_2]$ as CVD precursors. As part of this work, a new complex of empirical formula [Ag(hfac)(dmpm)], dmpm = $Me_2PCH_2PMe_2$, was prepared and characterized. It is not a useful precursor for CVD but its structure, which is reported below, provides another clue to explain the low volatility of β-diketonatosilver(I) complexes.

Experimental

All experiments were carried out under a nitrogen atmosphere by using standard Schlenk techniques. Infrared spectra were recorded by using a Perkin-Elmer System 2000 FT-IR spectrometer using KBr plates. A Perkin-Elmer DSC-7 Differential Scanning Calorimeter was used to obtain the decomposition temperature and melting point of the compound. The ^1H, $^{13}C\{^1H\}$, and $^{31}P\{^1H\}$ NMR spectra were measured by using a Varian 300 Spectrometer. References used were internal TMS for ^1H and ^{13}C NMR spectra and 85% H_3PO_4 for ^{31}P NMR spectra.

Preparation of $[Ag_2(hfac)_2(\mu\text{-dmpm})_2]$

Silver(I) oxide (0.992 g, 4.28 mmol) was suspended in THF (30 mL). To this was added 1,1,1,5,5,5-hexafluoropentanedione (1.25 mL, 8.85 mmol). Most of the suspended material dissolved immediately. The reaction mixture was stirred for 30 min, then filtered through a pad of Celite. The volume of the clear yellow filtrate was reduced *in vacuo* to a yield 1,1,1,5,5,5-hexafluoropentanedionatosilver(I) (2.48 g) as a pale yellow solid. This solid decomposes slowly at room temperature was not fully characterized. To a solution of the above product (0.416 g) in CH_2Cl_2 (30 mL) was added slowly bis(dimethylphosphino)methane (1.32 g). The reaction mixture was stirred for 30 min at room temperature and the solvent was then evaporated under vacuum to yield a brownish solid. This was dissolved in acetone and decolorised with charcoal. The solution was centrifuged to yield a clear yellow solution from which the product was obtained in >90% yield. The single crystals for X-ray structural studies were grown from acetone/hexane solution by slow diffusion. Mp 189°C (by DSC). Anal. calcd. for $C_{10}H_{15}AgF_6O_2P_2$: C 26.63, H 3.35; found: C 26.61, H 3.19. NMR (CD_2Cl_2): $\delta(^1H) = 5.61$ (s, 1H, hfac), 1.98 (broad s, 2H, CH_2P_2), 1.42 (s, 18H, PMe_3); $\delta(^{13}C) = 175.7$ (q, $^2J(CF) = 30.6$ Hz, $C\text{-}CF_3$), 132.3 (q, $^1J(CF) = 291.4$ Hz, CF_3), 86.0 (s, CH), 31.4 (d, $^1J(PC) = 3.5$

[1]To whom correspondence should be addressed.

Can. J. Chem. Downloaded from www.nrcresearchpress.com by EESC ESCOLA DE ENGENHARIA on 09/08/12
For personal use only.

Can. J. Chem. Downloaded from www.nrcresearchpress.com by EESC ESCOLA DE ENGENHARIA on 09/08/12
For personal use only.

Hz, CH_2P), 15.5 (d, ^1J(PC) = 4.5 Hz, PMe_3); $\delta(^{31}P) = -20.0$ (broad d, J(AgP) = ca. 500 Hz, dmpm). The coupling constants calculated from the low temperature ^{31}P NMR spectrum are $^1J(^{107}AgP)$ = 500 Hz, $^2J(PP)$ = 149 Hz, $^3J(^{107}AgP)$ = 1 Hz. Molar conductivity for a 10^{-3} M solution in CH_2Cl_2 at 25°C: $\Lambda_M = 2.0\ \Omega^{-1}\ cm^2\ mol^{-1}$.

X-ray structure determination of $[Ag_2(hfac)_2(\mu\text{-dmpm})_2]$, 2

A colourless crystal of dimensions 0.41 × 0.40 × 0.28 mm was wedged inside a Lindemann capillary tube, which was then flame sealed on both ends. The diffraction experiments were carried out by using an Enraf-Nonius CAD4F diffractometer at 295 K. Photo and automatic indexing routines, followed by least squares fits of 22 reflections ($23.9° \leq 2\theta \leq 29.7°$) gave cell constants (8) indicating an orthorhombic system. The Laue symmetry *mmm* was confirmed from an inspection of symmetry equivalent reflections. In total 4971 intensity data were collected in the 2θ range 0–55° ($-1 \leq h \leq 12$, $-1 \leq k \leq 19$, $-1 \leq l \leq 29$) in ω–2θ scan mode at variable scan speeds (1.18 to 4.12), so chosen as to optimize counting statistics within a maximum time per datum of 60 s. Background measurements were made by extending the scan by 25% on each side. Three standard reflections were monitored every 120 min of X-ray exposure time and crystal orientation checks were done for every 250 reflections measured. The data were processed using NRCVAX crystal structure programs (9) running on a SUN 3/80 workstation. An empirical absorption correction was applied to the data based upon the ψ scans of eleven reflections with θ ranging from 6.9 to 17.5 ($\mu = 13.36\ cm^{-1}$). The maximum and minimum correction factors were 0.999 and 0.911, respectively. The space group *Pbca* (No. 61) was uniquely determined from the systematic absences (10*a*). The equivalent reflections were averaged (R_{int} = 0.012) leaving 3769 ($I \geq 0\sigma(I)$) unique reflections. The structure was solved using the SHELXS-86 program (11) and subsequent difference Fourier techniques. The final full-matrix least-squares refinements on F were done using the SHELX-76 software (12). Scattering factors for neutral non-hydrogen atoms were taken from the International tables (10*b*). The hydrogen atoms were placed in the calculated positions (C—H = 0.95 Å) and they were included for the purpose of structure factor calculations only. A common thermal parameter was assigned and refined in the least-squares cycles. Anisotropic thermal parameters were assigned and refined for all the non-hydrogen atoms. In the final least-squares refinement cycles, the data converged at $R = 0.0495$ and $R_w = 0.0532$ for 2269 observations with $I \geq 2\sigma(I)$ and 192 variables using the weighting scheme $w = k/\sigma^2F + gF^2$, where $g = 0.000273$ and $w = 3.4623$. In the final difference Fourier synthesis the electron density fluctuated in the range from 0.84 to −1.13 e Å^{-3}; of these, the top five peaks were associated with F atoms. The maximum shift/esd in the final cycle was −0.0012. The secondary extinction coefficient was refined to $7.39(86) \times 10^{-4}$. The experimental details and crystal data are in Table 1, the positional and thermal parameters are in Table 2, anisotropic thermal parameters, calculated hydrogen atom coordinates, selected weighted least-squares planes and selected torsion angles have been included in the supplementary materials.

Results and discussion[2]

The compound $\{Ag(hfac)\}_n$, **1**, of unknown structure, was readily prepared by reaction of silver(I) oxide with 1,1,1,5,5,5-hexafluoropentanedione, hfacH, but, because it appears to have limited thermal stability, it was prepared and then used immediately. The complex $[Ag_2(hfac)_2(\mu\text{-dmpm})_2]$, **2**, which is an air-stable, colourless crystalline material, was synthesized by reaction of $\{Ag(hfac)\}_n$, **1**, with dmpm (reaction [1]). Compound **2** is soluble in chlorinated solvents and in acetone but is sparingly soluble in hexane. Unlike the complexes $[Ag(hfac)(PR_3)]$ (R = Me and Et) (4), compound **2** could not be sublimed under vacuum and so it is not useful as a precursor for CVD of silver. Complex **2** is decomposed thermally at 270°C, as measured by DSC.

The ^1H, ^{13}C, and ^{31}P NMR were used to characterize the solution properties of compound **2**. The ^1H NMR spectrum at room temperature contained a broad singlet resonance due to the CH_2P_2 protons for the dmpm ligands but at 0°C or below the resonance appeared as a quintet with J_{obs}(PH) = 5 Hz. This quintet appearance suggested the structure containing the $Ag_2(\mu\text{-dmpm})_2$ unit since the CH_2P_2 units should then give rise to an $[A_2X_2]_2$ spin system, for which a quintet appearance is possible and in which the observed coupling constant is $(1/2)\{^2J(PH) + {}^4J(PH)\}$. The room temperature ^{31}P NMR spectrum of **2** contained a broad doublet resonance but a much more complex spectrum was readily resolved at lower temperatures from +10°C to −90°C (Fig. 1). This indicates that compound **2** undergoes some form of exchange at room temperature, leading to partial loss of AgP coupling information. The complex ^{31}P NMR spectrum obtained at low temperature is due to overlapping spectra of isotopomers containing $^{107}Ag^{107}Ag$,

TABLE 1. Crystal data and experimental details[a]

Compound, formula weight	$C_{20}H_{30}Ag_2F_{12}O_4P_4$, 902.03
Crystal system, space group	Orthorhombic, *Pbca*(No. 61)
Cell dimensions	a = 9.960(2) Å
	b = 14.694(3) Å
	c = 22.548(3) Å
Temperature	295 K
Cell volume (Å^3), Z	3300(1), 4
Density, g cm^{-3} calcd.	1.816
F(000)	1776
Diffractometer, monochromator	Enraf Nonius CAD4F; graphite
Radiation, wavelength (Å)	MoKα, 0.71073
Absorption coefficient (cm^{-1})	13.36
No. of observations, variables	2269($I \geq 2\sigma(I)$), 192
Final model; R and R_w	0.0495, 0.0532

[a] $R = \Sigma(||F_o| - |F_c||)/\Sigma|F_o|$; $R_w = [\Sigma\sqrt{w}(||F_o| - |F_c||)^2/\Sigma\sqrt{w}|F_o|]$.

TABLE 2. Atomic coordinates and thermal parameters

Atom	x	y	z	B_{iso}
Ag	0.56133(6)	0.08913(4)	0.47205(2)	4.21(2)
P(1)	0.69975(19)	−0.01273(13)	0.41472(8)	3.89(7)
P(2)	0.48079(20)	0.17737(13)	0.55472(9)	4.17(8)
C(1)	0.7667(9)	0.0339(6)	0.3450(3)	6.0(4)
C(2)	0.8472(8)	−0.0589(6)	0.4519(3)	5.9(4)
C(3)	0.3592(11)	0.2613(6)	0.5293(4)	7.5(5)
C(4)	0.5977(9)	0.2437(7)	0.5979(3)	7.2(5)
C(5)	0.6049(8)	−0.1120(5)	0.3891(3)	4.3(3)
O(1)	0.3367(5)	0.0731(4)	0.4209(2)	5.8(3)
O(2)	0.5314(6)	0.2166(4)	0.3911(2)	5.5(3)
C(6)	0.2185(10)	0.0114(8)	0.3442(4)	6.8(5)
C(7)	0.3213(7)	0.0774(5)	0.3684(3)	4.1(3)
C(8)	0.3826(8)	0.1355(6)	0.3272(3)	4.9(4)
C(9)	0.4800(8)	0.2003(5)	0.3426(3)	4.6(3)
C(10)	0.5333(10)	0.2588(7)	0.2921(4)	5.7(5)
F(1)	0.2702(8)	−0.0492(5)	0.3089(4)	12.2(5)
F(2)	0.1367(8)	0.0487(6)	0.3038(4)	12.4(5)
F(3)	0.1460(9)	−0.0248(8)	0.3811(3)	17.4(7)
F(4)	0.6582(8)	0.2503(6)	0.2838(3)	13.1(5)
F(5)	0.4794(9)	0.2497(7)	0.2420(3)	15.8(6)
F(6)	0.5227(12)	0.3445(5)	0.3033(3)	14.9(6)

[2]Supplementary material includes calculated hydrogen atom positions, anisotropic parameters, weighted least-square planes and selected torsion angles. This supplementary material may be purchased from The Depository of Unpublished Data, Document Delivery CISTI, National Research Council Canada, Ottawa, ON K1A 0S2, Canada.

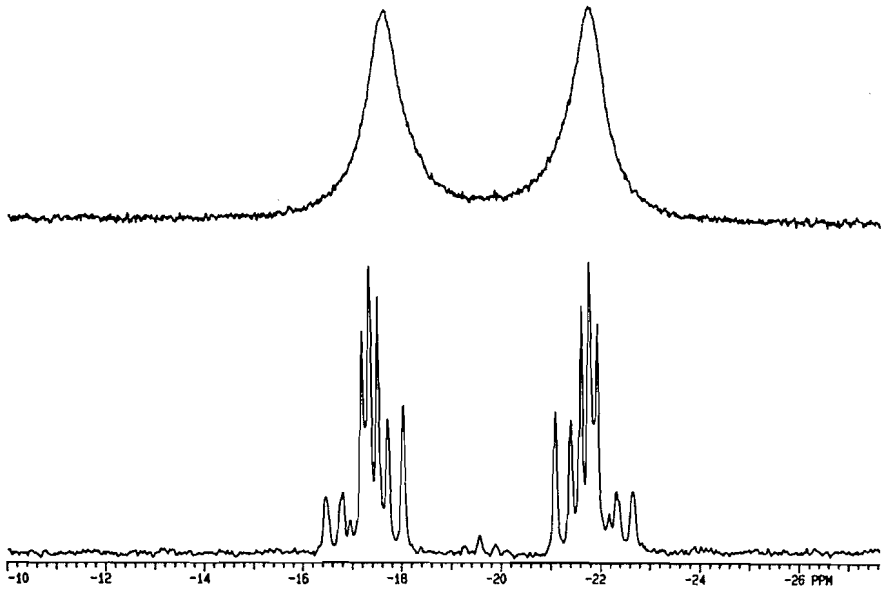

FIG. 1. The $^{31}P\{^1H\}$ NMR spectra of $[Ag_2(hfac)_2(\mu\text{-dmpm})_2]$, (*a*) at room temperature and (*b*) at −60°C.

[1] $\frac{2}{n}\{Ag(hfac)\}_n + 2dmpm \rightarrow$ 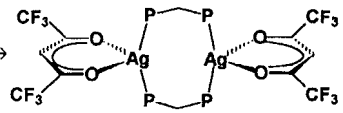

$^{109}Ag^{109}Ag$, and $^{107}Ag^{109}Ag$ pairs in the binuclear $Ag_2(\mu\text{-dmpm})_2$ structure (13). Note that both ^{107}Ag (48%) and ^{109}Ag (52%) each have nuclear spin $I = 1/2$, and the spectral analysis of similar complexes has been reported earlier (13). The calculated coupling constants, $^1J(^{107}AgP)$ and $^1J(^{109}AgP)$ are 500 and 579 Hz, respectively. The ratio of $^1J(^{109}AgP)/^1J(^{107}AgP) = 1.158$, in agreement with the theoretical ratio of $\gamma(^{109}Ag)/\gamma(^{107}Ag) = 1.150$ (14). The $^1J(^{107}AgP)$ value of 500 Hz is only slightly lower than those of the ionic compounds, $[Ag_2\mu\text{-dmpm})_2](BF_4)_2$ (515 Hz, complex prepared by reaction of $AgBF_4$ with dmpm in the required ratio, spectrum recorded at −60°C) and $[Ag_2(\mu\text{-dppm})_2](BF_4)_2$ (505 Hz) (13). In complexes in which silver(I) is bound strongly to three ligands the magnitude of $^1J(^{107}AgP)$ is lower; for example, in $[Ag_2(\mu\text{-dmpm})_3]^{2+}$ it is 317 Hz (13).

The NMR data indicated a binuclear structure for **2** but it was not clear if the $hfac^-$ group was coordinated to silver or not. Hence an X-ray structure determination was carried out. The molecular structure of compound **2** is illustrated in Fig. 2 and selected bond distances are given in Table 3. The proposed binuclear structure is confirmed and each molecule has a crystallographically imposed centre of symmetry. The conformation is shown schematically as **I**. There is an $Ag_2(\mu\text{-dmpm})_2$ core with each silver(I) atom chelated by two oxygen atoms from hfac. The Ag—P bond distances of 2.408(2) and 2.411(2) Å are in the normal range for silver(I)–phosphorus bonds. However, the silver–oxygen bond distances (Ag(1)—O(1), 2.528(5) Å; Ag(1)—O(2), 2.632(5) Å) are significantly different, and both of them are longer than the normal covalent silver(I)–oxygen bond length of ca. 2.3 Å. This indicates that the $hfac^-$ ligand is only weakly bonded to silver and raises the question of whether the complex should be considered covalent or ionic $[Ag_2(\mu\text{-dmpm})_2]^{2+}(hfac^-)_2$. The ideal bond angles for 2- and 4-coordinate silver(I) are 180° (*sp* hybridization) and 109.5° (sp^3 hy-

TABLE 3. Selected bond distances (Å) and angles (deg)

Bond	Distance	Bond	Distance
Ag—Ag[a]	3.153(1)	Ag—P(1)	2.411(2)
Ag—P(2)	2.408(2)	Ag—O(1)	2.528(5)
Ag—O(2)	2.632(5)	P(1)—C(1)	1.839(8)
P(1)—C(2)	1.822(8)	P(1)—C(5)	1.831(7)
P(2)—C(3)	1.821(9)	P(2)—C(4)	1.805(8)
P(2)—C(5)[a]	1.805(7)	O(1)—C(7)	1.195(8)
O(2)—C(9)	1.231(9)	C(6)—C(7)	1.51(1)
C(6)—F(1)	1.30(1)	C(6)—F(2)	1.34(1)
C(6)—F(3)	1.22(1)	C(7)—C(8)	1.40(1)
C(8)—C(9)	1.40(1)	C(9)—C(10)	1.52(1)
C(10)—F(4)	1.26(1)	C(10)—F(5)	1.26(1)
C(10)—F(6)	1.29(1)		

Bonds	Angle	Bonds	Angle
Ag[a]—Ag—P(1)	85.42(5)	Ag[a]—Ag—P(2)	90.50(5)
Ag[a]—Ag—O(1)	76.2(1)	Ag[a]—Ag—O(2)	145.5(1)
P(1)—Ag—P(2)	160.02(7)	P(1)—Ag—O(1)	101.8(1)
P(1)—Ag—O(2)	97.7(1)	P(2)—Ag—O(1)	96.2(1)
P(2)—Ag—O(2)	96.7(1)	O(1)—Ag—O(2)	69.5(2)
Ag—P(1)—C(1)	115.7(3)	Ag—P(1)—C(2)	116.4(3)
Ag—P(1)—C(5)	111.7(3)	C(1)—P(1)—C(2)	103.9(4)
C(1)—P(1)—C(5)	102.3(4)	C(2)—P(1)—C(5)	105.3(4)
Ag—P(2)—C(3)	110.1(3)	Ag—P(2)—C(4)	119.6(3)
Ag—P(2)—C(5)[a]	114.5(3)	C(3)—P(2)—C(4)	103.5(4)
C(3)—P(2)—C(5)[a]	105.5(4)	C(4)—P(2)—C(5)[a]	102.3(4)
P(1)—C(5)—P(2)[a]	116.5(4)	Ag—O(1)—C(7)	124.0(5)
Ag—O(2)—C(9)	121.7(5)	C(7)—C(6)—F(1)	113.1(8)
C(7)—C(6)—F(2)	113.3(9)	C(7)—C(6)—F(3)	115.7(9)
F(1)—C(6)—F(2)	96.0(8)	F(1)—C(6)—F(3)	110.5(10)
F(2)—C(6)—F(3)	106.3(9)	O(1)—C(7)—C(6)	114.2(7)
O(1)—C(7)—C(8)	129.3(7)	C(6)—C(7)—C(8)	116.5(7)
C(7)—C(8)—C(9)	123.4(7)	O(2)—C(9)—C(8)	129.7(7)
O(2)—C(9)—C(10)	114.2(7)	C(8)—C(9)—C(10)	116.1(7)
C(9)—C(10)—F(4)	113.5(8)	C(9)—C(10)—F(5)	117.6(9)
C(9)—C(10)—F(6)	112.2(8)	F(4)—C(10)—F(5)	106.0(8)
F(4)—C(10)—F(6)	102(1)	F(5)—C(10)—F(6)	104.2(9)

[a]Symmetry operator (1 − *x*, −*y*, 1 − *z*).

Can. J. Chem. Downloaded from www.nrcresearchpress.com by EESC ESCOLA DE ENGENHARIA on 09/08/12
For personal use only.

Can. J. Chem. Downloaded from www.nrcresearchpress.com by EESC ESCOLA DE ENGENHARIA on 09/08/12
For personal use only.

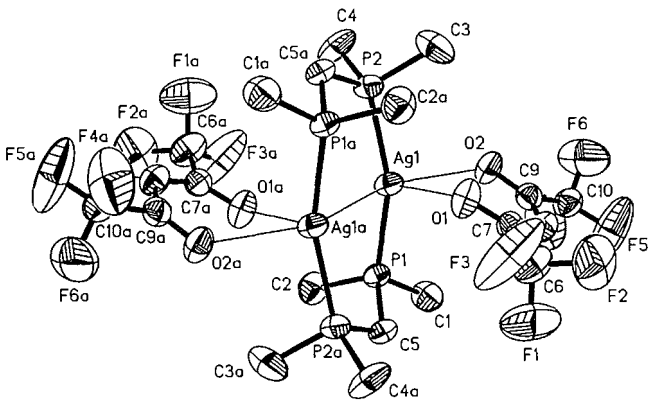

FIG. 2. The ORTEP representation of the molecular structure of $[Ag_2(hfac)_2(\mu\text{-dmpm})_2]$. 50% probability ellipsoids are shown and the hydrogen atoms are omitted for clarity.

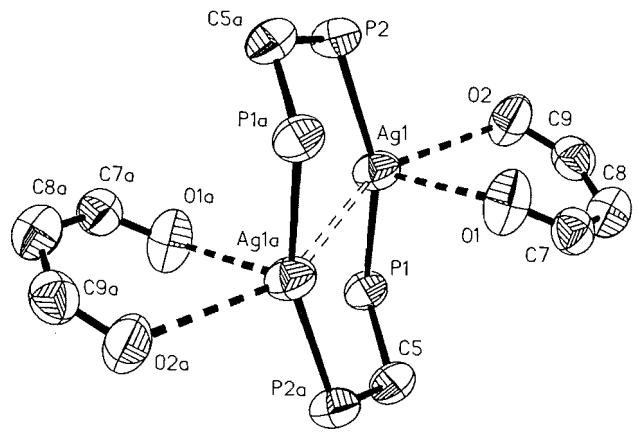

FIG. 3. The inner coordination sphere, emphasizing the distorted tetrahedral stereochemistry at silver(I) and the anti conformation.

bridization), respectively, and the P(1)—Ag—P(2) angle of 160.02(7)° is best considered as distorted linear. The O(1)—Ag(1)—O(2) angle is only 69.5(2)° as a result of the long AgO distances. In [Ag(hfac)(PMe_3)], the angle O—Ag—O is 80.0–80.7(3)° (there are several independent molecules in the unit cell) due to the much shorter Ag—O distances of 2.268(8)–2.309(8) Å (4). Although structure determinations have been reported for many binuclear complexes containing $M_2(\mu\text{-}R_2PCH_2PR_2)_2$ units, only one has M = Ag. This is for the binuclear $[Ag_2(\mu\text{-}dppm)_2(NO_3)_2]$, **3**, which has the conformation **II** (15). The Ag—P distances of 2.436(2) and 2.417(2) Å are similar to those in **2** but the P—Ag—P angle in **3** is 138.3(1)° and the Ag—O bond distance is 2.416(5) (there is also a longer Ag...O contact at 2.689(6) Å). The smaller angle P—Ag—P and shorter Ag—O distance in **3** indicates that nitrate in **3** is coordinated more strongly than the $hfac^-$ ion in **2**. Since nitrate is usually considered a weakly coordinating anion to silver(I) (16), it seems clear that the $hfac^-$ ligand is very weakly coordinated in **2**. The complex $[Ag_2(cod)_2(\mu\text{-}hfac)_2]$, **4**, also has long Ag—O distances of 2.47(1)–2.56(1) Å, with two Ag...O distances of 2.72 Å assigned as non-bonding (7). The molar conductivity for a 10^{-3} M solution of **2** in CH_2Cl_2 at 25°C was Λ_M = 2.0 Ω^{-1} cm^2 mol^{-1}, under which conditions the 1:1 conductor $[Pr_4N]Cl$ and covalent *t*-Bu_3PAgCl have Λ_M = 19.0 and 0.75 Ω^{-1} cm^2 mol^{-1}, respectively (14). Hence, at least in dichloromethane, the equilibrium appears to favor the non-ionic structure for **2** but some ionization is indicated. The Ag...Ag distances in **2**, **3**, and **4** are similar at 3.153(1), 3.085(1), and 2.955(2) Å (7, 15); all are probably best considered as non-bonding distances, although very weak bonding of the kind very commonly observed in gold(I) complexes cannot be dismissed.

Interestingly, the complexes **2** and **3** adopt different conformations. Complex **2** adopts the anti (staggered) conformation, **I** (Fig. 3), while **3** adopts the *syn* (eclipsed) conformation, **II** (15). There is no obvious reason for the difference and both probably undergo easy, reversible anionic ligand dissociation in solution to give $[Ag_2(\mu\text{-}R_2PCH_2PR_2)_2]^{2+}$, with linear AgP_2 coordination (13). The solid state structure of **2** contains no plane of

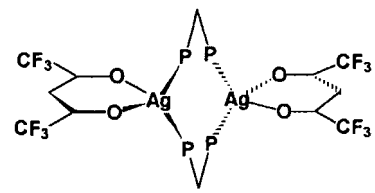

I II

symmetry and therefore should give two MeP resonances in the ^1H or ^{13}C NMR spectra and two CF_3 resonances in the ^{13}C or ^{19}F NMR spectra, whereas only one resonance was observed in each case. The most probable mechanism for the apparent equivalence is reversible dissociation of $hfac^-$ in solution, even at low temperature. The loss of fine structure in the ^{31}P NMR spectrum at room temperature, with retention of a broad doublet splitting (Fig. 1), due to *J*(AgP) coupling indicates that the dmpm ligands undergo exchange within the $Ag_2(dmpm)_2$ unit perhaps by undergoing end-over-end exchange (13).

Conclusions

The complexes [Ag(hfac)(PMe_3)] and $[Ag_2(hfac)_2(\mu\text{-}dmpm)_2]$, **2**, have coordination numbers at silver(I) of 3 and 4, respectively. There is a major difference in the strength of binding of the $hfac^-$ ligand in the two cases, this being much weaker for complex **2**. As well as the structural evidence discussed above, the NMR evidence also supports the conclusion of weak $hfac^-$ binding in **2**. Thus, for complexes $[Ag(PR_3)_2X]$ the magnitude of the coupling constant $^1J(^{107}AgP)$ depends markedly on the strength of covalent bonding of the ligand X^- (14). This coupling constant for complex **2** falls in the range usually found for ionic ligands X^-. For example, the magnitude of $^1J(^{107}AgP)$ for **2** (500 Hz) is similar to those for the ionic compounds $[Ag_2(\mu\text{-dmpm}))]_2(BF_4)_2$ (515 Hz) and $[Ag_2(\mu\text{-dppm})]_2(BF_4)_2$ (505 Hz) (13, 14). Covalent bonding of X^- causes a marked decrease in ^1J(AgP) as the hybridization at silver(I) changes from *sp* towards sp^2.

The partial ionic nature of the $hfac^-$ ligands in **2** was unexpected since the effect is not observed in related copper complexes $[Cu(hfac)(PR_3)_2]$ (6). Of course, the apparent greater ionic character in the Ag(hfac) compared to the Cu(hfac) unit in related complexes may account in a simple way for the much lower volatility of silver(I) compared to copper(I) complexes with $hfac^-$ ligands, since the more polar nature will lead to stronger intermolecular forces. It has been noted earlier that [Cu(hfac)(cod)] is a monomer whereas the silver(I) analogue has the binuclear structure $[Ag_2(\mu\text{-hfac})_2(cod)_2]$, **4**, and that the different degrees of aggregation may account for the lower volatility of the silver(I) complex (7). Complex **4** also has long

Ag—O bonds and the binuclear structure may result not only from the larger size of Ag(I) compared to Cu(I) but also from the more ionic nature of the $hfac^-$ ligands in combination with Ag(I). If this interpretation is correct, it suggests that the search for more volatile silver(I) complexes for use as precursors for CVD of silver should focus on ligands which bind in a more covalent fashion to silver(I) than the $hfac^-$ ligand.

Acknowledgments

We thank the Ontario Center for Materials Research (OCMR) and the NSERC (Canada) for financial support and Dr. N.C. Payne for the X-ray facilities.

1. (*a*) D. Lee, X. Chaud, and K. Salama. Jpn. J. Appl. Phys. **31**, 2411 (1992); (*b*) T.E. Jones, W.C. McGinnis, E.W. Jacobs, R.D. Boss, P.M. Thibado, J.S. Briggs, and W.E. Glad. Physica C, **201**, 279 (1992).
2. R. Gliem and G. Schlamp. Met. Tech. **41**, 34 (1987).
3. H. Liedberg and T. Lundeberg. Urol Res. **17**, 359 (1989).
4. N.H. Dryden, J.J. Vittal, and R.J. Puddephatt. Chem. Mater. **5**, 765 (1993).
5. (*a*) P.M. Jeffries, S.R. Wilson, and G.S. Girolami. J. Organomet. Chem. **449**, 203 (1993); (*b*) M.J. Shapiro, W.J. Lackey, J.A. Hanigofsky, D.N. Hill, W.B. Carter and E.K. Barefield. J. Alloys Compd. **187**, 331 (1992); (*c*) T.H. Baum and C.E. Larson. US Patent, 5,096,737, Mar. 17, 1992.
6. H.K. Shin, K.M. Chi, M.J. Hampden-Smith, T.T. Kodas, J.D. Farr, and M. Paffett. Chem. Mater. **4**, 788 (1992).
7. A. Bauley, T.S. Corbitt, M.J. Hampden-Smith, E.N. Duesler, and T.T. Kodas. Polyhedron, **12**, 1785 (1993).
8. CAD4 diffractometer manual. Enraf-Nonius: Delft, The Netherlands. 1988.
9. E.J. Gabe, Y. Le Page, J.-P. Charland, and F.C. Lee. J. Appl. Crystallogr. **22**, 384 (1989).
10. International tables for X-ray crystallography. (*a*) Vol. A.D. Reidel Publishing Co., Boston. 1983; (*b*) Vol. IV. Kynoch Press, Birmingham, England. 1974.
11. G.M. Sheldrick. SHELXS-86. University of Gottingen, Gottingen, F.D.R. 1986.
12. G.M. Sheldrick. SHELX-76. University of Cambridge, England. 1976.
13. (*a*) A.F.M.J. van der Ploeg and G. van Koten. Inorg. Chim. Acta, **51**, 225 (1981); (*b*) P.A.W. Dean, J.J. Vittal, and R.S. Srivastava. Can. J. Chem. **65**, 2628 (1987); (*c*) D. Obendorf, M. Probst, P. Peringer, H. Falk, and N. Muller. J. Chem. Soc. Dalton Trans. 1709 (1988).
14. (*a*) E.L. Muetterties and C.W. Alegranti. J. Am. Chem. Soc. **94**, 6386 (1972); (*b*) R.G. Goel adn R. Pilon. Inorg. Chem. **17**, 2876 (1978).
15. D.M. Ho and R. Bau. Inorg. Chem. **22**, 4073 (1983).
16. R.J. Lancashire. *In* Comprehensive coordination chemistry. Vol. 5. Pergamon Press, Oxford, U.K. 1987. Chap. 54.

Can. J. Chem. Downloaded from www.nrcresearchpress.com by EESC ESCOLA DE ENGENHARIA on 09/08/12
For personal use only.

Nitration of 3-aryl-4-acetylsydnones: preparation of 3-(3-nitroaryl)sydnones by using acetyl group as a blocking group

HSIEN-JU TIEN
Department of Chemistry, National Chung-Kung University, Tainan, Taiwan, 701, Republic of China
SHAW-TAO LIN
Department of Applied Chemistry, Providence University, Sha-Lu, Taichung Hsien, Taiwan, 433, Republic of China
AND
JINN-TSAIR SHEU
Department of Chemistry, National Chung-Kung University, Tainan, Taiwan, 701, Republic of China

Received October 14, 1993

HSIEN-JU TIEN, SHAW-TAO LIN, and JINN-TSAIR SHEU. Can. J. Chem. **72**, 1610 (1994).

The 3-(3-nitroaryl)sydnones were prepared in good yields by the nitration of 3-aryl-4-acetylsydnones followed by deacetylation with aqueous barium hydroxide.

HSIEN-JU TIEN, SHAW-TAO LIN et JINN-TSAIR SHEU. Can. J. Chem. **72**, 1610 (1994).

On a préparé les 3-(3-nitroaryl)sydnones avec de bons rendements en effectuant la nitration des 3-aryl-4-acétylsydnones et en procédant ensuite à une désacétylation à l'aide d'hydroxyde de baryum aqueux.

[Traduit par la rédaction]

Introduction

Much attention has been given to the preparation of sydnones because of their mesoionic character and biological activities (1). Ordinarily, 3-(nitrophenyl)sydnones are prepared from corresponding anilines via a series of reactions as in eq. [1] (2).

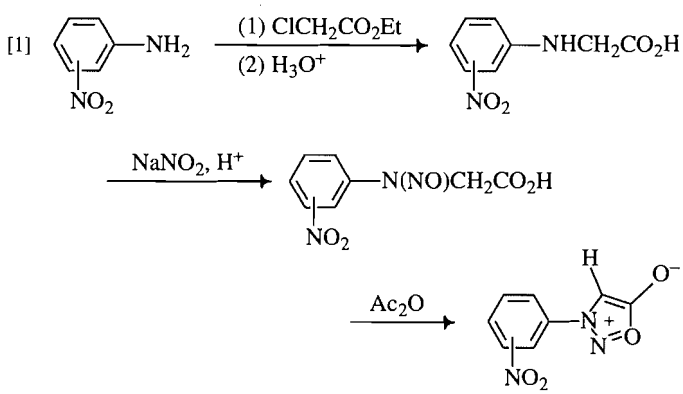

1

Some of the substituted anilines, unlike aniline, are not often commercially available. The mesoionic character exhibits an electron-withdrawing tendency at the N3 position and an electron-donating at the C4 position. These facts are reflected in the functionalization of sydnone derivatives, such as the nitration of 3-arylsydnones in eqs. [2] and [3]. With **2**, the nitronium

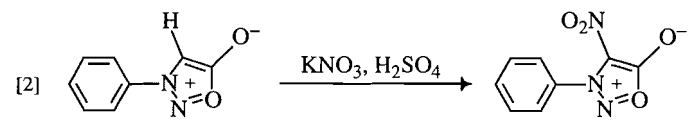

2 3

ion preferential reacts at C4 rather than at the phenyl ring (3). With **4**, electrophilic substitution occurs at position 4 of the C4-phenyl ring, followed by position 2 (4). Therefore, direct nitration of 3-arylsydnone is not a route to prepare 3-(nitroaryl)-

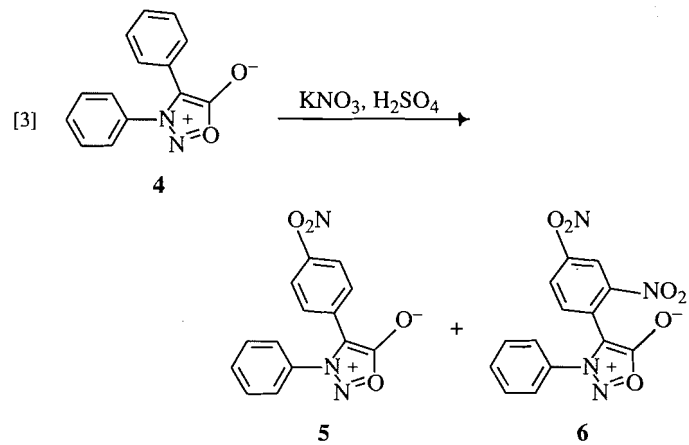

sydnones. Herein, we report a method to prepare 3-(nitroaryl)-sydnones by the nitration of 3-aryl-4-acetylsydnones, followed by the deacetylation using barium hydroxide as a catalyst (eq. [4]). Some of the PM3 calculation data will be used to explain the nitration results.

Results and discussion

The charge density distribution of the atoms of the sydnone ring has been discussed since this series of compounds has been known. However, the unequal distribution of electron density around the ring resulting in the mesoionic character is well accepted (5). The unequal electron densities of the atoms lead to the different nature between N3 and C4. We used a PM3 calculation package to obtain quantitative data for this feature of a series of compounds. The charge distributions at the carbons, nitrogens, and oxygens of compounds **2**, **4**, and **7–12** were calculated at the geometry with minimum potential energies and are listed in the Table 1. The charge at the atoms of sydnonyl rings reflect the nature of substituents of N3 and (or) C4. The electron-donating nature of methyl group decreases the positive charge of the N3 atom (**8**), while the phenyl ring decreases the negative charge of the C4 atom (**4**, **8**). The acetyl group

Can. J. Chem. Downloaded from www.nrcresearchpress.com by EESC ESCOLA DE ENGENHARIA on 09/08/12
For personal use only.

[4] 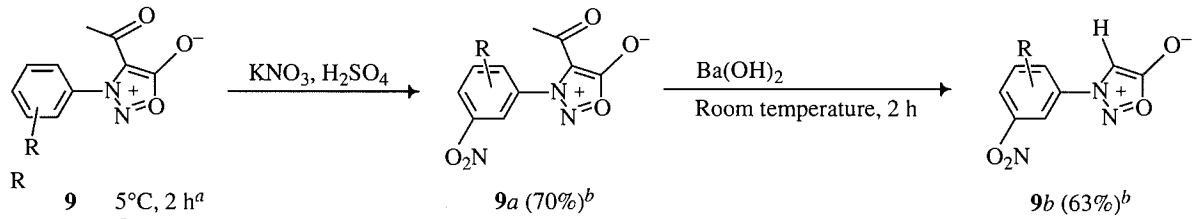

R				
H	**9**	5°C, 2 h[a]	**9***a* (70%)[b]	**9***b* (63%)[b]
4-OMe	**10**	−5°C, 1 h	**10***a* (92%)	**10***b* (67%)
4-OMe	**10**	−5°C, 1 h[c]	**10***a*' (74%)[d]	
4-OEt	**11**	−5°C, 1 h	**11***a* (89%)	**11***b* (62%)
4-Me	**12**	−5°C, 1 h	**12***a* (87%)	**12***b* (55%)
2-OEt	**13**	0°C, 1 h	**13***a* (47%)	**13***b* (60%)
2-Me	**14**	−10°C, 1 h	**14***a* (85%)	**14***b* (50%)
3-OMe	**15**	−10°C, 1 h	**15***a* (80%)[e]	**15***b* (65%)[f]

[a]Nitration condition.
[b]The number in parentheses is the isolated yield.
[c]Double amount of KNO_3 was used.
[d]3-(3,5-Dinitro-4-methoxyphenyl)-4-acetylsydnone.
[e]3-(2-Nitro-5-methoxyphenyl)-4-acetylsydnone.
[f]3-(2-Nitro-6-methoxyphenyl)sydnone.

TABLE 1. Charge distribution of sydnones obtained from the PM3 calculation

	Atom							
Compound	8	4	2	9	7	10	11	12
O1	−0.120	−0.123	−0.124	−0.129	−0.125	−0.131	−0.130	−0.129
N2	−0.286	−0.304	−0.306	−0.234	−0.322	−0.237	−0.236	−0.233
N3	+0.639	+0.738	+0.736	+0.758	+0.764	+0.773	+0.774	+0.786
C4	−0.480	−0.511	−0.595	−0.645	−0.610	−0.649	−0.653	−0.648
C5	+0.385	+0.388	+0.381	+0.401	+0.386	+0.399	+0.399	+0.399
O6	−0.326	−0.325	−0.332	−0.323	−0.334	−0.323	−0.325	−0.327
C31		−0.212	−0.213	−0.208	−0.274	−0.289	−0.266	−0.251
C32		−0.033	−0.030	−0.031	+0.020	+0.015	+0.023	+0.164
C33		−0.101	−0.099	−0.096	−0.149	−0.141	−0.146	−0.016
C34		−0.055	−0.055	−0.051	+0.152	+0.140	+0.153	−0.016
C35		−0.106	−0.103	−0.100	−0.201	−0.194	−0.193	−0.190
C36		−0.058	−0.058	−0.034	−0.024	−0.010	−0.004	−0.000
C41	+0.031	+0.021						
C42	−0.082	−0.086						
C43	−0.089	−0.095						
C44	−0.101	−0.099						
C45	−0.091	−0.098						
C46	−0.131	−0.111						
	−0.178[a]				−0.182[b]	−0.179[b]	−0.183[b]	−0.197[b]
					+0.058[c]	+0.045[d]	+0.058[c]	+0.067[c]
					−0.124[e]		−0.123[e]	−0.156[e]
				+0.405[f]		+0.404[f]	+0.406[f]	+0.404[f]
				−0.365[g]		−0.360[g]	−0.360[g]	−0.358[g]
				−0.164[h]		−0.160[h]	−0.159[h]	−0.158[h]

[a]N3—CH_3.
[b]Oxygen atom of alkoxyl group.
[c]Carbon atom of methylene of ethoxyl group.
[d]Carbon atom of methyl of methoxyl group.
[e]Carbon atom of methyl of ethoxyl group.
[f]sp^2 carbon atom of acetyl group.
[g]Oxygen atom of acetyl group.
[h]Carbon atom of methyl of acetyl group.

decreases the charge densities of O6 and C5 and the increase in the charge density of C4 might result from its strong electron-withdrawing nature (**9–12**). The higher charge density at C4 atom is well corroborated with the orientation of nitration of **2** where the C4-NO_2 is the only product (3, 6). Also, the positive charge at N3 causes the sydnone ring to behave as an electron-withdrawing group and directs the nitration of phenyl group at C33. The nitration of **4** occurs at C44 and C42 rather than at the N3-phenyl ring, reflecting the higher negative charge density of C4 atom as calculated.

Neither direct nitration of 3-arylsydnones nor preparation from multiple substituted anilines is a useful procedure to pre-

Can. J. Chem. Downloaded from www.nrcresearchpress.com by EESC ESCOLA DE ENGENHARIA on 09/08/12
For personal use only.

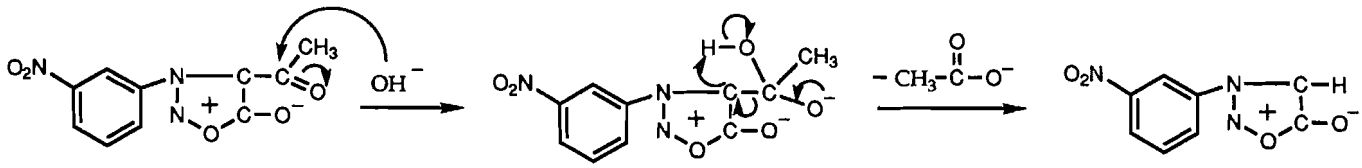

SCHEME 1

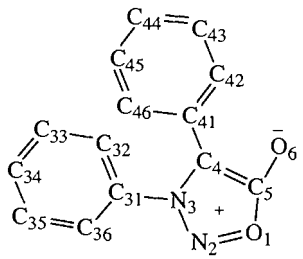

3-(4-Ethoxyphenyl)sydnone **7**
3-Methyl-4-phenylsydnone **8**

pare 3-(nitroaryl)sydnones. The title compounds are synthesized by nitrating 3-aryl-4-acetylsydnones, followed by removal of the blocking group. The methods of acetylation of sydnone at C4 are well established (7). The yields for nitration of C4-acetylsydnones to form 3-(3-nitroaryl)-4-acetylsydnones range from fair to good, depending upon the nature and position of the director group on the phenyl ring. Increasing the electron densities of the aryl ring by the C34-alkoxyl or -alkyl group enhances the yield of the nitration process and even produces the dinitro derivative **10***a*′ under a large excess of nitronium ion (Table 1). By contrast, under the same large excess of KNO_3, the nitration of methyl analogues yield only the mononitration product **12***a*. However, nitration of **13** is less facile than its methyl counterpart **14**. This result can be explained by

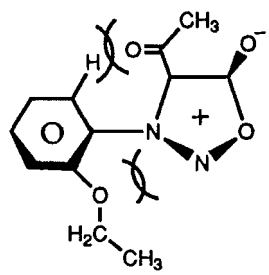

the steric hindrance of the *ortho* substituent causing more of an energy barrier for the coplanar between the phenyl and sydnone rings.

The sydnone ring is very labile in strong base. Therefore, the acetyl group cannot be removed while retaining the sydnone ring in the presence of either alkali hydroxide or alkoxide. Fortunately, the deacetylation can be carried out in a suspension of sydnone and barium hydroxide in water at room temperature. This involves the reaction of the hydroxyl ion with the carbon of the carbonyl group and transfer of a proton to C4, followed by the loss of an acetate ion (Scheme 1) (8). The carbonyl group of the sydnone ring must possess a normal carbonyl similar to that of β-di ketones or β-keto acids (8). However, the deacetylation reaction of **15***a* to yield 3-(2-nitro-6-methoxyl)sydnone (**15***b*) is mechanistically still unclear.

Experimental

All melting points were measured with a Yanaco MP-J3 apparatus and are uncorrected. ^1H NMR spectra were recorded on a Bruker AC-200 spectrometer, using tetramethylsilane as internal standard. Infrared spectra were recorded on a Hitachi 270-30 grating infrared spectrophotometer. Mass spectra were measured on a JMS-D100 spectrometer, using 70 eV ionization potential. Microanalysis were performed on a Heraeus CHN-O-Rapid analyzer. 3-Arylsydnones (2) and 3-aryl-4-acetylsydnones (7) were prepared according to the literature. The theoretical calculations were determined using a SGI workstation (model 4D20) and the PM3 software package from Biosym Technologies. The charge densities of atoms were recorded at their optimum geometry.

Nitration of 3-aryl-4-acetylsydnone: typical procedure

To an ice-cooled and stirred solution of 4-acetyl-3-phenylsydnone (1.50 g, 7.5 mmol) in H_2SO_4 (10 mL), KNO_3 (4.50 g, 30.0 mmol) was slowly added. After being stirred for 2 h at 5°C, the color of the solution changed from light brown to deep green. This solution was poured into ice water which yielded yellow precipitate. Following filtration, the crude product was recrystallized from 95% ethanol yielding **9***a* as white needles: 1.31 g (70% yield); mp 150–152°C; IR (KBr) $\nu_{C=O}$: 1776, 1656 cm^{-1}; IR (KBr) ν_{NO_2}: 1540, 1346 cm^{-1}; NMR (acetone-d_6) δ: 2.40 (s, 3H, Me), 8.02 (t, 1H, J = 8.0 Hz, aromatic), 8.21 (d, 1H, J = 8.0 Hz, aromatic), 8.68–8.59 (m, 2H, aromatic); MS *m/z* (relative intensity): 249 (M^+, 13), 149 (100). Anal. calcd. for $C_{10}H_7N_3O_5$: C 48.20, H 2.83, N 16.90; found: C48.10, H 2.83, N 16.90.

The following compounds were obtained according to this procedure.

3-(3-Nitro-4-methoxyphenyl)-4-acetylsydnone (***10***a)*:* mp 170–172°C; IR (KBr) $\nu_{C=O}$: 1798, 1668 cm^{-1}; IR (KBr) ν_{NO_2}: 1532, 1350 cm^{-1}; NMR (acetone-d_6) δ: 2.40 (s, 3H, C(O)Me), 4.15 (s, 3H, OMe), 7.64 (d, 1H, J = 9.1 Hz, aromatic), 8.04 (dd, 1H, J = 2.6, 9.1 Hz, aromatic), 8.33 (d, 1H, J = 2.6 Hz, aromatic); MS *m/z* (relative intensity): 279 (M^+, 1), 43(100). Anal. calcd. for $C_{11}H_9N_3O_6$: C 47.32, H 3.25, N 15.05; found: C 47.25, H 3.22, N 15.08.

3-(3,5-Dinitro-4-methoxyphenyl)-4-acetylsydnone (***10***a′) (same procedure, except 8 equiv. of KNO_3 was used): mp 161–162°C; IR (KBr) $\nu_{C=O}$: 1776, 1680 cm^{-1}; IR (KBr) ν_{NO_2}: 1548, 1348 cm^{-1}; NMR (acetone-d_6) δ: 2.42 (s, 3H, C(O)Me), 4.22 (s, 3H, OMe), 8.78 (s, 2H, aromatic); MS *m/z* (relative intensity): 324 (M^+, 5), 43(100). Anal. calcd. for $C_{11}H_8N_4O_8$: C 40.75, H 2.49, N 17.28; found: C 40.55, H 2.52, N 17.19.

3-(3-Nitro-4-ethoxyphenyl)-4-acetylsydnone (***11***a)*:* mp 150–152°C; IR (KBr) $\nu_{C=O}$: 1806, 1656 cm^{-1}; IR (KBr) ν_{NO_2}: 1538, 1286 cm^{-1}; NMR (acetone-d_6) δ: 1.48 (t, 3H, J = 6.9 Hz, CH_2CH_3), 2.40 (s, 3H, C(O)Me), 4.43 (q, 2H, J = 6.9 Hz, CH_2CH_3), 7.61 (d, 1H, J = 9.1 Hz, aromatic), 8.01 (dd, 1H, J = 2.6, 9.1 Hz, aromatic), 8.31 (d, 1H, J = 2.6 Hz, aromatic); MS *m/z* (relative intensity): 293 (M^+, 2), 43(100). Anal. calcd. for $C_{10}H_7N_3O_5$: C 48.20, H 2.83, N 16.86; found: C 48.10, H 2.83, N 16.90.

3-(3-Nitro-4-methyphenyl)-4-acetylsydnone (***12***a)*:* mp 126–128°C; IR (KBr) $\nu_{C=O}$: 1778, 1671 cm^{-1}; IR (KBr) ν_{NO_2}: 1532, 1357 cm^{-1}; NMR (acetone-d_6) δ: 2.41 (s, 3H, C(O)Me), 2.74 (s, 3H, Me), 7.82 (d, 1H, J = 8.3 Hz, aromatic), 8.00 (dd, 1H, J = 8.3, 2.1 Hz), 8.44 (d, 1H, J = 2.1 Hz, aromatic); MS *m/z* (relative intensity): 263 (M^+, 2), 43(100). Anal. calcd. for $C_{11}H_9N_3O_5$: C 50.20, H 3.45, N 15.96; found: C 50.17, H 3.41, N 15.97.

3-(5-Nitro-2-ethoxyphenyl)-4-acetylsydnone (***13***a)*:* mp 129–131°C; IR (KBr) $\nu_{C=O}$: 1806, 1793, 1758, 1665 cm^{-1}; IR (KBr) ν_{NO_2}: 1524, 1344 cm^{-1}; NMR (acetone-d_6) δ: 1.33 (t, 3H, J = 7.0 Hz, OCH_2CH_3), 2.40 (s, 3H, C(O)Me), 4.38 (m, 2H, OCH_2CH_3), 7.59 (d, 1H, J = 8.7

Can. J. Chem. Downloaded from www.nrcresearchpress.com by EESC ESCOLA DE ENGENHARIA on 09/08/12
For personal use only.

Hz, aromatic), 8.61 (dd, 1H, J = 8.7 Hz, aromatic), 8.63 (s, 1H, aromatic); MS *m/z* (relative intensity): 293 (M^+, 1), 43(100). Anal. calcd. for $C_{12}H_{11}N_3O_6$: C 49.15, H 3.78, N 14.33; found: C 49.04, H 3.73, N 14.34.

*3-(5-Nitro-2-tolyl)-4-acetylsydnone (**14**a):* mp 126–128°C; IR (KBr) $\nu_{C=O}$: 1776, 1666 cm^{-1}; IR (KBr) ν_{NO_2}: 1526, 1348 cm^{-1}; NMR (acetone-d_6) δ: 2.39 (s, 3H, Me), 2.41 (s, 3H, C(O)Me), 7.87 (d, 1H, J = 8.0 Hz, aromatic), 8.51 (dd, 1H, J = 8.0, 2.3 Hz, aromatic), 8.59 (d, 1H, J = 2.3 Hz, aromatic); MS *m/z* (relative intensity): 263 (M^+, 3), 43(100). Anal. calcd. for $C_{11}H_9N_3O_5$: C 50.20, H 3.45, N 15.96; found: C 50.10, H 3.43, N 15.94.

*3-(2-Nitro-5-methoxyphenyl)-4-acetylsydnone (**15**a):* mp 174–176°C; IR (KBr) $\nu_{C=O}$: 1792, 1658 cm^{-1}; IR (KBr) ν_{NO_2}: 1522, 1352 cm^{-1}; NMR (acetone-d_6) δ: 2.41 (s, 3H, C(O)Me), 4.04 (s, 3H, OMe), 7.52 (dd, 1H, J = 8.5, 2.0 Hz, aromatic), 7.81 (d, 1H, J = 2.0 Hz, aromatic), 8.13 (d, 1H, J = 8.5 Hz, aromatic); MS *m/z* (relative intensity): 279 (M^+, 3), 43(100). Anal. calcd. for $C_{11}H_9N_3O_6$: C 47.32, H 3.25, N 15.05; found: C47.07, H 3.27, N 14.98.

Deacetylation of 3-(Nitroaryl)-4-acetylsydnones: typical procedure

To a stirred solution of 3-(3-nitrophenyl)-4-acetylsydnone (**9***a*, 0.43 g, 1.7 mmol) in 95% EtOH, $Ba(OH)_2$ (0.49 g suspension in 15 mL of water) was added. After being stirred for 2 h at room temperature, the resultant solution was poured into ice water. Following filteration, the crude product was recrystallized from ethanol yielding **9**b as colorless crystals: 0.22 g (63% yield); mp 139–140°C. The IR spectrum was identical with the authentic sample (8). Compounds **10***b* (9), **12***b* (10), and **14***b* (9) were obtained from hydrolysis of the corresponding 4-acetylsydnones and identified by comparing the mp and IR spectra with authentic samples.

The following new compounds were obtained according to this hydrolysis procedure.

*3-(3-Nitro-4-ethoxyphenyl)sydnone (**11**d):* mp 126–128°C; IR (KBr) $\nu_{C=O}$: 1758 cm^{-1}; IR (KBr) ν_{NO_2}: 1532, 1362 cm^{-1}; NMR (acetone-d_6) δ: 1.46 (t, 3H, J = 6.8 Hz, OCH_2CH_3), 4.43 (q, 2H, J = 6.8 Hz, OCH_2CH_3), 7.42 (s, 1H, N—C4—H), 7.68 (d, 1H, J = 9.2 Hz, aromatic), 8.22 (dd, 1H, J = 9.2, 2.7 Hz, aromatic), 8.47 (d, 1H, J = 2.7 Hz, aromatic); MS *m/z* (relative intensity): 251 (M^+, trace), 193(100). Anal. calcd. for $C_{10}H_9N_3O_5$: C 47.82, H 3.61, N 16.73; found: C 47.77, H 3.57, N 16.73.

*3-(5-Nitro-2-ethoxyphenyl)sydnone (**13***b*): mp 144–146°C; IR (KBr) $\nu_{C=O}$: 1760 cm^{-1}; IR (KBr) ν_{NO_2}: 1528, 1346 cm^{-1}; NMR (acetone-d_6) δ: 1.46 (t, 3H, J = 7.1 Hz, OCH_2CH_3), 4.48 (q, 2H, J = 7.1 Hz, OCH_2CH_3), 7.22 (s, 1H, N—C4—H), 7.65 (d, 1H, J = 9.2 Hz, aromatic), 8.57 (dd, 1H, J = 9.2, 2.7 Hz, aromatic), 8.68 (d, 1H, J = 2.7 Hz, aromatic); MS *m/z* (relative intensity); 251 (M^+, 3), 165(100). Anal. calcd. for $C_{10}H_9N_3O_5$: C 47.82, H 3.61, N 16.73; found: C 47.74, H 3.53, N 16.78.

*3-(2-Methoxyl-6-nitrophenyl)sydnone (**15**b):* mp 156–158°C; IR (KBr) $\nu_{C=O}$: 1758 cm^{-1}; IR (KBr) ν_{NO_2}: 1532–1362 cm^{-1}; NMR (acetone-d_6) δ: 4.11 (s, 3H, OCH_3), 7.30 (s, 1H, aromatic), 7.64 (d, 1H, J = 8.0 Hz, aromatic), 7.79 (d, 1H, J = 8.0 Hz, aromatic), 7.95 (t, 1H, J = 8.0 Hz, aromatic); MS *m/z* (relative intensity): 237 (M^+, trace), 93(100%). Anal. calcd. for $C_9H_7N_3O_5$: C 45.37, H 3.00, N 17.61; found: C 45.58, H 2.97, N 17.72.

Acknowledgment

Financial support by the National Science Council of the Republic of China is gratefully acknowledged.

1. C.G. Newton and C.A. Ramsden. Tetrahedron, **38**, 2965 (1982).
2. R.A. Eade and J.C. Earl. J. Chem. Soc. 591 (1946).
3. W. Baker, W. Ollis, and V.D. Poole. J. Chem. Soc. 1542 (1950); M. Hashimoto and M. Ohta. Nippon Kagaku Kaishi, **78**, 181 (1957).
4. W. Schubert and W.J. Ellenrieder. J. Chem. Res. Synop. 256 (1984); J. Chem. Res. Miniprint, 2343 (1984).
5. H.J. Tien, T. Nonaka, T. Fuchigami, T. Sekine, and M. Ohta. Nippon Kagaku Kaishi, 1310 (1978).
6. F.H. Stewart. Chem. Ind. (London), 1718 (1962).
7. M.Y. Yeh, H.J. Tien, L.Y. Huang, and M.H. Chen. J. Chin. Chem. Soc. (Taipei), **30**, 29 (1983); M.Y. Yeh, H.J. Tien, and T. Nonaka. J. Org. Chem. **48**, 1382 (1983); H.J. Tien, G.M. Fang, S.T. Lin, and L.L. Tien. J. Chin. Chem. Soc. (Taipei), **39**, 107 (1992).
8. S. Boatman, T.M. Harris, and C.R. Hauser. Org. Synth. Coll. Vol. V, 187 (1973); S. Boatman and C.R. Hauser. Org. Synth. Coll. Vol. V, 767 (1973).
9. B.G. Ugarkar, B.V. Badami, G.S. Puranik, and K.G.S. Bhat. Arch. Pharm. (Weinheim, Ger.), **311**, 109 (1978).
10. P.M. Weintraub and R.E. Bambury. Tetrahedron Lett. 579 (1969).

Can. J. Chem. Downloaded from www.nrcresearchpress.com by EESC ESCOLA DE ENGENHARIA on 09/08/12
For personal use only.

Preparation and application of 4′-carboxybenzo-15-crown-5, a drift-type crown ether phase transfer catalyst

MING-SENG CHOU AND JENG-SHONG SHIH[1]

Department of Chemistry, National Taiwan Normal University, Taipei, Taiwan 11718, Republic of China

Received September 15, 1993

MING-SENG CHOU and JENG-SHONG SHIH. Can. J. Chem. **72**, 1614 (1994).

A new "drift-type" crown ether phase transfer catalyst, 4′-carboxybenzo-15-crown-5 adsorbed on poly(styrene/divinylbenzene)-NR_2 resin, was synthesized and applied to catalyze the oxidation of benzhydrol with $NaMNO_4$ as an oxidant. Before the reaction, the drift-type crown ether catalyst was adsorbed on the resin with ion-pair (resin-NR_2H^+ ^-O_2C-monobenzo-15-crown-5) formation. During the reaction period the crown ether catalyst was released from the resin into the reaction solution as a homogeneous catalyst by adjusting the acidity of the solution to 10^{-1} M HCl to destroy the ion pair between the catalyst and the resin. After the reaction, the crown ether catalyst could be readsorbed on the resin by adjusting the concentration of HCl to 10^{-5} M and could be readily recovered by filtration. The catalyst, 4′-carboxybenzo-15-crown-5, was found to be a more effective catalyst than other crown ethers, such as 15-crown-5, 18-crown-6, monobenzo-15-crown-5, and dibenzo-18-crown-5.

MING-SENG CHOU et JENG-SHONG SHIH. Can. J. Chem. **72**, 1614 (1994).

On a effectué la synthèse d'un nouvel éther-couronne de type «à la dérive» pouvant agir comme catalyseur par transfert de phase, l'éther 4′-carboxybenzo-15-couronne-5 adsorbé sur de la résine poly(styrène/divinylbenzène)-NR_2, et on l'a utilisé pour catalyser l'oxydation du benzhydrol par le $NaMnO_4$. Avant la réaction, le catalyseur éther couronne est adsorbé sur la résine avec formation d'une paire d'ions (résine-NR_2H^+/éther ^-O_2C-monobenzo-15-couronne-5). En ajustant l'acidité de la solution à 10^{-1} M de HCl afin de détruire la paire d'ions formée par le catalyseur et la résine, on libère le catalyseur éther couronne de la résine au cours de la réaction et on l'introduit dans le milieu réactionnel sous la forme d'un catalyseur homogène. Après la réaction, on peut réadsorber le catalyseur éther couronne sur la résine en ajustant la concentration de HCl à 10^{-5} M et on peut alors le récupérer facilement par filtration. On a trouvé que le catalyseur 4′-carboxybenzo-15-couronne-5 est plus efficace que d'autres éthers couronnes comme les éthers 15-couronne-5, 18-couronne-6, monobenzo-15-couronne-5 et dibenzo-18-couronne-6.

[Traduit par la rédaction]

Introduction

Crown ethers have demonstrated a remarkable ability to complex alkali metal ions (1–5). Owing to this complexing ability, they can not only increase the solubility of the metal salts (MX) in organic solvents but also cause activation (6–10) of the anion (X^-) of salts, which results in the catalysis of anion-involved organic reactions, such as displacements, oxidations, and reductions in organic solvents. Crown ethers are used as homogeneous catalysts in most instances. For such homogeneous catalysts, difficulty in recovery and separation of the catalyst from reactants and products after reaction is often encountered. On the other hand, heterogeneous crown ether catalysts, for example, poly(crown ether), are easily recovered after the reaction (11–15). However, heterogeneous catalysts generally exhibit poorer catalytic ability than do the homogeneous catalysts. A new type of "drift-type" crown ether catalyst, 4′-carboxybenzo-15-crown-5, is designed and synthesized in this study. The drift-type catalyst can be drifted out and in reversibly between a solid phase and a solution by adjusting the experimental conditions. The drift-type catalyst is easily recovered, similar to a heterogeneous catalyst, yet has the high catalytic activity of a homogeneous catalyst. Before the reaction, the drift-type crown ether catalyst is adsorbed on a poly(styrene/divinylbenzene)-NR_2 resin by ion-pair formation (resin-NR_2H^+ $-O_2C$-benzo-15-crown-5). The catalyst is re-leased from the resin as a homogeneous catalyst during the reaction period by adjusting the pH of the reaction solution. It is readsorbed on the resin after the reaction by pH readjustment.

[1]Author to whom correspondence may be addressed.

Experimental section

Apparatus

A Waters ALC 200 high-performance liquid chromatograph (HPLC) with a UV–visible detector was utilized to determine concentration of product (benzophenone) and reactant (benzhydrol) for the oxidation reaction as well as concentration of the crown ethers, 4′-carboxybenzo-15-crown-5 and mono-benzo-15-crown-5. FT-NMR (Jeol JNM-FX100), IR (Perkin–Elmer 735 B), and GC-MS (Jeol JMS-D300) spectrometers were employed for identification of the catalyst, products, reactants, crown ethers, and the chloromethylated as well as the alkylamine XAD, resins.

Chemicals

Dibenzo-18-crown-6, monobenzo-15-crown-5, and 15-crown-5 were synthesized as described by Gokel and Durst (16), Pedersen (1), and Cook (17) respectively. The 18-crown-6 was obtained from E. Merck. All other chemicals were of analytical reagent grade.

Preparation of the drift-type crown ether catalyst

The drift-type catalyst 4′-carboxybenzo-15-crown-5 was synthesized by oxidation of 4′-acetylbenzo-15-crown-5, which was prepared by acetylation of monobenzo-15-crown-5 (Fig. 1A).

4′-Acetylbenzo-15-crown-5 was prepared by stirring a mixture of 5.4 g (20 mmol) of benzo-15-crown-5 and 1.3 g (22 mmol) of acetic acid with 27 g of saturated diphosphorus pentoxide – methylsulfonic acid solution for 6 h (18), followed by extraction of the reaction mixture with chloroform (300 mL), evaporation of the chloroform, and recrystallization of the residue from hexane to give a 65% yield of 4′-cetylbenzo-15-crown-5 with mp 96–97°C; IR: 1680 (C=O) cm^{-1}; NMR ($CDCl_3$), δ: 2.55 (s), 4.0 (m), 6.6 (d), 7.0 (s), and 7.3 (d); MS: 310 (M^+).

4′-Carboxybenzo-15-crown-5 was obtained by dropwise addition of 150 mL of an aqueous solution of NaOH (22 g) to 7 mL of bromine water (138 mmol Br_2) at 0–10°C, mixing with 10.5 g (0.33 mmol) of 4′-acetylbenzo-15-crown-5 and stirring the solution at 20°C for 5 h. After extraction of the unreacted 4′-acetylbenzo-15-crown-5 with

Can. J. Chem. Downloaded from www.nrcresearchpress.com by EESC ESCOLA DE ENGENHARIA on 09/08/12
For personal use only.

Can. J. Chem. Downloaded from www.nrcresearchpress.com by EESC ESCOLA DE ENGENHARIA on 09/08/12
For personal use only.

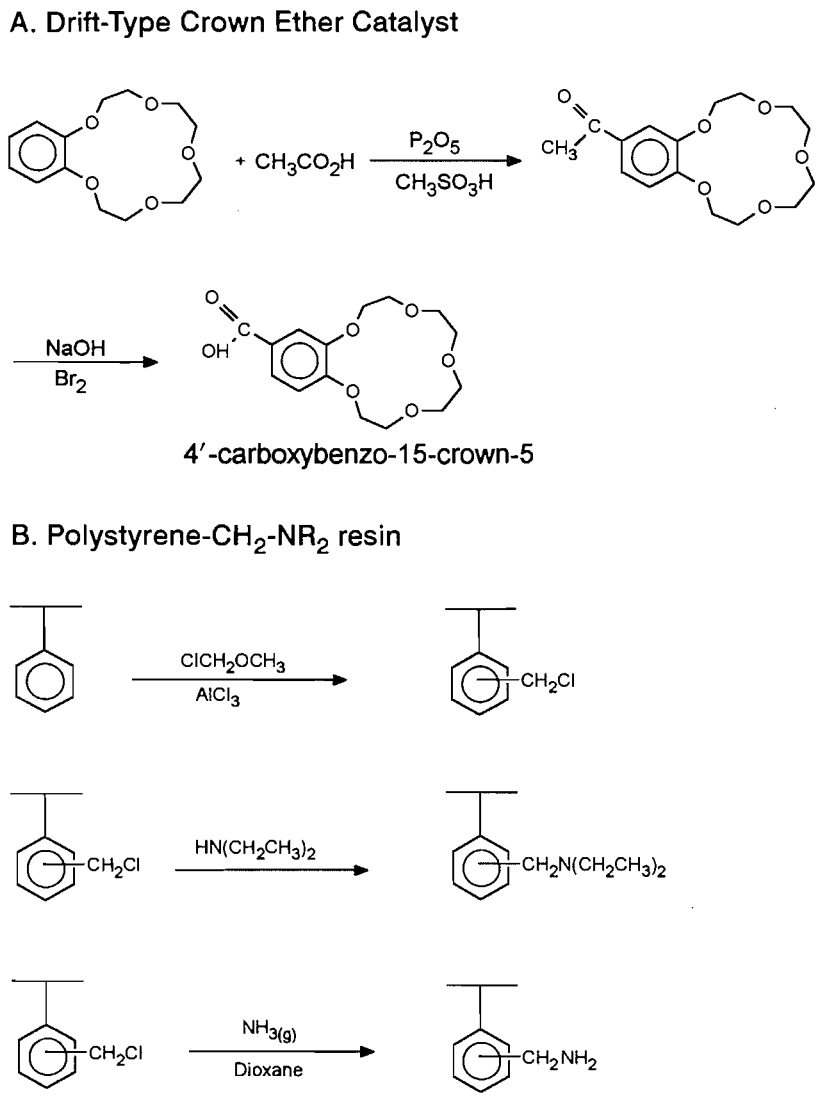

FIG. 1. Syntheses of drift-type crown ether catalyst and resin.

chloroform (300 mL), the aqueous solution was acidified with hydrochloric acid, which precipitated the product. Extraction with chloroform (300 mL), evaporation of the chloroform, and recrystallization of the residue from *n*-hexane gave an 83% yield of the desired product with mp 180°C; IR (KBr): 1720 (C=O) and 2800 (COOH) cm^{-1}; NMR ($CDCl_3$), δ: 3.6 (s), 4.0 (m), 7.0 (d), and 7.5 (m); MS: 312 (M^+).

Preparation of stationary resin

The scheme of synthesis of the alkylamine XAD resin is shown in Fig. 1B. A mixture of XAD-4 resin (poly(styrene/divinylbenzene), 200–400 mesh, 10 g), chloromethyl methyl ether (20 mL), dichloromethane (20 mL), and nitromethane (6 mL) was mixed well in an ice bath. Aluminum chloride ($AlCl_3$, 6 g) was slowly added as the catalyst for chloromethylation (19, 20) of XAD-4 resin. The chloromethylated resin (XAD-CH_2Cl) was mixed with diethylamine (20 mL) and refluxed for 72 h. After washing with methanol (300 mL), the XAD-$CH_2N(C_2H_5)_2$ resin was obtained and identified, with IR(KBr): 1390 (C—N) cm^{-1}. Similarly, other XAD-alkylamine resins, XAD-$CH_2N(CH_3)_3$ and XAD-CH_2NH_2, were prepared by the reactions of XAD-CH_2Cl with trimethylamine and NH_3, respectively. The ion exchange capacity of the alkylamine XAD resins was determined by titration of the -NH_2 or -NR_2 groups on the resins with HCl.

The adsorption capacity of a resin for 4′-carboxybenzo-B-15-crown-5 was determined by measuring the residual of crown ether in the aqueous solution after stirring an excess of crown ether and 1 g of the resin in water for 4 h and filtering. The concentration of crown ether was measured with a high-performance liquid chromatograph.

Catalysis and recovery of catalyst

A mixture of 120 mg of the drift-type catalyst 4′-carboxyl-B15C5 in 100 mL of dichloromethane or benzene and 5 g of XAD-$CH_2N(C_2H_5)_2$ resin was stirred for about 4 h for the adsorption of the catalyst on the resin (Fig. 2(1)). At the beginning of the reaction the crown ether catalyst was released into the dichloromethane or benzene solution by addition of 2 mL of 0.55 N HCl (Fig. 2(2)). The resin in the mixture was filtered and neutralized with 1 N NaOH, which resulted in the change of the resin from XAD-NR_2H^+ into XAD-NR_2. The acidified dichloromethane or benzene solution containing the crown ether catalyst was then mixed with 1 mmol (0.18 g) of benzhydrol (reactant) and 7 mmol (about 1 g) of $NaMnO_4$ as an oxidant (Fig. 2(3)). The mixture was stirred for 6 h for the oxidation of benzhydrol. The oxidation product, benzophenone, was determined with high-performance liquid chromatography. After the reaction, 2 mL of 1 N HCl was added to release the neutral form of the crown ether from the complex Na^+B15C5CO_2H. Sodium bisulfate was also added to decompose the unreacted $NaMnO_4$. The neutral XAD-NR_2 resin was then mixed with the acidified crown ether – dichloromethane or benzene solution to

Can. J. Chem. Downloaded from www.nrcresearchpress.com by EESC ESCOLA DE ENGENHARIA on 09/08/12
For personal use only.

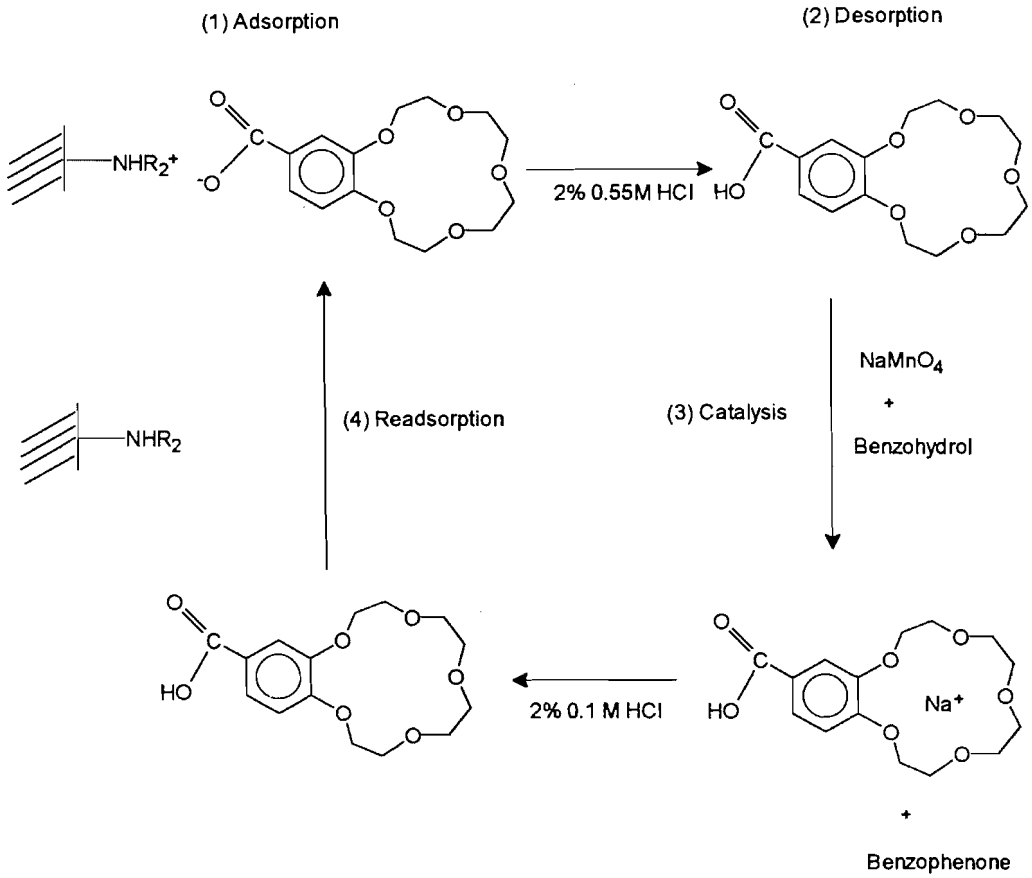

FIG. 2. Catalysis and recovery of 4′-carboxybenzo-15-crown-5 in organic solvents at 25°C.

readsorb the drift-type crown ether catalyst for recovery by filtration (Fig. 2(4)).

Results and discussion

The catalytic ability of the drift-type crown ether catalyst 4′-carboxy-B15C5 was first investigated.The crown ether compounds of 4′-carboxy-B15C5, benzo-15-crown-5(B15C5), 15-crown-5(15C5), dibenzo-18-crown-6(DB18C6), and 18-crown-6(18C6), were utilized as homogeneous catalysts for catalyzing the oxidation of benzhydrol with sodium permanganate ($NaMnO_4$) in benzene. Among the crown ethers, 4′-carboxy-B15C5 and B15C5 were found to exhibit better catalytic abilities than the other crown ether catalysts (Fig. 3). This finding indicates that the drift-type crown ether catalyst can perform very well as a homogeneous catalyst in relation to common crown ether catalysts. By use of the drift-type crown ether catalyst, the oxidation of benzhydrol in benzene can be dramatically catalyzed to give about a 95% yield of benzophenone in only 3 h at room temperature, as shown in Fig. 3. Crown ethers are well known to be sensitive to the size of the metal ions. Both 4′-carboxyl-B15C5 and B15C5 have cavity radii (ca. 1.1 Å) (21) that can fit the size (1.12 Å) (22) of the Na^+ ion of $NaMnO_4$ very well. This should lead to the formation of quite strong complexes between crown ethers and Na ions as well as an increase in the solubility of oxidant $NaMnO_4$ in benzene and activation of the MnO_4^-, which results in catalysis of the oxidation of benzhydrol.

The process of catalysis/recovery of the drift-type crown ether catalyst includes four steps (Fig. 2): (1) Adsorption of the catalyst on the resin; (2) releasing of the catalyst from the resin at the beginning of the reaction; (3) catalysis of the oxidation of benzhydrol; and (4) readsorption of the catalyst on the resin after the reaction. Each step of the process has been studied and is briefly discussed as follows:

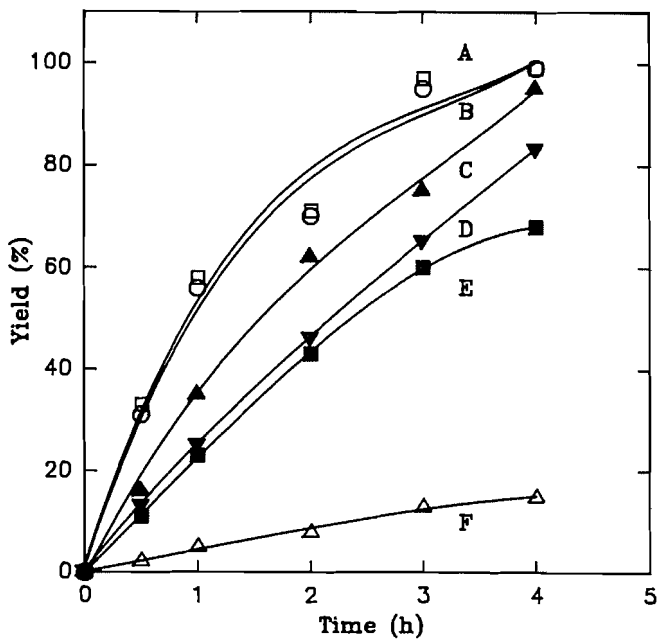

FIG. 3. Crown ether effect on oxidation of benzhydrol with $NaMnO_4$ in benzene at 25°C with (A) 4′-carboxybenzo-15-crown-5, (B) benzo-15-crown-5, (C) dibenzo-18-crown-6, (D) 18-crown-6, (E) 15-crown-5, and (F) without crown ether.

TABLE 1. Adsorption capacity of various XAD-amine resins for the crown ether 4′-carboxybenzo-15-crown-5 in dichloromethane

Resin	Ion exchange capacity (mequiv./g)	Adsorption of crown ether (mg/g)	Adsorption capacity of crown ether (mequiv./g)
XAD-NH_2	0.129	33.1	0.106
XAD-$N(C_2H_5)_2$	0.175	26.4	0.085
XAD-$N(CH_3)_3^+OH^-$	0.261	32.4	0.104

Step 1

The drift-type catalyst, 4′-carboxy-B15C5, is first adsorbed on a poly(styrene/divinylbenzene)-NR_2 (XAD-NR_2) resin prior to reaction. Various poly(styrene/divinylbenzene) resins, for example, XAD-$CH_2N(CH_3)_3^+{}^-OH$, XAD-$CH_2N(C_2H_5)_2$, XAD-CH_2NH_2, and XAD-CH_2Cl, are utilized for adsorbing the crown ethers, 4′-carboxy-B15C5, B15C5, and DB18C6, as well as benzoic acid. The study reveals that crown ethers B15C5 and DB18C6, which do not have the polar carboxylic acid group, are not adsorbed on these XAD resins. This indicates that the adsorption of crown ethers on these XAD resins cannot be attributed to nonpolar–nonpolar van der Waals forces. Resins such as XAD-CH_2Cl and XAD-4 that do not possess an ionized polar group cannot adsorb the crown ethers or benzoic acid. This also shows that the crown ethers, as well as benzoic acid, cannot be adsorbed on the resin by nonionic processes. Only 4′-carboxy-B15C5 and benzoic acid, which have carboxylic acid groups, can be adsorbed on the resins that have NR_2 groups. This suggests that adsorption of the drift-type crown ether catalyst 4′-carboxy-B15C5 on the XAD-NR_2 resins takes place by protonation of the amine group of the XAD-NR_2 resin and formation of ion pairs (resin-$NR_2H^+{}^-O_2C$-monobenzo-15C5).

The adsorption capacity of the resins for 4′-carboxy-B15C5 in dichloromethane was investigated. Results are listed in Table 1. Various XAD-NR_2 resins can absorb the drift-type catalyst with an adsorption capacity of about 0.1 mequiv./g (30 mg/g). About 0.4 mequiv. (120 mg) of the crown ether catalyst was used in most experiments of this study. This means that >4 g (actually, 5 g was used) of resin is necessary for complete adsorption of 120 mg (0.4 mequiv.) of the drift-type catalyst 4′-carboxy-B15C5. The adsorption of the crown ether by the XAD-$N(C_2H_5)_2$ resin (0.085 mequiv./g resin) is about half of the capacity of the resin (0.175 mequiv./g resin), which indicates that about 50% of amine sites on the resin can adsorb 4′-carboxy-B15C5 in dichloromethane.

Step 2

The catalyst 4′-carboxy-B15C5 is next released from the resin as a homogeneous catalyst at the beginning of the reaction by adding acid (HCl) to the dichloromethane solution. The pH (−log[acid added]) of aqueous dichloromethane solution was found to have a significant effect on the release of catalyst from the resin (Fig. 4). Thus an increase in concentration of H^+ (lower pH) in the solution results in enhanced release of the catalyst from the resin. This may be attributed to protonation of the carboxylate (COO^-) group of 4′-carboxy-B15C5 and decomposition of the ion-pair (resin-$NR_2H^+{}^-O_2C$-B15C5) between the catalyst and the resin, which results in the desorption and release of the catalyst from the resin. As indicated in Fig. 4, the crown ether catalyst is completely released from the resin at pH 2, which means that about 1 mmol of HCl must be added to the 100 mL dichloromethane solution. In the study of the oxidation reactions, 2 mL of 0.55 N HCl was added to the dichloromethane solution to release the catalyst.

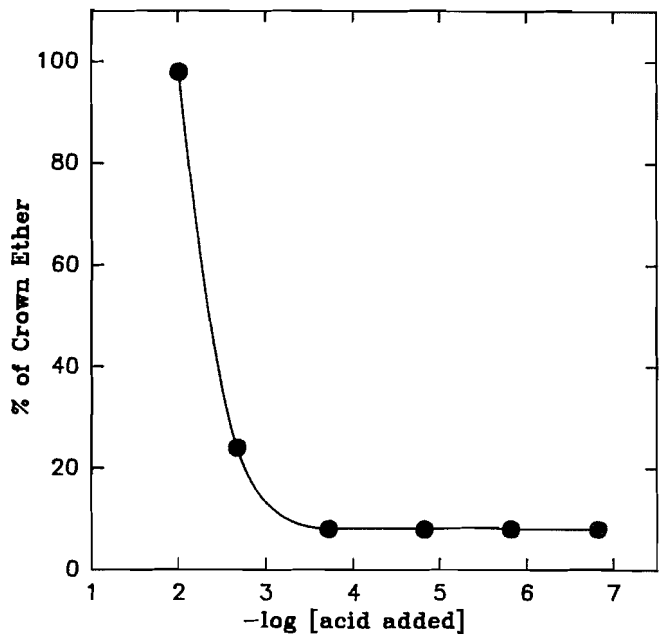

FIG. 4. Effect of the concentration of HCl acid added on desorption of the drift-type crown ether catalyst from the resin in 2% H_2O – CH_2Cl_2 solution.

Step 3

The drift-type catalyst 4′-carboxy-B15C5 is utilized as a homogeneous catalyst in the oxidation of benzhydrol. As mentioned above, 4′-carboxy-B15C5 has been shown to be as good a catalyst as B15C5 and better than any other crown ethers tested. Effects of crown ether concentration, cation of the oxidant, solvents, and temperature on the yield of the catalytic oxidation have been investigated in this study. The mechanism of the reaction can be expressed as follows.

(a) Anion activation

[1] $B15C5CO_2H + NaMnO_4 = Na^+B15C5CO_2H + MnO_4^-$

(b) Catalysis

[2] $2\,MnO_4^- + 5\,Bz_2CHOH = 2\,Mn^{2+} + 5\,Bz_2CO + 6\,OH^- + 2\,H_2O$

According to eqs. [1] and [2],

[3] $-d\,[B15C5CO_2H]/dt = d\,[MnO_4^-]/dt$

Can. J. Chem. Downloaded from www.nrcresearchpress.com by EESC ESCOLA DE ENGENHARIA on 09/08/12
For personal use only.

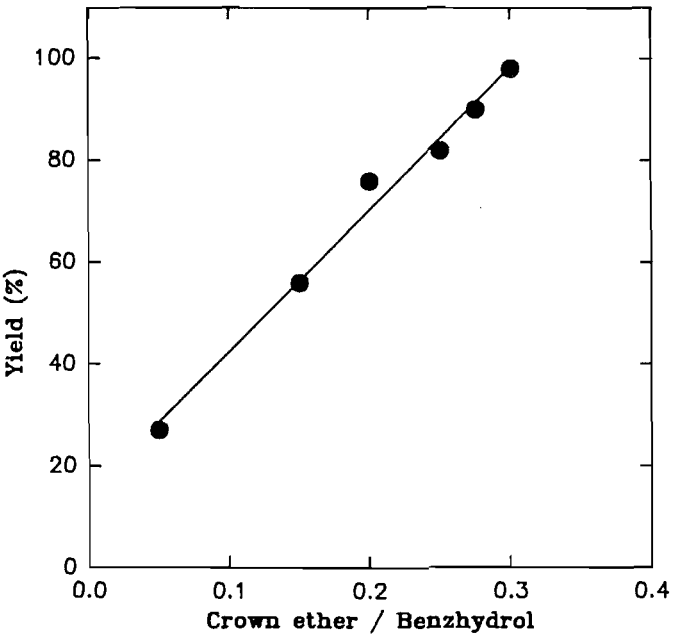

FIG. 5. Crown ether/benzhydrol mole ratio effect on oxidation of benzhydrol catalyzed by 4′-carboxybenzo-15-crown-5.

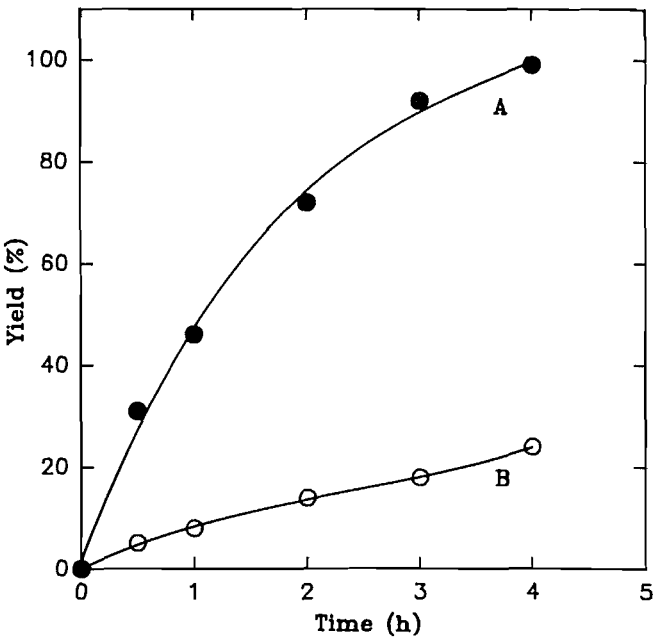

FIG. 6. Cation effect for oxidation of benzhydrol catalyzed by 4′-carboxybenzo-15-crown-5 with (A) $NaMnO_4$ and (B) $KMnO_4$.

and

[4] $-5\ d\ [MnO_4^-]/dt = 2\ d\ [Bz_2CO]/dt$

Therefore

[5] $d\ [Bz_2CO]/dt = 5/2\ d\ [B15C5CO_2H]/dt$

Division by $[Bz_2CHOH]$ gives

[6] $d\ ([Bz_2CO]/[Bz_2CHOH])/dt = 2.5\ d\ ([B15C5CO_2H]/[Bz_2CHOH])/dt$

Since $[Bz_2CO]/[Bz_2CHOH]$ = yield,

[7] $d\ (\text{yield})/dt = 2.5\ d\ ([B15C5CO_2H]/[Bz_2CHOH])/dt$

and

[8] $d\ (\text{Yield})/d([B15C5CO_2H]/[Bz_2CHOH]) = 2.5$

If this mechanism is correct, according to eq. [8] a plot of yield against ($[B15C5CO_2H]/[Bz2CHOH]$) should produce a straight line with a slope of 2.5. In agreement, a plot of yield against ($[B15C5CO_2H]/[Bz_2CHOH]$) gives a straight line with a slope of 2.54 (Fig. 5).

The cation effect of the oxidant on the reaction was also investigated. As shown in Fig. 6, $NaMnO_4$ is a superior oxidant to $KMnO_4$ in this reaction. The Na^+ ion (1.12 Å) can fit the cavity (ca. 1.1 Å) of the catalyst 4′-carboxy-B15C5 very well, which results in the formation of quite strong complexes between the Na^+ ion with the crown ether and dramatic catalysis of the reaction. In contrast, the K^+ ion with the size (radius) of 1.33 Å is too big for the cavity of the crown ether and leads toward a less activated MnO_4^- ion as well as a lower reactivity.

The solvent property is known to also be an important factor for the complexing ability of crown ethers with the metal ion. As shown in Fig. 7, benzene is a better solvent than dichloromethane or chloroform for the crown ether catalyzed oxidation of benzhydrol. Benzene with a dielectric constant (E) of 2.27 is less polar than chloroform (E = 4.80) or dichloromethane (E = 8.92) (23). This suggests that the catalytic ability of the crown ether is higher in less polar solvents. Since Na^+ ions are better solvated in more polar solvents such as chloroform, weaker crown ether – Na^+ complexes would be formed. In contrast, the solvation of Na^+ is weaker in a less polar solvent such as benzene, which results in the formation of strong complexes between the crown ether and the metal ion. This forma-

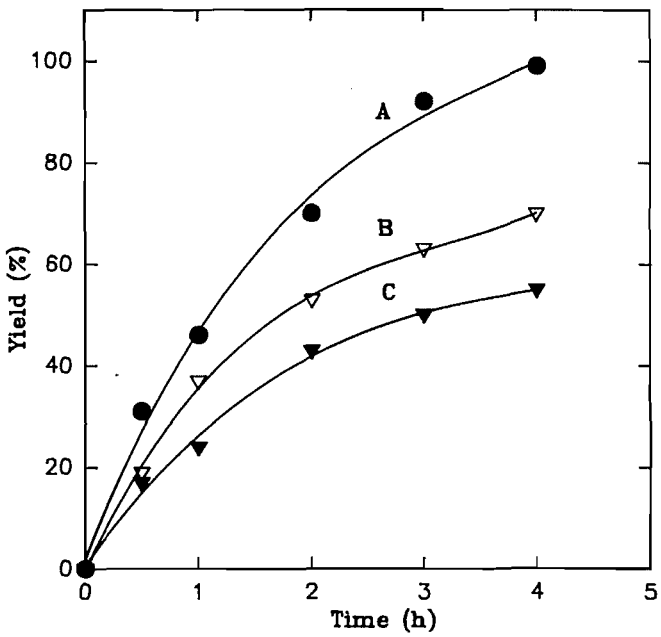

FIG. 7. Solvent effect on yield (%) of oxidation of benzhydrol catalyzed by 4′-carboxybenzo-15-crown-5 in (A) benzene, (B) dichloromethane, and (C) chloroform.

Can. J. Chem. Downloaded from www.nrcresearchpress.com by EESC ESCOLA DE ENGENHARIA on 09/08/12
For personal use only.

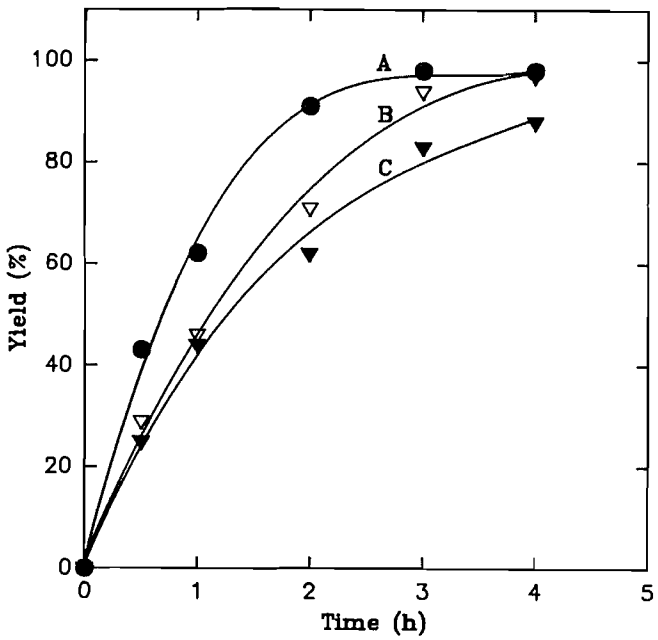

FIG. 8. Temperature effect on oxidation of benzhydrol catalyzed by 4′-carboxybenzo-15-crown-5 in benzene at (A) 60°C, (B) 25°C, and (C) 40°C.

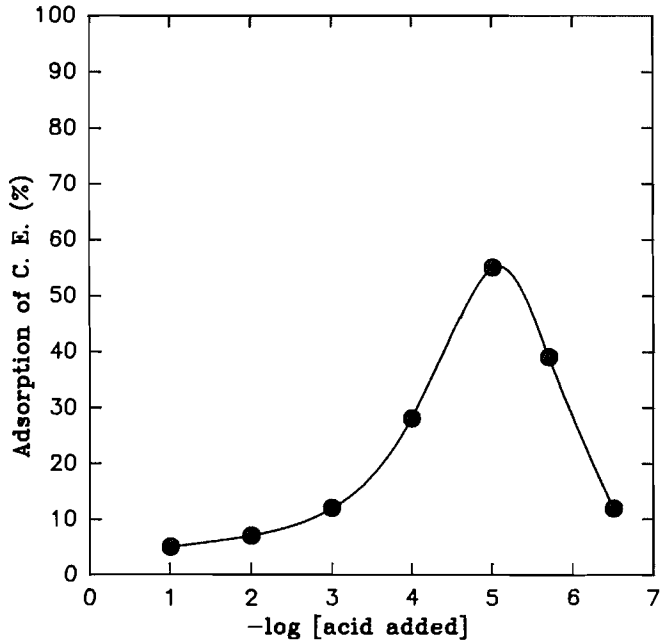

FIG. 9. Effect of the concentration of HCl added on readsorption of 50 mg of 4′-carboxybenzo-15-crown-5 with 1.0 g of XAD-N$(C_2H_5)_2$ resin in 102 mL of 2% $H_2O - CH_2Cl_2$ solution.

tion leads to more activated MnO_4^- anions and also more reactivity for the oxidation.

The temperature effect on the oxidation reaction was also investigated. Reaction at higher temperature (60°C) was found to be more rapid than at 25 and 40°C (Fig. 8).

Step 4

After the reaction, the drift-type crown ether is readsorbed on the XAD-N$(C_2H_5)_2$ resin. The crown ether is present in organic solvent as the complex Na^+B15C5CO_2H after the reaction. As was shown in Fig. 2, the crown ether can be produced in its neutral form B15C5CO_2H by the addition of 2% 0.1 M HCl. However, too large of an amount of HCl solution would drastically reduce the readsorption of the crown ether on the resin. The optimum acid concentration of the solution for readsorption of the crown ether was found to be 10^{-5} M HCl added (log[acid added] = 5) as shown in Fig. 9.

The identity of the organic solvent is also found to produce a significant effect on the readsorption of the crown ether (Table 2). Among the 10 solvents investigated, benzene, which has the lowest dielectric constant (2.27), appears to be the best solvent for the adsorption of the crown ether on the resin. As mentioned above, benzene is also the optimum solvent for the oxidation step. Therefore, benzene is identified as a good solvent for all of the drift-type catalytic processes, i.e., adsorption, release of the catalyst, catalysis of the oxidation, and readsorption of the catalyst.

The drift-type crown ether catalyst can theoretically be recycled forever. Some loss of the crown ether catalyst actually occurs after each cycle. The data in Table 3 show that the oxidation yield is 82.9% and 72.5% after the first and second cycles, respectively. The recovery of the crown ether is about 75% in each cycle.

TABLE 2. Solvent effect on adsorption of 4′-carboxybenzo-15-crown-5 with XAD-N$(C_2H_5)_2$ resin[a]

Solvent	Adsorption of C.E. (mg)[b]	Recovery of C.E. (%)[b]	Dielectric constant
Benzene	38.5	77.0	2.27
Dichloromethane	32.4	64.8	8.93
Chloroform	27.7	55.4	4.81
Diethyl ether	24.3	48.6	4.34
Dimethyl sulfoxide	Trace	≈0	46.7
Dimethyl formamide	Trace	≈0	36.7
Acetonitrile	3.3	6.6	36.0
Acetone	Trace	≈0	20.7
Ethyl acetate	Trace	≈0	6.02
Methanol	Trace	≈0	32.6

[a]XAD-N$(C_2H_5)_2$ resin (1.0 g).
[b]C.E. = 4′-carboxy-B15C5 (50 mg in 100 mL of the solvent).

TABLE 3. Recycle effect on the catalysis and recovery of 4′-carboxybenzo-15-crown-5 in benzene

Cycle	Catalytic yield (%)	Recovery of crown ether (%)[a]
Cycle 1	82.9	77.8
Cycle 2	72.5	57.1

[a]XAD-N$(C_2H_5)_2$ resin (5.0 g) and 4′-carboxy-B15C5 (120 mg) in 100 mL of benzene.

Conclusion

The drift-type crown ether 4′-carboxy-B15C5 can be used as an efficient homogeneous phase transfer catalyst for catalyzing an organic reaction, such as the oxidation of benzydrol. This drift-type crown ether can also be easily recovered by readsorption on the XAD-NR_2 resin after the reaction. Thus, the drift-type crown ether catalyst was found to possess both the high catalytic capability of a homogeneous catalyst and the ease of use of a heterogeneous catalyst. In addition to the drift-type

Can. J. Chem. Downloaded from www.nrcresearchpress.com by EESC ESCOLA DE ENGENHARIA on 09/08/12
For personal use only.

crown ether catalyst, other kinds of drift-type catalysts, such as modified drift-type enzymes, can be envisaged.

Acknowledgment

The authors would like to express their appreciation to the National Science Council of the Republic of China in Taiwan for financial support of this research.

1. C.J. Pedersen. J. Am. Chem. Soc. **89**, 7017 (1967).
2. J. Christensen, D.J. Eatough, and R.M. Izatt. Chem. Rev. **74**, 351 (1974).
3. I.M. Kelthoff. Anal. Chem. **51**, 1R (1979).
4. R.M. Izatt and J.J. Christensen. Progress in macrocyclic chemistry. Wiley–Interscience, New York. 1979.
5. R.M. Izatt and J.J. Christensen. Synthetic multidentate macrocyclic compounds. Academic, New York. 1978.
6. C.L. Liotta, H.P. Harris, M. McDermot, T. Gonazalez, and T. Smith. Tetrahedron Lett. 2417 (1974).
7. J.W. Znbrick, B.I. Dumbar, and H.D. Durst. Tetrahedron Lett. 71 (1975).
8. P.E. Stott, J.S. Bradshaw, and W.W. Parish. J. Am. Chem. Soc. **102**, 4810 (1980).
9. P.E. Viout. J. Mol. Catal. **10**, 231 (1981).
10. Y.S. Lin and J.S. Shih. J. Chin. Chem. Soc. (Taipei), **38**, 451 (1991).
11. S. Kopolow, T.E. Hogen, and J. Smid. Macromolecules, **6**, 133 (1973).
12. K. Kikukawa, K. Nagira, and T. Matsuda. Bull. Chem. Soc. Jpn. **50**, 2207 (1977).
13. A. Warshawsky and N. Kahana. Polym. Prepr. (Am. Chem. Soc. Div. Polym. Chem.), **21**, 114 (1980).
14. W.T. Ford. CHEMTECH, 437 (1984).
15. J. Lieto, D. Milsten, R.L. Albright, and B.C. Gates. CHEMTECH, 46 (1983).
16. G.W. Gokel and H.D. Durst. Synthesis, 168 (1976).
17. F.L. Cook. Tetrahedron Lett. 4029 (1972).
18. P.E. Stott and J.S. Bradshaw. J. Org. Chem. **45**, 4716 (1980).
19. D.J. Gjerde, J.S. Fritz, and G. Schmuckler. J. Chromatogr. **186**, 509 (1979).
20. S.J. Chen and J.S. Shih. J. Chin. Chem. Soc. (Taipei), **38**, 211 (1991).
21. C.J. Pedersen and H.K. Frensdroff. Angew. Chem. Int. Ed. Engl. **11**, 16 (1972).
22. F.L. Cotton and F.R. Wilkinson. *In* Advanced inorganic chemistry. 4th ed.Wiley–Interscience, New York. 1980. p. 14.
23. K. Kalyanasundaram and J.K. Thomas. J. Am. Chem. Soc. **99**, 2039 (1977).

Can. J. Chem. Downloaded from www.nrcresearchpress.com by EESC ESCOLA DE ENGENHARIA on 09/08/12
For personal use only.

The interaction of D-penicillamine with aldehydes and ketones: 2-phenyl-5,5-dimethylthiazolidine-4-carboxylic acid

R.A. BELL, J.F. BRITTEN, H.E. HOWARD-LOCK, C.J.L. LOCK,[1] AND M. SCHMIDT

Laboratories for Inorganic Medicine, Departments of Chemistry and Pathology, McMaster University, ABB-266A, Hamilton, ON L8S 4M1, Canada

Received October 4, 1993

R.A. BELL, J.F. BRITTEN, H.E. HOWARD-LOCK, C.J.L. LOCK, and M. SCHMIDT. Can. J. Chem. **72**, 1621 (1994).

The reaction of D-penicillamine and benzaldehyde yielded 2-phenyl-5,5-dimethylthiazolidine-4-carboxylic acid. The structure was determined by single crystal X-ray diffraction. Crystals were monoclinic, $P2_1$, $a = 9.785(2)$, $b = 6.941(1)$, $c = 10.399(2)$ Å, $\beta = 114.06(3)°$, $Z = 2$. Intensities were measured on a Rigaku AFC6R diffractometer with Cu Kα radiation and 1881 reflections were used to determine the structure. $R = 0.076$, $wR = 0.048$. The compound exists as an amino acid in the 2*S*,4*S* configuration. The conformation of the thiazolidine ring is determined by intermolecular hydrogen bonding. Bond lengths and angles are normal. ^{1}H and ^{13}C NMR spectra showed that epimerization takes place in d_4-CH_3OH solution, and the ratio of 2*S*,4*S* diastereomer to 2*R*,4*S* diastereomer at room temperature is 65:35.

R.A. BELL, J.F. BRITTEN, H.E. HOWARD-LOCK, C.J.L. LOCK et M. SCHMIDT. Can. J. Chem. **72**, 1621 (1994).

La réaction de la D-pénicillamine et du benzaldéhyde conduit à l'acide 2-phényl-5,5-diméthylthiazolidine-4-carboxylique. On a déterminé sa structure par diffraction des rayons X par un cristal unique. Les cristaux sont monocliniques, $P2_1$, avec a = 9,785(2), b = 6,941(1) et c = 10,399(2) Å, $\beta = 114,06(3)°$ et $Z = 2$. On a mesuré les intensité à l'aide d'un diffractomètre Rigaku, modèle AFC6R, à l'aide du rayonnement Kα du Cu et on a utilisé 1881 réflexions indépendantes pour déterminer la structure. $R = 0,076$ et $R_w = 0,048$. Le composé existe sous la forme d'un acide aminé de configuration 2*S*,4*S*. La conformation du noyau thiazolidine est déterminée par une liaison hydrogène intramoléculaire. Les longueurs et les angles des liaisons sont normaux. Les spectres de RMN du ^{1}H et du ^{13}C démontrent que, en solution dans le d_4-CH_3OH, il se produit une épimérisation et que, à la température ambiante, le rapport des diastéréoisomères 2*S*,4*S* et 2*R*,4*S* est de 65 : 35.

[Traduit par la rédaction]

Introduction

D-Penicillamine, when administered as a drug, interferes with a number of metabolic processes that involve vitamin B6. The fact that the interference is so general suggests that any interference occurs very early in any metabolic pathway or possibly even directly with the drug (1). Reaction of D-penicillamine with aldehydes and ketones is one of three types of biochemical reaction of the drug, and we have shown that D-penicillamine reacts directly with vitamin B6 forming a thiazolidine-4-carboxylic acid by condensation of the aldehyde group on vitamin B6 with the sulphydryl and amine groups on D-penicillamine, **1** (2).

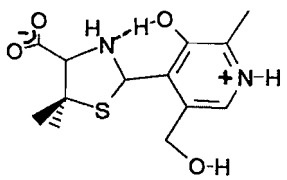

1

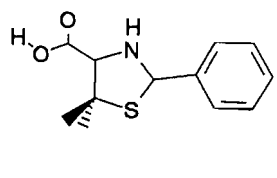

2

D-Penicillamine is used in the treatment of rheumatoid arthritis (RA), but the time taken for any beneficial effect to be seen can be long (weeks), so that, generally, a nonsteroidal anti-inflammatory drug (NSAID) is given as well, to deal with short-term inflammation until the D-penicillamine takes effect. Many of these NSAIDs contain ketone groups and we were interested in seeing whether thiazolidine-containing condensation complexes could be formed with D-penicillamine. We have examined ketoprofen and tiaprofenic acid, but did not obtain products under physiological conditions. We speculate that this might be because of steric hindrance. We also attempted reactions with the related molecules benzophenone and benzaldehyde. No product was obtained with the sterically more demanding benzophenone, but a product, **2**, was obtained with benzaldehyde (3). We have examined the structure of the product and compared it to the results from the vitamin B6 experiments. There are significant differences in the two structures and we think these may be caused by intra- and intermolecular hydrogen bonding.

Experimental section

All chemicals and solvents were newly purchased as reagent grade and were generally used as received. Benzaldehyde was distilled before use. To avoid unwanted side reactions all operations were carried out under an atmosphere of dry nitrogen. Melting points (mp) were measured on a Gallenkamp melting point apparatus in open capillaries and are reported as measured.

Solutions for NMR studies were prepared in d_4-CH_3OH (99.8 at.% D; MSD Isotopes, Montreal) and concentrations were about 25 mg (solid)/mL. Proton NMR spectra and ^{13}C NMR spectra were recorded on a Bruker AC-200 spectrometer (at 200.13 MHz) with the deuterated solvent as internal reference. All spectra were obtained on natural-abundance compounds. Proton NMR spectra were obtained in 32–128 scans at a spectral width of 2404 Hz (16K, 0.29 Hz/data point, 3.408 s acquisition time). ^{13}C NMR spectra were obtained in 7000 scans at a spectral width at 12 195 Hz (16K, 1.49 Hz/data point, 0.672 s acquisition time). Line-broadening parameters used in processing the free induction decays were set slightly higher than their respective data point resolutions. Proton–proton NOE difference spectra were acquired by subtraction of a control FID from an on-resonance FID. The decoupler in the control FID irradiated a position in the spectrum where there were no proton signals. The on-resonance FID was obtained by selectively saturating the proton of interest. In both cases the same decoupler power and duration of saturation (5.0 s) were used. This saturation period also served as the relaxation delay for both the control and on-resonance FIDs. The decoupler was gated off during acquisition. Eight scans were acquired for both the control and on-resonance FIDs. This cycle of alternate acquisition of control and

[1]Author to whom correspondence may be addressed.

Can. J. Chem. Downloaded from www.nrcresearchpress.com by EESC ESCOLA DE ENGENHARIA on 09/08/12
For personal use only.

Can. J. Chem. Downloaded from www.nrcresearchpress.com by ESC ESCOLA DE ENGENHARIA on 09/08/12
For personal use only.

on-resonance FIDs was repeated 12 times for a total of 96 scans for the final difference FID. A 90° ^{1}H pulse width of 9.4 μs was used. The difference FID was processed by use of exponential multiplication (line broadening: 4.0 Hz) and was zero-filled to 64K before Fourier transformation. The sample was not degassed.

5,5-Dimethyl-2-phenyl-thiazolidine-4-carboxylic acid, 2

D-(−)-Penicillamine (0.5 g) was added to a mixture of ethanol (6 mL) and benzaldehyde (0.5 mL, freshly distilled). The solution was stirred and heated for about 45 min. The almost clear mixture was filtered while hot and refrigerated for 4–5 h to yield colourless platelike crystals (0.64 g (83%), mp 145–146°C). NMR and vibrational spectra were similar to data in ref. 3. ^{1}H NMR (200 MHz, d_4-CH_3OH) 2*R*,4*S* diastereomer, δ: 7.57–7.51 (m, 5H, aromatic), 5.91 (s, 1H, C2-H), 3.97 (s, 1H, C4-H), 1.70 (s, 3H, C52-CH_3), 1.48 (s, 3H, C51-CH_3); *S*,*S* diastereomer, δ: 7.42–7.33 (m, 5H, aromatic), 5.67 (s, 1H, C2-H), 3.82 (s, 1H, C4-H), 1.73 (s, 3H, C52-CH_3), 1.44 (s, 3H, C51-CH_3). Ratio of diastereomers: 35% 2*R*,4*S* to 65% 2*S*,4*S*. ^{1}H NMR (200 MHz, d_6-DMSO) 2*R*,4*S* diastereomer, δ: 7.45 (m, 5H, aromatic), 5.83 (s, 1H, C2-H), 3.67 (s, 1H, C4-H), 1.32 (s, 3H, CH_3), 1.29 (s, 3H, CH_3); *S*,*S* diastereomer, δ: 7.45 (m, 5H, aromatic), 5.62 (s, 1H, C2-H), 3.56 (s, 1H, C4-H), 1.63 (s, 3H, CH_3), 1.51 (s, 3H, CH_3). Ratio of diastereomers: 70% 2*R*,4*S* to 30% 2*S*,4*S*. ^{13}C NMR (200 MHz, d_4-CH_3OH) 2*R*,4*S* diastereomer, δ: 170.97 (*C*OOH), 139.99 (C11), 74.57 (C2), 67.50 (C4), 58.41 (C5), 27.87 (C5-CH_3), 26.76 (C5-CH_3); *S*,*S* diastereomer, δ: 171.79 (*C*OOH), 139.08 (C11), 75.47 (C2), 69.50 (C4), 59.45 (C5), 29.98 (C5-CH_3), 28.71 (C5-CH_3). The remaining aromatic signals overlapped and could not be definitively assigned: they occurred at δ 129.88, 129.73, 128.86, 128.72.

Structure determination details for 2

For single crystal X-ray diffraction, crystals of 2-phenyl-5,5-dimethyl-thiazolidine-4-carboxylic acid were obtained by the slow evaporation (20°C) of an absolute ethanol solution. The unit cell was determined by least-squares refinement of 24 reflections between θ = 19.9° and θ = 55.7°. Hydrogen atoms were placed at calculated positions and constrained to ride on the atoms to which they were attached, except for atoms H(1) and H(3), which were placed at positions located in the electron density map and were not refined. The details of the structure determination follow, and positional parameters and isotropic temperature factors are given in Table 1.[2]

Crystal data

Empirical formula, $C_{12}H_{15}NO_2S$; colourless plate; crystal size, 0.30 × 0.30 × 0.03 mm^3; monoclinic, $P2_1$; a = 9.785 (2) Å, b = 6.941 (1) Å, c = 10.399 (2) Å, β = 114.06 (3)°; V = 644.9 (3) Å^3; Z = 2; formula weight, 237.3; density, calcd., 1.222 Mg m^{-3}; absorption coefficient, 2.121 mm^{-1}; F(000) = 252.

Data collection

Diffractomer used, Rigaku AFC6-R; CuKα (λ = 1.54178 Å); temperature 298 K; monochromator, highly oriented graphite crystal; 2θ range, 5.0–120.0°; scan type, ω–2θ; scan speed, 32° min^{-1} in ω, with up to 9 rescans; scan range (ω), 2° plus Kα separation; background measurement, stationary crystal and stationary counter at beginning and end of scan, each for 0.25 of total scan time; standard reflections, 3 measured every 100 reflections; index ranges, $0 \le h \le 11$, $0 \le k \le 8$, $-12 \le l \le 12$ and $-11 \le h \le 0$, $-8 \le k \le 0$, $-12 \le l \le 12$; reflections collected, 2232; independent reflections, 1881 (R_{int} = 3.93%); reflections used, 1881, absorption correction, by Ψ-scan, T_{min} = 0.7635, T_{max} = 1.000.

TABLE 1. Atomic coordinates (×10^4) and equivalent isotropic displacement coefficients (Å^2 × 10^3) for **2**

Atom	*x*	*y*	*z*	*U*(eq)[a]
S(1)	9403 (1)	0	8649 (1)	74 (1)
C(2)	7751 (4)	−1396 (7)	8502 (4)	55 (2)
N(3)	6455 (4)	−606 (6)	7298 (3)	53 (1)
C(4)	6963 (4)	237 (7)	6279 (4)	49 (2)
C(5)	8433 (5)	1378 (8)	7031 (5)	61 (2)
C(1)	5685 (5)	1420 (7)	5272 (4)	56 (2)
O(1)	5817 (3)	1948 (5)	4122 (3)	66 (1)
O(2)	4631 (4)	1836 (7)	5530 (4)	94 (2)
C(51)	9341 (5)	1451 (10)	6171 (6)	100 (3)
C(52)	8103 (7)	3418 (8)	7402 (6)	101 (3)
C(11)	7409 (5)	−1408 (8)	9794 (4)	60 (2)
C(12)	6835 (5)	−3047 (10)	10101 (5)	81 (3)
C(13)	6434 (6)	−3028 (13)	11257 (7)	101 (3)
C(14)	6611 (7)	−1472 (13)	12067 (6)	104 (4)
C(15)	7199 (6)	111 (13)	11752 (5)	100 (3)
C(16)	7623 (5)	208 (9)	10642 (5)	75 (2)

[a]Equivalent isotropic U defined as one third of the trace of the orthogonalized U_{ij} tensor.

Solution and refinement

System used, Siemens SHELXTL PLUS (PC Version) (4); solution, direct methods; refinement method, full-matrix least squares; quantity minimized, $\Sigma w(|F_o| - |F_c|)^2$; absolute structure, from known configuration of D-penicillamine, and confirmed by the Rogers parameter of 0.94(7); extinction correction, not applied; hydrogen atoms, riding model, fixed isotropic U; weighting scheme, $w^{-1} = (\sigma(F))^2$ (2); number of parameters refined, 144; final R indices, R = 0.076, wR = 0.048; goodness-of-fit, S, 1.62; largest and mean Δ/σ, 0.000, 0.000; data-to-parameter ratio, 13.1:1; largest difference peak, 0.41 e Å^{-3}; largest difference hole, −0.41 e Å^{-3}. $R = \Sigma||F_o| - |F_c||/\Sigma|F_o|$; $wR = [\Sigma w(|F_o| - |F_c|)^2/\Sigma wF_o^2]^{1/2}$; $S = [\Sigma w(|F_o| - |F_c|)^2/(n - m)]^{1/2}$.

Discussion

Attempts to react D-penicillamine with ketoprofen and tiaprofenic acid under physiological conditions (water, pH 7.6, 37°C) were unsuccessful, probably because of the low solubility of the NSAIDs. Reaction under more drastic conditions (refluxing ethanol) was also unsuccessful. The solid recovered after reaction was D-penicillamine. Reaction of D-penicillamine with benzophenone under similar conditions also yielded no product. Benzaldehyde did react, however, and yielded **2**.

The structure of 2-phenyl-5,5-dimethylthiazolidine-4-carboxylic acid, **2**, is shown in Fig. 1 and bond lengths and angles are given in Table 2. The compound is an amino acid, which is not unusual for solid thiazolidine-4-carboxylic acids derived from D-penicillamine, and in agreement with the predictions based on the vibrational spectra (3). The configuration is 2*S*,4*S*, in contrast to the similar compound 2*R*,4*S*-2-(2′-methyl-3′-hydroxy-5′-hydroxymethylenepyridine-C4′)-5,5-dimethyl-thiazolidine-4-carboxylic acid, **1** (2). The energy required to change the torsional angles about bonds is small and thus variations in the conformation of thiazolidine rings can occur (6, 7). The conformations of the thiazolidine rings in compounds **1** and **2** differ from previous compounds (6, 7) and from each other, as is shown by the torsional angles within the thiazolidine rings

[2]Tables of anisotropic temperature factors, hydrogen atom parameters, best planes, and torsional angles can be purchased from: The Depository of Unpublished Data, Document Delivery, CISTI, National Research Council Canada, Ottawa, ON K1A 0S2, Canada. Structure factor amplitudes are no longer being deposited and may be obtained directly from the author.

The hydrogen atom coordinates for **2** have also been deposited with the Cambridge Crystallographic Data Centre, and can be obtained on request from The Director, Cambridge Crystallographic Data Centre, University Chemical Laboratory, 12 Union Road, Cambridge, CB2 1EZ, U.K.

TABLE 2. Bond lengths (Å) and angles (deg) for **2**

S(1)—C(2)	1.837 (5)	C(2)—N(3)	1.477 (5)
N(3)—C(4)	1.463 (6)	C(4)—C(5)	1.546 (6)
C(5)—S(1)	1.829 (4)	C(4)—C(1)	1.506 (6)
C(1)—O(1)	1.306 (6)	C(1)—O(2)	1.202 (7)
C(5)—C(51)	1.497 (9)	C(5)—C(52)	1.536 (8)
C(2)—C(11)	1.511 (7)	C(11)—C(12)	1.363 (9)
C(12)—C(13)	1.408 (10)	C(13)—C(14)	1.337 (12)
C(14)—C(15)	1.341 (12)	C(15)—C(16)	1.378 (9)
C(16)—C(11)	1.389 (8)		
Hydrogen bond		O(1)...N(3)[a]	2.707 (6)
C(5)—S(1)—C(2)	95.2 (2)	S(1)—C(2)—N(3)	107.3 (3)
C(2)—N(3)—C(4)	109.6 (3)	N(3)—C(4)—C(5)	111.1 (3)
C(4)—C(5)—S(1)	103.0 (3)	S(1)—C(2)—C(11)	115.8 (3)
N(3)—C(2)—C(11)	109.3 (4)	N(3)—C(4)—C(1)	106.9 (4)
C(1)—C(4)—C(5)	114.2 (4)	C(4)—C(1)—O(1)	115.2 (4)
C(4)—C(1)—O(2)	121.4 (4)	O(1)—C(1)—O(2)	123.4 (4)
C(4)—C(5)—C(51)	111.8 (4)	C(4)—C(5)—C(52)	110.6 (4)
S(1)—C(5)—C(51)	110.8 (3)	S(1)—C(5)—C(52)	109.6 (3)
C(51)—C(5)—C(52)	110.8 (5)	C(2)—C(11)—C(12)	118.4 (5)
C(2)—C(11)—C(16)	122.0 (5)	C(16)—C(11)—C(12)	119.6 (5)
C(11)—C(12)—C(13)	118.5 (6)	C(12)—C(13)—C(14)	122.4 (8)
C(13)—C(14)—C(15)	117.8 (7)	C(14)—C(15)—C(16)	123.4 (7)
C(15)—C(16)—C(11)	118.3 (6)		

[a]Atom is related to that in Table 1 by $1 - x$, $-0.5 + y$, $1 - z$.

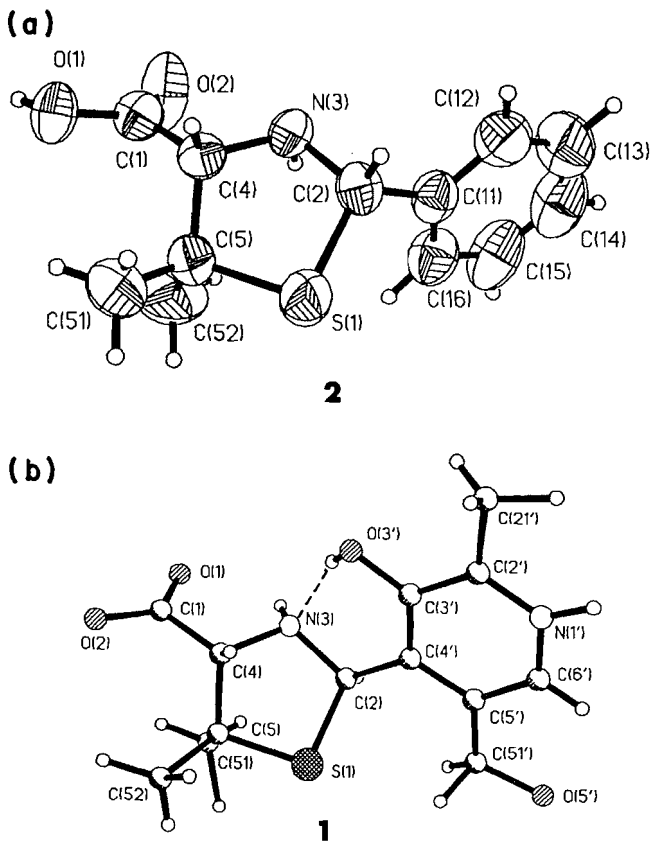

FIG. 1. (*a*) The structure of **2** showing the atom numbering. (*b*) The structure of **1**, oriented in roughly the same way, for comparison.

(Table 3). While both have the open-envelope conformation, for **1** S(1), C(2), N(3), C(4) are almost planar (max. dev. from plane 0.024 Å) and C(5) lies 0.689 Å below this plane, whereas for **2** the plane comprises C(5), S(1), C(2), N(3) (max. dev. from plane 0.046 Å) and C(4) lies 0.496 Å above this plane. The conformation in each case appears to be determined by hydrogen bonding. In the case of **1** there is a very strong intramolecular hydrogen bond between the 3′ hydroxy group on the vitamin B6 moiety and N(3) in the thiazolidine ring. This hydrogen bond determines the configuration at N(3). The alternative configuration at C(2), assuming the hydrogen bond was still present, would put all the bound hydrogen atoms at C(2), N(3), and C(4) on the same side of the thiazolidine ring and in essentially eclipsed conformations, giving rise to considerable steric hindrance. Even with the present conformation, the hydrogen atoms on C(2) and N(3) are eclipsed, but in this case the strength of the hydrogen bond must be sufficient to overcome the repulsion. No such hydrogen bonding is present in **2**, however, and steric hindrance is minimized by having the *S* configuration at C(2), such that the hydrogen atoms at C(2), N(3), and C(4) lie in a staggered *trans,trans* conformation. The configuration at N(3) is determined by the medium strong hydrogen bond between O(1) on one molecule and N(6) in a molecule related by the 2_1 axis at x, $z = 0.5$, as shown in Fig. 2. These hydrogen bonds connect molecules spiralling up the 2_1 axis in the *b* direction. Interactions between molecules in other directions are van der Waals.

TABLE 3. Torsional angles (deg) for **1** and **2**

Atoms	**1**	**2**
C(5)-S(1)-C(2)-N(3)	19.6	−6.4 (4)
S(1)-C(2)-N(3)-C(4)	4.0	27.6 (4)
C(2)-N(3)-C(4)-C(5)	−31.8	−41.5 (5)
N(3)-C(4)-C(5)-S(1)	43.1	34.0 (5)
C(4)-C(5)-S(1)-C(2)	−35.3	−14.8 (4)

Comparison of the corresponding bond lengths in the thiazolidine parts of **1** and **2** shows minimal differences (maximum deviation 1.53 σ, where $\sigma = (\sigma_1^2 + \sigma_2^2)^{1/2}$), except for C(4)—C(1), C(1)—O(1), and C(1)—O(2). For **1** the last two

Can. J. Chem. Downloaded from www.nrcresearchpress.com by EESC ESCOLA DE ENGENHARIA on 09/08/12
For personal use only.

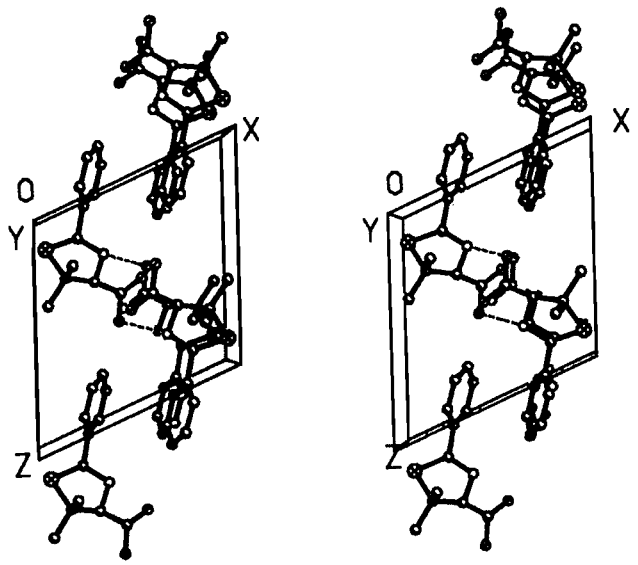

FIG. 2. The packing of **2** in the unit cell. The view is down *b*.

distances are nearly equal, (1.241(6), 1.260(6) Å), as expected for an ionized carboxylate group. For **2** there is a marked asymmetry (1.202(7), 1.306(6) Å), consistent with C=O and C—OH bonds. In addition, C(4)—C(1) in the latter compound is considerably shorter than in **1** (1.506(6) vs. 1.548(7) Å, 4.55σ).

There is considerably more variation in the corresponding angles between the two compounds. Differences of two or three degrees are common (2.00–9.72σ). There are significant differences in the C(4)—C(1)—O(1), C(4)—C(1)—O(1), and O(1)—C(1)—O(2) angles, as might be expected. The values for the angles observed for **2** are fairly close to those observed for the corresponding angles in the amino acid (*S*)-2,2,5,5-tetramethylthiazolidine-4-carboxylic acid (differences: +3.9°, −2.9°, −1.0°) (6), whereas those for **1** agree better with the zwitterionic (*R*)-thiazolidine-4-carboxylic acid (7). We assume the variations in the other sets of corresponding angles are caused by the different conformations of the thiazolidine rings.

The proton NMR spectral parameters are given in the experimental section. All peaks are doubled because of epimerization of the thiazolidine compound in solution. The ^{1}H NMR spectrum alone is not sufficient to distinguish which set of peaks belongs to which diastereomer. An attempt was made, therefore, to assign the resonances in the *S,R* and *S,S* diastereomers based on the work of McMillan and Stoodley (8). Writing about the protons at C2 and C4 in similar compounds, they state: "In particular, if both stereoisomers at C2 are available, the isomer in which the C4 proton appears at lowest field possesses the *trans* configuration." Applying this rule to the above spectrum, the 2*R*,4*S* diastereomer produces the set of signals with lower intensity and the *S,S* diastereomer the set with higher intensity.

To prove this statement, an NOE experiment was performed on the same sample. With saturation of the more intense proton signal of C2 at δ = 5.67 ppm, a signal at δ = 3.82 ppm was observed that corresponds to the more intense proton signal of C4. From these results it can be deduced that these two protons are on the same side of the molecule, which assigns this set of peaks of the *S,S* diastereomer. Saturation of the C2 proton signal at δ = 5.910 ppm, which is the one with lower intensity, caused no signal. From this result it can be gathered that the distance between the saturated proton and other protons, especially the one on C4, is too long for any through-space interaction. This occurs for a saturated proton in an equatorial position. Therefore the set of peaks with lower intensity belongs to the 2*R*,4*S* diastereomer. Thus, the *S,S* and the 2*R*,4*S* diastereomers of 2-phenyl-5,5-dimethylthiazolidine-4-carboxylic acid are found in d_4-H_3OH solution with a ratio of approximately 65:35 at room temperature. This is in contrast to the results found previously for a d_6-DMSO solution of the same compound, where the corresponding ratio was 30:70. It seems probable that the different hydrogen-bonding properties of the solvents are the cause of the difference since the free energy difference between the *S,S* and 2*R*,4*S* diastereomers is −1.52 kJ mol^{-1} in d_4-CH_3OH solution and 3.10 kJ mol^{-1} in d_6-DMSO solution.

An additional NOE experiment was carried out on a d_4-CH_3OH solution of the diastereomers to assign the two diastereotopic methyl groups on C5. Irradiation of the more intense C4-H proton signal at δ 3.82 showed a distinct positive NOE for the CH_3 signal at δ 1.73. Thus C52 was assigned as *cis* to C4-H and C51 at δ 1.44 as *trans* to C4-H in the major (2*R*,4*S*) diastereomer in d_4-methanol.

Acknowledgements

We acknowledge, with thanks, financial support from the Natural Sciences and Engineering Research Council of Canada, gifts of ketoprofen from Rhone Poulenc Rorer, Montreal, and tiaprofenic acid from Roussel-Hoechst, Montreal, and help in the acquisition of the NMR data from Dr. D. Hughes, McMaster University.

1. H.E. Howard-Lock, C.J.L. Lock, A. Mewa, and W.F. Kean. Semin. Arthrit. Rheum. **15**, 261 (1986).
2. R. Faggiani, H.E. Howard-Lock, C.J.L. Lock, and R. Orgias. Can. J. Chem. **69**, 1 (1991).
3. H.E. Howard-Lock, C.J.L. Lock, and M.L. Martins. Can. J. Chem. **69**, 1721 (1991).
4. G.M. Sheldrick. SHELXTL PC. Release 4.1 Siemens Analytical Instruments, Inc. Madison, Wis. 1990.
5. D. Rogers. Acta Crystallogr. Sect. A: Cryst. Phys. Diffr. Theor. Gen. Crystallogr. **A37**, 734 (1981).
6. H.E. Howard-Lock, C.J.L. Lock, and P.S. Smalley. Can. J. Chem. **63**, 2411 (1985).
7. J. Loscalzo, R.G. Kallen, and D. Voet. Arch. Biochem. Biophys. **157**, 426 (1973).
8. I. McMillan and R.J. Stoodley. Chem. Commun. 11, (1968).

Can. J. Chem. Downloaded from www.nrcresearchpress.com by EESC ESCOLA DE ENGENHARIA on 09/08/12
For personal use only.

Molecular shape effects on electron and ion behavior in dielectric liquids: *cis*- and *trans*-butene-2 between the freezing and critical points

SHINICHI SASAKAKI[1] AND GORDON R. FREEMAN
Department of Chemistry, University of Alberta, Edmonton, AB T6G 2G2, Canada
Received December 13, 1993

SHINICHI SASAKAKI and GORDON R. FREEMAN. Can. J. Chem. **72**, 1625 (1994).

Radiolysis free ion yields, electron mobilities, and ion mobilities were measured as functions of applied electric field strength in the liquids *cis*- and *trans*-butene-2 at temperatures from near their freezing points to near their critical points. The dielectric permittivities were also measured, to permit extraction of electron thermalization distances from free ion yield data. The thermalization distance distribution in each liquid was found to be the Gaussian YGP, rather than the exponential YE or YEP. This indicates that electrons are not captured before thermalization in either liquid. The density-normalized thermalization distances $b_{GP}d$ were ~40% larger in *cis*- than in *trans*-butene-2; this correlates with the more globular structure of the *cis*- molecules, which decreases the efficiency of electron energy loss collisions in the liquid phase. Electron mobilities were not appreciably different from those reported earlier. Cation mobilities in the liquids from the freezing points ($T/T_c \approx 0.35$, $d/d_c \approx 3.2$) up to ~400 K ($T/T_c \approx 0.92$, $d/d_c \approx 2.0$) are adequately described by the free-volume model. At densities $d/d_c < 2.0$ the mobilities are smaller than predicted by the free-volume model.

SHINICHI SASAKAKI et GORDON R. FREEMAN. Can. J. Chem. **72**, 1625 (1994).

Opérant à des températures allant de leurs point de congélation à leurs point critiques, on a mesuré les rendements en ions libres, les mobilités des électrons et les mobilités des ions produits, en fonction de la force du champ électrique appliqué, lors de la radiolyse des *cis*- et *trans*-but-2-ènes liquides. On a aussi mesuré les permittivités afin de pouvoir déterminer les distances de thermalisation des électrons à partir des données des rendements en ions libres. On a trouvé que la distribution des distances de thermalisation dans chaque liquide présente une forme gaussienne YGP plutôt qu'une exponentielle YE ou YEP. Ce résultat indique que, dans chacun des liquides, les électrons ne sont pas capturés avant la thermalisation. Les distances de thermalisation normalisées pour la densité, $b_{GP}d$, sont environ 40% plus grandes dans le *cis*- que dans le *trans*-but-2-ène; ce résultat est en bon accord avec la structure plus globulaire des molécules *cis* qui, en phase liquide, diminue l'efficacité des pertes d'énergie par collision. Les mobilités des électrons ne sont pas très différentes de celles rapportées antérieurement. Les mobilités des cations dans les liquides, des points de congélation ($T/T_c \approx 0{,}35$, $d/d_c \approx 3{,}2$) jusqu'à environ 400 K ($T/T_c \approx 0{,}92$, $d/d_c \approx 2{,}0$) sont décrites d'une façon adéquate par le modèle sans volume. À des densités d/d_c inférieures à 2,0, les mobilités sont plus faibles que celles prédites par le modèle de volume-libre.

[Traduit par la rédaction]

Introduction

The present work continues the study of distribution functions of secondary electron thermalization distances in X-irradiated liquids (1). The scattering of low energy electrons in a liquid is strongly dependent on the molecular structure (2). Comparison of electron behaviors in isomeric hydrocarbons is particularly useful, because physical properties such as molar volume and average polarizability are similar, so differences in electron scattering properties can be attributed to differences in molecular shape.

Isomers of special interest are *cis*- and *trans*-butene-2. Previous measurements showed remarkable differences in the radiolytic free ion yields (3, 4) and in the mobilities of thermal electrons (3, 5) in these liquids. It appears that electrons are captured to form transient anions in the *trans*- isomer. However, the free ion yields were measured over a smaller temperature range than more recent studies of other liquids, so it was desirable to extend the temperature range for these butenes.

In the present work, samples of *cis*- and *trans*-butene-2 were sufficiently purified that electrons generated in them had half lives up to 300 μs at low temperatures. Electron and ion mobilities were remeasured as functions of electric field strength at temperatures from the freezing point to near the critical region.

[1]Permanent address: Radiation Safety Control Center, National Laboratory for High Energy Physics (KEK), Oho 1-1, Tsukuba, Ibaraki, Japan 305.

Experimental

A. Sample preparation

cis-Butene-2 (Phillips Research Grade, 99.94%) or *trans*-butene-2 (Phillips Research Grade, 99.75%) was transferred from the cylinder into a grease-free vacuum line, and further purified. Air was removed and the liquid butene was stirred in a flask with lithium aluminum hydride powder for three or more days, then distilled under vacuum onto sodium hydroxide pellets and let stand for three days. Finally, the butene was transferred into a bulb containing sodium–potassium alloy, stirred gently for more than one week, then let sit on the alloy until transfer to the conductance cell. Between successive reagent treatments the butene was degassed by trap-to-trap distillation, with the receiver held at 77 K while pumping on the downstream side.

B. Apparatus and experimental method

Two types of conductance cell were used. The high-pressure conductance cell (HPC) was like that shown in ref. 6, and the low-pressure conductance cell (LPC) like that in ref. 7, except for the geometry of the metal pin lead-throughs. The separation between the electrode plates, 3.23 mm in HPC and 2.60 mm in LPC, were measured directly using precision calipers. The effective area of the collector plate, 2.62 cm^2 in HPC and 8.00 cm^2 in LPC, was determined from capacitance measurement (8) using liquid benzene and air as standards. The cell capacitances obtained using these two standards gave results that agreed within 0.2%.

Before filling with a liquid, the cell was heated to 600 K while evacuating to 10^{-5} Pa.

The temperature of the sample was controlled to within 0.2 K. Details of the cooling (9) and heating (10) systems, and of temperature control and measurement (11, 12) have been reported. The voltage sources and data collection system are described in ref. 12.

Can. J. Chem. Downloaded from www.nrcresearchpress.com by EESC ESCOLA DE ENGENHARIA on 09/08/12
For personal use only.

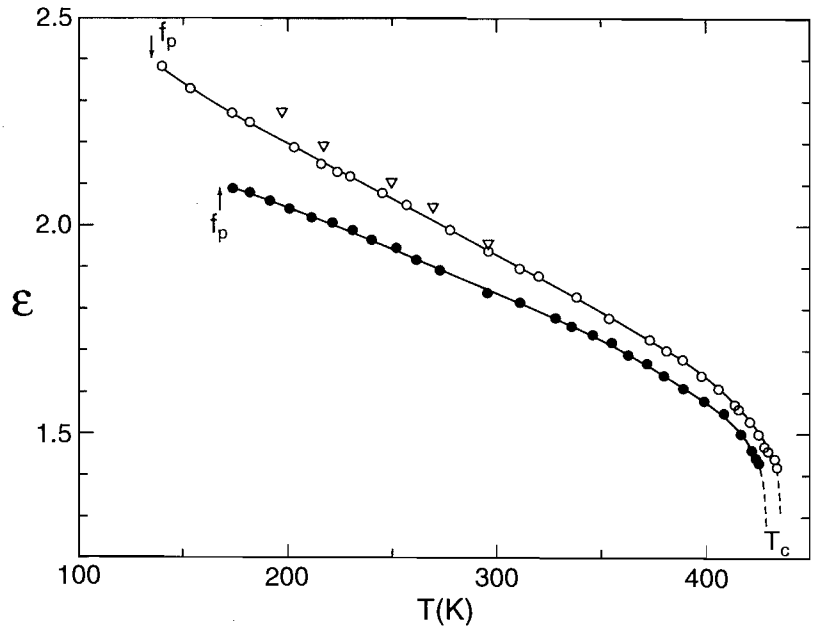

FIG. 1. Relative permittivities ϵ of *cis*- (○) and *trans*-butene-2 (●), measured as a function of temperature. ∇, Previous experimental values for *cis*-butene-2 (8).

To generate ion-electron pairs in the cell, a 0.10 or 1.0 μs pulse of 320 fJ (2 MeV) electrons from a van de Graaff accelerator was stopped in a 3 mm thick gold target to produce X rays. For each pulse a relative dose monitor measured the charge deposited on the gold target by the electron beam. The dose monitor was calibrated by LiF thermoluminescence (13) for each sample.

Ion mobilities were determined by time of flight (12). Electron mobilities were measured either by time of flight or by the electron conductance transient (ECT) method (14).

C. Physical properties

Static relative permittivities ϵ measured by the procedure of ref. 8 are plotted in Fig. 1 and listed in Table 1. The present values for *cis*-butene-2 are 1.0–2.7% lower than those at the same temperature reported in ref. 8.

Values of the liquid densities d of the 2-butenes reported in ref. 15*a* are only estimates; they do not vary sufficiently rapidly with T in the vicinity of the critical temperature T_c, and also the reported value of T_c for *cis*-butene-2 is 3 K lower than a more recent value (15*b*). Measured values of the density of liquid *n*-butane under its vapor pressure have recently been reported for the entire liquid range (15*c*). The liquids *cis*- and *trans*-butene-2 and *n*-butane have similar values of T_c (435.6, 428.6, 425.2 K) and d_c (240, 236, 228 kg/m^3) (15*b*), so densities of the two butenes were calculated from a plot of d/d_c against T/T_c made from the *n*-butane data (15*c*). Values of the densities are listed in Table 1. They are within 1% of those given in ref. 15*a* for *cis*-butene-2 at $226 < T/\mathrm{K} < 390$, and for *trans*- at $240 < T/\mathrm{K} < 400$.

Viscosities η were taken from ref. 15*a*, but they are unreliable near T_c.

Results and discussion

Free ion yields and electron thermalization distances

The electric field dependences of the free ion yields in *cis*- and *trans*-butene-2 at 296 K are shown in Fig. 2. Data obtained from the two cells HPC and LPC agree within 1%.

The lines in Fig. 2 were calculated from an extension (2) of the Onsager model (16). The model permits extrapolation of the yields to zero applied field strength and provides information about the distribution of thermalization distances of the secondary electrons. The free ion yield G_{fi}^E (ion pairs/16aJ) at applied field E(V/m) is given by

$$[1] \qquad G_{fi}^E = G_{tot} \int_{fi}^{\infty} \phi_{fi}^0(y)[1 + f(E, \epsilon, y, T)]F(y)dy$$

where G_{tot} is the total initial yield of ionizations, ϕ_{fi}^0 is fraction of the initial ion–electron pairs that escape geminate neutralization at $E = 0$, $f(E, \epsilon, y, T)$ is a function that describes the field dependence of escape, and $F(y)dy$ is the fraction of secondary electrons that have thermalization distances between y and $y + dy$. The model and eq. [1] are discussed in detail in ref. 2 and more briefly in ref. 17. The gas phase value of G_{tot} = 4.2 ionizations/16aJ was used (2, 18).

The electron thermalization distance distribution function that fits data from most liquids is a three-dimensional Gaussian with a power tail, and is denoted YGP (2):

$$[2] \qquad F(y) = \begin{cases} 0.96\ \mathrm{YG} & y < 2.4\ b_{GP} \\ 0.96[\mathrm{YG} + 0.5(b_{GP}^2/y^3)] & y > 2.4\ b_{GP} \end{cases}$$

where 0.96 is a normalization factor, $\mathrm{YG} = (4y^2/\pi^{1/2}b_{GP}^3)\exp(-y^2/b_{GP}^2)$, and b_{GP} is the most probable value of y.

The lines in Fig. 2 were calculated with eqs. [1] and [2], using b_{GP} = 6.46 nm in *cis*- and 4.72 nm in *trans*-butene-2. The fit is good for both compounds.

The measured yields at the lowest temperatures, near the freezing points, are shown in Fig. 3, and those at the highest temperatures, near the critical points, are shown in Fig. 4.

Several types of thermalization distance distribution function have been used from time to time (2, 19–24). The commonest alternatives to the three-dimensional Gaussian are one-dimensional exponentials. The simple exponential is designated YE:

$$[3] \qquad F(y) = \begin{cases} 0 & y < y_0 \\ b_E^{-1} \exp[(y_0 - y)/b_E] & y > y_0 \end{cases}$$

where y_0 is the reaction distance of the electron and ion and is

Can. J. Chem. Downloaded from www.nrcresearchpress.com by EESC ESCOLA DE ENGENHARIA on 09/08/12
For personal use only.

TABLE 1. Relative permittivities ϵ and densities d

T (K)	ϵ^a	d (kg/m^3)^b	T (K)	ϵ^a	d (kg/m^3)^b	T (K)	ϵ^a	d (kg/m^3)^b
				cis-Butene-2				
134.3^c	2.39^c	779						
140	2.38	773	276	1.99	636	406	1.61	442
153	2.33	761	296	1.94	614	414	1.57	418
173	2.27	742	311	1.90	595	416	1.56	410
182	2.25	733	320	1.88	586	421	1.53	394
203	2.19	712	338	1.83	562	425	1.50	374
216	2.15	698	355	1.78	540	426	1.49	372
224	2.13	691	373	1.73	509	428	1.47	360
230	2.12	684	381	1.70	494	430	1.46	346
245	2.08	670	389	1.68	479	633	1.44	322
257	2.05	658	398	1.64	461	434	1.42	305
						435.6^d	1.31^d	240^d
				trans-Butene-2				
167.6^c	2.11^c	732						
174	2.09	725	262	1.92	637	372	1.67	491
182	2.08	717	272	1.90	625	380	1.64	477
192	2.06	708	296	1.84	597	389	1.61	458
201	2.04	699	311	1.82	581	399	1.58	430
212	2.02	689	328	1.78	559	409	1.55	406
222	2.00	677	336	1.76	548	417	1.50	375
232	1.99	668	346	1.74	536	422	1.46	347
241	1.97	658	355	1.72	519	424	1.44	337
252	1.94	647	363	1.69	507	426	1.43	316
						428.6^d	1.28^d	236^d

[a]Measured.
[b]See text.
[c]Freezing point from ref. 15*b*; ϵ by extrapolation.
[d]Critical temperature and density from ref. 15*b*, p. 642, and ϵ calculated from the Clausius–Mosotti equation and the value of the molar polarization calculated from the other data: P (10^{-6} m^3/mol) = 20.7 for *trans*-, 22 for *cis*-.

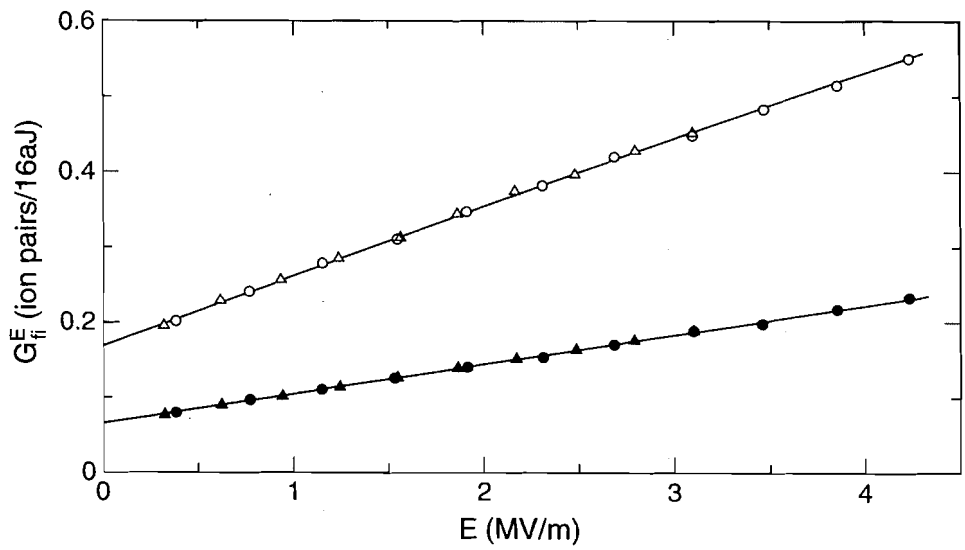

FIG. 2. Free ion yields in *cis*- (open symbols) and *trans*-butene-2 (solid symbols) at 296 K as a function of electric field strength. Results obtained in the LPC (○, ●) and HPC (△, ▲) are shown. The lines were calculated using distribution YGP and $G_{tot} = 4.2$, with $G^0_{fi} = 0.170$ and 0.068 ion pair/16aJ, and $b_{GP} = 6.46$ and 4.72 nm in *cis*- and *trans*-butene-2, respectively.

taken as 1 nm, and b_E is the attenuation coefficient. Another distribution, designated YEP, has a power tail added to YE for the outermost few percent of distances:

[4]
$$F(y) = \begin{cases} 0.97\ \mathrm{YE} & y - y_0 < 3.5\ b_{EP} \\ 0.97[\mathrm{YE} + 0.74\{b_{EP}^2/(y-y_0)^3\}] & y - y_0 > 3.5\ b_{EP} \end{cases}$$

where 0.97 is the normalization factor and b_{EP} replaces b_E in YE.

A Gaussian distribution of thermalization distances might arise from random scattering of electrons by the molecules to which they lose energy. An exponential distribution might arise from electron capture prior to thermalization (2, 21, 24).

Values of the yields calculated using these three distribution functions are shown in Figs. 3 and 4. Only YGP gave values

Can. J. Chem. Downloaded from www.nrcresearchpress.com by EESC ESCOLA DE ENGENHARIA on 09/08/12
For personal use only.

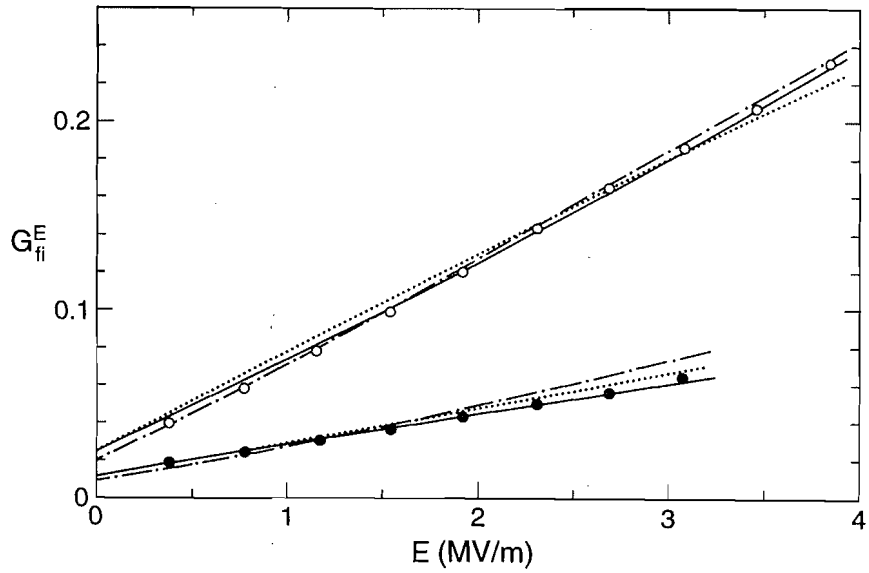

FIG. 3. Free ion yields in *cis*- (○, 140 K) and *trans*-butene-2 (●, 174 K) near the freezing points, as a function of electric field strength in the LPC. The lines were calculated using $G_{tot} = 4.2$ and: —, YGP, $b_{GP} = 5.26$ nm for *cis*-, 3.60 nm for *trans*-; ..., YEP, $y_0 = 1.0$ nm, $b_{EP} = 3.52$ nm for *cis*-, 2.26 nm for *trans*-: – · – ·, YE, $y_0 = 1.0$ nm, $b_E = 4.40$ nm for *cis*-, 3.14 nm for *trans*-.

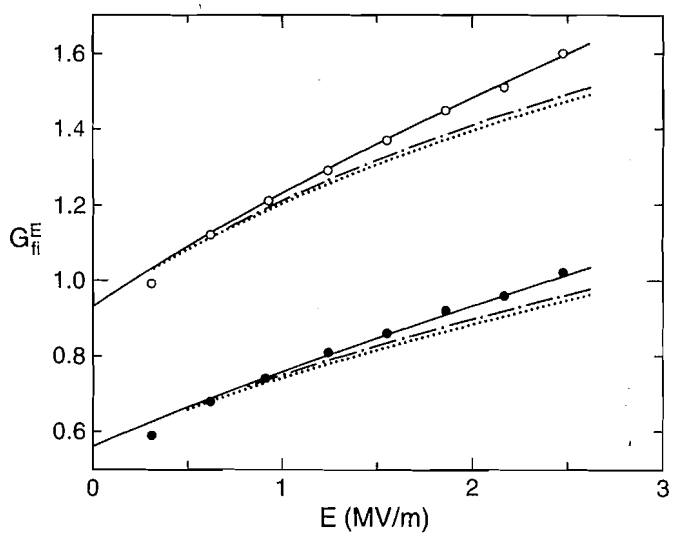

FIG. 4. Free ion yields in *cis*- (○, 434 K) and *trans*-butene-2 (●, 426 K) near the critical temperatures, as a function of electric field strength in the HPC. The lines were calculated using $G_{tot} = 4.2$ and: —, YGP, $b_{GP} = 15.5$ nm for *cis*- and 11.0 nm for *trans*-; ..., YEP, $y_0 = 1.0$ nm, $b_{EP} = 18.2$ nm for *cis*- and 11.2 nm for *trans*-: – · – ·, YE, $y_0 = 1.0$ nm, $b_E = 19.7$ nm for *cis*- and 12.4 nm for *trans*-.

that agreed with the experimental results over the entire temperature range. This indicates that the slowing-down electrons are not permanently captured before becoming thermalized in either *cis*- or *trans*-butene-2 (24).

The values of the most probable thermalization distances b_{GP} and the free ion yields extrapolated to zero applied electric field strength, G_{fi}^{0}, are listed in Table 2. Yields reported in 1973 (4) for these liquids at temperatures 183–293 K were about 25% higher than the present values, due to less accurate dosimetry.

If the efficiencies of the energy-loss collisions of the thermalizing electrons remained constant as the density of the liquid was changed, then the thermalization distance b_{GP} would be inversely proportional to the density; that is, the density-normalized thermalization distance $b_{GP}d$ would remain constant. The values of $b_{GP}d$ in *cis*-butene-2 are about 40% larger than those in the *trans*-isomer (Fig. 5), which means that electron energy-loss collisions are more effective in the latter. The lower efficiency in *cis*- correlates with the greater sphericity of the molecules (4, 25).

The efficiency of the energy-loss collisions increases ($b_{GP}d$ decreases) with increasing liquid density, except at the highest densities in *cis*-butene-2, near the freezing point, where the efficiency decreases ($b_{GP}d$ increases) again (Fig. 5). The behavior in *cis*-butene-2 is similar to that in propane, while that in *trans*-butene-2 is similar to that in ethene or cyclopropane (25). Transient anion formation has been suggested to occur in the latter three liquids (5, 25). Anion formation would be more favorable at the higher densities near the freezing points. The decrease of efficiency in *cis*-butene-2 or propane at the highest densities, as the crystalization temperature is approached, is attributed to a beginning of the ordering of the molecules in the liquid structure. The value of $b_{GP}d$ is larger in the ordered crystal than in the disordered liquid of the same compound (26).

The decrease of electron energy loss efficiency as the density decreases below 700 kg/m^3 is attributed to the looser packing of the liquid molecules, the resulting lower frequency of the intramolecular oscillations, and the reduced magnitude of the short-range electron–molecule interactions. The value of $b_{GP}d$ is determined mainly by inelastic collisions of the electrons at energies <0.1 aJ (2).

Electron mobilities

Electron mobilities in both liquids are independent of electric field strength up to the maximum used, 3.1 MV/m. The values obtained in the present work were virtually the same as those reported earlier (5), and nothing can yet be added to the discussion there.

Ion mobilities

Most of the samples contained a trace of impurity that scavenged some of the electrons. In those cases the ion conduc-

Can. J. Chem. Downloaded from www.nrcresearchpress.com by ESC ESCOLA DE ENGENHARIA on 09/08/12
For personal use only.

TABLE 2. Free ion yields and electron thermalization distances

T (K)	G_{fi}^{0} [a]	b_{GP} [b]	$b_{GP}d$ [c]	T (K)	G_{fi}^{0} [a]	b_{GP} [b]	$b_{GP}d$ [c]
			cis-Butene-2				
140	0.025	5.26	4.07	329	0.239	7.11	4.08
153	0.031	5.30	4.03	338	0.263	7.28	4.09
173	0.040	5.34	3.96	355	0.32	7.79	4.21
182	0.046	5.40	3.96	373	0.37	8.27	4.28
187	0.048	5.34	3.89	381	0.42	8.82	4.36
192	0.052	5.42	3.92	389	0.47	9.33	4.45
203	0.057	5.40	3.84	406	0.57	10.4	4.60
216	0.069	5.53	3.86	414	0.62	11.1	4.64
224	0.077	5.53	3.82	416	0.64	11.3	4.63
230	0.081	5.62	3.84	419	0.66	11.5	4.63
257	0.112	5.92	3.90	421	0.68	11.8	4.66
276	0.140	6.19	3.94	426	0.74	12.7	4.72
296	0.170	6.46	3.97	430	0.82	13.8	4.77
311	0.198	6.72	4.00	432	0.85	14.3	4.71
320	0.218	6.83	4.00	434	0.93	15.5	4.72
			trans-Butene-2				
174	0.012	3.60	2.61	328	0.100	5.06	2.83
182	0.014	3.70	2.65	336	0.114	5.26	2.88
191	0.016	3.69	2.61	346	0.129	5.44	2.91
201	0.018	3.78	2.64	355	0.158	5.88	3.05
212	0.023	3.97	2.74	372	0.188	6.23	3.06
222	0.026	3.96	2.72	380	0.213	6.52	3.14
232	0.029	4.02	2.72	389	0.244	6.98	3.20
241	0.033	4.08	2.73	399	0.293	7.53	3.24
252	0.038	4.25	2.75	409	0.36	8.25	3.35
262	0.044	4.37	2.79	417	0.43	9.24	3.47
272	0.050	4.45	2.78	422	0.48	10.0	3.46
296	0.068	4.72	2.82	424	0.51	10.4	3.51
311	0.081	4.82	2.82	426	0.56	11.1	3.50

[a]Yield at zero applied field strength (ion pairs/16aJ).
[b]Most probable thermalization distance (nm), distribution YGP, based on $G_{tot} = 4.2$.
[c]Density-normalized thermalization distance (10^{-6} kg/m^2).

Can. J. Chem. Downloaded from www.nrcresearchpress.com by EESC ESCOLA DE ENGENHARIA on 09/08/12
For personal use only.

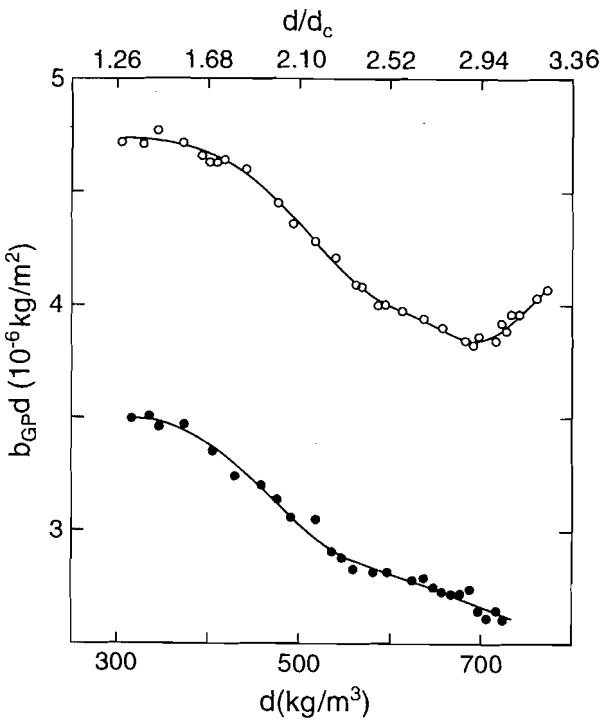

FIG. 5. Density-normalized thermalization distances $b_{GP}d$ plotted against density in *cis*- (○) and *trans*-butene-2 (●).

tance transient (ICT) consisted of a spike at the beginning due to electron conduction, followed by a "ramp" that corresponded to ion conduction, followed by a lower ramp that corresponded to slower ions. The ratio of the two ion mobilities obtained from the ratio of the ramp durations was 1.5 ± 0.1 at all temperatures in *cis*-, and for *trans*- it was 1.5 in the low temperature cell and 1.3 in the high temperature cell. Anion and cation mobilities in several alkanes and cycloalkanes under irradiation have been measured separately, and ratios $\mu_-/\mu_+ = 1.7$–2.2 were found (27, 28). The negative ions in these liquids resulted from electron capture by traces of impurities. We therefore assume that the slowest ions in the butenes were also cations; their mobilities are listed in Table 3.

The ion mobilities were independent of electric field strength up to the maximum used, 3.1 MV/m.

Arrhenius plots of μ_+ are slightly S-shaped (Fig. 6). The temperature coefficients E_μ between about 200 and 300 K are 4.9 kJ/mol in *cis*- and 4.6 kJ/mol in *trans*-; they increase at lower and higher temperatures. However, these temperature coefficients are relatively small, and densities of the liquids decrease greatly as the temperature is raised from near the freezing point to near the critical point. We therefore apply the free-volume model of ion transport (14):

$$[5] \qquad \mu_+ = \frac{A_+}{T^{1/2}} \left(\frac{V - V_0}{V_0} \right) \exp\left(-E_+/RT\right)$$

TABLE 3. Cation mobilities μ_+

T (K)	μ_+ (10^{-7} m^2/V·s)	T (K)	μ_+ (10^{-7} m^2/V·s)	T (K)	μ_+ (10^{-7} m^2/V·s)
			cis-Butene-2		
140	0.10	258	1.04	389	2.75
153	0.18	277	1.29	399	3.05
173	0.33	296	1.45	406	3.1
182	0.40	311	1.6	414	3.3
187	0.45	320	1.7	419	3.5
192	0.47	329	1.8	421	3.5
203	0.59	338	2.0	425	3.6
216	0.71	355	2.2	428	3.8
224	0.78	373	2.5	431	3.85
230	0.84	381	2.7	434	4.0
			trans-Butene-2		
174	0.37	262	1.28	375	2.8
182	0.46	272	1.37	385	3.0
192	0.55	296	1.61	399	3.5
201	0.66	311	1.74	409	3.7
212	0.77	328	2.0	417	4.1
222	0.86	337	2.1	422	4.3
232	0.99	346	2.25	425	4.5
241	1.09	355	2.4	426	4.5
252	1.16	363	2.6		

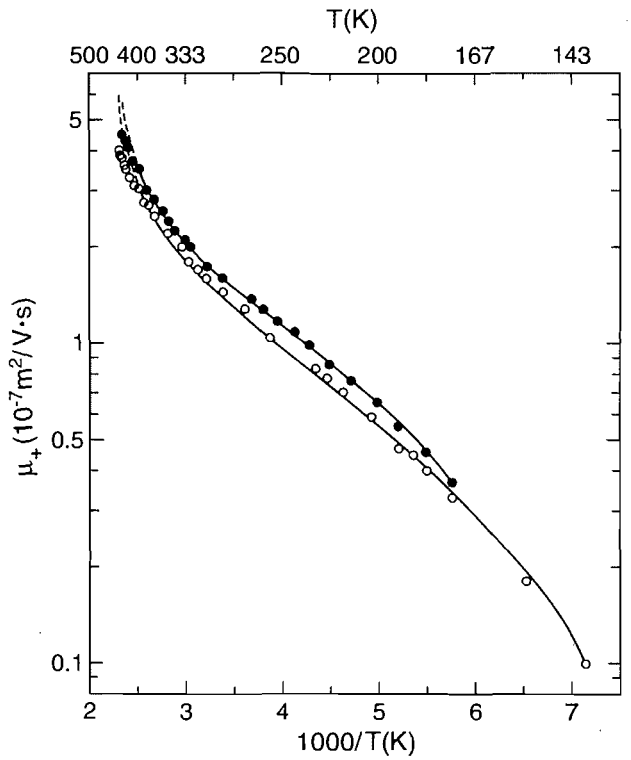

FIG. 6. Arrhenius plots of cation mobilities in *cis*- (○) and *trans*-butene-2 (●). The lines were calculated with eq. [5], using the parameters listed in Table 4.

where A_+ is a constant, V is the molar volume, V_0 is the molar volume at which the liquid molecules are too crowded for diffusion to occur, E_+ is a residual exponential temperature coefficient (see below), and R is the gas constant. Equation [5] provided an adequate description of the ion mobilities in the liquids from their freezing points up to 400 K, above which the calculated mobilities were too high (Fig. 6). The parameter

TABLE 4. Parameters for free-volume model (eq. [5]) of cation mobilities in *cis*- and *trans*-butene-2

Parameter	Value *cis*-	Value *trans*-
$A_+(10^{-6}$ K$^{1/2}\cdot$m^2/V·s)	9.9	7.4
$V_0(10^{-6}$ m^3/mol)	71.4	74.8
E_+(kJ/mol)	0.4	–0.9
E_+/RT_m[a]	0.2	–0.4
T_m(K)[a]	287	270

[a] T_m is the temperature in the middle of the range used to estimate E_+.

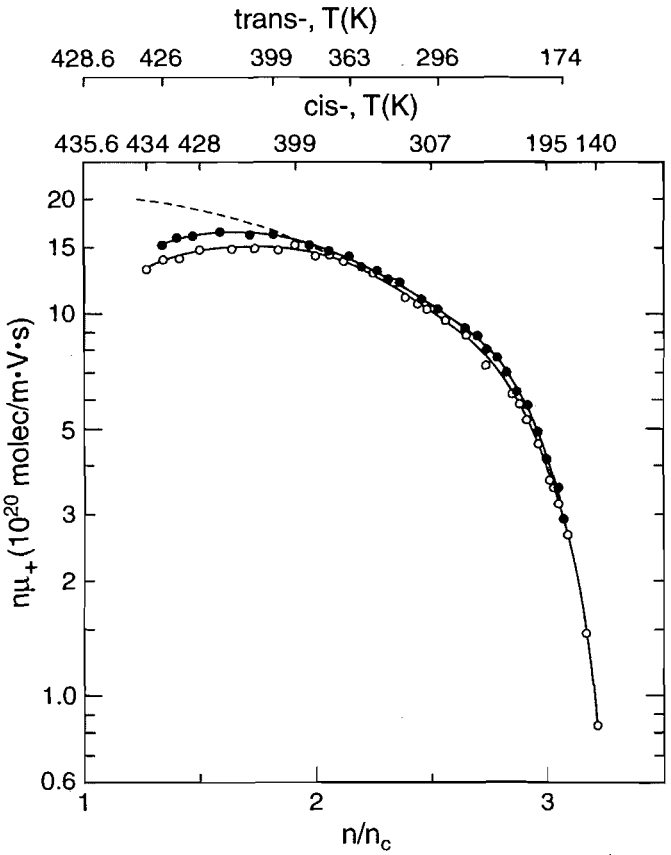

FIG. 7. Density-normalized mobilities as functions of relative number density (n_c is the number density in the critical fluid) in *cis*- (○) and *trans*-butene-2 (●). – – –, calculated from the free-volume model for both *cis*- and *trans*-.

values obtained by fitting eq. [5] to the experimental results up to 400 K are listed in Table 4.

The values $A_+ = 9.9$ and 7.4 (10^{-6} K$^{1/2}\cdot$ m^2/V·s) for radiolytic cations in *cis*- and *trans*-butene-2 are similar to those in the C_6 to C_{11} *n*-alkanes, which are 8–9 (10^{-6} K$^{1/2}\cdot$ m^2/V·s) (14). The value in a quite different liquid, CS_2, is also similar, 11×10^{-6} K$^{1/2}\cdot$ m^2/V·s (14). The similarity of A_+ values over such a wide range of nonpolar liquids (*cis*-butene-2 is slightly polar, with dipole moment 1.0×10^{-30} C·m (15*b*)) indicates that the cations are monomeric.

The values of V_0 correspond to 17.9 and 18.7 cm^3/mol per carbon atom in the molecules of *cis*- and *trans*-butene-2, respectively. They are similar to those for radiolytic cation mobilities in a series of *n*-alkanes, which range from 18.5 in C_6

Can. J. Chem. Downloaded from www.nrcresearchpress.com by EESC ESCOLA DE ENGENHARIA on 09/08/12
For personal use only.

Can. J. Chem. Downloaded from www.nrcresearchpress.com by EESC ESCOLA DE ENGENHARIA on 09/08/12
For personal use only.

to 18.3 (cm^3/mol carbon) in C_{11} (14). If the sulfurs in CS_2 are taken as equivalent in volume to methyl groups, the value $V_0/3 = 17.1$ (cm^3/mol C or S) is obtained. This similarity of values again suggests that the cations are monomeric.

The values of E_+ are smaller than the thermal agitation energy RT (Table 4), so they are not typical "activation" energies. The value for *trans*-butene-2 is slightly negative (Table 4), which produces the curvature of the plot near 180 K in Fig. 6. The small exponential term can be thought of as a modifier of the V_0 term; it corresponds to a slight increase of V_0 with T in *cis*-, and to a slight decrease of V_0 with increasing T in *trans*-. This might be related to the stick-like structure of the *trans*- molecules and the more globular structure of the *cis*-. The flexible C_6 to C_{11} *n*-alkane molecules all give positive values of E_+, with $E_+/RT_m = 0.4$–0.6; the relatively globular CS_2 has $E_+/RT_m = 0.3$ (14). This commonality of values again indicates a simplicity in the diverse systems.

At $T \gtrsim 400$ K ($T/T_c \gtrsim 0.92$, in the liquids under their vapor pressure) the free volume model breaks down, which means that liquid viscosity ceases to be the controlling factor for ion mobility (14). In the low density gas phase, the controlling factor for ion mobility is the collision frequency with the gas molecules. Thus the product of ion mobility and number density n of the gas tends to be constant in gases (29). The density-normalized mobilities $n\mu_+$ in the present liquids are plotted against the relative densities n/n_c, where n_c is the number density of the particular critical fluid, in Fig. 7. The dashed line in Fig. 7 indicates values estimated from the free-volume model for both liquids. The model predicts mobilities that are too high at $n/n_c < 2.0$, which corresponds to $T > 400$ K in the liquids under their vapor pressure.

The values of $n\mu_+$ pass through a maximum in the low density liquids at $n/n_c \approx 1.7$ (Fig. 7). This is consistent with earlier reports that the transition from the mechanism of ion transport in normal liquids, which is governed by viscosity or free volume, to the transport mechanism in normal gases, which is governed by collision rate or number density, occurs in the relative density region $2.0 > n/n_c > 0.4 \pm 0.1$ (29–31).

Acknowledgements

We thank Norman Gee for helpful discussions and a critical reading of this manuscript, and the staff of the Radiation Research Center for providing and maintaining the accelerator and electronic circuitry. One of us (S.S.) is grateful to the Japanese National Laboratory for High Energy Physics (KEK) and the Japanese Ministry of Education, Science and Culture for financial support during this work at the University of Alberta.

1. T. Yoshinari, N. Gee, and G.R. Freeman. Can. J. Chem. **70**, 327 (1992).
2. G.R. Freeman. *In* Kinetics of nonhomogeneous processes. *Edited by* G.R. Freeman. Wiley-Interscience, New York. 1987. Chap. 2.
3. J.-P. Dodelet, K. Shinsaka, and G.R. Freeman. J. Chem. Phys. **59**, 1293 (1973).
4. J.-P. Dodelet, K. Shinsaka, U. Kortsch, and G.R. Freeman. J. Chem. Phys. **59**, 2376 (1973).
5. J.-P. Dodelet and G.R. Freeman. Can. J. Chem. **55**, 2893 (1977).
6. J.-P. Dodelet and G.R. Freeman. Can. J. Chem. **55**, 2264 (1977).
7. T. Wada and G.R. Freeman. Phys. Rev. Lett. **42**, 715 (1979).
8. N. Gee, K. Shinsaka, J.-P. Dodelet, and G.R. Freeman. J. Chem. Thermodyn. **18**, 221 (1986).
9. M.A. Floriano, N. Gee, and G.R. Freeman. J. Chem. Phys. **84**, 6799 (1986).
10. M.A. Floriano and G.R. Freeman. J. Chem. Phys. **85**, 1603 (1986).
11. M.A. Floriano, N. Gee, and G.R. Freeman. Can. J. Chem. **66**, 1872 (1988).
12. N. Gee, M.A. Floriano, and G.R. Freeman. Z. Naturforsch. **A39**, 1225 (1984).
13. N. Gee, P.C. Senanayake, and G.R. Freeman. J. Chem. Phys. **89**, 3710 (1988).
14. N. Gee and G.R. Freeman. J. Chem. Phys. **90**, 5399 (1989).
15. (*a*) R.W. Gallant. Physical properties of hydrocarbons. Vol. 1. Gulf Publishing Co. Houston, TX. 1968; (*b*) R.C. Reid, J.M. Prausnitz, and T.K. Sherwood. The properties of gases and liquids. 3rd ed. McGraw-Hill, New York. 1977; (*c*) B.A. Younglove and J.F. Ely. J. Phys. Chem. Ref. Data, **16**, 758 (1987).
16. L. Onsager. Phys. Rev. **54**, 554 (1938).
17. G. Ramanan, N. Gee, and G.R. Freeman. Can. J. Phys. **68**, 925 (1990).
18. R.M. Leblanc and J.A. Herman. J. Chem. Phys. **63**, 1055 (1966).
19. G.C. Abell and K. Funabashi. J. Chem. Phys. **58**, 1079 (1973).
20. J.-P. Dodelet and G.R. Freeman. J. Chem. Phys. **60**, 4657 (1974).
21. A. Mozumder and M. Tachiya. J. Chem. Phys. **62**, 979 (1975).
22. P.M. Borsenberger and A.I. Ateya. J. Apply. Phys. **50**, 909 (1979).
23. H.T. Choi, D.S. Sethi, and C.L. Braun. J. Chem. Phys. **77**, 6027 (1982).
24. G. Ramanan and G.R. Freeman. J. Chem. Phys. **87**, 319 (1987).
25. N. Gee and G.R. Freeman. IEEE Trans. Electr. Insl. **EI-23**, 505 (1988).
26. K. Shinsaka and G.R. Freeman. Can. J. Chem. **52**, 3556 (1974).
27. A. Hummel and A.O. Allen. J. Chem. Phys. **44**, 3426 (1966).
28. P. Tewari and G.R. Freeman. J. Chem. Phys. **49**, 4394 (1968).
29. I. György, N. Gee, and G.R. Freeman. Can. J. Chem. **63**, 1105 (1985).
30. N. Gee and G.R. Freeman. Can. J. Chem. **59**, 2988 (1981).
31. N. Gee, G. Ramanan and G.R. Freeman. Can. J. Chem. **68**, 1527 (1990).

Vinyl ether hydrolysis. XXIX.[1] 1-Methoxy-1,3-butadiene: reaction mechanism and implication for hydrolysis of the mutagen fecapentaene-12

YVONNE CHIANG, ROBERT ELIASON,[2] GARY H.-X. GUO, AND A. JERRY KRESGE[3]

Department of Chemistry, University of Toronto, Toronto, ON M5S 1A1, Canada

Received January 28, 1994

YVONNE CHIANG, ROBERT ELIASON, GARY H.-X. GUO, and A. JERRY KRESGE. Can. J. Chem. **72**, 1632 (1994).

The hydrolysis of *cis*- and *trans*-1-methoxy-1,3-butadiene in aqueous solution occurs by hydron transfer to the δ-carbon atom with little or no β-hydronation to give crotonaldehyde as essentially the sole aldehyde product. The reaction gives appreciable hydronium-ion isotope effects in the normal direction (*cis*: $k_{H^+}/k_{D^+} = 2.60$, *trans*: $k_{H^+}/k_{D^+} = 3.52$) and shows general acid catalysis; five carboxylic acid catalytic coefficients for hydrolysis of the *trans* isomer give a good Brønsted relation with the exponent $\alpha = 0.59$. This is taken as evidence that these reactions occur by the conventional mechanism for vinyl ether hydrolysis involving rate-determining hydron transfer to substrate carbon followed by rapid formation and decomposition of a hemiacetal intermediate. Comparison of the reactivity of the present dienyl ethers with that of their monoenyl analog, methyl vinyl ether, shows that introduction of the second double bond decreases reactivity considerably: the hydronium-ion catalytic coefficient is reduced by a factor of 8.3 for the *trans* isomer and by a factor of 160 for the *cis* isomer. This reduction supports a hypothesis advanced to explain the occurrence of reaction by a different mechanism recently discovered in the hydrolysis of the strongly mutagenic polyenyl ether, fecapentaene-12.

YVONNE CHIANG, ROBERT ELIASON, GARY H.-X. GUO, et A. JERRY KRESGE. Can. J. Chem. **72**, 1632 (1994).

L'hydrolyse des *cis*- et *trans*-1-méthoxybuta-1,3-diènes en solution aqueuse se produit par un transfert d'hydron vers le carbone δ, avec peu ou pas de β-hydronation, et essentiellement il se forme uniquement du crotonaldéhyde comme produit aldéhydique. La réaction donne lieu à des effets isotopiques importants normaux de l'ion hydronium (k_{H^+}/k_{D^+} = *cis* 2,60 et *trans* = 3,52) et elle présente une catalyse acide généralisée; cinq coefficients catalytiques d'acide carboxylique pour l'hydrolyse de l'isomère *trans* donnent une bonne relation de Brønsted, avec un exposant $\alpha = 0,59$. On interprète ces données comme une preuve que ces réactions se produisent par le mécanisme conventionnel d'hydrolyse des éthers vinyliques impliquant, dans l'étape déterminante, un transfert d'hydron vers le carbone du substrat, puis la formation et la décomposition rapide d'un hémiacétal intermédiaire. Une comparaison de la réactivité des éthers diényles utilisés dans cette étude avec celle de leur analogue monoénylique, l'oxyde de méthyle et de vinyle, montre que l'introduction de la deuxième double liaison réduit considérablement la réactivité : le coefficient catalytique de l'ion hydronium est réduit par un facteur de 8,3 avec l'isomère *trans* et de 160 avec l'isomère *cis*. Cette réduction est en accord avec l'hypothèse préconisée pour expliquer l'existence d'une réaction impliquant un autre mecanisme qui a récemment été découverte lors de l'hydrolyse de l'éther polyénylique fortement mutagénique, le fécapentaène-12.

[Traduit par la rédaction]

The hydrolysis of simple vinyl ethers occurs through rate-determining hydron transfer from an acid catalyst to the β-carbon atom of the substrate, followed by rapid steps in which the alkoxycarbocation thus formed is hydrated and the ensuing hemiacetal is cleaved into aldehyde and alcohol products, eq. [1]. No exceptions to this reaction mechanism have so far been

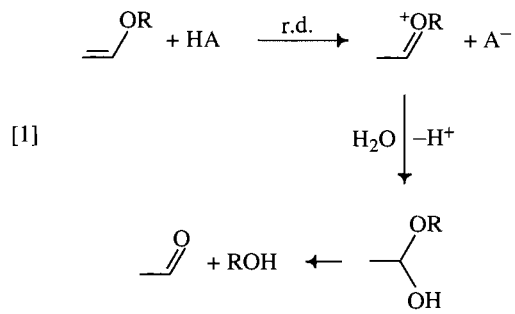

[1]

found for vinyl ethers containing only one carbon–carbon double bond (1, for a brief review of the evidence and references to earlier literature). Recently, however, it was discovered that the acid-catalysed hydrolysis of the polyenyl ether of glycerol, fecapentaene-12, **1**, a strongly mutagenic substance found in human feces and believed to be responsible for colon cancer, gives the unexpected hydroxyaldehyde **2** and allyl alcohol as reaction products, and a mechanism for this reaction involving hydronation of a glycerol hydroxyl group followed by nucleophilic attack of water at the far end of the polyene system, eq. [2], was proposed (2). Further investigation revealed that analogs of **1** containing only one or two double bonds conjugated with the glycerol oxygen reacted normally by the mechanism of eq. [1] and that at least three conjugated double bonds were required for the unusual reactivity (3). Semiempirical calculations were then performed whose results suggested that increasing the number of double bonds in the polyene system raised the rate of reaction by the unusual mechanism, eq. [2], and lowered that by the conventional route, eq. [1], thus rationalizing the observed reaction differences (4).

We have provided experimental support for this hypothesis by studying the hydrolysis of 1-methoxy-1,3-butadiene, **3**: we found that this substance undergoes acid-catalyzed hydrolysis by the conventional mechanism of eq. [1], and that its rate of reaction is indeed slower than that of the monoenyl analog, methyl vinyl ether **4**. This result corroborates a previous, less detailed investigation of the hydrolysis of 1-ethoxy-1,3-butadiene, (5) **5**, whose results, when combined with the rate of hydrolysis of ethyl vinyl ether, (6) **6**, also shows that introduction of the second double bond produces a rate retardation.

Experimental section

Materials

A sample of *trans*-1-methoxy-1,3-butadiene (Aldrich Chemical Company, Inc.) used for kinetic measurements was purified by gas

[1]Part XXVIII: ref. 15.

[2]On leave from Department of Chemistry, Southwest State University, Marshall, MN 56258, U.S.A.

[3]Author to whom correspondence may be addressed.

Can. J. Chem. Downloaded from www.nrcresearchpress.com by 85.192.166.187 on 09/08/12
For personal use only.

[2] 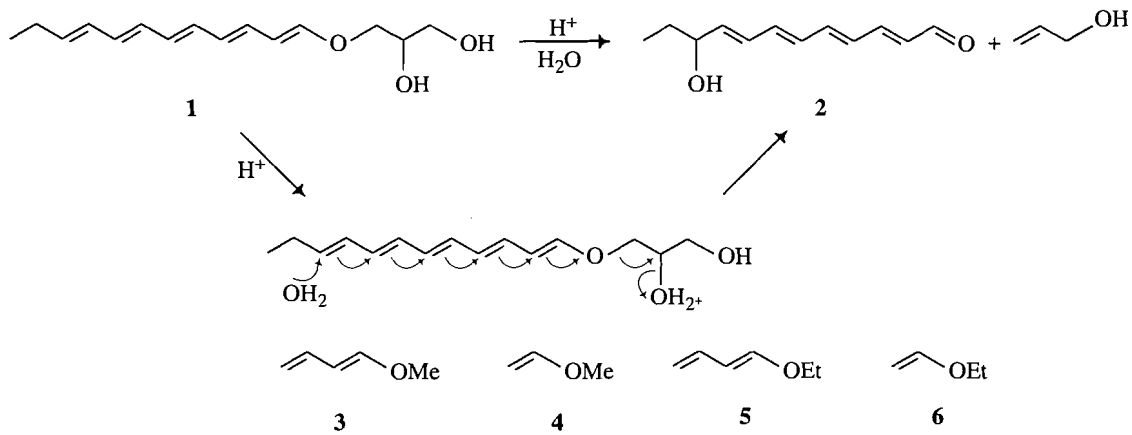

chromatography. The *cis* isomer was prepared by hydrogenation of *cis*-1-methoxybut-1-ene-3-yne (Aldrich Chemical Company, Inc.) using Lindlar catalyst (7), and a sample for kinetics was also purified by gas chromatography. The proton NMR spectra of both materials were consistent with their structures and with a previous report (8).

3-Butenal was prepared by controlled hydrolysis of its dimethyl acetal, itself obtained by reaction of allylmagnesium chloride with trimethylorthoformate (9). Two grams of the acetal (^{1}H NMR ($CDCl_3$), δ/ppm: 2.35–2.45 (2H, m), 3.31 (6H, s), 4.38–4.43 (1H, t), 5.08–5.19 (2H, m), 5.70–5.90 (1H, m)) was added to 10 mL H_2O containing a few drops of HCl (pH 5) and the mixture was shaken vigorously for 10 min. It was then immediately extracted with three 15 mL portions of diethyl ether, the ether extracts were dried with anhydrous $MgSO_4$, and the ether was removed by evaporation. The residue consisted of 60% 3-butenal plus 5% of the isomeric cronaldehyde (*trans*-2-butenal) and 35% of unreacted acetal. A pure sample of 3-butenal was obtained by distillation followed by preparative GC; ^{1}H NMR ($CDCl_3$), δ/ppm: 3.19–3.22 (2H, m), 5.17–5.34 (2H, m), 5.82–6.04 (1H, m), 9.63–9.73 (1H, t).

Cyanoacetic, chloroacetic, methoxyacetic, and acetic acids were purified by distillation; all other materials were best available commercial grades and were used as received.

Product analysis

The hydrolyses of *cis*- and *trans*-1-methoxy-1,3-butadiene were conducted separately by adding 4–6 drops of diene to 1 mL portions of 1.0 M aqueous $HClO_4$ and shaking the initially cloudy mixtures for several hours until they became clear. The mixtures were then extracted with 1 mL portions of $CDCl_3$ and the $CDCl_3$ extracts were dried with anhydrous Na_2CO_3 and their proton NMR spectra were taken.

Kinetics

Rates of hydrolysis of *cis*- and *trans*-1-methoxy-1,3-butadiene were measured spectroscopically by monitoring the decrease in absorbance of these dienyl ethers at λ = 245–250 nm. Measurements were made using a Cary model 2200 spectrometer whose cell compartment was thermostatted at 25.0 ± 0.1°C. Acid or buffer solutions were first allowed to reach temperature equilibrium with the spectrometer cell compartment, reactions were then initiated by injecting 2–5 μL portions of a methanol stock solution of dienyl ether substrate into the cuvette. Substrate concentrations in the reaction mixtures were ca. 10^{-4} M. Continuous recordings of absorbance, made over at least 4–5 half-lives, were fed into a computer and observed first-order rate constants were calculated by least-squares fitting of an exponential function. The data obeyed the first-order rate law well.

An initial-rate method was also used to determine rate constants for the slower reactions. Zero-order rates of change of absorbance, $\Delta A/\Delta t$, were measured for about 1% reaction, and these were then converted to first-order rate constants by dividing by the total absorbance change, $A_0 - A_\infty$, expected for 100% reaction: $k = (\Delta A/\Delta t)/(A_0 - A_\infty)$. Total absorbance changes were determined by first adding, to a cuvette containing only water, the same amount of substrate stock solution as used to determine $\Delta A/\Delta t$ and recording the absorbance of this solution; that gave a value of A_0. This solution was then acidified by adding a (known) small quantity of concentrated perchloric acid, waiting for a time corresponding to at least 10 hydrolysis half-lives, and then making another absorbance reading; this gave a value of A_∞. Substrate concentrations were chosen to make $A_0 - A_\infty$ equal to ca. one absorbance unit and an offset scale of the spectrometer was used to measure $\Delta A/\Delta t$. The method gave good results in agreement with rate determinations made by the conventional method (vide infra).

Results

Reaction products

Acid-catalyzed hydrolysis of 1-methoxy-1,3-butadiene by the route of eq. [1] can occur either by hydronation on the δ-carbon atom to give crotonaldehyde as the reaction product, eq. [3], or by hydronation on the β-carbon to give 3-butenal as the

[3] $CH_2{=}CHCH{=}CHOCH_3 \xrightarrow[H_2O]{H^+} CH_3CH{=}CHCHO + CH_3OH$

[4] $CH_2{=}CHCH{=}CHOCH_3 \xrightarrow[H_2O]{H^+} CH_2{=}CHCH_2CHO + CH_3OH$

reaction product, eq. [4]. We performed a product analysis for this reaction using a modification of a method employed before to determine the proportions of crotonaldehyde and 3-butenal formed in the ketonization of the corresponding enols (10). In that study, acid-catalyzed ketonization was followed by monitoring the absorbance increase at λ = 220 nm, where crotonaldehyde absorbs strongly but 3-butenal is transparent. Upon completion of the ketonization reaction, the final absorbance was recorded and the acidity was then changed to pH = 11, where 3-butenal is isomerized rapidly to crotonaldehyde. This produced an additional absorbance increase, from which, together with the final absorbance reading, the product composition could be calculated.

This method requires that no isomerization of 3-butenal to crotonaldehyde take place during the reaction being investigated. That condition was apparently satisfied in the ketonization study, but vinyl ether hydrolysis is a considerably slower process and we consequently could not assume that the requirement would be met in our case. We therefore determined the rate of acid-catalyzed isomerization of 3-butenal to crotonaldehyde[4] and found that, whereas only 1% isomerization occurred after 10

[4]Measurements at $[HClO_4]$ = 0.0095 and 0.095 M produced the rate law $k_{obs}/s^{-1} = (7.07 \pm 0.06) \times 10^{-6} + (1.11 \pm 0.01) \times 10^{-4}\ [HClO_4]$.

Can. J. Chem. Downloaded from www.nrcresearchpress.com by 85.192.166.187 on 09/08/12
For personal use only.

TABLE 1. Summary of catalytic coefficients for the hydrolysis of *cis*- and *trans*-1-methoxy-1,3-butadiene in aqueous solution at 25°C

	$k/10^{-3}$ M^{-1} s^{-1}	
Catalyst	*trans*-1-Methoxy-1,3-butadiene	*cis*-1-Methoxy-1,3-butadiene
H_3O^+	91.3	4.75
D_3O^+	26.0	1.83
CH_2CNCO_2H	1.62	0.0742
CH_2ClCO_2H	1.04	—
$CH_2(OCH_3)CO_2H$	0.413	—
HCO_2H	0.328, 0.318[a]	—
CH_3CO_2H	0.0714[a]	—

[a]Determined by the initial-rate method.

half-lives of the hydrolysis of *trans*-1-methoxy-1,3-butadiene, the extent of isomerization reached 20% after 10 hydrolysis half-lives of the more slowly reacting *cis*-1-methoxy-1,3-butadiene. Hydrolysis was therefore allowed to go to completion (10 half-lives) in the case of *trans*-1-methoxy-1,3-butadiene, but for *cis*-1-methoxy-1,3-butadiene it was stopped by pH adjustment to 11 after only 1 half-life (which corresponded to 1% isomerization). In the latter case, a minor correction for absorbance of the unreacted *cis*-1-methoxy-1,3-butadiene was included in calculating the product composition.

Determinations performed in 0.095 M $HClO_4$ solutions gave the following results: 99% crotonaldehyde and 1% 3-butenal for the hydrolysis of *trans*-1-methoxy-1,3-butadiene and 98% crotonaldehyde and 2% 3-butenal for the hydrolysis of *cis*-methoxy-1,3-butadiene. The uncertainties in these results are probably similar to the percentages of 3-butenal.

The essentially sole formation of crotonaldehyde as the initial product in these hydrolyses was confirmed by ^1H NMR examination of reactions performed in D_2O solution. Crotonaldehyde was the only aldehyde product detected, and the signal from its aldehydic proton was a clean doublet, produced by spin–spin coupling with a single adjacent vinyl proton, with no sign of the additional triplet structure expected from coupling with an adjacent vinyl deutron; deuterium would, of course, have entered and in part remained at this position if some of the crotonaldehyde observed had been formed by isomerization of initially produced 3-butenal.

This result is somewhat different from that obtained in a previous examination of the hydrolysis of *cis*- and *trans*-1-ethoxy-1,3-butadiene conducted in a 2/5 D_2O/diglyme solvent (5). NMR examination of deuterium incorporation into the crotonaldehyde produced there led to the conclusion that, whereas only crotonaldehyde was formed from the *trans* isomer, some 20% of 3-butenal was made initially from the *cis* isomer. The reason for this difference is not clear.

Kinetics

Rates of hydrolysis of *cis*- and *trans*-1-methoxy-1,3-butadiene were measured in dilute aqueous (H_2O and D_2O) solutions of perchloric and hydrochloric acids. Measurements were made over a range of acid concentrations and replicate determinations were made at each concentration. The data are summarized in supplementary table S1.[5]

[5]Tables S1 and S2 of rate data may be purchased from: The Depository of Unpublished Data, Document Delivery, CISTI, National Research Council Canada, Ottawa, Canada K1A O52.

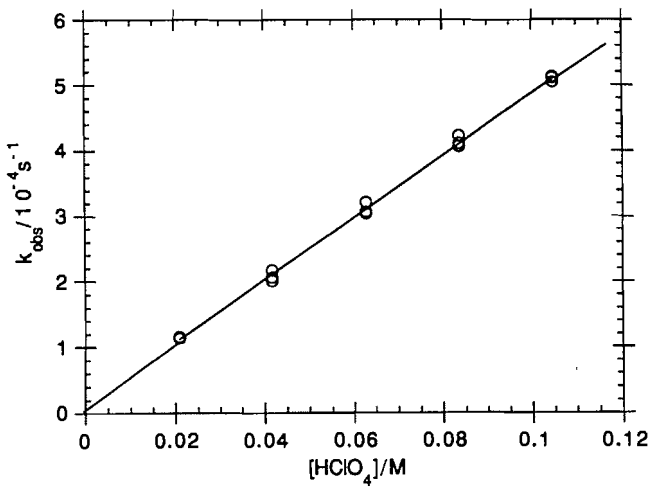

FIG. 1. Relationship between acid concentration and observed first-order rate constants for the hydrolysis of *cis*-1-methoxy-1,3-butadiene in perchloric acid solutions at 25°C.

As Fig. 1 illustrates, observed first-order rate constants proved to be accurately proportional to acid concentration, and second-order catalytic coefficients were therefore evaluated by linear least-square analysis. The results are summarized in Table 1. Combination of the catalytic coefficients for H_2O and D_2O solutions gives the isotope effects $k_{H^+}/k_{D^+} = 3.52 \pm 0.14$ for *trans*-1-methoxy-1,3 butadiene and $k_{H^+}/k_{D^+} = 2.60 \pm 0.09$ for *cis*-1-methoxy-1,3-butadiene.

Rate measurements were also made in carboxylic acid buffer solutions. Series of solutions of constant buffer ratio and constant ionic strength (0.10 M) but varying buffer concentration were used. The data are summarized in supplementary table S2.[5] With the weaker buffer acids this served to hold hydronium-ion concentrations constant, but with the stronger acids buffer failure occurred and hydronium-ion concentrations dropped regularly with decreasing buffer concentration (11). Observed rate constants were therefore adjusted to a common hydronium-ion concentrating using the known hydronium-ion catalytic coefficients determined in the perchloric acid solutions; hydronium-ion concentrations needed for this purpose were obtained by calculation using literature pK_a values for the carboyxlic acids and activity coefficients recommended by Bates (12).

Figure 2 shows that rate constants adjusted in this way are accurately proportional to buffer acid concentration, thus demonstrating the general acid catalysis expected for vinyl ether

Can. J. Chem. Downloaded from www.nrcresearchpress.com by 85.192.166.187 on 09/08/12
For personal use only.

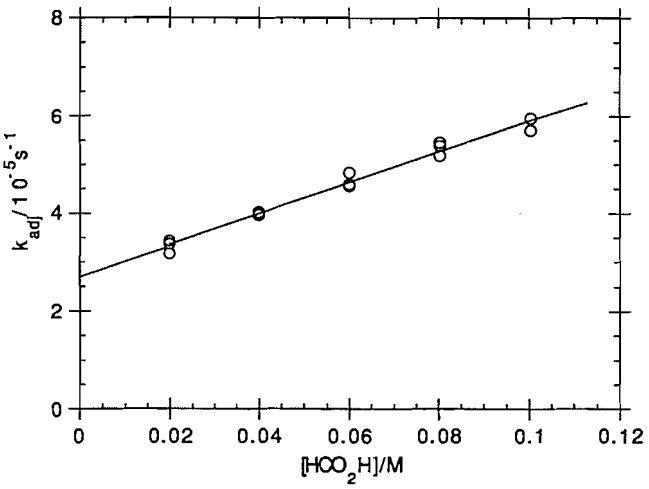

FIG. 2. Relationship between acid concentration and adjusted first-order rate constants for the hydrolysis of *trans*-1-methoxy-1,3-butadiene in formic acid buffer solutions at 25°C.

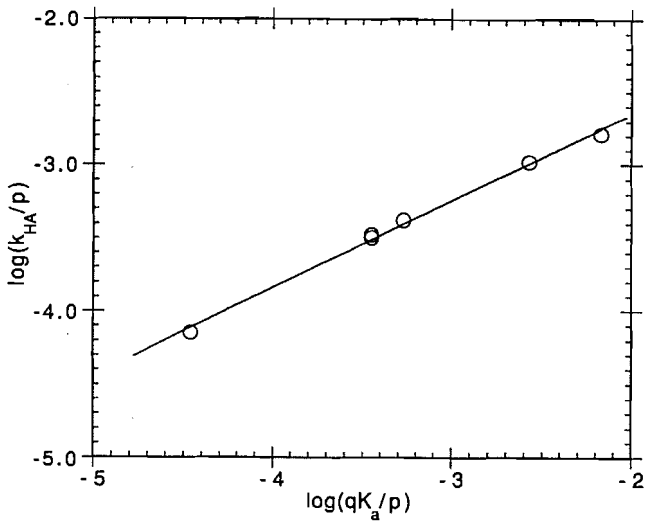

FIG. 3. Brønsted plot for the hydrolysis of *trans*-1-methoxy-1,3-butadiene in carboxylic acid buffer solutions at 25°C.

hydrolysis occurring by the conventional reaction mechanism of eq. [1]. The data were therefore analyzed by linear least-squares fitting of the rate law that applies in this situation, eq. [5]; the general acid catalytic coefficients obtained in this way

$$[5] \quad k_{adj}(\text{or } k_{obs}) = k_{H^+}[H^+] + k_{HA}[HA]$$

are listed in Table 1. They give a good Brønsted correlation, shown in Fig. 3, whose exponent is $\alpha = 0.59 \pm 0.02$.

Rates of hydrolysis of *trans*-1-methoxy-1,3-butadiene in formic acid solutions were determined by both the conventional technique, in which the reactions were allowed to run for several half-lives, and the initial-rate method. The results obtained by these two techniques are in excellent agreement: $k_{adj}/s^{-1} = (2.71 \pm 0.12) \times 10^{-5} + (3.28 \pm 0.17) \times 10^{-4}$ [HA] (conventional method) and $k_{adj}/s^{-1} = (2.72 \pm 0.08) \times 10^{-5} + (3.18 \pm 0.12) \times 10^{-4}$ [HA] (initial-rate method).

Hydronium-ion catalytic coefficients were also extracted from the buffer solution data by dividing the intercepts of eq. [5], $k_{H^+}[H^+]$, by the known hydronium-ion concentrations of these buffers. This produced six values for *trans*-1-methoxy-1,3-butadiene, whose average, $k_{H^+} = (9.50 \pm 0.40) \times 10^{-2}$ M^{-1} s^{-1}, agrees well with the result obtained in perchloric acid solutions, $k_{H^+} = (9.13 \pm 0.20) \times 10^{-2}$ M^{-1} s^{-1}. The single value obtained for *cis*-1-ethoxy-1,3-butadiene, $k_{H^+} = 5.21 \times 10^{-3}$ M^{-1} s^{-1}, is also consistent with the perchloric acid result for that substrate, $k_{H^+} = 4.75 \times 10^{-3}$ M^{-1} s^{-1}.

Discussion

Reaction mechanism

We have found that the hydrolysis of both *cis*- and *trans*-1-methoxy-1,3-butadiene gives strong hydronium-ion isotope effects in the normal direction ($k_H/k_D > 1$) and shows general acid catalysis. This is classic evidence for rate-determining hydron transfer to carbon (11), and it shows that these reactions occur by the conventional mechanism for vinyl ether hydrolysis shown in eq. [1]. This, of course, is the expected result, inasmuch as the newly discovered unusual mechanism of eq. [2] requires the presence of a hydroxyl group in the saturated alkyl portion of the vinyl ether, which is absent from the present substrates.

Reactivity

The hydronium-ion catalytic coefficients determined here show 1-methoxy-1,3-butadiene to be considerably less reactive than its monoenyl analog, methyl vinyl ether: comparison of $k_{H^+} = 0.76$ M^{-1} s^{-1} for the latter substance (13) with the present results gives a rate retardation of 1/8.3 for *trans*-1-methoxy-1,3-butadiene and 1/160 for *cis*-1-methoxy-1,3-butadiene. These rate ratios are similar to those that may be obtained from measurements of the rates of hydrolysis of *cis*- and *trans*-ethoxy-1,3-butadiene in 80% aqueous dioxane at single acid concentration (5) in combination with the rate constant reported for the hydrolysis of ethyl vinyl ether in the same medium (6); that comparison gives rate retardations of 1/7.2 and 1/103 for the *trans* and *cis* isomers, respectively, in the ethoxy series. These rate retardations provide good evidence for the hypothesis that the switch from the conventional mechanism for vinyl ether hydrolysis to the new mechanism shown in eq. [2] occurs in part because introduction of additional conjugated double bonds slows reaction by the conventional mechanism.

It is not clear, however, why hydrolysis of the present dienyl ethers should be slower than that of their monoenyl analog. Introduction of a second double bond in conjugation with the first will stabilize the vinyl ether, lowering the free energy of the initial state of the hydrolysis reaction. If this stabilization is lost in the transition state by hydron transfer to the α-carbon atom (eq. [4]), then the energy difference between initial state and transition state will increase and the reaction will be slowed. In the present case, however, hydronation takes place essentially exclusively on the δ-carbon atom, giving an allyl-type alkoxycarbocation, eq. [5]. The additional stabilization this will pro-

$$[5] \quad CH_2{=}CHCH{\equiv}CHOCH_3 \xrightarrow{H^+} CH_3\overset{+}{C}HCH{=}CHOCH_3 \leftrightarrow CH_3CH{=}\overset{+}{C}HCHOCH_3$$

duce should outweigh that conferred on the initial state, and that will lower the energy difference between initial state and transition state and raise the rate of reaction. We can offer no explanation for this apparent paradox.

Can. J. Chem. Downloaded from www.nrcresearchpress.com by 85.192.166.187 on 09/08/12
For personal use only.

It is curious that in both the methoxy and the ethoxy series, the *trans* butadienyl ethers are considerably more reactive than their *cis* counterparts. This is opposite to the reactivity pattern shown by alkyl-substituted monoenyl ethers: in the latter case the *cis* isomers are more reactive than the *trans* (6), a difference that can be attributed to the greater thermodynamic stability of the *trans* isomer (14). The *trans* isomers are also more stable than the *cis* in the case of the butadienyl ethers (14), which makes the greater reactivity of the *trans* isomers all the more surprising.

A similar difference in reactivity is shown by the butadienyl enols themselves: the *trans* isomer, **7**, has been found to

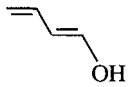

7

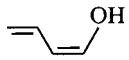

8

undergo acid-catalyzed ketonization by rate-determining hydron transfer from the hydronium ion 5.5 times more rapidly than the *cis* isomer, **8** (10). Hydronation here is also predominantly on the δ-carbon atom, and it has been suggested that the *trans* isomer is the more reactive because the incipient hydroxy-substituted allyl cation being formed in its transition state can more easily attain a planar configuration (10). It seems likely, however, that a Coulombic effect also operates, for the partial positive charges at oxygen and the γ-carbon atom of this cation will be farther apart in the ion formed from the *trans* isomer, **9**, than in that derived from the *cis*, **10**. This will make the *trans*

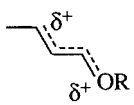

9

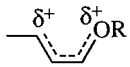

10

cation more stable than the *cis*, and a similar difference in the transition states leading to these cations will make the *trans* enol or enol ether more reactive than its *cis* counterpart.

Acknowledgements

We are grateful to the Natural Sciences and Engineering Research Council of Canada, the Donors of the Petroleum Research Fund, administered by the American Chemical Society, and the U.S. National Institutes of Health for financial support of this work.

1. A.J. Kresge. Acc. Chem. Res. **20**, 364 (1987).
2. L.B.J. Vertegaal, M. van der Steeg, and A. van der Gen. Tetrahedron Lett. **30**, 5639 (1989).
3. L.B.J. Vertegaal and A. van der Gen. Tetrahedron, **46**, 7301 (1990).
4. H. Zuilhof, L. Vertegaal, A. van der Gen, and G. Lodder. J. Org. Chem. **58**, 2804 (1993).
5. T. Okuyama, T. Sakagami, and T. Fueno. Tetrahedron, **29**, 1503 (1973).
6. T. Okuyama, T. Fueno, H. Nakatsuji, and F. Furukawa. J. Am. Chem. Soc. **89**, 5826 (1967).
7. S.M. Makin and S.D. Yablonoskaya. Zh. Org. Khim. (Engl. Transl.), **5**, 1696 (1969).
8. J.P. Dorie, M.L. Martin, S. Odiot, and F. Tonnard. Org. Magn. Reson. **5**, 265 (1973).
9. D. Kritchevsky. J. Am. Chem. Soc. **65**, 487 (1943).
10. B. Capon and B. Guo. J. Am. Chem. Soc. **110**, 5144 (1988).
11. J.R. Reefe and A.J. Kresge. *In* Techniques of chemistry. Vol. VI. Investigations of rates and mechanisms of reactions. *Edited by* C.F. Bernasconi. Wiley, New York. 1986. Part 1, Chap. XI.
12. R.G. Bates. Determination of pH. Theory and practice. Wiley, New York. 1973. p. 49.
13. A.J. Kresge, D.S. Sagatys. and H.L. Chen. J. Am. Chem. Soc. **99**, 7228 (1977).
14. T. Okuyama, T. Fueno, and J. Furukawa. Tetrahedron, **25**, 5409 (1969).
15. J. Jones and A.J. Kresge. Can. J. Chem. **71**, 38 (1993).

Can. J. Chem. Downloaded from www.nrcresearchpress.com by 85.192.166.187 on 09/08/12
For personal use only.

Oxidation of DL-penicillamine by chromium(VI). Kinetics of formation of the thioester intermediate

JOAQUIN F. PEREZ-BENITO, DRISS LAMRHARI, AND CONCHITA ARIAS

Departamento de Quimica Fisica, Facultad de Quimica, Universidad de Barcelona, Marti i Franques, 1

08028 Barcelona, Spain

Received January 12, 1994

JOAQUIN F. PEREZ-BENITO, DRISS LAMRHARI, and CONCHITA ARIAS. Can. J. Chem. **72**, 1637 (1994).

The kinetics of formation of the thioester involved as an intermediate in the reaction between chromium(VI) and DL-penicillamine in aqueous media (pH = 1–8) containing different buffers (acetate, citrate, and phosphate) has been studied by monitoring the disappearance of chromium(VI) at 370 nm and application of the initial-rates method. The initial rate is directly proportional to the initial concentrations of both oxidant and reductant, and the rate vs. pH plots show bell-shaped profiles. The reaction is catalyzed by the buffer present in the medium, the catalytic power of each buffer increasing in the order acetate < citrate < phosphate. This is explained in terms of a mechanism involving the formation of a complex between the acidic form of the buffer and $HCrO_4^-$ previous to the formation of the thioester. Potassium chloride and sodium sulfate do not seem to have important specific effects on the reaction rate, their effect being that of an acceleration of the reaction as the ionic strength increases. On the contrary, the sulfates of magnesium, manganese(II), and zinc (the latter only in the presence of acetate buffer) have specific effects, indicating the probable formation of several complexes. The spectrophotometric detection of the thioester at 430 nm has allowed to confirm some of the conclusions extracted from the measurement of initial rates, and suggests that this intermediate might approach a steady-state behavior in the three buffers at pH > 6.25, and also that a bimolecular reaction with DL-penicillamine might be involved in its destruction.

JOAQUIN F. PEREZ-BENITO, DRISS LAMRHARI et CONCHITA ARIAS. Can. J. Chem. **72**, 1637 (1994).

En examinant la vitesse de disparition du chrome(VI) à 370 nm et en appliquant la méthode des vitesses initiales, on a étudié la cinétique de formation du thioester impliqué comme intermédiaire dans la réaction du chrome(VI) et la DL-pénicillamine, en milieu aqueux (pH = 1 à 8) contenant divers tampons (acétate, citrate et phosphate). La vitesse initiale est directement proportionnelle aux concentrations à la fois de l'oxydant et du réducteur et les courbes des vitesses en fonction du pH présentent des profils en forme de cloche. La réaction est catalysée par le tampon présent dans le milieu, le pouvoir catalytique de chacun des tampons augmentant dans l'ordre acétate < citrate < phosphate. On peut expliquer ces résultats en fonction d'un mécanisme impliquant la formation, avant la formation du thioester, d'un complexe entre la forme acide du tampon et le $HCrO_4^-$. Le chlorure de potassium et le sulfate de sodium ne semblent pas avoir d'effets spécifiques importants sur la vitesse de la réaction; leur effet se limite à une accélération de la réaction lorsque la force ionique augmente. Au contraire, les sulfates de magnésium, de manganèse(II) et de zinc (dans ce dernier cas, uniquement en présence du tampon acétate) possèdent des effets spécifiques, suggérant la formation probable de plusieurs complexes. La détection spectrophotométrique du thioester à 430 nm a permis de confirmer quelques-unes des conclusions tirées des mesures des vitesses initiales et elle suggère que cet intermédiaire peut approcher un comportement d'état stationnaire dans les trois tampons, à des pH > 6,25, et aussi qu'une réaction bimoléculaire avec la DL-pénicillamine peut être impliquée dans sa destruction.

[Traduit par la rédaction]

Introduction

The kinetics of reduction of chromium(VI) by the aminoacid DL-penicillamine (DL-2-amino-3-mercapto-3-methylbutanoic acid) and other thiols was studied in perchloric acid media by McAuley and Olatunji (1), reporting the spectrophotometric detection of an oxidant–reductant thioester involved as a relatively-stable intermediate. More recently, some interest has arisen on the kinetics and mechanism of this and similar reactions at physiological pH, since it seems probable that the mutagenic effects of the well-known carcinogen chromium(VI) require its previous reduction inside the cell, and glutathione and other biological thiols seem to be likely candidates as reductants (2, 3).

We have studied the reaction between chromium(VI) and DL-penicillamine in aqueous solutions under slightly acidic or neutral conditions. Our results indicate that the kinetics of formation of the corresponding thioester depends notably on the nature and concentration of the buffer present in the medium, and that some electrolytes have important specific effects on that formation.

Experimental section

Materials and methods

The solvent water was purified by deionization followed by double distillation (the first time from a potassium permanganate solution). The oxidant was potassium dichromate (although, under the conditions of this work, most of it was present in the solutions in the monomeric forms, $HCrO_4^-$ and CrO_4^{2-}). The reductant was DL-penicillamine (DL-PA). Three types of buffer were used: citric acid (H_3Cit) – sodium citrate (Na_3Cit), acetic acid (HAc) – sodium acetate (NaAc), and KH_2PO_4–K_2HPO_4 (in some experiments, the acid of each buffer mixture was replaced by HCl). The ionic strength was controlled when necessary with KCl. Besides this electrolyte, the effects of Na_2SO_4, $MgSO_4$, $MnSO_4$, and $ZnSO_4$ on the reaction rate were also studied.

The kinetics of the reaction was followed by monitoring the chromium(VI) decay at 370 nm with a Varian Cary 219 UV-VIS spectrophotometer. The formation and decay of the thioester intermediate were detected by following the reaction at 430 nm. The pH of the solutions was measured with a Metrohm 605 pH-meter provided with a combination electrode.

Determination of initial rates

In order to avoid that the reaction be too fast to be followed with a conventional spectrophotometer, in most of the experiments the concentration of DL-penicillamine was not large enough to assure a first-order decay of the reaction rate as the concentration of chromium(VI) decreased. Moreover, in some of the experiments designed to study the effect of the buffer, the concentration of the latter was so low that the pH of the solution increased appreciably as the reaction proceeded. A further deviation from the behavior expected for a first-

Can. J. Chem. Downloaded from www.nrcresearchpress.com by 85.192.166.187 on 09/08/12
For personal use only.

Can. J. Chem. Downloaded from www.nrcresearchpress.com by 85.192.166.187 on 09/08/12
For personal use only.

order kinetics was provoked by the relative stability of the thioester involved as intermediate.

Because of these reasons, the kinetic data for the reaction were obtained by application of the initial-rates method. The absorbances measured at 370 nm from the beginning of the reaction until around 25% of the initial chromium(VI) was destroyed were fitted against time by nonlinear least squares to the equation:

$$[1] \qquad \ln (A_t - A_\infty) = a + bt + ct^2$$

A_t and A_∞ being the absorbances at time t and at the end of the reaction, respectively, whereas a, b, and c are fitting parameters. The initial rate was then obtained as:

$$[2] \qquad r_0 = -b[\mathrm{Cr(VI)}]_0$$

The kinetic data given in this work are the averages of two independent determinations. Their reproducibility was assured in most cases within ± 1%.

Results

Stoichiometry

A spectrophotometric search for the stoichiometry was undertaken, mixing chromium(VI) and DL-penicillamine (RSH) in different proportions in citrate buffer (pH = 6.01) and allowing the solutions to react until completion. After one week, the absorbance at 370 nm was measured and, when represented against the reductant/oxidant ratio, it led to a curve instead of to a linear plot. The minimum ratio required for total consumption of chromium(VI) was $[\text{DL-PA}]_0/[\mathrm{Cr(VI)}]_0 = 2.3$. The results of this study (deposited as supplementary material[1]) are in agreement with those found by McAuley and Olatunji (1) in perchloric acid media, and suggest that at low values of that ratio there is a deviation from the main stoichiometry:

$$[3] \qquad 2HCrO_4^- + 6RSH + 8H^+ = 2Cr^{3+} + 3RSSR + 8H_2O$$

probably due to overoxidation of the main organic product (the disulfide, RSSR).

Kinetic data

The initial rate (r_0) was directly proportional to the initial concentrations of both oxidant and reductant (Table 1), thus allowing the determination of the second-order rate constants as $k_2 = r_0/[\mathrm{Cr(VI)}]_0[\text{DL-PA}]_0$. The initial rate vs. pH plots showed a certain dependence on the nature of the buffer (acetate, citrate, or phosphate), although in the three cases they had a bell-shaped profile with a maximum at pH = 5.5–6.0 (Fig. 1); similar bell-shaped rate vs. pH plots were also obtained by Connett and Wetterhahn (4) for the chromium(VI) oxidation of other thiols.

At constant pH, the second-order rate constants increased with the total concentration of buffer ($[B]_T$) according to the law (Fig. 2):

$$[4] \qquad k_2 = \frac{a' + b'[B]_T}{1 + c'[B]_T}$$

The dependences of the fitting parameters a', b', and c' on the pH have been studied; the data corresponding to both a' and b' are shown in Fig. 3, whereas those for c' have been deposited.[1] Parameter b' is a good measurement of the catalytic power of each buffer, which is in the sequence acetate < citrate < phosphate. Due to the fact that the reaction in the presence of phosphate buffer was very fast, accurate values of parameters a' and c' could be obtained only for the other two buffers. Parameter a' is an extrapolation of the second-order rate constant at zero concentration of buffer, and it should thus be independent of the buffer used; however, we can see that there is a slight deviation in the values corresponding to acetate and citrate buffers, indicating the existence of a small systematic error, although the two sets of values seem to be rather consistent. For the same buffers, parameter c' increased with increasing pH, being this effect much more pronounced for acetate than for citrate.

The influences of several electrolytes on the reaction rate have been investigated. Given that addition of those electrolytes resulted either in an increase or a decrease of the pH,

[1]Copies of material on deposit may be purchased from the Depository of Unpublished Data, Document Delivery, CISTI, National Research Council Canada, Ottawa, ON K1A 0S2, Canada.

TABLE 1. Dependence of the initial rate on the initial concentrations of oxidant and reductant

$10^4[\mathrm{Cr(VI)}]_0$ (M)	$10^3[\text{DL-PA}]_0$ (M)	$10^7 r_0$ (M s^{-1})	k_2 (M^{-1} s^{-1})[a]
2.56	4.80	8.4 ± 0.1	0.68 ± 0.01[b]
5.12	4.80	17.4 ± 0.2	0.71 ± 0.01[b]
7.68	4.80	24.9 ± 0.3	0.68 ± 0.01[b]
10.25	4.80	34.7 ± 0.5	0.71 ± 0.01[b]
12.81	4.80	43.4 ± 1.0	0.71 ± 0.02[b]
15.37	4.80	52.7 ± 0.8	0.71 ± 0.01[b]
1.60	0.48	0.46 ± 0.02	0.60 ± 0.03[c]
1.60	1.44	1.47 ± 0.02	0.64 ± 0.01[c]
1.60	2.40	2.46 ± 0.04	0.64 ± 0.01[c]
1.60	3.36	3.55 ± 0.05	0.66 ± 0.01[c]
1.60	4.32	4.56 ± 0.07	0.66 ± 0.01[c]
1.60	4.80	5.2 ± 0.2	0.68 ± 0.03[c]
1.60	9.61	10.1 ± 0.5	0.66 ± 0.03[c]
1.60	14.41	15.0 ± 0.2	0.65 ± 0.01[c]
1.60	19.22	20.6 ± 0.6	0.67 ± 0.02[c]
1.60	24.02	24.6 ± 0.8	0.64 ± 0.02[c]

[a]Calculated as $k_2 = r_0/[\mathrm{Cr(VI)}]_0[\text{DL-PA}]_0$.
[b]$[H_3Cit] = 3.40 \times 10^{-2}$ M, $[Na_3Cit] = 6.80 \times 10^{-2}$ M, ionic strength 0.41 M, pH = 4.97 ± 0.02, 25.0°C.
[c]$[H_3Cit] = 7.32 \times 10^{-3}$ M, $[Na_3Cit] = 6.80 \times 10^{-2}$ M, ionic strength 0.41 M, pH = 6.00 ± 0.02, 25.0°C.

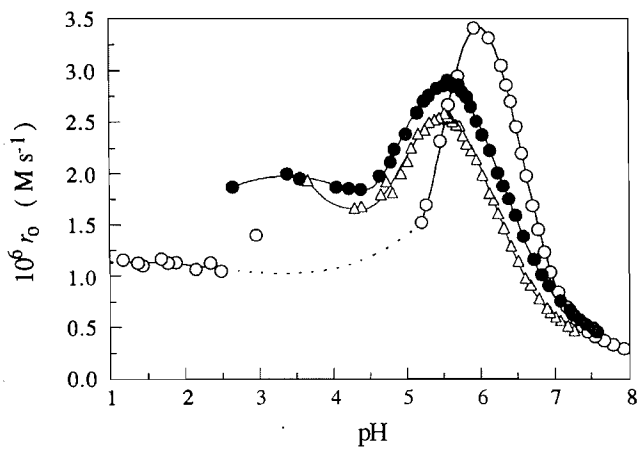

FIG. 1. Dependence of the initial rate on the pH for the reaction between chromium(VI) (5.15×10^{-4} M) and DL-penicillamine (4.80×10^{-3} M) at ionic strength 2.1 M (KCl) and 25.0°C. Buffers: NaAc (0.20 M) – HCl, triangles; Na_3Cit (6.80×10^{-2} M) – HCl, solid circles; and K_2HPO_4 (4.80×10^{-2} M) – HCl, open circles. The HCl concentration was changed for each buffer from 0 to 0.19 M.

Can. J. Chem. Downloaded from www.nrcresearchpress.com by 85.192.166.187 on 09/08/12
For personal use only.

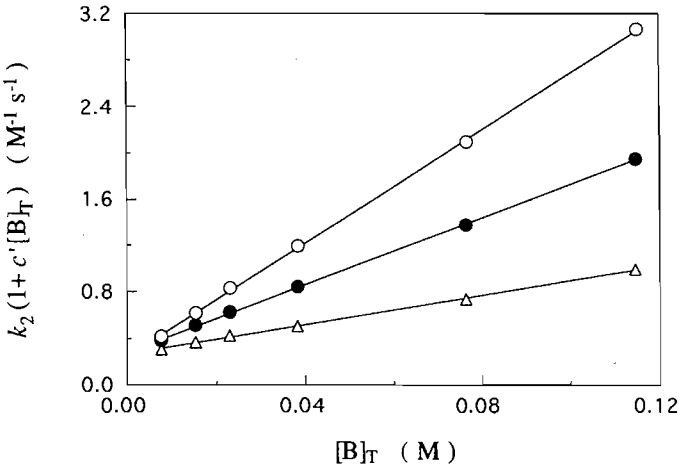

FIG. 2. Dependence of the second-order rate constant on the total concentration of buffer at constant pH for the reaction between chromium(VI) (5.15×10^{-4} M) and DL-penicillamine (4.80×10^{-3} M) at ionic strength 2.1 M (KCl) and 25.0°C. Buffers: HAc–NaAc ([acid]/[base] = 0.12, pH = 5.52), triangles; H_3Cit–Na_3Cit ([acid]/[base] = 0.13, pH = 5.59), solid circles; and KH_2PO_4–K_2HPO_4 (acid/base = 1.67, pH = 6.05), open circles.

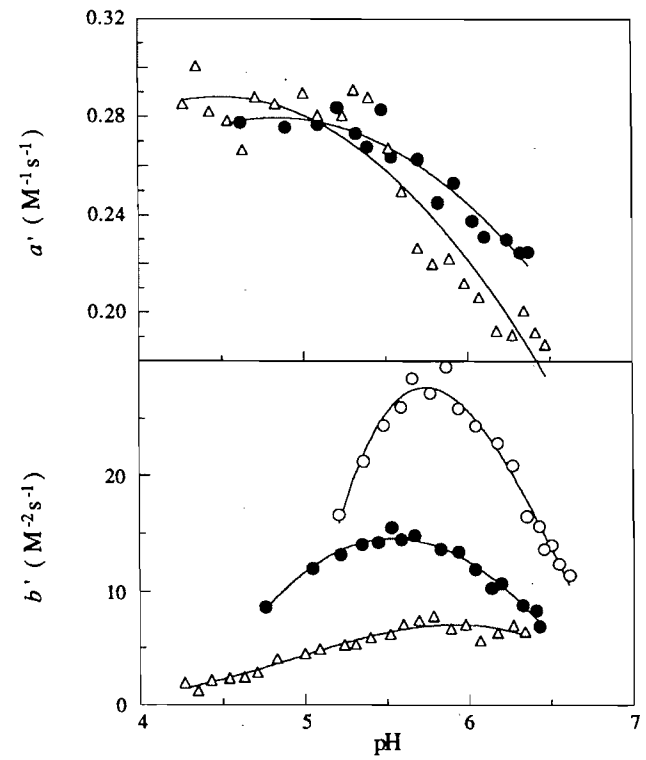

FIG. 3. Dependence of parameters a' (above) and b' (below) on the pH for the reaction between chromium(VI) (5.15×10^{-4} M) and DL-penicillamine (4.80×10^{-3} M) at ionic strength 2.1 M (KCl) and 25.0°C. Buffers: HAc–NaAc ([acid]/[base] = 0.01–2.44), triangles; H_3Cit–Na_3Cit ([acid]/[base] = 0.02–0.50), solid circles; and KH_2PO_4–K_2HPO_4 ([acid]/[base] = 0.50–12.50), open circles.

the effect of this change in pH was minimized by working near the maximum of the rate vs. pH plots (Fig. 1), where the rate is fairly independent of pH.

Potassium chloride accelerates the reaction both in acetate and citrate buffers, but much more in the latter case. The effect of sodium sulfate in acetate buffer is very similar to that of

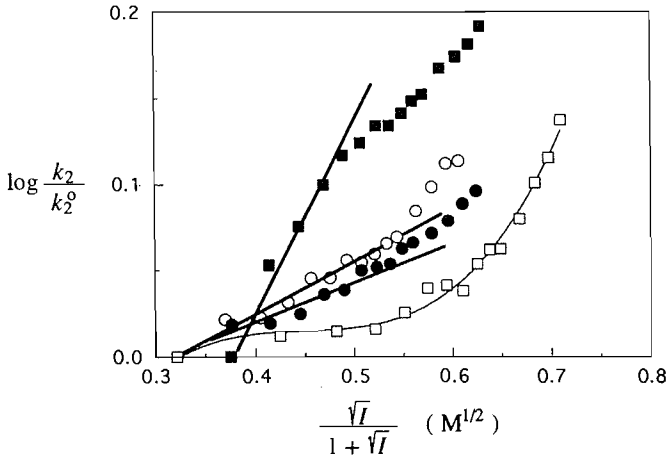

FIG. 4. Dependence of the second-order rate constant on the ionic strength for the reaction between chromium(VI) (5.15×10^{-4} M) and DL-penicillamine (4.80×10^{-3} M) at 25.0°C, k_2^0 being the value of the second-order rate constant corresponding to the ionic strength of the buffer, in the absence of any added electrolyte. Buffers: for the solid squares, Na_3Cit (5.58×10^{-2} M) – HCl (2.42×10^{-2} M); for the other three cases, NaAc (0.20 M) – HCl (2.42×10^{-2} M). Electrolytes: potassium chloride (solid squares, pH = 5.84–5.52, ionic strength 0.359 M + [KCl]; solid circles, pH = 5.53–5.62, ionic strength 0.224 M + [KCl]); sodium sulfate (open circles, pH = 5.53–5.48, ionic strength 0.224 M + 3 [Na_2SO_4]), and magnesium sulfate (open squares, pH = 5.53–5.07, ionic strength 0.224 M + 4 [$MgSO_4$]).

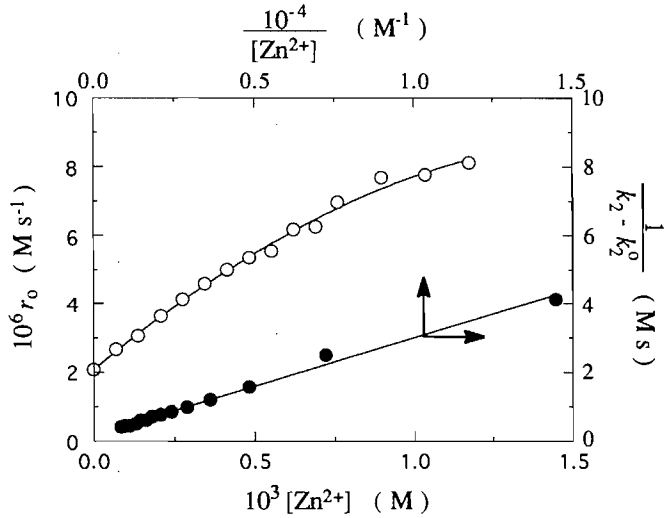

FIG. 5. Influence of the concentration of zinc sulfate on the kinetics of the reaction between chromium(VI) (5.15×10^{-4} M) and DL-penicillamine (4.80×10^{-3} M) in the presence of HAc (2.80×10^{-2} M) – NaAc (0.20 M) buffer at ionic strength 0.21 M, pH 5.50 ± 0.02 and 25.0°C. Open circles: r_0 vs. $[Zn^{2+}]$ plot. Solid circles: $1/(k_2 - k_2^0)$ vs. $1/[Zn^{2+}]$ plot, k_2^0 being the value of the second rate constant corresponding to the reaction in the absence of zinc ion. Except when indicated, the x and y axes are those situated below and on the left, respectively.

potassium chloride in the same buffer, but magnesium sulfate increases the reaction rate much less than expected from the ionic strength values (Fig. 4).

Zinc sulfate also accelerates the reaction in acetate buffer (Fig. 5), but this seems to be a catalytic effect, since it is much more pronounced than would be expected from the corresponding ionic strength values (this magnitude changed only a 2% between the extreme experiments). This effect seemed

TABLE 2. Dependence of the initial rate on the concentration of manganese(II) ion at various concentrations of DL-penicillamine[a]

$10^2[Mn^{2+}]$ (M)[b]	$10^6 r_0$ (M s^{-1})[c]						
0.00	0.66[d]	1.35[e]	2.08[f]	3.82[g]	5.92[h]	8.46[i]	10.61[j]
0.12	0.63	1.21	1.79	3.24	4.87	6.77	8.36
0.23	0.63	1.18	1.75	3.13	4.69	6.37	7.87
0.35	0.64	1.18	1.74	3.05	4.55	6.08	7.33
0.46	0.63	1.18	1.69	3.01	4.33	5.81	7.08
0.69	0.65	1.17	1.66	2.83	4.16	5.36	6.44
0.92	0.67	1.16	1.61	2.68	3.84	4.87	5.80
1.15	0.68	1.17	1.55	2.53	3.59	4.51	5.18
1.38	0.70	1.14	1.54	2.41	3.31	4.07	4.66
1.61	0.72	1.14	1.49	2.30	3.14	3.74	4.46
Ratio[k]	0.92	1.18	1.40	1.66	1.89	2.26	2.38

[a]$[Cr(VI)]_0 = 5.15 \times 10^{-4}$ M, $[H_3Cit] = 7.32 \times 10^{-3}$ M, $[Na_3Cit] = 6.80 \times 10^{-2}$ M, ionic strength 0.47 M, pH = 5.78 ± 0.05, 25.0°C.
[b]$[ZnSO_4] + [MnSO_4] = 1.61 \times 10^{-2}$ M.
[c]Average error in $r_0 = \pm 0.9\%$.
[d]$[DL\text{-}PA]_0 = 1.75 \times 10^{-3}$ M ([reductant]/[oxidant] = 3.4), pH = 5.76–5.83.
[e]$[DL\text{-}PA]_0 = 3.49 \times 10^{-3}$ M ([reductant]/[oxidant] = 6.8), pH = 5.76–5.84.
[f]$[DL\text{-}PA]_0 = 5.23 \times 10^{-3}$ M ([reductant]/[oxidant] = 10.2), pH = 5.75–5.84.
[g]$[DL\text{-}PA]_0 = 8.74 \times 10^{-3}$ M ([reductant]/[oxidant] = 17.0), pH = 5.75–5.84.
[h]$[DL\text{-}PA]_0 = 1.31 \times 10^{-2}$ M ([reductant]/[oxidant] = 25.4), pH = 5.73–5.84.
[i]$[DL\text{-}PA]_0 = 1.75 \times 10^{-2}$ M ([reductant]/[oxidant] = 34.0), pH = 5.73–5.84.
[j]$[DL\text{-}PA]_0 = 2.19 \times 10^{-2}$ M ([reductant]/[oxidant] = 42.5), pH = 5.73–5.85.
[k]Defined as the ratio between the values of the initial rate for $[MnSO_4] = 0$ and $[MnSO_4] = 1.61 \times 10^{-2}$ M at each reductant concentration.

to be specific of the acetate buffer, since it was not observed when the buffer was of the citrate type.

Manganese(II) ion is known to act either as a catalyst (5, 6) or (more frequently) as an inhibitor (7–9) of many chromium(VI) reactions. In the case of the Cr(VI)/DL-PA reaction, it seems to have both effects. At low reductant concentration an acceleratory effect of manganese(II) sulfate was observed, whereas at higher reductant concentrations the effect was clearly inhibitory (Table 2). In those experiments, both the total sulfate concentration and ionic strength were kept constant by adequate additions of zinc sulfate ($[ZnSO_4] + [MnSO_4] = 1.61 \times 10^{-2}$ M). To that end, it was first checked that zinc ion did not behave in the presence of citrate buffer as it did in that of acetate (see Fig. 5). Moreover, some of the series were repeated keeping the ionic strength constant with sodium sulfate instead of zinc sulfate, and the results obtained were notably similar, thus indicating that the kinetic effect shown in Table 2 was caused by manganese(II) ion.

The second-order rate constants fulfilled the Arrhenius law for the three buffers. The apparent activation parameters corresponding to the maximum in the rate vs. pH plot for each buffer (see Fig. 1) have been determined (deposited[1]).

Determination of the ionization constant of hydrogenchromate ion

The values of the initial absorbance at 370 nm, A^0_{370}, at different pHs (deposited[1]) allowed us to determine the value of the pK_a of hydrogenchromate ion at 2.1-M ionic strength (KCl). The buffer did not seem to affect significantly that equilibrium constant, since for the three buffers the value obtained was within the range $pK_a = 5.75 \pm 0.01$. This agrees well with the value reported by Connett and Wetterhahn at 0.5-M ionic strength (KCl), $pK_a = 5.98$ (4).

Detection of the thioester intermediate

As shown in Fig. 6, the oxidant–reductant thioester intermediate was stable enough for its accumulation and decay to be detected spectrophotometrically at 430 nm (1, 10). The influence of several experimental variables on the maximum absorbance observed at that wavelength was studied (deposited[1]). The maximum absorbance was directly proportional to the initial concentration of oxidant but was independent of that of reductant. In the presence of acetate buffer, it increased with additions of zinc sulfate to the solutions.

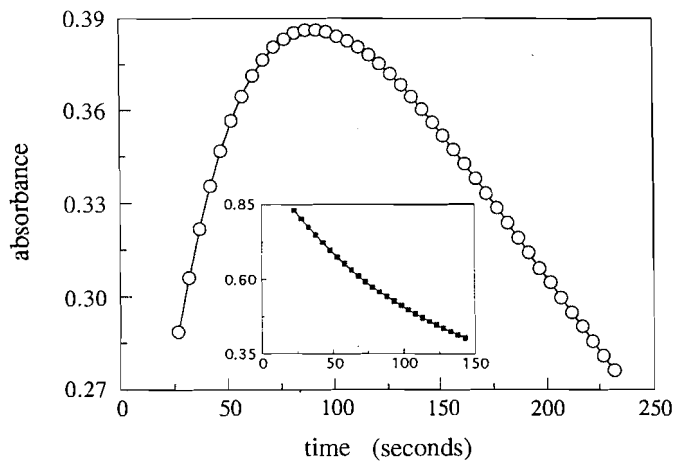

FIG. 6. Absorbance at 430 nm vs. time plot for the reaction between chromium(VI) (5.15×10^{-4} M) and DL-penicillamine (4.80×10^{-3} M) in the presence of HAc (2.80×10^{-2} M) – NaAc (0.20 M) buffer and zinc sulfate (2.77×10^{-4} M) at ionic strength 0.21 M, pH = 5.48 ± 0.01 and 25.0°C. Inset: absorbance at 370 nm vs. time plot for the same conditions.

At constant pH, the maximum absorbance increased with increasing concentration of buffer, the data being conveniently fitted to 2nd-degree polynomial:

[5] $$A^{max}_{430} = a'' + b''[B]_T + c''[B]_T^2$$

Can. J. Chem. Downloaded from www.nrcresearchpress.com by 85.192.166.187 on 09/08/12
For personal use only.

Can. J. Chem. Downloaded from www.nrcresearchpress.com by 85.192.166.187 on 09/08/12
For personal use only.

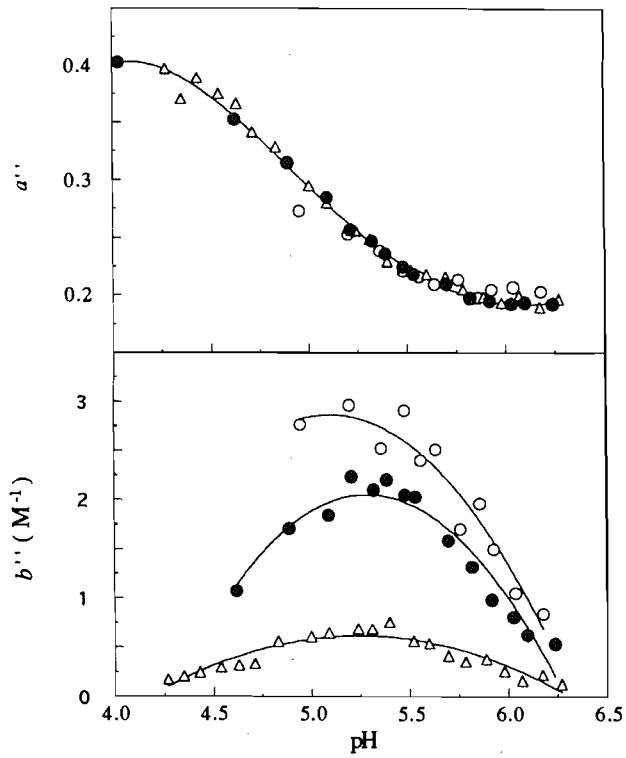

FIG. 7. Dependence of parameters a'' (above) and b'' (below) on the pH for the reaction between chromium(VI) (5.15×10^{-4} M) and DL-penicillamine (4.80×10^{-3} M) at ionic strength 2.1 M (KCl) and 25.0°C. Buffers: HAc–NaAc ([acid]/[base] = 0.01–2.44), triangles; H_3Cit–Na_3Cit ([acid]/[base] = 0.02–1.00), solid circles; and KH_2PO_4–K_2HPO_4 ([acid]/[base] = 1.25–25.00), open circles.

Parameter a'' is the value of the maximum absorbance that would be expected in the absence of any buffer, and the values extrapolated from the three buffers are quite consistent (Fig. 7, above). The stability of the intermediate decreased with increasing pH, and it could not be detected at pH > 6.25, suggesting that at neutral or basic pH the intermediate is in a steady state. On the other hand, it can also be seen in Fig. 7 (below) that the b'' vs. pH curves were very similar to the b' vs. pH plots (Fig. 3, below), since in both cases they showed bell-shaped profiles. Moreover, the sequence acetate < citrate < phosphate could be observed at any fixed pH for both parameters b' and b''.

Discussion

Mechanism in the absence of buffer

Given the pK_a values for hydrogenchromate ion (5.75, see above) and for the different ionizable groups of DL-penicillamine (1.8 for $-CO_2H$, 7.9 for $-NH_3^+$ and 10.5 for –SH) (11), within the pH range corresponding to the study of parameters a' and b' (pH = 4.3–6.5, see Fig. 3) there were two predominant forms of the oxidant (hydrogenchromate and chromate ions) and only one of the reductant (the zwitterionic form containing the groups $-CO_2^-$, $-NH_3^+$, and –SH). The mechanism that can be proposed for formation of the thioester intermediate in the absence of buffer is that corresponding to hydrogenchromate ion as the active form of the oxidant:

$$[6] \qquad CrO_4^{2-} + H^+ \overset{K_I}{\rightleftharpoons} HCrO_4^-$$

$$[7] \qquad HCrO_4^- + RSH \underset{\text{slow}}{\overset{k_{II}}{\longrightarrow}} RSCrO_3^- + H_2O$$

The rate law that can be deduced from this mechanism is:

$$[8] \qquad r = \frac{K_I k_{II}[Cr(VI)]_T[RSH][H^+]}{1 + K_I[H^+]}$$

where $[Cr(VI)]_T = [HCrO_4^-] + [CrO_4^{2-}]$. The expression corresponding to parameter a' (eq. [4]) is:

$$[9] \qquad a' = \frac{K_I k_{II}[H^+]}{1 + K_I[H^+]}$$

From eq. [9] it follows that parameter a' must increase with decreasing pH, reaching a plateau when $K_I[H^+] \gg 1$. Since the pK_a value for hydrogenchromate ion under the conditions of our work is 5.75, the plateau is expected to be found at pH < 4.75, in good agreement with Fig. 3 (above), leading to the value $k_{II} = 0.28 \pm 0.01$ M^{-1} s^{-1}. Moreover, the mechanism proposed also agrees well with the experimental data extrapolated for the maximum absorbance of the thioester intermediate in the absence of buffer, since a decrease in the pH is expected to result in an increase of the rate of formation of that intermediate (due to the protonation of CrO_4^{2-} to give the active form of the oxidant, $HCrO_4^-$), and the experimental data indicate that the intermediate accumulates much more at low values of the pH (Fig. 7, above).

Connett and Wetterhahn (2) have shown that there is a good correlation between the rate constant for formation of the thioester intermediate and the pK_a for ionization of the mercapto group of the thiol, so that the rate constant increases with increasing acidity of that group. The above mechanism can easily explain this finding if we take into consideration that in the transition state corresponding to the rate-determining step (eq. [7]) the hydrogen atom of the —SH group is already partially protonated to give (with an —OH group of the hydrogenchromate ion) a molecule of water.

Mechanism in the presence of buffer

We have seen in Fig. 1 that the pH dependence of the initial rate is rather complex, but the experimental data (Fig. 3) indicate that the complexity is not present if the reaction occurs in the absence of buffer, and can only be found when the reaction is performed in the presence of buffer. Therefore, the mechanism proposed for the reaction in the presence of buffer has to be more complex than that proposed above for the reaction in the absence of buffer. The catalytic effect that the different buffers can exert on the reaction (Fig. 2) can be explained in terms of the following mechanism:

$$[10] \qquad B + H^+ \overset{K_{III}}{\rightleftharpoons} A$$

$$[11] \qquad HCrO_4^- + A \overset{K_{IV}}{\rightleftharpoons} C + H_2O$$

$$[12] \qquad C + RSH \overset{K_V}{\rightleftharpoons} D$$

$$[13] \qquad D + OH^- \underset{\text{slow}}{\overset{k_{VI}}{\longrightarrow}} RSCrO_3^- + B + H_2O$$

where A and B stand, respectively, for the acidic and basic forms of the buffer, whereas C and D are two different complexes.

In the case of acetate buffer, A is a molecule of acetic acid and B an acetate ion. In the case of phosphate buffer, A = $H_2PO_4^-$ and B = HPO_4^{2-}. However, since the three pK_a

Can. J. Chem. Downloaded from www.nrcresearchpress.com by 85.192.166.187 on 09/08/12
For personal use only.

of citric acid differ from each other much less than those of phosphoric acid (12), in the case of citrate buffer the roles of A and B may be played by several species with different degrees of protonation.

Chromium(VI) is known to form condensation complexes similar to C with a great variety of organic (13) and inorganic (14) substances. In particular, condensation of $HCrO_4^-$ and $H_2PO_4^-$ leads to $[HO_3P—O—CrO_3]^{2-}$ (15, 16).

The rate law deduced from the mechanism proposed is

$$[14] \qquad r = \frac{K_W K_I K_{III} K_{IV} K_V k_{VI} [Cr(VI)]_T [RSH][B]_T [H^+]}{(1 + K_I[H^+])(1 + K_{III}[H^+])}$$

where K_W is the water ionic product, $[Cr(VI)]_T = [HCrO_4^-] + [CrO_4^{2-}]$ and $[B]_T = [A] + [B]$. Thus, the expression corresponding to parameter b' (eq. [4]) is

$$[15] \qquad b' = \frac{K_W K_I K_{III} K_{IV} K_V k_{VI} [H^+]}{(1 + K_I[H^+])(1 + K_{III}[H^+])}$$

From eq. [15] it follows that parameter b' must take near-zero values in both very acidic and very alkaline solutions, and it must present a maximum at a certain pH which is a function of the pK_a of both hydrogenchromate ion and the acidic form of the buffer (A), which agrees well with the b' vs. pH plots found for the three buffers (Fig. 3, below). When the solution is acidified starting from pH = 6.5, parameter b' is found to increase first and then to decrease; according to the mechanism proposed, the initial increase is due to protonation of both the oxidant (eq. [6]) and buffer (eq. [10]), since complex C formed from the acidic forms of those two species (eq. [11]) presents a strong reactivity toward the reductant (eq. [12]); however, complex D formed in eq. [12] needs to react with a hydroxyl ion to yield the thioester intermediate $RSCrO_3^-$ (eq. [13]), what explains that, at low values of the pH, a further increase of the acidity of the medium results in a decrease of parameter b'. Moreover, Fig. 7 (below) confirms the existence of a certain pH at which the effect of the concentration of each buffer on the accumulation of the thioester intermediate is optimal.

In the case of acetate buffer, since A is a molecule of acetic acid, complex C must be an anion with electrostatic charge −1 (see eq. [11]), and so must be complex D (see eq. [12]), since RSH is a zwitterionic molecule containing the groups $—CO_2^-$ and $—NH_3^+$. Therefore, the rate-determining step (eq. [13]) is a reaction between two like-charged ionic species, which explains the increase of the second-order rate constant with increasing ionic strength (Fig. 4). Moreover, the effect of potassium chloride is more intense with citrate buffer than with acetate, what suggests that the role of the acidic form of citrate buffer (A) is played by a negatively charged species (H_2Cit^- or $HCit^{2-}$) rather than by a neutral molecule (H_3Cit). Hence, in the case of citrate buffer, complexes C and D have an electrostatic charge of −2 or −3.

Although the mechanism proposed for the reaction in the presence of buffer is indeed in agreement with many experimental features of the reaction, the meaning of parameter c' (eq. [4]) is difficult to explain. At first view, one might think that this parameter is a consequence of the saturation that can be expected for the equilibrium depicted in eq. [11], since at high values of the buffer concentration the reaction must approach a situation where all the chromium(VI) has been complexed by the acidic form of the buffer and, so, a further increase in the total concentration of buffer does not result in an increase of the reaction rate. However, this interpretation does not agree well with the experimental behavior, since in that case a decrease of parameter c' with increasing pH would be expected (the complexation occurs between the acidic forms of the oxidant and buffer), and the situation observed was exactly the opposite.

An alternative explanation would be possible if we assume that there is a small reactivity between the basic form of the oxidant (CrO_4^{2-}) and the reductant (RSH), and that the contribution of this pathway to the total rate of formation of the thioester intermediate becomes important at pH > 6.5, where most of the chromium(VI) is present in the basic form. Furthermore, it has to be assumed also that CrO_4^{2-} can be complexed by the basic form of the buffer (B), and that the resulting complex is rather unreactive toward RSH, just the opposite of what occurs with complex C formed from the acidic forms of the oxidant ($HCrO_4^-$) and buffer (A) (see eqs. [11] and [12]). Although this explanation does not seem to us entirely satisfactory (the complexation cannot occur by condensation when B is an acetate ion), the A^0_{370} vs. pH plots indicated that the absorbance of the plateau corresponding to the basic form of the oxidant depends very definitely on the nature of the buffer present in the medium, what might indicate the existence of a complexation equilibrium between the basic forms of the oxidant and buffer. Moreover, the maximum absorbance was observed for acetate buffer, for which a rapid increase of parameter c' with increasing pH has been found.

Mechanism in the presence of zinc and acetate

We have seen in Fig. 5 that, when the reaction takes place in the presence of acetate buffer (but not in that of citrate), the initial rate increases very markedly with increasing concentration of zinc ion, and that this happens at concentrations of zinc sulfate too low to be explained by an effect of ionic strength. This catalytic effect can be explained by the following mechanism involving as intermediate a complex of zinc ion with both acetate and hydrogenchromate ions:

$$[16] \qquad Zn^{2+} + Ac^- + HCrO_4^- \overset{K_{VII}}{\rightleftharpoons} Ac^- - Zn^{2+} - HCrO_4^-$$

$$[17] \qquad Ac^- - Zn^{2+} - HCrO_4^- + RSH \underset{\text{slow}}{\overset{k_{VIII}}{\longrightarrow}} RSCrO_3^- + Zn^{2+} + Ac^- + H_2O$$

and leading to the following rate law:

$$[18] \qquad r = \frac{K_{VII} k_{VIII} [Cr(VI)]_T [RSH][Ac^-][Zn^{2+}]}{1 + K_{VII}[Ac^-][Zn^{2+}]}$$

where $[Cr(VI)]_T = [HCrO_4^-] + [Ac^-—Zn^{2+}—HCrO_4^-]$. Thus, the expression corresponding to the dependence of the second-order rate constant on the concentration of zinc ion is

$$[19] \qquad \frac{1}{k_2 - k_2^0} = \frac{1}{k_{VIII}} + \frac{1}{K_{VII} k_{VIII} [Ac^-]} \frac{1}{[Zn^{2+}]}$$

where k_2^0 is the value of the second-order rate constant in the absence of zinc ion. From the intercept and slope of the $1/(k_2 - k_2^0)$ vs. $1/[Zn^{2+}]$ linear plot (see Fig. 5), it can be deduced that $K_{VII} = (2.8 \pm 0.6) \times 10^3\ M^{-2}$ and $k_{VIII} = 5.6 \pm 1.0\ M^{-1}\ s^{-1}$. A comparison of the latter value to the above determined $k_{II} = 0.28 \pm 0.01\ M^{-1}\ s^{-1}$ indicates that the reaction between RSH and $Ac^-—Zn^{2+}—HCrO_4^-$ (eq. [17]) is

Can. J. Chem. Downloaded from www.nrcresearchpress.com by 85.192.166.187 on 09/08/12
For personal use only.

twenty times faster than that between RSH and free $HCrO_4^-$ (eq. [7]). Moreover, the measurements of A_{430}^{max} confirmed that the accumulation of the thioester intermediate increases with increasing concentration of zinc ion in the presence of acetate buffer.

Mechanism in the presence of manganese(II) ion

It can be seen in Table 2 that when the ratio between the initial concentrations of reductant and oxidant is about 3 (corresponding to the stoichiometric ratio, according to eq. [3]) manganese(II) has a slight catalytic effect on the reaction, but when that ratio equals 7 the effect of that ion is inhibitory instead, and the inhibition observed is more intense as the reductant/oxidant ratio increases. Actually, manganese(II) ion is known to be an inhibitor for many chromium(VI) redox reactions, due to its ability to act as a trapping agent for the intermediate chromium(IV) (17); however, the maximum decrease in the reaction rate that can be expected from this effect is 50% (9), and for a reductant/oxidant ratio ≥ 34 we have observed that the inhibitory effect of manganese(II) ion on the chromium(VI)/DL-PA reaction exceeds that limit (and it would be probably larger at higher values of the reductant/oxidant ratio). Therefore, we must conclude that manganese(II) ion has other effects on the reaction aside from the trapping of chromium(IV).

The experimental findings can be explained if we assume that manganese(II) ion may form two different complexes, one with both the oxidant and the reductant and the other only with the reductant. Then, the mechanism of formation of the thioester intermediate catalyzed by manganese(II) ion at low values of the reductant/oxidant ratio would be:

$$[20] \qquad Mn^{2+} + HCrO_4^- + RSH \overset{K_{IX}}{\rightleftharpoons} [Mn(HCrO_4)(RSH)]^+$$

$$[21] \qquad [Mn(HCrO_4)(RSH)]^+ \xrightarrow[slow]{k_X} RSCrO_3^- + Mn^{2+} + H_2O$$

leading to the following rate law:

$$[22] \qquad r = K_{IX}k_X[HCrO_4^-][RSH][Mn^{2+}]$$

However, as the reductant/oxidant ratio increases, the complex formed in eq. [20] would be replaced by the one formed in this other equilibrium:

$$[23] \qquad Mn^{2+} + 2RSH \rightleftharpoons [Mn(RSH)_2]^{2+}$$

and, if we assume that this new complex is much less reactive toward the oxidant to form the thioester intermediate than the free RSH molecule, the inhibitory effect of manganese(II) ion at high values of the reductant/oxidant ratio would be easily explained.

Moreover, we have seen in Fig. 4 that the increase observed in the second-order rate constant when magnesium sulfate was added to the solution (especially at low concentrations of this electrolyte) was much lower than the increase expected from the ionic strength values (compare the data corresponding to $MgSO_4$ to those corresponding to Na_2SO_4 and KCl in the same buffer). This suggests that magnesium ion might form a complex with DL-penicillamine similar to that formed in eq. [23], so that the increase of the second-order rate constant with increasing ionic strength might be partially compensated by the inhibitory effect caused by Mg^{2+}. We can thus conclude that DL-penicillamine seems to have a notable capacity for the complexation of divalent cations, which is probably due to the zwitterionic character of the predominant form of the reductant for the pH range studied.

Destruction of the thioester intermediate

Although the kinetic data reported in this work are related only to the formation of the thioester intermediate and not to its destruction, the data corresponding to the measurement of the accumulation of $RSCrO_3^-$ can give us some evidences (albeit indirect) on the way of disappearance of this intermediate. Effectively, we have observed that, for the conditions of our experiments, the maximum absorbance measured at 430 nm (A_{430}^{max}) was directly proportional to the initial concentration of oxidant but was independent of that of the reductant. This suggests that, whereas hydrogenchromate ion is involved only in the formation of the thioester intermediate (see eq. [7]), the thiol is involved in both its formation and destruction, the latter according to the reaction:

$$[24] \qquad RSCrO_3^- + RSH \longrightarrow HCrO_3^- + RSSR$$

It should be noticed that, although we have written the intermediate chromium(IV) formed in eq. [24] as $HCrO_3^-$, there is no information in the literature on the predominant form of this species in slightly acidic or neutral aqueous solutions. In fact, $HCrO_3^-$ might react with the solvent to yield CrO^{2+}, which is known to be the predominant form of chromium(IV) in perchloric acid media (9, 18).

The thioester intermediate may also disappear by the reaction opposite to its formation (the reaction depicted in eq. [7] is reversible). Furthermore, although a bimolecular reaction of the thioester with a second RSH molecule to yield chromium(IV) and the disulfide RSSR (eq. [24]) is in agreement with most reports on the reactions between chromium(VI) and several thiols (1, 2, 4), O'Brien and Wang (19) have indicated that at low thiol concentrations the predominant pathway for the redox disappearance of the thioester is its unimolecular decomposition to yield chromium(V) (20–22) and the free radical RS· (22). Therefore, eq. [24] would be predominant only at high concentrations of RSH.

Acknowledgment

This work was supported by a grant from the Spanish Ministry of Education and Science (DGICYT PB91-0243).

1. A. McAuley and M.A. Olatunji. Can. J. Chem. **55**, 3328 (1977); **55**, 3335 (1977).
2. P.H. Connett and K.E. Wetterhahn. J. Am. Chem. Soc. **107**, 4282 (1985).
3. D.Y. Cupo and K.E. Wetterhahn. Proc. Natl. Acad. Sci. USA. **82**, 6755 (1985).
4. P.H. Connett and K.E. Wetterhahn. J. Am. Chem. Soc. **108**, 1842 (1986).
5. T.J. Kemp and W.A. Waters. J. Chem. Soc. 3193 (1964).
6. C.F. Huber and G.P. Haight. J. Am. Chem. Soc. **98**, 4128 (1976).
7. N.K. Saran and R.C. Acharya. J. Indian Chem. Soc. **62**, 747 (1985).
8. J.F. Perez-Benito, C. Arias, and D. Lamrhari. J. Chem. Soc., Chem. Commun. 472 (1992).
9. J.F. Perez-Benito and C. Arias. Can. J. Chem. **71**, 649 (1993).
10. S.L. Brauer and K.E. Wetterhahn. J. Am. Chem. Soc. **113**, 3001 (1991).
11. S. Budavari (*Editor*). The Merck index. Merck, Rahway, NJ. 1989, p. 1122.
12. R.C. Weast (*Editor*). CRC handbook of chemistry and physics. CRC Press, Cleveland, OH. 1977. pp. D-150 and D-151.

13. G.P. Haight, T.J. Huang, and B.Z. Shakhashiri. J. Inorg. Nucl. Chem. **33**, 2169 (1971).
14. D.G. Lee and R. Stewart. J. Am. Chem. Soc. **86**, 3051 (1964).
15. F. Holloway. J. Am. Chem. Soc. **74**, 224 (1952).
16. S.A. Frennesson, J.K. Beattie, and G.P. Haight. J. Am. Chem. Soc. **90**, 6018 (1968).
17. J.K. Beattie and G.P. Haight. *In* Inorganic reaction mechanisms. Part II. *Edited by* J.O. Edwards. Wiley, New York. 1972. p. 102.
18. A.M. Al-Ajlouni, J.H. Espenson, and A. Bakac. Inorg. Chem. **32**, 3162 (1993).
19. P. O'Brien and G. Wang. J. Chem. Soc., Chem. Commun. 690 (1992).
20. P. O'Brien, J. Barrett, and F. Swanson. Inorg. Chim. Acta, **108**, L19 (1985).
21. S. Kitagawa, H. Seki, F. Kametani, and H. Sakurai. Inorg. Chim. Acta, **152**, 251 (1988).
22. X. Shi and N.S. Dalal. Biochem. Biophys. Res. Commun. **156**, 137 (1988).

Can. J. Chem. Downloaded from www.nrcresearchpress.com by 85.192.166.187 on 09/08/12
For personal use only.

Biosynthesis of 5-hydroxy-4-oxo-L-norvaline in *Streptomyces akiyoshiensis*

ROBERT L. WHITE,[1] KEVIN C. SMITH, AND ALPHONSE C. DEMARCO
Department of Chemistry, Acadia University, Wolfville, NS B0P 1X0, Canada

Received November 16, 1993

This paper is dedicated to Professors Ian Spenser and David B. MacLean

ROBERT L. WHITE, KEVIN C. SMITH, and ALPHONSE C. DEMARCO. Can. J. Chem. **72**, 1645 (1994).

The biosynthesis of 5-hydroxy-4-oxo-L-norvaline (HON) in *Streptomyces akiyoshiensis* has been investigated using ^{13}C-labelled substrates. Incorporations of ^{13}C label from sodium [1-^{13}C]-, [2-^{13}C]-, and [1,2-$^{13}C_2$]acetate indicated that HON was formed from a four-carbon compound derived from the citric acid cycle and the methyl carbon of acetate. Feeding experiments using DL-[4-^{13}C]- and DL-[2-^{13}C,^{15}N]aspartate demonstrated that aspartate served as the four-carbon precursor to HON. Both enantiomers of aspartate were metabolized by *S. akiyoshiensis*, but the D isomer was consumed at a slower rate. The distribution of ^{13}C label in the intracellular L-glutamic acid isolated in these feeding experiments is consistent with the operation of the citric acid cycle in *S. akiyoshiensis*. A biosynthetic hypothesis that involves a condensation reaction between acetyl or malonyl CoA and the β-carboxyl group of aspartate, and subsequent oxidative decarboxylation, is proposed to account for the incorporation results. An analogous condensation step has been proposed for the biosynthesis of other natural products, including the carbapenem antibiotics. DL-[2-^{13}C,^{15}N]Aspartate was synthesized from [2-^{13}C]diethylmalonate and potassium [^{15}N]phthalimide via diethyl [2-^{13}C,^{15}N]phthalimidomalonate.

ROBERT L. WHITE, KEVIN C. SMITH et ALPHONSE C. DEMARCO. Can. J. Chem. **72**, 1645 (1994).

Utilisant des substrats marqués au ^{13}C, on a étudié la biosynthèse de la 5-hydroxy-4-oxo-L-norvaline (HON) dans le *Streptomyces akiyoshiensis*. Les incorporations de marqueur ^{13}C des [1-^{13}C]-, [2-^{13}C]- et [1,2-$^{13}C_2$]-acétates de sodium indiquent que la HON se forme à partir d'un composé contenant quatre atomes de carbone qui serait dérivé du cycle de l'acide citrique et du carbone méthylique de l'acétate. Des expériences impliquant l'addition de DL-[4-^{13}C]- et DL-[2-^{13}C,^{15}N]aspartates ont permis de démontrer que l'aspartate sert de précurseur à quatre atomes de carbone pour la HON. Les deux énantiomères de l'aspartate sont métabolisés par le *S. akiyoshiensis*, toutefois l'isomère D est consommé plus lentement. La distribution du marqueur ^{13}C dans l'acide L-glutamique intracellulaire isolé de ces expériences est en accord avec l'opération du cycle de l'acide citrique dans le *S. akiyoshiensis*. Pour expliquer les résultats d'incorporation, on propose une hypothèse biosynthétique qui implique une réaction de condensation de l'acétyl ou du malonyl CoA avec le groupe β-carboxylique de l'aspartate, suivie d'une décarboxylation oxydante. Une étape de condensation analogue a été proposée pour la biosynthèse d'autres produits naturels, y compris des antibiotiques du carbapénème. On a synthétisé le DL-[2-^{13}C,^{15}N]aspartate à partir du [2-^{13}C]malonate de diéthyle et du [^{15}N]phtalimide de potassium, via le [2-^{13}C,^{15}N]phtalimidomalonate de diéthyle.

[Traduit par la rédaction]

Can. J. Chem. Downloaded from www.nrcresearchpress.com by EESC ESCOLA DE ENGENHARIA on 09/08/12
For personal use only.

Introduction

The amino acid 2-amino-5-hydroxy-4-oxopentanoic acid, also known as 5-hydroxy-4-oxonorvaline or HON (**1**), was discovered during a search for the production of antitubercular antibiotics by strains of Streptomyces (1). Subsequently, it was isolated from the culture broth of *Streptomyces akiyoshiensis*, and its structure was assigned (1, 2) and confirmed by chemical synthesis (3). More recently, other synthetic routes have been explored in several laboratories (4), and HON has been reisolated from a *Streptomyces* sp. as the antifungal agent RI-331 (5).

The antifungal activity of HON has been attributed to the inhibition of protein biosynthesis caused by depletion of amino acids in the aspartate family (6). More specifically, HON has been shown to inhibit homoserine dehydrogenase (7), an enzyme needed for the conversion of aspartate to isoleucine, methionine, and threonine. An earlier report that HON had no effect on the biosynthesis of aspartic acid and asparagine in tumour cells (8) is consistent with the above observations. Although no mechanism for the inhibition of *Mycobacterium tuberculosis* and *M. bovis* by HON was suggested by the initial investigators (9), it may have been also due to enzyme inhibition, since HON was subsequently shown to be a competitive inhibitor of δ-aminolevulinic acid dehydratase isolated from *M. phlei* (10), an enzyme required for the biosynthesis of porphyrins.

HON is a member of a group of natural products known as nonprotein or unusual amino acids. These amino acids, as a group, possess a wide array of chemical structures, and often contain functional groups not commonly present in natural products (11). The structural diversity of the group means that many different and unrelated biosynthetic routes are needed for their formation. The biosynthetic precursor(s) of HON are not obvious, even though HON contains only five carbon atoms. If another amino acid serves as a precursor, then three general biosynthetic routes to HON are possible: degradation of a larger amino acid, functional group modification of another five-carbon amino acid, and chain extension of a smaller amino acid. Also, because HON contains a hydroxyketone functional group that is present in many carbohydrates, routes starting from carbohydrate or polyketide precursors, with addition of nitrogen at a later stage, can be envisioned. The aim of this investigation was to establish the biosynthetic origin of HON (12, for a preliminary communication of this work).

Results and discussion

As a prelude to biosynthetic experiments, the production of HON (**1**) by *S. akiyoshiensis* (ATCC 13480) was confirmed and its parameters established. Analysis by hplc (13), using pre-column derivatization with *o*-phthalaldehyde (OPA), demonstrated

[1]Author to whom correspondence may be addressed. Present address: Department of Chemistry, Dalhousie University, Halifax, NS B3H 4J3, Canada. Telephone: (902) 494-6403. FAX: (902) 494-1310. E mail: RLWHITE@AC.DAL.CA.

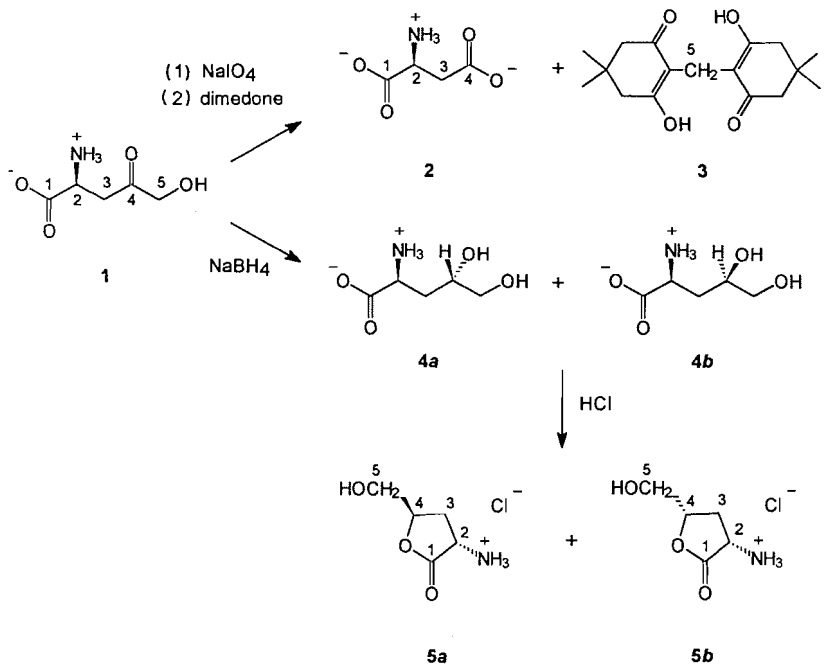

SCHEME 1. Degradation and derivatization of HON (**1**).

TABLE 1. Stereochemistry and enantiomeric purity of amino acids isolated from *S. akiyoshiensis*[a]

	Aspartic acid				β-Methyl aspartate				Glutamic acid			
	D Isomer		L Isomer		D Isomer		L Isomer		D Isomer		L Isomer	
Sample chromatographed	Ret. time (min)	%[b]	Ret. time (min)	%[b]	Ret. time (min)	%[b]	Ret. time (min)	%[b]	Ret. time (min)	(%)[b]	Ret. time (min)	%[b]
Standard D isomer	18.3	98.6	20.3	1.4	97.1	100	Not detected		23.2	100	Not detected	
Standard DL mixture	18.2	48.2	21.0	51.8	109.1	51.6	96.1	48.4				
Standard L isomer	18.5	0.3	21.4	99.7	Not detected		86.9	100	Not detected		15.5	100
Intracellular glutamate									21.7	0.9	16.3[c]	99.1
Aspartate product (Expt. 2) from periodate cleavage of HON	18.5	0.6	21.3[c]	99.4	Not detected		92.1[c]	100				
Reisolated aspartate (Expt. 4)												
Extracellular	18.3	96.5	21.0	3.5	104.5[d]	97.6	93.9	2.4				
Intracellular	18.4	98.0	20.4	2.0	102.9[d]	99.4	92.9	0.6				
Reisolated aspartate (Expt. 5)												
Extracellular					89.1[d]	98.8	80.3	1.2				
Intracellular					86.3[d]	98.6	77.4	1.4				

[a]Determined by hplc separation of diastereomeric OPA derivatives.
[b](Peak area of one enantiomer/peak area of the two enantiomers) × 100%.
[c]Two distinct peaks were obtained when this sample was co-chromatographed with the corresponding standard D isomer.
[d]Two distinct peaks were obtained when this sample was co-chromatographed with the corresponding standard L isomer.

that one major metabolite containing a primary amino group accumulated between 48 and 120 h of incubation in cultures of *S. akiyoshiensis* growing on a medium containing starch and Pharmamedia as carbon and nitrogen sources, respectively. The metabolite was isolated from the culture broth (1, 2) by cation-exchange chromatography (Amberlite IR-120, H^+ form, NH_3 elution) and was separated from acidic amino acids (14) by anion-exchange chromatography (Dowex 1-X8, CH_3COO^- form). Treatment of the metabolite with periodate generated aspartate (**2**) and formaldehyde (Scheme 1): a characteristic reaction (2) of HON (**1**). The formaldehyde was trapped as its dimedone derivative (**3**), and aspartate was separated by anion-exchange chromatography (Dowex 1-X8, CH_3COO^- form, CH_3COOH elution) from neutral and basic amino acids and salts. Each compound isolated was characterized by spectroscopic methods.

The stereochemistry of the aspartic acid isolated was determined by an hplc method for the separation of diastereomeric OPA/*N*-acetylcysteine derivatives of amino acids (15) in which the mobile phase was adjusted to provide a baseline separation of D and L enantiomers. As shown in Table 1, aspartate (**2**) obtained by periodate cleavage of HON eluted as a single peak with a retention time (21.3 min) corresponding to that of L-aspartate (21.4 min), and separated from D-aspartate when a mixture of the sample and authentic D-aspartic acid was chromatographed. Analogous results were obtained when the anal-

Can. J. Chem. Downloaded from www.nrcresearchpress.com by EESC ESCOLA DE ENGENHARIA on 09/08/12
For personal use only.

TABLE 2. Feeding experiments with isotopically labelled substrates

Expt. no.	Substrate added	Atom % ^{13}C, ^{15}N or ^{2}H	Amount fed[a] (mmol)	Time added (h)	Culture size (mL)	% HON formed[b]	Amount isolated (mmol)			
							HON	Glutamic acid	Aspartic acid	
									Extracellular	Intracellular
1	Sodium [1-^{13}C]acetate	99.5	8.01	67, 91	500	63	2.15[c]	0.40	—	—
2	Sodium [2-^{13}C]acetate	99.7	7.88	67, 91	500	61	2.35[c]	0.55	—	—
3	Sodium [1,2-$^{13}C_2$]acetate	99.3	6.01	46, 70	300	65	1.10[d]	0.30	—	—
4	DL-[4-^{13}C]-Aspartic acid	99	3.36	67, 91	300	70	1.58[c]	0.26	0.43	0.32
5	DL-[2-^{13}C,^{15}N]-Aspartic acid	99.3 99.5	1.88	45, 70	200	23	0.91[d]	0.08	0.43	0.04
6	Sodium [$^{2}H_3$]acetate	99.5	15.8	71, 95	500	60	1.48[c]	0.47	—	—
7	Sodium [$^{2}H_3$]acetate	99.5	15.8	47, 52 71, 76	500	77	1.58[d]	—	—	—

[a]Administered in equal portions at the times indicated.
[b]% HON formed in culture after the addition of labelled substrate. Calculated using chromatographic peak areas and based on the total amount of HON accumulated extracellularly during the experiment.
[c]Calculated from the amount of aspartic acid isolated.
[d]Calculated from the amount of 4,5-dihydroxynorvaline lactone HCl isolated.

ysis was repeated using the β-methyl ester of aspartate, but longer and more variable retention times were observed. These results confirmed the L configuration previously assigned (2) to HON (**1**) and, since the aspartate sample derived from HON contained less than 1% D-aspartic acid, established that *S. akiyoshiensis* produces only one enantiomer of the metabolite.

In subsequent experiments, HON (**1**) in culture supernatants was reduced with sodium borohydride (Scheme 1); the resulting mixture of 4,5-dihydroxynorvalines (**4***a* and **4***b*) was isolated by cation- and anion-exchange chromatography, and converted in concentrated HCl (2) to a mixture of diastereomeric γ-lactones (**5***a* and **5***b*). The presence of diastereomers was apparent in the ^{13}C nmr spectrum, which exhibited two peaks of similar chemical shift for each of the five γ-lactone carbons.

Glutamic acid was identified as the major intracellular amino acid of *S. akiyoshiensis* by hplc analysis of ethanolic mycelial extracts. The glutamic acid was isolated by anion-exchange chromatography (Dowex 1-X8, CH_3COO^- form, CH_3COOH elution), and its structure was confirmed by spectroscopic analysis. The L configuration was assigned to the intracellular glutamate after chiral hplc analysis as described for aspartate (Table 1). The sample isolated chromatographed as a single peak with a retention time (16.3 min) equivalent to that of authentic L-glutamic acid (15.5 min), and was separated from authentic D-glutamic acid. Moreover, more than 99% of the intracellular glutamic acid was present as the L enantiomer.

To distinguish among the speculative biosynthetic pathways to HON outlined above, aqueous solutions of ^{13}C-labelled substrates were administered to cultures of *S. akiyoshiensis*. As described in Table 2, the labelled substrates were added in two or more equal portions over a period of 24–30 h; the first addition was made after detection by hplc of a small amount of HON in the culture supernatant. Incubation was continued for an additional 24 h. HON was isolated from the resulting culture broth (Scheme 1) either as aspartic acid (C-1 to C-4 of HON) and formaldehyde (C-5 of HON) or as an intact five-carbon unit (i.e., 4,5-dihydroxynorvaline γ-lactone). Glutamate in mycelial extracts was separated from aspartate and recovered by chromatography on two successive anion-exchange columns. All ion-exchange separations were monitored by hplc. Isolated compounds were recrystallized prior to the determination of ^{13}C enrichments by nmr analysis, and sodium malonate was included in the amino acid samples as an internal standard because enrichment of all carbon atoms in these small molecules was possible.

As a general precursor of cellular metabolites, acetate provided an indication of the metabolic reactions involved in HON formation. As shown in Table 3, HON derived from [1-^{13}C]acetate (Expt. 1) was enriched in two carbons (C-1 and C-4), whereas in HON derived from [2-^{13}C]acetate all five carbons were enriched (Expt. 2). Equal enrichments (within the experimental error of nmr peak height comparisons) were evident for C-1 and C-4 in both experiments, and for C-2 and C-3 in the [2-^{13}C]acetate experiment. Also, the incorporation of label from [2-^{13}C]acetate into either C-2 or C-3 was larger than that into either C-1 or C-4. This enrichment pattern would be expected (16) if ^{13}C label from acetate were incorporated via the four-carbon intermediates of the citric acid cycle, and suggests that one of these (i.e., succinate, fumarate, malate, or oxaloacetate), or a substance derived from it (e.g., aspartate), is the precursor of C-1 to C-4 in HON. A more direct route from the methyl group of acetate to C-5 is suggested by the larger ^{13}C enrichment (2.8 versus ≤1.7%) observed at this position by both nmr and mass spectrometry (Expt. 2).

The C4 + C1 origin of HON indicated by the results of the initial experiments was tested by feeding [1,2-$^{13}C_2$]acetate (Expt. 3). Four-carbon intermediates generated by the first turn of the citric acid cycle would be expected to exhibit ^{13}C–^{13}C

Can. J. Chem. Downloaded from www.nrcresearchpress.com by EESC ESCOLA DE ENGENHARIA on 09/08/12
For personal use only.

TABLE 3. Incorporation of labelled substrates into HON and glutamate

Expt. no.	Substrate added	Isotopic enrichment (%)[a] of isolated amino acids										
		Carbon atoms in HON[b]						Carbon atoms in glutamate				
		1	2	3	4	5	5[c]	1	2	3	4	5
1	[1-^{13}C]Acetate	1.7	0.0	0.0	1.5	0.0 (0.1)	0.4 (0.2)	0.1	−0.2	0.1	0.0	−0.1
2	[2-^{13}C]Acetate	0.7	1.3	1.5	0.6	2.8 (0.2)	2.9 (0.2)	0.0	0.2	0.5	0.4	−0.4
3	[1,2-$^{13}C_2$]Acetate	1.2[d]	0.9[d]	1.1[e]	1.1[e]	1.5		0.5[f]	0.7[f]	1.0	0.9[g]	0.5[g]
4	DL-[4-^{13}C]Aspartate	0.5	−0.1	−0.1	2.3	0.0 (0.1)	0.2 (0.1)	0.7	−0.2	0.2	0.2	−0.2
5	DL-[2-^{13}C,^{15}N]Aspartate		1.3	0.1	0.0	−0.2		0.1	0.3	1.6	0.6	0.2

[a]Enrichment (%) = 1.1(enrichment factor) − 1.1. The enrichment factor is the ratio of the normalized intensity of an individual peak in the spectrum of the enriched sample to the normalized intensity of the corresponding peak in the natural abundance ^{13}C nmr spectrum acquired using identical instrumental parameters. Peak normalization is described in the experimental section. The standard deviation of the peak heights for the natural abundance carbons in formaldehyde dimethone is given in parentheses.

[b]For Expts. 1, 2, and 4, C-1–C-4 correspond to C-1–C-4, respectively, of aspartate and C-5 corresponds to the central methylene of formaldehyde dimethone. For Expts. 3 and 5, the five carbons of HON correspond to those in 4,5-dihydroxynorvaline γ-lactones.

[c]Calculated from the relative intensities of the M^+ and the M + 1 ions in the mass spectrum of formaldehyde dimethone (**3**). The standard deviation calculated from the intensities measured in several scans is given in parentheses.

[d]Coupled signals in 4,5-dihydroxynorvaline γ-lactones: $^1J_{CC}$ = 53.1 and 54.0 Hz.

[e]Coupled signals in 4,5-dihydroxynorvaline γ-lactones: $^1J_{CC}$ = 32.0 and 33.0 Hz.

[f]Coupled signals: $^1J_{CC}$ = 52.8 Hz.

[g]Coupled signals: $^1J_{CC}$ = 51.0 Hz.

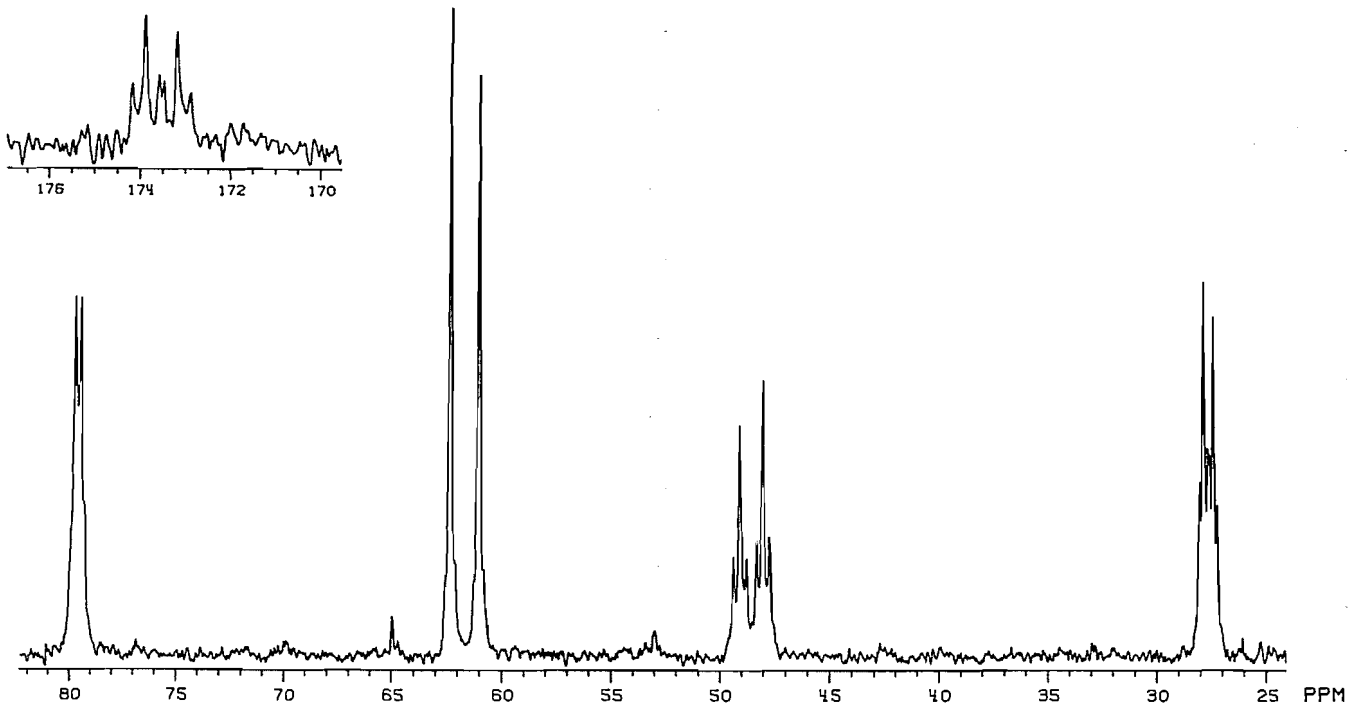

FIG. 1. The ^{13}C nmr spectrum of the mixture of diastereomeric 4,5-dihydroxynorvaline lactones showing coupled carbons derived from intact incorporation of [$^{13}C_2$]acetate into HON (Expt. 3).

coupling between C-1,C-2 and C-3,C-4 due to the symmetry of succinate and fumarate, and this pattern would be maintained on incorporation into HON. The fifth carbon in HON should not be coupled. The results of the feeding experiment (Table 3 and Fig. 1) support this interpretation. Coupling was observed between C-1,C-2 ($^1J_{CC}$ = 53.1 and 54.0 Hz) and C-3,C-4 ($^1J_{CC}$ = 32.0 and 33.0 Hz) in the 4,5-dihydroxynorvaline lactones (**5***a* and **5***b*) derived from HON, and C-5 was enriched (relative to the C-4 singlet), but not coupled.

Since *S. akiyoshiensis* accumulated relatively large amounts of L-glutamic acid, this provided an independent means of verifying that the labelled substrates were metabolized via the citric acid cycle. In each experiment, glutamate was isolated from 80% ethanol extracts of the mycelium and separated from aspartate by anion-exchange chromatography. The timing of the addition of labelled substrates was not optimized for incorporation into glutamate, and low or negligible incorporations of singly labelled acetates were observed (Expts. 1 and 2, Table 3). However, the ^{13}C nmr spectrum of glutamate isolated from *S. akiyoshiensis* fed [1,2-$^{13}C_2$]acetate (Expt. 3, Table 3) exhibited

Can. J. Chem. Downloaded from www.nrcresearchpress.com by EESC ESCOLA DE ENGENHARIA on 09/08/12
For personal use only.

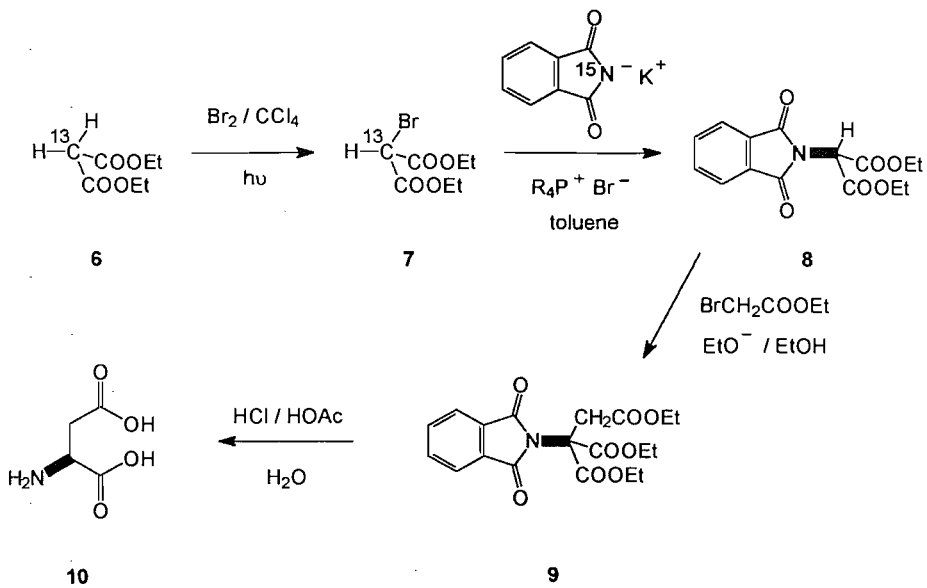

SCHEME 2. Synthesis of DL-[2-^{13}C,^{15}N]aspartic acid.

doublets superimposed on natural abundance singlets for C-1, C-2, C-4, and C-5, demonstrating the presence of ^{13}C–^{13}C coupling between C-1,C-2 (52.8 Hz) and C-4,C-5 (51.0 Hz)[2] and the intact incorporation of acetate units. Enrichment was observed for C-3, but no satellite signals were detected in the ^{13}C nmr spectrum. Incorporation of [1,2-$^{13}C_2$]acetate via the citric acid cycle (16) would provide α-ketoglutarate labelled at C-4,C-5 (coupled) on the first turn of the cycle, and at C-1,C-2 (coupled) and C-3 (not coupled) on the second turn. The coupled units would be broken up on subsequent turns of the cycle. Glutamate, formed from α-ketoglutarate by reductive amination or transamination, would maintain the pattern of coupling and enrichment in α-ketoglutarate. Therefore, the ^{13}C-incorporation patterns observed were consistent with the synthesis of glutamate from acetate via citrate, isocitrate, and α-ketoglutarate.

To distinguish among the possible four-carbon precursors of HON, label was introduced to this group using an asymmetric source, aspartic acid. Direct incorporation of aspartate (or another asymmetric precursor) labelled in one carbon should enrich a single carbon, whereas incorporation via a symmetrical molecule would place label equally in two positions. Of the four possible singly labelled aspartates, [4-^{13}C]aspartate was chosen (Expt. 4) because it was commercially available and no metabolic randomization of label was expected, since ^{13}C label in oxaloacetate derived from [4-^{13}C]aspartate would be lost as carbon dioxide after the first few steps of the citric acid cycle. As shown in Table 3, label from DL-[4-^{13}C]aspartate was incorporated mainly into C-4 of HON, but also to a smaller extent into C-1.[3] The incorporation of ^{13}C label mainly into C-4 of HON demonstrated that oxaloacetate, malate, or aspartate, and not a symmetrical four-carbon intermediate of the citric acid cycle, served as the C4 precursor of HON. The smaller ^{13}C enrichment at C-1 would be expected if a portion of the administered DL-[4-^{13}C]aspartate had been converted to a symmetrical citric acid cycle intermediate (e.g., fumarate) either via oxaloacetate and malate or directly by the action of carbon–nitrogen lyases such as aspartate ammonia lyase, EC 4.3.1.1 (18), argininosuccinate lyase, EC 4.3.2.1, and adenylosuccinate lyase, EC 4.3.2.2 (19). An equal distribution of ^{13}C at C-1 and C-4 would be obtained for the aspartate, malate, and oxaloacetate synthesized from carboxyl-labelled fumarate.

A distinction between aspartate and the citric acid cycle intermediates, oxaloacetate and malate, as HON precursors required a doubly labelled sample of aspartate to investigate the intact incorporation of the C—N bond in aspartate. The required DL-[2-^{13}C,^{15}N]aspartate (**10**) was synthesized (20–22) from diethyl [2-^{13}C]malonate (**6**) and potassium [^{15}N]phthalimide in a 65% overall yield (Scheme 2), and [2-^{13}C,^{15}N]glycine was recovered in a 19% overall yield. The $^1J_{CN}$ coupling of the synthesized aspartate was in agreement with that reported previously (23). The intact incorporation of this C—N unit, and thus the precursor role of aspartate, was demonstrated (Expt. 5) by the presence (Fig. 2) of two coupled ^{13}C nmr signals (centered at 49.1 and 48.1 ppm, $^1J_{CN}$ = ca 6 Hz for each), superimposed on the natural abundance signals in the mixture of diastereomeric γ-lactones of 4,5-dihydroxynorvaline. These signals are associated with C-2 in each of the diastereomeric γ-lactones, and consequently represent C-2 of HON. Similar spectra, in which only one of the coupled signals is separated from the uncoupled signals, have been used to support the incorporation of ^{13}C–^{15}N labelled precursors into naphthyridinomycin (24) and nocardicin A (25).

The samples of glutamate isolated from each of the aspartate feeding experiments were enriched with ^{13}C (Table 3). Enrichments at C-1 and C-3 from [4-^{13}C]- and [2-^{13}C,^{15}N]aspartate, respectively, and the absence of ^{13}C–^{15}N coupling are consistent with the synthesis of glutamate from aspartate via oxaloacetate, citrate, isocitrate, and α-ketoglutarate, and further

[2]Similar coupling constants for C-1,C-2 (52.7 Hz) and C-4,C-5 (54.9 Hz) have been reported for synthetically enriched glutamate samples (17).

[3]Note that the anion-exchange step in the purification sequence separated HON from acidic amino acids in the culture supernatant and that no aspartic acid was detected by hplc in the HON sample before it was cleaved by periodate. These steps were carried out carefully to ensure that the observed enrichment at C-4 of aspartate was not due to carry-over of the initial substrate.

Can. J. Chem. Downloaded from www.nrcresearchpress.com by EESC ESCOLA DE ENGENHARIA on 09/08/12
For personal use only.

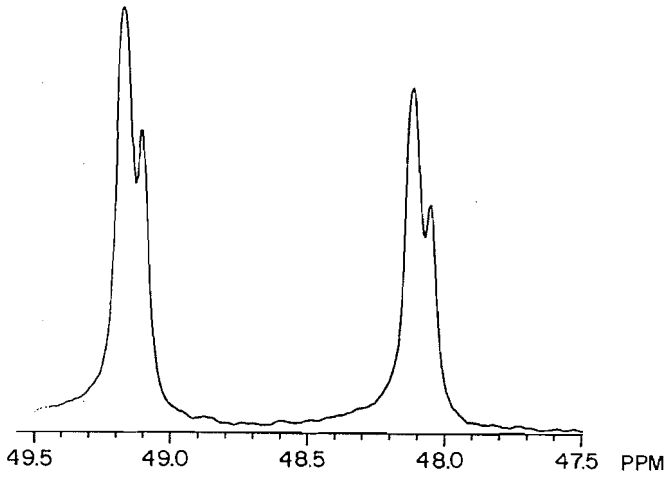

FIG. 2. The ^{13}C nmr spectrum of the mixture of diastereomeric 4,5-dihydroxynorvaline lactones derived from [2-^{13}C,^{15}N]aspartate showing ^{15}N coupling at carbon-2 (Expt. 5).

support the presence of the citric acid cycle in *S. akiyoshiensis*. The smaller ^{13}C enrichment observed at C-4 of glutamate derived from [2-^{13}C,^{15}N]aspartate can be explained by incorporation of label via the glyoxylate cycle (26).

In the aspartic acid feeding experiments (Expts. 4 and 5), significant amounts of the administered aspartic acid remained when the cultures were harvested; both the extra- and intracellular pools of this amino acid were isolated by ion-exchange chromatography and characterized. In each aspartic acid sample reisolated in Expt. 5, the nmr signal for C-2 appeared as a doublet ($^1J_{CN}$ = ca. 7 Hz) indicating that the coupling to ^{15}N had been maintained during transport through the cell membrane. Both the lack of an uncoupled signal for C-2 and the high enrichment of the doublet in the extracellular sample (96.5 times more intense than the corresponding signals for C-3) suggested that little or no dilution of the labelled aspartic acid had occurred. The enantiomeric compositions of the aspartic acids isolated in Expts. 4 and 5, determined by hplc separation of diastereomeric OPA derivatives (15), indicated that more than 96% of the extracellular and more than 98% of the intracellular aspartic acids were the D enantiomer in each experiment (Table 1). Thus L-aspartate was metabolized more quickly than D-aspartate; some metabolism of the D isomer was suggested by the partial recovery (approximately 50%) of the D-aspartate initially fed (Table 2).

The different rates of enantiomer metabolism were investigated in more detail by adding D- and L-aspartate to separate cultures of *S. akiyoshiensis*. Accumulation of HON and the levels of extra- and intracellular aspartate were monitored by hplc in duplicate cultures over 4 days. The extracellular concentration of HON increased over this period, but production of HON was not enhanced in any of the cultures supplemented with aspartic acid. The cultures supplemented with 3.8 and 7.5 mM L-aspartate were indistinguishable from unsupplemented control cultures after 17 and 41 h, respectively (Table 4). The failure to influence HON production was not due to rapid depletion of both aspartate enantiomers, since 89 h were needed for the initial 3.8 mM level of D-aspartate to fall to that of the control cultures, and about 15% of the D-aspartate added at 7.5 mM remained at 89 h after addition. Although intracellular accumulations of D- and L-aspartate were observed, they were not large enough to account for the extracellular decrease. Therefore,

TABLE 4. Extracellular concentrations of aspartate in cultures of *S. akiyoshiensis* supplemented with either D- or L-aspartate at 52 h after inoculation

Substrate added	[Aspartate] (mM)/time after addition				
	Initial	17 h	41 h	69 h	89 h
D-Aspartate	3.8	2.8	2.0	0.34	0.03
D-Aspartate	7.5	7.2	5.8	3.7	1.1
L-Aspartate	3.8	0.11	0.06	0.06	0.05
L-Aspartate	7.5	1.8	0.04	0.07	0.03
None	—	0.07	0.06	0.10	0.03

both enantiomers of aspartate were metabolized by *S. akiyoshiensis*, and the elevated intracellular levels in supplemented cultures vis-à-vis unsupplemented cultures indicated that transport across the cell membrane did not limit the rate of metabolism for either D- or L-aspartate. Thus the slower disappearance of D-aspartate must be due to a difference in metabolism.

Although D-aspartate is metabolized more slowly than L-aspartate, both are consumed by *S. akiyoshiensis* during the time that HON is formed in the culture. Thus the different rates of metabolism do not indicate which enantiomer is the more direct precursor of HON. Since L-aspartate and HON have identical configurations at C-2, direct incorporation of the L enantiomer (i.e., without bond cleavage at C-2) is the simplest explanation for intact incorporation of label from DL-[2-^{13}C,^{15}N]aspartate. On the other hand, a racemase-catalyzed inversion of stereochemistry without cleavage of the bond between C-2 and N could account for the incorporation of D-aspartate. This possibility was suggested to explain the incorporation of L-[^{14}C,^{15}N]aspartate into D-aspartate with maintenance of the $^{15}N/^{14}C$ ratio in *Streptococcus faecalis* (27); subsequently, an aspartate racemase (E.C. 5.1.1.13) was partially purified from this organism and characterized (28).

Of the three general routes referred to in the introduction for the biosynthesis of HON from another amino acid, only one is supported by the results of the isotopic feeding experiments. The incorporation of nitrogen and carbon atoms from aspartate and of one carbon atom from acetate are consistent with elongation of the carbon chain of aspartate via a Claisen or aldol condensation, followed by oxidation and decarboxylation (Scheme 3). Coupling of the condensation step to the hydrolysis of the thiolester group originally present in acetyl (**12***a*) or malonyl coenzyme A (**12***b*) to yield the β-ketoacid **13***b* would improve the energetics of this step. The product of the proposed aldol condensation, 2-amino-4-hydroxyadipic acid (**13***a*), has been isolated from *Vibrio cholera* (29), but its biosynthesis has not been investigated. The intermediacy of a β-ketoacid (**13***b*) is supported by the results of [$^2H_3$]acetate feeding experiments. Sodium [$^2H_3$]acetate was added to *S. akiyoshiensis* cultures and HON was isolated as either aspartic acid and formaldehyde (Expt. 6) or 4,5-dihydroxynorvaline (Expt. 7), which was subsequently cleaved to provide formaldehyde. Possible ^2H exchange of the hydrogens on C-5 of HON during isolation was minimized in Expt. 7 by reduction of HON directly in the culture supernatant to 4,5-dihydroxynorvaline. The formaldehyde derived from C-5 of HON was trapped as its dimedone derivative. Only 0.5 (±0.1)% and 0.7 (±0.2)% deuterium (Expts. 6 and 7, respectively) were found in these derivatives by mass spectrometry. The deuterium label was not exchanged during periodate cleavage and derivatization, as formaldehyde dime-

Can. J. Chem. Downloaded from www.nrcresearchpress.com by ESC ESCOLA DE ENGENHARIA on 09/08/12
For personal use only.

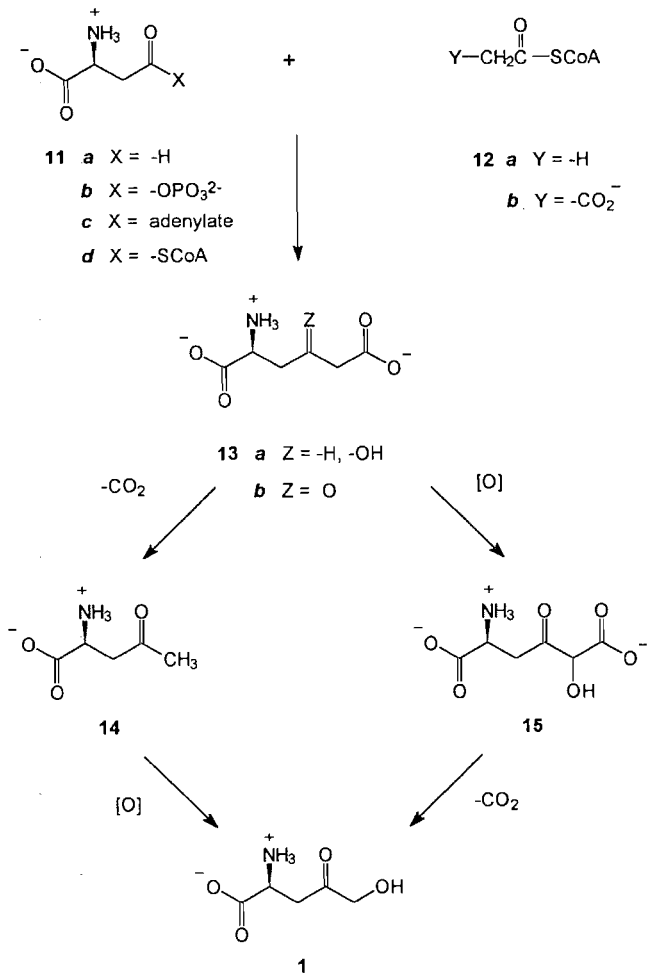

SCHEME 3. Hypothesis for the biosynthesis of HON (**1**) from aspartate and acetate derivatives.

thone isolated from the cleavage of 4,5-dihydroxynorvaline in D_2O (99.8% ^2H) contained only 1.3 (±0.5)% ^2H. In both experiments, the incorporation of deuterium was much lower than that of ^{13}C in Expt. 2 (Table 3). Since the methyl group of acetate is incorporated into C-5 of HON, deuterium should be located at C-5 in HON and in **13**. However, C-5 in **13***b* is located between two carbonyls, and the deuterium label would probably be lost rapidly by enolization.[4] Thus the lack of incorporation of the deuterium label is consistent with the intermediacy of a β-ketoacid such as **13***b*.

The presence of an oxidation step in the pathway is indicated by the observation that efficient aeration of *S. akiyoshiensis* cultures is required for HON production (31), but the oxidation and decarboxylation steps needed to convert the product of the condensation step (**13**) to HON (**1**) could occur simultaneously or in two alternative sequences (Scheme 3). There is some precedent for each of the latter. Decarboxylation of **13***b* yields 4-oxonorvaline (**14**),[5] an intermediate of ornithine degradation in *Clostridium sticklandii* (33), whereas an α-hydroxy-β-ketoacid (**15**) is formed if oxidation precedes decarboxylation. An analogous oxidation of a β-ketoacid to an α-chloro-β-ketoacid is catalyzed by a chloroperoxidase (34).

Several derivatives of aspartate (**11**) and acetate (**12**) are shown in Scheme 3 as possible substrates for the in vivo condensation reaction. Either a phospho anhydride, an adenylate derivative, a thiolester, or an aldehyde could serve as the activated aspartate derivative required for reaction with acetyl (**12***a*) or malonyl CoA (**12***b*). Both aspartyl phosphate (**11***b*) and aspartic semialdehyde (**11***a*) are well-known intermediates in the conversion of aspartate to homoserine in bacteria (35), and β-aspartyl adenylate (**11***c*) is known as an intermediate in the synthesis of asparagine from aspartate (36). Thiolesters are also well-known activated derivatives for carbon–carbon bond formation in fatty acid biosynthesis, and for the synthesis of peptide antibiotics (37). In the latter the thiolester is formed from the adenylate derivative of the amino acid, but formation of a thiolester from aspartyl phosphate is also possible.

A condensation between the carboxyl group of an amino acid (or the corresponding aldehyde) and a carbon derived from the methyl group of acetate has been proposed as a step in the biosynthesis of many natural products. Similar condensations extending the side chains of aspartate and glutamate have been proposed for fusaric acid (38) and thienamycin (39) biosynthesis, respectively, and condensations with the α-carboxyl of leucine, serine, lysine, phenylalanine, and picolinic acid have been suggested for the biosynthesis of pepstatin (40), elaiomycin (41), slaframine/swainsonine (42), tenellin (43), and caerulomycin (44), respectively. Also, on structural grounds, a Claisen condensation is a likely step in the biosynthesis of the modified amino acid residue in each of the peptides detoxin (45), galantin (46), and cyclotheonamide (47).

Other condensations that extend a carbon chain by one carbon are known. The formation of an α-aminoketone, δ-aminolevulinic acid, from glycine and succinyl CoA is catalyzed by δ-aminolevulinate synthase, EC 2.3.1.37 (48), and glyoxalate carboligase EC 4.1.1.47 (49) catalyzes the formation of an α-hydroxyaldehyde from two molecules of glyoxalate. Also, it has been suggested (26) that a thiamin-catalyzed condensation of glyoxalate with α-ketoglutarate to form 2-hydroxy-3-ketoadipate (a structure analogous to **15**) is the blocked step in type 1 hyperoxaluria (50), a disease in which large amounts of oxalate and L-glycerate are excreted in the urine. In each of these examples, C-2 of glycine or glyoxalate provides the one-carbon unit and, since C-2 of glyoxalate and glycine are labelled by [2-^{13}C]acetate, they are possible precursors of C-5 in HON. However, the highest ^{13}C enrichment was obtained at C-5, which suggests that acetate is incorporated via a more direct route.

Since the Claisen condensation in pepstatin biosynthesis occurs at the C-terminal leucine residue of a peptide (40) and *N*-acetylglutamate is an intermediate in the biosynthesis of ornithine from glutamate (51), it is conceivable that a derivative of aspartic acid or an aspartic acid residue in a peptide is involved in HON biosynthesis. Derivatization of the α-carboxyl group of aspartate would direct the Claisen condensation to the β position, and derivatization of nitrogen would serve as protection for the oxidation step. The modified amino acid, i.e., HON, could be liberated by hydrolysis in the final step of the pathway.

Experimental

Melting points were determined on a Mel Temp apparatus and are uncorrected. Nicolet 360 NB, Bruker AC250, and Varian EM-360L spectrometers were used to collect ^1H (361, 250, and 60 MHz) and ^{13}C

[4]The rate of enolization in another β-ketoacid, oxaloacetate, has been shown to be rapid (30).

[5]A peak that chromatographed with the same retention time as 4-oxonorvaline was discovered in *S. akiyoshiensis* cultures, but was subsequently shown to be due to another metabolite, as yet unidentified (32).

Can. J. Chem. Downloaded from www.nrcresearchpress.com by EESC ESCOLA DE ENGENHARIA on 09/08/12
For personal use only.

Can. J. Chem. Downloaded from www.nrcresearchpress.com by EESC ESCOLA DE ENGENHARIA on 09/08/12
For personal use only.

(90.8 and 62.9 MHz) nmr spectra. Chemical shifts are reported relative to either TMS in $CDCl_3$, HOD or external dioxane in D_2O. The ir spectra were obtained on a Perkin Elmer 683 infrared spectrometer and mass spectra were acquired by electron impact at 70 eV on a CEC 21-104 spectrometer. Labelled compounds were purchased from MSD Isotopes, Montreal, Que., and liquid cultures were incubated at 220 rpm in a Queue orbital shaker, model 4750.

Growth of Streptomyces akiyoshiensis

Streptomyces akiyoshiensis (ATCC 13480) was obtained from the American Type Culture Collection, Rockville, Md., U.S.A. It was maintained at −20°C in 20% glycerol as a spore suspension prepared from *S. akiyoshiensis* grown on semi-solid medium (malt extract 10 g/L, yeast extract 4 g/L, maltose 4 g/L, and agar 20 g/L) for 1 week at 27°C. Seed medium (malt extract 10 g/L, yeast extract 4 g/L, glucose 4 g/L, adjusted to pH 7.3 with aqueous NaOH prior to autoclaving) was inoculated with a loopful of spore suspension and incubated at 27°C with shaking for 48 to 72 h. Seed culture (1.0 mL) was added to starch–Pharmamedia medium (52) (100 mL, potato starch 50 g/L, Pharmamedia (Traders Protein, Fort Worth, Tex., U.S.A.) 30 g/L, $MgSO_4$ 10 g/L, KH_2PO_4 10.9 g/L, $Na_2HPO_4 \cdot 12\ H_2O$ 7.4 g/L) in a 2-L Erlenmeyer flask and incubated at 27°C with shaking for 96 h. The cultures were centrifuged (9600*g*, 30 min). The mycelial pellet was resuspended in a volume of water equal to the initial culture volume and centrifuged (9600*g*, 30 min). The water wash and the culture supernatant were combined.

HPLC analysis of amino acids

Portions (300 μL) of cultures were removed aseptically and centrifuged (15850*g*, 5 min). The supernatant was decanted and diluted with water (typically 50 μL was diluted to 500 μL). The pelleted mycelium was resuspended in ethanol (80% (v/v), 100 μL), allowed to stand at ambient temperature for 1 h, and centrifuged (15850*g*, 5 min). The ethanolic supernatant was decanted and diluted with water (typically 50 μL was diluted to 500 μL). Diluted culture broth or cell extract (20 μL) was mixed with an internal standard solution (20 μL, cysteic acid, 50 nmol/mL) and derivatized using a commercial *o*-phthalaldehyde reagent (Beckman Fluor-R, Beckman Instruments, Mississauga, Ont., or Sigma *o*-phthalaldehyde reagent, Sigma Chemical Company, St. Louis, Mo., U.S.A.) according to published conditions (13). The fluorescent OPA-derivatives were separated by gradient elution on a reversed-phase column as described previously (Figure 1b in ref. 13).

In addition to the analysis of extracellular and intracellular levels of amino acids, this hplc method was used to monitor all preparative separations of amino acids, as well as the periodate cleavage and borohydride reduction reactions described below. Aspartic acid, glutamic acid, and HON were identified by their retention times: 0.9, 1.5, and 1.2 min, respectively.

Feeding experiments

Labelled substrate was dissolved in sterile, deionized water (10 mL) and divided equally among production cultures of *S. akiyoshiensis* (100 mL/2-L Erlenmeyer flask, incubated with rotary shaking at 27°C) at 2 or 3 days after inoculation from the seed cultures (Table 2). At this point, the level of HON had reached ca. 40% of the maximum fermentation yield. In Expts. 1–6, an equal amount of labelled substrate was added in the same fashion 24 h later, and the incubation was continued for an additional 24 h. In Expt. 7, the sodium [$^2H_3$]acetate was added in four equal portions at the times given in Table 2.

*Isolation of extracellular HON (**1**) as aspartic acid (**2**) and formaldehyde*

The combined supernatants from a 500-mL culture (e.g., Expt. 2) were adjusted to pH 3.5 by the addition of oxalic acid, decolorized with charcoal, and filtered through Celite 545. The filtrate was applied to a column of Amberlite IR-120 (H^+ form, 2.5 × 45 cm). The column was washed with water (1 L) and eluted with ammonia (0.3 M). Fractions (200 mL) were collected and the amino acid-containing fractions were combined and concentrated in vacuo to ca. 150 mL to remove ammonia. The resulting solution was applied to a column of Dowex 1-X8 (acetate form, 2.5 × 45 cm) and the column was washed with water (500 mL). Aspartic acid and other acidic amino acids were retained on the column.

The sample effluent and the water wash, which contained HON and other neutral amino acids, were combined and concentrated in vacuo to ca. 100 mL. Solid $NaHCO_3$ was added to a final concentration of 0.5 M, and $NaIO_4$ (0.5 g) was added. The solution was swirled for 1 min and dimedone (5,5-dimethyl-1,3-cyclohexanedione, 0.85 g dissolved in 95% ethanol, 5 mL) was added. The reaction mixture was heated on a steam bath until a homogeneous solution was obtained. Upon storage of the solution at 4°C overnight, a white precipitate of formaldehyde dimethone (**3**) formed. It was collected by filtration and recrystallized twice from 70% aqueous ethanol to give 0.39 g. For unlabelled material isolated from cultures: mp 190–191°C (lit. (53) mp 189–190°C); ^1H nmr ($CDCl_3$, 60 MHz) δ: 3.10 (s, 2H), 2.26 (s, 8H), 1.08 (s, 12H); ^{13}C nmr ($CDCl_3$, 90.8 MHz) δ: 189.43 (s), 113.43 (s), 45.99 (t, $^1J_{CH}$ = 127 Hz), 31.77 (s), 29.48 (q, $^1J_{CH}$ = 123 Hz), 27.08 (q, $^1J_{CH}$ = 126 Hz), and 15.94 (t, $^1J_{CH}$ = 128 Hz); mass spectrum [*m/z* (relative intensity)] 292 (M^+, 100), 277 (10), 233 (6), 208 (10), 193 (6), 191 (8), 190 (6), 180 (12), 165 (47), 153 (6), 125 (10), 124 (14), 97 (10), 83 (16), 69 (13), 55 (16), 43 (13), 41 (12).

The filtrate from the formaldehyde derivatization reaction was applied to a column of Amberlite IR-120 (H^+ form, 2.5 × 45 cm) and the column was washed successively with water (500 mL) and ammonia (0.3 M). Fractions (200 mL) containing aspartic acid were combined, concentrated in vacuo, and applied to a column of Dowex 1-X8 (acetate form, 2.5 × 45 cm). The column was washed with water (500 mL) and eluted with acetic acid (0.5 M). Fractions (200 mL) containing aspartic acid (**2**) were combined and evaporated to dryness in vacuo. The resulting solid was recrystallized three times from aqueous ethanol to yield 235 mg. For unlabelled material isolated from cultures: ir: identical to authentic L-aspartic acid; ^1H nmr (D_2O, 250 MHz) δ: 4.07 (apparent t, 1H, splittings of 5.5 and 5.8 Hz), 3.1–2.9 (m, 2H); ^{13}C nmr (D_2O/NaOD, 90.8 MHz) δ: 182.36, 180.26, 53.99, 43.31.

*Isolation of extracellular HON (**1**) as 4,5-dihydroxynorvaline γ-lactone (**5**) and formaldehyde*

Sodium borohydride (150 mg) was added to the combined supernatants from a 300-mL culture (Expt. 3). The resulting solution, which contained 4,5-dihydroxynorvaline (**4**), was treated with oxalic acid and decolorizing charcoal, and chromatographed on Amberlite IR-120 and Dowex 1-X8 as described above. The sample effluent and water wash from the Dowex 1-X8 column were combined and evaporated in vacuo to dryness. The resulting oil was dissolved in concentrated HCl (50 mL) and heated on a steam bath for 30 min. The HCl was removed in vacuo, and the brown residue was dissolved in water (50 mL), treated with decolorizing charcoal, and filtered. The filtrate was evaporated to dryness in vacuo. The resulting hydrochloride salts of the diastereomeric γ-lactones of 4,5-dihydroxynorvaline (**5**) were stored in a desiccator over NaOH and washed with a mixture of isopropanol (25 mL) and methanol (4 mL) to yield 0.184 g. For unlabelled material isolated from culture: mp 206–210°C (lit. (2) mp 211–214°C); ir (Nujol): 3250 (N—H), 1770 (C═O) cm^{-1}; ^1H nmr (D_2O, 361 MHz) δ: 4.95–4.71 (m, 1H), 4.54 (dd, 1H, J = 10.9 and 9.7 Hz), 3.98–3.86 (m, 1H), 3.73–3.67 (m, 1H), 2.82–2.53 and 2.28–2.19 (m, 2H); ^{13}C nmr (D_2O, 90.8 MHz) δ: 173.83, 173.13, 79.72, 79.44, 62.32, 61.02, 49.04, 47.98, 27.83, 27.38.

In Expt. 7, a portion (20 mL) of the Dowex 1-X8 effluent, which contained 4,5-dihydroxynorvaline (**4**), was mixed with $NaHCO_3$ (0.84 g) and $NaIO_4$ (0.30 g). After 10 min, dimedone (5,5-dimethyl-1,3-cyclohexanedione, 0.50 g dissolved in 95% ethanol, 5 mL) was added, and the mixture was heated on a steam bath for 30 min. The solid product, which formed on cooling after the addition of 5 M acetic acid (1 mL), was collected by filtration and recrystallized from ethanol–water to provide formaldehyde dimethone (**3**, 142 mg) for mass spectrometric analysis: mp 188.5–189°C.

Reisolation of administered aspartic acid from extracellular fluids

In Expts. 4 and 5, in which labelled aspartic acids were administered

Can. J. Chem. Downloaded from www.nrcresearchpress.com by ESC ESCOLA DE ENGENHARIA on 09/08/12
For personal use only.

to *S. akiyoshiensis*, aspartic acid bound to the initial Dowex 1-X8 column (acetate form) was eluted with acetic acid (0.5 M). Aspartic acid-containing fractions were combined and evaporated to dryness in vacuo. The solid residue was dissolved in acetic acid (0.5 M, 5 mL), applied to a column of Dowex 1-X8 (acetate form, 2.5 × 48 cm) pre-equilibrated in acetic acid (0.5 M), and eluted with acetic acid (0.5 M). Fractions (25 mL) were collected. Fractions 30–56 were combined and evaporated to dryness in vacuo to give aspartic acid (58 mg). For aspartic acid isolated in Expt. 5: ^{13}C nmr (D_2O/DCl, 90.8 MHz) δ: 172.58, 170.20 (d, $^1J_{CC}$ = 61.5 Hz), 48.75 (d, $^1J_{CN}$ = 6.6 Hz), 33.25 (d, $^1J_{CC}$ = 37.9 Hz) (lit. (23) 49.2 (d, $^1J_{CN}$ = 7.0 Hz)).

Isolation of intracellular glutamic and aspartic acids

The mycelial pellet obtained by centrifugation of a 300-mL culture broth (e.g., Expt. 4) was suspended in 80% ethanol (300 mL) and allowed to stand at ambient temperature for 1 h. The mixture was centrifuged (9600*g*, 30 min) and the extraction was repeated on the pellet. The ethanol extracts were combined and concentrated in vacuo. The residue was dissolved in water (300 mL), and applied to a column of Dowex 1-X8 (acetate form, 2.5 × 45 cm). The column was washed with water (500 mL) and eluted with acetic acid (0.5 M). Amino acid-containing fractions were combined and evaporated to dryness in vacuo. The solid residue (114 mg) was dissolved in acetic acid (0.5 M, 5 mL), applied to a column of Dowex 1-X8 (acetate form, 2.5 × 48 cm) pre-equilibrated in acetic acid (0.5 M), and eluted with acetic acid (0.5 M). Fractions (25 mL) were collected. Glutamic acid-containing fractions (numbers 8–21) were combined and evaporated to dryness in vacuo. The residue (38 mg) was recrystallized from aqueous ethanol to give glutamic acid (25 mg). For unlabelled material isolated from cultures: mp 200–202°C (lit. (54) mp 211–213°C); ir: identical to authentic L-glutamic acid; ^{1}H nmr (D_2O, 250 MHz) δ: 3.81 (t, 1H, J = 6.3 Hz), 2.56 (apparent t, 2H, splittings of 7.5 and 7.8 Hz), 2.22–2.08 (m, 2H); ^{13}C nmr (D_2O/NaOD, 90.8 MHz) δ: 184.01, 183.82, 57.02, 35.26, 32.92.

In Expts. 4 and 5, aspartic acid-containing fractions (numbers 22–54) were combined and evaporated to dryness in vacuo. The residue (44 mg) was recrystallized from aqueous ethanol to give aspartic acid (34 mg). For aspartic acid isolated in Expt. 5: ^{13}C nmr (D_2O/DCl, 90.8 MHz) δ: 48.74 (d, $^1J_{CN}$ = 6.3 Hz) (lit. (23) 49.2 (d, $^1J_{CN}$ = 7.0 Hz)).

Determination of ^{13}C enrichments by nuclear magnetic resonance

Incorporation of isotopic label was determined from ^{13}C nmr spectra acquired at 90.8 MHz using 16k data points in a 10 kHz spectral window and processed using a line broadening of 2–5 Hz. Formaldehyde dimethone (**3**) samples were dissolved in $CDCl_3$ and the Lorentzian peak height of the signal (15.9 ppm) corresponding to the central methylene carbon was normalized to the average value of the Lorentzian peak heights of the carbons supplied by the dimedone reagent (55). Spectra of aspartate (**2**) and glutamate were obtained in D_2O–NaOH and sodium phosphate buffer (pH 11.5), respectively. Lorentzian peak heights in these samples were normalized to the Lorentzian peak height of the carboxyl signal of disodium malonate (177 ppm), which was added as an internal standard. Peak assignment of the carbons in the amino acids was based on the literature (56) and the assignment of C-4 (180 ppm) in aspartate was confirmed using the commercial, enriched sample. 4,5-Dihydroxynorvaline spectra were acquired in D_2O and peak heights were normalized relative to the average peak heights of the two uncoupled C-4 signals (79.4 and 79.7 ppm).

Determination of the enantiomeric composition of amino acids by high performance liquid chromatography

Synthesis of β-methyl aspartate standards (57, 58)

Aspartic acid (10.0 g, 0.075 mol) was added to a solution of concentrated sulfuric acid (4.2 mL) in methanol (110 mL, previously dried over 3Å molecular sieves), and the mixture was stirred and refluxed for 25 h. A solution of dimethylamine (18 mL) in methanol (62 mL) was added, and the reaction mixture was concentrated in vacuo. The resulting oil was dissolved in water (350 mL) and applied to a Dowex 1-X8 column (2.5 × 45 cm, CH_3COO^- form); the column was washed with water (750 mL). The sample effluent and the water wash were combined and evaporated to dryness in vacuo. The residue was dissolved in hot 95% ethanol; white crystals were obtained upon cooling.

β-Methyl D-aspartate (0.12 g, 11% from 1.0 g D-aspartic acid): mp 189–191°C (lit. (59) mp 188–190°C); ^{1}H nmr (D_2O, 250 MHz) δ: 4.05 (t, 1H, J = 5.5 Hz), 3.74 (s, 3H), 3.03 (d, 2H, J = 5.5 Hz); ^{13}C nmr (D_2O, 62.9 MHz) δ: 175.67, 175.32, 55.43, 53.48, 37.24.

β-Methyl DL-aspartate (3.80 g, 34%): mp 192–194°C (lit. (60) mp 201–202°C); ^{1}H nmr (D_2O, 250 MHz) δ: 4.04 (t, 1H, J = 5.5 Hz), 3.74 (s, 3H), 3.02 (d, 2H, J = 5.5 Hz); ^{13}C nmr (D_2O, 62.9 MHz) δ: 175.68, 175.31, 55.43, 53.48, 37.24.

β-Methyl L-aspartate (4.34 g, 39%): mp 187–189°C (lit. (61) mp 193–194°C, (62) mp 194–195°C); ^{1}H nmr (D_2O, 250 MHz) δ: 4.05 (t, 1H, J = 5.5 Hz), 3.74 (s, 3H), 3.03 (d, 2H, J = 5.5 Hz); ^{13}C nmr (D_2O, 62.9 MHz) δ: 175.66 (s), 175.31 (s), 55.43 (q), 53.47 (d), 37.23 (t).

Synthesis of β-methyl aspartate samples

Aspartic acid (1 mg) was heated at 65°C in a mixture of H_2SO_4 (8 μL) and methanol (200 μL) for 12 h. The solution was cooled to room temperature, diluted to 1.0 mL with water, and stored at 4°C until the hplc analysis was performed.

The hplc conditions (15)

Derivatization reagent (100 μL), prepared from incomplete *o*-phthalaldehyde reagent (1.0 mL, Sigma Chemical Co.) and *N*-acetylcysteine solution (0.20 mL, 5 mg/mL), were added to an amino acid solution and the reaction was allowed to proceed at ambient temperature for 15 min. The reaction was quenched by the addition of the mobile phase used for the separation (100 μL) and a portion of the resulting solution (20 μL) was chromatographed immediately on a Nucleosil 5 C18 column (4.6 × 250 mm, Phenomenex, Torrance, Calif., U.S.A.) using a mobile phase that contained acetonitrile, copper(II) acetate (2.5 mM), and L-proline (5 mM), adjusted to pH 6.0 with ammonium acetate. Enantiomers of aspartic acid and β-methyl aspartate were separated isocratically in mobile phases containing 1% and 5.8% acetonitrile, respectively, at a flow rate of 1.5 mL/min, whereas glutamic acid enantiomers separated in a mobile phase containing 2% acetronitrile at a flow rate of 2.5 mL/min.

*Synthesis of DL-[2-^{13}C,^{15}N]aspartic acid (**10**)*

*Diethyl [2-^{13}C]bromomalonate (**7**) (20, 21)*

A solution of bromine (1.01 g, 6.32 mmol) in CCl_4 (4 mL) was added dropwise to a stirred mixture of diethyl [2-^{13}C]malonate (**6**, 1.00 g, 6.24 mmol, 99.3 at.% ^{13}C) and CCl_4 (2.5 mL) in a two-necked flask equipped with a reflux condenser. After six drops of the bromine solution had been added, the reaction was initiated by irradiating the flask with a 100-W incandescent bulb. The remaining bromine solution was added over 15 min to maintain an orange-red color in the reaction mixture. The reaction mixture was refluxed for 1 h, diluted with an equal volume of CCl_4, washed with 5% $NaHCO_3$ (2 × 10 mL), dried over anhydrous $MgSO_4$, and evaporated in vacuo to yield diethyl [2-^{13}C]bromomalonate (**7**, 1.55 g). For unlabelled material: ^{1}H nmr (CCl_4, 60 MHz) δ: 4.6 (s, 1H), 4.2 (q, 4H, J = 7 Hz), 1.3 (t, 6H, J = 7 Hz).

*Diethyl [2-^{13}C,^{15}N]phthalimidomalonate (**8**) (21)*

Potassium [^{15}N]phthalimide (1.15 g, 6.21 mmol, 99.5 at.% ^{15}N) and hexadecyltri-*n*-butylphosphonium bromide (0.35 g, 0.69 mmol) were added to diethyl [2-^{13}C]bromomalonate (**7**, 1.55 g) in anhydrous toluene (20 mL), and the mixture was stirred for 20 h at 20°C. The mixture was filtered and the filtrate was concentrated in vacuo. The resulting yellow oil was dissolved in $CHCl_3$ (20 mL) and filtered through a column (0.7 × 10 cm) of silica gel (Aldrich grade 923, 100–200 mesh). The column was washed with $CHCl_3$ (125 mL). Column effluent was evaporated to dryness in vacuo to yield an oil (2.02 g) that crystallized immediately when seeded with a small crystal of diethyl phthalimidomalonate (**8**): ^{13}C nmr ($CDCl_3$, 90.8 MHz) δ: 54.42 (d, $^1J_{CN}$ = 13.1 Hz) (lit. (21) 54.5 (d, $^1J_{CN}$ 12.7 Hz)). For unlabelled material: mp 73.5–75°C (lit. (21) mp 75–76°C); ^{1}H nmr ($CDCl_3$, 361 MHz) δ: 7.91

Can. J. Chem. Downloaded from www.nrcresearchpress.com by ESC ESCOLA DE ENGENHARIA on 09/08/12
For personal use only.

(dd, 2H, J = 5.5 and 3.2 Hz), 7.81 (dd, 2H, J = 5.4 and 3.0 Hz), 5.49 (s, 1H), 4.37–4.27 (11 line m, 4 H), 1.32 (t, 6H, J = 7.2 Hz); ^{13}C nmr ($CDCl_3$, 90.8 MHz) δ: 166.47, 164.29, 134.39, 131.69, 123.81, 62.78, 54.42, 13.97.

*Triethyl [1-^{13}C,^{15}N]-1-phthalimido-1,1,2-ethanetricarboxylate (**9**) (22)*

Sodium ethoxide (190 mg of sodium in 4.3 mL absolute ethanol) was added to diethyl [2-^{13}C,^{15}N]phthalimidomalonate (**8**, 2.0 g) in absolute ethanol (20 mL). The mixture was stirred for 5 min at 20°C and the ethanol was removed in vacuo. Ethyl bromoacetate (8.00 g, 47.9 mmol) was added to the resulting orange oil and the mixture was heated for 2 h at 150°C. The excess ethyl bromoacetate was removed by vacuum distillation and the residue was extracted with ether (2 × 10 mL). The ether extracts were filtered and the collected solids were washed with ether (2 × 10 mL). The combined filtrates were evaporated to dryness in vacuo and placed under high vacuum to remove traces of ethyl bromoacetate. Triethyl [1-^{13}C,^{15}N]-1-phthalimido-1,1,2-ethanetricarboxylate (**9**) was obtained as an oil (3.17 g). For unlabelled material: ^1H nmr ($CDCl_3$, 361 MHz) δ: 7.85 (dd, 2H, J = 5.5 and 3.1 Hz), 7.74 (dd, 2H, J = 5.5 and 3.1 Hz), 4.36–4.28 (2 overlapped q, 4H, J = 7.1 Hz), 4.10 (q, 2H, J = 7.2 Hz), 3.46 (s, 2H), 1.29 (t, 6H, J = 7.1 Hz), 1.17 (t, 3H, J = 7.2 Hz); ^{13}C nmr ($CDCl_3$, 90.8 MHz) δ: 168.87, 167.09, 165.54, 134.19, 131.78, 123.52, 65.51, 63.02, 60.74, 36.39, 13.92, 13.79.

*DL-[2-^{13}C,^{15}N]Aspartic acid (**10**) (22)*

Water, concentrated HCl, and glacial acetic acid (7.0 mL of each) were added to the above oil. The mixture was refluxed for 43 h, concentrated in vacuo to two-thirds of its volume, diluted to 1 L with water, and applied to a column of Amberlite IR-120P (H^+ form, 2.5 × 46 cm). The column was washed with water (1.5 L) and eluted with ammonia (0.5 M). Fractions (200 mL) were collected and those containing aspartic acid (numbers 4–7) were combined, concentrated in vacuo to about 200 mL, and applied to a column of Dowex 1-X8 (acetate form, 1.5 × 25 cm). The column was washed with water (500 mL) and eluted with acetic acid (0.5 M). Fractions (75 mL) were collected and those containing aspartic acid (numbers 2–5) were combined and evaporated to dryness in vacuo. The white residue (577 mg) was recrystallized from aqueous ethanol to give DL-[2-^{13}C,^{15}N]aspartic acid (**10**, 543 mg, 65% yield from diethyl [2-^{13}C]malonate): ^{13}C nmr (D_2O/DCl, 90.8 MHz) δ: 49.06 (d, $^1J_{CN}$ = 7.1 Hz) (lit. (23) 49.2 (d, $^1J_{CN}$ = 7.0 Hz)).

The sample effluent and the water wash from the Dowex column were combined and evaporated to dryness in vacuo. The residue (165 mg) was recrystallized from aqueous ethanol to yield [2-^{13}C,^{15}N]glycine (89 mg, 19% yield from diethyl [2-^{13}C]malonate): ^1H nmr (D_2O, 250 MHz) δ: 3.54 (s and d, $^1J_{CH}$ = 143.4 Hz); ^{13}C nmr (D_2O, 62.9 MHz) δ: 175.15 (s and d, $^1J_{CC}$ = 53.4 Hz), 44.18 (d, $^1J_{CN}$ = 6.7 Hz).

Acknowledgements

We thank the Natural Sciences and Engineering Research Council of Canada (NSERC) for operating, equipment, and research development grants, Dr. D.L. Hooper and the Atlantic Region Magnetic Resonance Centre for NMR spectra, Dr. J.S. Grossert for mass spectra, and Dr. L.C. Vining for advice on the culturing of *S. akiyoshiensis*.

1. S. Tatsuoka, A. Miyake, H. Hitomi, J. Ueyanagi, H. Iwasaki, T. Yamaguchi, K.-I. Kanazawa, T. Araki, K. Tsuchiya, F. Hiraiwa, K. Nakazawa, and M. Shibata. J. Antibiot. **14**, 39 (1961).
2. A. Miyake. Chem. Pharm. Bull. **8**, 1071 (1960).
3. A. Miyake. Chem. Pharm. Bull. **8**, 1074 (1960).
4. (*a*) P.K. Chang, L.J. Sciarini, and R.E. Handschumacher. J. Med. Chem. **16**, 1277 (1973); (*b*) H.H. Mooiweer, K.W.A. Ettema, H. Hiemstra, and W.N. Speckamp. Tetrahedron, **46**, 2991 (1990); (*c*) R.F.W. Jackson, A. Wood, and M.J. Wythes. Synlett, 735 (1990); (*d*) R.F.W. Jackson, N. Wishart, A. Wood, K. James, and M.J. Wythes. J. Org. Chem. **57**, 3397 (1992); (*e*) U. Schmidt, F. Stäbler, and A. Lieberknecht. Synthesis, 482 (1992); (*f*) K. Burger, M. Rudolph, H. Neuhauser, and M. Gold. Synthesis, 1150 (1992); (*g*) J.E. Baldwin, R.M. Adlington, C.R.A. Godrey, D.W. Gollins, M.L. Smith, and A.T. Russel. Synlett, 51 (1993).
5. (*a*) S. Watanabe, K. Numata, S. Omura, and H. Yamaguchi. Jpn. Kokai Tokkyo Koho JP, 61,243,018 [86,243,018] (1986); Chem. Abstr. **106**, 72944r (1987); (*b*) H. Yamaguchi, K. Uchida, T. Hiratani, T. Nagate, N. Watanabe, and S. Omura. Ann. N.Y. Acad. Sci. **544**, 188 (1988).
6. (*a*) H. Yamaki, M. Yamaguchi, T. Nishimura, T. Shinoda, and H. Yamaguchi. Drugs Exp. Clin. Res. **14**, 467 (1988); (*b*) M. Yamaguchi, H. Yamaki, T. Shinoda, Y. Tago, H. Suzuki, T. Nishimura, and H. Yamaguchi. J. Antibiot. **43**, 411 (1990).
7. (*a*) H. Yamaki, M. Yamaguchi, H. Imamura, H. Suzuki, T. Nishimura, H. Saito, and H. Yamaguchi. Biochem. Biophys. Res. Commun. **168**, 837 (1990); (*b*) H. Yamaki, M. Yamaguchi, and H. Yamaguchi. Recent Prog. Antifungal Chemother. (Proc. Int. Conf. 1st, Oiso, Japan, 1990). 403 (1992).
8. T.C. Chou and R.E. Handschumacher. Biochem. Pharmacol. **21**, 39 (1972).
9. (*a*) K.-I. Kanazawa, K. Tsuchiya, and T. Araki. Am. Rev. Respir. Dis. **81**, 924 (1960); (*b*) A. Miyake. Chem. Pharm. Bull. **8**, 1079 (1960); (*c*) K. Tsuchiya, A. Imai, T. Tsuchiya, and T. Araki. Takeda Kenkyusho Nempo, **22**, 148 (1963) and **22**, 167 (1963); Chem. Abstr. **61**, 2335a (1964) and **61**, 2335d (1964); (*d*) K. Tsuchiya, A. Imai, T. Yamazaki, and T. Araki. Takeda Kenkyusho Nempo, **23**, 149 (1964); Chem. Abstr. **67**, 10221v (1967); (*e*) K. Tsuchiya, T. Yamazaki, A. Imai, and Y. Araki. Takeda Kenkyusho Nempo, **23**, 164 (1964); Chem. Abstr. **67**, 10222w (1967); (*f*) M. Kamada. Kyoto Daigaku Kekkaku Kyobushikkan Kenkyusho Kiyo, **2**, 124 (1968); Chem. Abstr. **72**, 87440b (1970).
10. H. Yamasaki and T. Moriyama. Biochim. Biophys. Acta, **227**, 698 (1971).
11. S. Hunt. *In* Chemistry and biochemistry of the amino acids. *Edited by* G.C. Barrett. Chapman and Hall, London. 1985. p. 55.
12. R.L. White, A.C. DeMarco, and K.C. Smith. J. Am. Chem. Soc. **110**, 8228 (1988).
13. R.L. White, A.C. DeMarco, and K.C. Smith. J. Chromatogr. **483**, 437 (1989).
14. C.H.W. Hirs, S. Moore, and W.H. Stein. J. Am. Chem. Soc. **76**, 6063 (1954).
15. S. Lam. J. Chromatogr. **355**, 157 (1986).
16. R.H. Abeles, P.A. Frey, and W.P. Jencks. Biochemistry. Jones and Bartlett Publishers, Boston. 1992. pp. 572–577.
17. W.J. Goux, L. Rench, and D.S. Weber. J. Labelled Comp. Radiopharm. **23**, 181 (1993).
18. K.R. Hanson and E.A. Havir. *In* The enzymes. 3rd ed. Vol. 7. *Edited by* P.D. Boyer. Academic Press, New York. 1972. pp. 75–166.
19. S. Ratner. *In* The enzymes. 3rd ed. Vol. 7. *Edited by* P.D. Boyer. Academic Press, New York. 1972. pp. 167–197.
20. C.S. Palmer and P.W. McWherter. Org. Synth. **7**, 34 (1927).
21. K.J. Martinkus, C.-H. Tann, and S.J. Gould. Tetrahedron, **39**, 3493 (1983).
22. M.S. Dunn and B.W. Smart. Org. Synth. **30**, 7 (1950).
23. (*a*) R.L. Baxter, E.M. Abbot, S.L. Greenwood, and I.J. MacFarlane. J. Chem. Soc. Chem. Commun. 564 (1985); (*b*) R.L. Baxter and E.M. Abbot. J. Labelled Comp. Radiopharm. **22**, 1211 (1985).
24. M.J. Zmijewski, Jr., V.A. Palaniswamy, and S.J. Gould. J. Chem. Soc. Chem. Commun. 1261 (1985).
25. C.A. Townsend and G.M. Salituro. J. Chem. Soc. Chem. Commun. 1631 (1984).
26. D.E. Metzler. Biochemistry. The chemical reactions of living cells. Academic Press, New York. 1977. pp. 649–651 and 837–838.
27. M. Rahmanian, G.R. Waller, and W.G. Smith. J. Biol. Chem. **246**, 823 (1971).
28. H.C. Lamont, W.L. Staudenbauer, and J.L. Strominger. J. Biol. Chem. **247**, 5103 (1972).

29. J. Blass and M. Macheboeuf. Helv. Chim. Acta, **29**, 1315 (1946).
30. C.I. Pogson and R.G. Wolfe. Biochem. Biophys. Res. Commun. **46**, 1048 (1972).
31. M.A. Glazebrook, L.C. Vining, R.L. White, K.C. Smith, and E.C. Chedrawy. Can. J. Microbiol. **39**, 536 (1993).
32. R.L. White, K.C. Smith, S.-Y. Shen, and L.C. Vining. *In* Molecular mechanisms in bioorganic processes. *Edited by* C. Bleasdale and B.T. Golding. The Royal Society of Chemistry, Cambridge, U.K. 1990. pp. 359–364.
33. (*a*) Y. Tsuda and H.C. Friedman. J. Biol. Chem. **245**, 5914 (1970); (*b*) I.M. Jeng, R. Somack, and H.A. Barker. Biochemistry, **13**, 2898 (1974).
34. P.D. Shaw and L.P. Hagar. J. Am. Chem. Soc. **81**, 1011 (1959).
35. P. Truffa-Bachi, M. Vernon, and G.N. Cohen. CRC Crit. Rev. Biochem. **2**, 379 (1974).
36. A. Meister. *In* The enzymes. 3rd ed. Vol. 10. *Edited by* P.D. Boyer. Academic Press, New York. 1974. pp. 561–580.
37. F. Lipmann. Science, **173**, 875 (1971).
38. W.B. Turner. Fungal metabolites. Academic Press, New York. 1971. pp. 314–315.
39. (*a*) J.M. Williamson, E. Inamine, K.E. Wilson, A.W. Douglas, J.M. Liesch, and G. Albers-Schönberg. J. Biol. Chem. **260**, 4637 (1985); (*b*) B.W. Bycroft, C. Maslen, S.J. Box, A.G. Brown, and J.W. Tyler. J. Chem. Soc. Chem. Commun. 1623 (1987).
40. H. Morishima, T. Sawa, T. Takita, T. Aoyagi, T. Takeuchi, and H. Umezawa. J. Antibiot. **27**, 267 (1974).
41. R.J. Parry and J.V. Mueller. J. Am. Chem. Soc. **106**, 5764 (1984).
42. E.C. Clevenstine, H.P. Broquist, and T.M. Harris. Biochemistry, **18**, 3658 (1979).
43. J.L.C. Wright, L.C. Vining, A.G. McInnes, D.G. Smith, and J.A. Walter. Can. J. Biochem. **55**, 678 (1977).
44. L.C. Vining, A.G. McInnes, A.W. McCulloch, D.G. Smith, and J.A. Walter. Can. J. Chem. **66**, 191 (1988).
45. K. Kakinuma, N. Ōtake, and H. Yonehara. Tetrahedron Lett. **21**, 167 (1972).
46. N. Sakai and Y. Ohfune. Tetrahedron Lett. **31**, 4151 (1990).
47. N. Fusetani, S. Matsunaga, H. Matsumoto, and Y. Takebayashi. J. Am. Chem. Soc. **112**, 7053 (1990).
48. P.M. Jordan and D. Shemin. *In* The enzymes. 3rd ed. Vol. 7. *Edited by* P.D. Boyer. Academic Press, New York. 1972. pp. 339–356.
49. S.-T. Chung, R.T.Y. Tan, and I. Suzuki. Biochemistry, **10**, 1205 (1971).
50. H.E. Williams and L.H. Smith, Jr. Science, **171**, 390 (1971).
51. G. Dénes. *In* The enzymes. 3rd ed. Vol. 9B. *Edited by* P.D. Boyer. Academic Press, New York. 1973. pp. 511–520.
52. T. Miyoshi, N. Miyairi, H. Aoki, M. Kohsaka, H.-I. Sakai, and H. Imanaka. J. Antibiot. **25**, 569 (1972).
53. R.E. Reeves. J. Am. Chem. Soc. **63**, 1476 (1941).
54. H. King. Org. Synth. Collect. Vol. **1**, 286 (1941).
55. T.J. Simpson. Chem. Soc. Rev. **4**, 497 (1975).
56. D.L. Rabenstein and T.L. Sayer. J. Magn. Reson. **24**, 27 (1976).
57. C.W. Waller and J.C. Paterson. U.S. Patent 2,561,323 (1951); Chem. Abstr. **46**, 1031c (1952).
58. R.E. Hill, R.L. White, and K.C. Smith. J. Nat. Prod. **56**, 1246 (1993).
59. R. Yoshioka, O. Ohtsuki, M. Senuma, and T. Tosa. Chem. Pharm. Bull. **37**, 883 (1989).
60. M.C. Khosla, R.R. Smeby, and F.M. Bumpus. Indian J. Chem. **5**, 279 (1967).
61. R. Albert, J. Danklmaier, H. Hönig, and H. Kandolf. Synthesis, 635 (1987).
62. P. Gmeiner, P.L. Feldman, M.Y. Chu-Moyer, and H. Rapoport. J. Org. Chem. **55**, 3068 (1990).

Can. J. Chem. Downloaded from www.nrcresearchpress.com by EESC ESCOLA DE ENGENHARIA on 09/08/12
For personal use only.

Indenone synthesis. Improved synthetic protocol and effect of substitution on the intramolecular Friedel–Crafts acylation

PAUL GALATSIS,[1] JEFFREY J. MANWELL, AND JAMES M. BLACKWELL
Department of Chemistry and Biochemistry, University of Guelph, Guelph, ON N1G 2W1, Canada

Received October 15, 1993

PAUL GALATSIS, JEFFREY J. MANWELL, and JAMES M. BLACKWELL. Can. J. Chem. **72**, 1656 (1994).

An improved protocol for the construction of substituted indenones is presented. Also the effect of substitution on the intramolecular Friedel–Crafts acylation was noted. Specifically, if there is no substitution at the 2-position of the indenone poor yields of cyclized material were obtained, if at all, while the substitution of a methyl or ethyl group greatly improved the yield of cyclized material. Placement of a large group (e.g., benzyl) resulted in a diminuation of the improved yield. The new synthetic procedure could, in principle, allow for the construction of 2,3-disubstituted indenones. One example of this reaction mode was presented.

PAUL GALATSIS, JEFFREY J. MANWELL et JAMES M. BLACKWELL. Can. J. Chem. **72**, 1656 (1994).

On présente un protocole amélioré pour la synthèse d'indénones substituées. On note l'effet de substitution sur l'acylation intramoléculaire de Friedel–Crafts. D'une façon spécifique, s'il n'y a pas de substituant en position 2 de l'indénone, on obtient, au mieux, de faibles rendements de produits cyclisés; par ailleurs, si cette position est substituée par un méthyle ou un éthyle, on obtient de bien meilleurs rendements en produits cyclisés. Si le substituant est volumineux (comme un benzyle), il y a une diminution du rendement amélioré. La nouvelle méthode de synthèse pourrait, au moins en principe, permettre d'obtenir des indénones substituées en positions 2 et 3.

[Traduit par la rédaction]

Introduction

We recently reported a general method for the construction of substituted cyclobutenone derivatives (1). To apply this methodology towards the construction of the natural product neofavelanone **1** (2), we required ready access to disubstituted indenone **2** (see Scheme 1). For the synthesis to be viable, the

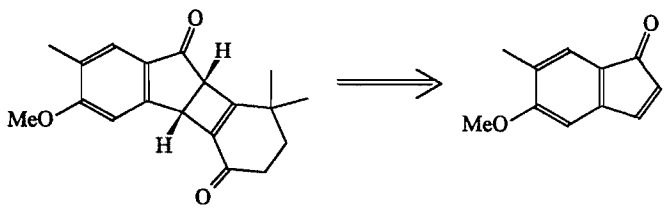

1 **2**

SCHEME 1

method for the synthesis would have to be rapid and proceed in good yield.

A great deal of work has been directed towards the synthesis of indanones (3). The methods include such procedures as intramolecular Friedel–Crafts acylation (3*a*, *c*) and a variation of the von Auwers reaction (3*d*). The interest in these compounds was twofold. Derivatives of indanone exhibited biological activity (e.g., antihypertensive or bronchodilatory activity) or they could serve as synthetic precursors to other natural products (e.g., steroids or gibberellic acid).

The synthesis of indenones is less well studied. A logical precursor to these compounds could be the corresponding indanone. However, poor yields, irreproducibility, or decomposition of the starting material were common outcomes. To our knowledge there exist only two general methods for the direct synthesis of indenone derivatives. The first one of these methods (4) is an aluminum chloride catalyzed addition of substituted benzoyl chlorides to acetylenic compounds (see reaction [1]). The second method (5) involves an intramolecular Friedel–Crafts acylation of β-chloro-β-arylpropionyl chlorides followed by a dehydrochlorination reaction (see reaction [2]).

[1]

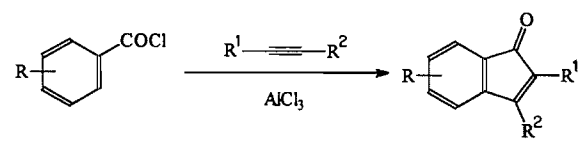

[2]

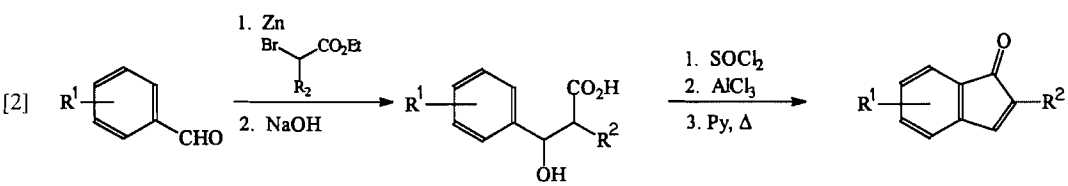

We felt the second method to be more synthetically amenable to our desired system. Thus we began an investigation of this chemistry and now wish to report an improvement in the synthetic protocol and the effect of substitution at the 2-position of the indenone on the cyclization step.

Results and discussion

Application of the second method (5) towards the synthesis of **2** required access to aldehyde **3***d*. This compound could be prepared in good overall yield following the reported procedure (6). With aldehyde **3***d* in hand, we wished to simplify the Reformatsky reaction – saponification sequence of the reported procedure (5). We set out to see if direct treatment of aldehyde **3***d*

[1]Author to whom correspondence may be addressed.

Can. J. Chem. Downloaded from www.nrcresearchpress.com by EESC ESCOLA DE ENGENHARIA on 09/08/12
For personal use only.

Can. J. Chem. Downloaded from www.nrcresearchpress.com by ESC ESCOLA DE ENGENHARIA on 09/08/12
For personal use only.

TABLE 1. Product formation from aldol reaction with dilithiocarboxylic acids

Entry	Compound	R^1	R^2	R^3	Yield (%)
1	**5***a*	H	H	H	95
2	**5***b*	Me	H	H	80
3	**5***c*	MeO	H	H	93
4	**5***d*	Me	MeO	H	93
5	**5***e*	H	H	Me	89
6	**5***f*	Me	H	Me	87
7	**5***g*	MeO	H	Me	81
8	**5***h*	Me	MeO	Me	86
9	**5***i*	H	H	Et	93
10	**5***j*	H	H	Bn	81

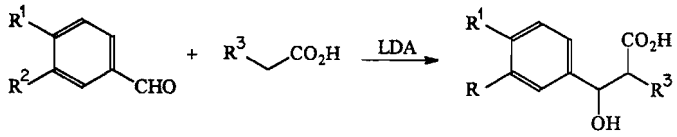

3 **4** **5**

with the dianion of acetic acid (**4**, R^3 = H) (7) would accomplish the equivalent transformation. This supposition was affirmed when we were able to isolate **5***d* in 93% yield (see Table 1). The generality of this approach to **5** was demonstrated by the fact that in addition to the dianion of acetic acid, we were able to carry out the aldol reaction with the dianions of propionic acid (**4**, R^3 = Me), butyric acid (**4**, R^3 = Et), and 3-phenylpropionic acid (**4**, R^3 = Bn). To obtain the yields presented in Table 1 for aldols **5**, one must allow the dianion to form at 0°C and then cool to −78°C before adding the desired aldehyde. With this protocol, one can routinely obtain these compounds. While compounds **5***e–j* were isolated as inseparable mixtures of diastereomers, this was not problematic, since both diastereomers gave rise to the same indenone derivative once the β-elimination step was completed.

With the formation of acid **5***d*, the Friedel–Crafts reaction – β-elimination sequence was attempted for the preparation of **2**. We were disappointed when only a 15% yield (see Table 2) was obtained for this transformation. However, when acid **5***h* was

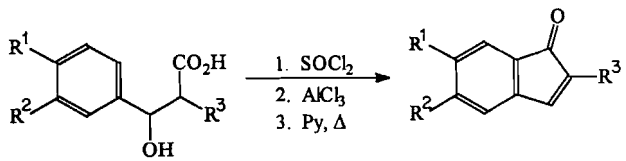

5 **6**

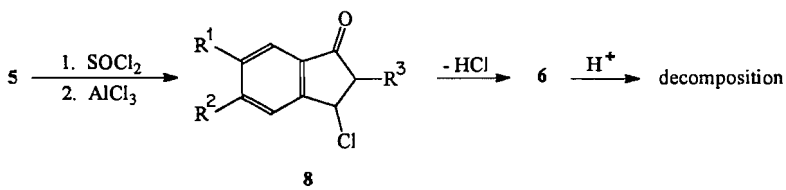

8

prior to treatment with pyridine. However, this mixture was routinely submitted to the elimination step in order to isolate the desired product under more favorable conditions. Furthermore, exposure of **6** to aluminum chloride under the standard reaction conditions resulted in a 20% decomposition of starting material after 30 min. While direct treatment of **5** with PPA or other Lewis acids resulted in no product formation, one could surmise that these acid conditions could also have resulted in destruction of any indenone that may have formed. This sensitivity of indenones has been previously described (3–5). In the case of **7***b*, *c*, subjected to these conditions, a 72% yield (see Table 2) of **6***h* was obtained. As one can see from Table 2, this trend was repeated for all the systems investigated. That is, only when a substituent was present at the 2-position of the indenone were synthetically acceptable levels of product formation witnessed. For compound **5***g*, treatment with thionyl chloride proceeded normally; however, upon treatment of this dichloro derivative with aluminum chloride only decomposition was observed. We are at a loss to provide an explanation for this result. For R^3 = H (Table 2, entries 1–4) one either isolates **6** in poor yield or a product of net dehydrochlorination from the dichloro derivative of **5**, in good yield, to afford the corresponding cinnamic acid derivative **7**.

TABLE 2. Results of intramolecular Friedel–Crafts acylation from acid **5**

Entry	Compound	R^1	R^2	R^3	Yield (%)
1	**6***a*	H	H	H	5
2	**7***b*	Me	H	H	79
3	**7***c*	MeO	H	H	65
4	**2**	Me	MeO	H	15
5	**6***e*	H	H	Me	74
6	**6***f*	Me	H	Me	63
7	**6***h*	Me	MeO	Me	72
8	**6***i*	H	H	Et	79
9	**6***j*	H	H	Bn	40

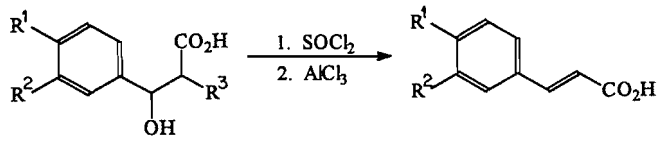

5 **7**

We feel these observations are consistent with the stability of the β-chloroindanone intermediate **8** in this two-step sequence. Exposure of **5** to thionyl chloride produces the corresponding β-chloro-acid chloride which under the influence of aluminum chloride gives rise to **8**. One could envisage that under the acidic conditions of this reaction an in situ β-elimination of chloride occurs to give **6**. These acidic conditions could then catalyze the decomposition of the indenone. With R^3 = H, this is a facile process; however, when R^3 = alkyl this process is stopped or at least slowed down enough to allow isolation of **8**. Treatment of **8** with pyridine then allows one to isolate **6** under basic conditions, which are more compatible with this functionality. Indeed, small amounts of **6** are found in the reaction mixture

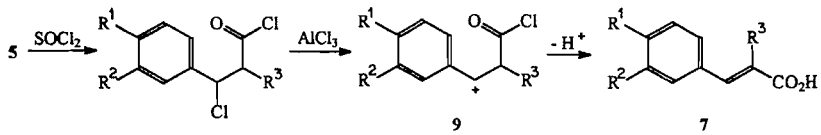

complexation of the β-chlorine with the aluminum chloride would result in formation of benzylic cation **9**. Loss of a proton would then give rise to the observed cinnamic acid derivatives **7**.

In addition, this method could be used to generate alternate substitution patterns if, for example, a ketone were used in place of aldehyde **3**. One example of this was demonstrated with acetophenone (**10**). Aldol reaction of **10** with the dianion of propionic acid, as before, produced hydroxy-acid **11** in excellent yield. Intramolecular Friedel–Crafts acylation of **11** then afforded indenone **12**.

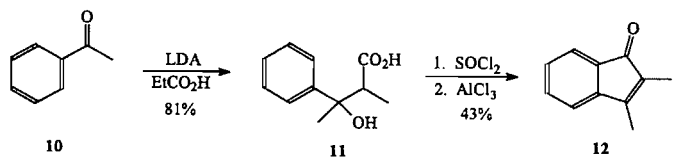

In summary, we have demonstrated that the aldol reaction of the dianion of carboxylic acids with aldehydes (and in principle ketones) provides direct access to acids **5** with improved yields. We have also shown that a substituent at the 2-position of the indenone appears to be necessary for optimal yields of indenones **6** by this method. Presently, an alternate method for the preparation of **2** is being pursued and this work will be reported when completed.

Experimental section

General procedures and materials

Melting points were taken on a Fischer–Johns melting point apparatus and are uncorrected. ^1H and ^{13}C NMR spectra were recorded in $CDCl_3$ at 400 and 100 MHz, respectively, unless specified otherwise.

All solvents used for chromatography were distilled prior to use. Reactions were monitored by TLC using E. Merck precoated silica gel 60 F-250 (0.25 mm thickness) aluminum backed plates. The plates were visualized by immersion in *p*-anisaldehyde solution and warming on a hotplate. E. Merck silica gel 60 (70–230 mesh) was used for column chromatography. All solvents were reagent grade and anhydrous solvents were dried prior to use as follows: diisopropylamine, pyridine, DMF, and CH_2Cl_2 were distilled from CaH_2; THF was distilled from benzophenone ketyl. Compounds obtained from commercial sources were used directly as received. Compounds **6***a*, **7***b*, and **7***c* are known compounds and commercially available. Also compounds **5***a*, **5***e*, **5***i*, **6***e*, **6***f*, **6***i*, and **12** have been reported in the literature (5, 8).

General procedure for the aldol reaction with dilithiocarboxylic acids

To a solution of diisopropyl amine (3.2 equiv.) in THF (20 mL) at −78°C was added *n*-BuLi (3.0 equiv., 2.5 M solution) and stirred for 30 min. Acid **4** (1.2 equiv.) in THF (2 mL) was added via cannula and the reaction was warmed to 0°C and stirred for 30 min. Cooling to −78°C preceded addition of the aldehyde **3** in THF (3 mL) via cannula. The reaction was allowed to slowly warm to room temperature and the stirring was maintained for 16–24 h. The reaction mixture was made basic with 15% NaOH solution and washed once with ether. The aqueous phase was acidified with 10% HCl solution and extracted five times with ether. The combined extracts were washed with brine solution, dried with anhydrous sodium sulfate, filtered, and the solvent removed in vacuo. The resulting product was recrystallized from ether–hexanes to afford a white solid.

3-Hydroxy-3-(4′-methylphenyl)propionic acid (5b)

Acetic acid (4.99 mmol, 0.287 mL) was deprotonated with LDA (diisopropylamine 13.31 mmol, 1.86 mL, and *n*-BuLi 12.48 mmol, 5.0 mL) and reacted with **3** (R^1 = Me, R^2 = H) (4.16 mmol, 0.50 g) according to the general procedure to afford after recrystallization 0.597 g (80%) of **5***b* (mp 93.5–95°C). IR ($CHCl_3$): 3550–2050, 1710, 1515, 1456, 1437, 1419, 1399, 1340, 1316, 1291, 1266, 1214, 1205, 1189, 1160, 1116, 1053, 1025, 1012, 953, 933, 895, 881, 852, 845, 819, 785, 727, 683, 628 cm^{-1}; ^1H NMR δ: 7.26 (d, 2H, J = 7.6 Hz), 7.17 (d, 2H, J = 8.0 Hz), 5.12 (dd, 1H, J = 9.6, 3.6 Hz), 2.78 (AB portion of ABX, 2H, J_{ab} = 16.4, J_{ax} = 9.2, J_{bx} = 3.6, Δνab = 31.72 Hz), 2.35 (s, 3H); ^{13}C NMR δ: 177.26, 139.08, 137.82, 129.32, 125.61, 70.07, 43.00, 21.12; HRMS calcd. for $C_{10}H_{12}O_3$: 180.0786; found: 180.0782.

3-Hydroxy-3-(4′-methoxyphenyl)propionic acid (5c)

Acetic acid (4.44 mmol, 0.254 mL) was deprotonated with LDA (diisopropylamine 11.80 mmol, 1.65 mL, and *n*-BuLi 11.10 mmol, 4.50 mL) and reacted with **3** (R^1 = MeO, R^2 = H) (3.70 mmol, 0.50 g) according to the general procedure to afford after recrystallization 0.667 g (93%) of **5***c* (mp 89–90°C). IR ($CHCl_3$): 3650–2350, 1710, 1612, 1514, 1404, 1303, 1251 cm^{-1}; ^1H NMR δ: 7.27 (d, 2H, J = 8.8 Hz), 6.87 (d, 2H, J = 8.0 Hz), 6.05 (br s, 1H), 5.08 (dd, 1H, J = 9.6, 3.6 Hz), 3.79 (s, 3H), 2.75 (AB portion of ABX, 2H, J_{ab} = 16.4, J_{ax} = 9.6, J_{bx} = 3.6, Δν_{ab} = 39.40 Hz); ^{13}C NMR δ: 176.87, 159.29, 134.24, 126.99, 114.00, 69.88, 55.27, 43.02; HRMS calcd. for $C_{10}H_{12}O_4$: 196.0735; found: 196.0727.

3-Hydroxy-3-(3′-methoxy-4′-methylphenyl)propionic acid (5d)

Acetic acid (1.60 mmol, 0.092 mL) was deprotonated with LDA (diisopropylamine 4.27 mmol, 0.60 mL, and *n*-BuLi 4.00 mmol, 1.60 mL) and reacted with **3** (R^1 = Me, R^2 = MeO) (1.33 mmol, 0.20 g) according to the general procedure to afford after recrystallization 0.261 g (93%) of **5***d* (mp 101.5–102.5°C). IR ($CHCl_3$): 3600–2440, 1710, 1614, 1588, 1506, 1462, 1418, 1315, 1260, 1180, 1134, 1066, 1038, 1004, 981, 901, 875, 818, 730, 668, 652 cm^{-1}; ^1H NMR δ: 7.11 (d, 1H, J = 7.6 Hz), 6.88 (s, 1H), 6.83 (d, 1H, J = 7.6 Hz), 5.13 (dd, 2H, J = 9.2, 3.2 Hz), 3.84 (s, 3H), 2.81 (AB portion of ABX, 2H, J_{ab} = 16.4, J_{ax} = 9.6, J_{bx} = 3.6, Δν_{ab} = 30.57 Hz), 2.20 (s, 3H); ^{13}C NMR δ: 177.19, 157.94, 140.99, 130.66, 126.52, 117.33, 107.21, 70.30, 55.30, 43.14, 15.98; HRMS calcd. for $C_{11}H_{14}O_4$: 210.0892; found: 210.0890.

2-Methyl-3-hydroxy-3-(4′-methylphenyl)propionic acid (5f)

Propionic acid (4.99 mmol, 0.372 mL) was deprotonated with LDA (diisopropylamine 13.31 mmol, 1.86 mL, and *n*-BuLi 12.48 mmol, 5.0 mL) and reacted with **3** (R^1 = Me, R^2 = H) (4.16 mmol, 0.50 g) according to the general procedure to afford a mixture of aldols 0.703 g (87%) of **5***f* (mp 71–73°C). IR ($CHCl_3$): 3650–2350, 1710, 1515, 1458, 1419, 1290, 1134, 1118, 1109, 1039, 1018, 986, 922 cm^{-1}; ^1H NMR δ: 7.26–7.12 (m, 10H), 5.12 (d, 1H, J = 3.6 Hz), 4.71 (d, 1H, J = 8.4 Hz), 2.88–2.76 (m, 2H), 2.35 (s, 3H), 2.34 (s, 3H), 1.14 (d, 3H, J = 7.2 Hz), 1.01 (d, 3H, J = 6.8 Hz); ^{13}C NMR δ: 181.14, 180.87, 138.05, 137.30, 129.27, 129.02, 126.66, 125.86, 76.17, 73.32, 47.05, 46.19, 21.14, 21.09, 14.33, 10.41; HRMS calcd. for $C_{11}H_{14}O_3$: 194.0943; found: 194.0947.

2-Methyl-3-hydroxy-3-(4′-methoxyphenyl)propionic acid (5g)

Propionic acid (4.44 mmol, 0.329 mL) was deprotonated with LDA (diisopropylamine 11.80 mmol, 1.65 mL, and *n*-BuLi 11.10 mmol, 4.5 mL) and reacted with **3** (R^1 = MeO, R^2 = H) (3.70 mmol, 0.50 g) according to the general procedure to afford a mixture of aldols 0.627 g (81%) of **5***g* (mp 50–52°C). IR ($CHCl_3$): 3650–2350, 1709, 1612, 1514, 1462, 1304, 1251, 1175, 1035, 1007, 919, 830 cm^{-1}; ^1H NMR δ:

Can. J. Chem. Downloaded from www.nrcresearchpress.com by EESC ESCOLA DE ENGENHARIA on 09/08/12
For personal use only.

Can. J. Chem. Downloaded from www.nrcresearchpress.com by ESC ESCOLA DE ENGENHARIA on 09/08/12
For personal use only.

7.27 (br d, 4H, J = 8.4 Hz), 6.89 (d, 2H, J = 8.4 Hz), 6.88 (d, 2H, J = 8.4 Hz), 5.09 (d, 1H, J = 4.0 Hz), 4.71 (d, 1H, J = 9.2 Hz), 3.81 (s, 3H), 3.80 (s, 3H), 2.88–2.75 (m, 2H), 1.16 (d, 3H, J = 7.2 Hz), 1.00 (d, 3H, J = 7.2 Hz); ^{13}C NMR δ: 180.65, 180.23, 159.39, 158.91, 133.25, 133.09, 127.96, 127.13, 113.84, 113.60, 75.88, 73.23, 55.15, 47.10, 46.28, 14.20, 10.51; HRMS calcd. for $C_{11}H_{14}O_4$: 210.0892; found: 210.0897.

*2-Methyl-3-hydroxy-3-(3′-methoxy-4′-methylphenyl)propionic acid (**5**h)*

Propionic acid (4.00 mmol, 0.298 mL) was deprotonated with LDA (diisopropylamine 10.67 mmol, 1.50 mL, and *n*-BuLi 10.00 mmol, 4.0 mL) and reacted with **3** (R^1 = Me, R^2 = MeO) (3.33 mmol, 0.50 g) according to the general procedure to afford a mixture of aldols 0.643 g (86%) of **5***h* (mp 96–98°C). IR ($CHCl_3$): 3650–2350, 1707, 1614, 1586, 1509, 1464, 1457, 1415, 1264, 1257, 1155, 1134, 1041, 1020, 993, 862, 819 cm^{-1}; ^{1}H NMR δ: 7.09 (br d, 2H, J = 8.0 Hz), 6.84 (br s, 2H), 6.80 (br, d, 2H, J = 7.2 Hz), 5.13 (d, 1H, J = 4.0 Hz), 4.71 (d, 1H, J = 9.2 Hz), 3.83 (s, 6H), 2.90–2.78 (m, 2H), 2.20 (br s, 6H), 1.16 (d, 3H, J = 7.2 Hz), 1.02 (d, 3H, J = 7.2 Hz); ^{13}C NMR δ: 181.11, 180.84, 157.98, 157.71, 139.96, 139.89, 130.50, 130.40, 126.85, 125.98, 118.78, 117.65, 107.92, 107.66, 76.48, 73.46, 55.31, 47.11, 46.28, 16.00, 15.94, 14.36, 10.50; HRMS calcd. for $C_{12}H_{16}O_4$: 224.1048; found: 224.1049.

*2-Benzyl-3-hydroxy-3-phenylpropionic acid (**5**j)*

Dihydrocinnamic acid (2.83 mmol, 0.425 g) was deprotonated with LDA (diisopropylamine 7.55 mmol, 1.06 mL, and *n*-BuLi 7.08 mmol, 2.8 mL) and reacted with **3** (R^1 = H, R^2 = H) (2.36 mmol, 0.250 g) according to the general procedure to afford a mixture of aldols 0.491 g (81%) of **5***i* (mp 151–153°C). IR ($CHCl_3$): 3650–2300, 1710, 1496, 1461, 1275, 1199, 1168, 1089, 1010, 979, 924, 896, 762, 704 cm^{-1}; ^{1}H NMR δ: 7.60–7.00 (m, 20H), 5.09 (d, 1H, J = 5.2 Hz), 4.82 (d, 1H, J = 7.2 Hz), 3.16–2.86 (m, 4H), 2.78–2.64 (m, 2H); ^{13}C NMR (CD_3COCD_3) δ: 175.27, 143.92, 140.15, 129.50, 129.03, 128.98, 128.37, 127.62, 126.89, 75.86, 56.40, 35.91; HRMS calcd. for $C_{16}H_{16}O_3$: 256.1099; found: 256.1085.

General procedure for the preparation of indenones

To a solution of acid **5** (1.0 equiv.) in CH_2Cl_2 (2 mL) was added a solution of $SOCl_2$ (2.4 equiv.) and DMF (0.03 equiv.) in CH_2Cl_2 (3 mL) via cannula over 30 min at room temperature. The reaction was stirred for 30 min and then heated at reflux for 15 min before removing the solvent in vacuo. This acid chloride in CH_2Cl_2 (2 mL) was added via cannula to a solution of $AlCl_3$ (1.1 equiv.) in CH_2Cl_2 (2 mL) at room temperature. After stirring for 30 min the reaction was poured into water, extracted four times with ether, and the combined extracts were washed successively with water, saturated $NaHCO_3$, and brine solution before drying with anhydrous Na_2SO_4. The solid was filtered, the solvent removed in vacuo. The crude **8** was dissolved in pyridine (1 mL) and heated at 70°C for 30 min to 2.5 h. After cooling to room temperature, the reaction was poured into water, extracted three times with ether, and the combined extracts were washed with 10% HCl solution, water, saturated $NaHCO_3$ solution, brine solution, and dried (Na_2SO_4). The solid was filtered, the solvent removed in vacuo, and the crude product purified by chromatography (20 g silica gel, EtOAc:hexanes = 1:9) to afford indenones **6**. Analytical samples were prepared by recrystallization from ether–hexanes.

*5-Methoxy-6-methyl-1-indenone (**2**)*

Treatment of **5***d* (0.51 mmol, 0.108 g) with $SOCl_2$ (1.23 mmol, 0.090 mL) and DMF (0.02 mmol, 0.002 mL) followed by $AlCl_3$ (0.56 mmol, 0.075 g) according to the general procedure afforded after chromatography 0.013 g (15%) of **2** as a yellow solid (mp 77–78°C). IR (CCl_4): 3001, 2957, 2927, 2856, 2836, 1710, 1610, 1587, 1506, 1488, 1464, 1456, 1296, 1281, 1270, 1244, 1168, 1160, 1151, 1131, 1115, 1095, 1067, 1043, 1001, 900, 856, 848 cm^{-1}; ^{1}H NMR δ: 7.40 (dd, 1H, J = 6.4, 0.4 Hz), 7.23 (s, 1H), 6.60 (s, 1H), 5.78 (d, 1H, J = 6.4 Hz), 3.89 (s, 3H), 2.16 (s, 3H); ^{13}C NMR δ: 197.95, 162.09, 147.87, 145.46, 127.30, 125.79, 122.30, 110.38, 105.63, 55.71, 16.27; HRMS calcd. for $C_{11}H_{10}O_2$: 174.06816; found: 174.0676.

*2,6-Dimethyl-5-methoxy-1-indenone (**6**h)*

Treatment of **5***h* (0.90 mmol, 0.200 g) with $SOCl_2$ (2.14 mmol, 0.156 mL) and DMF (0.03 mmol, 0.003 mL) followed by $AlCl_3$ (0.98 mmol, 0.131 g) according to the general procedure afforded after chromatography 0.122 g (72%) of **6***h* as an orange solid (mp 115–117°C). IR (CCl_4): 3055, 3003, 2957, 2938, 2919, 2855, 2839, 1717, 1608, 1478, 1466, 1344, 1269, 1243, 1078 cm^{-1}; ^{1}H NMR δ: 7.18 (s, 1H), 6.95 (s, 1H), 6.49 (s, 1H), 3.87 (s, 3H), 2.13 (s, 3H), 1.84 (d, 3H, J = 0.8 Hz); ^{13}C NMR δ: 198.12, 162.17, 145.81, 141.07, 136.24, 125.78, 124.13, 122.51, 104.79, 55.65, 16.11, 10.10; HRMS calcd. for $C_{12}H_{12}O_2$: 188.0837; found: 188.0849.

*2-Benzyl-1-indenone (**6**j)*

Treatment of **5***j* (0.39 mmol, 0.100 g) with $SOCl_2$ (0.94 mmol, 0.068 mL) and DMF (0.01 mmol, 0.001 mL) followed by $AlCl_3$ (0.43 mmol, 0.057 g) according to the general procedure afforded after chromatography 0.034 g (40%) of **6***j* as a solid (mp 98–99°C). IR (CCl_4): 3090, 3070, 3064, 3029, 2926, 2907, 2893, 1708, 1646, 1615, 1587, 1495, 1467, 1450, 1326, 1298, 1270, 1209, 1184, 1091, 959 cm^{-1}; ^{1}H NMR δ: 7.92 (d, 1H, J = 7.6 Hz), 7.68 (m, 2H), 7.62 (t, 1H, J = 7.6 Hz), 7.56 (d, 1H, J = 7.2 Hz), 7.51–7.37 (m, 5H), 4.06 (s, 2H); ^{13}C NMR δ: 194.32, 149.63, 138.02, 135.40, 134.72, 134.61, 133.92, 130.71, 129.65, 128.92, 127.67, 126.16, 124.45, 32.45; HRMS calcd. for $C_{10}H_{12}O_3$ (M − 1): 219.0810; found: 219.0806.

Acknowledgements

This research was supported by the Natural Sciences and Engineering Research Council of Canada (NSERC) to which we express our sincere gratitude. J.M.B. would also like to thank NSERC for an undergraduate student research award. Helpful comments by the reviewers are sincerely appreciated.

1. P. Galatsis, K.J. Ashbourne, J.J. Manwell, R. Dufault, K.L. Hatt, G. Ferguson, and J.F. Gallagher. J. Org. Chem. **58**, 1491 (1993).
2. Y. Endo, T. Ohta, and S. Nozoe. Tetrahedron Lett. **33**, 353 (1992).
3. (*a*) W.S. Johnson and W.E. Shelberg. J. Am. Chem. Soc. **67**, 1853 (1945); (*b*) R.V. Heinzelmann, H.G. Kolloff, and H.G. Hunter. J. Am. Chem. Soc. **70**, 1386 (1948); (*c*) W.S. Johnson and H.J. Glenn. J. Am. Chem. Soc. **71**, 1092 (1949); (*d*) R.A. Barnes, E.R. Kraft, and L. Gordon. J. Am. Chem. Soc. **71**, 3523 (1949); (*e*) J.F. Feeman and E.D. Amstutz. J. Am. Chem. Soc. **72**, 1526 (1950); (*f*) C.S. Marvel and C.W. Hinman. J. Am. Chem. Soc. **76**, 5435 (1954); (*g*) J. Sam and J.N. Plampin. J. Am. Chem. Soc. **82**, 5205 (1960); (*h*) H.O. House, V. Paragamian, R.S. Ro, and D.J. Wluka. J. Am. Chem. Soc. **82**, 1452 (1960); (*i*) H.O. House and J.K. Larson. J. Org. Chem. **33**, 448 (1968); (*j*) H.O. House and C.B. Hudson. J. Org. Chem. **35**, 647 (1970); (*k*) H.O. House and W.C. McDaniel. J. Org. Chem. **42**, 2155 (1977); (*l*) F.D. Bellamy, J.B. Chazan, and K. Ou. Tetrahedron, **39**, 2803 (1983).
4. (*a*) H. Martens and G. Hoornaet. Synth. Commun. **2**, 147 (1972); (*b*) Tetrahedron, **30**, 3641 (1974).
5. M.B. Floyd and G.R. Allen. J. Org. Chem. **35**, 2647 (1970).
6. H. Fukumi, H. Kurihara, and H. Mishima. Chem. Pharm. Bull. **26**, 2175 (1978).
7. (*a*) B. Angelo. Bull. Soc. Chim. Fr. 1848 (1970); (*b*) P.L. Creger. J. Org. Chem. **37**, 1907 (1972); (*c*) S. Danishefsky, T. Kitahara, P.F. Schuda, and S.J. Etheredge. J. Am. Chem. Soc. **98**, 3028 (1976); (*d*) S. Danishefsky, M.-Y. Tsai, and T. Kitahara. J. Org. Chem. **42**, 394 (1977); (*e*) J. Mulzer, G. Hartz, U. Kuhl, and G. Bruntrup. Tetrahedron Lett. 2949 (1978); (*f*) J. Mulzer, U. Kuhl and G. Bruntrup. Tetrahedron Lett. 2953 (1978).
8. (*a*) R.J. Murray and N.H. Cromwell. J. Org. Chem. **41**, 3540 (1976); (*b*) L.S. Liebeskind and M.S. South. J. Org. Chem. **45**, 5426 (1980).

Enamines from formamides. Synthesis of 1,2,3,4-tetrahydro-1-substituted β-carbolines[1]

RAHUL VOHRA AND DAVID B. MACLEAN[2]
Department of Chemistry, McMaster University, Hamilton, ON L8S 4M1, Canada

Received December 20, 1993

RAHUL VOHRA and DAVID B. MACLEAN. Can. J. Chem. **72**, 1660 (1994).

Pyridines and benzopyridines substituted with trimethylsilylmethyl groups, α or γ to the nitrogen atom, have been found to react with formamides by way of a Peterson reaction to form enamines. Trimethylsilylmethylbenzene behaved similarly. The enamines prepared from N^b-formyl-N^a,N^b-dimethyltryptamine cyclized readily to β-carbolines. The reaction of formamides with lithiated 4-methylpyridines as a route to enamines was examined but proved to be less general and proceeded in lower yield than the route by way of the Peterson reaction. The nuclear magnetic resonance and mass spectra of the enamines and β-carbolines derived from **3** are discussed.

RAHUL VOHRA et DAVID B. MACLEAN. Can. J. Chem. **72**, 1660 (1994).

On a trouvé que les pyridines et benzopyridines substituées par des groupes triméthylsilylméthyles en α ou en γ de l'azote réagissent avec les formamides, par le biais d'une réaction de Peterson, pour conduire à la formation d'énamines. Le triméthylsilylméthylbenzène se comporte de la même manière. Les énamines préparées à partir de la N^b-formyl-N^a,N^b-diméthyltryptamine se cyclisent facilement en β-carbolines. On a examiné la réaction des formamides avec les 4-méthylpyridines lithiées, comme voie d'accès aux énamines, mais on a montré que la réaction est moins générale et qu'elle se produit avec un rendement plus faible que la voie impliquant la réaction de Peterson. On discute des spectres de résonance magnétique nucléaire et de masse des énamines et des β-carbolines dérivés du produit **3**.

[Traduit par la rédaction]

Introduction

It is known that acyclic enamines derived from tryptamine derivatives are effective precursors of β-carbolines (1–4). Cyclization of the enamines is brought about by treatment with acid and very likely proceeds, mechanistically, through an iminium ion intermediate in the same manner as the Pictet–Spengler reaction (5). We describe here an investigation of the preparation of enamines from formamides. We report that pyridines and benzopyridines, bearing a trimethylsilylmethyl group α or γ to the nitrogen atom, will react, by way of a Peterson reaction (6), with N^b-formyl-N^a,N^b-dimethyltryptamine to form enamines, suitable for elaboration to 1,2,3,4-tetrahydro-β-carbolines. Trimethylsilylmethylbenzene behaves similarly, and other formamides are shown to undergo the Peterson reaction to form enamines. We investigated also the reaction of lithio derivatives derived from 4-methylpyridines with several formamides as an alternative route to enamines. This approach proved to be less general and to proceed in lower yield than that proceeding through the trimethylsilylmethylpyridines.

Results and discussion

Synthesis of enamine precursors of β-carbolines from 3

The general approach to enamine precursors of β-carbolines by way of the Peterson reaction is outlined in Scheme 1. The pyridines and benzopyridines bearing trimethylsilylmethyl groups α or γ to the nitrogen atom, **1***a–g*, in the form of their lithio derivatives, **2***a–g*, reacted readily with **3**, in solution in tetrahydrofuran (THF). The enamines so formed, **4***a–g*, were converted into 1,2,3,4-tetrahydro-β-carbolines, **5***a–g*, by treatment with a saturated solution of hydrogen chloride in methanol. Trimethylsilylmethylbenzene undergoes a similar series of reactions, under different experimental conditions, to afford **4***h*, which cyclized under similar conditions to those used for **4***a–g*. There are only a few examples of the Peterson reaction applied to amides. Intermolecular reactions of this type have been reported by Woodbury and Rathke (7*a*) and by Agawa et al. (7*b*) and intramolecular reactions by Snieckus and co-workers (7*c–e*).

The pyridines and benzopyridines bearing a trimethylsilylmethyl group, compounds **1***a–g*, were prepared from the corresponding methylpyridines and methylbenzopyridines by treatment with lithium diisopropylamine (LDA) in tetrahydrofuran (THF) followed by treatment with trimethylsilyl chloride. The procedure used in the preparation of **1***a*, **1***b*, and **1***d–g* was patterned on that reported for the preparation of **1***b* (8) whereas the preparation of **1***c* was based on a published procedure (9). Compounds **1***a*, **1***b*, and **1***c* were isolated and purified by distillation in vacuo, whereas **1***d–g* were not isolated but were employed in situ in the preparation of enamines. Trimethylsilylmethylbenzene **1***h* was prepared from benzyl chloride (10).

Compound **3** was isolated in 1974 (11) as a by-product of a photochemical reaction and was synthesized by the same group by treatment of N^a,N^b-dimethyltryptamine with ethyl formate. We prepared **3** from N^b-formyltryptamine (12). A solution of the latter in dimethyl sulfoxide (DMSO) was treated with a solution of dimsyl sodium (2.25 equiv.) in DMSO and the red solution was stirred for 3 h before addition of iodomethane (3.0 equiv.); processing of the reaction mixture afforded **3** (92%). The ^{1}H and ^{13}C nmr spectra of **3** confirmed the earlier observation (11) that it is a mixture of rotamers.

Enamines **4***a–h* were prepared by way of the Peterson reaction between **3** and the lithio derivatives **2***a–h*. Lithio derivatives **2***a–c* were prepared by dropwise addition of a solution of the trimethylsilylmethyl compounds **1***a–c* in THF into a solution of LDA in THF. The solutions of **2***a–c*, so generated, were treated directly with a solution of **3** in THF to afford **4***a–c*, respectively. The enamines **4***d–g* were prepared from the methylbenzopyridines in a one-pot reaction without isolation of the trimethylsilylmethyl compounds. The conversion of **1***h* to **4***h* did not proceed under conditions that led to the formation of **4***a–c*. However, **4***h* was obtained when a solution of **1***h* in hexamethylphosphoric triamide (HMPTA) was treated first with *n*-BuLi in hexane and subsequently with a solution of **3** in THF.

The enamines were prone to decomposition on chromatography on silica gel. Purification of **4***a* and **4***b* was achieved by this

[1]For a preliminary account of part of this research, see ref. 23.
[2]Author to whom correspondence may be addressed.

Can. J. Chem. Downloaded from www.nrcresearchpress.com by EESC ESCOLA DE ENGENHARIA on 09/08/12
For personal use only.

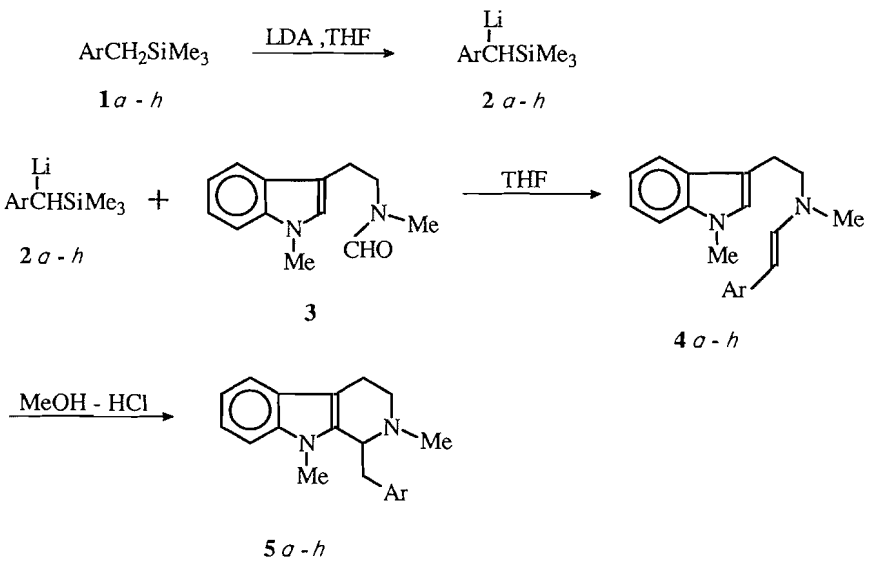

Ar = *a*, 3-ethylpyridin-4-yl; *b*, pyridin-4-yl; *c*, pyridin-2-yl; *d*, quinolin-4-yl; *e*, quinolin-2-yl; *f*, 3-methylquinolin-2-yl; *g*, 6,7-dimethoxyisoquinolin-1-yl; *h*, phenyl

SCHEME 1

method but with some loss of enamine. In other cases the crude enamines were used directly in the subsequent step. The 1,2,3,4-tetrahydro-β-carbolines, **5***a–h*, were prepared by treatment of the enamines with methanolic hydrogen chloride. The overall yields of the 1-substituted 1,2,3,4-tetrahydro-β-carbolines **5***a–c* and **5***h*, based on the trimethylsilyl derivatives **1***a–c* and **1***h*, were **5***a* (45%), **5***b* (44%), **5***c* (58%), and **5***h* (27%). The yields of **5***d–g* based on the methylated benzopyridines were **5***d* (34%), **5***e* (71%), **5***f* (63%), and **5***g* (61%). When **5***a* and **5***b* were prepared under the same conditions as **5***d–g*, namely, directly from 3-ethyl-4-methylpyridine and 4-methylpyridine, respectively, the yields of **5***a* and **5***b* were 58 and 56%, respectively. The preparation of **5***c* by this procedure was not attempted because of the tendency of 2-methylpyridine to form di-trimethylsilyl derivatives (8, 9). The preparation of **5***h* from toluene by this procedure was not considered feasible and was not attempted.

The structures assigned to all compounds are compatible with their ^{1}H nmr and mass spectra and their compositions. A characteristic feature of the ^{1}H nmr spectra of the enamines is the presence of an AB quartet ascribed to the vinylic protons of the enamine system, with coupling constants in the range 12.6–13.5 Hz, indicating that all compounds have the (*E*) configuration. The chemical shift of the higher field proton (H-2) in the spectra of **4***a–c* and **4***h* appeared in the range 4.90–5.17 and in the spectra of **4***d–g* in the range 5.28–5.77. The signals of the protons at H-1 appeared at lower field, lying in the range 6.88–7.92. In some cases the signals for this proton overlapped with those of aromatic protons in the same region and they could not be assigned definitively.

The ^{1}H nmr spectra of the 1,2,3,4-tetrahydro-β-carbolines, **5***a–h*, lack signals corresponding to H-1, H-2, and H-2″ present in the enamines. However, all exhibit a signal ascribed to H-1 of the 1,2,3,4-tetrahydro-β-carboline system and signals for the

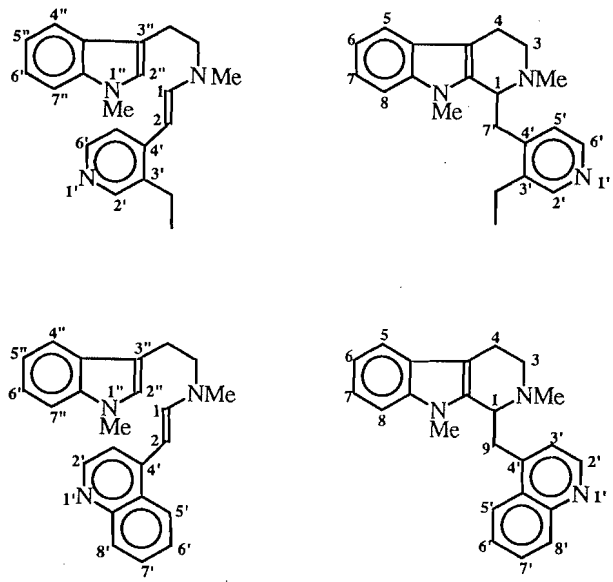

two diastereotopic protons of the adjacent methylene group. These protons are designated H-7′a and H-7′b in **5***a–c* and **5***h*, the β-carbolines derived from the methyl pyridines and from toluene. The corresponding methylene protons in the benzopyridines are designated H-9′a and H-9′b.

The ^{13}C spectra of β-carbolines **5***a–h* are characterized by the presence of a signal in the range δ 57.2–59.8 assigned to C-1. The spectra show only small variations in chemical shift for the NMe carbons and for the methylene carbons at C-3 and C-4. There is, however, a broader range of chemical shift for C-7′ (in **5***a–c* and **5***h*) and for its counterpart C-9′ in **5***d–g*.

The mass spectra of the enamines **4***a–h* show two major pathways of fragmentation, illustrated in Scheme 2 (see Table 1 for ion abundances), which support their structures. Fission at "x"

Can. J. Chem. Downloaded from www.nrcresearchpress.com by EESC ESCOLA DE ENGENHARIA on 09/08/12
For personal use only.

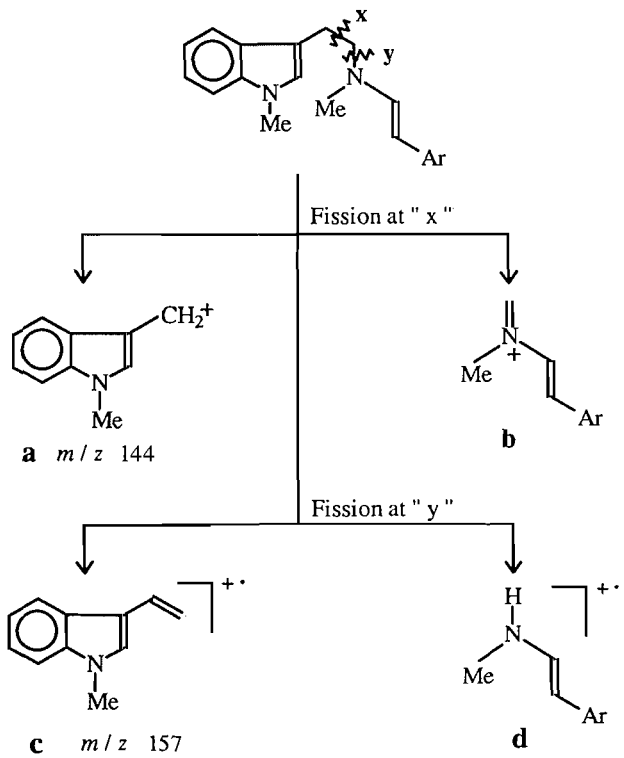

SCHEME 2

affords two even-electron ions **a** and **b**. Ion **a** at *m/z* 144, derived from the indole moiety, is the more abundant ion in the spectra of **4***a*, **4***b*, **4***d*, and **4***h*. Ion **b**, comprising the remainder of the molecule, is more abundant in the spectra of **4***c* and **4***e*–**4***g* and approximates the abundance of **a** in **4***h*. The greater abundance of **b** is observed in those compounds where the enamine function is situated α to the nitrogen atom of the pyridines, quinolines, and the isoquinoline (represented by Ar in the various formulas). It seems likely, therefore, that the aromatic nitrogen atom plays a part in charge stabilization as illustrated in the formula of **b** derived from **4***c*, Fig. 1. Analogous structures may be written for ion **b** derived from **4***e*–*g*. In the other compounds the enamine function is γ to the nitrogen atom and unable, sterically, to participate in charge stabilization. The relatively high abundance of **b** in **4***h* might result from charge stabilization through the structure illustrated in Fig. 1 for ion **b** derived from **4***h*.

Fission of the molecule at "y" affords two odd-electron ions, **c** and **d**. Ion **c** at *m/z* 157, derived from the indole moiety and the two-carbon side chain, has the same mass in **4***a*–*h*, and ion **d** comprises the remainder of the molecules plus a hydrogen atom, probably transferred from the indole moiety in the formation of ion **c**. In all but one instance, ion **c** is more abundant than **d**. Ion **d** is relatively more abundant in those compounds that have the enamine group situated α to the nitrogen atom than in those compounds where the enamine is γ to the nitrogen atom. Its stabilization in the α relative to their γ-substituted analogues may be a consequence of hydrogen bonding as illustrated for **d** derived from **4***c* in Fig. 1.

The molecular ion varies in intensity with the Ar group but never exceeds 40%. Previous reports (13–15) on the mass spectra of enamines have been concerned mainly with acyclic enamines derived from aliphatic aldehydes and ketones and secondary amines, e.g., morpholine, piperidine, pyrrolidine,

TABLE 1. Relative abundances of selected ions in the mass spectra of **4***a*–*h*

	Ion				
Enamine	M^+	**a**[a]	**b**	**c**[a]	**d**
4*a*	319(12)	100	175(46)	56	162(4)
4*b*	291(18)	100	147(45)	50	134(6)
4*c*	291(12)	45	147(100)	26	134(19)
4*d*	341(25)	100	197(68)	65	184(3)
4*e*	341(10)	31	197(100)	32	184(38)
4*f*	355(<1)	73	211(100)	65	198(31)
4*g*	401(38)	20	257(100)	42	244(32)
4*h*	290(18)	100	146(98)	50	133(1)

[a]In all compounds **a** appears at *m/z* 144 and **c** at *m/z* 157.

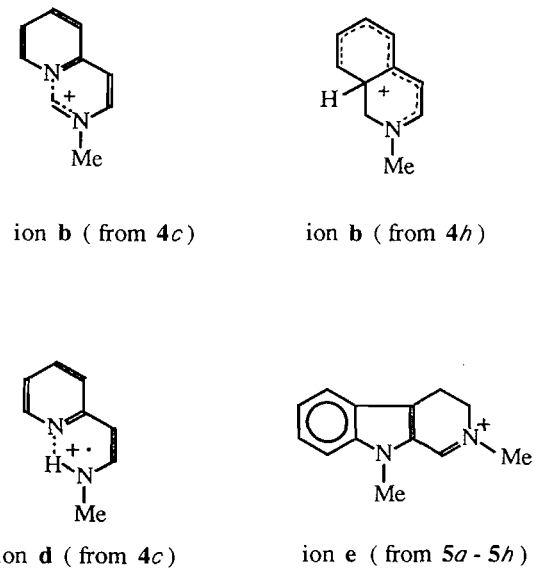

FIG. 1. Postulated structures of fragment ions in the EI spectra of enamines and β-carbolines.

and dialkyl amines. Formation of ions of type "**b**" was a dominant process in the spectra of those compounds as it is in the examples cited here. However, the presence of two aromatic systems in compounds **4***a*–*h* has a pronounced influence on their mode of fragmentation and leads to fragmentation pathways that were absent or not prominent in the compounds previously examined (13–15).

The mass spectra of the β-carbolines **5***a*–*h* are characterized by the presence of an abundant fragment ion at *m/z* 199 (ion **e**), the base peak in all spectra, derived from the 1,2,3,4-tetrahydro-β-carboline moiety. Fragment ions derived from the arylmethyl groups at C-1 of the β-carboline are uniformly of low abundance, as is the molecular ion. An ion at *m/z* 158 of low abundance is present in all spectra and, from its mass and composition, must be associated with the indole moiety.

Enamines from other formamides

We have found that dimethylformamide (DMF), *N*-formylmorpholine, and *N*-formyl-*N*-methyl-2-(3,4-dimethoxyphenyl)ethylamine undergo reactions under Peterson conditions to afford enamines in good yield. Like their counterparts derived from **3**, the enamines have the (*E*) configuration as evidenced by the coupling constants of the vinylic protons (J = 13.0–13.5 Hz). Compounds **6**, **7**, and **9** were derived from **1***a* as the tri-

Can. J. Chem. Downloaded from www.nrcresearchpress.com by EESC ESCOLA DE ENGENHARIA on 09/08/12
For personal use only.

methylsilylmethyl component and compound **10** from **1***b*. The facile formation of the enamines **4***a–h* and **6**, **7**, **9**, and **10** is very likely a consequence of the conjugation of the enamine function with the aromatic system. We have not applied the reaction to systems where conjugation of the putative enamine to an aromatic system would be precluded.

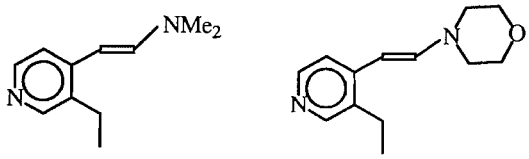

6 **7**

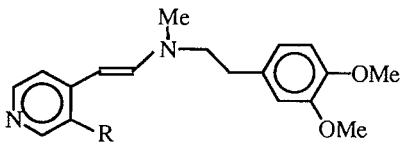

9 R = C_2H_5
10 R = H

N,N-Dimethylacetamide failed to yield an enamine under conditions that led to the formation of **6** from DMF. This result implies that amides, other than formamides, are unlikely to react under the conditions employed in this investigation. We found, also, that 3,4-dimethylquinoline failed to afford an enamine under conditions that were successful with 4-methylquinoline. Thus the reaction is sensitive to steric effects with respect to the amide employed and also to substitution on the aromatic ring, in the case of 4-methylquinolines.

Enamines by reaction of lithiated methyl pyridines with formamides

The reaction of organometallic reagents with formamides is a standard procedure for the introduction of an aldehyde function into an organic molecule. *N*-Formyl morpholine (16), *N*-formylpiperidine (17), and DMF (18) are often employed as the amide component. The reaction is considered to proceed through addition of the organometallic reagent to the amide carbonyl to afford a metalated hemiaminal. By quenching the reaction mixture with aqueous acid an aldehyde is liberated. This type of reaction has been applied also to enamine synthesis (19) using both Grignard and alkyl lithium reagents to add to dialkylformamides. It was reported that the adducts from Grignard addition afforded enamines spontaneously whereas those from alkyl lithium addition yielded enamines only after addition of a Lewis acid.

We considered that the hemiaminal intermediates that led to aldehydes upon quenching with aqueous acid might afford enamines upon quenching with aqueous alkali. In the event we found that enamines were formed from the reaction between lithiated 3-ethyl-4-methylpyridine with DMF, *N*-formylmorpholine, and **3**, when the reaction mixtures were processed under alkaline conditions. The yields of enamine were lower than those obtained by way of the Peterson reaction (for **6** (45% vs. 65%), for **7** (48% vs. 81%), and for **4***a* (33% vs. 60%)). However, we found that lithiated 4-methylpyridine failed to afford the desired enamine **4***b* under a variety of experimental conditions. Because of the lower yields of enamines and our failure to obtain **4***b*, this approach to enamine formation was not pursued further.

Conclusion

The preparation of enamines from formamides by way of the Peterson reaction has been investigated and shown to be applicable to formamides of different structural types. The main emphasis of this work has been directed to the preparation of enamines from **3** and their cyclization to 1,2,3,4-tetrahydro-β-carbolines bearing pyridylmethyl, benzopyridylmethyl, or benzyl groups at C-1. This method of preparation of β-carbolines complements the Pictet–Spengler reaction for 1,2,3,4-tetrahydro-β-carboline synthesis. It will find its main use in those cases where the aldehydes normally used in the Pictet–Spengler reaction are unstable or otherwise difficult to obtain.

Experimental

Apparatus, methods, and materials

The ^{1}H nmr spectra were recorded on Bruker AC 200, AC 300, and AM500 spectrometers at 200, 300, and 500 MHz, respectively, or on a Varian EM390 spectrometer at 90 MHz; $CDCl_3$ was the solvent and tetramethylsilane (TMS) was used as the internal standard, unless otherwise stated. Chemical shifts are reported in ppm (δ) downfield from the signal of TMS. The symbols, s (singlet), d (doublet), t (triplet), q (quartet), and m (multiplet), are used to report the multiplicity of signals. The ^{13}C nmr spectra were recorded at 125.76 MHz, at 75.46 MHz, and at 50.3 MHz on Bruker AM 500, AC 300, and AC 200 spectrometers, respectiveily, at ambient temperature. The carbon chemical shifts are quoted in ppm with reference to $CDCl_3$ (77.00 ppm). Spin decoupling and nuclear Overhauser experiments were employed to assign signals in the ^{1}H nmr spectra; selective proton decoupling, spin sort, and DEPT experiments were used to assign signals in the ^{13}C experiments.

EI (electron ionization) mass spectra were recorded at 70 eV on a VG Analytical ZAB-E mass spectrometer equipped with a VG 11-250 data system. Chemical ionization (CI) spectra were recorded on the same instrument using NH_3 at ~1 Torr (1 Torr = 133.3 Pa) as reagent gas. The peak intensities are given as a percent of the intensity of the base peak (100%). High-resolution mass spectra (hrms) measurements were performed on the above instrument under EI conditions.

All reactions involving lithiation were performed in apparatus dried in the oven at 120°C for at least 12 h and assembled hot under a stream of argon. Septa and syringes were used for transfer of reagents. Solvents and reagents were reagent grade and, when required, further purification was accomplished following published procedures. THF, used in lithiation reactions, was dried over sodium and distilled immediately before use. Trimethylsilylmethylbenzene (10), 6,7-dimethoxy-1-methylisoquinoline (20), and 2,3-dimethylquinoline (21) were prepared by methods described in the literature; 2- and 4-methylpyridine, 3-ethyl-4-methylpyridine, 2- and 4-methylquinoline, and *N*-formylmorpholine were obtained commercially.

Melting points were determined using a Fisher–Johns apparatus and are uncorrected. Thin-layer chromatography was performed using silica gel 60-F_{254} plates of 0.25 mm thickness. Samples were purified by preparative-layer, radial chromatography (2 or 4 mm layers) using silica gel PF_{254}. The plates were eluted sequentially with hexane, ethyl acetate, and methanol.

The homogeneity of the products was established on the basis of chromatographic and spectroscopic (^{1}H nmr and mass spectral) examination.

3-Ethyl-4-trimethylsilylmethylpyridine 1a

A solution of 3-ethyl-4-methylpyridine (500 mg, 4.13 mmol) in THF (5 mL) was added dropwise, under an argon atmosphere at −10°C, to a stirred solution of LDA (prepared from diisopropylamine

Can. J. Chem. Downloaded from www.nrcresearchpress.com by EESC ESCOLA DE ENGENHARIA on 09/08/12
For personal use only.

Can. J. Chem. Downloaded from www.nrcresearchpress.com by EESC ESCOLA DE ENGENHARIA on 09/08/12
For personal use only.

(0.58 mL, 4.13 mmol) in THF (5 mL) and *n*-BuLi (1.65 mL, 2.5 M in hexane)). When addition was complete, the reaction mixture was stirred at 0°C for 30 min and for an additional 1 h at ambient temperature. Then the reaction mixture was cooled to 0°C, trimethylsilyl chloride (0.53 mL, 4.13 mmol) was added dropwise, and the mixture was stirred for 30 min. The solution was allowed to warm to room temperature and stirring was continued for 1 h. Water (5 mL) was added, the mixture was stirred for 5 min, and then extracted with CH_2Cl_2 (30 mL). The extract was washed first with water and then with brine and dried over anhydrous sodium sulfate. Evaporation of the solvent afforded an oil, which was purified by bulb-to-bulb distillation to afford **1***a* as a colorless oil (680 mg, 85%); bp 110°C, 5 Torr; ^{1}H nmr (90 MHz, $CDCl_3$) δ: 0.03 (9H, s, SiMe_3), 1.17 (3H, t, J = 7.0 Hz, CH_3), 2.10 (2H, s, CH_2 Si), 2.55 (2H, q, J = 7.0 Hz, CH_2CH$_3$), 6.85 (1H, d, J = 5.0 Hz, H-5), 8.26 (1H, d, J = 5.0 Hz, H-6), 8.33 (1H, s, H-2); ms *m/z* (EI): 193 (100), 192 (68), 178 (20), 165 (13), 150 (7). Exact Mass (hrms) calcd. for $C_{11}H_{19}NSi$: 193.1287; found: 193.1297.

4-Trimethylsilylmethylpyridine **1**b

This compound was prepared by the procedure described for the preparation of **1***a*. Yield, 85%; bp 105°C, 40 Torr; ^{1}H nmr (90 MHz, $CDCl_3$) δ: 0.03 (9H, s, SiMe_3), 2.05 (2H, s, CH_2SiMe$_3$), 6.90 (2H, d, $J \approx$ 5.0 Hz, H-3 and H-5), 8.40 (2H, d, J ≈ 5.0 Hz, H-2 and H-6); ms *m/z* (EI): 165 (62), 150 (14), 93 (26), 73 (100); ms *m/z* (CI–NH_3): 166 (100) [M + H]$^+$. Exact Mass (hrms) calcd. for $C_9H_{15}NSi$: 165.0974; found: 165.0987.

2-Trimethylsilylmethylpyridine **1**c

A solution of 2-methylpyridine (4.42 g, 47.5 mmol) in THF (5 mL) was added dropwise, under an argon atmosphere at −65°C, to a stirred solution of LDA (prepared from diisopropylamine (6.65 mL, 47.5 mmol) in THF (57 mL) and *n*-BuLi (19 mL, 1.6 M in hexane)). When addition was complete, the reaction mixture was stirred at −65°C for 1 h and then for an additional 0.5 h at −40°C. The reaction mixture was cooled to −65°C, trimethylsilyl chloride (3.0 mL, 23.7 mmol) was added dropwise, and the mixture was stirred for 1.5 h at −65°C. The solution was allowed to warm to room temperature and stirring was continued for 1 h. Water (10 mL) was added and the mixture was extracted with ether (3 × 15 mL). The combined extract was washed with water and then with brine and dried over anhydrous sodium sulfate. Evaporation of the solvent afforded an oil, which was purified by vacuum distillation to afford **1***c* as a colorless oil (3.0 g, 77%, based on Me_3SiCl); bp 98°C, 40 Torr; ^{1}H nmr (200 MHz, $CDCl_3$) δ: 0.03 (9H, s, SiMe_3), 2.34 (2H, s, CH_2SiMe$_3$), 6.92–7.03 (2H, m, H-3, H-4), 7.44–7.56 (1H, m, H-5), 8.40–8.46 (1H, m, H-6); ms *m/z* (EI): 165 (18), 150 (100), 120 (9), 84 (18), 73 (63). ms *m/z* (CI–NH_3): 166 (M^+ + 1) (100), 150 (8). Exact Mass (hrms) calcd. for $C_9H_{15}NSi$: 165.0974; found: 165.0976.

N^b-*Formyl*-N^a,N^b-*dimethyltryptamine* **3**

Sodium hydride (2.32 g, 80% in mineral oil), suspended in dimethyl sulfoxide (38 mL), was heated at 80°C for 15 min to generate a 2 M solution of dimsylsodium. To a solution of *N*-formyltryptamine (6.1 g, 32.5 mmol) in dry DMSO (7 mL) was added dimsylsodium (37 mL, 73.4 mmol) at 20°C. The red solution was stirred for 3 h at 20°C, treated with MeI (4.7 mL, 75.8 mmol), and stirred an additional 30 min. Water (300 mL) was added to the reaction mixture and the resulting solution was extracted with CH_2Cl_2 (3 × 40 mL). The combined extract was washed with water and brine and dried over anhydrous Na_2SO_4. Evaporation of the dry extract afforded **3** (6.45 g, 92%) as an oil; ^{1}H nmr (500 Mz, $CDCl_3$) δ: 2.85 and 2.91 (3H, 2s, N^{b}Me), 2.96 and 2.99 (2H, 2 t, $J \approx$ 6.9 Hz and 7.6 Hz, CH_2CH$_2$N), 3.49 and 3.62 (2H, 2 t, $J \approx$ 6.9 and 7.6 Hz, CH$_2$CH_2N), 3.70 (3H, s, N^{a}Me), 6.80 and 6.89 (1H, 2 s, H-2), 7.10–7.13 (1H, t, H-5), 7.20–7.24 (1H, m, H-6), 7.26–7.29 (1H, overlapping d, H-7), 7.52 and 7.53 (1H, 2 d, $J \approx$ 7.5 Hz and 7.9 Hz, H-4), 7.78 and 8.03 (1H, 2 s, CH═O); ^{13}C nmr (125.8 MHz, $CDCl_3$) δ: 22.56 and 24.21 (CH_2CH$_2$N), 29.47 and 34.79 (N^{b}Me), 32.45 (N^{a}Me), 44.91 and 50.04 (CH$_2$CH$_2$N), 109.12 and 109.35 (C-7), 110.00 and 111.09 (C-3), 118.23, 118.60, 118.74, and 118.91 (C-4 and C-5), 121.49 and 121.68 (C-6), 126.59 and 126.96 (C-2), 127.30 and 127.71 (C-3a), 136.91 and 137.01 (C-7a), 162.29 and 162.53 (*C*H═O); ms *m/z* (EI): 216 (17), 157 (46), 144 (100), 115 (10), 44 (20); ms *m/z* (CI–NH_3): 234 [M + NH_4]$^+$ (100). Exact Mass (hrms) calcd. for $C_{13}H_{16}N_2O$: 216.1263; found: 216.1278.

(E)-*1-(*N^a,N^b-*Dimethyltryptaminyl)-2-(3-ethylpyridin-4-yl)ethene* **4**a

(a) From 3-ethyl-4-trimethylsilylmethylpyridine

A stirred solution of LDA, prepared from diisopropylamine (0.62 mmol) in THF (1 mL) and *n*-BuLi (0.4 mL, 1.6 M in hexane), was treated dropwise at −20°C under an argon atmosphere with a solution of **1***a* (100 mg, 0.52 mmol) in THF (1 mL). When the addition was complete, the temperature of the reaction mixture was raised to 25°C and the reddish-orange solution was stirred for 1 h before cooling to −60°C. The cooled solution was treated dropwise with a solution of **3** (118 mg, 0.54 mmol) in THF (1 mL) and stirred for 1 h. The temperature of the mixture was allowed to rise to 20°C and stirring was continued for 1 h more. The resulting mixture was processed in the usual manner to afford an oil, which was subjected to radial chromatography (silica gel, 60 PF_{254}, EtOAc). The major fraction **4***a* (100 mg, 60%) was obtained as a yellow oil; ^{1}H nmr (200 MHz, $CDCl_3$) δ: 1.21 (3H, t, J = 7.5 Hz, CH$_2$CH_3), 2.58 (2H, q, J = 7.5 Hz, CH_2CH$_3$), 2.89 (3H, s, N^{b}Me), 3.00 (2H, apparent t, $J \approx$ 7.0 Hz, CH_2CH$_2$N), 3.49 (2H, apparent t, J = 7.0 Hz, CH$_2$CH_2N), 3.70 (3H, s, N^{a}Me), 5.05 (1H, d, J = 13.5 Hz, CH═CHN), 6.60–7.80 (6H, m, H-2″, H-5″, H-6″, H-7″, H-5′, CH═CHN), 7.60 (1H, d, J = 7.6 Hz, H-4″), 8.09 (1H, d, J = 5.4 Hz, H-6′), 8.15 (1H, s, H-2′); ms *m/z* (EI): 319 (12), 175 (46), 162 (4), 157 (56), 144 (100), 117 (14). Exact Mass (hrms) calcd. for $C_{21}H_{25}N_3$: 319.2048; found: 319.2034.

(b) From 3-ethyl-4-methylpyridine

The procedure was the same as that in part (*a*) except that 3-ethyl-4-methyl pyridine (69 mg, 0.57 mmol) was used instead of **1***a*, along with appropriate amounts of other reagents. Compound **4***a* was obtained as a yellow oil (60 mg, 33%).

(±)-*1,2,3,4-Tetrahydro-*N^a,N^b-*dimethyl-1-[(3-ethylpyridin-4-yl)methyl]-*β-*carboline* **5**a

Enamine **4***a* (200 mg, 0.63 mmol) was added at 0°C to a saturated solution of HCl in MeOH (1.5 mL) and the mixture was stirred for 10 min. The temperature was raised to 20°C and stirring was continued for 1 h. The reaction mixture was made basic with ammonia, and was taken to dryness under vacuum. The residue was treated with CH_2Cl_2 (10 mL) and water (5 mL), the organic layer was separated, and the CH_2Cl_2 extract was washed, in succession, with water and brine. The extract was dried over anhydrous sodium sulfate and the solvent removed to afford **5***a* as a light yellow solid (150 mg, 75%), mp 118–119°C; ^{1}H nmr (500 MHz, $CDCl_3$) δ: 1.19 (3H, t, $J \approx$ 7.6 Hz, CH$_2$CH_3), 2.44 (3H, s, N^{b}Me), 2.60–2.65, 2.93–3.02, 3.11–3.16, 3.31–3.39 (8H, 4 m, CH_2CH$_3$, 2 H-7′, 2 H-3, 2 H-4), 3.35 (3H, s, N^{a}Me), 3.92–3.96 (1H, dd, H-1), 7.10 (1H, t, J = 7.8 Hz, H-6), 7.16 (1H, d, J = 5.0 Hz, H-5′), 7.19 (1H, t, J = 7.8 Hz, H-7), 7.23 (1H, d, J = 8.1 Hz, H-8), 7.52 (1H, d, J = 7.8 Hz, H-5), 8.36 (1H, d, J = 5.0 Hz, H-6′), 8.40 (1H, s, H-2′). ^{13}C nmr (125.8 MHz, $CDCl_3$) δ: 15.09 (CH$_2$CH_3), 16.76 (C-4), 23.30 (CH_2CH$_3$), 29.59 (N^{a}Me), 36.25 (C-7′), 41.81 (N^{b}Me), 44.29 (C-3), 58.18 (C-1), 106.78 (C-4a), 108.86 (C-8), 118.24 (C-5), 119.10 (C-6), 121.42 (C-7), 124.21 (C-5′), 126.85 (C-4b), 135.23 (C-3′), 137.27 (C-9a), 137.98 (C-8a), 146.02 (C-4′), 147.34 (C-6′), 149.94 (C-2′); ms *m/z* (EI): 319 (1), 199 (100); ms *m/z* (CI–NH_3): 320 [M + H]$^+$ (20), 199 (100), 122 (20). Exact Mass (hrms) calcd. for $C_{21}H_{25}N_3$: 319.2048; found: 319.2051.

(E)-*1-(*N^a,N^b-*Dimethyltryptaminyl)-2-(pyridin-4-yl)ethene* **4**b

4-Trimethylsilylmethylpyridine (83 mg, 0.5 mmol) was subjected to the reaction conditions (method (*a*)) used for the preparation of **4***a*. Compound **4***b* was isolated as a yellow oil (85 mg, 58%); ^{1}H nmr (200 MHz, $CDCl_3$) δ: 2.82 (3H, s, N^{b}Me), 2.92 (2H, apparent t, $J \approx$ 7.0 Hz, CH_2CH$_2$N), 3.43 (2H, apparent t, $J \approx$ 7.0 Hz, CH$_2$CH_2N), 3.63 (3H, s, N^{a}Me), 4.90 (1H, d, J = 13.5 Hz, CH═CHN), 6.73–6.82 (3H, m, H-2″,

Can. J. Chem. Downloaded from www.nrcresearchpress.com by EESC ESCOLA DE ENGENHARIA on 09/08/12
For personal use only.

H-3′, H-5′), 6.88 (1H, d, J = 13.5 Hz, CH═C*H*N), 7.05–7.30 (3H, m, H-5″, H-6″, and H-7″), 7.56 (1H, d, J = 7.7 Hz, H-4″), 8.10, 8.23 (2H, m, H-2′ and H-6′); ms *m/z* (EI): 291 (18), 276 (7), 157 (50), 147 (45), 144 (100), 134 (6). Exact Mass (hrms) calcd. for $C_{19}H_{21}N_3$: 291.1735; found: 291.1755.

*(±)-1,2,3,4-Tetrahydro-*N^a,N^b*-dimethyl-1-[(pyridin-4-yl)methyl]-*β*-carboline* **5**b

Enamine **4***b* (70 mg, 0.24 mmol) was subjected to the reaction conditions described for the preparation of **5***a*. Compound **5***b* was isolated as a crystalline solid (53 mg, 75%), mp 155–156°C (EtOAc); ^{1}H nmr (500 MHz, $CDCl_3$) δ: 2.45 (3H, s, *N*^{b}Me), 2.58–2.62, 2.92–3.01, 3.07–3.11, 3.30–3.36 (6H, 4 m, 2 H-3, 2 H-4, 2 H-7′), 3.51 (3H, s, *N*^{a}Me), 3.89 (1H, dd, H-1), 7.12 (1H, t, J = 7.6 Hz, H-6), 7.21 (1H, d, J = 5.9 Hz, H-3′ and H-5′), 7.22 (1H, d, J = 7.2 Hz, H-8), 7.27 (1H, t, J = 7.5 Hz, H-7), 7.52 (1H, d, J = 7.8 Hz, H-5), 8.52 (1H, d, J = 5.9 Hz, H-2′ and H-6′); ^{13}C nmr (125.8 MHz, $CDCl_3$) δ: 16.76 (C-4), 29.67 (*N*^{a}Me), 39.89 (C-7′), 41.84 (*N*^{b}Me), 44.40 (C-3), 58.83 (C-1), 107.01 (C-4a), 108.85 (C-8), 118.27 (C-5), 119.12 (C-6), 121.45 (C-7), 124.57 (C-3′ and C-5′), 126.79 (C-4b), 134.84 (C-9a), 137.29 (C-8a), 148.69 (C-4′), 149.66 (C-2′ and C-6′); ms *m/z* (EI): 291 (2), 199 (100), 158 (7). Exact Mass (hrms) calcd. for $C_{19}H_{21}N_3$: 291.1735; found: 291.1759.

*(E)-1-(*N^a,N^b*-Dimethyltryptaminyl)-2-(pyridin-2-yl)ethene* **4**c

A stirred solution of LDA, prepared from diisopropylamine (0.25 mL, 1.63 mmol) in THF (3.5 mL) and *n*-BuLi (1.12 mL, 1.6 M in hexane), was treated dropwise at −60°C under an argon atmosphere with a solution of **1***c* (270 mg, 1.63 mmol) in THF (1 mL). When the addition was complete, the reaction mixture was stirred for 30 min at −60°C, after which the solution was warmed to 20°C and the deep red solution was stirred for 1 h before cooling to −60°C. The cooled solution was treated dropwise with a solution of **3** (360 mg, 1.63 mmol) in THF (2 mL) and then stirred for 1 h. The temperature of the reaction mixture was allowed to rise to 20°C and stirring was continued for 5 h more. The resulting mixture was processed in the usual manner to afford an oil in almost quantitative yield that was used as such in the next step; ^{1}H nmr (200 MHz, $CDCl_3$) δ: 2.85 (3H, s, *N*^{b}Me), 2.98 (2H, apparent t, $J \approx$ 7.0 Hz, CH_2CH_2N), 3.47 (2H, apparent t, J = 7.0 Hz, CH$_2$CH_2N), 3.70 (3H, s, *N*^{a}Me), 5.17 (1H, d, J = 13.3 Hz, C*H*═CHN), 6.72–6.85 (3H, m, H-2″, H-3′, H-4′), 6.98–7.61 (5H, m, H-4″, H-5″, H-6″, H-7″, H-5′), 7.49 (1H, d, $J \approx$ 13.3 Hz, CH═C*H*N), 8.27 (1H, d, J = 5.9 Hz, H-6′); ms *m/z* (EI): 291 (12), 157 (26), 147 (100), 144 (45), 134 (19), 106 (13); ms *m/z* (CI–NH_3): 292 [M + 1]$^+$ (100), 189 (27), 147 (11). Exact Mass (hrms) calcd. for $C_{19}H_{21}N_3$: 291.1735; found: 291.1747.

*(±)-1,2,3,4-Tetrahydro-*N^a,N^b*-dimethyl-1-[(pyridin-2-yl)methyl]-*β*-carboline* **5**c

Enamine **4***c* (450 mg, 1.54 mmol) was subjected to the reaction conditions described for the preparation of **5***a*. Compound **5***c* was isolated as a colorless oil (260 mg, 58%); ^{1}H nmr (300 MHz, $CDCl_3$) δ: 2.40 (3H, s, *N*^{b}Me), 2.55–2.66, 2.90–3.04, 3.06–3.24, 3.29–3.42 (6H, 4 m, 2 H-3, 2 H-4, 2 H-7′), 3.54 (3H, s, *N*^{a}Me), 4.30–4.35 (1H, dd, H-1), 7.06–7.28, 7.48–7.61 (7H, 2 m, H-5, H-6, H-7, H-8, H-3′, H-4′, H-5′), 8.59 (1H, d, J = 3.0 Hz, H-6′); ^{13}C nmr (75.5 MHz, $CDCl_3$) δ: 16.98 (C-4), 29.62 (*N*^{a}Me), 41.82 (*N*^{b}Me), 42.74 (C-7′), 44.47 (C-3), 58.05 (C-1), 106.37 (C-4a), 108.77 (C-8), 118.07 (C-5), 118.84 (C-6), 126.85 (C-4b), 137.42 (C-8a), 121.04, 121.36, 124.13, 136.21 (C-7, C-3′, C-4′, C-5′), 149.26 (C-6′), 159.70 (C-2′); ms *m/z* (EI): 291 (3), 200 (15), 199 (100), 183 (9), 158 (11); ms *m/z* (CI–NH_3): 292 [M + H]$^+$ (72), 199 (100). Exact Mass (hrms) calcd. for $C_{19}H_{21}N_3$: 291.1735; found: 291.1747.

*(E)-1-(*N^a,N^b*-Dimethyltryptaminyl)-2-(quinolin-4-yl)ethene* **4**d

A stirred solution of LDA (prepared from diisopropylamine (0.2 mL, 1.43 mmol) in THF (2 mL) and *n*-BuLi (0.87 mL, 1.6 M in hexane)) was treated dropwise at −20°C under an argon atmosphere with a solution of lepidine (199 mg, 1.39 mmol) in THF (2 mL). When the addition was complete, the temperature of the reaction mixture was raised to 20°C and the reddish solution was stirred for 1 h before cooling to 0°C. The cooled solution was treated dropwise with trimethylsilyl chloride (0.18 mL, 1.39 mmol) and stirred for 30 min. The temperature of the reaction mixture was raised to 20°C and stirring was continued for 1 h more before cooling to −20°C. A cooled solution of LDA ((prepared from diisopropylamine (0.21 mL, 1.50 mmol) in THF (2.4 mL) and *n*-BuLi (0.95 mL, 1.6 M in hexane)) was added dropwise, after which the temperature was raised to 20°C. The reddish solution was stirred for 1 h before cooling to −60°C. The cooled solution was then treated with **3** (300 mg, 1.39 mmol) in THF (1.5 mL) and stirred for 1 h; then the temperature of the mixture was allowed to rise to 20°C and stirring was continued overnight. The resulting mixture was processed in the usual manner to afford **4***d* as an oil that was used as such in the next step; ^{1}H nmr (300 MHz, $CDCl_3$) δ: 2.99 (3H, s, *N*^{b}Me), 3.05 (2H, t, J = 7.0 Hz, CH_2CH$_2$N), 3.56 (2H, t, J = 7.0 Hz, CH$_2$CH_2N), 3.67 (3H, s, *N*^{a}Me), 5.64 (1H, d, J = 13.2 Hz, C*H*═CHN), 6.84 (1H, s, H-2″), 6.90 (1H, d, J = 4.8 Hz, H-3′), 7.05 (1H, d, J = 13.2 Hz, CH═C*H*N), 7.12–7.63 (6H, m, H-4″, H-5″, H-6″, H-7″, H-6′, H-7′), 7.94 (1H, d, J = 8.1 Hz, H-8′), 8.01 (1H, d, J = 8.1 Hz, H-5′), 8.49 (1H, d, J = 4.8 Hz, C-2′); ms *m/z* (EI): 341 (25), 197 (68), 184 (3), 182 (11), 157 (65), 144 (100), 115 (10); ms *m/z* (CI–NH_3): 342 [M + H]$^+$ (100), 189 (41), 172 (56), 158 (42), 144 (55), 130 (26). Exact Mass (hrms) calcd. for $C_{23}H_{23}N_3$: 341.1892; found: 341.1903.

*(±)-1,2,3,4-Tetrahydro-*N^a,N^b*-dimethyl-1-[(quinolin-4-yl)methyl]-*β*-carboline* **5**d

Crude enamine **4***d* (480 mg, 1.40 mmol) was subjected to the reaction conditions described for the preparation of **5***a*. Compound **5***d* was isolated as a crystalline solid (165 mg, 34%), mp 171–172°C (EtOAc); ^{1}H nmr (300 MHz, $CDCl_3$) δ: 2.49 (3H, s, *N*^{b}Me), 3.18 (3H, s, *N*^{a}Me), 2.65–2.72, 2.92–3.10, 3.35–3.56, 3.61–3.70 (6H, 4 m, 2 H-3, 2 H-4, 2 H-9′), 4.09–4.15 (1H, m, H-1), 7.08–7.22, 7.50–7.75 (6H, m, H-5, H-6, H-7, H-8, H-6′, H-7′), 7.31 (1H, d, J = 4.4 Hz, H-3′), 8.07 (1H, d, J = 8.2 Hz, H-8′), 8.14 (1H, d, J = 8.2 Hz, H-5′), 8.83 (1H, d, J = 4.4 Hz, C-2′); ^{13}C (75.5 MHz, $CDCl_3$) δ: 16.86 (C-4), 29.75 (*N*^{a}Me), 37.14 (C-9′), 41.76 (*N*^{b}Me), 44.30 (C-3), 57.97 (C-1), 108.88, 118.24, 119.08, 121.39, 121.77, 123.35, 126.35, 129.10, 130.40 (aromatic *C*H), 106.57, 126.77, 128.03, 135.43, 137.11, 145.20, 148.37 (aromatic quaternary), 150.16 (C-2′); ms *m/z* (EI): 341 (1), 199 (100), 183 (8), 158 (5), 143 (5), 115 (8); ms *m/z* (CI–NH_3): 342 (M + H)$^+$ (10), 199 (100), 185 (4), 144 (18). Exact Mass (hrms) calcd. for $C_{23}H_{23}N_3$: 341.1892; found: 341.1879.

*(E)-1-(*N^a,N^b*-Dimethyltryptaminyl)-2-(quinolin-2-yl)ethene* **4**e

Quinaldine (205 mg, 1.43 mmol) was subjected to the reaction conditions described for the preparation of **4***d*. Compound **4***e* was obtained as an oil, which was used as such in the next step; ^{1}H nmr (300 MHz, $CDCl_3$) δ: 2.90 (3H, s, *N*^{b}Me), 3.01 (2H, t, J = 7.0 Hz, CH_2CH$_2$N), 3.52 (2H, t, J = 7.0 Hz, CH$_2$CH_2N), 3.66, 3.70 (3H, 2 s, *N*^{a}Me), 5.36 (1H, d, J = 13.5 Hz, C*H*═CHN), 6.77–8.02 (12H, m, CH═C*H*N, ArH); ms *m/z* (EI): 341 (10), 197 (100), 184 (38), 157 (32), 144 (31), 128 (13); ms *m/z* (CI–NH_3): 342 [M + H]$^+$ (82), 189 (21), 172 (100), 144 (21). Exact Mass (hrms) calcd. for $C_{23}H_{23}N_3$: 341.1892; found: 341.1893.

*(±)-1,2,3,4-Tetrahydro-*N^a,N^b*-dimethyl-1-[(quinolin-2-yl)methyl]-*β*-carboline* **5**e

The crude enamine **4***e* (490 mg, 1.43 mmol) was subjected to the reaction conditions described for the preparation of **5***a*. Compound **5***e* was isolated as a colorless oil (350 mg, 71%); ^{1}H nmr (300 MHz, $CDCl_3$) δ: 2.42 (3H, s, *N*^{b}Me), 2.60–2.67, 2.92–3.04, 3.25–3.45 (6H, 3m, 2 H-3, 2 H-4, 2 H-9′), 3.55 (3H, s, *N*^{a}Me), 4.46–4.50 (1H, dd, H-1), 7.08–7.30, 7.45–7.78, 8.00–8.10, (10H, 3 m, ArH); ^{13}C (75.5 MHz, $CDCl_3$) δ: 17.58 (C-4), 30.12 (*N*^{a}Me), 42.25 (*N*^{b}Me), 43.67 (C-9′), 45.11 (C-3), 58.38 (C-1), 109.21, 118.48, 119.25, 121.45, 122.86, 126.16, 127.90, 129.45, 129.59, 136.25 (aromatic *C*H), 106.92, 127.31, 127.37, 136.50, 137.62, 148.46, 160.77 (aromatic quaternary); ms *m/z* (EI): 341 (3), 199 (100), 183 (7), 158 (8), 143 (8), 115 (5); ms *m/z* (CI–NH_3): 342 [M + H]$^+$ (15), 199 (100), 144 (10). Exact Mass (hrms) calcd. for $C_{23}H_{23}N_3$: 341.1892; found: 341.1906.

Can. J. Chem. Downloaded from www.nrcresearchpress.com by EESC ESCOLA DE ENGENHARIA on 09/08/12
For personal use only.

(E)-1-(N^a,N^b-Dimethyltryptaminyl)-2-(3-methylquinolin-2-yl)ethene **4***f*

The procedure described for the preparation of **4***d* was employed. From 2,3-dimethylquinoline (80 mg, 0.51 mmol), and appropriate amounts of other reagents, compound **4***f* was obtained as a yellow oil that was used as such in further steps; ^{1}H nmr (200 MHz, $CDCl_3$) δ: 2.32 (3H, s, CH_3), 2.91 (3H, s, N^bMe), 3.01 (2H, t, J = 8.0 Hz, CH_2CH_2N), 3.52 (2H, t, J = 8.0 Hz, CH_2CH_2N), 3.65 (3H, s, N^aMe), 5.28 (1H, d, J = 12.7 Hz, C*H*=CHN), 6.82 (1H, s, H-2″), 7.02–8.03 (10H, m, aromatic H, CH=C*H*N); ms *m/z* (EI): 355 (28), 211 (100), 198 (31), 168 (19), 157 (65), 144 (64); ms *m/z* (CI–NH_3): 356 $[M + H]^+$ (100). Exact Mass (hrms) calcd. for $C_{24}H_{25}N_3$: 355.2048; found: 355.2056.

*(±)-1,2,3,4-Tetrahydro-*N^a,N^b*-dimethyl-1-[-(3-methylquinolin-2-yl)methyl]-β-carboline* **5**f

Enamine **4***f* (200 mg, 0.56 mmol) was subjected to the reaction conditions described for the preparation of **5***a*. Compound **5***f* was isolated as a colorless crystalline solid (125 mg, 63%), mp 141–142°C (ether); ^{1}H nmr (200 MHz, $CDCl_3$) δ: 2.36 (3H, s, CH_3), 2.48 (3H, s, N^bMe), 2.62–2.72 (1H, m, H-4), 2.92–3.08 (2H, m, H-3, H-4), 3.14, 3.19 (1H, d, J = 3.8 Hz, H-9′), 3.33–3.44 (1H, m, H-3), 3.48 (3H, s, N^aMe), 3.44–3.54 (1H, m, H-9′), 4.90 (1H, dd, H-1), 7.08–7.26 (3H, m, H-6, H-7, H-8), 7.43–7.49 (1H, m, H-6′), 7.52–7.55 (1H, m, H-5), 7.60–7.65 (1H, m, H-7′), 7.72 (1H, d, J = 8.5 Hz, H-5′), 7.83 (1H, s, H-4′), 8.06 (1H, d, J = 8.5 Hz, H-8′); ms *m/z* (EI): 355 (5), 199 (100), 158 (5); ms *m/z* (CI–NH_3): 356 $(M + H)^+$ (5), 199 (100), 156 (3). Exact Mass (hrms) calcd. for $C_{24}H_{25}N_3$: 355.2048; found: 355.2050.

(E)-1-(N^a,N^b-Dimethyltryptaminyl)-2-(6,7-dimethoxyisoquinolin-1-yl)ethene **4**g

The procedure described for the preparation of **4***d* was employed. From 6,7-dimethoxy-1-methylisoquinoline (100 mg, 0.49 mmol), and appropriate amounts of other reagents, compound **4***g* was obtained as a yellow oil that was used without purification in the next step; ^{1}H nmr (200 MHz, $CDCl_3$) δ: 3.01 (3H, s, N^bMe), 3.08 (2H, apparent t, $J \approx 8.0$ Hz, CH_2CH_2N), 3.58 (2H, apparent t, $J \approx 8.0$ Hz, CH_2CH_2N), 3.69 (3H, s, N^aMe), 4.00, 4.01 (6H, 2 s, 2 OCH_3), 5.77 (1H, d, J = 12.6 Hz, C*H*=CHN) 6.88 (1H, s, H-2″), 6.96 (1H, s, H-5′), 7.04–7.34 (4H, m, H-4′, H-5″, H-6″, H-7″), 7.36 (1H, s, H-8′), 7.63 (1H, d, J = 7.0 Hz, H-4″), 7.92 (1H, d, J = 12.6 Hz, CH=C*H*N), 8.16 (1H, d, J = 5.6 Hz, H-3′); ms *m/z* (EI): 401 (38), 357 (3), 343 (17), 257 (100), 244 (32), 157 (42), 144 (20). Exact Mass (hrms) calcd. for $C_{25}H_{27}N_3O_2$; 401.2079; found: 401.2088.

*(±)-1,2,3,4-Tetrahydro-*N^a,N^b*-dimethyl-1-[(6,7-dimethoxyisoquinolin-1-yl)methyl]-β-carboline* **5**g

Enamine **4***g* (450 mg, 1.12 mmol) was subjected to the reaction conditions described for the preparation of **5***a*. Compound **5***g* was isolated as a yellow oil (275 mg, 61%), which was crystallized from EtOAc to afford yellow crystals, mp 101–102°C; ^{1}H nmr (300 MHz, $CDCl_3$) δ: 2.49 (3H, s, N^bMe), 2.66–2.75, 2.98–3.11, 3.41–3.52, 3.74–3.84 (6H, 2 H-3, 2 H-4, 2 H-9′), 3.20 (3H, s, N^aMe), 3.71, 3.98 (6H, 2 s, 2 OCH_3), 4.56–4.67 (1H, m, H-1), 7.02 (1H, s, H-5′), 7.20 (1H, s, H-8′), 7.05–7.53 (5H, m, H-5—H-8, H-4′), 8.40 (1H, d, J = 6.0 Hz, H-3′); ^{13}C nmr (75.5 MHz, $CDCl_3$) δ: 17.41 (C-4), 29.48 (N^aMe), 39.63 (C-9′), 41.70 (N^bMe), 45.00 (C-3), 55.70, 55.88 (2 OMe), 57.21 (C-1), 103.67, 104.96, 108.72, 117.87, 118.29, 118.67, 121.08 (aromatic *C*H), 105.95, 123.78, 132.98, 136.51, 137.13 (aromatic quaternary), 140.97 (C-3′), 149.74, 152.41 (C-6′ and C-7′), 156.79 (C-1′); ms *m/z* (EI): 401 (2), 343 (2), 199 (100), 183 (4), 158 (7); ms *m/z* (CI–NH_3): 402 $[M + H]^+$ (3), 204 (42), 199 (100). Exact Mass (hrms) calcd. for $C_{25}H_{27}N_3O_2$: 401.2103; found: 401.2084.

(E)-1-(N^a,N^b-Dimethyltryptaminyl)-2-phenylethene **4**h

To a stirred, ice-cooled solution of benzyltrimethylsilane (210 mg, 1.28 mmol) in HMPA (1.2 mL) was added *n*-BuLi (0.8 mL, 1.6 M in hexane). After the addition of *n*-BuLi was complete, the deep reddish solution was stirred for 1 h at 5–10°C before cooling to −10°C. The cooled solution was treated dropwise with a solution of **3** (290 mg, 1.34 mmol) in THF (1 mL) and then stirred for 30 min. The temperature of the reaction mixture was allowed to rise to 20°C and stirring was continued for 24 h. Water (50 mL) was added and the mixture was extracted with CH_2Cl_2 (3 × 5 mL). The extract was washed first with water, then with brine, and dried. Evaporation of the solvent afforded enamine **4***h* as an oil, which was used as such in the next step; ^{1}H nmr (200 MHz, $CDCl_3$) δ: 2.71 (3H, s, N^bMe), 2.88 (2H, t, J = 7.0 Hz, CH_2CH_2N), 3.28 (2H, t, J = 7.0 Hz, CH_2CH_2N), 3.59 (3H, s, N^aMe), 5.03 (1H, d, J = 13.4 Hz, C*H*=CHN), 6.60–7.21 (9H, m, CH=C*H*N, H-2′–H-6′, H-2″, H-5″, H-6″, H-7″), 7.47 (1H, d, J = 7.6 Hz, H-4″); ms *m/z* (EI): 290 (18), 157 (50), 146 (98), 144 (100), 133(1), 77 (34); ms *m/z* (CI–NH_3): 291 $[M + H]^+$ (100). Exact Mass calcd. for $C_{20}H_{22}N_2$: 290.1782; found: 290.1780.

*(±)-1,2,3,4-Tetrahydro-*N^a,N^b*-dimethyl-1-phenylmethyl-β-carboline* **5**h

Enamine **4***h* from the previous reaction was subjected to the reaction conditions described for the preparation of **5***a*. Compound **5***h* was isolated as a colorless oil (100 mg, 27%, based on benzyltrimethylsilane); ^{1}H nmr (300 MHz, $CDCl_3$) δ: 2.44 (3H, s, N^bMe), 2.53–2.65, 2.90–3.03, 3.08–3.17, 3.31–3.41 (6H, 4 m, 2 H-3, 2 H-4, 2 H-7′), 3.28 (3H, s, N^aMe), 3.84–3.90 (1H, dd, H-1), 7.05–7.31 (8H, m, H-2′–H-6′, H-6–H-8), 7.52 (1H, d, J = 7.5 Hz, H-5); ^{13}C nmr (75.5 MHz, $CDCl_3$) δ: 16.97 (C-4), 29.40 (N^aMe), 40.87 (C-7′), 41.88 (N^bMe), 44.30 (C-3), 59.79 (C-1), 106.23 (C-4a), 108.75 (C-8), 118.10 (C-5), 118.62 (C-6), 121.01, 126.24, 128.35, 129.25 (C-7, C-2′–C-6′), 126.91 (C-4b), 135.98 (C-1′), 137.16 (C-9a), 139.67 (C-8a); ms *m/z* (EI): 199 (100), 183 (5), 158 (9), 91 (9); ms *m/z* (CI–NH_3): 291 $[M + H]^+$ (100), 199 (40). Exact Mass calcd. for $C_{20}H_{22}N_2$: 290.1783; found: 290.1793.

(E)-1-Dimethylamino-2-(3-ethylpyridin-4-yl)ethene **6**

(a) From 3-ethyl-4-trimethylsilylmethylpyridine

The procedure described for the preparation of **4***a* was employed, except that DMF was substituted for **3**. From **1***a* (100 mg, 0.52 mmol), and appropriate amounts of other reagents, compound **6** (60 mg, 65%) was obtained as a viscous oil that solidified in the freezer; ^{1}H nmr (200 MHz, $CDCl_3$) δ: 1.21 (3H, t, J = 7.5 Hz, CH_2CH_3), 2.62 (2H, q, J = 7.5 Hz, CH_2CH_3), 2.89 (6H, s, NMe_2), 5.08 (1H, d, J = 13.5 Hz, C*H*=CHN), 6.98 (1H, d, J = 13.5 Hz, CH=C*H*N), 7.10 (1H, d, J = 5.4 Hz, H-5), 8.14 (1H, d, J = 5.4 Hz, H-6), 8.17 (1H, s, H-2); ^{13}C (50.3 MHz, $CDCl_3$) δ: 13.78 (CH_2CH_3), 23.40 (CH_2CH_3), 40.10 (NMe_2), 90.39 (*C*H=CHNMe$_2$), 114.9 (CH=*C*HNMe$_2$), 136.0 (C-3), 143.13, 145.89, 146.52 (C-2, C-5, and C-6), 145.29 (C-4); ms *m/z* (EI): 176 (100), 161 (17), 145 (22), 132 (45), 117 (20); ms *m/z* (CI–NH_3): 177 $[M + H]^+$ (100). Exact Mass (hrms) calcd. for $C_{11}H_{16}N_2$: 176.1313; found: 176.1317.

(b) From 3-ethyl-4-methylpyridine

3-Ethyl-4-methylpyridine (5.19 g, 42 mmol) was converted into its lithio derivative using the procedure described in the preparation of **1***a*. The reaction mixture was cooled to −60°C, treated with DMF (3.91 mL, 42 mmol), and stirred for 1 h at −60°C. The cooling bath was removed, the solution was brought to room temperature, and stirring was continued for 1 h more. Water (10 mL) and CH_2Cl_2 (100 mL) were added to the reaction mixture. The CH_2Cl_2 layer was separated and washed sequentially with water and brine. The extract was dried over anhydrous sodium sulfate. The drying agent was removed by filtration and the filtrate was evaporated to afford a brown oil; purification was effected by bulb-to-bulb distillation (bp 160°C, 0.1 Torr) to afford **6** (3.35 g, 45%).

(E)-1-Morpholinyl-2-(3-ethylpyridin-4-yl)ethene **7**

(a) From 3-ethyl-4-trimethylsilylmethylpyridine

The procedure was the same as that used for the preparation of **4***a* except that *N*-formylmorpholine was substituted for **3**. From **1***a* (100 mg, 0.52 mmol), and appropriate amounts of other reagents, compound **7** (90 mg, 81%) was obtained; mp 88–89°C; ^{1}H nmr (200 MHz, $CDCl_3$) δ: 1.23 (3H, t, J = 7.6 Hz, CH_2CH_3), 2.64 (2H, q, J = 7.6 Hz,

CH_2CH_3), 3.15–3.28 (4H, m, CH_2-N-CH_2), 3.75–3.85 (4H, m, CH_2-O-CH_2), 5.38 (1H, d, J = 13.5 Hz, CH=CHN), 6.95 (1H, d, J = 13.5 Hz, CH=CHN), 7.21 (1H, d, J = 5.5 Hz, H-5), 8.19 (1H, d, J = 5.5 Hz, H-6), 8.21 (1H, s, H-2); ^{13}C (50.3 MHz, $CDCl_3$) δ: 14.37 (CH_2CH_3), 23.72 (CH_2CH_3), 48.52 (CH_2-N-CH_2), 66.11 (CH_2-O-CH_2), 93.90 (CH=CH-N), 116.19 (CH=CH-N), 133.53 (C-3), 144.50 (C-4), 142.79, 146.7, 149.38 (C-2, C-5, C-6); ms *m/z* (EI): 218 (100), 173 (7), 159 (22), 145 (40), 132 (45), 112 (32); ms *m/z* (CI–NH_3): 219 $(M + H)^+$ (100), 150 (12). Exact Mass (hrms) calcd. for $C_{13}H_{18}N_2O$: 218.1419; found: 218.1420.

(b) From 3-ethyl-4-methylpyridine

The procedure described for the preparation of **6** (method (*b*)) was employed, except that *N*-formylmorpholine was substituted for DMF. From 3-ethyl-4-methylpyridine (100 mg, 0.52 mmol), and appropriate amounts of other reagents, compound **7** (55 mg, 48%) was obtained.

N-*Formyl*-N-*methyl-2-(3,4-dimethoxyphenyl)ethylamine* ***8***

N-Formyl-2-(3,4-dimethoxyphenyl)ethylamine (22) (500 mg, 2.42 mmol) was treated with dimsyl sodium and CH_3I using the procedure described for the preparation of **3**. Compound **8** was obtained as an oil (430 mg, 80%); ^{1}H nmr (90 MHz, $CDCl_3$) δ: 2.73 (2H, apparent t, J = 6.0 Hz, CH_2CH_2N), 2.80 2.84 (3H, 2s, NMe), 3.40 (2H, apparent t, J = 6.0 Hz, CH_2CH_2N), 3.80 3.83 (6H, 2 s, 2 OMe), 6.56–6.90 (3H, m, H-2′, H-5′, and H-6′), 7.80–8.00 (1H, 2s, CH=O); ms *m/z* (EI): 223 (8), 164 (100), 151 (67), 107 (10). Exact Mass (hrms) calcd. for $C_{12}H_{17}NO_3$: 223.1208; found: 223.1211.

(E)-1-[N-Methyl-β-(3,4-dimethyoxyphenylethylamino)]-2-(3-ethylpyridin-4-yl)ethene ***9***

The procedure described for the preparation of **4***a* (method (*a*)) was employed, except that compound **8** was substituted for **3**. From **8** (100 mg, 0.52 mmol), and appropriate amounts of other reagents, compound **9** (95 mg, 56%) was obtained; ^{1}H nmr (200 MHz, $CDCl_3$) δ: 1.21 (3H, t, J = 7.5 Hz, CH_3CH_2), 2.61 (2H, q, J = 7.5 Hz, CH_2CH_3), 2.79 (2H, apparent t, $J \approx$ 7.6 Hz CH_2CH_2N), 2.85 (3H, s, NMe), 3.40 (2H, t, J = 7.6 Hz, CH_2CH_2N), 3.86 (6H, s, 2 OCH_3), 5.06 (1H, d, J = 13.5 Hz, CH=CHN), 6.68–6.86 (3H, m, H-2′, H-5′, H-6′), 6.93 (1H, d, J = 13.5 Hz, CH=CHN), 7.01 (1H, d, J = 5.4 Hz, H-5″), 8.10 (1H, d, J = 5.6 Hz, H-6″), 8.15 (1H, s, H-2″); ms *m/z* (EI): 326 (22), 175 (100), 164 (42), 151 (20). Exact Mass (hrms) calcd. for $C_{20}H_{26}N_2O_2$: 326.1994; found: 326.2006.

(E)-1-N-Methyl-β-(3,4-dimethoxyphenyl)ethylamino-2-(pyridin-4-yl)ethene ***10***

The procedure was the same as that used for the preparation of **9**, except that **1***b* was substituted for **1***a*. From **1***b* (100 mg, 0.60 mmol), and appropriate amounts of other reagents, compound **10** (104 mg, 58%) was obtained; ^{1}H nmr (200 MHz, $CDCl_3$) δ: 2.78 (2H, apparent, t, $J \approx$ 6.85 Hz, CH_2CH_2N), 2.81 (3H, s, *N*Me), 3.39 (2H, apparent, t, J = 6.85, CH_2CH_2N), 4.95 (1H, d, J = 13.5 Hz, CH=CHN), 6.68–7.02 (6H, m, H-2′, H-5′, H-6′, CH=CHN, H-3″, H-5″), 8.24 (2H, apparent d, $J \approx$ 5.6 Hz, H-2″, H-6″); ms *m/z* (EI): 298 (10), 164 (40), 151 (22), 147 (100). Exact Mass (hrms) calcd. for $C_{18}H_{22}N_2O_2$: 298.1681; found: 298.1694.

Acknowledgements

We thank the Natural Sciences and Engineering Research Council of Canada for financial support of this research through a grant to D.B.M. We thank, also, Dr. D.W. Hughes and Dr. R.W. Smith of this department for assistance with the nmr and mass spectrometry experiments, respectively, and we are indebted to Professor V.A. Snieckus and Professor W.A. Szarek for helpful discussions.

1. M. Onanga and F. Khuong-Huu. Tetrahedron Lett. **24**, 3627 (1983).
2. L.R. McGee, G.S. Reddy, and P. Confalone. Tetrahedron Lett. **25**, 2115 (1984).
3. P.D. Bailey, S.P. Hollinshead, and Z. Dauter. J. Chem. Soc. Chem. Commun. 1507 (1985).
4. J. Vercauteren, C. Lavaud, J. Lévy, and G. Massiot. J. Org. Chem. **49**, 2278 (1984).
5. W.M. Whaley and T.R. Govindichari. Org. React. **6**, 74 (1951).
6. D.J. Peterson. J. Org. Chem. **33**, 780 (1968).
7. (*a*) R.P. Woodbury and N.W. Rathke. Tetrahedron Lett. 709 (1978); (*b*) T. Agawa, M. Ishikawa, M. Komatsu, and Y. Ohshiro. Bull. Chem. Soc. Jpn. **55**, 1205 (1982); (*c*) M.P. Sibi, J.W. Dankwardt, and V. Snieckus. J. Org. Chem. **51**, 273 (1986); (*d*) J.-C. Cuevas and V. Snieckus. Tetrahedron Lett. **30**, 5837 (1989); (*e*) J.-C. Cuevas, P. Patil, and V. Snieckus. Tetrahedron Lett. **30**, 5841 (1989).
8. R.I. Papasergio, B.W. Skelton, P. Twiss, A.H. White, and C.L. Raston. J. Chem. Soc. Dalton Trans. 1161 (1990).
9. T. Konakahara and Y. Takagi. Heterocycles, **14**, 393 (1980).
10. D.J. Coughlin and R.G. Solomon. J. Org. Chem. **44**, 3784 (1979).
11. M. Nakagawa, T. Kaneko, H. Yamaguchi, H. Kawashima, and T. Hino. Tetrahedron, **30**, 2591 (1974).
12. C. Schöpf and H. Steuer. Justus Liebigs Ann. Chem. **558**, 124 (1947).
13. H.J. Jakobsen, S.-O. Lawesson, J.T.B. Marshall, G. Schroll, and D.H. Williams. J. Chem. Soc. (B), 940 (1966).
14. P.P. Lynch. Gazz. Chim. Ital. **99**, 789 (1969).
15. A.G. Cook. *In* Enamines. 2nd ed. *Edited by* A.G. Cook. Marcel Dekker, Inc., New York. 1988. pp. 74–77.
16. G.A. Olah, L. Ohannesian, and M. Arvanaghi. J. Org. Chem. **49**, 3856 (1984).
17. G.A. Olah and M. Arvanaghi. Angew. Chem. Int. Ed. Engl. **20**, 878 (1981).
18. E.A. Evans. J. Chem. Soc. 4691 (1956); E.R.H. Jones, L. Skattebøl, and M.C. Whiting. J. Chem. Soc. 1054 (1958).
19. C. Hannson and B. Wickberg. J. Org. Chem. **38**, 3074 (1973).
20. G.N. Walker. J. Am. Chem. Soc. **76**, 3999 (1954).
21. S.G.P. Plant and R.J. Rosser. J. Chem. Soc. 1861 (1929).
22. W.M. Whaley and M. Meadow. J. Chem. Soc. 1067 (1953).
23. R. Vohra and D.B. Maclean. Tetrahedron Lett. **34**, 7673 (1993).

Can. J. Chem. Downloaded from www.nrcresearchpress.com by EESC ESCOLA DE ENGENHARIA on 09/08/12
For personal use only.

Electrochemical oxidation and kinetics of the decay of UV-absorbing intermediate of uric acid oxidation at pyrolytic graphite electrodes[1]

RAJENDRA N. GOYAL,[2] ALOK MITTAL,[3] AND DIVYA AGARWAL
Department of Chemistry, University of Roorkee, Roorkee, 247 667, India

Received May 14, 1993

RAJENDRA N. GOYAL, ALOK MITTAL, and DIVYA AGARWAL. Can. J. Chem. **72**, 1668 (1994).

The electrochemical oxidation of uric acid has been studied in 0.50 M NaCl and phosphate buffers of ionic strength 0.05 to 0.5 M. The kinetics of the decay of UV-absorbing intermediate generated during electrooxidation of uric acid (7,9-dihydro-1*H*-purine-2,6,8-(3*H*)-trione) has also been studied. On the basis of pseudo first order rate constants observed in different media, it has been concluded that the diimine species formed from the 2e, $2H^+$ oxidation of uric acid is attacked by water to give diol, which then decomposes in a series of reactions to give allantoin as the major product at pH 7.2. The possibility of attack by phosphate on diimine has been ruled out.

RAJENDRA N. GOYAL, ALOK MITTAL et DIVYA AGARWAL. Can. J. Chem. **72**, 1668 (1994).

On a étudié l'oxydation électrochimique de l'acide urique dans du NaCl 0,50 M et dans des tampons de phosphate, à des forces ioniques allant de 0,5 à 0,05 M. On a aussi étudié le cinétique de la décroissance de l'intermédiaire qui absorbe la lumière IV et qui est généré au cours de l'électrooxydation de l'acide urique (7,9-dihydro1*H*-purine-2,6,8-(3*H*)-trione). En se basant sur les constantes de vitesse de pseudo-premier order observé dans divers milieux, on en conclut que la diimine formée par une oxydation de l'acide urique par 2e– et $2H^+$ est attaquee par de l'eau pour donner un diol que se décompose alors par une série de réactons pour donner, à un pH de 7,2, l'allantoïne comme produit majeur. On a éliminé la possibilité d'une attaque de la diimine par le phosphate.

[Traduit par la rédaction]

Introduction

The electrochemical oxidation of biologically important purines has attracted considerable attention in the last decade in the expectation that the mechanisms observed at the electrode–solution interface can provide a more detailed understanding of the enzymic redox reactions of these molecules, leading to insight about biological reaction pathways. The on-line combination of mass spectrometry with electrochemistry has also been claimed as a powerful tool to get chemical informations about electrochemically generated species with excellent time resolution (1, 2). The electrochemical oxidation of uric acid (I) has been studied in 1 M acetic acid by Dryhurst (3) and more recently by Volk et al. (4). It is now generally accepted that the oxidation of uric acid proceeds by 2e, $2H^+$ mechanism (Scheme 1) to give an unstable diimine species (II). Owens et al. (5) determined the half life of the diimine using chronopotentiometry and found it to be ≅20 ms. It has also been proposed (6) that in high phosphate medium (0.5 M) the diimine species is attacked by phosphate, whereas, in low phosphate medium (5 mM) attack by H_2O is preferred during electrolysis at reticulated viterous carbon electrode; however, no species with phosphate attached (III_b) was ever isolated.

The work reported in this paper was undertaken to investigate the effect of phosphate concentration on the electrochemical behaviour as well as kinetics of the decay of UV-absorbing intermediate generated during electrooxidation of uric acid at pyrolytic graphite electrode. It was believed that if phosphate competes with OH^- in attacking species (II), the kinetics of decay in absence of phosphate will be very different than in presence of phosphate (Scheme 1). In particular, we were interested in finding out whether the electrochemical behaviour of uric acid is dependent on the amount of phosphate present and also whether the kinetics of decay changes significantly from 0 to 500 mM phosphate media. The role of phosphate on the kinetics of decomposition of UV-absorbing intermediate has been explained on the basis of Brønsted equation modified on the basis of Debye Hückle theory (7). The products of electrooxidation of uric acid formed at physiological pH (pH 7.2) in low and high phosphate buffers have also been separated and analysed.

Experimental

Uric acid was obtained from Reanal, Hungary and used as received. Phosphate buffers (8) of different ionic strengths were prepared in the pH range 2.1 to 10.6. The stock solution of uric acid was prepared in doubly distilled water.

The equipments used for linear and cyclic sweep voltammetry and spectral studies were essentially same as has been described earlier (9, 10). The pyrolytic graphite electrode used in the studies was fabricated in the laboratory by the reported method (11). The kinetics studies were carried out using Beckman DU-6 spectrophotometer. All experiments were carried out at an ambient temperature of 22 ± 1°C.

Voltammetric studies were carried out by mixing 5.0 mL of the stock solution with 5.0 mL of buffer of different ionic strengths. The solution was bubbled with nitrogen for 8–10 min and the curves were recorded. For monitoring the kinetics of the decay of UV-absorbing intermediate, the solution of uric acid in buffers of different ionic strengths was electrolysed in a three compartment cell using PGE (6×1 cm^2) as working, platinum gauze as auxiliary and SCE as reference electrode, respectively, at a potential 50 mV more positive than peak I_a. When absorbance at λ_{max} reduced to about 50%, the potential was turned off and 2.0 mL solution was immediately transferred in a 1.0 cm^3 quartz cell and the change in absorbance with time at selected wavelengths were monitored.

For the identification of products of electrooxidation of uric acid in 0.5 M NaCl, 5 mM phosphate, and 0.50 M phosphate buffers (pH 7.2), the electrolysis was carried out in appropriate solution. The 1 mM solution of uric acid generally took about 3 to 4 h for complete oxidation. When peak I_a completely disappeared, electrolysis was stopped and the electrolysed solution was removed from the cell and lyopholised. The freeze-dried material was dissolved in 1 mL of H_2O and passed through sephadex G-10 (Sigma, bead size 40–80 μm) using water as an eluent.

[1]Taken in part from the M.Phil. dissertation of Divya Agarwal.

[2]Author to whom all correspondence and reprint requests should be directed.

[3]Present address: Jiwagi University, Gwalior, India.

Can. J. Chem. Downloaded from www.nrcresearchpress.com by EESC ESCOLA DE ENGENHARIA on 09/08/12
For personal use only.

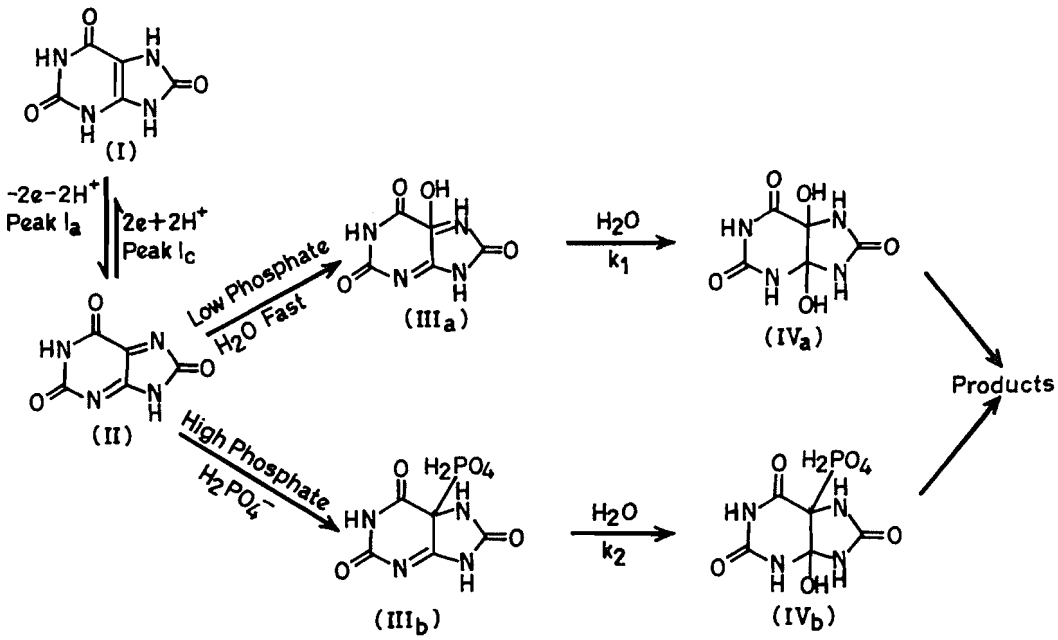

SCHEME 1. Oxidation of uric acid.

Fractions of 5 mL each were collected and their absorbance was monitored at 210 nm. The absorbance versus volume plot exhibited two peaks in gel permeation chromatography. The first peak between 110–190 mL was found to be due to phosphate and hence discarded. The second peak between 190–260 mL was collected, lyopholised, and analysed using mp, IR, mass and ^{1}H NMR spectra. Mass spectrum of the product was recorded on KRATOS model 50 mass spectrophotometer direct insertion probe at an electron beam voltage of 70 eV. NMR spectrum was obtained using Varian XL 300 spectrophotometer.

Results and discussion

Voltammetric studies

The linear sweep voltammograms of 1 mM uric acid (I) at a scan rate of 10 mV s^{-1} exhibited a single well-defined anodic peak (I_a) at pyrolytic graphite electrode in the entire pH range 2.1–10.6. The peak potential (E_p) was dependent on pH and shifted to less positive potential with increase in pH. A careful analysis of E_p vs. pH plot indicated two breaks at pHs 5.5 and 9.8 (Fig. 1) and dependence of E_p vs. pH can be represented by the following equations:

$$E_p = -0.1418\ \text{pH} + 1.6373\ (\text{pH } 2.14\text{–}5.75) \quad \text{V vs. SCE}$$

$$E_p = -0.0403\ \text{pH} + 0.6419\ (\text{pH } 5.75\text{–}9.80) \quad \text{V vs. SCE}$$

$$E_p = -0.0618\ \text{pH} + 0.7504\ (\text{pH } 9.80\text{–}10.63) \quad \text{V vs. SCE}$$

The earlier studies on electrooxidation of uric acid (3–5) indicated a linear E_p vs. pH graph without any break, whereas, in the present studies two clear breaks at pH 5.7 and 9.80 were noticed, which corresponds to the pK_a of uric acid. The dependence of E_p on pH clearly indicated that the species oxidized over the whole pH range is the conjugate base. This is the species predominating at pH > 9.80, and is rapidly formed from conjugate acid in the pH range 5.7–9.80 and from the species bearing two protons more than the conjugate base of pH < 5.7. As anodic mechanism involves oxidation of fully deprotonated species, the slop of E_p vs. pH plot becomes practically zero at pH > 9.80.

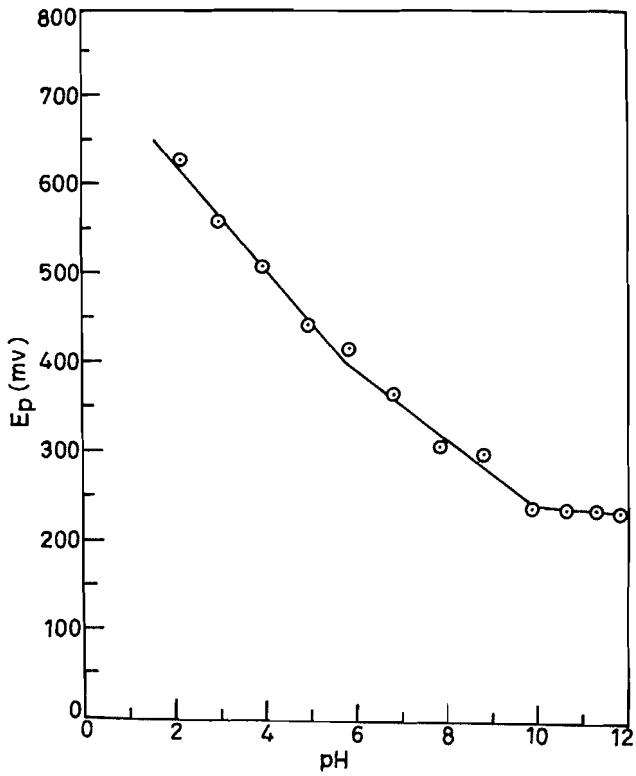

FIG. 1. Variation of the peak potential (E_p) with pH for the oxidation peak I_a of 1.0 mM uric acid, sweep rate 10 mV s^{-1}.

Cyclic voltammograms of (I) were recorded at a scan rate of 100 mV s^{-1} at different solid electrodes, viz., pyrolytic graphite, glassy carbon, and platinum electrodes. In phosphate buffer and at PGE, a well-defined pH dependent peak I_a was obtained during anodic sweep. Below pH 3.90, a bump close to background was also noticed. In the reverse sweep, two reduction peaks (I_c, II_c) were observed. Peak I_c formed a quasi reversible couple with peak I_a. Some typical cyclic voltammograms of uric acid are presented in Fig. 2. The cyclic voltammograms recorded in

Can. J. Chem. Downloaded from www.nrcresearchpress.com by EESC ESCOLA DE ENGENHARIA on 09/08/12
For personal use only.

Can. J. Chem. Downloaded from www.nrcresearchpress.com by EESC ESCOLA DE ENGENHARIA on 09/08/12
For personal use only.

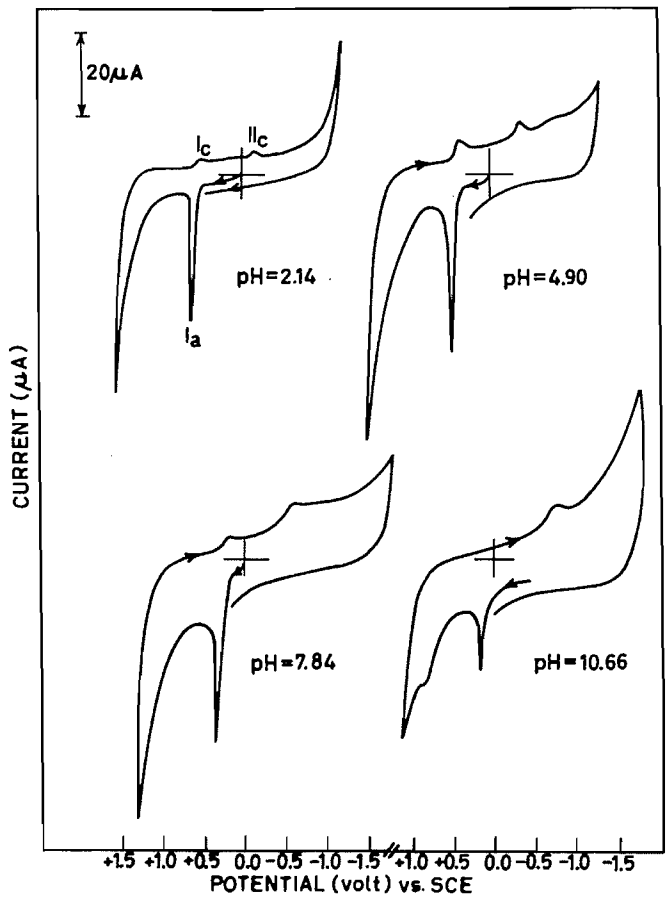

FIG. 2. Typical cyclic voltammograms of 1 mM uric acid in phosphate buffers (μ = 0.5 M) of different pH at pyrolytic graphite electrode (sweep rate 100 mV s^{-1}).

buffers of different ionic strength (5 mM – 0.5 M) were essentially similar with the only difference that at 5 mM ionic strength a post adsorption peak was noticed. The peak current of peak I_a was practically constant in the pH range 2.1–8.0, however, the peak current decreased at pH > 8.0 (Table 1). Peak current for peaks I_c and II_c were more or less constant in the entire pH range studied. The ratio of peak I_c/I_a was strongly dependent on pH and the ratio increased with increase in pH. The dependence of peak I_c on pH clearly suggested that the species involved in peak I_c reduction undergoes acid base catalyzed reaction. The ratio of peaks II_c/I_c was always close to 2.0 (Table 1). These peaks were also pH dependent and shifted to more negative potential with increase in pH. Their dependence on pH can be represented by the following equations:

$$E_p \text{ (pH 2.14–9.87)} = -0.051 \text{ pH} + 0.643 \quad \text{V vs. SCE (Peak } I_c\text{)}$$

$$E_p \text{ (pH 2.96–10.66)} = -0.061 \text{ pH} + 0.070 \quad \text{V vs. SCE (Peak } II_c\text{)}$$

At glassy carbon and platinum electrodes only peak I_a appeared during the anodic scan at a rate of 100 mV s^{-1}. However, no reduction peaks during cathodic scan were noticed. Hence, pyrolytic graphite was chosen for entire studies.

The effect of concentration on peak current of peak I_a was

TABLE 1. Effect of pH on the peak currents of 0.2 mM uric acid in 0.5 M phosphate solutions, sweep rate 100 mV s^{-1}

	Peak current (μA)			Peak ratio	
pH	I_a	I_c	II_c	I_c/I_a	II_c/I_c
2.14	60	5	11	0.08	2.2
2.96	50	6	13	0.12	2.1
3.90	45	5	10	0.11	2.0
4.90	45	6	11	0.13	1.8
5.86	45	5	12	0.11	2.4
6.80	45	5	12	0.11	2.4
7.84	45	6	12	0.13	2.0
8.79	35	5	12	0.14	2.4
9.87	25	5	11	0.20	2.2
10.66	20	6	12	0.30	2.0

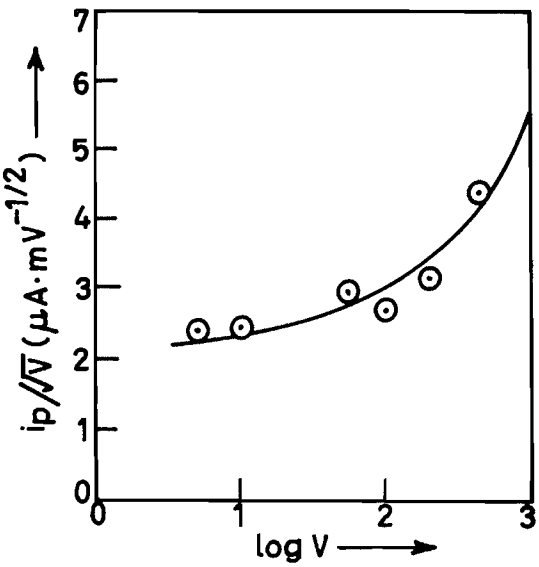

FIG. 3. Dependence of peak current function $i_p/\sqrt{v}$ with change in log (sweep rate).

studied in the concentration range 0.1 to 3 mM. The i_p vs. concentration plot was practically linear upto 2 mM but at higher concentration, the i_p values were more or less constant. The peak current for peaks I_c and II_c increased with increase in concentration of uric acid up to about 0.8 mM, however, at concentrations > 0.8 mM the peak currents became practically constant. The ratio of peaks II_c/I_c was always constant and equal to ~2.0 in the entire concentration range studied. This behavior indicated involvement of adsorption in the electrode reaction. Adsorption complications (12, 13) were further confirmed by the increase in peak current function ($i_p/v^{1/2}$) with increase in sweep rate as shown in Fig. 3.

It was interesting to observe that peak I_c increased with increase in sweep rate in the range 5–500 mV s^{-1}. The ratio of peak I_c/I_a increased from 0.17 at 5 mV s^{-1} to 0.45 at 500 mV s^{-1} (Table 2). The increase in peak I_c with increase in sweep rate suggested that the species responsible for peak I_c undergoes some type of follow up chemical reactions. The peak currents for peak II_c also increased with increase in sweep rate and the ratio of peaks II_c/I_c decreased from 0.24 to 0.20 with increase in sweep rate and at sweep rate >10 mV s^{-1} became almost constant.

TABLE 2. Effect of sweep rate on the peak currents of 0.5 mM uric acid in phosphate buffer (μ = 0.5 M) of pH 7.2

Sweep rate (mV s^{-1})	Peak current (μA)			Peak ratio	
	I_a	I_c	II_c	I_c/I_a	II_c/I_c
5	30	5	12	0.17	2.4
10	43	9	23	0.21	2.4
20	75	22	44	0.29	2.0
50	91	34	65	0.37	1.8
100	130	50	100	0.39	2.0
200	168	70	107	0.41	2.1
500	260	120	240	0.45	2.0

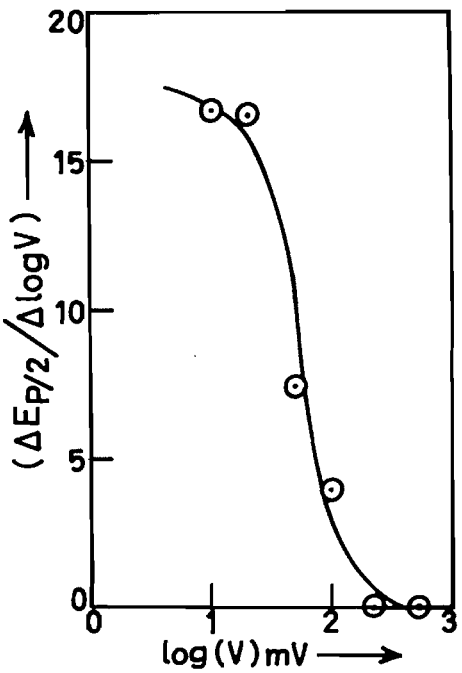

FIG. 4. Observed dependence of $\Delta E_{p/2}/\Delta$ log V on log V for the oxidation peak I_a of uric acid.

The peak potential of peak I_a also shifted to more positive potential with increase in sweep rate. The shift of E_p was 15 mV per ten fold increase in sweep rate in the range 5 to 100 mV s^{-1}, whereas the shift decreased to 8–10 mV at higher sweep rates. The plot of $\Delta E_{p/2}/\Delta$ log v vs. log v was S-shaped (Fig. 4) and clearly indicated that the nature of the electrode reaction is EC in which charge transfer is followed by an irreversible chemical reaction (14, 15). The EC nature of the reaction was further confirmed by the increase in I_c/I_a with sweep rate as expected for coupled chemical reactions (Fig. 5).

Spectral studies

Ultraviolet and visible spectra of compound (I) were monitored at different pH to determine the pK_a of the species. The absorbance at λ_{max} was plotted against pH and the resulting graph exhibited two breaks at around pH 5.5 and 10.1, indicating thereby the pK_{a1} and pK_{a2} of the compound (I). These values were essentially similar to the values obtained by E_p vs. pH relation (Fig. 1) and are similar to the pK_a values reported for uric acid in the literature (16, 17). Hence it is clear that below pK_{a1} uric acid exists mainly as a neutral species, whereas in the pH

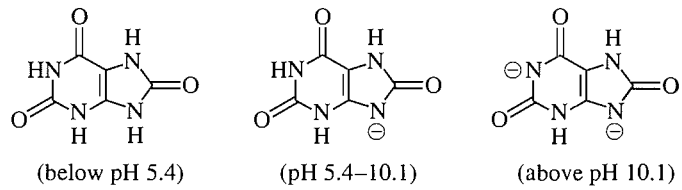

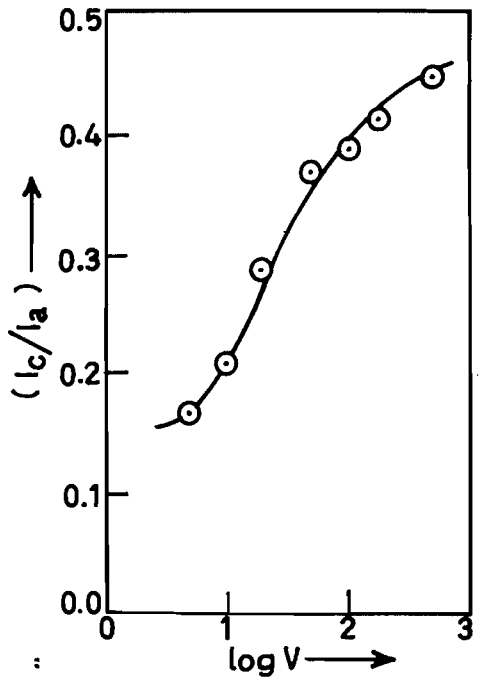

FIG. 5. Observed dependence of I_c/I_a on log V for 0.5 mM uric acid.

range 5.5–10.1, it exists as a mono anion. Out of the four hydrogen present in uric acid the hydrogen attached at position –9 has been found most acidic hence the anion has been suggested (16) to form at position –9.

UV/Visible spectra of 0.05 mM uric acid were also recorded during controlled potential electrolysis in acidic, neutral, and alkaline media to monitor the spectral changes during electrolysis. At pH 6.8, uric acid exhibited two well-defined λ_{max} at 240 nm and 292 nm. The peak at λ_{max} 240 nm was broad. With progress of electrolysis absorbance at these peaks decreased and almost vanished after an interval of 110 min (Fig. 6). The absorbance in the longer wavelength region (320–350 nm) also indicated some increase. Curve 10 in Fig. 6 represents the spectrum at the end of electrolysis with a broad shoulder at about 240 nm. This behavior indicated that π-chromophore system in the product has decreased. These spectral changes were practically similar to the ones observed in 0.5 M NaCl medium adjusted to desired pH with dilute HCl/NaOH.

Effect of ionic strength

The effect of ionic strength of the buffer constituents on the pseudo first order rate constant decay of the UV-absorbing intermediate was determined in the range 0.05–0.50 M at pHs 3.68, 6.75, and 10.0. The electrooxidation intermediate was generated by electrolysing the solution of uric acid in each ionic strength buffer (see Experimental) and then the decay of the intermediate was monitored by recording absorbance at selected wavelengths. These wavelengths were selected on the basis of UV/Vis spectral changes observed during electrolysis

Can. J. Chem. Downloaded from www.nrcresearchpress.com by EESC ESCOLA DE ENGENHARIA on 09/08/12
For personal use only.

TABLE 3. Observed rate constants for the decay of UV-absorbing intermediate of uric acid in buffers of different ionic strength

Ionic strength (μ)	$k \times 10^{-3}$/s					
	pH 3.68		pH 6.75		pH 10.0	
	λ_{230}	λ_{284}	λ_{237}	λ_{293}	λ_{240}	λ_{293}
Phosphate buffer						
0.05	6.07	6.10	0.61	1.09	4.52	1.96
0.10	5.51	5.47	0.83	1.01	5.48	2.74
0.20	5.30	6.34	1.11	1.37	7.43	3.34
0.30	4.99	7.08	0.92	1.43	11.13	6.10
0.40	4.82	7.10	1.26	1.90	14.31	5.52
0.50	5.80	6.06	1.66	2.47	13.62	8.65
NaCl						
0.50	5.80	6.05	1.66	2.46	14.05	8.60

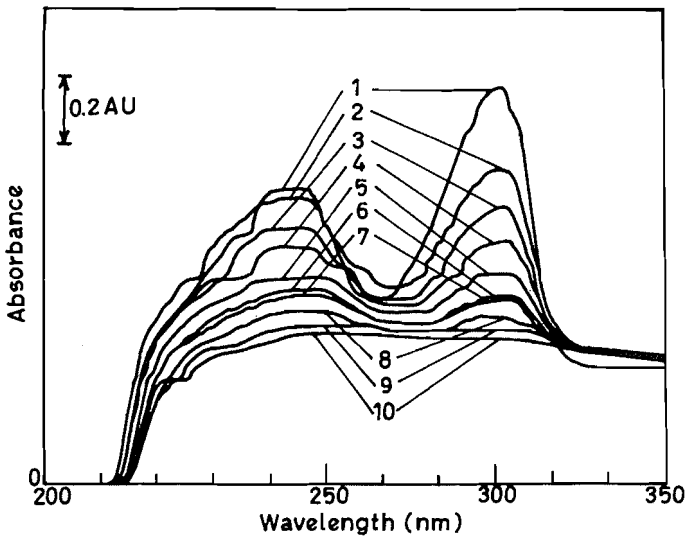

FIG. 6. Observed spectral changes during oxidation of uric acid at pH 6.80 (μ = 0.5). Curves were recorded at an interval of 10 min. Potential applied 0.5 V vs SCE.

as described earlier. In each case, time vs. absorbance profile showed an exponential decay in absorbance with increase in time, which then ultimately became constant and hence, the absorbance at this point was considered as A_∞. The values of rate constants were calculated by slope value of linear best fit equation of time vs. $\log_e (A-A_\infty)$ and are presented in Table 3.

At pH 3.68, the pseudo first order rate constant varied from 4.82×10^{-3} to 6.07×10^{-3} s^{-1} at 230 nm and 5.47×10^{-3} to 7.10×10^{-3} s^{-1} at 284 nm with change in the ionic strength of phosphate from 0.05 to 0.50 M. At pH 6.75, a significant increase in the rate constants were observed at both the wavelengths, whereas, at pH 10.0 the rate constants showed a large variation from 4.52×10^{-3} to 13.6×10^{-3} s^{-1} at λ = 240 nm and 1.96×10^{-3} to 8.65×10^{-3} s^{-1} at λ = 293 nm. The values of the rate constants observed are presented in the Table 1. To determine whether such a variation was due to attack of phosphate on diimine or simply due to ionic strength changes, Brønsted equation (7) was applied.

$$\log k = \log k_0 + 1.02\, Z_1 Z_2 \sqrt{\mu}$$

where k = rate coefficient at ionic strength μ, k_0 = rate coefficient at ionic strength zero, μ = ionic strength, and Z_1 and Z_2 = charges on ions.

In all the cases studied, it was found that the log k vs. $\sqrt{\mu}$ plot exhibited a straight line as shown in Fig. 7. This behavior indicated that the observed changes in the rate constants of the UV-absorbing intermediate are due to the changes in the ionic strength of phosphate and phosphate does not attack at the diimine intermediate as reported earlier. Figure 7 further indicated that at pH 3.68, the slope of plots of $\sqrt{\mu}$ and log k was zero, whereas at pH 6.7 and 10.0, the plots had positive slopes. The zero value of slope at pH 3.68 shows existence of one of the species in neutral form, however, a positive value of the slope indicates the presence of similar charges on both the species. As uric acid exists as a neutral species at pH 3.68 (below pK_{a1} 5.7) the values of Z_1Z_2 turns to zero and hence the slope of log k against $\sqrt{\mu}$ plot becomes zero as observed in Fig. 7. At pH 6.78, uric acid predominantly exists as a mono anion and a positive slope of (~1) in log k vs. $\sqrt{\mu}$ plot was observed. At pH 10.0, the slope of log k vs. $\sqrt{\mu}$ plot was found to increase significantly to ~2 (Fig. 7), due to the fact that at pH 10.0, which is higher than pK_{a2} of uric acid (9.80) the formation of dianion of uric acid increases the value of Z_1Z_2 to almost 2. Hence, the value of slope observed at this pH is double than at pH 6.78.

Thus, the observed changes in the rate constants were only due to changes in ionic strength was further confirmed by studying the oxidation of uric acid in 0.5 M NaCl solution adjusted to pH 3.68, 6.75, and 10.0 with dilute HCl/NaOH. The cyclic voltammetric behavior in 0.5 M NaCl was essentially similar to the corresponding buffer solution. Hence, the decay of UV-absorbing intermediate was monitored under conditions similar to the ones maintained for ionic strength studies. The rate constants were calculated at same wavelengths and are presented in Table 3. As the rate constants in 0.5 M NaCl did not show a significant variation from the solutions containing phosphate, it was concluded that the diimine species is attacked by water molecule to give diol and that the phosphate does not act as a nucleophile in this reaction. If phosphate competes with water in this reaction, it is expected that the rate constants will change significantly from 0.5 M NaCl to 0.5 M phosphate medium.

To further confirm that the phosphate moiety does not attack at diimine (II), the products of electrooxidation at pH 7.2 were characterized in 0.5 M NaCl adjusted to pH 7.2 with dilute NaOH; 0.05 M phosphate and 0.50 M phosphate buffers. In all

Can. J. Chem. Downloaded from www.nrcresearchpress.com by EESC ESCOLA DE ENGENHARIA on 09/08/12
For personal use only.

Can. J. Chem. Downloaded from www.nrcresearchpress.com by EESC ESCOLA DE ENGENHARIA on 09/08/12
For personal use only.

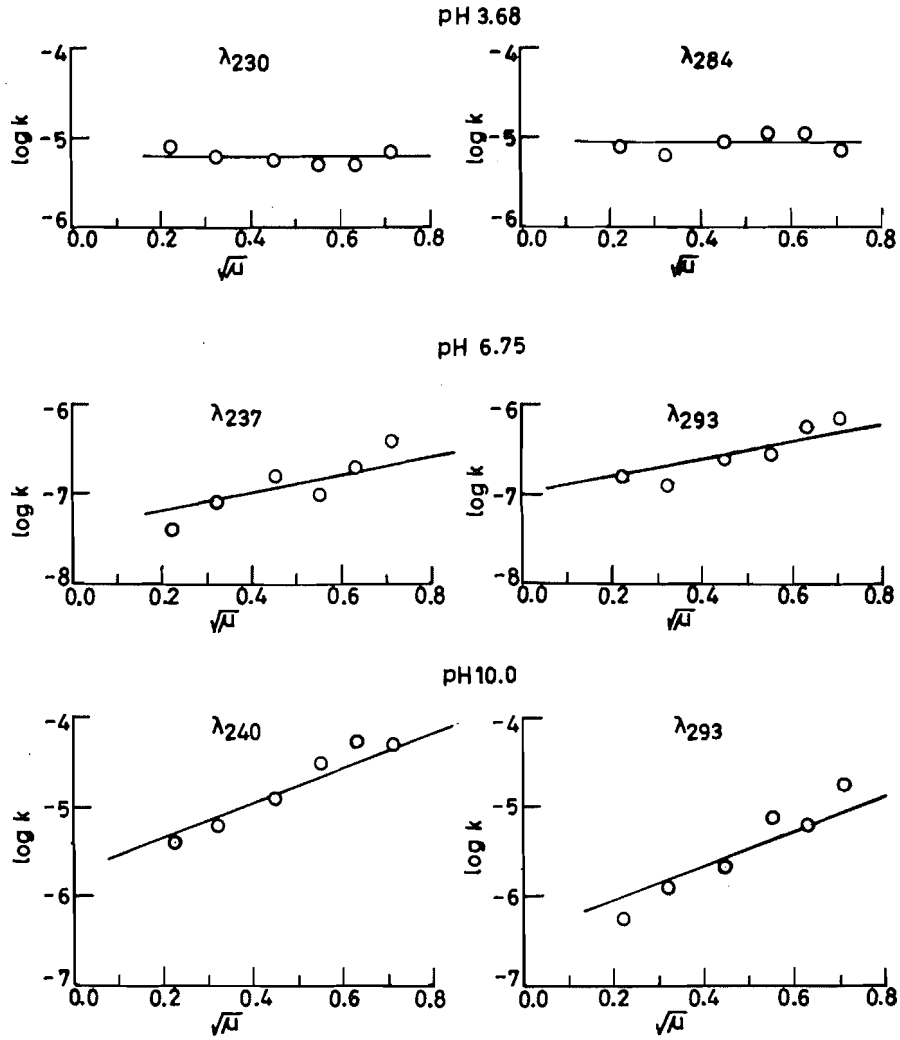

FIG. 7. Dependence of $\log_e k$ with increase in $\sqrt{\mu}$ for uric acid at different pHs.

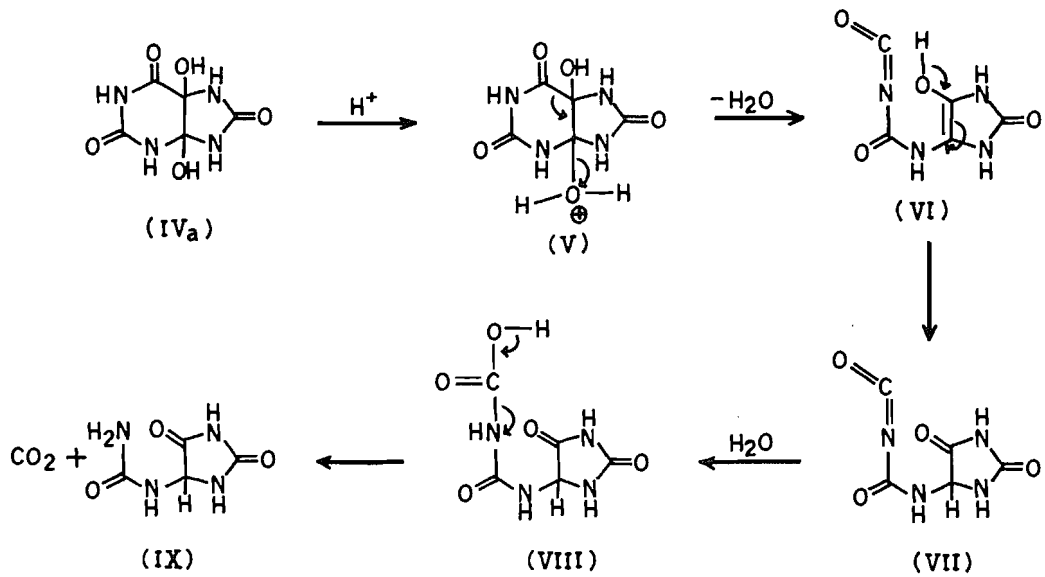

SCHEME 2. Tentative mechanism proposed for the formation of allantoin from uric acid at pH 7.2.

the cases only one chromatographic peak was observed in gel permeation chromatography. The colourless freeze dried material obtained had a mp 230°C. The mass spectra of the product exhibited a clear molecular ion peak at *m/e* 158 and indicated the product to be allantoin. The other high mass peaks observed in the fragmentation pattern were at 141 (8.6%); 140 (3.4%); 130 (32.3%); 129 (3.6%); 116 (4.8%); 115 (15.2%); 114 (10.8%); 113 (6.2%); 100 (4.0%); 99 (3.2%); 98 (14.3%). However, no attempt was made to explain the fragmentation pattern. The ^{1}H NMR spectrum indicated strong bands at δ = 5.28 (d, 1H); 5.8 (s, 3H); 8.04 (s, 1H) and 10.52 (s, 1H) and hence further supported the product as allantoin. Thus, the product of electrooxidation at pH 7.2 was found as allantoin in the presence or absenceof phosphate.

The observed results thus clearly indicate that the difference in rate constant values calculated for different phosphate concentrations is only due to change in ionic strength of the solutions and hence obeys Brønsted equations. Therefore, it is reasonable to conclude that phosphate moiety does not attack at diimine as suggested earlier (6) and only water attacks to give imine alcohol or diol, which in a series of reactions give allantoin as the product as shown in Scheme 2.

Acknowledgements

One of the authors (A.M.) is thankful to CSIR, India, for the award of Research Associateship. Financial assistance for this work was provided by the Department of Science and Technology, New Delhi, through grant no. SP/S1/G21/91.

1. H. Chang, D.C. Johnson, and R.S. Houk. Trends Anal. Chem. **8**, 328 (1989).
2. B. Bittins-Cattaneo, E. Cattaneo, P. Konigshoven, and W. Vielstich. *In* Electroanalytical chemistry. Vol. 17. *Edited by* A.J. Bard. Marcel Dekker, New York. 1991.
3. G. Dryhurst. J. Electrochem. Soc. **119**, 1659 (1972).
4. K.J. Volk, R.A. Yost, and A.B. Toth. Anal. Chem. **64**, 21A (1992).
5. J.L. Owens, H.A. Marsh, and G. Dryhurst. J. Electroanal. Chem. **91**, 231 (1978).
6. R.N. Goyal, A.B. Toth, G. Dryhurst, and N.T. Nguyen. Bioelectro. Bioenerg. **9**, 39 (1982).
7. J.N. Bronsted. Z. Physik Chem. **102**, 169 (1992).
8. G.D. Christian and W.C. Purdy. J. Electroanal. Chem. **3**, 363 (1962).
9. R.N. Goyal, A. Kumar, and A. Mittal. J. Chem. Soc. Perkin Trans, II, **9**, 1369 (1992).
10. R.N. Goyal, Rajeshwari, and N.C. Mathur. J. Electroanal. Chem. **220**, 311 (1987).
11. R.N. Goyal, S.K. Srivastava, and R. Agarawal. Bull. Soc. Chim. France, **41**, 281 (1985).
12. R.H. Wopschall and I. Shain. Anal. Chem. **39**, 1514 (1967).
13. R.S. Nicholson and I. Shain. Anal. Chem. **36**, 706 (1964).
14. R.S. Nicholson and I. Shain. Anal. Chem. **37**, 178 (1965).
15. E.R. Brown and R.F. Large. *In* Techniques of chemistry. *Edited by* A. Weissberger and R.W. Rossiter. Wiley Interscience. p. 423.
16. F. Bergman and S. Dikstein. J. Am. Chem. Soc. **77**, 691 (1955).
17. E.A. Johnson. Biochem. J. **51**, 133 (1952).

Can. J. Chem. Downloaded from www.nrcresearchpress.com by EESC ESCOLA DE ENGENHARIA on 09/08/12
For personal use only.

Reactions of 7-azaindole with niobium and tantalum pentachlorides and coupling to the azaindolyl-azaindolium cation

JACQUES POITRAS AND ANDRÉ L. BEAUCHAMP[1]

Département de chimie, Université de Montréal, C.P. 6128, Succ. centre-ville, Montréal, PQ H3C 3J7, Canada

Received January 10, 1994

JACQUES POITRAS and ANDRÉ L. BEAUCHAMP. Can. J. Chem. **72**, 1675 (1994).

The reaction of $NbCl_5$ and $TaCl_5$ with 7-azaindole (Haza) at room temperature in benzene or dichloromethane yielded MCl_5(Haza) addition compounds. Under more severe conditions, the same compound was obtained with $TaCl_5$. For $NbCl_5$, some reduction to Nb(IV) was observed and $NbCl_5$(Haza), $NbCl_4$(Haza)$_2$, and the $(H_2aza)^+$ ion were identified in the reaction mixture by infrared spectroscopy. Oxidative coupling of two azaindole units via N7—C6 also took place during the reaction, since the 7-(azaindol-6-yl)azaindolium cation was found as counter-ion in the crystal structures of two complex salts. In the crystals of $(H_2aza\text{-}aza)[NbOCl_4(Haza)]\cdot 0.5CH_2Cl_2$ ($P\bar{1}$, $a = 7.255$ Å, $b = 12.412$ Å, $c = 14.277$ Å, $\alpha = 89.03°$, $\beta = 85.60°$, $\gamma = 76.66°$, $Z = 2$, $R = 0.062$), the anion is the roughly octahedral $[NbOCl_4(azaindole)]^-$ species containing a neutral N7-coordinated azaindole *trans* to the Nb═O bond. The $[NbOCl_5]^{2-}$ salt ($P\bar{1}$, $a = 7.527$ Å, $b = 10.168$ Å, $c = 10.467$ Å, $\alpha = 66.41°$, $\beta = 84.07°$, $\gamma = 85.51°$, $Z = 1$, $R = 0.037$) contains the distorted octahedral $[NbOCl_5]^{2-}$ ion disordered over two orientations. The infrared spectra suggest monomeric octahedral structures for the MCl_5(Haza) and $NbCl_4$(Haza)$_2$ complexes. ^1H NMR spectroscopy shows that $NbCl_5$(Haza) is not dissociated in CD_2Cl_2.

JACQUES POITRAS et ANDRÉ L. BEAUCHAMP. Can. J. Chem. **72**, 1675 (1994).

La réaction de $NbCl_5$ et $TaCl_5$ avec le 7-azaindole (Haza) à température ambiante dans le benzène ou le dichlorométhane conduit au composé d'addition MCl_5(Haza). Dans des conditions plus vigoureuses, le même complexe est obtenu avec $TaCl_5$. Pour $NbCl_5$, il se produit une réduction en Nb(IV) et la spectroscopie infrarouge permet d'identifier $NbCl_5$(Haza), $NbCl_4$(Haza)$_2$ et l'ion $(H_2aza)^+$ dans le mélange réactionnel. Un couplage oxidant de deux motifs azaindole via N7—C6 se produit également durant la réaction, puisque le cation 7-(azaindol-6-yl)azaindolium est observé comme contre-ion dans les structures cristallines de deux sels complexes. Dans les cristaux de $(H_2aza\text{-}aza)[NbOCl_4(Haza)]\cdot 0.5CH_2Cl_2$ ($P\bar{1}$, $a = 7{,}255$ Å, $b = 12{,}412$ Å, $c = 14{,}277$ Å, $\alpha = 89{,}03°$, $\beta = 85{,}60°$, $\gamma = 76{,}66°$, $Z = 2$, $R = 0{,}062$), l'anion est l'espèce $[NbOCl_4(azaindole)]^-$ approximativement octaédrique, dans laquelle un azaindole neutre coordonné par N7 occupe un site *trans* à la liaison Nb═O. Le sel de $[NbOCl_5]^{2-}$ ($P\bar{1}$, $a = 7{,}527$ Å, $b = 10{,}168$ Å, $c = 10{,}467$ Å, $\alpha = 66{,}41°$, $\beta = 84{,}07°$, $\gamma = 85{,}51°$, $Z = 1$, $R = 0{,}037$) contient l'ion $[NbOCl_5]^{2-}$ de géométrie octaédrique déformée, désordonné selon deux orientations. La spectroscopie infrarouge indique une structure monomère octaédrique pour les composés MCl_5(Haza) et $NbCl_4$(Haza)$_2$. Le spectre RMN ^1H montre que $NbCl_5$(Haza) n'est pas dissocié dans CD_2Cl_2.

Can. J. Chem. Downloaded from www.nrcresearchpress.com by 85.192.166.187 on 09/08/12
For personal use only.

Introduction

Pyridine and related aromatic N-heterocyclic ligands are known to react with $NbCl_5$ and $TaCl_5$ (1). The simplest complexes expected to form with unidentate ligands are octahedral $MX_5\cdot L$ adducts, which have indeed been obtained with pyridines (2, 3) and, more recently, with imidazoles (4, 5). However, higher coordinations are possible with these metal centres (6–8) and other types of reactions often take place. The high affinity of Nb(V) and Ta(V) for oxygen donors makes the pentahalides extremely sensitive to moisture, leading to various oxo species and finally to the M_2O_5 oxides. Common oxygen-donor solvents tend to displace the nitrogen ligand from the coordination sphere. Oxygen abstraction from the solvent can also take place (9): for instance, MOX_3 adducts with bipyridine and phenanthroline were obtained when they were reacted with MX_5 in ether (10).

$NbCl_5$ can be reduced to the Nb(IV) state under relatively mild conditions by aromatic amines, but $TaCl_5$ is more resistant to reduction. McCarley et al. (2) have shown that the $NbCl_5$–pyridine system at room temperature yields 30% of $NbCl_5$(py) and 70% of the reduced $NbCl_4(py)_2$ complex. The oxidized species has been identified as the 4-pyridylpyridinium cation. When $NbBr_5$ was used as starting material, only 10% of $NbBr_5$(py) was obtained, whereas the redox pathway leading to $NbBr_4(py)_2$ represented 90% of the reaction. Metal reduction also took place with 4-picoline, bipyridine, and phenanthroline (6), but the oxidized species were not identified.

[1]Author to whom correspondence may be addressed.

7-Azaindole (Haza, **I**)[2] first attracted our attention because its N1-deprotonated anion is a potential binucleating agent, stabilizing pairs of nearby metal atoms (11–13). Monodentate coordination can also occur with both the anionic and the neutral forms (14–20). When protonated, the resulting H_2aza^+ cation simply acts as counter ion (20, 21). The present paper reports on the reactions of this ligand with $NbCl_5$ and $TaCl_5$, with special emphasis on the products generated by the redox pathway.

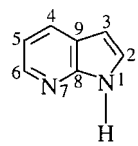

I

Experimental

Reactants and techniques

$NbCl_5$, $TaCl_5$, and $NbCl_4(THF)_2$ were stored in the glove box and used as received from Aldrich. 7-Azaindole (Aldrich) was used without further purification. The starting materials were transferred and weighed in Schlenk tubes under argon in the glove box. All reactions were carried out in a standard Schlenk system under dry argon. The solvents, dried over sodium (benzene, toluene, CH_2Cl_2) or $CaCl_2$ (acetonitrile) and distilled under argon, were vigorously outgassed im-

[2]1*H*-Pyrrolo[2,3-*b*]pyridine. Haza = neutral ligand, H_2aza^+ = N7-protonated cation, $(H_2aza\text{-}aza)^+$ = azaindolyl-azaindolium cation (IUPAC name: 7-(1*H*-Pyrrolo[2,3-*b*]pyridin-6-yl)-1*H*-pyrrolo[2,3-*b*]pyridin-7-ium).

Can. J. Chem. Downloaded from www.nrcresearchpress.com by 85.192.166.187 on 09/08/12
For personal use only.

mediately before use. Samples for analyses or physical measurements were prepared in the glove box.

For quantitative analysis, the samples were hydrolysed with 1 M NH_4OH and the mixture was acidified to pH 1 with 1.5 M HNO_3. Chlorine was then determined as AgCl by potentiometric titration with $AgNO_3$. For metal analysis, the hydrolysed mixture was heated to dryness on a hot plate, heated for 24 h in an oven at 1000°C (Nb) (22, 23) or 1100° (Ta) (22), and weighted as M_2O_5.

The IR spectra (4000–250 cm^{-1}) of Nujol mulls were recorded with a Perkin-Elmer 783 spectrophotometer by using KRS-5 windows. ^1H NMR spectra were taken in CD_2Cl_2 or $(CD_3)_2SO$ (Merck, Sharp & Dohme Canada) with Bruker WH-400 or Varian VXR-300 spectrometers. They were referenced to the residual solvent signal (δ = 5.30 ppm for CD_2Cl_2 and 2.50 ppm for $(CD_3)_2SO$) and converted to the usual TMS scale. Magnetic moments were determined at room temperature with an Evans magnetic susceptibility balance (Johnson-Matthey), calibrated with $HgCo(SCN)_4$ ($\chi = 16.44 \times 10^{-6}$ c.g.s.e.m.u.). The data were corrected for the diamagnetism of the ligands using Pascal's constants (24).

Preparative work

$TaCl_5$(Haza)

To azaindole (0.26 g, 2.2 mmol) were added $TaCl_5$ (0.72 g, 2.0 mmol) and dry benzene (15 mL). In the resulting orange solution, an orange precipitate appeared quickly. The mixture was stirred at room temperature for 12 h. The solid was filtered, washed with benzene, and dried in vacuo. Yield: 0.88 g, 92%. Anal. calcd. for $TaCl_5C_7H_6N_2$: Ta 38.0, Cl 37.2; found: Ta 38.6, Cl 36.9. The same compound was obtained with a similar yield (based on Ta) when a 1:2 $TaCl_5$:azaindole mixture was refluxed for 72 h.

$NbCl_5$(Haza)

Azaindole (0.54 g, 4.6 mmol) was added to the orange solution of $NbCl_5$ (1.22 g, 4.5 mmol) in benzene (25 mL). The solution turned brown quickly and a dark brown precipitate formed. The mixture was stirred at room temperature for 16 h. The product was filtered, washed twice with benzene, and dried in vacuo. Yield: 1.56 g, 89%. Anal. calcd. for $NbCl_5C_7H_6N_2$: Nb 23.9, Cl 45.7; found: Nb 23.8, Cl 44.4. The same product was obtained when dichloromethane was used as solvent. ^1H NMR (CD_2Cl_2): δ (ppm): 11.38 (s br, H1), 7.695 (d, H2), 6.878 (d, H3), 8.598 (dd, H4), 7.555 (dd, H5), 8.427 (dd, H6); coupling constants (Hz): ^3J(H2—H3) = 3.6, ^3J(H4—H5) = 7.9, ^4J(H4—H6) = 0.8, ^3J(H5—H6) = 6.0. The H2 and H3 signals sometimes appear as doublets of doublets, because of extra ^3J(H2—H1) and ^4J(H3—H1) couplings of 2.2 and 2.0 Hz, respectively.

$NbCl_4(Haza)_2$

The dark brown solution of $NbCl_4(THF)_2$ (1.32 g, 3.5 mmol) and azaindole (0.84 g, 7.1 mmol) in toluene (35 mL) was stirred for 24 h at room temperature. The orange precipitate was filtered, washed with toluene (15 mL), and dried in vacuo. Yield: 1.55 g, 94%. Anal. calcd. for $NbCl_4C_{14}H_{12}N_4$: Nb 19.7, Cl 30.1; found: Nb 19.5, Cl 29.9. Magnetic moment μ_{eff}: 1.36 B.M.

$(H_2aza)[NbCl_6]$

A mixture of $NbCl_5$ (1.35 g, 5.0 mmol) and azaindole (0.59 g, 5.0 mmol) in benzene (15 mL) was made as above for the preparation of $NbCl_5$(Haza). HCl gas was bubbled in the brown suspension, which turned orange. The orange precipitate was filtered, washed with benzene and dried in vacuo. Anal. calcd. for $NbCl_6C_7H_7N_2$: Nb 21.9, Cl 50.1; found: Nb 21.8, Cl 49.2.

$(H_2aza\text{-}aza)[NbOCl_4(Haza)]\cdot 0.5CH_2Cl_2$

A mixture of $NbCl_5$ (1.12 g, 4.2 mmol) and azaindole (1.00 g, 8.5 mmol) in dichloromethane (50 mL) was stirred for 4 days at room temperature. The brown precipitate was filtered and washed with dichloromethane. This light brown filtrate was left under argon and a few brown crystals appeared some weeks later. Their structure was determined by X-ray diffraction (see below).

$(H_2aza\text{-}aza)_2[NbOCl_5]$

To 60 mL of benzene was added 1.21 g (4.5 mmol) of $NbCl_5$ and 1.26 g (10.7 mmol) of azaindole, whereupon a brown precipitate of $NbCl_5$(Haza) formed. After refluxing for 72 h, a dark red suspension containing brown $NbCl_5$(Haza) and orange $NbCl_4(Haza)_2$ was obtained. The solid was then filtered and washed with 30 mL of dry acetonitrile. In the combined filtrate and washings kept under argon, a few air-stable colourless crystals appeared after a few days. The crystal structure was determined by X-ray diffraction (see below).

Crystallographic measurements and structure determination

The brown crystals of $(H_2aza\text{-}aza)[NbOCl_4(Haza)]\cdot 0.5CH_2Cl_2$ are very sensitive to moisture and the diffracted intensities were measured at low temperature, on a specimen transferred and sealed under dry argon in a Lindemann capillary. For the more stable colourless crystals of $(H_2aza\text{-}aza)_2[NbOCl_5]$, the data were collect at room temperature in open air. The crystallographic work was done with an Enraf-Nonius CAD-4 diffractometer, following similar procedures for the two compounds. The reduced triclinic cell was determined from 25 randomly distributed reflections, generated by the automatic search routine of the CAD-4 software and centred in the counter aperture. The cell was checked with axial photographs. The Niggli coefficients were not consistent with a symmetry higher than triclinic. Therefore, $P1$ and $P\bar{1}$ were the only possible space groups.

The crystal data and conditions for data collection are given in Table 1. Seven standard reflections were monitored every hour for crystal decay and every 200 reflections for misorientation. Half spheres of data were measured. For $(H_2aza\text{-}aza)[NbOCl_4(Haza)]\cdot 0.5CH_2Cl_2$, an absorption correction was not deemed necessary, considering the low absorption coefficient and small size of the crystal. In the case of $(H_2aza\text{-}aza)_2[NbOCl_5]$, the data were corrected for absorption (Gaussian integration, grid 10 × 10 × 10, transmission range = 0.38–0.63). Corrections for the effects of Lorentz and polarization were finally applied. The structures were solved by the direct methods of SHELX-76 (25). The nonhydrogen atoms were refined anisotropically by full-matrix least-squares procedures. The function minimized was $\Sigma w(|F_o| - |F_c|)^2$, with individual weights w based on counting statistics. In both structures, problems were encountered with disorder.

For $(H_2aza\text{-}aza)[NbOCl_4(Haza)]\cdot 0.5CH_2Cl_2$, an E map revealed positions for Nb and the attached Cl atoms. Nonhydrogen atoms for a coordinated Haza unit and a $(H_2aza\text{-}aza)^+$ "dimer" were located from subsequent ΔF maps. After refinement of this model, the ΔF map showed six residuals of 1.2–2.3 e $Å^{-3}$, which were obviously due to Cl atoms of a disordered solvent molecule. Refinement of positions and occupancies (fixed U_{iso} = 0.09 $Å^2$) yielded relative values for the occupancy factors, which were normalized to make the sum equal to unity, assuming that each site was fully occupied by a CH_2Cl_2 molecule: Cl(11) = 0.25; Cl(12) = Cl(13) = 0.20; Cl(14) = 0.15; Cl(15) = Cl(16) = 0.10. Extra peaks could not be detected in the ΔF map for the solvent fractional carbon and hydrogen atoms. Although many peak pairs show the expected Cl···Cl separation of ~2.9 Å, no model corresponding to a small number of orientations of CH_2Cl_2 could be determined. In the final cycles, azaindole hydrogen atoms were introduced at idealized positions (C—H = 0.95 Å, N—H = 0.87 Å, U_{iso} = 0.076 $Å^2$). Their parameters were not refined, but their coordinates were recalculated after each cycle. The final residuals were R = 0.062 and R_w = 0.052. The general background in the final ΔF map was below ±0.8 e $Å^{-3}$. Attempts to refine this structure in the non-centric $P1$ space group failed.

For $(H_2aza\text{-}aza)_2[NbOCl_5]$, the E map in space group $P\bar{1}$ showed a Nb atom near the cell origin, together with three peaks suitably oriented to define, with their centrosymmetric counterparts, an approximately octahedral arrangement of what first appeared to be a $[NbCl_6]^-$ unit. However, one "Cl" peak was much weaker than the other two and Nb was actually displaced from the origin by 0.4 Å in the direction of the weak peak. This suggested a $[NbOCl_5]^{2-}$ unit disordered over two orientations with the Cl—Nb═O direction reversed (Fig. 1), where the low "Cl" peak would actually correspond to statistical occupancy by either O or Cl. A Nb site with half occupancy, two fully occupied Cl

TABLE 1. Crystal data and conditions for data collection

Parameter	Value	
	$(H_2aza\text{-}aza)[NbOCl_4(Haza)]\cdot 0.5CH_2Cl_2$	$(H_2aza\text{-}aza)_2[NbOCl_5]$
Formula	$C_{21.5}H_{18}NbCl_5N_6O$	$C_{28}H_{22}NbCl_5N_8O$
Formula weight	646.59	756.71
Crystal system	Triclinic	Triclinic
Space group	$P\bar{1}$	$P\bar{1}$
a, Å	7.255(6)	7.527(2)
b, Å	12.412(11)	10.168(2)
c, Å	14.277(11)	10.467(2)
α, deg	89.03(7)	66.41(2)
β, deg	85.60(7)	84.07(2)
γ, deg	76.66(7)	85.51(2)
V, Å^3	1247.3	729.6
D_{calc}, g cm^{-3}	1.722	1.722
Z	2	1
Radiation, λ (Å)	MoKᾱ 0.71069	Cu-Kᾱ 1.54178
$F(000)$	646	380
μ, cm^{-1}	10.4	81.0
Crystal size, mm (faces)	0.09 (011–0$\bar{1}\bar{1}$)	0.11 (011–0$\bar{1}\bar{1}$)
	0.06 (001–00$\bar{1}$)	0.06 (001–00$\bar{1}$)
	0.14 (100–$\bar{1}$00)	0.19 (100–$\bar{1}$00)
$2\theta_{max}$, deg	40	140
Scan technique	ω/2θ	ω/2θ
Scan width, Δω, deg	1.00 + 0.35 tan θ	0.90 + 0.14 tan θ
Scan speed, °(ω) min^{-1}	3.30	3.30
No. unique reflections measured	2308	2758
No. observed reflections	1471	2076
Rejection criterion, $I/\sigma(I)$ <	3.0	3.0
T, K	190	293
R^a	0.062	0.037
$R_w{}^a$	0.052	0.043
Goodness-of-fit	2.59	2.04

$^aR = \Sigma||F_o| - |F_c||/\Sigma|F_o|$, $R_w = [\Sigma w(|F_o| - |F_c|)^2/\Sigma w|F_o|^2]^{1/2}$.

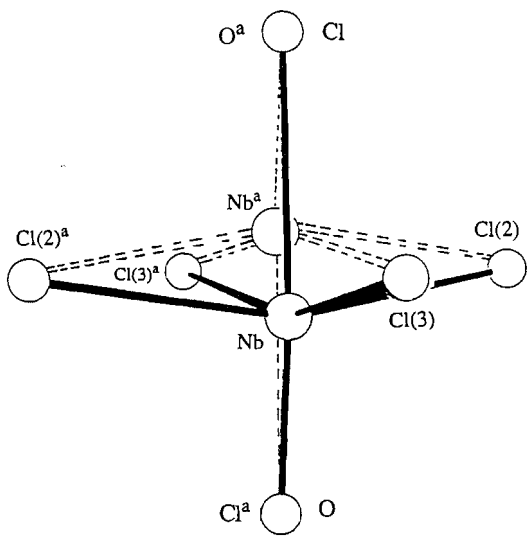

FIG. 1. $[NbOCl_5]^{2-}$ anion in the crystal of the $(H_2aza\text{-}aza)^+$ salt. Atoms are represented by spheres of arbitrary size. The central Nb atom is disordered over two symmetry-equivalent sites off the origin (occupancy 0.50) and the dashed bonds correspond to the alternate orientation of the anion. $a = -x, -y, -z$.

positions and a 12.5-electron "O/Cl atom" were introduced in the starting model. The $(H_2aza\text{-}aza)^+$ "dimer" clearly showed in the next ΔF map. Idealized hydrogen atoms were introduced and refinement was completed as described above. The final agreement factors were R = 0.037 and R_w = 0.043. The highest residual (0.38 e Å^{-3}) in the final ΔF map was near the disordered Nb atom.

Since an ordered $[NbOCl_5]^{2-}$ anion in a $P1$ unit cell could also have produced the features discussed above in an E map calculated in $P\bar{1}$ symmetry, structure determination and refinement were repeated in $P1$. However, the final results described the same structure as above with twice as many atomic positions and the anion remained disordered. Thus, the $P\bar{1}$ model was retained.

The scattering curves were taken from standard sources (26, 27). The anomalous dispersion coefficients of Nb and Cl were taken from Cromer (28). The refined coordinates for the two structures are listed in Tables 2 and 3, respectively.[3]

Results and discussion

When $TaCl_5$ is reacted with 7-azaindole in anhydrous ben-

[3]The supplementary material includes tables of refined temperature factors, hydrogen coordinates, geometry of hydrogen bonds, least-squares plane calculations, views of molecular packing and structure factor amplitudes for both structures, distances and angles for the $(H_2aza\text{-}aza)^+$ ion in the $[NbOCl_4(Haza)]^-$ salt, and infrared data for the Nb and Ta compounds (36 pages). Copies of material on deposit may be purchased from the Depository of Unpublished Data, Document Delivery, CISTI, National Research Council Canada, Ottawa, ON K1A 0S2, Canada.

Tables of hydrogen coordinates, and distances and angles for the $(H_2aza\text{-}aza)^+$ ion in the $[NbOCl_4(Haza)]^-$ compound have also been deposited with the Cambridge Crystallographic Data Centre and can be obtained on request from the Director, Cambridge Crystallographic Data Centre, University Chemical Laboratory, 12 Union Road, Cambridge, CB2 1EZ, U.K.

Can. J. Chem. Downloaded from www.nrcresearchpress.com by 85.192.166.187 on 09/08/12
For personal use only.

Can. J. Chem. Downloaded from www.nrcresearchpress.com by 85.192.166.187 on 09/08/12
For personal use only.

TABLE 2. Refined coordinates ($\times 10^4$, Cl(11)–Cl(16) $\times 10^3$) and equivalent isotropic temperature factors ($Å^2 \times 10^3$) for (H_2aza-aza)-[$NbOCl_4$(Haza)]·0.5CH_2Cl_2

Atom	x	y	z	U_{eq}
Nb(1)	2186(2)	8347(1)	7925(1)	31
Cl(1)	1041(6)	7385(3)	6738(3)	43
Cl(2)	5122(6)	8079(3)	6984(3)	49
Cl(3)	−986(6)	8955(4)	8612(3)	50
Cl(4)	3147(7)	9656(3)	8859(3)	53
Cl(11)[a]	118(3)	485(2)	503(2)	92
Cl(12)[b]	226(4)	464(2)	518(2)	95
Cl(13)[b]	279(4)	415(2)	478(2)	64
Cl(14)[c]	44(6)	500(3)	443(3)	97
Cl(15)[d]	154(6)	448(3)	449(4)	55
Cl(16)[d]	111(7)	488(3)	558(3)	65
O(1)	2738(13)	7258(7)	8661(7)	32
N(1)	−1735(18)	9731(9)	6413(8)	37
C(2)	−3077(22)	10232(12)	5810(11)	40
C(3)	−2533(21)	11113(12)	5383(10)	34
C(4)	450(22)	11835(12)	5638(10)	36
C(5)	2058(21)	11602(11)	6143(10)	32
C(6)	2335(20)	10693(10)	6751(11)	26
N(7)	1253(16)	10018(9)	6873(8)	24
C(8)	−372(20)	10290(11)	6396(11)	29
C(9)	−791(20)	11179(11)	5762(10)	25
N(11)	3981(18)	4884(9)	8235(8)	37
C(12)	4680(25)	4856(12)	7306(11)	49
C(13)	5534(22)	3822(13)	7060(12)	48
C(14)	6047(21)	2024(13)	8036(11)	38
C(15)	5691(20)	1679(12)	8917(12)	39
C(16)	4636(23)	2377(12)	9640(11)	40
N(17)	4041(15)	3484(9)	9435(8)	25
C(18)	4369(22)	3873(12)	8583(10)	37
C(19)	5489(19)	3150(11)	7838(10)	26
N(111)	820(18)	7002(10)	10511(8)	39
C(112)	−261(21)	7385(12)	11348(12)	39
C(113)	−369(23)	6562(12)	11964(11)	43
C(114)	1325(23)	4420(13)	11705(11)	47
C(115)	2359(24)	3777(13)	11030(12)	49
C(116)	2883(20)	4175(11)	10197(10)	26
N(117)	2514(16)	5244(9)	9940(9)	30
C(118)	1426(21)	5861(11)	10627(10)	30
C(119)	847(21)	5572(12)	11492(10)	32

[a]Occupancy factor = 0.25.
[b]Occupancy factor = 0.20.
[c]Occupancy factor = 0.15.
[d]Occupancy factor = 0.10.

zene or dichloromethane, the orange $TaCl_5$(Haza) adduct is the only complex isolated, even when the mixture is refluxed for several days and excess ligand is used. Infrared data are consistent with the monomeric octahedral structure observed for the 2-methylimidazole adduct (5). With $NbCl_5$, a related dark brown $NbCl_5$(Haza) complex is obtained when a 1:1 mixture is stirred at room temperature for a short time. These Nb and Ta compounds should be isostructural, since their infrared spectra are virtually identical.

The orange Nb(IV) adduct $NbCl_4(Haza)_2$ can be prepared by substitution on $NbCl_4(THF)_2$. The magnetic moment (1.36 BM) corresponds to a monomeric octahedral species (1). From the available data on $NbCl_4L_2$ and $TaCl_4L_2$ compounds (7, 22, 29–33), there seems to be a preference for small monodentate ligands to give the *cis* isomer, although *trans* compounds are also known. In the present case, a single slightly split ν(Nb—Cl) band near 325 cm^{-1} is more consistent with the *trans* structure (see below), but the stereochemistry cannot be regarded as firmly established.

TABLE 3. Refined coordinates ($\times 10^4$; Nb, Cl $\times 10^5$) and equivalent isotropic temperature factors ($Å^2 \times 10^3$) for (H_2aza-aza)$_2$[$NbOCl_5$]

Atom	x	y	z	U_{eq}
Nb(1)[a]	763(10)	34(6)	3614(5)	39
Cl(2)	14923(16)	−23368(10)	9984(12)	76
Cl(3)	28139(14)	10705(11)	−9139(12)	68
O/Cl[b]	206(2)	391(2)	1891(1)	58
N(11)	1685(4)	1567(3)	5311(3)	49
C(12)	1151(6)	2887(4)	5314(5)	61
C(13)	1658(6)	3942(4)	4084(5)	63
C(14)	3399(6)	3731(4)	1900(4)	59
C(15)	4156(7)	2721(5)	1433(4)	65
C(16)	4116(7)	1285(4)	2260(4)	60
N(17)	3304(4)	772(3)	3577(3)	44
C(18)	2546(5)	1760(3)	4066(3)	41
C(19)	2567(5)	3264(4)	3235(4)	49
N(111)	1766(5)	−3121(4)	7818(4)	62
C(112)	1913(6)	−4586(4)	8248(4)	63
C(113)	2697(6)	−4934(4)	7207(5)	63
C(114)	3737(6)	−3194(4)	4647(5)	62
C(115)	3818(6)	−1748(4)	3817(4)	54
C(116)	3230(5)	−769(3)	4399(3)	43
N(117)	2538(4)	−1112(3)	5709(3)	49
C(118)	2461(5)	−2515(4)	6469(4)	47
C(119)	3055(5)	−3622(4)	6031(4)	51

[a]Occupancy factor = 0.50.
[b]Site statistically occupied by O and Cl atoms.

When $NbCl_5$–Haza mixtures are stirred for 4 days at room temperature or refluxed for a few hours, the suspension turns dark red. The very strong and broad ν(Nb—Cl) absorption of $NbCl_5$(Haza) at ~350 cm^{-1} is observed, but it includes a well-defined shoulder at ~320 cm^{-1} not found for pure $NbCl_5$(Haza). The solid does not contain *oxo* species, since the characteristic bands for ν(Nb═O) at 920 cm^{-1} or ν(Nb—O—Nb) at ~840 cm^{-1} are absent. These data, together with other diagnostic bands, suggest that $NbCl_4(Haza)_2$ is a major component of this mixture. The two complexes cannot be separated because they are insoluble or decompose in common solvents. The extra infrared bands of the solid mixture are assigned to the azaindolium cation by comparison with those of the $(H_2aza)^+$ salts of $[NbCl_6]^-$ (see below), Cl^- and ClO_4^- (21). However, the particular salt present in the mixture cannot be identified.

By analogy with the Nb–pyridine system (2), Nb(V)/Nb(IV) reduction can be assumed to be produced by azaindole, but no clues concerning oxidation products are provided by the infrared spectra. From the X-ray diffraction work done on two compounds obtained in small amounts from the reaction filtrates, an oxidized form of azaindole is found to be the azaindolyl-azaindolium cation shown in Fig. 2. Thus, azaindole undergoes N—C coupling to give a quaternary ammonium cation like pyridine, with the difference that coupling occurs at the γ carbon with pyridine, but at the α position here. In these crystals, the metal is present as the *oxo*-chloro anions $[NbOCl_4(Haza)]^-$ and $[NbOCl_5]^{2-}$, respectively. Since all reactants are devoid of oxygen, the fresh filtrates undoubtedly contain fully chlorinated species and the apparently less soluble oxo compounds are produced by serendipitous introduction of moisture into the Schlenk tube over several weeks.

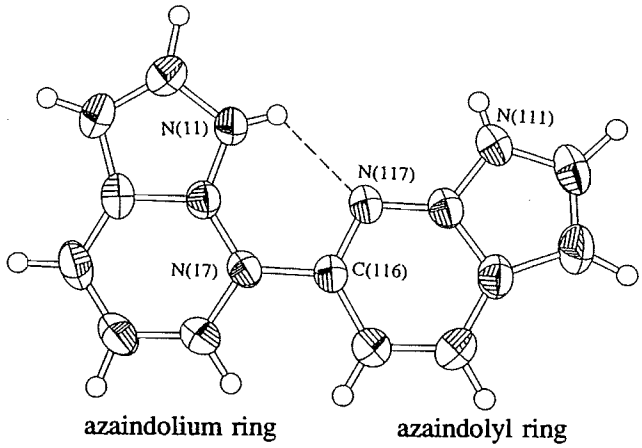

FIG. 2. ORTEP drawing of the $(H_2aza\text{-}aza)^+$ unit in $(H_2aza\text{-}aza)[NbOCl_4(Haza)]\cdot 0.5CH_2Cl_2$. Thermal ellipsoids correspond to 50% probability. Hydrogens are shown as spheres of arbitrary size. The dashed line represents a hydrogen bond.

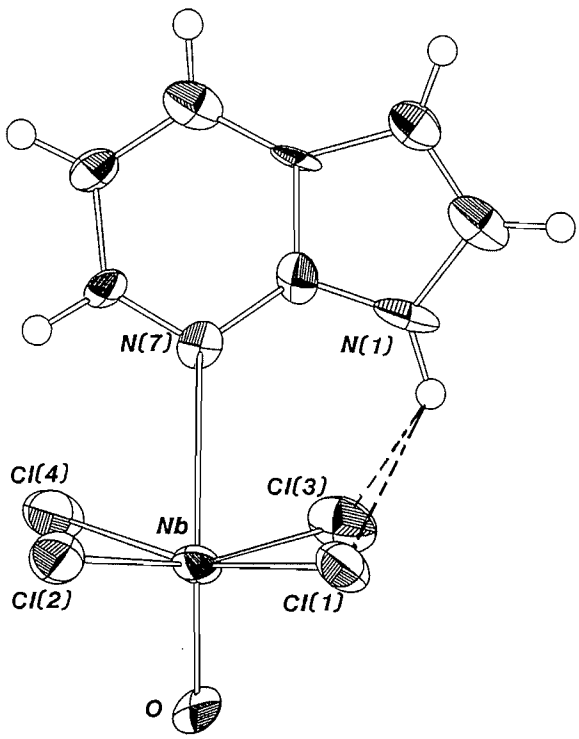

FIG. 3. ORTEP drawing of the $[NbOCl_4(Haza)]^-$ anion. Thermal ellipsoids correspond to 50% probability. Hydrogens are shown as spheres of arbitrary size. Dashed lines represent hydrogen bonds.

Crystal structures of $(H_2aza\text{-}aza)[NbOCl_4(Haza)]\cdot 0.5CH_2Cl_2$ and $(H_2aza\text{-}aza)_2[NbOCl_5]$

Both compounds contain the same $[H_2aza\text{-}aza]^+$ cation (Fig. 2) produced by N7—C6 coupling of two azaindole units. The metal is present as the six-coordinate *oxo*-chloro $[NbOCl_4(Haza)]^-$ (Fig. 3) and $[NbOCl_5]^{2-}$ anions (Fig. 1), respectively.

(a) $[H_2aza\text{-}aza]^+$ cation

The distance and angles observed for the $[NbOCl_5]^{2-}$ salt are compared with those of 7-azaindole in Table 4. The less accurate results from the $[NbOCl_4(Haza)]^-$ compound, provided as supplementary material (Table S-3)[3], are not significantly different. N7—C6 coupling does not appreciably affect bond lengths and angles in the azaindolyl unit, but greater differences are found in the azaindolium ring (14). The bond lengths are increased by ~0.02 Å in the C(16)—N(17)—C(18)—C(19) region, whereas N(11)—C(18) is shortened by the same amount. Also, the angle at N(17) in the six-membered ring increases by 3.0°, those at C(16) and C(18) decrease by 2.3 and 4.3°, respectively, whereas remote angles undergo smaller changes keeping the ring roughly planar: +1.5°, C(19); +2.1°, C(15). Similar changes are produced by protonation in $(H_2aza)_2[ZnCl_4]$ (25), the only structure containing a non-disordered 7-azaindolium ion, and an analogous pattern is observed in purines (34). The C(116)—N(17) distance of 1.456(5) Å is similar to those found in other N—C coupled systems (35, 36).

Each of the two units in $H_2aza\text{-}aza^+$ is approximately planar (Tables S-4 and S-9)[3]. In the $[NbOCl_5]^{2-}$ salt, no significant departure from planarity is noted for the azaindolium unit (mean atom-to-plane distance: 0.003 Å), but some distortion is detected in the azaindolyl ring (mean distance: 0.015 Å, maximum for C(115): 0.026 Å, σ = 0.004 Å). For the $[NbOCl_4(Haza)]^-$ salt, the mean distances calculated are ~0.016 Å for both units, but the standard deviations are greater (~0.015 Å) and the maximum deviation of 0.046 Å (for C(119)) is at the 3σ limit.

The dihedral angles between the two azaindole halves are 6.0(3) and 7(1)° for the $[NbOCl_5]^{2-}$ and $[NbOCl_4(Haza)]^-$ salts, respectively. A perfectly planar conformation would lead to severe steric hindrance, since the H(16)···H(115) separation of 1.95 Å, calculated from idealized hydrogen coordinates, is already below the normal van der Waals distance (2.1 Å). In principle, minimum non-bonded contact should rotate these two units as far apart as possible. The nearly coplanar structure, also approached in the 4-pyridylpyridinium cation (dihedral angle = 16.6°) (35), might be favored by the possibility for the π-electron system to encompass both rings if they are coplanar. More specific to the present case is the presence of a strong intramolecular N(11)—H(11)···N(117) hydrogen bond. This interaction is far from being linear (N—H—N ~115°, Tables S-5 and S-10)[3], but the short N···H distance (~2.07 Å) is highly favorable.

(b) $[NbOCl_4(Haza)]^-$

Crystal structures are known for $NbOCl_3L_2$ adducts with MeCN (37) and hexamethylphosphoramide (HMPA) (38), for $[NbOX_4L]^-$ compounds with L = MeCN (39), O_2PCl_2 (40), H_2O (40, 41), and THF (42), and for $[NbOCl_5]^{2-}$ salts (43–45). As observed in these systems, our equatorial Nb—Cl bonds are displaced away from Nb=O bond, despite the relatively large size of the azaindole ligand *trans* to the oxo group (Fig. 3): the O=Nb—Cl angles range from 94.1 to 99.3° (Table 5) and the Nb atom lies 0.261(2) Å above the plane through the four chlorines (Table S-4)[3]. The Nb=O distance of 1.691(9) Å is in the normal range (1.66–1.77 Å) (46) and consistent with a double bond. The Nb—Cl distances (2.375–2.395 Å, σ = 0.005 Å) compare well with those found for the above oxo compounds and for mutually *trans* Nb—Cl bonds in related species (47, 48). On the other hand, the Nb—N bond (2.534(11) Å) is much longer than those reported for $NbCl_5(NCH)$ (2.31 Å) (49) and $NbCl_5$(1-methylimidazole) (2.23 Å) (4), where the N-donor is *trans* to a chlorine. This is due to the high *trans* influence of the oxo group: in $NbOCl_3(MeCN)_2$ (37) and $NbOCl_3(HMPA)_2$ (38), for instance, the distances for the ligands *trans* to Nb=O

Can. J. Chem. Downloaded from www.nrcresearchpress.com by 85.192.166.187 on 09/08/12
For personal use only.

Can. J. Chem. Downloaded from www.nrcresearchpress.com by 85.192.166.187 on 09/08/12
For personal use only.

TABLE 4. Interatomic distances and bond angles for the $(H_2aza\text{-}aza)^+$ cation in the $[NbOCl_5]^{2-}$ salt

Azaindolyl-azaindolium cation				
Azaindolium ring		Azaindolyl ring		
Atoms	Distance	Atoms	Distance	7-Azaindole[a]
N(11)—C(12)	1.372(6)	N(111)—C(112)	1.372(6)	1.370(5)
N(11)—C(18)	1.341(5)	N(111)—C(118)	1.360(5)	1.361(4)
C(12)—C(13)	1.346(6)	C(112)—C(113)	1.343(6)	1.342(5)
C(13)—C(19)	1.423(6)	C(113)—C(119)	1.429(6)	1.419(5)
C(14)—C(15)	1.368(7)	C(114)—C(115)	1.379(6)	1.377(6)
C(14)—C(19)	1.380(5)	N(114)—C(119)	1.389(6)	1.383(6)
C(15)—C(16)	1.368(6)	C(115)—C(116)	1.385(6)	1.375(5)
C(16)—N(17)	1.359(5)	C(116)—N(117)	1.332(4)	1.337(5)
N(17)—C(18)	1.363(5)	N(117)—C(118)	1.329(5)	1.341(4)
C(18)—C(19)	1.425(5)	C(118)—C(119)	1.402(6)	1.398(5)
N(17)—C(116)	1.456(5)			
Bonds	Angle	Bonds	Angle	Angle
C(12)—N(11)—C(18)	108.6(3)	C(112)—N(111)—C(118)	108.4(4)	107.6(3)
N(11)—C(12)—C(13)	110.7(4)	N(111)—C(112)—C(113)	110.0(4)	110.6(3)
C(12)—C(13)—C(19)	106.7(4)	C(112)—C(113)—C(119)	107.2(4)	106.9(3)
C(15)—C(14)—C(19)	118.2(4)	C(115)—C(114)—C(119)	119.1(4)	117.9(4)
C(14)—C(15)—C(16)	121.5(4)	C(114)—C(115)—C(116)	118.7(4)	119.4(4)
N(17)—C(16)—C(15)	122.5(4)	N(117)—C(116)—C(115)	124.9(3)	124.8(3)
C(16)—N(17)—C(116)	120.6(3)	N(17)—C(116)—C(115)	121.2(3)	
C(18)—N(17)—C(116)	122.4(3)	N(17)—C(116)—N(117)	113.9(3)	
C(16)—N(17)—C(18)	116.9(3)	C(116)—N(117)—C(118)	114.5(3)	113.9(3)
N(11)—C(18)—N(17)	129.8(3)	N(111)—C(118)—N(117)	125.1(4)	125.2(3)
N(11)—C(18)—C(19)	108.2(3)	N(111)—C(118)—C(119)	108.2(3)	108.5(3)
N(17)—C(18)—C(19)	122.0(3)	N(117)—C(118)—C(119)	126.6(4)	126.3(3)
C(13)—C(19)—C(14)	135.3(4)	C(113)—C(119)—C(114)	137.8(4)	136.5(4)
C(13)—C(19)—C(18)	105.9(3)	C(113)—C(119)—C(118)	106.1(4)	106.4(3)
C(14)—C(19)—C(18)	118.8(4)	C(114)—C(119)—C(118)	116.1(4)	117.1(3)

[a]Reference 14. Data for non-disordered tetrameric unit E—H.

are ~0.2 Å longer than for those *trans* to Nb—Cl. A similar effect of the imide group in $[NbCl_4(NBu^t)(py)]^-$ leads to a Nb—pyridine distance of 2.48 Å (50).

The formally neutral 7-azaindole ligands is bonded via N7. The distances and angles in coordinated azaindole (Table 5) show no significant differences with those found in free azaindole and other complexes containing monodentate N7-bonded azaindole (14, 16, 18–20). The ligand two-ring system is planar: the mean atom-to-plane distance (0.012 Å) corresponds to 1σ with the largest deviation (0.023(10) Å) found for N(7) (Table S-4)[3]. The azaindole ring making a ~45° angle with the Cl(2)—Nb(1)—Cl(3) and Cl(1)—Nb(1)—Cl(4) directions, the N(1)—H proton can form a bifurcated intramolecular hydrogen bond with equatorial chlorines, as observed for $ReOCl_3(Haza)_2$ and $ReOCl_3(Haza)(PPh_3)$ (19). The N(1)···Cl(1) and N(1)···Cl(3) separations of 3.19 and 3.32 Å, respectively (Table S-5)[3], are well within the range (2.91–3.52 Å) suggested by Stout and Jensen (51). The 6° difference between the Nb(1)—N(7)—C angles likely results from this interaction.

(c) $[NbOCl_5]^{2-}$

The $[NbOCl_5]^{2-}$ ion (Fig. 1) is disordered over two orientations in the crystal. The atoms in the equatorial plane, namely Cl(2), Cl(3), and their symmetry-equivalent counterparts, are common to both orientations. Of the two symmetry-equivalent axial "O/Cl" sites, one is occupied by chlorine and the other by oxygen in one individual, whereas the distribution is opposite in the other. The difference between the Nb=O and Nb—Cl distances is large enough to produce two resolved half-niobium atoms off the origin. This type of disorder is also present in alkali metal salts (44, 45), but the anion is reported to be ordered in the Ph_4As^+ salt (43).

The metal in $[NbOCl_5]^{2-}$ is considerably displaced (0.386(1) Å) from the plane of the four equatorial chlorines, in the direction of oxygen, leading to O=Nb—Cl angles between 95.0(1) and 103.2(1)°. One equatorial bond (2.501(1) Å) is longer than the other three (2.392–2.422 Å, σ = 0.001 Å) (Table 6), which are similar to those discussed above. The axial Nb—Cl distance is much greater (2.576(2) Å) because of the Nb=O *trans* influence. Our Nb=O distance (1.808(2) Å) seems to be appreciably above the normal 1.66–1.77 Å range (46) and longer than those observed for $[NbOCl_4(Haza)]^-$ (Table 5) and $[NbOF_5]^{2-}$ (1.68 Å) (52). However, this distance should not be regarded as very reliable, since the refined "O/Cl" coordinates probably represent two not exactly coincident positions for O and Cl, and refinement is largely controlled by the more electron-rich Cl atom. In this respect, the very large Nb=O distance of 1.967(6) Å reported for the Ph_4As^+ salt (43) is puzzling. Besides orientation disorder of the $[NbOCl_5]^{2-}$ ion, the possibility of partial substitution by $[NbCl_6]^{2-}$ in this crystal should be checked. Similar cases of abnormal bond lengths, first ascribed to "distortional" isomerism, have recently been shown to originate

TABLE 5. Selected interatomic distances and bond angles in the $[NbOCl_4(Haza)]^-$ ion

Atoms	Distance	Atoms	Distance
Nb(1)—Cl(1)	2.395(5)	C(2)—C(3)	1.37(2)
Nb(1)—Cl(2)	2.388(5)	C(3)—C(9)	1.43(2)
Nb(1)—Cl3)	2.389(5)	C(4)—C(5)	1.39(2)
Nb(1)—Cl(4)	2.375(5)	C(4)—C(9)	1.35(2)
Nb(1)—O(1)	1.691(9)	C(5)—C(6)	1.40(2)
Nb(1)—N(7)	2.534(11)	N(7)—C(6)	1.28(2)
N(1)—C(2)	1.38(2)	N(7)—C(8)	1.38(2)
N(1)—C(8)	1.33(2)	C(8)—C(9)	1.41(2)

Bonds	Angle	Bonds	Angle
Cl(1)—Nb(1)—Cl(2)	87.7(2)	C(2)—N(1)—C(8)	109.0(12)
Cl(1)—Nb(1)—Cl(3)	89.7(2)	N(1)—C(2)—C(3)	109.5(13)
Cl(1)—Nb(1)—Cl(4)	166.6(2)	C(2)—C(3)—C(9)	106.4(13)
Cl(1)—Nb(1)—O(1)	96.4(4)	C(5)—C(4)—C(9)	118.4(14)
Cl(2)—Nb(1)—O(1)	99.3(4)	C(4)—C(5)—C(6)	118.9(14)
Cl(3)—Nb(1)—O(1)	94.1(4)	N(7)—C(6)—C(5)	125.6(13)
Cl(4)—Nb(1)—O(1)	97.0(4)	Nb(1)—N(7)—C(6)	119.8(9)
Cl(1)—Nb(1)—N(7)	84.5(3)	Nb(1)—N(7)—C(8)	125.8(9)
Cl(2)—Nb(1)—Cl(3)	166.6(2)	C(6)—N(7)—C(8)	114.4(12)
Cl(2)—Nb(1)—Cl(4)	90.0(2)	N(1)—C(8)—N(7)	126.2(13)
Cl(2)—Nb(1)—N(7)	82.9(3)	N(1)—C(8)—C(9)	109.0(13)
Cl(3)—Nb(1)—Cl(4)	89.5(2)	N(7)—C(8)—C(9)	124.7(13)
Cl(3)—Nb(1)—N(7)	83.7(3)	C(3)—C(9)—C(4)	136.1(14)
Cl(4)—Nb(1)—N(7)	82.1(3)	C(3)—C(9)—C(8)	106.1(12)
O(1)—Nb(1)—N(7)	177.6(4)	C(4)—C(9)—C(8)	117.8(13)

from substitution of the M=O-containing molecule by an "isostructural" species of the reduced metal center, containing an M—Cl bond at the same place (53).

(d) Molecular packing

In both structures, the $(H_2aza\text{-}aza)^{2+}$ cations form hydrogen bonds with Cl atoms in the anions. Details on these and other intermolecular contacts are discussed in detail in the supplementary material, where stereoviews of the unit cells are provided.

NMR spectroscopy

$NbCl_5(Haza)$ and $TaCl_5(Haza)$ are insoluble or decompose in common solvents. In DMSO, the ligand is quantitatively displaced by solvent molecules, leading to ^1H NMR spectra identical to those of free 7-azaindole (15). Solubility for $NbCl_5(Haza)$ in CH_2Cl_2 is high enough to obtain an interpretable spectrum (experimental section). The signals are assigned as described earlier (15), using the coupling constants to identify H4 and H6. Coordination to N7 results in downfield shifts on most of the protons, as recently found for Re complexes (19). The largest displacements occur for H4 and H5 (+0.54 and +0.39 ppm, respectively), whereas the H_6 proton, close to the coordination site, is barely affected (–0.02 ppm). A broad signal at 11.4 ppm is observed for the N—H proton. These signals definitely originate from the $NbCl_5(Haza)$ species, because fast exchange does not take place between the complex and free azaindole: two sets of peaks are found when azaindole is added to the solution. This also shows that higher-coordinated complexes do not form to any detectable extent under these conditions.

Infrared spectroscopy

A list of frequencies for $(H_2aza)[NbCl_6]$, $NbCl_5(Haza)$, $TaCl_5(Haza)$ and $NbCl_4(Haza)_2$ is provided in Table S-12[3]. Most of the changes already identified for N7-coordination (12, 15, 18) are observed, thereby confirming this binding mode here. As a particularity of the present systems, two medium features of free azaindole at 428 and 419 cm^{-1} are now found at ~440 and 400 cm^{-1}, respectively. The γ(C—H) pattern at 700–800 cm^{-1} can be used to distinguish between the two types of compounds: the strong peaks of Haza at 789/762/715 cm^{-1} are found at ~792/780/720 cm^{-1} for (Nb,Ta)Cl_5(Haza) and 796/779/730 cm^{-1} for $NbCl_4(Haza)_2$. In the ν(N—H) region, the very broad band of free Haza is replaced by two sharp bands of medium intensity at ~3430 and ~3290 cm^{-1} for (Nb,Ta)Cl_5(Haza) and a single sharp band at 3400 cm^{-1} for $NbCl_4(Haza)_2$. The weak γ(N—H) absorption, observed near

TABLE 6. Selected interatomic distances and bond angles in the $[NbOCl_5]^{2-}$ ion

Atoms	Distance	Atoms	Distance
Nb—O/Cl	1.808(2)	Nb—Cl(2)[a]	2.501(1)
Nb—O/Cl[a]	2.576(2)	Nb—Cl(3)	2.414(1)
Nb—Cl(2)	2.392(1)	Nb—Cl(3)[a]	2.422(1)

Bonds	Angle	Bonds	Angle
O/Cl—Nb—Cl(2)	103.2(1)	Cl(2)—Nb—O/Cl[a]	80.4(1)
O/Cl—Nb—Cl(3)	98.2(1)	Cl(2)—Nb—Cl(2)[a]	161.8(1)
O/Cl—Nb—O/Cl[a]	176.4(1)	Cl(2)—Nb—Cl(3)[a]	89.5(1)
O/Cl—Nb—Cl(2)[a]	95.0(1)	Cl(3)—Nb—O/Cl[a]	81.6(1)
O/Cl—Nb—Cl(3)[a]	99.1(1)	Cl(3)—Nb—Cl(2)[a]	87.2(1)
Cl(2)—Nb—Cl(3)	90.9(1)	Cl(3)—Nb—Cl(3)[a]	161.5(1)
Cl(2)[a]—Nb—Cl(3)[a]	87.4(1)		

[a] $-x\ -y\ -z$.

Can. J. Chem. Downloaded from www.nrcresearchpress.com by 85.192.166.187 on 09/08/12
For personal use only.

Can. J. Chem. Downloaded from www.nrcresearchpress.com by 85.192.166.187 on 09/08/12
For personal use only.

850 cm^{-1} in the free ligand, shifts to ~530 cm^{-1} and becomes much stronger in the three complexes.

No ligand vibrations occur in the 250–390 cm^{-1} region, which includes only strong features for metal-centred modes. $NbCl_4(Haza)_2$ exhibits a slightly split band at ~320 cm^{-1} for ν(Nb—Cl). More complex patterns are usually observed for $NbCl_4L_2$ and $TaCl_4L_2$ compounds and since four infrared-active bands are expected for the *cis* isomer (C_{2v}) (54, 55), this geometry has been proposed (22, 30, 31). The presence of a single band here would be consistent with a *trans* structure (D_{4h}), in which case the slight splitting of the only infrared-active E_u mode would be due to solid-state effects. The *trans* structure has been proposed for $NbCl_4L_2$ complexes with various pyridines on the basis of EPR spectra in solution (56) and for crystals of $TaCl_4(py)_2$ (32).

$TaCl_5$(Haza) exhibits a very strong complex band centered at ~330 cm^{-1} and a weaker sharp peak at 372 cm^{-1}. Patterns similar, but displaced by approximately +20 cm^{-1} and –10 cm^{-1} are reported for the analogous systems with nitriles (57, 58) and PPh_3 (59), respectively. The main band of $NbCl_5$(Haza) at ~350 cm^{-1} is very broad and the high-frequency vibration is not resolved, although it is clearly present as a shoulder near 380 cm^{-1}. These results are consistent with a metal–chlorine vibration for a six-coordinate complex (60).

Azaindole protonation in the $[NbCl_6]^-$ salt can be detected from a number of characteristic spectral modification previously noted for the Cl^- and the ClO_4^- salts (21). In the fingerprint region, the azaindole doublet at 428/419 cm^{-1} has moved to 411/397 cm^{-1}. A single infrared-active Nb—Cl stretching mode of symmetry T_{1u} is expected for an octahedral $[NbCl_6]^-$ ion. The very strong band centred at 339 cm^{-1} occurs at the position observed for other salts (22, 57, 61). The presence of several shoulders is likely due to low site symmetry.

Conclusion

Both $TaCl_5$ and $NbCl_5$ form the octahedral MCl_5(Haza) adduct and there is no evidence for higher coordination in these systems. Under vigourous reaction conditions, Nb(V) is reduced, yielding the monomeric $NbCl_4(Haza)_2$ compound probably as the *trans* isomer. Azaindole oxidation leads to the azaindolyl-azaindolium ion, which is found as counter-ion in two complex salts. Efforts are being made to determine if this cation is the only oxidation product and C—N coupling takes place exclusively at the C6 site. The anionic form of this coupled species would be of interest as a binucleating agent providing three donor atoms.

Acknowledgments

We wish to thank M. Simard and F. Bélanger-Gariépy for their assistance in solving the X-ray structures. The financial support of the Natural Sciences and Engineering Research Council of Canada is gratefully acknowledged.

1. L.G. Hubert-Pfalzgraf, M. Postel, and J.G. Riess, Comprehensive coordination chemistry. *Edited by* G. Wilkinson, R.D. Gillard, and J.A. McCleverty. Pergamon Press, New York. 1987. Chap. 34.
2. R.E. McCarley, B.G. Hughes, J.C. Boatman, and B.A. Torp. Adv. Chem. Ser. **37**, 243 (1963).
3. D.L. Kepert. The early transitions metals. Academic Press, London. 1972.
4. B. Therrien. M.Sc. Thesis, Université de Montréal, Montréal, Canada. 1993.
5. G. Levasseur. M.Sc. Thesis, Université de Montréal, Montréal, Canada. 1990.
6. M. Allbut, K. Feenan, and G.W.A. Fowles. J. Less-common Met. **6**, 299 (1964).
7. F.A. Cotton and W.J. Roth. Inorg. Chem. **23**, 945 (1984).
8. F.A. Cotton, M.P. Diebold, and W.J. Roth. Inorg. Chim. Acta, **105**, 41 (1985) and references therein.
9. D.B. Copley, F. Fairbrother, K.H. Grundy, and A. Thompson. J. Less-common Met. **6**, 407 (1964); M.S. Gill, H.S. Ahuja, and G.S. Rao. J. Less-common Met. **21**, 447 (1970).
10. C. Djordjevic and V. Katovic. J. Chem. Soc. A. 3382 (1970).
11. S.M. Peng and Y.N. Lin. Acta Crystallogr. **C42**, 1725 (1986); S.M. Peng and C.H. Lai. J. Chin. Chem. Soc. (Taipei). **35**, 325 (1988).
12. F. Allaire and A.L. Beauchamp. Inorg. Chim. Acta, **156**, 241 (1989).
13. J.J.H. Edema, S. Gambarotta, A. Meetsma, F. Van Bolhuis, A.L. Spek, and W.J.J. Smeets. Inorg. Chem. **29**, 2147 (1990); L.A. Oro, M.A. Ciriano, B.E. Villaroya, A. Tiripicchio, and F.J. Lahoz. J. Chem. Soc. Dalton Trans. 1891 (1985); F.A. Cotton, D.G. Lay, and M. Millar. Inorg. Chem. **17**, 186 (1978).
14. P. Dufour, Y. Dartiguenave, M. Dartiguenave, N. Dufour, A.M. Lebuis, F. Bélanger-Gariépy, and A.L. Beauchamp. Can. J. Chem. **68**, 193 (1990).
15. N. Dufour, A.M. Lebuis, M.C. Corbeil, A.L. Beauchamp, P. Dufour, Y. Dartiguenave, and M. Dartiguenave. Can. J. Chem. **70**, 2914 (1992).
16. F.A. Cotton and T.R. Felthouse. Inorg. Chem. **20**, 600 (1981).
17. F. Allaire. Ph.D. Thesis, Université de Montréal, Canada. 1987.
18. J. Poitras and A.L. Beauchamp. Can. J. Chem. **70**, 2846 (1992).
19. A.M. Lebuis and A.L. Beauchamp. Can. J. Chem. **71**, 2060 (1993); A.M. Lebuis and A.L. Beauchamp. Acta Crystallogr. In press.
20. W.S. Sheldrick. Z. Naturforsch. **37B**, 653 (1982).
21. J. Poitras, M. Leduc, and A.L. Beauchamp. Can. J. Chem. **71**, 549 (1993).
22. W.A. Fowles, D.J. Tidmarsh, and R.A. Walton. Inorg. Chem. **8**, 631 (1969).
23. N. Vuletic and C. Djordjevic. J. Chem. Soc. Dalton Trans. 550 (1973).
24. R.S. Drago. Physical methods in chemistry. Saunders, Philadelphia, U.S.A. 1977. p. 413.
25. G. Sheldrick. SHELX-76, Crystallographic Program System, Cambridge University, U.K. 1976.
26. International tables for X-ray crystallography. Vol. III. Kynoch Press, Birmingham, England. 1968.
27. D.T. Cromer and J.T. Waber. Acta Crystallogr. **18**, 104 (1965); R.F. Stewart, E.R. Davidson, and W.T. Simpson. J. Chem. Phys. **42**, 3175 (1965).
28. D.T. Cromer. Acta Crystallogr. **18**, 17 (1965).
29. F.A. Cotton, S.A. Duraj, and W.J. Roth. Inorg. Chem. **23**, 3592 (1984); **23**, 4046 (1984).
30. G.W.A. Fowles, D.J. Tidmarsh, and R.A. Walton. J. Inorg. Nucl. Chem. **31**, 2373 (1969).
31. J.B. Hamilton and R.E. McCarley. Inorg. Chem. **9**, 1333 (1970).
32. G.J. Miller, J. Lin, and V. Young Jr. Acta Crystallogr. **C49**, 1770 (1993).
33. A.J. Benton, M.G.B. Drew, R.J. Hobson, and D.A. Rice. J. Chem. Soc. Dalton Trans. 1304 (1981).
34. R. Taylor and O. Kennard. J. Mol. Struct. **78**, 1 (1982).
35. J. Lipkowski, P. Sgarabotto, and J.D. Andreetti. Cryst. Struct. Comm. **5**, 931 (1976).
36. A.J. Canty, C.V. Lee, N. Chaichit, and B. Gatehouse. Acta Crystallogr. **B38**, 743 (1982).
37. C. Chavant, J.C. Daran, Y. Jeannin, G. Constant, and R. Morancho. Acta Crystallogr. **B31**, 1828 (1975).
38. L.G. Hubert-Pfalzgraf and A.A. Pinkerton. Inorg. Chem. **16**, 1895 (1977).
39. W. Hiller, J. Strähle, H. Prinz, and K. Dehnicke. Z. Naturforsch. **39B**, 107 (1984).

40. P. Klingelhöfer and U. Müller. Z. Anorg. Allgem. Chem. **516**, 85 (1984).
41. H.N. Schäfer, H. Burzlaff, A.M.H. Grimmeiss, and R. Weiss. Acta Crystallogr. **C47**, 1808 (1991).
42. H.C. Aspinall, M.M. Roberts, and S.J. Lippard. Inorg. Chem. **23**, 1782 (1984).
43. U. Müller and I. Lorenz. Z. Anorg. Allgem. Chem. **463**, 110 (1980).
44. D. Brown. J. Chem. Soc. 4944 (1964).
45. M. Weishaupt and J. Strähle. Z. Anorg. Allgem. Chem. **429**, 261 (1977).
46. W.A. Nugent and J.M. Mayer. Metal–ligand multiple bonds. Wiley, New York. 1988. p. 163.
47. B. Therrien and A.L. Beauchamp. Acta Crystallogr. **C49**, 1303 (1993).
48. F.A. Cotton, M.P. Diebold, and W.J. Roth. Acta Crystallogr. **C46**, 1624 (1990).
49. C. Chavant, G. Constant, Y. Jeannin, and R. Morancho. Acta Crystallogr. **B31**, 1823 (1975).
50. W. Clegg, R.J. Errington, D.C.R. Hockless, and C. Redshaw. Polyhedron, **10**, 1959 (1991).
51. G.H. Stout and L.H. Jensen. X-ray structure determination, a practical guide. Macmillan, London. 1968.
52. E.M. Shustorovich, M.A. Porai-Koshits, and Yu. A. Buslaev. Coord. Chem. Rev. **17**, 32 (1975).
53. K. Yoon, G. Parkin, and A.L. Rheingold. J. Am. Chem. Soc. **114**, 2210 (1992).
54. R.J.H. Clark. Spectrochim. Acta, **21**, 955 (1965).
55. K. Nakamoto. Infrared and Raman spectra of inorganic and coordination compounds. 4th ed. Wiley-Interscience, NY. 1986.
56. D.P. Johnson, J. Wilinski, and R.D. Bereman. J. Inorg. Nucl. Chem. **35**, 2365 (1973).
57. J. Maccordick and G. Kaufmann. J. Mol. Struct. **6**, 305 (1970).
58. G.A. Ozin and R.A. Walton. J. Chem. Soc. A, 2236 (1970).
59. G. Jamieson and W.E. Lindsell. Inorg. Chim. Acta, **28**, 113 (1978).
60. A.R. Roy and A. Thompson. J. Less Comm. Met. **61**, 1 (1978).
61. I.R. Beattie, T.R. Gilson, and G.A. Ozin. J. Chem. Soc. A, **11**, 2765 (1968).

Can. J. Chem. Downloaded from www.nrcresearchpress.com by 85.192.166.187 on 09/08/12
For personal use only.

Acid-catalysed transformation of oleic acid, and 12-hydroxystearic acid, into γ-octadecanolactone. Evidence for the occurrence of a novel side reaction

ALESSANDRO GRANATA, FRANÇOISE SAURIOL, AND ARTHUR S. PERLIN[1]
Department of Chemistry, McGill University, Montreal, QC H3A 2A7, Canada

Received December 2, 1993

ALESSANDRO GRANATA, FRANÇOISE SAURIOL, and ARTHUR S. PERLIN. Can. J. Chem. **72**, 1684 (1994).

γ-Octadecanolactone is produced in the reaction between oleic acid (*cis*-9-octadecenoic acid) and concentrated sulfuric acid at 80°C. To account for its formation, two types of mechanism have been considered. Both begin with protonation at C-9/C-10 to give a carbocation, following which the positive charge is transmitted to C-4, where nucleophilic attack by the carboxyl group is facilitated. One of them invokes a "zipperlike" succession of 1,2-shifts of intervening methylenic protons, whereas the other amounts to a stepwise migration of the alkene function along the carbon chain. Results obtained through the use of deuterated sulfuric acid to catalyse formation of the lactone allow for the existence of both types. However, each is characteristic of a different region of the C_{18} structure. Of the total isotope incorporated (individual molecules contained from zero to nine atoms of deuterium), >85% had been distributed relatively uniformly over the chain segment from C-7 to C-17, according to ^2H nuclear magnetic resonance spectra recorded in the presence of the shift reagent Yb(fod)$_3$, and ^{13}C nuclear magnetic resonance data. This evidence is consistent with the occurrence of a side reaction that creates many protonation sites over that specific region of the lactone's precursors. By contrast, as very little of the isotope had reached the proximity of the lactone ring, the latter is more likely to have been formed via the 1,2 shift type of mechanism. These events can also be initiated at other sites, as shown by the preparation of γ-octadecanolactone, and a comparably deuterated form of it, from 12-hydroxystearic acid. Reactions of these three stearic acid derivatives with HI, HBr, and HCl are described, by way of comparison.

ALESSANDRO GRANATA, FRANÇOISE SAURIOL et ARTHUR S. PERLIN. Can. J. Chem. **72**, 1684 (1994).

La γ-octadécanolacone se forme lors de la réaction de l'acide oléique (*cis*-octadéc-9-ènoïque) avec de l'acide sulfurique concentré, à 80°C. Pour expliquer cette formation, on a envisagé deux mécanismes. Les deux débutent par la protonation de la double liaison C-9/C-10 conduisant à un carbocation qui est suivie par une transmission de la charge positive vers le C-4 où une attaque nucléophile par le groupe carboxyle est facilitée. Un des mécanismes fait appel à une succession de déplacements-1,2 d'hydrure, à la manière d'une fermeture éclair, impliquant les protons des méthylènes alors que l'autre correspond à une migration par étape de la fonction alcène le long de la chaîne carbonée. Les résultats obtenus lorsqu'on a utilisé de l'acide sulfurique deutéré comme catalyseur peuvent être accommodés par les deux mécanismes. Toutefois, chacun est caractéristique d'une région différente de la structure en C_{18}. De la quantité totale d'isotope incorporé (les molecules individuelles contenaient de zéro à neuf atomes de deutérium), les spectres en résonance magnétique nucléaire du ^2H enregistrés en présence de réactif à déplacement Yb(fod)$_3$ et les données de la résonance magnétique nucléaire du ^{13}C indiquent que plus de 85% est distribué d'une façon uniforme sur le segment de chaîne allant de C-7 à C-17. Ces données sont en accord avec la présence d'une réaction secondaire qui crée plusieurs sites de protonation dans cette région spécifique des précurseurs de la lactone. Par ailleurs, comme très peu d'isotope arrive à proximité du cycle lactonique, ce dernier est probablement plus facilement formé par le biais d'un mécanisme impliquant des déplacements-1,2. Ces événements peuvent aussi être initiés à d'autres sites, comme on l'a démontré par la préparation de la γ-octadécanolactone ainsi qu'une de ses formes deutérée de la même maniére, à partir de l'acide 12-hydroxystéarique. Pour fins de comparaison, on décrit les réactions de ces trois dérivés de l'acide stéarique avec le HI, le HBr et le HCl.
[Traduit par la rédaction]

Introduction

In 1924, Clutterbuck (1) reported the isolation of γ-octadecanolactone (**1**) in 30% yield by heating oleic acid (*cis*-9-octadecenoic acid (**2**)) in concentrated sulfuric acid and water at 80°C for 6 h. We repeated that preparation, to use the lactone in studies to be mentioned presently, and verified its identity by contemporary methods. That compound **1** contains a five-membered ring was confirmed by the presence in its EI-mass spectrum of a base peak at *m/z* 85 ($C_4H_5O_2^+$), as well as by diagnostic evidence from a ^1H-COSY spectrum that the methine-proton signal located furthest downfield (δ 4.4) is that of H-4.

A distinctive chemical characteristic of lactone **1** in comparison with its shorter-chain γ-(or δ)-*n*-alkanolactone homologs, is its relative inertness in reactions with hydrogen halides (2, 3). For example, in 48% HBr under reflux, **1** undergoes ring opening to give a 30% yield of one product, the 4-bromoacid, whereas, by contrast, δ-dodecanolactone affords in 75% yield a mixture of 4-, 5-, 6-, 7-, 8-, 9-, 10-, and 11-bromododecanoic acids; and γ-octanolactone gives a mixture of 4-, 5-, 6-, and 7-bromooctanoic acids in 65% yield. Analogous results are found in reactions with 57% HI. Most striking is the fact (2) that the longest monohaloalkanoic acid (C_{18}) formed from among the series of lactones examined ($C_{18} \rightarrow C_6$) is the least susceptible to the migration of a halogen atom introduced initially by ring opening at C-4.

Carbocationic and olefinic intermediates likely (2, 3) play a key role in these isomerizations and rearrangements, whereby the formation of each mixture of haloacids involves a progression of the center of positive charge along the carbon chain, in the direction *away from* the carboxyl group. However, in the conversion of oleic acid into lactone **1**, the carbocation formed initially by protonation at either C-9 or C-10 must migrate in the opposite direction, i.e., *towards* the carboxyl group. These two types of substitution reactions, both of which are examined here, could have some common intermediates but, otherwise, are controlled by different circumstances: one, favoring ring opening of the lactone followed by the introduction of halogen substituents along the alkanoic acid chain, and the other, the

[1]Author to whom correspondence may be addressed.

Can. J. Chem. Downloaded from www.nrcresearchpress.com by EESC ESCOLA DE ENGENHARIA on 09/08/12
For personal use only.

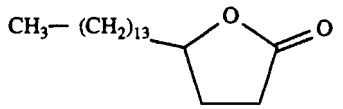

1

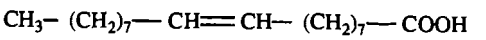

2

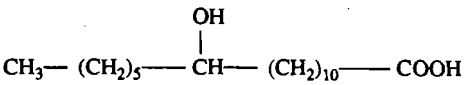

3

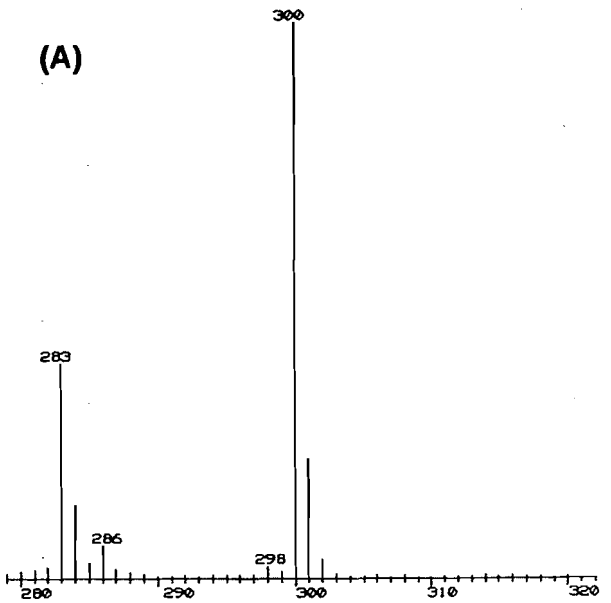

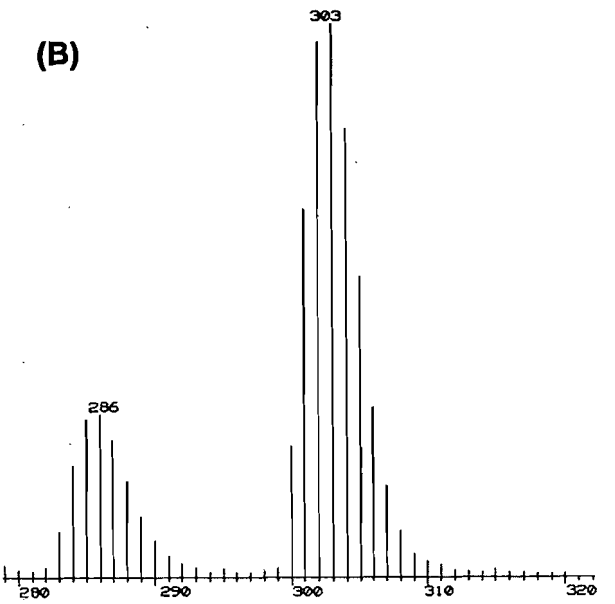

FIG. 1. High-mass region of the chemically induced (CI) mass spectrum (NH_3 induction) of (A) γ-octadecanolactone, and (B) deuterated γ-octadecanolactone, produced in the reaction of oleic acid with H_2SO_4 and $^2H_2SO_4$, respectively.

closure of a γ-lactone ring at the expense of the acid-labile alkene structure.

Results and discussion

The formation of γ-octadecanolactone from 12-hydroxystearic acid

Lactone **1** was also prepared by initiating its formation at a carbon atom beyond the C-9 or C-10 location on a C_{18} acid skeleton. Hence, the reaction of 12-hydroxystearic acid (**3**) with sulfuric acid under the same conditions as used with oleic acid gave **1** in 23% yield. This would be analogous to the use of a Δ^{11}- or a Δ^{12}-*n*-octadecenoic acid in place of oleic acid (although these variants were not tested). Therefore, it appears that a cationic charge generated in these reactions can be conducted with facility across sequences of at least eight methylene/methine groups (C-11 to C-4), until the interaction between a positive carbon atom and the carboxyl oxygen atom leads to closure of the lactone bridge. Although an earlier interaction at such centres as C-6 (ε-lactone) or C-5 (δ-lactone) also seems plausible, rearrangement to the more stable γ form should follow.

Reaction of oleic and 12-hydroxystearic acid with $^2H_2SO_4$

As already noted, the initial step in the formation of lactone **1** from oleic acid is assumed to be protonation of the Δ^9-alkene structure, with the formation of a carbocation intermediate. Subsequent steps, among possibilities to be discussed later, could include regeneration of the alkene repeatedly at new positions, Δ^8, Δ^7, etc., to allow for the eventual closure of the lactone bridge at C-4. Or, alternatively, the initial protonation could be simply followed by a succession of 1,2-hydride shifts, whereby the positive charge is transferred ultimately to the γ position. In the latter pathway, the proton is required only for initiation, whereas in the other type of sequence protons could be introduced anywhere between C-10 and C-4. Possibilities such as these were examined by the use of deuterosulfuric acid ($^2H_2SO_4$).

Isotopically labelled specimens of lactone **1** were prepared, and information about the level of incorporation of deuterium and its distribution within the molecule was obtained by mass spectrometry and nmr spectroscopy. A comparison of the chemical-ionization (CI) mass spectra of **1** and its deuterated analog showed that the latter consisted of a mixture of at least eight different compounds. As seen in the region of the molecular ion (Fig. 1A; NH_3 was the reagent gas), the peaks at *m/z* 283 and 300 correspond to MH^+ and MNH_4^+. The deuterated sample is represented in this region (Fig. 1B) by corresponding peaks that range from *m/z* 284 to 292 and from *m/z* 301 to 310. Most prominent among the latter group are the components that contain either two or three atoms of deuterium, i.e., of *m/z* 302 and 303, each representing about 20% of the total, whereas the 6% of unlabelled molecules of **1** represent a small content of hydrogen atoms in the medium (the incorporation of which should have been favored by the isotope effect).

Can. J. Chem. Downloaded from www.nrcresearchpress.com by EESC ESCOLA DE ENGENHARIA on 09/08/12
For personal use only.

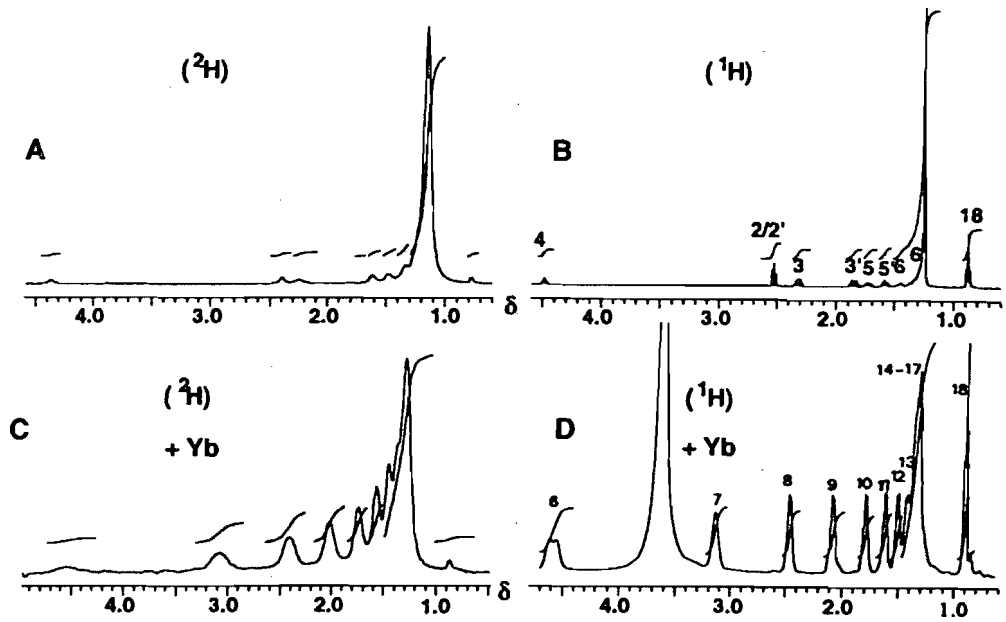

FIG. 2. The 76.7 MHz ^2H nmr spectra, and 500 MHz ^1H nmr spectra of deuterated γ-octadecanolactone: (A) the ^2H spectrum (solvent, $CHCl_3$); (B) the ^1H spectrum (solvent, C^2HCl_3); (C) and (D) the partial ^2H spectrum and the ^1H spectrum, respectively, following the introduction of $Yb(fod)_3$ (temp, 50°C). The ^1H assignments in (B) and (D) are based on COSY experiments.

The foregoing describes a reaction with $^2H_2SO_4$ for a 6 h period. However, samples of deuterated **1** recovered from reactions of 3 h and 20 h duration gave ms data differing by only a few percent from those in Fig. 1. Analogous experiments conducted with 12-hydroxystearic acid afforded lactone samples having similar isotopic compositions.

Patterns of ^2H-labelling within lactone 1-^2H

As to the location of the ^2H atoms within the lactone samples, it was readily apparent from EI mass spectra that little isotope had been introduced on the carbon atoms of the ring. That is, whereas both **1** and its deuterated analogs gave ion *m/z* 85 as the base peak (due to the ring moiety: $C_4H_5O_2^+$), the relative intensity of the *m/z* 86 peak, present as a minor component in all spectra, was only marginally higher in the spectra of the labelled species.

This was confirmed, and additional information obtained, from ^2H nmr spectra. Figure 2A represents the lactone recovered from a 20 h reaction with $^2H_2SO_4$. Using assignments based on the ^1H nmr spectrum (Fig. 2B), it is clear that a total of only ~10% of the isotope is accounted for by the minor signals associated with nuclei on the ring at C-2, -3, and -4, as well as at C-5, -6, and -18. The great majority of isotope is located in other methylene groups represented by the strong band at δ 1.2. Noteworthy is the evidence for stereoselective labelling, in that there is no ^2H resonance corresponding to signal ^1H-3 (δ 1.85 in Fig. 2B). It also appears likely, based on the relatively uniform intensities of the minor ^2H signals, that only one of the overlapping ^1H-2 signals in Fig. 2B has a ^2H-2 counterpart in Fig. 2A, and hence that a stereoselective replacement on C-2 had also occurred. Worth mentioning as well is the fact that a 3 h reaction with $^2H_2SO_4$ introduced less isotope into the minor sites represented in Fig. 2A, this being true especially of the methyl group, which produced only a barely detectable signal at δ 0.8. Hence, some isotope may be incorporated merely by prolonged treatment, and is unrelated to the formation of the lactone. As a "control," stearic acid was found to incorporate only a trace of ^2H, approximately one half of the isotope at C-2 according to ^2H nmr. (In striking contrast to this is the facile preparation of fully deuterated stearic acid (4) through isotopic exchange catalysed by Pt.)

The use of a shift reagent (5) was very helpful in the identification of the other sites of deuteration. Highly effective was Yb $(fod)_3$ (6) (the widely used Eu compound was far less so), which allowed for an extension of the range of individual ^1H and ^2H signals detectable, from those of the nuclei on C-6 (Figs. 2A and 2B) to those on C-13. The partial ^1H spectrum in Fig. 2D covers this region in which signal separation has become greatly enhanced; the methylene signal designations shown were obtained from a COSY experiment. Not included are the resonances for protons 2—5, already displayed in spectrum 2B, which were now shifted downfield over the region δ 22.0 (H-4) to δ 5.4 (H-5b). As a point of reference in the corresponding section of the ^2H spectrum (Fig. 2C), the ^2H-6 peak is observed at δ 4.6, in contrast to the value of δ 1.3 for the uncomplexed lactone (Fig. 2A), and it is far weaker than any of the peaks upfield of it (aside from that of the methyl group). From the appearance of the signals between δ 2.5 and 1.0, it is clear that the isotope had *not* been localized in a small number of sites, such as C-9/10, but was dispersed in a moderately uniform pattern over all carbon atoms from C-7 to, perhaps, C-17. This latter possibility seemed reasonable, because the integral for the major peak centered at δ 1.2 is sufficiently large to accommodate several ^2H signals comparable in size to those of the individual signals for the group ^2H-8 to ^2H-12. In fact, the inclusion of C-16 and C-17 was confirmed by ^{13}C data, presented below.

The ^1H nmr spectra of the deuterated lactone (Figs. 2B and 2D) differ in only minor respects from those of the unlabelled compound (not shown), because the ^2H atoms are so broadly distributed and are so greatly outnumbered by the protons remaining. More noticeable changes are observed in the ^{13}C nmr spectrum of the lactone (Fig. 3A) following the incorporation of the isotope (Fig. 3B). Most of the ^{13}C assignments are based on ^{13}C–^1H resonance correlations (HMQC) (7). Although

Can. J. Chem. Downloaded from www.nrcresearchpress.com by EESC ESCOLA DE ENGENHARIA on 09/08/12
For personal use only.

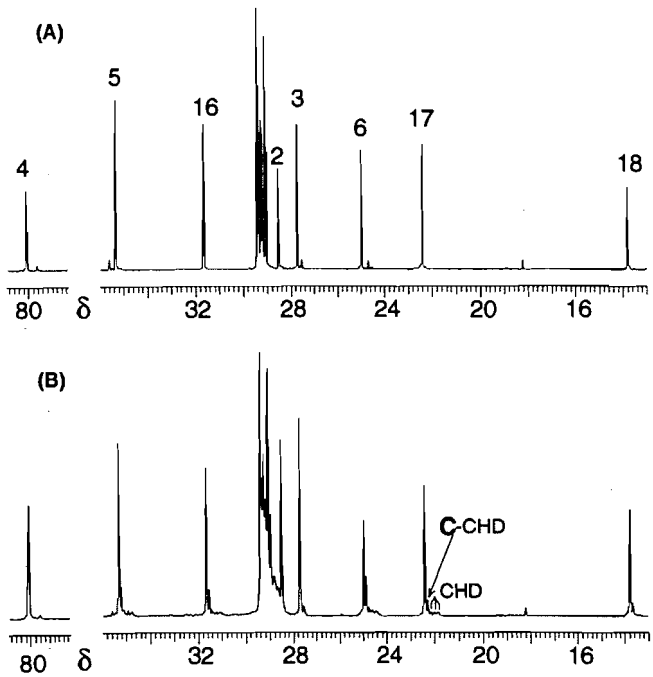

FIG. 3. The 125 MHz ^{13}C nmr spectra of (A) γ-octadecanolactone, and (B) deuterated γ-octadecanolactone. Representative of the signals in (B) is that of C-17, where *C*-CHD designates the portion of the signal affected by a β ^{2}H-isotope shift, and *C*HD the portion affected by an α ^{2}H-isotope shift (see text). The ^{13}CO signal appeared at δ 176.9. Based on HMBC experiments (see text), C-7 resonated at δ 29.1, and C-8 at δ 29.3.

the chemical shifts of the 7- and 8-protons were not available directly (see Fig. 2B), identification of the ^{13}C-7 and -8 signals in Fig. 3A was feasible through application of the HMBC sequence (8), which correlated H-5 and H-6 with the more distant C-7 and C-8 nuclei through their small $^{2}J_{CH}$ and $^{3}J_{CH}$ couplings.

Many of the signals in Fig. 3A have more complex counterparts in Fig. 3B, which is attributable in the latter to upfield displacements caused by the presence of ^{2}H atoms that are attached directly (α) to some carbons, and (or) to adjacent (β) carbons. Several of the signals have three components, as illustrated for the C-17 resonance in the vicinity of δ 22: a singlet at its normal position (no isotope shift), a small, broad, peak (^{13}C-CHD, due to a β-isotope shift), and a small triplet (^{13}C HD, due to an α-isotope shift). Hence, the presence of the triplet at δ 31.1 confirms that C-16 was also deuterated, whereas the fact that the C-18 signal exhibits only a β-isotope shift (due to the ^{2}H atom on C-17) confirms that the methyl group was not labelled. Analogously, other nondeuterated carbons (no triplet signal component) are C-1 (δ 176.9; not shown), C-2 (δ 28.6), C-3 (δ 27.8), and C-4 (δ 80.7), in agreement with the ^{2}H nmr data (Fig. 2A, wherein the corresponding signals are weak, but detectable). The complex pattern of signals observed between δ 29.6 and 28.6 in Fig. 3B, which accounts for the resonances of carbons 7–15, reflects both α and β ^{2}H-isotope shifts as well as related ^{13}C–^{2}H coupling.

Possible reaction pathways

Overall, these spectra show that although the deuterium is surely introduced initially at C-9/10 of oleic acid, almost all of the isotope incorporated into lactone **1** becomes scrambled broadly along the carbon chain from positions 7 to 17. According to the ms data, individual molecules of the lactone preparations may have from one to nine or ten of these specific positions labelled, although most contain 2–3 atoms of deuterium.

Two types of reaction mechanism have already been mentioned. One offers a possible way of accounting for the very broad distribution of ^{2}H atoms. It is based on the assumption that the alkene group of oleic acid (or that of the product of dehydration of 12-hydroxystearic acid) undergoes a succession of rearrangements that are followed by deuteration at each new site. For example, the incorporation of a deuteron at C-9, followed by rearrangement of the π bond in the direction of the methyl terminus, allows for the entry of a second ^{2}H atom at C-10 (**4**→**5**→**7**→**8**). (Repeated formation and decomposition of alkyl hydrogen sulfate intermediates could also give rise to alkenes that are positional isomers (**4** → **5** → **6** → **7**)). Some molecules then acquire a third atom of the isotope (at C-11) following a second rearrangement and, ultimately, deuteration extending to C-16 and C-17 would be found.

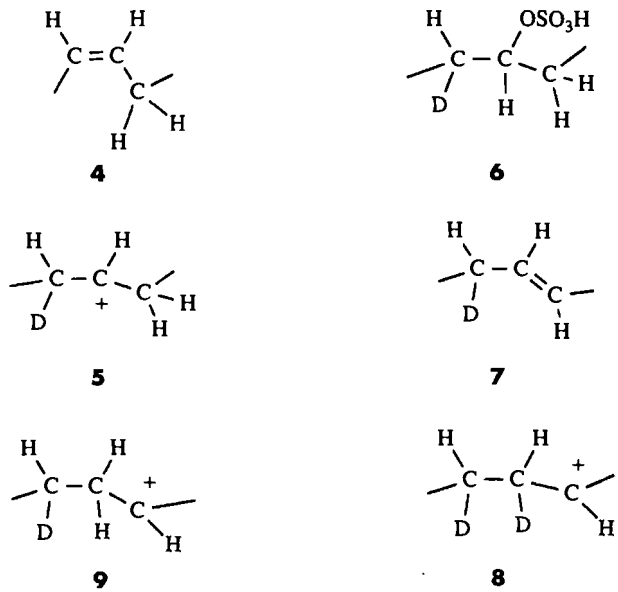

Operation of an analogous sequence in the direction of the carboxyl terminus is assumed to account for the ample presence of ^{2}H on C-8 and C-7 (Fig. 2C). These contributions to the total number of doubly and triply labelled species would make them, as observed, the most populous overall. However, as suggested by the progressive decrease in the levels of deuteration observed for C-7, C-6, C-5, etc., the alkene rearrangement is a "side reaction," rather than a process engaged in the formation of the lactone ring.

For the latter purpose, a different mechanism is proposed, i.e., a succession of 1,2-hydride shifts (**5** → **9**) along the bridge of methylene groups between C-9 and C-4 (for oleic acid), or between C-12 and C-4 (for 12-hydroxystearic acid). The term "zipper mechanism" may be a useful description for such a pathway, by analogy with the term "acetylene zipper" (9, 10) that characterizes extensive multipositional rearrangements of alkynes.

We assume that the "zipper" functions independently of the side reaction, although both share intermediates of the same type (e.g., **5**), and also that the side reaction is dependent upon it for the dissipation of cationic charges that are created (as in **8**) in the protonation (deuteration) step. Accordingly, the progress of

Can. J. Chem. Downloaded from www.nrcresearchpress.com by EESC ESCOLA DE ENGENHARIA on 09/08/12
For personal use only.

TABLE 1. ^{13}C Chemical shifts of products from reactions of γ-octadecanolactone, oleic acid, and 12-hydroxystearic acid with hydrogen halides

Reaction	^{13}C Chemical shift (δ) of methine ^{13}C of monobromoacid substituted at position							
	4	5	6	7	8	9	10	11
48% HBr with								
δ-dodecanolactone[a]	56.8	57.5	58.1	58.4	58.5	58.6	60.5	51.9
γ-octadecanolactone	56.9							
oleic acid						58.79,	58.84	
12-hydroxystearic acid							58.74	
	^{13}C Chemical shift (δ) of carboxyl group of monoiodo acid substituted at position							
	4	5	6	7	8	9	10	11
57% HI with								
δ-dodecanolactone[a]	179.50	179.98	180.19	180.40	180.50	180.55	180.60 – 180.62	
γ-octadecanolactone	179.00,	179.64						
oleic acid			(180.36,	180.45,	180.52,	180.55,	180.60)[b]	
12-hydroxystearic acid							180.55	

[a]Data from ref 2.
[b]In a ratio (from left to right) of approx. 1:3:4:5:5.

the side reaction along the carbon chain is terminated at various sites en route by operation of the zipper to transfer the positive charge to C-4, where the overall transformation is completed. (If the side reaction itself, through reversal, were to serve this purpose, higher levels of deuteration should be found than are observed.) Ultimately, the longest segment of the alkyl chain over which the zipper mechanism is presumed to function is that linking C-4 with C-17.

It is worth noting that, without the isotopic evidence, there would have been no reason to anticipate that the transformation of oleic acid into γ-octadecanolactone is accompanied by a side reaction that penetrates so deeply into the sequence of (ostensibly inert) methylene groups between C-10 and C-18. Deuteration was used specifically to scan the chain segment between C-9 and C-4 but, in fact, it provided evidence that nearly every other carbon in the molecule is affected in some manner. Also, the evidence that the methyl group was not appreciably labelled is consistent, according to Markovnikov's rule, with the proposal that an ionic type of mechanism is involved. For the same reason, and the absence of appreciable deuteration at C-2 to C-4, free-radical pathways appear to be less likely.

Increasing the level of deuteration of lactone ***1***

The amount of isotope incorporated into the lactone may be raised by using a higher $^2H_2SO_4$/oleic acid ratio, although at the expense of the formation of lactone: its yield was reduced by two thirds when a 1.5-fold increase in $^2H_2SO_4$ was employed. In the CI mass spectrum of the product, the molecular-ion region contained bell-shaped clusters of peaks similar in appearance to those in Fig. 1B. However, the most prominent ions in this instance were *m/z* 290, 291 (MH^+) and *m/z* 307, 308 (MNH_4^+), respectively, corresponding to molecules containing 7 and 8 atoms of ^2H, and among the lesser species were molecules containing up to 13 atoms of ^2H.

Despite this substantial increase overall, the C-7 to C-17 portion of the alkyl chain again accounted for the great majority of the isotope. In the ^2H nmr spectrum, for example, about 80% of the isotope was represented by the major peak centered at δ 1.2, which, according to the corresponding spectrum in Fig. 2A, comprises the resonances of ^2H atoms on carbons 7–17. The ^{13}C spectrum of the product, when compared to that in Fig. 3B, showed clearly that the use of extra $^2H_2SO_4$ had enhanced the degree of ^1H–^2H exchange on some carbons that previously had been relatively lightly deuterated, i.e., carbons 5, 6, 17, and 17, whereas it had made far less of an impact on the others, i.e., carbons 2, 3, 4, and 18.

Consequently, these observations reinforce the evidence that the side reaction is promoted along the carbon chain primarily in the direction of the methyl terminus, and hence the suggestion that it is probably incidental to the formation of the lactone. Also, the fact that, even under forcing conditions, the methyl group itself (as well as C-2, etc.) undergoes little isotopic exchange supports the proposal that the latter process involves carbocationic, rather than radical, intermediates.

Reactions with hydrogen halides

In contrast to the foregoing examples, in which positive charge appears to be transferred across long sections of the C_{18} *n*-alkanoic acid chain, is the exceptional resistance of lactone **1** towards the formation of higher-numbered haloacids in reactions with hydrogen halides. As already noted (2), 48% HBr was found to produce only the 4-bromo isomer (also, see Table 1), and it appears that in 57% hydriodic acid, a second isomer (likely the 5-isomer, see Table 1) is formed in low yield, which is in marked contrast to the fact that shorter chain lactone analogs give an abundance of isomeric mixtures in the carbocation-mediated reactions. As one possibility, we have suggested (2) that isomerization occurs least readily with **1** because its alkyl chain is the least effectively solvated within the series in the aqueous hydrogen halide medium.

Although this may be a contributing factor, it has now been found that in the reaction generated by a hydrogen halide at positions more remote than C-4 or C-5 from the carboxyl end of the C_{18} chain there is little tendency again for isomeric halides

Can. J. Chem. Downloaded from www.nrcresearchpress.com by EESC ESCOLA DE ENGENHARIA on 09/08/12
For personal use only.

Can. J. Chem. Downloaded from www.nrcresearchpress.com by EESC ESCOLA DE ENGENHARIA on 09/08/12
For personal use only.

to be produced. Evidence of this was provided by the reactions of oleic and 12-hydroxystearic acids in 48% HBr under reflux, whereby the olefin gave a 1:1 mixture of two products (90% yield), and the latter acid only one product. Most probably, the products were a mixture of the 9- and 10-bromoacids, and the 12-bromoacid, respectively, on the basis of their ^{13}C nmr spectra. As shown by data (2) for the methine ^{13}C (Br) nuclei of an array of monobromo acids, represented in Table 1 by those for a mixture of bromododecanoic acids, there is a progressive increase (and eventually a discontinuity) in chemical shift as the number of the carbon atom increases. Accordingly, the value of δ 56.9 for the product that was obtained from lactone **1** indicates bromination at C-4, whereas downfield shifts of δ 58.8–58.7 are equally consistent with the likelihood that oleic acid simply gives a mixture of the 9- and 10-bromides, and (less definitive) that 12-hydroxystearic acid yields the 12-bromide.

Reactions of the three octadecanoic acid derivatives (**1**, **2**, and **5**) in 57% HI under reflux exhibited similar characteristics. In this instance, ^{13}C signals of the carboxyl groups of the products (Table 1) were more informative, because not only do they exhibit characteristic variations, but the alternative, methinyl $^{13}C(I)$, resonances generally overlap upfield those of some methylene ^{13}C signals. Lactone **1**, as already noted, afforded an 80% yield of two iodoacids, and 12-hydroxystearic acid a quantitative yield of only one. The relatively downfield location of the latter's carboxyl signal is consistent with substitution at a high carbon number, and hence with the likelihood that the product was simply 12-iodostearic acid (it was *not* stearic acid, the reduction product). By comparison, the smaller chemical shifts of the products from **1** show that the iodine atoms were much closer to the carboxyl group, i.e., likely at C-4 and C-5.

There was a total of five $^{13}COOH$ signals in spectra of the products obtained in close to quantitative yield from the reaction of oleic acid with HI. Of those, by comparison with data for iododododecanoic acids (Table 1), the two major signals had chemical shifts commensurate with iodination at the feasible positions furthest from the carboxyl group, i.e., at C-9 and C-10, whereas the progressive decrease in chemical shift for the other three isomers suggests that they are the 8-, 7-, and 6-iodoacids, respectively. This reaction is noteworthy in that it is the only one of the six reactions compared here in which appreciable isomerization occurs.

An additional comment about the reactions of 12-hydroxystearic acid is merited. Although only one bromo, and one iodo, acid was isolated, the transient occurrence of at least one other product was detected in short-term (1–6 h) reaction mixtures, and it was more prominent with HBr. As the possibility of self-association seemed likely, and with the knowledge (2) that HCl is far less reactive towards alkanolactones, 12-hydroxystearic acid was heated under reflux with 37% HCl for 18 h. As expected, the product proved not to be a chloroacid, but a neutral, higher molecular weight species. Its FAB mass spectrum contained a peak at *m/z* 565, which is consistent with a dimeric structure (M, 564), and the relative simplicity of its ^{13}C spectrum suggested that the material isolated consisted mainly of the symmetrical diolide (**10**) (for other preparations of diolides see, e.g., ref. 11).

One conclusion to be drawn from these observations is how markedly the reaction of oleic acid in HBr (or HI) differs from that in H_2SO_4. One would expect both reactions to have an initiation step in common, i.e., protonation at C-9/C-10 to generate a carbocation. Yet the formation of lactone **1** is the tangible outcome in H_2SO_4, whereas the same compound cannot occur even as an intermediate in HBr, because it should then give rise (2) to the 4-bromide, rather than to the mixture of 9- and 10-bromides found. Presumably there is a facile transfer of positive charges from C-9 to C-4 (as well as from C-9 to C-17) in one instance, but little or no migration of the charge in the other. That is, the reactions of oleic and 12-hydroxystearic acids with hydrogen halides are confined largely to the locus of the initial attack by the reagents. Such stability seems analogous to that of γ-octadecanolactone because, in marked contrast (2, 3) to short-chain lactones, it fails to yield a mixture of isomeric haloacids. Perhaps, as suggested previously (2), the longer chain alkane derivatives are less likely to be reactive in the *aqueous* hydrogen halide media because they are relatively poorly solvated.

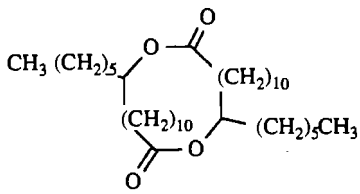

10

Experimental

Nuclear magnetic resonance spectra were recorded with a Varian Unity 500 spectrometer operating at 500 MHz for ^1H, 76.7 MHz for ^2H, and at 125 MHz for ^{13}C. The probe temperature was 23 ± 1°C, the solvent was $CDCl_3$, sample concentrations were approximately 100 mg/mL, and chemical shifts are given with respect to TMS. In the ^{13}C experiments, the digital resolution was 1 Hz. Mass spectra were recorded with a double focusing Kratos MS25RFA mass spectrometer. Chemical ionization mass spectra were obtained with ammonia as the ionizing reagent. Hydriodic acid (57%, <0.01% stabilizer) was obtained from ACP chemicals. Deuterosulfuric acid (98%; 99% atoms ^2H) and hydrobromic acid (48%) were obtained from Aldrich Chemical Co., as were shift reagents $Yb(fod)_3$ and $Eu(fod)_3$. DL-12-Hydroxystearic acid was obtained from Eastman Chemicals.

γ-*Octadecanolactone* (*1*) (γ-*stearic lactone*)

(*a*) Following the procedure of Clutterbuck (1), concentrated H_2SO_4 (3.8 mL) was mixed, dropwise, with oleic acid (14.0 g), accompanied by vigorous stirring and external cooling at 0°C. The dark brown reaction mixture was then heated with stirring at 80–85°C for 6 h, water (22 mL) was introduced, and the bath temperature was raised to 115–120°C for 30 min. At room temperature, ether (250 mL) and water (200 mL) were added to the dark solid product; the ether layer was separated, washed successively with 1 M NaOH (2 × 50 mL) and saturated NaCl (2 × 50 mL), dried over anhydrous $MgSO_4$, and concentrated. A greyish solid was obtained; yield, (20%); mp 45–47°C (lit. (1) mp 52–53°C); ir (film, cm^{-1}); 1751 (C=O), 1195; ^1H nmr data are given in Fig. 2 and ^{13}C nmr data in Fig. 3. EI mass spectrum *m/z*: 282 [M], 85 (100%). CI mass spectrum (NH_3 induction) *m/z*: 300 [M + 18] (100%), 283 [M + 1], 272 [M + 18 – CO], 267, 255 [M + 1 – CO], 244, 239, 227.

(*b*) Under the same reaction conditions as in (*a*), (±)-12-hydroxystearic acid (1.5 g) was also converted into crystalline lactone **1**; yield 0.33 g (23%); identity confirmed by EI and CI mass spectroscopy and by ^1H and ^{13}C nmr spectroscopy.

Preparation of deuterated γ-*octadecanolactone*

Several preparations of deuterated lactone were obtained by the use of concentrated (98%) $^2H_2SO_4$ in place of concentrated H_2SO_4, under reaction conditions comparable to those described in (*a*). In addition to the reaction time noted there, periods of 3 h and 18 h were also selected, and, in the subsequent dilution of the reaction mixture, the introduction of ^2H_2O vs. H_2O was compared in separate runs. An

experiment was conducted as well with DL-12-hydroxystearic acid, using an initial reaction period of 6 h and ^2H_2O as the diluent. In each instance a crystalline specimen of deuterated lactone was isolated. When compared by EI and CI mass spectroscopy as well as by ^1H, ^2H, and ^{13}C nmr spectroscopy, the samples were found to differ little in their content and distribution of the isotope. Representative data are contained in Figs. 1–3.

Reactions of oleic and 12-hydroxystearic acid with hydrogen halides

Representative are the following (the reactions were not protected against light or oxygen):

Reaction of oleic acid with HI

A solution of oleic acid (0.60 g) in HI (57%, 5 mL) containing a suspension of red phosphorus (0.15 g) was heated under reflux for 18 h, and then cooled to room temperature. Saturated aqueous NaCl (5 mL) was added, followed by dichloromethane (50 mL), and the mixture was decolorized with concentrated sodium thiosulfate solution during the extraction. The organic layer was separated, washed with sodium chloride solution (2 × 5 mL), dried over anhydrous magnesium sulfate, and concentrated. A yellow oil was obtained, 0.85 g (97% yield), that according to ^1H and ^{13}C nmr spectra (see Table 1) consisted of a mixture of five monoiodooctadecanoic acids.

Reaction of 12-hydroxystearic acid with HBr

A solution of 12-hydroxystearic acid (0.63 g) in HBr (48%, 5 mL) was heated under reflux for 18 h. The reaction mixture was worked up as above, with omission of the washing with thiosulfate. A yellow oil was obtained, 0.67 g (90%), that according to ^1H and ^{13}C nmr spectra (see Table 1) consisted almost entirely of 12-bromostearic (12-bromooctodecanoic) acid.

Reaction of 12-hydroxystearic acid with HCl

A solution of 12-hydroxystearic acid (0.63 g) in HCl (ca. 37%, 5 mL) was heated under reflux for 18 h, followed by work-up as above. A brown oil was recovered, 0.50 g (83% yield), that according to its ^{13}C nmr spectrum consisted mainly of one component that, likely, was a macrocyclic dimer (diolide); ^1H nmr, δ: 5.0 (H-C_{12}-O); ^{13}C nmr, δ: 173.69 (C═O), 74.02 (C_{12}—O), 34.64, 34.09, 31.60, 29.63, 29.60, 29.13, 25.30, 25.20, 25.15, 22.50, 13.99; FAB mass spectrum *m/z*: 565 [M + 1] (structure **10** requires M 564), 547, 283, 265 (100%).

Acknowledgements

We express our thanks to the Natural Sciences and Engineering Research Council of Canada for valuable support.

1. P.W. Clutterbuck. J. Chem. Soc. 2330 (1924).
2. A. Granata and A.S. Perlin. Can. J. Chem. **71**, 864 (1993).
3. Z. Liu, A. Granata, X. Shen, and A.S. Perlin. Can. J. Chem. **70**, 2081 (1992).
4. D.N. Nguyen, A. Raal, and E. Stenhagen. Chem. Scr. **2**, 171 (1972).
5. C.C. Hinkley. J. Am. Chem. Soc. **91**, 5160 (1969).
6. R.E. Rondeau and R.E. Sievers. Anal. Chem. **45**, 2145 (1983).
7. L. Muller. J. Am. Chem. Soc. **101**, 4481 (1979).
8. A. Bax and M.F. Summers. J. Am. Chem. Soc. **108**, 2093 (1986).
9. C.A. Brown and A. Yamashita. J. Am. Chem. Soc. **97**, 891 (1975).
10. S.R. Abrams. Can. J. Chem. **62**, 1333 (1984).
11. T. Mukaiyama, J. Izumi, M. Miyashita, and I. Shiina. Chem. Lett. 907 (1993).

Can. J. Chem. Downloaded from www.nrcresearchpress.com by EESC ESCOLA DE ENGENHARIA on 09/08/12
For personal use only.

Kinetics of electroreduction of Zn^{2+} at mercury in nonaqueous solutions

MARILÉA MANZINI AND ANDRZEJ LASIA[1]

Département de chimie, Université de Sherbrooke, Sherbrooke, QC J1K 2R1, Canada

Received August 23, 1993

MARILÉA MANZINI and ANDRZEJ LASIA. Can. J. Chem. **72**, 1691 (1994).

The electroreduction of Zn^{2+} was studied in propylene carbonate (PC), acetonitrile (ACN), and hexamethylphosphoramide (HMPA) on mercury at various concentrations of tetraethylammonium perchlorate as a supporting electrolyte using dc polarography, cyclic voltammetry, chronoamperometry, and ac polarography. It was found that in PC and ACN the electroreduction process proceeds in one step. In HMPA, however, the electroreduction proceeds through a CEE mechanism in which a chemical reaction is followed by a charge transfer in two steps. The heterogeneous rate constants, corrected for the double layer effects, decrease with increase in the solvent donor number. The electroreduction process proceeds through the cation transfer mechanism.

MARILÉA MANZINI et ANDRZEJ LASIA. Can. J. Chem. **72**, 1691 (1994).

L'électroréduction du Zn^{2+} a été étudié dans le carbonate de propylene (PC), l'acétonitrile (ACN) et l'hexaméthylphosphoramide (HMPA) sur une électrode de mercure en présence de concentrations différentes de perchlorate de tétraethylammonium en utilisant la polarographie classique, la voltampérométrie cyclique, la chronoamperométrie et la polarographie ac. Notre étude a demontré que dans le PC et l'ACN l'électroréduction procède en une étape. Dans le HMPA la réduction procède par le mécanisme CEE dans lequel la réaction chimique est suivie par deux transferts de charge distincts. Les constantes de vitesse hétérogènes, corrigées pour les effets de la double couche électrique, diminuent avec le nombre donneur de solvant. L'électroréduction procède par le mécanisme de transfert de cation.

[Traduit par la rédaction]

Introduction

The electroreduction of Zn^{2+} at a mercury electrode has been studied in aqueous (1–13), nonaqueous (14–20), and mixed solutions (21–25). In non-complexing media this reaction can be described as:

[1] $$Zn^{2+} + 2e^- + Hg \leftrightarrow Zn(Hg)$$

Two different mechanisms have been suggested to explain Zn^{2+} electroreduction in aqueous solutions. Several authors (5, 6, 8, 9, 12, 13) proposed a simple two-electron transfer mechanism in one step. Others (1–4, 7) proposed two successive electron transfer reactions. In the latter mechanism Zn^+ has to appear as an intermediate. Until now, this intermediate species has never been observed in aqueous solutions.

The behaviour of the $Zn^{2+}/Zn(Hg)$ system in nonaqueous solvents (14–19) was also explained by the two abovementioned mechanisms (17, 19, 20, 22–25). Recently, it was proposed (14, 15) that zinc electroreduction in DMF and DMSO can be explained by assuming a successive charge transfer in two steps (15). This charge transfer mechanism can be represented not only as a subsequent electron transfer but as an ion transfer through the double layer.

[2] $$Zn^{2+}{}_{dl} + e^- \leftrightarrow Zn^{+}{}_{dl}$$

[3] $$Zn^{+}{}_{dl} + e^- \leftrightarrow Zn(Hg)$$

In this case, the transfer of the first electron should be slower than that of the "subsequent electron" because the reorganization energy around the intermediate ion of lower charge requires less electrostatic work (26). In this mechanism the species Zn^+ and Zn^{2+} must be present in the double layer and the position of the reaction site does not change with respect to the interface in the overall process.

In another mechanism (15, 27–30) the slow process is a cation transfer through the double layer in two steps:

[4] $$Zn^{2+}{}_c \leftrightarrow Zn^{2+}{}_b$$

[5] $$Zn^{2+}{}_b \leftrightarrow Zn^{2+}{}_a$$

[6] $$Zn^{2+}{}_a + 2e^- \leftrightarrow Zn(Hg)$$

where the site c is located in the diffuse layer, close to the outer Helmholtz plane (o.H.p.), site b in the inner layer, and site a is an adsorption site at the interface.

Reactions [4] and [5] involve an ion transfer from one site in the double layer to another, without an electron transfer. This case represents a cation transfer mechanism. The transfer coefficient, α, depends on the relative positions of sites a, b, and c in the double layer (15, 27, 31).

In the present paper Zn^{2+} electroreduction at a mercury electrode in propylene carbonate, PC, acetonitrile, ACN, and hexamethylphosphoramide, HMPA, was studied over a wide range of potentials. Double layer and solvent effects were studied in order to better understand the electroreduction process (27–31).

Experimental

$Zn(ClO_4)_2 \cdot 6H_2O$ (Alfa) was dried for 24 h at 140°C in vacuo over P_2O_5. $Zn(CF_3SO_3)_2$ was prepared from stoichiometric quantities of zinc oxide (BDH) and trifluoromethanesulfonic acid (Aldrich). It was dried in the same way as $Zn(ClO_4)_2 \cdot 6H_2O$. The former salt was used in propylene carbonate and HMPA and the latter in acetonitrile. Zn^{2+} concentration was 0.8 mM in propylene carbonate (PC) and acetonitrile (ACN) and 3.0 mM in hexamethylphosphoramide (HMPA).

Tetraethylammonium perchlorate (TEAP) was prepared using tetraethylammonium bromide (Aldrich) and perchloric acid (70% ACS). The salt obtained was recrystallized from deionized water and dried for 48 h at 70°C in vacuo over P_2O_5. Purification of PC (Anachemia), ACN (Anachemia), and HMPA (Aldrich) is described elsewhere (34). The solvents were stored in a dry box. Because of its instability HMPA was distilled just before the experiment. The water content, determined by the Karl–Fischer method, was 0.017% in PC, 0.013% in ACN, and 0.02% in HMPA. The results obtained in ACN were very sensitive to traces of water, and voltammetric and ac polarographic measurements in this solvent were carried out in a dry box.

[1]Author to whom correspondence may be addressed.

Can. J. Chem. Downloaded from www.nrcresearchpress.com by EESC ESCOLA DE ENGENHARIA on 09/08/12
For personal use only.

Can. J. Chem. Downloaded from www.nrcresearchpress.com by EESC ESCOLA DE ENGENHARIA on 09/08/12
For personal use only.

A three-electrode cell was used during the experiments. The reference electrode was a silver wire in 0.05 M Ag^+ ($AgClO_4$ in PC and $AgNO_3$ in ACN and HMPA) + 0.1 M TEAP in the same solvent. A dropping mercury electrode was used as a working electrode in polarographic measurements. Chronoamperometric and voltammetric experiments were performed using a static mercury drop electrode, EG&G PAR model 303, radius 0.03 cm. All the potentials are given with respect to the reference redox system bis-biphenylchromium(I) tetraphenylborate/bis-biphenylchromium(0) ($BBCr^+/BBCr$) (32). The diffusion coefficient of zinc in mercury was taken as 1.4×10^{-5} cm^2 s^{-1} (33).

All the experiments were conducted at 25 ± 1°C. Dry ultrapure nitrogen presaturated with a solvent was bubbled through the solution to remove oxygen; during the measurements nitrogen flow was maintained over the solution surface.

The reversible half-wave, $E^r_{1/2}$, and the apparent standard, E^0, potentials were determined in PC and HMPA solutions from equilibrium potential, E_{eq}, measurements using the Nernst equation (35):

$$[7] \qquad E_{eq} = E^{0\prime} + \frac{RT}{2F} \ln \frac{[Zn^{2+}]}{[Zn(Hg)]}$$

and

$$[8] \qquad E^{0\prime} = E^r_{1/2} - \frac{RT}{nF} \ln \frac{D_r^{1/2}}{D_{ox}^{1/2}}$$

where R is the gas constant, T is the temperature, n is the number of electrons, F is the Faraday constant, $[Zn^{+2}]$ and [Zn(Hg)] are the concentrations of Zn^{2+} in the solution and Zn amalgam, and D_r and D_{ox} are the diffusion coefficients of the reduced and oxidized forms. Zinc amalgam was prepared by reducing Zn^{2+} on the static mercury drop electrode. The potentials were measured after stabilization.

Kinetic parameters were determined using dc polarography (in PC and HMPA), ac polarography (in ACN), cyclic voltammetry (all solvents), and chronoamperometry (in PC and ACN). The apparatus and data analysis used were described in previous papers (15, 36, 37).

Results and discussion

Polarography

PC and ACN

The electroreduction of Zn^{2+} at a mercury electrode in PC and ACN solutions with TEAP as a supporting electrolyte results in a single well-defined dc polarographic wave. The slopes of the logarithmic plots for Zn^{2+} electroreduction change from 52 to 73 mV in PC and from 34 to 67 mV in ACN as the TEAP concentration increases from 0.1 to 0.9 M. This behaviour suggests a quasi-reversible nature of the process in these solvents.

Figure 1 shows the dependence of the diffusion coefficients for Zn^{2+} on TEAP concentration in PC and ACN. The decrease in the diffusion coefficient, D_{ox}, with increasing ionic strength of the inert salt can be associated with the increase in the viscosity of the solutions (15, 34, 36). D_{ox} values for the pure solvents were determined from extrapolation to zero ionic strength. These values are 1.4×10^{-6} cm^2 s^{-1} and 1.14×10^{-5} cm^2 s^{-1} for PC and ACN, respectively.

HMPA

The electroreduction of Zn^{2+} at the mercury electrode in HMPA solutions results in a single ill-defined polarographic wave as shown in Fig. 2. The limiting current observed is much lower than that in other solvents. Subsequently, the Zn^{2+} concentration was increased to 3 mM because the polarographic waves were note well developed at lower concentrations.

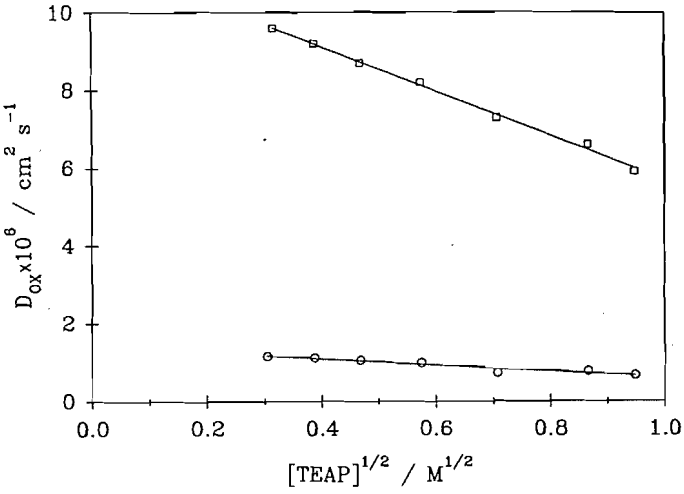

FIG. 1. Dependence of the Zn^{2+} diffusion coefficients on the TEAP concentration in (○) PC and (□) ACN solutions.

Another problem was the determination of the diffusion coefficient in this solvent. The value obtained from the polarographic measurements, Fig. 2, was 5.0×10^{-8} cm^2 s^{-1}. It is too low, compared with the one obtained by extrapolation of D_{ox} vs. inverse of the solvent viscosity, η^{-1} (9.0×10^{-7} cm^2 s^{-1}). When 10% of water was added to HMPA solutions, Fig. 3, the limiting current observed led to a diffusion coefficient of 5.6×10^{-7} cm^2 s^{-1}. Comparison of the diffusion coefficients of Cd(II) and Eu(III) (38, 39) determined in HMPA and HMPA + 10% H_2O solutions shows that addition of 10% of water does not affect their values. We concluded from this behaviour that the substantial decrease in the limiting current is caused by a chemical reaction preceding the electrochemical process. We therefore used the value determined in the presence of 10% of water in further analysis.

Kinetics of electroreduction

PC and ACN

The kinetic parameters, i.e., standard rate constants, k_s, and transfer coefficients, α, determined in PC and ACN solutions, are shown in Tables 1–3. They were obtained from voltammetric, chronoamperometric, and ac polarographic experiments. In ACN the voltammetric and ac polarographic experiments were obtained in a dry box because they were strongly affected by traces of humidity; however, the chronoamperometric measurements were carried out outside the dry box.

The rate constants determined decrease with increase in the supporting electrolyte concentration, and there is a small decrease in the value of the transfer coefficients. Results presented in Tables 2 and 3 confirm the influence of humidity on the kinetics in ACN; when the experiments were conducted in a dry box the rate constants measured were higher. In fact, studies performed in mixed solvents (40, 41) indicate that the rate constants decrease and pass through a minimum when water is added to the organic solvent.

The charge distribution in the double layer changes with change in the supporting electrolyte concentration. These changes affect the potential, ϕ_2, at the outer Helmholtz plane, o.H.p. The double layer effects can be taken into account using the Frumkin correction (42):

$$[9] \qquad \ln k_f = \ln k_{s,a} + (\alpha_a n - z) f \phi_2 - \alpha_a n f (E - E^{0\prime})$$

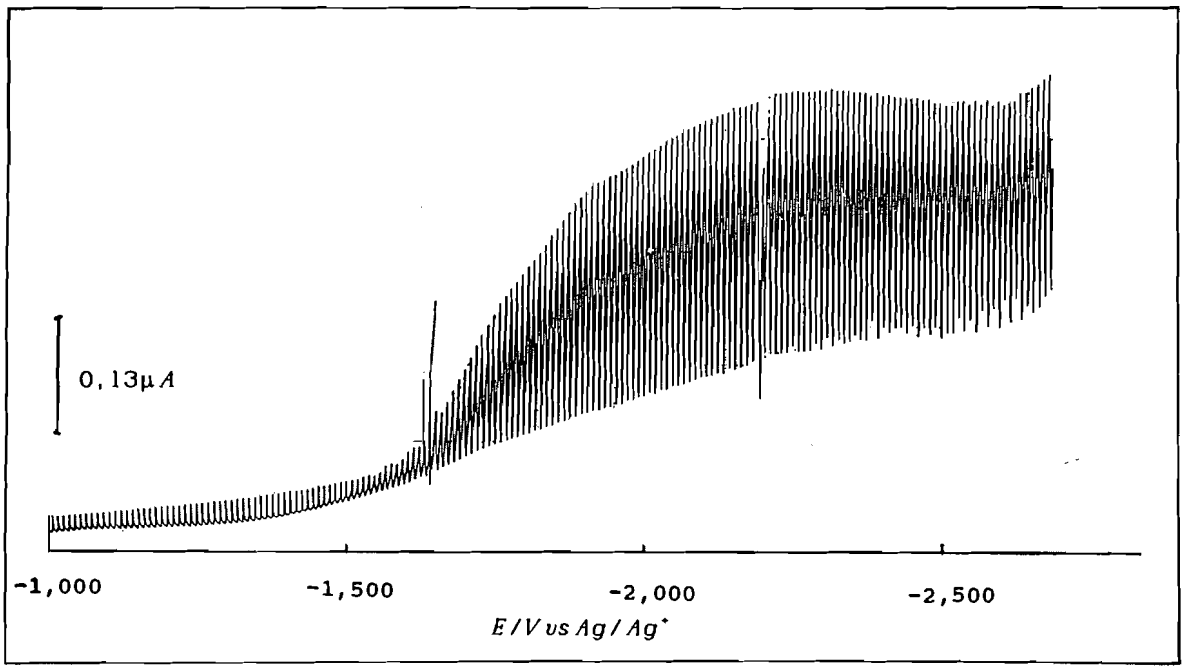

FIG. 2. Polarogram of Zn^{2+} electroreduction in pure HMPA solution; $[Zn^{2+}] = 3.0$ mM, [TEAP] = 0.1 M, $v = 5$ mV/s.

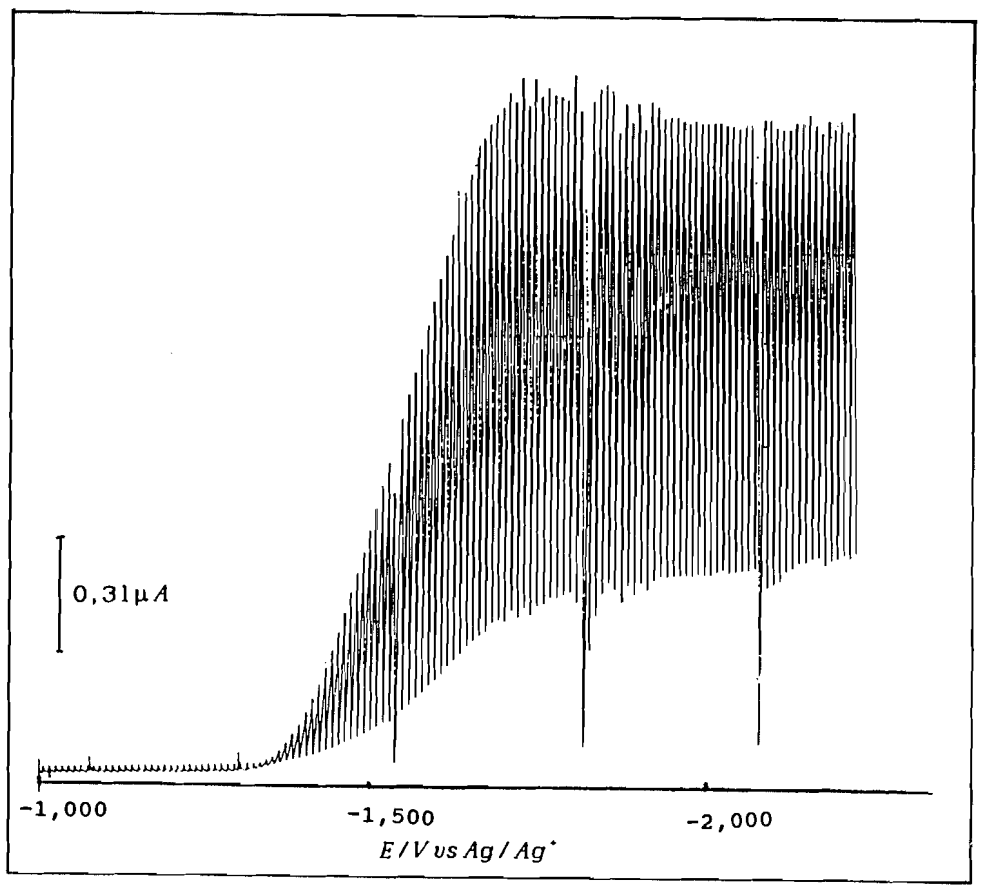

FIG. 3. Polarogram of Zn^{2+} electroreduction in HMPA + 10% H_2O; $[Zn^{2+}] = 3.0$ mM, [TEAP] = 0.1 M, $v = 5$ mV/s.

Can. J. Chem. Downloaded from www.nrcresearchpress.com by EESC ESCOLA DE ENGENHARIA on 09/08/12
For personal use only.

TABLE 1. Results of the kinetics analysis of Zn^{2+} electroreduction from the voltammetric and chronoamperometric curves in PC solutions; $[Zn^{2+}] = 0.8$ mM, $T = 25 \pm 1°C$

	Voltammetric		Chronoamperometric	
[TEAP], M	$10^4 k_s$, cm s^{-1}	α	$10^4 k_s$, cm s^{-1}	α
0.093	4.46	0.40	4.37	0.40
0.150	3.81	0.42	2.75	0.42
0.220	1.73	0.42	1.42	0.40
0.330	2.21	0.33	1.78	0.30
0.500	3.17	0.29	1.05	0.32
0.750	2.05	0.31	1.47	0.28
0.900	1.38	0.29	0.97	0.28

TABLE 2. Results of the kinetics analysis of the Zn^{2+} electroreduction from the voltammetric and chronoamperometric curves in ACN solutions; $[Zn^{2+}] = 0.8$ mM, $T = 25 \pm 1°C$; voltammetric measurements were carried out in a dry box

	Voltammetric		Chronoamperometric	
[TEAP], M	$10^2 k_s$, cm s^{-1}	α	$10^2 k_s$, cm s^{-1}	α
0.10	2.17	0.40	1.51	0.23
0.15	2.34	0.37	2.92	0.22
0.22	1.19	0.33	0.46	0.32
0.33	1.18	0.29	0.49	0.24
0.50	0.68	0.32	0.37	0.29
0.75	0.60	0.23	0.30	0.22
0.90	0.50	0.22	0.38	0.21

TABLE 3. Results of the kinetics analysis of Zn^{2+} electroreduction from ac polarographic measurements in ACN solutions; $[Zn^{2+}] = 0.8$ mM, $T = 25 \pm 1°C$; measurements carried out in a dry box

[TEAP], M	$10^2 k_s$, cm s^{-1}	α
0.10	2.04	0.34
0.15	1.13	0.36
0.22	0.65	0.32

and

$$[10] \qquad \ln k_s = \ln k_{s,a} + (\alpha_a n - z) f \phi_2$$

where $k_{s,a}$ is the standard rate constant corrected for the double layer effects, α_a is the apparent transfer coefficient, z is the ion charge, and $f = F/RT$.

Figures 4 and 5 show examples of the corrected rate constants as functions of the potential in PC and ACN solutions. These curves were obtained from voltammetric data. The ϕ_2 values in PC solutions are very small and they are not significantly affected by the increase in the supporting electrolyte concentration; they change only between -11 and -3 mV. This behaviour is connected with the fact that the reduction potentials of Zn^{2+} in PC are close to the potential of zero charge. However, in ACN, where the reduction potential is much more negative than the potential of zero charge, ϕ_2 decreases from -70 to -32 mV as the supporting electrolyte concentration increases from 0.1 M to 0.9 M. The ϕ_2 values were obtained from double layer studies carried out earlier in this laboratory

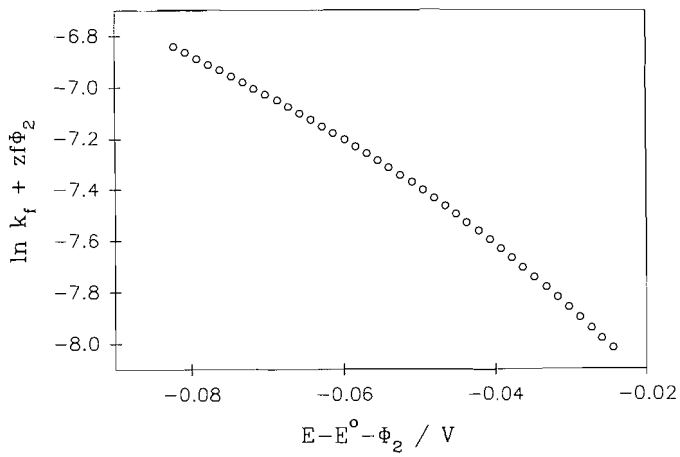

FIG. 4. Dependence of the corrected rate constants on potential for the $Zn^{2+}/Zn(Hg)$ system in PC; $[Zn^{2+}] = 0.8$ mM, [TEAP] = 0.1 M.

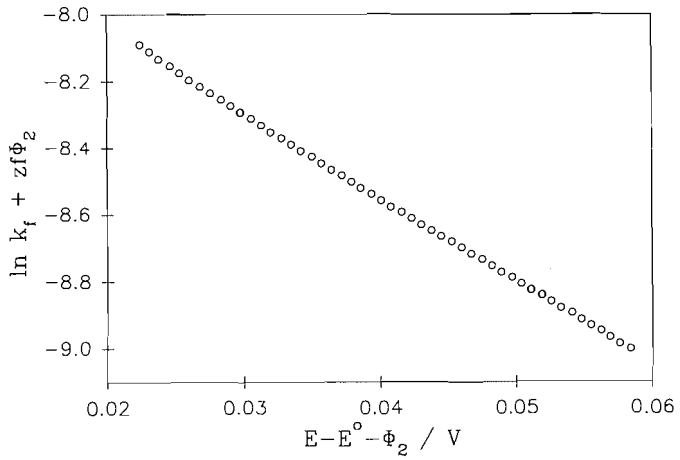

FIG. 5. Dependence of the corrected rate constants on potential for the $Zn^{2+}/Zn(Hg)$ system in ACN; $[Zn^{2+}] = 0.8$ mM, [TEAP] = 0.1 M.

TABLE 4. Kinetic parameters of Zn^{2+} electroreduction corrected for double layer effects obtained from the voltammetric and chronoamperometric experiments in PC; $[Zn^{2+}] = 0.8$ mM, $T = 25 \pm 1°C$

	Voltammetric		Chronoamperometric	
[TEAP], M	$10^4 k_{s,a}$, cm s^{-1}	α_a	$10^4 k_{s,a}$, cm s^{-1}	α_a
0.093	2.22	0.26	1.87	0.25
0.150	2.28	0.31	2.57	0.24
0.220	1.10	0.31	0.85	0.31
0.330	1.67	0.25	1.26	0.22
0.500	2.23	0.28	0.76	0.26
0.750	1.38	0.26	1.07	0.22
0.900	0.74	0.24	0.53	0.23

(35). The corrected kinetic parameters are displayed in Tables 4 and 5. It is evident that the transfer coefficients measured in PC and corrected for double layer effects are independent of the supporting electrolyte concentration, although some dependence exists in ACN. Such a dependence was earlier found for Cd^{2+} electroreduction (36, 37). The corrected rate constants in PC, after elimination of the two smallest values from voltam-

Can. J. Chem. Downloaded from www.nrcresearchpress.com by EESC ESCOLA DE ENGENHARIA on 09/08/12
For personal use only.

Can. J. Chem. Downloaded from www.nrcresearchpress.com by EESC ESCOLA DE ENGENHARIA on 09/08/12
For personal use only.

TABLE 5. Kinetic parameters of Zn^{2+} electroreduction, corrected for double layer effects, from the voltammetric experiments in ACN; $[Zn^{2+}] = 0.8$ mM, $T = 25 \pm 1$°C

[TEAP], M	$10^4 k_{s,a}$, cm s^{-1}	α_a
0.10	5.27	0.32
0.15	5.42	0.29
0.22	5.34	0.28
0.33	6.49	0.22
0.50	6.70	0.26
0.75	6.78	0.18
0.90	6.66	0.16

TABLE 6. Kinetic parameters obtained by the approximation of the cyclic voltammograms of Zn^{2+} in PC solutions, assuming a simple charge transfer in one step; $[Zn^{2+}] = 0.8$ mM, $T = 25 \pm 1$°C

[TEAP], M	$10^4 k_s$ (appr)[a], cm s^{-1}	α (appr)	$E^{0'}$ (appr), V
0.093	1.58	0.32	−1.046
0.150	1.70	0.31	−1.037
0.220	1.60	0.28	−1.059
0.330	1.30	0.28	−1.055
0.500	1.31	0.23	−1.031
0.750	1.34	0.23	−1.038
0.900	1.38	0.21	−1.041

[a]appr: obtained by approximation. Errors of k_s (appr) and α (appr) calculated by the program were quite small and for $E^{0'}$ (appr) the error was 0.001 V.

metric or the two extreme values from the chronoamperometric measurements, do not show any dependence on concentration and their variation may come from experimental error. Besides, the Frumkin correction in this solvent is not very precise because the reduction potential is located very close to the potential of zero charge where ϕ_2 changes rapidly with the electrode potential (small errors in $E^{0'}$ cause large errors in ϕ_2). The slight nonlinearity of the corrected kinetic plots may be caused by that factor. However, in ACN the corrected rate constants obtained are independent of the supporting electrolyte concentration. Corrected plots shown in Figs. 4 and 5 are linear, which indicates that the electroreduction process is limited by one step as far as the kinetics of the overall process is concerned.

To confirm the above results the cyclic voltammograms were approximated using a nonlinear least-squares (NLS) technique. In this method the experimental cyclic voltammograms were approximated by the solution of the diffusion–kinetic problem using the Cranck–Nicolson method in each step (36, 43, 44). Tables 6 and 7 present kinetic parameters obtained by approximation assuming simple charge transfer in one step. For both solvents a good approximation was obtained. An example of the approximation of the cyclic voltammogram obtained in PC is shown in Fig. 6. An attempt to use a more complex sequential charge transfer mechanism (EE) produced meaningless results (negative transfer coefficients).

In conclusion, the kinetic measurements in PC and ACN indicate that Zn^{2+} electroreduction at mercury proceeds in a two-step mechanism. The slowest step is probably a cation transfer through the electrical double layer, from the position *c* located in the solution close to the o.H.p., to the position *a* located at or close to the electrode surface, reaction [11], followed by a

TABLE 7. Kinetic parameters obtained by approximation of the cyclic voltammograms of Zn^{2+} in ACN solutions, assuming a simple charge transfer in one step; $[Zn^{2+}] = 0.8$ mM, $T = 25 \pm 1$°C

[TEAP], M	$10^2 k_s$ (appr)[a], cm s^{-1}	α (appr)	$E^{0'}$ (appr), V
0.10	3.05	0.21	−0.918
0.15	2.42	0.21	−0.912
0.22	1.19	0.23	−0.919
0.33	0.99	0.21	−0.925
0.50	0.48	0.26	−0.920
0.75	0.39	0.19	−0.930
0.90	0.34	0.19	−0.936

[a]appr: obtained by approximation. Errors of k_s (appr) and α (appr) calculated by the program were quite small and for $E^{0'}$ (appr) the error was 0.001 V.

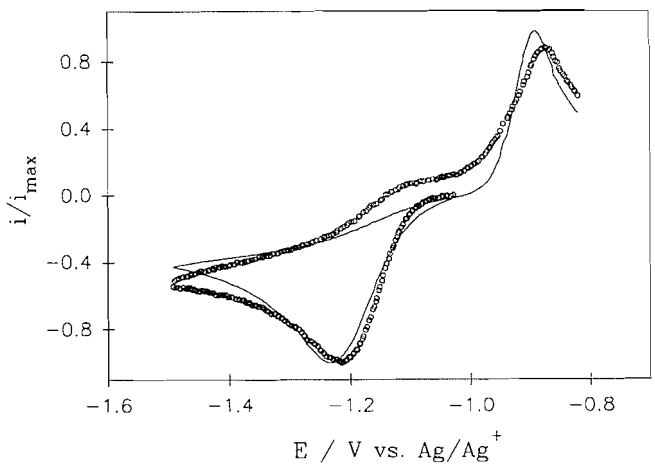

FIG. 6. Experimental (○) and approximated according to a simple charge transfer in one step (—) cyclic voltammogram of Zn^{2+} in PC; [TEAP] = 0.15 M, $[Zn^{2+}] = 0.8$ mM, $v = 2$ V s^{-1}, cathodic peak ~4 μA.

fast electroreduction with formation of the amalgam, reaction [12]:

[11] $Zn^{2+}{}_c \leftrightarrow Zn^{2+}{}_a$

[12] $Zn^{2+}{}_a + 2e^- \leftrightarrow Zn(Hg)$

The electron transfer mechanism, reactions [2] and [3], does not seem to be probable because it suggests formation of a neutral zinc atom in solution (close to the o.H.p.) that diffuses only towards the electrode surface. The latter fact is confirmed by coulometric experiments (15) in which 100% of zinc is found in mercury after electrolysis.

HMPA

The kinetic parameters obtained for the $Zn^{2+}/Zn(Hg)$ system in HMPA solutions were determined using the Koutecky analysis (45) and the approximation of cyclic voltammograms. Earlier studies of the electroreduction of alkali metal cations by Baranski and Fawcett (28, 29) indicated that the electrochemical behaviour in HMPA was different than that in other solvents. The authors attributed this differences to a slow partial cation desolvation reaction preceding the charge transfer process. This reaction was the rate-determining step in the electroreduction of Li^+. Because the desolvation step takes place in the double layer it can be considered as a heterogeneous process. The heterogeneous rate constant of the surface

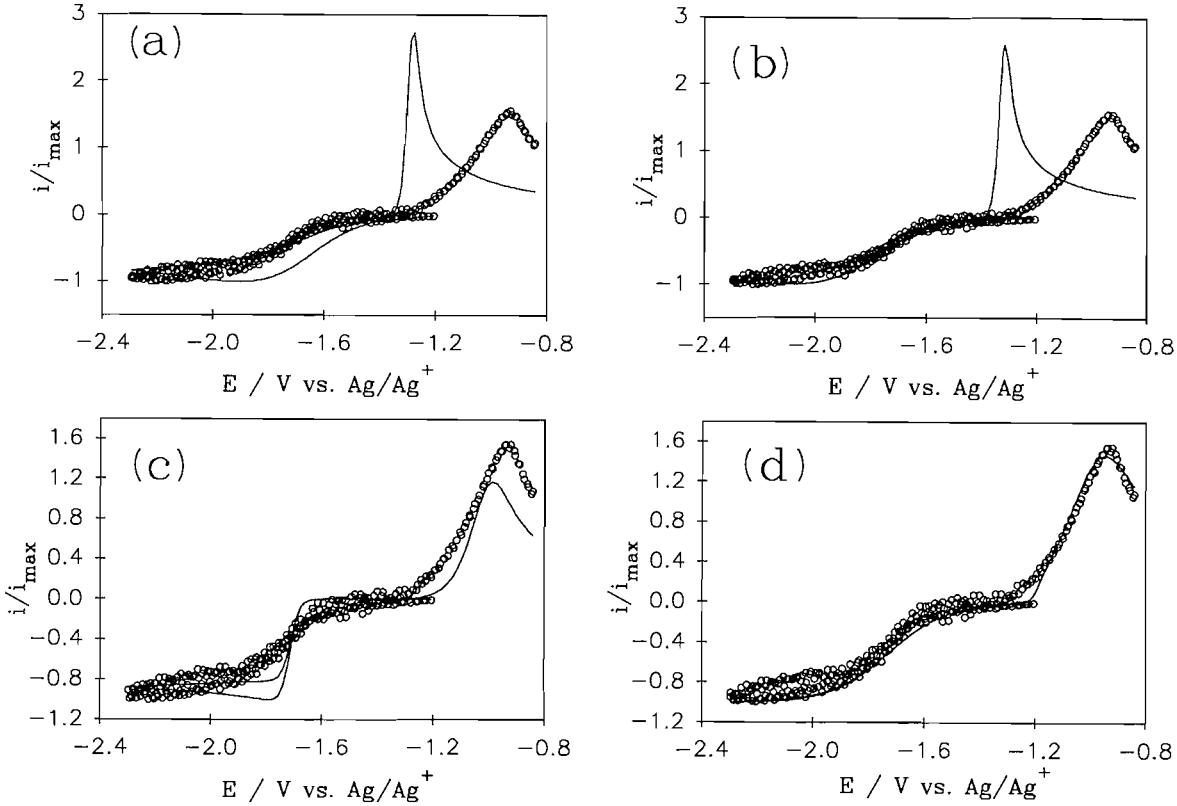

FIG. 7. Experimental (○) and (—) approximated cyclic voltammograms for the $Zn^{2+}/Zn(Hg)$ system in HMPA; $[Zn^{2+}] = 3.0$ mM, [TEAP] = 0.1 M, $v = 0.1$ V s^{-1}. (*a*) Simple charge transfer in one step (E); (*b*) mechanism EE; (*c*) mechanism CE; and (*d*) mechanism CEE, cathodic peak current ~1 μA.

chemical reaction, k_{1h}, may be obtained using the Koutecky method at the potentials of the polarographic plateau where the overall reaction kinetics is determined by the chemical reaction (rates of the heterogeneous charge transfer reactions are potential dependent and fast as negative potentials):

$$[13] \qquad F(\chi) = \frac{i_k}{i_g}$$

where $f(\chi)$ is a tabulated function (45), i_k is a kinetic current, i_g is a hypothetical limiting current in the absence of the preceding reaction limitations, and parameter χ is defined as:

$$[14] \qquad \chi = \left(\frac{12t}{7D_{ox}}\right)^{1/2} k_{1h}$$

For Zn^{2+} electroreduction the ratio of limiting currents in the absence and presence of 10% of water in HMPA was equal to ~0.3 and the value of the heterogeneous rate constant k_{1h} was determined as equal to 1.5×10^{-4} cm s^{-1}. The kinetic parameters were also determined by the NLS approximation of cyclic voltammograms assuming simple charge transfer in one step (E), subsequent charge transfer in two steps (EE), chemical reaction followed by a charge transfer (CE), and chemical reaction followed by two subsequent charge transfer processes (CEE). Figure 7 shows a few examples of these approximations. When the charge transfer in one or two steps was assumed, the NLS method approximated the anodic peak very poorly. In this case very low values of the transfer coefficient, which produced very asymmetrical peaks, were found, similar to those found earlier for Cd(II) in DMSO (36). In the case of mechanisms E, EE, and CE the parameters found did not have physical signficance because of the large errors of approximation. The best fit was obtained assuming the CEE mechanism (Fig. 7*d*) and the kinetic parameters obtained are shown in Table 8. The mechanism found is in agreement with the shape of the cathodic peak, which is characteristic for the chemically limited processes. The value of the first transfer coefficient, α_1, was assumed equal to 0.2 on the basis of polarographic measurements at the foot of the polarographic wave. The kinetic parameters obtained from approximation might be more reliable than those obtained from dc polarography because they were determined over a wider potential range. The large difference in values of the heterogeneous rate constant of the

TABLE 8. Kinetic parameters obtained by approximation of the cyclic voltammograms of Zn^{2+} in HMPA solutions, assuming a CEE mechanism; $[Zn^{2+}] = 3.0$ mM, $T = 25 \pm 1$°C; α_1 was supposed to be equal to 0.2

Kinetic parameter	Value
k_{1h}	$(4.5 \pm 2.7) \times 10^{-3}$ cm s^{-1}
k_{s1}	$(1.4 \pm 3.3) \times 10^{-7}$ cm s^{-1}
k_{s2}	$(2.3 \pm 1.9) \times 10^{-5}$ cm s^{-1}
α_2	0.690 ± 0.009
E^0	-1.208 ± 0.016 V

Can. J. Chem. Downloaded from www.nrcresearchpress.com by EESC ESCOLA DE ENGENHARIA on 09/08/12
For personal use only.

TABLE 9. Thermodynamic and kinetic parameters obtained from voltammetric experiments for Zn^{2+} reduction at a mercury electrode; [TEAP] = 0.1 M, T = 25 ± 1°C

Solvent	$10^6 D_{ox}$, cm^2 s^{-1}	$E^{\tau}_{1/2,BBCr}$, V	k_s, cm s^{-1}	α	$k_{s,a}$, cm s^{-1}	α_a
ACN	9.60	0.122	2.17×10^{-2}	0.40	5.27×10^{-4}	0.32
PC	1.15	0.180	4.46×10^{-4}	0.40	2.22×10^{-4}	0.26
DMSO[a]	2.00	−0.360	4.65×10^{-3}	0.20	5.96×10^{-6}	0.30
HMPA	0.56	−0.445	1.37×10^{-7}	0.20	9.52×10^{-10}	0.30

[a]From ref. 15.

preceding chemical reaction obtained from polarography and voltammetry may originate from the fact that the polarographic plateau in Fig. 2 is not well defined.

Therefore, the following mechanism of Zn^{2+} electroreduction in HMPA may be proposed:

$$[15] \quad [Zn(HMPA)_x]_c^{2+} \rightleftharpoons [Zn(HMPA)_y]_c^{2+} + (x-y)HMPA$$

$$[16] \quad [Zn(HMPA)_y]_c^{2+} \rightleftharpoons [Zn(HMPA)_y]_b^{2+}$$

$$[17] \quad [Zn(HMPA)_y]_b^{2+} \rightleftharpoons [Zn(HMPA)_y]_a^{2+}$$

$$[18] \quad [Zn(HMPA)_y]_a^{2+} + 2e \rightleftharpoons Zn(Hg) + yHMPA$$

where the heterogeneous desolvation reaction [15] is followed by a cation transfer through the double layer in two steps, reactions [16] and [17], and, at the electrode surface, the rate of amalgam formation, reaction [18], is fast. Therefore, the kinetic parameters k_{1h}, k_{s1}, and k_{s2} in Table 8 correspond to reactions [15]–[17], respectively. Similar mechanisms were observed for Zn^{2+} (EE) and Cd^{2+} (CE or CEE) electroreduction in DMSO (15, 37). The presence of a preceding chemical step in HMPA is connected with the strong solvating power of that solvent towards cations.

Solvent effects

Diffusion coefficients depend on the solvent viscosity according to the Stokes–Einstein equation (46):

$$[19] \quad D = \frac{k_B T}{6\pi r \eta}$$

where D is the diffusion coefficient, r is the particle radius, k_B the Boltzmann constant, and η the solvent viscosity. The dependence of D_{ox} on η^{-1} is shown in Fig. 8. Although the straight line is characterized by a high determination coefficient, $r^2 = 0.996$, there are no points in the middle region to better characterize that dependence.

The values of the half-wave potential depend on the solvent donor number, DN. The correlation between $E_{1/2}$ and DN has $r^2 = 0.947$; Gritzner (47) obtained $r^2 = 0.92$ for 13 solvents.

A comparison of the kinetic parameters of Zn^{2+} in different solvents is presented in Table 9. It is evident that solvent effects are very strong. The corrected rate constant changes 10^6 times as the solvent changes from ACN to HMPA. Figure 9 shows the dependence of ln $k_{s,a}$ on DN. Although there are only a few experimental points, a linear relation is fulfilled ($r^2 = 0.9$). Similar linear dependence was also observed for Cd^{2+} electroreduction in various solvents (34). However, no correlation was found between ln k_s (uncorrected) and DN ($r^2 = 0.56$).

Although the process was studied in four solvents only,

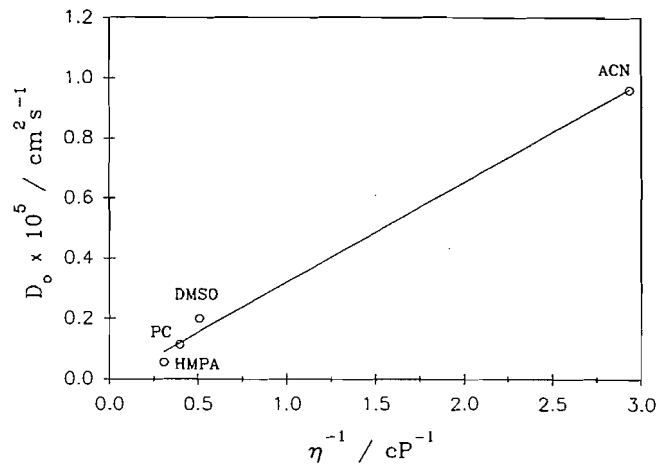

FIG. 8. Dependence of the Zn^{2+} diffusion coefficients on the inverse of the viscosity of the solvents.

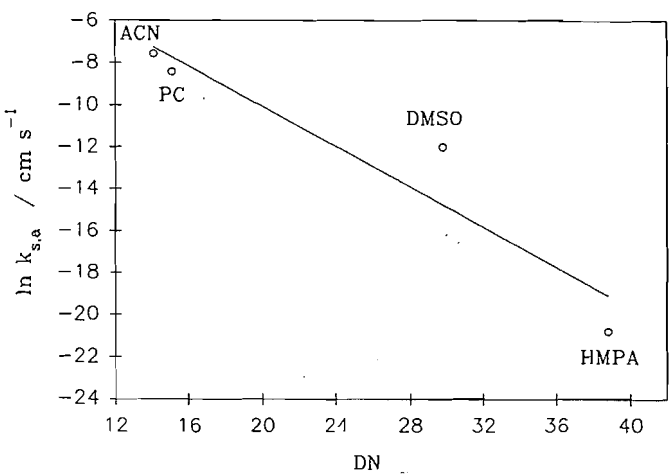

FIG. 9. Dependence of the corrected standard rate constant on the donor number solvents.

the results presented above indicate that the electroreduction mechanism and kinetics are strongly influenced by the nature of the solvent. In weakly solvating solvents (ACN, PC, small DN) Zn^{2+} is reduced in a mechanism containing one slow step. In more strongly solvating solvents (DMSO, HMPA) it is reduced in two (EE) or three (CEE) distinct steps. In HMPA there is a chemical reaction preceding the charge transfer reaction.

Conclusions

Electroreduction of Zn^{2+} was studied in PC, ACN, and HMPA using dc polarography, cyclic voltammetry, chronoam-

Can. J. Chem. Downloaded from www.nrcresearchpress.com by EESC ESCOLA DE ENGENHARIA on 09/08/12
For personal use only.

Can. J. Chem. Downloaded from www.nrcresearchpress.com by ESC ESCOLA DE ENGENHARIA on 09/08/12
For personal use only.

perometry, and ac polarography. It should be stressed that the measurements in these solvents were very difficult and much effort was required to obtain reproducible results. The measurements performed in ACN were very sensitive to the water content and different kinetic parameters outside and inside the dry box could be obtained. The reduction kinetics and mechanism are influenced by the solvent donor properties. In the solvents characterized by low values of donor number (ACN, PC) the charge transfer was controlled by the kinetics of one step. In DMSO (15), reaction proceeded through the EE mechanism and in HMPA the preceding heterogeneous chemical reaction was followed by the charge transfer in two steps (CEE mechanism). The preceding heterogeneous chemical reaction was earlier found for the electroreduction of alkali metal cations in HMPA (29) and Cd^{2+} in DMSO (37), and the EE mechanism was found for Zn^{2+} in DMSO (15).

The diffusion coefficients determined polarographically depend on the concentration of the supporting electrolyte; there is a linear relation between D_{ox} and the square root of the concentration of TEAP, Fig. 1, from which the diffusion coefficients in pure solvents were determined. In addition, the diffusion coefficients depend on the solvent viscosity, Fig. 8.

There is no dependence of the apparent rate constant, k_s, on the solvent donor number, $r^2 = 0.56$; however, the rate constants corrected for the double layer effects, $k_{s,a}$, correlate fairly well with DN ($r^2 = 0.9$). The results obtained may be explained by the cation transfer mechanism, in which the slow process is the cation transfer through the electrical double layer in one or two steps.

Acknowledgements

Financial support from the Natural Sciences and Engineering Research Council of Canada (NSERC) and the Conselho Nacional de Desenvolvimento Cientifico e Technologico (CNPq) (Brazilian Government) is gratefully acknowledged.

1. N.S. Hush and J. Blackledge. J. Electroanal. Chem. **5**, 420 (1963).
2. J. Blackledge and N.S. Hush. J. Electroanal. Chem. **5**, 435 (1963).
3. T. Hurlen and E. Eriksrud. J. Electroanal. Chem. **45**, 405 (1973).
4. F. Van Der Pol, M. Sluyters-Rehbach, and J.H. Sluyters. J. Electroanal. Chem. **58**, 177 (1975).
5. H.L. Jindal, K. Matsuda, and R. Tamamushi. J. Electroanal. Chem. **90**, 185 (1978).
6. S. Vavricka, J. Kuta, and L. Pospisil. J. Electroanal. Chem. **133**, 299 (1978).
7. R. Andreu, M. Sluyters-Rehbach, A.G. Remijnse, and J.H. Sluyters. J. Electroanal. Chem. **134**, 101 (1982).
8. S. Kang, K. Matsuda, and R. Tamamushi. Collect. Czech. Chem. Commun. **47**, 1433 (1982).
9. J.J. O'Dea, J. Osteryoung, and R.A. Osteryoung. J. Phys. Chem. **87**, 3911 (1983).
10. J. Hendrikx, A. Van Der Putten, W. Visscher, and E. Barendrecht. Electrochim Acta, **29**, 81 (1984).
11. L. Linder and K. Kordesch. Electrochim. Acta, **31**, 255 (1986).
12. S.W. Go and J. Osteryoung. J. Electroanal. Chem. **233**, 275 (1987).
13. S.W. Go, J.J. O'Dea, and J. Osteryoung. J. Electroanal. Chem. **255**, 21 (1988).
14. W.R. Fawcett and A. Lasia. J. Electroanal. Chem. **279**, 243 (1990).
15. A. Lasia and M. Bouderbala. J. Electroanal. Chem. **288**, 153 (1990).
16. J.S. Dunnett and D. Gearey. Electrochim. Acta, **19**, 907 (1974).
17. S. Fronaeus and B. Palm. Acta Chem. Scand. Ser. A: **A32**, 909 (1978).
18. R. Andreoli, L. Benedetti, G. Grandi, and G.B. Gavioli. Electrochim. Acta, **29**, 227 (1984).
19. S. Biallozor and E.T. Bandura. Electrochim. Acta, **32**, 891 (1987).
20. J. Stroka, K. Maksymiuk, and Z. Galus. J. Electroanal. Chem. **167**, 211 (1984).
21. J. Taraszewska and A. Walega. J. Electroanal. Chem. **171**, 243 (1984).
22. J. Taraszewska and A. Walega. J. Electroanal. Chem. **183**, 3 (1985).
23. C. Cronnolly, C. Pillai, and W.E. Waghorne. J. Electroanal. Chem. **207**, 177 (1986).
24. J. Taraszewska and J. Sledzik. J. Electroanal. Chem. **215**, 287 (1986).
25. J. Stroka and W. Gorski. J. Electroanal. Chem. **288**, 143 (1990).
26. V.V. Losev. *In* Modern Aspects of Electrochemistry. Vol. 7. *Edited by* J.O'M. Bockris and B.E. Conway. Plenum Press, New York. 1972. Chap. 5.
27. W.R. Fawcett. J. Electroanal. Chem. **302**, 13 (1991).
28. A.S. Baranski and W.R. Fawcett. J. Chem. Soc. Faraday Trans. 1, **76**, 1962 (1980).
29. A.S. Baranski and W.R. Fawcett. J. Chem. Soc. Faraday Trans. 1, **78**, 1279 (1982).
30. W.R. Fawcett and J. Jaworski. J. Chem. Soc. Faraday Trans. 1, **78**, 1971 (1982).
31. W.R. Fawcett. Langmuir, **5**, 661 (1989).
32. G. Gritzner and J. Kuta. Pure Appl. Chem. **56**, 259 (1984).
33. R.M. Rodriguez, E. Brillas, and J.A. Garrido. Can. J. Chem. **64**, 891 (1986).
34. G.M. Brisard and A. Lasia. J. Electroanal. Chem. **314**, 103 (1991).
35. A.J. Bard and L.R. Faulkner. Electrochemical methods. Fundamentals and applications. John Wiley and Sons, New York. 1980. p. 101.
36. A. Lasia and G.M. Brisard. J. Electroanal. Chem. **266**, 69 (1989).
37. G.M. Brisard and A. Lasia. J. Electroanal. Chem. **221**, 129 (1987).
38. M. Cetnarska and J. Stroka. J. Electroanal. Chem. **234**, 263 (1987).
39. J. Stroka, K. Maksymiuk, and A. Mital. J. Electroanal. Chem. **272**, 145 (1989).
40. T. Biegler, E.R. Gonzalez, and R. Parsons. Collect. Czech. Chem. Commun. **36**, 414 (1971).
41. K. Maksymiuk, J. Stroka, and Z. Galus. J. Electroanal. Chem. **226**, 315 (1987).
42. P. Delahay. Double layer and electrode kinetics. Interscience, New York. 1965. Chap. 9.
43. A. Lasia. Can. J. Chem. **64**, 2319 (1986).
44. A. Lasia. J. Electroanal. Chem. **191**, 185 (1985).
45. Z. Galus. Fundamentals of electrochemical analysis. John Wiley and Sons, New York. 1976. p. 196.
46. J. O'M. Bockris and A.K.N. Ready. *In* Modern electrochemistry. Vol. 1. Plenum Press, New York. 1970. p. 380.
47. G. Gritzner. J. Phys. Chem. **90**, 5478 (1986).

Enantioselective deprotonation of protected 4-hydroxycyclohexanones

MAREK MAJEWSKI[1] AND JOHN MACKINNON

Department of Chemistry, University of Saskatchewan, Saskatoon, SK S7N 0W0, Canada

Received January 10, 1994

MAREK MAJEWSKI and JOHN MACKINNON. Can. J. Chem. **72**, 1699 (1994).

A series of derivatives of 4-hydroxycyclohexanone (**1***a–g*) with the hydroxy group protected as a silyl ether (**1***a*, *b*), ether (**1***d*, *g*), an acetal (**1***c*), or an ester (**1***e*, *f*) were deprotonated with chiral, optically pure, lithium amides **3–9**. The resulting non-racemic enolates were trapped as enol acetates. The enantioselectivity of deprotonation was up to 74% ee.

MAREK MAJEWSKI et JOHN MACKINNON. Can. J. Chem. **72**, 1699 (1994).

On soumis une série de dérivés de la 4-hydroxycyclohexanone (**1***a–g*) dont l'hydroxyle était protégé par un ester silylique (**1***a* et **1***b*), un éther (**1***d* et **1***g*), un acétal (**1***c*) ou un ester (**1***e* et **1** *f*) à une déprotonation à l'aide d'amidures de sodium (**3–9**) chiraux, optiquement purs. On a piégé les énolates non racémiques obtenus sous la forme d'acétates énoliques. L'énantiosélectivité de la déprotonation s'élève jusqu'à 74% ee.

[Traduit par la rédaction]

Introduction

Deprotonation of cyclic ketones with chiral lithium amide bases is a topic of current interest (for a review see ref. 1). The reaction has been applied to enantioselective deprotonation of ketones having C_s symmetry (1), to kinetic resolution of racemic cyclic carbonyl compounds (2), and to regioselective deprotonation of cyclic, chiral ketones (3). In an imaginative recent paper Simpkins and co-workers brought together the two latter approaches to form a new concept, which was used to synthesize a chiral precursor to (+)-yohimbine (4).

Tactics based on deprotonation with chiral lithium amide bases were used in synthesis of several natural products and intermediates leading to natural products (5). To increase the usefulness of these tactics it is necessary that the scope and limitation of this deprotonation approach are more clearly defined, i.e., correlation between variables like structure of the base, structure of the ketone, reaction conditions (temperature, solvent, additives), and efficiency (enantiomeric excess) of enolization must be understood to the point that affords reasonable predictability. Alternatively, a large number of precedents might be substituted for understanding.

Cyclohexanone derivatives that were deprotonated enantioselectively in the past include several 4-alkylcyclohexanones (6*a–c*) as well as 2,6-dimethyl- and 3,5-dimethylcyclohexanone (6*d*, 7). All the above ketones are conformationally biased and it is reasonable to assume that "conformational anchoring" (1, 5*k*) would benefit enantioselective deprotonation by resulting in a system in which the base would have to differentiate between two enantiotopic axial hydrogens without interference from diastereotopic α-hydrogens (8). Experimental data, however, show that the extent of the conformational bias matters little, at least in some cases. Thus, 4-methyl-, 4-isopropyl-, and 4-*tert*-butylcyclohexanone when deprotonated with base **3**, in the presence of TMS-Cl, gave virtually identical optical purity (cf. Table 2) of the resulting TMS enol ethers (6*a*, 6*c*). Recently, 4-methyl-4-phenylcyclohexanone was deprotonated with base **3** and the TMS enol ether derived from this compound has shown 60% ee (5*j*). It should be noted that the degree of conformational bias for this compound is small; in 1-methyl-1-phenylcyclohexane the conformer with axial phenyl is more stable by only 0.32 kcal/mol (9).

Cyclohexanones substituted at the 4-position with alkyl groups have limited synthetic utility. Hoping to increase the synthetic appeal of enantioselective deprotonation of cyclic ketones, we decided to investigate enolization of cyclohexanone derivatives having a functional group containing oxygen at this position. We hoped that some derivatives of 4-hydroxycyclohexanone should be deprotonated with reasonable enantioselectivity despite the fact that, in general, alkoxy groups provide much less conformational bias than alkyl groups.

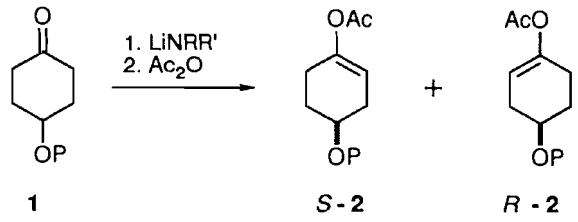

P = (*a*) $SiMe_2{}^tBu$ (*b*) $SiPh_2{}^tBu$ (*c*) CH_2OMe (*d*) Me
(*e*) $C(O){}^tBu$ (*f*) $C(O)C_6H_4$-p-OMe (*g*) CH_2Ph

SCHEME 1

Results and discussion

First, we searched for a product, derived from an enolate, that will allow measurement of enantiomeric excess (ee) of deprotonation. Several derivatives of 4-hydroxycyclohexanone (compounds **1***a–g*) (Scheme 1) were deprotonated with LDA and the racemic enolates were quenched with electrophiles. The resulting compounds were analyzed using NMR with chiral additives and (or) chiral shift reagents, and by chromatography (HPLC and GC) on chiral columns. Enol acetates (**2**), formed in 65–75% yield, proved suitable for estimating the ee by NMR using chiral shift reagents.

Next, each of the ketones **1***a–g* was treated with a chiral, optically pure, lithium amide. Lithium dialkylamides used in this study are shown in Scheme 2. In selecting these reagents we were conscious of the fact that it is difficult to make a sweeping statement regarding the correlation between the structure of a lithium amide and its effectiveness as a reagent for enantioselective deprotonation. We tried to choose representative compounds of each of the three categories of lithium amides which were used successfully in the past (1), i.e.:

[1]Author to whom correspondence may be addressed.

Can. J. Chem. Downloaded from www.nrcresearchpress.com by EESC ESCOLA DE ENGENHARIA on 09/08/12
For personal use only.

TABLE 1. Enantioselectivity of deprotonation of 4-substituted cyclohexanones **1***a–g* with lithium amides **3–9**[a]

	Compound						
Base	**1***a*	**1***b*	**1***c*	**1***d*	**1***e*	**1***f*	**1***g*
3	28 (55)	36 (63)	16 (64)	22 (60)	30 (76)	10 (6)	—
4	34 (60)	30 (68)	20 (92)	18 (66)	30 (69)	24 (57)	30 (63)
5	36 (50)	52 (60)	34 (88)	42 (75)	34 (61)	36 (63)	49 (71)
6	74 (65)	50 (90)	66 (77)	45 (64)	64 (89)	42 (71)	62 (56)
7	30 (55)	22 (71)	22 (87)	30 (65)	18 (67)	4 (65)	—
8	52 (74)	38 (69)	44 (72)	34 (69)	62 (60)	48 (78)	54 (66)
9	26 (39)	30 (55)	44 (81)	34 (72)	56 (73)	31 (75)	—

[a]Numbers represent enantiomeric excess (% ee) which was measured by NMR in the presence of a chiral shift reagent: $Eu(hfc)_3$ or $Pr(hfc)_3$. Yields of isolated products are given in parentheses.

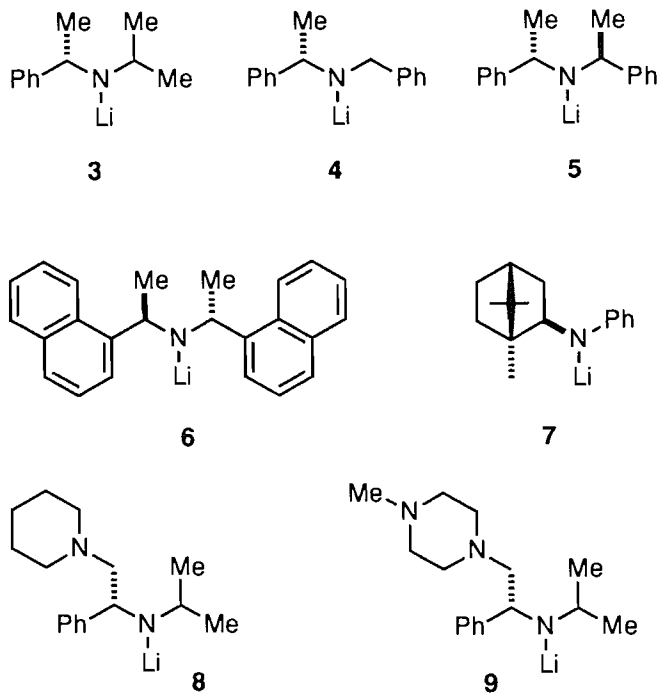

SCHEME 2

(*i*) Derivatives of 1-phenylethylamine (both enantiomers of this amine are commercially available). These amides are exemplified by structures **3–5** in Scheme 2. In this group of compounds amides with two stereogenic centers having C_2 symmetry (e.g., **5**) often proved the best in past studies on different models (1, 5*h*). Taking this into account we have synthesized a new C_2-symmetrical amide **6** from (*R*)-1-(1-naphthyl)ethylamine.

(*ii*) Lithiated secondary amines derived from terpenes. Only a few of such compounds have been investigated to date (5*h*, 7) and camphor-derived amides were found by Simpkins to work especially well when 2,6-dimethylcyclohexanone was the substrate (1). In our study one of these compounds was tested (**7**).

(*iii*) Lithiated secondary amines derived from tertiary amides of amino acids. The application of these compounds to enantioselective deprotonation was pioneered by Koga's group and it was found that bi- and tridentate amines derived from phenylglycine (e.g., compounds **8** and **9** used in our study) worked well on several cyclic ketones (6*a*).

The selectivities of deprotonation of compounds **1***a–g* with lithium amides **3–9** are summarized in Table 1. The yields of the acetate products were, with a few exceptions, in the 60–90% range but the selectivities were modest. The most selective reactions involved the new C_2 symmetrical base **6**, which turned out to be a very promising reagent. The highest ee observed was 74% (base **6**, ketone **1***a*), which compares favorably with results of enantioselective deprotonation of 4-alkylcyclohexanones (ref. 6*a*, Table 2) and 4-methyl-4-phenylcyclohexanone (5*j*). In general, the bigger the protecting group the larger the ee, although this trend is not very precisely defined. Among the ethers, for example, benzyl ether (**1***g*) was consistently the best and gave higher ee values (with one exception) than the methyl and methoxymethyl ethers (**1***d* and **1***c*). Similarly ester **1***e* showed greater efficiency in enantioselective deprotonation reactions than ester **1***f*.

It should be noted that the ee of deprotonation of 4-methoxycyclohexanone **1***d* was much lower than that of 4-methylcyclohexanone. Clearly, a certain measure of steric bias is necessary.

The efficiency of enantioselective deprotonation can be greatly influenced by reaction conditions. Both our group (7) and others (10) observed that the presence of lithium salts in the reaction mixture can increase the ee, sometimes substantially. It was also reported that lowering the reaction temperature often resulted in measurable increase in enantioselectivity (1) and that HMPA, used as an additive, often had an interesting effect on selectivity (1): in cases where bases of structures **3–5** (or similar) were used, addition of HMPA usually resulted in the decrease in enantioselectivity. Some amides derived from bidentate or tridentate amines derived from phenylglycine (e.g., **8**, **9**) showed increased enantioselectivity when HMPA was added (1, 6*a*). This interesting difference in behavior could, perhaps, be a result of different species being responsible for deprotonation in both cases; that is, dimers originating from amides **3–6** could be the actual reactive species (7) whereas the amides **8** and **9** might react in their monomeric forms (11).

The results of our investigations of the effects of lowering the temperature and applying additives (LiCl, HMPA) on the system in question are shown in Table 3. A small temperature effect was observed in only one case: compound **1***f*, deprotonated with amide **8** at −100°C showed an increase in enantioselectivity from 48 to 58%. Addition of HMPA either had no effect or resulted in decreased ee values. And finally, addition of LiCl led to a measurable increase of reaction enantioselectivity when base **4** was used to deprotonate ketones **1***a* and **1***f*.

Conclusion

Our study shows that cyclohexanones having a protected hydroxy group at the 4-position can be enantioselectively

Can. J. Chem. Downloaded from www.nrcresearchpress.com by EESC ESCOLA DE ENGENHARIA on 09/08/12
For personal use only.

TABLE 2. Deprotonation of 4-alkylcyclohexanones with chiral lithium amides

Alkyl group	Base	Observed[a] $[\alpha]_{365}$	$[\alpha]_{365}$ of pure *R* isomer[b]	Optical purity (%)[c]
	R-**3**	−181[d]		76
*t*Bu	**8**	+182[e]	+237	77
	9	+182[f]		77
i-Pr	*R*-**3**	−180[f]	+228	78
	9	+178[e]		79
Me	*R*-**3**	−175[f]	+238	64
	9	+152[e]		74

[a]Reference 6*a*.
[b]Reference 6*c*.
[c]Results (6*a*) recalculated taking into account recent reinvestigation of maximum optical rotation values for 4-alkyl-1-trimethylsilyloxycyclohexenes (6*c*); see also ref. 6*d*.
[d]HMPA (2 equiv.) was added.
[e]With HMPA (1 equiv.).
[f]Without HMPA.

TABLE 3. Effect of conditions (temperature, additives) on enantioselectivity for bases **4** and **8**[a]

	Conditions					
	−100°C		HMPA		LiCl	
Ketone	**4**	**8**	**4**	**8**	**4**	**8**
1*a*	36	50	14	33	45	27
1*f*	30	58	26	46	47	48

[a]Numbers represent enantiomeric excess (% ee), which was measured by NMR in the presence of a chiral shift reagent: $Eu(hfc)_3$ or $Pr(hfc)_3$.

deprotonated with a number of chiral lithium amides. The selectivities were modest (highest ee was 74%) and it was concluded that, for best results, the protecting group ought to be bulky.

Experimental

General methods

All air-sensitive reactions were carried out under argon. THF was dried with sodium and distilled under nitrogen from sodium benzophenone ketyl. Diisopropylamine, triethylamine, pyridine, HMPA, and CH_2Cl_2 were distilled from CaH_2. Benzene was distilled from P_2O_5, and methanol from magnesium. All chiral amines were distilled under reduced pressure and stored under argon. Ac_2O was fractionally distilled from P_2O_5 and stored under argon. Lithium chloride was dried at 130°C and used directly. *n*-BuLi was periodically titrated using 2,5-dimethoxybenzyl alcohol as the indicator (12).

Flash chromatography was carried out using Merck Kieselgel 60 (230–400 mesh) with TLC being performed on precoated plates (Merck, silica gel 60, F254). Detection was by using UV light, iodine, or phosphomolybdic acid visualizing solution. Gas chromatography was done on a Hewlett Packard 5890A instrument using a methyl silicone gum column (HP-1, 5 m × 0.53 mm). Melting and boiling points are uncorrected. Optical rotations were measured using Perkin Elmer 241 polarimeter, concentrations are given in g/100 mL. ^1H NMR and ^{13}C NMR spectra were measured on a Bruker AM-300 spectrometer at 300 MHz and 75 MHz, respectively. $CDCl_3$ was used as solvent unless otherwise stated, with tetramethylsilane being used as the internal standard. Infrared spectra were recorded on a Biorad FTS-40 interferometer using a diffuse reflectance cell. Mass spectra were recorded on a VG analytical retrofit of a single-sectored, magnetic scanning MS-12, linked to a Zenith computer. Electron impact was accomplished at 70 eV and chemical ionization at 50 eV with ammonia as the carrier gas.

*1,4-Dioxaspiro[4.5]decan-8-ol (**10**) (ref. 13)*

A solution of 1,4-cyclohexanedione monoethyleneketal (10.00 g, 64 mmol) in THF (50 mL) was added dropwise to a slurry containing lithium aluminum hydride (2.92 g, 76.8 mmol) in THF (100 mL) at 0°C. Stirring was carried out overnight at room temperature. The mixture was cooled to 0°C, water (2.9 mL) was then added followed by 15% NaOH (2.9 mL) and a further 8.8 mL of water. The mixture was then extracted with AcOEt (3 × 75 mL). The organic extracts were combined, washed with $NaHCO_3$ solution (2 × 10 mL), and dried over $MgSO_4$. The solvent was removed in vacuo, which yielded the alcohol **10** as a colorless liquid (9.91 g, 98%); bp 252–254°C; IR (KBr): 3400 (OH), 2940 (CH), 921 (C-O) cm^{-1}; ^1H NMR δ: 3.89 (s, 4H), 3.73 (m, 1H), 2.27 (br s, 1H), 1.84–1.72 (m, 4H), 1.62–1.51 (m, 4H); ^{13}C NMR δ: 108.2, 67.9, 64.2, 64.1, 31.8, 31.5; MS (CI, NH_3), *m/e* (relative intensity): 176 ([M + 18], 7), 159 ([M + 1], 100), 99 (41).

*4-Hydroxycyclohexanone (**11**) (ref. 14)*

A solution of **10** (9.91 g, 62.7 mmol) in H_2O (100 mL) containing a catalytic amount of *p*-TsOH was refluxed for 2 h. The solution was cooled to room temperature, neutralized with solid $NaHCO_3$, and extracted with AcOEt (5 × 70 mL). The organic extracts were then combined and dried over $MgSO_4$. The solvent was then removed in vacuo to yield **11** (7.21 g, 99%); IR (KBr): 3340 (OH), 2941 (CH), 1709 (C=O), 950 (C-O) cm^{-1}; ^1H NMR δ: 4.22–4.16 (m, 1H), 3.34 (br s, 1H), 2.66–2.57 (m, 2H), 2.37–2.28 (m, 2H), 2.12–1.95 (m, 4H); ^{13}C NMR δ: 211.9, 65.7, 37.1, 33.5; MS (CI, NH_3), *m/e* (relative intensity): 132 ($[M + 18]^+$, 100), 131 (3), 114 (5), 99 (6).

*4-(tert-Butyldimethylsiloxy)cyclohexanone (**1**a)*

A solution of **11** (3.73 g, 32.7 mmol) in CH_2Cl_2 (25 mL) was added to imidazole (2.66 g, 39.3 mmol) in CH_2Cl_2 (100 mL) at 0°C. After 15 min, TBDMSCl (5.92 g, 39.3 mmol) in CH_2Cl_2 (30 mL) was added dropwise to the mixture. After stirring the solution overnight at room temperature, the reaction mixture was quenched by addition of water (25 mL) and was extracted with AcOEt (3 × 50 mL). The organic phase was washed with H_2O (2 × 25 mL), brine (2 × 15 mL), and dried over $MgSO_4$. The product was purified via flash column chromatography (hex:AcOEt 8:1, R_f 0.30) to yield **1***a* (6.96 g, 93%); bp 261–262°C; IR (KBr): 2954 (CH), 1726 (C=O) cm^{-1}; ^1H NMR δ: 4.14–4.10 (m, 1H), 2.70–2.59 (m, 2H), 2.25–2.17 (dt, 2H, J = 14.4, 4.4 Hz), 1.97–1.60 (m, 4H), 0.95 (s, 9H), 0.07 (s, 6H); ^{13}C NMR δ: 211.9, 65.7, 36.9, 34.1, 25.7, 25.6, 18.0, −4.9; MS (CI, NH_3), *m/e* (relative intensity): 246 ($[M + 18]^+$, 100), 229 ($[M + 1]^+$, 15), 188 (13), 172 (10), 171 (68), 97 (12), 92 (16), 91 (20). Anal. calcd. for $C_{12}H_{24}SiO_2$: C 63.10, H 10.59; found: C 63.31, H 10.44.

*4-(tert-Butyldiphenylsilyloxy)cyclohexanone (**1**b)*

TBDPSCl (4.1 mL, 15.8 mmol) in CH_2Cl_2 (50 mL) was added drop-

Can. J. Chem. Downloaded from www.nrcresearchpress.com by ESC ESCOLA DE ENGENHARIA on 09/08/12
For personal use only.

Can. J. Chem. Downloaded from www.nrcresearchpress.com by EESC ESCOLA DE ENGENHARIA on 09/08/12
For personal use only.

wise to a solution of **11** (1.50 g, 13.2 mmol) and imidazole (2.66 g, 39.3 mmol) in CH_2Cl_2 (100 mL) at 0°C. The resulting solution was stirred overnight at room temperature. The reaction mixture was then quenched with H_2O (5 mL) and washed with H_2O (2 × 10 mL), brine (2 × 10 mL), and the washings were extracted with AcOEt (2 × 40 mL). The organic extracts were combined and dried over $MgSO_4$. The solvent was then removed in vacuo and the residue was purified by flash column chromatography (hex:AcOEt 4:1, R_f 0.37) to yield **1***b* (3.76 g, 81%); mp 107–108°C; IR (KBr): 3067 (CH), 2957 (CH), 1706 (C═O) cm^{-1}; ^1H NMR δ: 7.68–7.66 (m, 4H), 7.44–7.38 (m, 6H), 4.14 (m, 1H), 2.73 (m, 2H), 2.22–2.17 (m, 2H), 1.97–1.92 (m, 2H), 1.80–1.77 (m, 2H), 1.09 (s, 9H); ^{13}C NMR δ: 211.7, 135.7, 133.9, 129.8, 127.7, 66.9, 37.0, 33.7, 27.0, 19.3; MS (CI, NH_3), m/e (relative intensity): 370 ([M + 18], 98), 295 (65), 275 (46), 274 (59), 217 (20), 216 (100), 196 (69), 78 (17). Anal. calcd. for $C_{22}H_{28}SiO_2$: C 74.95, H 8.00; found: C 74.7, H 8.19.

*4-Methoxymethoxycyclohexanone (**1**c)*

Ketone **11** (2.00 g, 17.6 mmol) and ethyldiisopropyl amine (4.52 g, 35.8 mmol) were added to a 100-mL round-bottom flask containing CH_2Cl_2 (50 mL) and the mixture was cooled to 0°C. MOMCl (4.0 mL, 52.7 mmol) was added dropwise and the reaction mixture was stirred for 1 h at 0°C, then for another 8 h at room temperature. The reaction mixture was quenched by addition of H_2O (10 mL), followed by extraction with AcOEt (2 × 25 mL). The organic phase was washed with $NaHCO_3$ (3 × 15 mL), brine (2 × 10 mL), and was then dried over $MgSO_4$. The solvent was then removed in vacuo and the residue was purified by flash column chromatography (hex:AcOEt 5:1, R_f 0.19) yielding **1***c* (1.61 g, 58%); bp 58–59°C at 0.6 Torr (1 Torr = 133.3 Pa); IR (KBr): 2928 (CH), 1719 (C═O), 1148 (C-O) cm^{-1}; ^1H NMR δ: 4.74 (s, 2H), 4.03–3.98 (m, 1H), 3.41 (s, 3H), 2.65–2.54 (m, 2H), 2.35–2.26 (m, 2H), 2.11–1.95 (m, 4H); ^{13}C NMR δ: 211.1, 94.7, 70.6, 55.3, 37.2, 31.2; MS (CI, NH3) *m/e* (relative intensity): 176 ([M + 18], 100), 159 ([M + 1], 29), 96 (17), 58 (29). Anal. calcd. for $C_8H_{14}O_3$: C 60.74, H 8.92; found: C 60.47, H 9.05.

*4-Methoxycyclohexanone (**1**d) (ref. 15)*

Compound **10** (2.01 g, 12.68 mmol) in THF (25 mL) was added to NaH (0.91 g, 38 mmol) in THF (50 mL) at 0°C and the mixture was stirred until evolution of hydrogen had ceased. MeI (8.99 g, 63.4 mmol) was then added slowly and the mixture was refluxed for 12 h. The solution was cooled to room temperature and Et_2O (50 mL) was added and the resulting mixture extracted with Et_2O (2 × 50 mL). The organic phase was then washed with $NaHCO_3$ (2 × 25 mL) and brine (2 × 10 mL). The organic extracts were then dried over $MgSO_4$ and the solvent was removed in vacuo to yield the 1,4-dioxaspiro[4,5]decan-8-ol methyl ether (2.00 g, 92%). The crude methyl ether was then added to a solution of H_2O (50 mL) containing a catalytic amount of *p*-TsOH and the mixture was refluxed for 1 h. The solution was then extracted with AcOEt (3 × 30 mL) and the organic phase was washed with $NaHCO_3$ (2 × 15 mL). The combined organic extracts were dried over $MgSO_4$, the solvent was removed in vacuo, and the residue was purified by flash column chromatography (hex:AcOEt 4:1, R_f 0.18) to yield **1***d* (2.01 g, 89%); IR (KBr): 2941 (CH), 2825 (CH), 1716 (C═O), 1079 (C-O) cm^{-1}; ^1H NMR δ: 3.60–3.56 (m, 1H), 3.37 (s, 3H), 2.57–2.47 (m, 2H), 2.26–2.17 (m, 2H), 2.10–2.00 (m, 2H), 1.95–1.87 (m, 2H); ^{13}C NMR δ: 211.2, 74.2, 56.0, 37.0, 30.0; MS (EI), *m/e* (relative intensity): 128 ($[M]^+$, 100), 114 (15), 113 (18), 99 (33), 97 (24), 96 (77), 74 (86), 71 (92).

*4-(Trimethylacetoxy)cyclohexanone (**1**e)*

Pivaloyl chloride (3.24 mL, 26.3 mmol) was added to a solution of **11** (1.50 g, 13.2 mmol) in pyridine (3 mL) and THF (75 mL) at 0°C and the reaction mixture was stirred for 10 h at room temperature. AcOEt (50 mL) was then added and the crude mixture was washed with $NaHCO_3$ (3 × 20 mL), brine (2 × 10 mL), the layers were separated, and the combined aqueous washings were extracted with AcOEt (2 × 25 mL). The combined organic extracts were dried over $MgSO_4$ and the solvent was removed in vacuo and purified by flash chromatography (hex:AcOEt 8:1, R_f 0.25) to yield the protected hydroxy ketone (**1***e*), (2.01 g, 77%); mp 50–52°C; IR (KBr): 2964 (CH), 1721 (C═O), 1281 (C-O), 1162 (C-O) cm^{-1}; ^1H NMR δ: 5.15–5.09 (m, 1H), 2.57–2.47 (m, 2H), 2.38–2.29 (m, 2H), 2.14–1.95 (m, 4H), 1.20 (s, 9H); ^{13}C NMR δ: 209.9, 177.7, 68.0, 37.2, 30.3, 27.2; MS (CI, NH_3), *m/e* (relative intensity): 216 ([M + 18], 100), 199 ([M + 1], 42.6), 96 (34). Anal. calcd. for $C_{11}H_{18}O_3$: C 66.60, H 9.15; found: C 66.40, H 9.34.

*4-(4′-Methoxybenzoyloxy)cyclohexanone (**1**f)*

Ketone **11** (1.71 g, 15.0 mmol) was added to Et_3N (50 mL) and the solution was cooled at 0°C. Anisoyl chloride (3.03 g, 18.0 mmol) was added to the cooled solution and the mixture was stirred at room temperature for 24 h. AcOEt (100 mL) was added and the organic phase was washed with $NaHCO_3$ (3 × 20 mL), brine (2 × 20 mL), and dried over $MgSO_4$. The organic portions were then combined and the solvent was removed in vacuo; the residue was purified by flash column chromatography (PhH:AcOEt 8:1, R_f 0.32) yielding **1***f* (3.35 g, 90%); mp 53–55°C; IR (KBr): 3001 (CH), 2957 (CH), 1705 (C═O), 1276 (C-O), 1256 (C-O) cm^{-1}; ^1H NMR δ: 8.03–8.00 (d, 2H, J = 8.7 Hz), 6.96–6.93 (d, 2H, J = 8.7 Hz), 5.41 (m, 1H), 3.88 (s, 3H), 2.69–2.60 (m, 2H), 2.47–2.40 (m, 2H), 2.28–2.10 (m, 4H); ^{13}C NMR δ: 209.9, 165.5, 163.5, 131.6, 122.6, 113.7, 68.6, 55.4, 37.3, 30.6; MS, *m/e* (relative intensity): 248 ($[M]^+$, 26), 152 (100), 136 (22), 135 (99), 96 (22), 92 (26), 77 (31). Anal. calcd. for $C_{14}H_{16}O_4$: C 67.70, H 6.50; found: C 67.65, H 6.50.

*4-Benzyloxycyclohexanone (**1**g) (ref. 16)*

Compound **10** (0.35 g, 2.22 mmol) in THF (25 mL) was added to NaH (0.117 g, 2.44 mmol) in THF (50 mL) at 0°C and the mixture was stirred until evolution of hydrogen had ceased. Benzyl bromide (0.455 g, 2.66 mmol) in THF (5 mL) was then added slowly and the mixture was refluxed for 12 h. The solution was cooled to room temperature, quenched with H_2O (10 mL), and extracted with Et_2O (2 × 50 mL). The organic phase was then washed with $NaHCO_3$ (2 × 25 mL), and brine (2 × 10 mL). The organic extracts were then finally dried over $MgSO_4$. The solvent was then removed in vacuo to yield the benzyl ether of **10**.

The crude benzyl ether was added to a solution of H_2O (50 mL) containing a catalytic amount of *p*-TsOH and refluxed for 1 h. The solutions was then extracted with AcOEt (3 × 30 mL) and the organic phase was washed with $NaHCO_3$ (2 × 15 mL). The combined organic extracts were dried over $MgSO_4$. The solvent was then removed in vacuo and the residue purified by flash column chromatography (hex:AcOEt 4:1, R_f 0.28) to yield **1***g* (0.290 g, 64%); bp 140–141°C at 1.5 Torr; IR (KBr): 3024 (C-H), 2944 (C-H), 1712 (C═O), 1101 (C-O) cm^{-1}; ^1H NMR δ: 7.38 (m, 5H), 4.61 (s, 2H), 3.83 (m, 1H), 2.68–2.58 (m, 2H), 2.32–2.23 (m, 2H), 2.21–2.12 (m, 2H), 2.02–1.94 (m, 2H); ^{13}C NMR δ: 211.0, 138.5, 128.4, 127.6, 127.4, 72.3, 70.3, 37.2, 30.5; MS (EI), *m/e* (relative intensity): 204 ($[M]^+$, 7), 104 (64), 98 (48), 91 (100), 65 (19).

Chiral amines

Chiral amines used to generate lithium amides **3**–**9**, respectively, are numbered below with numbers **3***a*–**9***a* to distinguish them from the amides shown in Scheme 2. Amines **3***a*–**5***a* and **7***a*–**9***a* were synthesized as described in the literature (6*d*, 2*c*, 17).

*(R,R)-Bis-(1-naphthylethyl)amine (**6**a)*

A solution of (*R*)-(−)-(1-naphthylethyl)amine (10 mmol, 1.62 mL), 1-acetonaphthone (10 mmol, 1.52 mL), and a catalytic amount of *p*-TsOH in benzene (50 mL) was purged under argon and the mixture was refluxed for 5 days in a Dean–Stark apparatus. The resulting solution was cooled to 0°C and was washed with a solution of $NaHCO_3$ (50 mL), with brine (50 mL), and dried over $MgSO_4$. The crude imine was then purified via flash column chromatography (2% MeOH in $CHCl_3$). The imine was dissolved in THF (100 mL) and then hydrogenated on a Parr apparatus for 6 h (40 psi (1 psi = 6.9 kPa), 10% Pd/C). The suspension was filtered and the solvent was removed in vacuo. The crude product contained two diastereoisomers of **6***a*: *meso* and *R,R*

Can. J. Chem. Downloaded from www.nrcresearchpress.com by EESC ESCOLA DE ENGENHARIA on 09/08/12
For personal use only.

in a ratio of 7:93 (by GLC). Concentrated HCl was added carefully to convert the amine to its hydrochloride salt and the resulting salt was recrystallized from ethanol. The free amine was then regenerated by dissolving the salt in Et_2O (100 mL), followed by the slow addition of 2 M NaOH. The amine was then distilled under vacuum on a Kugelrohr apparatus (250°C at 0.1 Torr). Yield 1.52 g (47%); $[\alpha]_D^{22}$ −53.59 (*c* 3.9, MeOH); IR (KBr): 3294 (N-H), 3045 (C-H), 2956 (C-H), 776 (C=C) cm^{-1}; ^1H NMR δ: 7.84–7.72 (m, 8H), 7.54–7.49 (m, 2H), 7.40–7.35 (m, 2H), 7.25–7.18 (m, 2H), 4.54–4.47 (q, 2H, *J* = 6.6 Hz), 1.95–1.80 (br s, 1H), 1.46–1.44 (d, 6H, *J* = 6.6 Hz); ^{13}C NMR δ: 133.9, 131.5, 128.7, 127.1, 125.7, 125.4, 125.3, 125.2, 123.1, 122.8, 51.3, 24.4; MS (EI), *m/e* (relative intensity): 325 ($[M]^+$, 8), 170, (17), 156 (29), 155 (100), 148 (16), 113 (28). Anal. calcd. for $C_{24}H_{23}N$: C 88.57, H 7.12, N 4.30; found: C 88.29, H 7.02, N 4.11.

General procedure for synthesis of enol acetate derivatives

n-BuLi (0.39 mmol) was added dropwise to a solution of amine (0.39 mmol) in THF (25 mL) at 0°C and the resulting solution was stirred for 30 min. The solution was then cooled to −78°C, whereupon the ketone (0.45 mmol) in THF (2 mL) was added dropwise and stirred for 2 h. Ac_2O (0.76 mmol) was added and the reaction mixture was stirred for 30 min. NH_4Cl solution (2 mL) was added to quench the reaction and the mixture was then extracted with AcOEt (3 × 25 mL). The combined organic extracts were washed with NaCl solution (2 × 10 mL), $NaHCO_3$ solution (2 × 10 mL), and dried over $MgSO_4$. The solvent was removed in vacuo and the residue purified by column chromatography yielding a colorless oil (yields are shown in Table 1).

Modifications

(i) Lower temperature (−100°C): A solution of lithium amide (1.2 equiv.) was prepared in the usual manner and then cooled to −100°C. The ketone (1 equiv.) in THF was then added and the mixture was stirred at −100°C for 2 h. Ac_2O was then added at −78°C and the resulting solution was stirred for 30 min. The reaction was then quenched with saturated NH_4Cl solution.

(ii) Addition of HMPA: A solution of lithium amide (1.2 equiv.) was prepared as usual at 0°C. HMPA (1 equiv.) was added and the mixture was stirred at 0°C for 15 min. The solution was then cooled to −78°C and stirred for 2 h; Ac_2O was added and the mixture was stirred for 30 min before being quenched with NH_4Cl solution.

(iii) Addition of LiCl: A solution of lithium amide (1.2 equiv.) was generated at 0°C whereupon LiCl (0.4 equiv.) was added via a side arm and the cooled solution was stirred for 15 min. The temperature was lowered to −78°C, the ketone in THF was added, and the mixture was stirred for 2 h. Ac_2O was then added and, after stirring for a further 30 min the mixture was quenched with NH_4Cl solution.

Spectral data and analyses for enol acetates

*1-Acetyloxy-4-[(*tert*-butyldimethylsilyl)oxy]cyclohexene (**2**a):* IR (KBr): 2947 (CH), 2854 (CH), 1755 (CO), 1213 (C=C) cm^{-1}; ^1H NMR δ: 5.20 (m, 1H), 3.92 (m, 1H), 2.27–2.19 (m, 4H), 2.09 (s, 3H), 2.81–1.74 (m, 2H), 0.92 (s, 9H), 0.04 (s, 6H); ^{13}C NMR δ: 169.3, 147.6, 111.4, 66.6, 33.1, 31.3, 25.8, 25.0, 21.0, 18.1, −4.7; MS (CI, NH_3), *m/e* (relative intensity): 288 ([M + 18], 84), 271 ([M + 1], 100), 255 (11), 246 (19), 214 (14), 213 (63), 188 (18), 171 (48). Anal. calcd. for $C_{14}H_{26}SiO_3$: C 62.20, H 9.67; found: C 62.42, H 9.64.

*1-Acetyloxy-4-[(*tert*-butyldiphenylsilyl)oxy]cyclohexene (**2**b):* IR (KBr): 3061 (CH), 2930, 2854 (CH), 1755 (C=O), 1218 (C=C) cm^{-1}; ^1H NMR δ: 7.67–7.64 (m, 4H), 7.41–7.33 (m, 6H), 5.15 (s, 1H), 3.99 (s, 1H), 2.27–2.13 (m, 4H), 2.08 (s, 3H), 1.79–1.74 (m, 2H), 1.04 (s, 9H); ^{13}C NMR δ: 169.3, 147.6, 135.7, 134.5, 129.6, 127.5, 111.1, 104.2, 67.2, 32.7, 30.8, 26.9, 24.6, 21.0, 19.2; MS (CI, isobutane), *m/e* (relative intensity): 395 ([M + 1], 10), 338 (25), 337 (98), 317 (30), 275 (40), 221 (36), 217 (95), 199 (47), 139 (100). Anal. calcd. for $C_{24}H_{30}SiO_3$: C 73.10, H 7.66; found: C 72.96, H 7.44.

*1-Acetyloxy-4-(methoxymethoxy)cyclohexene (**2**c):* IR (KBr): 3018 (C=C), 2928 (C-H), 1758 (C=O), 1213 (C-O) cm^{-1}; ^1H NMR δ: 5.25–5.23 (m, 1H), 4.67 (s, 2H), 3.90–3.82 (m, 1H), 3.35 (s, 3H), 2.47–2.38 (m, 1H), 2.25–2.19 (m, 3H), 2.08 (s, 3H), 2.00–1.92 (m, 1H), 1.86–1.78 (m, 1H); ^{13}C NMR δ: 169.3, 147.7, 111.1, 94.9, 71.0, 55.3, 30.1, 28.0, 24.8, 21.0; MS (CI, NH_3), *m/e* (relative intensity): 218 ([M + 18], 100), 201 ([M + 1], 62), 141 (35), 138 (24), 113 (22), 96 (44), 95 (16), 60 (23). Anal. calcd. for $C_{10}H_{16}O_4$: C 60.0, H 8.05; found: C 60.0, H 8.16.

*1-Acetyloxy-4-methoxycyclohexene (**2**d):* IR (KBr): 2919 (CH), 1755 (C=O), 1210 (C-O) cm^{-1}; ^1H NMR δ: 5.26 (m, 1H), 3.50 (m, 1H), 3.38 (s, 3H), 2.42 (m, 1H), 2.24–2.21 (m, 2H), 2.15 (m, 1H), 2.10 (s, 3H), 1.97 (m, 1H), 1.76 (m, 1H); ^{13}C NMR δ: 169.3, 147.8, 111.0, 74.5, 56.0, 29.3, 27.1, 24.8, 21.0; MS (CI, NH_3), *m/e* (relative intensity): 188 ([M + 18], 100), 171 ([M + 1], 66), 146 (30), 128 (43), 96 (47), 60 (43). Anal. calcd. for $C_9H_{14}O_3$: C 63.51, H 8.29; found: C 63.59, H 8.44.

*1-Acetyloxy-4-(2,2,2-trimethylacetoxy)cyclohexene (**2**e):* IR (KBr): 2957 (CH), 1756 (C=O), 1720 (C=O), 1221 (C-O) cm^{-1}; ^1H NMR δ: 5.25 (m, 1H), 5.00 (m, 1H), 2.41 (m, 1H), 2.25–2.14 (m, 3H), 2.09 (s, 3H), 1.94–1.86 (m, 2H), 1.16 (s, 9H); ^{13}C NMR δ: 178.0, 169.2, 147.6, 110.5, 67.4, 38.7, 28.9, 27.1, 26.7, 23.8, 21.0; MS (CI, NH_3), *m/e* (relative intensity): 258 ([M + 18], 100), 241 ([M + 1], 72), 216 (16), 138 (13), 113 (24), 96 (44). Anal. calcd. for $C_{13}H_{20}O_4$: C 64.98, H 8.39; found: C 65.00, H 8.35.

*1-Acetyloxy-4-[(4′-methoxy)benzoyloxy]cyclohexene (**2**f):* IR (KBr): 3017 (CH), 2941 (CH), 1758 (C=O), 1707 (C=O), 1601 (C-O) cm^{-1}; ^1H NMR δ: 8.00–7.96 (d, 2H, *J* = 8.9 Hz), 6.92–6.87 (d, 2H, *J* = 8.7 Hz), 5.32–5.27 (m, 2H), 3.83 (s, 3H), 2.58–2.52 (m, 2H), 2.39–2.29 (m, 2H), 2.12 (s, 3H), 2.08–2.01 (m, 2H); ^{13}C NMR δ: 169.3, 165.8, 163.3, 147.7, 131.6, 123.0, 113.6, 110.7, 68.0, 55.4, 29.2, 27.0, 24.0, 21.0; MS (CI, NH_3), *m/e* (relative intensity): 308 ([M + 18], 55), 291 ([M + 1], 100), 266 (14), 249 (19), 152 (13), 135 (28), 113 (12), 96 (17). Anal. calcd. for $C_{16}H_{18}O_5$: C 66.19, H 6.25; found: C 65.97, H 5.99.

*1-Acetyloxy-4-benzyloxycyclohexene (**2**g):* IR (KBr): 3029 (CH), 2931 (CH), 1755 (C=O), 1224 (C=C), 1120 (C-O) cm^{-1}; ^1H NMR δ: 7.34–7.24 (m, 5H), 5.26 (m, 1H), 4.56 (s, 2H), 3.71 (m, 1H), 2.44 (m, 1H), 2.24–2.15 (m, 3H), 2.09 (s, 3H), 2.02 (m, 1H), 1.86 (m, 1H); ^{13}C NMR δ: 169.3, 147.8, 138.8, 128.4, 127.5, 127.4, 111.1, 72.6, 70.3, 29.7, 27.6, 25.0, 21.0; MS (CI-NH_3), *m/e* (relative intensity): 264 ([M + 18], 2.6), 205 (17), 203 (32), 113 (50), 95 (38), 91 (100).

Acknowledgements

We thank the Natural Sciences and Engineering Research Council of Canada and the University of Saskatchewan for financial support.

1. P.J. Cox and N.S. Simpkins. Tetrahedron: Asymmetry, **2**, 1 (1991).
2. (*a*) P. Coggins and N.S. Simpkins. Synlett, **3**, 313 (1992); (*b*) Synlett, **2**, 515 (1991); (*c*) H. Kim, H. Kawasaki, M. Nakayima, and K. Koga. Tetrahedron Lett. **30**, 6537 (1989).
3. M. Sobukawa, M. Nakajima, and K. Koga. Tetrahedron: Asymmetry, **1**, 295 (1990).
4. K. Bambridge, N.S. Simpkins, and B.P. Clark. Tetrahedron Lett. **33**, 8141 (1992).
5. (*a*) A.E. Greene, A.A. Serra, E.J. Barreiro, and P.R.R. Costa. J. Org. Chem. **52**, 1170 (1987); (*b*) C.N. Cain and N.S. Simpkins. Tetrahedron Lett. **28**, 3723 (1987); (*c*) T. Momose, N. Toyooka, S. Seki, and Y. Hirai. Chem. Pharm. Bull. **38**, 2072 (1990); (*d*) T. Momose, N. Toyooka, and Y. Hirai. Chem. Lett. 1319 (1990); (*e*) J. Leonard, D. Ouali, and S.K. Raman. Tetrahedron Lett. **31**, 739 (1990); (*f*) H. Izawa, R. Shirai, H. Kawasaki, H.-D. Kim, and K. Koga. Tetrahedron Lett. **30**, 7221 (1989); (*g*) P.J. Cox and N.S. Simpkins. Synlett, 321 (1991); (*h*) M. Majewski and G.-Z. Zheng. Can. J. Chem. **70**, 2618 (1992); (*i*) H. Wild and L. Born. Angew. Chem. Int. Ed. Engl. **30**, 1685 (1991); (*j*) T. Honda, N. Kimura, and M. Tsubuki. Tetrahedron: Asymmetry, **4**, 21 (1993); (*k*) B.J. Bunn, P.J. Cox, and N.S. Simpkins. Tetrahedron, **49**, 207 (1993).
6. (*a*) R. Shirai, M. Tanaka, and K. Koga. J. Am. Chem. Soc. **108**, 543 (1986); (*b*) R.P.C. Cousins and N.S. Simpkins. Tetrahedron Lett. **30**, 7241 (1989); (*c*) K. Aoki, M. Nakajima, K. Tomioka, and

K. Koga. Chem. Pharm. Bull. **41**, 994 (1993); (*d*) C.M. Cain, R.P.C. Cousins, G. Coumbarides, and N.S. Simpkins. Tetrahedron, **46**, 523 (1990).
7. M. Majewski and D.M. Gleave. J. Org. Chem. **57**, 3599 (1992).
8. P. Deslongchamps. Stereoelectronic effects in organic chemistry. Pergamon Press, Toronto. 1983. pp. 274–284.
9. E. Juaristi. Introduction to stereochemistry and conformational analysis. Wiley, Toronto. 1991. p. 265.
10. B.J. Bunn and N.S. Simpkins. J. Org. Chem. **58**, 533 (1993).
11. D. Sato, H. Kawasaki, I. Shimada, Y. Arata, K. Okamura, T. Date, and K. Koga. J. Am. Chem. Soc. **114**, 761 (1992).
12. M.R. Winkle, J.M. Lasinger, and R.C. Rolard. J. Chem. Soc. Chem. Commun. 87 (1980).
13. D.G. Cleary. Synth. Commun. **19**, 737 (1989).
14. T. Nakana, T. Terada, Y. Ishi, and M. Ogawa. Synthesis, 774 (1986).
15. C. Cauletti, G. DiMaio, W. Li, E. Vecchi, and T. Vondrak. Tetrahedron, **42**, 3677 (1986).
16. E. Ghera and Y. Ben-David. J. Org. Chem. **53**, 2972 (1998).
17. A. Ando and T. Shioiri. Tetrahedron, **45**, 4969 (1989).

Can. J. Chem. Downloaded from www.nrcresearchpress.com by EESC ESCOLA DE ENGENHARIA on 09/08/12
For personal use only.

Linkage isomerization and electrochemical behavior of two geometrical isomers of dichlorobis(dimethylsulfoxide)bis(*t*-butylpyridine)ruthenium(II)

DENISE O. SILVA AND HENRIQUE E. TOMA

Instituto de Química, Universidade de São Paulo, Caixa Postal 20780, CEP 01498-970, São Paulo, SP, Brazil

Received April 28, 1993

Can. J. Chem. Downloaded from www.nrcresearchpress.com by EESC ESCOLA DE ENGENHARIA on 09/08/12
For personal use only.

DENISE O. SILVA and HENRIQUE E. TOMA. Can. J. Chem. **72**, 1705 (1994).

The reaction of *cis*-[$RuCl_2(dmso)_4$] (dmso = dimethylsulfoxide) with 4-*tert*-butylpyridine (tbpy) in chloroform leads to the all *cis* (*ccc*) and the *cis,cis,trans* (*cct*) geometrical isomers of [$RuCl_2(S\text{-}dmso)_2(tbpy)_2$]. The *cct* isomer exhibits a reversible cyclic voltammogram, ascribed to the $Ru^{II/II}$ redox couple with $E_{1/2}$ = 1.12 V versus SHE. The *ccc* isomer can be oxidized at $E_{1/2}$ = 1.27 V; however, the oxidized species undergoes a relaxation equilibrium, ($K_{s\rightarrow o}$ = 1.59), involving the S-to-O linkage isomerization of a coordinated dmso ligand ($k_{s\rightarrow o}$ 1.9 s^{-1} and $k_{O\rightarrow S}$ = 1.2 s^{-1}). The isomerization reaction in the Ru^{III} *ccc* isomer is discussed in terms of the competitive effects between the S-bound dmso and the tbpy ligands.

DENISE O. SILVA et HENRIQUE E. TOMA. Can. J. Chem. **72**, 1705 (1994).

La réaction du *cis*-[$RuCl_2(dmso)_4$] (dmso = diméthylsulfoxyde) avec la 4-*tert*-butylpyridine (tbpy) dans le chloroforme conduit à la formation des isomères géométriques complètement *cis* (*ccc*) et *cis,cis,trans* (*cct*) du [$RuCl_2(dmso)_4(tbpy)_2$]. L'isomère *cct* présente un voltampérogramme cyclique réversible, attribué au couple rédox $Ru^{II/III}$, avec $E_{1/2}$ = 1,12 V versus SHE. L'isomère *ccc* peut être oxydé à $E_{1/2}$ = 1,27 V; toutefois, les espèces oxydées subissent un équilibre de relaxation ($K_{s\rightarrow o}$ = 1,59) impliquant l'isomérisation d'un coordinat dmso de la liaison S vers O ($k_{s\rightarrow o}$ = 1,9 s^{-1} et $k_{O\rightarrow S}$ = 1,2 s^{-1}). On discute de la réaction d'isomérisation de l'isomère *ccc* du Ru^{III} en fonction des effets compétitifs entres les coordinats tbpy et dmso lié par le S.

[Traduit par la rédaction]

Introduction

Recent publications have focused on the chemistry of geometrical isomers of ruthenium(II) sulfoxide complexes of the type [$RuX_2(dmso)_4$], where X = Cl, Br; dmso = dimethylsulfoxide, with special emphasis on their pronounced antitumor activity (1, 2). These complexes can strongly bind to guanine bases, and by analogy to cisplatin they seem to inhibit the restriction enzymes that recognize DNA sequences containing two or more adjacent guanines (3). We started investigating the chemistry of mixed ruthenium(II) sulfoxide complexes because of the biological (4) and catalytical activity (5–9) of this type of complex, and of the recent progress in the design of new drugs, such as those containing nitroimidazole, employed in radiosensitizing measurements (10). In the course of our studies on the reaction of *cis*-[$RuCl_2(dmso)_4$] with L = N-heterocyclic ligands (11, 12) we have observed a general tendency of forming a mixture of two geometrical isomers of [$RuCl_2(S\text{-}dmso)_2L_2$]. Such isomers can be detected by HPLC and characterized based on their contrasting electronic spectra and cyclic voltammograms. However, the isolation of the pure species and the determination of their chemical properties have never been reported before. Recently, we succeeded in isolating the geometrical isomers of the [$RuCl_2(S\text{-}dmso)_2(tbpy)_2$] complex, where tbpy = 4-*tert*-butylpyridine, and here we report a comparative study on their properties, including the elucidation of the Ru–dmso linkage isomerization reactions in solution.

Experimental section

The starting complex, *cis*-[$RuCl_2(dmso)_4$] was prepared according to the method previously reported in the literature (13). The *cis,cis,cis*-[$RuCl_2(dmso)_2(tbpy)_2$] complex, (isomer B) was prepared by reacting 1.6 mL (10.8 mmol) of 4-*tert*- butylpyridine with 1.0 g (2.0 mmol) of *cis*-[$RuCl_2(dmso)_4$] dissolved in 125 mL of chloroform, and refluxing the mixture for 4 h under an argon atmosphere. The resulting orange solution was evaporated to 3 mL, at room temperature, and diethyl ether (20 mL) was added. After 4 days in the freezer (−15°C), a yellow solid precipitated. The solid was collected on a filter, washed with diethyl ether, and dried under vacuum. Anal. calcd. for $C_{22}H_{38}O_2N_2S_2Cl_2Ru$: C 44.14, H 6.34, N 4.68; found: C 44.4, H 6.4, N 4.5. Infrared spectrum: 3040 w, 3020 w, 2950 s, 2920 sh, 2900 sh, 2860 m (ν CH_3 tbpy, dmso); 1610 s, 1530 w, 1500 s, 1470 sh, 1455 w (ν ring tbpy), 1435 sh, 1420 s, 1400 sh (δ CH_3 dmso, tbpy); 1365 m (ν ring tbpy); 1310 m, 1300 w, 1285 sh, 1270 m (δ CH dmso, tbpy); 1230 m, 1195 w, 1125 w (β CH tbpy); 1095 s, 1075 s (ν SO dmso), 1065 m (β CH tbpy); 1010 vs (ring breath, tbpy); 960 m, 925 m, 910 m (ρ CH_3 dmso); 840 sh, 830 s (γ CH tbpy); 720 m, 670 s (ν CSC dmso); 570 m, 545 sh (β ring); 380 w (δ dmso); 440 m, 420 m (ν RuS); 375 m, 345 w (ν RuN); 295 w, 240 m (ν RuCl); w = weak, vw = very weak, m = medium, s = strong, sh = shoulder. The *cis,cis,trans*-[$RuCl_2(dmso)_2(tbpy)_2$] complex (isomer A) was isolated from the filtrate of the *cis,cis,cis* isomer, which was kept in the freezer (−15°C) for two months. The yellow–orange solid was collected on a filter, washed with diethyl ether, and dried under vacuum. Anal. found: C 44.1, H 6.2, N 4.5. Infrared spectrum: 3060 w, 3030 w, 2950 s, 2920 sh, 2860 m (ν CH_3 tbpy, dmso); 1610 s, 1535 w, 1495 s, 1475 sh, 1470 w (ν ring tbpy); 1435 sh, 1415 s, 1390 sh (δ CH_3); 1365 m (ν ring tbpy); 1310 m, 1295 w, 1275 sh, 1265 m (δ CH_3 dmso, tbpy); 1220 m, 1195 w (β CH tbpy); 1080 vs (ν SO dmso); 1010 vs, 1000 s (ring breath, tbpy); 958 m, 930 m, 910 m (ρ CH_3 dmso); 830 s, 825 sh (γ CH tbpy); 710 sh, 705 m (ν CSC dmso); 570 m, 540 vw (β ring); 385 w (δ dmso); 430 sh, 420 s (ν RuS); 345 m (ν RuN); 295 w, 230 m (ν RuCl); Unfortunately, up to the present time, we have not obtained suitable crystals for X-ray studies.

The electronic spectra were recorded on a Hewlett-Packard model 8452-A diode-array spectrophotometer. High-performance liquid chromatography, infrared spectra, and cyclic voltammetry measurements were carried out as previously reported (11). ^1H NMR spectra (in $CDCl_3$ versus TMS) were recorded on a Brucker AC 200 FT spectrometer.

Results and discussion

Spectroscopic and analytical characterization

The [$RuCl_2(dmso)_2(tbpy)_2$] isomers exhibit quite different retention times in HPLC, e.g. 1650 s (isomer A) and 1135 s (isomer B), for an isocratic elution with a 60:40 methanol–water mixture. Under the conditions of this work, the retention times for *cis*-[$RuCl_2(dmso)_4$], dmso, and tbpy, were 135, 146, and 753 s, respectively. Therefore, the purity of the samples can be readily confirmed by means of HPLC, from the observation of a single peak in the chromatograms.

Can. J. Chem. Downloaded from www.nrcresearchpress.com by EESC ESCOLA DE ENGENHARIA on 09/08/12
For personal use only.

The isomers also exhibit contrasting ^1H NMR spectra. In the case of isomer A, a single resonance signal is observed for the $(CH_3)_2SO$ ligands at 3.257 ppm, and a single set of signals for the tbpy ligands at 8.970, 8.940 (*ortho*-H); 7.224, 7.190 (*meta*-H) and 1.264 ppm (CH_3). This result indicates that the two dmso and the two tbpy ligands occupy equivalent positions in the complex. In the case of isomer B, the resonance signals for the $(CH_3)_2SO$ ligands split into two doublets, at 3.695, 3.400 and 2.820, 2.694 ppm, indicating that the dmso ligands are non-equivalent, and exhibit little rotational freedom. For the coordinated tbpy ligands there are two peaks at 1.325 and 1.287 ppm (CH_3), a broad doublet at 8.763, 8.674 ppm (*ortho*-H) and two doublets at 7.335, 7.303, and 7.188, 7.156 ppm (*meta*-H), indicating two non-equivalent sites in the complex. In both cases, the relative intensities for the methyl protons of tbpy, dmso, and aromatic protons were consistent with the expected values, e.g. 4.5, 3.0, and 2.0, respectively.

Five geometrical isomers are theoretically possible for a pseudo-octahedral complex of the type $RuCl_2S_2N_2$. These isomers can be denoted, based on the corresponding sequence of ligands, as *cis,cis,cis* (*ccc*); *cis,cis,trans* (*cct*); *cis,trans,cis* (*ctc*); *trans,cis,cis* (*tcc*) and *trans,trans,trans* (*ttt*), respectively. The only species exhibiting two non-equivalent dmso and tbpy ligands in the coordination shell is the *ccc* isomer of C_1 symmetry, corresponding to the complex B. The results from the NMR spectra in this case are conclusive. The remaining isomers exhibit twofold rotational axis, and would lead to a single set of resonance signals for the dmso and tbpy ligands. The identification of isomer A, based exclusively on the NMR spectra, is not possible.

According to the literature (1), isomers containing *trans*-chloride ligands are less stable thermodynamically with respect to the *cis*-analogues, and their synthesis are usually carried out starting from the *trans*-$[RuCl_2(dmso)_4]$ complex, rather than from *cis*-$[RuCl_2(dmso)_4]$. Therefore, by ruling out the *tcc* and *ttt* configurations, one has to decide between *cct* and *ctc* configurations for isomer A. In this sense, it should be noted that a *trans*-cooperative interaction is favored when a π-donor ligand, such as Cl^-, is *trans* to a π-acceptor ligand, e.g. dmso, as in the case of the *cct* configuration. In the *ctc* case, the *trans*-dmso ligands would compete for the d_π electrons of ruthenium(II), leading to a less favorable configuration. According to the *trans*-competitive and *trans*-cooperative effects, the *cct* configuration for isomer A would be the most probable.

The infrared spectra for isomers A and B are complicated by the strong overlap of vibrational peaks of the dmso and tbpy ligands. A tentative assignment was carried out by comparison with the vibrational spectra of the free ligands, and of related complexes from the literature (10, 13–15). In general, the vibrational frequencies associated with the dmso and tbpy ligands are rather similar for both isomers; the main differences (Fig. 1) are in the ν-SO region (1100–1050 cm^{-1}) and in the region of the metal–ligand vibrations (430–350 cm^{-1}), which are more sensitive to the geometry of the complexes. Isomer B exhibits well resolved ν-SO peaks at 1095 and 1075 cm^{-1}, consistent with the presence of two non-equivalent dmso ligands, as expected for a *ccc* configuration. In contrast, isomer A exhibits a broad peak at 1080 cm^{-1}. Both isomers exhibit a composite peak in the region of 440–420 cm^{-1} ascribed to the ν-RuS vibrations. Isomer B exhibits two ν-RuN peaks at 375 and 345 cm^{-1}, in agreement with a *ccc* configuration, while isomer A exhibits only a single peak at 345 cm^{-1}, consistent with a *trans* configuration for the tbpy ligands. Therefore, according to the vibrational data, a *cct* configuration can be ascribed to isomer A.

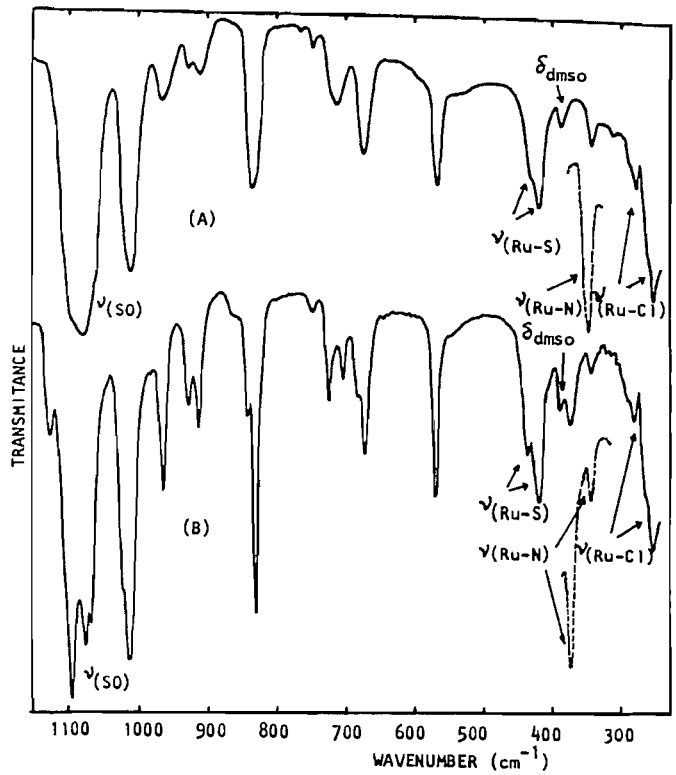

FIG. 1. Infrared spectra of (*A*) *cct*-$[RuCl_2(dmso)_2(tbpy)_2]$, and (*B*) of the *ccc* isomer, in KBr pellets (--- expanded scale).

The electronic spectra of the two isomers can be seen in Fig. 2. The absorption profiles for the two isomers are rather contrasting and can be deconvoluted into three Gaussian bands, located at 275, 315, and 366 nm for isomer B, and at 268, 316, and 430 nm for isomer A. Isomer B exhibits an additional shoulder at 240 nm, which is not resolved in the case of isomer A, ascribed to an internal π–π^* transition in the tbpy ligands. The visible–uv bands are relatively strong and consistent with ruthenium(II)-to-tbpy d_π–p_π^* charge transfer transitions, as in related systems reported in the literature (11, 16, 17). For isomer A, the occupied metal d_π orbitals transform according to the symmetry representations a_1, a_2, and b_1. The lowest unoccupied π^* orbitals of the tbpy ligands in *trans* configuration transform as a_1 and b_1. Based on symmetry and orbital overlap considerations (17), the strong bands at 268 and 316 nm can be ascribed to the $a_1(d_\pi) \rightarrow a_1$(tbpy) and $b_1(d_\pi) \rightarrow b_1$(tbpy) charge-transfer transitions. The third band at 430 nm is less intense and may be ascribed to a ligand field transition or to the $a_2(d_\pi) \rightarrow b_1$(tbpy) charge-transfer transition which is symmetry allowed, but involves weakly interacting orbitals. Isomer B has global C_1 symmetry; however, for comparison purposes, if one assumes a local C_{2v} symmetry for the two tbpy ligands in *cis* configuration, the lowest unoccupied π^* orbitals would transform according to a_2 and b_1. Analogously, the intense charge-transfer bands at 275 and 315 nm could be ascribed to the $a_2(d_\pi) \rightarrow a_2$(tbpy) and $b_1(d_\pi) \rightarrow b_1$(tbpy) transitions, while the weak band at 366 may be due to a ligand field transition

Can. J. Chem. Downloaded from www.nrcresearchpress.com by EESC ESCOLA DE ENGENHARIA on 09/08/12
For personal use only.

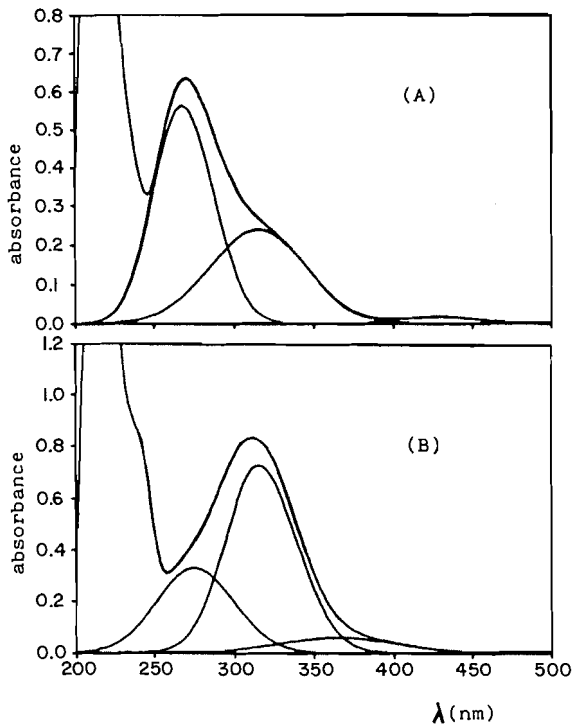

FIG. 2. Absorption spectra of (*A*) *cct*-$[RuCl_2(dmso)_2(tbpy)_2]$ (0.15 mmol dm^{-3}) and (*B*) of the *ccc* isomer (0.12 mmol dm^{-3}), in ethanol.

or to the $a_1(d_\pi) \rightarrow b_1(tbpy)$ transition, which is symmetry allowed, but involves weakly interacting orbitals.

Electrochemistry and linkage isomerization reactions

Typical cyclic voltammograms for isomers A and B can be seen in Fig. 3. Isomer A exhibits a normal voltammogram, consistent with a reversible monoelectronic process involving the $Ru^{III/II}$ redox couple, at $E_{1/2}$ = 1.12 V versus SHE. In contrast, the voltammograms of isomer B are much more interesting. By starting at 0.2 V, and scanning in the anodic direction, a single peak (ia_1) associated with the $Ru^{III/II}$ redox couple can be observed at $E_{1/2}$ = 1.27 V. In the reverse scan, the corresponding cathodic peak current (ic_1) becomes less intense, and a new peak (ic_2) grows up at $E_{1/2}$ = 0.55 V. This effect becomes very pronounced by starting at 1.8 V, as one can see in Fig. 3*C*. The ratios $[ic_1]/[ia_1]$ and $[ic_2]/[ia_2]$ are strongly dependent on the scan rates, and are consistent with the involvement of chemical reactions coupled to the electrochemical process.

The origin of ia_2 and ic_2 peaks might be due to a ligand dissociation or to an isomerization reaction. In the first case, the reaction would be repressed by an excess of the ligand, and the properties of the substituted product would depend on the nature of the solvent molecules. In the second case, the reaction would proceed independently of the presence of the ligands in solution, as in the case of a unimolecular process.

In order to test the hypothesis, the cyclic voltammograms were repeated in pure dmso solutions. The results were quite similar to those obtained in acetonitrile solutions, indicating the occurrence of a unimolecular reaction coupled to the electrochemical process.

The dramatic change of $E_{1/2}$ from 1.27 to 0.55 V associated with the chemical reaction is analogous to those previously reported (18) for the S- and O-bound linkage isomers of the $[Ru(NH_3)_5dmso]^{3/2+}$ complex. By analogy to the literature (18, 19), the pair of anodic and cathodic peaks at 0.55 V are ascribed to the O-bound isomer in the *ccc*-$[RuCl_2(dmso)_2(tpby)_2]$ complex, e.g.:

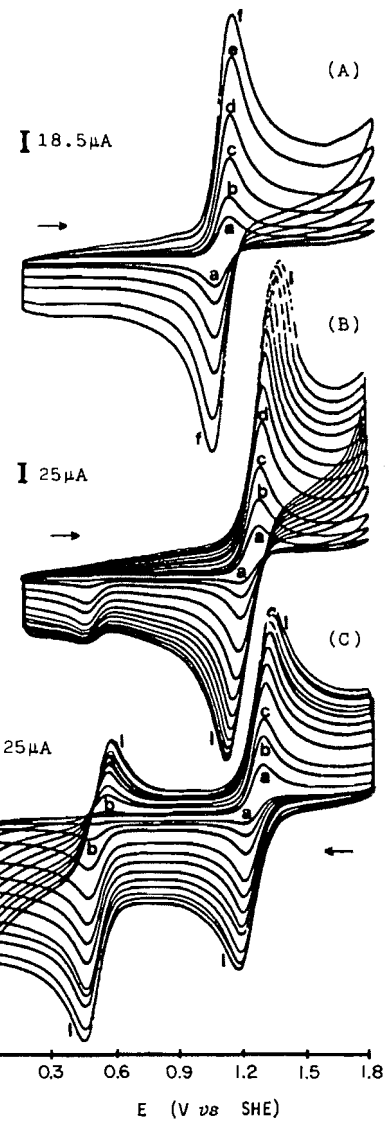

FIG. 3. Cyclic voltammograms of (*A*) *cct*-$[RuCl_2(dmso)_2(tbpy)_2]$ (1 mmol dm^{-3}) at (*a*) 10, (*b*) 20, (*c*) 50, (*d*) 100, (*e*) 200, (*f*) 300 mV s^{-1}, and of the *ccc* isomer, starting at (*B*) 0.2 V and (*C*) 1.8 V, at (*a*) 20, (*b*) 50, (*c*) 100, (*d*) 200, (*e*) 300, (*f*) 400, (*g*) 500, (*h*) 600, (*i*) 700, (*j*) 800, (*k*) 900, and (*l*) 1000 mV s^{-1} (acetonitrile, 25°C, [TEAP] = 0.10 mol dm^{-3}).

$$Ru^{III}—O \underset{k^{III}_{S\rightarrow O}}{\overset{k^{III}_{O\rightarrow S}}{\rightleftharpoons}} Ru^{III}—S$$

The equilibrium constant for the Ru^{III}—O/Ru^{III}—S reaction can be estimated from the cyclic voltammograms (Fig. 3*C*) starting at 1.8 V, after a few minutes, in order to ensure complete equilibration of the system. In the absence of kinetic effects, i.e. if the isomerization rates were much slower than the scan rates, the ratio $[ic_1]/[ic_2]$ would correspond to K^{III} = $[Ru^{III}—S]/[Ru^{III}—O]$, considering that the diffusion coefficients for the two isomers are practically the same. Unfortunately, because of the kinetic effects, this is only approximate, and K^{III} is better obtained from the plot of $[ic_1]/[ic_2]$ as a func-

tion of the inverse of the scan rates, v^{-1}, and extrapolating to $v \rightarrow \infty$. In this way, $K^{III}_{O\rightarrow S} = 0.63 \pm 0.04$.

The kinetic constants for the isomerization process were estimated from the working curves proposed by Shain and Nicholson (20), for a reversible chemical reaction preceding an electrochemical step (case III). The ratios i_k/i_d employed in this method, where i_k is the measured peak current and i_d is the corresponding diffusional current in the absence of chemical reactions, were obtained from $[ic_1] = i_k$, starting at 1.8 V, and from $[ia_1] = i_d$, starting at 0.2 V. The kinetic constants obtained in this way were:

$$k^{III}_{O\rightarrow S} = 1.2 \pm 0.3\ s^{-1} \text{ and } k^{III}_{S\rightarrow O} = 1.9 \pm 0.3\ s^{-1}$$

Based on the equilibrium constant $K^{III}_{O\rightarrow S}$ and on the electrochemical data, assuming $E^0 = E_{1/2}$, the following thermodynamic cycle can be solved in order to obtain $K^{II}_{O\rightarrow S}$,

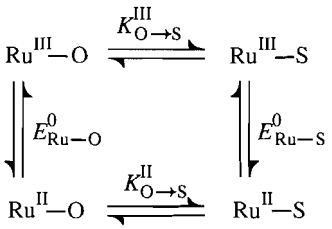

In this way, $K^{II}_{O\rightarrow S} = 2.1 \times 10^{12}$, indicating that Ru^{II} has a very strong preference for the S donor atom in dmso.

The evaluation of the kinetic constants for the isomerization reaction in the Ru^{II} complex depends on the detection of the unstable Ru^{II}—O species before it converts to the Ru^{II}—S form. A simple way of generating the Ru^{II}—O isomer is to start from the Ru^{III}—O and Ru^{III}—S species, in equilibrium, e.g., at 1.8 V, and applying a fast potential scanning in the cathodic direction. The Ru^{II}—O species generated in this way can be detected in the reverse scan as a function of time, from ia_2 measured at the several scan rates, or indirectly, from the changes in the anodic peak currents, ia_1, corresponding to the Ru^{II}—S isomer. The dependence of ln $(ia_1/v^{1/2})$ or ln $(ia_2/v^{1/2})$ against time was linear, yielding a rate constant $k^{II}_{O\rightarrow S} = 1.0 \times 10^{-2}\ s^{-1}$. The reverse rate constant can be calculated as $k^{II}_{S\rightarrow O} = k^{II}_{O\rightarrow S}/K^{II}_{O\rightarrow S} = 5 \times 10^{-14}\ s^{-1}$.

According to these results, the *cct* isomer exhibiting two *trans*-Cl—Ru^{III}—SO bonds does not undergo linkage isomerization reactions, presumably because of the *trans*-cooperative interactions. In contrast, the *ccc* isomer isomerizes very rapidly to the O-bound form when it is oxidized to Ru^{III}. The main difference between these two isomers is the occurrence of a dmso ligand *trans* to a tbpy ligand. In the oxidized state, this combination seems to destabilize the complex, since the S-bound dmso is a strong π-acceptor ligand, in contrast to the O-bound species, and the tbpy ligand is not a strong enough π donor to interact in a cooperative way with the dmso ligand.

Acknowledgements

The support from FAPESP, CNPq, and PADCT is gratefully acknowledged.

1. E. Alessio, G. Mestroni, G. Nardin, W.M. Attia, M. Calligaris, G. Sava, and S. Zorzet. Inorg. Chem. **27**, 4099 (1988).
2. J.S. Jaswall, S.J. Rettig, and B.R. James. Can. J. Chem. **68**, 1808 (1990).
3. S. Cauci, P. Viglino, G. Esposito, and F. Quadrifoglio. J. Inorg. Biochem. **43**, 739 (1991).
4. N.P. Farrell. Transition metal complexes as drugs and chemotherapeutic agents. Kluwer Academic Publication, Dordrecht. 1989.
5. B.R. James, E. Ochiai, and G.L. Rempel. Inorg. Nucl. Chem. Lett. **7**, 781 (1971).
6. D.P. Riley. Inorg. Chem. **22**, 1965 (1983).
7. D.P. Riley and R.E. Shumate. J. Am. Chem. Soc. **106**, 3179 (1984).
8. D.P. Riley and J.D. Oliver. Inorg. Chem. **25**, 1814 (1986).
9. R.S. Srivastava, B. Milani, E. Alessio, and G. Mestroni. Inorg. Chim. Acta, **191**, 15 (1992).
10. P.K.L. Chan, K.A. Skov, B.R. James, and N.P. Farrell. Chem. Biol. Interactions, **59**, 247 (1986).
11. H.E. Toma and D. Oliveira. Polyhedron, **10**, 1699 (1991).
12. H.E. Toma and D.O. Silva. Chromatographia, **32**, 54 (1991).
13. I.P. Evans, A. Spencer, and G. Wilkinson. J. Chem. Soc. Dalton, **2**, 204 (1973).
14. J.H.S. Green, W. Kynaston, and H.M. Paisley. Spectrochim. Acta, **19**, 549 (1963).
15. M.T. Forel and M. Tranquille. Spectrochim. Acta, **26**, 1023 (1970).
16. H.E. Toma, P.S. Santos, and A. Bolanos. J. Chem. Res. S, 124 (1988).
17. P. Day and N. Sanders. J. Chem. Soc. A, 1536 (1967).
18. A. Yeh, N. Scott, and H. Taube. Inorg. Chem. **21**, 2542 (1982).
19. G. Costa, G. Balducci, E. Alessio, C. Tavagnacco, and G. Mestroni. J. Electroanal. Chem.**296**, 57 (1990).
20. R.S. Nicholson and I. Shain. Anal. Chem. **36**, 706 (1964).

Can. J. Chem. Downloaded from www.nrcresearchpress.com by ESC ESCOLA DE ENGENHARIA on 09/08/12
For personal use only.

AM1 studies on the stabilities of anionic σ-complex regioisomers: thermodynamics of regioselectivity in the reaction of methide, methoxide, and hydroxide anions with electron-deficient aromatics

ERWIN BUNCEL[1] AND RICHARD M. TARKKA[2]

Department of Chemistry, Queen's University, Kingston, ON K7L 3N6, Canada

AND

JULIAN M. DUST[1]

Department of Chemistry, Sir Wilfred Grenfell College, Corner Brook, NF A2H 6P9, Canada

Received October 8, 1993

Can. J. Chem. Downloaded from www.nrcresearchpress.com by EESC ESCOLA DE ENGENHARIA on 09/08/12
For personal use only.

ERWIN BUNCEL, RICHARD M. TARKKA, and JULIAN M. DUST. Can. J. Chem. **72**, 1709 (1994).

Heats of formation (ΔH_f) for a series of aromatics that are progressively more electron deficient (benzene, **6**; nitrobenzene, **7**; 4-fluoronitrobenzene, **8**; 1,3-dinitrobenzene, **9**; 2,4,6-trinitroanisole, **2**; and 1,3,5-trinitrobenzene, **1**) were determined by semi-empirical AM1 calculations. As a probe of the factors that govern the regioselectivity exhibited in the formation of anionic σ-adducts (Meisenheimer complexes), experimental gas-phase ΔH_f values for the prototypical oxygen and carbon nucleophiles (hydroxide, methoxide, and methide anions) were used in a thermochemical calculation along with the calculated ΔH_f of the electrophiles and the adducts to determine the heats of complexation (ΔH_c). The present results show that for the series of nitroaryl electrophiles, **7**, **9**, and **1**, hydroxide and methide anions *exhibit the same regioselectivity based on thermodynamics of Meisenheimer complex formation.* Specifically, Meisenheimer complexes derived from attack at a position *para* to at least one nitro group (designated MC-4) are formed with the greatest exothermicity (ΔH_c). Exothermicity of complexation increases for both hydroxide and methide adduct formation as the number of nitro groups in the electrophile is increased, from **7** to **9** and to **1**, but formation of the methide adducts occurs uniformly with greater exothermicity than that of hydroxide adducts. These results are considered in light of solution calorimetric data that quantify adduct stability in condensed phases. Surprisingly, it is found that *regioselectivity inverts for CH_3^- as compared to OH^- and CH_3O^- in complexation with 2,4,6-trinitroanisole, 2.* Thus, while methoxide and hydroxide form adducts at C-1 of TNA with higher exothermicity than at C-3, methide preferentially forms an adduct at C-3 according to the same enthalpy criterion. These results arise from the degree of stereoelectronic stabilization that may be imparted to the respective Meisenheimer complexes formed from *ipso* attack, that is, the adducts (MC-1) that are geminally disubstituted with electronegative heteroatom groups. For the methoxide MC-1 of TNA, **2**, full stereoelectronic stabilization is provided by n–σ* donation from nonbonding electron pairs of the acetal-like methoxyl moieties to suitable C—O acceptor bonds. However, the methide moiety of the comparable MC-1 of TNA cannot partake in such an interaction and, so, with methide, MC-3 formation is preferred over MC-1. Further evidence is provided by consideration of the two energy minima obtained from optimization of the geometry of the oxygen-centred adducts formed by attack of methoxide at C-1 of TNA, **2**. In the presence of a point charge that simulates an ion-paired cation, an "M-shaped" conformer is favoured for MC-1, while in the absence of a counterion the "S-shaped" conformer is favoured. Without a complexing counterion M and S conformers are both local minima, while the "S" conformer constitutes the global minimum. The AM1 optimized structure for the "M" conformer compares favourably to published X-ray data. The greater exothermicity of formation of the "S" conformer in the absence of the counterion is indicative of stereoelectronic stabilization of the O-adduct. The geometry is rationalized as a result of minimizing steric repulsion and maximizing the n–σ* stabilization of the C-1 adduct.

ERWIN BUNCEL, RICHARD M. TARKKA et JULIAN M. DUST. Can. J. Chem. **72**, 1709 (1994).

Utilisant des calculs semi-empiriques AM1, on a déterminé les chaleurs de formation (ΔH_f) d'une série de composés aromatiques de plus en plus électrodéficients (benzène, **6**; nitrobenzène, **7**; 4-fluoronitrobenzène, **8**; 1,3-dinitrobenzène, **9**; 2,4,6-trinitroanisole, **2**; et 1,3,5-trinitrobenzène, **1**). Comme sonde des facteurs qui gouvernent la régiosélectivité exhibée lors de la formation d'adduits-σ anioniques (complexes de Meisenheimer), on a utilisé les valeurs de ΔH_f expérimentales de la phase gazeuse de nucléophiles oxygénés et carbonés typiques (anions hydroxyde, méthylate et méthylure) de concert avec les valeurs calculées des ΔH_f électrophiles et des adduits dans un calcul thermochimique effectué en vue de déterminer les chaleurs de complexation (ΔH_c). Les résultats obtenus démontrent que pour la série des nucléophiles nitroaryles **7**, **9** et **11**, les anions hydroxyde et méthylure *présentent la même régiosélectivité, si on se base sur la thermodynamique de la formation des complexes de Meisenheimer.* D'une façon spécifique, les complexes de Meisenheimer obtenus par une attaque en position *para* par rapport à au moins un groupe nitro (appelé MC-4) se forment avec la plus grande exothermicité (ΔH_c). Avec l'augmentation du nombre de groupes nitro, en passant du composé **7** à **9** et à **1**, l'exothermicité de la complexation augmente pour la formation de l'adduit hydroxyde ainsi que méthylure; toutefois, la formation des adduits méthylures se fait toujours avec une plus grande exothermicité que pour les adduits hydroxyde. On considère ces résultats à la lumière de données calorimétriques qui quantifient la stabilité des adduits en phase condensée. D'une façon surprenante, on a trouvé que *pour la complexation avec le 2,4,6-trinitroanisole, 2, la régiosélectivité s'inverse pour le CH_3^- par rapport avec le OH^- et le CH_3O^-.* Alors que les anions méthylate et hydroxyde forment des adduits en C-1 du TNA avec une plus grande exothermicité qu'en C-3, le méthylure formerait donc, suivant les mêmes critères, préférentiellement un adduit en C-3. Ces résultats découlent du degré de stabilisation stéréoélectronique qui peut être transmis aux complexes de Meisenheimer respectifs par une attaque *ipso*, c'est-à-dire aux adduits (MC-1) qui sont disubstitués d'une façon géminée avec des groupes hétéroatomiques négatifs. Pour le MC-1 du méthanolate du TNA, **2**, toute la stabilisation stéréoélectronique est fournie par un don n–σ* des paires d'électrons non liés d'un méthoxyle ressemblant à un acétal à des liai-

[1]Authors to whom correspondence may be addressed.

[2]Current address: Dept. of Chemistry, University of Illinois, Urbana-Champaign, IL 60801, U.S.A.

sons C—O appropriées agissant comme accepteur. Toutefois, la portion méthylure du MC-1 comparable du TNA ne peut pas prendre part à une telle interaction et avec le méthylure la formation d'un MC-3 est préférée à celle d'un MC-1. D'autres données sont obtenues par la considération des deux minima d'énergie obtenues par optimisation de la géométrie des adduits centrés sur l'oxygène et formées par l'attaque du méthylate en C-1 du TNA, **2**. En présence d'une charge ponctuelle qui simule un cation apparié, un conformère en «forme de M» est favorisé pour le MC-1 alors que, en l'absence d'un contre-ion, le conformère «en forme de S» est favorisé. En l'absence d'un contre-ion agissant comme complexant, les conformères M et S sont tous les deux des minima locaux alors que le conformère S est le minimum global. La structure optimisée par AM1 du conformère M se compare favorablement avec les données de diffraction des rayons x qui ont été publiées. L'exothermicité plus élevée observé pour la formation du conformère S en l'absence de contre-ion indique la présence d'une stabilisation stéréoélectronique de l'adduit-O. On rationalise la géométrie sur la base d'une minimisation de la répulsion stérique et une maximisation de la stabilisation n–σ^* avec l'adduit C-1.

[Traduit par la rédaction]

Introduction

Anionic σ-adducts, also termed Meisenheimer (1) or Jackson–Meisenheimer complexes (2), arise from σ-bond formation between nucleophiles ($Nu:^-$) and electron-deficient aromatic or heteroaromatic substrates, typified by 1-X-2,4,6-trinitrobenzene electrophiles (3). The interaction may be represented generally by Scheme 1. When X is a ring proton, the electrophile E is TNB (**1**) and a single adduct is formed by reaction at an unsubstituted site (solid boxed portion of Scheme 1); when X represents a substituent other than H, isomeric Meisenheimer complexes (i.e., MC-1 and MC-3) result from nucleophilic attack at C-1 and C-3 sites, respectively. Attack at C-1 of a substrate that bears a good leaving group leads to formation of a metastable MC-1 that decomposes to give a new 1-Nu-2,4,6-trinitrobenzene derivative. Thus, the pathway defined by attack at C-1 and expulsion of X^- represents the S_NAr mechanism of nucleophilic aromatic substitution (4) (dashed portion of Scheme 1), where k_1 (the rate coefficient for C-1 attack) is usually rate determining. However, if X is a relatively poor nucleofuge such as methoxy (E = 2,4,6-trinitroanisole, TNA, **2**), then both MC-1 and MC-3 may be observable, depending upon solvent and temperature (5, 6).

The kinetic preference (k_1 vs. k_3) shown by nucleophiles in such reactions with **2**, as well as the thermodynamic stability of the adducts ($K_1 = k_1/k_{-1}$ vs. $K_3 = k_3/k_{-3}$), yield patterns of regioselectivity that have constituted an important area of recent inquiry (7, 8). In the course of these investigations we have classified the various types of potential regioselectivity[3] in MC formation for 1-X-2,4,6-trinitrobenzenes (7), ranging from thermodynamic and kinetic preference for formation of MC-1 (termed K1T1, and exemplified by the reaction of TNA with phenoxide as an O-nucleophile) (*7a*), among other systems (9, 10), to the more commonly reported kinetic preference for MC-3 formation, coupled with formation of MC-1 as the product of thermodynamic control, i.e., K3T1 as illustrated by the TNA-alkoxide systems (5, 11). Most recently we have detailed K1T3 regioselectivity in the TNA – mesitoxide system (*7b*), the exact inverse of K3T1 behaviour (7). These patterns of reactivity are shown in Fig. 1 as qualitative energy profiles.

We have been especially interested in the formation of Meisenheimer complexes by electron-deficient substrates, such as **1** and **2**, with ambident nucleophiles, including phenoxide ion as a carbon- and oxygen-nucleophile (7, 11), aniline as a carbon- and nitrogen-nucleophile (12), and dopamine (3,4-dihydroxyphenylethylamine) as a carbon-, nitrogen-, and oxygen-nucleophile (13). Our recent finding that phenoxide, as an O-nucleophile, displays the K1T1 pattern of behaviour in its reaction with **2**, in contrast to the K3T1 behaviour exhibited by methoxide, has led us to scrutinize the connection between the type of nucleophile and the type of behaviour displayed. The present theoretical study thus probes the intrinsic reactivity of carbon- vs. oxygen-centred nucleophiles in Meisenheimer complex formation, as well as those features of the substrates and nucleophiles that govern the regioselectivity found in condensed phase studies of these systems.

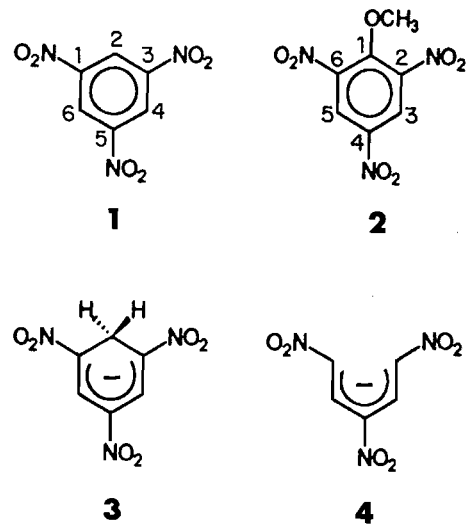

1 **2** **3** **4**

The historical development of theoretical calculations on Meisenheimer complexes (MCs), and their generally nitro-substituted parent compounds, parallels the development of computational chemistry. Early calculations were of the Hückel molecular orbital (HMO) type (14–16) or used the Pariser–Parr–Pople (PPP) self-consistent field (SCF) method to obtain information such as π-electron distribution in the MC, substituent effects, and electronic transition energies. Generally, these studies were limited to the anionic adduct that would arise from addition of hydride ion to TNB (**3**) or to model compounds such as the pentadienyl system, substituted with one or more electron-withdrawing groups (e.g., **4**).

More recently, theoretical studies have fallen into two broad categories: (*a*) ab initio calculations on MC models and (*b*) semi-empirical calculations on the Meisenheimer complexes themselves. For example, ab initio calculations at the STO-3G level have been run to delve into the question of structure of cyclohexadienate anions: planar or fully delocalized in a homocyclopentadienyl structure (17, 18). The semi-empirical stream has concentrated on the determination of fully optimized structures and physical properties (e.g., charge distribution) for

[3]Our previous terminology for K1T1 (Kinetic preference for C-1 attack, coupled with Thermodynamic preference for C-1 attack) was KC-1,1, indicating Kinetic Control favouring MC-1 formation (7). K1T1 now replaces KC-1,1 and similarly KC-1,3 is now designated as K3T3, TC-1,1 as K3T1, and TC-1,3 as K1T3. We thank Prof. J.F. Bunnett for suggesting this alternative classification.

Can. J. Chem. Downloaded from www.nrcresearchpress.com by EESC ESCOLA DE ENGENHARIA on 09/08/12
For personal use only.

Can. J. Chem. Downloaded from www.nrcresearchpress.com by EESC ESCOLA DE ENGENHARIA on 09/08/12
For personal use only.

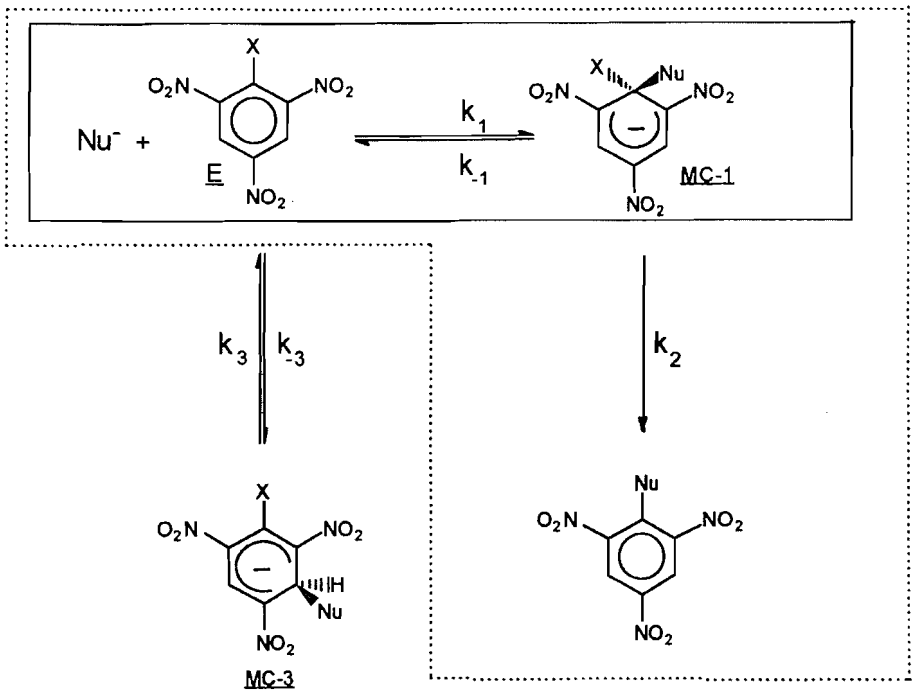

X = H, E = **1** = TNB; MC-1 = MC-3
X = OCH_3, E = **2** = TNA

SCHEME 1

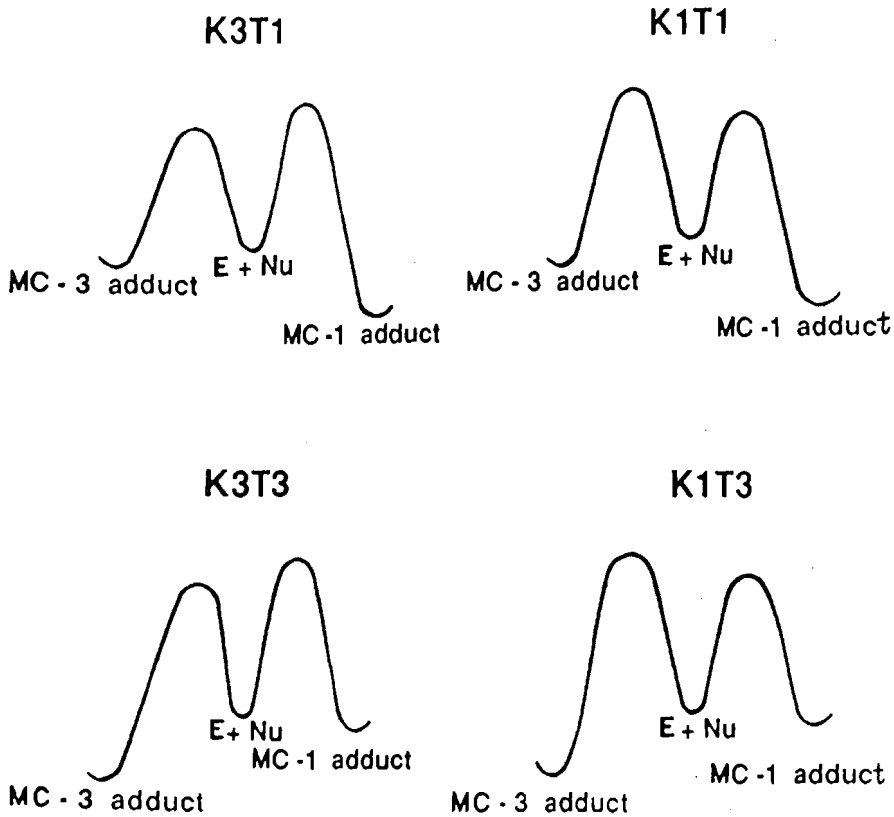

FIG. 1. Qualitative free energy profiles detailing the different patterns of regioselectivity: K3T1 represents the case where the MC-3 adduct is favoured kinetically, but the MC-1 adduct is the product of thermodynamic control; K1T1 describes kinetic and thermodynamic preference for the MC-1 adduct; K3T3 describes kinetic and thermodynamic preference for the MC-3 adduct; and K1T3 represents the case where the MC-1 adduct is favoured kinetically, but the MC-3 adduct is the product of thermodynamic control. The different classes of regioselectivity (K3T1, etc.) are discussed in the text. Energetics are exaggerated for clarity.

actual MCs. Our MNDO exploration of the structures, charge densities, and heats of formation of the hydroxide MCs formed from **1** and from the super-electrophile, 4,6-dinitrobenzofuroxan, **5**, is an example of this type of theoretical study (19).

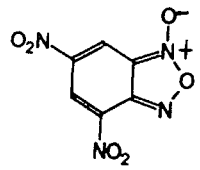

5

In comparing the two categories of calculations, it is generally found that ab initio calculations, performed with relatively sophisticated basis sets, yield better estimates of the values for physical properties than do semi-empirical methods. However, the requirement of relatively large basis sets (e.g., 6-31+G*) limits the systems suitable for study by high-level ab initio methods to relatively small molecules. As a result, semi-empirical methods are the methods of choice for investigating large MCs (20).

At the same time as the advent of high-speed computers has made larger molecules amenable to ab initio calculations, semi-empirical calculations have also improved. These SCF calculations, most commonly Dewar's MINDO/3 (21), MNDO (22), and AM1 (23) methods, are parameterized to experimental data and empirically adjusted for average correlation and thermal energies. AM1 represents an advance over the MNDO method in that the tendency of MNDO to overestimate core–core repulsions has been corrected by adjustment of the core repulsion function. This correction alleviates the MNDO weaknesses: failure to reproduce hydrogen bonds, overestimation of activation enthalpies, and incorrect formation enthalpies for crowded and strained molecules (23). As such, the calculations presented here represent a refinement over earlier calculation results performed at the MNDO and MINDO/3 levels.

To assess trends in MC stability as a function of both nucleophile and electrophile type, and of the site of addition to the electrophile, we have calculated the heats of formation of a variety of OH^-, CH_3O^-, and CH_3^- adducts formed with a wide range of nitroaromatics. The results, including fully optimized structures and comparative heats of formation, will be discussed in light of known X-ray structures of MCs and the condensed phase reactions of **1** and **2** with nucleophiles. The importance of stereoelectronic effects on the stability of MCs will emerge from the discussion.

Experimental

Method

All calculations were carried out using an IBM 3081 computer. The AMPAC version 2.10 of AM1 (23) was the program used for all calculations reported herein. All structures were fully optimized using a Fletcher–Powell minimization (24) to a self-consistent field (SCF) that satisfied Herbert's test and were characterized as local minima; no negative force constants were obtained after running the "FORCE" option. The restricted Hartree–Fock (RHF, closed shell) scheme was used throughout. All optimizations were carried out using the "PRECISE" option.

Input geometries

The input geometry for a given neutral nitroaromatic was constructed from the AM1 optimized geometry of a less highly substituted aromatic. For example, the AM1 optimized geometry for nitrobenzene (NB, **7**), which has been reported (20*a*), was used as the template for construction of the input geometry of 4-fluoronitrobenzene (4-FNB, **8**). Slightly perturbed geometries, obtained from initial optimization, were generally used as input for a second run to ensure convergence.

The input geometries of the MCs assumed standard sp^3 hybridization of the carbon at the site of addition, while the other ring carbons and nitro groups were entered as being perfectly coplanar. The O—CH_3 bonds were placed antiperiplanar to the sp^3 C—H (or C—OCH_3) bond, as suggested by X-ray data (25).

Systems studied

Full optimizations and calculations of the energetics were done for all possible regioisomers of the following systems (substrate:nucleophile): TNB:OH^-, TNB:OCH_3^-, TNB:CH_3^-, TNA:OH^-, TNA:OCH_3^-, TNA:CH_3^-, B:OH^-, B:CH_3^-, NB:OH^-, NB:CH_3^-, 4-FNB:OH^-, 4-FNB:CH_3^-, 1,3-DNB:OH^-, and 1,3-DNB:CH_3^-, where TNB, TNA, B,

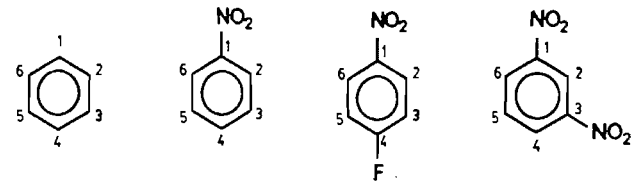

6 **7** **8** **9**

NB, 4-FNB, and 1,3-DNB refer to 1,3,5-trinitrobenzene, 2,4,6-trinitroanisole, benzene, nitrobenzene, 4-fluoronitrobenzene, and 1,3-dinitrobenzene, respectively. Summaries of the calculations, including fully optimized geometries, are available as Supplementary Material (Supplementary Figs. 1–37 and Supplementary Tables 1–37).[4] Supplementary Figs. 1–37 show the optimized structures and numbering schemes used in the AM1 calculations and correspond to the relevant Supplementary Table. For example, Fig. 4 illustrates the electrophile, nitrobenzene, while Table 4 contains the calculation results, including ΔH_f, dipole moment, ionization potential, bond lengths, and atomic charges.

Results

The enthalpies of formation of the series of fully optimized neutral nitroaromatics and fully optimized MCs are presented in Tables 1 and 2. Reaction enthalpies (heats of complexation, ΔH_c) were calculated for the following reaction:

[1] $Nu^-: + E \rightarrow MC$

where E represents the aromatic substrate, $Nu^-:$ is OH^-, CH_3^-, or CH_3O^-, and MC identifies the resultant Meisenheimer complex. The standard thermochemical eq. [2] follows from eq. [1]:

[2] $\Delta H_c = \Delta H_f(MC) - [\Delta H_f(E) + \Delta H_f(Nu^-:)]$

where the reaction enthalpy, ΔH_c, refers to eq. [1]. The reaction enthalpies for formation of the various adducts are listed in Table 2.

In determining the reaction enthalpies, experimental values for the gas-phase heats of formation of the nucleophiles were used rather than the values calculated by AM1. It is recognized that the heats of formation of small anions that bear a highly localized charge are not reproduced well by AM1 (20, 23*a*, *b*). Although the AM1 ΔH_f of CH_3O^- agrees well with the experi-

[4]Copies of the Supplementary Material may be purchased from: The Depository of Unpublished Data, Document Delivery, CISTI, National Research Council Canada, Ottawa, Canada K1A 0S2.

Can. J. Chem. Downloaded from www.nrcresearchpress.com by EESC ESCOLA DE ENGENHARIA on 09/08/12
For personal use only.

TABLE 1. AM1 heats of formation (kcal/mol) of electrophiles (E) and regioisomeric Meisenheimer complexes (MC(Nu^-))

E	ΔH_f	MC[a]	ΔH_f MC(OH^-)	MC(CH_3^-)	MC(OCH_3^-)
B, **6**	+22.0	MC-1	−35.2 −(35.2)[b]	+12.2	
NB, **7**	+25.3	MC-2	−66.2 (−65.2)[b]	−21.9	
		MC-3	−51.5	−5.7	
		MC-4	−69.2	−24.7	
4-FNB, **8**	−19.1	MC-2	−116.1	−72.3	
		MC-3	−101.5	−56.5	
		MC-4	−120.5	−69.5	
1,3-DNB, **9**	+33.1	MC-2	−79.9 (−78.5)[b]	−37.9	
		MC-4	−84.6 (−84.1)[b]	−42.2	
		MC-5	−61.3 −(68.2)[b]	−17.0	
TNB, **1**	+44.9	MC-2	−92.0 −(89.9)[b]	−51.2	−85.6
TNA, **2**	+12.5	MC-1	−131.3	−82.2	−120.6[c] (−116.2)[d]
		MC-3	−123.8	−82.3	−116.6

[a]The numbers following the designation "MC" refer to the positions of attack of the nucleophiles.
[b]Values in parentheses refer to previous AM1 calculations, refs. 20*a*, 23*a*, and 23*b*.
[c]Values refer to the S conformer.
[d]Values refer to the M conformer, calculated without simulated cation.

TABLE 2. AM1 heats of complexation (ΔH_c) for eq. [1], kcal/mol[a]

E	MC[b]	ΔH_c MC(OH^-)	MC(CH_3^-)	MC(OCH_3^-)
B, **6**	MC-1	−24.5	−43.0	
NB, **7**	MC-2	−58.8	−80.4	
	MC-3	−43.8	−64.2	
	MC-4	−61.8	−83.2	
4-FNB, **8**	MC-2	−64.3	−86.4	
	MC-3	−49.8	−70.6	
	MC-4	−68.8	−83.6	
1,3-DNB, **9**	MC-2	−80.3	−104.2	
	MC-4	−85.0	−108.5	
	MC-5	−61.7	−83.3	
TNB, **1**	MC-2	−104.2	−129.1	−97.3
TNA, **2**	MC-1	−111.1	−127.9	−99.9[c] (−95.5)[d]
	MC-3	−103.6	−128.0	−95.9

[a]Calculated according to thermochemical eq. [2], using AM1 heats of formation (ΔH_f) for the electrophiles, E, and Meisenheimer complexes, MC.Nu^- (Table 1), and gas-phase experimental ΔH_f for OH^- (−32.7), CH_3^- (+33.2 ± 1.9), and CH_3O^- (−33.2 ± 2.4 kcal/mol), ref. 23*c*.
[b]The numbers following the designation "MC" refer to the positions of attack of the nucleophiles.
[c]Values refer to the S conformer.
[d]Value refers to the M conformer, calculated without simulated cation.

Can. J. Chem. Downloaded from www.nrcresearchpress.com by EESC ESCOLA DE ENGENHARIA on 09/08/12
For personal use only.

Can. J. Chem. Downloaded from www.nrcresearchpress.com by EESC ESCOLA DE ENGENHARIA on 09/08/12
For personal use only.

mental value (20), we have chosen to use the experimental gas-phase ΔH_f of the nucleophiles as compiled in a recent critical review (−32.7 kcal/mol for OH^-, +33.2 kcal/mol for CH_3^-, and −33.2 kcal/mol for CH_3O^-) (23*c*) for calculating reaction enthalpies, for the sake of self-consistency.

The MCs are designated according to the site of addition, numbering from the nitro substituent, if present, according to the structures, **1**, **2** and **6**–**9**. Thus, attack of a nucleophile at C-2 would lead to the Meisenheimer complex, MC-2, attack at C-4 would lead to MC-4, and so on. For 2,4,6-trinitroanisole, **2**, MC-1 refers to the product of addition at C-1 while MC-3 represents the product of nucleophilic addition to the C-3 site, as per the numbering of structure **2**.

Hydroxide and methide Meisenheimer complexes (MCs) of benzene, nitrobenzene, 4-fluoronitrobenzene, and 1,3-dinitrobenzene

The heats of formation (ΔH_f) of a series of aromatic compounds, ranging from relatively electron-rich (B, **6**) to successively electron-poor (NB, **7**; 4-FNB, **8**; and 1,3-DNB, **9**) were calculated. These enthalpies of formation are tabulated, along with ΔH_f values for the corresponding regioisomeric OH^- and CH_3^- MCs, in Table 1. All optimized geometries, both for the neutral aromatics and the anionic σ-adducts, were deemed satisfactory; no bond lengths or angles were found to be unusually large or small and these were found to agree reasonably well with published AM1 results in the case of some of the neutrals (20*a*, 23*a*) and with X-ray data in the case of the MCs (16, 25), as discussed below. Importantly, the energetics for the few systems shared with previous AM1 studies were replicated satisfactorily. Thus, the calculated heats of formation for B, **6**; NB, **7**; and 1,3-DNB, **9**, are in accord with those reported by Dewar et al. (23*a*) and Bunton and co-workers (20*a*).

It is noteworthy that although attempts were made to calculate the structures of the hydroxide adducts that would arise from nucleophilic attack of hydroxide on the *ipso* carbon bearing a nitro group for substrates **8** and **9**, no local minima representing these putative adducts could be located on the potential energy surface. Instead, the inputs optimized to the phenols produced by nucleophilic displacement of nitrite from the ring.

Hydroxide, methoxide, and methide adducts of TNB and TNA

Fully optimized AM1 structures for the hydroxide, methoxide, and methide MCs of TNB, **1**, and TNA, **2**, were calculated (cf. Supplementary Figs. and Tables 26–28 for **1** and Supplementary Figs. and Tables 29–37 for **2**). The optimized structures derived from CH_3O^- attack on **1** and for the MC-1 derived from CH_3O^- attack on **2** are in good agreement with published X-ray structures (16, 25) (vide supra).

For the methoxide adduct MC-1 of TNA the calculation provided two local minima, corresponding to the "M-shaped" and "S-shaped" conformations (Supplementary Tables 34 and 35, respectively) shown in Fig. 2. The S conformer is the global minimum.

Discussion

Insightful information can be obtained from semi-empirical calculations for the minimum energy reaction pathways (MERPs) for formation of anionic σ-adducts (25), from the charge densities of the neutral substrates, and the resultant MCs (26), as well as intermediate species that potentially exist on the MERP to MC formation (20). Previous calculations of the

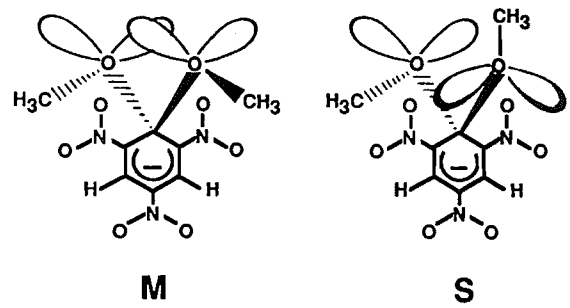

FIG. 2. The conformational minima for the CH_3O^- MC-1 of TNA, **2**. The "S-shaped" conformer, in which one methyl of the CH_3O-C(1)-OCH_3 moiety is pointed "down" and the other "up" and in which the lone pairs of the oxygens are staggered, is favoured by 4.4 kcal/mol over the "M-shaped" conformer, according to the AM1 calculations. In the M conformer both methyl groups point "down". The lone pairs of the oxygen of the "up" methoxyl in the S form can each participate partly in n–σ* stabilization, whereas the lone pairs of the oxygen of the "down" methoxyl cannot. Consequently, stereoelectronic stabilization in the M form is not possible. In this figure, the C(1)—O bond lengths are exaggerated for clarity. Note that in both the M and S forms the CH_3O-C(1)-OCH_3 moiety places the methyls in the same plane.

MERP at the MNDO (27) and AM1 (20) levels have located minima, of varying degrees of shallowness, for charge-transfer complexes and for complexes resulting from single electron transfer (i.e., radical–radical anion pairs). On the other hand, the factors governing the propensity of a given nucleophile and substrate to form one regioisomer over another, as a function of the nature of the substrate and nucleophile, have not hitherto been probed by AM1 on the basis of the energetics of formation of the regioisomeric MCs. The present study concentrates on these energetics; the heats of complexation, ΔH_c (eq. [1]), for various regioisomers were therefore calculated for the reaction of a series of nitroaromatic substrates with OH^-, CH_3O^-, and CH_3^- as nucleophiles.

1. Comparative trends in the reaction enthalpies for formation of Meisenheimer complexes

*(a) Effect of increasing NO_2 substitution (E = **6**, **7**, **9**, **1**)*

For comparable sets of both OH^- and CH_3^- MCs there is a definite increase in the exothermicity of adduct formation as a function of increasing nitro group substitution of the ring (Table 2). The overall order of decreasing exothermicity for formation of OH^- adducts (ΔH_c) when comparing the most stable regioisomer for each substrate–nucleophile pair, is MC-2 of **1** > MC-4 of **9** > MC-4 of **7** > MC-1 of **6**, with numerical differences in ΔH_c of 19.2, 23.2, and 37.3 kcal, respectively. A similar trend was found for the corresponding CH_3^- MCs.

Comparison of solution (CH_3O^-/CH_3OH) calorimetric data (28, 29) with our present calculations reveals a remarkable agreement between the experimental and the calculated energetics. In this regard, Strauss and co-workers (28) found nitro substitution of a cyclohexadienate ring in a position *ortho* to the site of nucleophilic attachment to be worth 9 kcal of stabilization, whereas *para* NO_2 substitution stabilized the Meisenheimer complex by 30 kcal/mol. Fendler et al. (29) later obtained values of 10.3 kcal/mol for *ortho* and 21.0 kcal/mol for *para* substitution, i.e., a ratio of 1:2 for *ortho* as compared to *para* substitution. On this basis one would expect MC-4 of **9** to be formed with an exothermicity of between 12 and 19 kcal/mol relative to MC-4 of **7** (33–50% of 37.3 kcal/mol, the difference

Can. J. Chem. Downloaded from www.nrcresearchpress.com by EESC ESCOLA DE ENGENHARIA on 09/08/12
For personal use only.

in ΔH_c between MC-1 of **6** and MC-4 of **7**). The $\delta\Delta H_c$ value, according to AM1, is 23.2 kcal/mol. Similarly, the second *ortho* NO_2 substitution that occurs on going from MC-4 of **9** to MC-2 of **1** should be worth 12–19 kcal/mol; the calculated difference is 19.2 kcal/mol. Therefore, the *proportionality* of the energetics is maintained in the calculations as in the solution calorimetric work.

Clearly, the trend to more exothermic ΔH_c values with increasing nitro group substitution arises from both the relative destabilization of the parent nitroaromatic and the relative stabilization of the resultant MC (ΔH_f) as seen from Table 1.

*(b) Effect of nucleophile (CH_3^- vs. OH^-) with **1**, **9**, **7**, and **6***

For a given aromatic substrate and a given site of attack the reaction enthalpy favours formation of the MC with CH_3^- compared with OH^-. Benzene, for example, forms MC-1 with CH_3^- with a ΔH_c of −43.0 kcal/mol, while formation of the corresponding OH^- MC has an associated reaction enthalpy of −24.5 kcal/mol. Besides the energetic preference for C-adduct formation over O-adduct formation, there is also a trend to greater MC stability with increased nitro substitution of the ring. It is interesting, then, that the "gap" in exothermicity between CH_3^- and OH^- adducts also increases with monotonic increase in the number of ring NO_2 groups. The differences in heats of complexation between the CH_3^- MC-2 of **1** and the OH^- MC-2 of **1** is 24.9 kcal in favour of the methide adduct. The ΔH_c gap between the OH^- and CH_3^- MC-4 of **9** narrows to 23.5 kcal, and further to 21.4 kcal favouring the C-adduct (MC-4) of **7** over the corresponding O-centred MC.

Significantly, Crampton and co-workers have reported kinetic and thermodynamic parameters for a series of nitro- and cyano-substituted carbanions with TNB, **1**, as well as 2,4,6-trinitrotoluene (30). The experiments clearly show the thermodynamic preference for C-adduct formation over O-adduct formation with TNB, when formation of the methoxide MC-2 of **1** was used as the reference. For example, the ratio of the equilibrium constants ($K(CH(CN)_2^-/K(MeO^-)$) for formation of MC-2 of **1** with malononitrile anion as compared to methoxide is approximately 2; adjustment for differences in Brønsted basicity increases the value of the ratio of the constants to ca. 10^3 (30*a*). Interestingly, when Marcus (31) intrinsic rate constants, k_0 (measured by extrapolation of log k vs. log K plots to $K = 1$) were compared for the nitroalkane anions, cyanoalkyl anions, and methoxide ion, the nitrocarbanions were found to be inherently less reactive in MC formation than the cyanoanions by a factor of 10^5 and less reactive than methoxide by a factor of 10^4 (30*b*). This was attributed to the greater requirement for electronic, structural, and solvent reorganization concomitant with MC formation by the nitroalkyl anions as compared to the cyanocarbanions and methoxide ion. The cyanocarbanions were considered more localized than the nitrocarbanions. Thus, our present AM1 results, which circumvent the need to consider solvent reorganization, are in accord with the observed greater exothermicity of complexation with carbanions as compared to oxyanions.

It is tempting, in light of the clear-cut thermodynamic preference for CH_3^- over OH^- adduct formation, to conclude that in the case of an ambident (C- and O-)nucleophile, C-attack at a given site should be more exothermic than O-attack. However, the differences in ground-state enthalpies between OH^- (ΔH_f = −32.7 kcal/mol) and CH_3^- (ΔH_f = +33.2 kcal/mol) (23*c*) that contribute to the relative exothermicities of adduct formation when these two nucleophiles are compared, are absent when an ambident nucleophile (e.g., phenoxide) is used. Therefore, if ground-state enthalpy differences ($\delta\Delta H_f$) of the nucleophiles are important in determining the thermodynamic stability of the Meisenheimer complexes, conclusions drawn from comparing individual O-nucleophiles and C-nucleophiles may not be valid for ambident O- and C-nucleophiles in Meisenheimer complexation. The relevance of the present findings to such ambident nucleophiles will emerge from the discussion of MC formation that results in geminal disubstitution with electronegative heteroatoms (below). Further, it is important to note that *there is no difference in regioselectivity shown by OH^- as compared to CH_3^- in formation of adducts with **7** and **9** as measured by ΔH_c for the various regioisomeric adducts.* In this regard, the most favoured regioisomeric adducts formed by reaction of OH^- or CH_3^- with either **7** or **9** are the MC-4 adducts that arise from attack at the site *para* to at least one nitro group. The MC-2 complexes of **7** and **9** are formed with the next greatest exothermicity; in these, CH_3^- and OH^- are attached to a site *ortho* to one, or both, NO_2 groups. The least thermodynamically favoured regioisomers are MC-3 of **7** and MC-5 of **9**, both of which are formed by attack of the nucleophiles at a site *meta* to all NO_2 functions.

In summary, in comparing **6**, **7**, **9**, and **1**, a series of progressively more electron-deficient substrates, it is apparent that complexes formed from either OH^- or CH_3^- at the same site of attack are increasingly stabilized by increasing NO_2 group substitution of the electrophile. For this same series of electrophiles, complexes formed by CH_3^- are favoured thermodynamically over those formed by OH^-, although both nucleophiles show the same regioselectivity.

2. Regioselectivity in Meisenheimer complex formation. The role of geminal disubstitution with electronegative heteroatoms

Further understanding accrues from examination of selected pairs of structurally related adducts involving electronegative atoms and hydrogen as substituents (Table 2). The OH^- MC-4 of 4-fluoronitrobenzene, **8**, is formed with an exothermicity of 7 kcal relative to the OH^- MC-4 of nitrobenzene, **7** (i.e., $\delta\Delta H_c$ = −7.0 kcal/mol). Replacement of H by F in the respective MC is thus worth 7 kcal of exothermicity. In fact, comparison of the OH^- MC-1 of **2** with OH^- MC-2 of **1** (Table 2) yields virtually the same enthalpy difference: 6.9 kcal favouring MC-1 of TNA, **2**, over MC-2 of **1**. Therefore, replacement of H by OCH_3 in the comparable MC is also worth 7 kcal. Further, with **8**, OH^- and CH_3O^- both form the most stable adduct at the position bearing F (i.e., *para* to the NO_2 group), whereas CH_3^- forms the most stable adduct *ortho* to the nitro group. These observations emphasize the stabilization that accompanies geminal disubstitution with electronegative heteroatoms.

Relief of internal strain has been suggested by us (7, 32) and others (33, 34; see also ref. 10) as a possible origin of the thermodynamic preference of the C-1 site of attack on TNA by nucleophiles. Thus, formation of an adduct by attack at a position substituted by an electronegative group, as in formation of the OH^- and CH_3O^- MC-1 of TNA, **2**, would be thermodynamically favoured since the process would convert a strained sp^2-hybridized carbon center (one bearing a substituent) to a less strained sp^3-hybridized center in the MC. Such strain is suggested, for example, by the X-ray structure of the ethyl ether, 2,4,6-trinitrophenetole, in which the *ortho* nitro groups flanking the ethoxy group are twisted from the plane of the ring by 33° and 62°, respectively, presumably as a result of accommo-

Can. J. Chem. Downloaded from www.nrcresearchpress.com by EESC ESCOLA DE ENGENHARIA on 09/08/12
For personal use only.

dating spatially the ethoxy group at C-1 (16). Since TNB, **1**, is not similarly substituted, formation of MC-2 of **1** would not involve such a release of strain and the difference in ΔH_c between MC-1 of **2**, which is substituted at C-1, and MC-2 of **1** could then reflect this stabilization due to relief of strain. On the other hand, the same enthalpy difference ($\delta\Delta H_c$) is exhibited by the CH_3O^- MC-4 pair formed from 4-fluoronitrobenzene (**8**), and nitrobenzene (**7**), even though **8** lacks any buttressing *ortho* nitro groups. It is difficult to see how **8** would be strained relative to **7** and, therefore, the observed $\delta\Delta H_c$ cannot be attributed to relief of strain in this case.

It is interesting that the present study indicates that the CH_3^- MC-1 of TNA (**2**) is slightly less stable than the C-3 adduct, although the OH^- MC-1 of TNA is 4.0 kcal more stable than the comparable C-3 adduct. Again, if relief of internal strain were the source of the regioselectivity shown by CH_3O^- (and OH^-), then the C-1 site should also be the preferred site of attack for CH_3^-. Therefore, even though the argument based on relief of internal strain may indeed be applicable in the comparison of **1** and **2** (and their adducts) it lacks generality as an explanation.

An alternative view to the internal-strain model holds that geminal substitution with two electronegative heteroatom groups is, in itself, stabilizing (35–37). The mechanism of this stabilization may be anionic hyperconjugation (38). However, qualitative molecular orbital theory would impute the stabilization to favourable n–σ^* interaction(s) between the lone pair electrons of one substituent and the antiperiplanar bond of the other substituent. The latter approach treats 1,1-dialkoxy MCs (such as the CH_3O^- MC-1 of **2**) as acetals (39); n–σ^* stabilization in acetals has been invoked to account for the anomeric effect on the preferred conformation of 2-alkoxytetrahydropyrans and related systems (40). In valence bond terms this constitutes a contribution to the resonance hybrid from a no-bond canonical form, as illustrated below for a 2-aryloxytetrahydropyran. The stabilization imparted by this no-bond form accounts for the preference of the aryloxy group for an axial position, as well as for the observed bond lengths, i.e., relatively short cyclic C—O bond. C—CH_3 bonds are relatively poor acceptors due to the high energy level of the fragment σ^* orbital (39); the lack of lone pairs clearly prohibits methide from acting as an "n" donor. Thus, stereoelectronic effects are not expected to stabilize the CH_3^- MC.[5]

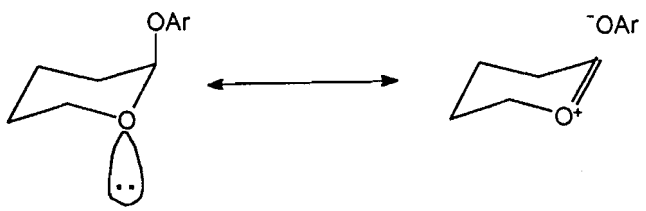

Examination of the adduct formation enthalpies for the TNA system, using the same approach, provides even more convincing evidence for the importance of stereoelectronic stabilization. Comparison of the CH_3^- MC-2 of **1** with the analogous MC-1 of **2** shows that formation of the C-1 methide adduct of TNA is actually 1.3 kcal less exothermic relative to MC-2 of TNB. As a result, in these cases, other regioisomeric Meisenheimer complexes become thermodynamically preferred. Consequently, the CH_3^- MC-2 of **8** is formed with an exothermicity of 2.8 kcal over the CH_3^- MC-4 of **8**. Similarly, the CH_3^- MC-3 of **2** has an associated reaction enthalpy that is slightly (0.1 kcal) more exothermic than that for MC-1 formation. *These results contradict the trend outlined above in which the regioselectivity exhibited by electrophiles **7** and **9** is invariant with the identity of the nucleophile.* Clearly, a significant change has followed from introduction of a substituent bound to the aromatic ring through a heteroatom, which leads to a difference in regioselectivity exhibited by the nucleophiles that is not found for substrates of the general formula $C_6H_n(NO_2)_{6-n}$ that do not contain other heteroatom substituents.

It is pertinent to note that in solution the CH_3O^- MC-3 of TNA is kinetically preferred, while the corresponding MC-1 of **2** is the product of thermodynamic control in a pattern of regioselectivity we have termed K3T1 (Fig. 1) (5, 7). It is equally important to note that with a carbon nucleophile, CH_3^-, the C-3 position is thermodynamically preferred over the C-1 site according to the present AM1 calculations. Further, we have found that TNA reacts with PhO^- as a C-nucleophile, to form the C-3 TNA phenoxide adduct (MC-3 of **2**) as the kinetic product of C-attack (7). Similar behaviour has been found with other ambident C-nucleophiles, such as acetonate anion in reaction with related picryl ethers where the only C-adduct observed in alkaline media by ^1H NMR is the acetonate MC-3 (42). However, in basic media, C-adducts are typically formed irreversibly and hence the relative thermodynamics associated with formation of these regioisomers is obscured. The present AM1 study suggests that these adducts are the products of *both kinetic and thermodynamic preference* and thus these cases can be designated as the first reported examples of K3T3 behaviour (cf. Fig. 1 and Introduction).

The extensive work of Makosza and co-workers (8) in elaborating the vicarious nucleophilic substitution (VNS) of hydrogen is also germane to the present discussion. In essence, a carbanion may attack an activated aromatic ring (typified by 4-fluoronitrobenzene, **8**, in Scheme 2) either at a site occupied by the substituent (e.g., fluorine) or occupied by hydrogen. In the former case the attack usually leads to formation of metastable MC and then to displacement of the ring substituent. In the latter case the addition is effectively reversible due to the poor nucleofugality of hydride ion. However, if the carbanion is itself substituted with a suitable leaving group, L, then attack at the position bearing the hydrogen can lead to a base-promoted β-elimination of HL after initial MC formation. (The immediate product is a nitrobenzylic carbanion that is usually protonated in work-up.) This second overall irreversible pathway constitutes the VNS mechanism (8) (solid boxed portion of Scheme 2).

For VNS to occur competitively with (or faster than) S_NAr displacement of a ring substituent, HL elimination, as the rate-determining step in the VNS process, must be faster than addition to a substituted ring position, the analogous usual S_NAr rate-determining step (4). By implication, the rate constant for attack at an unsubstituted position must be faster than the rate coefficient associated with HL elimination or with attack at a substituted position.

It is therefore important to note that in a recent review of the

[5]It is believed that n–σ^* donation into the C—CNO_2 system should be less favourable energetically due to the relatively high energy level of the C—Cσ^* orbitals (cf. ref. 41). Note also that stabilization due to such donation into antibonding orbitals of fragments of the trinitrocyclohexadienate ring would necessarily be constant and would apply equally to adducts like MC-3 of **2**; this factor would be the same in comparing regioisomers and cannot account for the observed regioselectivity in Meisenheimer complex formation.

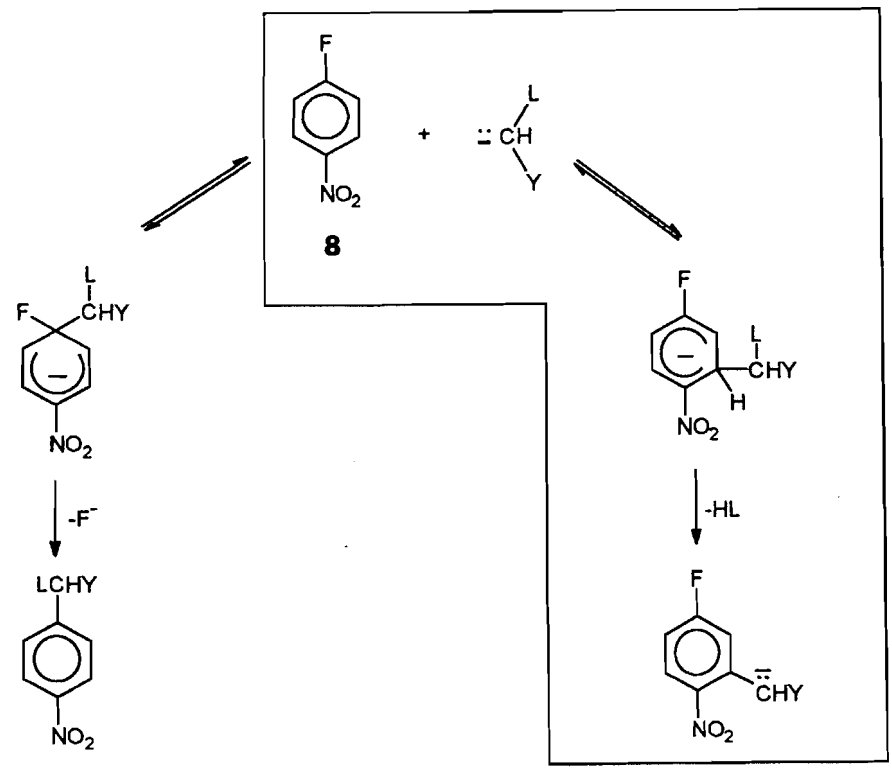

SCHEME 2

VNS reaction Maskosza generalized the regioselectivity of this reaction: "In 4-Z-nitrobenzenes, the reaction can only proceed *ortho* to the nitro group" (*8a*). Thus, for **8** (Scheme 2) VNS should yield a product in which the erstwhile carbanion is attached to C-2 (*ortho* to the nitro group and *meta* to the fluoro group). The present AM1 calculations predict an order of preference for addition of C-2 > C-4 > C-3, based on the exothermicity of MC formation for CH_3^- with **8**. Note, again, that OH^- and CH_3O^- prefer attack at C-4 over attack at any other position. As required by the VNS mechanism, the thermodynamics of regioselectivity for carbanions favours attack at the position *ortho* to the nitro group.

For more highly substituted aromatics the comparison becomes more difficult since substituents perforce affect both the competitive addition steps of VNS and S_NAr mechanisms, respectively, but also the rate-determining elimination step of the VNS route. Further, with more highly substituted electrophiles steric factors come into play to a greater extent.

Further evidence in support of stereoelectronic stabilization is found in comparison of the two minimum energy conformations of the CH_3O^- MC-1 of TNA, **2**, the "M-shaped" and "S-shaped" conformers. The "M-shaped" conformation that places both methyl groups over the trinitrocyclohexadienate ring is slightly less stable than the CH_3O^- MC-3 of TNA, **2**. On the other hand, rotation of one of the CH_3O groups by 180° to the "S-shaped" conformation stabilizes the C-1 adduct by 4.4 kcal, and makes the C-1 adduct the product of thermodynamic control. Because n–σ^* interactions are not possible in the M conformer, yet exist for the S conformer, stereoelectronic stabilization of the MC due to n–σ^* interaction(s) is the most likely source of the enhanced stability of CH_3O^- C-1 adduct of **2**. This result is discussed further with respect to the corresponding X-ray structures (vide infra).

What appears to distinguish the thermodynamics of K3T1 behaviour is stereoelectronic stabilization afforded by geminal diheterosubstitution. We have previously recognized the importance of such disubstitution as one factor in determining the regioselectivity of attack by phenoxide vs. methoxide in picryl derivatives (32). In a study of the reaction of CN^- with TNA, **2**, MC-1 was found to be thermodynamically less stable than the corresponding MC-3; overall K1T3 regioselectivity was observed in this system (*6a*). It could be argued, therefore, that whenever the two electronegative groups in a geminal disubstituted adduct are different (e.g., CN and OCH_3 in the CN^- MC-1 of TNA) the degree of stabilization may be diminished (*6a*). However, this view is challenged by the efficacy of stabilization found for the "unsymmetrical" OH^- MC-4 of **8** and by the fact that the symmetrical CH_3O^- MC-1 of **2** is only favoured by 2.6 kcal over the CH_3O^- MC-2 of **1** (as compared to the unsymmetrical OH^- of MC-1 of **2**, which is formed with an exothermicity of 6.9 kcal relative to the OH^- MC-2 of **1**).

Three factors are significant in assessing the degree of stereoelectronic stabilization that may be attained by a geminal disubstituted adduct. First, energy levels for lone pair and relevant acceptor bond should be similar for maximum interaction (refs. 7, 40, 41, and footnote 5). Secondly, though perhaps obviously, the optimum interaction can only be achieved if both substituents can act as donor and acceptor towards one another; both substituents require lone pairs to act as donors. Finally, steric hindrance may prevent the donor and acceptor groups from achieving optimal conformations. In this regard, we have previously noted (7) that a conformation that would maximize the n–σ^* stabilization for a complex such as the CH_3O^- MC-1 of TNA should orient donor lone pairs and acceptor C—O bonds antiperiplanar to each other, as in the structure OS (where OS indicates that the groups R and CH_3 are arranged on opposite

Can. J. Chem. Downloaded from www.nrcresearchpress.com by EESC ESCOLA DE ENGENHARIA on 09/08/12
For personal use only.

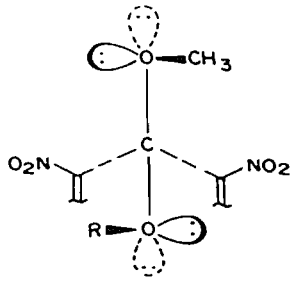

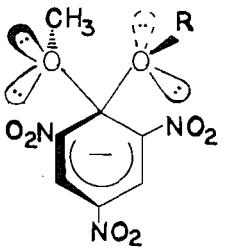

OS

sides of the O-(C-1)-O axis). OS is also drawn according to the "rabbit-ear" convention. The most suitable conformer of the CH_3O^- MC-1 of **2**, according to the present AM1 calculations, is the "S-shaped" conformer (Fig. 2), *which places neither lone pair of either acetal-like oxygen in the antiperiplanar position, but which permits partial interaction of* both *lone pairs with the relevant acceptor C—O bond.* In the S-shaped conformation a trade is made: n–σ^* stabilization for minimization of steric hindrance between the groups at C-1 and between these groups and the nitro groups of the trinitrocyclohexadienate ring (see discussion of X-ray structures below).

While the OH^- MC-1 of TNA has *not* been observed in solution by high-field ^1H NMR, the OH^- MC-3 of TNA, **2**, is readily observed (7, 43). How can this be reconciled with the present AM1 calculation results, which show that the OH^- MC-1 of **2** is formed with a 7.5 kcal/mol greater exothermicity than is the OH^- MC-3 of TNA? The key is that a favourable kinetic pathway exists for decomposition of the OH^- MC-1 of **2** in solution, namely, expulsion of methanol and formation of the delocalized picrate anion. No such facile route would be open to the OH^- MC-2 of **1**, given the poor leaving group ability of hydride anion, any more than this route is open to the OH^- MC-3 of TNA (refs. 11*a*, 44, and footnote 6). Hence, assuming that OH^- attack at C-3 is kinetically controlled leads to K3T1 behaviour for the TNA-OH^- system: initial formation of the OH^- MC-3 of **2** followed by conversion to picrate anion, *presumably via the OH^- MC-1* (7).

It should also be reiterated that the difference in enthalpy of adduct formation ($\delta\Delta H_c$) compares well with the solution calorimetric free energy differences ($\delta\Delta G$) reported previously (28, 29). Thus, based on the AM1 data, the difference in reaction enthalpy between the CH_3O^- MC-2 of **1** and the CH_3O^- MC-1 of **2** is 2.6 kcal in favour of the 1,1 TNA•OCH_3^- adduct (i.e., ΔH_c MC-1 of **2** − ΔH_c MC-2 of **1** for CH_3O^- as nucleophile = −2.6 kcal). Fendler et al. (29) assigned 4.2 kcal stabilization to geminal disubstitution with CH_3O^-, based on this and similar comparisons of free energy differences.

3. Structures of the Meisenheimer complexes

(a) Comparison of the X-ray and AM1 optimized structures of the CH_3O^- MC-2 of TNB (1)

Further evidence supporting the importance of stereoelectronic effects as factors affecting the relative adduct formation enthalpies derives from comparison of the calculated structures to available X-ray data, specifically the CH_3O^- MC-2 of TNB, **1**, and the MC-1 of TNA, **2**. The data given in the Supplementary Tables 28, 34, and 36 show that all AM1 bond lengths correspond well to those found by X-ray by Destro et al. (45); while C—C bond lengths were systematically overestimated in the theoretical study, the average error was only 0.014 Å or ca. 1%. Similarly, the C—N bond lengths were generally overestimated and the N—O bond lengths, by comparison to the X-ray structures, routinely underestimated, though again, the average error was small: only 0.03 Å (<3%).

The X-ray crystal structure of the CH_3O^- MC-2 of **1** contains an interesting structural feature: the adduct is boat-like, with C-1 and C-4 distorted from the plane defined by C-2:C-3:C-5:C-6. The "top" face of the molecule, (i.e., the side of substitution) is also the direction of pucker of the molecule (16). AM1 correctly predicts C-1 to be bent slightly out of this plane on the side of substitution, though the effect is small (Supplementary Table 28). The puckering of C-4 is not, on the other hand, reproduced by AM1. Given that Destro et al. (16) suggested that the C-4 puckering was an artifact induced by crystal packing forces, the absence of puckering about C-4 in the AM1 gas-phase calculations is not unexpected and, in fact, supports the previous interpretation of the role of packing forces on the structure (45).

Finally, the slight asymmetry found in the X-ray structure of the CH_3O^- MC-2 of **1** is not observed in the calculated AM1 structure. For example, in the X-ray structure the C—C bond between C-5 and C-6 is somewhat longer than the comparable bond between C-2 and C-3, while in the AM1 optimized structure these bonds are identical in length. These differences between X-ray and calculated structures have been noted previously (27) and also attributed to packing forces present in the crystal, but absent in the gas-phase structures predicted by AM1.

(b) Comparison of the X-ray and AM1 optimized structures of the CH_3O^- MC-1 of TNA (2)

The X-ray structure of the CH_3O^- MC-1 of TNA, **2**, was found to lack the puckering found for the CH_3O^- MC-2 of TNB (25). Both O—CH_3 bonds in the X-ray structure were found to be oriented antiperiplanar to the opposite C—O bonds. The plane defined by the bonding axis through CH_3-O-(C-1)-O-CH_3 is perpendicular to the trinitrocyclohexadienate ring (Supplementary Tables 34 and 36).

Contrary to the X-ray results, AM1 predicts the M conformation of C_{2v} symmetry about C-1, which places both methyl groups over the aryl ring to be 4.4 kcal less stable ($\delta\Delta H_{AF}$) than the S conformer, which places only one methyl group over the ring. Our above comparisons of heats of complexation, are therefore based on the more stable S conformation (Fig. 2). However, when a simulated counterion was added to the input geometry (SPARKLE option of AM1) only the M conformation was found to exist as a local minimum (Fig. 3). This result suggests that the positive counterion induces the M conformation in the solid phase, by coordination to the oxygen atoms not only of the acetal-like CH_3O^- groups at C-1, but also of the flanking *ortho* nitro groups. The attached methoxyl groups would thus be inhibited from rotating and prevented from taking up a conformation that permits n–σ^* interaction.

Complexation of the positive counterion has been proposed as a rationale for the high *ortho*:*para* ratio for the products that arise from displacement of a fluorine *ortho* to a nitro group in 2-fluoronitrobenzene by *tert*-butoxide (in *t*-BuOH) as compared to displacement of a *para* fluorine (46). Stabilization imparted to the incoming *tert*-butoxide anion by the bridging of the K^+

[6]E. Buncel and R.A. Manderville, unpublished work.

Can. J. Chem. Downloaded from www.nrcresearchpress.com by EESC ESCOLA DE ENGENHARIA on 09/08/12
For personal use only.

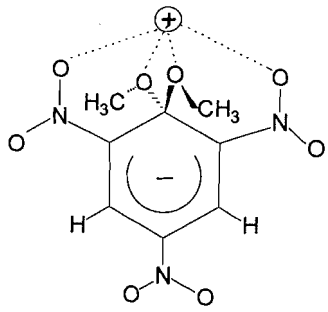

FIG. 3. The CH_3O^- MC-1 of TNA, **2**, ion paired to a hypothetical counterion simulated by a point charge (AM1 calculation using the SPARKLE option). Compare the structure to that of the "M-shaped" conformer (Fig. 2).

counterion to the *ortho* nitro group was suggested as providing a lower energy pathway for *ortho* displacement by *tert*-butoxide in *tert*-butyl alcohol solvent (46).

A more rigorous model for the cation association that apparently promotes the M conformation for the CH_3O^- MC-1 of **2** comes from the work of Crampton and co-workers who have studied the kinetics and thermodynamics of MC formation with a variety of O-nucleophiles and counterions (10, 47). While these studies show that the counterion is indeed complexed to the geminal diether oxygens and to the oxygens of the *ortho* nitro groups ("pseudo-crown-ether arrangement") in the CH_3O^- MC-1 of **2**, the CH_3O^- MC-2 of **1** does not show this type of association of the cation with the adduct, indicating that this ion pairing requires both O-CH_3 groups to be present (47, see also ref. 8*h*). More pertinent is the finding that the C-1 adduct is the product of thermodynamic control even when crown ethers are used to eliminate counterion complexation with the CH_3O^- MC-1 of TNA. No shift in the pattern of regioselectivity from K3T1 (see Fig. 1) to any other type of behaviour occurs. Consequently, while the M conformer is preferred in the solid state and possibly in some condensed media, the present results indicate that the S conformer is the more stable of the two structures. Again, this is consistent with the view that stereoelectronic stabilization via n–σ^* donation is important in assigning intrinsic thermodynamic stabilities of Meisenheimer complexes.

In solution it is reasonable to expect that the degree of complexation of cation to MC-1 of **2** will depend on the medium. Hydroxylic media along with a counterion that is relatively small, e.g., Na^+, would favour the M conformer (47), while the intrinsically more stable S conformer would be expected to predominate in a good cation-solvating solvent such as DMSO (48). Thus, in hydroxylic media, it is expected that with moderately small cations the CH_3O^- of **2** will be stabilized by ion pairing; MC-1 is then the thermodynamically preferred regioisomer.[7] The corresponding CH_3O^- MC-3, although formed first, would rearrange to the MC-1 regioisomer as is observed in solution (5, 7). When ion pairing is disrupted through the use of crown ethers, MC-1 is still preferred because this adduct can take up the inherently more stable S conformation. Recall that in the S-shaped conformation partial n–σ^* stabilization is possible for both O – lone pair orbitals interacting with the geminal C—O acceptor bonds. Therefore, there is no change in regioselectivity when crown ethers are present in these and related systems.

Clearly, a MC formed from CH_3^- attack must involve an insignificant degree of stereoelectronic stabilization compared to the MC formed from CH_3O^- attack since no lone pairs are present on the bonded CH_3 fragment; n–σ^* donation from CH_3 to the C-O-CH_3 antibonding orbital is energetically costly, regardless of the preferred conformation of the adduct (M or S). As well, the C—CH_3 bond would be less efficient as an acceptor than the O—CH_3 bond because of the comparatively high n–σ^* energy gap (40, 41). Neither conformation would confer any extraordinary stability on the CH_3^- MC-1; hence MC-3 becomes the preferred regioisomer (albeit only favoured by an exothermicity of 0.1 kcal in the present AM1 calculations).

Conclusions

Several important conclusions may be drawn from the present AM1 theoretical study. These are summarized as follows:

1. For a series of electrophiles that are progressively substituted with more electron-withdrawing nitro groups, that is, nitrobenzene, **7**, 1,3-dinitrobenzene, **9**, and 1,3,5-trinitrobenzene, **1**, hydroxide and methide anions, as model oxygen and carbon nucleophiles, *exhibit the same regioselectivity based on thermodynamics of Meisenheimer complex formation.* Thus, Meisenheimer complexes derived from attack at a position *para* to at least one nitro group (designated MC-4) are formed with the greatest exothermicity (ΔH_c).

2. Exothermicity of complexation increases for both OH^- and CH_3^- adduct formation as the number of nitro groups in the electrophiles is increased (**7** to **9** to **1**), but formation of the CH_3^- adducts occurs uniformly with greater exothermicity than that of OH^- adducts. The proportionality of stabilization, as a function of nitro group substitution, was shown to correspond well with that found by solution calorimetric methods (28, 29).

3. Unexpectedly, it is found that *regioselectivity inverts for CH_3^- as compared to OH^- and CH_3O^- in complexation with 2,4,6-trinitroanisole, 2.* Thus, while CH_3O^- and OH^- form MC-1 with TNA with higher exothermicity than MC-3, CH_3^- preferentially forms MC-3 on the basis of the same enthalpy criterion. Therefore, in adduct formation with **2**, CH_3O^- displays the thermodynamics associated with K3T1 regioselectivity, in accord with the known solution behaviour (5, 7), while CH_3^- exhibits the thermodynamics linked to K3T3 behaviour.

4. It is shown that stereoelectronic stabilization of geminally disubstituted Meisenheimer complexes, arising from significant overlap of donor substituent lone pairs with the acceptor σ-bond of the other substituent, accounts for the greater exothermicity of complexation of OH^- and CH_3O^- at C-1 as compared to C-3 of TNA. However, the methide moiety of the comparable MC-1 of TNA cannot partake in such an n–σ^* interaction and, consequently, with CH_3^-, MC-3 formation is preferred over MC-1.

5. Confirmation of this stereoelectronic stabilization for the oxygen geminal disubstituted adducts of TNA derives from examination of the optimized CH_3O^- MC-1 structures of TNA, which show that the preferred conformation, in a medium in which the counterion would be well separated from the adduct, has an "S-shape" rather than an "M-shape" (Fig. 2). In the S

[7]Bernasconi and Howard (39*a*) arrived at a complementary conclusion from the analysis of the kinetics of spiro Meisenheimer complex formation and ring-opening decomposition. In methanol solvent they argued in favour of the "M-shaped" conformer as the preferred geometry for the CH_3O^- MC-1 of TNA, although they recognized the S-shaped conformer as the more stable one in the absence of cation complexation and solvation effects.

Can. J. Chem. Downloaded from www.nrcresearchpress.com by EESC ESCOLA DE ENGENHARIA on 09/08/12
For personal use only.

conformation n–σ^* interaction is possible, whereas in the M conformation it is not.

The present study emphasizes the utility of the AM1 method to assess the thermodynamic stability of Meisenheimer complexes and thus to predict patterns of regioselectivity. Also revealed is the modulation of regioselectivity as a function of the nature of the nucleophile, specifically oxygen versus carbon nucleophiles. Stereoelectronic stabilization is recognized as a major factor in influencing regioselectivity in Meisenheimer complex formation.

Acknowledgements

We thank the Natural Sciences and Engineering Research Council for a grant in aid of research (E.B.). Funding from the Principal's Research Fund at Sir Wilfred Grenfell College (J.M.D.) and the award of an R.T. Mohan Fellowship (R.M.T.) are also gratefully acknowledged. Stimulating discussions with Professor M. Makosza are highly appreciated.

1. J. Meisenheimer. Justus Liebigs Ann. Chem. **323**, 205 (1902).
2. C.J. Jackson and P.H. Gazzolo. J. Am. Chem. Soc. **23**, 376 (1900).
3. (*a*) E. Buncel, M.R. Crampton, M.J. Strauss, and F. Terrier. Electron-deficient aromatic and heteroaromatic-base interactions. The chemistry of anionic sigma complexes. Elsevier, Amsterdam. 1984; (*b*) E. Buncel. The chemistry of amino, nitro and nitroso groups. *Edited by* S. Patai. Wiley, London. 1982; (*c*) F. Terrier. Chem. Rev. **82**, 77 (1982); (*d*) G.A. Artamkina, M.P. Egorov, and I.P. Beletskaya. Chem. Rev. **82**, 427 (1982); (*e*) M.J. Strauss. Chem. Rev. **70**, 667 (1970).
4. (*a*) F. Terrier. Nucleophilic aromatic displacement. The influence of the nitro group. VCH, New York. 1991; (*b*) J. Miller. Nucleophilic aromatic substitution. Elsevier, Amsterdam. 1968; (*c*) J.F. Bunnett. J. Chem. Educ. **51**, 312 (1974); (*d*) J.F. Bunnett, E.W. Garbisch, and K.M. Pruitt. J. Am. Chem. Soc. **79**, 385 (1957).
5. (*a*) K. L. Servis. J. Am. Chem. Soc. **87**, 5495 (1965); (*b*) J. Am. Chem. Soc. **89**, 1508 (1967).
6. (*a*) A.R. Norris. Can. J. Chem. **47**, 2895 (1969); (*b*) P. Caveng and H. Zollinger. Helv. Chim. Acta, **50**, 891 (1967).
7. (*a*) E. Buncel, J.M. Dust, A. Jonczyk, R.A. Manderville, and I. Onyido. J. Am. Chem. Soc. **114**, 5610 (1992); (*b*) R.A. Manderville and E. Buncel. J. Am. Chem. Soc. **115**, 8985 (1993).
8. (*a*) M. Makosza and J. Winiarski. Acc. Chem. Res. **20**, 282 (1987); (*b*) M. Makosza and J. Golinski. Tetrahedron Lett. 3495 (1978); (*c*) M. Makosza, J. Golinski, and J. Baran. J. Org. Chem. **49**, 1488 (1984); (*d*) M. Makosza and A. Kinowski. Bull. Pol. Acad. Sci. (Chem.) **37**, 127 (1989); (*e*) M. Makosza and Z. Owczarczyk. J. Org. Chem. **54**, 5094 (1989); (*f*) W. Wrobel and M. Makosza. Org. Prep. Proced. Int. **22**, 575 (1990); (*g*) M. Makosza, W. Danikiewicz, and K. Wojciechowski. Phosphorus, Sulfur Silicon, **53**, 457 (1990); (*h*) M. Makosza, A. Glinka, and A. Kinowski. Tetrahedron, **40**, 1863 (1984).
9. (*a*) L.B. Clapp, H. Lacey, G.G. Beckwith, R.M. Srivastava, and N. Muhammad. J. Org. Chem. **33**, 4262 (1968); (*b*) J.M. Dust and J.M. Harris. J. Polym. Sci. Part A: Polym. Chem. **28**, 1875 (1990).
10. A. Cooney and M.R. Crampton. J. Chem. Soc. Perkin Trans. 2, 1973 (1984).
11. (*a*) E. Buncel and R.A. Manderville. J. Phys. Org. Chem. **6**, 71 (1993); (*b*) E. Buncel and J.M. Dust. Can. J. Chem. **66**, 1712 (1988); (*c*) E. Buncel, R.A. Renfrow, and M.J. Strauss. J. Org. Chem. **52**, 488 (1987); (*d*) E. Buncel and W. Eggiman. Can. J. Chem. **54**, 2436 (1976); (*e*) E. Buncel, A. Jonczyk, and J.G.K. Webb. Can. J. Chem. **53**, 3761 (1975); (*f*) E. Buncel and J.G.K. Webb. Can. J. Chem. **95**, 8470 (1973).
12. (*a*) E. Buncel, C. Innis, and I. Onyido. J. Org. Chem. **51**, 3680 (1986); (*b*) E. Buncel and W. Eggiman. J. Chem. Soc. Perkin Trans. 2, 673 (1978); (*c*) J. Am. Chem. Soc. **99**, 5958 (1977); (*d*) E. Buncel and J.G.K. Webb. Can. J. Chem. **52**, 630 (1974).
13. E. Buncel, J.M. Dust, R.A. Manderville, and K.T. Park. Bull. Soc. Chim. Fr. 371 (1988).
14. (*a*) T. Abe. Bull. Chem. Soc. Jpn. **37**, 508 (1964); (*b*) Bull. Chem. Soc. Jpn. **39**, 627 (1966).
15. P. Caveng, P.B. Fischer, E. Heilbronner, A.L. Miller, and H. Zollinger. Helv. Chim. Acta, **50**, 848 (1967).
16. R. Destro, C.M. Grammiccioli, and M. Simonetta. Acta Crystallogr. Sect. B: Struct. Crystallogr. Cryst. Chem. **B24**, 1369 (1968).
17. (*a*) S. Sekiguchi, T. Hirose, K. Tsutsumi, T. Alizawa, and H. Shizuka. J. Org. Chem. **44**, 3921 (1979); (*b*) A.J. Birch, A.L. Hinde, and L. Radom. J. Am. Chem. Soc. **102**, 6430 (1980).
18. J. Burdon, I.W. Parsons, and E.J. Evramides. J. Chem. Soc. Perkin Trans. 1, 1268 (1979).
19. M.J. Strauss, S. Fleischman, and E. Buncel. J. Mol. Struct. (Theochem), **121**, 37 (1985).
20. (*a*) R. Bacaloglu, C.A. Bunton, and F. Ortega. J. Am. Chem. Soc. **111**, 1041 (1989); (*b*) R. Bacaloglu, A. Blasko, C.A. Bunton, E. Dorwin, F. Ortega, and C. Zucco. J. Am. Chem. Soc. **113**, 238 (1991).
21. (*a*) M.J.S. Dewar and W. Theil. J. Am. Chem. Soc. **99**, 7907 (1977); (*b*) M.J.S. Dewar. J. Mol. Struct. **100**, 41 (1983).
22. M.J.S. Dewar and E. Healy. J. Comput. Chem. **5**, 358 (1984).
23. (*a*) M.J.S. Dewar, E.G. Zoeblisch, E.F. Healy, and J.J.P. Stewart. J. Am. Chem. Soc. **107**, 3902 (1985); (*b*) M.J.S. Dewar and K.M. Dieter. J. Am. Chem. Soc. **108**, 8075 (1986); (*c*) S.G. Lias, J.E. Bartmess, J.F. Liebman, J.L. Holmes, R.D. Levin, and W.G. Mallard. J. Phys. Chem. Ref. Data, **17**, Suppl. **1**, 664 (1988); **1**, 666 (1988); **1**, 781 (1988).
24. R. Fletcher and M.J.D. Powell. Comput. J. **6**, 163 (1963).
25. J. Ueda, N. Sakabe, J. Tanaka, and A. Furusaki. Bull. Chem. Soc. Jpn. **41**, 2866 (1963).
26. S.K. Dotterer and R.L. Harris. J. Org. Chem. **53**, 777 (1988).
27. N.S. Nudelman and P. MacCormick. J. Chem. Soc. Perkin Trans. 2, 327 (1987).
28. R.M. Murphy, C.A. Wulff, and M.J. Strauss. J. Am. Chem. Soc. **96**, 2678 (1974).
29. J.H. Fendler, W.L. Hinze, and L.J. Liu. J. Chem. Soc. Perkin Trans. 2, 1768 (1975).
30. (*a*) M.R. Crampton, T.P. Kee, and J.R. Wilcox. Can. J. Chem. **64**, 1714 (1988); (*b*) J.P.L. Cox, M.R. Crampton, and P. Wight. J. Chem. Soc. Perkin Trans. 2, **25**, 1988.
31. (*a*) R.A. Marcus. J. Phys. Chem. **72**, 891 (1968); (*b*) A.O. Cohen and R.A. Marcus. J. Phys. Chem. **72**, 4249 (1968); (*c*) W.J. Albery. Annu. Rev. Phys. Chem. **31**, 227 (1980); (*d*) C.F. Bernasconi. Pure Appl. Chem. **54**, 2335 (1982); (*e*) D.B. Boyd. J. Org. Chem. **50**, 885 (1985).
32. E. Buncel, S.K. Murarka, and A.R. Norris. Can. J. Chem. **62**, 534 (1984).
33. (*a*) M.R. Crampton and V. Gold. J. Chem. Soc. 4293 (1964); (*b*) J. Chem. Soc. B, 893 (1966).
34. M.R. Crampton. Adv. Phys. Org. Chem. **7**, 211 (1969).
35. C.F. Bernasconi. J. Am. Chem. Soc. **92**, 4682 (1970).
36. M.R. Crampton and J.A. Stevens. J. Chem. Soc. Perkin Trans. 2, 1097 (1990).
37. E.J. Fendler, J.H. Fendler, C.E. Griffin, and J.W. Larsen. J. Org. Chem. **35**, 287 (1970).
38. (*a*) J. Hine. J. Am. Chem. Soc. **85**, 3239 (1963); (*b*) J. Hine, L.G. Mahone, and C.L. Liotta. J. Am. Chem. Soc. **89**, 5911 (1967).
39. (*a*) C.F. Bernasconi and K.A. Howard. J. Am. Chem. Soc. **104**, 7248 (1982); (*b*) J.F. Bunnett and A.V. Cartano. J. Am. Chem. Soc. **103**, 4861 (1981); (*c*) S. Sekiguchi, T. Suzuki, and M. Hosokawa. J. Chem. Soc. Perkin Trans. 2, 1783 (1989).
40. (*a*) P.G. Jones and A.J. Kirby. J. Am. Chem. Soc. **106**, 6207 (1984); (*b*) A.J. Kirby. The anomeric effect and related stereoelectronic effects at oxygen. Springer Verlag, Berlin. 1983; (*c*) R.D. Amos, N.C. Hardy, P.G. Jones, A.J. Kirby, J.K. Parker, J.M. Percy, and M. Der Su. J. Chem. Soc. Perkin Trans. 2, 549 (1992).
41. N.D. Epiotis. Theory of organic reactions. Springer Verlag, Berlin. 1978.

Can. J. Chem. Downloaded from www.nrcresearchpress.com by EESC ESCOLA DE ENGENHARIA on 09/08/12
For personal use only.

42. R.A. Foster, C.A. Fyfe, P.H. Emslie, and M.I. Foreman. Tetrahedron, **23**, 227 (1967).
43. R.A. Manderville. Ph.D. Thesis, Queen's University, Kingston, Ontario. 1992.
44. M.R. Crampton. J. Chem. Soc. B, 1208 (1968).
45. R. Destro, T. Pilati, and M. Simonetta. Acta Crystallogr. Sect. B: Struct. Crystallogr. Cryst. Chem. **B35**, 733 (1979).
46. F.D. Cima, G. Biggi, and F. Pietra. J. Chem. Perkin Trans. 2, 56 (1973).
47. (*a*) M.R. Crampton and H.A. Khan. J. Chem. Soc. Perkin Trans. 2, 1173 (1972); (*b*) M.R. Crampton, B. Gibson, and F.W. Gilmore. J. Chem. Soc. Perkin Trans. 2, 91 (1979); (*c*) P.C.M.F. Castilho, M.R. Crampton, and J. Yarwood. J. Chem. Soc. Perkin Trans. 2, 639 (1991).
48. (*a*) E. Buncel and H. Wilson. Adv. Phys. Org. Chem. **14**, 133 (1977); (*b*) A.J. Parker. Chem. Rev. **69**, 1 (1969).

Can. J. Chem. Downloaded from www.nrcresearchpress.com by EESC ESCOLA DE ENGENHARIA on 09/08/12
For personal use only.

A precise analysis of the ^{1}H nuclear magnetic resonance spectrum of 2-phenyl-1,3-dithiane. Ring pucker, signs of long-range J(H,H), internal rotational barrier, and van der Waals shifts

TED SCHAEFER,[1] JEREMY P. KUNKEL, ROBERT W. SCHURKO, AND GUY M. BERNARD
Department of Chemistry, University of Manitoba, Winnipeg, MB R3T 2N2

Received January 12, 1994

TED SCHAEFER, JEREMY P. KUNKEL, ROBERT W.J SCHURKO, and GUY M. BERNARD. Can. J. Chem. **72**, 1722 (1994).

The ^{1}H nuclear magnetic resonance spectrum of 2-phenyl-1,3-dithiane, as a dilute solution in a CS_2–C_6D_{12}–TMS solvent mixture at 300 K, is analyzed to yield 8 chemical shifts and 22 distinct coupling constants, ^nJ(H,H), n = 2–6. The coupling constant between H-2 and the *para* proton indicates, first, that the bisected conformer (phenyl plane perpendicular to the pseudo plane of the dithiane ring) is most stable and, second, that the apparent twofold barrier to rotation about the Csp^2—Csp^3 bond is 9.6 kJ/mol. The AM1, STO-3G, and STO-3G* computations confirm the twofoldedness of the barrier; the AM1 barrier is 9.4 kJ/mol. The empirical equation, ^3J(H,H) = 13.36 cos^2 ϕ + 9.59 cos ϕ − 0.43, reproduces the vicinal coupling constants of the $CH_2CH_2CH_2$ fragments and implies puckering angles ϕ_{ee}, ϕ_{ea}, and ϕ_{ae} of 54°, 61°, and 64°, respectively. It is implied that ^3J at ϕ = 0° is larger than at ϕ = 180°. This results is discussed in terms of the latest theoretical approach to ^3J in the HCCH fragment. The ^4J(H,H) signs and magnitudes for the $CH_2CH_2CH_2$ fragment agree reasonably well with theory. For the CH_2SCH fragment, ^4J(H,H) values are positive, in contrast to corresponding numbers in the propanic fragment, perhaps the first experimental values for certain rigid orientations about a heteroatom. INDO MO FPT computations on propane, dimethyl ether, and dimethyl sulfide confirm the experimental trend in ^4J(H,H). ^2J(H,H) and ^5J(H,H) values are compared to those in related molecules. The striking differential shifts of the axial and equatorial protons are attributed to differential van der Waals interactions with the 3p lone-pair orbital on sulfur. A comparison of the ring proton chemical shifts with those in phenylcyclohexane and isopropylbenzene implies that C—S bonds are weaker net electron donors by hyperconjugation than are C—C bonds. It is also proposed that the *ortho* protons are deshielded by intramolecular van der Waals interactions with the 3p orbitals on the sulfur atoms.

TED SCHAEFER, JEREMY P. KUNKEL, ROBERT W.J SCHURKO et GUY M. BERNARD Can. J. Chem. **72**, 1722 (1994).

Le spectre résonance magnétique nucléaire du ^{1}H du 2-phényl-1,3-dithiane, déterminé à 300 K, en solution diluée dans un mélange de solvants formé de CS_2, de C_6D_{12} et de TMS, a été analysé et on en a déduit 8 déplacements chimiques et 22 constantes de couplage distinctes, ^nJ(H,H), n = 2 – 6. La constante de couplage entre le proton H-2 et le proton en *para* indique, en premier lieu, que le conformère avec bissection (dans lequel le plan du phényle est perpendiculaire au pseudo plan du noyau dithiane) est le plus stable et, deuxièmement, que la barrière binaire apparente à la rotation autour de la liaison Csp^2—Csp^3 est de 9,6 kJ/mol. Des calculs AM1, STO-3G et STO-3G* confirment que la barrière est binaire; les calculs AM1 indiquent que la barrière est de 9,4 kJ/mol. L'équation empirique, ^3J(H,H) = 13,36 cos^2 ϕ + 0,59 cos ϕ − 0,43, permet de reproduire les constantes de couplage vicinales du fragment $CH_2CH_2CH_2$ et ceci implique que les angles de plissement ϕ_{ee}, ϕ_{ea} et ϕ_{ae} sont respectivement de 54°, 61° et 64°. On discute de ce résultat en fonction de l'approache théorique la plus récente concernant ^3J dans le fragment HCCH. Les signes et les amplitudes des ^4J(H,H) du fragment $CH_2CH_2CH_2$ sont en bon accord avec la théorie. Pour le fragment CH_2SCH, les valeurs de ^4J(H,H) sont positives et ce résultat est en opposition avec les valeurs correspondantes dans le fragment propanique et cette disparité est peut être due au fait qu'il s'agit des premières valeurs expérimentales pour certaines orientations rigides autour d'un hétéroatome. Des calculs d'OM FPT effectués sur le propane, l'éther méthylique et le disulfure de méthyle confirment la tendance expérimentale observée dans les ^4J(H,H). Les differences importantes observées pour les déplacements chimiques des protons axiaux et équatoriaux sont attribuées aux interactions de van der Waals différentes de ces atomes avec la paire d'électrons 3p libre du soufre. Une comparaison des déplacements chimiques des protons du noyau avec ceux observés dans le phénylcyclohexane et l'isopropylbenzène implique que, comparées aux liaisons C—C, les liaisons C—S sont d'une façon globale des donneurs d'électrons par hyperconjugaison qui sont plus faibles. On propose aussi que les protons en *ortho* sont plus déblindés par des interactions intramoléculaires de van der Waals avec les orbitales 3p des atomes de soufre.

[Traduit par la rédaction]

Introduction

A precise analysis of the ^{1}H nmr spectrum of 2-phenyl-1,3-dithiane, **1**, yields, not only the chemical shifts of the eight distinct types of protons and the larger coupling constants such as the vicinal coupling constants between the alkyl protons, but also a variety of long-range coupling constants. Thus, the proton in the methine bond can couple with all 11 other protons in the molecule in a stereospecific manner. For example, $^6J(H,H_p)$, the coupling constant over six formal bonds to the *para* proton of the phenyl group, depends on the angle of twist, θ, about the Csp^2—Csp^3 bond and can be related to the conformational minimum energy about that bond; an assessment of the barrier to rotation about the bond also follows from $^6J(H,H_p)$. Again, the

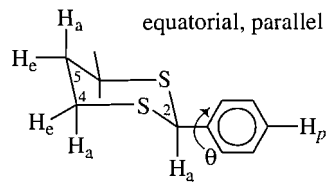

^3J(H,H) values for the alkyl protons provide measures of the flattening or pucker of the dithiane ring; in **1**, they suggest that ^3J is larger at a dihedral angle of 0° than at 180°. Because sulfur is considered to have an electronegativity equal to that of carbon in formulations of the substituent dependence of ^3J, this result is intriguing. The signs and magnitudes of ^4J(H,H) are also of interest, in that some involve a CCC, others a CSC fragment. An additional point of discussion is the striking variation in the chemical shifts of the axial and equatorial protons in **1**.

[1]Author to whom correspondence may be addressed.

Can. J. Chem. Downloaded from www.nrcresearchpress.com by EESC ESCOLA DE ENGENHARIA on 09/08/12
For personal use only.

TABLE 1. ^{1}H nmr spectral parameters for 2-phenyl-1,3-dithiane[a] at 300 K

Parameter	Value	Parameter	Value
ν_o	220.104[b,c]	$^3J_{4a,5a} = {}^3J_{5a,6a}$	12.423
ν_m	2159.372	$^3J_{4a,5e} = {}^3J_{5e,6a}$	2.423
ν_p	2147.603	$^3J_{4e,5a} = {}^3J_{5a,6e}$	2.945
ν_2	1507.1[d]	$^3J_{4e,5e} = {}^3J_{5e,6e}$	4.560
$\nu_{4a} = \nu_{6a}$	874.494	$^4J_{4a,6a}$	−0.248
$\nu_{4e} = \nu_{6e}$	826.411	$^4J_{4a,6e} = {}^4J_{4e,6a}$	−0.379
ν_{5a}	557.165	$^4J_{4e,6e}$	1.427
ν_{5e}	606.775	$^4J_{2a,4a} = {}^4J_{2a,6a}$	0.186
$^3J_{om}$	7.764	$^4J_{2a,4e} = {}^4J_{2a,6e}$	0.480
$^3J_{mp}$	7.458	$^5J_{2a,5a}$	±0.043[e]
$^4J_{oo}$	1.997	$^5J_{2a,5e}$	±0.078[e]
$^4J_{op}$	1.252	$^2J_{4a,4e} = {}^2J_{6a,6e}$	−13.990
$^4J_{mm}$	1.426	$^2J_{5a,5e}$	−13.858
$^5J_{om}$	0.582	No. of assigned transitions	16.375
$^4J_{20}$	−0.467	No. of peaks	337[f]
$^5J_{2m}$	0.271	Largest deviation	0.017
$^6J_{2p}$	−0.181	Root-mean-square deviation	0.007

[a]4.8 mol% in CS_2 containing also 10.0 mol% of C_6D_{12} and 0.5 mol% of TMS.
[b]In Hz at 300.135_2 MHz to high frequency of internal TMS.
[c]The standard deviations in the parameters were all ≤0.0003 Hz, but the latter are given here only to a precision of 0.001 Hz.
[d]Transitions in this spectral region could not be assigned reliably; see Experimental.
[e]Because of footnote *d* these signs are not certain, although the least-squares fitting procedure yielded positive signs.
[f]Not counting degeneracies of the many peaks in the band due to H-2.

Accordingly, we report precise ^{1}H nmr spectral parameters for **1** as a dilute solution in a CS_2–C_6D_{12}–TMS solvent mixture. A Karplus equation is deduced for ^3J(H,H). Its parameters are discussed in terms of the pucker of the dithiane moiety and in terms of the theory of vicinal coupling constants. The proton–proton coupling constants over four bonds within this moiety are compared with the ones available for a *tert*-butylcyclohexane derivative, and from theory. The apparent twofold barrier to rotation about the Csp^2—Csp^3 bond is reduced and compared with that for phenylcyclohexane. Semiempirical, AM1, as well as STO-3G and STO-3G* molecular orbital computations of this barrier are given. The chemical shifts of the alkyl protons are discussed in terms of the perturbations caused by the mainly 3*p* lone pair on sulfur and the ring proton shieldings in terms of van der Waals interactions. ^2J(H,H) and ^5J(H,H) for the dithiane ring are noted.

Experimental

A 4.8 mol% solution of **1** (Aldrich) in a CS^2–C_6D_{12}–TMS solvent mixture (see Table 1 for details) was filtered into a 5 mm o.d. nmr sample tube. The tube was degassed by five cycles of the freeze–pump–thaw procedure and was then flame-sealed under vacuum to produce a reasonably symmetrical top. The ^{1}H nmr spectra were acquired with an AM 300 nmr spectrometer at a probe temperature of 300 K, in the manner previously described in detail (1). The peak widths at half height in the aromatic region were less than 0.1 Hz, many being about 0.05 Hz. Similar remarks apply to the alkyl proton spectrum, but H-2, being coupled to 11 other protons with couplings constants of less than 0.5 Hz in magnitude, gave an unassignable band of peaks.

The AM1 (2), STO-3G(3), and STO-3G*(4) computations used the program GAUSSIAN 92 (5) and were done for various angles of twist about the Csp^2—Csp^3 bond in **1**. At each angle the geometry was optimized with the proviso that the phenyl group remain a planar entity.

Results and discussion

Spectral analysis

The ^{1}H nmr spectrum was analyzed with the computer program NUMARIT (6), greatly modified and arranged to be partially self-assigning by R. Sebastian. In all, 16 375 transitions were assigned to some 337 peaks for the 12-spin system. However, transitions could not be assigned in the H-2 region, that of the methine proton. This means that the signs of ^5J(H-2, H-5) in the dithiane ring are uncertain; those to the aromatic protons are, however, known, as are the signs of ^4J(H,H). The H-2 peaks coalesce to a broad band because H-2 couples to at least 10 protons with coupling constant magnitudes of less than 0.5 Hz. The final spectral parameters had standard deviations of 0.0003 Hz or less and are given in Table 1.

*The internal rotation barrier in **1***

The coupling constant over six formal bonds, ^6J(H-2, H_p) ≡ ^6J, is proportional to $\sin^2\theta$, as in **2** (7), and $^6J(\theta = 90°)$ is somewhat dependent on the electronegativity of the substituents at the sp^3 carbon atom (8). For isopropylbenzene, $^6J(\theta = 90°)$ is −1.12 Hz (9). The electronegativities of carbon and sulfur are

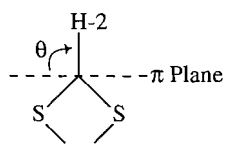

2

identical, to a first approximation, so that the same value of $^6J_{90}$ will here be taken for the dithiane. The expectation value of $\sin^2\theta$ follows at −0.181/−1.12 or 0.169 at 300 K. A hindered rotor model (7) then yields the apparent twofold barrier to rotation about the Csp^2—Csp^3 bond as 9.6 kJ/mol, as does a classical averaging procedure. This value for **1** is somewhat higher than that of 7.1 kJ/mol deduced for phenylcyclohexane (10). Both molecules clearly adopt the parallel or bisected conformation in the conformation of lowest energy, that in which the

Can. J. Chem. Downloaded from www.nrcresearchpress.com by EESC ESCOLA DE ENGENHARIA on 09/08/12
For personal use only.

C(2)—H bond lies in the phenyl plane. Certainly, this is true for **1** in the crystal (11).

The foldedness of the barrier to internal rotation was probed with the three basis sets above, with the results that

$$V_2/\text{kJ/mol} = 9.44 \sin^2\theta - 0.12 \sin^2 2\theta, \quad \text{AM1}$$

$$V_2/\text{kJ/mol} = 12.38 \sin^2\theta - 0.21 \sin^2 2\theta, \quad \text{STO-3G}$$

$$V_2/\text{kJ/mol} = 13.31 \sin^2\theta - 0.16 \sin^2 2\theta + 0.26 \sin^2 3\theta, \quad \text{STO-3G*}$$

The angle θ is zero for the bisected conformation. The assumption of a predominantly twofold barrier, in $\sin^2\theta$, is a good one apparently because any fourfold, in $\sin^2 2\theta$, and sixfold, in $\sin^2 3\theta$, terms are rather small. The AM1 results agrees closely with the twofold barrier deduced fro the solution of **1** in CS_2–C_6D_{12}. The solvent effect on the barrier is not known, of course. Calculations with much larger basis sets are not feasible at present for a molecule of this size.

The energy difference between the equatorial and axial conformers of **1** was also calculated. As expected (10), the axial conformer has the perpendicular orientation of the phenyl group instead of the bisected or parallel orientation in the equatorial conformer, as in **1**. As in phenylcyclohexane (10), repulsive interactions with the axial C(4)—H and C(6)—H bonds destabilize the bisected orientation of the phenyl group in the axial conformer. The axial is computed as 8.96, 13.21, and 13.47 kJ/mol less stable than the equatorial conformer by the AM1, STO-3G, and STO-3G* procedures, respectively. The most recent measurement of the free energy difference yields 9.8 kJ/mol (12). The inversion barrier for 1,3-dithiane in CS_2 solution is 39.3 ± 1.3 kJ/mol (13). The assumption in this paper of a negligible amount of the axial conformer of 2-phenyl-1,3-dithiane in solution at 300 K appears reasonable.

The pucker of the dithiane moiety

The vicinal coupling constant, ^3J(H,H), is sensitive to the dihedral angle, ϕ, between the protons (14, 15), but also depends on the CCH angles, the *s* character of the hybrid orbitals at the two carbon atoms in the HCCH fragment, on various overlap integrals, themselves dependent on the C—C distance, and on the effective nuclear charges at the carbon atoms (16, 17). It follows that substituents, X, at carbon will also perturb ^3J(H,H), a perturbation whose magnitude may well depend on the dihedral angle between the C—X and the vicinal C—H bonds. It is therefore not surprising that, while the Karplus equation relating ^3J(H,H) to ϕ is of great stereochemical significance, its quantitative application requires circumspection. The following discussion of the four ^3J(H,H) values in **1** illustrates this point (see **3**).

The ^3J values in Table 1 are ^3J(4a,5a) = 12.423, ^3J(4a,5e) = 2.422, ^3J(4e,5a) = 2.946, and ^3J(4e, 5e) = 4.560 Hz, differing by up to 0.3 Hz from earlier (18, 19) values. In cyclohexane, ^3J(a,a) is 12.85, ^3J(e,e) is 2.92, while ^3J(a,e) are 3.61 Hz in CS_2 solution (20, 21). These numbers were analyzed to yield a dihedral angle of 57°, the HCH angle being somewhat less than a tetrahedral value (22). The data for **1** therefore suggest that the dithiane ring is puckered, that is, that ψ is larger than the 56° commonly accepted for cyclohexane (22). In the crystal of **1** the value of ψ is 62.5 ± 2.5° (11).

Lambert defines the quantity, *R*, as $\{^3J(a, a) + {}^3J(e, e)\}/\{^3J(a, e) + {}^3J(e, a)\}$, a measure of the degree of pucker (23). The perturbation of ^3J caused by an electronegative substituent, if independent of the relative orientation of the C—H and C—X bonds, is removed by this division. For **1**, *R* is 3.16, compared to 2.16 for cyclohexane (23). Furthermore, if the S-CH_2CH_2-C fragment possesses pseudotrigonal projection symmetry, as in **3**, and if ^3J is given by the simplified expression, $A \cos^2\phi$, then ψ follows as 63° (23). It must also follow that ϕ_{aa} is 183°, ϕ_{ee} is 57°, and that ϕ_{ae} and $\phi_{e,a}$ are 63°.

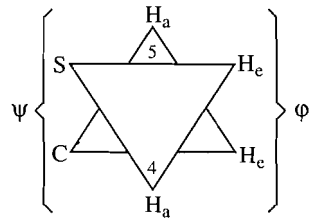

3

Note, however, that the values of ^3J(4a,5e) and ^3J(4e,5a), at 2.422 and 2.946 Hz, respectively, are not the same. The equal angles, ϕ_{ea} and ϕ_{ae}, underlying the derivation of *R*, imply the equality of the two coupling constants *unless* the electronegativity of sulfur differs from that of carbon. The generalized Karplus equation (24) would assume the equality of the two (Huggins) electronegativities.

In an attempt at a better assessment of the endocyclic torsion angles in **1**, the following approach is taken, somewhat similar to the discussion of Slessor and Tracey (25). The original formulation (14) writes $^2J = J_0 \cos^2\phi - 0.28$ for $0° \leq \phi \leq 90°$ and $^3J = {}^3J_{180} \cos^2\phi - 0.28$ for $90° \leq \phi \leq 180°$. This formulation will be used here because there is good reason (16, 17) to believe that ^3J is more sensitive to changes in CCH angles and C—C distances at torsion angles greater than 90° than it is for torsion angles less than 90°. Accordingly, the smaller ^3J values for **1**, corresponding to $\phi < 90°$, may well be the more reliable sources of ϕ_{ee}, ϕ_{ea}, and ϕ_{ae}. Furthermore, in cyclohexane the HCH angle is smaller than its tetrahedral value. In consequence, the pseudo-trigonal symmetry is lost. The projection angles, as in **3**, for example, are no longer 120° but may be as small as 115°. In **1**, these projection angles, ω, can be different at C-4 and C-5. We shall adjust their values so as to obtain a single J_0 and consistent values of the three ϕ values above. The adjustment proceeded with the result that ω at C-5 was 115° and was 118° at C-4, taking $\omega < 120°$. The former value is that found by Slessor and Tracy (25) for cyclohexane. In gaseous 1,3-dithiane (26) the HCH angles are somewhat smaller than in cyclohexane (22). An example of the calculations goes as follows. One has

$$^3J(4e,5e)/{}^3J(4e,5a) = (J_0 \cos^2 \phi_{ee} - 0.28)/[J_0 \cos^2 (115 - \phi_{ee}) - 0.28]$$

where $115 - \phi_{ee} = \phi_{ea}$ and the first subscript of ϕ refers to H-4, the second to H-5. Again,

$$^3J(4e,5e)/{}^3J(4a,5e) = (J_0 \cos^2 \phi_{ee} - 0.28)/[J_0 \cos^2 (118 - \phi_{ee}) - 0.28]$$

where $118 - \phi_{ee} = \phi_{ae}$, and 118° is the value for the CH_2 group at C-4. The upshot is that ϕ_{ee}, ϕ_{ea}, and ϕ_{ae} are 53.9 ± 0.1°, 61.1 ±

Can. J. Chem. Downloaded from www.nrcresearchpress.com by EESC ESCOLA DE ENGENHARIA on 09/08/12
For personal use only.

TABLE 2. Some theoretical and experimental values of ^4J(H,H) in Hz in the propanic fragment

	INDO/FPT[b]	MO + VB[c]	1-*tert*-Butylcyclohexane[d]	**1**
a,a(60,60)[a]	−0.76	−0.49	−0.31[e]	−0.25[g]
a,e(60,180)	−0.47	−0.02	−0.14[f]	−0.38[h]
e,e(180,180)	2.09	1.52	2.10[e]	1.43[i]

[a]The twist angles of the two C—H bonds out of the CCC plane.
[b]From ref. 27, column 3 of Table II.
[c]From ref. 27, column 6 of Table II.
[d]From ref. 28.
[e]An average of three values in *tert*-butylcyclohexane-3,3,4,4,5,5-d_6 and -3,3,5,5-d_4.
[f]An average of four values in the two compounds in footnote *e*.
[g]From Table 1, ^4J(4a, 6a).
[h]From Table 1, ^4J(4a, 6e) = ^4J(4e, 6a).
[i]From Table 1, ^4J(4e, 6e).

0.1°, and 64.1 ± 0.1°, respectively, corresponding to a J_0 of 13.97 ± 0.10 Hz; the significant figures indicate the error of fit only, of course. The average of ϕ_{ea} and ϕ_{ae} is 62.6°, very close to the ψ value give by the *R* value of Lambert. For 1,3-dithiane in the gas phase ψ is 64.1° (26).

With the values of ω as given above, two equations in J_{180} follow. They are

$$^3J(4a,5e)/^3J(4a,5a) = (J_0/J_{180}) \cos^2 \phi_{ae}/\cos^2 (115 + \phi_{ae})$$

and

$$^3J(4e,5a)/^3J(4a,5a) = (J_0/J_{180}) \cos^2 \phi_{ae}/\cos^2 (118 + \phi_{ea})$$

Use of $^3J_0$, ϕ_{ea} and ϕ_{ae} yields $^3J_{180}$ as 12.69 ± 0.16 Hz. The equation,

$$^3J(H,H) = 13.36 \cos^2\phi + 0.59 \cos \phi - 0.43$$

reproduces the four coupling constants with an average deviation of 0.04 Hz if the angles above are used; ϕ_{aa} is 179.1°. The striking conclusion is that the coefficient of cos ϕ is positive, that is, $^3J_{180} < {}^3J_0$. The following points are relevant to this conclusion.

First, even if ω is taken at 120° and (or) the term *C* in $A \cos^2\theta - C$ is omitted, the conclusion holds. The condition $\omega > 120°$ was not tested because $\omega < 120°$ for cyclohexane and because in 1,3-dithiane the HCH angle is quoted (26) as being even smaller than in cyclohexane. In cyclohexane, J_{180} is 12.94 Hz and J_0 = 12.50 Hz (20, 21) for an ω of 118°. Second, the coefficient of cos ϕ is not required to be negative by theory because it is the difference between large terms of opposite signs (16). In fact, for the latest formulating of ^3J(H,H), which takes CCH angles into consideration (16, 17), the *B* term is 0.3 Hz for tetrahedral angles and hence $J_{180} < J_0$ in the ideal case. Third, the exact values of ϕ for **1** above are not to be taken too literally; it does appear, however, that $\phi_{ae} > \phi_{ea} > \phi_{ee}$. Fourth, the formulations under consideration here apply to molecules without highly electronegative atoms; in their presence negative *B* terms may well occur.

^{4}J(*H,H*) *in the dithiane moiety*

Long-range coupling constants over four bonds are a result of competition among several coupling mechanisms and can be positive or negative (27). Table 2 presents some particular theoretical (27) and experimental values for ^4J(H,H) in the propanic fragment, those for axial and equatorial protons in the ideal chair form of a six-membered alicyclic ring. The theoretical values are for propane itself and of course, substituent effects can alter these numbers (27). However, neither carbon nor sulfur are strongly electronegative and hence the comparisons in Table 2 may be of some value even though, furthermore, the angles involved experimentally are clearly not exactly 60° or 180°. The early data for 1-*tert*-butylcyclohexane (28) are averages over a range of values. Those for **1** are single values of relatively high precision. Qualitatively, theory and experiment are in reasonable agreement.

Of greater interest here are the ^4J(H,H) values for **1** that involve the C—S—C fragment. ^4J(2,4a) = ^4J(2,6a) = 0.19 Hz and ^4J(2a,4e) = ^4J(2a,6e) = 0.48 Hz. Both are now positive, unlike such couplings in the propanic fragments in Table 2 (the second-order spectra **1** could not be reproduced with different signs of these coupling constants). These couplings constants are perhaps the first examples whose signs are know for definite orientations of the C—H bonds relative to the C—X—C plane (there are some examples for five-membered rings in which a dual pathway (29) is important for ^4J(H,H)).

The positive shift in $^4J_{aa}$ and $^4J_{ae}$ in fragment C—S—C is reproducible by INDO MO FPT (30) computations, as follows. The geometries of propane, dimethyl ether, and dimethyl sulfide were optimized using the STO-3G* basis and the ^4J values were computed with these geometries. The $^4J_{ae}$ values changed from −0.54 to −0.28 to −0.03 Hz in going from CH_2 to O to S, respectively, in the C—X—C fragment; for $^4J_{aa}$ the values are −0.79, −0.45, and 0.93 Hz. Thus, the qualitative theoretical trend bears out the experimental algebraic increase in the ^4J(H,H) values measured for the dithiane. It would be useful to measure signs of ^4J(H,H) for the C—O—C fragment in 1,3-dioxane derivatives. The INDO MO FPT computations also suggest positive shifts in $^4J_{ee}$; measurements would require axial substituents at position 2 in these six-membered rings or equatorial substituents at C-5.

The coupling constants, ^{2}J*(H,H) and* ^{5}*(H,H) in the dithiane ring*

^2J(H,H) in cyclohexane is −12.88(5) to −13.05(5) Hz (20, 21), not far from the −13.42 ± 0.26 Hz (31) in propane. In **1**, ^2J(H,H) at C-4 is −13.99 Hz and is −13.86 Hz at C-5. In the molecular orbital model (32) of substituent perturbations of ^2J(H,H), inductive electron withdrawal (donation) from the CH_2 fragment leads to an increase (decrease) in ^2J(H,H), whereas hyperconjugative electron shifts cause the opposite corresponding signs in the changes induced in ^2J(H,H). The lat-

Can. J. Chem. Downloaded from www.nrcresearchpress.com by EESC ESCOLA DE ENGENHARIA on 09/08/12
For personal use only.

TABLE 3. Proton chemical shift data in ppm for the alkyl protons of 2-phenyl-1,3 dithiane, **1**

	1		
Proton	δ^a	Δ^b	$\Delta\chi^c$
2a	5.021	3.885	0.52_3
2e	—	—	—
4a = 6a	2.914	1.778	0.00_2
4e = 6e	2.753	1.146	0.00_1
5a	1.856	0.720	0.12_6
5e	2.002	0.415	0.06_2

[a]From Table 1, 4.8 mol% in CS_2–C_6D_{12}–TMS.

[b]$\Delta = \delta - \delta_a$ or $\Delta = \delta - \delta_e$, where $\delta_a = 1.136$ and $\delta_e = 1.607$ for a 5% solution in CS_2 of 1,1,2,2,3,3,4,4-octadeuterocyclohexane at −103°C (20, 21).

[c]The deshielding due to the phenyl ring.

est computations on methane (33) imply that a decrease of one degree in the HCH angle entails a change of –0.72 Hz in ^2J(H,H). Because the electronegativities of carbon and sulfur are so similar, the small decrease of ^2J(H,H) in **1** relative to cyclohexane could be a result of hyperconjugative withdrawal of electron density by sulfur from both CH_2 moieties (the 3*p* orbital approaches the axial C(5)—H bond reasonably closely) and (or) of small decreases in the HCH angles in **1** relative to cyclohexane. The comparison in a previous section of HCH angles in 1,3-dithiane and cyclohexane suggests that changes in HCH angles are a distinct possibility as a cause of the smaller ^2J(H,H)values in **1**. More cannot be established at present.

Turning to ^5J(H,H), the magnitude of ^5J(2a,5e), at about 0.08 Hz, is nearly twice as large as that of ^5J(2a,5a), at about 0.04 Hz. These numbers can be compared to the magnitude of 0.9 Hz, for ^5J(2e,5e) in some 1,3-dioxane derivatives (34, 35); here larger rear-lobe interactions of C—H bonds are likely. Unfortunately, the signs of these couplings constants are not known.

The chemical shifts of the alkyl protons

In Table 3 the chemical shifts of the alkyl protons of **1** are compared with the chemical shifts of the axial and equatorial protons in cyclohexane. Because the electronegativities of sulfur and of the replaced methylene group are essentially equal, the relatively large deshieldings of H-4 and H-5 are remarkable., as is the fact that an axial proton is more deshielded than its equatorial partner. To isolate these differential shifts from those caused by the diamagnetic anisotropy, $\Delta\chi$, of the phenyl group in **1**, the model in ref. 36 was applied. This model relates the shift cause by $\Delta\chi$ to $\langle\sin^2\theta\rangle$, the expectation value of $\sin^2\theta$, where θ is the torsion angle about the Csp^3—Csp^2 bond in **1**. The value of $\langle\sin^2\theta\rangle$, deduced in a previous section, is required because it determines whether or not, on average, the alkyl proton lies in the shielding or deshielding region of the magnetic field from the induced dipole in the phenyl group. For example, if $<\sin^2\theta>$ is zero, then H-5a and H-5e lie in the phenyl plane and experience their maximum deshielding. These anisotropy shifts are given in Table 3. They are negligible for H-4 protons because of the average geometry of **1**.

The remaining differential shifts are here attributed to intramolecular van der Waals interactions (37) originating from the mainly 3*p* lone-pair orbital on sulfur, for the following reasons. In previous work (38–40) we have shown that a close approach of a C—H bond to a 3*p* orbital of sulfur leads to a marked deshielding of its proton. For example, in 2-methylthiobenzaldehyde, δ(CHO) is 10.27, the molecule existing as a mixture of planar O-*syn* and O-*anti* conformers in solution (39); the 3*p* orbital lies essentially perpendicular to the molecular plane. For 2-*tert*-butylbenzaldehyde, only the O-*anti* conformer exists and, furthermore, the bulky alkyl group is twisted nearly 90° out of the benzene plane. In consequence, the 3*p* orbital is now oriented in the benzene plane and δ(CHO) becomes 10.70, its larger value being attributed to the proximity of this lone pair and the C—H bond of the formyl group. In an independent and earlier discussion (41) it was noted that, in an axial orientation of the phenyl group in 2-methyl-2-phenyl-1,3-dithiane, the *ortho* protons were deshielded by about 0.6 ppm relative to the *meta* and *para* protons. An axial phenyl group was assumed to be predominantly oriented to bring the *ortho* C—H bonds close to the 3*p* lone pairs on the sulfur atoms (see the conformation deduced for a mimic of axial phenylcyclohexane (10)) and the deshielding of the *ortho* protons was attributed to interactions with the proximate 3*p* orbitals.

Of course, a quantitative treatment of intramolecular van der Waals shifts is difficult (42). They must depend on some power of the distance (45, 46) between the C—H bond and the 3*p* orbital on sulfur as well as on their relative orientation. It is possible to parameterize the proton shifts, in an additive fashion, in terms depending on the dihedral angles between the C—H bonds and the 3*p* orbitals on sulfur. Such a parameterization can also reproduce the proton shift differences observed (41) for the inverting molecule, 1,3-dithiane. However, it is possible that modern molecular orbital calculations (45, 46) will soon be able to reproduce such differential shifts. Therefore, it is simply noted here that the axial C—H bond of a given methylene group has a significantly greater proximity to the 3*p* lone pair than does the equatorial C—H bond (they point away from the 3*p* orbitals and (or) are oriented roughly in the nodal plane of these orbitals). The values of Δ–$\Delta\chi$ in Table 3 are then a measure of the differential van der Waals shifts at a given methylene moiety. As expected, the differential shift at C-5 is smaller than that, for example, at C-4.

The aromatic chemical shifts

For dilute solutions of benzene, phenylcyclohexane (10), and isopropylbenzene (9) in CS_2 solutions at 300 K, the δ values of the *para* protons are 7.218, 7.004, and 7.017, respectively; for **1**, it is 7.155. Accordingly, the C—S bond in **1** can be considered as a electron donor by a σ–π mechanism; the barriers to rotation about the Csp^2—Csp^3 bonds in these three molecules are similar, so that the α C—H bonds have very similar hyperconjugative interactions in these molecules. In these terms, the C—S bonds is only 30% as effective as a C—C bond in redistribution of electron density in the phenyl group. Again, relative to benzene, the *ortho* protons in phenylcyclohexane and isopropylbenzene are shielded by 0.172 and 0.144 ppm, respectively, as expected from the discussion of the *para* proton shifts. The *ortho* protons of **1**, however, are deshielded by 0.112 ppm. On the basis of the *para* proton shift in **1**, a shielding of about 0.05 ppm would have been expected. The net deshielding of about 0.16 ppm is attributed to van der Waals interactions with the 3*p* lone pair on sulfur, four formal bonds distant. In the bisected, most stable, conformation of **1**, one of the *ortho* protons and H-5a, three bonds distant from sulfur are essentially equidistant from sulfur; the other *ortho* proton is too far removed from the 3*p* orbital to undergo deshielding. Further averaging of shifts comes from oscillation about the Csp^2—Csp^3 bond. It is therefore plausible that the *ortho* protons undergo deshielding by intramolecular van der Waals interactions.

Can. J. Chem. Downloaded from www.nrcresearchpress.com by EESC ESCOLA DE ENGENHARIA on 09/08/12
For personal use only.

Acknowledgments

We thank the Natural Sciences and Engineering Research Council of Canada for a grant-in-aid of research.

1. T. Schaefer, R. Sebastian, R.W. Schurko, and F.E. Hruska. Can. J. Chem. **71**, 1384 (1993).
2. M.J.S. Dewar, E.J. Zoebisch, E.F. Healy, and J.J.P. Steward. J. Am. Chem. Soc. **107**, 3902 (1985).
3. W.J. Hehre, R. Ditchfield, R.F. Stewart, and J.A. Pople. J. Chem. Phys. **52**, 2796 (1970).
4. J.B. Collins, P.v.R. Schleyer, J.S. Binkley, and J.A. Pople. J. Chem. Phys. **64**, 5142 (1976).
5. M.J. Frisch, G.W. Trucks, M. Head-Gordon, P.M.W. Gill, M.W. Wong, J.B. Foresman, B.G. Johnson, H.B. Schlegel, M.A. Robb, E.S. Replogle, R. Gomperts, J.L. Andres, K. Raghavachari, J.S. Binkley, C. Gonzalez, R.L. Martin, D.J. Fox, D.J. Defrees, J. Baker, J.J.P. Stewart, and J.A. Pople. GAUSSIAN 92, Revision A. Gaussian, Inc., Pittsburgh, Pa. 1992.
6. J.S. Martin, A.R. Quirt, and K.W. Worvill. The NMR program library. Daresbury Laboratory, Daresbury, U.K.
7. W.J.E. Parr and T. Schaefer. Acc. Chem. Res. **13**, 400 (1980).
8. T. Schaefer, C. Beaulieu, R. Sebastian, and G.H. Penner. Can. J. Chem. **68**, 581 (1990).
9. T. Schaefer, R. Sebastian, and G.H. Penner. Can. J. Chem. **66**, 1495 (1988).
10. T. Schaefer, C. Beaulieu, and R. Sebastian. Can. J. Chem. **69**, 503 (1991).
11. H.T. Kalff and C. Romers. Acta Crystallogr. **20**, 490 (1966).
12. H. Köhler, C. Tschierske, H. Zaschke, and E. Kleinpeter. Tetrahedron, **46**, 4241 (1990).
13. H. Friebolin, S. Kabuss, W. Maier, and A. Lüttringhaus. Tetrahedron Lett. 683 (1962).
14. M. Karplus. J. Chem. Phys. **30**, 11 (1959).
15. M. Karplus. J. Am Chem. Soc. **85**, 2870 (1963).
16. M. Barfield and W.B. Smith. J. Am. Chem. Soc. **114**, 1574 (1992).
17. W.B. Smith and M. Barfield. Magn. Reson. Chem. **31**, 696 (1993).
18. J.-P. Albrand, D. Gagnaire, J. Martin, and J.B. Robert. Org. Magn. Reson. **5**, 33 (1973).
19. J. Martin and J.B. Robert. Org. Magn. Reson. **7**, 76 (1975).
20. E.W. Garbisch, Jr. and M.G. Griffith. J. Am Chem. Soc. **90**, 6543 (1968).
21. D. Höfner, S.A. Lesko, and G. Binsch. Org. Magn. Reson. **11**, 179 (1978).
22. H.R. Buys and H.J. Geise. Tetrahedron Lett. 2991 (1970).
23. J.B. Lambert. Acc. Chem. Res. **4**, 87 (1971).
24. C.A.G. Haasnoot, F.A.A.M. de Leeuw, and C. Altona. Tetrahedron, **36**, 2783 (1980).
25. K.N. Slessor and A.S. Tracey. Can. J. Chem. **49**, 2874 (1971).
26. W.J. Adams and L.S. Bartell. J. Mol. Struct. **37**, 261 (1977).
27. M. Barfield, A.M. Dean, C.J. Fallick, R.J. Spear, S. Sternhell, and P.W. Westerman. J. Am. Chem. Soc **97**, 1482 (1975).
28. V.R. Haddon and L.M. Jackman. Org. Magn. Reson. **5**, 333 (1973).
29. M. Barfield, R.J. Spear, and S. Sternhell. J. Am. Chem. Soc. **93**, 5322 (1971).
30. J.A. Pople, J.W. McIver, Jr., and N.S. Ostlund. J. Chem. Phys. **49**, 2960 (1968); **49**, 2965 (1968).
31. C. Schumann and H. Dreeskamp. J. Magn. Reson. **3**, 204 (1970).
32. J.A. Pople and A.A. Bothner-By. J. Chem. Phys. **42**, 1335 (1965).
33. J. Geertsen, J. Oddershede, and W.T. Raynes. Magn. Reson. Chem. **31**, 722 (1993).
34. K.C. Ramey and J. Messick. Tetrahedron Lett. 4423 (1965).
35. J. Delmau and J. Duplan. Tetrahedron Lett. 559 (1966).
36. T. Schaefer, R. Sebastian, and F.E. Hruska. Can. J. Chem. **71**, 639 (1993).
37. T. Schaefer, W.F. Reynolds, and T. Yonemoto. Can. J. Chem. **41**, 2969 (1963).
38. T. Schaefer, S.R. Salman, T.A. Wildman, and P.D. Clark. Can. J. Chem. **60**, 342 (1982).
39. T. Schaefer, G.H. Penner, K.J. Davie, and R. Sebastian. Can. J. Chem. **63**, 777 (1985).
40. T. Schaefer, L.B.-L. Lee, and R. Sebastian. Can. J. Chem. **70**, 2375 (1992).
41. H.T. Kalff and E. Havinga. Recl. Trav. Chem. Pays-Bas, **85**, 467 (1966).
42. T. Yonemoto. Can. J. Chem. **44**, 223 (1966).
43. B.B. Howard, B. Linder, and M.T. Emerson. J. Chem. Phys. **36**, 485 (1962).
44. M.J. Stephen. Mol. Phys. **1**, 223 (1958).
45. J. Gauss. J. Chem. Phys. **99**, 3629 (1993), and references therein.
46. T. Onak, D. Tran, J. Tseng, M. Diaz, J. Arias, and S. Herrera. J. Am. Chem. Soc. **115**, 9210 (1993).

Can. J. Chem. Downloaded from www.nrcresearchpress.com by EESC ESCOLA DE ENGENHARIA on 09/08/12
For personal use only.

Ditopic thiacyclophanes containing the $S(CH_2)_2X(CH_2)_2S$ (X = O, S) linkage. Synthesis and structures of 2,5,8,17,20,23-hexathia[9](1,2)[9](4,5)cyclophane and 5,20-dioxa-2,8,17,23-tetrathia[9](1,3)[9](4,6)-2,5-bis(ethoxy)cyclophane

STEPHEN J. LOEB[1] AND GEORGE K.H. SHIMIZU

Department of Chemistry and Biochemistry, University of Windsor, Windsor, ON N9B 3P4, Canada

Received January 28, 1994

STEPHEN J. LOEB and GEORGE K.H. SHIMIZU. Can. J. Chem. **72**, 1728 (1994).

The Cs^+/DMF mediated reactions of 1,2,4,5-tetra(bromomethyl)benzene and 1,2,4,5-tetra(bromomethyl)3,6-bis(ethoxy)benzene with dithiols $HSCH_2CH_2XCH_2CH_2SH$ (X = S,O) were explored in order in order to ascertain the effect of structural variations on the regioselectivity of double ring-closure. Although a structure with bis(*ortho*) geometry was the target molecule, the major products are those with a bis(*meta*) structure. Two crystal structures, one with a bis(*ortho*) structure, 2,5,8,17,20,23-hexathia[9](1,2)[9](4,5)cyclophane, **1**, and one with a bis(*meta*) structure, 5,20-dioxa-2,8,17,23-tetrathia[9](1,3)[9](4,6)-2,5-bis(ethoxy)cyclophane, **7**, are reported. **1** crystallized in the triclinic space group $P\bar{1}$ with a = 8.583(3), b = 11.806(3), c = 5.448(2) Å, α = 97.18(2), β = 107.18(2), γ = 99.40(2)°, V = 511.6(6) Å^3, and Z = 1. The structure refined to R = 6.48% and R_w = 7.13% for 1020 reflections with $F_o^2 > 3\sigma(F_o^2)$. **7** crystallized in the triclinic space group $P\bar{1}$ with a = 9.568(2), b = 9.577(2), c = 8.312(2) Å, α = 113.53(2), β = 94.58(2), γ = 114.94(2)°, V = 604.3(7) Å^3, and Z = 1. The structure refined to R = 3.86% and R_w = 4.20% for 1129 reflections with $F_o^2 > 3\sigma(F_o^2)$. Both compounds sit on a crystallographic centre of symmetry and have the thioether linkages oriented on opposite sides of the central aromatic ring.

STEPHEN J. LOEB et GEORGE K.H. SHIMIZU. Can. J. Chem. **72**, 1728 (1994).

Afin de déterminer l'effet des variations de structure sur la régiosélectivité de double cyclisation, on a étudié les réactions, catalysées par le Cs^+/DMF, du 1,2,4,5-tétra(bromométhyl)benzène et du 1,2,4,5-tétra(bromométhyl)-3,6-bis(éthoxy)benzène avec les dithiols $HSCH_2CH_2XCH_2CH_2SH$ (X = S ou O). Même si la molécule cible possédait une géométrie bis(*ortho*), les produits principaux sont ceux d'une structure bis(*méta*). On a déterminé les deux structures cristallines, soit celle de la structure bis(*ortho*), 2,5,8,17,20,23-hexathia[9](1,2)[9](4,5)cyclophane (**1**) et celle de la structure bis(*méta*), 5,20-dioxa-2,8,17,23-tétrathia[9](1,3)[9](4,6)-2,5-bis(éthoxy)cyclophane (**7**). Le composé **1** cristallise dans le groupe d'espace triclinique $P\bar{1}$, avec a = 8,586(3), b = 11,806(3) et c = 5,448(2)Å, α = 97,18(2), β = 107,18(2) et γ = 99,40(2)°, V = 511,6(6) Å^3 et Z = 1. On a affiné la structure jusqu'à des valeurs de R et R_w de 6,48% et 7,13% respectivement pour 1020 réflexions avec $F_o^2 > 3\sigma F_o^2$. Le composé **7** cristallise dans le groupe d'espace triclinique $P\bar{1}$, avec a = 9,568(2), b = 9,577(2) et c = 8,312(2)Å, α = 113,53(2), β = 94,58(2) et γ = 114,94(2)°, V = 604,3(7) Å^3 et Z = 1. On a affiné la structure jusqu'à des valeurs de R et R_w de 3,86% et 4,20% respectivement pour 1129 réflexions avec $F_o^2 > 3\sigma F_o^2$. Les deux composés se retrouvent sur un centre de symétrie crystallographique et ils possèdent tous les deux des liaisons thioéthers orientées dans des directions opposés du cycle aromatique central.

[Traduit par la rédaction]

Introduction

The synthesis of ditopic thioether macrocycles is currently an active area of research (1–9). One of the most successful approaches towards this goal has been the incorporation of a rigid durene fragment into the macrocyclic framework (5, 6). The durene fragment functions as a central spacing unit and serves to compartmentalize the two metal binding sites.[2] An appealing aspect of this design strategy is that, with the appropriate choice of starting materials, the resultant ligands would be ditopic analogs of the thiacyclophanes, TT[9]OC (11–15) and TT[9]MC (16).

The known coordination chemistry of these thiacyclophanes provides a good model for predicting the bonding preferences of the ditopic versions. Although both molecules have exodentate conformations, the *ortho* and *meta* substitution patterns have dramatically different effects on the coordinating ability of the ligand. The *o*-xylyl fragment introduces strain into the free ligand conformation, which favours an *exo*-to-*endo* conformational change and facial S_3-coordination to a single metal centre. In contrast, the *m*-xylyl group prevents this type of S_3-coordination by reinforcing a rigid exodentate conformation. Thus, TT[9]OC coordinates facially to transition metals with tetrahedral, trigonal bipyramidal, and octahedral geometry. Some structurally characterized examples include $[Ag(TT[9]OC)(PPh_3)]^+$ (12), $[Mo(CO)_3(TT[9]OC)]$ (11), $[Ir(COD)(TT[9]OC)]^+$ (17), and $[PdCl_2(TT[9]OC)]$ (16). The macrocycle, TT[9]MC is a much poorer ligand and the only structurally characterized complex of this thiacyclophane bound to a transition metal is $[PdCl_2(TT[9]MC)]$ (16) in which TT[9]MC acts as a bidentate chelate coordinating through one benzylic S-atom and the central aliphatic S-atom with the third sulphur exodentate. It would, therefore, be anticipated that the *ortho* isomer of the durene-based macrocycles, **1**, would exhibit a significantly richer coordination chemistry than the *meta* isomer, **4**.

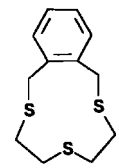

TT[9]OC

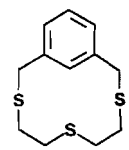

TT[9]MC

The difficulty lies with the synthesis of **1**. The preparation of thiacyclophanes **1** and **4**, employ a common starting material, 1,2,4,5-tetra(bromomethyl)benzene, and a bis-cyclization reac-

[1]Author to whom correspondence may be addressed. TEL: 519-253-4232 (ext 3529), FAX: 519-973-7098, E-MAIL: LOEB@UWINDSOR.CA.

[2]This design strategy has been employed by others towards the goal of ditopic macrocycle synthesis. Lee et al. reported the synthesis of a very similar group of oxo crown ethers. These authors incorporated an aromatic fragment between two polyether chains containing four, five and six oxygen donors and controlled the regioselectivity of the cyclization via the choice of alkaline base (10).

Can. J. Chem. Downloaded from www.nrcresearchpress.com by ESC ESCOLA DE ENGENHARIA on 09/08/12
For personal use only.

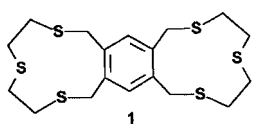

1

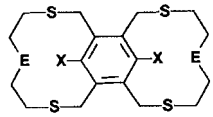

4 (X = H, E = S)
5 (X = H, E = O)
6 (X = OEt, E = S)
7 (X = OEt, E = O)

tion has the potential to produce any combination of *ortho*, *meta*, or *para* substituted cyclization products. Herein, we describe (*i*) our initial attempts to effect control over the cyclization reaction in order to exclusively produce **1** and (*ii*) the synthesis and single crystal X-ray structures of **1** and **7**.

Experimental section

General

Compound **1** was prepared as described previously (5). 1,2,4,5-Tetra(bromomethyl)benzene, 3-thiapentane-1,5-dithiol, 3-oxapentane-1,5-dithiol, cesium carbonate, duroquinone, $NaBH_4$, bromoethane, *N*-bromosuccinamide, benzoyl peroxide, and all deuterated solvents were purchased from Aldrich and used as received. All reactions were conducted under an atmosphere of N_2(g) using standard Schlenk techniques and all solvents were degassed prior to use. ^1H and $^{13}C\{^1H\}$ were recorded at 300.1 and 75.4 MHz, respectively, on a Brüker AC300 spectrometer locked to the deuterated solvent. Elemental analyses were performed by Canadian Microanalytical Services, Delta, British Columbia.

Preparation of 3,6-bis(ethoxy)-1,2,4,5-tetramethylbenzene, 2

$NaBH_4$ (5.980 g, 158 mmol) was suspended in anhydrous ethanol (120 mL). To this suspension was added dropwise, a solution of duroquinone (5.910 g, 36.0 mmol) in anhydrous ethanol (75 mL). This mixture allowed to stir for 12 h. Deionized water (150 mL) and two drops of concentrated HCl(aq) were then added and the solution stored for 12 h at −5°C resulting in the precipitation of durohydroquinone as a white fluffy solid. Yield: 5.42 g (94%). ^1H NMR ($CDCl_3$): δ (ppm) 4.20 (s, 2H, OH), 2.15 (s, 12H, CH_3). Na metal (1.58 g, 68.7 mmol) was dissolved in anhydrous ethanol (300 mL). The durohydroquinone, as prepared above (5.192 g, 31.2 mmol), was then added to this solution and the purple mixture warmed to 50°C for 2 h. Bromoethane (6.808 g, 62.5 mmol) was then slowly syringed into this reaction mixture and the ethanolic solution brought to reflux for 4 h. The ethanol was removed in vacuo and the residue treated with 0.1 M NaOH(aq) (100 mL). The NaOH solution was decanted and the residue dissolved in diethyl ether (100 mL) and extracted with deionized water (100 mL). The diethyl ether layer was then separated, dried over anhydrous $MgSO_4$ and the solvent removed in vacuo. The resulting yellow residue was then dissolved in a minimum volume of anhydrous ethanol and stored at −5°C for 24 h. The product precipitated as a white solid which was filtered and collected. The ethanol solution was then concentrated and again stored at −5°C resulting in the further precipitation of white solid which was filtered, dried, and combined with the first precipitate. Yield: 5.13 g (74%). ^1H NMR ($CDCl_3$): δ (ppm) 3.70 (q, 4H, OCH_2), 2.14 (s, 12H, $ArCH_3$), 1.38 (t, 6H, CH_3). $^{13}C\{^1H\}$ NMR ($CDCl_3$): δ (ppm) 151.76 (ArO), 127.62 (ArMe), 68.30 (CH_2), 15.60 ($ArCH_3$), 12.88 (CH_3). Anal. calcd. for $C_{14}H_{22}O_2$: C 75.62, H 9.99; found: C 75.55, H 9.92.

Preparation of 1,2,4,5-tetra(bromomethyl)-3,6-bis(ethoxy)benzene, 3

2 (1.450 g, 6.52 mmol), *N*-bromosuccinamide (5.108 g, 28.7 mmol), and a catalytic amount of benzoyl peroxide were combined in CCl_4 (40 mL). This mixture was brought to reflux while irradiating with a UV lamp. After 2 h, the white solid which had originally been suspended in the solution was dissolved and a precipitate was observed floating on the surface of the CCl_4 solution, indicating conversion of NBS to succinamide. The mixture was filtered and the CCl_4 removed in vacuo. The residue was recrystallized from ethanol giving **3** as a white microcrystalline solid. Yield: 2.98 g (85%). ^1H NMR ($CDCl_3$): δ (ppm) 4.74 (s, 8H, CH_2Br), 4.20 (q, 4H, OCH_2), 1.52 (t, 6H, CH_3). $^{13}C\{^1H\}$ NMR ($CDCl_3$): δ (ppm) 153.70 (C(Ar)—O), 133.15 (C(Ar)—Me), 70.89 (OCH_2), 23.27 (CH_2Br), 15.67 (CH_3). Anal. calcd. for $C_{14}H_{18}Br_4O_2$: C 31.26, H 3.38; found: C 31.19, H 3.33.

Preparation of 2,5,8,17,20,23-hexathia[9](1,3)[9](4,6)cyclophane, 4

A solution of 1,2,4,5-tetra(bromomethyl)benzene (7.558 g, 16.8 mmol) and 3-thiapentane-1,5-dithiol (7.55 g, 33.6 mmol) in DMF (400 mL) was added using a constant addition funnel to a stirred suspension of Cs_2CO_3 (12.01 g, 36.9 mmol) in DMF (900 mL) at 55°C over a period of 2 days. The DMF was removed in vacuo after completion of addition and the resulting orange residue extracted with CH_2Cl_2 (150 mL). The organic extract was filtered, washed with 0.1 M NaOH(aq) (2 × 100 mL), and dried over anhydrous $MgSO_4$. This fraction was concentrated to 50 mL and added dropwise to boiling absolute ethanol (300 mL) which was filtered while hot. The ethanol was then removed in vacuo and the resulting yellow residue dissolved in $CHCl_3$ (30 mL). Diffusion of *n*-hexane into this solution gave **4** as a microcrystalline white solid. Yield: 6.57 g (90%). mp 203–205°C. ^1H NMR ($CDCl_3$): δ (ppm) 7.03 (s, 2H, aromatic), 4.07 (s, 8H, benzylic), 2.20–2.50 (m, 16H, SCH_2CH_2S). $^{13}C\{^1H\}$ NMR ($CDCl_3$): δ (ppm) 135.33, 134.94 (aromatic), 32.67 (benzylic), 32.08, 30.84 (SCH_2CH_2S). Anal. calcd. for $C_{18}H_{26}S_6$: C49.71, H 6.04; found: C 49.80, H 5.99.

Preparation of 5,20-dioxa-2,8,17,23-tetrathia[9](1,3)[9](4,6)cyclophane, 5

1,2,4,5-Tetra(bromomethyl)benzene (2.164 g, 4.81 mmol) and 3-oxapentane-1,5-dithiol (1.370 g, 9.62 mmol) were dissolved in DMF (150 mL) and added, over 3 days, to a suspension of Cs_2CO_3 (6.89 g, 21.1 mmol) in DMF (800 mL) stirring at 55°C. Upon completion of addition, the DMF was removed in vacuo and the resulting yellowish residue dissolved in CH_2Cl_2 (100 mL) and filtered. The CH_2Cl_2 solution was washed with 0.1 M NaOH(aq) (2 × 100 mL) and deionized water (100 mL) then dried over anhydrous $MgSO_4$. The solvent was removed in vacuo and the ^1H NMR spectrum of this crude product mixture revealed the presence of three isomers in a 16:3:1 ratio. Recrystallization of the crude product from anhydrous ethanol yielded the major isomer, **5**, as a white microcrystalline solid. Yield 1.55 g (80%). ^1H NMR ($CDCl_3$): δ 7.44 (s, 2H, aromatic), 3.94 (s, 8H, benzylic), 3.05 (t, 8H, OCH_2), 2.47 (t, 8H, SCH_2). $^{13}C\{1H\}$ NMR ($CDCl_3$): δ 135.10, 133.68 (aromatic), 68.78 (OCH_2), 33.59 (benzylic), 29.19 (SCH_2). Anal. calcd. for $C_{18}H_{26}O_2S_4$: C 53.68, H 6.52; found: C 53.58, H 6.49. The minor products were assigned the structures of the *ortho* and *para* cyclization products based on the position of the aromatic singlet in the ^1H NMR ($CDCl_3$); *ortho* isomer δ 7.12 (s, 2H, aromatic) and *para* isomer δ 7.00 (s, 2H, aromatic).

Preparation of 2,5,8,17,20,23-hexathia[9](1,3)[9](4,6)-2,5-bis(ethoxy)cyclophane, 6

3-Thiapentane-1,5-dithiol (1.275 g, 8.26 mmol) and **3** (2.222 g, 4.13 mmol) were combined in DMF (150 mL) and added over 3 days, via constant addition funnel, to a suspension of Cs_2CO_3 (5.922 g, 18.1 mmol) in DMF (600 mL). Upon completion of addition, the DMF was removed in vacuo and the residue dissolved in CH_2Cl_2 (300 mL). The CH_2Cl_2 solution was washed with aqueous 0.1 M NaOH (2 × 100 mL) and deionized water (1 × 100 mL) then dried over anhydrous $MgSO_4$. The suspension was filtered and the CH_2Cl_2 solution evaporated slowly resulting in precipitation of the *meta* cyclization product, **6**, as a microcrystalline white solid. Yield: 1.94 g (90%); mp (dec) 245°C. ^1H NMR ($CDCl_3$): δ (ppm) 4.32 (d, 4H, benzylic), 4.09 (d, 4H, benzylic), 3.75 (q, 4H, OCH2), 2.71 (d of t, 4H, SCH_2), 2.56 (d of t, 4H, SCH_2), 2.24 (d of t, 4H, SCH_2), 1.99 (t, 6H, CH_3). $^{13}C\{^1H\}$ NMR ($CDCl_3$): δ (ppm) 154.58 (C(Ar)—O), 130.48 (C(Ar)), 72.58 (OCH_2), 31.88, 30.74, 25.50 ($CH_2SCH_2CH_2S$), 15.47 (CH_3). Anal. calcd. for $C_{22}H_{34}O_2S_6$: C 50.52, H 6.57; found: C 50.48, H 6.52.

Preparation of 5,20-dioxa-2,8,17,23-tetrathia[9](1,3)[9](4,6)-2,5-bis(ethoxy)cyclophane, 7

3-Oxapentane-1,5-dithiol (0.250 g, 1.81 mmol) and **3** (0.487 g, 1.81 mmol) were dissolved in DMF (125 mL) and added over 2 days via slow addition funnel to a suspension of Cs_2CO_3 (1.297 g,

Can. J. Chem. Downloaded from www.nrcresearchpress.com by EESC ESCOLA DE ENGENHARIA on 09/08/12
For personal use only.

Can. J. Chem. Downloaded from www.nrcresearchpress.com by EESC ESCOLA DE ENGENHARIA on 09/08/12
For personal use only.

TABLE 1. Crystal data and details of data collection and refinement for **1** and **7**

Parameter	Value	
	1	**7**
Formula	$C_{18}H_{26}S_6$	$C_{22}H_{34}S_4O_4$
Crystal colour and form	Colourless prism	Colourless prism
Formula weight	434.84	490.82
Crystal system	Triclinic	Triclinic
a (Å)	8.586(3)	9.568(2)
b (Å)	11.806(3)	9.577(2)
c (Å)	5.448(2)	8.312(2)
α (deg)	97.18(2)	113.53(2)
β (deg)	107.18(2)	94.58(2)
γ (deg)	99.40(2)	114.94(2)
V (Å^3)	511.6(6)	604.3(7)
Space group	$P\bar{1}$ (No. 2)	$P\bar{1}$ (No. 2)
Z	1	1
Density (g cm^{-3}), calcd.	1.41	1.35
Radiation, λ (Å)	0.71069	0.71069
Absorption coefficient, μ (cm^{-1})	6.42	4.20
Temperature (°C)	24	24
Data collected	1809 (+h, ±k, ±l)	2267 (+h, ±k, ±l)
Number of unique data	1020	1129
Significance test	$F_o^2 > 3\sigma(F_o^2)$	$F_o^2 > 3\sigma(F_o^2)$
Number of variables	109	136
Goodness of fit	2.10	1.65
$R(F_o)$, %	6.48	3.86
$R_w(F_o)$, %	7.13	4.20

3.70 mmol) in DMF (500 mL). Upon completion of addition, the DMF was removed in vacuo and the residue dissolved in CH_2Cl_2 (200 mL). This solution was washed with aqueous 0.1 M NaOH (2 × 100 mL) and deionized water (1 × 100 mL) then dried over $MgSO_4$. The $MgSO_4$ was filtered off and the CH_2Cl_2 removed on the rotary evaporator. The yellowish residue was recrystallized from ethanol giving the *meta* cyclization product, 5,20-dioxa-2,8,17,23-tetrathia[9](1,3)[9](4,6)-2,5-bis(ethoxy)cyclophane, **7**, as a crystalline white solid. Yield: 0.378 g (85%); mp dec. 235°C. ^{1}H NMR ($CDCl_3$): δ (ppm) 4.32 (d, 4H, benzylic), 3.95 (d, 4H, benzylic), 3.77 (q, 4H, $PhOCH_2$), 3.37 (d of t, 4H, SCH_2CH_2O), 2.60 (m, 8H, SCH_2CH_2O), 2.24 (d of t, 4H, SCH_2CH_2O), 1.47 (t, 6H, CH_3). $^{13}C\{^1H\}$ NMR ($CDCl_3$): δ (ppm) 154.45 (C(Ar)—O), 131.09 (C(Ar)), 72.54 ($PhOCH_2$), 67.91 (CH_2OCH_2), 27.37, 26.06 (CH_2SCH_2), 15.50 (CH_3). Anal. calcd. for $C_{22}H_{34}O_4S_4$: C 53.83, H 7.00; found: C 53.78, H 7.00.

General X-ray crystallography

Diffraction experiments were performed on a four-circle Rigaku AFC6S diffractometer with graphite monochromatized Mo Kα radiation. The unit cell constants and orientation matrices for data collection were obtained from 20 centred reflections ($15° < 2\theta < 35°$). Instrument parameters, crystal data, and data collection parameters are summarized in Table 1. The intensities of three standard reflections were recorded every 150 reflections and showed no statistically significant changes over the duration of the data collections. The intensity data were collected using the ω–2θ scan technique, in four shells ($2\theta < 30$, 40, 45, and 50°). Empirical absorption coefficients were small and thus, no absorption corrections were applied to the data. The data were processed using the TEXSAN software package running on a VAX 3520 computer (18). Refinements were carried out by using full-matrix least-squares techniques on *F* by minimizing the function $\Sigma w(|F_o| - |F_c|)^2$, where $w = 1/\sigma^2(F_o)$ and F_o and F_c are the observed and calculated structure factors. Atomic scattering factors (19) and anomalous dispersion terms (20, 21) were taken from the usual sources. Fixed H-atom contributions were included with C—H distances of 0.95 Å and thermal parameters 1.2 times the isotropic thermal parameter of the bonded C atoms. No H atoms were refined, but all values were updated as refinement continued.

X-ray structure determination of ***1***

Colourless crystals of **1** were grown by diffusion of *n*-hexane into a chloroform solution of the compound. Initial cell symmetries indicated a primitive triclinic cell which was checked by a cell reduction routine (18). A statistical analysis of intensity distributions was consistent with the centrosymmetric space group $P\bar{1}$ and this was confirmed by a successful solution refinement. A total of 1809 reflections were collected and 1020 unique reflections with $F_o^2 > 3\sigma(F_o^2)$ were used in the refinement. The positions of the sulphur atoms were determined by direct methods (SHELX86) (18) from the *E*-map with highest figure of merit. The remaining carbon atoms were located from a single difference Fourier map calculation. In the final cycles of refinement all non-hydrogen atoms were assigned anisotropic thermal parameters. This resulted in $R = 0.0648$ and $R_w = 0.0713$ at final convergence. A goodness-of-fit calculation resulted in a value of 2.095. The Δ/σ value for any parameter in the final cycle was less than 0.01. A final difference Fourier map calculation showed no peaks of chemical significance; the largest being 0.666 electrons/Å^3, which was associated with C(6). Atomic positional parameters and selected bonding parameters are summarized in Tables 2 and 3. Thermal parameters, hydrogen atom parameters and a listing of $10|F_o|$ vs. $10|F_c|$ are deposited as supplementary material in Tables S-1, S-2, and S-5.[3]

[3]Supplementary Tables S-1 through S-4 may be purchased from the Depository of Unpublished Data, Document Delivery, CISTI, National Research Council of Canada, Ottawa, Ont., Canada K1A 0S2.

Tables of hydrogen atom parameters for 1 and 7 have also been deposited with the Cambridge Crystallographic Data Centre, and can be obtained on request from The Director, Cambridge, Crystallographic Data Centre, University Chemical Laboratory, 12 Union Road, Cambridge, CB2 1EZ, U.K. 778.

Can. J. Chem. Downloaded from www.nrcresearchpress.com by EESC ESCOLA DE ENGENHARIA on 09/08/12
For personal use only.

TABLE 2. Positional parameters and B(eq) for **1**

Atom	x	y	z	B(eq)
S(1)	1.4933(2)	0.6415(2)	0.3534(4)	5.31(9)
S(2)	1.3101(3)	0.9388(2)	0.0531(5)	6.4(1)
S(3)	0.8850(2)	0.7936(2)	0.3009(4)	4.60(8)
C(1)	1.1480(8)	0.4703(5)	0.009(1)	3.5(2)
C(2)	0.9931(8)	0.5842(5)	0.199(1)	3.0(2)
C(3)	1.1446(8)	0.5551(5)	0.210(1)	3.1(2)
C(4)	1.3030(9)	0.6067(6)	0.431(1)	4.0(3)
C(5)	1.436(1)	0.740(1)	0.123(2)	9.8(5)
C(6)	1.452(1)	0.8494(8)	0.259(2)	8.5(5)
C(7)	1.084(2)	0.8505(8)	0.056(2)	12.7(6)
C(8)	1.095(1)	0.8966(8)	0.283(2)	9.1(5)
C(9)	0.9701(8)	0.6728(5)	0.409(1)	3.9(3)

TABLE 3. Selected bond parameters for **1**

Bond	Distance (Å)	Bond	Distance (Å)
S(1)—C(4)	1.802(7)	S(1)—C(5)	1.83(1)
S(2)—C(6)	1.94(1)	S(2)—C(7)	2.06(2)
S(3)—C(8)	2.04(1)	S(3)—C(9)	1.792(6)
C(1)—C(2)	1.386(9)	C(1)—C(3)	1.399(8)
C(2)—C(3)	1.386(8)	C(2)—C(9)	1.527(8)
C(3)—C(4)	1.499(9)	C(5)—C(6)	1.37(1)
C(7)—C(8)	1.26(1)		

Bonds	Angle (deg)	Bonds	Angle (deg)
C(4)—S(1)—C(5)	100.4(4)	C(6)—S(2)—C(7)	98.5(4)
C(8)—S(3)—C(9)	99.4(3)	C(2)—C(1)—C(3)	122.7(6)
C(1)—C(2)—C(3)	119.3(5)	C(1)—C(2)—C(9)	117.0(6)
C(3)—C(2)—C(9)	123.7(6)	C(1)—C(3)—C(2)	118.1(6)
C(1)—C(3)—C(4)	118.7(6)	C(2)—C(3)—C(4)	123.2(6)
S(1)—C(4)—C(3)	118.0(5)	S(1)—C(5)—C(6)	109.5(9)
S(2)—C(6)—C(5)	112(1)	S(2)—C(7)—C(8)	97(1)
S(3)—C(8)—C(7)	97(1)	S(3)—C(9)—C(2)	116.6(5)

X-ray structure determination of **7**

Colourless crystals of **7** were grown by slow evaporation of a chloroform solution of the compound. Initial cell symmetries indicated a primitive triclinic cell which was checked by a cell reduction routine (18). A statistical analysis of intensity distribution was consistent with the centrosymmetric space group $P\bar{1}$ and this was confirmed by a successful solution refinement. A total of 2267 reflections were collected and 1129 unique reflections with $F_o^2 > 3\sigma(F_o^2)$ were used in the refinement. The positions of the sulphur atoms were determined by direct methods (MITHRIL) (18) from the E-map with highest figure of merit. The remaining oxygen and carbon atoms were located from a series of difference Fourier map calculations. In the final cycles of refinement, all non-hydrogen atoms were assigned anisotropic thermal parameters. This resulted in $R = 0.0386$ and $R_w = 0.0420$ at final convergence. A goodness-of-fit calculation resulted in a value of 1.652. The Δ/σ value for any parameter in the final cycle was less than 0.01. A final difference Fourier map calculation showed no peaks of chemical significance; the largest being 0.291 electrons/Å^3, which was associated with the methyl carbon, C(5). Atomic positional parameters and selected bonding parameters are summarized in Tables 4 and 5. Thermal parameters, hydrogen atom parameters, and a listing of $10|F_o|$ vs. $10|F_c|$ are deposited as supplementary material in Tables S-3, S-4, and S-6.[3]

Results and discussion

The reaction of two equivalents of 3-thiapentane-1,5-dithiol with one equivalent of 1,2,4,5-tetra(bromomethyl)benzene, employing Kellogg's Cs^+-mediated cyclization method for the synthesis of macrocyclic thioethers (22), yields the bis-*meta* cyclization product, **4**, in a yield of 90%. No other cyclization products were isolated from this reaction nor observed in the ^{1}H NMR spectrum of the reaction mixture. Compound **1** could only be prepared employing a metal template method devised by Sellmann and Zapf (23) for the synthesis of 1,4,7-trithiacyclononane (9S3). This synthetic route relies on coordination of the $[SCH_2CH_2SCH_2CH_2S]^{2-}$ thiolate to Mo(0) to obtain the desired regioselectivity for bis(*ortho*) cyclization. Thus, the "$Mo(CO)_3$" templated cyclization of two equivalents of 3-thiapentane-1,5-dithiol with one equivalent of 1,2,4,5-tetra(bromomethyl)benzene proceeds in a bis-*ortho* fashion to give **1** in 20% isolated yield (5). We have previously reported this synthesis of **1** and the X-ray structures of complexes *anti*-$[Cu_2(PPh_2Me)_2(\mathbf{1})]$ $[ClO_4]_2$, *anti*-$[Ag_2(PPh_3)_2(\mathbf{1})][BF_4]_2$ and *syn*-$[Cu_2(\mu\text{-}Ph_2PCH_2CH_2PPh_2)(\mathbf{1})][PF_6]_2$ (5). For binuclear coordination and eventual activation of a single substrate, the *syn*-conformation of **1** is required so that both metal ions are bonded on the same side of the aromatic ring. Complexes of compound **1**, however, showed a tendency to adopt an *anti* conformation in the absence of a bridging ligand.

TABLE 4. Positional parameters and B(eq) for **7**

Atom	x	y	z	B(eq)
S(1)	0.6427(2)	0.7533(2)	0.0819(2)	3.29(5)
S(2)	0.0425(2)	0.8711(2)	0.3300(2)	3.32(5)
O(1)	0.2946(4)	0.6408(4)	0.3387(4)	2.2(1)
O(2)	0.2167(5)	0.7232(5)	−0.1020(5)	4.0(1)
C(1)	0.3976(6)	0.8211(6)	0.4206(6)	2.0(2)
C(2)	0.5560(6)	0.8843(7)	0.4053(6)	2.1(2)
C(3)	0.3395(6)	0.9347(7)	0.5101(6)	2.1(2)
C(4)	0.2989(7)	0.5690(7)	0.4606(7)	3.2(2)
C(5)	0.1893(8)	0.3770(8)	0.3607(8)	5.1(2)
C(6)	0.6063(6)	0.7538(7)	0.2969(6)	2.7(2)
C(7)	0.4982(7)	0.8050(8)	0.0030(7)	3.5(2)
C(8)	0.3237(7)	0.6641(8)	−0.0552(7)	3.6(2)
C(9)	0.1924(7)	0.8355(8)	0.0545(8)	3.7(2)
C(10)	0.0615(6)	0.7326(7)	0.1184(7)	3.5(2)
C(11)	0.1639(6)	0.8596(7)	0.5013(7)	2.7(2)

This work describes our initial investigation into the regioselectivity of this particular cyclization reaction with focus on finding a way to: (*i*) circumvent the template route for the preparation of bis(*ortho*) products and (*ii*) favour a *syn* conformation for these compounds. The first approach taken was to change the nature of the central donor atom of the tridentate chain from sulphur to oxygen. The rationale for this strategy was that since the donor atoms in oxa crown ethers preferentially adopt endodentate orientations (24, 25) this would decrease the strain associated with the $SCH_2CH_2XCH_2CH_2S$ bracket in an *ortho*-xylyl product. The resulting macrocycle, which would contain two S_2O donor sets, would still possess sufficient soft-acid character for coordination to transition metals (8, 9, 17).

The results of the cyclization of two equivalents of 3-oxapentane-1,5-dithiol and one equivalent of 1,2,4,5-tetra(bromomethyl)benzene revealed that the regioselectivity of the bis-cyclizations was altered slightly. A comparison of the aromatic resonances in the ^{1}H NMR spectrum of the crude product mixture to that of the respective monomeric analogs and integration of the aromatic region showed the yields of the three possible isomers to be 80, 15, and 5% for the *meta*, *ortho*, and *para* cyclization products, respectively. The *meta*-isomer, **5**, could be isolated in pure form by repeated, fractional crystallization, but

TABLE 5. Selected bond parameters for **7**

Bond	Distance (Å)	Bond	Distance (Å)
S(1)—C(6)	1.846(5)	S(1)—C(7)	1.811(6)
S(2)—C(10)	1.810(5)	S(2)—C(11)	1.833(5)
O(1)—C(1)	1.392(5)	O(1)—C(4)	1.439(6)
O(2)—C(8)	1.456(6)	O(2)—C(9)	1.430(6)
C(1)—C(2)	1.414(6)	C(1)—C(3)	1.406(6)
C(2)—C(3)	1.398(6)	C(2)—C(6)	1.511(6)
C(3)—C(11)	1.505(6)	C(4)—C(5)	1.479(7)
C(7)—C(8)	1.514(7)		

Bonds	Angle (deg)	Bonds	Angle (deg)
C(6)—S(1)—C(7)	103.6(2)	C(10)—S(2)—C(11)	101.6(2)
C(1)—O(1)—C(4)	113.4(4)	C(8)—O(2)—C(9)	113.6(4)
O(1)—C(1)—C(2)	118.8(4)	O(1)—C(1)—C(3)	119.1(4)
C(2)—C(1)—C(3)	122.0(4)	C(1)—C(2)—C(3)	118.9(4)
C(1)—C(2)—C(6)	118.9(5)	C(3)—C(2)—C(6)	122.2(4)
C(1)—C(3)—C(2)	119.0(4)	C(1)—C(3)—C(11)	119.5(5)
C(2)—C(3)—C(11)	121.3(5)	O(1)—C(4)—C(5)	109.5(4)
S(1)—C(6)—C(2)	114.8(4)	S(1)—C(7)—C(8)	114.2(4)
O(2)—C(8)—C(7)	110.2(5)	O(2)—C(9)—C(10)	112.1(5)
S(2)—C(10)—C(9)	113.0(4)	S(2)—C(11)—C(3)	113.5(4)

only small, contaminated samples of the *ortho* and *para* compounds have been obtained to date.

The second approach taken to alter the regioselectivity of the bis-cyclization reaction was to functionalize the vacant sites of the central durene fragment with an ethoxy group. It was hoped that since the substitution site would be "inside the ring" of a *meta*-isomer that these derivatives would offer some steric hindrance to the cyclization proceeding in a *meta* fashion. Thus, compound **2** was prepared from durohydroquinone by a Williamson ether synthesis with bromoethane and then brominated using NBS to yield **3**. The bis-cyclization reactions then proceeded, employing Kellogg's method, between two equivalents of either 3-thiapentane-1,5-dithiol or 3-oxapentane-1,5-dithiol and one equivalent of **3**. The ^{1}H NMR spectra of the product mixtures revealed that the ethoxy group has almost no effect on the regioselectivity of the cyclization. In the case of the all sulphur compound, only the *meta*-isomer **6** was produced and for the oxygen-containing products the product distribution was essentially identical to that observed in the absence of the ethoxy group. The *meta*-isomer, **7**, was isolated and the regiochemistry of this product confirmed by single crystal X-ray structure determination.

Compound **1** was crystallized by diffusion of *n*-hexane into a $CHCl_3$ solution of the compound. A perspective ORTEP drawing of **1** with the atom numbering scheme is shown in Fig. 1. The ditopic macrocycle, **1**, crystallizes with one molecule per unit cell such that the molecule resides on a crystallographic centre of symmetry. Figure 1 illustrates the compartmentalization of the S_6 donor set into two distinct S_3 sets while Fig. 2 shows the orientation of the two chelating rings with respect to one another and the aromatic ring. Clearly, the ligand adopts an *anti* conformation that places the aliphatic chains on opposite sides of the aromatic ring. The conformation of the $SCH_2CH_2SCH_2CH_2S$ linkages is very similar to that found for this same feature in the X-ray structure of TT[9]OC (11). The S—C—C—S torsional angles are 155.3(5) and 173.0(3)° and the C—C—S—C torsional angles are 80.5(7), 85.8(7), 77.9(7), and 71.9(7)°. The dihedral angle between the aromatic ring and

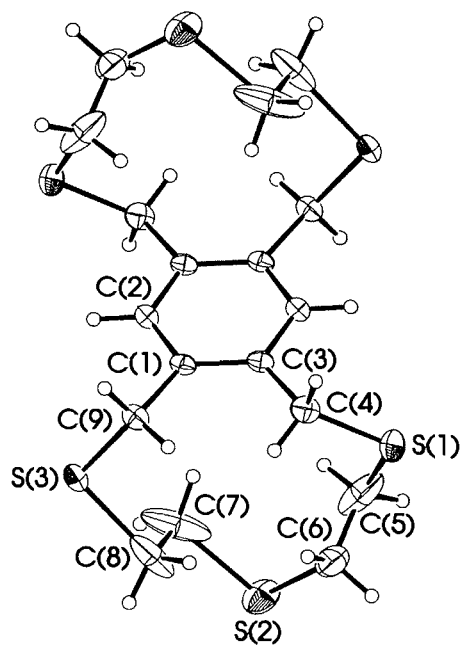

FIG. 1. Perspective ORTEP drawing of **1** showing the atom-numbering scheme. Thermal ellipsoids of 30% are shown.

the plane defined by the three sulphur atoms on one side of the ligand is 96.2°.

Crystals of **7** were grown by slow evaporation of a chloroform solution of the compound. Perspective ORTEP drawings of **7** are shown in Figs. 3 and 4. The macrocycle **7** crystallizes with one molecule per unit cell. The view of the structure shown in Fig. 3 confirms that the cyclization of the bis(ethoxy) substituted durene derivative does indeed proceed in a *meta* fashion and that the ethoxy group does not provide sufficient steric bulk to direct the cyclization otherwise. The ethoxy group simply folds out of the way of the tridentate donor chain enabling the cyclization to proceed relatively unimpeded. This molecule sits on a crystallographically imposed centre of sym-

Can. J. Chem. Downloaded from www.nrcresearchpress.com by EESC ESCOLA DE ENGENHARIA on 09/08/12
For personal use only.

Can. J. Chem. Downloaded from www.nrcresearchpress.com by EESC ESCOLA DE ENGENHARIA on 09/08/12
For personal use only.

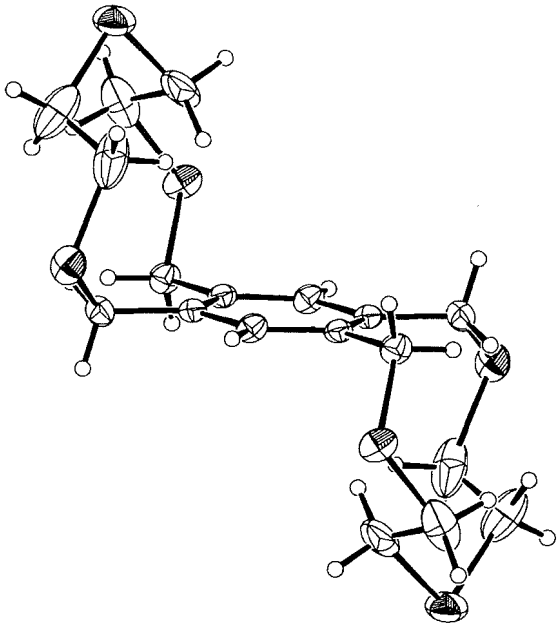

FIG. 2. Perspective ORTEP drawing of **1** showing an alternate view emphasizing the relative orientation of the aliphatic thioether chains.

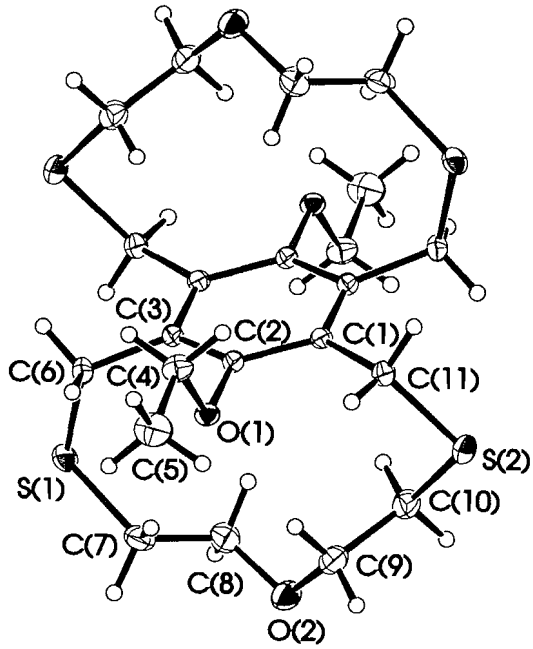

FIG. 3. Perspective ORTEP drawing of **7** showing the atom-numbering scheme. Thermal ellipsoids of 30% are shown.

metry. This molecule also adopts an *anti* conformation that places, not only the aliphatic chains, but also the ethoxy groups on opposite sides of the aromatic ring as shown in Fig. 4. The S—C—C—O torsional angles are 175.4(3) and 174.1(3)°, the C—C—O—C torsional angles are 81.0(6) and 83.6(6)° and the C—S—C—C torsion angles are 66.9(4) and 96.7(4)°. The dihedral angle defined by the aromatic ring and the three donor atoms on one side of the macrocycle is 76.1°.

It was noted during the isolation of macrocycles **6** and **7** that they possessed substantially lower solubility in solvents ($CHCl_3$, CH_2Cl_2, benzene) in which their non-functionalized analogs, **4** and **5** displayed very good solubility. Intuitively, this

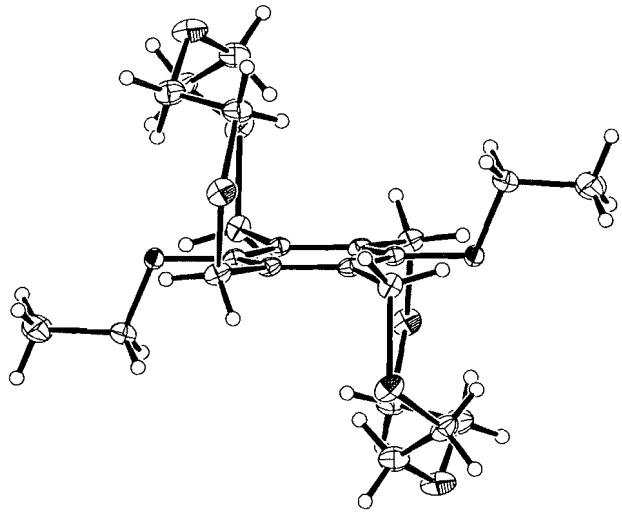

FIG. 4. Perspective ORTEP drawing of **7** showing an alternate view emphasizing the relative orientation of the aliphatic oxythioether chains and the ethoxy groups.

difference in solubility seemed too great to be accounted for strictly on the basis of the addition of two ethoxy groups. The principal cause of the reduced solubility was the greatly increased rigidity of the macrocycles as the effect of the ethoxy substitution was to confine the nine-membered, aliphatic chain to one side of the molecule. For compounds **4** and **5**, the ^1H NMR spectra show an AA′BB′ pattern with second order effects for the ethylene region and a single resonance for the benzylic protons due to rapid inversion at the sulphur atoms. For compounds **5** and **6**, the second order effects are removed for the AA′BB′ pattern and the benzylic protons are a pair of doublets consistent with a lack of inversion at sulphur and the chelate chain being restricted to one side of the molecule (26). Although both *syn* and *anti* isomers are possible, it is very likely that the *anti* isomer observed in the solid state is the "locked conformation" in solution.

The results of this study indicate the overwhelming preference of the $SCH_2CH_2XCH_2CH_2S$ (X = S, O) chelate chain to cyclize in a *meta* fashion for xylyl-based thioethers. From molecular modeling studies it was determined that an even bulkier alkoxy group would likely not provide a sufficient barrier to *meta* cyclization. In order for the functionality to serve as a more considerable barrier more bulk at the α-position to the central aromatic ring would be required. Interestingly, a similar reaction between two equivalents of the propylene-linked dithiol, 4-thiaheptane-1,7-dithiol, and one equivalent of 1,2,4,5-tetra(bromomethyl)benzene proceeds to give exclusively the bis-*ortho* cyclization product in ca. 60% yield. A study of the regioselectivities of these bis-cyclizations base on the length of the thioether chain was the subject of a previous publication (6). These investigations add to the body of information that will hopefully lead to control of the regioselectivity of thiacyclophane formation and produce desired ditopic ligands, such as **1**, for application in transition metal coordination chemistry.

1. J. Buter, R.M. Kellogg, and F. van Bolhuis. J. Chem. Soc. Chem. Commun. 292 (1992).
2. R.J. Smith, G.D. Admans, A.P. Richardson, H.J. Küppers, and P.J. Blower. J. Chem. Soc. Chem. Commun. 475 (1991).
3. A.J. Blake, A. Taylor, and M. Schröder. Polyhedron, **24**, 2911 (1990).

4. A.J. Blake, R.O. Gould, A.J. Holder, A.J. Lavery, and M. Schröder. Polyhedron, **24**, 2919 (1990).
5. S.J. Loeb and G.K.H. Shimizu. (*a*) J. Chem. Soc. Chem. Commun. 1119 (1991); (*b*) Inorg. Chem. **32**, 1001 (1993).
6. S.J. Loeb and G.K.H. Shimizu. Synlett. 823 (1992).
7. B. De Groot, S.J. Loeb, and G.K.H. Shimizu. Inorg. Chem. In press.
8. N. Atkinson, A.J. Blake, M.G.B. Drew, G. Forsyth, A.J. Lavery, G. Reid, and M. Schröder. J. Chem. Soc. Chem. Commun. 984 (1989).
9. G. Reid and M. Schröder. Coord. Chem. Rev. **19**, 239 (1990).
10. W. Lee, W. Sim, and O.S. Park, Synlett **2**, 157 (1992).
11. B. De Groot and S.J. Loeb. Inorg. Chem. **29**, 4080 (1990).
12. B. De Groot, G.R. Giesbrecht, S.J. Loeb, and G.K.H. Shimizu. Inorg. Chem. **30**, 177 (1991).
13. B. De Groot and S.J. Loeb. J. Chem. Soc. Chem. Commun. 1755 (1990).
14. B. De Groot, H.A. Jenkins, and S.J. Loeb. Inorg. Chem. **31**, 203 (1992).
15. L. Esriche, M.-P. Almjano, J. Casabo, F. Teixidor, J. Rius, C. Miravitlles, R. Kivekas, and R. Sillampaa. J. Chem. Soc. Dalton Trans. 2969 (1993).
16. B. De Groot, G.S. Hanan, and S.J. Loeb. Inorg. Chem. **31**, 4644 (1991).
17. H.A. Jenkins and S.J. Loeb. Organometallics. **13**, 1840 (1994).
18. Texsan-texray Structure Analysis Package, Molecular Structure Corp. (1985).
19. D.T. Cromer and J.T. Waber. International tables for X-ray crystallography. Vol. IV. Kynoch Press, Birmingham. 1974. Table 2.2A.
20. J.A. Ibers and W.C. Hamilton. Acta Crystallogr. **17**, 781 (1974).
21. D.T. Cromer. International tables for X-ray crystallography. Vol. IV. Kynoch Press, Birmingham. 1974. Tables 2.3.1.
22. (*a*) J. Buter and R.M. Kellogg. Org. Synth. **65**, 150. (1987); (*b*) J. Buter and R.M. Kellogg. J. Org. Chem. **46**, 4481 (1981).
23. D. Sellmann and L. Zapf. (*a*) Angew. Chem. Intl. Ed. Engl. **23**, 807 (1984); (*b*) J. Organomet. Chem. **289**, 57 (1985).
24. N.K. Dalley. *In* Synthetic multidentate macrocyclic compounds. *Edited by* R.M. Izatt and J.J. Christensen. Academic Press, New York. 1978.
25. I. Goldberg. *In* Chemistry of ethers, crown ethers, hydroxyl groups and their sulfur analogues. *Edited by* S. Patai. John Wiley and Sons, New York. 1980.
26. (*a*) F. Vögtle. Tetrahedron, **25**, 3231 (1969); (*b*) F. Vögtle, J. Grütze, R. Natscher, W. Wieder, E. Weber, and R. Grün. Chem. Ber. **108**, 1694 (1975); (*c*) E. Weber, W. Weber, and F. Vögtle. Chem. Ber. **109**, 1002 (1976).

Can. J. Chem. Downloaded from www.nrcresearchpress.com by EESC ESCOLA DE ENGENHARIA on 09/08/12
For personal use only.

Structural studies of organoboron compounds LXI.[1] Synthesis of (alkylideniminoxy)-diarylboranes and crystal and molecular structure of dimeric (ethylideniminoxy)-bis(4-methoxyphenyl)borane [3,3,6,6-tetrakis(4-methoxyphenyl)-2,5-diethylidene-1,4-dioxa-2,5-diazonia-3,6-diboratacyclohexane]

WOLFGANG KLIEGEL, DIERK NANNINGA, AND ULF RIEBE

Institut für Pharmazeutische Chemie der Technischen Universität Braunschweig, Beethovenstrasse 55, 38106 Braunschweig, Germany

AND

STEVEN J. RETTIG AND JAMES TROTTER

Department of Chemistry, University of British Columbia, 2036 Main Mall, Vancouver, BC V6T 1Z1, Canada

Received February 7, 1994

WOLFGANG KLIEGEL, DIERK NANNINGA, ULF RIEBE, STEVEN J. RETTIG, and JAMES TROTTER. Can. J. Chem. **72**, 1735 (1994).

Oxime diarylborinates, **4**, were obtained from several aliphatic and aromatic aldoximes as well as from cyclic ketoximes by acylation with a diarylborinic acid or anhydride (R_2B-X, R = aryl, X = OH or OBR_2). Compounds **4** could also be synthesized by condensation of an (aminoxy)-diarylborane, which supposedly has a cyclodimeric BONBON structure, with an aldehyde or with a ketone. Crystals of 3,3,6,6-tetrakis(4-methoxyphenyl)-2,5-diethylidene-1,4-dioxa-2,5-diazonia-3,6-diboratacyclohexane, **4***b*, are monoclinic, a = 7.9182(9), b = 19.7582(9), c = 9.6779(8) Å, β = 91.598(8)°, Z = 2, space group $P2_1/n$. The structure was solved by direct methods and refined by full-matrix least-squares procedures to R = 0.033 and R_w = 0.034 for 2344 reflections with $I \geq 3\sigma(F^2)$. A dimeric structure featuring a central six-membered BONBON ring has been established for the oxime diarylborinate **4***b*. This represents the first structurally characterized example of a monocyclic BONBON ring.

WOLFGANG KLIEGEL, DIERK NANNINGA, ULF RIEBE, STEVEN J. RETTIG et JAMES TROTTER. Can. J. Chem. **72**, 1735 (1994).

On a préparé les diarylborinates d'oximes, **4**, en procédant à l'acylation de plusieurs aldoximes aliphatiques et aromatiques ainsi que diverses cétoximes cycliques à l'aide d'un acide ou d'un anhydride diarylborinique (R_2B-X, R = aryle, X = OH ou OBR_2). On peut aussi synthétiser les composés **4** par condensation d'un (aminoxy)-diarylborane, qui possèderait une structure cyclodimère BONBON, avec un aldéhyde ou une cétone. Les cristaux du 3,3,6,6-tétrakis(4-méthoxyphényl)-2,5-diéthyléne-1,4-dioxa-2,5-diazonia-3,6-diboratacyclohexane, **4***b*, sont monocliniques, groupe d'espace $P2_1/n$, avec a = 7,9182(9), b = 19,7582(9) et c = 9,6779(8) Å, β = 91,598(8)° et Z = 2. On a résolu la structure par des méthodes directes et on l'a affinée par la méthode des moindres carrés jusqu'à des valeurs de R = 0,033 et R_w = 0,034 pour 2344 réflexions avec $I \geq 3\sigma(F^2)$. On a déterminé que, pour le composé **4***b*, il s'agit d'une structure dimère comportant un cycle central BONBON à six chaînons. Ceci correspond au premier exemple caractérisé d'un cycle BONBON monocyclique.

[Traduit par la rédaction]

Introduction

Over 100 years ago Beckmann (1) proposed the formation of oxime dimers in inert solvents. The dimerization of **1** was later recognized as a consequence of cyclic stabilization by O—H···N hydrogen bonding in associates like **2** (2). Six-membered dimers of the general formula **2** were also found in the solid state by X-ray crystallographic analyses of various oximes (3) and were further characterized (4) by ab initio calculations of the most simple example, formaldoxime (**2**, $R^1 = R^2$ = H), along with a neutron diffraction study of glyoxime at 9 K. It is known that iminoxyboranes **3**, which can be envisaged as borinic acid esters of oximes, are able to dimerize in an equilibrium reaction to the six-membered BONBON ring compounds **4** if steric and electronic conditions allow the formation of a twofold Lewis acid–base adduct (5–9).[2] Formally, in the cyclic dimer **4** both of the "chelated" protons in **2** are replaced by borenium ions (R_2B^+), in accordance with the concept of the chelation of "pseudometal" cations (10). In the solid state, the complete association of **3** should allow a structural characterization of the dimeric form **4** by X-ray crystallographic analysis. To the best of our knowledge, no structure analysis of a type **4** compound has been published to date with the exception of a preliminary report of some crystallographic data (without any details on the molecular structure) for the acetonoxime derivative **4** ($R = R^1 = R^2$ = Me) (5). In the course of our structural investigations of the BONBON ring systems only *B*-monoaryl derivatives (boronates) have been characterized thus far, the BONBON ring being part of a polycyclic skeleton in all reported cases (11).

To provide an example of a type **4** compound suitable for X-ray analysis we synthesized a series of oxime diarylborinates **3**/**4** (R = aryl). The reaction product from (dimethylamino)-diphenylborane and acetone oxime has been described in the literature (8) as the dimeric diphenylborinate **4** (R = Ph, $R^1 = R^2$ = Me). Using diarylborinic acid or the respective anhydride we did not succeed in preparing the acetone oxime derivative (12). We did, however, obtain the desired diarylborinates from several aliphatic and aromatic aldoximes (**4***a–j*) as well as from cyclic ketoximes (**4***k* and **4***l*) by acylation with a diarylborinic acid or anhydride (R_2B-X, R = aryl, X = OH or OBR_2). Compounds **4** could also be synthesized by condensation of an (aminoxy)-diarylborane, which supposedly has a cyclodimeric BONBON structure **5** (13), with an aldehyde leading to **4***b* or with a ketone leading to **4***k* and **4***l*, for example. Evidence for the cyclodimeric structure **4** comes from the ^{11}B nmr spectra, which show signals between $\delta(Et_2OBF_3)$ = 6.5 and 8.0 ppm, indicative

[1]Previous paper in this series: ref. 24.

[2](Ethylideniminoxy)-diethylborane, mp 79–81°C, was originally reported as a monomer (**3**, R = Et, R^1 = Me, R^2 = H) (6). The ^{11}B nmr signal at δ = 7.34 ppm, however, as already mentioned in the literature (7), contradicts a monomeric structure and supports that of a dimer of the type **4**.

Can. J. Chem. Downloaded from www.nrcresearchpress.com by ESC ESCOLA DE ENGENHARIA on 09/08/12
For personal use only.

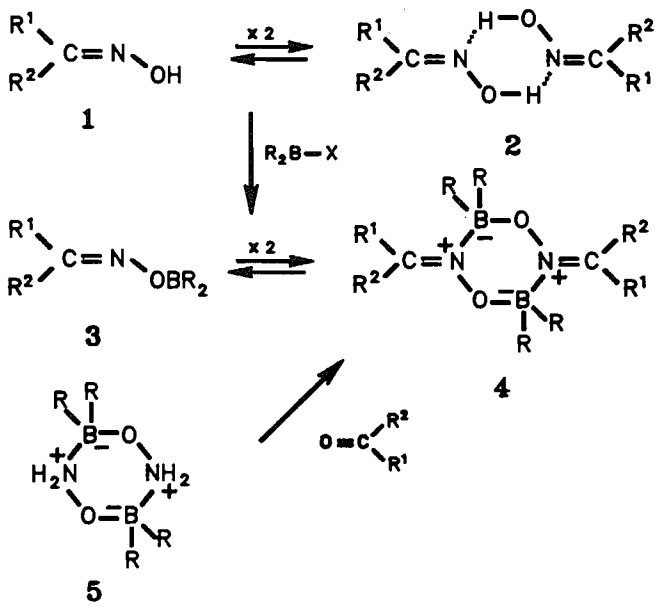

	R^1	R^2	R
4*a*	CH_3	H	C_6H_5
4*b*	CH_3	H	$4\text{-}CH_3OC_6H_4$
4*c*	CH_3	H	$4\text{-}FC_6H_4$
4*d*	CH_3	H	$4\text{-}ClC_6H_4$
4*e*	C_2H_5	H	C_6H_5
4*f*	C_3H_7	H	C_6H_5
4*g*	$CH(CH_3)_2$	H	C_6H_5
4*h*	$CH(C_2H_5)_2$	H	C_6H_5
4*i*	C_6H_5	H	C_6H_5
4*j*	C_6H_5	H	$4\text{-}CH_3OC_6H_4$
4*k*	$-(CH_2)_4-$		C_6H_5
4*l*	$-(CH_2)_5-$		C_6H_5

of the presence of tetracoordinate boron even in solution (14), and also from the solid state infrared spectra of the diphenylborinate derivatives, which display substantially weakened ν_{16} phenyl ring stretching vibrations at 1600 cm^{-1}, also consistent with tetracoordination at the phenylboron centres (11, 15). The C=N absorption bands between 1635 and 1662 cm^{-1} are not distinctly different from those of free oximes and thus give no hints about cycloadduct formation. The ^1H nmr spectra, as well, provide no evidence supporting the structure **4**. In both the EI and CI mass spectra of several examples, the highest mass feature with prominent abundance is the molecular ion of the monomer **3**, reminiscent of similar dissociations of BONBON dimers in the gas phase reported for oxime borinates (5, 7, 8, 11). The highest quality crystals were obtained by recrystallization of the dianisylborinate of acetaldoxime, **4***b*, which was characterized by an X-ray analysis to provide unambiguous proof of the cyclodimeric BONBON structure **4**.

Experimental

General procedures for the synthesis of dimeric (alkylideniminoxy)-diarylboranes, 4

Method A

Diarylborinic acid (R_2BX, R = aryl, X = OH, 2 mmol) or oxybis(diarylborane) (R_2BX, R = aryl, X = OBR_2, 1 mmol) and an oxime (2 mmol) are dissolved in 10 mL of ethanol and heated rapidly to a boil. Crystallization occurs spontaneously or upon cooling and (or) partial evaporation. Recrystallization is carried out from the solvent specified in each case.

Method B

2-(Diarylboryloxy)ethylamine (R_2BX, R = aryl, X = $OCH_2CH_2NH_2$, 5 mmol) is dissolved in 20 mL of aqueous sulfuric acid (25%) under stirring until complete dissolution, and then extracted with 4 × 50 mL of ether. The collected ether extracts are washed out with 3 × 10 mL of water, dried with Na_2SO_4, and the solvent is distilled off in vacuo. The residue (oily or solid) is dissolved in 20 mL of ethanol and mixed with a solution of an oxime (5 mmol) in 20 mL of ethanol. After rapid heating to boiling temperature the solution is cooled down, and if necessary partially evaporated, to induce crystallization.

Method C

3,3,6,6-Tetraaryl-1,4-dioxa-2,5-diazonia-3,6-diboratacyclohexane (**5**, R = aryl, 1 mmol) and an aldehyde or ketone (1 mmol) are heated in 30 mL of benzene under reflux for 30 min with continuous removal of water using a Dean–Stark trap. Partial evaporation and cooling of the solution yields crystals, which are washed, if necessary, with cold ethanol.

Method D

3,3,6,6-Tetraaryl-1,4-dioxa-2,5-diazonia-3,6-diboratacyclohexane (**5**, R = aryl, 1 mmol) is dissolved in 10 mL of absolute ethanol with slight heating and mixed with an aldehyde or ketone (2 mmol). After 15 min of refluxing the solution is partially evaporated and, if necessary, cooled down to induce crystallization.

All compounds of type **4** give a deep blue color reaction with diphenylcarbazone in methanolic solution, indicating the presence of diarylboron moieties (16).

*3,3,6,6-Tetraphenyl-2,5-diethylidene-1,4-dioxa-2,5-diazonia-3,6-diboratacyclohexane, 4*a

From oxybis(diphenylborane) and acetaldoxime (method A). Yield: 95%, colorless crystals, mp (dec.) 239–241°C (from benzene/diethyl ether). Infrared (KBr): 1665 cm^{-1} (C=N). EI mass spectrum (70 eV, 200°C), *m/z*: 223 (42%, 1/2 M^+), 222 (22%), 208 (48%), 181 (28%, Ph_2BO), 165 (34%, Ph_2B), 164 (12%), 163 (12%), 154 (6%), 153 (10%), 146 (4%, 1/2 $M^+ - C_6H_5$), 119 (14%), 105 (38%, PhBOH), 104 (24%, PhBO), 89 (8%), 77 (100%, C_6H_5). Anal. calcd. for $C_{28}H_{28}B_2N_2O_2$: C 75.38, H 6.33, B 4.85, N 6.28; found: C 75.37, H 6.38, B 4.88, N 6.27.

*3,3,6,6-Tetrakis(4-methoxyphenyl)-2,5-diethylidene-1,4-dioxa-2,5-diazonia-3,6-diboratacyclohexane, 4*b

From 2-[bis(4-methoxyphenyl)boryloxy]ethylamine (17) and acetaldehyde oxime (method B). Yield: 73%. From 3,3,6,6-tetrakis(4-methoxyphenyl)-1,4-dioxa-2,5-diazonia-3,6-diboratacyclohexane (**5**, R = $4\text{-}CH_3OC_6H_4$) (see below for preparation) and freshly distilled acetaldehyde (method C). Yield: 36%. Colorless crystals, mp (dec.) 195°C (from ethanol), 201–202°C (from CH_2Cl_2 – petroleum ether). Infrared (KBr): 1662 cm^{-1} (C=N); ^1H nmr (400 MHz, $CDCl_3$/TMS), δ (ppm): 2.10 (d, J = 6 Hz, 2 =C-CH_3), 3.79 (s, 4 OCH_3), 6.82 and 7.21 (d and d, AA′BB′, 16 aromatic H), 7.00 (q, J = 6 Hz, 2 N=CH); ^{11}B nmr (64 MHz, $CDCl_3/Et_2OBF_3$), δ (ppm): 7.8 ($w_{1/2}$ = 385 Hz). EI mass spectrum (70 eV, 120°C), *m/z*: 283 (100%, 1/2 M^+), 241 (64%, $OB(C_6H_4OCH_3)_2$), 225 (48%, $B(C_6H_4OCH_3)_2$), 183 (6%), 160 (10%), 149 (26%), 135 (14%), 119 (10%), 107 (18%, $C_6H_4OCH_3$), 92 (24%, C_6H_4O), 77 (30%, $C_6H_4OCH_3 - CH_2O$). Anal. calcd. for $C_{32}H_{36}B_2N_2O_6$: C 67.87, H 6.41, B 3.82, N 4.95; found: C 67.86, H 6.42, B 3.83, N 4.75.

Crystals suitable for X-ray crystallography were obtained by slow evaporation of a solution of **4***b* in CH_2Cl_2 – petroleum ether at room temperature.

Can. J. Chem. Downloaded from www.nrcresearchpress.com by ESC ESCOLA DE ENGENHARIA on 09/08/12
For personal use only.

Can. J. Chem. Downloaded from www.nrcresearchpress.com by EESC ESCOLA DE ENGENHARIA on 09/08/12
For personal use only.

3,3,6,6-Tetrakis(4-fluorophenyl)-2,5-diethylidene-1,4-dioxa-2,5-diazonia-3,6-diboratacyclohexane, ***4****c*

From 2-[bis(4-fluorophenyl)boryloxy]ethylamine (18) and acetaldehyde oxime (method B). Yield: 68%, colorless crystals, mp (dec.) 216–217°C (from ethanol). Infrared (KBr): 1663 cm^{-1} (C=N); ^1H nmr (400 MHz, $CDCl_3$/TMS), δ (ppm): 2.14 (d, J = 6 Hz, 2 CH_3), 6.93–7.02 (m, 8 aromatic H + 2 N=CH), 7.18–7.26 (m, 8 aromatic H). EI mass spectrum (70 eV, 90°C), *m/z*: 259 (100%, 1/2 M^+), 244 (96%, $(OBC_6H_4F)_2$), 217 (62%, $OB(C_6H_4F)_2$), 201 (76%, $B(C_6H_4F)_2$), 170 (10%), 151 (10%), 148 (18%), 137 (15%), 123 (66%, $HOBC_6H_4F$), 107 (14%), 95 (95%, C_6H_4F), 75 (38%). Anal. calcd. for $C_{28}H_{24}B_2F_4N_2O_2$: C 64.91, H 4.67, B 4.17, N 5.41; found: C 64.90, H 4.64, B 3.95, N 5.28.

3,3,6,6-Tetrakis(4-chlorophenyl)-2,5-diethylidene-1,4-dioxa-2,5-diazonia-3,6-diboratacyclohexane, ***4****d*

From 2-[bis(4-chlorophenyl)boryloxy]ethylamine (17) and acetaldehyde oxime (method B). Yield: 55%, colorless crystals, mp (dec.) 209–211°C (from ethanol). Infrared (KBr): 1660 cm^{-1} (C=N); ^1H nmr (400 MHz, $CDCl_3$/TMS), δ (ppm): 2.14 (d, J = 6 Hz, 2 CH_3), 7.00 (q, J = 6 Hz, 2 N=CH), 7.16 and 7.24 (d and d, AA′BB′, 16 aromatic H). EI mass spectrum (70 eV, 130°C), *m/z*: 414/416 (16/14%, $(OBC_6H_4Cl)_3$), 291/293 (92/60%, 1/2 M^+), 276/278 (94/64%, $(OBC_6H_4Cl)_2$), 249/251 (54/36%, $OB(C_6H_4Cl)_2$), 233/235 (47/30%, $B(C_6H_4Cl)_2$), 164 (24%), 153 (36%), 139 (76%, $HOBC_6H_4Cl$), 111 (100%, C_6H_4Cl), 75/77 (60/35%). Anal. calcd. for $C_{28}H_{24}B_2Cl_4N_2O_2$: C 57.59, H 4.14, B 3.70, Cl 24.29, N 4.80; found: C 57.33, H 4.14, B 3.62, Cl 24.92, N 4.61.

3,3,6,6-Tetraphenyl-2,5-dipropylidene-1,4-dioxa-2,5-diazonia-3,6-diboratacyclohexane, ***4****e*

From oxybis(diphenylborane) and propionaldehyde oxime (method A). Yield: 90%, colorless crystals, mp (dec.) 215–216°C (from ethanol). Infrared (KBr): 1660 cm^{-1} (C=N); ^1H nmr (90 MHz, $CDCl_3$/TMS), δ (ppm): 0.97 (t, J = 6 Hz, 2 CH_3), 2.66 (m, 2 $-CH_2-$), 6.87 (t, J = 6 Hz, N=CH), 7.24–7.28 (m, 20 aromatic H); ^{11}B nmr (64 MHz, $CDCl_3/Et_2OBF_3$), δ (ppm): 7.8 ($w_{1/2}$ = 425 Hz). Anal. calcd. for $C_{30}H_{32}B_2N_2O_2$: C 75.98, H 6.80, N 5.91; found: C 76.15, H 6.79, N 5.87.

3,3,6,6-Tetraphenyl-2,5-dibutylidene-1,4-dioxa-2,5-diazonia-3,6-diboratacyclohexane, ***4****f*

From oxybis(diphenylborane) and butyraldehyde oxime (method A). Yield: 92%, colorless crystals, mp (dec.) 199–200°C (from ethanol). Infrared (KBr): 1660 cm^{-1} (C=N); ^1H nmr (90 MHz, $CDCl_3$/TMS), δ (ppm): 0.84 (t, J = 7 Hz, 2 CH_3), 1.36 (m, 2 CH_2CH_3), 2.61 (m, 2 N=CH-CH_2), 6.88 (t, J = 6 Hz, N=CH), 7.21–7.36 (m, 20 aromatic H); ^{11}B nmr (64 MHz, $CDCl_3/Et_2OBF_3$), δ (ppm): 7.6 ($w_{1/2}$ = 385 Hz). Anal. calcd. for $C_{32}H_{36}B_2N_2O_2$: C 76.52, H 7.22, B 4.30, N 5.58; found: C 76.43, H 7.14, B 4.08, N 5.53.

3,3,6,6-Tetraphenyl-2,5-diisobutylidene-1,4-dioxa-2,5-diazonia-3,6-diboratacyclohexane, ***4****g*

From oxybis(diphenylborane) and isobutyraldehyde oxime (method A). Yield: 98%, colorless crystals, mp (dec.) 206-208°C (from ethanol). Infrared (KBr): 1655 cm^{-1} (C=N); ^1H nmr (90 MHz, $CDCl_3$/TMS), δ (ppm): 0.92 (d, J = 7 Hz, 4 CH_3), 3.54 (m, 2 N=CH-CH_2), 6.65 (d, J = 9 Hz, 2 N=CH), 7.22–7.36 (m, 20 aromatic H); ^{11}B nmr (64 MHz, $CDCl_3/Et_2OBF_3$), δ (ppm): 6.94 ($w_{1/2}$ = 340 Hz). EI mass spectrum (70 eV, 120°C), *m/z*: 251 (65%, 1/2 M^+), 208 (100%, 1/2 $M^+ - C_3H_7$), 181 (72%, Ph_2BO), 165 (26%, Ph_2B), 105 (38%, PhBOH), 77 (66%, C_6H_5). Anal. calcd. for $C_{32}H_{36}B_2N_2O_2$: C 76.52, H 7.22, N 5.58; found: C 75.99, H 7.20, N 5.30.

3,3,6,6-Tetraphenyl-2,5-bis(2-ethylbutylidene)-1,4-dioxa-2,5-diazonia-3,6-diboratacyclohexane, ***4****h*

From oxybis(diphenylborane) and 2-ethylbutyraldehyde oxime (method A). Yield: 68%, colorless crystals, mp (dec.) 188–189°C (from ethanol – diethyl ether). Infrared (KBr): 1657 cm^{-1} (C=N); ^1H nmr (400 MHz, $CDCl_3$/TMS), δ (ppm): 0.69 (t, J = 7 Hz, 4 CH_3), 1.13 (sept, J = 7 Hz, 2 CH_2CH_3), 1.33 (sept, J = 7 Hz, 2 CH_2CH_3), 3.11 (sext, J = 9 Hz, 2 N=CH-C*H*) , 6.65 (d, J = 9 Hz, 2 N=CH), 7.21–7.58 (m, 20 aromatic H); ^{11}B nmr (64 MHz, $CDCl_3/Et_2OBF_3$), δ (ppm): 8.0 ($w_{1/2}$ = 430 Hz). EI mass spectrum (70 eV, 110°C), *m/z*: 481 (3%, $M^+ - C_6H_5$), 447 (4%), 410 (24%), 312 (16%, $(PhBO)_3$), 306 (68%), 279 (100%, 1/2 M^+), 208 (54%, $(PhBO)_2$), 181 (53%, Ph_2BO), 165 (23%, Ph_2B), 146 (10%), 119 (16%), 105 (37%, PhBOH), 104 (22%, PhBO), 77 (36%, C_6H_5). Anal. calcd. for $C_{36}H_{44}B_2N_2O_2$: C 77.44, H 7.94, B 3.87, N 5.02; found: C 77.45, H 7.85, B 3.86, N 4.85.

3,3,6,6-Tetraphenyl-2,5-dibenzylidene-1,4-dioxa-2,5-diazonia-3,6-diboratacyclohexane, ***4****i*

From oxybis(diphenylborane) and benzaldehyde oxime (method A). Yield: 63%, colorless crystals, mp (dec.) 237–238°C (from tetrahydrofuran). Infrared (KBr): 1635 cm^{-1} (C=N). Poor solubility of the compound in appropriate solvents precluded nmr spectra. EI mass spectrum (70 eV, 190°C), *m/z*: 312 (9%, $(OBPh)_3$), 285 (38%, 1/2 M^+), 208 (80%, $(OBPh)_2$), 181 (40%, $OBPh_2$), 180 (46%), 165 (34%, BPh_2), 105 (26%, PhBOH), 104 (40%, PhBO), 97 (22%), 83 (20%), 77 (100%, C_6H_5). Anal. calcd. for $C_{38}H_{32}B_2N_2O_2$: C 80.03, H 5.66, B 3.79, N 4.91; found: C 79.79, H 5.79, B 3.69, N 4.46.

3,3,6,6-Tetrakis(4-methoxyphenyl)-2,5-dibenzylidene-1,4-dioxa-2,5-diazonia-3,6-diboratacyclohexane, ***4****j*

From bis(4-methoxyphenyl)borinic acid (17, 19) and (*Z*)-benzaldoxime (method A). Yield: 44%, colorless crystals, mp (dec.) 212–215°C (from ethanol). Infrared (KBr): 1635 cm^{-1} (C=N); ^1H nmr (400 MHz, d_6-DMSO/TMS), δ (ppm): 3.80 (s, 4 CH_3), 6.97 and 7.67 (d and d, AA′BB′, 16 aromatic H), 7.40–7.46 (m, 6 aromatic H + 2 N=CH), 7.94–7.99 (m, 4 aromatic H). CI mass spectrum (iso-butane, pos. mode, 120°C), *m/z*: 345 (18%, 1/2 M^+), 331 (60%, $M^+ - CH_2$), 303 (16%), 271 (22%), 242 (50%), 183 (27%), 169 (39%), 141 (21%), 122 (100%), 104 (40%), 78 (22%), 77 (20%). Anal. calcd. for $C_{42}H_{40}B_2N_2O_6$: C 73.07, H 5.84, B 3.13, N 4.06; found: C 72.57, H 5.84, B 3.16, N 4.08.

3,3,6,6-Tetraphenyl-2,5-dicyclopentylidene-1,4-dioxa-2,5-diazonia-3,6-diboratacyclohexane, ***4****k*

From oxybis(diphenylborane) and cyclopentanone oxime (method A). Yield: 89%. From 3,3,6,6-tetraphenyl-1,4-dioxa-2,5-diazonia-3,6-diboratacyclohexane (13) and cyclopentanone (method D). Yield: 63%. Colorless crystals, mp (dec.) 199–200°C (from ethanol). Infrared (KBr): 1661 cm^{-1} (C=N); ^1H nmr (400 MHz, $CDCl_3$/TMS), δ (ppm): 1.47 and 1.58 (quint and quint, J = 7 Hz, 2 C-CH_2-CH_2-C), 1.65 and 2.85 (t and t, J = 7 Hz, 2 N=C(CH_2)$_2$), 7.14–7.22 (m, 20 aromatic H); ^{11}B nmr (64 MHz, $CDCl_3/Et_2OBF_3$), δ (ppm): 6.5 ($w_{1/2}$ = 470 Hz). EI mass spectrum (70 eV, 70°C), *m/z*: 263 (66%, 1/2 M^+), 234 (48%), 221 (16%), 181 (70%, $OBPh_2$), 159 (43%), 130 (26%), 105 (60%, PhBOH), 77 (100%, C_6H_5). Anal. calcd. for $C_{34}H_{36}B_2N_2O_2$: C 77.59, H 6.89, B 4.11, N 5.32; found: C 77.72, H 6.90, B 4.16, N 5.24.

3,3,6,6-Tetraphenyl-2,5-dicyclohexylidene-1,4-dioxa-2,5-diazonia-3,6-diboratacyclohexane, ***4****l*

From oxybis(diphenylborane) and cyclohexanone oxime (method A). Yield: 68%. From 3,3,6,6-tetraphenyl-1,4-dioxa-2,5-diazonia-3,6-diboratacyclohexane (13) and cyclohexanone (method D). Yield: 40%. Colorless crystals, mp (dec.) 178–179°C (from ethanol). Infrared (KBr): 1641 cm^{-1} (C=N). ^1H nmr (90 MHz, $CDCl_3$/TMS), δ (ppm): 0.70–1.12 (m, 4 C-C-CH_2-C-C), 1.15-1.70 (m, 2 N=C(CH_2CH_2)$_2$), 1.93 and 2.75 (t and t, J = 6 Hz, 2 N=C(CH_2CH_2)$_2$), 7.1 (m_c, 20 aromatic H); ^{11}B nmr (64 MHz, $CDCl_3/Et_2OBF_3$), δ (ppm): 7.3 ($w_{1/2}$ = 430 Hz). EI mass spectrum (70 eV, 120°C), *m/z*: 277 (83%, 1/2 M^+), 234 (64%), 200 (25%), 181 (52%, $OBPh_2$), 173 (48%), 158 (17%), 130 (20%), 105 (35%, PhBOH), 96 (82%), 77 (100%, C_6H_5). CI mass spectrum (NH_3, pos. mode, 100°C), *m/z*: 278 (50%, 1/2 M^+ + H), 182 (45%, $OBPh_2$ + H), 114 (100%). Anal. calcd. for $C_{36}H_{40}B_2N_2O_2$: C 78.00, H 7.27, B 3.90, N 5.05; found: C 77.74, H 7.28, B 3.93, N 4.90.

Can. J. Chem. Downloaded from www.nrcresearchpress.com by EESC ESCOLA DE ENGENHARIA on 09/08/12
For personal use only.

TABLE 1. Crystallographic data[a]

Compound	**4***b*
Formula	$C_{32}H_{36}B_2N_2O_6$
fw	566.27
Crystal system	Monoclinic
Space group	$P2_1/n$
a, Å	7.9182(9)
b, Å	19.7582(9)
c, Å	9.6779(8)
β°	91.598(8)
V, Å^3	1513.5(2)
Z	2
ρ_{calc}, g cm^{-3}	1.242
F(000)	600
Radiation	Cu-K_α
μ, cm^{-1}	6.45
Crystal size, mm	0.25 × 0.27 × 0.35
Transmission factors (relative)	0.91–1.00
Scan type	ω–2θ
Scan range, deg in ω	1.15 + 0.20 tan θ
Scan speed, deg min^{-1}	32
Data collected	$+h$, $+k$, $\pm l$
$2\theta_{max}$, deg	155
Crystal decay	Negligible
Total reflections	3435
Total unique reflections	3093
R_{merge}	0.019
Reflections with $I \geq 3\sigma(F^2)$	2344
No. of variables	251
R	0.033
R_w	0.034
gof	2.69
Max Δ/σ (final cycle)	0.02
Residual density e Å^{-3}	−0.09 to 0.16

[a]Temperature 294 K, Rigaku AFC6S diffractometer, Cu-K_α (λ = 1.54178 Å) radiation, graphite monochromator, takeoff angle 6.0°, aperture 6.0 × 6.0 mm at a distance of 285 mm from the crystal, stationary background counts at each end of the scan (scan/background time ratio 2:1, up to 8 rescans), $\sigma^2(F^2) = [S^2(C + 4B)]/Lp^2$ (S = scan rate, C = scan count, B = normalized background count), function minimized $\Sigma w(|F_o|-|F_c|)^2$ where $w = 4F_o^2/\sigma^2(F_o^2)$, $R = \Sigma||F_o| - |F_c||/\Sigma|F_o|$, $R_w = (\Sigma w(|F_o| - |F_c|)^2/\Sigma w|F_o|^2)^{1/2}$, and gof = $[\Sigma w(|F_o| - |F_c|)^2/(m - n)]^{1/2}$. Values given for R, R_w, and gof are based on those reflections with $I \geq 3\sigma(F^2)$.

3,3,6,6-Tetrakis(4-methoxyphenyl)-1,4-dioxa-2,5-diazonia-3,6-diboratacyclohexane, 5 (R = 4-$CH_3OC_6H_4$)

Bis(4-methoxyphenyl)borinic acid (19) (1.21 g, 5 mmol) is dissolved in 5 mL of ethanol (with slight warming). After the addition of a solution of hydroxylamine (base, 0.17 g, 5 mmol) in 5 mL of ethanol the mixture is refluxed for 5 min. From the cooled solution colorless crystals are obtained. Yield: 0.87 g (68%), mp (dec.) 200–201°C. Infrared (KBr): 3250, 3200 cm^{-1} (N-H); ^{1}H nmr (90 MHz, d_6-DMSO/TMS), δ (ppm): 3.63 (s, 4 CH_3), 6.70 and 7.19 (d and d, 16 aromatic H), 7.66 (s, br, exchangeable, 2 NH_2). Anal. calcd. for $C_{28}H_{32}B_2N_2O_6$: C 65.41, H 6.27, B 4.21, N 5.45; found: C 65.29, H 6.43, B 4.26, N 5.10.

X-ray crystallographic analysis of **4***b*

Crystallographic data appear in Table 1. The final unit-cell parameters were obtained by least squares on the setting angles for 25 reflections with 2θ = 85.9–102.3°. The intensities of three standard reflections, measured every 200 reflections throughout the data collection, showed only small random fluctuations. The data were processed,[3] corrected for Lorentz and polarization effects, and absorption (empirical, based on azimuthal scans for three reflections).

[3]TEXSAN/TEXRAY structure analysis package (Version 5.1), Molecular Structure Corp. 1985.

TABLE 2. Final atomic coordinates (fractional) and B_{eq} (Å^2)*

Atom	*x*	*y*	*z*	B_{eq}[a]
O(1)	0.0623(1)	0.05630(4)	0.5816(1)	3.52(4)
O(2)	−0.4570(1)	0.30052(5)	0.4924(1)	5.54(6)
O(3)	0.4876(2)	0.09739(8)	0.0163(1)	7.14(7)
N(1)	0.1360(1)	−0.00723(6)	0.5944(1)	3.37(5)
C(1)	0.2879(2)	−0.00904(8)	0.6425(2)	4.02(6)
C(2)	0.3944(2)	0.04969(9)	0.6770(2)	5.18(8)
C(3)	−0.1254(2)	0.13680(7)	0.4535(1)	3.43(6)
C(4)	−0.2289(2)	0.14625(8)	0.5671(2)	3.95(6)
C(5)	−0.3359(2)	0.20101(8)	0.5779(2)	4.38(7)
C(6)	−0.3448(2)	0.24910(7)	0.4740(2)	4.10(6)
C(7)	−0.2441(2)	0.24207(7)	0.3600(2)	4.26(7)
C(8)	−0.1365(2)	0.18661(7)	0.3518(2)	4.01(7)
C(9)	0.1301(2)	0.07336(7)	0.3242(1)	3.55(6)
C(10)	0.2552(2)	0.12259(8)	0.3360(2)	4.17(7)
C(11)	0.3778(2)	0.13232(9)	0.2376(2)	4.56(7)
C(12)	0.3774(2)	0.0911(1)	0.1230(2)	4.77(8)
C(13)	0.2586(2)	0.0404(1)	0.1089(2)	5.22(8)
C(14)	0.1372(2)	0.03210(8)	0.2076(2)	4.38(7)
C(15)	−0.4667(3)	0.3512(1)	0.3889(3)	6.4(1)
C(16)	0.5967(3)	0.1538(2)	0.0174(3)	7.7(2)
B(1)	−0.0120(2)	0.07049(8)	0.4389(2)	3.37(6)

[a]$B_{eq} = (8/3)\pi^2\Sigma\Sigma U_{ij}a_i^*a_j^*(\mathbf{a}_i \cdot \mathbf{a}_j)$.

TABLE 3. Bond lengths (Å) with estimated standard deviations*

Atoms	Distance	Atoms	Distance
O(1)—N(1)	1.389(1)	C(4)—C(5)	1.380(2)
O(1)—B(1)	1.512(2)	C(5)—C(6)	1.384(2)
O(2)—C(6)	1.365(2)	C(6)—C(7)	1.386(2)
O(2)—C(15)	1.417(2)	C(7)—C(8)	1.392(2)
O(3)—C(12)	1.377(2)	C(9)—C(10)	1.391(2)
O(3)—C(16)	1.411(3)	C(9)—C(14)	1.395(2)
N(1)—C(1)	1.278(2)	C(9)—B(1)	1.604(2)
N(1)—B(1)*	1.616(2)	C(10)—C(11)	1.392(2)
C(1)—C(2)	1.468(2)	C(11)—C(12)	1.376(2)
C(3)—C(4)	1.402(2)	C(12)—C(13)	1.378(2)
C(3)—C(8)	1.393(2)	C(13)—C(14)	1.383(2)
C(3)—B(1)	1.597(2)		

*Here and elsewhere refers to symmetry operation: $-x$, $-y$, $1 - z$.

The structure was solved by direct methods, the coordinates of the non-hydrogen atoms being determined from an *E*-map. The molecule has crystallographic inversion symmetry. Non-hydrogen atoms were refined with anisotropic thermal parameters. The hydrogen atoms of the C(2) methyl group were found to be (6:4) disordered over two sites. These hydrogen atoms were fixed in calculated positions (C—H = 0.98 Å, $B_H = 1.2\ B_{bonded\ atom}$, methyl group orientations based on difference map positions) and the remaining hydrogen atoms were refined with isotropic thermal parameters. A correction for secondary extinction was applied (Zachariasen type), the final value of the extinction coefficient being $8.97(6) \times 10^{-4}$. Neutral atom scattering factors for all atoms and anomalous dispersion corrections for the non-hydrogen atoms were taken from the *International Tables for X-Ray Crystallography* (20). Final atomic coordinates and equivalent isotropic thermal parameters, bond lengths, and bond angles appear in Tables 2–4, respectively. A stereoview of the molecule is shown in Fig. 1. Hydrogen atom parameters, anisotropic thermal parameters, torsion angles, intermolecular contacts, and least-squares planes are included as sup-

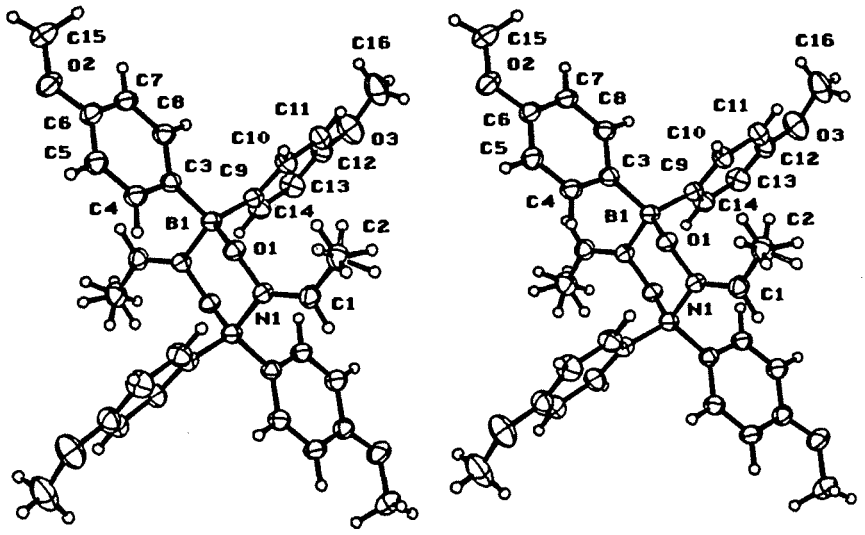

FIG. 1. Stereoview of **4***b*; 33% probability thermal ellipsoids are shown for the non-hydrogen atoms.

TABLE 4. Bond angles (deg) with estimated standard deviations

Atoms	Angle	Atoms	Angle
N(1)—O(1)—B(1)	113.6(1)	C(10)—C(9)—C(14)	115.5(1)
C(6)—O(2)—C(15)	117.1(2)	C(10)—C(9)—B(1)	118.7(1)
C(12)—O(3)—C(16)	117.9(2)	C(14)—C(9)—B(1)	125.8(1)
O(1)—N(1)—C(1)	116.5(1)	C(9)—C(10)—C(11)	123.3(1)
O(1)—N(1)—B(1)*	115.4(1)	C(10)—C(11)—C(12)	118.9(2)
C(1)—N(1)—B(1)*	127.7(1)	O(3)—C(12)—C(11)	124.3(2)
N(1)—C(1)—C(2)	126.2(1)	O(3)—C(12)—C(13)	115.9(2)
C(4)—C(3)—C(8)	115.7(1)	C(11)—C(12)—C(13)	119.8(1)
C(4)—C(3)—B(1)	121.4(1)	C(12)—C(13)—C(14)	120.2(2)
C(8)—C(3)—B(1)	122.8(1)	C(9)—C(14)—C(13)	122.3(2)
C(3)—C(4)—C(5)	122.5(1)	O(1)—B(1)—N(1)*	104.9(1)
C(4)—C(5)—C(6)	120.1(1)	O(1)—B(1)—C(3)	106.1(1)
O(2)—C(6)—C(5)	115.9(1)	O(1)—B(1)—C(9)	112.1(1)
O(2)—C(6)—C(7)	124.7(1)	N(1)*—B(1)—C(3)	108.2(1)
C(5)—C(6)—C(7)	119.4(1)	N(1)*—B(1)—C(9)	108.9(1)
C(6)—C(7)—C(8)	119.4(1)	C(3)—B(1)—C(9)	116.0(1)
C(3)—C(8)—C(7)	122.9(1)		

plementary material.[4] Measured and calculated structure factor amplitudes are available from the authors on request.

Results and discussion

The X-ray analysis of **4***b* establishes the postulated cyclic dimer form of the oxime diarylborinate. The centrosymmetric dimer manifests itself as a six-membered BONBON ring having a slightly flattened chair conformation. To the best of our knowledge, this structure represents the first example of a monocyclic BONBON ring structure established by an X-ray structure analysis. A similar BONBON ring system, also having a chair conformation, has recently been characterized as part of the tricyclic skeleton of compound **6** (11).

[4]Supplementary material mentioned in the text may be purchased from: The Depository of Unpublished Data, Document Delivery, CISTI, National Research Council Canada, Ottawa, Canada K1A 0S2.

Tables of hydrogen atom coordinates and bond lengths and angles involving hydrogen atoms have also been deposited with the Cambridge Crystallographic Data Centre and can be obtained on request from The Director, Cambridge Crystallographic Data Centre, University Chemical Laboratory, 12 Union Road, Cambridge CB2 1EZ, U.K.

The N→B coordinative bonds in **4***b* (1.616(2) Å) are 0.079(3) Å shorter than the corresponding bonds in the BONBON ring incorporated into the polycyclic ring system of compound **6** (1.695(2) Å) (11). The sum of the N—O and O—B bond distances in **4***b* (2.901(3) Å) is very similar to the corresponding sum for **6** (2.918(3) Å), but in **4***b* the N—O bonds are significantly shorter, and the O—B bonds significantly longer, than those in **6**. The relatively short N—O (1.389(1) Å) and long O—B (1.512(2) Å) bonds in **4***b* may be compared with those reported for another oxime derivative having a BONBON ring structure: the polycyclic phenylboronate of salicylaldoxime, **7** (N—O = 1.3865(14) and 1.3903(14) Å, O—B = 1.479(2) and 1.472(2) Å) (21). It should be noted, however, that the conformations of the BONBON rings in **4***b* and **7** are quite

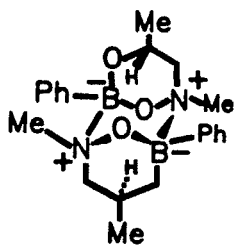

6

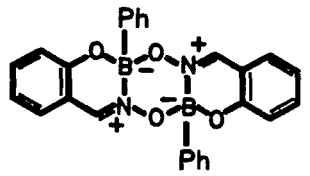

7

different. In compound **6** the N—O and O—B distances are 1.453(1) and 1.465(1) Å, respectively. The oxime C=N bonds in **4***b* (1.278(2) Å) are not significantly different from those in **7** (1.275(2) and 1.277(2) Å) (21) and in a number of dimeric hydrogen-bonded oximes of the type **2**: phenylpropane dioxime (1.278 Å) (3*b*), acetophenone oxime (1.278 Å) (3*d*), phenylpyridylketone oxime (1.276(2) Å) (3*e*), and methoxyindanone oxime (1.277(2) Å) (3*g*).

The substitution about the oxime function in **4***b* adopts the (*Z*) configuration, allowing more space for the bulky diarylboron group. The O(1)N(1)C(1)C(2)B(1)* oxime group is planar to within 0.032(1) Å, although this represents a statistically significant deviation from planarity. The torsion angles O(1)-N(1)-C(1)-C(2) = −4.2(2)° and C(2)-C(1)-N(1)-B(1)* = −177.2(1)° are also consistent with approximate planarity of the oxime group. The steric requirements of the planar oxime moieties

Can. J. Chem. Downloaded from www.nrcresearchpress.com by EESC ESCOLA DE ENGENHARIA on 09/08/12
For personal use only.

Can. J. Chem. Downloaded from www.nrcresearchpress.com by EESC ESCOLA DE ENGENHARIA on 09/08/12
For personal use only.

may be responsible for the widening of the O—N—B angles within the six-membered BONBON ring of **4***b* (115.4(1)°) relative to the corresponding angles in **6** (106.80(7)°) (11), in spite of the overall structural similarity of the six-membered heterocycles in these two molecules. The intracyclic N—O—B angles in **4***b* are also widened (113.6(1)°) relative to those in **6** (111.75(7)°), whereas the N—B—O angles in the two compounds are virtually identical (104.9(1)° in **4***b*, 104.98(8)° in **6**).

The slight flattening of the BONBON chair in the oxime derivative **4***b* resembles that reported for 1,4-bisacyl piperazines (22), which is thought to be controlled by the planarity about the partial C=N double bonds of the amide groups at the 1- and 4-positions of the six-membered ring. The oxime C=N bonds in **4***b* act in a similar way to produce the flattened chair conformation.

The B—C(aryl) bond lengths of **4***b* (1.597(2) and 1.604(2) Å) are within the range normally observed for tetracoordinated arylboron compounds (23). The geminal *B*-aryl rings are oriented roughly perpendicular to one another (the dihedral angle between normals to the mean planes is 71.3°), an arrangement normal for geminal substituents at small atoms. All intermolecular distances correspond to normal van der Waals interactions, the shortest nonbonded contact between non-hydrogen atoms being O(3)···C(2) = 3.475(2) Å.

From the X-ray crystallographic analysis of **4***b* and the chemical shifts from the ^{11}B nmr spectra of **4***b*,*e*,*f*,*g*,*h*,*k*, and *l* in deuterochloroform solution, it can be concluded that the (alkylideniminoxy)diarylboranes **3** exist predominantly in the cyclodimeric form **4** having a six-membered BONBON ring system that adopts a chair conformation. This conclusion is indirectly corroborated by the synthesis of the same materials from compounds **5**, bearing in mind that the BONBON ring structure for **5** is only assumed, although very probable. Under the conditions of EI and CI mass spectrometry experiments, these rings dissociate into monomers that represent the "molecular ions" ($1/2M^+$).[5]

Acknowledgments

We thank the Natural Sciences and Engineering Research Council of Canada and the Fonds der Chemischen Industrie, Frankfurt am Main, for financial support. We are grateful to the Chemische Institute der Technischen Universität Braunschweig for running the ^{11}B nmr and mass spectra.

1. E. Beckmann. Z. Phys. Chem. **2**, 715 (1888).
2. G. Geiseler. J. Mol. Struct. **1**, 305 (1967, 1968).
3. (*a*) S.J. Rettig and J. Trotter. Can. J. Chem. **53**, 765 (1975), and references therein; (*b*) H. Saarinen, J. Korvenranta, and E. Näsäkälä. Cryst. Struct. Commun. **6**, 557 (1977); (*c*) A. Gieren and B. Dederer. Acta Crystallogr. Sect. B: Struct. Crystallogr. Cryst. Chem. **B33**, 3296 (1977); (*d*) A. Gieren, T. Hübner, and C. Ruiz-Perez. Chem.-Ztg. **110**, 73 (1986); (*e*) T. Taga, A. Uchiyama, and K. Machida. Acta Crystallogr. Sect. C: Cryst. Struct. Commun. **C46**, 2241 (1990); (*f*) B. Jerslev and S. Larsen. Acta Crystallogr. Sect. C: Cryst. Struct. Commun. **C48**, 136 (1992); (*g*) W.V. Nicholson, L. Sawyer, P. Taylor, I. Dawson, and R.O. Gould. Acta Crystallogr. Sect. C: Cryst. Struct. Commun. **C49**, 101 (1993).
4. G.A. Jeffrey, J.R. Ruble, and J.A. Pople. Acta Crystallogr. Sect. B: Struct. Crystallogr. Cryst. Chem. **B38**, 1975 (1982).
5. J. R. Jennings and K. Wade. J. Chem. Soc. A: 1333 (1967).
6. O.P. Shitov, L.M. Leont'eva, S.L. Ioffe, B.N. Khasanov, V.M. Novikov, A.U. Stepanyants, and V. A. Tartakovskii. Izv. Akad. Nauk SSSR, Ser. Khim. 2782 (1974); Bull. Acad. Sci. USSR, Div. Chem. Sci. 2684 (1974).
7. W. Maringgele and A. Meller. Monatsh. Chem. **106**, 1369 (1975).
8. D.W. Palmer and K. Niedenzu. Synth. React. Inorg. Metal-Org. Chem. **9**, 13 (1979).
9. R. Köster and A. Deege. Unpublished results, cited in Houben-Weyl, Methoden der Organischen Chemie, Bd. 13/3b (Organobor-Verbindungen II). Thieme-Verlag, Stuttgart. 1983. pp 587–588.
10. L.H. Toporcer, R.E. Dessy, and S.I.E. Green. Inorg. Chem. **4**, 1649 (1965).
11. W. Kliegel, G. Lubkowitz, S.J. Rettig, and J. Trotter. Can. J. Chem. **70**, 2809 (1992), and references therein.
12. W. Kliegel, D. Nanninga, S.J. Rettig, and J. Trotter. Can. J. Chem. **61**, 2329 (1983).
13. H.J. Roth and B. Miller. Arch. Pharm. Ber. Dtsch. Pharm. Ges. **297**, 744 (1964).
14. H. Nöth and B. Wrackmeyer. Nuclear magnetic resonance spectroscopy of boron compounds. Springer-Verlag, Berlin. 1978.
15. (*a*) W. Kliegel. Liebigs Ann. Chem. **763**, 61 (1972); (*b*) W. Kliegel and E. Ahlenstiel. J. Organomet. Chem. **277**, 173 (1984).
16. (*a*) R. Neu. Z. Anal. Chem. **176**, 334 (1960); (*b*) B. Friese and F. Umland. Anal. Chim. Acta, **96**, 303 (1978).
17. (*a*) T.P. Povlock and W.T. Lippincott. J. Am. Chem. Soc. **80**, 5409 (1958); (*b*) Y. Rasiel and H.K. Zimmerman. Liebigs Ann. Chem. **649**, 111 (1961).
18. (*a*) J.B. Skaptason. U.S. Pat. 3,117,854 (14.1.1964); Chem. Abstr. **60**, 12602c (1964); (*b*) S.J. Rettig and J. Trotter. Acta Crystallogr. Sect. B: Struct. Crystallogr. Cryst. Chem. **B30**, 2139 (1974).
19. (*a*) W. König and W. Scharmbeck. J. Prakt. Chem. **128**, 153 (1930); (*b*) V.A. Sazanova, E.P. Serebryakov, and L.S. Kovaleva. Dokl. Akad. Nauk SSSR, **113**, 1295 (1957); Chem. Abstr. **52**, 354 (1958).
20. International tables for X-ray crystallography. Vol. IV. Kynoch Press, Birmingham, U.K. (present distributor: Kluwer Academic Publishers: Dordrecht, The Netherlands). 1974. pp. 99–102 and 149.
21. S.J. Rettig and J. Trotter. Can. J. Chem. **61**, 206 (1983).
22. (*a*) L. Olansky and J.W. Moncrief. Acta Crystallogr. Sect. B: Struct. Crystallogr. Cryst. Chem. **B29**, 357 (1973); (*b*) Tien-Ming Ko and J.W. Moncrief. Acta Crystallogr. Sect. B: Struct. Crystallogr. Cryst. Chem. **B31**, 2544 (1975); (*c*) I.W. Bassi and R. Scordamaglia. Makromol. Chem. **178**, 2063 (1977).
23. W. Kliegel, G. Lubkowitz, S.J. Rettig, and J. Trotter. Can. J. Chem. **70**, 2033 (1992).
24. W. Kliegel, G. Lubkowitz, S.J. Rettig, and J. Trotter. Can. J. Chem. **72**, 1154 (1994).

[5]Fragments of higher mass are detected in some of the mass spectra. These are supposed to be thermolytic artifacts of the organoboron moiety of the molecules, such as dimeric or trimeric anhydrides of arylboronic acids, $(ArBO)_n$

Systematic sequences of well-balanced Gaussian basis sets

MARIUSZ KLOBUKOWSKI
Department of Chemistry, University of Alberta, Edmonton, AB T6G 2G2, Canada

Received July 26, 1993[1]

MARIUSZ KLOBUKOWSKI. Can. J. Chem. **72**, 1741 (1994).

Systematic sequences of Gaussian basis sets with controlled energy errors for the studies of convergence of the basis set effects on the computed results of molecular calculations are presented. The basis sets were prepared for atoms H–Ne and Al–Ar and may be used in systematic *ab initio ad limitem* studies of molecular structure and properties.

MARIUSZ KLOBUKOWSKI. Can. J. Chem. **72**, 1741 (1994).

On présente des séquences systématiques d'ensembles de bases gaussiennes avec des erreurs d'énergie contrôlées qui peuvent être utilisées pour des études de convergence des effets d'ensembles de base sur les résultats de calculs moléculaires. On a préparé les ensembles de base des atomes H–Ne et Al–Ar et on peut les utiliser dans des études *ab initio ad limitem* de structures et de propriétés moléculaires.

[Traduit par la rédaction]

Can. J. Chem. Downloaded from www.nrcresearchpress.com by EESC ESCOLA DE ENGENHARIA on 09/08/12
For personal use only.

Introduction

Almost a decade ago, we have published the first compilation of the well-tempered basis sets (1) and used them in calculations of molecular structure and properties (2–5). The main stimulus for the development of these new basis sets was the perceived need to provide a collection of basis sets for use in molecular calculations devoid of basis set errors. This objective was achieved by using very large expansions in terms of primitive Gaussian functions. The realization of this goal leads thus to two problems, both connected with computational efficiency: The first one is the evaluation of the molecular integrals, and the second is the optimization of the exponential parameters of the basis sets (usually done in atomic calculations). Many of the frequently-used computer codes achieve savings in the integral and gradient evaluation times via utilizing the sharing of exponents within the shells of the atomic functions (6–8). We have therefore designed the well-tempered basis sets in which all exponents are *shared* between the *s*, *p*, *d*, and *f* spaces in atomic calculations. To address the second problem, we expanded the even-tempered formula, originally suggested by Reeves (9) and then extensively studied by Ruedenberg and co-workers (10–16):

$$[1] \quad \zeta_{k,l} = \alpha_l \beta_l^k \qquad k = 1, ..., N_l$$

where N_l is the number of primitive functions in symmetry l, and the parameters α_l and β_l are different for different l's. We modified this formula in order to improve the distribution of both the small and large exponential parameters, and called the resulting basis sets *well-tempered:*

$$[2] \quad \zeta_k = \alpha\beta^{N-k+1}\left[1 + \gamma\left(\frac{N-k+1}{N}\right)^{\delta}\right] \qquad k = 1, ..., N$$

In recent work, Huzinaga et al. (17, 18) used a modified version of eq. [2],

$$[3a] \quad \zeta_N = \alpha$$

$$[3b] \quad \zeta_{N-k+1} = \zeta_{N-k+2}\,\beta\left[1 + \gamma\left(\frac{k}{N}\right)^{\delta}\right] \qquad k = 2, ..., N$$

The idea that it may be advantageous to modify the even-tempered formula was independently proposed by Wilson who, discussing the even-tempered sequences of Gaussian functions in a review of the many-body perturbation theory of molecules (19), suggested the generalized recursion $\zeta_{k+1} = \zeta_k\,(\beta + \gamma k)$, which rewritten as $\zeta_{k+1} = \zeta_k\beta(1 + \gamma' k)$ has the form resembling eq. [3].

These basis sets, together with the ones developed by Schmidt and Ruedenberg (16), Partridge (20, 21), and Clementi et al. (22, 23), aimed at providing very large expansions which are essentially free of BSSE. However, these basis sets are almost intractable in the studies on larger molecular systems for which the smaller basis sets are still being used (24–29), the developments in computer hardware notwithstanding. These smaller basis sets are usually of a fixed size for the atoms in each row of the periodic table; this size was predetermined mainly on the basis of computational efficiency in the molecular calculations. However, these basis sets exhibit very nonuniform error with respect to the atomic number: the larger the value of Z for a basis set of fixed size the larger the error. Such basis sets are then not balanced, and when used in molecular calculations, may lead to differential basis set errors between the constituent atoms of a molecule. Furthermore, within each basis set for a given atom, it often happens that the *s*, *p*, etc. spaces are not represented with equal accuracy, thus potentially leading to differential basis set effects within each atomic basis set.

The present work constitutes an extension of the previous work on the Gaussian basis sets done in this laboratory and was undertaken in order to build a family of Gaussian expansions which would exhibit controlled basis set errors. These basis sets would be *well balanced* (30), and, in the words of Clementi, would provide "poor atomic sets for all atoms, medium sets for all atoms, good atomic set for all the atoms in the molecule" (31). Furthermore, their availability would establish the basis for systematic studies of convergence patterns in molecular energy and properties. Need for such basis has been stressed for the first time by Schwarz (32) and reiterated by Schmidt and Ruedenberg (16) (who developed the concept of *energy-balanced* even-tempered basis sets) and by Wilson (33) (who followed the convergence within the universal basis sets (34)). In addition, the systematic build-up of the basis sets was designed so as to assist in the understanding of the relationship and the role of the *s* and *p* spaces in approaching the Hartree–Fock limit of the total energy.

In our previous work we demonstrated that while for very

[1]Revision received March 14, 1994.

large basis sets, as the basis set approaches completeness, the quality of results does not depend on the formula used to generate the exponential parameters ζ of the basis set (35). However, as the size of basis is reduced, a device is needed to increase the large values of ζ, which are too small compared with the ones obtained in the full optimization. Furthermore, we also determined (35) that the errors in exponents generated with the original well-tempered formulas, eqs. [2] and [3], could be reduced by a factor of two if the exponents are not shared between the atomic symmetries. The best formula used int he present work is obtained when the fourth degree polynomial expansion of log ζ is used:

$$[4] \quad \log \zeta_{k,l} = \sum_{i=1}^{5} P_{i,l} k^{i-1}$$

This formula has the added advantage that the initial values of parameters, P_i required in the optimization process are readily obtained via the least-squares fitting to a set of exponents from a known basis set. (In this work, the procedure SVDFIT (36) was used for fitting.) Furthermore, as pointed out by Mezey and Hass, the use of ln ζ in the optimization instead of ζ is advantageous (37). From the comparison of eqs. [1] and [4] we see that $\alpha_l \approx 10^{P_{1,l}}$ and $\beta_l \approx 10^{P_{2,l}}$.

With only ten parameters per atom to be optimized, a large number of basis sets could be generated to provide a uniform description at each atomic site in molecular calculations. All calculations were performed on IBM RS/6000 workstations.

II. Calculations and results

The optimization of parameters in the generator formula was done using the Powell's method of conjugate directions as modified by Brent (38). As shown previously (35), the method is very efficient (despite the lack of derivatives) and sufficiently accurate: the errors in the atomic total energy were found to be only 1–2 μhartree.

The reference Hartree-Fock energies, computed with the Froese–Fischer code (39), are collected in Table 1. The errors ΔE, δs, and δp for the generated basis sets are shown in Tables 2–8 for the atoms hydrogen through neon and in Tables 12–16 for aluminum through argon. The error ΔE is defined as the difference between the total energy computed with a given basis set and the Hartree-Fock energy $\Delta E = E_{\text{basis}} - E_{\text{Hartree-Fock}}$. In order to measure whether each symmetry is represented equally well, we defined two parameters, δ_s and δ_p. The errors δ_s and δ_p indicate whether the basis set is internally balanced; they were evaluated by calculating how much the total energy is lowered upon addition of another s and p function, respectively. Specifically,

$$\delta_s = E(N_s.N_p) - E(N_s + 1.N_p)$$

$$\delta_p = E(N_s.N_p) - E(N_s.N_p + 1)$$

The notation $(N_s.N_p)$ is used to represent a basis set with N_s s-type and N_p p-type uncontracted functions. The values in italics were estimated using the observed regular behaviour of δs and δp. To save space, the tables are somewhat distorted from the optimum format of the quasi-diagonal matrix in which the columns are labeled by N_s and the rows by N_p. The results are arranged so that moving down a column results in simultaneous increase in the number of s and p functions; moving right along a row increases the number of s functions only; and moving along the lines parallel to the counter-diagonal increases the number of p functions.

TABLE 1. Hatree–Fock total energies[a] for atoms hydrogen through argon

Atom (state)	Energy	Atom (state)	Energy
H (^2S)	−0.5	Li (^2S)	−7.432727
He (^1S)	−2.861680	Be (^1S)	−14.573023
B (^2P)	−24.539061	Al (^2P)	−241.876707
C (^3P)	−37.688619	Si (^3P)	−288.854362
N (^4S)	−54.400934	P (^4S)	−340.718781
O (^3P)	−74.809398	S (^3P)	−397.504896
F (^2P)	−99.409349	Cl (^2P)	−459.482072
Ne (^1S)	−128.547098	Ar (^1S)	−526.817513

[a]All values in hartree.

A. *Hydrogen – beryllium*

The errors for the atoms hydrogen through beryllium are shown in Table 2. It is interesting to observe how quickly the

TABLE 2. Results for atoms hydrogen through beryllium

H (^2S)		He (^1S)		Li (^2S)		Be (^1S)	
N_s	ΔE[b]	N_s	ΔE[b]	N_s[a]	ΔE[b]	N_s[a]	ΔE[b]
4	721.6	10	7.3	8^2	1644.0	8^2	3252.6
5	190.2	11	2.8	9^2	606.6	9^2	1202.9
6	54.9	12	1.1	10^2	247.8	10^2	499.9
7	17.0	13	0.5	11^2	105.0	11^3	202.9
8	5.6	14	0.2	12^3	41.8	12^3	80.6
9	2.0	15	0.1	13^3	17.2	13^3	34.2
10	0.7	16	0.0	14^3	7.6	14^3	15.5
11	0.3	17	0.0	15^3	3.5	15^4	6.9
12	0.1	18	0.0	16^3	1.6	16^4	3.1
		19	0.0	17^3	0.7	17^4	1.4
				18^4	0.3	18^4	0.7
				19^4	0.2	19^4	0.3
				20^4	0.1	20^4	0.2

[a]The superscript denotes the number of primitive functions deployed in the valence region (i.e. the subscript of 3 indicates "triple zeta valence" quality of the basis set).
[b]$\Delta E = E_T$(Gaussian) − E_T(HF), μhartree.

Can. J. Chem. Downloaded from www.nrcresearchpress.com by EESC ESCOLA DE ENGENHARIA on 09/08/12
For personal use only.

TABLE 3. Results for B (^2P)[a]

	N_s									
	N_p + 4		N_p + 5		N_p + 6		N_p + 7		N_p + 8	
N_p	ΔE	(δs;δp)	ΔE	(δs;δp)	ΔE	(δs;δp)	ΔE	(δs;δp)	ΔE	(δs;δp)
4	6238	(3128;*980*)	3111	(1076;980)	2035	(442;980)	1593	(181;984)	1412	(*70*;987)
5	2131	(1077;*230*)	1055	(446;228)	608	(183;228)	425	(70;228)	356	(*28*;229)
6	826	(446;*56*)	380	(183;56)	197	(70;56)	127	(28;56)	99	(*13*;56)
7	325	(183;*14*)	141	(70;14)	71	(28;14)	43	(13;14)	30	(*6*;14)
8	128	(70;*4*)	57	(28;4)	29	(13;4)	16	(6;4)	10	(*3*;4)
9	53	(28;*1*)	25	(13;1)	12	(6;1)	6	(3;1)	4	(*1*;1)
10	24	(13;*0*)	11	(6;0)	5	(3;0)	3	(1;0)	2	(*1*;0)
11	11	(6;*0*)	5	(3;0)	2	(1;0)	1	(1;0)	1	(*0*;0)
12	5	(3;*0*)	2	(1;0)	1	(1;0)	1	(0;0)	0	(*0*;0)
13	2	(1;*0*)	1	(1;0)	1	(0;0)	0	(0;0)	0	(*0*;0)
14	1	(1;*0*)	0	(0;0)	0	(0;0)	0	(*0*;0)		
15	0	(0;*0*)	0	(0;0)	0	(0;0)	0	(*0*;0)		
16	0	(0;*0*)	0	(0;0)	0	(*0*;0)				
17	0	(0;*0*)	0	(*0*;0)						

[a]Energy differences in μhartree; see text for definitions.

TABLE 4. Results for C (^3P)[a]

	N_s									
	N_p + 4		N_p + 5		N_p + 6		N_p + 7		N_p + 8	
N_p	ΔE	(δs;δp)	ΔE	(δs;δp)	ΔE	(δs;δp)	ΔE	(δs;δp)	ΔE	(δs;δp)
4	11397	(4458;*3300*)	6939	(1538;3304)	5401	(621;3310)	4779	(253;3323)	4526	(*99*;3328)
5	3635	(1544;*769*)	2091	(634;769)	1457	(258;769)	1198	(99;770)	1099	(*40*;771)
6	1321	(634;*188*)	688	(259;188)	428	(100;188)	328	(40;188)	288	(*18*;188)
7	499	(259;*48*)	240	(100;48)	140	(40;48)	100	(18;48)	82	(*8*;48)
8	192	(100;*13*)	92	(40;13)	52	(18;13)	34	(8;13)	26	(*4*;13)
9	79	(40;*4*)	38	(18;4)	20	(8;4)	12	(4;4)	9	(*2*;4)
10	35	(18;*1*)	17	(8;1)	8	(4;1)	5	(2;1)	3	(*1*;1)
11	15	(8;*0*)	7	(4;0)	4	(2;0)	2	(1;0)	1	(*0*;0)
12	7	(4;*0*)	3	(2;0)	2	(1;0)	1	(0;0)	1	(*0*;0)
13	3	(2;*0*)	1	(1;0)	1	(0;0)	0	(0;0)	0	(*0*;0)
14	1	(1;*0*)	1	(0;0)	0	(0;0)	0	(*0*;0)		
15	1	(0;*0*)	0	(0;0)	0	(0;0)	0	(*0*;0)		
16	0	(0;*0*)	0	(0;0)	0	(*0*;0)				
17	0	(0;*0*)	0	(*0*;0)						

[a]Energy differences in μhartree; see text for definitions.

TABLE 5. Results for N (^4S)[a]

	N_s									
	N_p + 4		N_p + 5		N_p + 6		N_p + 7		N_p + 8	
N_p	ΔE	(δs;δp)	ΔE	(δs;δp)	ΔE	(δs;δp)	ΔE	(δs;δp)	ΔE	(δs;δp)
4	19364	(6036;*7500*)	13329	(2087;7466)	11242	(834;7480)	10408	(339;7506)	10069	(*133*;7514)
5	5863	(2101;*1739*)	3762	(859;1739)	2902	(347;1739)	2555	(133;1742)	2422	(*54*;1745)
6	2022	(859;*426*)	1163	(350;426)	813	(135;425)	678	(54;425)	623	(*24*;426)
7	737	(350;*109*)	387	(135;110)	252	(55;109)	197	(24;109)	173	(*11*;109)
8	278	(135;*31*)	143	(55;31)	88	(25;31)	63	(11;31)	52	(*5*;30)
9	112	(55;*9*)	57	(24;9)	33	(11;9)	22	(5;9)	17	(*2*;9)
10	48	(24;*3*)	24	(11;3)	13	(5;3)	8	(2;3)	6	(*1*;3)
11	21	(11;*1*)	10	(5;1)	5	(2;1)	3	(1;1)	2	(*0*;1)
12	9	(5;*0*)	5	(2;0)	2	(1;0)	1	(0;0)	1	(*0*;0)
13	4	(2;*0*)	2	(1;0)	1	(0;0)	1	(0;0)	0	(*0*;0)
14	2	(1;*0*)	1	(0;0)	1	(0;0)	0	(*0*;0)		
15	1	(0;*0*)	0	(0;0)	0	(0;0)	0	(*0*;0)		
16	0	(0;*0*)	0	(0;0)	0	(*0*;0)				
17	0	(0;*0*)	0	(*0*;0)						

[a]Energy differences in μhartree; see text for definitions.

Can. J. Chem. Downloaded from www.nrcresearchpress.com by EESC ESCOLA DE ENGENHARIA on 09/08/12
For personal use only.

TABLE 6. Results for O (^3P)[a]

	N_s									
	$N_p + 4$		$N_p + 5$		$N_p + 6$		$N_p + 7$		$N_p + 8$	
N_p	ΔE	(δs;δp)	ΔE	(δs;δp)	ΔE	(δs;δp)	ΔE	(δs;δp)	ΔE	(δs;δp)
4	31966	(7859;*14800*)	24106	(2725;14799)	21382	(1078;14820)	20303	(435;14861)	19868	(*172*;14876)
5	9307	(2746;*3500*)	6561	(1119;3500)	5442	(450;3497)	4993	(172;3502)	4821	(*71*;3506)
6	3062	(1117;*870*)	1945	(455;870)	1490	(176;869)	1314	(71;869)	1243	(*32*;869)
7	1075	(454;*226*)	622	(176;226)	446	(72;226)	374	(32;226)	342	(*14*;226)
8	395	(176;*63*)	219	(72;63)	148	(32;63)	116	(14;63)	102	(*6*;63)
9	156	(71;*18*)	85	(32;18)	53	(14;19)	39	(6;19)	32	(*3*;19)
10	66	(32;*6*)	34	(14;6)	20	(6;6)	14	(3;6)	11	(*1*;6)
11	29	(14;*2*)	14	(6;2)	8	(3;2)	5	(1;2)	4	(*1*;2)
12	12	(6;*1*)	6	(3;1)	3	(1;1)	2	(1;1)	2	(*0*;1)
13	6	(3;*0*)	3	(1;0)	2	(1;0)	1	(0;0)	1	(*0*;0)
14	3	(1;*0*)	1	(1;0)	1	(0;0)	0	(*0*;0)		
15	1	(1;*0*)	1	(0;0)	0	(0;0)	0	(*0*;0)		
16	1	(0;*0*)	0	(0;0)	0	(*0*;0)				
17	0	(0;*0*)	0	(*0*;0)						

[a]Energy differences in μhartree; see text for definitions.

TABLE 7. Results for F (^2P)[a]

	N_s									
	$N_p + 4$		$N_p + 5$		$N_p + 6$		$N_p + 7$		$N_p + 8$	
N_p	ΔE	(δs;δp)	ΔE	(δs;δp)	ΔE	(δs;δp)	ΔE	(δs;δp)	ΔE	(δs;δp)
4	49186	(9933;*25300*)	39253	(3447;25310)	35806	(1355;25343)	34451	(545;25403)	33096	(*217*;25425)
5	13944	(3480;*6030*)	10463	(1415;6030)	9048	(567;6026)	8482	(217;6034)	8265	(*90*;6040)
6	4433	(1411;*1510*)	3022	(574;1510)	2448	(223;1508)	2225	(90;1508)	2135	(*40*;1509)
7	1512	(572;*396*)	940	(223;396)	717	(91;395)	626	(40;395)	586	(*18*;395)
8	544	(222;*111*)	322	(90;111)	231	(40;111)	191	(18;111)	173	(*8*;111)
9	211	(91;*33*)	120	(40;33)	80	(18;33)	62	(8;33)	54	(*4*;33)
10	88	(40;*10*)	48	(18;10)	30	(8;10)	22	(4;10)	18	(*2*;10)
11	38	(18;*3*)	20	(8;3)	12	(4;3)	8	(2;3)	6	(*1*;3)
12	16	(8;*1*)	8	(4;1)	5	(2;1)	3	(1;1)	2	(*0*;1)
13	7	(4;0)	4	(2;0)	2	(1;0)	1	(0;0)	1	(*0*;0)
14	3	(2;*0*)	2	(1;0)	1	(0;0)	1	(0;0)	0	(*0*;0)
15	2	(1;*0*)	1	(0;0)	0	(0;0)	0	(*0*;0)		
16	1	(0;*0*)	0	(0;0)	0	(*0*;0)				
17	0	(0;*0*)	0	(*0*;0)						

[a]Energy differences in μhartree; see text for definitions.

TABLE 8. Results for Ne (^1S)[a]

	N_s									
	$N_p + 4$		$N_p + 5$		$N_p + 6$		$N_p + 7$		$N_p + 8$	
N_p	ΔE	(δs;δp)	ΔE	(δs;δp)	ΔE	(δs;δp)	ΔE	(δs;δp)	ΔE	(δs;δp)
4	71652	(12252;*39500*)	59400	(4255;39478)	55145	(1665;39528)	53480	(668;39609)	52812	(*267*;39638)
5	19922	(4305;*9443*)	15617	(1746;9443)	13871	(697;9439)	13174	(267;9449)	12907	(*111*;9457)
6	6175	(1742;*2374*)	4432	(708;2374)	3725	(275;2372)	3450	(111;2371)	3338	(*50*;2373)
7	2058	(705;*625*)	1353	(275;625)	1078	(112;625)	966	(50;624)	916	(*22*;624)
8	728	(275;*176*)	453	(112;176)	341	(50;176)	292	(22;176)	269	(*10*;176)
9	277	(112;*52*)	165	(49;52)	116	(22;52)	94	(10;52)	84	(*4*;52)
10	114	(49;*16*)	64	(22;16)	42	(10;16)	32	(4;16)	28	(*2*;16)
11	48	(22;*5*)	26	(10;5)	16	(4;5)	12	(2;5)	10	(*1*;5)
12	21	(10;2)	11	(4;2)	7	(2;2)	5	(1;2)	4	(*0*;2)
13	9	(4;*1*)	5	(2;1)	3	(1;1)	2	(0;1)	1	(*0*;1)
14	4	(2;*0*)	2	(1;0)	1	(0;0)	1	(*0*;0)		
15	2	(1;*0*)	1	(0;0)	1	(0;0)	0	(*0*;0)		
16	1	(0;*0*)	1	(0;0)	0	(*0*;0)				
17	0	(0;*0*)	0	(*0*;0)						

[a]Energy differences in μhartree; see text for definitions.

Can. J. Chem. Downloaded from www.nrcresearchpress.com by EESC ESCOLA DE ENGENHARIA on 09/08/12
For personal use only.

Can. J. Chem. Downloaded from www.nrcresearchpress.com by EESC ESCOLA DE ENGENHARIA on 09/08/12
For personal use only.

total energies converge to the limiting Hartree–Fock value: It requires only 10*s*, 13*s*, 17*s*, and 18*s* functions for H, He, Li, and Be, respectively, to reach the Hartree–Fock energy with sub-μhartree error. The comparison of the exponents generated with eq. [4] for hydrogen and those which were optimized using the gradient methods by Matsuoka and co-workers (40) shows that the formula gives very accurate rendering of the individually optimized exponents. These values are also rather close to the set generated by Huzinaga (41).

B. Boron – Neon

The collection of results for the atoms boron through neon is shown in Tables 3–8. For an increasing atomic number *Z*, the errors in the total energy, ΔE, also increase. As the number of Gaussian functions increases, the errors become smaller, and eventually reach sub-μhartree values, which are reached with larger basis sets for heavier atoms. The errors δ_s and δ_p of course are equal and very small for the largest basis sets; for the remaining ones it seems that the internal balance of the *s* and *p* spaces is observed for $N_s = N_p + 5$ for the smallest sets, and $N_s = N_p + 6$ or 7 for the medium-size basis sets.

The decoupling of the *s* and *p* exponents results in the variational freedom which is demonstrated in the constant errors δ_s and δ_p: The total energy is lowered by the same amount when one *p* functions is added to a basis set with any value of N_s. Taking as an example the series of basis sets (12.8), (13.8), (14.8), ..., for neon (Table 8), we observe $\delta_p = 176$ μhartree. The constancy still approximately holds even for the smallest basis with $N_p = 4$. Similarly, the addition of one s function to a basis set with any N_p results in identical lowering of the total energy (although the structure in the tables makes this effect a little more difficult to observe).

Inspection of the optimized values of the parameters in the generator formula of eq. [4] shows that the role of the cubic and quartic terms for the s space decreases with the increasing basis set size, while the values of the quadratic term remain almost constant. For the *p* space the changes are similar, although the values of the higher-order terms are larger. In other words, while it may be sufficient to truncate the series (4) at the cubic term for the *s* space, such truncation may lead to larger errors for the smaller basis sets due to inadequate flexibility in the *p* symmetry.

It is interesting to observe that, unlike in the case of the even-tempered basis sets studied by Schmidt and Rudenberg (16), the present basis sets of structure analogous to their (2*N*.*N*), or ($2N_p$.N_p) in our notation, are not necessarily energy balanced, as may be seen in the unequal values of δs and δp. The relationship $\delta s \approx \delta p$ seen for the basis sets ($2N_p$.N_p) of lighter atoms, deteriorates as the atomic number *Z* increases.

Finally, it may be interesting to compare the errors of some of the smaller basis sets with the ones determined using unconstrained optimization of exponents: Table 9 shows the results for the (9.5) and (10.6) basis sets in relation to basis sets of the same size optimized by Huzinaga (41). It is quite clear from Table 9 that the generator formula of eq. [4] is very effective in approximating the fully optimized basis set exponents. Furthermore, the difference between the total energies of the fully optimized Huzinaga's functions and the present ones is much smaller than the error with respect to the Hartree–Fock limit.

C. Aluminum – argon

The errors for the basis sets for atoms aluminum through argon are presented in Tables 10–15. It appears that in order to achieve similar errors as for the analogous atoms from the previous row of the periodic table, five additional functions are needed for the lighter atoms while only three suffice for the heavier ones. While for the larger basis sets the internal balance is observed for $N_s = N_p + 5$ or 6, in parallel with the behaviour seen for the second row atoms, the constraints on the p space in the smallest basis sets result in large δ_p errors and, in consequence, make them internally unbalanced. For the two sets of basis sets with $N_s = 2N_p$, namely those with $N_p = 7$ and 8, the errors in the p space are much larger than those in s space, making these basis sets internally unbalanced.

TABLE 9. Comparison of total energies (in hartree) and total energy errors (in mhartree) for B–Ne[a]

Atom	E_T (this work)	ΔE_1[a]	E_T (Huzinaga)	ΔE_2[b]
		Basis (9.5)		
B (^2P)	−24.526929	−0.218	−24.527130	−1.914
C (^3P)	−37.684984	−0.285	−37.685247	−3.350
N (^4S)	−54.395071	−0.402	−54.395336	−5.461
O (^3P)	−74.800092	−0.482	−74.800289	−8.824
F (^2P)	−99.395406	−0.520	−99.395586	−13.423
Ne (^1S)	−128.527176	−0.49	−128.52674	−19.43
		Basis (10.6)		
B (^2P)	−24.528235	−0.051	−24.528282	−0.775
C (^3P)	−37.687298	−0.037	−37.687324	−1.284
N (^4P)	−54.398912	−0.013	−54.398909	−2.009
O (^3P)	−74.806337	0.015	−74.806295	−3.076
F (^2P)	−99.404916	−0.030	−99.404870	−4.403
Ne (^1S)	−128.540923	−0.05	−128.54094	−6.13

[a] $\Delta E_1 = E_T$(Huzinaga) − E_T (this work).
[b] $\Delta E_2 = E_T$(Hartree–Fock) − E_T (Huzinaga).

The values of the optimized parameters, compared with analogous values for the first-row atoms, reveal diminished role of the cubic and quartic terms in the expansion of log ζ, especially for the *s* space. However, these terms appear to be required for the expansion in *p* space.

The results for two smaller basis sets, (11.7) and (12.8), are compared in Table 16 with the fully optimized basis sets of Huzinaga (42). As seen in the case of analogous atoms from the preceding row, the errors between the fully optimized and formula-based basis sets are much smaller that the energy differences between the fully optimized energies and the Hartree–Fock limit.

III. Conclusions

The perfect internal balance may be somewhat elusive goal: as the number of the primitive functions may increase only by an integer value, it is impossible to find the basis sets for which $\delta_s = \delta_p$. However, for practical purposes, the approximate relationship $\delta_s \approx \delta_p$ should be sufficient. The recommended basis sets which exhibit the approximate internal balance are the ones for which $N_s = N_p + 5$ or 6, provided that, for the atoms of the third row, $N_p > 9$.

With the help of the data presented in the Tables 2–8 and 10–15 it is now possible to choose, for each atomic site in molecular calculations, the basis sets with similar values of ΔE, and thus ensure external balance of the basis sets (31). For example, in the calculation of boron fluoride, the (9.5) basis for boron should be used with (10.6) or (11.6) basis for fluorine; all these basis sets have approximately the same value of ΔE (and approximate internal balance). The error for the (9.5) basis for fluorine is more than ten times larger than that for boron,

TABLE 10. Results for Al (^2P)[a]

	N_s									
	$N_p + 4$		$N_p + 5$		$N_p + 6$		$N_p + 7$		$N_p + 8$	
N_p	ΔE	(δs;δp)	ΔE	(δs;δp)	ΔE	(δs;δp)	ΔE	(δs;δp)	ΔE	(δs;δp)
7	25911	(6678;*8600*)	19233	(3045;8519)	16188	(1307;8735)	14882	(534;8662)	14348	(*240*;8654)
8	10714	(3260;*3430*)	7454	(1234;3435)	6220	(526;3519)	5694	(240;3531)	5454	(*131*;3533)
9	4019	(1318;1070)	2701	(538;1076)	2163	(243;1057)	1921	(131;1063)	1790	(*59*;1064)
10	1625	(519;*383*)	1106	(248;383)	858	(133;382)	725	(59;385)	666	(*27*;386)
11	723	(247;*147*)	476	(136;149)	340	(60;147)	280	(27;147)	253	(*13*;148)
12	327	(134;*49*)	193	(60;49)	133	(27;50)	106	(13;49)	93	(*6*;49)
13	143	(60;*18*)	83	(26;18)	57	(13;18)	43	(6;18)	37	(*4*;18)
14	65	(26;*8*)	39	(13;8)	25	(6;7)	19	(4;7)	15	(*2*;7)
15	31	(13;*3*)	18	(6;3)	12	(4;3)	8	(2;3)	6	(*1*;3)
16	15	(6;*1*)	9	(3;1)	5	(2;1)	4	(1;1)	3	(*0*;1)
17	8	(4;*0*)	4	(2;0)	3	(1;0)	2	(0;0)	1	(*0*;0)
18	4	(2;*0*)	2	(1;0)	1	(0;0)	1	(0;0)	1	(*0*;0)
19	2	(1;*0*)	1	(0;0)	1	(0;0)	0	(*0*;0)		
20	1	(0;*0*)	0	(0;0)	0	(*0*;0)				
21	0	(0;*0*)	0	(*0*;0)						
22	0	(0;*0*)	0	(*0*;0)						

[a]Energy differences in μhartree; see text for definitions.

TABLE 11. Results for Si (^3P)[a]

	N_s									
	$N_p + 4$		$N_p + 5$		$N_p + 6$		$N_p + 7$		$N_p + 8$	
N_p	ΔE	(δs;δp)	ΔE	(δs;δp)	ΔE	(δs;δp)	ΔE	(δs;δp)	ΔE	(δs;δp)
7	32854	(7509;*13000*)	25345	(3326;12982)	22019	(1411;13214)	20608	(556;13172)	20052	(*250*;13188)
8	12363	(3558;*4300*)	8805	(1369;4239)	7436	(572;4309)	6864	(250;4319)	6614	(*140*;4327)
9	4565	(1438;*1280*)	3127	(582;1278)	2545	(258;1277)	2287	(137;1282)	2150	(*64*;1286)
10	1850	(582;*484*)	1268	(263;484)	1005	(141;482)	864	(64;484)	800	(*29*;485)
11	784	(262;*168*)	523	(143;169)	380	(65;167)	315	(29;168)	286	(*14*;168)
12	354	(141;*56*)	213	(66;57)	147	(29;55)	118	(14;56)	104	(*7*;56)
13	156	(65;*21*)	91	(30;21)	62	(13;21)	48	(7;21)	42	(*4*;21)
14	70	(29;*8*)	41	(14;8)	27	(7;8)	21	(4;8)	17	(*2*;8)
15	33	(14;*3*)	19	(7;3)	12	(4;3)	9	(2;3)	7	(*1*;3)
16	16	(7;1)	9	(4;1)	6	(2;1)	4	(1;1)	3	(*0*;0)
17	8	(4;*0*)	5	(2;0)	3	(1;1)	2	(0;0)	1	(*0*;0)
18	4	(2;*0*)	2	(1;0)	1	(0;0)	1	(0;0)	1	(*0*;0)
19	2	(1;*0*)	1	(0;0)	1	(0;0)	0	(*0*;0)		
20	1	(0;*0*)	0	(0;0)	0	(*0*;0)				
21	0	(0;*0*)	0	(0;0)						
22	0	(0;*0*)	0	(*0*;0)						

[a]Energy differences in μhartree; see text for definitions.

TABLE 12. Results for P (^4S)[a]

	N_s									
	$N_p + 4$		$N_p + 5$		$N_p + 6$		$N_p + 7$		$N_p + 8$	
N_p	ΔE	(δs;δp)	ΔE	(δs;δp)	ΔE	(δs;δp)	ΔE	(δs;δp)	ΔE	(δs;δp)
7	39212	(8422;*16800*)	30791	(3675;16761)	27116	(1532;16969)	25584	(614;16958)	24970	(*280*;16971)
8	14030	(3883;*5000*)	10147	(1522;4968)	8626	(626;5021)	7999	(272;5031)	7727	(*150*;5040)
9	5179	(1574;*1530*)	3605	(637;1531)	2968	(281;1530)	2687	(148;1535)	2539	(*70*;1541)
10	2073	(636;*572*)	1437	(286;574)	1152	(153;572)	999	(71;573)	928	(*32*,574)
11	864	(284;*190*)	580	(154;190)	426	(72;189)	354	(32;189)	322	(*15*;189)
12	390	(153;*64*)	237	(73;64)	165	(32;63)	133	(15;64)	118	(*7*;64)
13	173	(72;*25*)	101	(32;25)	69	(15;24)	54	(7;24)	47	(*4*;24)
14	77	(32;*9*)	45	(15;9)	30	(7;9)	23	(4;9)	19	(*2*;9)
15	36	(15;*3*)	21	(7;3)	14	(4;3)	10	(2;3)	8	(*1*;3)
16	18	(7;*1*)	10	(4;1)	6	(2;1)	4	(1;1)	3	(*0*;1)
17	9	(4;*1*)	5	(2;1)	3	(1;1)	2	(0;1)	1	(*0*;1)
18	4	(2;*0*)	2	(1;0)	1	(0;0)	1	(0;0)	1	(*0*;0)
19	2	(1;*0*)	1	(0;0)	1	(0;0)	0	(*0*;0)		
20	1	(1;*0*)	1	(0;0)	0	(*0*;0)				
21	1	(0;*0*)	0	(*0*;0)						
22	0	(0;*0*)	0	(*0*;0)						

[a]Energy differences in μhartree; see text for definitions.

Can. J. Chem. Downloaded from www.nrcresearchpress.com by EESC ESCOLA DE ENGENHARIA on 09/08/12
For personal use only.

TABLE 13. Results for S (^3P)[a]

	N_s									
	N_p+4		N_p+5		N_p+6		N_p+7		N_p+8	
N_p	ΔE	(δs;δp)	ΔE	(δs;δp)	ΔE	(δs;δp)	ΔE	(δs;δp)	ΔE	(δs;δp)
7	46746	(9439;*21000*)	37307	(4103;20902)	33204	(1662;21034)	31542	(677;21091)	30866	(*310*;21105)
8	16405	(4234;*6100*)	12170	(1719;6094)	10451	(691;6105)	9761	(300;6116)	9461	(*170*;6128)
9	6076	(1730;*1950*)	4347	(702;1949)	3645	(312;1946)	3333	(163;1950)	3170	(*80*;1956)
10	2397	(699;*710*)	1698	(315;712)	1383	(169;709)	1214	(78;709)	1135	(*35*;710)
11	987	(313;*230*)	674	(169;230)	505	(80;229)	425	(35;229)	390	(*16*;229)
12	444	(168;*80*)	276	(79;81)	196	(35;80)	161	(16;80)	145	(*8*;80)
13	195	(79;*30*)	116	(35;30)	81	(16;30)	65	(8;30)	57	(*4*;30)
14	86	(35;*11*)	51	(16;11)	35	(8;11)	27	(4;11)	22	(*2*;11)
15	40	(16;*4*)	24	(8;4)	16	(4;4)	11	(2;4)	9	(*1*;4)
16	20	(8;*2*)	12	(4;2)	7	(2;2)	5	(1;2)	4	(*1*;2)
17	10	(4;*1*)	6	(2;1)	3	(1;1)	2	(1;1)	2	(*0*;1)
18	5	(2;*0*)	3	(1;0)	2	(1;0)	1	(0;0)	1	(*0*;0)
19	2	(1;*0*)	1	(1;0)	1	(0;0)	0	(*0*;0)		
20	1	(1;*0*)	1	(0;0)	0	(*0*;0)				
21	1	(0;*0*)	0	(*0*;0)						
22	0	(0;*0*)	0	(*0*;0)						

[a]Energy differences in μhartree; see text for definitions.

TABLE 14. Results for Cl (^2P)[a]

	N_s									
	N_p+4		N_p+5		N_p+6		N_p+7		N_p+8	
N_p	ΔE	(δs;δp)	ΔE	(δs;δp)	ΔE	(δs;δp)	ΔE	(δs;δp)	ΔE	(δs;δp)
7	54424	(10445;*25000*)	43979	(4575;25051)	39404	(1843;25126)	37561	(744;25178)	36817	(*340*;25195)
8	18928	(4651;*7300*)	14278	(1895;7277)	12383	(762;7280)	11621	(332;7292)	11289	(*180*;7306)
9	7000	(1898;*2380*)	5102	(773;2378)	4329	(346;2374)	3983	(180;2376)	3803	(*86*;2383)
10	2724	(769;*840*)	1956	(349;839)	1607	(187;836)	1420	(86;836)	1334	(*38*;837)
11	1117	(345;*270*)	771	(187;271)	584	(87;270)	497	(38;269)	459	(*18*;270)
12	500	(186;*97*)	314	(87;97)	227	(38;96)	189	(18;96)	171	(*9*;96)
13	218	(87;*36*)	131	(38;36)	93	(18;36)	75	(9;36)	66	(*5*;36)
14	95	(38;*13*)	57	(18;13)	39	(9;13)	31	(5;13)	26	(*2*;13)
15	44	(18;*5*)	27	(9;5)	18	(5;5)	13	(2;5)	10	(*1*;5)
16	22	(9;*2*)	13	(5;2)	8	(2;2)	6	(1;2)	4	(*1*;2)
17	11	(5;*1*)	6	(2;1)	4	(1;1)	2	(1;1)	2	(*0*;1)
18	5	(2;*0*)	3	(1;0)	2	(1;0)	1	(0;0)	1	(*0*;0)
19	3	(1;*0*)	1	(1;0)	1	(0;0)	1	(*0*;0)		
20	1	(1;*0*)	1	(0;0)	0	(*0*;0)				
21	1	(0;*0*)	0	(*0*;0)						
22	0	(0;*0*)	0	(*0*;0)						

[a]Energy differences in μhartree; see text for definitions.

TABLE 15. Results for Ar (^1S)[a]

	N_s									
	N_p+4		N_p+5		N_p+6		N_p+7		N_p+8	
N_p	ΔE	(δs;δp)	ΔE	(δs;δp)	ΔE	(δs;δp)	ΔE	(δs;δp)	ΔE	(δs;δp)
7	62571	(11573;*29400*)	50998	(5026;29370)	45972	(2024;29451)	43949	(822;29504)	43127	(*380*;29520)
8	21628	(5107;*8560*)	16521	(2077;8558)	14444	(837;8560)	13607	(370;8572)	13237	(*200*;8585)
9	7963	(2078;*2820*)	5885	(849;2818)	5035	(383;2813)	4652	(199;2815)	4454	(*95*;2823)
10	3066	(844;*965*)	2222	(385;968)	1838	(207;965)	1631	(94;964)	1537	(*42*;966)
11	1254	(381;*313*)	873	(206;314)	666	(95;312)	571	(42;312)	529	(*20*;312)
12	559	(205;*113*)	354	(95;113)	259	(42;112)	217	(20;112)	198	(*10*;112)
13	241	(95;*41*)	147	(42;41)	105	(19;41)	85	(10;41)	76	(*5*;41)
14	106	(42;*15*)	64	(19;15)	44	(10;15)	35	(5;15)	29	(*3*;15)
15	49	(19;*6*)	30	(10;6)	20	(5;6)	15	(3;6)	12	(*1*;6)
16	24	(10;*2*)	14	(5;2)	9	(3;2)	6	(1;2)	5	(*1*;2)
17	12	(5;*1*)	7	(3;1)	4	(1;1)	3	(1;1)	2	(*0*;1)
18	6	(3;*0*)	3	(1;0)	2	(1;0)	1	(0;0)	1	(*0*;0)
19	3	(1;*0*)	2	(1;0)	1	(0;0)	1	(*0*;0)		
20	1	(1;*0*)	1	(0;0)	0	(*0*;0)				
21	1	(0;*0*)	0	(*0*;0)						
22	0	(0;*0*)	0	(*0*;0)						

[a]Energy differences in μhartree; see text for definitions.

Can. J. Chem. Downloaded from www.nrcresearchpress.com by EESC ESCOLA DE ENGENHARIA on 09/08/12
For personal use only.

TABLE 16. Comparison of total energies (in hartree) and total energy errors (in mhartree) for Al–Ar[a]

Atom	E_T (this work)	ΔE_1[a]	E_T (Huzinaga)	ΔE_2[b]
		Basis (11.7)		
Al (^2P)	−241.850796	−4.75	−241.85555	−21.16
Si (^3P)	−288.821509	−8.53	−288.83004	−24.32
P (^4P)	−340.679568	−9.91	−340.68948	−29.30
S (^3P)	−397.458150	−10.45	−397.46860	−36.30
Cl (^2P)	−459.427648	−10.74	−459.43839	−43.68
Ar (^1S)	−526.754941	−10.00	−526.76494	−52.57
		Basis (12.8)		
Al (^2P)	−241.865993	−2.38	−241.86837	−8.34
Si (^3P)	−288.842000	−3.02	−288.84502	−9.34
P (^4P)	−340.704751	−3.15	−340.70790	−10.88
S (^3P)	−397.488491	−2.52	−397.49101	−13.89
Cl (^2P)	−459.463144	−1.48	−459.46462	−17.45
Ar (^1S)	−526.795884	−0.56	−526.79644	−21.07

[a]$\Delta E_1 = E_T$ (Huzinaga) − E_T (this work).
[b]$\Delta E_2 = E_T$ (Hartree–Fock) − E_T (Huzinaga).

TABLE 17. Recommended combinations of compatible basis sets[a]

	Error in total energy (in μhartree)				
Atom	10000	1000	100	10	1
H (^2S)	—	$(4)_{0.7}$	$(6)_{0.5}$	$(8)_{0.6}$	$(10)_{0.7}$
He (^1S)	—	—	—	$(10)_{0.7}$	$(13)_{0.5}$
Li (^2S)	—	$(9)_{0.6}$	$(11)_{1.0}$	$(14)_{0.8}$	$(17)_{0.7}$
Be (^1S)	—	$(10)_{0.5}$	$(12)_{0.8}$	$(15)_{0.7}$	$(18)_{0.7}$
B (^2P)	—	$(11.5)_{0.6}$	$(13.7)_{0.7}$	$(16.8)_{1.0}$	$(18.11)_{1.0}$
C (^3P)	$(8.4)_{1.1}$	$(11.6)_{0.7}$	$(14.8)_{0.5}$	$(16.9)_{1.2}$	$(19.11)_{1.0}$
N (^4S)	$(9.5)_{0.6}$	$(11.6)_{1.2}$	$(14.8)_{0.9}$	$(16.10)_{1.2}$	$(19.12)_{1.0}$
O (^3P)	$(9.5)_{0.9}$	$(12.7)_{0.6}$	$(15.9)_{0.5}$	$(17.10)_{1.4}$	$(20.13)_{1.0}$
F (^2P)	$(10.6)_{0.4}$	$(12.7)_{0.9}$	$(15.9)_{0.8}$	$(18.11)_{0.8}$	$(20.13)_{1.0}$
Ne (^1S)	$(10.6)_{0.6}$	$(13.8)_{0.4}$	$(15.10)_{0.6}$	$(18.12)_{0.7}$	$(20.14)_{1.0}$
Al (^2P)	$(13.9)_{0.4}$	$(15.10)_{1.1}$	$(18.13)_{0.8}$	$(21.15)_{1.2}$	$(24.18)_{1.0}$
Si (^3P)	$(13.9)_{0.5}$	$(16.11)_{0.5}$	$(18.13)_{0.9}$	$(22.15)_{0.9}$	$(24.18)_{1.0}$
P (^4S)	$(13.9)_{0.5}$	$(16.11)_{0.6}$	$(18.13)_{1.0}$	$(22.15)_{1.0}$	$(24.18)_{1.0}$
S (^3P)	$(13.9)_{0.6}$	$(16.11)_{0.7}$	$(19.14)_{0.5}$	$(22.16)_{0.7}$	$(25.18)_{1.0}$
Cl (^2P)	$(13.9)_{0.7}$	$(16.11)_{0.8}$	$(19.14)_{0.6}$	$(22.16)_{0.8}$	$(25.18)_{1.0}$
Ar (^1S)	$(13.9)_{0.8}$	$(16.11)_{0.9}$	$(19.14)_{0.6}$	$(22.16)_{0.9}$	$(25.18)_{1.0}$

[a]The subscript in the basis set label multiplied by the first entry in the column gives the actual total energy error.

mainly due to the inadequate expansion of the p space. Similarly, for the calculations on boron chloride, the (9.5) basis set of boron should be matched with chlorine's (14.10) basis set. The sets of matching basis sets with similar total energy errors (external balance) are suggested in Table 17 (the basis sets selected show approximate internal balance). For the selected basis sets, the parameters in the generator formula of eq. [4] are collected in Tables 18–22. The detailed tables containing the results of atomic calculations for these basis sets are available as supplementary material.[2]

For each atom, there is a number of basis sets exhibiting sub-μhartree accuracy in the total energy; choosing any of them for molecular calculations should give identical answers. However, for reasons of computational economy (if that notion may be brought up when discussing basis sets of the very large size required to reach sub-μhartree accuracy), one may select, for e.g. fluorine, the (22.14) basis set rather than (21.17). The matching basis sets may be useful in the studies of convergence of results of molecular computations, thus enabling conducting the first-principles, *ab initio*, calculations to their basis-set limit, *ad limitem*.

The performance of the internally balanced basis sets which also provide external energy balance can be ultimately evaluated only in molecular calculations. For the calculations on molecules, however, we need to study the contraction schemes for the primitive basis sets (the most efficient being the general contraction scheme (11)) and to investigate the polarization functions. Such work is now in progress.

[2]This supplementary material can be purchased from: The Depository of Unpublished Data, Document Delivery, CISTI, National Research Council Canada, Ottawa, ON K1A 0S2, Canada.

Can. J. Chem. Downloaded from www.nrcresearchpress.com by EESC ESCOLA DE ENGENHARIA on 09/08/12
For personal use only.

TABLE 18. Parameters of basis sets with total energy error of 10000 μhartrees[a]

Atom	Basis[b]	l[c]	P1	P2	P3	P4	P5
C (^3P)	(8.4)	*s*:	−1.31930379	5.66398187D-1	1.18937344D-3	−5.18921808D-3	6.57158651D-4
		p:	−1.40108934	5.92099530D-1	−1.48161822D-3	−1.03996272D-2	2.72351501D-3
N (^4S)	(9.5)	*s*:	−1.19504978	5.41905619D-1	−1.07646889D-3	−3.96599750D-3	4.69703340D-4
		p:	−1.29589229	5.45541927D-1	−7.26088276D-3	−5.22623232D-3	1.32650076D-3
O (^3P)	(9.5)	*s*:	−1.07526836	5.49348748D-1	−4.22751553D-3	−3.52082094D-3	4.49012699D-4
		p:	−1.22393756	5.65067040D-1	−3.10364131D-3	−8.01629453D-3	1.62566027D-3
F (^2P)	(10.6)	*s*:	−0.99479483	5.39782911D-1	−1.43114969D-2	−1.22742421D-3	2.54796155D-4
		p:	−1.18389612	5.31455428D-1	−7.38722226D-3	−4.77447430D-3	9.23101000D-4
Ne (^1S)	(10.6)	*s*:	−0.90446901	5.45148221D-1	−1.62249909D-2	−9.77783290D-4	2.43890414D-4
		p:	−1.10344893	5.41531785D-1	−8.49583104D-3	−4.98340430D-3	9.53138538D-4
Al (^2P)	(13.9)	*s*:	−1.66079484	5.52972250D-1	−1.86875738D-2	−7.65291722D-6	8.73696335D-5
		p:	−1.81850998	5.87395347D-1	−1.77964630D-2	−2.39366659D-3	3.47365532D-4
Si (^3P)	(13.9)	*s*:	−1.51446817	5.36659962D-1	−1.75387657D-2	−2.77326718D-6	8.54469859D-5
		p:	−1.62852860	5.23885780D-1	−2.40028501D-3	−4.13061551D-3	4.20629783D-4
P (^4S)	(13.9)	*s*:	−1.39660199	5.26260070D-1	−1.68718685D-2	−5.47549141D-7	8.45938867D-5
		p:	−1.49443424	5.05698003D-1	−1.36684218D-3	−3.99783807D-3	4.08758680D-4
S (^3P)	(13.9)	*s*:	−1.29703857	5.18747761D-1	−1.64130982D-2	7.53346747D-8	8.41551005D-5
		p:	−1.44681502	5.31406133D-1	−1.13380024D-2	−2.63377440D-3	3.46179840D-4
Cl (^2P)	(13.9)	*s*:	−1.21038081	5.13496995D-1	−1.61783184D-2	6.89454574D-6	8.37924582D-5
		p:	−1.37956112	5.39392138D-1	−1.63093673D-2	−1.85746514D-3	3.08244045D-4
Ar (^1S)	(13.9)	*s*:	−1.13288473	5.09029380D-1	−1.58917907D-2	−1.50529577D-6	8.40949802D-5
		p:	−1.30774496	5.39735167D-1	−1.86574408D-2	−1.43199055D-3	2.86450280D-4

[a]See eq. [4] for the definition of parameters.
[b]The notation (N_s·N_p) is used to represent a basis set with N_s *s*-type and N_p *p*-type uncontracted functions.
[c]Angular symmetry parameter.

TABLE 19. Parameters of basis sets with total energy error of 1000 μhartrees[a]

Atom	Basis	l	P1	P2	P3	P4	P5
H (^2S)	(4)	*s*:	−1.42084943	4.72864154D-1	4.30035601D-2	−1.15529468D-2	2.71493622D-3
Li (^2S)	(9)	*s*:	−1.94186004	4.70375737D-1	2.52156098D-2	−7.33068845D-3	6.13866200D-4
Be (^1S)	(10)	*s*:	−1.72869079	4.84844177D-1	6.48330016D-3	−3.92192975D-3	3.69974179D-4
B (^2P)	(11.5)	*s*:	−1.52371805	4.56895517D-1	7.47370817D-7	−2.02835890D-3	2.18712793D-4
		p:	−1.61941141	5.13887185D-1	−5.57246592D-3	−3.09675150D-3	1.05341804D-3
C (^3P)	(11.6)	*s*:	−1.36151236	4.71574863D-1	−4.45484407D-3	−1.53695775D-3	2.00442395D-4
		p:	−1.47088067	4.81968487D-1	−4.95774410D-3	−2.78303983D-3	6.93786783D-4
N (^4S)	(11.6)	*s*:	−1.22715113	4.80464601D-1	−7.01461497D-3	−1.26115911D-3	1.90292187D-4
		p:	−1.33175505	4.96091610D-1	−6.60989534D-3	−3.17331569D-3	7.49089533D-4
O (^3P)	(12.7)	*s*:	−1.12109648	4.54900069D-1	−5.21046542D-3	−1.12568783D-3	1.48119555D-4
		p:	−1.29458102	4.70612090D-1	−3.11090797D-3	−3.44614892D-3	5.75338323D-4
F (^2P)	(12.7)	*s*:	−1.02112404	4.61971438D-1	−7.16946626D-3	−9.21960600D-4	1.40940593D-4
		p:	−1.21920846	4.89768693D-1	−7.21543316D-3	−3.12275061D-3	5.68176350D-4
Ne (^1S)	(13.8)	*s*:	−0.94364991	4.47093018D-1	−7.14872367D-3	−7.42779488D-4	1.10450374D-4
		p:	−1.16990880	4.60179865D-1	−5.47963608D-3	−2.64707020D-3	4.07359665D-4
Al (^2P)	(15.10)	*s*:	−1.66892129	5.08864776D-1	−1.52879298D-2	−2.73828869D-5	5.78342360D-5
		p:	−1.83488131	5.53326710D-1	−1.68185619D-2	−1.73538222D-3	2.48464651D-4
Si (^3P)	(16.11)	*s*:	−1.53229686	4.65306542D-1	−1.25032911D-2	−2.01329110D-6	4.48695910D-5
		p:	−1.67644885	4.50907227D-1	−3.30062737D-3	−2.05072231D-3	1.94906835D-4
P (^4S)	(16.11)	*s*:	−1.41635792	4.58435293D-1	−1.22008985D-2	−1.57677372D-6	4.47775623D-5
		p:	−1.54737393	4.37972834D-1	−2.61345416D-3	−1.99338325D-3	1.90280888D-4
S (^3P)	(16.11)	*s*:	−1.32137170	4.53005473D-1	−1.19688835D-2	−1.36441855D-6	4.47432767D-5
		p:	−1.49429204	4.50785931D-1	−6.23892622D-3	−1.61589338D-3	1.76811941D-4
Cl (^2P)	(16.11)	*s*:	−1.23696576	4.47627902D-1	−1.16823460D-2	−1.04421060D-6	4.45235830D-5
		p:	−1.42398206	4.54075770D-1	−7.75399653D-3	−1.45714330D-3	1.71750123D-4
Ar (^1S)	(16.11)	*s*:	−1.16081191	4.43035472D-1	−1.14398796D-2	8.60800506D-8	4.42875580D-5
		p:	−1.35163810	4.55691800D-1	−9.22552396D-3	−1.27042494D-3	1.64701148D-4

[a]See Table 18 for notation.

Can. J. Chem. Downloaded from www.nrcresearchpress.com by EESC ESCOLA DE ENGENHARIA on 09/08/12
For personal use only.

TABLE 20. Parameters of basis sets with total energy error of 100 μhartrees[a]

Atom	Basis	*l*	P1	P2	P3	P4	P5
H (^2S)	(6)	*s*:	−1.49266972	4.45075832D-1	2.99488504D-3	−5.50547520D-4	5.79154953D-4
Li (^2S)	(11)	*s*:	−1.95613426	4.15012087D-1	1.30457355D-2	−3.49980125D-3	2.74500161D-4
Be (^1S)	(12)	*s*:	−1.74054810	3.98074871D-1	1.19989984D-2	−2.98248274D-3	2.14847517D-4
B (^2P)	(13.7)	*s*:	−1.54448519	4.15637003D-1	3.70622166D-4	−1.39915643D-3	1.29779822D-4
		p:	−1.67190340	4.21749195D-1	5.94460118D-5	−2.01227871D-3	4.18974226D-4
C (^3P)	(14.8)	*3*:	−1.39211293	4.06835583D-1	−2.05429714D-3	−9.68704649D-4	9.69939064D-5
		p:	−1.52819384	4.14648861D-1	−3.37703651D-3	−1.54017263D-3	3.02812620D-4
N (^4S)	(14.8)	*s*:	−1.25910821	4.14141899D-1	−3.77861396D-3	−8.19279852D-4	9.26292733D-5
		p:	−1.39528922	4.35748571D-1	−9.34606711D-3	−8.71666431D-4	2.75575823D-4
O (^3P)	(15.9)	*s*:	−1.16190945	4.03341362D-1	−6.14899617D-3	−3.46895533D-4	6.16821086D-5
		p:	−1.35269515	4.14067479D-1	−3.67126247D-3	−1.77061510D-3	2.61838527D-4
F (^2P)	(15.9)	*s*:	−1.06321936	4.08020606D-1	−6.91585926D-3	−3.02562311D-4	6.08983107D-5
		p:	−1.27477710	4.21335095D-1	−3.14990970D-3	−2.08125824D-3	2.83273026D-4
Ne (^1S)	(15.10)	*s*:	−0.97395621	4.07597876D-1	−6.25673673D-3	−4.02548184D-4	6.48460803D-5
		p:	−1.22171073	4.01275927D-1	−2.38212972D-3	−1.80295979D-3	2.15836859D-4
Al (^2P)	(18.13)	*s*:	−1.68412045	3.97726264D-1	−9.41518179D-4	−7.84754793D-4	5.14124047D-5
		p:	−1.87596260	4.25561901D-1	−3.40161306D-3	−1.49264683D-3	1.22580451D-4
Si (^3P)	(18.13)	*s*:	−1.55020122	4.05832878D-1	−5.50059829D-3	−3.19362685D-4	3.77376608D-5
		p:	−1.71660353	4.14432784D-1	−4.94671434D-3	−1.14290459D-3	1.07251779D-4
P (^4P)	(18.13)	*s*:	−1.43603356	4.04524753D-1	−6.75905725D-3	−1.70469187D-4	3.32019329D-5
		p:	−1.59063938	4.07626383D-1	−6.03154576D-3	−9.20890130D-4	9.79183678D-5
S (^3P)	(19.14)	*s*:	−1.35280221	3.95285486D-1	−7.37813911D-3	−6.70895029D-5	2.61794197D-5
		p:	−1.55720736	3.92458291D-1	−6.78406358D-3	−6.02856097D-4	7.13133136D-5
Cl (^2P)	(19.14)	*s*:	−1.27051882	3.93440116D-1	−7.45681393D-3	−5.83500562D-5	2.60694000D-5
		p:	−1.48761695	3.92658791D-1	−6.89617355D-3	−6.19317714D-4	7.27555912D-5
Ar (^1S)	(19.14)	*s*:	−1.19498195	3.91293121D-1	−7.42014176D-3	−5.87256709D-5	2.61752595D-5
		p:	−1.41556967	3.91414220D-1	−6.94221058D-3	−6.23546731D-4	7.33844421D-5

[a]See Table 18 for notation.

TABLE 21. Parameters of basis sets with total energy error of 10 μhartrees[a]

Atom	Basis	*l*	P1	P2	P3	P4	P5
H (^2S)	(8)	*s*:	−1.53265016	3.95897978D-1	2.48088530D-4	7.54639679D-5	2.26258442D-4
He (^1S)	(10)	*s*:	−1.25182630	3.85378033D-1	5.36105406D-3	−1.66791971D-3	2.20695411D-4
Li (^2S)	(14)	*s*:	−1.98277720	3.52047244D-1	1.25815702D-2	−2.35229919D-3	1.40357532D-4
Be (^1S)	(15)	*s*:	−1.77950235	3.59142632D-1	4.08347685D-3	−1.21819088D-3	8.66374470D-5
B (^2P)	(16.8)	*s*:	−1.58239013	3.60879384D-1	5.04704545D-4	−7.86791976D-4	6.35449793D-5
		p:	−1.69824249	3.95012127D-1	8.77295242D-4	−1.80847345D-3	3.04080421D-4
C (^3P)	(16.9)	*s*:	−1.42174411	3.73999536D-1	−2.82266178D-3	−4.79618689D-4	5.42552069D-5
		p:	−1.55131923	3.85190370D-1	−5.60243315D-4	−1.60775735D-3	2.36323155D-4
N (^4S)	(16.10)	*s*:	−1.28844800	3.80079568D-1	−4.26826387D-3	−3.43335370D-4	4.99836731D-5
		p:	−1.44016264	3.73447934D-1	−1.92276517D-3	−1.23193055D-3	1.74076656D-4
O (^3P)	(17.10)	*s*:	−1.19070170	3.76329882D-1	−4.98031447D-3	−2.65879834D-4	4.15548389D-5
		p:	−1.38003866	3.98948942D-1	−6.73301063D-3	−8.68513685D-4	1.65102861D-4
F (^2P)	(18.11)	*s*:	−1.10461200	3.71736238D-1	−5.77983092D-3	−1.57146899D-4	3.30425310D-5
		p:	−1.32320957	3.74626576D-1	−1.86539633D-3	−1.37225564D-3	1.55335347D-4
Ne (^1S)	(18.12)	*s*:	−1.01833179	3.74164172D-1	−6.11053942D-3	−1.40388439D-4	3.27617896D-5
		p:	−1.26898936	3.60440915D-1	−1.79140275D-3	−1.14787830D-3	1.20201170D-4
Al (^2P)	(21.15)	*s*:	−1.71227939	3.80342400D-1	−6.15867773D-3	−8.95089572D-5	1.99024146D-5
		p:	−1.91561087	3.94832222D-1	−7.32670746D-3	−4.41456650D-4	5.46093663D-5
Si (^3P)	(22.15)	*s*:	−1.59061078	3.58746850D-1	−5.64801827D-3	−2.53626971D-5	1.52282628D-5
		p:	−1.75756275	3.86512602D-1	−8.06898854D-3	−2.84895851D-4	4.86637280D-5
P (^4S)	(22.15)	*s*:	−1.47755327	3.52412171D-1	−5.31738698D-3	−2.55843692D-5	1.49975979D-5
		p:	−1.63160261	3.79239606D-1	−7.83160486D-3	−2.72955358D-4	4.81226449D-5
S (^3P)	(22.16)	*s*:	−1.39173654	3.52314264D-1	−5.46183718D-3	−2.60257387D-5	1.52732711D-5
		p:	−1.59297701	3.65421599D-1	−6.84897500D-3	−3.11149921D-4	4.28810627D-5
Cl (^2P)	(22.16)	*s*:	−1.31255355	3.51109548D-1	−5.54564930D-3	−2.03987870D-5	1.52359539D-5
		p:	−1.52458706	3.65138523D-1	−7.08395698D-3	−2.93383409D-4	4.25770236D-5
Ar (^1S)	(22.16)	*s*:	−1.23898301	3.48764829D-1	−5.43819495D-3	−2.33082775D-5	1.52990187D-5
		p:	−1.45391884	3.63095335D-1	−6.91396267D-3	−3.14804699D-4	4.35395787D-5

[a]See Table 18 for notation.

Can. J. Chem. Downloaded from www.nrcresearchpress.com by EESC ESCOLA DE ENGENHARIA on 09/08/12
For personal use only.

TABLE 22. Parameters of basis sets with total energy error of 1 μhartree[a]

Atom	Basis	l	P1	P2	P3	P4	P5
H (^2S)	(10)	s:	−1.56672499	3.60505862D-1	3.94108625D-4	−1.64110825D-5	1.32861210D-4
He (^1S)	(13)	s:	−1.30101633	3.32407390D-1	6.44907537D-3	−1.33647126D-3	1.16623076D-4
Li (^2S)	(17)	s:	−2.02612765	3.24830213D-1	4.52305567D-3	−9.08448791D-4	5.61972822D-5
Be (^1S)	(18)	s:	−1.81234732	3.29799515D-1	2.95794950D-3	−8.18787982D-4	4.96597038D-5
B (^2P)	(18.11)	s:	−1.60602838	3.54621179D-1	−4.34590560D-3	−1.27389841D-4	2.94904829D-5
		p:	−1.76851834	3.41159165D-1	−1.65161321D-3	−6.98595495D-4	1.10893721D-4
C (^3P)	(19.11)	s:	−1.45562901	3.51946256D-1	−5.00485661D-3	−9.39582097D-5	2.55754538D-5
		p:	−1.59651261	3.43044601D-1	−1.91498219D-3	−5.53825272D-4	9.91681004D-5
N (^4S)	(19.12)	s:	−1.32364683	3.53883232D-1	−5.04870386D-3	−1.03967796D-4	2.59967216D-5
		p:	−1.48531860	3.37659034D-1	−2.53575574D-3	−5.59883621D-4	8.55910796D-5
O (^3P)	(20.13)	s:	−1.22825362	3.43841147D-1	−4.40356015D-3	−1.29232280D-4	2.32735968D-5
		p:	−1.44222877	3.33531670D-1	−2.24666578D-3	−6.41766258D-4	7.69281767D-5
F (^2P)	(20.13)	s:	−1.13344272	3.48734356D-1	−4.97280763D-3	−1.13991429D-4	2.34011174D-5
		p:	−1.36771423	3.39776763D-1	−2.18214379D-3	−7.51665490D-4	8.30647783D-5
Ne (^1S)	(20.14)	s:	−1.04759384	3.47089289D-1	−4.55342898D-3	−1.44927791D-4	2.40984536D-5
		p:	−1.31104259	3.28021360D-1	−1.96345402D-3	−6.47030906D-4	6.63836494D-5
Al (^2P)	(24.18)	s:	−1.74750484	3.45733567D-1	−4.77157447D-3	−3.98613877D-5	1.18270291D-5
		p:	−1.95594166	3.34306876D-1	−3.83223502D-3	−2.63959442D-4	2.67698825D-5
Si (^3P)	(24.18)	s:	−1.61117197	3.42004922D-1	−4.87238717D-3	−2.65782885D-5	1.16049504D-5
		p:	−1.80336758	3.33661259D-1	−4.47323989D-3	−2.56517610D-4	2.81076377D-5
P (^4S)	(24.18)	s:	−1.49885148	3.40201823D-1	−4.97346023D-3	−2.74784593D-5	1.18659876D-5
		p:	−1.68128885	3.28614547D-1	−4.38291584D-3	−2.55394706D-4	2.82768696D-5
S (^3P)	(25.18)	s:	−1.42156725	3.34961375D-1	−4.97189133D-3	−3.30921027D-5	1.10009093D-5
		p:	−1.62687808	3.38573872D-1	−6.07792341D-3	−1.64620663D-4	2.68512809D-5
Cl (^2P)	(25.18)	s:	−1.34339184	3.33574098D-1	−5.08648930D-3	−2.31174642D-5	1.08204679D-5
		p:	−1.55793764	3.38779518D-1	−6.09624708D-3	−1.81065248D-4	2.77204066D-5
Ar (^1S)	(25.18)	s:	−1.27042346	3.31288154D-1	−4.96227119D-3	−3.16963655D-5	1.10621190D-5
		p:	−1.48773228	3.33365095D-1	−5.00820870D-3	−2.81339650D-4	3.07186810D-5

[a]See Table 18 for notation.

Can. J. Chem. Downloaded from www.nrcresearchpress.com by EESC ESCOLA DE ENGENHARIA on 09/08/12
For personal use only.

Acknowledgments

Grant of computer time on the workstation IBM RS/6000 model 580, hosted by the Computing and Network Services of the University of Alberta, is gratefully acknowledged. This work was partly supported by a grant from Natural Sciences and Engineering Research Council of Canada. The comments of Professor Huzinaga during a discussion of the present results are much appreciated.

1. S. Huzinaga, M. Klobukowski, and H. Tatewaki. Can. J. Chem. **63**, 1812 (1985).
2. M. Klobukowski and S. Huzinaga. Edited by V.H. Smith, Jr. et al. Applied quantum chemistry, Reidel, Dordrecht. 1986.
3. S. Huzinaga and M. Klobukowski. J. Mol. Struct. THEOCHEM, **167**, 1 (1988).
4. T.W. Dingle, S. Huzinaga, and M. Klobukowski. J. Comput. Chem. **10**, 753 (1989).
5. M. Klobukowski, T.W. Dingle, and S. Huzinaga. Theoret. Chim. Acta, **77**, 191 (1990).
6. M.W. Schmidt, K.K. Baldridge, J.A. Boatz, J.H. Jensen, S. Koseki, M.S. Gordon, K.A. Nguyen, T.L. Windus, and S.T. Elbert. QCPE Bull. **10**, 52 (1990).
7. M. Dupuis, J.D. Watts, H.O. Villar, and G.J.B. Hurst. QCPE Program No. 544, QCPE Bull. **8**, 79 (1988); M. Dupuis, A. Farazdel, S.P. Karna, and S.A. Maluendes. In MOTECC: Modern techniques in computational chemistry, ESCOM. Edited by E. Clementi. Leiden, 1990. Chap. 2.
8. M.J. Frisch, M. Head-Gordon, G.W. Trucks, J.B. Foresman, H.B. Schlegel, K. Raghavachari, M.A. Robb, J.S. Binkley, C. Gonzalez, D.J. DeFrees, D.J. Fox, R.A. Whiteside, R. Seeger, C.F. Melius, J. Baker, R.L. Martin, L.R. Kahn, J.J.P. Stewart, S. Topiol, and J.A. Pople. GAUSSIAN 90. Gaussian, Inc., Pittsburgh PA. 1990.
9. C.M. Reeves. J. Chem. Phys. **39**, 1 (1963); C.M. Reeves and M.C. Harrison. J. Chem. Phys. **39**, 11 (1963).
10. K. Ruedenberg, R.C. Raffenetti, and R.D. Bardo. Energy, structure and reactivity. Edited by D.W. Smith. Proceedings of the 1972 Boulder Seminar Research Conference on Theoretical Chemistry. Wiley, New York. 1972.
11. R.C. Raffenetti. J. Chem. Phys. **59**, 5936 (1973).
12. R.D. Bardo and K. Ruedenberg. J. Chem. Phys. **59**, 5956 (1973).
13. R.D. Bardo and K. Ruedenberg. J. Chem. Phys. **59**, 5966 (1973).
14. R.C. Raffenetti and K. Ruedenberg. J. Chem. Phys. **59**, 5978 (1973).
15. D.F. Feller and K. Ruedenberg. Theoret. Chim. Acta, **52**, 231 (1979).
16. M.W. Schmidt and K. Ruedenberg. J. Chem. Phys. **71**, 3951 (1979).
17. S. Huzinaga and B. Miguel. Chem. Phys. Lett. **175**, 289 (1990).
18. S. Huzinaga and M. Klobukowski. Chem. Phys. Lett. **212**, 260 (1993); S. Huzinaga, B. Miguel, and M. Klobukowski. Well-tempered Gaussian basis sets. Department of Chemistry, University of Alberta. 1993 (unpublished).
19. S. Wilson. In Theoretical chemistry. Vol. 4. A Specialist Periodical Report, The Royal Society of Chemistry, London. 1981. p. 1.
20. H. Partridge. J. Chem. Phys. **87**, 6643 (1987); NASA Technical Memorandum 89449.
21. H. Partridge. J. Chem. Phys. **90**, 1043 (1989); NASA Technical Memorandum 101044.
22. E. Clementi and G. Corongiu. Geometrical basis sets for molecular computations. Report Pok-11, IBM, Poughkeepsie, NY. 1982; Chem. Phys. Lett. **90** 359 (1982); E. Clementi, G. Corongiu, M. Gratarola, P. Habitz, C. Lupo, P. Otto, and D. Vercauteren. Int. J. Quantum Chem. Symp. **16**, 409 (1982).
23. E. Clementi, S.J. Chakravorty, G. Corongiu, J.R. Flores, and V.

Sonnad. In Modern techniques in computational chemistry, ESCOM. Edited by E. Clementi. Leiden, 1991. Chap. 2.
24. T.H. Dunning, Jr. and P.J. Hay. In Methods of electronic structure theory. Edited by H.F. Schaefer III. Plenum, New York. 1977.
25. S. Wilson. In Methods in computational molecular physics. Edited by G.H.F. Diercksen and S. Wilson Reidel, Dordrecht. 1983.
26. S. Huzinaga. Comput. Phys. Rep. **2**, 281 (1985).
27. E.R. Davidson and D. Feller. Chem. Rev. **86**, 681 (1986).
28. S. Wilson. Adv. Chem. Phys. **LXVII**, 439 (1987).
29. D. Feller and E.R. Davidson. In Reviews in computational chemistry. Vol. 1. Edited by K.B. Lipkowitz and D.B. Boyd. VCH Publishers, New York. 1990.
30. R.S. Mulliken. J. Chem. Phys. **36**, 3428 (1962).
31. E. Clementi and H. Popkie. J. Chem. Phys. **57**, 1077 (1972).
32. C.M. Schwarz. Meth. Comput. Phys. **2**, 241 (1963).
33. S. Wilson. Theoret. Chim. Acta, **57**, 53 (1980).
34. D.M. Silver, S. Wilson, and W.C. Nieuwpoort. Int. J. Quantum. Chem. **14**, 635 (1978); D.M. Silver and W.C. Nieuwpoort. Chem. Phys. Lett. **57**, 421 (1978); S. Wilson and D.M. Silver. J. Chem. Phys. **69**, 3787 (1978).
35. M. Klobukowski. Chem. Phys. Lett. **214**, 166 (1993).
36. W.H. Preuss, S.A. Teukolsky, W.T. Vetterling, and B.P. Flannery. Numerical recipes in FORTRAN: the art of scientific computing. 2nd ed. Cambridge University Press, Cambridge. 1992.
37. P.G. Mezey and E.-C. Hass. J. Comput. Chem. **4**, 482 (1983).
38. R.P. Brent. Algorithms for minimization without derivatives. Prentice-Hall, Englewood Cliffs, NJ. 1973.
39. C. Froese-Fisher. Comp. Phys. Commun. **14**, 145 (1978).
40. O. Matsuoka and K. Okamura. Bull. Univ. Electro-Comm. **2**, 313 (1989). H. Yamamoto and O. Matsuoka. Bull. Univ. Electro-Comm. **5**, 23 (1992).
41. S. Huzinaga. J. Chem. Phys. **42**, 1293 (1965); S. Huzinaga. Approximate atomic functions. Part I. Department of Chemistry, University of Alberta. 1971 (Unpublished).
42. S. Huzinaga. Approximate atomic functions. Part II. Department of Chemistry, University of Alberta. 1971 (Unpublished).

Can. J. Chem. Downloaded from www.nrcresearchpress.com by EESC ESCOLA DE ENGENHARIA on 09/08/12
For personal use only.

A ^{139}La NMR study of the interactions between the La(III) cation and D-ribose in aqueous solution

ZHIGANG CHEN

Ottawa-Carleton Chemistry Institute, University of Ottawa Campus, Ottawa, ON K1N 6N5, Canada

NICOLE MOREL-DESROSIERS AND JEAN-PIERRE MOREL[1]

Laboratoire de Chimie Physique des Solutions, U.R.A. au C.N.R.S. n° 434, Université Blaise Pascal (Clermond-Ferrand II), F-63177 Aubière Cedex, France

AND

CHRISTIAN DETELLIER[2]

Ottawa-Carleton Chemistry Institute, University of Ottawa Campus, Ottawa, ON K1N 6N5, Canada

Received February 11, 1994

ZHIGANG CHEN, NICOLE MOREL-DESROSIERS, JEAN-PIERRE MOREL, and CHRISTIAN DETELLIER. Can. J. Chem. **72**, 1753 (1994).

The interactions of the La(III) cation with D-ribose and with D-arabinose in aqueous solution were investigated by ^{139}La NMR spectroscopy. In the case of D-ribose, the formation of a La(III)–sugar complex was indicated by variations of the ^{139}La chemical shift and linewidth with an increase of the sugar concentration in solution. In contrast, the complexation of La(III) by arabinose is very weak and almost undetectable by ^{139}La NMR. On the basis of a 1:1 stoichiometry, the stability constant for the complex of La(III) with D-ribose was calculated from the observed ^{139}La chemical shift values. A similar treatment was done for the viscosity corrected ^{139}La linewidths using arabinose as an uninteractive reference. The stability constants, K, obtained independently from ^{139}La chemical shifts and linewidths are in good agreement, 2.8 ± 0.5 and 2.2 ± 0.6 M^{-1} respectively at 299.0 ± 0.5 K. The thermodynamic parameters for the complexation of La(III) by D-ribose could also be obtained: $\Delta H^0 = -12 \pm 2$ kJ mol^{-1}, and $\Delta S^0 = -31 \pm 5$ J K^{-1} mol^{-1}. These values are in very good agreement with those obtained by calorimetric measurements.

ZHIGANG CHEN, NICOLE MOREL-DESROSIERS, JEAN-PIERRE MOREL et CHRISTIAN DETELLIER. Can. J. Chem. **72**, 1753 (1994).

On a étudié par résonance magnétique nucléaire du ^{139}La les interactions du cation La(III) avec le D-ribose et avec le D-arabinose en solution aqueuse. Dans le cas du D-ribose, la formation d'un complexe La(III)-sucre fut mise en évidence par les variations des déplacements chimiques et largeurs de raie du ^{139}La lors d'un accroissement de la concentration du sucre dans la solution. Au contraire, la complexation du La(III) par l'arabinose est très faible et presque indétectable par RMN du ^{139}La. Sur la base d'une stoechiométrie 1:1, à partir des valeurs des déplacements chimiques du ^{139}La, on a calculé la constante de stabilité du complexe de La(III) avec le D-ribose. Une approche similaire a été utilisée dans le cas des largeurs de raie corrigées pour la viscosité, en se servant de l'arabinose comme d'une référence non interagissante. Les constantes de stabilité obtenues indépendamment à partir des deux séries de mesure sont en bon accord: 2,8 ± 0,5 et 2,2 ± 0,6 M^{-1} à 299,0 ± 0,5 K. Les paramètres thermodynamiques caractérisant la complexation du La(III) par le D-ribose ont pu aussi être obtenus: $\Delta H^0 = -12 \pm 2$ kJ mol^{-1}, et $\Delta S^0 = -31 \pm 5$ J K^{-1} mol^{-1}. Ces valeurs sont en bon accord avec celles obtenues par mesures calorimétriques.

Introduction

The formation of complexes between carbohydrates and metal cations in solution, topic reviewed by Angyal (1), has been of interest for a long time. The interaction between sugars and metal cations is weak: only those sugars (or isomers) with hydroxyl groups in a specific arrangement can compete with water molecules to form stable complexes with metal cations in aqueous solution. For example, the most favorable sites for the coordination are *axial-equatorial-axial* hydroxyl groups in a six-membered ring or vicinal *cis-cis*-triol groupings in a five-membered ring. The higher equilibrium constants of complexation are observed in the case of trivalent lanthanide cations (1).

Several techniques, such as paper electrophoresis (2), thin-layer ligand-exchange chromatography (3), and NMR of the ligands (4–6), have been used to characterize the interaction between sugars and metal cations in solution. However, the stability constants for the complex formation have still to be determined in a fully satisfactory manner. Some results obtained from different experimental methods differ significantly. For example, by using a calorimetric method, Morel and co-workers have determined the stability constants for the case of D-ribose (7–9). The value they find for Ca^{2+}-ribose in water is in excellent agreement with that determined electrochemically by using a liquid-membrane electrode selective to Ca^{2+} ions (10) but much smaller than other reported values (6, 11–13). This discrepancy is presumably due to the fact that the stability constants are comparatively small (<5 M^{-1} in most cases) and that, accordingly, their accurate determination is difficult. It probably also reflects the fact that the various determinations have been made under quite different concentration conditions. Whereas Morel and co-workers could keep the electrolyte at almost infinite dilution, the other experimental approaches, in particular the older NMR determinations, required high concentrations to observe complex formation. Under the latter conditions the activity coefficient effects can not be neglected: the stability constants calculated from the concentrations may indeed differ significantly from the actual ones. Moreover, the equilibrium between the sugar isomers present in solution may be shifted by the presence of a large quantity of salt; this, of course, makes the various results hardly comparable. It should be possible to avoid these problems by working with modern NMR instruments and hence to get spectroscopic results that can be compared with the calorimetric ones.

The metal cation NMR spectroscopy of quadrupolar nuclei has proved to be a powerful technique to characterize the com-

[1]Author to whom correspondence may be addressed. Phone: 33-73407162, fax: 33-73407185, e-mail: CLERM2@FRCPN11.

[2]Author to whom correspondence may be addressed. Phone: (613) 564 2967, fax: (613) 564 6793, e-mail: Detse@UOTTAWA.

Can. J. Chem. Downloaded from www.nrcresearchpress.com by ESC ESCOLA DE ENGENHARIA on 09/08/12
For personal use only.

Can. J. Chem. Downloaded from www.nrcresearchpress.com by EESC ESCOLA DE ENGENHARIA on 09/08/12
For personal use only.

plexation between metal cations and macrocyclic ligands in solution (14). More particularly, the stoichiometry of such complexes present in small amounts in solution could be determined (15, 16). However, a similar approach has been used very rarely for the study of metal cation – sugar interactions: for example, the binding of Na^+ to D-ribose and to *cis*-inositol in water was observed through the variation of the ^{23}Na spin–lattice relaxation rates in the presence of sugar (17). In pyridine, the large dissymmetry of the electronic distribution around the sugar-complexed sodium cation permitted to define precisely the complexation parameters (18, 19).

In the present work, ^{139}La NMR was used to investigate the interaction of La(III) with D-ribose and with arabinose in aqueous solution. These two sugars have been chosen because some of the ribose isomers present in aqueous solution readily bind La(III) whereas arabinose, following Morel et al. (7–10), can be considered as a noninteractive reference. The analysis of the ^{139}La chemical shifts and linewidths allowed the calculation of the thermodynamic parameters for the La(III)–D-ribose complex. The NMR values are in good agreement with the calorimetric determinations.

Experimental

D-Ribose (Aldrich), $LaCl_3.7H_2O$ (Aldrich, 99.999%), and D-arabinose (Pfanstiehl Labs.) were dried 24 h under vacuum over P_2O_5 prior to use. The lanthanum content of $LaCl_3.7H_2O$ was determined by titration with EDTA. The solutions for the NMR measurements were prepared by dissolving an appropriately weighted quantity of the lanthanum salt or of the sugar in triply distilled water. All spectra were recorded within 24 h of the preparation of the samples. The pH values (5.0 ± 0.1) for the stock solutions was adjusted by very small amounts of HCl or NaOH solutions.

The NMR samples were made by transferring the stock solutions into 10 mm NMR tubes which were then sealed under argon with Parafilm. ^{139}La NMR spectra were recorded at 42.37 MHz on a Varian XL-300 spectrometer. The ^{139}La chemical shifts were referenced to a 0.100 M $La(NO_3)_3$ aqueous solution containing 20% D_2O. The 90° pulse width was 16 μs. The temperature was measured with a thermocouple submerged in water in a non-spinning NMR tube. The temperature of the samples was estimated to be reliable to ±0.5 K.

Results and discussion

Figure 1 shows a series of ^{139}La NMR spectra for a 0.040 M $LaCl_3$ aqueous solution in the presence of various amounts of D-ribose. In the absence of sugar ($R = [\text{sugar}]_0 / [\text{La(III)}]_0 = 0$), the ^{139}La NMR spectrum is characterized by a chemical shift of 1.34 ppm and a linewidth of 110 Hz. The signal results from the population average of aquated La(III) and ion pair species (20). The percentage of ion pairing was previously calculated to be 3.8% for this concentration of lanthanum chloride (20). In the rest of this study, on the basis of this small percentage, the competitive effect of the ion pair formation on the sugar complexation was assumed to be negligible. The same assumption was previously made by Lenkinski and Reuben (6) since they observed that the complexation results did not depend upon the anion nature (chloride or perchlorate). In the presence of sugar ($R > 0$), the ^{139}La chemical shifts and linewidths increased with an increase of R, indicating theLa(III)–sugar complex formation. The chemical exchange was fast on the ^{139}La chemical shift time scale since only one Lorentzian signal was observed for all the values of R.

Similar experiments were done with arabinose, and the ^{139}La NMR spectra are shown on Fig. 2. In contrast with the case of D-ribose, the ^{139}La NMR chemical shifts were almost constant.

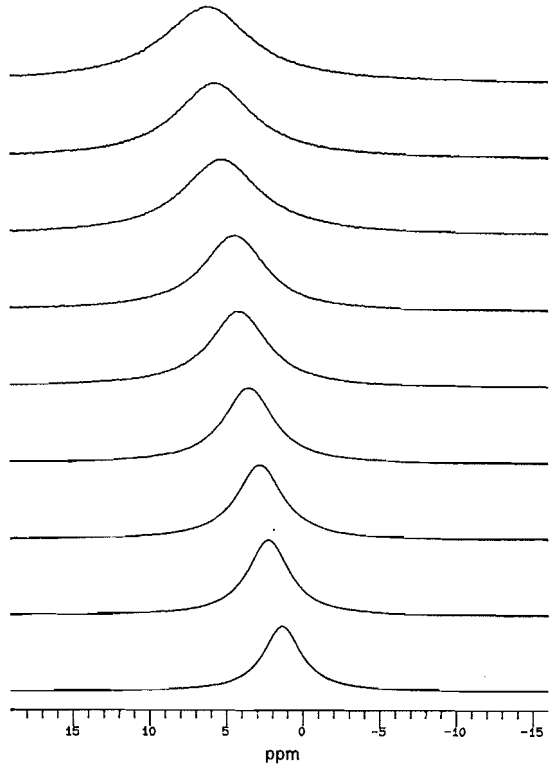

FIG. 1. ^{139}La NMR spectra of a 0.040 M $LaCl_3$ aqueous solution in the presence of D-ribose. From top to bottom: $R = ([\text{D-ribose}]_0 / [\text{La(III)}]_0) = 7.99, 7.10, 6.08, 5.07, 4.06, 3.04, 2.03, 1.01, 0$. $T = 299$ K.

This is in agreement with a very weak, almost undetectable by ^{139}La NMR, complexation of La(III) by arabinose. The linewidths, on the other hand, increase with an increase of R, due to an increase of the viscosity of the solution. These observations confirm (7–10) that arabinose can reasonably be used as an inactive reference and that the complexation between La(III) and D-ribose readily occurs. To calculate the stability constant for the complex of La(III) with D-ribose, the following equations were derived, on the basis of a 1:1 stoichiometry.

[1] $\underset{(A)}{\text{La(III)}} + \underset{(S)}{\text{ribose}} \rightleftharpoons \underset{(B)}{\text{(La(III) ribose)}}$

[2] $K = [B] / ([A] \times [S])$

where A ≡ La(III), B ≡ (La(III)ribose), and S ≡ ribose.

Since $[A] = [La]_0 - [B]$ and $[S] = R\,[La]_0 - [B]$, eq. [3] can be derived from eqs. [1] and [2].

[3] $[B] = 0.5\,C - (0.25\,C^2 - D)^{1/2}$

Here $C \equiv [La]_0 + R[La]_0 + K^{-1}$ and $D \equiv [La]_0^2$.

The observed ^{139}La chemical shifts, δ_{obs}, are the population-averaged values of δ_A and δ_B, the chemical shifts characterizing, respectively, the solvated and the 1:1 complexed La(III) cation

Therefore,

[4] $\delta_{obs} = ([B]/[La]_0) \times \delta_B + (([La]_0 - [B]) / [La]_0) \times \delta_A$

On the basis of eqs. [3] and [4], δ_A, δ_B, and K were determined from a non-linear regression on the observed ^{139}La

Can. J. Chem. Downloaded from www.nrcresearchpress.com by EESC ESCOLA DE ENGENHARIA on 09/08/12
For personal use only.

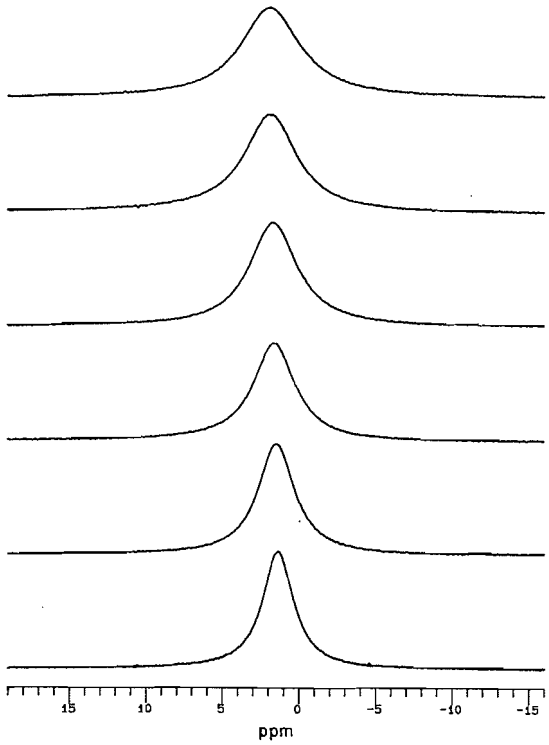

FIG. 2. ^{139}La NMR spectra of a 0.040 M $LaCl_3$ aqueous solution in the presence of D-arabinose. From top to bottom: R = ([arabinose]$_0$/[La(III)]$_0$ = 9.71, 7.77, 5.82, 3.88, 1.94, 0. T = 299 K.

chemical shifts values. Table 1 reports K values and the corresponding ^{139}La chemical shifts for the solvated and complexed La(III) cations at different temperatures. Figure 3 shows the ^{139}La chemical shifts as a function of R for both sugars at 300 K. The solid line in Fig. 3 is calculated from the parameters reported in Table 1 and the data points are experimental. Figure 4 gives the ^{139}La chemical shifts as a function of R in the case of D-ribose for various temperatures. In Fig. 4, the solid lines are calculated and the points reported are experimental .data.

As mentioned previously, the ^{139}La NMR linewidths increase with an increase of R for both sugars. The variations of the linewidthsis much larger in the case of ribose than in the case of arabinose. Since the chemical shift variation with R is very small in the case of arabinose, the increase of the linewidths might be considered as resulting from a viscosity increase. Assuming that the viscosity variations caused by the presence of different quantity of sugar in the solutions are the same in the cases of D-ribose and of arabinose, the ^{139}La NMR linewidths observed in the case of D-ribose were corrected by subtracting the viscosity effects. The viscosity reduced linewidths were analyzed by a procedure similar to the one used for the chemical shifts analysis, on the basis of eq. [5].

$$[5]\quad (\nu_{1/2})_{obs} = ([B] / [La]_0) \times (\nu_{1/2})_B + (([La]_0 - [B]) / [La]_0) \times (\nu_{1/2})_A$$

where $(\nu_{1/2})_B$ and $(\nu_{1/2})_A$ are the viscosity-corrected ^{139}La NMR linewidths for the La(III) cations, respectively, in the solvated site and in the site complexed by D-ribose.

The K value obtained for the temperature of 299 K is 2.2 ± 0.6 M^{-1}, which is compatible with the value obtained through the chemical shift analysis (see Table 1). Figure 5 shows the viscosity reduced linewidths as a function of R for the ribose. As above, the solid line is calculated and the data points are experimental.

TABLE 1. ^{139}La chemical shifts characterizing La(III) in the solvated and in the ribose-complexed sites and the stability constants, K, reported at different temperatures[a]

T(K)[b]	δ_A(ppm)[c]	δ_B(ppm)[d]	K[e]
299	1.19	11.4 ± 0.8	2.8 ± 0.5
303	1.14	10.8 ± 0.7	2.7 ± 0.5
312	0.61	10.2 ± 0.5	2.6 ± 0.3
320	0.32	10.7 ± 0.4	2.1 ± 0.2
328	0.08	10.4 ± 0.6	1.9 ± 0.2
336	−0.12	10.1 ± 0.5	1.6 ± 0.1

[a]The parameters reported in this table were obtained from a non-linear regression analysis (eqs. [1]–[4]).
[b]±0.5 K.
[c]^{139}La chemical shifts characterizing La(III) in the solvated δ_A sites.
[d]^{139}La chemical shifts characterizing La(III) in the ribose-complexed (δ_B) sites.
[e]Stability constants for the complex La(III)–ribose. The errors are reported as one σ.

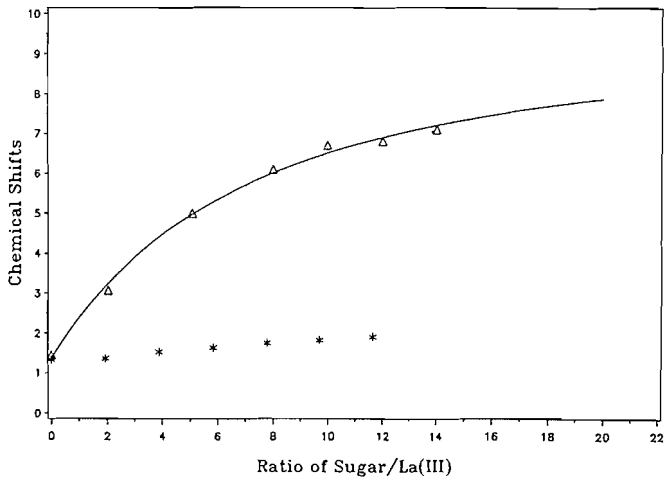

FIG. 3. ^{139}La chemical shifts as a function of R. (△): D-Ribose; (★): D-Arabinose. T = 299 K. The solid line is calculated, and the data points are experimental.

D-Ribose exists in solution as an equilibrium mixture of mainly six isomers: 21% of α-pyranose ($^1C_4$ and $^4C_1$ conformers), 59% of β-pyranose ($^1C_4$ and $^4C_1$ conformers), 6% of α-furanose and 14% of β-furanose (1). Among the ribopyranose forms, only the $^1C_4$ and $^4C_1$ conformers of the α-anomer and the $^1C_4$ conformer of the β-anomer bear a complexing site, while among the ribofuranose forms only the α-anomer does (8). However, in the present study, the metal cation NMR parameters (chemical shift and transverse relaxation) do not discriminate amongst the various complexes formed with the different isomers. In the treatment above, it was implicitely assumed that all complexes had the same chemical shift (δ_B) and the same characteristic linewidth ($(\nu_{1/2})_B$). Since, in all the complexes, the local geometries around the metal cation are expected to be very similar, the assumption seems reasonable. However, the treatment of the NMR data must be limited to a "global" phenomenon, considering only one type, averaged, of complexed site.Therefore, the stability constants given in Table 1 are overall values for the whole of ribose isomers present in solution.

Can. J. Chem. Downloaded from www.nrcresearchpress.com by EESC ESCOLA DE ENGENHARIA on 09/08/12
For personal use only.

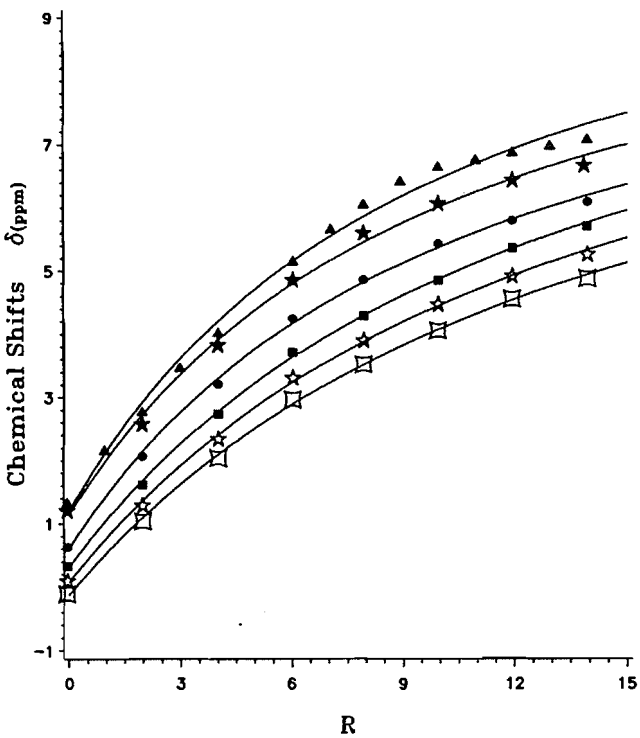

FIG. 4. ^{139}La chemical shifts as a function of R. From top to bottom: T = 336 K, 328 K, 320 K, 312 K, 303 K, and 299 K. The solid lines are calculated and the data points are experimental.

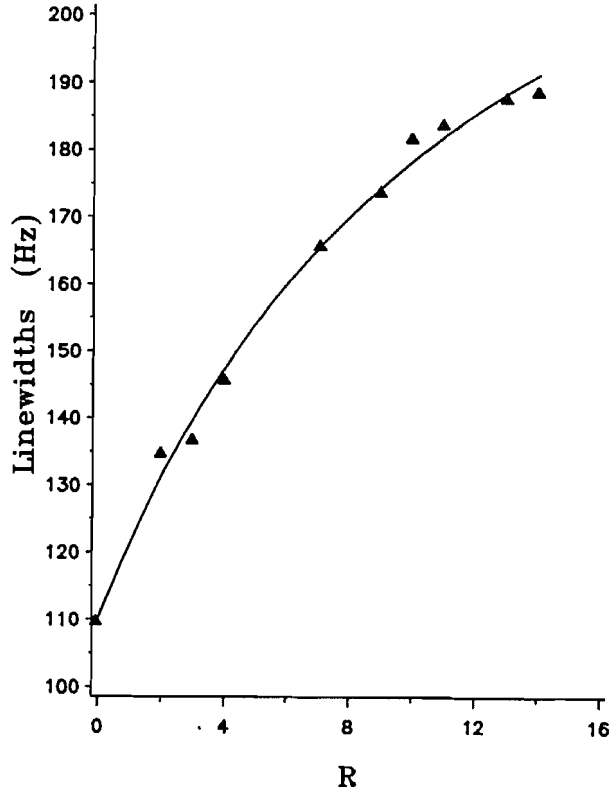

FIG. 5. Viscosity corrected ^{139}La linewidths as a function of R for the case of D-ribose. T = 299 K. The solid line is calculated and the data points are experimental.

Recently, Morel-Desrosiers et al. (21) have determined by calorimetry the thermodynamic properties of association of the trivalent lanthanide cations (La(III) → Tb(III)) with ribose in water. Through an approach based on the comparison of the behaviour of the complexing sugar with that of non-complexing epimer, they have isolated the properties characterizing solely the specific interactions between the cation and the complexing sequence of hydroxyl groups. Once converted to an overall value, their stability constant for La(III) is equal to 1.3 ± 0.2 M^{-1} at 298.15 K. This is relatively small compared to the value of 2.8 ± 0.5 M^{-1} given in Table 1. However, the agreement is better with the value of 2.2 ± 0.6 M^{-1} deduced from the analysis of the viscosity reduced linewidths. Values of 3.6 and 0.9 were reported by Lenkinski and Reuben (6) for La(III)–α-D-furanose and La(III)–β-D-pyranose, respectively, at 52°C: these values, once converted to the overall stability constant, appear, considering the temperature, to be compatible with the value given in the present work.

The enthalpy and entropy of complex formation were calculated from the temperature dependence of the equilibrium constants, given in Table 1: $\Delta H^0 = -12 \pm$ kJ mol^{-1} and $\Delta S^0 = -31 \pm 5$ J K^{-1} mol^{-1}. These values are in very good agreement with those directly obtained by calorimetric measurements (17) and converted here, for comparison, to overall values (that is, given with respect to the whole of ribose isomers): ΔH^0 = –9.6 kJ mol^{-1} and ΔS^0 = –30 J K^{-1} mol^{-1}.

Conclusions

Both chemical shifts and linewidths of the ^{139}La NMR spectra are very sensitive to complex formation, and can be used to characterize the complexation process. One of the most important advantages of this method is that the experiments can be done at a constant, low, salt concentration.The lanthanum chloride concentration used throughout the present work was 0.040 M; if necessary, given the high receptivity of ^{139}La, one could work at the subcentimolar level. Because, in water, the ^{139}La NMR signals are not too broad (100–500 Hz), the NMR observations can be performed in a reasonable amount of time. At such a low concentration, the activity coefficient effects are negligible. Moreover, the potential formation of complexes of higher stoechiometries, such as 2:1 or 1.2, is not favoured. Compared to other techniques, the metal cation NMR provides the information directly related to the cation coordination shell and thus allows to study the inner-sphere complexes. It was shown here that the effect of the other interactions on the chemical shifts is weak and that the viscosity correction of the linewidths leads to results in agreement with the chemical shifts ones. Obviously, ^{139}La NMR spectroscopy is particularly appropriate for the study of the interactions of La(III) with polyols in solution.

Acknowledgment

The Natural Sciences and Engineering Research Council of Canada (NSERCC) is gratefully acknowledged for financial support (Research grant to C.D.).

1. S.J. Angyal. Adv. Carbohydr. Chem. Biochem. **47**, 1 (1989).
2. E.J. Bourne, F. Searle, and H. Weigel. Carbohydr. Res. **16**, 185 (1971).
3. M.M. Hamalainen and H. Lonnberg. Carbohydr. Res. **215**, 357 (1991).
4. S.J. Angyal, D. Greeves, L. Littlemore, and V.A. Pickles. Aust. J. Chem. **29**, 1231 (1976).
5. S.J. Angyal. Adv. Chem. Ser. **117**, 106 (1973).
6. R.E. Lenkinski and J. Reuben. J. Am. Chem. Soc. **98**, 3089 (1976).

7. A.M. Alvarez, N. Morel-Desrosiers, and J.-P. Morel. Can. J. Chem. **65**, 2656 (1987).
8. N. Morel-Desrosiers and J.-P. Morel. J. Chem. Soc. Faraday Trans. **85**, 3461 (1989).
9. N. Morel-Desrosiers, C. Lhermet, and J.-P. Morel. J. Chem. Soc. Faraday Trans. **87**, 2173 (1991).
10. J.P. Morel, C. Lhermet, and N. Morel-Desrosiers. J. Chem. Soc. Faraday Trans. 1, **84**, 2567 (1988).
11. S.J. Angyal. Austr. J. Chem. **25**, 1957 (1972).
12. L.G. Ekström and A. Olin. Acta Chem. Scand. Part A, **31**, 838 (1977).
13. H. Lönnberg and A. Vesala. Carbohydr. Res., **78**, 53 (1980).
14. C. Detellier. *In* NMR of newly accessible nuclei. Vol. 2. *Edited by* Laszlo. Wiley, New York. 1983. Chap. 5.
15. Z. Chen, H. Dettman, and C. Detellier. Polyhedron, **8**, 2029 (1989).
16. C. Detellier, H.P. Graves, and K.M. Brière. Alkali metal NMR studies of synthetic and natural ionophore complexes. *Edited by* E. Buncel and J. Jones. Elsevier, New York. 1991. Chap. 5.
17. J. Andrasko and S. Forsen. Biochem. Biophys. Res. Commun. **52**, 233 (1973).
18. C. Detellier, J. Grandjean, and P. Laszlo. J. Am. Chem. Soc. **98**, 3375 (1976).
19. J. Grandjean and P. Laszlo. Helv. Chim. Acta. **60**, 259 (1977).
20. Z. Chen and C. Detellier. J. Solution Chem. **21**, 941 (1992).
21. N. Morel-Desrosiers, C. Lhermet, and J.P. Morel. J. Chem. Soc. Faraday Trans. **89**, 1223 (1993).

Can. J. Chem. Downloaded from www.nrcresearchpress.com by EESC ESCOLA DE ENGENHARIA on 09/08/12
For personal use only.

Cyclization of $Ph_2Si(NHNHMe)_2$. II. Reactions with methyl iodide, HCl, and Ph_2SiCl_2, and thermolysis

JILIANG HE AND JOHN F. HARROD[1]

Chemistry Department, McGill University, Montreal, QC H3A 2K6, Canada

Received January 10, 1994

JILIANG HE and JOHN F. HARROD. Can. J. Chem. **72**, 1759 (1994).

The reaction of $Ph_2Si(NHNHMe)_2$ (**1**) with MeI results in a mixture of two six-membered ring isomers, 1,2,4,5-tetraaza-1,4-dimethyl-3,3,6,6-tetraphenyl-3,6-disilacyclohexane (**2**), 45%, and 1,2,4,5-tetraaza-1,5-dimethyl-3,3,6,6-tetraphenyl-3,6-disilacyclohexane (**3**), 40%. The reaction of **1** with HCl or Ph_2SiCl_2 proceeds in a similar fashion. The thermolysis of **1** is studied from 25–600°C. In the range of 250–300°C, about 50% of **1** is converted into **2**, **3**, and 1,2,4-triaza-1-methyl-4-methylamino-3,3,5,5-tetraphenyl-3,5-disilacyclopentane, **8**. Possible pathways for the formation of **2**, **3**, and **8** in these cyclization reactions are discussed.

JILIANG HE et JOHN F. HARROD. Can. J. Chem. **72**, 1759 (1994).

La réaction du $Ph_2Si(NHNHMe)_2$ (**1**) avec le MeI conduit à la formation de deux cycles à six chaînons isomères, le 1,2,4,5-tétraaza-1,4-diméthyl-3,3,6,6-tétraphényl-3,6-disilacyclohexane (**2**), 45%, et le 1,2,4,5-tétraaza-1,5-diméthyl-3,3,6,6-tétraphényl-3,6-disilacyclohexane (**3**), 40%. La réaction du composé **1** avec le HCl ou le Ph_2SiCl_2 se produit d'une façon semblable. On a étudié la thermolyse du composé **1** entre 25 et 600°C. Entre 250 et 300°C, environ 50% du composé **1** se transforme en produis **2** et **3** et en 1,2,4-triaza-1-méthyl-4-méthylamino-3,3,5,5-tétraphényl-3,5-disilacyclopentane, **8**. On discute des diverses voies de formation des composés **2**, **3** et **8** dans ces réactions de cyclisation.

[Traduit par la rédaction]

Introduction

Silylhydrazine ring compounds, containing the Si—N—N unit, constitute an important family of cyclic silicon–nitrogen compounds (1). The most widely exploited synthetic method for the preparation of these compounds is the intermolecular reaction of a hydrazine with a dihalosilane with the elimination of hydrogen halide (2–5). They are also obtainable by a number of other synthetic routes (6–10). We recently reported the synthesis of bis(2-methylhydrazino)diphenylsilane, **1**, by a catalytic dehydrocoupling method (9). This novel silylhydrazine compound possesses several different functionalities, including two N—H groups of different acidities (11), labile Si—N bonds (12), and two different basic nitrogen atoms which can serve as nucleophiles.

In the present paper we report two modes of cyclization of **1**, brought about either by the reaction with reagents MeI, HCl, and Ph_2SiCl_2 or by thermolysis.

Results and discussion

Reactions of $PH_2Si(NHNHMe)_2$ with MeI, HCl, and Ph_2SiCl_2

The reaction of **1** with an equimolar amount of iodomethane in toluene unexpectedly yielded a mixture of two tetraazadisilacyclohexane isomers, 1,2,4,5-tetraaza-1,4-dimethyl-3,3,6,6-tetraphenyl-3,6-disilacyclohexane, **2**, and 1,2,4,5-tetraaza-1,5-dimethyl-3,3,6,6-tetraphenyl-3,6-disilacyclohexane, **3**, with no other detectable silylhydrazine formation. In a typical experiment, compounds **2** and **3** accounted for 56% and 44% in the product, respectively, measured by ^{1}H-NMR spectra. The separation of **2** from the mixture was accomplished by recrystallization from a hot hexane solution, cooled to ambient temperature. The isolated yield of **2** was 45%. Further recovery of **2** was effected by partial evaporation of the hexane and cooling the solution of 4°C. After this procedure, **3** was isolated in 40% yield by removing hexane under reduced pressure. This product was contaminated with about 15% of **2**. **3** was obtained in higher purity by recrystallization from pentane solution. ^{1}H and

[1] $Ph_2Si(NHNHMe)_2 + MeI \longrightarrow$

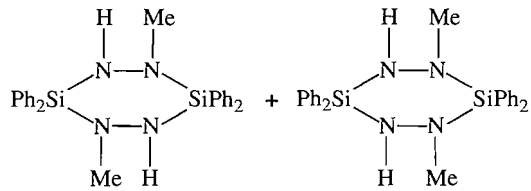

2 **3**

^{29}Si-NMR and EI-MS spectra were consistent with the assigned structures for the both compounds, as reported elsewhere (11). Both **2** and **3** were colorless crystalline solids. They are mildly moisture-sensitive but can be handled in air for a short period of time without significant decomposition.

In order to better understand the origin of the product distribution, the reaction was followed by ^{1}H-NMR spectroscopy. In the early stages of the reaction, **2** was the dominant product. The proportion of **3** in the product increased gradually as the reaction proceeded and finally accounted for 46% of the product. With an 0.6 to 1.0 mole equivalent of MeI to **1**, approximately same product distribution was obtained. The results are summarized in Table 1.

These experiments indicate that HI produced in the reaction can play the same role as MeI before the hydrazonium iodide salt precipitates completely. This was confirmed by the reaction of **1** with anhydrous HCl (in diethyl ether). A similar result to that with MeI was obtained, except for a small amount of a new unidentified compound (18%) in the product. For most silylhydrazines, the Si—N bond is readily cleaved solvolytically by acids, or by anhydrous hydrogen halides in solution, as shown in reaction [2] (13):

[2] 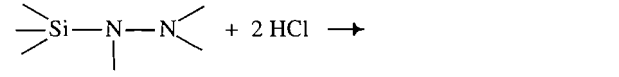

[1]Author to whom correspondence may be addressed. Phone: 514-398-6911; fax: 514-398-3797; e-mail: harrod@omc.lan.mcgill.ca.

Can. J. Chem. Downloaded from www.nrcresearchpress.com by 85.192.166.187 on 09/08/12
For personal use only.

TABLE 1. Reactions of $Ph_2Si(NHNHMe)_2$ with MeI, HCl, and Ph_2SiCl_2, and the product distribution

Reaction	Molar ratio	Time (h)	Product distribution (%)[a] 2	3
$Ph_2Si(NHNHMe)_2$ + MeI	1:1	3	47	10
		10	56	44
	1:0.8	12	55	45
	1:0.6	12	58	42
$Ph_2Si(NHNHMe)_2$ + HCl[b]	1:1	24	58	24
$Ph_2Si(NHNHMe)_2$ + Ph_2SiCl_2[c]	1:1	16	45	29

[a]Based on ^1H NMR measurement.
[b]The product also consists of 18% of unidentified compound(s).
[c]The product also consists of 26% of **6**.

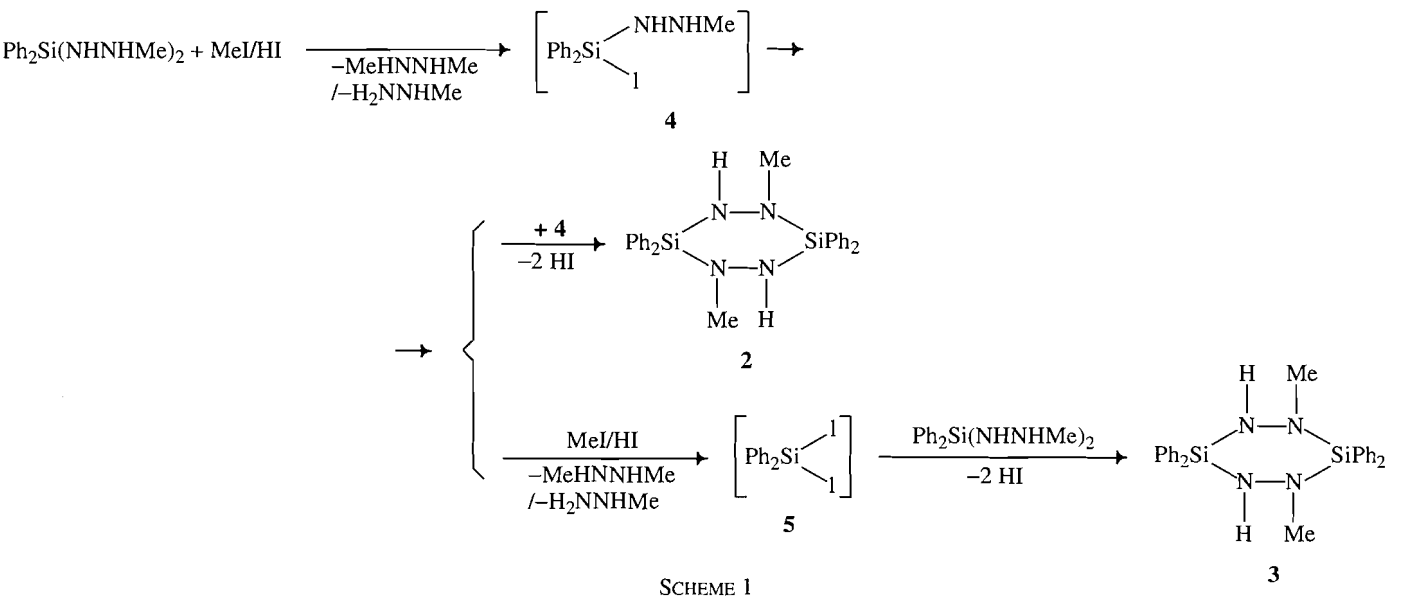

SCHEME 1

A possible pathway which accounts for the formation of **2** and **3** is shown in Scheme 1. The first step is the formation of an iodosilyl-substituted methylhydrazine, **4**, through the attack of MeI on **1**, with the elimination of MeHNNHMe. **4** is apparently a reactive intermediate since it is not observed and such a compound has not been synthesized, although fluorosilyl-substituted hydrazines have recently been prepared and isolated by Klingebiel (*7e*). **4** can either undergo autocondensation with another molecule of the same identity to yield **2** by the elimination of two molecules of HI, or it can be further attacked by MeI to form diiododiphenylsilane, **5**, which can react with **1**, with ring closure, to give **3** by HI elimination. In addition to precipitation as methylhydrazonium iodides, the HI formed in the reaction can also form **4**, or **5** by displacement of one, or two, moles of H_2NNHMe.

2 and **3** are also the products of the reaction of Ph_2SiCl_2 with **1**. In addition to **2** (45%) and **3** (29%), a third product, **6**, is also produced. In the early stages of reaction, compounds **3** and **6** predominate, but the amount of **2** increases gradually with the passage of time. Compound **6** was not isolated in a pure state, but it was tentatively assigned as $Ph_2Si(NHNMeSiPh_2Cl)_2$ based on its ^1H and ^{29}Si-NMR spectra. This compound is one of the expected products of reaction of Ph_2SiCl_2 with **1**. As the reaction proceeds, Ph_2SiCl_2 is depleted and the formation of **3** and **6** slows down. The reaction of **1** with HCl begins to compete and the relative rate of formation of **2** increases.

Thermolysis of $Ph_2Si(NHNHMe)_2$

A thermogravimetric analysis of **1** was performed from 25 to 600°C. Figure 1 shows the total weight loss which starts at ~200°C and ends at ~450°C. Within this temperature range, the weight loss at 265 and 332°C, respectively, occurs dramatically (as indicated by the DTG curve), while the DTA curve shows a slight exotherm at ~300°C. This fact suggests that a major decomposition (or structural change) occurs around 300°C.

In order to understand the thermal behavior, an NMR study of the thermal decomposition product at 250, 300, and 350°C was carried out. Figure 2 shows the ^1H-NMR spectra of the products at these temperatures. The results indicate that 52% of **1** is converted into **8** (31%), **2** (14%), and **3** (7%) at 250°C under the same heating conditions as that in Fig. 1. The remainder of the product was a mixture of unreacted **1** and an unidentified compound. **8** was assigned the structure 1,2,4-triaza-1-methyl-4-methylamino-3,3,5,5-tetraphenyl-3,5-disilacyclopentane, based on ^1H and ^{29}Si-NMR data, as reported elsewhere (11). The unknown compound is probably $Ph_2(MeHNHN)SiNHNMeSi(NHNHMe)Ph_2$, **7**. However, its structure

Can. J. Chem. Downloaded from www.nrcresearchpress.com by 85.192.166.187 on 09/08/12
For personal use only.

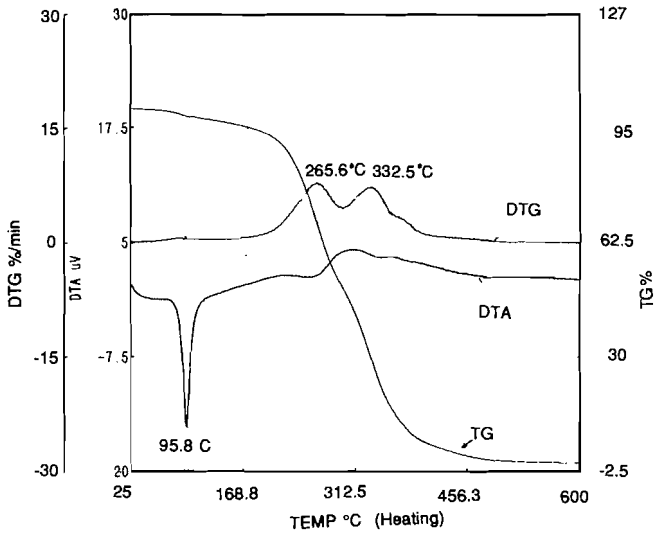

FIG. 1. Thermogravimetric analysis of $Ph_2Si(NHNHMe)_2$ at a heating rate of 10°C/min under a flow of N_2 (120 mL/min).

could not be assigned unequivocally on the basis of NMR data. At 300°C, **1** was completely converted to a mixture of **8** (16%), **2** (21%), and **3** (17%), and about 46% of uncharacterised oligomers.

$Si(NHR)_4$ has been previously reported to undergo polycondensation on heating, with the loss of amine to form complex polymers containing six- and /or four-membered $(SiN)_n$ rings (14). A similar condensation could occur with **1**. A proposal for the mechanism of formation of **8**, **2**, and **3** is shown in Scheme 2. In this scheme two molecules of **1** undergo self-condensation to form intermediate **7**. Under the same conditions, intramolecular condensation of **7** takes place to yield compounds **8**, **2**, and **3** by pathways, *1*, *2*, and *3*, in which three different nitrogen atoms serve as the species which can attack the two silicon atoms.

By comparison of the products of 250 and 300°C, it is evident that the formation of **8** (5-membered ring) is more favorable at 250°C. Because the 5-membered ring is kinetically favored at lower temperature and thermodynamically unstable at higher temperature. Indeed, when pure compound **8** was heated to 300°C under the same conditions, **2** and **3** were obtained.[2] In accordance with the mechanism in Scheme 2, the formation of **2** is favored over that of **3** (in which two NMe groups are on the same Si atom) due to the unfavorable steric effect. The weight loss (ca. 50%) at 300°C in the TGA does not correlate with that (17%) depicted in Scheme 2. This difference is probably due to the loss of **1**, or small ring compounds by sublimation or evaporation at high temperature under the flow of N_2.

The product at 350°C is more complicated. The ^{1}H-NMR spectrum shows that the composition of the residue is dominated by phenyl groups. Decomposition could be the main thermal behavior at this temperature, as a gaseous product was observed to evolve from the residue during heating. In a study of the gaseous pyrolysis products of silylhydrazines (from $MeRSiCl_2 + H_2NNH_2$), Colombier reported that the major species were CH_3SiH_3 (300°C), NH_3 (250–500°C), CH_4 (400–1000°C), and H_2 (maximum at 800°C), in addition to hydrazine (15). Similar products could result from our system at 350°C or higher temperature.

[2]When compound **8** was heated at 300°C under the same conditions as that of **1**, the pyrolysis residue consisted of **2** (27%), **3** (23%), oligomeric product (33%) and 17% of **8** remained, as measured by ^{1}H-NMR.

Experimental

Reagents and analytical methods

All reactions were carried out under an atmosphere of dry argon. The solvents used were dried over Na/benzophenone and distilled prior to use. Bis(2-methylhydrazino)diphenylsilane (**1**) was prepared by the catalytic dehydrocoupling reaction of diphenylsilane with methylhydrazine as described elsewhere (9). Other chemicals were used as received from Aldrich Chemical Co. All glassware was heated to at least 120°C and evacuated and purged several times with dry argon. ^{1}H (^{29}Si, ^{15}N)-NMR spectra were recorded on a Varian XL-200 (300, 500) FT-NMR at 20°C with internal TMS (^{1}H, ^{29}Si) and external CH_3NO_2 (^{15}N) as standards. Benzene-d_6 was used as solvent. Low resolution mass spectra were obtained on a Du Pont 21-492b spectrometer with an ionizing energy of 70 eV. IR spectra were recorded on a Bruker IFS-88 spectrometer with a resolution of 4 cm^{-1} under dry N_2 purge, using a mercury cadmium telluride detector.

Reactions of $Ph_2Si(NHNHMe)_2$ with MeI, HCl, and Ph_2SiCl_2

Reaction of $Ph_2Si(NHNHMe)_2$ with MeI

The reaction was carried out in a 50 mL Schlenk flask at ambient temperature under dry argon. **1** (1.28 g, 4.72 mmol) was dissolved in 20.0 mL of toluene–hexane (10:1), into which MeI (0.29 mL, 4.72 mmol) was added dropwise with stirring by a long needle syringe. Precipitation took place immediately in the solution upon the addition of MeI. Stirring was periodically stopped so that the clear layer of solution could be sampled for ^{1}H-NMR measurements. Compound **2** was the major product (ca. 80% in selectivity) in the first 3 h. After 10 h, the reaction was complete, and the salt was filtered under an argon atmosphere. The toluene–hexane was removed under reduced pressure. The final yields were 56% for **2** and 44% for **3**, as measured by ^{1}H-NMR. Various stoichiometric ratios of MeI with **1** were tried and the results were listed in Table 1.

The residue was redissolved in hot *n*-hexane (20 mL), and the solution was cooled to ambient temperature to give pure **2** in an isolated yield of 0.48 g (45%). After isolation of **2**, the solvent was stripped, the residue was redissolved in 10 mL of hexane, and the solution was cooled to 4°C to remove residual **2**. The mother liquor was then evaporated to yield **3** in 85% isomeric purity (0.43 g, 40%). **3** was further purified by recrystallization from concentrated pentane solution at 4°C.

Analytical data for **2**: ^{1}H-NMR (200 MHz): δ 2.89 (s, 6H, NCH), 3.44 (s, 2H, NH), 7.20 (m, 12H, Ph), 7.70 (m, 8H, Ph). ^{29}Si-NMR (56.9 MHz): −19.92. ^{15}N{^{1}H}-NMR (HMQC, 499.84 MHz): δ −311.82 (N{H}). EI-MS (*m/e*, abundance, fragmentation): 452(100) [M$^{\cdot+}$ − HNNHMe], 378(19) [M$^{\cdot+}$ − HNNHMe − NMe], 331(26) [M$^{\cdot+}$ − SiPh − MeH], 302(22) [M$^{\cdot+}$ − HNNHMe − SiPh], 226(12) [M$^{\cdot+}$ − HNNMe − $SiPh_2$]. IR (neat, ν cm^{-1}): 3331s, 3302s (N—H); 1018vs, 994s (Si—N). mp: 149–150°C.

Analytical data for **3**: ^{1}H-NMR (200 MHz): δ 2.83 (s, 6H, NCH), 3.39 (s, 2H, NH), 7.20 (m, 12H, Ph), 7.82 (m, 8H, Ph). ^{29}Si-NMR (56.9 MHz): δ − 18.52 (SiNH), −18.73 ($SiNCH_3$). IR (neat, ν cm^{-1}): 3373s, 3321s (N—H); 1022s, 998s (Si—N). mp: 102–104°C.

Reaction of $Ph_2Si(NHNHMe)_2$ with HCl

The general procedure was the same as in the previous experiment. **1** (1.36 g, 5.00 mmol) was dissolved in 20.0 mL of toluene–hexane (10:1), into which 5.0 mL of anhydrous HCl (5.00 mmol, 1.0 M in diethylether) was added dropwise with stirring by a long needle syringe. Fuming and precipitation took place immediately as HCl contacted the solution. The mixture was periodically sampled for ^{1}H-NMR measurement. The reaction was complete in 24 h. After work-up, the final product was **2** (58%), **3** (24%), and 18% of an unidentified product, by ^{1}H-NMR.

Can. J. Chem. Downloaded from www.nrcresearchpress.com by 85.192.166.187 on 09/08/12
For personal use only.

Can. J. Chem. Downloaded from www.nrcresearchpress.com by 85.192.166.187 on 09/08/12
For personal use only.

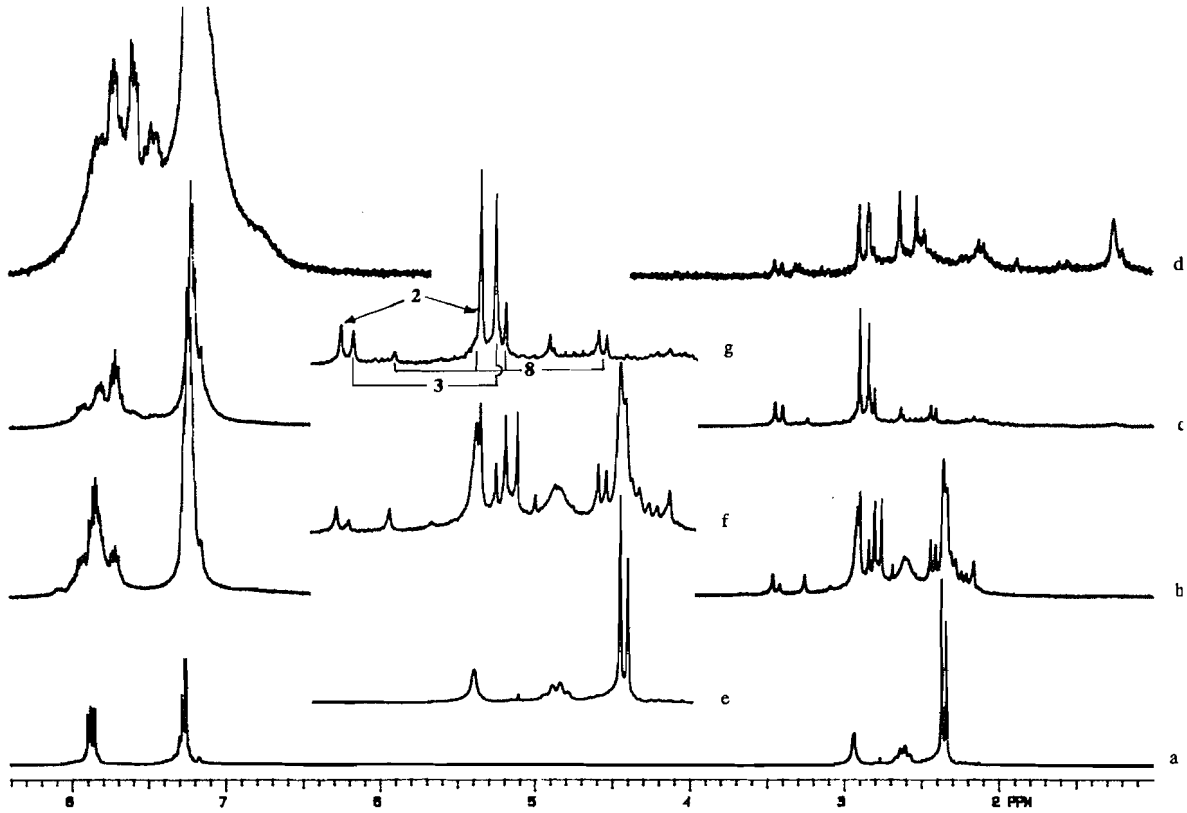

FIG. 2. ^{1}H-NMR spectra for the thermolysis of $Ph_2Si(NHNHMe)_2$: (*a*) before heating; (*b*) at 250°C; (*c*) at 300°C; (*d*) at 350°C; (*e*), (*f*), and (*g*) expansion of the region for N—H/N—Me from (*a*), (*b*), and (*c*), respectively.

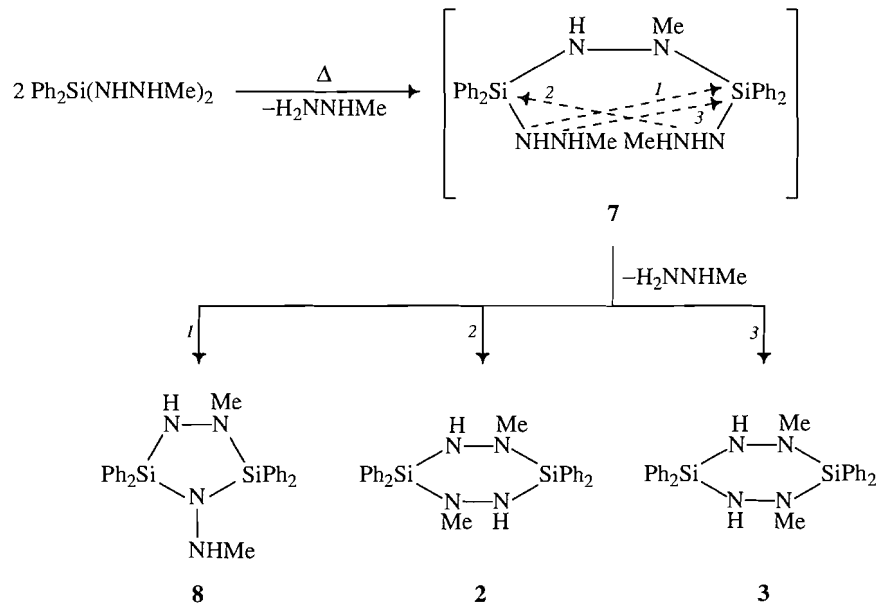

SCHEME 2

Reaction of $Ph_2Si(NHNHMe)_2$ with Ph_2SiCl_2

The procedure described above was followed. **1** (1.42 g, 5.20 mmol) was dissolved in 15.0 mL of toluene–hexane (10:1), into which 0.55 mL of Ph_2SiCl_2 (2.60 mmol) was added dropwise with stirring by a long needle syringe. Precipitation took place immediately in the solution upon the addition of Ph_2SiCl_2. The mixture was periodically sampled for ^{1}H-NMR measurement. Compound **3** was formed mainly in the early stages of the reaction, and the proportion of compound **2** increased gradually through the reaction. The formation of compound **6** occurred continuously throughout the reaction. The reaction was complete in 16 h. After work-up, the final product gave **2** (45%), **3** (29%), and **6** (26%), as measured by ^{1}H-NMR.

Analytical data for **6**: ^{1}H-NMR (200 MHz): δ 2.79 (s, 6H), 3.21 (s, 2H), 7.15 (m, 18H, Ph), 7.50 (m, 12H, Ph). ^{29}Si-NMR (56.9 MHz): −4.56 (SiCl), −8.75 (SiN_2).

Thermolysis of $Ph_2Si(NHNHMe)_2$

Thermogravimetric analysis (TGA) was performed on a Seiko 220 TG/DTA instrument. A flow of N_2 (~120 mL/min) was maintained during the TGA runs. The sample (8.80 mg) was heated in an alumi-

num pan at a rate of 10°C/min from 25 to 600°C. The result is shown in Fig. 1. The weight loss (5%) at 90–170°C was attributed to the presence of solvent (toluene) in the sample.

General procedure for preparing NMR samples

About 80 mg of $Ph_2Si(NHNHMe)_2$ was placed in an NMR tube, which was heated in a furnace at ca. 10°C/min up to a given temperature (250, 300, and 350°C, respectively) under argon atmosphere, and held at the desired temperature for 5 min. The furnace was then removed to let the tube cool to ambient temperature. The liquid formed during heating was removed under reduced pressure. C_6D_6 (0.5 mL) was then added into the tube to dissolve the residue and the sample was analysed by NMR spectroscopy.

In order to trap and identify the liquid formed on heating, a larger amount of **1** (ca. 1.00 g) was placed in a 10 mL Schlenk tube (1.5 cm in diameter) which was connected to a trap immersed in liquid nitrogen. The sample was heated to 300°C and the volatile product was collected under vacuum in the trap. This product was found to be H_2NNHMe. ^{1}H-NMR: d 2.32 (s, 3H, NCH), 3.05 (br, 3H, NH).

At 250°C, the residue was composed of **8** (31%), **2** (14%), **3** (7%), **1**, and some unidentified compound(s) (total 48%). Analytical data for **8**: ^{1}H-NMR (200 MHz): δ 2.41 (d, $^3J_{HNCH}$ = 4.2 Hz, 3H, N^4CH_3), 2.79 (s, 3H, N^1CH_3), 2.89 (q, $^3J_{HNCH}$ = 4.2 Hz, 1H, N^4H), 3.23 (s, 1H, N^2H), 7.20 (m, 12H, Ph_2Si), 7.86 (m, 8H, Ph_2Si). ^{29}Si-NMR (59.6 MHz): δ −16.38 (SiNH), −17.55 ($SiNCH_3$). $^{15}N\{^1H\}$-NMR (HMQC, 499.84 MHz, $^1J_{N—H}$ = 90 Hz): δ −307.02 ($N^2\{H\}$), −326.68 ($N^4\{H\}$). IR (neat, ν cm^{-1}): 3433–3315 br, (N—H); 994s, 934s (Si—N).

At 300°C, $Ph_2Si(NHNHMe)_2$ was completely converted to **8** (16%), **2** (21%), **3** (17%), and oligomeric product (46%).

At 350°C, a gaseous product was observed to evolve from the residue during heating. The pyrolysis residue consisted of **2** and **3** (total, 10%) and an uncharacterised oligomeric product.

Acknowledgements

This work was supported by grants from the Natural Sciences and Engineering Research Council of Canada and the Fonds F.C.A.R. du Québec.

1. (*a*) E.A.V. Ebsworth. Volatile silicon compounds. Pergamon Press, Oxford, New York, 1963. Chap 5; (*b*) D.A. Armitage. *In* The silicon–heteroatom bonds. *Edited by* S. Patai and Z. Rappaport. Wiley, Chichester, England. 1991. Chaps. 11, 12. pp. 367–485.
2. (*a*) U. Wannagat and H. Niederprum. Angew. Chem. **70**, 745 (1958); (*b*) U. Wannagat. Inorg. Nucl. Chem. Lett. **1**, 13 (1965); (*c*) U. Wannagat and M. Schlingmann. Z. Anorg. Allg. Chem. **406**, 7 (1974).
3. (*a*) C.G. Pitt and K.R. Skillern. Inorg. Nucl. Chem. Lett. **2**, 237 (1966); (*b*) C.G. Pitt and K.R. Skillern. Inorg. Chem. **6**, 865 (1967).
4. J.W. Connolly, B.F. Stockton, C.M. Emerick, and E.A. Bernheim. Inorg. Chem. **9**, 93 (1970).
5. N.W. Mitzel, P. Bissinger, J. Riede, K.H. Drieihaupl, and H. Schmidbaur. Organometallics, **12**, 413 (1993).
6. M.V. George, P.B. Talukar, and H. Gilman. J. Organomet. Chem. **5**, 397 (1966).
7. (*a*) J. Hluchy and U. Klingebiel. Angew. Chem. Int. Ed. Engl. **21**, 301 (1982); (*b*) W. Clegg, H. Hluchy, U. Klingebiel, and G.M. Sheldrick. Z. Naturforsch. **34B**, 1260 (1979); (*c*) W. Clegg, M. Haase, H. Hluchy, U. Klingebiel, and G.M. Sheldrick. Chem. Ber. **116**, 290 (1983); (*d*) C. Drost, U. Klingebiel, and M. Noltemeyer, J. Organomet. Chem. **414**, 307 (1991); (*e*) C. Drost and U. Klingebiel. Chem. Ber. **126**, 1413 (1993).
8. A. Sakakibara, Y. Kabe, T. Shimizu, and W. Ando. J. Chem. Soc. Chem. Commun. 43 (1991).
9. J. He, H.-Q. Liu, J.F. Harrod, and R. Hynes. Organometallics, **13**, 336 (1994).
10. J.R. Hwu and M. Wang. Tetrahedron, **44**, 4181 (1988).
11. J. He and J.F. Harrod. Heteroatom chemistry. In press.
12. J. He, J.F. Harrod, and R. Hynes. Organometallics. In press.
13. U. Wannagat. *In* Advances in inorganic and radiochemistry. Vol. 6. *Edited by* H.J. Emeleus and A.G. Sharpe. Academic Press, Inc. New York. 1964. pp. 244–251.
14. (*a*) K.A. Andrianov, M.M. Il'in, V.N. Talanov, L.S. Isakova, and N.A. Sidorenko. Vysokomol. Soedin, *A18*, 2752 (1975); (*b*) N.M. Narsavage, L.V. Interrante, P.S. Marchetti, and G.E. Maciel. Chem. Mater. **3**, 721 (1991).
15. C. Colombier. *In* Proceedings of the 1st European Ceramic Society Conference. Vol. 1. *Edited by* de G. With, R. Terpstra, and R. Metselaar. Elsevier Science Publisher Ltd., New York. 1989. pp. 143–152.

Can. J. Chem. Downloaded from www.nrcresearchpress.com by 85.192.166.187 on 09/08/12
For personal use only.

Electronic effects on crown ether conformation. X-ray crystal structure and ^{13}C NMR study in solution and the solid phase of 4-nitrobenzo-9-crown-3 ether[1]

G.W. Buchanan, A.B. Driega, A. Moghimi, and C. Bensimon

Ottawa–Carleton Chemistry Institute, Department of Chemistry, Carleton University, 1125 Colonel By Drive, Ottawa, ON K1S 5B6, Canada

Received November 10, 1993[2]

G.W. Buchanan, A.B. Driega, A. Moghimi, and C. Bensimon. Can. J. Chem. **72**, 1764 (1994).

The X-ray crystal structure of the title material has been determined and the results are compared to previous findings for benzo-9-crown-3 itself. The ^{13}C NMR spectrum in solution has been unambiguously assigned using COSY and HETCOR methods. The solid phase ^{13}C spectrum has been obtained and the 7,10-d_4 derivative has been examined to aid in spectral assignments.

G.W. Buchanan, A.B. Driega, A. Moghimi et C. Bensimon. Can. J. Chem. **72**, 1764 (1994).

On a déterminé la structure cristalline du composé mentionné dans le titre par diffraction des rayons x et on a comparé les résultats avec ceux obtenus au cours d'une étude antérieure sur l'éther benzo-9-couronne fondamental. Faisant appel aux méthodes COSY et HETCOR, on a pu attribuer sans ambiguïté le spectre rmn du ^{13}C. On a déterminé le spectre du ^{13}C en phase solide et, dans le but d'aider à faire des attributions spectrales spéciales, on a étudié le dérivé 7,10-d_4.

[Traduit par la rédaction]

Introduction

Despite the substantial number of studies of benz-annelated crown ether stereochemistry using X-ray crystallographic methods, little attention has been paid to the possible electronic effects of aromatic substituents on crown ether conformation. Such effects might be expected to be substantial due to the possibility of varying degrees of conjugative electron release by the oxygen atoms bonded directly to the aromatic moiety as a result of the influence of substituents with a variety of electronic demand. The influence of a 4-nitro group on the ^{13}C NMR chemical shifts of dibenzo-18-crown-6 has been explored (1) and the results have been discussed in terms of transmission of the electronic effects throughout the molecule, however no X-ray data are reported. Presently we report the X-ray crystal structure of 4-nitrobenzo-9-crown-3 ether and compare the findings to our earlier results (2) for benzo-9-crown-3 itself. The introduction of the 4-nitro group permits an unambiguous assignment of the solution phase ^{13}C NMR spectrum and subsequently aids in the assignment of the solid phase ^{13}C spectrum. Finally the geometrical dependence of the aryl—O—*CH_2—^{13}C chemical shift on the C—C—O—*C torsion angle in benz-annelated crown ethers is clarified.

Results and discussion

The structure and numbering scheme for 4-nitrobenzo-9-crown-3 (**1**) are shown in Fig. 1. The ORTEP diagram is illustrated in Fig. 2 and the ^{13}C NMR spectra are in Fig. 3. Table 1 contains bond lengths and bond angles while torsion angles are collected in Table 2. Crystallographic data are listed in Table 3 and atomic parameters in Table 4. In Table 5 are presented the ^{13}C NMR data.

(i) X-ray crystal structure

It is of interest to compare the torsion angle data for the C and O framework of **1** with those for benzo-9-crown-3, **2**, (2). Such a comparison shows that the overall geometries have many similarities, since only eight torsional networks change their geometries by more than 1° and the largest change is 9.6°. Details of the changes in excess of 1° are shown below.

	Torsion angle (deg)		
Network	**1**	**2**	Difference
C10—O1—C1—C2	−0.9	−10.5	9.6
C10—O1—C1—C6	179.0	170.3	8.7
C7—O2—C2—C3	73.9	79.9	6.0
C7—O2—C2—C1	−108.5	−105.0	3.5
O3—C9—C10—O1	−66.2	−63.3	2.9
O2—C7—C8—O3	−63.3	−66.7	3.4
C1—O1—C10—C9	91.4	98.4	7.0
C9—O3—C8—C7	111.7	108.7	3.0

The most pronounced effect of the introduction of the 4-nitro group is to induce a flattening effect in the C10—O—Cl—C2 and C10—O1—C1—C6 units so that there is essentially a planar conformation induced in the C10—O—aryl geometry. Such an effect is intuitively reasonable based on the known electron-withdrawing character of the nitro moiety. Thus the resonance structure **1***b* depicted below for **1** most accurately describes the electronic distribution in the molecule, with the C1—O1—C10 bond angle of 123.3° indicating sp^2 hybridized O1. The C2—O2—C7 angle of 115.4° is almost identical to the C8—O3—C9 angle of 114.4°. Thus the hybridization at O2 can be regarded as essentially sp^3.

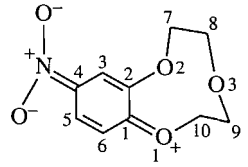

1*b*

As expected, less pronounced nitration induced changes occur in the geometry in the vicinity of O2 and C7, due to the *meta* disposition of O2. The nitro group is twisted by only about 3° out of the plane of the aromatic ring. The increase in sp^2 character at O1 upon nitration induces a slight expansion of the O3—C9—C10—O1 angle to 66.2° in **1** from 63.9° in **2**. The

[1]Taken in part from the M.Sc. thesis of A.B. Driega, Carleton University, January 1993.

[2]Revision received April 12, 1994.

Can. J. Chem. Downloaded from www.nrcresearchpress.com by 85.192.166.187 on 09/08/12
For personal use only.

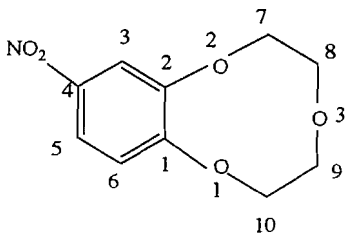

1

FIG. 1. Structure and numbering scheme for **1**.

normal *gauche* geometry (3, 4) for O—C—C—O torsional units in crown ethers is clearly retained in both compounds when sp^3 hybridized carbons are the central atoms of such units.

With respect to the bond angles of **1**, there is a large observed difference between the O1—C1—C2 angle of 128.1° and the O1—C1—C6 angle of 112.5°. Such a difference also occurs in the corresponding carbons of benzo-9-crown-3 itself and hence cannot be due to the introduction of the nitro group. From the ORTEP diagram and inspection of molecular models, it appears that the expansion of the O1—C1—C2 angle results from a molecular structural adjustment to minimize a potentially repulsive transannular interaction involving the equatorial H on C10 and O2.

TABLE 1. Atomic bond distances (Å) and bond angles (deg)

Bond	Distance	Bond	Distance
O1—C1	1.362(4)	C4—C5	1.381(6)
O1—C10	1.450(5)	C5—C6	1.373(6)
O2—C2	1.374(4)	O2—C7	1.444(5)
O3—C8	1.427(5)	C7—C8	1.504(6)
O3—C9	1.430(5)	C9—C10	1.496(6)
O4—N1	1.221(5)		
O5—N1	1.233(5)		
N1—C4	1.455(5)		
C1—C2	1.409(5)		
C1—C6	1.397(5)		
C2—C3	1.375(5)		
C3—C4	1.382(6)		

Bond	Angle	Bonds	Angle
C1—O1—C10	123.3(3)	O2—C7—C8	109.7(4)
C2—O2—C7	115.4(3)	O3—C8—C7	109.9(3)
C8—O3—C9	114.4(3)	O3—C9—C10	114.6(3)
O4—N1—O5	122.5(3)	O1—C10—C9	111.0(4)
O4—N1—C4	119.0(3)	O1—C1—C2	128.1(3)
O5—N1—C4	118.6(3)	O1—C1—C6	112.5(3)
C2—C1—C6	119.4(3)	O2—C2—C1	122.7(3)
O2—C2—C3	118.8(3)	C1—C2—C3	118.5(3)
C2—C3—C4	121.0(4)	N1—C4—C3	119.2(3)
N1—C4—C5	119.5(4)	C3—C4—C5	121.3(4)
C4—C5—C6	118.4(4)	C1—C6—C5	121.5(4)

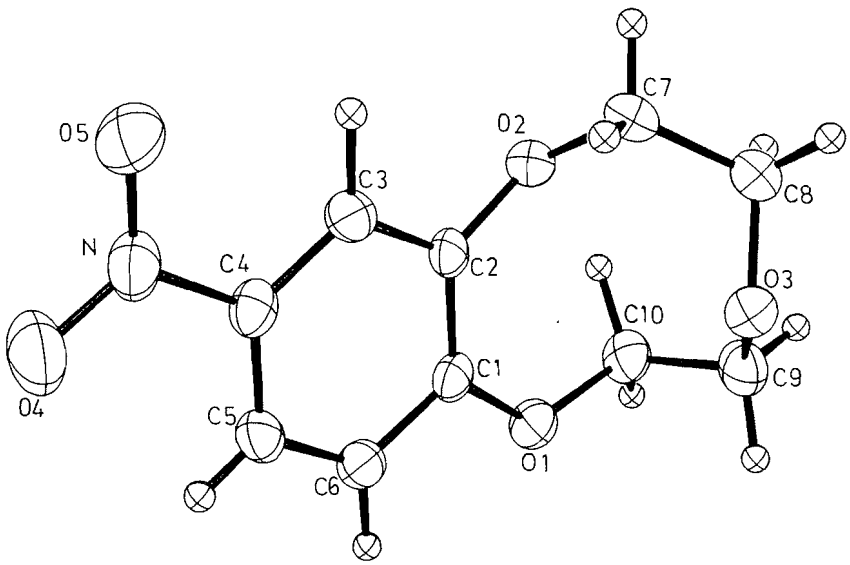

FIG. 2. ORTEP diagram of **1**.

TABLE 2. Selected torsion angles involving non-H atoms

Bonds	Torsion angle	Bonds	Torsion angle
C10—O1—C1—C2	−0.9(2)	C10—O1—C1—C6	179.0(4)
C1—O1—C10—C9	91.4(4)	C7—O2—C2—C1	−108.5(4)
C7—O2—C2—C3	73.9(3)	C2—O2—C7—C8	106.2(4)
C9—O3—C8—C7	111.7(4)	C8—O3—C9—C10	−73.7(3)
O4—N1—C4—C3	177.9(5)	O4—N1—C4—C5	−3.0(2)
O5—N1—C4—C3	−2.7(2)	O5—N1—C4—C5	176.5(5)
O1—C1—C2—O2	4.0(1)	O1—C1—C2—C3	−178.3(5)
C6—C1—C2—O2	−175.9(4)	O1—C1—C6—C5	178.3(5)
O2—C2—C3—C4	177.1(5)	C2—C3—C4—N1	178.5(5)
N1—C4—C5—C6	−178.5(5)	O2—C7—C8—O3	−63.3(3)
O3—C9—C10—O1	−66.2(3)		

Can. J. Chem. Downloaded from www.nrcresearchpress.com by 85.192.166.187 on 09/08/12
For personal use only.

Can. J. Chem. Downloaded from www.nrcresearchpress.com by 85.192.166.187 on 09/08/12
For personal use only.

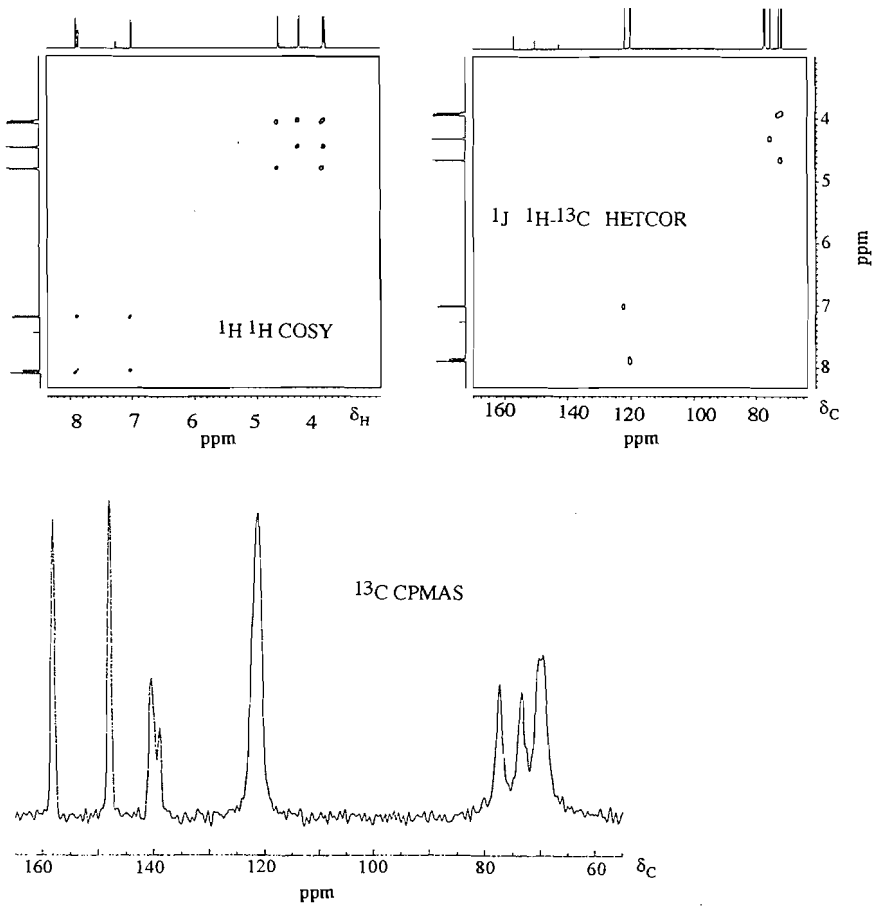

FIG. 3. 400 MHz ^{1}H^{1}H COSY, ^{1}H^{13}C HETCOR and 45.3 MHz ^{13}C CPMAS spectra of **1**.

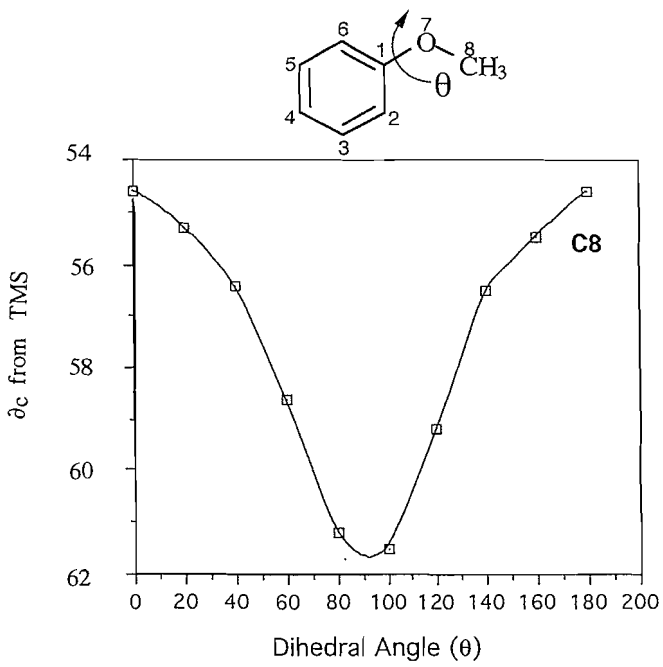

FIG. 4. Dependence of CH_3 shielding of anisole on the CH_3—O—C—C dihedral angle.

TABLE 3. Crystallographic data

Formula	$C_{10}H_{11}NO_5$
fw	225.20
Crystal system	Monoclinic
Space group	$P\ 2_1/c$
a, Å	4.3393 (14)
b, Å	12.562 (5)
c, Å	18.321 (4)
β	95.254 (24)
V, Å^3	994.5 (5)
Z (molecules/unit cell)	4
D_c, g cm^{-3}	1.504
Crystal dimensions, mm^3	0.10 × 0.10 × 0.30
Radiation (λ, Å)	MoKα (0.70932)
h, k, l ranges	−4, 4; 0, 14; 0, 20.
Maximum 2θ	46.9
No. reflections measured	1678
No. of unique reflections	1460
No. of reflections observed	1227
($I/\sigma(I)$ ratio)	0.055
F(000)	472.26
μ	0.13 mm^{-1}
R_f (sign. refl.)	0.052
R_w (sign. refl.)	0.070
S (GOF)	5.67

(ii) Solution ^{13}C NMR spectrum

The ^{13}C NMR spectrum of **1** at 100.6 MHz shows 10 lines as expected, with resonances for C3 and C5 being nearly identical in chemical shift. Assignments of all resonances can be done unambiguously using a combination of 1D and 2D NMR techniques. Initially, C1, being *para* to the nitro group, will be the most deshielded quaternary carbon (5). Using this as a starting

Can. J. Chem. Downloaded from www.nrcresearchpress.com by 85.192.166.187 on 09/08/12
For personal use only.

TABLE 4. Atomic parameters x, y, z and B_{iso}[a]

Atom	x	y	z	B_{iso}
O1	0.6609(6)	0.77547(20)	0.20823(13)	2.75(13)
O2	0.5696(6)	0.60959(20)	0.09095(13)	2.57(11)
O3	0.8710(6)	0.55039(20)	0.22997(13)	2.69(13)
O4	1.3688(8)	0.90156(25)	−0.05923(16)	4.25(16)
O5	1.2101(8)	0.74678(24)	−0.09618(15)	4.55(17)
N1	1.2249(8)	0.8196 (3)	−0.05086(17)	2.99(16)
C1	0.7796(9)	0.7769 (3)	0.14194(19)	2.08(15)
C2	0.7488(9)	0.6991 (3)	0.08637(19)	2.05(15)
C3	0.8956(9)	0.7154 (3)	0.02392(20)	2.34(17)
C4	1.0671(9)	0.8065 (3)	0.01530(19)	2.28(16)
C5	1.0948(10)	0.8845 (3)	0.06865(21)	2.43(18)
C6	0.9496(9)	0.8691 (3)	0.13131(21)	2.41(18)
C7	0.7380(12)	0.5110 (3)	0.10282(23)	2.92(21)
C8	0.7220(12)	0.4747 (3)	0.18058(22)	2.94(21)
C9	0.6664(11)	0.6069 (4)	0.27307(24)	3.03(20)
C10	0.4715(10)	0.6893 (3)	0.23200(23)	2.74(19)
H3	0.885 (8)	0.654 (3)	−0.0159 (19)	2.7 (8)
H5	1.209 (9)	0.940 (3)	0.0631 (19)	2.7 (9)
H6	0.958 (9)	0.924 (3)	0.1710 (19)	2.8 (8)
H7A	0.642 (9)	0.462 (3)	0.0683 (20)	2.6 (8)
H7B	0.957 (9)	0.524 (3)	0.0874 (18)	2.3 (8)
H8A	0.496 (10)	0.465 (3)	0.1880 (19)	3.0 (9)
H8B	0.835 (9)	0.405 (3)	0.1851 (20)	3.1 (9)
H9A	0.526 (10)	0.557 (3)	0.2894 (22)	3.9 (10)
H9B	0.804 (9)	0.648 (3)	0.3115 (20)	3.1 (9)
H10A	0.329 (8)	0.657 (3)	0.1848 (20)	2.9 (8)
H10B	0.349 (10)	0.725 (3)	0.2647 (22)	3.7 (10)

[a] B_{iso} is the mean of the principal axes of the thermal ellipsoid, esd's refer to the last digit in the table.

point, the C2 and C4 assignments follow directly. The aromatic proton on C6 is the most shielded due to its disposition *ortho* to oxygen and *meta* to the NO_2 function. Also its multiplicity in the ^1H spectrum is consistent with this assignment. The aromatic proton on C3 shows only long range (^4J) coupling to H5. With the aromatic proton assignments in hand, the protonated aromatic C's were assigned via ^1J HETCOR. The solution ^1H and ^{13}C NMR spectra of the C7,10-d_4 version of **1** permitted elucidation of the resonance positions of C7,10 protons and carbons. Distinction between C7 and C10 protons was made on the basis of long range ^{13}C—^1H HETCOR (J = 5.0 Hz) since the assignments for their respective vicinal carbons C2 and C1 are clear. Subsequently the C8 and C9 protons were assigned via $^1H^1H$ COSY and the C7, C8, C9, and C10 carbons via ^1J HETCOR. Data are collected in Table 5.

(iii) Solid phase ^{13}C NMR spectrum

This spectrum is shown in Fig. 3. The most deshielded aromatic carbons are attributed to C1 and C2, respectively, with chemical shifts within 1–2 ppm of those found in solution. The C4 resonance is an asymmetric doublet, characteristic of a carbon bonded to the quadrupolar N atom. Resonances for C3, C5, and C6 are overlapping. With respect to the aliphatic resonances, the range of chemical shifts observed is 7.5 ppm, which is within 1 ppm of that found previously for benzo-9-crown-3 (2). The dipolar dephased spectrum of **1**-C7,10-d_4, clearly indicated that resonances at 69.9 and 77.4 ppm arise from C7 and C10. In solution, C7 resonates at 75.7 and C10 at 71.7 ppm, respectively. Although clearly some conformational averaging will occur in solution, we feel confident that the solid phase shift for C7 of **1** is 77.4 ppm and that of C10 is at 69.9 ppm.

TABLE 5. Solution and solid phase ^{13}C NMR chemical shifts for **1** (∂_c from TMS)

	^{13}C NMR shift	
Position	Solution (0.2 M in $CDCl_3$)	Solid
C1	157.3	157.7
C2	150.6	148.0
C3	120.1	121.2
C4	142.6	140.0
C5	120.3	121.2
C6	122.1	121.2
C7	75.4	77.4
C8	72.8	73.5
C9	72.0	70.7
C10	71.7	69.9

It remains to examine the origin of the 7.5 ppm shift difference between C7 and C10, with C10 being the more shielded site. Recently (2), we have calculated the dependence of CH_3 shielding of anisole on the CH_3—O—C—C dihedral angle. The results are depicted in Fig. 4.

Clearly, the aryl—O—*C resonance is most shielded for the *cis*-coplanar ($\theta = 0°$) and *trans*-coplanar ($\theta = 180°$) situations, with maximum deshielding occuring in the perpendicular conformation. Examination of the two aryl—O—*C angles involving each of C7 and C10 reveals substantial differences. For C7, the C7—O2—C2—C3 angle is 73.9° while the C7—O2—C2—C1 angle is −108.5°. In contrast, the C10 site appears to be nearly coplanar with the aromatic ring, with the C10—O1—C1—C2 angle being −0.9° and the C10—O1—C1—C6 angle 179.0°. These solid state geometries, coupled with the results of the anisole calculations, would lead one to expect that C10 should be shielded relative to C7 by ca. 10 ppm. The experimental NMR difference is 7.5 ppm. We regard this as satisfactory agreement, given that the calculations are for a model compound rather than for **1**, and are for the gas phase situation, rather than the solid.

The fundamental origin of the angular dependence of the OCH_3 shielding in methoxybenzenes has been discussed by Grant and co-workers (6). For non-planar OCH_3, the C—O bond is destabilized by the absence of conjugation between the O lone pairs and the aromatic π system. Thus the antibonding C—O orbital has a lower energy in non-planar than planar conformers. This reduces the ΔE (average electronic excitation energy) term in the denominator of the paramagnetic shielding term. Since this is a negative shielding term, a deshielding results.

Experimental

(i) Materials

The synthesis of benzo-9-crown-3-d_4 has been reported previously (7). Nitration of this material to give **1** was carried out using the following procedure which is similar to that reported for the synthesis of dinitrodibenzo-18-crown-6 ether (8). Benzo-9-crown-3-d_4 (3.3 g, 0.018 mol) was dissolved in a mixture of CH_2Cl_2 (70 mL) and glacial acetic acid (50 mL) and 1 drop of 96% H_2SO_4 was added with stirring. To this solution was added 8.0 mL of 70% HNO_3 and the mixture was stirred at ambient temperature for 15 min before refluxing for 3 h. After cooling, the acidic reaction mixture was neutralized by the addition of aqueous Na_2CO_3 while keeping the mixture cool in an ice bath. Following extraction with CH_2Cl_2, the organic extracts were backwashed with saturated $NaHCO_3$ and H_2O and dried over $MgSO_4$. Solvent removal gave a crude yellow solid which was recrystallized from

absolute ethanol to yield 2.4 g (59%) of **1**, mp. 93.5–95.0°C. High resolution MS: *m/z* for $C_{10}H_7O_5N_1D_4(M^+)$, calcd 229.0888, found 229.0926.

(ii) Spectra

Solution NMR spectra were recorded using a Bruker AMX-400 spectrometer equipped with a 5 mm inverse probe and an Aspect X32 computer. An Aspect 3000 processing controller was employed and all standard microprograms used are in the Bruker Software Library.

$^1H^1H$ COSY experiments were run using N-type phase cycling with a 45° mixing pulse. Free induction decays were acquired over 1024 data points for each of the 256 values of the evolution time, with a digital resolution of 5 Hz/point. The raw data were zero filled in F1 prior to transformation using the qsine window function for both F1 and F2. The matrix was symmetrized about the diagonal.

For the $^1H^{13}C$ HETCOR experiments, the free induction decays were typically acquired over 1024 data points for each of the 512 values of the evolution time, with a digital resolution of ca. 8 Hz/point in F2 and 4 Hz/point in F1. The raw data were zero filled in F1 prior to transformation using the qsine window function for both F1 and F2. The proton relaxation delays were set to 1 s. For 1-bond couplings, delays were set to emphasize couplings of 104 Hz, while for the long range HETCOR experiment, delays were set to correspond to couplings of 5 Hz.

Solid phase ^{13}C NMR spectra were recorded at 45.3 MHz using a Bruker CXP-180 spectrometer using cross polarization magic angle spinning (CPMAS) conditions described previously (9). For the dipolar dephased spectra, the ^1H decoupler was gated off for a period of 40 μs during the delay before the ^{13}C acquisition.

(iii) X-ray crystallographic measurements and structure solution

A summary of the crystallographic data is given in Table 3. Diffraction intensities were collected on a Rigaku diffractometer using MoKα radiation at −90°C. The θ/2θ scan technique with profile analysis (10) was employed. The space group was determined by systematic absences. Unit cell parameters were obtained by refinement of the setting angles of 25 reflections with 2θ values in the range of 40–46.9°. Lorentz and polarization factors were applied but no correction for absorption was made. The structure was solved by direct methods plus Fourier maps and was refined by full-matrix least-squares analysis with weights based on counting statistics. Non-H atoms were refined anisotropically and H atoms were refined isotropically. All calculations were performed using the NRC VAX crystal structure programs (11). Anisotropic thermal parameters and structure factor tables are available as supplementary data.[3]

Acknowledgements

G.W.B. thanks the Natural Sciences and Engineering Research Council (NSERC) for continuing financial support. We thank Dr. C.I. Ratcliffe for obtaining the solid phase ^{13}C spectra.

1. V.F. Loktev, I.L. Mudrakovsky, A.K. Tashmukhamedova, I.A. Stempnevskyaya, and I.J. Morozova. Mag. Res. Chem. **28**, 176 (1990).
2. G.W. Buchanan, A.B. Driega, A. Moghimi, C. Bensimon, R.A. Kirby, and T.D. Bouman. Can. J. Chem. **71**, 1983 (1993).
3. A.C. Coxon, D.A. Laidler, R.B. Pettman, and J.F. Stoddart. J. Am. Chem. Soc. **100**, 8260 (1978).
4. M.J. Boill, D.J. Chadwick, and I.O. Sutherland. J. Chem. Soc. Perkin Trans. 2, 1529 (1980).
5. J.B. Stothers. Carbon-13 NMR spectroscopy. Academic Press, New York, NY. 1972. p. 197.
6. C.M. Carter, J.C. Facelli, D.W. Alderman, D.M. Grant, N.K. Dalley, and B.E. Wilson. J. Chem. Soc. Faraday Trans. I, **84**, 3673 (1988).
7. G.W. Buchanan, A.B. Driega, A. Moghimi, C. Benzimon, and K. Bourque. Can. J. Chem. **71**, 951 (1993).
8. W.M. Fiegenbaum and R.H. Michel. J. Polymer Sci. A-1 **9**, 817 (1970).
9. G.W. Buchanan, A. Rodrigue, C. Bensimon, and C.I. Ratcliffe. Can. J. Chem. **70**, 1033 (1992).
10. D.F. Grant and E.J. Gabe. J. Appl. Crystallogr. **11**, 114 (1978).
11. E.J. Gabe, F.L. Lee, and Y. Le Page. J. Appl. Crystallogr. **22**, 384 (1989).

[3]This supplementary material can be purchased from: The Depository of Unpublished Data, Document Delivery, CISTI, National Research Council Canada, Ottawa, ON K1A 0S2, Canada.

Can. J. Chem. Downloaded from www.nrcresearchpress.com by 85.192.166.187 on 09/08/12
For personal use only.

Stereoselective oxirane formation by reaction of diazomethane on 1-fluoro-3-[(4-methylphenyl)sulfinyl]-3-phenylpropan-2-one

PIERFRANCESCO BRAVO,[1] MASSIMO FRIGERIO, GIOVANNI FRONZA, VADIM SOLOSHONOK,[2] AND FIORENZA VIANI

Consiglio Nazionale delle Richerche – Centro di Studio per le Sostanze Organiche Naturali, Dipartimento di Chimica, Politecnico, Via Mancinelli 7, I-20131 Milano, Italy

GIANCARLO CAVICCHIO AND GIANCARLO FABRIZI

Dipartimento di Chimica, Ingegneria Chimica e Materiali, Università di L'Aquila, Via Assergi 6, I-67100 L'Aquila, Italy

AND

DORIANO LAMBA

Istituto di Strutturistica Chimica "Giordano Giacomello", Consiglio Nazionale delle Richerche, Area della Ricerca di Roma, Casella Postale N. 10, I-00016 Monterotondo Stazione (Roma), Italy

Received August 10, 1993[3]

Can. J. Chem. Downloaded from www.nrcresearchpress.com by 85.192.166.187 on 09/08/12
For personal use only.

PIERFRANCESCO BRAVO, MASSIMO FRIGERIO, GIOVANNI FRONZA, VADIM SOLOSHONOK, FIORENZA VIANI, GIANCARLO CAVICCHIO, GIANCARLO FABRIZI, and DORIANO LAMBA. Can. J. Chem. **72**, 1769 (1994).

(2*S*,2′*R*,R_S)-2-(Fluoromethyl)-2-{[(4-methylphenyl)sulfinyl][phenyl]methyl}oxirane (**4**) was obtained in high chemical yield and with high diastereoselectivity by reacting diazomethane with pure (3*R*,R_S)-1-fluoro-3-[(4-methylphenyl)sulfinyl]-3-phenylpropan-2-one (**3**), but also with its (3*S*,R_S)-**3**-diastereoisomer, in the latter case through inversion of the configuration at carbon 3. The corresponding methyl enol ethers **6** were isolated as by-products. NMR experiments and molecular modelling calculations were performed in order to clarify the equilibria in solution and the preferred conformations of both ketones **3**. Several variously substituted, sulfur-free tertiary α-(fluoromethyl)carbinols were obtained from the main reaction product (2*S*,2′*R*,R_S)-**4** through appropriate elaborations of the sulfinyl group and of the oxirane ring. The structure of (2*S*,2′*R*,R_S)-**4** was established by X-ray analysis of the open-chain derivative (2*S*,2′*R*,R_S)-1-bromo-3-fluoro-2′-{[(4-methylphenyl)sulfinyl][phenyl]methyl}propan-2-ol (**7**).

PIERFRANCESCO BRAVO, MASSIMO FRIGERIO, GIOVANNI FRONZA, VADIM SOLOSHONOK, FIORENZA VIANI, GIANCARLO CAVICCHIO, GIANCARLO FABRIZI et DORIANO LAMBA. Can. J. Chem. **72**, 1769 (1994).

Le (2*S*,2′*R*,R_S)-2-(fluorométhyl)-2-{[(4-méthylphényl)sulfinyl][phényl]méthyl}oxirane (**4**) fut obtenu avec d'excellents rendements chimiques et avec une diastéréosélectivité élevée en faisant réagir du diazométhane avec de la (3*R*,R_S)-1-fluoro-3-[(4-méthylphényl)sulfinyl]-3-phénylpropan-2-one (**3**) pure ou sous la forme de mélange avec le diastéréoisomère (3*S*,R_S)-(**3**); dans ce dernier cas, la réaction se fait par le biais d'une inversion de configuration au niveau du carbone 3. Les éthers énoliques méthyles correspondants (**6**) sont isolés comme sous-produits. Des expériences de RMN et des calculs de modelage moléculaire ont été exécutés pour clarifier les équilibres en solution et les conformations privilégiées des deux cétones **3**. On a préparé de nombreux α-(fluorométhyl)carbinols tertiaires sans soufre et portant divers groupes fonctionnels par élaborations appropriées du groupe fonctionnel sulfinyle et de l'anneau oxirane à partir du produit principal de la réaction le (2*S*,2′*R*,R_S)-**4**. La structure du (2*S*,2′*R*,R_S)-**4** a été déterminée par diffraction des rayons X du dérivé aliphatique (2*S*,2′*R*,R_S)-1-bromo-3-fluoro-2′-{[(4-méthylphényl)sulfinyl][phényl]méthyl)propan-2-ol (**7**).

[Traduit par la rédaction]

Introduction

The current surge of activity in the synthesis of fluoro analogs of organic natural substances and of biologically active molecules (1) has prompted searches for improved, easily accessible, fluorinated chiral building blocks (2). Our efforts in this area have centered on the preparation and use of sulfoxide-based fluorinated reagents. The 1-fluoro substituted-3-arylsulfinylpropan-2-ones **3** (R = H, alkyl, aryl; $R_F = CH_2F, CF_3$), easily accessible from fluorinated acetic acid esters **1** and chiral aryl alkyl sulfoxides **2** (Scheme 1), have been the chirons of choice for the construction of a number of target molecules of biological interest (3–5). In all cases the key step of the synthetic routes has been the transfer of chirality from sulfur to carbon, obtained by stereoselective hydride-promoted reduction of the carbonyl (6). Elimination of the chiral auxiliary sulfinyl group and carbon chain elaboration to the final target molecules followed. Some deoxyfluoro-pentoses and -hexoses, some fluoro-substituted acyclic nucleoside analogs, and the four diastereoisomers of 4-deoxy-4-fluoromuscarine (for biological testing) were obtained by that route (3–5).

While searching for an alternative route to achieve the chirality transfer from sulfur to the carbon chain, we found that, under appropriate reaction conditions, the transfer of the methylene group from diazomethane to the carbonyl can occur with excellent diastereofacial selectivity (7). This route yields some new highly versatile chirons (**4**, see Scheme 1) that may undergo a large number of transformations with high regio- and stereocontrol.

Expanding on this methodology, we will be reporting (P. Bravo et al., results to be published) on the high-yield preparation of a broad spectrum of chiral and enantiomerically pure 2,2-disubstituted oxiranes obtained by the action of diazomethane on a series of β-ketosulfoxides, some of them γ-polyhalogenated, as well as on a number of α-substituted and γ-mono- or polysubstituted β-ketosulfoxides.

In the present paper we wish to report (8) on the most remark-

---

[1]Author to whom correspondence may be addressed. Tel. No.: (39) 2-23993033.

[2]Recipient of a C.N.R. – Progetto Finalizzato Chimica Fine visiting professorship from Ukranian Academy of Sciences, Kiev.

[3]Revision received March 25, 1994.

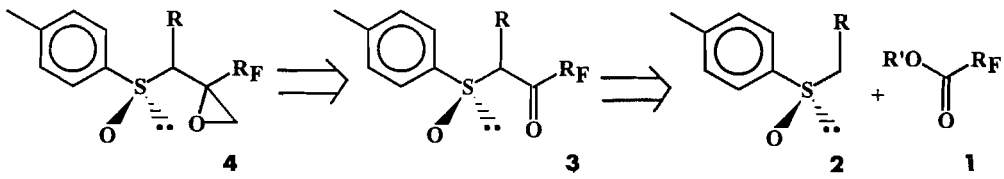

SCHEME 1

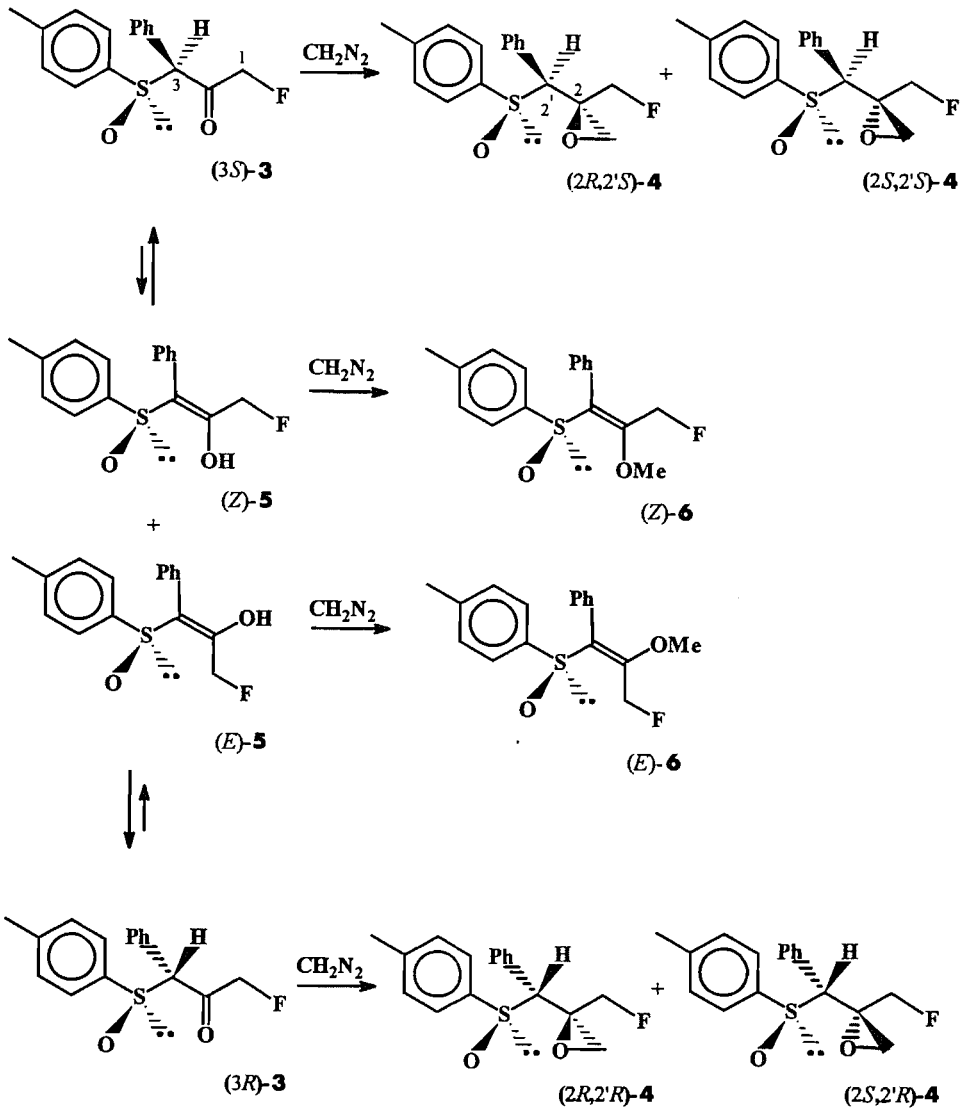

SCHEME 2

able case of diastereoselection found while studying these methylene transfer reactions, i.e., the synthesis of (2*S*,2′*R*,R_S)-2-fluoromethyl-2-{[(4-methylphenyl)sulfinyl]methyl}oxirane **4** from the corresponding ketones (2*S*,R_S)- and (2*R*,R_S)-**3** (Scheme 1, R = Ph, $R_F = CH_2F$) and on some synthetically useful transformations performed on **4**.

Results and discussion

As already described (9), 1-fluoro-3-[(4-methylphenyl)sulfinyl]-3-phenylpropan-2-one (**3**) is obtained by acylating the lithium salt of benzyl 4-methylphenyl sulfoxide (**2**) with ethyl fluoroacetate (**1**) in tetrahydrofuran (THF).

A mixture of the two diastereoisomers (3*R*,R_S)- and (3*S*,R_S)-**3** is obtained in a 1.0:1.8 ratio and both compounds can be obtained in optically pure form by fractional crystallization (see Experimental).

The reactivity towards diazomethane and the diastereoselectivity of the process were tested both on diastereoisomerically pure ketones and on mixtures, in three different solvents: methanol, THF, and ethyl ether. In all cases examined, a mixture of oxiranes **4** and of (*E*) and (*Z*) methyl enol ethers **6** was observed, in different relative ratio depending on the stereochemistry of the starting ketones and the reaction medium.

When an approximately 0.5 M ethereal solution of diazomethane (10) was added at 0°C to a methanolic solution of optically pure (3*R*,R_S)-1-fluoro-3-[(4-methylphenyl)sulfinyl]-

Can. J. Chem. Downloaded from www.nrcresearchpress.com by 85.192.166.187 on 09/08/12
For personal use only.

Can. J. Chem. Downloaded from www.nrcresearchpress.com by 85.192.166.187 on 09/08/12
For personal use only.

3-phenylpropan-2-one **3**, a fast reaction occurred (in less than 5 min) and the product mixture was isolated in about 96% overall yield. The ^1H and ^{19}F NMR analysis of the crude showed the presence of two oxiranes (^{19}F NMR δ: −228.5 and −227.4 ppm) and of two enol ethers (^{19}F NMR δ: −212.0 for (*E*)-**6** and δ: −217.3 ppm for (*Z*)-**6**). The main oxirane (δ: −228.5 ppm) was isolated in optically pure form in 83.8% yield and the (2*S*,2′*R*,R_S) absolute stereochemistry was determined as reported (vide infra). The other compounds mentioned were detected in amounts of less than 6% (see Experimental). When the ethereal solution of diazomethane was added to a 2:1 mixture of 3*R*/3*S* ketones **3** in three different solvents (methanol, THF, and ethyl ether) the resulting mixtures showed the following: (*a*) (2*S*,2′*R*,R_S)-**4** (^{19}F NMR δ: −228.5 ppm) was always the main product, being isolated in, respectively, 76, 70, and 65% yield; (b) another oxirane (^{19}F NMR δ: −229.2 ppm) was detectable in reaction mixtures in, respectively, 5, 8, and 4% yield; (*c*) the other two oxiranes (^{19}F NMR δ: −227.4 and −226.8 ppm) were only detectable in the third case by NMR analyses on the crude; (*d*) *E*/*Z*-**6** methyl enol ether mixtures were present in, respectively, 15, 16, and 13% yield. Comparable results were obtained starting from a ca. 1:1 mixture of diastereoisomeric ketones **3** (see Experimental). Moreover, when optically pure (3*S*,R_S)-**3** ketone was reacted with diazomethane in the same three solvents, (2*S*,2′*R*,R_S)-**4** was still the main reaction product although the stereochemistry at C-2′ was opposite to the corresponding stereochemistry of the starting ketone. The oxirane could be isolated in optically pure form in, respectively, 45, 60, and 62% yields whilst the remaining three oxiranes were present in slightly different relative ratios (27, 14, and 13% respectively, see Experimental). As the global yield was always nearly quantitative, the *E*/*Z*-**6** methyl enol ether mixtures accounted for the remaining reaction products.

In conclusion, the same (2*S*,2′*R*,R_S)-**4** oxirane was surprisingly obtained in all cases, both starting from an optically pure ketone or from different mixtures of the two diastereoisomers, in a largely prevailing amount. This implies that in the reaction medium an equilibrium between the two ketones may occur, that the reaction rate of diazomethane may be higher for one diastereoisomer than for the other, and that the approach to the carbonyl group may be preferred from one side rather than from the other.

Therefore, the final products ratio may be influenced by different factors: epimerization rates of the ketones, equilibrium composition, presence of enolic forms, preferred conformations of the diastereoisomeric ketones, and catalytic effect of methanol on the reaction of diazomethane on carbonyls (11).

The supposed species present in solution at equilibrium and the products isolated from the reaction are reported in Scheme 2.

To obtain further information on the nature of the reported equilibria, the reaction progress was monitored by ^{19}F NMR, through progressive spectral recordings of solutions of both diastereoisomeric ketones **3** in perdeuterated methanol. Moreover, to obtain some information about the different reactivity of diazomethane on both ketones **3**, their respective preferred conformations were investigated by molecular modelling calculations based on minimum energy convergence.

Equilibration experiments

The ^{19}F NMR spectrum of (3*S*)-**3**, just after dissolution in perdeuterated methanol, shows a triplet of doublets at −227.02 ppm (J(F, CH_2) = 16.6 Hz, J(F, H-3) = 2.4 Hz) (Fig. 1 (*a*′)) consistent with the presence of a single diastereoisomer. During this time two new triplets appear at −227.06 and −226.56 ppm (J(F, CH_2) = 46.6 Hz) lacking the long-range coupling ^4J(F, H-3) (Fig. 1 (b′), (c′)). The signal at −227.06 ppm can be assigned to the C-3 deuterated form of (3*S*)-**3**, the fluorine chemical shift being shifted to high field by 0.04 ppm with respect to (3*S*)-**3** because of the isotopic effect of the deuterium atom four bonds away. The second signal at −226.56 ppm can be attributed to the deuterated species of (3*R*)-**3** formed in solution by epimerization at position 3. The thermodynamic equilibrium is reached in about 30 h showing a ca. 4:6 ratio of the two epimeric forms (3*S*)- and (3*R*)-**3**, respectively (Fig. 1(*c*)).

The (3*R*)-**3** fluoroketone behaves similarly. Just after dissolution in methanol the ^{19}F NMR spectrum displays a triplet of doublets at −226.52 ppm (J(F, CH_2) = 46 Hz, J(F, H-3) = 2.1 Hz) (Fig. 1(*a*)). After some time two new signals appear at −226.56 and −227.06 ppm (Fig. 1(*b*)) that can be assigned to the C-3 deuterated species (3*R*)- and (3*S*)-**3**, respectively. In this case the equilibration rate is slower than that observed for (3*S*)-**3** and the thermodynamic equilibrium is reached after ca. 3 days (Fig. 1(*c*)). The enolic forms (*E*)- or (*Z*)-**5** were undetectable by ^1H and ^{19}F NMR measurements. These experiments show that the epimerization process at C-3 for (3*S*)- and (3*R*)-**3** is rather slow in solution.

On the contrary their reaction with diazomethane is very fast, leading in a few minutes to the formation of (2*S*,2′*R*,R_S)-**4** as main product. This was true both for the reactions reported in the Experimental and for test reactions run in an NMR tube. These findings suggest that in the presence of diazomethane the epimerization rate of ketones is much faster than that observed in methanol only. Incorporation of deuterium can be taken as positive evidence for the transient formation of enolic forms **5**.

Molecular modelling calculations

As outlined above, the fluoroketones (3*S*)-**3** and (3*R*)-**3** show a peculiar behaviour, which can be summarized as follows: (*i*) they epimerize slowly in solution to form a mixture of ca. 60% of (3*R*)-**3** and 40% of (3*S*)-**3** (methanolic solution); (*ii*) they react immediately with diazomethane, leading to the formation of the (2*S*,2′*R*)-**4** oxirane as main product. These observations suggest that diazomethane would react preferentially with the (3*R*)-**3** isomer, which is generated in a fast-catalysed reaction. Possibly a rationale of this behaviour may be found in the conformational properties of the two molecules, since a particular conformation may explain, in principle, the marked preference of the reactivity towards diazomethane.

To this end we performed some molecular mechanics calculations[4] on the two fluoroketones. The conformational space was explored starting from a minimized random structure and varying the two most significant torsional angles, OSC_3C_2 (ϕ_1) and SC_3C_2O (ϕ_2), over 360° in steps of 30°. Every conformation obtained in this way was minimized and the values of the strain energy have been reported as a function of ϕ_1 and ϕ_2 in a bidimensional plot. As a result of this searching procedure, the (3*R*)-**3** epimer shows two isoenergetic minima having ϕ_1,ϕ_2, defined according to Kline and Prelog, of ca. −45°,−90° and 60°,90°, respectively. The epimer (3*S*)-**3**

[4]The calculations were performed with the MMX Version 89.000 program (Serena Software, Box 3076, Bloomington, IN 47402-3076, U.S.A.).

Can. J. Chem. Downloaded from www.nrcresearchpress.com by 85.192.166.187 on 09/08/12
For personal use only.

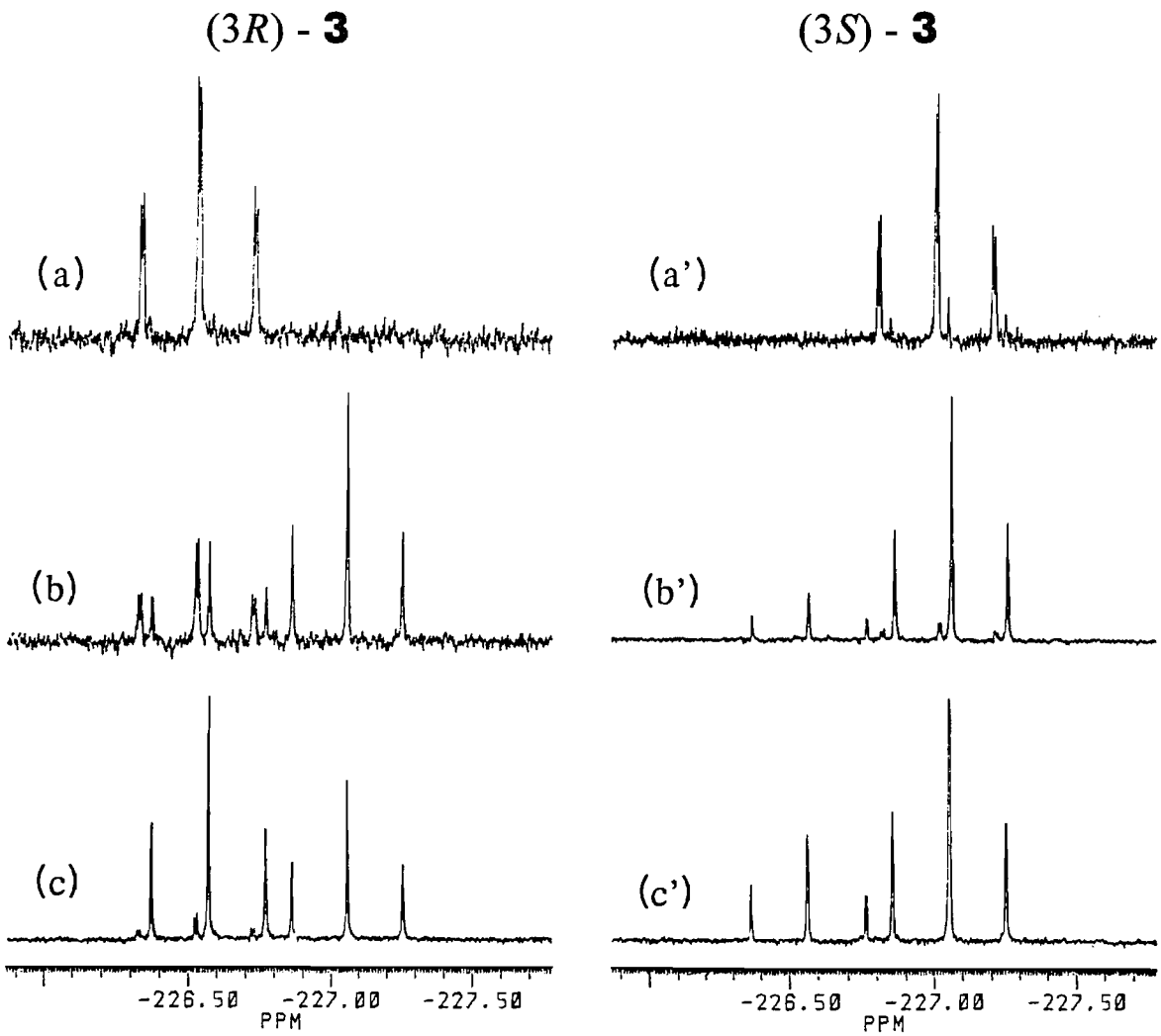

FIG. 1. ^{19}F NMR spectra of (3*R*,R_S)- and (3*S*,R_S)-**3** in CD_3OD. (3*R*,R_S)-**3**: (*a*) just after dissolution; (*b*) after 4 h; (*c*) after ca. 3 days (thermodynamic equilibrium). (3*S*,R_S)-**3**: (*a'*) just after dissolution; (*b'*) after 2 h; (*c'*) after 12 h; (*c*) after ca. 30 h.

shows only one minimum, having the same strain energy of the minima found for (3*R*)-**3**, with ϕ_1,ϕ_2 of ca. 180°,0°, respectively.

These results can help to tentatively explain the observed behaviour of the two ketones. Although the calculated energy minima are practically the same, the (3*R*)-**3** isomer shows two minimum energy conformations, while the (3*S*)-**3** shows only one, and this fact may account for the observation that in solution the equilibrium is shifted in favour of (3*R*)-**3**. Moreover, from the molecular mechanics calculations the conformation of (3*R*)-**3** (ϕ_1,ϕ_2 of ca. −45°, −90°) shows a side of the carbonyl group well exposed, while the other side is hindered by the presence of the *p*-tolyl group (Fig. 2). Thus, reasonably, for this molecular conformation, diazomethane has no difficulty to approach the carbonyl group, leading to the (2*S*,2'*R*)-**4** epoxide, the main reaction product.

The second conformation of (3*R*)-**3** (ϕ_1,ϕ_2 of ca. 60°,90°) may be considered less favoured to the attack of diazomethane, at least from the point of view of steric hindrance, since the carbonyl group has the sulfoxide group on one side and the phenyl residue on the other side (Fig. 3).

Finally, the conformational analysis of (3*S*)-**3** shows one minimum only, where the carbonyl is hindered on both sides by the presence of the two aromatic rings (Fig. 4). Furthermore, an inspection of Fig. 4 shows that the H—C(3) bond is nearly perpendicular to the carbonyl plane, and therefore enolization of (3*S*)-**3** should be a favored process.

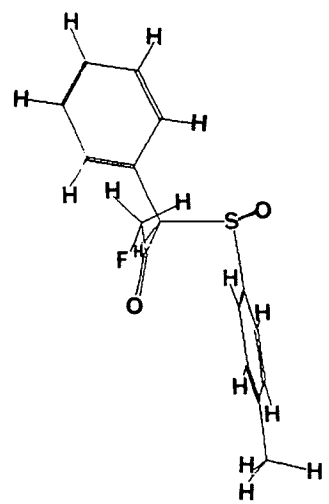

FIG. 2. Calculated first minimum-energy conformation of (3*R*)-**3**.

Can. J. Chem. Downloaded from www.nrcresearchpress.com by 85.192.166.187 on 09/08/12
For personal use only.

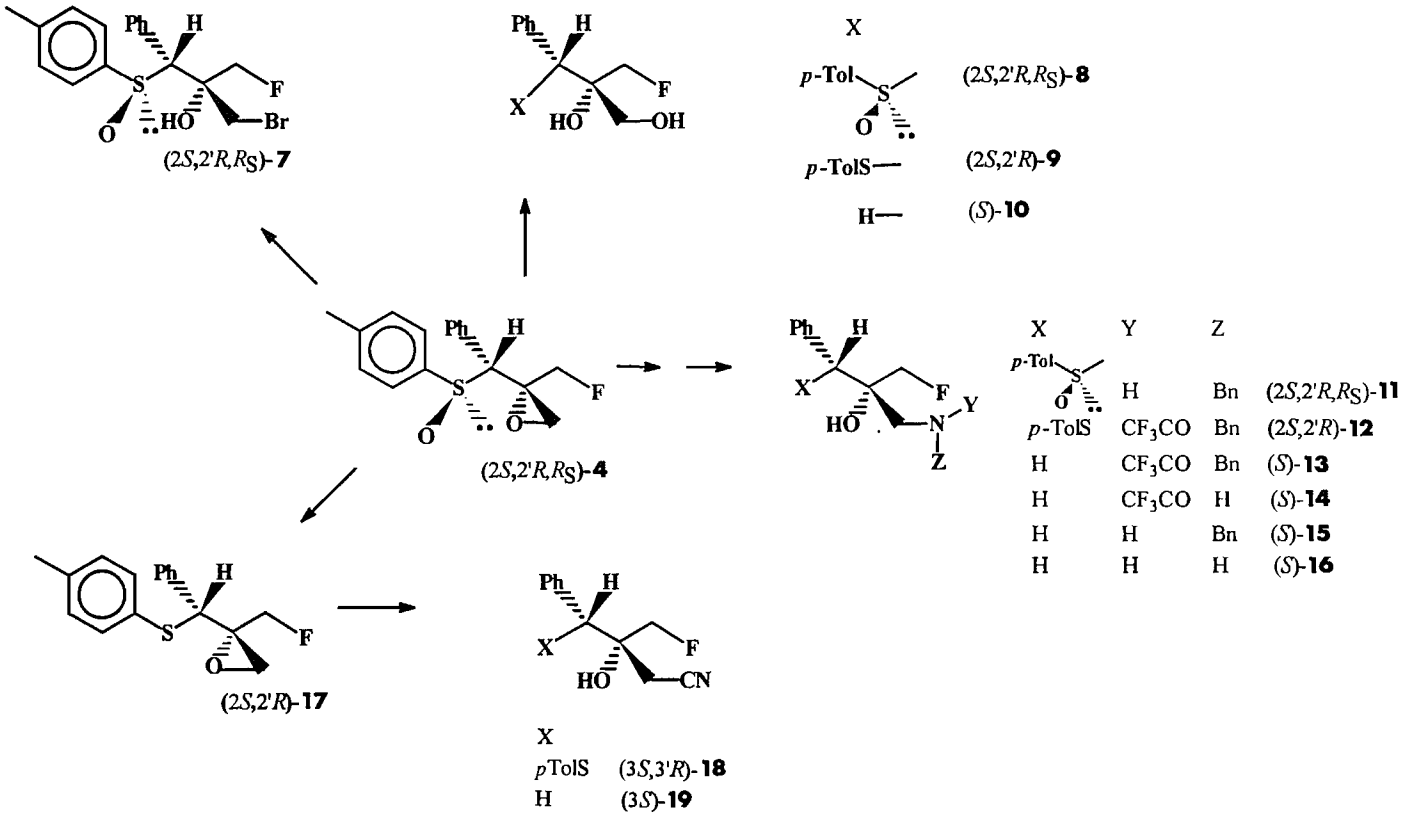

SCHEME 3

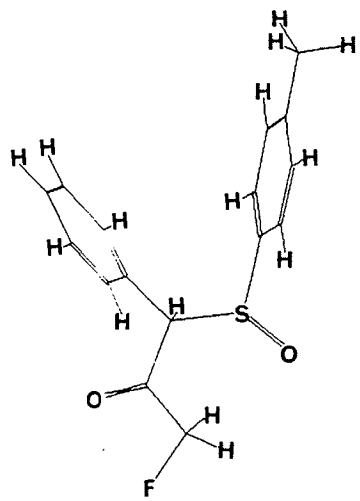

FIG. 3. Calculated second minimum-energy conformation of (3*R*)-**3**.

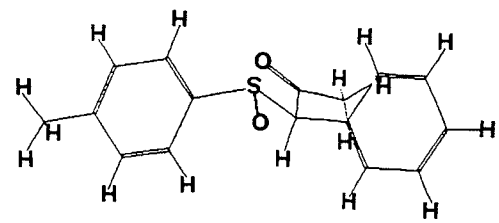

FIG. 4. Calculated minimum-energy conformation of (3*S*)-**3**.

Elaboration of the synthon

Some synthetically useful elaborations have been performed starting from the main reaction product (2*S*,2′*R*,R_S)-**4** in order to obtain differently substituted tertiary α-(fluoromethyl)carbinols, useful chiral building blocks for new fluorinated materials (12) (Scheme 3). Among the various reagents available to open the highly reactive oxirane ring (13) were chosen: bromide ion to introduce a halogen atom (14), water and benzylamine to introduce oxygen and nitrogen functions, and the cyanide ion to introduce to nitrile group (15). In all cases mentioned, the chiral auxiliary sulfinyl group was reductively removed.

Specifically, treatment of (2*S*,2′*R*,R_S)-**4** with cupric bromide and lithium bromide (1:2 molar ratio) in anhydrous THF afforded the (2*S*,2′*R*,R_S)-fluoromethyl bromohydrine **7** in 96% yield. X-ray analysis on a crystal sample of **7** gave stereochemical informations on the C-2 and C-2′ chiral centres (see below). Reaction of (2*S*,2′*R*,R_S)-**4** with water in THF and catalytic amounts of perchloric acid aqueous solution gave (2*S*,2′*R*,R_S)-fluoromethyl diol **8** in 90% yield, and treatment of the same starting oxirane **4** with benzylamine in THF gave (2*S*,2′*R*,R_S)-fluoromethyl aminoalcohol **11** in 95% yield.

Removal of the sulfur atom was carried out in two steps: first, reduction of the sulfinyl group to the thio group following the Oae procedure (16) (NaI, trifluoroacetic anhydride in acetone at −20°C) and, second, reductive desulfenylation promoted by Raney nickel in ethanol at reflux under a hydrogen atmosphere. Accordingly, fluorodiol **8** gave the thio derivative **9** in 90% yield, and (*S*)-2-benzyl-3-fluoropropan-1,2-diol (**10**) was obtained from the second step in 76.4% yield.

On the other hand, the fluoromethyl amino alcohol **11**, upon treatment with sodium iodide and trifluoroacetic anhydride, gave the corresponding trifluoroacetyl derivative **12**, which after reaction with Raney nickel afforded a nearly 1:1 mixture of *N*-trifluoroacetyl *N*-benzyl amino alcohol **13** and trifluoromethyl amino alcohol **14** in 62% global yield.

Can. J. Chem. Downloaded from www.nrcresearchpress.com by 85.192.166.187 on 09/08/12
For personal use only.

Finally, alkaline treatment of **13** and **14** gave, respectively, optically pure (*S*)-2-benzyl-1-benzylamino-3-fluoropropan-2-ol (**15**) and (*S*)-1-amino-2-benzyl-3-fluoropropan-2-ol (**16**).

A different strategy had to be employed for the synthesis of hydroxy fluoronitrile **19** because, due to the basic medium, the deprotonation at C-2′ became absolutely competitive with the opening of the oxirane ring by cyanide ion. To prepare **19**, the sulfoxide group was deoxygenated to (2*S*,2′*R*)-**17** and the oxirane ring was opened by potassium cyanide in the presence of lithium perchlorate to give (3*S*,3′*R*)-hydroxy nitrile **18** in 50% isolated yield. After removal of the *p*-tolylthio group with Raney nickel under a hydrogen atmosphere, (*S*)-3-benzyl-4-fluoro-3-hydroxybutanenitrile (**19**) was isolated in optically pure form in 65% yield.

Structural assignments

The reaction of (3*S*)-**3** and (3*R*)-**3** with diazomethane can give rise to the formation of four diastereoisomeric oxiranes, which have been recognized by NMR spectroscopy.

The oxiranes (2*S*,2′*R*)-**4**, the main reaction product, and (2*S*,2′*S*)-**4** were isolated and analysed separately, while (2*R*,2′*R*)-**4** and (2*R*,2′*S*)-**4**, the minor products of the reaction, were analysed as a mixture with the main isomers.

The presence of the oxirane ring in compounds **4** was recognized from the value of the geminal coupling constant $J(H_3, H'_3)$ of ca. 4 Hz (see Experimental), which is characteristic of the oxirane ring. Attempts to determine the relative stereochemistry of the epoxides **4** from long-range couplings or intramolecular NOE enhancements were unsuccessful. Only (2*R*,2′*S*)-**4** shows a long-range coupling $^4J(H_2, H_3)$ of 1.3 Hz, suggesting a rather rigid conformation around the C2—C2′ bond, but this coupling is not diagnostic for the configuration assignment. Thus the configuration of the main product (2*S*,2′*R*)-**4** was established by X-ray analysis after conversion to the bromo derivative **7** and that of (2*S*,2′*S*)-**4** by CD analysis of the corresponding sulfide (see below), while the configuration of the minor products (2*R*,2′*S*)-**4** and (2*R*,2′*R*)-**4** was not assigned. The reduction of the sulfoxides (2*S*,2′*R*)-**4** and (2*S*,2′*S*)-**4** led to the obtainment of the two diastereoisomeric sulfides (2*S*,2′*R*)- and (2*S*,2′*S*)-**17**, respectively, without the opening of the oxirane ring, as shown by the value of $J(H_3, H'_3)$ of ca. 4.6 Hz.

The reaction on the oxirane ring of many nucleophile reagents, performed on both sulfoxide- and sulfide-bearing moieties, led to the formation of the derivatives **7**–**19**. In all cases the oxirane ring is opened leaving a tertiary OH group linked to the carbon C-2, while the entering group (OH, $NHCH_2Ph$, CN, Br) is linked to the methylene carbon C-3. The opening of the oxirane ring was evidenced by the change in the $^2J(H_3, H'_3)$, which varies from ca. 4 Hz to 11–17 Hz, depending on the nature of the C-3 substituent.

X-ray crystallographic analysis of the bromohydrin 7

Colourless polyhedron-shaped crystals were grown by slow concentration of a isopropyl ether solution at 25°C. A crystal with approximate dimensions 0.35 × 0.30 × 0.25 mm was used for data collection and set on a Siemens R3m/V diffractometer. Accurate unit cell dimensions were determined by least-squares fit of the setting angles of 25 selected reflections (2θ = 60°–84°). Crystal data are as follows: $C_{17}H_{18}BrFO_2S$, FW = 385.3, orthorhombic, a = 8.637(2), b = 9.983(2), c = 19.798(2) Å, V = 1707.1(2) Å^3, Z = 4, ρ_c = 1.499 Mg m^{-3}, $F(000)$ = 784, μ(Cu-Kα) = 45.50 cm^{-1} (25°C, Cu-Kα radiation λ = 1.54178 Å), space group $P2_12_12_1$. Intensities were measured using graphite-monochromated Cu-Kα radiation with θ–2θ scans to 2θ = 136° (h −10/1, k −12/1, l −23/1). The intensities of three check reflections (0 0−2, −1−1−3, 0−4 0) measured every 100 reflections throughout the data collection showed only small random fluctuations. The data were corrected for Lorentz, polarization, and absorption effects (ψ scan, minimum and maximum transmission factors 0.658 and 0.936), no extinction correction.

Of the 2513 reflections measured, 2227 were unique (R_{int} = 0.0065) and 2049 had $F_o \geq 4\sigma(F_o)$. The structure was solved[5] by the use of the automatic Patterson solution method to locate the heavy atom. A Fourier phased on the bromine atom revealed all the remaining non-H atoms. The structure as then refined isotropically and anisotropically by full-matrix least-squares procedure. Difference Fourier maps, computed at the end of the anisotropic least-squares refinement, showed all H atoms in configurationally feasible positions; these were refined with isotropic displacement coefficients. The function minimized was $\Sigma w(|F_o| - |F_c|)^2$, with $w = [\sigma^2(F_o) + 0.0010F_o^2]^{-1}$. In the final cycles of refinement the maximum parameter shift corresponded to 0.366σ. A final difference Fourier map showed no features ≥0.50 e Å^{-3}. Refinement converged[6] with R = 0.0303, wR = 0.0439, and S = 1.14 for the 2049 $F_o \geq 4\sigma(F_o)$. The final positional and equivalent isotropic displacement parameters for the non-H atoms are given in Table 1. Bond lengths and valence angles are listed in Table 2. Anisotropic displacement parameters and tables of observed and calculated structure factors have been deposited.[7]

A perspective view of **7** is shown in Fig. 5. On the basis of the known absolute configuration at sulfur (*R*), the relative configurations at the new chiral centre C(2) and at C(3) are *S* and *R*, respectively. The Hamilton *R* test confirmed the absolute configuration assignment at higher than 99.5% confidence. The conformation around the central S(1)—C(3) bond is *transoid*, the torsional angle C(2)—C(3)—S(1)—C(30), defining the orientation of the phenyl ring and the fluoromethyl moiety, being 164.5(2)°. The molecular geometry at S(1) conforms to that found for related *p*-tolylsulfinyl derivatives (17–21).

Circular dichroism experiments

To establish the absolute stereochemistry at C-2 and C-2′ of the less abundant isolated oxirane **4** obtained from (3*R*,R_S)-**3**, circular dichroism measurements were made. For this purpose, both isolated epoxides **4** were reduced at the sulfur atom to give thio derivatives **17**.

By X-ray analyses on (2*S*,2′*R*,R_S)-**7**, information on the absolute stereochemistry at C-2 and C-2′ of the most abundant epoxide (2*S*,2′*R*,R_S)-**4** and, consequently, of its thio derivative (2*S*,2′*R*)-**17**, was obtained.

(2*S*,2′*R*)-**17** showed a negative maximum at 199 nm and a

[5]All calculations, including the drawing of Fig. 5, were performed with SHELXTL-Plus, Version 4.23 (1991), by G.M. Sheldrick and available from Siemens Analytical Instruments Inc. The scattering factors used were those employed by SHELXTL-Plus.

[6]$R = \Sigma(|F_o| - |F_c|)/\Sigma|F_o|$; $wR = \{\Sigma w(|F_o| - |F_c|)^2/\Sigma w(|F_o|^2\}^{1/2}$; $S = \{\Sigma w(|F_o| - |F_c|)^2/(n - m)\}^{1/2}$.

[7]A complete set of tables may be purchased from: The Depository of Unpublished Data, Document Delivery, CISTI, National Research Council Canada, Ottawa, Canada K1A 0S2. Tables of the H-atom coordinates have also been deposited with the Cambridge Crystallographic Data Centre and can be obtained on request from The Director, Cambridge Crystallographic Data Centre, University Chemical Laboratory, 12 Union Road, Cambridge, CB2 1EZ, U.K.

TABLE 1. Atomic coordinates (× 10^4) and equivalent isotropic displacement coefficients (Å^2 × 10^3) with esd's in parentheses for (2*S*,3*R*,R_S)-1-bromo-2-(fluoromethyl)-3-[(4-methylphenyl)sulfinyl]-3-phenylpropan-2-ol (**7**)

Atom	*x*	*y*	*z*	U_{eq}[a]
Br(1)	−4271(1)	158(1)	1585(1)	73(1)
S(1)	759(1)	−713(1)	1391(1)	43(1)
F(1)	−2874(4)	2777(3)	2554(1)	70(1)
O(1)	−154(3)	954(3)	2568(1)	51(1)
O(2)	−258(4)	−1844(3)	1617(1)	53(1)
C(1)	−2535(5)	130(4)	2216(2)	50(1)
C(2)	−1254(4)	1122(4)	2044(2)	40(1)
C(3)	−445(4)	829(3)	1358(2)	36(1)
C(20)	−1869(5)	2544(4)	2016(2)	49(1)
C(30)	962(4)	−906(3)	493(2)	40(1)
C(31)	−50(6)	−1716(4)	146(2)	50(1)
C(32)	74(5)	−1858(4)	−542(2)	55(1)
C(33)	1214(4)	−1200(4)	−905(2)	45(1)
C(34)	2257(5)	−414(4)	−544(2)	51(1)
C(35)	2146(5)	−272(4)	150(2)	50(1)
C(36)	1336(7)	−1314(6)	−1661(2)	63(1)
C(40)	617(5)	1929(3)	1127(2)	40(1)
C(41)	1983(5)	2220(5)	1470(2)	56(1)
C(42)	2960(7)	3225(6)	1245(3)	73(2)
C(43)	2549(8)	3971(6)	687(4)	86(2)
C(44)	1207(8)	3705(5)	347(3)	79(2)
C(45)	250(6)	2676(4)	552(2)	55(1)

[a]Equivalent isotropic *U* defined as one third of the trace of the orthogonalized U_{ij} tensor.

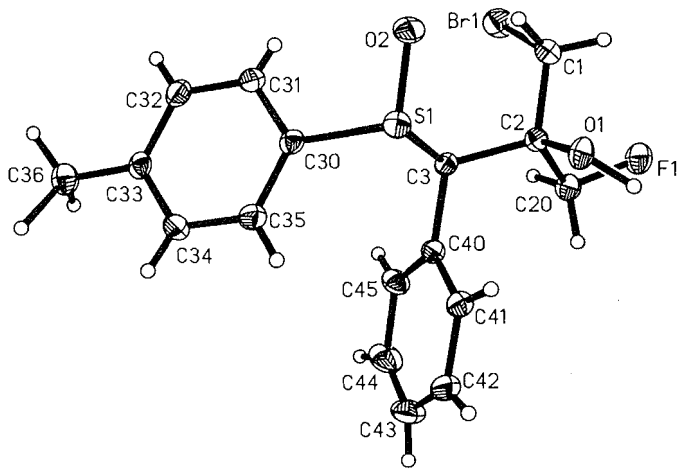

FIG. 5. Perspective view and atom labelling of X-ray structure (thermal ellipsoids are drawn at the 50% probability level).

second negative absorption at 230 nm. On the contrary, the investigated thio oxirane **17** showed a positive maximum at 199 nm and a second positive absorption at 231 nm.

Assuming that the absorption was mainly due to the electronic transitions of benzylic and sulfide chromophores (22) and that the opposite CD behaviour was the consequence of chromophores situated in an enantiomeric environment (23), an opposite stereochemistry at C-2′ was assigned.

By $[\alpha]_D^{20}$ measurements and NMR spectral analyses (see Experimental), a diastereoisomeric relationship was established: as a consequence, the absolute stereochemistry of the less abundant oxirane was assigned as (2*S*,2′*S*)-**17**.

TABLE 2. Bond lengths (Å) and angles (deg) with esd's in parentheses for (2*S*,3*R*,R_S)-1-bromo-2-(fluoromethyl)-3-[(4-methylphenyl)sulfinyl]-3-phenylpropan-2-ol (**7**)

Br(1)—C(1)	1.952(4)	S(1)—O(2)	1.499(3)
S(1)—C(3)	1.859(3)	S(1)—C(30)	1.798(3)
F(1)—C(20)	1.394(5)	O(1)—C(2)	1.416(4)
C(2)—C(20)	1.517(5)	C(2)—C(3)	1.555(5)
C(1)—C(2)	1.523(5)	C(3)—C(40)	1.502(5)
C(30)—C(31)	1.375(6)	C(30)—C(35)	1.380(5)
C(31)—C(32)	1.372(6)	C(32)—C(33)	1.385(6)
C(33)—C(34)	1.392(6)	C(33)—C(36)	1.504(6)
C(34)—C(35)	1.385(6)	C(40)—C(41)	1.392(6)
C(40—C(45)	1.397(5)	C(41)—C(42)	1.385(8)
C(42)—C(43)	1.378(9)	C(43)—C(44)	1.367(10)
C(44)—C(45)	1.380(8)		

O(2)—S(1)—C(3)	107.9(2)	O(2)—S(1)—C(30)	105.8(2)
C(3)—S(1)—C(30)	96.3(1)	O(1)—C(2)—C(1)	104.3(3)
O(1)—C(2)—C(20)	111.9(3)	C(1)—C(2)—C(20)	111.3(3)
O(1)—C(2)—C(3)	108.4(3)	C(1)—C(2)—C(3)	113.5(3)
C(20)—C(2)—C(3)	107.5(3)	Br(1)—C(1)—C(2)	114.0(3)
F(1)—C(20)—C(2)	110.2(3)	S(1)—C(3)—C(2)	112.1(2)
S(1)—C(3)—C(40)	105.9(2)	C(2)—C(3)—C(40)	113.8(3)
S(1)—C(30)—C(31)	119.7(3)	S(1)—C(30)—C(35)	120.6(3)
C(31)—C(30)—C(35)	119.7(4)	C(30)—C(31)—C(32)	120.4(4)
C(31)—C(32)—C(33)	121.5(4)	C(32)—C(33)—C(34)	117.4(4)
C(32)—C(33)—C(36)	122.1(4)	C(34)—C(33)—C(36)	120.5(4)
C(33)—C(34)—C(35)	121.5(4)	C(30)—C(35)—C(34)	119.5(4)
C(3)—C(40)—C(41)	121.4(3)	C(3)—C(40)—C(45)	120.0(3)
C(41)—C(40)—C(45)	118.6(4)	C(40)—C(41)—C(42)	120.7(4)
C(41)—C(42)—C(43)	119.5(5)	C(42)—C(43)—C(44)	120.5(6)
C(43)—C(44)—C(45)	120.5(6)	C(40)—C(45)—C(44)	120.1(5)

Can. J. Chem. Downloaded from www.nrcresearchpress.com by 85.192.166.187 on 09/08/12
For personal use only.

Can. J. Chem. Downloaded from www.nrcresearchpress.com by 85.192.166.187 on 09/08/12
For personal use only.

Experimental

Apparatus, materials, and methods

^1H, ^{13}C, and ^{19}F NMR spectra were recorded with a Bruker AC 250L spectrometer in $CDCl_3$. C_6F_6 was used as internal standard (δ_F = −162.90) for ^{19}F. The $[\alpha]_D^{20}$ values were determined on a Jasco DIP-181 polarimeter. Melting points are uncorrected and were obtained on a capillary apparatus. Thin-layer chromatography (TLC) was run on silica gel $60F_{254}$ Merck; flash column chromatography was performed with silica gel 60 (60–200 μm, Merck). THF was freshly distilled from lithium aluminium hydride, diisopropylamine was freshly distilled from calcium hydride, and a 2.6 M solution of *n*-butyllithium in hexanes (Aldrich) was employed. Diazomethane was distilled from an ethanol–water (3:1, 100 mL) solution of potassium hydroxide (15 g) to which an ethereal solution (400 mL) of Diazald (64.2 g) was added dropwise. Ethyl ether was previously washed with an acidic (H_2SO_4) aqueous solution of ferrous sulfate. In other cases, commercially available reagent grade solvents were employed without further purification.

Synthesis of 1-fluoro-3-[(4-methylphenyl)sulfinyl]-3-phenylpropan-2-one (3)

A solution of (+)-(*R*) benzyl 4-methylphenyl sulfoxide (**2**, 5.0 g, 21.7 mmol) was added to a solution of LDA (28.2 mmol, 4.0 mL) in THF (50 mL) at −78°C under argon. Into the resulting yellow solution at −60°C was dropped ethyl fluoroacetate (**1**, 6.3 mL, 65.1 mmol) in THF (5 mL); the reaction was quenched with a saturated aqueous solution of ammonium chloride, extracted with ethyl acetate (3 × 100 mL), dried over anhydrous sodium sulfate, and the solvent was evaporated. Flash chromatography of the residue (4:1 toluene:ethyl acetate as eluent) gave a 1.0:1.8 (^{19}F NMR ratio) mixture of (3*S*,R_S)- and (3*R*,R_S)-**3**. Crystallization of the crude mixture from ethyl acetate afforded (3*S*,R_S)-**3** in pure form. The mother liquors were treated with hexane, and the solid obtained was filtered, analysed by ^{19}F NMR, and identified as a ca. 1:1 mixture of the two diastereoisomers. The mother liquors thus enriched were treated with another portion of hexane to give pure (3*R*,R_S)-**3** as white crystals.

(3*S*,R_S)-**3**: mp 117–119°C (ethyl acetate); $[\alpha]_D^{20}$ +341.3 (*c* 0.1, $CHCl_3$); R_F (4:1 toluene:ethyl acetate) 0.35; ^1H NMR ($CDCl_3$) δ: 2.42 (s, 3H, CH_3), 4.58 (d, 2H, CH_2, $J(CH_2, F)$ 48.0 Hz), 4.96 (d, 1H, CH, J(CH, F) 2.0 Hz), 7.22–7.45 (m, 9H, aromatic hydrogens); ^{19}F NMR ($CDCl_3$) δ: −226.8 (td, $J(CH_2, F)$ 48.0, J(CH, F) 2.2 Hz); ^{19}F NMR (CH_3OH) δ: −227.0 (td, $J(CH_2, F)$ 46.5, J(CH, F) 2.1 Hz). Anal. calcd. for $C_{16}H_{15}FO_2S$: C 66.19, H 5,21; found: C 66.12, H 5.20%.

(3*R*,R_S)-**3**: mp 111–113°C (hexane); $[\alpha]_D^{20}$ −83.3 (*c* 0.5, $CHCl_3$); R_F (4:1 toluene:ethyl acetate) 0.35; ^1H NMR ($CDCl_3$) δ: 2.27 (s, 3H, CH_3), 4.92 (d, 2H, CH_2, $J(CH_2, F)$ 48.0 Hz), 4.96 (d, 1H, CH, J(CH, F) 2.0 Hz), 7.0–7.4 (m, 9H, aromatic hydrogens); ^{19}F NMR ($CDCl_3$) δ: −227.3 (td, $J(CH_2, F)$ 48.0, J(CH, F) 2.2 Hz; ^{19}F NMR (CH_3OH) δ: −226.5 (td, $J(CH_2, F)$ 46.5, J(CH, F) 2.1 Hz). Anal. calcd. for $C_{16}H_{15}FO_2S$: C 66.19, H 5.21; found: C 65.98, H, 5.19%.

Reaction of the ketones 3 with diazomethane

The reaction was run by dissolving ketones in three different solvents: methanol (method A), THF (method B), and ethyl ether (method C).

General procedure

A solution of the starting compound **3** (1 g, 3.3 mmol) dissolved in a solvent (100 mL) at 0°C was treated portionwise with an ethereal solution of diazomethane (ca. 0.5 M) and kept at the same temperature until the yellow colour of the diazomethane solution persisted (ca. 50 mL was needed). The reaction progress was monitored by TLC (3:2 chloroform:ethyl acetate as eluent), and after ca. 10 min all starting compound **3** disappeared. A few drops of acetic acid were added to destroy the diazomethane excess, the solvent was evaporated under reduced pressure (benzene (3 × 2 mL) was added to remove the acetic acid), and the residue was purified by flash chromatography (4:1 chloroform:ethyl acetate).

Method A

Starting from (3*R*,R_S)-**3**, a 1.0:1.8 mixture (the ratio was measured from the ^{19}F NMR spectrum) of (*E*)-(R_S)-3-fluoro-2-methoxy-1-phenyl-1-[(4-methylphenyl)sulfinyl]propene (*E*)-**6** (^{19}F NMR ($CDCl_3$) δ: −212.0 ppm) and (*Z*)-**6** (^{19}F NMR ($CDCl_3$) δ: −217.3 ppm) in 6.7% global yield was isolated along with a mixture of oxiranes **4** (89.3% global yield) whose ^{19}F NMR signals resonated at δ −228.5 and −227.4 ppm, respectively. After crystallization of the latter mixture (1:1 hexane:ethyl acetate) the major oxirane was obtained in pure form.

(2*S*,2′*R*,R_S)-**4**: mp (isopropyl ether) 89–91°C; $[\alpha]_D^{20}$ −197.4 (*c* 1.1, $CHCl_3$); R_F (4:1 chloroform:ethyl acetate) 0.35; ^1H NMR ($CDCl_3$) δ: 2.31 (s, 3H, CH_3), 3.08 (d, 1H, H-3, $J(H_3, H'_3)$ 4.0 Hz), 3.88 (td, 1H, H′-3, $J(H'_3, F)$ 4.0, $J(H'_3, CHF)$ 1.0 Hz), 4.18 (d, 1H, H-2′, $J(H_{2'}, F)$ 1.0 Hz), 4.31 (dd, 1H, CH*H*′F, J(H′, F) 47.1, J(H′, H) 10.1 Hz), 4.42 (ddd, 1H, C*H*H′F, J(H, F) 47.0 Hz), 6.95–7.30 (m, 9H, aromatic hydrogens); ^{19}F NMR ($CDCl_3$) δ: −228.5 (tdd, $J(F, H)_{gem}$ 47.0, $J(F, H'_3)$ 4.0, $J(F, H_{2'})$ 1.0 Hz). Anal. calcd. for $C_{17}H_{17}FO_2S$: C 67.08, H 5.63; found: C 67.27, H 5.61%.

Similar results were observed starting from mixtures in different ratios (1.0:1.3 or 1.0:2.0) of (3*S*,R_S)- and (3*R*,R_S)-**3**, respectively. From a 1.0:2.0 (3*S*)-/(3*R*)-**3** mixture, ^{19}F NMR analysis of the crude gave a 1.0:1.4 ratio of, respectively, (*E*) and (*Z*) enol ethers **6** in 15% global yield and 76.3% (isolated yield) of (2*S*,2′*R*,R_S)-**4** along with traces (<5%) of two different oxiranes whose ^{19}F NMR signals resonated at −227.4 and −229.2 ppm.

From a 1.0:1.3 (3*S*)/(3*R*)-**3** mixture, the same analysis on the crude gave a 1.0:1.5 ratio of (*E*)- and (*Z*)-**6** in 24.0% global yield, (2*S*,2′*R*,R_S)-**4** in 55.0% isolated yield, 9% of the oxirane **4** resonating at −229.2 ppm (^{19}F NMR), and 7.6% of a mixture of epoxides showing ^{19}F NMR signals at −226.8 and −227.4 ppm.

Starting from a solution of (3*S*,R_S)-**3**, a 1.0:1.1 mixture of (*E*)- and (*Z*)-**6** (21.9% yield) and a 1.7:1.0:10.0:3.3 ratio of all four possible oxiranes (^{19}F NMR ($CDCl_3$) signals being at δ −226.8, −227.4, −228.5 and −229.2 ppm, respectively) in 72.5% global yield were obtained.

Method B

When a solution of (3*S*,R_S)-**3** in THF was treated with diazomethane, a 1.0:1.5 mixture of (*E*)- and (*Z*)-**6** (16.3% global yield) and a 1.0:3.6:25.4:1.5 mixture of oxiranes **4** (^{19}F NMR ($CDCl_3$) signals being at δ −226.8, −227.4, −228.5, and −229.2 ppm, respectively) (73.6% global yield) were obtained. Similarly, from a 1.0:2.0 (3*S*)/(3*R*)-**3** mixture, a 1.0:1.4 (*E*)/(*Z*)-**6** mixture (16.3% global yield) and a 8.6:1.0 mixture of (2*S*,2′*R*,R_S)-**4** and oxirane resonating at −229.2 ppm in 77.7% global yield were obtained. Flash chromatography on the crude (7:3 toluene:ethyl acetate) afforded (2*S*,2′*S*,R_S)-**4**.

(2*S*,2′*S*)-**4**: $[\alpha]_D^{20}$ +311.9 (*c* 0.7, $CHCl_3$); ^1H NMR ($CDCl_3$) δ: 2.34 (s, 3H, CH_3), 2.95 (dt, 1H, H-3, $J(H_3, H'_3)$ 4.0, $J(H'_2, H_3)$ 1.3, $J(H_3, F)$ 1.3 Hz), 3.92 (dd, 1H, H′-3, $J(H'_3, F)$ 5.6 Hz), 4.00 (d, 1H, H-2′), 4.12 (dd, 1H, C*H*H′F, J(H, H′) 10.6, J(H, F) 47.5 Hz), 4.45 (dd, 1H, CH*H*′F, J(H′, F) 47.2 Hz), 6.75–7.30 (m, 9H, aromatic hydrogens); ^{19}F NMR ($CDCl_3$) δ: −229.15 (tdd, $J(F, H)_{gem}$ 47.3 Hz, $J(F, H'_3)$ 5.6, $J(F, H_3)$ 1.3 Hz).

Method C

Starting from a solution of (3*S*,R_S)-**3** in ethyl ether, a 1.0:2.3 mixture of (*E*)- and (*Z*)-**6** (15.1% global yield) and a 1.0:3.2:25.2:1.0 mixture of oxiranes **4** (^{19}F NMR ($CDCl_3$) signals being at δ −226.8, −227.4, −228.5, and −229.2 ppm, respectively) (75.6% global yield) were obtained. From the 1.0:2.0 (3*S*)/(3*R*)-**3** mixture, a 1.0:3.0 (*E*)- and (*Z*)-**6** mixture (12.9% yield) and a 1.0:2.1:15.5:1.0 mixture of the same oxiranes **4** in 81.3% global yield were obtained.

(2*R*,2′*S*)- or (2*R*,2′*R*)-**4**: ^1H NMR ($CDCl_3$) δ (mixture with other epoxides): 2.35 (s, 3H, CH_3), 2.82 (dd, 1H, H-3, $J(H_3, H'_3)$ 4.5, $J(H_3, F)$ 3.5 Hz), 2.97 (d, 1H, H′-3), 4.00 (d, 1H, H-2′, $J(H_{2'}, F)$ 1.0 Hz), 4.55 (dd, 1H, H-1, $J(H_1, H'_1)$ 10.2, $J(H_1, F)$ 47.3 Hz), 5.18 (dd, 1H, H′-1, $J(H'_1, F)$ 47.3 Hz), 6.3–7.2 (m, 9H, aromatic hydrogens); ^{19}F NMR ($CDCl_3$) δ: −227.43 (td, CH_2F, $J(CH_2, F)$ 47.3, $J(F, H_3)$ 3.5 Hz).

Can. J. Chem. Downloaded from www.nrcresearchpress.com by 85.192.166.187 on 09/08/12
For personal use only.

(2*R*,2′*R*)- or (2*R*,2′*S*)-**4**: ^{1}H NMR ($CDCl_3$) δ (analysed in mixture with other epoxides): 2.34 (s, 3H, CH_3), 2.97 (d, 1H, H-3, $J(H_3, H'_3)$ 4.0 Hz), 3.36 (dd, 1H, H-3′, $J(H'_3, F)$ 4.0 Hz), 3.81 (d, 1H, H-2′, $J(H_{2'}, F)$ 1.0 Hz), 4.68 (dd, 1H, H-1, $J(H_1, H'_1)$ 10.2 Hz, $J(H_1, F)$ 47.2 Hz), 4.48 (dd, 1H, H′-1, $J(H'_1, F)$ 47.0 Hz), 6.3–7.2 (m, 9H, aromatic hydrogens); ^{19}F NMR ($CDCl_3$) δ: −226.77 (td, CH_2F, $J(CH_2, F)$ 47.2 Hz, $J(H'_3, F)$ 4.0 Hz).

Synthesis of (2S,2′R,R$_S$)-1-bromo-3-fluoro-2′-{[(4-methylphenyl)-sulfinyl][phenyl]methyl]propan-2-ol (7)

Cupric bromide (2.3 g, 10.5 mmol) and lithium bromide (1.8 g, 21.0 mmol) were suspended in anhydrous THF (20 mL; distilled from $LiAlH_4$) cooled at 0°C under argon. A solution of (2*S*,2′*R*,*R*$_S$)-**4** (2.0 g, 6.6 mmol) in THF (10 mL) was added dropwise. Stirring was continued for up to 1 h, until disappearance of the starting oxirane, then 10 mL of a phosphate buffer solution (pH 10) was added, and the resulting mixture was diluted with water and extracted with ethyl acetate (3 × 20 mL). After drying over anhydrous sodium sulfate and solvent evaporation, the residue was purified by flash chromatography (3:2 hexane:ethyl acetate), and pure (2*S*,2′*R*,*R*$_S$)-**7** (1.7 g, 96% yield) was isolated; mp 119–120°C (isopropyl ether); $[\alpha]_D^{20}$ −76.2 (*c* 1.2, $CHCl_3$); R_F (3:2 hexane:ethyl acetate) 0.35; ^{1}H NMR ($CDCl_3$), δ: 2.31 (s, 3H, CH_3), 3.73 (dd, 1H, H-3, $J(H_3, F)$ 1.2, $J(H_3, H'_3)$ 10.8 Hz), 3.76 (dd, 1H, H′-3, $J(H'_3, F)$ 1.5 Hz), 4.17 (s, 1H, H-2′), 4.53 (dd, 1H, H-1, J(H-1, $J(H_1, F)$ 46.8, $J(H_1, H'_1)$ 10.2 Hz), 4.60 (dd, 1H, H′-1, $J(H'_1, F)$ 46.8 Hz), 5.38 (s, 1H, OH), 7.0–7.4 (m, 9H, aromatic hydrogens); ^{19}F NMR ($CDCl_3$) δ: −227.6 (t, CH_2F, $J(CH_2, F)$ 46.8 Hz). Anal. calcd. for $C_{17}H_{18}BrFO_2S$: C 53.00, H 4.71; found: C 52.87, H 4.69%.

Synthesis of (2S,2′R,R$_S$)-3-fluoro-2-{[(4-methylphenyl)sulfinyl]-[phenyl]methyl]propan-1,2-diol (8)

To a stirred solution of (2*S*,2′*R*,*S*$_S$)-**4** (2.0 g, 6.6 mmol) in THF (20 mL) and water (1 mL) at room temperature was added dropwise perchloric acid (0.5 mL of a 70% aqueous solution). The solution was stirred for 10 h at the same temperature, the solvent was removed under reduced pressure, water (10 mL) was added, and extraction was made with chloroform (3 × 20 mL). The organic layers were dried over anhydrous sodium sulfate, the solvent was removed, and the residue was purified by flash chromatography (1:1 hexane:ethyl acetate as eluent).

Pure (2*S*,2′*R*,*R*$_S$)-**8** was obtained as a solid: mp 130–132°C (isopropyl ether); $[\alpha]_D^{20}$ −174.4 (*c* 1.2, $CHCl_3$); ^{1}H NMR ($CDCl_3$) δ: 2.30 (s, 3H, CH_3), 3.61 (dd, 1H, H-3, $J(H_3, H'_3)$ 11.5, $J(H_3$, OH-3) 7.0 Hz), 3.78 (dd, 1H, H′-3, $J(H'_3$, OH-3) 7.0 Hz), 3.98 (t, 1H, OH-3), 4.07 (s, 1H, H-2′), 4.33 (dd, 1H, H-1, $J(H_1, F)$ 46.7, $J(H_1, H'_1)$ 9.5 Hz), 4.41 (dd, 1H, H′-1, $J(H'_1, F)$ 46.7 Hz), 7.0–7.3 (m, 9H, aromatic hydrogens); ^{19}F NMR ($CDCl_3$) δ: −231.4 (t, CH_2F, $J(CH_2, F)$ 46.7 Hz). Anal. calcd. for $C_{17}H_{19}FO_3S$: C 63.33, H 5.94; found: C 63.12, H 5.92%.

Synthesis of (S)-2-benzyl-3-fluoropropan-1,2-diol (10)

To a stirred solution of (2*S*,2′*R*,*R*$_S$)-**8** (1.0 g, 3.1 mmol) and sodium iodide (1.4 g, 9.3 mmol) in acetone at −40°C, under an argon atmosphere, a solution of trifluoroacetic anhydride (2.2 mL, 15.5 mmol) in the same solvent was added dropwise. When the starting compound **8** was no longer present, saturated aqueous solutions of sodium sulfite and sodium hydrogen carbonate were added, along with ethyl acetate. The organic phase was dried over anhydrous sodium sulfate and the solvent was evaporated under reduced pressure. The residue was purified by flash chromatography (4:1 hexane:ethyl ether) to give (2*S*,2′*R*)-**9** in 90% yield as a yellowish oil: $[\alpha]_D^{20}$ −307.2 (*c* 1.0, $CHCl_3$); R_F (4:1 hexane:ethyl ether) 0.35; ^{1}H NMR ($CDCl_3$) δ: 2.25 (s, 3H, CH_3), 2.90 (br s, 1H, OH-3), 3.28 (s, 1H, OH-2), 3.75 (d, 1H, H-3, $J(H_3, H'_3)$ 11.0 Hz), 2.84 (dd, 1H, H′$_3$, $J(H'_3, F)$ 2.0 Hz), 4.16 (dd, 1H, H-1, $J(H_1, H'_1)$ 9.5, $J(H_1, F)$ 47.0 Hz), 4.33 (s, 1H, H-2′), 4.50 (dd, 1H, H′-1, $J(H'_1, F)$ 47.0 Hz), 6.95–7.45 (m, 9H, aromatic hydrogens). Anal. calcd. for $C_{17}H_{19}FO_2S$: C 66.64, H 6.25; found: C 66.58, H 6.26%.

To the thio derivative (2S,2′R)-**9** (800 mg, 2.8 mmol) dissolved in absolute ethanol (10 mL) dry Raney nickel (2.4 g) was added and air was removed by vacuum pump. Ethanol was refluxed under a hydrogen atmosphere for 3 h and, after complete disappearance of the substrate, the Raney nickel was filtered off, the solvent was evaporated, and the residue was flash chromatographed (7:3 hexane:ethyl acetate as eluent) to give (S)-**10** (390 mg, 76.4% yield) as a yellow oil: $[\alpha]_D^{20}$ −2.65 (c 1.2, $CHCl_3$); R_F (7:3 hexane:ethyl acetate) 0.35; ^{1}H NMR ($CDCl_3$) δ: 2.65 (br s, 2H, OH-2 and OH-3), 2.82 (dd, 1H, H-2′, $J(H_{2'}, H'_{2'})$ 14.0, $J(H_{2'}, H_3)$ 2.0 Hz), 2.88 (dd, 1H, H′-2′, $J(H'_{2'}, F)$ 2.0 Hz), 3.51 (dd, 1H, H-3, $J(H_3, H'_3)$ 11.5 Hz), 3.59 (dd, 1H, H′-3, $J(H'_3, F)$ 1.5 Hz), 4.19 (dd, 1H, H-1, $J(H_1, F)$ 47.0, $J(H_1, H'_1)$ 9.5 Hz), 4.29 (dd, 1H, H′$_1$, $J(H'_1, F)$ 47.0 Hz), 7.2–7.4 (m, 1H, aromatic hydrogens); ^{19}F NMR ($CDCl_3$) δ: −231.3 (t, CH_2F, $J(CH_2, F)$ 47.0 Hz). Anal. calcd. for $C_{10}H_{13}FO_2$: C 65.20, H 7.11%; found: C 65.13, H 7.09%.

Synthesis of (S)-1-amino-2-benzyl-3-fluoropropan-2-ol (16)

To a stirred solution of sulfinyl oxirane (2*S*,2′*R*,*R*$_S$)-**4** (1.5 g, 4.93 mmol) in THF (20 mL) was added benzylamine (20 mL, 189.4 mmol) at room temperature. After 2 days, THF was evaporated off and the residue was purified by flash chromatography (3:2 hexane:ethyl acetate) to give the corresponding amino alcohol (2*S*,2′*R*,*R*$_S$)-**11** as a yellowish oil (95% yield): $[\alpha]_D^{20}$ −69.4 (*c* 1.1, $CHCl_3$); R_F (3:2 hexane:ethyl acetate) 0.30; ^{1}H NMR ($CDCl_3$) δ: 2.04 (s, 1H, OH-2), 2.30 (s, 3H, CH_3), 2.67 (d, 1H, H-3, $J(H_3, H'_3)$ 12.0 Hz), 2.85 (d, 1H, H′-3), 3.72 (d, 1H, NC*H*H′Ph, J(H, H′) 13.5 Hz), 3.79 (d, 1H, NCH*H*′Ph), 4.19 (s, 1H, H-2′), 4.39 (dd, 1H, H-1, $J(H_1, H'_1)$ 9.5, $J(H_1, F)$ 47.0 Hz), 4.44 (dd, 1H, H′-1, $J(H'_1, F)$ 47.0 Hz), 7.0–7.4 (m, 14H, aromatic hydrogens); ^{19}F NMR ($CDCl_3$) δ: −229.4 (t, CH_2F, $J(CH_2, F)$ 47.0 Hz). Anal. calcd. for $C_{24}H_{26}FNO_2S$: C 70.05, H 6.37, N 3.40; found: C 70.15, H 6.35; N 3.42%.

The derivative **11** (1.15 g, 2.7 mmol) was dissolved in acetone (25 mL), sodium iodide (1.25 g, 8.1 mmol) was added, and the mixture was cooled at −40°C under a nitrogen atmosphere. A solution of trifluoroacetic anhydride (1.87 mL, 13.5 mmol) in acetone (25 mL) was added dropwise. To the resulting reaction mixture a saturated aqueous solution of sodium sulfite and sodium hydrogen carbonate was added, acetone was evaporated off, and extraction was made with ethyl ether (3 × 20 mL). The collected organic layers were dried over anhydrous sodium sulfate and the solvent was evaporated to give a residue that by flash chromatographic purification (9:1 hexane:ethyl ether) afforded (2*S*,2′*R*)-1-(*N*-trifluoroacetyl)benzylamino-3-fluoro-2-{[(4- methylphenyl)thio][phenyl]methyl}propan-2-ol (**12**) (98% yield) as a yellowish oil: $[\alpha]_D^{20}$ −135.94 (*c* 1.2, $CHCl_3$); R_F (9:1 hexane:ethyl ether) 0.40; ^{1}H NMR ($CDCl_3$) δ: 2.22 (s, 3H, CH_3), 3.48 (d, 1H, H-3, $J(H_3, H'_3)$ 14.5 Hz), 3.97 (dd, 1H, H-1, $J(H_1, H'_1)$ 9.5, $J(H_1, F)$ 46.5 Hz), 4.04 (d, 1H, H-2′, $J(H_{2'}, H'_3)$ 2.0 Hz), 4.22 (s, 1H, OH), 4.27 (dd, 1H, H′-3), 4.28 (dd, 1H, H′-1, $J(H'_1, F)$ 46.5 Hz), 4.62 (d, 1H, NC*H*H′Ph, J(H, H′) 16.5 Hz), 5.02 (d, 1H, NCH*H*′Ph), 6.90–7.45 (m, 14H, aromatic hydrogens); ^{19}F NMR ($CDCl_3$) δ: −226.0 (t, 1F, CH_2F, $J(CH_2, F)$ 46.5 Hz), −68.9 (s, 3F, $COCF_3$). Anal. calcd. for $C_{26}H_{25}F_4NO_2S$: C 63.53, H 5.13, N 2.85; found: C 63.35, H 5.12, N 2.86.

The thio derivative **12** (1.0 g, 2.5 mmol) was dissolved in absolute ethanol (30 mL), Raney nickel (2.7 g) was added, and the mixture was heated at reflux under hydrogen atmosphere for 1 h and 40 min. Raney nickel was filtered off, the ethanol was evaporated, and flash chromatographic purification (65:35 hexane:ethyl ether as eluent) gave a mixture (1.7:1.0) of, respectively, the following products: (S)-2-benzyl-3-fluoro-1-[(N-trifluoroacetyl)benzylamino]propan-2-ol (**13**, 39% yield); $[\alpha]_{365}^{20}$ −7.42 (c 1.0, $CHCl_3$); R_F (65:35 hexane:ethyl ether) 0.45; ^{1}H NMR ($CDCl_3$) δ: 2.77 (dd, 1H, H-2′, $J(H_{2'}, H'_{2'})$ 13.8, $J(H_{2'}$, H′$_3$) 2.4 Hz), 2.86 (dd, 1H, H′-2′, $J(H'_{2'}, F)$ 2.0 Hz), 3.27 (s, 1H, H-2′), 3.46 (d, 1H, H-3, $J(H_3, H'_3)$ 14.7 Hz), 3.59 (dd, 1H, H′-3), 4.12 (dd, 1H, H-1, $J(H_1, H'_1)$ 9.6, $J(H_1, F)$ 46.8 Hz), 4.18 (dd, 1H, H′-1, $J(H'_1, F)$ 46.8 Hz), 4.74 (d, 1H, NC*H*H′Ph, J(H, H′) 16.2 Hz), 4.93 (d, 1H, NCH*H*′Ph), 7.12–7.45 (m, 10H, aromatic hydrogens); ^{19}F NMR ($CDCl_3$) δ: −225.4 (t, 1F, CH_2F, $J(CH_2, F)$ 46.8 Hz), −69.0 (s, 3F, $COCF_3$). Anal. calcd. for $C_{19}H_{19}F_4NO_2$: C 61.79, H 5.18, N 3.79; found: C 61.86, H 5.20, N 3.80%; and (S)-2-benzyl-3-fluoro-1-[(trifluoroacetyl)amino]propan-2-ol (**14**, 23% yield): $[\alpha]_D^{20}$ −13.91, $[\alpha]_{365}^{20}$ −53.60 (c 0.8, $CHCl_3$); R_F (same solvent) 0.35; ^{1}H NMR ($CDCl_3$) δ: 2.38 (s, 1H, OH-2), 2.85 (dd, 1H, H-2′, $J(H_{2'}, H'_{2'})$ 14.0, $J(H_{2'}, H_3)$ 2.0

Can. J. Chem. Downloaded from www.nrcresearchpress.com by 85.192.166.187 on 09/08/12
For personal use only.

Hz), 2.94 (dd, 1H, H′-2′, J(H′$_{2'}$, F) 1.8 Hz), 3.48 (ddd, 1H, H-3, J(H$_3$, H′$_3$) 14.0, J(H$_3$, NH) 5.5 Hz), 3.58 (dd, 1H, H′-3, J(H′$_3$, NH) 6.3 Hz), 4.17 (dd, 1H, H-1, J(H$_1$, H′$_1$) 9.5, J(H$_1$, F) 47.0 Hz), 4.30 (dd, 1H, H′-1, J(H′$_1$, F) 47.0 Hz), 6.70 (br, 1H, NH), 7.27–7.45 (m, 5H, aromatic hydrogens); ^{19}F NMR ($CDCl_3$) δ: −230.1 (t, 1F, CH_2F, J(CH_2, F) 47.0 Hz), −77.0 (s, 3F, $COCF_3$). Anal. calcd. for $C_{12}H_{13}F_4NO_2$: C 51.62, H 4.69, N 5.02; found: C 51.65, H 4.68, N 5.04%.

The trifluoroacetyl derivatives **13** (100 mg, 0.27 mmol) and **14** (100 mg, 0.36 mmol) were separately dissolved in THF (2 mL) and treated with a 2.5% aqueous solution of potassium hydroxide (1 mL). Stirring was continued for 5 h, the THF was evaporated, and the following compounds were obtained in pure form by flash chromatographic purification: (*S*)-2-benzyl-1-benzylamino-3-fluoropropan-2-ol (**15**) (95% yield): $[\alpha]^{20}_{365}$ −9.33 (*c* 0.5, $CHCl_3$); R_F (3:2 cyclohexane:ethyl acetate) 0.35; ^{1}H NMR ($CDCl_3$) δ: 1.70 (br, 2H, OH and NH), 2.58 (dd, 1H, H-3, *J*(H$_3$, H′$_3$) 12.5, *J*(H$_3$, H′$_{2'}$) 1.7 Hz), 2.78 (dd, 1H, H-2′, *J*(H$_2$, H′$_{2'}$) 13.5, *J*(H$_{2'}$, F) 2.0 Hz), 2.82 (dd, 1H, H′-3, *J*(H′$_3$, F) 1.1 Hz), 2.86 (dd, 1H, H′-2′), 3.75 (d, 1H, NC*H*H′Ph, *J*(H, H′) 13.5 Hz), 3.80 (d, 1H, NCH*H*′Ph), 4.18 (d, 2H, CH_2F, *J*(CH_2, F) 47.0 Hz), 7.20–7.40 (m, 5H, aromatic hydrogens); ^{19}F NMR ($CDCl_3$) δ: −228.5 (t, CH_2F, *J*(CH_2, F) 47.0 Hz). Anal. calcd. for $C_{17}H_{20}FNO$: C 74.70, H 7.37, N 5.12; found: C 74.64, H 7.39, N 5.10%; and (*S*)-1-amino-2-benzyl-3-fluoropropan-2-ol (**16**, 90% yield): $[\alpha]^{20}_D$ −9.33 (*c* 0.3, $CHCl_3$); R_F (1:1 ethyl acetate: methanol) 0.35; ^{1}H NMR ($CDCl_3$) δ: 2.80–2.90 (m, 3H, H-3, H′-3, and H-2′), 2.95 (d, 1H, H′-2′, *J*(H$_{2'}$, H′$_{2'}$) 13.5 Hz), 4.24 (d, 2H, CH_2F, *J*(CH_2, F) 47.0 Hz), 7.20–7.40 (m, 5H, aromatic hydrogens); ^{19}F NMR ($CDCl_3$ + CD_3OD) δ: −230.2 (t, CH_2F, *J*(CH_2, F) 47.0 Hz). Anal. calcd. for $C_{10}H_{14}FNO$: C 65.55, H 7.70, N 7.64; found: C 65.28, H 7.67, N 7.61%.

Synthesis of (2S,2′R)- and (2S,2′S)-2-fluoromethyl-2-{[(4-methylphenyl)thio][phenyl]methyl}oxirane (17)

(2*S*,2′*R*,*R*$_S$)-**4** (1.0 g, 3.3 mmol) was treated with sodium iodide and trifluoroacetic anhydride following the procedure already described. The thio oxirane (2*S*,2′*R*)-**17** was obtained in 98% yield; $[\alpha]^{20}_D$ −249.24 (*c* 1.0, $CHCl_3$); R_F (9:1 hexane:ethyl ether) 0.40; ^{1}H NMR ($CDCl_3$) δ: 2.29 (s, 3H, CH_3), 2.84 (d, 1H, H-3, *J*(H$_3$, H′$_3$) 4.5 Hz), 3.06 (t, 1H, H′-3, *J*(H′$_3$, F) 4.5 Hz), 4.49 (dd, 1H, H-1, *J*(H$_1$, F) 47.0, *J*(H$_1$, H′$_1$) 10.2 Hz), 4.54 (s, 1H, H-2′), 4.58 (dd, 1H, H′-1, *J*(H′$_1$, F) 47.0 Hz), 6.95–7.45 (m, 9H, aromatic hydrogens); ^{19}F NMR ($CDCl_3$) δ: −228.8 (td, CH_2F, *J*(CH_2, F) 47.0, *J*(F, H′$_3$) 4.5 Hz). Anal. calcd. for $C_{17}H_{17}FOS$: C 70.80, H 5.94; found: C 70.68, H 5.96%.

In the same way, (2*S*,2′*S*,*R*$_S$)-**4** was reduced to the corresponding thio derivative (2*S*,2′*S*)-**17** in 76% yield: $[\alpha]^{20}_D$ +268.6 (*c* 0.3, $CHCl_3$); R_F (9:1 hexane:ethyl ether) 0.35; ^{1}H NMR ($CDCl_3$) δ: 1.82 (s, 3H, CH_3), 2.32 (d, 1H, H-3, *J*(H$_3$, H′$_3$) 4.8 Hz), 2.54 (dd, 1H, H′-3, *J*(H′$_3$, F) 4.5 Hz), 4.12 (dd, 1H, H-1, *J*(H$_1$, H′$_1$) 10.2, *J*(H$_1$, F) 47.5 Hz), 4.48 (dd, 1H, H′-1, *J*(H′$_1$, F) 47.3 Hz), 4.54 (d, 1H, H-2′, *J*(H$_{2'}$, F) 1.1 Hz), 6.70–7.35 (m, 9H, aromatic hydrogens); ^{19}F NMR ($CDCl_3$) δ: −230.5 (t, CH_2F, *J*(CH_2, F) 46.8 Hz).

(2*S*,2′*R*)-3-fluoro-1-iodo-2-{[(4-methylphenyl)thio][phenyl]methyl}propan-2-ol (**20**) (19% yield) was also obtained: $[\alpha]^{20}_D$ +179.0 (*c* 0.2, $CHCl_3$); R_F (9:1 hexane:ethyl ether) 0.25; ^{1}H NMR ($CDCl_3$) δ: 2.29 (s, 3H, CH_3), 2.55 (s, 1H, OH), 3.23 (dd, 1H, H-3, *J*(H$_3$, H′$_3$) 10.5, *J*(H$_3$, F) 2.0 Hz), 3.35 (dd, 1H, H′$_3$, *J*(H′$_3$, F) 2.5 Hz), 4.42 (d, 1H, H-2′, *J*(H$_{2'}$, F) 1.2 Hz), 4.59 (dd, 1H, H-1, *J*(H$_1$, F) 47.0, *J*(H$_1$, H′$_1$) 9.5 Hz), 4.66 (dd, 1H, H′-1, *J*(H′$_1$, F) 47.0 Hz), 7.0–7.45 (m, 9H, aromatic hydrogens); ^{19}F NMR ($CDCl_3$) δ: −228.2 (t, *J*(CH_2, F) 47.0 Hz). Anal. calcd. for $C_{17}H_{18}FIOS$: C 49.05, H 4.36; found: C 48.92, H 4.35%.

Synthesis of (S)-3-benzyl-4-fluoro-3-hydroxybutanenitrile (19)

To a solution of sodium cyanide (96.7 mg, 1.97 mmol) in acetonitrile (10 mL) heated at 60°C under an Ar atmosphere for 15 min, lithium perchlorate (209 mg, 1.97 mmol) was added, followed in 10 min by dropwise addition of a solution of (2*S*,2′*R*)-**17** (380 mg, 1.32 mmol) in acetonitrile (1 mL). The mixture was stirred at 60°C for 1.5 h, then 10 mL of water was added, the solvent was removed under reduced pressure, and the organic layers were extracted with ethyl acetate (3 × 15 mL), washed with water (5 mL), and dried over anhydrous sodium sulfate. The crude was purified by flash chromatography (3:2 cyclohexane:ethyl acetate) to give (3*S*,3′*R*)-4-fluoro-3-hydroxy-3-{[(4-methylphenyl)thio][phenyl]methyl}butanenitrile (**18**, 187 mg, 45% yield): $[\alpha]^{20}_D$ −223.9 (*c* 0.8, $CHCl_3$): mp 80–82°C (ethyl acetate:hexane); ^{1}H NMR ($CDCl_3$) δ: 2.29 (s, 3H, CH_3), 2.90 (dd, 1H, H-3, *J*(H$_3$, H′$_3$) 16.5, *J*(H$_3$, F) 1.5 Hz), 2.99 (dd, 1H, H′-3, *J*(H′$_3$, F) 1.5 Hz), 2.99 (s, 1H, OH), 4.24 (dd, 1H, H-1, *J*(H$_1$, H′$_1$) 9.5, *J*(H$_1$, F) 46.5 Hz), 4.32 (d, 1H, H-2′, *J*(H$_{2'}$, F) 1.5 Hz), 4.30 (dd, 1H, H′-1, *J*(H′$_1$, F) 46.5 Hz), 7.0–7.45 (m, 9H, aromatic hydrogens); ^{19}F NMR ($CDCl_3$) δ: −229.6 (t, CH_2F, *J*(CH_2, F) 46.5 Hz). Anal. calcd. for $C_{18}H_{18}FNOS$: C 68.55, H 5.75, N 4.44; found: C 68.51, H 5.73, N 4.46%.

Into a mixture of Raney nickel (560 mg) and (3*S*,3′*R*)-**18** (187 mg, 0.59 mmol) in absolute ethanol (18 mL) was bubbled Ar for 10 min at room temperature. Then the mixture was heated at 75°C for 4 h. Raney nickel was filtered off, and ethanol was evaporated under reduced pressure. The residue was chromatographed on silica gel (4:1 hexane:ethyl acetate) to give (*S*)-**19** in 65% yield: $[\alpha]^{20}_D$ −15.8 (*c* 0.5, $CHCl_3$); ^{1}H NMR ($CDCl_3$) δ: 2.25 (br s, 1H, OH), 2.59 (m, 2H, H-3 and H′-3), 3.00 (m, 1H, H-2′ and H′-2′), 4.31 (dd, 1H, H-1, *J*(H$_1$, H′$_1$) 10.2, *J*(H$_1$, F) 47.1 Hz), 4.36 (dd, 1H, H′-1, *J*(H′$_1$, F) 47.1 Hz), 7.25–7.45 (m, 5H, aromatic hydrogens); ^{19}F NMR ($CDCl_3$) δ: −228.7 (t, CH_2F, *J*(CH_2, F) 47.1 Hz). Anal. calcd. for $C_{11}H_{12}FNO$: C 68.38, H 6.26, N 7.25; found: C 68.11, H 6.24, N 7.23%.

Acknowledgements

We thank Dr. Vecchio for skilled assistance in obtaining C.D. spectra and Progetto Finalizzato Chimica Fine for a Visiting Professor Fellowship.

1. (*a*) R. Filler and Y. Kobayashi (*Editors*). Biomedical aspects of fluorine chemistry. Kodansha, Tokyo, and Elsevier Biomedical Press, Amsterdam. 1982; (*b*) J.T. Welch and S. Eswarakrishnan. Fluorine in bioorganic chemistry. J. Wiley and Sons, New York. 1991.
2. (*a*) P. Bravo and G. Resnati. Tetrahedron: Asymmetry, **1**, 661 (1990); (*b*) P. Bravo, E. Piovosi, G. Resnati, and S. De Munari. Gazz. Chim. Ital. **115**, 118 (1988).
3. (*a*) P. Bravo, E. Piovosi, G. Resnati, and G. Fronza. J. Org. Chem. **54**, 5171 (1989); (*b*) P. Bravo, M. Frigerio, G. Fronza, A. Ianni, and G. Resnati. Tetrahedron, **46**, 997 (1990).
4. (*a*) P. Bravo, G. Resnati, and F. Viani. Tetrahedron, **49**, 713 (1993); (*b*) P. Bravo, G. Resnati, and F. Viani. Gazz. Chim. Ital. **122**, 493 (1992); (*c*) G. Resnati. Farmaco, **45**, 1043 (1990).
5. P. Bravo, G. Resnati, P. Angeli, M. Frigerio, F. Viani, A. Arnone, G. Marucci, and F. Cantalamessa. J. Med. Chem. **35**, 3102 (1992).
6. (*a*) G.H. Posner. *In* The chemistry of sulphones and of sulphoxides. *Edited by* S. Patai, Z. Rappaport, and C. Stirling. John Wiley and Sons, New York. 1988. p. 823; (*b*) G. Solladiè, D. Demailly, and C. Greck. J. Org. Chem. **50**, 1552 (1985); (*c*) P. Bravo, E. Piovosi, and G. Resnati. J. Chem. Soc. Perkin Trans. 1, 1201 (1989).
7. A. Arnone, P. Bravo, G. Cavicchio, M. Frigerio, V. Marchetti, F. Viani, and C. Zappalà. Tetrahedron Lett. **33**, 5609 (1992).
8. Presented at the 9th International Conference on Organic Synthesis, Montréal, June 28 – July 2, 1992.
9. P. Bravo, E. Piovosi, and G. Resnati. Gazz. Chim. Ital. **118**, 115 (1988).
10. A.H. Blatt. *In* Org. Synth. Coll. Vol. 2. John Wiley and Sons, New York. 1943. p. 461.
11. (*a*) S. Patai (*Editor*). The chemistry of diazonium and diazo groups. John Wiley and Sons, New York. 1978. pp. 575 and 598; (*b*) E. Müller (*Editor*). Methoden der Organischen Chemie, Houben-Weyl. Vol. VII/2b, part II. G. Thieme Verlag, Stuttgart. 1976. p. 1855; (*c*) Vol. X/4, part IV. G. Thieme Verlag, Stuttgart. 1968. p. 712.
12. (*a*) P. Bravo, G. Ganazzoli, E. Piovosi, and G. Resnati. Gazz. Chim. Ital. **119**, 323 (1989); (*b*) J.T. Welch, K. Seper, S. Eswarakrishnan, and J. Samartino. J. Org. Chem. **49**, 4720 (1984); (*c*) J.T. Welch and S. Eswarakrishnan. J. Org. Chem. **50**, 5403 (1985).
13. (*a*) A.S. Rao, S.K. Paknikar, and J.G. Kirtane. Tetrahedron, **39**,

2323 (1983); (*b*) J.G. Smith. Synthesis, **8**, 629 (1984); (*c*) M. Bartok and K.L. Lang. *In* Small ring heterocycles. Part 3. *Edited by* A. Weissberger and E.C. Taylor. John Wiley, New York. 1985; (*d*) B.B. Lohray. Synthesis, **11**, 1035 (1992).
14. J.A. Ciaccio, E. Heller, and A. Talbot. Synlett, **4**, 248 (1991).
15. M. Chini, P. Crotti. L. Favero, and F. Macchia. Tetrahedron Lett. **32**, 4775 (1991).
16. J. Drabowicz and S. Oae. Synthesis, 404 (1977).
17. U. de la Champ and H. Hope. Acta Crystallogr. Sect. B: Struct. Crystallogr. Cryst. Chem. **B26**, 846 (1970).
18. D.H. Hua, I. Badejo, P.J. McCann, and F. Takusagawa. Acta Crystallogr. Sect. C: Cryst. Struct. Commun. **C43**, 1112 (1987).
19. Robinson, D.H. Hua, J. Shan Chen, and S. Saha. Acta Crystallogr. Sect. C: Cryst. Struct. Commun. **C47**, 594 (1991).
20. C. Hamdouchi. Tetrahedron Lett. **33**, 1701 (1992).
21. G. Fabrizi, W. Fedeli, and D. Lamba. Acta Crystallogr. Sect. C: Cryst. Struct. Commun. **C48** 1131 (1992).
22. (*a*) A. La Manna and V. Ghislandi. Farmaco, **17**, 355 (1962); (*b*) **17**, 480 (1962); (*c*) C. Toniolo and A. Fontana. *In* The chemistry of the thiol group. *Edited by* S. Patai. John Wiley and Sons, London. 1974. Chap. 7, p. 355; (*d*) M.A. Adams, K. Nakanishi, W.C. Still, E.V. Arnold, J. Clardy, and C.J. Persoon. J. Am. Chem. Soc. **101**, 2495 (1979); (*e*) C. Djerassi, W. Klyne, T. Norin, G. Ohloff, and E. Klein. Tetrahedron, **21**, 163 (1965).
23. H.E. Smith. Chem. Rev. **83**, 359 (1983).

Can. J. Chem. Downloaded from www.nrcresearchpress.com by 85.192.166.187 on 09/08/12
For personal use only.

Does the Csp^2—Csp^3 barrier in ethylbenzene have a hyperconjugative component? An indirect experimental and theoretical approach

TED SCHAEFER,[1] ROBERT W. SCHURKO, AND GUY M. BERNARD
Department of Chemistry, University of Manitoba, Winnipeg, MB R3T 2N2, Canada

Received February 21, 1994

TED SCHAEFER, ROBERT W. SCHURKO, and GUY M. BERNARD. Can. J. Chem. **72**, 1780 (1994).

The proton chemical shifts and the proton spin–spin coupling constants are reported for 1-phenyl-1-butyne and 1-phenyl-1-pentyne dissolved in CS_2/C_6D_{12} and acetone-d_6. The long-range coupling constants between the methylene and ring protons are used to derive the twofold barriers to internal rotation in these molecules. They are 0.5 ± 0.1 kJ/mol; the perpendicular conformer is the most stable, the one in which the C(3)—C(4) bond of the side chain lies in a plane perpendicular to the phenyl group. This energetic preference is assigned to the difference between C—C and C—H hyperconjugative interactions with the aromatic π electron system, the C—C interaction being larger. Comparison of the twofold components of the internal rotational barriers in biphenyl and diphenylacetylene, that in the latter amounting to 40% of that in the former, implies that the hyperconjugative component of the internal barrier in ethylbenzene is 1.2 ± 0.3 kJ/mol, a minor component of the total magnitude. Molecular orbital computations of the conformational energies of 1-phenyl-1-butyne all agree that the perpendicular conformer has the lowest energy but only to the extent of 0.1 kJ/mol at most.

TED SCHAEFER, ROBERT W. SCHURKO et GUY M. BERNARD. Can. J. Chem. **72**, 1780 (1994).

On rapporte les déplacements chimiques et les constantes de couplage du proton des composés 1-phényl-1-butyne et 1-phényl-1-pentyne dissous dans du CS_2/C_6D_{12} et dans l'acétone-d_6. On a utilisé les constantes de couplage à longue distance entre les protons du méthylène et ceux du cycle pour déduire les barrières doubles à la rotation interne dans ces molécules. Elles sont de 0,5 ± 0,1 kJ/mol; le conformère perpendiculaire est le plus stable, celui dans lequel la liaison C(3)—C(4) de la chaîne latérale est dans un plan perpendiculaire au groupe phényle. On attribue cette préférence énergétique à la différence entre les interactions hyperconjuguées des liaisons C—C et C—H et le système d'électrons π, les interactions C—C étant plus grandes. La comparaison des composantes doubles des barrières de rotation internes dans le biphényle et le diphénylacétylène, cette interaction étant de 40% plus élevée dans le biphénylacétylène, implique que le constituant d'hyperconjugaison de la barrière interne de l'éthylbenzène, un constituant minoritaire, est de 1,2 ± 0,3 kJ/mol. Les calculs d'orbitales moléculaires des énergies conformationelles du 1-phényl-1-butyne confirment que le conformère perpendiculaire a la plus basse énergie mais la différence est tout au plus de 0,1 kJ/mol.

[Traduit par la rédaction]

Introduction

In a discussion of the first ab initio molecular orbital calculations of the barrier to rotation about the Csp^2—Csp^3 bond in ethylbenzene (1), it is suggested that a hyperconjugative component may be present in addition to a larger steric component. The stable perpendicular conformer of ethylbenzene, **1**, is analogous to the computed stable conformer of the propyl cation. Such stabilization will naturally be smaller in the neutral than in the charged molecule. Because the hyperconjugative, σ–π electron, interaction is proportional to $\sin^2\theta$, where θ is the angle by which a bond in the side chain twists out of the benzene plane (2), **1** represents the conformation in which the C—C bond interacts most strongly with the π electron system. The C—H bonds are situated such that their hyperconjugative interactions are rather small, $\sin^2\theta$ being 0.25. There is no agreement in the literature concerning the relative hyperconjugative abilities of C—H and C—C bonds (3–14). These have been variously assessed as C—C > C—H, C—C ~ C—H, or C—H > C—C.

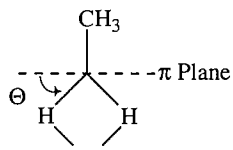

1

One comparison (10) of the conformational behaviour of alkylbenzene cations and anions suggests that C—H is greater than C—C hyperconjugation in the former but that the opposite is true for the anions. How much these conclusions would be altered by steric considerations is problematical. Another comparison, based on neutral 4-alkylbenzyl radicals, does not suffer from this uncertainty; it is concluded (14) that the C—C bond is 40–60% as effective as C—H hyperconjugation for delocalizing spin density and, furthermore, that it is 75–90% as effective in delocalizing charge density in 4-alkylcumyl cations. As another example of the many investigations of this topic, a simple molecular orbital analysis of magnetic circular dichroism data (4) for neutral alkylbenzenes concludes that there exists little, if any, difference between the hyperconjugative ability of C—H and C—C bonds.

An alternative approach to the matter would involve the measurement of the relative energetic contribution, $E_{C-C} - E_{C-H}$, to the hyperconjugative stabilization of a given conformation of a neutral alkylbenzene. Such a measurement is unknown to us and is difficult, simply because a separation of hyperconjugative (probably small) from other components, such as steric, is not straightforward.

Returning to ethylbenzene, the barrier is very likely dominated by steric repulsion between the methyl group and the *ortho* C—H bonds of the phenyl group. However, insertion of a C≡C bond between the ethyl and phenyl groups removes the steric repulsions during rotation about the Csp—Csp^2 and Csp—Csp^3 bonds. Hyperconjugation between the C—C and C—H bonds of the ethyl group and the π electrons of the phenyl group can still occur via the triple bond although, of course, it will be

[1]Author to whom correspondence may be addressed.

Can. J. Chem. Downloaded from www.nrcresearchpress.com by 85.192.166.187 on 09/08/12
For personal use only.

Can. J. Chem. Downloaded from www.nrcresearchpress.com by 85.192.166.187 on 09/08/12
For personal use only.

reduced in magnitude compared to ethylbenzene. Thus, the conjugational barrier to rotation in diphenylacetylene, at 2.4 kJ/mol (15, 16), is rather smaller than in biphenyl if the twofold component of the barrier in the latter is taken as a measure of the conjugational barrier in the absence of the triple bond. The twofold component of the internal barrier in biphenyl is about 6.1 kJ/mol (17). Again, in phenylpropynal, $C_6H_5{\equiv}CC\text{-}CHO$, the planar conformer is more stable than the perpendicular conformer by 6 ± 2 kJ/mol, attributable to conjugation between the formyl and phenyl π electron systems (18). The internal rotational barrier in benzaldehyde, also twofold, is >19 kJ/mol (19).

In 1-phenyl-1-butyne, **2**, the ethyl group can hyperconjugate with the aromatic π electron system via the triple bond. Any conformational preferences with respect to the aromatic plane will be reflected in the σ–π electron-mediated coupling constant between the methylene protons and the ring protons, $^8J(H, CH_2)$, as discussed previously (18, 20). This coupling constant varies as $^8J_{90}\sin^2\theta$ and an estimation of $^8J_{90}$ can be had (19). The measured ^8J then yields $\langle\sin^2\theta\rangle$, that is, the value of $\sin^2\theta$ averaged over the internal motion, which, in turn, is governed by the internal rotational potential. As an example, if in **2** a

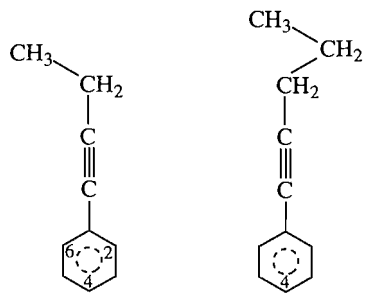

2 **3**

hyperconjugative interaction stabilizes a conformation analogous to **1** sufficiently strongly, then $\langle\sin^2\theta\rangle$ approaches 0.25; if, however, the internal motion about the C*sp*—C*sp*^{3} bond is unhindered, the associated value of $\langle\sin^2\theta\rangle$ is 0.5. It also turns out that $^6J(H, CH_2)$ in **2** and **3** can be used in this fashion.

Accordingly, the precise analyses of the ^{1}H nmr spectra of 1-phenyl-1-butyne, dissolved in a nonpolar and a polar solvent, are reported here. The ensuing ^6J and ^8J values are used to deduce the ease of internal motion of the ethyl group relative to the plane of the phenyl group. In addition, ^{1}H nmr spectral data are obtained for 1-phenyl-1-pentyne, **3**, affirming that the coupling constant data are not peculiar to the butyne derivative. Confirmation of the experimental results is also sought via molecular orbital computations of the relative energies of the planar and perpendicular conformers of the phenylbutyne.

Experimental

Dilute solutions (see Table 1 for details) of 1-phenyl-1-butyne and 1-phenyl-1-pentyne (Aldrich) in CS_2/C_6D_{12}/TMS and acetone-d_6/TMS solvent mixtures were transferred to 5 mm o.d. nmr sample tubes. These were degassed by five cycles of the freeze–pump–thaw procedure and were then flame-sealed to provide reasonably symmetric tops. The ^{1}H nmr spectra were acquired on an AM 300 nmr spectrometer using documented techniques (19, 21). Acquisition times of 50 s and some resolution enhancement (LB of −0.11 and a GB of 0.6) produced linewidths at half height of about 0.03 Hz in the aromatic region, so that splittings of 0.04 Hz were cleanly resolved.

Molecular orbital computations used the computer program GAUSSIAN 86 (22) and employed the AM1 parameterization (23) as well as the STO-3G (24), 6-31G (25), and 6-31G* (26) basis sets. The carbon and hydrogen atoms of the phenyl group in 1-phenyl-1-butyne were constrained to lie in a plane during the geometry optimization procedures, all other bond angles and lengths being allowed to vary. INDO MO FPT (27) computations of spin–spin coupling constants were done for STO-3G MO geometries of the butyne derivative.

Results and discussion

Spectral analyses

The ^{1}H nmr spectra were analyzed with a greatly modified version (R. Sebastian) of the computer program NUMARIT (28). The spectral parameters appear in Table 1. Signs of the long-range coupling constants between the ring protons and those in the side chain are known from previous work on 1-phenyl-1-propyne (18). The sign of $^4J(CH_2, CH_3)$ in 1-phenyl-1-pentyne follows from a comparison of simulated with experimental spectra, some of which are displayed in Fig. 1. Although the linewidths are considerably larger for the methyl protons than for the aromatic protons, these spectra illustrate how the sign of a very small coupling constant follows from a complete analysis.

*$^{6,8}J(H, CH_2)$ and the relative orientation of the alkyl and phenyl groups in **2** and **3***

The derivation of the internal barriers in **2** and **3** goes as follows. As discussed previously (18, 20), $^8J(H, CH_2)$ is a σ–π electron coupling constant and, as such, varies as $\sin^2\theta$ where θ is the angle by which the C—H bond of the methylene group twists out of the aromatic plane. This functional dependence is confirmed by our INDO MO FPT computations on 1-phenyl-1-propyne (18) and on **2**. Hence $^8J(H, CH_2) = {}^8J_{90}\langle\sin^2\theta\rangle$. Furthermore, the INDO MO FPT computations on **2**, using the optimized STO-3G MO geometries, yield the angle dependence of $^6J(H, CH_2)$ as dominated by a term, 0.270 $\sin^2\theta$, and containing a small term, 0.028 $\sin^2(\theta/2)$. For a twofold barrier, $\langle\sin^2(\theta/2)\rangle$ is 0.5. The magnitudes of the coefficients in these terms depend on the parameterization of the semiempirical algorithm. We shall assume that $^6J(H, CH_2)$ is also a pure σ–π coupling constant.[2]

For the propyne, the expectation value of $\sin^2\theta$ is 0.5 because the internal barrier is effectively zero (29). Because $^{6,8}J$ in 1-phenyl-propyne are known, the extremes in $^{6,8}J$, their values at θ = 90°, follow. However, the magnitudes of $^{6,8}J_{90}$ for the methylene group depend somewhat on the substituent, R, in CH_2R; in **2** and **3**, R is CH_3 and CH_2CH_3, respectively. If the electronegativity of R, E_R, is greater than that of hydrogen, the C—H bonds of the methylene group are polarized so as to reduce the σ–π (hyperconjugative) overlap with π electrons. Hence nuclear spin state information is not as effectively transmitted and $^{6,8}J_{90}$ decrease in magnitude, a calibration[3] yielding its value as $^8J(H, CH_2)/{}^8J(H, CH_3) = (1.15 \pm 0.01)/1.20$.

The experimental values of $\langle\sin^2\theta\rangle$ are then matched to values obtained from a hindered rotor model (34), which computes $\langle\sin^2\theta\rangle$ as a function of the internal barrier, the reduced moment of inertia of the molecule, and the temperature. At ambient tem-

[2]If a constant amounting to 10% of the ^6J values in Tables 1 and 2 is subtracted from their magnitudes, to account for a term in $\sin^2(\theta/2)$, the $\langle\sin^2\theta\rangle_{300}$ values are not significantly altered in Table 2.

[3]Thus, for the most electronegative R, fluorine, it has been shown experimentally (30) that $^6J_{90}(H, CH_2)$ is −0.94 Hz, as compared to a $^6J_{90}(H, CH_3)$ of −1.20 Hz in toluene (31). Again, for an oxygen substituent, $^6J_{90}(H, CH_2)$ is −1.02 Hz (32, 33). The assumption of a linear dependence of $^6J_{90}$ on E_R, and values of 4.0, 3.5, 2.5, and 2.1 for F, O, C, and H, respectively, yields a $^6J_{60}$ of −1.15 ± 0.01 Hz for R = CH_3 or CH_2CH_3.

Can. J. Chem. Downloaded from www.nrcresearchpress.com by 85.192.166.187 on 09/08/12
For personal use only.

TABLE 1. The ^{1}H nmr spectral parameters of 1-phenyl-1-butyne and 1-phenyl-1-pentyne at 300 K

Parameter	1-Phenyl-1-butyne		1-Phenyl-1-pentyne	
	$CS_2/C_6/D_{12}$[a]	Acetone-d_6[b]	CS_2/C_6D_{12}[a]	Acetone-d_6[b]
$\nu(CH_3)$	357.907[c]	357.113	308.333	306.180
$\nu(CH_2)$	—	—	474.095	475.651
$\nu(CH_2)$	702.069	720.017	693.022	708.612
ν_2	2171.618	2213.160	2171.465	2214.734
ν_3	2141.814	2193.640	2141.992	2188.524
ν_4	2137.708	2188.738	2137.547	2182.713
$^3J(CH_2, CH_3)$	7.484	7.489	7.353	7.375
$^3J(CH_2, CH_2)$	—	—	7.012[d]	7.006[d]
$^4J(CH_2, CH_3)$	—	—	−0.084	−0.095
$^3J_{23}$	7.751	7.768	7.749	7.776
$^3J_{34}$	7.523	7.551	7.528	7.551
$^4J_{24}$	1.283	1.269	1.287	1.270
$^4J_{26}$	1.751	1.784	1.747	1.785
$^4J_{35}$	1.400	1.403	1.400	1.405
$^5J_{25}$	0.625	0.637	0.625	0.635
$^6J(2, CH_2)$	−0.277	−0.280	−0.278	−0.281
$^7J(3, CH_2)$	0.133	0.136	0.133	0.129
$^8J(4, CH_2)$	−0.233	−0.240	−0.225	−0.238
Transitions calcd.	2264	2330	11848	11968
Transitions assigned	2049	2130	8066	9700
Peaks observed	214	223	270	256
Largest difference	0.016	0.024	0.018	0.020
RMS deviation	0.006	0.007	0.007	0.006

[a]5.0 mol% in CS_2, containing also 10.0 mol% C_6D_{12} and 0.5 mol% of TMS.
[b]5.0 mol% in acetone-d_6, containing also 0.5 mol% of TMS.
[c]In Hz at 300.135$_2$ MHz to high frequency of internal TMS; the standard deviations of the spectral parameters are all less than 0.001 Hz.
[d]This is the mean of ^3J and $^3J'$ in an AA'BB' analysis. ^3J and $^3J'$ do not differ by as much as 0.4 Hz while the ^2J values are strongly correlated. Hence only the sum of ^3J and $^3J'$ is very reliable. The *gauche* conformer is somewhat less stable than the *trans* by about 0.3 kJ/mol.

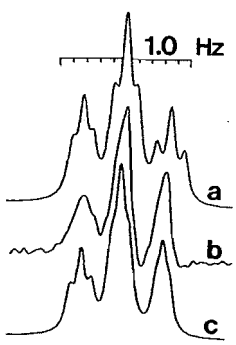

FIG. 1. Part of the ^{1}H nmr spectrum at 300 MHz and 300 K of the methyl protons in 1-phenyl-1-pentyne, as a 5.0 mol% solution in a CS_2/C_6D_{12}/TMS solvent mixture, is displayed in (*b*). In (*a*) the computed spectrum has $^4J(CH_2, CH_3)$ as +0.08 Hz and as −0.08 Hz in (*c*).

peratures, barriers of less than about 12 kJ/mol, and reduced moments of inertia of about 10^{-38} gm cm^2, the values of $\langle\sin^2\theta\rangle$ are insensitive to the precise value of the inertial properties. The barriers in **2** and **3** are assumed to be twofold, as expected intuitively (hyperconjugation), and confirmed by at least some of the molecular orbital computations described below.

Table 2 presents the internal barriers and experimental values of $\langle\sin^2\theta\rangle$. For **2** and **3**, $\langle\sin^2\theta\rangle$ is always less than 0.5, implying that the conformation analogous to **1** is most stable. In other words, if the internal barriers in **2** and **3** are hyperconjugative in origin, then C—C is larger than C—H hyperconjugation. More precisely, if the hyperconjugative stabilization, E(h.c.), is proportional to $\sin^2\theta$, where θ is the angle by which the C—H or C—C bonds twist out of the phenyl plane, and if the barrier is twofold, then **4** and **5** entail the relationship, $E_{C—C} > E_{C—H}$; the barriers in Table 2 are the measures of $E_{C—C} - E_{C—H}$.

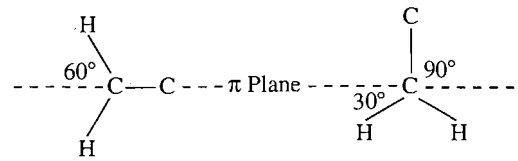

$E(h\cdot c) = 1.5E_{C—H}$ **4**

$E(h\cdot c) = E_{C—C} + 0.5E_{C—H}$ **5**

The errors quoted for the twofold barriers in Table 2 are based on an uncertainty of 0.01 Hz in the calibration of the correction factor for electronegativity and an error[4] of 0.001 Hz in the measured values of $^{6,8}J$; the standard form of error propagation was used.[5] On the assumption that the barrier values are the

[4]The standard deviations of $^{6,8}J$ ranged from 0.0002 to 0.0007 Hz, as obtained from the least-squares fit of many transitions (Table 1).

[5]The values of $\langle\sin^2\theta\rangle$, proportional to the measured values of $^{6,8}J(H, CH_2)$, are very sensitive to V_2 for small values of the latter. Thus, for an increase of V_2 from zero to 4.2 kJ/mol, $\langle\sin^2\theta\rangle$ changes from 0.500 to 0.405, whereas a further increase of V_2 from 4.2 to 13.4 kJ/mol is needed to cause a further decrease of 0.100 in $\langle\sin^2\theta\rangle$ at 300 K.

TABLE 2. The twofold internal rotational barriers in phenyl-C≡C-CH_2R (R = CH_3, CH_2CH_3) derived from $^{6,8}J$(H, CH_2)

R	$-^6J$/Hz	$\langle\sin^2\theta\rangle_{300}$	V_2^c (kJ/mol)	$-^8J$/Hz	$\langle\sin^2\theta\rangle_{300}$	V_2^c (kJ/mol)
			CS_2/C_6D_{12}			
H	0.295(1)	0.500[a]	0[a]	0.251(1)	0.500[a]	0[a]
CH_3	0.277(1)	0.490(6)[b]	0.4(2)	0.233(1)	0.484(6)[b]	0.6(2)
CH_2CH_3	0.278(1)	0.492(b)	0.3(2)	0.225(1)	0.468(6)	1.3(2)
			Acetone-d_6			
H	0.298(1)	0.500	0	0.254(1)	0.500	0
CH_3	0.280(1)	0.490(6)	0.4(2)	0.240(1)	0.493(6)	0.3(2)
CH_2CH_3	0.281(1)	0.492(6)	0.3(2)	0.238(1)	0.489(6)	0.4(2)

[a]It is assumed that the barrier in 1-phenyl-1-propyne, very likely sixfold if it were present, effectively vanishes (29).

[b]For R = CH_3 and R = CH_2CH_3, the expectation values of $\sin^2\theta$ come from $\langle\sin^2\theta\rangle = {}^{6,8}J(H, CH_2)/\{2 \times {}^{6,8}J(H, CH_3)\}$ (1.15 ± 0.01)/1.20}; see text. A value of $\langle\sin^2\theta\rangle$ <0.5 means that the perpendicular conformer is most stable.

[c]V_2 comes from tables giving $\langle\sin^2\theta\rangle_{300}$ as a function of V_2, derived from a hindered rotor model as referenced in the text; the temperature is 300 K.

same for **2** and **3** and that they do not depend on the solvent, the hyperconjugative barrier is then 0.5(1) kJ/mol (if the apparent outlier, 1.3 kJ/mol, is excluded, one has 0.4(1) kJ/mol, but there is no solid evidence for its exclusion). Clearly, the barrier is very small; nevertheless, all eight values of $\langle\sin^2\theta\rangle$ in Table 2 agree that the perpendicular, **4**, is more stable than **5**.

The estimated hyperconjugative barrier in ethylbenzene

The conjugational barrier favouring planarity in tolane (diphenylacetylene) is 2.4 kJ/mol, amounting to 40% of the twofold component of the barrier in biphenyl, presumably also arising from conjugation of the π electrons of the two phenyl groups.[6] The σ–π or hyperconjugative component of the barrier in ethylbenzene is then (0.5 ± 0.1) 2.5 or 1.2 ± 0.3 kJ/mol. The barrier height in ethylbenzene has been variously deduced (35, 36) and ranges from 4.8 to 9.2 kJ/mol, so that the hyperconjugative contribution amounts to a minor component of the barrier.

Molecular orbital computations on 1-phenyl-1-butyne, 2

The AM1 computations on **2**, done at intervals of 15° in the torsion angle, predict a twofold barrier with the perpendicular conformer, **4**, being most stable by 0.1 kJ/mol. The STO-3G MO optimizations agree formally with this conclusion, having **4** most stable by 0.02 kJ/mol. Again, the 6-31G and 6-31G* computations find **4** of lower energy than **5** by 0.07 and 0.06 kJ/mol, respectively. These last numbers are perhaps just within the level of significance of such computations. In this sense the computations are in qualitative agreement with the experimental deductions for the molecules in solution. Whether the inclusion of electron correlation would alter the theoretical prediction is unknown. It is true that C—H and C—C hyperconjugation in neutral molecules has been a subject of controversy, no doubt because it is small energetically, as also indicated by the present results. The most recent discussions concentrate on structural changes induced by this phenomenon. One (37), based on $^1J(^{13}C, ^{13}C)$ variations, concludes that C—C hyperconjugation is negligible; the other (8), based on a comparison of experimental bond lengths with their theoretical analysis, concludes that C—C and C—H bonds can hyperconjugate in neutral, ground-state molecules.

Further considerations

(a) Isopropylphenylacetylene

According to the present experimental measurements, for isopropylphenylacetylene the most stable conformer would be that in which the methine C—H bond lay in the aromatic plane. If the presence of a second methyl group does not alter $E_{C-C} - E_{C-H}$ (there are now two C—C bonds and only one C—H bond for hyperconjugative interactions), then the magnitude of the twofold internal barrier will equal that in **2**. The barrier should be accessible to the techniques described here as soon as the compound itself becomes available.

(b) $^3J(CH_2, CH_2)$ in 3

The apparently large value, 1.3(2) kJ/mol, for V_2 in 1-phenyl-1-pentyne dissolved in CS_2/C_6D_{12} arouses the suspicion that a steric component might be present. Models imply that, in a *gauche* arrangement of the CH_3 and $C_6H_5C{\equiv}C$ groups about the C—C bond of the CH_2-CH_2 fragment, the distance of closest approach of a methyl proton and a proton in an *ortho* C—H bond could be somewhat less than 3 Å, consistent with such a suspicion. In a *trans* arrangement of the two groups the closest distance would be 4 Å, that between the ring proton and the 4-methylene protons (just as in the butyne derivative). However, a larger population of the *gauche* conformer in the nonpolar solvent should be reflected in a change of $^3J(CH_2, CH_2)$ between the two solvents (38, 39). This change is not significant (Table 1). Furthermore, $^6J(H, CH_2)$ for **3** in the two solvents also indicates no change in barrier between the solutions. A longer alkyl chain could conceivably give rise to steric components of the barrier.

If the substituent dependence of the vicinal coupling constants in 1,2-disubstituted ethanes, as given by Phillips and Wray (39), is used with eq. 5c of Abraham and Gatti (38), then

[6]It is interesting that the σ–π transmitted coupling constant in 1-phenyl-1-propyne (18), a $^8J(H, CH_3)$ of −0.251(1) Hz in CS_2/C_6D_{12} (18), is 42% of the −0.602(2) Hz for $^6J(H, CH_3)$ in toluene dissolved (31) in the same solvent mixture. Exactly the same proportion holds for $^6J(H, CH_3)$ and $^4J(H, CH_3)$ in these molecules. Of course, while the transmission of the spin polarization giving rise to these coupling constants and the hyperconjugative energetics both arise from σ–π electron interactions, it does not follow that their magnitudes are directly proportional to one another.

Can. J. Chem. Downloaded from www.nrcresearchpress.com by 85.192.166.187 on 09/08/12
For personal use only.

the *gauche* conformer of **3** has a population of 0.64. This conformer is twofold degenerate, so that the *trans* conformer is favoured by an enthalpy of 0.3 kJ/mol. From a number of theoretical computations of ^4J(H, H) in propane (40), it is clear that the *gauche* conformer has a positive $^4J(CH_2, CH_3)$, the *trans* a negative. In **3**, ^4J is about -0.09 Hz, so that the presence of a significant population of the *trans* conformer seems assured.

(c) Solvent dependence of ^nJ(H, H) for the aromatic protons

The pattern of the solvent dependence of the aromatic proton coupling constants in Table 1 follows precisely that observed for a variety of monosubstituted benzenes in this laboratory. ^3J increases by about 0.02 Hz in passing from $CS_2/C_6/D_{12}$ to acetone-d_6 solutions; $^4J_{26}$ and $^5J_{25}$ increase as well, but $^4J_{24}$ decreases while $^4J_{35}$ is insensitive to solvent. These changes are not artifacts of the spectral analytical procedures; they are apparently not a function of the polarity or of other obvious properties of the substituents. The cause of these changes is not known and remains under investigation.

Acknowledgment

We are grateful to the Natural Sciences and Engineering Research Council of Canada for a grant-in-aid of research.

1. W.J. Hehre, L. Radom, and J.A. Pople. J. Am. Chem. Soc. **94**, 1496 (1972).
2. D.E. Sunko and W.J. Hehre. Prog. Phys. Org. Chem. **14**, 205 (1983), and references cited therein.
3. E. Glyde and R. Taylor. J. Chem. Soc. Perkin Trans. 2, 678 (1977), and references cited therein.
4. G.H. Weeks, W. Adcock, K.A. Klingensmith, J.W. Waluk, R. West, M. Vašak, J. Downing, and J. Michl. Pure Appl. Chem. **58**, 39 (1986).
5. S. Berger, B.W.K. Diehl, and H. Künzer. Chem. Ber. **120**, 1059 (1987).
6. W. Adcock and A.N. Abeywickrema. J. Org. Chem. **47**, 779 (1982), footnote 20, in particular.
7. L.M. Stock and M.R. Wasielewski. J. Am. Chem. Soc. **99**, 50 (1977).
8. T. Laube and T.-K. Ha. J. Am. Chem. Soc. **110**, 5511 (1988), and references cited therein.
9. B.T. Cooney and D.A.R. Happer. Aust. J. Chem. **40**, 1537 (1987).
10. M. Kira, H. Nakazawa, and H. Sakurai. Chem. Lett. 1841 (1985).
11. W.F. Reynolds, R.H. Kohler, and G.K. Hamer. Tetrahedron Lett. 4671 (1976).
12. S.D. Kan and W.J. Hehre. J. Am. Chem. Soc. **109**, 666 (1987).
13. F. Gerson and W. Huber. Angew. Chem. Int. Ed. Engl. **24**, 495 (1985).
14. D.D.M. Wayner and D.R. Arnold. Can. J. Chem. **63**, 2378 (1985).
15. K. Okuyama, M.C.R. Cockett, and K. Kimura. J. Chem. Phys. **97**, 1649 (1992), and references cited therein.
16. S. Saebø, J. Almlöf, J.E. Boggs, and J.G. Stark. J. Mol. Struct. (Theochem), **200**, 361 (1989).
17. S. Tsuzuki and K. Tanabe. J. Phys. Chem. **95**, 139 (1991), and references cited therein.
18. T. Schaefer, R. Sebastian, and R.W. Schurko. Can. J. Chem. **70**, 2365 (1992).
19. T. Schaefer, R. Sebastian, and F.E. Hruska. J. Mol. Struct. (Theochem), **281**, 269 (1993), and references cited therein.
20. C.J. Macdonald, G.K. Hamer, I.R. Peat, and W.F. Reynolds. Can. J. Chem. **50**, 2035 (1972).
21. T. Schaefer and R. Sebastian. Can. J. Chem. **70**, 2555 (1992).
22. M.J. Frisch, J.S. Binkley, H.B. Schlegel, K. Raghavachari, C.F. Melius, R.L. Martin, J.J.P. Steward, F.W. Bobrowicz, D.F. Rohlfing, L.R. Kahn, K.J. Defrees, R. Seeger, R.A. Whiteside, D.J. Fox, E.M. Fluder, and J.A. Pople. Carnegie-Mellon Quantum Publishing Unit, Pittsburgh, Pa. 1984.
23. M.J.S. Dewar, E.J. Zoebisch, E.F. Healy, and J.J.P. Stewart. J. Am. Chem. Soc. **107**, 3902 (1985).
24. W.J. Hehre, R.J. Stewart, and J.A. Pople. J. Chem. Phys. **51**, 2657 (1969).
25. W.J. Hehre, R. Ditchfield, and J.A. Pople. J. Chem. Phys. **56**, 2257 (1972).
26. P.C. Hariharan and J.A. Pople. Chem. Phys. Lett. **66**, 217 (1972).
27. J.A. Pople, J.W. McIver, Jr., and N.S. Ostlund. J. Chem. Phys. **49**, 2960 (1968); **49**, 2965 (1968).
28. J.S. Martin, A.R. Quirt, and K.E. Worvill. The NMR program library. Daresbury Laboratory, Daresbury, U.K.
29. W.B. Olson and D. Papousek. J. Mol. Spectrosc. **37**, 527 (1971).
30. T. Schaefer, C. Beaulieu, R. Sebastian, and G.H. Penner. Can. J. Chem. **68**, 581 (1990).
31. T. Schaefer, R. Sebastian, and G.H. Penner. Can. J. Chem. **63**, 2597 (1985).
32. R. Laatikainen. Magn. Reson. Chem. **24**, 588 (1986).
33. R. Laatikainen and K. Tuppurainen. J. Chem. Soc. Perkin Trans. 2, 121 (1987).
34. W.J.E. Parr and T. Schaefer. Acc. Chem. Res. **13**, 400 (1980).
35. T. Schaefer. G.H. Penner, and R. Sebastian. Can. J. Chem. **65**, 873 (1987), and references cited therein.
36. W. Caminati, D. Damiani, G. Corbelli, B. Velino, and C.W. Bock. Mol. Phys. **74**, 885 (1991).
37. J.B. Lambert and R.A. Singer. J. Am. Chem. Soc. **114**, 10246 (1992).
38. R.J. Abraham and G. Gatti. J. Chem. Soc. B, 961 (1969).
39. L. Phillips and V. Wray. J. Chem. Soc. Perkin Trans. 2, 536 (1972).
40. M. Barfield, A.M. Dean, C.J. Fallick, R.J. Spear, S. Sternhell, and P.W. Westerman. J. Am. Chem. Soc. **97**, 1482 (1975).

Can. J. Chem. Downloaded from www.nrcresearchpress.com by 85.192.166.187 on 09/08/12
For personal use only.

Nickel(II) and palladium(II) chelates of dehydroacetic acid Schiff bases derived from thiosemicarbazide and hydrazinecarbodithioate

ABDULLA AL KUBAISI[1] AND KAMAL Z. ISMAIL

Department of Chemistry, Faculty of Science, University of Qatar, Box 2713, Doha-Qatar

Received July 16, 1993[2]

ABDULLA AL KUBAISI and KAMAL Z. ISMAIL. Can. J. Chem. **72**, 1785 (1994).

Dehydroacetic acid Schiff bases DAE (**1**) and DATS (**2**) were isolated from the reaction of dehydroacetic acid (2-acetyl-5-hydroxy-3-oxo-4-hexenoic acid-δ-lactone) with hydrazine-*S*-methylcarbodithioate and the corresponding acid amide, thiosemicarbazide, respectively. Reaction of such Schiff bases with nickel(II) and palladium(II) ions afforded the dimeric monoligand chelates $[M(DAE\text{-}2H)]_2$ and $[M(DATS\text{-}2H)]_2$; M = Ni(II) or Pd(II). In the presence of monodentate Lewis bases, B, square-planar chelates [M(DAE-2H)B] and [M(DATS-2H)B], in which B = pyridine or triphenylphosphine, were isolated. The stoichiometry and structure of the isolated organic ligands and their chelates were confirmed through elemental analyses, molecular weight determination, and infrared, ultraviolet–visible, and ^1H and ^{13}C nuclear magnetic resonance spectroscopy.

ABDULLA AL KUBAISI et KAMAL Z. ISMAIL. Can. J. Chem. **72**, 1785 (1994).

On a isolé les bases de Schiff DAE (**1**) et DATS (**2**) de l'acide déhydroacétique en faisant réagir l'acide déhydroacétique (δ-lactone de l'acide 2-acétyl-5-hydroxy-3-oxo-hex-4-ènoïque) avec l'hydrazine du carbodithioate de *S*-méthyle et l'amide correspondant, la thiosemicarbazide, respectivement. Les réactions de telles bases de Schiff avec des ions nickel(II) et palladium(II) fournissent les chélates dimères monocoordinés $[M(DAE)\text{-}2H)]_2$ et $[M(DATS)\text{-}2H)]_2$ dans lesquels M = Ni(II) ou Pd(II). En présence des bases de Lewis monocoordinées, B, on isole des chélates plans carrés $[M(DAE)\text{-}2H)B]_2$ et $[M(DATS)\text{-}2H)B]_2$ dans lesquels B = pyridine ou triphénylphosphine. On a déterminé la stoechiométrie et la structure des coordinats organiques isolés en faisant appel à des analyses élémentaires, des déterminations de masses moléculaires et à des spectres infrarouges, ultraviolet–visible et résonance magnétique nucléaire du ^1H et du ^{13}C.

[Traduit par la rédaction]

Introduction

Dehydroacetic acid, DA, is an important and biologically active compound. Studies have shown that the compound has both antibiotic and fungicidal effects (1). In aqueous solutions, even at very low concentrations (0.02–0.2%), DA shows a strong antiseptic effect (2). The compound is widely used in food technology. It is used to enhance vitamin C stability and protect vegetables during food processing (3) and as a preservative in such products as fish sausages (4). Above all, the structure of DA appeals to inorganic chemists working in the field of coordination chemistry.

On the other hand, hydrazinecarbodithioates and the corresponding acid amide, thiosemicarbazide, and their corresponding Schiff bases show very interesting biological properties, such as antitumour (5, 6), antibacteria (7), and antiviral activities, in addition to a wide range of chemotherapeutic activities. Coordination of such compounds with metal ions such as nickel, iron, and copper often enhances their activity (7, 8), as reported for pathogenic fungi (9).

The antifungal activity of thiosemicarbazones and their corresponding metal chelates is substitution dependent, mainly upon the chemical nature of the segment attached to the C=S carbon atom (10–13). Similarly, substitution in the ring system of Schiff bases derived from compounds containing carbonyl groups attached to N-heterocyclic ring systems, thiosemicarbazides, and their corresponding metal chelates highly affects the biological activity of these compounds (13, 14). So, there is an important structure–activity relationship in these systems. In this manuscript, we use the carbonyl compound, DA, which is reported to have some biological activity, to form Schiff bases with both hydrazinecarbodithioate and thiosemicarbazide. The prepared Schiff bases may show enhanced biological activity. The corresponding nickel(II) and palladium(II) chelates were also prepared. We used elemental analyses and different spectroscopic techniques to elucidate both stoichiometry and structure for all isolated compounds. In future work we aim, with the assistance of our Zoology Department, to test our compound for biological activity.

Results and discussion

The reaction, in boiling ethanol, of hyrazine-*S*-methylcarbodithioate and its corresponding acid amide, thiosemicarbazide, with dehydroacetic acid, 2-acetyl-5-hydroxy-3-oxo-4-hexenoic acid-δ-lactone, afforded the corresponding Schiff bases DAE (**1**) and DATS (**2**), respectively (Scheme 1). Mass spectrometry fragmentation patterns as well as the infrared spectroscopic data revealed that condensation took place with the branched carbonyl group of the heterocyclic ring system of dehydroacetic acid. When mixed with metal acetates, compounds **1** and **2** reacted as dibasic tridentate anionic ligands. The coordination centres are the oxygen atom of the ring carbonyl, the sulphur atom, and the imine nitrogen $[ONS]^{2-}$.

Reaction of nickel(II) acetate with DAE and DATS in the molar ratio 1:1 gave brown crystalline chelates of stoichiometry $[Ni(DAE\text{-}2H)]_2$ and $[Ni(DATS\text{-}2H)]_2$, respectively, where (DAE-2H), and (DATS-2H) are the dinegative anion forms of the ligands DAE and DATS, respectively. The corresponding palladium chelates $[Pd(DAE\text{-}2H)]_2$ and $[Pd(DATS\text{-}2H)]_2$ were similarly isolated as orange solids. Elemental analyses of these chelates (Table 1) showed monoligand metal chelate stoichiometry, i.e., one ligand per metal center. Since our ligands **1** and **2** are only tridentate, one should expect dimerization to complete the coordination. The solution electronic spectra in $CHCl_3$ (Table 2) show several absorption bands. The uv absorption bands between ca. 270 and 320 nm are assigned to localized L–L* transitions of the dianion form of the ligands (in alkaline solution, the unchelated ligand absorbs at ca. 280 and 320 nm).

[1]Author to whom correspondence may be addressed.

[2]Revision received April 5, 1994.

Can. J. Chem. Downloaded from www.nrcresearchpress.com by 85.192.166.187 on 09/08/12
For personal use only.

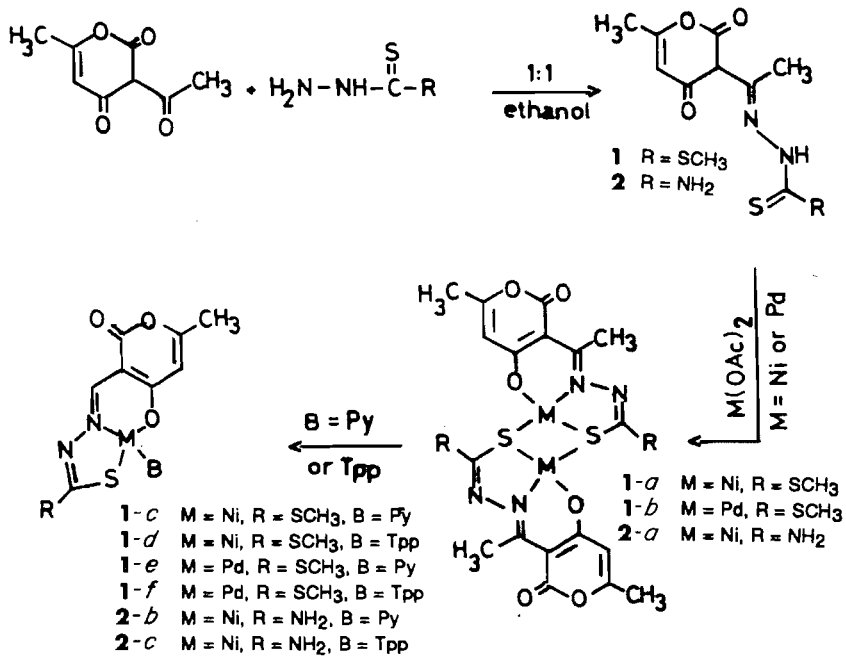

SCHEME 1

TABLE 1. Elemental analysis of DAE and DATS and their metal chelates

Compounds		Found (calculated) %				
		C	H	N	S	M
1	DAE	44.11 (44.40)	4.41 (4.31)	10.29 (10.22)	23.55 (24.05)	— —
1*a*	[Ni(DAE-2H)]$_2$	36.47 (37.47)	3.40 (3.60)	8.51 (7.91)	19.45 (19.51)	17.9 (18.20)
1*c*	[Ni(DAE-2H)Py]	44.11 (44.39)	3.67 (3.69)	10.30 (10.36)	15.68 (16.16)	14.38 (14.53)
1*d*	[Ni(DAE-2H)Tpp]	56.90 (57.25)	4.23 (4.26)	4.73 (4.85)	10.82 (10.90)	9.93 (9.98)
1*b*	[Pd(DAE-2H)]$_2$	31.83 (31.62)	2.65 (2.60)	7.42 (7.33)	16.97 (16.19)	28.11 (27.94)
1*e*	[Pd(DAE-2H)Py]	39.47 (39.19)	3.28 (3.26)	9.21 (9.05)	14.03 (13.74)	23.33 (23.00)
1*f*	[Pd(DAE-2H)Tpp]	52.66 (52.92)	3.91 (4.04)	4.38 (4.05)	10.03 (10.08)	16.67 (16.96)
2	DATS	44.81 (45.19)	4.56 (4.27)	17.42 (17.01)	13.27 (12.91)	— —
2*a*	[Ni(DATS-2H)]$_2$	36.24 (36.14)	3.02 (2.80)	14.07 (13.27)	10.73 (10.21)	17.71 (17.46)
2*b*	[Ni(DATS-2H)Py]	44.56 (44.41)	3.71 (3.71)	14.85 (14.13)	8.48 (8.05)	15.59 (15.61)
2*c*	[Ni(DATS-2H)Tpp]	57.85 (56.90)	4.28 (4.11)	7.5 (7.00)	5.71 (5.70)	10.53 (11.20)

The absorption around 370 nm is due to a charge transfer transition, whereas the *d–d* transition absorption manifold appears at ca. 460–510 nm. No absorption bands appeared beyond 550 nm, which is consistent with square-planar arrangements around the metal ion (15). Such arrangements can only be achieved through dimerization of the monoligand metal chelates (16), which was confirmed by determination of the molecular weights of the isolated chelates using freezing point depression. The reaction of these dimeric chelates with monodentate Lewis bases such as pyridine (Py) and triphenylphosphine (Tpp) in ethanol gave adducts of the general formula [M(DAE-2H)B] and [M(DATS-2H)B], where B is the monodentate Lewis base. The elemental analyses of the isolated compounds and their electronic spectra in $CHCl_3$, which are consistent with the square-planar structure, as well as their infrared spectra confirm the proposed structure for these chelates.

The infrared spectra of both ligands and selected metal chelates are listed in Table 2. The spectra of the chelates show no absorption bands corresponding to νN—H and νC=S (the two absorption bands appear at ca. 3100 cm^{-1} and 1530 cm^{-1}, respectively, in the free ligand), implying tautomerization followed by deprotonation of the thiol tautomer form of the ligand during complex formation. The spectra of the ligands, however, display a sharp νC=O absorption band at ca. 1700 cm^{-1} confirming that the condensation takes place on the side-chain carbonyl group of the acid; otherwise, two distinct bands would have been observed due to nonequivalent ring and side-chain carbonyl groups. The palladium center in **1***a*, **1***b*, and **1***f* exhibits a stronger tendency to shift the aromatic νC=C towards νC=O than does nickel in the analogous chelates. Because of nearby conjugation created by complex formation, the νC=N at ca. 1540 cm^{-1} is shifted about 100 cm^{-1} towards lower frequencies.

The isolated ligands and their corresponding chelates were studied by both ^{1}H and ^{13}C nmr spectroscopy. In their ^{1}H nmr spectra, both ligands **1** and **2** showed two signals in the methyl region. The first, at δ 2.25 ppm, is due to -N=C-CH_3 methyl and the second, at δ 2.6 ppm, is due to $OCCH_3$ protons. A third signal in **1** at δ 2.5 ppm is attributed to the methyl ester, SCH_3. While no significant shifts were observed with the first and sec-

Can. J. Chem. Downloaded from www.nrcresearchpress.com by 85.192.166.187 on 09/08/12
For personal use only.

TABLE 2. Electronic and selected infrared spectral data for ONS ligands and some metal chelates

	Compounds	Band maxima, nm (log ε, M^{-1} cm^{-1})					Infrared spectral bands, cm^{-1} (N—H)	(C—N)	(C=O)	(C=S)	(C—C)
1	DAE	252 (4.16)	285 (4.10)	373 (4.37)			3190	1647	1697	1547	1647
1*a*	$[Ni(DAE\text{-}2H)]_2$	276 (4.49)	328 (4.03)	386 (4.16)	480sh			1537	1678, 1666		1645
1*c*	[Ni(DAE-2H)Py]	274 (4.28)	320sh	460sh (4.07)	480	510sh		1541	1683		1655
1*d*	[Ni(DAE-2H)Tpp]	278 (4.45)	328 (4.43)	374 (4.12)	460sh	480sh		1539	1701		1655
1*e*	[Pd(DAE-2H)Py]	260 (4.50)	314sh (4.15)	375	510sh						
2	DATS	226 (3.54)	276 (3.44)	315 (3.58)			3190	1628	694	1537	1628
2*a*	$[Ni(DATS\text{-}2H)]_2$	242 (4.5)	376 (3.97)	490sh				1529	1691		1651
2*b*	[Ni(DATS-2H)Py]	240 (4.4)	263 (5.35)	370 (4.64)	460sh			1529	1686		1651

TABLE 3. The ^1H nmr spectra of ligands and metal chelates in $CDCl_3$

	Compound	δ, ppm SCH_3	$CN{=}C{-}CH_3$	$OC{-}CH_3$	CH	NH
1	DAE	2.5	2.25	2.6	5.96	9.87
1*a*	$[Ni(DAE\text{-}2H)]_2$	2.6	2.3	3.3	5.7	
1*c*	[Ni(DAE-2H)Py]	2.5	2.1	2.8	5.7	
1*d*	[Ni(DAE-2H)Tpp]	2.5	2.0	2.95	5.1	
1*e*	[Pd(DAE-2H)Py]	2.65	2.15	2.9	5.9	
1*f*	[Pd(DAE-2H)Tpp]	2.55	2.1	2.9	5.4	
2	DATS		2.15	2.55	6.0	9.9
2*a*	$[Ni(DATS\text{-}2H)_2$		2.5	3.45	5.7	
2*b*	[Ni(DATS-2H)Py]		2.0	3.3	5.75	
2*c*	[Ni(DATS-2H)Tpp]		2.0	3.3	5.1	

ond signals as a result of metal chelation or adduct formation, the third signal suffered downfield shifts upon chelation and was more sensitive to the nature of the base in the isolated adducts. The disappearance of the proton signal of both the C-H (the parafinic ring CH) and the N-H (they appear at δ 7.2 and δ 9.82 ppm in the free ligands) on chelation, along with the stoichiometry, confirms the dibasic tridentate nature of both ligands in their chelation. The olefinic proton shift was incoming base-dependent, with triphenylphosphine causing a larger upfield shift than pyridine. The notable shielding with triphenylphosphine may be attributed to a virtual effect, from the three sterically hindered phenyl groups. The pyridine base exhibited three symmetrical proton environments showing a doublet at ca. δ 8.7 ppm of the α-CH proton, a triplet centered at ca. δ 7.9 ppm of the γ-CH, and a triplet at ca. δ 7.4 ppm of the β-CH. The α-CH proton appeared downfield shifted with respect to the other protons and further splittings were observed upon resolution-enhanced measurements, uncovering a long-range coupling between the remote protons. The nature of the metal ion did not significantly affect the pyridine proton chemical shifts. However, slight downfield shifts were observed upon replacing the $-SCH_3$ with $-NH_2$. The dispersion of proton chemical shifts of the pyridine hydrogens was not observed for the phenyl protons of triphenylphosphine base in the isolated adducts. Only two wide unresolved bands centered at ca. δ 7.4 ppm and δ 7.75 ppm were detected, due to phenyl protons for both Ni(II) and Pd(II) chelates. The ^1H nmr data are listed in Table 3.

The ^{13}C nmr spectra of some selected chelates were recorded for comparison. The discussion is confined to carbon nuclei whose chemical shift is affected by complex formation. Upon complexation and regardless of the nature of base, both SCH_3 and $NC\text{-}CH_3$ signals were deshielded by ca. 2.5 ppm due to donation of electron density from S and N atoms as a result of coordination to the central metal ion. The ^{13}C nmr chemical shifts of compounds **1** and **2** are almost identical. Replacement of the $-SCH_3$ by $-NH_2$ in **2** caused an upfield shift for the *C*=S carbon by ca. 4.5 ppm due to shielding effects by back-donation from the N atom. Deprotonation of the OC-*C*H-CO carbon is unmistakably deduced by ^{13}C nmr; the OC-*C*H-CO carbon signal observed at ca. 97 ppm in the free ligands is severely shifted upon complexation. The conjugation in the ring system, resulting from complexation, severely deshielded the OC-*C*H-CO carbon. In general, coordinated triphenylphosphine exhibits a deshielding effect on the *C*-S and *C*-O-M carbons, due to its higher electron-withdrawing ability than is the case with pyridine.

Experimental

Preparation of organic ligands and their chelates

Preparation of ammonium hydrazinecarbodithioate (17)

The ammonium hydrazinecarbodithioate was prepared by treating

Can. J. Chem. Downloaded from www.nrcresearchpress.com by 85.192.166.187 on 09/08/12
For personal use only.

hydrazine hydrate (100%, 1.0 mol), in absolute ethanol (300 mL), with concentrated ammonium hydroxide (50 mL) in a 1-L beaker. The reaction mixture was cooled to 5°C in an ice bath and stirred for 15 min using a mechanical stirrer. The equivalent molar ratio of carbon disulphide (1.0 mol) was added dropwise. The reaction mixture was constantly stirred after each addition and the temperature was kept at or below 5°C. The white product was filtered off, washed with ethanol and ether, and dried.

Preparation of S*-methylhydrazinecarbodithioate (18)*

An aqueous solution of ammonium hydrazinecarbodithioate (12.5 g, 0.1 mol, in 100 mL water) was strongly shaken with methyl iodide (14.5 g, 0.1 mol). The latter was added in small portions and the mixture was shaken after each addition. The product was filtered off, washed with water, dried, and recrystallized from benzene – petroleum ether (mp = 82°CC).

Preparation of Schiff bases

A mixture of 0.1 mol of dehydroacetic acid and 0.1 mol of *S*-methylhydrazinecarbodithioate or thiosemicarbazide in ethanol was refluxed for 1 h. On evaporation and cooling, the corresponding Schiff bases **1** and **2** were isolated as yellowish solids.

Preparation of metal chelates

A clear hot solution of metal acetate (0.01 mol) in ethanol was mixed with a boiling solution of the Schiff base (0.01 mol) and the mixture was refluxed for ca. 2 h. The reaction mixture was then evaporated and cooled to yield the corresponding dimeric chelates, $[M(DAE\text{-}2H)]_2$ and $[M(DATS\text{-}2H)]_2$. The corresponding adducts were prepared by treating the resulting adducts [M(DAE-2H)B] and [M(DATS-2H)B] where B = Py or Tpp.

Measurements

The electronic spectra were recorded in chloroform on a Perkin–Elmer S22 spectrophotometer. Infrared spectra were measured in the solid state using the KBr disk technique and a Nicolet FT-IR 5IOP spectrometer. The ^1H and ^{13}C nmr spectra were measured on a 100 MHz Bruker nuclear magnetic resonance spectrometer. Finally, the formation of dimeric chelates was confirmed by determining the molecular weights cryoscopically by measuring the freezing point depression of nitrobenzene solution containing a known amount of the solute. The molal freezing point depression constant (K_f = 7.00°C/molal) for nitrobenzene was determined using benzil as a standard.

Acknowledgement

The authors would like to thank Professor Ahmed A. El-Toukhy for his assistance during this research work.

1. K. Kakemi, T. Arita, M. Sezaki, and T. Kiriyama. Yakuzaigaku, **18**, 77 (1958).
2. Y. Kato, M. Sugrura, and H. Yamada. Gifu Yakka Daigaku Kiyo, **8**, 37 (1958).
3. Wm. A. Sistrunk. Food Technol. **11**, 336 (1957).
4. S. Tanaka. Kolumin Eissei, **25**, 138 (1956).
5. M. Das and S.E. Livingstone. Inorg. Chim. Acta, **19**, 5 (1976).
6. M. Mohan, A. Agarwal, and N.K. Jha. J. Inorg. Biochem. **34**, 41 (1981).
7. A. Maiti, A.K. Guha, and S. Gosh. J. Inorg. Biochem. **33**, 57 (1988).
8. M. Das and S.E. Livingstone. J. Cancer, **37**, 463 (1978).
9. L. Sacconi. Trans. Met. Chem. (NY), **4** (1969).
10. D.X. West, C.S. Carlson, A.C. Whyte, and E.E. Liberta. Transition Met. Chem. (London), **15**, 43 (1990).
11. D.X. West, C.S. Carlson, G.P. Golloway, and C.R. Daniel. Transition Met. Chem. (London), **15**, 91 (1990).
12. D.X. West, C.S. Carlson, A.E. Liberta, and C.R. Daniel. Transition Met. Chem. (London), **15**, 341 (1990).
13. D.X. West, C.S. Carlson, A.E. Liberta, and J.P. Scovill. Transition Met. Chem. (London), **15**, 383 (1991).
14. D.X. West, C.S. Carlson, K.J. Bouck, and A.E. Liberta. Transition Met. Chem. (London), **16**, 271 (1991).
15. M. Akbar Ali, S.E. Livingstone, and D.J. Phillips. Inorg. Chem. Acta, **7**, 179 (1973).
16. L.A. Sargan, E. Anckel, and Krishnamurthi. Biochem. Pharmacol. **30**, 1595 (1981).
17. C.D. Johnsen, A.R. Katritzky, B.J. Ridgewell, N. Shakir, and H.N. White. Tetrahedron, **21**, 1055 (1965).
18. L. El-Sayed, M.F. Iskander, and A. El-Toukhy. J. Inorg. Nucl. Chem. **36**, 1739 (1974).

Can. J. Chem. Downloaded from www.nrcresearchpress.com by 85.192.166.187 on 09/08/12
For personal use only.

β-Deuterium kinetic isotope effects for identity processes: bromide ion substitution at 1-bromo-1-arylethanes and 2-bromooctane

ALLAN R. STEIN

Department of Chemistry, Memorial University of Newfoundland, St. John's, NF A1B 3X7, Canada

Received October 12, 1993

ALLAN R. STEIN. Can. J. Chem. **72**, 1789 (1994).

While deuterium kinetic isotope effects for solvolyses have been extensively studied, other nucleophilic substitutions have received less attention, and identity processes, that is, substitutions where the nucleophile and leaving group are the same, have rarely been examined. Identity reactions must pass through a truly symmetrical stage, a transition state or an intermediate, so that data will be of interest to both theoretical and experimental chemists. Values of k_H/k_D have been determined by polarimetry for bromide exchange– racemization at $ArCHBrCH_3/CD_3$ (Ar = C_6H_5, 4-Br- and 4-Me-C_6H_4, and 3,4,-dimethyl-C_6H_3) in acetone, acetonitrile, and nitromethane. Observed values are analogous to values seen in solvolyses. They range from 1.01 to 1.35 and, in some cases, increase markedly as the concentration of Bu_4NBr decreases. Solvolyses are either first order or pseudo first order whereas plotting observed racemization rate versus [Bu_4NBr] allows separation of first- and second-order components; those species giving more stable carbocations in the more dipolar solvents, the systems showing k_H/k_D variation with Br^- concentration, alone show an appreciable first-order component. The second-order k_H/k_D ratio averages 1.062 ±–0.018 at temperatures ranging from 25 to 50°C for all substrates in the three solvents, very analogous to the values seen for racemization of 1,1,1-d_3-2-bromooctane or solvolysis of ethyl substrates but considerably lower than the typical solvolysis values of 1.15–1.25 for *secondary*, and 1.35–1.5 for *tertiary* substrates. The first-order k_H/k_D values obtained are higher, 1.1–1.5. These and other results are discussed.

ALLAN R. STEIN. Can. J. Chem. **72**, 1789 (1994).

Les effets isotopiques cinétiques du deutérium sur les solvolyses ont fait l'objet de nombreuses études; toutefois, d'autres substitutions nucléophiles ont reçu beaucoup moins d'attention et les processus d'identité, les réactions de substitutions dans lesquelles le nucléophile et le nucléofuge sont les mêmes, ont rarement été examinés. Les réactions d'identité doivent nécessairement passer par une étape, un état de transition ou un intermédiaire, vraiment symétrique; ces données devraient donc présenter de l'intérêt pour les chimistes tant expérimentaux que théoriques. Faisant appel à la polarimétrie, on a déterminé les valeurs des k_H/k_D pour la réaction d'echange – racémisation des $ArCHBrCH_3/CD_3$ (Ar = C_6H_5, 4-Br-, 4-Me-C_6H_4 et 3,4-diméthyl-C_6H_3) dans l'acétone, l'acétonitrile et le nitrométhane. Les valeurs observées sont semblables à celles obtenues lors des solvolyses. Elles varient de 1,01 à 1,35 et, dans quelques cas, elles augmentent beaucoup avec une diminution de la concentration de Bu_4NBr. Les solvolyses sont soit du premier ordre ou du pseudo premier ordre alors que, dans notre cas, la courbe de la racémisation en fonction de la concentration de Bu_4NBr permet de séparer les composantes du premier et du deuxième ordre; seules les espèces conduisant à carbocations les plus stables dans les solvants les plus dipolaires, les systèmes présentant une variation du k_H/k_D en fonction de la concentration du Br^-, présentent une portion importante des réaction du premier ordre. Pour tous les substrats, dans les trois solvants, à des températures allant de 25 à 50°C, le valeur du rapport k_H/k_D des réactions du deuxième ordre rend une moyenne de 1,062 ± 0,018 et elles sont très semblables à celles observées lors de la racémisation du 1,1,1-d_3-2-bromoéthane ou de la solvolyse des substrats avec des groupes éthyles; elles sont toutefois beaucoup plus basses que les valeurs typiques de 1,15 à 1,25 ou 1,35 à 1,5 observées lors de solvolyses de substrats *secondaires* ou *tertiaires*. Les valeurs des k_H/k_D du premier ordre sont plus élevées (1,1–1,5). On discute de ces valeurs et d'autres résultats.

[Traduit par la rédaction]

A continuing research interest of ours has been the ion-pair mechanism for nucleophilic substitutions, especially bimolecular substitutions at saturated carbon (1,2). As part of the mechanistic evidence, β-deuterium kinetic isotope effects were desired. The empirical β-deuterium isotope effects reported here are apparently the first measured for an "identity process," which, in the case of a nucleophilic substitution, Scheme 1,

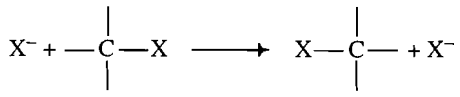

SCHEME 1. An identity process.

requires that the nucleophile and the leaving group are identical species. Such processes can, in principle, be followed by either of two methods: by isotopic exchange using *radio* or stable isotopes of the nucleophile/leaving group if they are available, or by optical activity changes, racemization, if the substrate has a chiral centre at the site of substitution. Both approaches have been used.

Radio-tracer studies were an essential part of the early evidence for the S_N2 reaction mechanism first proposed by Hughes and Ingold. Hughes et al. (3) followed *radio*-iodide exchange with 2-iodooctane, and *radio*-bromide exchanges with 1-bromo-1-phenylethane and 2-bromopropanoic acid in the mid-1930s. Others have also used *radio* tracers to follow exchanges (4–9). We employed the electrodeposition of silver halide at a silver anode, a method developed and extensively used by Beronius (5), to follow *radio*-halide exchanges (6, 7).

Racemization kinetics of chiral alkyl halides, together with halide exchanges, were used by Hughes to show that bimolecular nucleophilic substitutions are accompanied by inversion of stereochemistry (3). These studies were a major, if not *the* major, bulwark of the S_N2 mechanistic proposal. While isotopic exchange methods can, in principal, be used for any substrate, racemizations are limited to species that can show chirality, substrates such as those used in this study.

For the studies reported here, racemizations of chiral *protio* and *deutero* substrates were used. The principal system studied is indicated in Scheme 2. β-Deuterium kinetic isotope effects were determined in acetone, acetonitrile, and nitromethane over

Can. J. Chem. Downloaded from www.nrcresearchpress.com by 85.192.166.187 on 09/08/12
For personal use only.

TABLE 1. Observed inversion rate constants and apparent k_H/k_D for 1-phenyl-1-bromoethanes; 40°C, [Bu_4NBr] = 0.00500 M[a]

Solvent	Substrate	k_H[a] ($\times 10^{-3}$ L m^{-1} s^{-1})	k_H/k_D[b]
Acetone	4′-Bromo	9.521 ± 0.073	1.037 ± 0.010
	Unsubstituted	4.440 ± 0.055	1.046 ± 0.011
	4′-Methyl	9.905 ± 0.066	1.014 ± 0.009
	3′,4′-Dimethyl	11.43 ± 0.12	1.076 ± 0.011
Acetonitrile	4′-Bromo	9.634 ± 0.003	1.047 ± 0.009
	Unsubstituted	7.866 ± 0.009	1.066 ± 0.004
	4′-Methyl	25.809 ± 0.069	1.054 ± 0.024
	3′,4′-Dimethyl	40.502 ± 0.004	1.211 ± 0.008
Nitromethane	4′-Bromo	6.909 ± 0.003	1.059 ± 0.002
	Unsubstituted	6.455 ± 0.004	1.065 ± 0.006
	4′-Methyl[c]	40.218 ± 0.043	1.149 ± 0.023[c]
	3′,4′-Dimethyl	74.682 ± 0.068	1.172 ± 0.019

[a]In acetone, [Bu_4NBr] = 0.0200 M, T = 25.0°C.
[b]Average of 2–6 runs. Error limits are one standard deviation.
[c]Observed k_H/k_D at the concentration of Bu_4NBr indicated: 0.0200 M, 1.082 ± 0.021; 0.0100 M, 1.129 ± 0.003; 0.00500 M, 1.149 ± 0.006; 0.00100 M, 1.270 ± 0.012.

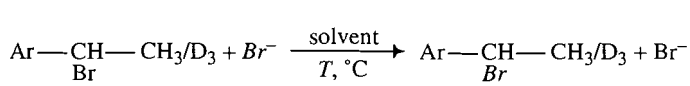

SCHEME 2. The identity process studied.

a range of temperatures and as a function of bromide ion concentration (as the tetrabutylammonium salt).

Results

The β-D_3-labelled 1-phenylethanols were made with *deutero*-methyl magnesium iodide and the corresponding benzaldehyde, where that was commercially available, or by metal hydride reduction of the β-*deutero*-acetophenone, which was either commercially available (acetophenone itself) or prepared by exchange using basic D_2O and a phase transfer agent (PTA). For such exchanges, the procedures of Starkes (11), modified as indicated, was used. Racemic alcohols with isotopic purities of 99.7–99.9% (by nmr) were obtained. These alcohols were converted to the corresponding $ArCHBrCH_3/D_3$ substrates used in these studies by procedures analogous to those already described (10, 12).

Racemizations with *protio* and *deutero* substrates, using the same batch of electrolyte solution, were alternated to minimize any effects due to variation in experimental conditions upon the measured isotope effects. Similarly, if one of the pair of unlabelled and labelled bromides had significantly greater optical activity than the other, it was diluted with racemic material to keep substrate concentrations approximately equal while using near full-scale deflections of the recorder at the same recorder and instrument settings. Two to seven runs were done at each temperature and ionic bromide concentration reported. Standard deviations within a run, from the weighted least-squares analysis of rotation versus time, were always considerably smaller than the differences between duplicate runs.

Second-order rate constants reported in this paper are for inversion (or substitution), that is, they are one half the observed racemization rate constants because substitution with inversion in an identity process results in the loss of two units of enantiomeric excess. First-order rate constants are those for racemization; there is no analogous factor of two here (16).

Actual, directly measured, rate constants and the calculated kinetic isotope effects are reported in Table 1 for 0.0200 M Bu_4NBr in acetone at 25°C and 0.00500 M Bu_4NBr in acetonitrile and nitromethane at 40°C.

Previous studies established that, in acetone, racemizations of all substrates examined are cleanly second order; a plot of observed racemization rate versus the concentration of added halide salt has a zero, or very near zero, intercept (7). The plot, however, is nonlinear because ion pairing of the bromide ion with its cation reduces the activity coefficient of the nucleophile as its concentration, a salt, is increased. The plot of rate versus the activity of the bromide ion was, thus, linear with a zero or very nearly zero intercept for all substrates. Consequently, deuterium kinetic isotope effect determinations were done at only a single concentration of tetrabutylammonium bromide in acetone.

In acetonitrile and nitromethane, in contrast to acetone, there is no evidence of ion pairing of the Bu_4NBr over the concentration ranges employed yet, especially those substrates giving more stable carbocations (i.e., 4′-methyl- and 3′,4′-dimethylphenyl-1-bromoethanes) show a marked dependence of the measured k_H/k_D upon the concentration of Bu_4NBr. Typical values for the methyl-substituted substrates in nitromethane are shown as a footnote to Table 1. A change in Bu_4NBr concentration from 0.02 to 0.001 M increases the observed isotope effect from 1.08 to 1.27! Even larger variations are seen for the 3′4′-dimethyl substrate in nitromethane, lower ones for these two substrates in acetonitrile.

As Fig. 1 clearly indicates, this apparent concentration dependence arises from mixed kinetics (1, 6). For such cases first- and second-order components of the reaction can be separated by plotting the observed rate versus the concentration of the nucleophile, or its salt. First- and second-order components were obtained by linear regression analysis of all data, Table 3 the activation parameters determined, Table 2, and used to recalculate the rate constants and kinetic isotope effects at 30.00°C included in Table 3. A comparison of the kinetic isotope effects in Tables 1 and 3 confirms the necessity of such a separation of the rate components. Note that, except for 4′-methyl and 3′,4′-dimethyl substrates in acetonitrile and nitromethane, the first-order component is very small, Table 3

Can. J. Chem. Downloaded from www.nrcresearchpress.com by 85.192.166.187 on 09/08/12
For personal use only.

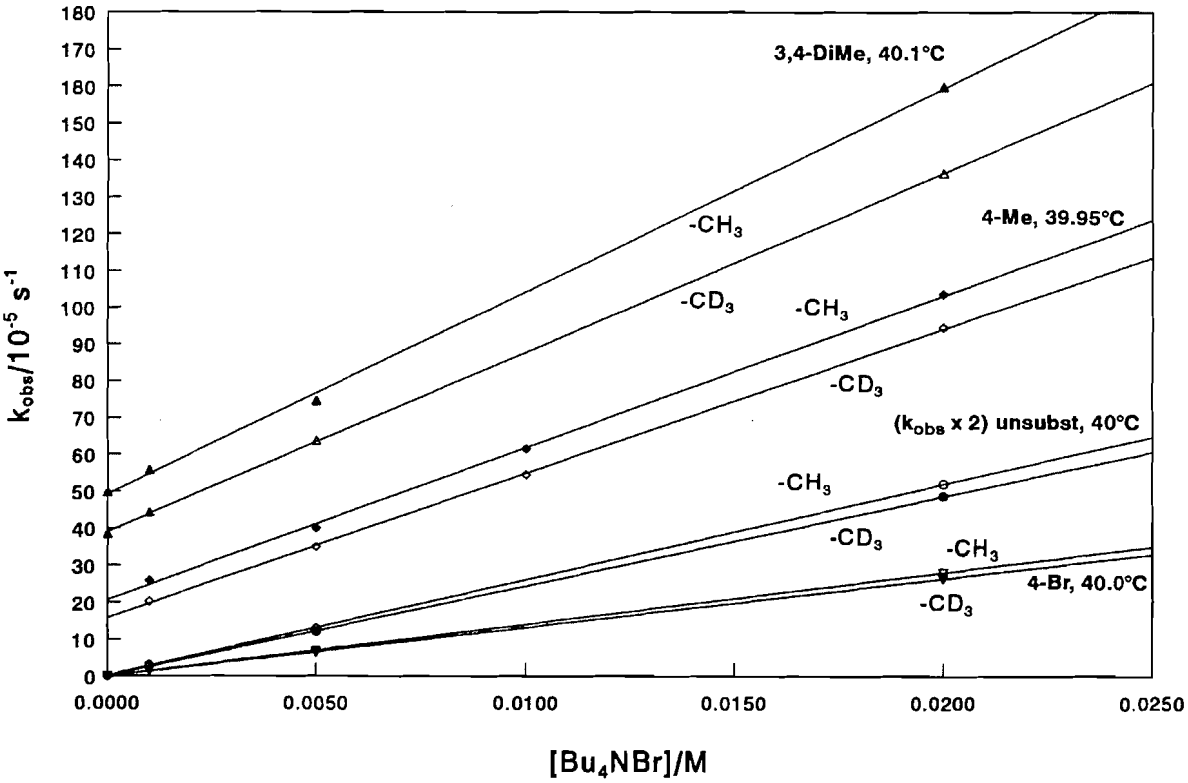

FIG. 1. Observed rate of racemization versus [Bu_4NBr]; separation of unimolecular (intercept) and bimolecular (slope) contributions in CH_3NO_2 at 40°C.

Uncertainties in these small rate constants are relatively large and the corresponding k_H/k_D is even more uncertain. Obviously, care must be exercised in attaching significance to such results.

For comparison, β-deuterium kinetic isotope effects for an identity process at a non-benzylic secondary carbon were desired. Chiral 1,1,1-d_3-2-bromooctane, and its *protio* analog, were prepared. In acetonitrile, a linear plot, with a zero intercept, for observed rate of racemization versus concentration of bromide ion was obtained so that a single Bu_4NBr concentration, 0.02500 M, was used for isotope effect measurements. Racemizations have, to date, only been done in acetonitrile at 60°C, giving $k_H = (5.923 \pm 0.040) \times 10^{-4}$ L mol^{-1} s^{-1} and $k_H/k_D = 1.084 \pm 0.006$.

Discussion

Deuterium kinetic isotope effects have commonly been determined and were the basis for much mechanistic discussion over the years. β-Deuterium effects are generally rather small secondary effects because the isotopically substituted atom is not directly involved in reaction progress. For the hydrolysis of *tert*-butyl chloride, presumedly a reaction through a carbocation, Robertson and co-workers (13) obtained an isotope effect of 2.387, or 1.101 per D. In our case, with three deuteriums, values of $(1.10)^3$ or 1.34 might be expected if the reactions were unimolecular. Such normal effects are usually attributed to hyperconjugative overlap of the C—H (or C—D) bond orbital with the empty, or electron deficient, developing *p*-orbital on the carbon undergoing the substitution. As such, the amount of overlap should reflect the degree of charge on the central carbon at the transition state. Isotope effects for reactions through a carbocation thus are larger than those following a concerted substitution, that is, the bimolecular mechanism. Consequently, the value of 1.34 per CD_3 group would represent a near-maximum value for substitution.

Shiner and Humphrey have confirmed that there is also an inductive effect, by using bridgehead deuteration where hyperconjugation is prohibited by stereochemistry. Inductive effects lead to smaller, inverse, effects, in Shiner's case about 0.986 per D (14). Of course, for a methyl group adjacent to the carbon undergoing substitution, only one of the C—D bonds can be appropriately orientated for hyperconjugation; the other two deuteriums on the methyl carbon exert inductive effects. Thus the measured k_H/k_D is the product of the normal hyperconjugative and inverse inductive contributions.

Almost all, or at the very least the vast majority, of k_H/k_D measurements for nucleophilic substitutions have been for solvolysis reactions. In fact, we have been unsuccessful in finding any reports of β-deuterium kinetic isotope effect measurements for identity processes. Unfortunately, in solvolysis, all reactions are kinetically first order, whether they are in fact first or actually pseudo first order. If first- and second-order processes are in competition and there is no way to determine the individual contributions, interpretation of the results is bound to be fraught with difficulty! Conversely, the lack of deuterium isotope effect data for identity processes, and the individual first- and second-order components for systems other than those reported here for the 1-phenylethyl system, makes interpretation of our results more difficult.

In fact the only published β-deuterium effects for identity processes have been obtained through force field calculations by McKenna et al. (15). Some of his results, those for the reaction RBr + Br^-, are presented in Table 4 along with the hydrolysis data of Robertson quoted in the paper. To facilitate comparison, both the calculated and measured effects are con-

Can. J. Chem. Downloaded from www.nrcresearchpress.com by 85.192.166.187 on 09/08/12
For personal use only.

TABLE 2. Activation parameters for uni- and bimolecular components of racemization of 1-phenyl-1-bromoethanes

Solvent	Substrate	Bimolecular racemization		Unimolecular racemization	
		$\Delta H^{\ddagger}$ (kJ mol^{-1})	$\Delta S^{\ddagger}$ (J deg^{-1} mol^{-1})	$\Delta H^{\ddagger}$ (kJ mol^{-1})	$\Delta S^{\ddagger}$ (J deg^{-1} mol^{-1})
Acetone	4′-Bromo, *protio*	69.49 ± 0.30	−50.6 ± 1.0		
	deutero	69.36 ± 0.33	−51.3 ± 1.1		
	Unsubstituted, *protio*	69.42 ± 0.41	−57.1 ± 1.3		
	deutero	69.55 ± 0.28	−57.08 ± 0.90		
	4′-Methyl, *protio*	65.60 ± 0.25	−63.28 ± 0.83		
	deutero	66.23 ± 0.23	−61.30 ± 0.77		
	3′,4′-DiMe, *protio*	64.36 ± 0.43	−66.3 ± 1.4		
	deutero	66.06 ± 0.41	−61.2 ± 1.5		
Acetonitrile	4′-Bromo, *protio*	71.93 ± 0.12	−54.26 ± 0.37	90.0 ± 29.0	−74.0 ± 91.0
	deutero	71.67 ± 0.14	−55.58 ± 0.45	105.0 ± 19.0	−24.0 ± 61.0
	Unsubstituted, *protio*	70.73 ± 0.39	−60.0 ± 1.3	106.0 ± 27.0	−20.0 ± 88.0
	deutero	70.41 ± 0.17	−61.46 ± 0.55	118.0 ± 29.0	14.0 ± 93.0
	4′-Methyl, *protio*	64.7 ± 1.7	−69.9 ± 5.6	80.8 ± 3.7	−71.0 ± 12.0
	deutero	65.79 ± 0.39	−66.9 ± 1.2	80.4 ± 2.6	−73.0 ± 8.4
	3′,4′-DiMe, *protio*	64.8 ± 2.6	−67.5 ± 8.4	77.9 ± 4.4	−71.0 ± 14.0
	deutero	67.2 ± 2.2	−60.1 ± 7.2	60.2 ± 1.2	−132.8 ± 4.0
Nitromethane	4′-Bromo, *protio*	70.59 ± 0.06	−61.14 ± 0.19	0.5 ± 12.0	−365.0 ± 38.0
	deutero	70.6 ± 1.4	−61.6 ± 4.3	12.9 ± 3.0	−328.2 ± 9.4
	Unsubstituted, *protio*	68.6 ± 1.3	−68.3 ± 4.1	92.0 ± 29.0	−61.0 ± 92.0
	deutero	68.6 ± 1.3	−68.9 ± 4.3	106.0 ± 34.0	−18.0 ± 108.0
	4′-Methyl, *protio*	62.52 ± 0.58	−78.1 ± 1.9	82.1 ± 2.8	−52.9 ± 8.8
	deutero	64.3 ± 1.1	−72.9 ± 3.4	80.7 ± 2.1	−60.3 ± 6.9
	3′,4′-DiMe, *protio*	64.62 ± 0.81	−68.6 ± 2.6	69.5 ± 4.7	−87.0 ± 15.0
	deutero	65.09 ± 0.76	−68.2 ± 2.5	75.4 ± 2.9	−69.8 ± 9.4

verted to the contribution for d_3 that is for one CD_3 group. McKenna's and Robertson's data (15) are somewhat more consistent with the values reported in Table 1 than with those in Table 3. Thus, in the more dipolar acetonitrile and nitromethane solutions, 4′-methyl- and 3′4′-dimethylphenyl-1-bromoethanes follow mixed kinetics with observed net isotope effects similar to an "ordinary" secondary substrate, isopropyl bromide, in the even more ionizing media, water. Does that imply that the latter reaction also has mixed kinetics?

Solvolyses data abound in the literature. A cross section of typical results is tabulated in Table 5 for comparison with the results reported in this paper. These studies are grouped according to the type of system studied. On a per CD_3 basis, for aqueous and mixed aqueous solvents, primary substrates show k_H/k_D values similar to those for the second-order component of the identity reaction reported here, that is about 1.03–1.04. Secondary substrates, that is isopropyl, 1-arylethyl, and other substrates, give hydrolysis isotope effects of about 1.15–1.26, more in line with those substrates showing mixed kinetics prior to separation of first- and second-order components as reported in Table 1. The effects reported for hydrolysis of *tert*-butylsubstrates, about 1.35 per CD_3, are more comparable to the unimolecular components of this study.

For racemizations of 2-bromooctane and 1,1,1-d_3-2-bromooctane in acetonitrile, a plot of observed rate versus nucleophile concentration is linear with a zero intercept. This identity process is cleanly second order. At 60°C, $k_H = (5.923 \pm 0.040) \times 10^{-4}$ L mol^{-1} s^{-1} and $k_H/k_D = 1.084 \pm 0.006$, which is not far from the average second-order component value for all the 1-phenyl-1-bromoethanes in acetonitrile as reported in Table 3, 1.065 ± 0.031 for the recalculated values at 30°C or 1.062 ± 0.012 for the actual values at various temperatures (25–50°C).

If the current results for identity processes give representatives values for "pure bimolecular" and "pure unimolecular" nucleophilic displacements at secondary carbon, then it appears that ethyl substrates alone hydrolyse by bimolecular substitution, *tertiary* substrates by unimolecular, and *secondary* substrates such as isopropyl and phenylethyl follow mixed kinetics apparently with a large first-order component. A number of the authors whose data are presented in Table 5 have reached conclusions that are not at variance with these observations.

For the phenylethyl substrates in the presence of the base lutidine, we have shown that the loss of optical activity could contain nucleophilic substitution and elimination components (6). Elimination, even in the presence of added base, was a relatively small component of the process except for 4-methyl and 3,4-dimethyl substrates at the lower Bu_4NBr concentrations especially in nitromethane. Except for an apparent solvent effect, the elimination rate was independent of lutidine concentration. Without added base, no elimination, as seen by increase in bromide concentration, was observed for any of the substrates in any of the solvents examined. Nor was the elimination rate with added lutidine affected by the initial bromide ion concentration. Thus, no second-order elimination component was detected. However, a first-order elimination–readdition process could contribute to the first-order isotope effect component reported in this paper. While deprotonation of the carbocation intermediate would, presumedly, show a primary kinetic isotope effect, that deprotonation is occurring *after* the transition state for the overall process and should contribute comparatively little to the observed isotope effects.

As is possible for our first-order component, part of the solvolytic isotope effect reported for some of the compounds in Table 5 is likely due to the much larger primary isotope effect associated with elimination rather than with substitution processes. The Sridharan and Vitullo (20) and the Humski, Sendi

Can. J. Chem. Downloaded from www.nrcresearchpress.com by 85.192.166.187 on 09/08/12
For personal use only.

TABLE 3. Uni- and bimolecular rate constants and deuterium kinetic isotope effects for racemization of 1-phenyl-1-bromoethanes[a]

Solvent	Substrate and temperature (°C)	Unimolecular		Bimolecular	
		k_H ($\times 10^{-5}$ s^{-1})	k_H/k_D	k_H, ($\times 10^{-3}$ L m^{-1} s^{-1})	k_H/k_D
Acetone	4′-Bromo, 32.5	—	—	19.326 ± 0.0011	1.037 ± 0.006
	25.0	—	—	9.5571 ± 0.0009	1.037 ± 0.010
	20.0	—	—	5.7803 ± 0.0003	1.035 ± 0.008
	Recalculated at 30[b]	—	—	15.341	1.037
	Unsubstituted, 40.0	—	—	17.880 ± 0.020	1.036 ± 0.019
	32.5	—	—	9.178 ± 0.008	1.066 ± 0.006
	25.0	—	—	4.4398 ± 0.0055	1.046 ± 0.011
	Recalculated at 30[b]	—	—	7.194	1.052
	4′-Methyl, 32.55	—	—	19.5481 ± 0.0015	1.012 ± 0.008
	25.0	—	—	9.9421 ± 0.0009	1.014 ± 0.009
	15.2	—	—	2.8906 ± 0.0003	1.027 ± 0.009
	Recalculated at 30[b]	—	—	15.551	1.013
	3′,4′-DiMe, 32.6	—	—	22.2665 ± 0.0017	1.059 ± 0.022
	25.0	—	—	11.3099 ± 0.0015	1.076 ± 0.011
	14.95	—	—	4.4411 ± 0.0006	1.103 ± 0.011
	Recalculated at 30[b]	—	—	17.730	1.064
Acetonitrile	4′-Bromo, 50.0	0.268 ± 0.071	—	23.261 ± 0.029	1.062 ± 0.003
	40.0	0.048 ± 0.021	—	9.611 ± 0.009	1.058 ± 0.002
	30.0	0.027 ± 0.032	—	3.731 ± 0.013	1.055 ± 0.004
	Recalculated at 30[b]	0.022[a]	0.733[a]	3.734	1.055
	Unsubstituted, 50.0	0.37 ± 0.10	1.60 ± 0.54	18.354 ± 0.044	1.063 ± 0.002
	40.0	0.183± 0.057	1.79 ± 0.84	7.608 ± 0.026	1.054 ± 0.004
	30.0	0.026 ± 0.014	2.2 ± 1.8	3.031 ± 0.006	1.054 ± 0.006
	Recalculated at 30[b]	0.031[a]	2.07[a]	3.023	1.053
	4′-Methyl, 50.0	12.2 ± 1.6	1.17 ± 0.17	51.68 ± 0.64	1.036 ± 0.013
	40.0	4.18 ± 0.99	1.02 ± 0.20	24.10 ± 0.43	1.099 ± 0.020
	30.0	1.57 ± 0.31	1.15 ± 0.20	9.91 ± 0.14	1.066 ± 0.013
	Recalculated at 30[b]	1.531	1.105	10.029	1.081
	3′,4′-DiMe, 40.0	12.6 ± 1.3	1.84 ± 0.43	30.30 ± 0.55	1.038 ± 0.029
	30.0	4.85 ± 0.44	1.42 ± 0.18	12.43 ± 0.20	1.064 ± 0.018
	25.0	2.62 ± 0.34	1.29 ± 0.13	8.32 ± 0.14	1.089 ± 0.017
	Recalculated at 30[b]	4.619	1.486	12.779	1.069
Nitromethane	4′-Bromo, 50.0	0.05 ± 0.13	—	16.742 ± 0.054	1.058 ± 0.003
	40.0	0.04 ± 0.20	—	7.020 ± 0.085	1.060 ± 0.010
	30.0	0.047 ± 0.028	—	2.775 ± 0.012	1.058 ± 0.004
	Recalculated at 30[b]	0.043[a]	1.593[a]	2.776	1.059
	Unsubstituted, 50.0	0.810 ± 0.069	1.07 ± 0.17	14.659 ± 0.031	1.067 ± 0.004
	40.0	0.14 ± 0.11	1.4 ± 1.3	6.461 ± 0.049	1.065 ± 0.007
	30.0	0.079 ± 0.014	1.52 ± 0.46	2.553 ± 0.007	1.066 ± 0.003
	Recalculated at 30[b]	0.065[a]	1.585[a]	2.576	1.066
	4′-Methyl, 49.95	61.5 ± 1.8	1.392 ± 0.042	43.36 ± 0.73	1.026 ± 0.016
	40.0	21.49 ± 0.87	1.350 ± 0.059	19.96 ± 0.33	1.011 ± 0.016
	29.95	7.74 ± 0.09	1.341 ± 0.038	8.82 ± 0.04	1.069 ± 0.008
	Recalculated at 30[b]	7.639	1.336	8.823	1.057
	3′,4′-DiMe, 40.1	47.8 ± 1.1	1.227 ± 0.034	28.31 ± 0.46	1.138 ± 0.021
	32.5	22.2 ± 1.2	1.142 ± 0.057	15.11 ± 0.41	1.144 ± 0.033
	25.0	11.75 ± 0.38	1.373 ± 0.044	7.67 ± 0.19	1.148 ± 0.027
	Recalculated at 30[b]	18.50	1.267	12.04	1.145

[a]The unimolecular component for these reactions was very small; uncertainties in the rate constants and the isotope effects are thus comparatively large.
[b]Recalculated values were obtained using the thermodynamic activation parameters reported in Table 2.

jarevevic, and Shiner (21) results make that most obvious. Unfortunately, the current study is the only one that allowed separation of uni- and bimolecular components — solvolyses and, under solvolysis conditions, also competing eliminations are first or pseudo first order.

Unfortunately, substituent, solvent, and temperature effects on the isotope effects are largely masked because the imperfect reproducibility of the kinetic data and the manipulation required to separate the first- and second-order components result in quite large standard deviations. Other approaches such as the differential methods (31), while they might improve the precision in measuring the observed k_H/k_D, would not allow separation of the first- and second-order components of the racemization. Consequently, any detailed discussion of identity kinetic isotope effects should await completion of the much more extensive study currently in progress.

However, it is apparent that the contribution of a β-CH_3/CD_3 in a bimolecular nucleophilic substitution is very nearly the same whether the reaction is hydrolysis of a primary substrate or bromide exchange at an aryl-substituted, or other secondary,

Can. J. Chem. Downloaded from www.nrcresearchpress.com by 85.192.166.187 on 09/08/12
For personal use only.

TABLE 4. β-Deuterium isotope effects predicted from force field calculations;[a] RBR + Br^-

R	Predicted	k_H/k_D hydrolysis[b]
Ethyl β-d_3	1.039	1.033
Propyl β-d_2	1.004 (d_3, 1.006)	1.054 (d_3, 1.082)
Isopropyl β-d_6	1.237 (d_3, 1.112)	1.366 (d_3, 1.169)
tert-Butyl β-d_9	1.508 (d_3, 1.147)	3.387 (d_3, 1.336)

[a]Reference 15.
[b]Results of R.E. Robertson, as quoted by McKenna for the corresponding hydrolysis.

centre. Solvolyses at secondary (and tertiary) centres give larger β-D_3 k_H/k_D effects, likely because the reactions are mixtures of substitution and elimination processes, either or both of which can have uni- and (or) bimolecular components.

Experimental

All solvents used for kinetics were HPLC or reagent grade, dried by final distillation from calcium hydride under nitrogen, which was dried with a train of concentrated H_2SO_4 and molecular sieves. Commercial anhydrous ether was used for Grignard reactions. Tetrahydrofuran (THF) was dried by shaking and storing over KOH, followed by refluxing over, then distillation from, $LiAlH_4$, again under dried nitrogen. The polarimeter cell was oven dried at about 60°C, other glassware used for the kinetics, at 125°C. Kinetics solutions were prepared, and all transfers made, in a nitrogen-flushed glove box.

Kinetics of racemization were followed with a Perkin Elmer model 141MC polarimeter fitted with a retransmitting potentiometer and a recorder. Actual rotations due to the solutions were not recorded; the rate of change alone was required. Temperature control was better than ±0.05° with a thermostated circulating constant temperature bath and a jacketed 10-cm quartz polarimeter cell. Times and rotations, as voltages, were read from the recorder trace and processed using standard weighted linear regression analysis. Generally 3–5 half-lives were used except for those cases with a significant first-order component, where the reaction accelerated with time due to increasing bromide ion concentration as competing elimination occurred (1, 6). Initial slopes from, generally, about a single half-life were used for such runs. Error limits, where reported, are one standard deviation. Standard deviations of one part in 5 000–40 000 were normal for individual kinetic runs and agreement between duplicate runs was generally better than one percent. For each solvent, at each temperature and nucleophile concentration, two to seven runs were averaged.

Preparation of substrates

Achiral alcohols and esters

Protio. Except for 1-phenylethanol, which was commercially avail-

TABLE 5. Representative β-deuterium kinetic isotope effects for solvolyses

Alkyl	Leaving group	Solvent	k_H/k_D (per CD_3)	References
Primary				
Ethyl	Br	H_2O	1.033	23
	I	H_2O	1.037	
	OTos	H_2O	1.018	
	$MeSO_3$	H_2O	1.027	
	OTf	HOAc	1.11	24
		TFE	1.09	
Secondary				
2-Propyl	Br	H_2O	1.148	23
	I	H_2O	1.146	
	OTos	H_2O	1.245	
	$MeSO_3$	H_2O	1.243	
	OBros	TFA	1.169	25
	$NaphSO_3$	EtOH to 97% F_6*i*PrOH	1.10–1.49	27
(2-Ad)Me	Cl	TFE	1.48	29
1-(1-Ad)Et	OBros	70–97% TFE	1.151	18
		79% EtOH	1.256	
	Me_5PhSO_3	90% F_6*i*PrOH	1.135	18
1-(1-Ar)Ethyl[a]	Cl, Br	Various aqueous	1.212 ± 0.011	25
Tertiary				
tert-Butyl	Cl	Various aqueous	1.35 ± 0.02	13, 23, 26
	$NaphSO_3$	EtOH	1.10	27
		TFE	1.33	
		97% HFIP	1.49	
2-(2-Bz)Pr	Cl	MeOH	1.30	22
2-(2-(*p*-FPh))Pr	Cl	60% EtOH	1.21	26
2-(2-CN)Pr	OTf	TFE	1.48	28
2-(2-CF_3)Pr	OTf	Various	~1.78	19
1-(1,1-Ph_2)Ethyl	Cl	MeOH/MeCN	0.84–0.96	17[b]
1-(1-Ph-1-CF_3)Ethyl	OTos	TFA to 80% EtOH	1.63–2.110	30

[a]Ar = *p*-Me, *p*-F, *p*-NO_2, *p*-PhO, *m*-Br, and unsubstituted phenyl in aqueous EtOH, acetone.
[b]Value quoted is for methanolysis; elimination gave 2.2–3.2 for a combined k_H/k_D of 1.81–1.58 with 1.96–9.09 vol% MeOH.

Can. J. Chem. Downloaded from www.nrcresearchpress.com by 85.192.166.187 on 09/08/12
For personal use only.

TABLE 6. Observed optical rotations[a] and boiling points[b]

Substrate	bp, °C/Torr	CH_3, at nm			CD_3, at nm		
		365	435	579	365	435	579
4′-Bromophenylethanol	118/5.0	25.70	15.09	7.31	25.90	15.15	7.28
4′-Bromophenylbromoethane	104/2.6	−43.5	−23.0	−10.2	−45.4	−24.0	−10.7
Phenylethanol	85.5/~8	14.23	8.84	4.47	13.13	8.19	4.18
Phenylbromoethane	73/5.3	−41.7	−22.0	−9.68	−52.4	−27.6	−22.2
4′-Methylphenylethanol	93/5.4	13.5	7.98	4.05	14.04	8.56	4.25
4′-Methylphenylbromoethane	83/3.9	−7.70	−3.98	−1.72	−20.3	−10.6	−4.35
3′,4′-Dimethylphenylethanol	85/1.4	12.76	7.38	3.91	13.76	8.45	4.24
3′,4′-Dimethylphenylbromoethane	85/1.6	4.65	2.40	1.01	1.63	0.82	0.34
2-Octanol	70/~6	−2.04	−1.36	−0.72	−1.93	−1.28	−0.63
2-Bromooctane	49/3.2	12.22	7.70	3.94	11.48	7.22	3.30

[a]Measured rotation for 1.00 cm of neat liquid at 25°C at the wavelength indicated for the material from the (+)-1-amino-1-phenylethane salt of the corresponding biphthalate.
[b]Boiling points for the *protio* material; those for the *deutero* materials were almost identical.

able (Aldrich), these were made, under dry nitrogen, from the corresponding ketone (Aldrich) by reduction, at reflux for several hours in THF, with 1.05 equivalents of $LiAlH_4$. The alcohol was not isolated. Phthalic anhydride (Fisher), which had been recrystallized from chloroform, 1.02 equivalents, was added to the cooled solution and reflux, with magnetic stirring, was continued overnight. The solution was concentrated and taken up in ether and ice-cold, approximately 2 M, HCl. The ethereal layer was washed 2–4 times with cold aqueous acid, water, and saturated brine. The ethereal solution was concentrated on a rotovac and the biphthalate allowed to crystallize. If desired, the half-ester was recrystallized from heptane but, generally, it was resolved directly.

1-Phenylethanol was converted to the lithium salt by refluxing with 1.1 equivalents of LiH in THF, phthalic anhydride was added, and the solution subsequently treated analogously.

Deutero. D_3-Acetophenone, which is commercially available (Aldrich), was treated analogously to the *protio* ketones.

To 4-bromobenzaldehyde (Aldrich), *p*-tolualdehyde (Anachemia), or heptanal (Aldrich) in anhydrous ether, 1.01 equivalents of CD_3MgI in ether (Aldrich) was added over 30 min at ice temperatures. The solution was refluxed for several hours and the acidified, washed several times with cold dilute acid, water, dilute Na_2CO_3 solution, and saturated brine. After drying over K_2CO_3, the ether was removed and the alcohol vacuum distilled: β-D_3-4′-bromophenylethanol, bp 100–102°C/2.0 Torr (1 Torr = 133.3 Pa); 4′-methylphenylethanol, bp 93–93.5°C/5.4 Torr; 2-octanol, bp 84–86°C/14.5 Torr. No, or at most a minute amount of, CD_2H group was detectable in the nmr. Yields were greater than 90%, and isotopic purities, as measured by nmr, were 99.7% or greater.

The β-D_3-alcohols were converted to their lithium salts by refluxing with 1.1 equivalents of LiH in THF and the biphthalate ester was prepared as for the *protio* equivalent above.

β-D_3-3′,4′-Dimethylacetophenone was made from the corresponding *protio* material by exchange (11). Under dry nitrogen, 25.0 g of 3′,4′-dimethylacetophenone and 1.95 g of tricaprylmethylammonium chloride was stirred at 30°C for about 30 min with four 15-mL batches of D_2O (99.95%) approximately 1.5 M in NaOD (Aldrich). After standing briefly to permit phase separation, each of the aqueous phases was removed from the pear-shaped flask by pipet. After exchange, three washes of the organic phase with 5-mL portions of D_2O saturated in KCl for anion exchange,[1] were followed by vacuum distillation of the product, bp 79–81.5°/1.6 Torr, 91.5%, greater than 99.7% CD_3 by nmr. The biphthalate ester was prepared, using LiH, as described above.

Optical resolutions

Using (+)- and (−)-1-amino-1-phenylethanes (Eastman), procedures analogous to those already described were used for both *protio* and *deutero* substrates (10). Ether was used as solvent for all but the 4′-bromo material, where acetone was used. With the *deutero* material, when difficulty was experienced in obtaining diastereomeric salt crystals in the resolutions, a small-scale sample was seeded with *protio* salt crystals and the resulting crystals used as seeds to initiate crystallization for the full-scale resolution. Combined yields of the two diastereomeric salts were greater than 80%, generally over 90%, based upon starting alcohol or ketone. The resolved materials were stored as the salts until required for kinetics.

Preparation of chiral bromides

Chiral alcohols were recovered from their diastereomeric salts by partition between ice-cold aqueous hydrochloric acid and ether, followed by base-catalyzed hydrolysis of the biphthalate esters as previously described (10).

Except for 3′,4′-dimethylphenyl-1-bromoethane, which was prepared using gaseous HBr in benzene as previously described (10), all of the chiral alcohols were converted to the bromides with diphos and bromine (12). (The dimethyl alcohol gave almost totally racemic product with the diphos procedure.) The clear, colourless bromides very slowly racemize and discolour even in the freezer, where they were stored between kinetic runs at −12°C. The 4′-methyl- and 3′,4′-dimethylphenyl-1-bromoethanes were prepared freshly every 7–10 days; the others, while much more stable, were prepared every 3 or 4 weeks.

Measured optical rotations for neat alcohol, and the resulting bromide, from the (+)-1-amino-1-phenylethane salt of the corresponding biphthalate, are reported in Table 6 together with the appropriate boiling points. All nmr and ir spectra were as expected. No OH was present in the ir of the bromides and the CD_2H signal in the nmr was, at most, barely detectable by nmr, generally representing >99.7% isotopic purity.

Kinetics of racemization

Bu_4NBr (Eastman) was dried at ~1 Torr and 50–60°C for 5–6 h and

[1]In initial runs, 3,4-dimethylacetophenone, about 87.5% CD_3-, 12.5% CD_2H-, as determined by nmr, was obtained whereas, based upon the amount of deuterium to hydrogen in the exchange cycles, the product should have been about 99.8% isotopically pure. The composition was essentially unchanged by recycling the substrate with fresh batches of D_2O and PTA. The counterion was no longer chloride, but rather deuteroxide, and heating for vacuum distillation caused Hoffman elimination of HOD from the tricaprylmethylammonium deuteroxide. Under the basic conditions, the HOD back-exchanges with the acetophenone to equilibrium. The ratio of D_2- to D_3-acetophenone was, in fact, almost exactly that expected after such equilibrium back-exchange. Anion exchange by washing the product several times with D_2O saturated in KCl before vacuum distillation solved the problem.

Can. J. Chem. Downloaded from www.nrcresearchpress.com by 85.192.166.187 on 09/08/12
For personal use only.

weighed and transferred in the glove box. Stock solutions, usually 0.0200 or 0.0500 M in electrolyte, were made, sealed in hypo vials with Teflon-lined caps, and diluted as required. Such stock solutions gave reproducible results for several months but were generally prepared freshly every few weeks. Diluted solutions were stored in volumetrics with glass stoppers and freshly prepared daily or, when the reactions were especially slow, after each pair of *protio* and *deutero* runs.

In the glove box, 25 mL of the diluted Bu_4NBr solution was prepared, 5.0 mL was pipetted into the polarimeter cell, and a weighted amount of chiral substrate added by syringe. The amount of substrate used was determined by the rotation of the resultant solution. A rotation of 0.4° gives near full-scale deflection on the recorder at moderate amplification. When rotations of a pair of substrates differed markedly, racemic material was added to the more active substrate so that similar total concentrations for the *protio* and *deutero* materials were used. The Teflon stoppers were inserted, the cell transferred to the circulating, constant temperature bath, and the contents of the cell thoroughly mixed while equilibrating to the pre-set temperature before the cell was inserted into the Perkin Elmer model 141MC polarimeter. Time was measured from the recorder trace, zero being when the pen crossed a dark time line. Runs with *protio* and *deutero* substrates, using the same solutions, were alternated.

About 60 data pairs of rotations, as recorder pen displacements or voltages, and times were read from the recorder chart and treated with standard weighted linear regression analysis routines. Half-lives ranged from about 12 min to several days. A linear regression of observed rate of racemization versus concentration of Bu_4NBr gave the first-order rate constant as the intercept, the second-order constant as the slope.

1. A.R. Stein. Can. J. Chem. **67**, 297 (1989).
2. D.J. McLennan, A.R. Stein, and B. Dobson. Can. J. Chem. **64**, 1201 (1986).
3. E.D. Hughes, F. Juliusburger, S. Masterman, B. Topley, and J. Weiss. J. Chem. Soc. 1525 (1935); E.D. Hughes, F. Juliusburger, A.D. Scott, B. Topley, and J. Weiss. J. Chem. Soc. 1173 (1936); W.A. Cowdrey, E.D. Hughes, T.P. Nevell, and C.L. Wilson. J. Chem. Soc. 209 (1938).
4. A. Ceccon, I. Papa, and A. Fara. J. Am. Chem. Soc. **88**, 4643 (1966).
5. P. Beronius. K. Tek. Hoegsk. Handl. no. 213 (1963); P. Beronius and R.P. Gupta. Acta Chem. Scand. Ser. A: **A30**, 477 (1976).
6. A.R. Stein. Can. J. Chem. **65**, 363 (1987); Tetrahedron Lett. 4145 (1974).
7. A.R. Stein and E. A. Moffatt. Can. J. Chem. **63**, 3433 (1985).
8. H.L. Goering and R.P. Anderson. J. Am. Chem. Soc. **100**, 6469 (1978).
9. M. Fujio, F. Sanematsu, Y. Tsuno, M. Sawada, and Y. Takai. Tetrahedron Lett. 93 (1988).
10. A.R. Stein, R.D. Dawe, and J.R. Sweet. Can J. Chem. **63**, 3442 (1985).
11. C.M. Starkes. J. Am. Chem. Soc. **93**, 195 (1971).
12. S.P. Schmidt and D.W. Brooks. Tetrahedron Lett. 767 (1987).
13. L. Hakka, A. Queen, and R.E. Robertson. J. Am. Chem. Soc. **87**, 161 (1965).
14. V.J. Shiner and J.S. Humphrey. J. Am. Chem. Soc. **85**, 2416 (1963).
15. J. McKenna, L.B. Sims, and I.H. Williams. J. Am. Chem. Soc. **103**, 268 (1981).
16. A.R. Stein. J. Org. Chem. **41**, 519 (1976).
17. A. Thibblin and H. Sidhu. J. Am. Chem. Soc. **114**, 7403 (1992).
18. V.J. Shiner, T.E. Neumann, and R.D. Fisher. J. Am. Chem. Soc. **104**, 354 (1982).
19. M.P. Jansen, K.M. Koshy, N.N. Mangru, and T.T. Tidwell. J. Am. Chem. Soc. **103**, 3863 (1981).
20. S. Sridharan and V.P. Vitullo. J. Am. Chem. Soc. **99**, 8093 (1977).
21. K. Humski, V. Sendijarevevic, and V.J. Shiner, Jr. J. Am. Chem. Soc. **95**, 7722 (1973).
22. A. Thibblin. J. Am. Chem. Soc. **111**, 5412 (1989).
23. K.T. Leffek, J.A. Llewellyn, and R.E. Robertson. Can. J. Chem. **38**, 2171 (1960).
24. A. Streitwieser, Jr., C.L. Wilkins, and E. Kiehlmann. J. Am. Chem. Soc. **90**, 1598 (1968); Tetrahedron Lett. 3159 (1970).
25. V.J. Shiner, Jr., W.E. Buddenhaum, B.L. Murr, and G. Lamty. J. Am. Chem. Soc. **90**, 418 (1968).
26. V.J. Shiner, Jr. ACS Monogr. **167**, 90 (1970).
27. H. Yamataka, S. Tamura, T. Hanafusa, and T. Ando. J. Am. Chem. Soc. **107**, 5429 (1985).
28. P.G. Gassman and J.T. Talley. J. Am. Chem. Soc. **102**, 1214 (1980).
29. D.E. Sunoko, I. Szele, and W.J. Hehre. J. Am. Chem. Soc. **99**, 5000 (1977).
30. A.D. Allen, M.P. Jansen, K.M. Koshy, N.N. Mangru, and T.T. Tidwell. J. Am. Chem. Soc. **104**, 207 (1982).
31. M. Tencer and A.R. Stein. Can. J. Chem. **56**, 2994 (1978); G. Bergson, O. Matsson, and S. Sjoberg. Chem. Scr. **11**, 25 (1977).

Can. J. Chem. Downloaded from www.nrcresearchpress.com by 85.192.166.187 on 09/08/12
For personal use only.

A ^{139}La and ^{17}O nuclear magnetic resonance study of the nature of La(III) first coordination sphere in acetonitrile solutions of hydrated lanthanum nitrate

ZHIGANG CHEN AND CHRISTIAN DETELLIER[1]

Ottawa–Carleton Chemistry Institute, University of Ottawa Campus, Ottawa, ON K1N 6N5, Canada

Received December 1, 1993[2]

ZHIGANG CHEN and CHRISTIAN DETELLIER. Can. J. Chem. **72**, 1797 (1994).

The nature of the first coordination sphere of the La(III) cation in acetonitrile solutions of $La(NO_3)_3.6H_2O$ was investigated by ^{139}La and ^{17}O NMR. All three nitrate anions are coordinated to La(III). There is a competition between water and acetonitrile molecules for the occupancy of the La(III) first coordination sphere. The ^{139}La and ^{17}O NMR results, obtained for various concentrations of $La(NO_3)_3.6H_2O$, were quantitatively interpreted through a chemical equilibrium model. It was shown that the presence of only two La(III) species, $\{La(III)\ (NO_3^-)_3\}$ and $\{La(III)\ (NO_3^-)_3.H_2O\}$, in rapid exchange in solution could account for all the NMR results. The variation of the ^{139}La and ^{17}O NMR parameters (chemical shifts and relaxation rates) with the concentration of $La(NO_3)_3.6H_2O$ results from the population increase of the species $\{La(III)\ (NO_3^-)_3.H_2O\}$. The chemical exchange between free and coordinated water molecules is also fast on the ^{17}O NMR time scale. The ^{17}O NMR signal of water is considerably broadened when it coordinates to the La(III) cation. This broadening was attributed to both direct and indirect interactions between the two quadrupolar nuclei ^{17}O and ^{139}La. The direct interaction comes from an increase of the electric field gradient at the ^{17}O nucleus when a water molecule coordinates to the La(III) cation. The indirect interaction results from an ^{17}O–^{139}La scalar coupling. The detailed analysis of the ^{17}O NMR spectra also allowed the determination of the indirect coupling constant between coordinated $^{17}OH_2$ and $^{139}La(III)$, $|^1J(^{17}O—^{139}La)|$: 88 ± 13 Hz.

ZHIGANG CHEN et CHRISTIAN DETELLIER. Can. J. Chem. **72**, 1797 (1994).

On a étudié par RMN du ^{139}La et de l'^{17}O la nature de la première couche de coordination de La(III) dans des solutions de $La(NO_3)_3.6H_2O$ dans l'acétonitrile. Les trois anions nitrate sont coordinés au La(III), alors que molécules d'eau et d'acétonitrile sont en compétition pour l'occupation de la première couche de coordination du La(III). On a proposé une interprétation quantitative des résultats de la RMN du ^{139}La et de l'^{17}O obtenus en variant la concentration de $La(NO_3)_3.6H_2O$. La présence de deux espèces chimiques, $\{La(III)\ (NO_3^-)_3\}$ et $\{La(III)\ (NO_3^-)_3.H_2O\}$, en échange rapide, rend compte des résultats de RMN. La variation des paramètres de RMN du ^{139}La et de l'^{17}O (déplacements chimiques et vitesses de relaxation) avec la concentration de $La(NO_3)_3.6H_2O$ résulte d'un accroissement de la population de l'espèce $\{La(III)\ (NO_3^-)_3.H_2O\}$. A l'échelle de temps de la RMN de l'^{17}O, l'échange chimique entre molécules d'eau "libres" et coordinées est, lui aussi, rapide. Le signal de RMN de l'^{17}O de l'eau est fortement élargi lorsque l'eau se coordine au cation La(III). Cet élargissement a été attribué à des interactions directes et indirectes entre les deux noyaux quadripolaires, ^{139}La et ^{17}O. L'interaction directe provient d'un accroissement du gradient de champs électrique au site du noyau d'^{17}O lors de la coordination d'une molécule d'eau sur le cation La(III). L'interaction indirecte résulte d'un couplage scalaire ^{17}O–^{139}La. L'analyse détaillée des spectres de la RMN de l'^{17}O a aussi permis la détermination de la constante de couplage indirecte entre $^{17}OH_2$ coordiné et $^{139}La(III)$, $|^1J(^{17}O—^{139}La)|$: 88 ± 13 Hz.

Lanthanide ions are increasingly used as spectroscopic probes in biochemical and biological systems (1, 2), and a more detailed knowledge of their coordination behavior in the presence of specific ligands in solutions is needed. However, many aspects of their coordination chemistry remain unclear. For example, the nature and the structure of the chemical species present in aqueous solutions of their salts are not yet fully understood (3–5).

It is likely that ion pairs be formed in the solutions of the tripositive lanthanoid ions ("Ln^{3+}": Y^{3+}, La^{3+}–Lu^{3+}), particularly in poorly coordinating solvents. Bunzli and co-workers (6, 7) have investigated the interactions between lanthanoid cations and the perchlorate anion in anhydrous acetonitrile solutions by FTIR spectroscopy. They found that inner sphere complexes of Ln^{3+} with ClO_4^- were formed in these systems (6, 7). The nature of the solutions of lanthanide chloride in methanol and methanol–water mixtures has been studied by several techniques, including X-ray diffraction (8, 9), NMR spectroscopy (8–11), ultrasonic absorption measurements (12), and UV-Visible spectroscopy (13). On the basis of these studies, evidences were found that contact ion pairs are formed between Ln^{3+} and Cl^- in water–methanol solutions. As the methanol molar fraction is larger, the degree of Ln–Cl inner sphere coordination increases. Inner sphere complexes of Ln^{3+} with nitrate and perchlorate anions were also found to be formed in methanol–water solutions (13).

Metal cation NMR in solution is a powerful and sensitive probe of the nature of the immediate electronic environment of the metal cation (5, 14). Among the lanthanide series, the quadrupolar ^{139}La nucleus ($I = 7/2$; $Q = 0.21 \times 10^{-28}$ m^2) is the best candidate for such studies (15) since its receptivity compared to ^{13}C is 342. In the present work, we investigate, by means of ^{139}La and ^{17}O NMR spectroscopies, the nature of the La^{3+} coordination sphere when the salt $La(NO_3)_3.6H_2O$ is dissolved in anhydrous acetonitrile. These NMR techniques permit one to characterize the competition between small amounts of water and bulk solvent molecules for the occupation of the La(III) first coordination shell. A model is proposed, and a quantitative interpretation of the results is given, allowing the calculation of the equilibrium constant of formation of the monohydrated species, $La(NO_3)_3.H_2O$. The coupling constant, $^1J_{^{139}La—^{17}O}$, between the La^{3+} cation and the water molecule in its first coordination sphere could be estimated.

[1]Author to whom correspondence may be addressed. Tel: (613) 564-2967, fax: (613) 564-6793, e-mail: DETSE@ACADVM1.UOTTAWA.CA.

[2]Revision received April 7, 1994.

Can. J. Chem. Downloaded from www.nrcresearchpress.com by 85.192.166.187 on 09/08/12
For personal use only.

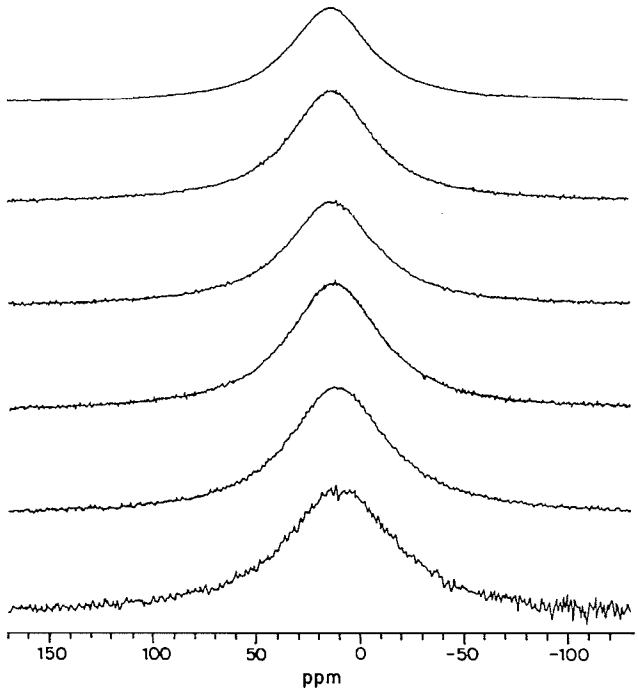

FIG. 1. A series of ^{139}La NMR spectra for various concentrations of $La(NO_3)_3.6H_2O$ in acetonitrile. Top to bottom [La(III)] = 0.100, 0.050, 0.040, 0.030, 0.020, and 0.010 M, T = 300 K.

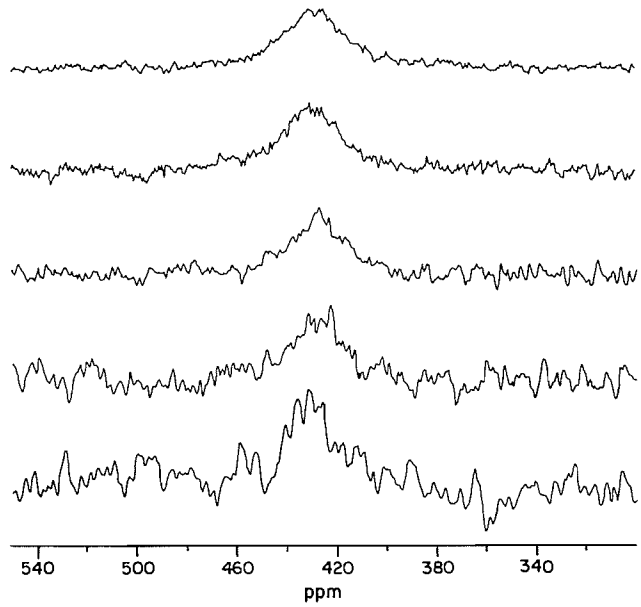

FIG. 2. A series of ^{17}O NMR spectra of the nitrate region for $La(NO_3)_3.6H_2O$ solutions in acetonitrile. Top to bottom [La(III)] = 0.090, 0.070, 0.050, 0.025, and 0.015 M, T = 300 K.

Experimental

$La(NO_3)_3.6H_2O$ (Aldrich 99.999%) was used without further purification. Acetonitrile (BDH Assured) was dried as previously reported (16).

The stock solutions for NMR investigations were prepared by dissolving an appropriately weighted quantity of hydrated lanthanum nitrate in dried acetonitrile. The lanthanum content of lanthanum nitrate was determined by titration with EDTA using xylenol orange as indicator. Results confirmed the hexahydrated lanthanum nitrate formula. The solutions thus made were transferred into 10 mm NMR tubes sealed under argon with Parafilm. ^{139}La NMR spectra were obtained at 42.37 MHz on a Varian XL-300 NMR spectrometer. A 0.10 M solution of $La(NO_3)_3$ in D_2O:H_2O 20:80 (v/v) was used as an external reference for the chemical shift measurements. The instrumental conditions were chosen as described previously (17). The linewidths at half-height and the chemical shifts were obtained from a complete lineshape analysis of the experimental Lorentzian lines. The errors on their determination was evaluated to be 40 Hz and 0.5 ppm, respectively.

The natural abundance ^{17}O NMR spectra were measured at 40.66 and at 67.77 MHz, respectively, on a Varian XL-300 and on a Bruker AMX-500 NMR spectrometers. The chemical shifts were referenced to external 100% D_2O. The error on their determination was evaluated to be 0.2 ppm.

The temperature in the probe was controlled, and all the experiments were performed at 300.0 ± 0.5 K.

Results

The chemical shifts and linewidths of the ^{139}La NMR spectra have been measured as a function of $La(NO_3)_3.6H_2O$ concentration in acetonitrile. In the range of concentrations studied, the ^{139}La NMR spectra consist of a single Lorentzian line. Figure 1 shows a series of ^{139}La NMR spectra for various concentrations, from 0.010 to 0.100 M. The ^{139}La NMR signals shift downfield, from 7.9 to 12.0 ppm, and the linewidths values decrease from 2750 to 1930 Hz, as the concentration of La(III) increases from 0.0050 to 0.10 M.

These results indicate that at least two different La(III) species, with different chemical environments, coexist and exchange rapidly in the solution. The formation of these different La(III) solution sites can result from the interactions of La(III) with the nitrate anion, water, and/or solvent molecules.

Figures 2 and 3 show series of ^{17}O NMR spectra for various concentrations of $La(NO_3)_3.6H_2O$ in acetonitrile. Two ^{17}O NMR signals were observed: one at 430 ppm, attributed to the nitrate anion (18, 20) (Fig. 2), and one at higher fields, in the range −3 to 11 ppm, attributed to water (19–21) (Fig. 3*a*). The ^{17}O NMR chemical shifts and linewidths of the nitrate anion are independent of the $La(NO_3)_3.6H_2O$ concentrations, in the limits of the experimental errors. The ^{17}O NMR chemical shifts of water, on the other hand, vary with the concentrations of hydrated lanthanum nitrate, from −2.26 to 10.6 ppm in the La(III) concentration range of 0.0050 to 0.100 M. These characteristics indicate the presence of one type of NO_3^- and of at least two types of water molecules. As it has been shown by several studies (12, 18, 19), all three nitrate anions are expected to be coordinated to the La(III) cation, while it is a variable number of water molecules which is expected to be in the first coordination sphere of the La(III). The different La(III) sites, which are observed on the ^{139}La NMR spectra (Fig. 1), are thus attributed to chemical species characterized by a different number of water molecules coordinated to La(III). The following model is proposed (eq. [1]–[7]). For more clarity, the number (unknown) of acetonitrile molecules directly coordinated to La(III) is not indicated.

$$[1] \qquad \{La(NO_3)_3.xH_2O\} + \{H_2O\} \rightleftharpoons \{La(NO_3)_3.(x+1)H_2O\}$$

Let us define [A] and [B] as [A] = $[La(NO_3)_3.xH_2O]$ and [B] = $[La(NO_3)_3.(x+1)H_2O]$, then

$$[2] \qquad K = \frac{[B]}{[A] \times [H_2O]}$$

Can. J. Chem. Downloaded from www.nrcresearchpress.com by 85.192.166.187 on 09/08/12
For personal use only.

Can. J. Chem. Downloaded from www.nrcresearchpress.com by 85.192.166.187 on 09/08/12
For personal use only.

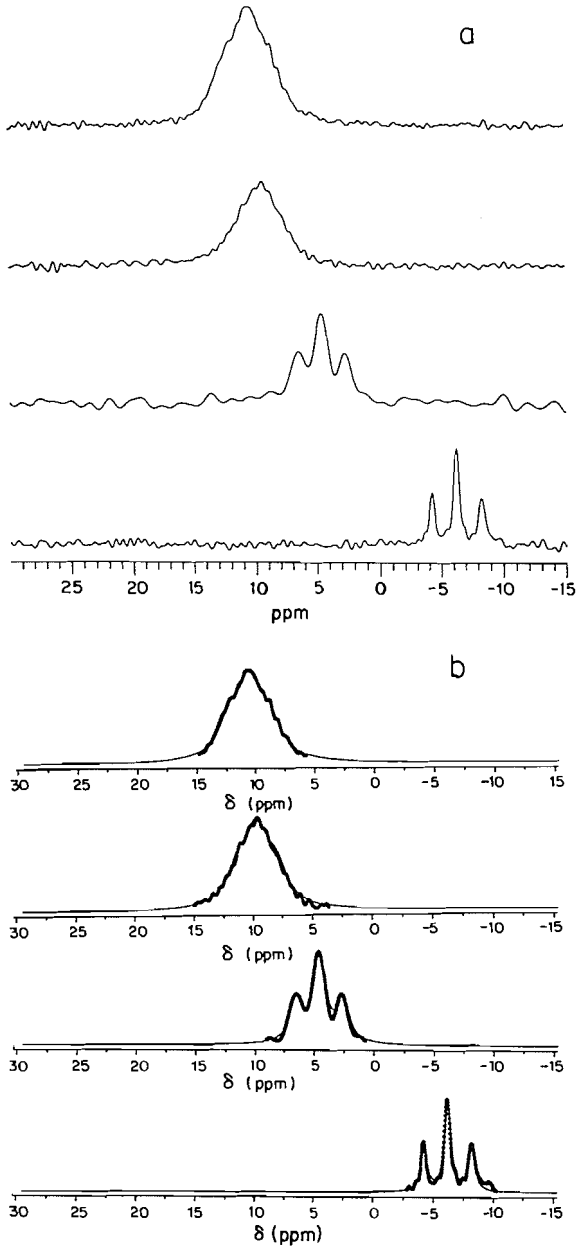

FIG. 3. A series of ^{17}O NMR spectra of the water region for $La(NO_3)_3.6H_2O$ solutions in acetonitrile. (*a*) Experimental spectra, top to bottom [La(III)] = 0.090, 0.070, 0.025 M. The spectrum of free water in acetonitrile ([H_2O] = 0.090 M) is given at the bottom. T = 300 K. (*b*) Calculated spectra, the data points are experimental (see text).

and

$$[3] \qquad (\delta_{obs})_{^{139}La} = \delta_A \times \left(1 - \frac{[B]}{[La]_0}\right) + \delta_B \times \frac{[B]}{[La]_0}$$

$$[4] \qquad (\delta_{obs})_{^{17}O} = \delta_f \times \frac{[H_2O]}{6[La]_0} + \delta_c \times \frac{[H_2O]_c}{6[La]_0}$$

where $[La]_0$ is the initial (or total) concentration of La(III), δ_A and δ_B are the chemical shifts for the sites A and B respectively, while δ_f and δ_c are the ^{17}O chemical shifts for free and complexed water molecules, respectively. In eq. [4], it is assumed that all the complexed water molecules have the same ^{17}O NMR chemical shift.

TABLE 1. Equilibrium constant and $H_2{}^{17}O$ NMR parameters characterizing the La(III) chemical species in acetonitrile solutions of $La(NO_3)_3.6H_2O$ (T = 300 K)

x^a	$\delta_c{}^b$ (ppm)	log K^c
-0.01 ± 0.06^d	120 ± 5	0.9 ± 0.3

[a]Number of water molecules in the first coordination shell of La(III); see eq. [1].
[b]^{17}O NMR chemical shift of the water molecule coordinated to La(III).
[c]Equilibrium constant (see eq. [2]).
[d]All errors are given as one standard deviation, σ, from the non-linear regression.

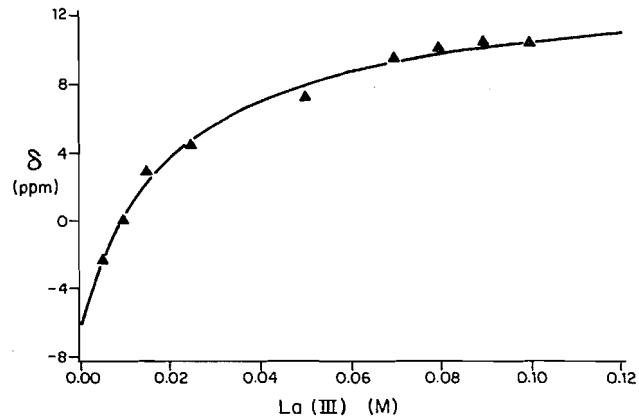

FIG. 4. ^{17}O chemical shifts as a function of [$La(NO_3)_3.6H_2O$] in acetonitrile. The data points are experimental and the curve is calculated from the values of the parameters reported in Table 1.

Since

$$[5] \qquad [A] = [La]_0 - [B]$$

$$[6] \qquad [H_2O] = (6 - x) \times [La]_0 - [B]$$

and

$$[7] \qquad [H_2O]_c = x\,[La]_0 + [B]$$

the observed ^{17}O NMR chemical shifts of water for $La(NO_3).6H_2O$ acetonitrile solutions can be fitted by a non-linear regression procedure through eqs. [2] and [4] to [7] using δ_c, K, and x as the adjustable parameters. In order to limit the number of adjustable parameters, the ^{17}O NMR chemical shift of free water, δ_f, was taken as an experimental value. Only a very slight dependence of δ_f upon the water concentration could be observed when given amounts of water were added to anhydrous acetonitrile. For water concentrations of 0.62 and 0.31 M, chemical shifts of −5.92 and −6.10 ppm were respectively observed: −6.00 ppm was choosen as the value of δ_f for the non-linear regression analysis. The results of this regression are reported in Table 1. In Fig. 4, the points are the experimental values of the ^{17}O NMR chemical shifts of water and the curve is calculated from the parameters reported in Table 1. The non-linear regression gave a value for x (see eq. 1) of zero.

Similarly, δ_A, δ_B, and K can be used as adjustable parameters in the series of eqs. [2], [3], [5], and [6]. Again, in order

TABLE 2. Equilibrium constant and ^{139}La NMR parameters characterizing the La(III) species in acetonitrile solutions of $La(NO_3)_3.6H_2O$ (T = 300 K); $x = 0$[a]

δ_A[b] (ppm)	δ_B[c] (ppm)	log K[d]	$(\nu_{1/2})_A$[e] (kHz)	$(\nu_{1/2})_B$[f] (kHz)	log K[g]
5.8 ± 0.6[h]	12.9 ± 0.2	1.1 ± 0.4	2.92 ± 0.05	1.60 ± 0.06	0.8 ± 0.2

[a]See eq. [1].
[b]^{139}La NMR chemical shift of species A ($La(NO_3)_3$).
[c]^{139}La NMR chemical shift of species B ($La(NO_3)_3.H_2O$).
[d]Equilibrium constant (eq. [2]) determined from chemical shift variation.
[e]^{139}La NMR linewidth of the species A.
[f]^{139}La NMR linewidth of the species B.
[g]Equilibrium constant (eq. [2]) determined from linewidth variation.
[h]All errors are given as one standard deviation, σ, from the nonlinear regression.

to limit the number of adjustable parameters, x is taken equal to zero, as found from the ^{17}O NMR data. The results are reported in Table 2. Figure 5 shows the observed ^{139}La NMR chemical shifts as a function of $La(NO_3)_3.6H_2O$ concentrations in acetonitrile solutions, in which the points are experimental and the line is calculated from the values of the adjustable parameters reported in Table 2, with $x = 0$.

A similar treatment was made for the ^{139}La NMR linewidths ($\nu_{1/2}$).

$$[8] \qquad (\nu_{1/2})_{obs} = (\nu_{1/2})_A \left(1 - \frac{[B]}{[La]_0}\right) + (\nu_{1/2})_B \frac{[B]}{[La]_0}$$

$(\nu_{1/2})_A$, $(\nu_{1/2})_B$, the linewidths respectively for site A and site B, and K are used as adjustable parameters. The results are also given in Table 2. It is worth stressing that the K values obtained independently from the ^{17}O NMR chemical shift data and from both ^{139}La NMR chemical shift and linewidth data are in good agreement (log K = 0.9 ± 0.3; 1.1 ± 0.4; 0.8 ± 0.2). Figure 6 gives the variations of $(\nu_{1/2})_{obs}$ with the concentration of hydrated lanthanum nitrate. The points are experimental and the curve is calculated on the basis of the values of the parameters of Table 2 with $x = 0$.

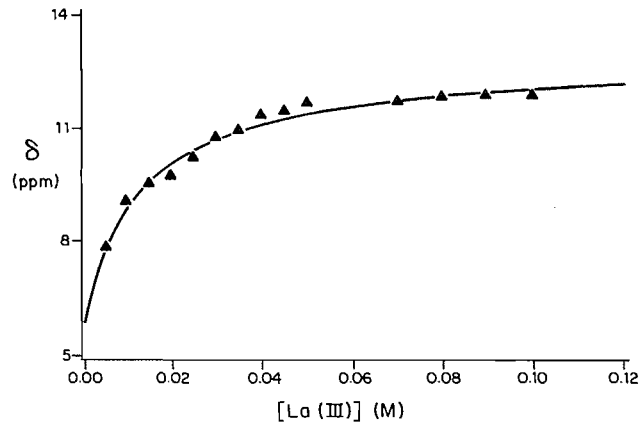

FIG. 5. ^{139}La chemical shifts as a function of $[La(NO_3)_3.6H_2O]$ in acetonitrile. The data points are experimental and the curve is calculated from the values of the parameters reported in Table 2.

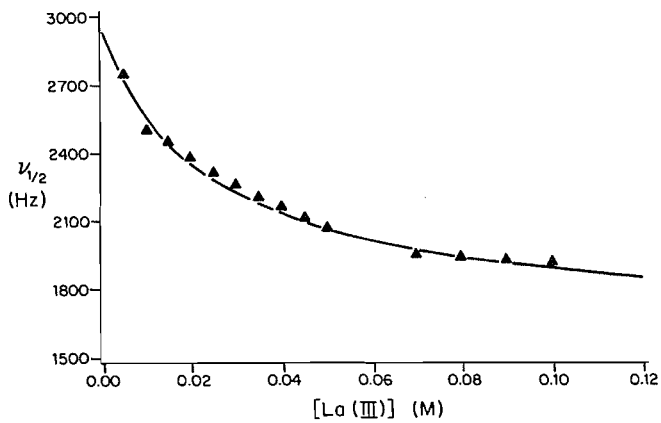

FIG. 6. ^{139}La transverse relaxation rates as a function of $[La(NO_3)_3.6H_2O]$ in acetonitrile. The data points are experimental and the curve is calculated from the values of the parameters reported in Table 2.

Discussion

The ^{139}La NMR chemical shift of $La(NO_3)_3$ in acetonitrile is 5.8 ± 0.6 ppm (Table 2). Evans and Missen (19) have investigated the interactions between NO_3^- and La(III) by progressively adding $(NBu_4)(NO_3)$ to anhydrous acetonitrile solutions of lanthanum perchlorate. They found that both ^{139}La NMR chemical shift and linewidth first increased then decreased as the ratio of NO_3^-/La(III) increased. For a ratio of 3:1 (NO_3^-/La(III)), the observed ^{139}La NMR chemical shift was 10 ± 2 ppm (see ref. 19, Fig. 3). This value is comparable with our result although the systems involved are not identical.

The ^{139}La NMR chemical shift of $La(NO_3)_3.H_2O$, 12.9 ± 0.2 ppm, is at higher frequency than the one of $La(NO_3)_3$. The shift is caused by the probable replacement of acetonitrile molecules in the first coordination shell of La(III) by water. A similar result was reported by Evans and Missen (19). They showed that the progressive addition of water to an anhydrous $La(ClO_4)_3$ solution in acetonitrile caused the ^{139}La NMR signals to shift downfield.

The value of the equilibrium constant of eq. [1] (with $x = 0$) ($K \approx 10$) is also in good agreement with the concept that less donating solvent molecule (acetonitrile) is replaced by a more donating one (water) in the first coordination sphere of La(III).

The calculated ^{139}La NMR linewidths for $La(NO_3)_3$ and $La(NO_3)_3.H_2O$ are 2.9 and 1.6 kHz, respectively. Again, the calculated linewidth value of $La(NO_3)_3$ is in the same order of magnitude than that reported by Evans and Missen (19) ($\nu_{1/2} \approx 3.8 \pm 0.2$ kHz for a ratio NO_3^-/La(III) of 3:1, estimated from Fig. 3 of ref. 19). The ^{139}La linewidth value for $La(NO_3)_3.H_2O$ is smaller than that for $La(NO_3)_3$. This indicates a higher symmetry of the electronic charge distribution around the ^{139}La nucleus in $La(NO_3)_3.H_2O$ than in $La(NO_3)_3$,

Can. J. Chem. Downloaded from www.nrcresearchpress.com by 85.192.166.187 on 09/08/12
For personal use only.

Can. J. Chem. Downloaded from www.nrcresearchpress.com by 85.192.166.187 on 09/08/12
For personal use only.

when an oxygenated ligand (water) replaces one or several acetonitrile molecules in the first coordination sphere of La(III) also coordinated by three nitrate groups.

The ^{17}O NMR chemical shift of free water in acetonitrile is about −6 ppm. This shift is understood on the basis of hydrogen bond breaking, resulting in an increased shielding of the ^{17}O nucleus (20). Values of -11.3 ± 0.6 and −6.8 ppm have been reported in the literature (18, 21) for the ^{17}O chemical shift of water in acetonitrile.

The ^{17}O NMR chemical shift of a water molecule coordinated to the lanthanum cation is 120 ± 4 ppm. Paramagnetic lanthanide cations have been used as "shift reagents" in ^{17}O NMR measurements (20), but, unfortunately, there is not any ^{17}O NMR data on water coordinated to diamagnetic lanthanide cation available in the literature, and a direct comparison of the δ_c (^{17}O) obtained in this work is not possible. However, ^{17}O NMR chemical shifts of coordinated water of +6 ppm in $Al(H_2O)_6^{3+}$ (22), −131.8 ppm in $Pd(H_2O)_4^{2+}$ (23), and 126 ppm in *cis*-$Co(en)_2(H_2O)_2^{2+}$ (24) have been reported. Even in diamagnetic systems, the ^{17}O NMR chemical shift of water varies widely upon complexation, and is very dependent upon the nature of the metal cation. From Fig. 3 it is also apparent that the ^{17}O signal of coordinated water is considerably broadened, compared to the signal of non-coordinated water (characterized by a linewidth of 25 Hz and a coupling constant $^1J_{^1H—^{17}O}$ of 80 Hz). From the data of Table 1, and on the basis of eq. [1], a simulation of the various ^{17}O NMR spectra as a function of the total water concentration was performed. Examples of this simulation are given on Fig. 3*b*, for the cases of Fig. 3*a*. The success of the simulation is consistent with the proposed model, a system of two species in very fast chemical exchange. The characteristic $^{17}OH_2$ NMR linewidth of the species $La(NO_3)_3.H_2O$ could be determined as an average value from the simulations: it is equal to (400 ± 50) Hz. Thus the coordination of a water molecule to the La(III) cation results in an increase of the $^{17}OH_2$ linewidth from 25 to 400 Hz. This broadening can result from three possible contributions which will be considered: chemical exchange, quadrupolar relaxation and scalar relaxation of the second kind. A moderately fast exchange between free and coordinated water molecules would result in a broadening of the ^{17}O NMR signal depending upon the square of the observation frequency (25). In order to test for this contribution, the ^{17}O NMR spectra of two samples, ($[La(NO_3)_3.6H_2O] = 0.050$ and 0.090 M), were recorded at 40.66 MHz and at 67.77 MHz (respectively 7.05 T and 11.75 T NMR spectrometers) (26). In the error limits of the experiments, the linewidths were identical and a chemical exchange contribution to the broadening could be ruled out.

An increase in the electric field gradient at the ^{17}O nucleus is expected when a water molecule coordinates to the La(III) cation. Since ^{17}O is a quadrupolar nucleus ($I = 5/2$, $|Q| = 0.026\ 10^{-28}\ m^2$), the interaction of this increased electric field gradient with the ^{17}O quadrupole moment will increase the quadrupolar relaxation and consequently the ^{17}O linewidth. This contribution to the ^{17}O linewidth is defined as $(\pi T_{2Q})^{-1}$ in the following discussion.

Since ^{139}La has a natural abundance of 99.91%, the line broadening of the coordinated water ^{17}O NMR signal could also result from the indirect quadrupolar interaction between the ^{17}O and ^{139}La nuclei (^{17}O–^{139}La coupling). The transverse relaxation rate of ^{139}La(III) in the species $La(NO_3)_3.H_2O$ is about 5 000 Hz (Table 2). Since the system is under extreme narrowing conditions, T_1 and T_2 are equal. From the known values of the coupling constants involving the ^{17}O nucleus (27), it is expected that $T_1^{-1}(^{139}La) \gg |^1J(^{139}La—^{17}O)|$. Under these conditions, an indirect coupling between ^{17}O and ^{139}La cannot be directly observed since the multiplet caused by the coupling would be collapsed (28). However, this coupling can provide a relaxation mechanism to the ^{17}O nucleus (scalar relaxation of the second kind), and its contribution to the ^{17}O linewidth, $(\nu_{1/2})_J$, is given by eq. [13] (29)

$$[13] \qquad (\nu_{1/2})_J = \tfrac{4}{3}\pi J^2 T_1(^{139}La) I(I+1)$$

where $T_1(^{139}La)$ is the ^{139}La longitudinal relaxation time, I is the ^{139}La nuclear spin number, and J is $|^1J(^{139}La—^{17}O)|$.

Combining the contributions from the direct quadrupolar interaction and the scalar relaxation, the ^{17}O linewidth for the coordinated H_2O molecule can be expressed as:

$$[14] \qquad (\nu_{1/2})_c = (\pi(T_{2Q})_c)^{-1} + 21\pi J^2 T_1(^{139}La)$$

where the subscript "c" refers to coordinated water. Under extreme narrowing conditions, $T_{1Q} = T_{2Q}$ for ^{17}O and $T_1 = T_2$ for ^{139}La, so that:

$$[15] \qquad (T_2^{-1})_c = (T_{1Q}^{-1})_c + 21\pi^2 J^2 T_2(^{139}La)$$

If $(T_{1Q}^{-1})_c$ was known, eq. [15] would allow the determination of the value of J, since $(T_2^{-1})_c$ and $T_2(^{139}La)$ are known ($\pi \times 400$ Hz and 5 000 Hz, respectively). Contrary to T_2, T_1 is generally not affected by the scalar relaxation of the second kind (except in the very rare cases where the frequencies of observation of the two nuclei are very close, which is not the case here) (29), so that a measurement of the ^{17}O longitudinal relaxation rate, $(T_1^{-1})_{obs}$, could provide $(T_{1Q}^{-1})_c$. The measurement gave 5.18×10^{-3} s for a $La(NO_3)_3.6H_2O$ concentration of 0.090 M. This value is an average of the characteristic relaxation rates of water in its two chemical sites, "free", $(T_1^{-1})_f$, and coordinated, $(T_1^{-1})_c$. This is expressed in eq. [16]:

$$[16] \qquad (T_1^{-1})_{obs} = P_f(T_1^{-1})_f + P_c(T_1^{-1})_c$$

where P_f and P_c are respectively the population of free and coordinated water molecules. $(T_1^{-1})_f$ was measured as 78.5 s^{-1}, and the populations are known from the data reported in Tables 1 and 2: in the conditions of the experiment, $P_f = 0.867$ and $P_c = 0.133$. It can be calculated that $(T_1^{-1})_c \doteq (T_{1Q}^{-1})_c = 938\ s^{-1}$. With this value, $|^1J(^{139}La—^{17}O)|$ can be calculated from eq. [15]: 88 ± 13 Hz. This is, to the best of our knowledge, the first reported value of a coupling $^{139}La—^{17}O$. It corresponds to a reduced coupling constant value of $K_{^{139}La—^{17}O} = 38\ N\ A^{-2}\ m^{-3}$, which is in the order of magnitude of other reduced coupling constants of transition metal nuclei with ^{17}O (for example, ^{95}Mo ($K = 38$), ^{99}Te ($K = 36$), or ^{99}Ru ($K = 31$)) (30).

In conclusion, the ^{139}La and ^{17}O NMR chemical shifts and linewidths have been measured as a function of the concentration of $La(NO_3)_3.6H_2O$ in acetonitrile. The results have been quantitatively interpreted through a chemical equilibrium model, in which two La(III) species, $La(NO_3)_3$ and $(La(NO_3)_3.H_2O)$ (with an unknown number of acetonitrile molecules coordinated to La(III), in both cases), coexist and exchange rapidly in solution. The detailed analysis of the ^{17}O NMR relaxation data allowed the evaluation of the indirect

coupling constant $|^1J(^{139}La—^{17}O)|$ for the coordinated water molecule.

Acknowledgments

The Natural Sciences and Engineering Research Council of Canada is gratefully acknowledged for financial support. Dr. Barbara Blackwell (Agriculture Canada, Ottawa) is gratefully acknowledged for the recording of the ^{17}O NMR spectra at 67.77 MHz (Bruker AMX-500).

1. M. Albin and W. DeW. Horrocks, Jr. Inorg. Chem. **24**, 895 (1985).
2. C.H. Evans. Biochemistry of the lanthanides. Plenum Press, New York. 1990.
3. S.F. Lincoln. Adv. Inorg. Bioinorg. Mechanisms, **4**, 217 (1986).
4. C. Cossy and A.E. Merbach. Pure Appl. Chem. **60**, 1785 (1988).
5. Z. Chen and C. Detellier. J. Solution Chem. **21**, 941 (1992).
6. (*a*) J.-C.G. Bunzli and M.M. Vuckovic. Inorg. Chim. Acta, **73**, 53 (1983); (*b*) J.-C.G. Bunzli and J.-R. Yersin. Inorg. Chim. Acta, **94**, 301 (1984); (*c*) J.-C.G. Bunzli, J.-R. Yersin, and C. Mabillard. Inorg. Chem. **21**, 1471 (1982); (*d*) J.-C.G. Bunzli, C. Mabillard, and J.-R. Yersin. Inorg. Chem. **21**, 4214 (1982).
7. J.-C.G. Bunzli and C. Mabillard. Inorg. Chem. **26**, 2750 (1986).
8. L.S. Smith, D.C. McCain, and D.L. Wertz. J. Am. Chem. Soc. **98**, 5125 (1976).
9. D.L. Wertz and S.T. Finch. Inorg. Chem. **18**, 1590 (1979).
10. D.C. McCain. J. Inorg. Nucl. Chem. **42**, 1185 (1980).
11. J.-C.G. Bunzli, A.E. Merbach, and R.M. Nielson. Inorg. Chim. Acta, **139**, 151 (1987).
12. H.B. Silber and T. Mioduski. Inorg. Chem. **23**, 1577 (1984).
13. H.B. Silber, R. Bakhshandeffar, L.A. Contreras, F. Gaizer, M. Gonsalves, and S. Ismail. Inorg. Chem. **29**, 4473 (1990).
14. C. Detellier. *In* NMR of newly accessible nuclei. Vol. 2. *Edited by* P. Laszlo. Academic Press, New York. 1983. Chap. 5.
15. D. Rehder. *In* Multinuclear NMR. *Edited by* J. Mason. Plenum Press, New York. 1987. Chap. 19.
16. H.P. Graves and C. Detellier. J. Am. Chem. Soc. **110**, 6019 (1988).
17. Z. Chen, H. Dettman, and C. Detellier. Polyhedron, **8**, 2029 (1989).
18. M. Frechette, I.R. Butler, R. Hynes, and C. Detellier. Inorg. Chem. **31**, 1650 (1992).
19. D.F. Evans and P.H. Missen. J. Chem. Soc. Dalton Trans. 1929 (1982).
20. J.P. Kintzinger. *In* O-17 NMR, basic principles and progress. *Edited by* P. Diehl, E. Fluck, and R. Kosfeld. Springer-Verlag Berlin, Heidelberg Press, New York. 1981.
21. Z. Luz and G. Yagil. J. Phys. Chem. **70**, 554 (1966).
22. D. Hugi-Cleary, L. Helm, and A.E. Merbach. Helv. Chim. Acta, **68**, 545 (1985).
23. L. Helm, L.I. Elding, and A.E. Merbach. Helv. Chim. Acta, **67**, 1453 (1984).
24. S. Aygen, H. Hanssum, and R. Van Eldik. Inorg. Chem. **24**, 2853 (1985).
25. C. Detellier. *In* Modern NMR techniques and their applications in chemistry. *Edited by* A.I. Popov and K. Hallenga. Practical spectroscopy series. Vol. 11. M. Dekker, New York. 1991. Pp. 521–566. Chap. 9.
26. Z. Chen. Ph. D. Thesis, University of Ottawa. Ottawa, Ont., Canada. 1993.
27. O. Lutz, W. Nepple, and A. Nolle. Z. Naturforsch. **31a**, 1046 (1976).
28. J. Virlet and G. Tantot. Chem. Phys. Lett. **44**, 296 (1976).
29. O. Howarth. *In* Multinuclear NMR. *Edited by* J. Mason. Plenum Press, New York. 1987. Chap. 5.
30. W. McFarlane and H.C.E. McFarlane. *In* Multinuclear NMR. *Edited by* J. Mason. Plenum Press, New York. 1987. Chap. 5.

Can. J. Chem. Downloaded from www.nrcresearchpress.com by 85.192.166.187 on 09/08/12
For personal use only.

Differential reactivity of carbohydrate hydroxyls in glycosylations. III. Structure, stability, and reactivity of 2′-deoxycytidine model compound-BF_3 complexes

TING-HUA TANG

Department of Chemistry, University of Toronto, Toronto, ON M5S 1A1, Canada and Protein Engineering Network of Centres of Excellence (PENCE)

DENNIS M. WHITFIELD, STEPHEN P. DOUGLAS, AND JIRI J. KREPINSKY

Department of Molecular and Medical Genetics, and Carbohydrate Research Centre, University of Toronto, Toronto, ON M5S 1A8, Canada and Protein Engineering Network of Centres of Excellence (PENCE)

AND

IMRE G. CSIZMADIA[1]

Department of Chemistry, University of Toronto, Toronto, ON M5S 1A1, Canada

Received February 11, 1994

TING-HUA TANG, DENNIS M. WHITFIELD, STEPHEN P. DOUGLAS, JIRI J. KREPINSKY, and IMRE G. CSIZMADIA. Can. J. Chem. **72**, 1803 (1994).

The possibility of complexation between an acidic promoter like BF_3 and the alcoholic aglycone has been studied as a key mechanistic intermediate in glycosylation reactions operating via an electron-deficient anomeric carbon. The BF_3 complexes at O3′, O4′, O5′, and N3 of the model compound of 3′-,4-*N*-diacetyl-2′-deoxyribocytosine (**1**) have been studied. The last regioisomer of the four BF_3 complexes was found to have the weakest hydrogen bond and yet was the most stable isomer energetically. Furthermore, the O5′ nucleophilicity of this isomer was the most pronounced, as evaluated by Bader-type charge density topological analysis at the HF/6-31G**//HF/3-21G level of theory. This indicates that such a complex will make glycosylation at the O5′ oxygen possible.

TING-HUA TANG, DENNIS M. WHITFIELD, STEPHEN P. DOUGLAS, JIRI J. KREPINSKY et IMRE G. CSIZMADIA. Can. J. Chem. **72**, 1803 (1994).

On a étudié la possibilité de complexation entre un promoteur acide comme le BF_3 et une aglycone alcoolique comme modèle de l'intermédiaire mécanistique des réactions de glycosylation se produisant par le biais d'un atome de carbone anomère déficient en électron. On a étudié les complexes du BF_3 avec les positions O3′, O4′, O5′, et N3 du composé modèle, la 3′-,4-*N*-diacétyl-2′-déoxyribocytosine (**1**). On a trouvé que le dernier des quatre complexes du BF_3 possède la liaison hydrogène la plus faible, mais que d'un point de vue énergétique il s'agit de l'isomère le plus stable. De plus, suivant une évaluation par une analyse topologique de la densité de charge du type Bader faite au niveau HF/6-31G**//HF/3-21G de la théorie, le caractère nucléophile du O5′ de cet isomère est le plus prononcé. Ces résultats indiquent qu'un tel complexe rend la glycosylation de l'oxygène O5′ possible.

[Traduit par la rédaction]

1. Introduction

Certain hydroxyl groups of carbohydrates do not undergo glycosylation (1,2) using Koenigs–Knorr conditions or its variants for the formation of glycosidic bonds. In some cases the secondary hydroxyl is far more reactive than the primary one. Such anomalous reactivity makes difficult the planning and execution of multistep oligosaccharides syntheses. Furthermore, the application of biologically active oligosaccharides, glycopeptides, and glycolipids in biomedical sciences, biotechnology industries, and new generation of therapeutic agents is becoming very important and therefore a deeper understanding of this unusual reactivity is essential for the rational development of oligosaccharide syntheses.

The reaction mechanism for Koenigs–Knorr type of glycosylation reactions (2) (see Scheme 1*a*) involves the activation of the glycosyl donor by the promoter to generate a reactive electron-deficient species which is approached by a nucleophilic alcohol acceptor, and after proton transfer the glycoside is formed.

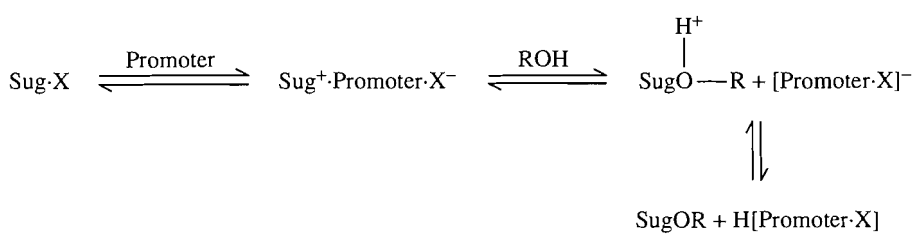

SCHEME 1*a*

Signs +, − do not necessarily describe separate charges. They just refer to electron deficiency (+) or surplus (−). Nowhere in this mechanism is an interaction of the promoter with the acceptor considered. Our recent observations (2, 3), however, suggest that complexation of the promoter by the acceptor can alter dramatically the glycosylation. This conclusion is further supported by our recent theoretical consideration (1). Somewhat similar observations were made a long time ago when certain deriva-

[1]To whom correspondence may be addressed.

Can. J. Chem. Downloaded from www.nrcresearchpress.com by 85.192.166.187 on 09/08/12
For personal use only.

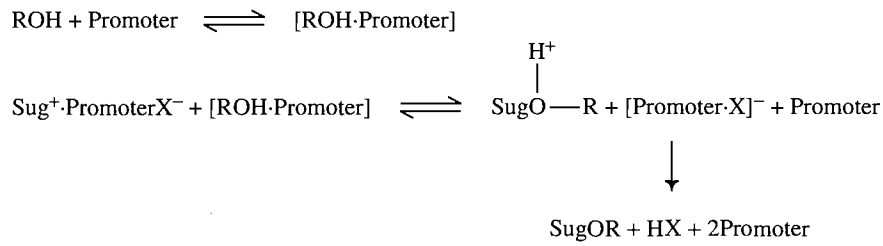

SCHEME 1*b*

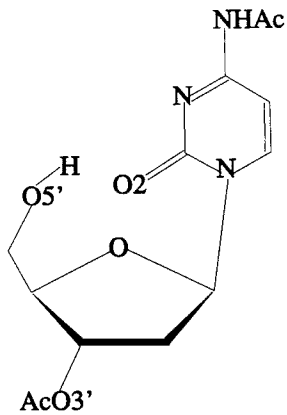

FIG. 1. The 3′-*O*-,4-*N*-diacetyl-2′-deoxyribocytosine (**1**) in its *syn* conformation.

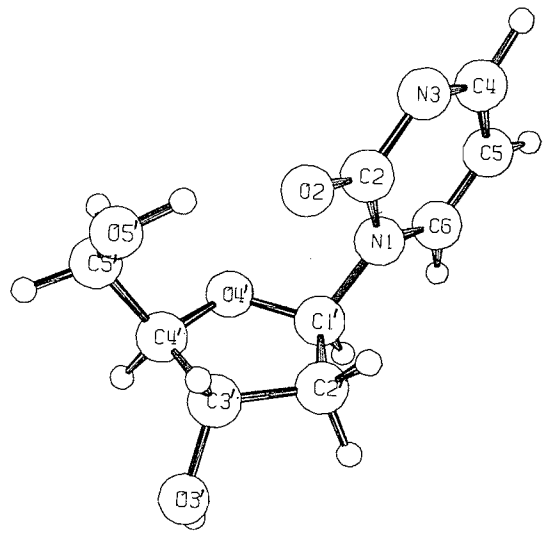

FIG. 2. Model compound (**3**) mimicing 2-deoxycytidine derivative (**1**) and the atomic labels of interest.

tives of the primary carbohydrate hydroxyl were found to enhance reactivity of the otherwise unreactive primary hydroxyls (4, 5). In the case of the galactosylation of the 5′-hydroxyl of nucleosides complexation of the nucleosides by the promoter has been suggested to favourably improve reactivity. In the present work we did a theoretical study on a prototypic Lewis acid promoter BF_3 and its complexes with the nucleoside (Scheme 1*b*).

2. Computational methods

The Gassian 92 program (6) has been used and the computations were carried out on an Apollo DN 10000 and an HP-750 minicomputer at the Department of Chemistry, University of Toronto. The starting or input geometries for the *ab initio* computation were constructed on the basis of model compound reported in our previous publication (1). *Ab initio* energies, reported in this paper, are for the fully optimized geometries, obtained by energy gradient optimization at the HF/3-21G level of theory (7). Single point calculations were performed at the HF/6-31G**//HF/3-21G level of theory (8).

The Bader-type topological analysis of charge density (9, 10) was performed at the HF/6-31G** polarized basis set on the HF/3-21G optimized geometries. The topological properties of the electronic density were determined by the atoms in molecules theory (9, 10) using the AIMPAC program.[2]

3. Results and discussion

I. Molecular Structure of Model Compounds

In our previous study (1) model compound **2** has been used to mimic 3′-*O*-,4-*N*-diacetyl-2′-deoxyribocytosine (**1**) (c.f. Figs. 1 and 2). Compound **1** has been shown to have a *syn* conformation in dichloromethane (DCM) that is stabilized by O5′—H···O2 hydrogen bonding. Our previous study (1) confirmed that model compound **2** (c.f. Fig. 3(*a*)) also has the same type of hydrogen bonding as compound **1** and that the hydrogen bonded structure is the global minimum energy conformation in the gas phase. However, model compound **2** has the shortcoming of not possessing a secondary OH at its 3′ position of the furanose ring.

We now wish to report the results of the computations on model compound **3**, which has an OH at C3′, thus the primary and secondary OH group may be compared (c.f. Fig. 2). Model compound **3** still lacks the 4-acetamido group from the heteroaromatic ring of the parent compound **1**. Presumably, this group does not significantly affect the molecular structure, complex stability and the hydroxyl reactivity studied here. Figure 3 and Table 1 clearly illustrate that the structures of the two model compounds (**2** and **3**) are very similar, both having the C5′—OH···O2 hydrogen bond.

II. Structure and stability of Lewis acid (BF_3) complexes with the model compounds

Lewis acids, such as BF_3 usually used as an ether complex, are frequently used as promoters in glycosylation reactions. In fact, such promoters have been shown to overcome the unreactivity of compound **1** in glycosylation reaction. It is postulated that this effect is caused by complexation with aglycone. There are a number of electronegative sites (lone pairs) in model compound **3** that may complex with the electropositive BF_3. Complexation of BF_3 by alcohols and amines is well known, for example see ref. 11. In the present study the following sites (labelled A, B, C, and D) were investigated.

[2]Available from Professor R.F.W. Bader's laboratory, McMaster University, Hamilton. ON L8S 4M1, Canada.

Can. J. Chem. Downloaded from www.nrcresearchpress.com by 85.192.166.187 on 09/08/12
For personal use only.

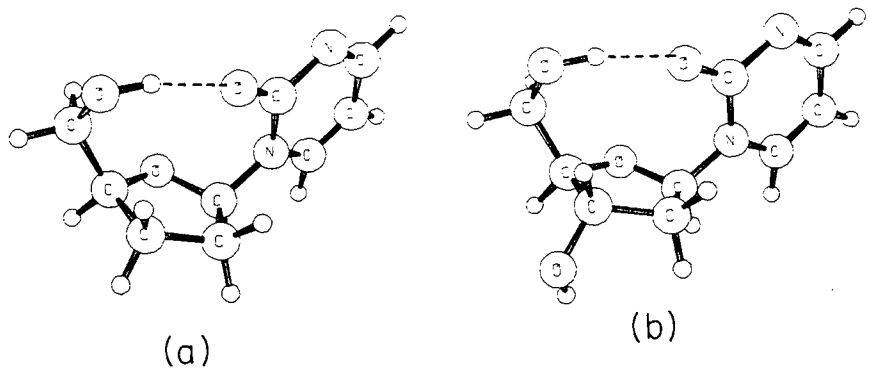

FIG. 3. 3-21G optimized geometries of model compounds **2** (*a*) and **3** (*b*).

TABLE 1. 3-21G optimized geometrical parameters of model compounds **2** and **3**

Geometrical parameters	Model compound 2	Model compound 3
	Bond lengths (Å)	
N1—C2	1.3975	1.3977
C2—N3	1.3820	1.3809
N3—C4	1.2880	1.2881
C4—C5	1.4217	1.4223
C5—C6	1.3429	1.3425
N1—C6	1.3609	1.3618
C2–O2	1.2177	1.2179
N1—C1′	1.4799	1.4760
H...O2	1.7479	1.7470
C1′—C2′	1.5497	1.5450
C2′—C3′	1.5511	1.5470
C3′—C4′	1.5419	1.5434
C1′—O4′	1.4125	1.4174
C4′—O4′	1.4627	1.4589
C4′—C5′	1.5422	1.5395
C5′—O5′	1.4266	1.4272
O5′—H	0.9724	0.9722
C5′—H5′	1.0838	1.0834
C5′—H5″	1.0802	1.0793
C3′—O3′		1.4405
O3′—H3′		0.9672
	Bond angles (deg)	
N1C1′O4′	110.14	109.87
C1′N1C6	119.62	119.86
N1C6C5	121.49	121.38
C4C5C6	115.96	116.01
N3C4C5	123.60	123.61
C2N1C1′	119.01	118.71
O2C2N3	123.23	123.40
C1′C2′C3′	105.42	106.35
C2′C3′C4′	106.46	105.65
C2′C1′O4′	108.27	107.74
C3′C4′C5′	113.86	113.87
C4′C5′O5′	115.16	114.75
C5′O5′H	109.56	109.90
C4′C5′H5′	106.82	107.00
C4′C5′H5″	108.31	108.31
C4′C3′O3′		112.63
C3′O3′H3′		110.71

TABLE 1. (*concluded*)

Geometrical parameters	Model compound 2	Model compound 3
	Dihedral angles (deg)	
C1′C2′C3′—C4′	−0.83	−1.20
O4′C1′C2′—C3′	1.70	2.65
C2′C3′C4′—C5′	−121.71	−122.59
C3′C4′C5′—O5′	20.38	22.46
C4′C5′O5′—H	63.93	64.28
C3′C2′C1′—N1	124.94	125.25
C3′C4′C5′—H5′	145.84	147.80
C3′C4′C5′—H5″	−97.58	−95.24
C2′C1′N1—C6	127.40	127.39
C5C6N1—C1′	176.72	176.61
C4C5C6—N1	−1.10	−1.14
N3C4C5—C6	−0.02	−0.03
C2N1C1′—04′	64.24	63.41
C4N3C2—O2	−180.30	−180.38
O3′C3′C2′—C1′		121.71
H3′O3′C3′—C4′		58.16

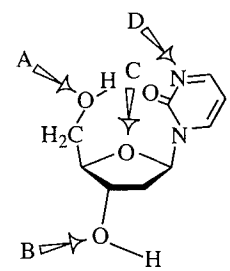

3

In the case of nitrogen there is only one lone pair; therefore only one BF_3 complex may be formed. However, in the case of oxygen there are two lone pairs and therefore two BF_3 complexes may be formed. These two complexes may be related to one another as enantiomeric pairs.[3] In the present study, arbitrarily, only one of these two structures was studied. When O3′ and O4′ were complexed the *S* configuration and when O5′ was complexed the *R* configuration were studied (details to be discussed

[3]Numbers 1, 2, and 3 represent the order of piorities the ligands are attached to the oxygen in assigning the *R* and *S* absolute configurations.

Can. J. Chem. Downloaded from www.nrcresearchpress.com by 85.192.166.187 on 09/08/12
For personal use only.

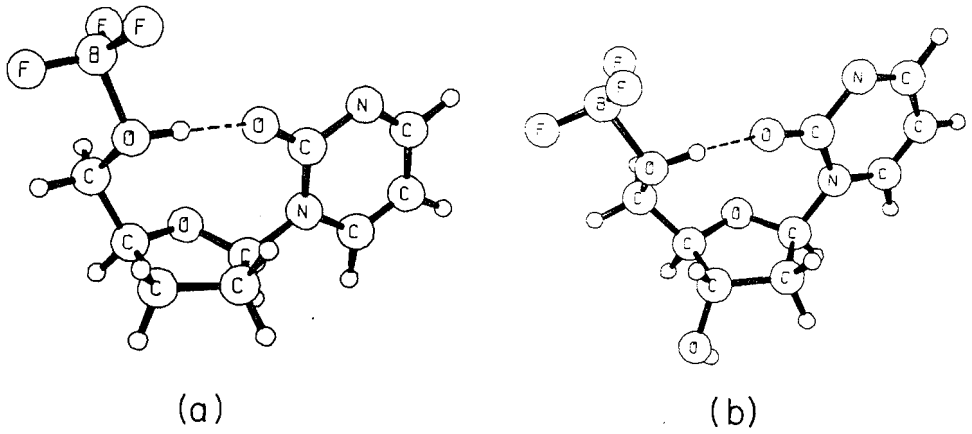

FIG. 4. 3-21G optimized geometries of BF_3 complexes with the model compounds **2** (**2***A*) and **3** (**3***A*).

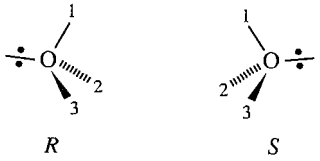

later). Figure 4 shows the BF_3 complexes of model compounds **2** and **3** with the BF_3 attached to O5′. These complexes are labelled as **2***A* and **3***A*. These two structures seem to be remarkably similar as can be judged graphically (Fig. 4) or numerically (Table 2). All four BF_3 complexes of model compound **3**, three of which (**3***A*, **3***B*, and **3***C*) involve complexation with the oxygen atoms (O5′, O3′, and O4′) of the furanose ring as well as the fourth complex, with complexation at nitrogen atom N3 (**3***D*) of the heteroaromatic ring, are shown in Fig. 5. All geometrical parameters are summarized in Table 2. The energetics associated with the complexation is given in Table 3. The stabilization energies associated with the Lewis complex formation are given in parenthesis in Table 3. It is noticeable that there is a marked change in these ΔE values on going from 3-21G//3-21G to the 6-31G**//3-21G level of theory. It is not clear at this stage which one of the two sets of numbers is more reliable. The values obtained at 6-31G**//3-21G level of theory could be more reliable because of the larger 6-31G** basis set but it was computed at a fixed geometry optimized at the 3-21G level of theory. For this reason a systematic basis set study has been carried out on a model complexation reaction:

$$C_2H_5OH + BF_3 \rightarrow C_2H_5O(H)\cdot BF_3$$

Geometry optimizations were carried out with three different basis sets (STO-3G, 3-21G, and 6-31G**) and the complexation energies were evaluated at these levels of theory. In addition, single point calculations were performed for the STO-3G and 3-21G geometry optimizations at several basis set levels up to 6-31G**. The results of a total of eight such computations are given in Table 4. Clearly, the single point calculations at the 6-31G** level of theory, irrespective of whether the STO-3G or 3-21G basis sets were used for the geometry optimization, are quite close to each other and they are also very close to the best results obtained by geometry optimization at the HF/6-31G**// HF/6-31G** level of theory. Thus we may regard the BF_3 complex formation energies for **3***A*, **3***B*, **3***C*, and **3***D* of −13.88, −8.57, −10.49, and −14.58 kcal/mol, respectively as the best estimates of the true values. Such semiquantitative results are expected to show the correct relative abundance of these BF_3 complexes (in percentage):

3*D*	>	**3***A*	>	**3***C*	>	**3***B*
88.3		11.6		0.1		0.0

with a very high population (p_i = 88.3%) calculated for **3***D* from the Boltzmann distribution at 25°C:

$$[1] \quad p_i = \frac{e^{-\Delta E_i/RT}}{\sum_{i=1}^{\text{all isomers}} e^{-\Delta E_i/RT}}$$

Transition metals like Ag(I) and Cu(II) are known experimentally to preferentially coordinate to the N3 of cytosine, suggesting a similarity with BF_3 complexes (12). On the basis of Boltzmann population (p_i) we can eliminate isomers **3***B* and **3***C* as likely candidates for glycosylation since they are present in minute proportions only. However, isomers **3***D* and **3***A* could, at least in principle, compete as nucleophiles in the glycosylation reaction. Whether they do or not depends on the relative nucleophilicities of the oxygen attached to C5′. It follows that the nucleophilicity of the O5′ lone pairs must be evaluated for the isomers of BF_3 complexes and that of the parent compound (II). Such an analysis can be performed using the Bader-type charge density analysis (6).

III. Charge density distribution analysis of Lewis acid (BF_3) complexes of model compounds

In addition to the energetic considerations mentioned above, there is an alternative way to analyse hydrogen bonding as has been discussed in the literature (1). This involves the topological analysis of the charge density distribution, which can be used to analyse intramolecular hydrogen bonding. Some insight should be gained concerning the reactivity of the furanose OH groups in particular.

Recently, inter- and intramolecular hydrogen bondings have been analysed by using Bader-type topological analysis of charge density distribution (9, 10, 13). The topological properties of the electronic density distribution is based on the gradient vector field of the electronic density $\nabla\rho(\boldsymbol{r})$, and on the Laplacian of the electronic density $\nabla^2\rho(\boldsymbol{r})$. Several excellent reviews have been published (9, 10) on this subject, therefore

Can. J. Chem. Downloaded from www.nrcresearchpress.com by 85.192.166.187 on 09/08/12
For personal use only.

Can. J. Chem. Downloaded from www.nrcresearchpress.com by 85.192.166.187 on 09/08/12
For personal use only.

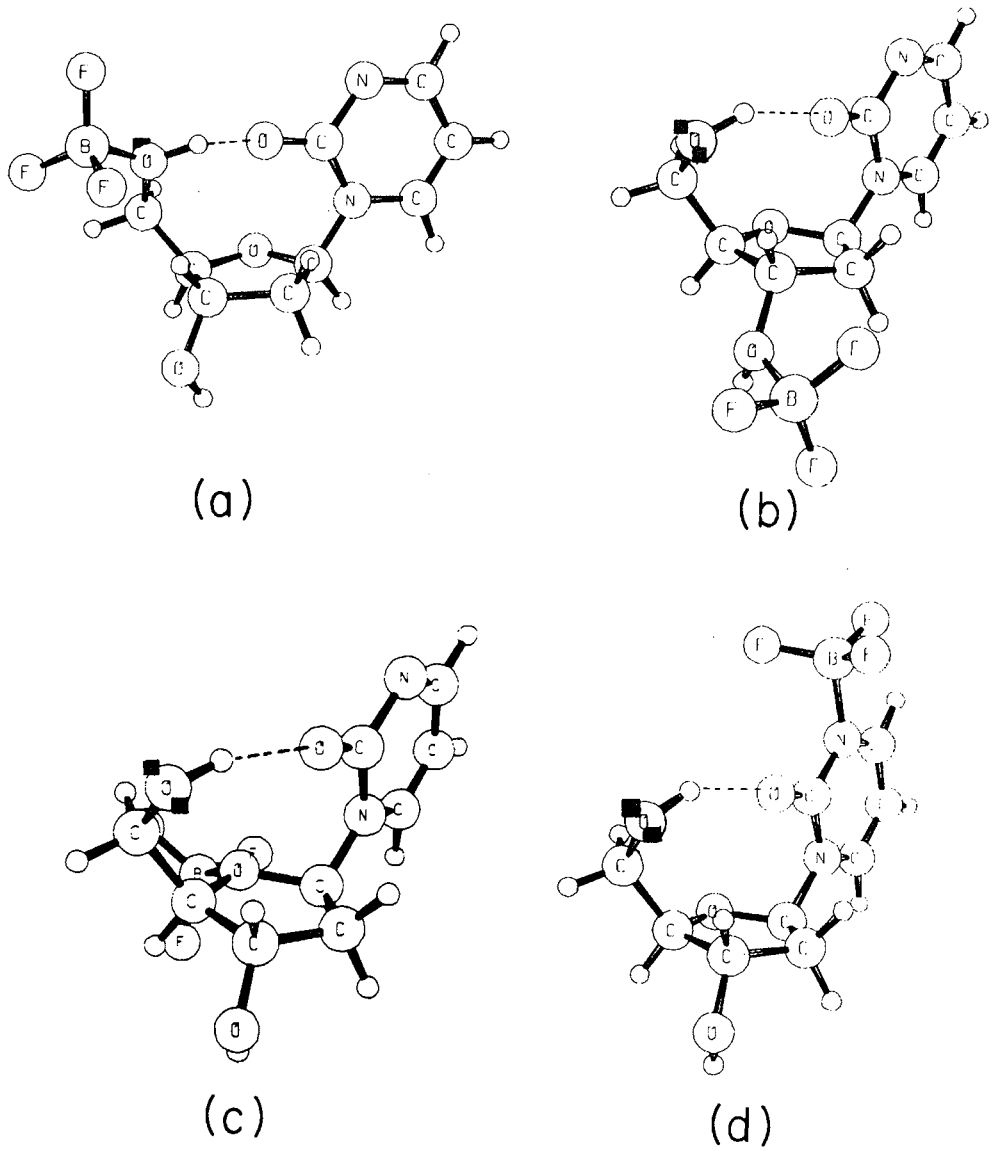

FIG. 5. 3-21G optimized geometries of BF_3 complexes with the model compound **3**: **3***A* (*a*), **3***B* (*b*), **3***C* (*c*), and **3***D* (*d*). The nonbonded Laplacian concentrations of O5′ are indicated by solid squares.

only a brief description of selected topological parameters, pertinent to the present work, is discussed here. The electronic charge distribution of a molecule is described by $\rho(\boldsymbol{r}, \boldsymbol{X})$ where **r** is a variable position vector in ordinary three-dimensional space with components r_1, r_2 and r_3 and $\boldsymbol{X}$ represents a particular set of nuclear coordinates in the space corresponding to the nuclear configurations of the molecule in question. An atom in a molecule is defined (9, 10) as a region of real three-dimensional space bounded by a zero-flux surface of the gradient vector field of $\rho(\boldsymbol{r})$; that is, a surface for which all points on this surface satisfy the equation

$$[2] \quad \nabla\rho(\boldsymbol{r})\cdot n(\boldsymbol{r}) = 0$$

where $n(\boldsymbol{r})$ is the unit vector normal to the surface at $\boldsymbol{r}$. Two interacting atoms in a molecule form a critical point in the electronic density, where

$$[3] \quad \nabla\rho(\boldsymbol{r}) = 0$$

called a bond critical point (BCP). The pairs of gradient paths, which originate at a BCP and terminate at the neighbouring nuclei ("attractor" in the gradient field of $\rho(\boldsymbol{r})$) define a line, through which electronic charge distribution, $\rho(\boldsymbol{r})$, is a maximum with respect to any lateral displacement, called an atomic interaction line. The presence of such a line, linking two nuclei in a molecule, which exists in a minimum energy geometry, implies that the two atoms are bounded to one another and in this instance this line is called a bond path. The necessary condition for two atoms to be bonded to one another is therefore that their nuclei be linked by a bond path. The network of bond paths for a molecule in a given nuclear configuration $\boldsymbol{X}$ defines the molecular graph which essentially is the union of the closures of the bond paths. Such a topological graph usually corresponds to the commonly drawn chemical bond network. The charge density, $\rho(r)$, at the bond critical point is related to the bond order and therefore the bond strength (14). The eigenvalues associated with the second derivatives of ρ, at the bond critical point (λ_1, λ_2, and λ_3) indicate how rapidly the density

TABLE 2. 3-21G optimized geometries of the BF_3 complexes of model compounds **2** and **3**

Geometrical parameters	Model compound complexes				
	2*A*	**3***A*	**3***B*	**3***C*	**3***D*
	Bond lengths (Å)				
N1—C2	1.3893	1.3895	1.3969	1.4024	1.3971
C2—N3	1.3720	1.3713	1.3774	1.3747	1.3858
N3—C4	1.2913	1.2912	1.2890	1.2890	1.3082
C4—C5	1.4191	1.4199	1.4228	1.4235	1.3958
C5—C6	1.3434	1.3428	1.3420	1.3394	1.3553
N1—C6	1.3630	1.3614	1.3633	1.3736	1.3450
C2—O2	1.2250	1.2251	1.2196	1.2189	1.2067
N1—C1′	1.4803	1.4761	1.4708	1.4510	1.4917
H…O2	1.5001	1.4994	1.7594	1.7635	1.8432
C1′—C2′	1.5492	1.5452	1.5450	1.5383	1.5428
C2′—C3′	1.5524	1.5489	1.5335	1.5529	1.5489
C3′—C4′	1.5487	1.5524	1.5364	1.5377	1.5432
C1′—O4′	1.4159	1.4207	1.4226	1.4577	1.4096
C4′—O4′	1.4571	1.4536	1.4525	1.4977	1.4652
C4′—C5′	1.5265	1.5229	1.5494	1.5433	1.5434
C5′—O5′	1.4565	1.4561	1.4258	1.4250	1.4279
O5′—H	1.0041	1.0038	0.9721	0.9718	0.9684
C5′—H5′	1.0776	1.0775	1.0815	1.0803	1.0823
C5′—H5″	1.0729	1.0731	1.0785	1.0785	1.0786
C3′—O3′		1.4357	1.4819	1.4341	1.4382
O3′—H3′		0.9673	0.9667	0.9675	0.9672
O5′—B5′	1.5687	1.5726			
O3′—B3′			1.6123		
N3—B3					1.6620
O4′—B4′				1.5823	
B5′—F′	1.3699	1.3893			
B5′—F″	1.3899	1.3812			
B5′—F‴	1.3828	1.3695			
B3′—F′			1.3771		
B3′—F″			1.3635		
B3′—F‴			1.3768		
B3—F′					1.3934
B3—F″					1.3735
B3—F‴					1.3740
B4′—F′				1.3721	
B4′—F″				1.3757	
B4′—F‴				1.3880	
	Bond angles (deg)				
N1C1′O4′	110.22	110.11	109.76	109.29	109.12
C1′N1C6	119.54	119.72	120.35	119.68	120.34
N1C6C5	121.30	121.20	121.13	120.57	121.98
C4C5C6	116.07	116.12	116.13	116.55	116.38
N3C4C5	123.36	123.36	123.61	123.66	122.05
C2N1C1′	119.38	119.16	118.17	118.95	117.64
O2C2N3	123.01	123.19	123.79	124.03	123.73
C1′C2′C3′	105.80	106.71	105.72	108.44	106.17
C2′C3′C4′	105.80	104.96	106.98	107.23	105.69
C2′C1′O4′	108.17	107.67	107.62	104.59	108.17
C3′C4′C5′	115.18	115.27	112.99	115.09	114.08
C4′C5′O5′	113.04	112.60	114.44	114.12	114.74
C5′O5′H	114.12	114.88	109.26	109.89	110.34
C4′C5′H5′	109.30	109.49	106.38	107.48	107.13
C4′C5′H5″	111.21	111.15	108.56	107.55	108.24
C4′C3′O3′		109.09	111.11	112.69	112.48
C3′O3′H3′		111.19	116.66	111.41	111.03
C5′O5′B5′	122.98	122.84			
C3′O3′B3′			120.23		
C4N3B3					118.60
C1′O4′B4′				121.37	

Can. J. Chem. Downloaded from www.nrcresearchpress.com by 85.192.166.187 on 09/08/12
For personal use only.

TABLE 2. (*concluded*)

Geometrical parameters	Model compound complexes				
	2*A*	**3***A*	**3***B*	**3***C*	**3***D*
O5′B5′F′	106.33	104.89			
O5′B5′F″	105.33	104.20			
O5′B5′F‴	104.29	106.09			
O3′B3′F′			102.04		
O3′B3′F″			107.64		
O3′B3′F‴			101.23		
N3B3F′					101.83
N3B3F″					106.95
N3B3F‴					106.91
O4′B4′F′				106.66	
O4′B4′F″				104.51	
O4′B4′F‴				102.53	
	Dihedral angles (deg)				
C1′C2′C3′—C4′	0.12	−0.39	1.21	−2.93	−1.58
O4′C1′C2′—C3′	2.03	3.21	−0.55	1.17	2.57
C2′C3′C4′—C5′	−123.57	−124.57	−122.76	−116.53	−122.06
C3′C4′C5′—O5′	33.56	37.41	13.25	13.50	16.47
C4′C4′O5′—H	51.33	49.50	72.69	72.62	74.31
C3′C2′C1′—N1	125.58	126.42	121.43	122.26	124.28
C3′C4′C5′—H5′	154.04	157.78	138.14	139.47	141.97
C3′C4′C5′—H5″	−83.63	−79.66	−104.69	−103.69	−100.97
C2′C1′N1—C6	123.93	123.79	126.77	135.91	126.51
C5C6N1—C1′	177.84	177.84	176.67	179.95	176.12
C4C5C6—N1	−1.00	−1.01	−1.14	−1.54	−1.19
N3C4C5—C6	−0.04	−0.02	0.80	−1.49	0.26
C2N1C1′—O4′	62.41	61.75	62.45	68.71	61.99
C4N3C2—O2	−180.70	−180.66	−180.46	−176.86	−180.27
O3′C3′C2′—C1′		121.37	121.20	121.10	121.54
H3′O3′C3′—C4′		62.11	43.18	59.30	56.60
C4′C5′O5′—B5′	250.04	248.85			
C5′O5′B5′—F′	216.30	94.63			
C5′O5′B5′–F″	95.99	−23.84			
C5′O5′B5′—F‴	−22.30	−145.26			
C4′C3′O3′—B3′			−171.09		
C3′O3′B3′—F′			−12.75		
C3′O3′B3′—F″			108.38		
C3′O3′B3′—F‴			−130.97		
H4C4N3—B3					−0.30
C4N3B3—F′					1.24
C4N3B3—F″					119.81
C4N3B3—F‴					−117.12
C3′C4′O4′—B4′				158.50	
C4′O4′B4′—F′				82.68	
C4′O4′B4′—F″				−38.46	
C4′O4′B4′—F‴				202.77	

TABLE 3. Total SCF energies of BF_3, model compounds **I**, **II** and their BF_3 complexes (**2***A*, **3***A*, **3***B*, **3***C*, and **3***D*)[a]

Molecule	3-21G//3-21G	6-31G**//3-21G
BF_3	−321.4658448	−323.1930349
2	−677.4817405	−681.2890036
2*A*	−999.0256713 (−49.00)	−1004.5070443 (−15.69)
3	−751.9135340	−756.1411984
3*A*	−1073.4544534 (−47.11)	−1079.3268314 (−13.38)
3*B*	−1073.4389882 (−37.41)	−1079.3478830 (−8.57)
3*C*	−1073.4475096 (−42.75)	−1079.3509503 (−10.49)
3*D*	−1073.4427618 (−39.77)	−1079.3574757 (−14.58)

[a]Total SCF energies are given in au (Lewis complex formation energies in parentheses are given in kcal/mol).

changes, away from the bond critical point (BCP), r_b. These three eigenvalues (λ_1, λ_2, and λ_3) represent the curvatures of charge density along the three different directions. For a normal single bond, such as C—C bond in ethane, the two negative curvatures (λ_1 and λ_2), perpendicular to the bond line, are equal. However, in the case of a double bond, one curvature (in the direction of the π bond) will be much smaller than the other. This difference may be described by the ellipticity of the bond, which is defined as

$$[4] \quad \epsilon = \lambda_1/\lambda_2 - 1$$

For a single bond $\lambda_1 \approx \lambda_2$, therefore $\epsilon \approx 0$. For a double bond $\lambda_1 > \lambda_2$, therefore $\epsilon > 0$. For an aromatic system, in general, ϵ is

Can. J. Chem. Downloaded from www.nrcresearchpress.com by 85.192.166.187 on 09/08/12
For personal use only.

TABLE 4. The SCF energies and Lewis complex formation energies of the model complexation reaction: $C_2H_5OH + BF_3 \rightarrow C_2H_5O(H) \cdot BF_3$

	EtOH[a]	BF_3[a]	EtO(H)BF_3[a]	ΔE[b]
STO-3G//STO-3G	−152.1326749	−318.6619373	−470.8164490	−16.10
3-21G//STO-3G	−153.2226809	−321.4644300	−474.7401289	−33.26
3-21G**//STO-3G	−153.2607916	−321.4644300	−474.7794731	−34.04
6-31G**//STO-3G	−154.0858413	−323.1952863	−477.2998506	−11.75
3-21G//3-21G	−153.2226809	−321.4658447	−474.7510240	−39.22
3-21G**//3-21G	−153.2642608	−321.4658447	−474.7890890	−37.01
6-31G**//3-21G	−154.0881899	−323.1930357	−477.2987230	−10.98
6-31G**//6-31G**	−154.0901617	−323.1954852	−477.3035598	−11.24

[a]SCF energies in atomic unit (au).
[b]Formation energies in kcal/mol.

Can. J. Chem. Downloaded from www.nrcresearchpress.com by 85.192.166.187 on 09/08/12
For personal use only.

the between a typical single and a typical double bond. Furthermore, for triple bonds, since $\lambda_1 \approx \lambda_2$, again ϵ is equal or close to zero. In practice, the trace or the sum of the second partial derivative values

$$[5] \quad \nabla^2\rho(\boldsymbol{r}_b) = \Sigma_{j=1,3}\partial^2\rho(\boldsymbol{r}_b)/\partial x_j^2$$

at the bond critical point (BCP), denoted by $\boldsymbol{r}_b$, is negative for a covalent interaction. The trace of $\nabla^2\rho(\boldsymbol{r}_b)$ is positive for an interaction between closed-shell system (including ionic interactions). For a very polar covalent bond the trace could be close to zero: either a small positive or a small negative value.

A critical point, at which $\rho(\boldsymbol{r})$ has one negative curvature and two positive curvatures, can be defined as a ring critical point. The existence of a ring critical point in a molecule indicates that the molecule contains a ring structure.

Of particular interest to this study is the Laplacian of the electronic charge density, the quantity at any point,

$$[6] \quad \nabla^2\rho(\boldsymbol{r}) = \Sigma_{j=1,3}\partial^2\rho(\boldsymbol{r})/\partial x_j^2$$

determines the regions of space wherein electronic charge is locally concentrated or depleted. From the definition of a second derivative, one finds that $\rho(\boldsymbol{r})$ is greater than the average of its values over an infinitesimal sphere centered on $\boldsymbol{r}$, when $\nabla^2\rho(\boldsymbol{r}) < 0$, and $\rho(\boldsymbol{r})$ is less than this average when $\nabla^2\rho(\boldsymbol{r}) > 0$. Thus a local maximum (or minimum) in $-\nabla^2\rho(\boldsymbol{r})$ signifies a local concentration (or depletion) of electronic charge. It has been reported (15) that these magnitudes of $-\nabla^2\rho(\boldsymbol{r})$ can be used to study the preferred orientation of electrophilic and nucleophilic attack. The site of Laplacian depletion favours nucleophilic and the site of Laplacian concentration favours electrophilic attack. Moreover, in some series of closely related molecules the Laplacian can give quantitative formation concerning relative protonation energies (16). The numbers, locations, and relative sizes of the bonded and nonbonded concentration of charge in the valence shell of a bonded atom as determined by the Laplacian of $\rho(\boldsymbol{r})$ are found to be in generally good agreement with corresponding properties that are ascribed to bonded and nonbonded pairs in Gillespie's VSEPR model of molecular geometry (17).

The theory of atoms in molecules has been widely applied to many chemical problems including the description of hydrogen-bonded systems (see for example refs. 6(*a*), 8, 9, and 10).

Table 5 shows the computed topological properties of electronic density for compounds **2**, **2***A*, **3**, **3***A*, **3***B*, **3***C*, and **3***D*. Comparing all the data in Table 5 (i.e. the ellipticity, ϵ; the density at the bond critical points (BCP), ρ_b; the Laplacian of the density at the BCP, $\nabla^2\rho(\boldsymbol{r}_b)$; and the two distances X—BCP and BCP—Y along the bond paths), it is clear that model compounds **2** and **3** as well as their BF_3 complexes at O5′ (**2***A* and **3***A*) are very similar in terms of the topological properties of the electronic density at the BCP. Furthermore, the ρ_b values associated with the O5′H···O2 hydrogen bond of **3***B*, **3***C*, and **3***D*, which are 0.0327, 0.0322, and 0.0268, respectively, are considerably smaller (about 50%) than that of the **3***A* complex (0.0604). Last, but not least, the magnitudes of the ρ_b values at the BCP of O5′H···O2 hydrogen bond have the following order:

$$3B \sim 3C > 3D$$

indicating that the above hydrogen bond is the weakest in the **3***D* isomer.

The outcome of any glycosylation reaction is critically dependent on the nucleophilicity of the electron pairs of the oxygen O5′. There is one lone pair in **3***A* since the other lone pair is tied up with the BF_3 complexation; however, all other isomers of the complex (**3***B*, **3***C*, and **3***D*) have two lone pairs. These two lone pairs are classified according to the location of these concentrations as *endo* and *exo* (cf. Fig. 6(*a*)). As a comparison, Fig. 6(*b*) shows the contour line diagram of calculated Laplacian concentrations of model compound **3** in a plane containing O5′— and the positions of concentrations associated with the two lone pairs. Also, Fig. 7(*a*) shows the projections of the two nonbonded Laplacian concentrations of O5′ are coincident on the C5′—O5′—H plane and Fig. 7(*b*) is the relief map of calculated Laplacian concentration of model compound **3** at the same C5′—O5′—H plane. Figure 5 shows the molecular structures and the locations of these concentrations that are associated with the *endo* and *exo* lone pairs. The magnitude of the concentrations, that can be used as a measure of O5′ nucleophilicity (15), are summarized in Table 6.

As may be judged from the values of these concentrations the "*exo* lone pair" (i.e. the *exo* sites) are more nucleophilic than the *endo* sites. Furthermore, **3***A* (in which O5′ is complexed) is not very nucleophilic. However, O5′ is more nucleophilic (larger magnitude of Laplacian concentration) in complex **3***D* than in any of the other isomers. The *exo* concentrations, measuring the nucleophilicities of O5′ at its *exo* site are plotted in Fig. 8. Clearly **3***A* is out of line since the nucleophilicity of O5′ cannot be compared to that of the other isomers simply because O5′ is the site of complexation. However, the other sites isomers (**3***B*, **3***C*, and **3***D*) show a reasonable trend.

TABLE 5. Topological properties at bond critical points of model compound **2**, **3** and their BF_3 complexes (6-31G**//3-21G)[a,b]

Molecule	Bond (X--Y)	ε	$\rho_b(r)$	$\nabla^2\rho(r_b)$	BCP → X (X = H, C, B)	BCP → Y (Y = O, N)
2	H---O5′	0.0236	0.3435	−2.1311	0.3409(0.1803)	1.5281(0.8086)
	H----O2	0.0407	0.0305	0.1244	1.1049(0.5845)	2.2129(1.1710)
	C5′--O5′	0.0284	0.2597	−0.4336	0.8771(0.4641)	1.8154(0.9607)
	C4′--C5′	0.0132	0.2167	−0.5141		
	C3′--C4′	0.0423	0.2492	−0.6462		
	C2′--C3′	0.0068	0.2461	−0.6224		
	C1′--C2′	0.0221	0.2477	−0.6483		
	C1′--O4′	0.1633	0.2620	−0.5793		
	C4′--O4′	0.0486	0.2371	−0.1847		
	Ring 1		0.0358	0.2512		
	C1′--N1	0.1576	0.2489	−0.7145		
	C6---N1	0.0086	0.3014	−0.7872		
	C5---C6	0.4289	0.3586	−1.2515		
	C4---C5	0.1382	0.2913	−0.8472		
	C4---N3	0.1153	0.3792	−0.8248		
	C2---N3	0.0656	0.2950	−0.9490		
	C2---O2	0.1089	0.4114	0.0186	0.7539(0.3989)	1.5564(0.8236)
	C2---N1	0.0618	0.2868	−1.0020		
	Ring 2		0.0198	0.1540		
2A	H---O5′	0.0220	0.3067	−2.1295	0.3096(0.1638)	1.5882(0.8402)
	H----O2	0.0425	0.0600	0.2172	0.8654(0.4578)	1.9797(1.0473)
	C5′--O5′	0.0906	0.2167	0.0426	0.8685(0.4594)	1.8843(0.9968)
	C4′--C5′	0.0090	0.2691	−0.7602		
	C3′--C4′	0.0391	0.2502	−0.6523		
	C2′--C3′	0.0133	0.2425	−0.6076		
	C1′--C2′	0.0209	0.2530	−0.6753		
	C1′--O4′	0.1861	0.2673	−0.4797		
	C4′--O4′	0.0270	0.2308	−0.2217		
	Ring 1		0.0362	0.2566		
	C1′--N1	0.1879	0.2522	−0.6653		
	C6---N1	0.0165	0.3205	−0.6363		
	C5---C6	0.3823	0.3514	−1.2053		
	C4---C5	0.1596	0.3130	−0.9656		
	C4---N3	0.0665	0.3794	−0.7814		
	C2---N3	0.0716	0.3445	−1.4346		
	C2---O2	0.0794	0.4066	−0.0134	0.7565(0.4002)	1.5586(0.8245)
	C2---N1	0.0302	0.3111	−0.8406		
	Ring 2		0.0224	0.1831		
	B5′--O5′	0.0305	0.1061	0.5406	0.9404(0.4975)	2.0249(1.0711)
	B5′--F	0.0121	0.1739	1.1347		
3	H---O5′	0.0239	0.3569	−2.3233	0.3304(0.1747)	1.5076(0.7676)
	H----O2	0.0604	0.0330	0.1397	1.1637(0.6156)	2.1683(1.1470)
	C5′--O5′	0.0329	0.2560	−0.4088	0.8795(0.4653)	1.8191(0.9623)
	C4′--C5′	0.0133	0.2616	−0.7239		
	C3′--O3′	0.0833	0.2430	−0.2849	0.8786(0.4648)	1.8459(0.9712)
	H---O3′	0.0286	0.3699	−2.1679	0.3671(0.1913)	1.4670(0.7760)
	C3′--C4′	0.0570	0.2608	−0.7099		
	C2′--C3′	0.0462	0.2521	−0.6602		
	C1′--C2′	0.0194	0.2554	−0.6868		
	C1′--O4′	0.1701	0.2679	−0.5164		
	C4′--O4′	0.0223	0.2283	−0.1827		
	Ring 1		0.0363	0.2596		
	C1′--N1	0.1704	0.2554	−0.6864		
	C6---N1	0.0138	0.3218	−0.6580		
	C5---C6	0.3923	0.3517	−1.2064		
	C4---C5	0.1586	0.3109	−0.9542		
	C4---N3	0.0800	0.3815	−0.7676		
	C2---N3	0.0633	0.3379	−1.3938		
	C2---O2	0.1033	0.4155	0.0297	0.7525(0.3981)	1.5491(0.8195)
	C2---N1	0.0212	0.3053	−0.8387		
	Ring 2		0.0222	0.1809		

Can. J. Chem. Downloaded from www.nrcresearchpress.com by 85.192.166.187 on 09/08/12
For personal use only.

TABLE 5. (*continued*)

Molecule	Bond (X–Y)	ε	$\rho_b(r)$	$\nabla^2\rho(r_b)$	BCP → X (X = H, C, B)	BCP → Y (Y = O, N)
3*A*	H---O5′	0.0223	0.3070	−2.1286	0.3098(0.1639)	1.5875(0.8398)
	H----O2	0.0443	0.0604	0.2177	0.8645(0.4573)	1.9783(1.0465)
	C5′--O5′	0.0930	0.2173	−0.0338	0.8558(0.4529)	1.8833(0.9963)
	C4′--C5′	0.0130	0.2740	−0.7671		
	C3′--O3′	0.0944	0.2470	−0.3085	0.8768(0.4638)	1.8386(0.9726)
	H---O3′	0.0286	0.3697	−2.1710	0.3612(0.1911)	1.4677(0.7764)
	C3′--C4′	0.0577	0.2560	−0.8736		
	C2′--C3′	0.0450	0.2511	−0.6551		
	C1′--C2′	0.0209	0.2550	−0.6853		
	C1′--O4′	0.1840	0.2649	−0.4948		
	C4′--O4′	0.0161	0.2325	−0.2043		
	Ring 1		0.0361	0.2577		
	C1′--N1	0.1839	0.2552	−0.6838		
	C6---N1	0.0175	0.3195	−0.6307		
	C5---C6	0.3840	0.3518	−1.2082		
	C4---C5	0.1575	0.3126	−0.6939		
	C4---N3	0.0656	0.3794	−0.7797		
	C2---N3	0.0712	0.3452	−1.4393		
	C2---O2	0.0790	0.4069	−0.0186	0.7566(0.4004)	1.5587(0.8245)
	C2---N1	0.0282	0.3107	−0.8334		
	Ring 2		0.0224	0.1830		
	B5′--O5′	0.0323	0.1047	0.5352	0.9425(0.4986)	2.0302(1.0740)
	B5′--F	0.0194	0.1632	1.0541		
3*B*	H---O5′	0.0240	0.3573	−2.3323	0.3301(0.1746)	1.5076(0.7975)
	H----O2	0.0809	0.0327	0.1397	1.2144(0.6424)	2.1626(1.1440)
	C5′--O5′	0.0411	0.2575	−0.4187	0.8791(0.4650)	1.8167(0.9610)
	C4′--C5′	0.0255	0.2565	−0.7002		
	C3′--O3′	0.1940	0.1980	0.1233	0.8795(0.4650)	1.9223(1.0169)
	H---O3′	0.0272	0.3609	−2.3333	0.3348(0.1771)	1.4927(0.7896)
	C3′--C4′	0.0596	0.2640	−0.7275		
	C2′--C3′	0.0471	0.2588	−0.6963		
	C1′--C2′	0.0264	0.2562	−0.6910		
	C1′--O4′	0.1702	0.2632	−0.4857		
	C4′--O4′	0.0289	0.2349	−0.2499		
	Ring 1		0.0308	0.2644		
	C1′--N1	0.1724	0.2594	−0.7148		
	C6---N1	0.0169	0.3201	−0.6413		
	C5---C6	0.3924	0.3520	−1.2510		
	C4---C5	0.1563	0.3108	−0.9540		
	C4---N3	0.0750	0.3080	−0.7692		
	C2---N3	0.0645	0.3408	−1.4128		
	C2---O2	0.1011	0.4140	0.0189	0.7533(0.3985)	1.5515(0.8207)
	C2---N1	0.0200	0.3057	−0.8305		
	Ring 2		0.0222	1.1813		
	B3′--O3′	0.0429	0.0933	0.4697	0.9637(0.5098)	2.0847(1.1028)
	B3′--F	0.0220	0.1777	1.7170		
3*C*	H---O5′	0.0241	0.3576	−2.3291	0.3306(0.1749)	1.5066(0.7970)
	H----O2	0.0730	0.0322	0.1358	1.2030(0.6364)	2.1735(1.1498)
	C5′--O5′	0.0553	0.2579	−0.4213	0.8790(0.4650)	1.8153(0.9603)
	C4′--C5′	0.0282	0.2582	−0.7137		
	C3′--O3′	0.0881	0.2486	−0.3271	0.8772(0.4640)	1.8351(0.9708)
	H---O3′	0.0282	0.3688	−2.1805	0.3589(0.1899)	1.4704(0.7778)
	C3′--C4′	0.0586	0.2631	−0.7282		
	C2′--C3′	0.0482	0.2488	−0.6447		
	C1′--C2′	0.0231	0.2573	−0.7077		
	C1′--O4′	0.2922	0.2242	−0.1383	0.8821(0.4666)	1.8737(0.9912)
	C4′--O4′	0.0337	0.1898	0.1399	0.8912(0.4714)	1.9408(1.0267)
	Ring 1		0.0344	0.2442		
	C1′--N1	0.2027	0.2757	−0.8489		
	C6---N1	0.0502	0.3120	−0.6095		
	C5---C6	0.3981	0.3539	−1.2235		
	C4---C5	0.1524	0.3106	−0.9555		

Can. J. Chem. Downloaded from www.nrcresearchpress.com by 85.192.166.187 on 09/08/12
For personal use only.

TABLE 5. (*concluded*)

Molecule	Bond (X–Y)	ε	$\rho_b(r)$	$\nabla^2\rho(r_b)$	BCP → X (X = H, C, B)	BCP → Y (Y = O, N)
	C4---N3	0.0682	0.3807	−0.7701		
	C2---N3	0.0661	0.3433	−1.4304		
	C2---O2	0.1001	0.4147	0.0256	0.7528(0.3982)	1.5507(0.8203)
	C2---N1	0.0135	0.3021	−0.8315		
	Ring 2		0.0220	0.1795		
	B4′--O4′	0.0234	0.1031	0.5158	0.9469(0.5009)	2.0437(1.0811)
	B4′--F	0.0157	0.1731	1.1227		
3D	H---O5′	0.0248	0.3623	−2.3322	0.3341(0.1767)	1.4967(0.7918)
	H----O2	0.0830	0.0268	0.1112	1.5191(0.6978)	2.2285(1.1789)
	C5′--O5′	0.0371	0.2552	−0.3999	0.8791(0.4650)	1.8207(0.9632)
	C4′--C5′	0.0204	0.2594	−0.7140		
	C3′--O3′	0.0892	0.2449	−0.2969	0.8779(0.4644)	1.8421(0.9745)
	H---O3′	0.0286	0.3697	−2.1704	0.3612(0.1911)	1.4677(0.7764)
	C3′--C4′	0.0577	0.2608	−0.7098		
	C2′--C3′	0.0475	0.2511	−0.6557		
	C1′--C2′	0.0175	0.2558	−0.6911		
	C1′--O4′	0.1788	0.2744	−0.5480		
	C4′--O4′	0.0203	0.2232	−0.1538		
	Ring 1		0.0364	0.2600		
	C1′--N1	0.1928	0.2426	−0.5830		
	C6---N1	0.0322	0.3329	−0.6395		
	C5---C6	0.3507	0.3445	−1.1793		
	C4---C5	0.1977	0.3253	−1.0483		
	C4---N3	0.0252	0.3610	−0.6525		
	C2---N3	0.0648	0.3261	−1.1919		
	C2---O2	0.1268	0.4269	0.0978	0.7474(0.3954)	1.5330(0.8110)
	C2---N1	0.0431	0.3090	−0.9213		
	Ring 2		0.0218	0.1801		
	B3′--N3	0.0071	0.1059	0.3510	0.9620(0.5092)	2.1783(1.1523)
	B3′--F	0.0010	0.1717	1.1254		

[a]All quantities, except the bond ellipticity, are given in atomic unit (au), the values of BPL in parentheses are given in angstrom.
[b]Ring #1 represents the ring critical point of the furanose ring and ring #2 represents the ring critical point of the heteroaromatic ring.

Can. J. Chem. Downloaded from www.nrcresearchpress.com by 85.192.166.187 on 09/08/12
For personal use only.

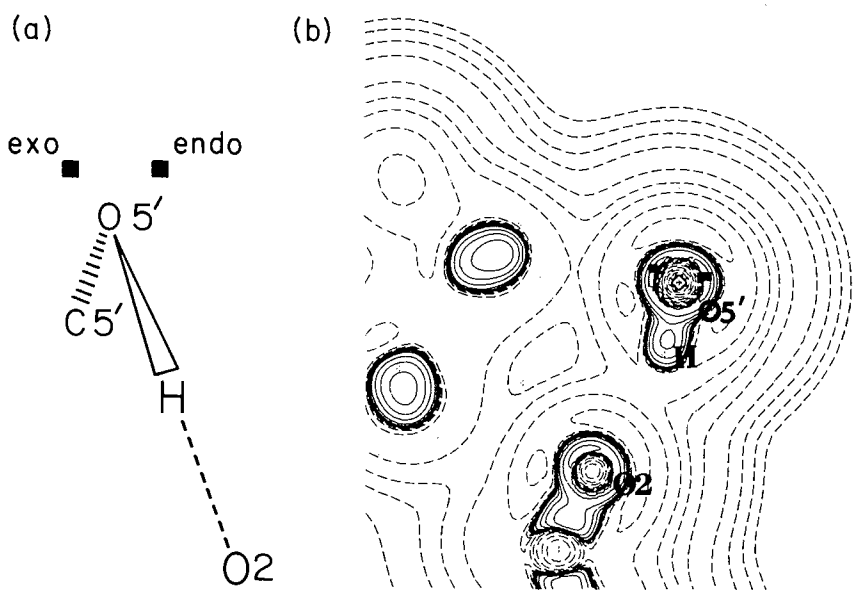

FIG. 6. (*a*) A schematic illustration of the two (*exo* and *endo*) nonbonded Laplacian concentrations of O5′ in BF_3 complexes (B, C, and D) with the model compound **3**. These nonbonded Laplacian concentrations are indicated by solid squares. (*b*) Contour line diagram of the calculated (6-31G**//3-21G) Laplacian concentrations ($-\nabla^2\rho(\boldsymbol{r})$) of model compound **3** in the plane containing O5′ atom and the positions of Laplacian concentrations associated with the two lone pairs of O5′. The two nonbonded Laplacian concentrations of O5′ are denoted by solid squares.

Can. J. Chem. Downloaded from www.nrcresearchpress.com by 85.192.166.187 on 09/08/12
For personal use only.

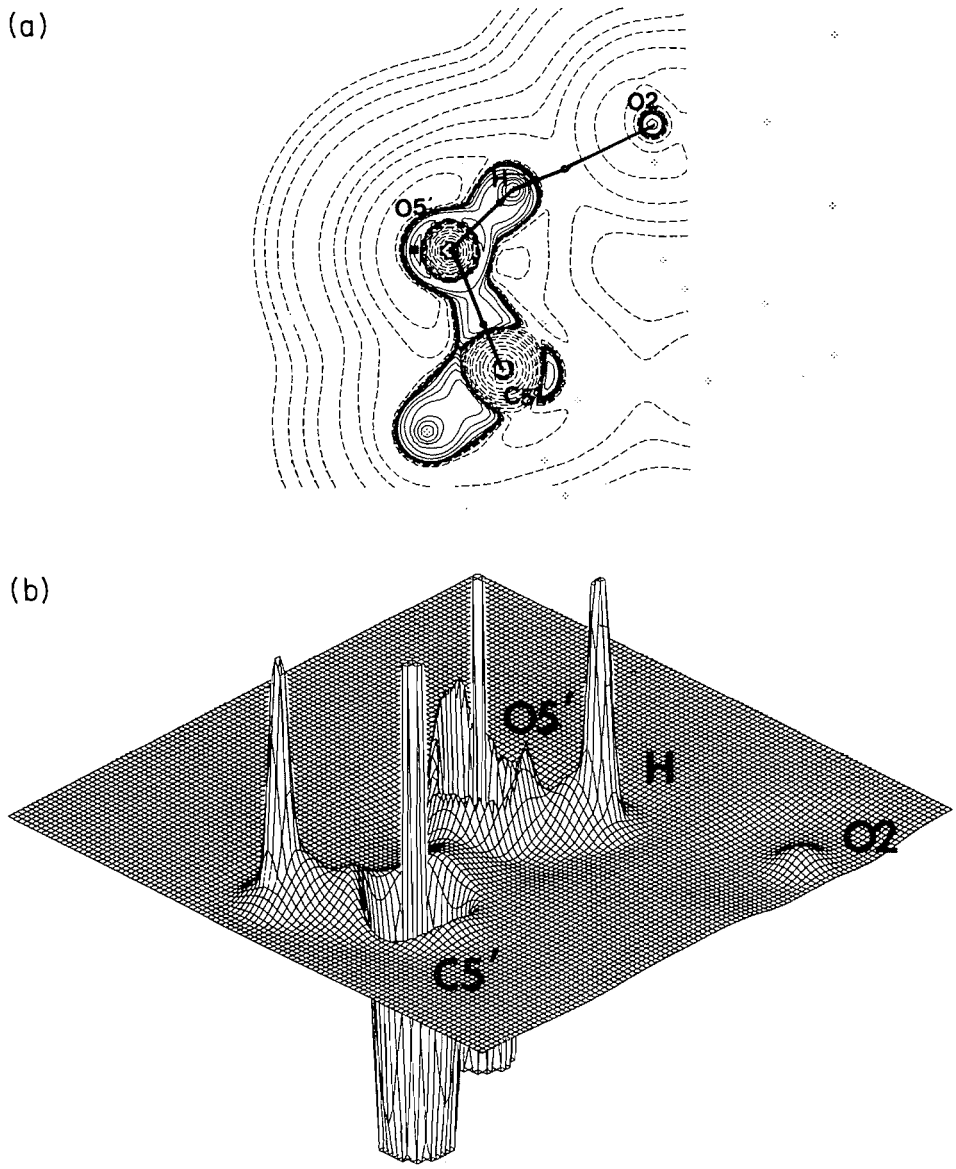

FIG. 7. (*a*) Contour line diagram of calculated (6-31G**//3-21G) Laplacian concentration ($-\nabla^2\rho(\boldsymbol{r})$) of model compound **3** in the plane of C5′—O5′—H. Bond paths (heavy solid lines) and BCPs (solid circles) are shown for $\rho(\boldsymbol{r})$. Regions of Laplacian concentration (depletion) as determined by $\nabla^2\rho < 0$ ($\nabla^2\rho > 0$) are denoted by solid (dashed) contours. The projections of the two nonbonded Laplacian concentrations of O5′ are coincident on the C5′—O5′—H plane (indicated by the solid square). (*b*) Relief map of $-\nabla^2\rho(\boldsymbol{r})$ representing the same information as (*a*).

TABLE 6. Nonbonded Laplacian concentrations at O5′ of model compounds **2**, **3** and their BF_3 complexes (**2***A*, **3***A*, **3***B*, **3***C*, and **3***D*)[a]

Molecule	*endo* concentration[b]	dl	*exo* concentration[b]	d2
2	−6.475684	0.6340	−6.512562	0.6337
2*A*	—	—	−6.570339	0.6320
3	−6.480095	0.6339	−6.527476	0.6335
3*A*	—	—	−6.361397	0.6336
3*B*	−6.441080	0.6342	−6.550981	0.6332
3*C*	−6.470822	0.6339	−6.547680	0.6333
3*D*	−6.503868	0.6336	−6.596710	0.6329

[a]Laplacian concentrations and their distances from nuclei O5′ (dl and d2) are given in Bohr atomic unit (au).

[b]The *exo* lone pair of O5′ points away from the furanose ring and the *endo* lone pair of O5′ points towards the furanose ring.

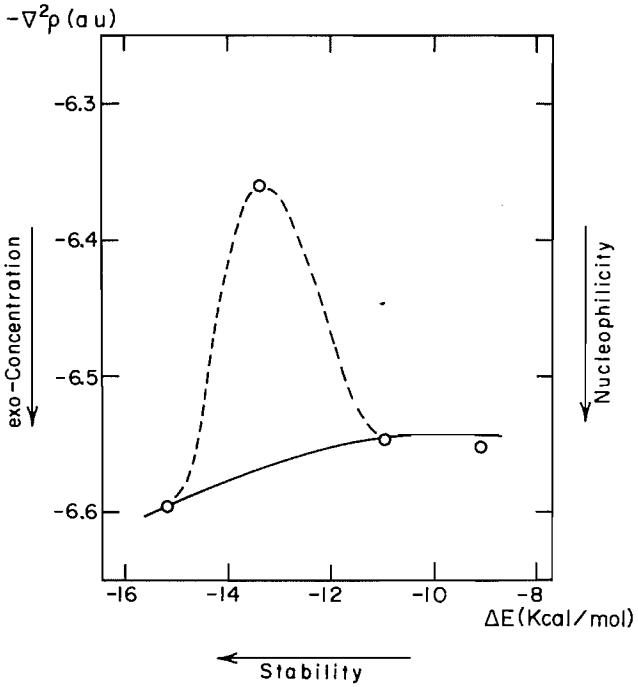

FIG. 8. The variation of *exo* concentration (i.e. $-\nabla^2\rho$) as a measure of nucleophilicity at the *exo* site of O5′ with the exothermic complexation energy of the BF_3 Lewis complexes of **3** (i.e. **3***A*, **3***B*, **3***C*, and **3***D*).

4. Conclusion

Model compound **3** used in the present study compared well with the model compound **2** used in the previous study (1) in terms of molecular geometry and their BF_3 complexes. These results suggests that both model compounds mimic well compound **1** studied experimentally.

The BF_3 complexes of **3** were studied at three oxygen sites (O5′, O3′, and O4′ denoted as **3***A*, **3***B*, and **3***C*) and one nitrogen site (N3) of the heteroaromatic aglycone denoted as **3***D*. The relative stability, as measured by the energy of complex formation, was found to be as

3*D*	>	**3***A*	>	**3***C*	>	**3***B*
88.3		11.6		0.1		0.0

with the percentage abundance shown above numerically.

The relative nucleophilicities of the *exo* lone pairs of O5′, as measured by the Laplacian concentration of the charge density ($-\nabla^2\rho$), was found in the following order:

← nucleophilicity			
3*D*	**3***B*	**3***C*	**3***A*
−6.597	−6.551	−6.548	−6.361

The combination of the above two qualities suggests that isomer **3***D* is the most likely species to be involved in the glycosylation reaction.

5. Acknowledgements

The continued financial support of the Natural Sciences and Engineering Research Council (NSERC) of Canada and the Protein Engineering Network of Centres of Excellence are gratefully acknowledged. The Carbohydrate Research Centre is partially supported by the Medical Research Council (MRC) of Canada.

1. T.-H. Tang, D.M. Whitfield, S.P. Douglas, J.J. Krepinsky, and I.G. Csizmadia. Can. J. Chem. **70**, 2434 (1992).
2. D.M. Whitfield, S.P. Douglas, T.-H. Tang, I.G. Csizmadia, H.Y. Pang, F.L. Moolten, and J.J. Krepinsky. Can. J. Chem. In press.
3. N. Lupescu, D.M. Whitfield, B.J. Underdown, and J.J. Krepinsky. To be submitted.
4. H. Bredereck, G. Wagner, H. Faber, H. Ott, and J. Rauther. Chem. Ber. **92**, 1135 (1959).
5. Y.V. Wozney and N.K. Kochetkov. Carbohydr. Res. **54**, 300 (1977).
6. M. Frisch, G.W. Trucks, M. Head-Gordon, P.M. Gill, M. Wong, J.B. Foresman, B.G. Johnson, H.B. Schlegel, M.A. Robb, E.S. Replogle, R. Gomperts, J.L. Andres, K. Raghavachari, J.S. Binkley, C. Gonzalez, R.L. Martin, D.J. Fox, D.J. Defrees, J. Baker, J.J.P. Stewart, and J.A. Pople. GAUSSIAN 92 (Revision C), Gaussian Inc., Pittsburg, PA. 1992.
7. J.S. Binkley, J.A. Pople, and W.J. Hedre. J. Am. Chem. Soc. **102**, 939 (1980).
8. (*a*) P.C. Hariharan and J.A. Pople. Chem. Phys. Lett. **66**, 217 (1972); (*b*) J.S. Binkley, J.A. Pople, and W.J. Hehre. J. Am. Chem. Soc. **102**, 939 (1980); (*c*) M.S. Gordon, J.S. Binkley, J.A. Pople, W.J. Pietro, and W.J. Hedre. J. Am. Chem. **104**, 2997 (1982); (*d*) W.J. Pietro, M.M. Francl, W.J. Hehre, D.J. Defrees, J.A. Pople, and J.S. Binkley. J. Am. Chem. Soc. **104**, 5039 (1982).
9. R.F.W. Bader. (*a*) Chem. Rev. **91**, 893 (1991); (*b*) Atoms in molecules: A quantum theory. Clarendon Press, Oxford. 1990.
10. R.F.W. Bader. Acc. Chem. Res. **18**, 9 (1985).
11. A.V. Topchiev, S.V. Zavgorodnii, and Ya. M. Paushkin. International series monographs on organic chemistry. Vol. 2. *Edited by* W. Doering and D.H.R. Barton. Pergamon Press, London. 1959. p. 64.
12. L.G. Marzilli. Advance in inorganic biochemistry Vol. 3. *Edited by* G.L. Eichhorn and L.G. Marzilli. Elsevier/North Holland, New York. 1981. p. 47.
13. (*a*) T.-H. Tang and X.-Y. Fu. Int. Quant. Chem. **24**, 317 (1983); (*b*) S.C. Choi and R.J. Boyd. Can. J. Chem. **64**, 2024 (1986); (*c*) R.J. Boyd. Stud. Org. Chem. (Amsterdam), **31**, 485 (1987); (*d*) J.R. Cheeseman, M.T. Carroll, and R.F.W. Bader. Chem. Phys. Lett. **143**, 450 (1988); (*e*) M.T. Carroll, C. Chang, and R.F.W. Bader. Mol. Phys. **63**, 387 (1988); (*f*) M.T. Carroll and R.F.W. Bader. Mol. Phys. **65**, 695 (1988); (*e*) T.-H. Tang, W.-J. Hu, D.-Y. Yan, and Y.-P. Cui. J. Mol. Struct. (THEOCHEM), **207**, 319 (1990); (*f*) E. Bosch, M. Moreno, and J.M. Lluch. Can. J. Chem. **70**, 1640 (1991).
14. R.F.W. Bader, T.-H. Tang, Y. Tal, and F.W. Biegler-Konig. J. Am. Chem. Soc. **104**, 940 (1982); **104**, 946 (1982).
15. (*a*) R.F.W. Bader, P.J. MacDougall, and C.D.H. Lau. J. Am. Chem. Soc. **106**, 1594 (1984); (*b*) R.F.W. Bader and P.J. MacDougall. J. Am. Chem. Soc. **107**, 6788 (1985); (*c*) R.F.W. Bader. Can. J. Chem. **64**, 1036 (1986); (*d*) J.P. MacDougall and R.F.W. Bader. Can. J. Chem. **64**, 1496 (1986); (*e*) R.F.W. Bader and C. Chang. J. Phys. Chem. **93**, 2946 (1989); (*f*) M.T. Carroll, J.R. Cheeseman, R. Osman, and H. Weinstein. J. Phys. Chem. **93**, 5120 (1989); (*g*) Z. Shi and R.J. Boyd. J. Phys. Chem. **95**, 4698 (1991); (*h*) T. Slee and R.F.W. Bader. J. Mol. Struct. (THEOCHEM), **255**, 173 (1992); (*i*) Z. Shi and R.J. Boyd. J. Am. Chem. Soc. **115**, 9614 (1993).
16. T.-H. Tang, W.-J. Hu, D.-Y. Yan, and Y.-P. Cui. J. Mol. Struct. (THEOCHEM), **207**, 327 (1990).
17. R.J. Gillespie. Molecular geometry. Van Nostrand-Reinhold, London. 1972.

Can. J. Chem. Downloaded from www.nrcresearchpress.com by 85.192.166.187 on 09/08/12
For personal use only.

A convenient procedure for the efficient preparation of alkyl (*Z*)-3-iodo-2-alkenoates

EDWARD PIERS,[1] TIMOTHY WONG, PHILIP D. COISH, AND CHRISTINE ROGERS
Department of Chemistry, University of British Columbia, 2036 Main Mall, University Campus, Vancouver, BC V6T 1Z1, Canada

Received February 1, 1994

EDWARD PIERS, TIMOTHY WONG, PHILIP D. COISH, and CHRISTINE ROGERS. Can. J. Chem. **72**, 1816 (1994).

Reaction of alkyl 2-alkynoates with sodium iodide (1.6–5.5 equiv.) in acetic acid (6.2–13 equiv.) at 115°C provides good to excellent yields of the corresponding alkyl (*Z*)-3-iodo-2-alkenoates.

EDWARD PIERS, TIMOTHY WONG, PHILIP D. COISH et CHRISTINE ROGERS. Can. J. Chem. **72**, 1816 (1994).

La réaction des 2-alkynoates d'alkyles avec l'iodure de sodium (1,6–5,5 équiv.) dans l'acide acétique (6,2–13 équiv.) à 115°C conduit aux (*Z*)-3-iodo-2-alkénoates d'alkyles correspondants avec des rendements allant de bon à excellent.

[Traduit par la rédaction]

Introduction

Alkyl (*Z*)-3-iodo-2-alkenoates (general structure **1**), along with substances that have been or could readily be derived therefrom, are useful intermediates for organic synthesis (1–20). Recently, it has been reported (17–20) that **1** (R^1 = H) can be produced by reaction of alkyl propynoates **2** with lithium or sodium iodide in acetic acid at 70°C. However, this protocol requires reaction times that are quite lengthy (12–24 h) and has been applied to only two higher homologs of **2**, namely **3** (R^2 = Me) (19) and **4** (R^2 = Et) (17). In the latter case, the yield of **1**

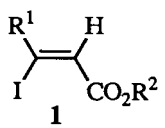

1

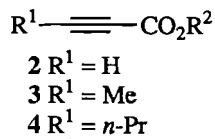

2 R^1 = H
3 R^1 = Me
4 R^1 = *n*-Pr
5 R^1 = alkyl or functionalized alkyl

(R^1 = *n*-Pr, R^2 = Et) was very low (22%) (17). Indeed, we have found that this procedure (17–20) generally works poorly or not at all for substrates of general structure **5** in which R^1 is larger than methyl.

In connection with current research projects in our laboratory, we required a number of substances of general structure **1** in which the R^1 group is more bulky than methyl and, in some instances, is functionalized. We report herein a procedure, significantly modified from those reported earlier (17–20), that effects the efficient conversion of α,β-acetylenic esters **5** into the alkyl (*Z*)-3-iodo-2-alkenoates **1**. Essentially, the procedure that we have developed employs sodium iodide, a limited amount of acetic acid, and a reaction temperature (115°C) considerably higher than that employed previously (17–20). Under these conditions, substrates **5**, including those with functionalized or bulky (e.g., *tert*-butyl) R^1 groups, are transformed smoothly and efficiently into iodo esters of general structure **1**.

Results and discussion

(a) The α,β-unsaturated acetylenic substrates

The acetylenic ester starting materials **6**–**15** employed in this study are listed in Chart 1. Of these materials, a number (**6**, **12**–**14**) are commercially available, while others have been reported previously: **7** (21), **8** (22), **9** (22), **11** (23), **15** (24). Compound **10** was prepared by treatment of methyl 6-(tetrahydropyranyloxy)-2-hexynoate (22) with ethanoyl chloride (25) (see Experimental). Collectively, these ester substrates contain a variety of functional groups and have alkyl groups attached to C-3 of the alkyl propynoate unit that are sterically small, medium, and large (see compounds **6**–**8**).

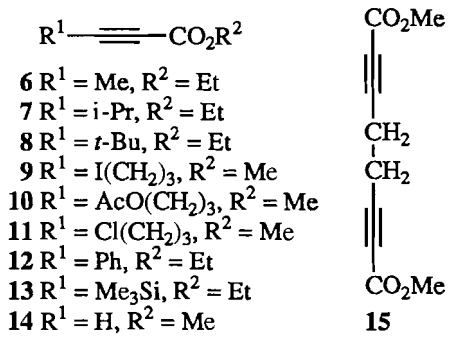

6 R^1 = Me, R^2 = Et
7 R^1 = i-Pr, R^2 = Et
8 R^1 = *t*-Bu, R^2 = Et
9 R^1 = $I(CH_2)_3$, R^2 = Me
10 R^1 = $AcO(CH_2)_3$, R^2 = Me
11 R^1 = $Cl(CH_2)_3$, R^2 = Me
12 R^1 = Ph, R^2 = Et
13 R^1 = Me_3Si, R^2 = Et
14 R^1 = H, R^2 = Me

15

CHART 1

(b) Preparation of alkyl (Z)-3-iodo-2-alkenoates and related substances

Initially, we carried out a series of experiments that involved treatment of ethyl 2-butynoate (**6**) with varying amounts of sodium iodide and acetic acid at a variety of temperatures. These studies quickly revealed that the rate of conversion of the substrate into ethyl (*Z*)-3-iodo-2-butenoate (**16**) (see Chart 2) increased significantly at temperatures above 100°C. Furthermore, it was found that the reaction product **16** was produced cleanly and efficiently (> 95% yield) when a stirred solution–suspension of **6** and sodium iodide (~1.6 equiv.) in a small amount of acetic acid (~6.7 equiv.) was heated at ~115°C for 90 min. Under these conditions, there was no indication of the formation of ethyl (*E*)-3-iodo-2-butenoate.

Subjection of the substrates **7**–**15** (Chart 1) to reaction conditions identical with or similar to those outlined above provided the results summarized in Table 1 (see Chart 2 for the structural formulas of the reaction products).

As shown by the data given in Table 1, the conversions investigated were generally efficient and complete in convenient reaction times. Of the reactions involving structurally "simple" substrates (Table 1, entries 1–3, 7, 9), the transformations of ethyl 4,4-dimethyl-2-pentynoate (**8**) and ethyl 3-phenylpropy-

[1]Author to whom correspondence may be addressed.

Can. J. Chem. Downloaded from www.nrcresearchpress.com by 85.192.166.187 on 09/08/12
For personal use only.

TABLE 1. Preparation of alkyl (*Z*)-3-iodo-2-alkenoates

Entry	Substrate[a] (amount: mg, mmol)	Equiv. of NaI	Equiv. of HOAc	Reaction time (h)	Product[a]	Distillation temperature (°C/Torr)	Yield[b] (g, %)
1	**6** (655, 5.8)	1.6	6.4	1.5	**16**	35–50/0.3	1.37, 98
2	**7** (674, 4.8)	1.6	6.4	1.5	**17**	60–80/0.3	1.14, 88
3	**8** (541, 3.5)	3.2	13.0	7.0	**18**	60–72/0.3	0.84, 85
4	**9** (929, 3.7)	1.6	6.2	1.5	**19**	90–100/0.3	1.08, 77[c]
5	**10** (550, 3.0)	1.6	6.4	1.5	**20**	90–100/0.3	0.76, 81
6	**11** (192, 1.2)	4.0	13.0	2.25	**19**	90–100/0.3	0.36, 80[d]
7	**12** (932, 5.3)	3.2	12.8	4.0	**21**	95–100/0.03	1.54, 95
8	**13** (178, 1.1)	5.5	9.5	3.25	**22**	40–45/0.08	0.11, 35[e]
9	**14** (5170, 61.5)	1.6	6.4	1.0	**24**	30–40/0.03	10.79, 83
10	**15** (194, 1.0)	3.2	12.8	1.75	**25**	—	0.34, 76

[a]See Charts 1 and 2 for the structural formulas of the substrates and products, respectively.
[b]Yield of purified, distilled (or crystallized) product.
[c]Also isolated, in 9% yield, was compound **20**.
[d]Also isolated, in 3% yield, was compound **20**.
[e]Also obtained were 19% of the starting material **13** and 28% of ethyl (*Z*)-3-iodopropenoate (**23**).

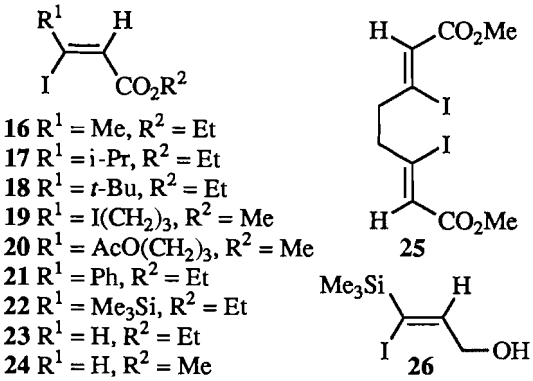

CHART 2

noate (**12**) into the corresponding (*Z*)-3-iodoalkenoates **18** and **21** (entries 3, 7) are particularly noteworthy. Because of the presence of the sterically bulky *tert*-butyl and phenyl groups in **8** and **12**, respectively, the reactions were, relatively speaking, quite slow and, in each case, the use of larger quantities of sodium iodide and acetic acid was found to be beneficial. Under these circumstances, the products **18** and **21** were produced cleanly and efficiently.

Functionalized substrates were also employed successfully (entries 4–6). Methyl (*Z*)-3,6-diiodo-2-hexenoate (**19**) could be derived from either the iodo ester **9** (entry 4) or the chloro ester **11** (entry 6). In each of these reactions, there was also produced a small amount of the acetoxy iodide **20**. The latter substance was also derived in very good yield from the α,β-acetylenic ester **10** (entry 5), thus showing that an acetoxy function is stable under the reaction conditions.

The use of this method for the conversion of ethyl 3-(trimethylsilyl)propynoate (**13**) into the structurally novel substance ethyl (*Z*)-3-iodo-3-(trimethylsilyl)propenoate (**22**) turned out to be quite inefficient (entry 8). A significant side reaction in this (sluggish) process involved protonative loss of the Me_3Si function to produce the iodo ester **23**.

More successful was the application of the developed procedure to a substrate possessing two α,β-acetylenic ester functions (entry 10). In this case, dimethyl 2,6-octadiyndioate (**15**) was converted in good yield into the structurally interesting diiodo ester **25**, a crystalline solid with melting point 73–74°C.

In each of a number of representative cases (substances **16**–**18**, **25**), the expected (17–20) configuration of the product was confirmed by use of nuclear Overhauser enhancement (nOe) difference experiments (see Experimental). To confirm the structure of product **22**, this material was reduced with diisobutylaluminum hydride to afford the known (26) alcohol **26** (Chart 2).

Finally, our procedure was employed to effect the conversion of propynoic acid (**27**) into (*Z*)-3-iodopropenoic acid (**28**)

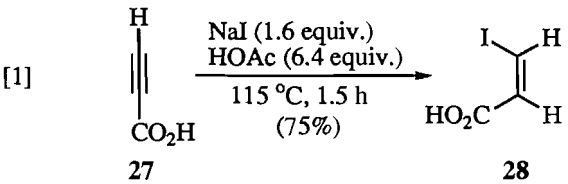

(eq.[1]). The required reaction time was quite short (1.5 h) and, following a simple workup procedure, crystalline **28** (2, 20, 27) was obtained in 75% yield.

Conclusion

This brief study resulted in the development of an effective general protocol for the conversion of alkyl 2-alkynoates into synthetically useful alkyl (*Z*)-3-iodo-2-alkenoates. The procedure is straightforward, the reaction times are conveniently short, and, importantly, the process works well for a structurally diverse set of substrates.

Experimental

General information

Distillation temperatures, which refer to short path (Kugelrohr) distillations, and melting points are uncorrected. Proton nuclear magnetic resonance (^{1}H nmr) spectra were recorded using $CDCl_3$ as the solvent. Signal positions (δ values) were measured relative to those of Me_4Si (δ = 0) or $CHCl_3$ (δ = 7.25). Carbon nuclear magnetic resonance (^{13}C nmr) spectra were recorded using $CDCl_3$ as the solvent and the signal positions are given relative to that of $CDCl_3$ (δ = 77.0). Infrared (ir) spectra were obtained on liquid films (NaCl plates), unless otherwise noted. Flash chromatography (28) was carried out with 230–400 mesh silica gel (E. Merck), while radial chromatography was performed with a Chromatotron model 7924, using plates coated with silica gel 60, PF_{254}, with $CaSO_4$ (E. Merck no. 7749).

Can. J. Chem. Downloaded from www.nrcresearchpress.com by 85.192.166.187 on 09/08/12
For personal use only.

Can. J. Chem. Downloaded from www.nrcresearchpress.com by 85.192.166.187 on 09/08/12
For personal use only.

Note: All reactions were carried out under an atmosphere of argon in flame- or oven-dried glassware.

*Methyl 6-acetoxy-2-hexynoate (**10**)*

Ethanoyl chloride (4.2 mL, 59 mmol) was added to a solution of methyl 6-(tetrahydropyranyloxy)-2-hexynoate (22) (2.68 g, 11.8 mmol) in dry THF (25 mL) and the resultant mixture was stirred at room temperature for 23 h. Saturated aqueous $NaHCO_3$ (50 mL) and diethyl ether (100 mL) were added and the phases were separated. The organic phase was washed with brine, dried ($MgSO_4$), and concentrated. Flash chromatography (150 g silica gel, 3:1 petroleum ether – Et_2O) of the crude product and distillation (90–110°C/0.3 Torr (1 Torr = 133.3 Pa)) of the acquired liquid afforded 1.51 g (70%) of the acetylenic ester **10**, a colorless oil that displayed ir (neat): 2239, 1737, 1719, 1255, 1046 cm^{-1}; ^1H nmr (400 MHz) δ: 1.88 (quintet, 2H, J = 7 Hz), 2.04 (s, 3H), 2.42 (t, 2H, J = 7 Hz), 3.73 (s, 3H), 4.13 (t, 2H, J = 7 Hz). Anal. calcd. for $C_9H_{12}O_4$: C 58.69, H 6.57; found: C 58.62, H 6.73. Exact Mass calcd. for $C_8H_9O_4(M^+ - Me)$: 169.0501; found: 169.0492.

*General procedure for the conversion of α,β-acetylenic esters **6–15** into alkyl (Z)-3-iodo-2-alkenoates*

An oil bath was preheated at 115°C for 15 min. A flask (argon atmosphere) containing a mixture (suspension) of the α,β-acetylenic ester, sodium iodide, and glacial acetic acid was placed in the oil bath and the mixture was stirred at 115°C for the specified time. The bath was removed and the brown mixture was transferred while hot to a separatory funnel containing water (~8–10 mL per mmol of ester substrate). The reaction flask was washed with a mixture of water (~2–5 mL) and diethyl ether (~25–30 mL per mmol of ester substrate). The washings were added to the separatory funnel. The phases were separated and the aqueous phase was washed with diethyl ether. The combined organic phases were washed sequentially with saturated aqueous sodium bicarbonate, 1 M aqueous sodium thiosulfate, and brine (~8–10 mL of each solution per mmol of ester substrate), and then were dried ($MgSO_4$ or Na_2SO_4) and concentrated. Distillation of the remaining material from basic alumina (~30–50 mg per mmol of ester substrate) provided the alkyl (Z)-3-iodo-2-alkenoate. Details regarding quantities of reactants, reaction times, distillation temperatures, and yields are given in Table 1.

The following substances were prepared via the general procedure. Any deviations from this protocol are noted in each case.

*Ethyl (Z)-3-iodo-2-butenoate (**16**) (16) (Table 1, Entry 1)*

Colorless oil, ir (neat): 1728, 1629, 1309, 1180 cm^{-1}; ^1H nmr (400 MHz) δ: 1.28 (t, 3H, J = 7 Hz), 2.71 (d, 3H, J = 1.5 Hz), 4.20 (q, 2H, J = 7 Hz), 6.27 (q, 1H, J = 1.5 Hz). In nOe difference experiments, irradiation at each of δ 2.71 and 6.27 caused enhancement of the signals at 6.27 and 2.71, respectively; ^{13}C nmr (50.3 MHz) δ: 14.2, 36.5, 60.5, 113.1, 125.6, 164.2. Anal. calcd. for $C_6H_9IO_2$: C 30.02, H 3.78, I 52.87; found: C 29.84, H 3.71, I 52.60. Exact Mass calcd.: 239.9648; found: 239.9646.

*Ethyl (Z)-3-iodo-4-methyl-2-pentenoate (**17**) (Table 1, Entry 2)*

Colorless oil, ir (neat): 1730, 1619, 1192, 1033 cm^{-1}; ^1H nmr (400 MHz) δ: 1.11 (d, 6H, J = 7 Hz), 1.29 (t, 3H, J = 7 Hz), 2.46 (septet, 1H, J = 7 Hz), 4.20 (q, 2H, J = 7 Hz), 6.39 (s, 1H). In nOe difference experiments, irradiation at each of δ 2.46 and 6.39 resulted in enhancement of the signals of 6.39 and 2.46, respectively; ^{13}C nmr (50.3 MHz) δ: 14.2, 23.0, 43.8, 60.5, 122.8, 131.8, 164.9. Anal. calcd. for $C_8H_{13}IO_2$: C 35.84, H 4.89; found: C 35.69, H 4.93. Exact Mass calcd.: 267.9961; found: 267.9955.

*Ethyl (Z)-3-iodo-4,4-dimethyl-2-pentenoate (**18**) (Table 1, Entry 3)*

Colorless oil, ir (neat): 1733, 1611, 1301, 1179, 1040 cm^{-1}; ^1H nmr (400 MHz) δ: 1.22 (s, 9H), 1.29 (t, 3H, J = 7 Hz), 4.21 (q, 2H, J = 7 Hz), 6.38 (s, 1H). In nOe difference experiments, irradiation at each of δ 1.22 and 6.38 caused enhancement of the resonances at 6.38 and 1.22, respectively; ^{13}C nmr (50.3 MHz) δ: 14.2, 30.3, 42.1, 60.7, 123.0, 136.0, 165.5. Anal. calcd. for $C_9H_{15}IO_2$: C 38.32, H 5.36, I 44.98; found: C 38.44, H 5.36, I 44.71. Exact Mass calcd.: 282.0118; found: 282.0111.

*Methyl (Z)-3,6-diiodo-2-hexenoate (**19**)*

*(a) From methyl 6-iodo-2-hexynoate (**9**) (Table 1, Entry 4)*

Radial chromatography (4 mm plate, 5:1 petroleum ether – diethyl ether) of the crude product, followed by distillation of the acquired oils, gave the diiodide **19** (77%) and the iodo acetate **20** (9%) (vide infra). Compound **19**, a colorless oil, displayed ir (neat): 1730, 1624, 1219, 1175 cm^{-1}; ^1H nmr (400 MHz) δ: 2.09 (quintet, 2H, J = 7 Hz), 2.80 (td, 2H, J = 7, 1 Hz), 3.13 (t, 3H, J = 7 Hz), 3.73 (s, 3H), 6.44 (t, 1H, J = 1 Hz); ^{13}C nmr (50.3 MHz) δ: 4.2, 32.0, 47.7, 51.7, 118.8, 126.0, 164.7. Anal. calcd. for $C_7H_{10}I_2O_2$: C 22.13, H 2.65, I 66.80; found: C 22.35, H 2.69, I 66.60. Exact Mass calcd. for $C_7H_{10}IO_2$ (M^+ – I): 252.9726; found: 252.9729.

*(b) From methyl 6-chloro-2-hexynoate (**11**) (Table 1, Entry 6)*

Radial chromatography (2 mm plate, 130 mL of 85:15 petroleum ether – diethyl ether and then 75:25 petroleum ether – diethyl ether) of the crude product gave compound **19** (80%) and the iodo acetate **20** (3%) (vide infra). The spectral data of **19** were found to be identical with those recorded above.

*Methyl (Z)-6-acetoxy-3-iodo-2-hexenoate (**20**) (Table 1, Entry 5)*

Colorless oil, ir (neat): 1734, 1624, 1243, 1174 cm^{-1}; ^1H nmr (400 MHz) δ: 1.92 (quintet, 2H, J = 7 Hz), 2.02 (s, 3H), 2.74 (t, 2H, J = 7 Hz), 3.70 (s, 3H), 4.03 (t, 2H, J = 7 Hz), 6.34 (s, 1H); ^{13}C nmr (50.3 MHz) δ: 20.9, 28.2, 44.4, 51.6, 62.5, 119.9, 125.3, 164.7, 170.9. Anal. calcd. for $C_9H_{13}IO_4$: C 34.64, H 4.20, I 40.66; found: C 35.00, H 4.22, I 40.37. Exact Mass calcd.: 311.9859; found: 311.9864.

*Ethyl (Z)-3-iodo-3-phenylpropenoate (**21**) (Table 1, Entry 7)*

Radial chromatography (4 mm plate, 9:1 petroleum ether – ethyl acetate) of the crude product, followed by distillation of the acquired liquid, produced the iodo ester **21**, a yellow oil that displayed ir (neat): 1724 cm^{-1}; ^1H nmr (400 MHz) δ: 1.31 (t, 3H, J = 7 Hz), 4.26 (q, 2H, J = 7 Hz), 6.61 (s, 1H), 7.32–7.33 (m, 3H), 7.49–7.52 (m, 2H); ^{13}C nmr (50.3 MHz) δ: 14.3, 60.8, 116.1, 126.9, 128.4, 128.8, 130.0, 143.3, 164.6. Anal. calcd. for $C_{11}H_{11}IO_2$: C 43.73, H 3.67, I 42.00; found: C 43.76, H 3.76, I 41.80. Exact Mass calcd.: 301.9804; found: 301.9803.

*Ethyl (Z)-3-iodo-3-(trimethylsilyl)propenoate (**22**) (Table 1, Entry 8)*

Radial chromatography (4 mm plate, 4:1 petroleum ether – dichloromethane) of the crude product, followed by distillation of the acquired liquids, gave 34 mg (19%) of the starting material **13**, along with the iodo silane **22** (35%) and ethyl (Z)-3-iodopropenoate (**23**) (20, 29) (65 mg, 28%). Compound **22**, a colorless oil, exhibited ir (neat): 1731, 1290, 1251, 1176, 844 cm^{-1}; ^1H nmr (400 MHz) δ: 0.23 (s, 9H), 1.31 (t, 3H, J = 7 Hz), 4.23 (q, 2H, J = 7 Hz), 6.89 (s, 1H); ^{13}C nmr (100.6 MHz) δ: –1.7, 14.2, 60.8, 125.6, 134.6, 164.1. Anal. calcd. for $C_8H_{15}IO_2Si$: C 32.22, H 5.07; found: C 32.27, H 5.00. Exact Mass calcd.: 297.9886; found 297.9890.

Ethyl (Z)-3-iodopropenoate (**23**) (20, 29), a colorless oil, displayed ir (neat): 1728, 1600, 1324, 1198, 1166, 1028, 807 cm^{-1}; ^1H nmr (400 MHz) δ: 1.30 (t, 3H, J = 7 Hz), 4.23 (q, 2H, J = 7.0 Hz), 6.86 (d, 1H, J = 9 Hz), 7.42 (d, 1H, J = 9 Hz); ^{13}C nmr (50.3 MHz) δ: 14.2, 60.8, 94.6, 129.9, 164.6.

*Methyl (Z)-3-iodopropenoate (**24**) (19, 20) (Table 1, Entry 9)*

The hot reaction mixture was poured into 200 mL of water (separatory funnel). The reaction flask was washed with a mixture of water (10 mL) and diethyl ether (60 mL) and the washings were added to the separatory funnel. The phases were separated and the aqueous phase was extracted with diethyl ether. The combined organic phases were washed (saturated aqueous sodium bicarbonate (20 mL), saturated aqueous sodium thiosulfate (20 mL), brine (20 mL)), dried ($MgSO_4$), and concentrated. Distillation of the derived oil gave methyl (Z)-3-iodopropenoate (**24**) (19, 20), a colorless oil that showed ^1H nmr (400

MHz) δ: 3.77 (s, 3H), 6.89 (d, 1H, J = 9 Hz), 7.45 (d, 1H, J = 9 Hz); ^{13}C nmr (50.3 MHz) δ: 51.6, 95.1, 129.4, 164.8.

Dimethyl (Z,Z)-3,6-diiodo-2,6-octadiendioate (25) (Table 1, Entry 10)

The crude product was passed through a short column of basic alumina (1 g, activity 1, elution with dichloromethane). Concentration (water aspirator, then vacuum pump) of the eluate afforded the diiodo diester **25**, a crystalline solid. This material exhibited mp 73–74°C (from petroleum ether – diethyl ether); ir (KBr): 1722, 1614, 1427, 1326, 1161, 1053, 875 cm^{-1}; ^{1}H nmr (400 MHz) δ: 2.95 (s, 4H), 3.71 (s, 6H), 6.38 (s, 2H). In nOe difference experiments, irradiation at each of δ 2.95 and 6.38 caused enhancement of the resonances at 6.38 and 2.95, respectively; ^{13}C nmr (50.3 MHz) δ: 46.5, 51.7, 117.2, 126.4, 164.5. Anal. calcd. for $C_{10}H_{12}I_2O_4$: C 26.69, H 2.69, I 56.40; found: C 26.87, H 2.75, I 56.46. Exact Mass calcd.: 449.8823; found: 449.8826.

(Z)-3-Iodo-3-trimethylsilyl-2-propen-1-ol (26)

To a cold (–78°C), stirred solution of ethyl (Z)-3-iodo-3-(trimethylsilyl)propenoate (**22**) (21 mg, 0.07 mmol) in 1.8 mL of dry diethyl ether was added a 1 M solution of diisobutylaluminum hydride in hexanes (0.21 mL, 0.21 mmol, 3 equiv.). The mixture was stirred at –78°C for 75 min and at 0°C for 95 min. Saturated aqueous ammonium chloride (1.5 mL) was added and the mixture was allowed to warm to room temperature. Water (15 mL) and diethyl ether (20 mL) were added and the phases were separated. The aqueous phase was extracted with diethyl ether (2 × 20 mL) and the combined organic phases were washed (brine), dried (Na_2SO_4), and concentrated. Radial chromatography (1 mm plate, 85:15 petroleum ether – diethyl ether) of the remaining liquid and subjection of the acquired oil to reduced pressure (0.3 Torr) afforded 13.5 mg (75%) of the alcohol **26** (26), a colorless oil that displayed ir (neat): 3331, 1250, 1031, 881, 842 cm^{-1}; ^{1}H nmr (400 MHz) δ: 0.18 (s, 3H), 1.6–1.7 (br s), 4.26 (d, 2H, J = 5 Hz), 6.49 (t, 1H, J = 5 Hz). In nOe difference experiments, irradiation at δ 6.49 caused enhancement of the signals at 0.18 and 4.26, while irradiation at δ 0.18 increased the intensity of the signal at 6.49; ^{13}C nmr (50.3 MHz) δ: –1.7, 69.5, 112.6, 146.4. Exact Mass calcd. for $C_6H_{13}IOSi$: 255.9780; found: 255.9787.

(Z)-3-iodopropenoic acid (28)

An oil bath was preheated to 115°C for 15 min. A flask (argon atmosphere) containing a solution–suspension of propynoic acid (**27**) (514 mg, 7.34 mmol), sodium iodide (1.76 g, 11.7 mmol), and glacial acetic acid (2.69 mL, 47.0 mmol) was placed in the oil bath and the mixture was stirred at 115°C for 90 min. The mixture was cooled to room temperature and the acetic acid was removed under reduced pressure (0.3 Torr, –78°C trap, ~10 min). The remaining dark oil was treated with dry diethyl ether (40 mL) and the resultant mixture was filtered. The collected material was washed with dry diethyl ether (~70 mL). The combined filtrate was washed with saturated aqueous sodium thiosulfate (20 mL) and the aqueous phase was extracted with diethyl ether (4 × 10 mL). The combined organic extracts were dried (Na_2SO_4) and concentrated (water aspirator pressure, followed by vacuum pump, 0.3 Torr). Crystallization of the remaining viscous oil from hot diethyl ether – petroleum ether (cooled to 0°C) gave 1.09 g (75%) of the iodo acid **28**, which exhibited mp 62–64°C (lit. (27) mp 63–65°C); ^{1}H nmr (400 MHz) δ: 6.96 (d, 1H, J = 9.5 Hz), 7.67 (d, 1H, J = 9.5 Hz), 11.95 (br s, 1H); ^{13}C nmr (100.6 MHz) δ: 98.0, 129.4, 169.7. Exact Mass calcd. for $C_3H_3IO_2$: 197.9177; found: 197.9181.

Acknowledgements

We are grateful to the Natural Sciences and Engineering Research Council of Canada for financial support, for a Postdoctoral Fellowship (to C.R.), and for a Postgraduate Scholarship (to P.D.C.).

1. K.S. Feldman. Tetrahedron Lett. **23**, 3031 (1982).
2. R.A. Moss, B. Wilk, K. Krogh-Jespersen, and J.D. Westbrook. J. Am. Chem. Soc. **111**, 6729 (1989).
3. S. Torii, H. Okumoto, T. Kotani, and F. Akahoshi. Chem. Lett. 1971 (1989).
4. K.C. Nicolaou, P. Maligres, J. Shin, E. de Leon, and D. Rideout. J. Am. Chem. Soc. **112**, 7825 (1990).
5. P.A. Wender, J.A. McKinney, and C. Mukai. J. Am. Chem. Soc. **112**, 5369 (1990).
6. B.H. Lipshutz, C. Ung, T.R. Elworthy, and D.C. Reuter. Tetrahedron Lett. **31**, 4539 (1990).
7. K.D. Kim and P.A. Magriotis. Tetrahedron Lett. **31**, 6137 (1990).
8. Y. Sato, T. Honda, and M. Shibasaki. Tetrahedron Lett. **33**, 2593 (1992).
9. Y. Masuda, M. Hoshi, and A. Arase. Bull. Chem. Soc. Jpn. **65**, 3294 (1992).
10. P. Knochel and C.J. Rao. Tetrahedron, **49**, 29 (1993).
11. S. Okamoto, S. Katayama, N. Ono, and F. Sato. Tetrahedron: Asymmetry, **3**, 1525 (1992).
12. A.G. Myers and N.S. Finney. J. Am. Chem. Soc. **114**, 10986 (1992).
13. E. Piers and J. Renaud. J. Org. Chem. **58**, 11 (1993).
14. E. Negishi, M. Ay, Y.V. Gulevich, and Y. Noda. Tetrahedron Lett. **34**, 1437 (1993).
15. M. Mori, N. Isono, N. Kaneta, and M. Shibasaki. J. Org. Chem. **58**, 2972 (1993).
16. C. Meyer, I. Marek, and J.-F. Normant. Synlett. 386 (1993).
17. S. Ma and X. Lu. J. Chem. Soc. Chem. Commun. 1643 (1990).
18. S. Ma and X. Lu. Tetrahedron Lett. **31**, 7653 (1990).
19. I. Marek, A. Alexakis, and J.-F. Normant. Tetrahedron Lett. **32**, 5329 (1991).
20. S. Ma, X. Lu, and Z. Li. J. Org. Chem. **57**, 709 (1992).
21. O. Hormi. Org. Synth. **66**, 173 (1988).
22. E. Piers, J.M. Chong, and H.E. Morton. Tetrahedron, **45**, 363 (1989).
23. E. Piers, T. Wong, and K.A. Ellis. Can. J. Chem. **70**, 2058 (1992).
24. R.T. Skerlj. Ph.D. Thesis, University of British Columbia, Vancouver, B.C. 1988. p. 183.
25. T. Bakos and I. Vincze. Synth. Commun. **19**, 523 (1989).
26. S.E. Denmark, K.L. Habermas, and G.A. Hite. Helv. Chim. Acta, **71**, 168 (1988).
27. M.E. Jung, J.A. Hagenah, and Z. Long-Mei. Tetrahedron Lett. **24**, 3973 (1983).
28. W.C. Still, M. Kahn, and A. Mitra. J. Org. Chem. **43**, 2923 (1978).
29. J. Biougne and F. Théron. C.R. Acad. Sci. Paris, **272C**, 858 (1971).

Can. J. Chem. Downloaded from www.nrcresearchpress.com by 85.192.166.187 on 09/08/12
For personal use only.

First transannular Diels–Alder reactions involving tetrasubstituted non-activated dienophiles

JACQUES Y. ROBERGE, PIERRE GIGUERE, PIERRE SOUCY, YVES L. DORY, AND PIERRE DESLONGCHAMPS[1]

Laboratoire de synthèse organique, Département de chimie, Faculté des sciences, Université de Sherbrooke, Sherbrooke, QC J1K 2R1, Canada

Received November 15, 1993

JACQUES Y. ROBERGE, PIERRE GIGUERE, PIERRE SOUCY, YVES L. DORY, and PIERRE DESLONGCHAMPS. Can. J. Chem. **72**, 1820 (1994).

Transannular Diels–Alder reactions of four 14-membered macrocyclic trienes (**27**, **28**, **43**, and **44**) possessing a dimethyl tetrasubstituted dienophile have been investigated. Macrocycles having a *cis-trans-cis* (CTC) (**27**), a CTT (**43**), and a TTT (**44**) geometry produced the predicted *trans-syn-cis* (TSC) (**45**), *cis-anti-cis* (CAC) (**48**), and TAC (**49**) tricycles, respectively. The TTC macrocycle (**28**) gave exclusively the TST tricycle (**46**), no CSC tricycle (**47**) being observed. TTT macrocycle (**44**) underwent macrocyclization at a lower temperature than the TTC isomer (**28**).

JACQUES Y. ROBERGE, PIERRE GIGUERE, PIERRE SOUCY, YVES L. DORY et PIERRE DESLONGCHAMPS. Can. J. Chem. **72**, 1820 (1994).

La réaction de Diels–Alder transannulaire de quatre triènes macrocycliques à 14 chaînons (**27**, **28**, **43** et **44**) possédant un diénophile tétrasubstitué contenant deux groupes méthyles est décrite. Les macrocycles ayant une géométrie *cis-trans-cis* (CTC) (**27**), CTT (**43**) et TTT (**44**) conduisent respectivement aux tricycles *trans-syn-cis* (TSC) (**45**), *cis-anti-cis* (CAC) (**48**) et TAC (**49**). Le macrocycle TTC conduit exclusivement au tricycle TST (**46**), l'autre produit possible, le tricycle CSC n'ayant pas été observé. Le macrocycle TTT donne le produit de cycloaddition au cours de la réaction de macrocyclisation; par contre, le macrocycle TTC requière une température beaucoup plus élevée pour la réaction.

Introduction

When looking at the strategy based on the transannular Diels–Alder reaction (Scheme 1) on macrocyclic trienes, one

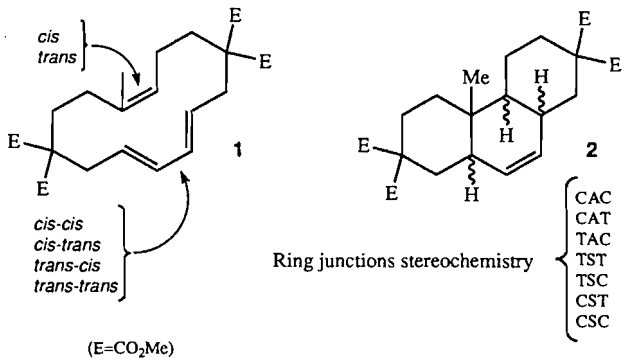

SCHEME 1

might wonder what the limitations of such an approach are. We have already shown (1) that transannular Diels–Alder reactions involving trisubstituted dienophiles (*cis* or *trans*) are limited only by the geometry of their diene counterparts: not surprisingly *cis-cis* dienes cannot lead neatly to their expected adducts because the required *cisoid* geometry of a *cis-cis* diene is extremely disfavored. On the other hand, *cis-trans* dienes give good yields of Diels–Alder adducts when the transannular Diels–Alder strategy is used. Very few intramolecular Diels–Alder examples involving this kind of *cis-trans* dienes have been reported in the literature (2), where the dienophile moiety was, moreover, activated. The transannular Diels–Alder reaction using *trans-trans* dienes is a very facile process indeed, since the corresponding macrocycles are not easily isolated due to their high reactivity.

The model study involving trisubstituted dienophiles was undertaken because the corresponding transannular Diels–Alder adducts are the cores of steroid or terpene natural or unnatural compounds. Triterpenes (Scheme 2) could similarly derive from transannular Diels–Alder reaction products from macrocyclic trienes featuring tetrasubstituted dienophiles.

We wish to report a study of such systems with *cis* and *trans* tetrasubstituted non-activated dienophiles and *cis-trans* and *trans-trans* dienes, the *cis-cis* diene being omitted for the reasons discussed above.

Results and discussion

The four required macrocycles (Scheme 3), whose general formula is summarized by the structure **8**, lead retrosynthetically to the two dienophile synthons **9** (*E* and *Z*) and the two diene synthons **10** (*EZ* and *EE*) where X, X′, Y, and Y′ are suitably protected alcohols or activated leaving groups. Such an approach is very convenient for the proposed study because of its high convergence. It is obvious that natural product syntheses based on the results of this model study could follow very different paths where the synthons would be chosen according to the desired targets.

Synthesis of the macrocyclic trienes 27 and 28 possessing a cis *dienophile (Schemes 4 and 6)*

The *Z* diol **11** (3) was monoprotected by means of *tert*-butyldiphenylsilyl chloride and imidazole (4) to yield the silyl ether **12** in 50% yield. The alcohol **12** was transformed into the mesylate **13**, which was subsequently treated with sodium dimethyl malonate to afford the substituted malonate **14** in 89% yield. The malonate anion of **14** generated by using sodium hydride was then left to react either with the requisite *EZ* allylic chloride (5) (chlorine on *E* side) or with its *EE* isomer (5) to afford the *ZEZ* and *EEZ* trienes **15** and **16**, respectively, in 76% and 70% yield. The silyl ether **15** was deprotected by means of tetrabutylammonium floride to give the alcohol **17** in 95% yield. The monosubstituted malonate **21** was synthesized from the alcohol **17** by the same two-step procedure used to prepare the malonate **14** from the alcohol **12**; subsequent cleavage of the tetrahydropyranyl ether with pyridinium *p*-toluenesulfonate (6) afforded

[1]Author to whom correspondence may be addressed. Tel: (819) 821-7002. Fax: (819) 821-7910.

Can. J. Chem. Downloaded from www.nrcresearchpress.com by 85.192.166.187 on 09/08/12
For personal use only.

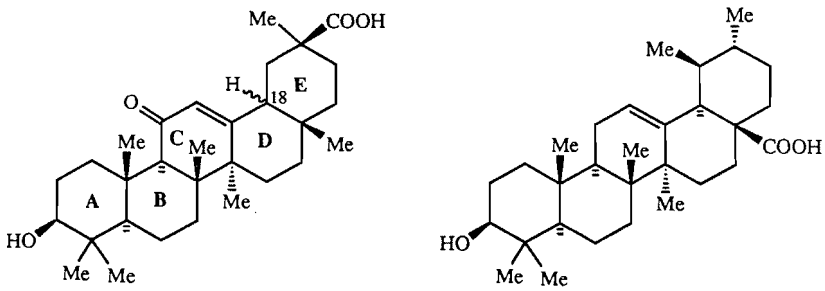

3 glycyrrhetinic acid (18α)
4 enoxolone (18β)

5 urshinic acid

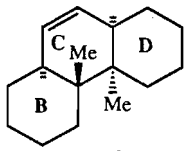

6

SCHEME 2

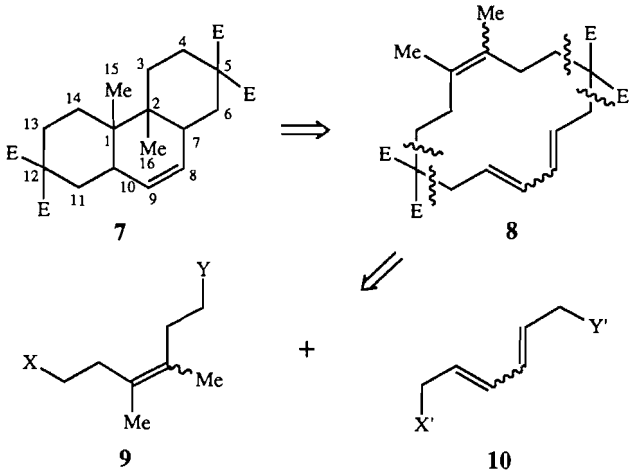

7 **8** **9** **10**

SCHEME 3

the allylic alcohol **23** (73% overall yield), which was transformed into the allylic chloride **25** using Meyers' conditions (7) in 71% yield.

Slow injection of the allylic chloride **25** into a suspension of cesium carbonate in a 1:1 mixture of *N,N*-dimethylformamide and tetrahydrofuran (high dilution conditions) to generate the malonate anion led to the CTC (or TCC) macrocyclic triene **27** in 83% yield.

The *EEZ* allylic chloride **26** was prepared from the silyl ether **16** by the same five-step sequence used to synthesize the isomeric allylic chloride **25** from **15**, and with similar yields. The crude allylic chloride **26** was slowly added to a suspension of cesium carbonate as in the case of the isomeric *ZEZ* allylic chloride **25**. However, the macrocyclization proved to be a difficult process; three macrocycles were observed. The desired TTC macrocycle **28** was obtained in 50% yield; the dimeric macrocycle **29** was also formed in 5% yield as well as the 12-membered ring macrocycle **30** (5% yield), generated through an S_N2 displacement of the allylic chlorine atom in **26**.

*Synthesis of the macrocyclic trienes **43** and **44** possessing a* trans *dienophile (Schemes 5 and 6)*

The *E* diol **31** (3) was transformed into the dimesylate **32**, which was then treated without purification with sodium dimethyl malonate and potassium iodide to give the dimalonate **33** in 76% overall yield. The *ZEE*, *EZE*, and *EEE* trienic alcohols **37**, **38**, and **39** were prepared from **33**, in the same way that **17** and **18** had been made from the malonate **14**, in 55, 52, and 64% yield from the corresponding allylic chlorides. The allylic alcohols **37** and **38** were transformed into the allylic chlorides **40** and **41**, which underwent internal SN_2 displacement of their allylic chlorine atoms when treated with cesium carbonate under high dilution conditions. Thus, the resulting CTT (or TCT) macrocyclic triene **43** was obtained in 54% yield from **37** and 76% yield from **38**. Similar treatment of the crude allylic chloride **42**, obtained from **39**, did not lead to the expected TTT macrocyclic triene **44** but rather, as already observed for other TTT systems (1, 8), directly to the corresponding TAC (or CAT) Diels–Alder adduct **49** in 28% yield from the allylic alcohol **39**.

For comparison, it has to be noted that *trans-trans* dienes usually undergo easy intramolecular Diels–Alder cyclization, as already observed for other TTT and TTC trienic systems possessing trisubstituted dienophiles (8). In these two cases, the TTC macrocycle could only be isolated when the macrocyclization was performed at 60°C. Such a temperature was found to be too low for the TTT macrocycle to be formed from its *EEE* allylic chloride precursor. Macrocyclization of the *EEE* system at 80°C led directly to the corresponding TAC and CAT tricycles; the TTC macrocycle also experienced Diels–Alder reaction at that temperature, thus showing how favored these Diels–Alder reaction processes are. In the present case, differing only by the heavier substitution of the dienophile moiety, the TTC macrocycle was isolated whereas the TTT isomer was not. Moreover, the TTC system required a temperature of 160°C for the cycloaddition reaction to take place, which is at least 80°C higher than that needed for the TTT isomeric system. Thus,

Can. J. Chem. Downloaded from www.nrcresearchpress.com by 85.192.166.187 on 09/08/12
For personal use only.

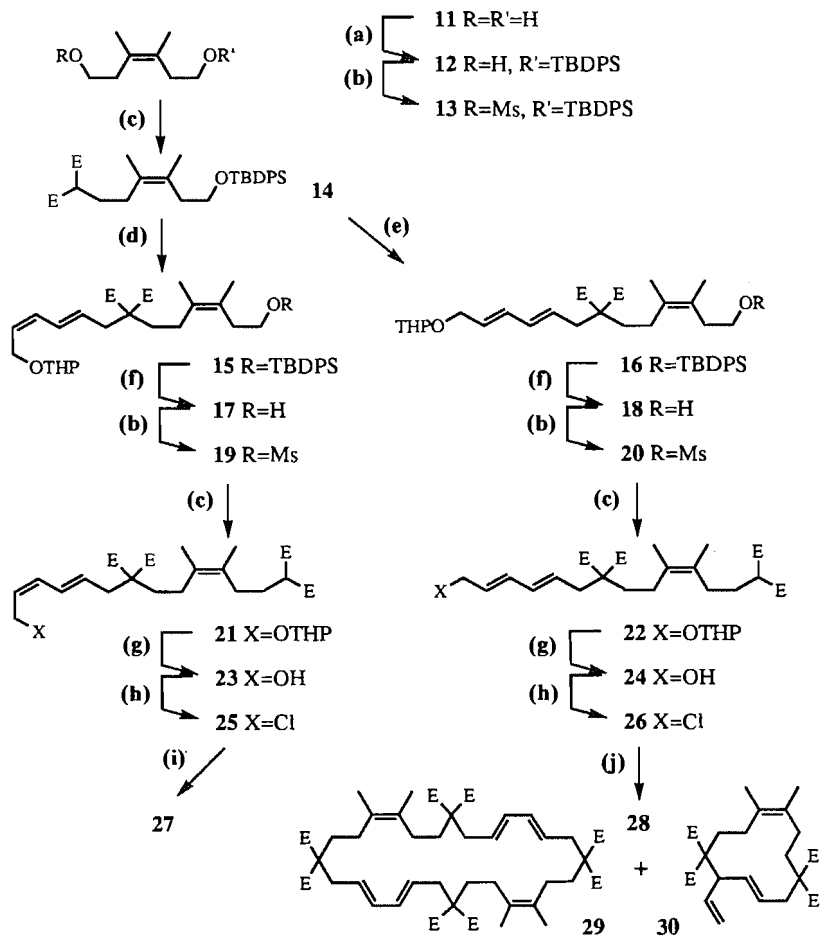

(a) TBDPSCl, imidazole, CH_2Cl_2, r.t. **(b)** NEt_3, MsCl, CH_2Cl_2, 0°C.
(c) **i:** CH_2E_2, NaH, KI, DMF, r.t. **ii:** **13** or **19** or **20**, THF, 95°C.
(d) **i:** **14**, NaH, DMF, THF, r.t. **ii:** *EZ* $ClCH_2CH{=}CHCH{=}CHCH_2OTHP$, THF, r.t.
(e) **i:** **14**, NaH, DMF, THF, r.t. **ii:** *EE* $ClCH_2CH{=}CHCH{=}CHCH_2OTHP$, THF, r.t.
(f) TBAF, THF, r.t. **(g)** PPTS, MeOH, 55°C. **(h)** LiCl, collidine, MsCl, DMF, 0°C.
(i) Cs_2CO_3, THF, DMF, 70°C. **(j)** Cs_2CO_3, MeCN, reflux

SCHEME 4

TTT macrocyclic trienes are shown to be more prone to Diels–Alder cyclization than their TTC isomers.

The Diels–Alder reaction (Schemes 6 and 7)

The CTC macrocycle **27** underwent the Diels–Alder reaction (yield 88%) when heated at 350°C for 3.5 h in toluene and in a sealed tube. The *trans-syn-cis* (TSC being identical to CST) structure of the only observed adduct **45** was determined by NMR analysis and comparison with other TSC and CST adducts (9) related to **45**; it corresponds to the expected Diels–Alder adduct obtained via the steric interaction free transition state **A** in a chair-boat-chair conformation (Scheme 7).

The macrocycle TTC **28** is the only one that can theoretically give rise to two adducts: namely, the TST tricycle **46** issued from the transition state **B** and the CSC tricycle **47** from the transition state **C**. Experimentally, the TTC macrocycle **28** was heated at 160°C for 90 min in toluene, the TST tricycle **46** only was formed in 100% yield; its geometry was determined by NMR analysis: the NMR spectrum shows that the molecule is symmetrical and that the protons at positions 7 and 10 (Scheme 3) are axial ($J_{H7,H6} = J_{H10,H11} = 3.5$ and 13.5 Hz). The TST tricycle **46**, having its B ring in a boat conformation, as in the transition-state-like structure **B**, is the only compound that can match these spectroscopic data. Thus, the highly favored chair-boat-chair transition state **B** alone is observed. The alternative transition state **C**, having two 1,3-diaxial steric interactions between the ester groups and the diene, is much too disfavored to compete with **B**. As a result no CSC tricycle **47** is obtained in the transannular Diels–Alder reaction of **28**.

The CTT macrocycle **43** was treated in the same way as the isomeric TTC macrocycle **28**; the CAC tricycle **48**, whose structure was confirmed by X-ray analysis (10) (Fig. 1), was obtained in 65% yield via the transition state **D**, which displays one 1,3-diaxial steric interaction between one ester and the E side of the diene. As discussed before, the TTT macrocycle [**44**] was not isolated, but rather the corresponding TAC (TAC = CAT) macrocycle **49**, whose structure was established by X-ray analysis[2] (Fig. 1), resulted from the cyclization of the chloride **42** (28% from the allylic alcohol **39**, Scheme 5). The transition

[2]A.G. Michel, P. Giguere, P. Deslongchamps, and N. Michel-Dewez. Unpublished results.

Can. J. Chem. Downloaded from www.nrcresearchpress.com by 85.192.166.187 on 09/08/12
For personal use only.

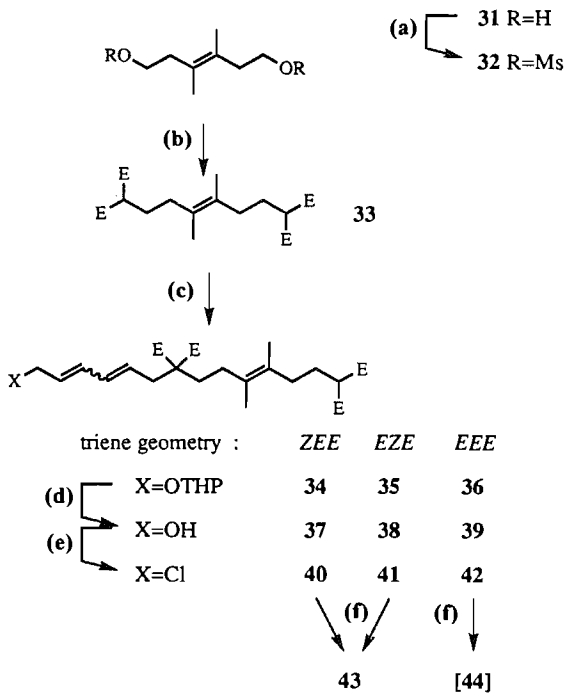

(a) NEt_3, MsCl, CH_2Cl_2, 0°C. **(b) i:** CH_2E_2, NaH, KI, DMF, r.t. **ii: 32**, THF, 95°C. **(c) i: 33**, NaH, DMF, THF, r.t. **ii:** *EZ* or *ZE* or *EE* $ClCH_2CH{=}CHCH{=}CHCH_2OTHP$, THF, r.t. **(d)** PPTS, MeOH, 55°C. **(e)** LiCl, collidine, MsCl, DMF, 0°C. **(f)** Cs_2CO_3, MeCN, reflux

SCHEME 5

state **E** that must arise to generate the tricycle **49** displays the same 1,3-diaxial steric interaction as already observed in the other *E* dienophile containing transition-state **D**. **E** is, however, much preferred to **D** because it involves an *EE* diene, whose *cisoid* conformation is sterically favored.

Conclusion

Transannular Diels–Alder reactions involving tetrasubstituted non-activated dienophiles are easy processes that lead neatly to the expected adducts. Of particular importance are the TTT trienic systems, which still undergo electrocyclization at low temperature, and which can then be handled on a large scale. Moreover, the TAC (or CAT) TTT adducts characterized by the basic skeleton **6** (Scheme 2) can be utilized in triterpene syntheses where the B, C, and D rings would be obtained in a stereospecific manner. Work in that direction is currently being carried out in our laboratories. The lower temperature necessary for TTT trienes to undergo Diels–Alder cyclization with regards to their TTC equivalents seems to be a general trend, since this intriguing phenomenon has once again been observed (9, 11). The reason remains unfortunately unclear: simple Dreiding model manipulation suggests that, in both the *transoid* and the *cisoid* diene ground state conformations, the dienophile is held close and parallel to the diene in TTT systems; such is not the case for TTC macrocycles, where both reacting centres are kept far apart and perpendicular to each other for minimum interactions to be reached. Molecular modelling calculations are currently underway to quantify these crude observations.

Experimental part

Melting points were recorded on a Rinco M-50 apparatus and are uncorrected. MS data were determined at 70 eV on a VG Micromass ZAB-1F spectrometer. The ir absorption spectra were measured on a Perkin Elmer 681 from neat compounds or chloroform solutions. Proton (^1H) and carbon (^{13}C) nmr spectra were recorded on a Bruker WM-250. Chemical shifts are reported relative to TMS (δ 0.00) with residual $CHCl_3$ (δ 7.26) or residual C_6D_6 (δ 7.21) as internal standard.

All reactions were conducted in oven-dried (120°C) or flame-dried glassware under an atmosphere of dry argon, unless otherwise stated. All reported compounds were homogeneous by thin-layer chromatography with at least two different solvent systems.

Silyl ether ***12***

To a solution of the diol **11** (100 mg, 0.69 mmol) in tetrahydrofuran (2.3 mL) was added imidazole (47 mg, 0.69 mmol) and *tert*-butylchlorodiphenylsilane (135 μL, 0.52 mmol) at room temperature. The resulting solution was stirred for 2 h, then more *tert*-butylchlorodiphenylsilane (45 μL, 0.17 mmol) was added and the mixture was stirred for a further 1 h. Solvent was removed and the product was purified by flash column chromatography using hexane and ethyl acetate (7:3) as eluent to give the title compound (132 mg, 50%); ir ($CHCl_3$) ν: 3620, 3450, 3060, 2950, 2850, 1110, 1080 cm^{-1}; ^1H nmr (80 MHz) δ (ppm): 1.05 (9H, s, Me_3CSi), 1.60 (3H, m, *Me*C=CMe), 1.64 (3H, m, MeC=C*Me*), 2.23 (2H, t, J = 6.5 Hz, CH_2CH_2OH), 2.37 (2H, t, J = 7 Hz, CH_2CH_2OSi), 3.57 (2H, t, J = 6.5 Hz, CH_2OH), 3.67 (2H, t, J = 7 Hz, CH_2OSi), 7.3–7.5 (6H, m, *Ph*), 7.6–7.8 (4H, m, *Ph*); ms *m/e*: 325 ($M^+ - CMe_3$).

Malonate ***14***

To a solution of the alcohol **12** (1.64 g, 4.28 mmol) and triethylamine (0.87 mL, 6.27 mmol) in dichloromethane (150 mL) was added methanesulfonyl chloride (0.39 mL, 5.04 mmol) at 0°C. The solution was stirred for 2.5 h at 0°C; water was added and the organic layer was washed with brine and dried ($MgSO_4$), solvent was removed, and the crude mesylate **13** (1.97 g) was used directly in the next step without further purification.

Can. J. Chem. Downloaded from www.nrcresearchpress.com by 85.192.166.187 on 09/08/12
For personal use only.

Can. J. Chem. Downloaded from www.nrcresearchpress.com by 85.192.166.187 on 09/08/12
For personal use only.

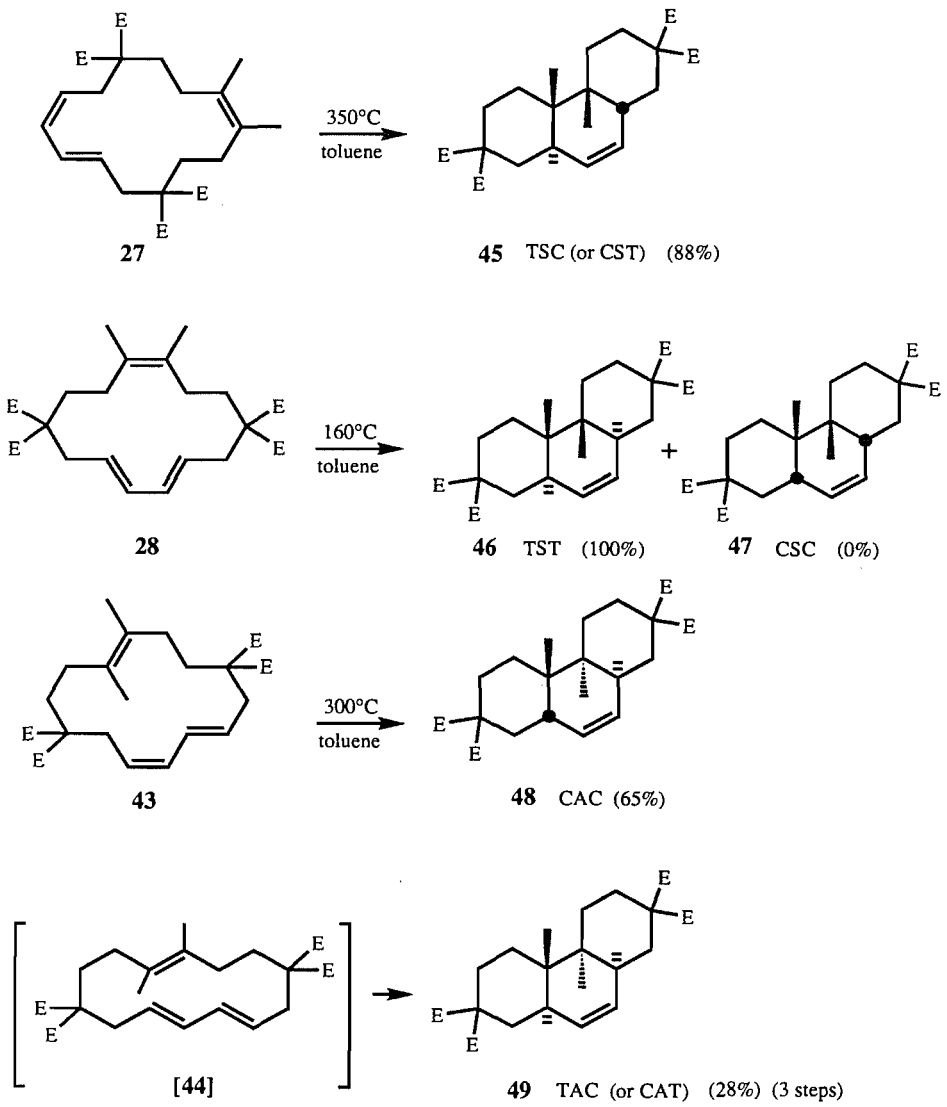

SCHEME 6

To a suspension of sodium hydride (60% in oil, 730 mg, 18.26 mmol) in tetrahydrofuran (30 mL) and *N,N*-dimethylformamide (30 mL) at 0°C was added dimethyl malonate (2.3 mL, 20.25 mmol). The mixture was stirred at 0°C for 15 min. Potassium iodide (0.31 g, 1.90 mmol) was first added, followed by a solution of the mesylate **13** (1.97 g) in tetrahydrofuran (30 mL). The resulting mixture was heated at 95°C for 6 h. The reaction was quenched with saturated aqueous ammonium chloride and the mixture was extracted several times with ether. The combined ether extract was washed with brine. Drying ($MgSO_4$) and removal of solvent under reduced pressure gave an oil, which was purified by chromatography on silica gel (hexane:ethyl acetate, 4:1) to yield the title compound as an oil (1.80 g, 89%); ir (neat) ν: 3050, 2950, 2860, 1735, 1110 cm^{-1}; ^1H nmr (250 MHz) δ (ppm): 1.03 (9H, s, Me_3CSi), 1.52 (3H, s, $MeC{=}CMe$), 1.59 (3H, s, $MeC{=}CMe$), 1.85–2.0 (4H, m, $(CH_2)_2C(CO_2Me)_2$), 2.27 (2H, t, J = 7 Hz, CH_2CH_2OSi), 3.28 (1H, t, J = 7.5 Hz, $CH(CO_2Me)_2$), 3.62 (2H, t, J = 7 Hz, CH_2OSi), 3.72 (6H, s, CO_2Me), 7.3–7.45 (6H, m, *Ph*), 7.6–7.7 (4H, m, *Ph*); ms *m/e*: 439 ($M^+ - CMe_3$).

Procedure for the preparation of trienic diethers

Triene ***15***

A solution of the malonate **14** (452 mg, 0.96 mmol) in tetrahydrofuran (4 mL) was slowly added to a suspension of sodium hydride (60% in oil, 47 mg, 1.16 mmol) in *N,N*-dimethylformamide (6 mL) and tetrahydrofuran (14 mL) at 0°C. The mixture was stirred for 20 min at 0°C and 10 min at room temperature. A solution of the required allylic chloride (5) (200 mg, 0.92 mmol) in tetrahydrofuran (4 mL) was added at 0°C and the resulting mixture was stirred for 23 h at room temperature. Saturated aqueous ammonium chloride was poured into the mixture and the aqueous phase was extracted several times with a mixture of ether and hexane (2:1). The combined organic extract was dried ($MgSO_4$) and solvent was removed. The residue was purified by flash column chromatography (hexane:ethyl acetate, 9:1) to give the title compound (496 mg, 76%); ir ($CHCl_3$) ν: 3010, 2945, 2855, 1735, 1197, 1110 cm^{-1}; ^1H nmr (80 MHz) δ (ppm): 1.03 (9H, s, Me_3CSi), 1.45–1.7 (12 H, m, $MeC{=}CMe$ and $(CH_2)_3$ THP), 1.85–2.0 (4H, m, $(CH_2)_2C(CO_2Me)_2$), 2.27 (2H, t, J = 7 Hz, CH_2CH_2OSi), 2.71 (2H, d, J = 7 Hz, $CH{=}CHCH_2C(CO_2Me)_2$), 3.60 (4H, m, OCH_2 THP and CH_2OSi), 3.70 (6H, s, CO_2Me), 4.24 (2H, m, $THPOCH_2$), 4.62 (1H, m, $OCHO$ THP), 5.4–5.7 (2H, m, $CH{=}CHCH{=}CH$), 6.0–6.3 (2H, m, $CH{=}CHCH{=}CH$), 7.35–7.5 (6H, m, *Ph*), 7.6–7.75 (4H, m, *Ph*); ms *m/e*: 619 ($M^+ - CMe_3$).

Triene ***16***. Yield: 70%; ir ($CHCl_3$) ν: 3005, 2955, 2860, 1730, 1215, 1110 cm^{-1}; ^1H nmr (250 MHz) δ (ppm): 1.03 (9H, s, Me_3CSi), 1.5–2.0 (16H, m, $MeC{=}CMe(CH_2)_2C(CO_2Me)_2$ and $(CH_2)_3$ THP), 2.26 (2H, t, J = 7 Hz, CH_2CH_2OSi), 2.68 (2H, d, J = 7.5 Hz, $CH{=}CHCH_2C(CO_2Me)_2$), 3.52 (2H, m, $OCHH$ THP), 3.63 (2H, t, J = 7 Hz, CH_2OSi), 3.71 (6H, s, CO_2Me), 3.87 (1H, m, $OCHH$ THP), 3.97

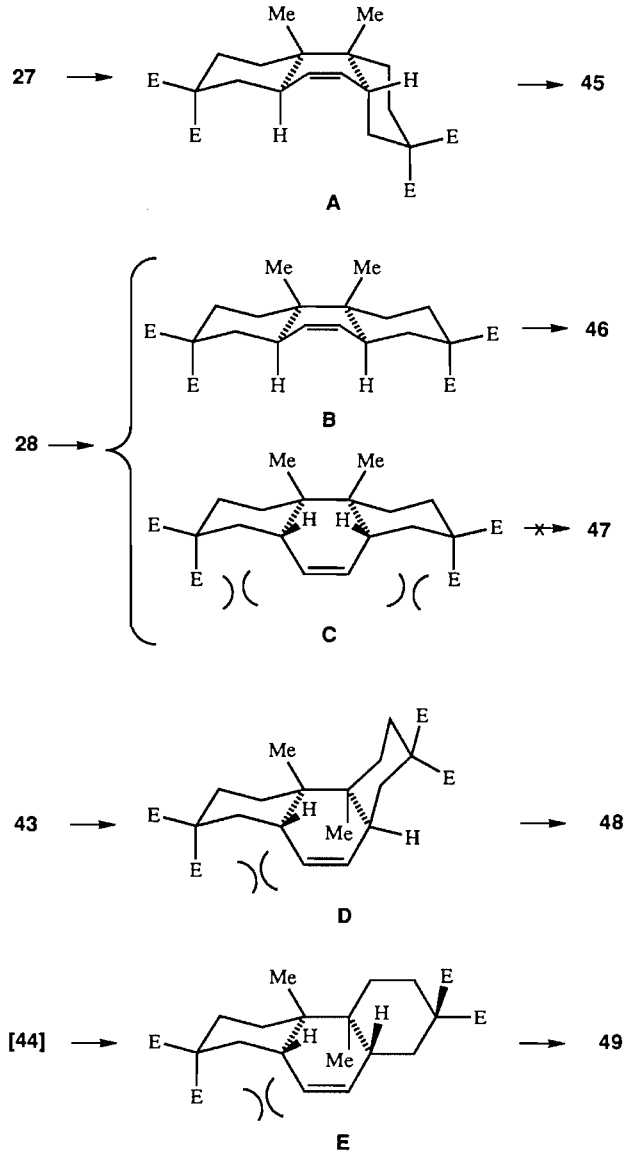

SCHEME 7

(1H, dd, J = 5.5, 13 Hz, THPOC*H*H), 4.23 (1H, dd, J = 5.5, 13 Hz, THPOCH*H*), 4.63 (1H, m, OC*H*O THP), 5.50 (1H, m, OCH_2CH=CHCH=C*H*), 5.68 (1H, m, OCH_2CH=CH), 6.0–6.25 (2H, m, CH=C*H*C*H*=CH), 7.35–7.45 (6H, m, *Ph*), 7.6–7.7 (4H, m, *Ph*); ms *m/e*: 619 ($M^+ - CMe_3$).

Procedure for the cleavage of silyl ethers

Alcohol ***17***

Tetrabutylammonium fluoride (1.47 mL, 1.47 mmol; 1 M in tetrahydrofuran) was slowly added at 0°C to a solution of the silyl ether **15** (496 mg, 0.73 mmol) in tetrahydrofuran (3 mL). The solution was stirred at room temperature for 2 h, solvent was removed, and the residue was purified by chromatography on silica gel (hexane:ethyl acetate, 1:1) to yield the title compound (305 mg, 95%); ir (neat) ν: 3460, 3020, 2862, 1730, 1200, 1030 cm^{-1}; ^1H nmr (80 MHz) δ (ppm): 1.6–1.65 (13H, m, *Me*C=C*Me*, $(CH_2)_3$ THP, and O*H*), 1.85–2.0 (4H, m, $(CH_2)_2C(CO_2Me)_2$), 2.25 (2H, t, J = 7 Hz, CH_2CH_2OH), 2.72 (2H, d, J = 7.5 Hz, CH=CH$CH_2C(CO_2Me)_2$), 3.45–3.7 (4H, m, OCH_2 THP and CH_2OH), 3.72 (6H, s, CO_2Me), 4.25 (2H, m, THPOCH_2), 4.61 (1H, m, OC*H*O THP), 5.4–5.7 (2H, m, C*H*=CHCH=C*H*), 6.05–6.3 (2H, m, CH=C*H*C*H*=CH).

Alcohol ***18***. Yield: 83%; ir ($CHCl_3$) ν: 3610, 3480, 3020, 2950, 2870, 1730, 1200, 1070 cm^{-1}; ^1H nmr (250 MHz) δ (ppm): 1.5–2.0 (11H, m, $(CH_2)_2C(CO_2Me)_2$, O*H*, and $(CH_2)_3$ THP), 1.63 (6H, s, *Me*C=C*Me*), 2.26 (2H, t, J = 6.5 Hz, CH_2CH_2OH), 2.70 (2H, d, J = 7.5 Hz, CH=CH$CH_2C(CO_2Me)_2$), 3.52 (1H, m, OC*H*H THP), 3.62 (2H, t, J = 6.5 Hz, CH_2OH), 3.73 (6H, s, CO_2Me), 3.85 (1H, m, OCH*H* THP), 3.98 (1H, dd, J = 13, 7.5 Hz, THPOC*H*H), 4.26 (1H, dd, J = 13, 6.5 Hz, THPOCH*H*), 4.64 (1H, m, OC*H*O THP), 5.51 (1H, dt, J = 15, 7 Hz, OCH_2CH=CHCH=C*H*), 5.72 (1H, dt, J = 14.5, 6 Hz, OCH_2CH=CH), 6.05–6.3 (2H, m, CH=C*H*C*H*=CH); ms *m/e*: 438 (M^+), 420 ($M^+ - H_2O$). Exact Mass ($M^+ - H_2O$), calcd.: 420.2512; found: 420.2509.

Procedure for the preparation of allylic alcohols

Alcohol ***23***

Methanesulfonyl chloride (65 μL, 0.84 mmol) was slowly added at 0°C to a solution of the alcohol **17** (305 mg, 0.70 mmol) and triethylamine (146 μL, 1.05 mmol) in dichloromethane (8 mL). The solution was stirred at 0°C for 2 h, treated with cold water, and extracted with dichloromethane. The combined organic extract was washed with water, dried ($MgSO_4$), and the solvent was removed to afford the mesylate **19** (350 mg), which was used in the next step without further purification.

To a suspension of sodium hydride (60% in oil, 126 mg, 3.15 mmol) in tetrahydrofuran (5 mL) and *N,N*-dimethylformamide (5 mL) at 0°C

Can. J. Chem. Downloaded from www.nrcresearchpress.com by 85.192.166.187 on 09/08/12
For personal use only.

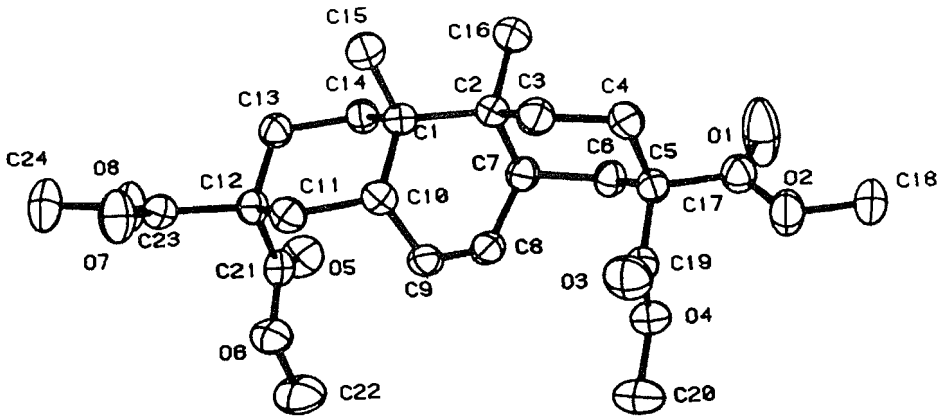

TRICYCLE **48**

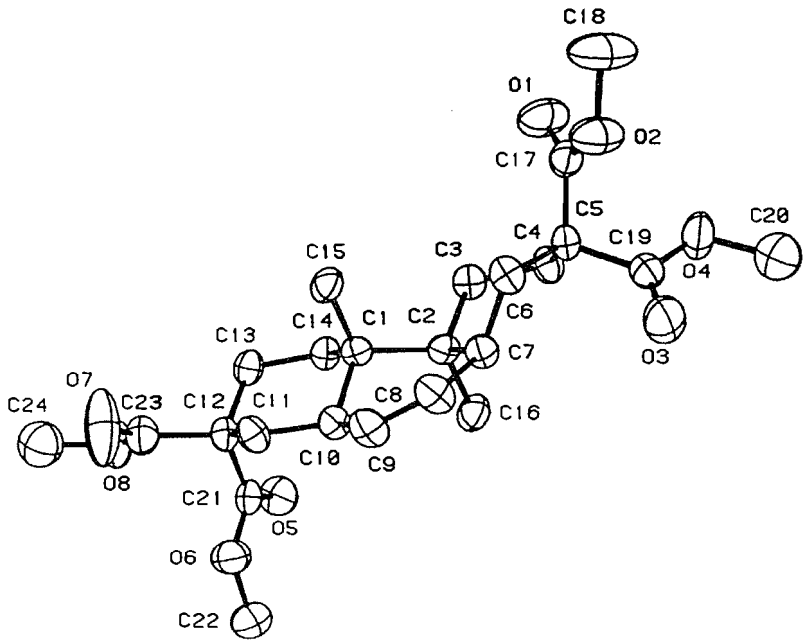

TRICYCLE **49**

FIG. 1. ORTEP perspective views (Johnson, 1976), molecular formulae, and atomic numbering of the tricycles **48** and **49** (10, 11).

was added dimethyl malonate (394 μL, 3.50 mmol). The mixture was stirred at 0°C for 15 min. Potassium iodide (50 mg, 0.31 mmol) was added together with a solution of the mesylate **19** (350 mg) in tetrahydrofuran (4 mL). The resulting reaction mixture was heated at 95°C for 16 h, treated with saturated aqueous ammonium chloride, then extracted several times with a mixture of ether and hexane (2:1). The organic extract was dried ($MgSO_4$), solvent was removed, and the residue was purified by chromatography on silica gel to afford the malonate **21** contaminated with residual dimethyl malonate (387 mg), which was used immediately in the next step.

The crude malonate **21** (387 mg) in methanol (6 mL) was treated with pyridinium paratoluenesulfonate (70 mg, 0.28 mmol) at 55°C for 1.3 h. The solvent was removed and the oily residue was purified by chromatography on silica gel (hexane:ethyl acetate, 6:4) to yield the title compound (237 mg, 73%); ir (neat) ν: 3500, 3010, 2950, 2860, 1730, 1435, 1200, 1040 cm^{-1}; ^1H nmr (80 MHz) δ (ppm): 1.58 (6H, s, *Me*C=C*Me*), 1.60 (1H, br, O*H*), 1.83 (4H, s, CH_2(Me)C=CMeCH_2), 1.9–2.0 (4H, m, CH_2CH_2(Me)C=CMeCH_2CH_2), 2.70 (2H, d, J = 7.5 Hz, CH=CHCH_2C(CO_2Me)$_2$), 3.28 (1H, m, C*H*(CO_2Me)$_2$), 3.72 (12H, s, CO_2*Me*), 4.28 (2H, m, CH_2OH), 5.4–5.7 (2H, m, C*H*=CHCH=C*H*), 6.1–6.3 (2H, m, CH=C*H*C*H*=CH); ms *m/e*: 450 ($M^+ - H_2O$). Exact Mass ($M^+ - H_2O$), calcd.: 450.2252; found: 450.2253.

Alcohol **24**. Yield: 80%; ir ($CHCl_3$) ν: 3600, 3500, 3055, 2955, 2865, 1730, 1205, 995 cm^{-1}; ^1H nmr (250 MHz) δ (ppm): 1.56 (1H, br, OH), 1.59 (6H, s, MeC=CMe), 1.83 (4H, s, CH_2(Me)C=CMeCH_2), 1.9–2.0 (4H, m, CH_2CH_2(Me)C=CMeCH_2CH_2), 2.70 (2H, d, J = 7.5 Hz, CH=CHCH_2C(CO_2Me)$_2$), 3.30 (1H, t, J = 7 Hz, CH(CO_2Me)$_2$), 3.73 (6H, s, CO_2Me), 3.74 (6H, s, CO_2Me), 4.16 (2H, t, J = 5.5 Hz, CH_2OH), 5.51 (1H, dt, J = 14, 7.5 Hz, OCH_2CH=CHCH=CH), 5.78 (1H, dt, J = 15, 5.5 Hz, OCH_2CH=CH), 6.05–6.3 (2H, m, CH=CHCH=CH); ms m/e: 450 ($M^+ - H_2O$), 435 (M^+ – Me), 417 ($M^+ - CO_2$Me). Exact Mass ($M^+ - H_2O$), calcd.: 450.2252; found: 450.2253.

Dimalonate 33

The diol **31** (1.68 g, 11.7 mmol) and triethylamine (4.9 mL, 35 mmol) were dissolved in dichloromethane (150 mL). The solution

Can. J. Chem. Downloaded from www.nrcresearchpress.com by 85.192.166.187 on 09/08/12
For personal use only.

Can. J. Chem. Downloaded from www.nrcresearchpress.com by 85.192.166.187 on 09/08/12
For personal use only.

was cooled to 0°C and methanesulfonyl chloride (2.16 mL, 28 mmol) was added dropwise. The solution was stirred for 2 h at 0°C. Then, water was added and the combined organic extract was washed with brine and dried ($MgSO_4$), the solvent was removed, and the crude dimesylate **32** (3.59 g) was used right away in the next step.

Dimethyl malonate (6.68 mL, 58.5 mmol) was slowly added to a suspension of sodium hydride (53 mmol) in a mixture of tetrahydrofuran and *N,N*-dimethylformamide (180 mL, 1:1) at 0°C. The resulting mixture was stirred for 20 min at room temperature. A solution of the dimesylate **32** (3.59 g) in dry tetrahydrofuran (70 mL) was added, followed by potassium iodide (1.94 g, 11.7 mmol). The resulting mixture was heated with an oil bath at 95°C for 12 h. The reaction vessel was cooled to room temperature and its content was poured into a separatory funnel containing saturated aqueous ammonium chloride and water (1:1). The solution was extracted with hexane and ether (1:1). The organic layers were combined, washed with water and brine, dried ($MgSO_4$), and concentrated under reduced pressure. The product was purified by flash column chromatography using hexane and ether (11:9) as eluent. The solid obtained was crystallized in hexane and ether to afford the title compound (3.31 g, 76%); mp 54–55°C; ir ($CHCl_3$) ν: 3030, 2960, 2870, 1740, 1440 cm^{-1}; ^1H nmr (80 MHz) δ (ppm): 1.58 (6H, s, *Me*C=C*Me*), 1.85–2.1 (8H, m, $(CH_2)_2$-(Me)C=CMe$(CH_2)_2$), 3.30 (2H, m, $CH(CO_2Me)_2$), 3.74 (12H, s, CO_2Me); ms *m/e*: 372 (M^+).

Procedure for the preparation of trienic alcohols

ZEE Trienol 37

A solution of the dimalonate **33** (1.56 g, 4.19 mmol) in tetrahydrofuran (20 mL) was slowly added to a suspension of sodium hydride (3.0 mmol) in tetrahydrofuran and *N,N*-dimethylformamide (60 mL, 2:1) at 0°C. The resulting mixture was stirred for 30 min at room temperature, then cooled to 0°C. A solution of the *EZ* chlorodiene (5) (567 mg, 2.62 mmol) in tetrahydrofuran (20 mL) was added and the reaction mixture was stirred for 20 h at room temperature. It was cooled to 0°C and quenched by adding saturated aqueous ammonium chloride and water. The mixture was extracted with hexane and ether (1:1). The organic layers were combined, washed with water and brine, dried ($MgSO_4$), and filtered on silica gel using hexane and ether (1:1) as eluent. The filtrate was concentrated under reduced pressure and the crude product was dissolved in dry methanol (100 mL). A catalytic amount of pyridinium paratoluenesulfonate was added and the solution was heated at 55°C for 3 h. Methanol was evaporated under reduced pressure. Flash column chromatography using dichloromethane and ethyl acetate (4:1) as eluent afforded the title compound (670 mg, 55% from the chlorodiene) and unreacted dimalonate **33** (738 mg); ir ($CHCl_3$) ν: 3610, 3015, 2950, 1757, 1435 cm^{-1}; ^1H nmr (250 MHz) δ (ppm): 1.58 (6H, s, *Me*C=C*Me*), 1.85 (4H, s, $(CH_2)_2C(CO_2Me)_2$), 1.9–2.1 (5H, m, $(CH_2)_2CH(CO_2Me)_2$ and O*H*), 2.73 (2H, d, J = 7.5 Hz, CH=CHC*H*$_2$C$(CO_2Me)_2$), 3.30 (1H, t, J = 7 Hz, C*H*$(CO_2Me)_2$), 3.72 (6H, s, CO_2Me), 3.73 (6H, s, CO_2Me), 4.28 (2H, t, J = 5.5 Hz, C*H*$_2$OH), 5.4–5.7 (2H, m, C*H*=CHCH=C*H*), 6.04 (1H, t, J = 11 Hz, OCH_2-CH=C*H*), 6.39 (1H, dd, J = 11, 15 Hz, OCH_2CH=CHC*H*=CH); ms *m/e*: 468 (M^+), 450 ($M^+ - H_2O$).

EZE *Trienol 38*. Yield: 52% from the chlorodiene; ir ($CHCl_3$) ν: 3610, 3020, 2955, 2860, 1760, 1470 cm^{-1}; ^1H nmr (250 MHz) δ (ppm): 1.56 (6H, s, *Me*C=C*Me*), 1.86 (4H, s, $(CH_2)_2C(CO_2Me)_2$), 1.8–2.1 (5H, m, $(CH_2)_2CH(CO_2Me)_2$ and O*H*), 2.82 (2H, d, J = 7.5 Hz, CH=CHC*H*$_2$C$(CO_2Me)_2$), 3.29 (1H, t, J = 6.5 Hz, C*H*$(CO_2Me)_2$), 3.71 (6H, s, CO_2Me), 3.73 (6H, s, CO_2Me), 4.21 (2H, m, C*H*$_2$OH), 5.29 (1H, dt, J = 7.5, 10.5 Hz, OCH_2CH=CHCH=C*H*), 5.86 (1H, dt, J = 6, 14.5 Hz, OCH_2C*H*=CH), 6.13 (1H, br t, J = 11 Hz, OCH_2-CH=CHC*H*=CH), 6.54 (1H, dd, J = 11, 14.5 Hz, OCH_2CH=C*H*); ms *m/e*: 450 ($M^+ - H_2O$).

EEE *Trienol 39*. Yield: 64% from the chlorodiene; ir ($CHCl_3$) ν: 3610, 3030, 3015, 2958, 1758, 1470 cm^{-1}; ^1H nmr (250 MHz) δ (ppm): 1.58 (6H, s, *Me*C=C*Me*), 1.84 (4H, s, $(CH_2)_2C(CO_2Me)_2$), 1.9–2.1 (5H, m, $(CH_2)_2CH(CO_2Me)_2$ and O*H*), 2.69 (2H, d, J = 7.5 Hz, CH=CHC*H*$_2$C$(CO_2Me)_2$), 3.30 (1H, t, J = 6.5 Hz, C*H*$(CO_2Me)_2$), 3.71 (6H, s, CO_2Me), 3.73 (6H, s, CO_2Me), 4.17 (2H, m, C*H*$_2$OH), 5.51 (1H, dt, J = 7, 14.5 Hz, OCH_2CH=CHCH=C*H*), 5.74 (1H, dt, J = 6, 14.5 Hz, OCH_2C*H*=CH), 6.05–6.25 (2H, m, CH=C*HCH*=CH); ms *m/e*: 468 (M^+), 450 ($M^+ - H_2O$).

Procedure for the macrocyclizations

Macrocycle 27

Methanesulfonyl chloride (50 μL, 0.64 mmol) was slowly added at 0°C to a solution of the trienol **23** (100 mg, 0.21 mmol), collidine (85 μL, 0.64 mmol), and lithium chloride (54 mg, 1.28 mmol) in *N,N*-dimethylformamide (4 mL). The mixture was stirred at 0°C for 5 h, then water (4 mL) was added, and the resulting mixture was extracted several times with ether and hexane (1:1). The organic extract was washed with saturated aqueous cupric nitrate. Drying ($MgSO_4$) and removal of solvent afforded an oil that was purified by flash chromatography (hexane:ethyl acetate, 4:1) to give the allylic chloride **25** (41 mg, 40%) and unreacted allylic alcohol **23** (44 mg); ir (CH_2Cl_2) ν: 3000, 2955, 2860, 1730, 1435, 1204 cm^{-1}; ^1H nmr (80 MHz) δ (ppm): 1.58 (6H, s, *Me*C=C*Me*), 1.84 (4H, s, CH_2(*Me*)C=CMeCH_2), 1.9–2.0 (4H, m, CH_2CH_2(*Me*)C=CMeCH_2CH_2), 2.73 (2H, d, J = 7.5 Hz, CH=CHCH_2C$(CO_2Me)_2$), 3.27 (1H, m, C*H*$(CO_2Me)_2$), 3.72 (12H, s, CO_2Me), 4.17 (2H, d, J = 8 Hz, ClCH_2), 5.45–5.75 (2H, m, C*H*=CHCH=C*H*), 6.05–6.3 (2H, m, CH=C*HCH*=CH).

The allylic chloride **25** (41 mg, 0.08 mmol) dissolved in tetrahydrofuran (5 mL) and *N,N*-dimethylformamide (5 mL) was slowly added, by means of a syringe pump, over a period of 5 h to a suspension of cesium carbonate in tetrahydrofuran (8 mL) and *N,N*-dimethylformamide (8 mL) at 70°C. The reaction mixture was stirred for a further 3 h at 70°C. The cold mixture was filtered and the solvent was removed under reduced pressure. Flash chromatography (dichloromethane:hexane:ethyl acetate, 30:19:1) of the residue afforded the title compound, which was crystallized from dichloromethane and hexane (32 mg, 83%); mp 246–247°C; ir (CH_2Cl_2) ν: 2950, 1730, 1435, 1205 cm^{-1}; ^1H nmr (250 MHz) δ (ppm): 1.56 (3H, s, *Me*C=CMe), 1.57 (3H, s, MeC=C*Me*), 1.7–1.95 (8H, m, $(CH_2)_2$(Me)C=CMe$(CH_2)_2$), 2.75 (4H, d, J = 9 Hz, CH_2CH=CHCH=CHCH_2), 3.73 (12H, s, CO_2Me), 5.01 (1H, dt, J = 11, 7.5 Hz, C*H*=CHCH=CH), 5.43 (1H, dt, J = 15, 7.5 Hz, CH=CHCH=C*H*), 6.16 (1H, t, J = 11 Hz, CH=C*H*-CH=CH), 6.53 (1H, dd, J = 15, 11 Hz, CH=CHC*H*=CH); ^{13}C nmr (62 MHz) δ (ppm): 171.44 (*C*O_2Me), 132.54 (CH=*C*HCH=CH), 129.55 (CH=CH*C*H=CH), 128.89 (*C*H=CHCH=CH), 128.00 (MeC=CMe), 127.26 (MeC=*C*Me), 124.36 (CH=CHCH=*C*H), 58.09 ($C(CO_2Me)_2$), 57.20 ($C(CO_2Me)_2$), 52.51 (CO_2Me), 52.40 (CO_2Me), 35.31 (CH_2CH=CHCH=CHCH_2), 30.50 (CH_2-CH=CHCH=CH*C*H_2), 29.35 (CH_2(Me)C=CMe*C*H_2), 28.76 (CH_2CH_2(Me)C=C), 28.56 (C=CMeCH_2*C*H_2), 18.49 (*Me*C=CMe), 18.11 (MeC=C*Me*). Exact Mass (M^+) calcd.: 450.2253; found: 450.2253.

Macrocycle 28

The allylic chloride **26** was used without purification. Injection time: 10 h, additional stirring: 9 h; solvent: acetonitrile; temperature: reflux. The crude product was purified by flash chromatography (ethyl acetate:hexane, 1:4) to yield the title compound **28** (50% yield from **24**) together with the macrocycles **29** (5%) and **30** (5%).

Macrocycle 28. Melting point 158–160°C (dichloromethane, ether, hexane); ir (neat) ν: 3020, 2950, 2860, 1730, 1435, 1230, 1000 cm^{-1}; ^1H nmr (250 MHz) δ (ppm): 1.52 (6H, s, *Me*C=C*Me*), 1.65–1.9 (8H, m, $(CH_2)_2$(Me)C=CMe$(CH_2)_2$), 2.63 (4H, d, J = 7.5 Hz, CH_2-CH=CHCH=CHCH_2), 3.73 (12H, s, (CO_2Me), 5.74 (2H, m, C*H*=CHCH=C*H*), 6.20 (2H, m, CH=C*HCH*=CH); ^{13}C nmr (62 MHz) δ (ppm): 172.11 (CO_2Me), 134.05 (CH=*C*HCH=CH), 128.73 (*C*H=CHCH=*C*H), 128.44 (MeC=*C*Me), 57.47 ($C(CO_2Me_2)_2$), 52.40 (CO_2Me), 38.91 (CH_2CH=CHCH=CH*C*H_2), 31.10 (CH_2(Me)C=CMe*C*H_2), 30.24 (CH_2CH_2(Me)C=CMeCH_2*C*H_2), 18.07 (*Me*C=C*Me*). Exact Mass (M^+) calcd.: 450.2253; found: 450.2258.

Macrocycle 29. Melting point 183–185°C (dichloromethane, ether, hexane); ir (neat) ν: 3020, 2955, 2860, 1730, 1435, 1195, 990 cm^{-1}; ^1H nmr (250 MHz) δ (ppm): 1.55 (12H, s, *Me*C=C*Me*), 1.85 (16H, s,

Can. J. Chem. Downloaded from www.nrcresearchpress.com by 85.192.166.187 on 09/08/12
For personal use only.

(CH_2)$_2$(Me)C=CMe(CH_2)$_2$), 2.62 (8H, d, J = 7 Hz, CH_2CH=CH-CH=CHCH_2), 3.68 (24H, s, CO_2Me), 5.46 (4H, m, CH=CHCH=CH), 6.01 (4H, m, CH=CHCH=CH); ^{13}C nmr (62 MHz) δ (ppm): 171.52 (CO_2Me), 133.66 (CH=CHCH=CH), 127.81 (MeC=CMe), 126.88 (CH=CHCH=CH), 58.18 (C(CO_2Me)$_2$), 52.24 (CO_2Me), 36.10 (CH_2CH=CHCH=CHCH_2), 31.80 (CH_2-(Me)C=CMeCH_2), 28.76 (CH_2CH_2(Me)C=CMeCH_2CH_2), 18.22 (MeC=CMe). Exact Mass (M$^+$) calcd.: 900.4507; found: 900.4507.

Macrocycle ***30***. Melting point 124–127°C (dichloromethane, ether, hexane); ir (neat) ν: 3025, 2950, 2860, 1730, 1435, 1200 cm^{-1}; ^{1}H nmr (250 MHz) δ (ppm): 1.53 (3H, s, MeC=CMe), 1.54 (3H, s, MeC=CMe), 1.4–2.25 (8H, 2m, (CH_2)$_2$(Me)C=CMe(CH_2)$_2$), 2.56 (1H, dd, J = 14.5, 8 Hz, CH=CHCHHC(CO_2Me)$_2$), 2.86 (1H, ddd, J = 14.5, 6.5, 1.5 Hz, CH=CHCHHC(CO_2Me)$_2$), 3.47 (1H, t, J = 7.5 Hz, CH_2=CHCHCH=CH), 3.59 (3H, s, CO_2Me), 3.67 (9H, s, CO_2Me), 4.9–5.05 (2H, m, CH_2=CH), 5.46 (1H, dt, J = 15.5, 6.5 Hz, CH_2=CHCH=CH), 5.75–6.0 (2H, m, CH_2=CHCHCH=CH); ^{13}C nmr (62 MHz) δ (ppm): 172.15 (CO_2Me), 171.71 (CO_2Me), 171.55 (CO_2Me), 170.86 (CO_2Me), 136.63 (CH_2=CHCHCH=CH), 131.85 (CH_2=CHCHCH=CH), 128.86 (MeC=CMe), 128.23 (MeC=CMe), 128.13 (CH_2=CH), 116.94 (CH_2=CH), 60.50 (C(CO_2Me)$_2$), 56.28 (C(CO_2Me)$_2$), 52.56 (CO_2Me), 52.39 (CO_2Me), 52.10 (CO_2Me), 51.97 (CO_2Me), 50.57 (CH_2=CHCHCH=CH), 36.83 (CH=CHCH_2C(CO_2Me)$_2$), 31.72 (CH_2(Me)C=C), 31.67 (C=CMeCH_2), 29.55 (CH_2CH_2(Me)C=C), 28.59 (C=CMeCH_2-CH_2), 18.65 (MeC=CMe), 18.39 (MeC=CMe); ms *m/e*: 450.

Macrocycle ***43***

The title compound was prepared from the *ZEE* allylic alcohol **37** or the isomeric *EZE* allylic alcohol **38**. The corresponding allylic chlorides **40** and **41** were not purified. From **37**: injection time: 24 h, additional stirring: 2 h; solvent: acetonitrile; temperature: reflux; yield: 54%. From **38**: injection time: 6 h, additional stirring: 2 h; solvent: acetonitrile; temperature: reflux; yield: 76%.

Melting point 158–161°C (dichloromethane, hexane, ethyl acetate); ir ($CHCl_3$) ν: 3020, 2955, 1765, 1458, 1440, 1278 cm^{-1}; ^{1}H nmr (250 MHz) δ (ppm): 1.35 (1H, ddd, J = 3, 10, 15.5 Hz, CHHCH$_2$), 1.62 (3H, s, MeC=CMe), 1.65 (1H, br, CHHCH$_2$), 1.80 (3H, s, MeC=CMe), 1.90 (1H, ttt, J = 3, 10, 14.5 Hz, CHHCH$_2$), 2.05–2.25 (4H, m, CH_2-CH_2), 2.47 (1H, m, CHHCH$_2$), 2.62 (1H, dd, J = 10, 14.5 Hz, *trans* C=CHCHH), 2.63 (1H, dd, J = 7, 14 Hz, *cis* C=CHCHH), 2.81 (1H, dd, J = 10.5, 14 Hz, *cis* C=CHCHH), 2.82 (1H, dd, J = 6, 14.5 Hz, *trans* C=CHCHH), 3.73 (6H, s, CO_2Me), 3.74 (6H, s, CO_2Me), 4.95 (1H, dt, J = 6.5, 9.5 Hz, *cis* CH=CHCH=CH), 5.26 (1H, m, *trans* CH=CHCH=CH), 6.0–6.15 (2H, m, CH=CHCH=CH). Exact Mass (M$^+$) calcd.: 450.2253; found: 450.2246.

Procedure for the Diels–Alder reactions

Tricycle ***45***

A solution of the macrocycle **27** (10.5 mg, 23.0 μmol) in toluene (0.4 mL) was heated at 350°C in a sealed Pyrex tube for 3.5 h. The solvent was removed under reduced pressure and the residue was purified by flash chromatography (dichloromethane:hexane:ethyl acetate, 12:7:1) to yield the title compound (9.2 mg, 88%); ir (neat) ν: 3020, 2955, 2860, 1730, 1435, 1250 cm^{-1}; ^{1}H nmr (250 MHz) δ (ppm): 0.79 (3H, s, *Me*, H15), 0.93 (3H, s, *Me*, H16), 1.20 (1H, dm, J = 13 Hz, H3e), 1.35 (1H, ddd, J = 3, 5, 13 Hz, H14e), 1.51 (1H, dt, J = 4.5, 13 Hz, H14a), 1.64 (1H, dt, J = 3, 13 Hz, H4a), 1.70 (1H, dm, J = 13 Hz, H3a), 1.88 (1H, ddd, J = 5, 13, 14.5 Hz, H13a), 1.92 (1H, t, J = 14 Hz, H11a), 2.12 (1H, ddd, J = 3, 1.5, 14 Hz, H10), 2.1–2.35 (5H, m, H11e, H6a, H7, H4e, and H13e), 2.37 (1H, dd, J = 6, 14.5 Hz, H6e), 3.65 (3H, s, CO_2Me), 3.68 (3H, s, CO_2Me), 3.69 (3H, s, CO_2Me), 3.76 (3H, s, CO_2Me), 5.21 (1H, td, J = 2.5, 10 Hz, H8), 5.30 (1H, ddd, J = 1.5, 3, 10 Hz, H9); ^{13}C nmr (62 MHz) δ (ppm): 173.10 (CO_2Me), 172.76 (CO_2Me), 171.67 (CO_2Me), 171.29 (CO_2Me), 130.68 (C9), 129.82 (C8), 54.94 (C12), 52.53 (CO_2Me), 52.27 (C5), 51.88 (CO_2Me), 38.45 (C7), 38.31 (C1), 36.51 (C2), 35.19 (C10), 31.38 (C11), 31.13 (C6), 26.93 (C4), 26.70 (C13 and C14), 24.16 (C3), 16.71 (C16), 11.91 (C15). Exact Mass (M$^+$) calcd.: 450.2253; found: 450.2253.

Tricycle ***46***. Temperature: 160°C, solvent: toluene, reaction time: 90 min; yield: 100%; ir (neat) ν: 3020, 2955, 1730, 1435, 1215 cm^{-1}; ^{1}H nmr (250 MHz, C_6D_6) δ (ppm): 0.77 (6H, s, *Me*, H15 and H16), 1.20 (2H, ddd, J = 13.5, 4.5, 3 Hz, H3e and H14e), 1.90 (2H, td, J = 13.5, 4.5 Hz, H3a and H14a), 2.14 (2H, td, J = 13.5, 4.5 Hz, H4a and H13a), 2.25 (2H, ddd, J = 13, 3, 2 Hz, H7 and H10), 2.39 (2H, t, J = 13 Hz, H6a and H11a), 2.57 (2H, dm, J = 13.5 Hz, H4e and H13e), 2.69 (2H, dt, J = 13, 3 Hz, H6e and H11e), 3.35 (6H, s, CO_2Me), 3.32 (6H, s, CO_2Me), 5.61 (2H, d, J = 2 Hz, H8 and H9); ^{13}C nmr (250 MHz, C_6D_6) δ (ppm): 172.62 (CO_2Me), 171.59 (CO_2Me), 133.85 (C8 and C9), 55.15 (C5 and C12), 52.02 (CO_2Me), 40.66 (C7 and C10), 40.55 (C1 and C2), 31.43 (C6 and C11), 31.14 (C3 and C14), 27.78 (C4 and C13), 17.26 (C15 and C16). Exact Mass (M$^+$) calcd.: 450.2253; found: 450.2258.

Tricycle ***48***. Temperature: 300°C, solvent: toluene, reaction time: 80 min; yield: 65%. The structure of the title compound was determined by X-ray analysis (10) (Fig. 1); ^{1}H nmr (250 MHz) δ (ppm): 0.94 (6H, s, *Me*), 1.2–1.35 (3H, m, CH_2), 1.55–1.8 (3H, m, CH_2), 2.2–2.4 (8H, m, CH and CH_2), 3.64 (6H, s, CO_2Me), 3.67 (6H, s, CO_2Me), 5.25 (2H, s, HC=CH).

Tricycle ***49***

The *EEE* trienol **39** (75 mg, 0.16 mmol), collidine (63 μL, 0.48 mmol), and lithium chloride (41 mg, 0.96 mmol) were dissolved in *N,N*-dimethylformamide (1.3 mL). The solution was stirred at room temperature until the salt dissolved, then cooled to 0°C. Methanesulfonyl chloride (37 μL, 0.48 mmol) was slowly added, and the resulting mixture stirred for 1 h at 0°C, 30 min at room temperature, quenched with cold water (7 mL), and extracted with hexane and ether (1:1). The combined organic extract was sequentially washed with saturated aqueous cupric nitrate, water, and brine. The organic solution was dried ($MgSO_4$) and filtered on silica gel using hexane and ether (1:1) as eluent. The filtrate was concentrated under reduced pressure and the crude allylic chloride **42** obtained (82 mg) was used immediately in the next step.

A solution of the allylic chloride **42** (82 mg) in acetonitrile (10 mL) was added over a period of 12 h with a syringe pump to a refluxing suspension of cesium carbonate (261 mg, 0.8 mmol) and 18-crown-6 (211 mg, 0.80 mmol) in acetronitrile (30 mL). The suspension was refluxed for another 2 h, cooled to room temperature, and filtered on silica gel using dichloromethane and ethyl acetate (4:1) as eluent. The filtrate was concentrated under reduced pressure and the product was purified by flash column chromatography (dichloromethane:hexane:ethyl acetate, 15:9:1) to afford the title compound (20 mg, 28%) whose structure was determined by X-ray analysis (footnote 2) (Fig. 1); ^{1}H nmr (250 MHz) δ (ppm): 0.86 (3H, s, *Me*), 0.88 (3H, s, *Me*), 1.05–2.3 (14H, m, CH and CH_2), 3.70 (3H, s, CO_2Me), 3.71 (3H, s, CO_2Me), 3.72 (3H, s, CO_2Me), 3.75 (3H, s, CO_2Me), 5.30 (1H, bd, J = 10 Hz, CH=CH), 5.51 (1H, dt, J = 3, 10 Hz, CH=CH). Exact Mass (M$^+$) calcd.: 450.2253; found: 450.2246.

Acknowledgements

This work was supported financially by the Natural Sciences and Engineering Research Council of Canada (NSERCC) and by the Fonds pour la Formation de Chercheurs et l'Aide à la Recherche (FCAR) du Québec.

1. (*a*) S. Lamothe, A. Ndibwami, and P. Deslongchamps. Tetrahedron Lett. **29**, 1639 (1988); (*b*) Tetrahedron Lett. **29**, 1641 (1988).
2. D. Craig. Chem. Soc. Rev. **16**, 187 (1987).
3. J.Y. Roberge and P. Deslongchamps. Synth. Commun. **19**, 817 (1989).
4. S. Hanessian and P. Lavallée. Can. J. Chem. **53**, 2975 (1975).
5. A. Ndibwami, S. Lamothe, D. Guay, R. Plante, P. Soucy, S. Goldstein, and P. Deslongchamps. Can. J. Chem. **71**, 695 (1993).
6. M. Miyashita, A. Yoshikoshi, and P.A. Grieco. J. Org. Chem. **42**, 3772 (1977).
7. E.W. Collington and A.I. Meyers. J. Org. Chem. **36**, 3044 (1971).
8. (*a*) P. Deslongchamps. Aldrichmica Acta, **24**, 43 (1991); (*b*) Pure Appl. Chem. **64**, 1831 (1992).

9. A. Ndibwami, S. Lamothe, P. Soucy, S. Goldstein, and P. Deslongchamps. Can. J. Chem. **71**, 714 (1993).
10. A.G. Michel, P. Giguere, P. Deslongchamps, and N. Michel-Dewez. Acta Crystallogr. Sect. C: Cryst. Struct. Commun. **C46**, 1254 (1990).
11. Y.-C. Xu, A.L. Roughton, R. Plante, S. Goldstein, and P. Deslongchamps. Can. J. Chem. **71**, 1152 (1993).

Can. J. Chem. Downloaded from www.nrcresearchpress.com by 85.192.166.187 on 09/08/12
For personal use only.

Synthesis and characterization of *O,O*-alkylene dithiophosphate derivatives of dimethyl- and trimethylgermane. Crystal structure of $Me_2Ge[S_2POCMe_2CMe_2O]_2$

JOHN E. DRAKE,[1] ANIL G. MISLANKAR, AND RAJU RATNANI[2]

Department of Chemistry and Biochemistry, University of Windsor, Windsor, ON N9B 3P4, Canada

Received February 14, 1994

JOHN E. DRAKE, ANIL G. MISLANKAR, and RAJU RATNANI. Can. J. Chem. **72**, 1830 (1994).

The *O,O*-alkylene dithiophosphate derivatives of dimethyl- and trimethylgermane $Me_2Ge[S_2POCMe_2CMe_2O]_2$, $Me_2Ge[S_2POCH_2CMe_2CH_2O]_2$, $Me_2Ge[S_2POCH_2CEt_2CH_2O]_2$, $Me_3Ge[S_2POCMe_2CMe_2O]$, $Me_3Ge[S_2POCH_2CMe_2CH_2O]$, and $Me_3Ge[S_2POCH_2CEt_2CH_2O]$ have been prepared in 70–85% yields by reaction of the salts of the appropriate *O,O*-alkylene dithiophosphoric acid with dichlorodimethyl- and chlorotrimethylgermane. The compounds were characterized by infrared, Raman, and ^1H, ^{13}C, and ^{31}P NMR spectroscopy. The crystal structure of $Me_2Ge[S_2POCMe_2CMe_2O]_2$ was determined and it crystallizes as monoclinic in the space group $P2_1/a$ (No. 14) with the cell parameters a = 12.368(6) Å, b = 6.897(2) Å, c = 17.923(3) Å, β = 99.00(3)°, V = 2450(2) Å^3, Z = 4, R = 0.0455, and R_w = 0.0394. The environment about germanium is essentially that of a distorted tetrahedron resulting in a S—Ge—S angle of 89.9(1)° and a C—Ge—C angle of 121.6(5)°. In contrast with analogous non-cyclic diorganodithiophosphatogermanes, the terminal sulfur atoms are oriented towards germanium rather than away from it to give an average Ge---S intramolecular distance of 3.49(3) Å. The spectra are interpreted as indicating that the dithiophosphate groups are linked in identical fashion in all compounds **1–6**. The ^1H and ^{13}C NMR spectra are of particular interest in that, unlike the spectra reported previously for related species, the substituents on the atoms in both the five- and six-membered rings maintain their non-equivalence in solution.

JOHN E. DRAKE, ANIL G. MISLANKAR et RAJU RATNANI. Can. J. Chem. **72**, 1830 (1994).

On a préparé les dérivés dithiophosphates des diméthyl et triméthylgermanes : $Me_2Ge[S_2POCMe_2CMe_2O]_2$, $Me_2Ge[S_2POCH_2CMe_2CH_2O]_2$, $Me_2Ge[S_2POCH_2CEt_2CH_2O]_2$, $Me_3Ge[S_2POCMe_2CMe_2O]_2$, $Me_3Ge[S_2POCH_2CMe_2CH_2O]_2$ et $Me_3Ge[S_2POCH_2CEt_2CH_2O]_2$, avec des rendements allant de 70 à 85% en faisant réagir les sels appropriés de l'acide *O,O*-alkylène dithiophosphorique avec les dichlorodimèthyl et chlorotriméthylgermanes. On a caractérisé les composés par spectroscopie infrarouge, Raman et par la RMN du ^1H, du ^{13}C et du ^{31}P. On a déterminé la structure cristalline du composé $Me_2Ge[S_2POCMe_2CMe_2O]_2$, il cristallise dans le groupe d'espace monoclinique $P2_1/a$ (No 14) avec a = 12,368(6) Å, b = 6,897(2) Å, c = 17,923(3) Å, β = 99,00(3)°, V = 2450(2) Å^3, Z = 4, R = 0,0455 et R_w = 0,0394. L'environnement autour de l'atome de germanium est essentiellement celui d'un tétraèdre déformé résultant d'un angle S—Ge—S de 89,9(1)° et d'un angle C—Ge—C de 121,6(5)°. Contrairement aux analogues diorganodithiophosphatogermanes non cycliques, les atomes de soufre terminaux sont plutôt orientés vers le germanium, au lieu de s'en éloigner, pour donner une distance intramoléculaire moyenne Ge---S de 3,49(3) Å. Les spectres révèlent que les groupes dithiophosphates sont liés de la même façon dans tous les composés **1–6**. Les spectres de RMN du ^1H et du ^{13}C sont d'un intérêt particulier en ce sens que contrairement aux autres spectres répertoriés pour les espèces apparentées, les substituants sur les atomes dans les cycles à cinq et à six chainons maintiennent leur non-équivalence en solution.

[Traduit par la rédaction]

Introduction

Earlier reports on a variety of sulfur-containing groups attached to germanium have included studies on dithiocarbamate, dithiophosphate, and dithiocarbonate (xanthate) derivatives (1–3). In general, a variety of modes of bonding through sulfur have been established for a wide range of both transition and main group elements (4–7). In germanium dithiocarbamates, although there is only one distinct Ge—S bond, the second sulfur atom is oriented towards germanium at distances that indicate anisobidentate and in some cases close to bidentate character (1, 8–10). By contrast, there are no secondary interactions between germanium and the terminal sulfur atom in germanium dithiocarbonates and *O,O*-dialkyldithiophosphates because the orientation of the groups result in an oxygen atom being closer to germanium rather than the second sulfur atom (2, 11–14). However, in related tin compounds such as $Ph_2Sn[S_2P(O\textit{i}\text{-}Pr)_2]_2$, the dithiophosphate groups are bidentate (15) and in $Sn(S_2COEt)_4$, two dithiocarbonates are bidentate and two are monodentate (16). There have been extensive reports of the use of cyclic dithiophosphates as ligands with transition metals (17–23) as well as a few with main group elements (24–27) but none with germanium.

We report on the synthesis and characterization of dimethyl- and trimethylgermanium dithiophosphates of the type $Me_2Ge[S_2POGO]_2$ and $Me_3Ge[S_2POGO]$, where G = —CMe_2CMe_2—, —$CH_2CMe_2CH_2$—, and —$CH_2CEt_2CH_2$—. The X-ray crystal structure of $Me_2Ge[S_2POCMe_2CMe_2O]_2$, **1**, shows the second sulfur atom of the dithiophosphate groups oriented toward germanium, in contrast to that found for the non-cyclic dithiophosphate analogues. The NMR spectra of all of these compounds show features that have not been reported previously for derivatives of these cyclic dithiophosphates and suggest that the solid state structure is maintained in solution.

Experimental

Materials

Dichlorodimethyl- and trichloromethylgermane were obtained from Alfa and were used as supplied. Sodium and ammonium salts of *O,O*-alkylene dithiophosphates were prepared in the manner described in the literature and their purity was checked by ^1H, ^{13}C, and ^{31}P NMR

[1]Author to whom correspondence should be addressed; tel.: (519)-253-4232 (ext. 3551); fax.: (519)-973-7098; e-mail: ak4@uwindsor.ca.

[2]Present address: Department of Chemistry, Dayanand College, Ajmer, India.

Can. J. Chem. Downloaded from www.nrcresearchpress.com by 85.192.166.187 on 09/08/12
For personal use only.

Can. J. Chem. Downloaded from www.nrcresearchpress.com by 85.192.166.187 on 09/08/12
For personal use only.

spectroscopy (28). Benzene, toluene, carbon disulfide, and *n*-hexane were dried and distilled prior to use. All the reactions were carried out under vacuum in air and moisture-free conditions to prevent the formation of germanium oxides.

Synthesis of dimethyl- and trimethylgermane derivatives of alkylene dithiophosphates

$Me_2Ge[S_2POCMe_2CMe_2O]_2$, 1

Typically, the sodium salt of *O,O*-2,3-dimethylbutylene dithiophosphate, $Na[S_2\overline{POCMe_2CMe_2O}]$ (0.476 g, 2.03 mmol) and benzene (10 mL) were placed in a reaction vessel and degassed at −196°C. Me_2GeCl_2 (0.1 mL, 0.87 mmol) was then distilled into the vessel and the contents were allowed to gradually warm up to ambient temperature and then stirred for 8 h. The reaction mixture was filtered to separate NaCl and any unreacted salt after which the solvent was evaporated off *in vacuo* to yield a white solid of the desired product. This was dissolved in toluene which was then layered with *n*-hexane. Crystals appeared after 3–5 days as the *n*-hexane diffused into the toluene solution at 0°C. Thus was formed $Me_2Ge[S_2\overline{POCMe_2CMe_2O}]_2$ (**1**): colorless crystals; mp 144–145°C; yield 82%; IR 1138 s, 953 s and 918 vs (compared with 1138 s, 955 s, and 902 vs in the corresponding starting salt). Unfortunately, the crystals grown in the toluene/*n*-hexane mixture were not suitable for X-ray diffraction studies. A few of these crystals were dissolved in CS_2 and slow evaporation of the CS_2 at 4°C produced colorless needle-like crystals which were of X-ray quality and were used for crystal structure determination.

$Me_2Ge[S_2\overline{POCH_2CMe_2CH_2O}]_2$, 2, $Me_2Ge[S_2\overline{POCH_2CEt_2CH_2O}]_2$, 3, $Me_3Ge[S_2\overline{POCMe_2CMe_2O}]$, 4, $Me_3Ge[S_2\overline{POCH_2CMe_2CH_2O}]$, 5, $Me_3Ge[S_2\overline{POCH_2CEt_2CH_2O}]$, 6

These compounds were prepared by essentially the same method as just described using Me_2GeCl_2 or Me_3GeCl and the sodium or ammonium salt of the appropriate dithiophosphoric acid in slight excess to ensure complete substitution of chlorine. Thus were formed the following compounds. $Me_2Ge[S_2\overline{POCH_2CMe_2CH_2O}]_2$, **2**, white solid; mp 155–157°C; yield 76%; IR 1048 vs and 990 vs (compared with 1051 s and 1001 s in the corresponding starting salt). Anal. calcd. for $C_{12}H_{26}O_4P_2S_4Ge$: C 29.33, H 5.51; found: C 30.08, H 5.79. $Me_2Ge[S_2\overline{POCH_2CEt_2CH_2O}]_2$, **3**; white solid; mp 94–95°C; yield 78%; IR 1070 s, 1019 vs, 991 s, and 934 s (compared with 1071 s, 1021 vs, 1000 vs, and 937 s in the corresponding starting salt). $Me_3Ge[S_2\overline{POCMe_2CMe_2O}]$, **4**; white solid; mp 70–72°C; yield 80%; IR 1140 s, 956 s, and 919 vs (compared with 1138 s, 955 vs, and 902 vs in the corresponding starting salt). $Me_3Ge[S_2\overline{POCH_2CMe_2CH_2O}]$, **5**; white solid; mp 93–95°C; yield 74%; IR 1048 s and 993 s (compared with 1051 s and 1001 s in the corresponding starting salt). $Me_3Ge[S_2\overline{POCH_2CEt_2CH_2O}]$, **6**; white solid; mp 56–57°C; yield 71%; IR 1070 s, 1019 s, 993 vs, and 933 s (compared with 1071 s, 1021 vs, 1000 vs, and 937 s in the corresponding starting salt). Anal. calcd. for $C_{10}H_{23}O_2PS_2Ge$: C 35.02, H 6.73; found: C 35.07, H 6.67. Unfortunately, despite extensive efforts to grow X-ray quality crystals, none were obtained for compounds **2**–**6**.

Physical measurements

All solvents were distilled prior to use. The elemental analyses were performed at Guelph Chemical Laboratories, Guelph, Ontario, Canada. The infrared spectra were recorded on a Nicolet 5DX FT spectrometer as KBr pellets and far infrared spectra on a Bomem IR Spectrometer between polyethylene films as Nujol mulls. The Raman spectra were recorded on a Spectra-Physics 164 spectrometer using the 5145-Å exciting line of an argon ion laser with samples sealed in capillary tubes. The ^1H and ^{13}C NMR spectra were recorded on a Bruker 300 FT NMR spectrometer in $CDCl_3$ solutions using Me_4Si as internal standard. The ^{31}P NMR spectra were recorded on a Bruker 200 FT NMR spectrometer in $CDCl_3$ using H_3PO_4 as external standard. The melting points were determined on a Fisher–Johns apparatus.

X-ray crystallographic analysis

A needle-like crystal of $Me_2Ge[S_2\overline{POCMe_2CMe_2O}]_2$, **1**, was sealed in a thin-walled glass capillary and mounted on a Rigaku AFC6S diffractometer, with graphite-monochromated MoKα radiation.

Cell constants and an orientation matrix for data collection, obtained from a least-squares refinement using the setting angles of 25 carefully centered reflections in the range $20° < 2\theta < 27°$ corresponded to a monoclinic cell whose dimensions are given in Table 1. The systematic absences ($h0l$, $h = 2n + 1$; $0k0$, $k = 2n + 1$) are observed. Based on packing considerations, statistical analyses of intensity distributions and the successful solution and refinement of the structure, the space group was determined to be $P2_1/a$ (No. 14).

The data were collected at a temperature of 23 ± 1°C using the ω–2θ scan technique to a maximum 2θ value of 50.0°. The ω scans of several intense reflections, made prior to data collection, had an average width at half-height of 0.34° with a takeoff angle of 6.0°. Scans of $(0.84 + 0.30 \tan\theta)°$ were made at a speed of 8.0°/min (in ω). The weak reflections ($I < 10.0\sigma(I)$) were rescanned (maximum of 2 rescans) and the counts were accumulated to assure good counting statistics. Stationary background counts were recorded on each side of the reflection. The ratio of peak counting time to background counting time was 2:1. The diameter of the incident beam collimator was 0.5 mm, and the crystal-to-detector distance was 285.0 mm.

Of the 3197 reflections which were collected, 3015 were unique ($R_{int} = 0.084$). The intensities of three representative reflections that were measured after every 150 reflections remained constant throughout data collection indicating crystal and electronic stability (no decay correction was applied).

The linear absorption coefficient for MoKα is 17.0 cm^{-1}. An empirical absorption correction, based on azimuthal scans of several reflections, was applied which resulted in transmission factors ranging from 0.84 to 1.00. The data were corrected for Lorentz and polarization effects.

The structure was solved by direct methods (for structure solution methods, see ref. 29). The non-hydrogen atoms other than oxygen and carbon atoms were refined anisotropically and the hydrogen atoms were included in their idealized positions with C—H set at 0.95 Å and with isotropic thermal parameters set at 1.2 times that of the carbon atom to which they were attached. The final cycle of full-matrix least-squares refinement[3] was based on 1178 observed reflections ($I > 3.00\sigma(I)$) (and 136 variable parameters and converged (largest parameter shift was 0.001 times its esd) with unweighted and weighted agreement factors of $R = \Sigma||F_o| - |F_c||/\Sigma|F_o| = 0.0455$ and $R_w = [(\Sigma w(|F_o| - |F_c|)^2/\Sigma w f_o^2)]^{1/2} = 0.0394$.

The standard deviations of an observation of unit weight[4] was 1.39. The weighting scheme was based on counting statistics and included a factor ($p = 0.01$) to downweight the intense reflections. Plots of $\Sigma w(|F_o| - |F_c|)^2$ versus $|F_o|$, reflection order in data collection, $\sin\theta/\lambda$, and various classes of indices showed no unusual trends. The maximum and minimum peaks on the final difference Fourier map corresponded to 0.35 and −0.33 e/Å^3, respectively.

Neutral-atom scattering factors were taken from Cromer and Waber (30). Anomalous dispersion effects were included in F_c (31); the values for $\Delta f'$ and $\Delta f''$ were those of Cromer (32). All calculations were performed using the TEXSAN (33) crystallographic software package of Molecular Structure Corp.

The final atomic coordinates and equivalent isotropic thermal

[3]Least-squares: function minimized: $\Sigma w(|F_o| - |F_c|)^2$, where $w = 4F_o^2(F_o^2)$, $\sigma^2(F_o^2) = [S^2(C + R^2B) + (pF_o^2)^2]/(Lp)^2$, S = scan rate, C = total integrated peak count, R = ratio of scan time to background counting time, Lp = Lorentz-polarization factor, and $p = p$ factor.

[4]Standard deviation of an observation of unit weight: $[\Sigma w(|F_o| - |F_c|)^2/N_o - N_v)^{1/2}$, where N_o = number of observations and N_v = number of variables.

Can. J. Chem. Downloaded from www.nrcresearchpress.com by 85.192.166.187 on 09/08/12
For personal use only.

TABLE 1. Summary of crystal data, intensity collection, and structural refinement for $Me_2Ge[S_2POCMe_2CMe_2O]_2$, **1**

Parameter	$C_{14}H_{30}O_4P_2S_4Ge$, **1**
Cell constants	
a (Å)	12.368(6)
b (Å)	10.164(1)
c (Å)	19.732(4)
β (deg)	99.00(3)
Cell volume (Å^3)	2450(2)
Space group	$P2_1/a$
Mol. wt. (g mol^{-1})	525.17
Z	4
ρ_{calcd} (g cm^{-1})	1.42
Absorption coefficient μ (cm^{-1})	17.04
Transmission factors	0.84–1.0
Temperature (°C)	23 ± 1
Radiation	MoKα 0.71069 Å
Monochromator	Highly oriented graphite
Total reflections measured	3197
Unique data used	1178
No. of parameters (NP)	136
$R = \Sigma\|\|F_o\| - \|F_c\|\|/\Sigma\|F_o\|$	0.0455
$R_w = [(\Sigma w(\|F_o\| - \|F_c\|)^2/\Sigma wF_o^2)]^{1/2}$	0.0394
Largest Δρ (e Å^{-3}) shift/error max.	0.0001
Largest residual electron density (e Å^{-3})	0.76
Atom associated with residual density	Ge

parameters for the non-hydrogen atoms are given in Table 2, important distances and bond angles in Tables 3 and 4, and an ORTEP diagram in Fig. 1. Tables of final thermal parameters of non-hydrogen atoms, final fractional coordinates, and thermal parameters of hydrogen atoms, and observed and calculated structure factors have been deposited.[5]

Results and discussion

Several cyclic dithiophosphate compounds of germanium were prepared in 70–85% yields by the action of a slight excess of the appropriate sodium or ammonium salt of *O,O*-alkylene dithiophosphoric acid with dichlorodimethyl- or chlorotrimethylgermane in benzene in accordance with the equations

$$Me_2GeCl_2 + 2MS_2\overline{POGO} \rightarrow Me_2Ge[S_2\overline{POGO}]_2 + 2MCl$$

$$Me_3GeCl + MS_2\overline{POGO} \rightarrow Me_3Ge[S_2\overline{POGO}] + MCl$$

where M = Na, NH_4; G = —CMe_2CMe_2—, —$CH_2CMe_2CH_2$—, and —$CH_2CEt_2CH_2$—. The reaction mixtures were stirred for approximately 8 h at room temperature followed by filtration to separate solid NaCl, NH_4Cl, or unreacted dithiophosphate salt. The solvent was pumped off to obtain a white solid which was recrystallized from fresh toluene at 4°C.

All of the compounds **1–6** are stable on exposure to atmospheric oxygen and moisture and in common organic solvents such as benzene, *n*-hexane, toluene, carbon disulfide, and chloroform; the latter being used as the preferred solvent for NMR spectroscopic studies. Solid samples of **1–6** are stable over a long period, particularly when kept refrigerated, as can be confirmed by the fact that NMR spectra recorded after several months show no changes from the spectra recorded initially. All of the compounds have sharp melting points and their ^{1}H NMR spectra confirm that they are 99% pure relative to any hydrogen-containing impurities.

Extensive attempts were made to grow X-ray quality crystals using a variety of solvents or solvent mixtures for **1–6**,

TABLE 2. Final fractional coordinates and B(eq) for non-hydrogen atoms of $Me_2Ge[S_2\overline{POCMe_2CMe_2O}]_2$, **1**, with standard deviations in parentheses

Atom	x	y	z	B(eq)
Ge(1)	0.6386(1)	0.2203(1)	0.23952(7)	3.10(7)
S(1)	0.7811(3)	0.1162(4)	0.2030(2)	5.0(2)
S(2)	0.5555(3)	0.0407(4)	0.0941(2)	5.3(2)
S(3)	0.7552(3)	0.3083(4)	0.3286(2)	4.2(2)
S(4)	0.5054(3)	0.4145(4)	0.3488(2)	6.2(2)
P(1)	0.7025(3)	0.0088(4)	0.1290(2)	3.6(2)
P(2)	0.6586(3)	0.4500(4)	0.3645(2)	3.7(2)
O(1)	0.7884(6)	0.0164(8)	0.0773(4)	4.0(2)
O(2)	0.7132(7)	0.1576(8)	0.1560(4)	4.6(2)
O(3)	0.6899(6)	0.5912(9)	0.3375(4)	4.7(2)
O(4)	0.7190(6)	0.4671(8)	0.4420(4)	3.6(2)
C(1)	0.584(1)	0.356(1)	0.1768(6)	4.8(3)
C(2)	0.543(1)	0.096(1)	0.2730(7)	5.5(4)
C(3)	0.818(1)	0.157(1)	0.0621(6)	4.2(3)
C(4)	0.806(1)	0.223(1)	0.1318(6)	4.2(3)
C(5)	0.729(1)	0.200(2)	0.0044(8)	6.8(4)
C(6)	0.930(1)	0.154(1)	0.0417(7)	6.3(4)
C(7)	0.910(1)	0.203(2)	0.1854(7)	6.6(4)
C(8)	0.779(1)	0.371(2)	0.1271(8)	7.5(4)
C(9)	0.771(1)	0.657(1)	0.3884(7)	4.8(3)
C(10)	0.746(1)	0.607(1)	0.4590(7)	4.4(3)
C(11)	0.752(1)	0.804(2)	0.3765(8)	7.8(4)
C(12)	0.884(1)	0.620(1)	0.3737(7)	6.8(4)
C(13)	0.646(1)	0.669(1)	0.4802(7)	5.4(4)
C(14)	0.843(1)	0.609(1)	0.5156(7)	6.2(4)

[5]Copies of material on deposit may be purchased from: The Depository of Unpublished Data, Document Delivery, CISTI, National Research Council Canada, Ottawa, ON K1A 0S2, Canada.

TABLE 3. Interatomic distances (Å) in $Me_2Ge[S_2\overline{POCMe_2CMe_2O}]_2$, **1**, with standard deviations in parentheses

Atoms	Distance	Atoms	Distance
Ge(1)—C(1)	1.91(1)	Ge(1)—C(2)	1.92(1)
Ge(1)—S(1)	2.268(4)	Ge(1)—S(3)	2.275(4)
S(1)—P(1)	2.061(5)	S(3)—P(2)	2.066(5)
S(2)—P(1)	1.909(5)	S(4)—P(2)	1.906(5)
P(1)—O(1)	1.587(8)	P(2)—O(3)	1.600(9)
P(1)—O(2)	1.603(9)	P(2)—O(4)	1.603(8)
O(1)—C(3)	1.51(1)	O(3)—C(9)	1.47(1)
O(2)—C(4)	1.47(1)	O(4)—C(10)	1.460(6)
C(3)—C(4)	1.56(2)	C(9)—C(10)	1.56(2)
C(3)—C(5)	1.52(2)	C(9)—C(11)	1.52(2)
C(3)—C(6)	1.51(2)	C(9)—C(12)	1.51(2)
C(4)—C(7)	1.55(2)	C(10)—C(13)	1.50(2)
C(4)—C(8)	1.53(2)	C(10)—C(14)	1.50(2)
Ge(1)---S(2)	3.471(4)	Ge(1)---S(4)	3.517(4)
P(1)---C(5)	3.19(1)	P(2)---C(12)	3.26(1)
P(1)---C(6)	3.82(1)	P(2)---C(11)	3.78(1)
P(1)---C(7)	3.29(1)	P(2)---C(13)	3.21(1)
P(1)---C(8)	3.80(1)	P(2)---C(14)	3.81(1)

but unfortunately it was only possible to do so for $Me_2Ge[S_2POCMe_2CMe_2O]_2$, **1**.

*The crystal structure of $Me_2Ge[S_2\overline{POCMe_2CMe_2O}]_2$, **1***

Dimethylbis(*O,O*-2,3-dimethylbutylene dithiophosphato)germane, **1**, crystallizes in the space group $P2_1/a$ and its ORTEP diagram (Fig. 1) illustrates that the immediate environment about germanium is that of a distorted tetrahedron. The C—Ge—C angle of 121.6(5)° is considerably larger than the all-tetrahedral angle but is essentially identical to that found in $Ph_2Ge[S_2CNEt_2]_2$ and in the starting material Me_2GeCl_2 (34). Naturally, the S—Ge—S angle is much smaller than the all tetrahedral angle but at 89.9(1)° it is wider than those in $Ph_2Ge[S_2CNEt_2]_2$ or $Me_2Ge[S_2CNMe_2]_2$ (35), which are 84.4(1) and 87.0(1)°, respectively. The distortions are considerably larger than that found in the related non-cyclic dithiophosphate, $Ph_2Ge[S_2P(OMe)_2]_2$, where the C—Ge—C and S—Ge—S angles are 115.8(3) and 103.5(1)°, respectively (2). The Ge—C bond distances in **1** are comparable to those in $Me_2Ge[S_2CNMe_2]_2$, 1.921(7) and 1.910(6) Å, $Ph_2Ge[S_2CNEt_2]_2$, 1.928(3) Å, and $Ph_2Ge[S_2P(OMe)_2]_2$, 1.931(7) Å. The Ge—S bond lengths of 2.268(4) and 2.275(4) Å in **1** are similar to those in $Ph_2Ge[S_2CNEt_2]_2$ and $Me_2Ge[S_2CNMe_2]_2$, but longer than those in $Ph_2Ge[S_2P(OMe)_2]_2$, 2.255(4), and $Ph_2Ge[S_2CO(i\text{-}Pr)]_2$, 2.252(3) Å. The xanthate and dithiophosphate ligands are undoubtedly monodentate, with Ge---S distances to the terminal sulfur atom averaging 4.754(1) Å in $Ph_2Ge[S_2CO(i\text{-}Pr)]_2$ and 5.38(2) Å in $Ph_2Ge[S_2P(OMe)_2]_2$. The longer Ge—S bonds in **1** and $Ph_2Ge[S_2CNEt_2]_2$ could arise because the ligands are mono- or anisobidentate, with the closing down of the S—Ge—S angle allowing room for the non-bonding, or anisobonding, sulfur atom to be oriented toward germanium. No such closing down of the angle is required or observed for the monodentate ligands in $Ph_2Ge[S_2P(OMe)_2]_2$ or $Ph_2Ge[S_2CO(i\text{-}Pr)]_2$, where the second sulfur atom is oriented away from germanium, and the S—Ge—S angles are similar to the X—Ge—X angles reported in the gas phase for Me_2GeCl_2 and Me_2GeBr_2 where no secondary intramolecular interactions can be involved. In $Me_2Ge[S_2CNMe_2]_2$ and $Ph_2Ge[S_2CNEt_2]_2$ (1, 9), the anisobonding sulfur atoms give Ge---S distances of 3.16(1) and 3.183(1) Å, respectively, which are well within the sum of the van der Waals radii of germanium and sulfur of 3.75 Å (36), whereas those in $Me_2Ge[S_2\overline{POCMe_2CMe_2O}]_2$, **1**, of 3.471(4) and 3.517(4) Å, are relatively long. In the related tin compounds, $Me_2Sn[S_2\overline{POCMe_2CMe_2O}]_2$ (25) and $Ph_3Sn[S_2\overline{POCMe_2CMe_2O}]$ (26), the aniso Sn---S distances are shorter, ranging from 3.130(1) to 3.411(3) Å, whereas in non-cyclic dithiophosphate tin derivatives, the dithiophosphate groups are fully bidentate as is illustrated by the structure of $Ph_2Sn[S_2P(Oi\text{-}Pr)_2]_2$, in which all four Sn—S bonds cover the range 2.678(1) to 2.689(1) Å (15). Thus, although non-cyclic dithiophosphate derivatives of tin are generally bidentate and those of germanium are monodentate, the cyclic dithiophosphates of tin appear to be anisobidentate and those of germanium, if not also anisobidentate, are at least oriented in a similar fashion.

The P—S(Ge) bonds in $Me_2Ge[S_2POCMe_2CMe_2O]_2$, **1**, are only slightly longer, 2.064(5) Å, than the P=S bonds, 1.908(5) Å. These relatively small differences are typical of all metal dithiophosphates, irrespective of their mode of bonding, and are similar to those reported for the diligands, $[OCMe_2CMe_2OP(S)S]_2$ (37) and $[(i\text{-}PrO)_2P(S)(S)]_2$ (38). In view of this insensitivity to changes in environment, it is not surprising that the distortion around phosphorus from all tetrahedral angles is similar to that found in $Ph_2Ge[S_2P(OMe)_2]_2$ (2). The orientation in the five-membered ring system is such that two of the carbon methyl atoms are at an average distance of 3.24(5) Å from the phosphorus atom and the other two are at 3.80(2) Å. A view down the C—C bond of the ring shows that the four methyl groups attached to them are in the staggered configuration expected for the more stable arrangement with the pair at 3.24(5) Å pointing above and below the approximate plane of the distorted ring in an arrangement essentially identical to that observed in $Me_2Te[S_2\overline{POCMe_2CMe_2O}]_2$ (27).

Infrared and Raman spectra

The infrared spectra of **1–6**, particularly in the region around 1000 cm^{-1}, contain distinctive strong bands which are similar, but not identical, to those of the starting salts. These are summarized in the Experimental section. The similarity of these characteristic features suggests either that the bonding within the dithiophosphate groups is essentially unchanged or that, in any case, the vibrational spectra are unlikely to provide definitive evidence as to the mode of attachment of the dithiophosphate.

Features in the infrared and Raman spectra involving bonding to germanium are summarized in Table 5. The Ge—C stretching vibrations in **1–3** are assignable to peaks at essentially the same positions and relative intensities in both effects as reported for Me_2GeCl_2, 638 and 579 cm^{-1} respectively, for the asymmetric and symmetric stretches (39). This is to be expected because the Ge—C bond lengths and C—Ge—C bond angles are similar in **1** and Me_2GeCl_2, as discussed above, and the similarity in structure presumably extends to **2** and **3**. The same comparison holds true when the assignments of the Ge—C stretching vibrations in compounds **4–6** are compared with those of Me_3GeCl (40). The assignments of the Ge—S stretching vibrations in **1–6** are made readily by comparisons with those reported for the analogous *O,O*-

Can. J. Chem. Downloaded from www.nrcresearchpress.com by 85.192.166.187 on 09/08/12
For personal use only.

TABLE 4. Bond angles (deg) in $Me_2Ge[S_2\overline{POCMe_2CMe_2O}]_2$, **1**, with standard deviations in parentheses

Bonds	Angles	Bonds	Angles
S(1)—Ge(1)—S(3)	89.9(1)	C(1)—Ge(1)—C(2)	121.6(5)
S(1)—Ge(1)—C(1)	110.3(4)	S(3)—Ge(1)—C(1)	109.6(4)
S(1)—Ge(1)—C(2)	110.7(4)	S(3)—Ge(1)—C(2)	110.1(4)
Ge(1)—S(1)—P(1)	102.0(2)	Ge(1)—S(3)—P(2)	102.0(2)
S(1)—P(1)—S(2)	114.3(2)	S(3)—P(2)—S(4)	115.2(2)
S(1)—P(1)—O(1)	101.3(3)	S(3)—P(2)—O(3)	109.1(4)
S(1)—P(1)—O(2)	110.0(4)	S(3)—P(2)—O(4)	101.2(3)
S(2)—P(1)—O(1)	118.5(4)	S(4)—P(2)—O(3)	113.7(4)
S(2)—P(1)—O(2)	113.2(4)	S(4)—P(2)—O(4)	118.6(4)
O(1)—P(1)—O(2)	98.0(5)	O(3)—P(2)—O(4)	96.9(5)
P(1)—O(1)—C(3)	112.2(7)	P(2)—O(3)—C(9)	110.0(8)
P(1)—O(2)—C(4)	110.5(8)	P(2)—O(4)—C(10)	111.9(7)
O(1)—C(3)—C(4)	100(1)	O(3)—C(9)—C(10)	104(1)
O(2)—C(4)—C(3)	106(1)	O(4)—C(10)—C(9)	100(1)
O(1)—C(3)—C(5)	105(1)	O(3)—C(9)—C(11)	105(1)
O(1)—C(3)—C(6)	107(1)	O(3)—C(9)—C(12)	108(1)
C(5)—C(3)—C(6)	113(1)	C(11)—C(9)—C(12)	110(1)
O(2)—C(4)—C(7)	109(1)	O(4)—C(10)—C(13)	108(1)
O(2)—C(4)—C(8)	107(1)	O(4)—C(10)—C(14)	108(1)
C(7)—C(4)—C(8)	109(1)	C(13)—C(10)—C(14)	112(1)
S(1)—Ge(1)—S(2)	68.4(1)	S(3)—Ge(1)—S(4)	66.8(1)
S(1)—Ge(1)—S(4)	156.7(1)	S(3)—Ge(1)—S(2)	158.3(1)
C(1)—Ge(1)—S(2)	79.2(4)	C(1)—Ge(1)—S(4)	80.7(4)
C(2)—Ge(1)—S(2)	79.4(4)	C(2)—Ge(1)—S(4)	77.7(4)
S(2)—Ge(1)—S(4)	134.9(1)		

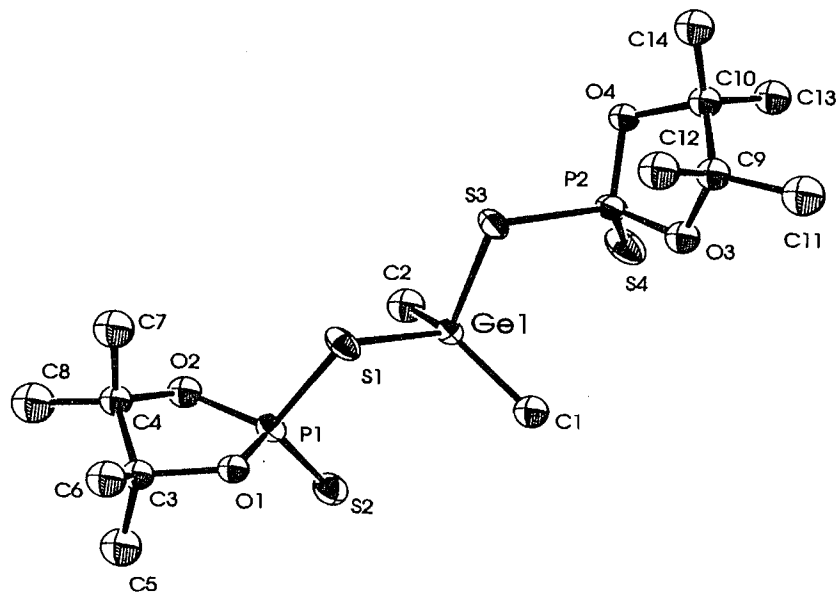

FIG. 1. ORTEP plot of the molecule $Me_2Ge[S_2\overline{POCMe_2CMe_2O}]_2$, **1**. The atoms are drawn with 25% probability ellipsoids. Hydrogen atoms are omitted for clarity.

dialkyldithiophosphates (41). The vibrational spectra are consistent with the dithiophosphate groups being bonded in similar fashion in all six derivatives.

Nuclear magnetic resonance spectra

The ^1H NMR spectra data for compounds **1–6** are presented in Table 6. The splitting patterns and relative intensities of peaks are consistent with the proposed structures. All of the derivatives show a sharp singlet assignable to the CH_3 groups attached to germanium. The chemical shifts in the $Me_2Ge[S_2\overline{POGO}]_2$ derivatives, **1–3**, are similar to that in Me_2GeBr_2, 1.47 ppm, whereas the values in the $Me_3Ge[S_2\overline{POGO}]$ species, **4–6**, are close to that of Me_3GeCl, 0.78 ppm. Changes in these chemical shifts have been related to changes in the electronegativity of the groups attached to germanium so the effective electronegativity of these cyclic dithiophosphate groups is presumably of a similar order of

Can. J. Chem. Downloaded from www.nrcresearchpress.com by 85.192.166.187 on 09/08/12
For personal use only.

TABLE 5. Selected features in the vibrational spectra (cm^{-1}) of compounds **1** to **6**[a,b]

Compound	$\nu(Ge—C)_{asym}$		$\nu(Ge—C)_{sym}$		$\nu(Ge—S)_{asym}$[c]		$\nu(Ge—S)_{sym}$[c]	
	IR[d]	Raman[e]	IR[d]	Raman[e]	IR[d]	Raman[e]	IR[d]	Raman[e]
$Me_2Ge[S_2\overline{POCMe_2CMe_2O}]_2$, **1**	630(w)	629(10)	570(w, sh)	574(40)	396(m)	395(80)	366(w)	364(30)
$Me_2Ge[S_2\overline{POCH_2CMe_2CH_2O}]_2$, **2**	630(w, sh)	625(25)	570(w, sh)	572(60)	395(ms)	394(30)	356(s)	364(50)
$Me_2Ge[S_2\overline{POCH_2CEt_2CH_2O}]_2$, **3**	630(m, sh)	625(25)	572(w, sh)	575(60)	395(s)	397(30)	374(m)	373(75)
$Me_3Ge[S_2\overline{POCMe_2CMe_2O}]$, **4**	616(m, sh)	616(45)	566(m, sh)	569(100)			380(s)	378(55)
$Me_3Ge[S_2\overline{POCH_2CMe_2CH_2O}]$, **5**	613(m)	617(50)	571(mw)	575(100)			375(s)	374(30)
$Me_3Ge[S_2\overline{POCH_2CEt_2CH_2O}]$, **6**	613(m)	619(50)	571(mw)	573(100)			371(s)	370(40)

[a]Parentheses denote relative intensities in the Raman effect.
[b]s = strong, m = medium, w = weak, v = very, sh = shoulder.
[c]Only one Ge—S stretching vibration in **4**–**6**.
[d]Run as KBr pellets to 400 cm^{-1} and as Nujol mulls below 450 cm^{-1}.
[e]Run as a solid in a glass capillary.

TABLE 6. ^1H and ^{31}P chemical shifts in the NMR spectra of compounds **1** to **6**[a,b,c]

Compounds	Ge—CH_3	O—CH_2[d]	OC—CH_3/—CCH_n[d]	$OCCCH_2CH_3$[d]	^{31}P[e]
$Me_2Ge[S_2\overline{POCMe_2CMe_2O}]_2$, **1**	1.59 (6 H, s)		1.46 (12 H, s) 1.42 (12 H, s)		98.27
$Me_2Ge[S_2\overline{POCH_2CMe_2CH_2O}]_2$, **2**	1.47 (6 H, s)	4.24 (4 H, m) [10.5; 5.7][e] 3.89 (4 H, m) [10.5; 25.5][f]	1.26 (6 H, s) 0.88 (6 H, s)		79.86
$Me_2Ge[S_2\overline{POCH_2CEt_2CH_2O}]_2$, **3**	1.47 (6 H, s)	4.23 (4 H, m) [11.4; 6.3][e] 4.04 (4 H, m) [11.4; 25.8][f]	1.72 (4 H, q) [7.5] 1.22 (4 H, q) [7.6]	0.88 (6 H, t) [7.5] 0.82 (6 H, t) [7.6]	81.15
$Me_3Ge[S_2\overline{POCMe_2CMe_2O}]$, **4**	0.77 (9 H, s)		1.46 (6 H, s) 1.42 (6 H, s)		101.57
$Me_3Ge[S_2\overline{POCH_2CMe_2CH_2O}]$, **5**	0.77 (9 H, s)	4.19 (2 H, m) [10.8; 6.6][e] 3.86 (2 H, m) [10.8; 24.3][f]	1.24 (3 H, s) 0.88 (3 H, s)		85.07
$Me_3Ge[S_2\overline{POCH_2CEt_2CH_2O}]$, **6**	0.76 (9 H, s)	4.18 (2 H, m) [11.1; 6.6][e] 4.00 (2 H, m) [11.1; 24.9][f]	1.70 (2 H, q) [7.5] 1.22 (2 H, q) [7.6]	0.86 (3 H, t) [7.5] 0.81 (3 H, t) [7.6]	86.07

[a]The spectra were recorded in $CDCl_3$ and reported in ppm from Me_4Si for ^1H and from H_3PO_4 for ^{31}P.
[b]Number of protons and multiplicities are in parentheses (s = singlet; t = triplet; q = quartet; m = multiplet).
[c]Coupling constants in Hz shown in square brackets [ ].
[d]Peaks attributable to the corresponding salts are seen in the ^1H NMR spectra of $Na[S_2\overline{POCMe_2CMe_2O}]$ at 1.46 (12 H, s); of $Na[S_2\overline{POCH_2CMe_2CH_2O}]_2$ at 4.03 (4 H, d [15.2]) and 1.05 (6 H, s); and of $NH_4[S_2\overline{POCH_2CEt_2CH_2O}]$ at 4.13 (4 H, d [15.4]), 1.44 (4 H, q [7.6]) and 0.88 (6 H, t [7.6]).
[e]Both $J(H_aH_b)$ and $J(PH_a)$ coupling are observed.

Can. J. Chem. Downloaded from www.nrcresearchpress.com by 85.192.166.187 on 09/08/12
For personal use only.

TABLE 7. ^{13}C NMR chemical shifts for the dimethyl- and trimethylgermanium dithiophosphates **1–6**[a,b,c]

Compound	Ge—CH_3	O—C^c	OC—C(ring)^c	OC—CH_3/—$CCH_n{}^c$	$OCCCH_2$—$CH_3{}^c$
$Me_2Ge[S_2\overline{POCMe_2CMe_2O}]_2$, **1**	11.13	90.50		24.52 23.96	
$Me_2Ge[S_2\overline{POCH_2CMe_2CH_2O}]_2$, **2**	9.49	77.56	32.61 [4.5]	22.25 20.87	
$Me_2Ge[S_2\overline{POCH_2CEt_2CH_2O}]_2$, **3**	9.51	74.93 [9.1]	37.31 [4.5]	23.35 22.36	7.19 6.18
$Me_3Ge[S_2\overline{POCMe_2CMe_2O}]$, **4**	3.62	89.90		24.62 [4.5] 24.10 [3.8]	
$Me_3Ge[S_2\overline{POCH_2CMe_2CH_2O}]$, **5**	3.58	76.84	32.52 [6.8]	22.32 21.03	
$Me_3Ge[S_2\overline{POCH_2CEt_2CH_2O}]$, **6**	3.58	74.28 [9.1]	37.31 [4.3]	23.36 22.38	7.18 6.85

[a]The spectra were recorded in $CDCl_3$ and reported in ppm from Me_4Si.
[b]Values of the coupling constants for the doublets arising from P-C coupling, J(P-C), are given in square brackets [ ].
[c]Peaks attributable to the corresponding salts are seen in $Na[S_2\overline{POCMe_2CMe_2O}]$ at 90.69 and 24.63 ppm, in $Na[S_2\overline{POCH_2CMe_2CH_2O}]$ at 77.92 [7.3], 34.55, and 23.20 ppm; and in $NH_4[S_2\overline{POCH_2CEt_2CH_2O}]$ at 75.29 [7.4], 39.58, 24.91, 8.79 ppm.

magnitude (9, 41). The shift of approximately 0.7 ppm per dithiophosphate group replacing a methyl group is close to that observed for related germanium derivatives with sulfur donating ligands (1) and the consistency of the chemical shifts reflects the fact that all of the compounds probably have identical linkages.

The observation of two peaks in the ^1H NMR spectrum of **1**, at 1.42 and 1.46 ppm, indicates that the eight methyl groups in the two dithiophosphates are in two different environments. This is in agreement with the structure of **1**, in which the carbon atoms in one set of four methyl groups are at an average distance of 3.24(5) Å from phosphorus and in the other set of four the average distance is 3.80(2) Å. However, the maintenance of the non-equivalence in solution is surprising because there have been no reports of such splitting in the NMR spectra of other derivatives containing similar cyclic dithiophosphates (17–24, 27) including those of $Me_2Sn[S_2\overline{POCMe_2CMe_2O}]_2$ and $Ph_2Sn[S_2\overline{POCMe_2CMe_2O}]_2$ where only single peaks were reported at 1.4 and 1.0 ppm, respectively (24).

The splitting patterns seen in the ^1H NMR spectra of all of these germanium derivatives are thus apparently unique for these cyclic dithiophosphates. Compounds **2**, **3**, **5**, and **6** all display the same complex pattern arising from the non-equivalence of the hydrogen atoms of the CH_2 groups in the six-membered ring. The feature is displayed in Fig. 2 for compound **2** where the eight CH_2 protons give two sets of multiplets that approximate to 1:1:1:1 quartets, one centered at 4.24 and the other at 3.89 ppm. The multiplet at 4.24 ppm is a doublet, which is the result of geminal spin–spin coupling with a value for $J(H_aH_b)$ of 10.5 Hz, and which is further split into a doublet by coupling with phosphorus to give a value for $J(PH_a)$ of 5.7 Hz. The second multiplet at 3.89 ppm is more

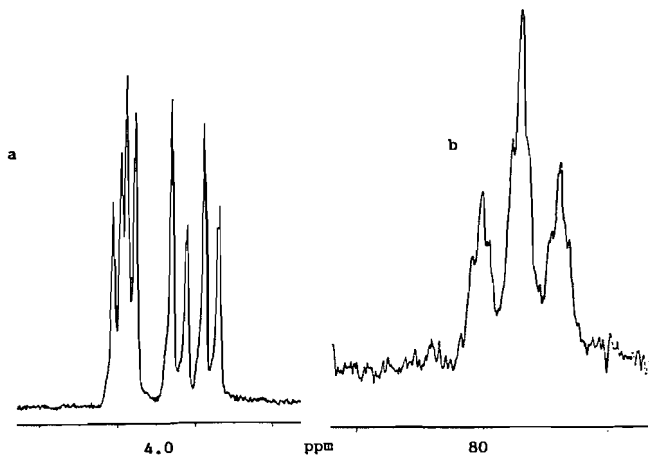

FIG. 2. Pertinent sections of the (*a*) ^1H and (*b*) ^{31}P NMR spectra of $Me_2Ge[S_2\overline{POCH_2CMe_2CH_2O}]_2$, **2**. The ^{31}P NMR spectrum illustrated is run without hydrogen decoupling.

clearly split into two doublets because the coupling to phosphorus is much larger with the value of the $J(PH_b)$ coupling constant being 25.5 Hz. The appearance of these two multiplets in the spectra of **3**, **5**, and **6** is essentially the same because the values of the chemical shifts and coupling constants are virtually identical in all four compounds. Thus the two protons on carbon are non-equivalent, as was observed for the two methyl groups substituted in the corresponding positions in the five-membered rings in **1** and **4**, and the values of the spin–spin coupling constants with phosphorus are different. It is reasonable to assume, by analogy with cyclohexane, that protons H_a and H_b occupy axial and equatorial positions respectively in a boat configuration and thus have different values for $J(PH)$. The ^{31}P NMR spectrum was recorded without

Can. J. Chem. Downloaded from www.nrcresearchpress.com by 85.192.166.187 on 09/08/12
For personal use only.

hydrogen decoupling and the resulting spectrum for **2**, which is a triplet of triplets, is also displayed in Fig. 2 to provide a representative sample. The larger triplet has a coupling constant of 25.5 Hz, as expected for coupling of phosphorus with the two equatorial protons, and the triplet is further split into a triplet from coupling of the phosphorus with the two axial protons with a value of 5.7 Hz for this coupling constant. It is worth noting that a typical value for J(PH) in the starting salts and related cyclic dithiophosphate derivatives that do not show the two separate couplings fall between those of these $J(PH_a)$ and $J(PH_b)$ values (18, 19, 22–24).

The $^{13}C\{H\}$ NMR spectra data for compounds **1–6** are presented in Table 7. The peaks attributable to CH_3—Ge are close to the value of 10.72 ppm found for Me_2GeCl_2 and for related dithio derivatives such as $Me_2Ge[S_2P(OEt)_2]_2$, 9.3 ppm (43), and $Me_2Ge[S_2CNMe_2]_2$, 13.7 ppm (1). Similarly, in compounds **4–6**, the CH_3—Ge peaks are comparable to 4.8 ppm in Me_3GeCl and to 3.6 and 3.2 ppm respectively in $Me_2Ge[S_2P(OEt)_2]$ and $Me_3Ge[S_2CNMe_2]$ (45, 1). All of the other peaks can be readily assigned to the various carbon atoms of the cyclic dithiophosphate groups at positions close to, but not identical to, those of the corresponding salts and acids. However, again in contrast to the features in the salts, acids, or metal derivatives where only single peaks are observed indicating identical or averaged positions, duplication of peaks is observed for compounds **1–6** for all of the atoms attached to the rings. In general, the values of the coupling constants, $J(P^2C)$ and $J(P^3C)$, which are included in Table 7, are typical of such groups in a variety of environments, as is the fact that these couplings are not observed in a consistent manner (18, 19, 22, 24, 27).

The $^{31}P\{H\}$ NMR spectra, which are presented in Table 6 along with the ^1H NMR data, show a single peak in all compounds **1–6**, consistent with both dithiophosphate groups being in identical environments. It has been proposed that the difference in the phosphorus chemical shift between a derivative and that of the free acid is an accurate indicator of the mode of binding, so that downfield shifts in the range 8–15 ppm are associated with bidentate ligands, and negligible shifts or even upfield shifts with monodentate linkages (42). In compounds **1–6** the downfield shifts range from 2.8 ppm in **2** to 9.2 ppm in **6**, and therefore are consistent with the ligands remaining aniso- or monodentate rather than becoming bidentate. In **1**, where the solid state structure suggests the presence of a monodentate ligand but with the second sulfur atom oriented toward rather than away from germanium, the shift is 6.2 ppm. This shift is considerably smaller than those observed for analogous dimethyltellurium derivatives, 11 to 16 ppm (27), which had similar solid state structures but were assumed to become bidentate in solution.

The similarities in the ^1H, ^{13}C, and ^{31}P NMR spectra of **1–6**, suggest that the weak anisobidenticity found in the solid state structure of **1**, is maintained in solution for all six compounds, in contrast to its tin and tellurium analogues where exchange of bonded and aniso-bonded sulfur apparently occurs (24, 27).

Acknowledgements

We thank the Natural Sciences and Engineering Research Council of Canada and Imperial Oil Canada for financial support.

1. R.K. Chadha, J.E. Drake, and A.B. Sarkar. Inorg. Chem. **25**, 2201 (1986).
2. R.K. Chadha, J.E. Drake, and A.B. Sarkar. Inorg. Chem. **24**, 3156 (1985).
3. J.E. Drake, A.G. Mislankar, and M.L.Y. Wong. Inorg. Chem. **30**, 2174 (1991).
4. H.B. Abrahamson, M.L. Freeman, M.B. Hossain, and D. van der Helm. Inorg. Chem. **23**, 2286 (1984) and references therein.
5. K.C. Molloy and J.J. Zuckermann. Acc. Chem. Res. **16**, 386 (1983).
6. R.P. Burns, F.P. McCullough, and C.A. McAuliffe. Adv. Inorg. Chem. Radiochem. **23**, 211 (1980).
7. R.C. Mehrotra, G. Srivastava, and B.P.S. Chauhan. Coord. Chem. Rev. **55**, 207 (1984).
8. R.K. Chadha, J.E. Drake, and A.B. Sarkar. Inorg. Chem. **23**, 4769 (1984).
9. R.K. Chadha, J.E. Drake, and A.B. Sarkar. Inorg. Chim. Acta, **143**, 31 (1988).
10. R.K. Chadha, J.E. Drake, A.B. Sarkar, and M.L.Y. Wong. Acta Crystallogr. Sect. C: Cryst. Struct. Commun. **C45**, 37 (1989).
11. R.K. Chadha, J.E. Drake, and A.B. Sarkar. Inorg. Chem. **26**, 2885 (1987).
12. J.E. Drake, A.B. Sarkar, and M.L.Y. Wong. Inorg. Chem. **29**, 785 (1990).
13. J.E. Drake, A.G. Mislankar, and J. Yang. Inorg. Chem. **31**, 5543 (1992).
14. J.E. Drake, A.G. Mislankar, and J. Yang. Inorg. Chim. Acta, **211**, 37 (1993).
15. K.C. Molloy, M.B. Hossain, D. van der Helm, J.J. Zuckermann, and I. Haiduc. Inorg. Chem. **19**, 2041 (1980).
16. C.L. Raston, P.R. Tennant, A.H. White, and G. Winter. Aust. J. Chem. **31**, 1493 (1978).
17. R. Ratnani, G. Srivastava, and R.C. Mehrotra. Transition Met. Chem. **17**, 137 (1992).
18. S.K. Pandey, G. Srivastava, and R.C. Mehrotra. Transition Met. Chem. **16**, 252 (1991).
19. R. Ratnani, G. Srivastava, and R.C. Mehrotra. Transition Met. Chem. **16**, 204 (1991).
20. R. Ratnani, G. Srivastava, and R.C. Mehrotra. Phosphorus, Sulfur, and Silicon, **48**, 245 (1990).
21. R. Ahmad, G. Srivastava, and R.C. Mehrotra. Inorg. Chim. Acta, **89**, 41 (1984).
22. R. Ratnani, G. Srivastava, and R.C. Mehrotra. Inorg. Chim. Acta, **161**, 253 (1989).
23. J.S. Yadav, R.K. Mehrotra, and G. Srivastava. Phosphorus, Sulfur, and Silicon, **62**, 169 (1991).
24. R.J. Rao, G. Srivastava, R.C. Mehrotra, B.S. Saraswat, and J. Mason. Polyhedron, **3**, 485 (1984).
25. H. Preut, V-D. Ngo, and F. Huber. Acta Crystallogr. Sect. C: Cryst. Struct. Commun. **C42**, 809 (1986).
26. H. Preut, V-D. Ngo, and F. Huber. Acta Crystallogr. Sect. C: Cryst. Struct. Commun. **C43**, 164 (1987).
27. J.E. Drake, L.N. Khasrou, A.G. Mislanka, and R. Ratnani. Can. J. Chem. **72**, 1328 (1994).
28. H.P.S. Chauhan, C.P. Bhasin, G. Srivastava, and R.C. Mehrotra. Phosphorus and Sulfur, **15**, 99 (1983).
29. (*a*) J.C. Calbrese. Ph.D. Thesis, University of Wisconsin, Maddison, 1972; (*b*) P.T. Beurskens. DIRDIF: direct methods for difference structures — an automatic procedure for phase extension and refinement of difference structure factors. Technical Report 1984/1; Crystallography Laboratory: Toernooiveld, 6525 Ed Nijmegen, Netherlands.
30. D.T. Cromer and J.T. Waber. International tables for X-ray crystallography. Vol. IV. The Kynoch Press: Birmingham, England. 1974. Table 2.2 A.
31. J.A. Ibers and W.C. Hamilton. Acta Crystallogr. **17**, 781 (1964).

Can. J. Chem. Downloaded from www.nrcresearchpress.com by 85.192.166.187 on 09/08/12
For personal use only.

32. D.T. Cromer. International tables for X-ray crystallography. Vol. IV. The Kynoch Press, Birmingham, England. 1974. Table 2.3.1.
33. Texsan-Texray structure analysis package. Molecular Structure Corp. 1985.
34. J.E. Drake, J.L. Hencher, and Q. Shen. Can. J. Chem. **55**, 1104 (1977).
35. J.E. Drake, R.T. Hemmings, J.L. Hencher, F.M. Mustoe, and Q. Shen. J. Chem. Soc. Dalton. Trans. 811 (1976).
36. A.J. Bondi. Phys. Chem. **68**, 441 (1964).
37. J.S. Yadav, R. Bohra, R.K. Mehrotra, A.K. Rai, and G. Srivastava. Acta Crystallogr. **C45**, 308 (1989).
38. P.R.H. Alderman, P.G. Owston, and J.M. Rowe. J. Chem. Soc. 668 (1962).
39. J.R. Durig, K.K. Lau, J.B. Turner, and J. Bragin. J. Mol. Spectrosc. **31**, 419 (1969).
40. J.E. Griffiths. Spectrochim. Acta, **20**, 1335 (1964).
41. R.K. Chadha, J.E. Drake, and A.B. Sarkar. J. Organomet. Chem. **323**, 271 (1987).
42. C. Glidewell. Inorg. Chim. Acta, **25**, 159 (1977).

Can. J. Chem. Downloaded from www.nrcresearchpress.com by 85.192.166.187 on 09/08/12
For personal use only.

Structure of the O-chain polysaccharide of three strains of *Pseudomonas syringae* ssp. *savastanoi*

MATTEO ADINOLFI, MARIA MICHELA CORSARO, ROSA LANZETTA, CARMELA ELSA MARCIANO, AND MICHELANGELO PARRILLI[1]

Dipartimento di Chimica Organica e Biologica, Università di Napoli Federico II, Via Mezzocannone 16, 80134 Napoli, Italy

ANTONIO EVIDENTE

Dipartimento di Scienze Chimico-Agrarie, Università di Napoli Federico II, Via Università 100, 80055 Portici, Italy

AND

GIUSEPPE SURICO

Istituto di Patologia e Zoologia Forestale ed Agraria, Università di Firenze, Piazzale delle Cascine 28, 50144 Firenze, Italy

Received January 21, 1994

MATTEO ADINOLFI, MARIA MICHELA CORSARO, ROSA LANZETTA, CARMELA ELSA MARCIANO, MICHELANGELO PARRILLI, ANTONIO EVIDENTE, and GIUSEPPE SURICO. Can. J. Chem. **72**, 1839 (1994).

The structure of the O-chain portion of the lipopolysaccharide isolated from three different strains of *Pseudomonas syringae* ssp. *savastanoi* has been determined by chemical and NMR spectral analysis. For all of the strains the O-chain consists of a tetrasaccharide repeating unit of three α-L-Rha*p* and one terminal nonreducing α-D-Fuc*p*3NAc. Two rhamnosyl residues are 3-linked and the third one is 2,3-linked. LPS from an olive strain, avirulent on oleander, was shown to attenuate the response of oleander plants inoculated with a homologous strain.

MATTEO ADINOLFI, MARIA MICHELA CORSARO, ROSA LANZETTA, CARMELA ELSA MARCIANO, MICHELANGELO PARRILLI, ANTONIO EVIDENTE et GIUSEPPE SURICO. Can. J. Chem. **72**, 1839 (1994).

Faisant appel à des analyses chimiques et de RMN, on a déterminé la structure de la partie de la chaîne oxygénée du lipopolysaccharide isolé des trois souches différentes de *Pseudomonas syringae* ssp. *savastanoi*. Pour chacune des souches, cette chaîne est formée d'un motif constitutif tétrasaccharidique formé de trois α-L-Rha*p* et d'une unité terminale non-réductrice α-D-Fuc*p*3NAc. Deux des résidus rhamnosyles sont liés par la position 3 alors que le troisième est lié par les positions 2,3. On a démontré que le lipopolysaccharide provenant d'une souche d'olive, avirulent sur l'oléandre, atténue la réponse des plants d'oléandre inoculés avec une souche homologue.

[Traduit par la rédaction]

Can. J. Chem. Downloaded from www.nrcresearchpress.com by 85.192.166.187 on 09/08/12
For personal use only.

Introduction

Pseudomonas syringae ssp. *savastanoi* (= *P. savastanoi*) is a bacterium that incites tissue overgrowth on an Apocynacea plant (oleander), olive, and some other Oleaceae plants (jasminum, ash, privet, phylirrea). Strains isolated from oleander also induce knots on Oleaceae but strains from Oleaceae are avirulent on oleander (1). The molecular basis of this host–pathogen specificity is poorly understood. Exopolysaccharides and the cell wall lipopolysaccharides (LPS) of phytopathogenic bacteria have been correlated with pathogenesis; the chemical structure and physical conformation of these complex molecules may play a role in the early infection process and in the determination of specificity of plant–bacterial interactions (2). For example, in the case of *Agrobacterium tumefaciens*, a bacterium that shares several features with *P. savastanoi* (3), LPS isolated from non-oncogenic strains inhibit tumor formation by virulent strains (4).

This report deals with the isolation and characterization of the O-chain of LPS from olive and oleander strains of *P. savastanoi*.

The role of LPS on the infectivity and virulence of the olive and oleander pathogen was also considered.

Results and discussion

Lipopolysaccharides were isolated from three strains (ITM519, ITM317, and PVF5) of *P. savastanoi* by extraction with phenol–water followed by gel-filtration chromatography, and the O-chain polysaccharide was obtained from LPS by hydrolysis with dilute acetic acid and purified by gel filtration. For the ITM519 and ITM317 O-chains an apparent molecular weight of 53 000 Da was estimated (see Experimental).

The ^{1}H NMR (Table 1) of the O-chain polysaccharide, obtained from all of the LPS, displayed in the anomeric zone, in addition to very minor signals (see Fig. 1*a*), four signals of similar intensities in the range 5.04–4.85 ppm, of which only one appeared as a doublet (3.9 Hz), while the others were broad singlets. Furthermore the presence of four methyl doublets in the range 1.00–1.18 ppm suggested the 6-deoxy nature of the monosaccharide residues. A fifth methyl signal at δ 1.87 indicated the presence of an acetyl group.

In agreement with the ^{1}H NMR data, the ^{13}C NMR spectrum (Table 1) showed four anomeric signals in the range 102.7–96.3 ppm, four methyl signals (C-6 of 6-deoxyhexoses) at δ 17.1–17.3 (three) and at δ 15.7 (one), and the signals of an *N*-acetyl group (Me at δ 22.5, CO at δ 174.9), in addition to one signal at δ 51.6, indicating a carbon bearing nitrogen (5).

The $^1J_{C,H}$ values (Table 1) of the anomeric signals, determined by a coupled DEPT experiment, indicated an α anomeric configuration for all of residues (6).

2D NMR H,H COSY and one-bond H,C COSY spectra allowed us to identify the chemical shifts of all protons and carbons of each residue (Table 1). In addition it was possible, starting from the anomeric proton doublet at δ 4.88, to identify the

[1]Author to whom correspondence may be addressed.

TABLE 1. NMR data of O-chain polysaccharide from coupled DEPT, H,H COSY, and H,C COSY experiments at 50°C [low-field glycosylation shift][a]

Assignment[b]	δ Carbon[c]	$^1J_{C,H}$ (Hz)	δ Proton	$^1J_{H,H}$ (Hz)
1 **F**	96.3	170.9	4.88	d 3.9
2 **F**	66.1		3.72	dd 3.9; 11.2
3 **F**	51.6		4.04	dd 2.7; 11.2
4 **F**	70.8		3.59	[d]
5 **F**	67.3		4.18	q 6.8
6 **F**	15.7		1.00	d 6.8
N-COOMe	174.9; 22.5		1.87	s
1 **N**	101.3	174.0	5.04	br s
2 **N**	75.1 [4.1]		4.04	d 2.9
3 **N**	76.2 [4.9]		3.80	dd 2.9; 9.3
4 **N**	71.3		3.45	t 9.3
5 **N**	69.6		3.70	[d]
6 **N**	17.3		1.18	d 6.3
1 **A**	102.1	177.0	4.95	br s
2 **A**	70.4		3.94	[d]
3 **A**	78.3 [7.0]		3.67	[d]
4 **A**	72.1		3.39	[d]
5 **A**	69.8		3.58	[d]
6 **A**	17.1		1.10	d 6.3
1 **B**	102.7	174.0	4.85	br s
2 **B**	70.4		3.96	[d]
3 **B**	78.3 [7.0]		3.74	[d]
4 **B**	71.9		3.40	[d]
5 **B**	69.8		3.68	[d]
6 **B**	17.1		1.10	d 6.3

[a]Valued by difference with respect to ^{13}C chemical shifts of methyl α-rhamnopyranoside from ref. 5.
[b]**F** = Fuc*p*3NAc, **N** = 2)3]Rha*p*, **A** = 3)Rha*p*(1→2), **B** = 3)Rha*p*(1→3).
[c]Internal standard 1,4-dioxane: δ 67.4.
[d]Overlapped signals.

patterns of the spin system for all of the connected protons, except for H-4, and the $^3J_{H,H}$ values. Therefore, the *galacto* configuration for the residue was recognized (7).

The above data suggested a polysaccharide built up of α-rhamnopyranosyl and 3-acetamido-3,6-dideoxy-α-galactopyranosyl (Fuc*p*3NAc) units in the 3:1 ratio. Furthermore, it was possible to identify the carbons of each residue involved in the interglycosidic linkage on the basis of the ^{13}C glycosylation shifts (Table 1) (8). In particular, two rhamnosyl residues are 3-linked and the other one is 2,3-linked, while the Fuc*p*3NAc is a nonreducing terminal unit.

Chemical analysis confirmed the above suggestion. Actually, the acid hydrolysis of the O-chain polysaccharide yielded rhamnose and Fuc*p*3NAc in a ca. 3.5:1 ratio (Fuc*p*3NAc standard was not available to establish the corrected response factor). The configuration for all of the rhamnose units was safely established to be L on the basis of the good agreement between the $[\alpha]_D$ value (+9) measured for the obtained rhamnose sample and the literature value (+8.7) (9). The configuration D for the Fuc*p*3NAc was suggested by the positive value (+6.5) of $[\alpha]_D$ of the O-chain polysaccharide, taking the strong positive $[\alpha]_D$ value (+238) (10) of methyl 3-acetamido-3,6-dideoxy-α-D-galactopyranoside into consideration.

The methylation analysis also gave the expected sugars, namely, 2,4-di-*O*-methyl-L-rhamnose, 4-*O*-methyl-L-rhamnose, and 3,6-dideoxy-2,4-di-*O*-methyl-3-*N*-methylacetamido-D-galactose, although the stoichiometry of the analysis was not very good.

To define the sequence of monosaccharides, a ROESY (11) experiment was performed. The projections of the ROESY experiment for each anomeric signal are given in Fig. 1, which shows the proton systems with which the anomeric protons establish NOE contacts. In addition to some internal NOEs, each anomeric proton displayed, almost exclusively, NOEs with the protons of only one unit, indicating its spatial proximity to this unit. Actually, the anomeric protons of the **N** units showed NOEs with the **B** protons (Fig. 1b), while both the **A** and **F** anomeric protons exhibited NOEs with those of nodal **N** units (Figs. 1*c* and 1*d*). In particular, the anomeric **A** proton displayed a very strong effect on H-2, suggesting that **A** was linked at C-2 and, consequently, **F** at C-3 of the **N** unit. Finally, the **B** anomeric proton showed NOEs with those of the **A** unit (Fig. 1*e*).

From these results, the structure **1** of the complete tetrasaccharide repeating unit can be defined.

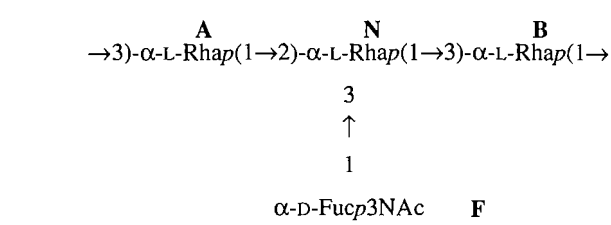

1

The configuration D for the Fuc*p*3NAc unit was substantiated

Can. J. Chem. Downloaded from www.nrcresearchpress.com by 85.192.166.187 on 09/08/12
For personal use only.

Can. J. Chem. Downloaded from www.nrcresearchpress.com by 85.192.166.187 on 09/08/12
For personal use only.

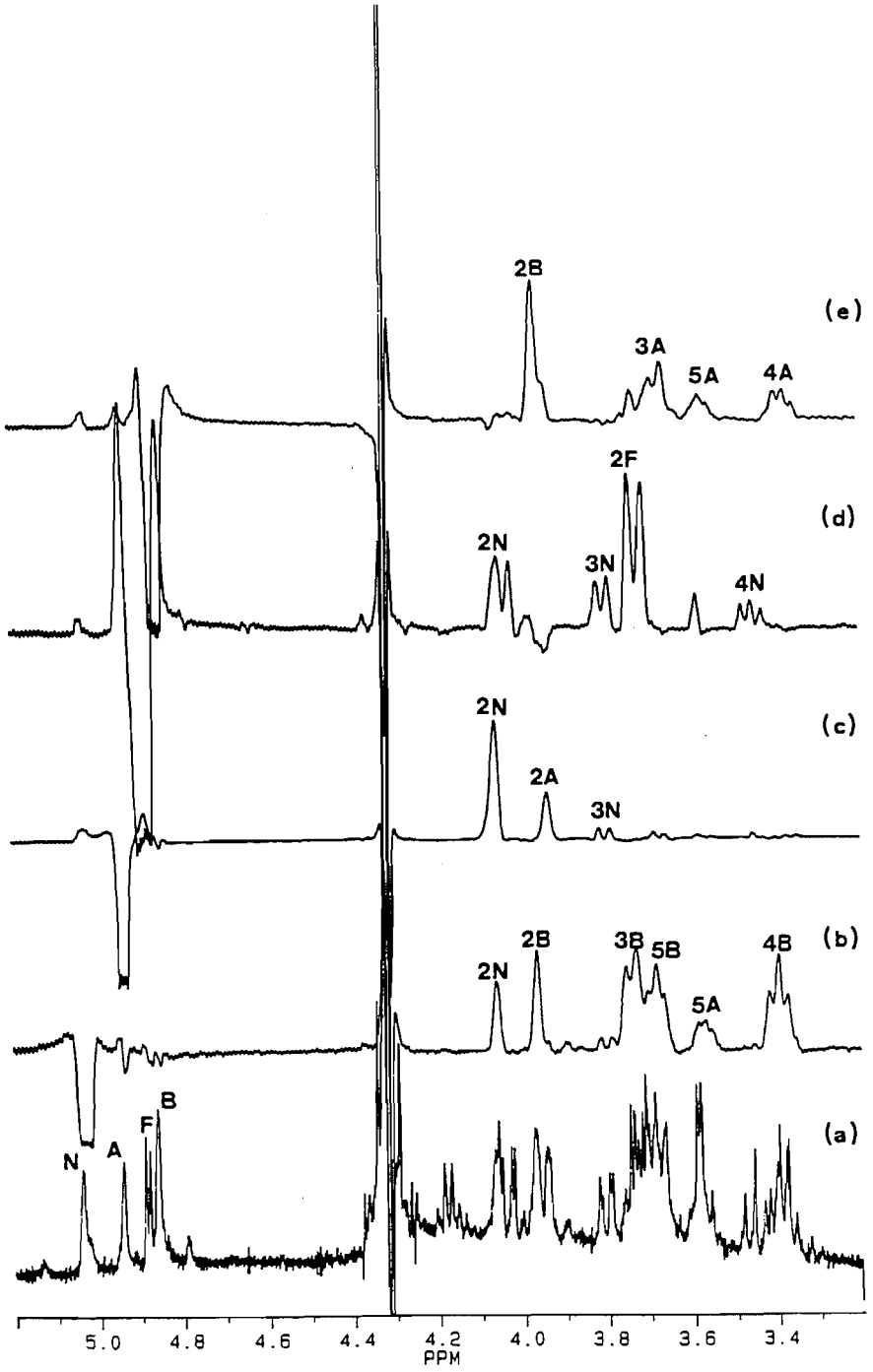

FIG. 1. ^{1}H NMR spectra (*a*) and ROESY projections (*b*)–(*e*) of O-chain polysaccharide between 3.2 and 5.2 ppm measured in D_2O at 50°C.

by analysis of the effects exerted (9) by the configuration of Fuc*p*3NAc on the ^{13}C NMR chemical shifts of the repeating unit (12, 13). The observed (corrected by +0.4 ppm in order to refer to internal standard methanol, δ 50.15) and calculated (12, 13) ^{13}C chemical shifts for structure **1** are given in Table 2. The normalized deviation ($S = \Sigma\Delta^2/n$) for structure **1** is 1.2, a lower value than the limit (≤ 1.5) taken as a measure of the good correspondence between observed and calculated ^{13}C NMR spectra (13). The alternative structure with L-Fuc*p*3NAc was safely ruled out, since the *S* value is 12.2.

When this work was completed, a paper describing the isolation of the same O-chain from *Pseudomonas syringae* pv. *tomato* was published (14). This latter result is not surprising because there is no direct correlation between O-chain structures and host–plant differentiation. Actually, strains of the same pv. of *P. syringae* show different O-chains, while different pv. of *P. syringae* show same O-chain (15). In accordance with this observation, our O-chain results are very different from that of LPS found in a strain of *P. s.* pv. *savastanoi* isolated from knots of diseased Spanish olive trees. Actually, this latter appeared to mainly contain rhamnose (38%) and glucose (33%) (16).

As far as the chemotaxonomic point of view is concerned, our strains may be classified in the I chemotype, as well as *P. s.* pv. *tabaci* (15).

TABLE 2. ^{13}C chemical shift data calculated (observed) for O-chain polysaccharide **1**

Constituents	Chemical shifts (ppm)					
	C1	C2	C3	C4	C5	C6
B →3)-α-L-Rha*p*-(1→	103.5 (103.1)	71.4 (70.8)	78.8 (78.7)	72.9 (72.3)	70.0 (70.2)	18.0 (17.5)
A →3)-α-L-Rha*p*-(1→	103.1 (102.5)	71.4 (70.8)	78.8 (78.7)	72.9 (72.5)	70.0 (70.2)	18.0 (18.5)
N →2,3)-α-L-Rha*p*-(1→	102.5 (101.7)	76.1 (75.5)	77.0 (76.6)	71.6 (71.7)	69.9 (70.0)	18.0 (17.8)
F α-D-Fuc*p*3NAc-(1→	97.0 (96.7)	66.7 (66.5)	52.2 (52.0)	71.65 (71.2)	68.0 (67.7)	16.9 (16.1)

Pure LPS isolated from olive strain ITM317 was used in a series of experiments to test the inhibition of tumor formation by virulent oleander strains.

The results of the inoculation experiments showed that *P. savastanoi* knot formation in oleander leaves is insensitive to exogeneously supplied LPS isolated from heterologous strains of the bacterium. Only when LPS was supplied in great weight excess relative to the amount of LPS on the surfaces of the bacterium in the inoculum was a somewhat inhibitory effect observed. Therefore, particles of bacterial cell envelopes other than purified LPS should be investigated in order to elucidate the failure of olive strains to infect oleander plants.

Experimental

General

The ^1H and ^{13}C NMR spectra were obtained at 400 and 100 MHz, respectively, with a spectrometer equipped with a dual probe, in the Fourier transform mode at 50°C. ^{13}C and ^1H chemical shifts were measured in D_2O solutions using 1,4-dioxane (67.4 ppm) and TSP, respectively, as internal standards. The DEPT experiment was performed using a polarization transfer pulse of 135° and a delay adjusted to an average C,H coupling of 160 Hz. The standard Bruker software (XHCORR) was used to perform the heteronuclear H,C COSY experiment under the following conditions: the time domain in f_2 was 1K, 128 spectra were collected with 1600 scans, the spectral width was 10 000 Hz in f_2 and 2000 Hz in the f_1 domain, delays were optimized for $^1J_{C,H}$ = 160 Hz. Fourier transformation was performed with a shifted sine-bell function in both dimensions. H,H COSY and ROESY experiments were performed with standard COSY, with a second pulse of 45°, and ROESYPH pulse sequences under the following conditions: the time domain in f_1 was 1K and in f_2 1K, SW = 2000 Hz. For the ROESY experiment the best results were obtained with a mixing time of 200 ms; the FID matrix was processed with a trapezoidal shifted function.

Total carbohydrates were determined by the phenol–H_2SO_4 test (17). UV absorbance was determined in H_2O solutions. Alditol acetates were separated on an SP-2330 capillary column (Supelco, 30 m × 0.25 mm i.d., flow rate 1 mL/min) at 240°C using N_2 as carrier gas, in a gas chromatograph equipped with a flame-ionization detector. Partially methylated alditol acetates were analysed by GLC–MS, using an SP-2330 capillary column (Supelco, 30 m × 0.25 mm i.d., flow rate 0.8 mL/min, He as carrier gas) with the temperature programme: 170°C for 3 min, 170 → 240°C at 4°/min, 240°C for 30 min (18). Methylation was performed according to Hakomori (19) with KCH_2SOCH_3, MeI in DMSO. Methylated product was recovered through adsorption on a C_{18} Sep-Pak. GLC of the partially methylated alditol acetates was carried out on a column identical with that used for GLC–MS. Paper chromatography was carried out on Whatman 3MM paper with 4:1:5 BuOH–AcOH–H_2O (upper phase) as the developer, and indication with aniline – diphenylamine phosphate. Optical rotations were determined in H_2O solutions.

Bacterial strains

Three strains of *P. savastanoi* were used in this study: strain ITM519 (collection of Istituto Tossine e Micotossine da Parassiti Vegetali del CNR, Bari, Italy) was isolated from infected oleander plants from South Italy; strains ITM317 and PVF5 (collection of Istituto di Patologia e Zoologia Forestale ed Agraria, Università di Firenze, Firenze, Italy) were isolated from infected olive plants from South and Central Italy, respectively. Colonies of strains ITM519 and ITM317 are typical of *P. savastanoi* while strain PVF5 is a naturally occurring, levan-positive nonfluorescent variant of the bacterium (20). Bacteria were stored on nutrient glycerol agar slants at 4°C and new stock cultures were established at monthly intervals.

Media and growth conditions

For solid cultures, bacteria were grown on plates (18 cm) containing nutrient glycerol agar medium (nutrient broth, 0.8%; glycerol, 1.5%; agar, 1.5%); distilled water, 1 L) laid on the top of the agar with a circular piece of dialysis tubing (cutoff of 3000). Following incubation at 26°C for 5–7 days, depending on the strain, bacteria were scraped off the upper side of the tubing, dispersed by shaking in 0.85% (w/v) NaCl, and centrifuged at 10 000 *g* for 30 min. Washing and centrifugation were repeated twice. Alternatively, bacteria were grown in shake culture (100 rpm) in nutrient glycerol broth or in King's medium B (21) to late log phase (after ca. 72 h at 26°C). The cells were harvested by centrifugation and washed three times with 0.85% (w/v) NaCl. Harvested cells from both solid and liquid cultures were frozen at –40°C and lyophilized.

Preparation of cellular lipopolysaccharides

Dry cells of *P. savastanoi* ITM 317 (1.83 g), obtained from colonies grown on nutrient glycerol agar solid culture, were suspended in 27 mL of distilled H_2O and extracted with phenol according to the conventional procedure (22). The resulting aqueous phase was dialyzed (cutoff 12 000 – 14 000) for 2 days. Contents of the tube were lyophilized; the residue was dissolved in distilled H_2O (40 mL) and brought to 1.5% (w/v) NaCl and 1.5% (w/v) Cetavlon (hexadecyltrimethylammonium bromide) while stirring at room temperature for 10 min. This mixture was then centrifuged and the supernatant was mixed with 10 volumes of 95% EtOH and left overnight at –20°C. The resulting precipitate was collected by centrifugation, dissolved in distilled H_2O, and dialyzed as described above. The contents were lyophilized to yield "crude" LPS (140 mg).

When the same procedure was used to extract the LPS from *P. savastanoi* strain ITM 519 (2.16 g, dry weight) and strain PVF5 (1.54 g), grown on King's medium B and on solid culture, respectively, 96 and 29 mg of "crude" LPS were obtained.

Purification of LPS (23)

Crude LPS samples (134 mg of ITM317, 80 mg of ITM519, and 20 mg of PVF5) were purified by chromatography on Bio-Gel A15m (Bio-Rad). The column (2.5 × 50 cm) was equilibrated and eluted with 300 mM triethylamine (TEA) neutralized to pH 7 with HCl. The samples were dissolved in a solution of 300 mM TEA and 10 mM EDTA,

Can. J. Chem. Downloaded from www.nrcresearchpress.com by 85.192.166.187 on 09/08/12
For personal use only.

adjusted to pH 7 with HCl prior to application to the column. Two-millilitre fractions were collected and monitored for hexose, KDO (24), and UV absorbance at 260 and 280 nm. Fractions containing both hexose and KDO were combined, dialyzed against distilled water for 1 week, and lyophilized to yield purified LPS (95 mg from ITM317, 58 mg from ITM519, and 16 mg from PVF5).

Isolation of the O-chain

The polysaccharide O-chain was obtained by hydrolysis of the purified ITM317 LPS (95 mg) in 23 mL of 1 N AcOH in a sealed tube for 3 h at 110°C. After cooling, the sample was centrifuged at 4000 *g* for 25 min. The supernatant liquid was adjusted to pH 5 with pyridine, evaporated to 6.5 mL in vacuo, and applied to a 2.5 × 50 cm Sephadex G-50 column. The sample was eluted with pyridine acetate buffer at pH 4.26, at a flow rate of 20 mL/h. The fractions (2 mL/tube) were analysed for hexose and KDO. The high molecular weight carbohydrate fractions (O-chain) were combined, lyophilized, and then applied to a Sephadex G-100 column (2.5 × 100 cm), eluting with pyridine acetate buffer at pH 4.26. The LPS of ITM519 (58 mg) and of PVF5 (10 mg) were hydrolysed with 16 mL and 3 mL of 1 N AcOH, respectively, and chromatographed as above. The carbohydrate-containing fractions in the included volume were combined, dialyzed, and lyophilized, yielding 26 mg ($[\alpha]_D$ +6.5 (*c* 0.4, H_2O, r.t.)) for ITM317, 28 mg for ITM519, and 6 mg for PVF5.

The molecular weight for the ITM519 and ITM317 O-chains was estimated to be 53 000 Da by gel filtration on a Bio-Gel P-100 column (50 mM NaOAc, pH 5.2), calibrated with dextran standards.

Hydrolysis of native and methylated materials (25)

A sample (1 mg) of the ITM317 native O-chain was suspended in 200 μL of 2 M H_2SO_4. Glacial AcOH (1.8 mL) was added and the solution was heated at 100°C for 9 h (sealed tube). After removal of AcOH by repeated codistillations with water in vacuo, H_2SO_4 was neutralized by the addition of water (1 mL) and $BaCO_3$ (120 mg). The slurry was centrifuged and the supernatant solution was filtered through at C_{18} Sep-Pak. $NaBD_4$ (5 mg) was added to the filtrate and the mixture was left for 1 h at room temperature. After evaporation of H_2O, the sample was acetylated with pyridine/Ac_2O (1:2 v/v, 20 min at 120°C). Methanol and then toluene were added. After evaporation in vacuo, alditol acetates were extracted with CH_2Cl_2 from the residue.

GLC–MS and GLC analysis of the sample revealed the presence of Fuc3NAc (26) and rhamnose in the ratio of ca. 1:3.5.

A sample of the ITM317 native O-chain (1 mg) was methylated (see General) and then treated as above. GLC–MS and GLC analysis gave 2,4-di-*O*-methylrhamnose, 4-*O*-methylrhamnose, and 3,6-dideoxy-2,4-di-*O*-methyl-3-*N*-methylacetamidogalactose.

The same procedures were used for the ITM519 and PVF5 samples and gave results identical with those from ITM317.

A sample of the ITM317 native O-chain (6 mg) was hydrolysed with 2 M H_2SO_4 as above. Paper chromatography (see General) of the crude yielded L-rhamnose (3.5 mg), $[\alpha]_D$ +9 (*c* 0.3, H_2O, r.t) (lit. $[\alpha]_D$ (9): +8.9).

Inoculation of plants

LPS from strain ITM317 was dissolved in distilled water at 50°C and the solution was mixed with viable cells of strain ITM519 (2×10^7 cells/mL) to obtain final concentrations of 40 μg/mL (an amount obtained from about 8.9×10^8 whole bacteria) and 80 μg/mL bacterial suspension. The purified LPS bacterial cells were injected into oleander leaves separately: first LPS and 15 min later ITM519. Control leaves were inoculated with LPS, ITM519, ITM317, and distilled water.

Can. J. Chem. Downloaded from www.nrcresearchpress.com by 85.192.166.187 on 09/08/12
For personal use only.

Acknowledgements

We thank the Centro di Metodologie Chimico-Fisiche of the University Federico II of Naples for the NMR spectra, and M.U.R.S.T. and C.N.R., Rome, for financial support.

1. J.D. Janse. Eur. J. For. Pathol. **11**, 425 (1981).
2. L.J. Halverson and J. Stacey. Microbiol. Rev. **50**, 193 (1986).
3. G. Surico and N.S. Iacobellis. *In* Molecular signals in plant–microbe communications. *Edited by* D.P.S. Verna. CRC Press, Boca Raton, Fla. 1992. p. 209.
4. M.H. Whatley, J.S. Bodwin, B.B. Lippincott, and J.A. Lippincott. Infect. Immun. **13**, 1080 (1976).
5. K. Boch and C. Pedersen. Adv. Carbohydr. Chem. Biochem. **41**, 27 (1983).
6. K. Boch and C. Pedersen. J. Chem. Soc. Perkin Trans. **2**, 293 (1974).
7. L.D. Hall. Adv. Carbohydr. Chem. **19**, 51 (1964).
8. K. Tori, S. Seo, Y. Yoshimura, H. Arita, and Y. Tomita. Tetrahedron Lett. 179 (1976).
9. P.M. Collins. Carbohydrates. Chapman and Hall, London. 1983. p. 433.
10. K. Čapek, J. Šteffková, and J. Jarí. Collect. Czech. Chem. Commun. **31**, 1854 (1966).
11. A.A. Bothner-By, R.L. Stephens, and J. Lee. J. Am. Chem. Soc. **106**, 811 (1984).
12. G.M. Lipkind, A.S. Shashkov, N.E. Nifant'ev, and N.K. Kochetkov. Carbohydr. Res. **237**, 11 (1992).
13. G.M. Lipkind, A.S. Shashkov, Y.A. Knirel, E.V. Vinogradov, and N.K. Kochetkov. Carbohydr. Res. **175**, 59 (1988).
14. Y.A. Knirel, A.S. Shashkov, N.A. Paramanov, G.M. Zdorovenko, L.P. Solyvanic, and L.M. Yakovleva. Carbohydr. Res. **243**, 199 (1993).
15. G.M. Zdorovenko, N.Y. Gubanova, L.P. Solyvanik, Y.A. Knirel, L.M. Yakovleva, and I.A. Zakorova. Proceedings of 4th International Working Group on *Pseudomonas syringae* Pathovars, Florence, Italy. 1991.
16. L.A. Cañas and M. Santaolalla. Can. J. Microbiol. **32**, 73 (1986).
17. M. Dubois, K.A. Gilles, J.K. Hamilton, P.A. Rebers, and F. Smith. Anal. Chem. **28**, 350 (1956).
18. W.S. York, A.G. Darvill, M. McNeil, T.T. Stevenson, and P. Albersheim. Methods Enzymol. **118**, 3 (1986).
19. S. Hakomori. J. Biochem. **55**, 205 (1964).
20. N.S. Iacobellis, A. Sisto, and G. Surico. Bull. OEPP, **23**, 429 (1993).
21. E.O. King, M.K. Ward, and D.E. Raney. J. Lab. Clin. Med. **44**, 303 (1954).
22. O. Westphal and K. Jann. Methods Carbohydr. Chem. **5**, 83 (1965).
23. P.A. Barton-Willis, M.C. Wang, M.J. Holliday, M.R. Long, and N.T. Keen. Physiol. Plant Pathol. **25**, 387 (1984).
24. Y.D. Karrkhanis, J.Y. Zeltner, J.J. Jackson, and D.J. Carlo. Anal. Biochem. **85**, 595 (1978).
25. C.G. Hellerquist and B.J. Sweetman. Methods Biochem. Anal. **34**, 91 (1990).
26. V.L. L'vov, N.V. Tochtamysheva, A.S. Shashkov, and B.A. Dimitriev. Carbohydr. Res. **112**, 233 (1983).

Stereospecific addition of aryltellurium(IV) trichlorides to 3-methylcyclohexene: the X-ray crystal structure of *p*-anisyl(*trans*-2-chloro-*trans*-3-methyl-1-cyclohexyl)tellurium(IV) dichloride

BOZENA BORECKA AND T. STANLEY CAMERON
Department of Chemistry, Dalhousie University, Halifax, NS B3H 4J3, Canada

AND

M. AZAD MALIK AND BARRY C. SMITH
Department of Chemistry, Birkbeck College (University of London), Gordon House, 29 Gordon Square, London WC1H 0PP, U.K.

Received January 7, 1994

BOZENA BORECKA, T. STANLEY CAMERON, M. AZAD MALIK, and BARRY C. SMITH. Can. J. Chem. **72**, 1844 (1994).

Aryltellurium(IV) trichlorides react with 3-methyl-1-cyclohexene to give aryl(*trans*-2-chloro-*trans*-3-methyl-1-cyclohexyl)tellurium(IV) dichlorides. The X-ray crystal structure of *p*-anisyl(*trans*-2-chloro-*trans*-3-methyl-1-cyclohexyl)tellurium(IV) dichloride is reported. Single crystals of *p*-$MeOC_6H_4$(*trans*-2-Cl-*trans*-3-MeC_6H_9)$TeCl_2$ are triclinic, space group $P\bar{1}$ (No. 2) with a = 10.419(2) Å, b = 10.906(3) Å, c = 8.285(3) Å, α = 92.40(3)°, β = 95.85(2)°, γ = 61.71(3)°, V = 824.6 Å^3, D(calcd) = 1.761 g cm^{-1} for Z = 2. The structure was refined to R = 0.0444 (R_w = 0.0458).

BOZENA BORECKA, T. STANLEY CAMERON, M. AZAD MALIK et BARRY C. SMITH. Can. J. Chem. **72**, 1844 (1994).

Les trichlorures d'aryltellure(IV) réagissent avec le 3-méthylcyclohex-1-ène pour donner des dichlorures d'aryl(*trans*-2-chloro-*trans*-3-méthylcyclohexan-1-yl)tellure(IV). Faisant appel à la diffraction des rayons X, on a déterminé la structure cristalline du dichlorure de *p*-anisyl((*trans*-2-chloro-*trans*-3-méthylcyclohexan-1-yl)tellure(IV). Les cristaux uniques du *p*-$MeOC_6H_4$(*trans*-2-Cl-*trans*-3-MeC_6H_9)$TeCl_2$ sont tricliniques, groupe d'espace $P\bar{1}$ (No. 2) avec a = 10,419(2), b = 10,906(3) et c = 8,285(3) Å, α = 92,40(3), β = 95,85(2) et γ = 61,71(3)°, V = 824,6 Å^3, D(calcd) = 1,761 g cm^{-1} pour Z = 2. On a affiné la structure jusqu'à des valeurs de R = 0,0444 et R_w = 0,0458.

[Traduit par la rédaction]

Introduction

Aryltellurium(IV) trichlorides behave as polar aryldichlorotellurium(IV) chlorides in addition reactions with cycloalkenes (1, 2). The X-ray crystal structures of *p*-tolyl(*trans*-2-chloro-1-cyclohexyl)tellurium(IV) dichloride (3) and *p*-anisyl(*trans*-2-chloro-1-cyclohexyl)tellurium(IV) dichloride (unpublished results) establish that tellurium has a pseudo trigonal bipyramidal configuration with chlorines occupying axial positions and aryl and cyclohexyl carbons occupying equatorial positions. The cyclohexyl groups have chair conformations with tellurium and chlorine in adjacent equatorial positions.

It is shown here that aryltellurium(IV) trichlorides undergo addition reactions with 3-methyl-1-cyclohexene to give aryl(*trans*-2-chloro-*trans*-3-methyl-1-cyclohexyl)tellurium(IV) dichlorides. A reaction mechanism is proposed. The structure of *p*-anisyl(*trans*-2-chloro-*trans*-3-methyl-1-cyclohexyl)tellurium(IV) dichloride has been determined by X-ray crystallography.

Experimental

A mixture of *p*-anisyltellurium(IV) trichloride (4) (2.00 g, 5.9 mmol) and 3-methyl-1-cyclohexene (0.58 g, 6.0 mmol) in chloroform (40 cm^3) was boiled under reflux (2 h). Some dark green decomposition products were removed by filtration. The yellow filtrate was shaken with charcoal and refiltered. The colourless filtrate was evaporated gently under reduced pressure. The transparent viscous residue crystallised from light petroleum (bp 40–60°C) to give colourless *p*-anisyl(*trans*-2-chloro-*trans*-3-methyl-1-cyclohexyl)tellurium(IV) dichloride (1.30 g, 3.0 mmol, 51%), mp 105–106°C. Other aryl(*trans*-2-chloro-*trans*-3-methyl-1-cyclohexyl)tellurium(IV) dichlorides were prepared similarly in chloroform or carbon tetrachloride although reactions of 3,5-dimethoxylphenyltellurium(IV) trichloride gave better yields in diethyl ether. Yields, mps, and analytical data are summarised in Table 1. NMR spectra were recorded on a Varian VXR 400 spectrometer.

Data collection

A suitable crystal of *p*-anisyl(*trans*-2-chloro-*trans*-3-methyl-1-cyclohexyl)tellurium(IV) dichloride was mounted on a glass fibre. An Enraf-Nonius CAD4 was used to measure the unit cell dimensions and collect data. The crystal and data collection parameters are listed in Table 2. The unit cell constants were obtained by least squares analysis of the diffractometer setting angles of 25 well centered reflections in the range 2θ = 30–36°. The intensities were reduced to a standard scale using routine procedures (5). Lorentz and polarisation corrections were applied and absorption corrections (6) were performed. Scattering factors for neutral atoms (7, 8) were corrected for the real part of anomalous dispersion. All calculations and refinements were performed with TEXSAN (5).

TABLE 1. Aryl(*trans*-2-chloro-*trans*-3-methyl-1-cyclohexyl)tellurium(IV) dichlorides

Product	Yield (%)	Mp (°C)	Found (%) C	Found (%) H	Found (%) Cl	Formula	Calculated (%) C	Calculated (%) H	Calculated (%) Cl
p-$MeOC_6H_4(ClMeC_6H_9)TeCl_2$	51	105–106	38.20	4.31	24.34	$C_{14}H_{19}Cl_3OTe$	38.46	4.38	24.32
p-$EtOC_6H_4(ClMeC_6H_9)TeCl_2$	70	Oil	40.17	4.61	23.72	$C_{15}H_{21}Cl_3OTe$	39.92	4.69	23.57
2′,4′-$(MeO)_2C_6H_3(ClMeC_6H_9)TeCl_2$	45	118	38.50	4.48	22.85	$C_{15}H_{21}Cl_3O_2Te$	38.56	4.53	22.76
3′,4′-$(MeO)_2C_6H_3(ClMeC_6H_9)TeCl_2$	55	115	38.49	4.44	22.86	$C_{15}H_{21}Cl_3O_2Te$	38.56	4.53	22.76
3′,5′-Me_2-4′-$HOC_6H_2(ClMeC_6H_9)TeCl_2$	42	128–130	39.82	4.62	23.62	$C_{15}H_{21}Cl_3OTe$	39.92	4.69	23.57

Can. J. Chem. Downloaded from www.nrcresearchpress.com by 85.192.166.187 on 09/08/12
For personal use only.

TABLE 2. Experimental details of crystal and X-ray data collection

(*A*) Crystal data

Empirical formula	$C_{14}H_{19}Cl_3OTe$
Formula weight	437.26
Crystal color, habit	Colourless, needle
Crystal dimensions (mm)	0.15 × 0.22 × 0.50
Crystal system	Triclinic
No. reflections used for unit cell determination (2θ range)	20 (30.0–45.5°)
Lattice parameters	a = 10.419(2) Å b = 10.906(3) Å c = 8.285(3) Å α = 92.40(3)° β = 95.85(2)° γ = 61.71(2)° V = 824.6(9) Å^3
Space group	$P\bar{1}$ (#2)
Z value	2
D_{calcd}	1.761 g/cm^3
F_{000}	428
$\mu_{(MoK\alpha)}$	22.88 cm^{-1}

(*B*) Intensity measurements

Diffractometer	Enraf-Nonius CAD-4
Radiation	MoKα (λ = 0.70926 Å)
Temperature	18°C
Attenuator	Zr foil, (factor = 19.0)
Take-off angle	2.8°
Detector aperture	2.0–2.5 mm horizontal 2.0 mm vertical
Crystal to detector distance	21 cm
Scan type	w–2θ
Scan rate	1.6–3.3°/min (in ω)
Scan width	(1.00 + 0.35 tan θ)°
$2\theta_{max}$	49.8°
No. of reflections measured	Total: 3102 Unique: 2885 (R_{int} = 0.031)
Corrections	Lorentz-polarization Absorption (trans. factors: 0.645–1.0) Decay (–21.00% decline)

Structural analysis and refinement

The cell dimensions and lack of systematically absent reflections confirmed the space group as $P\bar{1}$. The position of tellurium was determined from a Patterson map and the remaining non-hydrogen atoms were located in subsequent difference-Fourier syntheses. The structure was refined initially by a full-matrix least-squares procedure with independent isotropic temperature factors on the atoms. Absorption corrections were then applied (6). Hydrogen atoms were placed in their geometrically calculated positions, d(C—H) 0.95 Å and were not refined. The final refinements with anisotropic temperature factors on the non-hydrogen atoms and individual isotropic temperature factors on the hydrogen atoms gave R = 0.0455 and R_w = 0.0458 (on full data R = 0.0556). A full-matrix least-squares method was employed. The function minimised was $\Sigma w(|F_o| - |F_c|)^2$ where w is the weight. The details are given in Table 3. No correction for extinction was applied. The final difference map had no recognisable residual features other than several peaks of approximately 1 e Å^{-3} near tellurium. Figure 4 was produced with ORTEP (9).

Results and discussion

Aryltellurium(IV) trichlorides, $ArTeCl_3$(Ar = p-$MeOC_6H_4$, p-$EtOC_6H_4$, 2,4-$(MeO)_2C_6H_3$, 3,4-$(MeO)_2C_6H_3$, and 3,5-Me_2-4-HOC_6H_2), undergo addition reactions with a slight excess of 3-methyl-1-cyclohexene in boiling organic solvents. The products are identified as aryl(*trans*-2-chloro-*trans*-3-methyl-1-cyclohexyl)tellurium(IV) dichlorides.

TABLE 3. Experimental details of structure solution and refinement

Structure solution	Patterson
Refinement	Full-matrix least-squares
Function minimized	$\Sigma w (\|F_o\| - \|F_c\|)^2$
Least-squares weights	$4F_o^2/\sigma^2(F_o^2)$
p-factor	0.03
Anomalous dispersion	All non-hydrogen atoms
No. observations ($I > 3.00\sigma(I)$)	2000
No. variables	172
Reflection/parameter ratio	11.63
Residuals: R; R_w	0.0455; 0.0458
Goodness-of-fit indicator	2.708
Maximum shift/error in final cycle	0.00
Maximum peak in final diffraction map	1.164 e$^-$/Å^3
Minimum peak in final diffraction map	–1.390 e$^-$/Å^3

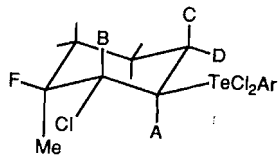

FIG. 1. Diagramatic representation of aryl(*trans*-2-chloro-*trans*-3-methyl-1-cyclohexyl)tellurium(IV) dichlorides with letters A to D and F assigned to five hydrogen atoms.

NMR spectra

Letters are assigned to five cyclohexyl hydrogens in Fig. 1 in order to assist discussion of the proton spectra of aryl(*trans*-2-chloro-*trans*-3-methyl-1-cyclohexyl)tellurium(IV) dichlorides.

The hydrogens that were alkenic originally appear as well-resolved multiplets. The cyclohexyl H-CTe protons (A) appear as a triplet through coupling with two adjacent *trans*-axial protons B and C, ^3J ca. 12 Hz, that is split further into doublets by the *cis*-equatorial proton D, ^3J ca. 5 Hz. The chemical shifts of H—CTe (A) protons show a greater dependence on aryl group and their signals are at higher field than those of cyclohexyl H—CCl (B) protons which appear as doublets of doublets through coupling with only one *trans*-axial proton A and one *cis*-equatorial proton F, ^3J(B—F) ca. 5 Hz. Coupling is not observed with protons from the C-methyl group (that replaces axial hydrogen E) which appear as a doublet near δ 1.2 ppm, ^3J ca. 7 Hz, through coupling with geminal proton F. The cyclohexyl A and B signals from *p*-anisyl(*trans*-2-chloro-*trans*-3-methyl-1-cyclohexyl)tellurium(IV) dichloride are reproduced in Fig. 2. Chemical shifts and coupling constants for cyclohexyl A and B protons in five aryl(*trans*-2-chloro-*trans*-3-methyl-1-cyclohexyl)tellurium(IV) dichlorides are summarised in Table 4. Coupling constants are at the high end of the expected range (2, 10). These patterns establish that tellurium and chlorine occupy adjacent *trans*-equatorial positions in solution whereas methyl has an axial position that is *cis* to chlorine.

The proton signals of cyclohexyl methylene groups, aryl groups, and alkyl, alkoxy, and hydroxy substituents resemble those of corresponding aryl(*trans* 2-chloro-1-cyclohexyl)tellurium(IV) dichlorides (2).

Aryl(*trans*-2-chloro-*trans*-3-methyl-1-cyclohexyl)tellurium-

Can. J. Chem. Downloaded from www.nrcresearchpress.com by 85.192.166.187 on 09/08/12
For personal use only.

TABLE 4. Proton NMR signals at 400 MHz for aryl(2-*trans*-chloro-3-*trans*-methyl-1-cyclohexyl)tellurium(IV) dichlorides

Compound	Solvent	H—CTe δ(A) (ppm)	H—CCl δ(B) (ppm)	^3J(A—B) ^3J(A—C) (Hz)	^3J(A—D) (Hz)	^3J(B—F) (Hz)
p-$MeOC_6H_4(ClMeC_6H_9)TeCl_2$	C_6D_6	4.40	4.88	11.7	4.7	4.7
p-$EtOC_6H_4(ClMeC_6H_9)TeCl_2$	$CDCl_3$	4.39	4.87	11.6	4.3	4.8
2′,4′-$(MeO)_2C_6H_3(ClMeC_6H_9)TeCl_2$	$CDCl_3$	4.60	4.94	10.0	4.8	4.3
3′,4′-$(MeO)_2C_6H_3(ClMeC_6H_9)TeCl_2$	C_6D_6	4.45	4.91	11.7	4.9	4.7
3′,5′-Me_2-4′-$HOC_6H_2(ClMeC_6H_9)TeCl_2$	$CDCl_3$	4.38	4.87	11.6	5.9	4.7

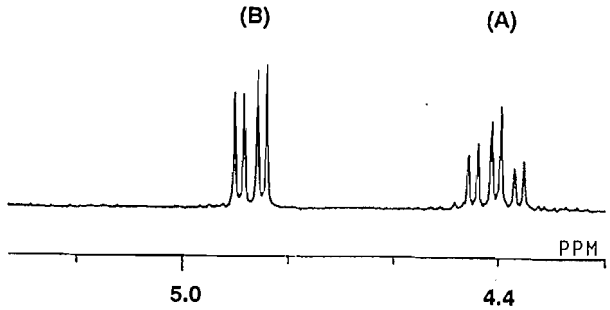

FIG. 2. Proton NMR spectrum at 400 MHz of axial H—CTe (A) and H—CCl (B) protons of *p*-anisyl(*trans*-2-chloro-*trans*-3-methyl-1-cyclohexyl)tellurium(IV) dichloride in C_6D_6.

(IV) dichlorides show carbon-13 NMR carbon-tellurium signals near δ 70 ppm relative to TMS and carbon—chlorine signals near δ 65 ppm. Methyl, methoxy, and six cyclohexyl carbons appear upfield and aryl carbons appear downfield with identical carbons showing signals of higher intensity.

Mechanism

The proposed mechanism is illustrated in Fig. 3. 3-Methylcyclohexene has a semi-chair conformation with methyl occupying an equatorial position in solution. Cationic aryldichlorotellurium(IV) reacts to form a bicyclo[4.1.0]heptane intermediate with cyclic telluronium and methyl on opposite sides of the cyclohexyl ring. Ring opening through bimolecular nucleophilic attack by chloride occurs at carbon with an axial hydrogen as predicted by the Furst–Plattner rule (see, for example, ref. 11). The conformationally unstable intermediate shown in square brackets is formed by Walden inversion of an approximately linear chloride—carbon—tellurium transition state. Ring-inversion leads to the favoured chair form of aryl(*trans*-2-chloro-*trans*-3-methyl-1-cyclohexyl)tellurium-(IV) dichloride having chlorine and bulky $TeCl_2Ar$ groups in equatorial positions and methyl in an axial position. Complete selectivity is achieved. No other cyclohexyltellurium derivatives were observed despite a thorough search of all the samples.

Crystal structure

The structure of *p*-anisyl(*trans*-2-chloro-*trans*-3-methyl-1-cyclohexyl)tellurium(IV) dichloride is shown in Fig. 4. Positional parameters and isotropic temperature factors are given in Table 5. Interatomic distances and angles are listed in Tables 6 and 7. Anisotropic temperature factors for non-hydrogen atoms are given in Table 8 (deposited).[1]

[1]Copies of material on deposit can be purchased from the Depository of Unpublished Data, Document Delivery, CISTI, National Research Council Canada, ON K1A 0S2, Canada.

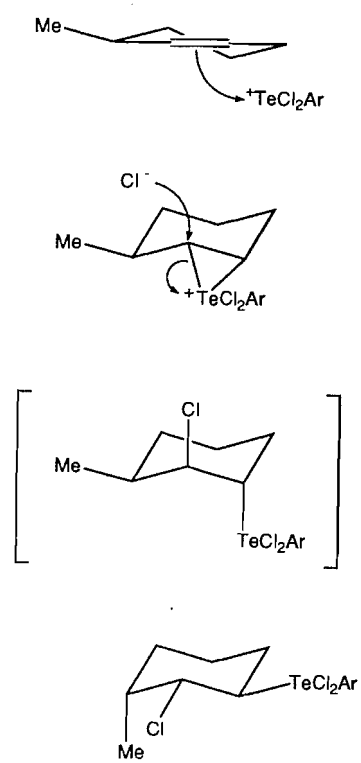

FIG. 3. Proposed scheme for reactions of aryltellurium(IV) trichlorides with 3-methylcyclohexene.

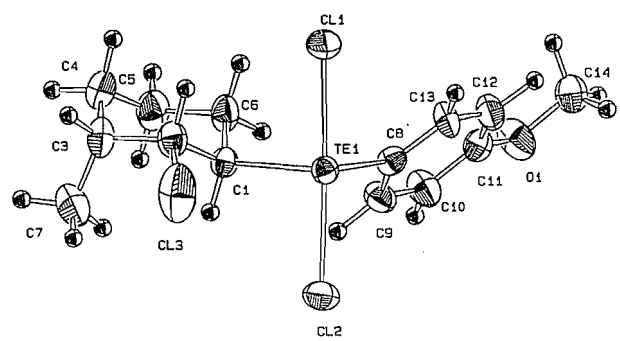

FIG. 4. X-ray crystal structure of *p*-anisyl(*trans*-2-chloro-*trans*-3-methyl-1-cyclohexyl)tellurium(IV) dichloride.

Tellurium has the expected pseudo trigonal bipyramidal configuration with two chlorines in axial positions, two carbon rings in equatorial positions, and the lone pair of electrons of tellurium in the third equatorial position. Internuclear distances within the co-ordination sphere are as follows: Te(1)—Cl(1)

Can. J. Chem. Downloaded from www.nrcresearchpress.com by 85.192.166.187 on 09/08/12
For personal use only.

TABLE 5. Positional parameters and B(eq) for p-$MeOC_6H_4(C_6H_9MeCl)TeCl_2$

Atom	x	y	z	B(eq)
Te(1)	0.28314(5)	0.06784(6)	0.06617(7)	2.43(4)
Cl(1)	0.4592(2)	0.0777(2)	0.2862(3)	3.6(2)
Cl(2)	0.1008(2)	0.0509(3)	−0.1427(3)	3.8(2)
Cl(3)	0.4726(4)	−0.2682(3)	0.0168(4)	6.6(2)
O(1)	−0.2165(6)	0.6083(6)	0.330(1)	4.7(5)
C(1)	0.2693(8)	−0.0911(8)	0.210(1)	2.5(5)
C(2)	0.4161(9)	−0.2207(9)	0.218(1)	3.5(6)
C(3)	0.415(1)	−0.340(1)	0.304(1)	3.8(6)
C(4)	0.370(1)	−0.291(1)	0.474(1)	4.6(7)
C(5)	0.222(1)	−0.159(1)	0.474(1)	4.3(7)
C(6)	0.227(1)	−0.0420(9)	0.381(1)	3.6(6)
C(7)	0.321(1)	−0.396(1)	0.216(1)	5.2(8)
C(8)	0.1112(8)	0.2534(8)	0.152(1)	2.6(5)
C(9)	−0.0253(9)	0.2628(9)	0.168(1)	3.3(6)
C(10)	−0.1307(9)	0.384(1)	0.227(1)	3.9(6)
C(11)	−0.1063(9)	0.496(1)	0.269(1)	3.5(6)
C(12)	0.030(1)	0.486(1)	0.244(1)	3.7(6)
C(13)	0.1368(9)	0.3636(8)	0.188(1)	3.2(6)
C(14)	−0.195(1)	0.723(1)	0.380(1)	4.3(7)

TABLE 6. Intramolecular distances involving the nonhydrogen atoms p-$MeOC_6H_4(C_6H_9MeCl)TeCl_2$

Atom	Atom	Distance (Å)	Atom	Atom	Distance (Å)
Te1	C11	2.487(2)	C3	C4	1.52(1)
Te1	C12	2.505(2)	C3	C7	1.50(1)
Te1	C1	2.212(8)	C4	C5	1.53(1)
Te1	C8	2.125(8)	C5	C6	1.54(1)
C13	C2	1.80(1)	C8	C9	1.40(1)
O1	C11	1.35(1)	C8	C13	1.36(1)
O1	C14	1.41(1)	C9	C10	1.37(1)
C1	C2	1.51(1)	C10	C11	1.38(1)
C1	C6	1.52(1)	C11	C12	1.40(1)
C2	C3	1.51(1)	C12	C13	1.37(1)

TABLE 7. Intramolecular bond angles involving the nonhydrogen atoms p-$MeOC_6H_4$-$(C_6H_9MeCl)TeCl_2$

Atom	Atom	Atom	Angle (deg)	Atom	Atom	Atom	Angle (deg)
C11	Te1	C12	176.38(8)	C4	C3	C7	111.3(8)
C11	Te1	C1	88.5(2)	C3	C4	C5	113.2(8)
C11	Te1	C8	90.7(2)	C4	C5	C6	109.7(8)
C12	Te1	C1	88.0(2)	C1	C6	C5	109.4(7)
C12	Te1	C8	88.8(2)	Te1	C8	C9	120.6(6)
C1	Te1	C8	100.9(3)	Te1	C8	C13	118.3(6)
C11	O1	C14	119.1(7)	C9	C8	C13	121.1(7)
Te1	C1	C2	108.2(5)	C8	C9	C10	117.9(8)
Te1	C1	C6	112.7(5)	C9	C10	C11	122.2(8)
C2	C1	C6	110.1(7)	O1	C11	C10	117.1(8)
C13	C2	C1	109.6(6)	O1	C11	C12	124.3(8)
C13	C2	C3	111.4(7)	C10	C11	C12	118.5(8)
C1	C2	C3	112.4(7)	C11	C12	C13	119.6(8)
C2	C3	C4	107.5(8)	C8	C13	C12	120.5(7)
C2	C3	C7	114.7(9)				

2.485(2), Te(1)—Cl(2) 2.503(2), Te(1)—C(1) 2.194(7), Te(1)—C(8) 2.101(7) Å. The bond lengths agree well with values reported earlier (3, 12) with Te—C(alkyl) longer than Te—C(aryl). The Cl(1)—Te(1)—Cl(2) bond angle of 176.39(7) is smaller than 180°, and the C(1)—Te(1)—C(8) bond angle of 100.7(3) is smaller than 120°, presumably because of the presence of nonbonding electrons on tellurium. The cyclohexyl ring adopts the usual chair conformation with tellurium and chlorine in adjacent equatorial positions but with methyl in an axial position.

Can. J. Chem. Downloaded from www.nrcresearchpress.com by 85.192.166.187 on 09/08/12
For personal use only.

Acknowledgement

We thank the Natural Sciences and Engineering Research Council of Canada for support to T.S.C.

1. M.M. Campos and N. Petragnani. Tetrahedon Lett. **6**, 11 (1959); Tetrahedron, **18**, 521 (1962).
2. M.A. Malik, M.E.S. Ali, F.J. Berry, J. Kaur, M. Rowshani, and B.C. Smith. Inorg. Chim. Acta, **180**, 251 (1991).
3. T.S. Cameron, R.B. Amero, and R.E. Cordes. Cryst. Struct. Commun. **9**, 539 (1980).
4. G.T. Morgan and R.E. Kellett. J. Chem. Soc. 1080 (1926).
5. TEXSAN–TEXRAY. Single crystal structure analysis package. Ver. 5.0. Molecular Structure Corporation, The Woodlands, Tex. 1989.
6. N. Walker and D. Stuart. Acta Crystallogr. **A39**, 158 (1983).
7. D.T. Cromer and J.T. Waber. *In* International tables for X-ray crystallography. Vol. IV. Kynoch Press, Birmingham, England. 1974. Table 2.2A, p. 71.
8. R.F. Stewart, E.R. Davison, and W.T. Simpson. J. Chem. Phys. **42**, 3175 (1965).
9. C.K. Johnson. *In* ORTEPII Report ORNL-5138. Oak Ridge National Laboratory, Oak Ridge, Tenn. 1976.
10. M.E.S. Ali, M.A. Malik, and B.C. Smith. Inorg. Chim. Acta Lett. **162**, 157 (1989).
11. S.J. Angyal. Chem. Ind. (London) 1230 (1954); R.J. Ferrier and P.M. Collins. Monosaccharide chemistry. Penguin Books Ltd., Harmondsworth. 1972.
12. N.W. Alcock and W.D. Harrison. J. Chem. Soc. Dalton Trans. 251 (1982); S. Husebye, E.A. Meyers, R.A. Zingaro, J.V. Comasseto, and N. Petragnani. Acta Crystallogr. **C43**, 1147 (1987); P.K. Bakshi, T.S. Cameron, M.E.S. Ali, M.A. Malik, and B.C. Smith. Inorg. Chim. Acta, **204**, 27 (1993).

Can. J. Chem. Downloaded from www.nrcresearchpress.com by 85.192.166.187 on 09/08/12
For personal use only.

Syntheses of 3-(substituted)-2,4,6-triphenylverdazyls

ALAN R. KATRITZKY[1] AND SERGEI A. BELYAKOV
Center for Heterocyclic Compounds, Department of Chemistry, University of Florida, Gainesville, FL 32611-2046, U.S.A.
H. DUPONT DURST
U.S. Army Edgewood Research, Development & Engineering Center, Aberdeen Proving Ground, MD 21010-5423, U.S.A.
AND
RUIXIN XU AND NARESH S. DALAL
West Virginia University, P.O. 6045, Morgantown, WV 26506, U.S.A.

Received December 21, 1993

ALAN R. KATRITZKY, SERGEI A. BELYAKOV, H. DUPONT DURST, RUIXIN XU, and NARESH S. DALAL. Can. J. Chem. **72**, 1849 (1994).

Two series of 2,4,6-triphenylverdazyls substituted at the C(3) position of the heterocyclic ring are obtained using new convenient synthetic methodology. Thus, crown ether assisted solid–liquid phase-transfer catalysis promotes the formation of 3-*n*-alkyl-substituted 2,4,6-triphenylverdazyls in the reactions of 1,3,5-triphenylformazan with *n*-alkyl bromides. Under PTC conditions, methylation of 3-(4-nitrophenyl)-1,5-diphenylformazan with methyl iodide exclusively gives the corresponding verdazyl radical. 3-Substituted 2,4,6-triphenylverdazyls containing various di(cyclo)alkylamino moieties at the C(3) position of the verdazyl ring are prepared by the reaction of 1,3,5-triphenylformazan with the corresponding 1-[*N*,*N*-di(cyclo)alkylaminomethyl]benzotriazoles under the efficient catalysis of barium hydroxide monohydrate. Sonication of this reaction allows the yields of the verdazyls to be substantially increased. A bis-verdazyl *N*,*N*-bonded in the C(3) positions was synthesized. All the radicals obtained were characterized by microanalysis, and by UV–visible and ESR spectroscopy.

ALAN R. KATRITZKY, SERGEI A. BELYAKOV, H. DUPONT DURST, RUIXIN XU et NARESH S. DALAL. Can. J. Chem. **72**, 1849 (1994).

Faisant appel à une nouvelle méthodologie de synthèse, on a obtenu deux séries de 2,4,6-triphénylverdazyles substitués en position C(3) de l'hétérocycle. La catalyse par transfert de phase solide–liquide assistée par un éther-couronne favorise la formation des 3-*n*-alkyl-2,4,6-triphénylverdazyles lors des réactions des 1,3,5-triphénylformazane avec des bromures de *n*-alkyles. Dans des conditions de transfert de phase, la méthylation du 3-(4-nitrophényl)-1,5-diphénylformazane par l'iodure de méthyle conduit uniquement au radical verdazyle correspondant. On a préparé des 2,4,6-triphénylverdazyles substitués par des portions di(cyclo)alkylamino en position (C)3 du cycle verdazyle en faisant réagir du 1,3,5-triphénylformazane avec les 1-[*N*,*N*-di(cyclo)alkylaminométhyl]benzotriazoles correspondants en présence de monohydrate d'hydroxyde de baryum comme catalyseur efficace. La sonication de cette réaction permet d'obtenir des rendements beaucoup plus élevés de verdazyles. On a synthétisé un bis-verdazyle lié aux positions C(3) par deux N. On a caractérisé tous les radicaux obtenus par des microanalyses, des spectres UV–visible et par spectroscopie RPE.

[Traduir par la rédaction]

Introduction

Verdazyls (1,2,3,4-tetrahydro-*s*-tetrazin-1-(2*H*)-yls), discovered by Kuhn and Trischmann (1, 2) represent a class of extraordinarily stable free radicals, in which the stability is enhanced by an extensive symmetrical delocalization of the unpaired electron. Only five atoms of the *s*-tetrazine ring participate in the delocalization of spin density, while the C(3) atom is generally believed to be excluded from the conjugated system (3). Based on this principle, one could expect that substituents at the C(3) atom of the heterocycle would not affect the properties of verdazyls. However, the properties of radicals in this series, especially their spectral characteristics, vary widely depending on the number (none, one, or two) and type (alkyl, alkenyl, alkynyl, aryl, oxo, amino, etc.) of the C(3) substituents (3).

Efficient methods for the preparation of the C(3)-substituted verdazyls include: (*i*) reaction of formazans with aliphatic aldehydes in acidic media followed by reduction of the intermediate verdazylium cations, and (*ii*) alkylation of formazans by primary alkyl halides in DMF in the presence of base. The latter is followed by two consecutive reactions: cyclization of the *N*-alkylformazan intermediates, and dehydrogenation of the cyclized leuco-verdazyls, frequently by atmospheric oxidation (2). Method (*i*) is more useful for the preparation of formazans with strongly electron-withdrawing substituents (O.M. Polumbrik, personal communication), but its applicability is limited to aliphatic aldehydes unbranched at the α-carbon atom (e.g., formaldehyde, acetaldehyde, and propionaldehyde), and it fails for aromatic aldehydes (3). Method (*ii*) is more general but has the significant disadvantage that a large excess of alkylating agent is required, which leads to alkylation of the intermediate tetrahydro-*s*-tetrazine (leuco-verdazyl) as a side reaction (2). For triarylformazans containing strongly electron-withdrawing substituents such as nitro groups in the phenyl rings, this side reaction predominates, and verdazyls of this type cannot be obtained by this method (4).

The alkylation of formazans is also limited to reactive electrophiles as reaction partners. Primary alkyl iodides have been used in most cases, although activated bromides such as propargyl (5) or benzyl bromide (1, 2) have also been utilized. These reactions generally require 6–12 h to reach completion (2). The successful use of *n*-alkyl bromides has not been described previously.

3-[*N*,*N*-Di(cyclo)alkylamino]-substituted verdazyls differ from the other verdazyls due to their unique chemical and physico-chemical properties, which include anomalous reaction with acids, enhanced solubility, and unusual spectral characteristics (5, 6). The reaction of formazans with formaldehyde and secondary alkyl or cycloalkyl amines has remained the primary

[1]Author to whom correspondence may be addressed.

Can. J. Chem. Downloaded from www.nrcresearchpress.com by 85.192.166.187 on 09/08/12
For personal use only.

Can. J. Chem. Downloaded from www.nrcresearchpress.com by 85.192.166.187 on 09/08/12
For personal use only.

method employed for their preparation (5) and can be classified as a variation of method (*ii*), i.e., Mannich-type alkylation of the formazan N—H group in the presence of base (barium oxide/barium hydroxide mixture). Unfortunately, this reaction requires a large excess of both formaldehyde (in the form of paraformaldehyde) and of the secondary amine. Moreover, the reaction is slow (in most cases 12–24 h) and, despite this, still gives poor yields (<16%). Only a few cyclic *sec*-amines were employed to obtain the 3-*N*-cycloalkylaminoverdazyls, and no 3-*N,N*-dialkylaminoverdazyls were isolated; it was mentioned, however, that open-chain *sec*-amines can react in a similar way (5).

The only other reported route to 3-*N,N*-dialkylaminoverdazyls involves the reaction of 1,3,5-triphenylformazan, *N,N,N′,N′*-tetramethyldiaminomethane, and paraformaldehyde in DMF (6). The latter two reagents apparently react with traces of water to give, initially, dimethylaminomethanol. Subsequent aminoalkylation leads to the 3-(*N,N*-dimethylamino)-2,4,6-triphenylverdazyl in 32% yield. However, the starting bis-(dialkylamino)methanes required for this method are not always easy to prepare, and the yield of radicals is only moderate.

One important general feature of the previous studies dealing with method (*ii*) is that a mixture of BaO and $Ba(OH)_2 \cdot 8H_2O$ is usually employed as the base, typically with a large excess of BaO (2, 4), while $Ba(OH)_2 \cdot 8H_2O$ is used in only catalytic amounts. Presumably, during the reaction, dehydration of the $Ba(OH)_2 \cdot 8H_2O$ by BaO occurs due to the latter's strong hydrophilic nature, but this is uncertain since both bases are insoluble in DMF. As shown by Sinisterra and co-workers, a modified barium hydroxide catalyst, C-200, which contains 80% $Ba(OH)_2 \cdot H_2O$ and 20% anhydrous BaO, is a versatile reagent for various organic reactions, and has found application in Michael additions (7), Claisen–Schmidt condensations (8), and the Wittig–Horner reaction (9). The superior catalytic activity of C-200 in comparison with $Ba(OH)_2 \cdot 8H_2O$ was indicated by the improved yields noted in the Michael addition of diethyl malonate to chalcone (7), the Horner reaction of furfural with triethyl phosphonoacetate (9), and also by the decrease in yield observed when the C-200 active sites were selectively poisoned (7). The two-step mechanism postulated for reactions of C-H active compounds in the presence of barium hydroxide (7) involves the adsorption of the substrate and formation of the corresponding carbanion at the active site of the catalyst. This is followed by the surface reaction of the adsorbed carbanion, i.e., reaction occurs at the solid–liquid interface.

It is also well known that reactions at solid–liquid interfaces are promoted by crown ethers (10) (solid–liquid phase-transfer catalysis, PTC). As established earlier (11), crown ethers are the preferred catalysts for solid–liquid PTC. Dicyclohexano-18-crown-6 (DC18C6) is one of the most widely used crown ethers for this purpose (10).

We have now found that the preparation of two series of 3-substituted verdazyls, 3-(*n*-alkyl)- and 3-[*N,N*-di(cyclo)alkylamino]-2,4,6-triphenylverdazyls, is significantly improved by the use of barium hydroxide monohydrate as an active catalyst. 3-(*n*-Alkyl)-2,4,6-triphenylverdazyls were prepared employing the $Ba(OH)_2 \cdot H_2O$/DC18C6 system in place of the earlier used combination of $BaO/Ba(OH)_2 \cdot 8H_2O$ in the alkylation of formazans by alkyl halides. This now permits the use of the *n*-alkyl bromides as alkylation substrates in the preparation of the 3-(*n*-alkyl)-2,4,6-triphenylverdazyls, thus circumventing the shortcomings of the previous procedures. Moreover, we found that the reaction of 1,3,5-triphenylformazan with 1-[*N,N*-di(cyclo)-alkylaminomethyl]benzotriazoles in DMF in the presence of $Ba(OH)_2 \cdot H_2O$ at ambient temperatures leads smoothly to 3-[*N,N*-di(cyclo)alkylamino]-2,4,6-triphenylverdazyls in yields of 37–69%. The limitations of the earlier routes are now effectively overcome by the use of Mannich reactants with preformed stoichiometry. In comparison with previous methods, our approach provides improved yields of verdazyls, and shortens reaction times.

Results and discussion

A possible general reaction sequence for these transformations is shown in Scheme 1. It includes the formation of formazan anions **2***a*, *b*, but by two different ways: in the case of our preparation of 3-*n*-alkylverdazyls the reaction occurs in the solution by crown-assisted transfer of anion **2***a* into the organic phase (solid–liquid PTC), while anion **2***b* is formed directly on the surface of the barium catalyst. After alkylation of the anions **2***a*, *b* by alkyl bromides **3**, or by Mannich bases **4**, respectively, the *N*-alkylformazans **5** are spontaneously cyclized into leucoverdazyls **6**. In situ oxidation of the latter finally gives the 3-substituted verdazyls **7**.

1. Syntheses of 3-(n-alkyl)-2,4,6-triphenylverdazyls 7a–f

Formazans, by virtue of their ability to react with both strong acids and bases, can be considered as amphoteric. In strongly acidic conditions they form formazanium cations (12), whereas in basic media they apparently give rise to the anionic species by loss of the acidic NH proton. This anion formation takes place at the surface of barium hydroxide, as does the subsequent alkylation. The catalyst's effectiveness decreases with time as the result of the elimination of hydrogen halide, which poisons the catalyst. Due to the heterogeneous character of the interaction, the reaction rate is low, and requires a large excess of $BaO/Ba(OH)_2 \cdot 8H_2O$ (10–15 mol/mol of formazan) and alkyl halide (ca. 30–40 mol/mol of formazan) (2).

It was anticipated that the transfer of the reaction into the liquid phase would accelerate the reaction. Crown ethers and solid bases (carbonates or hydroxides of alkaline or alkaline earth metals) in solid–liquid PTC form cation-complexed ion pairs (11), which are soluble in the organic phase in which the reaction occurs (10). No precise data for the solid–liquid phase transfer of barium hydroxides by DC18C6 are yet available. However, the ionic radius of Ba^{2+} fits the DC18C6 cavity very well (13), and the stability of the complex DC18C6:Ba^{2+} is quite high ($\log K > 5$; enthalpy of complex formation in acetonitrile, $\Delta H = -48.1$ kJ mol^{-1} (14)). At the same time, DC18C6 shows little or no interaction with the solvent molecules, which assists successful phase transfer (14). Indeed, DC18C6 was found to be an effective ligand for selective transport of Ba^{2+} in a competitive system (Mg^{2+}, Ba^{2+}, Ca^{2+}) from a chloroform liquid membrane system when crown ether cooperatively acts with *n*-alkanoic acids (15). DC18C6 also efficiently extracts barium nitrate (16) and barium picrate (17) from neutral solutions into chloroform. Recently the transfer process of KOH into a toluene phase through solid phase KOH in the presence of DC18C6 was described (18). Considering the similar ionic radii of K^+ and Ba^{2+} cations (13), it might be possible to use DC18C6 for the interfacial transfer of barium hydroxide.

In our case (Scheme 1), when a mixture of formazan **1**, $Ba(OH)_2 \cdot H_2O$, and DC18C6 in DMF was stirred for several

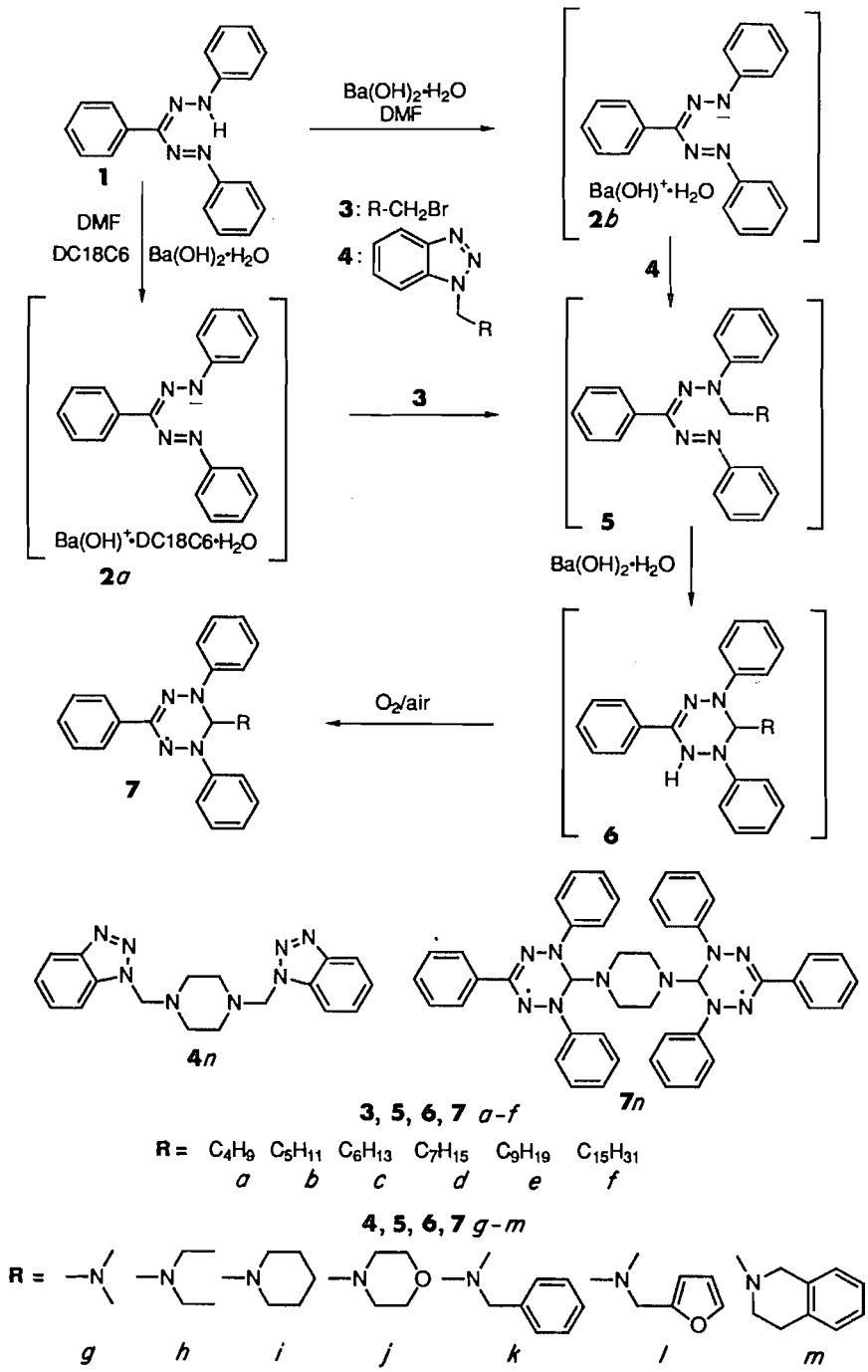

SCHEME 1

minutes, the color changed from red to crimson. This apparently indicates the formation of a soluble complex **2***a* that owes its deep color to its ionic character. Addition of an *n*-alkyl bromide leads to the *N*-alkylformazan **5**, and to the liberation of the DC18C6·Ba(OH)Br complex. Since the cyclization of **5** to leuco-verdazyl **6** occurs rapidly in the presence of strong bases, thermally, or in the presence of acids (4), we found that heating the mixture smoothly led to the leuco compound **6**, which, in turn, was oxidized to verdazyl **7** by passing a stream of air through the reaction medium. The consecutive nature of the reaction leads to various concentrations of *N*-alkylformazan **5**, leucoverdazyl **6**, and radical **7**. The presence of oxygen, however, prevents the undesirable formation of *s*-tetrazine anion from **6** by means of its reaction with the catalytic complex. This anion could otherwise be easily alkylated to give the side product, *N*-alkyl-*s*-tetrazine.

As was noted earlier (10), the presence of a small amount of water is very important in solid–liquid PTC; moreover, in some reactions involving the participation of C-200 barium hydroxide catalyst, a small amount of water must be added to the reaction mixture to increase the reaction rate to an acceptable level (9). Although the role of water in both cases is not clear, its presence is probably also important in the alkylation of formazans, and as such the addition of BaO (a strong dehydrating agent) is not necessary.

The reversibility of DC18C6 in the present procedure is illus-

Can. J. Chem. Downloaded from www.nrcresearchpress.com by 85.192.166.187 on 09/08/12
For personal use only.

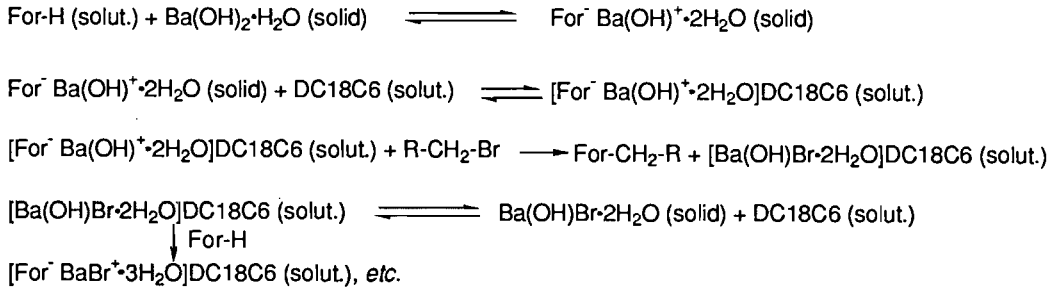

SCHEME 2

TABLE 1. 3-(*n*-Alkyl)-2,4,6-triphenylverdazyls **7***a–f*[a]

Radical **7**	Yield of isolated products, %	Melting point, °C	Molecular formula	Elemental analysis found (required), % C	H	N
a	58	180	$C_{24}H_{25}N_4$	78.02 (78.01	6.81 6.82	14.94 15.17)
b	72	154–155	$C_{25}H_{27}N_4$	78.37 (78.29	7.20 7.10	14.46 14.61)
c	63	132–133	$C_{26}H_{29}N_4$	78.57 (78.55	7.35 7.35	14.12 14.10)
d	71	111	$C_{27}H_{31}N_4$	78.83 (78.79	7.75 7.59	13.45 13.62)
e	77	110	$C_{29}H_{35}N_4$	79.18 (79.22	7.99 8.03	12.74 12.75)
f	75	94–95	$C_{35}H_{47}N_4$	80.22 (80.26	9.15 9.05	10.53 10.69)

[a]Molar ratio formazan **1** : *n*-alkyl bromide : $Ba(OH)_2 \cdot H_2O$: DC18C6 = 1 : 1.5 : 2.0 : 0.04.

TABLE 2. Spectral properties of verdazyls **7***a–f*

Radical **7**	λ_{max}, nm (log *E*)[a]	*g*-Value	ΔH_s, G[b]	a_N, G[c]
a	285 (4.38); 320 (4.23); 405 (4.03); 430 (4.03); 721 (3.83)	2.0031	1.62	5.72
b	284 (4.36); 320 (4.21); 405 (4.00); 430 (4.00); 718 (3.82)	2.0031	1.41	5.72
c	286 (4.37); 322 (4.17); 406 (4.03); 424 (4.03); 720 (3.83)	2.0032	1.41	5.72
d	286 (4.37); 322 (4.23); 408 (4.01); 430 (4.01); 716 (3.82)	2.0032	1.79	5.75
e	285 (4.35); 316 (4.21); 402 (4.01); 425 (4.00); 710 (3.81)	2.0032	2.03	5.80
f	283 (4.42); 318 (4.21); 401 (3.97); 426 (3.97); 712 (3.67)	2.0032	1.81	5.80

[a]5×10^{-5} mol/L, in benzene.
[b]Linewidth between points of maximum slope (solid samples), gauss.
[c]^{14}N Hyperfine coupling due to 4 nitrogens, in benzene, gauss.

trated in Scheme 2. The ion pair formed on the surface of $Ba(OH)_2 \cdot H_2O$ from the latter and formazan (For-H) is transferred into the liquid phase by DC18C6. The reaction proceeds in the solution. After alkylation, a complex of barium hydroxybromide with DC18C6 can either free the crown ether (thus involving it again in the catalytic cycle) or react to include another molecule of formazan in the catalytic alkylation process.

We have used this modified method to obtain in good yields a series of new 3-(*n*-alkyl)-2,4,6-triphenylverdazyls. All the verdazyls obtained (Table 1) form deeply colored (dark-green) crystals. Their melting points steadily decrease as the number of CH_2 units in the alkyl substituent increases. The spectral properties of the radicals are collected in Table 2.

The UV–VIS spectra of verdazyls **7***a–f* exhibit absorption bands typical for this class of compounds: (*i*) two intense bands with maxima at 285 and 320 nm in the UV region, (*ii*) two almost equal in intensity and wavelength (near 405 and

Can. J. Chem. Downloaded from www.nrcresearchpress.com by 85.192.166.187 on 09/08/12
For personal use only.

TABLE 3. 3-[*N,N*-Di(cyclo)alkylamino]-2,4,6-triphenylverdazyls **7***g–n*

Radicals **7**	Yield of isol. prod./lit. yield	Method of synthesis[a]	Molar ratio **1**:**4**:$Ba(OH)_2 \cdot H_2O$	Melting point/lit. mp, °C	Molecular formula	Elemental analysis, found (required), % C	H	N
g	37/32 (6)	A	1:2.0:2.0	155–157/156–157 (6)	$C_{22}H_{22}N_5$	—	—	—
						73.89	6.18	19.45
	63	D	1:2.0:2.0	157–159		(74.13	6.22	19.65)
h	33	A	1:2.0:2.0	122–124	$C_{24}H_{26}N_5$	—	—	—
						74.95	6.80	18.18
	48	C	1:2.0:2.0	124–125		(74.97	6.82	18.21)
i	63/16 (5)	B	1:1.5:1.5	165–166/170–171 (5)	$C_{25}H_{26}N_5$	75.40	6.71	17.32
						(75.73	6.61	17.66)
j	60	A	1:1.5:1.5	174–175	$C_{24}H_{24}N_5O$	71.99	5.98	17.46
						(72.34	6.07	17.57)
k	50	C	1:1.8:2.0	135–137	$C_{28}H_{26}N_5$	77.94	5.88	15.89
						(77.75	6.06	16.19)
l	52	C	1:1.8:2.0	98–100	$C_{26}H_{24}N_5O$	73.97	5.73	16.64
						(73.91	5.73	16.58)
m	48	C	1:1.8:2.0	123–125	$C_{29}H_{26}N_5$	78.00	5.85	15.85
	69	E	1:1.8:2.0	124–125		(78.35	5.89	15.76)
n	43[b]	B	2:1.1:5.0	176–177	$C_{44}H_{40}N_{10}$	74.33	5.71	19.36
						(74.55	5.69	19.76)

[a]A: 60°C, 30 min; B: 60°C, 3 h; C: r.t., 24 h; D: r.t., 2 h, ultrasound; E: r.t., 3 h, ultrasound.
[b]On the initial formazan.

Can. J. Chem. Downloaded from www.nrcresearchpress.com by 85.192.166.187 on 09/08/12
For personal use only.

425 nm), and (*iii*) one long-wave band responsible for the deep green color of such radicals (near 720 nm). This set of bands is characteristic for π–π^* transitions of a highly conjugated chromophoric chain. As expected, the length of the substituent at the C(3) atom of the heterocycle, which is not involved in the conjugation, exerts only minor influence on the position of the long-wave maximum.

Crystalline samples of the radicals **7***a–f* exhibited intense, single-peak, ESR spectra centered at the *g*-value of 2.0032 ± 0.0002 with a signal bandshape of Lorentzian form, as expected for concentrated free radical samples. The linewidth between points of maximum slope, ΔH_s, is quite narrow, varying from 1.41 to 2.03 G depending on the length of alkyl chain in radicals **7***a–f*. This indicates a strong exchange interaction between the unpaired electrons. ESR spectra of **7***a–f* obtained in well-degassed (10^{-4} Torr; 1 Torr = 133.3 Pa) benzene or hexane showed the nine-peak hyperfine patterns usual for verdazyls in the intensity ratio of 1:4:10:16:19:16:10:4:1, with an average spacing of approximately 5.75 G, in agreement with earlier studies (3).

Our modified method was also successfully used to obtain 6-(4-nitrophenyl)-2,4-diphenylverdazyl (**8**). As previously shown (4), alkylation of 3-(4-nitrophenyl)-1,5-diphenylformazan by methyl iodide in the presence of $BaO/Ba(OH)_2 \cdot 8H_2O$ in DMF led exclusively to 1-methyl-6-(4-nitrophenyl-1,2,3,4-tetrahydro-*s*-tetrazine. Radical **8** was obtained in 70% yield after a short reaction time with a small excess of the alkylating agent.

2. *Syntheses of 3-[N,N-di(cyclo)alkylamino]-2,4,6-triphenylverdazyls 7g–n*

Initial attempts to synthesize 3-(benzotriazol-1-yl)-2,4,6-triphenylverdazyl by the reaction of 1,3,5-triphenylformazan with 1-hydroxymethylbenzotriazole in both acidic and neutral media gave only 2,4,6-triphenylverdazyl. The well-known lability of the N—CH_2 bond in 1-hydroxymethylbenzotriazole and the leaving-group character of benzotriazole suggested the possible aminoalkylation of formazans (i.e., **1**) with benzotriazolyl derivatives **4**.

When amine **4**, formazan **1**, and $Ba(OH)_2 \cdot H_2O$ are stirred in DMF (Scheme 1), the *N'*-[*N,N*-di(cyclo)alkylaminomethyl]formazan, formed via aminoalkylation, immediately cyclizes into leuco-verdazyl **6** by the action of base (barium hydroxide) if heated to 60°C. Atmospheric oxygen was used to oxidize leuco compound **6** into radical **7**.

The optimum molar ratio of reagents depends on the reactivity of the amines **4** (Table 3). Dialkylamines (**7***g, h*) react more slowly than cycloalkylamines (**7***i, j*) and a larger excess of the former is required. Those dialkylamines in which the aromatic or heteroaromatic systems are connected with the carbon atom at the β position to the active methylene group show an intermediate reactivity (**7***k–m*). The same regularity is observed regarding the optimum preparative conditions. When di(cyclo)alkylamines **7***g, i, j* (**7***h* being the only exception) were employed, heating the reaction mixture for 0.5–3 h gave the corresponding leuco compounds **6** and then the radicals **7**, while in the case of **7***k–m* acceptable yields of verdazyls **7** were obtained only by extended stirring at room temperature.

1-[*N,N*-Di(cyclo)alkylaminomethyl]benzotriazoles **4** are solid compounds that can be easily prepared by a one-pot procedure from benzotriazole, formaldehyde, and the corresponding *sec*-amines in high yield (19, 20). Their use as aminoalkylation agents in Mannich-type reactions is of considerable interest because of the preformed stoichiometry between the reagents commonly used in Mannich reactions (i.e., formaldehyde and amine). Compounds **4** reversibly dissociate into iminium salts in polar solvents (21, 22), and these are the reactive entities in Mannich reactions. As shown for the case of radical **7***n*, we employed this strategy to obtain the first representative of a bis-verdazyl *N,N*-bonded in the C(3) position.

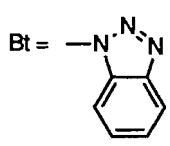

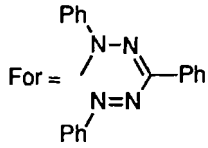

[1] $Bt\text{-}CH_2\text{-}N(R^1R^2) \rightleftharpoons [Bt^- + CH_2{=}\overset{+}{N}(R^1R^2)]$ (solut.)

[2] For-H (solut.) + $Ba(OH)_2\ H_2O$ (solid) $\rightleftharpoons$ [For$^-$ $Ba(OH)^+\ 2H_2O$] (solid)

[3] [For$^-$ $Ba(OH)^+\ 2H_2O$] (solid) + [$Bt^- + CH_2{=}\overset{+}{N}(R^1R^2)$] (solut.) $\longrightarrow$

$\longrightarrow$ [For-CH_2-$N(R^1R^2)$ + BtH] (solut.) + $Ba(OH)_2\ H_2O$ (solid)

SCHEME 3

TABLE 4. Spectral properties of verdazyls **7***g–n*

Radical **7**	λ_{max}, nm (log E)[a]	g-Value	ΔH_s, G[b]	a_N, G[c]
g	246 (4.14); 274 (4.31); 316 (4.20); 402 (3.99); 420[d] (3.98); 684 (3.81)	2.0033	1.29	5.56
h	246 (4.16); 273 (4.33); 316 (4.22); 402 (4.01); 422[d] (4.00); 687 (3.81)	2.0032	2.40	5.56
i	246 (4.12); 274 (4.14); 316 (4.21); 402 (4.03); 420[d] (4.00); 688 (3.82)	—[e]	—[e]	—[e]
j	246 (4.10); 271 (4.30); 314 (4.20); 392 (3.98); 420[d] (3.97); 678 (3.81)	2.0033	2.29	5.58
k	248[d] (4.21); 274 (4.37); 315 (4.27); 400 (4.07); 420[d] (4.05); 678 (3.87)	2.0033	1.95	5.54
l	250[d] (4.21); 273 (4.33); 315 (4.20); 400 (3.98); 420[d] (3.97); 684 (3.79)	2.0033	2.05	5.61
m	258[d] (430); 270 (4.34); 315 (4.18); 402 (3.92); 422[d] (3.91); 679 (3.75)	2.0033	2.92	5.60
n	252 (4.07); 279 (4.18); 320 (4.09); 416 (3.88); 435 (3.89); 693 (3.80)	2.0032	2.68	5.46

[a] 5×10^{-5} mol/L, in dioxane.
[b] Linewidth between points of maximum slope (solid samples), gauss.
[c] ^{14}N Hyperfine coupling due to 4 nitrogens, in toluene, gauss.
[d] Shoulder.
[e] Not determined.

A possible mechanism of the reaction is given in Scheme 3. In the dipolar aprotic solvent (DMF) **4** exists partly in the form of the iminium salt (eq. [1]). Formazan **1** reacts with the active sites of $Ba(OH)_2{\cdot}H_2O$ to give the corresponding salt, which remains bound to the insoluble catalyst surface (eq. [2]). Subsequently, 5-(*N,N*-dialkylaminomethyl)-1,3,5-triphenylformazan **5** (formed as the result of fast ion exchange) is transferred from the interfacial reaction site into the DMF solution (eq. [3]). A further transformation of **5** into radical **7** via leuco-verdazyl intermediate **6** occurs according to the established mechanism (1). Indeed, the formation of ion–molecule pairs from **4***g–n* and the distribution of the positive charge in their structure appear to play a key role in this reaction. Attempts to use benzotriazolyl derivatives **4** in which one of the hydrogens of the active methylene group is replaced by an alkyl or aryl substituent, or in which a nitrogen atom is bound to an aromatic system (aniline, carbazole, phenoxazine, etc.), failed.

Interestingly, radicals **7***g*, *m* were also obtained in yields higher than 60% after ultrasonic treatment of the reaction mixture containing formazan **1**, the corresponding benzotriazole derivative **4**, $Ba(OH)_2{\cdot}H_2O$, and DMF. As shown by Fuentes and Sinisterra, ultrasound positively affects the Canizzaro reaction carried out in heterogeneous (solid–liquid) phase in the presence of active barium hydroxide catalyst, which contains 80% of $Ba(OH)_2{\cdot}H_2O$ (23). It was suggested that the reaction takes place by single electron transfer by means of reducing sites of the solid catalyst; in our case, however, the process is apparently accelerated by the efficient degassing of the porous cavities of the catalyst. Since the reaction occurs on the catalyst surface, the role of surface accessibility is extremely important. Ultrasound increases it by (*i*) development of the surface of catalyst by cavitation; (*ii*) cleaning the surface of the catalyst by removal of gas bubbles trapped in the pores. Thus, while the detailed mechanism and nature of this ultrasonic process remain

Can. J. Chem. Downloaded from www.nrcresearchpress.com by 85.192.166.187 on 09/08/12
For personal use only.

Can. J. Chem. Downloaded from www.nrcresearchpress.com by 85.192.166.187 on 09/08/12
For personal use only.

to be investigated, its usefulness in our procedure is quite evident.

Spectral properties of the radicals **7***g–n* are collected in Table 4. The UV–VIS absorption spectra of the radicals **7***g–n* consist of three intense bands in the UV region and three bands of lower intensity in the visible region. The presence of the highly conjugated heterocyclic system containing an odd number of π-electrons dictates the position of the first electronic transition at about 680–685 nm. The hypsochromic shift of the long-wave absorption maxima of **7***g–m* (35–40 nm) from the position of the analogous maximum in the spectrum of unsubstituted 2,4,6-triphenylverdazyl (720 nm (3)) is explained by the steric interaction of the bulky di(cyclo)alkylamino substituent at the C(3) atom with the conjugated heterocyclic ring. However, the C(3) atom only fixes the cyanine-like system (four nitrogens and one C(6) carbon) in a *cis–cis* arrangement and does not take part in the unpaired electron density transfer (3). Therefore, the change of the substituent in the structure of **7***g–m* does not strongly affect the position of their long-wave maxima. The UV–VIS spectrum of bis-radical **7***n* differs slightly from the spectra of mono-radicals **7***g–m* in the visible region (bathochromic shift of all the three maxima is about 13–15 nm).

The ESR spectra of the radicals **7***g–n* (1 mM solutions of radicals in well-degassed toluene) exhibit well-resolved nine-line patterns in the intensity ratio 1:4:10:16:19:16:10:4:1, which is typical for verdazyl radicals. The *g*-values of **7***g–n* are (2.0032–2.0033) ± 0.0002, and the hyperfine coupling constants, a_N, of the four equivalent nitrogen atoms of the verdazyl ring are between 5.46 and 5.61 G (Table 4), which is also in good agreement with the data for other verdazyls (3). It should be mentioned that a good resolution in the ESR spectra of **7***g–n* can be achieved only when their solutions are well degassed; apparently the complexation of verdazyls with the oxygen of the air is an important factor. However, the ESR spectra of the solid verdazyls were single peaks. The ΔH_s, linewidth between points of maximum slope, values of the crystalline samples of **7***g–n* vary in the range from 1.30 G (**7***g*) to 2.92 G (**7***m*) (Table 4), due to rapid electron exchange among neighboring free radical molecules.

Conclusion

The enhanced catalytic activity demonstrated by the combination of $Ba(OH)_2 \cdot H_2O$ and DC18C6 under solid–liquid phase transfer catalysis results in improved preparation of 3-(*n*-alkyl)-2,4,6-triphenylverdazyls. In addition, this reagent combination substantially decreases the quantities of base and alkylating agent required and allows the use of the more available and more stable *n*-alkyl bromides in place of the iodides. *p*-Nitrophenyl-substituted triarylverdazyls can be easily obtained by alkylation of the corresponding formazans under the conditions of solid–liquid PTC with the use of the DC18C6/$Ba(OH)_2 \cdot H_2O$ system, whereas the previous method failed due to dominating side reactions (4). On the other hand, the Mannich-type reaction of 1,3,5-triphenylformazan with 1-[*N*,*N*-di(cyclo)alkylaminomethyl]benzotriazoles in the presence of the active catalyst, $Ba(OH)_2 \cdot H_2O$, carried out in a dipolar aprotic solvent (DMF), leads to the aminoalkylation of the formazan N—H bond followed by stepwise cyclization–oxidation reactions to yield 3-[*N*,*N*-di(cyclo)alkylamino]-2,4,6-triphenylverdazyls. The aminoalkylation reaction apparently takes place on the catalyst surface, whereas cyclization and oxidation occur in the solution. Reaction is promoted by the use of ultrasound, which positively affects the catalyst surface activity and results in higher yields of radicals. By comparison with previous procedures, the present method has the advantages of rapidity, versatility, ease of scale-up, and improved yields.

Experimental

The UV–visible spectra were obtained using a Perkin–Elmer 330 spectrophotometer. Melting points were determined on a Bristoline hot-stage microscope and are uncorrected. The ESR spectra were recorded on a Bruker ER 300 spectrometer (frequency 9.5 GHz). *g*-Values were determined by utilizing a digital frequency counter, Hewlett–Packard 5420, and DPPH as a standard. Nitrogen hyperfine coupling, a_N, were measured from 1 mM solutions in benzene (**7***a–f*) or toluene (**7***g–n*), and their comparison with computer simulations. Ultrasonic treatments (methods D, E) were performed by use of the compact high-performance ultrasonic system FS3 (Fisher Scientific Co., peak output 70 W, frequency 55 kHz). Methyl iodide, *n*-alkyl bromides, and DC18C6 (mixture of *cis-syn-cis* and *cis-anti-cis* isomers) were purchased from Aldrich, $Ba(OH)_2 \cdot H_2O$ from the J.T. Baker Chemical Co., and DMF from the Fischer Scientific Co. All reagents were used as received. 1,3,5-Triphenyl- and 3-(4-nitrophenyl)-1,5-diphenylformazans were synthesized following literature procedures (24). 1-[*N*,*N*-Di(cyclo)alkylaminomethyl]benzotriazoles **4***g–m* and the corresponding bis-derivative **4***n* were prepared by known methods (19, 20). Compounds **4***g–n* were recrystallized from ethanol and gave satisfactory microanalysis data, and ^1H and ^{13}C NMR spectra.

General procedure for the preparation of verdazyls 7a–f

A mixture of triphenylformazan (1.65 mmol), DC18C6 (0.067 mmol), and $Ba(OH)_2 \cdot H_2O$ (3.30 mmol) in DMF (25 mL) was stirred vigorously for 5 min. The appropriate *n*-alkyl bromide (3.30 mmol) was added in one portion, and the mixture was heated to 60°C under stirring. After 10 min, a fast stream of air was passed through the reaction mixture with stirring and heating. Completion of the reaction was monitored by TLC (phase: silica gel; eluent: chloroform). The reaction was stopped when the TLC no longer indicated the initial red formazan (this takes usually about 1.0–1.2 h). The reaction mixture was cooled, diluted with diethyl ether (75 mL), and the solid filtered. The filtrate was washed with water (3 × 50 mL), the organic layer was separated, dried over anhydrous sodium sulphate, removed under vacuum, and the residue triturated with a mixture of petroleum ether and methanol. The solid product obtained was filtered off and washed with a mixture of petroleum ether and methanol. Analytical samples of radicals **7***a–f* were obtained after column chromatography (phase: aluminum oxide basic, Brockmann activity I; solvent/eluent:hexane).

The general procedure for the synthesis of verdazyls **7***g–n* is illustrated with reference to compound **7***g*.

3-Dimethylamino-2,4,6-triphenyl-3,4-dihydro-2H-1,2,4,5-tetrazin-1-yl (3-N,N-dimethylamino-2,4,6-triphenylverdazyl) 7g

Method A

The solid **4***g* (0.59 g, 3.32 mmol) was added to a mixture of 1,3,5-triphenylformazan **1** (0.50 g, 1.66 mmol), $Ba(OH)_2 \cdot H_2O$ (0.63 g, 3.32 mmol), and DMF (25 mL), which was initially stirred at room temperature for 5 min. The mixture was heated to 60°C under stirring, while a stream of air was passed through it. After 0.5 h the mixture was cooled, ether (30 mL) was added, and organic phase was collected by filtration. Water (50 mL) was added, and the mixture was extracted with additional ether. The organic layer was dried over anhydrous sodium sulfate, concentrated under vacuum, and the oily crude product quickly triturated with methanol (10 mL). The resulting solid was collected by filtration and recrystallized from methanol–DMF to give black-green crystals of **7***g* (0.22 g, 37%).

Method D

A mixture of **1** (0.25 g, 0.83 mmol), **4***g* (0.29 g, 1.66 mmol), $Ba(OH)_2 \cdot H_2O$ (0.31 g, 1.66 mmol), and DMF (20 mL) was placed in a

round-bottom flask and sonicated at room temperature for 2 h while immersed in a water bath. After a standard work-up procedure (see above), radical **7***g* was isolated in 63% yield.

*6-(4-Nitrophenyl)-2,4-diphenyl-3,4-dihydro-2H-1,2,4,5-tetrazin-1-yl (6-(4-nitrophenyl)-2,4-diphenylverdazyl) **8***

A mixture of 3-(4-nitrophenyl)-1,5-diphenylformazan (0.150 g, 0.43 mmol), DC18C6 (0.005 g, 0.013 mmol), and $Ba(OH)_2 \cdot H_2O$ (0.164 g, 0.86 mmol) in DMF (10 mL) was stirred for 5 min followed by addition of methyl iodide (0.054 mL, 0.86 mmol) in one portion. After 2–3 min of stirring, the mixture became brown. Stirring was continued for 15 min at room temperature (TLC no longer indicated the presence of formazan) and then for 5–7 min at 40–50°C while an air stream was passed through the mixture. After cooling, benzene (30 mL) was added, the solid was filtered off, and the filtrate was washed with water (2 × 50 mL). The organic layer was evaporated under vacuum, and the crude product was triturated with methanol, yielding 0.108 g (70%) of **8**, mp 205–206°C (lit. (25) mp 206–207°C).

Acknowledgement

This work was supported by the U.S. Army Research Office (Contract no. DAAL03-92-G-0195).

1. R. Kuhn and H. Trischmann. Angew. Chem. Int. Ed. Engl. **2**, 155 (1963).
2. R. Kuhn and H. Trischmann. Monatsh. Chem. **95**, 457 (1964).
3. F.A. Neugebauer. Angew. Chem. Int. Ed. Engl. **12**, 455 (1973).
4. G. MacConnachie and F.A. Neugebauer. Tetrahedron, **31**, 555 (1975).
5. R. Kuhn, F.A. Neugebauer, and H. Trischmann. Monatsh. Chem. **97**, 846 (1966).
6. L.N. Markovskii, S.A. Belyakov, A.V. Misyura, and O.M. Polumbrik. J. Org. Chem. USSR (Engl. Transl.), **24**, 2018 (1988).
7. M. Iglesias, J.M. Marinas, and J.V. Sinisterra. Tetrahedron, **43**, 2335 (1987).
8. J.V. Sinisterra, A. Garsia-Laso, J.A. Cabello, and J.M. Marinas. Synthesis, 502 (1984).
9. J.V. Sinisterra, Z. Mouloungui, M. Demlas, and A. Gaset. Synthesis, 1097 (1985).
10. W.P. Weber and G.W. Gokel. Phase transfer catalysis in organic synthesis. Springer-Verlag, Berlin. 1977. pp. 9–11.
11. G.W. Gokel and H.D. Durst. Synthesis, 168 (1976).
12. S.A. Belyakov. Ukr. Khim. Zh. (Russ. Ed.), **55**, 1079 (1989); Chem. Abstr. **112**, 177876x (1990).
13. J.D. Lamb, R.M. Izatt, and J.J. Christensen. *In* Progress in macrocyclic chemistry. Vol. 2. *Edited by* R.M. Izatt and J.J. Christensen. J. Wiley & Sons, New York. 1981. pp. 52–59.
14. H.-J. Buschmann. J. Solution Chem. **17**, 277 (1988).
15. S. Inokuma, T. Hayase, and T. Kuwamura. Yukagaku, **36**, 340 (1987); Chem. Abstr. **107**, 84732m (1987).
16. T. Deloye, M. Burgard, and M.J.F. Leroy. New J. Chem. **13**, 139 (1989).
17. A. Yu. Tsivadze, V.V. Basmanov, and A.V. Levkin. Zh. Neorg. Khim. **35**, 2435 (1990); Chem. Abstr. **114**, 12922n (1991).
18. O.I. Kachurin, I.B. Frolova, and Z.A. Okhrimenko. Ukr. Khim. Zh. (Russ. Ed.), **55**, 749 (1989); Chem. Abstr. **112**, 63443y (1990).
19. A.R. Katritzky, S. Rachwal, B. Rachwal, and P.J. Steel. J. Org. Chem. **57**, 4932 (1992).
20. J.H. Burkhalter, V.C. Stephens, and L.A.R. Hall. J. Am. Chem. Soc. **74**, 3868 (1952).
21. A.R. Katritzky and K. Yannakopoulou. Heterocycles, **28**, 1121 (1989).
22. J.R. Lindsay Smith and J.S. Sadd. J. Chem. Soc. Perkin Trans. 1, 1181 (1975).
23. A. Fuentes and J.V. Sinisterra. Tetrahedron Lett. **27**, 2967 (1986).
24. J.N. Ashley, B.M. Davis, A.W. Nineham, and R. Slack. J. Chem. Soc. 3881 (1953).
25. F.A. Neugebauer and R. Bernhardt. Chem. Ber. **107**, 529 (1974).

Can. J. Chem. Downloaded from www.nrcresearchpress.com by 85.192.166.187 on 09/08/12
For personal use only.

A highly stereoselective preparation of *syn*-1,2-diols from secondary α-allenic alcohols via iodocyclization. Synthesis of (±)-*threo*-L-factor and (±)-disparlure

RICHARD W. FRIESEN[1] AND ANDRÉ GIROUX

Department of Medicinal Chemistry, Merck Frosst Centre for Therapeutic Research, P.O. Box 1005, Pointe Claire-Dorval, QC H9R 4P8, Canada

Received March 25, 1994

RICHARD W. FRIESEN and ANDRÉ GIROUX. Can. J. Chem. **72**, 1857 (1994).

The iodocyclization of the *N*-tosyl carbamates **5** of secondary α-allenic alcohols **4** is described. The reaction sequence involves the addition of iodine to the terminal olefin of the allene moiety of **5** resulting in the formation of an isomeric mixture of *Z* and *E* diiodides **6** and **7**. This initial process is followed, in the same pot, by reaction of the diiodides with silver carbonate. Hydrolysis of the resulting *trans* imino carbonates **8** provides *syn*-1,2-diols **10** in a highly diastereoselective (>50:1) and regioselective (>20:1) fashion. Oxazolidinones **9** are minor products that arise from the participation of the carbamate nitrogen atom in the cyclization reaction. The regioselectivity of the cyclization reaction from **6/7** to **8** is highly dependent upon the reaction solvent with the optimum results being obtained in ether/MeCN mixtures (10:1 to 50:1) or CH_2Cl_2. The synthetic utility of the vinyl iodo diols **10** is demonstrated by the synthesis of (±)-*threo*-5-hydroxy-4-decanolide (**17**) ((±)-*threo*-L-factor) and (±)-*cis*-7,8-epoxy-2-methyloctadecane (**24**) ((±)-disparlure). The key step in each synthesis involves the conversion of the vinyl iodide moiety of **10** into the alkynes **15** or **18** (from **10***j* and **10***k*, respectively) via a high-yielding dehydrohalogenation reaction.

RICHARD W. FRIESEN et ANDRÉ GIROUX. Can. J. Chem. **72**, 1857 (1994).

L'iodocyclisation des *N*-tosylcarbamates **5** des alcools α-alléniques secondaires **4** est décrite. La séquence des réactions implique l'addition de l'iode sur l'oléfine terminale de la portion allène du composé **5**, conduisant à la formation d'un mélange *Z* et *E* des diiodures isomères **6** et **7**. Cette première réaction est suivie d'une réaction unipot des diiodures avec du carbonate d'argent. L'hydrolyse des imino carbonates *trans* **8** qui en résultent, conduit aux *syn*-1,2-diols **10** de manières hautement diastéréosélective (>50 : 1) et régiosélective (>20 : 1). Les oxazalidinones **9** sont des produits secondaires provenant de la participation de l'atome d'azote du carbamate dans la réaction de cyclisation. La régiosélectivité de la réaction de cyclisation des composés **6/7** en composés **8** dépend fortement du solvant de la réaction, les meilleurs résultats étant obtenus avec des mélanges d'éther/MeCN (10:1 à 50:1) ou du CH_2Cl_2. L'utilité des iododiols vinyliques **10** est démontrée en synthétisant les composés suivants : le (±)-*thréo*-5-hydroxy-4-décanolide (**17**) (le (±)-*thréo*-L-facteur) et le (±)-*cis*-7,8-époxy-2-méthyloctadécane (**24**) ((±)-disparlure). L'étape fondamentale de chaque synthèse implique la transformation de la portion iodure vinylique du composé **10** en alcynes **15** ou **18** (respectivement à partir des composés **10***j* et **10***k*) par l'intermédiaire d'une réaction de déshydrohalogénation ayant un rendement élevé.

[Traduit par la rédaction]

Can. J. Chem. Downloaded from www.nrcresearchpress.com by 85.192.166.187 on 09/08/12
For personal use only.

Introduction

There has been a great deal of effort directed toward the stereocontrolled preparation of vicinal diols in the context of the total synthesis of polyoxygenated natural products. As a result of these studies, several useful and stereoselective methods have emerged for the synthesis of *anti*- and *syn*-1,2-diols including (*a*) the reduction (1) or alkylation (2) of α-hydroxy (or alkoxy) carbonyl compounds, (*b*) the reaction of a carbonyl group with α-hydroxy carbanions (3) or γ-alkoxyallyl organometallics (4),[2] (*c*) the dihydroxylation of *trans* disubstituted olefins (5),[3] and (*d*) the electrophile (E) induced cyclofunctionalization reactions of allylic alcohol derivatives (for two excellent reviews, see ref. 6). These latter reactions, illustrated by the conversion of **1** to **2**, have been performed on a variety of allylic alcohol derivatives **1** including trichloroacetaldehyde-derived hemiacetals (7), esters (7), carbamates (8), and carbonates (9). For those systems in which the internal asymmetric induction of the reaction has been addressed, the *trans*-substituted heterocycle **2** that leads to the *syn*-1,2-diol **3** usually predominates over the *cis* derivative of **2**. Typical cyclization diastereoselectivities for this process range from 4:1 to 13:1.

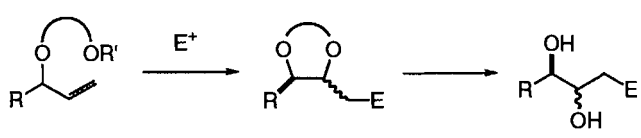

1 **2** **3**

In previous papers we (10, 11) and others (12) have demonstrated that α-allenic alcohols **4** are useful substrates with respect to cyclofunctionalization reactions. Carbamate derivatives of these alcohols can be converted in a highly diastereoselective fashion (27:1 to >50:1) into *syn*-1,2-amino alcohols **A**

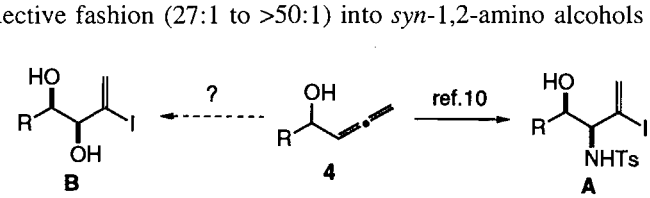

B **4** **A**

via an iodocyclization process (10*a*, *b*). Due to our general interest in the cyclofunctionalization reactions of α-allenic alcohol derivatives in the context of acyclic stereocontrol, we wished to determine whether α-allenic alcohol derivatives could also be used to prepare vicinal diols **B** via a similar strategy. If successful, the vicinal diol/vinyl iodide products would be potentially useful and versatile synthetic intermediates. Herein, we describe the details of the highly diastereoselective synthesis of *syn*-1,2-diols **10** from secondary α-allenic alcohols according to a cyclofunctionalization strategy employing car-

[1]Author to whom correspondence may be addressed. Phone: (514) 428-3164. Fax: (514) 695-0693.

[2]References 3 and 4 list examples of these types of reactions that provide *syn* diols as the major diastereomer.

[3]The reference most pertinent to this discussion is that of the dihydroxylation of 1,3-dienes (5) leading to 3,4-dihydroxy-1-alkenes.

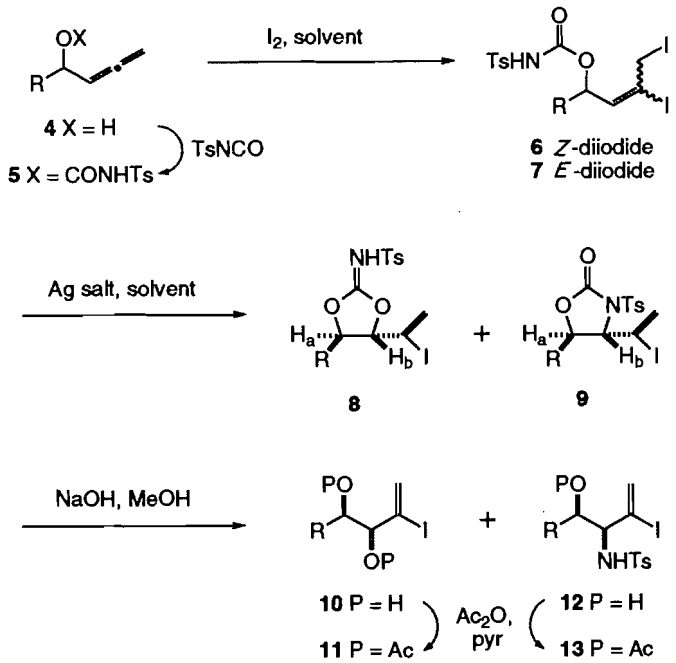

SCHEME 1

bamate derivatives of **4**.[4] The potential synthetic utility of the *syn*-1,2-diols **10** is demonstrated by short syntheses of (±)-*threo*-5-hydroxy-4-decanolide (**17**) (*threo*-(±)-L-factor) and (±)-*cis*-7,8-epoxy-2-methyloctadecane (**24**) ((±)-disparlure).

Results and discussion

The method whereby α-allenic alcohols **4** are converted into the *syn*-1,2-amino alcohols **12** (Scheme 1) involves the initial formation of *N*-toluenesulfonyl carbamates **5**, followed by a cyclofunctionalization reaction in the presence of iodine and base to form *trans* oxazolidinones **9** (10). This iodocyclization process involves the intermediacy of an isomeric mixture of diiodides **6/7** wherein iodine has added to the terminal double bond of the allene system. Under basic reaction conditions (K_2CO_3), intramolecular S_N2' displacement of the allylic iodide in each isomer by the carbamate nitrogen atom generates the *trans* oxazolidinone.

It is known (14) that carbamates can act as ambident nucleophiles in intramolecular displacement reactions, the regioselectivity that is observed (nitrogen vs. oxygen participation) being highly dependent on the nature of the reaction conditions. For example, the intramolecular opening of epoxides by carbamate nucleophiles under basic reaction conditions favours nitrogen participation (S_N2 like). However, under Lewis acidic conditions (S_N1 like) the regioselectivity is altered and the carbonyl oxygen becomes the participating nucleophile.[5] According to the latter mode of reactivity, we reasoned that treatment of the diiodide intermediates **6/7** with a silver salt might result in the generation and nucleophilic trapping of a cationic species by the carbamate carbonyl oxygen to form **8**.

(a) Iodocyclization regioselectivity and diastereoselectivity

Our initial efforts in this area were directed toward finding the optimal conditions for achieving regioselective participation of the carbamate carbonyl oxygen atom in the cyclization/displacement reaction of **6/7** as illustrated in Scheme 1. The *N*-tosyl carbamate **5***a* (R = *n*-heptyl) derived from α-allenic alcohol **4***a*[6] (TsNCO, ether) was treated with iodine as described previously (10) to afford a 1:1 *Z*/*E* mixture of diiodides **6***a* and **7***a* (Scheme 1). Using this diiodide mixture, a variety of cyclization reaction conditions were surveyed. The solvent (MeCN, Et_2O, CH_2Cl_2) and silver salt ($AgBF_4$, AgOTf, Ag_2CO_3, $AgNO_3$) were systematically varied and the resulting crude mixtures were inspected by ^1H NMR spectroscopy to determine the reaction regioselectivity. Although cyclized products **8***a* and **9***a* were observed in the majority of cases, it quickly became evident that Ag_2CO_3 was the salt of choice. In contrast to the other silver salts, many of the reactions using Ag_2CO_3 were extremely clean and gave excellent mass recovery. The solvent effect on the cyclization of **6***a*/**7***a* using this salt was then studied in detail and some of the results are summarized in Table 1, entries 1–7.

While no reaction was observed in ether (entry 1), presumably due to the insolubility of Ag_2CO_3 in this solvent, the cyclization that was carried out in MeCN (entry 2) did provide cyclized products **8***a* and **9***a* in a ratio of 1.4:1. Only a *single* stereoisomer of each cyclization product was observed in the spectrum of this reaction mixture. The ratio of **8***a* to **9***a* was easily established by integration of the vinyl proton resonances (δ 6.58 and 6.05 for **8***a*; δ 6.55 and 6.01 for **9***a*) and the methine proton resonances H_b (see table) in the ^1H NMR spectrum of the crude material. To facilitate isolation and purification, the crude mixture was hydrolyzed (aqueous NaOH, MeOH) and acetylated (Ac_2O, pyridine, DMAP) to provide **11***a* and **13***a* in yields of 55 and 34%, respectively, after chromatography. The isolated yield ratio correlated well with the integrated ratio observed in the ^1H NMR spectrum. None of the stereoisomeric products related to **11***a* and **13***a* could be found or isolated (diastereoselectivity >50:1).[7]

The relative stereochemistry in the cyclized products **8***a* and **9***a* was assigned as follows. While the *syn* amino acetate **13***a* was identical with material prepared previously (10), difference NOE experiments were performed on **8***a* in order to assess the stereochemistry of the oxygen cyclized product. Irradiation of the methylene proton resonance RCH_2CH_aO (δ 1.80, $CDCl_3$) resulted in the enhancement of the resonances of both protons H_a and H_b (δ 4.58 and 4.74, J_{ab} = 6.8 Hz), confirming the relative *trans* stereochemistry in **8***a*.

High degrees of regioselectivity favouring the production of **8***a* over **9***a* were observed in ether/MeCN solutions containing small amounts of MeCN (entries 3–5) as well as in CH_2Cl_2 solution (entry 7). In all cases, only a single stereoisomer **8***a* was observed in the crude mixture (by ^1H NMR) and only a single diacetate **11***a* was isolated. It should be noted that all of these reactions were repeated several times and the range of regioselectivities that were observed in each solvent are reported in the table. As can be seen in entry 6, there is a limit to the dilution of MeCN with ether that is successful; a 100:1 ratio of ether to MeCN does not provide cyclized products. In addition, there is some variability from one experiment to the next in the ratio of **8***a*:**9***a* that is observed in each of the 10:1 and 50:1

[4]For a preliminary account of this work, see ref. 13.

[5]For a more detailed discussion on the factors affecting regioselectivity in the reactions of ambident nucleophiles, see ref. 15.

[6]The α-allenic alcohols **4** were prepared according to the procedure described in ref. 16.

[7]We have been unable to isolate the *anti* diol. Thus, without an authentic standard and with the apparent lack of other resonances in the ^1H NMR spectra, we estimate the diastereoselectivity as >50:1.

Can. J. Chem. Downloaded from www.nrcresearchpress.com by 85.192.166.187 on 09/08/12
For personal use only.

TABLE 1. Preparation of *syn*-1,2-diols **10** and *syn*-1,2-diacetates **11** from secondary α-allenic alcohols **4**

Entry	Substrate **4** (R)	Cyclization reaction solvent[a]	Ratio **8**:**9**	H_b Chemical shift (δ)[b] **8**	**9**	$J_{a,b}$ in **8** (Hz)[b]	Overall yield (%) **10** or **11**[c]
1	**4***a* (*n*-heptyl)	E	nr[d]				**11***a* 0
2		A	1.4–3:1	4.74	4.40	6.8	**11***a* 55(34)
3		E/A (5:1)	2–10:1				**11***a* 62 (5)
4		E/A (10:1)	20–50:1				**11***a* 70(3)
5		E/A (50:1)	28–50:1				**11***a* 76(3)
6		E/A (100:1)	nr[d]				**11***a* 0
7		CH_2Cl_2	>50:1				**11***a* 82(0)
8	**4***b* ($TIPSOC_4H_8$)	A	1:1	4.75	4.41	5.5	**11***b* 40
9		CH_2Cl_2	14:1				**11***b* 80
10		E/A (10:1)	>50:1				**11***b* 78
11	**4***c* ($BnOCH_2OC_4H_8$)	E/A (10:1)	>50:1	4.75	—	6.1	**11***c* 75
12	**4***d* (i-butyl)	E/A (3:1)	13:1	4.68	4.35	6.8	**11***d* 74(4)
13		E/A (10:1)	20:1				**11***d* 70(3)
14		E/A (50:1)	30:1				**11***d* 60(2)
15	**4***e* (c-hexyl)	E/A (5:1)	10:1	4.86	4.58	5.3	**11***e* 70(8)
16		CH_2Cl_2	>50:1				**11***e* 70(0)
17	**4***f* (*tert*-butyl)	E/A (10:1)	>50:1	4.78	4.55	4.5	**11***f* 75(2)
18	**4***g* (3,4-$(OCH_2O)C_6H_3$)	E/A (10:1)	>50:1	4.86	—	6.1	**11***g* 75
19	**4***h* (4-$MeOC_6H_4$)	E/A (10:1)	[e]	4.90	—	6.3	**11***h* 29
20	**4***i* (*n*-butyl)	E/A (10:1)	30:1	4.73	4.40	6.1	**10***i* 80
21	**4***j* (*n*-pentyl)	E/A (4:1)	16:1	4.69	4.32	6.2	**10***j* 70
22		E/A (10:1)	20:1				**10***j* 75
23	**4***k* (*n*-decyl)	E/A (10:1)	40:1	4.69	4.31	5.6	**10***k* 85
24	**4***l* ($PhCH_2CH_2$)	E/A (10:1)	30:1	4.72	4.39	5.6	**10***l* 83
25	**4***m* ((*E*)-*n*-BuCH=CH)	E/A (10:1)	>50:1	4.69	4.38	6.5	**10***m* 81
26	**4***n* ((*E*)-MeCH=CH)	E/A (10:1)	nr[d]				**10***n* 0

[a]Cyclization reactions carried out according to the general procedure (see experimental section) in the solvents indicated. E = ether, A = acetonitrile.
[b]Crude reaction mixture in $CDCl_3$.
[c]Overall, isolated yields of analytically pure products **10** or **11** from allenic alcohols **4**. Value in parentheses refers to the isolated yield of the corresponding amine **13**, which was described previously (10*a*, *b*).
[d]No reaction.
[e]Unable to determine.

mixtures of ether:MeCN. The reason for this observation is unclear (other than experimental variability), but what is obvious from these data is that the cyclization regioselectivity is highly dependent upon the reaction solvent. The subtle differences in solvent polarity and the solubility of Ag_2CO_3 in the particular medium are presumably the key factors that affect the S_N2'/S_N1 nature of the cyclization reaction, and as a result the reaction regioselectivity.[5]

With these results in hand, the procedure was applied to a variety of α-allenic alcohols **4***b*–**4***n* (Scheme 1; Table 1, entries 8–26) wherein the steric size and makeup of the R group was varied (R = 1°, 2°, 3° alkyl, CH=CHR, and aryl) and in two cases included common alcohol protecting groups (entries 8–11). The conversion of the alcohols **4** to the imino carbonates **8** was carried out in one pot (see experimental section) with each of the cyclization reactions being performed in the standard solvent systems of 10:1 ether/MeCN or CH_2Cl_2. In some cases (entries 8–19) cyclization was followed by hydrolysis and acetylation to provide the *syn* diacetates **11** while in several other cases, the sequence was terminated prior to acetylation (entries 20–25) to afford the *syn*-1,2-diols **10**. The yields of **10** or **11** are good to excellent in the majority of cases (vide infra) and the reaction mixtures are extremely clean. In each case, a single imino carbonate **8** and a single *syn*-1,2-diol **10** or diacetate **11** was observed. The relative stereochemistry was assigned in the case of **8***f* by difference NOE experiments similar to those described previously for **8***a*. Irradiation at the frequency of the $(CH_3)_3C$ resonance (δ 0.86, $CDCl_3$) resulted in enhancement of the resonances of both of the protons H_a and H_b (δ 4.19 and 4.78, J_{ab} = 4.5 Hz), confirming the *trans* stereochemistry. Therefore, by analogy, the cyclization of **6**/**7** with Ag_2CO_2 produces solely (diastereoselectivity >50:1[7]) the *trans* diastereomers **8** (J_{ab} = 4.5–6.8 Hz) regardless of the steric size of the R group in the α-allenic alcohol **4**.

The reaction regioselectivity was consistently high, favouring the imino carbonates **8** over the oxazolidinones **9**. In certain cases (**4***b*, **4***d*, and **4***e*), alternative cyclization reaction solvent systems were tested and these conditions exhibited regioselectivity ratios in line with those observed for the cyclization of **6***a*/**7***a*. Again, the regioselectivity was established by integration of the vinyl proton resonances and (or) the resonances of H_b for each of **8** and **9** in the ^1H NMR spectra of the crude reaction mixtures. The chemical shift of H_b in **8** was typically 0.3–0.4 ppm downfield of the corresponding H_b resonance in **9** (see table). The vinyl proton resonances were less well separated but often proved to be useful for comparison purposes. Typically, the vinyl proton resonances of **8** were 0.03–0.04 ppm downfield of the corresponding resonances in **9**. In several cases, the amino acetates **13** had been previously prepared (10) and identified (entries 12–17). For

Can. J. Chem. Downloaded from www.nrcresearchpress.com by 85.192.166.187 on 09/08/12
For personal use only.

these examples, the isolated yield ratio of **11**:**13** corresponds well with the integrated ratios.

There are limitations to this methodology since certain highly unsaturated systems (allylic or benzylic alcohols) are not good substrates. As can be seen from entries 19 and 26, α-allenic alcohols **4***h* and **4***n* either produced the cyclized product **8***h* in low yield (entry 19) or did not provide any recognizable product (entry 26). However, a closely related analogue of each underwent iodocyclization successfully to provide the intermediate **8** (compare entries 18/19 and entries 25/26). Apparently, for each of **4***h* and **4***n*, the initial reaction to form the *N*-tosyl carbamate **5** is the problematic step. Decomposition upon treatment of the alcohol **4** with TsNCO is relatively rapid. Attempts at stabilizing the carbamate intermediate **5** in each case (treating with triethylamine for example (12*c*)) were not successful. The reason for the difference in stability between two closely related compounds is not known but it does put a small limitation on the generality of the reaction.

(b) Cyclization mechanism – rationale for stereoselectivity

Two related mechanisms merit consideration when attempting to rationalize the stereochemical outcome of the reaction from **6**/**7** to **8**. In this cyclization, iodide should be effectively removed from the reaction mixture by the precipitation of AgI. This precludes the involvement of iodide in a reversible process and suggests that the cyclization is under kinetic control.

In the first pathway, cyclization of **6**/**7** proceeds via attack of the carbamate carbonyl oxygen atom on the developing allylic cationic intermediate **14** that is formed by the reaction of **6**/**7** with Ag^+. Intermediate **14**, generated from either of the isomeric diiodides **6** or **7**, can cyclize out one of two rotomeric forms, **14A** or **14B**. Due to the large steric interactions between

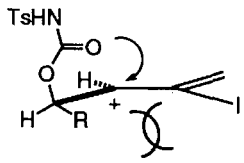

14A

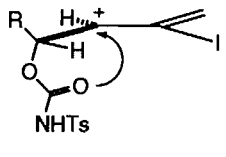

14B

the R group and the vinyl iodide moiety in the cyclization transition state arising out of conformer **14A**, the energetically more favourable pathway would derive from the alternative conformer, **14B**. The product of cyclization from **14B** is the *trans* imino carbonate **8**. Thus, regardless of the geometry of the starting diiodide **6** or **7**, cyclization via an S_N1-like mechanism occurs in a highly diastereoselective manner.

An alternative and closely related mechanism involves a process in which iodide departure and oxygen attack are more synchronous (S_N2' like). However, a S_N2' mechanism would appear to be less likely since **8** is formed regioselectively over **9**, a result that implies an S_N1-like pathway (14, 15). Nevertheless, this mechanistic possibility also predicts that the *trans* diastereomer **8** should be formed preferentially.[8] Thus, both the S_N2' mechanism and the S_N1 mechanism described above rationalize the observed *trans* diastereoselectivity in the formation of **8**.

In general, and irrespective of the actual mechanism of the iodocyclization, the transformation of the α-allenic alcohols **4** into either the *syn*-1,2-diols **10** or *syn*-1,2-diacetates **11** is a highly regio- (>20:1) and diastereoselective (>50:1) process and proceeds in synthetically useful yields. Furthermore, the presence of the vinyl iodide moiety enables one to consider a variety of synthetic operations. One possibility that exists is the conversion of this functionality into an alkyne via dehydrohalogenation (17). Using such a reaction, short and high-yielding syntheses of (±)-*threo*-L-factor (**17**) (Scheme 2) and (±)-disparlure (**24**) (Scheme 3) have been developed, illustrating the potential of the functionalized *syn*-1,2-diols **10** for the stereocontrolled synthesis of acyclic compounds.

*(c) Synthesis of (±)-*threo*-5-hydroxy-4-decanolide (**17**) ((±)-*threo*-L-factor)*

The isolation of two diastereomeric 5-hydroxy-4-decanolides (**17** and its diastereomer) from *Streptomyces griseus* was reported in 1982 (18*a*). These compounds were originally proposed to be autoregulators of the biosynthesis of the anthracycline antibiotic leukaeomomycin (hence the name L-factors). Although both the *erythro* and *threo* L-factors were subsequently shown to be biologically inactive (18*b*),[9] a variety of efficient synthetic approaches to these natural products have been described (20). The majority of these syntheses derive from carbohydrates in which the stereoselective formation of the preexisting diol moiety is not a key issue.

syn Diol **10***j* was converted to the corresponding acetonide (2-methoxypropene, CSA, DMF) and in the same pot was dehydrohalogenated by treatment with $NaN(TMS)_2$ to afford the alkyne **15** in 91% yield over two steps (Scheme 2). Deprotonation of **15** (MeLi, THF) followed by trapping of the resulting lithium acetylide with ethyl chloroformate provided the α,β-acetylenic ester **16** in 95% yield. Hydrogenation of **16** (H_2, Pd–C, EtOH) followed by acid-catalyzed lactonization (6 N HCl, MeOH) yielded (±)-*threo*-5-hydroxy-4-decanolide (**17**) in 93% yield.[10] The overall yield of **17** for the nine-step, six-pot sequence from **4***j* is 60%.

*(d) Synthesis of (±)-*cis*-7,8-epoxy-2-methyloctadecane (**24**) ((±)-disparlure)*

The sex attractant of the female gypsy moth *Porthetria dispar* (L.) was isolated in 1974 (21*a*) and the structure and absolute configuration were established as (+)-(7*R*,8*S*)-*cis*-7,8-epoxy-2-methyl-octadecane (**24**) ((+)-disparlure) (21). Many groups have reported the synthesis of **24** both in racemic and enantiomerically pure form (21, 22). In the majority of cases, these syntheses employ natural products as starting materials wherein the relative stereochemistry of the asymmetric centers is already established. Notable exceptions include syntheses that utilize the Sharpless asymmetric epoxidation (22*b*, *c*) or dihydroxylation (22*d*) as key reactions or employ chiral sulfoxides (22*e*, *f*) to introduce asymmetry. We have prepared (±)-disparlure **24** via a short, high-yielding sequence (Scheme 3) from diol **10***k*, further illustrating the synthetic utility of the vinyl iodo diols **10**.

syn Diol **10***k* was converted in 93% yield to the acetylenic

[8]Such an S_N2' mechanism has been described in detail for the *base-induced* cyclization of **6**/**7** to form **9** (10*b*). In this S_N2' pathway, the geometry of the starting diiodides is irrelevant to the stereochemical outcome of the reaction and the *trans* diastereomer **9** is the major product from each diiodide isomer. Thus, by analogy, the stereochemical outcome of an S_N2' mechanism in the present study is predicted to be *trans* as well.

[9]It is noteworthy that a related 5-hydroxy-γ-lactone named muricatacin has been isolated from the tropical fruit *Annona muricata L.* and exhibits cytotoxic activity (19).

Can. J. Chem. Downloaded from www.nrcresearchpress.com by 85.192.166.187 on 09/08/12
For personal use only.

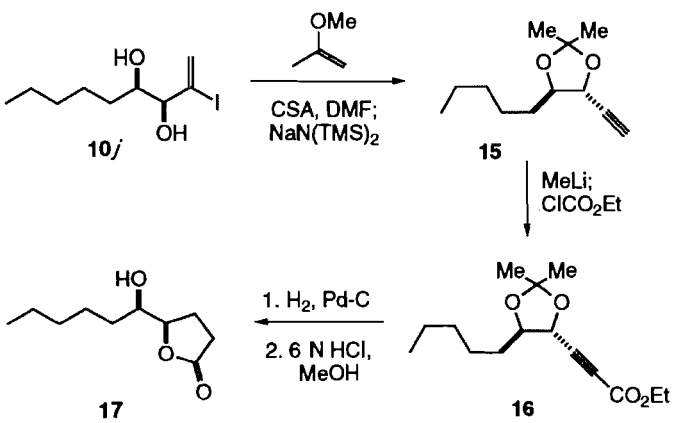

SCHEME 2

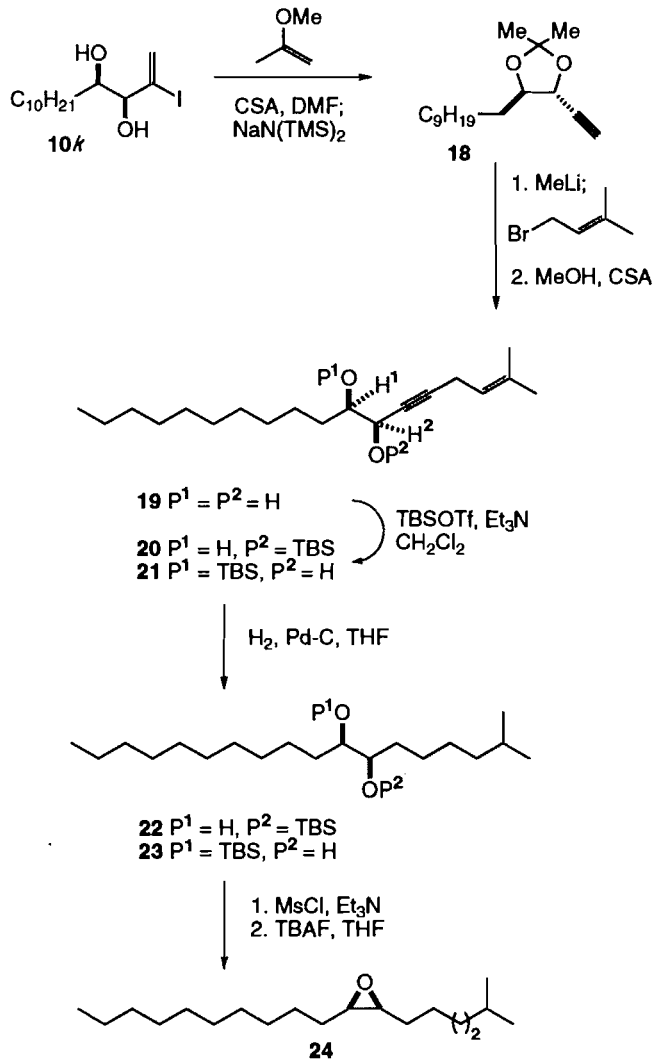

SCHEME 3

acetonide **18** as described above for the preparation of **15**. Deprotonation of **18** (MeLi, THF) was followed by trapping of the resulting lithium acetylide with 4-bromo-2-methyl-2-butene in the presence of HMPA. In the absence of HMPA, no alkylation occurred. The crude enyne acetonide was deprotected (MeOH, CSA) to yield diol **19** in 75% over two steps. The synthetic plan called for the monosilylation of diol **19** and the eventual formation of the *cis* epoxide of (±)-disparlure by an intramolecular displacement reaction of a suitably activated alcohol (22*g*). Treatment of **19** with TBSOTf (CH_2Cl_2, Et_3N) at −78°C provided **20** and **21** in 90% combined yield and in a ratio of 1.3:1, while at 0°C a 1:1.3 ratio of the same compounds was obtained in 87%. The regioselectivity of this reaction was not an issue since we were operating in the racemic mode. However, for the sake of simplicity these isomers were conveniently separated by column chromatography and used separately in the subsequent reactions.[11] The position of the silyl moiety in each isomer was readily established by decoupling experiments. The H^2 resonance (δ 4.16) in **21** was simplified upon irradiation at the resonance frequency of the both the O*H* proton (δ 2.44) and the allylic methylene protons (δ 2.87). Conversely, irradiation at the resonance frequency of the O*H* proton (δ 2.47) in **20** simplified the H^1 resonance (δ 3.48) while irradiation at the resonance frequency of the allylic methylene protons (δ 2.86) simplified the H^2 resonance (δ 4.06). Enynes **20** and **21** were hydrogenated (10% Pd–C, THF) individually to afford the corresponding alcohols **22** and **23** in yields of 96 and 97%, respectively. Epoxidation of each was accomplished by mesylation (MsCl, Et_3N, 0°C) of the free hydroxyl followed by treatment of the crude mixture with TBAF in THF at room temperature overnight (22*g*). (±)-Disparlure **24** was obtained in 83% yield from **22** and 78% yield from **23**.[12]

Experimental

General information

^1H NMR spectra were recorded in $CDCl_3$, unless stated otherwise, and are reported using TMS or $CHCl_3$ as internal standard. Broad band proton-decoupled ^{13}C NMR spectra were recorded in $CDCl_3$ using $CDCl_3$ as the internal standard. IR spectra were recorded on neat samples unless stated otherwise. Solvents were anhydrous and transferred via syringes under an argon atmosphere. Workup procedures involving the drying of organics was done with $MgSO_4$. Column chromatography was carried out on 230–400 mesh silica gel, eluting with the solvents indicated. Elemental analyses were performed by Oneida Research Services, Inc., Whitesboro, N.Y. The secondary α-allenic alcohols **4**, prepared by the two-step procedure of Landor and coworkers from the corresponding aldehydes and THP-protected propargyl alcohol in yields of 80–90% (16), were not characterized by combustion analysis but were homogeneous by TLC analysis and gave satisfactory spectroscopic data indicative of their purity. The alcohols **4** exhibited excellent stability when stored at −5°C (freezer temperature). Alcohols **4***a*, **4***d*, **4***e*, and **4***f* have been reported previously (10*b*).

8-Triisopropylsiloxy-1,2-octadien-4-ol (4b)

Colorless liquid; IR: 3600–3100, 1955, 835 cm^{-1}; ^1H NMR (400 MHz) δ: 1.00–1.10 (m, 21H), 1.40–1.65 (m, 6H), 1.78 (br s, 1H), 3.66 (t, 2H, J = 6.4 Hz), 4.15 (m, 1H), 4.80 (m, 2H), 5.20 (q, 1H, J = 6.5 Hz); ^{13}C NMR (100 MHz) δ: 12.0, 18.0, 21.7, 32.8, 37.2, 63.3, 69.7, 77.3, 94.8, 207.0. Exact Mass calcd. for $C_{17}H_{34}O_2Si$ (M^+): 298.2328; found: 298.2331.

8-Benzyloxymethoxy-1,2-octadien-4-ol (4c)

Colorless liquid; IR: 3700–3150, 1953 cm^{-1}; ^1H NMR (400 MHz) δ: 1.40–1.65 (m, 6H), 1.95 (br s, 1H), 3.58 (t, 2H, J = 6.5 Hz), 4.14 (m,

[10]This material exhibited spectra (^1H and ^{13}C NMR, IR) consistent with the data reported for natural **17** (18, 20).

[11]If one were operating in the enantiomerically pure series, the separation of **20** and **21** would allow one to prepare both enantiomers of disparlure from the same intermediate.

[12]This material exhibited spectra (^1H and ^{13}C NMR, IR) consistent with the data reported for natural **24** (21, 22).

Can. J. Chem. Downloaded from www.nrcresearchpress.com by 85.192.166.187 on 09/08/12
For personal use only.

Can. J. Chem. Downloaded from www.nrcresearchpress.com by 85.192.166.187 on 09/08/12
For personal use only.

1H), 4.58 (s, 2H), 4.73 (s, 2H), 4.83 (m, 2H), 5.21 (q, 1H, J = 6.5 Hz), 7.24–7.35 (m, 5H); ^{13}C NMR (100 MHz) δ: 22.1, 29.5, 37.1, 67.8, 69.2, 69.5, 77.3, 94.5, 94.8, 127.6, 127.8, 128.4, 137.9, 207.0. Exact Mass calcd. for $C_{16}H_{22}O_3$ (M^+): 262.1569; found: 262.1568.

*1-(3,4-Methylenedioxyphenyl)-2,3-butadien-1-ol (**4**g)*

Colorless liquid; IR: 3650–3100, 1953 cm^{-1}; ^{1}H NMR (300 MHz, acetone-d_6) δ: 4.51 (d, 1H, J = 4.6 Hz), 4.79 (m, 2H), 5.14 (m, 1H), 5.34 (q, 1H, J = 6.8 Hz), 5.95 (s, 2H), 6.76 (dd, 1H, J = 0.5, 7.9 Hz), 6.86 (dd, 1H, J = 1.7, 7.9 Hz), 6.91 (dd, 1H, J = 0.5, 1.7 Hz); ^{13}C NMR (100 MHz) δ: 71.7, 78.1, 95.1, 100.9, 106.7, 108.0, 119.5, 136.9, 147.0, 147.7, 207.0. Exact Mass calcd. for $C_{11}H_{10}O_3$ (M^+): 190.0630; found: 190.0625.

*1-(4-Methoxyphenyl)-2,3-butadien-1-ol (**4**h)*

Colorless liquid; IR: 3600–3100, 1955 cm^{-1}; ^{1}H NMR (200 MHz) δ: 2.09 (d, 1H, J = 4.5 Hz), 3.80 (s, 3H), 4.93 (m, 2H), 5.22 (m, 1H), 5.44 (q, 1H, J = 6.5 Hz), 6.88 (m, 2H), 7.33 (m, 2H). Exact Mass calcd. for $C_{11}H_{12}O_2$ (M^+): 176.0827; found: 176.0825.

*1,2-Octadien-4-ol (**4**i)*

Colorless liquid; IR: 3600–3100, 1955 cm^{-1}; ^{1}H NMR (300 MHz) δ: 0.91 (m, 3H), 1.25–1.50 (m, 4H), 1.55–1.65 (m, 2H), 1.72 (d, 1H, J = 4.7 Hz), 4.16 (m, 1H), 4.85 (m, 2H), 5.24 (q, 1H, J = 6.5 Hz); ^{13}C NMR (100 MHz) δ: 14.0, 22.6, 27.5, 37.2, 69.7, 77.4, 94.9, 207.0. Exact Mass calcd. for $C_8H_{14}O$ (M^+): 126.1045; found: 126.1047.

*1,2-Nonadien-4-ol (**4**j)*

Colorless liquid; IR: 3600–3100, 1958 cm^{-1}; ^{1}H NMR (300 MHz) δ: 0.86 (t, 3H, J = 7.0 Hz), 1.25–1.50 (m, 6H), 1.50–1.60 (m, 2H), 1.86 (br s, 1H), 4.13 (m, 1H), 4.82 (m, 2H), 5.20 (q, 1H, J = 6.5 Hz); ^{13}C NMR (100 MHz) δ: 14.0, 22.6, 25.0, 31.7, 37.4, 69.7, 77.3, 94.8, 207.0. Exact Mass calcd. for $C_9H_{16}O$ (M^+): 140.1201; found: 140.1998.

*1,2-Tetradecadien-4-ol (**4**k)*

Colorless liquid; IR: 3600–3100, 1954 cm^{-1}; ^{1}H NMR (300 MHz) δ: 0.85 (t, 3H, J = 7.0 Hz), 1.15–1.45 (m, 16H), 1.50–1.60 (m, 2H), 1.79 (d, 1H, J = 4.7 Hz), 4.13 (m, 1H), 4.82 (m, 2H), 5.20 (q, 1H, J = 6.4 Hz); ^{13}C NMR (100 MHz) δ: 14.1, 22.7, 25.4, 29.3, 29.5, 29.6, 31.9, 37.5, 69.7, 77.3, 94.9, 207.0. Exact Mass calcd. for $C_{14}H_{26}O$ (M^+): 210.1984; found: 210.1988.

*1-Phenyl-4,5-hexadien-3-ol (**4**l)*

Colorless liquid; IR: 3700–3100, 1952 cm^{-1}; ^{1}H NMR (300 MHz) δ: 1.71 (d, 1H, J = 4.8 Hz), 1.89 (m, 2H), 2.74 (m, 2H), 4.19 (m, 1H), 4.86 (m, 2H), 5.27 (q, 1H, J = 6.5 Hz), 7.15–7.30 (m, 5H); ^{13}C NMR (100 MHz) δ: 31.6, 38.9, 68.8, 77.6, 94.6, 125.8, 128.3, 128.4, 141.7, 207.0. Exact Mass calcd. for $C_{12}H_{14}O$ (M^+): 174.2426; found: 174.2426.

*1,2,5-Decatrien-4-ol (**4**m)*

Pale yellow liquid; IR: 3600–3100, 1955, 1660, 1615 cm^{-1}; ^{1}H NMR (300 MHz) δ: 0.87 (t, 3H, J = 7.1 Hz), 1.25–1.40 (m, 4H), 1.77 (br s, 1H), 2.02 (q, 2H, J = 6.6 Hz), 4.60 1M, 1H), 4.85 (dd, 2H, J = 2.5, 6.6 Hz), 5.25 (q, 1H, J = 6.5 Hz), 5.50 (dd, 1H, J = 6.6, 15.4 Hz), 5.69 (td, 1H, J = 6.6, 15.4 Hz); ^{13}C NMR (100 MHz) δ: 13.8, 22.1, 31.1, 31.7, 70.4, 77.6, 94.2, 130.9, 132.6, 207.1. Exact Mass calcd. for $C_{10}H_{16}O$ (M^+): 152.1201; found: 152.1206.

*1,2,5-Heptatrien-4-ol (**4**n)*

Colorless liquid; IR: 3650–3100, 1954, 1655, 1615 cm^{-1}; ^{1}H NMR (300 MHz) δ: 1.68 (ddd, 1H, J = 0.8, 1.5, 6.3 Hz), 1.91 (br s, 1H), 4.58 (m, 1H), 4.84 (m, 2H), 5.24 (q, 1H, J = 6.5 Hz), 5.53 (qdd, 1H, J = 1.5, 6.5, 15.3 Hz), 5.71 (dqd, 1H, J = 1.0, 6.5, 15.3 Hz); ^{13}C NMR (100 MHz) δ: 17.5, 70.4, 77.7, 94.1, 127.4, 132.3, 207.1. Exact Mass calcd. for $C_7H_{10}O$ (M^+): 110.0732; found: 110.0734.

General procedure A: preparation of syn *diacetates **11***

The procedures described below for the preparation of **11***a* are general. To a solution of 1,2-undecadien-3-ol (**4***a*) (210 mg, 1.25 mmol) in ether (5 mL; note that some of the reactions were carried out in alternative solutions, Table 1) at room temperature was added *p*-TsNCO (0.2 mL, 1.1 equiv.). After stirring for 30 min at room temperature, solid I_2 (350 mg, 1.1 equiv.) was added periodically until the solution stayed colored (~1 h). Ag_2CO_3 (344 mg, 1.1 equiv.) and MeCN (0.1 mL) were added sequentially and the resulting mixture was stirred for 15 h (3–15 h depending upon substrate) at room temperature. The reaction mixture was filtered through Celite, washing with ethyl acetate, and the filtrate was concentrated. The crude mixture was analyzed by ^{1}H NMR spectroscopy (Table 1, entry 5) and then was dissolved in methanol (10 mL) and 1 N NaOH (10 mL). After stirring at room temperature overnight, the methanol was removed and the solution was neutralized (to ~pH 7) by the addition of 1 N HCl. The mixture was extracted with CH_2Cl_2 (3 × 20 mL) and the combined organics were dried and concentrated to provide the crude diol **10***a*. The residual material containing the diol **10***a* was dissolved in pyridine (5 mL) and Ac_2O (0.6 mL, 5 equiv.) and DMAP (10 mg) were added. The mixture was stirred at room temperature for 15 h and then water (20 mL) was added. The aqueous layer was extracted with ethyl acetate (3 × 20 mL) and the combined organics were washed with 1 N HCl (2×), saturated $NaHCO_3$, and water, dried, and concentrated. The residual material was subjected to flash chromatography (hexane/ethyl acetate, 5:1, v/v) to provide **11***a* (377 mg, 76%), which was eluted first, followed by **13***a* (20 mg, 3%).

The diacetates **11**, prepared according to the above procedures, exhibited the following physical properties. The solvent used for the cyclization reaction is given below.

syn-*3,4-Diacetoxy-2-iodo-1-undecene (**11**a)*

Colorless oil; IR: 1742, 1615, 1245–1210 cm^{-1}; ^{1}H NMR (300 MHz) δ: 0.87 (t, 3H, J = 7.0 Hz), 1.25–1.35 (m, 10H), 1.40–1.60 (m, 2H), 2.05 (s, 3H), 2.10 (s, 3H), 4.99 (br d, 1H, J = 6.2 Hz), 5.26 (ddd, 1H, J = 5.3, 6.2, 7.5 Hz), 6.02 (d, 1H, J = 1.8 Hz), 6.47 (dd, 1H, J = 1.0, 1.8 Hz); ^{13}C NMR (100 MHz) δ: 13.8, 20.6, 22.4, 24.6, 28.8, 29.0, 30.2, 31.5, 72.5, 78.6, 104.4, 129.6, 169.3, 169.9. Anal. calcd. for $C_{15}H_{25}O_4I$: C 45.47, H 6.36; found: C 45.58, H 6.38.

syn-*3,4-Diacetoxy-2-iodo-8-triisopropylsilyloxy-1-octene (**11**b)*

Following general procedure A (ether:MeCN 10:1), alcohol **4***b* (264 mg, 0.86 mmol) was converted to **11***b* (365 mg, 78%). Colorless oil; IR: 1750, 1615, 1240–1210 cm^{-1}; ^{1}H NMR (300 MHz) δ: 0.99–1.23 (23H) 1.35–1.62 (m, 4H), 2.05 (s, 3H), 2.10 (s, 3H), 3.67 (m, 2H), 4.99 (dd, 1H, J = 0.7, 6.2 Hz), 5.27 (ddd, 1H, J = 5.0, 6.2, 7.5 Hz), 6.02 (d, 1H, J = 1.5 Hz), 6.48 (dd, 1H, J = 0.7, 1.5 Hz); ^{13}C NMR (100 MHz) δ: 12.0, 18.0, 20.7, 20.8, 21.3, 30.3, 32.5, 62.9, 72.6, 78.9, 104.6, 129.9, 169.4, 170.0. Anal. calcd. for $C_{21}H_{39}O_5SiI$: C 47.91, H 7.47; found: C 48.24, H 7.69.

syn-*3,4-Diacetoxy-8-benzyloxymethoxy-2-iodo-1-octene (**11**c)*

Following general procedure A (ether:MeCN 10:1), alcohol **4***c* (224 mg, 0.86 mmol) was converted to **11***c* (313 mg, 75%). Colorless oil; IR: 1745, 1615, 1240–1212 cm^{-1}; ^{1}H NMR (300 MHz) δ: 1.38–1.46 (m, 2H), 1.52–1.67 (m, 4H), 2.05 (s, 3H), 2.11 (s, 3H), 3.57 (t, 1H, J = 6.4 Hz), 4.60 (s, 2H), 4.74 (s, 2H), 5.00 (d, 1H, J = 6.1 Hz), 5.27 (m, 1H), 6.03 (d, 1H, J = 1.7 Hz), 6.48 (dd, 1H, J = 0.9, 2.5 Hz), 7.29 (m, 5H); ^{13}C NMR (100 MHz) δ: 20.8, 21.7, 29.3, 30.2, 67.5, 69.3, 72.5, 78.8, 94.6, 104.5, 127.6, 127.8, 128.4, 130.0, 137.9, 169.4, 170.1. Anal. calcd. for $C_{20}H_{27}O_6I$: C 48.99, H 5.55; found: C 49.21, H 5.52.

syn-*3,4-Diacetoxy-2-iodo-6-methyl-1-heptene (**11**d)*

Following general procedure A (ether:MeCN 3:1), alcohol **4***d* (189 mg, 1.49 mmol) was converted to **11***d* (393 mg, 74%). White solid; mp 72–73°C; IR (KBr): 1735, 1618, 1250–1218 cm^{-}; ^{1}H NMR (300 MHz) δ: 0.93 (d, 3H, J = 6.6 Hz), 0.94 (d, 3H, J = 6.5 Hz), 1.22–1.35 (m, 1H), 1.42–1.55 (m, 2H), 2.05 (s, 3H), 2.10 (s, 3H), 4.96 (dd, 1H, J = 0.8, 6.2 Hz), 5.37 (m, 1H), 6.02 (d, 1H, J = 1.7 Hz), 6.47 (dd, 1H, J = 1.0, 1.7 Hz); ^{13}C NMR (100 MHz) δ: 20.8, 21.7, 23.3, 24.3, 39.5, 71.2, 79.3, 104.7, 129.9, 169.5, 170.1. Anal. calcd. for $C_{12}H_{19}O_4I$: C 40.70, H 5.41; found: C 40.99, H 5.31.

Can. J. Chem. Downloaded from www.nrcresearchpress.com by 85.192.166.187 on 09/08/12
For personal use only.

syn-*1,2-Diacetoxy-3-iodo-1-cyclohexyl-3-butene (**11**e)*

Following general procedure A (ether:MeCN 5:1), alcohol **4***e* (254 mg, 1.66 mmol) was converted to **11***e* (435 mg, 70%). White solid; mp 37–38°C; IR (KBr): 1738, 1615, 1238–1210 cm^{-1}; ^1H NMR (300 MHz) δ: 1.00–1.30 (m, 6H), 1.55–1.80 (m, 5H), 2.06 (s, 3H), 2.11 (s, 3H), 5.16 (t, 1H, J = 5.4 Hz), 5.19 (d, 1H, J = 5.6 Hz), 6.00 (d, 1H, J = 1.8 Hz), 6.44 (dd, 1H, J = 0.9, 1.7 Hz); ^{13}C NMR (100 MHz) δ: 20.4, 20.5, 25.5, 25.6, 25.8, 27.0, 29.2, 37.6, 75.3, 77.4, 104.7, 128.8, 169.0, 169.7. Anal. calcd. for $C_{14}H_{21}O_4I$: C 44.23, H 5.57; found: C 44.51, H 5.68.

syn-*1,2-Diacetoxy-3-iodo-1-tert-butyl-3-butene (**11**f)*

Following general procedure A (ether:MeCN 10:1), alcohol **4***b* (225 mg, 1.78 mmol) was converted to **11***f* (476 mg, 75%). White solid; mp 74–75°C; IR (KBr): 1760, 1620, 1220; ^1H NMR (300 MHz) δ: 0.97 (s, 9H), 2.13 (s, 3H), 2.15 (s, 3H), 5.15 (d, 1H, J = 2.4 Hz), 5.43 (m, 1H), 5.89 (dd, 1H, J = 0.7, 1.9 Hz), 6.32 (dd, 1H, J = 1.3, 1.9 Hz); ^{13}C NMR (100 MHz) δ: 20.5, 20.8, 26.5, 34.5, 76.1, 76.7, 106.1, 126.7, 168.9, 169.9. Anal. calcd. for $C_{12}H_{19}O_4I$: C 40.69, H 5.41; found: C 41.11, H 5.30.

syn-*1,2-Diacetoxy-3-iodo-1-(3,4-methylenedioxyphenyl)-3-butene (**11**g)*

Following general procedure A (ether:MeCN 10:1), alcohol **4***g* (135 mg, 0.71 mmol) was converted to **11***g* (221 mg, 75%). White solid; mp 110–111°C; IR (KBr): 1735, 1615, 1248–1218 cm^{-1}; ^1H NMR (300 MHz) δ: 2.03 (s, 3H), 2.09 (s, 3H), 5.14 (dd, 1H, J = 0.7, 7.9 Hz), 5.84 (d, 1H, J = 1.8 Hz), 5.92 (d, 1H, J = 7.9 Hz), 5.93 (s, 2H), 6.23 (dd, 1H, J = 0.9, 1.8 Hz), 6.73 (dd, 1H, J = 0.5, 7.8 Hz), 6.87 (s, 1H), 6.91 (dd, 1H, J = 1.0, 7.8 Hz); ^{13}C NMR (100 MHz) δ: 20.8, 75.2, 79.2, 101.1, 104.1, 107.8, 108.1, 121.6, 129.4, 131.1, 147.6, 147.9, 169.2, 169.4. Anal. calcd. for $C_{15}H_{15}O_6I$: C 43.08, H 3.62; found: C 43.29, H 3.56.

syn-*1,2-Diacetoxy-3-iodo-1-(4-methoxyphenyl)-3-butene (**11**h)*

Following general procedure A (ether:MeCN 10:1), alcohol **4***h* (102 mg, 0.58 mmol) was converted to **11***h* (68 mg, 29%). Colorless oil; IR: 1740, 1615, 1240–1218 cm^{-1}; ^1H NMR (300 MHz) δ: 2.05 (s, 3H), 2.11 (s, 3H), 3.79 (s, 3H), 5.20 (d, 1H, J = 7.9 Hz), 5.84 (d, 1H, J = 1.8 Hz), 6.00 (d, 1H, J = 8.0 Hz), 6.21 (dd, 1H, J = 0.7, 1.6 Hz), 6.86 (d, 2H, J = 8.7 Hz), 7.34 (d, 2H, J = 8.7 Hz); ^{13}C NMR (100 MHz) δ: 21.0, 55.2, 76.2, 79.4, 104.3, 113.9, 127.8, 129.1, 131.2, 159.9, 169.4, 169.6. Anal. calcd. for $C_{15}H_{17}O_5I$: C 44.58, H 4.24; found: C 45.85, H 4.45.

General procedure B: preparation of syn-*diols **10***

Following general procedure A described above, 1,2-octadien-3-ol (**4***i*) (5.00 g, 39.6 mmol) was converted into the crude diol **10***i* using 10:1 ether:MeCN (60 mL:6 mL). The residual material was subjected to flash chromatography (toluene/acetone, 6:1, v/v) to provide the diol **10***i* (8.54 g, 80%) as a white solid.

The diols **10**, prepared according to the above procedures, exhibited the following physical properties.

syn-*3,4-Dihydroxy-2-iodo-1-octene (**10**i)*

White solid; mp 48–48°C; IR (KBr): 3600–3100, 1625, 1050; ^1H NMR (300 MHz) δ: 0.92 (t, 3H, J = 7.1 Hz), 1.30–1.55 (m, 6H), 2.37 (br s, 1H), 2.96 (br s, 1H), 3.58 (br m, 1H), 3.77 (br m, 1H), 6.00 (d, 1H, J = 1.7 Hz), 6.49 (dd, 1H, J = 1.1, 1.7 Hz); ^{13}C NMR (100 MHz) δ: 20.0, 22.5, 27.6, 32.5, 73.0, 80.2, 113.0, 127.6. Anal. Calcd. for $C_8H_{15}O_2I$: C, 35.57; H, 5.60. Found: C, 35.87; H, 5.46.

syn-*3,4-Dihydroxy-2-iodo-1-nonene (**10**j)*

Following general procedure B (ether:MeCN 10:1), alcohol **4***j* (953 mg, 6.80 mmol) was converted to **10***j* (1.45 g, 75%). White solid; mp 61–62°C; IR (KBr): 3500–3050, 1625, 1050; ^1H NMR (300 MHz) δ: 0.85 (t, 3H, J = 6.9 Hz), 1.20–1.50 (m, 8H), 3.17 (br s, 2H), 3.51 (dd, 1H, J = 0.7, 5.7 Hz), 3.70 (m, 1H), 5.94 (d, 1H, J = 1.6 Hz), 6.44 (dd, 1H, J = 1.1, 1.6 Hz); ^{13}C NMR (100 MHz) δ: 14.0, 22.5, 25.1, 31.6, 32.6, 73.0, 80.2, 113.1, 127.6. Anal. calcd. for $C_9H_{17}O_2I$: C 38.04, H 6.03; found: C 38.31, H 5.87.

syn-*3,4-Dihydroxy-2-iodo-1-tetradecene (**10**k)*

Following general procedure B (ether:MeCN 10:1), alcohol **4***k* (2.57 g, 12.22 mmol) was converted to **10***k* (3.68 g, 85%). White solid; mp 49–50°C; IR (KBr): 3600–3050, 1625, 1050; ^1H NMR (300 MHz) δ: 0.85 (t, 3H, J = 6.7 Hz), 1.20–1.50 (m, 18H), 2.26 (br s, 1H), 2.86 (br s, 1H), 3.55 (br d, 1H, J = 5.0 Hz), 3.75 (m, 1H), 5.97 (dd, 1H, J = 0.4, 1.7 Hz), 6.44 (dd, 1H, J = 1.1, 1.7 Hz); ^{13}C NMR (100 MHz) δ: 14.1, 22.7, 25.5, 29.3, 29.47, 29.52, 29.58, 31.9, 32.7, 73.0, 80.2, 112.9, 127.7. Anal. calcd. for $C_{14}H_{27}O_2I$: C 47.46, H 7.68; found: C 47.40, H 7.72.

syn-*3,4-Dihydroxy-5-iodo-1-phenyl-5-hexene (**10**l)*

Following general procedure B (ether:MeCN 10:1), alcohol **4***l* (280 mg, 1.61 mmol) was converted to **10***l* (424 mg, 83%). White solid; mp 77–77.5°C; IR (KBr): 3600–3050, 1720, 1610, 1050 cm^{-1}; ^1H NMR (300 MHz) δ: 1.70–1.85 (m, 2H), 2.56 (br s, 1H), 2.70 (ddd, 1H, J = 7.1, 9.3, 13.8 Hz), 2.86 (ddd, 1H, J = 5.6, 8.9, 13.8 Hz), 3.01 (br d, 1H, J = 5.6 Hz), 3.58 (br t, 1H, J = 5.2 Hz), 3.77 (m, 1H), 5.97 (d, 1H, J = 1.7 Hz), 6.45 (dd, 1H, J = 1.1, 1.7 Hz), 7.15–7.30 (m, 5H); ^{13}C NMR (100 MHz) δ: 31.8, 34.4, 72.6, 80.3, 112.6, 126.0, 127.9, 128.4, 141.5. Anal. calcd. for $C_{12}H_{15}O_2I$: C 45.30, H 4.75; found: C 45.13, H 4.79.

(E)-syn-*3,4-Dihydroxy-2-iodo-1,5-decadiene (**10**m)*

Following general procedure B (ether:MeCN 10:1), alcohol **4***m* (302 mg, 1.98 mmol) was converted to **10***m* (478 mg, 81%). Colorless oil; IR: 3600–3050, 1665, 1610, 1050; ^1H NMR (300 MHz) δ: 0.85 (t, 3H, J = 7.1 Hz), 1.20–1.40 (m, 4H), 2.01 (q, 2H, J = 6.7 Hz), 2.77 (br s, 1H), 3.28 (br s, 1H), 3.51 (d, 1H, J = 5.7 Hz), 4.15 (t, 1H, J = 6.7 Hz), 5.37 (m, 1H), 5.79 (m, 1H), 5.92 (d, 1H, J = 1.6 Hz), 6.41 (dd, 1H, J = 1.0, 1.6 Hz); ^{13}C NMR (100 MHz) δ: 13.8, 22.0, 30.9, 31.8, 74.7, 80.2, 112.4, 127.2, 127.9, 135.0. Anal. calcd. for $C_{10}H_{17}O_2I$: C 40.56, H 5.79; found: C 40.35, H 5.77.

*Acetylenic acetonide **15***

To a solution of the diol **10***j* (800 mg, 2.82 mmol) in DMF (7 mL) at room temperature was added 2-methoxypropene (0.4 mL, 1.5 equiv.) and CSA (5 mg). The mixture was stirred at room temperature overnight and then $NaN(TMS)_2$ (3.1 mL of a 1 M solution in THF) was added dropwise. The resulting mixture was stirred for 10 min at room temperature and then water (40 mL) was added. The mixture was extracted with ethyl acetate (3 × 50 mL) and the combined organics were washed twice with water, dried, and concentrated. The residual oil was subjected to flash chromatography (hexane/ethyl acetate, 15:1, v/v) to provide the alkyne **15** (502 mg, 91%) as a colorless liquid; IR: 3280, 2120 cm^{-1}; ^1H NMR (400 MHz) δ: 0.87 (t, 3H, J = 7.1 Hz), 1.25–1.55 (m, 6H), 1.38 (s, 3H), 1.44 (s, 3H), 1.60 (m, 2H), 2.49 (d, 1H, J = 2.1 Hz), 4.01 (td, 1H, J = 6.1, 7.8 Hz), 4.17 (dd, 1H, J = 2.1, 7.8 Hz); ^{13}C NMR (100 MHz) δ: 14.0, 22.5, 25.3, 26.1, 27.1, 31.7, 32.3, 70.3, 74.5, 80.9, 81.5, 109.8. Anal. calcd. for $C_{12}H_{20}O_2$: C 73.43, H 10.27; found: C 73.44, H 10.23.

α,β-*Acetylenic ester **16***

To a solution of alkyne **15** (209 mg, 1.07 mmol) in THF (4 mL) at −78°C was added MeLi (1.14 mL of a 1.4 M solution in ether, 1.5 equiv.) dropwise. The resulting solution was stirred for 10 min at −78°C followed by 30 min at 0°C, and then ethyl chloroformate (0.15 mL, 1.5 equiv.) was added. The cold bath was removed and the solution was stirred for 30 min. Water (25 mL) was added and the mixture was extracted with ethyl acetate (3 × 2 mL). The combined extracts were dried and concentrated. The residual material was subjected to flash chromatography (hexane/ethyl acetate, 11:1, v/v) and provided the ester **16** (271 mg, 95%) as a colorless oil; IR: 2218, 1715 cm^{-1}; ^1H NMR (400 MHz) δ: 0.87 (t, 3H, J = 7.1 Hz), 1.28 (t, 3H, J = 7.1 Hz), 1.25–1.50 (m, 6H), 1.39 (s, 3H), 1.43 (s, 3H), 1.61 (m, 2H), 4.09 (m, 1H), 4.21 (q, 2H, J = 7.1 Hz), 4.27 (d, 1H, J = 7.5 Hz);

Can. J. Chem. Downloaded from www.nrcresearchpress.com by 85.192.166.187 on 09/08/12
For personal use only.

^{13}C NMR (100 MHz) δ: 13.9, 22.5, 25.3, 25.8, 27.0, 31.7, 35.5, 62.2, 69.9, 77.7, 81.2, 83.7, 110.6, 153.1. Anal. calcd. for $C_{15}H_{24}O_4$: C 67.14, H 9.01; found: C 67.08, H 8.90.

*(±)-threo-5-Hydroxy-4-decanolide ((±)-threo-L-factor) (**17**)*

A mixture of the ester **16** (211 mg, 0.79 mmol) and 10% Pd–C (200 mg) in ethanol (5 mL) was stirred under H_2 (1 atm; 101.3 kPa) for 2 h at room temperature. The resulting mixture was filtered through Celite, washing with ethyl acetate, and then the filtrate was concentrated. The residual material was dissolved in methanol (5 mL) and 6 N HCl (1 mL) was added. The resulting mixture was heated gently (~50°C) for 2 h and then the methanol was removed on the rotary evaporator. Brine (20 mL) was added and the mixture was extracted with ethyl acetate (3 × 50 mL). The combined organics were dried and concentrated. The residual material was subjected to flash chromatography (hexane/ethyl acetate, 1:1 v/v) to provide the lactone **17** as a colorless oil (136 mg, 93%) that solidified in the freezer. This material, a white solid, exhibited mp 32–33°C; IR: 3700–3100, 2980–2850, 1760, 1455, 1180, 1030, 920 cm^{-1}; ^{1}H NMR (400 MHz) δ: 0.85 (t, 3H, J = 6.7 Hz), 1.21–1.40 (m, 5H), 1.40–1.54 (m, 3H), 2.10 (m, 1H), 2.20 (m, 1H), 2.30 (br d, 1H, J = 5.4 Hz), 2.45 (ddd, 1H, J = 8.7, 9.9, 17.9 Hz), 2.57 (ddd, 1H, J = 5.2, 9.9, 17.9 Hz), 3.53 (m, 1H), 4.38 (dt, 1H, J = 4.4, 7.4 Hz); ^{13}C NMR (100 MHz) δ: 13.9, 22.4, 24.0, 25.1, 28.6, 31.6, 32.8, 73.5, 82.9, 177.4. Anal. calcd. for $C_{10}H_{18}O_3$: C 64.49, H 9.74; found: C 64.48, H 9.63.

*Acetylenic acetonide **18***

Following the procedure described for the preparation of **15**, diol **10***k* (3.63 g, 10.2 mmol) was converted into alkyne **18** (2.55 g, 93%). This material, a colorless liquid, exhibited IR: 3300, 2115 cm^{-1}; ^{1}H NMR (300 MHz) δ: 0.86 (t, 3H, J = 6.6 Hz), 1.20–1.50 (m, 16H), 1.38 (s, 3H), 1.44 (s, 3H), 1.62 (m, 2H), 2.48 (d, 1H, J = 2.1 Hz), 4.01 (dt, 1H, J = 7.8, 6.0 Hz), 4.16 (dd, 1H, J = 2.1, 7.8 Hz); ^{13}C NMR (125 MHz) δ: 14.1, 22.7, 25.7, 26.1, 27.1, 29.3, 29.4, 29.5, 29.6, 31.9, 32.4, 70.3, 74.5, 80.9, 81.5, 109.8. Anal. calcd. for $C_{17}H_{30}O_2$: C 76.64, H 11.35; found: C 76.56, H 11.51.

syn-*7,8-Dihydroxy-2-methyl-2-octadecen-5-yne (**19**)*

To a solution of alkyne **18** (1.02 g, 3.83 mmol) in THF (20 mL) at −78°C was added MeLi (6.9 mL of a 1.4 M solution in ether, 2.5 equiv.) dropwise. The resulting solution was stirred for 10 min at −78°C followed by 30 min at 0°C, and then 4-bromo-2-methyl-2-butene (1.33 mL, 3 equiv.) and HMPA (2 mL) were added successively. The cold bath was removed and the solution was stirred for 90 min at room temperature. Water (50 mL) was added and the mixture was extracted with ethyl acetate (3 × 50 mL). The combined extracts were washed successively with 1 N HCl, water, brine, dried, and concentrated. The residual material and CSA (50 mg) were dissolved in MeOH (20 mL) and refluxed for 10 h. After cooling to room temperature, the solution was concentrated and the residue subjected to flash chromatography (hexane/ethyl acetate, 5:2, v/v). The diol **19** (847 mg, 75%) was obtained as a colorless solid; mp 42–43°C; IR ($CHCl_3$): 3580, 2920, 2845 cm^{-1}; ^{1}H NMR (300 MHz) δ: 0.84 (t, 3H, J = 6.7 Hz), 1.20–1.70 (m, 18H), 1.59 (br s, 3H), 1.67 (d, 3H, J = 1.1 Hz), 2.73 (br s, 1H), 2.83 (br s, 1H), 2.88 (d, 2H, J = 6.9 Hz), 3.53 (br m, 1H), 4.08 (br m, 1H), 5.12 (m, 1H); ^{13}C NMR (100 MHz) δ: 14.1, 17.7, 17.8, 22.7, 25.5, 25.6, 29.3, 29.53, 29.58, 29.60, 31.9, 32.4, 66.4, 75.1, 78.0, 85.9, 118.4, 134.1. Anal. calcd. for $C_{19}H_{34}O_2$: C 77.50, H 11.64; found: C 77.71, H 11.51.

syn-*7-tert-Butyldimethylsiloxy-2-methyl-2-octadecen-5-yn-8-ol (**20**) and* syn-*8-tert-butyldimethylsiloxy-2-methyl-2-octadecen-5-yn-7-ol (**21**)*

To a solution of diol **19** (700 mg, 2.38 mmol) and Et_3N (0.7 mL, 2.1 equiv.) in CH_2Cl_2 (20 mL) at 0°C was added TBSOTf (0.57 mL, 1.05 equiv.) dropwise over 5 min. The resulting mixture was stirred for 15 min and then the cooling bath was removed. After 15 min, water (50 mL) was added and the mixture was extracted with CH_2Cl_2 (3 × 50 mL). The combined organics were dried and concentrated and the residual material was subjected to column chromatography (hexane/ether, 15:1, v/v). Alcohol **20** (368 mg, 38%) eluted first and was obtained as a colorless oil; IR: 3575, 3600–3300, 830 cm^{-1}; ^{1}H NMR (300 MHz) δ: 0.11 (s, 3H), 0.13 (s, 3H), 0.85 (t, 3H, J = 6.8 Hz), 0.88 (s, 9H), 1.20–1.70 (m, 18H), 1.60 (br s, 3H), 1.68 (d, 3H, J = 0.9 Hz), 2.47 (d, 1H, J = 3.3 Hz), 2.86 (br d, 2H, J = 6.9 Hz), 3.48 (m, 1H), 4.06 (dt, 1H, J = 7.1, 2.0 Hz), 5.13 (m, 1H); ^{13}C NMR (100 MHz) δ: 14.1, 17.7, 17.8, 18.2, 22.7, 25.4, 25.7, 25.8, 29.3, 29.56, 29.63, 31.9, 32.2, 67.5, 75.1, 78.5, 85.5, 118.6, 133.9. Anal. calcd. for $C_{25}H_{48}O_2Si$: C 73.46, H 11.84; found: C 73.64, H 12.26.

The more polar alcohol **21** (478 mg, 49%) was obtained as a colorless oil; IR: 3650–3300, 830 cm^{-1}; ^{1}H NMR (300 MHz) δ: 0.07 (s, 3H), 0.10 (s, 3H), 0.85 (t, 3H, J = 6.9 Hz), 0.89 (s, 9H), 1.20–1.70 (m, 18H), 1.59 (s, 3H), 1.67 (d, 3H, J = 1.1 Hz), 2.44 (d, 1H, J = 7.1 Hz), 2.87 (br d, 2H, J = 6.9 Hz), 3.66 (br q, 1H, J = 6.0 Hz), 4.16 (m, 1H), 5.14 (m, 1H); ^{13}C NMR (100 MHz) δ: 14.1, 17.6, 17.9, 18.1, 22.6, 25.0, 25.4, 25.9, 29.3, 29.49, 29.53, 29.56, 29.7, 31.9, 33.8, 65.0, 75.8, 79.3, 84.3, 118.8, 133.5. Anal. calcd. for $C_{25}H_{48}O_2Si$: C 73.46, H 11.84; found: C 73.42, H 11.93.

syn-*7-tert-Butyldimethylsiloxy-2-methyl-8-octadecanol (**22**)*

A mixture of enyne **20** (340 mg, 0.83 mmol) and Pd–C (10%, 200 mg) in THF (15 mL) was stirred under a H_2 atmosphere (1 atm) for 24 h. The mixture was filtered through Celite, washing well with ethyl acetate, and concentrated. The residue was filtered through a short plug of silica eluting with hexane/ether (15:1, v/v) to provide alcohol **22** (332 mg, 96%) as a colorless oil; IR: 3560, 3650–3300, 830 cm^{-1}; ^{1}H NMR (300 MHz) δ: 0.04 (s, 3H), 0.05 (s, 3H), 0.83 (d, 6H, J = 6.6 Hz), 0.86 (t, 3H, J = 6.8 Hz), 0.87 (s, 9H), 1.10–1.70 (m, 27H), 2.10 (br s, 1H), 3.39 (br m, 1H), 3.47 (dt, 1H, J = 6.1, 4.2 Hz); ^{13}C NMR (100 MHz) δ: −4.1, 14.1, 18.1, 22.59, 22.60, 22.68, 25.3, 25.89, 25.95, 27.7, 27.9, 29.3, 29.6, 29.7, 31.9, 33.9, 34.1, 38.9, 72.7, 75.2. Anal. calcd. for $C_{25}H_{54}O_2Si$: C 72.39, H 13.12; found: C 72.23, H 12.84.

syn-*8-tert-Butyldimethylsiloxy-2-methyl-7-octadecanol (**23**)*

A mixture of enyne **21** (450 mg, 1.1 mmol) and Pd–C (10%, 300 mg) in THF (20 mL) was stirred under a H_2 atmosphere (1 atm) for 24 h. The mixture was filtered through Celite, washing well with ethyl acetate, and concentrated. The residue was filtered through a short plug of silica eluting with hexane/ether (15:1, v/v) to provide alcohol **23** (434 mg, 95%) as a colorless oil; IR: 3560, 3650–3250, 830 cm^{-1}; ^{1}H NMR (300 MHz) δ: 0.05 (s, 3H), 0.06 (s, 3H), 0.84 (d, 6H, J = 6.6 Hz), 0.87 (t, 3H, J = 6.8 Hz), 0.88 (s, 9H), 1.10–1.70 (m, 27H), 2.10 (d, 1H, J = 6.9 Hz), 3.39 (m, 1H), 3.47 (dt, 1H, J = 6.2, 4.1 Hz); ^{13}C NMR (100 MHz) δ: −4.1, 14.1, 18.1, 22.60, 22.65, 22.67, 25.0, 25.9, 26.2, 27.4, 27.9, 29.3, 29.6, 29.9, 31.9, 33.7, 34.1, 39.0, 72.6, 75.1. Anal. calcd. for $C_{25}H_{54}O_2Si$: C 72.39, H 13.12; found: C 72.53, H 13.55.

*(±)-cis-7,8-Epoxy-2-methyloctadecane ((±)-disparlure) (**24**)*

To a solution of alcohol **22** (233 mg, 0.56 mmol) and Et_3N (0.17 mL, 2.2 equiv.) in CH_2Cl_2 (10 mL) at 0°C was added MsCl (0.052 mL, 1.2 equiv.) and the mixture was stirred for 30 min. Water (20 mL) was added and the aqueous was extracted with CH_2Cl_2 (3 × 20 mL). The combined organics were dried and concentrated. The residue was dissolved in THF (10 mL) and TBAF (1.7 mL, 3 equiv.) was added. After stirring at room temperature for 15 h, water was added and the mixture extracted with ethyl acetate (3 × 50 mL). The combined organics were dried, concentrated, and subjected to flash chromatography (hexane/ether, 20:1, v/v) to provide (±)-disparlure (**24**) (132 mg, 83%) as a colorless oil; IR: 2920, 2850, 1460, 1360, 1320, 1260, 725 cm^{-1}; ^{1}H NMR (300 MHz) δ: 0.84 (d, 6H, J = 6.6 Hz), 0.85 (t, 3H, J = 6.4 Hz), 1.10–1.60 (m, 27H), 2.86 (app quintet, 2H, J = 4.2 Hz); ^{13}C NMR (100 MHz) δ: 14.0, 22.56, 22.64, 26.6, 26.8, 27.3, 27.81, 27.85, 27.86, 29.3, 29.5, 29.6, 31.9, 38.9, 57.2. Anal. calcd. for $C_{19}H_{38}O$: C 80.78, H 13.56; found: C 80.94, H 13.10.

In a similar manner, alcohol **23** (450 mg, 1.1 mmol) was converted into (±)-**24** (269 mg, 88%).

Acknowledgment

We would like to thank Drs. L. Trimble and M. Bernstein for carrying out the NOE experiments on **8***a* and **8***f*.

1. T. Oishi and T. Nakata. Acc. Chem. Res. **17**, 338 (1984).
2. M.T. Reetz. Angew. Chem. Int. Ed. Engl. **23**, 556 (1984).
3. (*a*) G.J. McGarvey and M. Kimura. J. Org. Chem. **47**, 5422 (1982); (*b*) J. Yamada, H. Abe, and Y. Yamamoto. J. Am. Chem. Soc. **112**, 6118 (1990).
4. *Allylboron*: (*a*) P.G.M. Wuts and S.S. Bigelow. J. Org. Chem. **47**, 2498 (1982); (*b*) R.W. Hoffmann and B. Kemper. Tetrahedron Lett. **23**, 845 (1982); (*c*) P.G.M. Wuts and S.S. Bigelow. J. Chem. Soc. Chem. Commun. 736 (1984); (*d*) R. Metterich and R.W. Hoffmann. Tetrahedron Lett. **25**, 4095 (1984); (*e*) W.R. Roush and M.R. Michaelides. Tetrahedron Lett. **27**, 3353 (1986); (*f*) H.C. Brown, P.K. Jadhav, and K.S. Bhat. J. Am. Chem. Soc. **110**, 1535 (1988). *Allylaluminum*: (*g*) M. Koreeda and Y. Tanaka. J. Chem. Soc. Chem. Commun. 845 (1982); (*h*) Y. Yamamoto, H. Yatagai, Y. Saito, and K. Maruyama. J. Org. Chem. **49**, 1096 (1984); (*i*) M. Yamaguchi and T. Mukaiyama. Chem. Lett. 237 (1982). *Allyltin*: (*j*) G.E. Keck, D.E. Abbott, and M.R. Wiley. Tetrahedron Lett. **28**, 139 (1987); (*k*) M. Koreeda and Y. Tanaka. Tetrahedron Lett. **28**, 143 (1987); (*l*) J.A. Marshall and W.Y. Gung. Tetrahedron Lett. **30**, 2183 (1989); (*m*) Y. Yamamoto, K. Kobayashi, H. Okano, and I. Kadota. J. Org. Chem. **57**, 7003 (1992).
5. D. Xu, G.A. Crispino, and K.B. Sharpless. J. Am. Chem. Soc. **114**, 7570 (1992).
6. (*a*) G. Cardillo and M. Orena. Tetrahedron, **46**, 3321 (1990); (*b*) K.E. Harding and T.H. Tiner. *In* Comprehensive organic synthesis. Vol. 4. *Edited by* B.M. Trost and I. Fleming. Pergamon Press, Oxford. 1991. Chap. 1.9. pp. 363–421.
7. (*a*) L.E. Overman and C.B. Campbell. J. Org. Chem. **39**, 1474 (1974); (*b*) B. Giese and D. Bartmann. Tetrahedron Lett. **26**, 1197 (1985).
8. M. Hirama and M. Uei. Tetrahedron Lett. **23**, 5307 (1982).
9. (*a*) G. Cardillo, M. Orena, G. Porzi, and S. Sandri. J. Chem. Soc. Chem. Commun. 465 (1981); (*b*) A. Bongini, G. Cardillo, M. Orena, G. Porzi, and S. Sandri. J. Org. Chem. **47**, 4626 (1982).
10. *Vicinal amino alcohols*: (*a*) R.W. Friesen. Tetrahedron Lett. **31**, 4249 (1990); (*b*) R.W. Friesen and A.E. Kolaczewska. J. Org. Chem. **56**, 4888 (1991); (*c*) R.W. Friesen, A. Giroux, and K.L. Cook,. Tetrahedron Lett. **34**, 5983 (1993).
11. *Vinyl epoxides:* R.W. Friesen and M. Blouin. J. Org. Chem. **58**, 1653 (1993).
12. (*a*) M. Kimura, K. Fugami, S. Tanaka, and Y. Tamaru. Tetrahedron Lett. **32**, 6359 (1991); (*b*) J. Org. Chem. **57**, 6377 (1992); (*c*) M. Kimura, N. Saeki, S. Uchida, H. Harayama, S. Tanaka, K. Fugami, and Y. Tamaru. Tetrahedron Lett. **34**, 7611 (1993).
13. R.W. Friesen and A. Giroux. Tetrahedron Lett. **34**, 1867 (1993).
14. (*a*) E.J. Corey, P.B. Hopkins, J.E. Munroe, A. Marfat, and S. Hashimoto. J. Am. Chem. Soc. **102**, 7987 (1980); (*b*) N. Minami, S.S. Ko, and Y. Kishi. J. Am. Chem. Soc. **104**, 1109 (1982); (*c*) W.R. Roush and M.A. Adam. J. Org. Chem. **50**, 3752 (1985).
15. J. March. *In* Advanced Organic Chemistry. 3rd ed. John Wiley & Sons, New York. 1985. pp. 322–325.
16. J.S. Cowie, P.D. Landor, and S.R. Landor. J. Chem. Soc. Perkin Trans. 1, 720 (1973).
17. G. Köbrich and P. Buck. *In* Chemistry of acetylenes. *Edited by* H.G. Viehe. Marcel Dekker, New York. 1969. Chap. 2.
18. (*a*) U. Gräfe, G. Reinhardt, W. Schade, D. Krebs, I. Eritt, W.F. Fleck, E. Heinrich, and L. Radics. J. Antibiot. **35**, 609 (1982); (*b*) U. Gräfe and I. Eritt. J. Antibiot. **36**, 1592 (1983).
19. M.J. Rieser, J.F. Kozlowski, K.V. Wood, and J.L. McLaughlin. Tetrahedron Lett. **32**, 1137 (1991).
20. (*a*) J.-R. Pougny. Tetrahedron Lett. **25**, 2363 (1984); (*b*) R.D. Cooper, V.B. Jigajinni, and R.H. Wightman. Tetrahedron Lett. **25**, 5215 (1984); (*c*) L. Stamatatos, P. Sinay, and J.-R. Pougny. Tetrahedron, **40**, 1713 (1984); (*d*) K. Mori and T. Otsuka. Tetrahedron, **41**, 3253 (1985); (*e*) J. Yadav, B.V. Joshi, and M.K. Gurjar. Carbohydr. Res. **165**, 116 (1987); (*f*) H. Kotsuki, I. Kadota, and M. Ochi. J. Org. Chem. **55**, 4417 (1990); (*g*) S.-K. Kang, H.-S. Cho, H.-S. Sim, and B.-K. Kim. J. Carbohydr. Chem. **11**, 807 (1992); (*h*) A.G. Tolstikov, N.V. Khakhalina, E.E. Savateena, R.Kh. Yamilov, L.V. Spirikhin, and G.A. Tolstikov. Bioorg. Khim. **18**, 981 (1992); Chem. Abstr. **119**, 249739z (1993).
21. (*a*) B.A. Bierl, M. Beroza, and C.W. Collier. Science, **170**, 87 (1970); (*b*) S. Iwaki, S. Marumo, T. Saito, M. Yamada, and K. Katagiri. J. Am. Chem. Soc. **96**, 7842 (1974).
22. (*a*) K. Mori. Tetrahedron, **45**, 3233 (1989); (*b*) B.E. Rossiter, T. Katsuki, and K.B. Sharpless. J. Am. Chem. Soc. **103**, 464 (1981); (*c*) K. Mori and T. Ebata. Tetrahedron, **42**, 3471 (1986), and references cited therein; (*d*) E. Keinan, S.C. Sinha, A. Sinha-Bagchi, Z.-M. Wang, X.-L. Zhang, and K.B. Sharpless. Tetrahedron Lett. **33**, 6411 (1992), and references cited therein; (*e*) T. Sato, T. Itoh, and T. Fujisawa. Tetrahedron Lett. **28**, 5677 (1987); (*f*) T. Sato, T. Oohara, Y. Ueda, and K. Yamakawa. Tetrahedron Lett. **29**, 313 (1988); (*g*) S. Pikul, M. Kozlowska, and J. Jurczak. Tetrahedron Lett. **28**, 2627 (1987).

Can. J. Chem. Downloaded from www.nrcresearchpress.com by 85.192.166.187 on 09/08/12
For personal use only.

One-pot synthesis of precocene I and II and a formal synthesis of robustadial A and B via 2-phenyl-4*H*-1,3,2-benzodioxaborin

SUZANNE BISSADA, CHEUK K. LAU, MICHAEL A. BERNSTEIN, AND CLAUDE DUFRESNE[1]

Medicinal Chemistry Department, Merck Frosst Centre for Therapeutic Research, P.O. Box 1005, Pointe Claire-Dorval, QC H9R 4P8, Canada

Received March 16, 1994

SUZANNE BISSADA, CHEUK K. LAU, MICHAEL A. BERNSTEIN, and CLAUDE DUFRESNE. Can. J. Chem. **72**, 1866 (1994).

The reaction of a phenol, an α,β-unsaturated aldehyde, and phenylboronic acid yields a 2-phenyl-4*H*-1,3,2-benzodioxaborin. Upon heating, this compound decomposes to an orthoquinone-methide intermediate, which undergoes an electrocyclization reaction to a chromene ring system. This method has been applied to the synthesis of precocenes **I** and **II** and the robustadial A and B.

SUZANNE BISSADA, CHEUK K. LAU, MICHAEL A. BERNSTEIN et CLAUDE DUFRESNE. Can. J. Chem. **72**, 1866 (1994).

La réaction d'un phénol avec un aldéhyde α,β-insaturé et de l'acide phénylboronique fournit une 2-phényl-4*H*-1,3,2-benzodioxaborine. Par chauffage, ce composé se décompose en un intermédiaire orthoquinone-méthane qui subit une réaction d'électrocyclisation conduisant à un système cyclique du chromène. On a appliqué cette méthode à la synthèse des précocènes **I** et **II** et des robustadials A et B.

[Traduit par la rédaction]

Introduction

The benzopyran family, of which the title compounds are part, is widely distributed in nature and plays an important role in a number of biological processes (1). Precocene I and II, isolated from *Ageratum houstonianum*, exert strong antihormonal activity in sensitive insects (2, 3) whereas robustadial A and B (5), isolated as a Chinese herbal medicinal extract of *Eucalyptus robusta* leaves, are useful in the treatment of malaria (4).

The most challenging task in synthesizing robustadials is the stereoselective construction of the spiro ring junction at the 2-position of a benzopyran ring, while preserving the integrity of the 6,6-dimethylbicyclo[3.1.1]heptane ring systems known to be sensitive to rearrangement under the acid conditions of the classical method for chromene ring system synthesis. This method requires three steps: (*a*) an acid-catalyzed cyclization to chromanone from a phenol and an α,β-unsaturated acid, (*b*) a reduction, and (*c*) a dehydration (6).

We have shown (7) that the reaction of α,β-unsaturated aldehydes, phenols, and phenylboronic acid results in the formation of the chromene ring system. 2-Phenyl-4*H*-1,3,2-benzodioxaborins are produced in situ, and they decompose to orthoquinone-methide intermediates. The latter undergo an electrocyclization reaction resulting in the formation of a chromene ring. We now report on the successful use of this methodology in the preparation of precocene I and II, and in a formal synthesis (8) of robustadial A and B.

Results and discussion

Precocene I was prepared by heating 3-methoxyphenol (**1**), 3-methyl-2-butenal (**2**), phenylboronic acid and propanoic acid in benzene with azeotropic removal of water. The desired product **3** was isolated in 95% yield. Precocene II was prepared similarly using 3,4-dimethoxyphenol (**4**) as starting material, affording **5** in 97% yield (Scheme 1). It is interesting to note that a single regioisomer was formed in each case. The boronic acid catalyzed condensation therefore exhibits a strong regioselectivity, probably for steric reasons. The reaction is believed to proceed via the intermediates **6** and **7**.

This process may now be applied to the synthesis of the robustadial skeleton. In this case, the α,β-unsaturated aldehyde **11** was required in order to form the desired 2-spiropinene-2*H*-1-benzopyran ring system. The aldehyde **11** was prepared from (1*R*)-(+)-nopinone (**8**) (Scheme 2). Homologation by a Wadsworth–Emmons reaction with triethyl phosphonoacetate and sodium hydride afforded **9**,[2] which in turn was reduced with DIBAL-H at –78°C to give **10**.[2] The alcohol **10** was oxidized with tetra-*n*-propylammonium perruthenate and *N*-methyl morpholine *N*-oxide (9), giving the desired **11**.[2] Using the reaction conditions described above, with 3,5-dimethoxyphenol (**12**) and **11**, we obtained a 3:2 diastereoisomer ratio of **13***a* and **13***b* in 66% combined yield.[3] With the spiropinene 2*H*-1-benzopyran ring system in hand, the next transformation towards robustadials was the replacement of the chromene C=C bond with a carbonyl at C4. To explore the desired transformation, the model compound **14** (Scheme 3) was subjected to oxymercuration (10) and bromohydrin formation reactions without success. On the other hand, hydrogenation to the 2,3-dihydro-4*H*-1-benzopyran ring system **15** and oxidation with ceric ammonium nitrate (CAN) (11) gave the desired chromanone **16** (6*a*, 6*b*). Applying this method to the spiro chromene system of robustadial precursors, the mixture of **13***a* and **13***b* was hydrogenated with 10% Pd on charcoal to give **17***a* and **17***b*[3] and this mixture was oxidized with CAN in a biphasic system to yield 52% of **18***a* and **18***b*. The two diastereoisomers were separated by hplc (Scheme 4) and correlated with the literature ^{1}H nmr, nOe and 2D-nmr spectral data for these precursors of robustadial A and B (8).

In summary, we have disclosed a novel and efficient route to precocene I and II via a 2-phenyl-4*H*-1,3,2-benzodioxaborin intermediate. This method was also applied to the synthesis of the robustadial skeleton, which was elaborated into a key chromanone intermediate, therefore constituting a formal synthesis of robustadial A and B.

[1]Author to whom correspondence may be addressed. Telephone: (514) 428-3037. Fax: (514) 695-0693.

[2]Compounds **9**, **10**, **11**, ^{1}H, ^{13}C nmr data were extracted from mixture. Identity of which isomer is *E* or *Z* was undetermined.

[3]Compounds **13***a,b*, **17***a,b*, ^{1}H, ^{13}C nmr assignments were achieved using characteristic bridge-head 6 axial, equatorial methyls chemical shift differences for the major/minor isomer and correlation with nmr data in refs. 8, 12, and 13.

Can. J. Chem. Downloaded from www.nrcresearchpress.com by 85.192.166.187 on 09/08/12
For personal use only.

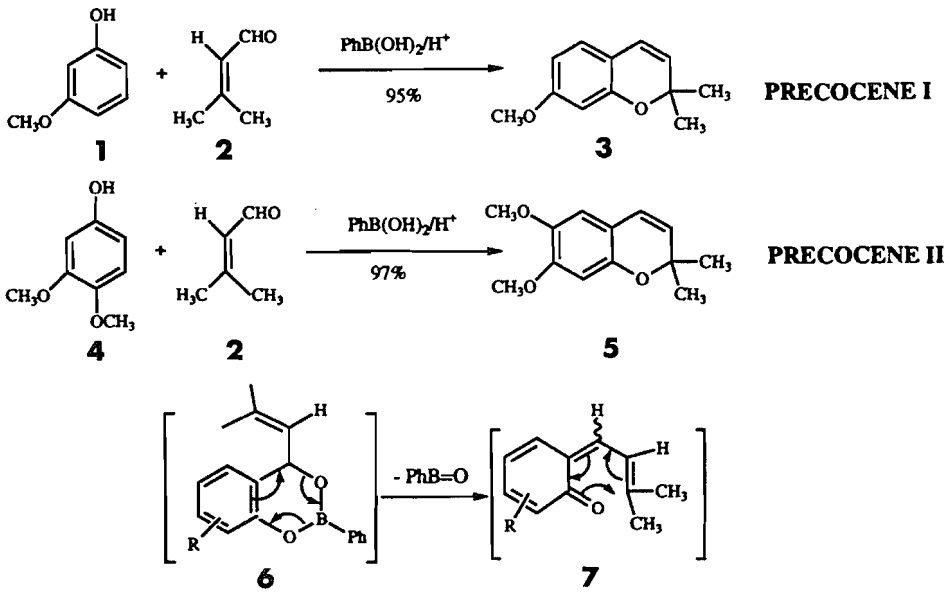

SCHEME 1

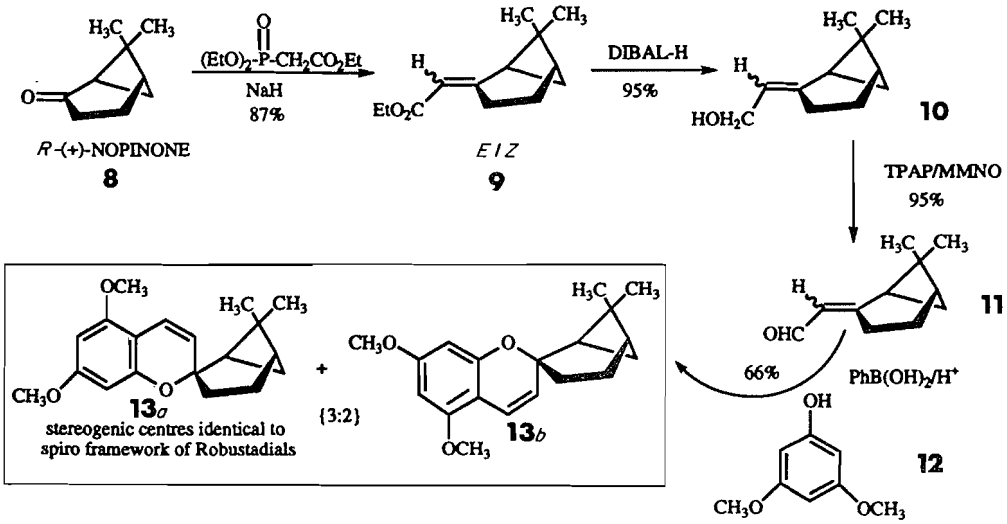

SCHEME 2

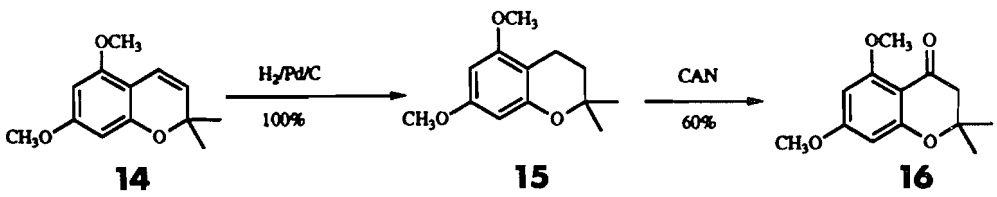

SCHEME 3

Experimental

General information

Proton and carbon nuclear magnetic resonance spectra were obtained on a Bruker AM250 spectrometer or AM300 spectrometer. Elemental analyses were performed by Guelph Chemical Laboratories Ltd, Guelph, Ontario. Flash chromatography was performed using Merck silica gel 60, 230–400 mesh.

7-Methoxy-2,2-dimethyl-2H-1-benzopyran — precocene I, 3

A mixture of 3-methoxyphenol (0.565 g, 4.56 mmol), phenylboronic acid (0.889 g, 7.30 mmol), 3-methyl-2-butenal (0.766 g, 9.12 mmol), and propanoic acid (0.1 g, 1.36 mmol) in benzene was heated under reflux for 20 h, with azeotropic removal of water using a Dean–Stark trap. The reaction mixture was quenched with cold ammonium acetate (20%) and extracted with ethyl acetate. The extract was dried over Na_2SO_4 and evaporated to dryness. The residue was chromatographed, using 10% ethyl acetate in hexane as the eluent. The title compound was obtained in 95% yield (0.82 g) as an oil; ir (neat): 3050, 1630, 1600, 1450 cm^{-1}; ^1H nmr (300 MHz, $CDCl_3$), δ: 1.40 (s, 6H), 3.77 (s, 3H), 5.49 (d, 1H, J = 10 Hz), 6.19 (d, 1H, J = 10 Hz), 6.60–6.80 (m,

Can. J. Chem. Downloaded from www.nrcresearchpress.com by 85.192.166.187 on 09/08/12
For personal use only.

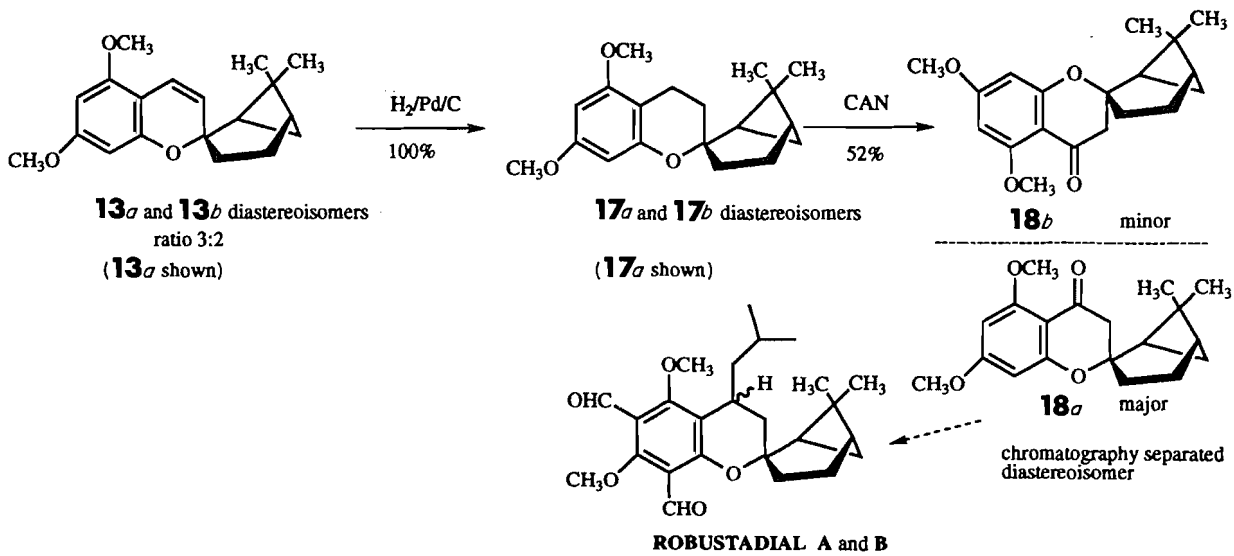

SCHEME 4

3H). Anal. calcd. for $C_{12}H_{14}O_2$: C 75.76, H 7.42; found: C 75.54, H 7.26. Exact Mass calcd. for $C_{12}H_{14}O_2$ (M + 1): 191.10720; found: 191.10710.

6,7-Dimethoxy-2,2-dimethyl-2H-1-benzopyran — precocene II, 5

According to the previous procedure, using 3,4-dimethoxyphenol, the title compound was obtained in 97% yield after chromatography; ^{1}H nmr (300 MHz, $CDCl_3$), δ: 1.42 (s, 6H), 3.75 (s, 3H), 3.80 (s, 3H), 5.45 (d, 1H, J = 10 Hz), 6.02 (m, 2H), 6.57 (d, 1H, J = 10 Hz). Anal. calcd. for $C_{13}H_{16}O_3$: C 70.89, H 7.32; found: C 71.24, H 7.44. Exact Mass calcd. for $C_{13}H_{16}O_3$ (M + 1): 221.11776; found: 221.11775.

E/Z Ethyl 6,6-dimethylbicyclo[3.1.1]-2-heptylidene acetate, 9

Triethyl phosphonoacetate (34.5 g, 154 mmol) was added dropwise to a suspension of NaH (3.71 g, 154 mmol) in THF (225 mL) at 0°C, followed by a rapid addition of (1*R*)-(+)-nopinone (12.54 g, 90.8 mmol). The solution was heated at 50°C for 20 h. The reaction mixture was quenched with cold ammonium acetate (20%) and extracted with ethyl acetate. The extract was dried over Na_2SO_4 and evaporated to dryness. The residue was chomatographed with 5% ethyl acetate in hexane. The title compound was obtained in 87% yield (16.44 g) as an oil; ir (neat): 3090, 2980, 1725, 1680 cm^{-1}; ^{1}H nmr (300 MHz, $CDCl_3$), *E/Z* isomers, δ: 0.74 (s, 3H), 1.20–1.34 (m, 6H), 1.39 (d, 1H, J = 10 Hz), 1.80–2.72 (m, 4H), 3.14–3.21 (m, 1H), 3.99 (m, 1H), 4.1 (m, 3H), 5.47 (s, 1H); resolved signals of the minor isomer: 1.45 (d, 1H, J = 10 Hz), 5.6 (s, 1H); ^{13}C nmr ($CDCl_3$), major isomer, δ: 168.88, 166.62, 113.00, 112.57, 59.24, 53.73, 40.40, 27.21, 26.02, 23.62, 22.40, 22.06, 14.36. Anal. calcd. for $C_{13}H_{20}O_2$: C 74.96, H 9.68; found: C 75.24, H 9.77. Exact Mass calcd. for $C_{13}H_{20}O_2$ (M + 1): 209.15410; found: 209.15410.

E/Z-2-(6,6-Dimethylbicyclo[3.1.1]-2-heptylidene)ethanol, 10

To a solution of **9** (8.6 g, 41.3 mmol) in toluene (40 mL) at –78°C was added dropwise DIBAL-H 1.5 M in toluene (66 mL, 99.12 mmol). The reaction mixture was stirred for 15 min, then quenched with 0.5 M HCl (150 mL), and extracted with ethyl acetate. The organic phase was dried over Na_2SO_4, filtered, and evaporated. The residue was chromatographed using 30% ethyl acetate in hexane. The title compound was obtained as an oil in 95% yield (0.63 g) as a mixture of isomeric olefins; ir (neat); 3600, 3010, 1514, 1430 cm^{-1}; ^{1}H nmr (300 MHz, $CDCl_3$,), *E/Z* isomers, δ, isomer 1: 0.70 (s, 3H), 1.2 (s, 3H), 1.36 (s, 1H, J = 10 Hz), 1.84 (m, 3H), 2.1–2.2 (dd, 1H, J = 8 Hz, J = 12 Hz), 2.3–2.5 (m, 2H), 2.52–2.65 (m, 1H), 2.8 (t, 1H, J = 5 Hz), 3.95–4.20 (m, 2H), 5.2 (m, 1H); resolved signals of the minor isomer: 0.72 (s, 3H), 1.25 (s, 3H), 1.46 (d, 1H, J = 10 Hz), 2.00 (m, 2H), 5.40 (t, 1H, J = 5 Hz); ^{13}C nmr ($CDCl_3$), major isomer, δ: 146.86, 120.50, 58.79, 52.30, 45.17, 40.72, 40.66, 24.47, 26.00, 21.89, 19.43. Anal. calcd. for $C_{11}H_{18}O$: C 79.46, H 10.91; found: C 79.36, H 10.80. Exact Mass calcd. for $C_{11}H_{18}O+H^+$; 167.14359; found: 167.14355.

E/Z-2-(6,6-Dimethylbicyclo[3.1.1]-2-heptylidene)ethanal, 11

To **10** (0.50 g, 3.0 mmol), *N*-methyl morpholine *N*-oxide (0.52 g, 4.5 mmol), and 4Å molecular sieve (1.50 g) in dichloromethane (6 mL) was added tetra-*N*-propylammonium perruthenate (0.053 g, 0.15 mmol). The reaction was stirred for 5 min at room temperature. The reaction mixture was then filtered through a pad of Celite and concentrated. The residue was chromatographed using 20% ethyl acetate in hexane. The title compound was isolated as an oil in 95% yield (0.46 g); ir (neat): 2970, 1710, 1600, 1390; ^{1}H nmr (300 MHz, $CDCl_3$), *E/Z* isomers, δ, isomer 1: 0.77 (s, 3H), 1.31 (s, 3H), 1.49 (d, 1H, J = 10 Hz), 1.90–2.13 (m, 3H), 2.2–2.65 (m, 1H), 2.74–2.83 (m, 1H), 3.16 (d, 1H, J = 8 Hz), 3.55 (t, 1H, J = 5 Hz), 5.7 (d, 1H, J = 8 Hz), 9.98 (d, 1H, J = 8 Hz); resolved signals of the minor isomer: 0.78 (s, 3H), 1.55 (d, 1H, J = 10 Hz), 5.9 (d, 1H, J = 8 Hz), 9.85 (d, 1H, J = 8 Hz); ^{13}C nmr ($CDCl_3$), major isomer, δ: 190.35, 124.48, 57.95, 53.71, 40.37, 32.76, 26.55, 25.54, 25.87, 23.45, 22.10. Thermally unstable for MS or combustion analysis.

5,7-Dimethoxy-2-(6,6-dimethylbicyclo[3.1.1]-2-heptylidene)-2H-1-benzopyran, 13a, 13b

A mixture of **11** (0.555 g, 3.3 mmol), 3,5-dimethoxyphenol (0.521 g, 3.3 mmol), phenylboronic acid (0.825 g, 6.7 mmol), and propanoic acid (0.68 mL, 0.66 mmol) in benzene (7 mL) was heated under reflux for 3 h with azeotropic removal of water using a Dean–Stark trap. The reaction mixture was quenched with cold ammonium acetate (20%) and extracted with ethyl acetate. The extract was dried over Na_2SO_4 and evaporated to dryness. The residue was chromatographed eluting with 5% ethyl acetate in hexane. The title compound was obtained as a 3:2 mixture of **13***a* and **13***b* as oil in 66% yield (0.65 g). Major isomer, ^{1}H nmr (300 MHz, $CDCl_3$), δ: 0.98 (s, 3H), 1.19 (s, 3H), 1.68 (d, 1H, J = 10 Hz), 1.84–2.2 (m, 6H), 2.36 (t, 1H, J = 5 Hz), 3.76–3.78 (m, 6H), 5.59–5.05 (m, 1H), 5.99–6.03 (m, 2H), 6.51–6.56 (m, 1H). Anal. calcd. for $C_{19}H_{24}O_3$: C 75.97, H 8.05; found: C 75.79, H 8.17. Exact Mass calcd. for $C_{19}H_{24}O_3$ (M + 1): 301.18036; found: 301.18038.

2,3-Dihydro-5,7-dimethoxy-2,2-dimethoxy-4H-1-benzopyran, 15

5,7-Dimethoxy-2,2-dimethyl-2*H*-1-benzopyran (**14**) (*6a*) (0.6 g, 2.72 mmol) was dissolved in ethanol (6 mL), and 10% palladium on charcoal (60 mg) was added. The reaction mixture was hydrogenated using a Parr apparatus at 40 psi (1 psi = 6.9 kPa) for 40 min. The mix-

Can. J. Chem. Downloaded from www.nrcresearchpress.com by 85.192.166.187 on 09/08/12
For personal use only.

ture was filtered on a pad of Celite, and then was evaporated to dryness. The title compound was obtained in 100% yield (0.6 g) as an oil; ^{1}H nmr (300 MHz, $CDCl_3$), δ: 1.35 (s, 6H), 1.75 (t, 2H, J = 7.5 Hz), 2.58 (t, 2H, J = 7.5 Hz), 3.78 (s, 3H), 3.82 (s, 3H), 6.05 (s, 2H). Anal. calcd. for $C_{13}H_{18}O_3$: C 70.24, H 8.16; found: C 69.98, H 8.25. Exact Mass calcd. for $C_{13}H_{18}O_3$ (M + 1): 223.13341; found: 223.13361.

2,3-Dihydro-5,7-dimethoxy-2,2-dimethyl-4H-1-benzopyran-4-one, ***16***

To 2,3-dihydro-5,7-dimethoxy-2,2-dimethyl-4*H*-1-benzopyran (**15**) (0.300 g, 1.35 mmol) in acetic acid (14 mL) and water (14 mL) was added, in small portions, ceric ammonium nitrate (4.5 g, 8.20 mmol). The resulting mixture was heated in bath oil at 100°C for 20 min. The reaction mixture was quenched with ammonium acetate (20%) and extracted with ethyl acetate. The organic phase was dried over sodium sulfate and filtered, then chromatographed using 19:1 hexane in ethyl acetate to yield 60% (0.19 g) of an oil, which has a ^{1}H nmr spectrum corresponding to that previously described in ref. 6*a*.

2,3-Dihydro-5,7-dimethoxy-2-(6,6-dimethylbicyclo[3.1.1]-2-heptylidene)-4H-1-benzopyran, ***17a 17b***

To **13**a, **13**b (0.30 g, 1.09 mmol) in ethanol was added 0.3 g of palladium on charcoal 10%. The mixture was hydrogenated using a Parr apparatus at 40 psi for 40 min. The reaction mixture was filtered through a pad of Celite to yield 0.30 g or 100% of the title compounds. Major isomer, ^{1}H nmr, δ: 1.00 (s, 3H), 1.26 (s, 3H), 1.73–2.3 (m, 10H), 2.50–2.56 (m, 2H), 3.74 (s, 3H), 3.77 (s, 3H), 6.0 (m, 2H); resolved signals of the minor isomer: 1.17 (s, 3H), 1.21 (s, 3H); ^{13}C nmr ($CDCl_3$), major isomer, δ: 159.29, 158.25, 155.28, 103.19, 93.99, 90.67, 81.15, 55.30, 49.36, 41.25, 40.77, 38.51, 32.52, 31.87, 28.31, 27.70, 26.48, 24.94, 16.42. Anal. calcd. for $C_{19}H_{26}O_3$; C 75.46, H 8.66; found: C 75.26, H 8.74. Exact Mass calcd. for $C_{19}H_{26}O_3$ (M + 1); 303.19601; found: 303.19603.

2,3-Dihydro-5,7-dimethoxy-2-(6,6-dimethylbicyclo[3.1.1]-2-heptylidene)-4H-1-benzopyran-4-one, ***18a, 18b***

Using the procedure described for compound **16**, the title compound was obtained, in 52% yield, as an oil, which was purified by a hplc reverse-phase C_{18}, 8 × 10 Waters RCM column, solvent: 10% H_2O, 90% MeOH; λ = 280 nm sens 1; RT: **18***a*, 4.68 min; **18***b*, 7.35 min. "The isomers **18***a* and **18***b* were identified by correlation with reported spectra data (8):" minor isomer, precursor of the unnatural isomer of robustadial **18***b*: ir (neat): 3060, 1684, 1595, 1460 cm^{-1}; ^{1}H nmr (500 MHz, $CDCl_3$), δ: 6.06 (d, 1H, J = 2.2 Hz), 5.95 (d, 1H, J = 2.2 Hz), 3.85 (s, 3H), 3.79 (s, 3H), 2.62 (m, 2H), 1.75–2.34 (m, 7H), 1.17 (s, 3H), 1.11 (s, 3H), 1.02–1.04 (m, 1H); ^{13}C nmr (500 MHz, $CDCl_3$), δ: 190.54 (s), 166.01 (s), 163.35 (s), 161.85 (s), 105.84 (s), 93.99 (d), 92.17 (d), 86.24 (s), 56.07 (q), 55.25 (q), 50.00 (t), 48.17 (d), 40.63 (d), 38.38 (s), 28.36 (t), 27.29 (q), 26.73 (t), 23.85 (t), 23.18 (q). Anal. calcd. for $C_{19}H_{24}O_4$: C 72.12, H 7.64; found: C 72.05, H 7.50. Exact Mass calcd. for $C_{19}H_{24}O_4$ (M + 1): 317.17528; found: 317.17527.

Major isomer (**18***a*), precursor of the natural isomer of robustadial; ir (neat); 3062, 1684, 1595, 1465 cm^{-1}; ^{1}H nmr (500 MHz, $CDCl_3$), δ: 5.98 (s, 2H), 3.85 (s, 3H), 3.79 (s, 3H), 2.82 (d, 1H, J = 16.1 Hz), 2.74 (d, 1H, J = 16.1 Hz), 1.84–2.32 (m, 7H), 1.50–1.60 (m, 1H), 1.21 (s, 3H), 0.96 (s, 3H). ^{13}C nmr (500 MHz, $CDCl_3$) δ: 190.11 (s), 165.88 (s), 163.43 (s), 161.63 (s), 105.74 (s), 93.99 (d), 92.14 (d), 85.60 (s), 55.94 (q), 55.41 (q), 50.88 (t), 48.72 (d), 40.31 (d), 37.97 (s), 28.43 (t), 27.27 (q), 26.50 (t), 24.46 (t), 23.13 (q). Anal. calcd. for $C_{19}H_{24}O_4$: C 72.12, H 7.64; found: C 72.25, H 7.41. Exact Mass calcd. for $C_{19}H_{24}O_4$ (M + 1): 317.17528; found: 317.17530.

1. (*a*) F.M. Dean. Naturally occurring oxygen ring compounds. Butterworths, London. 1963; (*b*) Chemistry of heterocyclic compounds. Vol. 31. Chromenes, chromanone and chromones. *Edited by* G.P. Ellis. Wiley, New York. 1977; (*c*) T. Swain. *In* Chemistry and biochemistry of plant pigments. *Edited by* T.W. Goodwin. Academic Press, London. 1976.
2. S.Y. Dike, J.R. Merchant, and N.Y. Sapre. Tetrahedron, **47**, 4775 (1991).
3. T. Timar, S. Hosztafi, J.C. Jaszberényi, and J. Csaba. Acta Chim. Hung, **125**, 617 (1988).
4. G.W. Quin, H.C. Chen, H.C. Wang, and M.K. Quian. Acta Chim. Sin. **39**, 83 (1981).
5. Q. Cheng, and J.K. Snyder. J. Org. Chem. **53**, 4562 (1988).
6. (*a*) T. Timar, J. Csaba, and J.C. Jaszberényi. J. Heterocycl. Chem. **25**, 871 (1988); (*b*) H. Seliger, A. Cascaval, and E. Happ. Rev. Roum. Chim. **37**, 485 (1992).
7. J. Chambers, J. Crawford, H.W.R. Williams, C. Dufresne, J. Scheigetz, M.A. Bernstein, and C.K. Lau. Can. J. Chem. **70**, 1717 (1992).
8. R.G. Salomon, S.M. Mazza, and K. Lal. J. Org. Chem. **54**, 1562 (1989).
9. W.P. Griffith and S.V. Ley. Aldrichimica Acta, **23**, 13 (1990).
10. G.T. Rodeheaver and D.F. Hunt. Chem. Commun. 818, 1971.
11. M.N. Kavinde, S.A. Kulkarni, and M. V. Paradkar. Synth. Commun. **20**, 3259 (1990).
12. M. Krause and H.M.R. Hoffmann. Tetrahedron Lett. **31**, 6629 (1990).
13. S. Koser and H.M.R. Hoffman. J. Org. Chem. **58**, 6163 (1993).

Can. J. Chem. Downloaded from www.nrcresearchpress.com by 85.192.166.187 on 09/08/12
For personal use only.

Crystal chemistry of tetraradial species. Part 5. Interaction between cation lone pairs and phenyl groups in tetraphenylborates: crystal structures of Me_3S^+, Et_3S^+, Me_3SO^+, Ph_2I^+, and 1-azoniapropellane tetraphenylborates[1,2]

OSVALD KNOP,[3] T. STANLEY CAMERON, PRADIP K. BAKSHI,[4] ANTONY LINDEN,[5] AND STEPHEN P. ROE
Department of Chemistry, Dalhousie University, Halifax, NS B3H 4J3, Canada

Received March 18, 1994

OSVALD KNOP, T. STANLEY CAMERON, PRADIP K. BAKSHI, ANTONY LINDEN, and STEPHEN P. ROE. Can. J. Chem. **72**, 1870 (1994).

Determination of the crystal structures of the tetraphenylborates of the trimethylsulfonium (Me_3S^+, $P2_1/n$), triethylsulfonium (Et_3S^+, *Cmcm*), trimethylsulfoxonium (Me_3SO^+, $P2_1/m$), diphenyliodonium (Ph_2I^+, *Pnma*), and 1-azoniapropellane ($C_{10}H_{18}N^+$, $P2_1/n$) cations has shown that when regions of high local electron density (lone electron pairs) are present in the cation, the cation orients itself so as to minimize the repulsion between the lone pair(s) and the nearest anion phenyl groups, i.e. the cation orientation responds to the lone pair – aromatic π system interaction. This behaviour contrasts with the formation of H...π hydrogen bonds in tetraphenylborates of organic ammonium cations containing *N*-hydrogens and provides corroborative evidence for our previous finding: (*1*) given the opportunity, a cation *N*-hydrogen will form a hydrogen bond to a phenyl group(s) of the anion; (2) the orientation of the cation to form the N—H(N)...π bond is thus a manifestation of a *positive* hydrogen-bonding tendency rather than a passive response to overall packing requirements in the crystal. The geometries of the above cations are compared to those reported in the literature and those of Me_3S^+ and Me_3SO^+ have also been optimized by *ab initio* (RHF/6-31G*) methods.

OSVALD KNOP, T. STANLEY CAMERON, PRADIP K. BAKSHI, ANTONY LINDEN et STEPHEN P. ROE. Can. J. Chem. **72**, 1870 (1994).

La détermination de la structure cristalline des tetraphénylborates des cations suivants: triméthylsulfonium (Me_3S^+, $P2_1/n$), triéthylsulfonium (Et_3S^+, *Cmcm*), triméthylsulfoxonium ($Me_3\ SO^+$, $P2_1/m$), diphényliodonium (Ph_2I^+, *Pnma*) et 1-azoniapropellane ($C_{10}H_{18}N^+$, $P2_1/n$), montre qu'en présence de régions à forte densité électronique locale (doublet électronique libre) dans le cation, ce dernier s'oriente de façon à minimiser la répulsion entre le doublet libre et les groupes phényles de l'anion les plus rapprochés, i.e. l'orientation du cation répond à l'interaction doublet libre avec le système π aromatique. Ce comportement contraste avec la formation des liaisons hydrogène H...π dans les tétraphénylborates des cations ammonium organiques contenant des liaisons N—H et fournit des preuves qui confirment nos résultats antérieurs à savoir: (*1*) si l'opportunité se présente, un cation ayant une liaison N—H formera des liaisons hydrogène avec le ou les groupes phényles de l'anion; (2) l'orientation du cation en vue de former la liaison N—H(N)...π est alors une manifestation d'une tendance positive à former une liaison hydrogène plutôt qu'une réponse passive à l'entassement global inévitable dans le cristal. On compare les géométries de ces cations avec celles répertoriées dans la littérature et on a optimisé les géométries des cations Me_3S^+ et Me_3SO^+ par les méthodes *ab initio* (RHF/6-31G*).

[Traduit par la rédaction]

Can. J. Chem. Downloaded from www.nrcresearchpress.com by 85.192.166.187 on 09/08/12
For personal use only.

Previously (1, 3) we have shown that, given the opportunity, a cation *N*-hydrogen, H(N), will form a hydrogen bond to a phenyl group(s) of the tetraphenylborate (TB) counter anion, and that the orientation of the cation to form the H-bond is a manifestation of a *positive* H-bonding tendency (reinforced by ion charge interaction) rather than a passive response to overall packing requirements in the crystal. We now offer evidence that when regions of high local electron density (lone electron pairs, LP or L for short) are present in the cation in place of an H(N) atom, the orientation which the cation assumes with respect to the nearest phenyl ring(s) is significantly different from (sometimes the opposite of) that which would be expected if an H(N) atom were present.

The compositions and geometries of the five title cations were chosen to illustrate to maximum effect how the cation orientation depends on the nature of the interactive end of the cation. The cations discussed in the following (Table 1) and intended to provide contrast to the H-bonding cations (1, 3) are either of the quaternary ammonium variety, in which the N atom is sterically shielded from the anion by CH_3 or CH_2 groups (4MTB, ImB, AzPpTB), or they contain one or more oriented LPs on the terminal (central) atom (3MSTB, 3ESTB, 3MTeTB, 3MSOTB, 2PhITB). The sources of the structural information are listed in Table 1.

To provide comparison with the results of the previously (4) so treated Me_3S^+ cation, we have also optimized (RHF/6-31G*) the equilibrium molecular geometry of the Me_3SO^+ ion in C_3 and C_{3v} symmetries. The optimized geometries are compared in some detail with those from experiment, both in the title compound and in crystal structures reported in the literature.

The crystal data of the five title compounds are assembled in Table 2. Details of the crystal structure and other determinations (Tables A–F) have been deposited[6] (see also Experimental). The following tables and figure are available: Table A. Posi-

[1]For Part 4 see ref. 1. A preliminary account of the present investigation was presented at the 3rd Chemical Congress of North America, Toronto, ON, June 5–10, 1988 (2).

[2]Corrigenda for Part 3 (3): p. 1496, read $[LL'C{=}NL''L''']^+$ instead of $[LL'C{=}NL''L'']^+$. Page 1498, Table 3, compound **A**, read C(C1)′ instead of C(1)′, and C(C2) instead of C(2); compound **B**, read C(C2) instead of C(2). Page 1510, Table 9: the third footnote is [c], not [d]; read −0.136 instead of −0136.

[3]To whom correspondence may be addressed (telephone: (902) 494-3317 or 494-3305, facsimile: (902) 494-1310).

[4]Holder of a graduate scholarship, Canadian Commonwealth Scholarship and Fellowship Plan, and a Killam Graduate Scholarship.

[5]Present address: Organisch-Chemisches Institut, Universität Zürich, CH-8057 Zürich, Switzerland.

[6]This material may be purchased from: The Depository of Unpublished Data, Document Delivery, CISTI, National Research Council Canada, Ottawa, ON K1A 0S2 Canada. Tables A to D have also been deposited with the Cambridge Crystallographic Data Centre, and can be obtained on request from the Director, CCDC, University Chemical Laboratory, 12 Union Road, Cambridge CB2 1EZ, U.K.

TABLE 1. Tetraphenylborates discussed in this work

Compound	Code	Reference
1 $Me_4N^+TB^-$ (*Cmcm*, $Z = 4$)	4MTB	5
2 $Me_3NH^+TB^-$ ($P2_1$, $Z = 2$)	3MTB	1
3 Trimethylsulfonium TB, $Me_3S^+TB^-$ ($P2_1/n$, $Z = 4$)	3MSTB	This work
4 Trimethyltelluronium TB, $Me_3Te^+TB^-$ (*Cmcm*, $Z = 4$)[a]	3MTeTB	6
5 Triphenyltelluronium TB, $Ph_3Te^+TB^-$ (($P1$ or $P\bar{1}$, $Z = 8$)	3PhTeTB	6
6 Tetraphenylarsonium TB, $Ph_4As^+TB^-$ ($I4_122$? $Z = 4$)	4PhAsTB	[b]
7 Tetraphenylstibonium TB, $Ph_4Sb^+TB^-$ ($I4_122$? $Z = 4$)	4PhSbTB	7[b]
8 $Et_3NH^+TB^-$ ($P2_1$, $Z = 2$)	3ETB	1
9 Triethylsulfonium TB, $Et_3S^+TB^-$ (*Cmcm*, $Z = 4$)	3ESTB	This work
10 Trimethylsulfoxonium TB, $Me_3SO^+TB^-$ ($P2_1/m$, $Z = 4$)	3MSOTB	This work
11 $Me_2NH_2^+TB^-\cdot Et_2CO$ ($P2_1/n$, $Z = 4$)	2MTB.Et_2CO	1
12 $Et_2NH_2^+TB^-$ ($P2_12_12_1$, $Z = 4$)	2ETB	1
13 Diphenyliodonium TB, $Ph_2I^+TB^-$ (*Pnma*, $Z = 4$)	2PhITB	This work
14 1-Azoniapropellane TB ($P2_1/n$, $Z = 4$)[c]	AzPpTB	This work
15 $[Me_2C{=}NHMe]^+TB^-$ (*Cmcm*, $Z = 4$)	ImA	3
16 $[Me_2C{=}NMe_2]^+TB^-$ (*Cmca*, $Z = 8$)	ImB	3

[a]Cation disordered across a mirror plane; refinement in *Ama*2 did not resolve the disorder.
[b]O. Knop, T.S. Cameron, and P.K. Bakshi. Unpublished work.
[c]Tetrahydro-1*H*,5*H*-4,7*a*-propanopyrrolizinium TB, $C_{10}H_{18}N^+TB^-$.

TABLE 2. Crystal data of the title tetraphenylborates[a]

Parameter	Value				
	3MSTB[b]	3ESTB[b]	3MSOTB[b]	2PhITB[c]	AzPpTB[c]
Formula	$BC_{27}H_{29}S$	$BC_{30}H_{35}S$	$BC_{27}H_{29}OS$	$BC_{36}H_{30}I$	$BC_{34}H_{38}N$
fw	396.4	438.5	412.4	630.4	471.5
Crystal size, mm^3	$0.2 \times 0.25 \times 0.15$	$0.3 \times 0.35 \times 0.35$	$0.2 \times 0.3 \times 0.5$	$0.2 \times 0.25 \times 0.3$	$0.35 \times 0.32 \times 0.42$
μ_{Mo}, cm^{-1}	1.54	1.46	1.60	11.2	0.61
θ-range, deg[d]	2–25/25	2–23/25	2–23/25	2–30/22	2–25/25
Max/min[e]	1.11/0.80	1.29/0.77	1.23/0.70	1.64/0.57	—
a, Å	9.837(4)	10.939(2)	9.482(3)	17.731(4)	9.903(2)
b, Å	15.593(12)	16.173(4)	12.790(2)	16.382(6)	19.897(2)
c, Å	15.112(5)	14.097(3)	9.713(3)	9.982(4)	13.630(2)
β, deg	102.71(6)	90	106.48(3)	90	92.33(1)
V, $Å^3$	2261(4)	2494(2)	1130(2)	2899(3)	2683(1)
Z	4	4	2	4	4
ρ_c, g/cm^3	1.164(1)	1.134(1)	1.177(2)	1.444(1)	1.167(1)
Space group	$P2_1/n$ (no. 14)	*Cmcm* (no. 63)	$P2_1/m$ (no. 11)	*Pnma* (no. 62)	$P2_1/n$ (no. 14)
F(000), e	848	944	440	1276	1016
Reflections:					
Total measured	4239	1238	2637	4710[f]	5186
Unique total	3951	813	2091	4710	4891
Unique used[g]	1154	601	1156	1370	2134
$100R_{merg}$	3.1	3.4	2.4	—	4.0
d/*p*	4.4	4.8	7.8	7.0[h]	6.6
$100R$; $100R_w$	5.1; 5.3	5.5; 5.5	6.9; 7.5	6.9; 6.9[h]	4.6; 4.6
G.O.F.	1.51	1.48	2.76	3.05[h]	2.56
Residual e.d.[i]	−0.23/0.36	−0.19/0.20	−0.42/0.34	−0.99/1.05[h]	−0.14/0.26

[a]For details of weighting schemes and other information see Experimental. $T \sim 18°C$.
[b]CAD-4, $\lambda = 0.70926$ Å (graphite monochromator).
[c]Rigaku AFC5R, $\lambda = 0.71069$ Å (graphite monochromator).
[d]$\theta_{min} < \theta < \theta_{max}/n$. The lattice parameters and orientation matrices were obtained by least squares from the setting angles θ of suitable *n* reflections.
[e]Maximum and minimum empirical absorption corrections from DIFABS (8).
[f]Decay correction applied.
[g]$I > 3\sigma(I)$.
[h]On modelling disorder (see text), *d*/*p* = 5.4, $100R = 6.3$, $100R_w = 6.3$, G.O.F. = 2.87, residual electron density, −0.88/1.03.
[i]Minimum and maximum residual electron density ($e/Å^3$) in final difference map.

Can. J. Chem. Downloaded from www.nrcresearchpress.com by 85.192.166.187 on 09/08/12
For personal use only.

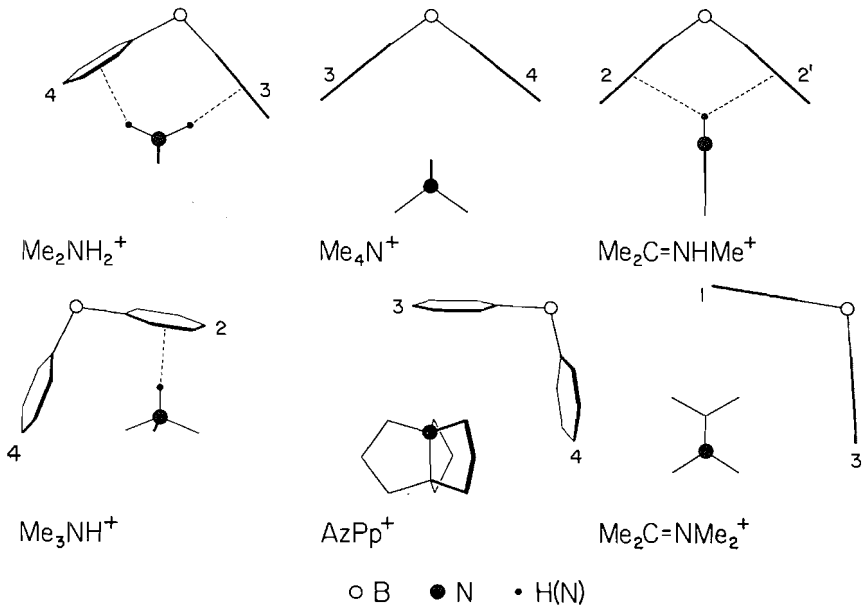

FIG. 1. The effect of replacing H(N) by a methyl group(s). Synoptic representation (to scale) of the cation–anion pair interactions in 2MTB.Et_2CO, 3MTB, 4MTB, AzPpTB, ImA, and ImB. The geometric feature of interest in the cation (C_3 or C_2 axis, C=N bond) is oriented vertically in the page. The N atom is in black; N—H...π_c bonds are indicated by broken lines (π_c, ring centre).

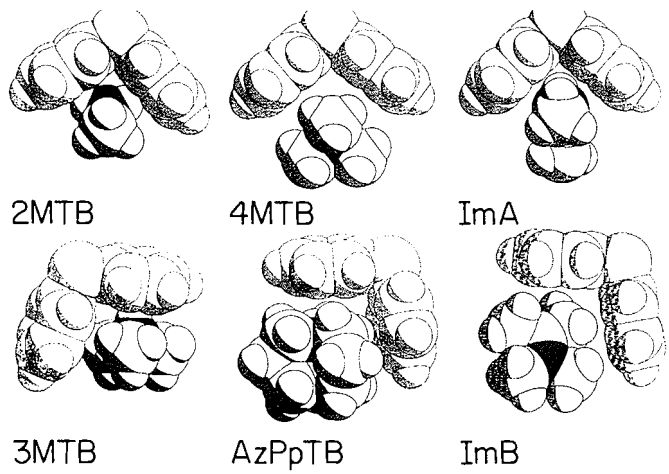

FIG. 2. Space-filling representation (van der Waals radii) of the cation–anion pairs of Fig. 1. The N atoms are shown in black.

tional parameters of the nonhydrogen atoms; Table B. Positional parameters and isotropic temperature factors of the H atoms; Table C. Anisotropic thermal parameters of the nonhydrogen atoms; Table D. Interatomic distances and angles; Table E. Deviations of the C and B atoms from the best planes through the phenyl rings and angles between the ring planes; Table F. Parameters of the RHF/6-31G* optimized equilibrium molecular geometries of the Me_3S^+ and Me_3SO^+ cations in C_{3v} symmetry; Fig. A. Projection of the AzPpTB structure on (100).

Hydrogen-bonded vs. nonbonded cations

The crystal structures of TBs of small cations are dominated by the packing of the anions. In the case of small *organic* cations this packing, which tends to be quite symmetric, is often based on the space group *Cmcm* or subgroup (1, 3). The freedom the cation has in these structures is restricted essentially to its orientability inside the wedge-shaped spaced formed by the phenyl rings.[7] These anion systems are therefore well suited for testing the propensity of the cation to interact with the phenyl groups and the nature of the cation–anion pair interaction. When a cation tends to form a H bond(s) to a phenyl group(s), this tendency is reinforced by the ionic charge. However, because of the large size of the anion the single charge is spatially greatly diluted, and while the net charge on the interacting cation hydrogen is larger than that on a CH_3 or CH_2 hydrogen in the cation, it is not dramatically so (cf. ref. 3). A cation orientation suggestive of H-bonding can therefore be legitimately interpreted as arising from a H-bonding interaction and not from Coulombic interaction as such. This is demonstrated by the following examples, in which geometries of the situations involving H bonding are compared side by side with the corresponding situations involving only ionic charge interaction.

In Figs. 1 and 2 the orientations of the H-bonding cations in 2MTB, 3MTB, and ImA are contrasted with the orientations of the cations in 4MTB, AzPpTB, and ImB, which do not contain *N*-hydrogens and thus are incapable of forming N—H...π bonds. A dramatic display of the effect of the presence of H(N) on cation orientation results when $Me_2NH_2^+$ is compared with Me_4N^+, and $Me_2C{=}NHMe^+$ with $Me_2C{=}NMe_2^+$. In the first pair the cations are rotated about their respective N...B axes so as to achieve bonding in $Me_2NH_2^+$ but "antibonding" of the corresponding two Me groups in Me_4N^+. In the iminium pair, the planar cation in ImA orients itself, in the plane bisecting the angle between the two phenyl rings, in such a way that the solitary H(N) forms a symmetrically bifurcated N—H...2π bond. In ImB the Me groups facing the rings are more or less equidistant, with the *N*-Me groups (one of which would correspond to H(N) in ImA) directed away from the rings. Since all the drawings in Fig. 1 are on the same scale (and similarly in Fig. 2), it is

[7] Thus the crystal structure of the TB is not determined (or even significantly influenced) by the presence of (oriented) LPs on the cation, the latter affecting only the cation orientation but not the packing as a whole (cf. ref. 4).

Can. J. Chem. Downloaded from www.nrcresearchpress.com by 85.192.166.187 on 09/08/12
For personal use only.

TABLE 3. Shortest interatomic distances (Å) between the cation and the centre π_c of the associated phenyl ring(s) or the boron atoms in tetraphenylborates[a]

Compound	Z...B	Distance	Z...π_c	Distance	Other contacts	Distance
2MTB.Et_2CO	N...B	4.53	N...π_c(3)	3.26	H(N1)...π_c(3)	2.26
			N...π_c(4)	3.19	H(N2)...π_c(4)	2.34
3MTB	N...B	4.74	N...π_c(2)	3.25	H(N)...π_c(2)	2.38
			N...π_c(4)	4.21	H(N)...π_c(4)	4.17
4MTB	N...B	5.58	N...π_c(2)	4.37	C(1)...π_c(2)	3.90
					H(1')...π_c(2)	3.10
3MeTeTB[b]	Te...B	6.03	Te...π_c(2)	4.38	C(1)...π_c(2)	3.92
	Te*...B	6.03	Te*...π_c(2)	5.05	C(1*)...π_c(2)	3.92
AzPpTB	N...B	5.78	N...π_c(3)	4.32	H(1, 11)...π_c(3)	2.82
			N...π_c(4)	4.63	H(1, 22)...π_c(4)	3.47
	C...B	6.95	C...π_c(3)	5.82	C(1, 1)...π_c(3)	3.75
			C...π_c(4)	5.21	C(1, 2)...π_c(4)	4.39
ImA[c]	N...B	4.32	N...π_c(2)	3.32	H(N)...π_c(2)	2.70
ImB[d]	N(C)...B	6.21	N...π_c(1)	4.54		
			N...π_c(4A)	5.13		
3MSTB	S...B	5.54	S...π_c(2)	3.89		
			S...π_c(4)	4.72		
3MSOTB[e]	O...B	4.50	O...π_c(2)	3.68	O...H(15A)	3.68
	S...B	5.74	O...π_c(1A)	4.29	O...H(14A)	3.23
	O...B(A)	6.50	O...π_c(1)	4.96	S...H(14A)	3.76
	S...B(A)	6.46			O...H(16)	2.59
					S...H(16)	3.57
2PhITB[f]	I...B	4.38	I...π_c(1)	3.49	I...C(16)	3.35
					I...C(15)	3.50
					I...C(11)	3.65
					I...C(14)	3.88
2ETB	N...B	4.23	N...π_c(1)	3.26	H(N1)...π_c(1)	2.24
			N...π_c(3)	3.16	H(N1)...π_c(3)	2.24
3ETB	N...B	5.11	N...π_c(2)	3.52	H(N)...π_c(2)	2.61
3ESTB[g]	S(B)...B(A)	5.18	S(B)...π_c(2)	3.94		
	S(B)...B	5.72	S(B)...π_c(4)	4.89		
			S(B)...π_c(1A)	5.15		

[a]Atom numbering as in original description (cf. Table 1). π_c(2) stands for centre of phenyl ring 2 etc.
[b]Cation disorder.
[c]Bifurcated hydrogen bond.
[d]A: $-\frac{1}{2} + x, \frac{1}{2} + y, z$. C: $-\frac{1}{2} + x, y, \frac{1}{2} - z$.
[e]A: $1 - x, \frac{1}{2} + y, 2 - z$.
[f]Free refinement.
[g]A: $\frac{1}{2} + x, \frac{1}{2} + y, \frac{1}{4}$. B: $x, 1 - y, \frac{1}{4}$.

Can. J. Chem. Downloaded from www.nrcresearchpress.com by 85.192.166.187 on 09/08/12
For personal use only.

immediately evident that the H-bonded cations are closer to the phenyl rings than the nonbonded ones. The difference in the cation–ring distances is reflected in the comparison of the N...π_c (π_c, ring centre) and N...B separations for the H-bonded and nonbonded cations (Table 3).

The N...π_c vs. N...B points in Fig. 3 correspond to situations (1, 3) in which the cation is contained in the wedge-shaped space between two phenyl rings of an anion that are related by a pseudo-S_4 axis passing through the B atom. The points for the cations containing two H(N) atoms, both engaged in N—H...π bonds, fall in a relatively small area with N...B separations below ~4.8 Å. This region is well separated from that for the cations which contain no H(N) and thus no N—H...π bonds, and in which the N atom is isolated from the associated phenyl rings by CH_3 or CH_2 groups. For cations containing a *single* H(N) atom one ring is engaged in a N—H...π bond while the other is nonbonded. For each such cation there are thus two points in the plot. The points corresponding to bonding interaction fall in the general 2H(N)—cation region, albeit at somewhat longer N...B distances, while the others have d(N...π_c) > 4

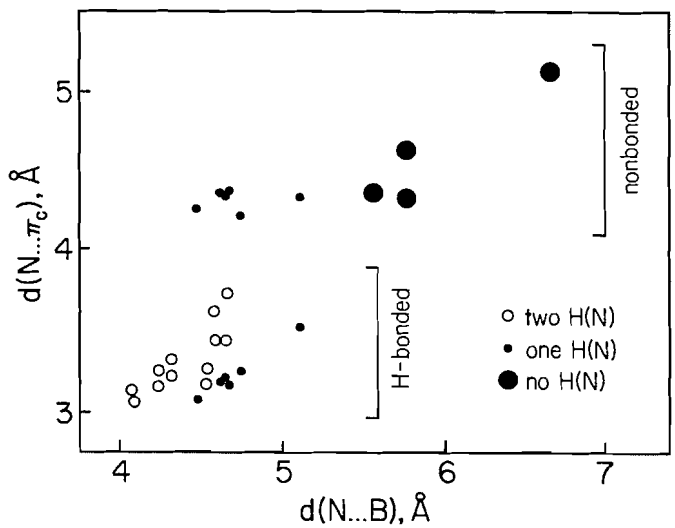

FIG. 3. Correlation of the shortest N...π_c and N...B distances in the tetraphenylborates of Table 3 and of refs. 1 and 3.

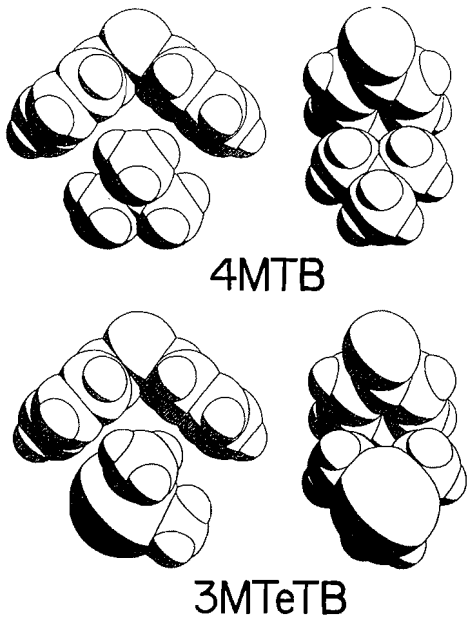

FIG. 4. Cation orientation in the isostructural pair 4MTB/3MTeTB. (Left) The proximal Me pair is oriented sideways in the wedge-shaped space formed by the nearest phenyl rings. Only one of the two cation orientations in 3MTeTB is shown; the other is obtained by reflection in the mirror plane through the B atom and perpendicular to the page. (Right) Side view with the front phenyl ring omitted for clarity. The four figures are to scale.

Å, consistent with the absence of H bonding. These $d(N...\pi_c)$ separations are greater than or equal to the sums of the van der Waals radii of the atoms in the CH_3 or CH_2 groups interposed between the N atom and the associated phenyl ring. There is no overlap between the H-bonded and the nonbonded region of the $N...\pi_c$ vs. N...B plot. The difference between the situations for which N—H...π bonding is claimed and those in which such bonding is absent is therefore clear-cut and significant, leaving no doubt that a difference in kind indeed exists between the two.

Effect of oriented lone electron pairs

In 4MTB the proximal pair of Me groups is oriented sideways in the wedge-shaped space formed by the two nearest phenyl groups (Figs. 1 and 2). In this cation orientation the Me hydrogens avoid the rings and the distance of the cation centroid from the anion is minimized. We now ask, how does this situation change when a Me group is replaced by an oriented lone pair?

The answer is provided by comparing 4MTB with Me_3TeL^+ in 3MTeTB. These two TBs are closely isostructural (*Cmcm*, $(a_N/a_{Te}):(b_N/b_{Te}):(c_N/c_{Te}) = 1.010:1.006:0.993$) and their structures are spatially completely determined by the anion packing. The cations are fully ordered in 4MTB but in 3MTeTB they are in a twofold orientational disorder across a mirror plane. Juxtaposition of $Me_2NMe_2^+$ and Me_2TeMeL^+ (Fig. 4) shows that the LP is oriented away from the phenyl rings, in preference to an orientation in which it would replace one of the (presumably bulkier) proximal Me groups in 4MTB. The reason for the orientational disorder and for 4MTB and 3MTeTB being isostructural is thus apparent.[8]

The reluctance of the LP to face a phenyl ring is demonstrated in a somewhat different way by the cation orientations in 3MSTB and 2PhITB (Figs. 5 and 6). In 3MSTB the unique LP on the S atom points *between* phenyl rings from three anions, one from each. The two LPs on the iodine atom in Ph_2I^+ are expected to be oriented tetrahedrally relative to the two I—C(α) bonds, i.e. with their axes in Figs. 5 and 6 in the page. Indeed, these directions are seen to skirt the nearest rings, in the plane bisecting the ring pair 1,1′ and clear of rings 2 and 3.

A similar avoidance of the phenyl rings by the oriented LP is displayed by Et_3S^+ in 3ESTB (Figs. 7 and 8). The shortest $S...\pi_c$ distances in 3MSTB and 3ESTB, 3.89 and 3.94 Å, are greater than the estimated van der Waals contact of 3.7 Å. In 3MSOTB the ring-avoiding tendency of the LPs on the O atom is more difficult to visualize, but it is undoubtedly present. The shortest $O...\pi_c$ distance, $O...\pi_c(2) = 3.68$ Å (Table 3, Figs. 5 and 6), is well above the value estimated for a van der Waals contact, 3.3 Å.

To facilitate recognition of the spatial relationships involving the LPs in the structures under discussion, Fig. 9 shows projections of the immediate cation environments that are designed to emphasize the orientation(s) of the pertinent LPs. The gap between the O atom and ring 2 (perpendicular to the S—O bond) in 3MSOTB is particularly noticeable: the $O...\pi_c(2) = 3.68$ Å separation is only ~0.2 Å smaller than the shortest $S...\pi_c$ distance in 3MSTB, 3.89 Å, a fact to consider in conjunction with the equality of the volumes V_1 per formula unit of 3MSOTB and 3MSTB (see under 3MSOTB below).

Individual crystal structures

None of the five title structures appears to have been reported previously.

3MSTB

Unlike in the corresponding Te compound 3MTeTB (6), the cations in 3MSTB are fully ordered. The two compounds are not isostructural: the 3MTeTB (*Cmcm*) structure is of a distorted NaCl type, while 3MSTB may be regarded as a highly distorted zincblende arrangement.

The anisotropic thermal parameters of the cation atoms are all reasonable and can be accounted for moderately well on the rigid-body-motion (RBM) model: $R(U_{ij}) = 13.2\%$, $R_w(U_{ij}) = 13.0\%$, $\text{rms}(U_{ij}) = 0.0060$, $\text{rms}[\text{esd}(U_{ij})] = 0.0047$ Å^2. The principal axis L_1 of libration coincides approximately with the quasi-C_3 axis of the cation, with L_2 and L_3 perpendicular to it. The mean librational amplitudes about these axes are 3.4°, 6.5°, and 7.5°, respectively. The bond lengths corrected on this model are S—C(1), 1.776(9) → 1.791 Å; S—C(2), 1.772(8) → 1.795 Å; S—C(3), 1.776(8) → 1.795 Å.

3ESTB

The cation in this structure is positionally disordered. The disorder was treated as a twofold orientational disorder across a mirror plane ||(001). Attempts to refine the structure as fully ordered in $Cmc2_1$ were not successful.

[8]It would be of interest to investigate why 3PhTeTB is not isostructural with 4PhAsTB and 4PhSbTB (Table 1). 3PhTeTB is triclinic, with a large unit cell ($V = 6483$ Å^3, $Z = 8$), while the other two are tetragonal ($V = 3600$ and 3628 Å^3, respectively, $Z = 4$). The structure of 3PhTeTB has not been determined; attempts to determine the structures of 4PhAsTB and 4PhSbTB have so far been unsuccessful (ref. 7; Knop et al., unpublished results). It appears likely that all three structures derive from a primitive CsCl-type tetragonal cell with $a \sim 11$, $c \sim 7$ Å, $Z = 1$ 4PhAsTB and 4PhSbTB, $a\sqrt{2} \times a\sqrt{2} \times 2c$; 3PhTeTB, $a\sqrt{2} \times a\sqrt{2} \times$ 4c.

Can. J. Chem. Downloaded from www.nrcresearchpress.com by 85.192.166.187 on 09/08/12
For personal use only.

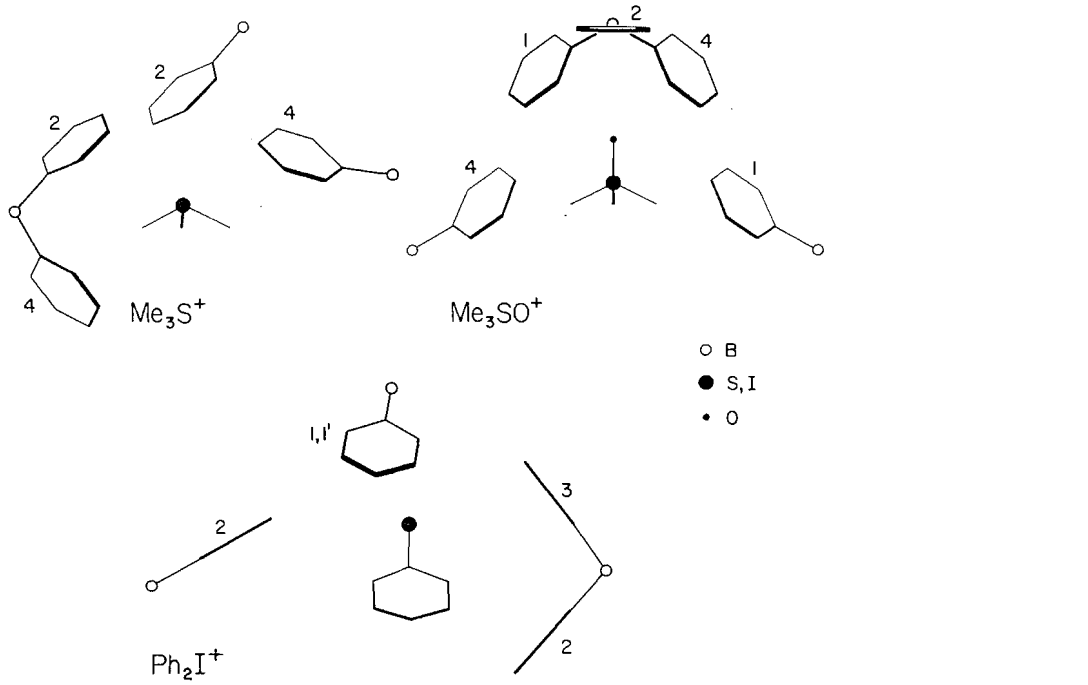

FIG. 5. Orientation of the presumed lone electron pair(s) on the S, O, and I atoms relative to the phenyl rings of the nearest anion(s) in 3MSTB, 3MSOTB, and 2PhITB, respectively. The crystallographic mirror plane passing through the I atom of 2PhITB and through the B atoms of the anions is in the page.

The anion packing is of the same type as in 4MTB and 3MTeTB (both *Cmcm*, cf. Fig. 3 of ref. 3), and in 3MSOTB ($P2_1/m \subset Cmcm$) if the unit cell is properly transformed (see under 3MSOTB). The ion packing in these structures is of a distorted NaCl type. The difference in the volumes per formula unit, V_1(3ESTB) − V_1(3MSTB), is 58.3 Å^3, i.e. 19.4 Å^3/CH_2, an unexceptionable value.

3MSOTB

When the $P2_1/m$ unit cell of Table 2 (a, b, c, β) is doubled to a B-centred cell (a', b', c', β') by the transformation $\boldsymbol{a'} = \boldsymbol{a} + \boldsymbol{c}$, $\boldsymbol{b'} = \boldsymbol{b}$, $\boldsymbol{c'} = -\boldsymbol{a} + \boldsymbol{c}$, a nearly orthogonal cell results, β' = 91.4°. On change of setting ($\boldsymbol{a''} = \boldsymbol{a'}$, $\boldsymbol{b''} = \boldsymbol{c'}$, $\boldsymbol{c''} = \boldsymbol{b}$) this cell can be directly related to an orthorhombic cell that is obtained from *Cmcm* by a dichromatic subgroup descent in symmetry (9, 10): $Cmcm \rightarrow Cm'c'm$ (no. 63/462), $P2_1/m \subset Cmcm$. The dimensions of the transformed cell are similar to those of other *Cmcm* TB structures:

Compound	a, Å	b, Å	c, Å	β, deg	V, Å^3
3MSOTB	11.489	15.379	12.790	91.4	2260
4MTB	11.565	15.635	12.868	90	2327
3MTeTB	11.445	15.539	12.955	90	2304
3ESTB	10.939	16.173	14.097	90	2494

i.e. these structures differ only in the way the cations are accommodated in the fixed anion arrangement.

The anion in 3MSOTB is of symmetry C_s, but geometrically it is close to a C_{2v} or even D_{2d} conformation (Table D). The geometry of the cation is discussed in some detail below.

Remarkably, the volume per formula unit V_1(3MSOTB) is the same as V_1(3MSTB), 565 Å^3. This would seem to indicate that in both 3MSTB and 3MSOTB it is the bulk of the methyl groups rather than the effective size of the S or O atom as such

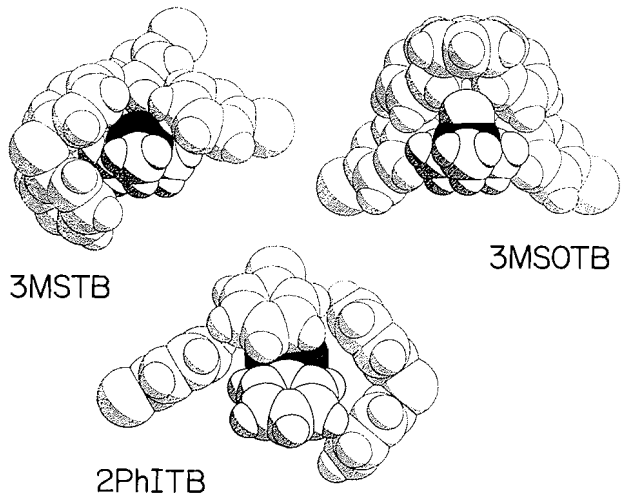

FIG. 6. Space-filling representation of the cation–anion pairs of Fig. 5. The S and I atoms are shown in black.

that governs the closeness of approach of the oriented cation to its associated phenyl rings. In other words, the observed S...π and O...π distances do not represent the "true" such distances but are controlled by external factors that make them too long, in such a way that both the S atom and the S—O group can be accommodated in the structure without the difference between the two manifesting itself in the unit volume. This would also apply to 3ESTB.

The thermal motion of the cation is consistent with RBM: $R(U_{ij}) = 5.9\%$, $R_w(U_{ij}) = 6.6\%$, rms(U_{ij}) = 0.0032, rms[esd(U_{ij})] = 0.0029. The largest-amplitude (mean, ~9°) libration is about an axis perpendicular to the S—O bond, i.e. to (010). The bond lengths corrected on the RBM model are S—O, 1.422(6) → 1.445 Å; S—C(1), 1.737(7) → 1.757 Å; S—C(2), 1.730(10) → 1.760 Å. The corrections to the bond angles are within 0.3°.

Can. J. Chem. Downloaded from www.nrcresearchpress.com by 85.192.166.187 on 09/08/12
For personal use only.

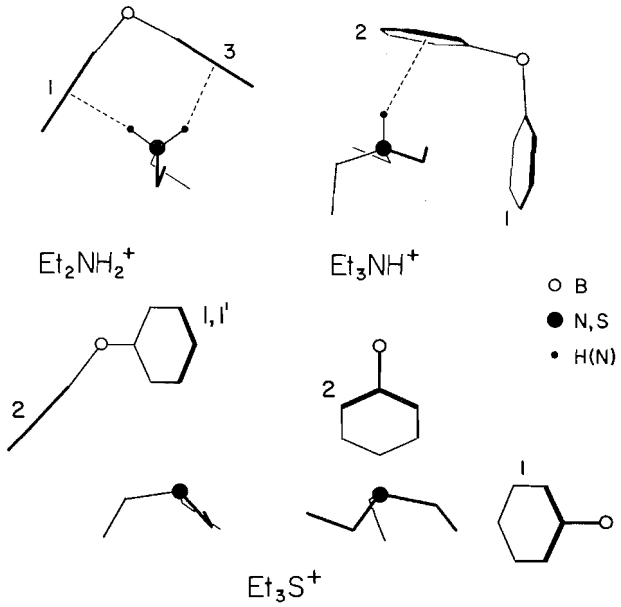

FIG. 7. Comparison of the hydrogen-bonding orientations in 2ETB and 3ETB with the "antibonding" orientation in 3ESTB. The N and S atoms are shown in black. The side view of the cation–anion pair in 3ESTB (left) shows the avoidance of the nearest phenyl rings by the lone pair on the S atom.

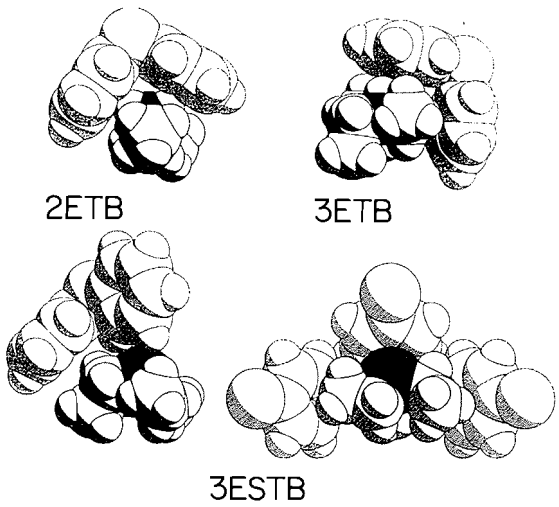

FIG. 8. Space-filling representation of the cation–anion pairs of Fig. 7. The N and S atoms are shown in black.

2PhITB

The free refinement of 2PhITB was characterized by large temperature factors, not only on the cation atoms, but also on some of the anion carbons (Table C; U_{33} of C(32) and C(33), ~0.26 Å^2). This is quite exceptional for a TB ion. The crystal did undergo slow deterioration during the data acquisition and an analytic decay correction had to be applied, but it is difficult to see how the gradual loss of crystal integrity would have affected the outcome of the structure determination *selectively*, by singling out a ring-carbon U_{ii} here and there in the structure. A more plausible explanation is to be sought in the particulars of the local structural arrangement.

Ring 3 of the anion is perpendicular to m||(010) and almost parallel to (001) (fig. 10). The largest U_{ii} are associated with atoms C(32) and C(33) and correspond to translations ||c, i.e. perpendicular to the ring. The nearest cation phenyl rings are 1′

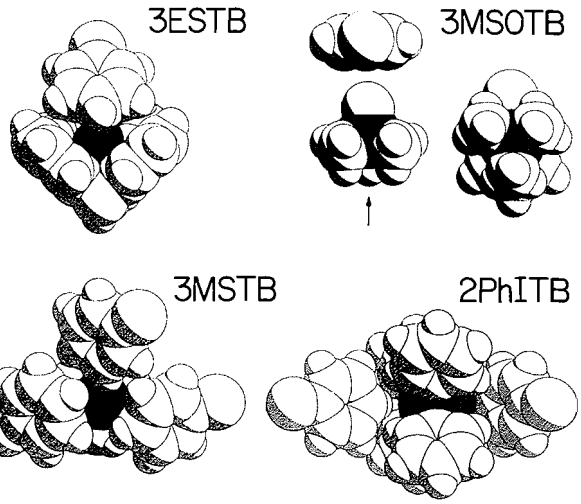

FIG. 9. Avoidance of the phenyl rings by the lone pairs on the S and I atoms. 3MSTB and 3ESTB: projection down the threefold cation axis, LP on the S atom pointing upward from the page. 3MSOTB: (left) the S—O bond is vertical in the page; (right) projection down the S—O bond (arrow), the O atom eclipsed by the S atom and points downward from the page. 2PhITB: projection down the bisector of the cation; the two LPs on the iodine point downward and sideways from the page. The S and I atoms are in black, the cations are in heavier line.

and 1″, and from Fig. 10 it is immediately evident that the C and H atoms closest to ring 3 are C(4)′ and H(4)′ of ring 1′. In fact, H(32)...H(4)′ ~ 1.76 Å is the shortest (static) H(anion)...H(cation) distance in the structure, well below the van der Waals contact of ~2.4 Å; all the other distances between the placed phenyl hydrogens are longer than 2.3 Å. The unusually short distance of 1.76 Å appears to be the direct cause of the large U_{33} values on C(32) and C(33). Seeking to minimize the repulsion between H(32) and H(4)′ (and between the symmetry counterparts of these hydrogens, Fig. 10), ring 3 undergoes a librational motion about its C(31)—C(34) axis, which is approximately parallel to a. Support for this assumed shutter mechanism (not necessarily cooperative though possibly correlated by a lattice mode) comes from TLS analysis of the thermal parameters of ring 3. While the motion of the ring is not too well accounted for on an RBM model (carbons only, $R(U_{ij})$ = 11.9%, $R_w(U_{ij})$ = 8.7%, rms(U_{ij}) = 0.0085 Å^2; carbons plus boron, $R(U_{ij})$ = 13.4%, $R_w(U_{ij})$ = 9.5%, rms(U_{ij}) = 0.0087, rms[esd(U_{ij})] = 0.0036 Å^2),[9] the directions of the principal libration axes $\boldsymbol{L}$ and the relative magnitudes of the mean librational amplitudes about these axes leave little doubt that the above explanation of the large U_{33} values is better than qualitatively valid: L_1||c, ~1°; L_2||b, ~3°; L_3||a, ~22° (cf. inset of Fig. 10). Since the proposed repulsion-minimizing mechanism involves the cation rings, the large U_{ii} values on the cation come as no surprise.

Several attempts to model the separate pivoting motions of the rings in terms of twofold positional disorder were only partially successful, indicating that the complexity of the dynamic disorder in this crystal resists a simple treatment. The best attempt to resolve the disorder, by splitting the C(32) and C(33) positions and those of all six cation carbons (Tables A–C) produced an overall improvement (Table 2) and significantly lowered the largest U_{ii} in both the anion and the cation.

The cation is of C_s symmetry, with an angle of 100.4°

[9]When U_{ij} = 0 for atoms in special positions are included, rms[esd(U_{ij})] = 0.0030 Å^2.

Can. J. Chem. Downloaded from www.nrcresearchpress.com by 85.192.166.187 on 09/08/12
For personal use only.

TABLE 4. Bond lengths (Å) and bond angles (deg) in the trimethylsulfonium cation[a]

Anion	6-31G*	I^- (11)	TB^-	$SnCl_6^{2-}$ (4)	$Cu_2Cl_6^{2-}$ (12)	an-1[b]
P.G.	C_{3v}[c]	C_s	C_1	C_3	C_1	C_s
S—C(1)	1.8074	1.805(6)	1.776(9)	1.769(7)	1.782(4)	1.804(14)
S—C(2)	1.8074	1.785(3)	1.772(8)	1.769(7)	1.796(4)	1.796(12)
S—C(3)	1.8074	1.785(3)	1.776(8)	1.769(7)	1.783(4)	1.796(12)
C(1)—S—C(2)	103.1	101.1(2)	102.6(4)	101.5(3)	101.9(2)	101.6(5)
C(1)—S—C(3)	103.1	101.1(2)	102.5(4)	101.5(3)	102.1(2)	101.6(5)
C(2)—S—C(3)	103.1	101.8(1)	103.9(4)	101.5(3)	101.3(2)	102.9(6)

	$CuCl_4^{2-}$ (12)					
Anion	1	2	3	4	an-2[d]	an-3[e]
P.G.	C_1	C_1	C_1	C_1	C_1	C_1
S—C(1)	1.780(6)	1.749(6)	1.781(6)	1.776(6)	1.774(2)	1.79(1)
S—C(2)	1.785(8)	1.775(8)	1.785(6)	1.789(6)	1.777(2)	1.79(1)
S—C(3)	1.773(6)	1.766(11)	1.779(6)	1.770(6)	1.781(2)	1.81(1)
C(1)—S—C(2)	101.2(4)	102.3(3)	101.3(3)	101.8(4)	102.0(1)	101.9(6)
C(1)—S—C(3)	101.1(3)	102.0(3)	101.7(3)	101.5(3)	101.5(1)	103.0(6)
C(2)—S—C(3)	100.8(3)	101.6(5)	101.1(3)	101.6(3)	101.3(1)	102.5(6)

[a]Not corrected for thermal motion. P.G., crystallographic point-group symmetry at the S atom. 6-31G*, *ab initio* calculation for the free ion. The atom numbering in this table may differ from that in the original description. In particular, a C atom in a mirror plane is C(1), and in cations of C_s symmetry, C(3) is the mirror image of C(2).

[b]$[MoBr_4(SMe_2)_2]^-$ (13).

[c]C—H, 1.0809 Å (2×); C—H′, 1.0807 Å; S—C—H, 107.7°; S—C—H′, 110.5° (2×); H—C—H, 109.4°; H—C—H′, 110.8° (2×). See Experimental and Table F.

[d]$[HO(O_2)PCH_2NH_2CH_2COO]^-$ (14).

[e]$[Cl_3W(\mu\text{-}Me_2S)_2(\mu\text{-}Cl)WCl_3]^-$.EtCN (15).

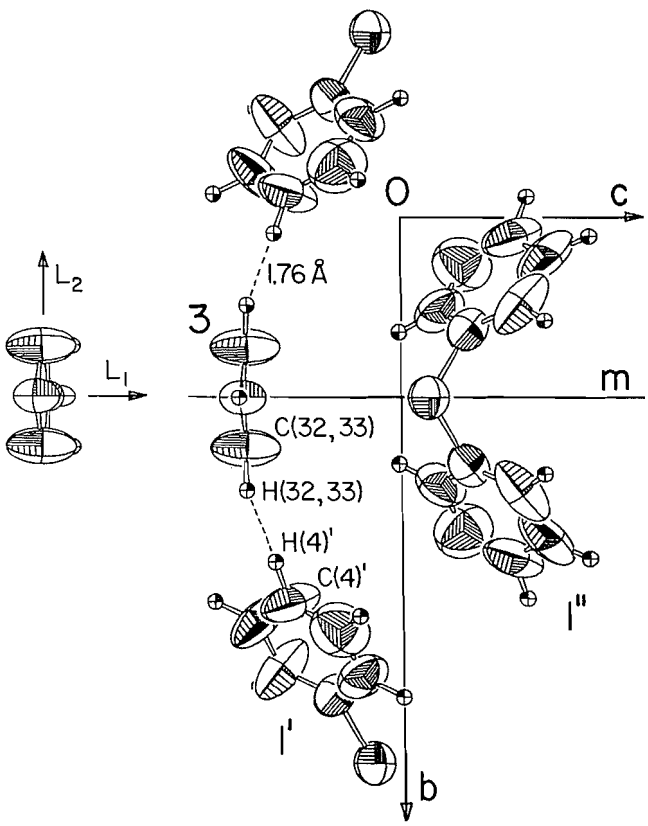

FIG. 10. Thermal motion in 2PhITB (projection on (100); 50% probability ellipsoids). Atoms C(32) and H(32) in ring 3 of the anion are eclipsed by atoms C(33) and H(33), respectively. The H(cation...H(anion) distance of 1.76 Å is between H(32) and H(4)′ (see text). Inset (left): projection of ring 3 down its principal libration axis L_3, as obtained from a TLS analysis.

between the best planes through the ring skeletons (mean deviation $\bar{\delta}$(C) from planarity, 0.023 Å). The iodine atom is 0.113 Å out of the ring planes. The cation geometry is compared with that of the handful of reported Ph_2I^+ cations below.

AzPpTB

The anions in this structure are arranged in an approximate fc packing, but the positions of the cation centroids cannot be described as corresponding to the NaCl or the zincblende arrangements without invoking severe, unnatural distortions.

The cation symmetry is very close to C_{3v} with the unique N—C axis ⊥(100) (Fig. A).[6] The mean deviations of the C and N atoms from the best planes corresponding to m_v of C_{3v} are 0.149, 0.150, and 0.142 Å for rings 1 (N — C(1, *n*) — C), 2 (N — C(2, *n*) — C), and 3 (N — C(3, *n*) — C), respectively (cf. Table A); the respective inter-ring angles 2/1, 3/1, and 3/2 are 120.0°, 120.3°, and 119.7°. The means of the endocyclic angles in rings 1–3 are 104.7(5)°, 104.7(5)°, and 104.8(10)°, respectively, with the corresponding sums of 523.5°, 523.5°, and 524.0° (ideal sum for a planar pentagon, 540°).

The thermal motion of the cation approximates only moderately well to the RBM model: $R(U_{ij}) = 12.5\%$, $R_w(U_{ij}) = 11.7\%$, $\text{rms}(U_{ij}) = 0.0059$, $\text{rms}[\text{esd}(U_{ij})] = 0.0028$ Å^2. Corrections to the bond lengths calculated on this model amount to ~0.02 Å; those to the bond angles are within 0.15°. The mean librational amplitudes about the principal axes of libration are 4.6°, 5.7°, and 6.6°.

Ion geometry

Title cations

The bond lengths and angles in the cations are listed in Table D. In Tables 4–7 the geometries of these less common cations

Can. J. Chem. Downloaded from www.nrcresearchpress.com by 85.192.166.187 on 09/08/12
For personal use only.

Can. J. Chem. Downloaded from www.nrcresearchpress.com by 85.192.166.187 on 09/08/12
For personal use only.

TABLE 5. Bond lengths (Å) and bond angles (deg) in the trimethylsulfoxonium cation[a]

Anion	6-31G*	$Cl^-·H_2O$ (16)	Br^- (17)	I^- (4)	I^- (17)
P.G.	C_{3v}[b]	C_3	C_s	C_s	C_s
S—O	1.4360	1.436(8)	1.433(2)	1.426(5)	1.436(3)
S—C(1)	1.7770	1.742(3)	1.732(4)	1.735(7)	1.749(3)
S—C(2)	1.7770	1.742(3)	1.743(2)	1.748(7)	1.747(3)
S—C(3)	1.7770	1.742(3)	1.743(2)	1.748(7)	1.747(3)
O—S—C(1)	112.46	112.6(1)	112.7(1)	112.1(3)	112.4(1)
O—S—C(2)	112.46	112.6(1)	112.5(1)	112.9(3)	112.6(1)
O—S—C(3)	112.46	112.6(1)	112.5(1)	112.9(3)	112.6(1)
C(1)—S—C(2)	106.33	106.2(1)	106.1(2)	106.2(3)	105.9(1)
C(1)—S—C(3)	106.33	106.2(1)	106.1(2)	106.2(3)	105.9(1)
C(2)—S—C(3)	106.33	106.2(1)	106.3(2)	106.1(3)	106.8(2)

Anion	SCN^- (18)	NO_3^- (19)	TB^-	$CdCl_3^-$ (20)	$CdBr_3^-$ (20)
P.G.	C_s	C_1	C_s	C_s	C_s
S—O	1.439(2)	1.436(3)	1.422(6)	1.439(2)	1.440(4)
S—C(1)	1.756(3)	1.752(4)	1.730(10)	1.756(3)	1.755(6)
S—C(2)	1.750(2)	1.736(5)	1.737(7)	1.747(2)	1.744(5)
S—C(3)	1.750(2)	1.749(4)	1.737(7)	1.747(2)	1.744(5)
O—S—C(1)	113.6(1)	112.3(2)	112.7(5)	112.9(1)	112.7(3)
O—S—C(2)	112.6(1)	112.0(2)	113.1(3)	112.8(1)	112.4(2)
O—S—C(3)	112.6(1)	111.6(2)	113.1(3)	112.8(1)	112.4(2)
C(1)—S—C(2)	105.6(1)	106.5(2)	105.8(5)	105.5(1)	105.7(2)
C(1)—S—C(3)	105.6(1)	106.8(2)	105.8(5)	105.5(1)	105.7(2)
C(2)—S—C(3)	105.9(1)	107.3(2)	105.7(5)	107.0(2)	107.8(3)

		CrO_4^{2-} (21)	
Anion	$SnCl_6^{2-}$ (4)	1	2
P.G.	C_s	C_1	C_1
S—O	1.435(5)	1.439(3)	1.438(3)
S—C(1)	1.750(9)	1.745(3)	1.747(4)
S—C(2)	1.746(5)	1.746(3)	1.745(3)
S—C(3)	1.746(5)	1.741(3)	1.742(2)
O—S—C(1)	113.0(4)	112.3(1)	112.9(1)
O—S—C(2)	112.0(2)	112.8(1)	113.2(1)
O—S—C(3)	112.0(2)	112.1(1)	112.5(1)
C(1)—S—C(2)	105.5(3)	106.7(1)	106.0(1)
C(1)—S—C(3)	105.5(3)	106.5(1)	105.9(1)
C(2)—S—C(3)	107.7(3)	106.0(1)	105.9(1)

[a]See footnote *a* of Table 4.
[b]C—H, 1.0822 Å (2×); C—H′, 1.0816 Å; S—C—H, 107.4°; S—C—H′, 110.3° (2×); H—C—H, 109.6°; H—C—H′, 111.0° (2×). See Experimental and Table F.

are also compared with the available literature reports[10] as well as (for Me_3S^+ and Me_3SO^+) with the RHF/6-31G* optimized geometries of the free cations (Table F).

The experimental means for Me_3S^+ (Table 4) are d(S—C) = 1.782(12) Å, C—S—C = 101.8(7)° (n = 33; uncorrected for thermal motion). Both values are within 2σ of the *ab initio* values. The geometry of the free Me_3S^+ configuration converged in the optimization from an initial C_3 to C_{3v} symmetry, with the six H atoms directed toward and the three H′ atoms away from the LP on the S atom.

The geometry of the Me_3SO^+ ion is like that of Me_3S^+ with the oxygen atom symmetrically added. The three H′ atoms are below the plane of the C atoms, away from the S atom (Figs. 6 and 9). The means for the uncorrected experimental data sets of

[10]The accuracy of some of the older structure determinations involving Me_3S^+ (24), Et_3S^+ (25), Me_3SO^+ (26, 27), and Ph_2I^+ (28) is limited and those determinations have not been considered here.

TABLE 6. Bond lengths (Å) and bond angles (deg) in the triethylsulfonium cation[a]

Anion	I^- (4)	TB^-	$SnCl_6^{2-}$ (4)
P.G.	C_1	C_s[b]	C_1
S—C(11)	1.792(9)	1.820(20)	1.801(4)
S—C(21)	1.815(7)	1.755(14)	1.795(3)
S—C(31)	1.818(8)	1.705(14)	1.798(4)
C(11)—C(12)	1.453(12)	1.54(2)	1.491(7)
C(21)—C(22)	1.491(10)	1.55(3)	1.494(6)
C(31)—C(32)	1.487(10)	1.53(3)	1.500(5)
C(11)—S—C(21)	102.3(3)	105.4(7)	103.3(2)
C(11)—S—C(31)	100.4(4)	102.2(7)	104.1(2)
C(21)—S—C(31)	100.7(4)	115.0(6)	103.3(2)
S—C(11)—C(12)	118.5(6)	124.3(11)	117.1(3)
S—C(21)—C(22)	110.5(5)	95.0(11)	110.7(3)
S—C(31)—C(32)	110.4(6)	120.8(12)	109.8(3)

[a]See footnote *a* of Table 4.
[b]Unresolved disorder of ethyl groups.

TABLE 7. Bond lengths (Å) and bond angles (deg) in the cations of $(Ph_2I)^+X^-$ compounds[a]

X	P.G.	d(I—C)	C—I—C	C(2)—C(1)—C(6)	R2/R1[b]
TB	C_s	2.069(11)	95.1(4)	120.4(12)	100.4
NO_3 (22)	C_1	2.114(7)	92.0(4)	122.4(9)	98.0[c]
		2.114(9)		122.5(9)	
Cl[d] (23)	C_1	2.078(6)	92.6(3)	—	98.9[c]
		2.096(7)			
Br[d] (23)	C_1	2.071(10)	91.8(6)	—	84.5[e]
		2.095(13)			
I[d] (23)	C_1	2.095(9)	93.2(5)	—	93.5[c]
		2.103(9)			

[a]Not corrected for thermal motion. P.G., site symmetry at the I atom.
[b]Angle between best planes through the carbon skeletons of the phenyl rings.
[c]R2/R1 angle calculated from the published atom coordinates.
[d]Centrosymmetric $Ph_2I—(X)_2—IPh_2$ μ_2-dimers. Phenyl rings constrained to regular hexagons.

Table 5 are d(S—O) = 1.435(6) Å (n = 12), d(S—C) = 1.745(6) Å, O—S—C = 112.6(4)°, C—S—C = 106.2(6)° (n = 36). These means compare well with the calculated values. The optimization process for Me_3SO^+ likewise proceeded from an initial C_3 symmetry to C_{3v}

The mean S—C bond length in Me_3SO^+, 1.745(6) Å, is shorter than in Me_3S^+, 1.782(12) Å. Statistical tests (t test and analysis of variance) show that this difference is significant at the 99.5% level: t = 15.7, $t_{0.005,60}$ = 2.92; F = 245, $F_{0.005,1,60}$ = 8.49). Similarly, the mean C—S—C angle in Me_3S^+, 101.8(7)°, is smaller than that in Me_3SO^+, 106.2(6)°, a highly significant difference (t = −29.2, $t_{0.005,60}$ = 2.92; F = 854, $F_{0.005,1,60}$ = 8.49). These differences are also present in the 6-31G* values of d(S—C) and C—S—C as well as in the electron densities at the critical points in the S—C bonds, 1.296 e/Å^3 for Me_3S^+ and 1.441 e/Å^3 for Me_3SO^+, the lower electron density corresponding to the longer bond. The reduction of the C—S—C angle in Me_3S^+ relative to Me_3SO^+ can be regarded as reflecting a greater lateral repulsion exerted by the LP on the S atom compared to that of the S—O bond, in accordance with the tenets of the VSEPR model.

The geometry of the Et_3S^+ ion in 3ESTB is not as well defined as that of Me_3S^+ because of the orientational disorder. However, the mean S—C bond length for the cations in Table 6, 1.789(35) Å, is indistinguishable from the corresponding mean for Me_3S, 1.782(12) Å; with 3ESTB excluded, the mean bond length is 1.803(10) Å, i.e. still well within the 2σ statistics.

Structural information on the diphenyliodonium ion, Ph_2I^+, is far from abundant (Table 7). The means for the available values are $\bar{d}$(I—C) = 2.093(16) Å, ⟨C—S—C⟩ = 93.0(12)°, and the mean angle ⟨C(2)—C(1)—C(6)⟩ at the α carbon is 121.8(10)°, i.e. essentially undistorted (cf. refs. 29–32). The dihedral angles R2/R1 between the ring planes range from ~85° to ~100°; they undoubtedly are sensitive to packing and secondary binding forces. The geometry of the I atom is thus tetrahedral.[11]

Our search of the Cambridge Crystallographic Data file failed to uncover a previous structure determination involving the 1-azoniapropellane cation, hence no comparison can be made.

traphenylborate anion

The geometry of the anion in the five title compounds is not exceptional. These structures contain five distinct TB ions, corresponding to 16 distinct phenyl groups. Although one of the anions is of symmetry C_{2v}, two of symmetry C_s and two of symmetry C_1, the actual anion geometry is always recognizably close to D_{2d}. The overall means of the B—C bond lengths, the C—B—C valence angles α and α′, and the endocyclic C(2)—C(1)—C(6) angles at the α carbon are indistinguishable from the corresponding means reported for 20 TB anions in ref. 1, and statistically more homogeneous:[12]

Parameter	Value	
	This work	Ref. 1
$\bar{d}$(B—C), Å	1.644(2)	1.646(10)
α	104.2(2)°	104.4(17)°
α′	112.2(2)°	112.1(17)°
⟨C(2)—C(1)—C(6)⟩	114.8(2)°	115.0(9)°

The planarity of the 16 phenyl rings is satisfactory (Table E). The overall mean deviation of the C atoms from the best planes through the ring skeleton is 0.006(3) Å (0.007(4) Å in ref. 1). The corresponding deviations of the B atom from the ring plane are listed in Table E, which also contains the interplane angles.

Conclusions

The organization of the crystal structures of the tetraphenylborates of small organic ammonium cations is dominated by the anion packing. The cations are accommodated in the wedge-shaped spaces formed by the phenyl rings of the nearest anion neighbour or sometimes by rings from two or more anion neighbours. The orientation of the cation in this space depends on whether or not the cation contains one or more *N*-hydrogen atoms. When an H(N) atom is present, it will engage in a H-bond to the nearest phenyl group. The resulting N—H(N)...π bond(s) can be of a variety of types (cf. ref. 1). When other contenders for H-bonds are simultaneously present in the structure (e.g. a solvent molecule, Cl^-), the cation may engage in H-bonds to these as well as to phenyl groups.

When the H(N) atom(s) is replaced by an alkyl or an alkyl-like group, the cation will orient itself in such a way that the repulsion between the alkyl and the phenyl groups as well as the

n $(C_5H_5N)_2I^+$ (33) donation of the LP on the N atom to the iodine
this ion to be centrosymmetric.

[12]The number in parentheses is the standard deviation for the sample population; it does not include the esd's from the individual structure determinations.

Can. J. Chem. Downloaded from www.nrcresearchpress.com by 85.192.166.187 on 09/08/12
For personal use only.

cation–anion distance are minimized. When the cation nitrogen is replaced by an atom X containing an oriented LP (e.g. S, Te, I) but with no H(X) atom attached to it, the LP will tend to avoid the phenyl groups. The strength of the ring-avoiding tendency decreases in the order LP > [CH_3, CH_2] > H(N), i.e. from a positive ring-avoiding tendency to a positive H-bonding tendency.

As a result of this and the preceeding investigations in this series (1, 3) the case for the existence of N—H(N)...π bonding as a positive H-bonding tendency to the delocalized π systems of the phenyl groups can be regarded as established.

Experimental

Preparation

The desired TB was precipitated from an aqueous or aqueous-alcoholic solution of the requisite cation halide by adding aqueous solution on $NaBPh_4$ at room temperature. The precipitate was washed with water and redissolved in acetone. Water was then added dropwise until reprecipitation occurred. The solution was restored by adding a minimum amount of acetone and set aside for recrystallization by slow evaporation at room temperature.

Structure determination

An Enraf-Nonius CAD-4 four-circle diffractometer and a Rigaku AFC5R diffractometer were used in the data acquisition (cf. Table 2). The intensities ($\omega/2\theta$) were reduced and corrected for Lorentz and polarization effects by routine procedures (34, 35). Low-angle reflections were examined for possible second-order intensity leakage from their respective strong $2h2k2l$ homologues. Empirical absorption corrections (8) were applied; extinction corrections were obtained where they seemed indicated. Scattering factors for neutral atoms and anomalous dispersion corrections were taken from ref. 36.

The structures were solved by the direct method. The function minimized in the refinement was $\Sigma w(|F_o| - |F_c|)^2$. Unit weights were used throughout. The temperature factor is defined as $\exp[-2\pi^2(U_{11}h^2a^{*2} + U_{22}k^2b^{*2} + U_{33}l^2c^{*2} + 2U_{23}klb^*c^* + 2U_{13}hla^*c^* + 2U_{12}hka^*b^*)]$. The hydrogen atoms were placed geometrically (C—H, 1.08 Å) and not refined ($U_{iso}(H) = 1.2B_{eq}(C)$ of the attached C atom). The computer programs of refs. 8, 35, and 37–39 were used in the structure solving, refinement, and presentation.

It must again be emphasized that in general organic cation TB crystals are weak and fickle scatterers (3). Significant reflections were seldom observed above a $(\sin\theta)/\lambda$ limit of 0.48 $Å^{-1}$ ($\theta \simeq 20°$ for Mo radiation). Since in this laboratory X-ray data collection routinely extends to a limit of 0.55 $Å^{-1}$ ($\theta = 23°$), the ratio of observed reflections to total measured unique reflections never exceeded 50%. When attempts were made to collect the data at lower temperatures they produced little if any improvement in these ratios.

Tables of structure factors are available from the Senior Editor (Tables G–L).

Systematic absences. *Cmcm* (3ESTB): hkl, $h + k$ odd; $0kl$, k odd; $h0l$, h, l odd; $hk0$, $h + k$ odd; $h00$, h odd; $0k0$, k odd; $00l$, l odd. *Pnma* (2PhITB): $0kl$, $k + l$ odd; $hk0$, h odd; $h00$, h odd; $0k0$, k odd; $00l$, l odd. $P2_1/n$ (3MSTB, AzPpTB): $h0l$, $h + l$ odd; $0k0$, k odd; $h00$, h odd; $0k0$, k odd; $00l$, l odd. $P2_1/m$ (3MSOTB): $0k0$, k odd.

Other comments. The 2PhITB crystal showed signs of progressive deterioration during the intensity collection. An analytic decay correction was therefore applied.

Ab initio *calculations*

The equilibrium molecular geometries of the Me_3S^+ and Me_3SO^+ cations were optimized, at the RHF/6-31G* level, using GAUSSIAN 86 (40) supplemented by AIMPAC (41). The optimizations were started in configurations of C_3 symmetry but in both cases converged to C_{3v} conformations. As a check, the two geometries were also optimized, independently, with C_{3v} as the imposed symmetry, but the differences between the C_3 and the $C_3 \rightarrow C_{3v}$ calculations were very minor.[13] The results of the C_{3v} optimizations are listed in Table F and partially also in Tables 4 and 5.

The present result for Me_3S^+ supersedes that of the earlier (Table 7 of ref. 4) calculation. The small discrepancies between the latter and Table F are attributable to the use of an earlier version of GAUSSIAN implemented on a different computer.

[13] Me_3S^+: $E(C_{3v}) = -516.11091$ au $\sim E(C_3 \rightarrow C_{3v})$. Me_3SO^+: $E(C_{3v}) = -590.90229$ au $\sim E(C_3 \rightarrow C_{3v})$.

Acknowledgments

We thank S.C. Choi for performing the *ab initio* calculations. This investigation was supported by grants from the Natural Sciences and Engineering Research Council of Canada to O.K. and T.S.C.

1. P.K. Bakshi, A. Linden, B.R. Vincent, S.P. Roe, D. Adhikesavalu, T.S. Cameron, and O. Knop. Can. J. Chem. **72**, 1273 (1994).
2. A. Linden, K.N. Robertson, O. Knop, and T.S. Cameron. Abstract 505. Book of abstracts. 3rd Chemical Congress of North America, Toronto, ON, June 5–10, 1988.
3. O. Knop, T.S. Cameron, P.K. Bakshi, W. Kwiatkowski, S.C. Choi, and D. Adhikesavalu. Can. J. Chem. **71**, 1495 (1993).
4. O. Knop, A. Linden, B.R. Vincent, S.C. Choi, T.S. Cameron, and R.J. Boyd. Can. J. Chem. **67**, 1984 (1989).
5. K. Hoffmann and E. Weiss. J. Organomet. Chem. **67**, 221 (1974).
6. R.F. Ziolo and J.M. Troup. Inorg. Chem. **18**, 2271 (1979).
7. G. Ferguson, C. Glidewell, D. Lloyd, and S. Metcalfe. J. Chem. Soc. Perkin Trans. II, 731 (1988).
8. N. Walker and D. Stuart. Acta Crystallogr. **A39**, 158 (1983).
9. V.A. Koptsik. Shubnikovskie gruppy. Moscow University Press, Moscow. 1966.
10. C.J. Bradley and A.P. Cracknell. The mathematical theory of symmetry in solids. Representation theory for point groups and space groups. Clarendon Press, Oxford. 1972.
11. M. Jannin, R. Puget, C. de Brauer, and R. Perret. Acta Crystallogr. **C47**, 982 (1991).
12. M.R. Bond and R.D. Willett. Acta Crystallogr. **C48**, 1189 (1992).
13. C. Schumacher, R.E. Schmidt, and K. Dehnicke. Z. Anorg. Allg. Chem. **520**, 25 (1985).
14. P.H. Smith, F.E. Hahn, A. Hugi, and K.N. Raymond. Inorg. Chem. **28**, 2052 (1989).
15. P.M. Boorman, X. Gao, G.K.W. Freeman, and J.F. Fait. J. Chem. Soc. Dalton, 115 (1991).
16. M. Jannin, R. Puget, C. de Brauer, and R. Perret. Acta Crystallogr. **C47**, 2228 (1991).
17. M. Jannin, R. Puget, C. de Brauer, and R. Perret. Acta Crystallogr. **C47**, 1687 (1991).
18. R. Puget, M. Jannin, R. Perret, and C. de Brauer. Acta Crystallogr. **C47**, 2232 (1991).
19. M. Jannin, R. Puget, C. de Brauer, and R. Perret. Acta Crystallogr. **C47**, 2229 (1991).
20. R. Puget, M. Jannin, C. de Brauer, and R. Perret. Acta Crystallogr. **C47**, 1803 (1991).
21. C. de Brauer, M. Jannin, R. Puget, and R. Perret. Acta Crystallogr. **C47**, 2231 (1991).
22. W.B. Wright and E.A. Meyers. Cryst. Str. Commun. **1**, 95 (1972).
23. N.W. Alcock and R.M. Countryman. J. Chem. Soc. Dalton, 217 (1977).
24. F. Mussgnug. Naturwiss. **29**, 256 (1941).
25. F. Mussgnug. Naturwiss. **28**, 366 (1940).
26. C.L. Coulter, P.K. Gantzel, and J.D. McCullough. Acta Cr[illegible] logr. **16**, 676 (1963).
27. I.C. Zimmermann, M. Barlow, and J.D. McCullough. Ac[illegible] tallogr. **16**, 883 (1963).
28. Yu. T. Struchkov and T.L. Khotsyanova. Acta Cryst[illegible] 1140 (1960).
29. A. Domenicano, A. Vaciago, and C.A. Coulson. Act[illegible] **B31**, 221 (1975).

Can. J. Chem. Downloaded from www.nrcresearchpress.com by 85.192.166.187 on 09/08/12
For personal use only.

30. A. Domenican, A. Vaciago, and C.A. Coulson. Acta Crystallogr. **B31**, 1630 (1975).
31. A. Domenicano, P. Mazzeo, and A. Vaciago. Tetrahedron Lett. 1029 (1976).
32. A. Domenicano, P. Murray-Rust, and A. Vaciago. Acta Crystallogr. **B39**, 457 (1983).
33. O. Hassel and H. Hope. Acta Chem. Scand. **15**, 407 (1961).
34. T.S. Cameron and R.E. Cordes. Acta Crystallogr. **B35**, 749 (1979).
35. TEXSAN-TEXRAY. Single crystal structure analysis package. Molecular Structure Corporation, The Woodlands, TX. 1989.
36. International tables for X-ray crystallography. Vol. IV. The Kynoch Press, Birmingham, U.K. 1974.
37. G.M. Sheldrick. SHELX-76. Program for crystal structure determination. University of Cambridge, Cambridge, U.K. 1976.
38. G.M. Sheldrick. SHELXS-86. In Crystallographic computing. Edited by G.M. Sheldrick, C. Kruger, and R. Goddard. Oxford University Press. 1985.
39. J.R. Carruthers and D.L. Watkins. CRYSTALS, issue 8. Chemical Crystallography Laboratory, Oxford, U.K. 1989.
40. M.J. Frisch, J.S. Binkley, H.B. Schlegel, K. Raghavachari, C.F. Melius, R.L. Martin, J.J.P. Stewart, F.W. Bobrowicz, C.M. Rohlfing, L.R. Kahn, D.J. Defrees, R. Seeger, R.A. Whiteside, D.J. Fox, E.M. Fleuder, and J.A. Pople. GAUSSIAN 86. Carnegie–Mellon Quantum Chemistry Publishing Unit, Pittsburgh PA. 1984.
41. R.W.F. Bader. AIMPAC series of programs. Department of Chemistry, McMaster University, Hamilton, ON. 1983.

Can. J. Chem. Downloaded from www.nrcresearchpress.com by 85.192.166.187 on 09/08/12
For personal use only.

ADDITIONS AND CORRECTIONS/AJOUTS ET CORRECTIONS

Alessandro Granata and Arthur S. Perlin. Formation of isomeric monohalo-*n*-alkanoic acids in the reactions of γ- and δ-*n*-alkanolactones with hydrogen halides. Can. J. Chem. **71**, 864 (1993).

On page 867, the first line of the caption to Fig. 1 should read "the mixture of monobromononanoic acids" rather than "the mixture of monobromooctanoic acids."

Can. J. Chem. Downloaded from www.nrcresearchpress.com by 85.192.166.187 on 09/08/12
For personal use only.

Face-selective Diels–Alder reactions of (1*R*,5*R*)-3-formyl-6,6-dimethylbicyclo[3.1.1]hept-3-en-2-one

HSING-JANG LIU, YANHONG LI,[1] AND ERIC N.C. BROWNE[2]

Department of Chemistry, The University of Alberta, Edmonton, AB T6G 2G2, Canada

Received March 15, 1994

HSING-JANG LIU, YANHONG LI, and ERIC N.C. BROWNE. Can. J. Chem. **72**, 1883 (1994).

The stereofacially differentiated enone aldehyde **11** was chosen to study the effects of steric and electronic influence on the Diels–Alder reaction. Under Lewis acid catalysis, **11** adds to dienes at low temperatures at a reasonable rate. Yields of desired chiral adducts are good to high with zinc chloride and boron trifluoride etherate catalysis. In all cases only products of addition to the *Re* face of general type **27** were observed. The regiochemistry of the adducts is exclusively that predicted by the *ortho* and *para* rules. The stereochemistry shows a very high selectivity in favour of aldehyde-*endo* transition state products. Unusual by-products were also obtained in some examples and mechanisms of these unexpected reactions are discussed.

HSING-JANG LIU, YANHONG LI et ERIC N.C. BROWNE. Can. J. Chem. **72**, 1883 (1994).

On a choisi le cétoaldéhyde insaturé **11**, différencié stéréofacialement, pour étudier les effets stériques de l'influence électronique sur la réaction de Diels–Alder. En présence d'un catalyseur de Lewis et à basse température, le composé **11** s'additionne sur les dièenes avec un rendement raisonnable. Les rendements en adduits chiraux désirés varient de bon à élevé avec le chlorure de zinc et l'éthérate trifluorure de bore comme catalyseurs. Dans tous les cas, on n'observe que les produits d'addition sur la face *Re* du type général **27**. La régiochimie des adduits est exclusivement celle prédite par les règles *ortho* et *para*. La stéréochimie montre une très grande sélectivité en faveur d'un aldéhyde-*endo* dans l'état de transition. On a également obtenu des produits secondaires inhabituels dans certains cas et on discute des mécanismes de ces réactions inattendues.

[Traduit par la rédaction]

Introduction

In recent years we have reported on a series of Diels–Alder reactions of 4,4-dimethyl-2-cyclohexenones **1** (1), **2** (1, 2), **3** (1, 3, 4), **4** (5) and several closely related cross-conjugated cyclic unsaturated carbonyl compounds **5** (6), **6** (7), **7** (8, 9), **8** (10, 11), **9** (12), and **10** (12). These studies showed that structural features in the dienophile and the nature of the Lewis acid strongly influence the regio- and stereoselectivity of the reaction. The use of various directing components such as cross-conjugated carbalkoxy groups or additional double bonds has provided a probe into the effect of structural, steric, and electronic features on the course of Diels–Alder additions by the study of their influence on the relative stabilities of the various possible orientational transition states. We also explored diastereofacial selectivity of some of these dienophiles (**8–10**). Additions to **8** and **9** ($n = 1, 2$) take place preferentially from the less hindered face while additions to **9** ($n = 0$) and **10** are from the more hindered face.

One of the most interesting features apparent in comparing this assemblage of dienophiles is the effect of the carbonyl directing substituents on the *exo* or *endo* orientation of addition. Dienophiles **4–8** exhibit preferential additions with diene orientation *endo* to the exocyclic ester directing substituent. Compounds **3** and **10** are preferentially keto-*endo* directed while the few examples we have reported to date for **9** ($n = 0$) exhibit reversal of selectivity depending on the diene used. Although the unusual behavior of **9** ($n = 0$) remains to be thoroughly explored and reported, the contrasting *exo–endo* orientation differences between the other groups of dienophiles raise important questions. What is the relative directing influence of the possible exocyclic substituents (alkyl, ketone, ester, aldehyde, halogen, nitrile, heteroatom, etc.)? Is the contribution of additional conjugation to the endocyclic carbonyl (such as the second cyclic double bond of **3** and **10**) the principal directing influence, overriding any contribution from the exocyclic directing substituent (in the same qualitative way that *ortho*-rule addition tyically supersedes *para*-rule addition of appropriately substituted dienes)? From a theoretical perspective, could secondary orbital effects really be the sole mechanism through which these orientational effects are manifested? From a practical viewpoint, can semi-empirical or theoretically based rules be identified to predict products in various novel systems in such a way as to allow strategic placement of directing influences into synthetic plans?

As a lead-in to the wider examination of Diels–Alder reactivity that these questions demand, and to improve on the stereoselectivity and yields of additions to **8**, we have turned our attention to enone aldehyde **11**. The formyl group is more strongly electron withdrawing and sterically smaller than the corresponding ester group in **8**. On these accounts alone the aldehyde-*endo* transition state **11***a* should be more strongly favoured over the keto-*endo* transition state **11***b* than the preference (11) for the corresponding ester-*endo* transition state of **8***a* over its keto-*endo* transition state **8***b*. The study also offers an interesting opportunity for comparison of the secondary oribital effect between the ester and aldehyde substituents. The elaboration[3] or removal[4] of the formyl group from the adducts can be addressed with a wider variety of methods than the carbalkoxy group so that **11** might prove to be even more synthetically useful than **8**.[5] The results of our investigations of Diels–Alder reactions of **11** are presented.

Results and discussion

*1. Preparation of enone aldehyde **11***

Enone aldehyde **11** was synthesized in high yield from (−)-

[1]Taken in part from the M.Sc. thesis of Y. Li, the University of Alberta, 1993.

[2]Present address: Wyeth–Ayerst Research Inc., 1025 Laurentian Blvd., St. Laurent, QC H4R 1J6, Canada.

[3]For selected examples see refs. 13–17.

[4]For selected example see refs. 18–21.

[5]The full synthetic application of **8** and **11** to natural product targets will be reported in separate publications.

Can. J. Chem. Downloaded from www.nrcresearchpress.com by 85.192.166.187 on 09/08/12
For personal use only.

Can. J. Chem. Downloaded from www.nrcresearchpress.com by 85.192.166.187 on 09/08/12
For personal use only.

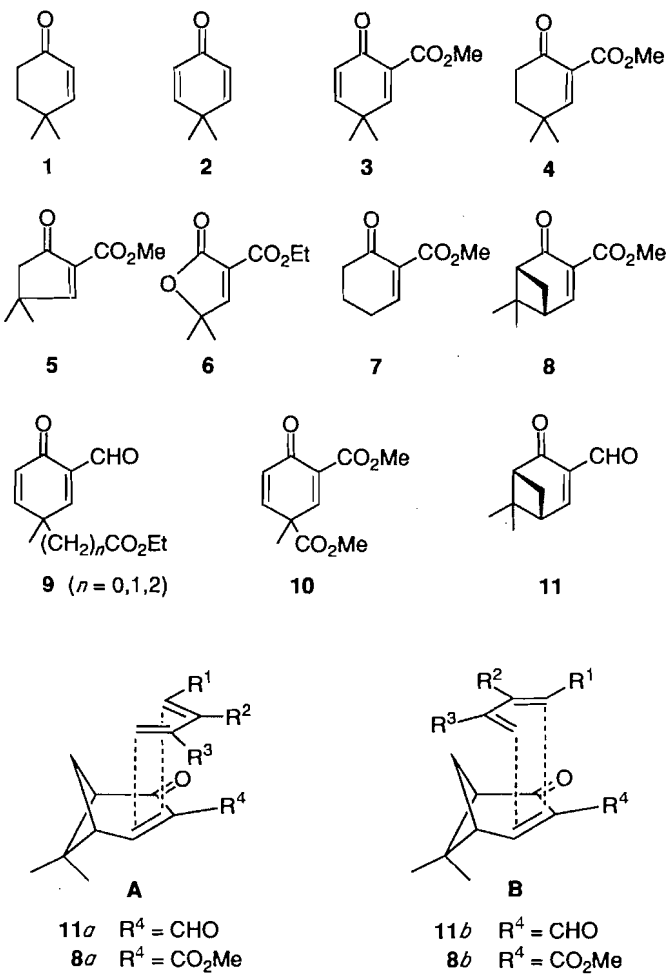

β-pinene **12**[6] in three steps (Scheme 1). We have already described the ozonolysis of β-pinene and its hazards[7] in reporting on the preparation of enone ester **8**. In the present study a modified procedure for ozonolysis of (−)-β-pinene in dichloromethane–methanol at higher concentration followed by reductive work-up with dimethyl sulfide gave (+)-nopinone (**13**) in an improved yield of 93%. Its spectral data were identical to those previously reported (11). We repeated the preparation several times and once, instead of chromatography, carried out purification by vacuum distillation without incident. The problems reported by others (22, 23) might be due to incomplete reduction of the ozonolysis products or improper handling of the work-up procedure. The following are some important precautions to consider in conducting this reaction: (*i*) A persistent blue or purple colour of the reaction solution can not serve as an indication of completion of the ozonolysis. We found that even when the purple colour remained, there was still considerable starting material remaining in the reaction mixture. Typically, only about 78% yield of product was formed (11). On the other hand, when tlc analysis showed the complete consumption of starting material, ketone **13** was obtained in 93% isolated yield. (*ii*) After the ozonolysis is complete, oxygen gas must be blown through the reaction mixture (5–10 min) to remove the excess of ozone. (*iii*) The reducing agent (dimethyl sulfide) must be added at low temperature (−78°C) and then the reaction mixture should be allowed to warm slowly over 2–4 h to room temperature. (*iv*) The amount of the reducing agent should be in excess and the reduction time should be suficiently long (overnight) to ensure the completion of the reaction.

The formyl group was introduced by the method of Watt and co-workers (24), treating **13** with sodium hydride and ethyl formate. The reaction was catalyzed by a few drops of ethanol and proceeded smoothly to give keto aldehyde **14** in 93% yield. Spectral data indicated that compound **14** was a mixture (7:2.5:1) of its tautomer and epimers. The ratio of the three components varied with the purity of the compound or with different solvents or temperatures. Dehydrogenation of **14** was carried out in two steps using the approach of Liotta et al. (25): phenylselenenylation followed by oxidative elimination of the resulting selenide to give enone aldehyde **11** in about 70% yield.

The desired product was always accompanied by epoxide **15**, presumably as a result of overoxidation. The epoxidation was very sensitive to the pH of the reaction media. When the oxidation was carried out under neutral conditions, the amount of epoxide increased rapidly and even became the major product (**11**:**15** = 1:1.2). When the selenide solution was oxidized immediately after washing with 1 N hydrochloric acid, only a small amount of epoxide was formed (**11**:**15** = 8:1). Compounds **11** and **15** were not separable by either column chromatography or bulb-to-bulb distillation. Pure epoxide **15** was recovered after the subsequent Diels–Alder reaction in which enone aldehyde **11** was totally consumed.

The mechanism for the generation of epoxide **15** remains unclear. The accepted mechanism for epoxidation of an α,β-unsaturated ketone or aldehyde by hydrogen peroxide, by 1,4-addition of hydroperoxide followed by ring closure with elimination of hydroxide (26–28), does not fit very well in this case. An alkaline medium would be required to deprotonate hydrogen peroxide and generate the hydroperoxide. In this case, there was no base present. If any hydroperoxide was present, it must have come from equilibrium dissociation of hydrogen peroxide (29). Such a process would not be sufficient to induce epoxidation of a normal α,β-unsaturated ketone or aldehyde. But in compound **11** the double bond is doubly activated and thus more highly reactive to Michael addition. Under neutral conditions, once the epoxidation is initiated by a trace of hydroperoxide, the epoxidation could be catalyzed by the hydroxide generated in the ring closure reaction. This process could lead to epoxide **15** as the major product. When the reaction is carried out under acidic conditions the hydroxide would be neutralized, the epoxidation process inhibited, and epoxide **15** would be obtained as only a minor by-product.

Recently, Reich suggested an alternative mechanism for the oxidation step.[8] In his opinion the rate of oxidation of the selenide to selenoxide is relatively slow. The observed rapid oxidation rate usually observed is attributed to perseleninic acid ($RSeO_3H$), which is generated during the reaction (30). It is perseleninic acid that acts as the true oxidant which enables the reaction to proceed at the fast rate observed. This is reasonable since perseleninic acid is a very strong oxidant. It should be possible to accelerate the oxidation by adding seleninic acid to the reaction mixture as a catalyst, thus reducing the amount of epoxidation so that a higher yield of the desired product may be achieved. To confirm this proposal several reactions were carried out using benzeneseleninic acid as a reagent. The results

[6]Commercial (−)-β-pinene was obtained from Aldrich Chemical Co. and had an optical purity of 92%.

[7]See footnote 11 in ref. 11.

[8]H.J. Reich. Personal communication.

TABLE 1. Oxidation of the selenide in the presence of benzeneseleninic acid

	With $PhSeO_2H$ added				Control		
Entry	$PhSeO_2H$ (equiv.)	Time (min)	Yield (%)	Ratio (**26**:**30**)	Time (min)	Yield (%)	Ratio (**26**:**30**)
1	0.1	60	65	8:1	120	66	7:1
2	0.5	35	67	5:1	100	61	7:1

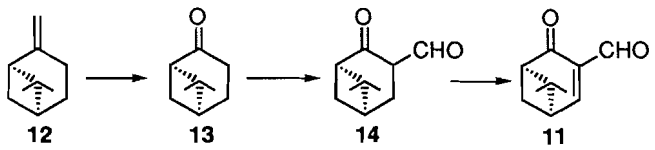

SCHEME 1

are listed in Table 1. We did observe a significant increase in the reaction rate but no obvious improvement in yield or product ratio. It is conceivable that the seleninic acid catalyzed both oxidation and epoxidation and thus the rates of both reactions increased to about the same extent. In fact, when 0.5 equivalents of seleninic acid was used, the ratio of the two products dropped to 5:1. Of many runs using this preparation, the best **11**:**15** ratio obtained was 12:1 after purification by bulb-to-bulb distillation.

Another side reaction also occurred during the oxidation. A small amount (3–8%) of **14** was always recovered. The intermediate selenide and selenoxide are both sterically congested at the C-3 position and may be relatively labile. Attack by a nucleophile such as hydrogen peroxide at the selenium atom could result in displacement of the selenium center, leaving a carbanion **16** and leading to formation of **14** after protonation. Several other methods were examined to improve on the production of enone aldehyde **11**, including 2,3-dichloro-5,6-dicyanobenzoquinone (DDQ) (31), sodium periodate (30), magnesium mono-perphthalate (MMPP),[9] hydrogen peroxide (30), and ozone (30) oxidation of **14** as well as non-oxidative elimination of the selenide (32). These alternative procedures gave no useful yield of product.

*2. Diels–Alder reactions of enone aldehyde **11***

A variety of Lewis acids and conditions were explored for the Diels–Alder reaction of enone aldehyde **11** with isoprene. The results of these investigations are summarized in Table 2. The particular Lewis acids chosen were previously noted as particularly suitable catalysts for related cross-conjugated enone dienophiles (6, 33). The Diels–Alder reaction of **11** was very sensitive to the choice of Lewis acid catalyst. The milder Lewis acid catalysts gave better yields. Good yields of product **17** were obtained with zinc chloride and boron trifluoride etherate. When ferric chloride and stannic chloride were used, the yields dropped drastically. This result may be due to greater stability of the strained ring system of the reactant and the product under the relatively mild acidic conditions of boron trifluoride etherate and zinc chloride catalysis and degradation by the stronger Lewis acids. In further investigations of the scope of the Diels–Alder reaction of **11**, only boron trifluoride etherate and zinc chloride were used as catalysts. Adducts were obtained in good to high yields and the results are summarized in Table 3.

[9]The experiment was made using MMPP in the manner used in ref. 30 for *m*-chloroperbenzoic acid.

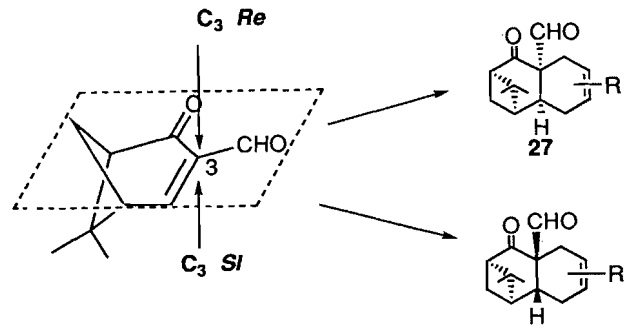

TABLE 2. Lewis acid catalyzed Diels–Alder addition of isoprene to enone aldehyde **11**

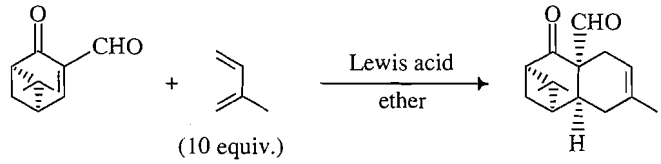

11 **17**

Lewis acid (equiv.)	Temp. (°C)	Time (h)	Yield (%)
$ZnCl_2$ (2.0)	–20	18	74
$ZnCl_2$ (1.0)	–20	18	71
$ZnCl_2$ (1.0)	–20 + 25	15 + 2	72
$SnCl_4$ (1.0)	–20	6	0
$FeCl_3$ (1.0)	–20	1	19
$BF_3{\cdot}OEt_2$ (1.0)	–20	2	84

In principle, Diels–Alder addition to enone aldehyde **11** could occur from either the sterically more hindered *Si* face or the less hindered *Re* face to give stereochemically distinct products (Scheme 2). In all cases, only the products of the addition to the *Re* face (general structure **27**) were obtained. The *gem*-dimethyl group in **11** presumably served to direct the Diels–Alder addition to the less hindered *Re* face, as indicated by the stereochemistry of the ring junction of the adducts. The structures of the adducts were established using spectroscopic methods including ^1H nmr, ^1H decoupling, and nOe experiments. The results of the nOe experiments are summarized in Table 4.

A. Addition to isoprene

The reaction of enone aldehyde **11** with isoprene under zinc chloride catalysis in ether at –20°C gave the adduct in 74% yield after 18 h. When boron trifluoride etherate was used as a

Can. J. Chem. Downloaded from www.nrcresearchpress.com by 85.192.166.187 on 09/08/12
For personal use only.

TABLE 3. Diels–Alder additions of dienes to enone aldehyde **11**

Entry	Diene (equiv.)	Lewis acid (1 equiv.)	Temp (°C)	Time (h)	Product(s)	(Ratio)	Yield (%)
1	(10)	$ZnCl_2$	−20	16	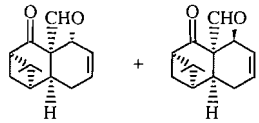 **18** + **19**	(170:1)	60
2		$BF_3{\cdot}OEt_2$	−20	1		(64:1)	71
3	(10)	$BF_3{\cdot}OEt_2$	−40	3	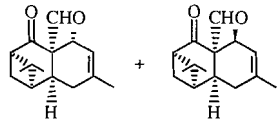 **20** + **21**	(133:1)	82
4	(10)	$BF_3{\cdot}OEt_2$	−20	1.5	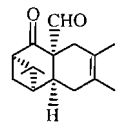 **22**		92
5	(10)	$ZnCl_2$	−20	4	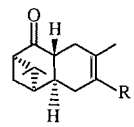		70
6	(5)	$ZnCl_2$	−40 → −15	3.5 1.5			68
	R = OTBDMS **23**				R = OTBDMS **24**		
7	(10)	$BF_3{\cdot}OEt_2$	−20	1.5	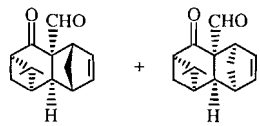 **25** + **26**	(20:1)	0
8		$BF_3{\cdot}OEt_2$	−40	0.5			0
9		$ZnCl_2$	−20	4			52

catalyst the reaction was finished in 2 h to give 84% yield of the adduct. Structure **17** could be assigned to the adduct if the Diels–Alder addition followed the normal *para* rule. However, orientational reversal, in violation of the *para* rule, in the Diels–Alder reaction of a 2-substituted diene has been observed (1, 2, 4). To rule out the possibility that the addition of isoprene to **11** could produce the regioisomer **28**, extensive ^1H decoupling experiments were carried out and all the protons of the adduct were assigned. A doublet of doublets assigned to H4e was observed to couple to H5 with a coupling constant of 7.0 Hz, as expected for the $CH_3C{=}CH_xCH_yH$ system (J_{xy} = 4–10 Hz). The regioisomeric adduct **28** would be expected to show a smaller coupling constant for the $CH_x{=}C(CH_3)CH_yH$ system (J_{xy} = 0–3 Hz) (34). On the basis of this ^1H nmr spectral data, structure **17** rather than **28** was assigned to the Diels–Alder adduct.

The stereochemistry of the ring junction was determined by nOe experiments. Irradiation of the ring junction proton (H8) signal at δ 2.94 resulted in enhancements of the formyl proton and the *endo*-methyl protons at δ 0.73. This implied that the formyl group and the *gem* dimethyl were on the same face as the ring junction proton. Thus the addition of isoprene obeyed the *cis* principle and occurred on the less hindered *Re* face of **11** to give adduct **17**. When the methyl at δ 1.32 was irradiated, nOe enhancements of H1, H11*exo*, H9 and the *endo*-methyl at δ 0.73 were observed. From this experiment, the *gem*-dimethyl and the *exo* and *endo* protons of the methylene bridge were assigned. The appearance of the *exo* methyl signal further down field than the *endo* methyl signal is probably due to shielding of the *endo* methyl by the ketone carbonyl. The signal at δ 2.52 (H11*exo*, dddd) was coupled to H1 (J = 5.5 Hz), H9 (J = 8.5 Hz), H11*endo* (J = 11.0 Hz) and H8 (W-coupling, J = 2.0 Hz). On the other hand the signal at δ 1.89 (H11*endo*), which was strongly shielded relative to H11*exo*, appeared as a readily recognizable doublet (J = 11.0 Hz) as the dihedral angles of H11*endo* to H1 and H9 were each about 90°.

B. Addition to trans*-piperylene*

When enone aldehyde **11** was reacted with *trans*-piperylene at −20°C under zinc chloride catalysis two adducts in a ratio of 170:1 were obtained in 60% yield. With boron trifluoride etherate catalysis two adducts in a ratio of 64:1 were formed in 71% yield. The adducts showed only one spot on the tlc plate and could not be separated by flash chromatography. The adducts displayed two sets of signals in the ^{13}C nmr APT spectrum and in the ^1H nmr spectrum. Since the product obtained was a mixture of two inseparable diastereomers the specific rotation was not measured. If the Diels–Alder reaction followed the normal *ortho* rule, then the structures of the adducts could tentatively be assigned as **18** and **19**. To conclusively determine the regiochemistry of the adducts, extensive ^1H decoupling experiments were carried out on the major isomer and a complete spectral assignment was made. The ring junction proton (H8), which appeared as a dddd at δ 2.80, was coupled to H7ax (J =

Can. J. Chem. Downloaded from www.nrcresearchpress.com by 85.192.166.187 on 09/08/12
For personal use only.

TABLE 4. The nOe data for Diels–Alder adducts

Compound	Irradiation	δ (ppm)	% Enhancement (H)
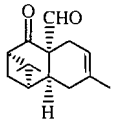 **17**	H8	2.94	3.7 (CHO), 2.7 (*endo* CH_3)
	exo CH_3	1.32	4.7 (*endo* CH_3), 14.5 (H1), 17.7 (H11*exo*), 18.4 (H9)
	C6-CH_3	1.74	9.2 (H5), 16.0 (H7)
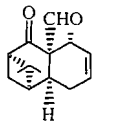 **18**	H8	2.80	4.8 (H7), 3.9 (H9), 5.8 (*endo* CH_3),
	endo CH_3	0.71	4.8 (*exo* CH_3), 7.0 (H8)
	C4-CH_3	1.40	9.7 (CHO), 9.8 (H5), 9.3 (H4)
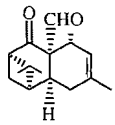 **20**	H8	2.82	5.8 (*endo* CH_3)
	C4-CH_3	1.40	5.3 (H5), 6.4 (CHO), 5.9 (H4)
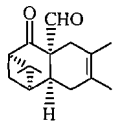 **22**	*endo* CH_3	0.71	3.7 (CHO), 5.3 (H8) 4.9 (*exo* CH_3)
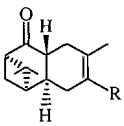 R = OTBDMS **24**	*exo* CH_3	0.89	16.5 (H1), 10.2 (H9) 13.0 (H11*exo*)
	C5-CH_3	1.43	5.6 (H4), 2.8 (Si-CH_3)
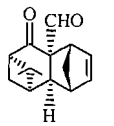 **25**	*endo* CH_3	0.82	2.3 (CHO), 8.2 (*exo* CH_3), 6.8 (H8)

10.5 Hz), H7e (J = 7.5 Hz), H9 (J = 2.0 Hz), and H11*exo* (W-coupling, J = 2.0 Hz). This coupling pattern indicated that two hydrogen atoms were attached to C7. Thus the methyl substituent could only be located at C4 and the major isomer was assigned the regiochemistry of structure **18**.

The stereochemistry of **18** was determined by nOe experiments. Irradiation of the *endo* methyl (δ 0.71) resulted in nOe enhancement of H8. According to the *cis* principle the formyl group should be on the same face as H8. This indicated that the addition of *trans* piperylene occurred from the *Re* face. Saturation of the methyl doublet (δ 1.40) produced enhancement of the formyl proton, indicating that the C4 methyl is on the same face as the aldehyde group. These experiments conclusively established the stereochemistry of the major adduct as that shown by **18**.

The presence of a trace amount of a minor isomer could only be detected by high-resolution nmr. Some ^{1}H nmr signals of the minor isomer were separated from those of the major isomer. The rest were buried under the signals of the major isomer. Therefore nOe and decoupling experiments were not performed on the minor adduct since it was impossible to complete all the spectral assignments. Compared to previous results obtained from our group (11), the two adducts should be epimers, so the minor isomer was tentatively assigned structure **19**.

In addition to adducts **18** and **19**, an unexpected product was formed during the Diels–Alder reaction between enone aldehyde **11** and *trans*-piperylene, with either boron trifluoride etherate or zinc chloride catalysis, in 14 and 15% isolated yield, respectively. This compound showed an intense spot under the uv lamp (short wavelength) on a tlc plate and greater polarity than the Diels–Alder adducts. It was isolated as a white crystalline compound by column chromatography. Based on the spectral data, structure **29** was assigned to the by-product, which

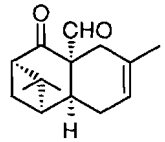
28

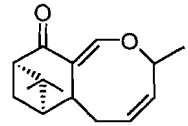
29

might have formed by a stepwise 1,4-cyclization process (see Scheme 3) instead of a Diels–Alder reaction. The reason for generation of this unexpected type of by-product in this partic-

Can. J. Chem. Downloaded from www.nrcresearchpress.com by 85.192.166.187 on 09/08/12
For personal use only.

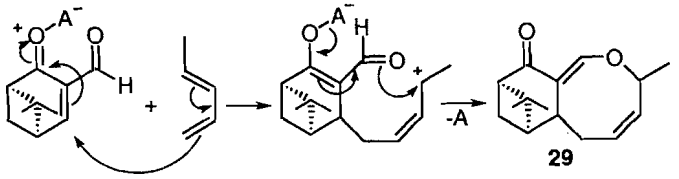

SCHEME 3

ular case and not in any other example described here is not clear to us at this time.

C. Addition to trans-*2-methyl-1,3-pentadiene*

At –40°C the boron trifluoride etherate catalyzed Diels–Alder reaction of enone aldehyde **11** with *trans*-2-methyl-1,3-pentadiene proceeded smoothly to give a colourless liquid in 82% yield. Although the products showed only one spot on tlc and could not be separated by flash chromatography, the ^{1}H nmr spectrum indicated the presence of two compounds in a ratio of 133:1. Assuming that the reaction followed the normal *ortho* and *para* rules, the structures of the two adducts could be tentatively assigned as keto aldehydes **20** and **21**. Previous observations indicated that the coupling pattern of the ring junction proton (H8) could be used to determine the regiochemistry of the Diels–Alder adducts of 1-substituted dienes. Detailed ^{1}H decoupling experiments of the major isomer showed that irradiation of the signal at δ 2.82 (H8, dddd) led to a change in multiplicity of the signals at δ 2.47 (H11*exo*), 2.10–2.30 (two protons, H7ax and H9), and 1.98 (H7e). As for the previous cases, this coupling pattern indicated that two hydrogen atoms were attached to C7 and consequently the methyl substituent must be at C4, confirming the regiochemistry of the major isomer as shown by structure **20**.

To determine the stereochemistry of the ring junction and the C4 methyl, nOe experiments were carried out on the major isomer. When proton H8 (δ 2.82) was irradiated, enhancement on the *endo* methyl (δ 0.66) was observed. This indicated that the H8 proton was on the same face as the *gem*-dimethyl group and therefore the addition of the diene occurred from the *Re* face of **11**. The stereochemistry of the formyl group was then assigned in accordance with the *cis* principle. When the signal at δ 1.40 (C4 methyl) was irradiated nOe enhancements of H5, H4 and the formyl proton signals were observed. This confirmed the position and the stereochemistry of the methyl substituent of the major isomer as that specified by structure **20**.

The ^{1}H nmr spectral data of the minor isomer were incomplete. Therefore we could not unambiguously assign the structure of the minor isomer. The tentative assignment as structure **21** was based on the previous findings on a similar system (11).

D. Addition to 2,3-dimethylbutadiene

Enone aldehyde **11** reacted with 2,3-dimethylbutadiene using boron trifluoride etherate as a catalyst to give a colourless liquid in 92% yield. The spectral data were consistent with the proposed structure **22**. Again the stereochemistry was determined by nOe experiments. Irradiation of the *endo* methyl at δ 0.71 resulted in enhancement of H8 (δ 2.88), the formyl proton (δ 9.71), and the *exo* methyl (δ 1.70). These findings supported the assigned stereochemistry of **22** resulting from the addition of the diene exclusively from the *Re* face of enone aldehyde **11**.

E. Addition to 2-tert-*butyldimethylsiloxy-3-methyl-1,3-butadiene*

To examine the addition of more highly functionalized dienes we considered silyloxydiene **23**. We previously observed (6) that silyloxy dienes such as **23** and **30** are extremely sensitive to the acidity of some Lewis acids and only zinc chloride produces useful yields. The reaction of **23** (10 equiv.) with **11** catalyzed by zinc chloride was much faster than other additions to **11** reported here. The product was obtained in 70% yield after purification by column chromatography. The spectral data supported the general structural features of the expected Diels–Alder adduct except that the formyl group was absent. Evidently the formyl group was eliminated during the reaction or work-up and so the *cis* principle could not be applied directly to the structure assignment. In addition, several signals were at unexpected downfield shifts in the ^{1}H nmr spectrum.

To determine the regio- and stereochemistry of this adduct, nmr decoupling studies were carried out. Irradiation of the protons at δ 4.00 (H4e and H7e) led to a change in multiplicity of the signals at δ 3.38 (H4ax), 2.34 (H7ax) and 1.43 (C5-CH_3). When the signal at δ 3.31 (H8) was irradiated, the signal at δ 3.38 (H4ax) was also irradiated, due to their close proximity. Changes in multiplicity of the signals at δ 4.00 (H4e), 3.71 (H3), 1.94 (H9), and 1.43 (C5-CH_3) were observed. Irradiation of the proton at δ 2.29 (H1) led to a change in multiplicity of the signals at δ 1.94 (H9) and 1.73 (H11*exo*). These results confirmed that structure **24** expressed the correct regiochemistry of the adduct.

To determine the stereochemistry of the ring junction, nOe experiments were carried out. From the spectral data of other compounds in this series the methyl singlet at higher field (δ 0.89 for this compound) usually represented the *endo* methyl group. When the singlet at δ 0.89 was irradiated, nOe enhancements of the signals at δ 2.29 (H1), δ 1.94 (H9), and δ 1.73 (H11*exo*) were observed. These results indicated that the methyl singlet at δ 0.89 was due to the *exo* methyl. The absence of the formyl group could cause the exchange of the chemical shifts between the two geminal methyl groups. We tried to irradiate proton H8 at δ 3.31; however, proton H4ax at δ 3.38 was so close to H8 that it was also irradiated and the results of this experiment were inconclusive. Therefore the stereochemistry of the ring junction could not be determined by nOe experiments. The large coupling constant (11 Hz) observed for H3 suggested a *trans* ring junction as depicted by structure **24**; however, we do not consider this assignment to be conclusive since this coupling could be to the adjacent H4ax.

Since the diene **23** was used in large excess (10 equiv.), 19.4% of the diene was recovered intact after column chromatography. Diels–Alder dimerization of diene **23** also occurred during the reaction and 12% yield of the dimeric adduct **31** was obtained. We wanted to determine if the formyl group was lost from an initial adduct such as **32** to give **24**. It could have been eliminated during the reaction or during the work-up. Also, since this addition was faster than other zinc chloride catalyzed additions of **11**, there was a possibility that the excess of the relatively costly diene **23** could be reduced without lowering the yield. We ran the reaction again with 5 equivalents of diene **23**. The reaction was monitored carefully to observe when the formyl group was removed. After complete conversion a sample of the reaction mixture was concentrated and the ^{1}H nmr spectrum of the residue was recorded before addition of saturated sodium bicarbonate solution. The spectrum showed the absence of a formyl group in the crude mixture, indicating its loss during the cycloaddition reaction. The yield of product **24** was not affected by the reduction in the amount of the diene used.

Can. J. Chem. Downloaded from www.nrcresearchpress.com by 85.192.166.187 on 09/08/12
For personal use only.

Can. J. Chem. Downloaded from www.nrcresearchpress.com by 85.192.166.187 on 09/08/12
For personal use only.

F. Addition to 1,3-cyclopentadiene

Attempts to induce addition of 1,3-cyclopentadiene to **11** with boron trifluoride etherate as catalyst were unsuccessful due to rapid polymerization of the diene. When zinc chloride was used, the Diels–Alder reaction produced a mixture of two inseparable adducts (20:1 by ^{1}H nmr) in 52% yield. Preliminary analysis of the spectral data indicated that the structures of the adducts could be assigned as **25** and **26**. Extensive ^{1}H decoupling experiments on the major isomer led to the assignment of all its protons. The ring junction proton (H8) appeared at δ 3.17 as a multiplet. Irradiation of the signals at δ 3.01 (H7) and 2.30 (H9) led to a small change in multiplicity of the signal at δ 3.17. In an nOe experiment, when the *endo* methyl at δ 0.82 of the major isomer was irradiated, enhancement of the signals at δ 3.17, δ 9.81 and δ 1.32 were observed. Therefore the major product was assigned with both H8 and the formyl group in the α-orientation. Previous observations indicated that the addition of dienes to enone aldehyde occurred exclusively from the *Re* face of **11**. It was therefore expected that exclusive addition of cyclopentadiene to the *Re* face of **11** would also occur, so the minor isomer would most likely contain an α-H8 and an α-formyl group as well.

The stereochemistry of the methylene bridge of the bicyclo[2.2.1]heptene ring system was determined by comparing the difference in chemical shifts between the two vinylic protons with the known compounds **33** and **34** (11). Since the major isomer exhibited a larger difference in chemical shift between the two vinylic protons (Δδ 0.30) than the minor isomer (Δδ 0.11), it was assigned structure **25** while the minor isomer was assigned structure **26**.

G. endo*-Selectivity of the addition*

All dienes in this study added to enone aldehyde **11** with very high diastereomeric excess and mention of this *endo*-selectivity is appropriate. As we have described for related dienophiles (1, 7, 8, 11), there are two dienophilic components in **11**: the α,β-unsaturated ketone (**11***c*) and the α,β-unsaturated aldehyde (**11***d*). It would be unnecessary to distinguish between these two moieties except in certain cases for 1- and 4-substituted dienes. *endo*-Addition to either the enone or the α,β-unsaturated aldehyde moiety would give stereochemically distinguishable products. Determining which dienophilic moiety would control the reaction pathway should be a function of the secondary orbital overlap with the diene. The addition of 1-substituted dienes (Table 3, Entries 1–3 and 9) to **11** occurred predominantly with secondary orbital overlap with the aldehyde (as in aldehyde-*endo* transition state **11***a*) rather than with the ketone carbonyl (as in keto-*endo* transition state **11***b*). Comparison of the two transition states indicates that the addition by **11***b* would encounter some steric interaction between the C2–C3 zone of the diene and the methylene bridge of the dienophile. We believe that the enhanced aldehyde-*endo* selectivity exhibited by **11** over the moderate ester-*endo* selectivity of keto-ester **8** is a reflection of improved secondary orbital effect participation by the aldehyde carbonyl. The dramatic increase in reaction rate for additions to **11** over additions to **8** reflects the greater electron-withdrawing character of the aldehyde group of **11** over the ester group of **8** which we had predicted.

H. Optical purity

The (−)-β-pinene used to prepare enone aldehyde **11** had an optical purity of 92%. Optically active nmr shift reagents such as Eu(hfc)$_3$ have been used to evaluate the optical yield of reactions (35, 36). Direct application of Eu(hfc)$_3$ to adduct **17** showed separation of the signals for the *gem*-dimethyl groups. The chemical shift difference (Δδ) increased with an increase in the amount of Eu(hfc)$_3$ added. In all experiments the integrals of the split signals were consistently in the ratio of 96:4. Thus the optical purity of the starting material (92%) was retained in the Diels–Alder adducts. The enantiomeric set of adducts that would be obtained from the relatively unavailable enantiomeric (+)-β-pinene could nevertheless be prepared easily using the conversion of (+)-α-pinene to (−)-nopinone reported by Lavallee and Bouthillier (37). The (−)-nopinone so obtained would provide the enantiomer of **11** by the method we have described.

3. Removal of the formyl group

Having successfully generated various Diels–Alder adducts of enone aldehyde **11**, we wished to demonstrate that the formyl group, as an effective tool for controlling stereoselectivity, is not only easily introduced but also easily removed. Treatment of **17** with saturated aqueous potassium carbonate in a methanol mixture at room temperature for 18 h gave a single product in quantitative yield. The spectral data for this product were comparable with those previously reported for ketone **35** (11).

Treatment of the mixture of adducts **18** and **19** (64:1) under the same conditions for 18 h did not give any detectable amount of product. The starting material was recovered intact. However, after refluxing for 15 h a colourless liquid was isolated in 92% yield. After chromatographic separation, two products were obtained in a ratio of 1:6. Based on the spectral data and the ratio of the two products, structures **36** and **37** were assigned to the two compounds. Starting with a 64:1 mixture of **18** and **19**, it is impossible that the minor product in the 6:1 mixture originated from the minor component of the starting material. The two deformylation products must both be derived from the major starting material and must be epimeric at C3. The stereochemistry of C3 remained to be determined. Extensive ^{1}H COSY experiments of the major isomer resulted in the assignment of all the protons. The ring junction proton (H8) appeared at δ 2.71 as a multiplet. Its multiplicity changed when the H3 (δ 2.55) and H11*exo* (δ 2.40) protons and the multiplet at δ 1.98–2.20 (H9, H7, and other) were irradiated individually. Attempted nOe irradiation of proton H8 at δ 2.71 did not provide useful information since H3 was simultaneously irradiated. However, the ^{1}H nmr spectrum showed proton H3 as a doublet of doublets with coupling constants of 12.0 and 5.5 Hz. This large coupling constant (12 Hz) indicated that the major isomer had a *trans* ring junction (**36**) while the minor isomer could be assigned with a *cis* ring junction (**37**).

Conclusion

The Diels–Alder reaction of enone aldehyde **11** with various dienes provided good to high yields of chiral adducts in very high diastereomeric excess with complete diastereofacial selectivity. The observed regiochemistry was as predicted by the *ortho* and *para* rules. The formyl substituent of the adducts can be removed or elaborated to achieve synthetic goals. Enone aldehyde **11** is a potentially versatile intermediate for chiral synthesis by asymmetric Diels–Alder reactions.

Experimental

General

Melting points were recorded on a Kofler hot stage apparatus and are not corrected. Elemental analyses were performed by the microan-

Can. J. Chem. Downloaded from www.nrcresearchpress.com by 85.192.166.187 on 09/08/12
For personal use only.

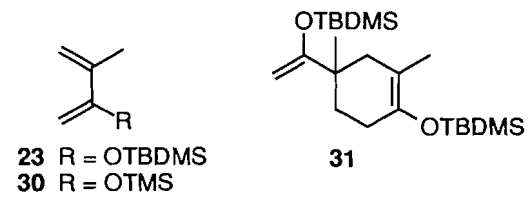

23 R = OTBDMS
30 R = OTMS

31

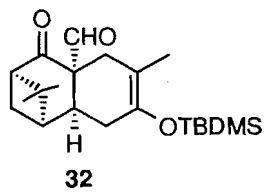

32

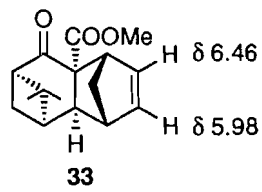

33

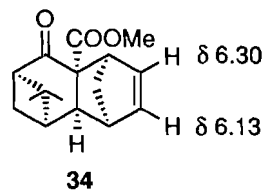

34

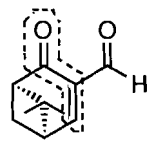

11*c*

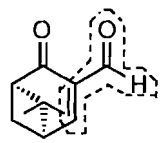

11*d*

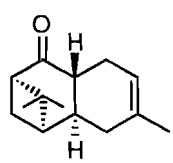

35

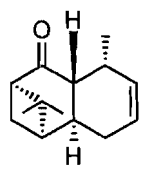

36

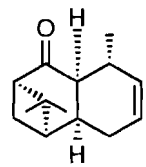

37

alytical laboratory of this department. Fourier transform infrared spectra (ir) were recorded on a Nicolet 7199 or Nicolet MX-1 FT-IR spectrophotometer, and unless otherwise stated, were obtained in chloroform cast. Proton nuclear magnetic resonance (^{1}H nmr) spectra were recorded on a Bruker WH-80, Bruker WH-200, Bruker WH-300, Bruker WH-400, or Bruker AM-400 spectrometer using deuteriochloroform ($CDCl_3$) as solvent unless otherwise stated. Tetramethylsilane (TMS) was used as an internal reference. Coupling constants are reported to ±0.5 Hz. Chemical shift measurements are reported in ppm downfield from TMS in delta (δ) units. The following abbreviations are used: s = singlet, δ = doublet, t = triplet, q = quartet, m = multiplet, and br = broad. Carbon-13 nuclear magnetic resonance (^{13}C nmr) spectra were recorded on a Bruker WH-300 (75 MHz) or Bruker WH-400 (125 MHz) spectrometer, and were obtained on solutions in deuteriochloroform as the internal reference, setting the central peak at 77.00 ppm. The ^{13}C nmr multiplicities were derived from APT (Attached Proton Test) experiments (38, 39). Methyl and methine groups are shown as signals possessing an antiphase (a) with respect to the deuteriochloroform signal, whereas methylene groups, quaternary carbons, and carbonyl groups appear in phase (p) with it. Nuclear Overhauser enhancement (nOe) experiments were determined in the difference mode in which a control (undecoupled) spectrum was computer subtracted from the irradiated spectrum after Fourier transformation. Positive enhancements are defined as signals possessing antiphase with respect to the irradiated signal. Samples for nOe measurements were deoxygenated with argon gas for 10 min. High resolution electron impact mass spectra (ms) were recorded using an A.E.I. model MS-50 mass spectrometer. Optical rotations were determined on a Perkin–Elmer 241 polarimeter. Specific rotations ($[\alpha]_D$) are reported in degrees at the specified temperature and concentration (*c*) is given in grams per 100 millilitre in the specified solvent.

All reactions were carried out under slight positive pressure of argon. Bulb-to-bulb distillation was performed using a Kugelrohr distillation apparatus. Flash chromatography (40) was used routinely for purification and separation of product mixtures using silica gel (Merck, 230–400 mesh). All solvents for chromatography were distilled prior to use. Concentrations of solvent systems used in column chromatography are given by volume. Analytical thin layer chromatography (tlc) was carried out on aluminum sheets precoated (0.2 mm layer thickness) with Merck silica gel 60 F_{254}. Ultraviolet-active materials were detected by visualization under a uv lamp (254 or 350 nm). Visualization of tlc chromatograms was completed by dipping in an ethanol solution of vanillin (5% w/v) and sulfuric acid (5% v/v), followed by charring on a hot plate. Alternatively, an aqueous solution of phosphomolybdic acid (3% w/v) containing ceric sulfate (0.5% w/v) and sulfuric acid (3% v/v) was used as the dipping solution, followed by charring on a hot plate.

Materials

Anhydrous reaction solvents were distilled under argon from the appropriate drying agents before use. Tetrahydrofuran (THF) was freshly distilled from a solution of sodium and benzophenone. Pyridine and dichloromethane were distilled from calcium hydride. Ether was distilled from lithium aluminum hydride. Reactions requiring anhydrous conditions were performed in oven- or flame-dried glassware that was assembled and allowed to cool while being purged with argon. Argon was passed through a column of 4 Å molecular sieves and self-indicating silica gel. Unless otherwise stated, anhydrous magnesium sulfate was used for drying organic solutions.

*(1R,5S)-(+)-6,6-Dimethylbicyclo[3.1.1]heptan-2-one (**13**)*

WARNING: See footnote 11 in ref. 11. Ozone was passed through a −78°C solution of (1*S*,5*S*)-(−)-β-pinene[6] (10.0 g, 73.5 mmol) in dichloromethane–methanol (1:1, 30 mL). After 3.5 h a persistent blue

Can. J. Chem. Downloaded from www.nrcresearchpress.com by 85.192.166.187 on 09/08/12
For personal use only.

colour appeared. The reaction was stopped after a further 40 min when tlc showed no starting material remaining. Excess ozone was purged with oxygen for 10 min and the reaction mixture turned colourless. Dimethyl sulfide (27.5 mL, 0.37 mol) was added to the reaction mixture at –78°C, then the mixture was allowed to gradually warm to room temperature while stirring overnight. The solvent was removed under reduced pressure on a rotary evaporator. Flash chromatography of the residue, eluting with 2–10% ether in petroleum ether, gave pure **13** (7.2 g) as a colourless oil. A second chromatography of impure fractions gave additional **13** (2.2 g, total yield 9.4 g, 93%): $[\alpha]_D^{23}$ +15.0 (neat), +29.6 (*c* 1.32, $CHCl_3$);[10] ir: 1708 (C=O) cm^{-1}; ^1H nmr (300 MHz) δ: 2.47–2.64 (complex, 3H), 2.34 (ddd, 1H, *J* = 19.0, 9.0, 2.5 Hz, C-3 H_α), 2.21 (m, 1H), 1.87–2.10 (complex, 2H), 1.55 (d, 1H, *J* = 10.0 Hz), 1.40 (s, 3H, *exo* CH_3), 0.82 (s, 3H, *endo* CH_3); ^{13}C nmr (75 MHz) δ: 215.0 (C=O), 58.0 (*C*HC=O), 41.2 (CMe_2), 40.5 (*C*HCMe_2), 32.8 (*C*H_2C=O), 25.9 (*exo* CH_3), 25.3 (CH_2), 22.2 (*endo* CH_3), 21.5 (CH_2); ms M^+ calcd. for $C_9H_{14}O$: 138.1045; found: 138.1046. Anal. calcd. for $C_9H_{14}O$: C 78.21, H 10.21; found: C 78.06, H 10.21.

*(1R,5R)-3-Formyl-6,6-dimethylbicyclo[3.1.1]heptan-2-one (**14**)*

Sodium hydride (60% oil dispersion, 800 mg, 20.0 mmol) was suspended in tetrahydrofuran (30 mL) under argon. Ethyl formate (25 mL, 0.31 mol) was added at 0°C and stirred for 10 min. A solution of nopinone (**13**) (1.38 g, 10.0 mmol) in tetrahydrofuran (25 mL) containing 98% ethanol (7 drops) was added dropwise at 0°C over 30 min. The reaction mixture was allowed to gradually warm to room temperature. After 3 h at room temperature a saturated aqueous solution of ammonium chloride (25 mL) was added. The mixture was separated and the aqueous phase was extracted with ether – petroleum ether (1:1, 3 × 20 mL). The combined organic phases were washed with water and saturated aqueous sodium chloride, dried, filtered, and concentrated. Flash chromatography of the residue, eluting with 5–10% ether in petroleum ether, gave keto aldehyde **14** (1.55 g, 9.34 mmol, 93% yield) as a colourless oil that solidified on standing. This compound was a 7:2.5:1 mixture of isomers. The major isomer gave the following signals: ^1H nmr (300 MHz) δ: 13.35 (br s, 1H, enol *OH*), 7.18 (br s, 1H, enol =*CH*), 2.41–2.58 (complex, 6H), 1.41 (s, 3H, *exo* CH_3), 0.90 (s, 3H, *endo* CH_3). The two minor isomers also showed distinguishable signals in the nmr spectrum: δ 9.65, 9.40 (s, 1H each, C*H*O), 1.44, 1.40 (s, 3H each, *exo* CH_3), 0.93, 0.82 (s, 3H each, *endo* CH_3). The mixture also gave the following analytical data: ir: 3310 (enol OH), 1725 (CHO), 1713 (C=O), 1653 (chelated β-hydroxy-α,β-unsaturated ketone carbonyl), 1598 (C=C) cm^{-1}; ^{13}C nmr (75 MHz) δ: 209.4 (C=O), 163.9 (=CHOH), 107.2 (=*C*C=O), 54.1 (*C*HC=O), 39.6 (*C*Me_2), 39.4 (*C*HCMe_2), 27.5 (CH_2), 26.0 (CH_3), 25.3 (CH_2), 21.5 (CH_3); ms M^+ calcd. for $C_{10}H_{14}O_2$: 166.1004; found: 166.1009. Anal. calcd. for $C_{10}H_{14}O_2$: C 72.25, H 8.49; found: C 72.43, H 8.73.

*(1R,5R)-3-Formyl-6,6-dimethylbicyclo[3.1.1]hept-3-en-2-one (**11**) and (1R,3R,5S,6R)-3-formyl-7,7-dimethyl-4-oxatricyclo-[4.1.1.0^{3,4}]heptan-2-one (**15**)*

Pyridine (0.53 mL, 6.5 mmol) was added to a solution of phenylselenenyl chloride (1.37 g, 7.15 mmol) in dichloromethane (30 mL) at 0°C under argon. The colour of the solution changed from dark red to yellow-brown and white fumes were generated. After stirring for 10 min a solution of keto aldehyde **14** (1.08 g, 6.5 mmol) in dichloromethane (10 mL) was added. At the end of the addition, which took about 3 min, an instantaneous colour change from yellow-brown to bright yellow occurred, indicating completion of the selenenylation reaction; tlc analysis confirmed that no starting material remained. After 5 min the reaction mixture was washed with aqueous 1 N hydrochloric acid (2 × 30 mL). The organic layer was cooled to 0°C and aqueous 30% hydrogen peroxide solution (0.5 mL) was added dropwise. After stirring for 5 min aqueous 30% hydrogen peroxide (0.5 mL) was added. Another portion of aqueous hydrogen peroxide solution (15%, 1.0 mL) was added dropwise 7 min later. The resulting mixture was stirred for 1.5 h, then water (5 mL) was added and the phases were separated. The organic phase was washed with saturated aqueous sodium bicarbonate and brine, dried, filtered, and concentrated. Flash chromatography of the residue, eluting with 2–30% ether in petroleum ether, gave a light yellow oil (746 mg) as a mixture of enone aldehyde **11** and epoxide **15** (7:1, ca. 70% yield). The following nmr data were attributed to the enone aldehyde **11**: ^1H nmr (300 MHz) δ: 10.00 (s, 1H, C*H*O), 8.31 (dd, 2H, *J* = 6.5, 1.5 Hz, =C*H*), 2.75–2.95 (complex, 3H, C*H*C*H*$_{exo}$C*H*), 2.12 (d, 1H, *J* = 9.0 Hz, CH*H*$_{endo}$), 1.57 (s, 3H, *exo* CH_3), 1.02 (s, 3H, *endo* CH_3); ^{13}C nmr (75 MHz) δ: 200.7 (C=O), 168.6 (CHO), 165.4 (CH=), 132.2 (C=), 58.3 (*C*HC=O), 54.8 (C), 44.7 (*C*HCMe_2), 40.4 (CH_2), 26.6 (CH_3), 21.5 (CH_3). The mixture showed the following spectral data: ir: 2830, 2710 (CHO, weak), 1724, 1691, 1657 (saturated and conjugated C=O), 1593 (C=C) cm^{-1}; ms M^+ calcd. for $C_{10}H_{12}O_2$: 164.0833; found: 164.0837; calcd. for $C_{10}H_{12}O_3$: 180.0786; found: 180.0781. Epoxide **15** was recovered in pure form from a typical Diels-Alder reaction mixture after dienophile **11** was totally consumed. It showed the following spectral data: ir: 1741 (CHO), 1710 (C=O), 1100 (C-O) cm^{-1}; ^1H nmr (300 MHz) δ: 9.65 (s, 1H, C*H*O), 3.89 (d, 1H, *J* = 4.5 Hz, CHC*H*O), 2.71 (dd, 1H, *J* = 11.0, 6.0 Hz, CH*H*$_{exo}$), 2.58 (dd, 1H, *J* = 6.0, 6.0 Hz, C*H*C=O), 2.38 (ddd, 1H, *J* = 11.0, 6.0, 4.5 Hz, C*H*CMe_2), 2.09 (dd, 1H, *J* = 11.0, 11.0 Hz, CHC*H*$_{endo}$), 1.49 (s, 3H, *exo* CH_3), 1.09 (s, 3H, *endo* CH_3); ^{13}C nmr (75 MHz) δ: 201.8 (C=O), 194.7 (CHO), 58.9 (CH), 56.7 (*C*HC=O), 50.0 (C), 40.7 (*C*HCMe_2), 26.5 (CH_3), 21.1 (CH_3), 20.7 (CMe_2), 20.4 (CH_2); ms M^+ + 1 calcd. for $C_{10}H_{13}O_3$: 181.0865; found: 181.0863.

General procedure for boron trifluoride etherate catalyzed reactions

The Diels–Alder reactions of enone aldehyde **11** with boron trifluoride etherate as catalyst were carried out in a manner similar to the following example.

*(1R,3R,8S,9R)-(−)-3-Formyl-6,10,10-trimethyltricyclo-[7.1.1.0^{3,8}]-undec-5-en-2-one (**17**)*

Isoprene (0.54 mL, 5.4 mmol, 10 equiv.) in ether (7 mL) was added to a solution of a mixture of **11** and **15** (9:1, 100 mg) at –20°C under argon, followed by addition of boron trifluoride etherate (0.07 mL, 0.54 mmol). After stirring for 2 h a saturated aqueous sodium bicarbonate solution (7 mL) was added. The mixture was separated and the aqueous layer was extracted with ether (3 × 7 mL). The combined organic layers were washed with water and brine, dried, filtered, and concentrated. Flash chromatography of the residue, eluting with 2–30% ether in petroleum ether, gave **17** as a colourless oil (105.2 mg, 84% yield): $[\alpha]_D^{23}$ –115.87 (*c* 0.75, $CHCl_3$); ir: 1730 (CHO), 1698 (C=O), 1600 (C=C) cm^{-1}; ^1H nmr (300 MHz) δ: 9.70 (s, 1H, C*H*O), 5.33 (m, 1H, C*H*=), 2.94 (dddd, 1H, *J* = 10.0, 7.5, 2.0, 2.0 Hz, CHC*H*CH$_2$), 2.83 (dd, 1H, *J* = 16.0, 7.0 Hz, CH*H*$_{ax}$CH=), 2.61 (dd, 1H, *J* = 5.5, 5.5 Hz, C*H*C=O), 2.52 (dddd, 1H, *J* = 11.0, 8.5, 5.5, 2.0 Hz, CH*H*$_{exo}$), 2.22 (dddd, 1H, *J* = 16.0, 8.0, 2.5, 2.5 Hz, CH*H*$_e$CH=), 2.15 (complex, 2H, C*H*CMe_2, CH*H*$_{ax}$C=), 1.91 (m, 1H, CH*H*$_e$C=), 1.89 (d, 1H, *J* = 11.0 Hz, CH*Hendo*), 1.74 (br s, 3H, CH_3C=), 1.32 (s, 3H, *exo* CH_3), 0.73 (s, 3H, *endo* CH_3); ^{13}C nmr (75 MHz) δ: 212.9 (C=O), 200.9 (CHO), 139.8 (CH_3C=), 116.4 (CH=), 68.2 (C), 61.9 (C), 57.5 (*C*H), 47.8 (CH), 33.4 (CH_2), 33.0 (CH_2), 30.4 (CH), 26.5 (=C*C*H$_3$), 25.3 (CH_2), 23.1 (CH_3), 21.7 (CH_3); ms M^+ calcd. for $C_{15}H_{20}O_2$: 232.1464; found: 232.1462. Anal. calcd. for $C_{15}H_{20}O_2$: C 77.55, H 8.68; found: C 77.43, H 8.94.

General procedures for zinc chloride, ferric chloride, and stannic chloride catalyzed reactions

The Diels–Alder reactions of enone aldehyde **11** with isoprene using ferric chloride and stannic chloride as catalysts were carried out by the method of the example procedure described above. Specific temperatures and times are reported in Table 4. The general procedure for zinc chloride catalyzed reactions was slightly different from the boron trifluoride catalyzed reactions. Zinc chloride (91.4 mg, 0.67 mmol, 1 equiv.) was flame-dried under vacuum and dissolved in ether (5 mL) at room temperature under argon to give a clear solution. A solution of a

[10]See analytical data and footnote 15 in ref. 11.

Can. J. Chem. Downloaded from www.nrcresearchpress.com by 85.192.166.187 on 09/08/12
For personal use only.

mixture of **11** and **15** (10:1, 110 mg, 0.60 mmol of **11**) in ether (2 mL) was added dropwise and a thick pale yellow precipitate formed. After a few minutes, the precipitate stuck onto the wall of the round-bottomed flask and the solution became clear again. After stirring for 10 min, the reaction mixture was cooled to –20°C and then isoprene (0.7 mL, 6.7 mmol, 10 equiv.) was added. The work-up procedure and purification were the same as those described above. Specific times and temperatures are reported in Tables 2 and 3.

*(1R,3R,4R,8S,9R)-3-Formyl-4,10,0-trimethyltricyclo[7.1.1.0^{3,8}]-undec-5-en-2-one (**18**) and (1R,3R,4S,8S,9R)-3-formyl-4,10,10-trimethyltricyclo[7.1.1.0^{3,8}]undec-5-en-2-one (**19**)*

After purification, the reaction with *trans*-piperylene gave a mixture of isomers **18** and **19** (64:1 ratio). The nmr spectra showed two sets of signals; the major set for isomer **18**: ^{1}H nmr (300 MHz) δ: 10.04 (s, 1H, C*H*O), 6.00 (m, 1H, C*H*═), 5.42 (ddd, 1H, *J* = 9.5, 3.0, 3.0 Hz, ═C*H*), 2.80 (dddd, 1H, *J* = 10.5, 7.5, 2.0, 2.0 Hz, CHC*H*CH$_2$), 2.62 (dd, 1H, *J* = 5.5, 5.5 Hz, C*H*C═O), 2.58 (m, 1H, CH$_3$C*H*CH═), 2.48 (dddd, 1H, *J* = 11.0, 5.5, 5.5, 2.0 Hz, CHH_{exo}), 2.34 (ddd, 1H, *J* = 15.0, 7.5, 7.5 Hz, CHH_eCH═), 2.10 (ddd, 1H, *J* = 5.5, 5.5, 2.0 Hz, C*H*CMe$_2$), 1.89 (d, 1H, *J* = 11.0 Hz, CHH_{endo}), 1.85 (m, 1H, CHH_{ax}CH═), 1.40 (d, 3H, *J* = 7.5 Hz, CH_3CH), 1.31 (s, 3H, *exo* CH_3), 0.71 (s, 3H, *endo* CH_3); ^{13}C nmr (75 MHz) δ: 211.0 (C═O), 204.3 (CHO), 130.9 (═CH), 127.9 (CH═), 68.3 (CH), 57.6 (CH), 56.2 (CH), 50.3 (C), 41.9 (CMe$_2$), 39.7 (CH), 32.4 (CH$_3$), 28.1 (CH$_2$), 26.3 (CH$_3$), 24.2 (CH$_2$), 21.4 (CH$_3$); the minor set for isomer **19**: ^{1}H nmr (300 MHz) δ: 9.63 (s, 1H, C*H*O), 6.00 (m, 1H, C*H*═), 5.75 (dddd, 1H, *J* = 9.5, 6.0, 1.5, 1.5 Hz, ═C*H*), 3.0 (m, 1H, CHC*H*CH$_2$), 2.88 (ddd, 1H, *J* = 14.0, 7.0, 7.0 Hz, CH$_3$C*H*CH═), 2.20 (ddd, 1H, *J* = 15.5, 7.0, 7.0 Hz, C*H*HCH═), 2.03 (ddd, 1H, *J* = 6.0, 6.0, 2.5 Hz, C*H*CMe$_2$), 1.32 (s, 3H, *exo* CH_3), 1.05 (d, 3H, *J* = 7.0 Hz, CH_3CH), 0.66 (s, 3H, *endo* CH_3); ^{13}C nmr (75 MHz) δ: 131.1, 128.3 (CH═CH), 71.5 (CH), 57.2 (CH), 48.1 (CH$_3$), 40.7 (CH), 26.7 (CH$_3$), 26.5 (CH$_2$), 20.8 (CH$_2$), 19.1 (CH$_3$). The following data are reported for the mixture of **18** and **19**: ir: 1723 (CHO), 1693 (C═O) cm^{-1}; ms M$^+$ calcd. for $C_{15}H_{20}O_2$: 232.1463; found: 232.1461. Anal. calcd. for $C_{15}H_{20}O_2$: C 77.55, H 8.68; found: C 77.30, H 8.77.

*(1R,10S,11R)-6,12,12-Trimethyl-5-oxatricyclo[9.1.1.0^{3,10}]undeca-3,7-dien-2-one (**29**)*

Compound **29** (colourless crystals): ir: 1684 (C═O), 1602 (C═C) cm^{-1}; ^{1}H nmr (300 MHz) δ: 7.40 (s, 1H, ═C*H*-O), 5.82 (m, 1H, C*H*═), 5.53 (dddd, 1H, *J* = 15.5, 7.0, 7.0, 1.5 Hz, ═C*H*), 4.59 (dddd, 1H, *J* = 12.0, 7.0, 3.0, 1.5 Hz, O-C*H*Me), 2.81 (ddd, 1H, *J* = 12.0, 4.5, 2.0 Hz, CHC*H*CH$_2$), 2.36–2.50 (complex, 2H, CH_2CH═), 2.10 (dd, 1H, *J* = 5.5, 5.5 Hz, C*H*C═O), 1.73 (complex, 3H, CH_2C*H*), 1.39 (d, 3H, *J* = 7.5 Hz, CHCH_3), 1.35 (s, 3H, CH_3), 0.95 (s, 3H, CH_3); ^{13}C nmr (75 MHz) δ: 203.8 (C═O), 151.8 (═CH-O), 129.8, 129.6 (CH═CH), 113.0 (C═), 79.1 (CH), 56.3 (CH), 43.2 (CH), 40.9 (C), 32.4 (CH), 31.4 (CH$_2$), 26.5 (CH$_3$), 24.2 (C), 21.5 (CH$_3$), 17.8 (CH$_3$); ms M$^+$ calcd. for $C_{15}H_{20}O_2$: 232.1463; found: 232.1462.

*(1R,3R,4R,8S,9R)-3-Formyl-4,6,10,10-tetramethyltricyclo-[7.1.1.0^{3,8}]undec-5-en-2-one (**20**) and (1R,3R,4S,8S,9R)-3-formyl-4,6,10,10-tetramethyltricyclo[7.1.1.0^{3,8}]undec-5-en-2-one (**21**)*

Compounds **20** and **21** were obtained as a 133:1 mixture (colourless oil) after flash chromatography. The nmr spectra displayed two sets of signals. The major set for isomer **20**: ^{1}H nmr (300 MHz) δ: 10.04 (s, 1H, C*H*O), 5.08 (m, 1H, ═C*H*), 2.82 (dddd, 1H, *J* = 10.0, 8.0, 2.0, 2.0 Hz, CHC*H*CH$_2$), 2.61 (dd, 1H, *J* = 5.5, 5.5 Hz, C*H*C═O), 2.56 (m, 1H, CH$_3$C*H*CH═), 2.47 (m, 1H, CHH_{exo}), 2.10–2.30 (complex, 2H, CHH_eC═, C*H*CMe$_2$), 1.98 (dm, 1H, *J* = 14.5 Hz, CHH_{ax}C═), 1.90 (d, 1H, *J* = 11.0 Hz, CHH_{endo}), 1.78 (br s, 3H, CH_3C═), 1.41 (d, 3H, *J* = 7.5 Hz, CHCH_3), 1.32 (s, 3H, *exo* CH_3), 0.66 (s, 3H, *endo* CH_3); ^{13}C nmr (75 MHz) δ: 211.9 (C═O), 204.2 (CHO), 138.5 (C), 124.6 (CH═), 64.1 (C), 55.8 (CH), 48.0 (CH), 42.0 (CMe$_2$), 40.3 (CH), 33.5 (CH$_2$), 32.4 (CH), 26.4 (CH$_3$), 24.1 (CH$_2$), 22.8 (CH$_3$), 21.4 (CH$_3$), 16.2 (CH$_3$); the minor set for isomer **21**: ^{1}H nmr (300 MHz) δ 9.63 (s, 1H, C*H*O), 5.37 (m, 1H, C*H*═), 3.05 (m, 1H, CHC*H*CH$_2$), 2.93 (dd, 1H, *J* = 7.5, 7.5 Hz, C*H*C═O), 1.89-2.00 (m, 3H), 1.82 (d, 1H, *J* = 10.5 Hz, CHH_{endo}), 1.73 (br s, 3H, CH_3C═), 1.33 (s, 3H, *exo* CH_3), 1.20 (d, 3H, *J* = 7 Hz, CHCH_3), 1.02 (s, 3H, *endo* CH_3); ^{13}C nmr (75 MHz) δ 129.4 (C═), 123.6 (CH═), 61.6 (C), 57.3 (CH), 41.5 (CH), 31.5 (CH$_2$), 26.8 (CH$_3$), 23.1 (CH$_3$), 21.0 (CH$_3$), 20.7 (CH$_2$), 18.8 (CH$_3$). The following data are reported for the mixture of **20** and **21**. ir 1713 (CHO), 1694 (C═O cm^{-1}); ms M$^+$ 246.1619 (calcd. for $C_{16}H_{22}O_2$: 246.1619);

*(1R,3R,8S,9R)-(+)-3-Formyl-5,6,10,10-tetramethyltricyclo-[7.1.1.0^{3,8}]undec-5-en-2-one (**22**)*

Adduct **22** (colourless oil): $[\alpha]_D^{23}$ +25.0 (*c* 1.0, CHCl$_3$); ir: 1729 (CHO), 1698 (C═O) cm^{-1}; ^{1}H nmr (300 MHz) δ: 9.71 (s, 1H, C*H*O), 2.88 (dddd, 1H, *J* = 10.5, 6.0, 2.0, 2.0 Hz, CHC*H*CH$_2$), 2.67 (d, 1H, *J* = 15.0 Hz, CCHH_{ax}C═), 2.61 (dd, 1H, *J* = 5.5, 5.5 Hz, C*H*C═O), 2.51 (dddd, 1H, *J* = 11.0, 6.0, 5.5, 2.0 Hz, CHH_{exo}), 2.33 (br d, 1H, *J* = 15.0 Hz, CCHH_eC═), 1.97-2.17 (complex, 3H, CHC*H*HC═, CHCH*H*C═, C*H*CMe$_2$), 1.86 (d, 1H, *J* = 11 Hz, CHH_{endo}), 1.70 (br s, 3H, CH_3C═), 1.61 (br s, 3H, CH_3C═), 1.31 (s, 3H, *exo* CH_3), 0.71 (s, 3H, *endo* CH_3); ^{13}C nmr (75 MHz) δ: 213.4 (C═O), 200.6 (CHO), 130.0 (CH$_3$C═), 122.7 (CH$_3$*C*═), 63.0 (C), 57.5 (CH), 47.5 (CH), 41.3 (C), 39.9 (CH$_2$), 34.7 (CH$_2$), 30.2 (CH), 26.5 (CH$_3$), 25.1 (CH$_2$), 21.7 (CH$_3$), 19.1 (CH$_3$), 19.0 (CH$_3$); ms M$^+$ calcd. for $C_{16}H_{22}O_2$: 246.1619; found: 246.1619. Anal. calcd. for $C_{16}H_{22}O_2$: C 78.01, H 9.00; found: C 77.95, H 8.87.

*(1R,3R,8S,9R)-6-(tert-Butyldimethylsiloxy)-5,10,10-trimethyl-tricyclo[7.1.1.0^{3,8}]undec-5-en-2-one (**24**)*

Ketone **24** (colourless oil): ir: 1715 (C═O) cm^{-1}; ^{1}H nmr (300 MHz, C_6D_6)[11] δ: 4.00 (complex, 2H, CHH_e(CH$_3$)C═, CHH_eCOSi), 3.71 (dd, 1H, *J* = 11.0, 3.5 Hz, O═CC*H*CH$_2$), 3.38 (dm, 1H, *J* = 15.0 Hz, CHH_{ax}(CH$_3$)C═), 3.31 (m, 1H, CHC*H*CH$_2$), 2.34 (dm, 1H, *J* = 15.0 Hz, CHH_{ax}COSi), 2.29 (dd, 1H, *J* = 6.0, 6.0 Hz, C*H*C═O), 2.01 (d, 1H, *J* = 10.5 Hz, CHH_{endo}), 1.94 (m, 1H, C*H*CMe$_2$), 1.73 (m, 1H, CHH_{exo}), 1.43 (br s, 3H, CH_3C═), 1.01 (s, 3H, *endo* CH_3), 0.98 (s, 9H, C(CH_3)$_3$), 0.89 (s, 3H, *exo* CH_3), 0.22 (s, 3H, SiCH_3), 0.07 (s, 3H, SiCH_3); ^{13}C nmr (75 MHz, C_6D_6) δ: 204.2 (C═O), 140.9 (═C-OSi), 109.3 (CH$_3$*C*═), 75.7 (CH), 69.3 (CH$_2$), 58.6 (CH), 58.2 (C), 57.6 (CH), 49.0 (C), 40.9 (CH), 32.2 (CH$_2$), 34.7 (CH$_2$), 26.5 (CH$_3$), 25.1 (3 × CH$_3$), 21.7 (2 × CH$_3$), 19.1 (CH$_3$), 18.99 (CH$_3$); ms M$^+$ calcd. for $C_{20}H_{34}O_2Si$: 334.2328; found: 334.2324.

*1-(tert-Butyldimethylsiloxy)-4-[1-(tert-butyldimethylsiloxy)-ethenyl]-2,4-dimethylcyclohexene (**31**)*

Compound **31** (colourless oil): ^{1}H nmr (300 MHz) δ: 4.20 (d, 1H, *J* = 3.0 Hz, ═C*H*H), 4.18 (d, 1H, *J* = 3.0 Hz, ═CH*H*), 1.39 (s, 3H, CH_3C═), 1.30 (complex, 6H), 1.03 (s, 3H, CCH_3), 0.89 (s, 9H, C(CH_3)$_3$), 0.84 (s, 9H, C(CH_3)$_3$), 0.09 (s, 3H, SiCH_3), 0.07 (s, 3H, SiCH_3), 0.02 (s, 3H, SiCH_3), 0.01 (s, 3H, SiCH_3).

*(1R,3R,4S,7R,8S,9R)-3-Formyl-10,10-dimethyltetracyclo-[7.1.1.1.^{4,7}0^{3,8}]dodec-5-en-2-one (**25**) and (1R,3R,4R,7S,8S,9R)-3-Formyl-10,10-dimethyltetracyclo[7.1.1.1.^{4,7}0^{3,8}]dodec-5-en-2-one (**26**)*

The nmr spectra of the two inseparable products (as a colourless oil) exhibited two sets of signals: the major set for isomer **25**: ^{1}H nmr (300 MHz) δ: 9.81 (s, 1H, C*H*O), 6.40 (dd, 1H, *J* = 5.5, 3.0 Hz, CHCHC*H*═), 6.10 (dd, 1H, *J* = 5.5, 3.0 Hz, CCHC*H*═), 3.33 (m, 1H, CHC*H*CH═), 3.17 (m, 1H, CHC*H*CH), 3.01 (br s, 1H, CC*H*CH═), 2.42 (d, 1H, *J* = 12.0 Hz, CHH_{endo}), 2.36 (dd, 1H, *J* = 6.6, 6.0 Hz, C*H*C═O), 2.19–2.35 (complex, 2H, CHH_{exo}, CH$_2$C*H*CH), 1.70 (br d, 1H, *J* = 8.5 Hz, CHCH*H*CH), 1.32 (s, 3H, *exo* CH_3), 1.27 (ddd, 1H, *J* =

[11]The ^{1}H nmr spectrum of **24** in deuteriochloroform gave an unexpectedly complex pattern. When the solution in the nmr tube was examined by tlc, two new spots appeared, indicating that the adduct had decomposed under the mildly acidic conditions of deuteriochloroform. Subsequent nmr spectra of **24** were run in deuteriobenzene.

Can. J. Chem. Downloaded from www.nrcresearchpress.com by 85.192.166.187 on 09/08/12
For personal use only.

8.5, 4.0, 2.0 Hz, CHC*H*HCH), 0.82 (s, 3H, *endo* CH_3); ^{13}C nmr (125 MHz) δ: 217.7 (C=O), 199.9 (CHO), 142.3 (HC=), 134.0 (=CH), 68.2 (C), 65.9 (C), 57.8 (CH), 52.3 (CH), 48.2 (CH), 47.2 (CH_2), 45.4 (CH), 39.1 (CH), 27.0 (CH_3), 22.4 (CH_2), 15.3 (CH_3); the minor set for isomer **26**: ^{1}H nmr (300 MHz) δ: 10.08 (s, 1H, C*H*O), 6.21 (m, 1H, C*H*=), 6.10 (m, 1H, C*H*=), 1.31 (s, 3H, CH_3), 0.81 (s, 3H, CH_3); ^{13}C nmr (125 MHz) δ: 130.9 (HC=), 128.8 (=CH), 71.6 (C), 43.3 (C), 38.8 (CH), 30.4 (CH_2), 29.0 (CH_2), 14.1 (CH_3), 11.0 (CH_3). The mixture also showed the following spectral data: ir: 1723 (CHO), 1694 (C=O) cm^{-1}; ms M$^+$ calcd. for $C_{15}H_{18}O_2$: 230.1307; found: 230.1308.

(1R,3R,8S,9R)-(−)-6,10,10-Trimethyltricyclo[7,1,1,0^{3,8}]undec-5-en-2-one (35)

Keto aldehyde **17** (70 mg, 0.30 mmol) was dissolved in methanol (10 mL). A saturated aqueous potassium carbonate solution (10 mL) was added. After stirring for 18 h at room temperature, the reaction mixture was extracted with a solution of ether and petroleum ether (1:1; 3 × 10 mL). The combined organic layers were washed with water and brine, dried, filtered, and concentrated. Flash chromatography of the residue, eluting with 0–3% ether in petroleum ether, gave **35** (60 mg, 0.295 mmol, 98% yield); $[\alpha]_D^{23}$ –47.7 (*c* 2.286, $CHCl_3$); mp 53–54°C (crystallization from petroleum ether); ir: 1713 (C=O) cm^{-1}; ^{1}H nmr (300 MHz) δ: 5.48 (br s, 1H, =C*H*), 2.60 (dd, 1H, *J* = 5.0, 5.0 Hz, C*H*C=O), 2.30-2.50 (complex, 3H), 1.83–2.20 (complex, 6H), 1.71 (br s, 3H, =CCH_3), 1.38 (s, 3H, *exo* CH_3), 0.79 (s, 3H, *endo* CH_3); ^{13}C nmr (125 MHz) δ: 214.8 (C=O), 135.4 (=C), 121.2 (=CH), 58.6 (CH), 46.4 (CH), 45.0 (CH), 44.7 (C), 36.6 (CH_2), 36.5 (CH), 26.8 (CH_3), 25.0 (CH_2), 24.0 (CH_2), 23.7 (CH_3), 22.0 (CH_3); ms M$^+$ calcd. for $C_{14}H_{20}O$: 204.1514; found: 204.1511. Anal. calcd. for $C_{14}H_{20}O$: C 82.29; H 9.87; found: C 82.04, H 9.97.

(1R,3R,4R,8S,9R)-4,10,10-Trimethyltricyclo[7.1.1.0^{3,8}]undec-5-en-2-one (36) and (1R,3S,4R,8S,9R)-4,10,10-trimethyltricyclo[7,1,1,0^{3,8}]undec-5-en-2-one (37)

A mixture of keto aldehydes **18** and **19** (64:1, 45.0 mg, 0.194 mmol) was dissolved in methanol (20 mL). Saturated aqueous potassium carbonate (20 mL) was added. After refluxing for 15 h, the reaction mixture was cooled to room temperature and extracted with ether and petroleum ether (1:1; 3 × 15 mL). The combined organic phases were washed with water and brine, dried, filtered, and concentrated. Flash chromatography of the residue, eluting with 0–3% ether in petroleum ether, gave isomer **37** (5.2 mg, 0.025 mmol, 13% yield): ir: 1710 (C=O) cm^{-1}; ^{1}H nmr (300 MHz) δ: 5.55 (m, 1H, =C*H*), 5.49 (m, 1H, C*H*=), 2.60 (dd, 1H, *J* = 5.0, 5.0 Hz, C*H*C=O), 2.30–2.45 (complex, 3H), 2.00–2.15 (complex, 4H), 1.70 (d, 1H, *J* = 11.0 Hz, CHH_{endo}), 1.37 (s, 3H, *exo* CH_3), 1.22 (d, 3H, *J* = 7.0 Hz, CHCH_3), 0.78 (s, 3H, *endo* CH_3); ^{13}C nmr (75 MHz) δ: 215.7 (C=O), 135.3 (HC=), 130.0 (=CH), 59.2 (CH), 52.6 (CH), 45.3 (CH), 45.0 (C), 36.3 (CH), 31.6 (CH_2), 30.1 (CH), 26.8 (CH_3), 24.2 (CH_2), 21.5 (CH_3), 16.0 (CH_3); ms M$^+$ calcd. for $C_{14}H_{20}O$: 204.1514; found: 204.1512. Continued elution gave isomer **36** (31.2 mg, 0.153 mmol, 79% yield): ir 1714 (C=O) cm^{-1}; ^{1}H nmr (300 MHz) δ: 5.77–5.63 (complex, 2H, C*H*=C*H*), 2.71 (m, 1H, CHC*H*CH$_2$), 2.64 (dd, 1H, *J* = 5.0, 5.0 Hz, C*H*C=O), 2.55 (dd, 1H, *J* = 12.0, 5.5 Hz, O=CC*H*CH), 2.40 (m, 1H, CHH_{exo}), 1.98–2.20 (complex, 4H, C*H*CMe$_2$, C*H*HCH=, CH*H*CH=, MeC*H*CH=), 1.82 (d, 1H, *J* = 11 Hz, CHH_{endo}), 1.36 (s, 3H, *exo* CH_3), 1.10 (d, 3H, *J* = 7.0 Hz, CHCH_3), 0.87 (s, 3H, *endo* CH_3); ^{13}C nmr (75 MHz) δ: 214.6 (C=O), 134.3 (HC=), 126.0 (HC=), 58.5 (CH), 49.4 (CH), 45.1 (CH), 44.5 (C), 32.3 (CH), 31.5 (CH_2), 29.9 (CH), 27.2 (CH_3), 24.4 (CH_2), 21.5 (CH_3), 15.5 (CH_3); ms M$^+$ calcd. for $C_{14}H_{20}O$: 204.1514; found: 204.1513.

Acknowledgements

We are grateful to the Natural Sciences and Engineering Research Council of Canada and the University of Alberta for financial support.

1. H.J. Liu and E.N.C. Browne. Can. J. Chem. **65**, 1262 (1987).
2. H.J. Liu and E.N.C. Browne. Can. J. Chem. **57**, 377 (1979).
3. H.J. Liu and E.N.C. Browne. Tetrahedron Lett. 2929 (1977).
4. H.J. Liu and E.N.C. Browne. Can. J. Chem. **59**, 601 (1981).
5. H.J. Liu, E.N.C. Browne, and S.Y. Chew. Can. J. Chem. **66**, 2345 (1988).
6. H.J. Liu, G. Ulibarri, and E.N.C. Browne. Can. J. Chem. **70**, 1545 (1992).
7. H.J. Liu, E.N.C. Browne, and P.R. Pednekar. Can J. Chem. **60**, 921 (1982).
8. H.J. Liu, T.K. Ngooi, and E.N.C. Browne. Can. J. Chem. **66**, 3143 (188).
9. H.J. Liu and T.K. Ngooi. Synth. Commun. **12**, 715 (1982).
10. H.J. Liu, E.N.C. Browne, and S.Y. Chew. Tetrahedron Lett. **32**, 2005 (1991).
11. H.J. Liu, S.Y. Chew, E.N.C. Browne, and J.B. Kim. Can. J. Chem. **72**, 1193 (1994).
12. H.J. Liu and Y. Han. Tetrahedron Lett. **34**, 423 (1993).
13. H. Chikashita, H. Yasuda, Y. Kimura, and K. Itoh. Chem. Lett. 195 (1992).
14. D.D. Sternbach, J.W. Hughes, and D.F. Burdi. J. Org. Chem. **49**, 201 (1984).
15. M. Ceruti, I. Degani, and R. Fochi. Synthesis, 79 (1987).
16. V. Kumar and S. Dev. Tetrahedron Lett. 1289 (1983).
17. P. Bravo, P. Carrera, G. Resnati, and C. Ticoggi. J. Chem. Soc. Chem. Commun. 19 (1984).
18. J. Iriarte, J. Hill, K. Schaffner, and O. Jeger. Proc. Chem. Soc. 114 (1963).
19. G.D. Ryerson, R.L. Wasson, and H.O. House. Org. Synth. **39**, 70 (1959).
20. K. Wiesner and J. Santroch. Tetrahedron Lett. 5939 (1966).
21. A.L. Wilds and C. Djerassi. J. Am. Chem. Soc. **68**, 1715 (1946).
22. P. M. Gordon. Chem. Eng. News, **68** (32), 2 (1990).
23. J.T.B. Ferreira. Chem. Eng. News, **68** (50), 4 (1990).
24. M. Kim, R.S. Gross, H. Sevestre, and D.S. Watt. J. Org. Chem. **53**, 93 (1988).
25. D. Liotta, C. Barnum, and R. Puleo. J. Org. Chem., **46**, 2920 (1981).
26. G.B. Payne and P.H. Williams. J. Org. Chem., **26**, 651 (1961).
27. B. Zwanenburg and J. ter Wiel. Tetrahedron Lett. 935 (1970).
28. Y. Apeloig, M. Karni, and Z. Rappoport. J. Am. Chem. Soc. **105**, 2784 (1983).
29. C.A. Bunton and G.J. Minkoff. J. Chem. Soc. 665 (1945).
30. D.L.J. Clive. Tetrahedron, **34**, 1088 (1978).
31. D. Walker and J.D. Hiebert. Chem. Rev. **67**, 153 (1967).
32. G. Zima and D. Liotta. Synth. Commun. **9**, 697 (1979).
33. Y.X. Han. Ph. D. Thesis, Department of Chemistry, University of Alberta, Edmonton. (1992).
34. R.M. Silverstein, G.C. Bassler, and T.C. Morrill. Spectrometric identification of organic compounds. Wiley, New York. (1980).
35. L.M. Sweeting, D.C. Crans, and G.M. Whitesides. J. Org. Chem. **52**, 2273 (1987).
36. T.J. Wenzel. NMR Shift Reagents, CRC Press, Boca Raton, Fla. 1987.
37. P. Lavallee and G. Bouthillier. J. Org. Chem. **51**, 1362 (1985).
38. D.R. Rabenstein and T.T. Nakashima. Anal. Chem. **51**, 1465A (1979).
39. S.K. Patt and T.N. Shoolery. J. Magn. Reson. **46**, 535 (1982).
40. C.W. Still, M. Kahn, and A. Mitra. J. Org. Chem. **43**, 2923 (1978).

Porphyrin chemistry pertaining to the design of anti-cancer drugs; part 1, the synthesis of porphyrins containing *meso*-pyridyl and *meso*-substituted phenyl functional groups

GUANGZHEN G. MENG AND BRIAN R. JAMES[1]

Department of Chemistry, University of British Columbia, Vancouver, BC V6T 1Z1, Canada

AND

KIRSTEN A. SKOV

Department of Medical Biophysics, B.C. Cancer Research Centre, Vancouver, BC V5Z 1L3, Canada

Received March 31, 1994

GUANGZHEN G. MENG, BRIAN R. JAMES, and KIRSTEN A. SKOV. Can. J. Chem. **72**, 1894 (1994).

Condensation of pyrrole with a benzaldehyde and 4-pyridinecarboxaldehyde mixture yields the six possible *meso*-substituted phenyl or pyridyl porphyrins. Nitration of four of these has yielded 13 other porphyrins containing one to four 4-nitrophenyl moieties, and $SnCl_2$ reduction of eight of these nitrophenylporphyrins gives the corresponding 4-aminophenyl(phenyl)- or 4-aminophenyl(phenyl)(4-pyridyl)-porphyrins. Twelve of the porphyrins are new, but all 27 are fully characterized by ^1H NMR; resonances for every proton within each of the phenyl, pyridyl, and pyrrole rings are assigned. Trends in UV–VIS data are discussed, while IR and mass spectral data are noted for selected porphyrins.

GUANGZHEN G. MENG, BRIAN R. JAMES et KIRSTEN A. SKOV. Can. J. Chem. **72**, 1894 (1994).

La condensation du pyrrole avec un mélange de benzaldéhyde et de 4-pyridinecarboxyaldéhyde conduit à un mélange des six porphyrines possibles substituées en *méso* par des groupes phényle ou pyridyle. La nitration de quatre de ces isomères a fourni 13 autres porphyrines comportant de une à quatre portions 4-nitrophényles et la réduction de huit de ces dérivés nitrés par du $SnCl_2$ a fourni les porphyrines correspondantes portant des substituants 4-aminophényl(phényle) ou 4-aminophényl(phényl)(4-pyridyle). Douze de ces porphyrines sont des produits nouveaux, mais on a complètement caractérisé les 27 par RMN du ^1H; on a attribué chacun des protons de chaque noyau phényle, pyridyle ou pyrrole. On discute des tendances dans les spectres UV alors que l'on a déterminé les spectres IR et de masse de certaines porphyrines.

[Traduit par la rédaction]

Introduction

A limitation of radiotherapy is the lack of selectivity toward tumor cells, especially toward the hypoxic tumor cells (1). Porphyrin drugs used in photodynamic therapy (PDT) have good selectivity toward tumors because of accumulation in cancer cells, but the therapy has a limitation governed by tissue penetration of the light (2). The rationale for the work described here was that the radiosensitization abilities of porphyrins (3–5) might be improved by introduction of certain groups (including nitro groups and metal ions, which have been shown in non-porphyrin systems to act as radiosensitizers (6)), with the tumor accumulation abilities being retained or improved, possibly by balancing lipophilicity and hydrophilicity of the porphyrin or by introducing nitro group(s) (6). Use of such a drug, which first accumulates in tumors, then kill cells via sensitization of the cells to ionizing radiation, may overcome the noted limitations of both radiotherapy and PDT because hypoxic cells might be selectively sensitized and X-rays are known to penetrate tissues well. If appropriate porphyrin compounds can be synthesized, they may also have potential for use in other aspects of cancer treatments and diagnosis, including PDT (7), chemotherapy (8), boron neutron capture therapy (9), and magnetic resonance imaging diagnosis (10). This paper reports the synthesis and characterization of porphyrins containing within *meso* substituents some functional groups that might possibly be beneficial for DNA binding ($-NH_2$, pyridine), and for radiosensitization ($-NO_2$ (6)). The *meso* substituents, phenyl and pyridine, can also be further functionalized to give water solubility by sulfonation of the phenyl (11*a*) or methylation of the pyridine (11*a*).

Early studies on natural porphyrin free-bases suggested that their use as radiosensitizers was not promising (3, 4). Some encouraging results for use of synthetic porphyrins and metalloporphyrins as radiosensitizers were published recently by O'Hara et al. (5); the highest radiosensitization efficiencies were found for cobalt(III) complexes of Tet(MPy)P (5,10,15,20-tetrakis(4-methylpyridinium)porphyrin) and Tet(SPh)P (5,10,-15,20-tetrakis(4-sulfonatophenyl)porphyrin), although no details were given on the synthesis or characterization of the porphyrin species. Figure 1 shows the porphyrin structures and abbreviations use in the present work.

Based on the findings in various laboratories on the importance of the presence of a nitro aromatic group in an electron affinic radiosensitizer (6), the work reported here evolved from an initial study focused on synthesis of nitrophenyl-containing porphyrins. The porphyrins were synthesized via a method combining monopyrrole/aromatic aldehyde condensation with subsequent modifications of the *meso* phenyls. Thus, condensation of pyrrole, benzaldehyde, and 4-pyridinecarboxaldehyde gives a mixture of six porphyrins (**1**–**6**, Fig. 1), which is separated by column chromatography. The subsequent modifications, determined by structure design of the required porphyrins, are nitration of phenyls (giving compounds **7**–**19**, Fig. 1), and reduction of the nitro groups to form amines (giving compounds **19**–**27**, Fig. 1). Sulfonation of the phenyl groups, methylation of the pyridyls, metallation of the porphyrins, and biological testing of selected porphyrin bases and metalloporphyrins are reported elsewhere (11).

Experimental section

Pyrrole, benzaldehyde, and 4-pyridinecarboxaldehyde were purchased from Aldrich Chemical Company. Other chemicals (including nitric acid, sulfuric acid, etc.) were analytical grade, and were used

[1]Author to whom correspondence may be addressed. Tel: (604) 822-6645. Fax: (604) 822-2847.

Can. J. Chem. Downloaded from www.nrcresearchpress.com by 85.192.166.187 on 09/08/12
For personal use only.

Can. J. Chem. Downloaded from www.nrcresearchpress.com by 85.192.166.187 on 09/08/12
For personal use only.

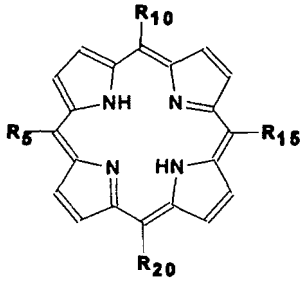

Ph=phenyl

NPh=4-nitrophenyl; APh=4-aminophenyl

Py=4-pyridyl 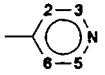

R_5= R_{10}=R_{15}=R_{20}=Ph	TetPhP [5,10,15,20-tetraphenylporphyrin]	1
R_5=R_{10}=R_{15}=Ph, R_{20}=Py	TPhPyP [5,10,15-triphenyl-20-(4-pyridyl)porphyrin]	2
R_5=R_{10}=Ph, R_{15}=R_{20}=Py	*cis*-DPhBPyP [5,10-diphenyl-15,20-bis(4-pyridyl)porphyrin]	3
R_5=R_{15}=Ph, R_{10}=R_{20}=Py	*trans*-DPhBPyP [5,15-diphenyl-10,20-bis(4-pyridyl)porphrin]	4
R_5=Ph, R_{10}=R_{15}=R_{20}=Py	PhTPyP [5-phenyl-10,15,20-tris(4-pyridyl)porphyrin]	5
R_5=R_{15}=R_{10}=R_{20}=Py	TetPyP [tetrakis(4-pyridyl)porphyrin]	6
R_5=NPh, R_{10}=R_{15}=R_{20}=Ph	(NPh)TPhP [5-(4-nitrophenyl)-10,15,20-triphenylporphyrin]	7
R_5=R_{10}=NPh, R_{15}=R_{20}=Ph	*cis*-B(NPh)DPhP [5,10-bis(4-nitrophenyl)-15,20-diphenyl-porphyrin]	8
R_5=R_{15}=NPh, R_{10}=R_{20}=Ph	*trans*-B(NPh)DPhP [5,15-bis(4-nitrophenyl)-10,20-diphenyl-porphyrin]	9
R_5=R_{10}=R_{15}=NPh, R_{20}=Ph	T(NPh)PhP [5,10,15-tris(4-nitrophenyl)-20-phenylporphyrin]	10
R_5=R_{10}=R_{15}=R_{20}=NPh	Tet(NPh)P [5,10,15,20-tetrakis(4-nitrophenyl)porphyrin]	11
R_5=NPh, R_{10}=R_{15}=Ph, R_{20}=Py	*cis*-(NPh)DPhPyP [5-(4-nitrophenyl)-10,15-diphenyl-20-(4-pyridyl)porphyrin]	12
R_5=R_{10}=NPh, R_{15}=Ph, R_{20}=Py	*cis*-B(NPh)PhPyP [5,10-bis(4-nitrophenyl)-15-phenyl-20-(4-pyridyl)porphyrin]	13
R_5=R_{15}=NPh, R_{10}=Ph, R_{20}=Py	*trans*-B(NPh)PhPyP [5,15-bis(4-nitrophenyl)-10-phenyl-20-(4-pyridyl)porphyrin]	14
R_5=R_{10}=R_{15}=NPh, R_{20}=Py	T(NPh)PyP [5,10,15-tris(4-nitrophenyl)-20-(4-pyridyl)porphyrin]	15
R_5=NPh, R_{10}=Ph, R_{15}=R_{20}=Py	*cis*-(NPh)PhBPyP [5-(4-nitrophenyl)-10-phenyl-15,20-bis(4-pyridyl)porphyrin]	16
R_5=R_{10}=NPh, R_{15}=R_{20}=Py	*cis*-B(NPh)BPyP [5,10-bis(4-nitrophenyl)-15,20-bis(4-pyridyl)-porphyrin]	17
R_5=R_{15}=NPh, R_{10}=R_{20}=Py	*trans*-B(NPh)BPyP [5,15-bis(4-nitrophenyl)-10,20-bis(4-pyridyl)-porphyrin]	18
R_5=NPh, R_{10}=R_{15}=R_{20}=Py	(NPh)TPyP [5-(4-nitrophenyl)-10,15,20-tris(4-pyridyl)porphyrin]	19
R_5=APh, R_{10}=R_{15}=R_{20}=Ph	(APh)TPhP [5-(4-aminophenyl)-10,15,20-triphenylporphyrin]	20
R_5=R_{10}=APh, R_{15}=R_{20}=Ph	*cis*-B(APh)DPhP [5,10-bis(4-aminophenyl)-15,20-diphenyl-porphyrin]	21
R_5=R_{15}=APh, R_{10}=R_{20}=Ph	*trans*-B(APh)DPhP [5,15-bis(4-aminophenyl)-10,20-diphenyl-porphyrin]	22
R_5=R_{10}=R_{15}=APh, R_{20}=Ph	T(APh)PhP [5,10,15-tris(4-aminophenyl)-20-phenylporphyrin]	23
R_5=APh, R_{10}=R_{15}=Ph, R_{20}=Py	*cis*-(APh)DPhPyP [5-(4-aminophenyl)-10,15-diphenyl-20-(4-pyridyl)porphyrin]	24
R_5=R_{15}=APh, R_{10}=Ph, R_{20}=Py	*trans*-B(APh)PhPyP [5,15-bis(4-aminophenyl)-10-phenyl-20-(4-pyridyl)porphyrin]	25
R_5=APh, R_{10}=Ph, R_{15}=R_{20}=Py	*cis*-(APh)PhBPyP [5-(4-aminophenyl)-10-phenyl-15,20-bis-(4-pyridyl)porphyrin]	26
R_5=APh, R_{10}=R_{15}=R_{20}=Py	(APh)TPyP [5-(4-aminophenyl)-10,15,20-tris(4-pyridyl)porphyrin]	27

FIG. 1. Porphyrin structures and abbreviations; B = bis, D = di, T = tri(s), Tet = tetra(kis), P = porphyrin.

TABLE 1. ^{1}H NMR data for **1–6**[a]

Porphyrin	Pyrrole	3,4,5-Ph	2,6-Ph	3,5-Py	2,6-Py	*N*-Pyrrole
1, TetPhP	8.85 s (8)	7.78 m (12)	8.23 m (8)	—	—	−2.78 s (2)
2, TPhPyP	8.90 d, 8.87 s, 8.81 d (2, 4, 2)	7.78 m (9)	8.23 m (6)	9.04 q (2)	8.18 q (2)	−2.80 s (2)
3, *cis*-DPhBPyP	8.92 d, 8.88 s, 8.85 s, 8.81 d, (2, 2, 2, 2)	7.80 m (6)	8.22 m (4)	9.05 q (4)	8.18 q (4)	−2.84 s (2)
4, *trans*-DPhBPyP	8.91 d, 8.81 d, (4, 4)	7.80 m (6)	8.22 m (4)	9.05 q (4)	8.18 q (4)	−2.84 s (2)
5, PhTPhP	8.94 d, 8.86 s, 8.83 d (2, 4, 2)	7.81 m (3)	8.22 m (2)	9.06 m (6)	8.18 m (6)	−2.88 s (2)
6, TetPyP	8.88 s (8)	—	—	9.08 q (8)	8.19 q (8)	−2.92 s (2)

[a]In $CDCl_3$ at ~20°C; δ signal pattern (number of protons).

without further purification. TLC plates (0.2 cm) of alumina (neutral, activity I) and of silica gel, and silica gel were BDH products. The alumina activity I (neutral, Fisher Chemicals) was converted to activity III and IV types by mixing with 10 and 15% water, respectively, 24 h before using.

NMR spectra were recorded on a Varian XL-300 or a Bruker WH-400 instrument operating in the Fourier transform mode, using TMS as reference (s = singlet, d = doublet, q = quartet, m = multiplet). UV–VIS spectra were recorded on a Perkin Elmer 552A spectrometer, with quartz cells (0.100 or 1.00 cm). Mass spectroscopy (NH_3 chemical ionization) was performed by the mass spectroscopy laboratory, Department of Chemistry, U.B.C. Infrared spectra (Nujol mulls) were recorded on a Nicolet 5DX FTIR spectrometer. Microanalyses were performed by Mr. P. Borda of the Department of Chemistry, U.B.C.

Porphyrins 1–6

These porphyrins, comprising TetPhP (**1**), TPhPyP (**2**), *cis*-DPhBPyP (**3**), *trans*-DPhBPyP (**4**), PhTPyP (**5**), and TetPyP (**6**), with phenyl and (or) pyridyl *meso* substituents, were synthesized from condensation of pyrrole, benzaldehyde, and 4-pyridinecarboxaldehyde (2:1:1) as described generally by Little et al. (12). Benzaldehyde (3.0 mL), 4-pyridinecarboxaldehyde (4.0 mL), and pyrrole (4.4 mL) were added to hot propionic acid (250 mL) in a 500 mL round-bottom flask, and the mixture was refluxed for 1 h. A precipitate (0.55 g) was filtered off from the cooled reaction mixture. The filtrate was concentrated to about 50 mL and then acetone (500 mL) was added with stirring; the mixture was filtered to yield another 1.78 g of precipitate, which was combined with the precipitate collected earlier. A portion of this crude product (0.5 g), a mixture of the six porphyrins, was dissolved in $CHCl_3$ (180 mL) and loaded on a column of silica gel (5 × 30 cm); **1** and **2** were eluted off successively with $CHCl_3$ (~1.5 L), while the mixture of **3–6** was eluted off using a mixed solvent (9:1 $CHCl_3$/MeOH). The solution of **3–6** was evaporated to dryness, and then the residue was dissolved in minimum $CHCl_3$ (~150 mL), loaded on a column of alumina activity III (3 × 70 cm), and eluted with $CHCl_3$ (~2 L). Four purple bands appeared on the column. *trans*-DPhBPyP (**4**) was first eluted and then the solvent in the column was forced out under N_2 pressure. The bands were removed using a spatula ("digging out" the bands saved time and eluant), and the alumina portions containing porphyrin were washed on fret filters using a mixed solvent to dissolve the porphyrins (9:1 $CHCl_3$/MeOH, ca. 0.2 L for each portion). The bands in order from top to bottom on the column contained TetPyP (**6**), PhTPyP (**5**), and *cis*-DPhBPyP (**3**). All the porphyrin solutions were washed with 5% Na_2CO_3 solution and then water; the organic phases containing the porphyrins were evaporated to dryness. Acetone (~10 mL) was added to the residues, and these were filtered off and air-dried. The yields (%) for the porphyrins were 7.5 (**1**), 9.0 (**2**), 4.5 (**3**), 1.5 (**4**), 2.0 (**5**), and 1.0 (**6**).

TetPyP (**6**) was also synthesized by the condensation of pyrrole and 4-pyridinecarboxaldehyde (1:1) in propionic acid as described above. The main portion of the propionic acid was evaporated off first, and then the porphyrin product was precipitated by addition of acetone; this precipitate was filtered, washed with acetone, and air-dried (25% yield).

^{1}H NMR data for **1–6** are shown in Table 1. UV–VIS data for these and other porphyrins are shown in Table 2. Samples of **3** and **5** obtained from the alumina column were contaminated by alumina, and gave low C and N values by elemental analysis. Alumina was found to be slightly soluble in $CHCl_3$, and in 9:1 $CHCl_3$/MeOH, probably to ~20 mg L^{-1} at ambient conditions. Further purification of **3** and **5** was not attempted. Elemental analyses for **1–6** are given in Table 3, together with data for other porphyrins. Mass spectral data for **3** and **5** are given in the footnote *c* of Table 3.

Nitrations

The nitration reactions were performed with concentrated HNO_3. Generally, a porphyrin (0.2–0.5 g) was dissolved in, or mixed with, acetic acid (30–50 mL) in a Schlenk tube, which was placed in an ice-bath. Concentrated H_2SO_4 (10 mL), which was used as dehydration reagent in some cases, was added dropwise with stirring, and then concentrated HNO_3 (10–20 mL) was added similarly before the ice-bath was removed. A stopcock on the side arm of the Schlenk tube was left open to avoid buildup of pressure. The reaction mixture changed from purple to green when either H_2SO_4 or HNO_3 was added. The ratio of the reactants and the reaction time used depend on the porphyrin and the intended degree of nitration, which was monitored by TLC (silica gel or alumina). Samples for TLC were first neutralized with Na_2CO_3 solution and extracted with $CHCl_3$; then the $CHCl_3$ solutions were introduced onto the TLC plates, which were developed using $CHCl_3$. The retention time of a porphyrin increased with the number of nitro groups.

When the intended nitration was complete, cold water (about the same volume as the reaction mixture) was added slowly to quench the reaction with liberation of heat. The hot mixture was cool by an ice-bath and neutralized first with concentrated NaOH, then with dilute Na_2CO_3 to pH ~8 (the color of the reaction mixtures changed from green to purple or brown at pH ≥4). The product was extracted with $CHCl_3$ (100–200 mL), the $CHCl_3$ portion was washed with water (3 × 100 mL), and the $CHCl_3$ layer was evaporated to dryness. The residue was washed with acetone (~50 mL), filtered off, and dried.

Nitration usually gave a mixture of products, and column chromatography was used to separate them. The compositions of the reaction mixtures, reaction times, details about column chromatography, and other experimental conditions for each porphyrin are described below.

7, (NPh)TPhP

TetPhP (0.5 g) was dissolved in acetic acid (50 mL), and concentrated HNO_3 (20 mL) was added with stirring. Reaction was monitored using TLC (silica gel, 0.2 cm) and, when no TetPhP could be detected

Can. J. Chem. Downloaded from www.nrcresearchpress.com by 85.192.166.187 on 09/08/12
For personal use only.

TABLE 2. UV–VIS data for the porphyrins[a]

Porphyrin	Soret	Visible IV	Visible III	Visible II	Visible I
1, TetPhP	416.7 (427)	513.6 (17.7)	548.7 (7.6)	590.7 (6.8)	649.7 (6.2)
2, TPhPyP	416.5 (474)	512.9 (22.6)	548.3 (10.7)	588.5 (9.2)	645.5 (8.5)
3, *cis*-DPhBPyP[b]	416.0 (354)	512.5 (15.6)	546.5 (5.1)	588.5 (4.7)	641.8 (2.0)
4, *trans*-DPhBPyP	415.5 (350)	511.5 (16.2)	546.0 (6.6)	587.1 (5.6)	642.5 (3.3)
5, PhTPyP[b]	415.7 (301)	511.6 (14.9)	545.1 (5.4)	588.2 (5.7)	641.8 (2.5)
6, TetPyP	415.0 (348)	510.4 (18.3)	542.8 (6.2)	588.0 (7.3)	642.0 (2.8)
7, (NPh)TPhP	418.0 (418)	515.3 (17.8)	550.5 (8.7)	589.3 (6.4)	646.6 (5.3)
8 and **9**, B(NPh)DPhP[b,c]	419.5 (314)	514.5 (19.3)	550.3 (9.3)	588.0 (6.3)	645.0 (3.7)
10, T(NPh)PhP	421.3 (262)	515.5 (17.5)	550.4 (8.7)	590.0 (6.2)	646.5 (3.8)
12, *cis*-(NPh)DPhPyP	417.6 (345)	513.9 (19.0)	549.8 (8.0)	587.6 (6.5)	645.5 (3.5)
13, *cis*-B(NPh)PhPyP	418.6 (301)	513.0 (19.7)	547.5 (8.0)	587.7 (7.1)	644.5 (3.4)
14, *trans*-B(NPh)PhPyP	419.0 (295)	513.5 (18.9)	548.5 (8.5)	588.9 (7.1)	644.1 (3.7)
15, T(NPh)PyP[b]	419.4 (306)	514.0 (19.7)	549.0 (9.3)	590.1 (7.7)	644.9 (4.1)
16, *cis*-(NPh)PhBPyP	416.4 (316)	512.7 (18.0)	548.0 (7.2)	589.0 (6.6)	644.0 (4.3)
17, *cis*-B(NPh)BPyP	418.9 (360)	513.3 (22.2)	548.5 (8.1)	591.6 (7.7)	645.5 (3.0)
18, *trans*-B(NPh)BPyP	418.8 (258)	514.6 (17.2)	548.0 (7.3)	589.3 (6.8)	642.4 (2.9)
19, (NPh)TPyP	416.8 (290)	512.2 (17.2)	545.7 (6.2)	588.5 (6.4)	642.5 (2.6)
20, (APh)TPhP	419.5 (395)	515.0 (18.7)	551.7 (10.6)	590.0 (6.8)	645.5 (5.8)
21, *cis*-B(APh)DPhP	421.5 (330)	517.5 (15.4)	555.0 (10.9)	592.5 (6.4)	650.0 (6.2)
22, *trans*-B(APh)DPhP	421.0 (336)	517.0 (15.8)	555.0 (11.0)	591.9 (6.1)	649.7 (5.9)
23, T(APh)PhP	423.8 (311)	518.2 (13.0)	558.3 (10.6)	593.5 (5.2)	651.5 (6.1)
24, *cis*-(APh)DPhPyP	418.8 (403)	515.3 (20.7)	551.0 (13.4)	589.4 (9.6)	648.4 (9.7)
25, *trans*-B(APh)PhPyP	422.3 (314)	518.0 (18.0)	555.0 (12.8)	592.0 (8.0)	650.0 (9.6)
26, *cis*-(APh)PhBPyP[b]	419.8 (308)	515.4 (16.4)	552.7 (8.4)	590.0 (5.6)	648.3 (3.8)

[a]In $CHCl_3$, ~20°C at 1×10^{-5} M; λ_{max} (extinction coefficient ($\varepsilon \times 10^{-3}$, M^{-1} cm^{-1})).
[b]Samples contaminated with alumina; thus, the ε values are minimum ones.
[c]A mixture of the *cis* and *trans* isomers.

TABLE 3. Elemental analyses of the porphyrins[a]

Porphyrin	C (%)	H (%)	N (%)
1, TetPhP	85.86(85.99)	4.82(4.89)	8.95(9.12)
2, TPhPyP	83.81(83.90)	4.69(4.72)	11.34(11.38)
3, *cis*-DPhBPyP[b,c]	78.40(81.84)	4.70(4.55)	12.74(13.64)
4, *trans*-DPhBPyP·H_2O	79.66(79.48)	4.64(4.76)	13.12(13.23)
5, PhTPyP[b,c]	77.13(79.73)	4.38(4.40)	15.09(15.87)
6, TetPyP·1/2H_2O[d]	76.56(76.56)	4.34(4.56)	17.86(17.67)
7, (NPh)TPhP	80.03(80.12)	4.46(4.40)	10.63(10.62)
8 and **9**, B(NPh)DPhP (a mixture)	74.96(75.00)	3.95(3.98)	11.79(11.93)
10, T(NPh)PhP·1/2H_2O	69.51(69.66)	3.85(3.69)	12.82(12.93)
12, *cis*-(NPh)DPhPyP·1/2H_2O	77.46(77.20)	4.22(4.33)	12.58(12.56)
13, *cis*-B(NPh)PhPyP·H_2O	71.51(71.37)	3.90(4.01)	13.61(13.55)
14, *trans*-B(NPh)PhPyP·H_2O	71.74(71.37)	3.80(4.01)	13.61(13.55)
15, T(NPh)PyP[b]	63.95(68.25)	4.35(3.44)	11.45(15.61)
16, *cis*-(NPh)PhBPyP·1/2H_2O[c]	75.22(75.66)	4.21(4.18)	14.63(14.40)
17, *cis*-B(NPh)BPyP·H_2O	69.49(69.61)	3.72(3.87)	15.18(15.48)
18, *trans*-B(NPh)BPyP[c]	71.19(71.38)	4.00(3.70)	15.52(15.85)
19, (NPh)TPyP·1/2H_2O	73.20(73.33)	4.09(4.05)	16.78(16.68)
20, (APh)TPhP	83.81(83.94)	4.83(4.92)	10.98(11.13)
21, *cis*-B(APh)DPhP·H_2O	80.79(80.86)	5.13(5.05)	12.87(12.86)
22, *trans*-B(APh)DPhP·H_2O	81.06(80.86)	5.13(5.05)	12.60(12.86)
23, T(APh)PhP·1/2H_2O	79.34(79.04)	5.23(5.09)	14.58(14.67)
24, *cis*-(APh)DPhPyP·H_2O	79.63(79.63)	4.91(4.94)	12.59(12.96)
25, *trans*-B(APh)PhPyP	77.89(77.83)	5.03(4.98)	14.46(14.78)
26, *cis*-(APh)PhBPyP[b,c]	75.78(79.87)	4.49(4.60)	14.56(15.53)

[a]Presented as found (calculated).
[b]Samples were contaminated by alumina.
[c]CI (NH_3) mass spectra (peaks with >20% relative intensity), *m/z*, assignment (relative intensity). For **3**: 616[M]$^+$ (81), 617 [M + 1]$^+$ (100), 618 [M + 2]$^+$ (38). For **5**: 617 [M]$^+$ (57), 618 [M + 1]$^+$ (100), 619 [M + 2]$^+$ (38). For **16**: 661 [M]$^+$ (25), 662 [M + 1]$^+$ (100), 663 [M + 2]$^+$ (44). For **18**: 706 [M]$^+$ (35), 707 [M + 1]$^+$ (100), 708 [M + 2]$^+$ (39). For **26**: 631 [M]$^+$ (80), 632 [M + 1]$^+$ (100), 633 [M + 2]$^+$ (41), 646 [M + NH]$^+$ (20), 647 [M + NH_2]$^+$ (28).
[d]Sample was synthesized from condensation of pyrrole and 4-pyridinecarboxaldehyde.

Can. J. Chem. Downloaded from www.nrcresearchpress.com by 85.192.166.187 on 09/08/12
For personal use only.

Can. J. Chem. Downloaded from www.nrcresearchpress.com by 85.192.166.187 on 09/08/12
For personal use only.

(~1 h), the reaction was stopped and the crude product was collected as described above. This was passed through alumina (activity III, 3 × 10 cm) with $CHCl_3$ as eluant to separate out some non-porphyrin materials, which remained on the top of the column. The eluted solution was evaporated to dryness, and 0.51 g crude product was collected; this was loaded onto alumina (activity I, 3 × 30 cm), and eluted with $CHCl_3$, when three brown bands were observed. After a trace of TetPhP was eluted, solutions of **7** and *cis*- and *trans*-B(NPh)DPhP (**8** and **9**) were collected successively. The solutions were evaporated to dryness and the residues were washed with acetone and air-dried; **7** (0.40 g, 74% yield), and **8** and **9** (~0.03 g as a by-product) were isolated.

8 and 9, cis- *and* trans-*B(NPh)DPhP*

All conditions were as described above for the synthesis of **7**, except that the reaction time was ~5 h, when no **7** could be detected by TLC (silica gel). After a trace of **7** was eluted, **8** and **9** were eluted together from alumina (activity I, 3 × 30 cm); 0.40 g, 70% yield. Attempts to separate **8** and **9** on an alumina column failed.

10, T(NPh)PhP

Conditions were as described above for the synthesis of **7**, but the reaction mixture was stirred for ~2 d, when no **8** and **9** were present according to TLC (silica gel); **10** was collected in ~30% yield via the major eluted band from alumina (activity I, 3 × 30 cm). Traces of **8** and **9**, and the tetra-nitro product **11**, were also separated and isolated in small quantities (~2% yield each).

An attempt to prepare Tet(NPh)P (**11**) failed because the required, lengthy reaction time (≥ 7 d) damaged the porphyrin structure. Purification of **11**, isolated as by-product from the synthesis of **10**, failed because of its low solubility in common solvents; **11** was identified only by ^1H NMR of a dilute solution in $CDCl_3$ (see Table 4 below).

12, cis-*(NPh)DPhPyP*

Conditions and procedures were as used for the synthesis of **7**, except that TPhPyP (**2**) (0.50 g) was used as precursor; the reaction was stopped after 5 h when no **2** could be detected by TLC (alumina, activity I, 0.2 cm). After a trace of **2**, **12** was eluted by $CHCl_3$ from alumina (activity III, 3 × 30 cm); the solution of **12** was collected, washed with water, and the $CHCl_3$ layer was separated and evaporated to dryness. The residue was then washed with acetone and air-dried (60% yield).

13 and 14, cis- *and* trans-*B(NPh)PhPyP*

Conditions and precursor were as described above for the synthesis of **12**, but the reaction was stopped after 20 h when no **12** could be detected by alumina TLC. After a trace of **12** eluted, **13** and **14**, and a small amount of T(NPh)PyP (**15**), were eluted from alumina (activity III, 3 × 30 cm). The *cis* and *trans* isomers were observed as the two major bands on the column, but were collected together because of poor separation (~60% yield). A smaller amount (20 mg) of this mixture was separated using a longer column (2 × 40 cm), the *trans* isomer being eluted first; about equal amounts of the two isomers were obtained.

15, T(NPh)PyP

Conditions were again the same as described for the synthesis of **12**, but the reaction was stopped after 40 h when a significant amount of **15** could be detected by alumina TLC. After **13** and **14** were eluted by $CHCl_3$, **15** was eluted out with 9:1 $CHCl_3$/MeOH from alumina (activity III, 3 × 30 cm) (~30% yield).

16, cis-*(NPh)PhBPyP*

cis-DPhBPyP (**3**) (0.20 g) was mixed with acetic acid (30 mL) and concentrated H_2SO_4 (10 mL), and then concentrated HNO_3 (10 mL) was added dropwise, and the mixture was stirred. The reaction was stopped after 20 h when no **3** could be detected by alumina TLC. The isolated crude product was separated using alumina (activity IV, 2 × 60 cm). After a trace of **3** was eluted, **16** and a trace of *cis*-B(NPh)BPyP (**17**) were collected; the yield of **16** was 55%.

17, cis-*B(NPh)BPyP*

The conditions were the same as those given for the synthesis of **16**. The reaction was stopped after 24 h when no **3** or **16** could be detected by alumina TLC. The crude product was separated on alumina (activity IV, 2 × 40 cm). After a trace of **16** was eluted, **17** was collected (~70% yield).

18, trans-*B(NPh)BPyP*

Conditions were again the same as described for the synthesis of **16**, but *trans*-DPhBPyP (**4**) (0.20 g) was used as precursor and the reaction was stopped after 24 h when no **4** and no mono-nitration product could be detected by alumina TLC. The solubilities of the crude product (70% yield) in $CHCl_3$ or CH_2Cl_2 were low. The crude product looked ~90% pure by TLC and ^1H NMR data; a portion (20 mg) was purified on alumina activity IV (2 × 40 cm) using $CHCl_3$ as eluent (~200 mL).

19, (NPh)TPyP

Conditions were the same as for the synthesis of **16**, but PhTPyP (**5**) was used as precursor. The reaction was stopped after 2 d when no **5** could be detected by alumina TLC. The pure product (~60% yield) was separated from a green impurity using alumina (activity IV, 2 × 40 cm) with $CHCl_3$ as eluent (~200 mL).

Elemental analyses of the nitrated porphyrins (for samples stored and weighed in air) are shown in Table 3; footnote *c* contains some mass spectral data for **16** and **18**. The ^1H NMR and UV–VIS data are given in Tables 4 and 2, respectively.

Reductions of the nitroporphyrins

Reductions were performed according to a literature method (13). Generally, the nitroporphyrin (0.1 g) was dissolved in $CHCl_3$ (20 mL) in a 250 mL round-bottom flask with magnetic stirring; acetic acid (30 mL) and then a solution of $SnCl_2$ (0.3 g in 30 mL concentrated HCl) were added. The mixture was stirred and refluxed overnight, and then was neutralized with concentrated NaOH and dilute Na_2CO_3 solutions to pH 8–9, an ice-bath being used for cooling; H_2O (100 mL) and $CHCl_3$ (100 mL) were then added. The organic layer was separated, filtered, washed with water (3 × 100 mL), and then evaporated to dryness. The crude product was purified on alumina (activity IV, 2 × 30 cm), using ~250 mL $CHCl_3$ or a 9:1 mixture of $CHCl_3$/MeOH as eluent. The yield was ≥ 90% for all the porphyrins.

To synthesize *cis*- and *trans*-B(APh)DPhP (**21** and **22**), a mixture of *cis*- and *trans*-B(NPh)DPhP (**8** and **9**) was used as the precursor, but a separation of the aminophenyl isomers was achieved on alumina ($CHCl_3$ as eluent). The *trans* isomer was eluted first from the column.

The (APh)TPyP (**27**) compound was synthesized from (NPh)TPyP (**19**), but only the ^1H NMR spectrum was recorded. A pure sample of **27** was not obtained because its low solubilities in common solvents made column chromatography impractical.

The more polar *cis*-(APh)PhBPyP (**26**) prepared from **16** was purified on an alumina column using $CHCl_3$/MeOH as eluent. The other aminophenylporphyrins, (APh)TPhP (**20**), T(APh)PhP (**23**), *cis*-(APh)DPhPyP (**24**), and *trans*-B(APh)PhPyP (**25**), prepared from **7**, **10**, **12**, and **14**, respectively, were purified using $CHCl_3$ as eluent.

The UV–VIS and ^1H NMR data and elemental analyses (for samples stored and weighed in air) for these aminophenylporphyrins are shown in Tables 2, 5, and 3, respectively; some mass spectral data for **26** are given in footnote *c* of Table 3.

Table 6 lists the ^1H NMR assignments for each pyrrole proton of all 27 porphyrins, while some infrared data for selected porphyrins are summarized in Table 7 (deposited).[2]

Results and discussion

Hydration of porphyrins

Associated water molecules of hydration are commonly

[2]Table 7 can be purchased from: The Depository of Unpublished Data, Document Delivery, CISTI, National Research Council Canada, Ottawa, ON K1A 0S2, Canada.

TABLE 4. ^{1}H NMR data for the nitroporphyrins[a]

Porphyrins	Pyrrole	2,6-Ph 3,4,5-Ph	3,5-Py 2,6-Py	3,5-NPh 2,6-NPh	*N*-Pyrrole
7, (NPh)TPhP	8.90 d, 8.87 s, 8.74 d, (2, 4, 2)	8.22 m (6) 7.78 m (9)	—	8.64 d (2) 8.41 d (2)	−2.80 s (2)
8 and **9**, B(NPh)DPhP[b]	8.90 d, 8.86 s, 8.77 s, 8.73 d (5/2, 3/2, 3/2, 5/2)	8.21 m (4) 7.80 m (6)	—	8.64 m (4) 8.38 m (4)	−2.83 s (2)
10, T(NPh)PhP	8.91 d, 8.79 s, 8.75 d, (2, 4, 2)	8.19 m (2) 7.99 m (3)	—	8.63 d (6) 8.38 d (6)	−2.83 s (2)
11, Tet(NPh)P[c]	8.88 s (8)	—	—	8.63 d (8) 8.38 d (8)	−2.84 s (2)
12, *cis*-(NPh)DPhPyP	8.89 d, 8.86 s, 8.82 d, 8.79 d, 8.76 d, 8.73 d, (2, 2, 1, 1, 1, 1)	8.20 m (4) 7.77 m (6)	9.04 q (2) 8.15 q (2)	8.62 d (2) 8.37 d (2)	−2.88 s (2)
13, *cis*-B(NPh)PhPyP	8.91 d, 8.85 d, 8.81 d, 8.79 d, 8.78 s, 8.75 d, (2, 1, 1, 1, 2, 1)	8.20 m (2) 7.78 m (3)	9.04 q (2) 8.14 q (2)	8.63 m (4) 8.37 m (4)	−2.87 s (2)
14, *trans*-B(NPh)PhPyP	8.92 d, 8.84 d, 8.79 d, 8.75 d, (2, 2, 2, 2)	8.19 m (2) 7.78 m (3)	9.04 d (2) 8.14 d (2)	8.63 m (4) 8.37 m (4)	−2.85 s (2)
15, T(NPh)PyP	8.86 d, 8.80 m (2, 6)	—	9.04 d (2) 8.15 d (2)	8.64 d (6) 8.38 d (6)	−2.87 s (2)
16, *cis*-(NPh)PhBPyP	8.90 d, 8.83 d, 8.83 s, 8.80 d, 8.78 d, 8.74 d, (2, 1, 2, 1, 1, 1)	8.19 q (2) 7.77 m (3)	9.04 q (4) 8.14 q (4)	8.63 m (2) 8.38 m (2)	−2.84 s (2)
17, *cis*-B(NPh)BPyP	8.86 m, 8.80 m (4, 4)	—	9.05 d (4) 8.14 d (4)	8.65 d (4) 8.38 d (4)	−2.90 s (2)
18, *trans*-B(NPh)BPyP[d]	8.86 d, 8.80 d	—	9.05 m 8.14 m	8.65 m 8.38 m	−2.90 s
19, (NPh)TPyP	8.82 m, 8.77 d (6, 2)	—	9.02 d (4) 8.10 d (4)	8.61 d (2) 8.34 d (2)	−2.99 s (2)

[a]In $CDCl_3$ at ~20°C; δ signal pattern (number of protons).
[b]A mixture of the *cis* and *trans* isomers.
[c]**11** was isolated in trace amounts, and was not pure (see experimental section, under **10**).
[d]Low concentration of the compound in the NMR sample.

found in samples of porphyrin free-bases (14, 15). Our samples were only dried under vacuum at room temperature, and elemental analyses were carried out on samples stored in air; hydration is evident, as judged by elemental analyses, by the intensity of the water signals in the ^{1}H NMR spectra, and by IR spectra in the 3200 cm^{-1} region. The hydration is probably related to the possibility of H-bonding between associated water molecule(s) and the pyrrole -N or -NH, the phenyl $-NH_2$ or $-NO_2$, or the pyridyl moieties. The elemental analyses for (NPh)TPhP (**7**), B(NPh)DPhP (**8** and **9**), and (APh)TPhP (**20**) were reported previously and are consistent with no hydration (13*a*) as found in the present work. The porphyrins TPhPyP (**2**) (14) and (NPh)TPyP (**19**) (15) have been reported as hydrated, with one-half and one water molecule, respectively, while the present data support zero and one-half water molecule, respectively. Comparison of the elemental analysis data with those of identical porphyrins (**1**, **3–6**, **10**, and **23**) reported in the literature cannot be made because such data were not reported (13*a*, 14, 16).

*Synthesis of the porphyrins **1–6***

The syntheses of these porphyrins were reported recently (16), following the earlier procedure described by Little et al. (12). The present work differs from that recent report (16), in that a significant amount of porphyrin product, besides that precipitated directly from the reaction mixture, was collected by precipitation from the concentrated condensation-reaction mixture using acetone, and therefore the yield was higher. Further, for the separation of the six porphyrins, alumina (activity III) and silica gel chromatographies with $CHCl_3$ as eluent were used instead of those reported using silica gel with a mixed solvent, $CHCl_3$–acetone–MeOH (16). All six porphyrins could be separated on a single alumina column, although use of silica gel to first separate TetPhP (**1**) and TPhPyP (**2**), followed by use of the alumina to separate the other four porphyrins, was more efficient. There is an advantage in using a single solvent because it can be readily recovered.

Mass, ^{1}H NMR (in $CDCl_3$), and UV–VIS (in CH_2Cl_2) spectroscopy data for **1–6** have been reported recently (16). The present ^{1}H NMR data (Table 1) are in good agreement with the reported data, but there are some differences in the UV–VIS data: e.g., the ε values for **3–6** are 10–20% lower in the present work, while for **2** the values were ~8% higher than the reported values (16). The alumina impurity in samples of **3** and **5** would

Can. J. Chem. Downloaded from www.nrcresearchpress.com by 85.192.166.187 on 09/08/12
For personal use only.

TABLE 5. ^{1}H NMR data for the aminoporphyrins[a]

Porphyrin	Pyrrole	2,6-Ph 3,4,5-Ph	3,5-Py 2,6-Py	2,6-APh 3,5-APh	-NH_2	*N*-Pyrrole
20, (APh)TPhP	8.93 d (2), 8.82 m (6)	8.25 m (6) 7.74 m (9)	—	7.98 d (2) 7.05 d (2)	4.00 s (2)	−2.78 s (2)
21, *cis*-B(APh)DPhP	8.91 m (4), 8.80 m (4)	8.20 q (4) 7.74 m (6)	—	7.98 d (4) 7.04 d (4)	4.00 s (4)	−2.74 s (2)
22, *trans*-B(APh)DPhP	8.91 d (4), 8.81 d (4)	8.20 q (4) 7.75 m (6)	—	7.98 d (4) 7.04 d (4)	4.00 s (4)	−2.73 s (2)
23, T(APh)PhP	8.89 s (6), 8.77 d (2)	8.19 q (2) 7.73 m (3)	—	7.97 d (6) 7.04 d (6)	4.01 s (6)	−2.73 s (2)
24, *cis*-(APh)DPhPyP	8.99 d (1), 8.95 d (1), 8.88 d (1), 8.84 s (2), 8.83 d (1), 8.78 d (2)	8.21 m (4) 7.77 m (6)	9.02 d (2) 8.16 d (2)	7.98 d (4) 7.05 d (4)	4.05 s (4)	−2.77 s (2)
25, *trans*-B(APh)PhPyP	8.98–8.67 m (8)	8.19 d (4) 7.75 m (6)	9.01 d (2) 8.15 d (2)	7.97 d (4) 7.06 d (4)	4.05 s (4)	−2.80 s (2)
26, *cis*-(APh)PhBPyP	8.99 d (1), 8.95 d (1) 8.88 d (1), 8.84 d (1) 8.81 s (2), 8.77 d (2)	8.19 q (2) 7.77 m (3)	9.04 q (4) 8.15 q (4)	7.98 d (2) 7.06 d (2)	4.05 s (2)	−2.82 s (2)
27, (APh)TPyP[b]	9.00 d, 8.81 s, 8.79 d	—	9.03 m 8.14 m	7.97 d 7.08 d	4.05 s	−2.85 s

[a]In $CDCl_3$ at ~20°C; δ signal pattern (number of protons).
[b]A dilute solution sample resulting from low solubility.

TABLE 6. The assignments of the pyrrole protons[a]

Porphyrin	Pattern	H_2	H_3	H_7	H_8	H_{12}	H_{13}	H_{17}	H_{18}
1 TetPhP	**I**				8.85 s				
2 TPhPyP	**II**	8.81 d	8.90 d	8.87 s	8.87 s	8.87 s	8.87 s	8.90 d	8.81 d
3 *cis*-DPhBPyP	**III**	8.81 d	8.92 d	8.88 s	8.88 s	8.92 d	8.81 d	8.85 s	8.85 s
4 *trans*-DPhBPyP	**IV**	8.81 d	8.91 d	8.91 d	8.81 d	8.81 d	8.91 d	8.91 d	8.81 d
5 PhTPyP	**II**	8.83 d	8.93 d	8.86 s	8.86 s	8.86 s	8.86 s	8.93 d	8.83 d
6 TetPyP	**I**				8.88 s				
7 (NPh)TPhP	**II**	8.90 d	8.74 d	8.74 d	8.90 d	8.87 s	8.87 s	8.87 s	8.87 s
8 *cis*-B(NPh)DPhP	**III**	8.90 d	8.73 d	8.77 s	8.77 s	8.73 d	8.90 d	8.86 s	8.86 s
9 *trans*-B(NPh)DPhP	**IV**	8.90 d	8.73 d	8.73 d	8.90 d	8.90 d	8.73 d	8.73 d	8.90 d
10 T(NPh)PhP	**II**	8.75 d	8.91 d	8.79 s	8.79 s	8.79 s	8.79 s	8.91 d	8.75 d
11 Tet(NPh)P	**I**				8.88 s				
12 *cis*-(NPh)DPhPyP	**V**	8.82 d	8.76 d	8.73 d	8.89 d	8.86 s	8.86 s	8.89 d	8.79 d
13 *cis*-B(NPh)PhPyP	**V**	8.85 d	8.79 d	8.78 s	8.78 s	8.75 d	8.91 d	8.91 d	8.81 d
14 *trans*-B(NPh)PhPyP	**VI**	8.84 d	8.79 d	8.75 d	8.92 d	8.92 d	8.75 d	8.79 d	8.84 d
15 T(NPh)PyP	**II**	8.86 d	8.80 d	8.80 s	8.80 s	8.80 s	8.80 s	8.80 d	8.86 d
16 *cis*-(NPh)PhBPyP	**V**	8.83 d	8.78 d	8.74 d	8.90 d	8.90 d	8.80 d	8.83 s	8.83 s
17 *cis*-B(NPh)BPyP	**V**	8.86 d	8.80 d	8.80 s	8.80 s	8.80 d	8.86 d	8.86 s	8.86 s
18 *trans*-B(NPh)BPyP	**VI**	8.86 d	8.80 d	8.80 d	8.86 d	8.86 d	8.80 d	8.80 d	8.86 d
19 (NPh)TPyP	**II**	8.82 d	8.77 d	8.77 d	8.82 d	8.82 s	8.82 s	8.82 s	8.82 s
20 (APh)TPhP	**II**	8.82 d	8.93 d	8.93 d	8.82 d	8.82 s	8.82 s	8.82 s	8.82 s
21 *cis*-B(APh)DPhP	**III**	8.80 d	8.91 d	8.91 s	8.91 s	8.91 d	8.80 d	8.80 s	8.80 s
22 *trans*-B(APh)DPhP	**IV**	8.81 d	8.91 d	8.91 d	8.81 d	8.81 d	8.91 d	8.91 d	8.81 d
23 T(APh)PhP	**II**	8.89 d	8.77 d	8.89 s	8.89 s	8.89 s	8.89 s	8.77 d	8.89 d
24 *cis*-(APh)DPhPyP	**V**	8.78 d	8.99 d	8.95 d	8.83 d	8.84 s	8.84 s	8.88 d	8.78 d
26 *cis*-(APh)PhBPyP	**V**	8.77 d	8.99 d	8.88 d	8.77 d	8.95 d	8.84 d	8.81 s	8.81 s
27 (APh)TPyP	**II**	8.79 d	9.00 d	9.00 d	8.79 d	8.81 s	8.81 s	8.81 s	8.81 s

[a]Chemical shift in ppm, peak pattern; in $CDCl_3$ unless stated otherwise.

account for our low ε values, although minor differences may also result from the difference in solvent used ($CHCl_3$ vs. CH_2Cl_2). Our UV–VIS and ^{1}H NMR data for **2** agree with those reported by another group (14), although there is some disagreement about the assignments of the NMR signals for **2** (see below).

Synthesis of nitroporphyrins 7–19

The reagents used for nitrations of the porphyrins varied according to the structures of the porphyrins. Generally, the more pyridyl and nitrophenyl groups present, the stronger the reagent needed. For example, the nitration of TPhPyP (**2**) is more difficult than that of TetPhP (**1**), the protonated pyridyl in

Can. J. Chem. Downloaded from www.nrcresearchpress.com by 85.192.166.187 on 09/08/12
For personal use only.

Can. J. Chem. Downloaded from www.nrcresearchpress.com by 85.192.166.187 on 09/08/12
For personal use only.

the reaction medium presumably reducing activity for electrophilic substitution. The first nitration of **2** gives almost solely the *cis* isomer **12** (as judged by ^{1}H NMR), which means that the phenyl *trans* to the pyridyl is more inert. However, the nitration of **12** results a mixture of the *cis*- and *trans*-B(NPh)PhPyP, **13** and **14**, in approximately equal amounts; this simply means that a phenyl group that is *trans* to the pyridyl or *trans* to the nitrophenyl has similar reactivity for a nitration under these experimental conditions. The reaction times for nitration were significantly dependent on temperature, and were even subject to variation within room temperature. Thus, it was more reliable to monitor the reaction by TLC than to control the reaction time at room temperature.

Strong nitration reagents such as NO_2 in acetone, and nitronium tetrafluoroborate, have been used for the nitration of 2,3,7,8,12,13,17,18-octaethylporphyrin (OEP) (17, 18) and fuming nitric acid has been used for the nitration of TetPhP (13*a*). These reagents are strong oxidants and the low nitration yields probably result from destruction of the porphyrin ring structure. Under reaction conditions used in present work, NO_2 was produced gradually by using nitric acid mixed with a dehydration reagent such as acetic acid or a mixture of acetic acid and sulfuric acid; the relatively mild reaction conditions generally gave 55–75% yields from the porphyrin precursors, but **10** and **15** were obtained in only 30% yield because of prolonged reaction times.

The (NPh)TPhP (**7**) and Tet(NPh)P (**11**) porphyrins were synthesized previously by direct condensation of the appropriate aldehyde(s) and pyrrole, but the yields were very low (<3%) (13*b*, 19), while (NPh)TPyP (**19**) was synthesized by direct condensation with 7% yield (15); the low yields probably result from the high activity of 4-nitrobenzaldehyde (19). Porphyrin **7** (55% yield), a mixture of *cis*- and *trans*-B(NPh)DPhP (**8** and **9**) (28% yield), and T(NP)PhP (**10**) (no yield reported), were synthesized previously by nitration of TetPhP (**1**) using fuming nitric acid (13*a*).

The ^{1}H and ^{13}C NMR, UV–VIS, IR, and mass spectra of **7** and the **8/9** mixture have been reported before (no physical data were reported for **10**) (13*a*, 13*b*). The more limited spectral data obtained in the present work agree with those reported except that the ϵ value for the Soret band of **7** obtained here (in $CHCl_3$) was about 25% lower than the reported value (in CH_2Cl_2) (13*a*). The synthesis and ^{1}H NMR and UV–visible spectra of (NPh)TPyP (**19**) were reported (15) during the course of the present work; our ϵ values were all about 100% higher than those reported (in the same solvent) and there are some disagreements about the assignments of the ^{1}H NMR signals (see below).

The methods used in the present work gave higher overall yields of porphyrins **7–10** and **19** and seven other new nitrophenylporphyrins (**12–18**).

*Synthesis of aminophenylporphyrins **20–27***

The (APh)TPhP (**20**), T(APh)PhP (**23**), and (APh)TPyP (**27**) porphyrins were synthesized and characterized previously by elemental analysis, ^{1}H NMR, and mass spectroscopy (13*a*, 13*b*, 15); the data obtained here for these porphyrins agree with those in the literature. The other five aminophenylporphyrins (**21**, **22**, **24–26**) are new compounds.

^{1}H NMR spectra

The chemical shifts, patterns, and relative intensities of the ^{1}H NMR signals, plus the information from the syntheses, were used to assign a structure to a synthesized porphyrin. In the following discussion, a pyrrole proton refers to a proton bonded to a pyrrole carbon atom, while the proton associated with the pyrrole nitrogen is referred to as an *N*-pyrrole proton.

A nitration always occurs at the *para* position of a *meso* phenyl. This was evident by the characteristic two doublets of the ^{1}H NMR spectrum corresponding to the *meta* and *ortho* protons of a 4-nitrophenyl group. The formation of a 4-aminophenyl derivative was confirmed by the two doublets for the *meta* and *ortho* protons of the aminophenyl, and the appearance of a singlet for the amine protons at δ 4.00–4.05 in $CDCl_3$, the singlet disappearing when D_2O was added to the NMR samples.

All substituents at the *meso* positions have characteristic chemical shifts: NPh gives two doublets or multiplets at about 8.4 and 8.6 ppm (J_{HH} = 8.6 Hz); APh gives two doublets at about 8.0 and 7.1 ppm (J_{HH} = 8.1 Hz) and one singlet at about 4.0 ppm (-NH_2 protons); Py gives two doublets or quartets at about 9.1 and 8.2 ppm; and Ph usually gives two multiplets at about 8.2 and 7.8 ppm. The ^{1}H NMR spectrum within a 4-substituted phenyl ring (APh, NPh) or a 4-pyridyl ring is strictly an AA′BB′ type, which is usually too complex to be analyzed for *J* values (20). However, the spectra of APh and NPh appear as AB quartets with significant coupling between only the 2 and 3 and the 5 and 6 protons, other couplings being negligible. The coupling constants noted above were obtained in this manner, and do not vary with porphyrin type. The same approximation cannot be applied to the 4-Py and Ph systems because more complex spectra are obtained.

The assignments of the coupled signals for a *meso* substituent are achieved simply by comparisons with related spectra. For instance, a comparison of the spectrum of TetPhP (**1**) to that of TPhPyP (**2**) (Table 1) shows that **2** has a new set of signals (8.18 and 9.04) for the pyridyl group, while the phenyl signals at 7.78 and 8.23 ppm reduce in intensity from 12 and 8H to 9 and 6H, respectively, and the pyrrole signal of **1** at 8.85 ppm splits into two doublets and one singlet; the *N*-pyrrole signal at –2.8 ppm scarcely changes. The signals of the nitro- and aminophenyl protons are assigned similarly.

Assignments of ^{1}H NMR signals to specific protons of the meso *substituent*

The signals for the phenyl protons (2,6 or 3,4,5) in the spectrum of TetPhP (**1**) (Table 1) are easily assigned by consideration of their intensities and the distances from the protons to the porphyrin ring, which provides deshielding effects (21). When the 4-phenyl proton is replaced by a nitro or an amino group, the chemical shifts for the 2,6 or 3,5 set can be calculated according to the shielding parameters of the group within aromatic compounds (Fig. 2) (22). Thus, for example, the calculated value for the 2,6-NPh protons is 8.41, i.e., 0.17 + 8.23 (the value for the 2,6-protons of the unsubstituted phenyl, Table 1), while the average observed value is 8.38 (Table 4). Similarly, the other calculated (observed) values from Tables 1, 4, and 5 are: 3,5-NPh 8.73 (8.63), 2,6-APh 7.99 (7.98), and 3,5-APh 7.03 (7.05). The parameters have been used similarly by Sun et al. (23) to calculate the shifts for the protons of the 3-nitrophenyl group of 5-(3-nitrophenyl)-10,15,20-triphenylporphyrin. Thus, a doublet is readily assigned to each kind of proton type (2,6- or 3,5-) for either the nitrophenyl or aminophenyl group; the "least satisfactory" agreement (within 0.1 ppm) is seen for 3,5-NPh protons. Figure 3 exemplifies a spectrum (for (NPh)TPhP, **7**) in the δ 7.6–9.0 region, and the assignments of the signals (see Table 4).

The shielding parameters for the N atom within a pyridine are

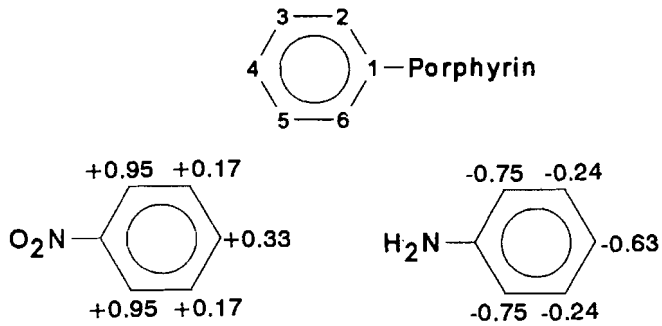

FIG. 2. Diagram illustrating shielding parameters for the $-NO_2$ and $-NH_2$ groups.

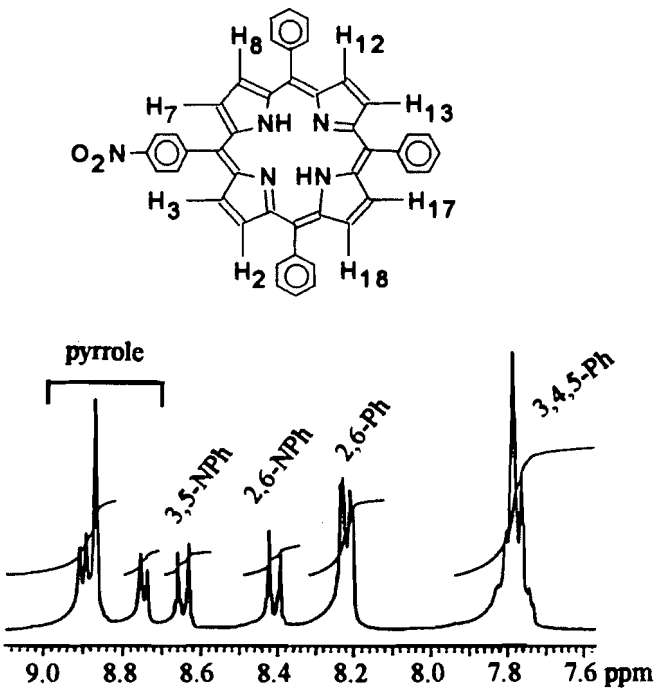

FIG. 3. ^1H NMR spectrum (δ 7.6–9.0) of (NPh)TPhP (**7**) in $CDCl_3$ at ~20°C; the pyrrole protons show the expected pattern (see Fig. 7).

not listed in the literature (22). The spectrum of pyridine in $CDCl_3$ was thus recorded, and the shielding parameters were calculated using δ 7.27 as the chemical shift for benzene (22); the chemical shifts of the 4-pyridyl in a porphyrin were calculated (see Fig. 4) using the chemical shifts for the phenyl groups of TetPhP as described above for the NPh and APh groups. These calculated data agree very well with the observed data, which show average values of 9.04 and 8.15 ppm for the 3,5 and 2,6-pyridyl protons, respectively (see Tables 1, 4, and 5).

The signals of the pyridyl protons within pyridylporphyrins have been assigned (without reasoning) in a few literature reports. In contrast to our assignments, Williams et al. (14) assigned signals at δ 9.01 and 8.22 to the 2,6- and 3,5-Py protons of TPhPyP (**2**), respectively, and Ding et al. (15) similarly assigned signals at δ 9.06 and 8.15 to the 2,6- and 3,5-Py protons of (NPh)TPyP (**19**), respectively. Consistent with our work, Sari et al. (16) have assigned signals at δ 9.1–9.4 and 8.2 to the 3,5 and 2,6-Py protons, respectively, for porphyrins **1–6**. Ding et al. (15) assigned the signals of the nitrophenyl protons within (NPh)TPyP (**19**) as δ 8.66 and 8.38 for the 2,6-NPh and

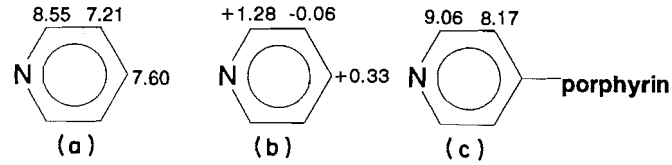

FIG. 4.Diagram illustrating chemical shifts (*a*) and shielding parameters (*b*) for pyridine, and calculated chemical shifts (*c*) for a 4-pyridyl substituent in a porphyrin.

3,5-NPh protons, respectively, the reverse of those assignments given by us which are also consistent with the assignments for the 3-nitrophenyl porphyrin given by Sun et al. (23). The signals of the aminophenyl protons within (APh)TPyP (**27**) were also assigned by Ding et al. (15) and are consistent with those given here.

Identification of isomers using ^1H NMR

The ^1H NMR spectral patterns of the pyrrole protons readily distinguish between *cis* and *trans* isomers. Figure 5 shows the C_2 symmetry elements of the two isomers of the A_2B_2P type; the treatment ignores the *N*-pyrrole protons because there is fast tautomer interconversion at room temperature in organic solvents (24). For the *cis* isomer, the four types of pyrrole protons give rise to two singlets (for $H_{7(8)}$, $H_{17(18)}$) and two coupled doublets (for $H_{3(12)}$, $H_{2(13)}$), while the two types of pyrrole protons of the *trans* isomer give two doublets for any pair of adjacent protons, e.g., H_2, H_3. Figure 6 shows the spectra of *cis*- and *trans*-DPhBPyP (**3** and **4**) for the pyrrole protons.

It is straightforward to predict the expected patterns for the pyrrole protons for the various combinations of *meso* substituents, and the patterns shown in Fig. 7 are those found experimentally. For example, the pyrrole protons for (NPh)TPhP (**7**) (Fig. 3) correspond to pattern **II**. In some cases, the signals overlap; for example, T(APh)PhP (**23**) of pattern **II** shows only one of the doublets, the second one overlapping with the singlet to give a broad "singlet" corresponding to six protons (Table 5). Figure 8 shows the spectra for *cis*- and *trans*-B(APh)DPhP (**21** and **22**); the *cis* spectrum (type **III**) is readily distinguished from the *trans* (type **IV**) even though the two singlets overlap the two doublets. Figure 9 shows a more complex example for *cis*- and *trans*-B(NPh)PhPyP (**13** and **14**) of types **V** and **VI** respectively; the four doublets of type **VI** are easily seen, but more imagination is needed to recognize the six doublets and a singlet of type **V** for the *cis* isomer!

Assignments of the signals for the pyrrole protons

For this discussion the numbering scheme of Fig. 7 is used; also, as shown by the full names of the porphyrins in Fig. 1, the 5,10,15,20-*meso* positions are assigned in alphabetical order to the *meso* substituents, if possible (thus, an aminophenyl substituent is always in the 5-*meso* position). The *J* value for two coupled protons on the same pyrrole ring is 4.7 Hz, and is independent of porphyrin type.

The singlet for pyrrole protons in the spectrum of (NPh)TPhP (**7**) (Fig. 3, Table 4) is assigned to H_{12}, H_{13}, H_{17}, and H_{18} because of their equivalence. The two doublets have been assigned using NOE experiments. When the 2,6-NPh protons (doublet at δ 8.41) are irradiated, positive enhancements are observed for the δ 8.74 pyrrole doublet and for the δ 8.64 doublet of the 3,5-NPh protons, while no enhancement is observed for the other pyrrole doublet at δ 8.90; when irradiation is on the

Can. J. Chem. Downloaded from www.nrcresearchpress.com by 85.192.166.187 on 09/08/12
For personal use only.

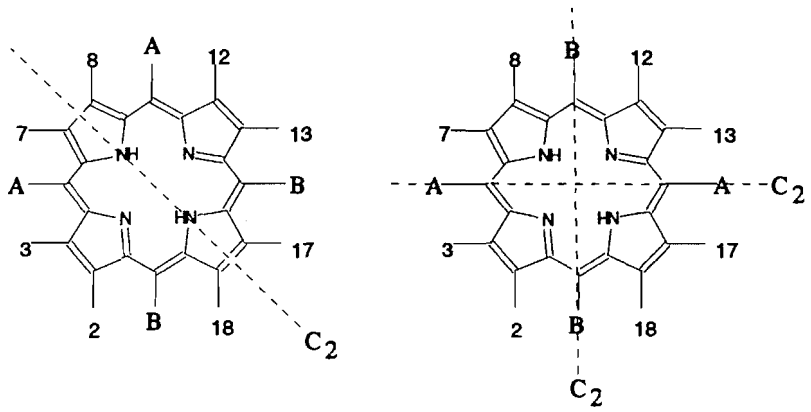

FIG. 5. The C_2 symmetry elements of *cis*- and *trans*-A_2B_2P type porphyrins.

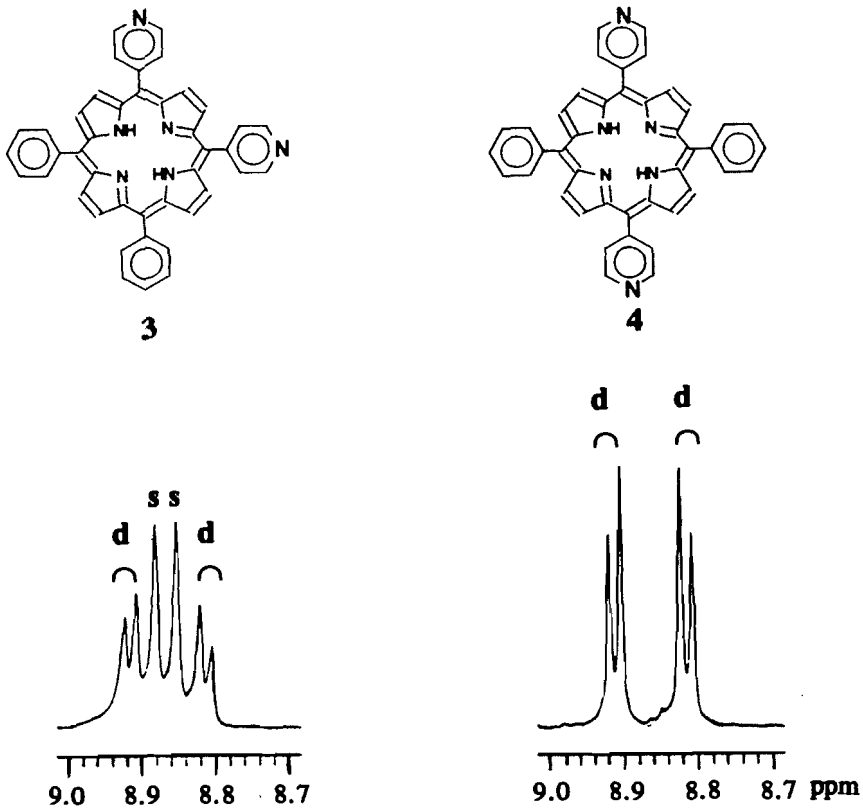

FIG. 6. H NMR spectrum (δ 8.7–9.0) of *cis*- and *trans*-DPhBPyP (**3** and **4**) in $CDCl_3$ at ~20°C.

pyrrole signal at δ 8.74, an enhancement results in the δ 8.41 signal of the 2,6-NPh protons, but not in the other phenyl or nitrophenyl signals. These data show clearly that the doublet at δ 8.74 corresponds to the pyrrole protons H_3 and H_7, because they are closer to the 2,6-NPh protons than H_2 and H_8, to which the other pyrrole doublet at δ 8.90 is thus assigned. Of several resonance structures that can be drawn, those shown in Fig. 10 predict lower electron density at C_2 and C_8 than at C_3 and C_7, and correlate with the NMR assignments. The same predictions pertain for any electron-withdrawing *meso* substituent, including 4-Py: the pyrrole proton adjacent to such a substituent resonates at a higher field than the other, same-ring pyrrole proton (and vice versa). For the electron-donating 4-APh group, resonance structures akin to those in Fig. 10 now reveal increased electron density at C_2 and C_8, and thus for (APh)TPhP (**20**) the H_2 and H_8 resonances are assigned within the δ 8.82 m, and the H_3, H_7 resonances to the δ 8.93 d (the integrations are also consistent with these assignments, the two "more unique" H_3 and H_7 protons giving the 8.93 doublet of relative intensity 2 (Table 5)).

Use of the rationalizations given above allows for assignment of the signals in patterns **II** and **IV**, and the doublets of pattern **III**. For the assignments of the singlets of pattern **III**, some observations summarized in Fig. 11 were used. In the spectrum of TPhPyP (**2**), the δ 8.87 singlet for the pyrrole protons "between" two phenyls is closer to the δ 8.90 doublet at lower field, while in the spectrum of PhTPyP (**5**), the δ 8.86 singlet for the pyrrole protons "between" two pyridyls is closer to the δ 8.83 doublet at higher field. A conclusion drawn is that in the spectrum of *cis*-DPhBPyP (**3**), the δ 8.88 singlet at lower field corresponds to the pyrrole protons "between" the two phenyls, while the δ 8.85 singlet at higher field relates to the

Can. J. Chem. Downloaded from www.nrcresearchpress.com by 85.192.166.187 on 09/08/12
For personal use only.

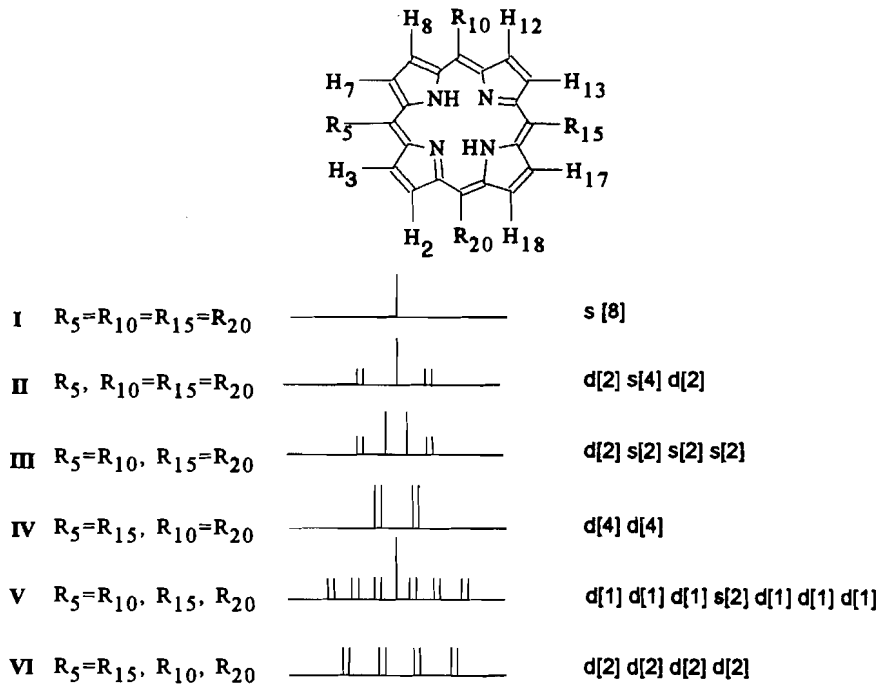

FIG. 7. The basic patterns for the ^{1}H NMR spectra of the pyrrole protons; the relative position of the singlet may vary.

protons "between" the two pyridyls. This is confirmed by an NOE experiment. When the 2,6-Py protons (the quartet at δ 8.18) are irradiated, positive enhancements are observed for the δ 8.85 (s) and δ 8.81 (d) pyrrole signals, and for the signal of 3,5-Py protons (quartet at δ 9.05), while no enhancements are observed for the pyrrole signals at δ 8.92 (d) and δ 8.88 (s). This experiment simply means that the pyrrole protons corresponding to the signal at δ 8.85 (s) and δ 8.81 (d) are closer to the 2,6-Py protons than the protons corresponding to the signals at δ 8.92 (d) and δ 8.88 (s). Thus, noting that the singlet for the pyrrole protons "between" two phenyls within TPhPyP (**2**), (NPh)TPhP (**7**), and *cis*-(NPh)DPhPyP (**12**) is at δ 8.86–8.88, while the singlet for the pyrrole protons "between" two nitrophenyls within T(NPh)PhP (**10**) and *cis*-B(NPh)PhPyP (**13**) is at δ 8.78–8.79, it is reasonable to assign the δ 8.77 s and 8.86 s resonances of the spectrum of a mixture of *cis*- and *trans*-B(NPh)DPhP (**8** and **9**), respectively, to the pyrrole protons (H_7 and H_8) "between" the two nitrophenyls and those (H_{17} and H_{18}) "between" the two phenyls of **8**. Thus, even from the spectrum of a mixture of **8** and **9** (Table 4), complete assignment of the pyrrole protons of each isomer can be made: Fig. 12 summarizes the data for **8**, while **9** just gives the two doublets at δ 8.90 (adjacent to the Ph) and δ 8.73 (adjacent to the NPh).

The resonances for the pyrrole protons of the porphyrins containing two different *meso* substituents, **2–5**, **7–10**, **15**, **17–23**, and **27** (patterns **II–IV**), are thus readily assigned, and these are summarized in Table 6.

For the porphyrins having three different *meso* substituents, **12–14**, **16**, and **24–26** (patterns **V** and **VI**), the problem of the assignment was more challenging. However, it is noted that the difference in chemical shifts (Δ) between the coupled doublets of the two protons on the same pyrrole ring was characteristic of the two adjacent *meso* substituents; the actual shifts differ somewhat within similar type porphyrins but Δ is essentially constant. For phenyl/pyridyl substituents Δ = 0.10 ppm (e.g., for **2–5**, **12–14**, **16**, **24–26**, Δ = 0.10 ± 0.01, see Tables 1, 4, and 5); similarly for nitrophenyl/phenyl (**7–10**, **12–14**, **16**), Δ = 0.165 ± 0.005; for aminophenyl/phenyl (**20–26**), Δ = 0.11 ± 0.01; for nitrophenyl/pyridyl (**12–19**), Δ = 0.055 ± 0.005; and for aminophenyl/pyridyl (**24–27**), Δ = 0.215 ± 0.005. Further, the coupled doublets have more intense peaks for the "inside" signals, because of second-order coupling. Using this information and the Δ correlation, the coupled doublets can be selected and assigned to specific protons within a particular pyrrole ring. For example, the assignments of the pyrrole protons of *cis*-(NPh)DPhPyP (**12**) and *cis*-(APh)PhBPyP (**26**) are shown in Figs. 13 and 14, respectively. In Fig. 13, the 2H doublet at δ 8.89 is composed of two 1H doublets that are part of couplings with the doublets at δ 8.79 (Δ = 0.10) and at δ 8.73 (Δ = 0.16); similarly, in Fig. 14 the broad 2H doublet pattern centred at δ 8.77 is seen to be composed of two overlapping 1H doublets. Standard 2D-NMR experiments have been carried out to confirm the coupling of the doublets. Table 6 lists also the pyrrole resonances for the pattern **V** and **VI** porphyrins.

Split signals for pyrrole protons have been recorded by many authors (12*b*, 13*a*, 14–16), but only the pyrrole signals for 5-(2-nitro-5-hydroxy-phenyl)-10,15,20-tris(4-tolyl)porphyrin have been assigned; Little (12*b*) suggested that the H_3 and H_7 resonate at higher fields than H_2 and H_8, which agrees with the assignments of the nitroporphyrins presented here.

UV–VIS, infrared, and mass spectra

The synthesized porphyrin free-bases show typical optical spectra, consisting of a dominant Soret band around 400 nm and four visible bands (from 500 to 650 nm) labeled as I, II, III, and IV on going from longer to shorter wavelengths (24, 25). Of the types of spectra classified as etio, rhodo, oxorhodo, and phyllo, according to the relative intensities of the four visible bands (24), the porphyrins synthesized in this work generally

Can. J. Chem. Downloaded from www.nrcresearchpress.com by 85.192.166.187 on 09/08/12
For personal use only.

Can. J. Chem. Downloaded from www.nrcresearchpress.com by 85.192.166.187 on 09/08/12
For personal use only.

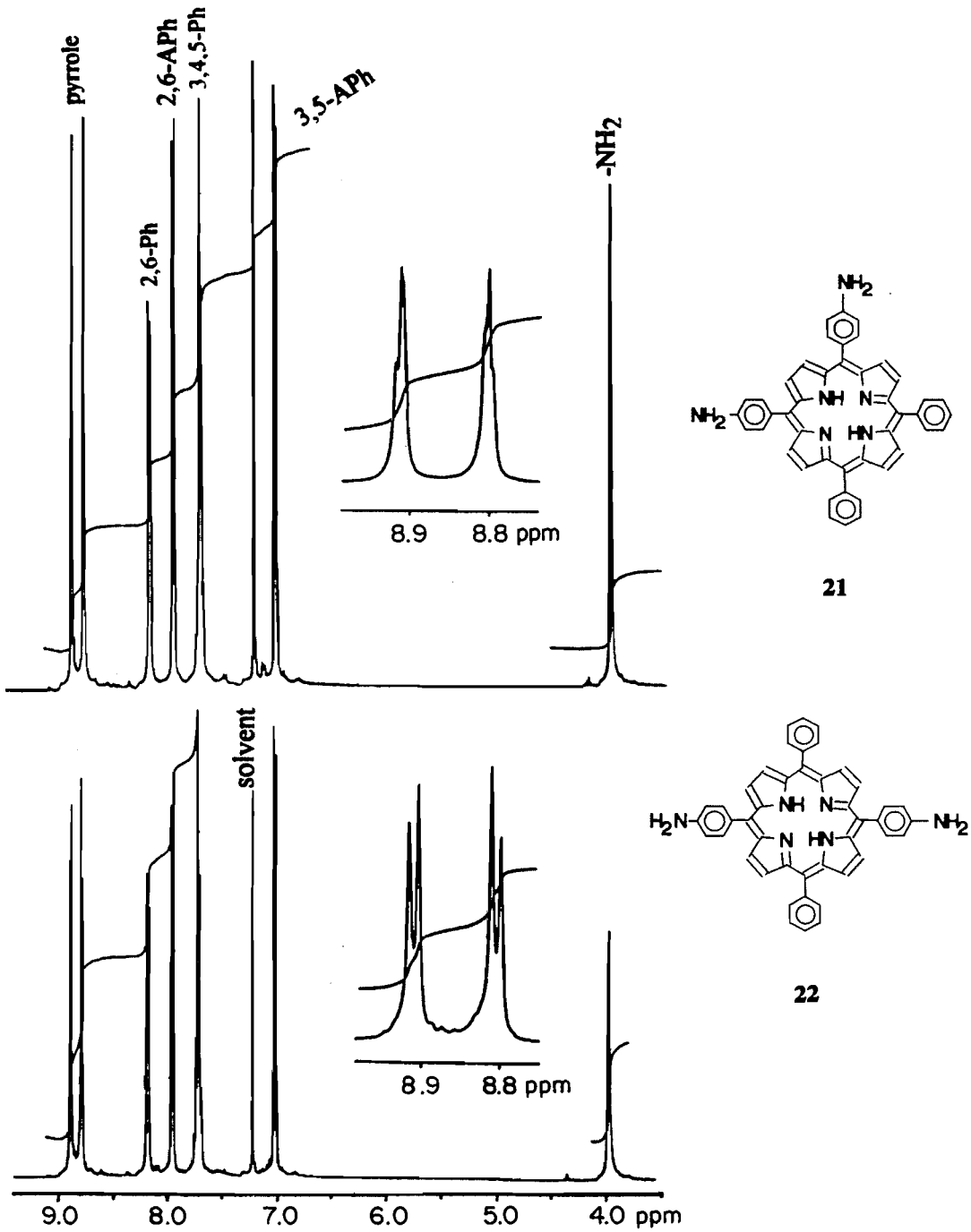

FIG. 8. ^{1}H NMR spectra (δ 4.0–9.0) of *cis*- and *trans*-B(APh)DPhP (**21** and **22**) in $CDCl_3$ at ~20°C.

give etio spectra (with intensities: IV > III > II > I, Table 2), but there are a few exceptions, porphyrins **5** (PhTPyP), **6** (TetPyP), and **19** (NPh)TPyP) having phyllo-type spectra (IV > II > III > I). Phyllo-type spectra are believed to result from the presence of asymmetry in the π-electron cloud (24); however, the fact that **2** (TPhPyP) has an etio-type and **6** (PhTPyP) a phyllo-type spectrum suggests that other factors are involved, because these porphyrins have the same symmetry. Porphyrins **24** (*cis*-(APh)DPhPyP) and **25** (*trans*-B(APh)PhPyP) are exceptional in that band I is more intense than band II, a trend that does not fit any of the four standard types.

The data of Table 2 show that the Soret band shifts to longer wavelength with nitration of a phenyl substituent, the shift increasing with the number of NPh groups (compare data for **1**, **7–10**, and **2**, **12–15**). The same trends are seen on reduction of the NPh groups to the aminophenyls (cf. data for **7–10** vs. **20–23**, **12** vs. **24**, and **14** vs. **25**). Such red shifts observed on alkylation of pyrrole hydrogen have been attributed to the electron-donor properties of the substituents (25), but, as we observe such a shift for the electron-withdrawing $-NO_2$ and for the electron-donating $-NH_2$ group, increasing conjugation on going from Ph→NPh→APh offers a more general rationalization (19). The resonance forms (Fig. 15) cannot come fully into play because the phenyl moieties are sterically prevented from

Can. J. Chem. Downloaded from www.nrcresearchpress.com by 85.192.166.187 on 09/08/12
For personal use only.

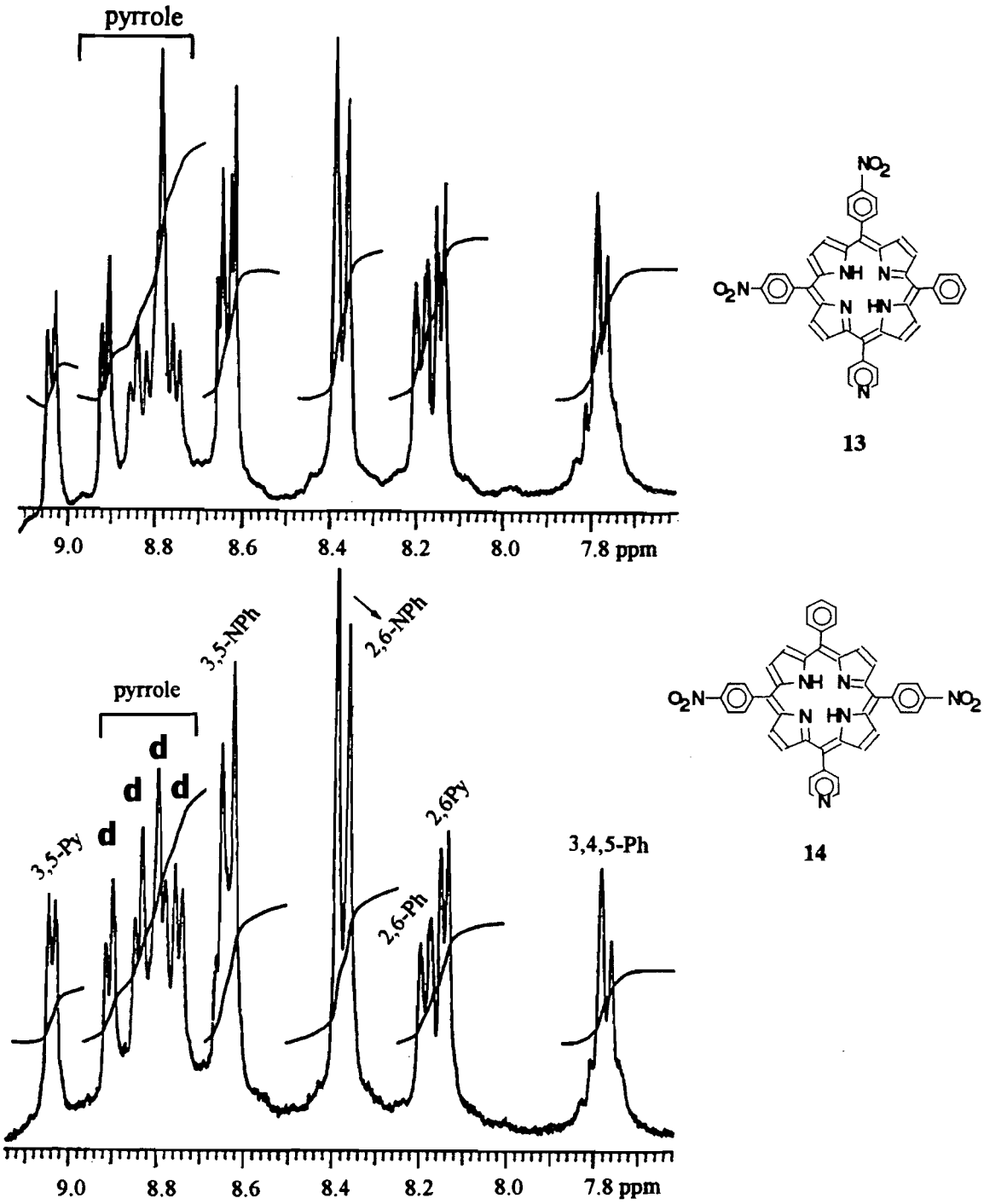

FIG. 9. ^{1}H NMR spectra (δ 7.7–9.5) of *cis*- and *trans*-B(NPh)PhPyP (**13** and **14**) in $CDCl_3$ at ~20°C.

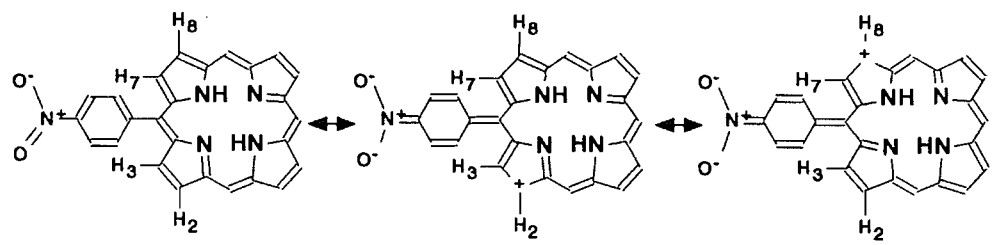

FIG. 10. Resonance structures of a 4-nitrophenylporphyrin.

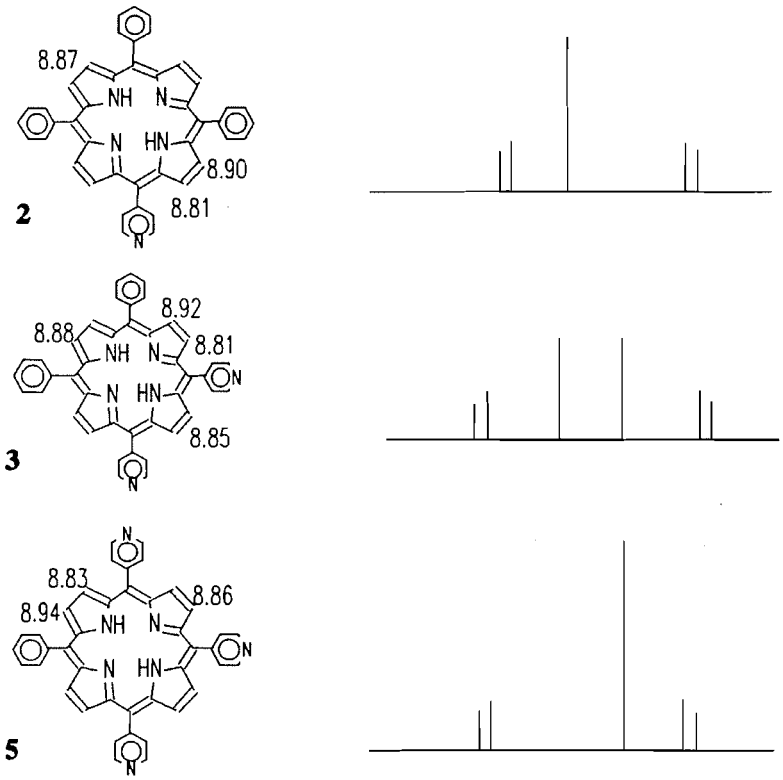

FIG. 11. A comparison of the schematic spectra of TPhPyP (**2**), *cis*-DPhBPyP (**3**), and PhTPyP (**5**).

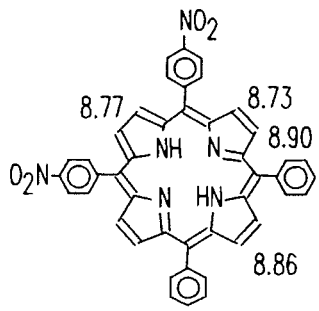

FIG. 12. Illustration of the chemical shifts of the pyrrole protons of *cis*-B(NPh)DPhP (**8**).

becoming coplanar with the porphyrin ring (19, 26), but more effective conjugation (and therefore a lower excitation energy) is apparent through the resonance forms shown for the NPh and APh groups. The only trends noticed in the visible bands are generally small red shifts on going from Ph to NPh to APh substituents for all four bands.

Little can be said about the differences noted between the extinction coefficients recorded in the present work for the isolated pure porphyrins and those reported in the literature (13*a*, 13*b*, 14–16). Our ϵ values were measured at 1×10^{-5} M concentration, and Beer's law studies (the classic method for investigating possible aggregation (27)) were not performed for these particular porphyrins, while the literature data in most cases did not give the concentration used. Beer's law and ^{1}H NMR studies on the water-soluble, sulfonated, and methylpyridinium porphyrin derivatives reveal "significant deviations" because of aggregation phenomena (11, 28).

Table 7 (deposited)[2] lists IR data for porphyrins **1–6**, **16**, **17**, **26**, **27**; the assignments of the common peaks for the porphyrin ring structure can be found in the literature (19, 29). The spectrum of TetPhP agrees with that given in the literature (19). Peaks at about 1517 and 1348 cm^{-1}, attributed to ν_{NO_2} (13*b*), are found for *cis*-(NPh)PhBPyP (**16**) (medium intensity) and *cis*-B(NPh)BPyP (**17**) (very strong) within the nitro porphyrins, and peaks at around 1618 cm^{-1} (δ_{NH} (13*b*)) are seen for aminoporphyrins. The intensity of the ν_{CN} band found for the pyrrole and pyridyl rings at ~1595 cm^{-1} (29, 30) naturally increases with increasing pyridyl content.

CI (NH_3) mass spectra were recorded for a few representative porphyrins, **3**, **5**, **16**, **18**, and **26**; the data listed (footnote *c*, Table 3) give peaks with relative intensity >20%. The major peaks seen are $[M]^+$, $[M + 1]^+$, and $[M + 2]^+$, which are common in porphyrin mass spectra (31); the $[M + NH]^+$ and $[M + NH_2]^+$ peaks, observed also for the aminoporphyrins, presumably arise from the ionizing chemical (NH_3) fragments, possibly associating with the aminophenyl groups.

Can. J. Chem. Downloaded from www.nrcresearchpress.com by 85.192.166.187 on 09/08/12
For personal use only.

Can. J. Chem. Downloaded from www.nrcresearchpress.com by 85.192.166.187 on 09/08/12
For personal use only.

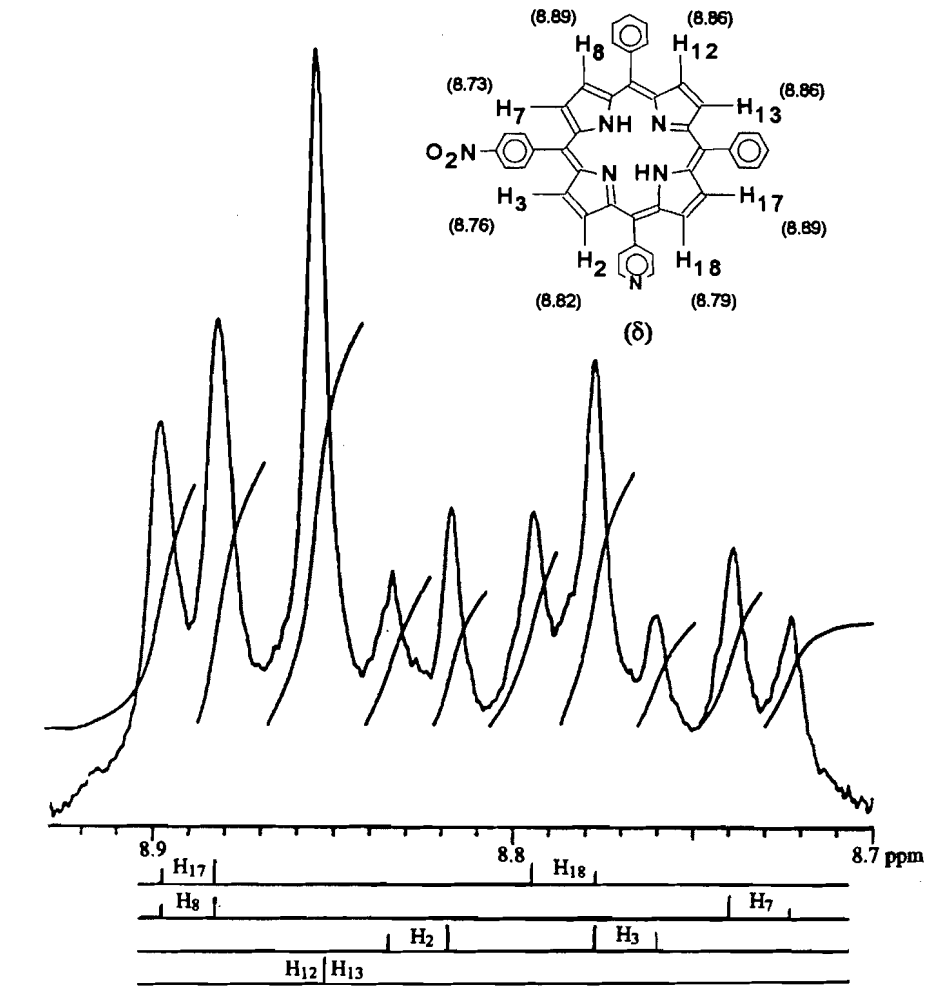

FIG. 13. Assignment of the pyrrole protons in the ^{1}H NMR spectrum of *cis*-(NPh)DPhPyP (**12**) in $CDCl_3$; pattern **V**.

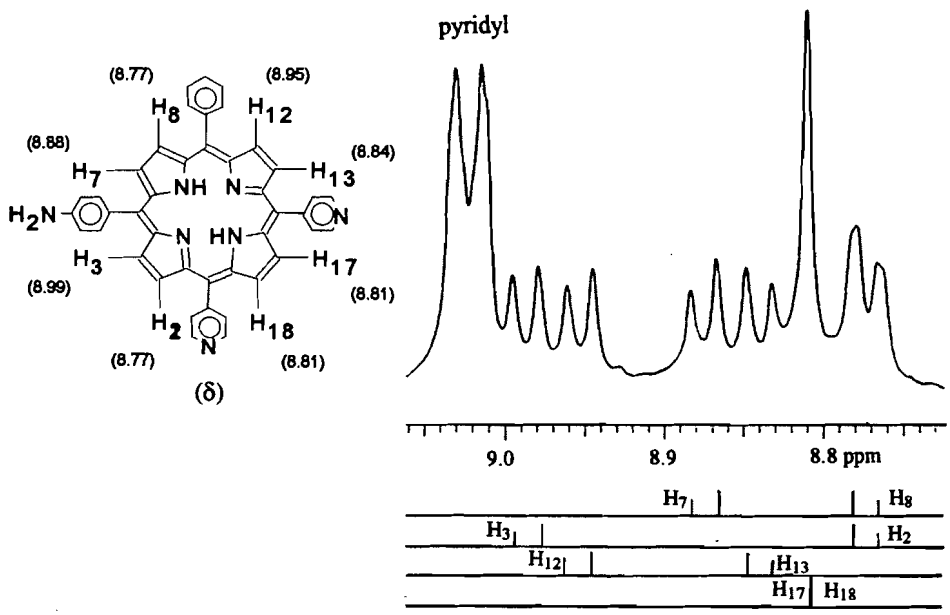

FIG. 14. ^{1}H NMR spectrum of *cis*-(APh)PhBPyP (**26**) in $CDCl_3$; pattern **V**.

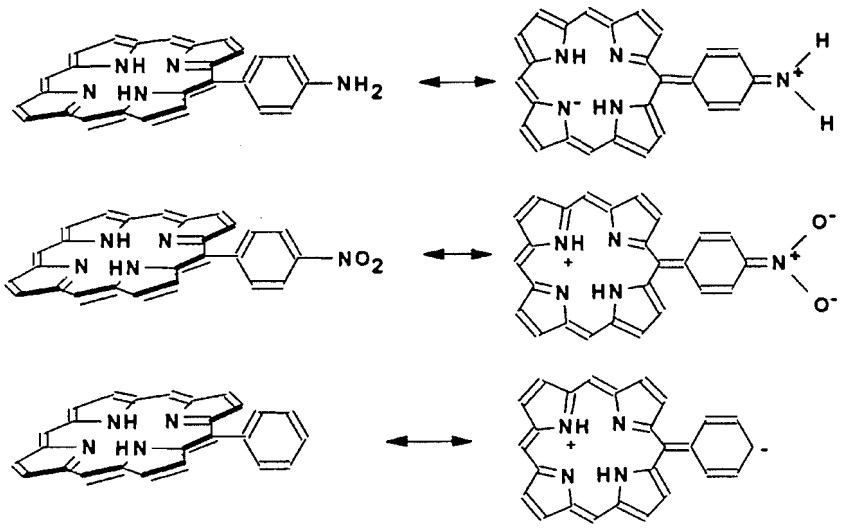

FIG. 15. Resonance forms of an aminophenylporphyrin and a nitrophenylporphyrin compared to that of a phenylporphyrin.

Acknowledgements

We thank the Natural Sciences and Engineering Research Council of Canada and the Medical Research Council of Canada for financial support.

1. L.H. Gray, A.D. Conger, M. Ebert, S. Hornsey, and O.C.A. Scott. Br. J. Radiol. **26**, 638 (1953); G. Adams and I.J. Stratford. *In* Radiobiology in radiotherapy. *Edited by* N.M. Bleehen. Springer-Verlag, London. 1988. p. 153.
2. T.J. Dougherty. *In* Advances in photochemotherapy. *Edited by* T. Hasan. SPIE, Bellingham. 1988. p. 2.
3. J. Moan and E.O. Pettersen. Int. J. Radiat. Biol. **40**, 107 (1981); H.P. Mack, W.K. Diehl, G.C. Peck, and F.H.J. Figge. Cancer, **10**, 529 (1957).
4. S. Schwartz, M. Keprios, J. Modelevsky, H. Freyholtz, R. Walters, and L. Larson. *In* Diagnosis and therapy of porphrias and lead intoxication. *Edited by* M. Doss. Springer-Verlag, Berlin. 1978. p. 227.
5. J.A. O'Hara, E.B. Douple, M.J. Abrams, D.J. Picker, C.M. Giandomenico, and J.F. Vollano. Int. J. Radiat. Oncol. Biol. Phys. **16**, 1049 (1989).
6. G.E. Adams, E.D. Clarke, I.R. Flockhart, R.S. Jacobs, D.S. Sehmi, I.J. Stratford, P. Wardman, M.E. Watts, J. Parrick, R.G. Wallace, and C.E. Smithen. Int. J. Radiat. Biol. **35**, 133 (1979); K.E. Linder, Y. Chan, J.E. Cyr, M.F. Malley, D.P. Nowotnik, and A.D. Nunn. J. Med. Chem. **37**, 9 (1994), and references therein.
7. R. Bonnett and M. Berenhaum. *In* Photosensitizing compounds: their chemistry, biology and clinical use. *Edited by* G. Bock and S. Harnett. John Wiley & Sons, Chichester. 1989. p. 40.
8. Y. Sun, A.E. Martell, D. Chen, R.D. Macgarlane, and C.J. McNeal. J. Heterocycl. Chem. **23**, 565 (1986); L. Ding, G. Etemad-Moghadam, S. Cros, C. Auclair, and B. Meunier. J. Med. Chem. **34**, 900 (1991).
9. J.S. Hill, S.B. Kahl, A.H. Kaye, S.S. Stylli, M. Koo, M.F. Gonzales, N.J. Vardaxis, and C.I. Johnson. Proc. Natl. Acad. Sci. U.S.A., **89**, 1785 (1992).
10. D.A. Place, P.J. Faustino, K.K. Berghmans, P.C.M. van Zijl, A.S. Chesnick, and J.S. Cohen. Magn. Reson. Imaging, **10**, 919 (1992); R. Ernestus, L.J. Wilmas, and M. Hoehem-Berlage. Clin. Exp. Metastasis, **10**, 345 (1992); R.J. Fiel, D.A. Musser, E.H. Mark, R. Mazurchuk, and J.J. Alletto. Magn. Reson. Imaging, **8**, 255 (1990).
11. (*a*) G.G. Meng, B.R. James, K.A. Skov, and M. Kerbelik. Can. J. Chem. Submitted; (*b*) G.G. Meng, B.R. James, and K.A. Skov. To be published; (*c*) G.G. Meng. Ph.D. dissertation, University of British Columbia, Vancouver. 1993.
12. (*a*) R.G. Little, J.A. Anton, P.A. Loach, and J.A. Ibers. J. Heterocycl. Chem. **12**, 343 (1975); (*b*) R.G. Little. J. Heterocycl. Chem. **18**, 129 (1981).
13. (*a*) W.J. Kruper, Jr., T.A. Chamberlin, and M. Kochanny. J. Org. Chem. **54**, 2753 (1989); (*b*) E. Tsuchida, E. Hasegawa, and T. Kanayama. Macromolecules **11**, 947 (1978); (*c*) J.P. Collman, R.R. Gagne, C.A. Reed, T.R. Halbert, G. Lang, and W.T. Robinson. J. Am. Chem. Soc. **97**, 1427 (1975); (*d*) J.P. Collman, R.R. Gagne, T.R. Halbert, J. Marchon, and C.A. Reed. J. Am. Chem. Soc. **95**, 7868 (1973).
14. G.N. Williams, R.F.X. Williams, A. Lewis, and P. Hambright. J. Inorg. Nucl. Chem. **41**, 41 (1979).
15. L. Ding, C. Casas, G. Etemad-Moghadam, and B. Meunier. New J. Chem. **14**, 421 (1990).
16. M.A. Sari, J.P. Battioni, D. Mansuy, and J.B. Le Pecq. Biochemistry, **29**, 4205 (1990).
17. L. Gong and D. Dolphin. Can. J. Chem. **63**, 401 (1985).
18. J. Cavaleiro, M. Neves, M. Hewline, and A. Jackson. J. Chem. Soc. Perkin Trans. 1, 575 (1986).
19. D.W. Thomas and A.E. Martell. J. Am. Chem. Soc. **78**, 1335 (1956); **78**, 1338 (1956).
20. E.D. Becker. High resolution NMR. Academic Press, Orlando. 1980. p. 167.
21. C.B. Storm, T. Teklu, and E.A. Sokolski. Ann N.Y. Acad. Sci. **63**, 206 (1973).
22. M. Zanger. Org. Magn. Reson. **4**, 1 (1972).
23. Y. Sun, A.E. Martell, and M. Tsutsui. J. Heterocycl. Chem. **23**, 561 (1986).
24. K.M. Smith. *In* Porphyrins and metalloporphyrins. *Edited by* H.E. Falk. Elsevier Scientific Publishing Co., Amsterdam. 1975. p. 3.
25. M. Gouterman. *In* The porphyrins. Vol. III. *Edited by* D. Dolphin. Academic Press, New York. 1978. p. 1; M. Gouterman and G.H. Wagniere. J. Mol. Spectrosc. **11**, 108 (1963); M. Gouterman. J. Mol. Spectrosc. **6**, 138 (1961).
26. E.G. Fleischer, C.K. Miller, and L.E. Webb. J. Am. Chem. Soc. **86**, 2342 (1964).
27. W.I. White. *In* The porphyrins. Vol. V. *Edited by* D. Dolphin. Academic Press, New York. 1978. p. 303.
28. K.M. Kadish, B.G. Maiya, and C. Araullo-McAdams. J. Phys. Chem. **95**, 427 (1991).
29. J.O. Alben. *In* The porphyrins. Vol. III. *Edited by* D. Dolphin. Academic Press, New York. 1978. p. 323.
30. R.J.H. Chan, Y.O. Su, and T. Kuwana. Inorg. Chem. **24**, 3777 (1985).
31. H. Budzikiewicz. *In* The porphyrins. Vol. III. *Edited by* D. Dolphin. Academic Press, New York. 1978. p. 395.

Can. J. Chem. Downloaded from www.nrcresearchpress.com by 85.192.166.187 on 09/08/12
For personal use only.

The cyclization of 2-substituted imidazolines in sulfuric acid[1]

ROBIN A. COX[2]
Department of Chemistry, University of Toronto, 80 St. George St., Toronto, ON M5S 1A1, Canada

AND

DAVID B. MOORE AND ROBERT S. MCDONALD
Department of Chemistry, Mount Saint Vincent University, 166 Bedford Highway, Halifax, NS B3M 2J6, Canada

Received February 15, 1994

ROBIN A. COX, DAVID B. MOORE, and ROBERT S. MCDONALD. Can. J. Chem. **72**, 1910 (1994).

A study of the rates of the cyclizations **1** → **3** and **2** → **4** as a function of medium acidity and temperature in aqueous sulfuric acid has been performed. The latter reaction is five times faster at all acidities. An excess acidity kinetic analysis reveals the probable involvement of a water molecule in the reaction in both cases. Mechanistic possibilities suggested by the observations are discussed; it is proposed that the water molecule acts as a base catalyst during the rate-determining ring closure.

ROBIN A. COX, DAVID B. MOORE et ROBERT S. MCDONALD. Can. J. Chem. **72**, 1910 (1994).

On a effectué une étude des vitesses des cyclisations **1** → **3** et **2** → **4** en fonction de l'acidité du milieu et de la température, dans de l'acide sulfurique aqueux. À tous les niveaux d'acidité, la deuxième réaction est cinq fois plus rapide. Une analyse de l'acidité cinétique en excès révèle qu'une molécule d'eau est probablement impliquée dans la réaction, dans chacun des cas. On discute des diverses possibilités de mécanismes suggérées par ces observations; on suggère que la molécule d'eau agit comme catalyseur basique au cours de l'étape déterminant la vitesse de la fermeture du cycle.

[Traduit par la rédaction]

Introduction

Many important drugs are guanidine derivatives, for example: cimetidine, a histamine H_2-receptor antagonist (1), clonidine, an antihypertensive (2), and amiloride, a diuretic (3). Cyclic compounds containing the guanidine unit result when suitably substituted imidazolines are treated with acids (4). This paper concerns the mechanisms of the ring closures of the 2-substituted imidazolines **1** and **2**, giving **3** and **4**, respectively (4), as shown below, which take place in aqueous sulfuric acid solution. Few studies of ring-closure reactions in this medium exist; two exceptions are the hydantoic acid to hydantoin ring closure studied by Güler and Moodie (5), and the reversible cyclization of 3-ureidopropanoic acid derivatives studied by Pojarlieff and co-workers (6).

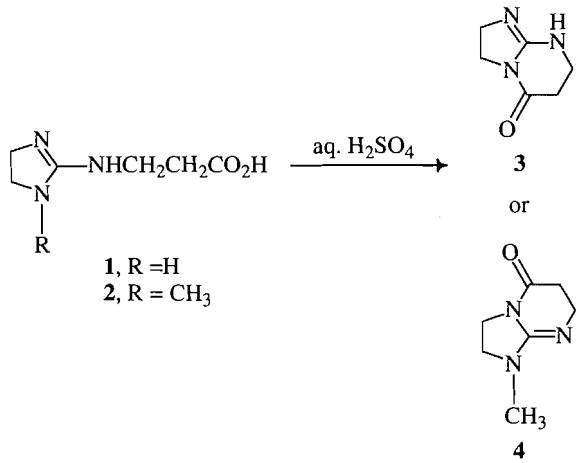

The rate data obtained are analyzed using the excess acidity method (7, 8), which has been successfully applied to many reactions in aqueous sulfuric acid, for instance, ester (9), thioester (10), amide (11), and acylhydrazine (12) hydrolyses, enolizations (13, 14), aldol condensations (14), hydrations of alkenes and alkynes (15, 16), and most recently aromatic hydrogen exchange (17) and phenylazo ether cleavage (18).

Experimental

Materials

Samples of *N*-(2-imidazolin-2-yl)-β-alanine **1** and *N*-(1-methyl-2-imidazolin-2-yl)-β-alanine **2** (4) were kindly supplied by Dr. John V. Greenhill of the University of Bradford, and were used without further purification. Aqueous sulfuric acid solutions were prepared by dilution of reagent grade acid (Fisher) with glass-distilled water and were left to mix and cool overnight. The solutions were then thoroughly mixed and the concentrations determined by titration of accurately weighed portions with aqueous sodium hydroxide that had been standardized against primary standard potassium acid phthalate.

Spectra

Ultraviolet spectra were recorded on either a Beckman model 24 or a Gilford Response spectrophotometer. The imidazolines **1** and **2** showed only end absorption in the UV region in water and aqueous sulfuric acid, no λ_{max} above 200 nm being observed. The final UV spectra after the reaction was complete were essentially identical to those quoted by Greenhill et al. (4) for the reaction products 2,3,7,8-tetrahydroimidazo[1,2-*a*]pyrimidin-5(6*H*)-one **3** or 1-methyl-1,2,3,7-tetrahydroimidazo[1,2-*a*]pyrimidin-5(6*H*)-one **4**. The UV spectral data were as follows (λ_{max} (log ε)): **3**, 221 (4.37); **4**, 217 (4.23). No systematic changes in the UV spectrum were observed for either **1** or **2** over the range of sulfuric acid concentrations used in the kinetic study.

Kinetics

Kinetic runs were initiated by injecting 2.5–10 μL of a stock solution of the substrate in water (9.4 mg/mL) into 3 mL of an acid solution in a cuvette that had been temperature pre-equilibrated for 20–30 min in the cell compartment of the Gilford spectrophotometer. Circulating constant temperature water was supplied by a Haake bath. Successive scans revealed the appearance of the product absorption maximum as given above. For both compounds the analytical wavelength chosen was 218 nm; both reactions exhibited low-wavelength isosbestic points, at 201 nm for **1** and 206 nm for **2**.

Kinetic runs were monitored over at least three half-lives, and a final absorbance reading (A_∞) was taken after at least 10 half-lives. Rate

[1]Presented in part at the 3rd Chemical Conference of North America, Toronto, June 1988, paper no. ORGN-429.

[2]Author to whom correspondence may be addressed. Phone: (416) 978-4581. Fax: (416) 978-8775.

Can. J. Chem. Downloaded from www.nrcresearchpress.com by 85.192.166.187 on 09/08/12
For personal use only.

TABLE 1. Rate constants for the cyclization of **1** in aqueous sulfuric acid

H_2SO_4, % w/w	T, °C	X^a	log $C_{H^+}{}^a$	log $a_{H_2O}{}^b$	k_ψ, s^{-1}
52.08	40.0	2.392	0.949	1.164	1.37×10^{-4}
56.86	40.0	2.791	0.993	1.001	2.53×10^{-4}
60.56	40.0	3.138	1.023	0.848	5.25×10^{-4}
67.70	40.0	3.940	1.075	0.456	9.49×10^{-4}
69.26	25.0	4.353	1.107	0.292	4.32×10^{-4}
69.26	30.0	4.281	1.099	0.313	6.72×10^{-4}
69.26	35.0	4.211	1.092	0.332	1.10×10^{-3}
69.26	40.0	4.144	1.086	0.350	1.95×10^{-3}
69.26	45.0	4.079	1.080	0.367	2.67×10^{-3}
76.62	40.0	5.265	1.128	−0.265	6.59×10^{-3}
80.30	40.0	5.909	1.139	−0.666	1.31×10^{-3}
84.81	40.0	6.720	1.116	−1.238	1.68×10^{-2}
89.90	40.0	7.586	0.983	−1.970	2.53×10^{-2}

[a]Reference 19.
[b]Reference 20, converted to units of molarity (pure water is 55.34 M at 25°C).

TABLE 2. Rate constants for the cyclization of **2** in aqueous sulfuric acid

H_2SO_4, % w/w	T, °C	X^a	log $C_{H^+}{}^a$	log $a_{H_2O}{}^b$	k_ψ, s^{-1}
52.08	40.0	2.392	0.949	1.164	7.80×10^{-4}
56.86	40.0	2.791	0.993	1.001	1.51×10^{-3}
60.56	40.0	3.138	1.023	0.848	2.99×10^{-3}
67.70	40.0	3.940	1.075	0.456	5.34×10^{-3}
69.26	25.0	4.353	1.107	0.292	3.14×10^{-3}
69.26	30.0	4.281	1.099	0.313	4.93×10^{-3}
69.26	35.0	4.211	1.092	0.332	7.16×10^{-3}
69.26	40.0	4.144	1.086	0.350	1.06×10^{-2}
69.26	45.0	4.079	1.080	0.367	1.44×10^{-2}
76.62	40.0	5.265	1.128	−0.265	3.65×10^{-2}
80.30	40.0	5.909	1.139	−0.666	6.42×10^{-2}

[a,b]See Table 1.

constants k_ψ were obtained from the slopes of semilogarithmic plots of $(A_\infty - A_t)$ vs. time in the usual way. Any runs that did not give linear plots over at least 80% of the reaction, or that gave correlation coefficients of less than 0.999, were discarded. Normally at least four replicate runs were obtained at each acidity, generally giving rate constants agreeing within 6–7%. The k_ψ values were found to be independent of the initial substrate concentration over the range 1.9×10^{-4} to 4.5×10^{-5} M.

Results

The observed pseudo-first-order rate constants k_ψ for **1** → **3** are given in Table 1, and those for **2** → **4** in Table 2. These are averages of three to seven replicate runs, in most cases at 40°C. Product formation was quantitative. Results were also obtained at four other temperatures in 69.26% H_2SO_4, enabling calculation of activation parameters as before (9, 11, 17), see Table 3.

The rate data were analyzed using the excess acidity method (8), and to this end plots of log k_ψ − log C_{H^+} against X are given for **1** and **2** in Fig. 1. As before, X was corrected to the measurement temperature (9), 40°C for the Fig. 1 results; values of X and log C_{H^+} were taken from Cox and Yates (19). If linear, these plots would indicate an A-1 or an A-S_E2 mechanism for these reactions, but they curve downwards, which means an A-2 mechanism is operative. The species reacting with the substrate can be identified by subtracting, for example, the log water activity from the Fig. 1 y-axis, and this is done in Fig. 2, using temperature-correct literature water activities calculated from the thermodynamic data in ref 20. The observed linearity means that the transition state contains one water molecule as well as the substrate and a proton (8). The statistical information regarding these lines is given in Table 3 with the activation parameters. Points at one X-value were rejected as being off the line for each compound (17), probably due to an acid concentration error.

TABLE 3. Activation parameters, slopes, and intercept log k_2 values for the cyclizations **1** → **3** and **2** → **4**

Quantity	Compound **1**	Compound **2**
$\Delta H^\ddagger$, kcal mol^{-1}	22.31 ± 0.58	18.50 ± 0.42
$\Delta S^\ddagger$, cal mol^{-1} K^{-1}	−25.9 ± 2.0	−34.3 ± 1.4
$m^\ddagger m^*$	1.023 ± 0.004	1.006 ± 0.004
log k_2, 40°C	−8.42 ± 0.03	−7.69 ± 0.02
r^a	0.9997	0.9997
σy^b	±0.042	±0.031

[a]Correlation coefficient. One point was not included in the fit for both compounds (17), see Fig. 2.
[b]Root-mean-square error of the fit.

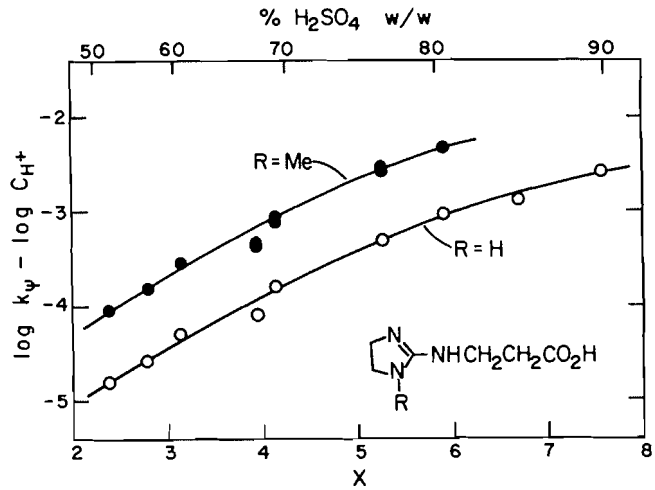

FIG. 1. Excess acidity plots of log k_ψ − log C_{H^+} against X for the cyclizations of **1** and **2** in aqueous sulfuric acid at 40°C, assuming an A-1 or A-S_E2 reaction; for convenience a % H_2SO_4 w/w scale is given at the top of the figure.

Discussion

The curves in Fig. 1 clearly show an upward trend, due to the acid catalysis. This means that a second proton must be involved in the reaction, since molecules like **1**–**4** all protonate on the imino nitrogen in the pH range. For instance the pK_{BH^+} values of the acylguanidines **3** and **4** are 8.36 and 8.56 (4), and the values for **1** and **2** would most likely be nearer the 14 or so of ordinary guanidines (21). The most logical place to expect the second protonation is on the side-chain CO_2H group, as shown in eq. [1], rather than in the guanidine system, in which further protonation would be very difficult; for instance the pK_a of $RC(=NH_2^+)—NH_3^+$ has been estimated to be about −19 (22), and that of diprotonated tetramethylguanidine to be about −11 (23).

The curvature in Fig. 1 could be caused by the variation of the extent of protonation with acidity, if the $pK_{SH_2{}^{2+}}$ values of the substrates are within the range of acidity covered by the rate

Can. J. Chem. Downloaded from www.nrcresearchpress.com by 85.192.166.187 on 09/08/12
For personal use only.

Can. J. Chem. Downloaded from www.nrcresearchpress.com by 85.192.166.187 on 09/08/12
For personal use only.

[1] 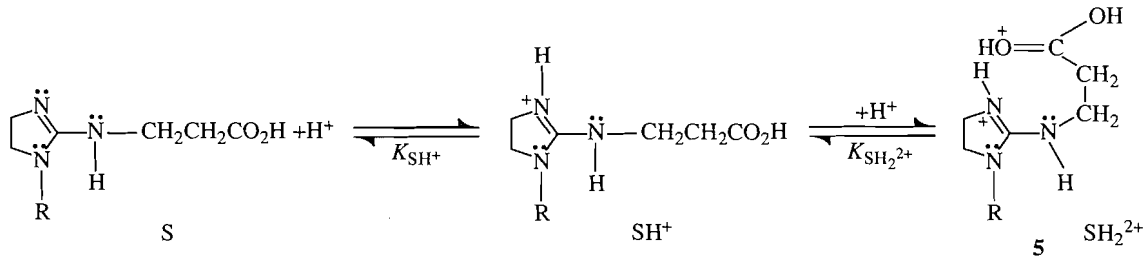

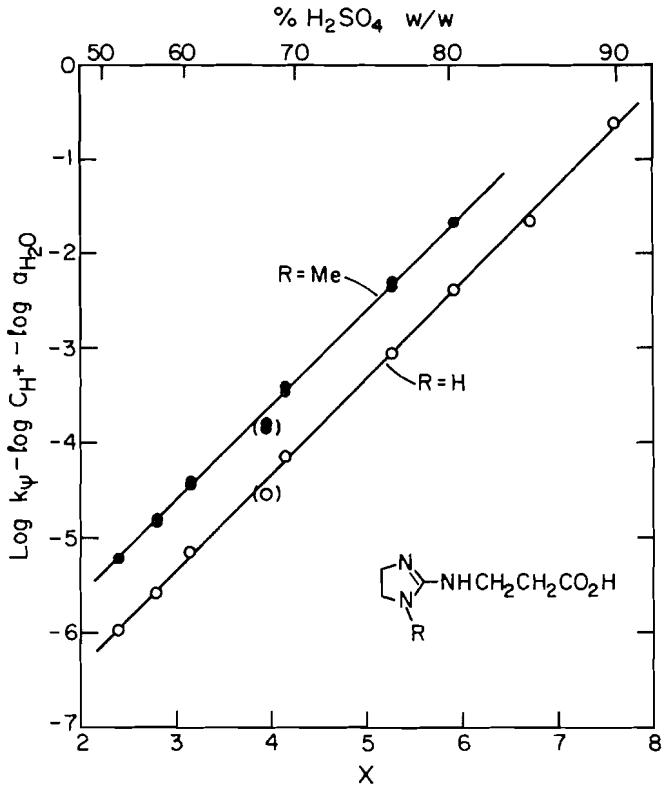

FIG. 2. Excess acidity plots for the cyclizations of **1** and **2** in aqueous sulfuric acid at 40°C, assuming an A-2 reaction with one water molecule; see Fig. 1.

measurements. Uncharged carboxylic acids are half-protonated at an acidity corresponding to about 80% H_2SO_4 (9, 24), already in the upper range of our measurements, and for a charged acid still stronger acid would be expected to be necessary. Also, no changes in the initial spectra of **1** and **2** were observed over the entire acidity range studied. Thus this possibility did not seem likely; however, it is not difficult to analyze the rate data on this basis by curve-fitting eq. [2] (8) using standard techniques (25), and this was done.

$$[2]\quad \log k_\psi - \log(C_{SH^+}/(C_{SH^+} + C_{SH_2^{2+}})) - \log C_{H^+} = \log (k_1/K_{SH_2^{2+}}) + m^\ddagger m^* X$$

$$[3]\quad \log(C_{SH_2^{2+}}/C_{SH^+}) - \log C_{H^+} = m^* X + pK_{SH_2^{2+}}$$

In this procedure the curvature in the Fig. 1 plots is ascribed to the protonation correction term in eq. [2], $\log(C_{SH^+}/(C_{SH^+} + C_{SH_2^{2+}}))$, and this is then used in the curve-fit to give values of m^* as slopes and $pK_{SH_2^{2+}}$ as intercepts according to the excess acidity equation for basicities, eq. [3] (19). When this is done the following values are obtained: for **1**, $pK_{SH_2^{2+}} = -3.84 \pm 0.15$, $m^* = 0.510 \pm 0.015$; and for **2**, $pK_{SH_2^{2+}} = -2.61 \pm 0.08$, $m^* = 0.495 \pm 0.046$. These are reasonable values for the protonation of *uncharged* carboxylic acids (26), but the basicities seem insufficiently negative for the second protonation of one that is already positively charged. However, the 1.23 pK units difference between the two basicities seems quite unreasonable, considering that the only difference between **1** and **2** is the presence of an *N*-methyl group in **2** a *long* way away from the protonation site. Thus we attribute all of the curvature in Fig. 1 to an A-2 reaction involving water, as stated above, and not to the onset of the second protonation within the acidity range of the measurements.

[4] 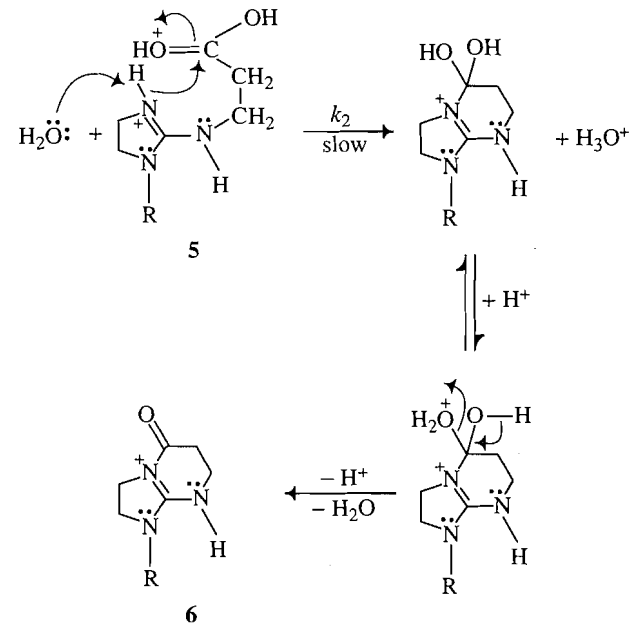

Having established the involvement of water, the mechanism given in eq. [4] is proposed. The diprotonated substrate **5** ring-closes, assisted by a water molecule acting as a base, in the rate-determining step. Base assistance is necessary to provide a pair of electrons for the ring closure, because the nitrogen lone pairs in **5** are involved in guanidinium resonance. (Consequently, base attack on the exocyclic N-H in **5**, rather than on the one shown, is less likely, because in this case guanidinium resonance would be lost in the ring-closed product.) The proton loss from nitrogen shown is concerted with ring closure because the pK_a changes from about +13 to about −11 as the C—N bond forms, so the energy of the transition state is considerably reduced by transferring it (27).[3] Protonation on the *gem*-diol then leads to essentially irreversible water loss, giving the sta-

[3]C.L. Perrin, personal communication, 1991. We would like to thank Professor Perrin for assistance with the analysis in this paragraph.

Can. J. Chem. Downloaded from www.nrcresearchpress.com by 85.192.166.187 on 09/08/12
For personal use only.

ble species **6**, which undergoes no further reaction in the acidic reaction medium.

[5] $k_\psi C_{SH^+} = k_2 a_{SH_2^{2+}} a_{H_2O}/f_\ddagger$

[6] $K_{SH_2^{2+}} = a_{SH^+} a_{H^+}/a_{SH_2^{2+}}$

[7] $k_\psi C_{SH^+} = (k_2/K_{SH_2^{2+}}) C_{SH^+} C_{H^+} a_{H_2O} (f_{SH^+} f_{H^+}/f_\ddagger)$

[8] $\log k_\psi - \log C_{H^+} - \log a_{H_2O} = \log(k_2/K_{SH_2^{2+}}) + m^\ddagger m^* X$

The excess acidity rate equations that apply are readily derived as follows (8). Absolute rate theory requires the equality of eq. [5], essentially all of S being in the monoprotonated form SH^+ as discussed above. The definition of $K_{SH_2^{2+}}$ given in eq. [6] enables substitution for $a_{SH_2^{2+}}$, and separation of activities a into molar concentrations C and molar activity coefficients f results in eq. [7]. Taking logarithms and rearranging, and making the usual excess acidity assumption about the log activity coefficient ratio being linear in X (8), leads to the rate equation for the reaction, eq. [8]; this is accurately obeyed, see Fig. 2 and the information in Table 3.

Differentiation to **3** and **4** evidently takes place during work-up, as shown in eq. [9]; the C=N arrangement in **3** must be the more stable of the two possibilities, since it is the only product observed from the reaction of **1** (4). (We do not mean to imply that the resonance structures in eq. [9] are different species; this is simply a convenient illustration of product formation.) The reaction of **2**, with an *N*-methyl, is faster than that of **1** (R = H) by a factor of 5–6, and has an enthalpy of activation about 4 kcal mol^{-1} lower (see Table 3). This seems reasonable; the electron-releasing methyl group in **2** will stabilize the ring-closed product, and should therefore also stabilize the transition state leading to it, increasing the reaction rate. The activation entropies are large and negative, consistent with a bimolecular reaction that is also a cyclization. The $m^\ddagger m^*$ slopes are around one, quite typical for A-2 reactions like this (7).

[9]

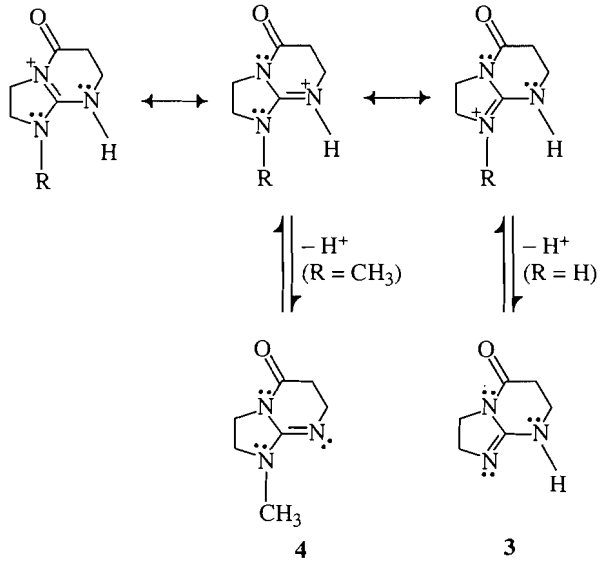

4 **3**

To find water acting in the role of base is actually not very common in reactions in sulfuric acid. In fact it had recently become doubtful as to whether water acting as a base would show up at all in the kinetics when using the excess acidity method. It had been reported that the curvature found in excess acidity plots for some acid-catalyzed enolization processes, as followed by enol bromination, was due to two water molecules acting as a base (13). However, this has subsequently been shown to be wrong, the curvature being an artifact caused by insufficiently effective bromine scavenging by the enol; once this was taken into account, plots of $\log k_\psi - \log C_{H^+}$ against X for this reaction were in fact linear, not curved (28). The only other reported case of water acting as a base in the excess acidity treatment occurs in the acid-catalyzed aldol condensation of acetaldehyde (14), and this is a bit shaky due to the second-order nature of the reaction causing an extra f_S term to appear in the activity coefficient ratio, which causes an unknown amount of curvature. Thus the precedents for this role for water in reactions in strong acids are not good, despite the often-quoted early work of Bunnett (29), before the present study.

[10]

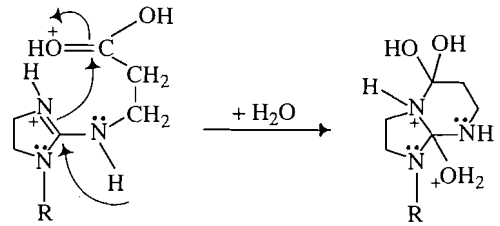

Another role is possible for the water molecule, and that is to have it act as a nucleophile, as shown in eq. [10]. This also supplies a pair of electrons for the ring closure, but it is regarded as a less likely mechanism for a number of reasons. (*a*) The amidinium ion resonance is lost during the eq. [10] process, and the product has two localized positive charges in close proximity. This seems improbable. (*b*) Comparing **1** with **2**, the electron-donating methyl group in **2** would make **5** *less* susceptible to nucleophilic attack, resulting in slower reaction rather than the faster one observed. (*c*) Nucleophilic additions by water in sulfuric acid usually involve more than one water molecule; for instance, ester hydrolysis needs two (9) and amide hydrolysis three, at least in less concentrated acid (11). Only one is needed here.

In summary, it is seen that ring-closure reactions are possible, albeit slow, in the sulfuric acid medium, and that a water molecule is necessary as a base catalyst. This reaction should prove to be a useful synthesis for cyclic guanidine derivatives and related compounds.

Acknowledgments

We would like to thank Dr. J.V. Greenhill for the gift of compounds **1** and **2**, Professors C.L. Perrin and A.J. Kresge for valuable discussions, and the Natural Sciences and Engineering Research Council of Canada and the Committee on Research and Publications of Mount Saint Vincent University for financial support.

1. J.A. Bristol and J.F. Long. Annu. Rep. Med. Chem. **16**, 83 (1981).
2. C.W. Thornber. Annu. Rep. Med. Chem. **12**, 60 (1977).
3. R.L. Smith, D.W. Cochran, P. Gund, and E.J. Cragoe, Jr. J. Am. Chem. Soc. **101**, 191 (1979).
4. J.V. Greenhill, M.J. Ismail, P.N. Edwards, and P.J. Taylor. J. Chem. Soc. Perkin Trans. 2, 1255 (1985).
5. F. Güler and R.B. Moodie. J. Chem. Soc. Perkin Trans. 2, 1752 (1980).
6. V. Rachina, I.B. Blagoeva, I.G. Pojarlieff, and K. Yates. Can. J. Chem. **68**, 1676 (1990).
7. R.A. Cox and K. Yates. Can. J. Chem. **57**, 2944 (1979).
8. R.A. Cox. Acc. Chem. Res. **20**, 27 (1987).

9. R.A. Cox, M.F. Goldman, and K. Yates. Can. J. Chem. **57**, 2960 (1979).
10. R.A. Cox and K. Yates. Can. J. Chem. **60**, 3061 (1982).
11. R.A. Cox and K. Yates. Can. J. Chem. **59**, 2853 (1981).
12. R.A. Cox and K. Yates. Can. J. Chem. **62**, 1613 (1984).
13. R.A. Cox, C.R. Smith, and K. Yates. Can. J. Chem. **57**, 2952 (1979).
14. L.M. Baigrie, R.A. Cox, H. Slebocka-Tilk, M. Tencer, and T.T. Tidwell. J. Am. Chem. Soc. **107**, 3640 (1985).
15. R.A. Cox, M. McAllister, K.A. Roberts, P.J. Stang, and T.T. Tidwell. J. Org. Chem. **54**, 4899 (1989).
16. (*a*) R.A. Cox, E. Grant, T. Whitaker, and T.T. Tidwell. Can. J. Chem. **68**, 1876 (1990); (*b*) V. Lucchini and G. Modena. J. Am. Chem. Soc. **112**, 6291 (1990).
17. R.A. Cox. J. Phys. Org. Chem. **4**, 233 (1991).
18. (*a*) E. Buncel and I. Onyido. Can. J. Chem. **64**, 2115 (1986); (*b*) R.A. Cox, I. Onyido, and E. Buncel. J. Am. Chem. Soc. **114**, 1358 (1992).
19. R.A. Cox and K. Yates. J. Am. Chem. Soc. **100**, 3861 (1978).
20. W.F. Giauque, E.W. Hornung, J.E. Kunzler, and T.R. Rubin. J. Am. Chem. Soc. **82**, 62 (1960).
21. D.D. Perrin, B. Dempsey, and E.P. Serjeant. pK_a prediction for organic acids and bases. Chapman and Hall, London. 1981.
22. C.L. Perrin, E.R. Johnston, and J.L. Ramírez. J. Am. Chem. Soc. **102**, 6299 (1980).
23. S. Limatibul and J.W. Watson. J. Org. Chem. **36**, 3805 (1971).
24. R. Stewart. The proton: applications to organic chemistry. Academic Press, Toronto. 1985. pp. 118–119.
25. P.R. Bevington. Data reduction and error analysis for the physical sciences. McGraw–Hill, Toronto. 1969. p. 237.
26. D.G. Lee and M.H. Sadar. Can. J. Chem. **54**, 3464 (1976).
27. W.P. Jencks. Acc. Chem. Res. **9**, 425 (1976).
28. Y. Chiang, A.J. Kresge, R.A. More O'Ferrall, B.A. Murray, N.P. Schepp, and J. Wirz. Can. J. Chem. **68**, 1563 (1990).
29. J.F. Bunnett. J. Am. Chem. Soc. **83**, 4956 (1961); **83**, 4968 (1961); **83**, 4973 (1961); **83**, 4978 (1961).

Can. J. Chem. Downloaded from www.nrcresearchpress.com by 85.192.166.187 on 09/08/12
For personal use only.

Surface and interfacial tensions of aqueous dispersions of charged colloidal (clay) particles

LAURIER L. SCHRAMM[1]
Syncrude Canada Ltd., Research Department, P.O. Box 5790, Edmonton, AB, T6C 4G3 Canada

AND

LOREN G. HEPLER
AOSTRA Strategic Program and Departments of Chemistry and Chemical Engineering, University of Alberta, Edmonton, AB, T6G 2G2 Canada

Received February 4, 1994

LAURIER L. SCHRAMM and LOREN G. HEPLER. Can. J. Chem. **72**, 1915 (1994).

We have measured (du Nouy ring and maximum bubble pressure methods) suspension–air surface tensions of aqueous suspensions of montmorillonite and have observed that these surface tensions are larger than those of pure water at the same temperatures. Further measurements have shown that dispersed montmorillonite also increases the suspension–toluene interfacial tension compared with that of pure water–toluene. Similar measurements on aqueous suspensions of kaolinite have yielded suspension–air interfacial tensions with uncertainties as large as the observed (small) effect, and also shown that the suspension–toluene interfacial tension is decreased (opposite to the effect of montmorillonite) by amounts larger than the experimental uncertainties. Measurements of maximum bubble pressures at different flow rates have provided information about the effect of surface age on observed surface tensions.

LAURIER L. SCHRAMM et LOREN G. HEPLER. Can. J. Chem. **72**, 1915 (1994).

On a mesuré (par les méthodes du cercle de Nouy et de la pression maximale de la bulle) les tensions de surface suspension/air de suspensions aqueuses de montmorillonite et on a observé que, aux mèmes températures, ces tensions de surface sont plus importantes que celle de l'eau pure. Des mesures additionnelles ont permis de montrer que la montmorillonite dispersée augmente aussi la tension interfaciale de la suspension/toluène par rapport à celle de l'eau pure/toluène. Des mesures semblables sur des suspensions aqueuses de kaolinite ont fourni des tensions interfaciales suspension/air pour lesquelles les incertitudes sont aussi importantes que le (faible) observé et on aussi permis de démontrer que la tension interfaciale suspension/toluène diminue (effet opposé à celui de la montmorillonite) par des quantités plus importantes que les incertitudes expérimentales. Des mesures par la méthode des pressions maximales de la bullel à diverses vitesses d'écoulement ont fourni de l'information concernant l'effet de l'age de la surface sur les tensions de surface observées.

[Traduit par la rédaction]

Introduction

Many aqueous systems found in industry and in nature contain dispersed clays or other finely divided solids. Examples include heat and mass transfer operations, the casting of ceramics, mineral flotation, and solids-stabilized emulsions. Several properties (such as viscosities, light scattering, and electrophoretic mobilities) of such systems have been investigated many times. On the other hand, the surface tensions (suspension–air) and interfacial tensions (suspension–liquid) of systems containing finely dispersed solids (such as clays) have not received much attention. In fact it is quite common, when dealing with such systems, to remove the solids and measure and report surface and interfacial tensions on a solids-free basis. This is in spite of evidence that such properties for the *suspensions* can be important in various fields.

Our specific interest in this problem arose in two connections: (*i*) the effects of clays on recovery of bitumen from oil (tar) sands by the hot water flotation process used commercially in Canada by Syncrude and Suncor, and (*ii*) the properties and possible treatment of the tailings "sludge" that is a troublesome by-product of the hot water flotation process.

In addition to the above specific interests there is a general interest in measuring and understanding surface and interfacial tensions of systems that consist of dispersions of finely divided particles. Some reasons for such interests are as follows.

Surface tensions of aqueous solutions of inorganic electrolytes are well-known to be larger than the surface tension of pure water at the same temperature. For example, the surface tension of 2M (10.5 mass%) sodium chloride solution is about 3.3 mN/m larger than the surface tension of water at the same (room) temperature. Such elevated surface tensions are not limited to solutions of inorganic electrolytes; aqueous solutions of sucrose and some other organic non-electrolyte solutes have larger surface tensions than does water at the same temperature. It is commonly believed that these increased surface tensions are due to strong interactions (hydration) of water with many ionic solutes and also with many non-ionic solutes. Chaudhury and Good (1) have reported their theory of negative adsorption and increased surface tension due to solutes such as sucrose.

Many other solutes (both electrolytes and non-electrolytes) cause the surface tensions of their solutions to be smaller than the surface tension of water at the same temperature. Among these solutes are substances that are called surfactants because of their dramatic effects on surface tension and some other properties (2).

In contrast to these well-known effects of solutes (*dissolved* substances) on the surface tension of water, consider the non-effect of a rock sitting on the bottom of a beaker of water. Consideration of the differences between solutes (NaCl, sucrose, etc.) and the rock leads to interesting questions about aqueous polymers ("small" polymers are similar to conventional solutes, but sufficiently large polymers may be regarded as small suspended particles) and about aqueous suspensions of finely divided solids. It is easy to observe that some such finely divided solids reside on or near the surface of water, and it is also easy to observe that solids in some dispersions settle (rapidly or slowly) away from the surface to become systems that

[1]Present address: Petroleum Recovery Institute, 100-3512-33rd St. N.W., Calgary, AB T2L 2A6, Canada.

Can. J. Chem. Downloaded from www.nrcresearchpress.com by 85.192.166.187 on 09/08/12
For personal use only.

Can. J. Chem. Downloaded from www.nrcresearchpress.com by 85.192.166.187 on 09/08/12
For personal use only.

are similar in some ways to the beaker of water with a rock at the bottom. These considerations made us suspect that some systems containing finely divided solids dispersed in water would exhibit surface and/or interfacial tensions different from those of pure water.

The exploratory measurements described in this paper were undertaken to answer some of the general questions mentioned above, and also to lead in the direction of data that would be relevant to specific problems with oil sand flotation and processing.

It is appropriate to mention several other investigations that are directly or indirectly related to the surface and interfacial tensions that are the subject of this investigation.

Salmang et al. (3) and Taylor and Howlett (4) have investigated physical properties of ceramic casting slips, which typically consist of suspensions of kaolinite in water in the presence of deflocculating agents. They found that the commonly used casting slip suspensions can have surface tensions that are several mN/m greater than that of pure water. Surface tensions slightly smaller than that of pure water were observed after wetting agents were added to the casting slip suspensions, whereas much larger surface tensions were observed when "skins" of particles formed at the suspension-air interface. In the oil sands industry, Gewers (5) has reported on the effects of clay "skins" at the oil–water interface.

Brian and Chen (6) have measured the surface tensions of suspensions of iron oxide and silicon dioxide particles in two liquids (water and isoparaffin). Their surface tensions for suspensions of these solids in water were larger than for pure water, while suspensions in isoparaffin had surface tensions that were smaller than for the pure liquid. These authors wrote "In conclusion, while some statistically significant effects were observed, for practical purposes the surface tension of the liquid was unaffected by the addition of solid particles." We do not disagree with their experimental results, but we do suggest that results of several other investigations and our own results reported here show that their conclusion is too restrictive; some finely divided solids do have a "practical" effect on surface tensions.

Adam (7) has written "Powdered solids are very useful emulsifiers, and are frequently used, and it is found that emulsions of either the oil-in-water or water-in-oil type can be stabilized by them." Adam has gone on to discuss stabilization in terms of contact angles and points out the systematic investigation by Pickering, published in 1907, that has led to the use of the term "Pickering emulsions" to denote emulsions stabilized by fine particles (see also refs. 2 and 8). Levine et al. (9–11) have provided a theoretical analysis of the stabilization of emulsions by fine particles at the interface, including some specific consideration of the bitumen–water interface. Menon et al. (12–17) have published several accounts of their investigations of emulsions stabilized by finely divided solids; these papers provide convincing evidence that such solids can have important effects on interfacial tensions. Finally, we note that Goldenberg et al. (18) have reported on the effects of suspended clays on transport in porous media containing gas bubbles.

Experimental

Wyoming montmorillonite ("Upton Wyoming montmorillonite", A.P.I. 25, Wards Natural Science Est., Rochester, N.Y.) and Georgia kaolinite ("Georgia kaolin", well crystallized, KGa-1, Clay Minerals Soc., Source Clay Repository) were used. The <2 μm equivalent spherical diameter fraction was isolated and prepared in the sodium form by treatments described previously by Ewin et al. (19) and Schramm and Kwak (20). Typical samples of the montmorillonite have cation exchange capacities of about 97 meq/100g and specific surface areas in the range 40–45 m^2/g (21–23), while the kaolinite has a CEC of about 2 mequiv./100 g and a specific surface area of about 10 m^2/g (24). Extensive characterizations have been given elsewhere for the Upton Wyoming montmorillonite (21) for the Georgia kaolinite (24). The suspensions were adjusted to pH 9.4 ± 0.2 with NaOH.

TABLE 1. Suspension–air and suspension–toluene interfacial tensions of systems containing Na-montmorillonite suspended in water at 24.5°C[a]

Mass% clay in water	Suspension–air surface tension (mN/m)	Suspension–toluene interfacial tension (mN/m)
0	72.1	36.0
0.15	73.5	37.3
0.30	73.8	39.5
0.98	73.7	39.0
1.49	73.9	38.8
2.14	74.1	39.1
3.00	74.1	39.5

[a]Measurements were made with the du Nouy ring method. Uncertainties are estimated to be about ±0.6 mN/m.

Some surface (liquid–air) and some interfacial (liquid–liquid) tensions were measured with the classical du Nouy ring method (Fisher Scientific, Surface Tensiometer Model 20) as described by Adamson (25), Harkins and Alexander (26), and Padday (27). Pure liquid standards used were methanol, ethylene glycol, toluene, and distilled-deionized water. Some surface tensions were measured with a modified differential maximum bubble pressure method that uses carefully displaced capillaries so that the measurements are independent of density, the importance of which has been discussed by Schramm (28). The flow arrangement allowed for continuously variable, stable gas flow rates capable of producing bubble periods ranging from 0.1 s to longer than 90 s. The waveforms characterizing the gas-pressure changes during bubble growth and breakaway cycles were recorded and used in the evaluation of effective surface ages (29). Each capillary was stainless-steel, with a carefully machined round orifice and a smooth 45° knife edge tip. For both measurement techniques uncertainties are estimated to be about ±0.6 mN/m for the Na-montmorillonite suspensions and about ±0.9 mN/m for the Na-kaolinite suspensions.

Densities of the suspensions were measured using a vibrating reed densitometer (Anton Paar, Graz, Austria, Model DMA 46) and also with 25 mL pychnometers.

Results

Measurements (by the du Nouy ring technique) on suspensions of Na-montmorillonite in water showed that the surface tension is increased compared with that of pure water. Similar measurements showed that the suspension–toluene interfacial tension is also increased by Na-montmorillonite, compared with that of pure water. These results are shown in Table 1 and illustrated in Fig. 1.

The qualitative reliability of the surface tensions cited above was confirmed by the application of the maximum bubble pressure method. The results, shown in Fig. 2 for a surface age of 50 s, again show that the surface tension of water is increased by Na-montmorillonite, with the amount of increase being nearly independent of temperature. The surface age of 50 s was long enough that there was minimal dependence of measured surface tension on bubble flow rate (age). Other illustrations of the increase in surface tension over that of pure water caused by the Na-montmorillonite are shown in Fig. 3, while Fig. 4 shows

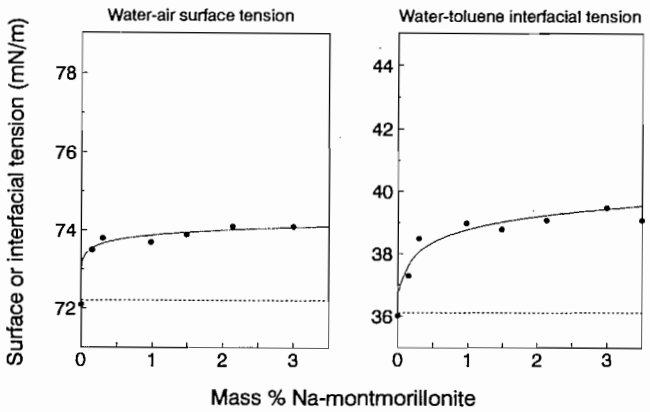

FIG. 1. Suspension–air and suspension–toluene surface and interfacial tensions for aqueous suspensions of Na-montmorillonite, as measured with the du Nouy ring technique at 24.5°C. The broken lines show the values measured for pure water.

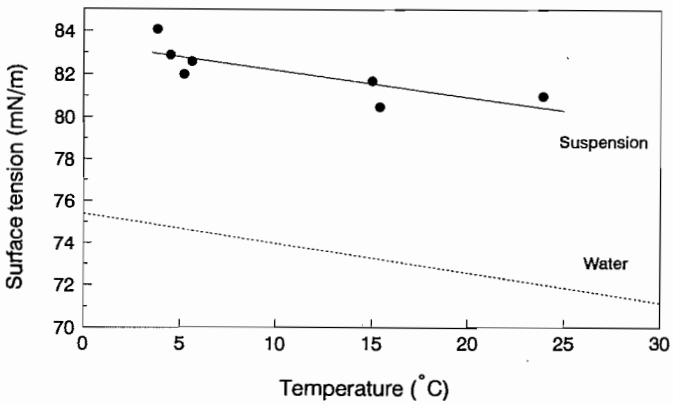

FIG. 2. Suspension–air surface tensions for aqueous suspensions of Na-montmorillonite (5 mass%), as measured with the maximum bubble pressure technique at different temperatures. The broken line shows the values measured for pure water.

a comparison of results obtained with the two independent methods (du Nouy ring and maximum bubble pressure).

We next consider the effect of Na-kaolinite on surface and interfacial tensions. The suspension–toluene interfacial tensions for Na-kaolinite are clearly lower than for pure water (Table 2 and Fig. 5), which is opposite to the effect of the Na-montmorillonite. On the other hand, the suspension–air surface tensions measured by du Nouy ring (Table 2 and Fig. 6) are not changed significantly (considering experimental uncertainties) from those for pure water.

The results of measurements by the maximum bubble pressure method show that surface tensions of Na-kaolinite suspensions are dynamic; they depend on the gas flow rate (surface age) as shown in Figs. 7 and 8. The Na-kaolinite suspensions showed decreased surface tension at fast flow rates (short surface ages) and larger surface tensions at slower flow rates (older surfaces).

Uncertainties in our results for suspensions of kaolinite are larger than for similar experiments with montmorillonite, presumably because the suspensions of kaolinite settle more rapidly than do the suspensions of montmorillonite.

Discussion

It was stated in the Introduction that surface tensions of aqueous solutions of inorganic electrolytes are larger than the surface tension of pure water at the same temperature. Therefore suspending sodium-form clays in water should have a positive effect on surface tension due to the counterions. For 5 mass% suspensions, the highest clay concentration used in this work, Na-montmorillonite contributes a sodium ion concentration of 5.1×10^{-2} M while Na-kaolinite contributes a sodium ion concentration of 1.05×10^{-3} M. But the anion must be considered as well. As an illustration we consider the addition to water

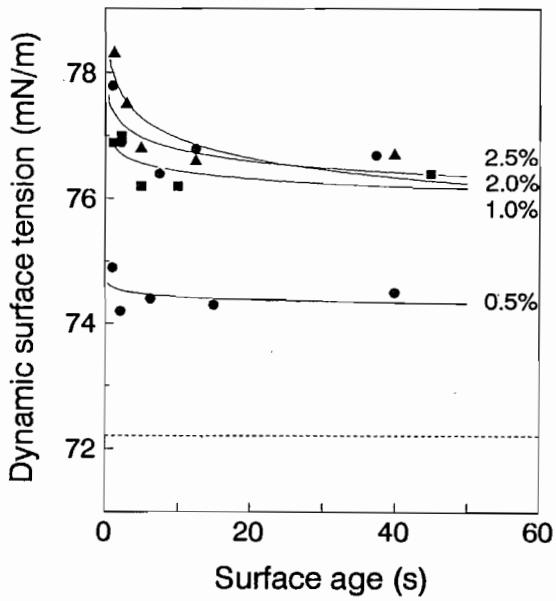

FIG. 3. Suspension–air surface tensions for aqueous suspensions of Na-montmorillonite, as measured with the maximum bubble pressure technique at 23.0°C for different surface ages. The solid curves indicate results for different concentrations (expressed as mass%) of clay. The broken line shows the value measured for pure water (it is independent of surface age).

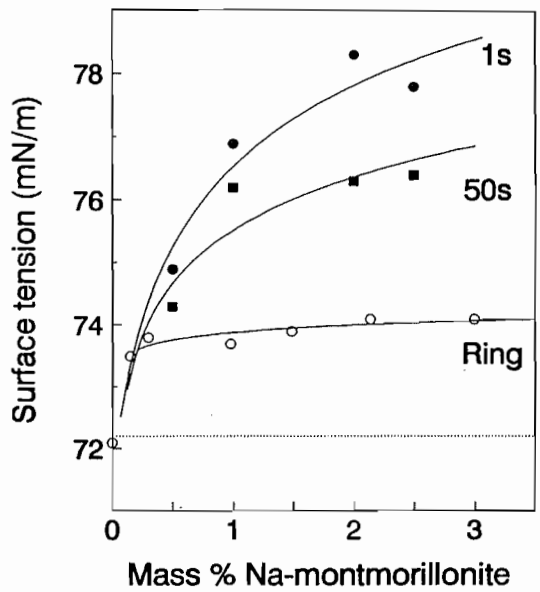

FIG. 4. Comparison of suspension–air surface tensions for aqueous suspensions of Na-montmorillonite, as measured with the du Nouy ring and maximum bubble pressure techniques. The curves with solid symbols represent bubble pressure results for two different surface ages. The broken line shows the value measured for pure water.

Can. J. Chem. Downloaded from www.nrcresearchpress.com by 85.192.166.187 on 09/08/12
For personal use only.

TABLE 2. Suspension–air and suspension–toluene interfacial tensions of systems containing Na-kaolinite suspended in 0.01 mol/L NaOH (aq) at 24.5°C[a]

Mass% clay in water	Suspension–air surface tension (mN/m)	Suspension–toluene interfacial tension (mN/m)
0	72.2	34.1
0.13	72.5	35.5
0.47	72.2	34.3
1.00	72.5	33.9
1.30	71.9	33.8
2.00	72.1	32.3

[a]Measurements were made with the du Nouy ring method. Uncertainties are estimated to be about ±0.9 mN/m.

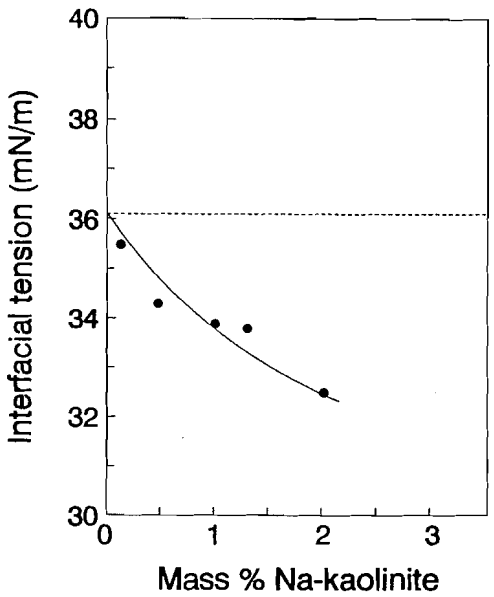

FIG. 5. Suspension–toluene interfacial tensions for aqueous suspensions of Na-kaolinite, as measured with the du Nouy ring technique at 24.5°C. The broken line shows the value measured for pure water.

of these concentrations of sodium in the form of NaCl. A 5.1×10^{-2} M NaCl solution (representing the ionic concentration of a 5% suspension of Na-montmorillonite) has a surface tension of 72.84 mN/m at 20°C which is only 0.09 mN/m larger than the surface tension of pure water at the same temperature. Similarly, the surface tension of 1.05×10^{-3} M NaCl solution at 20°C (representing the ionic concentration of a 5% suspension of Na-kaolinite) is only 0.002 mN/m larger than that of pure water at the same temperature. All of the changes in surface tension due to the presence of clay particles and their counterions determined in this work are of much greater magnitude than would be expected based on the addition of the same number of equivalents of the clay-counterions with simple anions.

There are at least two ways to interpret the observation that colloidal clays dispersed in water can raise or lower surface and interfacial tensions. The first can be expressed in terms of the Gibbs adsorption equation

$$d\gamma^\circ = -RT\Gamma \, d \ln a$$

where Γ is the surface excess adsorption per area and a is the activity of adsorbing species. From this point of view one might

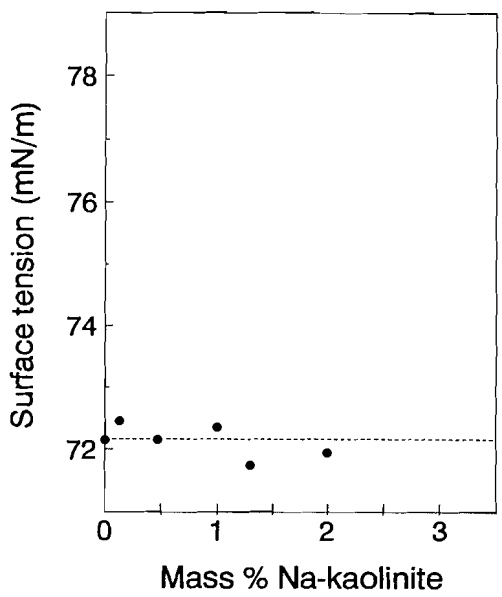

FIG. 6. Suspension–air surface tensions for aqueous suspensions of Na-kaolinite, as measured with the du Nouy ring technique at 24.5°C. All surface tensions are within experimental uncertainty equal to the value measured for pure water (broken line).

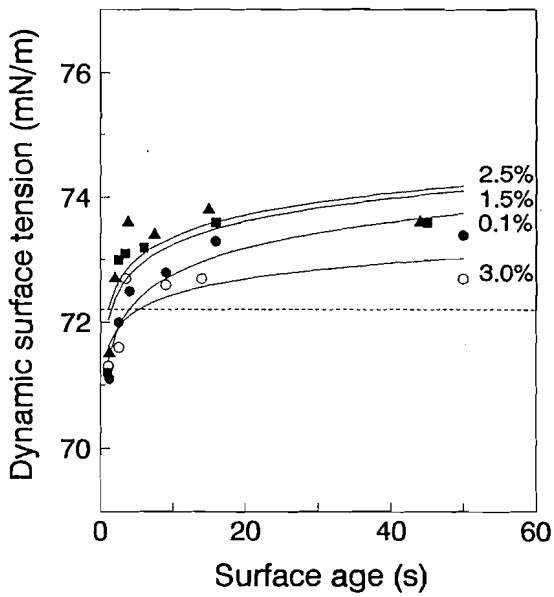

FIG. 7. Suspension-air surface tensions for aqueous suspensions of Na-kaolinite, as measured with the maximum bubble pressure technique at 23.0°C for different surface ages. The broken line shows the value measured for pure water.

conclude that the montmorillonite particles tend to be negatively adsorbed while the kaolinite particles tend to positively adsorb. This is consistent with a study of adhesion of small particles to large air bubbles in suspensions by Goldenberg et al. (18). They found that in dilute electrolyte solutions clays of low cation exchange capacity (kaolinite) adhered to bubble surfaces and formed surface structures. In contrast, clays of high cation exchange capacity (smectite) tended not to adhere to the bubble surfaces.

An alternative point of view can be drawn from the work of Menon et al. (12–14) who found that when fine solids were

Can. J. Chem. Downloaded from www.nrcresearchpress.com by 85.192.166.187 on 09/08/12
For personal use only.

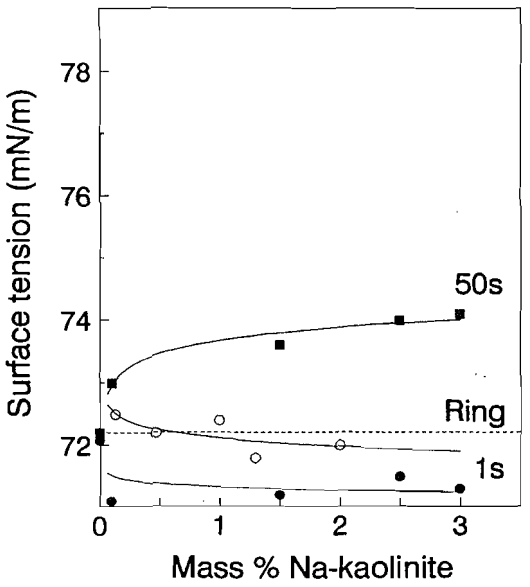

FIG. 8. Comparison of suspension–air surface tensions for aqueous suspensions of Na-kaolinite, as measured with the du Nouy ring and maximum bubble pressure techniques. The curves with solid symbols represent bubble pressure results for two different surface ages. The broken line shows the value measured for pure water.

forced to accumulate at the oil–water interface the presence of the solids at the interface could either raise or lower interfacial tension. Menon et al. associate changes in interfacial tension with degrees of repulsive interaction among particles present at the interface. High interfacial coverages with shale dust particles (clays coated with asphaltic material) were found to raise or lower interfacial tension depending on the extent of surface coverage and particle orientations. At high particle coverages the interfacial tensions were raised, presumably due to net electrostatic repulsions. When the negative charge of the clay was almost completely countered by the adsorption of asphaltenes, interfacial tension lowering was observed.

Another feature of the particle interaction model is that dynamic effects (dynamic surface or interfacial tensions) might be expected, due to the formation of a monolayer followed by particle rearrangements. Support for this can be found in a recent paper by Williams and Berg (30) that describes the phenomenon of adsorption and aggregation of colloidal particles at air–liquid interfaces.

Results of our measurements by the du Nouy ring method and the maximum bubble pressure method are in good qualitative agreement. Each method leads to measured surface tensions for aqueous suspensions of Na-montmorillonite that are larger than the surface tension of water without suspended clay at the same temperature. There are, however, quantitative disagreements. For example, extrapolation of the surface tensions shown in the left hand diagram of Fig. 1 leads to a predicted surface tension amounting to a little less than 75 mN/m for a 5 mass% suspension of Na-montmorillonite, whereas the value from the maximum bubble pressure method (Fig. 2) is a little more than 80 mN/m at the same temperature. For du Nouy ring measurements the effective surface ages are not well known. The ring was initially equilibrated with the solution (or suspension) but some changes still can take place at the meniscus surface where new surface is created as the ring is raised, even when the ring is raised as slowly as possible. By assuming that the surface age was older for the ring method than for the bubble pressure method, we can account for part (only part) of the discrepancy noted above.

In the present systems the extent to which the particles may have been present at the interfaces is not known for certain. Our results are, however, consistent with the available literature in that it seems that where the interfacial properties of suspensions are concerned – significant interparticle repulsive forces (high charge density particles such as montmorillonite) can cause surface or interfacial tension elevation while near-zero or attractive forces (low or zero charge density particles such as kaolinite) can cause surface or interfacial tension lowering. A related aspect is the effect of particle size on the results. The particle sizes were not measured in this work. However, it is known from the results of other investigations that the Na-kaolinite particles were larger than the Na-montmorillonite particles. The latter would be expected from other work to have a major dimension of about 300 nm and a minor dimension of about 2.4 nm (31). The possible effect of particle size on the surface or interfacial tensions of suspensions should be investigated in future work. This is an important aspect because different exchange cations will influence the particle sizes in suspension. In montmorillonite suspensions particularly, tactoid formation is very much dependent on the counterion (31).

For the present we conclude only that colloidal clays dispersed in water can raise or lower surface and interfacial tensions by amounts significantly larger than experimental uncertainties, and that the time-dependence of suspension surface tensions can be appreciable. These effects of suspended clay particles (and possibly other colloidal solids) on surface and interfacial tensions are surely important in connection with stabilities of certain emulsions and may be important in other systems.

Acknowledgements

We are grateful to Brian Turnbull and Z.M. Ding for assistance with the measurements, and to Visiting Professor Shmuel Yariv and the journal's manuscript reviewers for helpful advice. We thank Syncrude Canada Ltd. and the Alberta Oil Sands Technology and Research Authority (Strategic Program) for their support of this research and for their permission to publish this report. L.L.S. also thanks the Petroleum Recovery Institute for providing the facilities and time needed to do some of the bubble pressure measurements and to prepare part of this report.

1. M.K. Chaudhury and R.J. Good. Langmuir, **1**, 673 (1985).
2. L.L. Schramm. The language of colloid and interface science. Am. Chem. Soc. Washington. 1993.
3. H. Salmang, W. Deen, and A. Vroemen. Ber. Deutsch Keram. Ges. **34**, 33 (1957).
4. D. Taylor and D.J. Howlett. Trans. J. Brit. Ceram. Soc. **73**, 19 (1974).
5. C.W.W. Gewers. J. Can. Petrol. Technol. **7**, 85 (1968).
6. B.W. Brian and J.C. Chen. AIChE J. **33**, 316 (1987).
7. N.K. Adam. The physics and chemistry of surfaces. 4th. ed., Dover Publ., New York. 1968.
8. L.L. Schramm (*Editor*). Emulsions: Fundamentals and applications in the petroleum industry. Am. Chem. Soc. Washington. 1992.
9. S. Levine, B.D. Bowen, and S.J. Partridge. Colloids and Surfaces **38**, 325 (1989).
10. S. Levine, B.D. Bowen, and S.J. Partridge. Colloids and Surfaces **38**, 345 (1989).

Can. J. Chem. Downloaded from www.nrcresearchpress.com by 85.192.166.187 on 09/08/12
For personal use only.

11. S. Levine and E. Sanford. Can. J. Chem. Eng. **63**, 258 (1985).
12. V.B. Menon, A.D. Nikolov, and D.T. Wasan. J. Colloid Interface Sci. **124**, 317 (1988).
13. V.B. Menon, A.D. Nikolov, and D.T. Wasan. J. Dispersion Sci. Technol. **9**, 575 (1988/89).
14. V.B. Menon and D.T. Wasan. Colloids Surf. **29**, 7 (1988).
15. V.B. Menon and D.T. Wasan. Colloids Surf. **19**, 89 (1986).
16. V.B. Menon and D.T. Wasan. Colloids Sur. **19**, 107 (1986).
17. V.B. Menon and D.T. Wasan. Colloids Surf. **23**, 353 (1987).
18. L.C. Goldenberg, I. Hutcheon, and N. Wardlaw. Transp. Porous Media **4**, 129 (1989).
19. G.J. Ewin, B.P. Erno, and L.G. Hepler. Can. J. Chem. **59**, 2927 (1981).
20. L.L. Schramm and J.C.T. Kwak. Can. J. Chem. **60**, 486 (1982).
21. American Petroleum Institute. Clay mineral standards, Preliminary Reports, Project 49. Columbia University, New York, 1951.
22. L.A.G. Aylmore, I.D. Sills, and J.P. Quirk. Clays Clay Miner. **18**, 91 (1970).
23. M.S. Stul and L. van Leemput. Surf. Technol. **16**, 89 (1982).
24. H. van Olphen and J.J. Fripiat (*Editors*). Data handbook for clay materials and other non-metallic minerals. Pergamon Press, Oxford. 1979.
25. A.W. Adamson. Physical chemistry of surfaces. 5th. ed. Wiley, New York. 1990.
26. W.D. Harkins and A.E. Alexander. *In* Technique of organic chemistry. Vol. 1, Pt. 1. *Edited by* A. Weissberger. Interscience, New York. 1959.
27. J.F. Padday. *In* Surface and colloid science. Vol. 1. *Edited by* E. Matijevic. Wiley-Interscience, New York. 1969. p. 101.
28. L.L. Schramm. J. Colloid Interface Sci. **133**, 534 (1989).
29. L.L. Schramm and W.H.F. Green. Colloid Polymer Sci. **270**, 694 (1992).
30. D.F. Williams and J.C. Berg. J. Colloid Interface Sci. **152**, 218 (1992).
31. L.L. Schramm and J.C.T. Kwak. Clays Clay Miner. **30**, 40 (1982).

Can. J. Chem. Downloaded from www.nrcresearchpress.com by 85.192.166.187 on 09/08/12
For personal use only.

Excess volumes and excess viscosities of binary mixtures of 2-chloro-2-methylpropane with isomeric butanols at 298.15 K

PILAR CEA, CARLOS LAFUENTE, HECTOR ARTIGAS, FELIX M. ROYO, AND JOSE S. URIETA[1]

Departamento de Química Orgánica-Química Física, Facultad de Ciencias, Universidad de Zaragoza. Ciudad Universitaria, Zaragoza 50009, Spain

Received December 23, 1993

PILAR CEA, CARLOS LAFUENTE, HECTOR ARTIGAS, FELIX M. ROYO, and JOSE S. URIETA. Can. J. Chem. **72**, 1921 (1994).

Excess volumes V^E, excess viscosities η^E, and excess free energies of activation of flow G^{*E} of binary mixtures of 2-chloro-2-methylpropane with isomeric butanols have been calculated from experimental measurements of density and viscosity at 298.15 K. The results are correlated by means of a Redlich–Kister type equation and explained in terms of molecular interactions.

PILAR CEA, CARLOS LAFUENTE, HECTOR ARTIGAS, FELIX M. ROYO et JOSE S. URIETA. Can. J. Chem. **72**, 1921 (1994).

Utilisant des mesures expérimentales de densité et de viscosités obtenues à 298,15 K, on a calculé les volumes en excès, V^E, les viscosités en excès, η^E, et les énergies libres d'activation d'écoulement en excès, G^{*E}, de mélanges binaires du 2-chloro-2-méthylpropane avec les butanols isomères. On a établi une corrélation entre les résultats et une équation du type de Redlich–Kister et on les a expliqués en fonction d'interactions moléculaires.

[Traduit par la rédaction]

Can. J. Chem. Downloaded from www.nrcresearchpress.com by 85.192.166.187 on 09/08/12
For personal use only.

Introduction

The study of the thermodynamics and transport properties of liquid mixtures provides information about intermolecular forces and the microscopic structure of liquids. As a continuation of previous work in our laboratory (1–5), we here report excess volumes V^E, excess viscosities η^E, and excess free energies of activation of flow G^{*E}, at 298.15 K for binary mixtures of 2-chloro-2-methylpropane with isomeric butanols. These compounds have several uses in the chemical industry (e.g., 2-chloro-2-methylpropane is used in Friedel–Crafts reactions).

We have found only one reference for excess volumes of 2-chloro-2-methylpropane with alkanols (ethanol, 1-hexanol, and 1-decanol) (6) but no references about isomeric butanols.

Experimental

Materials

The liquids used, 1-butanol (better than 99.8 mol%), 2-methyl-1-propanol and 2-methyl-2-propanol (better than 99.5 mol%), and 2-butanol and 2-chloro-2-methylpropane (better than 99 mol%) were obtained from Aldrich. The purity of these chemicals was checked by GLC and exceeded 99 mol%. All isomeric butanols were dried over activated molecular sieves type 0.3 nm from Merck and no further purification was considered necessary.

Table 1 shows the experimental values of density and viscosity for the pure components at 298.15 K compared with those found in the literature (7).

Methods

Densities were determined with an Anton Paar DMA-58 vibrating tube densimeter. The uncertainty of density measurements was ± 0.01 kg m^{-3}. Viscosities were determined using an Ubbelhode viscosimeter with a Schott–Geräte automatic measuring unit model AVS-440, the accuracy of the time flow measurement is ± 0.01 s. Details of calibrations and procedures can be found in an earlier paper (5).

Results and discussion

Measured data of density and viscosity are used to calculate V^E, η^E, and G^{*E} using the following equations:

$$[1] \quad V^E = x_1M_1(\rho^{-1} - \rho_1{}^{-1}) + x_2M_2(\rho^{-1} - \rho_2{}^{-1})$$

$$[2] \quad \eta^E = \eta - (x_1\eta_1 + x_2\eta_2)$$

$$[3] \quad G^{*E} = RT(\ln \nu M - (x_1 \ln \nu_1M_1 + x_2 \ln \nu_2M_2))$$

where M_1 and M_2 are the molecular masses of the components ρ, ρ_1, and ρ_2 are the densities (kg m^{-3}) of the mixture and of the pure components, η, η_1, and η_2 are the absolute viscosities (Pa s) of the mixtures and of the pure components, ν, ν_1, and ν_2 are the corresponding kinematic viscosities (m^2 s^{-1}), calculated as the quotient between η and ρ, M is the molar mass of the mixture, and x_i is the mole fraction of component i in the mixture.

Excess properties are given in Tables 2–4 and are graphically presented in Figs. 1–3. The results were fitted to a Redlich–Kister-type equation:

$$[4] \quad Y^E = x_1(1 - x_1) \Sigma\, a_i(2x_1 - 1)^i$$

where a_0, a_1, etc., are adjustable parameters and x_1 is the mole fraction of 2-chloro-2-methylpropane. The values of the parameters computed by the least squares method are shown in Table 5, together with standard deviation $\sigma(Y^E)$.

The excess volumes for the mixtures containing 2-butanol and 2-methyl-2-propanol are positive, the latter giving a symmetrical curve. For those with 1-butanol V^E are negative over the entire composition range. The mixtures containing 2-methyl-1-propanol have negative values of V^E between $0 < x_1 < 0.7$. V^E values increase in the sequence: 1-butanol < 2-methyl-1-propanol < 2-butanol < 2-methyl-2-propanol.

The butanols are self-associated compounds by hydrogen bonding (8). In the pure state exists an equilibrium between the monomers and linear and cyclic polymers (9). On the other hand, 2-chloro-2-methylpropane is a polar liquid but not self-associated. When the compounds are mixed the behaviour of the mixture may be due to several factors: (*i*) the breaking of the self-association by hydrogen-bonds existing in butanols, this loss of self-association is greater for 2-methyl-2-propanol than for the others. This is supported by the H^E values for the mixtures of n-hexane + isomeric butanols (10); (*ii*) the breaking of the dipole–dipole interactions between chloroalkane molecules. These two effects contribute in a positive way to excess volume; (*iii*) the specific interaction between the Cl group in chloroalkane and the OH group in butanol which has a negative effect on excess volume due to a dipole–dipole interaction with inter-

Can. J. Chem. Downloaded from www.nrcresearchpress.com by 85.192.166.187 on 09/08/12
For personal use only.

TABLE 1. Densities, ρ, and viscosities, η, of pure components at 298.15 K and comparison with literature data

Component	ρ / kg m^{-3}		η / 10^{-3} Pa s	
	This paper	Literature	This paper	Literature
2-Chloro-2-methylpropane	836.78	836.1	0.4842	—
1-Butanol	805.75	805.75	2.550	2.5710
2-Butanol	802.41	802.41	3.084	2.998
2-Methyl-1-propanol	797.84	797.8	3.363	3.330
2-Methyl-2-propanol	781.00	781.2	4.394	4.438

TABLE 2. Excess volumes V^E of binary mixtures 2-chloro-2-methylpropane(1) + isomeric butanols(2) at 298.15 K

x_1	V^E / 10^{-6} m^3 mol^{-1}	x_1	V^E / 10^{-6} m^3 mol^{-1}	x_1	V^E / 10^{-6} m^3 mol^{-1}
2-Chloro-2-methylpropane(1) + 1-butanol(2)					
0.1057	−0.1041	0.4171	−0.1928	0.6992	−0.0993
0.2305	−0.1715	0.5080	−0.1701	0.8089	−0.0560
0.3039	−0.1883	0.6179	−0.1334	0.9065	−0.0131
2-Chloro-2-methylpropane(1) + 2-butanol(2)					
0.1051	0.0425	0.4047	0.1949	0.7072	0.2473
0.2086	0.0982	0.5160	0.2327	0.8076	0.2179
0.3015	0.1508	0.6269	0.2484	0.8945	0.1643
2-Chloro-2-methylpropane(1) + 2-methyl-1-propanol(2)					
0.1094	−0.0662	0.4165	−0.0625	0.7144	0.0042
0.2102	−0.0812	0.5124	−0.0431	0.8138	0.0279
0.3071	−0.0784	0.6249	−0.0214	0.9052	0.0277
2-Chloro-2-methylpropane(1) + 2-methyl-2-propanol(2)					
0.1055	0.2883	0.4077	0.6379	0.6949	0.5630
0.2059	0.4665	0.5319	0.6559	0.8015	0.4396
0.3102	0.5897	0.6277	0.6203	0.8962	0.2809

TABLE 3. Excess viscosities η^E of binary mixtures 2-chloro-2-methylpropane(1) + isomeric butanols(2) at 298.15 K

x_1	η^E / 10^{-3} Pa s	x_1	η^E / 10^{-3} Pa s	x_1	η^E / 10^{-3} Pa s
2-Chloro-2-methylpropane(1) + 1-butanol(2)					
0.0989	−0.2458	0.4011	−0.6360	0.7014	−0.4504
0.1970	−0.4571	0.4996	−0.6214	0.8031	−0.3213
0.2993	−0.5922	0.6077	−0.5484	0.9062	−0.1675
2-Chloro-2-methylpropane(1) + 2-butanol(2)					
0.1031	−0.7517	0.4030	−1.1008	0.7005	−0.6672
0.1995	−1.0489	0.5024	−0.9934	0.8024	−0.4591
0.2984	−1.1303	0.6025	−0.8440	0.9008	−0.2430
2-Chloro-2-methylpropane(1) + 2-methyl-1-propanol(2)					
0.1015	−0.5646	0.4027	−1.0576	0.7041	−0.6842
0.2007	−0.9005	0.4989	−0.9984	0.8059	−0.4712
0.3042	−1.0430	0.6030	−0.8581	0.9027	−0.2492
2-Chloro-2-methylpropane(1) + 2-methyl-2-propanol(2)					
0.1044	−1.4879	0.4097	−1.8337	0.7064	−1.0275
0.2058	−1.9427	0.5117	−1.5998	0.8074	−0.6924
0.3124	−1.9712	0.6109	−1.3217	0.9096	−0.3355

TABLE 4. Excess free energies of activation of flow G^{*E} of binary mixtures 2-chloro-2-methylpropane(1) + isomeric butanols(2) at 298.15 K

x_1	G^{*E} / J mol^{-1}	x_1	G^{*E} / J mol^{-1}	x_1	G^{*E} / J mol^{-1}
		2-Chloro-2-methylpropane(1) + 1-butanol(2)			
0.0989	−72.7	0.4011	−459.8	0.7014	−491.0
0.1970	−211.5	0.4996	−527.4	0.8031	−402.8
0.2993	−358.9	0.6077	−536.7	0.9062	−252.3
		2-Chloro-2-methylpropane(1) + 2-butanol(2)			
0.1031	−517.2	0.4030	−1093.1	0.7005	−847.4
0.1995	−835.1	0.5024	−1072.5	0.8024	−630.8
0.2984	−1004.2	0.6025	−991.0	0.9008	−373.3
		2-Chloro-2-methylpropane(1) + 2-methyl-1-propanol(2)			
0.1015	−239.4	0.4027	−726.3	0.7041	−676.9
0.2007	−467.0	0.4989	−785.8	0.8059	−514.1
0.3042	−627.6	0.6030	−752.5	0.9027	−310.2
		2-Chloro-2-methylpropane(1) + 2-methyl-2-propanol(2)			
0.1014	−820.3	0.4097	−1515.6	0.7064	−1038.8
0.2058	−1293.4	0.5117	−1425.8	0.8074	−748.6
0.3124	−1488.9	0.6109	−1253.6	0.9096	−397.6

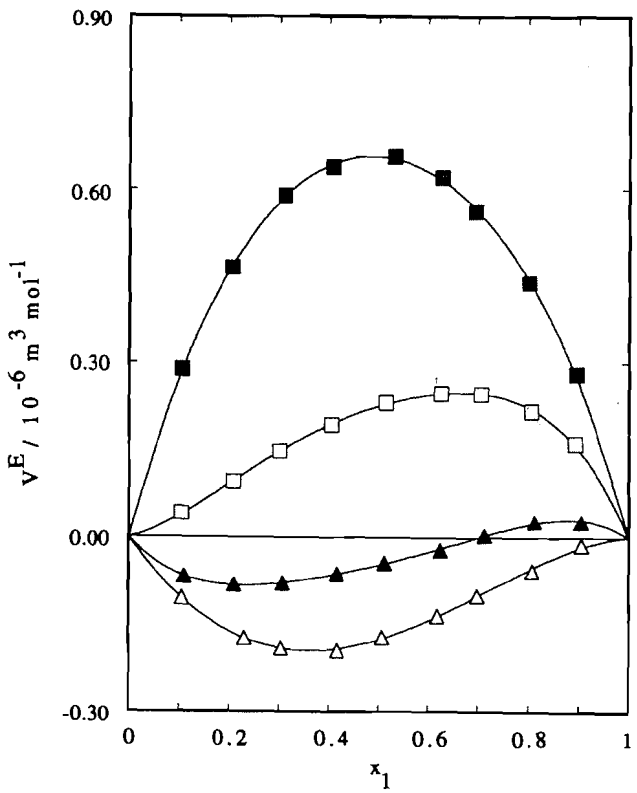

FIG. 1. Excess volumes, V^E, of 2-chloro-2-methylpropane(1) + an isomeric butanol(2) at 298.15 K as a function of mole fraction x_1: (△) 1-butanol; (□) 2-butanol; (▲) 2-methyl-1-propanol; (■) 2-methyl-2-propanol.

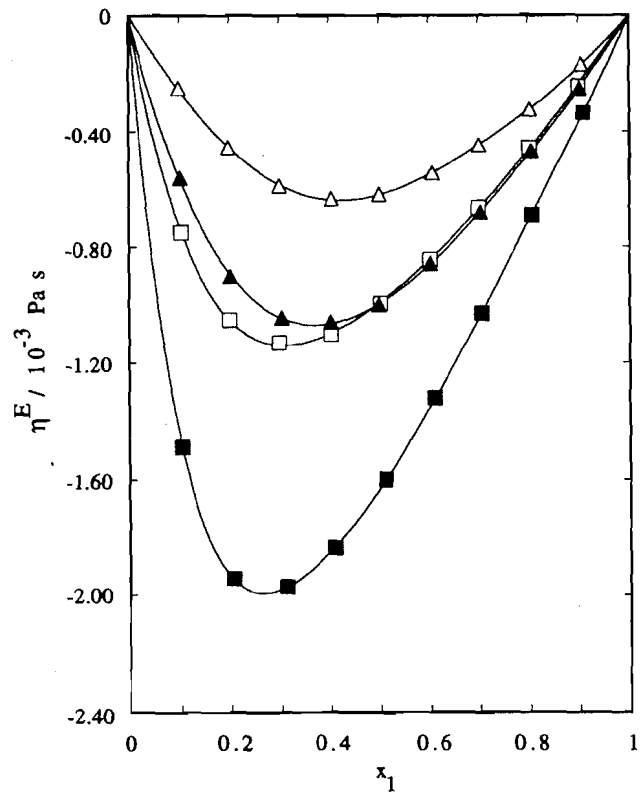

FIG. 2. Excess viscosities, η^E, of 2-chloro-2-methylpropane(1) + an isomeric butanol(2) at 298.15 K as a function of mole fraction x_1: (△) 1-butanol; (□) 2-butanol; (▲) 2-methyl-1-propanol; (■) 2-methyl-2-propanol.

molecular complex formation (11), and (*iv*) structural factors due to the difference between the shape and size of the two components in the mixture which influence the interstitial positioning of 2-chloro-2-methylpropane between the butanols. In our mixtures the main factors which affect excess volume are the loss of self-association of the butanols and the specific Cl–OH interaction. In the mixture with 1-butanol these effects are compensated for and small excess volume are obtained due to the

Can. J. Chem. Downloaded from www.nrcresearchpress.com by 85.192.166.187 on 09/08/12
For personal use only.

TABLE 5. Coefficients, a_i, of equation [4] and standard deviations, determined by the method of least squares

Function	a_0	a_1	a_2	a_3	a_4	σ
			2-Chloro-2-methylpropane(1) + 1-butanol(2)			
$V^E/10^{-6}$ m^3 mol^{-1}	−0.6963	0.5167	0.0623	0.0752		0.0030
$\eta^E/10^{-3}$ Pa s	−2.4938	0.9279	0.1309	−0.6473		0.0046
G^{*E}/J mol^{-1}	−2094.6	−660.8	381.6	−984.9		5.5
			2-Chloro-2-methylpropane(1) + 2-butanol(2)			
$V^E/10^{-6}$ m^3 mol^{-1}	0.9060	0.5099	0.2601	0.4706		0.0029
$\eta^E/10^{-3}$ Pa s	−3.9645	2.5616	−2.1669	1.3341		0.0078
G^{*E}/J mol^{-1}	−4296.5	1014.4	−872.9	−112.2		7.0
			2-Chloro-2-methylpropane(1) + 2-methyl-1-propanol(2)			
$V^E/10^{-6}$ m^3 mol^{-1}	−0.1885	0.4089	0.0150	0.3706		0.0022
$\eta^E/10^{-3}$ Pa s	−3.9779	2.0745	−0.9000	0.1031		0.0052
G^{*E}/J mol^{-1}	−3106.7	−248.9	46.7	−390.7		8.5
			2-Chloro-2-methylpropane(1) + 2-methyl-2-propanol(2)			
$V^E/10^{-6}$ m^3 mol^{-1}	2.6225	−0.1090	0.5926	0.1022		0.0057
$\eta^E/10^{-3}$ Pa s	−6.5167	4.9270	−3.9391	3.9840	−2.6316	0.0049
G^{*E}/J mol^{-1}	−5757.8	2554.6	−1708.6	−11.2		6.4

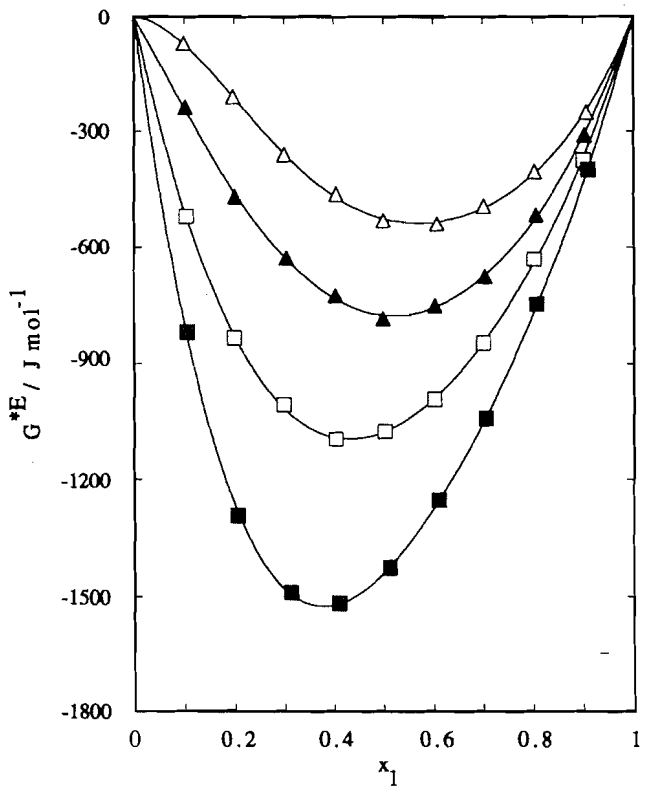

FIG. 3. Excess free energies of activation of flow, G^{*E}, of 2-chloro-2-methylpropane(1) + an isomeric butanol(2) at 298.15 K as a function of mole fraction x_1: (△) 1-butanol; (□) 2-butanol; (▲) 2-methyl-1-propanol; (■) 2-methyl-2-propanol.

fact that the breaking of the molecular order is not very great. On the other hand, with 2-methyl-2-propanol the breaking of the order is greater because the hydrogen bonds are broken to a greater extent, as previously mentioned, and the excess volume is greater. The influence of the molecular structure of the components on volumetric behaviour is shown by the smaller excess volumes for the mixtures containing 1-butanol and 2-methyl-1-propanol which have more open structures to enable the 2-chloro-2-methylpropane, a quasi globular molecule, to situate itself better than the 2-butanol and 2-methyl-2-propanol. It is also noteworthy that the mixture containing 2-methyl-2-propanol gives a symmetrical curve, given the similar shape and size of the two components, this does not apply to the rest of the mixtures studied. The influence of these structural factors can also be seen by comparing the V^E values for the mixtures studied with those of the mixtures containing 1-chlorobutane (3) whose excess volume is greater.

Excess viscosities and excess free energies of activation of flow are negative over the entire composition range. η^E and G^{*E} decrease in the sequence 1-butanol < 2-methyl-1-propanol < 2-butanol < 2-methyl-2-propanol, although η^E values for the mixtures containing 2-methyl-1-propanol and 2-butanol are similar.

The values of η^E and G^{*E} can be interpreted in a similar way to the V^E values. Thus a breaking of the association and the dipole–dipole interactions results in greater fluidity of the molecules, that is to say, a decrease in the viscosity of the mixture with regard to ideal behaviour. On the other hand, the appearance of a specific Cl–OH interaction leads to an increase in viscosity, although this solute–solvent interaction is not very marked.

Acknowledgement

This project was financially supported by the Dirección General de Investigación Científica (DGICYT), Project N° PS90-0115, for which the authors are very grateful.

1. M.A. Gallardo, M.C. López, J.S. Urieta, and C. Gutiérrez Losa. Can. J. Chem. **68**, 435 (1990).
2. J. Pardo, V. Rodríguez, M.C. López, F.M. Royo, and J.S. Urieta. J. Chem. Thermodyn. **17**, 371 (1985).
3. H. Artigás, J. Santafé, M.C. López, F.M. Royo, and J.S. Urieta. J. Chem. Thermodyn. **25**, 1403 (1993).
4. C. Lafuente, J. Pardo, V. Rodríguez, F.M. Royo, and J.S. Urieta. J. Chem. Eng. Data, **38**, 554 (1993).
5. D. Blasco, C. Lafuente, J. Santafé, F.M. Royo, and J.S. Urieta. Themochim. Acta, **55**, 230 (1993).
6. P. Pérez, M. Gracia, and C. Gutiérrez Losa. J. Chem. Thermodyn. **17**, 1067 (1985).

Can. J. Chem. Downloaded from www.nrcresearchpress.com by 85.192.166.187 on 09/08/12
For personal use only.

7. J.A. Riddick, W.B. Bunger, and T.K. Sakano. Techniques of chemistry; organic solvents. Vol 2. 4th ed. Wiley–Interscience, New York. 1986.
8. G.C. Pimentel and A.L. McClellan. The hydrogen bond. W.H. Freeman and Co., San Francisco. 1960.
9. J.C. Davis Jr., K.S. Pitzer, and C.N.R. Rao. J. Phys. Chem. **64**, 1744 (1960).
10. I. Brown, W. Fock, and F. Smith. J. Chem. Thermodyn. **1**, 273 (1969).
11. I. Progogine. The molecular theory of solutions. North Holland Publishing Co., Amsterdam, Holland. 1975.

Can. J. Chem. Downloaded from www.nrcresearchpress.com by 85.192.166.187 on 09/08/12
For personal use only.

Weiss's *endo*- and *exo*-tetracyclo[5.5.1.0.^{2,6}.0^{10,13}]tridecane-4,8,12-trione: analysis of ^{1}H NMR couplings in a system of fused 5-membered rings[1]

STEVEN H. BERTZ,[2] WEIJIANG ZHANG,[3] JAMES M. COOK,[3] MARTHA D. BRUCH,[4] AND LYNN W. JELINSKI[5]

AT&T Bell Laboratories, Murray Hill, NJ 07974, U.S.A., and Department of Chemistry, University of Wisconsin–Milwaukee, Milwaukee, WI 53201, U.S.A.

Received November 18, 1993

STEVEN H. BERTZ, WEIJIANG ZHANG, JAMES M. COOK, MARTHA D. BRUCH, and LYNN W. JELINSKI. Can. J. Chem. **72**,1926 (1994).

The configurational isomers of the title compounds consist of four fused five-membered rings. They contain tightly coupled ^{1}H NMR spin systems, which provide excellent models for establishing the relationships between coupling constants and conformation. Complete chemical shift assignments and spin–spin coupling constants are reported for the title compounds by using high-field (500 MHz) ^{1}H NMR techniques (e.g., 2D homonuclear and heteronuclear experiments, difference NOE enhancements, and computational spin simulations). In addition to the more familiar two- and three-bond couplings, the spectra of **1** and **2** also contain a number of long-range (four- and five-bond) couplings, which provide a stringent test of Barfield's theoretical treatment of four-bond couplings.

STEVEN H. BERTZ, WEIJIANG ZHANG, JAMES M. COOK, MARTHA D. BRUCH et LYNN W. JELINSKI. Can. J. Chem. **72**, 1926 (1994).

Les isomères de configuration des composés mentionnés dans le titre comportent quatre cycles condensés à cinq chaînons. En RMN du ^{1}H, ils contiennent des systèmes de spin fortement liés qui fournissent d'excellents modèles pour établir des relations entre les constantes de couplage et la conformation. Faisant appel à des techniques de RMN du ^{1}H à haut champ (500 MHz) (par exemple, des expériences homonucléaires et hétéronucléaires en 2-D, des rehaussements des différences d'eOn et des simulations de spin par calculs) on a fait les attributions complètes des déplacements chimiques ainsi que des constantes de couplages des composés mentionnnés dans le titre. En plus des couplages bien connus à travers deux et trois liaisons, les spectres des composés **1** et **2** comportent aussi un certain nombre de couplages à longue distance (quatre et cinq liaisons) qui fournissent une méthode stricte de valider le traitement théorique de Barfield des couplages à travers quatre liaisons.

[Traduit par la rédaction]

Can. J. Chem. Downloaded from www.nrcresearchpress.com by 85.192.166.187 on 09/08/12
For personal use only.

Compounds that consist of multiple fused five-membered rings were named "polyquinanes" by Jacobson (2*a*), who studied their graph-theoretical properties. Muller (3), Jacobson (2*b*), and Woodward (4) proposed that one fascinating polyquinane, triquinacene, could be dimerized to another: dodecahedrane (5). The exceptionally interesting C_{13}-tetraquinane, *endo*-tetracyclo[5.5.1.0.^{2,6}.0^{10,13}]tridecane-4,8,12-trione (**1**), was first prepared by Weiss and Edwards in 1968 (6), and its structure was definitively established by X-ray crystallography in 1973 (7). Shortly thereafter, Bertz proposed **1** as a starting material for dodecahedrane (8*a*),[6] and Baldwin and Beckwith used it to prepare a C_{19}-heptaquinane that might be suitable for "further elaboration towards dodecahedrane" (5*c*).

exo-Tetracyclo[5.5.1.0.^{2,6}.0^{10,13}]tridecane-4,8,12-trione (**2**) was isolated independently by Weiss and co-workers (9) and by Bertz (8*a*, *b*). Its X-ray structure has yet to be determined; its structure was established by the similarity of its spectral data to that of **1** (8*a*, 9). The preparation of molecules as complex as **1** and **2** in two easy steps from simple starting materials (glyoxal and dimethyl 3-ketoglutarate) is remarkable, even among reactions that quickly build molecular complexity (8*c*, 10).

Interest in **1** and **2** was renewed because they provide excellent models for the study of the relationship between ^{1}H NMR coupling constants (*J*) and stereochemistry in five-membered ring systems (8*d*). Furthermore, these molecules exhibit tightly coupled spin systems and, therefore, provide a challenging test of the utility of 2D *J*-resolved NMR techniques. Herein we report complete analyses of the ^{1}H NMR spectra of **1** and **2** based on the Karplus relationship (11), as well as Barfield's theoretical treatment of four-bond coupling constants (12).

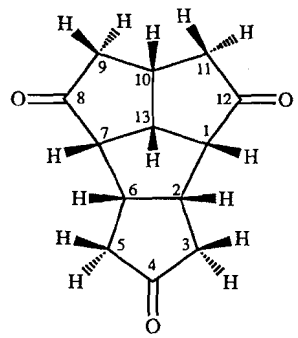

1

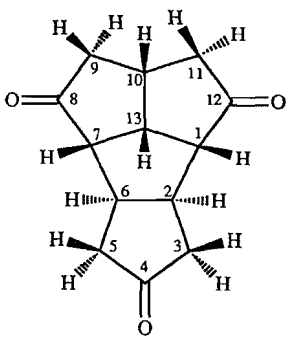

2

Results and discussion

The ^{1}H NMR spectra of **1** and **2** are sufficiently complex to require analysis at high magnetic field strengths. The 500 MHz ^{1}H NMR spectra of compounds **1** and **2** are shown in Fig. 1. Although these spectra are considerably simpler than the corresponding spectra obtained at 200 MHz, they nevertheless defy direct analysis. Homonuclear ^{1}H–^{1}H correlated 2D-FT NMR experiments (13) provided qualitative information concerning the proton spin system; however, no quantitative data could be obtained. Difference nuclear Overhauser effect (NOE) enhance-

[1]Part 11 in the Bertz series on the Weiss Reaction. For part 10 see ref. 1*a*. Part 16 in the Cook series on the Weiss Reaction. For part 15 see ref. 1*b*. For part 14 see ref. 1*c*.

[2]Author to whom correspondence may be addressed. Current address: Lonza Inc., 79 Rt. 22 E, Annandale, NJ 08801, U.S.A. Telephone: (908) 730-1581. Fax: (908) 730-1546.

[3]Department of Chemistry, University of Wisconsin–Milwaukee.

[4]Current address: Department of Chemistry, University of Delaware, Newark, DE 19716, U.S.A.

[5]Current address: Department of Chemistry, Cornell University, Ithaca, NY 14853, U.S.A.

[6]S.H. Bertz. Conversation with R.B. Woodward, 1974.

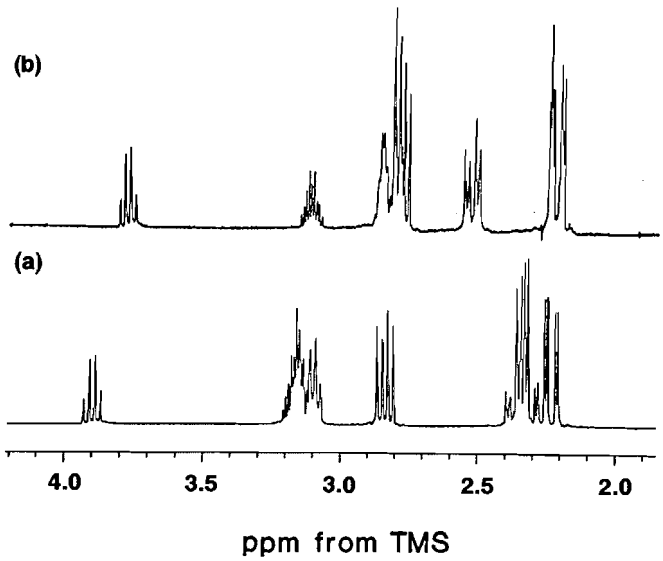

FIG. 1. 500 MHz ^{1}H NMR spectra of (*a*) *endo* isomer **1** and (*b*) *exo* isomer **2**.

ments, heteronuclear correlated 2D experiments, and *J*-resolved 2D studies were performed in order to obtain unambiguous assignments of the ^{1}H NMR spectra. Computer spin simulations also provide support for our assignments.

In contrast, the ^{13}C NMR spectra are straightforward to assign (8*a*, 9). Taking advantage of this fact, heteronuclear ^{13}C–^{1}H correlated 2D-FT experiments (14) provided direct assignment of the proton resonances. This technique identified the CH groups, and the protons of the CH_2 groups were associated with their respective carbons, but an unambiguous distinction between the geminal α- and β-protons could not be made with this technique.

Difference NOE experiments (15) in one dimension at 500 MHz were found to provide the best method for distinguishing between the resonances due to the geminal α and β protons. The increased chemical shift separations (in Hz) at the high magnetic field strength (500 MHz) were necessary to avoid saturation of nearby resonances. Two-dimensional NOE experiments did not pick up the small enhancements that provided the key to the assignment of α or β configuration. These assignments were confirmed by the four-bond coupling constants (vide infra).

TABLE 1. Chemical shifts of **1** and **2**

Protons	δ **1** (ppm)	δ **2** (ppm)	δ **1** − δ **2** (ppm)
1, 7	3.10	2.80	0.30
2, 6	3.15	2.86	0.29
3α, 5α	2.36	2.22	0.14
3β, 5β	2.31	2.52	−0.21
9α, 11α	2.23	2.22	0.01
9β, 11β	2.83	2.78	0.05
10	3.17	3.11	0.06
13	3.90	3.78	0.12

Initial estimates for the larger (>5 Hz) coupling constants were obtained from *J*-resolved 2D-FT proton spectra (16, 17). The actual coupling constants and shifts must be obtained from computer simulation of the spin system. Due to the large number of spins (14), isomers **1** and **2** do not lend themselves to complete spin simulations. However, by taking advantage of the apparent symmetry of these molecules, the spin systems can be calculated in two parts and, taken together with the data from the 2D-FT experiments, a fine-tuning of the chemical shift and coupling constant data can be achieved.

The chemical shifts of **1** and **2** are summarized in Table 1, and the coupling constant data are listed in Tables 2 and 3, which also contain information on distances and angles. These were calculated for the minimum energy structures as determined by molecular mechanics (MM2) (18). As shown in Fig. 2, the optimal structures for **1** and **2** are chiral. The validity of these results is confirmed by the X-ray structure of **1**, which is very similar to the calculated structure (Fig. 3). The root mean square distance $r^2 = 0.132$, which was calculated by including all atoms. For a more detailed comparison, the distances and angles calculated from the X-ray coordinates are given in Table 10 in the Supple-

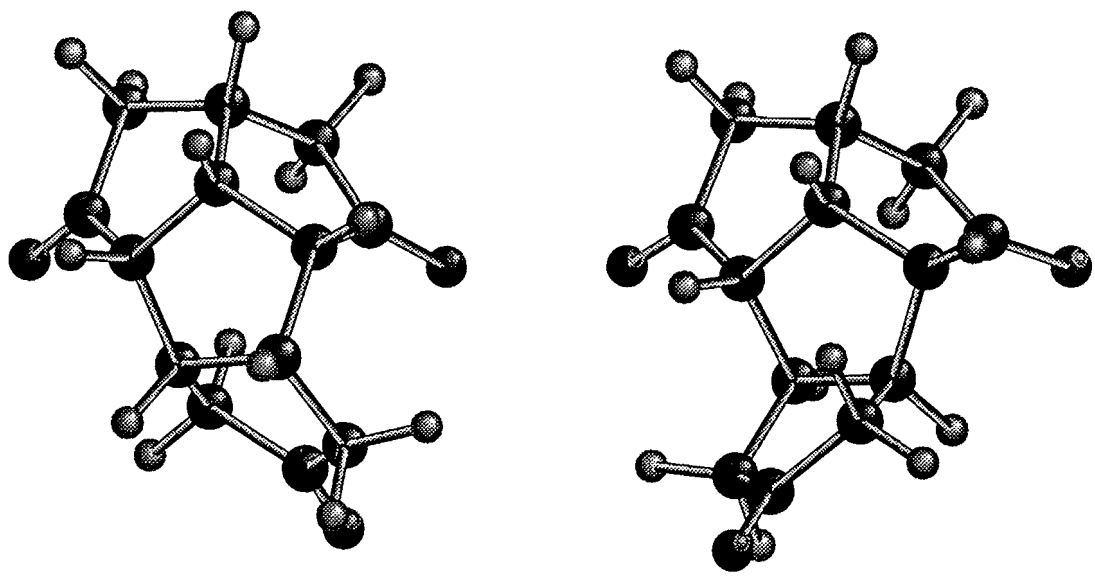

FIG. 2. Computer-generated ball and stick drawings of the minimum energy conformations of (*a*) *endo* isomer **1** and (*b*) *exo* isomer **2**.

Can. J. Chem. Downloaded from www.nrcresearchpress.com by 85.192.166.187 on 09/08/12
For personal use only.

Can. J. Chem. Downloaded from www.nrcresearchpress.com by 85.192.166.187 on 09/08/12
For personal use only.

TABLE 2. Coupling constant data for **1** (MM2 minimized structure)

	Protons	J (Hz)	Distance (Å)	θ (°)	ϕ_1 (°)	ϕ_2 (°)	ϕ_3 (°)
Two-bond	3α, 3β	18.9	1.82	108			
	5α, 5β	18.9	1.81	109			
	9α, 9β	19.5	1.82	109			
	11α, 11β	19.5	1.81	108			
Three-bond	1, 2	10.1	2.39	39	39		
	7, 6	10.1	2.34	18	18		
	1, 13	9.8	2.40	336	336		
	7, 13	9.8	2.30	1	1		
	2, 3α	8.5	2.81	267	267		
	6, 5α	8.5	3.08	155	155		
	2, 3β	5.5	2.37	28	28		
	6, 5β	5.5	2.38	32	32		
	9α, 10	4.6	2.78	88	88		
	11α, 10	4.6	3.02	225	225		
	9β, 10	9.9	2.42	325	325		
	11β, 10	9.9	2.34	347	347		
	10, 13	10.4	2.38	22	22		
Four-bond	1, 3α	0.9	3.02	312	88	31	
	7, 5α	0.9	3.78	155	217	28	
	1, 3β	0.7	3.91	65	88	153	
	7, 5β	0.7	3.88	47	217	265	
	1, 10	0	3.40	358	260	258	
	7, 10	0	3.93	21	121	143	
	1, 11α	0.5	4.04	159	112	244	
	7, 9α	0.5	4.08	223	256	149	
	1, 11β	1.8	3.65	9	112	126	
	7, 9β	1.8	3.17	11	256	269	
	2, 13	0	3.04	9	83	98	
	6, 13	0	3.86	17	223	242	
	9α, 13	0.8	4.10	144	152	261	
	11α, 13	0.8	4.14	209	255	141	
	9β, 13	0.3	3.14	351	275	261	
	11β, 13	0.3	4.03	9	133	141	
Five-bond	2, 10	0	4.93	42	83	221	102
	6, 10	0	5.45	63	223	120	217
	2, 11α	0	5.05	207	198	122	116
	6, 9α	0	5.32	246	105	228	211
	2, 11β	0	5.44	66	198	122	234
	6, 9β	0	5.08	39	105	228	91
	3α, 13	0.5	4.89	271	329	151	262
	5α, 13	0.5	4.39	169	332	262	118
	3β, 13	0.3	5.17	41	207	151	262
	5β, 13	0.3	5.24	68	95	262	118

mentary Material.[7] In both the solid state and in solution, there must be equal numbers of both enantiomers. The calculated MM2 energies for **1** and **2** are 38.7 and 36.3 kcal mol^{-1}, respectively. The fact that **1** predominates over the more stable **2**, under all reaction conditions (8*a*, 9), remained a mystery until the mechanism of formation was elucidated with the aid of glyoxal-d_2 (8*b*, 8*e*).

As expected, the largest chemical shift differences (δ **1** − δ **2** = 0.3 ppm) occur where the C1—C2 and C6—C7 bonds connect the bicyclo[3.3.0]octanedione subunit and the cyclopentanone subunit. The chemical shifts of the 1, 2, 6, 7, and 13 protons in **1** are downfield from the corresponding protons in **2**

[7]Tables of coupling constant data and angular information (from X-ray and MM2 structures) for **1** and **2** have been deposited and can be purchased from: The Depository of Unpublished Data, Document Delivery, CISTI, National Research Council Canada, Ottawa, ON K1A 0S2, Canada.

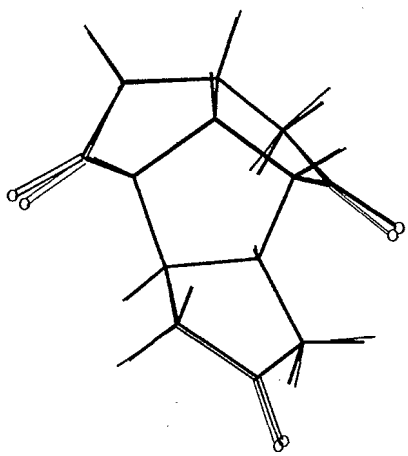

Fig. 3. Comparison of X-ray crystallographic structure (thick lines) and MM2 structure (thin lines) of *endo* isomer 1.

TABLE 3. Coupling constant data for **2** (MM2 minimized structure)

	Protons	J (Hz)	Distance (Å)	θ (°)	ϕ_1 (°)	ϕ_2 (°)	ϕ_3 (°)
Two-bond	3α, 3β	19.7	1.82	109			
	5α, 5β	19.7	1.82	109			
	9α, 9β	18.7	1.82	109			
	11α, 11β	18.7	1.82	109			
Three-bond	1, 2	1.3	2.76	275	275		
	7, 6	1.3	3.07	146	146		
	1, 13	9.6	2.42	343	343		
	7, 13	9.6	2.32	352	352		
	2, 3α	6.0	2.40	31	31		
	6, 5α	6.0	2.41	32	32		
	2, 3β	7.0	3.08	153	153		
	6, 5β	7.0	2.80	269	269		
	9α, 10	5.3	2.78	88	88		
	11α, 10	5.3	3.07	212	212		
	9β, 10	9.3	2.43	325	325		
	11β, 10	9.3	2.38	334	334		
	10, 13	9.1	2.39	27	27		
Four-bond	1, 3α	0.5	3.05	314	320	264	
	7, 5α	0.5	3.72	164	341	158	
	1, 3β	1.4	2.61	62	320	27	
	7, 5β	1.4	2.49	50	341	35	
	1, 10	0	3.42	6	253	263	
	7, 10	0	4.03	20	129	148	
	1, 11α	0	4.01	161	125	259	
	7, 9α	0	4.15	224	249	145	
	1, 11β	1.7	3.92	12	125	140	
	7, 9β	1.7	3.32	13	249	266	
	2, 13	0.6	4.15	222	209	107	
	6, 13	0.6	4.01	169	94	231	
	9α, 13	0.8	4.06	147	152	266	
	11α, 13	0.8	4.04	205	267	145	
	9β, 13	0.1	3.08	354	275	266	
	11β, 13	0.1	4.14	2	145	145	
Five-bond	2, 10	0	5.13	258	209	230	97
	6, 10	0	4.59	206	94	110	212
	2, 11α	0	3.86	68	322	110	101
	6, 9α	0	4.01	4	337	236	215
	2, 11β	0	4.76	300	322	110	220
	6, 9β	0	4.54	158	337	236	94
	3α, 13	0	4.27	272	96	276	253
	5α, 13	0	5.30	204	202	139	129
	3β, 13	0.2	2.77	4	333	276	253
	5β, 13	0.2	4.60	69	325	139	129

due to the mutual deshielding effect of eclipsed C—H bonds (19). The 3β and 5β protons also show a significant difference (−0.2 ppm) between **1** and **2**, since they are on a convex surface in **1**, but on a concave surface in **2**.

Looking at protons within the same molecule, it may be noted that the α and β protons next to the C4-carbonyl differ by only 0.05 ppm in **1**, but by 0.3 ppm in **2**. This is evidence for a conformational change in this relatively flexible five-membered ring upon going from **1** to **2** that, on average, puts the β protons further into the region of deshielding and the α protons further into the cone of shielding (19). This change is not observed in the much more rigid rings of the bicyclo[3.3.0]octanedione subunit, where the α − β differences at C9 and C11 are the same (ca. 0.6 ppm). In fact, the chemical shift of the magnetically equivalent 9α and 11α protons in **1** is virtually identical to the chemical shift of the corresponding protons in **2**, which is also true for the β protons.

In addition to the coupling constants ^nJ (n = 2, 3, 4, 5), where the superscript refers to the number of bonds between the coupled protons (i.e., the graph-theoretical distance), Tables 2 and 3 contain the Euclidean distances between them, as well as the angles θ and ϕ_i (i = 1, 2, 3). We define θ as the angle between the vectors containing the C—H bonds, where the C lies towards the origin of the vector; ϕ_i is a dihedral angle, as defined by Barfield (illustrated for **1** and **2** in Fig. 4). It may be noted that for ^2J, θ is the usual valence angle, and for ^3J, $\phi = \phi_1$ is the usual dihedral angle.

The proton coupling constants for the *endo* and *exo* isomers are similar in many respects. For both **1** and **2**, the values of ^2J are large (19–20 Hz), as expected for geminal protons on a five-membered ring (19). Moreover, the coupling constants for the protons belonging to the bicyclo[3.3.0]octanedione subunit (9α, 11α; 9β, 11β; 10 and 13) are not markedly different in either isomer.

Can. J. Chem. Downloaded from www.nrcresearchpress.com by 85.192.166.187 on 09/08/12
For personal use only.

Can. J. Chem. Downloaded from www.nrcresearchpress.com by 85.192.166.187 on 09/08/12
For personal use only.

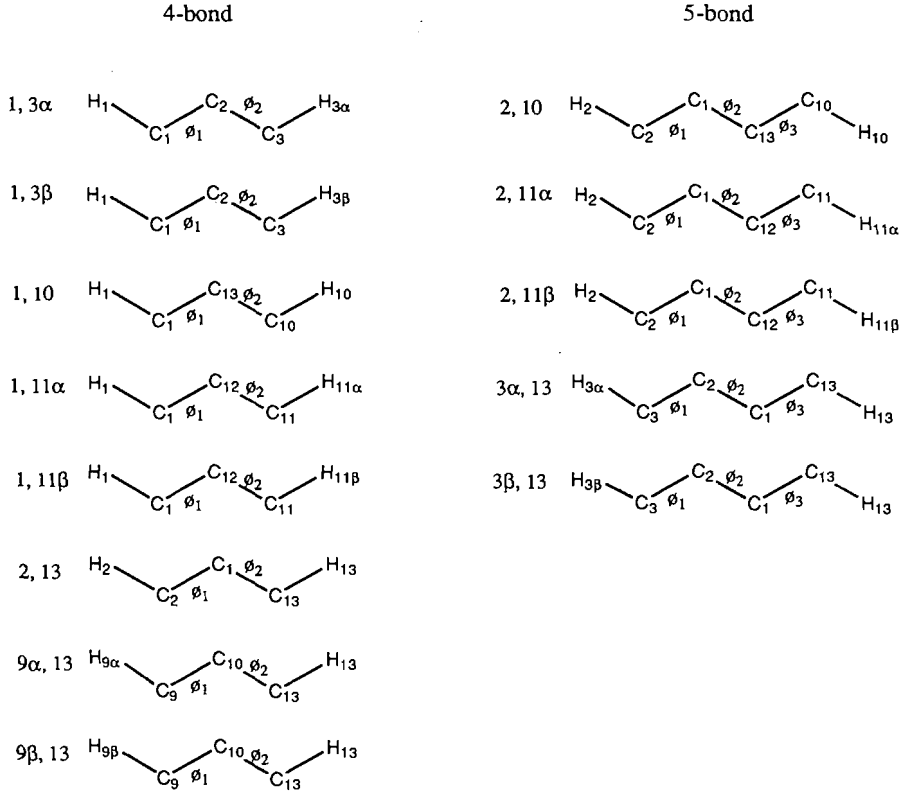

FIG. 4. Coupling paths between pairs of protons with definitions of ϕ_1, ϕ_2 (and ϕ_3) for ^4J (and ^5J).

However, there are marked differences between the isomers in the coupling constants between the 1 and 2 (or 6 and 7) protons. The dihedral angle between these protons in the *endo* isomer is small (ca. 30° average) and the coupling constant is large (10.1 Hz), consistent with the Karplus relation, $^3J = A + B\cos\phi + C\cos 2\phi$ (11*a*). The corresponding coupling constant in the *exo* isomer is small (1.3 Hz), reflecting the ca. 115° (average) dihedral angle between these protons. This information establishes the stereochemistry at the critical ring junction between the triquinancene moiety and the fused cyclopentanone ring. As mentioned above, this stereochemistry is vouchsafed by X-ray crystallography (7).

For **1** the other values of ^3J correlate with the values predicted by the Karplus equation, except for ^3J(H2–H3α) = 8.5 Hz and ^3J(H2–H3β) = 5.5 Hz, which are definitely out of line whether one uses the parameters proposed by Karplus (11*a*) or Bothner-By (11*b*). The ^3J values for **1** calculated for both the minimum energy structure and the symmetrically constrained one are summarized in Table 4, which shows that the best results are obtained by using Bothner-By's parameters in conjunction with the minimum energy (MM2) structure. Since the minimum energy structure is chiral, each value of ^3J is the average of two values, one calculated for each enantiomer. This analysis assumes that the observed spectrum is the time average of the spectra of the enantiomers, to a first approximation. The corresponding data for **2** are summarized in Table 5.

The fact that the couplings between H2 and H3 are opposite to the predictions of the Karplus equation would be of great concern in six-membered rings, perhaps even requiring the revision of the stereochemical assignments. However, in the case of flexible five-membered rings, sometimes $^3J_{cis} > {}^3J_{trans}$ and sometimes $^3J_{trans} > {}^3J_{cis}$, as previously reported for a 3,4-disubstituted cyclopentanone (8*d*). In this case the configurational assignments of the 3α and 3β protons, originally based on the observed NOEs, are confirmed by four-bond couplings ^4J (vide infra).

TABLE 4. Observed and calculated ^3J values for **1**

Protons	$^3J_{obs}$ (**1**)	$^3J_{calc}$ (Karplus)[a]	$^3J_{calc}$ (Bothner-By)[b]
1, 2 (7, 6)	10.1	5.86[c] (7.90)[d]	8.67[c] (10.90)[d]
1, 13 (7, 13)	9.8	7.27 (7.41)	10.21 (10.36)
2, 3α (6, 5α)	8.5	3.45 (0.07)	6.60 (2.73)
2, 3β (6, 5β)	5.5	5.81 (6.98)	8.62 (9.89)
9α, 10 (11α, 10)	4.6	1.92 (5.00)	4.84 (8.45)
9β, 10 (11β, 10)	9.9	6.34 (7.41)	9.20 (10.36)
10, 13	10.4	6.77 (8.00)	9.67 (11.00)

[a]Calculated using $A = 4$, $B = -0.5$, and $C = 4.5$ in the Karplus equation.
[b]Calculated using $A = 7$, $B = -1$, and $C = 5$ in the Karplus equation.
[c]MM2 minimum energy structure.
[d]MM2 symmetrically constrained structure.

A critical points analysis (20) of Barfield's equations (12) for the "indirect" (through-bond) contributions to $^4J = f(\phi_1, \phi_2)$ is given in Table 6. The dependence of ^4J on the dihedral angles ϕ_1 and ϕ_2 is much more complicated than the relatively simple functional dependence of $^3J = f(\phi)$, commonly known as "the Karplus equation" (vide supra). Whereas the Karplus equation has a true maximum ($\phi = 180°$), a true minimum ($\phi = 90°$), and one local maximum ($\phi = 0°$), the Barfield equations have a true maximum ($\phi_1, \phi_2 = 180°, 180°$), a true minimum ($\phi_1, \phi_2 = 90°, 90°$), and many local maxima and minima. It is assumed that the "direct" (through-space) contribution to long-range coupling is negligible. (Before proceeding, it should be noted that the labels ϕ_1 and ϕ_2 are interchangeable by symmetry. Thus, if one

TABLE 5. Observed and calculated ^3J values for **2**

Protons	$^3J_{obs}$ (**2**)	$^3J_{calc}$ (Karplus)[a]	$^3J_{calc}$ (Bothner-By)[b]
1, 2 (7, 6)	1.3	2.81[c] (0.01)[d]	5.84[c] (2.64)[d]
1, 13 (7, 13)	9.6	7.54 (6.32)	10.50 (9.18)
2, 3α (6, 5α)	6.0	5.61 (6.77)	8.41 (9.67)
2, 3β (6, 5β)	7.0	3.30 (0.08)	6.42 (2.55)
9α, 10 (11α, 10)	5.3	2.95 (0.31)	6.01 (2.27)
9β, 10 (11β, 10)	9.3	5.72 (6.55)	8.53 (9.43)
10, 13	9.1	6.20 (8.00)	9.05 (11.00)

[a]Calculated using $A = 4$, $B = -0.5$, and $C = 4.5$ in the Karplus equation.
[b]Calculated using $A = 7$, $B = -1$, and $C = 5$ in the Karplus equation.
[c]MM2 minimum energy structure.
[d]MM2 symmetrically constrained structure.

TABLE 6. Selected Barfield points

ϕ_1 (°)	ϕ_2 (°)	^4J (Hz)	Description
0	**0**	**0.9**	Local max.
0	60	0.5	
0	**90**	**0.3**	Local min.
0	120	0.5	
0	150	0.9	
0	**180**	**1.0**	Local max.
30	0	0.5	
30	30	0.5	
30	60	0.2	
30	90	0.2	
30	120	0.5	
30	150	0.8	
30	180	0.9	
90	**0**	**0.3**	Local max.
90	45	0.0	
90	**90**	**−0.3**	True min.
90	130	0.0	
90	150	0.3	
90	**180**	**0.5**	Local max.
120	90	−0.1	
120	120	0.1	
120	150	0.5	
150	60	0.5	
150	150	0.8	
180	**0**	**1.0**	Local max.
180	60	0.6	
180	**90**	**0.5**	Local min.
180	120	0.7	
180	150	1.0	
180	**180**	**1.2**	True max.

is looking for ^4J corresponding to angles near $\phi_1, \phi_2 = 120°, 30°$ and does not find it listed in Table 6, one should look at 30°, 120°. Also, the use of $\phi' = 360 - \phi$ is made possible by the fact that the family of curves is symmetrical about $\phi = 180°$ to within ±10°.) For the most accurate predictions, Barfield's original work should be consulted (12). The ^4J values for the protons related by symmetry in **1** and **2** (planar representations) must be determined independently for their (nonplanar) lowest energy structures and then averaged, as done for ^3J (above). The calculated ^4J values are summarized in Table 7 along with the measured ones. In six of eight cases for **1**, relatively large values of $^4J_{calc} > 0.1$ Hz correspond to relatively large values of $^4J = 0.5$–0.9 Hz, and small values of $^4J_{calc} < 0.1$ Hz correspond to $^4J \approx 0$. The two exceptions involve $^4J_{calc} \approx \pm 0.07$ Hz and $^4J = 0.3$ or 1.8 Hz. Interestingly, the larger discrepancy is the more easily explained: the 1.8 Hz coupling is across a carbonyl group, which is known to enhance the coupling between α and α′ protons (19). The other discrepancy involves the smallest non-zero value of ^4J. Thus, the overall correlation is very good for **1**.

TABLE 7. Observed and calculated ^4J values

Protons	$^4J_{obs}$ (**1**)	$^4J_{obs}$ (**2**)	$^4J_{calc}$ (**1**)	$^4J_{calc}$ (**2**)
1, 3α (7, 5α)	0.9	0.5	0.4	0.5
1, 3β (7, 5β)	0.7	1.4	0.4	0.5
1, 10 (7, 10)	0	0	0.07	0.2
1, 11α (7, 9α)	0.5	0	0.2	0.1
1, 11β (7, 9β)	1.8	1.7	−0.07	0.1
2, 13 (6, 13)	0	0.6	0.05	0.2
9α, 13 (11α, 13)	0.8	0.8	0.3	0.3
9β, 13 (11β, 13)	0.3	0.1	0.07	0.2

In the case of **2**, the largest discrepancy again involves ^4J(H1–H11β), across a carbonyl group. Overall, the correlation is not quite as good as it is for **1**. For example, ^4J(H2–H13) = 0.6 and ^4J(H9β–H13) = 0.1, even though $^4J_{calc} \approx 0.2$ Hz for both.

The alternative approach of calculating angles for a (hypothetical) symmetrical planar structure and then using these angles to determine ^4J gives satisfactory results, but not as good as the more rigorous method presented above. (See Tables 8 and 9, Supplementary Material,[7] for the angles of the planar structures.)

Of special importance is the fact that the ^4J(H1–H3α) and ^4J(H1–H3β) values of **1** and **2** are consistent with the NOE results, which were used to assign the configurations (α vs. β) of the protons on C3 and C5. As discussed above, the values of ^3J(H2–H3α) and ^3J(H2–H3β) are opposite to the predictions of the Karplus equation. This provides dramatic confirmation of our earlier conjecture that ^4J is more reliable than ^3J for flexible five-membered rings (8*d*).

It is easy to see that θ, the angle between the C–H vectors, does not correlate ^4J. For example, in the case of **1**, both the largest (1.8 Hz) and the smallest (0 Hz) values of ^4J have nearly the same value of θ. The Euclidean distance also does not predict the order of ^4J: pairs of protons that are more than 4 Å apart (e.g., H9α–H13 and H11α–H13) have high values for ^4J (0.8 Hz), whereas some protons with shorter distances have $^4J = 0$. Our results support the assumption that the direct, through-space term is negligible for ^4J. In contrast, it has recently been reported that NMR information can be transmitted through up to 14 saturated C—C bonds (21).

The only way we have found to rationalize the large five-bond couplings in **1** involves looking at ϕ_1 and ϕ_3 in the planar structure and noting that ^5J is only observed in those cases for which ϕ_1 and ϕ_3 give a significant value of ^4J. Barfield and Chakrabarti have shown that ^5J is independent of ϕ_2 (12*b*).

Conclusion

The structures of **1** and **2** have been uniquely assigned on the basis of ^{1}H NMR spectroscopy: ^3J can be used to determine stereochemistry about the key C2–C6 ring fusion, but does not correctly assign stereochemistry on the flexible five-membered ring. The relative configurations (α vs. β, as drawn) of the protons on C3 and C5 and on C9 and C11 were determined by NOE experiments and confirmed by ^4J values. A "critical points" analysis of Barfield's equations provides a practical method of estimating the magnitude of ^4J for both "W" and "non-W" spin

Can. J. Chem. Downloaded from www.nrcresearchpress.com by 85.192.166.187 on 09/08/12
For personal use only.

systems. The use of ^4J values to predict whether ^5J should be observable is proposed.

Experimental

The ^{1}H NMR spectra were obtained in chloroform-*d* by using Varian XL-200 or JEOL GX-500 NMR spectrometers. The Nicolet spin simulation program NMCSIM was used to calculate the spectra in two parts, since this program can only accommodate seven spins. Molecular mechanics calculations were performed using MM2 (MacroModel version 3.5, Columbia University, New York) on a Silicon Graphics Personal Iris 4D/35 workstation.

Acknowledgment

Samples of compounds **1** and **2** were the gracious gifts of Dr. U. Weiss (National Institutes of Health), to whose memory this paper is dedicated.

1. (*a*) S.H. Bertz, J.M. Cook, A. Gawish, and U. Weiss. Org. Synth. **64**, 27 (1986) (Coll. Vol. **VII**, 50 (1990)); (*b*) X. Fu, G. Kubiak, W. Zhang, W. Han, A.K. Gupta, and J.M. Cook. Tetrahedron, **49**, 1511 (1993); (*c*) X. Fu and J.M. Cook. J. Org. Chem. **57**, 5121 (1992).
2. (*a*) I.T. Jacobson. Ph.D. Dissertation, University of Lund, Sweden. 1973. See also ref. 5*i*; (*b*) Acta Chem. Scand. **21**, 2235 (1967).
3. F.M. Muller. Chem. Weekbl. **59**, 334 (1963).
4. R.B. Woodward, T. Fukunaga, and R.C. Kelly. J. Am. Chem. Soc. **86**, 3162 (1964).
5. (*a*) L.A. Paquette. Chem. Rev. **89**, 1051 (1989); (*b*) P.E. Eaton. Tetrahedron, **35**, 2189 (1979); (*c*) J.E. Baldwin and P.L.M. Beckwith. J. Chem. Soc. Chem. Commun. 279 (1983); (*d*) E. Carceller, M.L. Garcia, A. Moyano, M.A. Pericas, and F. Serratosa. Tetrahedron, **42**, 1831 (1986); (*e*) W.-D. Fessner, B.A.R.C. Murty, J. Wörth, D. Hunkler, H. Fritz, H. Prinzbach, W.D. Roth, P.v.R. Schleyer, A.B. McEwen, and W.F. Maier. Angew. Chem. Int. Ed. Engl. **26**, 452 (1987); (*f*) D.G. Farnum and T. Monego. Tetrahedron Lett. **24**, 1361 (1983); (*g*) M.A. McKervey, P. Vibuljan, G. Ferguson, and P.Y. Siew. J. Chem. Soc. Chem. Commun. 1981, 912; (*h*) W.P. Roberts, S. Srivastava, and W.J. le Noble. Ind. Chem. News, August 1984, p. 24; (*i*) L.A. Paquette. Top. Curr. Chem. **119**, 1984.
6. J.M. Edwards and U. Weiss. Tetrahedron Lett. **9**, 4885 (1968).
7. (*a*) J.M. Edwards, I.H. Qureshi, U. Weiss, T. Akiyama, J.V. Silverton. J. Org. Chem. **38**, 2919 (1973); (*b*) T. Akiyama and J.V. Silverton. Acta Crystallogr. Sect. B: Struct. Crystallogr. Cryst. Chem. **B31**, 2336 (1975).
8. (*a*) S.H. Bertz. Ph.D. Dissertation, Harvard University, 1978; (*b*) S.H. Bertz, J. Kouba, and N.E. Sharpless. J. Am. Chem. Soc. **105**, 4116 (1983); (*c*) S.H. Bertz. J. Am. Chem. Soc. **103**, 3599 (1981); (*d*) S.H. Bertz, L.W. Jelinski, and G. Dabbagh. J. Chem. Soc. Chem. Commun. 388 (1983); (*e*) S.H. Bertz. J. Org. Chem. **46**, 4088 (1981).
9. K.C. Rice, N.E. Sharpless, U. Weiss, and R.J. Highet. Tetrahedron Lett. **16**, 3763 (1975).
10. G.H. Posner. Chem. Rev. **86**, 831 (1986).
11. (*a*) M. Karplus. J. Chem. Phys. **30**, 11 (1959); J. Am. Chem. Soc. **85**, 2870 (1963); (*b*) A.A. Bothner-By. Adv. Magn. Reson. **1**, 195 (1965).
12. (*a*) M. Barfield. J. Chem. Phys. **41**, 3825 (1964); (*b*) M. Barfield and B. Chakrabarti. Chem. Rev. **69**, 757 (1969); (*c*) M. Barfield, A.M. Dean, C.J. Fallick, R.J. Spear, S. Sternhell, and P.W. Westerman. J. Am. Chem. Soc. **97**, 1482 (1975).
13. A. Bax, R. Freeman, and G. Morris. J. Magn. Reson. **42**, 164 (1981).
14. R. Freeman and G.A. Morris. J. Chem. Soc. Chem. Commun. 684 (1978).
15. J.H. Noggle and R.E. Schirmer. The nuclear Overhauser effect: chemical applications. Academic Press, New York. 1971.
16. W.P. Aue, J. Karhan, and R.R. Ernst. J. Chem. Phys. **64**, 4226 (1976).
17. G. Wider, R. Baumann, K. Nagayama, R.R. Ernst, and K. Wüthrich. J. Magn. Reson. **42**, 73 (1981).
18. U. Burkert and N.L. Allinger. ACS Monogr. **117**, 1982.
19. (*a*) L.M. Jackman and S. Sternhell. Applications of NMR spectroscopy in organic chemistry. 2nd ed. Pergamon, New York. 1969; (*b*) E.D. Becker. High resolution NMR. 2nd ed. Academic Press, New York. 1980.
20. J. Casti. Connectivity, complexity, and catastrophe in large-scale systems. John Wiley & Sons, New York. 1979.
21. G. Bianchi, O.W. Howarth, C.J. Samuel, and G. Vlahov. J. Chem. Soc. Chem. Commun. 627 (1994).

Can. J. Chem. Downloaded from www.nrcresearchpress.com by 85.192.166.187 on 09/08/12
For personal use only.

Solvation and metal ion effects on structure and reactivity of phosphoryl compounds. Part 4.[1] Dealkylation of phosphate esters by thiophenoxide ion in methanol

MARIAN MENTZ, AGNES M. MODRO, AND TOMASZ A. MODRO[2]

Centre for Heteroatom Chemistry, Department of Chemistry, University of Pretoria, Pretoria 0002, South Africa

Received February 10, 1994

MARIAN MENTZ, AGNES M. MODRO, and TOMASZ A. MODRO. Can. J. Chem. **72**, 1933 (1994).

Second-order rate constants for the demethylation of three phosphate esters by thiophenoxide salts, PhS^-M^+ ($M^+ = Me_4N^+$, K^+, Na^+ Li^+) in methanol-d_4 at 25°C have been measured. In contrast to the demethylation by iodide salts, metallic counterions do not exhibit any catalytic effects on the demethylation rate. The absence of the catalysis indicates that the salts react exclusively as ion pairs, in which an alkali metal ion is not available for the interactions with the phosphoryl group in the transition state.

MARIAN MENTZ, AGNES M. MODRO et TOMASZ A. MODRO. Can. J. Chem. **72**, 1933 (1994).

On a mesuré les constantes de vitesse d'ordre deux de la réaction de déméthylation de trois esters phosphoriques par des thiophénolates, PhS^-M^+ ($M^+ = Me_4N^+$, K^+, Na^+, Li^+), dans le méthanol-d_4 à 25°C. Contrairement à la déméthylation par les iodures, l'ion métallique n'a aucun effet catalytique sur la vitesse de déméthylation. L'absence d'effet catalytique indique que les sels réagissent exclusivement comme des paires d'ions dans lesquels l'ion du métal alcalin n'est pas disponible pour les interactions avec le groupe phosphoryle dans l'état de transition.

[Traduit par la rédaction]

We recently reported that the nucleophilic demethylation of methyl phosphinates (1) and phosphates (2) by iodide ion in acetone is catalyzed by alkali metal ions, the effect increasing in the order $R_4N^+ < K^+ < Na^+ < Li^+$. In the discussion of the observed catalytic effects we applied to our reaction the model proposed by Buncel and co-workers for the substitution at phosphorus by ethoxide ion (3), but we did not specify whether the reaction involved free ions (iodide as a nucleophile and the metal ion as a catalyst), or the M^+I^- ion pair. The decrease of the observed rate constants with increase in the iodide salt concentration (4), as well as the dramatic variation of the specific rate constant k_{I^-} with the nature of the counterion, indicated, however, that the interactions of free metal ions, rather than ion pairs, with the organophosphorus substrate are responsible for the catalysis. In this work we report on the results of the O-dealkylation of three phosphate esters by another nucleophilic reagent, thiophenoxide ion, which is frequently used as a demethylating agent in the "triester method" in the synthesis of oligonucleotides (5). The results of this work demonstrate that the phenomenon of metal ion catalysis may depend critically on the state of the Nu^-M^+ salt in the reaction medium.

Results and discussion

Trimethyl (**1**), dimethylbenzyl (**2**), and dimethyl(2-pyridylmethyl) (**3**) phosphates were used as substrates. All three esters reacted smoothly with the thiophenoxide ion in methanolic solution yielding products shown in Scheme 1. The ionic dealkylation products **4** and **5***a*, **5***b* could be easily identified by

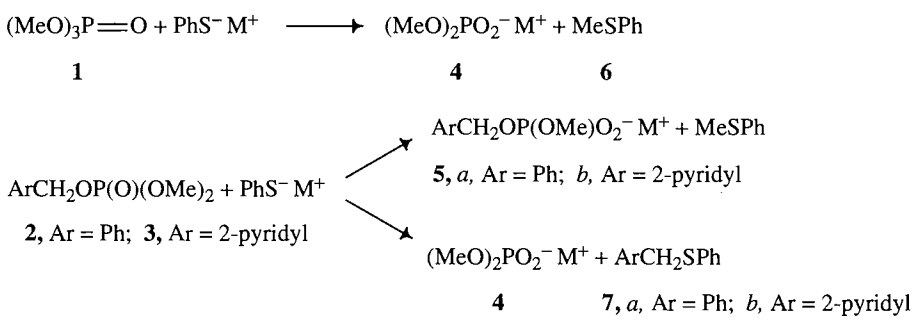

SCHEME 1

NMR (^1H and ^{31}P) spectroscopy by comparison with authentic samples. The alkylation products, thioethers **6** and **7***a*, **7***b* were isolated and characterized by ^1H NMR spectroscopy and by oxidation and full characterization of the corresponding sulfones. Since substrates **2** and **3** gave upon dealkylation two pairs of products, intramolecular selectivity of the attack by PhS^- ion was of interest. For **2**, the demethylation/debenzylation ratio (corrected to a single methyl group) is ca. 0.4, contrasting sharply with the negligible contribution of demethylation observed in the reaction of the same nucleophile with dimethylbenzylphenylammonium ion (6). This difference points to the importance of the leaving group in the selectivity of the substitution, which was further confirmed by the results obtained for ester **3**. In this case the (corrected) ratio of the attack at the Me and CH_2 carbon atoms is ca. 0.8, twice the value obtained for **2**. Since the electrophilicity of the methylene α-carbon in **3** is higher than that in **2** (the polar effect of the **2**-pyridyl vs. phenyl

[1]For previous papers of this series see refs. 1 and 2.

[2]Author to whom correspondence may be addressed.

Can. J. Chem. Downloaded from www.nrcresearchpress.com by 85.192.166.187 on 09/08/12
For personal use only.

Can. J. Chem. Downloaded from www.nrcresearchpress.com by 85.192.166.187 on 09/08/12
For personal use only.

substituents), the higher Me/CH_2 ratio obtained for **3** indicates that other factors than the electrophilicity of the reaction centre determine the selectivity of substitution. On the other hand, the leaving group **5***b* is the anion of a stronger acid than the conjugate acid of **5***a*; thus **5***b* represents the best leaving group in those two phosphates, and this seems to determine the relative rates of substitution. In the case of much poorer leaving groups involved in the dealkylation of quaternary ammonium salts (tertiary amines), the observed intramolecular selectivity (6) is consequently much higher.

The kinetics of the dealkylation reaction were measured and the rate constants for the demethylation determined from the total dealkylation rates and the product distribution. For rates and product studies ^1H NMR spectroscopy was found most reliable. The signals of the methyl and methylene groups of all species shown in Scheme 1, as well as the pyridyl hydrogens of **3**, **5***b*, and **7***b*, were sufficiently separated in the spectra, so it was possible to monitor the concentration changes of both substrates and products in a single sample. The rate data obtained for the dealkylation of **1–3** by four different thiophenoxide salts are summarized in Table 1. For comparison, the last column of the table includes the previously determined (2) effect of the counterions on the relative rate of demethylation of **1** and **3** by iodide salts in acetone. The most obvious result is that for each substrate the nature of the counterion in the PhS^-M^+ reagent, as well as the $[PhS^-M^+]/[ester]$ ratio, has negligible effect on the rate of demethylation. This absence of any metal ion catalysis remains in sharp contrast with the demethylation of **1** and **3** by iodide, where the rate increased dramatically in the order $R_4N^+ \ll K^+ < Na^+ < Li^+$. Westaway and co-workers presented a detailed study on the effect of the form of the reacting nucleophile on the transition state structure of an S_N2 reaction using sodium thiophenoxide in methanol as a nucleophilic system (7). One of their conclusions was that, at concentrations higher than 1.0×10^{-4} M, PhSNa exists in methanol primarily as a solvent-separated ion pair complex of the general formula $[Na^+(solvent)_nPhS^-]_m$. In consequence, depending on the concentration of the nucleophile, they proposed two distinct models for the transition states, one involving a free PhS^- ion, and the other involving the $PhS^-/MeOH/Na^+$ ion pair complex. Since our rate constants were determined for solutions with $[PhS^-M^+]_0 \geq 7.5 \times 10^{-4}$ M, we can assume that all sodium thiophenoxide existed in the reaction medium as a solvent-separated ion pair complex, even at 99% conversion. The same is most likely true for other PhS^- M^+ salts where $M^+ = Li^+$, K^+, but, considering facile dissociation of tetraalkylammonium salts in organic media,[3] it may be only partially true for $M^+ = Me_4N^+$. We have recorded the UV spectra of sodium, lithium, and tetramethylammonium thiophenoxides in methanol in the concentration range 10^{-5}– (4×10^{-4}) M (Fig. 1). For the Na^+ and Li^+ salts, we confirmed Westaway's conclusions by observing the dramatic changes of the value of ϵ_{max} up to the concentrations of ca. (9×10^{-5})–(2×10^{-4}) M, above which no further changes in the ϵ_{max} were observed. The corresponding plot for the Me_4N^+ salt, on the other hand, shows the variation of the ϵ_{max} over the whole concentration range, indicating more complex behavior of this thiophenoxide in methanolic solution. This difference in the behavior of the thiophenoxide salts may be reflected in the rates of the demethylation, which for all substrates used are slightly lower for $M^+ = Li^+$, Na^+, K^+ (av. $k_{rel} = 0.82$) than for $M^+ = Me_4N^+$. It is possible that tetramethylammonium thiophenoxide reacts partially as the free ion, which leads to the rate increase. This is in agreement with the reported (7) slightly higher reactivity of the free ion than the solvent-separated ion pair complex of the ArS^- nucleophile.

We conclude therefore that the alkali metal thiophenoxides

[3]Solvent activity coefficient for the transfer of a cation from MeOH to water is -1.5 for K^+, but $+3.7$ for Bu_4N^+ (8).

TABLE 1. Kinetic data on the demethylation of phosphates **1**, **2**, and **3** by thiophenoxide salts, MSPh, in methanol-d_4 at 25°C

[Ester] (M)	M^+ in MSPh (M)	Select[a]	$10^4 k_2$[b] ($M^{-1} s^{-1}$)	k_{rel} (PhS^-)	k_{rel} (I^-)[c]
1					
0.075	Me_4N^+ 0.075		2.2	1.0	1.0
0.075	Me_4N^+ 0.19		2.1	0.9	
0.075	K^+ 0.075		1.9	0.9	27.5
0.075	Na^+ 0.075		1.7	0.8	51.4
0.075	Li^+ 0.075		1.6	0.7	242
0.17	Li^+ 0.17		1.7	0.8	
0.075	Li^+ 0.15		1.7	0.8	
2					
0.075	Me_4N^+ 0.075	0.43	2.7	1.0	
0.075	K^+ 0.075	0.42	2.4	0.9	
0.075	Na^+ 0.075	0.37	2.1	0.8	
0.075	Li^+ 0.075	0.43	2.4	0.9	
3					
0.075	Me_4N^+ 0.075	0.75	5.2	1.0	1.0
0.075	K^+ 0.075	0.76	4.6	0.9	43.5
0.075	K^+ 0.15	0.78	4.4	0.8	
0.075	Na^+ 0.075	0.82	4.1	0.8	91.0
0.075	Li^+ 0.075	0.81	4.2	0.8	1930
0.17	Li^+ 0.17	0.98	4.3	0.8	
0.089	Li^+ 0.17	0.80	4.7	0.9	

[a]Selectivity of dealkylation; 0.5[**5**]/[**4**].

[b]Second-order rate constants k_2 for the demethylation only; corrected to a single methyl group. Since the k_2 values were obtained from rate constants for the decomposition of the substrate and from the product ratio, they are given only to two significant figures.

[c]Taken from ref. 2. The standard of reference ($k_{rel} = 1.0$) was obtained for demethylation by $Bu_4N^+I^-$.

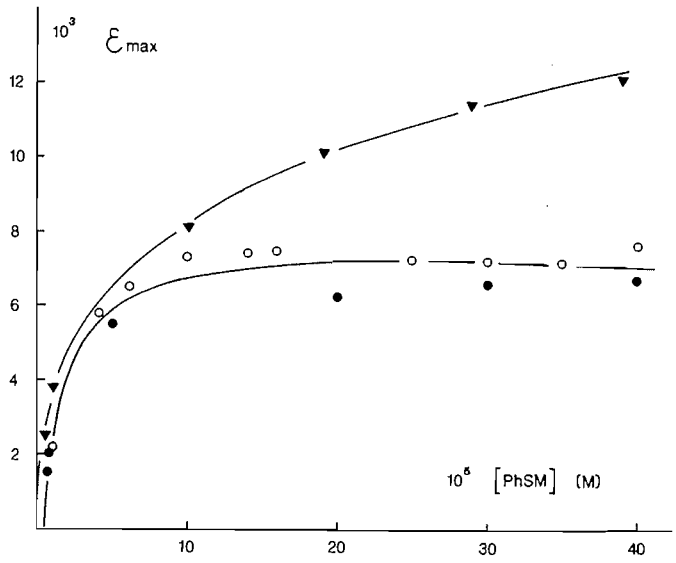

FIG. 1. Variation of the ϵ_{max} (λ_{max} = 265 nm) for the thiophenoxide salts, PhS^-M^+, in methanol; ○, $M^+ = Na^+$; ●, $M^+ = Li^+$; ▼, $M^+ = Me_4N^+$.

react with phosphate esters under the conditions of our experiments exclusively as solvent-separated ion pair complexes, in which the cation cannot be involved with the leaving group, hence is not capable of catalyzing the displacement. In agreement with this conclusion, the product ratio should not vary significantly with the cation; this was, indeed, observed for both substrates. On the other hand, strong catalysis by the same ions observed for the demethylation by iodide suggests the involvement of free metal ions in stabilizing interactions with the leaving group. By applying Westaway's model for the S_N2 transition states (*7b*) to our system, we propose the following models for the transition states for the demethylation of methyl phosphates by iodide ions in acetone, and by thiophenoxide ions in methanol, respectively (Fig. 2).

Experimental section

Methanol-d_4 (Merck, ≥99 at.% D) was dried over molecular sieves (Merck, 0.4 nm) and used without further purification. The thiophenoxide salts were prepared by adding an equimolar amount of the respective hydroxide, M^+OH^-, to an ethanolic solution of thiophenol, removing the solvent, drying the salt under high vacuum and storing in a desiccator over P_4O_{10}. The NMR spectra were recorded on a Bruker AC 300 MHz spectrometer at a probe temperature of 30°C. Chemical shifts are given relative to $SiMe_4$ (^1H) or 85% H_3PO_4 (^{31}P). Coupling constants are given in Hz. UV spectra were recorded on a Varian Cary 2390 spectrophotometer. The mass spectrum was recorded on a Varian MAT-212 double-focusing direct-inlet spectrometer at an ionization potential of 70 eV. Only the major fragments are listed. The oxidizing agent, oxodiperoxymolybdenum(aqua)hexamethylphosphoric triamide, MoO_5H_2OHMPA, was prepared according to the literature procedure (9). Trimethyl phosphate (**1**) (Merck) was distilled immediately before use. Dimethylbenzyl phosphate (**2**) was prepared from dimethylphosphorochloridate and sodium benzylate in toluene; 59%, bp 108°C/0.3 Torr (1 Torr = 133.3 Pa); δ_H ($CDCl_3$): 3.70 (6H, d, J_{HP} 11.2), 5.05 (2H, d, J_{HP} 8.3), 7.31–7.39 (5H, m); δ_P: 1.98. Dimethyl(2-pyridylmethyl) phosphate (**3**) was prepared as described before (10).

Lithium methyl(2-pyridylmethyl)phosphate (5b)

A sample of **3** (0.50 g, 2.29 mmol) was incubated at room temperature in acetone solution (33 mL) containing LiCl (0.32 g, 2.41 mmol) and the progress of the reaction was followed by TLC ($CHCl_3$/EtOH, 9:1). After 30 h the solution was concentrated to a volume of 5 mL and separated by column chromatography ($CHCl_3$/EtOH, 9:1). Fractions containing single product (R_f 0.5) were combined, evaporated, and the residue was recrystallized from ethanol. White powder, mp (dec.) 227°C; δ_H (D_2O): 3.50 (3H, d, J_{HP} 10.8), 4.94 (2H, d, J_{HP} 7.8), 7.38 (1H, dd, J_{HH} 7.9, 4.8), 7.55 (1H, d, J_{HH} 7.9), 7.88 (1H, t, J_{HH} 7.9), 8.46 (1H, d, J_{HH} 4.8); δ_P: 2.43. Anal. calcd. for $C_7H_9LiNO_4P$: C 40.22, H 4.34, N 6.70; found: C 39.8, H 4.1, N 6.45%.

Sodium methylbenzylphosphate (5a) was prepared in the same way from **2** and NaCl; δ_H (D_2O): 3.47 (3H, d, J_{HP} 10.8), 4.84 (2H, d, J_{HP} 7.2), 7.37–7.40 (5H, m); δ_P: 3.74.

Methylphenyl sulphide (6) and phenyl(2-pyridylmethyl) sulphide (7b)

A solution of **3** (1.01 g, 4.65 mmol) and PhSLi (0.54 g, 4.65 mmol) in acetone (30 mL) was kept at room temperature for 2 h. Acetone was removed and the residue was partitioned between chloroform (35 mL) and water (35 mL). The chloroform solution was dried, concentrated to a volume of 5 mL, and the solution was separated by column chromatography (silica gel, $CHCl_3$/EtOH, 9:1). First fraction: **6**, 0.31 g (54%); δ_H ($CDCl_3$): 2.48 (3H, s), 7.13 (1H, m), 7.26 (4H, m). Second fraction: **7b**, 0.36 g (37%); δ_H ($CDCl_3$): 4.23 (2H, s), 7.10–7.30 (7H, m), 7.55 (1H, dt, J_{HH} 7.6, 1.9), 8.50 (1H, d, J_{HH} 1.9).

Methylphenyl (6) and benzylphenyl sulphide (7a) were not isolated but were identified as the corresponding sulfones after oxidation of a mixture of **6** and **7a** obtained in reaction of **2** with PhSLi.

Oxidation of **6**, **7a**, **7b** to sulfones by MoO_5H_2OHMPA was carried out following the literature procedure (11), as described below for the oxidation of **7b**. To a solution of **7b** (0.35 g, 1.74 mmol) in CH_2Cl_2 (10 mL), MoO_5H_2OHMPA (0.91 g, 2.43 mmol) was added and the reaction mixture was stirred at room temperature for 22 h. Another portion of the oxidating agent (0.41 g) was added and the stirring was continued until TLC (CH_2Cl_2/Et_2O, 1:1) showed complete disappearance of **7b** (24 h). After filtration, the CH_2Cl_2 solution was washed with water (30 mL), the water layer was extracted with CH_2Cl_2 (2 × 20 mL), and the combined organic phases were washed with 10%

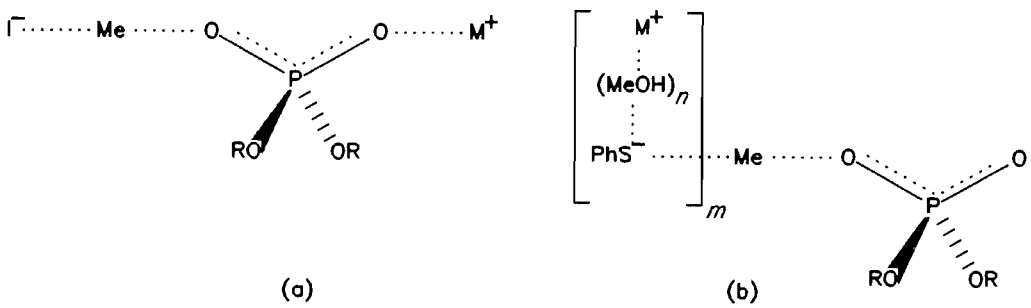

FIG. 2. The S_N2 transition states for the reaction between methyl phosphates and (*a*) free ions of an iodide salt in acetone; (*b*) solvent-separated ion pair complex of a thiophenoxide salt in methanol.

Can. J. Chem. Downloaded from www.nrcresearchpress.com by 85.192.166.187 on 09/08/12
For personal use only.

aqueous K_2CO_3, dried, and evaporated. The crude product (87%) was crystallized twice from CH_2Cl_2/Et_2O (1:1) yielding pure phenyl(2-pyridylmethyl) sulfone; mp 156–157°C; δ_H (acetone-d_6): 4.99 (2H, s), 7.30 (2H, m), 7.58 (3H, m), 7.69 (1H, t, J_{HH} 6.0), 7.78 (2H, d, J_{HH} 5.8), 8.03 (1H, d, J_{HH} 6.0); ms, *m/z*: 233 (M^+, 0.01%), 168 ($M^+ - HSO_2$, 78%), 92 ($M^+ - PhSO_2$, 100%). Anal. calcd. for $C_{12}H_{11}NSO_2$: C 61.78, H 4.75, N 6.01; found: C 61.6, H 4.7, N 5.9%.

The mixture of **6** and **7***a* obtained in the reaction of **2** with PhSLi was oxidized in the same way and the products were separated by column chromatography (silica gel, ethyl acetate/CH_2Cl_2, 1:1).

Methylphenyl sulfone, mp 82.5–84.5°C; δ_H ($CDCl_3$): 3.04 (3H, s), 7.56 (2H, dd, J_{HH} 7.7, 7.3), 7.63 (1H, dd, J_{HH} 7.3, 1.2), 7.94 (2H, dd, J_{HH} 7.7, 1.2). Anal. calcd. for $C_7H_8O_2S$: C 53.83, H 5.16; found: C 53.5, H 5.2%.

Phenylbenzyl sulfone, mp 148–149°C; δ_H ($CDCl_3$): 4.29 (2H, s), 7.06 (2H, dd, J_{HH} 8.2, 1.6), 7.20–7.30 (3H, m), 7.42 (2H, t, J_{HH} 9.6), 7.55–7.63 (3H, m). Anal. calcd. for $C_{13}H_{12}O_2S$: C 67.22, H 5.21; found: C 66.9, H 5.0%.

Kinetic measurements

Rate constants were determined as before (1), following the changes of the intensities of the methoxy group signals of substrates and products in the ^1H NMR spectra of reaction mixtures. The methoxy groups gave rise to sharp doublets at the following values of δ_H: **1**, 3.76; **2**, 3.72; **3**, 3.78; **4**, 3.55; **5***a*, 3.53; **5***b*, 3.58. The runs were carried out to at least 75% conversion, and good second-order linear plots were obtained ($r^2 = 0.995–0.999$).

Acknowledgment

Financial support from the University of Pretoria and the Foundation for Research Development is gratefully acknowledged.

1. A.M. Modro and T.A. Modro. Can. J. Chem. **71**, 469 (1993).
2. M. Mentz, A.M. Modro, and T.A. Modro. J. Chem. Res. (S), 46 (1994).
3. (*a*) E.J. Dunn and E. Buncel. Can. J. Chem. **67**, 1440 (1989); (*b*) E.J. Dunn, R.Y. Moir, E. Buncel, J.G. Purdon, and R.A.B. Bannard. Can. J. Chem. **68**, 1837 (1990).
4. I.P. Beletskaya. Russ. Chem. Rev. **44**, 1067 (1975).
5. W.G. Daub and E.E. van Tamelen. J. Am. Chem. Soc. **99**, 3526 (1977).
6. Z-G. Lai and K.C. Westaway. Can. J. Chem. **67**, 21 (1989).
7. (*a*) K.C. Westaway and Z-G. Lai. Can. J. Chem. **66**, 1263 (1988); (*b*) Can. J. Chem. **67**, 345 (1989); (*c*) Y-R. Fang and K.C. Westaway. Can. J. Chem. **69**, 1017 (1991).
8. A.J. Parker. Chem. Rev. **69**, 1 (1969).
9. A.R. Daniewski and W. Wojciechowska. Synth. Commun. **16**, 535 (1986).
10. S. Cocks, K.R. Koch, and T.A. Modro. J. Org. Chem. **51**, 265 (1986).
11. G. Keilen, T. Bennecke, K. Gaare, and K. Undheim. Acta Chim. Scand. **46**, 867 (1992).

Can. J. Chem. Downloaded from www.nrcresearchpress.com by 85.192.166.187 on 09/08/12
For personal use only.

Densities and viscosities of binary aqueous mixtures of nonelectrolytes: *tert*-Butyl alcohol and *tert*-butylamine

PIUS K. KIPKEMBOI AND ALLAN J. EASTEAL

Department of Chemistry, The University of Auckland, Private Bag 92019, Auckland, New Zealand

Received February 4, 1994

PIUS K. KIPKEMBOI, and ALLAN J. EASTEAL. Can. J. Chem. **72**, 1937 (1994).

The density and shear viscosity of mixtures of *tert*-butyl alcohol (BuOH) and *tert*-butylamine (TBA) with water have been determined for various temperatures (288 to 318 K for H_2O + BuOH and 288 to 308K for H_2O + TBA) over the whole composition range. Excess molar volumes and apparent molar volumes of the components of each system were calculated from the density data. In both systems the apparent molar volume of the organic component passes through a minimum in the water-rich region. Both systems exhibit large negative excess molar volumes which are essentially independent of temperature at all compositions. The two systems show pronounced maxima in their shear viscosity isotherms.

PIUS K. KIPKEMBOI et ALLAN J. EASTEAL. Can. J. Chem. **72**, 1937 (1994).

On a déterminé les densités et les viscosités de cisaillement de mélanges d'alcool *tert*-butylique (BuOH) et de *tert*-butylamine (TBA) avec de l'eau, sur l'ensemble des compositions possibles et à diverses températures (allant de 288 K à 318 Kj pour H_2O + BuOH et de 288 K à 308 pour H_2O + TBA). Utilisant les données de densité, on a calculé les volumes molaires en excès et les volumes molaires apparents des composants de chaque système. Dans les deux systèmes, le volume molaire apparent du composant organique passe par un minimum dans la région riche en eau. Les deux systèmes présentes des volumes molaires en excès largement négatifs qui sont essentiellement indépendants de la température, à toutes les compositions. Les deux systèmes présents des maxima importants dans leurs isothermes de viscosité de cisaillement.

[Traduit par la rédaction]

Introduction

There have been a large number of studies on the behaviour of mixtures of water with nonelectrolytes. Most of them have been concerned with water-rich solutions and have discussed structural changes of the solvent water caused by the introduction of nonpolar groups. The unusual thermodynamic properties of nonpolar solutes in water were interpreted by Frank and Evans (1) in terms of the ordering of water molecules around the solute ("iceberg" formation). The molecular phenomena comprise two related processes. First, apolar solutes promote a stabilization of the extensive, but thermally sensitive, hydrogen-bonded network of liquid water, an effect known as "hydrophobic hydration". Second, apolar solutes in water exhibit a tendency to aggregate, i.e., "hydrophobic interaction". Solutes which impose order (promote iceberg formation) are considered to be structure makers, and solutes which decrease order are said to be structure breakers. Importantly, simple hydrocarbons have been shown to increase the order of surrounding water molecules to relatively long range (2).

Organic cosolvents (with polar functional groups such as OH and NH_2) exhibit much larger solubilities in water than do hydrocarbons. However, in dilute solutions the behaviour of organic cosolvents frequently shows features similar to those of hydrocarbons (3). Studies of such features (hydrophobic hydration and interaction) have attracted considerable attention since they have been shown to influence protein conformation and thermodynamic stability (3). The pivotal biological role of H_2O is attributed to its ability to promote aggregation of nonpolar molecules.

As part of an ongoing program in the studies of molecular interactions in aqueous–organic mixtures, we are pursuing detailed thermodynamic investigations on selected water–cosolvent systems (4, 5). The cosolvents studied were chosen because they are relatively hydrophobic yet completely miscible with water in all proportions. Both water + *tert*-butyl alcohol and water + *tert*-butylamine systems are potentially extremely interesting. The large compact hydrocarbon moieties must promote a hydrophobic interaction, while the OH and NH_2 groups can no doubt form hydrogen bonds to water.

Being relatively hydrophobic cosolvents, both BuOH and TBA are attractive compounds in the study of hydration phenomena and may serve as models for more complicated aqueous systems like surfactants, emulsions, and biopolymers. In the hope of obtaining an overall picture of these aqueous binary solutions we have studied the whole composition range. In particular, comparison between the hydroxyl group (—OH) and the amine group (—NH_2) has been investigated since the cosolvents are structurally similar. Although the H_2O + BuOH system has been investigated extensively, there are few data available in the literature for H_2O + TBA mixtures.

The physical properties of water and aqueous mixtures of organic solvents are important for many reasons. In particular, mixing volumes and viscosity effects have theoretical and practical significance, and strong deviations from linearity are often encountered in aqueous liquid mixtures. Precise measurements of volumes and shear viscosities over the whole composition range are necessary to understand the nature of interactions between nonpolar groups and water, the so-called hydrophobic solvation. There have been no previous measurements, so far as we know, of the volumes and viscosities of H_2O + TBA system covering the whole composition range. Also, while many researchers have reported determinations of the partial molar volume of BuOH in the water-rich region of aqueous solutions (6–17) there have been few measurements at high alcohol concentrations over a wide temperature range. In view of the scatter of data found in the literature, measurements of shear viscosity of H_2O + BuOH mixtures were performed for the whole range of concentrations at 288, 298, 308, and 318 K, with special attention paid to the region highly dilute with respect to water.

Experimental

Materials

Tert-Butylamine was supplied by Aldrich or Merck and *tert*-butyl alcohol by Riedel-de Haën. The stated purity of these materials exceeded 99.0 mol%. The solvents were stored over freshly activated

Can. J. Chem. Downloaded from www.nrcresearchpress.com by 85.192.166.187 on 09/08/12
For personal use only.

TABLE 1. Density of *tert*-butyl alcohol and *tert*-butylamine

	ρ/kg m^{-3}						
T/K	This work	Ref. 15	Ref. 16	Ref. 38	Ref. 7	Ref. 8	Ref. 17
				tert-Butyl alcohol			
288	790.88						
298	780.43				782.20	780.40	780.53
308	770.22	770.08	769.97	770.90			
318	759.65	759.39	759.37				
				tert-Butylamine			
288	698.16						
293	692.61						
298	686.64						
303	681.73						
308	675.80						

molecular sieves (Union Carbide type 3 Å) for several weeks before use. Ultra-pure water from a Milli-Q reagent-grade water system was used to prepare the aqueous mixtures, and as a calibrating liquid.

Binary mixtures were prepared by mass in 50-cm^3 Erlenmeyer flasks with ground-glass stoppers using a balance with an accuracy of ±0.1 mg. To minimise errors due to evaporation of the organic component, water was weighed in first, followed by the organic solvent. Density and viscosity measurements were carried out soon after sample preparation in order to avoid preferential evaporation and consequential composition changes.

Apparatus

Densities of the pure components and the binary mixtures were measured with an Anton Paar Model DMA 02C vibrating-tube digital densimeter operated in the static mode. The reference liquids used for calibration of the densimeter were 2,2,4-trimethylpentane (99.7+%, HPLC grade), cyclohexane (99+%, spectrograde), and Milli-Q water whose densities were taken from ref. 18. Water and cyclohexane were used as calibrating fluids for H_2O + BuOH while water and 2,2,4-trimethylpentane were used for H_2O + TBA mixtures. The calibration liquids were selected to span a wide density range. Moreover, they can be obtained in high purity and their densities are known with high accuracy for all the temperatures which were investigated. The densities of each pair bracketed the densities of the binary mixtures investigated. The densimeter was calibrated daily and at each temperature.

Kinematic viscosities were measured with factory-calibrated Cannon Ubbelhode suspended-level viscometers. Flow times were measured with a stop watch, and measurements were repeated until flow times agreed within a few tenths of a second. The values of kinematic viscosity were converted to shear viscosities using densities measured at the same time. To check the calibration at each temperature, each viscometer used was recalibrated against water, and in each case the measured viscosity of water agreed to within experimental uncertainty with literature values. A kinematic energy correction was considered to be not necessary on account of long flow times obtained by proper selection of the capillary. The estimated error in the viscosity measurements was within ±0.005 mPa s. All glassware was thoroughly cleaned with warm chromic acid cleaning solution.

Prior to any readings, solutions were thermostatted for at least 20 min. The temperature of the thermostat bath was monitored continuously at each temperature with a precision digital thermometer (Ebro TEX-492). Temperatures were constant to ±0.005 K during measurements at each temperature, and the accuracy of temperature measurement was ±0.05 K. Densities of the pure and mixed fluids were obtained at the temperatures at which viscosity measurements were done.

Results and discussion

The densities of the pure cosolvents are given in Table 1 together with values from the literature, and generally show good agreement with literature data. The densities were estimated by linear extrapolation of the measured dilute solution densities to zero water content by the method of least squares. From the experimental densities, excess molar volumes V^E and single-component apparent molar volumes V_Φ for the two systems were calculated using the equations:

$$[1] \quad V^E = \frac{X_1M_1 + X_2M_2}{\rho} - \frac{X_1M_1 + X_2M_2}{\rho}$$

$$[2] \quad V_\Phi(2) = \frac{X_1M_1(\rho_1 - \rho)}{X_2\rho_1\rho} + \frac{M_2}{\rho}$$

where ρ represents solution density, M, X, and V_Φ denote respectively molar mass, mole fraction, and apparent molar volume, for either mixture component. The measured densities for the two systems at various temperatures are listed in Tables 2 and 3 as a function of the mole fraction of the organic component.

The excess molar volume of a mixture is the consequence of the coupling of different contributions deriving from structural modifications of the pure components, changes in the free volume, interstitial accommodation, and hydrogen bonding of unlike molecules and from other non-specific physical effects. The excess volumes for H_2O + BuOH mixtures at 288, 298, 308, and 318 K are shown in Fig. 1, and for H_2O + TBA mixtures at 288, 293, 298, 303, and 308 K in Fig. 2. Previously reported excess volumes (for the H_2O + BuOH system) are mostly for 298 K. For both systems V^E is large and negative, and not strongly temperature dependent. The sign of V^E for liquid aqueous mixtures can be accounted for by occupation of the free volume of cavities in the open water structure by the other component. For both systems V^E is much larger than for H_2O + CH_3CN mixtures (4) in which it is believed that water–cosolvent interactions are very weak. For the H_2O + BuOH system, the maximum (negative) value of V^E is approximately equal to that for the H_2O + CH_3OH system (5) where the cosolvent molecule has one hydrogen bonding site in each case. It seems likely that the much larger volume contraction in H_2O + TBA mixtures arises at least in part from the additional hydrogen bonding site afforded by the NH_2 group.

Most of the significant changes occurring in aqueous–

Can. J. Chem. Downloaded from www.nrcresearchpress.com by 85.192.166.187 on 09/08/12
For personal use only.

TABLE 2. Density and viscosity data for the H_2O + BuOH system

	ρ/kg m^{-3}				η/mPa s			
X^a	288 K	298 K	308 K	318 K	288 K	298 K	308 K	318 K
0.00[b]	999.10	997.05	994.04	990.21	1.139	0.890	0.719	0.596
0.10	998.37	996.28	993.30	989.66			0.731	0.606
0.50	995.63	993.44	990.42	986.80		0.976	0.783	0.644
1.00	992.59	990.41	987.34	983.46		1.076	0.855	0.711
2.00	987.53	984.98	981.47	977.31	1.817		1.007	0.804
3.00	983.36	980.15	976.16	971.20	2.270	1.566	1.175	0.916
4.00	979.63	975.61	97.78	965.38			1.336	1.038
5.00	975.75	970.76	965.05	958.93	3.288	2.117	1.501	1.153
6.00	971.15	965.05	958.79	952.36			1.651	1.234
8.00		953.60	945.87	939.44		2.777	1.926	1.430
10.0	949.51	942.10	934.91	927.33	5.180	3.243	2.178	1.602
15.0	925.11	917.47	906.49	901.46	6.417	3.857	2.724	1.935
20.0	905.09	896.99	888.83	880.42	7.194	4.342	2.944	2.091
25.0	888.60	880.40	871.89	863.33	7.683	4.615	3.109	2.190
30.0	874.72	866.23	857.75	849.01	7.929	4.747	3.209	2.235
35.0	862.75	854.53	845.60	836.62	7.984	4.838	3.209	2.233
40.0	852.65	844.08	835.31	826.10	8.003	4.815	3.208	2.224
50.0	835.91	827.62	817.88	808.43	7.823	4.698	3.077	2.139
60.0	822.72	813.73	804.33	794.64	7.542	4.494	2.957	2.032
70.0	811.68	802.84	793.36	783.26	7.277	4.298	2.801	1.926
80.0	803.17	793.84	784.24	773.95	7.114	4.152	2.678	1.832
85.0	799.43	789.96	780.17	769.99	7.132	4.106	2.636	1.803
88.0	797.36	787.83	778.00	767.69	7.202	4.108	2.613	1.771
90.0	796.04	786.44	776.61	766.27	7.302	4.113	2.603	1.758
92.0	795.02	785.20	775.26	764.83	7.432	4.114	2.594	1.747
95.0		783.31	773.12	762.75		4.167	2.590	1.728
97.0		782.27	772.10	761.55		4.215	2.592	1.719
98.0		781.59	771.48	760.85		4.249	2.597	1.710
99.0		781.11	770.87	760.27		4.284	2.601	1.706
100.0		780.43	770.22	759.65		4.324	2.606	1.702

[a] X = mol% BuOH.
[b] For sources of data for pure water, see footnotes to Tables 3 and 4.

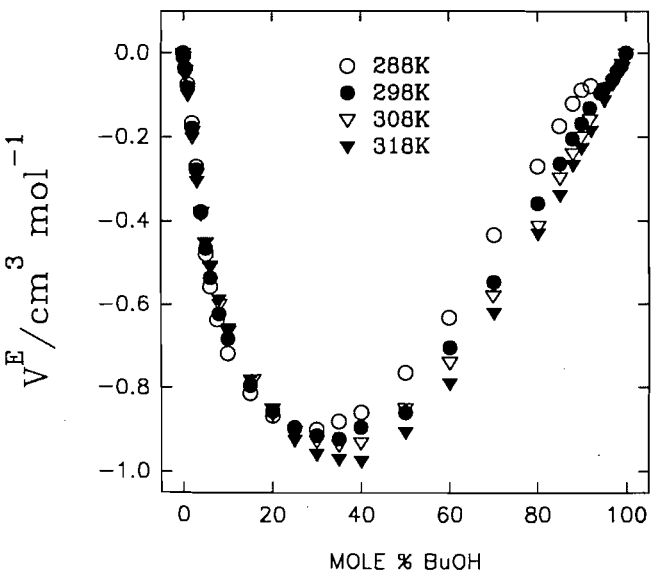

FIG. 1. Excess molar volume for H_2O + *tert*-butyl alcohol mixtures as a function of composition and temperature.

organic mixtures are in the water-rich region. Although molar excess functions give information on interactions occurring in mixtures, since they vanish at the composition extremes they may not reveal phenomena in dilute solutions where structural changes of pure components imposed by the interactions between like and unlike molecules can occur. Apparent and partial molar properties, on the other hand, reflect more appropriately characteristic interactions and structural changes induced by the addition of small, increasing amounts of the second component (11). Figures 3 and 4 show that the apparent molar volumes of BuOH and TBA in water vary with composition in a similar fashion, and the sharp V_Φ(cosolvent) minimum in the water-rich region is common to many aqueous non-electrolyte solutions. The trends of the apparent molar volumes of BuOH and TBA in the water-rich region with composition and temperatures are shown in more detail in Figs. 5 and 6. The shapes of the curves for both cosolvents are essentially the same at all temperatures, but the minimum becomes more pronounced and shifts to higher concentration as the temperature is lowered. Similar behaviour is found for $V_\Phi(H_2O)$ in the BuOH-rich region (Fig. 7) where the minimum is also very pronounced and shifts to a higher concentration with decreasing temperature, though it is not as sharp as for V_Φ(BuOH). The volumetric behaviour of H_2O in TBA-rich mixtures is quite different: $V_\Phi(H_2O)$ gradually decreases from a higher value in water to a small value at infinite dilution in TBA as the proportion of amine increases. The volumetric behaviour of H_2O + BuOH mixtures is unusual at both ends of the concentration range, as was also noted by Sakurai (15), whose results are in excellent agreement with ours. A minimum in the apparent molar volume of water in the organic cosolvent-rich region has been observed also in H_2O + tetrahydrofuran mixtures (19). The well-known characteristics of volumetric properties in water-rich regions of

Can. J. Chem. Downloaded from www.nrcresearchpress.com by 85.192.166.187 on 09/08/12
For personal use only.

TABLE 3. Density data for the H_2O + TBA system

	ρ/kg m^{-3}				
X^a	288 K	293 K	298 K	303 K	308 K
0.00[b]	999.1016	998.2063	997.048	995.6511	994.0359
0.10	998.18	997.37	996.20	994.74	993.13
0.50	994.80	993.82	992.56	991.07	989.41
1.00	990.93	989.78	988.33	986.80	985.11
2.00	983.74	982.51	980.81	978.93	976.94
3.00	977.56	975.74	973.68	971.43	969.16
4.00	971.36	968.97	966.46	963.55	960.80
5.00	964.57	961.59	958.59	955.40	952.19
6.00	956.88	953.60	950.54	947.22	944.21
8.00			934.81	931.50	927.93
10.0	927.82	924.07	920.54	916.71	913.05
15.0	897.36	893.40	888.74	885.73	874.95
20.0	872.51	868.38	863.41	860.32	855.93
25.0	851.83	847.54	843.44	839.13	834.64
30.0	834.09	829.59	824.89	821.10	816.62
40.0	805.02	799.96	794.44	791.02	786.44
50.0	780.87	776.05	770.85	766.20	761.31
60.0	760.34	755.39	750.31	745.26	740.09
70.0	742.31	737.15	731.86	726.81	721.77
80.0	726.31	720.97	715.90	710.51	705.36
90.0	711.69	706.37	700.99	695.76	690.05
92.0	708.94	703.45	697.74	692.92	687.27
95.0	704.89	699.44	693.85	688.61	682.99
97.0	702.19	696.62	691.11	685.84	680.13
98.0			690.23	684.51	678.93
99.0	699.53	693.99	688.46	683.00	677.59
100.0	698.16	692.61	686.64	681.73	675.80

[a]X = mol% TBA.
[b]Data from ref. 18.

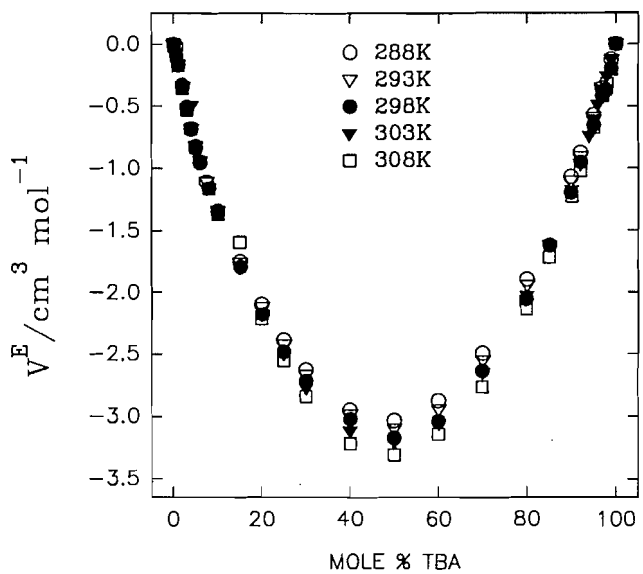

FIG. 2 Excess molar volume for H_2O + *tert*-butylamine mixtures as a function of composition and temperature.

many aqueous non-electrolyte solutions, represented typically by aqueous BuOH and TBA solutions, have been interpreted in terms of the hydrophobic hydration concept (1, 20), although the exact nature of hydrophobic hydration is still unclear. The occurrence of a minimum has been attributed to a balance between the effects of interstitial solution of organic cosolvent

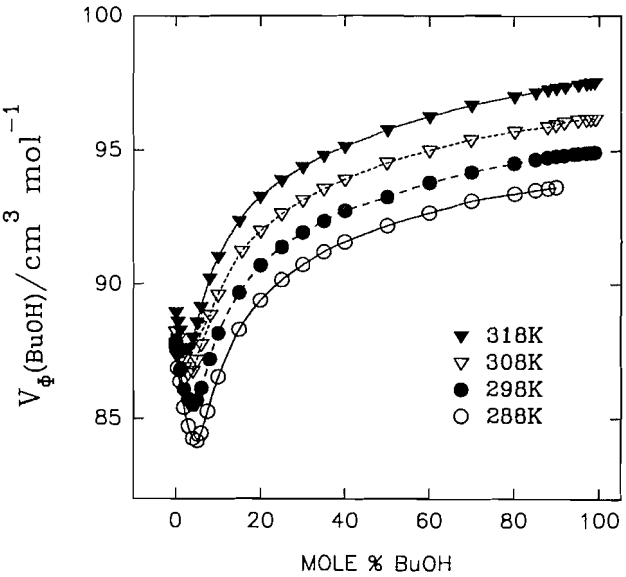

FIG. 3. Apparent molar volume of *tert*-butyl alcohol in water as function of composition and temperature.

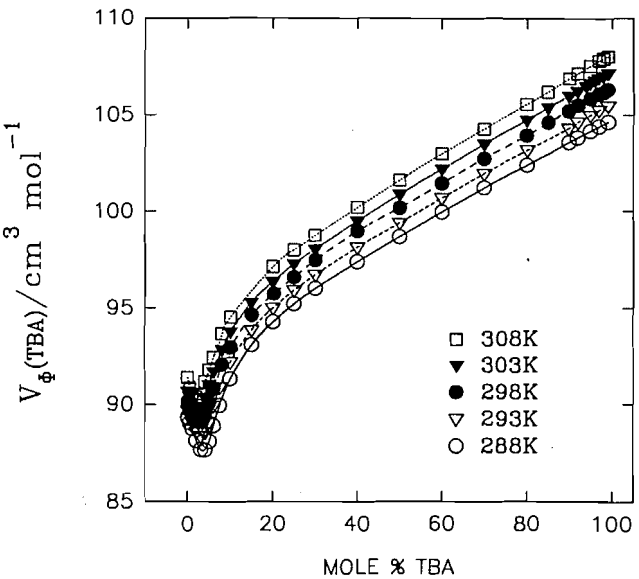

FIG. 4. Apparent molar volume of *tert*-butylamine in water as a function of composition and temperature.

molecules with accompanying enhancement of an ice-like structure in the water, and a breaking of this structure due to loss of free space with increasing concentration of the solute (8, 21). Initially, the addition of BuOH or TBA to water will result in the formation of stronger H-bonds between water molecules that would bring about volume contraction. At the same time, the bulky tertiary alkyl groups of BuOH or TBA occupying cavities in the network structure of water will tend to associate because this causes a free energy decrease. This tendency is known as hydrophobic interaction (8). The structural stabilization produced by the cosolvent becomes more pronounced and eventually reaches a minimum beyond which further addition of solute results in a fairly rapid breakdown of the structural integrity of water. Although the interpretation of the minimum is not unequivocal it probably corresponds to the upper limit of the region where the stabilization of the water structure can take place. Packing of the cosolvent molecules evidently takes place

Can. J. Chem. Downloaded from www.nrcresearchpress.com by 85.192.166.187 on 09/08/12
For personal use only.

Can. J. Chem. Downloaded from www.nrcresearchpress.com by 85.192.166.187 on 09/08/12
For personal use only.

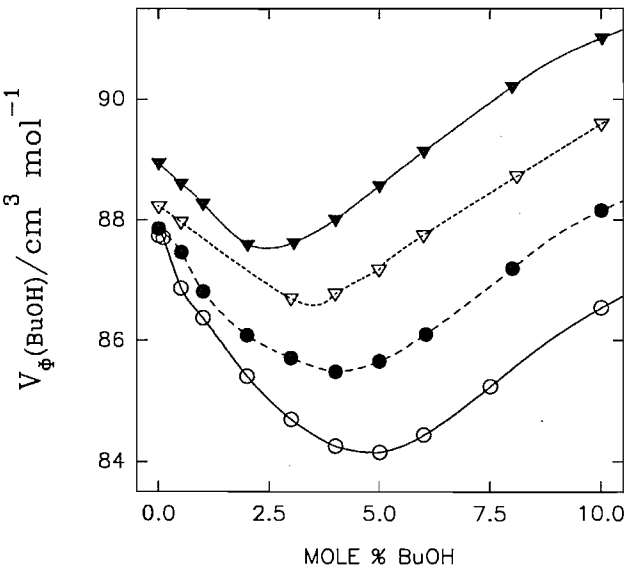

FIG. 5. Apparent molar volume of *tert*-butyl alcohol in the water-rich region at various temperatures: 318 K (▼), 308 K (▽), 298 K (●), 288 K (○).

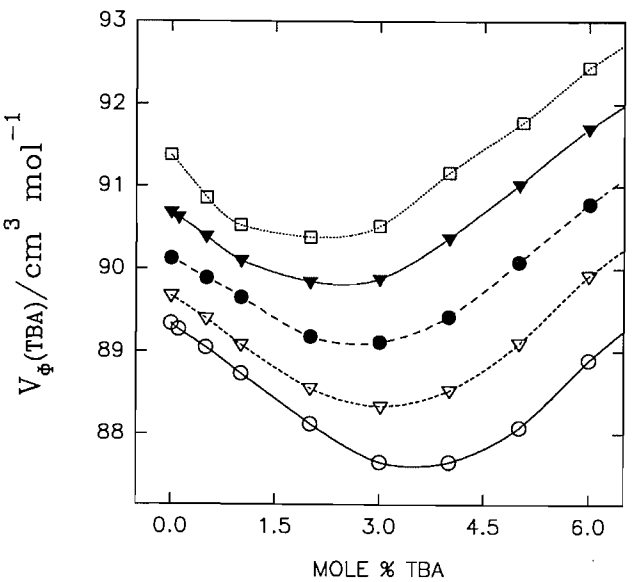

FIG. 6. Apparent molar volume of *tert*-butylamine in the water-rich region at various temperatures (K): 308 (□), 303 (▼), 298 (●), 293 (▽), 288 (○).

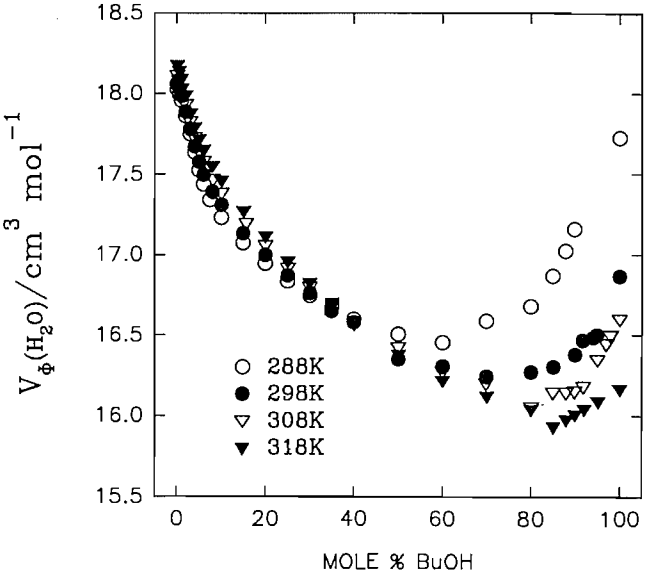

FIG. 7. Apparent molar volume of water in *tert*-butyl alcohol as a function of composition and temperature.

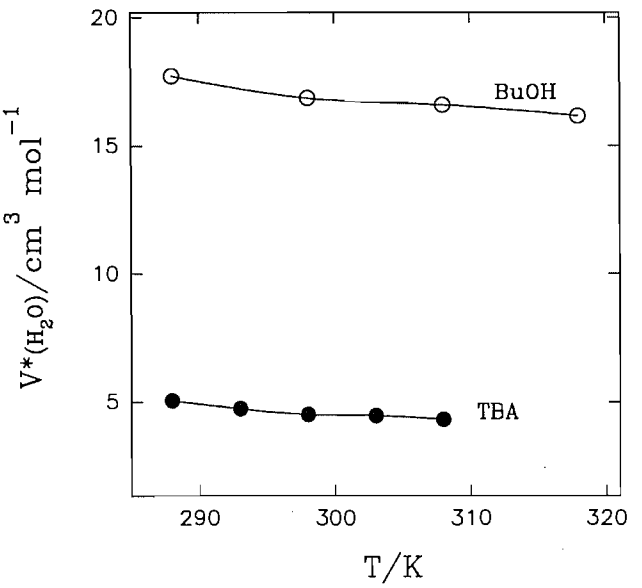

FIG. 8. Limiting partial molar volume of water in *tert*-butyl alcohol and *tert*-butylamine as a function of temperature.

more effectively up to this concentration due to the interstitial accommodation of the solute molecules within the water structure. The minimum in the $V_\phi(H_2O)$ curve shown in Fig. 7, on the other hand, cannot be attributed to such a structural influence because the open structure of water no longer exists in the BuOH-rich region. It is noteworthy that structure promoting interactions of the two cosolvents persist over a considerable range of temperature, so that at 318 K BuOH is still a powerful structure promoter.

Limiting partial molar volumes of BuOH, TBA, and H_2O, i.e. the infinite-dilution apparent molar volumes, are given in Tables 5 and 6 together with literature data. Our values for both components in the H_2O + BuOH system are in good agreement with published data. For the H_2O + TBA system, the only published data are those of Kaulgud and co-workers (22), which are based on the differential float balance method. Their values for the limiting partial molar volume, V^*(TBA), for TBA in water are 0.75 and 1.11 cm^3 mol^{-1} higher than our results at 288 and 298 K, respectively. These differences can be ascribed to impurities in TBA, their extrapolation method and the different techniques employed in the measurements. The limiting partial molar volumes of water in BuOH and TBA are plotted as a function of temperature in Fig. 8. In both cosolvents $V^*(H_2O)$ is smaller than the molar volume of water. The decrease in volume relative to pure water may be related to the loss of the open structure of bulk water and to the formation of H-bonds between water and solvent molecules (19). $V^*(H_2O)$ in TBA is very small, and at present we cannot offer a convincing explanation of the large difference in the values of $V^*(H_2O)$ in BuOH and TBA, though it must be borne in mind that the amine

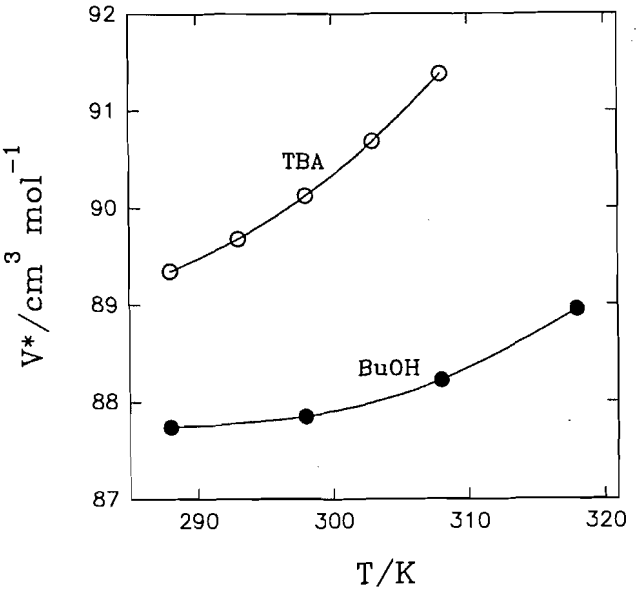

FIG. 9. Limiting partial molar volume of *tert*-butyl alcohol and *tert*-butylamine in water as a function of temperature.

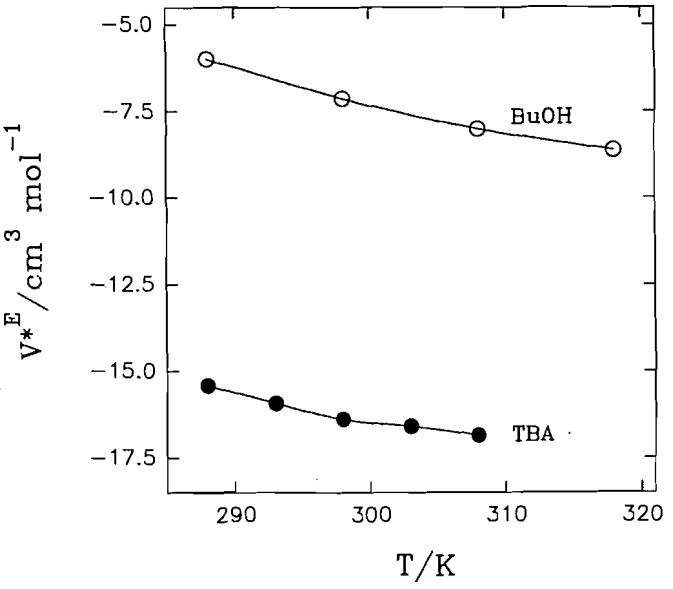

FIG. 10. Excess limiting partial molar volume of *tert*-butyl alcohol and *tert*-butylamine in water as a function of temperature.

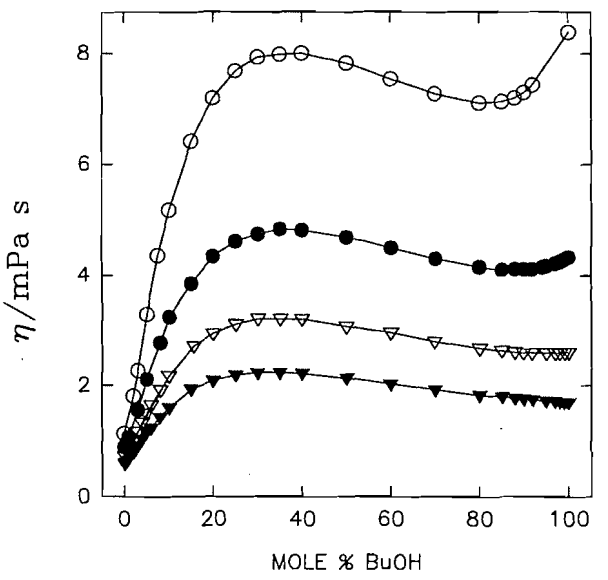

FIG. 11. Viscosity of H_2O + *tert*-butyl alcohol mixtures as a function of composition and temperature (K): 288 (○), 298 (●), 308 (▽), 318 (▼).

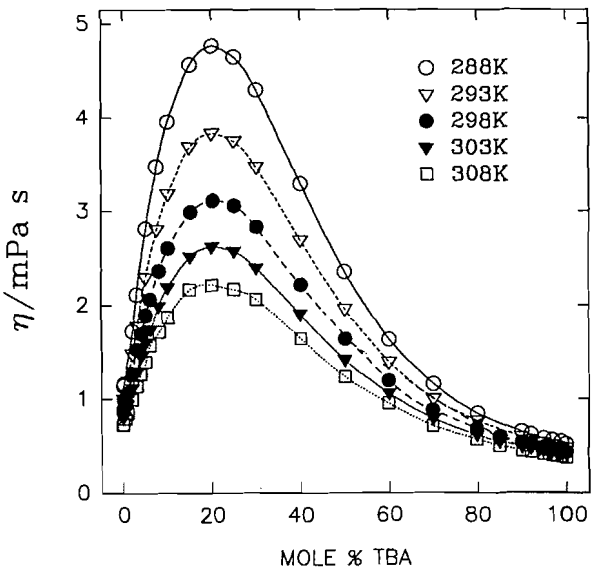

FIG. 12. Viscosity of H_2O + *tert*-butylamine mixtures as a function of composition and temperature.

becomes significantly protonated at low concentration in water, and the extent of protonation increases with increasing dilution. Similarly, as for other organic liquid + water mixtures both V^*(BuOH) and V^*(TBA) are smaller than the molar volumes of the respective pure components at all temperatures. This contraction in volume on mixing organic cosolvent and H2O is surprising at first, since hydrophobic hydration around the organic cosolvent causes an increase in ice-likeness of the solvent, and consequently should cause a decrease in density of the solution. The explanation offered by Nemethy and Scheraga (23) is that hydrophobic hydration occurs with an overall economy of space. As shown in Fig. 9, V^*(BuOH) and V^*(TBA) in water increase with temperature, more significantly for V^*(TBA) than for V^*(BuOH). Both the alcohol and amine show (Fig. 10) negative excess limiting partial molar volumes defined by

$$[3]\quad V^{*E}(i) = V^*(i) - V_m(i)$$

where V_m is the molar volume of pure component i. The magnitude of V^{*E} is larger for TBA than for BuOH, suggesting that the extent of accommodation of TBA in the open cage structure existing in water is greater than for BuOH. Also, the excess limiting partial molar volumes of BuOH and TBA are strongly temperature-dependent, becoming more negative as the temperature increases.

Shear viscosities for aqueous binary mixtures of BuOH and TBA are given in Tables 2 and 4 respectively, and viscosity isotherms are shown in Figs. 11 and 12. Extensive viscosity data at 298 K have been reported for H_2O + BuOH, and our data compare favourably with the literature values. In particular, the val-

Can. J. Chem. Downloaded from www.nrcresearchpress.com by 85.192.166.187 on 09/08/12
For personal use only.

TABLE 4. Viscosity data for the H_2O + TBA system

	η/mPa s				
X^a	288 K	293 K	298 K	303 K	308 K
0.00[b]	1.139	1.002	0.8902	0.7975	0.7194
0.10	1.163		0.993	0.810	0.730
1.00			1.068	0.947	0.846
2.00	1.725	1.479	1.269	1.116	0.990
3.00	2.109	1.773	1.527	1.290	1.132
4.00			1.698	1.455	1.263
5.00	2.814	2.287	1.890	1.606	1.394
6.00			2.059	1.745	1.571
8.00			2.363	1.986	1.718
10.0	3.960	3.188	2.604	2.189	1.871
15.0	4.572	3.684	2.992	2.516	2.168
20.0	4.770	3.833	3.112	2.622	2.211
25.0	4.644	3.746	3.057	2.570	2.160
30.0	4.299	3.466	2.832	2.392	2.061
40.0	3.294	2.689	2.211	1.901	1.643
50.0	2.358	1.961	1.642	1.419	1.240
60.0	1.634	1.393	1.195	1.060	1.100
70.0	1.160	1.003	0.881	0.787	0.712
80.0	0.841	0.762	0.677	0.609	0.566
85.0			0.594	0.543	0.499
90.0	0.649	0.593	0.534	0.490	0.451
92.0	0.616	0.561	0.523	0.470	0.433
95.0	0.575	0.526	0.480	0.442	0.410
97.0	0.558	0.504	0.462	0.426	0.396
98.0			0.456	0.419	0.389
99.0	0.543	0.483	0.445	0.417	0.383
100.0	0.517	0.473	0.434	0.403	0.375

[a]X = mol% TBA.
[b]Reference 39.

ues given by Kenttamaa and co-workers (24) agree with the present data within experimental error but are slightly lower than those of Senanayake and Freeman (25), although the general shape of the curve obtained in all three cases is the same.

Solute–solvent interactions in binary liquid mixtures can lead to extrema in viscosity–composition isotherms, and most binary aqueous mixtures have the characteristic feature that at a particular composition, the viscosity of the solution reaches a value that is larger than the viscosities of either pure component. Addition of BuOH or TBA to H_2O increases the viscosity of the mixture rapidly and the viscosity reaches a maximum at a composition in the water-rich region (Figs. 11 and 12). The viscosities at the maxima are nearly 7.0 and 4.2 times the viscosity of water and appear around 40 and 20 mol% of BuOH and TBA, respectively, at 288 K. Viscosity maxima observed for aqueous mixtures of different organic solvents have been attributed to the formation of association complexes (26–29). An alternative interpretation is that the ascending part of the viscosity–composition curve (water-rich region in Figs. 11 and 12) represents structural promotion in the mixture by gradual formation of clusters of associated species via hydrogen bonding. At lower concentrations, BuOH and TBA molecules are accommodated in cavities within the H_2O structure leading to an enhancement of H_2O network structure. At moderate concentrations, however, there is insufficient free volume for all of the cosolvent molecules in the structural cavities of water, and this results in the BuOH or TBA molecules participating in strong hydrogen bonding with H_2O, producing a more strongly bonded and less compressible structure than in H_2O itself. A gradual aggregation of different types of clusters, viz. H_2O–H_2O, H_2O–cosolvent, and cosolvent–cosolvent, would lead to an increase in viscosity and a maximum value when aggregation is maximum, i.e. maximum structuredness (5, 30). The viscosity maxima sharpen and the heights of the maxima (as in other systems) increase with decreasing temperature. Increased temperature undoubtedly weakens BuOH–H_2O and TBA–H_2O interactions in H_2O-rich mixtures, leading to decomposition of cosolvent–H_2O complexes.

For most water + alcohol systems addition of water decreases the viscosity of the alcohol, whereas for the lower members of a homologous series there is an increase in viscosity. Thus the decrease in viscosity when water is added to *n*-butanol, *n*-pentanol, and *n*-hexanol contrasts sharply with the increase showed by methanol, ethanol, and *n*-propanol (31). *tert*-Butyl alcohol shows both types of behaviour; increased viscosity with initial addition of water at higher temperature, and decreased viscosity at low. The behaviour at 298 K in the alcohol-rich region is very similar to that found for the dielectric constant (32) of this system (Fig. 13). The minima of both properties correspond to the same alcohol content, and it is concluded that the minima are due to solvent structure changes. This conclusion is in accordance with ideas about the formation of Brown–Ives "centrosymmetric" associates, composed of one water and four alcohol molecules (33).

According to Kauzman and Eyring (34) the viscosity of a liquid can be expressed in terms of its activation parameters by the equation

TABLE 5. Limiting partial molar volumes for H_2O + BuOH mixtures

	V^*/cm^3 mol^{-1}						
T/K	This work	Ref. 15	Ref. 8	Ref. 9	Ref. 10	Ref. 11	Ref. 12
				BuOH			
288	87.74	87.66					
298	87.85	87.81	87.82	87.90	87.73	87.76	88.30
308	88.22	88.20					
318	88.95	88.75					
				H_2O			
288	17.73						
298	16.87						
308	16.60	16.56					
318	16.17	16.05					

Can. J. Chem. Downloaded from www.nrcresearchpress.com by 85.192.166.187 on 09/08/12
For personal use only.

TABLE 6. Limiting partial molar volumes for H_2O + TBA mixtures

	$V^*/cm^3\ mol^{-1}$		
	V^*(TBA)		
T/K	This work	Ref. 22	$V^*(H_2O)$
288	89.35	90.10	5.06
293	89.68		4.75
298	90.13	91.24	4.53
303	90.69		4.48
308	91.38		4.34

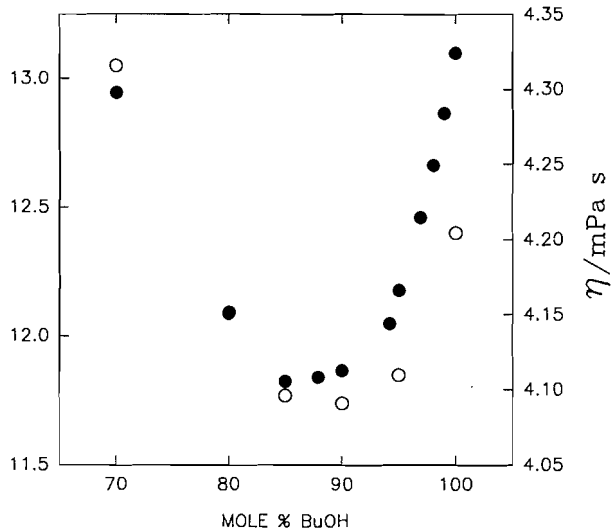

FIG. 13. Viscosity and dielectric constant (32) for H_2O + *tert*-butyl alcohol mixtures at 298 K. The shaded symbols denote viscosity, and the open circles dielectric constant values.

$$[4]\quad \eta = \frac{hN}{V}\exp\frac{\Delta H^*}{RT}\exp\frac{-\Delta S^*}{R}$$

where V/N is the molecular volume of the liquid, ΔH^* is the activation enthalpy for viscous flow, i.e., the energy required for a molecule to reach the top of a potential energy barrier so as to jump into a neighbouring hole, ΔS^* is the corresponding entropy of activation, T is temperature, and R is the gas constant. Since V and ΔS^* do not vary greatly with temperature the above equation can be simplified to the form suggested by Arrhenius (35)

$$[5]\quad \eta = A\exp\frac{E_a}{RT}$$

E_a is the "activation energy" for successive passage of individual molecules from one equilibrium position to another, that is the energy required to create a hole (36). In a hydrogen-bonded system, the motion will involve the breaking of a series of bonds and the formation of new bonds, and since viscous flow may involve the motion of clusters of molecules from one cage structure to another, the activation energy is a mean value for the processes which occur in the fluid. The large viscosity of water, relative to other molecular liquids with similarly sized molecules, can be attributed to the fact that in addition to the energy

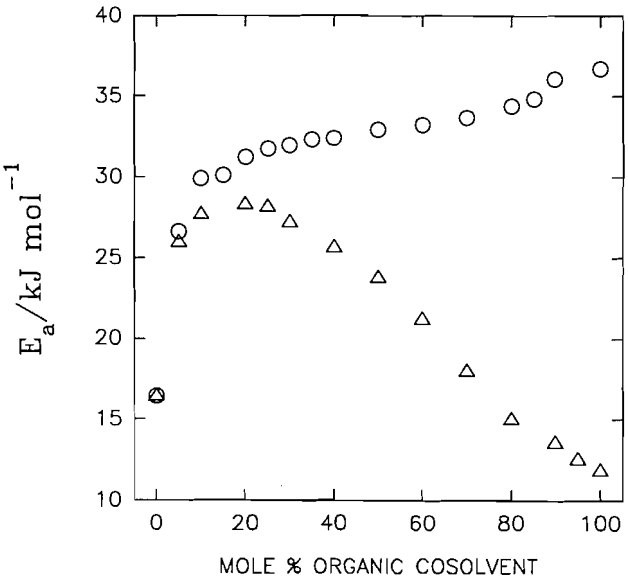

FIG. 14. Activation energies for viscous flow for H_2O + BuOH (○) and H_2O + TBA (▽) mixtures.

required for the formation of holes, the hydrogen bonds between the water molecules have to be broken to achieve an activated state for viscous flow.

Figure 14 shows the activation energies for viscous flow for the two binary systems studied, calculated from linear least squares fits of ln η vs. $1/T$. The estimated uncertainty in E_a is of the order 0.2 kJ mol^{-1}. Whereas E_a progressively increases as the TBA concentration increases up to 20 mol% (also the composition of maximum viscosity) and thereafter regularly decreases for further increase in the amine concentration, in the H_2O + BuOH system the activation energy increases monotonically with the concentration of BuOH. This trend is indicative of the larger energy required to induce translational motion in the alcohol molecule relative to the smaller water or lighter amine molecule. However, the change is larger at both extremes of the solvent composition. The present values are consistent with the limited data reported in the literature (25, 37). Other data appear not to be available for the H_2O + TBA system.

Acknowledgements

The authors are indebted to the New Zealand government for the award of a Commonwealth Scholarship to Pius Kipkemboi, and to the University of Auckland Research Committee for equipment funding.

1. H.S. Frank and M.W. Evans. J. Chem. Phys. **13**, 507 (1945).
2. B.C.R. Guillaume, D. Yogev, and J.H. Fendler. J. Chem. Soc. Faraday Trans. **88**, 1281 (1992).
3. Y. Cheng, M. Page, and C. Jolicoeur. J. Phys. Chem. **97**, 7359 (1993).
4. A.J. Easteal and L.A. Woolf. J. Chem. Thermodyn. **14**, 755 (1982).
5. A.J. Easteal and L.A. Woolf. J. Chem. Thermodyn. **17**, 49 (1985).
6. K. Nakanishi. Bull. Chem. Soc. Jpn. **33**, 793 (1960).
7. K. Nakanishi, N. Kato, and M. Maruyama. J. Phys. Chem. **71**, 814 (1967).
8. F. Franks and H.T. Smith. Trans. Faraday Soc. **64**, 2962 (1968); J. Chem. Eng. Data, **13**, 538 (1968).
9. L. Avedikian, G. Perron, and J.E. Desnoyers. J. Solution Chem. **4**, 331 (1975).
10. C. Jolicoeur and G. Lacroix. Can. J. Chem. **54**, 624 (1976).

Can. J. Chem. Downloaded from www.nrcresearchpress.com by 85.192.166.187 on 09/08/12
For personal use only.

11. C. de Visser, G. Perron, and J.E. Desnoyers. Can. J. Chem. **55**, 856 (1977).
12. A. Hvidt, R. Moss, and G. Nielsen. Acta Chem. Scand. **B32**, 274 (1978).
13. G. Perron and J.E. Desnoyers. J. Chem. Thermodyn. **13**, 1105 (1981).
14. J.F. Alary, M.A. Simard, J. Dumont, and C. Jolicoeur. J. Solution Chem. **11**, 755 (1982).
15. M. Sakurai. Bull. Chem. Soc. Jpn. **60**, 1 (1987).
16. E.S. Kim and K.N. Marsh. J. Chem. Eng. Data, **33**, 288 (1988).
17. T.L. Broadwater and R.L. Kay. J. Phys. Chem. **74**, 3802 (1970).
18. G. Girard. *In* Recommended reference materials for the realization of physicochemical properties. *Edited by* K.N. Marsh. Blackwell Scientific Publications, Oxford. 1987. pp. 25–32.
19. M. Sakurai and T. Nakagawa. Bull. Chem. Soc. Jpn. **55**, 1641 (1982).
20. F. Franks and J.E. Desnoyers. Water Sci. Rev. **1**, 171 (1985).
21. F. Franks and D.S. Reid. *In* Water: A comprehensive treatise. Vol. 2. *Edited by* F. Franks. Plenum Press, New York. 1973. pp. 330–374.
22. M.V. Kaulgud, V.S. Bhagde and A. Shrivastava. J. Chem. Soc. Faraday Trans. I, **18**, 313 (1982).
23. G. Nemethy and H.A. Scheraga. J. Chem. Phys. **36**, 3401 (1962).
24. J. Kenttamaa, E. Tommila, and M. Martti. Ann. Acad. Sci. Fenn. Ser. A, **2**, 1 (1959).
25. P.C. Senanayake and G.R. Freeman. J. Phys. Chem. **91**, 2123 (1987).
26. P. Assarsson and F.R. Eirich. J. Phys. Chem. **72**, 2710 (1968).
27. M.V. Ramanamurti and L. Bahadur. J. Chem. Soc., Faraday Trans. I, **76**, 1409 (1980).
28. R.L. Kay and T.L. Broadwater. J. Solution Chem. **5**, 57 (1976).
29. R.L. Kay and T.L. Broadwater. Electrochim. Acta, **16**, 667 (1971).
30. M.V. Ramanamurti, P.V. Prabhu, and L. Bahadur. Bull. Chem. Soc. Jpn. **59**, 2341 (1986).
31. A. D'Aprano, I.D. Donato, E. Caponetti, and V. Agrigento. J. Solution Chem. **8**, 793 (1979).
32. P.K. Kipkemboi and A.J. Easteal. Aust. J. Chem. In press.
33. A.C. Brown and D.I.G. Ives. J. Chem. Soc. 1608 (1962).
34. W. Kauzman and H. Eyring. J. Am. Chem. Soc. **62**, 3113 (1940).
35. S. Arrhenius. Medd. Vetensk. Nobel **3**, 20 (1916).
36. S. Glasstone, K.J. Laidler, and H. Eyring. The theory of rate processes. McGraw-Hill, New York. 1941. pp. 480–481.
37. M. Tabellout, P. Lanceleur, J.R. Emery. D. Hayward, and R. Pethrick. J. Chem. Soc. Faraday Trans. **86**, 1493 (1990).
38. J. Timmermans, Physico-chemical constants of pure organic compounds. Elsevier, Amsterdam. 1950. p. 324.
39. W. Künzel, H.F. van Wijk, and K.N. Marsh. *In* Recommended reference materials for the realization of physicochemical properties. *Edited by* K.N. Marsh. Blackwell Scientific Publications, Oxford. 1987. pp. 59–61.

Can. J. Chem. Downloaded from www.nrcresearchpress.com by 85.192.166.187 on 09/08/12
For personal use only.

Substituent dependency in pentaamminemetal(II) complexes (M = Ru, Os) of styrenes probed by using carbon-13 nuclear magnetic resonance spectroscopic method and voltammetrical analysis

SHAW-TAO LIN[1] AND JIN-TSUEY JONG

Department of Applied Chemistry, Providence University, Sha-Lu, Taichung Hsien, Taiwan 433-01

Received October 10, 1993[2]

SHAW-TAO LIN and JIN-TSUEY JONG. Can. J. Chem. **72**, 1946 (1994).

The ^{13}C NMR spectra of $[M(NH_3)_5(styrene)]^{2+}$ (M = Ru, Os) demonstrate the substituent dependency of the interaction between the vinyl group and the metal moiety which suggests the modes of bonding. This phenomenon is also observed from the voltammetric analytical results which confirm the substituent dependency of the oxidation potential.

SHAW-TAO LIN et JIN-TSUEY JONG. Can. J. Chem. **72**, 1946 (1994).

Les spectres de RMN du ^{13}C du $[M(NH_3)_5(Styrène)]^{2+}$ (M = Ru, Os) mettent en évidence l'influence des substituants sur l'interaction entre le groupe vinyle et la portion métallique, et cette influence fournit des renseignements sur les modes de liaison. Ce phénomène a été également observé à partir des résultats des analyses voltamétriques qui confirment l'effet des substituants sur le potentiel d'oxydation.

[Traduit par la rédaction]

Introduction

Ruthenium and osmium complexes play an important role in catalytic processes, hence their characteristics have been widely studied (1). The olefin pentaammineruthenium complexes have been synthesized and studied using electrochemical and spectroscopic techniques (2). The cyclic voltammetric (CV) analysis of styrene pentaammineruthenium(II) chloride shows that the interaction between the vinyl group of styrene and ruthenium is independent of the substituent on the phenyl ring (2). NMR spectrometry is a very sensitive tool which can determine the electron density of nucleus in organic as well as organometallic compounds. Certain Pd–styrene and Pt–styrene complexes have been studied by NMR spectroscopic technique (3–6). The correlation between Hammett constants (σ_p or σ^+, σ^-) and $\Delta\delta$ for neutral, anionic and cationic Pt–styrenes were reported (4). We took advantage of this relationship in our study to investigate the substituent dependency of the bonding of styrenes with ruthenium and osmium, we have also used voltammetric analysis in our study.

The $[Ru(NH_3)_5(styrene)]Cl_2$ series was prepared by reducing $RuCl_3(NH_3)_5$ with amalgamated zinc in the presence of styrene (7). After stirring at room temperature for 3 h, the residue was removed by filtration and the excess styrene and solvent were removed under a reduced pressure. The resultant complexes were characterized by ^1H NMR and ^{13}C NMR spectroscopy. The ^1H NMR resonance of the vinyl hydrogens of styrenes shifted upfield by 3 ppm, exhibiting identical coupling patterns as the free styrenes. The chemical shifts of NH_3 protons appeared as two broad signals near 2.0 ppm and 3.9 ppm with an intensity ratio of 4:1 (Table 1). The four *cis* NH_3 ligands were located upfield. The chemical shifts of NH_3 protons and vinyl group protons were found to be substituent dependent. This substituent dependency indicates that the bonding between the metal and the vinyl group is influenced by the substituent and the phenyl ring. The equal chemical shifts of the four NH_3 ligands imply equal shielding by the phenyl ring, indicating free rotation between the metal and the vinyl group.

$[Os(NH_3)_5(styrene)]_2tfms$ (tfms:CF_3SO_3) was prepared by reducing $(NH_4)_2OsCl_6$ with NH_2NH_2, then substituting the chloride by trifluoromethylsulfonate, and finally reducing with amalgamated zinc in the presence of styrene. The resultant yellow complexes exhibited relatively poor solubility in water. The proton chemical shifts of the vinyl protons on the chelated styrene were observed to be similar to their Ru analogues except for an upfield shift of approximately 0.2 ppm (Table 1). The resonances of the aromatic protons were well separated from each other; meanwhile, unresolved patterns from Ru counterpart frequently appeared. A rapid exchange between NH_3 protons and D_2O protons was reported by Shepherd et al. (2). However, we observed NH_3 resonances near 2.3 and 3.25 ppm with relative intensities of 4:1 from the fresh D_2O solution. The lines disappear within 1 h and 16 h for the proton resonances at 2.3 and 3.25 ppm, respectively. Styrene protons showed no change in their resonance, suggesting that the disappearance of the NH_3 proton signal was due to an H–D exchange. Differences in NMR patterns in the aromatic region could imply that there are different bonding modes for styrene–Ru and styrene–Os complexes.

^{13}C chemical shifts are well correlated with the electron density of carbon nucleus (8). Relationships between substituent chemical shifts (SCS) and Hammett constants in aromatic systems have been previously studied (9). We have examined the substituent-dependency of vinyl carbons on styrenes. All chemical shifts were measured relative to NaTMPS in proton–noise decoupled spectra. The chemical shifts of free styrenes and their complexes of Ru and Os are tabulated in Tables 2, 3, respectively. The differences in chemical shifts ($\Delta\delta$) of C_α, C_β between free styrenes and chelated styrenes as shown in Table 2 range from 50 to 60 ppm upfield of the free ligand. On this series of Os complexes, the upfield shifts for C_α and C_β are 70–77 and 80–88 ppm, respectively (Table 3). These could have resulted from a change in the carbon character from sp^2 to sp^3 and from the influence of metal atoms.

The SCS (α, β) values are shifted upfield whenever the substituents on the aromatic rings are electron-donating groups, and vice versa. The substituent dependency of chemical shifts ($\Delta\Delta\delta$) for C_β and C_α varied from +3.09 to −3.42 ppm and +0.72 to −0.83 ppm for 4-Me_2N- to 4-CN groups (Table 2). Inverse substituent effects might possibly result from the altered back-bonding of metal rather than directly from the substituent.

[1]To whom correspondence should be addressed.

[2]Revision received April 13, 1994.

Can. J. Chem. Downloaded from www.nrcresearchpress.com by 85.192.166.187 on 09/08/12
For personal use only.

TABLE 1. The elemental analysis and ^{1}H NMR resonances for $(NH_3)_5Ru(styrene)Cl_2$ and $[(NH_3)_5Os(styrene)](CF_3SO_3)_2$ complexes

Compd no.	Anal. calcd (found) C	H	N	^{1}H NMR(D_2O)
1*A*	26.59 (26.02	6.42 6.44	19.39 19.35)	2.03 (s, 12H, *cis*-NH_3), 3.51 (d, J = 10.0 Hz, 1H, vinyl), 3.89 (s, 3H, *trans*-NH_3), 4.16 (d, J = 12.5 Hz, 1H, vinyl), 4.52 (dd, J = 1.0, 12.5 Hz, vinyl), 7.23–7.43 (m, 5H, aromatic)
2*A*	29.70 (29.78	6.98 6.91	20.79 20.54)	2.00 (s, 12H, *cis*-NH_3), 2.86 (m, 6H, $N(CH_3)_2$), 3.42 (d, J = 8.4 Hz, 1H, vinyl), 3.88 (s, 3H, *trans*-NH_3), 4.06 (d, J = 12.4 Hz, 1H, vinyl), 4.53 (dd, J = 8.4, 12.4 Hz), 7.00–7.36 (m, 4H, aromatic)
3*A*	27.62 (27.65	6.44 6.40	17.90 17.73)	1.96 (s, 12H, *cis*-NH_3), 3.40 (d, J = 8.6 Hz, 1H, vinyl), 3.76 (s, 3H, OCH_3), 3.85 (s, 3H, *trans*-NH_3), 3.99 (d, J = 12.5 Hz, vinyl), 4.51 (dd, J = 8.6, 12.5 Hz), 6.94 (d, J = 8.7 Hz, 2H, aromatic), 7.15 (d, J = 8.7 Hz, 2H, aromatic)
4*A*	28.80 (28.88	6.71 6.78	18.66 17.36)	1.90 (s, 12H, *cis*-NH_3), 2.23 (s, 3H, CH_3), 3.38 (d, J = 7.5 Hz, vinyl), 3.81 (s, 3H, *trans*-NH_3), 4.02 (d, J = 12.3 Hz, 1H, vinyl), 4.44 (dd, J = 7.5, 12.3 Hz, 1H, vinyl), 7.02 (d, J = 8.1 Hz, 2H, aromatic), 7.14 (d, J = 8.1 Hz, 2H, aromatic)
5*A*	25.33 (25.18	5.85 5.79	18.47 18.55)	2.03 (s, 12H, *cis*-NH_3), 3.52 (d, J = 8.5 Hz, 1H, vinyl), 3.94 (s, 3H, *trans*-NH_3), 4.11 (d, J = 12.2 Hz, 1H, vinyl), 4.55 (dd, J = 8.5, 12.2 Hz), 7.09–7.27 (m, 4H, aromatic)
6*A*	24.28 (24.40	5.60 5.65	17.70 17.65)	2.03 (s, 12H, *cis*-NH_3), 3.56 (d, J = 8.3 Hz, 1H, vinyl), 3.96 (s, 3H, *trans*-NH_3), 4.16 (d, J = 12.3 Hz, vinyl), 4.53 (dd, J = 8.3, 12.3 Hz, 1H, vinyl), 7.20 (d, J = 7.8 Hz, 2H, aromatic), 7.39 (d, J = 7.8 Hz, 2H, aromatic)
7*A*	21.83 (21.68	5.04 4.95	15.91 15.98)	2.01 (s, 12H, *cis*-NH_3), 3.57 (d, J = 8.0 H, 1Hz, vinyl), 3.93 (s, 3H, *trans*-NH_3), 4.16 (d, J = 10.1 Hz, vinyl), 4.48 (dd, J = 8.0, 10.1 Hz, vinyl), 7.15 (d, J = 8.1 Hz, 2H, aromatic), 7.54 (d, J = 8.1 Hz, 2H, aromatic)
8*A*	25.18 (25.22	5.17 5.25	16.32 16.40)	2.04 (s, 12H, *cis*-NH_3), 3.67 (d, J = 7.8 Hz, 1H, vinyl), 3.99 (s, 3H, *trans*-NH_3), 4.29 (d, J = 11.7 Hz, 1H, vinyl), 4.66 (dd, J = 7.8, 11.7 Hz, vinyl), 7.37 (d, J = 8.0 Hz, 2H, aromatic), 7.68 (d, J = 8.0 Hz, 2H, aromatic)
9*A*	27.98 (23.10	5.74 5.68	21.21 21.14)	2.10 (s, 12H, *cis*-NH_3), 3.71 (d, J = 7.8 Hz, 1H, vinyl), 4.04 (s, 3H, *trans*-NH_3), 4.30 (d, J = 11.8 Hz, 1H, vinyl), 4.55 (dd, J = 7.8, 11.8 Hz, 1H, vinyl), 7.61 (d, J = 8.3 Hz, 2H, aromatic), 7.72 (d, J = 8.3 Hz, 2H, aromatic)
1*B*	17.72 (17.81	3.42 3.44	10.34 10.27)	3.39 (d, J = 6.5 Hz, 1H, vinyl), 4.14 (d, J = 11.0 Hz, 1H, vinyl), 4.40 (dd, J = 6.5, 11.0 Hz, 1H, vinyl, 7.14 (d, J = 7.5 Hz, 2H, aromatic), 7.26 (t, J = 7.5 Hz, 1H, aromatic), 7.37 (d, J = 7.5 Hz, 2H, aromatic)
2*B*	20.00 (20.13	3.92 4.01	11.66 11.50)	2.99 (s, 6H, $N(CH_3)_2$), 3.35 (d, J = 6.6 Hz, 1H, vinyl), 4.07 (d, J = 10.3 Hz, 1H, vinyl), 4.39 (dd, J = 6.6, 10.3 Hz, vinyl), 7.05 (d, J = 8.5 Hz, aromatic), 7.12 (d, J = 8.5 Hz, aromatic)
3*B*	18.67 (18.74	3.56 3.63	9.90 9.72)	3.41 (d, J = 7.5 Hz, 1H, vinyl), 3.92 (s, 3H, OCH_3), 4.11 (d, J = 10.0 Hz, 1H, vinyl), 4.45 (dd, J = 7.5, 10.0 Hz, 1H, vinyl), 7.04 (d, J = 7.5 Hz, 2H, aromatic), 7.17 (d, J = 7.5 Hz, 2H, aromatic)
4*B*	19.10 (19.22	3.64 3.76	10.13 10.02)	2.23 (s, 3H, CH_3), 3.35 (d, J = 7.5 Hz, 1H, vinyl), 4.09 (d, J = 10.1 Hz, 1H, vinyl), 4.38 (dd, J = 7.5, 10.1 Hz), 7.04 (d, J = 7.7 Hz, 2H, aromatic), 7.21 (d, J = 7.7 Hz, 2H, aromatic)
5*B*	17.27 (17.25	3.19 3.24	10.07 10.01)	3.42 (d, J = 7.3 Hz, 1H, vinyl), 4.17 (d, J = 8.8 Hz, 1H, vinyl), 4.43 (dd, J = 7.3, 8.8 Hz, 1H, vinyl), 7.15 (d, J = 7.5 Hz, 2H, aromatic), 7.37 (d, J = 7.5 Hz, 2H, aromatic)
6*B*	16.86 (16.81	3.11 3.02	9.83 9.70)	3.42 (d, J = 7.7 Hz, 1H, vinyl), 4.17 (d, J = 9.8 Hz, 1H, vinyl), 4.40 (br.s. 1H, vinyl), 7.16 (d, J = 7.0 Hz, 2H, aromatic), 7.37 (d, J = 7.0 Hz, 2H, aromatic)
7*B*	15.87 (15.98	2.97 3.05	9.26 9.11)	3.42 (d, J = 7.8 Hz, 1H, vinyl), 4.18 (d, J = 9.6 Hz, 1H, vinyl), 4.43 (br.s. 1H, vinyl), 7.15 (d, J = 7.1 Hz, 2H, aromatic), 7.36 (d, J = 7.1 Hz, 2H, aromatic)
8*B*	17.93 (17.84	3.01 2.88	9.51 9.59)	3.56 (d, J = 7.3 Hz, 1H, vinyl), 4.22 (d, J = 9.6 Hz, 1H, vinyl), 4.50 (dd, J = 7.3, 9.6 Hz, 1H, vinyl), 7.65 (d, J = 8.0 Hz, 2H, aromatic), 7.74 (d, J = 8.0 Hz, 2H, aromatic)
9*B*	18.86 (18.99	3.17 3.28	12.00 12.24)	3.51 (d, J = 7.4 Hz, 1H, vinyl), 4.03 (d, J = 9.3 Hz, 1H, vinyl), 4.59 (br.s. 1H, vinyl), 7.25 (d, J = 7.5 Hz, 2H, aromatic), 7.68 (d, J = 7.5 Hz, 2H, aromatic)

Can. J. Chem. Downloaded from www.nrcresearchpress.com by 85.192.166.187 on 09/08/12
For personal use only.

TABLE 2. ^{13}C NMR resonances for $(NH_3)_5Ru(styrene)Cl_2$ complexes[a]

	ppm					
Compound	C_α	C_β	C_1	C_2	C_3	C_4
1	113.68	136.88	137.50	126.15	128.45	127.72
1*A*	59.43	75.65	144.18	128.29	132.55	129.94
Δδ	−53.85	−61.23	5.88	1.34	3.30	1.42
1*A*[b]	59.68	75.43	143.98	128.10	132.33	129.71
1*A*[c]	59.89	75.63	144.20	128.32	132.55	129.92
1*A*[d]	59.81	75.68	144.17	128.28	132.57	129.98
2	109.14	136.53	126.62	127.01	112.20	150.13
2*A*	58.38	76.02	131.55	128.96	118.43	152.90
Δδ	−50.76	−60.51	4.96	1.95	6.23	2.74
ΔΔδ	3.09	0.72	−0.95	0.61	2.93	1.32
3	111.54	136.31	130.48	127.43	113.96	159.45
3*A*	58.82	75.54	136.19	129.30	117.71	160.51
Δδ	−52.72	−60.77	5.71	1.87	3.75	1.06
ΔΔδ	1.13	0.46	−0.17	0.53	0.45	−0.36
4	112.63	136.72	134.79	126.06	129.16	137.51
4*A*	59.11	75.55	140.60	127.96	132.81	139.89
Δδ	−53.53	−61.18	5.81	1.89	3.65	2.38
ΔΔδ	0.33	0.05	−0.07	0.55	0.35	0.96
5	113.35	135.70	133.72	127.68	115.32	162.45
5*A*	59.55	74.50	139.86	129.56	119.29	164.38
Δδ	−53.80	−61.25	6.14	1.87	3.97	1.93
ΔΔδ	0.05	−0.02	0.26	0.57	0.67	0.51
6	114.32	135.59	135.96	127.35	128.58	133.36
6*A*	59.84	74.29	142.90	129.37	132.18	134.55
Δδ	−54.48	−61.30	6.94	2.02	3.60	1.19
ΔΔδ	−0.63	−0.07	1.06	0.68	0.30	−0.23
7	114.51	135.67	136.36	127.69	131.53	121.53
7*A*	59.72	74.12	143.40	129.63	134.91	122.30
Δδ	−54.78	−61.55	7.03	1.94	3.38	0.77
ΔΔδ	−0.93	−0.32	1.15	0.60	0.08	−0.65
8	116.35	135.64	140.98	126.37	125.46	130.43
8*A*	60.76	73.76	149.96	128.31	129.28	130.68
Δδ	−55.59	−61.88	8.99	1.94	3.82	0.25
ΔΔδ	−1.73	−0.65	3.11	0.60	0.52	−1.17
9	118.16	135.73	142.25	127.18	132.73	111.38
9*A*	60.70	73.49	148.88	128.26	136.21	113.37
Δδ	−57.27	−62.05	6.63	1.08	3.48	1.99
ΔΔδ	−3.42	−0.83	0.75	−0.26	0.12	0.57

[a]Resonances measured in D_2O at 25°C with NaTPMS as internal reference. Concentration of complexes: 0.22 mM. Δδ represent the shifts from free styrenes to chelated styrenes. Negative values indicate upfield shifts. ΔΔδ represent the difference in Δδ from unsubstituted styrene system.

[b]Concentration of **1***A*: 0.44 mM.

[c]Concentration of **1***A*: 0.66 mM.

[d]The complex was isolated as salt containing PF_6^-. Their chemical shifts of 25.9, 81.5, and 150.3 ppm were assigned for C_α, C_β, and C_1, respectively, with *p*-dioxane as internal reference (66.5 ppm).

The electron-donor groups enhance the electron density of vinyl group through the phenyl ring so as to resist the back-bonding from metal. Figure 1 illustrates the correlation between this dependency and the Hammett substituent constant (σ_p). An inflection apparently arises in the correlation lines with slopes −4.620 (r = 0.9448) and −1.218 (r = 0.9408) for C_β and C_α, respectively. When a substituent is changed, C_β shows a change in chemical shift with a higher sensitivity than C_α, indicating a preferential coordination of the metal centers to the *exo* vinyl substituents of the styrene rather than ring coordination, as stated previously by Shepherd et al. (2). This fact resembles that of anionic Pt–styrene compound series (4). On the Os complexes, for the same substituent the ΔΔδ of C_α and C_β varies from +4.01 to −3.53 ppm, and from −5.34 to +2.74 ppm, respectively (Table 3). The correlation between C_α and C_β on ΔΔδ and resonance parameter (σ^+, σ^-) shows slopes of −2.8777 (r = 0.9773) and +3.1596 (r = 0.9807), respectively (Fig. 2). The σ+ or σ− parameters are used for a better correlation with ΔΔδ indicating that the resonance effects are important for the Os series (10). This phenomenon is similar to that

Can. J. Chem. Downloaded from www.nrcresearchpress.com by 85.192.166.187 on 09/08/12
For personal use only.

Can. J. Chem. Downloaded from www.nrcresearchpress.com by 85.192.166.187 on 09/08/12
For personal use only.

TABLE 3. ^{13}C chemical shifts for $(NH_3)_5Os(styrene)CF_3SO_3)_2$ in D_2O (ppm from NaTPMS as internal standard)[a]

	ppm					
Compound	C_α	C_β	C_1	C_2	C_3	C_4
1	113.68	136.88	137.50	126.15	128.45	127.72
1*B*	39.76	54.14	147.30	132.29	127.47	128.02
Δδ	−73.92	−82.74	9.80	6.14	−0.98	0.30
2	109.14	136.53	126.62	127.01	112.20	150.13
2*B*	39.23	48.45	132.00	128.28	120.13	143.15
Δδ	−69.91	−88.08	5.38	1.27	7.93	−6.62
ΔΔδ	4.01	−5.34	−4.42	−4.87	8.91	−6.92
3	111.54	136.31	130.48	127.43	113.96	159.45
3*B*	38.08	53.52	139.17	128.52	117.74	153.25
Δδ	−73.46	−82.79	8.69	1.09	3.78	−6.20
ΔΔδ	0.46	−0.05	−1.11	−5.05	4.76	−6.50
4	112.63	136.72	134.79	126.06	129.16	137.51
4*B*	38.84	53.80	143.79	127.42	132.75	129.60
Δδ	−73.79	−82.92	8.96	1.36	3.59	−7.91
ΔΔδ	−0.13	0.18	−0.84	−4.78	4.57	−8.21
5	113.35	135.70	133.72	127.68	115.32	102.45
5*B*	39.69	53.05	142.70	127.85	118.60[b]	[c]
Δδ	−73.66	−80.65	8.98	0.17	3.28	
ΔΔδ	0.26	0.08	−0.82	−5.97	4.26	
6	114.32	135.59	135.96	127.35	128.58	133.36
6*B*	39.53	53.61	142.81	127.39	132.14	129.91
Δδ	−74.79	−81.98	6.85	0.04	3.56	−3.45
ΔΔδ	−0.87	0.76	−2.96	−6.10	4.54	−3.75
7	114.51	135.67	136.36	127.69	131.53	121.53
7*B*	39.81	54.09	149.54	127.41	132.14	128.31
Δδ	−74.70	−81.58	13.18	−0.28	0.61	6.78
ΔΔδ	−0.94	1.16	3.38	−6.42	1.59	6.48
8	116.35	135.64	140.98	126.37	125.46	130.43
8*B*	39.75	55.46	148.02	127.41	127.96	132.17
Δδ	−76.60	−80.18	7.04	1.04	2.50	1.74
ΔΔδ	−2.68	2.55	−2.76	−5.10	3.48	1.44
9	118.16	135.73	142.25	127.18	132.73	111.38
9*B*	40.71	55.73	146.64	127.64	135.92	114.14
Δδ	−77.45	−80.00	4.39	0.46	3.19	2.76
ΔΔδ	−3.53	2.74	−5.41	−5.68	4.17	2.44

[a]Resonance measure in D_2O at 25°C with NaTPMS as the internal reference. Concentration of analyte: 0.11 mM.
[b]J = 23.3 Hz.
[c]Too weak to assign.

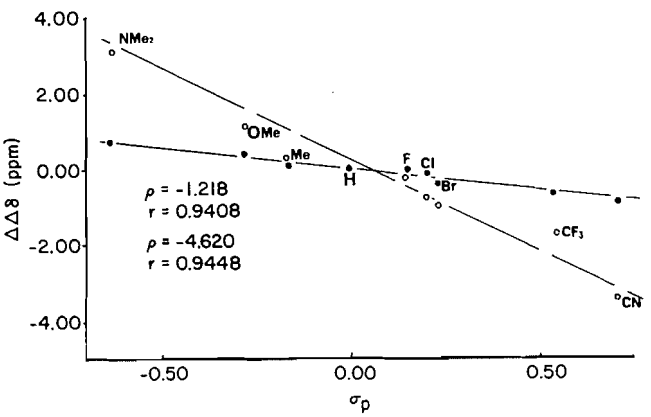

FIG. 1. ^{13}C SCS(α)(○), SCS(β)(●) values in ppm for $(NH_3)_5Ru(styrene)Cl_2$ vs. Hammett substituent constants (σ_p).

shown by neutral and cationic Pt–styrene complexes (4). The σ^+ and σ^- values are larger than that from ethylbenzenes (11) ethenylbenzenes (12). No significant change in chemical shifts is observed from varying concentrations of the analyte **1*A***, suggesting that no change in the dissociation of the ligand (styrene or NH_3) polarizability occurs in this series. Furthermore, no $\eta^2 \rightarrow \eta^4$ interconversion is observed as in (styrene)-Fe(dfepe)$(CO)_2$ (13).

Electrochemical methods are widely used in the study of organometallic compounds to understand their bonding patterns and chemistry. The oxidation potential for a specific electroactive species is expected to be related to their electron density as modulated by metal complexation. Ligands with a higher electron-donating nature would enhance the electron density of metal and lower the oxidation potential. The phenyl ring is capable of transmitting the electron cloud from the substituent

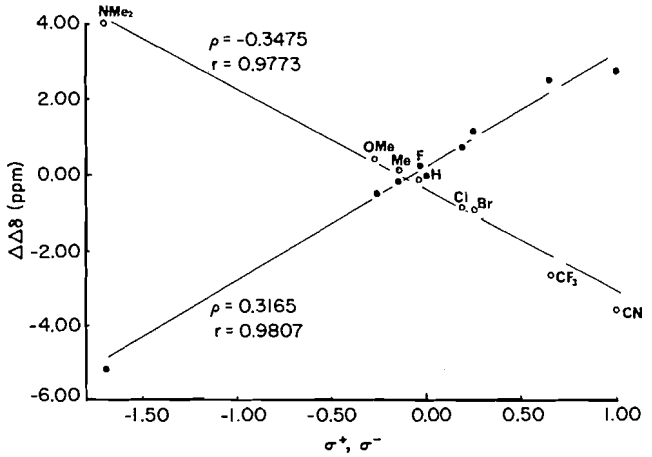

FIG. 2. ^{13}C SCS(α)(○), SCS(β)(●) values in ppm for $[(NH_3)_5Os(styrene)](CF_3SO_3)_2$ vs. Hammett substituents (σ^+, σ^-). The requirement of σ^+, σ^- parameter to obtain a better correlation infers that the resonance mechanism dominates the substituent effect on the bonding between Os and styrenes (10).

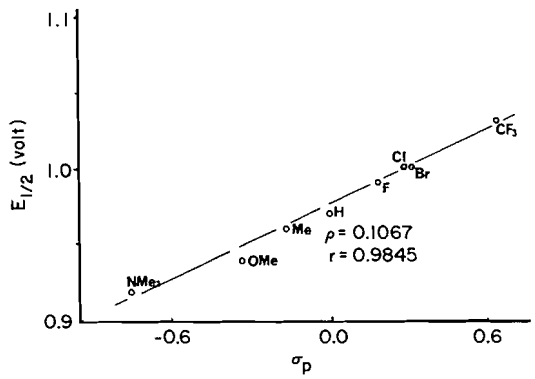

FIG. 3. Oxidation potential $E_{1/2}$ values in volt for $(NH_3)_5Ru(styrene)Cl_2$ vs. Hammett substituent constants (σ_p).

TABLE 4. $E_{1/2}$ values for $(NH_3)_5Ru(styrene)^{3+/2+}$ (**A**) and $(NH_3)_5Os(styrene)^{3+/2+}$ (**B**) complexes

	$E_{1/2}$, V	
Styrene	**A**	**B**
H	0.97	0.49
4-NMe_2	0.92	−0.10
4-OMe	0.94	0.46
4-Me	0.96	0.47
4-F	0.99	0.50
4-Cl	1.00	0.51
4-Br	1.00	0.58
4-CF_3	1.03	0.67
4-CN	0.72	0.61

to the vinyl group in this series of complexes. Therefore, the oxidation potentials of styrene–Ru and styrene–Os should be substituent dependent.

Some electrochemical studies dealing with Ru–styrene and Os–styrene complexes have been previously reported (2). Our results are similar to those found in literature (2). The ruthenium complex exhibits a quasi-reversible $Ru^{3+/2+}$ redux couple at +0.98 V vs. NHE. The osmium complex exhibits reversible redox behavior with $Os^{3+/2+}$ potential of 0.49 V vs. NHE. The $E_{1/2}$ values of series styrenes complexed with either Ru^{2+} or

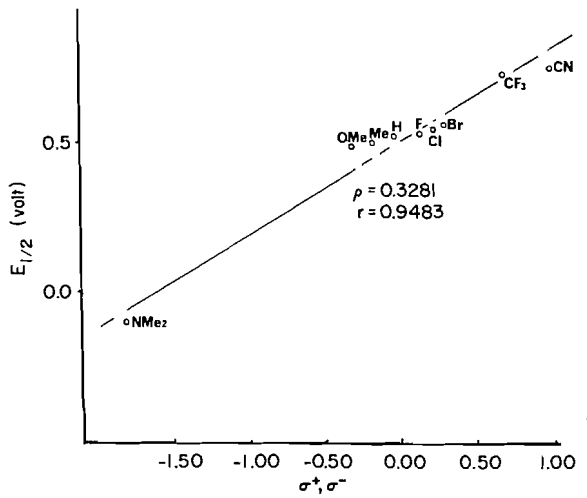

FIG. 4. Oxidation potential $E_{1/2}$ values in volts for $[(NH_3)_5Os(styrene)](CF_3SO_3)_2$ vs. Hammett substituent constant (σ^+, σ^-).

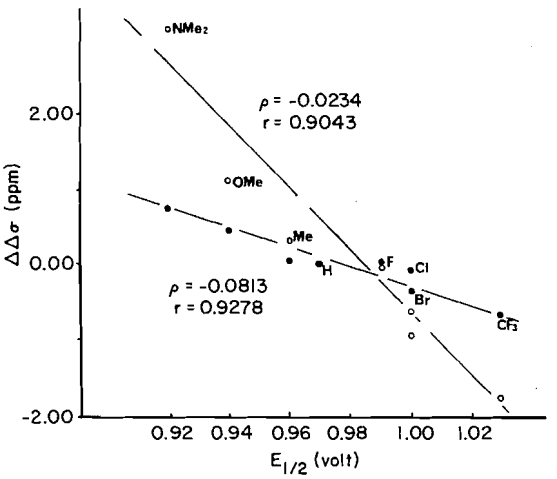

FIG. 5. ^{13}C SCS(α)(○), SCS(β)(●) values in ppm for $(NH_3)_5Ru(styrene)Cl_2$ vs. oxidation potential $E_{1/2}$ in volt.

Os^{2+} are listed in Table 4. The $E_{1/2}$ values in our study vary from +0.92 to +1.03 V and −0.1 to 0.67 V for Ru-, and Os-complexes in the study as the substituent changes from electron-donating character group (NMe_2) to electron-withdrawing group (CF_3). These $E_{1/2}$ values correlate well with the Hammett substituent constant σ corresponding to a slope of 0.1067 (r = 0.9845) and 0.3281 (r = 0.9483) for Ru^{2+} and Os^{2+}, respectively (Figs. 3, 4). The large ρ value indicates that the binding between metal–styrene is more substituent dependent. The correlation between the ΔΔδ and the $E_{1/2}$ are also shown in Figs. 5 and 6. The ΔΔδ of C_α and C_β shows the same correlation relationships with $E_{1/2}$ for Ru series; meanwhile the ΔΔδ of $C_{(\alpha)}$ and C_β displays different relationships with $E_{1/2}$ in the case of Os.

The differences in the substituent dependencies between ruthenium and osmium complexes infer the various fashions in bonding between styrene with ruthenium and osmium. The C_α and C_β display the same substituent dependency implying that both carbons bind with Ru, with back-bonding from the metal influenced by the substituent on the phenyl ring. In the case of Os, while the same substituent dependence on C_α infer that the bonding between C_α and Os is the same as their Ru counterpart. The difference in substituent dependency for C_β suggests

Can. J. Chem. Downloaded from www.nrcresearchpress.com by 85.192.166.187 on 09/08/12
For personal use only.

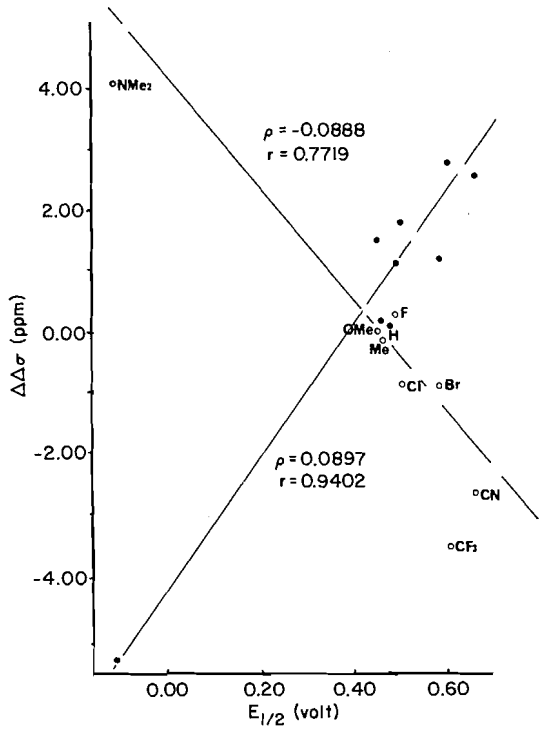

FIG. 6. ^{13}C SCS(α)(○), SCS(β)(●) values in ppm for $[(NH_3)_5Os(styrene)](CF_3SO_3)_2$ vs. oxidation potential $E_{1/2}$ in volt.

another type of interaction between C_β and Os. This interaction is consistent with the previous reports (2) in which a vinyl and an allyl type bonding for the Ru and Os complexes of olefine are proposed. The difference in bonding between the vinylic ligand and metal for Os(II) or Ru(II) is observed in this work by ^{13}C NMR variation in C_α or C_β upon changing of the substituents of the phenyl ring.

Experimental section

Styrenes were obtained either commercially or prepared from the corresponding benzaldehyde via the Wittig reaction (14) $[Ru(NH_3)_5Cl]Cl_2$ and $(NH_4)_2[OsCl_6]$ were obtained from Aldrich Co. $[Ru(NH_3)_5Cl]Cl_2$ (15), $[Ru(NH_3)_5(styrene)]Cl_2$ (2), $[Os(NH_3)_5\text{-}N_2]Cl2$ (16), $[Os(NH_3)_5(tfms)](tfms)_2$ (17), and $[Os(NH_3)_5(styrene)]\text{-}(tfms)_2$ (2) were prepared according to literature.

The ^{13}C NMR data of 0.22 mM of analyte in D_2O were recorded on a Bruker AC-250 spectrometer at 62.9 MHz; 128 K data points were collected within a range of 12 kHz. All chemical shifts were measured relative to NaTMPS in proton–noise decoupled spectra.

Electrochemical studies were performed on an EG&G Princeton Applied Research Model 362, operating in the cyclic voltammetry mode. A glassy-carbon working electrode, potassium chloride calomel electrode (SSCE) as reference, and a Pt-wire auxilliary electrode were employed. The $E_{1/2}$ values were obtained at 4.03×10^{-4} M in 0.1 F NaCl solution with a scan rate of 50 mV/s, $t = 25°C$.

Acknowledgment

We thank the National Science Council of the Republic of China for financial support.

1. W.D. Harman, D.P. Fairlie, and H. Taube. J. Am. Chem. Soc. **108**, 8223 (1986).
2. M.G. Elliott, S. Zhang, and R.E. Shepherd. Inorg. Chem. **28**, 3036 (1989).
3. E. Ban, R.P. Hughes, and J. Powell. J. Organomet. Chem. **69**, 455 (1974).
4. D.G. Cooper, and J. Powell. Inorg. Chem. **15**, 1959 (1976).
5. H. Kurosawa and N. Asada. J. Organomet. Chem. **217**, 259 (1981).
6. H. Kurodsawa, A. Urabe, and M. Emoto. J. Chem. Soc. Dalton Trans. 891 (1986).
7. (*a*) W.D. Harman and H. Taube. J. Am. Chem. Soc. **110**, 7555 (1988); (*b*) D.J. Brauer and C. Kruger. Inorg. Chem. **16**, 884 (1977).
8. (*a*) R.H. Kohler and W.F. Reynolds. Can. J. Chem. **55**, 530 (1977); (*b*) M.J. Arnoey, K.E. Calderband, and H.J. Stootman. J. Chem. Soc. Perkin, Trans. 2, 2060 (1973).
9. (*a*) W.F. Reynolds, R.H. Kohler, and G.K. Hamer. Tetrahedron Lett. 4671 (1976); (*b*) C. Dell'Erba, F. Sancassen, M. Novi, G. Petrillo, A. Mugnoli, D. Spinelli, G. Consiglio, and P. Latti. J. Org. Chem. **53**, 3564 (1988).
10. C. Hansch, A. Leo, and R.W. Taft. Chem. Rev. **91**, 165 (1991).
11. L.F. Blackwell, P.D. Buckley, and K.W. Jolley. Aust. J. Chem. 29, 2423 (1976).
12. Y. Kusuyama, C. Dyllick-Brenzinger, and J.D. Roberts. Org. Magn. Reson. 13, 372 (1980).
13. M. Brookhart, W.A. Chandler, A.C. Pfister, C.C. Santini, and P.S. White. Organometallics, **11**, 1263 (1992).
14. E. Vedejs, G.P. Meier, and K.A. Snoble. J. Am. Chem. Soc. **103**, 2823 (1981).
15. W.W. Henderson and R.E. Shepherd. Inorg. Chem. **24**, 2398 (1985).
16. S. Siddiqui, W.W. Henderson, and R.E. Shepherd. Inorg. Chem. **26**, 3101 (1987).
17. N.E. Dixon, G.A. Lawrance, P.A. Lay, and A.M. Sargeson. Inorg. Chem. **23**, 1851 (1984).

Can. J. Chem. Downloaded from www.nrcresearchpress.com by 85.192.166.187 on 09/08/12
For personal use only.

Crystal structure – reactivity correlations in the solid state photochemistry of *N*-(*tert*-butyl)succinimide

TAI Y. FU, JOHN R. SCHEFFER,[1] AND JAMES TROTTER

Department of Chemistry, University of British Columbia, 2036 Main Mall, Vancouver, BC V6T 1Z1, Canada

Received January 25, 1994

TAI Y. FU, JOHN R. SCHEFFER, and JAMES TROTTER. Can. J. Chem. **72**, 1952 (1994).

In order to provide experimental evidence on the stereoelectronic requirements for intramolecular hydrogen atom abstraction by carbonyl oxygen, *N*-(*tert*-butyl)succinimide, **1**, was investigated by the crystal structure – reactivity correlation method. In this method, the success or failure of a given reaction in the crystalline state is correlated with the geometric parameters associated with the process as determined by X-ray crystallography. In the case of *N*-(*tert*-butyl)succinimide, the crystal and molecular structure shows that the molecule adopts a conformation in which there are very close contacts (d = 2.17–2.24 Å) between the carbonyl oxygen atoms and certain γ-hydrogen atoms on the *tert*-butyl group. In accord with these close contacts, ultraviolet irradiation of *N*-(*tert*-butyl)succinimide in the crystalline state leads to transfer of one of the γ-hydrogen atoms from carbon to oxygen. This produces a 1,4-biradical which closes to form a cyclobutanol, and the cyclobutanol undergoes ring opening to afford the final stable product, tetrahydro-1*H*-azepine-2,5-dione, **2**. The crystal and molecular structure of photoproduct **2** is also reported. In contrast to many solid state transformations, there was no discernable melting of the crystals during reaction, and complete conversions of **1** into **2** could be achieved. The isolated chemical yield of photoproduct **2** from the solid state reaction (79%) is in fact considerably higher than that reported by Kanaoka and Hatanaka for the corresponding solution phase process (49%). This permitted the solid state reaction to be followed to 100% conversion by X-ray powder diffractometry, which showed that the process is a single crystal-to-polycrystalline transformation involving a regular and progressive conversion of **1** into **2** with no obvious diffraction peaks that might be attributable to the intermediate cyclobutanol.

TAI Y. FU, JOHN R. SCHEFFER et JAMES TROTTER. Can. J. Chem. **72**, 1952 (1994).

On a utilisé la méthode de corrélation structure-réactivité du cristal dans le but d'obtenir des preuves expérimentales des conditions stéréoélectroniques nécessaires pour l'abstraction intramoléculaire d'un atome d'hydrogène par l'oxygène du carbonyle de la *N*-(*tert*-butyl)succinimide, **1**. Dans cette méthode, le succès ou l'échec d'une réaction donnée dans l'état cristallin est relié aux paramètres géométriques associés au processus réactionnel tels que déterminés par cristallographie de rayons X. Dans le cas de la *N*-(*tert*-butyl)succinimide, la structure cristalline et moléculaire montre que la molécule adopte une conformation dans laquelle les atomes d'oxygène du carbonyle se rapprochent de très près (d = 2,17–2,24 Å) de certains des atomes d'hydrogène en position du groupe *tert*-butyle. Conformément à ces rapprochements étroits, l'irradiation ultraviolette de la *N*-(*tert*-butyl)succinimide à l'état cristallin conduit au transfert d'un des atomes d'hydrogènes en position γ de l'atome de carbone vers l'atome d'oxygène. Ce transfert donne un biradical-1,4 qui par cyclisation conduit au cyclobutanol, et le cyclobutanol par ouverture du cyle conduit au produit final stable la tétrahydro-1*H*-azépine-2,5-dione, **2**. On rapporte également la structure cristalline et moléculaire du produit photochimique **2**. Contrairement à beaucoup de transformations à l'état solide, on n'a pas observé la fusion des cristaux pendant la réaction et on a pu réaliser la transformation complète du composé **1** en composé **2**. Le rendement en produit photochimique **2** isolé à partir de la réaction en phase solide (79%) est en fait considérablement plus élevé que celui rapporté par Kanaoka et Hatanaka pour la réaction correspondante en solution (49%). Ce qui permet de suivre la réaction en phase solide jusqu'à sa transformation à 100% par diffraction de rayons X des poudres laquelle révèle que le processus est la transformation d'un monocristal en un polycristal faisant intervenir une transformation régulière et progressive du composé **1** en composé **2** sans la présence évidente de pics que l'on pourrait attribuer à un intermédiaire cyclobutanol.

[Traduit par la rédaction]

Introduction

One of the goals of our research in solid state organic photochemistry has been to delineate the stereoelectronic requirements for intramolecular hydrogen atom abstraction by carbonyl oxygen. The most widely known general reaction that involves such a process is the photochemical Norrish type II reaction of ketones containing accessible γ-hydrogen atoms (1). Following n,π* excitation of such compounds, the γ-hydrogen atom is transferred from carbon to oxygen through a six-membered transition state, and the resulting 1,4-biradical can revert to starting material or react further to give one or more stable products.

Despite extensive work on the details of this synthetically and mechanistically important reaction, direct experimental evidence on the preferred geometry for the hydrogen atom transfer step is rare. This stems from the fact that most studies have been carried out on conformationally mobile systems for which the exact geometric disposition of the atoms involved in the six-membered transition state is not known. Leaving aside for the moment the important question of ground state versus excited state geometry, if one could establish ground state geometric guidelines for successful hydrogen atom abstraction, one could hope to make the Norrish type II reaction and other similar intramolecular hydrogen abstraction processes predictable through MM2-type force field calculations.

Our approach to this problem has been to study the hydrogen abstraction reactions in the *solid state* and to correlate the success or failure of the reactions with the geometric parameters as determined by X-ray crystallography, the so-called crystal structure – reactivity correlation method. The advantage of this approach is that the ketone reactants are locked in well-defined conformational minima in the solid state for which the intramolecular C=O···Hγ geometry can be accurately measured. A review article summarizing some of our initial results in this area has been published (2).

In this paper we report an application of the crystal structure – reactivity correlation method to the hydrogen abstraction reaction of *N*-(*tert*-butyl)succinimide **1** (Scheme 1). This compound was chosen because it is crystalline and is known to

[1]Author to whom correspondence may be addressed.

Can. J. Chem. Downloaded from www.nrcresearchpress.com by 85.192.166.187 on 09/08/12
For personal use only.

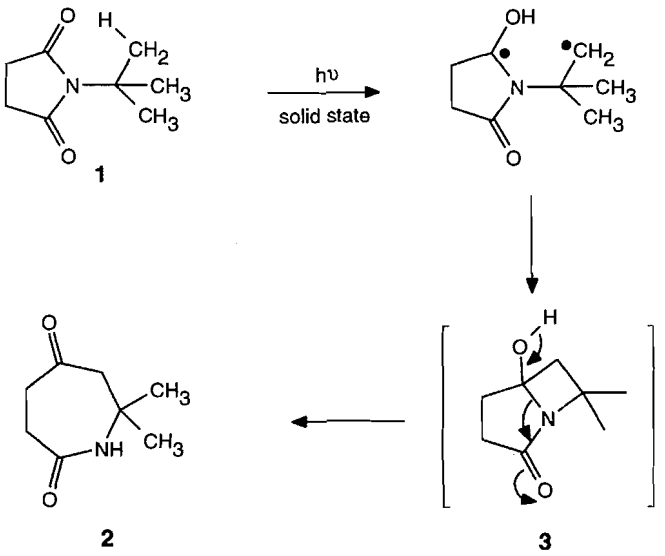

SCHEME 1

undergo a Norrish type II-like photorearrangement in solution (3). A further consideration was that, because the molecule has nine γ-hydrogen atoms, it seemed virtually certain that one or more of them would be located favorably for abstraction in the solid state, regardless of the conformation adopted by the molecule in the crystal.

Experimental

Melting points were taken on a Fisher Johns melting point apparatus and are uncorrected. Infrared spectra were recorded on a Perkin-Elmer 1710 Fourier transform spectrophotometer, and the X-ray powder diffraction measurements were carried out on a Rigaku Geigerflex PMG-VH diffractometer using Ni-filtered Cu-Kα radiation (λ = 1.54184 Å), scan range $5° \leq 2\theta \leq 50°$. Gas chromatographic analyses were performed on a Hewlett-Packard 5890 capillary instrument fitted with a 15 m DB-1 column, flame ionization detector and 3392A integrator. *N*-(*tert*-butyl)succinimide, **1**, was prepared according to the procedure of Schreiber and Fernandez (4) and recrystallized from hexane to afford prisms, mp 44°C (lit. (4) mp 49–50°C).

Photolysis of N-(tert-*butyl)succinimide* ***1*** *in the solid state*

N-(*tert*-Butyl)succinimide, **1** (1.00 g, 6.5 mmol), was ground into a fine powder by means of an agate mortar and pestle and then distributed in a thin layer between two quartz plates. The plates were sealed inside a nitrogen-filled polyethylene bag and irradiated by using a 12 W Canrad-Hanovia low pressure mercury lamp available from Ace Glass, Inc. At intervals, powder diffraction and gas chromatographic analyses were taken of the reaction mixture, the results of which are shown in Figs. 1 and 2. After 12 h, reaction was complete and the product was chromatographed on silica gel (eluting solvent 10% acetone in hexanes) to afford 0.79 g (79%) of tetrahydro-1*H*-azepine-2,5-dione, **2**. The material thus obtained was recrystallized from acetone to afford plates, mp 174.5–175.5°C (lit. (3) mp 175–176°C).

X-ray crystallographic analyses of N-(tert-*butyl)succinimide,* ***1****, and tetrahydro-1*H*-azepine-2,5-dione,* ***2***

Crystallographic data for compounds **1** and **2** appear in Table 1. The final unit-cell parameters were obtained by least-squares on the setting angles for 23 reflections with $2\theta = 7.9–19.8°$ for **1** and 17 reflections with $2\theta = 89.7–105.8°$ for **2**. The data for **1** and **2** were processed,[2] corrected for Lorentz and polarization effects. A linear decay correction was applied for **2** based on the intensities of three standard reflections, measured every 200 reflections throughout the data collection. Absorption (empirical, based on azimuthal scans for three reflections) correction was also applied for **2**. No decay or absorption corrections were applied for **1**.

Structure analyses of **1** and **2** were initiated in the space groups $P2_1/n$ and $P2_1/c$ respectively on the basis of *E*-statistics, the choices being confirmed by subsequent successful solutions and refinements of the structures. The asymmetric unit of **1** contains two molecules. The structures were solved by direct methods, the non-hydrogen atoms being determined from *E*-maps or from subsequent difference Fourier synthesis. The non-hydrogen atoms were refined with anisotropic thermal parameters. The amide hydrogen atom, H(13), in **2** was refined with isotropic thermal parameters. All the other hydrogen atoms in **1** and **2** were fixed in idealized positions (C—H = 0.95 Å, $B_H = 1.2B_{\text{bonded atom}}$). Corrections for secondary extinction were applied for both structures, the final values of the extinction coefficients being 7.39×10^{-7} for **1** and 1.37×10^{-5} for **2**. Neutral atom scattering factors for all atoms and anomalous dispersion corrections for the non-hydrogen atoms were taken from the International tables for X-ray crystallography (5). Final atomic coordinates and equivalent isotropic thermal parameters, bond lengths, and angles appear in Tables 2–4, respectively. Hydrogen atom parameters, anisotropic thermal parameters, torsion angles, intermolecular contacts, least-squares planes, and measured and calculated structure factor amplitudes for both structures are included as supplementary material.[3]

Results and discussion

The first study of the photochemistry of *N*-(*tert*-butyl)succinimide **1** was by Kanaoka and Hatanaka in 1976 (3). They reported that irradiation of this compound at 2537 Å in acetonitrile solution leads to a 49% yield of ketolactam **2** and suggested that the reaction involves a Norrish type II γ-hydrogen abstraction, Yang cyclization of the resulting 1,4-biradical to give cyclobutanol **3** (not isolated), and ring opening of **3** to afford **2** (Scheme 1). Similar results were obtained for a number of other succinimide derivatives.

Our first task was to ascertain whether the same reaction can be induced photochemically in the solid state. It can. Crystals of *N*-(*tert*-butyl)succinimide **1**, mp 44°C from hexane, $n \rightarrow \pi^*$ UV $\lambda_{\text{shoulder}}$(MeCN) = 242 nm (ε 112), were irradiated in a Rayonet reactor at 2537 Å under nitrogen. When carefully grown, transparent single crystals of **1** were photolyzed, the extent of conversion to photoproduct **2** (as indicated by gas chromatography) leveled off at approximately 60%, and continued irradiation led to little additional product. The crystals did not change in appearance except for the development of an overall light yellow tinge and an opaque center; no melting was detectable. Gas chromatographic analysis of the crystals indicated a very clean reaction with compound **2** as the only photoproduct. As it seemed likely that the limiting conversion was due to a surface reaction that screens the interior of the crystal, the crystals were ground in a mortar and pestle and photolyzed as a finely divided powder dispersed between two quartz plates. Under these conditions, complete conversions of **1** to **2** could be achieved, and photoproduct **2** could be isolated in 79% yield

[2]TEXSAN/TEXRAY structure analysis package which includes versions of the following: DIRDIF, direct methods for difference structures, by P.T. Beurskens; ORFLS, full-matrix least-squares, and ORFFE, function and errors, by W.R. Busing, K.O. Martin and H.A. Levy; ORTEP II, illustrations by C.K. Johnson.

[3]Supplementary material mentioned in the text may be purchased from The Depository of Unpublished Data, Document Delivery, CISTI, National Research Council, Canada, Ottawa, Canada K1A 0S2.

Tables of hydrogen atom coordinates and bond lengths and angles involving hydrogen atoms have also been deposited with the Cambridge Crystallographic Data Centre and can be obtained on request from The Director, Cambridge Crystallographic Data Centre, University Chemical Laboratory, 12 Union Road, Cambridge CB2 1EZ, U.K.

Can. J. Chem. Downloaded from www.nrcresearchpress.com by 85.192.166.187 on 09/08/12
For personal use only.

Can. J. Chem. Downloaded from www.nrcresearchpress.com by 85.192.166.187 on 09/08/12
For personal use only.

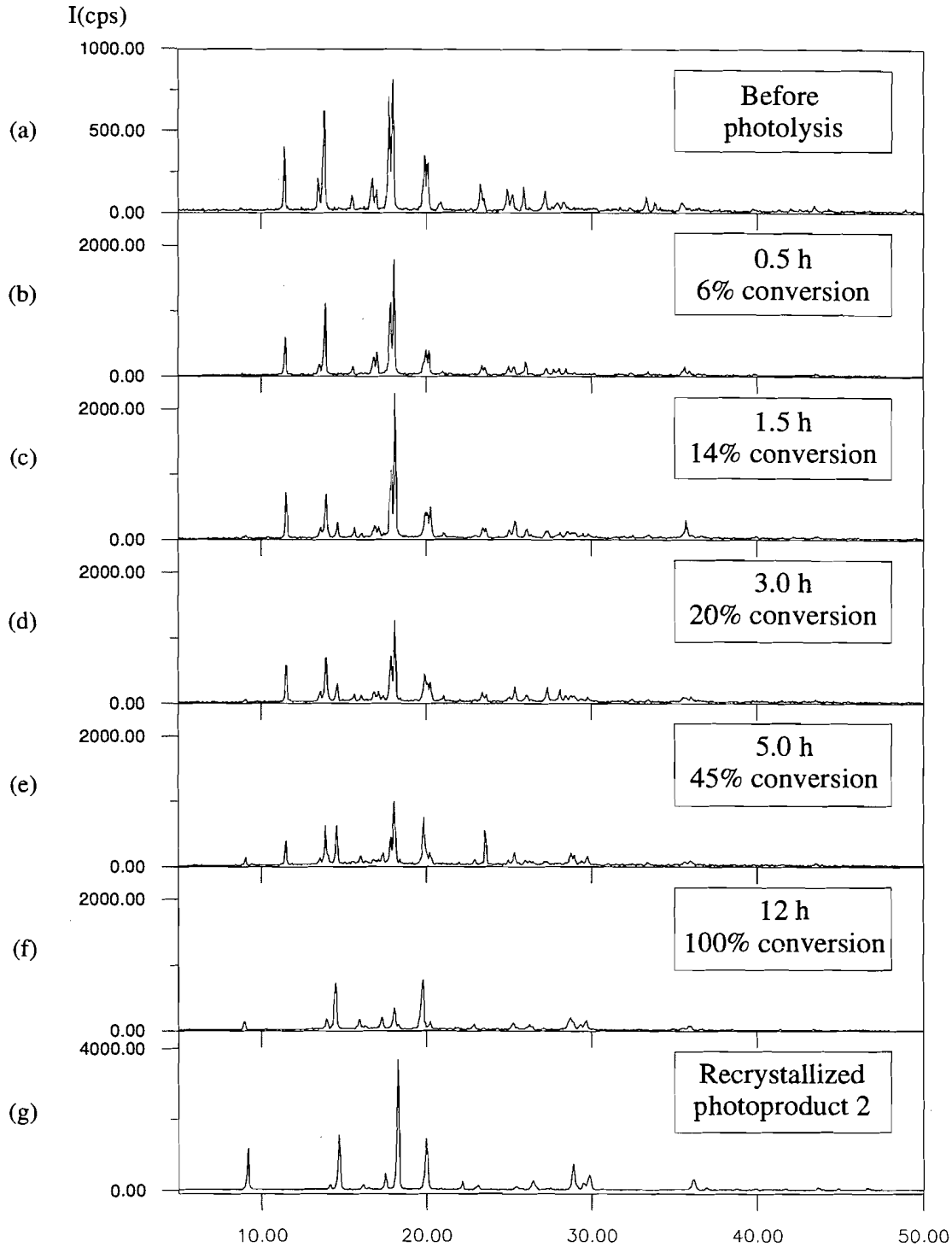

FIG. 1. X-ray powder diffraction pattern at different stages of photolysis of compound **1** ($5° \leq 2\theta \leq 50°$).

following column chromatography to remove traces of the unknown yellow material. The solid state chemical yield is considerably higher than the reported solution phase yield of 49%. Microscopic examination of the polycrystalline sample following complete conversion runs revealed that the majority of the crystallites remained transparent (albeit slightly yellow) with no evidence of melting.

Concomitant with the chemical studies, single crystal X-ray diffraction studies of *N*-(*tert*-butyl)succinimide, **1**, were undertaken. In order to confirm its structure as well as to be able to interpret the X-ray powder diffraction data (vide infra), the X-ray single crystal structure of photoproduct **2** was also determined. Figure 3 shows the results of these investigations. Compound **1** crystallizes in space group $P2_1/n$ with two independent molecules in the asymmetric unit, only one of which is shown in Fig. 3; the other has a very similar (but not identical) conformation. Photoproduct **2** crystallizes in space group $P2_1/c$ with one molecule per asymmetric unit. Details of the crystal structure determinations are given in the Experimental section.

Careful examination of the crystal structure of **1** reveals the

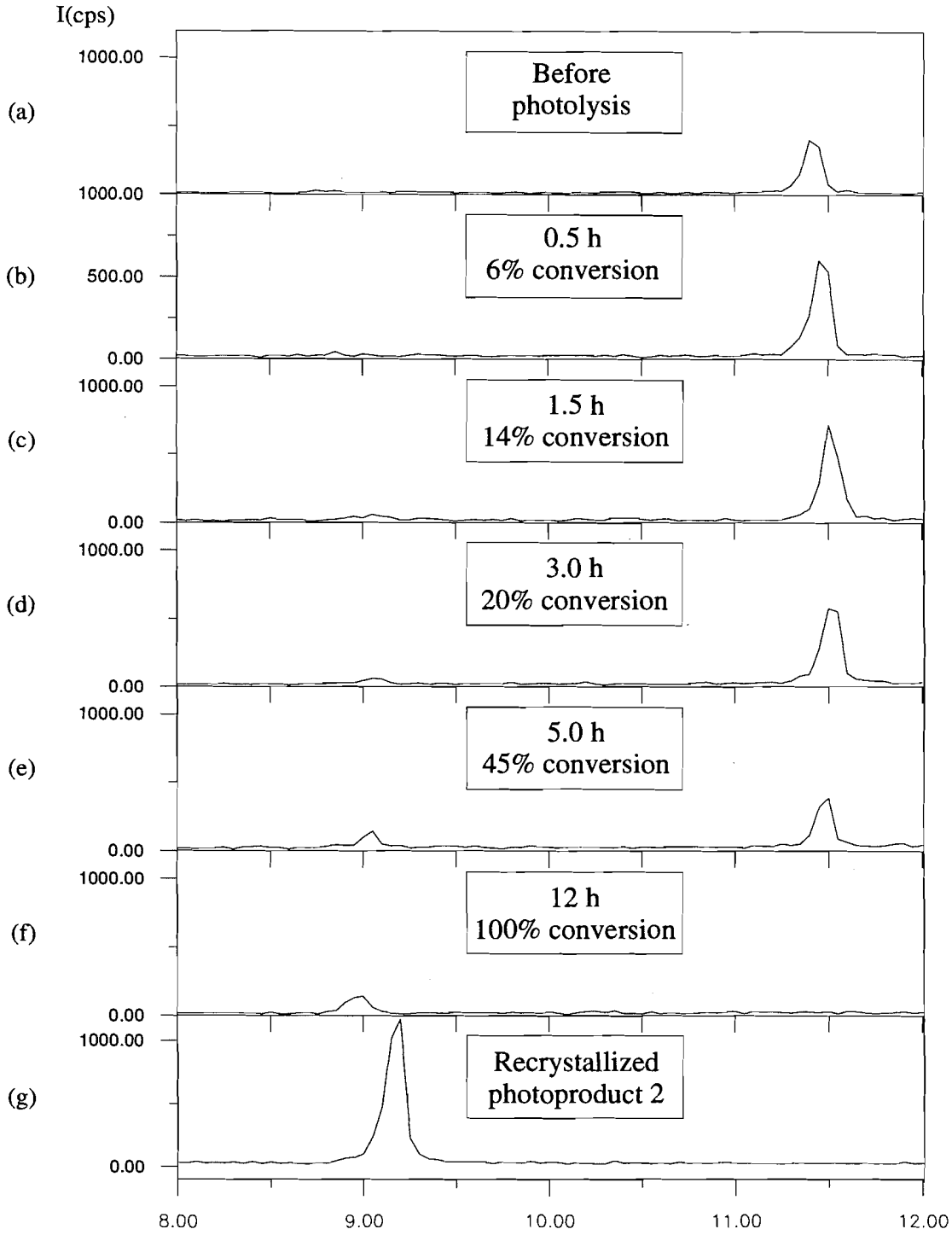

FIG. 2. X-ray powder diffraction pattern at different stages of photolysis of compound **1** ($8° \leq 2\theta \leq 12°$).

approximate planarity of the imide moieties: O1—C1—N1—C4 = 172.8(7)° and O2—C4—N1—C1 = 168.1(6)° (independent molecule 1); O3—C9—N2—C12 = −167.4(6)° and O4—C12—N2—C9 = 166.3(6)° (independent molecule 2). The imide C—N bond lengths are found to be around 1.4 Å and are longer than a normal amide C—N bond distance (1.32 Å). The introduction of an additional carbonyl group clearly results in a decrease in delocalization of the amide nitrogen lone pair. Such an effect has been suggested to be important in the photoreactivity of imides in hydrogen abstraction reactions (6). The crystal structure of photoproduct **2** shows that the amide hydrogen and the ketone carbonyl are held together by intermolecular H bonding: O(1)...H(13) = 2.14 Å; O(1)...N(1) = 2.95 Å.

With the photochemical and crystallographic results in hand, we are now ready to correlate the two in terms of the hydrogen abstraction geometry. As shown in Fig. 4, intramolecular hydrogen atom abstraction may be characterized geometrically by four parameters: d, the C═O···Hγ abstraction distance; ω, the degree to which the abstracted hydrogen atom lies outside the mean plane of the carbonyl group; Δ, the C═O···Hγ angle; and θ, the C—H···O angle (1, 2).

The crystallographically-determined values of these four

Can. J. Chem. Downloaded from www.nrcresearchpress.com by 85.192.166.187 on 09/08/12
For personal use only.

TABLE 1. Crystallographic data[a]

Parameter	Value	
	1	**2**
Formula	$C_8H_{13}NO_2$	$C_8H_{13}NO_2$
fw	155.20	155.20
Crystal system	Monoclinic	Monoclinic
Space group	$P2_1/n$	$P2_1/c$
a, Å	10.551(4)	9.868(2)
b, Å	8.342(3)	7.725(1)
c, Å	19.992(3)	10.963(2)
β (deg)	97.65(2)	98.78(2)
V	1744.0(9)	825.9(3)
Z	8	4
ρ_{calcd}, g/cm^3	1.182	1.248
$F(000)$	672	336
Radiation	Mo-K_α (λ = 0.71069 Å)	Cu-K_α (λ = 1.54178 Å)
μ, cm^{-1}	0.79	6.94
Crystal size, mm	0.15 × 0.15 × 0.20	0.05 × 0.30 × 0.40
Transmission factors	—	0.85–1.00
Scan type	ω–2θ	ω–2θ
Scan range, deg in ω	1.10 + 0.35 tan θ	1.05 + 0.20 tan θ
Scan speed, deg/min	32	16
Data collected	$+h$, $+k$, $\pm l$	$+h$, $+k$, $\pm l$
$2\theta_{max}$, deg	45	155
Crystal decay	Negligible	2.1%
Total reflections	2631	1913
Total unique reflections	2477	1813
R_{merge}	0.058	0.030
No. of reflections with $I \geq 3\sigma(I)$	938	1354
No. of variables	200	105
p-factor	0.02	0.05
R	0.049	0.043
R_w	0.062	0.061
Goodness-of-fit (gof)	1.70	3.07
Maximum Δ/σ (final cycle)	0.02	0.00
Residual density e/Å^3	−0.14 to +0.17	−0.16 to +0.21

[a]Temperature 294K, Rigaku AFC6S diffractometer, take-off angle 6.0°, aperature 6.0 × 6.0 mm at a distance of 285 mm from the crystal, stationary background counts at each end of the scan (scan/background time ratio 2:1, up to 8 rescans), $\sigma^2(F^2) = [S^2(C + 4B) + (pF^2)^2]/Lp^2$ (S = scan rate, C = scan count, B = normalized background count), function minimized $\Sigma w(|F_o| - |F_c|)^2$ where $w = 4F_o^2/\sigma^2(F_o^2)$, $R = \Sigma||F_o| - |F_c||/\Sigma|F_o|$, $R_w = (\Sigma w(|F_o| - |F_c|)^2/\Sigma w|F_o|^2)^{1/2}$, and gof = $[\Sigma w(|F_o| - |F_c|)^2/(m - n)]^{1/2}$. Values given for R, R_w, and gof are based on those reflections with $I \geq 3\sigma(I)$.

parameters for *N*-(*tert*-butyl)succinimide, **1**, are compiled in Table 5. There are six separate values for each parameter because there are three "abstractable" hydrogen atoms for each of the two independent molecules in the crystallographic asymmetric unit. The term "abstractable" refers to hydrogens for which the abstraction distance d is less than 3.1 Å, since our experience (2) and that of others (7) have been that hydrogen atoms that exceed this distance are unreactive towards intramolecular abstraction. Also included in Table 5 are the hypothetical "ideal" values for d, ω, Δ, and θ. The value for d of 2.72 Å comes from the sum of the Van der Waals radii for hydrogen and oxygen (8), and the value of 0° for ω is based on the well-established principle that oxygen utilizes its in-plane n,π* n-orbital for abstraction (9). This orbital makes an angle of between 90° and 120° with the C=O axis depending on the model selected (2), hence the same range of values for Δ; the value of 180° for θ is theoretically based (10).

Four of the six values of d recorded in Table 5 are remarkably short, ranging from 2.17–2.24 Å. These represent the shortest hydrogen abstraction distances yet measured by the crystal structure – reactivity correlation method. These contacts are so short that they should, in fact, be considered as C—H···O hydrogen bonds (11). In other type II systems that we have investigated by the crystal structure – reactivity correlation method, average values for d have been much closer to the hypothetical ideal value of 2.72 Å (2, 12, 13). The four γ-hydrogen atoms that are favored for abstraction in *N*-(*tert*-butyl)succinimide by low values of d are also associated with much more favorable values of ω, Δ, and θ (Table 5). In overall terms, these four hydrogen atoms are better situated for abstraction than any that have been reported heretofore. Of course, there is no way of determining experimentally which of the six hydrogen atoms listed in Table 5 is abstracted, since abstraction of any one of them leads to the same product. Based on literature analogy, however, it seems likely that H(8) (d = 2.88 Å) and H(20) (d = 2.98 Å) are *not* abstracted. This stems from our work with 1,8-cyclohexadecanedione (14), in which it was demonstrated through product studies that abstraction of a γ-hydrogen for which d = 2.72 Å, ω = 53°, Δ = 81°, and θ = 116° completely dominates abstraction of a different γ-hydrogen atom for which d = 2.99 Å, ω = 59°, Δ = 66°, and θ = 117° (Fig. 4). It is necessary at this point to remind the reader that the geometric data

Can. J. Chem. Downloaded from www.nrcresearchpress.com by 85.192.166.187 on 09/08/12
For personal use only.

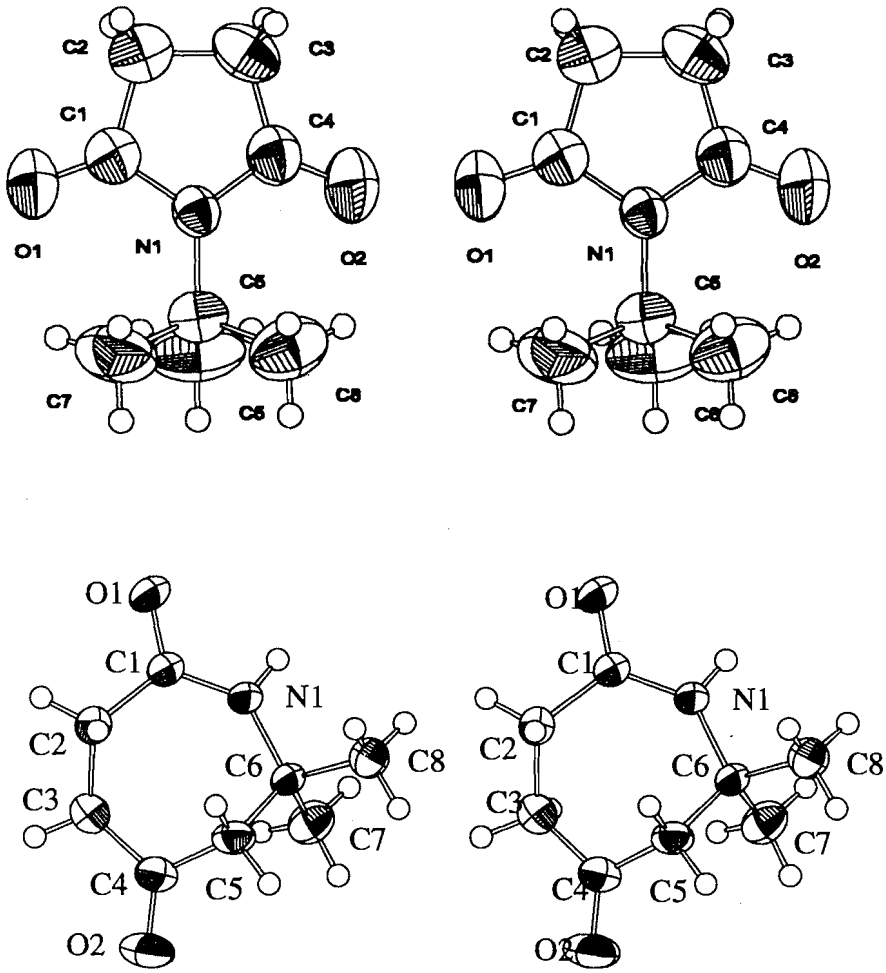

FIG. 3. Stereoscopic views of *N*-(*tert*-butyl)succinimide, **1**, (top) and its photoproduct, tetrahydro-1*H*-azepine-2,5-dione, **2**, (bottom) showing atom labeling; 50% probability thermal ellipsoids are shown for the non-hydrogen atoms.

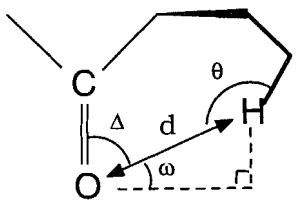

FIG. 4. Definition of geometric parameters *d*, ω, Δ, and θ for intramolecular hydrogen atom abstraction.

reported in Table 5 and discussed above are ground state data. Recent theoretical calculations by Houk et al. indicate that excitation of amides and imides results in pyramidalization of both the carbonyl and amine groups (15). If confirmed, this means that the present crystallographic data should serve as only a rough guideline to hydrogen abstractability in similar compounds.

We turn now to a second aspect of the solid state photochemistry of *N*-(*tert*-butyl)succinimide that interested us, namely the question of whether cyclobutanol **3** could be detected at intermediate stages of the reaction. The course of the photoreaction was followed by solid state Fourier transform infrared spectroscopy and X-ray powder diffractometry. The infrared studies were carried out by recording the FTIR spectra of KBr discs of compound **1** as a function of irradiation time. This showed a regular and progressive transformation of *N*-(*tert*-butyl)succinimide into keto-lactam **2** with no obvious absorptions for cyclobutanol **3**; the final infrared spectrum was identical to that of pure **2**. We tentatively conclude from these results that cyclobutanol **3** undergoes ring opening to **2** nearly as rapidly as it is formed and is present, if at all, only in small steady-state amounts.

A similar conclusion was reached from the X-ray powder diffraction studies. Figure 1 shows the powder diffraction patterns as a function of the extent of conversion as determined by gas chromatography. We interpret the powder patterns in terms of a two component phase diagram in which the starting material **1** and the photoproduct **2** are only partially soluble in the solid state (16). Thus, initial photolysis induces small shifts in the diffraction peaks that correspond to changes in the cell dimensions of the primary solid solution formed between compound **1** and a small amount of photoproduct **2**. Figure 2 shows an expansion of the powder patterns in the region $8° \leq 2\theta \leq 12°$. New diffraction peaks corresponding to a second phase rich in compound **2** (the terminal solid solution) begin to grow in between 6% and 14% conversion as the solubility limit of compound **2** in the primary solid solution is reached. At the same time, the diffraction peaks due to the primary solid solution stop shifting at this two phase stage, and gradually decrease in intensity as reaction proceeds. At complete conversion, the powder pattern indicates that the reaction mixture retains the crystal structure of the

Can. J. Chem. Downloaded from www.nrcresearchpress.com by 85.192.166.187 on 09/08/12
For personal use only.

Can. J. Chem. Downloaded from www.nrcresearchpress.com by 85.192.166.187 on 09/08/12
For personal use only.

TABLE 2. Final atomic coordinates (fractional) and B(eq) (Å^2)[a]

Atom	x	y	z	B(eq)
		1		
O(1)	0.8492(5)	0.2982(6)	0.5009(2)	10.0(3)
O(2)	0.9258(5)	0.2769(6)	0.7285(2)	9.3(3)
O(3)	0.2883(4)	0.0619(7)	0.8100(3)	10.1(3)
O(4)	−0.0855(4)	0.0909(6)	0.8953(2)	7.4(3)
N(1)	0.8645(4)	0.2436(6)	0.6156(2)	4.1(2)
N(2)	0.1130(4)	0.0319(5)	0.8660(2)	3.9(2)
C(1)	0.8629(6)	0.3416(9)	0.5584(4)	5.7(4)
C(2)	0.8818(5)	0.5122(8)	0.5814(4)	5.9(4)
C(3)	0.8963(5)	0.5075(9)	0.6561(4)	6.0(4)
C(4)	0.8979(6)	0.3334(9)	0.6732(3)	5.6(4)
C(5)	0.8526(5)	0.0647(7)	0.6137(3)	4.9(3)
C(6)	0.9843(6)	−0.0057(8)	0.6196(4)	8.9(4)
C(7)	0.7669(7)	0.0098(8)	0.5507(4)	9.1(4)
C(8)	0.7836(7)	0.0107(9)	0.6722(4)	8.2(4)
C(9)	0.2053(6)	0.1192(8)	0.8385(3)	5.6(4)
C(10)	0.1823(6)	0.2936(9)	0.8473(3)	6.6(4)
C(11)	0.0608(6)	0.3034(8)	0.8776(3)	5.7(3)
C(12)	0.0167(6)	0.1348(8)	0.8820(3)	4.8(3)
C(13)	0.1105(6)	−0.1470(7)	0.8712(3)	4.7(3)
C(14)	0.2459(7)	−0.212(1)	0.8835(4)	9.6(5)
C(15)	0.0404(7)	−0.2148(8)	0.8061(3)	8.9(4)
C(16)	0.0460(8)	−0.1997(9)	0.9305(4)	9.3(5)
		2		
O(1)	0.5139(1)	0.2290(2)	0.2614(1)	4.13(5)
O(2)	0.9083(2)	0.2333(2)	−0.0612(1)	6.27(8)
N(3)	0.6455(1)	0.4224(2)	0.1861(1)	2.72(5)
C(1)	0.6108(2)	0.2595(2)	0.2051(1)	2.88(6)
C(2)	0.6881(2)	0.1083(2)	0.1624(2)	3.96(7)
C(3)	0.7291(2)	0.1206(2)	0.0351(2)	4.54(8)
C(4)	0.8447(2)	0.2434(2)	0.0246(2)	3.73(7)
C(5)	0.8766(1)	0.3796(2)	0.1216(2)	3.11(6)
C(6)	0.7591(1)	0.5048(2)	0.1341(1)	2.51(5)
C(7)	0.7023(2)	0.5855(2)	0.0098(2)	3.88(7)
C(8)	0.8158(2)	0.6465(2)	0.2247(2)	3.72(7)

TABLE 3. Bond lengths (Å) with estimated standard deviations

Atom	Atom	Distance	Atom	Atom	Distance
		1			
O(1)	C(1)	1.196(7)	C(2)	C(3)	1.481(8)
O(2)	C(4)	1.201(7)	C(3)	C(4)	1.492(9)
O(3)	C(9)	1.205(6)	C(5)	C(6)	1.499(8)
O(4)	C(12)	1.202(6)	C(5)	C(7)	1.521(8)
N(1)	C(1)	1.404(7)	C(5)	C(8)	1.525(8)
N(1)	C(4)	1.381(7)	C(9)	C(10)	1.489(8)
N(1)	C(5)	1.498(7)	C(10)	C(11)	1.492(8)
N(2)	C(9)	1.387(7)	C(11)	C(12)	1.488(8)
N(2)	C(12)	1.400(7)	C(13)	C(14)	1.516(8)
N(2)	C(13)	1.497(7)	C(13)	C(15)	1.519(8)
C(1)	C(2)	1.501(9)	C(13)	C(16)	1.508(8)
		2			
O(1)	C(1)	1.238(2)	C(3)	C(4)	1.501(3)
O(2)	C(4)	1.211(2)	C(4)	C(5)	1.495(3)
N(1)	C(1)	1.329(2)	C(5)	C(6)	1.532(2)
N(1)	C(6)	1.477(2)	C(6)	C(7)	1.526(2)
C(1)	C(2)	1.508(2)	C(6)	C(8)	1.526(2)
C(2)	C(3)	1.514(3)			

TABLE 4. Bond angles (deg) with standard deviations

Atom	Atom	Atom	Angle	Atom	Atom	Atom	Angle
			1				
C(1)	N(1)	C(4)	109.7(5)	C(6)	C(5)	C(7)	113.0(6)
C(1)	N(1)	C(5)	124.6(6)	C(6)	C(5)	C(8)	110.9(6)
C(4)	N(1)	C(5)	124.9(6)	C(7)	C(5)	C(8)	104.8(5)
C(9)	N(2)	C(12)	109.8(5)	O(3)	C(9)	N(2)	124.9(7)
C(9)	N(2)	C(13)	124.8(5)	O(3)	C(9)	C(10)	125.7(7)
C(12)	N(2)	C(13)	125.1(5)	N(2)	C(9)	C(10)	109.4(6)
O(1)	C(1)	N(1)	126.4(7)	C(9)	C(10)	C(11)	105.3(6)
O(1)	C(1)	C(2)	125.2(7)	C(10)	C(11)	C(12)	105.3(6)
N(1)	C(1)	C(2)	108.4(6)	O(4)	C(12)	N(2)	124.3(6)
C(1)	C(2)	C(3)	106.0(6)	O(4)	C(12)	C(11)	126.8(7)
C(2)	C(3)	C(4)	104.7(5)	N(2)	C(12)	C(11)	108.9(5)
O(2)	C(4)	N(1)	124.0(7)	N(2)	C(13)	C(14)	110.0(5)
O(2)	C(4)	C(3)	126.0(7)	N(2)	C(13)	C(15)	108.8(5)
N(1)	C(4)	C(3)	110.1(6)	N(2)	C(13)	C(16)	111.1(5)
N(1)	C(5)	C(6)	108.3(5)	C(14)	C(13)	C(15)	110.3(6)
N(1)	C(5)	C(7)	111.0(5)	C(14)	C(13)	C(16)	106.4(6)
N(1)	C(5)	C(8)	108.8(5)	C(15)	C(13)	C(16)	110.3(6)
			2				
C(1)	N(1)	C(6)	134.2(1)	C(3)	C(4)	C(5)	118.0(1)
O(1)	C(1)	N(1)	119.7(1)	C(4)	C(5)	C(6)	115.3(1)
O(1)	C(1)	C(2)	118.3(1)	N(1)	C(6)	C(5)	113.0(1)
N(1)	C(1)	C(2)	122.0(1)	N(1)	C(6)	C(7)	108.9(1)
C(1)	C(2)	C(3)	117.1(2)	N(1)	C(6)	C(8)	106.4(1)
C(2)	C(3)	C(4)	115.1(2)	C(5)	C(6)	C(7)	111.0(1)
O(2)	C(4)	C(3)	120.6(2)	C(5)	C(6)	C(8)	107.7(1)
O(2)	C(4)	C(5)	121.4(2)	C(7)	C(6)	C(8)	109.7(1)

TABLE 5. Hydrogen abstraction geometry for *N*-(*tert*-butyl)succinimide, **1**

C=O···H	*d* (Å)	ω (deg)	Δ (deg)	θ (deg)
"Ideal"[a]	2.72	0	90–120	180
O(1)···H(9)[b]	2.24	6.51	101.6	115.9
O(1)···H(8)	2.88	33.5	83.7	74.8
O(2)···H(13)	2.19	21.7	100.0	123.4
O(3)···H(19)	2.17	17.5	100.7	121.4
O(3)···H(20)	2.98	39.1	79.7	68.8
O(4)···H(25)	2.24	19.1	100.3	120.2

[a]See text for origin of ideal values.

[b]O(1) and O(2) refer to one independent molecule in the asymmetric unit and O(3) and O(4) refer to the other.

terminal solid solution, which is different from (but very similar to) the crystal structure of the recrystallized photoproduct **2** (Fig. 1*g*). Analysis of other regions of the powder diffraction data lead to identical conclusions.

It seems likely that the single crystal-to-polycrystalline nature of the phototransformation of **1** to **2** is due to the extensive molecular reorganization that is associated with the process along with the polar nature of the photoproduct and its relatively high melting point (174.5–175.5°C). In contrast to single crystal-to-single crystal transformations, which occur when the product molecules form solid solutions with the unreacted starting material in all proportions (17), single crystal-to-polycrystalline reactions take place when the solubility limit of the product in the reactant lattice is reached at a relatively early stage of reaction, and the product begins to "precipitate out" in its own crystal structure (17, 18). In the present instance, it seems quite reasonable that compounds **1** and **2**, which have very different geometries, polarities, and melting points, would have limited mutual solubility.

Acknowledgements

Acknowledgement is made to the donors of the Petroleum Research Fund, administered by the American Chemical Society, for partial support of this research. Financial support by the Natural Sciences and Engineering Research Council of Canada is also gratefully acknowledged. We thank Professor Helen M. Burt for assistance with the X-ray powder diffraction measurements.

1. P. Wagner and B-S. Park. *In* Organic photochemistry. Vol. 11. *Edited by* A. Padwa. Marcel Dekker, New York. 1991. Chap. 4.
2. J.R. Scheffer. *In* Organic solid state chemistry. *Edited by* G.R. Desiraju. Elsevier, New York. 1987. Chap. 1.
3. Y. Kanaoka and Y. Hatanaka. J. Org. Chem. **41**, 400 (1976).
4. K.C. Schreiber and V.P. Fernandez. J. Org. Chem. **26**, 1744 (1961).
5. International tables for X-ray crystallography. Vol. IV. Kynoch Press, Birmingham, U.K. (present distributor: Kluwer Academic Publishers. Dordrecht, The Netherlands). 1974. pp. 99–102 and 149.
6. E. Sato and Y. Kanaoka. Chem. Pharm. Bull. **33**, 3006 (1985).
7. A. Weisz, M. Kaftory, I. Vidavsky, and A. Mandelbaum. J. Chem. Soc. Chem. Commun. 18 (1984).
8. A. Bondi. J. Phys. Chem. **68**, 441 (1964).
9. N.J. Turro and D.S. Weiss. J. Am. Chem. Soc. **90**, 2185 (1968).
10. A.E. Dorigo, M.A. McCarrick, R.J. Loncharich, and K.N. Houk. J. Am. Chem. Soc. **112**, 7508 (1990) and references therein.
11. (*a*) R. Taylor and O. Kennard. J. Am. Chem. Soc. **104**, 5063 (1982); (*b*) G.R. Desiraju. Acc. Chem. Res. **24**, 290 (1991); (*c*) G.R. Desiraju. Mol. Cryst. Liq. Cryst. **211**, 63 (1992).
12. T.J. Lewis, S.J. Rettig, J.R. Scheffer, J. Trotter, and F. Wireko. J. Am. Chem. Soc. **112**, 3679 (1990).

Can. J. Chem. Downloaded from www.nrcresearchpress.com by 85.192.166.187 on 09/08/12
For personal use only.

13. T.J. Lewis, S.J. Rettig, J.R. Scheffer, and J. Trotter. J. Am. Chem. Soc. **113**, 8180 (1991).
14. T.J. Lewis, S.J. Rettig, J.R. Scheffer, and J. Trotter. Mol. Cryst. Liq. Cryst. **219**, 17 (1992).
15. Y. Li, R.L. Garrell and K.N. Houk. J. Am. Chem. Soc. **113**, 5895 (1991).
16. B.D. Cullity. Elements of X-ray diffraction. Addison-Wesley, Reading, Mass. 1956. Chap. 12.
17. M.D. Cohen. Tetrahedron, **43**, 1211 (1987).
18. I.C. Paul and D.Y. Curtin. Acc. Chem. Res. **6**, 217 (1973).

Can. J. Chem. Downloaded from www.nrcresearchpress.com by 85.192.166.187 on 09/08/12
For personal use only.

Photolysis of 3-chloro-3-aryldiazirines in the presence of amines and allyl alcohol

MICHAEL T.H. LIU,[1] YURI N. ROMASHIN, AND T.K. VENKATACHALAM
Department of Chemistry, University of Prince Edward Island, Charlottetown, PE C1A 4P3, Canada

Received March 1, 1994

This paper is dedicated to Professor Charles W. Jefford on the occasion of his 65th birthday

MICHAEL T.H. LIU, YURI N. ROMASHIN, and T.K. VENKATACHALAM. Can. J. Chem. **72**, 1961 (1994).

When photolysis of arylchlorodiazirines is performed in the presence of either alkyl- or allyl-substituted amines, either *N*-alkyl- or *N*-allyl-substituted amines result as the sole high-yield (64–93%) products. Photolysis in the presence of phenylallylamine produces a rearranged product in poor yield (11–15%) whereas the reaction of allyl alcohol with arylchlorocarbene gives exclusively diallyl acetals in high yield (70%). The rate constants for these reactions were obtained by laser flash photolysis. Allyl phenyl ether forms a cyclopropanated product when treated with arylchlorocarbene. The different behaviour of these compounds may be attributed to the nucleophilicity at the nitrogen and oxygen centres of these compounds, when the latter are subjected to the substitutions described above. The formation of a cyclopropanated product when allyl phenyl ether is used differs from the reaction of bis (methoxycarbonyl) carbene with allyl ethers, as reported in the literature. The formation of this cyclopropanated product demonstrates the absence of an oxonium ylide intermediate during the reaction.

MICHAEL T.H. LIU, YURI N. ROMASHIN et T.K. VENKATACHALAM. Can. J. Chem. **72**, 1961 (1994).

La photolyse d'arylchlorodiazirines en présence soit d'amines alkyl- ou allyl-substituées, les seuls produits qui se forment (avec d'excellents rendements allant de 64 à 93%) sont les imines *N*-alkyl- ou *N*-allyl-substituées. La photolyse en présence de phénylallylamine conduit à un produit de transposition, avec un faible rendement (11–15%) alors que la réaction de l'alcool allylique avec l'arylchlorocarbène fournit exclusivement les acétals diallylique avec d'excellents rendements (70%). On a déterminé les constantes de vitesse de ces réactions en faisant appel à la photolyse éclair. Lorsqu'on traite l'oxyde d'allyle et de phényle avec de l'arylchlorocarbène, il se forme un produit cyclopropane. Les comportements divers de ces composés peut être attribué au caractère nucléophile des centres azote et oxygène de ces composés lorsqu'ils sont soumis aux réactions de substitutions décrites plus haut. La formation du dérivé cyclopropane lorsqu'on utilise l'oxyde d'allyle et de phényle diffère de ce qui est rapporté dans la littérature pour la réaction du bis-méthoxycarbonyl-carbène avec des éthers allyliques. La formation de ce dérivé cyclopropane démontre l'absence d'un intermédiaire oxonium ylure durant cette réaction.

[Traduit par la rédaction]

Introduction

The reactions of some carbenes with allyl-substituted ethers, amines, and halides have been studied (1) and reviewed (2). In the case of allyldimethylamine and allyldiethylamine, the reactions go through nitrogen ylides as intermediates and are completed by either a 1,2 allylic shift (3) or a 2,3-sigmatropic rearrangement (4). Reactions of carbenes with allylic ethers such as allyl methyl ether, γ-methylallyl ether, and γ, γ-dimethylallyl ether yield products derived from 2,3-sigmatropic rearrangement of an oxonium ylide and a cyclopropanated product (1). Ylide formation in the above cases was favoured by a factor of 3:2 and the steric factor greatly influences the ratio of insertion to addition products.

Earlier reports described the reaction of phenylchlorocarbene with secondary amines such as diethylamine (5a) and of benzylchlorocarbene with alcohols (5*b*,*c*). These reactions led to products derived from the insertion of carbenes into N—H and O—H bonds. The present study investigates the products resulting from the reaction of phenylchlorocarbene with primary amines such as allylamine and a primary alcohol, namely, allyl alcohol.

Results and discussion

3-Chloro-3-aryldiazirines **1** were synthesized by Graham oxidation of the corresponding amidine hydrochlorides (6). Irradiation (350 nm) of the diazirines **1** in hexane (0.1 M) at 25°C yielded arylchlorocarbenes, **2**, which in the presence of a 10-fold excess of allylamine gave *N*-allyl imines **4** in high yield (64–93%) as the only product. These products were isolated by column chromatography, and their structure confirmed by IR, NMR, GC–MS, and by comparison with authentic samples prepared according to literature procedures (7). The formation of imines **4** probably occurs through a three-stage process of ylide **3** formation, followed by 1,2-hydrogen migration and subsequent elimination of HCl (Scheme 1). Several amines of various structures, for example, propylamine, isopropylamine, *n*-butylamine, ethanolamine, and aniline, reveal that a similar mechanism is operating in all cases since the Schiff bases were the only observed product in these reactions.

The reaction of arylchlorocarbene **2** with allyl aniline yields *N*-phenylimines **6** as the only detectable product to be isolated, in poor yield, by column chromatography on alumina (11% for phenylchlorocarbene and 15% for *p*-chlorophenylchlorocarbene). Scheme 2 shows the plausible pathway through which the reaction proceeds in the example cited above.

The formation of imines such as **6** probably proceeds via the nitrogen ylide intermediate **5**, followed by either 1,2-allyic or 2,3-sigmatropic shift and subsequent HCl elimination. The latter process is the possible driving force for product formation in the reaction of arylchlorocarbenes **2** with both primary and secondary amines. The insertion of singlet carbenes, such as arylchlorocarbenes, into the N—H bond of amines likely proceeds via the formation of an ammonium ylide followed by the migration of the hydrogen atom from the nitrogen to the carbon center. Laser flash photolysis (LFP) of 3-chloro-3-aryldiazirine in the presence of diethylamine (5*a*) enabled direct observation of the UV spectrum of ammonium ylide (λ = 340 nm). As a result, the formal insertion into the N—H bond is classified as a two-step process. The lifetime of the ylide is ~30 ns at 25°C when the concentration of diethylamine is 0.05 M. Furthermore, the kinetic parameters for the 1,2 hydrogen shift in this ylide: E_a = 5.9 kcal mol^{-1} and log A = 12.0, have recently been determined (5*d*). In addition, the 1,2-H shift in the ylide was catalyzed by

[1]Author to whom correspondence may be addressed. Telephone: (902) 566-0565 Fax: (902) 566-0420.

Can. J. Chem. Downloaded from www.nrcresearchpress.com by 85.192.166.187 on 09/08/12
For personal use only.

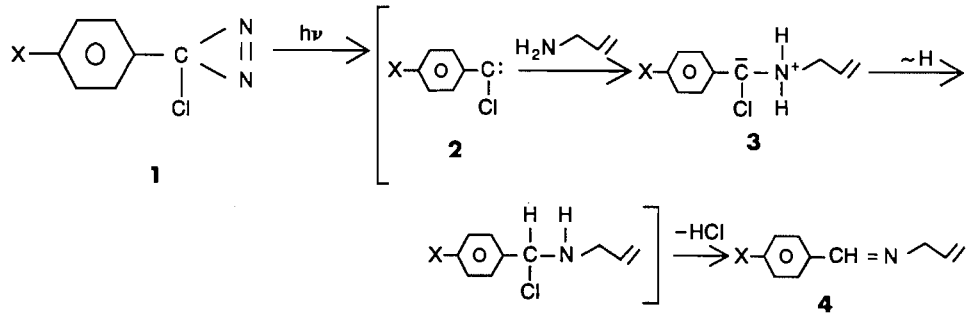

a, X = H; *b*, X = Cl; *c*, X = CH_3

SCHEME 1

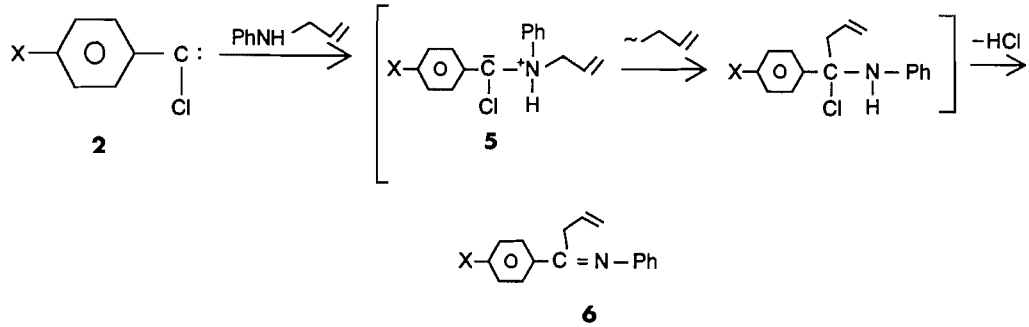

SCHEME 2

the external diethylamine molecule at low temperature. Similarly, we attempted to detect the formation of the ammonium ylide in the LFP of arylchlorodiazirines in isooctane with allylamine and allylaniline. Unfortunately, the ylides **3** or **5** could not be observed in LFP, probably because the rates of disappearance of these ylides are faster than the rates of their formation. Monitoring the C_6H_5–C–Cl and *p*–ClC_6H_4–C–Cl absorptions (5*a*) at 310 nm enabled us to determine the quenching rate constants for the reactions of the carbenes and amine substrates. The reactions were first order with respect to allylamine or allylaniline, as evidenced by the excellent linearity of plots obtained by using eq [1]

$$[1] \quad k_{obs} = k_o + k_q [\text{amine}]$$

where k_{obs} is the observed pseudo-first-order rate constant for transient decay, k_o is the rate constant for decay in the absence of the substrate, and k_q is the rate constant for the reaction of carbene with the substrate.

C_6H_5-$\ddot{C}$-Cl	allylamine	$(1.4 \pm 0.1) \times 10^9\ M^{-1}\ s^{-1}$
C_6H_5-$\ddot{C}$-Cl	allylaniline	$(4.4 \pm 0.2) \times 10^9\ M^{-1}\ s^{-1}$
p-ClC_6H_4-$\ddot{C}$-Cl	allylamine	$(1.6 \pm 0.1) \times 10^9\ M^{-1}\ s^{-1}$
p-ClC_6H_4-$\ddot{C}$-Cl	allylaniline	$(6.3 \pm 0.2) \times 10^9\ M^{-1}\ s^{-1}$

In general, the rate of formation of the ylide is rapid and is close to diffusion controlled. In these cases, the ylide spectra cannot be observed. This suggests that the 1,2 shifts in ylides **3** or **5** must be in the sub-nanosecond range.

The reaction of allyl alcohol with phenylchlorocarbenes indicated that irradiation of diazirines **1** in hexane (0.1 M) at 25°C in the presence of a 10-fold excess of allyl alcohol gave the diallyl acetals **7** in 74–79% yield. The structure of products was confirmed by comparison with authentic samples prepared according to the literature (8). From the results it was clear that cyclopropanes were not detected in GC, GC–MS, and NMR. In search of a mechanism for the reaction of carbenes **2** with allyl alcohol, kinetic studies were carried out by LFP. LFP of 3-chloro-3-*p*-chlorophenyl-diazirine (10^{-3} M) in isooctane (N_2-purged) at 25°C gave rise to a transient (λ = 310 nm) attributed to the absorption of the singlet *p*-$ClC_6H_4\ddot{C}Cl$. The transient was quenched when allyl alcohol was added to the sample in the LFP experiments. When the observed pseudo-first-order rate constants, k_{obs}, for the decay of the transient were plotted against the concentration of allyl alcohol, a pronounced curvature (concave upward) was observed, Fig. 1. This conforms to the observation that the reactions of chlorocarbenes are not first order in alcohol. In fact, Griller et al. (9) have shown that the chlorocarbenes have strong discrimination in their activity toward the monomers and oligomers of various alcohols. For example, *p*-$CH_3OC_6H_4\ddot{C}Cl$ is more reactive toward hydrogen-bonded oligomers than methanol monomers. As well, the reactions of methoxycarbenes with hydroxylic substrates demonstrate that the carbene's activity depends on the function of the alcohol's structure and acidity (10). Since there was no cyclopropane formation in the reaction of *p*-$ClC_6H_4\ddot{C}Cl$ with allyl alcohol, presumably the carbene attacks the oxygen atom rather than the allylic double bond. This assumption is also confirmed by a comparison of the quenching rate constant for *p*-$ClC_6H_4\ddot{C}Cl$ with allyl alcohol at very low concentration, $k_q \sim 10^7 M^{-1}\ s^{-1}$, whereas the rate of cyclopropanation reaction for *p*-$ClC_6H_4\ddot{C}Cl$ with allyl bromide is of an order of lesser magnitude, namely, $k_q \sim 10^6\ M^{-1}\ s^{-1}$ (11). The data for the oligomerization of allyl alcohol are not known, but an excellent straight-line plot, Fig. 1, was obtained when the observed rate constants

Can. J. Chem. Downloaded from www.nrcresearchpress.com by 85.192.166.187 on 09/08/12
For personal use only.

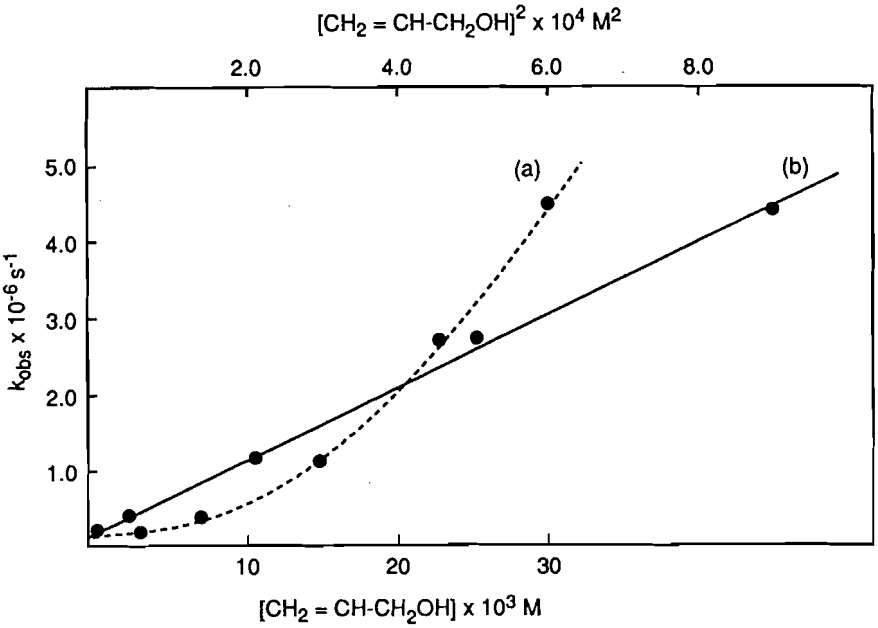

FIG. 1. Plots of pseudo-first-order rate constants vs. allyl alcohol concentrations. (*a*) k_{obs} vs. [CH_2=$CHCH_2OH$]; (*b*) k_{obs} vs. [CH_2=$CHCH_2OH$]^2.

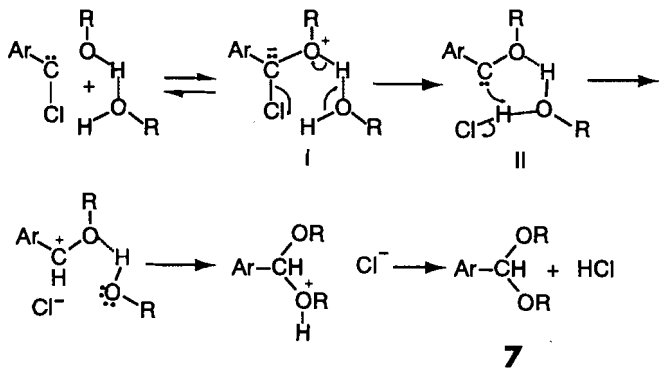

SCHEME 3

were plotted against the square of the allyl alcohol concentration. The slope of the line yielded a third-order rate constant, $\sim 5 \times 10^9$ L^2 mol^{-2} s^{-1}, which agrees with the value derived for the reaction of $C_6H_5CH_2\ddot{C}Cl$ vs. [MeOH]^2 (5*c*).

For the reaction of chlorocarbenes with allyl alcohol, two facts must be taken into consideration: first, no cyclopropanation products were formed; second, the overall reaction is second order in alcohol. It appears that the electrophilic carbene reacts with the nucleophilic alcohol dimer or oligomer by a rate-determining ylide-type interaction (carbene LUMO and alcohol HOMO), as depicted in Scheme 3.

Loss of chloride ion via a six-membered transition state leads to the concomitant formation of a new alkoxycarbene intermediate, which further reacts with a second alcohol molecule to give the final acetal by a variety of mechanisms as discussed in an earlier publication (5*b*). It is also possible to envisage an alternative mechanism involving proton transfer in the ylide, yielding ArCH(Cl)OR and ROH, followed by solvolysis.

These investigations also attempt to establish whether a similarity exists between the reactivity of allylaniline and that of allyl phenyl ether towards arylchlorocarbenes. An examination of the reaction of arylchlorocarbenes **2** with allyl phenyl ether (Scheme 4) shows that the reaction yields chlorocyclopropane **8**, as the only product, in 60% yield.

The total absence of products derived from the 2,3-sigmatropic shift of an oxonium ylide shows that the reaction of arylchlorocarbenes **2** with allyl phenyl ether does not proceed via an oxonium ylide intermediate. This is in marked contrast to the behaviour of bis(methoxycarbonyl)carbene towards allyl-substituted ethers (1). The formation of a cyclopropanated product in this experiment may be due to a change in nucleophilicity at the oxygen centre caused by the introduction of an electron-withdrawing phenyl group in the structure. The difference in the reactivity of arylchlorocarbenes towards ethers in comparison with the reactivity of diazomalonate carbenes with ether could cause such a change in product formation. Also, the difference between the reactivity of allylaniline and allyl phenyl ether towards arylchlorocarbenes may be explained by invoking the nucleophilicity of nitrogen and oxygen centres in stabilizing the ylide intermediate. However, in several instances, the carbene attack was found to favour the nitrogen rather than the oxygen centre. This analogy is in accord with the suggestion of Ando et al. (1) who reported that nucleophilicity differences can cause a variation in the ratio of insertion to addition products.

In conclusion, the behaviour of allyl-substituted amines, such as allylamine and allylaniline, as well as allyl alcohol and allyl phenyl ether, differs when treated with arylchlorocarbenes. This is principally due to the nucleophilicity at the nitrogen and oxygen centres, respectively. This report has also demonstrated that allyl phenyl ether does not react with arylchlorocarbenes via the oxonium ylide intermediate.

Experimental

All of the chemicals used were purchased from the Aldrich Chemical Company. Allylamine, propylamine, butylamine, *sec*-butylamine, and aniline were dried over KOH pellets and distilled prior to use. Solvents such as THF and hexane were refluxed over Na wire and distilled. Solvents were stored over Na wire under argon. All the diazirines were synthesized according to literature procedures (6). Irradiation was performed with a battery of 350-nm lamps in a Rayonet photoreactor until all the diazirine was destroyed. ^{1}H NMR spectra were recorded using a Varian T-60 spectrometer using tetramethylsi-

Can. J. Chem. Downloaded from www.nrcresearchpress.com by 85.192.166.187 on 09/08/12
For personal use only.

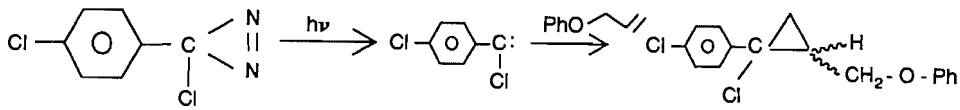

8

SCHEME 4

lane as a reference. GC analysis was done on a Varian 6000 series gas chromatograph fitted with a CSP-2 (20m Carbowax) column using a flame ionization detector. Peak areas were integrated using a Hewlett-Packard 3390 integrator and chart recorder. All of the products obtained were subject to GC analysis using proper calibration methods and authentic samples as references. IR spectra were recorded using a Perkin–Elmer 1600 series FTIR instrument. GC–MS were carried out on a Hewlett–Packard HP 5927A MSD instrument. The LFP apparatus in Austin uses a crossed-beam arrangement. A mode-locked Nd: YAG (~10 mJ, pulse width 200 ps) laser provided excitation at 355 nm with a pulsed xenon lamp as monitoring source. The system has a response time of 2 ns. All data collected were signal averaged over 3 shots.

General procedure

A solution of a diazirine (1 mmol), amine (5 mmol), and hexane (10 mL) was irradiated using a battery of 350-nm lamps in a Rayonet photoreactor at 25°C for 7 h. The solution was degassed by bubbling AR through it for a period of 10 min prior to irradiation. The solvent and excess amine were removed in vacuo. The residue was diluted with diethyl ether (30 mL), washed with water (3 × 10 mL), and dried over Na_2SO_4. The products were purified by column chromatography.

Reaction between allylamine and phenylchlorodiazirine. *N*-Allyl benzilidine, **4***a*: yield 90%. IR ν: 1648 cm^{-1}. ^1H NMR (60 MHz, $CDCl_3$) δ: 4.13–4.36 (m, CH_2), 5.0–5.42 (m, CH_2), 5.76–6.47 (m, CH), 7.23–7.96 (m, C_6H_5), 8.20–8.34 (m, CH).

Reaction between allylamine and p-*chlorophenylchlorodiazirine.* *N*-Allyl-*p*-chlorobenzilidine, **4***b*: yield 64%. IR ν: 1649 cm^{-1}. ^1H NMR (60 MHz, $CDCl_3$) δ: 4.13–4.36 (m, CH_2), 5.00–5.42 (m, CH_2), 5.76–6.47 (m, CH), 7.27–7.85 (m, C_6H_4), 8.23–8.37 (m, CH). MS, *m/e*: 181(7), 179(23), 178(65), 153(9), 151(27), 140(8), 138(22), 127(10), 125(30), 113(13), 111(14), 89(52), 75(33), 41(100).

Reaction between allylamine and p-*methylphenylchlorodiazirine.* *N*-Allyl-*p*-methylbenzilidine, **4***c*: yield 93%. IR ν: 1649 cm^{-1}. ^1H NMR (60 MHz, $CDCl_3$) δ: 2.33(s, CH_3), 4.13–4.36 (m, CH_2), 5.00–5.42 (m, CH_2), 5.76–6.47 (m, CH), 5.76–6.47 (m, CH), 7.07–7.81 (m, C_6H_4), 8.18–8.32 (m, CH). MS, *m/e*: 159(32), 158(93), 144(64), 131(27), 130(26), 118(41), 117(28), 105(44), 104(30), 103(28), 91(43), 77(31), 41(100).

Reaction between propylamine and phenylchlorodiazirine. *N*-Propyl benzilidine: yield 75%. IR ν:1648 cm^{-1}. ^1H NMR (60 MHz, $CDCl_3$) δ: 0.93 (t, J = 7 Hz, CH_3), 1.71 (sex, J = 7 Hz, CH_2), 3.40–3.71 (m, CH_2), 7.26–7.92 (m, C_6H_5), 8.16–8.30 (m, CH). MS, *m/e*: 147(6), 146(23), 119(15), 118(59), 104(15), 91(100), 90(11), 89(14), 77(17).

Reaction between propylamine and p-*chlorophenylchlorodiazirine.* *N*-Propyl-p-chlorobenzilidine: yield 71%. IR ν: 1644 cm^{-1}. ^1H NMR (60 MHz, $CDCl_3$) δ: 0.93 (t, J = 7 Hz, CH_3), 1.70 (sex, J = 7 Hz, CH_2), 3.40–3.71 (m, CH_2), 7.26–7.77 (m, C_6H_4), 8.16–8.30 (m, CH). MS, *m/e*: 183(2), 182(5), 181(45), 180(15), 154(22), 152(63), 140(5), 138(12), 127(33), 125(100), 113(4), 111(9), 89(33).

Reaction between propylamine and p-*methylphenylchlorodiazirine.* *N*-Propyl-*p*-methylbenzilidine: yield 93%. IR ν: 1647 cm^{-1}. ^1H NMR (60 MHz, $CDCl_3$) δ: 0.93 (t, J = 7 Hz, CH_3), 1.73 (sex, J = 7 Hz, CH_2), 2.32 (s, CH_3), 3.39–3.70 (m, CH_2), 7.07–7.77 (m, C_6H_4), 8.16–8.30 (m, CH).

Reaction between butylamine and phenylchlorodiazirine. *N*-Butylbenzilidine: yield 78%. IR ν: 1646 cm^{-1}. ^1H NMR (60 MHz, $CDCl_3$) δ: 0.93 (t, J = 7 Hz, CH_3), 1.13–1.87 (m, $2CH_2$), 3.44–3.75 (t, CH_2), 7.26–7.92 (m, C_6H_5), 8.20–8.34 (m, CH).

Reaction between sec-*butylamine and phenylchlorodiazirine.* *N*-sec-Butylbenzilidine: yield 75%. IR ν: 1645 cm^{-1}. ^1H NMR (60 MHz, $CDCl_3$) δ: 0.85 (t, J = 7 Hz, CH_3), 1.25 (d, J = 7 Hz, CH_3), 1.32–1.90 (m, CH_2), 2.90–3.50 (m, CH), 7.23–7.89 (m, C_6H_5), 8.23–8.37 (m, CH). MS, *m/e*: 161(2), 160(5), 146(33), 132(100), 105(47), 104(21), 91(20), 90(13), 89(19), 77(25).

Reaction between ethanolamine and p-*chlorophenylchlorodiazirine.* *p*-Chloro-*N*-benzilidine ethanolamine: yield 61%. IR ν: 1647 cm^{-1}. ^1H NMR (60 MHz, $CDCl_3$) δ: 3.14 (s, OH), 3.58–4.08 (m, CH_2), 7.29–7.86 (m, C_6H_4), 8.23–8.37 (m, CH). MS, *m/e*: 185(2), 183(5), 182(2), 154(22), 152(71), 140(2), 138(5), 127(32), 125(100), 113(2), 111(6), 89(32).

Reaction between aniline and p-*chlorophenylchlorodiazirine.* *N*-Phenyl-*p*-chlorobenzilidine: yield 91%. IR ν: 1645 cm^{-1}. ^1H NMR (60 MHz, $CDCl_3$) δ: 7.30–7.89 (m, C_6H_4 and C_6H_5), 8.4–8.5 (m, CH). MS, *m/e*: 217(25), 216(37), 215(79), 214(86), 89(18), 77(100).

Reaction between allylaniline and phenylchlorodiazirine. Phenyl allyl-*N*-phenylimine, **6***a*: yield 11%. ^1H NMR (60 MHz), $CDCl_3$) δ: 3.50–3.70 (m, CH_2), 5.20–5.40 (m, CH), 7.20–7.70 (m, C_6H_4), 7.70–8.00 (m, C_6H_5). MS, *m/e*: 221 (M^+, 23), 220(100), 206(13), 193(6), 144(23), 130(8), 117(25), 115(35), 104(15), 91(27), 89(23), 77(20), 65(20), 51(22), 39(26).

Reaction between allylaniline and p-*chlorophenylchlorodiazirine.* *p*-Chlorophenylallyl-*N*-phenylimine, **6***b*: yield 15%. ^1H NMR (60 MHz, $CDCl_3$) δ: 3.70–4.20 (m, CH_2), 5.60–6.20 (m, CH), 7.02–7.90 (m, C_6H_4), 8.18–8.30 (m, C_6H_5). MS, *m/e*: 257(9), 256(37), 225(M^+, 25), 254(100), 242(4), 240(13), 227(4), 144(23), 138(11), 130(11), 125(10), 115(36), 91(21), 89(27), 77(17), 65(19), 39(23).

Reaction between allylalcohol and phenylchlorodiazirine. Phenyl diallyl acetal, **7***a*: yield 79%. IR ν: 1647 cm^{-1}, ^1H NMR (60 MHz, $CDCl_3$) δ: 4.00–4.20 (m, $2CH_2$), 5.00–5.60 (m, $2CH_2$), 5.67 (s, CH), 5.70–6.40 (m, 2CH), 7.30–7.70 (m, C_6H_5). MS, *m/e*: 147(M^+ – $OCH_2CH{=}CH_2$ 25), 106(4), 105(44), 91(21), 89(2), 77(24), 41(100).

Reaction between allylalcohol and p-*chlorophenylchlorodiazirine.* *p*-Chlorophenyl diallyl acetal, **7***b*: yield 77%. IR ν: 1647 cm^{-1}. ^1H NMR (60 MHz, $CDCl_3$) δ: 4.00–4.20 (m, $2CH_2$), 5.00–5.60 (m, $2CH_2$), 5.63 (s, CH), 5.70–6.40 (m, 2CH), 7.43 (bs, C_6H_4). MS, *m/e*: 183(6), 181 (M^+–$OCH_2CH{=}CH_2$, 18) 142(1), 141(9), 140(3), 139(25), 113(3), 111(6), 41(100).

Reaction between allylalcohol and p-*nitrophenylchlorodiazirine.* *p*-Nitrophenyl diallyl acetal, **7***d*: yield 74%. IR ν: 1646 cm^{-1}. ^1H NMR (60 MHz, $CDCl_3$) δ: 4.00–4.20 (m, $2CH_2$), 5.00–5.60 (m, $2CH_2$), 5.75 (s, CH), 5.75–6.40 (m, 2CH), 7.50–8.60 (m, C_6H_4). MS, *m/e*: 192 (M^+–$OCH_2CH{=}CH_2$, 13), 151(1), 150(9), 41(100).

Reaction between phenyl allyl ether and p-*chlorophenylchloridiazirine.* 1-*p*-Chlorophenyl-1-chloro-2-phenoxymethyl cyclopropanes, **8**: yield 60%. IR ν: 1600 cm^{-1}. ^1H NMR (60 MHz, $CDCl_3$) δ: 1.20–1.90 (2H, m, CH_2), 1.80–2.40 (1H, m, CH), 3.20–3.80 (2H, m, CH_2O), 6.80–7.20 (m, C_6H_4), 7.20–7.60 (m, C_6H_5).

The two isomers (50:50) are well separated in GC, which gave similar fragmentation patterns in the MS *m/e*: 294(2), 292(3), 203(2), 201(11), 199(17), 166(3), 165(26), 164(11), 163(77), 151(4), 149(10), 139(4), 137(9), 129(31), 128(100), 127(67), 77(26).

Acknowledgements

The experiments and analyses of the data produced were performed at the Center for Fast Kinetics Research, which is supported jointly by the Biomedical Research Technology Program of the Division of Research Resources of the National Institutes of Health (RR00886) and by The University of Texas at Austin. The financial support of the Natural Sciences and Engineering

Can. J. Chem. Downloaded from www.nrcresearchpress.com by 85.192.166.187 on 09/08/12
For personal use only.

Research Council of Canada (NSERC) is gratefully acknowledged. We wish to thank Professors M.P. Doyle and J.C. Scaiano for helpful discussion.

1. W. Ando, S. Kondo, K. Nakayama, K. Ichibori, H. Kohoda, H. Yamoato, I. Imai, S. Nakaido, and T. Migita. J. Am. Chem. Soc. **94**, 3870 (1972).
2. A. Padwa and S.F. Hornbuckle. Chem. Rev. **91**, 263 (1991).
3. Y. Hata and M. Watanabe. Tetrahedron Lett. 4659 (1972); W.E. Parham and J.R. Potoski. J. Org. Chem. **32**, 275 (1967).
4. (*a*) J. Auerbach and S.M. Weinreb. J. Am. Chem. Soc. **94**, 7172 (1972); (*b*) M.P. Doyle, W.H. Tamblyn, and V. Bagheri. J. Org. Chem. **46**, 5094 (1981).
5. (*a*) R. Bonneau and M.T.H. Liu. J. Am. Chem. Soc. **113**, 9872 (1991); (*b*) M.T.H. Liu and R. Subramanian. J. Chem. Soc. Perkin Trans. 2, 1233 (1986); (*c*) J. Chem. Soc. Chem. Commun. 1062 (1984); (*d*) R. Bonneau, I. Reuter, and M.T.H. Liu. J. Am. Chem. Soc. **116**, 3145 (1994).
6. W.H. Graham. J. Am. Chem. Soc., **87**, 4396 (1965).
7. R. Tiollais. Bull. Soc. Chim. Fr., **14**, 706 (1947); **14**, 716 (1947).
8. F. Stasiuk, W.A. Sheppard, and A.N. Bourns. Can. J. Chem. **34**, 123 (1956).
9. D. Griller, M.T.H. Liu, and J.C. Scaiano. J. Am. Chem. Soc. **104**, 5549 (1982).
10. X-M, Du, H. Fan, J.L. Goodman, M.A. Kesselmeyer, K. Krogh-Jespersen, J.A. LaVilla, R.A. Moss, S. Shen, and R.S. Sheridan. J. Am. Chem. Soc. **112**, 1920 (1990).
11. R. Bonneau, M. Grobys, M.T.H. Liu, M. Himori, K. Fukushima, and T. Ibata. Res. Chem. Intermed. **20**, 141 (1994).

Can. J. Chem. Downloaded from www.nrcresearchpress.com by 85.192.166.187 on 09/08/12
For personal use only.

On the positional reactivity order in the sulfur trioxide sulfonation of benzene, halogenobenzenes, halogenonaphthalenes, and chloroanthracenes[1,2]

HANS CERFONTAIN,[3] YOUSI ZOU,[4] BERT H. BAKKER, AND FREEK VAN DE GRIENDT
Laboratory of Organic Chemistry, University of Amsterdam, Nieuwe Achtergracht 129, 1018 WS Amsterdam, The Netherlands

Received April 29, 1994

HANS CERFONTAIN, YOUSI ZOU, BERT H. BAKKER, and FREEK VAN DE GRIENDT. Can. J. Chem. **72**, 1966 (1994).

The reaction of sulfur trioxide with benzene, the four halogenobenzenes, and six halogenonaphthalenes in dichloromethane as solvent, and with four chlorinated anthracenes in nitromethane as solvent, has been studied by analysis of the resulting mixture of the sulfo derivatives with ^{1}H NMR. The sulfonation of benzene yields initially benzenesulfonic acid and subsequently the 1,3-disulfonic acid (1,3-S_2). The initial sulfonation of the four halogenobenzenes yields ≥98% of the 4-S. Their subsequent sulfonation gives the 2,4-S_2 and in the case of fluoro- and iodobenzene also the 2,4,6-S_3. Monosulfonation of 1-fluoronaphthalene yields only the 4-S, whereas the three other 1-halogenonaphthalenese yield in addition some 5-S. Further sulfonation on any of the four 1-halogenonaphthalene-4-sulfonic acids yields a mixture of the 2,4-S_2 and 4,7-S_2, and eventually also some 2,4,7-S_3, whereas the 1-halogeno-5-sulfonic acids give the corresponding 5,7-S_2. Sulfonation of 2-chloro- and 2-bromonaphthalene yields initially 85% 8-S and 15% 4-S, which are subsequently converted into the 6,8-S_2 and 4,7-S_2, respectively. On reaction with 1.0 mol-equiv. of SO_3, 2-chloroanthracene gives the 9-S, and 9-chloroanthracene gives an 18:82 mixture of the 4-S and 10-S. Both 1,5- and 1,8-dichloroanthracene yield initially the 4-S and subsequently the 4,8-S_2 and 4,5-S_2, respectively.

HANS CERFONTAIN, YOUSI ZOU, BERT H. BAKKER et FREEK VAN DE GRIENDT. Can. J. Chem. **72**, 1966 (1994).

En se basant sur une analyse par RMN du ^{1}H des dérivés sulfoniques des mélanges obtenus, on a étudié la réaction du trioxyde de soufre avec le benzène, les quatre halogénobenzènes et six halogénonaphtalènes dans le dichlorométhane comme solvant et avec quatre anthracènes chlorés dans le nitrométhane comme solvant. La sulfonation du benzène conduit initialement à l'acide benzènesulfonique et subséquemment à l'acide 1,3-disulfonique (1,3-S_2). La sulfonation initiale des quatre halogénobenzènes conduit à ≥98% du 4-S. Leur sulfonation subséquente conduit aux 2,4-S_2 et, dans le cas des fluoro- et iodobenzène, il y a aussi formation des 2,4,6-S_3. La monosulfonation du 1-fluoronaphtalène conduit seulement aux 4-S alors que les trois autres halogénonaphtalènes fournissent aussi un peu du 5-S. La sulfonation subséquente de chacun des acides 1-halogénonaphtalène-4-sulfoniques fournit un mélange des 2,4-S_2 et 4,7-S_2 et éventuellement un peu du 2,4,7-S_3 alors que les acides 1-halogénonaphtalène-5-sulfoniques conduisent aux 5,7-S_2 correspondants. La sulfonation des 2-chloro- et 2-bromonaphtalènes conduit initialement à 85% de 8-S et 15% de 4-S qui sont subséquemment transformés respectivement en 6,8-S_2 et 4,7-S_2. La réaction de 1,0 équivalent molaire de SO_3 avec le 2-chloroanthracène fournit le 9-S alors que le 9-chloroanthracène fournit un mélange 18 : 82 des 4-S et 10-S. Les 1,5- et 1,8-dichloroanthracènes fournissent initialement le 4-S et ultérieurement ils fournissent respectivement le 4,8-S_2 et 4,5-S_2.

[Traduit par la rédaction]

Introduction

The sulfonation of halogenoarenes with chlorosulfuric acid and with concentrated aqueous and fuming sulfuric acid has been studied extensively (2–7). In aromatic substitution, the directing effect of a halogeno substituent is determined by three factors. First, the mesomeric electron release, which decreases in the order F > Cl > Br > I, and which is far more effective in the transition state for *para* than for *ortho* substitution (8, 9). Second, the negative inductive effect, which decreases in the order F > Cl > Br > I, is most effective at the *ortho* and least effective at the *para* position, and third, substitution *ortho* to the halogen is inhibited by steric hindrance, which increases in the order F < Cl < Br < I, as was established by Brand for sulfonation with fuming sulfuric acid (7). The sulfonation of the monohalogenobenzenes in concentrated aqueous sulfuric acid takes place almost exclusively at the 4-position.[5] Under both aprotic and strongly protic sulfonation conditions dehalogenation may occur with substituted bromoarenes and, in particular, with substituted iodoarenes (4, 5, 14).

To allow a proper comparison of the halogenoarenes we have studied the sulfonation of benzene, the four halogenobenzenes, six halogenonaphthalenes, and four chloro-substituted anthracenes under aprotic conditions using sulfur trioxide as reagent.

Results and discussion

The sulfonation of benzene, Hlg-benzene (Hlg = F, Cl, Br, I), 1-Hlg-naphthalene (Hlg = F, Cl, Br and I), and 2-Hlg-naphthalene (Hlg = Cl, Br) with sulfur trioxide using dichloromethane as solvent at ≈22°C has been studied. The results are collected in Tables 1 and 2. In addition a study was made of the sulfona-

[1]Aromatic sulfonation, part 123. Preceding paper: see ref. 1.

[2]For reasons of convenience, all sulfo products have been numbered as for the parent substrate.

[3]Author to whom correspondence may be addressed.

[4]Present address: Department of Chemical Engineering, Xiamen University, Xiamen, Fujian, P.R. China.

[5]For the sulfonation of fluoro-, chloro-, bromo-, and iodobenzene in 98.1% H_2SO_4 at 25°C the relative contents of the 4-sulfonic acids (4-S's) are 99.1, 99.1, 98.8, and 97.7%, respectively, and the corresponding partial rate factors for the *para* position in 83–95 wt.% H_2SO_4 are 3.3 ± 0.5, 0.48 ± 0.05, 0.29 ± 0.03, and 0.57 ± 0.12, respectively (10).[6] The small variations of these values illustrate the near balance between the mesomeric and inductive effects of the halogens for substitution at the 4-position.

[6]For the chlorination and bromination of the 1-halogenonappthalenes (1-Hlg-Naph's) the sequence of the relative rates, presuming the halogenation to occur very substantially at the 4-position (11, 12), is very similar to that of the halogenobenzenes, the data for the bromination decreasing in the order 1-F-Naph (3.7) > NaphH (1.00) > 1-I-Naph (0.22) > 1-Cl-Naph (0.13) > 1-Br-Naph (0.09) (13).

Can. J. Chem. Downloaded from www.nrcresearchpress.com by 85.192.166.187 on 09/08/12
For personal use only.

TABLE 1. Sulfonation of benzene and the halogenobenzenes with SO_3 in dichloromethane at 22°C

Benzene substituent	SO_3 (equiv., ±0.1)	Reaction time (min)	Product mixture composition[a] (%, ±3)		
—	1.0	1020	1-S (≥98)		
	3.0	35	1-S (94)	1,3-S_2 (6)	
	4.0	90	1-S (63)	1,3-S_2 (37)	
1-F	1.0	30	4-S (≥98)		
	4.0	30	4-S (≥98)		
	4.0	1020	4-S (86)	2,4-S_2 (10)	2,4,6-S_3 (4)
	6.0	1020	4-S (64)	2,4-S_2 (27)	2,4,6-S_3 (9)
	8.0	1020	4-S (64)	2,4-S_2 (17)	2,4,6-S_3 (19)
	10.0	1660	4-S (51)	2,4-S_2 (21)	2,4,6-S_3 (28)
1-Br	1.0	30	4-S (≥98)		
	4.0	30	4-S (≥98)		
	8.0	1020	4-S (85)	2,4-S_2 (15)	
1-Cl	1.0	30	4-S (≥98)		
	4.0	30	4-S (≥98)		
	8.0	1020	4-S (80)	2,4-S_2 (20)	
1-I	1.0	30	4-S (≥98)		
	4.0	30	4-S (≥98)		
	4.0	265	4-S (85)	2,4-S_2 (9)	2,4,6-S_3 (6)
	6.0	265	4-S (66)	2,4-S_2 (27)	2,4,6-S_3 (7)
	8.0	1020	4-S (44)	2,4-S_2 (38)	2,4,6-S_3 (18)

[a]S stands for $SO_3^- K^+$.

tion of four chloro-substituted anthracenes with SO_3 in nitromethane at 20°C, the results of which are given in Table 3.

The sulfonation of benzene with 4.0 mol-equiv. of SO_3 yields initially benzenesulfonic acid and subsequently the 1,3-disulfonic acid (1,3-S_2) as the water soluble products. In the halogenobenzene series the initial sulfonation yields very predominantly the 4-S, irrespective of the type of halogen (Table 1).[7] The positional reactivity order in the sulfonation of the four halogenobenzenes is similar to that of $PhOSO_2Me$[8] and $PhOSO_2OMe$ (18), the substituents of which also exhibit both a −I and +M effect.[9]

The further sulfonation of the four halogenobenzene-4-sulfonic acids is very much slower than that of the starting halogenobenzene and leads to the formation of the corresponding 2,4-S_2, and with fluoro- and iodobenzene even to the 2,4,6-S_3. The rates of sulfonation of both the 4-S and 2,4-S_2 are lower for 1-fluoro- and 1-iodobenzene than for 1-chloro- and 1-bromobenzene. This behaviour is in line with the partial rate factor sequence for the bromination of the four 1-halogenonaphthalenes (13).[6]

Halogenonaphthalenes

Sulfonation of 1-fluoronaphthalene with 1.0 mol-equiv. of SO_3 gives only the 4-S, whereas the other three 1-Hlg-naphthalenes yield in addition ≈7% 5-S (Table 2). Again 1-naphthyl methanesulfonate behaves like 1-fluoronaphthalene in that only the 4-S is formed (19). For protiodetritiation of the mono[^{3}H]-1-halogenonaphthalenes the partial rate factors decrease for Hlg = F in the order f_4 (5320) ≫ f_2 (81) ≈ f_8 (62) ≈ f_5 (50) ≫ f_3 (0.2), for Hlg = Cl in the order f_4 (307) ≫ f_8 (50) ≈ f_5 (33) > f_2 (11) > others, and for Hlg = Br in the order f_4 (157) > f_8 (54) > f_5 (29) > f_2 (6.6) > others (20). The very predominant sulfonation of 1-fluoronaphthalene at the 4-position is in line with the partial rate factor sequence for protiodetritiation. Steric effects in hydrogen exchange are significantly smaller than in any other electrophilic substitution, if not entirely absent (21, 22). The very low content of the 1-fluoro-2-S and 8-S is therefore due to electronic effects of the fluorine substituent. Studies with Catalin Stuart space-filling molecular models do predict that the degree of steric hindrance for sulfonation *peri* to the 1-fluoro substituent is only moderate, but that it is very much larger with the other halogens, rendering sulfonation *peri* to these three halogens impossible.

Sulfonation of any of the four 1-halogenonaphthalene-4-sulfonic acids yields a mixture of the 2,4-S_2 and 4,7-S_2. With the 1-fluoro compound the ratio of [2,4-S_2]:[4,7-S_2] is 0.40 ± 0.02, irrespective of the amount of reagent and the reaction time. With 1-chloronaphthalene, using 2.0 and 4.0 mol-equiv. of SO_3, the [2,4-S_2]:[4,7-S_2] ratio decreases from 0.89 to 0.10 (Table 2). These two data are thought to be the kinetically determined and the thermodynamically controlled isomer distributions, respectively. The driving force for the apparent isomerization of the 2,4-S_2 is relief of steric strain between the 1-chloro and 2-sulfo substituents.[10] With 1-bromo- and 1-iodonaphthalene the [2,4-

[7]The sulfonation of chlorobenzene in 1,2-dichloroethane at −12°C (15) and that of bromo- (16) and iodobenzene (17) in liquid sulfur dioxide at −10°C is reported to yield predominantly the 4-S with, in addition, the 2-S and 3-S in yields of 4 ± 2 and 15 ± 2, 0.6 and 3.6, and 0.8 and 0.6%, respectively.

[8]P. de Wit. Private communication.

[9]The 2-fluoro, 2-chloro, and 2-methyl derivatives of $PhOSO_2Me$ react with 2.0 mol-equiv. of SO_3 to give the 4-S and 5-S in ratios of 33:67, 98: ≤2, and 98: ≤2, respectively (18). This infers that, as a first approximation, the *para*-directing effects of the methanesulfonate and fluoro substituents are quite comparable in size, and that these effects are both substantially greater than the *para*-directing effects of the chloro and methyl substituents.

[10]Upon sulfonation of 1,3-dimethoxynaphthalene with SO_3 in nitromethane a similar type of isomerization of the initially formed 4-S into the thermodynamically more stable 7-S was observed (23).

Can. J. Chem. Downloaded from www.nrcresearchpress.com by 85.192.166.187 on 09/08/12
For personal use only.

TABLE 2. Sulfonation of halogenonaphthalenes with SO_3 in dichloromethane at 22°C

Halogen substituent	SO_3 (equiv., ±0.1)	Reaction time (min)	Product mixture composition[a] (%, ±3)					
1-F	1.0	110	4-S (≥98)					
	2.0	40	4-S (44)		2,4-S_2 (17)	4,7-S_2 (39)		
	4.0	5			2,4-S_2 (27)	4,7-S_2 (69)		2,4,7-S_3 (4)
	4.0	1680			2,4-S_2 (26)	4,7-S_2 (68)		2,4,7-S_3 (6)
	4.0	4145			2,4-S_2 (26)	4,7-S_2 (67)		2,4,7-S_3 (7)
	6.0	25			2,4-S_2 (26)	4,7-S_2 (66)		2,4,7-S_3 (8)
1-Cl	1.0	60	4-S (93)	5-S (7)				
	2.0	40	4-S (29)		2,4-S_2 (31)	4,7-S_2 (35)	5,7-S_2 (5)	
	4.0	5	4-S (13)		2,4-S_2 (24)	4,7-S_2 (58)	5,7-S_2 (5)	
	4.0	1240			2,4-S_2 (9)	4,7-S_2 (78)	5,7-S_2 (7)	2,4,7-S_3 (6)
	6.0	1500			2,4-S_2 (8)	4,7-S_2 (80)	5,7-S_2 (6)	2,4,7-S_3 (6)
1-Br	1.0	15	4-S (85)	5-S (6)		4,7-S_2 (9)		
	2.0	40	4-S (34)	5-S (6)		4,7-S_2 (60)		
	4.0	5			2,4-S_2 (7)	4,7-S_2 (88)	5,7-S_2 (5)	
	4.0	1240			2,4-S_2 (6)	4,7-S_2 (84)	5,7-S_2 (5)	2,4,7-S_3 (5)
	6.0	1500			2,4-S_2 (5)	4,7-S_2 (81)	5,7-S_2 (6)	2,4,7-S_3 (8)
1-I	1.0	15	4-S (74)	5-S (8)		4,7-S_2 (18)		
	2.0	40	4-S (57)	5-S (8)		4,7-S_2 (35)		
	4.0	5	4-S (10)		2,4-S_2 (12)	4,7-S_2 (72)	5,7-S_2 (6)	
	4.0	1240			2,4-S_2 (11)	4,7-S_2 (78)	5,7-S_2 (6)	2,4,7-S_3 (5)
	6.0	280			2,4-S_2 (14)	4,7-S_2 (75)	5,7-S_2 (5)	2,4,7-S_3 (6)
2-Cl	1.0	85	4-S (17)	8-S (83)				
	2.0	5	4-S (9)	8-S (27)		6,8-S_2 (64)		
	2.0	40	4-S (7)	8-S (15)		6,8-S_2 (78)		
	4.0	5	4-S (9)	8-S (8)		6,8-S_2 (83)		
	4.0	120			4,7-S_2 (8)	6,8-S_2 (92)		
2-Br	1.0	8	4-S (14)	8-S (86)				
	2.0	5	4-S (7)	8-S (24)		6,8-S_2 (69)		
	2.0	40	4-S (9)	8-S (12)		6,8-S_2 (79)		
	4.0	5	4-S (8)	8-S (9)		6,8-S_2 (83)		
	4.0	20	4-S (7)		4,7-S_2 (8)	6,8-S_2 (85)		
	4.0	120			4,7-S_2 (16)	6,8-S_2 (84)		
	6.0	120			4,7-S_2 (14)	6,8-S_2 (86)		

[a]S stands for SO_3^- K^+.

TABLE 3. Sulfonation of chloroanthracenes with 1.0 mol-equiv. of SO_3 in nitromethane at 22°C[a]

Anthracene substituents	Product mixture composition (%, ±3)[b]	
2-Cl	9-S (>90)	
9-Cl	4-S (18)	10-S (82)
1,5-Cl_2	4-S (53)	4,8-S_2 (47)
1,8-Cl_2	4-S (50)	4,5-S_2 (50)

[a]Reaction time 45 min.
[b]S stands for SO_3^- Na^+.

S_2]:[4,7-S_2] ratio appears to be independent of the reaction conditions, with values of 0.07 and 0.16, respectively. These values, which are fairly similar to the eventual ratio found for 1-chloronaphthalene, accordingly indicate that the conversion of 1-bromo- and 1-iodobenzene-4-S into the 2,4-S_2 and 4,7-S_2 is thermodynamically controlled.[11]

Sulfonation of the 1-Hlg-naphthalene-5-sulfonic acids (Hlg = Cl, Br, I) yields the corresponding 5,7-S_2. On reaction of the four 1-halogenonaphthalenes with ≥4.0 mol-equiv. of SO_3, some 2,4,7-S_3 is eventually formed.[12]

Sulfonation of 2-chloro- and 2-bromonaphthalene with 1.0 mol-equiv. of SO_3 yields a mixture containing predominantly 8-S (≈85%) with a small amount of 4-S (≈15%). The eventual products on using 4.0–6.0 mol-equiv. of SO_3 are 6,8- and 4,7-S_2, formed for the 2-chloro and 2-bromo isomer in ratios of 92:8 and 85:15, respectively. The monosulfonation of 2-naphthyl methanesulfonate also yields the 8-S as the predominant product (75%) and in addition small amounts of the 5-S and 6-S (19). Sulfonation of 2-methylnaphthalene with 1.0 mol-equiv. of SO_3 yields mainly the 8-S (49%) with, in addition, 1-S (8%), 4-S (15%), 5-S (15%), and 6-S (14%) (24).

Chloroanthracenes

Sulfonation of 2-chloroanthracene with 1.0 mol-equiv. of SO_3 in nitromethane as solvent gives the 9-S as the very predominant product (cf. Table 3). 2-Methylanthracene behaves quite similarly, the sulfonation product mixture consisting of

[11]Sulfonation of 4-sulfo-1-naphthyl methanesulfonate with SO_3 yields only 4,7-S_2 (19).

[12]It cannot be rigorously excluded that *ipso* sulfodehalogenation (5) has occurred with 1-bromo- and 1-iodonaphthalene-4,7-S_2 with formation of naphthalene-1,4,6(≡1,4,7)-S_3 (cf. Table 5, last entry).

Can. J. Chem. Downloaded from www.nrcresearchpress.com by 85.192.166.187 on 09/08/12
For personal use only.

TABLE 4. ^{1}H NMR data of benzene, the halogenobenzenes, and their sulfonates

Benzene substituents[a]	Solvent	δ (ppm, ±0.03)[b] 1	2	3	4	5	6
—	$CDCl_3$	7.39					
	D_2O	7.42					
1-S	D_2O		7.81	7.55	7.55		
1,3-S_2	D_2O		8.19		7.98	7.70	
1-F	$CDCl_3$		7.07	7.34	7.14		
1-F-4-S	D_2O		7.28	7.85			
1-F-2,4-S_2	D_2O			8.19		8.00	7.43
1-F-2,4,6-S_3	D_2O			8.45			
1-Cl	$CDCl_3$		7.27	7.33	7.31		
1-Cl-4-S	D_2O		7.57	7.78			
1-Cl-2,4-S_2	D_2O			8.36		7.93	7.71
1-Br	$CDCl_3$		7.52	7.27	7.29		
1-Br-4-S	D_2O		7.72	7.72			
1-Br-2,4-S_2	D_2O			8.37		7.81	7.79
1-I	$CDCl_3$		7.72	7.12	7.34		
1-I-4-S	D_2O		7.93	7.55			
1-I-2,4-S_2	D_2O			8.36		7.61	8.28
1-I-2,4,6-S_3	D_2O			8.47			

[a]S stands for SO_3^- K^+.
[b]All $^3J_{H,F}$ and $^4J_{H,F}$ values were found to be 8.5–9.0 and 6.5–7.0 Hz, respectively.

TABLE 5. ^{1}H NMR data of the halogenonaphthalenes and their sulfo products

Naphthalene substituents[a]	Solvent	δ (ppm, ±0.03)[b] 1	2	3	4	5	6	7	8
—	$CDCl_3$	7.88	7.51						
F	D_2O	7.91	7.54						
1-F	$CDCl_3$		7.55	7.17	7.90	7.66	7.40	7.55	8.13
1-F-4-S	D_2O		7.16	8.02		8.55	7.70	7.60	8.10
1-F-2,4-S_2	D_2O			8.43		8.60	7.66	7.80	8.20
1-F-4,7-S_2	D_2O		7.36	8.25		8.73	8.08		8.62
1-F-2,4,7-S_3	D_2O			8.25		8.30	8.01		8.52
1-Cl	$CDCl_3$		7.59	7.41	7.88	7.79	7.59	7.59	8.30
1-Cl-4-S	D_2O		7.54	7.93		8.60	7.72	7.72	8.38
1-Cl-5-S	D_2O		7.62	7.58	8.58		8.17	7.78	8.45
1-Cl-2,4-S_2	D_2O			8.42		8.63	7.72	7.72	8.27
1-Cl-4,7-S_2	D_2O		7.62	8.02		8.80	8.09		8.76
1-Cl-5,7-S_2	D_2O		7.73	7.68	8.48		8.65		9.13
1-Cl-2,4,7-S_3	D_2O			8.50		8.86	8.19		9.03
1-Br	$CDCl_3$		7.87	7.37	7.87	7.87	7.63	7.63	8.37
1-Br-4-S	D_2O		7.92	7.98		8.65	7.75	7.75	8.47
1-Br-5-S	D_2O		7.81	8.03	8.65		8.18	7.68	8.23
1-Br-2,4-S_2	D_2O			8.48		8.61	7.67	7.57	8.73
1-Br-4,7-S_2	D_2O		7.87	8.03		8.81	8.08		9.20
1-Br-5,7-S_2	D_2O		8.07	8.21	8.70		8.59		9.13
1-Br-2,4,7-S_3	D_2O			8.39		8.90	8.18		
1-I	$CDCl_3$		7.85	7.20	8.13	7.80	7.55	7.55	8.13
1-I-4-S	D_2O		7.80	8.22		8.59	7.71	7.71	8.22
1-I-5-S	D_2O		7.88	7.38	8.66		8.15	7.62	8.32
1-I-2,4-S_2	D_2O			8.20		8.87	7.83	7.75	7.97
1-I-4,7-S_2	D_2O		7.78	7.98		8.76	8.05		8.58
1-I-5,7-S_2	D_2O		8.0	7.75	8.70		8.49		9.15
1-I-2,4,7-S_3	D_2O			8.54		8.33	8.20		9.10
2-Cl	$CDCl_3$	7.80		7.55	7.80	7.86	7.53	7.53	7.86
2-Cl-4-S	D_2O	7.82		8.27		8.43	7.64	7.58	8.03
2-Cl-8-S	D_2O	8.56		7.56	7.91	8.02	7.52	8.12	
2-Cl-4,7-S_2	D_2O	7.68		8.22		8.38	8.09		8.18
2-Cl-6,8-S_2	D_2O	8.47		7.63	8.04	8.42		8.62	

Can. J. Chem. Downloaded from www.nrcresearchpress.com by 85.192.166.187 on 09/08/12
For personal use only.

TABLE 5 (*Concluded*)

Naphthalene substituents[a]	Solvent	δ (ppm, ±0.03)[b] 1	2	3	4	5	6	7	8
2-Br	$CDCl_3$	8.02		7.56	7.82	7.76	7.51	7.51	7.72
2-Br-4-S	D_2O	7.82		8.25		8.42	7.72	7.72	7.92
2-Br-8-S	D_2O	8.74		7.63	7.78	7.97	7.53	8.09	
2-Br-4,7-S_2	D_2O	7.85		8.28		8.38	7.87		8.26
2-Br-6,8-S_2	D_2O	8.80		7.77	7.98	8.40		8.50	
1,4,6-S_3(≡1,4,7-S_3)[c]	D_2O		8.15	8.15		8.91		8.01	8.45

[a]S stands for $SO_3^- K^+$.
[b]All $^3J_{H,H}$, $^4J_{H,H}$, $^3J_{H,F}$, $^4J_{H,F}$, and $^5J_{H,F}$ values were found to be 8.0–10.0, 1.0–3.0, 9.5–10.6, 5.4–7.1, and 1.5–2.0 Hz, respectively.
[c]Calculated data from the ^1H chemical shifts of potassium naphthalene-1-sulfonate and the naphthalene substituent shifts of the 1- and 2-SO_3^- groups.

TABLE 6. ^1H NMR data of anthracene and some sulfo and chloro derivatives

Anthracene substituents[a]	Solvent[b]	δ (ppm) 1	2	3	4	5	6	7	8	9	10
—	TCM	8.02(m)	7.46(m)							8.42(s)	
	DMSO	8.12(m)	7.54(m)							8.61(s)	
1-S[c]	DMSO	—	8.08(m)	7.51(m)	← 8.08(m)	→	← 7.51(m)	→ 8.08(m)		9.53(s)	8.57(s)
2-S[c]	DMSO	8.52(s)	—	7.71(dd)	← 8.06(m)	→	← 7.49(m)	→ 8.06(m)		8.64(s)[d]	8.55(s)[d]
9-S[c]	DMSO	9.71(m)	← 7.48(m)	→	8.03(m)					—	8.57(s)
2-Cl	TCM	7.98(m)	—	7.47(m)	← 7.98(m)	→	← 7.47(m)	→ 7.98(m)		8.31(s)[e]	8.40(s)[e]
2-Cl-9-S	DMSO	9.76(d)[f]	—	7.49(m)	← 8.05(m)	→	← 7.49(m)	→ 9.76(m)		—	8.65(s)
9-Cl	TCM	8.48(dd)[g]	← 7.52(m)	→	7.96(m)					—	8.33(s)
9-Cl-4-S	DMSO				—					—	9.60(s)
9-Cl-10-S	DMSO	8.49(m)	← 7.64(m)	→	9.82(m)					—	—
1,5-Cl_2	TCM	—	← 7.49(m)	→	8.00(dd)[h]		—			8.84(s)	
1,5-Cl_2-4-S	DMSO	—				—	—		8.27(d)[i]	8.99(s)	10.02(s)
1,5-Cl_2-4,8-S_2	DMSO	—				—	—			10.05(s)	
1,8-Cl_2	TCM	—	7.58(dd)[j]	7.34(m)	7.86(d)[k]				—	9.18(s)	8.37(s)
1,8-Cl_2-4-S	DMSO	—			—		7.89(d)[l]		9.17(s)	9.72(s)	
1,8-Cl_2-4,5-S_2	DMSO	—			—		—		—	9.29(s)	10.61(s)

[a]S stands for $SO_3^- Na^+$.
[b]TMC and DMSO stand for trichloromethane-*d* and dimethyl sulfoxide-d_6, respectively.
[c]Data from ref. 31.
[d,e]The data may be reversed.
[f]*J* 1.4 Hz.
[g]*J* 1.4 and 8.0 Hz.
[h]*J* 1.5 and 8.5 Hz.
[i]*J* 8.5 Hz.
[j]*J* 1.5 and 7.0 Hz.
[k]*J* 8.4 Hz.
[l]*J* 7.5 Hz.

81% 9-S and 19% 10-S (25). 9-Chloroanthracene gives 18% 4-S and 82% 10-S; the sulfonic acid isomer ratio is very similar to that of 9-neopentylanthracene, giving 15% 4-S and 85% 10-S (26).[13] The f_4/f_{10} partial rate factor ratio for the SO_3 sulfonation of 9-chloroanthracene (0.11) is smaller than the f_1/f_9 ratio for anthracene (0.20) (27), indicating that the mesomeric stabilization by the 9-chloro substituent is greater for the transition state leading to the 10-S than for that leading to the 4-S. 1,5-Dichloro- and 1,8-dichloroanthracene undergo sulfonation "*para*" to one of the chlorine atoms giving 4-S; further sulfonation yields the 4,8-S_2 and 4,5-S_2, respectively. The absence of any 9-S in the sulfonation of 1,5-dichloroanthracene may be ascribed to prohibitive steric hindrance by the chlorine substituents. The absence of any 10-S with 1,8-dichloroanthracene then remains notable. The sulfonation of 1-methylanthracene does yield 10% of 10-S, but the main monosulfonation product formed in 90% yield is the 4-S (24). For the sulfonation of both 9-chloro- and 1,8-dichloroanthracene, the mesomeric stabilization of the transition state by chlorine appears to be most effective at the ring containing the chlorine substituent, thus directing the entering sulfo group to the same ring.

Experimental

The halogenobenzenes, halogenonaphthalenes, and 9-chloroanthracene were obtained commercially and used as such. 2-Chloro-, 1,5- and 1,8-dichloroanthracene were synthesized from the corre-

[13]A comparison with 9-methylanthracene would not be significant, since this substrate on reaction with SO_3 undergoes exclusively methyl sulfonation to yield quantitatively 9-anthrylmethanesulfonic acid (27).

Can. J. Chem. Downloaded from www.nrcresearchpress.com by 85.192.166.187 on 09/08/12
For personal use only.

sponding anthraquinones by the Meerwein–Ponndorf–Verley reduction (28) and subsequent dehydration, using Al(*O*-cyclohexyl)$_3$ in dry cyclohexanol as solvent at 180°C in yields of 36, 20, and 43%, respectively. The ^{1}H NMR spectra of the substrates and their sulfo product mixtures were recorded using Varian XL-100 and Bruker AC-200 spectrometers.

Sulfonation procedures and analyses

The procedure for the SO_3 sulfonation of all the chloroanthracenes in nitromethane as solvent is as described under Method B in ref. 29. The procedure for all the other substrates is as follows. The desired amount of SO_3 was added to a homogeneous solution of 0.14 mmol of substrate in 0.5 mL of dry dichloromethane at ≈22°C under an argon atmosphere. During the sulfonation, the reaction mixture turned heterogeneous. After the appropriate reaction time, 0.5 mL of water was added, and the mixture heated at 70–80°C for 30 min to hydrolyse any sulfonic anhydride formed (30). The aqueous layer was isolated and neutralized with 10% aqueous potassium or sodium hydroxide and the water was removed by freeze-drying. Subsequently, an ^{1}H NMR spectrum of the resulting potassium or sodium sulfonate salt mixture dissolved in ^2H_2O was recorded for product assignment and the quantitative analysis.

The structural assignments of the sulfo products in the sulfonation mixtures were made on the basis of the observed chemical shifts, absorption area ratios, coupling constants, and excessive spin decoupling through double-resonance experiments. The structural assignments are compiled in Tables 4–6. The compositions of the sulfonation product mixtures were determined by multicomponent ^{1}H NMR analysis on the basis of specific absorptions of the various components (32).

1. H. Cerfontain, A. Koeberg-Telder, E. Vogel, and O. Wilmes. Recl. Trav. Chim. Pays-Bas, **113**, 288 (1994).
2. C.M. Suter. The organic chemistry of sulfur. John Wiley & Sons, New York. 1944. pp. 214–215, 277–279, 302.
3. H. Cerfontain. Mechanistic aspects of aromatic sulfonation and desulfonation. Interscience, New York. 1968. pp. 87–93.
4. C.W.F. Kort and H. Cerfontain. Recl. Trav. Chim. Pays-Bas, **88**, 860 (1969).
5. H. Cerfontain, A. Koeberg-Telder, K. Laali, H.J.A. Lambrechts, and P. de Wit. Recl. Trav. Chim. Pays-Bas, **101**, 390 (1982).
6. H. Cerfontain, A. Koeberg-Telder, H.J.A. Lambrechts, and P. de Wit. J. Org. Chem. **49**, 4917 (1984).
7. J.C.D. Brand and W.C. Horning. J. Chem. Soc. 3922 (1952).
8. R. Baker, C. Eaborn, and R. Taylor. J. Chem. Soc. 4927 (1961).
9. P.B.D. de la Mare. J. Chem. Soc. 2871 (1949).
10. C.W.F. Kort and H. Cerfontain. Recl. Trav. Chim. Pays-Bas, (*a*) **86**, 865 (1967); (*b*) **88**, 860 (1969).
11. H. Hirtz. Chem. Ber. **29**, 1404 (1896).
12. G. Schiemann, W. Gueffroy, and W. Winkelmüller. Liebigs Ann. **487**, 270 (1931).
13. P.B.D. de la Mare and P.W. Robertson. J. Chem. Soc. 100 (1948).
14. L.I. Smith and C.M. Moyle. J. Am. Chem. Soc. (*a*) **55**, 1676 (1933); (*b*) **58**, 1 (1936).
15. A.A. Spryskov and O.I. Kachurin. J. Gen. Chem. USSR, **28**, 2250 (1958).
16. K.L. Nelson and J.C. Robertson. *Cited in* Friedel–Crafts and related reactions. Vol. III. *Edited by* G.A. Olah. Interscience, New York. 1964. Chap. 42, p. 1388, ref. 251.
17. K.L. Nelson, T.G. Davies, and J.A. Knight. *Cited in* Friedel–Crafts and related reactions. Vol. III. *Edited by* G.A. Olah. Interscience, New York. 1964. Chap. 42, p. 1388, ref. 248.
18. P. de Wit, A.F. Woldhuis, and H. Cerfontain. Recl. Trav. Chim. Pays-Bas, **107**, 668 (1988).
19. H.R.W. Ansink, E. Zelvelder, and H. Cerfontain. Recl. Trav. Chim. Pays-Bas, **112**, 210 (1993).
20. C. Eaborn, P. Goldborn, R.E. Spillett, and R. Taylor. J. Chem. Soc. B, 1112 (1968).
21. R. Taylor. Electrophilic aromatic substitution. John Wiley and Sons Inc., New York. 1990. p. 61.
22. R. Baker, C. Eastborn, and R. Taylor. J. Chem. Soc. 4927 (1961).
23. H.R.W. Ansink, E. Zelvelder, and H. Cerfontain. Recl. Trav. Chim. Pays-Bas, **111**, 499 (1992).
24. K. Lammertsma and H. Cerfontain. J. Chem. Soc. Perkin Trans. 2, 673 (1979).
25. F. van de Griendt, C.P. Visser, and H. Cerfontain. J. Chem. Soc. Perkin Trans. 2, 911 (1980).
26. F. van de Griendt and H. Cerfontain. J. Chem. Soc. Perkin Trans. 2, 13 (1980).
27. H. Cerfontain, A. Koeberg-Telder, C. Ris, and C. Schenk. J. Chem. Soc. Perkin Trans. 2, 966 (1975).
28. A.I. Vogel. A text-book of practical organic chemistry. 3rd ed. Longmans, Green and Co. Ltd., London. 1958. p. 882 ff.
29. H.R.W. Ansink, E.J. de Graaf, E. Zelvelder, and H. Cerfontain. Can. J. Chem. **71**, 210 (1993).
30. N. Hesselbjerg Christensen. Acta Chem. Scand. **15**, 1507 (1961).
31. A. Koeberg-Telder and H. Cerfontain. Recl. Trav. Chim. Pays-Bas, **91**, 22 (1972).
32. H. Cerfontain, A. Koeberg-Telder, C. Kruk, and C. Ris. Anal. Chem. **46**, 72 (1974).

Can. J. Chem. Downloaded from www.nrcresearchpress.com by 85.192.166.187 on 09/08/12
For personal use only.

Concerning the internal rotational barrier and the experimental and theoretical $^nJ(^{13}C,^{13}C)$ and ^nJ $(^1H,^{13}C)$ in ethylbenzene-β-^{13}C

TED SCHAEFER,[1] WING K. CHAN, RUDY SEBASTIAN, ROBERT SCHURKO, AND FRANK E. HRUSKA
Department of Chemistry, University of Manitoba, Winnipeg, MB R3T 2N2, Canada

Received March 15, 1994

TED SCHAEFER, WING K. CHAN, RUDY SEBASTIAN, ROBERT SCHURKO, and FRANK E. HRUSKA. Can. J. Chem. **72**, 1972 (1994).

The ^1H nuclear magnetic resonance spectra of ethylbenzene-β-^{13}C in CS_2/C_6D_{12} and acetone-d_6 solutions yield long-range $^1H,^1H$ and $^1H,^{13}C$ coupling constants. The $^{13}C\{^1H\}$ NMR spectra yield $^{13}C,^{13}C$ couplings. The conformational dependence of some of these coupling constants is compatible with two values of the barrier to internal rotation about the exocyclic Csp^2—Csp^3 bond. If the fourfold component of the internal rotational potential is not larger than about 20% of the twofold component and the perpendicular conformer is most stable, then the barrier height is probably less than 6 kJ/mol. However, if the stable conformer has a torsion angle of 60° for the exocyclic C—C bond, then the coupling constants are consistent with a twofold barrier of about 23 kJ/mol. Experimental values of $\langle\sin^2\psi\rangle$ and $\langle\sin^2\theta\rangle$, where ψ and θ are the torsion angles for the exocyclic C—C and C—H bonds, respectively, are compared to those obtained from INDO MO FPT computations of the angular dependence of ^nJ(H,C), and ^nJ(H,H), ^nJ(C,C) for $n \geq 3$. For example, the computations very likely give the correct qualitative ψ dependence of ^5J(C,C), yet overestimate its extremum by about a factor of two, either because of an overestimate of the σ–π exchange integrals or because of too large a valence orbital density at the carbon nucleus. Other ^nJ values are discussed in a similar manner and, because optimized geometries are used in the computations, a somewhat more reliable treatment arises for some coupling constants; an example is ^3J(C,C) at small torsion angles.

TED SCHAEFER, WING K. CHAN, RUDY SEBASTIAN, ROBERT SCHURKO et FRANK E. HRUSKA. Can. J. Chem. **72**, 1972 (1994).

Les spectres de résonance magnétique du ^1H de l'éthylbenzène-β-^{13}C en solutions dans le CS_2/C_6D_{12} et dans l'acétone-d_6 ont permis d'obtenir les constantes de couplage à longue distance $^1H,^1H$ et $^1H,^{13}C$. Les spectres RMN $^{13}C\{^1H\}$ fournissent les couplages $^{13}C,^{13}C$. La dépendance conformationnelle de quelques unes de ces constantes de couplage est compatible avec deux valeurs pour la barrière à la rotation interne autour de la liaison Csp^2—Csp^3. Si la valeur de composante quaternaire du potentiel rotationnel interne n'est pas supérieure à 20% de la composante binaire et si le conformère perpendiculaire est le plus stable, la hauteur de la barrière est probablement inférieure à 6 kJ/mol. Toutefois, si l'angle de torsion de la liaison C—C exocyclique du conformère stable est égale à 60°, les constantes de couplage sont alors en accord avec une barrière binaire d'environ 23 kJ/mol. On a comparé les valeurs expérimentales de $\langle\sin^2\psi\rangle$ et $\langle\sin^2\theta\rangle$, dans lesquelles ψ et θ sont respectivement les angles de torsion des liaisons C—C et C—H exocycliques, avec celles obtenues par des calculs INDO MO FPT de la dépendance angulaire de ^nJ(H,H), ^nJ(H,C), et ^nJ(C,C) pour $n \geq 3$. Par exemple, les calculs donnent vraisemblablement la dépendance qualitative correcte de ψ de ^5J(H,H) même s'ils surévaluent ses extrêmes par un facteur d'environ deux, soit par une surévaluation des intégrales d'échange σ–π soit par une trop grande densité orbitalaire de valence au niveau du noyau de carbone. On discute de la même manière d'autres valeurs de ^nJ et, parce que l'on utilise de géométries optimisées dans les calculs, on obtient un traitement un peu plus certain pour quelques unes des constantes de couplage; par exemple, ^3J(C,C) à des angles de torsion faibles.

[Traduit par la rédaction]

Introduction

The long-range spin–spin coupling constants between the methylene and ring protons, $^nJ(H,CH_2)$, in ethylbenzene have been precisely determined for a variety of solvent conditions (1). In particular, $^6J(H,CH_2)$ is a σ–π coupling constant and, as such, is proportional to $\sin^2\theta$, θ being the torsion angle about the Csp^2—Csp^3 bond, as in **1**. If the extrema in $^6J(H,CH_2)$ can be

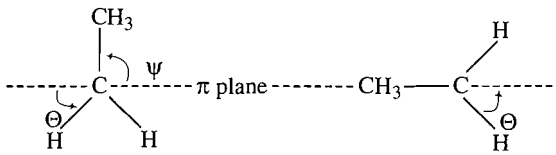

1, Θ = 30°, ψ = 90° **2**, Θ = 60°, ψ = 0°

assessed, those for 0° and 90° in θ, then the measured value of $^6J(H,CH_2)$ provides the average or expectation value, $\langle\sin^2\theta\rangle$, at the temperature of the measurement. The value of $\langle\sin^2\theta\rangle$ indicates the conformation of lowest energy (1), namely, **1**, but can also be related to the barrier to rotation about the Csp^2—Csp^3 bond via classical or quantum mechanical averaging procedures. In this way the apparent sixfold barrier, V_2, is deduced as 5.0 kJ/mol; **2** is then the conformation of highest energy.

Computations at various levels of ab initio molecular orbital theory (1, 2) agree that **1** and **2** represent the conformers of lowest and highest energy, respectively, but predict the presence of a minor fourfold, in addition to the major twofold, component of the internal rotational potential. For example, if a theoretical fourfold component of 0.9 kJ/mol is used to fit the rotational spectrum in the vapor phase (2), then the twofold component is 4.9 ± 0.7 kJ/mol; alternatively, the latter is 7.8 ± 0.7 kJ/mol if the former vanishes. A combined molecular mechanics – molecular orbital method (3) arrives at 4.2 kJ/mol for the energy difference between **1** and **2**. Reference 3 also collects citations to all previous, somewhat contradictory, experimental work on the conformational properties of ethylbenzene. In addition, supersonic molecular jet spectroscopy (4) strongly implies **1** as the most stable conformer.

By way of contrast, the ^1H nmr spectra of 3,5-dibromoethylbenzene, dissolved in a nematic solvent (5), are interpreted to yield a minimum in the internal rotational potential at θ = 60°. It is possible, though perhaps improbable, that the bromine substituents cause a shift in the phase of the potential, although molecular orbital computations on the free molecule do not detect such a shift. It may therefore be that intermolecular forces from the partially ordered solvent molecules are respon-

[1]Author to whom correspondence may be addressed.

Can. J. Chem. Downloaded from www.nrcresearchpress.com by 85.192.166.187 on 09/08/12
For personal use only.

sible for a change in the conformational minimum. The parent molecule has not been studied in the same nematic medium.

While the magnitude of the internal rotational potential in ethylbenzene very likely lies between 4.2 and 9.2 kJ/mol (1–4, 6), and is therefore somewhat uncertain, the further apparent uncertainly in the phase of the potential is also disconcerting. The experimental estimates of the phase favor either **1** or **3** as

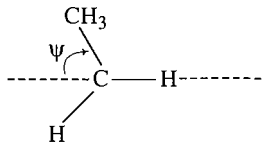

3, $\Theta = 60°, 0°$
$\psi = 60°$

the conformer of minimum energy, examples of each alternative being found for the molecule in the vapor as well as in solution.

Now, $^6J(H,CH_2)$ is dominated by a certain region of the internal rotational potential (see **1** and **2**); being proportional to $\sin^2\theta$ it depends on the probability that the two α C—H bonds take on the various angles, θ. The α C—C bond, on the other hand, samples a different region of the internal potential. Because $^6J(H,C)$ and $^5J(C,C)$ are very likely σ, π coupling constants (7) and therefore proportional to $\sin^2\psi$, their measurement should help to further characterize the internal barrier in ethylbenzene. The first purpose of the present work is therefore the analysis of the ^1H nmr spectrum of ethylbenzene-β-^{13}C, yielding the long-range $^nJ(H,H)$ and $^nJ(H,C)$. The ^{13}C $\{^1H\}$ spectra provide the magnitudes of $^nJ(C,C)$. It turns out that $^6J(H,H)$ and $^6J(H,C)$ are consistent with two magnitudes of the internal barrier, one high and corresponding to **3** as the conformer of lowest energy, the other much lower and consistent with **1** as most stable.

INDO MO FPT (8) computations of long-range, σ–π coupling constants have been reasonably successful in the prediction of their qualitative conformational dependence (7, 9, 10). The quantitative predictions are usually less successful, that is, those of the extrema in relationships such as $^nJ = {}^nJ_{90} \sin^2\theta$; hence the need for the use of model compounds in which the conformations are well defined (large barriers). Of course, once the internal potential is known, then, together with experimental values of ^nJ, it is a source of the extrema in ^nJ. Consequently, a comparison with INDO MO FPT computations of ^nJ as a function of conformational angle yields hints as to the causes of disparities between experiment and the semiempirical model. This will be so particularly for long-range coupling constants for which the σ–π electron interactions have a direct dependence on conformational angle. A semiquantitive indication of the disparities can they be had.

While real progress is being made in the ab initio molecular orbital calculations of J, the computational investment (11) is rather high, so that the speed of the INDO MO FPT procedure is of great utility, particularly if estimates of its qualitative and quantitative behaviour are available. Hence the second purpose of this work is a comparison of semiempirical computations of $^nJ(H,C)$ and $^nJ(C,C)$ for ethylbenzene with the experimentally indicated extrema for such coupling constants.

Experimental

The ethylbenzene-β-^{13}C (99% enriched) from Isotec was prepared as 8.0 mol% solutions in CS_2/C_6D_{12}/TMS and acetone-d_6/TMS solvent mixtures (see Table 1 for details). The solutions were filtered into 5 mm o.d. nmr sample tubes, which were then degassed by five freeze–pump–thaw cycles and flame-sealed to provide reasonably symmetric tops. The ^1H nmr spectra were obtained with an AM 300 nmr spectrometer in a manner previously described (7, 12). Acquisition times of the free induction decays ranged from 41 to 51 s for various response regions; as many as 64 decays were coadded in digital form and the digital resolution was 0.012 Hz/point or better. Modest amounts of resolution enhancement were applied by means of convolution and produced satisfactory spectra in the frequency domain. Figure 1 displays an example of such spectra.

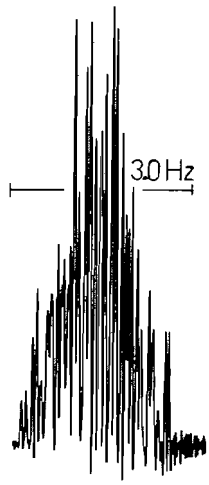

FIG. 1. One of the eight multiplets, near 779 Hz relative to TMS, of the ^1H nmr spectrum at 300 K and 300 MHz of the methylene protons in ethylbenzene-β-^{13}C, dissolved as an 8.0 mol% solution in a CS_2/C_6D_{12}/TMS solvent mixture, is displayed. The splitting of the doublet at the far right is 0.05 Hz. The acquisition times of 32 free induction decays were 51.2 s, the digital resolution was <0.01 Hz/point, and some resolution enhancement procedures were applied. In a first-order spectrum this multiplet would consist of 18 peaks due to the five phenyl protons (3 × 3 × 2). At least 32 peaks are resolved.

STO-3G molecular orbital computations (13) utilized GAUSSIAN 92 (14) and were done at 15° intervals in the conformational angle, ψ (see **1**). All bond angles and lengths were optimized with the constraint that the nuclei of the phenyl group remained in a plane. These geometries were employed in the CNDO/2 and INDO MO FPT (8, 15) computations of ^nJ.

Results and discussion

Spectral analyses

The ^1H nmr spectra were analyzed with the computer program NUMARIT (16), greatly modified by R. Sebastian. The ensuing spectral parameters are found in Table 1. Those coupling constants in common with isotopically unenriched ethylbenzene agree reasonably well with previous values for the latter (1), obtained at different dilutions in the solvents in question.

The ^{13}C nmr chemical shifts and $^nJ(C,C)$ appear in Table 2. The indicated signs of $^nJ(C,C)$ are based on theory as well as on experimental signs for related molecules (8).

The barrier to rotation about the Csp^2—Csp^3 bond

$^6J(H,CH_2)$ is –0.455 Hz in CS_2/C_6D_{12} and –0.454 Hz in acetone-d_6 solutions (Table 1), essentially the same as the corresponding values of –0.455 and –0.451 Hz for more dilute solutions (1) of the unenriched ethylbenzene. As before (1), the apparent twofold barrier follows from a $\langle\sin^2\theta\rangle$ of 0.455/1.16 or 0.392, which, at 300 K, corresponds to 5.0 kJ/mol if **1** is indeed the conformer of lowest energy. For a tetrahedral geometry at the methylene carbon atom, $\langle\sin^2\psi\rangle = 1.5–2\langle\sin^2\theta\rangle$. Then $\langle\sin^2\psi\rangle$

Can. J. Chem. Downloaded from www.nrcresearchpress.com by 85.192.166.187 on 09/08/12
For personal use only.

TABLE 1. The ^{1}H nmr spectral parameters for ethylbenzene-β-^{13}C at 300 K and 300.135 MHz

Parameter[c]	Solvent CS_2/C_6D_{12}[a]	Solvent Acetone-d_6[b]	Parameter	Solvent CS_2/C_6D_{12}[a]	Solvent Acetone-d_6[b]
$\nu(CH_3)$[d,e]	359.845	358.259	^5J(H, CH_2)	0.298	0.301
$\nu(CH_2)$	773.137	784.662	^6J(H, CH_2)	−0.455	−0.454
$\nu_2 = \nu_6$	2113.746	2159.101	^1J(H, C)	126.264	126.226
$\nu_3 = \nu_5$	2136.994	2176.494	^2J(H, C)	−4.906	−4.984
ν_4	2106.014	2143.751	^4J(H, C)	−0.245	−0.194
$^3J(CH_2, CH_3)$	7.596	7.605	^5J(H, C)	0.186	0.189
$^3J_{23} = {}^3J_{56}$	7.677	7.690	^6J(H, C)	−0.460	−0.467
$^3J_{34} = {}^3J_{45}$	7.419	7.444	Root-mean-square deviation	0.013	0.010
$^4J_{26}$	1.932	1.948			
$^4J_{24} = J_{46}$	1.256	1.250	Largest absolute difference	0.032	0.024
$^4J_{35}$	1.454	1.452			
$^5J_{25} = {}^5J_{36}$	0.604	0.595	Transitions assigned	4561	3738
^4J(H, CH_2)	−0.639	−0.637	Transitions calculated	5561	5738

[a]For an 8.0 mol% solution in CS_2 containing also 10 mol% of C_6D_{12} and 0.5 mol% of TMS.
[b]For an 8.0 mol% solution in acetone-d_6 containing also 0.5 mol% of TMS.
[c]The standard deviations were all less than 0.001 Hz.
[d]In Hz to high frequency of internal TMS.
[e]The spectral analyses imply that the magnitudes of ^nJ(H, CH_3) are 0.027(3), 0.014(2), and 0.001(1) Hz, respectively, for n = 5, 6, 7, in agreement with earlier results for ethylbenzene (1). ^5J(H, CH_3) was partially resolved in the methyl proton region, appearing as triplets.

TABLE 2. The ^{13}C nmr chemical shifts and ^nJ(C, C) for ethylbenzene-β-^{13}C at 75.48 MHz and 300 K

Parameter	Solvent[a] CS_2/C_6D_{12}	Solvent[a] Acetone-d_6	Parameter	Solvent[a] CS_2/C_6D_{12}	Solvent[a] Acetone-d_6
$\nu(CH_3)$	15.840	16.086	^1J	(+) 33.92[b]	(+) 33.90
$\nu(CH_2)$	29.306	29.367	^2J	(−) 2.32	(−) 2.37
ν_1	143.521	144.897	^3J	(+) 2.27	(+) 2.24
$\nu_2 = \nu_6$	127.628	128.517	^4J	(−) 0.51	(−) 0.54
$\nu_3 = \nu_5$	128.187	129.040	^5J	(+) 0.74	(+) 0.76
ν_4	125.534	126.324			

[a]For the samples described in Table 1.
[b]Estimated errors in ^nJ(C, C) are 0.02 Hz.

is 0.716 and, because ^6J(H,C) is −0.463(3) Hz, $^6J_{90}$(H,C) follows as −0.647(5) Hz. A check on this number follows from an experiment with 2,6-dimethoxyethylbenzene (80 vol.% in acetone-d_6), in which the ^{13}C nmr spectrum of the methyl group (1905 free induction decays, acquisition times of 20.5 s, a digital resolution of 0.024 Hz/point) gave ^6J(H,C) as (−)0.65(2) Hz on the basis of a first-order interpretation. By comparison with the internal barrier in 2,6-difluoroethylbenzene (17), which may be as large as 33 kJ/mol and is expected to be very similar to that in the dimethoxy derivative, ^6J(H,C) in the latter is a reasonable approximation to $^6J_{90}$(H,C).

An alternative interpretation of ^6J(H,CH_2) and ^6J(H,C) is based on **3** as the most stable conformer and a twofold barrier. One may note that $\langle\sin^2\theta\rangle$ would then vary between 0.375, for a rigid **3**, and 0.5, for unhindered rotation; the corresponding numbers for $\langle\sin^2\psi\rangle$ would be 0.75 and 0.5. The experimental values of the expectation values would then imply an apparent V_2 of 22.6 kJ/mol. This value appears unreasonably high in view of the fairly high-level molecular orbital computations described in the introduction in this paper.

A third interpretation allows for a substantial fourfold component in the Csp^2—Csp^3 barrier. If V_2 and V_4 have the same sign, as indicated by all available molecular orbital calculations (1, 2), then a $\langle\sin^2\psi\rangle$ of 0.716 at 300 K is compatible with, for example, V_2/V_4 ratios of 6.02/2.0, 8.5/5.0, and 12.0/7.8; it is assumed, as implied by all the theoretical models, that **1** is the most stable conformer. As V_4 increases in magnitude so must V_2, because a pure V_4 barrier entails a $\langle\sin^2\psi\rangle$ of 0.5. The rotational spectrum (2) is compatible with V_2/V_4 of 7.8(7)/0 and 4.9(7)/0.9; the experimental data were not extensive enough to fit V_2 and V_4 simultaneously. It appeared, however, that **1** was the most stable conformer in the vapor. The ratio 4.9(7)/0.9 implies a $\langle\sin^2\psi\rangle$ of 0.70(1) at 300 K, very close to its value in solution, whether in polar or nonpolar solvents (ref. 1 and Table 1). The potential function deduced from dipolar couplings for a solution of 3,5-dibromoethylbenzene in a liquid-crystalline solvent (5) has a $V_2/V_4/V_6$ of 4.4/2.2/−0.8, corresponding to a $\langle\sin^2\psi\rangle$ of 0.66_7 at 300 K, with **3**, however, as the least energetic conformer. This disagreement with the internal potential for ethylbenzene is remarkable in that the bromine substituents, placed symmetrically with respect to the site of the ethyl group, are not expected to change the phase of the potential. Hence intermolecular forces remain as the possible cause of the shift in phase in the nematic solvent.

If, as strongly indicated by the molecular orbital computations for the free molecule, V_4 is of the same sign as V_2 and not

Can. J. Chem. Downloaded from www.nrcresearchpress.com by 85.192.166.187 on 09/08/12
For personal use only.

Can. J. Chem. Downloaded from www.nrcresearchpress.com by 85.192.166.187 on 09/08/12
For personal use only.

larger than about 20% of the latter's magnitude, and if the barrier is independent of the isotropic solvent, as indicated by the long-range coupling constants, then the barrier height is probably less than 6 kJ/mol, with **1** as the minimum in energy.

The extrema in ^6J(H,C) and ^5J(C,C)

^6J(H,H) has a $\sin^2\theta$ dependence and its extremum, $^6J_{90}$, is -1.20_4 Hz in toluene (12). If the angle-independent contribution is neglected as an artifact, as discussed in other connections (9, 10, 18), then this magnitude is close to that computed with INDO MO FPT parameterization (9), namely, -1.14_4Hz. As discussed previously (9, 19, 20), this σ–π coupling can be written as ^6J(H,H) α $Q^{H}CHQ^{C}CH$, where $Q^{H}CH$ is the hyperfine interaction parameter representing the coupling between the proton in an aromatic C—H bond and unpaired π electron density (spin density) in a $p\pi$ orbital on the carbon atom of the bond; $Q^{H}CH$ is negative. $Q^{H}CCH$ represents the hyperfine interaction between a β-proton, as in toluene, and the $p\pi$ spin density on the contiguous aromatic carbon atom. $Q^{H}CCH$ is positive and proportional to $\sin^2\theta$. Experimentally, $^6J(H,CH_3)$ in toluene and $^7J(CH_3, CH_3)$ in *p*-xylene, at –0.602(2) Hz(12) and +0.596(9) Hz (recent unpublished measurement for a 50vol./vol.% solution in acetone in this laboratory), are essentially equal in magnitude. The $\sin^2\theta$ dependence of $^7J(CH_3,CH_3)$, as computed by INDO MO FPT methods (9), entails $Q^{H}CCHQ^{H}CCH$ α 1.378 Hz, while the experimental value is 1.200 Hz. These theoretical and experimental data reduce to the relationships, $(Q^{H}CH)^e = -1.00(Q^{H}CCH)^e$, $(Q^{H}CCH)^t = 1.07(Q^{H}CCH)^e$, and $(Q^{H}CH)^t = 0.88_6(Q^{H}CH)^e$; the superscripts refer to theoretical or experimental values.

The theoretical and experimental values of ^5J(C,C) and ^6J(H,C) in ethylbenzene can also be discussed in such a manner. Thus, ^6J(H,C) $\propto$ $Q^{H}CHQ^{C}CCC$ and ^5J(C,C) $\propto$ $Q^{C}CHQ^{C}CCC$ and therefore one has $^5J(C,C)/^6J(H,C)$ α $Q^{C}CH/Q^{H}CH$. In aromatic free radicals, $Q^{C}CH$ is positive and represents the hyperfine interaction between the $p\pi$ electron on the carbon atom of a C—H bond and its ^{13}C nucleus (21). In ethylbenzene (Tables 1 and 2), $^5J(C,C)/^6J(H,C)$ = (+)0.75(1)/–0463(3) or –1.62(3). The INDO MO FPT calculations do indeed predict that both coupling constants are proportional to $\sin^2\psi$, as expected for σ–π interactions, but find $^5J_{90}$(C,C) as 1.60 and $^6J_{90}$(H,C) as –0.49 Hz. The theoretical value of $Q^{C}CH/Q^{H}CH$ is therefore –3.26, the experimental value is –1.62(3). It follows that $(Q^{C}CH)^t = 1.78(3)(Q^{C}CH)^e$ and $(Q^{C}CCC)^t = 0.85_8(Q^{C}CCC)^e$. A reparameterization of the theoretical model would involve consideration of the magnitudes of valence *s* orbital densities at carbon and hydrogen and (or) the relevant σ–π exchange integrals, among other matters.

In summary, $(Q^{H}CH)^t = 0.88_6(Q^{H}CH)^e$, $(Q^{H}CCH)^t = 1.07(Q^{H}CCH)^e$, $(Q_{CH})^t = 1.78(Q^{C}CH)^e$, $(Q^{C}CCC)^t = 0.85_8(Q^{C}CCC)^e$, and $(Q^{H}CH)^e = -1.00(Q^{H}CCH)^e = -2.90(Q^{C}CCC)^e = -0.61_7(Q^{C}CH)^e$. These proportionalities will depend somewhat on the geometries assumed for the computations. They will now be used in adjusting the computed π electron contributions to other ^nJ(H,C) and ^nJ(C,C) in ethylbenzene.

$^5J(H,CH_2)$, ^5J(H,C), and ^4J(C,C)

The long-range coupling constant between methyl and *meta* protons in toluene has been written (12) as $^5J(H,CH_3) = 0.336 \sin^2\theta + 0.332 \sin^2(\theta/2) = {}^5J^{\pi} \sin^2\theta + {}^5J^{\sigma} \sin^2(\theta/2)$. Applied to ethylbenzene, one has $^5J(H,CH_2) = 0.336(1.16/1.20)\sin^2\theta + 0.332 \sin^2(\theta/2)$. For an evenfold barrier, $\langle\sin^2(\theta/2)\rangle$ is 0.5 and, because $\langle\sin^2\theta\rangle$ is 0.392, $^5J(H,CH_2)$ is calculated as 0.289 Hz, considered as adequate in that the measured value is 0.299(2) Hz.

A similar parameterization of ^5J(H,C) goes as follows. The INDO MO FPT values are represented by $^5J(H,C) = 0.155 \sin^2\psi + 0.287 \sin^2(\psi/2)$. According to the conclusions in the previous section, one has the correct $^5J^{\pi}$(H,C) as 0.155(1/0.858)(1/0.886) or 0.204 Hz. The measured ^5J(H,C) is 0.187(2) Hz, so that $^5J(H,C) = 0.187(2) = 0.204 \langle\sin^2\psi\rangle + {}^5J^{\sigma} \langle\sin^2(\psi/2)\rangle$, from which $^5J^{\sigma}$ follows as 0.084 Hz. The final relationship is thus $^5J(H,C) = 0.20 \sin^2\psi + 0.08 \sin^2(\psi/2)$. The assumption that ^5J(H,C) vanishes at $\psi = 0°$ is based on the behaviour of ^5J(H,CH) and also on our CNDO/2 computations, which have it as zero; such computations are in agreement with the known numbers for ^5J(H,CH) at $\psi = 0°$ and $\psi = 180°$ (9, 22). In the 2,6-dimethoxyethylbenzene, the magnitude of the splitting, approximating to ^5J(H,C), is 0.21(3) Hz; $\langle\sin^2\psi\rangle$ must be near 1.0. Turning to ^4J(C,C), the INDO MO FPT calculations are reproduced by $^4J(C,C) = -0.130 - 1.561 \sin^2\psi + 0.246 \sin^2(\psi/2)$ while the CNDO/2 numbers have $^4J(C,C) = 0.074 - 0.098 \sin^2\psi + 0.076 \sin^2(\psi/2)$. What ^4J(C,C) is at $\psi = 0°$, the so-called dipper conformation (23), is problematic. It is computed as positive for pentane (23). Here, arbitrarily, the mean of the two computed values at $\psi = 0°$ is taken. Further, the INDO MO FPT value for $^5J^{\pi}$, negative as expected, is too large in magnitude by a factor of 0.858 (1.78). The measured value of ^4J(C,C) is (–)0.53(2) Hz, so that one has $^4J(C,C) = -0.03 - 1.02 \sin^2\psi + 0.46 \sin^2(\psi/2)$. This equation must be regarded as rather tentative; certainly, ^4J(C,C) is expected to be negative for large ψ values where the σ–π contribution is dominant (see **4**). In 2,6-

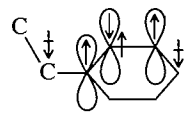

crossed arrows: nuclear spin rate

4

dichloroanisole, ^4J(C,C) is –0.69(3) Hz(7) and $\langle\sin^2\psi\rangle$ cannot be much less than unity, whereas $\langle\sin^2(\psi/2)\rangle$ is 0.5. Of course, here one has an O—C bond, as opposed to a C—C bond in **4**. Perturbations by the chlorine substituent are also a possibility.

$^4J(H,H)$ and $^4J(H,C)$

The original INDO MO FPT computations (9) of $^4J(H,CH_3)$ in toluene can be found from $-0.34 - 1.01 \sin^2\theta - 0.23 \sin^2(\theta/2)$. Hence $^4J(H,CH_3)$ is predicted to be –0.95 Hz, $\langle\sin^2\theta\rangle$ and $\langle\sin^2(\theta/2)\rangle$ being 0.5. The experimental value is –0.702(1) Hz (12). The coefficient of $\sin^2\theta$ above is to be multiplied by (1/0.886)(1/1.07) or 1.05, becoming –1.06 Hz, according to the approach developed in this work. Of course, the disagreement with experiment is then even larger. A detailed investigation (24) of $^4J(H,CH_3)$ concluded that it should be written as $-1.08 \sin^2\theta - 0.32 \cos^2\theta$, the latter term accounting for other than σ–π interactions. This relationship reproduces the later (12) experimental number exactly; it is also interesting that –1.06 and –1.08 are so similar in magnitude. For ethylbenzene, $\langle\sin^2\theta\rangle$ is –0.392 at 300 K. One then has –0.62 Hz predicted for $^4J(H,CH_2)$, compared to –0.644 Hz in Table 1. It appears that the angle-independent term in the INDO formulation is much too large.

Turning to ^4J(H,C), the INDO MO FPT data again overestimate its value, being reproduced by $-0.27 - 0.43 \sin^2\psi - 0.024 \sin^2(\psi/2)$. The multiplier of $\sin^2\psi$ is to be altered by a factor of (1/0.858)(1/0.886) or 1.31. To obtain agreement with the exper-

Can. J. Chem. Downloaded from www.nrcresearchpress.com by 85.192.166.187 on 09/08/12
For personal use only.

imental value of –0.22(3) Hz would require a substantial change in the theoretical formulation, possibly a positive coefficient, as large as 0.36, of $\sin^2(\psi/2)$; the negative angle-independent term, apparently spurious, is reminiscent of a similar one for $^4J(H,CH_2)$.

The ψ dependence of $^3J(C,C)$

The INDO MO FPT results can be written as one of the Karplus forms, $^3J(C,C)/Hz = 0.86 \cos^2\psi - 0.41 \cos\psi + 2.28$ or, equivalently, as $^3J(C,C)/Hz = -0.86 \cos^2\psi - 0.41 \cos\psi + 2.28$ or, again equivalently, as $^3J(C,C)/Hz = -0.86 \sin^2\psi + 0.71 \sin^2(\psi/2) + 2.80$. The negative coefficient of cos ψ entails a larger $^3J(C,C)$ in the *trans* than in the *cis* arrangement of the vicinal C—C bonds, unlike the results of a previous computation (25) that, however, also indicate that other than contact contributions to $^3J(C,C)$ are very small. The disagreement at small dihedral angles is very likely a result of the use of a standard geometrical model, leading to unrealistic "close-range nonbonded interactions" (25), in the earlier work.

The large computed values in the vicinity of ψ = 90°C indicate a substantial σ–π electron contribution to $^3J(C,C)$, as previously discussed (24). Its magnitude depends on the degree of π electron spin correlation in the partial double bond, as well as on Q^CCCC Q^CCH; the latter is too large by a factor of 0.86(1.78), according to the discussion above of $^3J(C,C)$. Judging by computations of $^3J(C,C)$ in butane and of the σ–π component of $^3J(C,C)$ in 1-butane (25), $^3J(C,C)$ at 90°C is near zero[2] in the absence of the latter, expected to go as $\sin^2\psi$. If $^3J = {}^3J^\sigma + {}^3J^\pi$ and $^3J^\sigma$ vanishes at 90°, then the theoretical values become $^3J = (3.14 \cos^2\psi - 0.41 \cos\psi) + (2.28 \sin^2\psi)$. Because $\langle\sin^2\psi\rangle$ is 0.716 and $\langle\cos\psi\rangle$ vanishes for an evenfold potential, ^3J becomes 2.52 Hz, as opposed to the experimental value of 2.26 Hz. If it is further assumed that $^3J^\pi$ is to be reduced by the above factor of 1.53, then ^3J become 1.97 Hz, now lower than experiment. Of course, accommodations between the computed values and the present two-mechanism model could be made to reproduce the experimental number for $^3J(C,C)$. In any event, it is remarkable that the original, theoretical equation does not overestimate $^3J(C,C)$ by much. In terms of the present approach it is likely that the σ electron contributions to $^3J(C,C)$ are underestimated by theory; those from the π electrons, overestimated.

Some other $^nJ(H,C)$ and $^nJ(C,C)$ numbers

The CNDO/2 and INDO MO FPT computations agree with the sign indicated in Table 2 for $^2J(C,C)$. The available evidence (7) implies an increase in the magnitude of $^2J(C,C)$ as ψ increases; the INDO values are $^2J(C,C) = -4.84 - 0.95 \sin^2\psi$, in qualitative agreement with the experimental evidence. In line with the previous sections, the coefficient of $\sin^2\psi$ should be reduced by a factor (1/0.858)(1/1.78) or 0.65 because it represents the coupling mechanism in **5**. The value of $^2J(C,C)$ there-

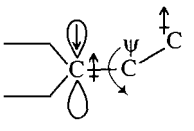

5

fore becomes –4.84 – 0.62 (0.716) or –5.28 Hz. The experimental value of (–) 2.3_5 Hz implies much too large a magnitude of the theoretical through-bond, angle-independent, term (one-centre exchange integrals (15)). The CNDO/2 numbers are given by $^2J(C,C) = -1.55 + 0.41 \sin^2\psi$ and fail to reproduce the correct sign of the angle dependence of $^2J(C,C)$, as might be expected (15).

$^1J(C,C)$ is 33.91(3) Hz in ethylbenzene, as compared to 34.6(3) Hz in ethane (26) in CCl_4 solution. Post Hartree–Fock computations of the contact contribution yield 34.1 for ethane (26). $^1J(C,C)$ does not correlate with the C—C bond length in various molecules (27). $^2J(H,C)$ is –4.95(4) Hz in ethylbenzene and –4.5(3) Hz in ethane (26), while $^1J(H,C)$ is 126.24(3) in the former and 124.93(3) in the latter (26). To within experimental error, the substituent perturbation by the phenyl group is only to 1–2% of the magnitudes of the three coupling constants.

In summary, a comparison of the experimental conformational dependence of at least some of the long-range coupling constants involving ^1H and ^{13}C nuclei in ethylbenzene with INDO MO FPT computations illustrates the need for modifications of the standard algorithm. Examples are given in which theory underestimates or overestimates certain components of the coupling mechanisms.

Solvent perturbations of ^nJ

The intraring $^{3,4,5}J(H,H)$ values display solvent perturbations typical of many phenyl X compounds, as measured in this laboratory; they are not artifacts of the spectral analyses. Thus, $^3J(H,H)$ is larger in acetone-d_6 solution, as is $^4J_{26}$, but $^4J_{24}$ and $^4J_{35}$ either decrease or do not change. $^4J(H,C)$ appears to decrease significantly in magnitude in passing to the polar solvent; a repeated set of experiments is necessary to confirm this result.

Acknowledgement

We are grateful to the Natural Sciences and Engineering Research Council of Canada for financial assistance.

1. T. Schaefer, G.H. Penner, and R. Sebastian. Can. J. Chem. **65**, 873 (1987).
2. W. Caminati, D. Damiani, G. Corbelli, B. Velino, and C.W. Bock. Mol. Phys. **74**, 885 (1911).
3. J. Kao. J. Am. Chem. Soc. **109**, 3817 (1987).
4. P.J. Breen, E.R. Bernstein, and J.I. Seeman. J. Chem. Phys. **87**, 3269 (1987).
5. G. Celebri, M. Longeri, N. Russo, A.G. Avent, J.W. Emsley, and V.N. Singleton. Mol. Phys. **65**, 391 (1988).
6. P. Scharfenberg. J. Chem. Phys. **77**, 4791 (1982).
7. T. Schaefer and G.H. Penner. Can. J. Chem. **66**, 1229 (1988).
8. J.A. Pople, J.W. McIver, Jr., and N.S. Ostlund. J. Chem. Phys. **49**, 2960 (1968); **49**, 2965 (1968).
9. R. Wasylishen and T. Schaefer. Can. J. Chem. **50**, 1852 (1972).
10. T. Schaefer, J. Peeling, G.H. Penner, A. Lemire, and R. Sebastian. Can. J. Chem. **63**, 24 (1985), and references therein.
11. I. Carmichael. J. Phys. Chem. **97**, 1789 (1993).
12. T. Schaefer, R. Sebastian, and G.H. Penner. Can. J. Chem. **63**, 2597 (1985).
13. W.J. Hehre, D. Ditchfield, R.F. Stewart, and J.A. Pople. J. Chem. Phys. **52**, 2796 (1970).
14. M.J. Frisch, G.W. Trucks, M. Head-Gordon, P.M.W. Gill, M.W. Wong, J.B. Foresman, B.G. Johnson, H.B. Schlegel, M.A. Robb, E.S. Replogle, R. Gomperts, J.L. Andres, K. Raghavachari, J.S. Binkley, C. Gonzalez, R.L. Martin, D.J. Fox, D.J. Defrees, J. Baker, J.J.P. Stewart, and J.A. Pople. GAUSSIAN 92, Revision C. Gaussian, Inc., Pittsburgh, Pa. 1992.
15. J.A. Pople and D.L. Beveridge, Approximate molecular orbital theory. McGraw Hill Book Co., New York. 1970.

[2]That $^3J^\sigma$ is close to zero is suggested by the CNDO/2 value for $^3J(C,C)$ at 90°, namely, 0.04 Hz. Such calculations ignore σ–π interactions.

16. A.R. Quirt and J.S. Martin. J. Magn. Reson. **5**, 318(1971); J.S. Martin, A.R. Quirt, and K.E. Worvill. The NMR program library. Daresbury Laboratory, Daresbury, U.K.
17. T. Schaefer, R.P. Veregin, R. Laatikaineu, R. Sebastian, K. Marat, and J.L. Charlton. Can. J. Chem. **60**, 2611 (1982).
18. T. Schaefer, J. Peeling, and G.H. Penner. Can. J. Chem. **61**, 2773 (1983).
19. H.M. McConnell. J. Chem. Phys. **30**, 126 (1959).
20. R. Wasylishen and T. Schaefer. Can. J. Chem. **49**, 94 (1971).
21. M. Karplus and G.K. Fraenkel. J. Chem. Phys. **35**, 1312 (1961).
22. B.J. Fuhr, B.W. Goodwin, H.M. Hutton, and T. Schaefer. Can. J. Chem. **48**, 1558 (1970), and references therein.
23. S.R. Walter, J.L. Marshall, C.R. McDaniel, Jr., E.D. Canada, Jr. and M. Barfield. J. Am. Chem. Soc. **105** 4185 (1983).
24. M. Barfield, C.J. Fallick, K. Hata, S. Sternhell, and P.W. Westerman. J. Am. Chem. Soc. **105**, 217 (1983).
25. M.L. Severson and G.E. Maciel. J. Magn. Reson. **57**, 248 (1984).
26. R.M. Lynden-Bell and N. Sheppard. Proc. R. Soc. London, A: **269**, 385 (1962).
27. K. Kamienska-Trela, L. Kania, and E. Bednarek. Magn. Reson. Chem. **31**, 268 (1993).

Can. J. Chem. Downloaded from www.nrcresearchpress.com by 85.192.166.187 on 09/08/12
For personal use only.

Heterocyclic analogs of nucleosides: synthesis and biological evaluation of novel analogs of puromycin[1]

PHILIP G. HULTIN AND WALTER A. SZAREK[2]
Department of Chemistry, Queen's University, Kingston, ON K7L 3N6, Canada

Received July 20, 1993[3]

PHILIP G. HULTIN and WALTER A. SZAREK. Can. J. Chem. **72**, 1978 (1994).

The diastereomeric 1-(piperidin-3′-yl)uracil compounds **20***a*, *b*, and the N^6-dimethyl-9-(piperidin-3′-yl)adenine compounds **21***a*, *b*, have been prepared as analogs of the naturally occurring aminoacyl nucleoside antibiotic puromycin. The diastereomers were separated using high-pressure liquid chromatography, and the absolute configuration of the more mobile diastereomer **20***a* was assigned as (3′*S*,5′*R*) by ^{1}H and ^{13}C nuclear magnetic resonance analysis, and by molecular modelling. Therefore, the less mobile diastereomer **20***b* had the (3′*R*,5′*S*) configuration. The configurations of **21***a* and **21***b* were assigned by analogy with **20***a* and **20***b*. These puromycin analogs have been tested for anti-HIV and antitumor activity in vitro.

PHILIP G. HULTIN et WALTER A. SZAREK. Can. J. Chem. **72**, 1978 (1994).

On a préparé les composés 1-(pipéridin-3′-yl) uracilee **20***a*, *b*, et N^6-diméthyl-9-(pipéridin-3′-yl) adénines **21***a*, *b*, comme analogues de la puromycine, un antibiotique naturel de type aminoacyle nucléoside. On a séparé les diastéréoisomères par chromatographie liquide á haute pression et on a attribué au diastéréoisomère le plus mobile, **20***a*, la configuration absolue (3′*S*,5′*R*) en se basant sur les résultats de la RMN du ^{1}H et du ^{13}C et sur les modèles moléculaires. Par conséquent, le diastéréoisomère le moins mobile, **20***b*, a la configuration (3′*R*,5′*S*). Par analogie avec les composés **20***a* et **20***b* on attribue les configurations des composés **21***a* et **21***b*. On a testé ces analogues de la puromycine in vitro pour leur activité anti-HIV et anti-tumorale.

[Traduit par la rédaction]

Introduction

The nucleoside derivative puromycin (Fig. 1) has been the focus of consistent interest since its discovery 40 years ago in the fermentation broth of *Streptomyces alboniger* (1). This

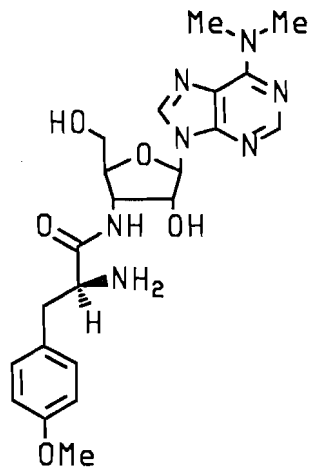

FIG. 1. Puromycin.

potent antibiotic mimics the 3′-end of aminoacyl-tRNA, interrupting protein synthesis on the ribosome (2). Puromycin has antimicrobial, antitumor (3), and antimalarial (4) activities, and is a reversible inhibitor of DNA synthesis (5). However, its therapeutic use is precluded by its extreme toxicity, particularly towards the kidney (6).

To address the problem of toxicity, many analogs of puromycin have been prepared. The ribosyl ring has been replaced by a 3-aminopentopyranose unit (7) or a daunosaminyl group (8), or modified by attachment of the N^6-dimethyladeninyl moiety at the sugar 5′-carbon rather than at the anomeric center (9); however, these modifications afforded no significant biological activities. 2′-Deoxypuromycin was found to be ineffective as an antimicrobial agent (10), as was the 2′,3′-*seco* analog (11). Carbocyclic analogs of puromycin have also been examined. The replacement of the furanose-ring oxygen by a methylene group yielded drugs whose cytotoxicities towards P-388 leukemia were found to be equal to that of puromycin itself (12). The carbocyclic 8-aza analog was identified also as an effective antibiotic (13), whereas a 7-deaza version was not (14). Hydroxycyclopentyl analogs displayed some antitumor effects in *HeLa* cells (15), while the cyclohexyl carbocyclic analog of puromycin was found to be somewhat less active than the cyclopentyl compounds (16).

As part of our ongoing investigation of the synthesis, structure, and biological activities of nucleoside analogs containing a variety of 5- and 6-membered heterocycles in place of the carbohydrate moiety (17), we wished to prepare puromycin analogs **20***a*, *b* and **21***a*, *b* incorporating a piperidine ring. Such compounds should be resistant to removal of the N^6-dimethyladeninyl group in vivo, since the base moiety is not attached by a glycosidic linkage. We wished to look for antitumor effects and activity against HIV. While this work was in progress, Peterson and Vince (18) reported the synthesis of a structurally similar pyrrolidinyl analog.

Results and discussion

Our synthetic strategy involved the construction of a pyrimidine- or purine-ring system on a *cis*-3-amino-5-(hydroxymethyl)piperidine precursor. There are few synthetic approaches available leading to such compounds;[4] however, we felt that lactam **1** (19) would offer the best starting point. Although both enantiomers of this lactam are commercially available,[5] the

[1]A portion of this work was presented at the 2nd Ontario–Québec Minisymposium in Synthetic and Bioorganic Chemistry, Montréal, Québec, October 26–27, 1991.

[2]Author to whom correspondence may be addressed.

[3]Revision received May 2, 1994.

[4]A route which was examined but discarded is described in ref. 32.

[5]Enzymatix Inc., Rosedale, NY 11422, U.S.A.

Can. J. Chem. Downloaded from www.nrcresearchpress.com by 85.192.166.187 on 09/08/12
For personal use only.

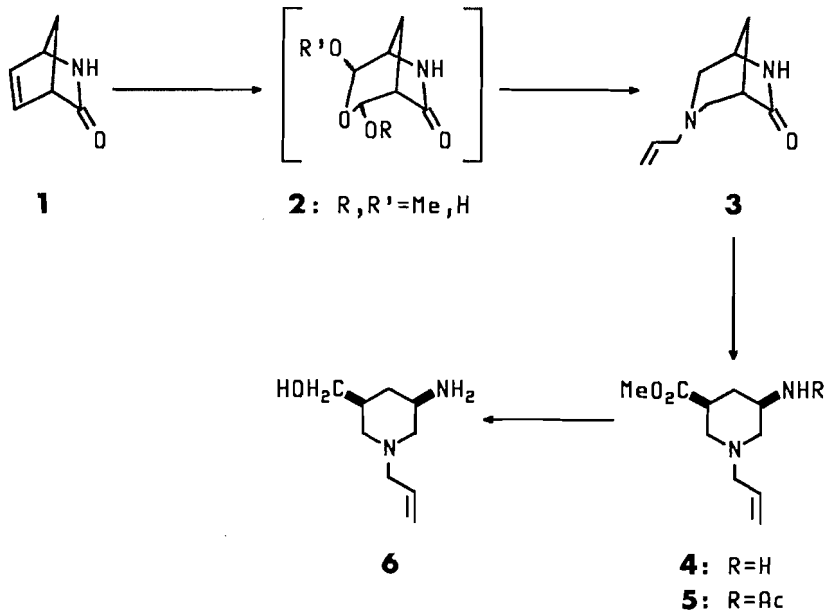

SCHEME 1

price of this material dictated that our nucleoside precursors would be racemic. The diastereomers produced by condensation with the amino acid could be separated and identified at the end of the sequence.

Initial attempts, based on our synthesis of *cis*-3-amino-5-(hydroxymethyl)thiane from **1** by nucleophilic displacement on the derived ditosylate (17), were unsuccessful; elimination products were obtained. Therefore, a reductive amination approach was tried (Scheme 1). Ozonolysis of **1** in methanol, followed by dimethyl sulfide processing, did not produce the expected dialdehyde. The product appeared to be **2**, identified by its ^1H and ^{13}C nmr spectra, which contained signals characteristic of the cyclic ketal structure, as well as by its positive reaction to a 2,4-dinitrophenylhydrazine test. This ketal was immediately subjected to reductive amination with allylamine hydrochloride and sodium cyanoborohydride. Standard conditions (20) failed to give the desired product; however, after considerable experimentation, **3** was obtained in 35% overall yield from **1**. No improvement in the yield could be achieved, and the remainder of the product of the reaction consisted of unidentifiable, highly polar material.

The lactam product **3** proved to be rather unstable, discoloring and decomposing on standing overnight. Accordingly, it was immediately converted into amino ester **4** (69%) by acid-promoted methanolysis. A sample of the amino ester was converted into its crystalline acetamido derivative **5** for analysis, while the bulk of the material was reduced, using lithium aluminium hydride, to afford the key amino alcohol, **6** (67%).

Synthesis of uracil-containing puromycin analogs

The construction of the uracil ring is shown in Scheme 2. Condensation of **6** with the acylisocyanate **7** (21), prepared in situ from the corresponding acid chloride, provided the acylurea derivative **8** (80%). Closure of the ring was effected with dilute sulfuric acid, yielding **9**, which was protected for easier purification as the *tert*-butyldimethylsilyl (TBDMS) ether **10** (82% from **8**).

The allyl blocking group was smoothly removed in 74% yield by a tris(triphenylphosphine)rhodium chloride-promoted hydrolysis, using the method of Laguzza and Ganem (22). The free piperidine was then acylated with *N*-(*tert*-butoxycarbonyl)-L-*p*-methoxyphenylalanine (**12**) (23), using 1-(3-dimethylaminopropyl)-3-ethylcarbodiimide hydrochloride (EDC), to provide a 1:1 mixture of diastereomeric protected analogs **13***a*, *b* in 77% yield. It was not possible to separate these diastereomers by chromatographic means.

Synthesis of puromycin analogs

Reaction of **6** with 5-amino-4,6-dichloropyrimidine (Scheme 3) provided the chloropyrimidine derivative **14** in 80% yield. Closure of the purine-ring system with triethyl orthoformate and hydrochloric acid gave the chloropurine **15** (69%), which afforded the N^6-dimethyladenine derivative **16** (93%) on treatment with aqueous dimethylamine. This reaction proved difficult to monitor by tlc, as **15** and **16** co-eluted and had similar responses to visualizing agents. The alcohol group of **16** was silylated to give **17** in 87% yield, and the piperidine ring was deblocked to provide **18** (68%). A quantitative yield of diastereomeric adducts **19***a*, *b* was obtained on treatment of **18** with **12**–EDC. These also proved resistant to chromatographic separation.

Removal of both the silyl ether and *tert*-butyl carbamate protecting groups of **13** and **19** was achieved by treatment with trifluoroacetic acid in either dichloromethane or methanol solution (Scheme 4). Anisole was added as a scavenger for *tert*-butyl cation; *tert*-butylated material was recovered from an experiment on **13** in the absence of scavenger. The resulting diastereomeric uracil-puromycin analogs **20***a*, *b* (87%) and puromycin analogs **21***a*, *b* (93%) were then separated by reverse-phase hplc.

Identification of product diastereomers

With samples of the diastereomeric products in hand, it remained to ascertain their configurations. For this purpose we turned to ^1H nmr spectroscopy. The problem seemed initially to be complicated by the presence of two stable rotamers in all of the spectra, as a result of hindered rotation around the amide C—N bond. Moreover, while spectra of both diastereomers of

Can. J. Chem. Downloaded from www.nrcresearchpress.com by 85.192.166.187 on 09/08/12
For personal use only.

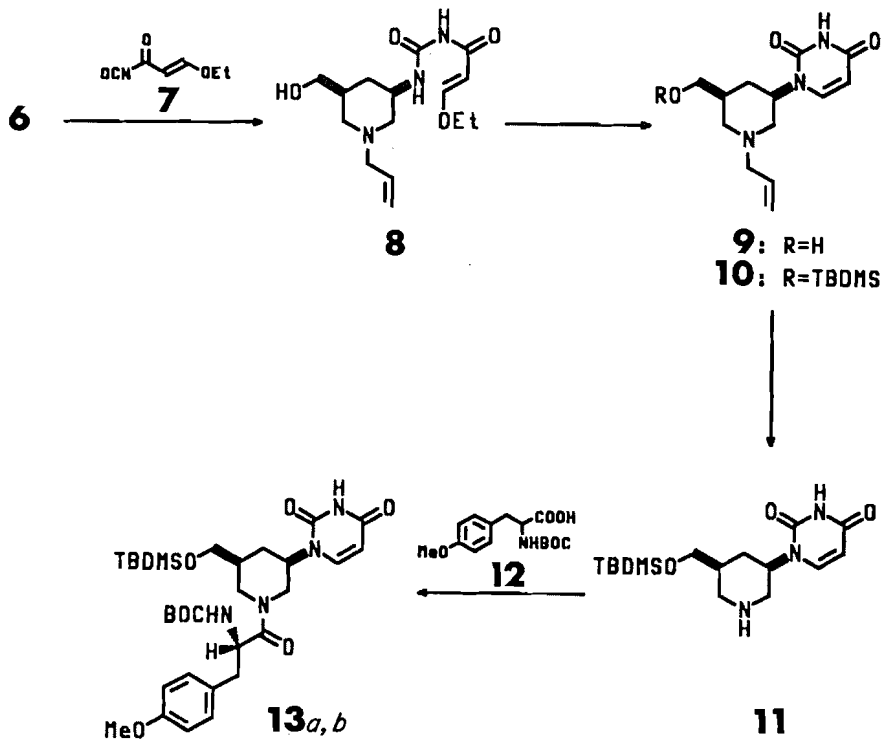

SCHEME 2

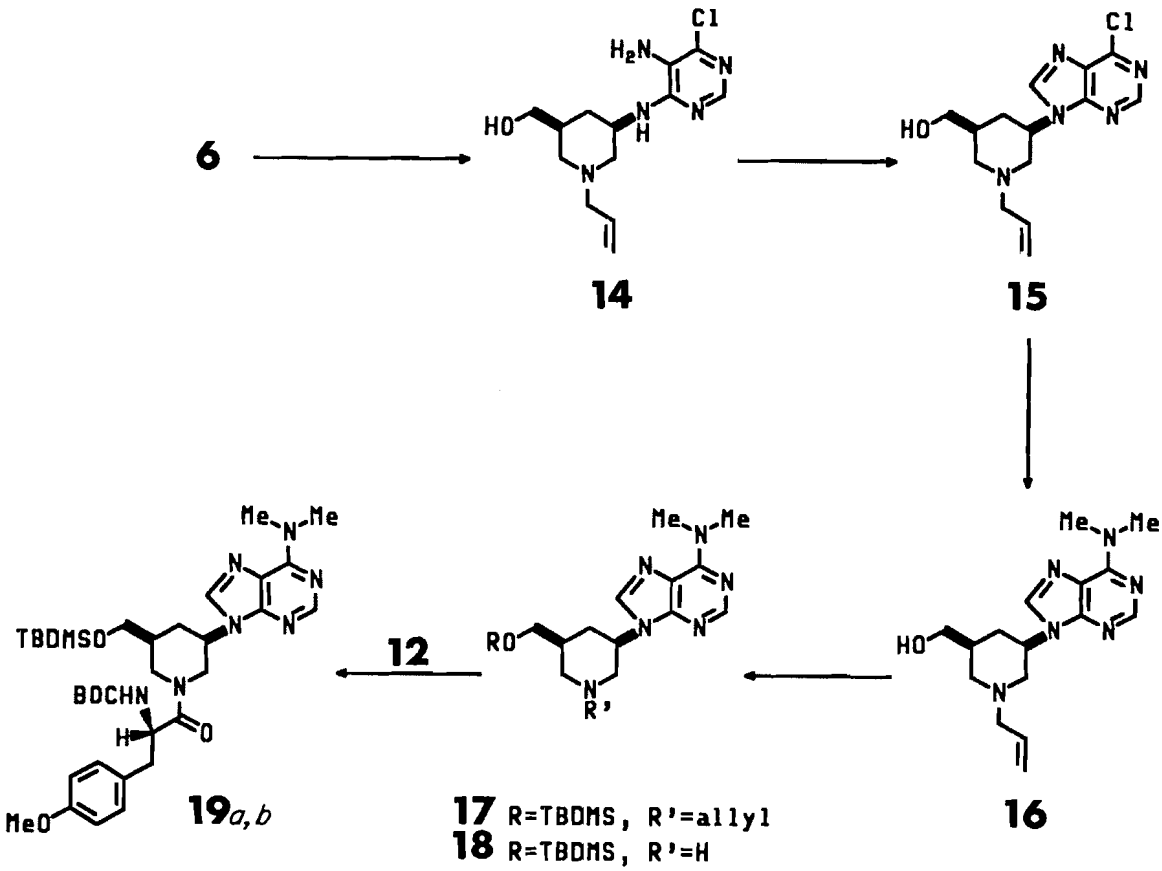

SCHEME 3

20 in D_2O solution were well resolved, the N^6-dimethyladenine compounds **21***a*, *b* were not soluble in this solvent, and gave severely broadened spectra in either $CDCl_3$ or DMSO-d_6 solutions. However, we were intrigued by the presence of the extremely high-field signal (δ 0.249 ppm) in the spectrum of the first-eluting fraction of **20** (Fig. 2(*A*)), which was lacking in

Can. J. Chem. Downloaded from www.nrcresearchpress.com by 85.192.166.187 on 09/08/12
For personal use only.

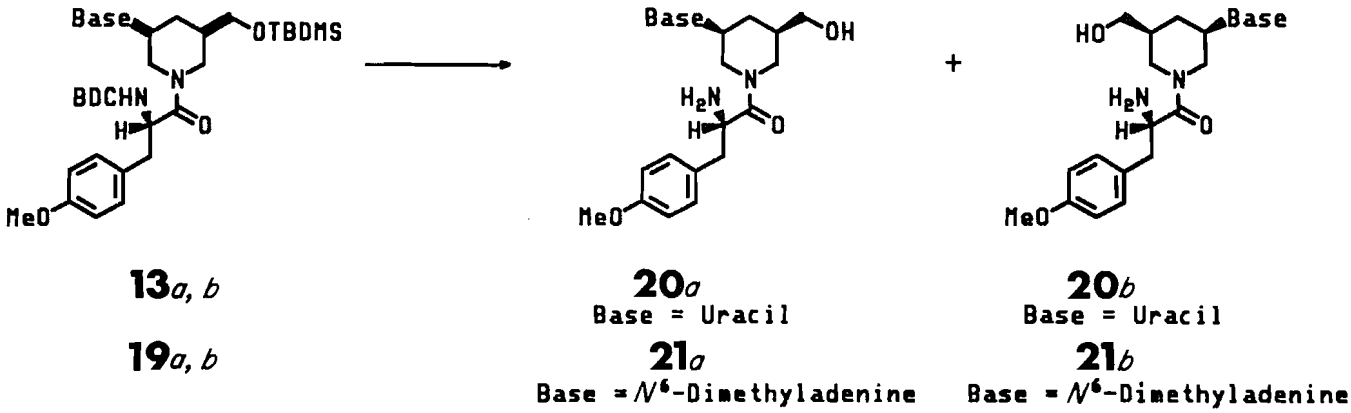

SCHEME 4

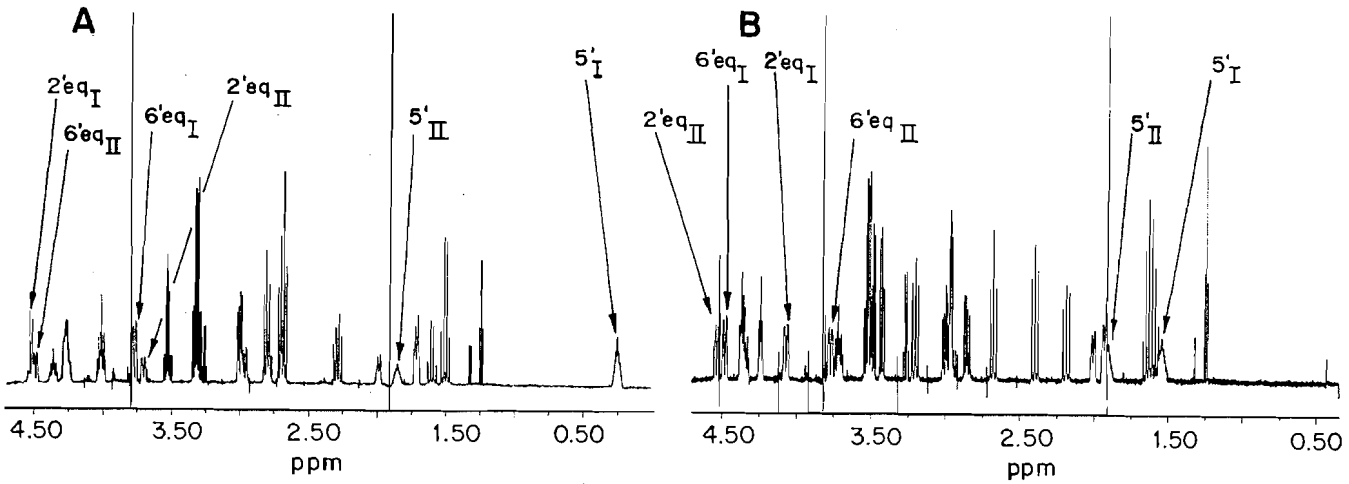

FIG. 2. Aliphatic regions of resolution-enhanced 600-MHz ^{1}H nmr spectra of (*A*) the first-eluting and (*B*) the second-eluting fractions of **20**. Peaks due to the major rotamer are labelled I, and those due to the minor rotamer are labelled II. The triplet at δ 1.142, singlet at δ 1.808, and quartet at δ 3.161 are attributable to $Et_3NH(OAc)$ from the HPLC buffer.

that of the second fraction (Fig. 2(*B*)), and we soon realized that this signal held the solution to our configurational problem.

A ^{1}H-COSY spectrum proved that this anomalously high-field signal arose from the H-5′ proton[6] of the major rotameric form (rotamer I) of the first fraction of **20**. The corresponding signal from H-5′ of the minor rotamer, II, was observed at δ 1.85 ppm. Such a high-field position for a methine proton most likely was due to shielding by the phenyl ring. Such shielding would occur if the ring were "tucked under" the piperidinyl ring. That this situation was only possible for *one* rotamer was evident from the ^{1}H nmr spectra, as was the fact that neither rotamer of the second fraction could adopt such a conformation (Fig. 2(*B*): H-5′$_I$ δ 1.50–1.58 ppm; H-5′$_{II}$ δ 1.87–1.95 ppm). It was clear from the ^3J values of the ring protons that the conformation of the piperidinyl ring was a chair having the 3′ and 5′ substituents equatorially oriented. Therefore, we needed to determine whether the major rotamer of fraction 1 had the carbonyl *syn* to the pyrimidinedione ring, or *anti*. We required also coupling constant and nOe information to set limits on possible side-chain conformations. With these data, we could construct models to ascertain which configuration could adopt the required orientation of the phenyl ring.

The chemical shifts of protons on *N*,*N*-dialkylamides depend on the orientation of the carbonyl: the signals of protons *syn* to the carbonyl are downfield of those of protons *anti* (24). In fraction 1, the signal of H-2′$_{eq}$ (I) is 0.82 ppm downfield of that of H-2′$_{eq}$ (II) and the signal of H-6′$_{eq}$ (I) is 0.72 ppm upfield of that of H-6′$_{eq}$ (II) (see Fig. 2). Carbon chemical shifts also are indicative of amide conformation; however, the *syn* carbon signal occurs *upfield* of that of the *anti* carbon (24). A heteronuclear correlation spectrum showed that the signal of C-2′ (I) is 2.83 ppm upfield of that of C-2′ (II), while the signal of C-6′ (I) is 3.27 ppm downfield from that of C-6′ (II). Further, irradiation of the side-chain H-α produced a 3.3% nOe in the signal of H-6′$_{eq}$ of rotamer I, and a 1.4% nOe in the signal of H-2′$_{eq}$ of rotamer II. These results are consistent with the carbonyl being *syn* to C-2′ and the pyrimidinedione ring in the major rotamer of fraction 1. Similar arguments allowed assignment of the rotamers of fraction 2.

The structures shown in Fig. 3 represent calculated local minima[7] relevant to our nmr observations of carbonyl orienta-

[6]The piperidine-ring system has been numbered according to IUPAC rules.

[7]Computations were performed on an IBM RS/6000 RISC 550 computer operating under AIX. Initial structures approximating the "tucked" and "extended" conformers were constructed based on our ^{1}H nmr data, and minimized using the Dreiding force field as implemented in the program BIOGRAF, from Biodesign, Inc. Energy minimization was accomplished using the conjugate-gradient method with an energy cutoff criterion of 0.001 kcal mol^{-1}. The resulting gas-phase minima were

Can. J. Chem. Downloaded from www.nrcresearchpress.com by 85.192.166.187 on 09/08/12
For personal use only.

Can. J. Chem. Downloaded from www.nrcresearchpress.com by 85.192.166.187 on 09/08/12
For personal use only.

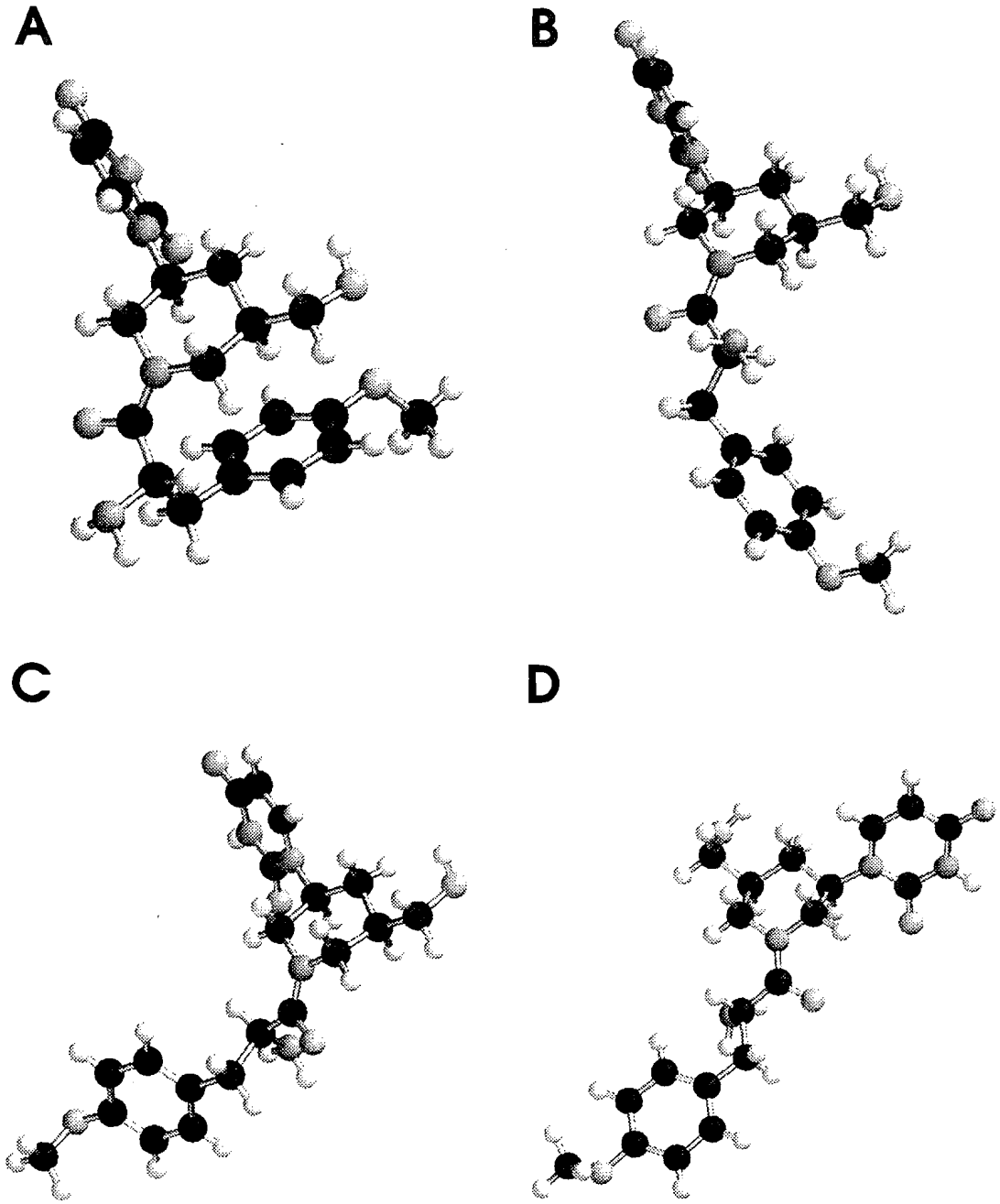

FIG. 3. Possible conformations of analogs **20**. (*A*) The "tucked" conformation of **20***a* with the carbonyl *syn* to the uracil ring. (*B*) An "extended" conformation of **20***a* with the carbonyl *syn*. (*C*) An "extended" conformation of **20***a* with the carbonyl *anti*. (*D*) An "extended" conformation of **20***b* with the carbonyl *syn*. The corresponding "tucked" conformer (not shown) would require overlap of the α-amino group with the C-6′ methylene.

tion and side-chain conformation in **20**. Only the (3′*S*,5′*R*) configuration affords a stable conformation with the carbonyl *syn* and the phenyl ring in the correct position to shield H-5′ (Fig. 3(*A*)). The *anti* rotamer cannot adopt this type of conformation, and must have the side chain extended away from the piperidine ring (Fig. 3(*C*)). The "tucked" conformer shown in Fig. 3(*A*) is the lowest in energy of the structures found for the (3′*S*,5′*R*) configuration, and the calculated torsional angles between H-α and the benzylic H's (55.8° and 171.1°) correspond well to those estimated from ^3J values of rotamer I of the first fraction of **20**, using a modified Karplus equation (25) (50° and 168°).

In the (3′*R*,5′*S*) configuration with the carbonyl *syn*, the α-amino group and the 6′-methylene group would come into contact if the side chain was "tucked under"; both rotamers must exist in conformations having the side chain extended (Fig. 3(*D*)). Therefore, we assign the (3′*S*,5′*R*) stereochemistry **20***a* to fraction 1, and the (3′*R*,5′*S*) stereochemistry **20***b* to the second fraction.

Analogs **21** were not soluble in D_2O, as noted above. The broadened ^1H nmr spectra obtained in $CDCl_3$ solution indicated the presence of an approximately 1:1 mixture of rotamers for both diastereomers; however, there was no high-field signal as

then solvated in a hexagonal lattice of water. The inner cutoff distance was 2.8 Å, the outer cutoff was 8.4 Å, and the lattice spacing was 2.8 Å to give ~3 layers of water. Re-minimization then provided the structures shown in Fig. 3.

Can. J. Chem. Downloaded from www.nrcresearchpress.com by 85.192.166.187 on 09/08/12
For personal use only.

in **20***a*. Lowering the temperature failed to "freeze-out" the rotamers above the freezing point of $CDCl_3$. Spectra in DMSO-d_6 solution were also broad; however, raising the temperature to 383 K allowed confirmation of the structure, at the cost of any conformational information. We assigned (tentatively) the (3′*S*,5′*R*) stereochemistry **21***a* to the first-eluting fraction, and the (3′*R*,5′*S*) configuration **21***b* to the second-eluting fraction, by analogy with the pyrimidinedione analogs **20**.

The absence of a "tucked-under" conformation analogous to that of Fig. 3(*A*) for **21** can be explained by the difference in solvents used for the nmr spectra. Such a conformation should be favored in water solutions since it minimizes contact of hydrophobic portions of the molecule with the solvent. In organic solvents, this effect would be unimportant, and extended conformations would result. It is interesting to note that puromycin itself does not adopt such a tucked conformation either in water solution (26), or in the crystal (27), although the phenyl ring is oriented near the 5′-hydroxymethyl group in both states.

Anti-HIV and antitumor assays

Samples of **20***a*, **20***b*, **21***a*, and **21***b* were submitted to the U.S. National Cancer Institute (N.C.I.) for anti-HIV screening by the soluble-formazan assay in human T4 lymphocytes (28). All compounds were inactive in this assay. Some toxicity was observed at high concentrations of **21***a* (1.4×10^{-4} M) but otherwise the compounds had no effect on infected or uninfected cells. Analogs **20***a*, **20***b*, **21***a*, and **21***b* were tested also by N.C.I. against a panel of human leukemia, lung cancer, colon cancer, CNS cancer, melanoma, ovarian cancer, and renal cancer cell cultures. No useful activity was observed in these assays, although **20***a* displayed a weak effect against HL-60(TB) leukemia ($GI_{50} = 5.84 \times 10^{-5}$ M), and **21***a* had a similarly low activity against HL-60(TB) ($GI_{50} = 7.34 \times 10^{-5}$ M) and against non-small-cell lung cancers HOP-18 ($GI_{50} = 4.57 \times 10^{-5}$ M) and HOP-92 ($GI_{50} = 5.70 \times 10^{-5}$ M).

The pyrrolidinyl puromycin analog of Peterson and Vince (18) was reported to be inactive in an assay against P-388 leukemia cells. The authors suggested that the absence of a 2′-OH group may explain this result, as this hydroxyl has been shown to be essential in puromycin itself (10). The lack of activity of the pyrrolidinyl and our piperidinyl analogs **20**–**21** may also be due to differences in conformation. Our compounds prefer to orient the aminoacyl chain below the mean plane of the piperidine ring, while puromycin exists in a C-3′ *endo* conformation in the solid phase (27) and in solution (26), in which the aminoacyl chain lies near or above the plane of the ribosyl ring.

Experimental

The ^{1}H nmr spectra were recorded on a Bruker AMX-600, AM-400, or AC-F 200 spectrometer at 600.140, 400.136, or 200.132 MHz. The signals due to residual protons in the deuterated solvents indicated were used as internal standards except for spectra recorded in D_2O, in which case 3-(trimethylsilyl)propane sulfonic acid sodium salt was added as an internal standard. Chemical shifts are reported in ppm (δ) downfield from the position of tetramethylsilane (TMS). The symbols s (singlet), d (doublet), t (triplet), q (quartet), m (multiplet), and br (broadened) are used to describe the multiplicity and shape of the signals. The ^{13}C nmr spectra were obtained at 100.6 MHz on the AM-400 spectrometer or at 50.323 MHz on the AC-F 200 spectrometer, using the JMOD spin-echo sequence (29) to aid in peak identification. Chemical shifts in ppm (δ) downfield from the position of TMS were measured using the solvent signals as internal standards, except for spectra measured in D_2O, where 1,4-dioxane-H_8 (δ 66.5) (30) was added as a standard.

EI mass spectra were recorded on a VG Micromass 7070F mass spectrometer at an ionizing voltage of 70 eV, or on a VG Analytical ZAB-E mass spectrometer, and CI spectra were recorded using NH_3 at ~1 Torr (133.3 Pa) as reagent gas; data are given as *m/z* (% relative intensity). The exact masses were determined under EI conditions. The high-resolution measurements were performed by peak matching using perfluorokerosene as a reference standard.

Melting points were determined using a Fisher–Johns apparatus, and are uncorrected. Flash chromatography was performed on Kieselgel 60 (230–400 mesh), and thin-layer chromatography (tlc) was performed on glass plates coated with Kieselgel 60. High-pressure liquid chromatography (hplc) was carried out using a Beckman System Gold instrument.

The homogeneity of the products was established on the basis of chromatographic, spectroscopic (^{1}H and ^{13}C nmr), and melting point determinations.

(±)-3,6-Diaza-7-oxo-3-(2-propenyl)bicyclo[3.2.1]octane (3)

A solution of freshly recrystallized lactam **1** (see ref. 19) (3.00 g, 27.49 mmol) in dry methanol (300 mL) was purged with oxygen, while being cooled to −70°C in a Dry Ice – acetone bath. Ozone was passed through the solution, maintaining a temperature of −70°C or below, until tlc analysis (0.5% methanol in ethyl acetate as eluant) and the presence of the blue color of an excess of ozone indicated completion. The solution was purged of ozone with a stream of nitrogen. Dimethyl sulfide (10 mL) was added and the mixture was stirred for 1 h. The temperature was allowed to rise to 23°C, the solvents were evaporated, and the residue was left in vacuo for several hours. The oily product (6.934 g) was identified as the mixed ketal **2** by ^{1}H and ^{13}C nmr spectroscopy, and by a positive response to a 2,4-dinitrophenylhydrazine test.

The oil **2** was dissolved in *N*,*N*-dimethylformamide (150 mL). To this solution were added 4 Å molecular sieves (15 g), allylamine hydrochloride (2.57 g, 27.5 mmol), and glacial acetic acid (1.6 mL, 27.5 mmol). The stirred mixture was cooled on ice under a nitrogen atmosphere, and sodium cyanoborohydride (3.45 g, 54.96 mmol) was added. The reaction was allowed to proceed overnight, gradually warming to 23°C. Methanol (150 mL) was added, and the mixture was filtered. The filter cake was washed thoroughly with methanol, and the combined filtrates were evaporated. The residue was dissolved in chloroform (100 mL) and the solution was washed with a 10% aqueous solution of potassium carbonate (50 mL). The aqueous layer was extracted with chloroform (2 × 50 mL), and the combined organic layers were dried ($MgSO_4$) and evaporated. The residue was evaporated twice more from toluene to remove residual *N*,*N*-dimethylformamide, before being chromatographed on silica gel (5% (v/v) methanol in chloroform as eluant) to afford **3** as an oil (1.607 g, 35%). The oil could be distilled (bp 130°C, 0.25 Torr) but even carefully purified material was found to discolor and decompose on standing overnight; ^{1}H nmr ($CDCl_3$, 200 MHz) δ: 1.59 (1H, dd, J_{gem} = 11.0 Hz, J_{vic} = 3.0 Hz, H-8_{eq}), 2.19–2.41 (4H, m, H-1, H-2_{ax}, H-4_{ax}, H-8_{ax}), 2.88 (1H, m, H-4_{eq}), 3.06–3.16 (3H, m, H-2_{eq}, =CHCH_2N), 3.71 (1H, m, H-5), 5.06–5.20 (2H, m, H_2C=), 5.69–5.95 (2H, m, =C*H*CH_2, NH); ^{13}C nmr ($CDCl_3$, 50 MHz) δ: 37.548 (C-8), 40.188 (C-1), 50.989 (C-5), 53.444 (C-2), 54.242 (C-4), 59.955 (=CHCH_2N), 117.512 (H_2C=), 134.749 (=*C*HCH_2), 179.942 (C-7).

(±)-(3β,5β)-3-Amino-5-(methoxycarbonyl)-1-(2-propenyl)piperidine (4)

To a solution of lactam **3** (2.80 g, 16.8 mmol) in methanol (50 mL) was added concentrated aqueous hydrochloric acid (3 mL), and the mixture was heated at reflux temperature for 2 h. A further portion of hydrochloric acid (1 mL) was added, and heating was continued. After 5 h, the mixture was cooled, and concentrated. The residue was dissolved in water (40 mL), and the solution was adjusted to pH 9.0 with solid potassium carbonate. The aqueous solution was extracted with chloroform (3 × 50 mL), and the organic extracts were dried ($MgSO_4$) and evaporated. The residual oil was distilled (bp 75–85°C, 0.01 Torr) using a Kugelrohr apparatus, to afford the aminoester **4** (2.29 g, 69%);

Can. J. Chem. Downloaded from www.nrcresearchpress.com by 85.192.166.187 on 09/08/12
For personal use only.

^{1}H nmr ($CDCl_3$, 400 MHz) δ: 1.13 (1H, ddd, $J_{3,4ax}$ = 11.0 Hz, $J_{4ax,5}$ = 12.5 Hz, $J_{4ax,4eq}$ = 12.5 Hz, H-4_{ax}), 1.24 (2H, br s, NH_2), 1.60 (1H, dd, $J_{2ax,3}$ = 10.0 Hz, $J_{2ax,2eq}$ = 10.5 Hz, H-2_{ax}), 1.93 (1H, dd, $J_{5,6ax}$ = 11.4 Hz, $J_{6ax,6eq}$ = 11.1 Hz, H-6_{ax}), 2.20 (1H, m, H-4_{eq}), 2.65 (1H, dddd, $J_{4ax,5}$ = 12.5 Hz, $J_{5,6ax}$ = 11.4 Hz, J_{vic} = 4.0 Hz, J_{vic} = 3.8 Hz, H-5), 2.85 (1H, dddd, $J_{2ax,3}$ = 10.0 Hz, $J_{3,4ax}$ = 11.0 Hz, J_{vic} = 4.5 Hz, J_{vic} = 4.0 Hz, H-3), 2.96 (1H, m, H-2_{eq}), 2.99–3.02 (2H, m, =CHCH_2N), 3.07 (1H, m, H-6_{eq}), 3.65 (3H, s, OCH_3), 5.11–5.19 (2H, m, H_2C=), 5.82 (1H, m, =CHCH_2); ^{13}C nmr ($CDCl_3$, 50 MHz) δ: 37.060 (C-4), 41.061 (C-5), 47.639 (C-3), 51.542 (OCH_3), 54.402 (C-6), 61.275 (=CHCH$_2$N), 62.065 (C-2), 117.940 (H_2C=), 134.618 (=CHCH$_2$), 173.791 (C=O).

(±)-(3β,5β)-3-Acetamido-5-(methoxycarbonyl)-1-(2-propenyl)piperidine (5)

Aminoester **4** (85 mg, 0.43 mmol) was dissolved in dry pyridine (1 mL) and the solution was cooled on ice as acetic anhydride (4 drops, excess) was added. The mixture was stirred at 23°C for 1 h, at which point tlc analysis (15% (v/v) methanol in chloroform as eluant) indicated complete reaction. The pyridine was evaporated, and the residue was dissolved in chloroform (10 mL). The solution was washed with a 10% aqueous solution of sodium hydrogen carbonate (2 × 2 mL) and then with brine (2 mL). The organic layer was dried ($MgSO_4$) and concentrated to yield a solid product, 110 mg (quant.). A sample recrystallized from diisopropyl ether had mp 98–100°C; ^{1}H nmr ($CDCl_3$, 400 MHz) δ: 1.53 (1H, br m, H-4_{ax}), 1.95 (3H, s, C(O)CH_3), 1.95–2.13 (2H, br m, H-4_{eq} and H-6_{ax}), 2.34 (1H, br m, H-2_{ax}), 2.70 (1H, m, H-5), 2.79–2.86 (2H, br m, H-2_{eq} and H-6_{eq}), 2.99 (1H, dddd, J_{gem} = 13.5 Hz, J_{vic} = 6.5 Hz, 2 × allylic J's ~1 Hz each, =CHCH_2N), 3.05 (1H, dddd, J_{gem} = 13.5 Hz, J_{vic} = 6.35 Hz, 2 × allylic J's ~1 Hz each, =CHCH_2N), 3.678 (3H, s, OCH_3), 4.02 (1H, m, H-3), 5.13–5.20 (2H, m, H_2C=), 5.81 (1H, m, =CHCH$_2$), 5.88 (1H, br s, NH); ^{13}C nmr ($CDCl_3$, 100 MHz) δ: 23.441 (C(O)CH$_3$), 31.812 (C-4), 40.035 (C-5), 45.124 (C-3), 51.892 (OCH_3), 54.264 (C-6), 57.858 (C-2), 61.194 (=CHCH$_2$N), 118.179 (H_2C=), 134.487 (=CHCH$_2$), 169.376 (amide C=O), 174.38 (ester C=O); ms (EI): 241 (M + H)$^+$ (3.3%), 209 ($M^{+\cdot}$ − $^{\cdot}OCH_3$)$^+$ (5.5%), 181 ($M^{+\cdot}$ − CH_3CONH_2)$^{+\cdot}$ and (or) ($M^{+\cdot}$ − $^{\cdot}COOCH_3$)$^+$ (100%), 140 ($C_7H_{12}N_2O$: $M^{+\cdot}$ − H_2C=$CHCH_2^{\cdot}$ − $^{\cdot}COOCH_3$)$^{+\cdot}$ (89.3%), 122 ($C_8H_{12}N$: 181 − CH_3CONH_2 or $^{\cdot}COOCH_3$)$^+$ (36.9%). Exact Mass calcd. for ($C_{12}H_{20}N_2O_3$ + H): 241.1553; found (hrms): 241.15419. Anal. calcd. for $C_{12}H_{20}N_2O_3$: C 59.98, H 8.39, N 11.66; found: C 59.89, H 8.29, N 11.43.

(±)-(3β,5β)-3-Amino-5-(hydroxymethyl)-1-(2-propenyl)piperidine (6)

A solution of aminoester **4** (2.20 g, 11.1 mmol) in dry oxolane (15 mL) was added dropwise to a suspension of lithium aluminium hydride (0.50 g, 13.2 mmol) in oxolane (10 mL) at 0°C. The reaction mixture was stirred under a nitrogen atmosphere for 30 min. A further portion of lithium aluminium hydride (255 mg, 6.7 mmol) was added, and stirring was continued for 15 min; tlc analysis (plate pretreated with NH_3 vapor, 15% (v/v) methanol in chloroform as eluant) indicated complete reaction had occurred. The reaction was quenched by cautious addition of water (1 mL), then a 15% (w/v) aqueous solution of sodium hydroxide (1 mL), followed by more water (3 mL), was added. The mixture was warmed to 23°C and stirred for 40 min. Magnesium sulfate was added, and the mixture was filtered. The filter cake was washed with oxolane (25 mL), and the combined filtrates were concentrated to afford an oil. Chromatography on silica gel using the organic layer of a 12:6:1 (v/v/v) chloroform–isopropanol – aqueous ammonium hydroxide mixture as eluant afforded the amino alcohol **6** as a solid (1.251 g, 67%). A sample recrystallized from diisopropyl ether had mp 74–75°C; ^{1}H nmr ($CDCl_3$, 200 MHz) δ: 0.73 (1H, apparent q, J_{app} = 12.0 Hz, H-4_{ax}), 1.47–2.00 (7H, m, H-2_{ax}, H-4_{eq}, H-5, H-6_{ax}, OH, NH_2), 2.83–3.13 (5H, m, H-2_{eq}, H-3, H-6_{eq}, =CHCH_2N), 3.44 (1H, dd, J_{gem} = 10.7 Hz, J_{vic} = 6.6 Hz, CHOH), 3.53 (1H, dd, J_{gem} = 10.7 Hz, J_{vic} = 5.5 Hz, CHOH), 5.06–5.24 (2H, m, H_2C=), 5.86 (1H, m, =CHCH$_2$); ^{13}C nmr ($CDCl_3$, 50 MHz) δ: 37.599 (C-4), 38.361 (C-5), 48.076 (C-3), 56.355 (C-6), 61.761 (C-2), 62.834 (=CHCH$_2$N), 65.895 (CH_2OH), 117.968 (H_2C=), 134.946 (=CHCH$_2$); ms (EI): 170 (M)$^{+\cdot}$ (12.8%), 152 ($M^{+\cdot}$ − H_2O)$^{+\cdot}$ (7.1%), 127 ($M^{+\cdot}$ − H_2C=$CHNH_2$)$^{+\cdot}$ (24.0%), 122 ($M^{+\cdot}$ − H_2O − $^{\cdot}CH_2NH_2$)$^+$ (9.8%), 96 (15.2%), 84 ($C_5H_{10}N$)$^+$ (100%). Exact Mass calcd. for $C_9H_{18}N_2O$: 170.14204; found (hrms): 170.14316. Anal. calcd. for $C_9H_{18}N_2O$: C 63.49, H 10.66, N 16.45; found: C 63.45, H 10.55, N 16.50.

*(±)-*trans*-3-Ethoxy-*N*-{N′-[(3′β,5′β)-5′-(hydroxymethyl)-1′-(2-propenyl)piperidin-3′-yl]carbamoyl}propenamide (8)*

Following the procedure of Shealy and O'Dell (21*a*), silver cyanate was dried at 60°C and <1 Torr in the dark for 12 h. Distilled *N,N*-dimethylformamide was dried over 4 Å molecular sieves. All glassware was dried overnight at 110°C, and assembled while hot, under a nitrogen atmosphere.

A suspension of silver cyanate (1.055 g, 7.04 mmol) in dry benzene (5 mL) was heated to reflux temperature under a nitrogen atmosphere. After 30 min, a solution of *trans*-3-ethoxypropenoyl chloride (21*b*) (475 mg, 3.52 mmol) in benzene (5 mL) was added. The mixture was boiled for 45 min more. Heating and stirring were stopped, and the suspended solids were allowed to settle from the solution of acylisocyanate **7** over 2 h.

A solution of amino alcohol **6** (400 mg, 2.35 mmol) in *N,N*-dimethylformamide (15 mL) was cooled to −75°C under a nitrogen atmosphere. An 8-mL portion of the solution of **7** (~2.82 mmol) was removed with a syringe, and was added dropwise to the amine solution. The mixture was rapidly warmed to −30°C, and was then stirred for 6 h as the temperature slowly rose to 23°C. The solvents were evaporated under high vacuum, and the residue was chromatographed on silica gel using a gradient of 5% → 7% → 10% (v/v) methanol in chloroform as eluant. Acylurea derivative **8** was obtained as a glassy foam (588 mg, 80%). A sample obtained by recrystallization from diisopropyl ether had mp 113°C; ^{1}H nmr ($CDCl_3$, 400 MHz) δ: 0.97 (1H, ddd, $J_{3',4'ax}$ = 11.8 Hz, $J_{4'ax,5'}$ = 12.8 Hz, J_{gem} = 10.9 Hz, H-$4'_{ax}$), 1.35 (3H, t, J = 7.1 Hz, CH_3), 1.71 (1H, dd, $J_{5',6'ax}$ = 11.1 Hz, J_{gem} = 10.7 Hz, H-$6'_{ax}$), 1.78 (1H, dd, $J_{2'ax,3'}$ = 10.4 Hz, J_{gem} = 10.6 Hz, H-$2'_{ax}$), 1.66–1.82 (1H, br s, OH), 1.88–1.99 (1H, m, H-5′), 2.07 (1H, m, H-$4'_{eq}$), 2.99 (1H, br dd, J_{gem} = 10.7 Hz, $J_{5',6'eq}$ = 3.5 Hz, H-$6'_{eq}$), 2.99–3.08 (2H, m, =CHCH_2N), 3.13 (1H, br dd, J_{gem} = 10.6 Hz, $J_{2'eq,3'}$ = 4.2 Hz, H-$2'_{eq}$), 3.46 (1H, dd, J_{gem} = 10.5 Hz, J_{vic} = 5.6 Hz, CHOH), 3.58 (1H, dd, J_{gem} = 10.5 Hz, J_{vic} = 7.1 Hz, CHOH), 3.92–4.01 (1H, m, H-3′), 3.96 (2H, q, J = 7.1 Hz, OCH_2CH$_3$), 5.11–5.20 (2H, m, H_2C=), 5.34 (1H, d, J = 12.2 Hz, H-2), 5.84 (1H, m, =CHCH$_2$), 7.61 (1H, d, J = 12.2 Hz, H-3), 8.59 (1H, d, J = 7.9 Hz, CHNH), 9.45 (1H, s, C(O)NHC(O)); ^{13}C nmr ($CDCl_3$, 100 MHz) δ: 14.440 (CH_3), 33.928 (C-4′), 37.977 (C-5′), 46.570 (C-3′), 56.057 (C-6′), 58.496 (C-2′), 61.532 (=CHCH$_2$N), 65.593 (CH_2OH), 67.453 (OCH$_2$CH$_3$), 98.030 (C-2), 118.160 (H_2C=), 134.609 (=CHCH$_2$), 154.696 (urea C=O), 162.635 (C-3), 168.376 (C-1); ms (EI): 311 (M)$^{+\cdot}$ (3.1%), 153 ($C_9H_{15}NO$: $M^{+\cdot}$ − EtOCH=CHCONHCONH$_2$)$^{+\cdot}$ (100%), 122 (153 − $^{\cdot}CH_2OH$)$^+$ (18.5%), 99 (EtOCH=CHC≡O)$^+$ (10.6%); ms (CI): 312 (M + H)$^+$ (100%), 272 (M − H_2C=$CHCH_2^{\cdot}$ + 2H)$^+$ (3.6%), 214 ($C_{10}H_{20}N_3O_2$)$^+$ (2.0%), 197 (214 − NH_3)$^+$ (8.8%), 171 ($M^{+\cdot}$ − EtOCH=CHCONHCO$^{\cdot}$)$^+$ (35.0%), 116 (EtOCH=CHCONH$_2$ + H)$^+$ (21.4%). Exact Mass calcd. for $C_{15}H_{25}N_3O_4$: 311.1845; found (hrms): 311.18593. Anal. calcd. for $C_{15}H_{25}N_3O_4$: C 57.86, H 8.09, N 13.49; found: C 57.89, H 8.03, N 13.52.

*(±)-1-{(3′β,5′β)-1′-(2-Propenyl)-5′-(*tert*-butyldimethylsilyloxymethyl)piperidin-3′-yl}-2,4(1H,3H) pyrimidinedione (10)*

Enol ether **8** (311 mg, 1 mmol) was dissolved in water (10 mL). The solution was adjusted to pH 1.0 with 1 M sulfuric acid, and then heated at reflux temperature for 20 min. The cooled reaction mixture was stirred at 23°C for 1.5 h more, before being neutralized with solid potassium carbonate. The solvent was removed by freeze-drying, and the solid residues were extracted with 20% (v/v) methanol in chloroform until no further product could be detected in the extracts. The solvent was evaporated to afford pyrimidinedione **9** as its H_2SO_4 salt (337 mg, 93%).

The salt (297 mg, 0.817 mmol) was suspended in dry *N,N*-dimethylformamide (5 mL). Imidazole (218 mg, 3.2 mmol) and *tert*-

Can. J. Chem. Downloaded from www.nrcresearchpress.com by 85.192.166.187 on 09/08/12
For personal use only.

butyldimethylsilyl chloride (180 mg, 1.2 mmol) were added, followed by a catalytic amount of 4-(dimethylamino)pyridine. After stirring under a nitrogen atmosphere for 1.5 h, a further portion of *tert*-butyldimethylsilyl chloride (100 mg, 0.66 mmol) was added, and the reaction was allowed to proceed overnight. Water (10 mL) was added, followed by dichloromethane (10 mL), and the phases were separated. The aqueous layer was extracted with dichloromethane (2 × 10 mL). The combined organic layers were washed with a 10% (w/v) aqueous solution of sodium hydrogen carbonate (2 × 10 mL), and with brine (10 mL). The dried ($MgSO_4$) organic solution was evaporated, and the residue was evaporated once more from toluene to remove traces of *N,N*-dimethylformamide. Chromatography of the residue on silica gel (5% (v/v) methanol in chloroform as eluant) afforded **10** as a foam (314 mg, 82% overall), which became a crystalline solid on a further evaporation from chloroform. A sample recrystallized from water–acetonitrile formed needles; mp 142–143°C; ^{1}H nmr ($CDCl_3$, 200 MHz) δ: 0.03 (6H, s, $Si(CH_3)_2$), 0.87 (9H, s, $SiC(CH_3)_3$), 1.29 (1H, apparent q, J_{app} = 12.2 Hz, H-4′$_{ax}$), 1.69 (1H, dd, $J_{5',6'ax}$ = 11.0 Hz, J_{gem} = 11.1 Hz, H-6′$_{ax}$), 1.87–2.10 (3H, m, H-2′$_{ax}$, H-4′$_{eq}$, H-5′), 2.93–3.16 (4H, m, H-2′$_{eq}$, H-6′$_{eq}$, =CHC*H*$_2$N), 3.49 (2H, apparent d, J_{app} = 5.6 Hz, CH_2OSi), 4.69 (1H, m, H-3′), 5.10–5.23 (2H, m, H_2C=), 5.70 (1H, d, *J* = 8.0 Hz, H-5), 5.82 (1H, m, =C*H*CH$_2$), 7.21 (1H, d, *J* = 8.0 Hz, H-6), 9.49–9.71 (1H, br, NH); ^{13}C nmr ($CDCl_3$, 50 MHz) δ: −5.47 ($Si(CH_3)_2$), 18.252 ($SiC(CH_3)_3$), 25.861 ($SiC(CH_3)_3$), 32.116 (C-4′), 38.278 (C-5′), 52.529 (C-3′), 55.882 (C-6′), 56.912 (C-2′), 61.331 (=CH*C*H$_2$N), 65.522 (CH_2OSi), 102.178 (C-5), 118.207 (H_2C=), 134.520 (=*C*HCH$_2$), 140.846 (C-6), 150.818 (C-2), 163.189 (C-4); ms (EI): 380 (M + H)$^+$ (3.8%), 379 (M)$^{+\cdot}$ (4.0%), 364 (M$^{+\cdot}$ − ·CH$_3$)$^+$ (5.2%), 322 (M$^{+\cdot}$ − *tert*-Bu·)$^+$ (5.5%), 268 (M − pyrimidinedione + H)$^+$ (26.0%), 267 (M$^{+\cdot}$ − pyrimidinedione)$^{+\cdot}$ (100%), 226 (267 − H_2C=CHCH$_2$·)$^+$ (34.5%), 210 (267 − *tert*-Bu·)$^+$ (17.3%), 170 (13.9%), 134 (19.7%), 122 (267 − *tert*-BuSiMe$_2$OCH$_2$·)$^+$ (26.2%). Exact Mass calcd. for $C_{19}H_{33}N_3O_3Si$: 379.2293; found (hrms): 379.2281. Anal. calcd. for $C_{19}H_{33}N_3O_3Si$: C 60.12, H 8.76, N 11.07; found: C 60.15, H 8.67, N 11.05.

*(±)-1-[(3′*β*,5′*β*)-5′-(*tert*-Butyldimethylsilyloxymethyl)piperidin-3′-yl]-2,4(1*H*,3*H*)pyrimidinedione (**11**)*

Using the procedure and apparatus described by Laguzza and Ganem (22), a solution of allyl amine derivative **10** (310 mg, 0.82 mmol) in 84:16 (v/v) acetonitrile–water (15 mL) was heated at reflux temperature under a stream of nitrogn, in the presence of tris(triphenylphosphine)rhodium chloride (20 mg). Fresh solvent was added during the reaction to maintain a constant volume. After 2.5 h, tlc analysis (10% (v/v) methanol in chloroform as eluant) showed that the reaction was essentially complete. The mixture was cooled, and the solvents were evaporated. The residue was evaporated several times from acetonitrile before being purified by preparative tlc on a 2 mm × 20 cm × 20 cm silica gel plate (E. Merck no. 5717) using 10% (v/v) methanol in chloroform as eluant. The free amine **11** was obtained as a yellowish solid (205 mg, 74%); ^{1}H nmr (CD_3OD, 200 MHz)[8] δ: 0.06 (6H, s, $Si(CH_3)_2$), 0.89 (9H, s, $SiC(CH_3)_3$), 1.55 (1H, apparent q, J_{app} = 12.4 Hz, H-4′$_{ax}$), 1.80–2.01 (2H, m, H-4′$_{eq}$ and H-5′), 2.28 (1H, br dd, Σ*J* = 23.9 Hz, H-6′$_{ax}$), 2.66 (1H, br dd, Σ*J* = 23.4 Hz, H-2′$_{ax}$), 3.01–3.16 (2H, m, H-2′$_{eq}$ and H-6′$_{eq}$), 3.51 (1H, dd, J_{gem} = 10.2 Hz, J_{vic} = 6.2 Hz, CHOSi), 3.55 (1H, dd, J_{gem} = 10.2 Hz, J_{vic} = 5.3 Hz, CHOSi), 4.50 (1H, m, H-3′), 5.67 (1H, d, *J* = 8.0 Hz, H-5), 7.64 (1H, d, *J* = 8.0 Hz, H-6); ^{13}C nmr (CD_3OD, 50 MHz)[8] δ: −5.337 ($Si(CH_3)_2$), 19.334 ($SiC(CH_3)_3$), 26.352 ($SiC(CH_3)_3$), 33.004 (C-4′), 41.400 (C-5′), 49.136 (C-6′), 49.940 (C-2′), 54.474 (C-3′), 66.780 (CH_2OSi), 102.550 (C-5), 143.525 (C-6), 152.699 (C-2), 166.177 (C-4); ms (EI): 340 (M + H)$^+$ (4.0%), 324 (M$^{+\cdot}$ − ·CH$_3$)$^+$ (4.2%), 282 (M$^{+\cdot}$ − *tert*-Bu·)$^+$ (7.1%), 227 (M$^{+\cdot}$ − pyrimidinedione)$^{+\cdot}$ (65.3%), 170 (227 − *tert*-Bu·)$^+$ (100%), 95 (60.1%); ms (CI): 340 (M + H)$^+$ (100%), 228 (7.5%), 227 (9.6%), 170 (8.6%), 113 (pyrimidinedione + H)$^+$ (4.7%), 95 (10.5%). Exact Mass calcd. for ($C_{16}H_{29}N_3O_3Si$ + H): 340.2058; found (hrms): 340.2029.

[8]In $CDCl_3$, all of the nmr signals were observed to be very broad.

*1-[(3′*RS*,5′*SR*)-1′-(2*S*-[*tert*-Butoxycarbamoyl]-3-(4-methoxyphenyl)propanoyl)-5′-(*tert*-butyldimethylsilyloxymethyl)-piperidin-3′-yl]-2,4(1*H*,3*H*)pyrimidinedione (**13**a, b)*

The amine **11** (190 mg, 0.56 mmol) and amino acid derivative **12** (23) (185 mg, 0.63 mmol) were dissolved in dry dichloromethane (15 mL) and the solution was cooled to 0°C. 1-(3-Dimethylaminopropyl)-3-ethylcarbodiimide hydrochloride (140 mg, 0.73 mmol) was added, with a further portion of dichloromethane (2 mL). The reaction was stirred under nitrogen for 1.5 h at 0°C. Water (5 mL) was added to quench the reaction. The phases were separated, and the organic layer was washed successively with water (10 mL), a 10% (w/v) aqueous sodium hydrogen carbonate solution (10 mL), and with brine (10 mL) before being dried ($MgSO_4$) and evaporated. The resulting thick yellow oil was chromatographed on silica gel using a slow gradient of 0% → 5% (v/v) methanol in chloroform as eluant. No separation of the product diastereomers was observed, and a 1:1 mixture of **13***a* and **13***b* was obtained as a glassy solid (265 mg, 77%); ^{1}H nmr ($CDCl_3$, 200 MHz)[9] δ: 0.01 (6H, br s, $Si(CH_3)_2$), 0.86 (9H, br s, $SiC(CH_3)_3$), 1.34–1.37 (9H, 2 × s, $OC(CH_3)_3$), 3.73 (3H, 2 × s, $ArOCH_3$), 5.64–5.72 (1H, 2 × d, H-5), 6.74–7.16 (5H, m, phenyl H's and H-6); ^{13}C nmr ($CDCl_3$, 50 MHz)[9] δ: −5.482 ($Si(CH_3)_2$), 18.259 ($SiC(CH_3)_3$), 25.885 ($SiC(CH_3)_3$), 28.329 ($OC(CH_3)_3$), 32.167 (C-4′), 38.060 (C-5′), 45.051 (CH_2Ar), 51.14–51.60 (C-3′), 55.19–55.37 ($ArOCH_3$), 64.41–64.70 (CH_2OSi), 79.66 ($OC(CH_3)_3$), 102.5–102.67 (C-5), 113.48–114.23 (phenyl C-3), 123.24–128.48 (phenyl C-1), 130.44–130.76 (phenyl C-2), 140.34–140.89 (C-6), 150.49–150.62 (C-2), 155.11 (phenyl C-4), 158.51–158.82 (NHC(O)O), 163.24 (C-4), 170.70–171.12 (amide C=O); ms (EI): 617 (M + H)$^+$ (4.9%), 559 (M$^{+\cdot}$ − *tert*-Bu·)$^+$ (2.9%), 543 (M$^{+\cdot}$ − *tert*-BuO·)$^+$ (3.9%), 517 (M − CO_2 − $(CH_3)_2C$=CH_2 + H)$^+$ (11.0%), 499 (M$^{+\cdot}$ − *tert*-BuOC(O)NH$_2$)$^{+\cdot}$ (10.5%), 442 (499 − *tert*-Bu·)$^+$ (100%), 395 ($C_{18}H_{31}N_4O_4Si$)$^+$ (15.7%), 387 (499 − pyrimidinedione)$^{+\cdot}$ (17.1%), 330 (442 − pyrimidinedione)$^+$ (34.7%), 282 (18.8%), 226 (15.6%), 194 (15.0%), 170 (26.9%), 161 (4-OMeArCH=CHC≡O)$^+$ (37.5%), 150 (4-OMeArCH$_2$CH=NH$_2$)$^+$ (50.2%), 121 (4-OMeArCH$_2$)$^+$ (85.4%). Exact Mass calcd. for ($C_{31}H_{48}N_4O_7Si$ + H): 617.3373; found (hrms): 617.3353.

*(±)-5-Amino-6-chloro-4-[[(3′*β*,5′*β*)-5′-(hydroxymethyl)-1′-(2-propenyl)piperidin-3′yl]amino]pyrimidine (**14**)*

Following the method of Daluge and Vince (19), a solution of amino alcohol **6** (500 mg, 2.93 mmol), 5-amino-4,6-dichloropyrimidine (971 mg, 5.92 mmol), and triethylamine (2 mL) in *n*-butanol (15 mL) was heated at reflux temperature under a calcium chloride drying tube for 20 h. The solvent was evaporated from the cooled mixture, and a solution of the residue in chloroform was adsorbed onto a small amount of silica gel. This material was applied to a short column of silica gel and eluted with a gradient of ethanol in ethyl acetate (0% → 2% → 5% → 10% → 20% (v/v)). The product-containing fractions were dissolved in a small amount of ethyl acetate, filtered, and the filtrate was evaporated. This process was repeated, to afford **14** (569 mg). The combined insoluble material was rechromatographed on silica gel using 5% (v/v) methanol in chloroform as eluant, to give a further 132 mg of **14**, for a total yield of 701 mg (80%). Recrystallization from water, after treatment with decolorizing carbon, provided very hygroscopic white needles, mp 88–93°C; ^{1}H nmr (CD_3OD, 200 MHz) δ: 1.04 (1H, apparent q, J_{app} = 12.0 Hz, H-4′$_{ax}$), 1.72 (1H, dd, J_{gem} = 11.0 Hz, $J_{5',6'ax}$ = 11.0 Hz, H-6′$_{ax}$), 1.79 (1H, dd, J_{gem} = 10.5 Hz, $J_{2'ax,3'}$ = 10.5 Hz, H-2′$_{ax}$), 1.80–2.17 (2H, m, H-4′$_{eq}$ and H-5′), 3.04–3.15 (3H, m, H-6′$_{eq}$ and =CHC*H*$_2$N), 3.27 (1H, m, H-2′$_{eq}$), 3.40 (1H, dd, J_{gem} = 11.0 Hz, J_{vic} = 6.5 Hz, C*H*OH), 3.50 (1H, dd, J_{gem} = 11.0 Hz, J_{vic} = 6.0 Hz, C*H*OH), 4.25 (1H, dddd, $J_{2'ax,3'}$ = 11.0 Hz, $J_{3',4'ax}$ = 12.0 Hz, $J_{2'eq,3'}$ = 4.0 Hz, $J_{3',4'eq}$ = 4.0 Hz, H-3′), 5.15–5.29 (2H, m, H_2C=), 5.91 (1H, m, =C*H*CH$_2$), 7.77 (1H, s, H-2); ^{13}C nmr (CD_3OD, 50 MHz) δ: 34.671 (C-4′), 39.140 (C-5′), 48.817 (C-3′), 57.355 (C-6′), 59.204 (C-

[9]The ^{1}H and ^{13}C nmr spectra were complicated by hindered rotation in each of the two diastereomers present. Only key diagnostic signals could be distinguished.

Can. J. Chem. Downloaded from www.nrcresearchpress.com by 85.192.166.187 on 09/08/12
For personal use only.

2′), 62.610 (=CHCH$_2$N), 65.932 (CH$_2$OH), 119.223 (H$_2$C=), 124.773 (C-5), 135.320 (=CHCH$_2$), 147.651 (C-2), 153.576 (C-4), pyrimidine C-6 not observed; ms (EI): 298 (M + H)$^+$ (1.6%), 169 (4.9%), 153 (C$_9$H$_{15}$NO: M$^{+\cdot}$ − chlorodiaminopyrimidine)$^{+\cdot}$ (100%), 124 (14.4%), 122 (153 − $\cdot$CH$_2$OH)$^+$ (23.4%), 112 (153 − H$_2$C=CHCH$_2\cdot$)$^+$ (10.6%), 96 (12.1%); ms (CI): 298 (M + H)$^+$ (100%), 145 (chlorodiaminopyrimidine + H)$^+$ (15.5%), 111 (19.7%), 94 (12.0%). Exact Mass calcd. for (C$_{13}$H$_{20}$^{35}ClN$_5$O + H): 298.1435; found (hrms): 298.1434. Anal. calcd. for C$_{13}$H$_{20}$ClN$_5$O: C 52.43, H 6.77, N 23.52; found: C 52.31, H 6.83, N 23.70.

*(±)-6-Chloro-9-[(3′β,5′β)-5′-(hydroxymethyl)-1′-(2-propenyl)-piperidin-3′-yl]purine (**15**)*

A solution of chloropyrimidine **14** (546 mg, 1.8 mmol), triethyl orthoformate (10 mL), and concentrated aqueous hydrochloric acid (0.5 mL) was stirred at 23°C for 2 h (31). The excess of the orthoformate was removed by evaporation in vacuo, and the remaining solid was stirred in the presence of 0.5 M aqueous hydrochloric acid (5 mL) for 1 h. The solution was then adjusted to pH 11 with a 15% (w/v) aqueous solution of sodium hydroxide, and extracted with chloroform (3 × 10 mL). The combined organic extracts were washed with brine (5 mL) and dried (MgSO$_4$). Evaporation of the solvent afforded a greasy foam that could not be induced to crystallize. Addition of an excess of aqueous hydrochloric acid followed by evaporation of the solvent provided the hydrochloride salt, which likewise resisted crystallization. The desired chloropurine **15** was obtained by chromatography on silica gel using the organic layer of a 12:6:1 (v/v/v) chloroform–isopropanol – concentrated aqueous ammonia mixture (385 mg, 69%); ^{1}H nmr (CDCl$_3$, 200 MHz) δ: 1.82 (1H, apparent q, J_{app} = 11.7 Hz, H-4′$_{ax}$), 1.93 (1H, dd, ΣJ = 35.09 Hz, H-6′$_{ax}$), 2.03–2.33 (2H, m, H-4′$_{eq}$ and H-5′), 2.43 (1H, dd, J_{gem} = 10.5 Hz, $J_{2'ax,3'}$ = 11.1 Hz, H-2′$_{ax}$), 2.88–3.18 (4H, m, H-6′$_{eq}$, =CHCH_2N, OH), 3.26 (1H, m, H-2′$_{eq}$), 3.62 (2H, apparent d, J_{app} = 5.7 Hz, CH_2OH), 4.79 (1H, dddd, $J_{2'ax,3'}$ = 11.1 Hz, $J_{3',4'ax}$ = 12.0 Hz, $J_{2'eq,3'}$ = 4.0 Hz, $J_{3',4'eq}$ = 4.0 Hz, H-3′), 5.11–5.24 (2H, m, H$_2$C=), 5.84 (1H, m, =CHCH$_2$), 8.16 (1H, s, H-2), 8.71 (1H, s, H-8); ^{13}C nmr (CDCl$_3$, 50 MHz) δ: 33.183 (C-4′), 38.312 (C-5′), 53.136 (C-3′), 55.697 (C-6′), 57.492 (C-2′), 61.249 (=CHCH$_2$N), 65.016 (CH$_2$OH), 118.716 (H$_2$C=), 131.761 (C-5), 134.051 (=CHCH$_2$), 143.45 (C-8), 151.091 (C-4 or C-6), 151.576 (C-6 or C-4), 151.697 (C-2); ms (EI): 308 (M + H)$^+$ (4.7%), 155 (chloropurine + H)$^+$ (3.4%), 153 (C$_9$H$_{15}$NO: M$^{+\cdot}$ − chloropurine)$^{+\cdot}$ (100%), 124 (12.0%), 122 (153 − $\cdot$CH$_2$OH)$^+$ (21.6%), 112 (153 − H$_2$C=CHCH$_2\cdot$)$^+$ (8.7%); ms (CI): 310 (^{37}Cl or ^{18}O M + H)$^+$ (34.4%), 309 (^{13}C or ^{2}H or ^{15}N or ^{17}O M + H)$^+$ (17.7%), 308 (M + H)$^+$ (100%), 157 (^{37}Cl chloropurine + H)$^+$ (3.6%), 155 (^{35}Cl chloropurine + H)$^+$ (10.6%), 154 (C$_9$H$_{15}$NO + H: M − chloropurine + H)$^+$ (19.9%), 153 (M$^{+\cdot}$ − chloropurine)$^{+\cdot}$ (27.1%). Exact Mass calcd. for (C$_{14}$H$_{18}$^{35}ClN$_5$O + H): 308.1278; found (hrms): 308.1264.

*(±)-6-(Dimethylamino)-9-[(3′β,5′β)-5′-(hydroxymethyl)-1′-(2-propenyl)piperidin-3′-yl]purine (**16**)*

Chloropurine **15** (301 mg, 0.98 mmol) was dissolved in 40% (w/v) aqueous dimethylamine (10 mL) and heated at 80°C in a sealed Pyrex tube for 28 h. At this point, tlc analysis (15% (v/v) methanol in chloroform as eluant) apparently indicated no reaction had occurred. The reaction mixture was then heated at reflux temperature for 2 h more, and left at 23°C for 24 h. Again tlc indicated no visible change. The aqueous solution was extracted with chloroform (3 × 10 mL), and the organic extracts were dried (MgSO$_4$) and concentrated. The residue was chromatographed on silica gel (using 10% (v/v) ethanol in ethyl acetate as eluant) to afford a brown oil (290 mg) that proved on ^{1}H nmr analysis to be the desired derivative **16** (93%); ^{1}H nmr (CDCl$_3$, 200 MHz) δ: 1.66 (1H, apparent q, J_{app} = 11.4 Hz, H-4′$_{ax}$), 1.86 (1H, dd, ΣJ = 21.6 Hz, H-6′$_{ax}$), 1.96–2.44 (4H, m, H-2′$_{ax}$, H-4′$_{eq}$, H-5′, OH), 3.00–3.25 (4H, m, H-2′$_{eq}$, H-6′$_{eq}$, =CHCH_2N), 3.50 (6H, br s, N(CH$_3$)$_2$), 3.55 (2H, apparent d, J_{app} = 5.7 Hz, CH_2OH), 4.67 (1H, m, H-3′), 5.06–5.20 (2H, m, H$_2$C=), 5.83 (1H, m, =CHCH$_2$), 7.72 (1H, s, H-2), 8.30 (1H, s, H-8); ^{13}C nmr (CDCl$_3$, 50 MHz) δ: 33.522 (C-4′), 38.515 (N(CH$_3$)$_2$ and C-5′), 51.788 (C-3′), 55.886 (C-6′), 57.949 (C-2′), 61.314 (=CHCH$_2$N), 65.136 (CH$_2$OH), 118.226 (H$_2$C=), 120.272 (C-5), 134.521 (=CHCH$_2$), 136.176 (C-8), 150.213 (C-6), 152.111 (C-2), 154.933 (C-4); ms (EI): 317 (M + H)$^+$ (4.3%), 164 (N^6-dimethyladenine + H)$^+$ (25.5%), 153 (C$_9$H$_{15}$NO: M$^{+\cdot}$ − N^6-dimethyladenine)$^{+\cdot}$ (100%), 124 (14.2%), 122 (153 − $\cdot$CH$_2$OH)$^+$ (24.6%), 112 (153 − H$_2$C=CHCH$_2\cdot$)$^+$ (11.0%). Exact Mass calcd. for (C$_{16}$H$_{24}$N$_6$O + H): 317.2090; found (hrms): 317.2081.

*(±)-6-(Dimethylamino)-9-[(3′β,5′β)-5′-(*tert*-butyldimethylsilyloxymethyl)piperidin-3′-yl]purine (**18**)*

A mixture of **16** (249 mg, 0.79 mmol) and imidazole (107 mg, 1.57 mmol) in dry dichloromethane (5 mL) was treated with *tert*-butyldimethylsilyl chloride (132 mg, 0.87 mmol). After 1 h of stirring at 23°C, a second portion of *tert*-butyldimethylsilyl chloride (50 mg, 0.33 mmol) was added. After a further 1 h, the reaction was quenched by the addition of water (2 mL). The phases were separated, and the organic layer was washed with water (2 mL). The combined aqueous layers were extracted with dichloromethane (5 mL) and the combined organic layers were dried (MgSO$_4$) and evaporated. The oily residue was applied to a short column of silica gel and eluted with a gradient of methanol in chloroform (0% → 10% (v/v)). The product was allowed to stand in vacuo until all traces of silicon-containing impurities had evaporated. Silyl ether **17** was obtained as an oil (295 mg, 87%); ^{1}H nmr (CDCl$_3$, 200 MHz) δ: 1.65 (1H, apparent q, J_{app} = 11.7 Hz, H-4′$_{ax}$), 1.82 (1H, dd, ΣJ = 21.6 Hz, H-6′$_{ax}$), 1.95–2.23 (2H, m, H-4′$_{eq}$ and H-5′), 2.29 (1H, dd, J_{gem} = 11.5 Hz, $J_{2'ax,3'}$ = 11.0 Hz, H-2′$_{ax}$), 2.97–3.15 (3H, m, H-6′$_{eq}$ and =CHCH_2N), 3.21 (1H, m, H-2′$_{eq}$), 4.69 (1H, dddd, $J_{2'ax,3'}$ = 11.0 Hz, $J_{3',4'ax}$ = 12.0 Hz, $J_{2'eq,3'}$ = 4.0 Hz, $J_{3',4'eq}$ = 4.0 Hz, H-3′), 5.08–5.23 (2H, m, H$_2$C=), 5.85 (1H, m, =CHCH$_2$), 7.74 (1H, s, H-2), 8.34 (1H, s, H-8).

Without further purification, the silyl ether **17** was treated with tris(triphenylphosphine)rhodium chloride (50 mg) in an 84:16 acetonitrile–water solvent mixture (22) (20 mL) as described above for the preparation of **11**. Complete reaction, as judged by tlc analysis (15% (v/v) methanol in chloroform eluant), was obtained after 7 h of heating at reflux temperature. After removal of the solvents in vacuo, the residue was purified by preparative tlc on a 2 mm × 20 cm × 20 cm silica gel plate (E. Merck no. 5717) using 10% (v/v) methanol in toluene as eluant. It was necessary to extract the product from the plate by Soxhlet extraction using an 87:13 (v/v) chloroform–methanol mixture, to obtain **18** as an oil (181 mg, 68%); ^{1}H nmr (CDCl$_3$, 200 MHz) δ: 0.034 (6H, s, Si(CH$_3$)$_2$), 0.88 (9H, s, SiC(CH$_3$)$_3$), 1.78 (1H, apparent q, J_{app} = 11.5 Hz, H-4′$_{ax}$), 1.84–2.08 (2H, m, NH and H-5′), 2.24 (1H, m, H-4′$_{eq}$), 2.44 (1H, dd, J_{gem} = 12.6 Hz, $J_{5',6'ax}$ = 10.8 Hz, H-6′$_{ax}$), 2.87 (1H, dd, J_{gem} = 11.6 Hz, $J_{2'ax,3'}$ = 11.6 Hz, H-2′$_{ax}$), 3.23 (1H, m, H-6′$_{eq}$), 3.36–3.60 (9H, m, H-2′$_{eq}$, N(CH$_3$)$_2$, CH$_2$OSi), 4.55 (1H, m, H-3′), 7.74 (1H, s, H-2), 8.33 (1H, s, H-8); ^{13}C nmr (CDCl$_3$, 50 MHz) δ: −5.672 (SiCH$_3$), −5.701 (SiCH$_3$), 18.018 (SiC(CH$_3$)$_3$), 25.638 (SiC(CH$_3$)$_3$), 33.564 (C-4′), 38.237 (br, N(CH$_3$)$_2$), 40.138 (C-5′), 48.572 (C-6′), 51.248 (C-2′), 52.322 (C-3′), 65.275 (CH$_2$OSi), 120.087 (C-5), 135.585 (C-8), 150.056 (C-4), 151.880 (C-2), 154.716 (C-6); ms (EI): 391 (M + H)$^+$ (8.5%), 375 (M$^{+\cdot}$ − $\cdot$CH$_3$)$^+$ (3.4%), 333 (M$^{+\cdot}$ − *tert*-Bu$\cdot$)$^+$ (3.2%), 227 (C$_{12}$H$_{25}$NOSi: M$^{+\cdot}$ − N^6-dimethyladenine)$^{+\cdot}$ (25.3%), 190 (6.3%), 170 (227 − *tert*-Bu$\cdot$)$^+$ (19.0%), 164 (N^6-dimethyladenine + H)$^+$ (100%), 134 (6.9%). Exact Mass calcd. for (C$_{19}$H$_{34}$N$_6$OSi + H): 391.2642; found (hrms): 391.2629.

*6-(Dimethylamino)-9-[(3′RS,5′SR)-1′-(2S-[*tert*-butoxycarbamoyl]-3-[4-methoxyphenyl]propanoyl)-5′-(*tert*-butyldimethylsilyloxymethyl)piperidin-3′-yl]purine (**19**a, b)*

As described above for the preparation of **13**, purine derivative **18** (180 mg, 0.46 mmol) and *N*-(*tert*-butoxycarbonyl)-L-*p*-methoxyphenylalanine (**12**) (23) (152 mg, 0.51 mmol) were dissolved in dry dichloromethane (5 mL) and treated with 1-(3-dimethylaminopropyl)-3-ethylcarbodiimide hydrochloride (108 mg, 0.56 mmol) at 0°C. Processing as previously described afforded, after chromatography on silica gel (0% → 2% (v/v) methanol in chloroform as eluant), a 1:1 mixture of the title compounds **19***a*, *b* (309 mg, quant.) as an oil; ^{1}H nmr (CDCl$_3$, 200 MHz)[9] δ: 0.032, 0.045 (6H, 2 × s, Si(CH$_3$)$_2$), 0.886,

Can. J. Chem. Downloaded from www.nrcresearchpress.com by 85.192.166.187 on 09/08/12
For personal use only.

0.893 (9H, 2 × s, $SiC(CH_3)_3$), 1.36, 1.40, 1.42 (9H, 3 × s, $OC(CH_3)_3$), 3.33–3.60 (9H, m + br s, $N(CH_3)_2$, CH_2OSi, H-2′$_{eq}$ or H-6′$_{eq}$), 3.75, 3.78, 3.79 (3H, 3 × s, OCH_3), 5.29–5.41 (1H, m, NH), 6.73–6.91 (2H, m, phenyl H-3), 7.02–7.25 (2H, m, phenyl H-2), 7.53, 7.62, 7.68 (1H, 3 × s, H-2), 8.28, 8.31, 8.32 (1H, 3 × s, H-8); ^{13}C nmr ($CDCl_3$, 50 MHz)[9] δ: −5.76 ($Si(CH_3)_2$), 17.91 ($SiC(CH_3)_3$), 25.57 ($SiC(CH_3)_3$), 28.03 ($OC(CH_3)_3$), 32.2, 33.1 (C-4′), 37.6, 37.7 (C-5′), 38.14 (br, $N(CH_3)_2$), 38.6, 39.0 (ArCH_2), 44.1, 44.3, 45.5, 45.6, 47.7, 48.0, 48.5, 49.0 (C-2′ and C-6′), 50.8, 51.1, 52.0 (C-α and C-3′), 54.82, 54.96 (OCH_3), 64.11, 64.25, 64.45 (CH_2OSi), 79.17 ($OC(CH_3)_3$), 113.49, 113.78, 113.8 (phenyl C-3), 120.1, 120.27, 120.37 (C-6), 128.07, 128.20, 128.48 (phenyl C-1), 130.09, 130.30, 130.58 (phenyl C-2), 135.7, 136.0 (C-8), 150.05, 150.15 (C-4), 151.80 (C-2), 154.64, 154.65 (phenyl C-4 and C-5), 158.20, 158.30, 158.35, 158.46 (carbamate C═O), 170.20, 170.56 (amide C═O); ms (EI): 667 $(M)^{+\cdot}$ (4.2%), 446 ($C_{21}H_{36}N_7O_2Si$: $M^{+\cdot}$ − CO_2 − $(CH_3)_2C{=}CH_2$ − 4-OMeArCH$_2^{\cdot}$)$^+$ (40%), 387 ($C_{22}H_{33}NO_3Si$: $M^{+\cdot}$ − CO_2 − $(CH_3)_2C{=}CH_2$ − NH_3 − N^6-dimethyladenine)$^{+\cdot}$ (8.3%), 330 (387 − *tert*-Bu$^{\cdot}$)$^+$ (21.2%), 283 ($C_{14}H_{27}N_2O_2Si$: 446 − N^6-dimethyladenine)$^+$ (8.1%), 227 (27.9%), 164 (N^6-dimethyladenine + H)$^+$ (100%), 121 (4-OMeArCH$_2$)$^+$ (62.2%). Exact Mass calcd. for $C_{34}H_{53}N_7O_5Si$: 667.3877; found (hrms): 667.3849. Exact Mass calcd. for $C_{21}H_{36}N_7O_2Si$: 446.2700; found (hrms): 446.2700. Exact Mass calcd. for $C_{22}H_{33}NO_3Si$: 387.2230; found (hrms): 387.2242. Exact Mass calcd. for $C_{18}H_{24}NO_3Si$: 330.1525; found (hrms): 330.1506. Exact Mass calcd. for $C_{14}H_{27}N_2O_2Si$: 283.1842; found (hrms): 283.1833.

*1-{(3′S,5′R)-1′-(2S-Amino-3-(4-methoxyphenyl)propanoyl)-5′-(hydroxymethyl)piperidin-3′-yl}-2,4(1H,3H)pyrimidinedione (**20**a) and 1-{(3′R,5′S)-1′-(2S-amino-3-(4-methoxyphenyl)propanoyl)-5′-(hydroxymethyl)piperidin-3′-yl}-2,4(1H,3H)pyrimidinedione (**20**b)*

The *N*-BOC *O*-TBDMS precursors **19***a,b* (252 mg, 0.41 mmol) were dissolved in dichloromethane (1 mL) and the solution was cooled in an ice bath. A mixture of trifluoroacetic acid (3 mL), anisole (1 mL), and water (0.5 mL) was added, and the mixture was stirred at 0°C for 30 min. It was then allowed to warm to 23°C over 2.5 h. Monitoring by tlc using a 2-butanone–water – acetic acid eluant (40:1:1 (v/v/v)) showed rapid conversion into an intermediate product followed by slow conversion to a ninhydrin-positive, highly polar material. The solvents were evaporated, and the residue was allowed to stand in vacuo to remove traces of anisole. The residual material was then dissolved in a 1:1 (v/v) water–ethanol mixture and applied to a short column of Dowex 50-X2 400 (H^+) ion-exchange resin (~5 mL of resin). The column was thoroughly washed with 1:1 (v/v) water–ethanol, and then eluted with 1:1 (v/v) 1 M aqueous ammonium hydroxide – ethanol. The product-containing fractions were pooled and the solvents were evaporated to give an amorphous mixture of diastereomers **20***a, b* (144 mg, 87%).

The diastereomeric mixture was resolved by reverse-phase hplc on a 300 mm × 7.0 mm Hamilton PRP-1 column. Small portions of the sample were injected onto the column and eluted with a linear gradient of 0.33 M aqueous triethylammonium hydrogen carbonate buffer (pH ~8) and acetonitrile (1.5 mL min^{-1}, 90:10 → 80:20 (v/v) over 20 min, then isocratic for 5 min), monitoring at 254 nm. Fractions were collected and the process was repeated until all of the mixture had been resolved. The fractions containing each product were combined, concentrated on a rotary evaporator to remove the organic solvent, and finally freeze-dried. To remove traces of buffer salts, it was necessary to pass each sample down a Dowex 50 column once more, as previously described, followed by freeze-drying. Samples of leading fraction **20***a* (34 mg, 41%, ~100% diastereomeric excess), and second fraction **20***b* (26 mg, 31%, ~100% diastereomeric excess) were obtained as fluffy solids.

First fraction (**20***a*); $[\alpha]_D^{25}$ +68.04 (*c* 1.02, H_2O); ^{1}H nmr spectra indicated the presence of two rotamers in a 2.26:1.00 ratio. The spectral data for the rotamers are listed separately for clarity.

Major rotamer (amide carbonyl *syn* with respect to the pyrimidinedione ring): ^{1}H nmr (D_2O, 600 MHz, 300 K) δ: 0.249 (1H, m, H-5′), 1.502 (1H, apparent q, J_{app} = 12.2 Hz, H-4′$_{ax}$), 1.711 (1H, m, H-4′$_{eq}$), 2.681 (1H, dd, J_{gem} = 12.2 Hz, $J_{2'ax,3'}$ = 9.1 Hz, H-2′$_{ax}$), 2.70 (1H, dd, J_{gem} = 12.0 Hz, $J_{6'ax,5'}$ = 10.5 Hz, H-6′$_{ax}$), 2.807 (1H, dd, J_{gem} = 12.9 Hz, J_{vic} = 10.4 Hz, ArCH_2), 3.003 (1H, dd, J_{gem} = 12.9 Hz, J_{vic} = 5.1 Hz, ArCH_2), 3.301 (1H, dd, J_{gem} = 11.5 Hz, J_{vic} = 6.07 Hz, C*H*OH), 3.331 (1H, dd, J_{gem} = 11.5 Hz, J_{vic} = 5.5 Hz, C*H*OH), 3.768 (1H, m, H-6′$_{eq}$), 3.801 (3H, s, OCH_3), 4.011 (1H, m, H-3′), 4.23–4.29 (1H, m, H-α), 4.524 (1H, m, H-2′$_{eq}$), 5.808 (1H, d, *J* = 8.01 Hz, H-5), 7.006 (2H, d, *J* = 8.61 Hz, 2 × phenyl H-3), 7.227 (2H, d, *J* = 8.61 Hz, 2 × phenyl H-2), 7.598 (1H, d, *J* = 8.01 Hz, H-6); ^{13}C nmr (D_2O, 100 MHz, 300 K) δ: 30.516 (C-4′), 37.272 (C-5′), 40.213 (ArCH_2), 44.833 (C-2′), 47.765 (C-6′), 51.267 (C-α), 51.419 (C-3′), 55.464 (OCH_3), 62.732 (CH_2OH), 101.850 (C-5), 114.540 (2 × phenyl C-3), 129.132 (phenyl C-1), 130.687 (2 × phenyl C-2), 142.894 (C-6), 152.169 (C-2), 158.065 (phenyl C-4), 166.492 (C-4), 174.157 (amide C═O).

Minor rotamer (amide carbonyl *anti* with respect to pyrimidinedione ring): ^{1}H nmr (D_2O, 600 MHz, 300 K) δ: 1.599 (1H, apparent q, J_{app} = 12.2 Hz, H-4′$_{ax}$), 1.85 (1H, m, H-5′), 1.99 (1H, m, H-4′$_{eq}$), 2.275 (1H, dd, J_{gem} = 13.0 Hz, $J_{5',6'ax}$ = 10.0 Hz, H-6′$_{ax}$), 2.296 (1H, dd, J_{gem} = 12.6 Hz, $J_{2'ax,3'}$ = 9.5 Hz, H-2′$_{ax}$), 2.77–2.83 (1H, dd, J_{gem} = 13.5 Hz, J_{vic} obscured by overlap, ArCH_2), 2.964 (1H, dd, J_{gem} = 13.5 Hz, J_{vic} = 5.6 Hz, ArCH_2), 3.52 (1H, dd, J_{gem} = 11.7 Hz, J_{vic} = 7.2 Hz, C*H*OH), 3.54 (1H, dd, J_{gem} = 11.7 Hz, J_{vic} = 6.0 Hz, C*H*OH), 3.70 (1H, m, H-2′$_{eq}$), 3.794 (3H, s, OCH_3), 4.23–4.29 (1H, m, H-α), 4.36 (1H, m, H-3′), 4.49 (1H, m, H-2′$_{eq}$), 5.808 (1H, d, *J* = 8.01 Hz, H-5), 6.911 (2H, d, *J* = 8.59 Hz, 2 × phenyl H-3), 7.113 (2H, d, *J* = 8.59 Hz, 2 × phenyl H-2), 7.514 (1H, d, *J* = 8.01 Hz, H-6); ^{13}C nmr (D_2O, 100 MHz, 300 K) δ: 30.392 (C-4′), 37.272 (C-5′), 39.421 (ArCH_2), 44.491 (C-6′), 47.661 (C-2′), 51.671 (C-α), 52.600 (C-3′), 55.261 (OCH_3), 63.280 (CH_2OH), 101.850 (C-5), 114.032 (2 × phenyl C-3), 128.475 (phenyl C-1), 130.586 (2 × phenyl C-2), 142.697 (C-6), 152.169 (C-2), 157.966 (phenyl C-4), 166.762 (C-4), 173.586 (amide C═O); ms (EI): 403 (M + H)$^+$ (3.8%), 385 (M + H − H_2O)$^+$ (8.8%), 332 (M + H − HNCO − CO)$^+$ (14.2%), 281 ($M^{+\cdot}$ − 4-OMeArCH$_2^{\cdot}$)$^+$ (84.8%), 150 (4-OMeArCH$_2$CH═NH_2)$^+$ (100%), 121 (4-OMeArCH$_2$)$^+$ (51.5%); ms (CI): 403 (M + H)$^+$ (100%), 226 ($C_{10}H_{16}N_3O_3$: M − aminoacyl + 2H)$^+$ (32.8%), 150 (4-OMeArCH$_2$CH═NH_2)$^+$ (35.3%). Exact Mass calcd. for ($C_{20}H_{26}N_4O_5$ + H): 403.1981; found (hrms): 403.1979.

Second fraction (**20***b*); $[\alpha]_D^{25}$ +51.51 (*c* 1.06, H_2O); ^{1}H nmr spectra indicated the presence of two rotamers in a 1.00:0.91 ratio. The spectral data for the two rotamers are listed separately for clarity.

Predominant rotamer (amide carbonyl *anti* with respect to base): ^{1}H nmr (D_2O, 600 MHz, 300 K) δ: 1.50–1.58 (1H, br m, H-5′), 1.64 (1H, apparent q, J_{app} = 12.2 Hz, H-4′$_{ax}$), 1.93 (1H, m, H-4′$_{eq}$), 2.399 (1H, dd, J_{gem} = 13.5 Hz, $J_{5',6'ax}$ = 11.6 Hz, H-6′$_{ax}$), 2.856 (1H, dd, J_{gem} = 13.6 Hz, J_{vic} = 8.18 Hz, ArCH_2), 3.001 (1H, dd, J_{gem} = 13.6 Hz, J_{vic} = 5.95 Hz, ArCH_2), 3.200 (1H, dd, J_{gem} = 13.7 Hz, $J_{2'ax,3'}$ = 11.1 Hz, H-2′$_{ax}$), 3.504 (1H, dd, J_{gem} = 11.5 Hz, J_{vic} = 6.6 Hz, C*H*OH), 3.531 (1H, dd, J_{gem} = 11.5 Hz, J_{vic} = 5.46 Hz, C*H*OH), 3.716 (1H, m, H-3′), 3.815 (3H, s, OCH_3), 4.169 (1H, m, H-2′$_{eq}$), 4.367 (1H, dd, J_{vic} = 5.95 Hz, $J_{vic'}$ = 8.18 Hz, H-α), 4.481 (1H, m, H-6′$_{eq}$), 5.820 (1H, d, *J* = 8.07 Hz, H-5), 6.972 (2H, d, *J* = 8.64 Hz, 2 × phenyl H-3), 7.211 (2H, d, *J* = 8.64 Hz, 2 × phenyl H-2), 7.561 (1H, d, *J* = 8.07 Hz, H-6); ^{13}C nmr (D_2O, 100 MHz, 300 K) δ: 30.416 (C-4′), 37.442 (C-5′), 39.101 (ArCH_2), 44.577 (C-6′), 47.934 (C-2′), 51.50 (C-α), 53.120 (C-3′), 55.289 (OCH_3), 63.244 (CH_2OH), 101.889 (C-5), 114.287 (2 × phenyl C-3), 128.477 (phenyl C-1), 130.70 (2 × phenyl C-2), 143.02 (C-6), 153.28 (C-2), 157.89 (phenyl C-4), 167.79 (C-4), 174.69 (br, amide C═O).

Second rotamer (amide carbonyl *syn* with respect to pyrimidinedione ring): ^{1}H nmr (D_2O, 600 MHz, 300 K) δ: 1.60 (1H, apparent q, J_{app} = 12.3 Hz, H-4′$_{ax}$), 1.87–1.95 (1H, m, H-5′), 2.01 (1H, m, H-4′$_{eq}$), 2.185 (1H, dd, J_{gem} = 13.3 Hz, $J_{5',6'ax}$ = 12.4 Hz, H-6′$_{ax}$), 2.676 (1H, dd, J_{gem} = 13.7 Hz, $J_{2'ax,3'}$ = 10.5 Hz, H-2′$_{ax}$), 2.95 (1H, dd, J_{gem} = 13.2 Hz, J_{vic} = 7.7 Hz, ArCH_2), 2.97 (1H, dd, J_{gem} = 13.2 Hz, J_{vic} = 6.0 Hz, ArCH_2), 3.424 (1H, dd, J_{gem} = 11.3 Hz, J_{vic} = 6.87 Hz, C*H*OH), 3.485 (1H, dd, J_{gem} = 11.3 Hz, J_{vic} = 5.48 Hz, C*H*OH), 3.771 (1H, m, H-6′$_{eq}$), 3.820 (3H, s, OCH_3), 4.239 (1H, dd, J_{vic} = 7.7 Hz, $J_{vic'}$ = 6.0 Hz, H-α), 4.347 (1H, m, H-3′), 4.534 (1H, m, H-2′$_{eq}$), 5.835 (1H, d, *J* = 8.06 Hz, H-5), 6.960 (2H, d, *J* = 8.64 Hz, 2 × phenyl H-3), 7.156 (2H, d, *J* = 8.64 Hz, 2 × phenyl H-2), 7.624 (1H, d, *J* = 8.06 Hz, H-6); ^{13}C nmr (D_2O,

Can. J. Chem. Downloaded from www.nrcresearchpress.com by 85.192.166.187 on 09/08/12
For personal use only.

100 MHz, 300 K) δ: 30.742 (C-4′), 38.207 (C-5′), 38.899 (ArCH_2), 44.760 (C-2′), 47.544 (C-6′), 51.47 (C-α), 51.992 (C-3′), 55.289 (OCH_3), 62.926 (CH_2OH), 101.600 (C-5), 114.108 (2 × phenyl C-3), 128.124 (phenyl C-1), 130.62 (2 × phenyl C-2), 142.98 (C-6), 152.98 (C-2), 157.915 (phenyl C-4), 167.79 (C-4), 174.69 (br, amide C=O); ms (EI): identical to that obtained for **20***a*; ms (CI): identical to that obtained for **20***a*. Exact Mass calcd. for ($C_{20}H_{26}N_4O_5$ + H): 403.1981; found (hrms): 403.1971.

*6-(Dimethylamino)-9-[(3′S,5′R)-(2S-amino-3-[4-methoxyphenyl]propanoyl)-5′-(hydroxymethyl)piperidin-3′-yl]purine (**21**a) and 6-(dimethylamino)-9-[(3′R,5′S)-(2S-amino-3-[4-methoxyphenyl]propanoyl)-5′-(hydroxymethyl)piperidin-3′-yl]purine (**21**b)*

The diprotected precursors **19***a*, *b* (250 mg, 0.37 mmol) and anisole (1 mL) were dissolved in methanol (1 mL), and the solution was cooled in an ice bath. Trifluoroacetic acid (2 mL) was added, and the mixture was stirred at 0°C for 30 min. The reaction was then allowed to warm to 23°C over 2 h, at which point tlc analysis (10% (v/v) methanol in chloroform as eluant, plate pretreated with ammonia vapor) indicated only about 10% conversion. A further portion of trifluoroacetic acid (1 mL) was added, and the reaction was allowed to proceed overnight. The solvents were evaporated, and the residue was processed as described above to give a mixture of diastereomers **21***a*, *b* (158 mg, 93%).

Reverse-phase hplc separation of the diastereomers was carried out by isocratic elution at 2 mL min^{-1} with 20% (v/v) acetonitrile in 0.3 M aqueous triethylammonium hydrogen carbonate buffer (pH ~8). Further processing of the product fractions as previously described gave samples of leading fraction **21***a* (27 mg, 31%, 95% diastereomeric excess) and second fraction **21***b* (23 mg, 27%, 95% diastereomeric excess) as fluffy solids. These products were only minimally soluble in water but dissolved readily in alcohol, chloroform or DMSO.

First fraction (**21***a*); $[\alpha]_D^{25}$ +60.3 (*c* 0.58, $CHCl_3$); ^{1}H nmr (DMSO-d_6, 400 MHz, 383 K)[10] δ: 1.52–1.69 (2H, br m, H-5′ and H-6′$_{ax}$), 1.980 (1H, apparent, q, J_{app} = 11.1 Hz, H-4′$_{ax}$), 2.12 (1H, m, H-4′$_{eq}$), 2.62 (1H, dd, J_{gem} = 13.7 Hz, J_{vic} = 7.2 Hz, ArCH_2), 2.834 (1H, dd, J_{gem} = 13.6 Hz, J_{vic} = 6.1 Hz, ArCH_2), 3.117 (1H, dd, ΣJ = 23.7 Hz, H-2′$_{ax}$) 3.354 (1H, dd, J_{gem} = 10.8 Hz, J_{vic} = 7.4 Hz, C*H*OH), 3.422 (1H, dd, J_{gem} = 10.8 Hz, J_{vic} = 5.5 Hz, C*H*OH), 3.468, (6H, s, $N(CH_3)_2$), 3.735 (3H, s, OCH_3), 3.936 (1H, dd, J_{vic} = 6.1 Hz, $J_{vic'}$ = 7.2 Hz, H-α), 4.25–4.55 (3H, br m, H-2′$_{eq}$, H-3′, H-6′$_{eq}$), 6.822 (2H, d, J = 8.5 Hz, 2 × phenyl H-3), 7.132 (2H, d, J = 8.5 Hz, 2 × phenyl H-2), 8.074 (1H, s, H-2), 8.213 (1H, s, H-8); ^{13}C nmr (DMSO-d_6, 100 MHz, 298 K)[11] δ: 32.464, 32.880 (C-4′), 38.107, 38.805 (C-5′), 40.696, 41.101 (ArCH_2), 44.503, 45.289, 47.620, 48.419 (C-2′ and C-6′), 50.263, 51.587 (C-3′), 52.120, 52.290 (C-α), 54.917, 55.002 (OCH_3), 62.805, 63.288 (CH_2OH), 113.352, 113.645 (2 × phenyl C-3), 119.336, 119.537 (C-6), 130.255, 130.372 (2 × phenyl C-2), 130.503 (phenyl C-1), 149.872, 150.035 (C-4), 151.7 (C-2), 154.280 (phenyl C-4), 157.655, 157.824 (C-5), 173.058, 173.373 (amide C=O); ms (EI): 454 $(M + H)^+$ (3.7%), 453 $(M)^{+\cdot}$ (3.6%), 436 $(M^{+\cdot} - NH_3)^{+\cdot}$ or $(M + H - H_2O)^+$ (1.3%), 332 ($C_{15}H_{22}N_7O_2$: $M^{+\cdot}$ − 4-OMeArC$H_2^{\cdot}$)$^+$ (100%), 304 (14.4%), 164 (*N*^{6}-dimethyladenine + H)$^+$ (67.7%), 150 (4-OMeArCH_2CH=NH_2)$^+$ (7.8%), 134 (9.0%), 121 (4-OMeArCH_2)$^+$ (12.6%). Exact Mass calcd. for $C_{23}H_{31}N_7O_3$: 453.2488; found (hrms): 453.2484.

Second fraction (**21***b*); $[\alpha]_D^{25}$ +13.0 (*c* 0.23, $CHCl_3$); ^{1}H nmr (DMSO-d_6, 400 MHz, 383 K) δ: 1.80 (1H, m, H-5′), 1.987 (1H, apparent q, J_{app} = 12.0 Hz, H-4′$_{ax}$), 2.16 (1H, m, H-4′$_{eq}$), 2.519 (1H, dd, partly obscured by solvent, H-6′$_{ax}$), 2.645 (1H, dd, J_{gem} = 13.6 Hz, J_{vic} = 7.4 Hz, ArCH_2), 2.900 (1H, dd, J_{gem} = 13.6 Hz, J_{vic} = 5.9 Hz, ArCH_2), 3.208 (1H, dd, ΣJ = 24.04 Hz, H-2′$_{ax}$), 3.373 (1H, dd, J_{gem} = 10.8 Hz, J_{vic} = 6.3 Hz, C*H*OH), 3.446 (1H, dd, J_{gem} = 10.8 Hz, J_{vic} = 5.3 Hz, C*H*OH), 3.470 (6H, s, $N(CH_3)_2$), 3.744 (3H, s, OCH_3), 3.937 (1H, dd, J_{vic} = 5.9 Hz, $J_{vic'}$ = 7.4 Hz, H-α), 4.26–4.40 (2H, m, H-3′ and H-2′$_{eq}$ or H-6′$_{eq}$), 4.52 (1H, m, H-6′$_{eq}$ or H-2′$_{eq}$), 6.831 (2H, d, J = 8.6 Hz, 2 × phenyl H-3), 7.165 (2H, d, J = 8.6 Hz, 2 × phenyl H-2), 8.058 (1H, s, H-2), 8.202 (1H, s, H-8); ^{13}C nmr (DMSO-d_6, 100 MHz, 300 K)[12] δ: 32.330, 33.018 (C-4′), 38.128 (C-5′), 40.745, 41.004 (ArCH_2), 44.354, 45.425, 47.493, 48.728 (C-2′ and C-6′), 50.282, 51.425 (C-3′), 51.801, 52.102 (C-α), 54.958 (OCH_3), 62.870, 63.286 (CH_2OH), 113.446, 113.491 (2 × phenyl C-3), 119.323, 119.525 (C-6), 130.289, 130.533 (phenyl C-1 and 2 × phenyl C-2), 137.537, 137.737 (C-8), 149.877, 150.042 (C-4), 151.625 (C-2), 154.297 (phenyl C-4), 157.708 (C-5), 173.244 (amide C=O); ms (EI): identical to that obtained for the diastereomer **21***a*. Exact Mass calcd. for $C_{23}H_{31}N_7O_3$: 453.2488; found (hrms): 453.2479.

[10]The product **21***a* was insoluble in D_2O. Its ^{1}H nmr spectra in $CDCl_3$ or DMSO-d_6 indicated the presence of an approximately 1:1 rotameric mixture, but all resonances were severely broadened. Lowering the temperature to the freezing point of $CDCl_3$ did not allow the rotamers to be resolved. The ^{1}H nmr spectra were therefore acquired in DMSO-d_6 solution at 383 K, at which temperature most but not all signals were well resolved at the expense of any conformational information. Over 1–2 h at this elevated temperature, however, the samples discolored. Two-dimensional spectra were therefore not obtained. The ^{13}C nmr spectra could be obtained at room temperature; however, it was not possible to assign signals to individual rotamers.

[11]The signals due to the $N(CH_3)_2$ group were obscured by the DMSO solvent signal. The signal of the purine C-8 (δ 135–137 ppm) was not observed due to slow relaxation.

[12]The signals attributable to the NCH_3 groups are obscured by the solvent signal.

Acknowledgements

We thank the Natural Sciences and Engineering Research Council of Canada for financial support of this work. We also extend gratitude to Professor G.R.J. Thatcher of Queen's University for access to HPLC facilities, to Professor D.F. Weaver, Mr. A.Y. Jin, and Dr. D.R. Cameron of Queen's for assistance with computer modelling, to Professor D.B. MacLean of McMaster University for mass spectra, and to Dr. J.-R. Brisson of the National Research Council of Canada for providing 600-MHz nmr spectra.

1. J.N. Porter, R.I. Hewitt, G.W. Hesseltine, G. Krupka, J.A. Lowery, W.S. Wallace, N. Bohonos, and J.H. Williams. Antibiot. Chemother. **2**, 409 (1952).
2. V. Betina. The chemistry and biology of antibiotics. Elsevier, Amsterdam. 1983. pp. 427, 485–486.
3. M. Grayson. Antibiotics, chemotherapeutics, and antibacterial agents for disease control. Wiley, New York. 1982. pp. 195–198, and references therein.
4. R.M. Ekong, G.C. Kirby, G. Patel, J.D. Phillipson, and D.C. Wardhurst. Biochem. Pharmacol. **40**, 297 (1990).
5. D. Suciu. Int. J. Biochem. **23**, 1245 (1991).
6. D. Nathans. *In* Antibiotics I. Mechanism of action. *Edited by* G. Gottlieb and P.D. Snow. Springer-Verlag, New York. 1967. pp. 259–277.
7. G. Carret, N. Sarda, M. Abou-Assali, D. Anker, and H. Pachéco. J. Heterocycl. Chem. **20**, 697 (1983).
8. E. Lazzari, A. Vigevani, and F. Arcamone. Carbohydr. Res. **56**, 35 (1977).
9. V. Nair and D.J. Emmanuel. J. Am. Chem. Soc. **99**, 1571 (1977).
10. F. Koizumi, T. Oritani, and K. Yamashita. Agric. Biol. Chem. **54**, 3093 (1990).
11. G. Beaton, A.S. Jones, and R.T. Walker. Tetrahedron, **44**, 6419 (1988).
12. (*a*) R. Vince, S. Daluge, and J. Brownell. J. Med. Chem. **29**, 2400 (1986); (*b*) R. Vince and S. Daluge. J. Med. Chem. **17**, 578 (1974).
13. P.H. Duquette, C.L. Ritter, and R. Vince. Biochemistry, **13**, 4855 (1974).
14. M. Legraverend, E. Bisagni, and B. Ekert. Eur. J. Med. Chem. **20**, 127 (1985).

15. T. Suami, K. Tadano, M. Ayabe, and Y. Emori. Bull. Chem. Soc. Jpn. **51**, 855 (1978).
16. R. Vince and S. Daluge. J. Med. Chem. **20**, 930 (1977).
17. P.G. Hultin and W.A. Szarek. Can. J. Chem. **72**, 208 (1994), and references therein.
18. M.L. Peterson and R. Vince. J. Med. Chem. **34**, 2787 (1991).
19. S. Daluge and R. Vince. J. Org. Chem. **43**, 2311 (1978).
20. R.F. Borch, M.D. Bernstein, and H.D. Durst. J. Am. Chem. Soc. **93**, 2897 (1971).
21. (*a*) Y.F. Shealy and C.A. O'Dell. J. Heterocycl. Chem. **13**, 1015 (1976); (*b*) G. Shaw and R.N. Warrener. J. Chem. Soc. 153 (1958).
22. B.C. Laguzza and B. Ganem. Tetrahedron Lett. **22**, 1483 (1981).
23. R. Vince, H. Lee, A.S. Narang, and F.N. Shirota. J. Med. Chem. **24**, 1511 (1981).
24. (*a*) W. Walter, W. Ruback, and C.O. Meese. Org. Magn. Reson. **11**, 612 (1978); (*b*) G.C. Levy and G.L. Nelson. J. Am. Chem. Soc. **94**, 4897 (1972); (*c*) D.A. Torchia, J.R. Lyerla, Jr., and C.M. Deber. J. Am. Chem. Soc. **96**, 5009 (1974); (*d*) B.M. Pinto, W.A. Szarek, and T.B. Grindley. Org. Magn. Reson. **22**, 676 (1984).
25. C.A.G. Haasnoot, F.A.A.M. de Leeuw, and C. Altona. Tetrahedron, **36**, 2783 (1980).
26. H.P.M. de Leeuw, J.R. de Jager, H.J. Koeners, J.H. van Boom, and C. Altona. Eur. J. Biochem. **76**, 209 (1977).
27. M. Sundaralingam and S.K. Arora. J. Mol. Biol. **71**, 49 (1972).
28. O.W. Weislow, R. Kiser, D. Fine, J. Bader, R.H. Shoemaker, and M.R. Boyd. J. Natl. Cancer Inst. **81**, 577 (1989).
29. C. Le Cocq and J.-Y. Lallemand. J. Chem. Soc. Chem. Commun. 150 (1981).
30. R.M. Silverstein, G.C. Bassler, and T.C. Morrill. Spectrometric identification of organic compounds. 4th ed. Wiley, New York. 1981. p. 269.
31. R. Vince and M. Hua. J. Med. Chem. **33**, 17 (1990).
32. P. Jacobsen, K. Schaumburg, J.-J. Larsen, and P. Krogsgaard-Larsen. Acta Chem. Scand. B, **35**, 289 (1981).

Can. J. Chem. Downloaded from www.nrcresearchpress.com by 85.192.166.187 on 09/08/12
For personal use only.

The syntheses of 2,9,16,23- and 1,8,15,22-tetrahydroxyphthalocyanines

CLIFFORD C. LEZNOFF,[1] MOUGANG HU, COLIN R. MCARTHUR, AND YONGNIAN QIN
Department of Chemistry, York University, North York (Toronto), ON M3J 1P3, Canada

AND

JOHAN E. VAN LIER
Medical Research Council Group in the Radiation Sciences, Faculty of Medicine, University of Sherbrooke, Sherbrooke, QC J1H 5M4, Canada

Received March 31, 1994

CLIFFORD C. LEZNOFF, MOUGANG HU, COLIN R. MCARTHUR, YONGNIAN QIN, and JOHAN E. VAN LIER. Can. J. Chem. **72**, 1990 (1994).

2,9,16,23-Tetra-*p*-*n*-butylbenzyloxy-, 2,9,16,23-tetradiphenylmethoxy-, 2,9,16,23-tetramethoxymethoxy-, and 1,8,15,22-tetra-*p*-*n*-butylbenzyloxyphthalocyanines were synthesized from the appropriate phthalonitriles. Metal-free phthalocyanines were converted to their zinc derivatives. Cleavage from the appropriate precursor with trifluoroacetic acid produced 2,9,16,23-tetrahydroxyphthalocyanine and 1,8,15,22-tetrahydroxyphthalocyanine and their zinc derivatives. NMR spectroscopy revealed that all the 2,9,16,23-tetrasubstituted phthalocyanines are the usual mixtures of the 2,9,16,23, 2,9,16,24, 2,9,17,24, and 2,10,16,24 isomers, but the two 1,8,15,22-tetrasubstituted phthalocyanines were formed as *pure single isomers*.

CLIFFORD C. LEZNOFF, MOUGANG HU, COLIN R. MCARTHUR, YONGNIAN QIN et JOHAN E. VAN LIER. Can. J. Chem. **72**, 1990 (1994).

Utilisant les phtalonitriles appropriés comme produits de départ, on a synthétisé les 2,9,16,23-tétra-*p*-*n*-butylbenzyloxy-, 2,9,16,23-tétraphénylméthoxy-, 2,9,16,23-tétraméthoxyméthoxy- et 1,8,15,22-tétra-*p*-*n*-butylbenzyloxyphtalocyanines. On a transformé les phtalocyanines libres de métal en dérivés zinciques. Le clivage du précurseur approprié avec de l'acide trifluoroacétique conduit à la 2,9,16,23-tétrahydroxyphtalocyanine et à la 1,8,15,22-tétrahydroxyphtalocyanine et à leurs dérivés zinciques. La RMN révèle que toutes les phtalocyanines tétrasubstituées en 2,9,16,23 sont formées des mélanges habituels des isomères 2,9,16,23, 2,9,16,24, 2,9,17,24 et 2,10,16,24; toutefois, les deux phtalocyanines substituées en 1,8,15,22 sont des *isomères purs*.

[Traduit par la rédaction]

Introduction

The first synthesis of 2,9,16,23-tetrahydroxyphthalocyanine was reported in 1987 (1) and its phototoxicity in the photodynamic therapy (PDT) of cancer tumours (2–5) investigated (1, 6–8). Previously, it was shown that changes in the length of the spacer group (8) on hydroxyphthalocyanine affected the phototoxicity and in this study we also wished to show variation in the *position* of the hydroxy group on the phthalocyanine ring. The above compound was prepared by the boron tribromide cleavage of 2,9,16,23-tetraneopentoxyphthalocyanine, as the desired synthesis from a hydroxyphthalonitrile only resulted in decomposition of the starting material (1). Although the preparation was basically successful, the reaction conditions were quite critical and the yields were sometimes inadequate because of the incomplete cleavage of the substituted phthalocyanine precursor and the slow decomposition of the tetrahydroxyphthalocyanine under the attempted reaction conditions. In addition, purification of 2,9,16,23-tetrahydroxyphthalocyanine was performed on a silica gel column and the tetrahydroxyphthalocyanine either decomposes on silica gel or is poorly recovered from that media. For example, when a small-scale sample (50 mg) of 2,9,16,23-tetrahydroxyphthalocyananine was purified, the recovery achieved was only 53%, while on a larger scale (1.26 g), the recovery from the column was only 22% (1). Thus, new synthetic and purification methods need to be discovered for the preparation of tetrahydroxyphthalocyanines. Since 2,9,16,23-tetrahydroxyphthalocyanine was originally obtained as a mixture of related isomers, the development of new methods to easily prepare other polyhydroxyphthalocyanines, these mixtures or, more desirably, pure single isomers for PDT were sought.

Benzyl (9), diphenylmethyl (10), and trityl (11) groups are often used to protect phenolic and hydroxy groups (12). These protecting groups are more easily removed than neopentyl moieties to give free phenolic-type functional groups using different methods (13). The methoxymethyl ether moiety (MOM) (or its analogs) is also a useful protecting group for phenols (14). We examined the possibility of preparing tetrahydroxyphthalocyanines by using different kinds of reagents to deprotect the hydroxy blocking groups of the substituted phthalocyanines. In addition, a new procedure was developed to purify tetrahydroxyphthalocyanine.

Identically tetrasubstituted phthalocyanines are almost always synthesized as mixtures of statistical isomers consisting of the 2,9,16,23, 2,9,16,24, 2,9,17,24, and 2,10,16,24 isomers, and very few studies have been directed toward the exclusive formation of one isomer of a tetrasubstituted phthalocyanine (15). Although the 2,9,16,23-tetraneopentoxyphthalocyaninato zinc(II) (16) and 2,9,17,24-tetra-*tert*-butylphthalocyaninato zinc(II) (17) were produced as pure isomers, several reaction steps were used and only low yields were obtained. The synthesis of a single isomer of 1,2-naphthalocyanine has been achieved (18) due to the steric constraints of the benzo substituents, but other 1,8,15,22-tetrasubstituted phthalocyanines gave mixtures of isomers that in one example could be separated by high performance liquid chromatography (HPLC) (19). In this paper we report the exclusive synthesis of two 1,8,15,22-tetrasubstituted phthalocyanines and their zinc derivatives as pure single isomers in high yields under common conditions. We examined the ^{1}H NMR and ^{13}C NMR spectra of these pure compounds and compared these spectra with those of the phthalocy-

[1]Author to whom correspondence may be addressed.

Can. J. Chem. Downloaded from www.nrcresearchpress.com by 85.192.166.187 on 09/08/12
For personal use only.

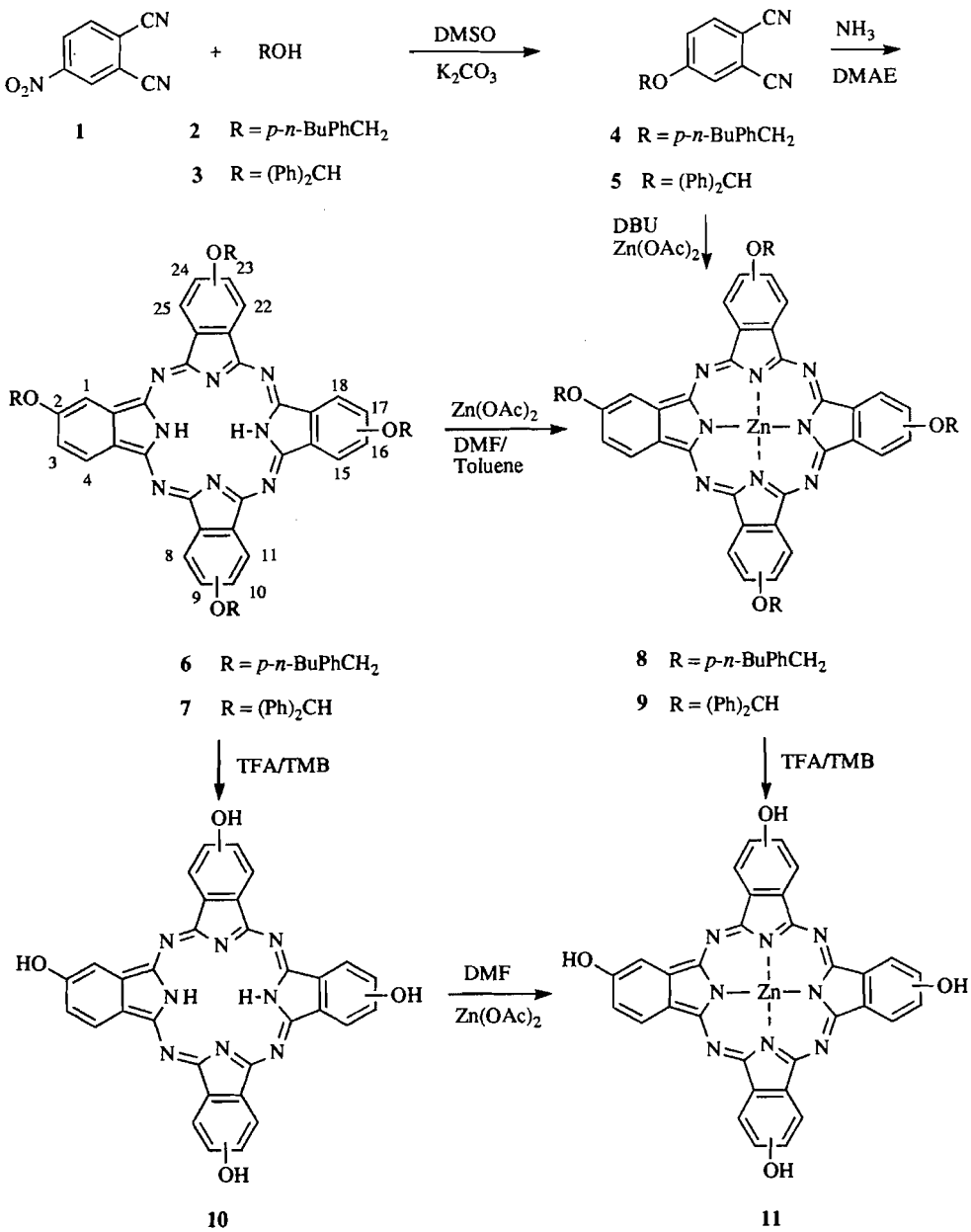

SCHEME 1

anines produced as mixtures of statistical isomers. Analyses of these spectra revealed that all the 2,9,16,23-tetrasubstituted phthalocyanines were indeed mixtures of isomers (for convenience numbered as the 2,9,16,23 derivatives only) but that the 1,8,15,22-tetrasubstituted phthalocyanines were produced as *pure single compounds*.

Results and discussion

The preparation of 2,9,16,23-tetrasubstituted phthalocyanines as mixtures of isomers

Using a new procedure developed in our laboratory (20, cf. ref. 21), 4-nitrophthalonitrile (**1**) reacted with *p*-*n*-butylbenzyl alcohol (**2**) or diphenylmethanol (**3**) in dimethyl sulfoxide (DMSO) at room temperature to give 4-*p*-*n*-butylbenzyloxyphthalonitrile (**4**) or 4-diphenylmethoxyphthalonitrile (**5**) in 90 or 92% yield, respectively (Scheme 1). The self-condensation of **4** or **5** in dimethylaminoethanol gave 2,9,16,23-tetra(*p*-*n*-butylbenzyloxy)phthalocyanine (**6**) or 2,9,16,23-tetra(diphenylmethoxy)phthalocyanine (**7**) in 17 or 25% yield, respectively. Refluxing the metal-free phthalocyanines (Pcs) **6** or **7** with zinc acetate in DMF and toluene gave 2,9,16,23-tetra(*p*-*n*-butylbenzyloxy)phthalocyaninato zinc(II) (**8**) or 2,9,16,23-tetra(diphenylmethoxy)phthalocyaninato zinc(II) (**9**), both in 90% yield. The zinc derivatives **8** and **9** could be prepared directly from **4** and **5**, respectively (22), in an improved procedure. Thus **4** or **5** reacted at 100°C with 1,8-diazabicyclo[5.4.0]undec-7-ene (DBU) (23) as a base and zinc acetate as a template during which ammonia gas was introduced into the reaction. Using this one-step improved procedure, **4** and **5** were produced in overall yields of 65 and 70%, respectively (Scheme 1).

Although catalytic hydrogenation (24), catalytic transfer hydrogenation (25), iodotrimethylsilane and chlorotrimethylsilane (26) couldn't efficiently cleave the alkyoxyphthalocyananines **6** and **7**, cleavage of the metal-free protected Pcs under reflux conditions with trifluoroacetic acid (TFA) (27) in the

Can. J. Chem. Downloaded from www.nrcresearchpress.com by 85.192.166.187 on 09/08/12
For personal use only.

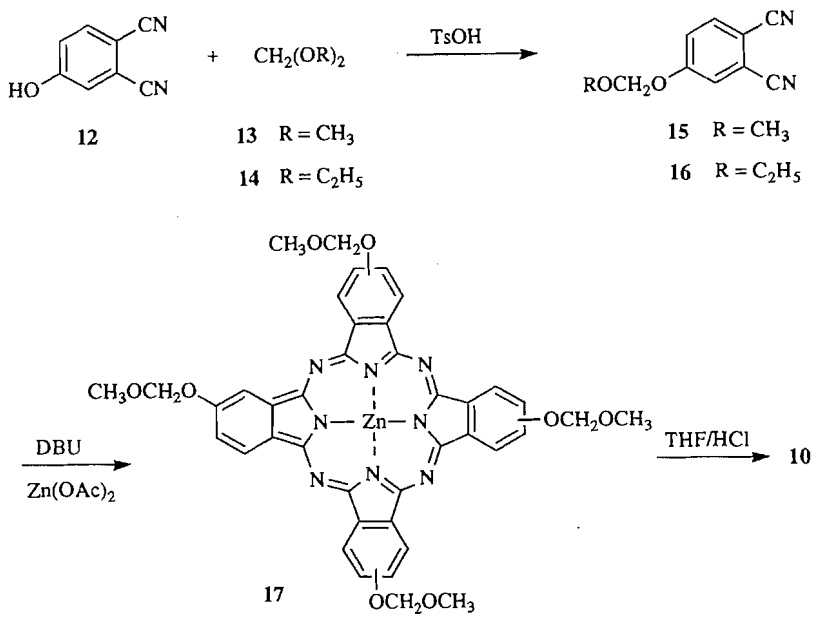

SCHEME 2

presence of a polyalkylbenzene (1,2,4,5-tetramethylbenzene (TMB) in this instance) as a benzyl cation scavenger (28) gave the desired 2,9,16,23-tetrahydroxyphthalocyanine (**10**) in 60–70% yield. Similarly, cleavage for 5 h of the protected zinc Pcs **8** or **9** gave 2,9,16,23-tetrahydroxyphthalocyaninato zinc(II) (**11**) in 84–88% yield. Alternatively, metal-free **10** can be metallated with zinc acetate in DMF–toluene as for **8** to give the zinc Pc **11**. The poor solubility of **10** contributes to the fact that **11** is more easily prepared via **8** or **9** (Scheme 1).

Phenols are usually converted to trityl or methoxymethyl (MOM) ethers by treatment with base and trityl chloride or methoxymethyl chloride. Since 4-hydroxyphthalonitrile (**12**) is unable to react with trityl chloride to give the corresponding ether and is unstable to basic conditions, **12** was treated with dimethoxymethane (**13**) or diethoxymethane (**14**) under acidic conditions (29) to give 4-methoxymethoxyphthalonitrile (**15**) and 4-ethoxymethoxyphthalonitrile (**16**) in 92 and 95% yield, respectively. 2,9,16,23-Tetra(methoxymethoxy)phthalocyaninato zinc(II) (**17**) was prepared from **15** in 30% yield in a previous procedure (23), but similar treatment of **16** gave mostly decomposition products. When the improved procedure as described for **8** and **9** was used, compound **17** was prepared in 60% yield. Treatment of **17** with HCl–THF under reflux conditions gave **10** in 31% yield (Scheme 2). The acidic cleavage conditions resulted in demeltallation of the zinc Pc so that **10** and not **11** was isolated.

Although classical chromatography on silica gel is not suitable for the purification of tetrahydroxyphthalocyanines because of either decomposition on silica gel or poor recovery from that media, gel permeation chromatography resolved this problem and **10** and **11** were readily purified by this latter method.

The preparation of 1,8,15,22-tetrahydroxyphthalocyanine as a pure single isomer

3-Nitrophthalonitrile (**18**) reacted with *p-n*-butylbenzyl alcohol (**2**) as for **4** and **5** to give 3-*p-n*-butylbenzyloxyphthalonitrile (**20**) in 95% yield. The usual procedures for preparation of 2,9,16,23-tetrasubstituted phthalocyanines did not subsequently give 1,8,15,22-tetra(*p-n*-butylbenzyloxy)phthalocyanine (**21**) and its zinc derivative (**22**). Phthalocyanines **21** and **22** could be prepared by heating **20** in a solution of lithium octoxide in *n*-octanol (Scheme 3). Quenching the reaction mixture with water and methanol gave the metal-free phthalocyanine **21** in 40% yield. When zinc acetate was added to the reaction mixture at 100°C and the temperature was controlled below or at 100°C, the zinc derivative **22** of the metal-free phthalocyanine could be obtained in 80% yield. 1,8,15,22-Tetrahydroxyphthalocyanine (**23**) and its zinc derivative (**24**) can be prepared as above by cleavage of **21** and **22** with TFA and TMB in 25 and 85% yield, respectively. Pc **22** can easily be prepared from Pc **21** by refluxing it with zinc acetate in DMF–toluene in 85% yield.

Spectroscopic and physical properties

NMR spectroscopy of 2,9,16,23-tetrasubstituted phthalocyanines generally exhibits broad absorptions in the aromatic and other spectral regions due to the presence of four isomers, but occasionally the resonances can be resolved (15, 30). Similarly, 1,8,15,22-tetrasubstituted phthalocyananines or analogs can exist as a distribution of four isomers (15, 31) but in this substitution pattern steric effects can afford a nonstatistical distribution of the four products. More recently, Hanack et al. actually separated all four isomers of 1,8,15,22-, 1,11,15,25-, 1,8,18,22-, and 1,8,15,25-tetrasubstituted phthalocyanines (19). In contrast, in our research, the 1,8,15,22-tetra(*p-n*-butylbenzyloxy)phthalocyanine (**21**) and its zinc derivative (**22**) were produced *exclusively*, presumably due to the greater steric constraints of the *p-n*-butylbenzyloxy substituent. ^{1}H NMR spectra of this phthalocyanine (**21**) and its zinc derivative (**22**) (Fig. 1) show doublet, triplet, and doublet absorbance peaks for protons of the phthalocyanine ring in the downfield region, and only one single peak at 5.9 ppm for protons of the -OCH_2- of the benzyl group in **21** and at 6.3 ppm for protons of the -OCH_2 of the benzyl group in **22** (Fig. 1). The ^{1}H NMR spectrum of 1,8,15,22-tetrahydroxyphthalocyaninato zinc(II) (**24**) (Fig. 1) shows a singlet at 10.56 ppm (phenol group), a doublet at 8.58–8.56, a triplet at 8.28–8.22, and a doublet at 7.83–7.81 ppm for

Can. J. Chem. Downloaded from www.nrcresearchpress.com by 85.192.166.187 on 09/08/12
For personal use only.

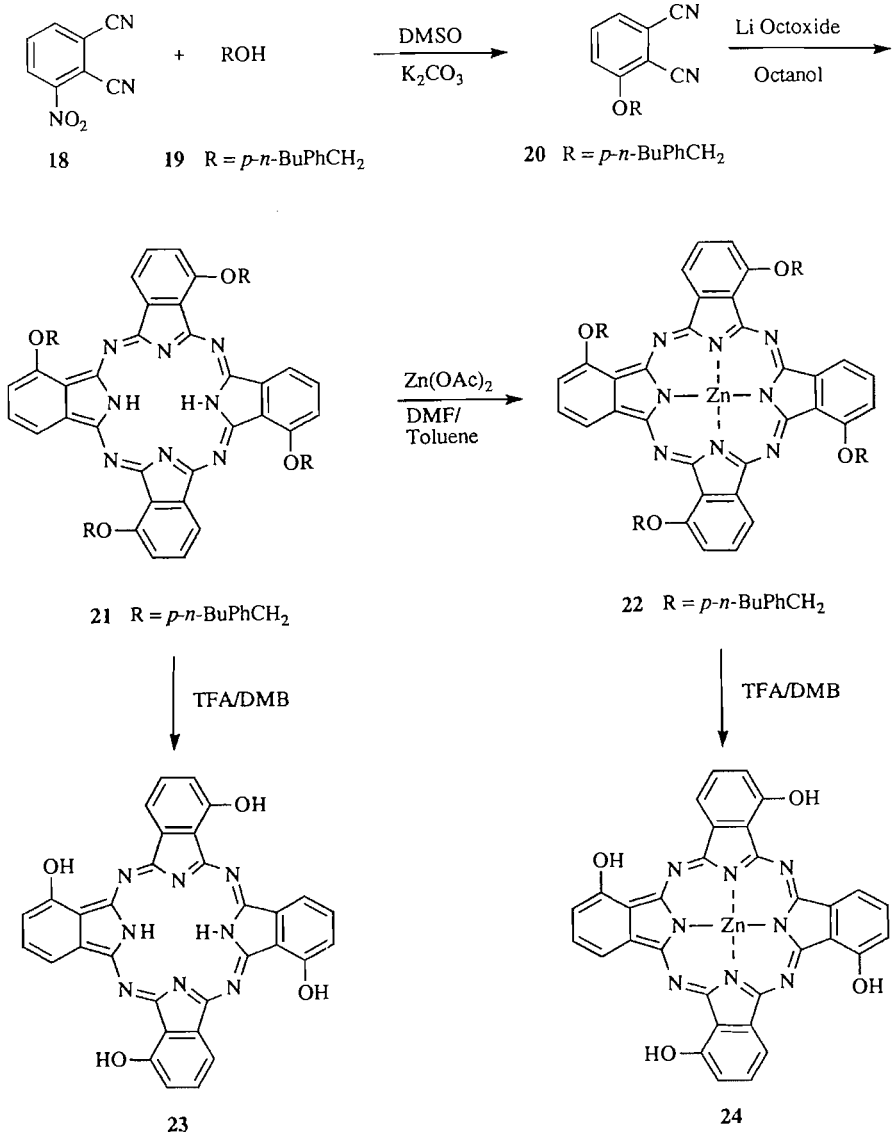

SCHEME 3

the three other protons attached to the phthalocyanine ring, while 2,9,16,23-tetrahydroxyphthalocyaninato zinc(II) (**11**) and its precursor **8** and its isomers show multiplets at 10.65–10.63 ppm (phenol group), 9.19–9.15, 8.70–8.68, and 7.67–7.63 ppm for the other three protons (Fig. 1). The *J*-modulated spin echo (JMOD) ^{13}C NMR spectrum of compound **22** shows only singlet NMR absorbance peaks for those identical carbons that make up the Pc ring. Thus, the NMR spectra support the conclusion that **21–24** exist as single isomers.

Some other physical properties of **21–24**, such as the formation of crystals and their relatively low solubility, support this conclusion. In general, tetrasubstituted Pcs are polymorphic solids due to the presence of statistically produced isomers, 1,8,15,22-Tetra-(*p*-*n*-butylbenzyloxy)phthalocyaninato zinc(II) (**22**) was directly produced as crystalline needles while recrystallization from THF gave square crystals. The solubilities of **21–24** are informative. For example, 2,9,16,23-tetra-(*p*-*n*-butylbenzyloxy)phthalocyanine (**6**) is very soluble in many organic solvents such as dichloromethane, chloroform, DMF, THF, and ethyl acetate, but 1,8,15,22-tetra-(*p*-*n*-butylbenzyloxy)phthalocyanine, its constitutional isomer, does not dissolve in most solvents and only slightly in THF and pyridine. The UV–visible spectra of **21–24** contrast strongly with those of **6**, **8**, **10**, and **11**. For example, **24** exhibits a strong *Q*-band at 719 nm compared to **10** at 684 nm (1, 32). Although tetrahydroxyphthalocyanines cannot be made directly from hydroxyphthalonitriles, the use of appropriate blocking groups can lead to their syntheses both as mixtures of isomers or, in the case of **23** or **24**, as pure single isomers.

Experimental

Matheson high-purity argon was used to maintain inert atmosphere conditions. Thin-layer chromatography (TLC) was performed using silica gel G as the adsorbent. Flash chromatography was performed using silica gel of particle size 20–45 μm. Gel permeation chromatography was performed using Bio-beads, SX-2, 200–400 mesh. Melting points (mp) were determined using a Kofler hot stage melting point apparatus and are uncorrected. Infrared (IR) spectra were recorded on a Pye Unicam SP1000 infrared spectrophotometer using KBr disks. Nuclear magnetic resonance (NMR) spectra for protons and carbons were recorded on a Bruker AM300 NMR spectrometer. The positions of signals are reported in δ units. (The splitting of the signal is described as singlets (s), doublets (d), triplets (t), quartets (q), doublets

Can. J. Chem. Downloaded from www.nrcresearchpress.com by 85.192.166.187 on 09/08/12
For personal use only.

Can. J. Chem. Downloaded from www.nrcresearchpress.com by 85.192.166.187 on 09/08/12
For personal use only.

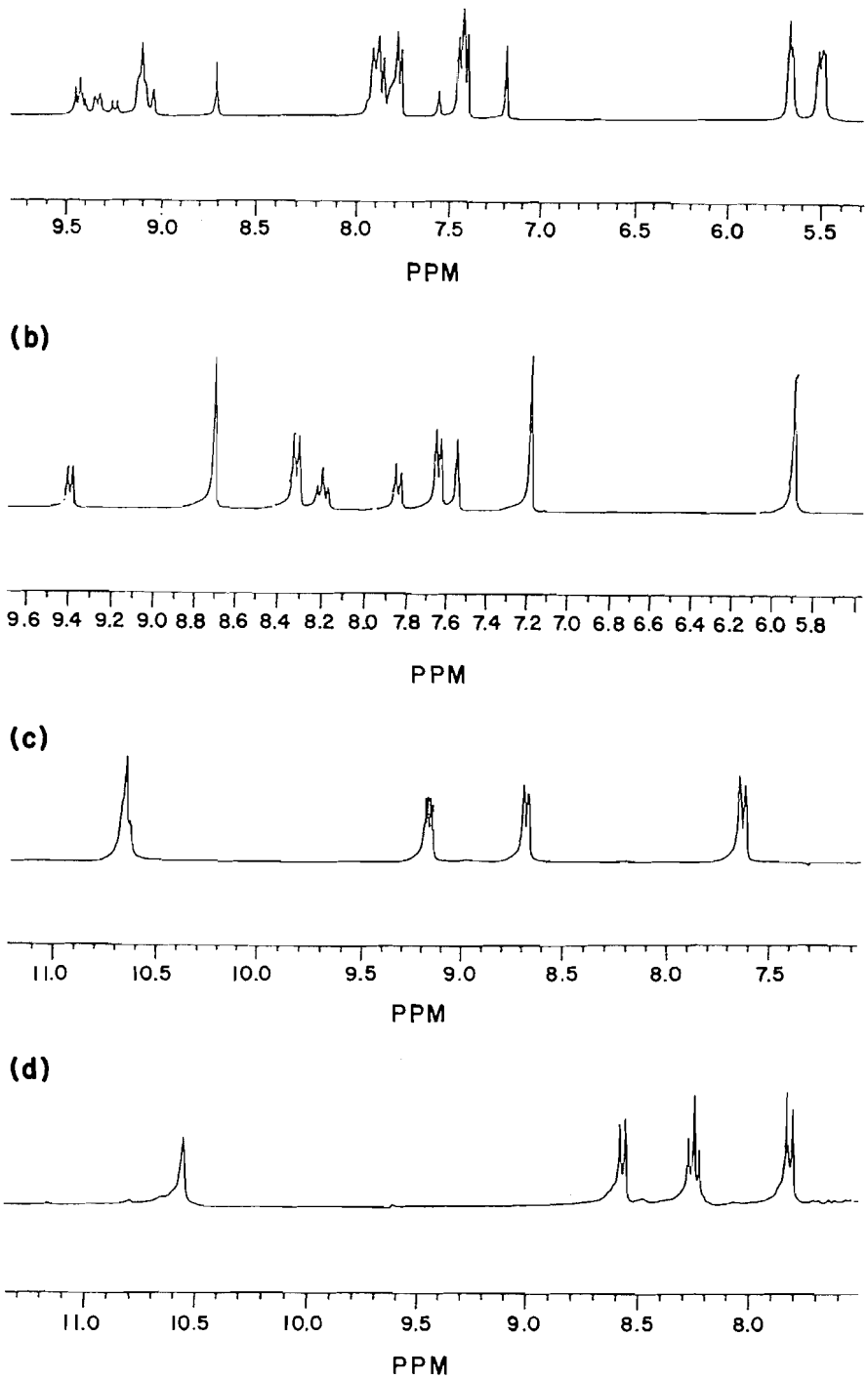

FIG. 1. The ^{1}H nmr spectra of tetrasubstituted phthalocyaninato zinc(II) compounds in pyridine-d_5 (*a*, *b*) and DMSO-d_6 (*c*, *d*); (*a*) 2,9,16,23-tetra(*p*-*n*-butylbenxyloxy)phthalocyaninato zinc(II) (**8**); (*b*) 1,8,15,22-tetra(*p*-*n*-butylbenzyloxy)phthalocyaninato zinc(II) (**22**); (*c*) 2,9,16,23-tetrahydroxyphthalocyaninato zinc(II) (**11**); (*d*) 1,8,15,22-tetrahydroxyphthalocyaninato zinc(II) (**24**); *: peaks of solvent.

of doublets (dd), or multiplets (m).) The ultraviolet–visible spectra (UV) were recorded on a Hewlett–Packard HP8451A diode array spectrophotometer. Mass spectra (MS) were recorded at 70 eV on a VG Micromass 16F mass spectrometer in the EI mode. The FAB spectra were obtained with a Kratos MS-50 triple analyzer mass spectrometer equipped with a FAB ion source of standard Kratos design and Ion Tech atom gun. Microanalyses were performed by Guelph Chemical Laboratories Ltd., Guelph, Ontario.

4-p-n-*Butylbenzyloxyphthalonitrile (4)*

Method I (21)

To a solution of 0.52 g (3.0 mmol) of 4-nitrophthalonitrile (**1**) in 10 mL of dimethylformamide (DMF) was added 0.41 g (2.5 mmol) of *p*-*n*-butylbenzyl alcohol (**2**) and 1.05 g (7.5 mmol) of finely ground potassium carbonate. This reaction mixture was stirred at room temperature for 96 h and poured into 30 mL of ice-water to give a yellow precipitate. The precipitate was collected by filtration, washed with cold water, and dried, The crude product was purified by column chromatography on silica gel, using THF–hexane (15:85) as eluant. Evaporation of the solvent gave a pale-yellow solid. Recrystallization of the solid in THF–hexane 3:7 gave 0.54 g (75%) of **4** as white crystals.

Method II

A improved method was used to prepare **4**. To a solution of 0.52 g

Can. J. Chem. Downloaded from www.nrcresearchpress.com by 85.192.166.187 on 09/08/12
For personal use only.

(3.0 mmol) of **1** in 10 mL of dimethyl sulfoxide (DMSO) was added 0.41 g (2.5 mmol) of **2** and 0.25 g (1.88 mmol) of finely ground potassium carbonate. The mixture was stirred for 96 h. Then another three 0.25-g portions of potassium carbonate were added to the mixture in 20-h intervals and the mixture was pumped under vacuum (20) for 5 min in 10-h intervals during the reaction. Ice-water (30 mL) was added with stirring to the mixture. The precipitate was collected by filtration, washed with cold water, and dried. After column chromatography on silica gel and recrystallization in THF and hexane (3:7), 0.65 g of a white crystalline material **4** was obtained in 90% yield, mp 64.5–65.5°C; IR (KBr, cm^{-1}): 3095, 3040, 2960, 2930, 2860, 2230 (CN), 1590, 1490, 1320, 1250, 1085, 990, 875, 845; ^1H NMR ($CDCl_3$) δ: 7.71–7.68 (d, $J = 4$ Hz, 1H), 7.32–7.21 (m, 6H), 5.11 (s, 2H), 2.65–2.60 (t, $J = 15$ Hz, 2H), 1.65–1.55 (m, 2H), 1.42–1.33 (m, 2H), 0.95–0.90 (t, $J = 15$ Hz, 3H); ^{13}C NMR ($CDCl_3$) δ: 161.89, 143.82, 135.20, 131.78, 128.97, 127.71, 120.09, 119.80, 117.44, 115.69, 107.43, 71.14, 35.37, 33.50, 22.34, 13.90; MS for ($C_{19}H_{18}N_2O$), *m/z* (relative intensity): 291 ($(M + 1)^+$, 18), 247 (19), 147 ($(C_4H_9PhCH_2)^+$, 100), 127 (24), 116 (35), 104 (47), 91 (41), 78 (30), 64 (27), 51 (25). Anal. calcd. for $C_{19}H_{18}N_2O$: 78.59, H 6.25, N 9.65; found: C 78.21, H, 6.47, N 9.50.

4-Diphenylmethoxyphthalonitrile (5)

A procedure previously described for the preparation of **4** (Method II) was used to prepare **5** in 92% yield as white crystals, mp 156–157°C; IR (KBr, cm^{-1}) 3080, 3020, 2950, 2920, 2848, 2230, 2220, 1575, 1468, 1295, 1180, 1040, 820, 790; ^1H NMR ($CDCl_3$) δ: 7.92–7.89 (d, $J = 9$ Hz, 1H), 7.70–7.68 (d, $J = 2.5$ Hz, 6H), 7.55–7.57 (m, 5H), 7.40–7.29 (m, 6H), 6.78 (s, 1H); ^{13}C NMR ($CDCl_3$) δ: 161.09, 139.00, 135.15, 129.05, 128.64, 126.74, 121.14, 120.68, 117.44, 115.54, 115.17, 107.71, 83.16; MS for $C_{21}H_{14}N_2O$, *m/z* (relative intensity): 310 (M^+, 6%), 285 (48), 237 (32), 167 (Ph_2CH^+, 100), 152 (58), 115 (54), 89 (50), 82 (73), 63 (32), 51 (16). Anal. calcd. for $C_{21}H_{14}N_2O$: C 81.27, H 4.55, N 9.03; found: C 81.50, H 4.48, N 9.21.

*2,9,16,23-Tetra(*p-n-*butylbenzyloxy)phthalocyanine (6)*

Compound **4** (0.405 g, 1.4 mmol) was suspended in 5 mL of 2-dimethylaminoethanol (DME). The suspension was heated to 80°C and the phthalonitrile dissolved. A steady stream of ammonia gas was introduced into the solution for 2 h. The temperature was raised to reflux and maintained, along with ammonia introduction, for 10 h. The mixture was cooled to room temperature and centrifuged to give a blue solid. The solid was washed with hexane and methanol. Further purification was performed on a flash silica gel column, eluting with THF and hexane (2:8). Evaporation of the solvent gave 0.069 g (17%) of a shining blue solid, mp >320°C; UV–vis (THF) λ_{max} (log ε): 702 (5.00), 666 (4.97), 638 (4.72), 608 (3.60); IR (KBr, cm^{-1}): 3300 (N-H), 3040, 3020, 2960, 2940, 2862, 1614, 1505, 1480, 1460, 1380, 1320, 1250, 1120, 1100, 1015, 940, 825, 750; ^1H NMR ($CDCl_3$) δ: 7.79–6.95 (m, br, 28H), 4.81–4.70 (m, br, 8H), 2.82–2.68 (t, 8H), 1.69–1.58 (p, 8H), 1.37–1.22 (m, 8H), 1.05–1.01 (t, 12H), −5.95 (s, br, 2H); MS (FAB) for $C_{76}H_{74}O_4$, *m/z* (relative intensity): 1164 ($(M + 2)^+$, 48), 1017 {$((M + 2)680 - R)^+$, 39}, 870 {$((M + 2)680 - 2R)^+$, 56}, 724 {$((M + 2\ 680 - 3R)^+$, 85}, 580 ($(M - 4R)^+$, 79. Anal. calcd. for $C_{79}H_{74}N_8O_4$: C 78.46, H 6.41, N 9.63; found: C 78.79, H 6.60, N 9.45.

2,9,16,23-Tetra(diphenylmethoxy)phthalocyanine (7)

A method previously described for the preparation of **6** was used to prepare **7**. After collection by centrifugation and washing, the crude product was applied onto a flash silica gel column and eluted with toluene. Evaporation of the solvent gave a shining, blue solid in 25% yield, mp >320°C; UV–vis (THF) λ_{max} (log ε): 704 (471), 668 (4.64), 641 (4.20), 605 (4.02), 390 (4.13), 351 (4.34); IR (KBr, cm^{-1}): 3300 (N-H), 3030, 3010, 2820, 1690, 1610, 1500, 1480, 1460, 1400, 1350, 1325, 1235, 1120, 1100, 1020, 750, 700; ^1H NMR ($CDCl_3$) δ: 8.38–808 (m), 7.99–7.80 (m), 7.77–7.29 (m), 7.20–7.10 (m), 6.80–6.71 (m, 8H), −3.92 (b, 2H); MS (FAB) for $C_{85}H_{58}N_8O_4$, *m/z* (relative intensity): 1243 ($(M + 1)^+$, 13), 1076 {$((M + 1)680 - 2R)^+$, 55}, 742 {$((M + 1)680 - 3R)^+$, 65}, 576 {$((M + 1)680 - 4R)^+$, 100}. Anal. calcd. for $C_{84}H_{58}N_8O_4$: C 81.14, H 4.66, N 9.01; found: C 81.21, H 4.03, N 9.15.

*2,9,16,23-Tetra(*p-n-*butylbenzyloxy)phthalocyaninato zinc(II) (8)*

Method I

Compound **4** (0.81 g, 2.8 mmol) was suspended in 10 mL of DME. The suspension was heated to 100°C and a steady stream of ammonia gas passed into the solution for 2 h. To the solution was added 1.5 mL of 1,8-diazatricyclo[5.4.0]undec-7-ene (DBU) followed by 546 mg (3.0 mmol) of zinc acetate after 0.25 h. The introduction of ammonia was continued for 10 h at 100–115°C. The mixture was cooled to room temperature and 30 mL of methanol and water (1:1) was added. The precipitate was collected by centrifugation, and washed with water, methanol, and hexane. Further purification was performed in a flash silica gel column by eluting with THF and hexane (2:8). Evaporation of the solvent gave 0.557 g of a shining, blue solid in 65% yield.

Method II

Compound **8** could also be prepared from **6**. To 116 mg (0.1 mmol) of **6** in 5 mL of toluene and DMF (1:1) was added 91 mg (0.4 mmol) of zinc acetate. The mixture was refluxed for 24 h. The mixture was cooled to room temperature and 10 mL of methanol and water (1:1) was added. The precipitate was collected by centrifugation, and washed with water, methanol, and hexane. The solid was put onto a flash silica gel column and eluted with THF and hexane (3:7). Evaporation of the solvent gave 110 mg (90% yield) of a shining, blue solid as pure **8**, mp >320°C; UV–vis (THF) λ_{max} (log ε): 682 (5.34), 610 (4.41), 350 (4.89); IR (KBr, cm^{-1}): 3040, 3010, 2950, 2930, 2860, 1910, 1735, 1705, 1580, 1532, 1450, 1400, 1325, 1250, 1160, 1100, 1030, 950, 850; ^1H NMR (pyridine-d_5) δ: 9.45–9.05 (m, 8H), 7.95–7.77 (m, 12H), 7.46–7.19 (m, 8H), 5.67–5.49 (m, 8H), 2.67–2.63 (t, 8H), 1.66–1.57 (p, 8H), 1.40–1.28 (m, 8H), 0.93–0.88 (t, 12H); JMOD ^{13}C NMR (pyridine-d_5) δ: 161.41–161.16 (m, 1 × 4C), 153.80–152.84 (m, 2 × 4C), 143.16–143.12 (d, 1 × 4C), 141.30–141.03 (m, 1 × 4C); 135.11–135.08 (d, 1 × 4C), 132.47–132.20 (m, 1 × 4C), 129.22–129.15 (d, 2 × 4C), 128.67–128.59 (d, 2 × 4C), 124.17 (m, b, 1 × 4C), 118.53 (m, b, 1 × 4C), 106.98 (m, b, 1 × 4C), 71.09 (s, 4C), 35.65 (s, 4C), 33.92 (s, 4C), 22.65 (s, 4C), 14.12 (s, 4C); MS (FAB) for $C_{76}H_{72}N_8O_4Zn$, *m/z* (relative intensity): 1226 ($(M + 2)^+$, 62), 1079 {$((M + 2)680 - R)^+$, 63}, 932 {$((M + 2)680 - 2R)^+$, 57}, 785 {$((M + 2)680 - 3R)^+$, 67}, 638 {$((M + 2)680 - 4R)^+$, 100}. Anal. calcd. for $C_{76}H_{72}N_8O_4Zn$: C 74.41, H 5.92, N 9.13; found: C 74.00, H 5.80, N 8.82.

2,9,16,23-Tetra(diphenylmethoxy)phthalocyaninato zinc(II) (9)

The methods (Method I and Method II) previously described for the preparation of **8** were used to prepare **9** in 70 and 90% yield, respectively, as a shining, blue solid, mp >320°C; UV–vis (THF) λ_{max} (log ε): 679 (5.74), 611 (4.71), 351 (5.31); IR (KBr, cm^{-1}): 3030, 3010, 2870, 1610, 1530, 1450, 1380, 1325, 1250, 1210, 1155, 1100, 1025, 845, 785; ^1H NMR (pyridine-d_5) δ: 9.55–9.50 (m, 8H), 8.72–8.07 (m, 4H), 7.94–7.69 (m, 16H), 7.52–7.37 (m, 28H); ^{13}C NMR (pyridine-d_5) δ: 160.68–160.46 (m, 1 × 4C), 154.91–153.15 (m, 2 × 4C), 142.29 (s, 2 × 4C), 141.16–140.9 (m, 1 × 4C), 132.77–132.64 (m, 1 × 4C), 129.26 (s, 4 × 4C), 128.32 (s, 2 × 4C), 127.64 (s, 4 × 4C), 124.44 (m, 1 × 4C), 119.48–119.39 (m, 1 × 4C), 109.50 (m, 1 × 4C), 82.57 (s, 1 × 4C); MS (FAB) for $C_{85}H_{56}N_8O_4Zn$, *m/z* (relative intensity): 1305 ($(M + 1)^+$, 100), 1139 {$((M + 2)680 - R)^+$, 62}, 972 {$((M + 2)680 - 2R)^+$, 33}, 805 {$((M + 2)680 - 3R)^+$, 20}, 638 {$((M + 2)680 - 4R)^+$, 18}. Anal. calcd. for $C_{84}H_{56}N_8O_4Zn$: C 77.21, H 4.32, N 8.58; found: C 76.88, H 3.85, N 8.70.

2,9,16,23-Tetrahydroxyphthalocyanine (10) (1)

To 60 mg (0.052 mmol) of **6** in 5 mL of trifluoroacetic acid (TFA) was added 27.9 mg (0.208 mmol) of 1,2,4,5-tetramethylbenzene (TMB). The mixture was refluxed for 15 h. The TFA was evaporated and the residue was washed with hexane. The residue was dissolved in THF and the solution was put onto a gel permeation column, eluting with THF. Evaporation of the solvent gave 18 mg (60%) of **10** as a green solid. When **7** was used to prepare **10**, the reaction time was 10 h and the yield was 70%; UV–vis (2-methoxyethanol) λ_{max} (log ε): 708 (4.89), 672 (4.85), 639 (4.53), 614 (4.32), 390 (4.40), 342 (4.72), 292 (4.54), 232 (4.45); IR (KBr, cm^{-1}): 3100–3500 (phenolic group), 1610,

Can. J. Chem. Downloaded from www.nrcresearchpress.com by 85.192.166.187 on 09/08/12
For personal use only.

1480, 1310, 1200, 1250, 1095, 1010, 930, 820, 740, 710; ^{1}H NMR (DMSO-d_6) δ: 10.45 (br, 4H (phenolic group)), 8.48 (m, 4H), 8.10 (m, 4H), 7.43 (br, 4H), −3.10 (br, 2H); MS (FAB) for $C_{32}H_{18}N_8O_4$, *m/z* (relative intensity): 578 (M^+, 100). Anal. calcd. for $C_{32}H_{18}N_8O_4$: C 66.43, H 3.14, N 19.37; found: C 66.28, H 3.21, N 19.01.

*2,9,16,23-Tetrahydroxyphthalocyaninato zinc(II) (**11**) (1)*

Treatment of **8** and **9** as previously described for the preparation of **10** gave **11**. The reaction times were 5 h for both cleavage reactions and gave **11** in 84 and 88% yield, respectively. Alternatively, compound **11** could be prepared from **10** by refluxing **10** with zinc acetate in DMF in 88% yield. Compound **11** was a blue solid, mp >320°C; UV–vis (THF) λ_{max} (log ε): 684 (5.00), 672 (4.90), 614 (4.44), 348 (4.83); IR (KBr, cm^{-1}): 3100–3500 (broad signal, phenolic group), 1600, 1475, 1300, 1240, 1085, 1040, 945, 745; ^{1}H NMR (DMSO-d_6) δ: 10.65–10.63 (m, 4H (phenolic group)), 9.19–9.15 (m, 4H), 8.70–8.68 (m, 4H), 7.67–7.63 (m, 4H); MS (FAB) for $C_{32}H_{16}N_8O_4Zn$, *m/z* (relative intensity): 640 (M^+, 100). Anal. calcd. for $C_{32}H_{16}N_8O_4Zn$: C 59.88, H 2.51, N 17.46, Zn 10.18; found: C 59.70, H 2.80, N 16.99, Zn 10.51.

*4-Methoxymethoxyphthalonitrile (**15**)*

Toluenesulfonic acid (TsOH, 150 mg), 4-hydroxyphthalonitrile (**12**) (33) (1.50 g, 10.4 mmol), and dimethoxymethane (**13**) (10 mL) were mixed with 200 mL of dry dichloromethane in a round-bottom flask, equipped with a Soxhlet extractor, in which there was a thimble containing 30 g of 4 Å molecular sieves (29). The suspension was protected under argon and heated under reflux with stirring. After every 12 h, 5 mL of fresh **13** was added. After 24 h, the molecular sieves were replaced with fresh sieves. As the reaction proceeded, the solid gradually dissolved. After 48 h under reflux conditions, the mixture was washed twice with 30 mL of a 0.5 M sodium hydroxide solution, twice with 30 mL of distilled water, and was dried with magnesium sulfate. After filtration and evaporation, 1.81 g of a crude yellowish product was obtained. It was then chromatographed on neutral alumina, eluting with ethyl acetate and hexane (4:6), to give 1.80 g (92%) of pure **15** as white yellowish crystals, mp 80–81°C; UV–vis (dichlorobenzene) λ_{max} (log ε): 304 (3.16), 286 (2.60), 278 (2.54); IR (KBr, cm^{-1}): 3100, 3060, 2980, 2960, 2920, 2220 (CN), 1940, 1780, 1600, 1560, 1495, 1450, 1420, 1320, 1310, 1290, 1240 (C-O-C), 1230, 1170, 1090, 990, 920, 890, 850, 730, 700, 660; ^{1}H NMR ($CDCl_3$) δ: 7.72 (d, J = 8.7 Hz, 1H), 7.45 (d, J = 2.4 Hz, 1H), 7.36 (dd, J = 8.7, 2.5 Hz, 1H), 5.27 (s, 2H), 3.50 (s, 3H); ^{13}C NMR ($CDCl_3$) δ: 160.41, 135.20, 121.23, 120.93, 117.44, 115.58, 115.21, 108.34, 94.62, 56.76; MS for $C_{10}H_8N_2O_2$, *m/z* (relative intensity): 188 (M^+, 60), 157 (60), 144 (100), 127 (90), 115 (30), 100 (60). Anal. calcd. for $C_{10}H_8N_2O_2$: C 63.82, H 4.38, N 14.93; found: C 63.82, H 4.29, N 14.88.

*4-Ethoxymethoxyphthalonitrile (**16**)*

4-Hydroxyphthalonitrile (**12**) (1.50 g, 10.4 mmol) was mixed with 200 mL of dry dichloromethane in a round-bottom flask equipped with a Soxhlet extractor containing molecular sieves (4 Å, 30 g). Diethoxymethane (**14**) (10 mL) and 150 mg of TsOH were added to the above suspension. The mixture was then heated under reflux with stirring. After every 12 h, 5 mL of fresh diethoxymethane was added. After 24 h, the molecular sieves were replaced by fresh sieves. As the reaction proceeded, the solid gradually dissolved. After 48 h, the mixture was washed twice with 30 mL of sodium hydroxide solution (0.5 M), twice with 30 mL distilled water, and was dried with magnesium sulfate. After filtration and evaporation, 2.01 g of a yellowish solid was obtained. This solid was then further purified on neutral alumina by column chromatography using ethyl acetate and hexane (4:6). After evaporation of the solvent, the residue was recrystallized from methanol and water to give 2.00 g (95% yield) of pure compound **16** as white or yellowish crystals, mp 56–57°C; UV–vis (dichlorobenzene) λ_{max} (log ε): 306 (3.22), 286 (2.71), 282 (2.64); IR (KBr, cm^{-1}): 3120, 3075, 2980, 2935, 2900, 2200 (-CN), 1935, 1590, 1560, 1495, 1480, 1410, 1400, 1320, 1290, 1240 (C-O-C), 1090, 960, 910, 870, 850, 740; ^{1}H NMR ($CDCl_3$) δ: 7.72 (d, J = 8.7 Hz, 1H), 7.45 (d, J = 2.5 Hz, 1H), 7.36 (dd, J = 8.7, 2.5 Hz, 1H), 5.32 (s, 2H), 3.74 (q, J = 7.0 Hz, 2H), 1.22 (t, J = 7.0 Hz, 3H, 3H); ^{13}C NMR (NMR ($CDCl_3$) δ: 160.62, 135.19, 121.23, 120.93, 117.41, 115.63, 108.19, 93.39, 65.39, 16.01; MS for $C_{11}H_{10}N_2O_2$, *m/z* (relative intensity): 202 (M^+, 10), 157 (40), 144 (100), 127 (40), 116 (20), 100 (20). Anal. calcd. for $C_{11}H_{10}N_2O_2$: C 65.35, H 5.27, N 13.80; found: C 65.34, H 4.99, N 13.85.

*2,9,16,23-Tetra(methoxymethoxy)phthalocyaninato zinc(II) (**17**)*

A suspension of 500 mg (2.66 mmol) of **15** and 2.5 mL of DBU in 2.5 mL of 1-butanol was stirred and heated under reflux. The phthalonitrile dissolved after 10–20 min. Then, 170 mg (0.93 mmol) of dried zinc acetate was added to the solution. After 24 h under reflux, the dark mixture was poured into 150 mL of methanol and water (1:1) to form a precipitate. The precipitate was collected by centrifugation, and washed with water, methanol, and hexane. The crude product was then purified by column chromatography on neutral alumina, eluting with ethyl acetate and hexane (9:1). Evaporation of the solvent gave 197 mg (36.2%) of a dark blue solid **17**. When the procedure previously described for the preparation of **8** was used to prepare the compound, the yield was 60%; UV–vis (2-methoxyethanol) λ_{max} (log ε): 680 (5.15), 672 (5.16), 610 (4.50), 350 (4.85), 286 (4.46), 240 (4.56); IR (KBr, cm^{-1}): 2950 (br), 1610, 1490, 1400, 1350, 1240 (C-O-C), 1210, 1160, 1050, 1000, 930, 830, 780, 750, 730; ^{1}H NMR (DMSO-d_6) δ: 9.10–7.70 (br, 12H), 5.76 (m, 8H), 3.67 (m, 12H); (pyridine-d_5) δ: 9.54–9.36 (m, br, 8H), 8.71 (m, 4H), 5.79–5.70 (d, 8H), 3.64–3.61 (d, 12H); ^{13}C NMR ($CDCl_3$) δ: 108–158; JMOD ^{13}C NMR (pyridine-d_5) δ: 159.6 (m, 1 × 4C), 153.9–153.2 (m, 2 × 4C), 141.0–140.8 (m, 1 × 4C), 133.1 (m, 1 × 4C), 124.3–123.5 (m, 1 × 4C), 119.6 (m, 1 × 4C), 109.1 (m, 1 × 4C), 95.3 (s, 1 × 4C), 56.3 (s, 1 × 4C). Anal. calcd. for $C_{40}H_{32}N_8O_8Zn$: C 58.72, H 3.94, N 13.70, Zn 7.99; found: C 58.55, H 4.10, N 13.62, Zn 8.12.

*2,9,16,23-Tetrahydroxyphthalocyanine (**10**) from **17***

A solution of 82 mg (0.1 mmol) of **17** in 50 mL of hydrochloric acid solution (HCl and 2-methoxyethanol 1:9) was stirred at 80°C overnight and then neutralized with 10% aqueous solution of sodium hydroxide. The solution was then poured into a saturated solution of sodium chloride (150 mL) to precipitate the phthalocyanine. The precipitate was washed twice with water to get rid of sodium chloride and then dissolved in a small portion of DMF and precipitated from toluene to get rid of any incompletely hydrolysed phthalocyanine species. This precipitate was then preabsorbed onto 2 g of classical silica gel and subjected to a classical column chromatography on silica gel, eluting with ethyl acetate and DMF in increasing amounts of DMF. After evaporation of the solvent and precipitation from toluene, 47 mg (31%) of **10** was obtained.

*3-p-n-Butylbenzyloxyphthalonitrile (**20**)*

A procedure previously described for the preparation of **4** (Method II) was used to prepare **20** in 95% yield as white crystals, mp 70–71°C; IR (KBr, cm^{-1}): 3080, 3020, 2950, 2920, 2850, 2250, 2220, 1575, 1470, 1295, 1280, 1180, 1040, 840, 790; ^{1}H NMR ($CDCl_3$) δ: 7.62–7.56 (t, J = 15 Hz, 1H), 7.54–7.16 (m, 7H), 5.24 (s, 2H), 2.64–2.62 (t, J = 15.4 Hz, 2H), 1.62–1.57 (m, 2H), 1.39–1.31 (m, 2H), 0.95–0.90 (t, J = 14.6 Hz, 2H); ^{13}C NMR ($CDCl_3$) δ: 161.14, 143.68, 134.44, 131.75, 128.98, 127.34, 125.30, 117.62, 117.22, 115.32, 113.02, 105.53, 71.57, 35.38, 33.51, 22.34, 13.91; MS for $C_{19}H_{18}N_2O$, *m/z* (relative intensity): 291 ($(M + 1)^+$, 18), 247 (20), 147 ($C_4H_9PhCH_{2+}$, 100), 127 (22), 116 (33), 104 (44), 91 (40), 78 (27), 64 (23), 51 (20). Anal. calcd. for $C_9H_{18}N_2O$: C 78.60, H 6.25, N 9.65; found: C 78.92, H 6.12, N 9.83.

*1,8,15,22-Tetra(p-n-butylbenzyloxy)phthalocyanine (**21**)*

Lithium (0.30 g) was suspended in 30 mL of *n*-octanol. The suspension was heated to 170°C under stirring and kept for 4 h. The homogenous solution was cooled to 40°C, at which point was added 0.35 g (1.2 mmol) of **20** in 4 mL of dried THF. The temperature was raised to 60°C and the mixture kept stirring for 2 h. Then, the temperature was raised to 100°C and stirring was continued for 12 h. The temperature was further raised to 120°C, and stirring continued for another 2 h. The mixture was cooled to room temperature and the reaction was

Can. J. Chem. Downloaded from www.nrcresearchpress.com by 85.192.166.187 on 09/08/12
For personal use only.

quenched with methanol and water (1:1) to form a blue precipitate. The precipitate was collected by centrifugation, washed successively with water, methanol, and hexane, and dried to give 126.7 mg (40%) of a dark-green solid **21**, mp >320°C; UV–vis (THF) λ_{max} (log ϵ): 724 (4.70), 690 (4.71), 658 (4.02), 627 (2.95), 395 (3.46), 351 (3.96); IR (KBr, cm^{-1}): 3310 (N-H), 3010, 2960, 2920, 2860, 1665, 1530, 1440, 1385, 1240, 1175, 1145, 1110, 1010, 925, 850; ^1H NMR (pyridine-d_5) δ: 9.48–9.45 (d, J = 7.5 Hz, 4H), 8.34–8.32 (d, J = 7.8 Hz, 8H), 8.27–8.22 (t, J = 15 Hz, 4H), 7.91–7.89 (d, J = 8 Hz, 4H), 7.66–7.63 (d, J = 7.7 Hz, 8H), 5.93 (s, 8H), 2.85–2.80 (t, J = 15 Hz, 8H), 1.83–1.73 (m, 8H), 1.51–1.42 (m, 8H), 1.01–0.96 (t, J = 15 Hz, 12H), −4.2 (br, 2H); MS (FAB) for $C_{79}H_{74}N_8O_4$, *m/z* (relative intensity): 1164 ((M + 2)$^+$, 68), 1017 {((M + 2)680 − R)$^+$, 56}, 870 {((M + 2)680 − 2R)$^+$, 23}, 723 {((M + 2)680 − 3R)$^+$, 100}, 578 {((M + 2)680 − 4R)$^+$, 91}. Anal. calcd. for $C_{76}H_{74}N_8O_4$: C 78.46, H 6.41, N 9.63; found: C 78.22, H 6.63, N 9.24.

1,8,15,22-Tetra(p-n-*butylbenzyloxy*)*phthalocyaninato zinc(II) (22)*

Lithium (0.60 g) was suspended in 60 mL of *n*-octanol. The mixture was heated to 170°C and kept stirring for 4 h. The homogeneous solution was cooled to 40°C, at which point was added 0.52 g (1.79 mmol) of **20** in 5 mL of THF. The solution was slowly heated to 100°C and underwent a colour change from colourless to green. To the green solution was added 326 mg (1.79 mmol) of zinc acetate and the solution was kept stirring for 12 h at 100°C. The temperature was raised to 120°C and stirring was continued for another 2 h. The mixture was cooled to room temperature and quenched with methanol and water (1:1) to form a shining, blue precipitate. The precipitate was collected by centrifugation, washed successively with water, methanol, and hexane, and dried. The blue solid was examined under a microscope and exhibited crystalline needles. Further recrystallization from THF gave 0.44 g (80%) of shining, blue, square crystals **22**.

Compound **22** can also be prepared from **21**. A mixture of 80 mg (0.069 mmol) of **15** and 50 mg of zinc acetate in 5 mL of DMF and toluene (1:1) was refluxed for 24 h. To the mixture was added 10 mL of water, and it was then centrifuged to separate a shining, blue solid. The solid was washed with water, methanol, and hexane, and dried to give 76 mg (90%) of a shining, blue solid **22** as needle or square crystals, mp >320; UV–vis (THF) λ_{max} (log ϵ): 696 (5.34), 665 (4.37), 626 (4.46), 369 (4.45); IR (KBr, cm^{-1}): 3010, 2940, 2920, 2840, 1580, 1485, 1335, 1260, 1235, 1130, 1090, 1060, 1040, 1020, 800, 760, 735; ^1H NMR (pyridine-d_5) δ: 9.44–9.41 (d, J = 7.5 Hz, 4H), 8.34–8.31 (d, J = 6.6 Hz, 8H), 8.24–8.19 (t, J = 15.4 Hz, 4H), 7.88–7.86 (d, J = 8.0 Hz, 4H), 7.68–7.63 (d, J = 7.7 Hz, 8H), 5.91 (s, 8H), 2.85–2.80 (t, J = 15.2 Hz, 8H), 1.83–1.73 (p, 8H), 1.51–1.39 (m, 8H), 1.01–0.96 (t, J = 14.6 Hz, 12H); JMOD ^{13}C NMR (pyridine-d_5) δ: 156.85 (s, 1 × 4C), 154.18 (s, 1 × 4C), 154.07 (s, 1 × 4C), 143.01 (s, 1 × 4C), 142.25 (s, 1 × 4C), 135.20 (s, 1 × 4C), 130.91 (s, 1 × 4C), 129.20 (s, 2 × 4C), 128.62 (s, 2 × 4C), 126.41 (s, 1 × 4C), 116.79 (s, 1 × 4C), 113.68 (s, 1 × 4C), 71.40 (s, 14C), 35.84 (s, 4C), 34.20 (s, 4C), 22.72 (s, 4C), 14.25 (s, 4C); MS (FAB) for $C_{76}H_{72}N_8O_4$, *m/z* (relative intensity): 1226 ((M + 2)$^+$, 100), 1079 {((M + 2)fs20 − R)$^+$, 88}, 932 {((M + 2)fs20 − 2R)$^+$, 96}, 785 {((M + 2)fs20 − 3R)$^+$, 84}, 638 {((M + 2)fs20 − 4R)$^+$, 68}. Anal. calcd. for $C_{76}H_{72}N_8O_4Zn$: C 74.41, H 5.92, N 9.13; found: C 74.21, H 5.18, N 9.07.

1,8,15,22-Tetrahydroxyphthalocyanine (23)

To a suspension of 50 mg (0.043 mmol) of **21** in 10 mL of TFA was added 25 mg (0.19 mmol) of TMB. The suspension was refluxed for 50 h. The TFA was evaporated and the residue was washed with hexane. The green residue was dissolved in THF and put onto a gel permeation column, eluting with THF. Evaporation of the solvent gave 6.2 mg of **23** (25% yield) as a green solid; UV–vis (THF): λ_{max} (log ϵ): 743 (4.69), 7.10 (4.69), 680 (4.00), 648 (2.98), 350 (3.40); IR (KBr, cm^{-1}): 3100–1500 (broad signal, phenolic group), 1620, 1482, 1310, 1284, 1220, 1200, 1095, 1000, 930, 820, 745, 710 cm; ^1H NMR (DMSO-d_6) δ: 10.50 (s, 4H), 8.51–8.45 (d, J = 7.5 Hz, 4H), 8.07–8.05 (t, J = 15 Hz, 4H), 7.68–7.65 (d, J = 7.5 Hz, 4H), −3.5 (br, 2H); MS (FAB) for $C_{32}H_{18}N_8O_4$, *m/s* (relative intensity): 578 (M$^+$, 100).

1,8,15,22-Tetrahydroxyphthalocyaninato zinc(II) (24)

To 109 mg (0.086 mmol) of **22** in 5 mL of TFA was added 46 mg (0.35 mmol) of TMB. The mixture was refluxed for 15 h. The TFA was evaporated and the residue was washed a few times with hexane. The blue solid was dissolved in THF and the solution was put onto a gel permeation column, eluting with THF. Evaporation of the solvent gave 46.8 mg (85%) of **24** as a blue solid; UV–vis (THF) λ_{max} (log ϵ): 719 (4.85), 686 (4.12), 646 (4.13), 344 (4.06); IR (KBr, cm^{-1}): 3100–3500 (broad signal, phenolic group), 1650, 1520, 1430, 1360, 1275, 1215, 1060, 925, 840; ^1H NMR (DMSO-d_6) δ: 10.56 (s, 4H), 8.58–8.56 (d, J = 7.5 Hz, 4H), 8.28–8.22 (t, J = 15 Hz, 4H), 7.83–7.81 (d, J = 7.7 Hz, 4H); MS (FAB) for $C_{31}H_{16}N_8O_4Zn$, *m/z* (relative intensity): 640 (M$^+$, 100). Anal. calcd. for $C_{32}H_{16}N_8O_4Zn$: C 59.88, H 2.51, N 17.46; found: C 59.74, H 2.33, N 16.89.

Acknowledgements

This research was supported by grants from the Natural Sciences and Engineering Research Council of Canada (NSERC).

1. I. Rosenthal, E. Ben-Hur, S. Greenberg, A. Concepcion-Lam, D.M. Drew, and C.C. Leznoff. Photochem. Photobiol. **46**, 959 (1987).
2. B. Paquette and J.E. van Lier. *In* Photodynamic therapy: basic principles and clinical aspects. *Edited by* B.W. Henderson and T.J. Dougherty. Marcel Dekker, New York. 1992. p. 145.
3. I. Rosenthal. Photochem. Photobiol. **53**, 859 (1991).
4. J.E. van Lier. *In* Photodynamic therapy of neoplastic disease. Vol. 1. *Edited by* D. Kessel. CRC Press, Boca Raton, Fla. 1990. p. 279.
5. I. Rosenthal and E. Ben-Hur. *In* Photodynamics: properties and applications. Vol. 1. *Edited by* C.C. Leznoff and A.B.P. Lever. VCH, New York. 1989. p. 393.
6. E. Ben-Hur, I. Rosenthal, and C.C. Leznoff. J. Photochem. Photobiol. B: **2**: 243 (1988).
7. C.C. Leznoff, S. Vigh, P.I. Svirskaya, S. Greenberg, D.M. Grew, E. Ben-Hur, and I. Rosenthal. Photochem. Photobiol. **49**, 79 (1989).
8. R.W. Boyle, C.C. Leznoff, and J.E. van Lier. Br. J. Cancer, **67**, 1177 (1993).
9. M.C. Venuti, B.E. Loe, G.H. Jones, and J.M. Young. J. Med. Chem. **31**, 2132 (1988); H. Schmidhammer and A. Brossi. J. Org. Chem. **48**, 1469 (1983); J.D. White and J.C. Amedio, Jr. J. Org. Chem. **54**, 736 (1989).
10. L. Lapatsanis. Tetrahedron Lett. 3943 (1978); V.G. Miranovski. Angew. Chem. Int. Ed. Engl. **15**, 281 (1976).
11. S.K. Chaudhary and O. Hernandez. Tetrahedron Lett. 95 (1979); S. Hanessian and A. P.A. Staub. Tetrahedron Lett. 95 (1973).
12. C.B. Reese. *In* Protective groups in organic chemistry. *Edited by* J.F.W. McOmie Plenum Press, New York. 1973. p. 104; T.W. Greene. *In* Protective groups in organic synthesis. Wiley, New York. 1981. p. 187.
13. R.C. Larock. Comprehensive organic transformations. VCH, New York. 1989.
14. L.F. Fieser and M. Fieser. Reagents for organic synthesis. Vol. 1. Wiley, New York. 1967. p. 132; J.F.W. McOmie. Adv. Org. Chem. **3**, 191 (1963); R.L. Edwards and I. Mir. J. Chem. Soc. [C], 411 (1967).
15. C.C. Leznoff. *In* Phthalocyanines — properties and applications. Vol. 1. *Edited by* C.C. Leznoff and A.B.P. Lever. VCH, New York. 1989.
16. S. Greenberg, A.B.P. Lever, and C.C. Leznoff. Can. J. Chem. **66**, 1059 (1988).
17. I.G. Oksengendler, N.V. Kondratenko, E.A. Luk'yanets, and L.M. Yagupol'skii, Zh. Org. Khim. **13**, 2234 (1977).
18. M. Hanack, G. Rene, J. Strahle, and S. Schmid. J. Org. Chem. **66**, 3501 (1991).
19. M. Hanack, G. Schmid, and M. Sommerauer. Angew. Chem. Int. Ed. Engl. **32**, 1422 (1993).
20. D.M. Drew and C.C. Leznoff. Synlett. In press. 1994.
21. W.O. Siegl. J. Heterocycl. Chem. **18**, 1613 (1981).

22. S.W. Oliver and T.D.J. Smith. Heterocycles, **22**, 2407 (1984).
23. H. Tomoda, S. Saito, S. Ogawa, and S. Shiraishi. Chem. Lett. 1277 (1980).
24. R. Davis and J.M. Muchowski. Synthesis, 987 (1982); T. Katsuki, A.W.M. Lee, P. Ma, V.S. Martin, S. Masamune, K.B. Sharpless, D. Tuddenham, and F.J. Walker. J. Org. Chem. **47**, 1378 (1982).
25. J.R. Medich, K.B. Kunnen, and C.R. Johnson. Tetrahedron, 4131 (1987); S. Hanessian, T.J. Liak, and B. Vanasse. Synthesis, 396 (1981); V.S. Rao and A.S. Perlin. Carbohydr. Res. **83**, 175 (1980); A.M. Felix, E.P. Heimer, T.J. Lambros, C. Tzougraki, and J. Meienhofer. J. Org. Chem. **43**, 4194 (1978).
26. H. Sakuri, A. Shirahata, K. Sasaki, and A. Hosomi. Synthesis, 740 (1979); M.E. Jung and M.A. Lyster. J. Org. Chem. **42**, 3761 (1977); G.A. Olah, S.C. Narang, B.G. Gupta, and R. Malhotra. Angew. Chem. Int. Ed. Engl. **18**, 612 (1979); J. Org. Chem. **44**, 1247 (1979).
27. J. Mayrargue, M. Essamkaou, and H. Moskowitz. Tetrahedron Lett. 6867 (1989); Y. Kiso, K. Ukawa, K. Nakamura, K. Ito, and T. Akita. Chem. Pharm. Bull. **28**, 673 (1980); C.N.. Kornblum and A. Scott. J. Am. Chem. Soc. **96**, 590 (1974).
28. H. Yoshino, Y. Tsuchiya, I. Saito, and M. Tsujii. Chem. Pharm. Bull. 3438 (1987).
29. J.P. Yardley. U.S. Patent 3,987,105 (1976); Chem. Abstr. **86**, 5148q (1977).
30. S.M. Marcuccio, P.I. Svirskaya, S. Greenberg, A.B.P. Lever, C.C. Leznoff, and K.B. Tomer. Can. J. Chem. **63**, 3057 (1985).
31. D. Wöhrle, J. Gitzel, I. Okuro, and S. Aono. J. Chem. Soc. Perkin Trans. 2, 1171 (1985).
32. P.J. Duggan and P.F. Gordon. Eur. Pat. Appl. Ep 155780 (1985); Chem. Abstr. **105**, 72642 (1987).
33. V.A. Ustinov, V.V. Plakhtinskii, G.S. Mironov, and N.S. Ryabukhina. Zh. Org. Kh. **15**, 1775 (1979).

Can. J. Chem. Downloaded from www.nrcresearchpress.com by 85.192.166.187 on 09/08/12
For personal use only.

The photochemistry of 2,3-benzobicyclo[4.2.0]octa-2,4,7-triene

CHARLOTTE LEE ASPLUND, CHRISTOPHER OWEN BENDER,[1] AND DOUGLAS DOLMAN
Department of Chemistry, University of Lethbridge, Lethbridge, AB T1K 3M4, Canada

Received June 1, 1994

CHARLOTTE LEE ASPLUND, CHRISTOPHER OWEN BENDER, and DOUGLAS DOLMAN. Can. J. Chem. **72**, 1999 (1994).

2,3-Benzobicyclo[4.2.0]octa-2,4,7-triene (**11**) was prepared by Shapiro reaction from 2,3-benzobicyclo[4.20]octa-2,7-dien-4-one (**10**). Triene **11** was found to be thermally and photochemically reactive. Benzocyclooctatetraene (i.e., COT **12**) was the unique product formed when solutions of **11** were heated at 150°C for 5.5 h. The direct irradiation of triene **11** gave benzosemibullvalene (i.e., SB **14**, 23%, $\Phi = 0.069$), COT **12** (39%, $\Phi = 0.11$), and naphthalene (8%, $\Phi = 0.025$). Sensitized irradiations of **11** gave SB **14**, (54%, $\Phi = 0.082$), COT **12** (2%, $\Phi = 0.003$), and naphthalene (4%, $\Phi = 0.009$). Studies with deuterium-labelled triene (**11***a*) indicated that the formation of SB **14** from the direct irradiation of triene **11** derives from the operation of two reaction pathways, the major one (83%) of which appears to be a Zimmerman di-π-methane rearrangement; the minor pathway involves a 1,2-shift of the C_1—C_6 bond to C_1—C_5. By contrast, SB **14** formed from sensitized irradiation appears to be provided uniquely by a Zimmerman di-π-methane rearrangement.

CHARLOTTE LEE ASPLUND, CHRISTOPHER OWEN BENDER et DOUGLAS DOLMAN. Can. J. Chem. **72**, 1999 (1994).

On a préparé le 2,3-benzobicyclo[4.2.0]octa-2,4,7-triène (**11**) par la réaction de Shapiro effectuée à l'aide de la 2,3-benzobicyclo[4.2.0]octa-2,7-dièn-4-one (**10**). Le triène **11** est réactif thermiquement et photochimiquement. Le benzocyclooctatétraène (soit, le COT **12**) est l'unique produit formé lorsqu'on chauffe des solutions du composé **11** à 150°C pendant 5.5 h. L'irradiation directe du triène **11** conduit au benzosemibullvalène (soit, le SB **14**, 23%, $\Phi = 0.069$), le COT **12** (39%, $\Phi = 0.11$), et le naphtalène (8%, $\Phi = 0.025$). Des irradiations sensibilisées du composé **11** conduisent au SB **14**, (54%, $\Phi = 0.082$), au COT **12** (2%, $\Phi = 0.003$), et au naphtalène (4%, $\Phi = 0.009$). Des études avec du triène marqué au deutérium (**11***a*) démontrent que pendant des irradiations directe il y a deux mécanismes qui entrent en jeu dans la formation du produit SB **14** : le mécanisme majeur (83%) dérive d'une transposition di-π-méthane de Zimmerman; le mécanisme proposé pour la voie mineure comporte la migration-1,2 de la liaison C_1—C_6 à la liaison C_1—C_5. Par contre, l'isomérie due triène **11** → SB **14** qu'on observe pendant des irradiations sensibilisée se produisent uniquement par la voie d'une transposition di-π-méthane de Zimmerman.

Can. J. Chem. Downloaded from www.nrcresearchpress.com by 85.192.166.187 on 09/08/12
For personal use only.

Introduction

Since Sasse's pioneering study of the photochemistry of 7,8-diphenyl-2,3-benzobicyclo[4.2.0]octa-2,4,7-triene, which was reported over 25 years ago (1), the photoreactivities of more than 20 derivatives of this benzo-triene system have been investigated (2). In many cases the trienes convert to complex polycyclic photoproducts. For example, the methyl derivative **1** gives the isomeric mixture **2**–**5** (Scheme 1) (2*d*). Of particular

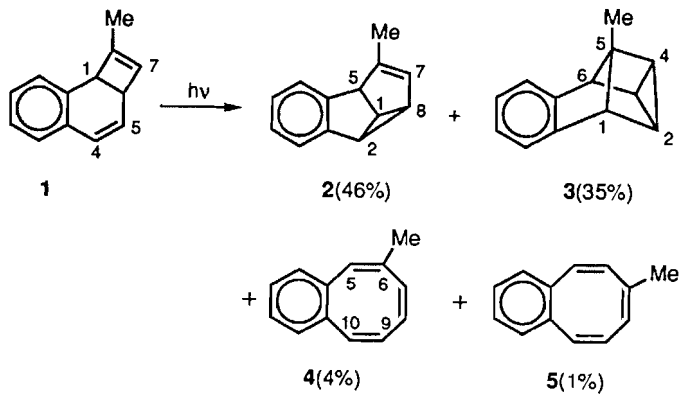

SCHEME 1

interest to us was the observation that semibullvalenes (e.g., SB **2**) are often the major products of sensitized and (or) direct irradiation, and hence the trienes offer a synthetic point of entry to the biologically important cyclopentanoid class of compounds.

To date, the unsubstituted benzo-triene has not been reported. We now describe the preparation and photoreactivity of 2,3-benzobicyclo[4.2.0]octa-2,4,7-triene (**11**), and present evidence that the semibullvalene formation from this parent compound arises from two mechanistic pathways.

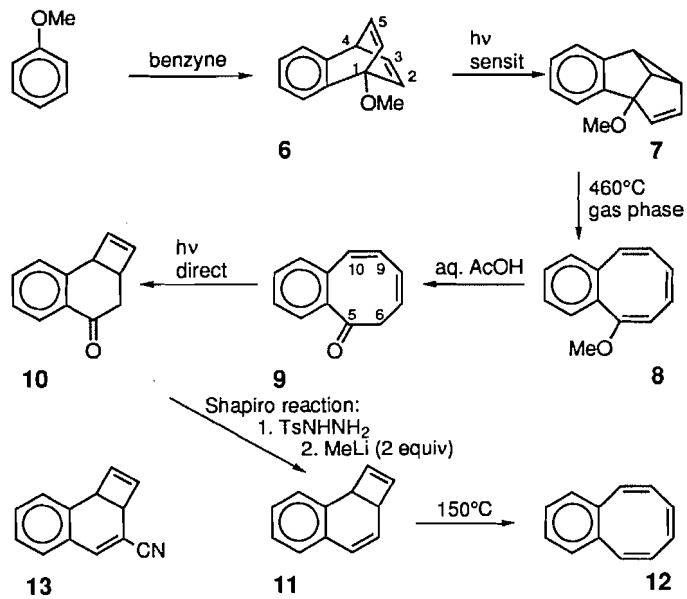

SCHEME 2

Results

The triene **11** was obtained by a synthetic sequence that paralleled the approach developed by us to prepare the 8-methyl derivative **1**(2*d*). The six-step synthesis, which starts with the Diels–Alder addition of benzyne to anisole, is outlined in Scheme 2. The identification of compounds **6**, **7**, **9**, and **10** was

[1]Author to whom correspondence may be addressed. Telephone: (403) 329-2307. Fax: (403) 329-2057.

TABLE 1. The ^{1}H NMR of 8-methyl (**1**), 5-cyano (**13**), and unsubstituted (**11**) triene

	Description and signal positions of ring protons, $\delta^{a,b}$		
Assignment	8-Me triene (**1**)	5-CN triene (**13**)	Triene **11**
Aromatics	6.99–7.26 m	7.15–7.35 m	6.98–7.13 m
H-1	3.91 d	4.27 d	4.10 d
H-4	6.22 d	6.99 br s	6.25 d
H-5	5.90 dd	—	5.86 dd
H-6	3.48 br s	3.82 br d	3.63 t
H-7	5.84 br s	6.25 br d	6.12 d
H-8	—	6.13 dd	6.01 d

[a]Run in $CDCl_3$ solvent.

[b]Coupling constants for **11** are: $J_{1,6} = J_{5,6} = 4.5$, $J_{4,5} = 10$, $J_{1,8}$ and $J_{6,7} < 1.0$, and $J_{7,8} = 2.7$ Hz; corresponding coupling constants for the methyl (**1**) and cyano (**13**) derivatives are within 0.5 Hz.

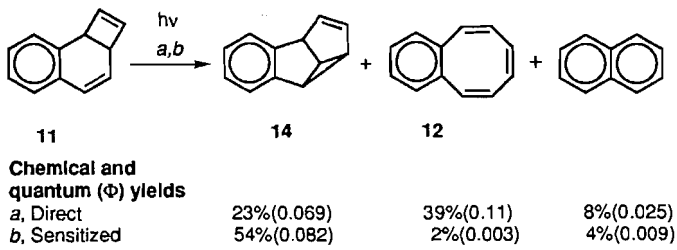

SCHEME 3

straightforward and the spectroscopic details (see Experimental) are analogous to those of the corresponding methyl derivatives encountered in the preparation of the triene **1** (*2d*). In the case of the cyclooctatetraene **8**, the characterization was not carried out because of its ready conversion to the ketone **9** upon attempts at purification with column chromatography.

The structure of triene **11** was assigned mainly on the basis of spectral evidence. Importantly, the ^{1}H NMR signal descriptions, given in Table 1, were in accord with those of the equivalent protons reported for the 8-methyl (**1** (*2d*)) and 5-cyano derivatives (**13**, note structure in Scheme 2 (3)). Further support for structure **11** was provided by the observation that the triene was converted to the known (4) benzocyclooctatetraene **12** on heating in refluxing nonane for 5.5 h. Thus, the parent triene conforms to the normal behaviour of other triene derivatives, all of which undergo thermolysis to give COT product (*2d*, 3, 5). For **11**, the rearrangement is noticeable on GC columns only at temperatures above 110°C.

The photochemistry of triene **11** was investigated on the preparative scale using direct irradiation (Corex filter; $\lambda \geq 280$ nm) and by sensitization with *p*-dimethylaminobenzophenone (at $\lambda \geq 345$ nm). Although both modes of excitation generated benzosemibullvalene (i.e., benzotricyclo[3.3.0.$0^{2,8}$]octa-3,6-diene, **14**), it was the dominant product only in the sensitized runs. The photoproducts are all known compounds (4), and their structures, analytical yields (based on consumed substrate; GC and NMR analysis), and quantum efficiencies are given in Scheme 3.

Mechanistically, the SB product **14** could be produced, in principle, from at least three different routes, all of which have literature precedent in triene derivatives. The pathways (routes i–iii) are outlined in Scheme 4. Route i, the most commonly encountered triene → SB mechanism (*2d*, 6), is a Zimmerman

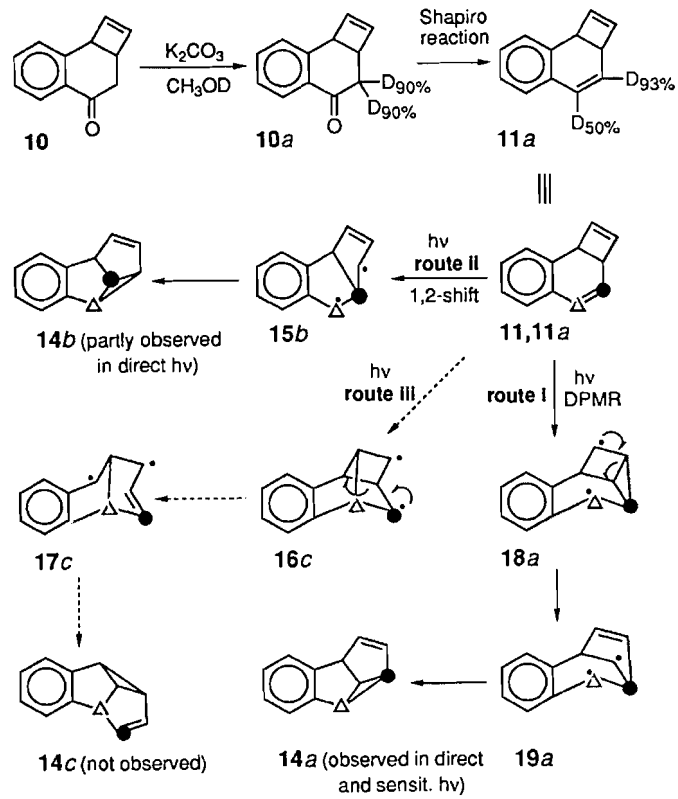

Structures denoted by "a" and "b" represent compounds doubly labelled with deuterium at positions marked by △ and ●. For structures denoted by a number only (e.g., **11**) △ and ● = H.

SCHEME 4

di-π-methane rearrangement (i.e, DPM rearrangement (7)); route ii is a 1,2-shift process, and has been observed in two cases (6, 8). The third, and least observed, pathway (route iii (3)), involves initial bridging between the distal carbons (i.e., C-4 and C-8) of the vinyl groups.

A convenient method of assessing the possible contributions of these pathways in the formation of SB **14** was provided by determining the label distributions resulting from irradiation of the deuterated triene material **11***a*. The labelled triene was prepared as shown in Scheme 4, starting from deuterium exchange of the methylene protons of the cyclohexanone **10**. The product from the Shapiro reaction was unexceptional in that deuterium incorporation was observed at both C-4 (50%) and C-5 (93%); similar two-site labelling from the tosylhydrazone–alkyllithium procedure was observed and commented on by us in the case of other members of the triene system (*2d*, 9), and a mechanistic rationalization for this phenomenon was proposed by Shapiro (10).

The most important result from the irradiation of the deuterated triene was that the label distributions in the semibullvalene product, as determined by ^{1}H NMR analyses, depended on the mode of excitation used. Thus, direct photolysis led to deuterium attachment at C-1 (16%), at C-2 (50%), and at C-8 (78%), and corresponded to a ca. 5:1 mixture of the isotopic isomers **14***a* and **14***b*. However, the SB product isolated from sensitized irradiation revealed labelling at only two locations: at C-2 (51%) and C-8 (92%), which accords with the presence of 100% of structure **14***a*.

In the case of the COT product, whether generated by direct

Can. J. Chem. Downloaded from www.nrcresearchpress.com by 85.192.166.187 on 09/08/12
For personal use only.

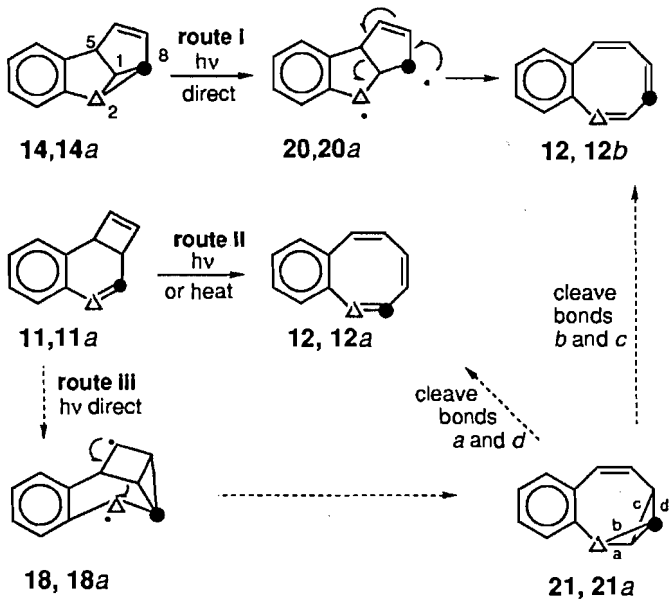

Structures denoted by "a" and "b" represent compounds doubly labelled with deuterium at positions marked by △ and ●. For structures denoted by a number only (e.g., **14**) △ and ● = H.

SCHEME 5

or sensitized irradiation, the deuterium was positioned at the C-5,10 (51%) and C-6,9 (92%) carbons only. This labelling pattern was the same as that observed in the COT product obtained from thermolysis of triene **11***a*, and corresponds to structure **12***a* (see Scheme 5, route ii).

Lastly, in connection with the labelling results, control experiments were carried out to determine the interconvertibility of the SB and COT photoproducts. We note that, although previous work on the photoisomerizations of SB **14** and COT **12** has been reported, (4), the conditions used were not the same as those employed in the present study. Here, the direct irradiation of SB **14** led to the inefficient formation of COT **12** ($\lambda \geq 280$ nm; $\Phi = 0.007$), and when labelled SB **14***a* was the substrate (Corex filter) the only product (by GC and NMR analysis) was COT **12***b* (48%); Scheme 5, route i). The transformation of SB **14** → COT **12** was first noted by Zimmerman, Givens, and Pagni (4), and involves cleavage of bonds C1—C5 and C2—C8, as shown in route i, Scheme 5. However, the reaction does not interfere as a secondary photoprocess in the conversion of triene **11** → COT **12** since no deuterium was found at the C-7,8 carbons of the labelled COT isolated from irradiations of triene **11***a* (i.e., COT **12***a* is formed, but not COT **12***b*). Attempts at sensitization of SB with *p*-dimethylaminobenzophenone (at $\lambda \geq 345$ nm) failed to produce product. Also, the direct and sensitized irradiations of COT **12**, under the same conditions used for triene **11**, did not lead to observable photochemistry.

Discussion

The deuterium-labelling studies suggest that SB **14**, the major product formed in sensitized irradiations of triene **11**, derives from a sole mechanism that is most reasonably interpreted as a Zimmerman DPM rearrangement from T_1.

In the case of the direct irradiations, the labelling results indicate that the SB is provided by two pathways: a 1,2-shift mechanism (17% route ii, Scheme 4); and a Zimmerman DPM rearrangement (83% route i, Scheme 4). One conclusion from this observation is that the excited state involved in the minor pathway must be S_1 since the same labelling pattern is not observed in the SB product formed in sensitized runs, and it is not formed from the secondary photochemistry of the major primary product COT **12**. Unfortunately, the excited state assignment for the more preferred route to SB **14** (route i) is ambiguous. Analysis of the quantum yield data is consistent with all, part, or none of the DPM rearrangement product being formed from S_1. This latter results stems from application of the expression (11) ${}^1\Phi_{SB} = {}^{dir}\Phi_{SB} - (\Phi_{isc})({}^3\Phi_{SB})$, which sets the limits of the $S_1 \rightarrow T_1$ intersystem crossing efficiency at $0 \leq \Phi_{isc} \leq 0.84$. Use of these same limits for the remaining products from the direct irradiation suggests that at least 98% of COT **12** and at least 68% of the naphthalene must derive from the singlet excited state of triene **11**.

The major S_1 product (COT **12**) from the direct irradiation of triene **11** may arise by a simple $2\sigma_s + 2\pi_s$ electrocyclic opening (12) of the cyclobutene ring (note Scheme 5, route ii). The deuterium-labelling results are in accord with this interpretation. Interestingly, the labelling results do rule out the operation of a pathway to COT **12** that was previously invoked to account for part of the formation of the COT **4** (Scheme 1) from the direct irradiation of the methyl triene **1** (2*d*). The mechanism in question is a variation of a DPM rearrangement, and is shown as route iii in Scheme 5; the thermal isomerization of the proposed octavalene intermediate **21** would be expected to lead to a 1:1 mixture of the COT label isomers **12***a* and **12***b*. Since the deuterium distributions observed in the COT product from **11***a* indicate no labelling at C-7,8, support for the utilization of this pathway in the case of the unsubstituted triene is lacking.

In conclusion, we note that, to date, the semibullvalenes that result from sensitized irradiations of the benzo-trienes appear to be universally provided by a Zimmerman DPM rearrangement (7), and it is only from the S_1 excited state that mechanistic variations in SB production have been observed.

Experimental

Instrumentation and materials

Unless otherwise stated, the ^1H and ^{13}C NMR spectra were recorded in $CDCl_3$ solvent at 250 and 62.9 MHz, respectively. The chemical shifts are in δ units and the coupling constants (*J*) in Hz. The abbreviations br, s, d, t, q, and m refer to broad, singlet, doublet, triplet, quartet, and multiplet, respectively. Maxima in the UV spectra are given in nm, with λ_{max} values in parentheses; sh = shoulder. Elemental analyses were performed by Galbraith Labs, Inc., Knoxville, Tenn. Column chromatography was carried out on Silica Gel 60 (Merck; 230–400 mesh) or on Lobar columns (Merck; size B, LiChroprep Si 60). The GC analyses were determined by FID on a DB-23 fused silica capillary column (30 m × 0.25 mm; J&W Scientific). Melting points are uncorrected. Cyclohexane solvent for quantum yields was prepared by scrubbing with 20% fuming sulfuric acid, followed by washing with 10% aqueous sodium hydroxide, drying ($MgSO_4$), and finally distilling from calcium hydride.

General procedures for preparative photolyses

The apparatus consisted of a 450-W Hanovia medium-pressure mercury arc surrounded by a water-cooled quartz immersion well. Unless otherwise stated, the light was filtered through either a cylindrical sleeve of Pyrex or Corex glass. Three types of sample cell were used. Cell A (250-mL sample volume) consisted of a cylindrical well, which surrounded the aqueous filter jacket. Cell A was fitted with gas inlet and exit ports, and sample solutions were magnetically stirred, and purged with argon prior to and during irradiations. Cell B (40-mL sample volume) and Cell C (3.5 mL) were a quartz test-tube-like vessel

Can. J. Chem. Downloaded from www.nrcresearchpress.com by 85.192.166.187 on 09/08/12
For personal use only.

Can. J. Chem. Downloaded from www.nrcresearchpress.com by 85.192.166.187 on 09/08/12
For personal use only.

and a quartz cuvette, respectively; sample solutions contained therein were deoxygenated by flushing with argon and sealed under a positive pressure; the solutions were magnetically stirred throughout the course of the irradiations.

Diels–Alder addition of benzyne to anisole

Benzene diazonium carboxylate (15), prepared from 10.9 g (79.7 mmol) of anthranilic acid, 18 mL of isoamylnitrite, and 70 mg of trifluoroacetic acid, was added to 500 mL of anisole and stirred at 45–60°C overnight. The resulting mixture was concentrated in vacuo and the residue was taken up in 30 mL of acetone, which was then diluted with 500 mL of hexane. The precipitate was filtered, the filtrate concentrated, and the residue was chromatographed on Silica Gel 60 (0.9 cm × 30 cm) with 1% ethyl acetate–hexane. The main band was concentrated and the residue was rechromatographed on a Lobar Silica Gel column with 1% ethyl acetate–hexane. Crude, yellow barrelene (**6**) was obtained from early fractions. Crystallization from ethanol gave 3.51 g (24%) of colourless 1-methoxy-4-hydro-1,4-ethenonaphthalene (**6**), mp 38–40°C; UV (hexane): 276 (360), 269 (390), 261 (330), 253 sh (380), and 231 sh (1000); ^{1}H NMR; 7.37 (dd, 1H, 1 aromatic, $J = 7$, $J = 1.3$), 7.14 (dd, 1H, 1 aromatic, $J = 7$, $J = 1.3$), 6.82–6.99 (m, 6H, 2 aromatics and 4 olefinics), 4.61 (tt, 1H, H-4, $J_{4,3} = J_{4,5} = 6$; $J_{4,2} = J_{4,6} = 1.5$), 3.83 (s, 3H, methoxyl); ^{13}C NMR: 48.3 (C4), 54.5 (OCH_3), 89.8 (C1), 119.2, 121.9, 123.4, 123.5, 138.4, 140.2, 145.8, and 147.7. Mass spectrum showed molecular ion at *m/e* = 184.08894 (100%); $C_{13}H_{12}O$ requires 184.08882. Anal. calcd. for $C_{13}H_{12}O$: C 84.75, H 6.57; found: C 84.83, H 6.68.

*Sensitized photolysis of barrelene **6***

A 250 mL solution of cyclohexane containing 1.0077 g (5.5 mmol) of barrelene **6** and 30 mL of acetone sensitizer in Cell A was photolyzed with Pyrex-filtered light for 4.5 h. The photolysate was concentrated and the residue chromatographed on Silica Gel 60 (0.9 cm × 20 cm) with 5% ethyl acetate–hexane solvent. The main band was rechromatographed on a Lobar column (3% ethyl acetate–hexane solvent). Short-path distillation (60°C/0.1 Torr; 1 Torr = 133.3 Pa) of the contents of the second band gave 523.5 mg (52%) of 5-methoxybenzotricyclo[3.3.0.0^{2,8}]octa-3,6-diene (**7**), mp 32–34°C; UV (hexane): 281 (720), 274 (790), and 268 sh (600); ^{1}H NMR; 7.14–7.33 (m, 4H, aromatics), 5.65 (d, 1H, H-6, $J_{6,7} = 5$), 5.18 (dd, 1H, H-7, $J_{7,6} = 5$, $J_{7,8} = 2.5$), 3.42 (t, 1H, H-1, $J_{1,2} = J_{1,8} = 6$), 3.38 (s, 3H, methoxyl), 3.24 (t, 1H, H-2, $J_{2,1} = J_{2,8} = 6.5$), and 2.90 (dt, 1H, H-8, $J_{8,1} = J_{8,2} = 6.5$; $J_{8,7} = 2.5$); ^{13}C NMR: 38.0 (C1), 40.2 (C8), 51.1, (C2), 53.1 (methoxyl), 99.2 (C5), 119.6, 120.9 (C7), 125.2, 125.6, 127.3, 135.5, 136.6 (C6), and 148.4; assignments were based on Hetcorr experiments. Mass spectrum showed molecular ion at *m/e* = 184.08870 (100%). Anal. found: C 84.82, H 6.48.

*Thermolysis of semibullvalene **7***

A total of 2.48 g (13.5 mmol) of SB **7** was divided into three equal portions, and each was separately distilled (during 1.5 h) into a Pyrex tube (2 cm × 30 cm) packed with glass beads (0.5 cm diameter) maintained at ca. 460°C by a tube furnace. The pressure was kept at 4 Torr by the passage of nitrogen. The combined thermolysis products, mostly COT **8**, collected in an ice-cooled U-trap, were not purified, but treated directly with 14 mL of 80% aqueous acetic acid. The solution was stirred at room temperature for 48 h, then neutralized with 200 mL of 15% aqueous $NaHCO_3$, and extracted with 300 mL hexane. The extract was washed (2 × 100 mL water), dried ($MgSO_4$), concentrated, and chromatographed on Silica Gel 60 (0.9 cm × 7 cm) with 5% ethyl acetate–hexane solvent. The main band was rechromatographed on a Lobar column (3% ethyl acetate–hexane). Short-path distillation (90°C/0.1 Torr) of the contents of the first fraction gave 787.8 mg (32%) of ketone **9**; IR (Nujol): 1670 (C=O) cm^{-1}; UV (hexane): 369 sh (260), 352 sh (670), 335 sh (1040), 315 sh (2850), and 301 sh (3620); ^{1}H NMR: 8.39 (d, 1H, H-4, $J = 8$), 7.27–7.53 (m, 3H, aromatics), 6.82 (d, 1H, H-10, $J_{10,9} = 12.5$), 6.34 (dd, 1H, H-9, $J_{9,8} = 4.5$, $J_{9,10} = 12.5$), 6.24 (dd, 1H, H-8, $J_{8,9} = 4.5$, $J_{8,7} = 10$), 5.82 (br q, 1H, H-7, $J_{7,9} = 10$, $J_{7,6} = J_{7,6'} = 8$), and 3.37 (d, 2H, H-6 and H-6′, $J_{6,7} = J_{6,7'} = 8$); ^{13}C NMR: 43.7, 127.0, 127.8, 128.7, 130.1, 130.9, 132.0, 132.2, 134.3, 136.7, 137.2, 193.4. Mass spectrum showed molecular ion at *m/e* = 170.07359 (96%), 141 (100%); $C_{12}H_{10}O$ requires 170.07317. Anal. calcd. for $C_{12}H_{10}O$: C 84.68, H 5.92; found: C 85.00, H 5.92.

*Cyclohexanone **10** from photoclosure of ketone **9***

A 250 mL solution of hexane containing 40 mL of piperylene quencher and 392.9 mg (2.31 mmol) of ketone **9** was photolyzed with Pyrex-filtered light for 13 min in Cell A. The photolysate was concentrated and the residue chromatographed on Silica Gel 60 (0.9 cm × 10 cm) with 100 mL of 8% ethyl acetate–hexane solvent. The main band was rechromatographed on a Lobar column with 3% ethyl acetate–hexane solvent. The first band gave 119.8 mg (30%) of recovered ketone **9**; the second band contained 222.4 mg (57%) of colourless cyclohexanone **10**, mp 37–38°C (from hexane); IR (Nujol): 1694 (C=O) cm^{-1}; UV (cyclohexane): 325 (85), 288 (1130); ^{1}H NMR: 7.86 (dd, 1H, aromatic, $J = 1.5$, $J = 7$), 7.51 (dt, 1H, aromatic, $J = 1.5$, $J = 7$), 7.26–7.35 (m, 2H, 2 aromatics), 6.23 (d, 1H, H-8, $J_{8,7} = 2.5$), 6.16 (d, 1H, H-7, $J_{7,8} = 2.5$), 4.13 (d, 1H, H-1, $J_{1,6} = 4$), 3.69 (sym m, 1H, H-6,), 2.89 (dd, 1H, H-5′, $J_{5',5} = 16$, $J_{5',6} = 2$), and 2.74 (dd, 1H, H-5, $J_{5,5'} = 16$, $J_{5,6} = 7.5$); ^{13}C NMR: 38.6, 41.1, 44.7, 126.4, 127.2, 128.5, 133.1, 133.3, 139.0, 144.4, 144.5, and 198.1. Mass spectrum showed molecular ion at *m/e* = 170.07468 (100%). Anal. found: C 85.04, H 5.94.

*Triene **11** from cyclohexanone **10***

A solution of 117.6 mg (0.64 mmol) of *p*-toluenesulfonylhydrazide, 104.2 mg (0.61 mmol) of cyclohexanone **10**, and 0.15 mL of acetic acid in 2 mL of methanol was stirred at room temperature for 72 h. The colourless crystalline product was filtered off and dried in vacuo to give 157.6 mg (76%) of the tosylhydrazone, mp 174–176°C (dec.). The Shapiro reaction (13) was carried out under a nitrogen atmosphere. A stirred slurry of 226.0 mg (0.67 mmol) of the tosylhydrazone in 8 mL of dry ether was cooled to −12°C and 2.0 mL (2.8 mmol) of 1.4 M methyllithium in ether was added during 2 min whereupon an orange solution formed. The solution was stirred at room temperature for 1.25 h, refluxed for 10 min, cooled, and then made slightly acidic by the addition of aqueous ammonium chloride solution. The organic layer was diluted with ether to 20 mL, then washed twice with water and dried ($MgSO_4$). The ether was evaporated and the residue chromatographed on Silica Gel 60 (0.9 cm × 10 cm) with hexane solvent. The first band gave 100.2 mg (97%) of triene **11** as a colourless oil (mp 0–5°C); UV (hexane): 301 sh (520), 291 sh (2390), 279 (5135), 273 sh (5210), and 269 (5690); ^{1}H NMR (400 MHz; $CDCl_3$): see Table 1; ^{13}C NMR: 43.3, 44.2, 125.9, 126.6, 127.6, 127.7, 127.8, 128.2, 131.9, 135.6, 139.8, one carbon missing. Mass spectrum showed molecular ion at *m/e* = 154.07825 (82%), 153 (100%); $C_{13}H_{12}$ requires 154.07825. Anal. calcd. for $C_{12}H_{10}$: C 93.46, H 6.54; found: C 93.46, H 7.61.

*Direct irradiation of triene **11***

A solution of 47.4 mg (0.30 mmol) of **11** and 35.1 mg of dodecane (GC standard) in 40 mL of hexane was irradiated (Corex filter) for 50 min in Cell B (84% conversion by GC). The photolysate composition analysed (as determined by GC peak areas calibrated (peak area versus mass) for the dodecane internal standard against individual photolysate components) for 3.3 mg (7%) of naphthalene, 15.6 mg (33%) of COT **12**, 7.5 mg (16%) of triene **11**, and 9.3 mg (20%) of SB **14**. The polymeric materials were removed from the photolysate by chromatography on Silica Gel 60 (0.9 cm × 10 cm; 100 mL hexane). The elute was rechromatographed on a Labor column with hexane solvent. The first band contained ca. 1 mg (2%) of naphthalene (identified by GC and TLC comparison with an authentic sample); the second band gave 6.1 mg (13%) of recovered triene; the third band gave 13.8 mg (29%) of the known benzocyclooctatetraene (i.e., COT **12**), mp 47–49°C (lit. (4) mp 48–50°C), which was identified by comparison of the ^{1}H NMR spectrum with that reported for authentic **12** (4). The fourth and last band gave 7.9 mg (17%) of a colourless oil (GC purity >98%), which was identified as 3,4-benzotricyclo[3.3.0.0^{2,8}]octa-3,6-diene (i.e., SB

Can. J. Chem. Downloaded from www.nrcresearchpress.com by 85.192.166.187 on 09/08/12
For personal use only.

14) by comparison of the ^{1}H NMR spectrum with that reported for authentic **14** (4).

*Sensitized irradiation of triene **11***

A solution of 45.0 mg (0.29 mmol) of **11**, 42.1 mg (0.19 mmol) of *p*-dimethylaminobenzophenone, and 31.2 mg of dodecane (GC standard) in 40 mL of cyclohexane was irradiated for 50 min in Cell B, with light filtered through a Pyrex and WG 345 glass (Schott) filter (88% conversion by GC). The photolysate composition analysed (as determined by GC peak areas calibrated (peak area versus mass) for the dodecane internal standard against the individual photolysate components) for 1.5 mg (3%) of naphthalene, 5.4 mg (12%) of triene **11**, ca. 0.7 mg (1.5%) of COT **12**, and 21.4 mg (48%) of SB **14**. The photolysate was first chromatographed on Silica Gel 60 (0.9 cm × 10 cm; 100 mL hexane) to remove polymeric materials and sensitizer, and then rechromatographed on a Lobar column with hexane solvent. The first band contained a trace of naphthalene (identified by GC and TLC comparison with an authentic sample). The second band gave 4.1 mg (9%) recovered triene **11**; the third band gave ca. 0.5 mg (1%) of COT **12**; and the final band gave 19.4 mg (43%) of SB **14** (GC purity >98%).

*Labelled cyclohexanone **10a***

A mixture of 123.0 mg (0.72 mmol) of cyclobutene **10**, 14 mg of potassium carbonate, and 25 mL of methanol-d_1 (99.5% deuterium) was stirred at room temperature during 42 h. The solvent was removed under vacuum (oil pump) and the residue was taken up in hexane (20 mL), washed with D_2O (2 mL), and chromatographed on SG 60 (0.9 cm × 10 cm) with 10% ethyl acetate–hexane. The main band gave 112 mg (91%) of deuterated cyclohexanone **10***a* (90%-d_2 labelled at C-5); ^{1}H NMR: 7.86 (dd, 0.91H, aromatic, J = 1.5, J = 7), 7.51 (dt, 0.99H, aromatic, J = 1.5, J = 7), 7.26–7.35 (m, 1.93H, 2 aromatics), 6.23 (d, 1.11H, H-8, $J_{8,7}$ = 2.5), 6.16 (d, 1.00H, H-7, $J_{7,8}$ = 2.5), 4.13 (d, 1.01H, H-1, $J_{1,6}$ = 4), 3.69 (br d, 0.98H, H-6, $J_{6,1}$ = 4), 2.89 (br, s, 0.09H), and 2.74 (br d, 0.11H, H-5, $J_{5,6}$ = 7.5).

*Deuterium-labelled triene **11** from cyclohexanone **10a***

A solution of 130 mg (0.63 mmol) of *p*-toluenesulfonylhydrazide, 112 mg (0.66 mmol) of cyclohexanone **10***a* and 0.05 mL of acetic acid-d_1 in 0.5 mL of methanol-d_1 was stirred at room temperature for 24 h, and then cooled to –12°C for 18 h. The resulting white crystals were filtered, and dried in vacuo to give 155 mg (70%) of labelled tosylhydrazone, which was then converted to 39.5 mg (56%) of deuterated triene **11***a* by the procedure described above for the preparation of unlabelled triene **11**; ^{1}H NMR: 7.00–7.17 (m, 4.33H, aromatics and residual $CHCl_3$), 6.26 (br s, 0.50H, H-4), 6.13 (d, 0.99H, H-7, $J_{8,7}$ = 2.7), 6.02 (dd, 1.00H, H-8, $J_{7,8}$ = 2.7, $J_{7,6}$ = 0.9), 5.88 (q, 0.07H, H-5, $J_{5,4}$ = $J_{5,6}$ = 4.5), 4.11 (d, 1.06H, H-1, $J_{1,6}$ = 4.5), and 3.64 (d, 1.02H, H-6, $J_{6,1}$ = 4.5), i.e., triene **11***a* is 93%-d_1 labelled at C-5 and 50%-d_1 labelled at C-4.

*Thermolysis of deuterium-labelled triene **11a***

A solution of 8.5 mg (0.055 mmol) of triene **11***a* in 1 mL of *n*-nonane was refluxed (ca. 150°C) for 5.5 h. The thermolysis product was chromatographed on Silica Gel 60 (0.9 cm × 10 cm; hexane), to give 7.3 mg (86%) of COT **12***a*; ^{1}H NMR: 7.17–7.24 (m, 2.07H, aromatics), 6.93–6.99 (m, 2.00H, aromatics), 6.55 (d + br s, 1.49H, H-10 and H-5, $J_{10,9}$ = 11.8), 6.03 (dm, 1.08H, H-6 + H-9, $J_{9,10}$ = 11.5), and 5.88 (d, 2.00H, H-7 and H-8, J = 1.8).

*Direct irradiation of deuterium-labelled triene **11a***

A solution of 15.8 mg (0.10 mmol) of **11***a* in 12 mL of hexane was irradiated (Corex filter) for 50 min in Cell B. The photolysate was worked up as described in the case of the direct irradiation of unlabelled triene **20** to give ca. 0.9 mg (6%) of naphthalene and 2.1 mg (13%) of recovered triene **11***a*, ^{1}H NMR: 7.00–7.17 (m, 4.23H, aromatics and residual $CHCl_3$), 6.26 (br s, 0.50H, H-4), 6.13 (d, 0.99H, H-7, $J_{8,7}$ = 2.7), 6.02 (dd, 0.99H, H-8, $J_{7,8}$ = 2.7, $J_{7,6}$ = 0.9), 5.88 (q, 0.10H, H-5, $J_{5,4}$ = $J_{5,6}$ = 4.5), 4.11 (d, 1.02H, H-1, $J_{1,6}$ = 4.5), and 3.64 (d, 1.01H, H-6, $J_{6,1}$ = 4.5); 4.3 mg (27%) of labelled COT **12***a*, ^{1}H NMR: 7.17–7.24 (m, 2.05H, aromatics), 6.93–6.99 (m, 2.00H, aromatics), 6.55 (d + br s, 1.49H, H-10 and H-5, $J_{10,9}$ = 11.8), 6.03 (dm, 1.10H, H-6 + H-9, $J_{9,10}$ = 11.6), and 5.88 (d, 1.97H, H-7 and H-8, J = 1.6); and 2.2 mg (14%) of a mixture of ca. 83% SB **14***a* and 17% SB **14***b*, ^{1}H NMR: 7.31–7.35 (m, 1.00H, aromatic), 7.04–7.18 (m, 3.19H, aromatics), 5.60 (dd, 0.99H, H-6, $J_{6,7}$ = 5, $J_{6,5}$ = 2.2), 5.21 (d, 1.00H, H-7, $J_{7,6}$ = 5), 3.90 (dd, 1.01H, H-5, $J_{5,1}$ = 6.3, $J_{5,6}$ = 2.3), 3.29 (br t, 0.84H, H-1, $J_{1,5}$ = $J_{1,2}$ = 6), 3.04 (br d, 0.50H, H-2, $J_{2,1}$ = 6.3), and 2.70–2.76 (m, 0.22H, H-8).

*Sensitized irradiation of deuterium-labelled triene **11a***

A solution of 23.7 mg (0.15 mmol) of triene **11***a*, 22.8 mg (0.38 mmol) of *p*-dimethylaminobenzophenone, and 17.4 mg of dodecane (GC standard) in 20 mL of hexane was irradiated for 55 min in Cell B, with light filtered through a Pyrex and WG 345 glass (Schott) filter (69% conversion by GC). The photolysate was worked up as in the case of the sensitized irradiation of unlabelled triene **11**, to give a trace of naphthalene; 6.6 mg (28%) of recovered triene **11***a*, ^{1}H NMR: 7.00–7.17 (m, 4.16H, aromatics and residual $CHCl_3$), 6.26 (br s, 0.48H, H-4), 6.13 (d, 1.00H, H-7, $J_{8,7}$ = 2.7), 6.02 (dd, 1.00H, H-8, $J_{7,8}$ = 2.7 $J_{7,6}$ = 0.9), 5.88 (q, 0.08H, H-5, $J_{5,4}$ = $J_{5,6}$ = 4.5), 4.11 (d, 1.02H, H-1, $J_{1,6}$ = 4.5), and 3.64 (d, 1.02H, H-6, $J_{6,1}$ = 4.5); ca. 0.3 mg (1%) of COT **12***a*, ^{1}H NMR: 7.17–7.24 (m, 2.58H, 2 aromatics and residual $CHCl_3$), 6.93–6.99 (m, 2.00H, aromatics), 6.55 (d + br s, 1.49H, H-10 and H-5, $J_{10,9}$ = 11.8), 6.03 (dm, 1.08H, H-6 + H-9, $J_{9,10}$ = 11.6), and 5.88 (d, 2.00H, H-7 and H-8, J = 1.6); and 8.7 mg (37%) of SB **14***a*, ^{1}H NMR: 7.31–7.35 (m, 1.00H, aromatic), 7.04–7.18 (m, 3.09H, aromatics), 5.60 (dd, 0.99H, H-6, $J_{6,7}$ = 5, $J_{6,5}$ = 2.3), 5.21 (d, 0.99H, H-7, $J_{7,6}$ = 5), 3.90 (dd, 1.02H, H-5, $J_{5,1}$ = 6.3, $J_{5,6}$ = 2.2), 3.29 (br t, 0.98H, H-1, $J_{1,2}$ = $J_{1,5}$ = 6), 3.04 (br d, 0.50H, H-2, $J_{2,1}$ = 6.2), and 2.70–2.76 (m, 0.08H, H-8).

*Direct irradiation of deuterium-labelled SB **14a***

A solution of 4.6 mg (0.03 mmol) of **11***a* in 4 mL of cyclohexane was irradiated (Corex filter) for 11.5 h in Cell C. The photolysate was chromatographed on a Lobar column with hexane solvent. The first band contained ca. 1.0 mg (22%) of COT **12***b* (>98% pure by GC); ^{1}H NMR: 7.17–7.24 (m, 2.13H, aromatics), 6.93–6.99 (m, 2.00H, aromatics), 6.55 (d, 1.56H, H-10 and H-5, $J_{10,9}$ = 11.7), 6.03 (dm, 1.94H, H-6 + H-9, $J_{9,10}$ = 11.7), and 5.88 (d, 1.10H, H-7 and H-8, J = 1.5); the second band gave 2.5 mg (54%) of recovered SB **14***a*.

Quantum efficiencies

Potassium ferrioxalate actionometry (14) was used to determine quantum efficiencies on an optical bench apparatus previously described (15). Cyclohexane solutions (3.0 mL) of reactants (ca. 8.7×10^{-3} M) and sensitizer, if any (*p*-dimethylaminobenzophenone, 5.0×10^{-3} M), were deoxygenated prior to irradiation by flushing with argon. A positive pressure of argon was maintained over the stirred solutions throughout the course of the irradiations. For the direct irradiations of triene **11** and the semibullvalene **14**, light of wavelength 280 nm was used. For sensitized runs the *p*-dimethylaminobenzophenone absorbed >95% of the incident light (366 nm) employed. The quantum yields (Φ's) were obtained from several runs extrapolated to zero conversion. Product analyses were determined by GC (internal dodecane standard).

Acknowledgements

The authors thank the Agriculture and Agri-Food Canada Research Centre at Lethbridge for the 400-MHz NMR spectrum. Financial support from the Natural Sciences and Engineering Research Council of Canada is gratefully acknowledged.

1. P.J. Collin and W.H.F. Sasse. Tetrahedron Lett. 1689 (1968).
2. (*a*) T. Teitei, D. Wells, and W.H.F. Sasse. Aust. J. Chem. **28**, 571 (1975); (*b*) W.H.F. Sasse, P.J. Collin, D.B. Roberts, and G. Sugowdz. Aust. J. Chem. **24**, 2151 (1971); (*c*) J.R. Scheffer and M. Yap. J. Org. Chem. **54**, 2561 (1989); (*d*) C.O. Bender, D.L. Bengtson, D. Dolman, and R.T. McKay. Can. J. Chem. **72**, 1556 (1994).

3. C.O. Bender and D. Dolman. Can. J. Chem. **67**, 82 (1989).
4. H.E. Zimmerman, R.S. Givens, and R.M. Pagni, J. Am. Chem. Soc. **90**, 6096 (1968).
5. J.A. Elix, M.V. Sargent, and F. Sondheimer, J. Am. Chem. Soc. **89**, 5081 (1967)).
6. C.O. Bender, D. Dolman, and N. Tu. J. Org. Chem. **56**, 5015 (1991).
7. (*a*) H.E. Zimmerman, *In* Rearrangements in ground and excited states. Vol. 3. *Edited by* P. de Mayo. Academic Press, New York. 1980. Essay 16, pp. 131–166; (*b*) S.S. Hixson, P.S. Mariano, and H.E. Zimmerman. Chem. Rev. **73**, 531 (1973).
8. C.O. Bender, D.S. Clyne, and D. Dolman. Can. J. Chem. **69**, 70 (1991).
9. C.O. Bender, I.M. Cassis, D. Dolman, L.D. Heerze, and F.L. Schultz. Can. J. Chem. **62**, 2769 (1984).
10. R.H. Shapiro and E.C. Hornaman. J. Org. Chem. **39**, 2302 (1974).
11. H.E. Zimmerman and R.A. Bunce. J. Org. Chem. **47**, 3377 (1982).
12. R.B. Woodward and R. Hoffmann. *In* The conservation of orbital symmetry. Verlag Chemie, Weinheim, and Academic Press, New York. 1970. p. 63.
13. (*a*) R.H. Shapiro and M.J. Heath. J. Am. Chem. Soc. **89**, 5734 (1967); (*b*) R.M. Adlington and A.G.M. Barrett. Acc. Chem. Res. **16**, 55 (1983).
14. C.G. Hatchard and C.A. Parker. Proc. R. Soc. London, A: **235**, 518 (1956).
15. C.O. Bender, D.L. Bengtson, D. Dolman, C.E.L. Herle, and S.F. O'Shea. Can. J. Chem. **60**, 1942 (1982).

Can. J. Chem. Downloaded from www.nrcresearchpress.com by 85.192.166.187 on 09/08/12
For personal use only.

A mild and efficient methodology for the synthesis of 5-halogeno uracil nucleosides that occurs via a 5-halogeno-6-azido-5,6-dihydro intermediate

RAKESH KUMAR, LEONARD I. WIEBE, AND EDWARD E. KNAUS[1]

Faculty of Pharmacy and Pharmaceutical Sciences, University of Alberta, Edmonton, AB T6G 2N8, Canada

Received April 29, 1994

RAKESH KUMAR, LEONARD I. WIEBE, and EDWARD E. KNAUS. Can. J. Chem. **72**, 2005 (1994).

A mild and efficient methodology for the synthesis of 5-halogeno (iodo, bromo, or chloro) uracil nucleosides has been developed. 5-Halo-2′-deoxyuridines **4***a–c* (84–95%), 5-halouridines **7***a–c* (45–95%), and 5-haloarabinouridines **8***a–c* (65–95%) were synthesized in good to excellent yields by the reaction of 2′-deoxyuridine (**2**), uridine (**5**), and arabinouridine (**6**), respectively, with iodine monochloride, or *N*-bromo (or chloro)succinimide, and sodium azide at 25–45°C. These C-5 halogenation reactions proceed via a 5-halo-6-azido-5,6-dihydro intermediate (**3**), from which HN_3 is eliminated, to yield the 5-halogeno uracil nucleoside. The 5-halo-6-azido-5,6-dihydro intermediate products (**10***a*, **10***b*) could be isolated from the reaction of 3′,5′-di-*O*-acetyl-2′-deoxyuridine (**9**) with iodine monochloride or *N*-bromosuccinimide and sodium azide at 0°C. The isolation of **10***a*, **10***b* indicates that the C-5 halogenation reaction proceeds via a 5-halo-6-azido-5,6-dihydro intermediate.

RAKESH KUMAR, LEONARD I. WIEBE et EDWARD E. KNAUS. Can. J. Chem. **72**, 2005 (1994).

On a mis au point une méthodologie douce et efficace de synthèse des nucléosides des 5-halogéno (iodo, bromo ou chloro) uraciles. On a synthétisé les 5-halo-2′-désoxyuridines (**4***a–c*, 84–95%), 5-halouridines (**7***a–c*, 45–95%) et 5-halorarabinouridines (**8***a–c*, 65–95%) par réactions respectivement de la 2′-désoxyuridine (**2**), de l'uridine (**5**) et de l'arabinouridine (**6**) avec du monochlorure d'iode ou de *N*-bromo(ou chloro)succinimide et de l'azoture de sodium à des températures allant de 25 à 45°C. Ces réactions d'halogénation en C-5 se produisent par le biais d'un intermédiaire 5-halo-6-azido-5,6-dihydro (**3**) à partir duquel il y a élimination de HN_3 et formation du nucléoside du 5-halogénouracile. On a pu isoler les intermédiaires 5-halo-6-azido-5,6-dihydro (**10***a*, **10***b*) lors de la réaction du 3′,5′-di-*O*-acétyl-2′-désoxyuridine (**9**) avec le monochlorure d'iode ou le *N*-bromosuccinimide et l'azoture de sodium à 0°C. En isolant les intermédiaires **10***a*, **10***b*, on confirme que la réaction d'halogénation en C-5 se produit par le biais d'un intermédiaire 5-halo-6-azido-5,6-dihydro.

[Traduit par la rédaction]

Analogs of 5-halouracils constitute a biologically important class of compounds, which possess interesting biochemical and biophysical properties (1), and which have been investigated extensively as antineoplastic and antiviral agents (2). In addition, some 5-chlorouracil nucleoside analogs, which are less cytotoxic, exhibit selective anti-HIV activity (3). Studies utilizing 5-halouracil derivatives have also provided important biochemical information pertaining to their cellular biochemistry, affinity for a nucleoside transporter, enzyme–substrate specificity, and the nature of enzyme–substrate interaction(s). Radiohalogenated uracil nucleosides are useful mechanistic probes to study DNA metabolism (4). Halogenated nucleosides have also been used as synthons for the synthesis of biologically active nucleoside analogs (5–10). Therefore, new methods for the efficient synthesis of 5-halouracil nucleoside derivatives, using mild reaction conditions, are of great interest in medicinal chemistry.

A variety of methods have been developed for electrophilic halogenation at the electron-rich C-5 position of uracil nucleosides (for an excellent review, see ref. 11). Prusoff et al. reported the first 5-iodination of uracil using molecular iodine, generated in situ by oxidation of KI with H_2SO_4 and KIO_3 (12). Prusoff also developed methods involving the reaction of I_2, prepared by oxidation of iodide using HNO_3, or molecular iodine in an organic solvent and water to prepare 5-iodo-2′-deoxyuridine (13). However, these harsh reaction conditions and (or) methodologies often afford a moderate yield of the target 5-iodo product due to decomposition and (or) formation of undesirable side product(s). Iodination of 5-mercurouridine derivatives in aqueous alcohol has been described by Dale et al. (14). *N*-Iodosuccinimide and iodine monochloride (ICl) have also been used for the efficient iodination of some uracil nucleosides (15, 16). An effective conversion of protected or unprotected uracil nucleosides to their 5-halo derivatives has been reported using elemental iodine, or a lithium halide, in the presence of ceric ammonium nitrate (CAN) (17). A number of methods have been reported for the synthesis of 5-bromouracil analogs using bromine–water (18, 19), or bromine in either acetic anhydride (20), dimethyl formamide (21), or pyridine (22). The C-5 chlorination of uracil nucleosides has been reported using Cl_2–H_2O under UV irradiation (23) or Cl_2–HOAc (24). Chlorination of uracil analogs has also been effected using elemental chlorine or *N*-chlorosuccinimide in acetic acid at reflux temperatures (25–27), iodobenzene dichloride in warm acetic acid (16), or 3-chloroperoxybenzoic acid in aprotic solvents containing hydrogen chloride (28).

It has been proposed by Wang (29) that the formation of 5-bromouracil analogs upon reaction of uracils with aqueous bromine proceeds via a 5-bromo-6-hydroxy-5,6-dihydro intermediate (**1**) that dehydrates to afford the 5-bromouracil. It was found that 5-bromo-6-hydroxy-5,6-dihydrouracil (**1***a*) dehydrated to 5-bromouracil in less than 10 min at room temperature. In contrast, only 10% dehydration of the 5-bromo-6-

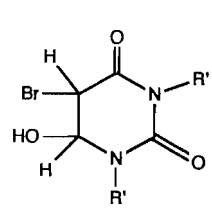

1*a*, R' = H; **1***b*, R' = CH_3

[1]Author to whom correspondence may be addressed. Telephone: (403) 492-5993. Fax: (403) 492-1217.

Can. J. Chem. Downloaded from www.nrcresearchpress.com by 85.192.166.187 on 09/08/12
For personal use only.

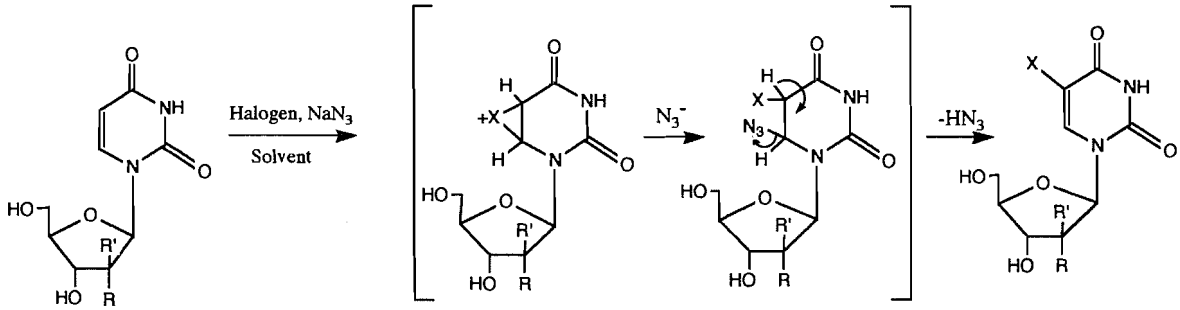

2, R = R' = H
5, R = OH, R' = H
6, R = H, R' = OH

3

4*a*, R = R' = H, X = I
4*b*, R = R' = H, X = Br
4*c*, R = R' = H, X = Cl
7*a*, R = OH, R' = H, X = I
7*b*, R = OH, R' = H, X = Br
7*c*, R = OH, R' = H, X = Cl
8*a*, R = H, R' = OH, X = I
8*b*, R = H, R' = OH, X = Br
8*c*, R = H, R' = OH, X = Cl

SCHEME 1

hydroxy-5,6-dihydro derivative of uridine to give 5-bromouridine was observed in 24 h at room temperature. However, when the 5,6-dihydro derivative of uridine was heated on a steam bath, it was quantitatively dehydrated to yield 5-bromouridine. It was observed by Moore and Anderson (30) that the conversion of 5-bromo-6-hydroxy-5,6-dihydrouracil to 5-bromouracil was accelerated by heating or by acid catalysis. The existence of the 5-bromo-6-hydroxy-5,6-dihydrouracil intermediate (**1***b*) was later confirmed by Tee and Banerjee, using ^{1}H NMR spectroscopy (31). 5-Iodo-6-hydroxy-5,6-dihydrouridine was the major product obtained upon reaction of uridine with iodine monochloride in aqueous DMF, along with the minor product 5-iodouridine (32). A 5-iodo-6-methoxy-5,6-dihydro derivative was formed in appreciable yield during the C-5 iodination of 3′,5′-protected-2′-fluoro-2′-deoxyuridine using iodine monochloride in methanol, and on further heating at reflux temperature was converted to the desired 5-iodo-2′-fluoro-2′-deoxyuridine analog (33). A similar reaction of bromine with a 2′,3′-protected uridine in methanol has also been reported to give 5-bromo-6-methoxy-5,6-dihydrouridine (34). During the C-5 chlorination of 2′-fluoro-2′-deoxyuridine with chlorine in acetic acid, 5-chloro-6-acetoxy-5,6-dihydro-1-(2-fluoro-2-deoxy-β-D-ribofuranosyl)uracil was obtained as the major product, which was subsequently converted to 5-chloro-2′-fluoro-2′-deoxyuridine by treatment with aqueous or methanolic ammonia (24). These studies suggest that the electrophilic halogenation of uracil nucleoside derivatives in the presence of water, alcohol, or acetic acid proceeds via a 5-halo-6-hydroxy (alkoxy or acetoxy)-5,6-dihydro intermediate that requires heating or acid–base catalysis for conversion to the 5-halouracil nucleoside. These results indicate that 5-halo-6-hydroxy (alkoxy or acetoxy)-5,6-dihydro derivatives of uracil nucleosides are relatively stable, and that the stability of the 5,6-dihydro intermediate is dependent upon the C-6 substituent.

We now report a mild and efficient procedure for the C-5 halogenation (iodination, bromination, or chlorination) of 2′-deoxyuridine (**2**), uridine (**5**), and arabinouridine (**6**) that proceeds via a 5-halo-6-azido-5,6-dihydro intermediate (**3**) (Scheme 1). The halogenation of **2**, **5**, and **6** was effected using iodine monochloride, or *N*-bromo (or chloro)succinimide, and sodium azide in acetonitrile or 1,2-dimethoxyethane at 0–45°C. The results are summarized in Table 1.

Reaction of 2′-deoxyuridine (**2**), uridine (**5**), or arabinouridine (**6**) with 2.5 mol equiv. of iodine monochloride (ICl) and 4.0 mol equiv. of sodium azide (NaN_3) in acetonitrile at 25°C afforded the corresponding 5-iodo product **4***a*, **7***a*, or **8***a* in 90–96% isolated yields. The corresponding 5-bromo analogs **4***b*, **7***b*, and **8***b* were synthesized in high yield using *N*-bromosuccinimide (NBS) and NaN_3 in 1,2-dimethoxyethane (DME) at 25°C for 24 h. A similar chlorination reaction of **2**, **5**, and **6** using *N*-chlorosuccinimide (NCS) and NaN_3 in DME at 45°C gave the 5-chloro products **4***c*, **7***c*, and **8***c* in 84, 45, and 65% yields, respectively. The chlorination of **2**, **5**, and **6** using NCS and NaN_3 in DME at 25°C proceeded slowly. The 5-chloro-6-azido-5,6-dihydro intermediates are significantly more stable at 25°C than the corresponding 5-iodo (or bromo)-6-azido-5,6-dihydro intermediates. Increasing the reaction temperature from 25°C to 45°C accelerated the rate of the chlorination reaction and the conversion of the 5-chloro-6-azido-5,6-dihydro intermediate to the 5-chloro product. These results suggest the enhanced stability of the 5-chloro-6-azido-5,6-dihydro intermediate, relative to the bromo and iodo analogs, is dependent upon the steric size of the halogen atom at the C-5 position and (or) the relative configurations at the C-5 and C-6 positions. Iodination or bromination of 2′-deoxyuridine (**2**) with ICl or NBS, in the absence of NaN_3, gave a low yield of the respective products. In contrast, chlorination of **2** using NCS, in the absence of NaN_3, did not occur, which indicates that an azido group at the C-6 position plays an important role in these C-5 halogenation reactions. The azido group at the C-6 position of these 5-halo-6-azido-5,6-dihydro intermediates is an excellent leaving group for regeneration of the 5,6-olefinic bond and it provides an attractive alternative to C-6 OH, OMe, or OAc substituents.

The C-5 halogenation of uracil nucleosides using an electrophilic halogen reagent and sodium azide proceeded efficiently under mild reaction conditions. Halogenation of the uracil nucleosides **2**, **5**, and **6** using this methodology in MeCN or DME was assumed to occur via a 5-halo-6-azido-5,6-dihydro intermediate (**3**) as illustrated in Scheme 1. Subsequent elimination of HN_3 would then afford the 5-halogeno products. The 5-

Can. J. Chem. Downloaded from www.nrcresearchpress.com by 85.192.166.187 on 09/08/12
For personal use only.

TABLE 1. C-5 halogenation of 2′-deoxyuridine (**2**), uridine (**5**), arabinouridine (**6**), and 3′,5′-di-*O*-acetyl-2′-deoxyuridine (**9**)[a]

Entry	Substrate	Halogenation reagents (mol equiv.)	NaN_3 (mol equiv.)	Solvent	Temp. (°C)	Time (h)	Product (yield, %)[b]
1	**2**	ICl (2.5)	4.0	CH_3CN	25	24.0	**4***a* (96)
2	**2**	ICl (2.0)	0	CH_3CN	25	24.0	**4***a* (20)[c]
3	**5**	ICl (2.5)	4.0	CH_3CN	25	24.0	**7***a* (93)
4	**6**	ICl (2.5)	4.0	CH_3CN	25	36.0	**8***a* (90)
5	**2**	NBS (1.1)	3.0	DME	0	12.0	**4***b* (68)
6	**2**	NBS (1.1)	4.0	DME	25	24.0	**4***b* (90)
7	**2**	NBS (1.1)	0	DME	25	20.0	**4***b* (60)[d]
8	**5**	NBS (1.1)	4.0	DME	25	24.0	**7***b* (95)
9	**6**	NBS (1.3)	4.0	DME	25	24.0	**8***b* (95)
10	**2**	NCS (4.0)	8.0	DME	25	48.0	**4***c* (35)[d]
11	**2**	NCS (4.0)	8.0	DME	45	8.0	**4***c* (84)
12	**5**	NCS (4.0)	8.0	DME	25	48.0	**7***c* (15)[d]
13	**5**	NCS (4.0)	8.0	DME	45	12.0	**7***c* (45)[d]
14	**6**	NCS (4.0)	8.0	DME	25	48.0	**8***c* (25)[d]
15	**6**	NCS (4.0)	8.0	DME	45	12.0	**8***c* (65)
16	**9**	ICl (2.5)	4.0	CH_3CN	25	48.0	**11***a* (94)
17	**9**	ICl (1.5)	3.0	CH_3CN	0	12.0	**11***a* (0)[d]
18	**9**	ICl (2.0)	4.0	CH_3CN	25	24.0	**11***a* (85)
19	**9**	NBS (1.0)	4.0	DME	0	1.0	**11***b* (20)
20	**9**	NBS (1.1)	4.0	DME	25	24.0	**11***b* (95)
21	**9**	NCS (4.0)	8.0	DME	25	48.0	**11***c* (50)[d]
22	**9**	NCS (4.0)	8.0	DME	45	3.0	**11***c* (89)

[a]Halogenation reactions were effected using 0.1 mmol of **2**, **5**, **6**, or **9** at 0–45°C.
[b]Isolated yield of purified product.
[c]Several products were formed (TLC analysis), some starting material and cleavage product (5-iodouracil) were isolated.
[d]Some starting material remained.

bromo (or iodo)-6-azido-5,6-dihydro intermediate product was isolated in 75 and 29% yields, respectively when 3′,5′-di-*O*-acetyl-2′-deoxyuridine (**9**) was allowed to react with ICl, or NBS, and NaN_3 at a reaction temperature of 0 to −5°C (Scheme 2). The addition of halogenoazides to unsymmetrical olefins has been reported to favor an unsymmetrical bridged halonium intermediate (35, 36) of the type illustrated in Scheme 2. The isolation of the 5-halo-6-azido-5,6-dihydro products (**10***a*,*b*), which existed as a mixture of two diastereomers that differ in configuration at the C-5 and (or) C-6 positions, confirmed the reaction mechanism for the formation of the C-5 halogenated pyrimidine nucleosides prepared using the methodology described. The configuration at the C-5 and C-6 positions ($J_{5,6}$ = 3.0 Hz) was not elucidated for **10***a*, **10***b* since these chiral centers are removed upon regeneration of the 5,6-olefinic bond.

Similar halogenations of 3′,5′-di-*O*-acetyl-2′-deoxyuridine (**9**) could also be effected using an electrophilic halogen reagent and sodium azide in MeCN or DME at 25–45°C. Thus, treatment of **9** with 2.5 mol equiv. of ICl and 4.0 mol equiv. of NaN_3 in MeCN at 25°C proceeded well and gave an excellent yield of 3′,5′-di-*O*-acetyl-5-iodo-2′-deoxyuridine (**11***a*, 94% isolated yield). 3′,5′-Di-*O*-acetyl-5-bromo-2′-deoxyuridine (**11***b*) was synthesized in 95% yield using NBS and NaN_3 in DME at 25°C for 24 h. A similar chlorination of **9** using NCS and NaN_3 in DME at 45°C afforded 3′,5′-di-*O*-acetyl-5-chloro-2′-deoxyuridine (**11***c*) in 89% yield.

In summary, the new and facile halogenation methods described herein have several advantages over most procedures currently available. These advantages include readily available reagents, mild reaction conditions (25–45°C), facile isolation procedures, and high product yields. This methodology avoids the use of acidic and (or) high reaction temperature conditions, which results in the decomposition of labile substrates. This methodology is applicable to the radioiodination (^{123}I, ^{125}I, ^{131}I) of uracil nucleosides and the potential halogenation of oligonucleosides under mild conditions. Robins et al. (17) developed an efficient method for the synthesis of 3′,5′-di-*O*-acetylated and unprotected 5-halouracil nucleosides using elemental iodine, or a metal halogenide (LiI, LiBr, LiCl) and CAN at 80°C. Our methodology provides marginally higher yields using the unprotected uracil nucleosides, and similar yields using 3′,5′-di-*O*-acetyl-2′-deoxyuridine (**9**). Although the Robins procedure is efficient for the chlorination of **9**, chlorination of 2′-deoxyuridine afforded multiple and (or) decomposition products. Halogenated solvents such as dichloromethane must not be used in this methodology since its reaction with sodium azide may lead to potentially explosive polyazidomethane (37, 38).

Experimental

Melting points were determined with a Buchi capillary apparatus and are uncorrected. Nuclear magnetic resonance spectra (^1H NMR, ^{13}C NMR) were determined on a Bruker AM-300 spectrometer using Me_4Si as an internal standard (^1H NMR). The assignment of all exchangeable protons (OH, NH) was confirmed by the addition of D_2O. ^{13}C NMR spectra were acquired using the *J* modulated spin echo technique where methyl and methine carbon resonances appear as positive peaks, and methylene and quaternary carbon resonances appear as negative peaks. Microanalyses were within ±0.4% of theoretical values for all elements listed, unless otherwise indicated. Silica gel column chromatography was carried out using Merck 7734 (60–200 mesh) silica gel. 3′,5′-Di-*O*-acetyl-2′-deoxyuridine (**9**) was prepared according to the reported procedure (39). 2′-Deoxyuridine (**2**), uridine (**5**), and arabinouridine (**6**) were purchased from the Aldrich Chemical Co.

5-Iodo-2′-deoxyuridine (4a)

Iodine monochloride (40 mg, 0.25 mmol) was added slowly during a 5 min period to a suspension of sodium azide (26 mg, 0.4 mmol) in

Can. J. Chem. Downloaded from www.nrcresearchpress.com by 85.192.166.187 on 09/08/12
For personal use only.

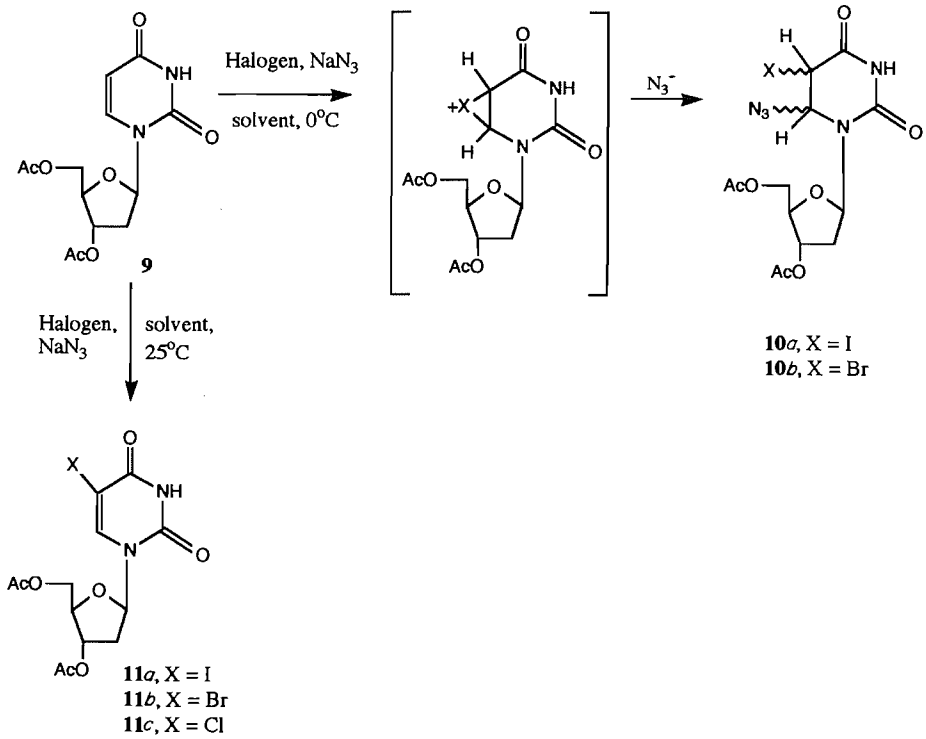

SCHEME 2

acetonitrile (10 mL) at ice-bath temperature with stirring. This mixture was stirred for a further 5 min, a solution of **2** (22.8 mg, 0.1 mmol) in acetronitrile (10 mL) was added and the reaction was warmed to 25°C and stirred for 24 h. Removal of the solvent in vacuo (bath temperature 50°C) and purification of the residue obtained by elution from a silica gel column using chloroform–methanol (85:15, v/v) as eluent afforded **4***a* (34 mg, 96%) (entry 1, Table 1), mp 170–180°C (dec.) (lit. (13) mp 160–180°C (dec.)). The ^{1}H NMR spectrum for **4***a* was identical to that reported (13).

5-Bromo-2′-deoxyuridine (4b)

N-Bromosuccinimide (NBS, 20 mg, 0.11 mmol) was added at 25°C to a suspension prepared by mixing a solution of **2** (22.8 mg, 0.1 mmol) in 1,2-dimethoxyethane (15 mL) with a solution of sodium azide (26 mg, 0.4 mmol) in water (0.1 mL). After stirring the reaction mixture for 24 h at 25°C, the solvent was removed in vacuo (bath temperature 45°C) and the residue was purified by silica gel column chromatography using chloroform–methanol (90:10, v/v) as eluent to give **4***b* (28 mg, 90%) as a solid (entry 6, Table 1), mp 175–179°C (dec.) (lit. (41) mp 187–189°C (dec.)). The ^{1}H NMR spectrum for **4***b* was identical to that reported (41).

5-Chloro-2′-deoxyuridine (4c)

N-Chlorosuccinimide (NCS, 26.6 mg, 0.2 mmol) was added at 25°C to a suspension prepared by mixing a solution of **2** (22.8 mg, 0.1 mmol) in 1,2-dimethoxyethane (10 mL) with a solution of sodium azide (26 mg, 0.4 mmol) in water (0.1 mL) with a solution of sodium azide (26 mg, 0.4 mmol) in water (0.1 mL). The reaction mixture was stirred for 4 h at 45°C. Additional aliquots of NCS (0.2 mL) and sodium azide (0.4 mmol) were added to the reaction mixture. The reaction was allowed to proceed for 4 h at 45°C with stirring. Removal of the solvent in vacuo (bath temperature 45°C) gave a residue that was purified by silica gel column chromatography using chloroform–methanol (90:10, v/v) as eluent to yield **4***c* (22 mg, 84%) as a solid (entry 11, Table 1), mp 173–176°C (lit. (42) mp 178–179.5°C)). The ^{1}H NMR spectrum for **4***c* was identical to the reported spectral data (42).

Iodination of nucleosides 5 and 6

A mixture of **5** or **6** (0.1 mmol), iodine monochloride (0.25 mmol), sodium azide (0.4 mmol), and acetonitrile (10 mL) was stirred at 25°C. After iodination was complete, the products were isolated by column chromatography as described for **4***a*.

5-Iodouridine (7a)

The white solid product was recrystallized from MeOH to give 35 mg (93%) of **7***a* (entry 3, Table 1), mp 207–209°C (dec.) (lit. (12) mp 205–208°C (dec.)).

5-Iodoarabinouridine (8a)

The white solid was recrystallized from MeOH to give 33 mg (90%) of **8***a* (entry 4, Table 1), mp 190–197°C (dec.) (lit. (43) mp 224–227°C (dec.)); ^{1}H NMR (DMSO-d_6) δ: 3.54–3.68 (m, 2H, H-5′), 3.70–3.78 (m, 1H, H-4′), 3.90–4.06 (m, 2H, H-2′, H-3′), 5.18, (t, $J_{5',OH}$ = 4.0, $J_{5'',OH}$ = 4.0 Hz, 1H, 5′-OH), 5.50 and 5.64 (2 br s, 1H each, 2′-OH, 3′-OH), 5.96 (d, $J_{1',2'}$ = 4.5 Hz, 1H, H-1′), 8.10 (s, 1H, H-6), 11.68 (s, 1H, NH). Anal. calcd. for $C_9H_{11}IN_2O_6$: C 29.20, H 2.99, N 7.57; found: C 29.36, H 2.69, N 7.85.

Bromination of nucleosides 5 and 6

A mixture of **5** or **6** (0.1 mmol), *N*-bromosuccinimide, sodium azide, and 1,2-dimethoxyethane (see Table 1) was stirred at 25°C for 24 h. After the bromination reaction was complete, the products were isolated by column chromatography as described for **4***b*.

5-Bromouridine (7b)

This compound was obtained in 95% yield (entry 8, Table 1), mp 190–198°C (dec. (lit. (18) mp 181–184°C (dec.)).

5-Bromoarabinouridine (8b)

This compound was obtained in 95% yield (entry 9, Table 1), mp 182–187°C (dec.) (lit. (43) mp 195–198°C (dec.)); ^{1}H NMR (DMSO-d_6) δ: 3.56–3.66 (m, 2H, H-5′), 3.70–3.80 (m, 1H, H-4′), 3.90–4.08 (m, 2H, H-2′, H-3′), 5.20, 5.52, 5.68 (3 br s, 1H each, 5′-OH, 3′-OH, 2′-OH), 5.96 (d, $J_{1',2'}$ = 4.5 Hz, 1H, H-1′), 8.06 (s, 1H, H-6). Anal. calcd. for $C_9H_{11}BrN_2O_6$: C 33.45, H 3.42, N 8.67; found: C 33.25, H 3.78, N 9.04.

Chlorination of nucleosides 5 and 6

A mixture of **5** or **6** (0.1 mmol), *N*-chlorosuccimide (NCS,

Can. J. Chem. Downloaded from www.nrcresearchpress.com by 85.192.166.187 on 09/08/12
For personal use only.

Can. J. Chem. Downloaded from www.nrcresearchpress.com by 85.192.166.187 on 09/08/12
For personal use only.

0.2 mmol), sodium azide (0.4 mmol), and 1,2-dimethoxyethane (10 mL) was stirred at 45°C for 6 h. Additional aliquots of NCS (0.2 mmol) and sodium azide (0.4 mmol) were added to the reaction mixture, which was stirred at 45°C for an additional 6 h. The products were purified by silica gel column chromatography as described for **4***c*.

5-Chlorouridine (7c)

Compound **7***c* was obtained in 45% yield (entry 13, Table 1), mp 215–220°C (dec.) (lit. (27) mp 220–223°C (dec.)).

5-Chloroarabinouridine (8c)

Compound **8***c* was obtained in 65% yield (entry 15, Table 1), mp 224–230°C (dec.) (lit. (43) mp 235–237°C (dec.)); ^{1}H NMR (DMSO-d_6) δ: 3.55–3.67 (m, 2H, H-5′), 3.70–3.80 (m, 1H, H-4′), 3.90–4.07 (m, 2H, H-2′, H-3′), 5.20, 5.60, 5.68 (3 br s, 1H each, 5′-OH, 3′-OH, 2′-OH), 5.97 (d, J = 4.5 Hz, 1H, H-1′), 8.06 (s, 1H, H-6), 11.60 (s, 1H, NH). Anal. calcd. for $C_9H_{11}ClN_2O_6$: C 38.78, H 3.97, N 10.05; found: C 38.76, H 3.98, N 10.22.

5-Iodo-6-azido-5,6-dihydro-3′,5′-di-O-acetyl-2′-deoxyuridine (10a)

A mixture of **9** (31.2 mg, 0.1 mmol), sodium azide (20 mg, 0.3 mmol), iodine monochloride (24 mg, 0.15 mmol), and acetonitrile (10 mL) was stirred at −5°C for 12 h. Evaporation of the solvent, work-up and purification of crude product as described for **11***a* yielded **10***a* (14 mg, 29%) as solid and unreacted starting material (**9**). Compound **10***a* was obtained as a mixture of two diastereomers, which could not be separated by silica gel column chromatography; mp 100–105°C (dec.); ^{1}H NMR ($CDCl_3$) (mixture of two diastereomers in a ratio of 2:1) δ: 2.10 and 2.12 (2 s, 3H each, CH_3CO), 2.22–2.3 and 2.32–2.42 (2 m, 1H each, H-2′), 4.16–4.44 (complex m, 3H, H-4′, H-5′), 4.58 and 4.68 (2 d, $J_{5,6}$ = 3.0 Hz, 1H total, H-5), 5.14–5.20 (m, 1H, H-3′), 5.30 and 5.36 (2 d, $J_{5,6}$ = 3.0 Hz, 1H total, H-6), 6.17 and 6.30 (2 t, $J_{1',2'} = J_{1',2''}$ = 6.0 Hz, 1H, H-1′), 8.20 (s, 1H, NH). ^{13}C NMR ($CDCl_3$) δ: 13.15 and 15.37 (C-5), 20.89 (CH_3CO), 35.45 and 36.67 (C-2′), 63.87 and 63.96 (C-5′), 69.93 and 71.07 (C-6), 74.09 (C-3′), 81.61 and 81.88 (C-4′), 83.80 and 84.72 (C-1′), 149.45 and 149.63 (C-2), 165.45 and 165.70 (C-4), 170.41 and 170.15 (CH_3CO). Anal. calcd. for $C_{13}H_{16}IN_5O_7$: C 32.44, H 3.35, N 14.55; found: C 32.47, H 3.63, N 14.92.

5-Bromo-6-azido-5,6-dihydro-3′,5′-di-O-acetyl-2′-deoxyuridine (10b)

A mixture of **9** (31.2 mg, 0.1 mmol), *N*-bromosuccinimide (18 mg, 0.1 mmol), sodium azide (26 mg, 0.4 mmol) in water (0.1 mL), and 1,2-dimethoxyethane (10 mL) was stirred at 0°C for 1 h. Removal of the solvent in vacuo and purification of crude product by silica gel column chromatography with chloroform–methanol (98:2, v/v) as eluent afforded **10***b* (32 mg, 75%) as a solid. The compound **10***b* was obtained as a mixture of two diastereomers, which could not be separated by silica gel column chromatography; mp 140–142°C (dec.); ^{1}H NMR ($CDCl_3$) (mixture of two diastereomers in a ratio of 3:1) δ: 2.13 and 2.15 (2 s, 3H, each, CH_3CO), 2.16–2.26 and 2.32–2.46 (2 m, 1H each, H-2′), 4.20–4.48 (complex m, 4H, H-5, H-4′, H-5′), 5.17–5.22 (m, 1H, H-3′), 5.37 and 5.42 (2 d, $J_{5,6}$ = 3.0 Hz, 1H total, H-6), 6.18 and 5.34 (2 t, $J_{1',2'} = J_{1',2''}$ = 6.0 Hz, 1H total, H-1′), 7.54 (s, 1H, NH). ^{13}C NMR ($CDCl_3$) δ: 20.80 (CH_3CO), 35.64 and 36.47 (C-2′), 37.61 and 38.91 (C-5), 63.82 and 63.91 (C-5′), 68.76 and 69.51 (C-6), 74.06 (C-3′), 81.52 and 81.91 (C-4′), 83.86 and 84.70 (C-1′), 149.52 (C-2), 163.71 (C-4), 170.14 and 170.36 (CH_3CO). Anal. calcd. for $C_{13}H_{16}BrN_5O_7$: C 36.21, H 3.03, N 16.24; found: C 36.51, H 3.24, N 15.98.

5-Iodo-3′,5′-di-O-acetyl-2′-deoxyuridine (11a)

This compound was synthesized by the reaction of **9**, according to the iodination procedure reported for **4***a*. Purification of the residue obtained by elution from a silica gel column using chloroform–methanol (95:5, v/v) as eluent afforded **11***a* (41 mg, 94%) (entry 16, Table 1), mp 157–158°C (lit. (40) mp 158–160°C).

5-Bromo-3′,5′-di-O-acetyl-2′-deoxyuridine (11b)

Compound **11***b* was synthesized by the reaction of **9**, according to the bromination procedure reported for **4***b*. Purification of the residue obtained by silica gel column chromatography using chloroform–methanol (95:5, v/v) as eluent afforded **11***b* (37 mg, 95%) as a viscous oil that did not crystallize (entry 20, Table 1) (lit. (17) mp 152.5–153°C); ^{1}H NMR ($CDCl_3$) δ: 2.10–2.24 (m, 7H, H-2′, CH_3CO), 2.50–2.60 (m, 1H, H-2″), 4.26–4.44 (complex m, 3H, H-4′, H-5′), 5.20–5.26 (m, 1H, H-3′), 6.28 (t, $J_{1',2'} = J_{1',2''}$ = 6.0 Hz, 1H total, 1H, H-1′), 7.90 (s, 1H, H-6), 8.78 (s, 1H, NH). ^{13}C NMR δ: 20.73 (CH_3CO), 38.05 (C-2′), 63.66 (C-5′), 73.88 (C-3′), 82.55 (C-4′), 85.53 (C-1′), 97.29 (C-5), 138.59 (C-6), 149.66 (C-2), 158.89 (C-4), 170.09 (CH_3CO) and 170.30 (CH_3CO). Anal. calcd. for $C_{13}H_{15}BrN_2O_7$: C 39.91, H 3.86, N 7.16; found: C 39.84, H 3.83, N 7.08.

5-Chloro-3′,5′-di-O-acetyl-2′-deoxyuridine (11c)

Compound **11***c* was synthesized by the reaction of **9**, according to the chlorination procedure reported for **4***c*. Purification of the product as described for **11***b* yielded **11***c* (31 mg, 89%) as a viscous oil that did not crystallize (entry 22, Table 1) (lit. (17) mp 174.5–175°C); ^{1}H NMR ($CDCl_3$) δ: 2.10–2.26 (m, 7H, H-2′, CH_3CO), 2.50–2.62 (m, 1H, H-2″), 4.28–4.40 (complex m, 3H, H-4′, H-5′), 5.20–5.25 (m, 1H, H-3′), 6.30 (t, $J_{1',2'} = J_{1',2''}$ = 6.0 Hz, 1H total, H-1′), 7.88 (s, 1H, H-6), 8.80 (s, 1H, NH). Anal. calcd. for $C_{13}H_{15}ClN_2O_7$: C 45.03, H 4.36, N 8.08; found: C 45.08, H 4.70, N 8.08.

Acknowledgement

We are grateful to the Medical Research Council of Canada (Grant No. MT-12304) for financial support of this research.

1. (*a*) P.L. Stetson, D.P. Normolle, J.A. Knol, N.J. Johnson, Z. Yang, E. Sakmar, D. Prieskorn, P. Terrio, C.A. Knutsen, and W.D. Ensminger. J. Natl. Cancer Inst. **83**, 1659 (1991); (*b*) D.B. Davies. *In* Progress in nuclear magnetic resonance spectroscopy. Vol. 12. *Edited by* J.W. Emsley, J. Feeney, and L.H. Suteliffe. Pergamon Press, New York. 1978. pp. 135–225; (*c*) L. Goodman. *In* Basic principles in nucleic acid chemistry. Vol. 1. *Edited by* O.P. Ts'o. Academic Press, New York. 1974. pp. 146–152; (*d*) S. Uesugi and M. Ikehara. Chem. Pharm. Bull. **26**, 3040 (1978); (*e*) E. Harbers, N.K. Chaudhuri, and C. Heidelberger. J. Biol. Chem. **234**, 1255 (1959); (*f*) W.H. Prusoff. Cancer Res. **20**, 92 (1960); (*g*) S. Zamenhof, B. Reiner, R. De Giovanni, and K. Rich. J. Biol. Chem. **219**, 165 (1956); (*h*) D.B. Dunn and J.D. Smith. Biochem. J. **67**, 494 (1957).
2. (*a*) E. De Clercq, J. Balzarini, P.F. Torrence, M.P. Mertes, C.L. Schmidt, D. Shugar, P.J. Barr, A.S. Jones, G. Verhelst, and R.T. Walker. Mol. Pharmacol. **19**, 321 (1981); (*b*) E. De Clercq, J. Descamps, G. Verhelst, R.T. Walker, A.S. Jones, P.F. Torrence, and D. Shugar. J. Infect. Dis. **141**, 563 (1980); (*c*) W.H. Prusoff and P.H. Fischer. *In* Nucleoside analogues: chemistry, biology and medical applications. *Edited by* R.T. Walker, E. De Clercq, and F. Eckstein. NATO Adv. Study Inst. Ser. A: Vol. 26. 1979. pp. 281–318; (*d*) T.S. Lin, M.S. Chen, C. McLaren, Y.S. Gao, I. Ghazzouli, and W.H. Prusoff. J. Med. Chem. **30**, 440 (1987); (*e*) E. De Clercq. Arch. Int. Physiol. Biochim. **87**, 353 (1979).
3. A.V. Aerschot, D. Everaert, J. Balzarini, K. Augustyns, L. Jie, G. Janssen, O. Peeters, N. Blaton, C. De Ranter, E. De Clercq, and P. Herdewijn. J. Med. Chem. **33**, 1833 (1990).
4. (*a*) J.R. Mercer. Ph.D. Thesis. University of Alberta, Edmonton, 1985; (*b*) J.R. Mercer, L.H. Xu, E.E. Knaus, and L.I. Wiebe. J. Med. Chem. **32**, 1289 (1989).
5. Y. Kobayashi, I. Kumadaki, and K. Yamamoto. J. Chem. Soc. Chem. Commun. 536 (1977).
6. R. Kumar, L.I. Wiebe, E.E. Knaus, T.M. Allen, and M.L. Tempest. Drug Des. Discovery, **8**, 179 (1992).
7. T. Iwashina, D.R. Tovell, L. Xu, D.L. Tyrrell, E.E. Knaus, and L.I. Wiebe. Drug Des. Delivery, **3**, 309 (1988).
8. T.K. Bradshaw and D.W. Hutchinson. Chem. Soc. Rev. **6**, 43 (1977).
9. R.A. Long, R.K. Robins, and L.B. Townsend. J. Org. Chem. **32**, 2751 (1967).

10. S.G. Rahim, M.J.H. Duggan, R.T. Walker, A.S. Jones, R.L. Dyer, J. Balzarini, and E. De Clercq. Nucleic Acids Res. **10**, 5285 (1982).
11. T. Ueda. *In* Chemistry of nucleosides and nucleotides. Vol. 1. *Edited by* L.B. Townsend. Plenum Press. New York. 1988. pp. 1–95.
12. W.H. Prusoff, W.L. Holmes, and A.D. Welch. Cancer Res. **13**, 221 (1953).
13. W.H. Prusoff. Biochim. Biophys. Acta, **32**, 295 (1959).
14. R.M.K. Dale, D.C. Ward, D.C. Livingston, and E. Martin. Nucleic Acids Res. **2**, 915 (1975).
15. D. Lipkin, F.B. Howard, D. Nowotny, and M. Sano. J. Biol. Chem. **238**, 2249 (1963).
16. M.J. Robins, P.J. Barr, and J. Giziewicz. Can. J. Chem. **60**, 554 (1982).
17. J. Asakura and M.J. Robins. J. Org. Chem. **55**, 4928 (1990).
18. P.A. Levene and F.B. La Forge. Chem. Ber. **45**, 608 (1912).
19. R.E. Beltz and D.W. Visser. J. Am. Chem. Soc. **77**, 736 (1955).
20. D.W. Visser. *In* Synthetic procedures in nucleic acid chemistry. Vol. 1. *Edited by* W.W. Zorbach and R.S. Tipson. Wiley, New York. 1968. p. 409.
21. J. Duval and J.P. Ebel. Bull. Soc. Chim. Biol. **46**, 1059 (1964).
22. T.S. Lin, J.H. Yang, M.C. Liu, Z.Y. Shen, Y.C. Cheng, W.H. Prusoff, G.I. Birnbaum, J. Giziewicz, I. Ghazzouli, V. Brankovan, J.S. Feng, and G.D. Hsiung. J. Med. Chem. **34**, 693 (1991).
23. T.K. Fukuhara and D.W. Visser. J. Am. Chem. Soc. **77**, 2393 (1955).
24. J.R. Mercer, E.E. Knaus, and L.I. Wiebe. J. Med. Chem. **30**, 670 (1987).
25. R.A. West and H.W. Barrett. J. Am. Chem. Soc. **76**, 3146 (1954).
26. B.C. Pal. J. Am. Chem. Soc. **100**, 5170 (1978).
27. K. Kikugawa, I. Kawada, and M. Ichino. Chem. Pharm. Bull. **23**, 35 (1975).
28. E.K. Ryu and M. MacCoss. J. Org. Chem. **46**, 2819 (1981).
29. S.Y. Wang. J. Org. Chem. **24**, 11 (1959).
30. A.M. Moore and S.M. Anderson. Can. J. Chem. **37**, 590 (1959).
31. O.S. Tee and S. Banerjee. Can. J. Chem. **57**, 626 (1979).
32. H. Yoshida, J. Duval, and J.P. Ebel. Biochim. Biophys. Acta, **161**, 13 (1968).
33. K.W. Morin, L.I. Wiebe, and E.E. Knaus. Carbohydr. Res. **259**, 109 (1993).
34. J.M.J. Tronchet, K. Mekhael. J.G. Poncet, R. Benhamza, and M. Geoffroy. Helv. Chim. Acta, **68**, 1893 (1985), and references therein.
35. D.R. Dalton, V.P. Dutta, and D.C. Jones. J. Am. Chem. Soc. **90**, 5498 (1968).
36. A. Hassner, F.P. Boerwinkle, and A.B. Levy. J. Am. Chem. Soc. **92**, 4879 (1970).
37. A. Hassner and M. Stern. Angew. Chem. Int. Ed. Engl. **25**, 479 (1986).
38. A. Hassner, M. Stern, H.E. Gottlieb, and F. Frolow. J. Org. Chem. **55**, 2304 (1990).
39. M.J. Robins, M. MacCoss, S.R. Naik, and G. Ramani. J. Am. Chem. Soc. **98**, 7381 (1978).
40. P.K. Chang and A.D. Welch. J. Med. Chem. **6**, 428 (1963).
41. R.E. Beltz and D.W. Visser. J. Am. Chem. Soc. **77**, 736 (1955).
42. D.W. Visser, D.M. Frisch, and B. Huang. Biochem. Pharmacol. **5**, 157 (1960).
43. K. Ono, M. Ogasawara, A. Ohashi, A. Matsukage, T. Takahashi, C. Nakayama, and M. Saneyoshi. Biochemistry, **21**, 1019 (1982).

Can. J. Chem. Downloaded from www.nrcresearchpress.com by 85.192.166.187 on 09/08/12
For personal use only.

Excited state acid catalysis of the 2 + 2 photocycloaddition of methyl 2-naphthoate and acetylacetone; the interaction of a nonfluorescent exciplex with H_2SO_4

YUAN L. CHOW[1] AND CARL I. JOHANSSON
The Department of Chemistry, Simon Fraser University, Burnaby, BC V5A 1S6, Canada
Received June 2, 1994

YUAN L. CHOW and CARL I. JOHANSSON. Can. J. Chem. **72**, 2011 (1994).

In this paper, the striking acid catalysis of the photocycloaddition of methyl 2-naphthoate (2MN) to acetylacetone (AA) to give **1** and **2** was traced to the enhanced conversion of the nonemissive *(2MN–AA) exciplex to **1** and **2** by H_2SO_4. The partial reversibility of the exciplex in CH_3CN and CH_3OH was established by extended fluorescence-quenching analysis using oxygen to perturb the system, whereas time-resolved fluorescence kinetics failed to reveal the presence of this exciplex. A similar analytical method demonstrated the interaction of the nonfluorescent *(2MN–AA) exciplex and H_2SO_4 with the rate constants of $k_{ap} = (2 \pm 1) \times 10^9$ M^{-1} s^{-1} in CH_3CN and $(4 \pm 1) \times 10^9$ M^{-1} s^{-1} in CH_3OH. The quantum yield of photocycloadducts was significantly enhanced at high 2MN conversions owing to the retardation of the competing excimer $*(2MN)_2$ formation. In the range of low conversion (<15%) and $[H_2SO_4] \leq 1$ mM, the quantum yield was shown to be proportional to H_2SO_4 concentration; the slope from such plots was analyzed to give k_{ap} values similar to those obtained from the extended fluorescence-quenching analysis. This agreement, along with the elimination of other potential acid catalytic routes, unambiguously proves that the acid catalysis originates from the interaction of the *(2MN–AA) exciplex with H_2SO_4.

YUAN L. CHOW et CARL I. JOHANSSON. Can. J. Chem. **72**, 2011 (1994).

Dans ce travail, on identifie que la catalyse acide remarquable de la photocycloaddition du 2-naphtoate de méthyle (2MN) à l'acétylacétone (AA) conduisant aux composés **1** et **2** est causée par une conversion plus importante de l'exciplexe non radiatif *(2MN–AA) en **1** et en **2** sous l'influence de H_2SO_4. On a mis en évidence la réversibilité partielle de l'exciplexe dans le CH_3CN et le CH_3OH en procédant à une analyse de la désactivation de la fluorescence étendue en utilisant de l'oxygène pour perturber le système alors que la cinétique de la fluorescence résolue en fonction du temps n'a pas révélé la présence de cet exciplexe. Une méthode analytique semblable a permis de démontrer l'existence de l'interaction de l'exciplexe non fluorescent *(2MN–AA) et du H_2SO_4 qui ont des constantes de vitesse de $k_{ap} = (2 \pm 1) \times 10^9$ M^{-1} s^{-1} dans le CH_3CN et de $(4 \pm 1) \times 10^9$ M^{-1} s^{-1} dans le CH_3OH. Dû à une retardement de la formation de l'excimère compétitif $*(2MN)_2$, le rendement quantique des photocycloadduits est grandement augmenté à des conversions élevées de 2MN. À de faibles taux de conversion (<15%) et $[H_2SO_4] \leq 1$ mM, on a démontré que le rendement quantique est proportionnel à la concentration en H_2SO_4; on a analysé la pente de telles courbes pour obtenir des valeurs de k_{ap} semblables à celles obtenues à partir de l'analyse de la désactivation de la fluorescence étendue. Cet accord, pris de concert avec l'élimination des autres routes catalytiques acides potentielles, prouve d'une façon non ambiguë que la catalyse acide trouve son origine dans l'interaction de l'exciplexe *(2MN–AA) avec H_2SO_4.

[Traduit par la rédaction]

Introduction

Upon absorption of light in the UV and visible region there are profound changes in a compound's electronic distribution where this difference may result in an acidity or basicity change from a few to tens of pK_a units (1). Such changes in acidity or basicity can be manipulated to promote reactions or initiate new chemistry. Indeed, a number of groups have taken advantage of the enhanced acidity or basicity in the excited state to promote difficult molecular transformations with high selectivity and regiospecificity (2–4). Mechanistic studies have shown that acid–base reactions can occur with either the excited state species (2) or an intermediate derived from the excited state species (3). The excited state acid–base behaviour is a general phenomenon and its utility has been discussed in a recent review (4).

We have shown that singlet excited naphthoate esters undergo 2 + 2 cycloaddition presumably with the acetylacetone (AA) *cis*-enol tautomer to give adduct **1** and a trace amount (5) of **2** through a cycloaddition intermediate, such as **3**. In the presence of a trace amount (>0.5 mM) of acid, **2** became the major product and this cycloaddition became a synthetically useful reaction when the low quantum yield was enhanced by about an order of magnitude in the presence of Brønsted acids at the millimolar level, wherein H_2SO_4 gave the largest enhancement (5).

Singlet excited state methyl 2-naphthoate (*2MN) has been shown, through product and emission studies (5–7), to interact with H_2SO_4 and AA in CH_3CN and CH_3OH. The fluorescence of *2MN is quenched by H_2SO_4, through associative interaction resulting in the formation of emissive $*2MNH^+$ species by a partially reversible reaction in CH_3CN and a fully reversible reaction in CH_3OH (6). While steady-state as well as time-resolved fluorimetry has demonstrated that the fluorescent $*2MNH^+$ intermediate interacts with AA in both CH_3CN and CH_3OH (6), this pathway has been shown not to be responsible for the acid enhancement of the formation of **1** and **2**, since the quantum yield of photocycloaddition computed from the rate constants gained from fluorimetry can account for, at most, only a small fraction of the observed value (6). The association of *2MN with an acid is therefore most likely an energy-wasting process, or a minor route to **1** and **2** at best. In the concentration range for preparative photocycloaddition (0.01 – 0.1 M), *2MN in CH_3CN forms a weakly fluorescing excimer, which could be quenched by H_2SO_4 but not by AA (7). Examples exist where an excimer could play a key role in photoreactions (8). In the present case, the 2MN excimer is formed with full reversibility, the reverse reaction being so fast that the excimer quenching by H_2SO_4 could not notice-

[1]Author to whom correspondence may be addressed.

Can. J. Chem. Downloaded from www.nrcresearchpress.com by 85.192.166.187 on 09/08/12
For personal use only.

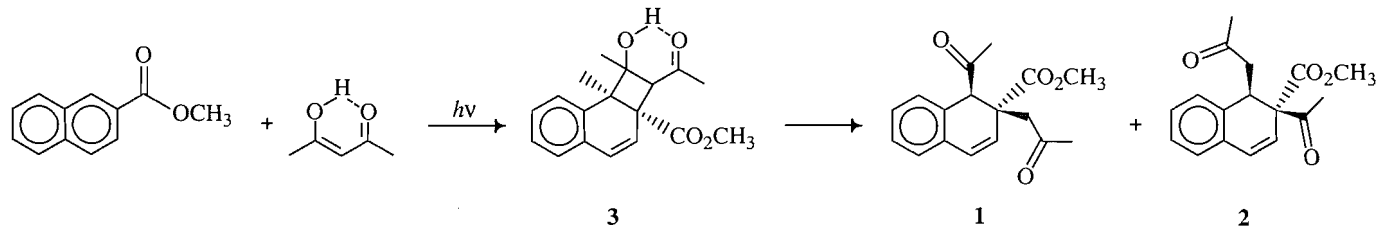

3 1 2

ably contribute to acid catalysis of the formation of **1** and **2** (7).

It is also possible that the observed acid catalysis has nothing to do with excited species but arises from acid catalysis of the ground state intermediates, such as **3** and its analogues, to promote the product formations. This line of enquiries was not pursued on account of the lack of acid effects on the photocycloaddition of AA to cyclohexene; in this case a cyclobutane analogous to **3** is the intermediate (6).

The overall mechanism of the reaction of *2MN in the presence of AA and H_2SO_4 is summarized in Scheme 1, which contains known processes determined previously (EE and EP pathways (5–7), and the reaction pathway to be discussed in this paper (EA pathway). To avoid complexity, the sum of all first-order reactions for an intermediate is represented as Σk_{e1}, Σk_{p1}, Σk_{d1}, and Σk_{a1}, each of which includes the rate constant of fluorescence (k_f) for the respective species. While it has been suspected that the *(2MN–AA) exciplex could be responsible for the acid catalysis by reacting with H_2SO_4, its lack of fluorescence has prevented access to examine this possibility. In this paper, we describe the detailed kinetic analysis of both fluorescence-quenching and product quantum yield studies that identified the EA pathway as the acid catalysis route. In addition, this paper describes the use of an "extended fluorescence-quenching analysis" on the quenching of 2MN fluorescence to probe this nonemitting exciplex.

Experimental section

Steady-state and dynamic fluorescence study

CH_3CN (BDH, spectrograde), CH_3OH (Mallinckrodt, SpectrAL), cyclohexane, dioxane (Fisher, spectrograde), ethyl ether (Caledon, anhydrous), 2-propanol (Fisher), and H_2SO_4 (Fisher, ACS reagent grade) were used as received. 2MN preparation and AA (Aldrich, 99+%) purification have been discussed previously (6).

Fluorescence-quenching spectra were recorded on either a Perkin–Elmer MPF-44B or Photon Technology International (PTI, South Brunswick, N.J.) LS-100 fluorimeter employing a right-angle cell arrangement at room temperature (25°C). Fluorescence-quenching experiments were performed as previously described (6, 7). Weak exciplex emission was checked for by normalizing the spectra at 2MN's fluorescence λ_{max} such that any change in the emission profile on the low-energy side could be visually inspected. For fluorescence quenching at 77 K (liquid nitrogen), the MPF-44B phosphorescence accessory (Hitachi) was attached with the chopper removed. The low-temperature glass was made from a mixture of 2-propanol and ethyl ether (1:3 v/v) with [2MN] = 0.3 mM and [AA] ranging from 0 to 0.4 M. The fluorimetry cell was a quartz tube with an i.d. of 3 mm. The samples were excited at 338 nm (room temperature) or 335 nm (77 K) and the fluorescence intensity was corrected for the percentage excitation light absorption by AA (9). Fluorescence decay measurements of *2MN were determined by a time-correlated single-photon counting method (10) and described elsewhere (6).

Product quantum yields

The quantum yield measurement method was similar to that previously described (5*a*) except that RPR 3500 Å lamps (16 × 24 W)

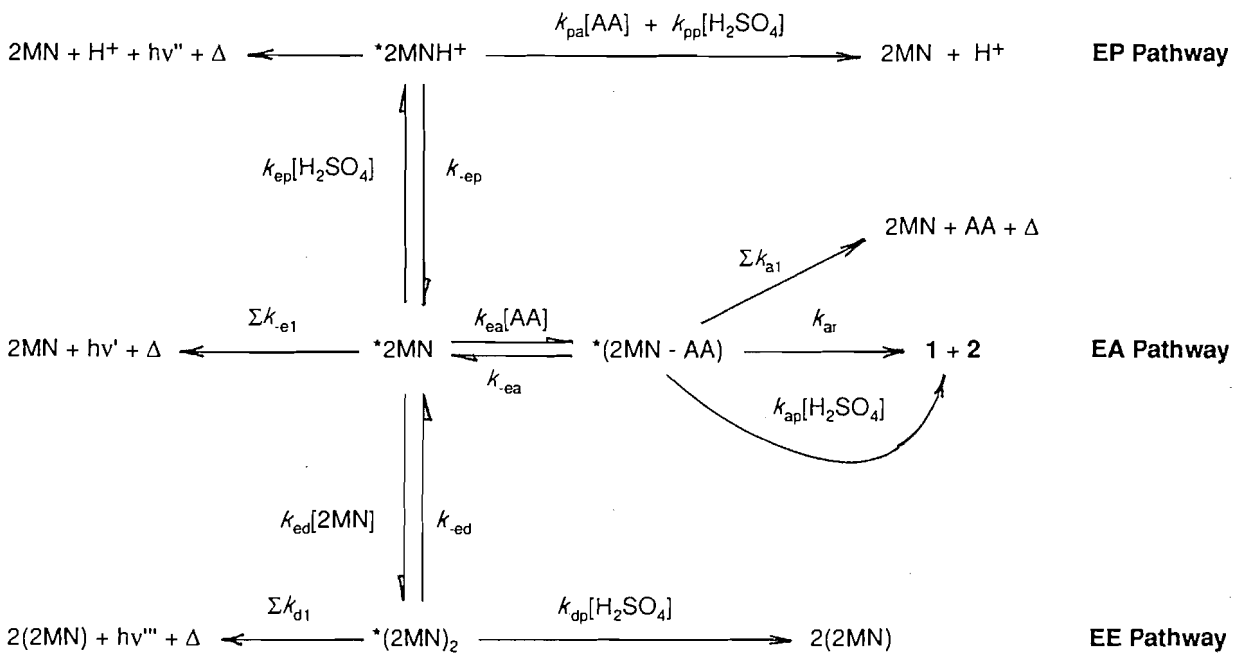

SCHEME 1

Can. J. Chem. Downloaded from www.nrcresearchpress.com by 85.192.166.187 on 09/08/12
For personal use only.

Can. J. Chem. Downloaded from www.nrcresearchpress.com by 85.192.166.187 on 09/08/12
For personal use only.

were used in place of RPR 3000 Å lamps. The concentrations were [2MN] = 0.02 M, [AA] = 0.08 M, and [H_2SO_4] ranged from 0 to 1 mM. The product formation was determined by GC analysis using octadecane as the internal standard with a 2MN conversion of ca. 12 ± 2% in CH_3CN and 6 ± 2% in CH_3OH. The relative quantum yields were calculated by the definition shown below under the condition of constant light intensity.

$$\Phi_P^T = \frac{\text{(moles of P formed)}}{\text{(number of quanta absorbed)}}$$

$$\Phi_P^T/(\Phi_P^T)^0 = \frac{\text{(moles of product formed) } t^0}{\text{(moles of product formed)}^0 t} = \frac{R_P t^0}{R_P^0 t}$$

The superscript (^{0}) refers to the reference solution ([H_2SO_4] = 0 mM and $(\Phi_P^T)^0 = 0.005$), t is the irradiation time, and R is the GC response relative to the internal standard (i.e., the product GC area divided by the internal standard GC area).

Results

*Quenching of *2MN fluorescence by AA*

2MN fluoresces strongly in various solvents showing a λ_{max} of 356 nm in CH_3CN and 360 nm in CH_3OH with a reported fluorescence quantum yield (Φ_e^0) of 0.30 in either solvent (11). The lifetime of singlet excited 2MN (0.4 mM) in CH_3CN solutions was determined by the single-photon counting technique at 370 nm. The fluorescence decay was adequately fitted by a single exponential, $I_e(t) = A\exp(-t/\tau)$, to give 7.7 ± 0.1 ns (= τ_e) under air and 13.2 ± 0.1 (= τ_e^0) under argon; in CH_3OH they were 7.0 ± 0.1 (= τ_e) and 11.6 ± 0.1 (= τ_e^0), respectively, by a similar determination. These lifetimes were fed into the Stern–Volmer equation, eq. [1*a*], to give the pseudo-first-order rate constants for quenching of 2MN fluorescence by dissolved oxygen, $k_{ox}[O_2]$, that is assumed to be the same for oxygen quenching of any excited state species (12, 13) in the same solvents by a diffusion-controlled process: $k_{ox}[O_2]$ are calculated to be 5.4×10^7 s^{-1} and 5.7×10^7 s^{-1} in CH_3CN and CH_3OH, respectively.

$$[1a] \qquad \tau_e^0/\tau_e = 1 + k_{ox}\tau_e^0[O_2] = 1 + K_{SV}^0[O_2]$$

$$[1b] \qquad = 1 + K_{SV}^a[AA]$$

Applying Henry's law and the known percentage of O_2 in air (20.9%) (14), these figures were multiplied by 4.78 to afford the pseudo-first-order rate constants under pure (100%) O_2; i.e., $k_{ox}[O_2] = 25.8 \times 10^7$ s^{-1} and 27.2×10^7 s^{-1} in CH_3CN and CH_3OH. In this calculation, Henry's law is expected to be obeyed since the O_2 concentration in CH_3CN or CH_3OH is extremely dilute ($x_{O_2} < 0.01$) (15). These rate constants will be used later in the evaluation of the *2MN + AA interaction and *(2MN–AA) exciplex decay rate constants.

The fluorescence decay kinetics of *2MN in the presence of AA (2–14.1 mM) in argon-purged CH_3CN solutions also unexpectedly showed single exponential decay kinetics to afford τ_e^a. The lifetimes listed in Table 1 were plotted according to eq. [1*b*] to give the Stern–Volmer constant (22.6 ± 0.5 M^{-1}) for the interaction of *2MN with AA (see supplementary material,[2] Fig. 6), the nature of which is clarified below. It must be pointed out that a single exponential decay would generally imply irreversible fluorescence quenching (10). However, under certain conditions, partially reversible fluorescence quenching may also show single exponential behaviour due to the failure of deconvolution procedures to resolve a biexponential decay; the present case is another example (6) (vide infra).

TABLE 1. Fluorescence decay kinetics of *2MN in the absence and presence of AA under argon in CH_3CN

[AA] (mM)	DW[a]	$\chi^{2,a}$	τ_e^a (± 0.1 ns)	τ_e^0/τ_e^a
0	1.8	1.05	13.2[b]	1.00
2.0	1.5	1.05	12.6	1.05
4.0	1.8	1.08	12.0	1.10
7.1	2.2	1.00	11.3	1.17
14.1	2.0	1.19	10.0	1.32

[a]Statistical parameters for the fitting of a single exponential to the 2MN fluorescence decay curves. DW = Durbin–Watson statistical fit parameter (7).
[b]τ_e^0.

In frozen solution at 77 K, 2MN fluorescence was not affected by [AA] ≤ 0.4 M, within experimental error, after correction for excitation light absorption by AA. In contrast, at room temperature the 2MN fluorescence intensity was quenched rapidly by AA in cyclohexane, dioxane, and CH_3CN without showing a new emission at up to 50% quenching.

The interaction of *2MN with AA has been shown to give the cycloaddition products (5), where the nonfluorescent *(2MN–AA) exciplex was proposed as the immediate precusor. A steady-state assumption on the process shown in Scheme 1 (EA pathway) afforded eq. [2] describing the quenching of 2MN fluorescence by AA (see Inset Fig. 1). Note that eq. [2] was derived by assuming that both *2MN and *(2MN–AA) are quenched by oxygen with a rate constant k_{ox} (8, 16). The plots of the data under argon, air, and pure oxygen are shown in Fig. 1 (supplementary material,[2] Fig. 7).

$$[2a] \qquad I_e^0/I_e = 1 + K_{SV}^0[O_2] + K_{SV}^a[AA]$$

where $K_{SV}^a = k_{ea}\alpha\tau_e^0$, $K_{SV}^0 = k_{ox}\tau_e^0$ and

$$[2b] \qquad \alpha = (\Sigma k_{a1} + k_{ox}[O_2])/(k_{-ea} + k_{ox}[O_2] + \Sigma k_{a1})$$

$$[2c] \qquad \alpha^0 = \Sigma k_{a1}/(k_{-ea} + \Sigma k_{a1})$$

$$\alpha/\alpha^0 = (k_{-ea} + \Sigma k_{a1})(\Sigma k_{a1} + k_{ox}[O_2])/(k_{-ea} + k_{ox}[O_2]$$

$$[2d] \qquad + \Sigma k_{a1})\Sigma k_{a1}$$

$$= K_{SV}^a(\text{presence of } O_2)/K_{SV}^a(\text{absence of } O_2)$$

I_e^0 and I_e are the *2MN fluorescence intensities in the absence

[2]Supplementary material available: Four pages: Plot of τ_e^0/τ_e^a against [AA] for the fluorescence quenching of 2MN by AA in argon-purged CH_3CN (Fig. 6); modified Stern–Volmer plots for the steady-state fluorescence quenching of 2MN (0.4 mM, monitored at 360 nm) by AA in CH_3OH under argon, air, and O_2 (Fig. 7); plot of $(I_p^0/I_p) \div (I_e^h/I_e)$ against [AA] for the fluorescence quenching of *2MNH$^+$ by AA in argon-purged CH_3CN (Fig. 8); plot of $\Phi_P^T/(\Phi_P^T)^0$ against 2MN percent conversion for the photocycloaddition of 2MN with AA at various levels of H_2SO_4 in argon-purged CH_3CN (Fig. 9). This material can be purchased from: The Depository of Unpublished Data, Document Delivery, CISTI, National Research Council Canada, Ottawa, ON K1A 0S2, Canada.

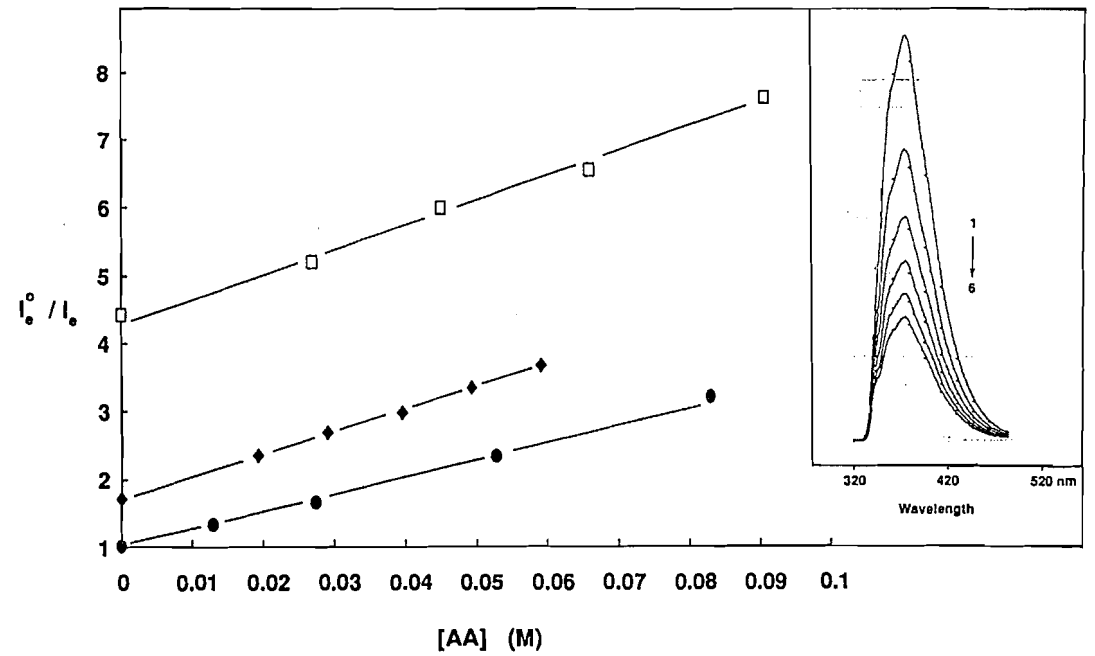

FIG 1. Modified Stern–Volmer plots for the steady-state fluorescence quenching of 2MN (0.4 mM, monitored at 356 nm) by AA in CH_3CN under argon (●), air (♦), and O_2 (□). Inset shows a typical steady-state fluorescence-quenching experiment: fluorescence quenching of 2MN (0.4 mM) by AA in CH_3OH (under air) at room temperature: [AA] are 0, 19.4, 38.8, 55.7, 77.3, and 96.4 mM for spectra 1 → 6.

TABLE 2. Stern–Volmer constants for 2MN[a] fluorescence quenching by AA; perturbation of the steady-state kinetics with O_2

Condition	K_{SV}^a (M^{-1})	$k_{ea}\alpha^{b,c}$ (10^9 M^{-1} s^{-1})	k_{ea} (10^9 M^{-1} s^{-1}) (calcd.)[d]	$\frac{\alpha}{\alpha^0}$
		CH_3CN		
Ar purged	23.4 ± 1.2	1.77 ± 0.09	2.5	(1.0)
Aerated	29.1 ± 1.5	2.20 ± 0.11	2.5	1.24
O_2 purged	31.4 ± 1.6	2.39 ± 0.12	2.5	1.35
		CH_3OH		
Ar purged	25.1 ± 1.3	2.16 ± 0.11	4.0	(1.0)
Aerated	31.0 ± 1.5	2.67 ± 0.13	4.0	1.24
O_2 purged	39.0 ± 2.0	3.36 ± 0.17	4.0	1.56

[a]All experiments were run with [2MN] = 0.4 mM.
[b]$k_{ea}\alpha = K_{SV}^a \div \tau_e^0$ using τ_e^0 = 13.2 ns in CH_3CN.
[c]As in (*a*) but τ_e^0 = 11.6 ns in CH_3OH.
[d]Rate constant for the interaction of *2MN with AA; calculated from the determined *(2MN–AA) exciplex decay rate constants (see text).

and presence of both AA and oxygen, respectively. For the sake of brevity, the reaction rate constant k_{ar} shown in Scheme 1 is included as part of Σk_{al} in the above equations. As defined in eq. [2*b*], α is the efficiency factor with which the exciplex decays to the ground state and $k_{ea}\alpha$ is the apparent fluorescence-quenching rate constant; τ_e^0 is the *2MN fluorescence decay lifetime at low 2MN concentration ($\cong 10^{-4}$ M where excimer formation is negligible) without AA and oxygen as shown above. The slopes in Fig. 1 (K_{SV}^a) were divided by τ_e^0 to give the apparent quenching rate constants, $k_{ea}\alpha$, which increased at higher oxygen concentrations indicating that the α values also increased; the perturbation of the system by oxygen is measured from the α/α^0 ratio in eq. [2*b*] (Table 2). The intercepts of the plots in Fig. 1 must be equal to $1+K_{SV}^0[O_2]$ as required by eq. [2*a*]. Equation [2*a*] was derived by factoring out the oxygen quenching from the *2MN's lifetime; therefore the K_{SV}^a values can be directly compared. It is immediately clear, from the α/α^0 ratio being greater than unity, that exciplex formation is reversible as required by eq. [2*d*], i.e., k_{-ea} must be significant with respect to Σk_{al}.

*Quenching kinetics of *2MN by AA in the presence of H_2SO_4*

In the presence of a fixed concentration of H_2SO_4 both the fluorescence of *2MN and *2MNH$^+$ (at 466 nm) were reduced by AA (Fig. 2). The modified Stern–Volmer plots for the *2MN fluorescence quenching by AA under argon were

Can. J. Chem. Downloaded from www.nrcresearchpress.com by 85.192.166.187 on 09/08/12
For personal use only.

Can. J. Chem. Downloaded from www.nrcresearchpress.com by 85.192.166.187 on 09/08/12
For personal use only.

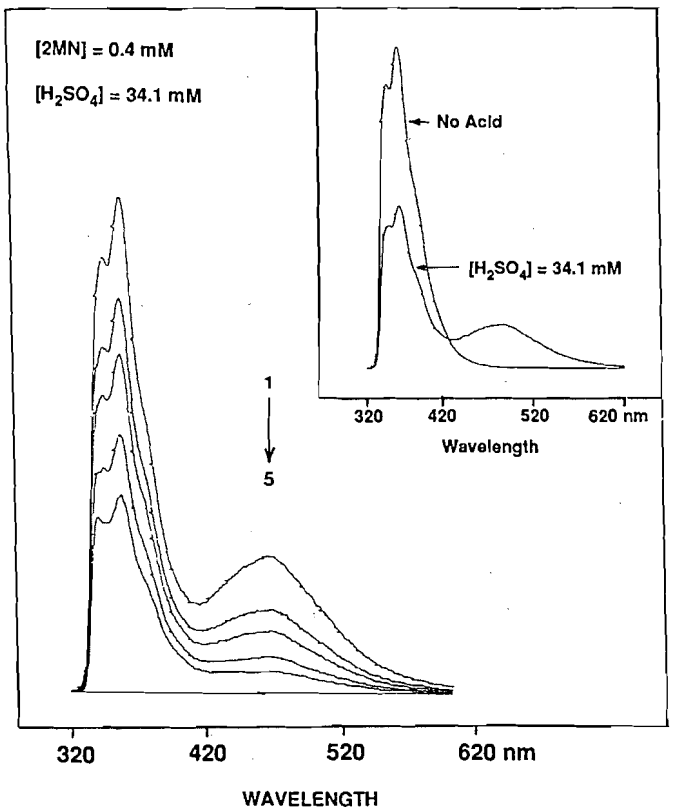

FIG. 2. Example of steady-state fluorescence quenching of 2MN (0.4 mM) by AA in the presence of constant $[H_2SO_4]$ (34.1 mM) in CH_3CN under argon. 2MN fluorescence in the presence of $[H_2SO_4]$ = 34.1 mM where the AA concentrations are 0, 16.4, 28.4, 54.5, and 84.1 mM for spectra 1 → 5. Inset shows the 2MN fluorescence spectra in the absence (I_e^0) and presence of $[H_2SO_4]$ = 34.1 mM.

constructed (Fig. 3); the resemblance to Fig. 1 under oxygen perturbation was obvious.

In analogy to the derivation of eq. [2], eq. [3] was obtained in the presence of the H_2SO_4 perturber for *2MN fluorescence quenching by AA:

$$[3a] \qquad I_e^0/I_e = 1 + k_{ep}\tau_e^0[H_2SO_4] + K_{SV}^h[AA]$$

where $K_{SV}^h = k_{ea}\beta\tau_e^0$

$$[3b] \qquad \beta = (\Sigma k_{a1} + k_{ap}[H_2SO_4])/(k_{-ea} + k_{ap}[H_2SO_4] + \Sigma k_{a1})$$

As the extent of H_2SO_4 dissociation in CH_3CN and CH_3OH is negligible (vide infra), the *(2MN–AA) exciplex is regarded to interact with the undissociated H_2SO_4 as defined by $k_{ap}[H_2SO_4]$. The Stern–Volmer constants (K_{SV}^h) were given from the slopes of these plots (Fig. 3) and were divided by τ_e^0 to give $k_{ea}\beta$ (Table 3). Both these slopes (K_{SV}^h) and the corresponding $k_{ea}\beta$ definitely increased with increasing $[H_2SO_4]$. At this stage our preliminary conclusion was that (*i*) the exciplex must interact with H_2SO_4 to increase the slope, (*ii*) the term $k_{ap}[H_2SO_4]$ in eq. [3*b*] must be significant relative to Σk_{a1} for such an increase to be observed, and (*iii*) the *2MN + AA reaction must be reversible; i.e., k_{-ea} is not insignificant in comparison to Σk_{a1} as we have concluded above.

The quenching of $^*2MNH^+$ fluorescence by AA was determined from Fig. 2*b* according to eq. [4] originally described

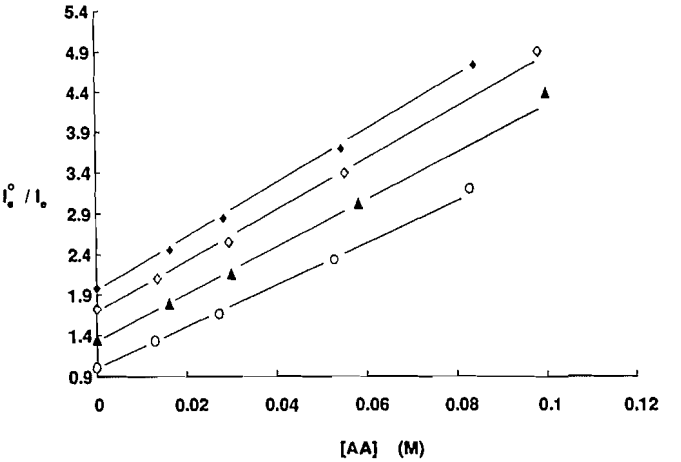

FIG. 3. Modified Stern–Volmer plot for the steady-state fluorescence quenching of 2MN by AA (CH_3CN under argon) in the presence of constant $[H_2SO_4]$: $[H_2SO_4]$ = 0 mM (○); 12.7 mM (▲); 23.5 mM (◇); 34.1 mM (◆).

by Caldwell et al. (17) (Fig. 4), where τ_p is the lifetime of the association species $^*2MNH^+$, and, I_p^0 and I_p represent the $2MNH^+$ fluorescence intensity (monitored at 466 nm in CH_3CN and 470 nm in CH_3OH) in the absence and presence of AA, respectively. I_e^h and I_e represent the *2MN fluorescence intensity in the presence of H_2SO_4 without and with AA.

$$[4a] \qquad (I_p^0/I_p) \div (I_e^h/I_e) = 1 + k_{pa}\tau_p[AA]$$

$$[4a] \qquad \tau_p = (\Sigma k_{p1} + k_{-ep} + k_{pp}[H_2SO_4])^{-1}$$

The $^*2MNH^+$ lifetime (τ_p) was calculated from eq. [4*b*] using the rate constants obtained from the decay kinetics of *2MN in the presence of H_2SO_4 cited from previous papers (Table 4) (6, 7); it must decrease as the $[H_2SO_4]$ increases due to the $k_{pp}[H_2SO_4]$ term. The rate constants for the interaction of $^*2MNH^+$ with AA (k_{pa}) at each $[H_2SO_4]$ were calculated from the slopes ($k_{pa}\tau_p$; see supplementary material,[2] Fig. 8) and the calculated τ_p. These values for k_{pa} are in excellent agreement with those obtained from fluorescence decay measurements (2.1×10^9 M^{-1} s^{-1}) (6). The constancy of k_{pa} (Table 3) in spite of the two different experimental probes, and the use of dynamic and steady state kinetics, is indeed remarkable; this provides support for the proposed mechanism. However, this pathway is unrelated to the acid-catalyzed photocycloaddition as shown previously (6).

Quantum yields of 2MN + AA photocycloaddition promoted by H_2SO_4

The product quantum yield ratios, $\Phi_P^T/(\Phi_P^T)^0$, of solutions containing [2MN] = 0.02 M and [AA] = 0.08 M were determined in the absence and presence of a trace amount of H_2SO_4 with 2MN conversion of ca. 12% (except one) in CH_3CN and ca. 6% in CH_3OH and the results are listed in Table 5. The quantum yield ratios varied linearly with respect to $[H_2SO_4]$ (Fig. 5) with a slope of 6700 ± 300 M^{-1} in CH_3CN and 8900 ± 400 M^{-1} in CH_3OH. The quantum yields rapidly increased by nearly an order of magnitude at about 1×10^{-3} M H_2SO_4; at the 1 mM level the photocycloaddition becomes preparatively useful with a projected quantum yield of 0.04 in CH_3CN and 0.045 in CH_3OH. The use of these slopes to correlate the quantum yield and fluorescence-quenching results (k_{ap} calculation) will be discussed later.

TABLE 3. Fluorescence quenching of *2MN and *2MNH$^+$ by AA in the presence of constant $[H_2SO_4]$

$[H_2SO_4]$ (mM)	K^h_{SV} (M^{-1})	$k_{ea}\beta$ ($\times 10^9$ M^{-1} s^{-1})[a]	$k_{pa}\tau_p$ (M^{-1})[b]	τ_p (ns)[c]	k_{pa} ($\times 10^9$ M^{-1} s^{-1})
		CH_3CN			
0[d]	22.6 ± 0.5	1.71 ± 0.04	—	—	—
0	23.4 ± 1.2	1.77 ± 0.09	(26.4)[e]	(13.2)[e]	—
12.7	26.0 ± 1.3	1.97 ± 0.10	22.5 ± 1.1	11.4	2.0 ± 0.1
23.5	27.0 ± 1.4	2.05 ± 0.10	20.4 ± 1.0	10.3	2.0 ± 0.1
34.1	28.9 ± 1.4	2.19 ± 0.11	18.6 ± 0.9	9.3	2.0 ± 0.1
52.5	29.0 ± 1.5	2.20 ± 0.11	17.3 ± 0.9	8.1	2.1 ± 0.1
		CH_3OH			
0	25.1 ± 1.3	2.16 ± 0.11	—	(1.4)	—
53.4	37.2 ± 1.9	3.21 ± 0.16	5.2 ± 0.3	1.4	3.7 ± 0.2

[a] $k_{ea}\beta = K^h_{SV} \div \tau^0_c$ using τ^0_c = 13.2 ns in CH_3CN and 11.6 ns in CH_3OH.
[b] $k_{ap}\tau_p$ obtained from Fig. 8 (supplementary material) according to eq. [5*a*]. All experiments were run with [2MN] = 0.4 mM.
[c] 2MNH$^+$ lifetime calculated from eq. [4*b*] using the rate constants listed in Table 4.
[d] Fluorescence decay kinetic results.
[e] A value extrapolated to $[H_2SO_4]$ = 0 M.

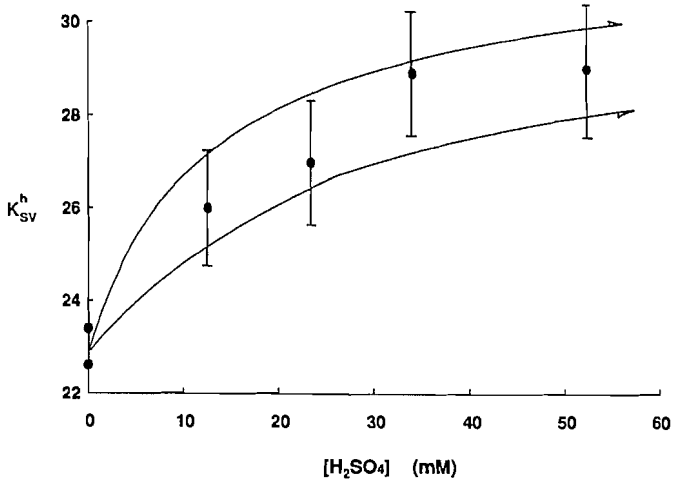

FIG. 4. Plot of the Stern–Volmer constants obtained from Table 3 as a function of $[H_2SO_4]$ in CH_3CN. The upper and lower solid lines are calculated from eq. [4] using the rate constants listed in Table 4 and $k_{ap} = 3 \times 10^9$ M^{-1} s^{-1} and 1×10^9 M^{-1} s^{-1}, respectively.

An examination of the relative quantum yields as a function of percentage conversion indicated a substantial increase at higher conversions (see supplementary material,[2] Fig. 9); i.e., the quantum efficiency increased as the product accumulated. In other words, the product yield was accelerated as the reaction proceeded; any factor that causes higher conversions (e.g., long irradiation time or higher acid concentration) will automatically enhance the quantum yield significantly. It was earlier reported that the acid catalysis asymptotically approaches a maximum at an acid concentration level of 1 mM with a projected quantum yield of 0.16 (5*a*). In that experiment, the high-end data were shown now to have a conversion as high as 50%, though the low-end data remained in the range of only 10–12% conversion. Owing to this apparent self-catalysis, the conversion of 2MN for the photoreactions in Table 5 was controlled in the low and narrow range of 12 ± 2% in CH_3CN and 6 ± 2% in CH_3OH. The self-catalysis is peculiar and reflects the complicated dynamics of the excited state reactions (vide infra).

Discussion

Fluorescence-quenching mechanism

From our earlier reported results (5), we identified that only singlet excited 2MN is the reacting species; i.e., neither singlet excited AA nor triplet excited 2MN is responsible for producing **1** and **2**. In this regard the photocycloaddition of 2MN with AA is quite different mechanistically from that of AA with cyclohexene (de Mayo reaction) (18). The fact that β-diketones exist as two equilibrated tautomers (19) and form ground-state aggregates at low concentrations ($\approx 10^{-3}$ M) (20) may complicate the mechanistic interpretation presented in this paper, hence their relevance must be addressed. The *cis*-enol percentage of AA at infinite dilution is 52.9% in CH_3CN, 68.0% in CH_3OH, and 97.0% in cyclohexane (19). These values roughly parallel the observed Stern–Volmer constants for the quenching of *2MN fluorescence by AA in these solvents (i.e., K^a_{SV} = 68 M^{-1} in cyclohexane (5*b*), 25.1 M^{-1} in CH_3OH, and 23.4 M^{-1} in CH_3CN), thus hinting that the *cis*-enol is the quenching species. From the work of Emsley and Freeman (19*a*), the *cis*-enol percentage does not significantly change over the concentration range used in this study; i.e., for AA mole fractions less than 0.01, the change in *cis*-enol percentage is calculated to be less than 1%. At higher AA concentrations the *cis*-enol percentage is known to decrease for solvents of low dielectric constant ($\epsilon < 26$) and increase for solvents of high dielectric constant ($\epsilon > 26$). In addition, UV absorption experiments have shown that the absorption of AAs is not affected by the presence of H_2SO_4 up to 0.1 M (5*b*); however, at higher concentrations a new absorption band at 430 nm was observed. Of the β-diketones investigated by Nikolov et al. only AA does not form ground state dimers (20). It is clear that there are no substantial changes in the AA *cis*-enol percentage under the conditions of the present investigation in the same solvent.

The lack of fluorescence quenching of *2MN by AA in frozen solution suggested that physical collision between *2MN and AA is required for the quenching act. Evidence for an exciplex was originally concluded by the observations

Can. J. Chem. Downloaded from www.nrcresearchpress.com by 85.192.166.187 on 09/08/12
For personal use only.

TABLE 4. Calculated rate constants for the interaction of *2MN with AA in CH_3CN and CH_3OH and related rated constants

Rate constant	CH_3CN	CH_3OH	Ref.
k_{ea} ($\times 10^9$ M^{-1} s^{-1})	2.5 ± 0.5	4.0 ± 0.8	This work
k_{-ea} ($\times 10^7$ s^{-1})	1.0 ± 0.2	7.0 ± 1.4	This work
Σk_{al} ($\times 10^7$ s^{-1})	2.5 ± 0.4	8.2 ± 1.6	This work
k_{ap} ($\times 10^9$ M^{-1} s^{-1})	2 ± 1	4 ± 1	This work
	(1.5 ± 0.4)[a]	(3.1 ± 0.7)[a]	This work
k_{ar} ($\times 10^5$ s^{-1})	2.2 ± 0.4	3.5 ± 0.8	This work
k_{ox} [O_2] ($\times 10^7$ s^{-1})			
aerated	5.4 ± 0.2	5.7 ± 0.2	This work
under O_2	25.8 ± 1.0[b]	27.2 ± 1.0[b]	This work
k_{ep} ($\times 10^9$ M^{-1} s^{-1})	2.7 ± 0.2	8.0 ± 0.7	2
k_{-ep} ($\times 10^7$ s^{-1})	1.7 ± 0.4	61 ± 4	2
Σk_{pl} ($\times 10^7$ s^{-1})	5.9 ± 0.4	11 ± 1	2
k_{pp} ($\times 10^8$ M^{-1} s^{-1})	9.1 ± 0.7	(0)[c]	2
Σk_{el} ($\times 10^7$ s^{-1})	7.6 ± 0.1	8.6 ± 0.1	2
k_{ed} ($\times 10^{10}$ M^{-1} s^{-1})	2.9 ± 0.7	—	3
k_{-ed} ($\times 10^9$ s^{-1})	6.0 ± 1.5	—	3
Σk_{dl} ($\times 10^8$ s^{-1})	2.7 ± 0.5	—	3
k_{dp} ($\times 10^9$ M^{-1} s^{-1})	6.5 ± 1.5	—	3

[a]The values are obtained from quantum yield studies, listed as comparisons with those obtained from extended fluorescence quenching analysis.
[b]Calculated by multiplying the values in aerated solution value by 4.78 (see Results).
[c]k_{pp} was found to be negligible in CH_3OH.

TABLE 5. Relative quantum yields of product formation (**1** + **2**) for the photocycloaddition of 2MN (0.02 M) and AA (0.08 M)[a]

$[H_2SO_4]$ (mM)	$\Phi_P^T/(\Phi_P^T)^0$	$[H_2SO_4]$ (mM)	$\Phi_P^T/(\Phi_P^T)^0$
CH_3CN[b]		CH_3OH[c]	
0[d]	1.0 ± 0.1	0[d]	1.0 ± 0.1
0.21	2.5 ± 0.1	0.22	2.6 ± 0.1
0.41	3.7 ± 0.2	0.41	3.8 ± 0.2
0.57	4.6 ± 0.2	0.60	6.0 ± 0.3
0.76	6.2 ± 0.3	0.80	7.6 ± 0.4
0.98	7.2 ± 0.4	1.00	8.4 ± 0.4

[a]Samples were irradiated with RPR 3500 Å lamps in a merry-go-round photoreactor (see experimental).
[b]Percent 2MN conversion was controlled to 12 ± 2%.
[c]Percent 2MN conversion controlled to 6 ± 2%.
[d]Quantum yield is 0.005 (5).

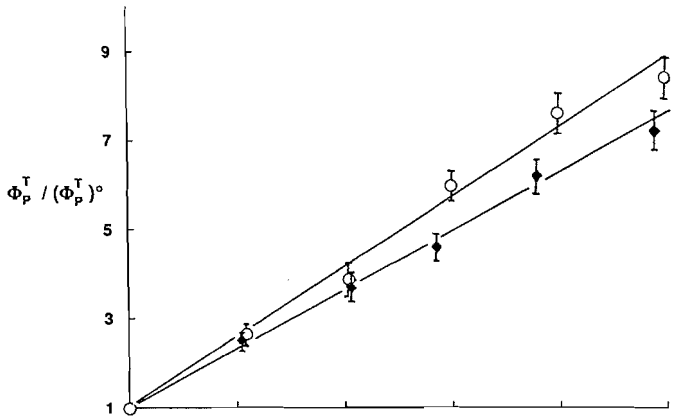

FIG. 5. Plot of the relative quantum yields as a function of $[H_2SO_4]$ in CH_3CN (◆) and CH_3OH (○).

of a negative temperature effect in fluorescence quenching (5) (in CH_3CN) and an inverse relation of fluorescence-quenching rate constants vis-à-vis increasing solvent dielectric constant (5*b*). While these observations also qualitatively parallel the change in *cis*-enol percentage with temperature and solvent polarity, respectively, it is certain that the variance in *cis*-enol content alone cannot account for them. Using the data of Emsley and Freeman (19*a*) and Mills and Beak (19*b*), the change in *cis*-enol content was estimated to account for only 20% of the observed Stern–Volmer constant variance with temperature and solvent polarity. Therefore, the original conclusion of exciplex formation between *2MN and AA is reasonable and will be validated below as a nonfluorescing intermediate under the conditions of the photocycloaddition.

Fluorescence-quenching kinetic analysis

The oxygen perturbation method, which was originally used by Saltiel and co-workers (16*a*) to probe the reversibility and kinetics for the nonfluorescent benz[*a*]anthracene–*cis*-1,3-pentadiene exciplex, serves nicely to evaluate the quenching pattern of the EA pathway processes in Scheme 1. We have expanded this method to examine the kinetics of an exciplex as a corollary to a reversibility probe (21); this method is particularly useful in unravelling the kinetics of a nonemissive exciplex such as *(2MN–AA). The first step is to obtain the kinetic parameters of the exciplex by eq. [2*d*] where the $k_{ox}[O_2]$ is provided by lifetime measurements and to establish the degree of exciplex formation reversibility. As eq. [2*d*] cannot be rearranged to a convenient linear form, the target data k_{-ea}

Can. J. Chem. Downloaded from www.nrcresearchpress.com by 85.192.166.187 on 09/08/12
For personal use only.

Can. J. Chem. Downloaded from www.nrcresearchpress.com by 85.192.166.187 on 09/08/12
For personal use only.

and Σk_{a1} were evaluated by trial and error to converge upon the experimental α/α^0 ratio in Table 2. The computation gave only one unique solution as given in Table 4, indicating that $k_{-ea} < \Sigma k_{a1}$. The efficiency factors α and α^0 can be calculated from eqs. [2*b*] and [2*c*], respectively, and are used to calculate the true rate constant of 2MN fluorescence quenching by AA, k_{ea} (Table 2), which has an error margin of ±20%. This error is not unreasonable in view of examining the H_2SO_4 interactions occurring at a remote site from the actual quenching event. The ratio of $k_{-ea}/\Sigma k_{a1} \cong 1/2.5$ in CH_3CN must indicate that the exciplex is reversible, at least partially, and in direct conflict with the observation of single exponential fluorescence decay profiles (Table 1) that would suggest irreversible fluorescence quenching. The failure of deconvolution methods to resolve biexponential fluorescence decay profiles (6, 18*a*, 22) is known and has been shown to arise from masking of one exponential by the more dominant exponential (vide supra) (22). A similar situation was observed in the partially reversible interaction of *2MN with H_2SO_4 in CH_3CN (6).

Using the same methodology applied to probe the kinetics of the derivative exciplex (a method that we wish to call "extended fluorescence-quenching analysis"), the reaction of the invisible exciplex *(2MN–AA) with H_2SO_4 in a low-concentration region can be probed by eq. [3]; the occurrence of such a reaction is clearly indicated by the increasing slopes (K^h_{SV}) in Fig. 3. A plot of K^h_{SV} values against $[H_2SO_4]$ in CH_3CN can be analyzed by fitting of eq. [3*b*] and shown, with the associated error margins, in Fig. 4. Using the necessary rate constants in Table 4, the upper line is calculated using $k_{ap} = 3 \times 10^9$ M^{-1} s^{-1} and the lower line $k_{ap} = 1 \times 10^9$ M^{-1} s^{-1}; i.e., $k_{ap} = (2 \pm 1) \times 10^9$ M^{-1} s^{-1}. In CH_3OH, K^h_{SV} from two steady-state experiments (Table 3) allows an estimate of $k_{ap} = (4 \pm 1) \times 10^9$ M^{-1} s^{-1} by the same procedure. As $[H_2SO_4]$ becomes larger, $k_{ap}[H_2SO_4]$ becomes the dominant term in eq. [3*b*] with $\beta \cong 1$, where K^h_{SV} approaches $k_{ea}\tau^0_e$: the plot in Fig. 4 indeed asymptotically approaches a limiting value of $k_{ea}\tau^0_e$ at about $[H_2SO_4] \geq 0.05$ M.

Product quantum yields

The multitudinous interactions of *2MN in the presence of AA and H_2SO_4 lead to a complex dynamic system for which Scheme 1 is probably a skeletal pattern that adequately represents the observed reactions. It remains to correlate the kinetic data obtained by fluorescence quenching with the experimental quantum yields for **1** and **2** to identify the route of acid catalysis. Previously (6, 7) the maximum possible contributions to the total quantum yield Φ^T_P from (*i*) the *2MNH$^+$ quenching by AA (EP pathway) and (*ii*) 2MN excimer quenching by H_2SO_4 (EE pathway) have been determined to be 10% and nil, respectively; in short, these pathways are either insignificant at most or nonexistent. To estimate the maximum possible contribution from the EA pathway in Scheme 1, it is assumed that the exciplex *(2MN–AA) interacts with H_2SO_4 to give product with unit efficiency. This assumption conveniently circumvents considering a triplex intermediate that may exist but is not experimentally demonstrated. Under photostationary conditions, the product quantum yield derived from the EA pathway can be shown to be given by the expression eq. [5] (2*a*):

$$[5a] \qquad \Phi^T_P = \Phi^{ea}_P + \Phi^{ap}_P = \frac{\varphi(k_{ar} + k_{ap}[H_2SO_4])}{(k_{-ea} + \Sigma k_{a1} + k_{ar} + k_{ap}[H_2SO_4])}$$

$$[5b] \qquad \varphi = \frac{k_{ea}[AA]}{\Sigma k_{e1} + k_{ea}(1 - R_{-ea})[AA] + k_{ep}(1 - R_{-ep})[H_2SO_4] + k_{ed}(1 - R_{-ed})[2MN]}$$

where

$$R_{-ea} = k_{-ea}/(k_{-ea} + \Sigma k_{a1} + k_{ap}[H_2SO_4])$$

$$R_{-ep} = k_{-ep}/(k_{-ep} + \Sigma k_{p1} + k_{pp}[H_2SO_4])$$

$$R_{-ed} = k_{-ed}/(k_{-ed} + \Sigma k_{d1} + k_{dp}[H_2SO_4])$$

φ represents the quantum efficiency of *(2MN–AA) exciplex formation, which is secondarily affected by H_2SO_4 (eq. [5*b*]). R_{-ea}, R_{-ep}, and R_{-ed} represent the dissociation efficiencies of the *(2MN–AA) exciplex, *2MNH$^+$, and 2MN excimer, respectively. Equation [5] is rather formidable but can be simplified under certain conditions as shown below.

From the rate constants in Table 4 and the experimental conditions used in the quantum yield study ([2MN] = 0.02 M and [AA] = 0.08 M) the *(2MN–AA) exciplex formation efficiency φ increases by a calculated 2% over the $[H_2SO_4]$ range of 0–1 mM. Therefore, to a good approximation φ can be considered constant in order to simplify eq. [5]. Under this approximation the ratio of quantum yields in the presence and absence of H_2SO_4, $\Phi^T_P/(\Phi^T_P)^0$, is given by eq. [6].

$$[6] \qquad \Phi^T_P/(\Phi^T_P)^0 \cong \left(\frac{k_{ar} + k_{ap}[H_2SO_4]}{k_{-ea} + \Sigma k_{a1} + k_{ar} + k_{ap}[H_2SO_4]}\right)\left(\frac{k_{-ea} + \Sigma k_{a1} + k_{ar}}{k_{ar}}\right)$$

In addition, within this $[H_2SO_4]$ range the condition $k_{-ea} + \Sigma k_{a1} \gg k_{ar} + k_{ap}[H_2SO_4]$ prevails, hence eq. [6] is further simplified to eq. [7].

$$[7] \qquad \Phi^T_P/(\Phi^T_P)^0 \cong 1 + (k_{ap}/k_{ar})[H_2SO_4]$$

The plot of $\Phi^T_P/(\Phi^T_P)^0$ vs. $[H_2SO_4]$ (Fig. 5) bears out a linear relationship as predicted by eq. [7] under the limiting conditions. This allows us to evaluate k_{ap} directly from these slopes if k_{ar} is known; $k_{ar} = (2.2 \pm 0.4) \times 10^5$ s^{-1} in CH_3CN and $(3.5 \pm 0.8) \times 10^5$ s^{-1} in CH_3OH were calculated from the quantum yield of the photocycloadduct without H_2SO_4 (0.005) (5*a*) using the necessary rate constants in Table 4. In CH_3CN, using the experimental slope of 6700 ± 300 M^{-1}, k_{ap} is calculated to be $(1.5 \pm 0.4) \times 10^9$ M^{-1} s^{-1}. Similarly in CH_3OH (slope = 8700 M^{-1}), $k_{ap} = (3.1 \pm 0.7) \times 10^9$ M^{-1} s^{-1} is obtained. These results agree well with k_{ap} obtained from fluorescence analysis as listed in Table 4. At high H_2SO_4 concentrations where $k_{ap}[H_2SO_4]$ dominates the exciplex reaction, the plot of the quantum yield ratios (eq. [6], such as Fig. 5, should asymptotically approach a limiting value; however, complications from other pathways in solution dynamics would modify the reaction pattern and the quantum yields.

Exciplex involvement in excited state acid catalysis

The convergence of the extended fluorescence-quenching analysis with the quantum yield analysis in terms of the close agreement of the estimated k_{ap} values confirms not only the physical presence of transparent *(2MN–AA) exciplex, but also that its protonation is responsible for the observed acid

Can. J. Chem. Downloaded from www.nrcresearchpress.com by 85.192.166.187 on 09/08/12
For personal use only.

catalysis. Though it is logical and predictable that an exciplex, having a certain charge transfer character, is more susceptible to protonation, acid–base interactions of exciplexes with Brønsted acids are likely to be a general phenomenon. The present discovery is, to our knowledge, *the first demonstration of an exciplex participation in intermolecular acid catalysis.* There are some relevant observations. First, the acid catalysis presented in this paper is reminiscent of the effect of acid on the photoaddition of benzene with electron acceptors, such has maleic anhydride (23). In these reactions, the excited ground-state complex is captured by acid and new chemistry is observed. Second, the photonitrosation of 1-naphthol (1-NpOH) by *N*-nitrosodimethylamine (NND) proceeds by intramolecular proton transfer within the *(1-NpOH–NND) exciplex (24). Third, intramolecular proton transfer is known for a number of bimolecular photoreactions involving radical ion pairs (25). What is fascinating in the present case is the size of the molar catalytic efficiency (6700 M^{-1} in CH_3CN and 8900 M^{-1} in CH_3OH), which is experimentally determined in Fig. 5 and approximated to k_{ap}/k_{ar} by eq. [7] under the defined limiting conditions; it shows that the catalytic effect is clearly visible at the 10^{-3} M level. The high catalytic efficiencies and close to diffusion-controlled rate constants of k_{ap} (see Table 4) also require that the reacting species is a highly reactive excited state, but not likely a ground-state species. For comparison, the photohydration of styrenes and phenylacetylenes (26) is reported to have a molar catalytic efficiency of 460 M^{-1} in polar aqueous media that require much larger acid concentrations to show catalytic effect.

Some pertinent comments remain to be made. For the analysis of fluorescence-quenching rate constants described in this paper, the total AA concentration (i.e., [AA] = [*cis*-enol] + [diketone]) has been used as a variable without any correction for the actual *cis*-enol tautomer concentration. We deem it an unnecessary exercise to correct the [AA] since such a correction will only affect the magnitudes of k_{ea} and k_{pa} (Table 4); k_{ea} and k_{pa} can be corrected by dividing by the *cis*-enol tautomer mole fraction. Equations [2*b*]–[2*d*], [3*b*], and [7] are independent of [AA]; hence the rate constants derived from these equations are unaffected.

Secondly, the kinetic parameters in CH_3CN and CH_3OH (Table 4) can be interpreted in terms of the effects from protic and aprotic solvents. The increase in k_{ap} on going from CH_3CN to CH_3OH follows the acid strength of H_2SO_4 in these solvents; i.e., $pK_a = 7.3$ in CH_3CN (27) and 3 in CH_3OH (28), hence H_2SO_4 is not significantly dissociated in these solvents (vide supra). Similarly, it has been shown that the amount of the cycloadducts in CH_3CN, under identical conditions, also follows the pK_a variation; i.e., decreases in the order of $H_2SO_4 > HCl > CF_3CO_2H \sim H_3PO_4$ (5*a*).

The increase in the quantum yields in the high-conversion range obviously arises from changes in kinetic pattern owing to a decrease of the excimer formation process, k_{ed}[2MN], at high conversion; i.e., the EE pathway becomes less important owing to reduced 2MN concentration (vide supra). However, an approximate estimation of the enhancement is less than 5% around the vicinity of 10% conversion where the quantum yield ratios in Fig. 5 were obtained. The estimated enhancement grows very rapidly beyond 20% conversions. More quantitative treatment of the retardation by excimer formation is hampered by reversibility and complex multi-manifold kinetics. Undoubtedly this unproductive EE pathway causes the reduction in the quantum yield; this leads to an unusual conclusion that the quantum yield of photocycloaddition becomes smaller with larger initial 2MN concentrations.

Conclusion

The acid catalysis of the photocycloaddition of singlet excited state 2MN with AA in CH_3CN and CH_3OH is the first demonstration of an interaction of the nonemissive *(2MN–AA) exciplex with a Brønsted acid (H_2SO_4). In contrast, the interaction of the emissive intermediate (*2MNH$^+$) with AA (EP pathway in Scheme 1) (6), or that of the excimer with H_2SO_4 (EE pathway) (7) is not an acid catalytic route to **1** and **2** for this system. The *(2MN–AA) exciplex is formed reversibly, which allows us to use extended fluorescence-quenching analysis to probe the reaction pattern of this nonfluorescent exciplex. This unambiguously identifies the reaction of the exciplex *(2MN–AA) with H_2SO_4 as the key step in the present catalytic process. Exciplex acid–base behaviour is believed to be a general but unrecognized phenomenon. The extended fluorescence-quenching analysis is shown to be a useful technique to perform kinetic analysis of a nonemissive exciplex provided it is reversibly formed.

Acknowledgements

The authors wish to thank the Natural Sciences and Engineering Research Council of Canada for generous financial support of this research project. We are grateful to Dr. P. Wan, Dr. E. Krogh, and Mr. D. Shukla of the University of Victoria for training and use of the PTI LS-1. We are grateful to one of the referees for numerous and valuable comments.

1. (*a*) J.F. Ireland and P.A.H. Wyatt, Adv. Phys. Org. Chem, **12**, 131 (1976); (*b*) R. Stewart. The proton: applications to organic chemistry. Academic, New York. 1985.
2. Examples where the proton is involved in the primary step: (*a*) G.G. Wubbles. Acc. Chem. Res. **16**, 285 (1983), and papers cited therein; (*b*) F.D. Saeva and G.R. Olin. J. Am. Chem. Soc. **97**, 5631 (1975); (*c*) J.A. Marshall and A.R. Hochstetler. J. Am. Chem. Soc. **91**, 648 (1969); (*d*) P. Wan and K. Yates. Rev. Chem. Intermed. **5**, 157 (1984), and papers cited therein; (*e*) P. Wan, K. Yates and M.K. Boyd. J. Org. Chem. **50**, 2881 (1985); (*f*) P.J. Kalanderopoulos and K. Yates. J. Am. Chem. Soc. **108**, 6290 (1986); (*g*) K. Rafizadeh and K. Yates. J. Org. Chem. **51**, 2777 (1986); (*h*) R.A. McClelland, F. Cozens, and S. Steenken. Tetrahedron Lett. 3821 (1990); (*i*) R.A. McClelland, C. Chan, F. Cozens, A. Modro, and S. Steenken. Angew. Chem. Int. Ed. Engl. **30**, 1337 (1991); (*j*) N.J. Turro and P. Wan. J. Photochem. **28**, 93 (1985).
3. Examples where the proton is involved in a secondary step: (*a*) ref. 2*a*; (*b*) G.G. Wubbles, D.P. Susens, and E.B. Coughlin. J. Am. Chem. Soc. **110**, 2538 (1988); (*c*) G.G. Wubbles, E.J. Snyder, and E.B. Coughlin. J. Am. Chem. Soc. **110**, 2543 (1988); (*d*) F.D. Lewis, D.K. Howard, S.V. Barancky, and J.D. Oxman. J. Am. Chem. Soc. **108**, 3016 (1986); (*e*) P.J. Kropp, E.J. Reardon, Z.L.F. Gailbel, K.F. Willard, and J.H. Hattaway. J. Am. Chem. Soc. **95**, 7058 (1973); (*f*) P. Kropp. J. Mol. Photochem. **9**, 39 (1978–79); (*g*) W.G. Dauben, H.C.H.A. van Riel, J.D. Robbins, and G.J. Wagner. J. Am. Chem. Soc. **101**, 6383 (1979); (*h*) A. Rudolph and A.C. Weedon. J. Am. Chem. Soc. **111**, 8756 (1989); (*i*) R.M. Duhaine and A.C. Weedon. J. Am. Chem. Soc. **109**, 2479 (1987).
4. P. Wan and D. Shukla. Chem. Rev. **93**, 571 (1993), and papers cited therein.
5. (*a*) Y.L. Chow and X.-Y. Liu. Can. J. Chem. **69**, 1261 (1991); (*b*) X.-Y. Lui. Ph.D. Thesis, Simon Fraser University. 1990.

6. Y.L. Chow and C.I. Johansson. J. Photochem. Photobiol. A: **74**, 171 (1993).
7. Y.L. Chow and C.I. Johansson. Res. Chem. Intermed. **19**, 191 (1993).
8. (*a*) R.O. Campbell and R.S.H. Liu. J. Chem. Soc. Chem. Commun. 1191 (1970); (*b*) C. Pac. Pure Appl. Chem. **9**, 1249 (1986); (*c*) Y.L. Chow and X. Cheng. Can. J. Chem. **69**, 1575 (1991).
9. S.A. Tucker, V.L. Amszi and W.E. Acree, Jr. J. Chem. Educ. **69**, A8 (1982).
10. D.V. O'Connor and D. Phillps. Time-correlated single photon counting. Academic, New York. 1984.
11. S.A. Green, D.J. Simpson, G. Zhou, P.S. Ho, and N.V. Blough. J. Am. Chem. Soc. **112**, 7337 (1990).
12. (*a*) J.A. Barltrop and J.D. Coyle. Principles of photochemistry. Wiley, New York. 1978; (*b*) N.J. Turro. Modern molecular photochemistry. Benjamin/Cummings, Reading. 1978.
13. (*a*) J.B. Birks. Photophysics of aromatic molecules. Wiley, New York. 1970. p. 508, (*b*) I.B. Berlman. Handbook of fluorescence spectra of aromatic molecules. Academic, New York. 1971.
14. R.C. Weast (*Editor*). CRC handbook of chemistry and physics. 64th ed. CRC Press, Boca Raton, Fla. 1983.
15. P.G.T. Fogg and W. Gerrard. Solubility of gases in liquids. Wiley, New York. 1991. pp. 24, 294.
16. (*a*) J.L. Charlton, D.E. Townsend, B.D. Watson, P. Shannon, J. Kowalewska, and J. Saltiel. J. Am. Chem. Soc. **99**, 5992 (1977); (*b*) W.K. Smothers, M.C. Meyer, and J. Saltiel. J. Am. Chem. Soc. **105**, 545 (1983); (*c*) T. Majima, C. Pac and H. Sakurai. Bull. Chem. Soc. Jpn. **51**, 1881 (1978).
17. R.A. Caldwell, D. Creed, L.A. Melton, H. Ohta, and P.H. Wine. J. Am. Chem. Soc. **102**, 2369 (1981).
18. (*a*) P. de Mayo. Acc. Chem. Res. **4**, 41 (1971); (*b*) A.C. Weedon. Synthetic organic photochemistry. *Edited by* W. Horspool. Plenum, New York. 1984. p. 61; (*c*) I. Ninomiya and T. Naito. Photochemical synthesis. Academic, New York. 1989.
19. (*a*) J. Emsley and N.J. Freeman. J. Mol. Struct. **161**, 193 (1987); (*b*) S.G. Mills and P. Beak. J. Org. Chem. **50**, 1216 (1985).
20. P. Nikolov, F. Fratev, I. Petkov, and P. Markov. Chem. Phys. Lett. **83**, 170 (1981).
21. Y.L. Chow and C.I. Johansson. Chinese J. Chem. **40**, 531 (1993).
22. (*a*) A.E. Mckinnon, A.G. Szabo, and D.R. Miller. J. Phys. Chem. **81**, 1564 (1977); (*b*) E. Gardini, S. Dellonte, L. Flamigini, and F. Barigelletti. Gazz. Chim. Ital. **110**, 533 (1980).
23. D. Bryce-Smith and A. Gilbert. Tetrahedron, **33**, 2459 (1977).
24. (*a*) Y.L. Chow, Z.-Z. Wu, M.L.W. Thewalt, and T.W. Steiner. J. Am. Chem. Soc. **110**, 5543 (1988); (*b*) Y.L. Chow and Z.-Z. Wu. J. Am. Chem. Soc. **109**, 5260 (1987); (*c*) J. Am. Chem. Soc. **107**, 3338 (1985).
25. A. Gilbert and J. Baggott. Essentials of molecular photochemistry. CRC Press, Boca Raton, Fla. 1991. Chaps. 6.7 and 8.3.
26. (*a*) P. Wan and K. Yates. J. Org. Chem. **48**, 869 (1983); (*b*) J. McEwan and K. Yates. J. Am. Chem. Soc. **109**, 5800 (1987).
27. O. Popovych and R.P.T. Tomkins. Nonaqueous solution chemistry. Wiley, New York. 1981. p. 62.
28. I.M. Kolthoff and M.K. Chantooni, Jr. Treatise on analytical chemistry. Part 1, 2nd ed. *Edited by* I.M. Kolthoff and P.J. Elving. Wiley, New York. 1979. pp. 246–247.

Can. J. Chem. Downloaded from www.nrcresearchpress.com by 85.192.166.187 on 09/08/12
For personal use only.

1994 R.U. Lemieux Award Lecture
Hydrolysis of acetals and ketals. Position of transition states along the reaction coordinates, and stereoelectronic effects[1]

PIERRE DESLONGCHAMPS,[2] YVES L. DORY, AND SHIGUI LI

Laboratoire de synthèse organique, Département de chimie, Faculté des sciences, Université de Sherbrooke, Sherbrooke, QC J1K 2R1, Canada

Received June 1, 1994

PIERRE DESLONGCHAMPS, YVES L. DORY, and SHIGUI LI. Can. J. Chem. **72**, 2021 (1994).

Past and recent experimental results on the formation or hydrolysis (or isomerization) of various acetals and ketals including α- and β-glycoside models are presented. Ab initio investigations of simple acetals are also briefly reviewed as well as recent experimental and theoretical support evidence for a synperiplanar effect. A detailed study using the semi-empirical Hamiltonian AM1 defining the reaction pathway in the hydrolysis of various acetals and ketals is reported. This overall study shows that the hydrolysis of acetals and ketals is controlled by powerful stereoelectronic effects.

PIERRE DESLONGCHAMPS, YVES L. DORY et SHIGUI LI. Can. J. Chem. **72**, 2021 (1994).

Des résultats expérimentaux anciens et nouveaux sur la formation ou l'hydrolyse (ou l'isomérisation) de divers acétals et cétals incluant des modèles d'α- et β-glycosides sont présentés. Des études ab initio d'acétals simples sont aussi brièvement rapportées ainsi que de récentes évidences expérimentales supportées théoriquement de l'effet synpériplanaire. Une étude détaillée, à l'aide de l'Hamiltonian semi-empirique AM1, des chemins réactionnels d'hydrolyse de divers acétals et cétals est rapportée. Cette étude globale montre que l'hydrolyse d'acétals et de cétals est contrôlée par de puissants effets stéréoélectroniques.

Can. J. Chem. Downloaded from www.nrcresearchpress.com by 85.192.166.187 on 09/08/12
For personal use only.

Introduction

It has been generally accepted that stereoelectronic effects play a major role in acetal hydrolysis (1, 2). We previously postulated (1), on the basis of the antiperiplanar lone-pair hypothesis, that α-glycosides (axial anomer) are hydrolyzed via their ground state chair conformation whereas β-glycosides (equatorial anomer) must first assume a twist-boat conformation in order to have the ring oxygen with a lone pair properly oriented to eject the leaving group. Since it is well known (3, 4) that α- and β-glycosides are hydrolyzed at similar rates, it follows that these compounds must be hydrolyzed via transition states that resemble more closely the geometry of the cyclic oxocarbonium ions rather than that of the protonated glycosides. It was therefore necessary to obtain experimental evidence and theoretical support to establish the position of the transition state along the reaction coordinates in the hydrolysis of acetals and related functions. In this paper, we wish to review our recent published work in this area and to present an AM1 molecular modelling study (5).

We recently discovered (6–8) that a series of hydroxy-enol ethers can undergo cyclization to provide the corresponding spiroketals either under kinetically (CH_3COOH–benzene) or thermodynamically (CF_3COOH–benzene) controlled conditions. For instance, taking bicyclic hydroxy-enol **1** as an example (Scheme 1), this compound gave exclusively spiroketal **8** under thermodynamic control and a 2:3 mixture of **5** and **8** under kinetic control. Spiroketal **8** being much more stable than **5** for steric and stereoelectronic reasons (9), it is the only isomer observed under equilibrating conditions. Under kinetically controlled conditions, upon protonation, **1** must first give the cyclic oxocarbonium ion **2**, which can then be converted into spiroketals **5** and **8** while respecting the antiperiplanar hypothesis. On that basis, **5** is formed via a twist-boat (**3** → **4**) and **8** via a chair pathway (**6** → **7**). If the transition states were late, their geometry would be near that of **4** and **7**, their energy difference would be quite large due to steric reasons, and the exclusive formation of **8** would have resulted. The 2:3 ratio of **5** and **8** observed can only be explained by transition states that are near the structures of the oxocarbonium ions **3** and **6**, respectively. Thus, these results can be explained by postulating early transition states, the early chair-like (near **6**) transition state being slightly favored over the early boat-like (near **3**) transition state.

The above results differ from those previously observed (10, 11) with hydroxypropyl acetal **9** (Scheme 2), as this compound led to the exclusive formation of *cis*-tricyclic acetal **13** under kinetically controlled conditions (*p*-TSOH–CH_3OH, room temperature). An equilibrium mixture (45:55) of *cis* and *trans* acetals **13** and **16** was obtained under reflux conditions. The kinetically controlled formation of **13** can be explained in the following way: upon protonation, **9** gave the cyclic oxocarbonium ion **10**, which can then lead to the *cis* and the *trans* acetals **13** and **16**, respectively, via a chair-like (**11** → **12**) pathway and a twist-boat-like (**14** → **15**) pathway while assuming the antiperiplanar hypothesis. Again, it is relatively easy to understand the exclusive formation of *cis* acetal **13** via an early transition state provided that the incoming hydroxyl group is properly aligned with the π-orbital of the cyclic oxocarbonium ion. Such an alignment, which corresponds closely to the Bürgi–Dunitz angle of attack of a nucleophile on a π-system (12, 13), can be easily attained with **11** but not with **14**, a conclusion that was supported by a molecular modelling study (6).

Concurrent to these experiments, a theoretical study on the anomeric effect in acetals was started in collaboration with F. Grein. In the first study (14), geometry optimizations at the 6-31G** level were performed on various conformers of H_nX-CH_2-YH_m and their protonated counterparts H_nX-CH_2-YH_{m+1}^+ where X and Y are N and O. The relative energies for the neutral systems are shown in Table 1. As expected, conformers having two anomeric effects are more stable than those having only

[1]This is an invited review article based on the R.U. Lemieux Award Lecture presented by Professor Pierre Deslonghcamps at the annual conference of the Canadian Society for Chemistry, Winnipeg, Manitoba, June 1994.

[2]Author to whom correspondence may be addressed. Telephone: (819) 821-7002. Fax: (819) 821-7910.

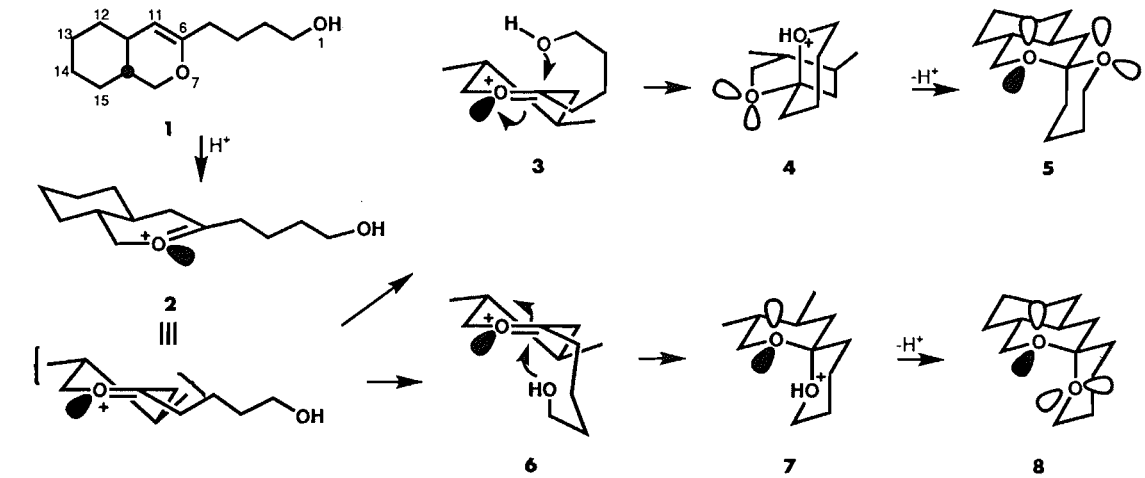

SCHEME 1

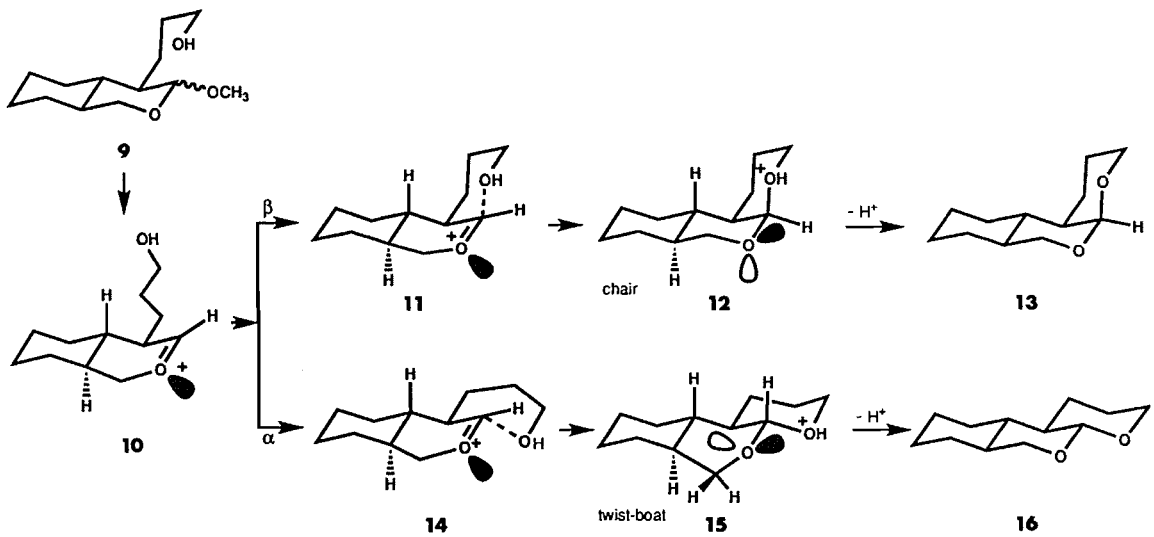

SCHEME 2

TABLE 1. Relative energy ΔE in kcal/mol obtained by 6-31G** geometry optimization on system XH_m-CH_3-YH_n. Values in parentheses come from a simple energy decomposition model

Simple model parameters

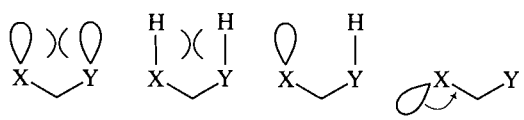

$l = +1$ $r = +1$ $h = -1$ $e_O = -2$ $e_N = -2.5$

XH_m-CH_2-YH_n	0 ae	1 ae(X)	1 ae(Y)	2 ae
OH-CH_2-OH	8.35 (8)	3.86 (4)	3.86 (4)	0.0 (0)
NH_2-CH_2-OH	5.06 (4.5)	0.17 (0)	0.95 (0.5)	0.0 (0)
NH_2-CH_2-NH_2	0.82 (1)	0.64 (0.5)	0.64 (0.5)	0.0 (0)

one, which in turn are more stable than conformers without an anomeric effect. The energy difference does not vary a great deal when oxygen is replaced by nitrogen. Using simple parameters, an energy analysis was performed to explain such different behavior. Energy differences between various conformers can be explained by taking into account an electronic stabilizing term (e_O or e_N), a 1,3-diaxial H—H repulsion term (r), a 1,3-diaxial lone pair – lone pair repulsion term (l), and an intramolecular hydrogen bonding term (h) (see Table 1). Based on ab initio calculations, approximate values $r \cong l \cong -h \cong 1$ kcal/mol were obtained. Applying this model to the systems given in Table 1 led to $e_O = -2$ kcal/mol and $e_N = -2.5$ kcal/mol. The energy values obtained by this simple model are shown in parentheses in Table 1 and are remarkably close to the ab initio values. Overall, this study led to a simple model from which it was possible to estimate qualitatively the underlying electronic energy of stabilization due to the anomeric effect and to separate it from other forms of energy, such as steric and electrostatic energy. The validity of this simple model was confirmed by application to methanetriol and aminomethanediol. Studies of the protonated systems led to a theoretical interpretation of the reverse anomeric effect (15), which would be the result of an electrostatic attraction between a positively charged heteroatom and the electron lone pairs of the neighboring heteroatom.

In a second article (16), more detailed studies were performed on systems H_mX-CH_2-OH with X = N, O, F, C where the OH group was rotated about the C—O bond. This was followed by a Fourier analysis of the energy as a function of the rotation

Can. J. Chem. Downloaded from www.nrcresearchpress.com by 85.192.166.187 on 09/08/12
For personal use only.

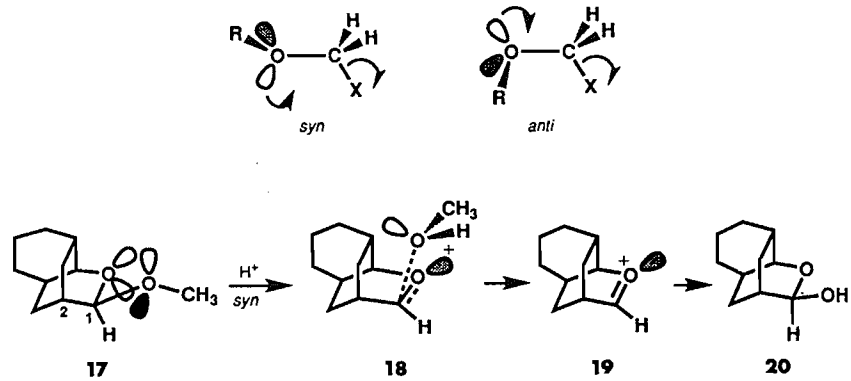

SCHEME 3

TABLE 2. Energy parameters e_O, e_N for electronic component of anomeric effect due to O, N and v_O, v_N, for reverse anomeric effect due to O, N, in kcal/mol

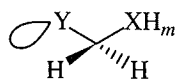

Y = OH, NH_2

XH_m\Y	e_O	e_N	v_O	v_N
F	−2.0	−3.6		
a-OH	−1.0	−1.9		
s-NH_2	−0.7	−1.0		
a-FH^+	−20.5	−30.6	C[a]	C[a]
s-OH_2^+	−6.2	−17.3	−7.5	C[a]
s-NH_3^+	−3.5	−5.7	−8.0	−7.5

[a]C stands for complex formation, which prevents the reverse anomeric effect from taking place.

angle. Again, a decomposition of the energy into a stabilizing electronic component, as a steric component (interaction of rotating OH with neighboring CH_2X group) and a steric–electrostatic component (interaction of OH with XH_m) was performed. The stabilizing electronic component considered to be the fundamental driving force of the anomeric effect was related to the ability of the CH_2OH portion of the molecule to form a double bond. The mechanism leading to anomeric stabilization is thus explained by partial π-bonding. The ideas described in these two papers were combined and extended by Grein (17), leading to much improved values for the electronic portion of the anomeric stabilization energy, which are summarized in Table 2.

These values are larger for nitrogen (e_N) than for oxygen (e_O) because the former is a better electron donor. The e_N and e_O values also increase with the leaving-group ability of the XH_m group. In the protonated series, these values become quite large and in some cases protonation of XH_m leads to the formation of π-complexes due to the high electronegativity of the protonated group. As a result, stereoelectronic effects in acetals are put on a more solid theoretical basis. The π-bonding model also indicated that the *syn* and the *anti* periplanar effects are energetically similar, although processes with the aid of the former are normally sterically disfavored over the latter, eclipsed conformers (*syn* process) being higher energetically than *gauche* conformers (*anti* process) (Scheme 3). Also, due to the large C-XH_{m+1}^+ bond increase found in the protonated species, these calculations suggested that in acetal hydrolysis the geometry of the transition state for the cleavage reaction is likely to be closer to the oxocarbonium ion than to the acetal.

Having obtained theoretical evidence for the synperiplanar effect, tricyclic acetal **17** was synthesized in order to verify whether this effect is operative both in the ozonolysis and the hydrolysis of acetals. Due to its bridged nature, tricyclic acetal **17** has the two lone pairs of the ring oxygen oriented *syn* to both the anomeric C(1)—H and the C(1)—OCH_3 bonds. The CH_3—O bond must also be antiperiplanar to the C(1)—C(2) bond as a result of the *exo* anomeric effect and minimal steric interaction for the CH_3 group. Thus, acetal **17** has one lone pair synperiplanar and one lone pair antiperiplanar to the C(1)—H bond. Normally, acetals that have a lone pair on each oxygen atom antiperiplanar to the C—H bond are very reactive toward ozone (18–20). Since it was observed (21) that acetal **17** is also already oxidized at −78°C, this result constitutes unequivocal experimental evidence that a *syn* stereoelectronic effect can also be operative in the ozonolysis of acetals.

It was also found (22) that tricyclic acetal **17** undergoes hydrolysis under mild acidic conditions (HCl, 0.01 N in water–acetone), yielding the corresponding lactol **20**. Since the endocyclic oxygen of **17** has one lone pair synperiplanar to the C—OCH_3 bond, this result constitutes the first unambiguous experimental evidence that a synperiplanar lone pair can accelerate the hydrolysis of acetals. Accepting the fact that acetals are hydrolyzed via a late transition state, the hydrolysis of **17** must take place via a transition state (**18**) having a geometry near the tricyclic oxocarbonium ion **19**.

Following this work, we studied the reaction pathway for the acid hydrolysis of various acetals using the semi-empirical Hamiltonian AM1.[3] We have examined specific conformations of acetals, their protonated forms, and corresponding oxocarbonium ions, and have looked for transition structures (23) for the cleavage steps. We first examined the hydrolytic pathway of acetals **13** and **16** (Fig. 1). In acetal **13**, the C—O(1) bond is shorter (1.41 Å) than the C—O(2) bond (1.43 Å) due to the anomeric effect (O(1) has one lone pair antiperiplanar to the C—O(2) bond). O(2) is thus more basic, and upon protonation (**21**) the C—O(1) bond shortens (1.36 Å) and the C—O(2) bond

[3]Computational procedure: All the calculations were done at the RHF level. The first input files for MOPAC 6.00 were created by means of SYBYL 6.01 (Tripos Associates, Inc.: 16995 Hanley Rd., Suite 303, St. Louis, Missouri 63144-2913) for IBM RISC 6000 computers. The gradients of the norm of these draft structures were then fully optimized using EF or TS subroutines. Finally, all the transition structures were characterized by only one negative force constant. The calculations were carried out on IBM RISC 6000 computers.

Can. J. Chem. Downloaded from www.nrcresearchpress.com by 85.192.166.187 on 09/08/12
For personal use only.

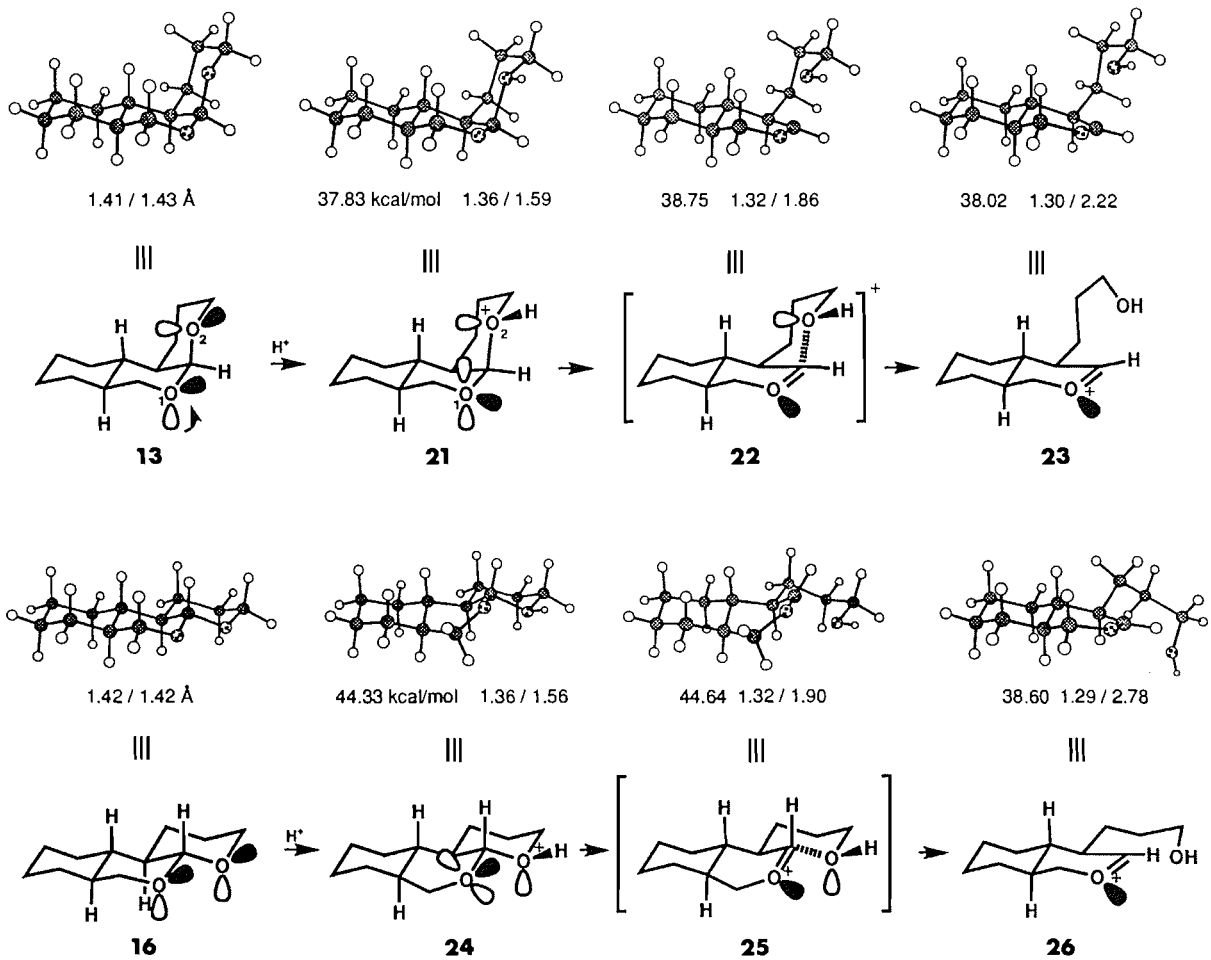

FIG. 1

lengthens (1.59 Å) considerably. This is in agreement with Grein's findings (14, 16, 17) that the anomeric electronic stabilizing effect greatly increases in protonated acetals. As a result, the middle ring flattens considerably and it appears better to draw, for this protonated acetal, an sp_2 hybridized O(1) and a p orbital periplanar to the C—O(2) bond. Transition structure **22** was then found with C—O(1)/C—O(2) bond distances of 1.32 and 1.86 Å with an energy of 38.75 kcal/mol. The geometry of this transition structure is now very close to that of the cyclic oxocarbonium ion **23** found at 38.02 kcal/mol and with C—O(1)/C—O(2) distances of 1.30 and 2.22 Å. The transition structure **22** is about 1.0 kcal/mol higher than the protonated acetal **21** and 0.7 kcal/mol higher than the oxocarbonium ion **23**.

Having no anomeric effect, the two C—O bonds in acetal **16** are of equal length. Upon protonation, **16** provides **24**, with ring B now appearing in a boat form as a result of a strong anomeric effect and a periplanar p orbital. In this case, there is a very small energy barrier after protonation, **24** being at 44.33 and **25** at 44.64 kcal/mol. What is even more important is the comparison between the *cis* and *trans* acetal transition structures. It can be seen that **25** from the *trans* acetal **16** is at a much higher energy (44.64 kcal/mol) than **22** (38.75 kcal/mol) from *cis* acetal **13**. This large difference, which is steric in nature, is a direct consequence of the required periplanar alignment of the p orbital with the neighboring C—O bond. The specific formation of *cis* acetal **13** under kinetically controlled conditions is thus well understood on this basis.

A similar analysis was made for the hydrolysis of spiroketals **5** and **8** (Fig. 2). Each oxygen having one anomeric effect, the two C—O bonds are of equal length in **8**. In **5**, the ring C oxygen having one anomeric effect, the C—O bond lengths vary accordingly (C—O(2)/C—O(1) = 1.42/1.43). Upon protonation, **8** gives **27** at 29.92 kcal/mol; then there is essentially no further energy barrier (**28** = 29.96 kcal/mol) to yield the oxocarbonium ion **29** (25.55 kcal/mol). It can be seen that ring B in **27** (or **28**) is almost a half-chair (or the end of a chair form), which completely flattens in oxocarbonium ion **29**. Upon protonation, **5** provides **30**, with a flattened boat-like conformation, which then provides the half-chair oxocarbonium ion **31**. In this case, no energy barrier was observed between **30** and **31**. Since **30** is about 1 kcal/mol higher than **27**, it follows that the formation of acetal **8** should be slightly favored over acetal **5**, a result in accord with experimentation (**8**:**5** ratio = 3:2).

The most stable conformers **32** and **36** (Fig. 3) of the axial and equatorial methoxytetrahydropyrans were next examined as theoretical models for α- and β-glycosides. The bond length difference in **36** is due to the *exo* anomeric effect. In **32**, each oxygen has one anomeric effect, but the C—OMe bond length was found to be slightly longer. This may be due to a stronger *endo* anomeric effect and (or) to the fact that the C—OMe bond is not part of a ring. As expected, **33** corresponds to a flattened chair and **37** to a flattened boat, **33** and **37** giving then the cyclic oxocarbonium ions **35** and **39** via their respective transition structures **34** and **38**. Since transition structure **38** is slightly higher in energy (≈0.4 kcal/mol) than **34**, it follows that the rate

Can. J. Chem. Downloaded from www.nrcresearchpress.com by 85.192.166.187 on 09/08/12
For personal use only.

Can. J. Chem. Downloaded from www.nrcresearchpress.com by 85.192.166.187 on 09/08/12
For personal use only.

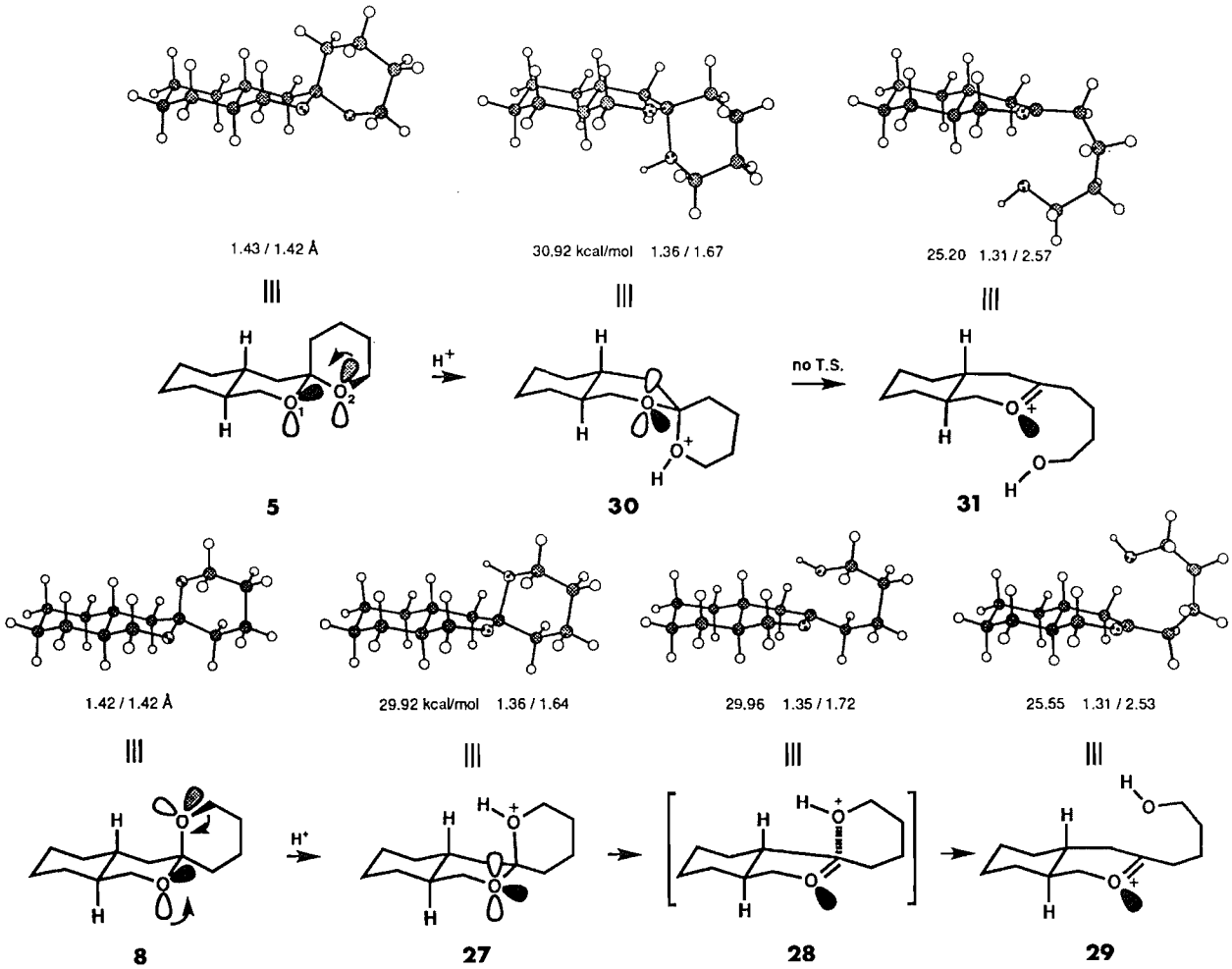

FIG. 2

of hydrolysis of **32** should be slightly faster than **36**. This is in complete accord with the reported hydrolysis of bicyclic acetals **40** and **41** (Scheme 4), which was reported by Eikeren (24). Indeed, the α-anomer **40** is more stable than the β-anomer **41** by 0.45 kcal/mol; on the other hand, **40** is hydrolyzed faster by a factor of 1.5 (≈0.25 kcal/mol). The difference in energy between the two transition states should thus be approximately 0.7 kcal/mol in favor of the α-anomer **40**, in complete agreement with the AM1 calculation. The relative rates of hydrolysis of α- and β-glycosides (3, 4) can thus be explained on the basis that the geometries of their late transition states are close to the half-chair cyclic oxocarbonium ion. In β-glycoside, this transition state can be reached either from a half-chair with a synperiplanar lone pair or via a twist-boat conformation with an antiperiplanar lone pair. Since the twist-boat is attained from the chair via the half-chair, it is thus likely that β-glycosides are hydrolyzed via a *syn* pathway. Such a pathway was previously suggested by Fraser-Reid and co-workers (25, 26) for the hydrolysis of a conformationally rigid β-*n*-pentenylglycoside under neutral conditions by the use of an electrophilic reagent. On the other hand, in α-glycoside the transition state geometry can be obtained directly from the chair conformation with an antiperiplanar lone pair.

Conclusion

The above experimental and molecular modelling studies confirm that proper alignment of an oxygen lone pair periplanar to the leaving group is one of the main driving forces in acetal and ketal hydrolysis.

In acetals, molecular modelling indicates that there is an energy barrier for the cleavage of the protonated form and the transition structure should be late, having a geometry near that of the oxocarbonium ion. More specifically, this transition structure corresponds to a flattened chair in α-glycosides and to a flattened boat in β-glycosides. Also, the hydrolysis of the α-isomer takes place via an antiperiplanar pathway whereas that of the β-isomer probably follows a synperiplanar route. The relative rate hydrolysis of α- and β-glycosides (3, 4) can be readily explained on that basis.

In ketals, AM1 calculations indicate that there is essentially no energy barrier after the protonation step (see Fig. 2); the transition state for the ketal hydrolysis must be very early, having a geometry close to that of their protonated form. The fact that there would be essentially no energy barrier after protonation would be the result of a steric decompression effect of the two alkyl groups present in ketal. As a result and in accord with experimental results, ketals are hydrolyzed at a much faster rate than acetals (27). Also, this rationalization is in accord with the fact that spiroketals such as **5** and **8** are very readily equilibrated with mild acid, whereas isomeric acetals such as **13** and **16**, or the α- and β-glycoside models **40** and **41**, require stronger acidic conditions for equilibration.

Work is now in progress to establish that the slow steps in acetals and ketals are not the same.

Can. J. Chem. Downloaded from www.nrcresearchpress.com by 85.192.166.187 on 09/08/12
For personal use only.

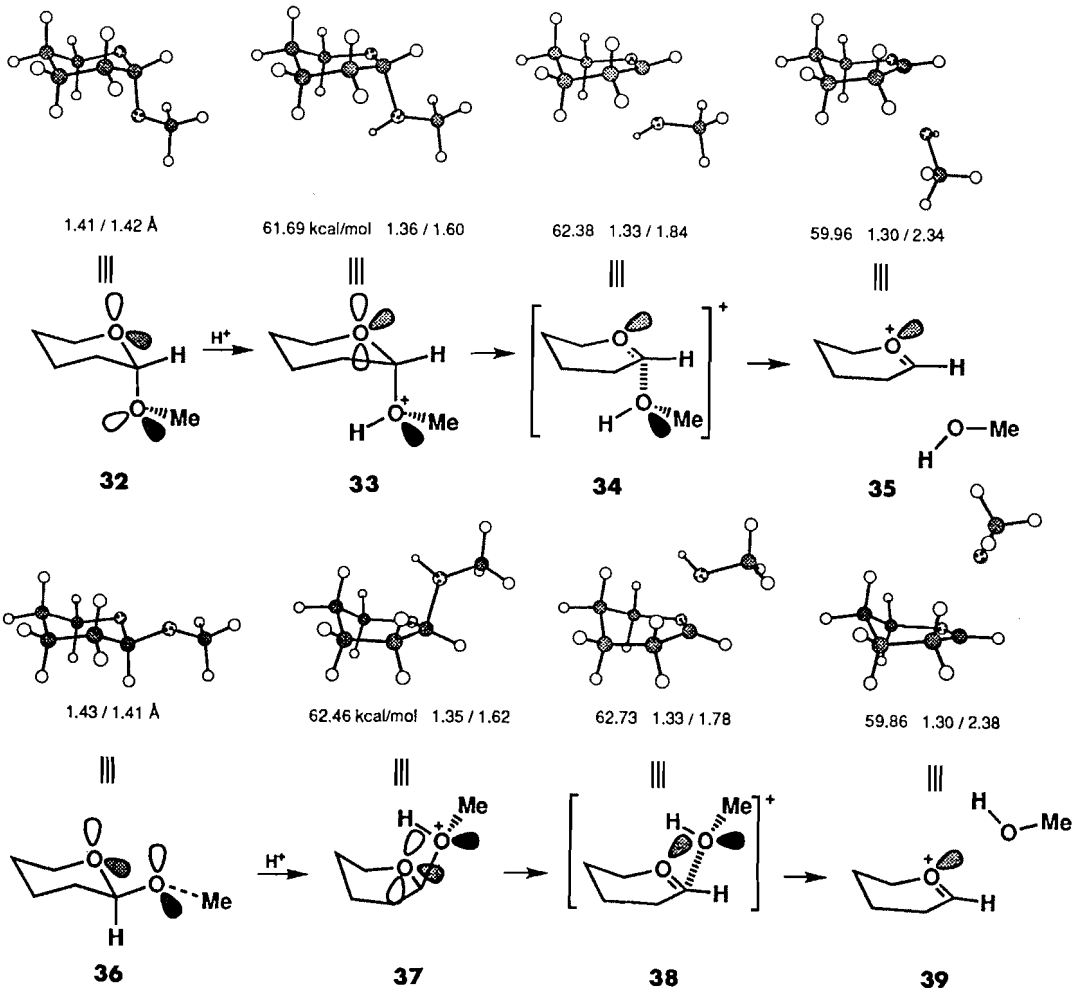

FIG. 3

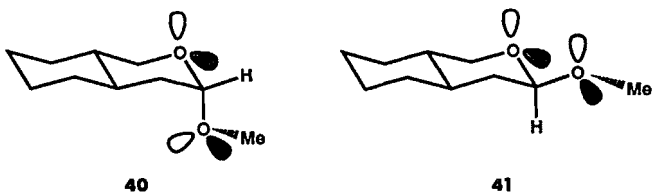

SCHEME 4

Acknowledgements

This work was supported financially by the Natural Sciences and Engineering Research Council of Canada (NSERCC) and by the Fonds pour la Formation de Chercheurs et l'Aide à la Recherche (FCAR) du Québec.

1. P. Deslongchamps. *In* Stereoelectronic effects in organic chemistry. *Edited by* J.E. Baldwin. Organic Chemistry Series. Vol. 1. Pergamon Press, Oxford, England. 1983.
2. A.J. Kirby. *In* The anomeric effect and related stereoelectronic effects at oxygen. Springer-Verlag, Berlin. 1983.
3. J.N. BeMiller. Adv. Carbohydr. Chem. **22**, 25 (1967).
4. J.N. BeMiller. Adv. Carbohydr. Chem. **25**, 544 (1970).
5. M.J.S. Dewar, E.G. Zoebisch, E.F. Healy, and J.J.P. Stewart. J. Am. Chem. Soc. **107**, 3902 (1985).
6. N. Pothier, S. Goldstein, and P. Deslongchamps. Helv. Chim. Acta, **75**, 604 (1992).
7. P. Deslongchamps. Pure Appl. Chem. **65**, 1161 (1993).
8. P. Deslongchamps. *In* The anomeric effect and associated stereoelectronic effects. Intramolecular strategies and stereoelectronic effects. Glycosides and orthoesters hydrolysis revisited. *Edited by* G.R.J. Thatcher. ACS Symp. Ser. 539, Washington, D.C. 1993. pp. 26–54. Chap. 3.
9. P. Deslongchamps, D.D. Rowan, N. Pothier, G. Sauvé, and J.K. Saunders. Can. J. Chem. **59**, 1105 (1981).
10. N. Beaulieu, R.A. Dickinson, and P. Deslongchamps. Can. J. Chem. **58**, 2531 (1980).
11. P. Deslongchamps and D. Guay. Can. J. Chem. **63**, 2757 (1985).
12. H.B. Bürgi, J.D. Dunitz, and E. Shefter. J. Am. Chem. Soc. **95**, 5065 (1973).
13. H.B. Bürgi and J.D. Dunitz. Acc. Chem. Res. **16**, 153 (1983).
14. F. Grein and P. Deslongchamps. Can. J. Chem. **70**, 1562 (1992).
15. R.U. Lemieux and A.R. Morgan. Can. J. Chem. **43**, 2205 (1965).
16. F. Grein and P. Deslongchamps. Can. J. Chem. **70**, 604 (1992).
17. F. Grein. *In* The anomeric effect and associated stereoelectronic effects. Anomeric and reverse anomeric effect in acetals and related functions. *Edited by* G.R.J. Thatcher. ACS Symp. Ser. 539, Washington, D.C. 1993. pp. 205–225. Chap. 11.
18. P. Deslongchamps and C. Moreau. Can. J. Chem. **49**, 2465 (1971).
19. P. Deslongchamps, C. Moreau, D. Fréhel, and P. Atlani. Can. J. Chem. **50**, 3402 (1972).
20. P. Deslongchamps, P. Atlani, D. Fréhel, A. Malaval, and C. Moreau. Can. J. Chem. **52**, 3651 (1974).
21. S. Li and P. Deslongchamps. Tetrahedron Lett. **34**, 7759 (1993).
22. S. Li, A.J. Kirby, and P. Deslongchamps. Tetrahedron Lett. **34**, 7757 (1993).

23. K.N. Houk, Y. Li, and J.D. Evanseck. Angew. Chem. Int. Ed. Engl. **31**, 682 (1992).
24. P.v. Eikeren. J. Org. Chem. **45**, 4641 (1980).
25. A.J. Ratcliffe, D.R. Mootoo, C.W. Andrews and B. Fraser-Reid. J. Am. Chem. Soc. **111**, 7661 (1989).
26. C.W. Andrews, B. Fraser-Reid, and J.P. Bowen. *In* The anomeric effect and associated stereoelectronic effects. Involvement of *ns** interactions in glycoside cleavage. *Edited by* G.R.J. Thatcher. ACS Symp. Ser. 539, Washington, D.C. 1993. pp. 114–125. Chap. 7.
27. E.H. Cordes and H.G. Bull. Chem. Rev. 584 (1974).

Can. J. Chem. Downloaded from www.nrcresearchpress.com by 85.192.166.187 on 09/08/12
For personal use only.

Structural studies of ligands for the glycine binding site of the excitatory amino acid receptor complex: 2. 6-bromo-, 6-methyl-, and 6-styryl-1,8-ethano-4-hydro-2,3-quinoxalinedione

MACIEJ KUBICKI,[1] TERESA W. KINDOPP, MARIO V. CAPPARELLI,[2] AND PENELOPE W. CODDING[3]

Departments of Chemistry and of Pharmacology and Therapeutics, University of Calgary, Calgary, AB T2N 1N4, Canada

Received January 7, 1994

MACIEJ KUBICKI, TERESA W. KINDOPP, MARIO V. CAPPARELLI, and PENELOPE W. CODDING. Can. J. Chem. **72**, 2028 (1994).

The crystal structures of three tricyclic quinoxalinedione derivatives, 6-bromo-1,8-ethano-4-hydro-2,3-quinoxalinedione (**1**), 6-methyl-1,8-ethano-4-hydro-2,3-quinoxalinedione hydrate (**2**), and 6-styryl-1,8-ethano-4-hydro-2,3-quinoxalinedione (**3**), are reported. For **1** and **2**, the space groups are $P2_1/n$ with the unit cell parameters for **1**: a = 7.4003(5) Å, b = 8.5799(5) Å, c = 14.3127(9) Å, β = 90.639(6)°, and for **2**: a = 7.0590(2) Å, b = 10.7483(3) Å, c = 13.9509(7) Å, β = 103.290(3)°. For **3**, the space group is $P2_1/c$, with a = 19.3683(10) Å, b = 8.0962(16) Å, c = 19.5801(16) Å, β = 114.028(6)°. Compound **3** crystallizes with two molecules in the asymmetric part of the unit cell; in one of them the styryl group is disordered. The geometries of the 1,8-ethano-4-hydro-2,3-quinoxalinedione fragments are similar in all observations, with the differences mainly caused by the different nature of the substituents in the 6-position. Hydrogen bonds connect the molecules into three-dimensional networks. Head-to-tail π-stacking between molecules connected by a center of symmetry determines the packing modes in **1** and **2** but there is no π-stacking in the crystal structure of **3**. The crystal structures of the three quinoxaline derivative ligands for the glycine receptor suggest a mode of recognition that involves an N—H···*receptor* hydrogen bond, a three-centre hydrogen bond to the neighboring carbonyl groups on the ligand, and π-stacking between ligand and receptor. This mode is consistent with the geometric constraints of the current binding site model but places greater emphasis on hydrogen-bond interactions.

MACIEJ KUBICKI, TERESA W. KINDOPP, MARIO V. CAPPARELLI et PENELOPE W. CODDING. Can. J. Chem. **72**, 2028 (1994).

On a déterminé les structures cristallines de trois dérivés tricycliques de la quinoxalinedione, la 6-bromo-1,8-éthano-4-hydro-2,3-quinoxalinedione (**1**), l'hydrate de la 6-méthyl-1,8-éthano-4-hydro-2,3-quinoxalinedione (**2**) et la 6-styryl-1,8-éthano-4-hydro-2,3-quinoxalinedione (**3**). Les composés **1** et **2** cristallisent dans le groupe d'espace $P2_2/n$ avec, pour **1**, a = 7,4003(5), b = 8,5799(5) et c = 14,3127(9) Å et β = 90,639(6)° et, pour **2**, a = 7,0590(2), b = 10,7483(3) et c = 13,9509(7) Å et β = 103,290(3)°. Le composé **3** cristallise dans le groupe d'espace $P2_1/c$, avec a = 19,3683(10), b = 8,0962(16) et c = 19,5801(16) Å, β = 114,038(6)°. Le composé **3** cristallise avec deux molécules de solvant dans la partie asymétrique du motif de la maille dans un desquels le groupe styryle est désordonné. Les géométries des fragments 1,8-éthano-4-hydro-2,3-quinoxalinedione sont semblables dans tous les composés examinés; les différences sont principalement causées par la nature différente des substituants en position 6. Des atomes d'hydrogène relient les molécules dans des réseaux tridimensionnels. Un entassement π tête-à-queue entre les molécules reliées par un centre de symétrie détermine les modes d'empilement dans les composés **1** et **2**; toutefois, il n'y a pas d'entassement π dans la structure cristalline du composé **3**. Les structures cristallines des trois coordinats dérivés de la quinoxaline pour le récepteur glycine suggère un mode de reconnaissance qui implique une liaison hydrogène N—H···*recepteur*, une liaison à trois centres hydrogènes avec les groupes carbonyles voisins sur le coordinat et l'empilement π entre le ligand et le récepteur. Ce mode est en accord avec les contraintes géométriques du modèle courant du site de liaison, mais il met plus d'emphase sur les interactions des liaisons hydrogène.

[Traduit par la rédaction]

Introduction

Quinoxalinedione (QD) derivatives are highly potent antagonists of the strychnine-insensitive glycine modulatory site of the NMDA receptor contained in the excitatory amino acid receptor complex (1); QD derivatives also show significant antagonistic activity for non-NMDA (i.e., kainate and AMPA) receptors (2). Excitatory amino acids (EAA) are the main neurotransmitters mediating synaptic excitation in the central nervous system (3); therefore, antagonists and agonists for EAA receptors are regarded as potential therapies for numerous CNS disorders, including ischemic brain damage (4) and epilepsy (5). The QD family is particularly useful for structure–activity studies because, in contrast to the other known NMDA receptor antagonists, they do not contain the glycine structural element, and small structural changes produce large differences in biological response. Our previous X-ray crystallographic studies (6, 7) show that there at least two important structural features responsible for biological action: hydrogen bonding and the charge distribution in the molecule. These studies identified a symmetrical pattern of hydrogen bonding for all 6,7-disubstituted QD derivatives, which featured both two-centre hydrogen bonds to the two carbonyl groups and a shared three-centre hydrogen bond in nearly equal proportions. An unsymmerical hydrogen-bonding pattern for the highly active 5,7-dinitro QD compound was observed due to an intramolecular hydrogen bond. Further investigation of these hydrogen-bonding patterns is required to refine the current model of the NMDA receptor glycine modulatory site pharmacophore (8), particularly since the model focuses on an ionic interaction with the glycine carboxyl group rather than hydrogen bonds to the QD carbonyl groups.

We studied the X-ray crystallographic structures of three tricyclic QD derivatives: 6-bromo- (**1**), 6-methyl- (**2**), and the hydrate of 6-styryl-1,8-ethano-4-hydro-2,3-quinoxalinedione (**3**). These compounds display a range of activity against ^{3}H glycine binding; the IC_{50} value for **1** is equal to 13 μM, for **2** 85 μM, and **3** is not active in the binding experiments.[4] The

[1]Present address: Department of Chemistry, Adam Mickiewicz University, 60-780 Poznan, Poland.

[2]Present address: Escuela de Quimica, Universidad Central de Venezuela, Caracas 1051, Venezuela.

[3]Author to whom correspondence may be addressed.

[4]Dr. Linda M. Pullan. ICI Pharmaceuticals. Private communication.

Can. J. Chem. Downloaded from www.nrcresearchpress.com by 85.192.166.187 on 09/08/12
For personal use only.

TABLE 1. Crystal data

Parameter	1	2	3
Formula	$C_{10}H_7N_2O_2Br$	$C_{11}H_{10}N_2O_2 \cdot H_2O$	$C_{18}H_{14}N_2O_2$
M_r	267.08	220.23	290.32
V(Å^3)	908.7(1)	1030.1(1)	2804.4(6)
d_x(Mg m^{-3})	1.95	1.42	1.38
μ(cm^{-1})	60.50	8.33	6.97
Crystal dimensions (mm)	0.46 × 0.34 × 0.30	0.38 × 0.36 × 0.64	0.15 × 0.15 × 0.35
θ range for cell parameters	22.18°–42.01°	19.56°–59.70°	19.97°–31.01°
hkl ranges	−8/8; 0/19; −16/16	−7/7; 0/12; 0/15	0/24; 0/10; −24/24
Max sin θ/λ (Å^{-1})	0.63	0.63	0.63
No. of unique reflections	1870	2117	5762
No. of observed reflections ($I \geq 2\sigma(I)$)	1854	2044	3198
No. of parameters refined	165	206	2 × 278
Weighting scheme (w^{-1})	$\sigma^2(F_o) + 0.0002F_o^2$	$\sigma^2(F_o)$	$\sigma^2(F_o)$
Final R	0.043	0.033	0.066
Final wR	0.061	0.045	0.066
S (goodness-of-fit)	3.50	2.81	1.40
Extinction correction (x in $F_c' = F_c(1 - xF_c^2/\sin\theta)$)	19(2) × 10^{-7}	28(2) × 10^{-7}	12(3) × 10^{-7}
Max. shift/error	0.017	0.004	0.004
Max./min.$\Delta\rho$ (e Å^{-3})	0.46/−0.45	0.32/−0.28	0.22/−0.22

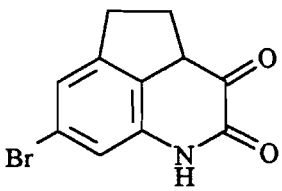

1

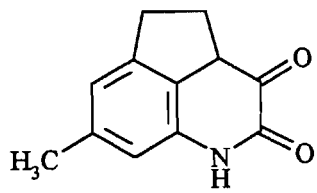

2

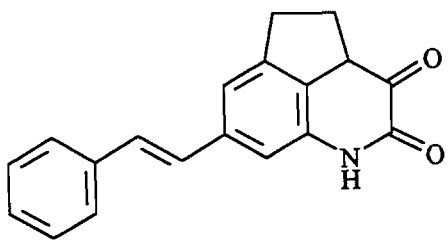

3

main reason for these studies was to determine the hydrogen-bonding schemes and the packing modes and to search for an explanation of the activity profile of these compounds.

Experimental

Samples were provided by ICI Americas Inc., Wilmington, Del. Colorless prisms of the three compounds were obtained by slow evaporation from dimethylformamide (**1** and **2**), and an acetone–water mixture (**3**). X-ray intensity data were collected at room temperature on an Enraf–Nonius CAD-4F automated diffractometer with Ni-filtered CuK_α radiation (λ = 1.54178 Å), using an $\omega/2\theta$ scan mode. Accurate unit-cell parameters were obtained by least-squares treatment of the setting angles of 25 reflections Three standard reflections were measured after 2000 s of exposure, the intensities decreased by 12% for **1**, 3.5% for **2**, and 8% for **3** and the data were corrected for this linear decay. Both Lorentz and polarization corrections were applied. An empirical absorption correction was made for compound **1** due to the large μ value (T_{max} = 0.331, T_{min} = 0.199). Additional crystal data are in Table 1.

All three structures were solved by direct methods using SHELXS86 (9). Full-matrix refinement was performed for **1** and **2** and block-matrix refinement for **3** (one symmetrically independent molecule in each block) using the least-squares program of SHELX-76 (10); the function $\Sigma w(|F_o| - |F_c|)^2$ was minimized. All non-hydrogen atoms were refined with anisotropic thermal parameters. For **1**, all hydrogen atoms were found in a ΔF map and their positional and isotropic thermal parameters were refined. For **2**, the hydrogen atoms of the methyl group were disordered and two positions with refined occupancies of 0.5 were defined. In the final cycles the occupancies of the disordered atoms were fixed and the positional and isotropic thermal parameters of all hydrogen atoms were refined. Molecule B of compound **3** showed disorder in the positions of C61 and C62 with occupancies of 0.7 and 0.3 for the two components. Although visible in the ΔF map, the disordered hydrogen atoms were not refined but were allowed to move with the carbon atoms and have U_{iso} values calculated from the respective carbon atom U_{eq} values. All of the other hydrogen atoms were refined with the isotropic thermal parameters. For each structure, an isotropic extinction correction was made during the final stages of refinement.

The atomic scattering factors for non-hydrogen atoms were taken from Cromer and Mann (11), and for hydrogen atoms from Stewart et al. (12). Other computer programs used: ORTEP (13), PLUTO (14), and CSU88 (15). The final atomic coordinates for all structures are given in Table 2.[5] The bond lengths and angles are listed in Table 3.

[5]Tables of anisotropic thermal parameters for non-hydrogen atoms, hydrogen atom fractional coordinates and isotropic thermal parameters, bond lengths and angles involving hydrogen atoms, dihedral angles for non-H atoms, least-squares plane data, and the packing scheme of compound **3** may be purchased from: The Depository of Unpublished Data, Document Delivery, CISTI, National Research Council Canada, Ottawa, ON K1A 0S2, Canada. Structure factor amplitudes are no longer being deposited and may be obtained directly from the author.

Tables of H-atom coordinates, bond lengths and angles for H-atoms, and the packing scheme of **3** have also been deposited with the Cambridge Crystallographic Data Centre, and can be obtained on request from The Director, Cambridge Crystallographic Data Centre, 12 Union Road, Cambridge CB2 1EZ, U.K.

Can. J. Chem. Downloaded from www.nrcresearchpress.com by 85.192.166.187 on 09/08/12
For personal use only.

Can. J. Chem. Downloaded from www.nrcresearchpress.com by 85.192.166.187 on 09/08/12
For personal use only.

TABLE 2. Non-hydrogen fractional atomic parameters ($\times 10^4$ and for Br, $\times 10^5$), equivalent thermal parameters ($\times 10^4$ Å^2) with esd's in parentheses, and site occupancy factors (if not equal to one). U_{eq} is defined as: $U_{eq} = (1/3)\Sigma_i\Sigma_j U_{ij} a_i a_j \boldsymbol{a}_i^* \boldsymbol{a}_j^*$

Compound **1**

Atom	x/a	y/b	z/c	U_{eq}
N1	3624(3)	7193(2)	5407(1)	318(4)
C2	3856(3)	7514(3)	6316(2)	339(5)
O2	4436(4)	8738(2)	6624(2)	471(5)
C3	3264(4)	6224(3)	6987(2)	345(5)
O3	3380(5)	6468(2)	7823(2)	558(7)
N4	2559(3)	4883(3)	6627(1)	340(4)
C4a	2377(3)	4608(3)	5667(2)	283(4)
C5	1672(3)	3267(3)	5257(2)	311(4)
C6	1544(3)	3208(3)	4292(2)	312(4)
Br6	5254(4)	13769(3)	37519(2)	380(1)
C7	2036(3)	4434(3)	3705(2)	333(5)
C8	2738(3)	5761(3)	4122(2)	306(5)
C8a	2926(3)	5793(3)	5081(2)	278(4)
C9	3319(4)	7330(3)	3742(2)	412(6)
C10	3899(4)	8266(3)	4616(2)	396(6)

Compound **2**

Atom	x/a	y/b	z/c	U_{eq}
N1	1725(1)	3537(1)	4493(1)	379(2)
C2	1622(2)	2661(1)	5164(1)	386(3)
O2	1122(2)	1578(1)	4974(1)	522(2)
C3	2225(2)	3084(1)	6237(1)	387(2)
O3	2186(2)	2332(1)	6888(1)	564(3)
N4	2819(2)	4278(1)	6430(1)	379(2)
C4a	2849(2)	5157(1)	5700(1)	337(2)
C5	3375(2)	6402(1)	5860(1)	405(3)
C6	3331(2)	7190(1)	5057(1)	451(3)
C61	3873(3)	8557(1)	5226(2)	615(5)
C7	2756(2)	6728(1)	4088(1)	486(3)
C8	2237(2)	5491(1)	3928(1)	427(3)
C8a	2291(2)	4749(1)	4741(1)	350(2)
C9	1567(2)	4702(2)	3017(1)	536(4)
C10	1312(2)	3379(2)	3414(1)	510(3)
O1w	373(2)	−38(1)	6677(1)	602(3)

Compound **3**

Atom	x/a	y/b	z/c	U_{eq}	Occ. fac.
N1A	3019(2)	8599(3)	6485(1)	421(7)	
C2A	3661(2)	9361(4)	6933(2)	445(9)	
O2A	3930(2)	9313(3)	7610(1)	650(8)	
C3A	4058(2)	10348(4)	6525(2)	441(9)	
O3A	4631(1)	11117(3)	6886(1)	564(7)	
N4A	3753(2)	10292(3)	5761(2)	402(7)	
C4aA	3054(2)	9574(4)	5337(2)	392(8)	
C5A	2669(2)	9664(4)	4558(2)	432(9)	
C6A	1962(2)	8925(4)	4200(2)	445(8)	
C61A	1545(2)	9098(5)	3389(2)	497(10)	
C62A	895(2)	8411(5)	2968(2)	493(9)	
C63A	433(2)	8672(4)	2173(2)	421(8)	
C64A	584(2)	9855(5)	1740(2)	485(9)	
C65A	103(2)	10066(5)	1000(2)	550(11)	
C66A	−541(2)	9123(5)	677(2)	552(10)	
C67A	−698(2)	7942(5)	1096(2)	555(10)	
C68A	225(2)	7733(5)	1832(2)	521(10)	
C7A	1639(2)	8066(4)	4626(2)	487(9)	
C8A	2019(2)	7955(4)	5388(2)	430(8)	

TABLE 2 (*Concluded*)

Compound **3**

Atom	x/a	y/b	z/c	U_{eq}	Occ. fac.
C8aA	2712(2)	8718(4)	5721(2)	397(8)	
C9A	1846(2)	7153(5)	6001(2)	515(10)	
C10A	2521(2)	7602(5)	6733(2)	512(10)	
N1B	5378(2)	12198(4)	9952(1)	430(7)	
C2B	4741(2)	12961(4)	9521(2)	456(9)	
O2B	4324(1)	13695(3)	9756(1)	616(7)	
C3B	4527(2)	12873(5)	8683(2)	486(9)	
O3B	3959(2)	13592(4)	8253(1)	734(8)	
N4B	4971(2)	11957(4)	8441(2)	502(8)	
C4aB	5612(2)	11111(4)	8917(2)	442(9)	
C5B	6085(3)	10113(5)	8709(3)	575(12)	
C6B	6718(2)	9385(5)	9250(3)	641(14)	
C61B	7322(5)	8365(9)	9155(4)	521(19)	0.7
C61B′	7019(9)	8524(17)	8734(11)	407(42)	0.3
C62B	7262(5)	8037(8)	8482(3)	460(16)	0.7
C62B′	7667(7)	7642(16)	9011(9)	442(35)	0.3
C63B	7898(3)	7084(5)	8365(4)	761(18)	
C68B	8563(4)	6432(7)	8892(3)	811(17)	
C67B	9085(3)	5653(6)	8671(3)	757(15)	
C66B	8926(3)	5539(5)	7924(3)	713(15)	
C65B	8262(3)	6167(6)	7415(3)	722(14)	
C64B	7753(3)	6937(6)	7630(4)	762(16)	
C7B	6885(3)	9599(5)	10008(3)	619(13)	
C8B	6421(2)	10562(5)	10219(2)	508(10)	
C8aB	5802(2)	11280(4)	9671(2)	411(9)	
C9B	6441(3)	11052(6)	10967(2)	637(12)	
C10B	5727(3)	12115(6)	10791(2)	562(11)	

TABLE 3. (*a*) Bond lengths (Å) with esd's in parentheses

Bond	**1**	**2**	**3***a*	**3***b*
N1—C2	1.339(3)	1.342(2)	1.345(4)	1.330(4)
N1—C8a	1.386(3)	1.383(2)	1.370(4)	1.377(6)
N1—C10	1.475(3)	1.476(2)	1.483(6)	1.502(4)
C2—O2	1.216(3)	1.228(2)	1.212(4)	1.233(5)
C2—C3	1.533(4)	1.529(2)	1.539(6)	1.522(5)
C3—O3	1.217(3)	1.220(2)	1.217(4)	1.226(4)
C3—N4	1.362(3)	1.357(2)	1.367(5)	1.359(6)
N4—C4a	1.399(3)	1.394(2)	1.395(4)	1.392(4)
C4a—C5	1.391(3)	1.393(2)	1.401(5)	1.401(7)
C4a—C8a	1.382(3)	1.376(2)	1.375(6)	1.375(5)
C5—C6	1.385(3)	1.398(2)	1.394(5)	1.384(6)
C6—Br6	1.903(2)			
C6—C61		1.523(2)	1.466(5)	1.504(11)
				1.525(23)[a]
C6—C7	1.397(3)	1.410(2)	1.413(6)	1.395(8)
C7—C8	1.384(3)	1.383(2)	1.372(5)	1.374(7)
C8—C8a	1.379(3)	1.379(2)	1.377(5)	1.371(4)
C8—C9	1.516(4)	1.511(2)	1.517(6)	1.503(6)
C9—C10	1.543(4)	1.551(2)	1.539(4)	1.544(8)
C61—C62			1.315(5)	1.302(11)
				1.351(20)[a]
C62—C63			1.461(5)	1.548(11)
				1.570(20)[a]
C63—C64			1.387(6)	1.355(11)
C63—C68			1.398(5)	1.386(8)
C64—C65			1.377(5)	1.370(10)
C65—C66			1.377(5)	1.365(6)
C66—C67			1.372(6)	1.370(8)
C67—C68			1.367(5)	1.401(10)

Can. J. Chem. Downloaded from www.nrcresearchpress.com by 85.192.166.187 on 09/08/12
For personal use only.

TABLE 3. (*b*) Bond lengths (°) with esd's in parentheses

Bonds	1	2	3*a*	3*b*
C2—N1—C8a	123.3(2)	123.0(1)	123.7(3)	123.2(3)
C2—N1—C10	126.9(2)	127.0(1)	126.0(3)	127.1(3)
C8a—N1—C10	109.7(2)	110.0(1)	110.2(3)	109.7(3)
N1—C2—O2	124.9(2)	124.9(1)	124.8(3)	124.5(3)
N1—C2—C3	115.2(2)	115.3(1)	115.1(3)	116.0(3)
O2—C2—C3	119.9(2)	119.7(1)	120.1(3)	119.5(3)
C2—C3—O3	118.4(2)	118.8(1)	119.6(3)	119.5(4)
C2—C3—N4	118.9(2)	118.6(1)	117.8(3)	117.9(3)
O3—C3—N4	122.7(3)	122.5(1)	122.6(3)	122.5(4)
C3—N4—C4a	123.1(2)	123.5(1)	123.2(3)	123.6(4)
N4—C4a—C5	125.8(2)	125.6(1)	125.7(3)	126.9(4)
N4—C4a—C8a	116.5(2)	116.4(1)	116.9(3)	116.5(3)
C5—C4a—C8a	117.7(2)	117.9(1)	117.4(3)	116.7(4)
C4a—C5—C6	118.2(2)	119.8(1)	120.3(3)	120.2(5)
C5—C6—Br6	117.2(2)			
C5—C6—C61		120.1(1)	119.9(3)	129.1(5)
				98.4(8)[a]
C5—C6—C7	123.8(2)	120.2(1)	119.7(3)	120.7(5)
Br6—C6—C7	118.8(2)			
C61—C6—C7		119.6(1)	120.4(3)	110.2(5)
				140.9(8)[a]
C6—C7—C8	117.4(2)	120.0(1)	120.3(3)	119.6(5)
C7—C8—C8a	118.7(2)	117.9(1)	118.3(3)	118.4(4)
C7—C8—C9	133.0(2)	134.0(1)	134.0(3)	133.0(4)
C8a—C8—C9	108.3(2)	108.1(1)	107.7(3)	108.6(4)
N1—C8a—C4a	123.0(2)	123.0(1)	122.8(3)	122.7(3)
N1—C8a—C8	112.7(2)	112.8(1)	113.1(3)	112.9(3)
C4a—C8a—C8	124.2(2)	124.2(1)	124.1(3)	124.4(4)
C8—C9—C10	104.4(2)	104.8(1)	105.0(3)	105.3(4)
N1—C10—C9	105.0(2)	104.2(1)	104.1(3)	103.4(4)
C6—C61—C62			127.1(4)	118.9(7)
				121.3(14)[a]
C61—C62—C63			128.4(4)	120.2(7)
				110.6(12)[a]
C62—C63—C64			124.1(3)	111.6(6)
				151.3(8)[a]
C62—C63—C68			118.3(3)	129.4(6)
				89.6(7)[a]
C64—C63—C68			117.5(3)	119.0(6)
C63—C64—C65			120.5(4)	120.2(6)
C64—C65—C66			120.8(4)	121.8(5)
C65—C66—C67			119.4(4)	119.4(5)
C66—C67—C68			120.0(4)	118.9(5)
C63—C68—C67			121.7(4)	120.7(6)

TABLE 3. (*c*) Selected torsion angles (°) for **3**

	Molecular A	Molecule B
C4a—C5—C6—C61	176.8(3)	−175.9(6)
		−178.6(8)[a]
C5—C6—C61—C62	176.3(4)	−2.2(11)
		178.5(14)[a]
C6—C61—C62—C63	174.0(4)	176.2(6)
		−172.8(11)[a]
C61—C6—C7—C8	−177.7(4)	177.0(5)
		179.3(12)[a]
C61—C62—C63—C64	−6.6(7)	−176.8(7)
		−7.5(23)[a]
C61—C62—C63—C68	176.8(4)	2.0(11)
		175.1(12)[a]
C62—C61—C6—C7	−6.1(6)	−179.9(7)
		−1.7(24)[a]

[a]Refers to the other position of disordered atoms.

Results

Hydrogen-bond networks connect the molecules into three-dimensional structures. In **1**, the N-H group acts as a donor in a three-centered hydrogen bond with both of the carbonyl oxygen atoms of the molecule and there is a relatively strong C—H···O hydrogen bond. In **2**, the oxygen atom of the water molecule accepts an N—H···O bond and acts as a donor for a three-centre and a two-centre hydrogen bond with the carbonyl oxygen atoms. The N-H group of compound **3** is bonded with one carbonyl oxygen atom (molecule A) or with both carbonyl oxygen atoms (molecule B) in an unsymmetrical three-centre hydrogen bond. Overall, all N-H groups are involved in hydrogen bonds and the carbonyl oxygen atoms are in all but one case involved in three-centre hydrogen bonds. The hydrogen-bond geometry is listed in Table 4 and illustrated in Figs. 1, 2, and 3.

Additionally, as shown in Figs. 4 and 5, there is head-to-tail π-stacking between the neighboring molecules connected by a centre of symmetry in the crystals of **1** and **2**. The distances between the least-squares planes of the molecules at (x, y, z) and ($-x$, $1-y$, $1-z$) are 3.379(2) Å for **1**, and 3.387(2) Å for **2**; and between the molecules at (x, y, z) and ($1-x$, $1-y$, $1-z$) are 3.466(2) Å for **1**, and 3.420(2) Å for **2**. The packing modes of these two compounds are similar.

For compound **3**, the packing mode is quite different. There are two molecules in the asymmetric part of the unit cell; the dihedral angle between the mean planes of the quinoxalinedione moieties is 68.88(4)°, and between the planes of the phenyl rings in the styryl groups is 74.10(10)°. There is no stacking between the molecules, and hydrogen bonds and van der Waals forces are the only factors determining the packing mode.

The quinoxaline fragments in all molecules are nearly planar (the maximum deviation is in molecule **3***b*, which has a dihedral angle of 4.75(9)° between the mean planes). The five-membered rings are approximately coplanar with the quinoxaline fragments (the maximum deviation in molecule **1** shows a interplane angle of 4.84(9)°). The carbonyl oxygen atoms are in the plane of the quinoxaline fragment except in the strong hydrogen bonds in compound **3** where the oxygen atoms deviate by 0.110(2) Å for O3A and 0.104(2) Å for O2B. The bond lengths and angles in the 1,8-ethano-2,3-quinoxalinedione fragments are similar in the four molecules. The attached five-membered ring causes strain in the molecule which is taken up by changes in the geometry of quinoxaline fragment as compared with the compounds without an attached ring (6, 7, 16–18); these changes are mainly visible in the bond angles, as has been observed in acenaphthene derivatives (19–21). In the phenyl ring, the substituent at C6 affects the bond angles; the effects of the methyl and the styryl groups are almost identical (22).

The crystal structure of **3** contains two independent molecules in the asymmetric part of the unit cell. One of these molecules (B) is significantly disordered; the disorder is caused by a rotation of a styryl group. The relevant torsion angles are listed in Table 3 (*c*). Alternative positions for the disordered atoms of the phenyl ring could not be identified due to the nature of the disorder; this failure is reflected in relatively large values for the U_{eq}'s and in the shapes of the thermal ellipsoids, in the poor geometry of ethene bridge in molecule B, and in the large thermal parameters for C5, C6, and C7. Similar disorder was also observed in the crystal structures of related compounds, *trans*-stilbene (23) and *trans*-azobenzene (24). The geometries of the quinoxalinedione moieties in both unique molecules and of the styryl group in molecule A are reasonable;

TABLE 4. Hydrogen bond data

D	H	A	D—H (Å)	A···H (Å)	D···A (Å)	D—H···A (deg)
			Compound **1**			
N4	H4	O2^{i}	0.77(4)	2.40(4)	3.080(3)	148(4)
N4	H4	O3^{i}	0.77(4)	2.46(4)	3.115(3)	144(4)
C5	H5	O3^{i}	1.06(4)	2.28(4)	3.151(3)	138(3)
			Compound **2**			
N4	H4	O1w^{ii}	0.98(1)	1.78(1)	2.756(1)	171(2)
O1w	H1w	O2^{iii}	1.03(2)	1.82(2)	2.835(1)	170(2)
O1w	H2w	O2	0.87(2)	2.37(3)	3.085(2)	141(2)
O1w	H2w	O3	0.87(2)	2.09(2)	2.835(2)	144(2)
*C5	H5	O3^{ii}	1.01(2)	2.51(2)	3.406(2)	148(1)
*C10	H102	O3^{iv}	0.99(2)	2.39(2)	3.278(2)	150(2)
			Compound **3**			
N4A	H4A	O2B^{v}	1.00(5)	1.81(5)	2.746(5)	156(4)
N4B	H4B	O2A	1.03(4)	2.54(4)	2.937(4)	102(3)
N4B	H4B	O3A	1.03(4)	1.90(4)	2.921(4)	171(3)
*C5A	H5A	O2B^{v}	1.03(4)	2.56(4)	3.344(4)	133(3)
*C64B	H64B	O3B^{vi}	1.11(5)	2.28(5)	3.333(6)	159(4)
*C9B	H92B	O2A^{vii}	1.01(5)	2.53(5)	3.162(6)	121(3)
*C10B	H101B	O2A^{vii}	1.14(5)	2.69(3)	3.144(5)	103(2)

Symmetry codes:

i 0.5 − *x*, −0.5 + *y*, 1.5 − *z*
ii 1/2 − *x*, −1/2 + *y*, 3/2 − *z*
iii −*x*, −*y*, 1 − *z*
iv −0.5 + *x*, 0.5 − *y*, −0.5 + *z*
v *x*, 2.5 − *y*, −0.5 + *z*
vi 1 − *x*, −0.5 + *y*, 1.5 − *z*
vii 1 − *x*, 2 − *y*, 2 − *z*

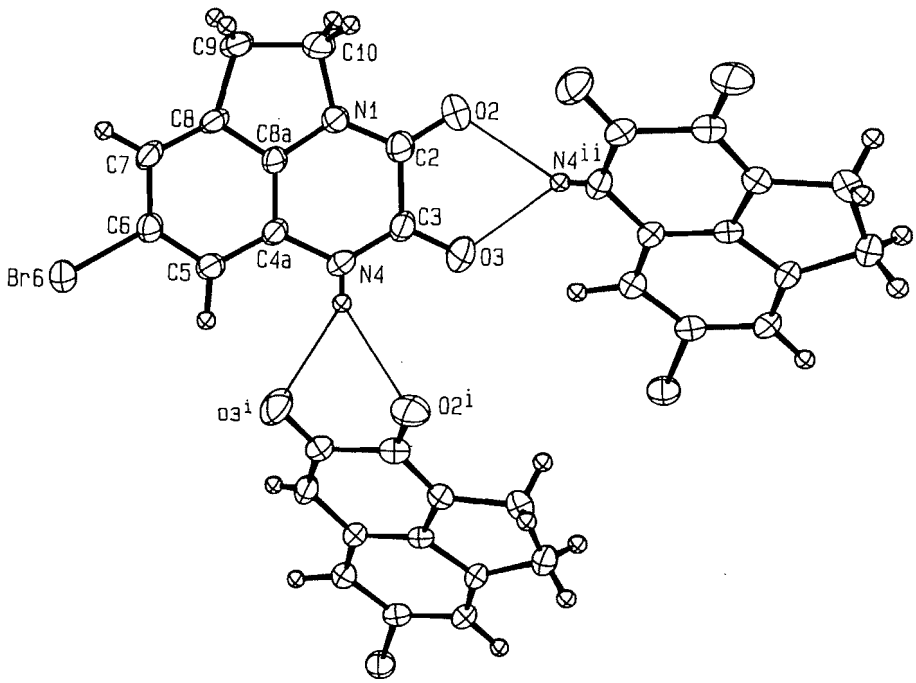

FIG. 1. The hydrogen-bonding scheme for **1**. The thermal ellipsoids are drawn at the 50% probability level, hydrogen atoms are represented as the spheres of arbitrary radius, and the hydrogen bonds are depicted as the thin lines. The symmetry codes: (*i*) 0.5 − *x*, −0.5 + *y*, 1.5 − *z*; (*ii*) 0.5 − *x*, 0.5 + *y*, 1.5 − *z*.

Can. J. Chem. Downloaded from www.nrcresearchpress.com by 85.192.166.187 on 09/08/12
For personal use only.

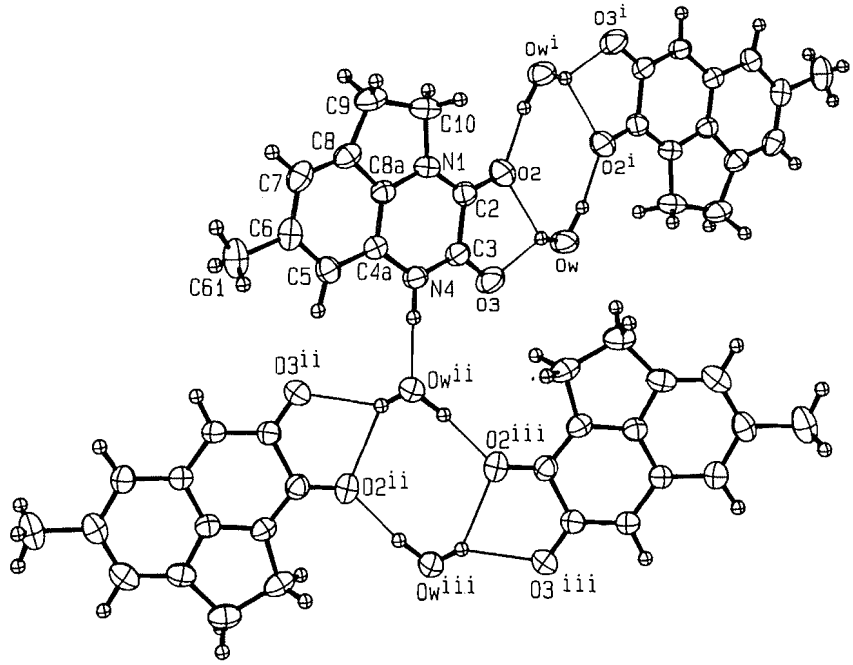

FIG. 2. The hydrogen-bonding scheme for **2**. The thermal ellipsoids are drawn at the 50% probability level, hydrogen atoms are represented as the spheres of arbitrary radius, and the hydrogen bonds are depicted as the thin lines. The symmetry codes: (*i*) $-x, -y, 1-z$, (*ii*) $0.5-x, -0.5+y, 1.5-z$; (*iii*) $-0.5+x, 0.5-y, 0.5+z$.

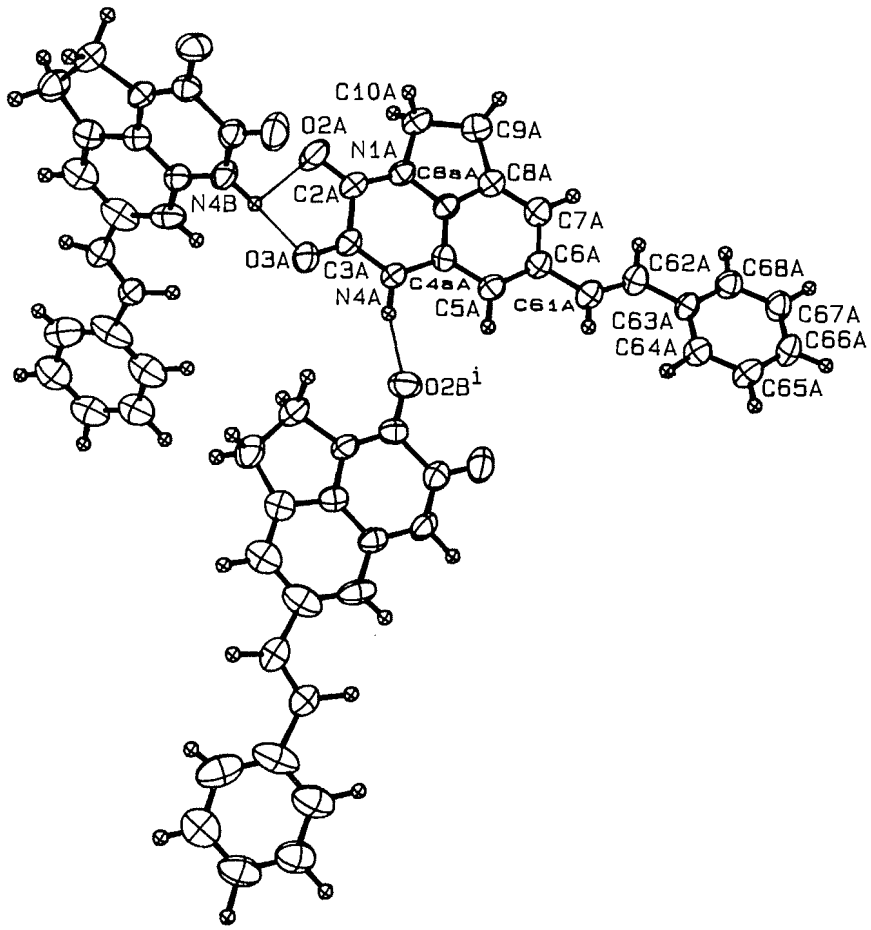

FIG. 3. The hydrogen-bonding scheme for **3**. The thermal ellipsoids are drawn at the 50% probability level, hydrogen atoms are represented as the spheres of arbitrary radius, and the hydrogen bonds are depicted as the thin lines. The symmetry codes: (*i*) $x, 2.5-y, -0.5+z$.

Can. J. Chem. Downloaded from www.nrcresearchpress.com by 85.192.166.187 on 09/08/12
For personal use only.

Can. J. Chem. Downloaded from www.nrcresearchpress.com by 85.192.166.187 on 09/08/12
For personal use only.

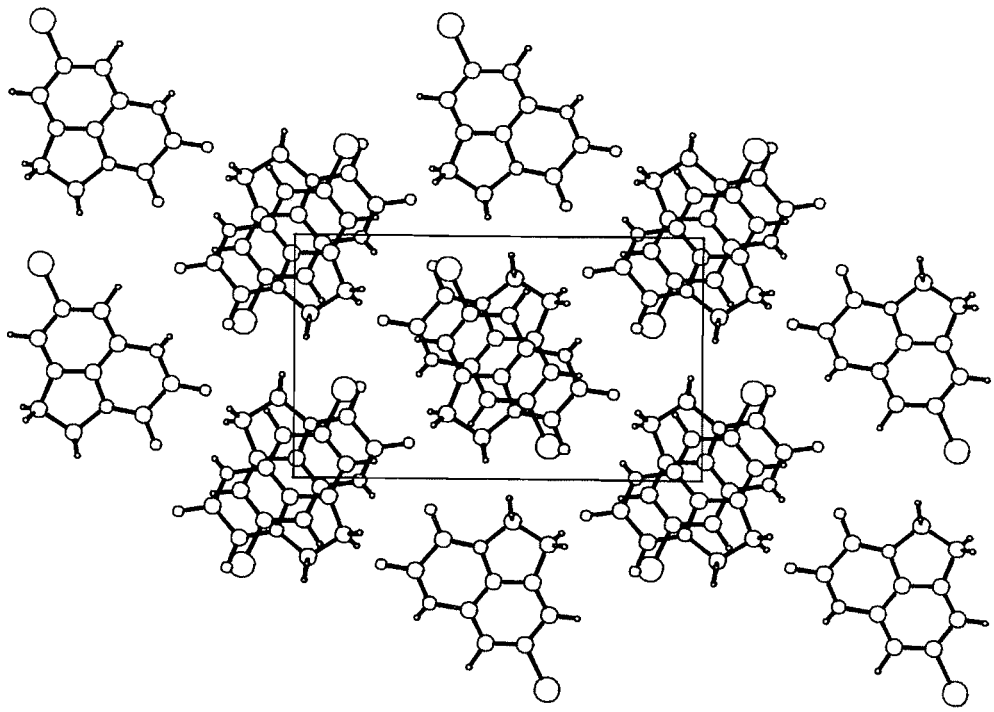

FIG. 4. The molecular packing of **1**, as seen along [100] direction.

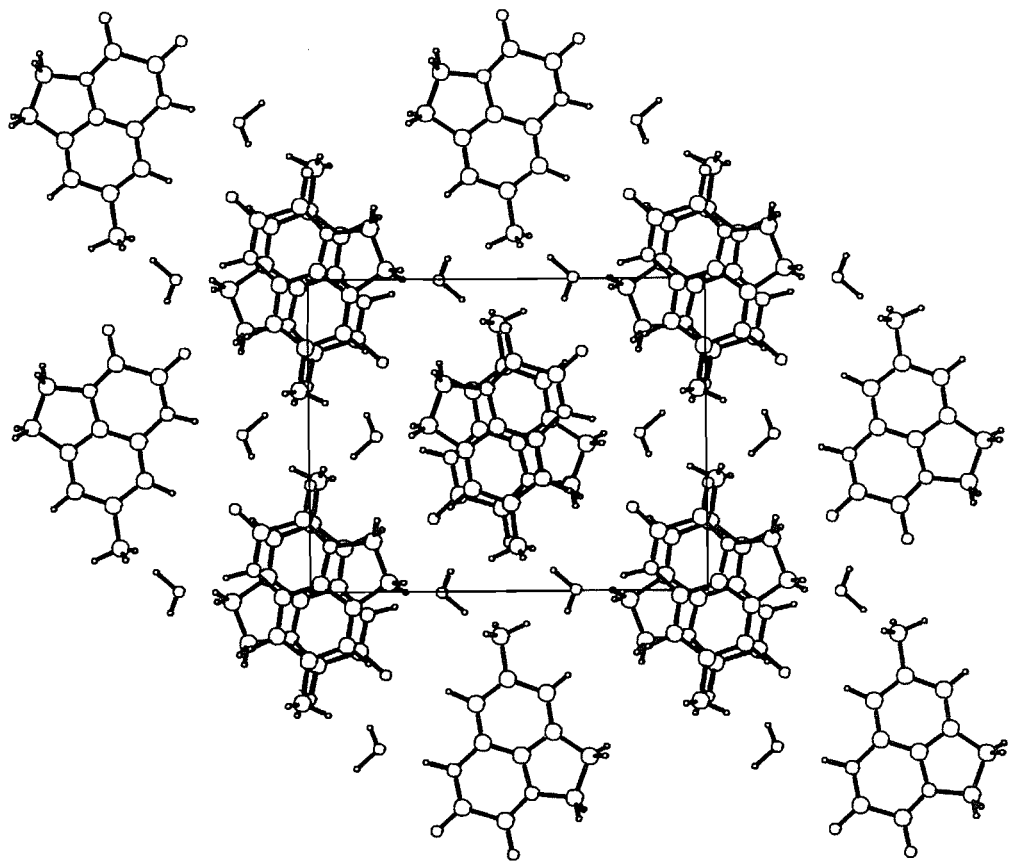

FIG. 5. The molecular packing of **2**, as seen along [100] direction.

Can. J. Chem. Downloaded from www.nrcresearchpress.com by 85.192.166.187 on 09/08/12
For personal use only.

a normal probability plot for the ordered part of the molecules (25, 26) shows statistical, not systematic, differences in geometry (correlation coefficient of 0.98).

Discussion

Structural analysis of QD derivatives shows that the N-H groups and the carbonyl oxygen atoms are maximally involved in hydrogen bonds (6, 7); these observations, coupled with structure–activity data, suggest that the N-H groups and the carbonyl groups are involved in receptor binding. The most active compound at the glycine receptor is an unsymmetrically substituted QD, 5,7-dinitro-1,4-dihydro-2,3-quinoxalinedione, which shows a hydrogen-bonding pattern that does not involve both N-H groups because of an intramolecular hydrogen bond between the 5-nitro group and one N-H group. This intramolecular bond effectively eliminates one hydrogen-bond donor from molecular "recognition-type" hydrogen bond (7) and suggests that the minimal pharmacophore for QD ligands contains one N-H group and two carbonyl groups; blocking both N-H groups eliminates activity.[4] This suggestion is supported by computations that show that the intramolecular hydrogen bond persists over a wide range of conformations (7). In the compounds reported herein, only one N-H group is present and available for hydrogen bonding; therefore the bonding patterns observed in these structures provide models for the key interactions of the postulated pharmacophoric fragment. All three reported structures shows a consistent pattern of a hydrogen bond involving the N-H groups and a shared three-centre hydrogen bond to the two carbonyl groups. The three-centre hydrogen bond was only present in 50% of the crystal packing patterns of QD derivatives that contain two N-H groups (6, 7), yet is the predominant pattern in the structures with only one N-H group, even when solvent is present in the crystal. The three-centre bond provides some variability in the geometry of recognition because the two sides of the three-centre bond do not have to be equivalent, as is apparent in structure **3**, and may allow accommodation of different sizes of ligand in the receptor site. Thus, these crystal structures provide a model of the key recognition interactions for the minimum molecular features of glycine receptor ligands: (*i*) the donation of an H atom by a single N-H group; and (*ii*) a three-centre hydrogen bond formed by the two contiguous carbonyl groups.

Compound **3** and some QD derivatives with 6,7 phenyl substituents are inactive, either because the binding site has a limited size constraining the distance between the hydrogen-bonding groups and the opposite end of the molecule or because the styryl or phenyl groups are not coplanar with the quinoxaline fragment and ring stacking is disfavored. The crystal structures of all active compounds (6, 7, and this work) show π interactions between planar moieties as a major intermolecular interaction and suggest that this mode of interaction may be important for recognition. Inactive compound **3** does not display π-stacking in the crystal structure.

The results of these studies are consistent with the structural features proposed for the antagonistic pharmacophore of the NMDA receptor glycine modulatory site (5, 27, 28). However, we propose a hydrogen-bond interaction instead of a Coulombic attraction for the carbonyl group. Although partial ionization of the carbonyl group would allow a similar interaction for QD and glycine-like antagonists, the hydrogen-bond interaction is probably favored for the carbonyl group. The hydrogen-bond interaction is directional and spatially restricted by the aromatic nature of the QD framework; thus, the geometric interaction of QD derivatives with the binding site is more specific and more clearly defines the structural features of the binding site.

In summary, the crystal structures of three quinoxaline derivative ligands for the glycine receptor suggest a mode of recognition that involves a N-H···*receptor* hydrogen bond, a three-center hydrogen bond to the neighboring carbonyl groups on the ligand, and π-stacking between ligand and receptor. This mode is consistent with the geometric constraints of the current binding site model but places greater emphasis on hydrogen-bond interactions.

Acknowledgements

The authors thank Dr. James Resch of ICI Pharmaceuticals for providing the compounds, the Medical Research Council of Canada (grant to P.W.C.) for financial support, and the Alberta Heritage Foundation for Medical Research for a summer studentship to T.W.K.

1. M.J. Sheardown, J. Drejer, L.H. Jensen, C.E. Stidsen, and T. Honoré. Eur. J. Pharmacol. **174**, 197 (1989).
2. T. Honoré, S.N. Davies, J. Drejer, E.J. Fletcher, P. Jacobsen, D. Lodge, and F.E. Nielsen. Science, **241**, 701 (1988).
3. J.C. Watkins and R.H. Evans. Annu. Rev. Pharmacol. Toxicol. **21**, 165 (1981).
4. B.S. Meldrum. Clin. Sci. **68**, 113 (1985).
5. M.J. Croucher, J.F. Collins, and B.S. Meldrum. Science, **216**, 899 (1982).
6. M. Kubicki, and P.W. Codding. Can. J. Chem. **71**, 68 (1993).
7. M. Kubicki, T.W. Kindopp, M.V. Capparelli, and P.W. Codding. Acta Crystallogr. Sect. B. Submitted.
8. J.A. Kemp and P.D. Leeson. Trends Pharmacol. Sci. **14**, 20 (1993).
9. G.M. Sheldrick. Acta Crystallogr. Sect. A: Found. Crystallogr. **A46**, 467 (1990).
10. G.M. Sheldrick. SHELX-76. Program for crystal structure determination. Univ. of Cambridge, Cambridge, England. 1976.
11. D.T. Cromer and J.B. Mann. Acta Crystallogr. Sect. A: Cryst. Phys. Diffr. Theor. Can. Crystallogr. **A24**, 321 (1968).
12. R.F. Stewart, E.R. Davidson, and W.T. Simpson. J. Chem. Phys. **42**, 3175 (1965).
13. C.K. Johnson. ORTEPII. Report ORNL-5138, Oak Ridge National Laboratory, Tenn. 1976.
14. W.D.S. Motherwell and W. Clegg. PLUTO78. Program for drawing molecular and crystal structures. Univ. of Cambridge, Cambridge, England. 1978.
15. I. Vickovic. CSU88. Geometry calculation program for X-ray analysis. Univ. of Zagreb, Yugoslavia. 1988.
16. C. Svensson. Acta Crystallogr. Sect. B: **30**, 581 (1976).
17. M.J. Grabowski, A. Stepien, M. Cygler, and E. Wajsman. Acta Crystallogr. Sect. B: Struct. Crystallogr. Cryst. Chem. **B33**, 2851 (1977).
18. A. Stepien. Acta Crystallogr. Sect. B: Struct. Crystallogr. Cryst. Chem. **B33**, 2854 (1977).
19. A.C. Hazell, R.G. Hazell, L. Nørskov-Lauritsen, C.E. Briant, and D.W. Jones. Acta Crystallogr. Sect. C: Cryst. Struct. Commun. **42**, 690 (1986).
20. R.L. Clough, W.J. Kung, R.E. Marsh, and J.D. Roberts. J. Org. Chem. **41**, 3603 (1976).
21. G. Bernardinelli and R. Gerdil. Acta Crystallogr. Sect. B: Struct. Crystallogr. Cryst. Chem. **B30**, 1594 (1974).
22. A. Domenicano and P. Murray-Rust. Tetrahedron Lett. **24**, 2283 (1979).
23. J. Bernstein. Acta Crystallogr. Sect. B: Struct. Crystallogr. Cryst. Chem. **B31**, 1268 (1975).
24. J.A. Bouwstra, A. Schouten, and J. Kroon. Acta Crystallogr. Sect. C: Cryst. Struct. Commun. **39**, 1121 (1983).
25. S.C. Abrahams and E.T. Keve. Acta Crystallogr. Sect. A: Cryst. Phys. Diffr. Theor. Can. Crystallogr. **A27**, 157 (1971).

26. International tables for X-ray crystallography. Vol. IV. Kynoch Press, Birmingham. 1969. pp. 293–309.
27. P.D. Leeson, R. Baker, R.W. Carling, N.R. Curtis, K.W. Moore, B.J. Williams, A.C. Foster, A.E. Donald, J.A. Kemp, and G.R. Marshall. J. Med. Chem. Chem. **34**, 1243 (1991).
28. P.D. Leeson, R.W. Carling, K.W. Moore, A.M. Moseley, J.D. Smith, G. Stevenson, T. Chan, R. Baker, A.C. Foster, S. Grimwood, J.A. Kemp, G.R. Marshall, and K. Hoogsteen. J. Med.

Can. J. Chem. Downloaded from www.nrcresearchpress.com by 85.192.166.187 on 09/08/12
For personal use only.

Photodissolution of iron oxides in malonic acid

MARTA I. LITTER, MARINA VILLEGAS, AND MIGUEL A. BLESA,[1]
Departamento Química de Reactores, Comisión Nacional de Energía Atómica, Av. del Libertador 8250, 1429 Buenos Aires, Argentina
Received December 8, 1993[2]

MARTA I. LITTER, MARINA VILLEGAS, and MIGUEL A. BLESA. Can. J. Chem. **72**, 2037 (1994).

The influence of 254-nm irradiation on the dissolution rate of magnetite (Fe_3O_4) and maghemite (γ-Fe_2O_3) suspended in aqueous solutions of malonic acid is analyzed and compared with the dark reaction. The effect of the addition of Fe^{3+}, reductants such as ascorbic acid and oxidants such as Ag^+ or O_2 is described. Photochemical initiation involves the production of $>Fe^{II}$ by electrons photogenerated on the oxide, which triggers thermal dissolution. Experimental results are fitted by analytical and numerical solutions of the set of kinetic equations. The calculated fitting parameters reflect the lower activity of iron oxides in malonic acid compared to EDTA media.

MARTA I. LITTER, MARINA VILLEGAS et MIGUEL A. BLESA. Can. J. Chem. **72**, 2037 (1994).

On a analysé l'influence de l'irradiation à 254 nm sur la vitesse de dissolution de la magnétite (Fe_3O_4) et de la maghémite (γ-Fe_2O_3) en suspension dans des solutions aqueuses d'acide malonique et on l'a comparée aux vitesses de réaction en l'absence de lumière. On décrit aussi l'effet de l'addition du Fe^{3+}, d'agents réducteurs comme l'acide ascorbique et d'oxydants tels que le Ag^+ et le O_2. L'initiation photochimique implique la production de $>Fe^{II}$ par des électrons photogénérés sur l'oxyde et qui provoque la dissolution thermique. On a ajusté les résultats expérimentaux des solutions analytiques et numériques de l'ensemble des équations cinétiques. Les paramètres d'ajustement calculés sont un reflet de l'activité plus faible des oxydes de fer dans l'acide malonique par comparaison avec les milieux contenant de l'EDTA.

[Traduit par la rédaction]

Introduction

Photocorrosion of semiconducting metal oxides in aqueous solutions is a well-documented process (1). Depending on the desired application, corrosion can be an interfering process in photocatalysis or a convenient tool for removal of oxides from surfaces by chemical attack (2). Iron oxides, compared with other more photostable materials such as TiO_2, present quite clearly both possibilities and, depending on the chosen conditions, one will prevail over the other. Some examples of photocatalysis on iron oxides have been reported, including the decomposition of saturated carboxylic acids (3, 4). According to Kormann et al. (5), only compounds which are prone to thermal oxidation and adsorb strongly onto the oxide surface, as sulfite or oxalate, are photooxidized at enhanced rates. On the other hand, photodissolution by carboxylic acids and reductants has been amply documented (6). Photoredox reactions involving iron oxides are also a matter of interest in atmospheric (7) and aquatic environmental chemistry (8–10).

EDTA and oxalic acid in iron oxide suspensions are photooxidized (8, 9, 11–13) in parallel with oxide dissolution. For hematite (α-Fe_2O_3), low dissolution rates are associated with low photooxidation rates. However, Siffert and Sulzberger (9) found relatively high oxalic acid photooxidation rates on α-Fe_2O_3 in strong aerobic conditions, with little corrosion of the oxide. Recent results from one of us (14) showed that maghemite is a good photocatalyst for oxalic acid and EDTA autoxidation, malonic acid being less extensively degraded under the same conditions.

The mechanism of maghemite, magnetite, and hematite photodissolution by oxalic acid and EDTA solutions has been reported previously (8, 11, 12). In this paper, we study the effect of 254-nm irradiation on maghemite and magnetite suspended in malonic acid solutions. Malonic acid is also able to form stable complexes with Fe^{III} in homogeneous solutions ($\log \beta_{101} = 7.50$; $\log \beta_{102} = 13.04$; $\log \beta_{103} = 16.6$; ref. 15), suggesting the possibility of a considerable extent of adsorption and the consequent formation of surface complexes with iron oxides. Some results of iron oxide thermal dissolution in malonic acid have been reported by Suter et al. (16), and a more detailed study has been completed in our laboratories (17). As in analogous systems, aggressitivity is found to be largest at an intermediate pH value, governed by the pH-dependency of the adsorption of weak acids (17, 18), that responds to the stability of iron–malonate complexes and to the need to protonate the surface.

The results presented here are important in the context of the development of solvents for iron oxides in the decontamination of nuclear reactor components. Oxalic acid is a reagent of choice, and the possibility of replacing it by malonic acid has been a matter of interest because of the potential danger of corrosion by oxalic acid. Photochemical initiation of dissolution is presently a possible way to overcome the high passivity of special pieces.

Experimental

Maghemite was the same commercial sample used in previous studies (8, 11, 12). It was composed of acicular particles, its specific surface area being 25 $m^2\ g^{-1}$. Magnetite was prepared in our laboratories as previously described (19). Its specific surface area was 9.7 $m^2\ g^{-1}$ and it was composed by cubo-octahedral particles.

The oxides were characterized by chemical analyses, X-ray diffractometry, SEM and BET surface area measurements.

Malonic acid (Mallinckrodt 99%) was dried under reduced pressure before use. Fresh aqueous solutions in boiled water were prepared in every case immediately before each experiment. All other reagents were of analytical purity and used without further purification. Water was bidistilled in a quartz apparatus.

Thermal and photochemical (254 nm) experiments were carried out as previously described (8, 12). In thermal experiments, N_2 (bubbled through alkaline pyrogallol and water) was passed through the reactor

[1]To whom all correspondence should be addressed.
[2]Revision received June 15, 1994.

Can. J. Chem. Downloaded from www.nrcresearchpress.com by 85.192.166.187 on 09/08/12
For personal use only.

Can. J. Chem. Downloaded from www.nrcresearchpress.com by 85.192.166.187 on 09/08/12
For personal use only.

for 20 min before the run, and sampling was started after the addition of the oxide. In some experiments, Fe^{2+} was added in the form of weighed amounts of Mohr salt ($Fe(NH_4)_2(SO_4)_2 \cdot 6H_2O$) previously dissolved in some drops of boiled water. Photochemical runs were performed in deoxygenated atmosphere (unless indicated), bubbling N_2 for 10 min and closing the cell before irradiation. Experiments in oxygenated media were carried out by bubbling a water-saturated oxygen stream. Temperature was kept at 55°C (±0.1°C) in all cases. The experiments were performed at pH 4, using NaOH for pH adjustment. When applicable, fresh concentrated deareated ascorbic acid aqueous solution or solid silver nitrate were added in appropriate amounts. Due to the large excess of $Hmal^-$, ionic strength remains constant within 3% in the whole course of the dissolution reaction.

The results of the dissolution experiments were analyzed following the amount of iron dissolved after the runs. No efforts were made to measure the amount of malonic acid decomposed. Malonic acid is potentially capable of reducing Fe^{III}, in a fashion similar to oxalic acid. However, it has been documented that in the course of low temperature thermal dissolution of Fe^{III} oxides, the extent of the redox reaction to yield Fe^{II} is minor. Only at high temperatures (20) or under UV-irradiation, the redox reaction takes place. In the case of oxalic acid, the reaction products of the photochemical reaction with dissolved Fe^{III} are Fe^{II} plus CO_2; in the case of malonic acid, no information is available. The photo-Kolbe reaction, yielding CO_2 plus CH_3COOH, is a well-known decomposition pathway in the course of heterogeneous photolysis (14, 21) that can be viewed as a parallel, competing pathway with reductive photodissolution. At the high levels of malonic acid used in this work, the photo-Kolbe reaction does not deplete the ligand appreciably in the time span of our experiments. Iron was determined by the thioglycolate method (22) after filtration of the samples through 0.2 μm filter membrane. When Ag^+ was added, the suspension was first poured on a diluted NaCl solution, the mixture filtered, and the analysis performed as usual on the filtrate. In the measuring media, the red Fe^{III} species decomposes slowly, but the resulting Fe^{II} complex is rapidly reoxidized in the presence of air and excess ligand; the method therefore measures total iron:

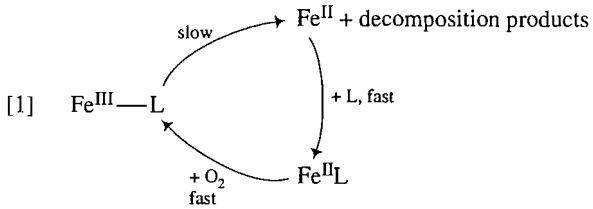

Absorbances were measured in a Shimadzu 210 A spectrophotometer.

Results

The dissolution experiments were performed at pH 4, with 0.6 mol dm^{-3} malonic acid at 55°C. These conditions allow to attain the highest rates of dissolution (17). To supplement the previous study of magnetite dissolution by malonic acid and malonic acid/ferrous salt mixtures (17), some thermal maghemite experiments were performed. The results are summarized in Figs. 1–4. The thermal rates of dissolution (curve 1*a* for γ-Fe_2O_3 and curve 2*f* for Fe_3O_4) are enhanced by ascorbic acid (cf. curves 1*a* vs. 1*e* and 1*f* for γ-Fe_2O_3), and almost completely arrested by O_2 and Ag^+ (not shown). Ferric ion does not change the thermal dissolution rate (not shown).

Irradiation enhances largely the rate of dissolution in the absence of oxidants or reductants (cf. curves 1*a* vs. 3*a*, and 2*f* vs. 2*a*). In the presence of ascorbic acid, photochemical rates are enhanced (cf. curves 3*e* and 3*f* vs. 3*a*), whereas O_2 and Ag^+ are effective to quench dissolution even under light. At a concentration of 2×10^{-4} mol dm^{-3}, Fe^{III} does not influence photochemical rates; at higher concentrations, the effect is uncertain and shall not be further discussed (* in Fig. 2).

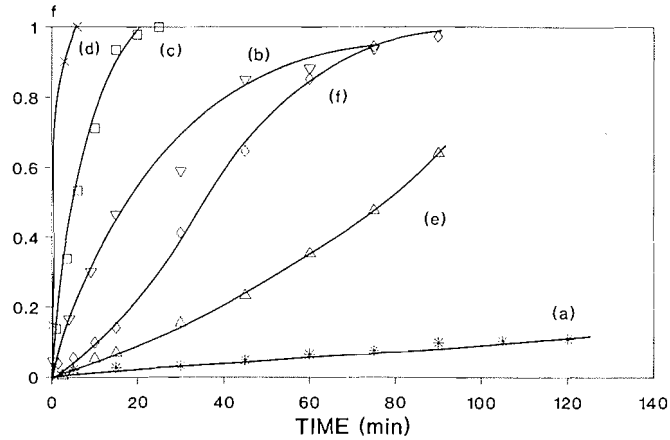

FIG. 1. Iron fraction thermally dissolved from γ-Fe_2O_3 (0.2 g dm^{-3}) by malonic acid (0.6 mol dm^{-3}) at 55°C and pH 4, N_2 atmosphere, as a function of time. (*a*): no other additives (*); (*b*): $[Fe^{2+}]_0 = 6.8 \times 10^{-5}$ mol dm^{-3} (▽); (*c*): $[Fe^{2+}]_0 = 2.0 \times 10^{-4}$ mol dm^{-3} (□); (*d*): $[Fe^{2+}]_0 = 1.0 \times 10^{-3}$ mol dm^{-3} (×); (*e*): [ascorbic acid] = 1.0×10^{-4} mol dm^{-3} (△); (*f*): [ascorbic acid] = 1.0×10^{-3} mol dm^{-3} (◇).

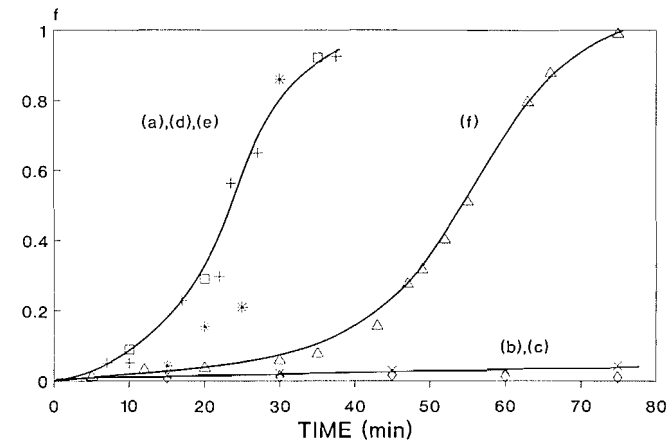

FIG. 2. Iron fraction photochemically (254 nm) dissolved from Fe_3O_4 (0.2 g dm^{-3}) by malonic acid (0.6 mol dm^{-3}) at 55°C and pH 4, N_2 atmosphere except (*c*), as a function of time. (*a*): no other additives (+); (*b*): $[Ag^+] = 3.0 \times 10^{-3}$ (◇); (*c*): no other additives, O_2 atmosphere (×); (*d*): $[Fe^{3+}] = 2.0 \times 10^{-4}$ mol dm^{-3} (□); (*e*): $[Fe^{3+}] = 1.0 \times 10^{-3}$ mol dm^{-3} (*); (*f*): thermal curve, no other additives (from ref. 17) (△).

Discussion

General mechanism

The general mechanism for the dissolution of an iron oxide in the presence of a reductive ligand in acid media can be described through the following steps (6):

(*a*) Chemisorption preequilibrium:

$$[2] \qquad > Fe^{III} + L^{n-} \overset{H^+}{\rightleftharpoons} > Fe^{III}\text{—}(L^{n-})(H^+)$$

where > denotes the lattice surface of the oxide.

(*b*) Slow acid dissolution of $>Fe^{III}$—L surface complexes:

$$[3] \qquad > Fe^{III}\text{—}(L^{n-})(H^+) \overset{R_H}{\underset{H^+}{\longrightarrow}} (Fe^{III} - L)^{3-n}_{aq}(+H^+)$$

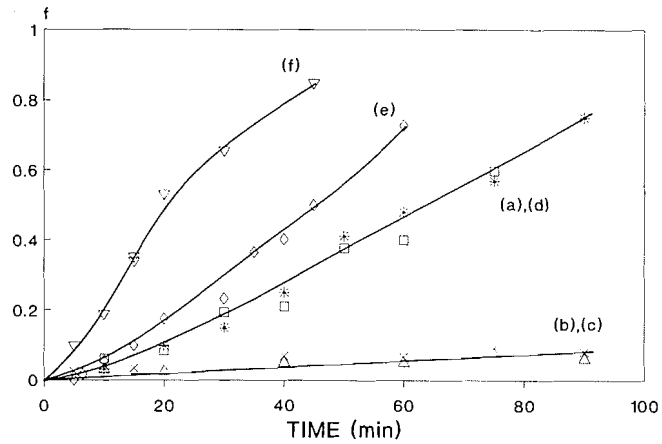

FIG. 3. Iron fraction photochemically (254 nm) dissolved from γ-Fe_2O_3 (0.2 g dm^{-3}) by malonic acid (0.6 mol dm^{-3}) at 55°C and pH 4, N_2 atmosphere except (*c*), as a function of time. (*a*): no other additives (∗); (*b*): $[Ag^+] = 3.0 \times 10^{-3}$ mol dm^{-3} (△); (*c*): no other additives, O_2 atmosphere (×); (*d*): $[Fe^{3+}] = 2.0 \times 10^{-4}$ mol dm^{-3} (□); (*e*): [ascorbic acid] $= 1.0 \times 10^{-3}$ mol dm^{-3} (◇); (*f*): [ascorbic acid] $= 1.0 \times 10^{-2}$ mol dm^{-3} (▽).

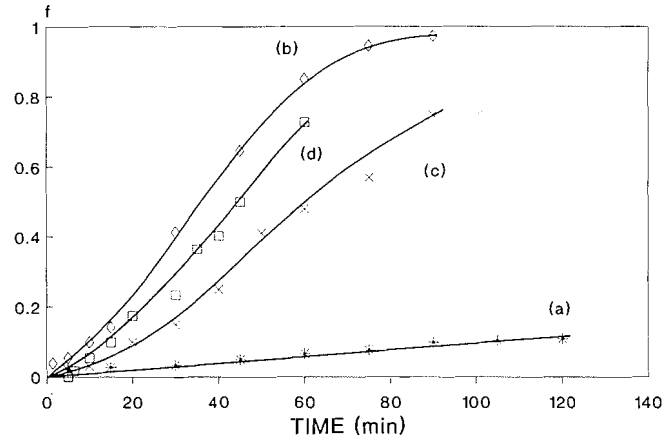

FIG. 4. Effect of ascorbic acid on the thermal and photochemical dissolution of γ-Fe_2O_3 (0.2 g dm^{-3}) by malonic acid (0.6 mol dm^{-3}) at 55°C and pH 4, N_2 atmosphere. (*a*): thermal, [ascorbic acid] = 0 (∗); (*b*): thermal, [ascorbic acid] $= 1.0 \times 10^{-3}$ mol dm^{-3} (◇); (*c*) photochemical, [ascorbic acid] = 0 (×); (*d*) photochemical, [ascorbic acid] $= 1.0 \times 10^{-3}$ mol dm^{-3} (□).

(*c*) Slow reductive dissolution of $>Fe^{III}$—L surface complexes:

$$[4] \qquad >Fe^{III}—(L^{n-})(H^+) \xrightarrow[L]{R_R} >Fe^{II}—(L^{(n-1)})^{\bullet -}(H^+) \longrightarrow Fe^{II}_{aq} + L^{(n-1)})^{\bullet -} + (H^+) \downarrow L^{n-} \; (Fe^{II} - L)^{2-n}_{aq}$$

(*d*) Fast charge transfer reaction between Fe^{II}—L complexes and $>Fe^{III}$ surface centers:

$$[5] \qquad >Fe^{III}—(L^{n-}) + (Fe^{II} - L)^{2-n}_{aq} \xrightarrow[H^+]{k_{Th}} >Fe^{II}—L^{n-}(H^+) + (Fe^{III}—L)^{3-n}_{aq} \downarrow L^{n-} \; (Fe^{II} - L)^{2-n}_{aq}$$

In addition, ferrous complexes in solution suffer fast autoxidation by oxygen or by other oxidants (Ox):

$$[6] \qquad (Fe^{II}—L)^{2-n}_{aq} \xrightarrow[Ox]{k_{Ox}} (Fe^{III}—L)^{3-n}_{aq}$$

For slowly dissolving oxides, traces of O_2 may become important in arresting dissolution through the efficient removal of Fe^{II}.

Under 254-nm irradiation, photochemical initiation produces Fe^{2+}, which triggers thermal dissolution. Equations [7] to [10] must be added to the previous thermal equations [2] to [6]. Also, homogeneous photolysis of Fe^{III}-complexes in solution can take place, after some amount of Fe^{III} is put in solution (eq. [11]).

$$[7] \qquad \text{oxide} + h\nu \xrightarrow{I_a^p} e^-_{cb} + h^+_{vb}$$

$$[8] \qquad e^-_{cb} + h^+_{vb} \xrightarrow{R_C} \text{recombination}$$

$$[9] \qquad >Fe^{III} + e^-_{cb} \xrightarrow{R_{Ph}} >Fe^{II} \longrightarrow Fe^{II}_{aq}$$

$$[10] \qquad h^+ + L \longrightarrow \text{Oxidation products of L}$$

$$[11] \qquad (Fe^{III}—L)^{3-n}_{aq} \xrightarrow{k_h} (Fe^{II}—L)^{(2-n)}_{aq}$$

where I_a^p is the light intensity absorbed by the solid. If S is the instantaneous surface area and V the suspension volume, calling ϕ_1 and ϕ_2 the quantum yields of e^-/h^+ pair formation and recombination respectively, $R_{Ph}S/V = I_a^p\phi_1$ is the rate of heterogenous $>Fe^{II}$ photoproduction (considering recombination negligible), and $R_C = I_a^p\phi_2$. In eq. [11], $k_h = I_a^s\phi_3$ is the specific rate constant, ϕ_3 being the quantum yield of Fe^{II} production in solution through the homogeneous photolysis, and I_a^s the light intensity absorbed by the complex in solution.[3] If S_0 is the initial oxide surface area and f is the dissolved fraction of total iron ($f = (m_0 - m)/m_0$, m_0 and m being the initial and instantaneous oxide mass), for magnetite (cubo-octahedral particles) $S = S_0(1-f)^{2/3}$ and for maghemite (acicular particles) $S = S_0(1-f)^{1/2}$. Therefore, the general rate expressions derived from this mechanism are given by eqs. [12]–[14] for magnetite and [18]–[20] for maghemite.

$$[12] \qquad \frac{d[Fe^{2+}]}{dt} = (0.5R_H + 1.5R_R + 1.5R_{Ph} + 0.5k_{Th}[Fe^{2+}])\frac{S_0}{V}(1-f)^{2/3} - k_{ox}[Ox][Fe^{2+}] + k_h[Fe^{3+}]$$

$$[13] \qquad \frac{d[Fe^{3+}]}{dt} = (R_H + k_{Th}[Fe^{2+}])\frac{S_0}{V}(1-f)^{2/3} + k_{Ox}[Ox][Fe^{2+}] - k_h[Fe^{3+}]$$

[3]Sometimes, direct photolysis of surface $>Fe^{III}$ complexes in their LTMCT band has been invoked, but not documented. A simple analysis of the relative probabilities of exciting the oxide through creating of (e^-, h^+) pairs and through the LTMCT band can be made on the basis of the absorptivity and availability of chromophores (see refs. 11 and 23). The results strongly favor the former pathway. In a very special case (thiocyanate) (24), the LTMCT band could be directly measured; even here, no ensuing photochemistry could be demonstrated (25). Anyhow, even if operative, this alternative pathway leads to the same kinetic expressions.

Can. J. Chem. Downloaded from www.nrcresearchpress.com by 85.192.166.187 on 09/08/12
For personal use only.

$$[14] \qquad \frac{df}{dt} = \left(1.5\frac{MV}{m_0}\right)(R_H + R_R + R_{Ph} + k_{Th}[Fe^{2+}])\frac{S_0}{V}(1-f)^{2/3}$$

where M is the FeO_x molar mass. This equation further simplifies when [Ox] = 0 and $k_h[Fe^{3+}] = 0$ to yield

$$[15] \qquad \frac{df}{dt} = \left[\left(1.5\frac{MV}{m_0}\right)(R_H + R_R + R_{Ph}) + 0.5k_{Th}f\right]\frac{S_0}{V}(1-f)^{2/3}$$

It should be noted that eq. [14] is inadequate to describe the length of the induction period whenever an oxidant is present; this issue has been discussed in ref. 8.

Magnetite photodissolution

According to the literature (26), the quantum yield of the photochemical decomposition of aqueous trismalonato–iron(III) complex under near-UV irradiation is three orders of magnitude lower than that of the trisoxalate complex in the same conditions. In agreement, the irradiation at 254 nm of 0.6 mol dm^{-3} malonic acid and 2.0×10^{-4} mol dm^{-3} Fe^{3+} at pH 4 and 55°C under N_2 atmosphere (to simulate the conditions of the heterogeneous system), gives a quantum yield of Fe^{II} production of 5.6×10^{-4} mol $einstein^{-1}$. Thus, the contribution of the k_h term in eqs. [12] and [13] can be neglected and, in the absence of oxidants, the k_{ox} term is also zero; therefore, the approximate eq. [15] is valid. The low quantum yields of Fe^{III}—malonate photodecomposition also explain why the addition of 2×10^{-4} mol dm^{-3} Fe^{3+} does not cause any effect on the rate of photodissolution (see curve *d* in Fig. 2), in contrast to the behavior in EDTA and oxalic acid media (8, 12). Some data suggest that Fe^{III} at higher concentration may also inhibit the onset of photodissolution (see curve 2*e*).

Numerical solution of eq. [15], using the data from the thermal experiments (17) to derive R_R, R_H, and k_{Th}, fits reasonably well the experimental values with $R_{Ph} = 1.0 \times 10^{-11}$ mol cm^{-2} s^{-1} for magnetite photodissolution (Fig. 5).

The addition of strong oxidants such as Ag^+ or O_2 to the irradiated systems almost suppresses dissolution (see curves *b* and *c* in Figs. 2 and 3). The effect is not the simple homogeneous Fe^{2+} oxidation included in the rate eqs. [12] and [13]. Silver salts (under N_2) can produce the following effects: (*i*) oxidation of Fe^{II} to Fe^{III}, not only in bulk solution but also on the oxide surface and (*ii*) competition with $>Fe^{3+}$ for created photoelectrons, thus reducing R_{Ph} (eq. [9]):

As in other cases (27), SEM and EDS examination demonstrated that silver particles are formed by reduction of Ag^+ (Fig. 6).

In the case of oxygen, (*i*) and (*ii*) are again operative. Photoelectron scavenging is represented by eq. [17]:

$$[17] \qquad O_2 + e^-_{cb} \longrightarrow O_2^-$$

The potential of the conduction bandedge of iron oxides (E_{cb} = +0.18 V at pH 4) is not adequate to reduce oxygen to superoxide radical (E = −0.268 E at pH 4) (5), and oxidation of $>Fe^{II}$ to $>Fe^{III}$ before Fe^{II} can be detached from the surface is the main cause of dissolution inhibition. This oxidation implies previous direct interaction between $>Fe^{II}$ and O_2, and a subsequent pathway that obviates the need to form free $\cdot O_2H$ radicals.

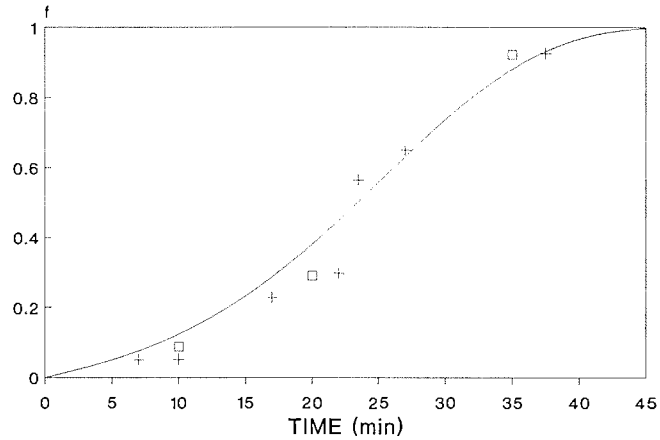

FIG. 5. Fitting of the 254-nm photodissolution curve for Fe_2O_4 in malonic acid at 55°C and pH 4. Experimental data (+) and (□) are those of Fig. 2 (*a*) and (*d*). Solid curve was obtained through the numerical solution of eq. [15] with the parameters of Table 1.

In both cases (Ag^+ or O_2 addition), the low amount of photoproduced $iron_{dissolved}$ hinders a quantitative analysis to evaluate kinetic parameters.

Maghemite dissolution

There was no previous information on the thermal dissolution of maghemite by malonic acid, and we explored this system to obtain the parameters required to describe photodissolution.

Thermal dissolution of maghemite is slower than that of magnetite, due to the lack of structural Fe^{II} in the lattice. In this case, eqs. [18]–[20] apply, which take into account the acicular shape of the particles.

$$[18] \qquad \frac{d[Fe^{2+}]}{dt} = R_R\frac{S_0}{V}(1-f)^{1/2} - k_{ox}[Ox][Fe^{2+}]$$

$$[19] \qquad \frac{d[Fe^{3+}]}{dt} = (R_H + k_{Th}[Fe^{2+}])\frac{S_0}{V}(1-f)^{1/2} + k_{Ox}[Ox][Fe^{2+}]$$

$$[20] \qquad \frac{df}{dt} = \left(\frac{MV}{m_0}\right)(R_H + R_R + k_{Th}[Fe^{2+}])\frac{S_0}{V}(1-f)^{1/2}$$

In the absence of added Fe^{2+}, dissolution is extremely slow, and $S \approx S_0$ in the whole time span of our experiments. The analytical solution of eqs. [18] and [19] setting $k_{ox}[Ox] = 8.3 \times 10^{-3}$ s^{-1}, leads to the values $R_R = 1.5 \times 10^{-14}$ mol cm^{-2} s^{-1}, $R_H = 8.6 \times 10^{-13}$ mol cm^{-2} s^{-1}, $k_{Th} = 4.4 \times 10^{-7}$ dm^3 cm^{-2} s^{-1}. These values fit all the experimental data, submitted to large error margins in the first two values (Fig. 7). Numerical solution of eq. [20], considering area changes and assuming that $[Fe^{2+}]$ is very low, also fits the data (see Fig. 7). The low extent of maximum observed dissolution results in linear f/t predicted relationships that do not warrant further elaborate discussion. Alternatively, a better fitting may be achieved, if the dissolution factors at very short times (<5 min) are attributed essentially to an R_H-type pathway involving fine and very reactive particles. In such a case, a slightly decreased R_H value may be derived (lower by ca. 15%) without sensibly altering other kinetic parameters.

When a ferrous salt is added, such that the contribution to $[Fe^{2+}]$ from [4] and [5] can be neglected, eq. [20] can be integrated assuming an exponential decay of the initial Fe^{2+}

Can. J. Chem. Downloaded from www.nrcresearchpress.com by 85.192.166.187 on 09/08/12
For personal use only.

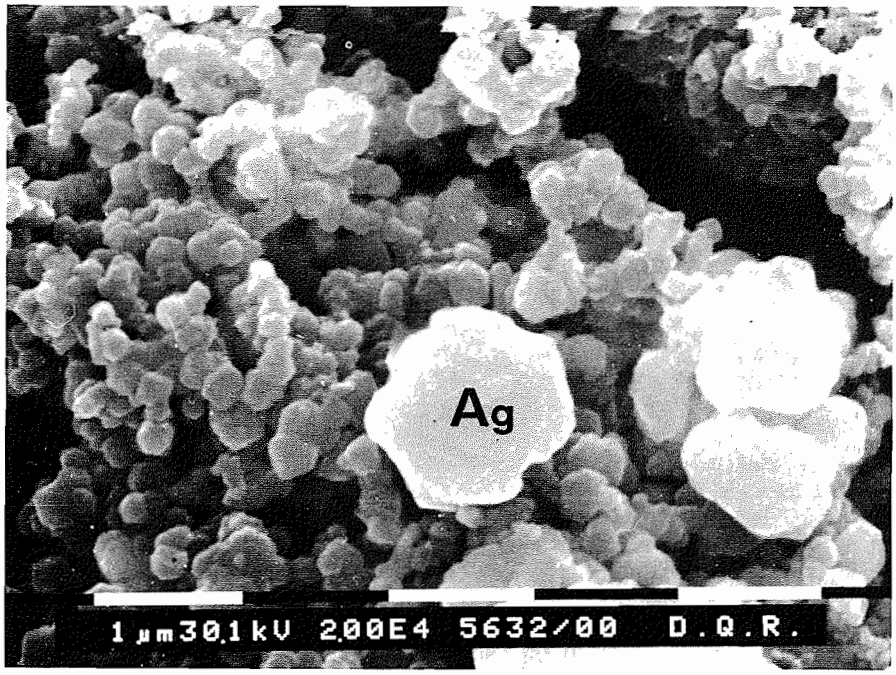

FIG. 6. SEM picture of Fe_3O_4 treated with malonic acid under light in the presence of $AgNO_3$, under retrodispersed illumination; brighter larger particles are shown by EDS to be composed essentially of Ag, whereas smaller darker ones are magnetite.

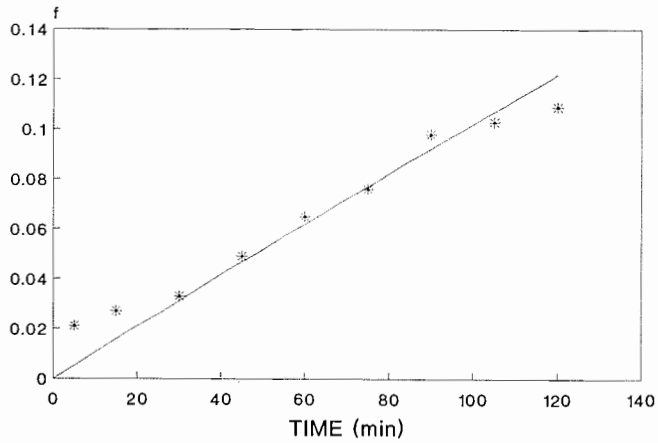

FIG. 7. Fitting of the thermal dissolution curve for γ-Fe_2O_3 in malonic acid at 55°C and pH 4. Experimental data (∗) are those of Fig. 1 (*a*). Solid curve was obtained through the numerical solution of eq. [20] with the parameters of Table 1.

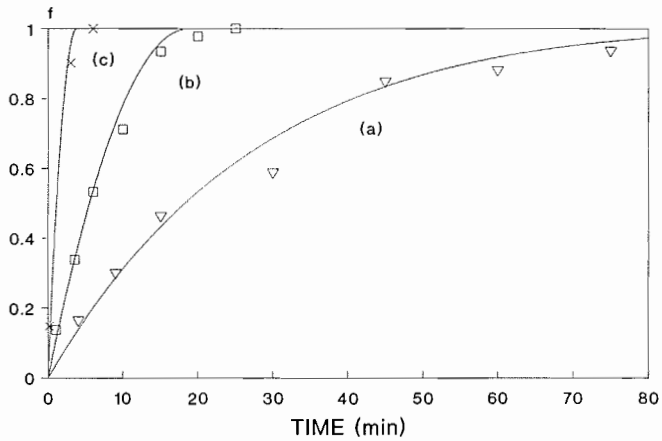

FIG. 8. Fitting of the thermal dissolution curve for γ-Fe_2O_3 in malonic acid at 55°C and pH 4 in the presence of Fe^{2+}. Experimental data (▽), (□), and (×) are those of Fig. 1 (*b*), (*c*), and (*d*), respectively. Solid curves were obtained through the numerical solution of eq. [22] with the parameters of Table 1 and $[Fe^{2+}]_0 = 6.8 \times 10^{-5}$ mol dm^{-3} (*a*), 2.0×10^{-4} mol dm^{-3} (*b*), and 1.0×10^{-3} mol dm^{-3} (*c*), respectively.

concentration with time, due to the entrance of oxygen or the presence of other oxidants, i.e.:

$$[21] \qquad [Fe^{2+}] = [Fe^{2+}]_0 \, e^{-t/\tau}$$

where $\tau = (k_{ox}[Ox])^{-1}$. Equation [20] becomes

$$[22] \qquad \frac{df}{dt} = \left(\frac{MV}{m_0}\right)(R_R + R_H + k_{Th}[Fe^{2+}]_0 \, e^{-t/\tau}) \frac{S_0}{V} (1-f)^{1/2}$$

Using the boundary condition $[Fe^{2+}]_0 = c$, corresponding to experiments with added ferrous salts, the experimental data can be fitted with the same above parameters R_R, R_H, and k_{Th} (see Fig. 8). For the numerical solution of eq. [22], when $[Fe^{2+}]_0 = 6.8 \times 10^{-5}$ mol dm^{-3}, a value of $\tau = 3.6 \times 10^3$ s ($k_{ox}[Ox] = 2.8 \times 10^{-4}$ s^{-1}) was taken, whereas for $[Fe^{2+}]_0 = 2.0 \times 10^{-4}$ and 1.0×10^{-3} mol dm^{-3}, $\tau = \infty (k_{ox}[Ox = 0)$; in this last case, the decay of $[Fe^{2+}]$ due to its oxidation is negligible.

In the presence of ascorbic acid, dissolution rates increase noticeably; the shape of the f/t profile is sigmoidal (see Fig. 1, curves *e* and *f*). Ascorbic acid is a strong reductant known to reduce both dissolved Fe^{III} and iron oxides (28, 29); the original reaction products are dehydroascorbic acid and Fe^{II}. Therefore, it not only prevents oxidation of Fe^{2+} produced through pathway [6] and the reductive pathway, but also reduces any Fe^{3+} produced through reaction [3]. Therefore, eqs.

Can. J. Chem. Downloaded from www.nrcresearchpress.com by 85.192.166.187 on 09/08/12
For personal use only.

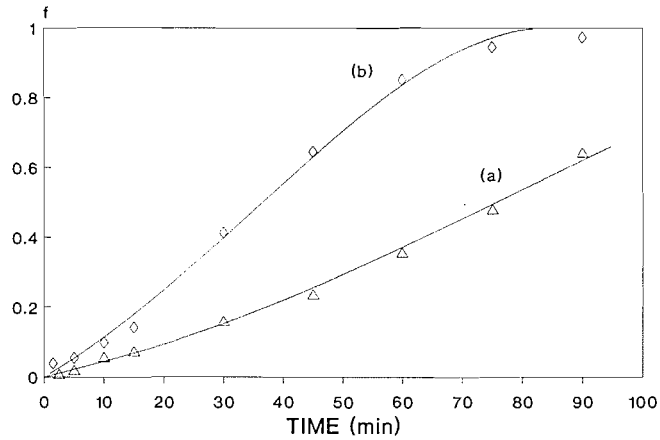

FIG. 9. Fitting of the thermal dissolution curve for γ-Fe_2O_3 in malonic acid at 55°C and pH 4, in the presence of ascorbic acid. Experimental data (△) and (◇) are those of Fig. 1 (*e*) and (*f*). Solid curves were obtained through the numerical solution of eq. [27] (see text); (*a*) [ascorbic acid] = 1.0×10^{-4} mol dm^{-3} (△); (*b*): [ascorbic acid] = 1.0×10^{-3} mol dm^{-3} (◇).

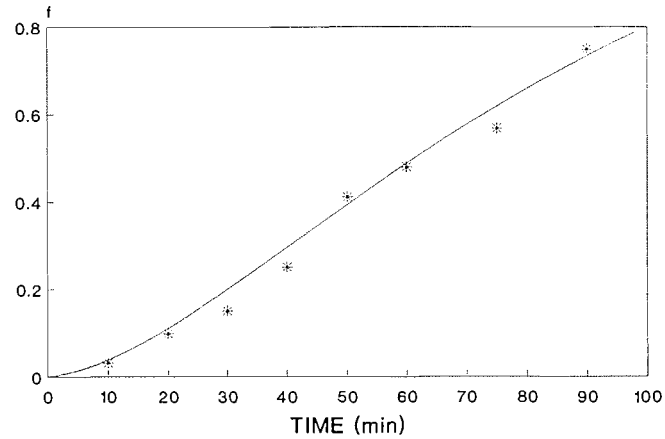

FIG. 10. Fitting of the 254-nm photodissolution curve for γ-Fe_2O_3 in malonic acid at 55°C and pH 4. Experimental data (*) are those of Fig. 3(*a*). Solid curve was obtained through the numerical solution of eq. [30] with the parameters of Table 1.

[4] and [5] prevail from the very beginning. Also, [Ox] = 0 can be safely assumed. Previous studies (29) demonstrated that ascorbate produces large enhancements in R_R, related with the labilizing effect of a facile intramolecular charge transfer in the surface $>Fe^{III}—(L^{n-})$ (H^+) complex (6, 30). Also, the surface complexation equilibrium [2] results in an apparent fractional order of R_R on ascorbate concentration:

$$[23] \qquad R_R = k[LH_n]^{0.5}$$

Equations [18]–[20] simplify to

$$[24] \qquad \frac{d[Fe^{2+}]}{dt} = R_R \frac{S_0}{V}(1-f)^{1/2}$$

$$[25] \qquad \frac{d[Fe^{3+}]}{dt} = k_{Th}[Fe^{2+}] \frac{S_0}{V}(1-f)^{1/2}$$

$$[26] \qquad \frac{df}{dt} = \left(\frac{MV}{m_0}\right)(R_R + k_{Th}[Fe^{2+}]) \frac{S_0}{V}(1-f)^{1/2}$$

Assuming that generation of Fe^{2+}, described by eq. [24], does not depend very much on area changes, we can integrate this equation with $S = S_0$, and rewrite eq. [26]:

$$[27] \qquad \frac{df}{dt} = \left(\frac{MV}{m_0}\right)\left(R_R + k_{Th}R_R \frac{S_0}{V}t\right) \frac{S_0}{V}(1-f)^{1/2}$$

The numerical solution of eq. [27] that fits the experimental data for an initial ascorbic acid concentration of 1.0×10^{-4} mol dm^{-3}, gives $R_R = 3.0 \times 10^{-12}$ mol cm^{-2} s^{-1}. In the case of 1.0×10^{-3} mol dm^{-3} ascorbic acid initial concentration, R_R is somewhat higher (8.5×10^{-12} mol cm^{-2} s^{-1}). The results of the fitting can be seen in Fig. 9. The dependence of R_R on ascorbic acid concentrations is in agreement with eq. [23].

The best fitting k_{Th} value is $1.0 - 1.1 \times 10^{-8}$ dm^3 cm^{-2} s^{-1} for both ascorbic acid concentrations, appreciably lower than the value found in ascorbate-free malonate media. The difference probably indicates a much more efficient bridging between the two metallic centers ($>Fe^{III}$ and Fe^{II}) by malonate.

Under 254-nm irradiation, the applicable kinetic expressions are

$$[28] \qquad \frac{d[Fe^{2+}]}{dt} = (R_R + R_{Ph}) \frac{S_0}{V}(1-f)^{1/2} - k_{ox}[Ox][Fe^{2+}] + k_h[Fe^{3+}]$$

$$[29] \qquad \frac{d[Fe^{3+}]}{dt} = (R_H + k_{Th}[Fe^{2+}]) \frac{S_0}{V}(1-f)^{1/2} + k_{ox}[Ox][Fe^{2+}] - k_h[Fe^{3+}]$$

$$[30] \qquad \frac{df}{dt} = \left(\frac{MV}{m_0}\right)(R_R + R_H + R_{Ph} + k_{Th}[Fe^{2+}]) \frac{S_0}{V}(1-f)^{1/2}$$

The analytical solutions of eqs. [28] and [29] (neglecting area changes) with the previous calculated values of R_R, R_H, and k_{Th} from thermal experiments, fit reasonably well the experimental data up to $f = 0.25$ with $k_{ox}[Ox] = 1.4 \times 10^{-3}$ s^{-1}, when R_{Ph} is set at 3.3×10^{-13} mol cm^{-2} s^{-1}. The numerical solution of eq. [30] with these parameters also fits the data for the whole dissolution curve (see Fig. 10).

As in the magnetite system, the addition of 2×10^{-4} mol dm^{-3} Fe^{3+} does not change the photochemical behavior, and the addition of Ag^+ or O_2 practically suppresses photodissolution (see Fig. 3).

The addition of 1.0×10^{-2} mol dm^{-3} ascorbic acid greatly accelerates photodissolution (see curve *f* from Fig. 3). However, irradiation in fact decreases somewhat the dissolution rates in 1.0×10^{-3} mol dm^{-3} ascorbic acid (cf. curves *b* and *d* from Fig. 4), probably because light essentially produces the direct photolysis or photocatalytic oxidation of ascorbic acid under 254-nm irradiation.

Comparison between magnetite and maghemite in malonic acid, and with EDTA systems

Table 1 shows the kinetic parameters for the thermal and photochemical reactions of malonic acid and EDTA with Fe_3O_4 and γ-Fe_2O_3. R_H value for γ-Fe_2O_3 is derived from curve 1*a* and is believed to be correct to ±5%; the fitting procedure for the other curves in Figs. 1 and 2 is not very sensitive to R_H, but depend crucially on the values assigned to R_R and R_{Ph}; because of the compromise involved in fitting various curves

Can. J. Chem. Downloaded from www.nrcresearchpress.com by 85.192.166.187 on 09/08/12
For personal use only.

TABLE 1. Comparison of the kinetic parameters for Fe_3O_4 and γ-Fe_2O_3 in malonic acid and in EDTA

(*a*) Malonic acid / 55°C

Parameter	Fe_3O_4	γ-Fe_2O_3
R_H/mol cm^{-2} s^{-1}	4.2×10^{-14}	8.6×10^{-13}
R_R/mol cm^{-2} s^{-1}	4.2×10^{-13}	1.5×10^{-14}
R_{Ph}/mol cm^{-2} s^{-1}	1.0×10^{-11}	3.3×10^{-13}
$R_H + R_R + R_{Ph}$/mol cm^{-2} s^{-1}	1.1×10^{-11}	1.2×10^{-12}
k_{Th}/dm^3 cm^{-2} s^{-1}	1.8×10^{-7}	4.4×10^{-7}

(*b*) EDTA / 30°C

Parameter	Fe_3O_4	γ-Fe_2O_3
$R_H + R_R + R_{Ph}$/mol cm^{-2} s^{-1}	8.5×10^{-12}	3.5×10^{-12}
k_{Th}/dm^3 cm^{-2} s^{-1}	2.3×10^{-7}	1.2×10^{-7}

with a single set of parameters, the error estimated for R_R and R_{Ph} reflects essentially the changes in the best-fit values in different experiments, and can be set at 10%; the thermal parameters for magnetite, as well as k_{Th} for γ-Fe_2O_3 were obtained in separate experiments and are correct to ±5%. R_{Ph} for magnetite is again correct within 10%.

Even though the interfacial regions on magnetite and maghemite are probably similar (31), the trends in the non-reductive (R_H) and reductive (R_R) pathways are reversed in these oxides. A probable rationale is the better electronic conductivity of Fe_3O_4 coupled with the more defective crystalline framework of γ-Fe_2O_3 that facilitates Fe^{III} transfer.

To photochemical initiation parameter R_{Ph} is lower for γ-Fe_2O_3 as also found in EDTA solutions, a fact that can be explained (12) by a faster recombination of e^-/h^+ pairs, facilitated by defects or vacancies in the oxide structure. In malonic acid, the value of k_{Th} is slightly higher for γ-Fe_2O_3 than for Fe_3O_4. The origin of the difference is not obvious, and does not seem to warrant elaborate interpretations.

As experiments in the malonic acid systems were carried out at higher temperatures than those in EDTA, the similarities in the values of the fitting parameters for both systems reflect the higher reactivity of iron oxides in EDTA media.

Acknowledgements

M.I.L. and M.A.B. are members of CONICET.

1. P.V. Kamat and N.M. Dimitrijevic. Sol. Energy, **44**, 83 (1990).
2. P. Mulvaney, F. Grieser, and D. Meisel. *In* Kinetics and catalysis in microheterogeneous systems. *Edited by* M. Grätzel and K. Kalyanasundaram. M. Dekker, Inc., New York. 1991. pp. 303–373.
3. H. Miyoshi, H. Mori, and H. Yoneyama. Langmuir, 7, 503 (1991).
4. J.-M. Herrmann, M.-N. Mozzanega, and P. Pichat. J. Photochem. **22**, 333 (1983).
5. C. Kormann, D.W. Bahnemann, and M.R. Hoffmann. J. Photochem. Photobiol. A: Chem. **48**, 161 (1989).
6. M.A. Blesa, P.J. Morando, and A.E. Regazzoni. *In* Chemical dissolution of metal oxides. CRC Press, Boca Raton, FL. 1994.
7. S.O. Pehkonen, R. Siefert, Y. Erel, S. Webb, and M.R. Hoffmann. Environ. Sci. Technol. **27**, 2056 (1993).
8. M.I. Litter, E.C. Baumgartner, G.A. Urrutia, and M.A. Blesa. Environ. Sci. Technol. **25**, 1907 (1991).
9. C. Siffert and B. Sulzberger. Langmuir, **7**, 1627 (1991).
10. M.C. Goldberg, K.M. Cunningham, and E.R. Weiner. J. Photochem. Photobiol. A: Chem. **73**, 105 (1993).
11. M.I. Litter and M.A. Blesa. J. Coll. Interface Sci. **125**, 679 (1988).
12. M.I. Litter and M.A. Blesa. Can. J. Chem. **70**, 2502 (1992).
13. J.K. Leland and A.J. Bard. J. Phys. Chem. **91**, 5076 (1987).
14. M.I. Litter and J.A. Navío. J. Photochem. Photobiol. A: Chem. In press.
15. I. Dellien. Acta Chem. Scand. A, **31**, 473 (1977).
16. D. Suter, S. Banwart, and W. Stumm. Langmuir, **7**, 809 (1991).
17. E.B. Borghi, P.J. Morando, and M.A. Blesa. VIIIth Argentine Meeting on Physical Chemistry, April 1993. Mar del Plata, Argentina. To be published.
18. E.B. Borghi, P.J. Morando, and M.A. Blesa. Langmuir, **7**, 1652 (1991).
19. A.E. Regazzoni, G.A. Urrutia, M.A. Blesa, and A.J.G. Maroto. J. Inorg. Nucl. Chem. **43**, 1489 (1981).
20. R.M. Sellers and W.J. Williams. Faraday Discuss. Chem. Soc. **77**, 265 (1984).
21. D.N. Furlong, D. Wells, and W.H.F. Sasse. Aust. J. Chem. **39**, 757 (1986).
22. D.L. Leussing and I.M. Kolthoff. J. Am. Chem. Soc. **75**, 390 (1953).
23. B. Faust and M.R. Hoffmann. Environ. Sci. Technol. **20**, 947 (1986).
24. A.E. Regazzoni and M.A. Blesa. Langmuir, **7**, 473 (1991).
25. M.I. Litter and M.A. Blesa. Can. J. Chem. **68**, 728 (1990).
26. R. Van Eldik and J.A. Van den Berg. J. S. Afr. Chem. Inst. **23**, 96 (1970).
27. J.-M. Herrmann, J. Disdier, and P. Pichat. **113**, 72 (1988).
28. M.M. Taqui Khan and A.E. Martell. J. Am. Chem. Soc. **89**, 7104 (1967).
29. M. Dos Santos Afonso, P.J. Morando, M.A. Blesa, S. Banwart, and W. Stumm. J. Coll. Interface Sci. **138**, 74 (1990).
30. M.A. Blesa, W. Stumm, and A.E. Regazzoni. To be published.
31. E.R. Vago and E.J. Calvo. J. Electroanal. Chem. **339**, 41 (1992).

Can. J. Chem. Downloaded from www.nrcresearchpress.com by 85.192.166.187 on 09/08/12
For personal use only.

Synthèses et caractérisations structurales de complexes perchlorato et triflato anhydres de praseodyme(III)

JEAN LOUIS PASCAL,[1] MUSTHAPHA EL HADDAD, HEICKO RIECK ET FREDERIC FAVIER

Laboratoire des agrégats moléculaires et matériaux inorganiques, Unité de recherche associée au Centre national de la recherche scientique, n° 79, Case Courrier 015, Université Montpellier II, Sciences et Techniques du Languedoc, 34095 Montpellier Cédex 5, France

Reçu le 19 avril 1994

JEAN LOUIS PASCAL, MUSTHAPHA EL HADDAD, HEICKO RIECK et FREDERIC FAVIER. Can. J. Chem. **72**, 2044 (1994).

Les synthèses de $Pr(ClO_4)_3$, $Pr(OTf)_3$ (OTf = CF_3SO_3), $Pr(ClO_4)_3,Cl_2O_6$ et $NO_2Pr(ClO_4)_4$ sont décrites. La spectroscopie de vibration, la diffraction des rayons X sur poudre et l'EXAFS (pour $Pr(ClO_4)_3$) sont utilisés pour caractériser la structure des complexes. $[ClO_4]$ et [OTf] sont tridentés dans $Pr(ClO_4)_3$ et $Pr(OTf)_3$ et Pr est énéacoordiné. Dans $Pr(ClO_4)_3,Cl_2O_6$, le trioxyde de chlore est inséré dans la maille de $Pr(ClO_4)_3$ et présente l'équilibre ionique ↔ covalent. Dans NO_2 $Pr(ClO_4)_4$, on retrouve la structure de $Pr(ClO_4)_3$, le groupement $[ClO_4]$ supplémentaire est faiblement lié à Pr. $Pr(ClO_4)_3$ cristallise dans le système monoclinique ($P2_1/m$), a = 8,608; b = 11,827; c = 7,416 Å; β = 106,29° et V = 724,79 Å^3. L'EXAFS montre que Pr—O = 2,51 Å et Pr—Cl = 3,90 Å. $Pr(ClO_4)_3$ présente des phénomènes de fluorescence intenses lors d'une excitation par la radiation 488 nm d'un laser à argon ionisé.

JEAN LOUIS PASCAL, MUSTHAPHA EL HADDAD, HEICKO RIECK, and FREDERIC FAVIER. Can. J. Chem. **72**, 2044 (1994).

The syntheses of $Pr(ClO_4)_3$, $Pr(OTf)_3$ (OTf = CF_3SO_3), $Pr(ClO_4)_3{\cdot}Cl_2O_6$, and $NO_2Pr(ClO_4)_4$ are described. Vibrational spectroscopy, X-ray powder diffraction, and EXAFS (for $Pr(ClO_4)_3$) are used to characterize the structure of the complexes. $[ClO_4]$ and [OTf] appear as tridentate in $Pr(ClO_4)_3$ and $Pr(OTf)_3$ and Pr is 9-coordinated. In $Pr(ClO_4)_3{\cdot}Cl_2O_6$, chlorine trioxide is included in the lattice of $Pr(ClO_4)_3$ and shows the ionic ↔ covalent equilibrium. In $NO_2Pr(ClO_4)_4$, $Pr(ClO_4)_4^-$ retains the structure of $Pr(ClO_4)_3$, the extra $[ClO_4]$ is weakly bonded to Pr. $Pr(ClO_4)_3$ crystallizes in the monoclinic system ($P2_1/m$), a = 8.608; b = 11.827; c = 7.416 Å; β = 106.29°, and V = 724.79 Å^3. Distances Pr—O = 2.51 Å and Pr—Cl = 3.90 Å are determined by EXAFS. Strong fluorescence phenomena are observed when $Pr(ClO_4)_3$ is excited with the 488 nm line of an ionized Ar laser.

Introduction

Les connaissances sur les complexes perchlorato $[ClO_4]$ ou triflato $[CF_3SO_3]$ ou [OTf] anhydres sont restées pendant longtemps très limitées. La mise au point de méthodes de synthèses efficaces a permis d'entreprendre une étude systématique de ces composés. Citons les travaux de l'école Rosolovskii $[ClO_4]$ (1), de Lawrance et coll. [OTf] (2), Aubke et coll. [OTf] (3) et notre groupe $[ClO_4]$ et [OTf] (4, 5). Un certain nombre de complexes perchlorato et triflato anhydres de lanthanides(III) ont été analysés (6), mais des lacunes subsistent notamment parmi les éléments pouvant présenter un degré d'oxydation IV comme le cérium, le praséodyme... Une étude partielle des complexes de cérium(IV) a été réalisée (7), mais les données sur les complexes de praséodyme se limitent aux complexes solvatés de Pr(III) (8).

Dans les lignes suivantes, les synthèses de $Pr(ClO_4)_3$, $Pr(OTf)_3$, $Pr(ClO_4)_3,Cl_2O_6$ et $NO_2Pr(ClO_4)_4$ sont décrites. La caractérisation structurale par diffraction X sur poudres et spectroscopie de vibration IR et Raman est développée. Une première analyse EXAFS de $Pr(ClO_4)_3$ est proposée. Les phénomènes de fluorescence intenses, observés plus particulièrement lors de l'excitation de $Pr(ClO_4)_3$ et $Pr(OTf)_3$ par un rayonnement laser à la fréquence 488 nm, sont présentés.

Partie expérimentale

Attention : Le trioxyde de chlore et les perchlorates anhydres sont des composés particulièrement réactifs; ils doivent être manipulés avec beaucoup de prudence. Les quantités utilisées doivent être faibles et les réactions étroitement surveillées. Le manipulateur doit être protégé. Les mises en solution dans des solvants organiques sont hasardeuses.

1. Auteur à qui adresser toute correspondance. Téléphone : (33) 67 14 33 32. Télex : USTMONT 490944 F. Télécopie : (33) 67 14 33 04. E-mail : DEBTOJA@FRMOP22.CNUCS.FR

Produits de base

Cl_2O_6, agent perchloratant, est préparé par oxydation de ClO_2 par un mélange O_3/O_2 puis purifié (6). Une distillation fractionnée préablable de HOTf (Fluka) est nécessaire. Les mises en solution aqueuse sont effectuées avec précaution (5). Pr_6O_{11} (Aldrich) est utilisé sans purification préalable. $Pr(ClO_4)_3,nH_2O$ est préparé par réaction de $HClO_4$ (OSI, 70%) sur Pr_6O_{11} et évaporation lente de la solution. Un processus analogue est utilisé pour obtenir $Pr(NO_3)_3,6H_2O$ à partir de HNO_3 (BDH, 70%). Dans ce dernier cas, la température ne doit pas dépasser 72°C afin de prévenir la formation d'oxo–hydroxo nitrato complexes.

La qualité des produits est vérifiée par diffraction X sur poudres ou (et) par spectroscopie Raman. L'analyse chimique des complexes est effectuée selon des méthodes déjà décrites (5, 6).

Préparation des complexes anhydres

Les réactions sont effectuées, sauf indications contraires, sur rampe à vide (9). Les évaporations d'acides se déroulent sous hotte aspirante. Les composés sont manipulés en boite à gants sous azote AGA «4,5» (<5 ppm en H_2O et O_2).

(a) Perchlorates de praséodyme

Pr_6O_{11} est aisément et totalement transformé, par un excès de Cl_2O_6, entre 5 et 15°C, en $Pr(ClO_4)_3,Cl_2O_6$, un solide orange (0,646 g de Pr_6O_{11} donnent 2,288 g de $Pr(ClO_4)_3,Cl_2O_6$ (attendu 2,299 g, soit un rendement par rapport à Pr_6O_{11} ≅ 99,5%). Ce dernier perd Cl_2O_6, sous vide dynamique, dès 50°C, pour donner $Pr(ClO_4)_3$, un solide vert jaune (calc. Pr: 32,08, ClO_4: 67,92; exp. Pr: 31,64, ClO_4: 68,35).

$Pr(ClO_4)_3$ anhydre peut être également obtenu par déshydratation de $Pr(ClO_4)_3,nH_2O$, soit par Cl_2O_6, soit par thermolyse à 200°C sous vide dynamique. Ce dernier processus est souvent décrit dans la littérature pour préparer des perchlorates de lanthanides anhydres (10). On préfère l'éviter car il est aléatoire et risque de conduire à des oxo–hydroxo perchlorato complexes.

$Pr(ClO_4)_3$ se transforme dès 295°C en Pr_2O_3. La décomposition est totale à 320°C.

Par action de Cl_2O_6 sur $Pr(NO_3)_3,6H_2O$, on aboutit à des perchlorato praséodymates de nitryle selon un processus déjà décrit (9) :

Can. J. Chem. Downloaded from www.nrcresearchpress.com by 85.192.166.187 on 09/08/12
For personal use only.

Can. J. Chem. Downloaded from www.nrcresearchpress.com by 85.192.166.187 on 09/08/12
For personal use only.

[1] $Pr(NO_3)_3,6H_2O + 12\ Cl_2O_6 \xrightarrow{5\text{–}15°C} (NO_2)_3Pr(ClO_4)_6 + 6\ ClO_2 + 3/2\ O_2 + 6\ HClO_4 + 6\ HClO_3$

[2] $(NO_2)_3Pr(ClO_4)_6 \xrightarrow{110\text{–}130°C} NO_2Pr(ClO_4)_4 + 2\ NO_2ClO_4$ (se sublime)

Note : Comme observé précédemment pour des complexes du même type (11), la spectroscopie de vibration et la diffraction de rayons X sur poudres montrent que $(NO_2)_3Pr(ClO_4)_6$ est le mélange $NO_2Pr(ClO_4)_4$–2 NO_2ClO_4. Il est délicat d'obtenir $NO_2Pr(ClO_4)_4$ parfaitement pur, il subsiste toujours des traces de NO_2ClO_4. $NO_2Pr(ClO_4)_4$ se décompose en $Pr(ClO_4)_3$ si l'on essaye de les faire disparaître à $T > 130°C$ (cf. figure 3).

(b) Triflate de praséodyme

Une solution de HOTf (0.5–1 N) contenant Pr_6O_{11}, en quantité légèrement inférieure à la stœchiométrie, est portée à ébullition, sous hotte ventilée. La poudre verte obtenue après évaporation à sec est placée sous vide dynamique (10^{-2} Torr (1 Torr = 133,3 Pa)), à 200°C durant 3 jours. On obtient $Pr(OTf)_3$ anhydre (calc. Pr: 23,96, OTf: 75,43; exp. Pr: 24,57, OTf: 76,03).

HOTf ou AnOTf ($(CF_3SO_2)_2O$) ne conduisent qu'à des mélanges de $Pr(OTf)_3$ et de NO_2OTf lorsqu'ils réagissent avec $Pr(NO_3)_3,6H_2O$,

Note : Devant l'échec de la préparation d'un complexe perchlorato anhydre de Pr(IV) par réaction de l'oxydant énergique Cl_2O_6 sur Pr_6O_{11} et le danger d'une réaction avec le mélange instable $HClO_4$–Cl_2O_7, nous avons essayé de synthétiser un triflate de Pr(IV) suivant : Pr_6O_{11} + HOTf + AnOTf. Après un mois en tube scellé à 130°C, des tests IR et de diffraction X sur poudres indiquent la formation de $Pr(OTf)_3$ et de PrO_2.

Appareillage

Les spectres IR sont enregistrés sur un spectromètre Bomen FTIR DA8. Les échantillons finement broyés sont placés entre deux faces en silicium (111) de 1 mm d'épaisseur, un porte échantillon dont l'étanchéité est assurée par deux joints toriques, les maintient durant l'analyse.

En Raman, on utilise un spectromètre Dilor piloté par un ordinateur PC 286 équipé d'un convertisseur analogique Digimetrix PC Lab 12 bits. La resolution est de 1 cm^{-1}. Les produits, scellés dans des tubes en Pyrex, de faible épaisseur, de 4 mm de diamètre extérieur, sont excités par un laser Spectra Physics à argon ionisé (514,5 ou 488,0 nm, puissance utilisée ≅140 mW). Le sel de chloryle, $Pr(ClO_4)_3,Cl_2O_6$, est refroidi à −180°C pour éviter la décomposition.

Les phénomènes de fluorescence et les raies Raman sont observés simultanément. Les conditions d'échantillonage sont identiques. La largeur des fentes est réduite étant donné la forte intensité des bandes de fluorescence.

$Pr(OTf)_3$ présentant un fond continu de fluorescence parasite à 488 ou 514,5 nm, les spectres Raman sont analysés grâce à un dispositif à transformée de Fourier relié au spectromètre infrarouge cité plus haut. La source lumineuse, 1064 nm, est un laser YAG CVI.

Les diagrammes de diffraction X sur poudres sont enregistrés sur un goniomètre Philips PW 1965/30 automatisé (12). Le porte échantillon est muni d'une fenêtre en beryllium de 0,25 mm d'épaisseur. L'étanchéité est assurée par une graisse inerte au Kelf et du ruban Téflon.

Les enregistrements d'absorption X (EXAFS) ont été effectués au LURE (13) sur DCI (ligne EXAFS 3) avec des caractéristiques de faisceau incident classiques : 1,85 GeV, 200 mA. Le monochromateur utilisé est constitué de deux monocristaux de silicium (311). Leur réglage optimum est réalisé avec une feuille de cuivre étalon de 25 μm en se plaçant au maximum du seuil K : 8979 eV. Avec le praséodyme, on travaille au seuil L_{III} : 5964 eV. Les échantillonnages sont effectués sous azote très sec en boite à gant. $Pr(ClO_4)_3$ finement broyé est intimement mélé à du nitrure de bore et du Nujol très sec. La pâte obtenue est placée dans un intercalaire entre deux feuilles de parafilm. Les spectres sont entregistrés à −180°C.

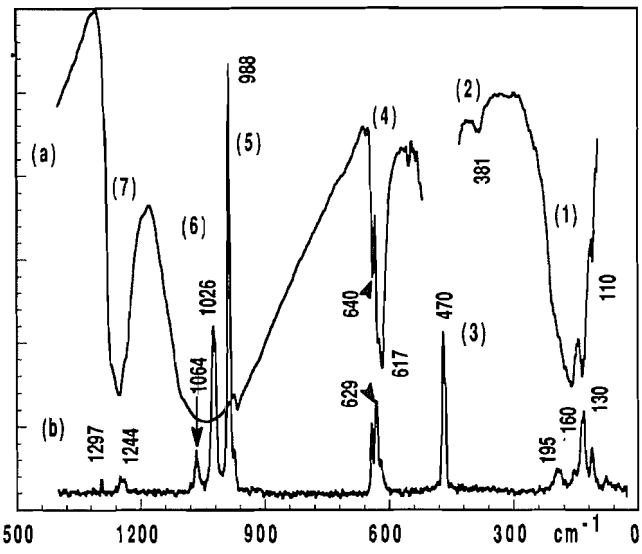

FIG. 1. Spectres IR (*a*) et Raman (*b*) de $Pr(ClO_4)_3$. (1) Réseau + νPr-O; (2) νPr-O (?); (3) $\delta_s ClO_{3p}$; (4) $\delta_{as} ClO_{3p}$ + ρ_r; (5) $\nu_s ClO_p$; (6) $\nu_{as} ClO_p$; (7) νClO_t (O_p : oxygène lié à Pr, O_t : oxygène terminal libre).

Résultats et discussions

Synthèses

La réaction «facile» de Cl_2O_6 sur Pr_6O_{11} est surprenante, en général Cl_2O_6 réagit très difficilement avec les oxydes étant donné leur arrangement cristallin compact (11). Aucune réaction n'est observée avec des oxydes de type Ln_2O_3 (Ln : lanthanides). La formation d'un complexe perchlorato à partir de Pr_6O_{11}, où Pr(IV) prédomine est, semble-t'il, favorisée par le caractère oxydant de Pr(IV) et l'existence d'un Cl(V) dans Cl_2O_6.

La formation d'un sel de nitryle à partir d'un nitrate est normale dans le milieu très acide $HClO_4$–Cl_2O_6 (11). La préparation de $Pr(OTf)_3$ est classique (5).

Note : La synthèse de Pr_2O_3 par décomposition thermique de $Pr(ClO_4)_3$ dès 300°C est intéressante car cet oxyde n'existe pas dans le commerce et est souvent préparé par des méthodes complexes (14).

Analyse structurale

(a) Spectroscopie de vibration

(i) $Pr(ClO_4)_3$. Les spectres de vibration IR et Raman de ce composé sont représentés sur la figure 1. Ils sont analogues à ceux des complexes $M(ClO_4)_2$ (M = Mn (15), Co, Ni (16), Zn (17) et Cd (18)) et $Ln(ClO_4)_3$ (Ln = Y, La, Nd, Sm, Gd et Er) (6). Ils sont caractéristiques d'un engagement tridenté du groupement ClO_4. Étant donné la stœchiométrie et le mode de coordination des perchlorates, Pr est énéacoordiné.

Les principales attributions déduites des résultats précédents sont notées dans la légende de la figure 1. La perte de symétrie du groupement $[ClO_4]$ ($T_d \rightarrow C_{3v}$) entraine des levées de dégénérescence ($\nu_{as} ClO_p$, déformations). La multiplicité de $\nu_s ClO_p$ ou de νClO_t peut s'expliquer par des effets de correlations liés à la symétrie locale autour de Pr (D_3) ou à l'état solide. Ces phénomènes se retrouvent sur les autres spectres de vibrations analysés plus loin.

Les vibrations Pr–O sont localisées autour de 160 cm^{-1} : fréquence inférieure à celles relevées pour les complexes de Ni ou Co (220 cm^{-1}) et Mn ou Zn (≅ 240 cm^{-1}). Ceci implique,

Can. J. Chem. Downloaded from www.nrcresearchpress.com by 85.192.166.187 on 09/08/12
For personal use only.

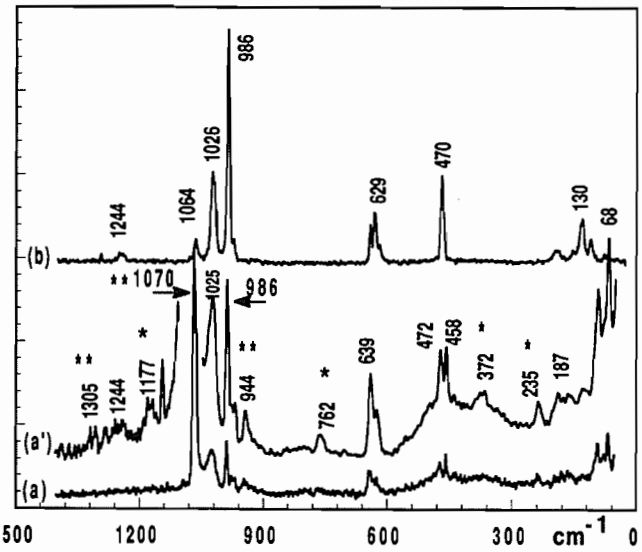

FIG. 2. Spectre Raman de $Pr(ClO_4)_3,Cl_2O_6$ (*a*) et (*a'*) comparé à celui de $Pr(ClO_4)_3$ (*b*). * Cl_2O_6 covalent, ** Cl_2O_6 ionique.

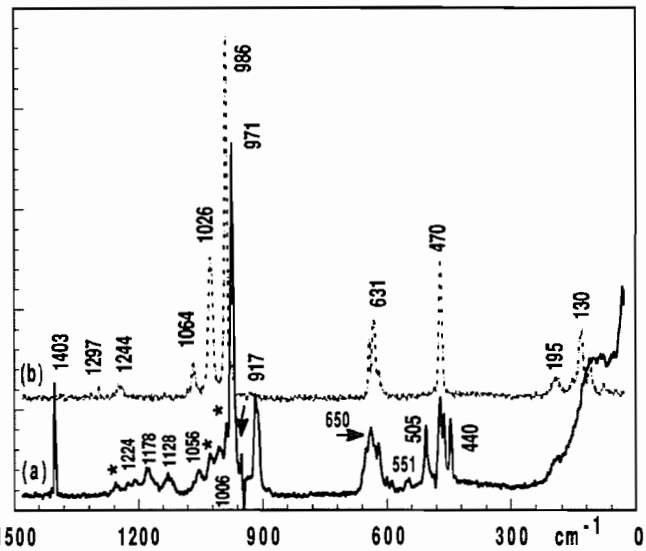

FIG. 3. Spectres Raman de $NO_2Pr(ClO_4)_4$ (*a*) et de $Pr(ClO_4)_3$ (*b*). Traces de NO_2ClO_4 (↓), et de $Pr(ClO_4)_3$ (*) dans $NO_2Pr(ClO_4)_4$.

étant donné le rayon ionique effectif élevé de Pr (128,4 pm pour une coordinance 9 (19)), une liaison Pr—O longue (cf. analyse EXAFS) et corrélativement, un caractère ionique important pour le complexe.

(ii) $Pr(ClO_4)_3,Cl_2O_6$. Le spectre Raman de $Pr(ClO_4)_3,Cl_2O_6$ est représenté sur la figure 2 (*a* et *a'*). On observe, sur la figure 2*a'*, la raie intense à 986 cm^{-1} ($\nu_s ClO_p$) et les raies à 1025 cm^{-1} ($\nu_{as} ClO_p$), 470 cm^{-1} ($\delta_s ClO_p$) et 1244 cm^{-1} (νClO_t) (O_p : oxygène lié à Pr, O_t : oxygène terminal libre), caractéristiques de $Pr(ClO_4)_3$. On relève également, les raies de Cl_2O_6 ionique à 1070 cm^{-1} ($\nu_s ClO_2^+$), 1305 cm^{-1} ($\nu_{as} ClO_2^+$) et 944 cm^{-1} ($\nu_s ClO_4^-$) et celles relatives à Cl_2O_6 covalent, $O_2ClOClO_3$ (20), à 762 cm^{-1} (νClO_p) 1025 et 1177 cm^{-1} (νClO_t), 372 cm^{-1} (ρ_r) et 235 cm^{-1} (ρ_r + δClOCl). On déduit de ces observations que $Pr(ClO_4)_3,Cl_2O_6$ est un mélange de $Pr(ClO_4)_3$ et de Cl_2O_6. Le trioxyde de chlore covalent est en équilibre avec la forme ionique $ClO_2^+ClO_4^-$. $\nu_s ClO_4^-$ apparait ici à 944 cm^{-1} au lieu de 918 cm^{-1} dans l'état solide (21), ClO_4^- ne présente pas d'interactions avec ClO_2^+ comme dans Cl_2O_6 solide pur. Au cours de la thermolyse de $Pr(ClO_4)_3,Cl_2O_6$ on peut isoler, à 55°C, un intermédiaire $Pr(ClO_4)_3,nCl_2O_6$ ($n \cong 0.333$) avec des caractéristiques spectroscopiques analogues au sel initial. L'existence de Cl_2O_6 libre après ce traitement thermique (Cl_2O_6 pur se décompose à la température ambiante) indique que celui-ci est relativement protégé donc vraisemblablement inséré dans la maille de $Pr(ClO_4)_3$. Ceci est en faveur d'une structure présentant des cavités d'accueil pour $Pr(ClO_4)_3$. Un modèle à canaux dérivé de ceux trouvés pour $PrCl_3$ (22) ou $Yb(ReO_4)_3$ (23) est probable.

Le comportement particulier de $Pr(ClO_4)_3,Cl_2O_6$ nous a incité à étudier le sel de nitryle voisin.

(iii) $NO_2Pr(ClO_4)_4$. Le spectre $NO_2Pr(ClO_4)_4$ est comparé à celui de $Pr(ClO_4)_3$ sur la figure 3. NO_2^+ apparait en Raman à 1403 cm^{-1} (ν_s) et 551 cm^{-1} (δ), en IR à 2349, 2365 cm^{-1} (ν_{as}) et 3732, 3740 cm^{-1} (ν_s + ν_{as}). Autour de 1000 cm^{-1}, on relève pour $[ClO_4]$ une séquence de raies : 971, 1006 et 1056 cm^{-1} comparable à celle observée pour $Pr(ClO_4)_3$ (986, 1026 et 1064 cm^{-1}). L'arrangement structural de $Pr(ClO_4)_3$ est conservé. L'abaissement des fréquences est provoqué par un perchlorate faiblement engagé (917, 1128 et 1178 cm^{-1}), analogue

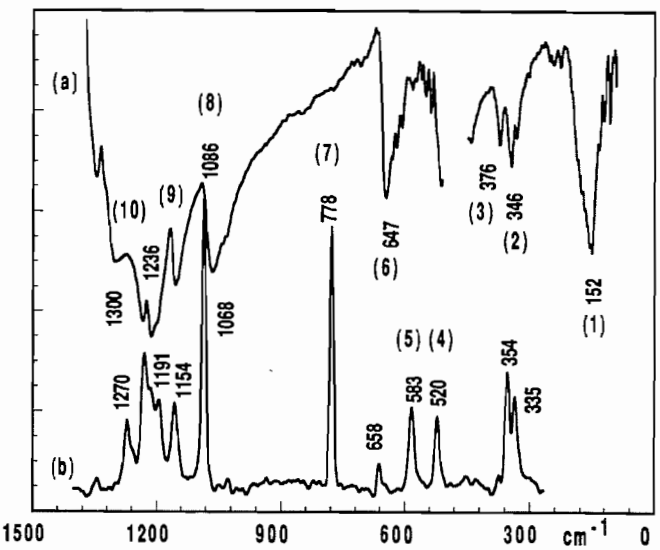

FIG. 4. Spectres IR (a) et Raman (b) de $Pr(CF_3SO_3)_3$. (1) Réseau + νPr-O; (2) $\rho_w SO_3$; (3) ρCS + $\delta_s CF_3$; (4) $\delta_{as} CF_3$; (5) $\delta_s SO_3$; (6) $\delta_{as} SO_3$; (7) $\delta_s CF_3$ + νCS; (8) $\nu_s SO_3$; (9) $\nu_{as} SO_3$; (10) ν_s + ν_{as} CF_3.

à ClO_4^- dans Cl_2O_6 solide (21), où les interactions $ClO_2 \leftrightarrow ClO_4$ sont fortes. Le comportement de $NO_2Pr(ClO_4)_4$ est différent des sels de type $AM(ClO_4)_3$ ($A = ClO_2^+, NO_2^+$; M = Mn, Co, Ni ....) (18), dans lesquels le squelette de $M(ClO_4)_2$ a disparu et où tous les perchlorates bidentés pontants sont équivalents et forment des chaînes $[M(ClO_4)_3]_\infty$.

(iv) $Pr(CF_3SO_3)_3$. Les spectres IR et Raman de $Pr(OTf)_3$ sont représentés sur la figure 4. Dans le domaine des vibrations de [OTf], 200–1500 cm^{-1}, les spectres sont voisins de ceux des composés ioniques (24). Le groupement [OTf] a donc une symétrie C_{3v}. On remarque que les fréquences νCS + δCF_3 : 354 (R). 376 cm^{-1} (IR) et de $\nu_s SO$: 1086 (R), 1068 cm^{-1} (IR) sont plus élevées que celles observées dans l'ion (respectivement $\Delta\nu$ = 14 et 40 cm^{-1}). Cet accroissement de fréquence est caractéristique d'un engagement tridenté du groupement [OTf] autour du métal (5).

Les principales attributions sont signalées dans la légende du

TABLEAU 1. Indexation du diagramme de diffraction X sur poudres de $Pr(ClO_4)_3$

	$Pr(ClO_4)_3$		
hkl	d_{calc}	d_{obs}	I/I_0
0 1 0	8,26	8,37	18
1 2 0	4,81	4,81	25
1 0 1	4,77	4,77	25
−2 0 1	4,11	4,11	25
1 2 1	3,71	3,70	52
−2 1 1	3,37	3,37	100
2 1 1	3,09	3,09	34
0 4 0	2,96	2,95	18
0 4 1	2,73	2,73	70
3 2 0	2,49	2,49	5
3 0 1	2,35	2,35	15
3 3 0	2,26	2,26	28
1 5 1	2,12	2,12	23 (ep)
−3 0 3	2,11	2,11	27
2 3 2	2,04	2,04	5
−2 3 3	2,03	2,03	(ep)

TABLEAU 2. Données de diffraction X sur poudres pour $Pr(OTf)_3$

	$Pr(OTf)_3$		
d_{obs}	I/I_0	d_{obs}	I/I_0
11,07	60	2,93	32
5,88	50	2,81	26
5,58	15	2,70	35
5,46	25	2,64	72
5,17	73	2,57	39
4,50	10	2,44	36
4,19	75	2,27	10
3,98	86	2,23	12
3,67	100	2,17	10
3,57	20	2,13	10
3,31	35	2,14	17
3,18	62	2,02	26
3,06	10		

spectre. Les fréquences νM–O sont très proches de celles notées pour les perchlorates, les interactions ligand–praséodyme sont similaires.

(b) Diffraction X sur poudres

Les diagrammes de diffraction X de $Pr(ClO_4)_3$ et de $Pr(OTf)_3$ sont analogues respectivement à ceux des complexes $Ln(ClO_4)_3$ et $Ln(OTf)_3$ (Ln = La, Nd, Sm, Gd, Er) étudiés précédemment (6, 5*b*). Pour un même ligand, les complexes sont isostructuraux, mais vu l'encombrement plus important des triflates, ces derniers diffèrent des perchlorates. Le diagramme de $Pr(ClO_4)_3$ est indexé en fonction des paramètres de maille des complexes $Ln(ClO_4)_3$ (6) (tableau 1). Il cristallise dans le système monoclinique, groupe d'espace $P2_1/m$, a = 8,608; b = 11,827; c = 7,416 Å; β = 106,29°; V = 724,79 Å^3. Avec Z = 4, ceci conduit à une densité de 4,02, plus élevée que celle du complexe hydraté : 3,8 (8*a*).

L'indexation du diagramme de $Pr(OTf)_3$ (tableau 2) est plus délicate étant donné la qualité médiocre du spectre. Le programme de résolution statistique, TREOR (25), en se basant sur

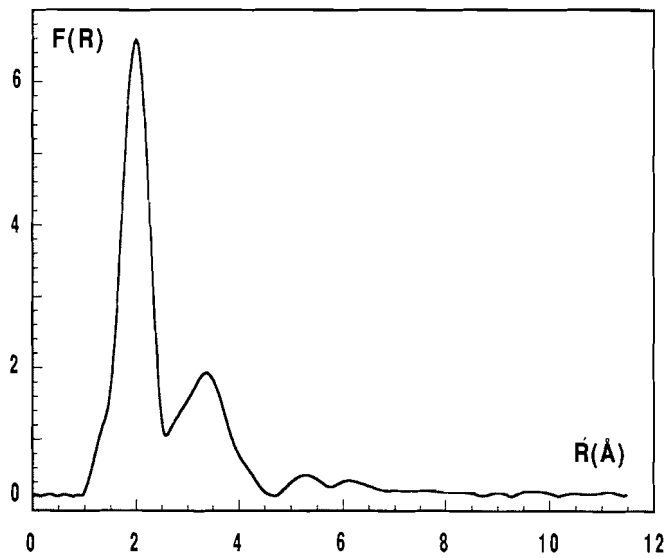

FIG. 5. Transformée de Fourier du spectre EXAFS de $Pr(ClO_4)_3$.

12 raies intenses, ne donne jamais de figures de mérite élevées (≤20%). Une solution possible est le système monoclinique et les paramètres : a = 11,56; b = 10,406; c = 7,346 Å; β = 103,73°; V = 858,55 Å^3.

Les diagrammes de $Pr(ClO_4)_3,Cl_2O_6$ et de $NO_2Pr(ClO_4)_4$ sont trop complexes pour être exploités.

(c) Spectroscopie d'absorption X (EXAFS) de $Pr(ClO_4)_3$

Les données sont analysées en utilisant «EXAFS pour le Mac» de Michalowicz (26). Les différentes étapes de calcul suivent celles décrites dans diverses publications de notre groupe (5*a*–27) (analyse du spectre d'absorption, normalisation, soustraction de l'énergie du préseuil, extraction par polynôme de degré 5 du spectre EXAFS, étude de la transformée de Fourier de ce spectre en utilisant une fenêtre de Kaiser et une pondération en k^3, filtrage des différentes contributions et recherche du meilleur accord théorie–experience en faisant varier les divers paramètres, N : nombre de proches voisins, σ : facteur de Debye–Waller, R : distance atome diffuseur – atome rétrodiffuseur). Les fonctions de phase et d'amplitude sont celles de McKale calculées par une méthode ab initio (28). La transformée de Fourier du spectre EXAFS de $Pr(ClO_4)_3$ est représentée sur la figure 5. Le premier maximum correspond à neuf atomes d'oxygènes à 2,51 Å du praséodyme. On retrouve l'environnement prévu par la stœchiométrie et la coordination tridentée de $[ClO_4]$. Le deuxième maximum est plus complexe mais neuf atomes de chlore à 3,90 Å de Pr sont suffisants pour affiner cette couche (Fig. 6). Ils sont significatifs d'une structure polymère. Si l'on se réfère aux données cristallographiques de $Pr(OH)_2NO_3$ (29) ou $PrCl_3$ (22) et de divers acétates de praséodyme (30), on devrait pouvoir trouver des atomes de Pr autour de 4,20 Å. Il est possible de placer trois atomes de Pr à 4,32 Å d'un autre Pr mais cela n'apporte pas d'amélioration dans l'affinement final (fig. 6). La présence de Pr à cette distance est contredite par les résultats acquis lors de l'analyse EXAFS de $Ni(ClO_4)_2$ et de $Co(ClO_4)_2$ (16), dans lesquels la distance métal–métal est de 4,80 Å, distance nettement plus longue que dans les chlorures correspondants (≅3,54 Å), d'autre part dans $Yb(ReO_4)_3$, la distance minimum Yb–Yb est de 6,07 Å (23). Notons également qu'il est difficile de placer

Can. J. Chem. Downloaded from www.nrcresearchpress.com by 85.192.166.187 on 09/08/12
For personal use only.

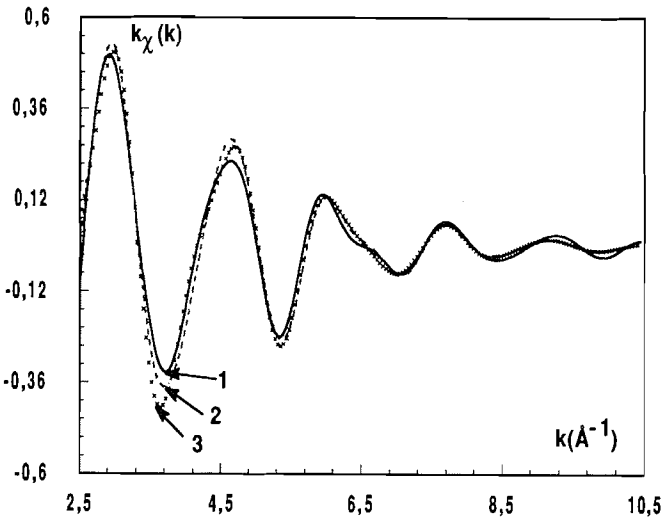

FIG. 6. Spectre EXAFS filtré (1ère et 2ème couche) dans l'espace L_{III} (1) comparé au spectres calculés : (2) contribution de Cl et de Pr dans la 2ème couche (R* = 4,8%); (3) contribution de Cl dans la 2ème couche (R* = 3,8%). * Qualité de l'affinement estimée à partir du facteur résiduel R. ($R = \Sigma_k(k[\chi_{exp}(k)] - k[\chi_{th}(k)])^2k^3/\Sigma_k(k[\chi_{exp}(k)]^2)k^3$)

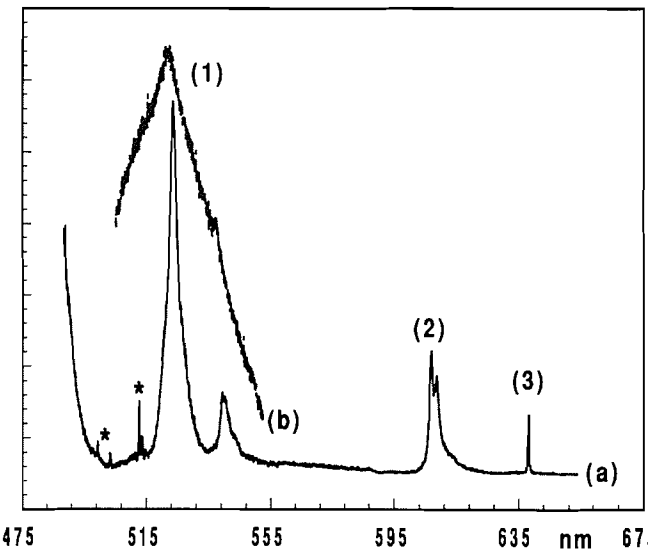

FIG. 7. Spectres de fluorescence de $Pr(ClO_4)_3$ (a) et de $Pr(OTf)_3$ (b). (1) $^3P_0 \rightarrow {}^3H_5$; (2) $^3P_0 \rightarrow {}^3H_6$; (3) $^3P_0 \rightarrow {}^3F_2$. * Raies caractéristiques des vibrations du ligand.

des atomes d'oxygène aux environs de 4 Å. Si l'on considère la somme des distances Pr—O + Cl—O (2,51 + 1,44 Å) (la distance Cl—O est déduite de la relation $((\nu_s^2 + \nu_{as}^2)/2)^{1/2} = f(d(Cl—O))$ (31)), on constate que celle ci est très voisine de la distance Cl—Pr, or comme Pr—O—Cl ne peut être linéaire, les groupements $[ClO_4]$ sont donc distordus comme dans de nombreux complexes perchlorato (32).

(d) Phénomènes de fluorescence

Lorqu'on excite $Pr(ClO_4)_3$ avec la radiation 488 nm (bleu) d'un laser à argon ionisé, on observe des raies très intenses et larges, attribuées sans ambiguité à des phénomènes de fluorescence (fig. 7). De tels effets avaient déjà été notés avec les complexes d'erbium (*5b*, 6). Ils sont plus difficilement observables pour $Pr(OTf)_3$ du fait d'un fond continu de fluorescence parasite important, mais les transitions caractéristiques autour de 530 nm sont présentes. Les attributions sont effectuées en fonction des données de la littérature (33), elles sont données dans la légende du spectre.

Conclusion

Au cours de cette étude, il n'a pas été possible d'isoler de complexes de praséodyme(IV), ce dernier se révélant plus oxydant que les réactifs utilisés tel Cl_2O_6. Malgrè cet échec, l'étude de la famille des complexes à ligands faibles de la série des lanthanides a été enrichie. À côté des complexes «classiques» $Pr(ClO_4)_3$ et $Pr(OTf)_3$, où $[ClO_4]$ et [OTf] jouent le rôle de ligands assembleurs pour donner des structures polymères, on a pu mettre en évidence sans ambiguité, pour la première fois, des sels particuliers : $Pr(ClO_4)_3,Cl_2O_6$ et $NO_2Pr(ClO_4)_4$. Dans le premier, Cl_2O_6 est libre et montre l'équilibre ionique–covalent, alors que dans le second, un $[ClO_4]$ interagit faiblement avec le squelette de $Pr(ClO_4)_3$. Ceci est semble-t'il du à la présence de larges cavités d'accueil au sein de $Pr(ClO_4)_3$ et au comportement différent de ClO_2^+ et NO_2^+. Le premier est souvent en interaction forte avec ClO_4^- (21) alors que ce n'est jamais le cas avec le second (18).

La basicité (ou dureté) très proches de ClO_4^- et de OTf^- $(34)^2$ entraine un comportement identique de $Pr(ClO_4)_3$ et de $Pr(OTf)_3$. Par contre, l'encombrement stérique de [OTf] ne permet pas de préparer de sels analogues à ceux obtenus avec les perchlorates.

Malgré l'absence de modèle, les résultats EXAFS pour $Pr(ClO_4)_3$ sont en accord avec les données de la spectroscopie de vibration et de la littérature (16, 22, 23). Ils permettent d'accroître les connaissances pour des intéractions faibles $[ClO_4] \leftrightarrow$ métal.

Bien que pauvres en informations structurales, les phénomènes de fluorescence méritent d'être signalés, car ils sont rarement observés pour ce type de complexes.

Les résultats structuraux devraient permettre de comprendre et d'étendre la réactivité de ces complexes. Cl_2O_6 «inséré» donne lieu à une chimie plus douce que Cl_2O_6 pur (35) et bon nombre de ces complexes, tels les triflates, voient leur utilisation s'accroître dans le domaine de la catalyse (36).

Remerciements

Les auteurs remercient A. Michalowicz et J. Rozière pour leur aide lors de l'enregistrement des données EXAFS au LURE, D.J. Jones pour des discussions fructueuses et S. Barguès pour sa collaboration scientifique. Ils remercient également le personnel du LURE qui assure la maintenance de l'appareillage. Ils sont gré au CNRS des aides financières accordées.

1. L.S. Skogareva, N.V. Kristov, A.V. Dudin et V.P. Babaeva. Russ. J. Inorg. Chem. (Trad. Anglaise), **37**, 873 (1992) et références citées.
2. G.A. Lawrance. Chem. Rev. **37**, 17 (1986).
3. S.P. Mallela, S. Tomic, S. Lee, S. Karunamithy, H.A. Carter, J.R. Sams et F. Aubke. J. Fluorine Chem. **44**, 309 (1989) et références citées.
4. F. Favier et J.L. Pascal. C.R. Acad. Sci. Paris Ser. II, **313**, 619 (1991) et références citées.
5. (*a*) K. Boumizane, M.H. Herzog-Cance, D.J. Jones, J.L. Pascal, J. Potier et J. Rozière. Polyhedron, **10**, 2757 (1991); (*b*) M. El M. Hamidi et J.L. Pascal. Polyhedron, **13**, 1787 (1994).

2. Aussi, A. Potier et J. Potier, résultats non publiées.

Can. J. Chem. Downloaded from www.nrcresearchpress.com by 85.192.166.187 on 09/08/12
For personal use only.

6. F. Favier et J.L. Pascal. J. Chem. Soc. Dalton Trans. 1997 (1992).
7. (*a*) L.S. Skogareva, V.P. Bavaeva et V. Ya Rosolovskii. Russ. J. Inorg. Chem. (Trad. Anglaise), **32**, 503 (1987); (*b*) M. Aouri. Diplôme d'Études Approfondies, Université de Montpellier II, 1987; (*c*) T. Imamoto, Y. Koide et S. Hiyama. Chem. Lett. 1445 (1990).
8. (*a*) T. Scheild, G. Meyer, G. Oczko et J. Legedziewicz. J. Alloys Compounds, **176**, 337 (1991); (*b*) G. Vicentini et V.M. De Bellis, J. Less-Common Met. **94**, 285 (1983).
9. J.L. Pascal, J. Potier et C.S. Zhang. J. Chem. Soc. Dalton Trans. 297 (1985).
10. J.C.G. Bunzli, J.R. Yersin et C. Mabillard. Inorg. Chem. **21**, 1471 (1982).
11. C.S. Zhang. Thèse d'état, Université de Montpellier II, 1984.
12. B. Ducourant, R. Fourcade et G. Mascherpa. Université de Montpellier II, Sciences et Techniques du Languedoc, Montpellier. Licence CNRS/ANVAR 1993. Vente : CEDRIS, F30170, St Hippolyte du Fort.
13. LURE : Laboratoire pour l'Utilisation du Rayonnement Électromagnétique, Centre Universitaire de Paris Sud. F91405.
14. T. Moeller, V.P. Affandilian et G.W. Cullen. Inorg. Synth. **5**, 39, 1957.
15. J.L. Pascal, J. Potier et C.S. Zhang. C.R. Acad. Sci. Paris, Sér. II, **298**, 579 (1984).
16. J.L. Pascal, J. Potier, D.J. Jones, J. Rozière et A. Michalowicz. Inorg. Chem. **24**, 238 (1985).
17. J.L. Pascal, J. Potier et C.S. Zhang. C.R. Acad. Sci. Paris, Sér. II, **295**, 1097 (1982).
18. M. Fourati, M. Chaabouni, J.L. Pascal et J. Potier. Can. J. Chem. **65**, 2783 (1987).
19. J.E. Huheey. Inorganic chemistry. Principles of structure and reactivity. 2^{e} ed. Harper and Row, New York. 1978. p. 71.
20. (*a*) J.L. Pascal. Thèse d'état. Université de Montpellier II. 1978; (*b*) M. Jansen, G. Schatte, K.M. Tobias et H. Willner. Inorg. Chem. **27**, 1703 (1988).
21. A.C. Pavia, J.L. Pascal et A. Potier. C.R. Acad. Sci. Paris, Sér. C, **272**, 1795 (1971).
22. B. Schmid, B. Halg, A. Furrer, W. Urland et R. Kremer. J. Appl. Phys. **61**, 3426 (1987).
23. V.N. Krustalev, M.B. Varfolomeev, N.B. Shamrai, Y.T. Stuchkov et A.P. Pisarevskii. Koord. Khim. **19**, 871 (1993).
24. D.H. Johnston et D.F. Shriver. Inorg. Chem. **32**, 1045 (1993) et références citées.
25. TREOR : Trial and Error Program for Indexing Unknown Pattern. Werner PE, Department of Structural Chemistry, Arrhenius Laboratory, University of Stockholm. Suède. 1982.
26. A. Michalowicz. Structures fines d'absorption X en chimie. Vol. 3. Logiciel d'Analyse de Données d'absorption X : EXAFS pour le Mac. Presse du CNRS, A. Michalowicz, H. Dexpert, M. Verdaguer Éd. 1988.
27. D.J. Jones, J. Rozière, L.E. Aléandri, B. Bogdanovic et S.C. Huckett. Chem. Mater. **4**, 620 (1992).
28. A.G. McKale. J. Am. Chem. Soc. **110**, 3763 (1988).
29. M. Lundberg et A.J. Skarnalius. Acta. Crystallogr. Sect. B: Struct. Crystallogr. Cryst. Chem. **B32**, 2944 (1976).
30. A. Lossin et G. Meyer. Z. Anorg. Allg. Chem. **620**, 438 (1994) et références citées.
31. M. Fourati, M. Chaabouni, C. Belin, M. Charbonnel, J.L. Pascal et J. Potier. Inorg. Chem. **25**, 1386 (1986).
32. J.L. Pascal et J. Potier. Le Courrier du CNRS, Images de la Chimie. supp. **60**, 14 (1985).
33. E.Y. Wong et I. Richman. J. Chem. Phys. **36**, 1889 (1962).
34. G.A. Olah, G.K.S. Prakash and J. Sommer. Superacids. John Wiley, New York. 1986. Chap. 1.
35. F. Favier et J.L. Pascal. Congrès du Groupe Français d'Étude des Composés d'Insertion. Montpellier – Cap d'Agde, 23–25 Mars 1994.
36. (*a*) J. Colomb, P. Arlaud, A. Gandini et H. Chéradame. Cationic polymerisation and related processes. IUPAC Éd., Publishers Academic. Londres, U.K. 1980. p. 49; (*b*) H. Chéradame, G. Rissoan, F. Favier, J.L. Pascal et F.J. Chen. C.R. Acad. Sci. Paris, Sér. II, **318**, 329 (1994); (*c*) A. Kawada, S. Mitamura et S. Kobayashi. J. Chem. Soc. Chem. Commun. 1157 (1993) et références citées.

Can. J. Chem. Downloaded from www.nrcresearchpress.com by 85.192.166.187 on 09/08/12
For personal use only.

Peptide models. IX. A complete conformational set of For-Ala-Ala-NH_2 from *ab inito* computations

ANDRÁS PERCZEL
Department of Chemistry, University of Toronto, Toronto, ON M5S 1A1, Canada
and
Department of Organic Chemistry, Eötvös University, 112 Budapest POB 32, Hungary

MICHAEL A. MCALLISTER
Department of Chemistry, University of Toronto, Toronto, ON M5S 1A1, Canada

PÁL CSÁSZÁR
Department of Chemistry, University of Toronto, Toronto, ON M5S 1A1, Canada
and
Apotex Inc., 150 Signet Drive, Weston, ON M9L 1T9, Canada

AND

IMRE G. CSIZMADIA
Department of Chemistry, University of Toronto, Toronto, ON M5S 1A1, Canada

Received November 15, 1993[1]

ANDRÁS PERCZEL, MICHAEL A. MCALLISTER, PÁL CSÁSZÁR, and IMRE G. CSIZMADIA. Can. J. Chem. **72**, 2050 (1994).

This paper reports the complete set of minimum energy (i.e. stable) conformations of For-Ala-Ala-NH_2 (containing three peptide bonds), computed by *ab initio* geometry optimization. A more confident *structure and relative energy comparison* of the 49 different relaxed geometries was possible using the HF/3-21G method as compared to empirical (force field) methods. The analysis of the different conformers resulted in a useful structure database, incorporating 30 different β-turns, which will have some relevance to the description of peptide folding. Spectroscopic (e.g. NMR) consequences of the reported *ab initio* calculations are also discussed, and a 3D-structure assignment method for proteins is provided.

ANDRÁS PERCZEL, MICHAEL A. MCALLISTER, PÁL CSÁSZÁR et IMRE G. CSIZMADIA. Can. J. Chem. **72**, 2050 (1994).

Dans ce travail, on rapporte un ensemble complet de conformations d'énergie minimale (c'est-à-dire stable) du For-Ala-Ala-NH_2 (contenant trois liaisons peptidiques), telles que calculées par une optimisation *ab initio* de la géométrie. En utilisant la méthode HF/3-21G plutôt que les méthodes empiriques (de champ de force) il a été possible d'établir une *comparaison plus certaine de la structure et de l'énergie relative* de 49 géométries différentes. L'analyse des différents conformères a conduit à une base de données utile de structures comportant 30 β-tours différents qui présentent un intérêt dans la description du plissement des peptides. On discute aussi des conséquences spectroscopiques (par exemple en RMN) des calculs *ab initio* rapportés et on fournit une méthode d'attribution des structures 3D des protéines.

[Traduit par la rédaction]

Introduction

The conformational analysis of small peptides not only has challenging spectroscopic aspects, it also has a role in the understanding of protein folding. Theoretical calculations revealed that for each peptide residue in vacuo, only a limited number of discrete ϕ, ψ backbone torsional angle combinations exist (1, 2). The structure of small peptides in solution is often quoted as "random" (3, 4), since conformational "mixtures" are generally observed in solution. Introducing special experimental conditions (low temperature, special solvation etc.), the population of a single conformer can be increased to such an extent that crystals can be obtained, usually incorporating a single conformer (5–10). Unfortunately, the solid state conformation is not necessarily identical to the dominant structure observed in liquid or gas phase. Unless specific stabilizing effects are present in solution, such as intermolecular H-bonds and/or ion pairs, a detailed conformational analysis of the structures in an equilibrium mixture is rather difficult (3, 4). By contrast, it is possible to investigate the geometrical properties of any *conformer* via theoretical calculations. In addition to earlier molecular mechanics and semi-empirical approaches (11–13), *ab initio* calculations of these systems are now possible (2, 14–16). Such calculations result in a more faithful description of the geometries as well as relative stabilities (i.e. relative energies: ΔE_i). Although these calculations may yield all possible minimum energy structures, regardless of their relative energy, the identification of *all the possible conformers* is still problematic, since it is not known (*i*) how many minima are on a potential energy surface (PES), (*ii*) where these minima are located.

There are two systematic methods to find all minima, regardless of whether molecular mechanics (MM), semi-empirical or *ab initio* calculations are used: (*i*) the analysis of a suitably chosen function fitted to the calculated grid points can result in finding the location of all the minima on a PES (17*a*, footnote 2); (*ii*) multidimensional conformational analysis (MDCA)

[1]Revision received June 27, 1994.

[2]The grid method is thorough but quite expensive since grid points must be generated at least by 30° intervals requiring 12 points along each of the torsional angles (ϕ_i and ψ_i where ($1 \leq i \leq n$). This involves the computation of 12^{2n} grid points where n is the number of amino acid residues in the peptide. For the analysis of For-Ala-Ala-NH_2, where n = 2, the total number of 12^4 = 20736 grid points are expected to be computed. (The planarity of the amide group, ω_1 and/or ω_2 = 180° or 0°, is usually presumed but nevertheless explicitly optimized.)

Can. J. Chem. Downloaded from www.nrcresearchpress.com by 85.192.166.187 on 09/08/12
For personal use only.

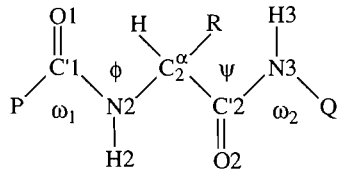

$E_{\omega = \text{const}} = E(\phi, \psi)$

SCHEME 1

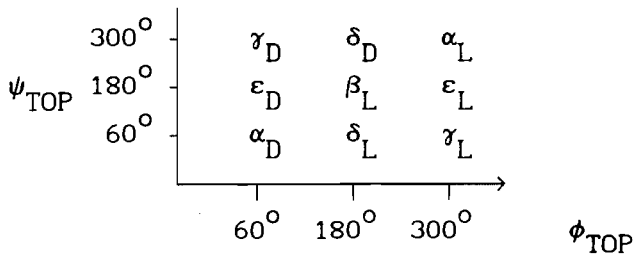

SCHEME 2

(footnote 3, ref. 17*c*) of an ideal PES can also yield the total number of legitimate minima, as well as their approximate locations.

Multidimensional conformational analysis (footnote 3, ref. 17*c*) as applied to *amino acid diamide systems* (e.g. For-Ala-NH_2), predicted (2) the existence of nine minima on the 2D-Ramachandran map (18). Each of these nine minima represents the only energy minimum in a given catchment region (19). The torsional angles are defined according to IUPAC-IUB (footnote 4, ref. 20) as shown on Scheme 1.

The occurrence of the nine minima (labelled as: α_L, α_D, β_L, γ_L, γ_D, δ_L, δ_D, ϵ_L, ϵ_D), are shown in an idealized fashion in Scheme 2 (footnote 4) and Fig. 1. It should be emphasized that Fig. 1 shows the topology of the 2D-Ramachandran map for two full cycles of rotation. Each of the four quadrants, presented in Fig. 1, is the same as the pattern given in Scheme 2. The central square in Fig. 1, defined by broken lines, is the conventional Ramachandran map, but for topological reasons the representation shown in Scheme 2, corresponding to the upper right hand corner of Fig. 1, is suggested.

The large number of *ab initio* points computed by Pople and co-workers (16*g*, *h*), involving 12 × 12 = 144 grid points, yielded the same seven minima (α_D, β_L, γ_L, γ_D, δ_L, δ_D, and ϵ_D) for For-L-Ala-NH_2 as determined using SCF gradient geometry optimizations at the MDCA predicted locations (2, 16*h*). Two conformations (α_L and ϵ_L) from the nine MDCA predicted minima were not found at the HF/3-21G level of theory. This is to be taken as diagnostic of the non-ideal nature of the PES. In order to underline the utility of MDCA let us reemphasize that the 9 set of input data, generated by MDCA, resulted in the same 7 minima (2) as the PES-generated based on the 144 grid points determined by Pople and co-workers (16*h*).

In the solid state, slightly distorted forms of the γ_L backbone substructure (also called C_7^{equ}) or its conformational neighbors (β_L, ϵ_L and δ_L) were extensively observed (22–27) for small

[3]See ref. 17*b* (part of the series The chemistry of functional groups) particularly pages 36–41 including Figs. 23 and 24 as well as Table 20.

[4]It should be noted that according to the IUPAC-IUB convention (19) ϕ and ψ vary between −180° and +180°. For various reasons (2), during conformational analysis it is convenient to use a different cut of the same PES, namely any of the four identical quadrants encircled by solid lines in Fig. 1, ref. 2.

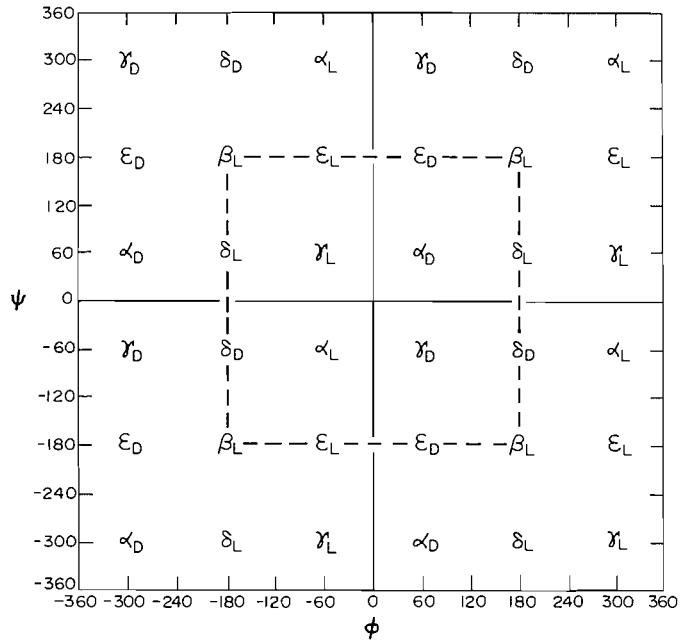

FIG. 1. Idealized PES topology for a single amino acid diamide residue involving two complete cycles of rotation in both ϕ and ψ. Locations of the minima are specified by their names in terms of subscribed greek letters.

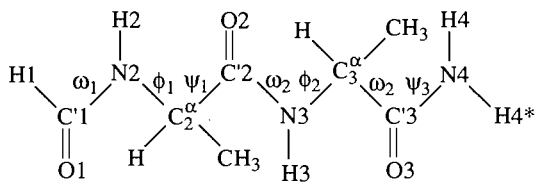

SCHEME 3

β-turn type	Backbone torsional angle values ϕ_1	ψ_1	ϕ_2	ψ_2	conformation type(s)
I	−60	−30	−90	0	$\alpha_L\alpha_L$, $\alpha_L\gamma_L$,$\alpha_L\delta_L$
I′	60	30	90	0	$\alpha_D\alpha_D$, $\alpha_D\gamma_D$, $\alpha_D\delta_D$
II	−60	120	80	0	$\epsilon_L\alpha_D$, $\epsilon_L\gamma_D$, $\epsilon_L\delta_D$
II′	60	−120	−80	0	$\epsilon_D\alpha_L$, $\epsilon_D\gamma_L$, $\epsilon_D\delta_L$
III	−60	−30	−60	−30	$\alpha_L\alpha_L$
III′	60	30	60	30	$\alpha_D\alpha_D$
VI*a*	−60	120	−90	0	$\epsilon_L\alpha_L$, $\epsilon_L\gamma_L$, $\epsilon_L\delta_L$
VI*b*	−120	120	−60	0	$\beta_L\alpha_L$, $\beta_L\gamma_L$, $\beta_L\delta_L$
VIII	−60	−30	−120	120	$\alpha_L\beta_L$

SCHEME 4

amide systems. In solution the presence of the above structures for amino acid diamides has not been confirmed by NMR, CD, or IR spectroscopy. Usually a conformational mixture of an "undefined" number of structures are present; these structures are labelled "random".

Peptides, incorporating three amide functional groups, such as the For-L-Ala-L-Ala-NH_2 (cf. Scheme 3), a representative element of the *diamino acid triamide* system, may adopt a larger variety of backbone conformations, such as type I and/or type II β-turns (21), etc. The existence of the turns, as typical triamide conformations, has been the target of many investigations (28–30), since, in addition to the α-helix ($\phi_i = (-60 \pm 30)°$, $\psi_i = (-45 \pm 30)°)_n$ and the β-pleated sheet ($\phi_i = (-150 \pm$

Can. J. Chem. Downloaded from www.nrcresearchpress.com by 85.192.166.187 on 09/08/12
For personal use only.

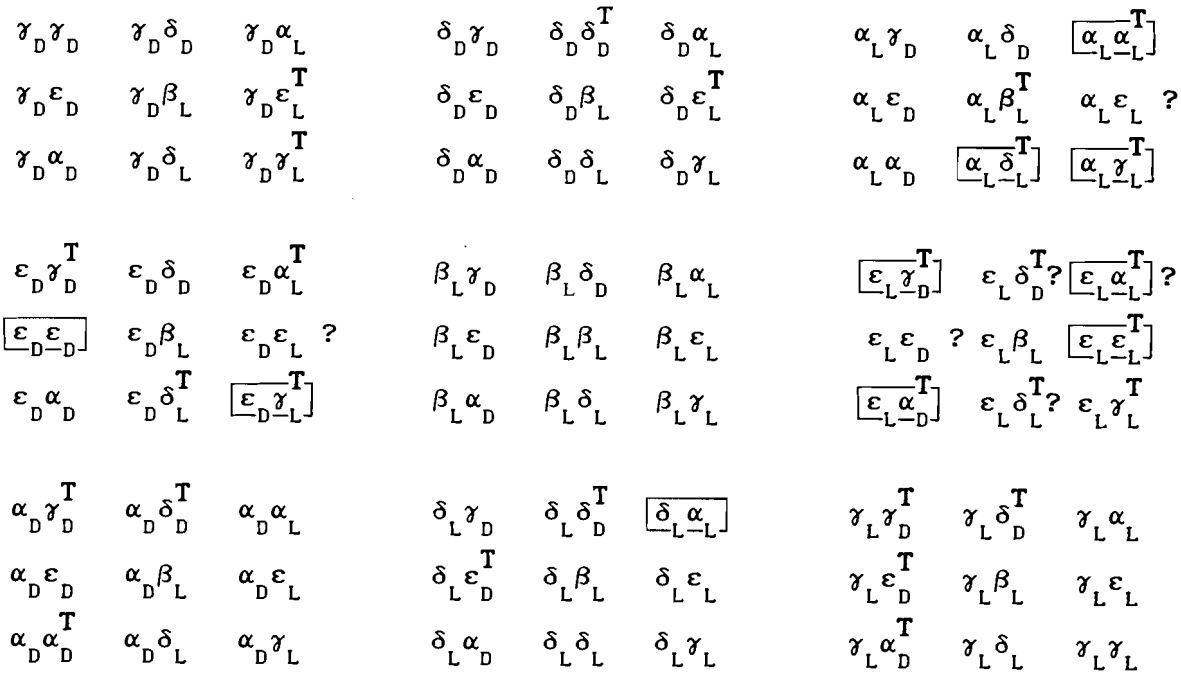

SCHEME 5

30)°, $\psi_i = (+150 \pm 30)°)_n$, the hairpin conformations or β-turns are the third most frequently found (30–37) structural unit in globular proteins (22, 33, 34).

In general β-turn types are defined according to the values of the four torsional angles (ϕ_1, ψ_1, ϕ_2, and ψ_2) as specified by Scheme 4. Only types I, II and III are frequently assigned in globular proteins based on their X-ray structures, but their conformational mirror images, i.e. conformational enantiomers (I, II, and III) as well as the type VI*a,b* and VIII β-turns have only sporadic occurrences. Since types IV, V, and VII β-turns are defined ambiguously their determination is rather questionable in globular proteins since they incorporate β-turns with very different backbone torsional angles (21). The X-ray analysis of protected dipeptides revealed that these structures incorporate intermolecular hydrogen bonds (21–27) which are typical for solid state conformations. Up to the present, the *direct* structural analyses of N- and C-protected dipeptides in the solid state has revealed the existence of approximately 10 different typical conformations of diaminoacid triamides (21).

In contrast to the few recognized structures of triamide systems, as discussed above, a total of 81 distinctly different conformations (38) were predicted by MDCA as shown in Scheme 5. Analysis (38) of a large crystallographic protein data base revealed that all 81 conformations do exist in globular proteins. A total of 30 from these 81 MDCA predicted conformations would qualify (37) as β-turns or reverse turns (36), marked by the **T** superscript in Scheme 5 (cf. ref. 37, Table 1). MDCA, without considering destabilizing or stabilizing interactions, yields 81 legitimate minima. The analysis of triamide substructures in a large protein data base, where all stabilizing interactions are present, suggests the existence of all 81 conformations (38). On the other hand, Molecular Mechanics (MM) calculations confirmed 75 out of the 81 MDCA legitimized conformations. The 6 non-existing conformations at the MM level are marked by question marks (?) in Scheme 5. When we tried to locate these 6 conformations during the MM optimization process using the ECEPP/2 method, the initial minima were shifted to other nearby minima as illustrated in Scheme 6.

Due to the large dimensionality of peptides, force field calculations have traditionally been used to estimate the energetic and geometrical properties of these bio-molecules. The favorable speed and size-tolerance have made these calculations popular. The inherent inaccuracies of these parameterized methods can induce errors in the structure analyses of polypeptides and therefore limit their applicability. The theoretical probability occurrence (p_i^{theo}) of the *i*th conformer is proportional to its relative energy (ΔE_i). The energy of all the conformations can only be obtained by theoretical computations since no experimental method is available to measure all ΔE_i. The purpose of this paper is to evaluate how many of the 81 legitimate conformations (Scheme 5) have intrinsic stability *without* the influence of stabilizing environmental effects. Only *ab initio* type molecular orbital computations can answer such a question accurately and determine the number of N_0 of the 81 legitimate conformations as having an intrinsic stability, while $(81 - N_0)$ conformations will be intrinsically unstable. Nevertheless, these $(81 - N_0)$ unstable, but otherwise legitimate conformations, may be restabilized through H bonds, long-range interactions, or other effects typical in large proteins. This paper

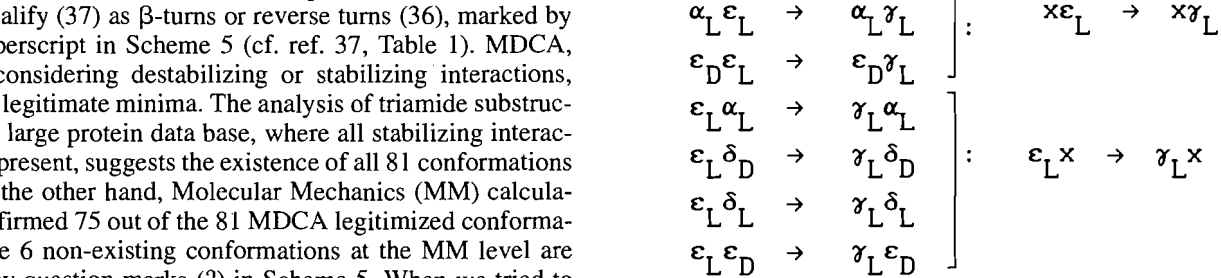

SCHEME 6

Can. J. Chem. Downloaded from www.nrcresearchpress.com by 85.192.166.187 on 09/08/12
For personal use only.

TABLE 1. Comparison of the ϕ and ψ torsional angles obtained in *ab initio* calculations under "normal" and "tight" optimization on selected conformations of For-L-Ala-NH_2 and For-L-Ala-L-Ala-NH_2

Compound	Conformation	Torsional angle[a] Type	Normal optimization[b]	Tight optimization[c]	Change
For-Ala-NH_2	α_D	ϕ	+63.8	+63.8	0.0
		ψ	+32.7	+32.7	0.0
	β_L	ϕ	−168.4	−168.3	0.1
		ψ	+170.9	+170.5	0.4
	γ_L	ϕ	−84.4	−84.5	0.1
		ψ	+67.7	+67.3	0.4
For-Ala-Ala-NH_2	$\gamma_L\gamma_L$	ϕ	−84.2	−84.2	0.0
		ψ	+67.0	+67.0	0.0
		ϕ	−84.9	−85.0	0.1
		ψ	+66.4	+66.4	0.0

[a]In degrees.
[b]Maximum force $\leq 3 \times 10^{-4}$ au.
[c]Maximum force $\leq 1 \times 10^{-5}$ au.

TABLE 2. A comparison of the ϕ, ψ torsional angles (degree), total energies, E (hartree), and relative energies, ΔE (kcal/mol) associated with the β_L and γ_L conformations of For-L-Ala-NH_2 computed at HF/3-21G and MP2/5-311++(d, p) levels of theory

Method	β_L ϕ	ψ	E	γ_L ϕ	ψ	E	ΔE
HF/3-21G	−168.3	+170.6	−412.472783	−84.5	+67.3	−412.474780	1.25
MP2/6-311++(d, p)	−157.1	+163.2	−416.382776	−82.8	+80.6	−416.384696	1.21

reports *all the* N_0 *ab initio* minimum energy conformations of For-L-Ala-L-Ala-NH_2, since the geometry optimization of all 81 structures was attempted.

Methods

Ab initio SCF computations

The fully relaxed minimum energy conformations were gradient geometry optimized using the GAUSSIAN 90 program (39*a*) on a Cray X-MP/28 super computer. It was found that the HF-SCF method with the 3-21 G basis set (39*b*) provides a reasonably accurate reproduction of experimentally observed geometrical parameters. The $\gamma_L\gamma_L$ conformation was found as the global minimum (E[RHF] = −656.963681 hartree) and was used as a reference point for all relative energy (ΔE_i) calculations.

For *ab initio* SCF computations, the initial geometries of selected triamides were generated on the basis of previously SCF-optimized For-L-Ala-NH_2 structures (2, 16*g*, *h*) and with the use of the 75 ECEPP/2 For-L-Ala-L-Ala-NH_2 geometries (38). Geometry optimizations were carried out under "normal" rather than "tight" conditions. Absolute values of the actual maximum forces along any internal coordinate in the relaxed structures ranged from 2.2×10^{-6} to 2.1×10^{-4} au, while RMS forces ranged between 5.4×10^{-7} and 5.7×10^{-5} au for the gradient-optimized conformations. One may be concerned about the geometry optimization convergency under these "normal" conditions (39*a*) when the optimization is carried out in an internal coordinate system. The ultimate test of accuracy, in this particular case, is not so much the magnitude of the residual force but the "self consistency" of the ϕ and ψ values as these torsional angles characterize peptide conformations. As a test "normal" and "tight" optimizations have been carried out on selected conformations as reported previously (37), and the results are summarized in Table 1. Also, in addition to the $\gamma_L\gamma_L$ conformation reported in Table 1, another one dipeptide conformations ($\delta_L\epsilon_D$) were reoptimized under "tight" optimization conditions and no dramatic changes were observed as discussed towards the end of this paper and summarized in footnote 5. The other usual concern is the role of the basis set size and the omission or inclusion of the correlation energy in determining the accuracy of the computed results. The β_L and γ_L conformations of the For-L-Ala-NH_2 have been reoptimized (40) at the MP2/6311++G[d, p] level of theory and the results are summarized in Table 2. Since, along the torsional mode of motion the conformational regions are separated from each other by several tens of degrees (on the idealized surface the separation is 120°) the variations in torsional angles are not considered to be very dramatic on going from the HF/3-21G to the MP2/6-311++(d, p) levels of theory. In addition, the relative energies are practically the same at these two levels of theory.

[5]To avoid artifact of partial optimization the optimized $\delta_L\epsilon_D$ (more precisely the $\delta_L^*\epsilon_D$) conformation was reoptimized under "tight" optimization criteria. Such a "sever" criterion resulted in $E = -656.954077$ hartrees, maximum force = 5.3E-6 au, and RMS force = 1.5E-6 au. The final torsional angles associated with the ϵ_D subconformation after "tight" optimization changed less than 0.5° (ϕ_2 = +62.4°, ψ_2 = +173.4°), while in the δ_L^* part ϕ_1 was identical with the value reported in Table 6 but ψ_1 changed 3°.

Can. J. Chem. Downloaded from www.nrcresearchpress.com by 85.192.166.187 on 09/08/12
For personal use only.

Can. J. Chem. Downloaded from www.nrcresearchpress.com by 85.192.166.187 on 09/08/12
For personal use only.

INPUT CONFORMATIONS

$\gamma_D\gamma_D$	$\gamma_D\delta_D$	$\gamma_D\alpha_L$	$\delta_D\gamma_D$	$\delta_D\delta_D$	$\delta_D\alpha_L$	$\alpha_L\gamma_D$	$\alpha_L\delta_D$	$\alpha_L\alpha_L$
$\gamma_D\varepsilon_D$	$\gamma_D\beta_L$	$\gamma_D\varepsilon_L$	$\delta_D\varepsilon_D$	$\delta_D\beta_L$	$\delta_D\varepsilon_L$	$\alpha_L\varepsilon_D$	$\alpha_L\beta_L$	$\alpha_L\varepsilon_L$
$\gamma_D\alpha_D$	$\gamma_D\delta_L$	$\gamma_D\gamma_L$	$\delta_D\alpha_D$	$\delta_D\delta_L$	$\delta_D\gamma_L$	$\alpha_L\alpha_D$	$\alpha_L\delta_L$	$\alpha_L\gamma_L$
$\varepsilon_D\gamma_D$	$\varepsilon_D\delta_D$	$\varepsilon_D\alpha_L$	$\beta_L\gamma_D$	$\beta_L\delta_D$	$\beta_L\alpha_L$	$\varepsilon_L\gamma_D$	$\varepsilon_L\delta_D$	$\varepsilon_L\alpha_L$
$\varepsilon_D\varepsilon_D$	$\varepsilon_D\beta_L$	$\varepsilon_D\varepsilon_L$	$\beta_L\varepsilon_D$	$\beta_L\beta_L$	$\beta_L\varepsilon_L$	$\varepsilon_L\varepsilon_D$	$\varepsilon_L\beta_L$	$\varepsilon_L\varepsilon_L$
$\varepsilon_D\alpha_D$	$\varepsilon_D\delta_L$	$\varepsilon_D\gamma_L$	$\beta_L\alpha_D$	$\beta_L\delta_L$	$\beta_L\gamma_L$	$\varepsilon_L\alpha_D$	$\varepsilon_L\delta_L$	$\varepsilon_L\gamma_L$
$\alpha_D\gamma_D$	$\alpha_D\delta_D$	$\alpha_D\alpha_L$	$\delta_L\gamma_D$	$\delta_L\delta_D$	$\delta_L\alpha_L$	$\gamma_L\gamma_D$	$\gamma_L\delta_D$	$\gamma_L\alpha_L$
$\alpha_D\varepsilon_D$	$\alpha_D\beta_L$	$\alpha_D\varepsilon_L$	$\delta_L\varepsilon_D$	$\delta_L\beta_L$	$\delta_L\varepsilon_L$	$\gamma_L\varepsilon_D$	$\gamma_L\beta_L$	$\gamma_L\varepsilon_L$
$\alpha_D\alpha_D$	$\alpha_D\delta_L$	$\alpha_D\gamma_L$	$\delta_L\alpha_D$	$\delta_L\delta_L$	$\delta_L\gamma_L$	$\gamma_L\alpha_D$	$\gamma_L\delta_L$	$\gamma_L\gamma_L$

OUTPUT CONFORMATIONS

$\gamma_D\gamma_D$	$\gamma_D\delta_D$	$\gamma_D\delta_L{}^*$	$\delta_D\gamma_D$	$\delta_D\delta_D$	$\delta_D\gamma_L{}^*$	$\delta_L\gamma_D{}^*$	$\delta_L\delta_D{}^*$	$\alpha_L\delta_L{}^*$
$\gamma_D\varepsilon_D$	$\gamma_D\beta_L$	$\gamma_D\varepsilon_L$	$\delta_D\varepsilon_D$	$\delta_D\beta_L$	$\delta_D\varepsilon_L$	$\delta_L\varepsilon_D{}^*$	$\delta_L\beta_L{}^*$	$\delta_L\beta_L{}^*$
$\varepsilon_D\alpha_D{}^*$	$\gamma_D\delta_L$	$\gamma_D\gamma_L$	$\delta_D\alpha_D$	$\delta_D\gamma_L{}^*$	$\delta_D\gamma_L$	$\delta_L\alpha_D{}^*$	$\alpha_L\delta_L$	$\delta_L\gamma_L{}^*$
$\varepsilon_D\gamma_D$	$\varepsilon_D\delta_D$	$\varepsilon_D\delta_L{}^*$	$\beta_L\gamma_D$	$\beta_L\delta_D$	$\beta_L\delta_L{}^*$	$\delta_D\gamma_D{}^*$	$\delta_D\delta_D{}^*$	$\beta_L\delta_L{}^*$
$\varepsilon_D\varepsilon_D$	$\varepsilon_D\beta_L$	$\varepsilon_D\gamma_L{}^*$	$\beta_L\varepsilon_D$	$\beta_L\beta_L$	$\beta_L\beta_L{}^*$	$\delta_D\varepsilon_D{}^*$	$\beta_L\beta_L{}^*$	$\beta_L\beta_L{}^*$
$\varepsilon_D\alpha_D$	$\varepsilon_D\delta_L$	$\varepsilon_D\gamma_L$	$\beta_L\alpha_D$	$\beta_L\delta_L$	$\beta_L\gamma_L$	$\delta_D\alpha_D{}^*$	$\beta_L\delta_L{}^*$	$\beta_L\gamma_L{}^*$
$\alpha_D\gamma_D$	$\alpha_D\delta_D$	$\alpha_D\delta_L{}^*$	$\delta_L\gamma_D$	$\delta_L\delta_D$	$\alpha_L\delta_L{}^*$	$\gamma_L\gamma_D$	$\gamma_L\delta_D$	$\gamma_L\delta_L{}^*$
$\gamma_D\varepsilon_D{}^*$	$\alpha_D\beta_L$	$\alpha_D\beta_L{}^*$	$\delta_L\varepsilon_D$	$\delta_L\beta_L$	$\delta_L\beta_L{}^*$	$\gamma_L\varepsilon_D$	$\gamma_L\beta_L$	$\gamma_L\varepsilon_L$
$\alpha_D\alpha_D$	$\alpha_D\delta_L$	$\alpha_D\gamma_L$	$\delta_L\alpha_D$	$\alpha_L\delta_L{}^*$	$\delta_L\gamma_L$	$\gamma_L\alpha_D$	$\gamma_L\delta_L$	$\gamma_L\gamma_L$

SCHEME 7

Protein data base

As a comparison to the *ab initio* computed peptide conformations, the description of the backbone conformation of 78 selected proteins (41*a*) was also performed. X-ray data of proteins were taken from Brookhaven Protein Structure Databank (BPSD) (41*b*, *c*). Their stereo chemical parameters such as the resolution, the *R* factor, and the core% were taken as recommended (41*d*).

Conformation assignment algorithm

An *A*mino acid *C*onformation *A*ssignment of *P*roteins (ACAP) algorithm was coded in Pascal, which assigns all the amino acid residue backbone conformations to one of the appropriate conformational (α_L, α_D, β_L, γ_L, γ_D, δ_L, δ_D, ϵ_L, and ϵ_D) clusters. The IBM/PC program is available from the authors upon request.

Results and discussions

Minima on the 4D-Ramachandran map

The upper limit (81) of the number of legitimate backbone conformations on the four- dimensional (4D) Ramachandran map associated with For-L-Ala-L-Ala-NH_2 was previously determined by MDCA (38). According to *ab initio* (SCF) geometry optimizations (using a 3-21G basis set) 49 intrinsically stable conformations were found, while 32 migrated (marked by * on Scheme 7) to one of the above 49 stable structures (Scheme 7 and Tables 3–9).

Ab initio calculations of single amino acid diamides (2, 16) revealed that on a 2D-Ramachandran map the α_L and ϵ_L backbone conformations should be regarded as annihilated minimum energy structures. All triamides, incorporating the α_L and/or the ϵ_L substructures, such as [($\alpha_L x_L$, $\alpha_L x_D$), ($x_L\alpha_L$, $x_D\alpha_L$), ($\epsilon_L x_L$, $\epsilon_L x_D$) and ($x_D\epsilon_L$, $x_L\epsilon_L$)], were investigated here with pre-

TABLE 3. Optimized *ab initio* SCF (3-21G) geometries[a] for $\alpha_L x_L$, $\alpha_L x_D$,[b] $\alpha_D x_L$, and $\alpha_D x_D$[c] conformations of For-L-Ala-L-Ala-NH_2

INI.[d]	$\alpha_L\alpha_L$		$\alpha_D\varepsilon_L$		$\alpha_D\alpha_L$		
	$\alpha_L\delta_L$	$\alpha_D\alpha_D$	$\alpha_D\beta_L$	$\alpha_D\delta_D$	$\alpha_L\delta_L$	$\alpha_D\gamma_D$	$\alpha_D\gamma_L$
CONV.[e]	$\alpha_L\delta_L$	$\alpha_D\alpha_D$	$\alpha_D\beta_L$	$\alpha_D\delta_D$	$\alpha_D\delta_L$	$\alpha_D\gamma_D$	$\alpha_D\gamma_L$
ω_1	−171.7	+171.2	+176.2	+171.0	+173.0	+173.52	+173.7
ϕ_1	−68.6	+60.4	+60.2	+64.1	+57.0	+62.3	+63.4
ψ_1	−17.5	+28.3	+33.0	+16.8	+39.4	+37.0	+30.4
ω_2	+177.8	+179.0	−177.5	−175.6	−166.3	−172.9	−175.9
ϕ_2	−113.1	+62.3	−173.6	+150.8	−131.4	+74.1	−87.3
ψ_2	+21.3	+24.9	+169.8	−40.0	+29.7	−58.0	+67.4
ω_3	+176.0	+179.1	+177.5	−174.2	+175.7	+174.9	−179.1
MODEL DIS[f]	4.83	5.33	7.03	4.30	7.35	6.06	7.79
τ	+41.1	−66.9	+61.6	−11.0	+125.3	−79.3	+164.3
CRIT DIS[g]	5.32	5.97	7.42	4.64	8.05	6.64	8.56
τ	+43.7	−70.8	+57.8	−12.7	+122.7	−80.4	+160.1
O1...HN4	2.11	2.03	6.42	2.16	5.49	3.76	5.39
O1...N4	3.07	3.03	6.06	3.11	5.85	4.00	5.90
O1...HN4...N4	+162.5	+172.4	−64.5	+160.3	+106.3	+97.1	+116.1
O1...HN3	3.01	3.03	3.18	2.87	3.12	3.20	3.17
O1...N3	3.15	3.10	3.19	3.05	3.15	3.27	3.22
O1...HN3...N3	−89.0	−84.5	−81.5	+90.7	−83.0	−85.3	−84.1
O2...HN4	3.50	3.06	5.11	4.10	3.51	1.93	2.02
O2...N4	3.98	3.23	5.16	4.61	4.08	2.83	2.87
O2...HN4...N4	+111.9	+91.1	−87.1	+114.9	+118.2	+147.1	+142.0
MAX. FORCE	1.5 E-5	1.8 E-5	3.6 E-5	8.4 E-5	1.9 E-4	1.1 E-4	9.3 E-5
RMS. FORCE	5.8 E-6	6.5 E-6	1.1 E-5	2.7 E-5	3.5 E-5	3.6 E-5	2.8 E-5
E	0.958677	0.956139	0.954609	0.949915	0.950469	0.950869	0.956058
ΔE	3.13	4.73	5.69	8.64	8.29	8.04	4.78
STRUC.[h]	330	[i]	73	10	28	15	44

[a]Torsion angles (ω, ϕ, ψ) in degrees, distances in Ångstroms, forces in au, energy (E) in hartrees, and energy difference (ΔE) in kcal/mol compared to $E(\gamma_L\gamma_L)$ = −656.963681.

[b]The $\alpha_L\alpha_D \rightarrow \delta_L\alpha_D$, $\alpha_L\beta_L \rightarrow \delta_L\beta_L$, $\alpha_L\delta_D \rightarrow \delta_L\delta_D$, $\alpha_L\varepsilon_D \rightarrow \delta_L\varepsilon_D$, $\alpha_L\varepsilon_L \rightarrow \delta_L\beta_L$, $\alpha_L\gamma_D \rightarrow \delta_L\gamma_D \rightarrow \delta_L\gamma_D$ and $\alpha_L\gamma_L \rightarrow \delta_L\gamma_L$ conformation shifts are observed.

[c]The $\alpha_D\varepsilon_D$ conformation was shifted to $\gamma_D\varepsilon_D$.

[d]INI: initial backbone conformation (calculated by ECEPP/2).

[e]CONV: converged backbone conformation.

[f]MODEL DIS.: C^α_i and C^α_{i+3} in accordance to classical β-turn definition must be shorter than 7 Å. In For-Ala-Ala-NH_2 the two C^α atoms are replaced by hydrogens (H1 and H4*) (cf. Scheme 2), therefore the model distance (d_{model}) is shorter than C^α_i—C^α_{i+3} (Fig. 1) no more than 1.1 Å. In such a case τ is H1—$C2^\alpha$—$C3^\alpha$—H4*.

[g]CRIT DIS.: critical distances for β-turn assignment (C^α_i—C^α_{i+3}) were extrapolated using *ab initio* resulted bond lengths and bond angles, on the basis of the determined N—H and C′—H distances. In such a case τ is $C1^\alpha$—$C2^\alpha$—$C3^\alpha$—$C4^\alpha$.

[h]Number of structures assigned in the 78 selected proteins.

[i]50 $\alpha_D\alpha_D$, 3 $\alpha_D\alpha_D\alpha_D$, and 1 $\alpha_D\alpha_D\alpha_D\alpha_D$ were assigned.

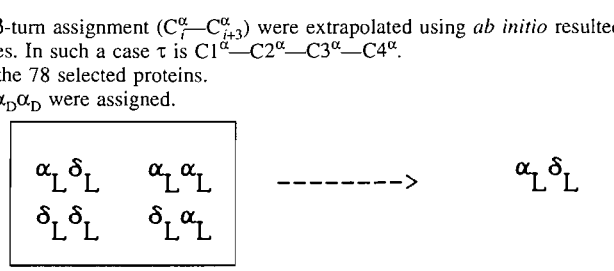

SCHEME 8

caution. Of these, only four conformations ($\alpha_L\delta_L$, $\gamma_L\epsilon_L$, $\gamma_D\epsilon_L$, and $\delta_D\epsilon_L$) turned out to be intrinsically stable. These four unexpectedly stable triamide conformations incorporate for the first time, as stable substructures, the α_L and the ϵ_L subunits, previously annihilated on the 2D-Ramachandran map. It should be noted that among the 32 unstable triamide conformations of the predicted 81 backbone arrangement (Scheme 7), only four ($\alpha_D\epsilon_D$, $\epsilon_D\alpha_D$, $\delta_D\delta_L$, and $\delta_L\delta_L$) are associated with neither the α_L nor the ϵ_L substructures.

At this level of the theory, the $\alpha_L\delta_L$ conformation (type I β-turn) is the only intrinsically stable backbone conformation of the For-Ala-Ala-NH_2 molecule which incorporates the α_L substructure. It is most probable that the intramolecular H-bond (1 ← 4 type H-bond (21), interconnecting the carbonyl oxygen of the formyl group with the amide proton located at the C terminal) (37) plays a crucial role in the stability of the $\alpha_L\delta_L$ conformation. According to earlier X-ray data set analysis (38), the $\alpha_L\delta_L$ was the sixth most frequent conformation among the 81 possible dipeptide structures, preceded only by the $\alpha_L\alpha_L$, $\beta_L\beta_L$, $\epsilon_L\epsilon_L$, $\beta_L\epsilon_L$, and $\epsilon_L\beta_L$ type backbone orientations (see Small Data Base in ref. 38). Some of these structures are the building units of the most frequently observed typical secondary structural elements of proteins; $(\alpha_L\alpha_L)_n \rightarrow$ α helix, $(\beta_L\beta_L)_n \rightarrow$ β-pleated sheet and $(\epsilon_L\epsilon_L)_n \rightarrow$ Poly(L-Proline)II. With the exception of the $\delta_D\alpha_L \rightarrow \delta_D\gamma_L$ conformational shift the α_L substructure is always transformed to the δ_L conformation (in 15 cases out of the total 17 [$\alpha_L x_L$, $\alpha_L x_D$, $x_L\alpha_L$, $x_D\alpha_L$] possibilities). On the other hand, the optimization of any combination of the α_L and δ_L substructures (see Scheme 8) yielded a single conformation, which is the $\alpha_L\delta_L$ (type I β-turn). The intrinsic stability of

Can. J. Chem. Downloaded from www.nrcresearchpress.com by 85.192.166.187 on 09/08/12
For personal use only.

TABLE 4. Optimized *ab initio* SCF (3-21G) geometries for $\beta_L x_L$, $\beta_L x_D$ conformations of For-L-Ala-L-Ala-NH_2[a]

INI.[b]	$\beta_L\alpha_L$	$\beta_L\varepsilon_L$	$\beta_L\delta_D$	$\beta_L\alpha_L$	$\beta_L\varepsilon_D$	$\beta_L\gamma_D$	$\beta_L\gamma_L$
CONV.[c]	$\beta_L\alpha_L$	$\beta_L\beta_L$	$\beta_L\delta_D$	$\beta_L\delta_L$	$\beta_L\varepsilon_D$	$\beta_L\gamma_D$	$\beta_L\gamma_L$
ω_1	+179.2	+179.0	−179.1	−178.7	+178.0	+179.2	+178.9
ϕ_1	−167.6	−168.6	−167.4	−168.2	−169.0	−167.2	−167.7
ψ_1	+168.4	+171.1	+169.2	+171.6	+172.4	+168.4	+169.3
ω_2	+172.1	+177.4	+173.8	−175.5	−171.5	+172.1	−177.5
ϕ_2	+62.1	−167.6	−173.7	−128.6	+65.7	+75.6	−85.1
ψ_2	+35.3	+170.3	−47.1	+29.6	−175.5	−57.2	+68.2
ω_3	+179.1	+177.9	−177.0	+176.1	−179.2	−178.2	−178.8
MODEL DIS[d]	7.13	10.01	9.03	8.64	8.43	7.27	7.67
τ	+49.2	−177.0	+145.0	−133.1	+40.2	+28.0	−83.0
CRIT DIS[e]	7.56	10.76	9.84	9.40	8.83	7.73	8.22
τ	+49.0	−177.0	+148.0	+131.8	+42.8	+31.1	−83.0
O1...HN4	5.96	9.12	6.74	6.43	8.81	6.29	6.53
O1...N4	6.69	8.75	7.33	7.28	8.17	6.96	7.16
O1...HN4...N4	+134.8	−68.1	+122.9	+146.7	−47.3	+128.8	+125.5
O1...HN3	5.06	5.14	5.06	5.05	5.05	4.99	5.08
O1...N3	5.15	5.17	5.15	5.16	5.18	5.13	5.15
O1...HN3...N3	−89.7	−86.0	−89.5	+90.6	+91.6	+92.7	−88.8
O2...HN4	3.20	5.09	4.57	3.58	4.55	1.93	2.04
O2...N4	3.24	5.14	4.86	4.13	4.14	2.82	2.89
O2...HN4...N4	−83.0	−87.1	+100.7	+117.0	−59.8	+146.7	+140.7
MAX. FORCE	1.5 E-4	3.2 E-5	7.6 E-5	9.0 E-5	2.1 E-4	1.7 E-4	1.0 E-4
RMS. FORCE	3.6 E-5	1.2 E-5	2.4 E-5	2.3 E-5	4.5 E-5	4.4 E-5	2.7 E-5
E	0.952663	0.960419	0.949998	0.955673	0.949539	0.956752	0.961052
ΔE	6.91	2.05	8.59	5.03	8.87	4.34	1.65
STRUC.[f]	33	[g]	38	56	48	11	186

[a]The $\delta_D\varepsilon_L$ conformation contains an 8-membered intramolecular H-bond, where O3...H2 = 2.07 Å, O3...N2 = 3.05 Å with an H-bond angle (O3—H2—N2) = +163.1°. Torsion angles (ω, ϕ, ψ) in degrees, distances in Ångstroms, forces in au, energy (*E*) in hartrees, and the energy difference (ΔE) in kcal/mol compared to $E(\gamma_L\gamma_L)$ = −656.963681.

[b]INI: initial backbone conformation (calculated by ECEPP/2).

[c]CONV: converged backbone conformation.

[d]MODEL DIS: C_i^α and C_{i+3}^α in accordance to classical β-turn definition must be shorter than 7 Å. In For-Ala-Ala-NH_2 the two C^α atoms are replaced by hydrogens (H1 and H4*) (cf. Scheme 2), therefore the model distance (d_{model}) is shorter than C_i^α—C_{i+3}^α (Fig. 1) more than 1.1 Å. In such a case τ is H1—$C2^\alpha$—$C3^\alpha$—H4*.

[e]CRIT DIS.: critical distances for β-turn assignment (C_i^α—C_{i+3}^α) were extrapolated using *ab initio* resulted bond lengths and bond angles, on the basis of the determined N—H and C′—H distances. In such a case τ is $C1^\alpha$—$C2^\alpha$—$C3^\alpha$—$C4^\alpha$.

[f]Number of structures assigned in the 78 selected proteins.

[g]191 $\beta_L\beta_L$, 67 $\beta_L\beta_L\beta_L$, 26 $\beta_L\beta_L\beta_L\beta_L$, 6 $\beta_L\beta_L\beta_L\beta_L\beta_L$, 1 $\beta_L\beta_L\beta_L\beta_L\beta_L\beta_L$ were assigned.

the $\alpha_L\delta_L$ conformation, as established by the present *ab initio* SCF computations, in accordance with the frequent occurrence of this structural type in globular proteins, may provide some explanation why type I β-turns are believed to play a cornerstone role in protein folding (21, 42, 43).

The ϵ_L subconformation, which is the other computationally "missing" backbone conformational type in amino acid diamides, was also found for the first time as a legitimate substructure among the For-Ala-Ala-NH_2 conformations. *Ab initio* calculations showed that the unfavorable eclipsed H—N—C^α—C^β orientation ($\approx -20°$) in the ϵ_L backbone conformation results in the annihilation of such a backbone geometry in For-Gly-NH_2, For-Ala-NH_2, For-Val-NH_2 and probably in the other amino acid diamides as well. In contrast, increasing the peptide chain length with an additional amino acid residue resulted in the stabilization of the ϵ_L substructure in three conformations ($\gamma_L\epsilon_L$, $\gamma_D\epsilon_L$, and $\delta_D\epsilon_L$). While $\delta_D\epsilon_L$ and $\gamma_D\epsilon_L$ geometries are perfect β-turns, in accordance with both the distance[6] and the angularity[7] criteria, the $\gamma_L\epsilon_L$ has an extended backbone conformation. Although these are only 3 conformations from the 17 possibilities (Scheme 7), they represent solid evidence that a "favorable" backbone/backbone interaction may "re-stabilize" the "annihilated" ϵ_L minimum. There is no direct influence (like an intramolecular hydrogen bond) between the third and the second amide groups of the molecule, oriented as an ϵ_L conformation. At this stage of the investigation we are not certain about the nature of the interaction that could stabilize the ϵ_L conformation substructure in triamide systems; however, it is conceivable that the negative polarity of the carbonyl oxygen in the central amide moiety may have some indirect stabilizing effect. The increased negative charge on the oxygen may have an influence to stabilize the ϵ_L conformation at the "second half" of the molecule, yielding the stable $\gamma_L\epsilon_L$, $\gamma_D\epsilon_L$, and $\delta_D\epsilon_L$ structures. In the other 14 initial geometries incorporating the ϵ_L substructure ($\epsilon_L x_L$, $x_D\epsilon_L$, $x_L\epsilon_L$, and $\epsilon_L x_D$), generally the $\epsilon_L \rightarrow \beta_L$ conformational shift was observed, resulting in the $\beta_L x_L$, $x_D\beta_L$, and $x_L\beta_L$ conformations in three out of the four cases. However, when the initial geometry falls in the $\epsilon_L x_D$ category the $\delta_D x_D$ backbone conformation was obtained ($\epsilon_L x_D \rightarrow \delta_D x_D$).

[6]According to the distance criterion the C_i^α—C_{i+3}^α distance must be shorter than 7 Å.

[7]According to the angularity (or twisting) parameter (τ), the value of τ (torsional angle involving C_i^α, C_{i+1}^α, C_{i+2}^α, C_{i+3}^α peptide backbone atoms) must be in the $-90° \leq \tau \leq +90°$ range for reverse turns (49).

Typical and unusual conformations

The monitoring of the ϕ and ψ torsional angle variation in

Can. J. Chem. Downloaded from www.nrcresearchpress.com by 85.192.166.187 on 09/08/12
For personal use only.

TABLE 5. Optimized *ab initio* SCF (3-21G) geometries for $\varepsilon_L x_L$, $\varepsilon_L x_D$,[a] $\varepsilon_D x_L$, and $\varepsilon_D x_D$ conformations of For-L-Ala-L-Ala-NH_2[b]

INI.[c]	$\varepsilon_D\alpha_D$	$\varepsilon_D\beta_L$	$\varepsilon_D\delta_D$	$\varepsilon_D\delta_L$ $\varepsilon_D\alpha_L$	$\varepsilon_D\varepsilon_D$	$\varepsilon_D\gamma_D$	$\varepsilon_D\varepsilon_L$ $\varepsilon_D\gamma_L$
CONV.[d]	$\varepsilon_D\alpha_D$	$\varepsilon_D\beta_L$	$\varepsilon_D\delta_D$	$\varepsilon_D\delta_L$	$\varepsilon_D\varepsilon_D$	$\varepsilon_D\gamma_D$	$\varepsilon_D\gamma_L$
ω_1	+174.6	−170.3	+172.6	+177.4	−169.6	−171.3	−171.9
ϕ_1	+73.8	+66.7	+62.6	+56.1	+67.7	+66.9	+64.0
ψ_1	+119.1	+156.5	−157.7	−129.7	−178.2	−178.1	−172.8
ω_2	−176.4	+179.3	+178.4	+177.2	−166.1	+174.9	−175.3
ϕ_2	+62.7	−166.9	−175.0	−112.4	+63.7	+75.8	−86.0
ψ_2	+35.3	+169.8	−42.9	+26.6	−170.6	−86.0	+66.2
ω_3	+178.9	+178.2	−176.2	+176.5	−179.0	−177.7	−176.2
MODEL DIS[e]	7.70	9.36	8.68	5.29	8.00	6.97	5.99
τ	−149.4	−137.8	−151.7	−35.0	+77.8	+71.3	−36.7
CRIT DIS[f]	8.57	10.17	9.53	5.82	8.56	7.52	6.52
τ	−153.3	−142.4	−153.1	−36.9	+75.4	+69.5	−41.5
O1...HN4	4.41	7.27	6.16	1.99	7.79	5.04	3.58
O1...N4	5.15	7.19	6.29	2.98	7.14	5.91	4.19
O1...HN4...N4	+133.9	−81.4	+92.69	+169.9	−71.7	+148.6	+121.6
O1...HN3	1.90	4.67	3.93	3.33	4.72	4.64	4.46
O1...N3	2.81	4.24	3.81	3.21	4.28	4.23	4.09
O1...HN3...N3	+150.2	−58.7	−75.5	−74.6	−58.2	−59.9	−62.1
O2...HN4	3.25	5.07	4.52	3.34	4.61	1.91	2.05
O2...N4	3.27	5.12	4.83	3.89	4.02	2.80	2.90
O2...HN4...N4	−82.3	−87.5	+102.5	+115.9	−62.1	+146.5	+141.9
MAX. FORCE	1.8 E-4	3.0 E-5	1.4 E-4	1.4 E-4	8.0 E-6	1.8 E-4	1.3 E-4
RMS. FORCE	6.3 E-5	2.8 E-5	3.8 E-5	4.9 E-5	2.8 E-6	3.9 E-5	4.6 E-5
E	0.9524580	0.950278	0.939187	0.955958	0.940468	0.947257	0.952062
ΔE	7.04	8.41	15.37	4.85	14.57	10.31	7.29
STRUC.[g]	10	56	7	21	16[h]	6	28

[a]The $\varepsilon_L\alpha_D \rightarrow \delta_D\alpha_D$, $\varepsilon_L\alpha_L \rightarrow \beta_L\beta_L$, $\varepsilon_L\beta_L \rightarrow \beta_L\beta_L$, $\varepsilon_L\delta_D \rightarrow \delta_D\delta_D$, $\varepsilon_L\delta_L \rightarrow \beta_L\delta_L$, $\varepsilon_L\varepsilon_D \rightarrow \delta_D\varepsilon_D$, $\varepsilon_L\varepsilon_L \rightarrow \beta_L\beta_L$, $\varepsilon_L\gamma_D \rightarrow \delta_D\gamma_D$, and $\varepsilon_L\gamma_L \rightarrow \beta_L\gamma_L$ conformational shifts are observed.

[b]Torsion angles (ω, ϕ, ψ) in degrees, distances in Ångstroms, forces in au, energy (*E*) in hartrees and the energy difference (ΔE) in kcal/mol compared to $E(\gamma_L\gamma_L)$ = −656.963681.

[c]INI: initial backbone conformation (calculated by ECEPP/2).

[d]CONV: converged backbone conformation.

[e]MODEL DIS: C_i^α and C_{i+3}^α in accordance to classical β-turn definition must be shorter than 7 Å. In For-Ala-Ala-NH_2 the two C^α atoms are replaced by hydrogens (HI and H4*) (cf. Scheme 2), therefore the model distance (d_{model}) is shorter than C_i^α—C_{i+3}^α (Fig. 1) no more than 1.1 Å. In such a case τ is H1—C2$^\alpha$—C3$^\alpha$—H4*.

[f]CRIT DIS.: critical distances for β-turn assignment (C_i^α—C_{i+3}^α) were extrapolated using *ab initio* resulted bond lengths and bond angles, on the basis of the determined N—H and C′—H distances. In such a case τ is C1$^\alpha$—C2$^\alpha$—C3$^\alpha$—C4$^\alpha$.

[g]Number of structures assigned in the 78 selected proteins.

[h]No $\varepsilon_D\varepsilon_D\varepsilon_D$ or longer fragments were assigned.

different conformations as a function of the side chain type can reveal the so-called "backbone/side chain effect". Also, the analysis of selected geometrical parameter changes in homopolymers as a function of the peptide chain length (e.g. For-[Ala]$_i$-NH_2; $1 \le i \le n$) will help in our understanding of the nature of interactions in polypeptides. The third type of data comparison performed in this study was to extract the geometrical parameters of the 9 legitimate backbone conformations of the optimized 49 conformations of For-Ala-Ala-NH_2. The 49 stable triamide conformations yield a total of $49 \times 2 = 98$ single amino acid residue subconformations classified as α_L, β_L, δ_L etc. Scheme 9 demonstrates the grouping of the triamide backbone geometries in order to extract typical ϕ and ψ torsional angle pairs of the 9 legitimate backbone conformations.

Figures 2 and 3 show the distribution of (ϕ, ψ) angle pairs as found in triamides. (Data in Fig. 2 are reported in the conventional $-180° \le \phi \le 180°$, $-180° \le \psi \le 180°$ representation, while a topologically more useful plot is shown in Fig. 3.) The arrangement of the 98 calculated backbone subconformations determines nine clusters, as expected (Fig. 3), where only two of the δ_L-type conformations are shifted away from the anticipated square representing the borders of the appropriate idealized catchment region. However, even these two cases are due to the fact that the average δ_L position (ϕ = −126.2°, ψ = +26.5°) is shifted substantially away from the idealized (ϕ = −180°, ψ = +60°) position of δ_L towards the lower right hand corner of the square. The concentric circles around the cluster "centers" show areas where the deviations from the average structure (Table 10) is smaller than 20°, 40°, or 60°. Many of the points in Fig. 3 are very close to their average value (denoted by the center of a small square in each of the clusters). For example all β_L, ϵ_L, and γ_L points are well within a 20° circle, suggesting

$\alpha_D x$ and $x\alpha_D$ → α_D

$\alpha_L\delta_L$ → α_L

$\beta_L x$ and $x\beta_L$ → β_L

$\gamma_D x$ and $x\gamma_D$ → γ_D

$\gamma_L x$ and $x\gamma_L$ → γ_L

$\delta_D x$ and $x\delta_D$ → δ_D

$\delta_L x$ and $x\delta_L$ → δ_L

$\varepsilon_D x$ and $x\varepsilon_D$ → ε_D

$\gamma_L\varepsilon_L$, $\gamma_D\varepsilon_L$ and $\delta_D\varepsilon_L$ → ε_L

SCHEME 9

Can. J. Chem. Downloaded from www.nrcresearchpress.com by 85.192.166.187 on 09/08/12
For personal use only.

TABLE 6. Optimized *ab initio* SCF (3-21G) geometries for $\delta_L x_L$, $\delta_L x_D$ and $\delta_L x_D$ conformations of For-L-Ala-L-Ala-NH_2[a]

INI.[c]	$\delta_L\alpha_D$	$\delta_L\varepsilon_L$ $\delta_L\beta_L$	$\delta_L\delta_D$	$\delta_L\varepsilon_D$[b]	$\delta_L\gamma_D$	$\delta_L\gamma_L$
CONV.[d]	$\delta_L\alpha_D$	$\delta_L\beta_L$	$\delta_L\delta_D$	$\delta_L\varepsilon_D$	$\delta_L\gamma_D$	$\delta_L\gamma_L$
ω_1	−172.4	−175.9	−172.8	−177.0	−172.7	−173.4
ϕ_1	−122.4	−121.3	+126.8	+161.8	+121.2	+124.9
ψ_1	+24.0	+17.6	+23.8	+55.7	+21.8	+20.6
ω_2	+168.8	+176.4	+171.1	−152.1	+172.4	−178.1
ϕ_2	+63.1	−169.4	−173.7	+62.6	+74.9	−84.7
ψ_2	+35.1	+169.6	−45.6	−173.8	−58.0	+67.0
ω_3	+179.6	+178.1	−176.5	+179.1	+177.8	+178.5
MODEL DIS[e]	7.12	7.25	5.66	6.47	7.67	7.54
τ	−106.3	+19.5	−9.9	−62.3	−127.3	+124.0
CRIT DIS[f]	7.71	7.56	5.95	6.60	8.27	8.24
τ	−105.1	+20.8	−5.6	−59.8	−123.0	+125.1
O1...HN4	5.89	7.55	5.49	8.05	6.42	5.84
O1...N4	6.60	6.98	5.74	7.33	6.88	6.03
O1...HN4...N4	+132.3	−51.9	+99.4	−40.7	+113.7	+96.5
O1...HN3	3.46	3.63	3.55	4.01	3.48	3.60
O1...N3	4.06	4.12	4.15	4.57	4.05	4.15
O1...HN3...N3	+121.0	+112.7	+121.2	+118.8	+117.8	+117.1
O2...HN4	3.19	5.10	4.55	4.56	1.91	2.02
O2...N4	3.24	5.15	4.85	4.18	2.80	2.88
O2...HN4...N4	−83.9	−87.31	+101.8	−61.79	+146.7	+141.9
MAX. FORCE	7.5 E-5	5.6 E-5	8.7 E-5	1.1 E-4	5.2 E-5	1.3 E-4
RMS. FORCE	2.3 E-5	1.6 E-5	2.7 E-5	2.9 E-5	1.4 E-5	4.2 E-5
E	0.948190	0.95657	0.945712	0.954077	0.954474	0.958063
ΔE	9.72	4.46	11.28	6.11	5.78	3.52
STRUC.[g]	75	97	28	44	15	51

[a]Torsion angles (ω, ϕ, ψ) in degrees, distances in Ångstroms, forces in au, energy (*E*) in hartrees, and the energy difference (ΔE) in kcal/mol compared to $E(\gamma_L\gamma_L)$ = −656.963681. The $\delta_L\alpha_L \rightarrow \alpha_L\delta_L$ and $\delta_L\delta_L \rightarrow \alpha_L\delta_L$ conformational shifts are observed. The $\delta_L\varepsilon_D$ conformation contains an 8-membered intramolecular H-bond, where O3...H2 = 2.07 Å, O3...N2 = 2.99 Å with an H-bond angle (O3—H2—N2) = +151.2°.

[b]The $\delta_L\varepsilon_D$ conformation contains an 8-membered intramolecular H-bond, where O3...H2 = 2.07 Å, O3...N2 = 2.99 Å with an H-bond angle (O3–H2—N2) = +151.2°.

[c]INI: initial backbone conformation (calculated by ECEPP/2).

[d]CONV: converged backbone conformation.

[e]MODEL DIS.: C^α_i and C^α_{i+3} in accordance to classical β-turn definition must be shorter than 7 Å. In For-Ala-Ala-NH_2 the two C^α atoms are replaced by hydrogens (H1 and H4*) (cf. Scheme 2), therefore the model distance (d_{model}) is shorter than C^α_i—C^α_{i+3} (Fig. 1) by no more than 1.1 Å. In such a case τ is H1—$C2^\alpha$—$C3^\alpha$—H4*.

[f]CRIT DIS.: critical distances for β-turn assignment (C^α_i—C^α_{i+3}) were extrapolated using *ab initio* resulted bond lengths and bond angles, on the basis of the determined N—H and C′—H distances. In such a case τ is $C1^\alpha$—$C2^\alpha$—$C3^\alpha$—$C4^\alpha$.

[g]Number of structures assigned in the 78 selected proteins.

that these substructure types are not influenced dramatically by conformational changes in the preceding or following subunit. With the exception of two (2) points, one δ_L and one ϵ_D, all 98 points are within a 40° circle. These two points are called "ghost" conformations and are marked by an asterisk, e.g., δ^*_L and ϵ^*_D. The substructure comparison of homopolymers (e.g. For-$[Ala]_i$-NH_2; $1 \leq i \leq n$) (44–49) in homo subconformations (e.g. $(\gamma_L)_i$; $1 \leq i \leq n$) resulted in small ϕ, ψ deviations in the case of $(\gamma_L)_i$ (44–47) and $(\beta_L)_i$ (44–48) ($1 \leq i \leq 4$) conformations. In contrast, the actual geometry of the α_L backbone type depends strongly on the length of the investigated homopolymer in its $(\alpha_L)_i\delta_L$ (49) conformation (Table 11).

Conformational folding

The importance of some triamide conformations, especially type I (or III) and type II β-turns, is continuously emphasized in the literature (21). Indeed, these conformations are frequently assigned secondary structural elements of globular proteins. Although the classification of β-turns in traditionally given on the basis of the backbone torsional angle values (ϕ_i, ψ_i), as specified in Scheme 4, the degree of folding or unfolding of a β-turn can be defined in a simpler way, based on the twisting of the hairpin conformation. We recently re-introduced (37) the C^α_i—C^α_{i+1}—C^α_{i+2}—C^α_{i+3} torsional angle labelled as τ (see Fig. 2 in ref. 37 and Fig. 1 in ref. 44), that describes the overall angularity of the backbone conformation with values $-180° \leq \tau \leq +180°$. The global minimum (the $\gamma_L\gamma_L$ conformation) has a $\tau_{\gamma L\gamma L}$ = +168.4°, which can quantitatively describe the degree of backbone unfolding since for a perfectly unfolded conformation τ must be ±180°. Considering the traditional criterion that the C^α_1—C^α_4 distance (*d*) must be shorter than 7 Å, only a fraction (18) of the total β-turn conformations (30 structures) should be assigned as β-turn. This paper summarizes all the 49 conformations of the model compound resulting in 30 structures within the $-90° \leq \tau \leq 90°$ angularity range and 19 backbone geometries with $-180° \leq \tau \leq -90°$ or $+90° \leq \tau \leq +180°$ values (see Fig. 4). Depending on the *d* or τ type of "conformation selection rule", both groups of hairpin geometries of For-Ala-Ala-NH_2 consist of a large number of elements. A total of 18 structures are assigned as turns if both the angularity and the distance criteria are applied simultaneously, but as many as 30 conformations are considered folded structures when only the angularity (τ) selection rule ($-80° \leq \tau \leq 90°$) is considered. All the calculated conformations have been observed previously (38), by X-ray data-base analysis of globular proteins. However, the extraction of all the β-turn conformations fulfill-

Can. J. Chem. Downloaded from www.nrcresearchpress.com by 85.192.166.187 on 09/08/12
For personal use only.

TABLE 7. Optimized *ab initio* SCF (3-21G) geometries for $\delta_D x_L$ and $\delta_D x_D$ conformations of For-L-Ala-L-Ala-NH_2[b]

INI.[c]	$\delta_D\alpha_D$	$\delta_D\beta_L$	$\delta_D\delta_D$	$\delta_D\varepsilon_D$	$\delta_D\varepsilon_L$[b]	$\delta_D\gamma_D$	$\delta_D\alpha_L$ $\delta_D\delta_L$ $\delta_D\gamma_L$
CONV.[d]	$\delta_D\alpha_D$	$\delta_D\beta_L$	$\delta_D\delta_D$	$\delta_D\varepsilon_D$	$\delta_D\varepsilon_L$	$\delta_D\gamma_D$	$\delta_D\gamma_L$
ω_1	+174.0	+176.6	+174.2	+175.3	+175.2	+174.7	+174.7
ϕ_1	+178.6	−176.6	+178.0	−179.4	−174.2	+179.2	+178.9
ψ_1	−47.0	−43.6	−45.6	−40.3	−55.0	−41.4	−44.3
ω_2	+177.1	−178.5	+178.7	−163.4	+154.1	+178.3	−173.2
ϕ_2	+61.5	−167.4	−172.9	+63.8	−79.0	+74.3	−85.5
ψ_2	+34.3	170.2	−49.7	−171.6	+171.7	−57.7	+68.8
ω_3	+179.3	+177.7	−173.0	−179.0	+179.7	−178.2	−179.3
MODEL DIS[e]	8.02	7.74	6.54	8.81	6.36	8.30	6.89
τ	−149.2	−16.2	−51.5	−149.1	+45.2	−163.1	+85.2
CRIT DIS[f]	8.77	8.00	6.87	9.44	6.42	9.03	7.23
τ	−152.2	−18.4	−51.4	−149.3	+43.3	−162.9	+82.2
O1...HN4	6.08	8.72	6.23	8.73	8.11	6.71	6.63
O1...N4	6.90	8.20	6.65	8.16	7.37	7.25	7.01
O1...HN4...N4	+142.6	−55.7	+110.7	−51.8	−39.0	+119.2	+108.8
O1...HN3	4.42	4.57	4.41	4.44	4.46	4.43	4.45
O1...N3	4.85	4.87	4.84	4.85	4.85	4.85	4.85
O1...HN3...N3	+109.6	+102.1	+109.8	+108.5	+107.7	+109.6	+108.0
O2...HN4	3.19	5.09	4.61	4.44	4.53	1.92	2.04
O2...N4	3.24	5.14	4.87	4.06	4.31	2.81	2.88
O2...HN4...N4	−84.1	−87.2	+99.7	−61.8	−71.0	+146.4	+140.3
MAX. FORCE	2.0 E-4	4.7 E-5	3.1 E-6	1.1 E-4	1.3 E-4	6.0 E-4	1.2 E-4
RMS. FORCE	5.7 E-5	1.5 E-5	9.7 E-7	4.0 E-5	3.8 E-5	2.5 E-5	3.3 E-5
E	0.943013	0.951769	0.940844	0.941230	0.954315	0.948000	0.952531
ΔE	12.97	7.47	14.33	14.09	5.88	9.84	7.00
STRCT.[g]	12	37	[h]	8	31	4	16

[a]Torsion angles (ω, ϕ, ψ) in degrees, distances in Ångstroms, forces in au, energy (E) in hartrees, and the energy difference (ΔE) in kcal/mol compared to $E(\gamma_L\gamma_L)$ = −656.963681.

[b]The $\delta_D\varepsilon_L$ conformation contains an 8-membered intramolecular H-bond, where O3...H2 = 2.07 Å, O3...N2 = 3.05 Å with an H-bond angle (O3—H2—N2) = +163.1°.

[c]INI: initial backbone conformation (calculated by ECEPP/2).

[d]CONV: converged backbone conformation.

[e]MODEL DIS.: C^α_i and C^α_{i+3} in accordance to classical β-turn definition must be shorter than 7 Å. In For-Ala-Ala-NH_2 the two C^α atoms are replaced by hydrogens (H1 and H4*) (cf. Scheme 2), therefore the model distance (d_{model}) is shorter than C^α_i—C^α_{i+3} (Fig. 1) by no more than 1.1 Å. In such a case τ is H1—$C2^\alpha$—$C3^\alpha$—H4*.

[f]CRIT DIS.: critical distances for β-turn assignment (C^α_i—C^α_{i+3}) were extrapolated using *ab initio* resulted bond lengths and bond angles, on the basis of the determined N—H and C′—H distances. In such a case τ is $C1^\alpha$—$C2^\alpha$—$C3^\alpha$—$C4^\alpha$.

[g]Number of structures assigned in the 78 selected proteins.

[h]11 $\delta_D\delta_D$, 6 $\delta_D\delta_D\delta_D$, 4 —$(\delta_D)_4$—, 1 —$(\delta_D)_5$—, 1 —$(\delta_D)_7$—, 1 —$(\delta_D)_9$—, 2 —$(\delta_D)_{10}$—, 1 —$(\delta_D)_{12}$—, 1 —$(\delta_D)_{17}$—, 1 —$(\delta_D)_{22}$—, and 1 —$(\delta_D)_{23}$— were assigned.

ing the angularity ($-90° \leq \tau \leq +90°$) or distance ($d \leq 7$ Å) criteria is not possible by an approach such as an X-ray data-base analysis. All existing β-turn conformations can be assigned on the corresponding 4D-Ramachandran (38) type PES; however, many of these conformations that do occur in globular proteins cannot be extracted from X-ray data, because some of these structures have a rare occurrence (small p_i and large ΔE_i).

The functional role of intramolecular hydrogen bonds in the formation of folded conformations is a subject of some controversy. It is shown here that if an α_L substructure is incorporated in a β-turn conformation (e.g. $\alpha_L\delta_L$ in type I β-turn), a favorable H-bond interaction is required to stabilize such a β-turn. By contrast, for β-turns not containing an α_L conformational subunit, the existence of such an $1 \leftarrow 4$ H-bond is not required. Consequently, although the $\alpha_D\alpha_D$ hairpin conformation contains a $1 \leftarrow 4$ type H-bond, in the $\delta_L\delta_D$ conformation (type II′ β-turn) such an intramolecular H-bond is not present. Therefore, it may be concluded, on the basis of these *ab initio* calculations, that while the $1 \leftarrow 4$ H-bond may be present in β-turns, it is not a necessary condition for the intrinsic stability of these structures. Only 5 structures ($\alpha_L\delta_L$, $\alpha_D\alpha_D$, $\alpha_D\delta_D$, $\epsilon_D\delta_L$, and $\gamma_L\delta_D$) of the 30 β-turns, located in this study, incorporate the intramolecular $1 \leftarrow 4$ H-bond ($d_{O..HN} \leq 2.2$ Å).

Spectroscopic aspects of ab initio calculations

The X-ray analysis of crystalline compounds, where typically a single conformer is observed (6–10), can yield extremely valuable information. However, the solid-state structure of a peptide is often modified by "crystal" forces. Therefore, these geometries are not necessarily identical with the dominant conformation adopted in solution, or in the gas phase. Although calculations can yield any minimum energy structure in the environment-free state, the spectroscopic identification of these conformers, or at least conformational regions, is still problematic in solution. The application of the results obtained by *ab initio* calculations may have some relevance to conformational analyses performed by vibrational (50, 51), circular dichroism (52), microwave (53), electron diffraction (54) and NMR (55) spectroscopy. The time scale of the experiment performed in solution has a cornerstone role. The applicability of *ab initio* structures can be different when the time-scale is long (e.g.; NMR) or when spectroscopy reflects a time-resolved structure set (e.g.; CD, FT-IR).

Nuclear Overhauser effect (NOE), such as the ^1H-{^1H}-NOE experiment is the most frequently applied NMR measurement to determine the folding pattern of peptide or protein backbone. It was shown that interproton distances (d_i) can be determined

Can. J. Chem. Downloaded from www.nrcresearchpress.com by 85.192.166.187 on 09/08/12
For personal use only.

TABLE 8. Optimized *ab initio* SCF (3-21G) geometries for $\gamma_L x_L$ and $\gamma_L x_D$ conformations for For-L-Ala-L-Ala-NH_2[a]

INI.[b]	$\gamma_L\alpha_D$	$\gamma_L\beta_L$	$\gamma_L\delta_D$	$\gamma_L\alpha_L$ $\gamma_L\delta_L$	$\gamma_L\varepsilon_D$	$\gamma_L\varepsilon_L$	$\gamma_L\gamma_D$	$\gamma_L\gamma_L$
CONV.[c]	$\gamma_L\alpha_D$	$\gamma_L\beta_L$	$\gamma_L\delta_D$	$\gamma_L\delta_L$	$\gamma_L\varepsilon_D$	$\gamma_L\varepsilon_L$	$\gamma_L\gamma_D$	$\gamma_L\gamma_L$
ω_1	−172.4	−176.1	−177.5	−174.6	+176.5	−174.8	−174.3	−174.4
ϕ_1	−85.8	−86.8	−79.3	−84.6	−80.9	−83.9	−84.5	−84.2
ψ_1	+64.0	+71.4	+75.8	+71.0	+75.8	+65.3	+68.6	+67.0
ω_2	+176.6	−179.7	−173.6	−171.5	−156.8	+172.9	+176.6	−174.1
ϕ_2	+62.4	−164.0	+176.7	−128.8	+64.3	−71.4	+72.7	−84.9
ψ_2	+33.0	+168.6	−35.2	+23.8	−176.5	+162.8	−57.3	+66.4
ω_3	+178.9	+177.8	−178.2	+177.3	+178.9	+178.7	+177.6	−178.9
MODEL DIS[d]	5.50	7.66	5.28	7.34	5.54	8.53	6.27	7.92
τ	−65.5	+77.7	+43.7	+117.3	−51.2	+166.0	−83.5	+167.8
CRIT DIS[e]	5.97	8.25	5.84	8.15	5.70	9.32	6.74	8.76
τ	−64.9	+78.4	+47.0	+119.4	−47.9	+166.6	−79.9	+168.4
O1...HN4	3.76	6.40	2.20	4.24	5.90	6.67	5.22	5.57
O1...N4	4.64	5.74	3.14	4.74	5.27	6.32	5.33	5.71
O1...HN4...N4	+148.5	−45.0	−157.4	+114.5	−47.1	−65.4	+90.7	+93.1
O1...HN3	2.01	2.16	2.07	2.00	1.99	2.03	1.98	2.02
O1...N3	2.88	2.96	2.82	2.88	2.85	2.88	2.87	2.88
O1...HN3...N3	+143.6	+135.4	+130.4	+145.6	+142.8	+141.0	+146.6	+142.4
O2...HN4	3.21	4.99	4.58	3.66	4.62	4.14	1.90	2.00
O2...N4	3.27	5.07	4.89	4.17	4.22	3.94	2.79	2.86
O2...HN4...N4	−84.7	−88.9	+102.0	+114.3	−60.2	−71.5	+146.9	+142.6
MAX. FORCE	1.2 E-4	3.3 E-5	1.2 E-4	5.9 E-5	1.7 E-4	1.5 E-5	1.6 E-4	6.4 E-5
RMS. FORCE	4.0 E-5	1.0 E-5	3.1 E-5	1.7 E-5	5.1 E-5	4.1 E-5	4.0 E-5	2.1 E-5
E	0.955569	0.957037	0.956465	0.958574	0.955072	0.954742	0.959946	0.963681
ΔE	5.09	4.17	4.53	3.20	5.40	5.61	2.34	0.00
STRCT.[f]	42	117	19	68	20	331	14	[g]

[a]Torsion angles (ω, ϕ, ψ) in degrees, distances in Ångstroms, forces in au, energy (E) in hartrees and energy difference (ΔE) in kcal/mol compared to $E(\gamma_L\gamma_L)$ = −656.963681.

[b]INI: initial backbone conformation (calculated by ECEPP/2).

[c]CONV: converged backbone conformation.

[d]MODEL DIS.: C_i^α and C_{i+3}^α in accordance to classical β-turn definition must be shorter than 7 Å. In For-Ala-Ala-NH_2 the two C^α atoms are replaced by hydrogens (H1 and H4*) (cf. Scheme 2), therefore the model distance (d_{model}) is shorter than C_i^α—C_{i+3}^α (Fig. 1) by no more than 1.1 Å. In such a case τ is H1—$C2^\alpha$—$C3^\alpha$—H4*.

[e]CRIT DIS.: critical distances for β-turn assignment (C_i^α—C_{i+3}^α) were extrapolated using *ab initio* resulted bond lengths and bond angles, on the basis of the determined N—H and C′—H distances. In such a case τ is $C1^\alpha$—$C2^\alpha$—$C3^\alpha$—$C4^\alpha$.

[f]Number of structures assigned in the 78 selected proteins.

[g]93 $\gamma_L\gamma_L$, 13 $\gamma_L\gamma_L\gamma_L$, 1 $\gamma_L\gamma_L\gamma_L\gamma_L$, 1 $\gamma_L\gamma_L\gamma_L\gamma_L\gamma_L$ were assigned.

(Fig. 5) on the basis of quantitative NOE even for multiple spin systems (55), as accurate as ±0.1 Å[8] For an interpretation of these experimentally determined distances, selected interproton distances are also calculated (usually by Molecular Mechanics and/or Molecular Dynamics calculations), but the empirical nature of the applied parameters used in MM and/or MD computations could introduce significant uncertainties in the distance-data set. Table 12 summarizes 10 possible marker distance values of the 49 different conformers of For-Ala-Ala-NH_2, useful for a quantitative structure assignment (Fig. 5) by NMR. The $d_{N\alpha}(d_{NH(i)/H\alpha(i)})$, $d_{NN}(d_{NH(i)/NH(i+1)})$, and $d_{\alpha N}(d_{H\alpha(i)/NH(i+1)})$ interproton distances have a specific role in the conformation assignment performed by NOE's. While the $d_{N\alpha}$ is a COSY-type connectivity, the $d_{\alpha N}$ and the d_{NN} are sequential NOE information. Although d_{NN} values vary the most ($d_{NN}^{\delta D} \approx 1.9$ Å, $d_{NN}^{\epsilon L} \approx 4.6$ Å) among these three marker distances, they are not too conformation-sensitive since they adopt similar values for the conformationally enantiomeric pairs (e.g. $d_{NN}^{\gamma L} \approx d_{NN}^{\gamma D} \approx 3.7 \pm 0.1$ Å (Table 12). Moreover, for β_L, γ_L, γ_D, ϵ_L, ϵ_D backbone conformations, where distances are large ($d_{NN} > 3.5$ Å), the intensities of the adjacent NOE's are weak or even indistinguishable from noise. In contrast, the other two sequential marker distances ($d_{N\alpha}$, $d_{\alpha N}$) can distinguish between conformational enantiomers since values range between 2.3 and 3.6 Å (e.g. $d_{N\alpha}^{\gamma L} \approx 2.9 \pm 0.1$ Å, $d_{N\alpha}^{\gamma D} \approx 2.25 \pm 0.1$ Å and $d_{\alpha N}^{\gamma L} \approx 2.35 \pm 1$ Å, $d_{\alpha N}^{\gamma D} \approx 3.6 \pm 0.1$ Å). Not counting the occasionally large variation of the $d_{\alpha N}$ (±0.5 Å in ϵ_D and ±0.3 Å in δ_L), the calculated marker distances are typical and indicative of the backbone conformational type, *regardless*

[8]Neglecting the cross-correlation between spins with a high irradiation power (49), all dipolar interactions may be characterized by a single relaxation time, therefore the ratio between two interproton distances (d_j and d_{ref}) is

$$\left(\frac{d_j}{d_{ref}}\right)^6 = \frac{\sigma_{ref}}{\sigma_j}$$

where σ_j and σ_{ref} are the individual cross-relaxation rates via dipole–dipole interaction. The σ_{ref} value is determined as a reference, using for example an appropriate methylene interproton distance d_{ref}. Applying a large pre-irradiation time, compared to T_{1i}, then the individual cross-relaxation rates via dipole–dipole interaction (σ_j) (in the absence of solvent-solute NOE) is

$$\sigma_j = \eta^i(j)/T_{1i}$$

where $\eta_i(j)$ is the enhancement of H_i's proton intensity when H_j is irradiated and T_{1i} is the relaxation time of H_i.

Can. J. Chem. Downloaded from www.nrcresearchpress.com by 85.192.166.187 on 09/08/12
For personal use only.

TABLE 9. Optimized *ab initio* SCF (3-21G) geometries for $\gamma_D x_L$ and $\gamma_D x_D$ conformations for For-L-Ala-L-Ala-NH_2[a]

INI.[b]	$\gamma_D\beta_L$	$\gamma_D\delta_D$	$\gamma_D\alpha_L$ $\gamma_D\delta_L$	$\gamma_D\varepsilon_D$	$\gamma_D\varepsilon_L$	$\gamma_D\gamma_D$	$\gamma_D\gamma_L$
CONV.[c]	$\gamma_D\beta_L$	$\gamma_D\delta_D$	$\gamma_D\delta_L$	$\gamma_D\varepsilon_D$	$\gamma_D\varepsilon_L$	$\gamma_D\gamma_D$	$\gamma_D\gamma_L$
ω_1	+175.0	+174.1	+172.0	+174.4	−177.2	+173.6	+174.3
ϕ_1	−76.1	+73.8	+75.5	+73.2	+72.6	+73.9	+73.8
ψ_1	−51.2	−57.6	−52.7	−59.7	−66.7	−55.7	−58.3
ω_2	−178.7	+178.9	−171.9	−161.0	+160.6	+176.7	−173.7
ϕ_2	−161.6	−170.5	−122.1	+63.3	−73.7	+74.4	−83.6
ψ_2	+169.2	−45.4	+22.9	−179.9	+168.8	−56.7	+67.1
ω_3	+177.6	−179.3	+176.9	−179.7	+179.0	−178.0	−179.4
MODEL DIS[d]	7.06	5.81	5.34	8.49	5.87	7.97	6.33
τ	−0.5	−46.7	+40.4	−151.5	+57.0	−165.7	+84.4
CRIT DIS[e]	7.51	6.34	5.77	9.28	6.09	8.83	6.80
τ	−4.7	−47.3	+38.3	−152.8	+53.2	−166.4	+80.6
O1...HN4	6.23	3.19	3.61	6.44	5.99	5.45	5.26
O1...N4	5.54	3.62	4.20	6.09	5.34	5.63	5.28
O1...Hn4...N4	−42.5	+107.7	+120.1	−65.2	−45.9	+95.3	−85.3
O1...HN3	2.01	1.88	1.91	1.91	1.90	1.89	1.90
O1...N3	2.88	2.81	2.83	2.82	2.80	2.81	2.81
O1...HN3...N3	+144.3	+151.8	+149.5	+149.6	+147.8	+151.0	+149.1
O2...HN4	4.95	4.62	3.54	4.65	4.35	1.90	1.99
O2...N4	5.04	4.89	4.06	4.20	4.12	2.79	2.85
O2...HN4...N4	−89.2	+99.7	+114.5	−57.6	−70.1	+147.4	+142.3
MAX. FORCE	1.1 E-4	1.6 E-4	6.7 E-5	1.4 E-4	1.6 E-4	1.4 E-5	6.0 E-5
RMS. FORCE	3.0 E-5	3.6 E-5	2.6 E-5	4.7 E-5	4.7 E-5	3.0 E-6	1.9 E-5
E	0.952732	0.949771	0.953949	0.949096	0.953218	0.956213	0.960326
ΔE	6.87	8.73	6.11	9.15	6.57	4.69	2.11
STRUCT.[f]	9	6	15	5	55	4	9[g]

[a]The $\gamma_D\alpha_D \rightarrow \varepsilon_D\alpha_D$ conformational shift is observed. Torsion angles (ω, ϕ, ψ) in degrees, distances in Ångstroms, forces in au, energy (*E*) in hartrees, and energy differences (ΔE) in kcal/mol compared to $E(\gamma_L\gamma_L) = -656.963681$.

[b]INI: Initial backbone conformation (calculated by ECEPP/2).

[c]CONV: converged backbone conformation.

[d]MODEL DIS.: C_i^α and C_{i+3}^α in accordance to classical β-turn definition must be shorter than 7 Å. In For-Ala-Ala-NH_2 the two C^α atoms are replaced by hydrogens (H1 and H4*) (cf. Scheme 2), therefore the model distance (d_{model}) is shorter than C_i^α—C_{i+3}^α (Fig. 1) no more than 1.1 Å. In such a case τ is H1—$C2^\alpha$—$C3^\alpha$—H4*.

[e]CRIT DIS.: critical distances for β-turn assignment (C_i^α—C_{i+3}^α) were extrapolated using *ab initio* resulted bond lengths and bond angles, on the basis of the determined N—H and C′—H distances. In such a case τ is $C1^\alpha$—$C2^\alpha$—$C3^\alpha$—$C4^\alpha$.

[f]Number of structures assigned in the 78 selected proteins.

[g]93 $\gamma_L\gamma_L$, 13 $\gamma_L\gamma_L\gamma_L$, 1 $\gamma_L\gamma_L\gamma_L\gamma_L$, 1 $\gamma_L\gamma_L\gamma_L\gamma_L\gamma_L$ were assigned, no $\gamma_D\gamma_D\gamma_D$ or longer fragments were assigned.

TABLE 10. Average torsional angles (ϕ, ψ) and number of conformations induced in the averaging of For-Ala_n-NH_2 where $1 \le n \le 4$ computed at the HF/3-21 G level of theory

Conformation[a] type	For-$(Ala)_1$-NH_2[b]		For-$(Ala)_2$-NH_2[c]			For-$(Ala)_3$-NH_2[d]			For-$(Ala)_4$-NH_2[e]		
	ϕ	ψ	ϕ	ψ	*n*	ϕ	ψ	*n*	ϕ	ψ	*n*
α_D	63.8	32.7	61.8	31.9	12	59.3	23.6	3	—	—	—
α_L	—	—	−68.6	−17.5	1	−67.4	−15.7	2[f]	−65.5	−17.5	3[f]
β_L	−168.3	170.5	−167.6	169.9	14	−168.1	170.8	3	−168.4	170.8	4
γ_L	−84.5	67.3	−84.5	68.7	15	−84.5	66.3	3	−84.5	66.6	4
γ_D	74.0	−57.4	74.3	−59.5	14	—	—	—	—	—	—
δ_L	−128.1	29.8	−126.2	26.5	12	—	—	—	—	—	—
δ_D	−178.6	−44.1	−179.6	−43.7	14	−173.8	−49.1	3	—	—	—
ε_L	—	—	−74.7	167.8	3	—	—	—	—	—	—
ε_D	67.2	−171.9	64.7	−178.3	13	65.7	−172.7	3	—	—	—

[a]Substructure type. *n* = number of points included in the averaging.

[b]Taken from ref. 14.

[c]This work.

[d]Taken from ref. 47.

[e]Taken from refs. 49 (γ_L), 50 (β_L), nd 51 (α_L).

[f]The α_L subconformation located next to the δ_L subconformation is far away from its anticipated value, it is therefore ignored from the averaging.

Can. J. Chem. Downloaded from www.nrcresearchpress.com by 85.192.166.187 on 09/08/12
For personal use only.

Can. J. Chem. Downloaded from www.nrcresearchpress.com by 85.192.166.187 on 09/08/12
For personal use only.

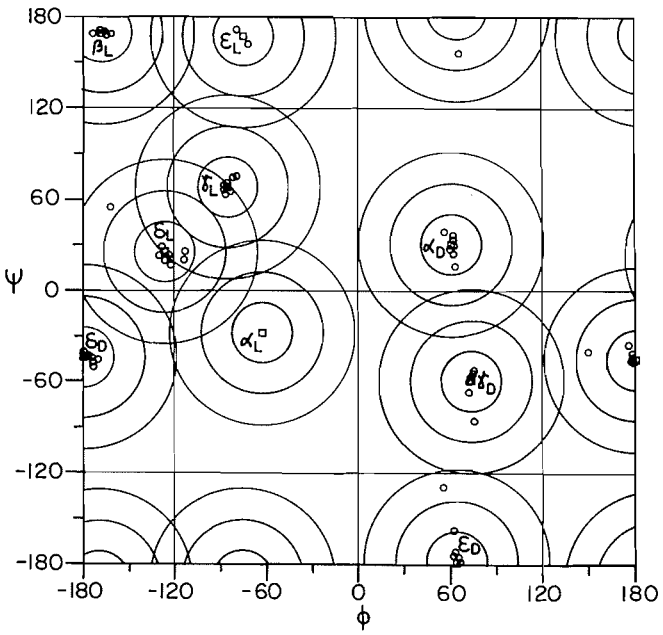

FIG. 2. The location of the "extracted" 9 basic conformations of an amino acid diamide by averaging the appropriate substructures (*) of For-L-Ala-L-Ala-NH_2 obtained from *ab initio* calculations: α_L, −63.9, −23.3; α_D, 61.8, 31.9; β_L, −167.6, 169.9; δ_L, −126.2, 26.5; δ_D, −179.6, −43.7; ϵ_L, −74.7, 167.8; ϵ_D, 64.7, −178.3; γ_L, −84.5, 68.7; γ_D, 74.3, −59.5. The potential energy surface of a single amino acid diamide involves 9 catchment regions in an idealized case (see for details ref. 2). The 9 sets of concentric cycles (3 for each minima) incorporate the area around the "averaged" structure located on a ϕ,ψ map, using a radius of 40°, 50°, and 60°.

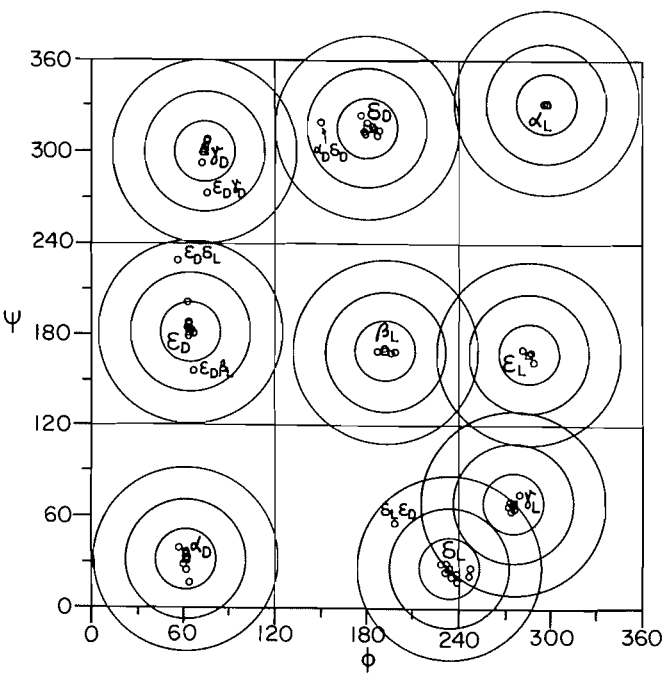

FIG. 3. The same as Fig. 2, using a topologically more useful representation of the same PES (see ref. 2 for the transformation). Note that such a representation of the PES makes the plot of the 9 catchment region possible without truncation.

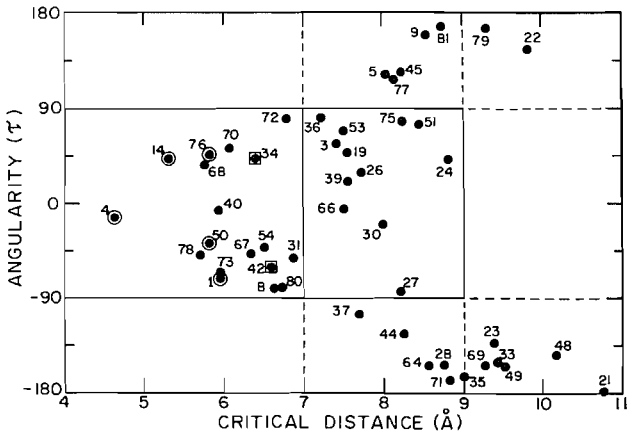

FIG. 4. The angularity τ of the conformation is plotted against the critical distance for the 49 For-Ala-Ala-NH_2 conformations, calculated by HF/3-21G method. (A critical distance, d, which is the separation of the non-bonded C_i^α—C_{i+3}^α atoms, that can be determined from the *ab initio* optimized geometry. The value of τ is also determined from the *ab initio* optimized geometry by calculating the relative orientation of $C1^\alpha$—$C2^\alpha$—$C3^\alpha$—$C4^\alpha$ atoms (see also ref. 37). Since only 49 from the 81 initial conformations was found as stable structures, during *ab initio* geometry optimization only 49 [d, τ] points were plotted:

1, $\alpha_D\alpha_D$; 2, $\alpha_D\alpha_L$; 3, $\alpha_D\beta_L$, 4, $\alpha_D\delta_D$; 5, $\alpha_D\delta_L$; 6, $\alpha_D\epsilon_D$; 7, $\alpha_D\epsilon_L$; 8, $\alpha_D\gamma_D$; 9, $\alpha_D\gamma_L$; 10, $\alpha_L\alpha_D$; 11, $\alpha_L\alpha_L$; 12, $\alpha_L\beta_L$; 13, $\alpha_L\delta_D$; 14, $\alpha_L\delta_L$; 15, $\alpha_L\epsilon_D$; 16, $\alpha_L\epsilon_L$; 17, $\alpha_L\gamma_D$; 18, $\alpha_L\gamma_L$; 19, $\beta_L\alpha_D$; 20, $\beta_L\alpha_L$; 21, $\beta_L\beta_L$; 22, $\beta_L\delta_D$; 23, $\beta_L\delta_L$; 24, $\beta_L\epsilon_D$; 25, $\beta_L\epsilon_L$; 26, $\beta_L\gamma_D$; 27, $\beta_L\gamma_L$; 28, $\delta_D\alpha_D$; 29, $\delta_D\alpha_L$; 30, $\delta_D\beta_L$; 31, $\delta_D\delta_D$; 32, $\delta_D\delta_L$; 33, $\delta_D\epsilon_D$; 34, $\delta_D\epsilon_L$; 35, $\delta_D\gamma_D$; 36, $\delta_D\gamma_L$; 37, $\delta_L\alpha_D$; 38, $\delta_L\alpha_L$; 39, $\delta_L\beta_L$; 40, $\delta_L\delta_D$; 41, $\delta_L\delta_L$; 42, $\delta_L\epsilon_D$; 43, $\delta_L\epsilon_L$; 44, $\delta_L\gamma_D$; 45, $\delta_L\gamma_L$; 46, $\epsilon_D\alpha_D$; 47, $\epsilon_D\alpha_L$; 48, $\epsilon_D\beta_L$; 49, $\epsilon_D\delta_D$; 50, $\epsilon_D\delta_L$; 51, $\epsilon_D\epsilon_D$; 52, $\epsilon_D\epsilon_L$; 53, $\epsilon_D\gamma_D$; 54, $\epsilon_D\gamma_L$; 55, $\epsilon_L\alpha_D$; 56, $\epsilon_L\alpha_L$; 56, $\gamma_L\alpha_L$; 57, $\epsilon_L\beta_L$; 58, $\epsilon_L\delta_D$; 59, $\epsilon_L\delta_L$; 60, $\epsilon_L\epsilon_D$; 61, $\epsilon_L\epsilon_L$; 62, $\epsilon_L\gamma_D$; 63, $\epsilon_L\gamma_L$; 64, $\gamma_D\alpha_D$; 65, $\gamma_D\alpha_L$; 66, $\gamma_D\beta_L$; 67, $\gamma_D\delta_D$; 68, $\gamma_D\delta_D$; 69, $\gamma_D\epsilon_D$; 70, $\gamma_D\epsilon_D$; 71, $\gamma_D\gamma_D$; 72, $\gamma_D\gamma_L$; 73, $\gamma_L\alpha_D$; 75, $\gamma_L\beta_L$; 76, $\gamma_L\delta_D$; 77, $\gamma_L\delta_D$; 78, $\gamma_L\epsilon_D$; 79, $\gamma_L\epsilon_L$; 80, $\gamma_L\gamma_D$; 81, $\gamma_L\gamma_L$.

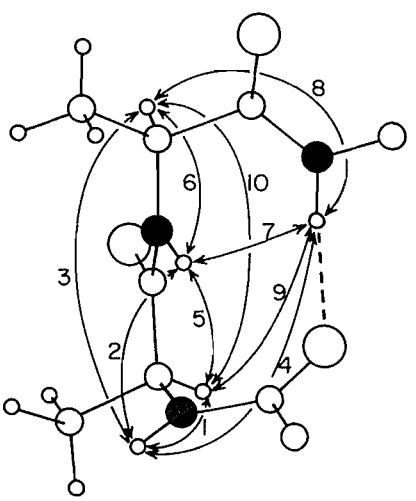

FIG. 5. The 10 marker interproton distances (d_i's) of For-Ala-Ala-NH_2: 1, NH_{i+1}—H_{i+1}^α; 2, NH_{i+1}—H_{i+2}; 3, NH_{i+1}—H_{i+2}^α; 4, NH_{i+1}—H_{i+3}; 5, NH_{i+2}—H_{i+1}^α; 6, NH_{i+2}—H_{i+2}^α; 7, NH_{i+2}—H_{i+3}; 8, NH_{i+3}—H_{i+2}; 9, NH_{i+3}—H_{i+2}^α; 10, H_{i+1}^α—H_{i+2}^α. The distance values are different for each conformer as reported in Table 11.

TABLE 11. Selected stereochemical parameters of 78 proteins from BPSD

Code[a]	Res.[b]	R^c	%core[d]	Code	Res.	R	%core	Code	Res.	R	%core
1BP2	1.7	0.171	89.3	1TGS	1.8	0.186	84.9	2RHE	1.6	0.149	90.3
1CC5	2.5	0.290	69.7	1TGSi	1.8	0.186	84.9	2SGA	1.5	0.126	88.3
1CCR	1.5	0.190	87.9	2ABX	2.5	0.240	14.5	2SNS	1.5	—	57.1
1CTF	1.7	0.174	95.1	2ACT	1.7	0.171	87.4	2SOD	2.0	0.256	65.4
1ECA	1.4	—	95.0	2ALP	1.7	0.131	86.4	351C	1.6	0.195	91.3
1FC2	2.8	—	78.6	2APP	1.8	0.136	90.4	3C2C	1.7	0.175	81.2
1FC2d	2.8	—	78.6	2AZA	1.8	0.157	90.4	3DFR	1.7	0.152	86.9
1FDX	2.0	—	80.0	2CAB	2.0	0.193	88.4	3ICB	2.3	0.178	92.4
1GCR	1.6	0.230	89.5	2CCY	1.7	0.188	92.7	3PGM	2.8	0.290	48.3
1HIP	2.0	0.240	81.1	2CDV	1.8	0.176	87.1	3RP2	1.9	0.191	84.8
1HMQ	2.0	0.173	89.7	2CTS	2.0	0.161	88.5	3RXN	1.5	—	78.0
1LH1	2.0	—	95.0	2CYP	1.7	0.202	92.9	3SGBe	1.8	0.125	86.4
1LZ1	1.5	0.177	88.0	2EST	2.5	0.210	85.2	3SGBi	1.8	0.125	86.4
1LZT	2.0	0.254	83.5	2GN5	2.3	0.217	44.6	3TLN	1.6	0.213	89.7
1MBD	1.4	—	92.0	2INSa	2.5	0.180	81.1	4APE	2.1	0.158	89.2
1NXB	1.4	0.240	60.4	2INSb	2.5	0.180	81.1	4DFR	1.7	0.155	89.2
1PCY	1.6	0.170	88.1	2LHB	2.0	0.142	92.0	4FXN	1.8	0.200	86.0
1PP2	2.5	0.178	86.8	2LZM	1.7	0.193	94.0	4HHBa	1.7	0.135	87.7
1PPD	2.0	0.145	85.6	2OVO	1.5	0.199	91.8	4HHBb	1.7	0.135	87.7
1PPT	1.4	—	86.7	2PAD	2.8	—	74.3	5CPA	1.5	—	86.9
1SBT	2.5	—	73.7	2PKA	2.0	0.220	82.5	5LDH	2.7	0.196	55.9
1SN3	1.8	—	88.5	2PKAb	2.0	0.220	82.5	5RXN	1.2	0.115	90.7

[a]BPSD code.
[b]Resolution of the X-ray measurement.
[c]R factor calculated from the observed and model-based structure factors.
[d]For the definition of core region, see ref. 40*d*. The stereochemical parameters of the additional 12 proteins (1CPV, 1CRND, 1FB41, 1FBJ1, 1FB4h, 1FBJh, 1INSa, 1INSb, 4ADH, 4ATCa, 4ATCb, 4CYT) incorporated in the analyses are not reported in ref. 40*d*.

Can. J. Chem. Downloaded from www.nrcresearchpress.com by 85.192.166.187 on 09/08/12
For personal use only.

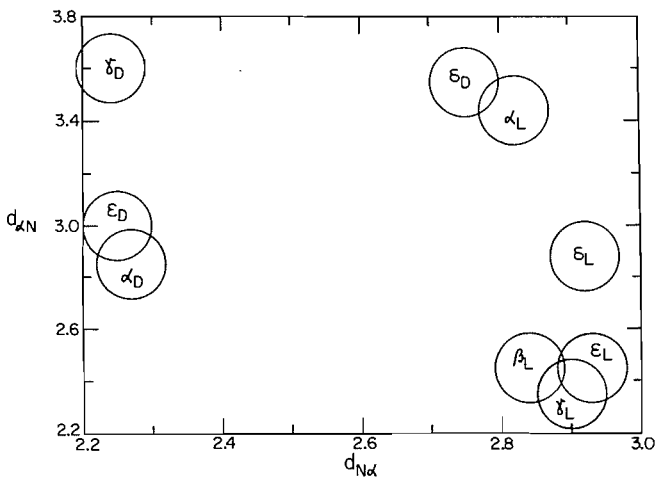

FIG. 6. The location of the 9 different backbone conformations on a $d_{N\alpha}d_{\alpha N}$ space. (The two marker distances are defined as $d_{N\alpha} = d_{NH(i)/H\alpha(i)}$ and $d_{\alpha N} = d_{H\alpha(i)/NH(i+1)}$.) Using also the d_{NN} marker distances further ambiguities can be eliminated.

of the conformation of the preceding or following structural unit. A representation of the 9 backbone conformations based on their $d_{N\alpha}$ and $d_{\alpha N}$ values (Fig. 6) yields 5 significantly different conformational clusters. The inherent error when 1D- and/or 2D-NOE type data are quantified, and converted to interproton distances (58), is large enough that $\beta_L/\gamma_L/\epsilon_L$ structures or the ϵ_D/α_D and δ_D/α_L conformations may not be distinguished simply using their $d_{N\alpha}$ and $d_{\alpha N}$ values. However, with the incorporation of the additional d_{NN} distance type (e.g. $d_{NN}^{\beta L} \approx 4.3 \pm 0.1$ Å/$d_{NN}^{\gamma L} \approx 3.7 \pm 0.2$ Å/$d_{NN}^{\epsilon L} \approx 4.6 \pm 0.1$ Å), all 9 conformers can be reliably assigned (see also Table 12). The conformation of any diamide-type subunit of a protein backbone can be characterized by one of the 9 conformational types (see below). The assignment of these substructures using a combination of the three well known $d_{N\alpha}$, $d_{\alpha N}$, and d_{NN} distances has great importance. Although the determination of interproton distances based on ^{1}H-{^{1}H}-NOE or NOESY spectra is problematic, the secondary structure of a polypeptide can now be assigned not only in term of helices, sheets, or turns but also as accurately as α_L, β_L, γ_L, δ_L, ϵ_L etc.

In the case of a single conformation these d_j's (eq. [1]) are typical for the investigated conformation and are therefore regarded as marker distances. However, in the case of a conformational mixture, these marker distances d_{ji} (that is the interproton distance in the ith conformer) have to be determined by computation for each of the conformers. The experimentally determined interproton distances in the case of conformational mixtures reflect the average interproton distance due to the time scale of the NMR experiment, which makes structure determination of small or medium size peptides extremely difficult. Consequently, the application of NOE-based structural constraints for small or mid-size peptides has serious limitations and requires sophisticated calculations. The reciprocal of the sixth power of the average interproton distance (d_j which is an experimental distance) is the weighted average of the reciprocal of the sixth power of the individual marker distance (d_{ji} which are calculated distances) as shown by the following equation:

$$[1] \quad \frac{1}{d_j^6} = \sum_{i=1} p_i \frac{1}{d_{ji}^6}$$

The weighing coefficient (p_i) is the probability occurrence of the ith conformation in the mixture. Consequently, the spectroscopic determination of peptide conformations requires the

TABLE 12. The 10 marker interproton distances in the 49 different conformers of For-Ala-Ala-NH_2

	NH_{i+1} NH^{α}_{i+1}	NH_{i+1} NH_{i+2}	NH_{i+1} NH^{α}_{i+2}	NH_{i+1} NH_{i+3}	NH_{i+2} NH^{α}_{i+1}	NH_{i+2} NH^{α}_{i+2}	NH_{i+2} NH_{i+3}	NH_{i+3} NH^{α}_{i+2}	NH_{i+3} NH^{α}_{i+1}	$NH_{i+1}{}^{\alpha}$ NH^{α}_{i+2}
Abbrev.[b]	$d_{N\alpha}$	d_{NN}			$d_{\alpha N}$	$d_{N\alpha}$	d_{NN}	$d_{\alpha N}$		
$\alpha_D\alpha_D$	2.27	2.88	5.12	4.48	2.91	2.25	2.82	3.09	4.48	4.84
$\alpha_D\beta_L$	2.27	2.81	5.40	7.10	2.90	2.85	4.29	2.51	6.61	4.38
$\alpha_D\delta_D$	2.25	2.84	5.33	4.28	2.99	2.64	2.35	3.59	4.78	4.64
$\alpha_D\delta_L$	2.29	2.87	5.40	4.99	2.81	2.93	2.72	2.92	3.70	4.45
$\alpha_D\gamma_D$	2.28	2.80	5.02	5.53	2.80	2.24	3.64	3.59	4.61	4.65
$\alpha_D\gamma_L$	2.27	2.83	5.35	5.66	2.90	2.89	3.70	2.43	4.00	4.60
$\alpha_L\delta_L$	2.82	2.83	5.39	4.39	3.44	2.94	2.57	3.10	3.81	4.44
$\beta_L\alpha_D$	2.85	4.28	5.67	4.52	2.49	2.26	2.84	2.88	3.56	4.57
$\beta_L\beta_L$	2.84	4.31	4.69	7.15	2.55	2.84	4.29	2.52	6.60	4.62
$\beta_L\delta_D$	2.84	4.28	4.83	5.96	2.50	2.79	2.28	3.60	4.09	4.65
$\beta_L\delta_L$	2.84	4.27	4.42	5.03	2.46	2.94	2.64	2.94	4.40	4.43
$\beta_L\varepsilon_D$	2.83	4.24	5.65	6.56	2.43	2.25	4.60	2.76	6.32	4.54
$\beta_L\gamma_D$	2.85	4.24	5.71	3.74	2.40	2.22	3.66	3.59	4.31	4.54
$\beta_L\gamma_L$	2.84	4.28	4.50	3.93	2.50	2.90	3.71	2.43	4.75	4.33
$\delta_D\alpha_D$	2.71	2.30	4.15	4.76	3.55	2.26	2.80	2.90	4.46	5.33
$\delta_D\beta_L$	2.79	2.19	3.95	5.81	3.60	2.86	4.31	2.53	7.05	4.66
$\delta_D\delta_D$	2.71	2.26	3.89	4.51	3.54	2.82	2.28	3.61	5.51	4.72
$\delta_D\varepsilon_D$	2.74	2.23	4.09	6.42	3.52	2.26	4.60	2.83	6.69	5.33
$\delta_D\varepsilon_L$	2.78	2.27	4.00	5.01	3.53	2.93	4.52	2.54	6.49	4.61
$\delta_D\gamma_D$	2.72	2.25	3.94	4.96	3.51	2.24	3.64	3.60	4.23	5.31
$\delta_D\gamma_L$	2.72	2.27	4.52	4.10	3.55	2.89	3.74	2.42	4.16	4.64
$\delta_L\alpha_D$	2.94	2.67	4.72	3.53	2.94	2.27	2.86	2.88	4.75	4.85
$\delta_L\beta_L$	2.94	2.50	5.00	6.65	3.09	2.83	4.29	2.51	6.65	4.36
$\delta_L\delta_D$	2.94	2.62	5.08	3.69	2.92	2.78	2.28	3.59	5.11	4.30
$\delta_L\varepsilon_D$	2.90	2.49	3.96	5.10	2.52	2.26	4.57	2.80	6.60	4.66
$\delta_L\gamma_D$	2.94	2.54	4.67	4.77	2.98	2.23	3.67	3.59	4.58	4.81
$\delta_L\gamma_L$	2.94	2.57	4.60	5.42	3.00	2.91	3.67	2.44	3.96	4.64
$\varepsilon_D\alpha_D$	2.23	3.66	5.64	5.69	3.57	2.27	2.82	2.86	4.41	5.32
$\varepsilon_D\beta_L$	2.26	4.60	5.55	7.91	2.73	2.83	4.28	2.51	6.66	4.64
$\varepsilon_D\delta_D$	2.26	4.65	5.61	6.34	3.06	2.73	2.27	3.59	4.35	4.79
$\varepsilon_D\delta_L$	2.26	4.62	5.38	4.71	3.31	2.93	2.60	3.02	4.60	4.45
$\varepsilon_D\varepsilon_D$	2.26	4.48	6.14	7.06	2.58	2.24	4.63	2.85	6.16	4.56
$\varepsilon_D\gamma_D$	2.26	4.50	6.26	4.52	2.60	2.21	3.67	3.59	4.14	4.66
$\varepsilon_D\gamma_L$	2.26	4.62	5.26	4.93	2.79	2.91	3.63	2.46	4.69	4.27
$\gamma_D\beta_L$	2.24	3.62	5.12	7.25	3.63	2.89	4.38	2.49	6.94	4.54
$\gamma_D\delta_D$	2.23	3.62	5.14	5.69	3.57	2.84	2.14	3.60	5.43	4.67
$\gamma_D\delta_L$	2.23	3.64	5.41	3.96	3.57	2.95	2.57	3.03	4.43	4.47
$\gamma_D\varepsilon_D$	2.23	3.67	5.73	7.76	3.55	2.26	4.60	2.68	6.70	5.31
$\gamma_D\varepsilon_L$	2.25	3.61	5.24	6.40	3.56	2.94	4.56	2.47	6.47	4.63
$\gamma_D\gamma_D$	2.23	3.63	5.50	5.64	3.54	2.23	3.68	3.59	4.10	5.31
$\gamma_D\gamma_L$	2.23	3.66	5.61	4.80	3.58	2.91	3.70	2.44	4.09	4.58
$\gamma_L\alpha_D$	2.90	3.67	5.52	3.62	2.42	2.27	2.77	2.90	4.33	4.52
$\gamma_L\beta_L$	2.91	3.78	5.46	7.50	2.44	2.88	4.36	2.48	6.39	4.31
$\gamma_L\delta_D$	2.90	3.82	5.69	4.72	2.26	2.82	1.94	3.62	3.95	4.41
$\gamma_L\delta_L$	2.90	3.68	5.12	5.73	2.40	2.95	2.55	3.02	3.46	4.40
$\gamma_L\varepsilon_D$	2.93	3.61	5.26	6.23	2.30	2.26	4.56	2.75	6.50	4.47
$\gamma_L\varepsilon_L$	2.90	3.70	5.06	7.29	2.43	2.92	4.66	2.36	6.19	4.54
$\gamma_L\gamma_D$	2.90	3.64	5.59	4.50	2.38	2.23	3.68	3.59	4.65	4.42
$\gamma_L\gamma_L$	2.90	3.69	4.91	5.55	2.41	2.91	3.71	2.45	4.26	4.53

[a]Backbone interproton distances calculated by *ab initio* (HF/3-21G) geometry optimization.
[b]Standard NMR type abbreviations of the marker distances.

quantitative knowledge of these marker distances (d_{ji}) in all the participating conformers (Table 12).

The IR and UV type spectra, containing time-resolved structural information, are rather complex due to the presence of multiple conformations and/or the dynamic aspects of backbone conformation in solution. Moreover, the IR and/or CD spectra provides no insight to structure-sequence correlation. Therefore, the deconvolution of the complex spectra must be followed by the assignment of the component curves to individual conformations, using external data (e.g. calculations resulting in probability occurrences (p_j), NOE structural constraints, etc.).

Description of the proteins 3D structure on the basis of ab initio calculations

At present, no relationship between the amino acid sequence of proteins and their three- dimensional conformation has been

Can. J. Chem. Downloaded from www.nrcresearchpress.com by 85.192.166.187 on 09/08/12
For personal use only.

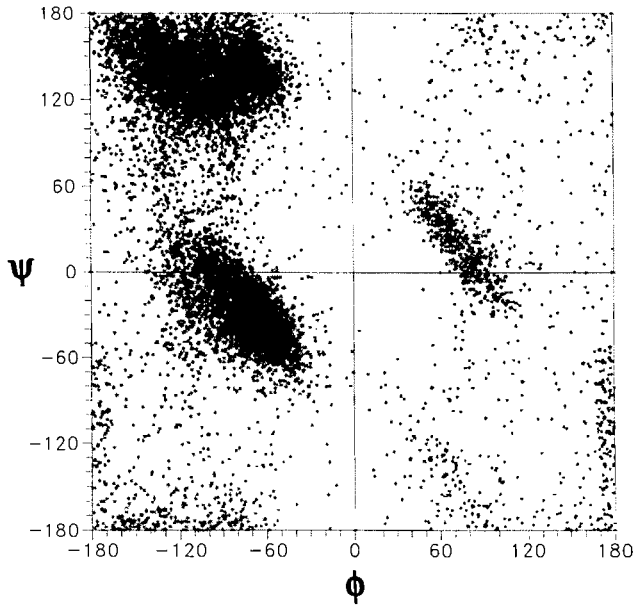

FIG. 7. The ϕ,ψ distribution of 11786 amino acid residues of 78 selected proteins on the basis of their solid state conformations determined by X-ray crystallography. (For the list of the proteins see the Protein Database section.)

found. Although many different approaches have been attempted, resulting in a variety of prediction algorithms, a reliable a priori prediction of protein 3D-structure from its amino acid sequence is still not in sight. A less glamorous but more fundamental task is to classify the already determined backbone conformations. This task is not only useful but could very well be a prerequisite to the discovery of a 3D structure predicting algorithm. The determination of several "central" points on the Ramachandran map, where all the possible backbone conformations of proteins are represented (c.f. Fig. 8), is equivalent to the recognition that certain conformations are playing some "key" role during protein folding. In the past the division of the $-180° < \phi < +180°$, $-180° < \psi < +180°$ space was achieved by the fragmentation of the X-ray determined protein structures (method A), as well as on the basis of the conformations determined by MM calculations (method B). The frequency ratios of subconformations in the investigated protein data set influenced the statistical analyses, introducing inaccuracies into method A. On the other hand, parameterization of the force fields, partially based on X-ray data, can induce errors in the geometrical and energetic description of the resulting structures. Although the two methods differ from each other, their arbitrary character may well be the cause of their limitations. We propose here a third method for the division of the ϕ,ψ surface on the basis of multidimensional conformational analysis combined with *ab initio* calculations. Because all published *ab initio* calculations on amino acid diamides, regardless of the applied basis set or calculation type, resulted in 9 (or fewer) backbone conformations, this value is considered the upper limit. Although HF calculations also have limitations, they can describe conformational properties quite accurately, which is not the case for the semi empirical or force field methods. Therefore, the Ramachandran map ($0° < \phi < +360°$, $0° < \psi < +360°$) was divided into 9 conformation regions labelled for their minima (2). All the 49 different optimized conformations of For-Ala-Ala-NH_2 are also the combination of these 9 (α_L, α_D, β_L, γ_L, γ_D, δ_L, δ_D, ϵ_L, and ϵ_D) legitimate conformations. However, the application of these minima as "central points" on the PES was previously questionable, because two of the 9 minima were annihilated in the case of simple amino acid diamides (2). Also, the degree of conformational distorting effects of the nearest neighbors was unknown. The analysis of the torsional angle distributions of the 12 α_D, 14 β_L, 15 γ_L, 14 γ_D, 12 δ_L, 14 δ_D, 3 ϵ_L, 13 ϵ_D, and 1 α_L subconformations (Scheme 9) yielded a set of average or "central" conformations with high confidence (Table 10 and Figs. 3 and 4). Although conformation-dependent alterations of some substructures was observed (e.g. 4 of the 14 ϵ_D substructures deviate significantly from the average value), in general they are located close to each other as well as to the ϕ, ψ values computed for the appropriate For-Ala-NH_2. The ϕ,ψ distribution of 11786 amino acids incorporated in the 78 selected proteins is reported in Fig. 7. The population of the different regions agrees well with the general expectation that locations around the helical ($\phi = -60°$, $\psi = -30°$) and the extended (β) regions ($\phi = -150°$, $\psi = +150°$) are highly populated. The dimension and the shape of the spot at the top left region (β region) of the Ramachandran map, compared to the "helical area", underlines our interpretation that this is an area that consists of three "centers" such as the β_L, ϵ_L, and γ_L (see Figs. 7 and 3). The location of the 9 "conformational centers" determined by *ab initio* calculations (Figs. 2 and 3) compared with the position of the dense area obtained by simply plotting the ϕ,ψ values of the selected 78 proteins (Fig. 7) resulted in an impressive similarity. The backbone distorting effect of the side chains can also be ignored to some extent since the analysis of other amino acid diamides (e.g. For-Ser-NH_2, For-Gly-NH_2, and For-Val-NH_2) yielded similar locations of backbone conformations.

As an example, the assignment of the 3D structure of a Cytochrome C (1CCR) fragment (Fig. 8) is reported. Using only the classical terms to describe the folding of the backbone (α-helices, β-turns and β-pleated sheets), the 22–23, 26–29, and 32–40 regions of this protein backbone cannot be assigned. The "structure-describing" method reported here, on the other hand, makes the description of the overall backbone structure possible (c.f. Fig. 9.)

The applicability of the "structure-describing" method was checked for all the 78 protein backbone conformations. The structure-assigning power of this method was calculated as a function of the allowed deviation from the "conformation centers" (see Table 12 and Fig. 9). The larger the circles drawn around the 9 centers, the higher the percentage of the ϕ,ψ points determined by X-ray crystallography was accounted for. For example, applying a deviation of 60° (which is the case when all 9 circles have a radius equal to 60°, more than 85% of all the 78 protein backbones can be assigned to one of the 9 conformation types (solid square). By decomposing the total profile into individual conformations (Fig. 9), it is clear that certain conformational types can be described more accurately than others. For example, more than 95% of the ϕ,ψ pairs assigned to right-handed helices in the 78 proteins deviate less than 60° from the *ab initio* determined (and averaged) α_L conformation center. On the other hand, conformational types such as the δ_D or the ϵ_D alternate more, less than 65% of the "total" backbone can be described with a smaller deviation than 60°.

Four points should be emphasized in closing.

(1) The observation that certain substructures have ϕ,ψ torsional angle pairs far away (>40°) from the "conformational centers" does not indicate the failure of the method. In fact, it is

Can. J. Chem. Downloaded from www.nrcresearchpress.com by 85.192.166.187 on 09/08/12
For personal use only.

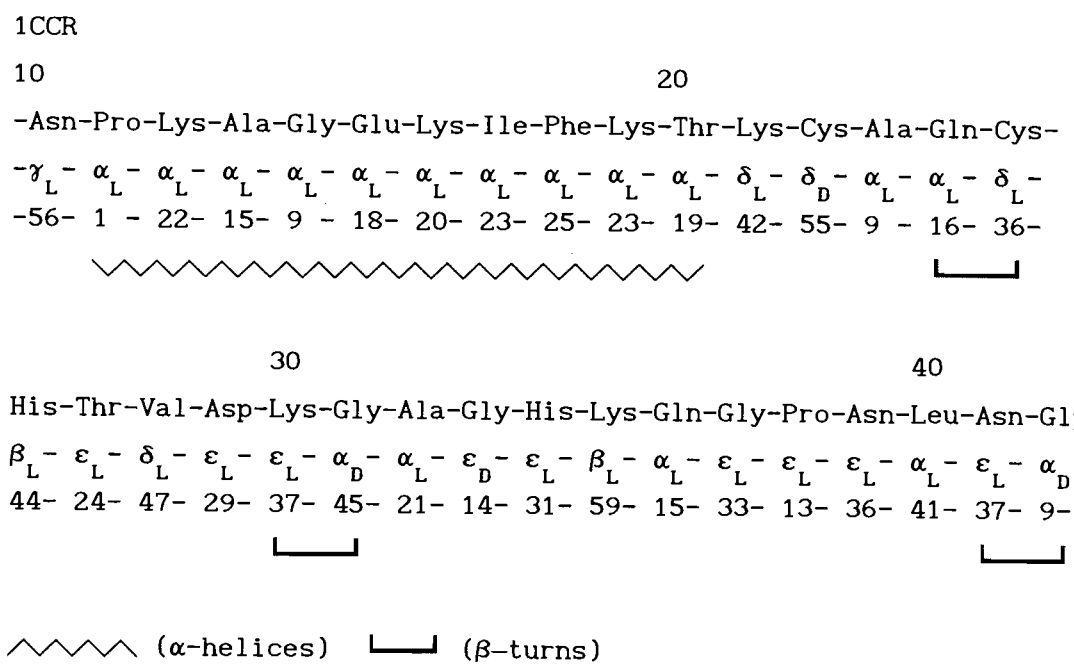

FIG. 8. The structural assignment of a Cytochrome C (1CCR) fragment (between residues 10, 42). Below the amino acid sequence, the structure codes as well as their deviations from the *ab initio* calculated (and averaged) conformations are reported. (According to classical folding description, the 21–23, 26–29, and 32–39 regions cannot be assigned.)

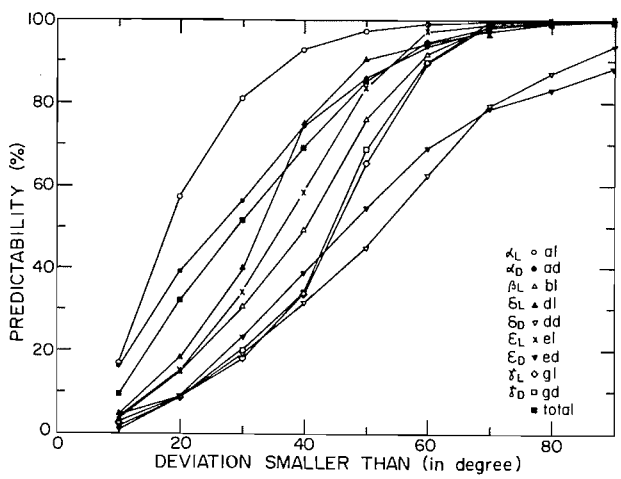

FIG. 9. Describability of the 78 selected protein backbone conformations, using 9 amino acid diamide conformation types. The upper limit of the allowed deviation is plotted against the desirability expressed in percentages. (E.g. 81.2% of the ϕ,ψ pairs assigned in the helical region of the 78 proteins deviate less than 30° from the ab initio determined (and averaged) ϕ,ψ value.

diagnostic that some unusual stabilizing or destabilizing interaction is operative at that particular amino acid residue. For example, the one and only "ghost" δ_L conformation assigned in $\delta_L\epsilon_D$ structure (c.f. Table 6) is located between the circles corresponding to the 40° and 60° radii, while all other 11 δ_L subconformations are located within a 20° radius measured from the δ_L "conformational center". Such an anomaly is diagnostic and indicative of some special intramolecular interaction.[5] In fact the $\delta_L\epsilon_D$ conformation incorporates an "unusual" 8-membered ring (Fig. 10) with all trans amide bonds. In contrast to the familiar 10-membered intramolecular H-bond, such as in $\alpha_L\delta_L$, the more stressful hydrogen bond can be characterized by (*i*) bent N—H...O system, with an angularity of 151.2°; (*ii*) with a significant pyramidalization of the N atom incorporated in the middle amide group; (*iii*) distorted δ_L subconformation. Therefore we think that "ghost" structures, assigned in proteins (Fig. 7) are diagnostic of special intra- or intermolecular interactions.

(*2*) The increase in polypeptide chain length. For a For-$(Ala)_i$-NH_2 ($1 \leq i \leq 4$) molecule, the average $\{\phi,\psi\}$ torsional angle pairs do not change dramatically with i (c.f. Table 10). The increase in basis set size and/or the inclusion of electron correlation did not result in significant conformational changes as demonstrated by Schafer and co-workers (15) in small systems, even when MP2/6-311++G(*d*, *p*) was applied. The observed standard deviation (i.e. $0.5[\Delta\phi + \Delta\psi]^{1/2}$) on the $\{\phi,\psi\}$ PES was smaller than 8° for selected backbone structures, while the largest alteration in the torsional angles was for the γ_L conformation was found to be $\Delta\psi = 15.2°$ on going from HF/3-21G to MP2/6-311++G(*d*, *p*). Our own study (40) showed, as may be seen from Table 2, the maximum alteration is $\Delta\phi = 13.3°$ on going from HF/3-21G to MP2/6-311++G(*d*, *p*) levels of theory with a standard deviation of only 6.7°. All these values are well within the smallest circles of 20° radii shown in Figs. 2 and 3. Certainly, precise determination of the 9 conformational centers depends upon the applied basis set, and could well be modified in future, when high computational power is available, but the basic concept of the conformational assignment will remain intact.

(*3*) All "conformational centers" were determined on the basis of *ab initio* calculations performed on For-$(Ala)_i$-NH_2 ($1 \leq i \leq 4$) molecules. It is obvious that the very simple side chain of such a model compound cannot be representative of the large variety of polar and apolar side chains. However, polyalanine models are the best systems for the investigation of purely backbone/backbone-type interactions. From this perspective all backbone/sidechain interactions are treated as indicative backbone modifying effects. Therefore, when the

Can. J. Chem. Downloaded from www.nrcresearchpress.com by 85.192.166.187 on 09/08/12
For personal use only.

TABLE 13. Observed deviations of the 9 backbone conformation types during structure description of 78 selected proteins. The describability ( ) in percentage of the conformation type using an upper limit (expressed in degree) were calculated.[a]

Dev.	α_L	α_D	β_L	δ_L	δ_D	ε_L	ε_D	γ_L	γ_D	Total
10	16.9	16.5	3.6	4.7	1.6	4.1	0.7	2.8	4.4	9.4
20	57.4	39.5	14.8	18.3	8.5	15.1	9.1	9.0	8.9	32.2
30	81.2	56.6	30.7	40.0	19.2	34.2	23.2	18.0	20.0	51.6
40	92.8	74.7	49.3	75.0	31.6	58.4	38.8	33.9	34.1	69.2
50	97.3	86.2	76.0	90.4	45.0	83.6	54.7	65.5	68.9	85.3
60	99.0	93.8	91.6	94.3	62.5	97.2	69.2	89.4	89.6	94.6
70	99.6	97.3	98.6	96.9	79.2	99.1	78.6	99.5	98.5	98.1
80	99.9	99.2	99.8	99.7	87.0	99.5	83.0	99.9	100.0	99.0
90	100	99.6	99.9	100	93.5	100	88.4	100	100	99.5

[a]For example, when the allowed deviation is smaller then 30°, 51.6% of the total backbone conformation can be described. However, at this limit 81.2% of all the helical regions can be determined.

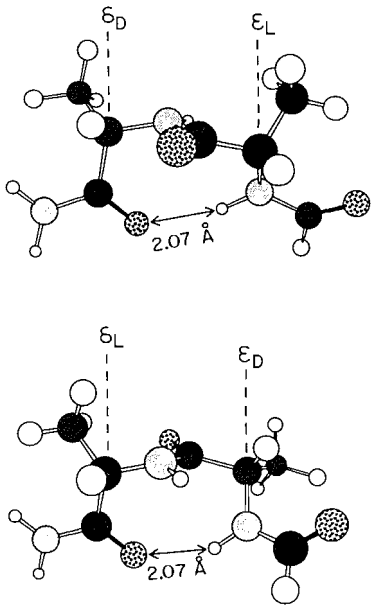

FIG. 10. The $\delta_L^*\epsilon_D$ conformation, where an unusual 8-membered H-bond ring was assigned. The same 8-membered H-bond ring was observed in its conformational enantiomer $\epsilon_L\delta_D$ (not shown).

conformation of an amino acid residue is classified by the ACAP algorithm (introduced here), and when a noticeable deviation is observed we may be certain that the resulted deviation reflects, as a global indicator, all types of interactions that are exerted on the backbone of the protein.

(*4*) All computations reported in this paper were carried out on individual conformations of the For-(L-Ala)$_2$-NH$_2$ molecule without taking into account the explicit or implicit effect of any solvent. Consequently, the present results provide a scale for intrinsic stability (ΔE) with respect to the global minimum ($\gamma_L\gamma_L$) of the 4D-Ramachandran potential energy hypersurface. When at a future date solvation effects on the conformations of For-(L-Ala)$_2$-NH$_2$ molecule are studied, the present results can be used, as a primary standard, to measure the energy lowering due to solvation.

Conclusion

For the first time, *ab initio* type calculations on the multidimensional conformational problem of a diamino acid triamide system resulted in a complete set of relaxed conformations. A large part of the For-Ala-Ala-NH$_2$ geometries are intrinsically stable hairpin (β-turns) conformations 18(30) depending on the applied criteria. This suggests that more β-turn types than expected exist on the basis of X-ray type secondary structure assignment. The 30 β-turn conformations are depicted in ref. 37 and the molecular graphics of the 19 non-β-turn conformations are shown in Fig. 11. Examples for all 49 calculated substructures were found in proteins by analzying the X-ray data of globular proteins. All 9 theoretically predicted backbone conformational types (α_L, α_D, β_L, γ_L, γ_D, δ_L, δ_D, ϵ_L, and ϵ_D) can be adopted as a substructure even for the simple For-Ala-Ala-NH$_2$ molecule. The preceding or following diamide unit can stabilize the α_L and ϵ_L conformations, as substructures, which were found to be intrinsically unstable geometries in the For-Ala-NH$_2$ molecule.

The *ab initio* calculations resulted in structures that can also be analyzed in terms of interproton distances, which are useful parameters for the interpretation of NMR spectra. The calculated marker distances (e.g. $d_{N\alpha}$, $d_{\alpha N}$, d_{NN}) are *typical* for the backbone conformational type, regardless of the conformation of the preceding or following structural unit. Moreover, by simply using the three common, $d_{N\alpha}$, $d_{\alpha N}$, d_{NN} marker distances all 9 different backbone conformers can be distinguished.

The ϕ,ψ distribution of 11786 amino acids, incorporated in 78 selected proteins with known X-ray structures, was analyzed. The conformation of all the 11786 residues were assigned, demonstrating the applicability of the "structure-description" method proposed in this paper.

Hudson, in his editorial article, examined the possibilities of X-ray and NMR protein backbone conformation determination, and concluded (56) that the "story of protein structure (mis)interpretation unfolds with every new β-turn". We believe that the enumeration of all β-turns on the basis of *ab initio* calculations, as well as their assignment in globular protein's X-ray structure, can further enhance structure assignments in the future.

Acknowledgements

The authors wish to thank the Ontario Center for Large Scale Computing (OCLSC) for a generous allocation of Cray X-MP/28Super computer time.

The continued finnancial support of the NSERC of Canada is gratefully acknowledged.

This research was also supported in part by a grant from the Hungarian Scientific Research Foundation (OTKA n° III-2245).

Can. J. Chem. Downloaded from www.nrcresearchpress.com by 85.192.166.187 on 09/08/12
For personal use only.

Can. J. Chem. Downloaded from www.nrcresearchpress.com by 85.192.166.187 on 09/08/12
For personal use only.

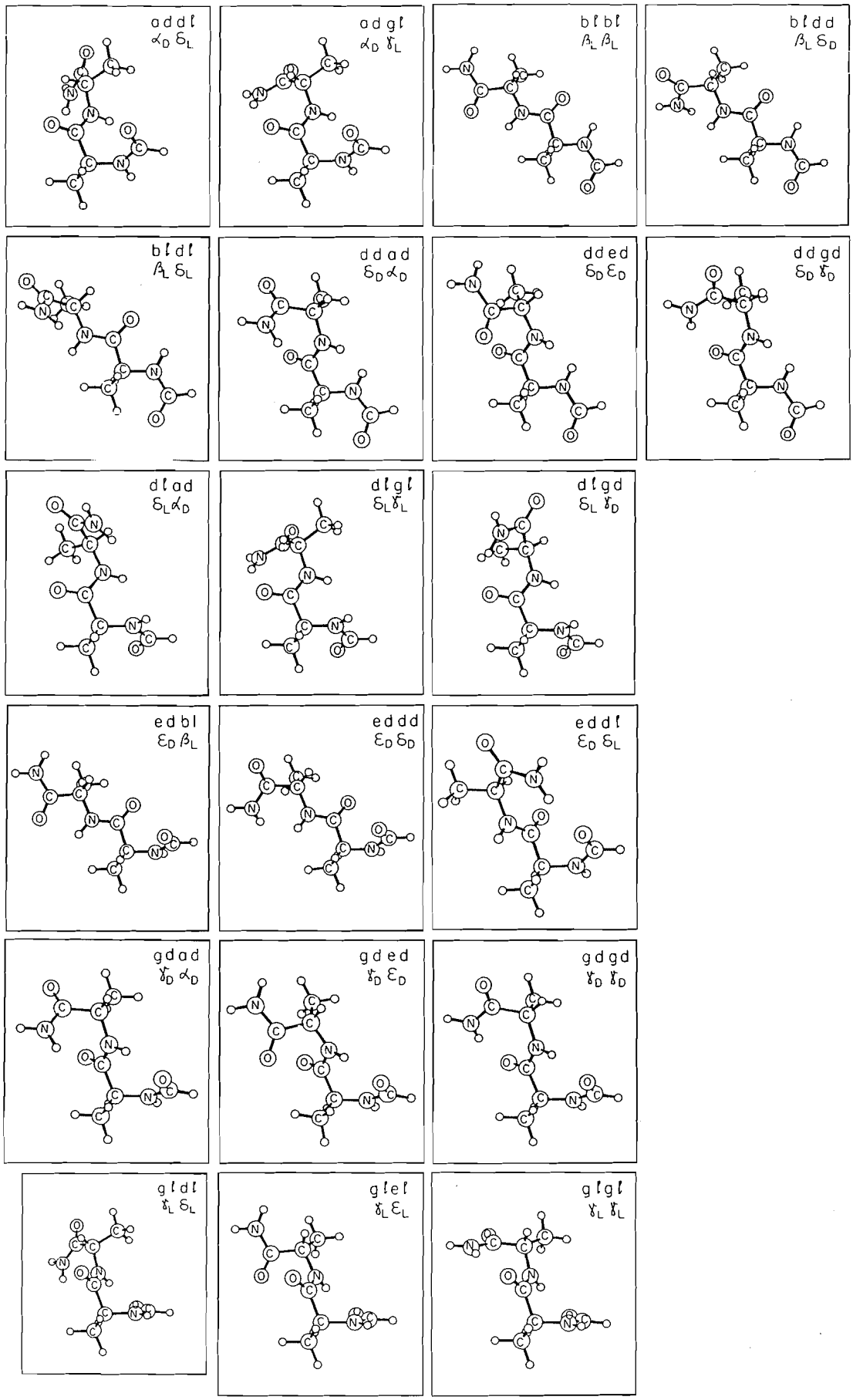

FIG. 11. The molecular graphics of the 19 non-β-turn conformations. (The 30 β-turn conformations are depicted in ref. 37.)

Can. J. Chem. Downloaded from www.nrcresearchpress.com by 85.192.166.187 on 09/08/12
For personal use only.

1. S.S. Zimmerman, M.S. Pottle, G. Nemethy, and H.A. Scheraga. Macromolecules **10**, 1 (1977).
2. A. Perczel, J.G. Angyan, M. Kajtar, W. Viviani, J.-L. Rivail, J.-F. Marcoccia, and I.G. Csizmadia. J. Am. Chem. Soc. **113**, 6256 (1991).
3. H.J. Dyson, M. Rance, R.A. Houghten, R.A. Lerner, and P.A. Wright. J. Mol. Biol. **201**, 161 (1988).
4. P.E. Wright, H.J. Dyson, and R.A. Lerner. Biochemistry, **27**, 7167 (1988).
5. *In* The peptides. Vol. 4. I.L. Karle. *Edited by* V.J. Hruby. Academic Press, New York, NY. 1981. pp. 1–53.
6. I.L. Karle. Byopolymers, **28**, (1981).
7. A. Aubry, N. Ghermani, and M. Marraud. Int. J. Peptide, Protein Res. **23**, 113 (1984).
8. A. Aubry, J. Protas, G. Boussard, and M. Marraud. Acta Crystallogr. **B36**, 2825 (1980).
9. A. Aubry, C. Lecomte, G. Boussard, and M. Marraud. J. Chim. Phys. Chim. Biol. **80**, 609 (1983).
10. A. Aubry and M. Marraud. Acta Crystallogr. **C41**, 65 (1985).
11. A.M. Liquori. Quart. Rev. Biophysics, **2**, 65 (1969).
12. E. Ralston and J.-L. Decoen. J. Mol. Biol. **83**, 393 (1974).
13. Roterman, I.K., M.H. Laubert, K.D. Gibson, and H.A. Scheraga. J. Biomol. Struct. Dyn. **7**, 421 (1989).
14. M.A. McAllister, A. Perczel, P. Csárzár, W. Vladia, J.-L. Rivail, and I.G. Csizmadia. J. Mol. Struct. (THEOCHEM) **288**, 161 (1993).
15. R.F. Frey, J. Coffin, S.Q. Newton, M. Ramek, V.K.W. Chen, F.A. Momany, and L. Schafer. J. Am. Chem. Soc. **114**, 5369 (1992).
16. (*a*) H.L. Sellers and L. Schafer. J. Am. Chem. Soc. **100**, 7728 (1978); (*b*) L. Schafer, H.L. Sellers, F.J. Lovas, and R.D. Suenram. J. Am. Chem. Soc. **102**, 6566 (1980); (*c*) L. Schafer, C. Van Alsenoy, and J.N. Scarsdale. J. Chem. Phys. **76**, 1439 (1982); (*d*) V.J. Klimkowski, L. Schafer, F.A. Momany, C. Van Alsenoy. J. Mol. Struct. **124**, 143 (1985); (*e*) J.N. Scarsdale, C. Van Alsenoy, V.J. Klimkowski, L. Schafer, and F.A. Momany. J. Am. Chem. Soc. **105**, 3438 (1983); (*f*) L. Schafer, V.J. Klimkowski, F.A. Momany, H. Chuman, and C. Van Alsenoy. Biopolymers, **23**, 2335 (1984); (*g*) T. Head Gordon, M. Head Gordon, M.J. Frish, C. Brooks II, J.A. Pople. Int. J. Quantum Chem. Quantum Biol. Symp. 16, 311 (1989); (*h*) T. Head Gordon, M. Head Gordon, M.J. Frish, C. Brooks II, and J.A. Pople. J. Am. Chem. Soc. **113**, 5989 (1991).
17. (*a*) M.R. Peterson and I.G. Csizmadia. *In* Progress of theoretical organic chemistry. Elsevier. **3**, 190 (1982); (*b*) I.G. Csizmadia. *In* The chemistry of the thiol group. J. Wiley and Sons. 1974. pp. 1–109; (*c*) I.G. Csizmadia and J.D. Bertran. (*Editors*). *In* New theoretical concept for understanding organic reactions. Reidel Publishing Co. 1989. pp. 1–31.
18. G.N. Ramachandran, C. Ramakrishnan, and V. Sasisekharan. J. Mol. Biol. 7, 95 (1963).
19. P.G. Mezey (*Editor*). Potential energy hypersurfaces. Elsevier Science Publishers. 1987.
20. IUPAC-IUB Commission on Biochemical Nomenclature. Biochemistry, **9**, 3471 (1970).
21. J. Smith and L. Pease. Crit. Rev. Biochem. **8**, 315 (1980).
22. A. Aubry, M. Marraud, J. Protas, and J. Neel. Compt. Rend. Acad. Sci. Paris, **287C**, 163 (1974).
23. A. Aubry, M. Marraud, J. Protas, and J. Neel. Compt. Rend. Acad. Sci. Paris, **276C**, 1089 (1973).
24. A. Aubry. Thèse pour Docteur et Sciences Physiques, Université de Nancy, Nancy, France. 1976. pp. 102–107.
25. A. Aubry, M.T. Cung, and M. Marraud. Cryst. Struct. Commun. **11**, 129 (1982).
26. A. Aubry, J. Protas, and M. Marraud. Acta. Crystallogr. **B33**, 2534 (1977).
27. A. Aubry, J. Protas, M. Marraud, and J. Neel. Acta. Crystallogr. **B32**, 2749 (1976).
28. L. Pauling and R. Corey. Proc. Natl. Acad. Sci. U.S.A. **37**, 729 (1951).
29. L. Pauling, R. Corey, and H. Branson. Proc. Natl. Acad. Sci. U.S.A **37**, 205 (1951).
30. M. Levitt and C. Chothia. Nature (London), **261**, 552 (1976).
31. J.L. Crawford, W.N. Lipscomb, and C.G. Schellman. Proc. Natl. Acad. Sci. U.S.A. **70**, 538 (1973).
32. S.S. Zimmerman and H.A. Scheraga. Proc. Natl. Acad. Sci. U.S.A. **74**, 4126 (1977).
33. C. Venkatachalam. Biopolymers, **6**, 1425 (1968).
34. B.L. Sibanda and J.M. Thorton. Nature (London), **316**, 170 (1985).
35. M. Levitt. J. Mol. Biol. **104**, 59 (1976).
36. C.M. Wilmot and J.M. Thornton. Protein Eng. **3**, 479 (1990).
37. A. Perczel, M.A. Mcallister, P. Császár, and I.G. Csizmadia. J. Am. Chem. Soc. **115**, 4849 (1993).
38. A. Perczel, M. Kajtar, J.-F. Marcoccia, and I.G. Csizmadia. J. Mol. Struct. (THEOCHEM) **232**, 291 (1991).
39. (*a*) M. Frisch, M. Head-Gordon, G.W. Trucks, J.B. Foresman, H.B. Schelegel, K. Raghavachari, M.A. Robb, J.S. Brinkley, C. Gonzalez, D.J. Defrees, D.J. Foz, J.J.P. Stewart, S. Topiol, and J.A. Pople. GAUSSIAN 90 (Revision F. Version), Gaussian Inc., Pittsburgh, PA. 1990; (*b*) J.S. Binkley, J.A. Pople, and W.L. Hehre. J. Am. Chem. Soc. **102**, 939 (1980).
40. G. Endredi, A. Perczel, M.A. McAllister, P. Császár, I. Ladik, and I.G. Csizmadia. To be published.
41. (*a*) M.J. McGregor, I.A. Suhail, and J.E. Sternberg. J. Mol. Biol. 198, 295 (1987); (*b*) F.C. Bernstein, T.F. Kkoetzle, G.J.B. Williams, E.F. Mayer, M.D. Jr. Brice, J.R. Rodgers, O. Kennard, T. Shimanouchi, and M. Tasumi. J. Mol. Biol. 112, 535 (1977); (*c*) E.E. Abola, F.G. Bernstein, S.H. Bryant, I.F. Koetzle, and J. Weng. *In* Data Commission of the International Union of Crystallography. *Edited by* F.H. Allen, G. Bergerhoff, and R. Sievers. Bonn/Cambridge/Chester. pp. 107–132; (*d*) A.L. Morris, M.W. MacArthur, E.G. Hutchinson, and M.J. Thornton. Proteins: Struct. Fun. and Gen. 12, 345 (1982).
42. Sundaralingham and Sukharudu. Nature (1991).
43. A. Perczel, B.M. Foxman, and G.D. Fasman. Proc. Natl. Acad. Sci. (1992).
44. M.A. McAllister, A. Perczel, P. Császár, I.G. Csizmadia. J. Mol. Structure (THEOCHEM) **288**, 181 (1983).
45. M. Cheng, M.E. McGovern, T.J. Danchman, C. Zhao, M.A. McAllister, A. Perczel, P. Császár, I.G. Csizmadia. J. Mol. Structure (THEOCHEM), **309**, 151 (1994).
46. L. Schafer, S.Q. Newton, M. Cao, A. Peeters, C. VanAlsenoy, K. Wolinsky, and F.A. Momany. J. Am. Chem. Soc. **115**, 272 (1993).
47. C.-M. Liegener, G. Endredi, M.A. McAllister, A. Perczel, J. Ladik, and I.G. Csizmadia. J. Am. Chem. Soc. **115**, 8275 (1983).
48. G. Endredi, C.-M. Liegener, M.A. McAllister, A. Perczel, J. Ladik, and I.G. Csizmadia. J. Mol. Struct. (THEOCHEM), **306**, 1 (1994).
49. A. Perczel, G. Endredi, M.A. McAllister, O. Farkas, P. Csaszar, J. Ladik, and I.G. Csizmadia. J. Am. Chem. Soc. Submitted.
50. K. Wolinsky, J.F. Hinton, and P. Pulay. J. Am. Chem. Soc. **112**, 8251 (1990).
51. (*a*) G. Fogarasi and P. Pulay. *In* Vibrational spectra and structure. Vol. 14. *Edited by* J.R. During. Elsevier, Amsterdam. 1985. p. 215. (*b*) R.S. Grev and H.F.J. Schafer III. J. Am. Chem. Soc. **111**, 5687 (1989).
52. (*a*) R.W. Woody. Biopolymers, **17**, 1451 (1978); (*b*) R.W. Woody. The peptides. Vol. 7. *Edited by* V.J. Hruby. Academic Press. 1985. pp. 15–113.
53. T.D. Norden, S.W. Staley, W.H. Taylor, and M.D. Harmony. J. Am. Chem. Soc. **109**, 7641 (1978).
54. H.J. Geise and W. Pyckhout. *In* Stereochemical application of gas phase electron diffraction. *Edited by* I. Hargittai and M. Hargittai. 1988. p. 321.
55. (*a*) M.D. Bruch, J.H. Noggle, and L.M. Gierasch. J. Am. Chem. Soc. **107**, 1400 (1985); (*b*) H. Kessler, U. Anders, and M. Schudok. J. Am. Chem. Soc. **112**, 5908 (1990); (*c*) L.M. Gierasch, C.M. Deber, V. Madison, C.-H. Niu, and E.R. Blout. Biochemistry, **20**,

4730 (1981); (*d*) J.H. Noggle and R.E. Schirmer. The nuclear Overhauser effect, chemical applications. Academic Press, New York; (*e*) D. Neuhaus and M. Williamson. The nuclear Overhauser effect in structural and conformational analysis. Verlagsgesellschaft (VCH).

56. J. Hudson. Bio-Technology, **11**, 36 (1983).

Can. J. Chem. Downloaded from www.nrcresearchpress.com by 85.192.166.187 on 09/08/12
For personal use only.

Acetal formation from methyl formate, pinacolone, and benzophenone: equilibrium constants in methanol and water determined by a chain of transacetalization equilibria

J. Peter Guthrie[1] and Junan Guo

Department of Chemistry University of Western Ontario, London, ON N6A 5B7, Canada

Received December 16, 1993[2]

J. Peter Guthrie and Junan Guo. Can. J. Chem. **72**, 2071 (1994).

Transacetalization equilibrium constants can be measured in methanol solution. This allows a ladder of equilibrium constants to be constructed from acetophenone, for which the equilibrium constant for acetal formation has been measured in methanol, to methyl formate, for which it has not. This is the first direct measurement of an equilibrium constant for formation of an acetal of an acyclic ester. We have also determined equilibrium constants for acetal formation from benzophenone and pinacolone. The value for benzophenone is inconsistent with the value reported for the diethyl acetal by Pfeiffer and Adkins (G.J. Pfeiffer and H. Adkins. J. Am. Chem. Soc. **53**, 1043 (1931)). We must conclude that their analytical method was subject to systematic errors.

J. Peter Guthrie et Junan Guo. Can. J. Chem. **72**, 2071 (1994).

On a mesuré les constantes d'équilibre de transacétalisation en solution dans le méthanol. On peut maintenant définir une échelle de constantes d'équilibre allant de l'acétophénone, pour laquelle la constant d'équilibre de formation de l'acétal a été mesurée dans le méthanol, au formate de méthyle, pour lequel cette mesure n'a pas été faite. Il s'agit de la première mesure directe d'une constante d'équilibre pour la formation d'un acétal d'un ester acyclique. On a aussi déterminé les constantes d'équilibre pour la formation d'un acétal à partir de le benzophénone et de la pinacolone. La valeur pour la benzophénone n'est pas en accord avec la valeur rapportée, pour l'acétale de diéthyle, par Pfeiffer et Adkins (G.J. Pfeiffer et H. Adkins. J. Am Chem. Soc. **53**, 1043 (1931)). On doit en conclure que leur méthode analytique devait être l'object d'erreurs systématiques.

[Traduit par la rédaction]

Introduction

Equilibrium constants for acetal formation can often be determined directly (1–7), but for less reactive carbonyl compounds this becomes increasingly difficult. Although there are several independent determinations of the equilibrium constant for acetophenone dimethyl acetal formation (2, 7), there are no values for compounds much less reactive than acetophenone: *p*-methoxyacetophenone is the least reactive compound for which an equilibrium constant has been measured directly (2). Pfeiffer and Adkins (8) extended the study of acetal formation to much less reactive compounds by using transacetalization, with formation of triethyl orthoformate from ethyl formate and ethanol as the reference equilibrium, although in fact they did not know this equilibrium constant and could only determine relative values. This pioneering work was hampered by the limited means available for analyzing the composition of the equilibrium solutions. In fact, the analyses were based on determination of the amount of ethyl formate in solution in ethanol by reaction with sodium metal, leading to production of carbon monoxide.

We have used the free energy of formation of trimethyl orthoformate, based on thermochemical data, as the starting point for calculation of the free energy of formation of orthoformic acid and its mono and dimethyl esters (9). We used the Pfeiffer and Adkins value for the transacetalization equilibrium constant to estimate the free energy of formation of benzophenone dimethyl acetal, from which we estimated the free energy of formation of the hydrate, and hence the equilibrium constant for covalent hydration of benzophenone (10). It was of interest to see if modern analytical methods would allow a more direct determination of the free energy of formation of trimethyl orthoformate and benzophenone dimethyl acetal by equilibrium measurements. We wish now to report the results of such studies. The equilibrations were carried out in methanol, but of greater interest are equilibrium constants in aqueous solution. To determine the free energies of transfer from methanol to water we used the approach of Toullec et al. (2), i.e., using dodecane as an intermediate solvent, not miscible with either water or methanol.

Results

Equilibrium constants for transacetalization

We used acetophenone as our anchor compound, but found that for nmr analysis, the equilibrium constant for transacetalization between acetophenone and trimethyl orthoformate was too far on the side of acetophenone dimethyl acetal to allow us to measure the equilibrium constant. Accordingly we used pinacolone as a bridge compound; from the work of Pfeiffer and Adkins (8) we knew that pinacolone had a considerably smaller tendency to form an acetal than acetophenone. Both the transacetalization equilibria relating pinacolone and acetophenone and pinacolone and methyl formate, could be measured conveniently. All equilibria were followed from both directions, and gave the same equilibrium constant in each case. For benzophenone we expected, based on the results of Pfeiffer and Adkins in ethanol solution (8), that the acetalization would be even more difficult than for methyl formate. However, we found that in fact benzophenone is similar to acetophenone in its reactivity. The results of these experiments are found in Table 1.

$$R^1R^2C(OMe)_2 + R^3R^4C{=}O \rightleftharpoons R^1R^2C{=}O + R^3R^4C(OMe)$$

$$K_{\text{transacetalization}} = \frac{[R^1R^2C=O][R^3R^4C(OMe)_2]}{[R^1R^2C(OMe)_2][R^3R^4C{=}O]}$$

$$= \frac{[R^1R^2C{=}O][MeOH]^2[R^3R^4C(OMe)_2][H_2O]}{[R^1R^2C(OMe)_2][H_2O][R^3R^4C{=}O[MeOH]^2}$$

$$= \frac{K^{R^3R^4CO}_{\text{acetalization}}}{K^{R^1R^2CO}_{\text{acetalization}}}$$

[1]Author to whom correspondence may be addressed.

[2]Revision received July 7, 1994.

Can. J. Chem. Downloaded from www.nrcresearchpress.com by 85.192.166.187 on 09/08/12
For personal use only.

TABLE 1. Transacetalization equilibrium constants in methanol, dodecane, and water[a]

Equation	K_f	K_r	K_{meoh}[b]	K_{dod}[c]	K_{water}[c]
[1]	115.9 ± 5.6	113.3 ± 7.3	114.6	108.6	115.6
[2]	55.5	46.5	51.0	35.6	59.1
[3]	6.1 ± 0.1	5.3 ± 0.4	5.7	34.8	1.5

[a]For transacetalization equilibrium:
Ketone-1 + acetal-2 ⇌ ketone-2 + acetal-1

[1] $PhCOMe + Me_3CC(OMe)_2Me \rightleftharpoons Me_3CCOMe + PhC(OMe)_2Me$

[2] $PhCOPh + Me_3CC(OMe)_2Me \rightleftharpoons Me_3CCOMe + PhC(OMe)_2Ph$

[3] $Me_3CCOMe + HC(OMe)_3 \rightleftharpoons HCOOMe + Me_3CC(OMe)_2Me$

The equilibrium constant was defined as: K = [ketone-2][acetal-1]/[ketone-1][acetal-2]. The activity coefficient ratio did not differ significantly from unity. This was confirmed by experiments showing that the equilibrium constant was concentration independent and that dilution of a system at equilibrium did not change the apparent value of the equilibrium constant.

[b]K_{meoh} is the equilibrium constant in methanol and was measured by ^1H NMR. K_{meoh} is the average of K_f and K_r, which were obtained from reactions run in the forward and reverse directions, respectively.

[c]K_{dod} and K_{water} stand for equilibrium constants in dodecane and water, respectively, and were calculated by the use of free energies of transfer from Table 3.

TABLE 2. Equilibrium constants for acetal formation in methanol, dodecane, and water[a]

	$10^6 K_X$		
Compound	K_{meoh}	K_{dod}	K_{water}
PhCOMe	632.0[b]	328.0[b]	43.8[b]
PhCOPh	281.0[c]	107.0[d]	22.4[d]
Me_3CCOMe	5.51[c]	3.02[d]	0.379[d]
HCOOMe	0.968[c]	0.0869[d]	0.257[d]

[a]K_{meoh}, K_{dod}, and K_{water} are equilibrium constants in methanol, dodecane, and water, respectively, based on the mole fraction standard state for all species.

[b]The values for acetophenone were from ref. 2.

[c]Calculated by combining transacetalization equilibrium constants from Table 1 and the equilibrium constant for acetal formation from acetophenone (2).

[d]Calculated using K_{meoh} and partition constants from Table 3.

Equilibria for acetalization in methanol

By combining the equilibrium constant for the acetalization of acetophenone with the equilibrium constants for transacetalization that we determined, we could calculate equilibrium constants for the acetalization of pinacolone, methyl formate, and benzophenone. These calculations are summarized in Table 2.

Partition constants

Equilibrium constants for partitioning of compounds from methanol to dodecane and from dodecane to water were determined in order to allow the calculation of the free energy of transfer from methanol to water. These results are summarized in Table 3, which also contains data from the literature on the free energies of transfer for water, methanol, acetophenone, and its dimethyl acetal.

Equilibria for acetalization in water

From the free energy of transfer data in Table 3 and the equilibrium constants for acetalization in methanol in Table 2 we have calculated equilibrium constants in water for each of the acetalizations; these values are in Table 2. The value for methyl formate represents the first equilibrium constant for formation of an acetal of an acyclic ester to be directly determined.

Free energies of formation

From the equilibrium constants determined in this work, and the thermodynamic data available in the literature for the carbonyl compounds, we are able to calculate the free energies of formation of the acetals. These values are found in Table 4, along with thermodynamic data for all compounds discussed in this paper. In the case of trimethyl orthoformate this new value, $\Delta G_f(aq) = -88.35 \pm 0.70$ kcal/mol, can be compared with the value previously calculated from thermochemical data, -87.80 ± 0.81 kcal/mol. The agreement is excellent. The value of the equilibrium constant for acetal formation from benzophenone allows determination of another group contribution to the free energy of formation in aqueous solution (11), namely $[C(C_B)_2(O)_2]$.[3] It is also possible to calculate a value for $[CO(C_B)_2]$, which has not previously been reported. Using group contributions from ref. (11) and the free energies of formation in Table 4 we calculate that $[CO(C_B)_2] = -30.1$ and $[C(C_B)_2(O)_2] = 5.47$. Since each value is based on only one compound, they can only be regarded as provisional.

Discussion

Our method for determining transacetalization equilibrium constants should be general. The main limitations are the limited dynamic range of NMR analysis and the problem of overlap between the peaks used for analysis and other peaks from species in solution. The former problem forces us to use integration of a peak from a minor species relative to a ^{13}C satellite of a peak from a major species. With more intermediate compounds, and more steps to the ladder, this could be overcome. The latter problem will restrict application to more elaborate structures but will become less important as higher field NMR instruments become more available.[4]

We were distressed to find that our results did not bear out those of Pfeiffer and Adkins (8). The discrepancy is shown in Fig. 1, which contrasts the results from the two methods. To allow direct comparison we calculated equilibrium constants for transacetalization involving methyl formate/trimethyl orthoformate as the reference reaction. Admittedly Pfeiffer and Adkins (8) worked in ethanol with triethyl orthoformate and diethyl acetals, but the discrepancies seem too large for the relatively modest effects expected for replacement of methyl by ethyl. Adkins and Adams found very similar equilibrium constants for acetal formation from acetaldehyde and methanol, ethanol, propanol, or butanol (1). We are forced to conclude that there were systematic errors in the work of Pfeiffer and Adkins (8). The problem doubtless lies in their analytical procedure, the conversion of ethyl formate to carbon monoxide by the action of sodium on the ethanol solution. Although the mechanism of this reaction does not appear to have been elucidated, it is not hard to imagine that benzophenone could interfere, by transient formation of a ketyl. An investigation of the kinetics of this reaction found that there is a smooth decomposition of ethyl formate under the influence of ethoxide ion in ethanol, which leads to a temperature-dependent equilibrium with carbon mon-

[3]Following Benson (24) we use C_B to mean aromatic carbon; thus $\{C(C_B)_2(O)_2\}$ is the contribution from a carbon bonded to two aromatic rings and two oxygen functions.

[4]We currently have routine access to 200 or 300 MHz NMR instruments. Preliminary experiments at 60 MHz were less promising because of problems of peak overlap and sensitivity. Still higher fields would be even better.

Can. J. Chem. Downloaded from www.nrcresearchpress.com by 85.192.166.187 on 09/08/12
For personal use only.

TABLE 3. Partition constants and free energies of transfer[a]

(*a*) Compounds for which ΔG_{m-w} was determined in this work

Compound	P_{m-d}	ΔG_{m-d} (kcal/mol)	P_{d-w}	ΔG_{d-w} (kcal/mol)	ΔG_{m-w} (kcal/mol)
PhCOPh[b]	0.383 ± 0.005	0.57	$(1.253 \pm 0.074) \times 10^{-3}$	3.96	4.42
$PhC(OMe)_2Ph$[b]	1.630 ± 0.035	−0.29	$(6.651 \pm 0.508) \times 10^{-5}$	5.70	5.40
Me_3CCOMe[b]	0.259 ± 0.020	0.80	0.155 ± 0.016	1.10	1.90
$Me_3CC(OMe)_2Me$[c]	1.58 ± 0.21	−0.27	$(4.89 \pm 0.20) \times 10^{-3}$	3.15	2.88
HCOOMe[c]	0.16 ± 0.04	1.09	2.94 ± 0.06	−0.64	0.45
$HC(OMe)_3$[c]	0.16 ± 0.01	1.09	2.19 ± 0.23	−0.46	0.62

(*b*) Compounds for which ΔG_{m-w} was already available[d]

Compound	ΔG_{m-w}
H_2O	1.67[e]
MeOH	−2.19[f]
PhCOMe	2.47
$PhC(OMe)_2Me$	3.45

[a] P_{m-d} and P_{d-w} are the partition constants from methanol to dodecane and those from dodecane to water. G_{m-d}, G_{d-w}, and G_{m-w} are the free energies of transfer from methanol to dodecane, from dodecane to water, and from methanol to water, respectively. Both the partition constants and the free energies of transfer are based on the molar concentration. In the determination of partition constants, activity coefficients were assumed to be unity and this was confirmed by the observation that the measured values were concentration independent. Free energies of transfer are given in kcal/mol.

[b] Measured by UV.

[c] Measured by ^{1}H NMR.

[d] Calculated from values in ref. 2, correcting to the standard states used in this paper.

[e] 1 M water in methanol to liquid water.

[f] Liquid methanol to 1 M methanol in water.

TABLE 4. Free energy of formation data for compounds discussed in this paper[a]

Compound	ΔG_f Water	ΔG_f Methanol
H_2O	−56.69	−58.36
CH_3OH	−41.88	−39.69
$HCOOCH_3$	−73.29 ± 0.23	−73.74 ± 0.27
$HC(OCH_3)_2$	−87.80 ± 0.81 −88.35 ± 0.70[b]	−88.42 ± 0.81
$C_6H_5COCH_3$	−2.22 ± 0.41	−4.69 ± 0.41
$C_6H_5C(OCH_3)_2CH_3$	−20.36 ± 0.48	−23.80 ± 0.48
$(CH_3)_3CCOCH_3$	−31.61 ± 0.13	−33.52 ± 0.15
$(CH_3)_3CC(OCH_3)_2CH_3$	−46.93 ± 0.94[b]	−49.81 ± 0.65
$(C_6H_5)_2CO$	−37.01 ± 0.88[c]	32.48 ± 0.88
$(C_6H_5)_2C(OCH_3)_2$	19.27 ± 1.10[b]	13.85 ± 1.10

[a] Standard states are ideal 1 M solutions in water or methanol, with an infinitely dilute reference state. For water in water or methanol in methanol, the standard state is the pure liquid. Except as noted, ΔG_f in water is taken from ref. 11 and ΔG_f in methanol is calculated from ΔG_f in water using the free energies of transfer from Table 2. Free energies are given in kcal/mol.

[b] Calculated from the equilibrium constants for transacetalization, found in Table 1, and the free energies of formation of the other reactants, taken from this table.

[c] Reference 10.

oxide (12). Methyl formate is produced industrially by the reaction of carbon monoxide with methanol and a catalytic amount of sodium methoxide at 70°C and 20–200 bar (1 bar = 100 kPa) (13). An unavoidable conclusion is that the set of transacetalization equilibrium constants reported by Pfeiffer and Adkins (8) must be considered unreliable, and should be redetermined.

Initially we had used the Pfeiffer and Adkins (8) value for acetal formation from benzophenone as the basis for an estimate of the equilibrium constant for hydration of benzophenone (10). This value was considerably less favorable than for the hydration of acetophenone, as seemed reasonable from a naive assumption that *two* conjugated phenyl groups would favor the carbonyl group relative to acetal more effectively than one. From this perspective the observation that the equilibrium constants for acetalization (and hence for hydration) of benzophenone and acetophenone are quite similar seems most surprising. There is, however, general agreement, both from theoretical calculations (14, 15), and from experimental investigations (16, 17), that the benzene rings in benzophenone are twisted substantially away from coplanarity with the carbonyl. The exact angle in solution is not yet well established, with estimates varying from 26.2° (14) to 36° (16), and the angle in the solid, a twist angle of 33° with respect to the plane of the carbonyl (18), may well be influenced by packing. Benzophenone adopts a nonplanar conformation in order to relieve nonbonded interactions of the *ortho* hydrogens. As a consequence the conjugative stabilization in benzophenone need not be greater than in acetophenone. Ab initio calculations (3-21G) suggested that conjugation becomes more important as the benzophenone molecule twists toward planarity; the planar conformation was calculated to be more stable than the book conformation[5] by 7 kcal (14), although both are less stable than the twisted form. Although there will not be extra conjugation in benzophenone, there is an extra electron withdrawing substituent relative to acetophenone. Thus it should not be surprising that benzophenone and acetophenone have similar equilibrium constants for acetalization.

With revised equilibrium constants for acetalization in hand,

[5] In the book conformation both dihedral angles about the C_B—CO bonds are 90°.

Can. J. Chem. Downloaded from www.nrcresearchpress.com by 85.192.166.187 on 09/08/12
For personal use only.

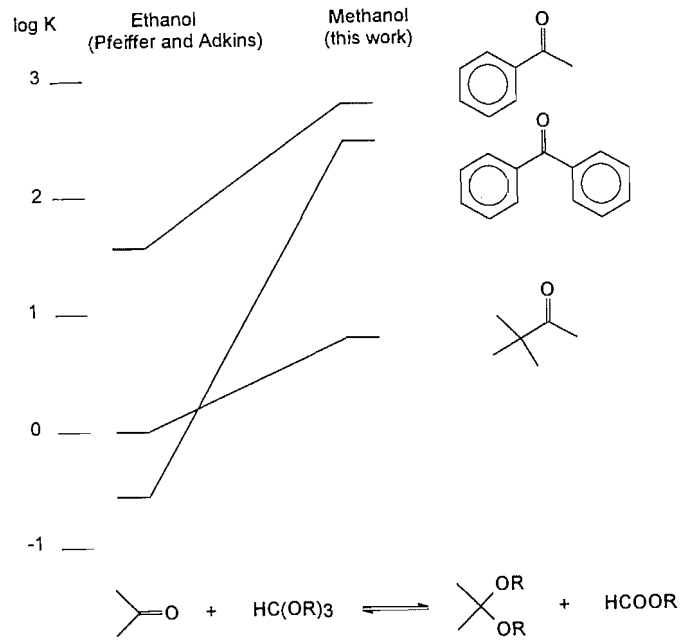

FIG. 1. Comparison of log K values for transacetalization in ethanol and methanol.

we can now calculate the equilibrium constants for hydration of the carbonyl compounds. We do this by means of the correlation we found between the free energy for the hypothetical hydrolysis (corrected for steric and symmetry effects) and the sum of the σ^* values for the other three groups on the central carbon (19).

$$R^1R^2R^3C\text{-}OCH_3 + H_2O \rightleftharpoons R^1R^2R^3C\text{-}OH + CH_3OH$$

$$\Delta G = 0.54 - 0.63\Sigma\sigma^* + \text{steric correction} + \text{symmetry correction}$$

Applying this procedure twice we obtain the equilibrium constant for hydrolysis of an acetal to the corresponding covalent hydrate, and from this and the equilibrium constant for acetal formation it is easy to calculate the equilibrium constant for hydration. The values so calculated are found in Table 5. The calculation requires values for the difference in strain between acetal and hemiacetal and between hemiacetal and hydrate. These strain energies were calculated as before (19) using the scheme introduced by Pihlaja (20, 21).

What are the prospects for extension of this transacetalization procedure? We have examined the question of whether transacetalization equilibrium constants could be measured for other, less reactive esters by similar experiments. It seems probable that it will be possible, but only if a suitable ladder can be constructed, because transacetalization equilibrium constants must be in the range from 0.01 to 100, in order to be practical for NMR analysis. By the use of more hindered ketones (which might react very slowly) and esters with electron-withdrawing groups it should be possible to do this. On the other hand, extension to amides appears unlikely, because of the need for acid catalysis of the transacetalization reaction. Acid, except at very low concentrations (high pH values), would protonate the amine, pulling alcoholysis of the amide or amide acetal to completion. At very low acid concentrations, transacetalization would be very slow, and substantial concentrations of amine would need to be present to maintain the concentration of amide.

TABLE 5. Equilibrium constant for addition of water to ketones

Ketone	log K	
	Liquid water[a]	1 M water[b]
$(CH_3)_3C\text{-}CO\text{-}CH_3$	−6.18	−7.93
$(C_6H_5)_2CO$	−5.04	−6.78
		−8.68[c]

[a] $K = [R^1R^2C(OH)_2]/[R^1R^2C{=}O]$, dimensionless.
[b] $K = [R^1R^2C(OH)_2]/[R^1R^2C{=}O][H_2O]$, M^{-1}.
[c] Reference 10, based on data from ref. 8.

It is of interest to see how well the acetalization equilibrium for pinacolone could have been predicted by simple additivity schemes such as we have recently published. When we calculate the free energy of formation of pinacolone dimethyl acetal using the published group contributions and an estimate of strain derived from MM3 (22) calculations,[6] we obtain a value of −46.82 kcal/mol, which may be compared with the value derived from our transacetalization equilibrium constant, −46.93. In calculating the strain in pinacolone dimethyl acetal we must allow for the strain inevitably present in the groups $[C(C)_2(O)_2]$ and $[C(C)_4]$. We do this by using the disproportion reaction:

$$(CH_3)C\text{-}C(OCH_3)_2\text{–}CH_3 + CH_3\text{–}CH_3 \rightleftharpoons C(CH_3)_4 + (CH_3)_2C(OCH_3)_2$$

This allows us to calculate the extra strain in pinacolone dimethyl acetal that is not implied by the groups in ethane, neopentane, and acetone dimethyl acetal. The net strain so calculated is 10.18 kcal/mol. These calculations are detailed in the Appendix.

The provisional group contributions for $[CO(C_B)_2]$ and $[C(C_B)_2(O)_2]$ that we have calculated should provide a guide for estimating free energies of other diaryl ketones and the corresponding acetals, but until further data are available they should be used with caution.

Experimental

Materials

1 M methanolic HCl solution was made by adding 0.7 mL of acetyl chloride to 10 mL of methanol at 0°C. All reagents were from BDH or Aldrich and were used without further purification except as follows: Acetophenone, pinacolone, methyl formate, and trimethyl orthoformate were purified by distillation. The dimethyl acetals of acetophenone, pinacolone, and benzophenone were synthesized by acid-catalyzed reaction of the ketone with trimethyl orthoformate in methanol, and purified by distillation (acetophenone and pinacolone diemthyl acetals) or by recrystallization from methanol (benzophenone dimethyl acetal). Methanol was dried by reaction with magnesium followed by distillation under nitrogen. The water concentration was checked by Karl Fischer titration using a Metrohm 684KF coulometer; the value found was 68 μg/mL.

[6] As contained in MM3(89) obtained through QCPE, without further parameterization.

Can. J. Chem. Downloaded from www.nrcresearchpress.com by 85.192.166.187 on 09/08/12
For personal use only.

Can. J. Chem. Downloaded from www.nrcresearchpress.com by 85.192.166.187 on 09/08/12
For personal use only.

Partition constant determination

For each compound a stock solution was prepared (volumetric flask) in the solvent in which it is less soluble. This stock solution (4–7 mL) was mixed with 7–4 mL of the other solvent in a volumetric tube with a standard taper stopper, shaken vigorously for 10 min, transferred into a centrifuge tube, and sealed using foil and parafilm; it was then placed in a constant temperature bath set at 25°C and left overnight. Finally, the two partition phases were separated carefully by centrifugation and the relative concentrations of the two phases were measured by UV or H NMR. In the determination of partition constants of benzophenone or its dimethyl acetal between dodecane and water and of pinacolone dimethyl acetal, the test compound was introduced in dodecane instead of in water because of the large difference in limiting solubilities. Also in these cases the partition systems were stirred overnight at 25°C instead of just shaken for 10 min to make sure that partition equilibrium was reached.

In the case of acetals, 0.1 M aqueous NaOH solution was used as the water phase to inhibit acetal hydrolysis. pH 7 buffer (from BDH, contains 5.775 g/L of Na_2HPO_4 and 3.538 g/L of KH_2PO_4) was used as the water phase for methyl formate for analogous reasons. Usually the relative concentration was measured directly except that benzophenone dimethyl acetal was first hydrolysed to benzophenone.

In the UV determination of benzophenone, benzophenone dimethyl acetal, and pinacolone, samples of the two partition phases were usually diluted in a common solvent: methanol and a 0.1 M $HClO_4$ solution in 90% methanol:10% water were used for benzophenone and its dimethyl acetal, respectively. For pinacolone, however, the samples of the two partition phases were diluted in the corresponding solvent and then analyzed using the appropriate molar extinction coefficients: λ = 288, log ϵ = 1.32 in dodecane (this work), λ = 278, log ϵ = 1.48 in water (23); and λ = 282, log ϵ = 1.40 in methanol (23).

In the H NMR determination of methyl formate, methyl orthoformate, and pinacolone dimethyl acetal, 0.35 mL of the dodecane or methanol phase was added to 0.35 mL of $CDCl_3$ containing methyl acetate as internal reference, and 0.35 mL of the water phase was added to 0.35 mL D_2O containing methyl acetate as internal reference for methyl formate determination and sodium acetate for the other cases. In the determination of the partition constant of pinacolone dimethyl acetal between dodecane and water, the relative concentration in the water phase was obtained by the use of ^{13}C-satellite of the methyl group in sodium acetate as reference because the concentration of pinacolone dimethyl acetal was very low.

Transacetalization equilibrium constant determination

To an NMR tube was added the appropriate amount of each reactant, 0.38 mL of a 1 M solution of HCl in methanol, and enough methanol to give a total volume of 1.5 mL. Then the NMR tube was sealed using a torch and put into the constant temperature bath at 25°C. The transacetalization equilibrium reactions were carried out in the NMR tube and the approach to equilibrium was followed by NMR using a Gemini-200. Relative concentrations of all species at equilibrium were measured by the NMR integrations. For most of the cases, protio methanol was used to prevent the deutero–proton exchange between CD_3OD and CH_3COR and consequently an external deuterium lock was used. However, for the equilibrium starting with pinacolone and benzophenone dimethyl acetal, because the relative equilibrium concentration of the pinacolone dimethyl acetal was very low, 15% of CD_3OD was added to the system after equilibrium was reached, in order to give an internal lock. Analysis was carried out by measuring the ratio of the ^{13}C-satellite of the *tert*-butyl group in pinacolone and the peak of the *tert*-butyl group in pinacolone dimethyl acetal. Some typical initial concentrations of the reactants for both directions are listed as follows:

Me_3CCOMe + $HC(OMe)_3$ ⇌	$Me_3CC(OMe)_2Me$ +	HCOOMe
1.01 M	2.01 M	0 M 0 M
0 M	0 M	0.5 M 1.5M

PhCOMe + $Me_3CC(OMe)_2Me$ ⇌	$PhC(OMe)_2Me$ +	Me_3CCOMe
1.01 M	1.01 M	0 M 0 M
0 M	0 M	1.48 M 1.01 M

PhCOPh + $Me_3CC(OMe)_2Me$ ⇌	$PhC(OMe)_2Ph$ +	Me_3CCOMe
0.10 M	0.20 M	0 M 0 M
0 M	0 M	0.11 M 0.22 M

Acknowledgments

We thank the Natural Sciences and Engineering Research Council of Canada for financial support of this work.

1. H. Adkins and E.W. Adams. J. Am. Chem. Soc. **47**, 1368 (1925).
2. J. Toullec, M. El-Alaoui, and P. Kleffert. J. Org. Chem. **48**, 4808 (1983).
3. K.B. Wiberg and R.R. Squires. J. Am. Chem. Soc. **101**, 5512 (1979).
4. H. Maltz. J. Chem. Soc. Chem. Commun. 843 (1968).
5. R. Garrett and D.G. Kubler. J. Org. Chem. **31**, 2665 (1966).
6. T.S. Davis, P.D. Feil, D.G. Kubler and D.J. Wells. J. Org. Chem. **40**, 1478 (1975).
7. R.P. Bell, J.P. Millington and J.M. Pink. Proc. R. Soc. London, A: **303**, 1 (1968).
8. G.J. Pfeiffer and H. Adkins. J. Am. Chem. Soc. **53**, 1043 (1931).
9. J.P. Guthrie. J. Am. Chem. Soc. **95**, 6999 (1973).
10. J.P. Guthrie. Can. J. Chem. **56**, 962 (1978).
11. J.P. Guthrie. Can. J. Chem. **70**, 1042 (1992).
12. F. Adickes and G. Schaefer. Chem. Ber. **65**, 950 (1932).
13. K. Weissermel and H. J. Arpe. Industrial organic chemistry. Verlag Chemie, Weinheim.
14. J. Kendrick. J. Chem. Soc. Faraday Trans. **86**, 3995 (1990).
15. K.M. Gough and T.A. Wildman. J. Am. Chem. Soc. **112**, 9141 (1990).
16. R.J. Abraham and I.S. Haworth. J. Chem. Soc., Perkin Trans. 2, 1429 (1988).
17. P. Jin and T.A. Wildman. J. Phys. Chem. **95**, 20 (1991).
18. E.B. Fleischer, N. Sung, and S. Hawkinson. J. Phys. Chem. **72**, 4311 (1968).
19. J.P. Guthrie. Can. J. Chem. **53**, 898 (1975).
20. K. Pihlaja. Acta Chem. Scand. **25**, 451 (1971).
21. K. Pihlaja and J. Kankare. Acta Chem. Scand. **23**, 1745 (1969).
22. N.L. Allinger, Y.H. Yuh, and J. H. Lii. J. Am. Chem. Soc. **111**, 8551 (1989).
23. W.P. Hayes and C.J. Timmons. Spectrochim. Acta, **21**, 529 (1965).
24. S.W. Benson. Thermochemical kinetics. Wiley, New York. 1976.

Appendix

Estimation of the free energy of formation in aqueous solution of the dimethyl acetal of pinacolane.

$$\Delta G_f^\circ(aq) = 4[CH_3(C)] + 2[CH_3(O)] + [C(C)_4] + [C(C)_2(O)_2] + RT\ln(\text{symmetry number}) + \text{strain correction} + \text{standard state correction}$$

$$= 4[-3.93] + [-3.95] + 2[10.40] + [-5.30] + 2[-22.49] + 0.593\ln(3^7) + 10.18 + 1.90$$

$$= -46.86 \text{ kcal/mol}$$

To calculate the strain correction we use the disproportionation reaction

$(CH_3)_3C–C(OCH_3)_2–CH_3 + CH_3–CH_3 \rightleftharpoons C(CH_3)_4 + (CH_3)_2C(OCH_3)_2$

MM3	20.11	3.39	4.30	9.02
Benson	x	0	0	0

for which the difference in strain energy must be the same whether it is calculated by use of MM3 steric energies, or by using Benson strain corrections. Simple arithmetic then gives the Benson strain correction for pinacolone dimethyl acetal as 10.18.

Can. J. Chem. Downloaded from www.nrcresearchpress.com by 85.192.166.187 on 09/08/12
For personal use only.

On the water-promoted mechanism of peptide cleavage by carboxypeptidase A. A theoretical study

SILVIA ALVAREZ-SANTOS, ANGELS GONZÁLEZ-LAFONT, AND JOSÉ M. LLUCH[1]
Departament de Química, Universitat Autònoma de Barcelona, 08193 Bellaterra, Barcelona, Spain

AND

BALDOMERO OLIVA AND FRANCESC X. AVILÉS
Institut de Biologia Fonamental i Departament de Bioquímica, Universitat Autònoma de Barcelona, 08193 Bellaterra, Barcelona, Spain

Received March 21, 1994

SILVIA ALVAREZ-SANTOS, ANGELS GONZÁLEZ-LAFONT, JOSÉ M. LLUCH, BALDOMERO OLIVA, and FRANCESC X. AVILÉS. Can. J. Chem. **72**, 2077 (1994).

The water-promoted pathway of peptide cleavage by carboxypeptidase A has been studied by semiempirical (AM1) quantum mechanical calculations. A relatively large model for the CPA-active site elements plus substrate has been designed, using two imidazoles and one acetate as the Zn^{2+} ligands, acetate as the proton acceptor (simulating Glu-270), and *N*-ethylacetamide as the peptide-like substrate. This model, although simpler than the natural one, is one of the largest used for theoretical calculations on CPA catalytic mechanisms. To ensure that this model is able to mimic the natural system, it has been compared with the structure of the $(Gly)_3$-L-Tyr + water + CPA complex resulting from several molecular dynamics/energy minimization simulations. Among the different steps involved in the water-promoted pathway proposed by Lipscomb's group, the attack of the oxygen atom that comes from the activated water molecule to the carbon atom of the peptide bond of the substrate has been found to be the rate-determining step, with a high enthalpy barrier of 37.9 kcal/mol. However, this enthalpy barrier is dramatically decreased when a positive charge, simulating Arg-127, is included near the scissile carbonyl. The reported results seem to favour the occurrence of the mechanism studied and indicate the limitations of using simple elements for the theoretical analysis of enzyme-catalyzed reactions.

SILVIA ALVAREZ-SANTOS, ANGELS GONZÁLEZ-LAFONT, JOSÉ M. LLUCH, BALDOMERO OLIVA et FRANCESC X. AVILÉS. Can. J. Chem. **72**, 2077 (1994).

Utilisant des calculs semiempiriques de mécanique quantique (AM1), on a étudié la voie de clivage des peptides par la carboxypeptidase A (CPA), catalysée par l'eau. On a mis au point un modèle relativement grand des éléments du site actif de la CPA avec le substrat qui utilise deux imidazoles et un acétate comme ligands du Zn^{2+}, un acétate comme accepteur de proton (simulant le Glu-270) et le *N*-éthylacétamide comme substrat semblable à un peptide. Ce modèle, même s'il est plus simple que le modèle naturel, est un des plus grand qui a été utilisé pour des calculs théoriques sur les mécanismes catalytiques de la CPA. Afin de s'assurer que ce modèle peut imiter le comportement du système naturel, on l'a comparé avec la structure du complexe $(Gly)_3$-L-Tyr + eau + CPA qui résulte de plusieurs simulations de dynamique moléculaire et minimisation de l'energie. Parmi les différentes étapes impliquées dans la voie catalysée par l'eau proposée par le groupe de Lipscomb, on a trouvé que l'étape déterminant la vitesse de la réaction est l'attaque de l'atome d'oxygène, provenant de la molécule d'eau activée, sur l'atome de carbone de la liaison peptidique du substrat et qu'elle est accompagnée d'une barrière enthalpique élevée (37,9 kcal/mol). Toutefois, il se produit une diminution dramatique de cette barrière lorsqu'on introduit une charge positive, ressemblant à celle de l'Arg-127, près du carbonyle à être scindé. Les résultats rapportés antérieurement semblent favoriser l'existence du mécanisme étudié et ils indiquent les limitations à l'usage d'éléments simples pour l'analyse théorique des réactions catalysées par les enzymes.

[Traduit par la rédaction]

Introduction

Bovine carboxypeptidase A (peptidyl-L-amino acid hydrolase; EC 3.4.17.1, abbrev. CPA) is a zinc metalloexopeptidase of 307 residues (MW = 34 472), and a well-studied enzyme (1–6). This protease preferentially hydrolyzes peptide or ester bonds at the C-terminus of polypeptide substrates with hydrophobic (aromatic or aliphatic) residues. The three-dimensional structure of CPA, alone and bound to different organic or organopeptidase inhibitors, has been determined by X-ray diffraction at high resolution (1,7–10). These studies allowed definition of four of the five previously proposed substrate binding sites from kinetic analyses (S1′, S1, S2, S3, and S4) (2, 4, 11, 12).

In contrast, the experimental characterization of the CPA catalytic site (S1) and of the catalytic intermediates has been more controversial (5, 13–16). In addition to the indirect evidence from the above-mentioned X-ray analyses (5, 7), enzyme kinetics studies together with chemical modification and site-directed mutagenesis experiments (17–22) indicated the residues involved in the hydrolytic mechanism. Glu-270 and Arg-127 (besides the Zn^{2+} at the active site) appear as the most directly involved, while Arg-145, Asn-144, Tyr-248, and Arg-71, among others, seem to be important for conferring the proper position, distortion, and environment to the substrate (23, 24).

Two alternative pathways have been proposed for the catalytic mechanism, both involving a precatalytic interaction between the C-terminal carboxyl with Arg-145/Asn-144 and between the carboxyl of the scissile C-terminal peptide bond with the zinc. The first is a nucleophilic pathway in which Glu-270 acts as an active base that attacks the scissile carbonyl to form a water-labile intermediate (25). The second is a water-promoted pathway in which zinc, assisted by Glu-270, forms a hydroxyl with a nearby water molecule, followed by the attack

[1]Author to whom correspondence may be addressed.

Can. J. Chem. Downloaded from www.nrcresearchpress.com by 85.192.166.187 on 09/08/12
For personal use only.

Can. J. Chem. Downloaded from www.nrcresearchpress.com by 85.192.166.187 on 09/08/12
For personal use only.

of the hydroxyl on the scissile carbonyl (15, 26, 27). A significant amount of experimental material about one or the other mechanism has been found (28). The accumulation of intermediates with the substrate bound to the enzyme (presumably the acyl enzyme) in hydrolytic experiments on ester substrates at low temperature is one of the most conclusive pieces of evidence in favour of the nucleophilic pathway for ester substrates, but not for peptidic substrates (29). On the other hand, experiments on peptide substrates are generally more in favour of the water-promoted pathway (30).

Theoretical approaches have also been used to throw light on the above mechanistic problems. Several authors have made molecular orbital calculations on the catalytic mechanism of CPA. Hayes and Kollman (31) studied the electrostatic environment effect on the scissile peptide bond of a substrate. Scheiner and Lipscomb (32) showed that the action of an electrophile at the carbonyl group of a substrate was effective in enhancing the hydrolysis. Nakagawa and Umeyama (23) showed that three arginine residues were important for the binding of a substrate to CPA. Subsequently, simulating some ligands of zinc with point fractional charges, Nakagawa and co-workers demonstrated that the Zn-coordinated water molecule acts as a proton donor for Glu-270 (33). In addition, the electrostatic effect of Zn^{2+} and its ligands and the electron delocalization between Zn^{2+} and the water seem to play a significant role in lowering the barrier height of the proton transfer mentioned above, which is the first step of the water-promoted pathway.

Recently Alex and Clark (34) reported an AM1 study of the water-promoted mechanism of peptide cleavage by CPA. They used a rather complete set of ligands for the Zn^{2+} atom, with two imidazoles (representing His-196 and His-69), an acetate molecule (representing Glu-72), and a formiate (which represents Glu-270). However, the substrate simulated by the authors, a formamide molecule, is too simple to be able to mimic the behaviour of natural, long, peptide substrates in the active site of the enzyme. Oversimplified substrate-like molecules in their interaction with CPA have also been studied by Kollman and co-workers (24) using molecular dynamics approaches.

The purpose of the present paper is to study the water-promoted pathway of peptide cleavage by CPA in such a way that some of the limitations of the previous studies can be overcome. We have combined molecular dynamics and quantum mechanical calculations and used longer peptide-like substrates towards this aim.

Computational details

Quantum mechanical calculations

The calculations were carried out by using the standard AM1 (35) procedure, as implemented in the AMPAC (36) package of computer programs.

All geometry minima were obtained by minimizing the energy with respect to all geometrical variables by using the Davidon–Fletcher–Powell (DFP) method (37, 38). The location of transition states was done by using the McIver–Komornicki gradient minimization technique (39). The characterization of both kinds of stationary points, minima and transition states, was carried out by diagonalizing their Hessian (force constant) matrices and looking for zero or one-negative eigenvalues, respectively.

Molecular dynamics calculations

The X-ray crystallographic coordinates of CPA with crystallographic water molecules (ref. 5cpa (7) in the Protein Data Bank; PDB) and Gly-L-Tyr/CPA complex (ref. 3cpa (40) in the PDB) were used to build the model of CPA with a substrate. Two glycines were added to the substrate (Gly-L-Tyr) found in 3cpa to build the $(Gly)_3$-L-Tyr tetrapeptide. This tetrapeptide substrate alone was then energy-minimized by 1000 steps of steepest descent without SHAKE (41, 42) and with position constraints over all the atoms of the crystallographic Gly-L-Tyr. The optimized tetrapeptide was positioned in the active site of CPA (3cpa) by superimposition over all the atoms of the crystallographic Gly-L-Tyr.

The substrate was added to CPA (5cpa) by superimposition of the main-chain atoms of CPA (3cpa) over the main-chain atoms of CPA (5cpa). The crystallographic water molecules (5pca) were removed, with the exception of the water molecule number 571, which was bound to the Zn atom of CPA (5cpa). The structure resulting from these steps was taken as the initial model to seed a molecular dynamics simulation of the active site of CPA plus substrate. Hereafter in this paper, this structure will be called **MD-0**.

The Zn atom and the atoms that are bound to it (one nitrogen of the imidazole groups of His-69 and His-196, the two oxygens of the carbonyl group of Glu-72, and the oxygen of the water molecule number 571) were constrained in their crystallographic position throughout all of the following steps of the procedure to model the active site of CPA plus the substrate.

Molecular dynamics (MD) and energy minimization (EM) were derived with the GROMOS program package (42). The standard GROMOS NIS (Non Inertial Solvent) (D4) potential energy function was used to simulate the effect of solvent waters for the MD simulations and energy minimizations in a simplified way. In the NIS force field (43, 44), the acidic and basic side chains, which may be charged species in solution, are neutralized to mimic the presence of surrounding counterions. His-196 and His-69 have their exchanging imidazole proton not at the Nδ, but rather at the Nε position (HisB in the GROMOS topology file definitions); thus the coordination to the Zn atom is done by the pair of free electrons of the nitrogen sp^2 orbital.

Electrostatic forces were evaluated with a clean twin-range cutoff technique. All nonbonded forces within 8 Å were evaluated at each simulation step. Electrostatic forces at distances between 8 and 13 Å were reevaluated every 10 steps. A 2-fs time step was used in the integration when the bond lengths were constrained by SHAKE, and a time step of 0.5 fs was used in the integration when the bond lengths were not constrained. The temperature of the MD simulations analyzed was set at 293 K, and a temperature relaxation time of 0.1 ps was used to maintain the system in a weak coupling bath (45).

Results and discussion

To study the chemical mechanism of peptide cleavage by CPA by means of the semiempirical, quantum mechanical AM1 procedure, we had to design a simplified model of the active site of CPA plus the substrate.

Design and validation of the substrate/CPA-active site complex

The following compounds were considered as key elements for the design of the active site of CPA plus the substrate: Zn^{2+} and its ligands (two imidazoles and one acetate) and a proton acceptor (one acetate) for the active site of CPA; and a simplified peptide-like species (*N*-ethylacetamide) for the substrate. The system defined with these key elements was optimized by

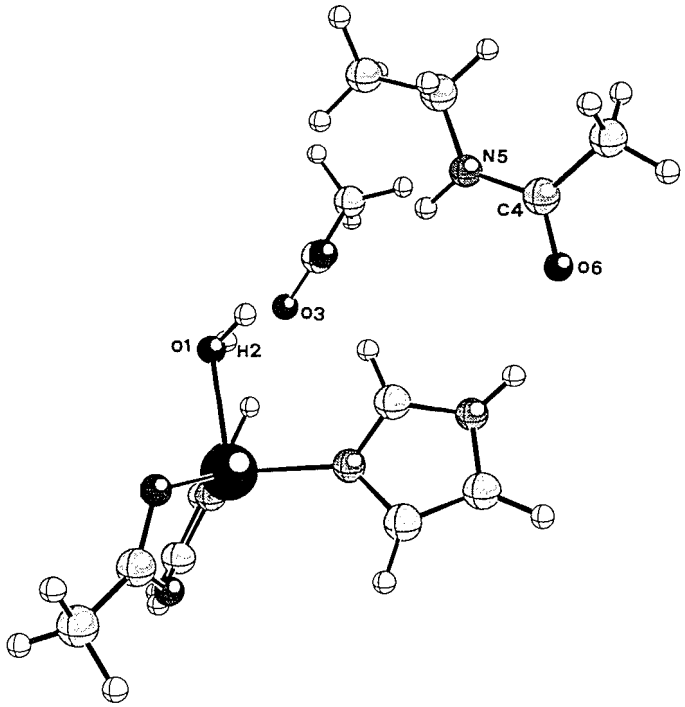

FIG. 1. AM1 optimized structure of the quantum mechanical model (**QM-1**) for the substrate/CPA-active site complex.

an AM1 semiempirical procedure. The optimization provided the initial structure **QM-1** (see Fig. 1), which was used to seed the quantum mechanical analyses of the catalytic mechanism of peptide cleavage.

To ensure that the **QM-1** structure was able to mimic the natural system, we wished to compare this structure with the real conformation of the substrate/CPA-active site complex. However, this experimental substrate/CPA complex does not exist (there are several crystallographic structures of complexes of CPA with inhibitors, but there is none with a substrate). As an alternative procedure we decided to compare the **QM-1** structure with the model resulting from applying MD and EM on the **MD-0** structure (the optimized tetrapeptide $(Gly)_3$-L-Tyr + water 571 + CPA structure) as defined in the Computational Details section.

We found that the initial **MD-0** structure was not in equilibrium, the energy being extremely high due to the nonbonded interactions between the substrate and the CPA. A new structure where the substrate became relaxed within the active site, but assuring that the whole system remains at the same region of the potential energy surface, is required. For this purpose we used a 10 ps MD run with the NIS force field, without SHAKE, and with no other restrictions other than those defined in the Computational Details section for the MD and EM simulations. Subsequently, a further optimization run of 5000 steps of steepest descent with SHAKE and with position constraints over the carbonyl carbon of Gly-3 of the substrate was used to approximate the substrate towards the proper positions in the active site, giving rise to the **MD-1** structure (it should be noted that Gly-3 is of functional importance in the above model because it is linked to Tyr-4, with which it establishes the scissile peptide bond). However, in the NIS force field the Zn atom did not have any charge, while the atoms that are coordinated to Zn had negative partial charges. As a consequence, the minimization was not enough to properly pull Gly-3 into the active site and the hydrogens of the water molecule 571 were incorrectly oriented.

From the former results it became evident that the NIS force field used was unable to simulate the natural substrate/CPA system in which the substrate is within the active site. Two overcome this limitation we decided to submit the **MD-1** structure to a further EM/MD procedure in order to reach a new state of equilibrium, but now to use the partial charges provided by the semiempirical approach (AM1) for the atoms of the active site, while the partial charges of the rest of the system were taken from the NIS force field (hereafter the new force field will be called NIS-AM1-cpa). In this procedure two consecutive EM runs of 5000 steps of steepest descent with the NIS-AM1-cpa force field (and with SHAKE) were used to pull and relax, respectively, the substrate into the active site. In the first run the position of the carbonyl carbon of Gly-3 of the substrate was still constrained at the position of the **MD-0** structure, while in the second run this constraint was removed. The structures obtained were designated **MD-2** and **MD-3**, respectively.

In the **MD-2** structure the distance between the carbonyl carbon of Gly-3 of the substrate and the oxygen of water 571 was 2.6 Å, and we observed that the hydrogens of water 571 were reoriented to face the carbonyl oxygens of the side chain of the Glu-270 of CPA. The **MD-3** structure became more relaxed, with the substrate kept in a proper position (the distance between the scissile carbonyl atom of the substrate and the oxygen of water 571 was 2.8 Å).

A further 10 ps MD simulation of the system (with SHAKE, and the NIS-AM1-cpa force field), involving the sampling of 5000 conformers, was performed to obtain an average **MD** structure (defined as the **MD-4** structure). At this structure the distance between the scissile carbonyl carbon of the substrate and the oxygen of water 571 slightly increased to 3.4 Å. It is interesting to note that the hydrogen bonds between the carbonyl oxygen of Glu-270 and the hydrogens of water 571 were observed to be present from the **MD-2** to the **MD-4** structures.

Finally, the **MD-4** structure was used to test the adequacy of the **QM-1** model. A comparison between both structures clearly shows that **QM-1** reproduces the relative orientation and the hydrogen bond network of the main groups that intervene in the active center – substrate interaction quite well. This fact justifies the choice of the **QM-1** structure as a model to study the reaction mechanism of the cleavage of the substrate by CPA.

Reactivity at the active site

Once the quantum model (**QM-1**) has been validated by means of MD/EM simulations, we can initiate the study of the different steps of the mechanism involved in the water-promoted pathway proposed by Lipscomb's group for the CPA-catalyzed proteolysis. For the sake of clarity we present the relative energies of reactants, transition states, and intermediates schematically over the course of the process in Fig. 2. In Figs. 1 and 3 the different localized stationary points are presented with a tridimensional perspective. These pictures will be very useful in describing the Lipscomb mechanism as follows.

The first step of the complete process is the water activation promoted by zinc and assisted by acetate. This consists of the hydrogen (H2) extraction by O3, one of the acetate oxygen atoms, from O1 of the water molecule coordinated to zinc. The second step of the mechanism is the attack of O1, which comes from the activated water molecule, on the carbon atom (C4) of

Can. J. Chem. Downloaded from www.nrcresearchpress.com by 85.192.166.187 on 09/08/12
For personal use only.

Can. J. Chem. Downloaded from www.nrcresearchpress.com by 85.192.166.187 on 09/08/12
For personal use only.

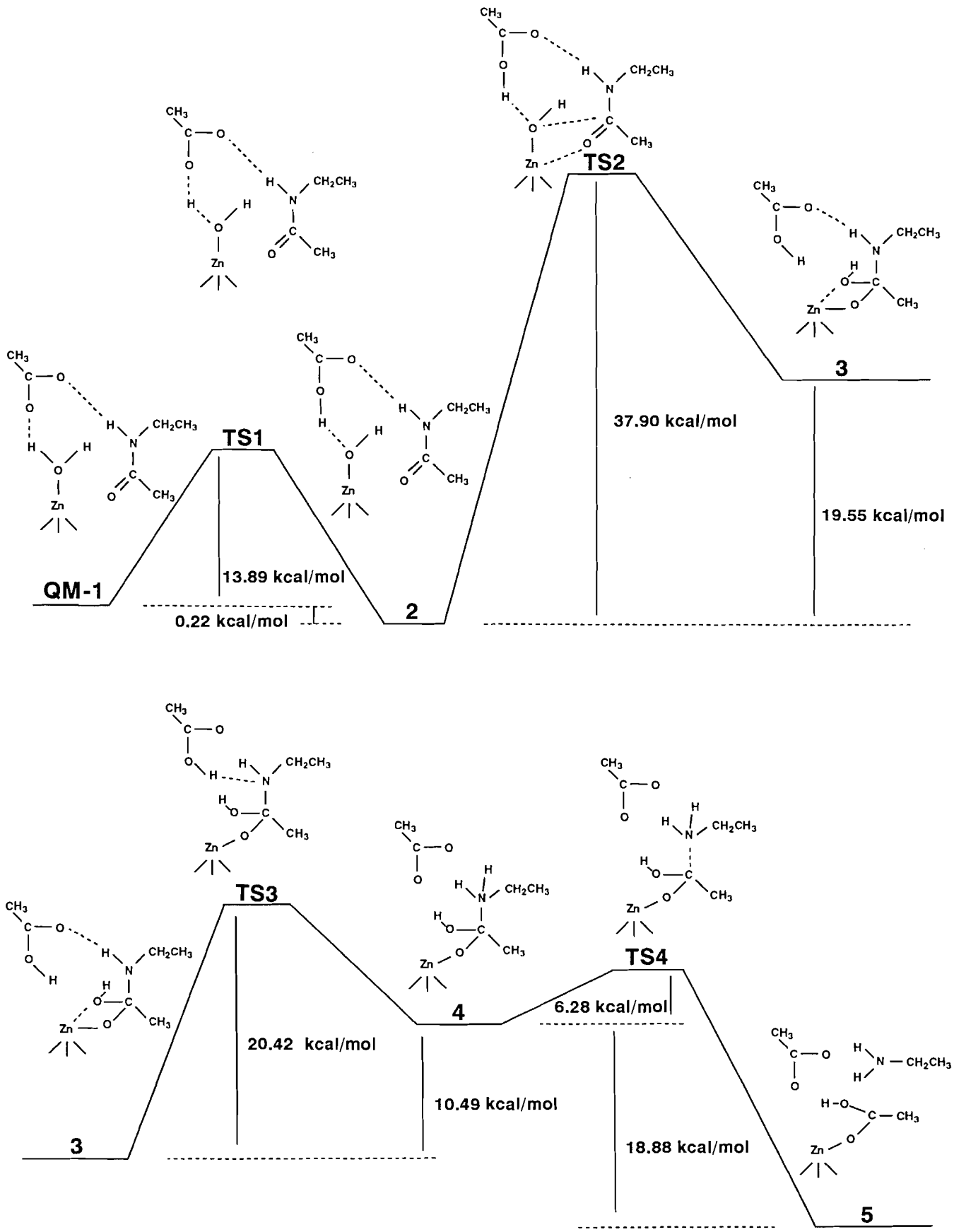

FIG. 2. Relative energies and geometries of reactants, transition states, and intermediates along the water-promoted pathway for the peptide cleavage by carboxypeptidase A.

Can. J. Chem. Downloaded from www.nrcresearchpress.com by 85.192.166.187 on 09/08/12
For personal use only.

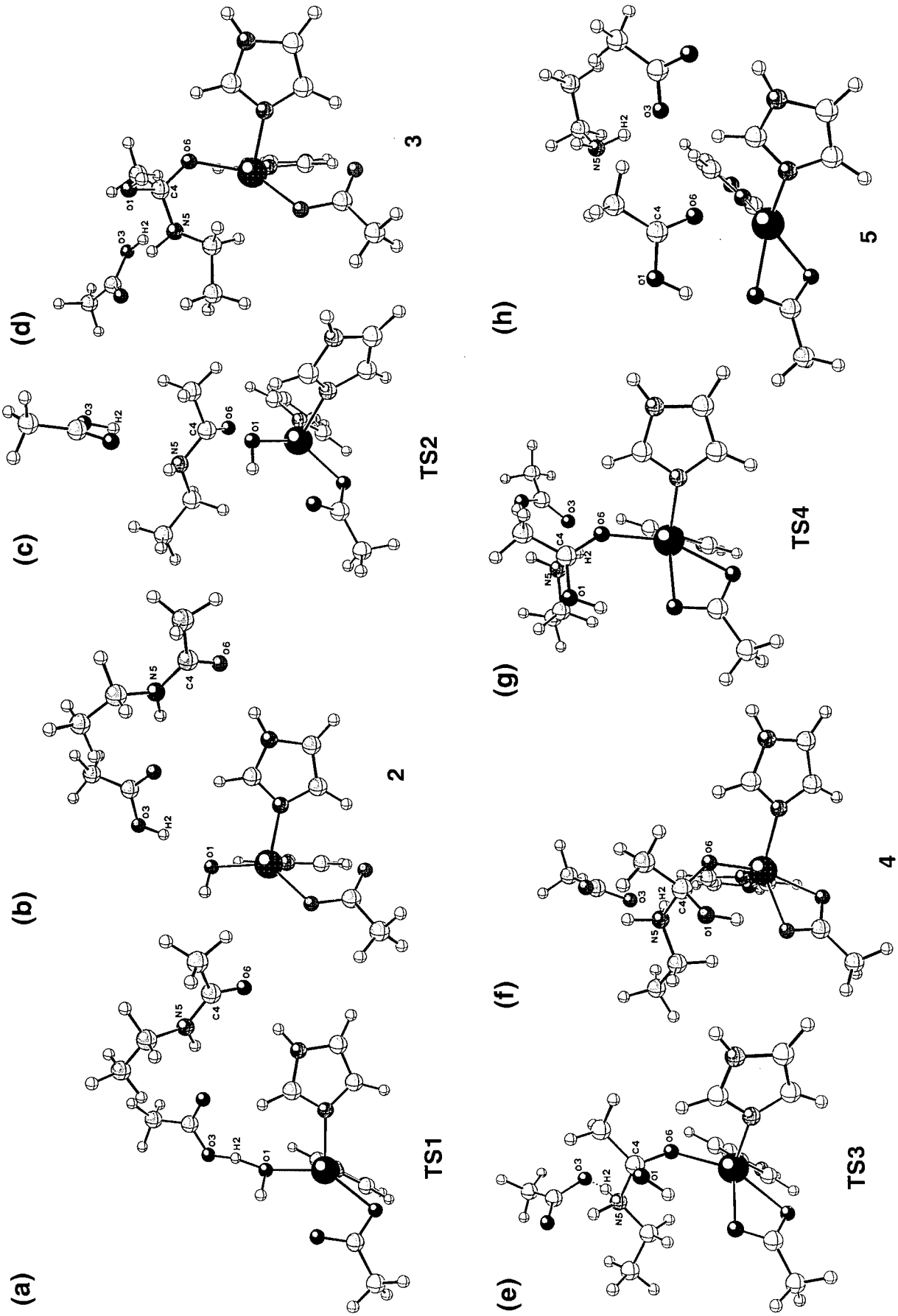

FIG. 3. 3-D optimized structures for the stationary points ((*a*) **TS1**; (*b*) **2**, (*c*) **TS2**, (*d*) **3**, (*e*) **TS3**, (*f*) **4**, (*g*) **TS4**, (*h*) **5**) drawn schematically in Fig. 2.

the peptide bond of the substrate. As a consequence of this attack the zinc atom changes from coordination to O1 to coordination to O6, the carbonyl oxygen atom of the substrate, in order to stabilize the increase of the negative charge of that oxygen atom. This process, with an enthalpy barrier of 37.9 kcal/mol, is the rate-determining step of the mechanism.

The third step consists of the hydrogen (H2) transfer from O3 to the nitrogen (N5) atom of the peptide bond of the substrate. In spite of this hydrogen transfer, the C4—N5 peptide bond does not break at this stage although the C4—N5 distance increases up to 1.58 Å. The peptide bond cleavage takes place at the next step with an energy barrier of 6.28 kcal/mol. The resulting amine molecule remains at the active site in structure **5** by means of a hydrogen bond formed with the acetate molecule: N5—H2···O3.

The global process is endothermic with an enthalpy change of 10.9 kcal/mol. As we have already mentioned, the enthalpy barrier obtained for the rate-determining step is nearly 38 kcal/mol, about twice the corresponding value previously obtained by Alex and Clark (34) using their more simplified system.

Taking into account the limitations of the AM1 semiempirical method, AM1 values of about 20 kcal/mol have recently been considered reasonable to theoretically validate a reaction mechanism (34, 46). However, we think that the rate-determining enthalpy barrier obtained in the present paper clearly exceeds the error that can be attributed to the AM1 methodology. At this point two alternatives can be envisaged: first, that the mechanism proposed by Lipscomb's group for the CPA-catalyzed proteolysis is not valid; secondly, that our model system is still too simplified, missing key functional groups positioned near the scissile peptide bond. For instance, crystallographic and site-directed mutagenesis studies (10, 19) suggest that Arg-127 is a key amino acid in the hydrolysis of peptides by carboxypeptidase A. The guanidinium group of Arg-127 is hypothesized to stabilize the oxyanion of the tetrahedral intermediate (structure **3** in Fig. 2) formed by the attack of water on the scissile carbonyl bond.

To perform a preliminary test of that hypothesis we have recalculated the second step of the mechanism, introducing a positive charge of 1.0 au located at 3.2 Å from O6 (according to X-ray crystallographic data (10)). This positive charge, attempting to represent the effect of the Arg-127 molecule, has been used in this test to avoid the huge increase of computational time that would be involved if a complete arginine side chain was introduced. Now the enthalpy barrier of the rate-determining step dramatically decreases to 22.7 kcal/mol. This stabilization comes from the combined interaction of Zn^{2+}, as mentioned above, and the positive charge with the scissile carbonyl oxygen (O6) in structure **3**.

This preliminary result using a positive charge suggests that the inclusion of more chemical groups may justify the water-promoted pathway proposed by Lipscomb and co-workers for the CPA-catalyzed peptide cleavage. More theoretical work is required to confirm this assumption. Towards this aim, further calculations on the complete mechanism, including additional key residues (as Arg-127), are now in progress in our laboratory.

Finally, from the results obtained in the present work, an important and interesting warning emerges. It is clear that quantum mechanical studies on biochemical systems are unattainable, unless drastic simplifications are imposed. In cases like the one treated here, these simplifications refer to both the substrate and the active site of the enzyme, and have to be chosen with caution. The substrate has to be modelled in such a way that the main features of the active center – substrate interaction (i.e., relative orientation and hydrogen bond network) are reproduced. In this sense, the comparison of quantum mechanical structures with experimental or numerical simulation data (Monte Carlo or Molecular Dynamics methods) are very useful in order to warrant the validity of the model. The substrate (a formamide) used by Alex and Clark (34) is probably too simple for the real, active center – substrate interactions to be correctly reproduced; in this way it is unable to provide a suitable representation of the CPA-active site plus the substrate. This fact leads to an enthalpy barrier for the rate-determining step that is not comparable with the value corresponding to our longer, more realistic, peptide-like substrate: *N*-ethylacetamide.

On the other hand, the main residues involved in the reaction mechanism have to be identified and taken into account in the design of the active center. It should be emphasized that the catalytic properties of the enzyme are a consequence of the stabilizing interactions of the substrate with several key residues. If one of these key groups is not included, the catalytic behaviour is not reproduced by the theoretical calculations, this fact suggesting that the real enzyme would not work in absence of this residue. The role of arginine 127 in the hydrolysis of peptides catalyzed by CPA can be a good example of this point.

1. F. Quiocho and W.N. Lipscomb. Adv. Protein Chem. **25**, 1, (1971).
2. S. Blackburn. Enzymes: Struct. Funct. **3**, 169 (1976).
3. M.W. Makinen, G.B. Wells, and S.O. Kang. Adv. Inorg. Biochem. **6**, 1 (1984).
4. D.S. Auld and B.L. Vallee. New Compr. Biochem. **16**, 201 (1987).
5. D.W. Christianson and W.N. Lipscomb. Acc. Chem. Res. **22**, 62 (1989).
6. J. Suh. Bioorg. Chem. **18**, 345 (1990).
7. D.C. Rees, M. Lewis, and W.N. Lipscomb. J. Mol. Biol. **160**, 367 (1983).
8. D.W. Christianson and W.N. Lipscomb. J. Am. Chem. Soc. **108**, 4998 (1986).
9. H. Kim and W.N. Lipscomb. Biochemistry, **29**, 5546 (1990).
10. H. Kim and W.N. Lipscomb. Biochemistry, **30**, 8171 (1991).
11. L.C. Kuo, J.M. Kukuyama, and M.W. Makinen. J. Mol. Biol. **163**, 63 (1983).
12. N. Abramowitz and I. Schechter. Isr. J. Chem. **12**, 543 (1974).
13. N. Abramowitz, I. Schechter, and A. Berger. Biochem. Biophys. Res. Commun. **29**, 862 (1967).
14. I. Schechter. Eur. J. Biochem. **14**, 516 (1970).
15. D.C. Rees, M. Lewis, R.B. Honzatko, and W.N. Lipscomb. Proc. Natl. Acad. Sci. U.S.A. **78**, 3408 (1981).
16. L.C. Kuo and M.W. Makinen. J. Am. Chem. Soc. **107**, 5255 (1986).
17. S.J. Gardell, C.S. Craik, D. Hilbert, M.S. Urdeo, and W.J. Rutter. Nature, **317**, 551 (1985).
18. S.J. Gardell, D. Hilbert, J. Barnett, E.T. Kaisser, and W.J. Rutter. J. Biol. Chem. **262**, 576 (1987).
19. M.A. Phillips, R. Fletterick, and W.J. Rutter. J. Biol. Chem. **265**, 20692 (1990).
20. M.A. Phillips, A.R. Kaplan, W.J. Rutter, and P.A. Barlett. Biochemistry, **31**, 959 (1992).
21. M.A. Phillips, L. Hedstrom, and W.J. Rutter. Protein Sci. **1**, 517 (1992).
22. D. Hilbert, S.J. Gardell, W.J. Rutter, and E.T. Kaisser. J. Am. Chem. Soc. **108**, 5298 (1986).
23. S. Nakagawa and H. Umeyama. J. Am. Chem. Soc. **100**, 7716 (1978).
24. L. Banci, S. Schröder, and P.A. Kollman. Proteins, **13**, 288 (1992).
25. B.M. Britt and W.L. Peticolas. J. Am. Chem. Soc. **114**, 5295 (1992).

Can. J. Chem. Downloaded from www.nrcresearchpress.com by 85.192.166.187 on 09/08/12
For personal use only.

26. W.L. Mock and T.Z. Zhang. J. Biol. Chem. **266**, 6393 (1991).
27. A. Schepartz and R. Breslow. J. Am. Chem. Soc. **109**, 1814 (1987).
28. M.E. Sander and H. Witzel. Biochem. Biophys. Res. Commun. **132**, 681 (1985).
29. J. Suh, T.H. Park, and B.K. Hwang. J. Am. Chem. Soc. **114**, 5141 (1992).
30. D.S. Auld, A. Galdes, K.F. Geoghegan, B. Holmquist, R.A. Martinelli, and B.L. Vallee. Proc. Natl. Acad. Sci. U.S.A. **81**, 5041 (1984).
31. D.M. Hayes and P.A. Kollman. J. Am. Chem. Soc. **98**, 7811 (1976).
32. S. Scheiner and W.N. Lipscomb. J. Am. Chem. Soc. **99**, 3466 (1977).
33. S. Nakagawa, H. Umeyama, K. Kitaura, and K. Morokuma. Chem. Pharm. Bull. **29**, 1 (1981).
34. A. Alex and T. Clark. J. Comput. Chem. **13**, 704 (1992).
35. M.J.S. Dewar, E.G. Zoebisch, E.F. Healy, and J.J.P. Stewart. J. Am. Chem. Soc. **107**, 13 (1985).
36. D.A. Liotard, E.F. Healy, J.M. Ruiz, and M.J.S. Dewar. AMPAC version 2.1. Quantum Chemistry Program Exchange, Program 506, QCPE Bull. **9**, 123 (1989).
37. R. Fletcher and M.J.D. Powell. Comput. J. **6**, 163 (1963).
38. W.C. Davidon. Comput. J. **10**, 406 (1968).
39. J.W. McIver and A. Komornicki. J. Am. Chem. Soc. **94**, 2625 (1972).
40. D.C. Rees, and W.N. Lipscomb. Proc. Natl. Acad. Sci. U.S.A. **80**, 7151 (1983).
41. J.P. Ryckaert, G. Ciccotti, and H.J.C. Berendsen. J. Comput. Phys. **23**, 327 (1977).
42. W.F. Van Gunsteren and H.J.C. Berendsen. Groningen molecular simulation (GROMOS) library manual. Biomos, Groningen, The Netherlands. 1987.
43. T. Åqvist, W.F. Van Gunsteren, M. Leijonmark, and O. Tapia. J. Mol. Biol. **83**, 461 (1985).
44. O. Nilsson, O. Tapia, and W.F. Van Gunsteren. Biochem. Biophys. Res. Commun. **171**, 581 (1990).
45. H.J.C. Berendsen, J.P.M. Postma, W.F. Van Gunsteren, A. Dinola, and T.R. Haak. J. Chem. Phys. **81**, 3684 (1984).
46. A. Ritter von Onciul and T. Clark. J. Comput. Chem. **14**, 392 (1993).

Can. J. Chem. Downloaded from www.nrcresearchpress.com by 85.192.166.187 on 09/08/12
For personal use only.

Structural studies on dioxan-2-ylium ions; intramolecular attack of an oxygen atom on a carbenium ion centre

RONALD F. CHILDS,[1] GUOGONG J. KANG, TERESA A. WARK, AND CHRISTOPHER S. FRAMPTON
Department of Chemistry, McMaster University, Hamilton, ON L8S 4M1, Canada

Received January 18, 1994

RONALD F. CHILDS, GUOGONG J. KANG, TERESA A. WARK, and CHRISTOPHER S. FRAMPTON. Can. J. Chem. **72**, 2084 (1994).

As models for the ionization of orthoesters, a series of 1,3-dioxan-2-ylium salts have been prepared and characterized. The properties of 1,3-dioxan-2-ylium hexachloroantimonate **1**, 5-ethoxymethyl-1,3-dioxan-2-ylium hexachloroantimonate **2**, 2-methyl-5-ethoxymethyl-1,3-dioxan-2-ylium hexachloroantimonate **3**, and 2-phenyl-5-ethoxymethyl-1,3-dioxan-2-ylium hexachloroantimonate **4**, have been studied by ^{1}H and ^{13}C NMR spectroscopy. The structures of **3** and **4** have been determined using X-ray crystallography. Salts **3** and **4** both crystallize in monoclinic crystal systems. For **3**, the space group is *C*2/*c*, with a = 30.192(4) Å, b = 9.613(2) Å, c = 12.742(2) Å, β = 109.71(1)°, V = 3482(1) Å^3, and Z = 8. Complex **4** crystallizes in the space group $P2_1/n$, with a = 10.638(2) Å, b = 11.849(2) Å, c = 16.970(3) Å, β = 106.84(1)°, V = 2047(1) Å^3, and Z = 4. The geometries of **3** and **4** are similar with the ether oxygen disposed over the dioxan-2-ylium ring. However, the interaction between the ether oxygen and the cationic centre is not significant due to the large internuclear distance observed. The cation **5**, in which the carbon chain length between the ether oxygen and C(5) was increased, was prepared. This ion was found to undergo a reversible, intramolecular rearrangement resulting in the formation of 1-methyl-4-acetoxymethyl-tetrahydrofuranyl oxonium hexachloroantimonate **11**.

RONALD F. CHILDS, GUOGONG J. KANG, TERESA A. WARK et CHRISTOPHER S. FRAMPTON. Can. J. Chem. **72**, 2084 (1994).

On a préparé et caractérisé une série de sels 1,3-dioxan-2-ylium comme modèles pour l'ionisation des orthoesters. Faisant appel à la RMN du ^{1}H et du ^{13}C, on a étudié les propriétés de l'hexachloroantimonate du 5-éthoxyméthyl-1,3-dioxan-2-ylium (**1**) de l'hexachloroantimonate du 5-éthoxyméthyl-1,3-dioxan-2-ylium (**2**), de l'hexachloroantimonate du 2-méthyl-5-éthoxyméthyl-1,3-dioxan-2-ylium (**3**) et de l'hexachloroantimonate du 2-phényl-5-éthoxyméthyl-1,3-dioxan-2-ylium (**4**). On a déterminé les structures des composés **3** et **4** par diffraction des rayons X. Les sels **3** et **4** cristallisent tous les deux dans le système monoclinique. Pour le composé **3**, le groupe d'espace est *C*2/*c*, avec a = 30,192(4), b = 9,613(2) et c = 12,742(2) Å, β = 109,71(1)°, V = 3482(1) Å^3 et Z = 8. Pour le composé **4**, le groupe d'espace est $P2_1/n$, avec a = 10,638(2), b = 11,849(2) et c = 16,970(3) Å, β = 106,84(1)°, V = 2047(1) Å^3 et Z = 4. Les géométries des composés **3** et **4** sont semblables et l'oxygène de l'éther est disposé au-dessus du cycle dioxan-2-ylium. Toutefois, l'interaction entre l'oxygène de l'éther et le centre cationique n'est pas important du à la grande distance internucléaire qui est observée. On a préparé le cation **5** dans lequel la longueur de la chaîne carbonée entre l'oxygène de l'éther et le C(5) est augmentée. On a trouvé que cet ion subit un réarrangement intramoléculaire réversible conduisant à la formation de l'hexachloroantimonate du 1-méthyl-4-acétoxyméthyl-tétrahydrofuranyl oxonium.

[Traduit par la rédaction]

Introduction

The acid-catalysed reactions of carboxylic acids, carboxylic acid derivatives, and orthoesters involve the transient formation of carbenium ions with two oxygen-containing substituents (1). These substituents can be either hydroxy, alkoxy, aryloxy, or combinations of these groupings depending on the nature of the reaction under consideration. The overall acid-catalysed transformations of the carboxylic acid family of functional groups normally involves the formation and reaction of a cascade of di-oxygen-substituted carbenium ions. A commonly encountered reversible step in these transformations involves the reaction of an intermediary cation with a Lewis base to give a tri-oxygen-substituted species, eq. [1].

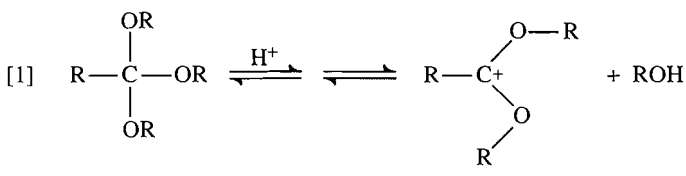

The formation and reverse ionization of orthoesters is a good example of the acid-catalyzed transformation of carboxylic acid derivatives. The steric requirements of this type of reaction have been extensively studied by Deslongchamps and co-workers (2). These workers have advanced the theory of stereoelectronic control in order to account for the selectivities observed in the reactions of cyclic materials (3).

In previous papers in this series we have reported the determination of the structures of a series of oxygen-substituted carbenium ions using X-ray diffraction techniques (4, 5). Not only are these structures informative about the geometry and charge distribution of the cations but the crystal packing in the lattice provides information on the attack of a nucleophile on this type of cation. In most crystal lattices a planar carbenium-ion carbon is found to be situated between two anions, one above and one below the carbenium-ion plane, with a Lewis base atom in the anion interacting with the positive centre. A limited number of examples have been found where a carbenium-ion centre has only a single Lewis base atom in close proximity and in these instances there is a small degree of pyramidalization of the cationic centre (6). In all the instances studied thus far it has been found that the cation–anion distances are not only very similar, but are typically close to the sum of the van der Waals radii of the carbenium carbon and the "attacking" Lewis base atom of the counterion.

In principle, if examples of carbenium ions could be found in which the distance between the cationic centre and a Lewis base atom was significantly reduced from the sum of the appropriate van der Waals radii, then the geometric changes associated with movement along the reaction coordinate of one of these ionization reactions could be probed. Such a study would not only par-

[1]Author to whom correspondence may be addressed. Telephone: (905)525-9140 ext. 27270.

Can. J. Chem. Downloaded from www.nrcresearchpress.com by 85.192.166.187 on 09/08/12
For personal use only.

TABLE 1. ^{1}H NMR data for 1,3-dioxan-2-ylium hexachloroantimonate and derivatives[a] (*J*, Hz)

	C(2)	C(4)/C(6)	C(5)	C(7)	C(9)[e]	C(10)	C(11)
1[b]	9.13	5.23	2.81				
2[c]	8.98	5.35(4.6, 11.8) 5.18(4.2, 11.8)	3.11	3.82(3)	3.49(7)	1.14(7)	
3[c]		5.18(4.5, 11.7) 5.04(4.2, 11.7)	2.99	3.81(3)	3.49(7)	1.15(7)	2.69
4[c,d]		5.39(4.5, 11.8) 5.24(4.0, 11.8)	3.05	3.83(3)	3.38(7)	0.80(7)	
5[b]		5.16(4.8, 11.5) 4.83(10.8, 11.5)	2.90	1.78	3.49	3.33	2.72

[a]Chemical shifts given in ppm.
[b]CD_3NO_2, −10°C.
[c]CD_2Cl_2, −10°C.
[d]Chemical shifts for the phenyl ring protons: C(12)/C(16) 8.18 ppm, C(13)/C(15) 7.67 ppm, C(14) 7.97 ppm.
[e]For **5**, the chemical shift is given for the protons on C(8).

allel in cationic systems the pioneering work of Dunitz and co-workers on the reactions of a neutral carbonyl compound with a nitrogen nucleophile (7) but would provide a greatly expanded dimension to the structural work on ionization processes reported by Kirby and co-workers (8).

In the work described in this present paper we describe the preparation and structure determination of some stable dialkoxy-substituted carbenium ions in which there is an intramolecular ether oxygen atom positioned so that it can undergo nucleophilic attack on the positive centre. It was our hope, by providing an appropriately positioned intramolecular Lewis base, to be able to prepare a series of cations in which there could be a close association of the cationic centre and the "attacking" atom. The cyclic systems chosen for study should also provide information on the related orthoester ionizations studied by Deslongchamps and co-workers (2).

Results and discussion

The strategy used in this work was to prepare a series of 5-substituted 1,3-dioxan-2-ylium cations in which the substituent at C(5) would contain an ether oxygen atom. By varying the chain length of the C(5) group and altering the stability of the carbenium ion by changing the substituent on C(2), the cationic centre, it was hoped to be able to control the degree of interaction between the ether oxygen and the charged centre.

The preparation and characterization of 1,3-dioxan-2-ylium ions has previously been described (9). In this work we attempted to prepare the cations **1–5** by ionization of the corresponding 2-ethoxy-1,3-dioxanes **6–10** with $SbCl_5$ in CH_2Cl_2, eq. [2].

[2] 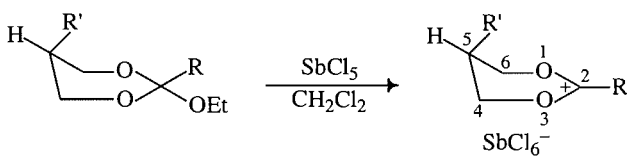

6	R = R' = H	**1**
7	R = H, R' = $CH_2OCH_2CH_3$	**2**
8	R = CH_3, R' = $CH_2OCH_2CH_3$	**3**
9	R = C_6H_5, R' = $CH_2OCH_2CH_3$	**4**
10	R = CH_3, R' = $CH_2CH_2OCH_3$	**5**

The dioxane **6** is a known compound (10). In the case of **7–10** the dioxanes were prepared via a method similar to that of Boering and Levy (11) involving reaction of the appropriately substituted 1,3-propanediol with an orthoester, eq. [3].

[3] $R'—CH(CH_2OH)_2 \xrightarrow[R—C(OEt)_3]{} \mathbf{6–10}$

R = H, CH_3, C_6H_5
R' = H, $CH_2OCH_2CH_3$, $CH_2CH_2OCH_3$

Cations **1–4** were readily prepared as stable, moisture-sensitive solids by using a similar procedure to that described by Meerwein et al. (9*a*). The salts were purified by washing several times with carbon tetrachloride, yielding colourless solids. Proton and carbon-13 NMR spectra of solutions of **1–4** were obtained and in each case the spectra were consistent with the assigned structures, Tables 1 and 2. The ^{1}H and ^{13}C chemical shifts found here for the dioxanylium ring atoms are similar to those described by Chalova et al. (9*b*) for 1,3-dioxan-2-ylium tetrafluoroborate and by Paulsen and Schuttpelz for 2-methyl- and 2-phenyl-1,3-dioxan-2-ylium perchlorates (5*c*). The ring proton NMR shifts of **1** and **3** are shifted downfield as compared to those of the corresponding 1,3-dioxanes (12).

Paulsen and Schuttpelz suggested, on the basis of MINDO calculations and an analysis of coupling constants, that 1,3-dioxan-2-ylium cations adopt an envelope conformation in which C(4)-C(5)-C(6) forms the flap and the 5-alkyl substituents preferentially adopt a pseudo-equatorial position, eq. [4]

[4] 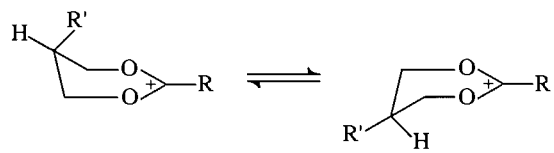

(9*b*). In the case of **2**, **3**, and **4** it would appear from the ^{1}H NMR spectra that each of these cations adopts a single conformation in solution. The resonances of the methylene protons at C(4) (and C(6)) of **2–4** are different, occurring at different chemical shifts from each other (9*b*). Each of the methylene proton resonances occurs as a doublet of doublets. The largest coupling constant observed (11.7–11.8 Hz) corresponds to the geminal coupling constant between the two methylene protons. The smaller coupling constant (4.0–4.6 Hz) represents coupling between the proton on C(5) and each of the methylene protons. The magnitude of this smaller coupling constant and the fact that the cou-

Can. J. Chem. Downloaded from www.nrcresearchpress.com by 85.192.166.187 on 09/08/12
For personal use only.

TABLE 2. ^{13}C NMR data for 1,3-dioxan-2-ylium hexachloroantimonate and derivatives[a]

	C(2)	C(4)/C(6)	C(5)	C(7)	C(9)[e]	C(10)	C(11)
1[b]	176.9	75.6	21.5				
2[c]	174.6	76.6	30.2	69.9	67.7	14.9	
3[c]	187.9	76.6	29.8	70.7	67.9	15.1	22.8
4[c,d]	177.3	75.8	30.0	70.5	67.5	14.6	122.4
5[b]	Not observed	78.3	29.6	28.0	70.4	59.0	22.4

[a]Chemical shifts given in ppm.
[b]CD_3NO_2, −10°C.
[c]CD_2Cl_2, −10°C.
[d]Chemical shifts for the phenyl ring carbon atoms: C(12)/C(16) 131.8 ppm, C(13)/C(15) 130.2 ppm, C(14) 140.2 ppm.
[e]For **5**, the chemical shift is given for C(8).

pling constants between either C(5)-H and the pseudo-equatorial or pseudo-axial methylene protons is almost the same indicates that for cations **2**–**4** the C(5) substituents are in the pseudo-axial positions (13). Thus the oxygen-containing C(5) substituents in **2**–**4** adopt a different conformation to that found by Paulsen and Schuttpelz for 5-alkyl-substituted 1,3-dioxan-2-ylium cations (9*b*). It would seem clear that some form of interaction of the oxygen substituent in the C(5) substituent of these cations with the positive centre at C(2) is sufficient to overcome the steric preference for the equatorial conformation in 5-alkyl-substituted 1,3-dioxan-2-ylium ions.

Comparison of the ^1H NMR spectra of **2** with its precursor **7** is instructive in determining the nature of the interaction of the oxygen-containing C(5) substituent with the cationic centre. As can be seen from the data in Table 1, the largest downfield shifts occurring on ionization of **7** are those associated with H(2), H(4), and H(6). Such downfield shifts are expected in the formation of a cation such as **2**. On the other hand, little perceptible change in chemical shift is observed with H(9), suggesting that there is no significant transfer of positive charge to the ether oxygen in **2**. This conclusion is substantiated by the structural work described later. Comparison of the ^1H and ^{13}C NMR chemical shifts, Tables 1 and 2, respectively, of the various resonances associated with the C(5) substituent indicates that there are no significant differences attributable to substituent variation at C(2).

Structure determinations

The crystal structures of **3** and **4** were determined by X-ray crystallographic methods with diffraction data being collected at low temperatures. Crystal data, atomic positional parameters, and selected bond distances and angles for the two salts are given in Tables 3, 4, and 5, respectively. The structures of the two cations are shown in Figs. 1 and 2. Data on important planes are summarized in Table 6. Full details of the structure solutions are given in the experimental section and the supplementary material deposited with this paper (see footnote 4).

Examination of Figs. 1 and 2 shows that in each cation the dioxanylium ring adopts an envelope conformation with C(4)-C(5)-C(6) forming the flap. The conformation of both cations can be understood in terms of three planes. Atoms O(1), C(2), O(3), and C(11) lie in a plane (plane *A*) with a maximum deviation of 0.006 Å. A second plane, *B*, is formed by O(3), C(4), C(6), and O(1) and the third plane, *C*, by C(4), C(5), and C(6). The angles between planes *A* and *B* in **3** and **4** are 3.3° and 6°, respectively, whereas those between planes *A* and *C* are 129.1° for **3** and 126.3° for **4**. It is interesting that the dihedral angle between the envelope flap (C(4)-C(5)-C(6)) and the base of the envelope (O(1)-O(3)-C(4)-C(6)) for trimethylene carbonate is 47°, which is the same as found for **3** and **4** (47.8°) (14).

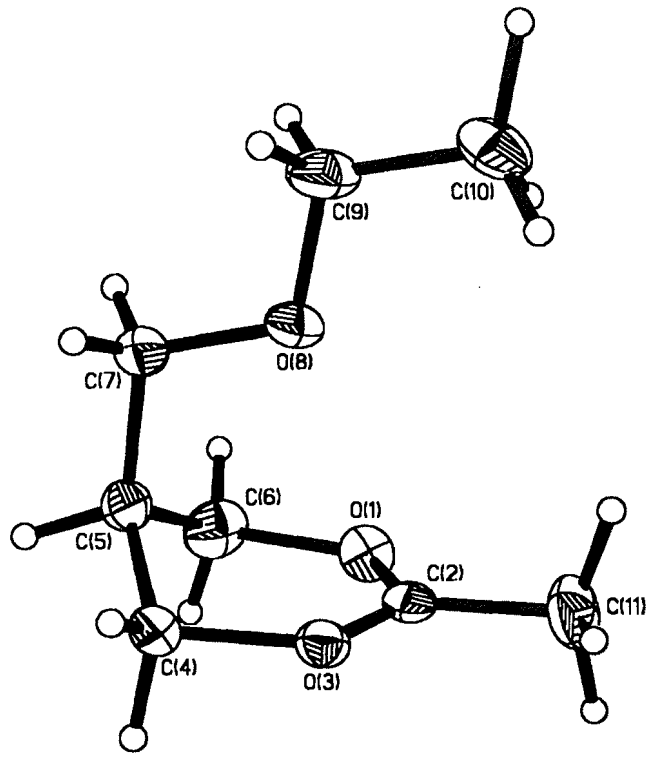

FIG. 1. Thermal ellipsoid plot for **3**.

Within the ring for **3** and **4**, the corresponding bond lengths found are not significantly different from one another. The O(1)—C(6) bond distances of 1.491(8) Å in **3** and 1.471(5) Å in **4** and the O(3)—C(4) bond distances of 1.470(7) Å in **3** and 1.481(5) Å in **4** are similar to one another, but longer than those found in corresponding neutral esters.[2] The average $-H_2C—O-$ distance in **3** and **4** is 1.478(17) Å,[2] significantly greater than that of 1.428 Å found in the silver hexafluoroantimonate complex of 1,3-dioxane $\{[Ag(1,3\text{-}C_4H_8O_2)_3]AsF_6\}$. However, in this silver complex the oxygen atoms are bonded to the metal centre.

The O(1)—C(2)/O(3)—C(2) bond distances in both cations are intermediate between those of C—O single and double

[2]The errors for mean bond lengths are given by $\sigma_D = (\Sigma_n(D - d_n)^2/n(n-1))$, where D is the mean bond distance of n independent variables.

Can. J. Chem. Downloaded from www.nrcresearchpress.com by 85.192.166.187 on 09/08/12
For personal use only.

TABLE 3. Crystal data for 2-methyl-5-ethoxymethyl-1,3-dioxan-2-ylium hexachloroantimonate and 2-phenyl-5-ethoxymethyl-dioxan-2-ylium hexachloroantimonate

Formula	$C_8H_{15}O_3SbCl_6$	$C_{13}H_{17}O_3SbCl_6$
FW, g mol^{-1}	493.65	555.7
Colour; habit	Colourless; plate	Colourless; plate
Crystal size, mm	0.25 × 0.20 × 0.15	0.5 × 0.5 × 0.2
System	Monoclinic	Monoclinic
Space group	*C2/c*	$P2_1/n$
a, Å	30.192(4)	10.638(2)
b, Å	9.613(2)	11.849(2)
c, Å	12.742(2)	16.970(3)
β, deg	109.71(1)	106.84(1)
V, Å^3	3482(1)	2047(1)
Z	8	4
D_c, g cm^{-1}	1.88	1.80
F(000)	1920	1088
Diffractometer	Nicolet P3	Siemens R3m/V
Temperature, K	187	173
Radiation	MoKα (λ = 0.710 69 Å)	AgKα (λ = 0.560 86 Å)
μ, cm^{-1}	25.07 (MoKα)	21.39 (AgKα)
No. of reflections used in cell determination	15 (22.5° < 2θ < 29.9°)	23 (14.6° < 2θ < 35.0°)
Standard reflections	2 every 48 reflections	3 every 97 reflections
Data collected	*h*, ±*k*, ±*l*	*h*, *k*, ±*l*
Maximum 2θ reflections collected	45°	45°
Reflections collected	5043	5748
Independent reflections	2279	5443
Observed reflections	1991 $I > 2.5\sigma(I)$	3355 $F > 6.0\sigma(F)$
Absorption correction	N/A	Semi-empirical
Min/Max transmission	N/A	0.4579/0.5461
R_{int}[a]	0.0144	0.0143
Largest and mean *D*/*R*	0.055, 0.002	0.004, 0.000
No. of variables	211	267
R_1, R_2 (%)	3.13, 3.35	2.97, 4.04
Weighting scheme	$\omega = (\sigma^2F + 0.000322F^2)^{-1}$	$\omega = (\sigma^2F + 0.0035F^2)^{-1}$
Highest peak, e Å^{-3}	0.735	0.83
Lowest peak, e Å^{-3}	−0.70	−0.40

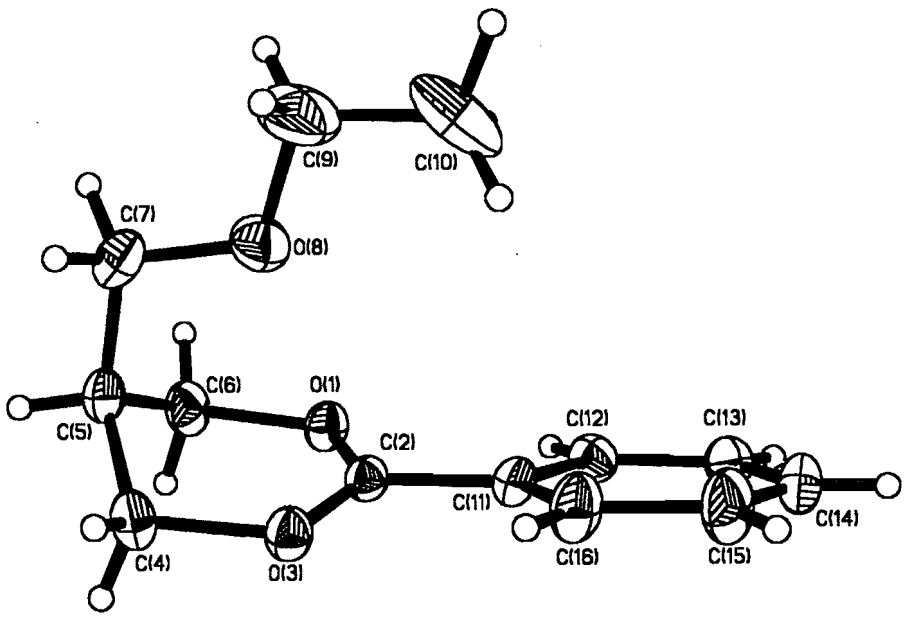

Fig. 2. Thermal ellipsoid plot for **4**.

bonds (15). It is interesting that the O(1)—C(2) bond distances (1.281(7) Å in **3** and 1.279(5) Å in **4**) and O(3)—C(2) (1.274(7) Å in **3** and 1.276(5) Å in **4**) are all the same within the error limits of the structure determinations. The average C—O bond length is 1.276(6) Å, which is significantly smaller than the corresponding value of 1.386 Å found for the silver complex of 1,3-dioxane (16).

The C^+—O and -H_2C—*O*- distances within the ring do not

Can. J. Chem. Downloaded from www.nrcresearchpress.com by 85.192.166.187 on 09/08/12
For personal use only.

Can. J. Chem. Downloaded from www.nrcresearchpress.com by 85.192.166.187 on 09/08/12
For personal use only.

TABLE 4. Atomic coordinates ($\times 10^4$) and equivalent isotropic displacement coefficients ($Å^2 \times 10^3$)

(*a*) 2-Methyl-5-ethoxymethyl-1,3-dioxan-2-ylium hexachloroantimonate

	x	*y*	*z*	*U*(eq)[a]
Sb(1)	0	3219(1)	2500	30(1)
Sb(2)	7500	2500	0	20(1)
Cl(1)	507(1)	1454(2)	2237(1)	45(1)
Cl(2)	−412(1)	3189(3)	578(1)	77(1)
Cl(3)	513(1)	4944(2)	2269(2)	81(1)
Cl(4)	2597(1)	9011(2)	8618(1)	43(1)
Cl(5)	2342(1)	5658(2)	8688(1)	54(1)
Cl(6)	3304(1)	6949(3)	10602(1)	65(1)
O(1)	863(1)	3311(4)	10060(3)	38(2)
O(3)	1048(1)	1031(4)	10397(3)	32(1)
O(8)	1481(1)	2308(4)	8975(3)	34(2)
C(2)	773(2)	2011(7)	9901(5)	33(2)
C(4)	1512(2)	1344(8)	11219(5)	42(3)
C(5)	1696(2)	2697(7)	10934(5)	38(2)
C(6)	1332(3)	3789(8)	10820(6)	50(3)
C(7)	1868(2)	2583(8)	9947(5)	39(3)
C(9)	1615(3)	2179(8)	8007(6)	46(3)
C(10)	1193(3)	1952(9)	7013(6)	52(3)
C(11)	323(3)	1651(9)	9050(7)	55(3)

(*b*) 2-Phenyl-5-ethoxymethyl-1,3-dioxan-2-ylium hexachloroantimonate

	x	*y*	*z*	*U*(eq)[a]
Sb	113(1)	1828(1)	2317(1)	30(1)
Cl(1)	−1481(1)	3260(1)	2165(1)	48(1)
Cl(2)	1704(1)	370(1)	2497(1)	38(1)
Cl(3)	1289(1)	2553(1)	3620(1)	49(1)
Cl(4)	−1160(1)	674(1)	2931(1)	42(1)
Cl(5)	1355(1)	2979(1)	1688(1)	50(1)
Cl(6)	−1002(1)	1064(1)	1006(1)	42(1)
O(1)	−4182(3)	3405(2)	4629(2)	34(1)
O(3)	−3102(3)	3207(2)	3661(2)	36(1)
O(8)	−3556(3)	1176(3)	4360(2)	51(1)
C(2)	−3146(3)	3408(3)	4391(2)	30(1)
C(4)	−4288(4)	2805(4)	3025(3)	40(1)
C(5)	−5218(4)	2236(4)	3428(3)	41(1)
C(6)	−5433(4)	3024(4)	4059(3)	41(1)
C(7)	−4764(6)	1079(4)	3754(4)	58(2)
C(9)	−2932(9)	159(5)	4701(5)	79(3)
C(10)	−1651(8)	407(7)	5293(4)	94(3)
C(11)	−1913(4)	3676(3)	5009(3)	33(1)
C(12)	−1920(4)	4174(4)	5750(3)	38(1)
C(13)	−730(5)	4417(4)	6318(3)	44(2)
C(14)	437(5)	4131(5)	6175(3)	53(2)
C(15)	436(5)	3617(6)	5449(3)	57(2)
C(16)	−737(4)	3398(5)	4850(3)	47(2)

[a]Equivalent isotropic *U* defined as one third of the trace of the orthogonalized U_{ij} tensor.

display a significant dependence on the substituent at C(2). Previous results obtained with 2-phenyl-1,3-dioxolan-2-ylium trifluoromethanesulfonate and 2-methyl-1,3-dioxolan-2-ylium perchlorate showed a significant difference between the corresponding bond lengths in the methyl- and phenyl-substituted ions (4*c*). It is not clear why no corresponding difference in the C^+—O bonds is observed with **3** and **4**.

Compound **4** has a twist angle of 17.3° between the -O-C^+-O- portion of the molecule and the phenyl ring. This is larger than the corresponding angle of 2° found from the single crystal study of 2-phenyl-1,3-dioxolan-2-ylium trifluoromethanesulfonate (4) and from MM2 calculations for the corresponding neutral benzoates (17). However, the twist angle in **4** is smaller than the twist angle found between the dialkoxycarbenium fragment and the aryl portion of the molecules for diethoxyphenylmethylium hexachloroantimonate (38.9°), dimethoxy-*p*-methoxyphenylmethylium hexachloroantimonate (30.5°), and diethoxy-2,4,6-trimethyphenylmethylium hexachloroantimonate (64.6°) (18).

As can be seen from Figs. 1 and 2, in both **3** and **4** the 5-ethoxymethyl substituent has adopted a pseudo-axial conformation in the crystal lattice. This conformation is in accord with the finding of the solution NMR studies discussed above. In each case the oxygen atom of the ethoxymethyl substituent is located over the top of the cationic centre of the ions. Atoms C(7), O(8), C(9), and C(10) of the ethoxymethyl groups form a

TABLE 5. Selected bond lengths (Å) and angles (degrees) for **3** and **4**

Atoms	3	4	Atoms	3	4
		Bond lengths (Å)			
O(1)—C(2)	1.281(7)	1.279(5)	C(2)—O(3)	1.274(7)	1.276(5)
C(2)—C(11)	1.465(9)	1.458(5)	O(3)—C(4)	1.470(7)	1.481(5)
O(1)—C(6)	1.491(8)	1.471(5)	C(4)—C(5)	1.506(9)	1.514(7)
C(5)—C(6)	1.491(10)	1.488(7)	C(5)—C(7)	1.519(9)	1.505(7)
C(7)—O(8)	1.412(7)	1.398(6)	O(8)—C(9)	1.427(7)	1.415(7)
C(9)—C(10)	1.478(11)	1.469(10)	O(8)..O(1)	2.840	2.794
O(8)..C(2)	2.783	2.679	O(8)..O(3)	2.846	2.788
		Bond angles (degrees)			
O(1)—C(2)—C(11)	116.3(6)	116.9(4)	O(3)—C(2)—C(11)	118.6(6)	117.4(4)
O(1)—C(2)—O(3)	125.1(5)	125.7(3)	C(2)—O(3)—C(4)	120.5(5)	120.3(3)
C(2)—O(1)—C(6)	120.5(5)	119.4(3)	O(3)—C(4)—C(5)	110.2(5)	110.1(3)
O(1)—C(6)—C(5)	110.7(5)	111.6(3)	C(4)—C(5)—C(7)	113.3(6)	112.9(4)
C(6)—C(5)—C(7)	114.7(6)	114.0(4)	C(4)—C(5)—C(6)	108.2(5)	107.6(4)
C(5)—C(7)—O(8)	109.0(5)	108.9(4)	C(7)—O(8)—C(9)	112.5(5)	116.9(4)
O(8)—C(9)—C(10)	109.9(6)	110.0(6)			

TABLE 6. Least-squares planes for **3** and **4**

	Planes[a]				Dihedral angle between planes[b]		
Compound	*A*	*B*	*C*	*D*	*A* and *B*	*A* and *C*	*A* and *D*
3	O(1) −0.002	O(3) −0.018	C(4) 0.00	C(7) 0.013	3.3	129.0	86.2
	C(2) 0.006	C(4) 0.017	C(5) 0.00	O(8) −0.013			
	O(3) −0.002	C(6) −0.017	C(6) 0.00	C(9) −0.011			
	C(11) −0.002	O(1) 0.018		C(10) 0.012			
4	O(1) 0.001	O(3) 0.002	C(4) 0.00	C(7) −0.017	6.0	126.3	86.4
	C(2) −0.004	C(4) −0.002	C(5) 0.00	O(8) 0.020			
	O(3) 0.001	C(6) 0.002	C(6) 0.00	C(9) 0.014			
	C(11) 0.001	O(1) −0.002		C(10) −0.016			

[a]Displacements given in angstrom units (Å).
[b]Angles given in degrees.

fourth plane, *D*, in each cation. The angles between planes *D* and *A* in **3** and **4** are 86.2° and 86.4°, respectively. The conformation of the ethoxymethyl group in each cation is such that plane *D* bisects the six-membered dioxanylium ring in such a way as to place the ether oxygen atom O(8) approximately equidistance from O(1) and O(2) and over C(2).

Examination of the bond distances and angles for the ethoxymethyl substituent gives an indication of the degree of interaction between the oxygen in this fragment and the cationic centre. The angle at C(7)-O(8)-C(9) is 112.5(5)° for **3** and 116.9(4)° for **4**. These values are similar to those reported for diethyl ether in a crystal lattice (19). As well, the corresponding C—C and C—O bond lengths in **3** and **4** are similar to those found for diethyl ether (19). This would indicate that the interaction between the ether oxygen of the dioxan-2-ylium cation and the cationic centre is not strong enough to perturb the ether geometry. The C(2)—O(8) distances in **3** (2.783 Å) and **4** (2.679 Å) are long and close to the sum of the van der Waals radii of the two atoms. In oxonium ions the C—O distances are typically short. For example, in Et_3O^+ the average C—O distance is 1.47 Å, while in Ph_3O^+ it is 1.50 Å (20).

It is interesting that the ether oxygen atoms in both **3** and **4** are arranged nearly symmetrically over the carbenium carbon. This can be seen by examining the displacement of O(8) from the plane defined by C(2)-C(7)-C(9). The geometry of O(8) is planar with the oxygen out of the plane by 0.059 Å for **3** and 0.040 Å for **4**. Alkyl-substituted oxonium ions generally adopt a pyramidal conformation, while the triaryl-substituted oxonium ions are nearly planar. The conformations of **3** and **4** provide models of the early stages of the attack of an oxygen nucleophile on a dialkoxy-substituted carbenium ion.

The anions and cations in **3** and **4** pack as discrete molecules, as seen in Figs. 3 and 4, respectively. This is in contrast to other oxygen-substituted carbenium systems in which there is interaction between the cationic centre and the anion (4*c*). For **3**, the rows of cations pack with the six-membered rings parallel with the ether bridge directed toward the ring of the next ion. The direction of the rows alternates throughout the lattice. The two distinct anions pack between the cations rows as alternate rows. The closest nonbonded anion and cation interaction is 2.544 Å, between Cl(2) and one of the 2-methyl protons. However, the closest approach of the anion to the cationic centre is 3.381 Å (C(2) and Cl(1)).

For **4**, the cations pack as pairs of ions with the ether portions directed toward one another with the phenyl rings parallel, but not directly under one another. The closest nonbonded interaction between the anions and cations is Cl(3) and the phenyl ring proton H(6′) with a distance of 2.801 Å. The closest anion–cation contact involving the cationic centre is C(2) and Cl(6) at a distance of 3.290 Å. The closest distances between cations and

Can. J. Chem. Downloaded from www.nrcresearchpress.com by 85.192.166.187 on 09/08/12
For personal use only.

Can. J. Chem. Downloaded from www.nrcresearchpress.com by 85.192.166.187 on 09/08/12
For personal use only.

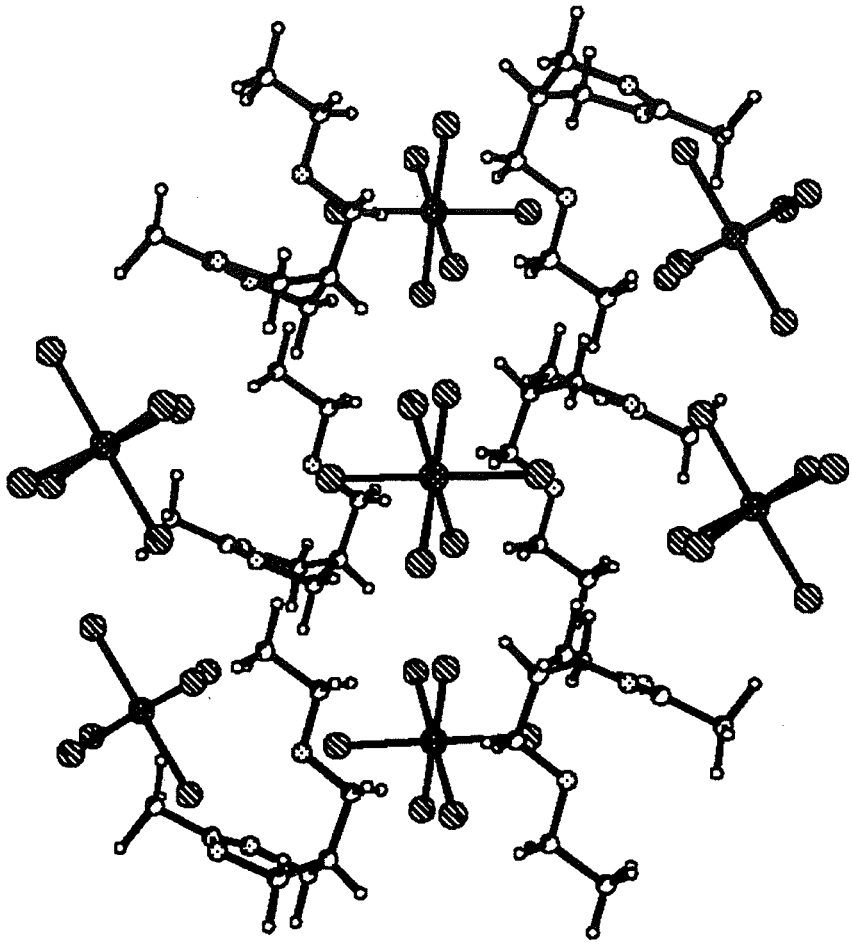

FIG. 3. Packing diagram for **3**.

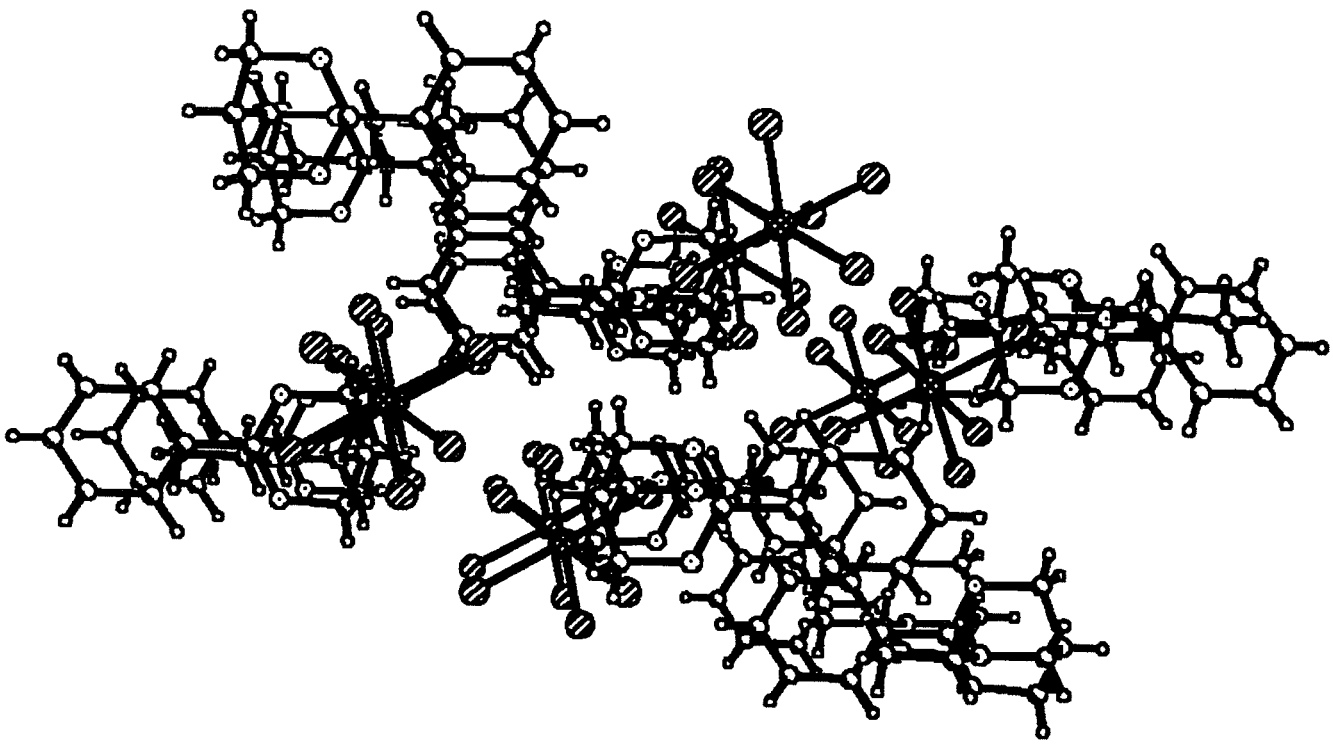

FIG. 4. Packing diagram for **4**.

Can. J. Chem. Downloaded from www.nrcresearchpress.com by 85.192.166.187 on 09/08/12
For personal use only.

anions for **3** and **4** are close to the sum of the van der Waals radii of the appropriate atoms. No significant interactions occur between the cations and anions and thus the anions do not help to stabilize the positive charge as was found for other systems (4).

Intramolecular rearrangement of 5

The ionization of dioxane **10** with $SbCl_5$ in CH_2Cl_2 appeared to proceed in the same manner as the reactions of **6–9** described above, with the formation of a colourless solid. However, ^1H NMR analysis of solutions of this solid in CD_2Cl_2 at −10°C revealed the presence of a mixture of cations, the minor component of which appeared to be **5**.

Recrystallization of the solid, followed by its careful dissolution at low temperatures in SO_2, and recording of its ^1H NMR spectrum at temperatures below −70°C showed that only a single cation was present. As the temperature of the solution was warmed above −70°C this cation isomerized to the same mixture as was isolated from the reaction mixture produced on the attempted formation of **5**. The cation obtained after dissolution of the recrystallized solid was identified as **11** on the basis of its ^1H NMR, ^{13}C NMR, and IR spectra. The proton NMR of **11** is similar to that of methyl tetrahydrofuranyl oxonium (21). From the peak at 1720 cm^{-1} in the IR spectrum and the resonance at 172.5 ppm in the ^{13}C NMR spectrum, it was determined that **11** contains a carbonyl group. The equilibrium is shown in eq. [5].

[5] 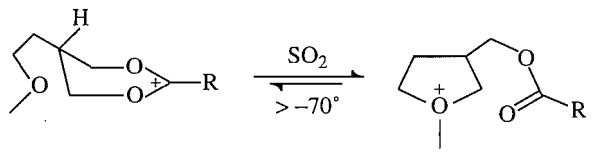

20% 80%

5 **11**

Comparison of the NMR spectra of the mixture of **5** and **11** with those of **11** on its own allowed for the determination of the NMR spectra for **5**. The spectra obtained were found to be similar to those reported for **1–4** with the exception of the resonances due to the terminal ether portion of the molecule. The major difference between the proton spectra for **5** and the other cations is the coupling of the ring methylene protons to the proton on C(5). A large coupling constant was found between H(5) and the protons on C(4)/C(6) (10.8 Hz/11.5 Hz). This large coupling constant indicates that the C(5) substituent of **5** preferentially adopts a pseudo-equatorial conformation.

The interconversion of **5** and **11** can be viewed as intramolecular nucleophilic substitution by an oxygen atom on a $-CH_2-O-$ fragment where the displaced oxygen atom formally carries a positive charge. Previous work in this laboratory has shown that the C—O bond of an alkoxy-substituted carbenium ion is longer than would normally be expected in a neutral system and that there is considerable transfer of positive charge onto the alkyl group, eq. [6] (4).

[6] 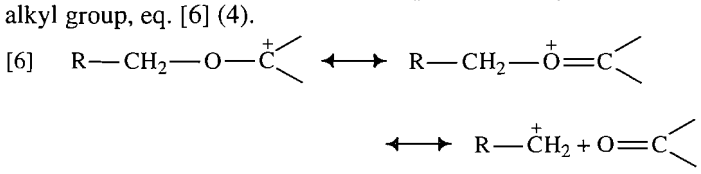

Experimental section

General methods

All manipulations were carried out under an N_2 atmosphere. Solvents were reagent grade, distilled from the appropriate drying agent prior to use. NMR experiments were recorded on a Bruker AM500 or a Bruker WM250 spectrometer using internal standards and chemical shifts are reported in δ (ppm).

Preparation of ethyl-2-ethoxymethyl malonate

To a suspension of 5.29 g of NaH in 150 mL of dry ether was slowly added 35.3 g of ethyl malonate with mechanical stirring at room temperature. The reaction was stirred for 3 h, cooled to 0°C, and $C_2H_5OCH_2Cl$ (25 g in 25 mL of dry ether) was added slowly with vigorous stirring. After the mixture was stirred for 1 h, water was added, the ether layer was separated, and the aqueous layer was washed with ether. The combined ethereal extracts were washed with water and dried with $MgSO_4$. After the ethereal extracts were dry, the solution was concentrated by rotary evaporator and the vacuum distilled with a short fractionating column; bp 74–76°C/0.5 Torr (1 Torr = 133.3 Pa). Yield: 44%. ^1H NMR ($CDCl_3$): 4.17 (q, 4H, J = 7 Hz), 3.47 (q, 2H, J = 7 Hz), 3.55–3.80 (m, 3H), 1.32 (t, 6H, J = 7 Hz), 1.20 (t, 3H, J = 7 Hz).

Preparation of ethyl methoxyethylmalonate

Ethyl methoxyethylmalonate was prepared following the method described for ethyl-2-ethoxymethyl malonate; bp 92–95°C/0.5 Torr (lit. (22) bp 110–111°C/6 Torr). Yield: 45%.

Preparation of 2-ethoxymethyl-1,3-propanediol

Ethyl ethoxymalonate (21.0 g) in 50 mL of dry THF was added dropwise to a suspension of 6.9 g of $LiAlH_4$ in 100 mL of dry THF at 0°C with stirring. The mixture was refluxed for 5 h, after which 7 mL of water was added, followed by 7 mL of 15% KOH and 21 mL of water. The mixture was again refluxed for 0.5 h and the solid was then removed by filtration. The THF and water were removed by rotary evaporator. The residue was then dissolved in ether and dried with $MgSO_4$. After the $MgSO_4$ was removed by filtration, the solvent was removed and the remaining oil was distilled under vacuum; bp 84–88°C/0.5 Torr. Yield: 54%. ^1H NMR ($CDCl_3$): 3.20–3.70 (m, 10H), 2.80 (m, 1H) 1.03 (t, 3H, J = 7 Hz).

Preparation of 2-methoxyethyl-1,3-propanediol

2-Methoxyethyl-1,3-propanediol was prepared following the method described for 2-ethoxymethyl-1,3-propanediol from ethylmethoxyethyl malonate; bp 86–90°C/0.5 Torr. Yield: 59%. ^1H NMR ($CDCl_3$) 3.30–3.65 (m, 8H), 3.23 (s, 3H), 1.40–1.85 (m, 3H).

Preparation of 2-ethoxy-1,3-dioxane, 6

A mixture of ethyl orthoformate (4.44 g) and 1,3-propanediol (2.28 g) was distilled at 150°C. After the theoretical amount of ethanol had been distilled, the residue was distilled under vacuum; bp 49–50°C/10 Torr (lit. (9*b*) bp 156°C). Yield: 40%. ^1H NMR ($CDCl_3$): 5.23 (s, 1H), 4.25–3.60 (m, 4H), 3.63 (q, 2H, J = 7 Hz), 1.67 (m, 2H), 1.20 (t, 3H, J = 7 Hz).

Preparation of 2-ethoxy-5-ethoxymethyl-1,3-dioxane, 7

2-Ethoxy-5-ethoxymethyl-1,3-dioxane was prepared from 2-ethoxymethyl-1,3-propanediol and ethyl orthoformate following the method described for 2-ethoxy-1,3-dioxane; bp 62–66°C/0.5 Torr. Yield: 37%. ^1H NMR ($CDCl_3$): 5.18 (s, 1H), 3.50–4.30 (m, 4H), 3.60 (q, 2H, J = 7 Hz), 3.40 (q, 2H, J = 7 Hz), 3.35 (d, 2H, J = 7 Hz), 1.75–2.08 (m, 1H), 1.15 (t, 3H, J = 7 Hz), 1.03 (t, 3H, J = 7 Hz).

Preparation of 2-ethoxy-2-methyl-5-ethoxymethyl-1,3-dioxane, 8

Compound **8** was prepared from 2-ethoxymethyl-1,3-propanediol and ethyl orthoacetate following the method described for 2-ethoxy-1,3-dioxane; bp 92–100°C/0.5 Torr. Yield: 40%. ^1H NMR ($CDCl_3$): 3.10–4.20 (m, 10H), 1.42–2.0 (m, 1H), 1.36, 1.33 (2 singlets, 3H), 0.97–1.23 (m, 6H). ^1H NMR suggests a mixture of *cis* and *trans* isomers.

Preparation of 2-ethoxy-2-phenyl-5-ethoxymethyl-1,3-dioxane, 9

2-Ethoxy-2-phenyl-5-ethoxymethyl-1,3-dioxane was prepared from 2-ethoxymethyl-1,3-propanediol and ethyl orthobenzoate following

Can. J. Chem. Downloaded from www.nrcresearchpress.com by 85.192.166.187 on 09/08/12
For personal use only.

the method described for 2-ethoxy-1,3-dioxane; bp 104–108°C/0.5 Torr. Yield: 53%. ^{1}H NMR ($CDCl_3$): 7.22–7.63 (m, 5H), 3.13–4.96 (m, 10H), 1.65–2.10 (m, 1H), 1.0–1.17 (m, 6H).

Preparation of 2-ethoxy-2-methyl-5-methoxyethyl-1,3-dioxane, ***10***

2-Ethoxy-2-methyl-5-methoxyethyl-1,3-dioxane was prepared from 2-methoxyethyl-1,3-propanediol and ethyl orthobenzoate following the method described for 2-ethoxy-1,3-dioxane; bp 68–70°C/0.5 Torr. Yield: 44%. ^{1}H NMR ($CDCl_3$): 3.25–4.23 (m, 8H), 1.73–2.10 (m, 1H), 1.66–1.95 (m, 2H), 1.35 (s, 3H), 1.13 (t, 3H, J = 7 Hz).

Preparation of 1,3-dioxan-2-ylium hexachloroantimonate, ***1***

The preparation of the hexachloroantimonate salts was performed in a similar manner for each species. A sample procedure, which is a modification of Meerwein's method, is described below (9). 2-Ethoxy-1,3-dioxane (444 mg) in 1.5 mL of dry CH_2Cl_2 was added slowly to 1.8 g of $SbCl_5$ in 1 mL of dry CH_2Cl_2 at −30°C with stirring under a nitrogen atmosphere. The reaction mixture was stirred for 2 h at −10°C. CCl_4 was then added and the white precipitate was collected by filtration. The solid was washed 3 times with CCl_4 and dried by vacuum. Yield: 55%. 5-Ethoxymethyl-1,3-dioxan-2-ylium hexachloroantimonate, **2**, yield 20%; 2-methyl-5-ethoxymethyl-1,3-dioxan-2-ylium hexachloroantimonate, **3**, yield 35%; 2-phenyl-5-ethoxymethyl-1,3-dioxan-2-ylium hexachloroantimonate, **4**, yield 58%; 5-ethoxymethyl-1,3-dioxan-2-ylium hexachloroantimonate, **5**, yield 20% (as determined by NMR spectroscopy); 1-methyl-4-acetoxymethyltetrahydrofuranyl oxonium hexachloroantimonate, **11**, yield 36%. IR (KBr): 1720 cm^{-1}. ^{1}H NMR (SO_2, −70°C): 5.08 (J = 7.8, 5.8 Hz), 4.97 (J = 7.8, 7.8 Hz), 4.94 (J = 7.8, 7.8 Hz), 4.84 (J = 6.4, 7.8 Hz), 4.17, 4.57 (s, 3H), (doublet of multiplets, 2H), 3.30 (s, 1H), 2.59 (doublet of multiplets, 2H), 2.13 (s, 3H). ^{13}C NMR (CD_3NO_2, −10°C): 172.5 (s), 90.9 (s), 90.6 (s), 74.0 (s), 64.3 (s), 38.5 (s), 28.6 (s), 20.7 (s).

X-ray data collection and reduction

Crystals of **3** and **4** were obtained by vapour diffusion of hexanes into methylene chloride solutions of the respective compounds at room temperature. Suitable crystals were selected and sealed in Lindemann capillaries under a nitrogen atmosphere. Diffraction experiments were performed at low temperature on a Nicolet P3 diffractometer for **3** (187 K) and a Siemens R3m/V for **4** (173 K), using MoKα (λ = 0.710 69 Å) and AgKα (λ = 0.56086 Å) radiation, respectively. The initial orientation matrices were obtained from 15 reflections for **3** (22.5° < 2θ < 29.9°) and 23 (14.59° < 2θ < 34.99°) reflections for **4**. The observed extinctions were consistent with a triclinic space group for **3** and the monoclinic space group $P2_1/n$ for **4**. For **3**, h, $\pm k$, $\pm l$ data (2θ ≤ 45°) were collected with two standard reflections monitored every 48 reflections, while $+h$, $+k$, $\pm l$ data (2θ ≤ 45°) were collected for **4** with three standard reflections recorded every 97 reflections. The standard reflection intensities showed no statistically significant change over the duration of the data collection for either **3** or **4**. The methods of selection of scan rates and initial data treatment for **3** have been described (23). For **4**, data were collected with a scan range of 1.0° below $K\alpha_1$ and 1.0° above $K\alpha_2$, using a background to scan time ratio of 0.5. Corrections were made for Lorentz-polarization factors for all data. A semiempirical absorption correction was applied to the data for **4**. The triclinic cell found for **3** was subsequently revealed to be a $C2/c$ monoclinic cell, which is related to the original cell by the matrix (1, 0, 2; 1, 0, 0; 0, 1, 0).

Structure solution and refinement

The coordinates of the antimony atoms were found from a three-dimensional Patterson synthesis with use of the program SHELX-86 (24) for **3** and SHELXTL PLUS (25) for **4**. Full-matrix least-squares refinement of these coordinates, followed by a three-dimensional electron density synthesis revealed the positional parameters of all the non-hydrogen atoms and confirmed those of the heavy atoms. The refinement was carried out using full-matrix least-squares techniques on F, minimizing the function $\Sigma w(F_o - F_c)^2$, where the weight, w, is defined as $4F_o^2/2\sigma(F_o^2)$ and F_o and F_c are the observed and calculated structure factor amplitudes, respectively. The temperature factors of the non-hydrogen atoms, which were previously isotropic, were made anisotropic, and further cycles of refinement revealed the positional parameters of the hydrogen atoms. The hydrogen atoms for **3** were included in the final cycles with U fixed at 0.05 Å, while all of the hydrogen thermal parameters for **4**, except for the ethyl fragment, were allowed to refine. The methyl group was defined as a rigid rotor, while the methylene protons of the ethyl group were fixed to have the same thermal parameter. The difference map showed no other chemically reasonable site for C10 of compound **4**; therefore, any disorder present at C10 was unresolvable. Correction for secondary extinctions was not necessary. Throughout the refinement, scattering curves (26), and anomalous dispersion corrections (27) were applied to the curves for antimony and chlorine. Calculations for **3** were performed on a Vax 6420 computer, while for **4** the initial data reduction was performed on a Vax 6420 computer, but the structure solution was accomplished using a Comptech 486/33 computer. Programs used for **3** include XTAL (28) for data reduction and least-squares plane calculations, SHELX-86 (24) for structure solution, and SHELX-76 (29) for structure refinement. For **4**, the program used was SHELX-86 (24) for data reduction and the PC version of SHELXTL PLUS (30) for structure solution and refinement. Crystal data are given in Table 3, positional parameters are given in Table 4, and selected bond lengths and angles are given in Table 5. Anisotropic displacement coefficients (Table S1), anion bond lengths and angles (Table S2), phenyl ring bond lengths and angles (Table S3), hydrogen atom parameters (Table S4), and bond lengths and angles involving hydrogen atoms (Table S5), have been deposited as supplementary material.[3]

Conclusion

The NMR spectroscopy and X-ray crystallography results have shown that there is no significant interaction between the oxygen of the ethoxymethyl substituent and the carbon carrying the positive charge. The planarity of the O(1)-C(2)-C(11)-O(3) fragment, the distance from the oxygen of the ether substituent to the cationic centre, and the structural similarity of the ethoxymethyl portion of the molecule to diethyl ether show that the ether oxygen does not interact with the cationic centre in a manner that would model ionization of an orthoester. However, the disposition of the ethoxymethyl ligand demonstrates that there is a stabilization energy associated with the adopted conformation, as one would expect the ether fragment to be oriented away from the dioxan-2-ylium ring, as was found for 2-methyl-5-methoxyethyl-1,3-dioxan-2-ylium hexachloroantimonate **5**. The challenge remaining for this study is to find a system in which O(8), the ether oxygen, is more tightly bound to the carbenium-ion centre. In principle, changing its C(2) substituent to an electron-withdrawing one could effect this change; however, we have been unsuccessful in our attempts to generate such ions.

Acknowledgement

This work was supported by a grant from the Natural Sciences and Engineering Research Council of Canada.

[3]This supplementary material can be purchased from: The Depository of Unpublished Data, Document Delivery, CISTI, National Research Council Canada, Ottawa, ON K1A 0S2, Canada.

Structure factor amplitudes are no longer being deposited and may be obtained directly from the author.

With the exception of the anisotropic displacement coefficients, the supplementary data have also been deposited with the Cambridge Crystallographic Data Centre, and can be obtained on request from The Director, Cambridge Crystallographic Data Centre, University Chemical Laboratory, 12 Union Road, Cambridge, CB2 1EZ, U.K.

1. C.U. Pitman, S.P. McManus, and J.W. Larsen. Chem. Rev. **72**, 357 (1972).
2. (*a*) P. Deslongchamps, P. Atlani, D. Frehel, and A. Malaval. Can. J. Chem. **50**, 3405 (1972); (*b*) P. Deslongchamps, R. Chênevert, R.J. Taillefer, C. Moreau, and J.K. Saunders. Can. J. Chem. **53**, 1601 (1972); (*c*) P. Deslongchamps, D. Guay, and R. Chenevert. Can. J. Chem. **63**, 2493 (1985); (*d*) N. Beaulieu and P. Deslongchamps. Can. J. Chem. **58**, 875 (1980).
3. P. Deslongchamps. *In* Stereoelectronic effects in organic chemistry; Organic Chemistry Series. Vol. 1. *Edited by* J.E. Baldwid. Pergamon Press, Oxford, England. 1983.
4. (*a*) S.K. Chadda, R.F. Childs, R. Faggiani, and C.J.L. Lock. J. Am. Chem. Soc. **108**, 1694 (1986); (*b*) R.F. Childs, R. Faggiani, C.J.L. Lock, M. Mahendran, and S.D. Zweep. J. Am. Chem. Soc. **108**, 1692 (1986); (*c*) R.F. Childs, R.M. Orgias, C.J.L. Lock, and M. Mahendran. Can. J. Chem. **71**, 836 (1993); (*d*) R.F. Childs, M. Mahendran, S.D. Zweep, G.S. Shaw, S.K. Chadda, N.A. Burke, B.E. George, R. Faggiani, and C.J.L. Lock. Pure Appl. Chem. **58**, 111 (1986).
5. (*a*) H. Paulsen and R. Dammeyer. Chem. Ber. **109**, 1837 (1976); (*b*) H. Paulsen and R. Dammeyer. Chem. Ber. **106**, 2324 (1973); (*c*) H. Paulsen and E. Schuttpelz. Chem. Ber. **112**, 3214 (1979).
6. R.F. Childs, M.D. Kostyk, C.J.L. Lock, and M. Mahendran. J. Am. Chem. Soc. **112**, 8912 (1990).
7. (*a*) H.B. Bürgi and J.D. Dunitz. Acc. Chem. Res. **16**, 153 (1983); (*b*) H.B. Bürgi, J.D. Dunitz, and E. Shefler. J. Am. Chem. Soc. **95**, 5065 (1973); (*c*) H.B. Bürgi, J.D. Dunitz, and E. Shefler. Acta Crystallogr. Sect. B: Struct. Crystallogr. Cryst. Chem. **B30**, 1517 (1974).
8. (*a*) A.J. Kirby. Acc. Chem. Res. **17**, 305 (1984); (*b*) P.G. Jones and A.J. Kirby. J. Chem. Soc. Chem. Commun. 288 (1979); (*c*) A.J. Briggs, R. Glenn, P.G. Jones, A.J. Kirby, and P. Ramaswamy. J. Am. Chem. Soc. **106**, 6200 (1984); (*d*) P.G. Jones and A.J. Kirby. J. Am. Chem. Soc. **106**, 6207 (1984); (*e*) M.R. Edwards, P.G. Jones, and A.J. Kirby. J. Am. Chem. Soc. **108**, 7067 (1986); (*f*) A.J. Kirby. Pure Appl. Chem. **59**, 1605 (1987).
9. (*a*) H. Meerwein, V. Hedrich, and K. Wunderlich. Arch. Pharm. Ber. Dtsch. Pharm. Ges. **291**, 41 (1958); H. Meerwein, K. Bodenbenner, P. Borner, F. Kunert, and K. Wunderlich. Justus Liebigs Ann. Chem. **38**, 632 (1960); Chem. Abstr. **55**, 546h (1961); (*b*) H. Baganz and L. Domaschke. Chem. Ber. **91**, 650 (1958); O.B. Chalova, E.S. Kurmaeva, T.K. Kiladze, and D.L. Rakhmankulov. J. Org. Chem. USSR, **18**, 1434 (1982); H. Paulsen and E. Schuttpelz. Org. Magn. Reson. **12**, 616 (1979); H. Paulsen. Pure Appl. Chem. **69**, 41 (1975).
10. Y.Y. Samitov and R.M. Aminova. Zh. Strukt. Khim. **5**, 207 (1964).
11. W.E. Boering and L.K. Levy. J. Am. Chem. Soc. **77**, 512 (1958).
12. E.V. Pastushenko, L.F. Lapuka, I.I. Khatuntsev, S.S. Zlot'skii, and D.L. Rakhmankulov. J. Gen. Chem. USSR, **56**, 50 (1986).
13. E.L. Eliel and M.C. Knoeber, Sr. J. Am. Chem. Soc. **90**, 3444 (1968).
14. O.N. Kataeva, I.A. Litvinov, and V.A. Naumov. Zh. Strukt. Khim. **29**, 186 (1988).
15. F.H. Allen and A.J. Kirby. J. Am. Chem. Soc. **106**, 6197 (1984).
16. P.C. Jones, H.W. Roesky, J. Liebermann, and G.M. Sheldrick. Z. Naturforsch. B: Anorg. Chem. Org. Chem. **39**, 1729 (1984).
17. A.L. Baumstark, P. Balakrishnan, M. Dotrong, C.J. McCloskey, M.G. Oakley, and D.W. Boykin. J. Am. Chem. Soc. **109**, 1059 (1987).
18. R.F. Childs, C.S. Frampton, G.J. Kang, and T.A. Wark. J. Am. Chem. Soc. In press.
19. (*a*) A.L. Rheingold, C.J. Baldacchini, P.D. Macklin, and G.L. Geoffroy. Acta Crystallogr. Sect. C: Cryst. Struct. Commun. **C46**, 496 (1990); (*b*) P.N. Rodier, J. Courant, and G. Le Baut. Acta Crystallogr. Sect. C: Cryst. Struct. Commun. **C45**, 1444 (1989).
20. M.I. Watkins, W.M. Ip, G.A. Olah, and R. Bau. J. Am. Chem. Soc. **104**, 2365 (1982).
21. A. Kirrmann and L. Wartski. Bull. Soc. Chim. Fr. 3825 (1966).
22. M.H. Palomaa and A. Kenetti. Ber. Dtsch. Chem. Ges. B: **54**, 797 (1931).
23. B. Lippert, C.J.L. Lock, B. Rosenberg, and M. Zavagulis. Inorg. Chem. **16**, 1525 (1977).
24. G.M. Sheldrick. SHELX-86, Program for crystal structure solution. University of Gottingen, Federal Republic of Germany. 1986.
25. SHELXTL-PC 4.1. Siemens Crystallographic Research Systems, Siemens Analytical X-ray Instruments, Inc. May, 1990.
26. D.T. Cromer and J.B. Mann. Acta Crytallogr. Sect. A: Cryst. Phys. Diffr. Theor. Gen. Crystallogr. **A24**, 231 (1968).
27. D.T. Cromer and J.T. Waber. International tables for X-ray crystallography. Vol. IV. *Edited by* J.A. Ibers and W.C. Hamilton. Birmingham, England. 1975.
28. J.M. Stewart and S.R. Hall. The XTAL system of crystallographic programs. Tech. Rept. TR-1364, University of Maryland, College Park, Md. 1983.
29. G.M. Sheldrick. SHELX-76, Program for crystal structure determination. University of Cambridge, Cambridge, England. 1976.
30. SHELXTL PLUS 4.2. Siemens Crystallographic Research Systems, Siemens Analytical X-ray Instruments, Inc. May, 1990.

Can. J. Chem. Downloaded from www.nrcresearchpress.com by 85.192.166.187 on 09/08/12
For personal use only.

On *N*-acetylcysteine. Part I. Experimental and theoretical approaches of the *N*-acetylcysteine/H_2O_2 complexation

JLIL ARROUB
Laboratoire de Chimie Physique, Université René Descartes, 45, rue des Saints-Pères, 75270 Paris, Cedex 06, France

JACQUELINE BERGÈS[1]
Dynamique des Interactions Moléculaires, Université Pierre et Marie Curie, 4 Place Jussieu, 75005 Paris, France

ZOHREH ABEDINZADEH
Laboratoire de Chimie Physique, Université René Descartes, 45, rue des Saints-Pères, 75270 Paris, Cedex 06, France

JACQUELINE LANGLET
Dynamique des Interactions Moléculaires, Université Pierre et Marie Curie, 4 Place Jussieu, 75005 Paris, France

AND

MONIQUE GARDÈS-ALBERT
Laboratoire de Chimie Physique, Université René Descartes, 45, rue des Saints-Pères, 75270 Paris, Cedex 06, France

Received March 12, 1993[2]

JLIL ARROUB, JACQUELINE BERGÈS, ZOHREH ABEDINZADEH, JACQUELINE LANGLET, and MONIQUE GARDÈS-ALBERT. Can. J. Chem. **72**, 2094 (1994).

The complexation of *N*-acetylcysteine (RSH) with hydrogen peroxide has been studied experimentally and theoretically. Experimentally we have measured the evolution of RSH, H_2O_2, and RSSR (*N*-acetylcystine) as a function of time. Surprisingly, H_2O_2 decays by a biphasic process, which is not the case for RSH and RSSR. In the first stage of the kinetics, H_2O_2 disappears without oxidizing the thiol function of RSH. By analogy with glutathione (GSH), the formation of a complex between RSH and H_2O_2 has been proposed. The thermodynamic equilibrium constant of complex formation has been determined. Theoretical calculations were performed within the SIBFA method to pinpoint the sites of complexation in isolated and hydrated states. A mixed "discrete–continuum" model was used to evaluate the solvent effect. The two stable complexes found in isolated state have different behaviour under the influence of the solvent. Comparison with complexed GSH is discussed.

JLIL ARROUB, JACQUELINE BERGÈS, ZOHREH ABEDINZADEH, JACQUELINE LANGLET et MONIQUE GARDÈS-ALBERT. Can. J. Chem. **72**, 2094 (1994).

Nous avons effectué l'étude expérimentale et théorique de la réaction de complexation de la *N*-acétylcystéine (RSH) avec l'eau oxygénée. Au point de vue expérimental, nous avons mesuré l'évolution de RSH, H_2O_2 et RSSR (*N*-acetylcystine) en fonction du temps. D'une manière surprenante, H_2O_2 décroit par un processus biphasique alors qu'il n'en est pas de même pour RSH et RSSR. Dès le début de la cinétique, H_2O_2 disparaît sans oxyder la fonction thiol de RSH. Par analogie avec le glutathion (GSH), la formation d'un complexe entre RSH et H_2O_2 a été proposée. La constante d'équilibre de formation de ce complexe a été déterminée. Des calculs théoriques menés selon la méthode SIBFA ont été effectués afin de préciser les sites de complexation des états isolé et hydraté. Un modèle mixte "discret-continuum" a été utilisé pour évaluer l'effet de solvant. Les deux complexes stables calculés dans l'état isolé ont des comportements différents en présence de solvant. La comparaison de ces résultats avec ceux du glutathion complexé est discutée.

Introduction

N-acetylcysteine, RSH (Fig. 1*a*), is a drug that counteracts oxidative stress and replenishes glutathione, GSH (1). It is also considered a therapeutic agent for AIDS (1–5). Furthermore, RSH structure is similar to the central part of GSH (Fig. 1*b*). Thus as a contrast to GSH/H_2O_2 complexation (6), complexation of *N*-acetylcysteine with hydrogen peroxide was studied. As we know, GSH is an intracellular cysteine-containing tripeptide (γ-glutamylcysteinylglycine) which plays many essential roles in vivo, particularly as a defence against electrophylic xenobiotics and intracellular oxidants (free radicals, reactive oxygen intermediates, i.e. H_2O_2) (1).

In our previous work (6) on the oxidation kinetics of glutathione (GSH) by hydrogen peroxide at neutral pH and in the absence of glutathione peroxydase, we have shown that an important amount of H_2O_2 disappears without oxidizing the thiol function. The formation of a chelate (hydrogen bonds) between GSH and H_2O_2 is presumed to follow

[1] $GSH + H_2O_2 \rightleftarrows [GSH]...H_2O_2]$

The equilibrium constant has been determined as 1950 ± 50 (6). It has also been shown that glutathione disulfide, GSSG, is the main product formed via two different routes of oxidation, one contributing 80–85% and the other 10–15% (2) of the overall process.

Moreover, theoretical calculations in the framework of the SIBFA (Sum of Interactions Between Fragments computed Ab-initio) and CHARMm methods have been performed to investigate the possibility of intermolecular hydrogen bonds between glutathione and hydrogen peroxide (7–9). According to these studies, the GSH ionized glutamyl NH_3^+ and COO^- groups as well as glycyl COO^- group and to a certain extent CO and NH of peptide groups are the privileged interaction sites for forming complexes with H_2O_2.

In this work we have studied experimentally and theoreti-

[1]Author to whom correspondence should be addressed.
[2]Revision received June 13, 1994.

Can. J. Chem. Downloaded from www.nrcresearchpress.com by 85.192.166.187 on 09/08/12
For personal use only.

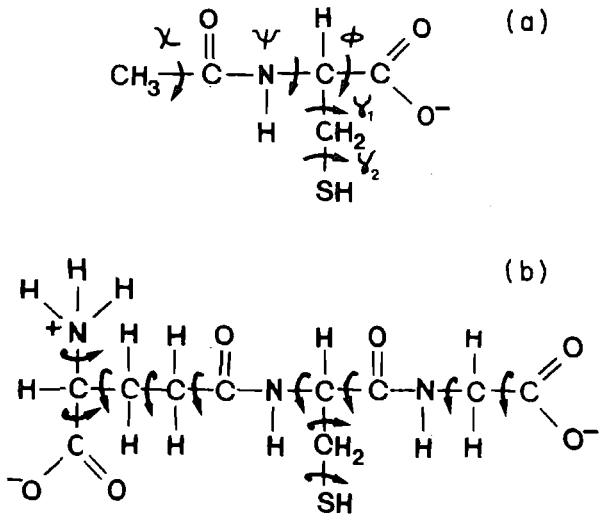

FIG. 1. (*a*) *N*-acetylcysteine (RSH) anion. Definition of the degrees of rotational freedom. (*b*) Glutathione (GSH) anion.

cally the possibilities and sites of complexation of *N*-acetylcysteine with hydrogen peroxide (this paper). As can be seen, the drug molecule contains GSH, thiol, glycyl COO^- and one peptide group, but it contains neither the second peptide part nor the glutamyl groups as the GSH molecule. In the following paper (26) we have performed a kinetic analysis of the overall process in the oxidation of RSH with H_2O_2.

Materials and method

A. Chemicals

Chemicals were the purest grade available and were used without further purification. The only exception was *N*-acetylcystine (RSSR) which was synthesized by acetylation of L-cystine according to ref. 10. RSH and 5,5′-dithiobis(2-nitrobenzoic acid) were supplied by Sigma Chemical Co.; hydrogen peroxide, sodium acid phosphate were from Merck. All solutions were prepared with Millipore water, the purity of which was confirmed by conductivity measurements ($10^{-6}\ \Omega^{-1}\ cm^{-1}$).

Thiol concentration was determined with Ellman's reagent (11), 5,5′-dithiobis(2-nitrobenzoïc acid) which undergoes a thiolate disulphide exchange reaction to yield 2-nitromercaptobenzoïc acid. This product was measured spectrophotometrically (λ_{max} = 412 nm, ϵ_{412} = 13600 ± 600 $mol^{-1}\ L\ cm^{-1}$) against an appropriate blank. Notice that Ellman's reagent characterizes all free SH groups and we have tested that this assay is not modified in presence of H_2O_2.

Hydrogen peroxide concentrations were measured spectrophotometrically by the titanium sulfate method (12, 13) using ϵ_{410} = 700 $mol^{-1}\ L\ cm^{-1}$. We can see later that in this method only free hydrogen peroxide is measured, complexed hydrogen peroxide or peroxide bonds in a molecule are excluded in the measurement. Moreover, it should be noted that titanium reagent does not react with RSH. Dilute buffered aqueous hydrogen peroxide solutions (5×10^{-4} to 5×10^{-3} mol L^{-1}) were stable at least for one day, showing nonspontaneous metallic cations induced dismutation.

N-Acetylcystine (RSSR) concentration was determined by spectrophotometric absorption at 250 nm where the thiol, RSH, does not absorb. According to Beer's law the differential extinction coefficient of *N*-acetylcystine, RSSR, 330 ± 4 $mol^{-1}\ L\ cm^{-1}$ at 250 nm has been obtained. Note that at this wavelength, the extinction coefficient of RSH equals zero and for H_2O_2, ϵ_{250} = 25 $mol^{-1}\ L\ cm^{-1}$ (14). Figure 2 shows the differential absorption spectrum of RSSR versus RSH. As can be seen, this spectrum gives two absorption bands at 214 and 250 nm, both differential bands are characteristic of RSSR.

For differential spectrophotometric measurements of reaction mixtures, we used two chamber cells; each has an optical path of 0.4375 cm. The reference cell contained H_2O_2 in one chamber (the concentration of H_2O_2 in this chamber is double that in the mixture, $[H_2O_2] = 2[H_2O_2]_{reaction\ mixture}$) and RSH in the other chamber (the concentration of RSH in this chamber is double that in the reaction mixture, $[RSH] = 2\ [RSH]_{reaction\ mixture}$. The measure cell contained the same reaction mixture, in each chamber.

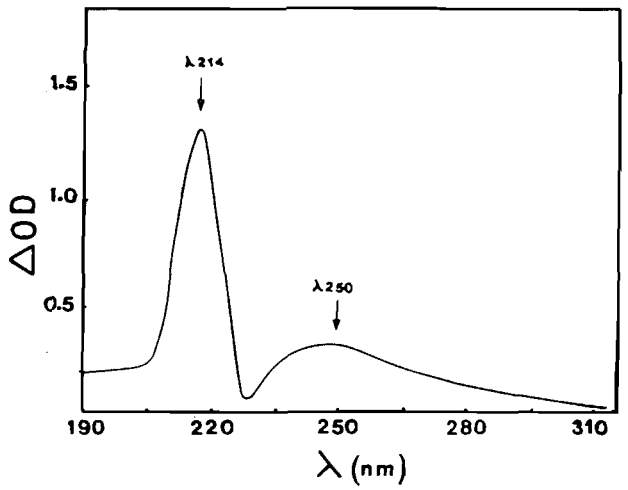

FIG. 2. Differential absorption spectra of the disulfide form and *N*-acetylcysteine.

Oxygen concentration was determined by Gilson oxygraph model IC TS-KI.

All solutions were prepared just prior to use and buffered at pH7 in a 10^{-2} mol L^{-1} phosphate medium.

B. Method of calculations

Both intra- and intermolecular energies have been calculated simultaneously within the framework of the SIBFA method (Sum of Interactions Between Fragments computed Ab-initio) (15–17).

1. Intermolecular energy (15, 16)

Following an additive procedure, the intermolecular energy is expressed as the sum of five contributions:

$$[1] \quad E_{Inter} = E_{El} + E_{Pol} + E_{Rep} + E_{Disp} + E_{CT}$$

This method has the following characteristic features: (*a*) Use of a multicenter (atom and middle of bonds), multipolar (up to quadrupoles) expansion derived (18) from an ab-initio SCF molecular function for the calculations of *electrostatic* and *polarization* components, E_{El} and E_{Pol}. (*b*) Computation of the *repulsion* term, E_{Rep}, as a sum of "bond–bond", "bond–lone pair" and "lone pair – lone pair" interactions. (*c*) *Dispersion*, E_{Disp}, is decreased because of an overestimation of energy at short distances. (*d*) Explicit evaluation of the *charge-transfer*, E_{CT}, contribution between lone pairs in the molecule that behaves as an electron donor and the hydrogen atom in the molecule that behaves as an electron acceptor.

2. Intramolecular energy (17).

In the SIBFA method, a molecule is built out of constituting molecular fragments separated by single bonds. In fact, one calculates the variation in conformational energy as a sum of interaction energies from inter fragments

$$[2] \quad E_{Intra} = \sum_{i=1}^{N} \sum_{j=i+1}^{N} E'_{Inter}(i,j)$$

where N is now the number of fragments.

E'_{Inter} is calculated as a sum of the four first terms in eq. [1], plus a term denoted E_{Tor} which is a transferable torsional energy contribution, calibrated for elementary rotations around single bonds (for more details concerning this method see refs. 15 to 17).

Can. J. Chem. Downloaded from www.nrcresearchpress.com by 85.192.166.187 on 09/08/12
For personal use only.

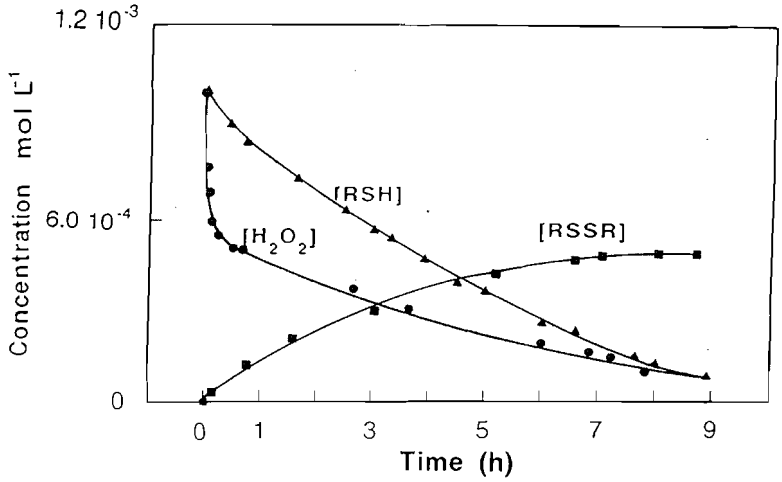

FIG. 3. Kinetic evolutions of hydrogen peroxide (●), *N*-acetylcysteine (▲), and *N*-acetylcystine (■) as a function of time. $[RSH]_0 = [H_2O_2] = 10^{-3}$ mol L^{-1}, phosphate buffer 10^{-2} mol L^{-1}, pH 7.

3. Solvent effect

Two models may be used: (*a*) The *microscopic (or discrete)* model in which the water molecules surrounding the solute are explicitly taken into account and the solute–water and water–water interaction energies are calculated within the SIBFA framework. (*b*) The *macroscopic (or continuum)* model. In this model, the solute molecule is represented by a charge distribution inside a cavity. It is surrounded by a continuous medium (the solvent) characterized by macroscopic properties (dielectric constant, molecular volume...). The details of this model are given in refs. 19 and 20. The following is a summary of this methodology. A thermodynamic quantity involved in the solvation process are separated into three terms, cavitation, dispersion–repulsion, and electrostatic. *The cavitation energy* is calculated using the Reiss–Pierrotti expressions (21). The *dispersion–repulsion terms* are calculated using the potential functions for pairs of atoms, *i* and *j*, that belong to the solvent and the solute molecules, respectively (this is consistent with the methodology initially proposed for pure liquid hydrocarbons (22). *The electrostatic* interaction between the solute and the solvent is expressed in terms of the reaction potential of the solvent polarized by the solute. The solvent is represented by a dielectric medium and a simple method is used to calculate the fictive charge density to represent the reaction potential.

To evaluate these three terms, we must first choose the shape of the cavity. Here we follow Huron and Claverie's proposal (22) by using the exact molecular shape of the solute. In practice this shape is made of the Van der Waals spheres of atoms that form the solute.

Experimental results and discussion

The oxidation of *N*-acetylcysteine, RSH (initial concentrations from 0.4×10^{-3} to 4×10^{-3} mol L^{-1}) by hydrogen peroxide (initial concentrations from 0.5×10^{-3} to 2.5×10^{-3} mol L^{-1}) has been studied in buffered aqueous medium at pH 7 (phosphate concentration 10^{-2} mol L^{-1}) as a function of time. Ten different experiments have been performed (see Table 1, the three first columns), each characterized by different initial concentrations of RSH and H_2O_2. The initial concentration ratio, $[RSH]_0/[H_2O_2]_0$, ranged between 0.2 and 8. Thus we have studied the cases with $[RSH]_0$ higher than $[H_2O_2]_0$ and $[H_2O_2]_0$ higher than $[RSH]_0$.

Moreover, we have tested the eventual decomposition of H_2O_2 according to the Haber–Weiss reaction by adding a transition metal chelator (EDTA) to the reaction mixture. However, we did not observed any modification in the kinetic experiments.

As an example, we reported in Fig. 3 the changes in the concentration of RSH, H_2O_2, and RSSR (the disulfide form of *N*-acetylcysteine) as a function of time, when the initial concentrations of RSH and H_2O_2 are equimolar (10^{-3} mol L^{-1}) (phosphate buffer 10^{-2} mol L^{-1}, pH 7). The decay of *N*-acetylcysteine and the appearance of its oxidized disulfide form are concomitant processes while the decrease in hydrogen peroxide is characterized by biphasic kinetics. During a very short time (~10 min) a significant quantity of H_2O_2 ($\sim[H_2O_2]_0/2$) disappears, then the remaining hydrogen peroxide decays slowly until the end of the reaction. Neither the disulfide RSSR, nor *N*-acetylcysteine, RSH, present a similar initial fast kinetic phase. The differential absorption spectra recorded as a function of time (Fig. 4) for the same experiment ($[RSH]_0 = [H_2O_2]_0 = 10^{-3}$ mol L^{-1}, phosphate buffer 10^{-2} mol L^{-1}, pH 7) exhibit two increasing absorption bands around 214 and 250 nm that characterize RSSR (see Materials and Methods). To confirm that both differential absorption bands at 214 and 250 nm are related to RSSR, we have compared the inapparent first order kinetics at 214 and 250 nm (see Fig. 4 inset). The similarity in the two slopes of the straight lines at 214 and 250 nm ($(1.1 \pm 0.2) \times 10^{-4}$ s^{-1} and $(1.3 \pm 0.2) \times 10^{-4}$ s^{-1} respectively at 214 nm and 250 nm) implies first order kinetics and hence the formation of only one product RSSR.

Nearly the end of the reaction (~9 h), the concentrations in RSH, H_2O_2, and RSSR are 0.5×10^{-4} mol L^{-1}, ≈0 mol L^{-1}, and 0.5×10^{-3} mol L^{-1}. Hence 95% of RSH and H_2O_2 have disappeared and [RSSR] formed equals $[RSH]_0/2$. Therefore 2 moles of RSH consume 2 moles of H_2O_2 to give 1 mol of RSSR, in contrast to the classical stoichiometry in which 2 mol of RSH react with 1 mol of H_2O_2 to give 1 mol of RSSR. According to our observation, it seems 1 mol of hydrogen peroxide has disappeared without oxidizing the thiol function.

To understand what has happened with hydrogen peroxide, the following experiments have been performed:

(*1*) The eventual formation of oxygen during the reaction of RSH with hydrogen peroxide has been tested using a Gilson Oxygraph (see Experimental section). Samples were prepared at equimolar concentrations ($[RSH]_0 = [H_2O_2]_0 = 10^{-3}$ mol L^{-1}, phosphate buffer 10^{-2} mol L^{-1}, pH 7). However, we observed no formation of oxygen at the beginning or during the reaction. Hence H_2O_2 does not oxidize or disproportionate.

Can. J. Chem. Downloaded from www.nrcresearchpress.com by 85.192.166.187 on 09/08/12
For personal use only.

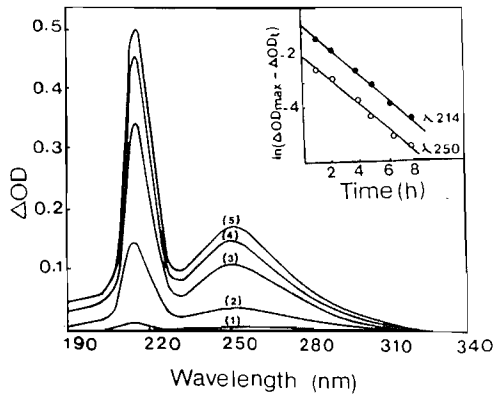

FIG. 4. Differential absorption spectra recorded as a function of time. $[RSH]_0 = [H_2O_2]_0 = 10^{-3}$ mol L^{-1}, phosphate buffer 10^{-2} mol L^{-1}, pH 7, optical path 4.375 mm. (*1*) 4 min after mixing, (*2*) 47 min, (*3*) 184 min, (*4*) 312 min, (*5*) 420 min. In inset, first order kinetic plots against time at 214 and 250 nm.

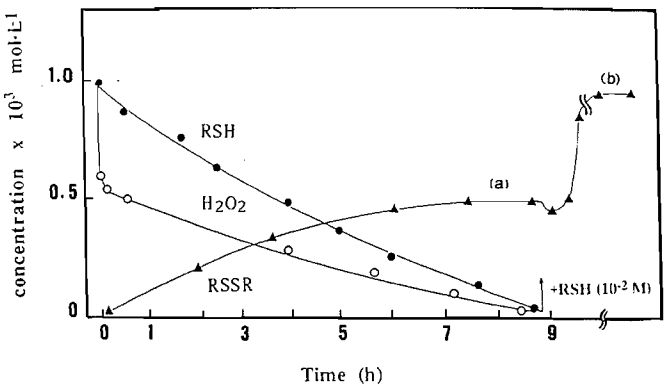

FIG. 5. Addition of RSH at the end of a reaction. Initial reaction: $[RSH]_0 = [H_2O_2]_0 = 10^{-3}$ mol L^{-1}, phosphate buffer 10^{-2} mol L^{-1}, pH 7. (*a*) [RSSR] before addition of RSH, (*b*) [RSSR] after addition of RSH.

(*2*) If an excess of RSH ($\approx 10^{-2}$ mol L^{-1}) was added at the end ($\approx$ 9 h) of the experiment ($[RSH]_0 = [H_2O_2]_0 = 10^{-3}$ mol L^{-1}, phosphate buffer 10^{-2} mol L^{-1}, pH 7), we could observe an extra amount of RSSR ($\approx 4.5 \times 10^{-4}$ mol L^{-1}), which involved consuming almost the entire initial concentration of H_2O_2 (see Fig. 5).

(*3*) The addition of catalase 10^{-7} mol L^{-1}, 9 h after the start of the reaction ($[RSH]_0 = [H_2O_2]_0 = 10^{-3}$ mol L^{-1}, phosphate buffer 10^{-2} mol L^{-1}, pH 7), leads to the formation of $\approx 5 \times 10^{-4}$ mol L^{-1} oxygen, whereas there was no free H_2O_2 (determined by the titanium method) detected.

(*4*) The classical stoichiometry has been observed when [RSH] was in large excess (2×10^{-2} mol L^{-1}) compared with $[H_2O_2]_0$ (10^{-3} mol L^{-1}) see Experimental results in ref. 26).

Thus, these experiments explain the residual oxidizing power of the end product, which could proceed from a "bound hydrogen peroxide" [RSSR...H_2O_2].

These experiments could be summarized as follows:

[2] $2RSH + 2H_2O_2 \rightarrow [RSSR...H_2O_2] + 2H_2O$

[3] $[RSSR...H_2O_2] + 2RSH \rightarrow 2RSSR + 2H_2O$

Reaction [2] represents the overall oxidation of RSH by H_2O_2

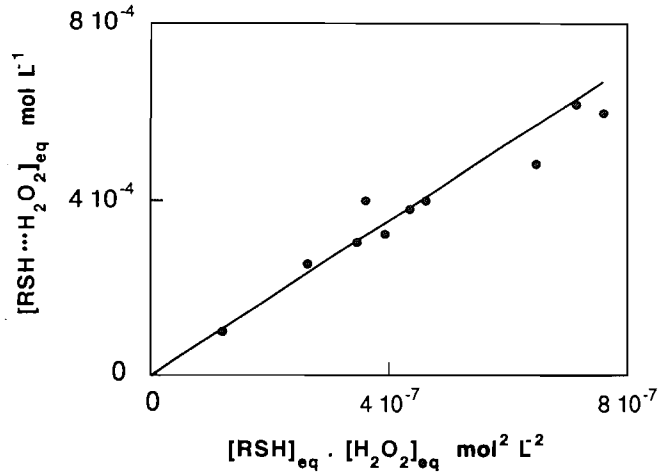

Fig. 6. Chelate concentration at equilibrium as a function of $[RSJ]_{eq} \times [H_2O_2]_{eq}$. Phosphate buffer 10^{-2} mol L^{-1}, pH 7.

leading to the final complexed product [RSSR...H_2O_2] (when the initial concentration of RSH and H_2O_2 are of the same order or magnitude). Reaction [3] explains the stoichiometric oxidation of RSH when it is in large excess. These overall reactions composed of several steps.

In this work, we have focused our attention on the fast initial decay of hydrogen peroxide in the presence of *N*-acetylcysteine. In the case of glutathione, the hypothesis of the initial formation of a chelate (hydrogen bonds) between glutathione and hydrogen peroxide, according to reaction [1], had been proposed. A similar process could be invoked to explain our experimental results with *N*-acetylcysteine, the fast initial decay of H_2O_2 resulting from the formation of a chelate between *N*-acetylcysteine and hydrogen peroxide:

[4] $RSH + H_2O_2 \rightleftarrows [RSH...H_2O_2]$.

The reaction could be considered the first step of the overall reaction [2].

We have determined the equilibrium constant K_4 by measuring [RSH], $[H_2O_2]$, and [RSH...H_2O_2] at equilibrium. These values are reported in Table 1. It has been established that the titanium sulfate method allowed one to measure only the free hydrogen peroxide and not bound hydrogen peroxide in the chelate. Concentration of H_2O_2 at equilibrium, $[H_2O_2]_{eq}$, has been determined by extrapolating to $t = 0$ the slow decay of H_2O_2. The concentration of chelate at equilibrium is deduced from $[H_2O_2]_0 - [H_2O_2]_{eq}$. Ellman's reagent, which measures the thiol concentration, gives the sum of concentrations of free *N*-acetylcysteine and its chelated form. Hence the concentration of *N*-acetylcysteine at equilibrium is calculated as the difference between the initial concentration of RSH and the concentration of chelate at equilibrium. In Fig. 6 are reported the values of $[RSH—H_2O_2]_{eq}$ as a function of the product $[RSH]_{eq} \times [H_2O_2]_{eq}$. The slope of the straight line following is the equilibrium constant: 880 ± 80 (Table 1). This number is of the same order of magnitude as that for glutathione (1950 ± 50 (2)).

Theoretical results and discussion

To formulate a model for the formation of a molecular complex in a solvent requires the following information: (*1*) *intermolecular energy*, to identify the geometrical arrangement of the molecules entering into the complex and the interaction

Can. J. Chem. Downloaded from www.nrcresearchpress.com by 85.192.166.187 on 09/08/12
For personal use only.

TABLE 1. Determination of equilibrium constants for the formation of complex [RSH...H_2O_2]

$[H_2O_2]_0$[a]	$[RSH]_0$[a]	$R = \frac{[RSH]_0}{[H_2O_2]_0}$	$[H_2O_2]_{eq}$[a]	$[RSH]_{eq}$[a]	$[complex]_{eq}$[a]	K
2.5	0.5	0.2	2.16	0.16	0.34	984
2.5	1	0.4	1.88	0.38	0.62	867
1	0.6	0.6	0.75	0.35	0.25	952
0.5	0.4	0.8	0.4	0.3	0.1	833
1	1	1	0.6	0.6	0.4	1100
1	2.5	2.5	0.4	1.9	0.6	789
0.8	2.5	3	0.32	2.02	0.48	742
0.62	2.5	4	0.22	2.1	0.4	865
0.5	2.5	5	0.18	2.18	0.32	815
0.5	4	8	0.12	3.62	0.38	874

[a]All concentrations are in 10^{-3} mol L^{-1}.

energy; (*2*) *intramolecular energy*, to account for the conformation of each partner forming the complex; and (*3*) *the solvent effect.*

In the discrete model, the number of water molecules surrounding the solute is important because of their long range effects. The water molecules may interact strongly with the solute (these are the "hydration" water molecules) or they may form several solvation shells. Here, computation time within the SIBFA framework is considerable. For example, in GSH complexation (3–5), water molecules in the first solvation shell interact strongly with the solute; they are therefore not at random but are extremely oriented with respect to the solute. After the first solvation shell, interaction with the solute weakens and bulk solvent may be used as a first approximation. In the continuum model, the orientation effects exerted by the solute on the water molecules in the first shell are not taken into account. A good compromise is therefore the "discrete–continuum model": i.e. a solute + *N*w strongly interacting water molecules surrounded by a continuum (*N*w is the number of "hydration water molecules").

In this work, N_w is chosen according to a criterion on energy, i.e. $E_{s-w} \leq -5.4$ kcal/mol (-22.6 kJ/mol), since 5.4 kcal/mol is the water dimer interaction energy. We called "hydration energy" (E_{Hydra}), the intermolecular energy between solute and the *N*w hydration molecules. The system "solute + N_w water molecules" is fully optimized (intra + inter energies) within the SIBFA method.

We have not calculated the free enthalpy energy, so we cannot directly correlate our theoretical to our experimental association constant *K*. We correlated the calculated energy values to enthalpy, thus we evaluated the stability of a complex.

1. Conformation of RSH

There are no experimental data on the geometry of RSH. However, since RSH is very similar to the central part of GSH (cystein unit), we have used the geometry and the special dihedral angles as determined (for this unit) in the glutathione crystal structure (23) (conformation A in Table 2).

(i) Isolated state

We have performed a complete automatic optimization of the five dihedral angles (Fig. 1*a*) and picked several conformations from an energy sub-map $E = f(\Phi, \Psi)$. From these conformations we got a unique optimized conformation O, characterized by a weak intramolecular H-bond between the carboxylate and the NH groups (d_{OH} = 2.51 Å) (Table 2). This conformation is stabilized with respect to the initial conformation A: $\Delta E_{intra} = E_{intra_O} - E_{intra_A} = -10.2$ kcal/mol (-42.6 kJ/mol).

TABLE 2. Dihedral angles in the initial and optimized conformations of RSH

Conformations	Φ	Ψ	γ_1	γ_2	χ
A	29.17	57.98	185.29	180.0	103.32
O	305.33	64.53	170.80	185.15	275.33

(ii) Hydrated state

According to the energetics criterion there are eleven hydration water molecules interacting with RSH in the O conformation. For comparison, we performed an intermolecular energy optimization of the system RSH + eleven water molecules, RSH being present in the initial conformation A (structure A′).

The total energies ($E_{tot} = E_{intra} + E_{inter}$) for the two structures A′ and O′ were compared. We define $\Delta E_{tot} = E_{tot_O} - E_{tot_A}$. In fact, even when considering a 2.6 kcal/mol (10.9 kJ/mol) intramolecular energy loss, the optimized hydrated structure O′ lies 16.9 kcal/mol (70.6 kJ/mol) below A′.

Note that apart from the usual "hydration" water molecules that are linked to the CO_2^-, CO, NH, or SH group, there are other water molecules that form H bonds with the two interaction sites at the RSH molecule of O′ structure (Fig. 7). These water molecules interact more strongly than the other water molecules; they form what we call a "water bridge". The first water molecule interacts with both the CO_2^- and NH groups while the second one is located between the CO_2^- and SH groups. Furthermore, in both structures A′ and O′, a water molecule acts as a proton donor towards the two oxygens of the carboxylate group, forming a cyclic dimer.

Similar strong water bridges have been suggested for the hydrated structures of GSH (3–5). Some of them contribute to the stabilization of the folded conformations, strengthening the intramolecular H bonds between polar and charged groups. However, we wish to emphasize the fact that the distance between the oxygen in the water molecule and SH group in RSH (2.86 Å) is longer than any other H-bond distance in RSH and in GSH ($d < 2.5$ Å).

2. Conformation of H_2O_2

We did not attempt any optimization of the isolated state of H_2O_2 since a number of experimental and theoretical data (*ab initio* calculations using extended basis) yield a dihedral angle τ of 120° (24).

Can. J. Chem. Downloaded from www.nrcresearchpress.com by 85.192.166.187 on 09/08/12
For personal use only.

Can. J. Chem. Downloaded from www.nrcresearchpress.com by 85.192.166.187 on 09/08/12
For personal use only.

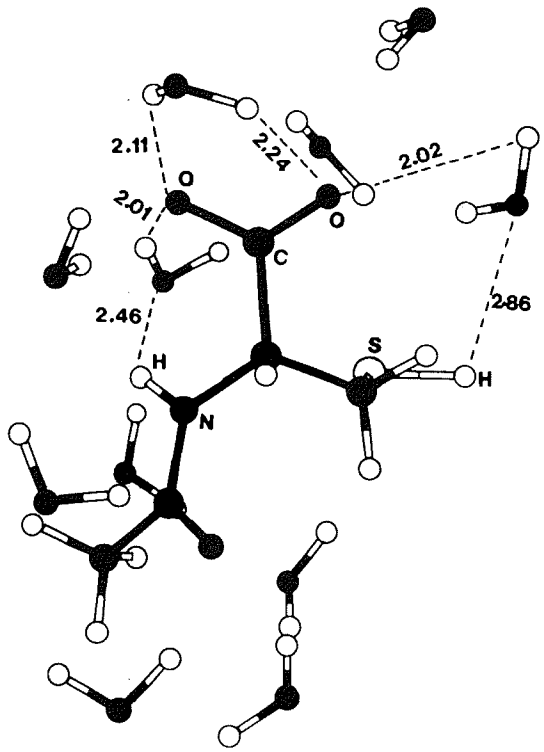

FIG. 7. Hydrated structure O′ of RSH. Intermolecular H-bonds are represented by dashed lines, lengths are in Å.

TABLE 3. Intermolecular energies of RSH...H_2O and RSH...H_2O_2 complexes in which the entity X (H_2O or H_2O_2) forms a bridge between the two interacting sites in RSH[a]

Interaction sites	X between NH...CO_2^-	X between SH...CO_2^-
E_{inter} (H_2O)	−14.6	−12.8
E_{inter} (H_2O_2)	−16.4	−15.0

[a]All energies in kcal/mol.

In the hydrated state, three water molecules satisfy the energetics criterion and yield a stable conformation.

3. *RSH...H_2O_2 complexes*

(i) Isolated state

As shown in a previous work concerning glutathione complexation (3–5), the preferred sites for H_2O_2 are the ones occupied by the water molecules that form H-bonded bridges. Thus we adopted these as our initial positions while keeping RSH and H_2O_2 in their "hydrated" form, and then performed a complete optimization of intra- and intermolecular energies. Table 3 gives an insight to the stability of these complexes. It can be seen that, when the H_2O_2 molecule replaces the water molecule, the interaction energies are lowered by ≅ 2 kcal/mol (8.4 kJ/mol). Furthermore, it can be noticed that the two cyclic complexes that involve either the NH and CO_2^- groups (I) or the SH and CO_2^- groups (II) in the RSH, have nearly the same stability.

In complex I, the CO_2^- and NH groups have rather similar relative positions as in the glycyl residue of GSH. Thus this complex is nearly the same as the one denoted Cgly—gly for [GSH...H_2O_2] (8) but is lower in energy (−16.4 kcal/mol (−68.6 kJ/mol)) by −12.9 kcal/mol (−53.9 kJ/mol) calculated for Cgly—gly. The less favourable interaction energy obtained for GSH probably arises from repulsive contributions between H_2O_2 and the rest of GSH molecule.

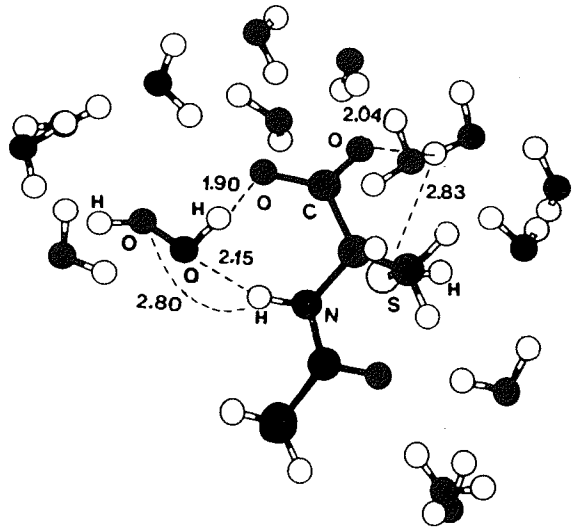

FIG. 8. Hydrated structure of the stable structure of [RSH...H_2O_2] complex. Intermolecular H-bonds are represented by dashed lines, lengths are in Å.

We cannot compare complex II for RSH with that for GSH since the relative positions of CO_2^- and SH groups are different in the two molecules. Effectively, in GSH, H_2O_2 forms a bridge between the glutamyl and cysteyl residues whereas in RSH, both CO_2^- and SH groups belong to the cystein molecule.

Though the two complexes are comparable in stability, we may note that the intermolecular H bonds in complex II are longer than those calculated for complex I (similar results have been obtained in the hydrated state, see Fig. 7).

(ii) Hydrated state

The two stable complexes obtained in the isolated state were surrounded by fourteen water molecules. We have performed complete intra- and intermolecular optimizations on these complexes. Let us define $\Delta E_{hydra} = E_{hydra}(RSH...H_2O_2) - E_{hydra}(RSH) - E_{hydra}(H_2O_2)$, $\Delta E_{tot_1} = \Delta E_{intra} + \Delta E_{hydra} + E_{inter}(RSH...H_2O_2)$; ($\Delta E_{intra}$ is calculated with respect to the complex in the isolated state).

When hydration water molecules are taken into account, it may be noticed that both complexes I and II are destabilized. In fact, this effect is more important for complex II, for which the total energy (ΔE_{tot_1}) is calculated to be ≅ −2 kcal/mol (−8.4 kJ/mol) versus a value of −15 kcal/mol (−62.7 kJ/mol) in vacuo. Thus we may conclude that such a complex cannot really exist in water. The behaviour of complex I is quite different, complexation leads to a 1.8 kcal/mol (7.5 kJ/mol) intramolecular energy gain and to a 9.2 kcal/mol (38.5 kJ/mol) hydration energy loss. However, as a whole, this complex remains stable $\Delta E_{tot_1} = -9.0$ kcal/mol (−37.6 kJ/mol). In Fig. 8 it can be noticed that, apart from the H bonds between H_2O_2 and RSH, there is still a water molecule located between SH and CO_2^- groups.

We are conscious of the fact that the hydration water molecules represent only a part of the whole solvent, so we explore the total effect upon complex I. We therefore performed calculations within the discrete–continuum model. The different energy contributions (including both intermolecular and solvation energies) are calculated following the scheme defined in Fig. 9 and their values are listed in Table 4.

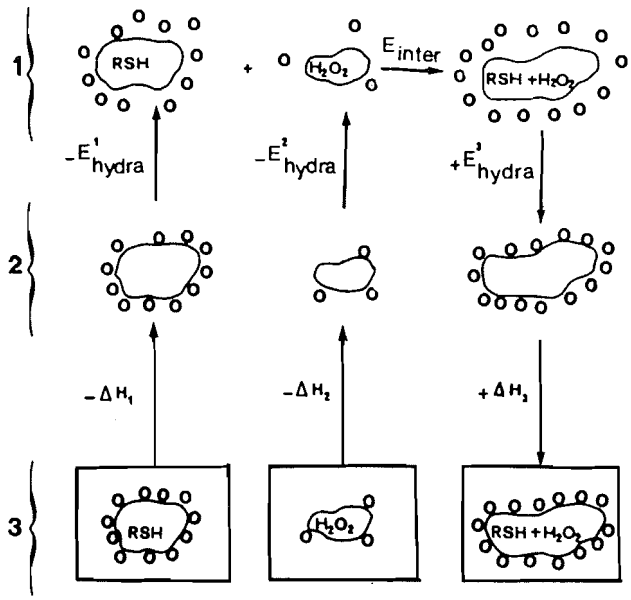

FIG. 9. Scheme of the intermolecular and solvation energies for the RSH and H_2O_2 molecules and [RSH...H_2O_2] complex in the isolated state (level 1), in the hydrated state: with the "hydration water molecules" (level 2) + the bulk solvent (level 3). Water molecules are represented by small circles.

TABLE 4. Variation in intermolecular energies for two solvation models: discrete (model 1), discrete–continuum (model 2)[a]

Model	$-E^1_{Hydra}$	$-E^2_{Hydra}$	E^3_{Hydra}	ΔE_{Intra}	ΔE_{Tot_1}
1	138.6	21.1	−167.0	−1.8	−9.0
Model	ΔH_1	ΔH_2	ΔH_3	ΔH_s	ΔE_{Tot_2}
2	−102.6	−29.8	−130.1	2.3	−6.7

[a]Energy contributions are defined in Fig. 8. $\Delta H_s = \Delta H_3 - \Delta H_1 - \Delta H_2$; $\Delta E_{tot_2} = \Delta E_{tot_1} + \Delta H_s$ (all values in kcal/mol).

From our results (Table 4) it appears that there is an additional energy loss (ΔH_s = 2.3 kcal/mol (9.6 kJ/mol) due to the bulk solvent effect. In fact, the effect of hydration water molecules upon complexes represents the major portion (≅80%), but not the total, of the solvent effect. However, this complex remains stable with ΔE_{tot_2} = −6.7 kcal/mol (−28 kJ/mol) which must remain as the energy of the hydrated complex (versus −16.4 kcal/mol (−68.6 kJ/mol) in the isolated state).

At this stage of our work, let us point out that our energies values are related to the change in enthalpy for binding but not to change in free enthalpy since we did not take entropic effects into account. However, we must emphasize the fact that the orders of magnitude of these enthalpy values are comparable to those obtained experimentally for molecular interactions involving cyclic H bonds between two nucleic bases (25).

Conclusion

Our objectives were (*i*) to examine the possibility for *N*-acetylcysteine to complex with hydrogen peroxide in the first stage of the kinetics and (*ii*) to determine theoretically the most probable site(s) of complexation.

From an experimental kinetic point of view, we have shown that there is a fast initial decay of hydrogen peroxide without a concomitant oxidation of thiol function of RSH. By analogy with the kinetic reaction of GSH/H_2O_2, we attributed this initial decay of H_2O_2 to the formation of a chelate between RSH and H_2O_2. We have determined the corresponding equilibrium constant (880 ± 80), which is of the same order of magnitude as that for GSH/H_2O_2 (1950 ± 50).

Moreover, it can be noticed that, when the initial concentrations of RSH and H_2O_2 are of the same order of magnitude, the end product could be RSSR...H_2O_2 since the final solution exhibits a strong oxidizing power. Since we have established the possible existence of the RSH...H_2O_2 complex, we can reasonably suppose a similar complex for RSSR. Furthermore, the interaction sites for RSSR should be more or less similar to those for RSH.

From a theoretical point of view, we have proposed a model for the complex by studying the intermolecular and intramolecular energies and evaluating the solvent effect. Let us look at two main features: (*i*) in the isolated state there are isoenergetic complexes, in which H_2O_2 form an H-bonded bridge between CO_2^- and either NH (I) or SH (II) groups and (*ii*) the solvent has a rather strong destabilizing effect, which is more influential in complex II that has longer H bonds than in the complex I which remains stable in water.

When we compare the formation of the complexes RSH...H_2O_2 and GSH...H_2O_2, we note that (*i*) the sites of complex formation are similar although they are more numerous in GSH (up to four possible sites, depending on whether the conformation was extended or folded) and (*ii*) the binding energies for the both complexes in vacuo are of the same order of magnitude (between −13 and −25 kcal/mol (−54 and −105 kJ/mol)) and are reasonable. These observations could explain qualitatively the slight difference between the two equilibrium constants. However, at this stage of our work, we cannot explain our experimental equilibrium constants because of we do not know the entropic factors.

We therefore conclude that both RSH and GSH can rapidly complex H_2O_2. We are tempted to speculate or the protective effect of RSH/GSH against the toxicity of H_2O_2. Since the complexation occurs before the reduction of H_2O_2, we might infer a secondary antioxidant defence mechanism against the excess H_2O_2.

Acknowledgments

We thank Pr. C. Ferradini for her keen interest in our work and her constant encouragement. We thank Dr. R. Azerad for helpful discussion and for the synthesis of the disulfide. We are indebted to Dr. J. Caillet for valuable discussions. We also wish to thank the Groupement Scientifique "Modelisation Moléculaire" IBM-CNRS for providing us with computer facilities on 3090-600E.

1. F.J.T. Staal, S.W. Ela, M. Roederer, M.T. Anderson, L.A. Herzenberg, and L.A. Herzenberg. The Lancet, **339**, 909 (1992).
2. M. Roederer, F.J.T. Staal, P.A. Raju, S.W. Ela, L.A. Herzenberg, and L.A. Herzenberg. Proc. Natl. Acad. Sci. USA, **87**, 4884 (1990).
3. T. Kalebic, A. Kinter, G. Poli, M.E. Anderson, A. Meister, and A.S. Fausi. Proc. Natl. Acad. Sci. USA, **88** 986 (1991).
4. S. Mihm, J. Ennen, U. Pessara, R. Kurth, and W. Droge. AIDS, **5**, 497 (1991).
5. B. Halliwell and C.E. Cross. Arch. Intern. Med. **151**, 29 (1991).
6. Z. Abedinzadeh, M. Gardès-Albert, and C. Ferradini. Can. J. Chem. **67**, 1247 (1989).
7. J. Bergès, J. Caillet, J. Langlet, Z. Abedinzadeh, and M. Gardès-Albert. *In* Studies in physical and theoretical chemistry. Vol. 71.

Can. J. Chem. Downloaded from www.nrcresearchpress.com by 85.192.166.187 on 09/08/12
For personal use only.

Edited by J.L. Rivail. Elsevier Science Publishers. 1990. pp. 233–243.
8. J. Bergès, J. Caillet, J. Langlet, and Z. Abedinzadeh. Theor. Chim. Acta, **85**, 87 (1993).
9. Z. Abedinzadeh, M. Gardès-Albert, C. Ferradini, J. Bergès, J. Caillet, and J. Langlet. J. Chim. Phys. **88**, 1003 (1991).
10. J.P. Greenstein and M. Winitz. Chemistry of amino acids. Vol. 3. John Wiley and Sons, Inc., New York. 1961. pp. 1917, 1918.
11. G.L. Ellman. Arch. Biochem. Biophys. **74**, 443 (1958).
12. G. Eisenberg. Ind. Eng. Chem. Anal. Ed. **15**, 327 (1948).
13. M.P. Bonét-Maury. C.R. de l'Academie des Sciences. 1944. pp. 117–119.
14. R. Curci and J.O. Edwards. *In* Organic peroxides. Vol. 1. *Edited by* D. Swern. Wiley Interscience, New York. 1970.
15. N. Gresh, P. Claverie, and A. Pullman. Int. J. Quantum Chem. Symp. **13**, 243 (1979).
16. N. Gresh, P. Claverie, and A. Pullman. Int. J. Quantum Chem. 2, 101 (1986).
17. N. Gresh, P. Claverie, and A. Pullman. Theor. Chim. Acta, **66**, 1 (1984).
18. F. Vigné-Maeder, and P. Claverie. J. Chem. Phys. **88**, 4934 (1988).
19. J. Langlet, P. Claverie, J. Caillet, and A. Pullman. J. Phys. Chem. **92**, 1617 (1988).
20. B. Deprick-Côte, J. Langlet, J. Caillet, J. Bergès, E. Kassab, and R. Constanciel. Theor. Chem. Acta, **82**, 435 (1992).
21. R.A. Pierrotti. J. Phys. Chem. **69**, 281 (1965).
22. M.J. Huron, and P. Claverie. J. Phys. Chem. **78**, 1853 (1974).
23. W.B. Wright. Acta Crystallogr. **11**, 632 (1958).
24. D. Cremer. *In* The chemistry of functional groups, peroxides. *Edited by* S. Patai. John Wiley and Sons Ltd., New York. 1983.
25. I.K. Yanson, A.B. Teplitsky, and L.F. Sukhodub. Biopolymers, **18**, 1149 (1979).
26. Z. Abedinzadeh, J. Arroub, and M. Gardès-Albert. Can. J. Chem. **72**, 2102 (1994).

Can. J. Chem. Downloaded from www.nrcresearchpress.com by 85.192.166.187 on 09/08/12
For personal use only.

On *N*-acetylcysteine. Part II. Oxidation of *N*-acetylcysteine by hydrogen peroxide: kinetic study of the overall process

ZOHREH ABEDINZADEH,[1] JLIL ARROUB, AND MONIQUE GARDÈS-ALBERT

Laboratoire de Chimie Physique, URA 400 CNRS, Université René Descartes, 45, rue des Saints-Pères, 75270 Paris, Cedex 06, France

Received February 1, 1994

ZOHREH ABEDINZADEH, JLIL ARROUB, and MONIQUE GARDÈS-ALBERT. Can. J. Chem. **72**, 2102 (1994).

The oxidation kinetics of *N*-acetylcysteine (RSH) by hydrogen peroxide has been studied at neutral pH at different concentration ratios from 0.2 to 20 (4×10^{-4} mol $L^{-1} \leq [RSH]_0 \leq 2 \times 10^{-2}$ mol L^{-1}, 10^{-4} mol $L^{-1} \leq [H_2O_2]_0 \leq 10^{-2}$ mol L^{-1}). In all the cases studied, *N*-acetylcystine (RSSR) is the only oxidized product formed. Our kinetic data have focused on the importance of the concentration ratio to reach the stoichiometric oxidation of *N*-acetylcysteine by hydrogen peroxide. Indeed non-stoichiometric oxidation of RSH occurs at relatively low concentration ratios ($R < 2.5$) whereas stoichiometric oxidation is observed when $R > 2.5$. Moreover, it has been shown that in the first minutes of the reaction there is the formation of a complex between RSH and H_2O_2, the stoichiometry of the complex being RSH concentration-dependent for a given R ($R > 2.5$). Reaction mechanisms have been quantitatively established and the k values of each step determined.

ZOHREH ABEDINZADEH, JLIL ARROUB et MONIQUE GARDÈS-ALBERT. Can. J. Chem. **72**, 2102 (1994).

On a étudié la cinétique de l'oxydation de la *N*-acétylcystéine (RSH) par le peroxyde d'hydrogène, à un pH neutre, à divers rapports de concentration allant de 0,2 à 20 (4×10^{-4} mol $L^{-1} \leq [RSH]_0 \leq 2 \times 10^{-2}$ mol L^{-1}, 10^{-4} mol $L^{-1} \leq [H_2O_2]_0 \leq 2 \times 10^{-2}$ mol L^{-1}). Dans tous les cas étudiés, le seul produit formé est la *N*-acétylcystine (RSSR). Nos données cinétiques mettent l'accent sur l'importance du rapport de concentrations nécessaire à l'atteinte de la stoechiométrie. En effet, l'oxydation non stoechiométrique de RSH se produit pour des rapports de concentrations relativement faibles ($R < 2,5$) alors que l'oxydation stoechiométrique est observée lorsque $R > 2,5$. De plus, on a montré que dans les premières minutes de la réaction, il y a formation d'un complexe entre le RSH et le H_2O_2 dont la stoechiométrie, pour une valeur donnée de R ($R > 2,5$), dépend de la concentration du RSH. On a établi quantitativement les mécanismes de réaction et on a déterminé les valeurs de k de chacune des étapes.

[Traduit par la rédaction]

Introduction

The univalent reduction of molecular oxygen results in the formation of reactive oxygen intermediates, so-called reactive oxygen species, that may disrupt cellular function by direct or indirect oxidation of cellular lipids, proteins, and nucleic acids (1–7). It is clear that the cells have developed an extensive collection of antioxidant defence. However, there are situations, both physiological and pathological, in which cells are exposed to an unusually high load of oxidants and free radicals (oxidative stress). Elevated quantities of reactive oxygen species, including H_2O_2, are also produced during the metabolism of certain xenobiotics and are often associated with the initiation of lipid peroxidation and acute toxicity (8, 9). Many authors have implicated reactive oxygen species as important causative agents of aging and of several human diseases. Inactivations of unusual quantities of reactive oxygen species by antioxidant therapy has been proposed by many authors (10–12).

In this framework *N*-acetylcysteine (RSH) has been widely used as an antioxidant in vivo and in vitro. For example, it decreases the toxicity of diquat to hepatocytes (13), protects animals against paracetamol hepathotoxicity (14), and it serves as the antidote of choice for paracetamol overdose in humans (15). It has received attention as an antioxidant for components of cigarette smoke (16, 17) and for treatment of various respiratory diseases (18). Recently, there have been several reports suggesting that *N*-acetylcysteine is cardioprotective against ischemia/reperfusion injury (19, 20) and finally several authors have proposed *N*-acetylcysteine as a therapeutic agent in AIDS (Acquired Immunodeficiency Syndrome) (21–25).

Although it is not clear the mechanisms by which *N*-acetylcysteine might be able to act as an oxidant scavenger in vivo, some authors suggest that the antioxidant properties of RSH come as a result of direct of oxidant species and others propose that RSH acts as a precursor of the natural antioxidant glutathione; or a combination of these two modes of action.

Concerning the antioxidant action of *N*-acetylcysteine towards hydrogen peroxide, it has been shown to react slowly with H_2O_2 (26), and an approximate rate of reaction of *N*-acetylcysteine with H_2O_2 was given by Aruoma et al. (27) (0.85 mol^{-1} L s^{-1}) by following only the loss of *N*-acetylcysteine in the reacting mixture in less than one half-live.

We have therefore investigated the mechanism of oxidation of RSH by H_2O_2 to better understand the process by which RSH might be able to act as a direct oxidant scavenger. The kinetics of this reaction has been studied in neutral aerated aqueous medium at different concentrations: 4×10^{-4} mol $L^{-1} \leq [RSH]_0 \leq 2 \times 10^{-2}$ mol L^{-1}, 10^{-4} mol $L^{-1} \leq [H_2O_2]_0 \leq 10^{-2}$ mol L^{-1}, and at different ratios of $[RSH]_0/[H_2O_2]_0$ (0.2 to 20).

Materials and methods

See ref. 29 for the experimental and theoretical approaches of the *N*-acetylcysteine/H_2O_2 complexation.

Experimental results

Kinetics for the reaction of *N*-acetylcysteine with hydrogen peroxide are functions of the concentration ratios R ($R = [RSH]_0/[H_2O_2]_0$). For a given value of R, they depend on the

[1]Author to whom correspondence should be addressed.

Can. J. Chem. Downloaded from www.nrcresearchpress.com by 85.192.166.187 on 09/08/12
For personal use only.

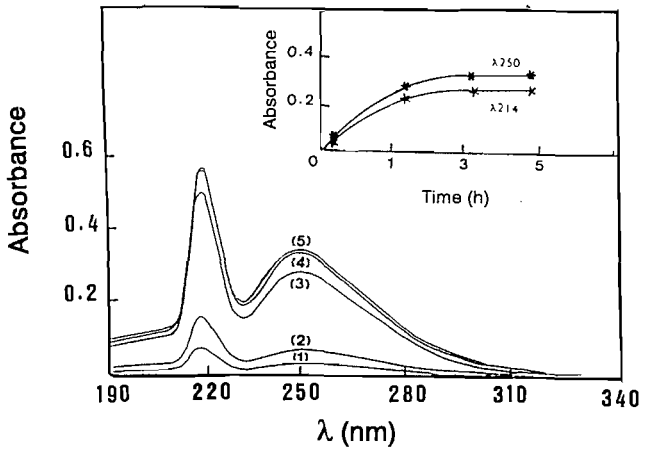

FIG. 1. Differential absorption spectra of the reaction mixture: $R = [RSH]_0/[H_2O_2]_0 = 0.2$, $[RSH]_0 = 2 \times 10^{-3}$ mol L^{-1}, $[H_2O_2]_0 = 10^{-2}$ mol L^{-1}, phosphate buffer 10^{-2} mol L^{-1}, pH 7, $l = 0.875$ cm. Reference: $[RSH]_0 = 4 \times 10^{-3}$ mol L^{-1}, $[H_2O_2]_0 = 2 \times 10^{-2}$ mol L^{-1} ($l = 0.4375$ cm) (two chambers cell, see ref. 29, Materials and methods section). (*1*) 03 min, (*2*) 0.9 min, (*3*) 1 h 10 min, (*4*) 2 h 10 min, (*5*) 3 h after the start of the reaction. In inset, evolutions of the absorbances as a function of time at λ 250 nm and λ 214 nm.

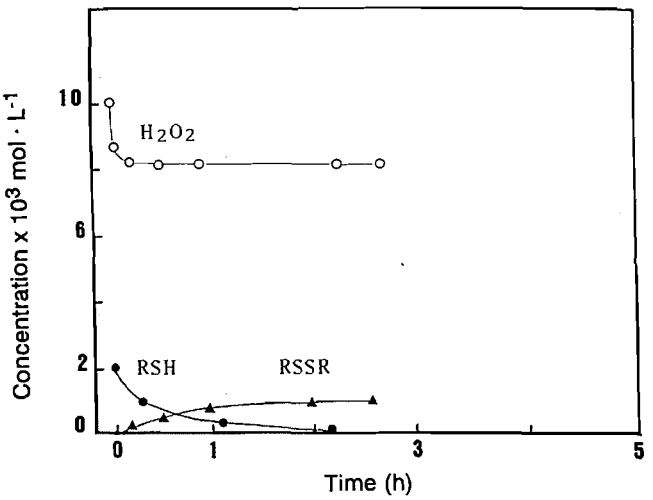

FIG. 2. Kinetic evolution of hydrogen peroxide (○), *N*-acetylcysteine (●), and *N*-acetylcystine (▲) as a function of time. $R = [RSH]_0/[H_2O_2]_0 = 0.2$, $[RSH]_0 = 2 \times 10^{-3}$ mol L^{-1}, $[H_2O_2]_0 = 10^{-2}$ mol L^{-1}, phosphate buffer 10^{-2} mol L^{-1}, pH 7.

concentrations of RSH. Thus we have studied reactions corresponding to $R < 2.5$ (see § I); $R \geq 2.5$ (see § II); and finally for a given R ($R > 2.5$), the effect of the thiol concentration (see § III).

I. Kinetic results for R < 2.5

(a) Differential absorption spectra of the reaction mixture

In Fig. 1, as an example, are reported the differential absorption spectra of a solution containing $[RSH]_0$ 2×10^{-3} mol L^{-1} and $[H_2O_2]_0$ 10^{-2} mol L^{-1} ($R = 0.2$, phosphate buffer 10^{-2} mol L^{-1}, pH 7) at various times after mixing. The differential absorption spectrum (*1*) recorded 3 min after mixing shows two maxima at 214 and 250 nm. These absorptions increase until the end of reaction (spectra (*2*) to (*5*)).

The kinetics at 250 and 214 nm are reported in the inset of Fig. 1. These curves appear to increase rather quickly for an hour, then they grow slowly until the end of reaction. These absorptions have been attributed to RSSR ($\Delta\epsilon_{250} = 330$ mol^{-1} L cm^{-1}). At the end of the reaction, the disulfide concentration is 1×10^{-3} mol L^{-1} which corresponds to the total transformation of RSH into RSSR. Consequently, we can assume that the thiol is stoichiometrically oxidized into RSSR.

(b) Evolution of RSH, H_2O_2, and RSSR

For the same experiment ($[RSH]_0 = 2 \times 10^{-3}$ mol L^{-1}, $[H_2O_2]_0 = 10^{-2}$ mol L^{-1}, $R = 0.2$, phosphate buffer 10^{-2} mol L^{-1}, pH 7) we have reported in Fig. 2, the simultaneous changes in $[H_2O_2]$, [RSH], and [RSSR] as a function of time. Note that the concentration of RSSR has been determined as previously described in I(*a*). As can be seen, the concentration of hydrogen peroxide decreases abruptly, while RSH disappears slowly and RSSR emerges slowly. Indeed, the changes in concentration end in about 2 h for RSH and RSSR whereas for H_2O_2 the change ends in about 30 min after reaction starts. Moreover, the initial drop in H_2O_2 (75% of the total H_2O_2 decay) occurs in less than 2 min. Similar trends have also been observed in $R = 1$ (see ref. 29, Experimental results). This drop has been attributed to the rapid complexation of H_2O_2 by RSH without oxidizing the thiol group in RSH. Thermodynamic equilibrium constant of complexation has been estimated using the method described in ref. 29. In the case of $R = 0.2$ we have found $K = 850$, which is in agreement with the results in ref. 29 (Discussion) ($K = 900 \pm 100$).

At the end of the reaction (~2 h), the final concentrations of RSH, H_2O_2, and RSSR equal to 0, 8×10^{-3} mol L^{-1} and 10^{-3} mol L^{-1}. Hence the amounts of RSH and H_2O_2 consumed are 2×10^{-3} mol L^{-1} and 2×10^{-3} mol L^{-1}. At the end of the reaction, 1 mol of RSH reacts with 1 mol of H_2O_2 to give half a mole of RSSR. The same has been observed for three other experiments ($R = 0.4$, 0.6, 1, see Table 1).

To follow the course of the hydrogen peroxide, we performed the following tests: (*i*) At the end of an experiment ($R = 1$) when no free H_2O_2 was present we have added catalase (10^{-7} mol L^{-1}). We observed the formation of the dioxygen whose concentration equals to the final concentration of RSSR. (*ii*) When we added an excess of RSH at the end of the experiment ($R = 1$) when no free H_2O_2 was present we observed the formation of extra RSSR. (*iii*) We have tested the eventual formation of dioxygen during our kinetic studies ($R = 1$) by Gilson Oxygraph. Any formation of dioxygen observed was due to disproportionation.

Thus, these tests demonstrated the residual oxidizing power of the end product, which might come from the presence of a "bound hydrogen peroxide compound" or from a peroxide bond in the final oxidized product [RSSR...H_2O_2]. It should be noted that these three tests were performed at $R = 1$, since in other cases ($R = 0.2$, 0.4, 0.6) there is always free H_2O_2 remaining in the medium at the end of the reaction. The free H_2O_2 may interfere with the bound hydrogen peroxide.

II. Kinetic results for R > 2.5

(a) Differential absorption spectra of the reaction mixture

As can be seen in Fig. 3 ($[RSH]_0 = 4 \times 10^{-3}$ mol L^{-1}, $[H_2O_2]_0 = 5 \times 10^{-4}$ mol L^{-1} ($R = 8$, phosphate buffer 10^{-2} mol L^{-1}, pH 7) the differential spectra exhibit two maxima at 214 and 250 nm, showing the formation of RSSR as a function of

Can. J. Chem. Downloaded from www.nrcresearchpress.com by 85.192.166.187 on 09/08/12
For personal use only.

TABLE 1. The final balance of the reactions having the concentration ratios R ($R = [RSH]_0/[H_2O_2]_0$) greater than 2.5[a]

$[H_2O_2]_0$ 10^3 mol L^{-1}	$[RSH]_0$ 10^3 mol L^{-1}	$R = [RSH]/[H_2O_2]$	$[RSH]_c$ 10^3 mol L^{-1}	$[H_2O_2]_c$ 10^3 mol L^{-1}	$[RSSR]_f$ 10^3 mol L^{-1}
10	2	0.2	2	2	1
5	2	0.4	2	2	1
1	0.6	0.6	0.6	0.5	0.3
1	1	1	1	1	0.5
1	2.5	2.5	1.73	0.9	0.73
0.8	2.5	3	2	0.75	0.75
0.5	4	8	1	0.5	0.42
0.5	5	10	1	0.5	0.46
0.1	1.5	15	0.18	0.10	0.10
0.125	2.5	20	0.25	0.125	0.12

[a]$[RSH]_c$ = [RSH] consumed, $[H_2O_2]_c$ = $[H_2O_2]$ consumed, and $[RSSR]_f$ = final value of [RSSR].

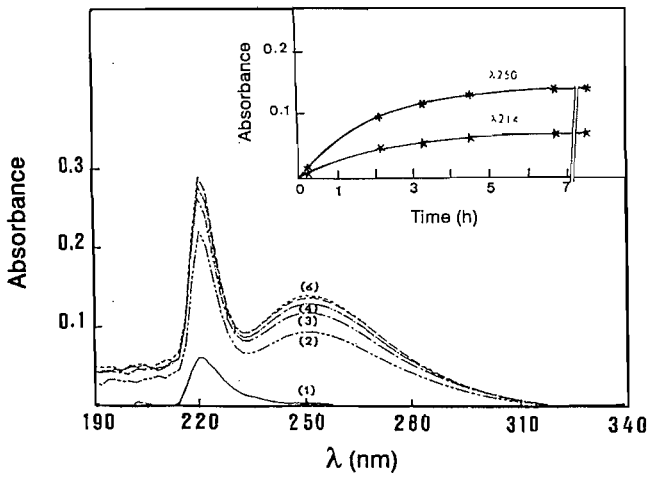

FIG. 3. Differential absorption spectra of the reaction mixture: $R = [RSH]_0/[H_2O_2]_0 = 8$, $[RSH]_0 = 4 \times 10^{-3}$ mol L^{-1}, $[H_2O_2]_0 = 5 \times 10^{-4}$ mol L^{-1}, phosphate buffer 10^{-2} mol L^{-1}, pH 7, l = 0.875 cm. Reference: $[RSH]_0 = 8 \times 10^{-3}$ mol L^{-1}, $[H_2O_2]_0 = 10^{-3}$ mol L^{-1} (l = 0.4375 cm) (two chambers cell, ref. 29 Materials and methods section). (*1*) 3 min, (*2*) 2 h 10 min, (*3*) 3 h 15 min, (*4*) 4 h 30 mn, (*5*) 5 h 20 min, (*6*) 6 h 40 mn after the start of the reaction. In inset, evolutions of the absorbances as a function of time at λ 250 nm and λ 214 nm.

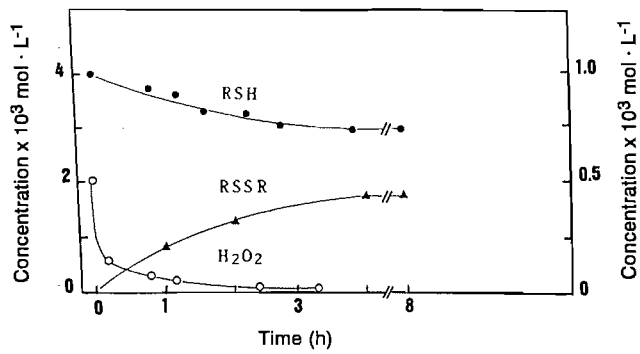

FIG. 4. Kinetic evolution of hydrogen peroxide (○), *N*-acetylcysteine (●), and *N*-acetylcystine (▲) as a function of time. $R = [RSH]_0/[H_2O_2]_0 = 8$, $[RSH]_0 = 4 \times 10^{-3}$ mol L^{-1} (left scale), $[H_2O_2]_0 = 5 \times 10^{-4}$ mol L^{-1} and [RSSR] (right scale), phosphate buffer 10^{-2} mol L^{-1}, pH 7.

time (spectra (*1*)–(*5*)). Figure 3 inset shows the absorbances at 214 and 250 nm. These absorptions increase as a function of time, until they reach a plateau in ~7 h. Notice that these spectra are similar to that observed for $R < 2.5$, meaning that the only oxidized final product is RSSR. At the end of the reaction, the concentration of RSSR is found to be 4.2×10^{-4} mol L^{-1}, showing that 84% of H_2O_2 have oxidized RSH to RSSR.

(b) Changes in [RSH], [H_2O_2], and [RSSR]

For the same experiment ($[RSH]_0 = 4 \times 10^{-3}$ mol L^{-1}, $[H_2O_2]_0 = 5 \times 10^{-4}$ mol L^{-1}, $R = 8$, phosphate buffer 10^{-2} mol L^{-1}, pH 7) it is reported in Fig. 4 the changes in [RSH], $[H_2O_2]$, and [RSSR] with time. We notice the decrease in $[H_2O_2]$ and the slow changes in [RSH], [RSSR], as in the case of $R < 2.5$. The rapid disappearance of H_2O_2 is related to the initial complexation of RSH by H_2O_2. Thermodynamic equilibrium constant of complexation in this case is 875, which is in agreement with the equilibrium constant determined in ref. 29, Discussion section.

At the end of the reaction (~7 h), the final concentrations of RSH, H_2O_2, and RSSR equal to 3×10^{-3}, 0, and 4.2×10^{-4} mol L^{-1}. Thus at the end of the reaction, 2 mol of RSH have reacted with 1 mol of H_2O_2 to give 1 mol of RSSR. The same has been observed for all experiments having concentration ratios of $R > 2.5$. This is the normally accepted stoichiometry when excess thiol reacts with hydrogen peroxide.

III. Effect of different concentrations of RSH on a given R ($R > 2.5$)

We have studied the effect of higher RSH concentrations when R = 10, 15, and 20 ($[RSH]_0 \geq 10^{-2}$ mol L^{-1}). Figure 5 ($[RSH]_0 = 2 \times 10^{-2}$ mol L^{-1}, $[H_2O_2]_0 = 1.33 \times 10^{-3}$ mol L^{-1} (R = 15, phosphate buffer 10^{-2} mol L^{-1}, pH 7) shows the changes in concentrations of H_2O_2, RSH, and RSSR with time. As in previous experiments (see § I and II), there is an initial fast drop in $[H_2O_2]$, and while about 65% of H_2O_2 disappears, RSH does not oxidize into RSSR. Then, the thiol concentration decreases slowly for 4 h while at the same time RSSR is slowly formed and H_2O_2 slowly disappears. The overall reaction shows that 2 mol of RSH react with 1 mol of H_2O_2 to give 1 mol of RSSR, a stoichiometry characteristic of $R > 2.5$. However, complexation of H_2O_2 cannot be explained by 1 mol of H_2O_2 reacting with 1 mol of RSH (reaction [1]). Indeed, with reaction [1], the thermodynamic equilibrium constant for complexation is found to be smaller by one order of magnitude (≈100 instead of 900 ± 100). It is the same observation for the two R's (R = 10, $[RSH]_0 = 10^{-2}$ mol L^{-1}, $[H_2O_2]_0 = 10^{-3}$ mol L^{-1}; and $R = 20$, $[RSH]_0 = 2 \times 10^{-2}$ mol L^{-1}, $[H_2O_2]_0 = 10^{-3}$ mol

Can. J. Chem. Downloaded from www.nrcresearchpress.com by 85.192.166.187 on 09/08/12
For personal use only.

TABLE 2. Determination of equilibrium constant for the formation of the complex $[RSH...H_2O_2...RSH] : [C]_{eq}$

$[RSH]_0$ 10^3 mol L^{-1}	$[H_2O_2]_0$ 10^3 mol L^{-1}	R	$[RSH]_{eq}$ 10^3 mol L^{-1}	$[H_2O_2]_{eq}$ 10^3 mol L^{-1}	$[C]_{eq}$ 10^3 mol L^{-1}	K
10	1	10	9	0.5	0.5	111
20	1.33	15	18.2	0.45	0.88	107
20	1	20	19.4	0.32	0.68	110

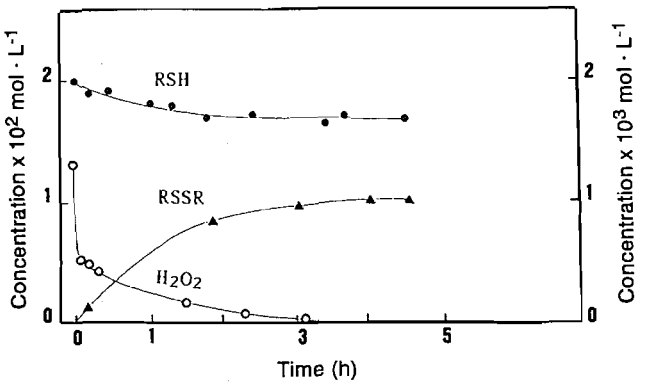

FIG. 5. Kinetic evolution of hydrogen peroxide (○), *N*-acetylcysteine (●), and *N*-acetylcystine (▲) as a function of time. $R = [RSH]_0/[H_2O_2]_0 = 15$, $[RSH]_0 = 2 \times 10^{-2}$ mol L^{-1} (left scale), $[H_2O_2]_0 = 1.33 \times 10^{-3}$ mol L^{-1} and [RSSR] (right scale), phosphate buffer 10^{-2} mol L^{-1}, pH 7.

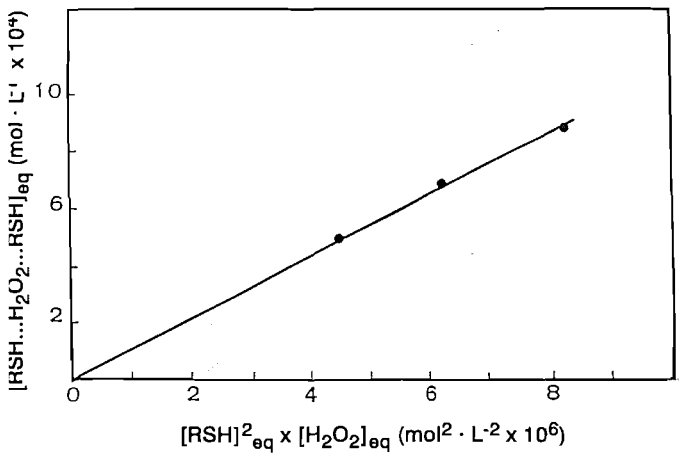

FIG. 6. Chelate concentration at equilibrium $[RSH...H_2O_2...RSH]_{eq}$ as a function of $[RSH]_{eq}^2 \times [H_2O_2]_{eq}$. Phosphate buffer 10^{-2} mol L^{-1}, pH 7.

L^{-1}) for which the equilibrium constants are the same order of magnitude (≈ 100). Hence we propose yet another type of complexation reaction in which 2 mol of RSH complex with 1 mol of H_2O_2 (reaction [2]). This mechanism is compatible with high concentrations of RSH in the medium.

[2] $2\ RSH + H_2O_2 \rightleftarrows [RSH...H_2O_2...RSH]$

Equilibrium constant K_2 is determined by measuring [RSH], $[H_2O_2]$, and $[RSH...H_2O_2...RSH]$ at equilibrium. These values are shown in Table 2. Note that the titanium sulphate method allows one to assay only the free hydrogen peroxide and not the bound hydrogen peroxide in the chelate. Concentration of H_2O_2 at equilibrium, $[H_2O_2]_{eq}$, has been determined by extrapolating to $t = 0$ the subsequent slow decrease in $[H_2O_2]$. The concentration of chelate at equilibrium has been deduced from the difference $[H_2O_2]_0 - [H_2O_2]_{eq}$. Ellman's reagent, which assays the thiol concentration, gives the sum of free *N*-acetylcysteine and its chelated form. Hence the concentration of *N*-acetylcysteine at equilibrium is calculated as the difference between the initial concentration of RSH and two times concentration of the chelate at equilibrium. In Fig. 6 are reported the values of $[RSH...H_2O_2...RSH]_{eq}$ as a function of the product $[RSH]^2_{eq} \times [H_2O_2]_{eq}$. The slope of the straight line is 110 ± 5.

Discussion

We propose the following scheme to interpret our results:

[1] $RSH + H_2O_2 \rightleftarrows [RSH...H_2O_2]$

[2] $RSH + H_2O_2 \rightleftarrows [RSH...H_2O_2...RSH]$

[3] $2\ [RSH...H_2O_2] \rightarrow [RSSR...H_2O_2] + 2H_2O$

[4] $[RSSR...H_2O_2] + 2RSH \rightarrow 2\ RSSR + 2H_2O$

[5] $[RSH...H_2O_2...RSH] \rightarrow RSSR + 2H_2O$

Reaction [1] represents the complexation of H_2O_2 by RSH to yield $[RSH...H_2O_2]$. This reaction has already been discussed in ref. 29, the preceding paper. The equilibrium constant at low concentrations of RSH ($<10^{-2}$ mol L^{-1}) has been determined. Experimental K_1 is 880 ± 80 (see preceding paper). The overall reaction [2] is the complexation of H_2O_2 by 2 mol of RSH when [RSH] is high ($\geq 10^{-2}$ mol L^{-1}). The equilibrium constant K_2 has been found to equal 110 ± 5. Reaction [3] involves the formation of complexed RSSR from the reaction of $[RSH...H_2O_2]$ with itself. Similar reaction has been proposed for glutathion (28). The formation of RSSR is consistent with the following experimental results: (*i*) at the end of the reaction, when there is no free H_2O_2, the addition of catalase stimulates the formation of oxygen and (*ii*) the addition of an excess of RSH leads to the formation of an extra RSSR equal to bounded H_2O_2 (see Experimental results and discussion in preceding paper). Reaction [3] takes place when a non-stoichiometric process is observed, that is, $R < 2.5$. Reaction [4] represents the action of RSH with the complexed RSSR. This occurs when R is > 2.5 (the concentration of the remaining thiol is less than 10^{-2} mol L^{-1}). Similar reaction has been suggested for glutathion (28). We propose that reaction [5] is an unimolecular decay of the second complex $[RSH...H_2O_2...RSH]$ to give the non-complexed disulfide RSSR.

The corresponding rate constants have been determined by numerical analyses of the kinetic differential equations using an iteration program. This calculation has been performed for three different experimental conditions: (*1*) $R < 2.5$, [RSH] < 10^{-2} mol L^{-1}; (*2*) $R > 2.5$, [RSH] < 10^{-2} mol L^{-1}; (*3*) $R > 2.5$, [RSH] > 10^{-2} mol L^{-2}.

In the first case ($R < 2.5$, [RSH] < 10^{-2} mol L^{-1}) we only take reactions [1], [−1], and [3] into consideration since the oxida-

Can. J. Chem. Downloaded from www.nrcresearchpress.com by 85.192.166.187 on 09/08/12
For personal use only.

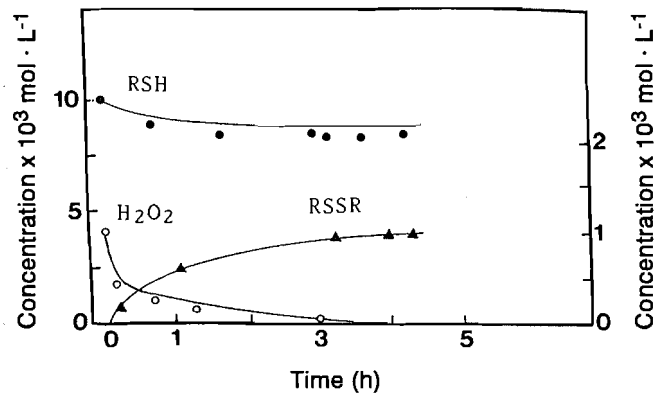

FIG. 7. Comparison between the computed kinetic curves and the experimental points [RSH] + [RSH...H_2O_2] (●), [H_2O_2] (○), [RSSR...H_2O_2] (▲): $R = [RSH]_0/[H_2O_2]_0 = 10$, $[RSH]_0 = 10^{-2}$ mol L^{-1} (left scale), $[H_2O_2]_0 = 10^{-3}$ mol L^{-1} and [RSSR] (right scale), phosphate buffer 10^{-2} mol L^{-1}, pH 7 (points are experimental).

tion of RSH by H_2O_2 is non-stoichiometric, the final product is the chelate [RSSR...H_2O_2]. Using this kinetic scheme we have calculated the three rate constants k_1, k_{-1}, and k_3 (using a known experimental equilibrium constant $K_1 = 880 \pm 80$): $k_1 = 25 \pm 5$ mol^{-1} L s^{-1}, $k_{-1} = 0.03 \pm 0.1$ s^{-1}, $K_1 = 900 \pm 100$, $k_3 = 0.5 \pm 0.2$ mol^{-1} L s^{-1}.

The calculated curves (R = 0.2, 0.4, 0.6, 1) are in perfect agreement with experimental curves, (see as an example for R = 0.2, Fig. 2 where curves are calculated).

Hence the kinetic scheme [1], [−1], and [3] seems to be consistent with the overall oxidation process (reaction I)

[I] $2\ RSH + 2\ H_2O_2 \rightarrow [RSSR...H_2O_2] + 2\ H_2O$

In the second case ($R > 2.5$, [RSH] < 10^{-2} mol L^{-1}) we have determined the rate constant of reaction [4], k_4. Under these conditions, reactions [1], [−1], [3], and [4] are taken into considerations, since the overall oxidation is stoichiometric. Using k_1, k_{-1}, and k_2 reported above, $k_4 = 40 \pm 10$ mol^{-1} L s^{-1} provides the best agreement with all the experimental curves. As an example, see Fig. 4 for R = 8 (the curves are calculated).

Consequently, the kinetic sequence [1], [−1], [3], and [4] is consistent with the overall stoichiometric oxidation process (reaction II).

[II] $2RSH + H_2O_2 \rightarrow RSSR + 2\ H_2O_2$

In the third case ($R > 2.5$, [RSH] > 10^{-2} mol L^{-1}) the rate constants k_2, k_{-2} (given that the experimental equilibrium constant $K_2 = 110 \pm 5$) and k_5 have been determined. Here we used the kinetic scheme [2], [−2], and [5]. The following k values provide the best agreement with the experimental curves (as an example see Fig. 7 for R = 10): $k_2 = 90 \pm 20$ mol^{-2} L^2 s^{-1}; $k_{-2} = 0.9 \pm 0.1$ s^{-1}; $K_2 = 110 \pm 20$; $k_5 = 0.03 \pm 0.01$ s^{-1}.

Thus the kinetic scheme [2], [−2], and [5] is in agreement with the overall stoichiometric oxidation process (reaction II)

[II] $2RSH + H_2O_2 \rightarrow RSSR + 2\ H_2O$

However, it should be noted that the fits are equally good using the full kinetic scheme (reactions [1], [−1], [2], [−2], [3], [4], and [5]) with the same theoretical rate constants used as above.

As to reaction [2], it is obvious that it is not an elementary step. It has been suggested[2] that another way of expressing reaction [2] is

[2′] $[RSH...H_2O_2] + RSH \rightleftarrows [RSH...H_2O_2...RSH]$

Nevertheless, we have no experimental proof to support [2′]. However, we have put the hypothesis to test, since K_2 would be $K_1K_{2'}$. Indeed the fits agree reasonably well with the reaction sequence [1], [−1], [2′], [−2′], [3], [4], and [5]. It should be noted that only k_5 is different by a factor of 3 (0.1 ± 0.05).

Conclusion

Our purpose was to quantitatively determine the mechanism and the kinetic parameters describing the action of hydrogen peroxide with *N*-acetylcysteine in aqueous medium buffered at pH 7. The analysis of the reaction mixture as a function of time, was performed using (*1*) Ellman's reagent to assay the thiol function of RSH and of the eventual complexes [RSH...H_2O_2] and [RSH...H_2O_2...RSH], (*2*) the titanium method to determine free H_2O_2, and (*3*) the differential absorbances of the aqueous solution in the UV region to assay the concentration of the disulfide of *N*-acetylcysteine, RSSR and of the eventual complex [RSSR...H_2O_2]. Thus the overall reaction is known at each stage of the kinetics and particularly at the end of the reaction.

The striking features of the reaction of *N*-acetylcysteine with hydrogen peroxide are summarized as follows. First of all, we have shown the importance of the concentration ratio R ($[RSH]_0/[H_2O_2]_0$) in the kinetic evolution since non-stoichiometric oxidation of RSH occurs when $R < 2.5$ whereas stoichiometric oxidation occurs when $R > 2.5$. Secondly, we have confirmed the formation of a complex between H_2O_2 and RSH in the first minutes of the reaction under all experimental conditions as described in the preceding paper. However, stoichiometry of the complex is dependent on the concentration of RSH at the highest R values ($R > 2.5$).

The rate constants for each step in the reaction mechanism have been calculated and they are in very good agreement with all experimental kinetic data.

The comparison of these results with those obtained with another thiol, the glutathione GSH (28) shows several similarities: (*i*) the formation of a complex between GSH and H_2O_2, [GSH...H_2O_2], with a K value of the same order of magnitude ($K = 2000 \pm 700$ (28)) as in the case of *N*-acetylcysteine ($K = 900 \pm 100$); (*ii*) a non-stoichiometric oxidation process for the lowest values of $R = [GSH]/[H_2O_2]$ (28) as for RSH.

The scavenging of H_2O_2 by RSH and GSH before reacting to give the disulfide certainly contributes to the antioxidant properties of the two biological systems. It is tempting to contemplate if other molecules with similar structures might exhibit similar interesting properties.

Acknowledgments

The authors wish to thank Professor C. Ferradini for her keen interest in their work and her constant encouragement and invaluable participation in this project. They thank Dr. R. Azerad for helpfull discussion and for the synthesis of the disulfide. They also thank B. Champion for NMR technical assistance.

[2]This reaction was suggested by an anonymous referee.

Can. J. Chem. Downloaded from www.nrcresearchpress.com by 85.192.166.187 on 09/08/12
For personal use only.

1. K. Brawn and I. Fridovich. Arch. Biochem. Biophys. **206**, 414 (1981).
2. B. Halliwell and J.M.C. Gutterige. Arch. Biochem. Biophys. **246**, 501 (1986).
3. I. Fridovich. Science, **201**, 875 (1978).
4. K.J.A. Davies. *In* Oxidation damage and repair. *Edited by* K.J.A. Davies. Pergamon Press, Oxford. 1990. pp. xvii–xxvii.
5. K.J.A. Davies. J. Biol. Chem. **262**, 9895 (1987).
6. J.F. Mead. *In* Free radicals in biology. *Edited by* W.A. Pryor. Academic Press, New York. 1976. pp. 51–68.
7. R. Adelman, R.L. Saul, and B.N. Ames. Proc. Natl. Acad. Sci. USA, **961**, 316 (1988).
8. J.S. Bus and J.E. Gibson. *In* Drug metabolism and drug toxicity. *Edited by* J.R. Mitchell, M.D. Horning. Raven Press, New York. 1984. pp. 21–31.
9. M.T. Smith, C.G. Evans, H. Thor, and S. Orrenius. *In* Oxidative stress. *Edited by* H. Sies. Academic Press, New York. 1985. p. 91*ff*.
10. C. Ceconi, S. Curello, A. Cargoni, G.M. Boffa, and R. Ferrari. Cardioscience, **3**, 191 (1990).
11. H.J. Schiller, P.M. Reilly, and G.B. Bulkley. *In* Oxidative damage and repair. *Edited by* K.J.A. Davies. Pergamon Press, Oxford. 1990. pp. 673–682.
12. P.D. Wagner, O. Mathieu-Costello, D.E. Bebout, A.T. Gray, P.D. Natterson, C. Glennow. Eur. Respir. J. **2**, 116 1989.
13. I.A. Cotgreave, M.S. Sandy, M. Berggren, P.W. Moldéus, and M.T. Smith. Biochem. Pharmacol. **36**, 2899 (1987).
14. J.O. Miners, R. Drew, and D.J. Birkett. Biochem. Pharmacol. **33**, 2995 (1984).
15. M.J. Smilkstein, G.L. Knapp, K.W. Kulig, and B.H. Rumack. N. Engl. J. Med. **319**, 1557 (1988).
16. H. Sprince. Eur. J. Respir. Dis. **66** (suppl. 139), 102 (1985).
17. P. Moldéus, M. Berggren, and R. Graftstrom. Eur. J. Respir. Dis. **66**, (suppl. 139), 123 (1985).
18. I. Ziment. Respiration, **50** (suppl. 1), 31 (1986).
19. Y. Qiu, M. Bernier, D.J. Hearse. **1**, 65 (1990).
20. M.B. Forman, D.W. Puett, C.U. Cates, D.E. McCroskey, J.K. Beckman, H.L. Greene, and R. Virmani. Circulation, **78**, 202 (1988).
21. M. Roederer, F.J.T. Staal, P.A. Raju, S.W. Ela, L.A. Herzenberg, and L.A. Herzenberg. Proc. Natl. Acad. Sci. USA, **87**, 4884 (1990).
22. Kalebic, T., A. Kinter, G. Poli, M.E. Anderson, A. Meister, and A.S. Fausi. Proc. Natl. Acad. Sci. USA, **88**, 986 (1991).
23. S. Mihm, J. Ennen, U. Pessara, R. Kurth, and W. Dröge. AIDS, **5**, 497 (1991).
24. B. Halliwell and C.E. Cross. Arch. Intern. Med. **151**, 29 (1991).
25. F.J.T. Staal, S.W. Ela, M. Roederer, M.T. Anderson, L.A. Herzenberg, and L.A. Herzenberg. The Lancet, **339**, 909 (1992).
26. P. Moldéus, I.A. Cotgreave, and M. Berggren. Respiration, **50** (suppl. 1), 31 (1986).
27. O.I. Aruoma, B. Halliwell, B.M. Hoey, and J. Butler. Free Radical Biol. Med. **6**, 593 (1989).
28. Z. Abedinzadeh, M. Gardès-Albert, and F. Ferradini. Can. J. Chem. **67**, 1247 (1989).
29. J. Arroub, J. Bergès, Z. Abedinzadeh, J. Langlet, and M. Gardès-Albert. Can. J. Chem. **72**, 2094 (1994).

Can. J. Chem. Downloaded from www.nrcresearchpress.com by 85.192.166.187 on 09/08/12
For personal use only.

1,3-Dipolar cycloaddition reactions of monocyclic aziridines with dimethyl 1-cyclobutene-1,2-dicarboxylate

KIYOSHI MATSUMOTO[1] AND HIROKAZU IIDA
Graduate School of Human and Environmental Studies, Kyoto University, Kyoto 606-01, Japan

TAKANE UCHIDA AND YOSHIMI YABE
Faculty of Education, Fukui University, Fukui 910, Japan

AKIKAZU KAKEHI
Faculty of Engineering, Shinshu University, Nagano 380, Japan

AND

J. WILLIAM LOWN[1]
Department of Chemistry, University of Alberta, Edmonton, AB T6G 2G2, Canada

Received February 15, 1994

KIYOSHI MATSUMOTO, HIROKAZU IIDA, TAKANE UCHIDA, YOSHIMI YABE, AKIKAZU KAKEHI, and J. WILLIAM LOWN. Can. J. Chem. **72**, 2108 (1994).

The thermally induced [2+3] cycloadditions of certain monocyclic aziridines to dimethyl 1-cyclobutene-1,2-dicarboxylate are described. The structures of the resulting bicyclic adducts were established unambiguously by X-ray analyses. The stereochemistries of the [2+3] adducts were interpreted in terms of dipole–dipole interactions and secondary orbital interactions. In certain cases an initial thermal conrotatory ring opening of the cyclobutene to 2,3-di(methoxycarbonyl)-1,3-butadiene precedes the [2+3] cycloaddition, affording the unexpected pyrrolidine adducts **12***a* and **12***b*. The structures and stereochemistries of the latter established by X-ray analysis strongly suggest that secondary orbital interactions between the phenyl and ester groups control and stereochemistry of the reactions.

KIYOSHI MATSUMOTO, HIROKAZU IIDA, TAKANE UCHIDA, YOSHIMI YABE, AKIKAZU KAKEHI et J. WILLIAM LOWN. Can. J. Chem. **72**, 2108 (1994).

On décrit les cycloadditions[2+3] induites thermiquement de certaines aziridines monocycliques sur le cyclobut-1-ène-1,2-dicarboxylate de diméthyle. On a déterminé les structures des adduits bicycliques formés par diffraction des rayons X. On interprète les stéréochimies des adduits [2+3] en fonction d'interactions dipôles et d'interactions orbitalaires secondaires. Dans certains cas, l'ouverture initiale conrotatoire thermique du cyclobutène en 2,3-di(méthoxycarbonyl)buta-1,3-diène précéde la cycloaddition [2+3] et fournit les adduits inattendus **12***a* et **12***b*, dérivés de la pyrrolidine. Les structures et les stéréochimies de ces derniers, déterminées par diffraction des rayons X, suggèrent fortement que des interactions orbitalaires secondaires entre les groupes phényle et ester contrôlent la stéréochimie des réactions.

[Traduit par la rédaction]

Introduction

The thermal and photochemically induced electrocyclic opening of aziridines **1** and their subsequent [2+3] cycloaddition to a variety of dienophiles are of considerable theoretical and synthetic interest (1). Several cyclobutenes have been found to serve as effective dienophiles and dipolarophiles in such reactions (2). Indeed, monocyclic aziridines **1** undergo 1,3-dipolar cycloaddition with dimethyl 1-cyclobutene-1,2-dicarboxylate **2** to give the corresponding 1:1 adducts (3), whereas reactions of 1,1a-dihydro-1,2-diarylazirino[1,2-*a*]quinoxalines, bicyclic aziridines, with **2** gave the 1,2-fused 4,5-dihydro-1*H*-azepines (4). We now describe in full detail the former reactions including the confirmed stereochemistry of representative 1:1 adducts by X-ray analyses (5).

Results and discussion

Refluxing a solution of 2-benzoyl-1-cyclohexyl-3-phenylaziridine (**1***a*) with an equimolar amount of dimethyl 1-cyclobutene-1,2-dicarboxylate (**2**) in dry benzene for 7 h under nitrogen produced only one (**3***a*) of the two possible isomers in 50% yield (Scheme 1). Similarly, smooth cycloadditions of *p*-substituted aroylaziridines **1***b–e* to **2** gave the corresponding 1:1 adducts (Scheme 2) in moderate to good yields (Table 1). It is well documented that *cis*- and *trans*-aroylaziridines cycloadd even with powerful dipolarophiles by equilibration via the *trans*-azomethine ylide intermediate (6, 7). Indeed, reaction of the stereochemically pure samples of *cis*- and *trans*-2-benzoyl-1-cyclohexyl-3-phenylaziridines gave the same adducts in approximately the same yields. When **1** was treated with the deuterated aziridine (**1***a*; 63% labeled at the 2-position), the ^{1}H NMR spectrum of the adduct showed a singlet with intensity of ca. 0.4 H, at δ6.00 which allowed an unambiguous assignment of H_b. The assignment of the geometry is based upon the ^{1}H NMR data (Table 1) and the well-documented observation that a ring proton or ester methyl protons are shielded by a *cis-vic*-phenyl group (8, 9). Furthermore, the chemical shifts of H_a, H_b, and the ester methyl protons have values in accord with those of the reported pyrrolidine adducts (10, 11). The stereochemistry of the adducts was unambiguously confirmed in the cases of **3***a* and **3***c* by their single crystal X-ray diffraction analyses (Fig. 1).

Interpretations of the stereochemistry of [2+3] and [2+4] (Diels–Alder reactions) and related 1,3-dipolar reactions have been made in terms of secondary orbital interactions, dispersion forces, steric repulsion, dipole–dipole interaction, charge transfer interaction, and inductive effects. The present results may be

[1]Authors to whom correspondence may be addressed. Tel: (403) 492-3646; FAX: (403) 492-8231 (J.W.L.). Tel: 81 (75) 753-2955; FAX: 81 (75) 753-2969 (K.M.).

Can. J. Chem. Downloaded from www.nrcresearchpress.com by 85.192.166.187 on 09/08/12
For personal use only.

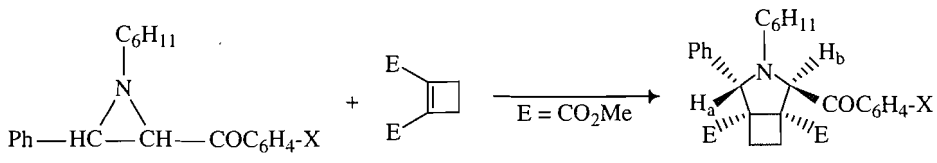

1*a*: X = H
b: X = Me
c: X = MeO
d: X = Cl
e: X = NO_2

2 **3**

SCHEME 1

TABLE 1. Cycloadducts from aziridines **1**, **5**, **7**, and the cyclobutene **2**

(X)	Reaction time (h)	Yield (%)	Melting point (°C)	^{1}H NMR chemical shifts (ppm)	
				Ester methyl	Pyrolidine ring
3*a* (H)	7[a]	59	150.0–151.0	3.16, 3.63	4.66, 6.05
3*b* (Me)	7[a]	80	134.0–135.0	3.14, 3.64	4.59, 5.93
3*c* (MeO)	7[a]	66	123.5–124.5	3.16, 3.68	4.65, 6.02
3*d* (Cl)	7[a]	60	136.5–137.5	3.16, 3.17	4.64, 6.00
3*e* (NO_2)	7[a]	31	142.0–143.0	3.15, 3.65	4.65, 6.08
8*a*	24 (14)[b]	24 (74)	154.0–155.2	3.06, 3.72	4.13, 5.08
8*b*	43[b]	46	171.2–172.3	3.10	4.07
8*c*	331 (168)[b]	17 (7)	182.5–183.8	3.20, 3.81	5.40, 6.12
12*a*	(207)[c]	38 (52)	194.0–195.3	3.17, 3.75	5.36, 5.66
8*d*	257[b]	26 (50)	144.3–145.1	3.23	5.17
12*b*	(157)[c]	10 (19)	173.8–174.5	3.25, 3.54	4.62, 5.08

[a]In refluxing benzene.
[b]In refluxing toluene.
[c]In refluxing xylene.

explained by dipole–dipole interactions (Scheme 3) (1).[2] Alternatively, the results can also be interpreted by the secondary orbital interaction between aryl and ester group and local dipole–dipole interaction between ester and aroyl groups. An unfavorable interaction between ester and aroyl groups exists in the transition state complex leading to **6**. The observed stereochemistry of addition of maleic anhydride or *N*-phenylmaleimide and dimethyl maleate to 2-aroylaziridines (10, 12) is consistent with either of these interpretations.

cis- and *trans*-1-Benzyl-2,3-diphenylaziridines (**7***a*, **7***b*) underwent completely stereospecific cycloaddition with **2** to give the adducts **8***a* and **8***b*, respectively (Scheme 4).[3] The determinations of the stereochemistries were made by the same rule as above by ^{1}H NMR (Experimental) and were confirmed by X-ray analyses (Fig. 2). The thermal conrotatory ring-opening of symmetrical *cis*-aziridine **7***a* to *trans*-**7***a* is structurally unambiguous. In contrast, the conrotation of *trans*-aziridine **7***b* can take place in two senses (Scheme 5), leading to the *cis*-azomethine ylide in either the **10** or the **11** conformations. The W-form is reported to be generally more stable (13). Thus, the exclusive formation of **8***b* can be interpreted by the secondary orbital interaction between ester and phenyl groups (Scheme 6).

[2]According to CNDO/2 calculations of **2** (LUMO), **1**(*trans*) (HOMO), and **1**(*cis*) (HOMO), there were no significant differences (X = H, MeO, and NO_2) between $\Delta E_{2\text{-}1trans}$ and $\Delta E_{1cis\text{-}2}$ (K. Matsumoto, H. Konishi, and X. Shi, unpublished results), suggesting that electrostatic interaction might be more important. More sophisticated calculations are planned.

[3]In another experiment, a higher yield of adduct was obtained (see Table 1); the degree of purity of **1** seems to be crucial to the yield.

Next, *cis*- and *trans*-1,2,3-triphenylaziridines, less reactive aziridines than 1-benzyl-2,3-diphenylaziridines, were investigated. Reaction of *cis*-1,2,3-triphenylaziridine (**7***c*) with dimethyl 1-cyclobutene-1,2-dicarboxylate (**2**) in refluxing dry toluene gave two types of 1:1 adducts in 17 and 38% yields. The latter product was readily proven to be the normal 1:1 adduct (**8***c*) based upon the ^{1}H and ^{13}C NMR spectra. Similarly, from *trans*-1,2,3-triphenylaziridine (**7***d*) and **2** in refluxing dry toluene, the normal 1:1 adduct (**8***d*) and an unidentified 1:1 adduct were obtained in 26 and 10% yields, respectively.[2] The structure of the former adduct was established by X-ray analysis (Fig. 3). Preliminary assignment of these other unidentified adducts was based upon their ^{1}H and ^{13}C NMR spectra (14). However, the reaction steps that would lead to these products were so unusual that we decided to perform X-ray analyses of these adducts. Fortunately, suitable crystals for the X-ray analyses were obtained by recrystallization from ethanol. Based upon their X-ray analyses, the structures of these adducts were confirmed to be **12***a* and **12***b* (Scheme 7), respectively (Fig. 4). The formation of **12***a* and **12***b* is readily explained by thermal ring-opening of the cyclobutene to 2,3-di(methoxycarbonyl)-1,3-butadiene (**11**) (15), followed by 1,3-dipolar cycloaddition to the azomethine ylides (**13**, **14**) generated from **7***c* and **7***d*. The reactions were completely stereospecific with respect to the aziridines.

It is interesting to note that the phenyl and ester groups are in *cis* relationship in all the adducts (**3**, **8**, and **12**) described here, suggesting that the secondary orbital interaction between phenyl and ester groups is important in controlling the stereochemistry of the reactions, though steric hindrance due to the

Can. J. Chem. Downloaded from www.nrcresearchpress.com by 85.192.166.187 on 09/08/12
For personal use only.

Can. J. Chem. Downloaded from www.nrcresearchpress.com by 85.192.166.187 on 09/08/12
For personal use only.

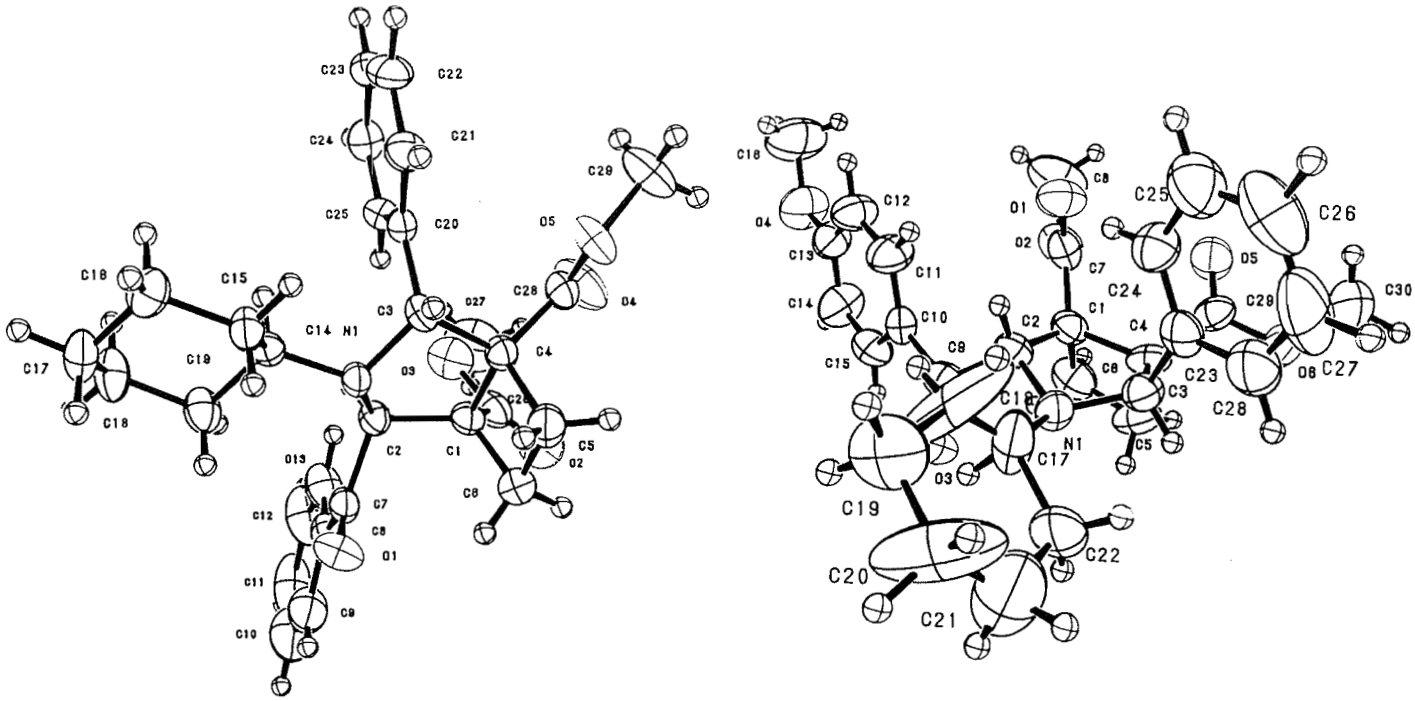

FIG. 1. ORTEP drawings of compounds **3***a* and **3***c*.

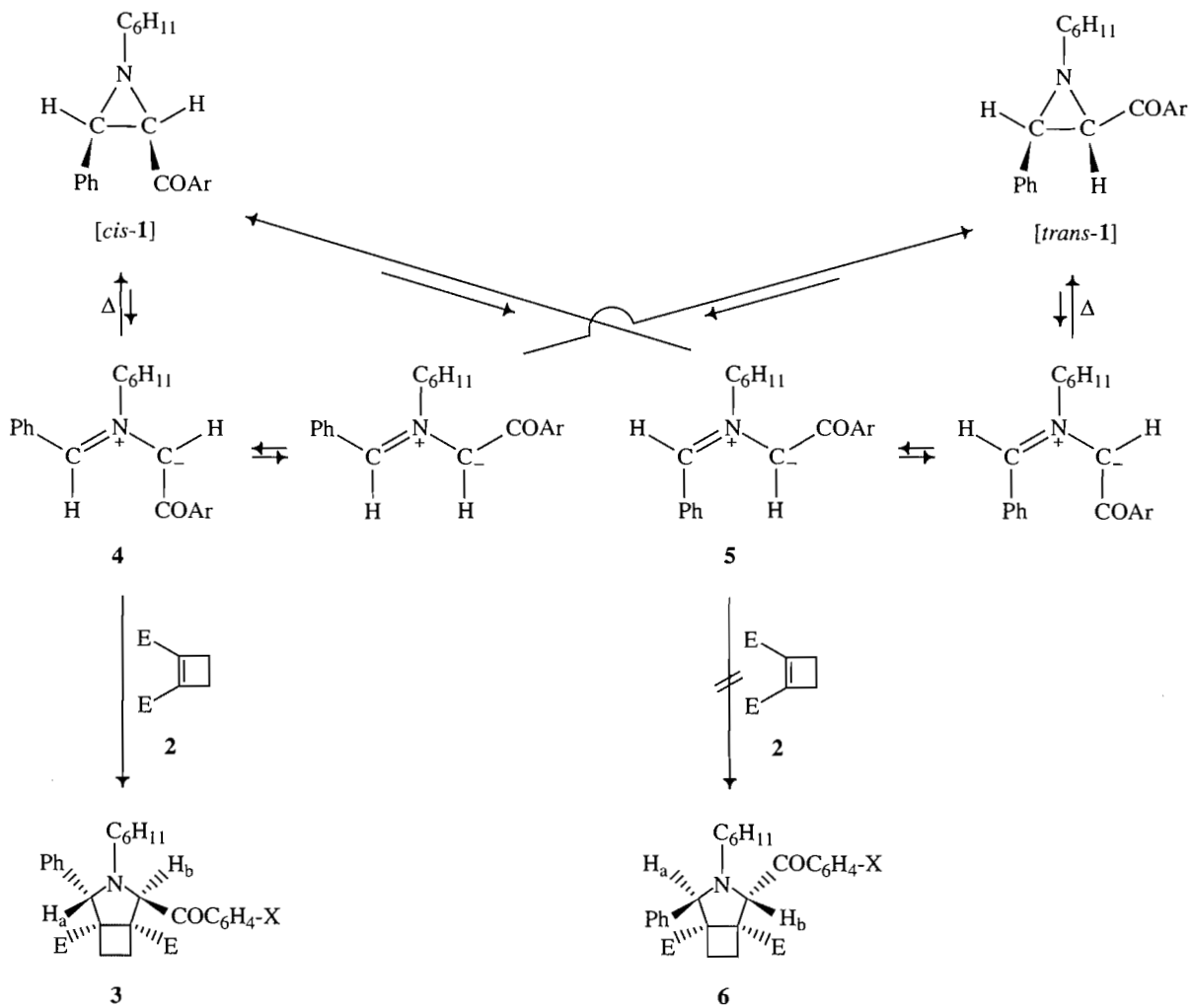

SCHEME 2

Can. J. Chem. Downloaded from www.nrcresearchpress.com by 85.192.166.187 on 09/08/12
For personal use only.

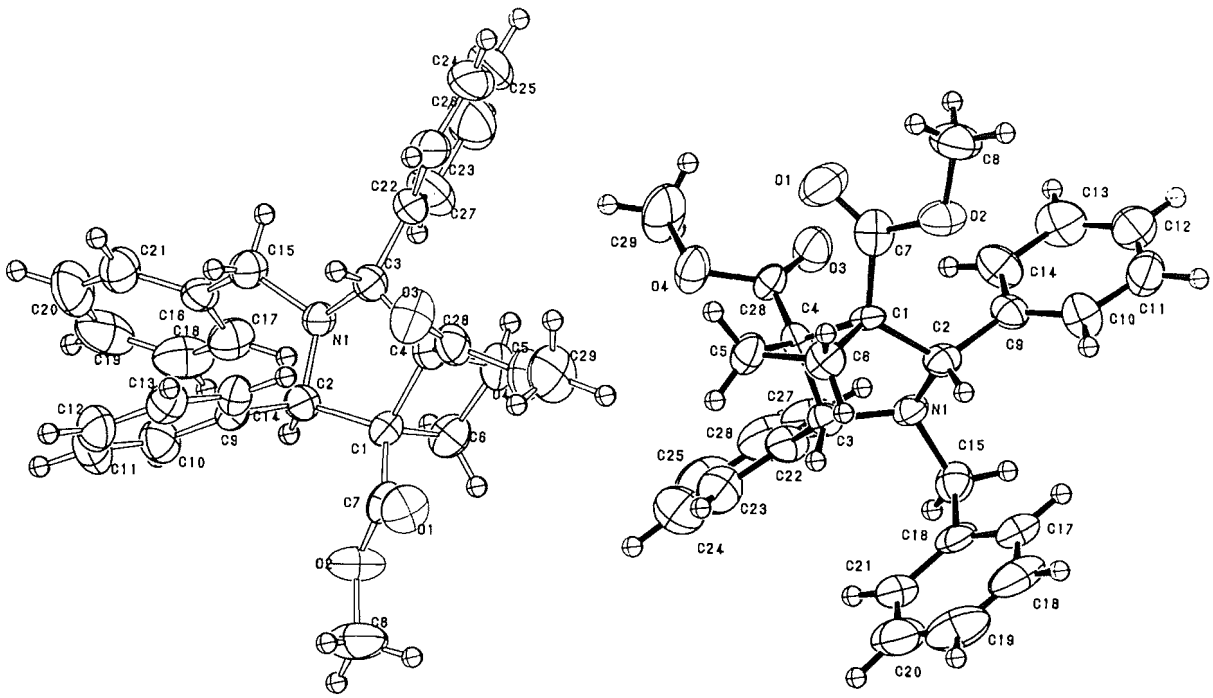

FIG. 2. ORTEP drawings of compounds **8***a* and **8***b*.

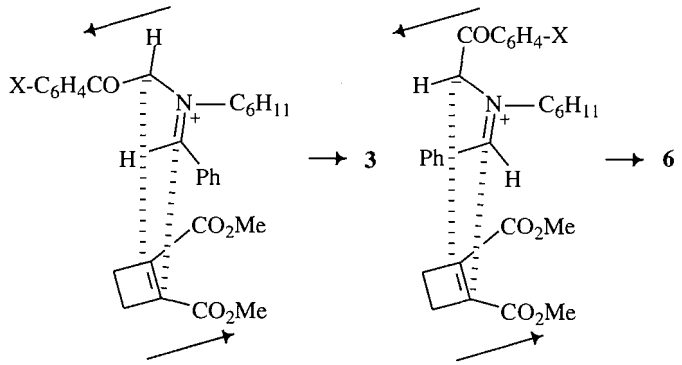

SCHEME 3

cyclobutene methylene moiety and the phenyl group cannot be excluded at present. This interpretation is in agreement with the stereochemical result that 2,3-diphenylindenone oxide (**15**) (16) undergoes thermal-symmetry-forbidden disrotatory 1,3-dipolar cycloadditions via a carbonyl ylide with **2** to give the adduct **16** (Scheme 9) whose structure was also determined by X-ray analysis (Fig. 5). Furthermore, the stereochemical results (16) obtained from **15** and symmetrical olefinic dipolarophiles are also in accord with the above interpretation.

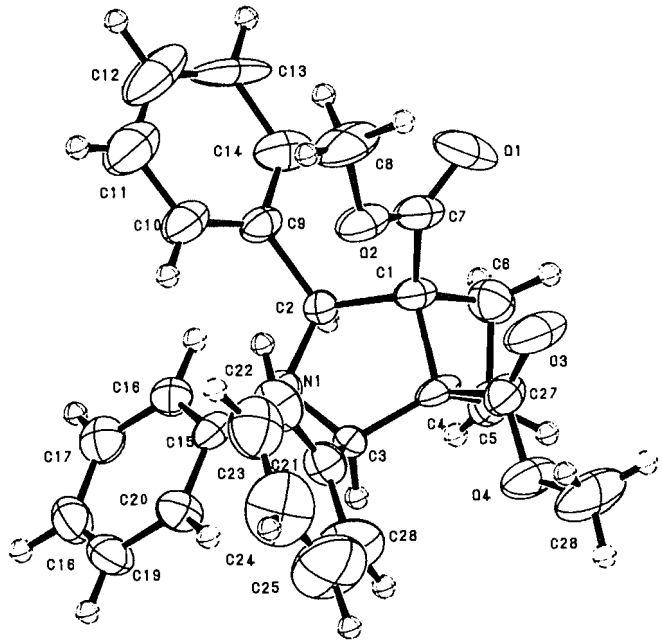

FIG. 3. ORTEP drawings of compounds **8***d*.

Experimental

General

Melting points were taken on a Yanagimoto micro-melting point apparatus and are uncorrected. The ^{1}H NMR spectra were measured either on a Hitachi R40 (90 MHz) or on a JEOL JNM EX270 (270 MHz), or JNM-ALPHA500 (500 MHz) instrument. ^{13}C NMR spectra were recorded either on a JEOL JNM-FX90Q or JNM-EX270 or JNM-ALPHA500 pulsed Fourier transform spectrometer operating at 22.49 MHz, 67.80 Hz, and 125.65 Hz, respectively. Aziridines were prepared following the procedures described in ref. 9. The cyclobutene was prepared according to the procedure of McDonald and Reitz (17). Chemical shifts are expressed in parts per million dowfield from internal tetramethylsilane. Partial proton decoupling was used to distinguish between individual carbon atoms. Preparative medium-pressure liquid chromatography was carried out using a column (25 × 310 mm) prepacked with silica gel (Lobar, LiChroprep Si60, Merck).

Reaction of 2-aroyl-1-cyclohexyl-3-phenylaziridine (1) with dimethyl 1-cyclobutene-1,2-dicarboxylate (2): general procedure

A solution of **1** (3 mmol) and **2** (3.1 mmol) in dry benzene (20 mL) was heated under reflux for 7 h. After evaporation of the solvent, the residue was chromatographed on silica (Wako Gel C-200) using benzene as eluent, giving the adducts **3**. The analytical samples were obtained by recrystallization from petroleum ether.

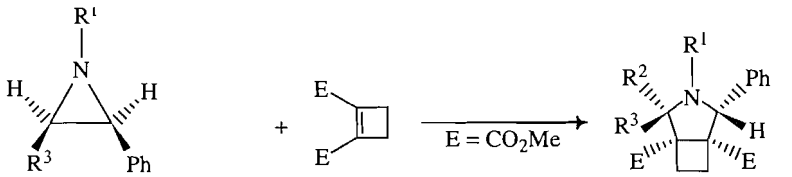

7*a*: (R^1 = Bz, R^2 = H, R^3 = Ph)
b: (R^1 = Bz, R^2 = Ph, R^3 = H)
c: (R^1 = Ph, R^2 = H, R^3 = Ph)
d: (R^1 = Ph, R^2 = Ph, R^3 = H)

2 **8***a–d*

SCHEME 4

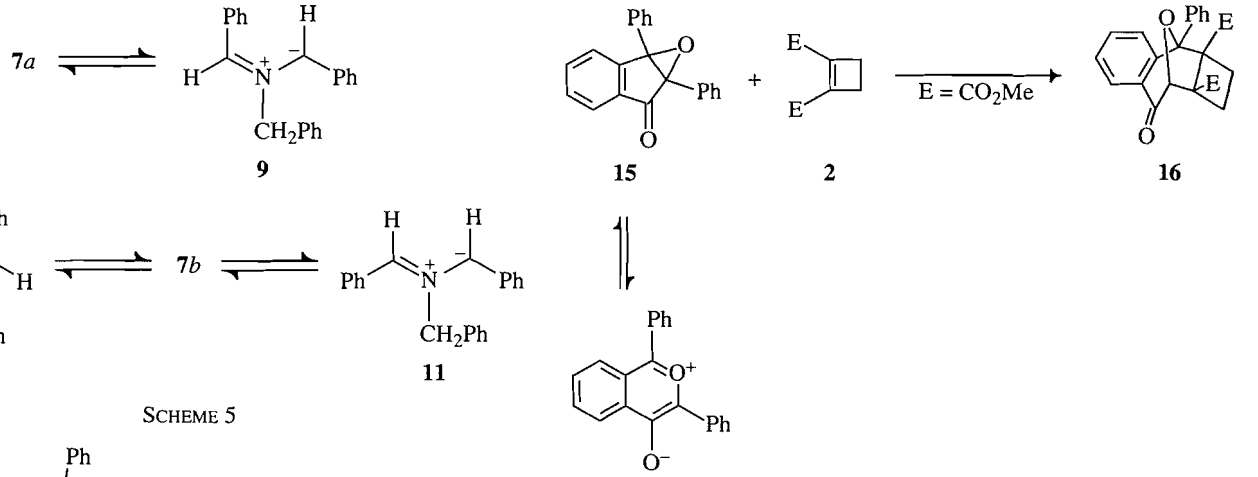

9 **15** **2** **16**

10 **11**

SCHEME 5

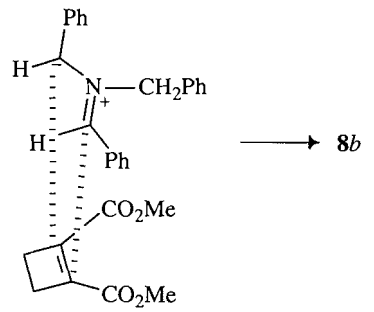

8*b*

SCHEME 6

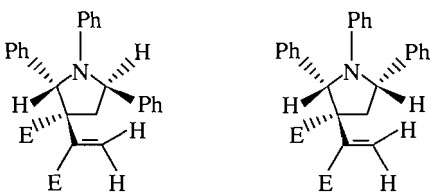

12*a* **12***b*

SCHEME 7

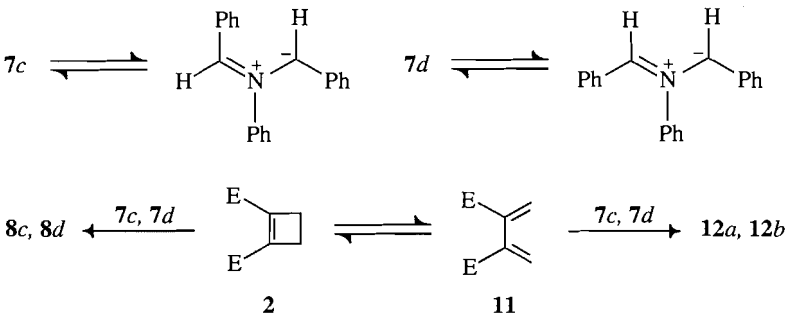

SCHEME 8

SCHEME 9

Dimethyl 2,4-trans-*2-benzoyl-3-cyclohexyl-4-phenyl-3-azabicyclo[3.2.0]heptane-1,5-dicarboxylate (3a; X = H)*

IR (KBr): 1735, 1684 cm^{-1}; ^1H NMR ($CDCl_3$) δ: 0.70–2.80 (m, 15H, cyclohexyl and H-6,7), 3.16 (s, 3H, OCH_3), 3.63 (s, 3H, OCH_3), 4.66 (s, 1H, H-2), 6.05 (s, 1H, H-4), 7.20–7.60 (m, 8H, Ar-H), 7.96 (br d, 2H, J = 3.4 Hz, benzoyl *ortho*-H); ^{13}C NMR ($CDCl_3$) δ: 20.3, 25.6 (each t, C-6,7), 25.9 26.4 (each t, phenyl C-3″), 128.6, 129.4 (each d, C-phenyl C-2″), 137.0, 140.3 (each s, C-phenyl C-1″), 172.0, 172.9 (each s, COO), 199.6 (s, C=O). Anal. calcd. for $C_{29}H_{33}O_5N$: C 73.24, H 6.99, N 2.95, found: C 73.05, H 7.12, N 2.91.

Dimethyl 2,4-trans-*2-p-methylbenzoyl-3-cyclohexyl-4-phenyl-3-azabicyclo[3.2.0]heptane-1,5-dicarboxylate (3b; X = Me)*

IR (KBr): 1730, 1679 cm^{-1}; ^1H NMR ($CDCl_3$) δ: 0.60–2.80 (m, 15H, cyclohexyl and H-6,7), 2.40 (s, 3H, Ph-CH_3), 3.14 (s, 3H, OCH_3), 3.64 (s, 3H, OCH_3), 4.59 (s, 1H, H-2), 5.93 (s, 1H, H-4), 7.00–7.60 (m, 7H, Ar-H), 7.85 (br d, 2H, J = 7.8 Hz, benzoyl *ortho*-H); ^{13}C NMR ($CDCl_3$) δ: 20.4, 25.6 (each t, C-6,7), 21.7 (q, CH_3), 25.9, 26.4 (each t, N-cyclohexyl C-2′, 6′), 51.4, 52.4 (each q, OCH_3), 57.1 (d, N-cyclohexyl C-1′), 56.1, 63.5 (each s, C-1, 5), 68.6, 73.6 (each d, C-2, 4),

Can. J. Chem. Downloaded from www.nrcresearchpress.com by 85.192.166.187 on 09/08/12
For personal use only.

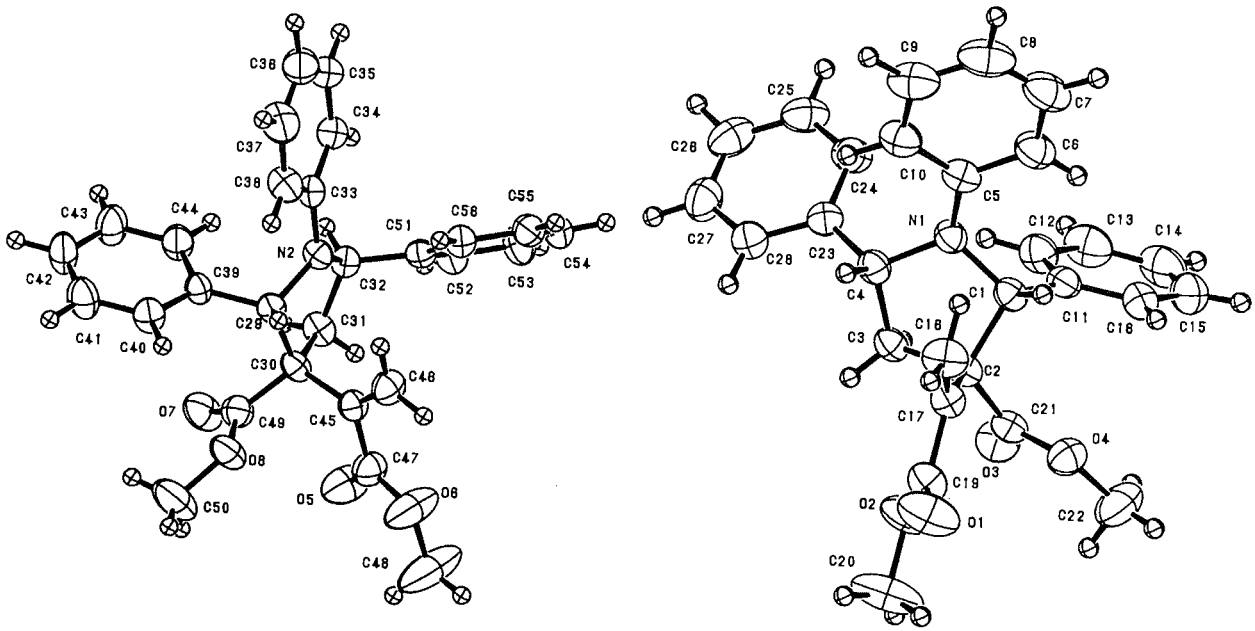

FIG. 4. ORTEP drawings of compounds **12***a* and **12***b*.

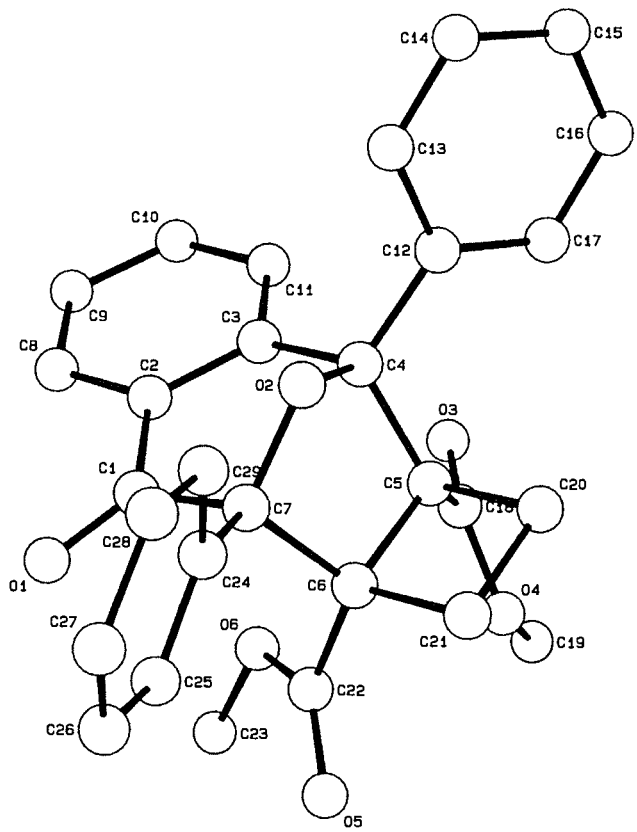

FIG. 5. Crystal structure of compound **16**.

127.3, 144.1 (each d, C-phenyl C-4″), 127.8, 128.5 (each d, C-phenyl C-3″), 129.3, 129.4 (each d, C-phenyl C-2″), 134.5, 140.4 (each s, C-phenyl- C-1″), 172.1, 173.0 (each s, COO), 198.7 (s, C=O). Anal. calcd. for $C_{30}H_{35}O_5N$: C 73.60, H 7.21, N 2.86; found: C 73.68, H 7.26, N 2.86.

Dimethyl 2,4-trans-*2*-p-*methoxybenzoyl-3-cyclohexyl-4-phenyl-3-azabicyclo[3.2.0]heptane-1,5-dicarboxylate (3c; X = MeO)*

IR (KBr): 1730, 1675 cm^{-1}; ^1H NMR ($CDCl_3$) δ: 0.70–2.95 (m, 15H, cyclohexyl and H-6,7), 3.16 (s, 3H, OCH_3) 3.68 (s, 3H, OCH_3), 3.87 (s, 3H, OCH_3), 4.65 (s, 1H, H-2), 6.02 (s, 1H, H-4), 7.20–7.60 (m, 7H, Ar-H), 7.89 (br d, 2H, J = 8.8 Hz, benzoyl *ortho*-H); ^{13}C NMR ($CDCl_3$) δ: 20.5, 25.7 (each t, C-6, 7), 26.0 26.5 (each t, N-cyclohexyl C-3′, 5′), 28.8 (t, *N*-cyclohexyl C-4′), 30.4, 32.8 (each t, N-cyclohexyl C-2′, 6′), 51.5, 52.2 (each q, OCH_3), 55.5 (q, OCH_3), 57.2 (d, N-cyclohexyl C-1′), 56.4, 63.7 (each s, C-1, 5), 68.4, 73.8 (each d, C-2, 4), 127.4, 163.9 (each d, C-phenyl C-4″), 113.9, 127.8 (each d, C-phenyl C-3″), 129.6, 130.9 (each d, C-phenyl C-2″), 130.1, 130.9 (each s, C-phenyl C-1″), 172.2, 173.2 (each s, COO), 197.5 (s, C=O). Anal. calcd. for $C_{30}H_{35}O_6N$: C 71.27, H 6.98, N 2.77; found: C 71.13, H 6.96, N 2.81.

Dimethyl 2,4-trans-*2*-p-*chlorobenzoyl-3-cyclohexyl-4-phenyl-3-azabicyclo[3.2.0]heptane-1,5-dicarboxylate (3d; X = Cl)*

IR (KBr): 1720, 1679 cm^{-1}; ^1H NMR ($CDCl_3$) δ: 0.70–2.80 (m, 15H, cyclohexyl and H-6, 7), 3.16 (s, 3H, OCH_3) 3.67 (s, 3H, OCH_3), 4.64 (s, 1H, H-2), 6.00 (s, 1H, H-4), 7.20–7.50 (m, 7H, Ar-H), 7.93 (Abq, 2H, J = 9.0, 30 Hz, benzoyl *ortho*-H); ^{13}C NMR ($CDCl_3$) δ: 20.3, 25.6 (each t, C-6, 7), 25.9, 26.4 (each 6, N-cyclohexyl C-3′, 5′), 28.5 (t, N-cyclohexyl C-4′), 30.2, 32.7 (each t, N-cyclohexyl C-1′), 56.1, 63.4 (each s, C-1, 5), 68.6, 73.7 (each d, C-2, 4), 127.5, 139.9 (each d, C-phenyl C-4″), 127.9, 128.9 (each d, C-phenyl C-3″), 129.4, 129.9 (each d, C-phenyl C-2″), 135.2, 139.9 (each s, C-phenyl C-1″), 171.9, 172.8 (each s, COO), 197.9 (s, C=O). Anal. calcd. for $C_{29}H32O_5NCl$: C 68.29, H 6.32, N 2.75; found: C 68.14, H 6.22, N 2.79.

Dimethyl 2,4-trans-*2*-p-*nitrobenzoyl-3-cyclohexyl-4-phenyl-3-azabicyclo[3.2.0]heptane-1,5-dicarboxylate (3e; X = NO_2)*

IR (KBr): 1721, 1690 cm^{-1}; ^1H NMR ($CDCl_3$) δ: 0.75–2.80 (m, 15H, cyclohexyl and H-6, 7), 3.15 (s, 3H, OCH_3), 3.65 (s, 3H, OCH_3), 4.65 (s, 1H, H-2), 6.08 (s, 1H, H-4), 7.20–7.50 (m, 7H, Ar-H), 8.14, 8.29 (ABq, 2H, J = 9.0, 30 Hz, benzoyl *ortho*-H); ^{13}C NMR ($CDCl_3$) δ: 20.3, 25.9 (each t, C-6, 7), 25.5, 26.4 (each t, N-cyclohexyl C-3′, 5′), 28.4 (t, N-cyclohexyl C-4′), 30.2, 32.8 (each t, N-cyclohexyl C-2′, 6′), 51.5 52.6 (each q, OCH_3), 57.1 (d, N-cyclohexyl C-1′), 56.2, 63.2 (each s, C-1, 5), 69.0, 73.8 (each d, C-2, 4), 127.6, 150.5 (each d, C-phenyl C-4″), 127.8, 128.0 (each d, C-phenyl C-3″), 129.3, 129.6 (each d, C-phenyl C-2″), 139.8, 141.5 (each s, *C*-phenyl C-1″), 171.8, 172.6 (each s, COO), 18.2 (s, C=O). Anal. calcd. for $C_{29}H_{32}O_7N_2$: C 66.91, H 6.20, N 5.38; found: C 67.11, H 6.37, N 5.62.

Can. J. Chem. Downloaded from www.nrcresearchpress.com by 85.192.166.187 on 09/08/12
For personal use only.

Can. J. Chem. Downloaded from www.nrcresearchpress.com by 85.192.166.187 on 09/08/12
For personal use only.

TABLE 2. Crystal data for **3***a*

Formula	$C_{29}H_{33}NO_5$
Crystal dimensions (mm)	0.22 × 0.34 × 0.28
M	475.58
Monoclinic space group	$P2_1/c$ (no. 14)
a (Å)	8.06 (1)
b (Å)	37.72 (1)
c (Å)	8.458 (4)
β	100.58 (7)
U (Å^3)	2526 (3)
Z	4
D_c (g cm^{-3})	1.250
μ (cm^{-1})	0.79
F (000)	1016
Radiation Mo-K_α, graphite monochromatized	λ = 0.71069 Å
Diffractometer	Rigaku AFC5S
Orienting reflections, range	7, 8.85° < 2θ < 10.43°
T (K)	293
Scan method	ω
Data collection range	6.0° < 2θ < 55.1°
No. unique reflections	5919
No. of observed reflections with $I > 3\sigma(I)$	1942
No. of parameters	316
R_a [b]	5.2%
R_w [b]	5.3%
Largest shift/esd, final cycle	0.04
Largest positive peak (e Å^{-3})	0.43
Largest negative peak (e Å^{-3})	−0.19

[a] $R = [\Sigma||F_o| - |F_c||]/\Sigma|F_o|$.
[b] $R_w = \{[\Sigma_w(|F_o| - |F_c|)^2]/[\Sigma_w(|F_o|)^2]\}^{1/2}$. Weighting scheme: $w = 4F_o^2/\sigma_2(F_o^2)$.

TABLE 3. Crystal data for **3***c*

Formula	$C_{30}H_{35}NO_6$
Crystal dimensions (mm)	0.22 × 0.34 × 0.28
M (amu)	505.61
Monoclinic space group	$P2_1/c$ (no. 14)
a (Å)	11.05 (4)
b (Å)	8.093 (8)
c (Å)	30.128 (8)
β	97.37 (8)
U (Å^3)	2672 (1)
Z	4
D_c (g cm^{-3})	1.257
μ (cm^{-1})	0.81
F (000)	1081
Radiation Mo-K_α, graphite monochromatized	λ = 0.71069 Å
Diffractometer	Rigaku AFC5S
Orienting reflections, range	25, 20.06° < 2θ < 25.47°
T (K)	297
Scan method	ω
Data collection range	6.0° < 2θ < 55.0°
No. unique reflections	5489
No. of observed reflections with $I > 3\sigma(I)$	1391
No. of parameters	370
R_a [b]	6.7%
R_w [b]	7.3%
Largest shift/esd, final cycle	0.28
Largest positive peak (e Å^{-3})	0.33
Largest negative peak (e Å^{-3})	−0.27

[a] $R = [\Sigma||F_o| - |F_c||]/\Sigma|F_o|$.
[b] $R_w = \{[\Sigma_w(|F_o| - |F_c|)^2]/[\Sigma_w(|F_o|)^2]\}^{1/2}$. Weighting scheme: $w = 4F_o^2/\sigma_2(F_o^2)$.

*Reaction of 1-benzyl-2,3-diphenylaziridines (**5**) with dimethyl 1-cyclobutene 1,2-dicarboxylate (**2**): general procedure*

A solution of **7** (4 mmol) and **2** (4.1 mmol) in dry benzene (20 mL) was heated under reflux for 14 h. After evaporation of the solvent, the residue was chromatographed on silica (Wako Gel C-200) using benzene as eluent, giving the adducts **8**. The analytical samples were obtained either by recrystallization from petroleum ether or ethanol–hexane.

Dimethyl trans*-2,4-diphenyl-3-benzyl-3-azabicyclo[3.2.0]heptane-1,5-dicarboxylate (**8**a)*

IR (KBr): 1700, 1598, 1512, 1260, 1225, 1205, 1118, 665 cm^{-1}; ^{1}H NMR ($CDCl_3$) δ: 1.60–2.60 (m, 4H, C-6, 7-CH_2 × 2), 2.81, 3.65 (q, 2H, *J* = 14.4 Hz, C*H*$_2$-Ph), 3.06 (s, 3H, OCH_3), 3.72 (s, 3H, OCH_3), 4.13 (s, 1H, C-4H), 5.08 (s, 1H, C-2H), 6.70–7.30 (m, 15H, Ar-H); ^{13}C NMR ($CDCl_3$) δ: 18.5, 29.2 (each t, C-6, 7), 50.8 (t, *C*H$_2$Ph), 51.3 (q, OCH_3), 52.3 (q, OCH_3) 57.6, 607 (each s, C-1, 5), 70.9, 72.8 (each d, C-2, 4), 126.7, 127.4, 127.6, 128.1, 128.3, 128.4, 130.1 (each d, Ph-*o*, *m*, *p*), 137.3, 137.6, 139.3 (each s, Ph-*ipso*), 172.4 (s, C=O), 173.1 (s, C=O); MS *m/z*: 455 (M$^+$), 396, 364. Anal. calcd. for $C_{29}H_{29}O_4N$: C 76.46, H 6.41, N 3.08; found: C 76.43, H 6.45, N 3.08.

Dimethyl cis*-2,4-diphenyl-3-benzyl-3-azabicyclo[3.2.0]heptane-1,5-dicarboxylate (**8**b)*

IR (KBr): 2970, 1740, 1500, 1443, 1320, 1280, 1245, 1200, 1150, 1125, 760, 705 cm^{-1}; ^{1}H NMR ($CDCl_3$) δ: 1.90–2.50 (m, 4H, C-6, 7-CH_2 × 2), 3.10 (s, 6H, OCH_3 × 2), 3.55 (s, 2H, C*H*$_2$Ph), 4.07 (s, 2H, C-2, 4-H), 6.70–7.40 (m, 15H, Ar-H); ^{13}C NMR ($CDCl_3$) δ: 28.2 (t, C-6, 7), 50.7 (q, OCH_3), 51.0 (t, Ph*C*H$_2$), 60.7 (s, C-1, 5), 73.2 (d, C-2, 4), 115.5, 127.2, 127.7, 128.0, 128.1, 129.0, 130.4 (each d, Ph-*o*, *m*, *p*), 133.9, 139.1 (each s, Ph-*ipso*), 171.5 (s, C=O); MS *m/z*: 455 (M$^+$), 364. Anal. calcd. for $C_{29}H_{29}O_4N$: C 76.46, H 6.41, N 3.08; found: C 76.31, H 6.41, N 3.07.

TABLE 4. Crystal data for **8***a*

Formula	$C_{29}H_{29}NO_4$
Crystal dimensions (mm)	0.26 × 0.48 × 0.48
M (amu)	455.55
Monoclinic space group	$P2_1/c$ (no. 14)
a (Å)	11.164 (5)
b (Å)	17.65 (1)
c (Å)	12.900 (6)
β	104.93 (4)
U (Å^3)	2456 (2)
Z	4
D_c (g cm^{-3})	1.232
μ (cm^{-1})	0.76
F (000)	968
Radiation Mo-K_α, graphite monochromatized	λ = 0.71069 Å
Diffractometer	Rigaku AFC5S
Orienting reflections, range	25, 34.7° < 2θ < 39.0°
T (K)	297
Scan method	ω–2θ
Data collection range	6.0° < 2θ < 54.9.1°
No. unique reflections	5806
No. of observed reflections with $I > 3\sigma(I)$	1699
No. of parameters	307
R_a [b]	5.0%
R_w [b]	5.0%
Largest shift/esd, final cycle	0.08
Largest positive peak (e Å^{-3})	0.19
Largest negative peak (e Å^{-3})	−0.21

[a] $R = [\Sigma||F_o| - |F_c||]/\Sigma|F_o|$.
[b] $R_w = \{[\Sigma_w(|F_o| - |F_c|)^2]/[\Sigma_w(|F_o|)^2]\}^{1/2}$. Weighting scheme: $w = 4F_o^2/\sigma_2(F_o^2)$.

Can. J. Chem. Downloaded from www.nrcresearchpress.com by 85.192.166.187 on 09/08/12
For personal use only.

TABLE 5. Crystal data for **8***a*

Formula	$C_{29}H_{29}NO_4$
Crystal dimensions (mm)	0.12 × 0.32 × 0.40
M (amu)	455.55
Monoclinic space group	$P2_1/a$ (no. 14)
a (Å)	11.11 (2)
b (Å)	12.595 (6)
c (Å)	17.890 (6)
β	98.25 (7)
U (Å^3)	2478 (5)
Z	4
D_c (g cm^{-3})	1.221
μ (cm^{-1})	0.75
F (000)	968
Radiation Mo-K_α, graphite monochromatized	λ = 0.71069 Å
Diffractometer	Rigaku AFC5S
Orienting reflections, range	25, 20.8° < 2θ < 27.9°
T (K)	297
Scan method	ω–2θ
Data collection range	6.0° < 2θ < 55.0°
No. unique reflections	4981
No. of observed reflections with $I > 3\sigma(I)$	1085
No. of parameters	307
R_a [b]	5.3%
R_w [b]	5.2%
Largest shift/esd, final cycle	0.03
Largest positive peak (e Å^{-3})	0.17
Largest negative peak (e Å^{-3})	−0.19

[a] $R = [\Sigma|F_o| - |F_c|]/\Sigma|F_o|$.
[b] $R_w = \{[\Sigma_w(|F_o| - |F_c|)^2]/[\Sigma_w(|F_o|)^2]\}^{1/2}$. Weighting scheme: $w = 4F_o^2/\sigma_2(F_o^2)$.

TABLE 6. Crystal data for **8***d*

Formula	$C_{28}H_{27}NO_4$
Crystal dimensions (mm)	0.24 × 0.36 × 0.68
M (amu)	441.53
Monoclinic space group	$P2_1/n$ (no. 86)
a (Å)	24.037 (3)
b (Å)	17.890 (3)
c (Å)	8.557 (7)
β	98.25 (7)
U (Å^3)	4944 (2)
Z	8
D_c (g cm^{-3})	1.186
μ (cm^{-1})	0.74
F (000)	1872
Radiation Mo-K_α, graphite monochromatized	λ = 0.71069 Å
Diffractometer	Rigaku AFC5S
Orienting reflections, range	25, 20.4° < 2θ < 29.0°
T (K)	295
Scan method	ω–2θ
Data collection range	6.0° < 2θ < 55.0°
No. unique reflections	6083
No. of observed reflections with $I > 3\sigma(I)$	1689
No. of parameters	330
R_a [b]	9.2%
R_w [b]	12.7%
Largest shift/esd, final cycle	2.01
Largest positive peak (e Å^{-3})	1.31
Largest negative peak (e Å^{-3})	−0.28

[a] $R = [\Sigma|F_o| - |F_c|]/\Sigma|F_o|$.
[b] $R_w = \{[\Sigma_w(|F_o| - |F_c|)^2]/[\Sigma_w(|F_o|)^2]\}^{1/2}$. Weighting scheme: $w = 4F_o^2/\sigma_2(F_o^2)$.

TABLE 7. Crystal data for **12***a*

Formula	$C_{28}H_{27}NO_4$
Crystal dimensions (mm)	0.36 × 0.58 × 0.76
M (amu)	441.53
Monoclinic space group	$P2_1/n$ (no. 14)
a (Å)	11.391 (9)
b (Å)	20.570 (2)
c (Å)	20.090 (3)
β	95.80 (7)
U (Å^3)	4683 (3)
Z	8
D_c (g cm^{-3})	1.252
μ (cm^{-1})	0.78
F (000)	1872
Radiation Mo-K_α, graphite monochromatized	λ = 0.71069 Å
Diffractometer	Rigaku AFC5S
Orienting reflections, range	25, 30.25° < 2θ < 36.87°
T (K)	295
Scan method	ω–2θ
Data collection range	6.0° < 2θ < 54.9°
No. unique reflections	11038
No. of observed reflections with $I > 3\sigma(I)$	4010
No. of parameters	595
R_a [b]	5.3%
R_w [b]	5.8%
Largest shift/esd, final cycle	0.01
Largest positive peak (e Å^{-3})	0.19
Largest negative peak (e Å^{-3})	−0.25

[a] $R = [\Sigma|F_o| - |F_c|]/\Sigma|F_o|$.
[b] $R_w = \{[\Sigma_w(|F_o| - |F_c|)^2]/[\Sigma_w(|F_o|)^2]\}^{1/2}$. Weighting scheme: $w = 4F_o^2/\sigma_2(F_o^2)$.

TABLE 8. Crystal data for **12***b*

Formula	$C_{28}H_{27}NO_4$
Crystal dimensions (mm)	0.36 × 0.82 × 0.94
M (amu)	441.53
Monoclinic space group	$P\bar{1}$ (no. 2)
a (Å)	11.587 (3)
b (Å)	11.649 (4)
c (Å)	10.876 (3)
β	116.44 (2)
U (Å^3)	1179.9 (7)
Z	2
D_c (g cm^{-3})	1.243
μ (cm^{-1})	0.77
F (000)	468
Radiation Mo-K_α, graphite monochromatized	λ = 0.71069 Å
Diffractometer	Rigaku AFC5S
Orienting reflections, range	25, 39.62° < 2θ < 40.00°
T (K)	293
Scan method	ω–2θ
Data collection range	6.0° < 2θ < 55.0°
No. unique reflections	5417
No. of observed reflections with $I > 3\sigma(I)$	3386
No. of parameters	407
R_a [b]	4.4%
R_w [b]	5.1%
Largest shift/esd, final cycle	0.10
Largest positive peak (e Å^{-3})	0.23
Largest negative peak (e Å^{-3})	−0.19

[a] $R = [\Sigma|F_o| - |F_c|]/\Sigma|F_o|$.
[b] $R_w = \{[\Sigma_w(|F_o| - |F_c|)^2]/[\Sigma_w(|F_o|)^2]\}^{1/2}$. Weighting scheme: $w = 4F_o^2/\sigma_2(F_o^2)$.

Can. J. Chem. Downloaded from www.nrcresearchpress.com by 85.192.166.187 on 09/08/12
For personal use only.

TABLE 9. Crystal data for **16**

Formula	$C_{29}H_{24}O_6$
M (amu)	468.51
Crystal system	Monoclinic
Space group	$C2/c$ (no. 15)
a (Å)	34.426 (6)
b (Å)	8.092 (6)
c (Å)	17.047 (5)
β	105.61 (2)
U (Å^3)	4752 (4)
Z	8
D_c (g cm^{-3})	1.360
μ (cm^{-1})	7.37
F (000)	1968
Radiation Mo-K$_\alpha$, graphite monochromatized	λ = 1.54178 Å
Diffractometer	Rigaku AFC5S
Orienting reflections, range	25, 43.6° < 2θ < 120.1°
T (K)	295
Scan method	ω–2θ
Data collection range	6.0° < 2θ < 120.1°
No. unique reflections	3142
No. of observed reflections with $I > 3\sigma(I)$	1894
No. of parameters	389
R_a [a]	5.4%
R_w [b]	6.2%
Largest shift/esd, final cycle	0.16
Largest positive peak (e Å^{-3})	0.23
Largest negative peak (e Å^{-3})	−0.21

[a] $R = [\Sigma||F_o| - |F_c||]/\Sigma|F_o|$.

[b] $R_w = \{[\Sigma_w(|F_o| - |F_c|)^2]/[\Sigma_w(|F_o|)^2]\}^{1/2}$. Weighting scheme: $w = 4F_o^2/\sigma_2(F_o^2)$.

*Reaction of 1,2,3-triphenylaziridines (**7**) with dimethyl 1-cyclobutene-1,2-dicarboxylate (**2**): general procedure*

A solution of **7** (5 mmol, 1.9 mmol) and **2** (5.1 mmol, 9.3 mmol) in dry toluene (30 mL, 50 mL) was heated under reflux. After evaporation of the solvent, the residue was chromatographed on silica (Wako Gel C-100) using ethyl acetate–hexane (15:75) as eluent, giving the adducts **8** and **12**.

The analytical samples were obtained by recrystallization from ethanol–hexane. In another run, a solution of **7** (3.7 mmol) and **2** (13.3 mmol) in dry xylene (90 mL) was refluxed and worked up as above.

Dimethyl trans-*2,3,4-triphenyl-3-azabicyclo[3.2.0]heptane-1,5-dicarboxylate (**8**c)*

IR (KBr): 1732, 1598, 1500, 1453, 1260, 1205, 1155, 1118, 750, 693 cm^{-1}; ^{1}H NMR ($CDCl_3$) δ: 1.68–1.80, 2.26–2.70 (4H, C-6, 7-CH_2 × 2), 3.20 (s, 3H, OCH_3), 3.81 (s, 3H, OCH_3), 5.40 (s, 1H, C-4H), 6.12 (s, 1H, C-2H), 6.71–7.33 (m, 15H, Ar-H); ^{13}C NMR ($CDCl_3$) δ: 20.3, 29.0 (each t, C-6, 7), 51.5 (q, OCH_3), 52.4 (q, OCH_3), 59.2, 61.8 (each s, C-1, 5), 68.8, 75.5 (each d, C-2, 4), 118.4, 119.2, 127.1, 127.2, 127.4, 127.6, 128.0, 128.3, 128.7 (each d, Ph-*o*, *m*, *p*), 138.5, 138.6, 145.4 (each s, Ph-*ipso*), 171.8 (s, C═O), 173.2 (s, C═O); MS *m/z*: 441 (M$^+$), 381, 226, 180. Anal. calcd. for $C_{28}H_{27}O_4N$: C 76.17, H 6.16, N 3.17; found: C 76.35, H 6.26, N 3.19.

Dimethyl cis-*2,3,4-triphenyl-3-azabicyclo[3.2.0]heptane-1,5-dicarboxylate (**8**d)*

IR (KBr): 1740, 1597, 1495, 1455, 1300, 1240, 1195, 1125, 750, 697 cm^{-1}; ^{1}H NMR ($CDCl_3$) δ: 2.38–2.48, 2.66–2.74 (m, 4H, C-6, 7-CH_2 × 2), 3.23 (s, 6H, OCH_3 × 2), 5.17 (s, 2H, C-2, 4-H), 6.45–7.62 (m, 15H, Ar-H); ^{13}C NMR ($CDCl_3$) δ: 29.1 (5, C-6, 7), 51.1 (q, OCH_3 × 2), 62.1 (s, C-1, 5), 75.8 (d, C-2,4), 115.5, 118.5, 127.4, 127.6, 127.9, 128.6 (each d, Ph-*o*, *m*, *p*), 140.1, 147.9 (each s, Ph-*ipso*), 171.9 (s, C═O); MS *m/z*: 441 (M$^+$), 293, 270, 180. Anal. calcd. for $C_{28}H_{27}O_4N$: C 76.17, H 6.16, N 3.17; found: C 76.05, H 6.44, N 3.07.

*3-Methoxycarbonyl-3-(1′-methoxycarbonylvinyl)-2,5-*trans*-1,2,5-triphenylpyrrolidine (**12**a)*

IR (KBr): 1725, 1593, 1498, 1450, 1320, 1242, 1214, 1062, 743, 694 cm^{-1}; ^{1}H NMR ($CDCl_3$) δ: 2.35 (d, 1H, J = 14.0 Hz, C-4H), 3.25 (s, 3H, OCH_3), 3.54 (s, 3H, OCH_3), 3.70–3.83 (m, 1H, C-4H), 5.36 (d, 1H, J = 10.5 Hz, C-5H), 5.66 (s, 1H, C-2H), 6.20 (s, 1H, C-2′H), 6.38 (s, 1H, C-2′H), 6.40–7.25 (m, 15H, Ar-H); ^{13}C NMR ($CDCl_3$) δ: 49.5 (t, C-4), 51.9 (q, OCH_3), 52.0 (q, OCH_3), 59.7 (s, C-3), 62.3 (d, C-5), 68.7 (d, C-2), 115.3, 116.9, 126.2, 127.1, 127.7, 128.0, 128.1, 128.3, 128.7 (each d, Ph-*o*, *m*, *p*), 126.5 (t, C-2′), 138.6, 140.4, 142.1 (each s, Ph-*ipso*), 144.9 (s, C-1′), 166.5 (s, C═O), 170.8 (s, C═O); MS *m/z*: 441 (M$^+$), 271. Anal. calcd. for $C_{28}H_{27}O_4N$: C 76.17, H 6.16, N 3.17; found: C 76.15, H 6.01, N 3.13.

*3-Methoxycarbonyl-3-(1′-methoxycarbonylvinyl)-2,5-*cis*-1,2,5-triphenylpyrrolidine (**12**b)*

IR (KBr): 1725, 1597, 1503, 1320, 1285, 1240, 1210, 1135, 750, 695 cm^{-1}; ^{1}H NMR ($CDCl_3$): δ: 2.53 (dd, 1H, J = 5.9, 13.0 Hz, C-4H), 3.05 (dd, 1H, J = 11.1, 13.0 Hz, C-4H), 3.17 (s, 3H, OCH_3), 3.75 (s, 3H, OCH_3) 4.62 (dd, 1H, J = 5.9, 11.1 Hz, C-5H), 5.08 (s, 1H, C-2H), 5.28 (s, 1H, C-2′H), 6.47 (s, 1H, C-2′H), 6.48–7.60 (m, 15H, Ar-H); ^{13}C NMR ($CDCl_3$) δ: 40.7 (t, C-4), 51.7 (q, OCH_3), 52.2 (q, OCH_3), 60.5 (s, C-3), 61.5 (d, C-5), 73.9 (d, C-2), 114.3, 118.2, 126.0, 126.9, 128.0, 128.1, 128.3, 128.7, 128.8 (each d, Ph-*o*, *m*, *p*), 125.9 (t, C-2′) 141.0, 141.1, 141.3 (each s, Ph-*ipso*), 147.0 (s, C-1′), 166.5 (s, C═O), 170.4 (s, C═O); MS *m/z*: 441 (M$^+$), 374, 270. Anal. calcd. for $C_{28}H_{27}O_4N$: C 76.17; H 6.16; H 3.17; found: C 76.02, H 6.25 3.15.

*Reaction of 2,3-diphenylindenone oxide (**15**) with **2***

A solution of **15** (3 mmol) and **2** (6 mmol) in dry toluene (30 mL) was heated under reflux for 3 days. After evaporation of the solvent, the residue was titrated with ethanol to give the 1:1 adduct **16** as colorless crystals in 60% yield. An inspection of the residue by TLC and NMR showed only the 1:1 adduct **16**. Yield 60%; mp 272–273°C; ^{1}H NMR ($CDCl_3$) δ: 1.70–1.82, 2.34–2.67 (4H, C-8, 9-CH_2 × 2), 3.53 (s, 3H, OCH_3), 3.58 (s, 3H, OCH_3), 6.90–6.98, 7.35–7.70, 8.02–8.08 (m, 14H, Ar-H); ^{13}C NMR ($CDCl_3$) δ: 22.2, 24.9 (each t, C-8, 9), 52.1 (q, OCH_3), 52.2 (q, OCH_3), 62.7, 65.9 (each s, C-1, 7), 89.1, 91.9 (each d, C-2, 6), 126.1, 127.0, 127.9, 127.9, 128.0, 128.2, 128.4, 128.9, 132.1 (each d, Ph-*o*, *m*, *p*), 130.7, 135.1, 139.0, 146.0 (each s, Ph-*ipso*), 171.5, 171.7 (each s, C═O), 192.4 (s, C═O). Anal. calcd. for $C_{29}H_{24}O_6$: C 74.35, H 5.16, found: C 74.23, H 5.13.

Crystal structure determination

Summaries of the crystal data and structure refinement details are given in Tables 2–9.[4] The structure was solved by a direct method (18), and refined by full-matrix least squares. The atoms other than hydrogen were refined anisotropically. The atomic scattering factors for all atoms and the anomalous dispersion correction factors for atoms other than hydrogen were taken from the literature (19–21). All calculations were performed using the TEXSAN (22) crystallographic software package of the Molecular Structure Corporation.

Acknowledgements

This work was supported in part by a Grant-in-Aid (to K.M.) for Scientific Research from the Ministry of Education, Sci-

[4]Tables of atomic coordinates, fractional atomic coordinates, bond lengths, bond angles, and thermal parameters have been deposited. Complete sets of data may be purchased from: The Depository of Unpublished Data, Document Delivery, CISTI, National Research Council Canada, Ottawa, Canada K1A 0S2.

Tables of atomic coordinates and of bond lengths and bond angles have also been deposited with the Cambridge Crystallographic Data Centre and can be obtained on request from The Director, Cambridge Crystallographic Data Centre, University Chemical Laboratory, 12 Union Road, Cambridge, CB2 1EZ, U.K.

Structure factor tables are no longer being deposited and may be obtained directly from the author.

ence, and Culture, Japan (No. 04453023). The authors are also grateful to the Ministry of Education, Science, and Culture, Japan for purchasing the high-field NMR instruments (JEOL JNM-ALPHA500 and JNM EX270) by the special fund (to K.M. as a representative in 1992). We thank Dr. Mituo Toda and Mr. Yukio Ikemi (Kyoto University) for some technical assistance.

This work is also in part supported by a grant from The Kyoto University Foundation (to J.W.L.) which is gratefully acknowledged, and by the Natural Sciences and Engineering Research Council of Canada. Thanks are also extended to Professor Toshio Sakurai (Shinshu University) and to Dr. Motoo Shiro (Rigaku Corporation) for their useful advice in the X-ray analyses.

1. J.W. Lown. *In* 1,3-Dipolar cycloaddition chemistry. *Edited by* A. Padwa. John Wiley and Sons, New York. 1984. Chap. 6; K. Matsumoto. Kagaku no Ryoiki, **27**, 148 (1973); Chem. Abstr. **76**, 42,253 (1972) J.W. Lown and K. Matsumoto. Yuki Gosei Kagaku Kyokaishi, **29**, 760 (1971); Chem. Abstr. **75**, 140,563 (1971), K. Matsumoto, Y. Ikami, M. Shiro, T. Uchida, and J.W. Lown. Can. J. Chem. **71**, 529 (1993).
2. A. Rastelli, M. Bagatti, A. Ori, R. Gandolfi, and M. Burdisso. J. Chem. Soc. Faraday Trans. **89**, 29 (1993); H. Landen, B. Margraf, H-D. Martin, and A. Steigel. Tetrahedron Lett. **29**, 6597 (1988), and references cited therein.
3. K. Matsumoto, T. Uchida, and K. Maruyama. Chem. Lett. 327 (1974).
4. K. Matsumoto, Y. Ikemi, C. Takayama, K. Aoyama, and T. Uchida. Chem. Lett. 1647 (1990).
5. K. Matsumoto, H. Iida, T. Uchida, Y. Yabe, and A. Kakehi. Chem. Express, **8**, 609 (1993).
6. R. Huisgen and H. Mader. J. Am. Chem. Soc. **93**, 1777 (1971).
7. A. Padwa, D. Dean, A. Mazzu, and E. Vega. J. Am. Chem. Soc. **95**, 7168 (1973).
8. A. Padwa, M. Dharanm, J. Smolanoff, and S.I. Wetmore, Jr. J. Am. Chem. Soc. **95**, 1945 (1973); R. Sustmann, R. Huisgen, and H. Huber. Chem. Ber. **100**, 1802 (1967).
9. R. Huisgen, K. Matsumoto, and C.H. Ross. Heterocycles, **15**, 1131 (1981); J.H. Hall and R. Huisgen. Chem. Commun. 1187 (1971).
10. J.W. Lown and K. Matsumoto. Can. J. Chem. **48**, 2215 (1970).
11. H.W. Heine, R. Peavy, and A.J. Durbetaki. J. Org. Chem. **31**, 3924 (1966).
12. P.N. Woller and N.H. Cromwell. J. Org. Chem. **35**, 888 (1970).
13. R. Huisgen, W. Scheer, H. Mader, and E. Brunn. Angew Chem. Int. Ed. Engl. **8**, 604 (1969).
14. T. Uchida, M. Toda, Y. Ikemi, Y. Yabe, K. Aoyama, A. Kakehi, and K. Matsumoto. 65th Annual Meeting of the Chemical Society of Japan, Tokyo. March 28, 1993. 1A533.
15. R.B. Woodward and R. Hoffmann. J. Am. Chem. Soc. **87**, 395 (1965); **87**, 2046 (1965); **87** 2511 (1965).
16. J.W. Lown and K. Matsumoto. Can. J. Chem. **49**, 3443 (1971).
17. R.N. McDonald and R.R. Reitz. J. Org. Chem. **37**, 2418 (1972).
18. MITHRIL: C.J. Gilmore. J. Appl. Crystallogr. **17**, 42 (1984); DIFDIR: P.T. Beurskens. Technical Report 1984/1, Crystallography Laboratory, Toernooiveld, 6525 Ed Nijmegen, Netherlands.
19. D.T. Cromer and J.T. Weber. International tables for X-ray crystallography. Vol. IV. The Kynoch Press, Birmingham, U.K. 1974. Table 2.2A.
20. J.A. Ibers and W.C. Hamilton. Acta Crystallogr. **17**, 781 (1964).
21. D.T. Cromer. International tables for X-ray crystallography. Vol. IV. The Kynoch Press, Birmingham, U.K. 1974. Table 2.3.1.
22. TEXRAY structure analysis package, Molecular Structure Corporation, 1985.

Can. J. Chem. Downloaded from www.nrcresearchpress.com by 85.192.166.187 on 09/08/12
For personal use only.

Structural studies of organoboron compounds LXII.[1] Synthesis and structure of various *N*-alkylated 1,3-dioxa-4-aza-2-boracyclohexanes

WOLFGANG KLIEGEL, HENNING AMT, HARALD BECKER, UTE LAUTERBACH, AND GOTTFRIED LUBKOWITZ

Institut für Pharmazeutische Chemie der Technischen Universität Braunschweig, Beethovenstrasse 55, 38106 Braunschweig, Germany

AND

STEVEN J. RETTIG AND JAMES TROTTER

Department of Chemistry, University of British Columbia, 2036 Main Mall, Vancouver, BC V6T 1Z1, Canada

Received March 21, 1994

WOLFGANG KLIEGEL, HENNING AMT, HARALD BECKER, UTE LAUTERBACH, GOTTFRIED LUBKOWITZ, STEVEN J. RETTIG, and JAMES TROTTER. Can. J. Chem. **72**, 2118 (1994).

The synthesis of a number of variously substituted *N*-alkyl 2-hydroxyaminoalkanols **3** and their reactions with phenylboronic acid are detailed. The crystalline products proved to be 1:2 condensates **4** in a few cases and 1:1 condensates **5** in all the other cases studied. Crystals of 2-mesityl-6,6-pentamethylene-1,3-dioxa-4-aza-2-boracyclohexane, **5***l*, are triclinic, $a = 11.540(2)$, $b = 10.402(3)$, $c = 8.440(2)$ Å, $\alpha = 108.86(2)°$, $\beta = 97.62(2)°$, $\gamma = 89.36(2)°$, $Z = 2$, space group $P\bar{1}$; and those of 4,4′-methylenebis(6,6-pentamethylene-2-phenyl-1,3-dioxa-4-aza-2-boracyclohexane) benzene solvate, **15a**·C_6H_6, are monoclinic, $a = 22.690(1)$, $b = 16.867(1)$, $c = 8.4783(9)$ Å, $\beta = 104.912(8)°$, $Z = 4$, space group $C2/c$. The structures were solved by direct methods and refined by full-matrix least-squares procedures to $R = 0.037$ and 0.035 ($R_w = 0.035$ and 0.044) for 3190 and 2084 reflections with $I \geq 3\sigma(F^2)$. respectively.

WOLFGANG KLIEGEL, HENNING AMT, HARALD BECKER, UTE LAUTERBACH, GOTTFRIED LUBKOWITZ, STEVEN J. RETTIG et JAMES TROTTER. Can. J. Chem. **72**, 2118 (1994).

On décrit la synthèse d'un certain nombre de *N*-alkyl 2-hydroxyaminoalcanols substitués (**3**) ainsi que leurs réactions avec l'acide phénylboronique. Il s'avère que, dans quelques cas, les produits cristallins obtenus sont les produits de condensation 1 : 2 (**4**) alors que, dans tous les autres cas étudiés, ce sont les produits de condensation 1 : 1 (**5**). Les cristaux du 2-mésityl-6,6-pentaméthylène-1,3-dioxa-4-aza-2-boracyclohexane, **5***l*, sont tricliniques, groupe d'espace $P\bar{1}$, avec $a = 11,540(2)$, $b = 10,402(3)$, $c = 8,440(2)$ Å, $\alpha = 108,86(2)°$, $\beta = 97,62(2)°$ et $\gamma = 89,36(2)°$ et $Z = 2$; ceux du 4,4′-méthylènebis(6,6-pentaméthylène-2-phényl-1,3,-dioxa-4-aza-2-boracyclohexane) solvaté par le benzène, **15***a*·C_6H_6, sont monocliniques, groupes d'espace $C2/c$, avec $a = 22,690(1)$, $b = 16,867(1)$ et $c = 8,4783(9)$ Å, $\beta = 104,912(8)°$ et $Z = 4$. On a résolu les structures par des méthodes directes et on les a affinées par la méthode des moindres carrés jusqu'a des valeurs de $R = 0,037$ et 0,035 ($R_w = 0,035$ et 0,044) pour respectivement 3190 et 2084 reflexions avec $I \geq 3\sigma(F^2)$.

[Traduit par la rédaction]

Introduction

In a previous work (1) we described the synthesis of two *N*-alkylated 2-hydroxylaminoalkanols of type **3**, and the products of their reactions with phenylboronic acid. These products turned out to possess different molecular structures: in one case a bicyclic pyroboronate structure **4**, formed by the incorporation of two phenylboronic acid moieties and a transannular N→B coordinative bond, and in another a monocyclic phenylboronate structure **5** that exists in the solid state as a BONBON dimer of type **8**, in which two chair-form BONCCO rings are joined by a pair of N→B bonds. Both molecular structures, **4** and **8**, have been established by X-ray crystallographic analyses (1). The monomeric BONCCO boronate ring system of type **5** had already been obtained from certain hydroxamic acid derivatives **3** (R = acyl) (2) as well as from the use of the sterically hindered mesitylboronic acid in the condensation reaction with *N*-unsubstituted 2-hydroxyaminoalkanols **3** (R = H) (3). The semiplanar "sofa" conformation adopted by these BONCCO cycloboronates **5** is consistent with that reported for other diol-boronates (cf. refs. 2, 3). In order to produce additional examples of the six-membered BONCCO cycloboronate ring system we synthesized a number of variously substituted *N*-alkyl 2-hydroxyaminoalkanols **3**(*a–p*) by reduction of the nitrones **1** or **2** with KBH_4 or $LiAlH_4$, and reacted them with phenylboronic acid. The crystalline products proved to be 1:2 condensates in a few cases (**4***a–c*) and 1:1 condensates in all the other cases studied (**5***d–p*). The bicyclic structure of **4**, characterized in detail by an X-ray crystallographic study (1), is confirmed by the ^{11}B nmr spectra that display two signals of equal peak area: one near $\delta(Et_2OBF_3) \approx 29$ ppm indicative of a trivalent sp^2 boron, and another near 15 ppm, indicative of the presence of a tetracoordinated sp^3 boron in the compounds **4**.

The 1:1 reaction products give ^1H nmr spectra consistent with the different possible structures **5–9**. From the considerations and findings discussed in our previous work (1) it could be assumed that the constitution **5** and its dimeric form **8**, respectively, are the most probable ones. The ^{11}B nmr spectra of the examples **5***h,i,k,l,m*, and *n* show the expected signals for tricoordinated (sp^2) boron at $\delta(Et_2OBF_3) = 27.5$, 27.3, 27.5, 28.3, 27.6 and 27.9 ppm, respectively, confirming the cycloboronate structure **5**, at least in solution. Dimeric associates of type **8** in the solid state, however, could not be ruled out. The infrared spectra (KBr pellets) corroborate the monomeric character of **5** in the solid state (with the exception of **5***d* and **5***e*, see Experimental) because of the strong ν_{16} phenyl ring stretching vibrations at 1600 cm^{-1} which are normally found in the spectra of trigonal planar phenylboronates (ref. 1, and references therein). An X-ray crystallographic analysis of one of the 1:1 condensation products, **5***l*, has been performed in order to provide unambiguous proof of the cycloboronate structure **5** in the solid state.

[1]Previous paper in this series; ref. 13.

Can. J. Chem. Downloaded from www.nrcresearchpress.com by 85.192.166.187 on 09/08/12
For personal use only.

Can. J. Chem. Downloaded from www.nrcresearchpress.com by 85.192.166.187 on 09/08/12
For personal use only.

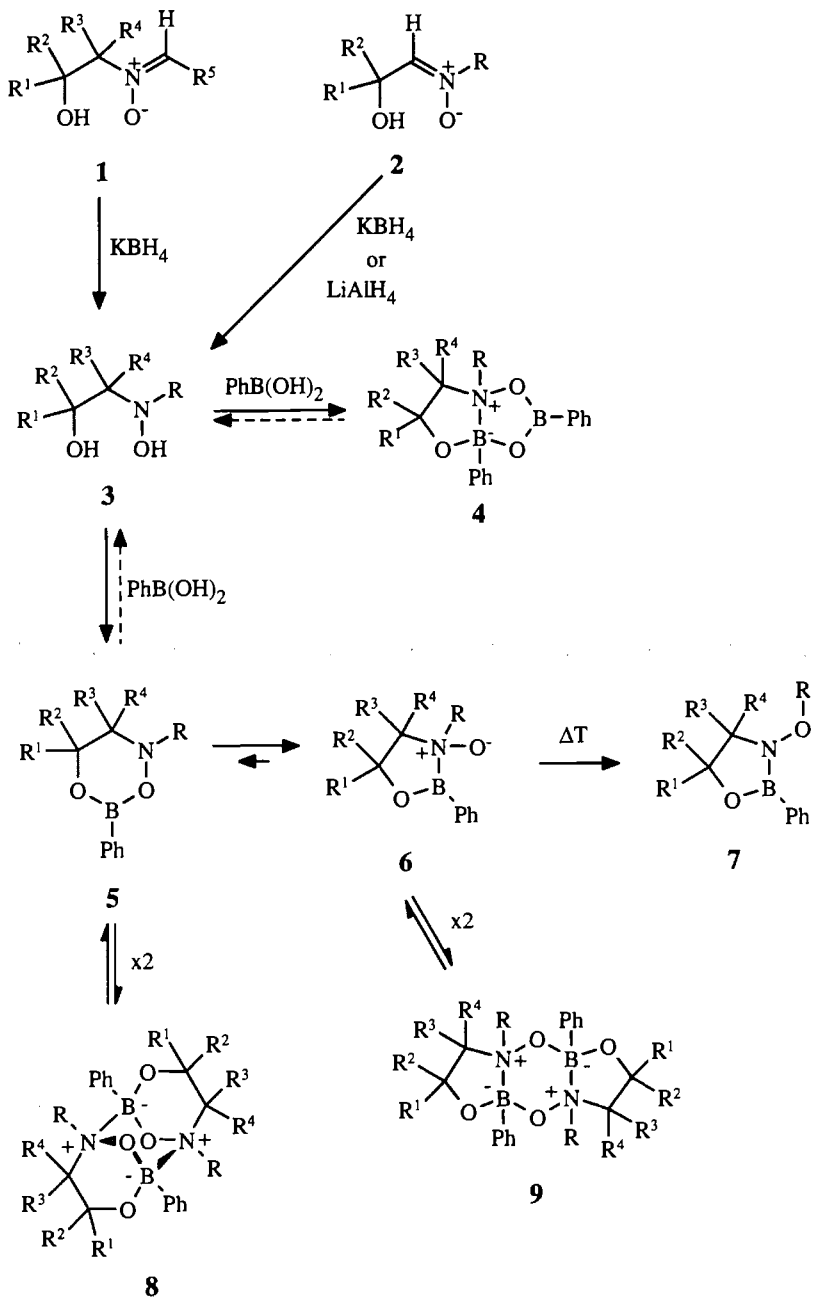

3 and 4/5	R	R^1	R^2	R^3	R^4
a	C_6H_{11}	H	CH_3	H	H
b	$CH_2C_6H_5$	H	H	H	H
c	$CH_2C_6H_5$	H	H	H	CH_3
d	CH_3	H	H	H	H
e	CH_3	—$(CH_2)_5$—		H	H
f	C_2H_5	—$(CH_2)_5$—		H	H
g	C_6H_{11}	H	H	H	H
h	$CH_2C_6H_{11}$	—$(CH_2)_5$—		H	H
i	$CH_2C_6H_5$	H	H	CH_3	CH_3
j	$CH_2C_6H_5$	H	CH_3	CH_3	CH_3
k	$CH_2C_6H_5$	—$(CH_2)_5$—		H	H
l	$CH_2C_6H_4$-4-Cl	—$(CH_2)_5$—		H	H
m	$CH_2C_6H_4$-4-NO_2	H	H	CH_3	CH_3
n	$CH_2C_6H_4$-4-NO_2	—$(CH_2)_5$—		H	H
o	$CH_2C_6H_4$-4-$N(CH_3)_2$	—$(CH_2)_5$—		H	H
p	$CH(C_6H_5)_2$	H	CH_3	H	H

Can. J. Chem. Downloaded from www.nrcresearchpress.com by 85.192.166.187 on 09/08/12
For personal use only.

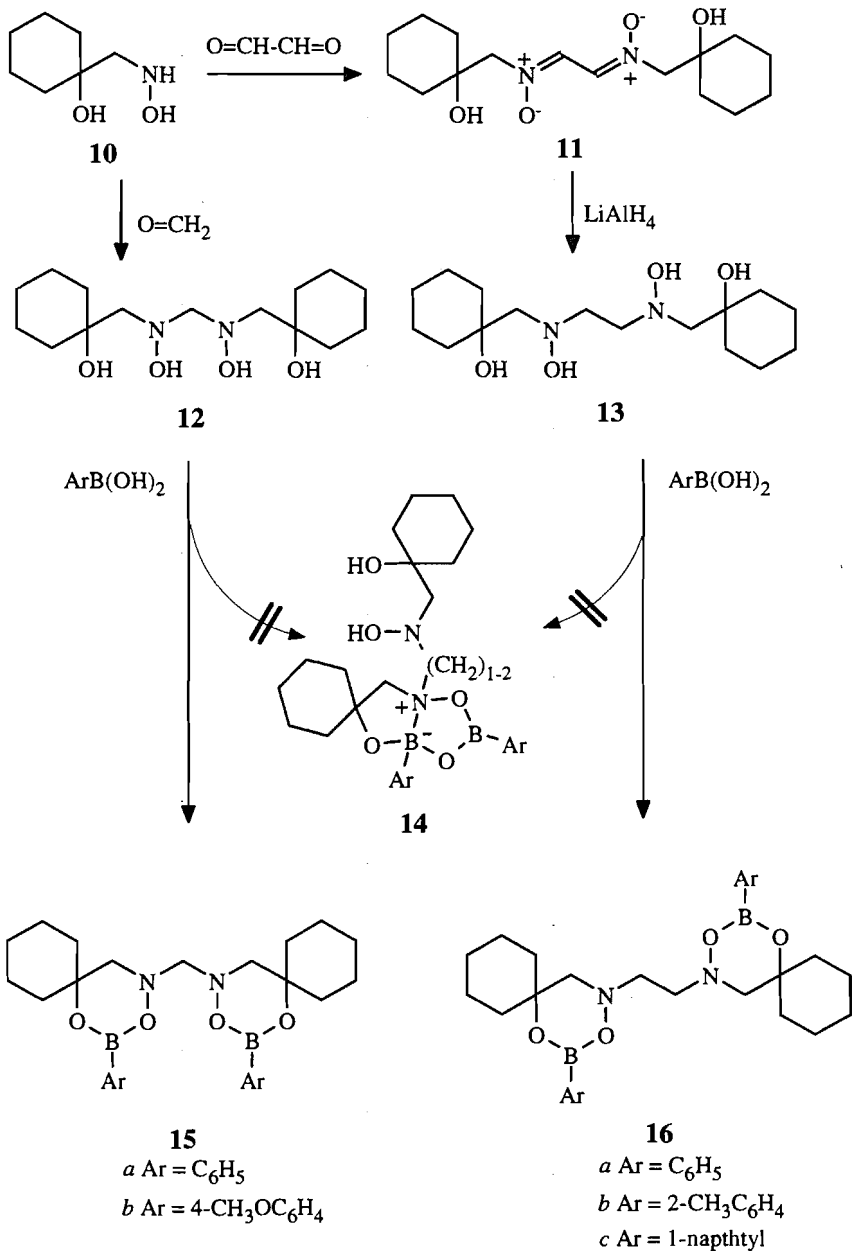

15
a Ar = C_6H_5
b Ar = 4-$CH_3OC_6H_4$

16
a Ar = C_6H_5
b Ar = 2-$CH_3C_6H_4$
c Ar = 1-napthtyl

A related structural problem arose from the reaction of arylboronic acids with compounds containing two *N*-alkylhydroxylaminoalkanol groups in a geminal or vicinal arrangement, namely the aminal **12** and the ethylenediamine derivative **13**. The aminal **12** could be prepared as a 2:1 condensation product of the hydroxylamine **10** and formaldehyde.[2] Compound **13** was synthesized by reduction of the glyoxal-bisnitrone **11** with $LiAlH_4$. Both of the tetrahydroxy compounds, **12** and **13**, gave bisarylboronates upon reaction with arylboronic acids. The elemental analyses as well as the infrared, ^1H nmr, and ^{11}B nmr spectra show that all of the four hydroxyl functions in each molecule are involved in the condensation reaction, so that a pyroboronate formation at only one of the "1,3-diol" groupings (**14**), as for type **4** compounds, can be excluded. Thus, structures **15** and **16** seemed very likely, although there are other possibilities of biscycloboronate condensation products as formulated in **17**–**20**. Further support for **15** and **16** comes from the strong ν_{16} phenyl ring stretching bands at 1600 cm^{-1} in the infrared spectra that are typical for non-tetracoordinated phenylboronates (like compound **5** (ref. 1, and references therein)). The EI mass spectra of **15** and **16**, however, give only very small molecular peaks (M^+). Both types of compound display a parent peak of a methyleniminium ion (Fig. 1), indicating an

[2]As shown by ^1H nmr and mass spectrometry, the aminal **12** dissociates easily into a formaldehyde nitrone and the hydroxylamine **10**, in an elimination/addition equilibrium:

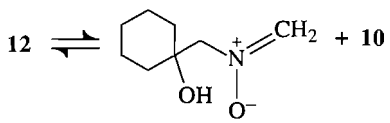

This kind of dissociation in solution or gaseous state has been reported for other *N*,*N*′-dihydroxyaminals (4).

Can. J. Chem. Downloaded from www.nrcresearchpress.com by 85.192.166.187 on 09/08/12
For personal use only.

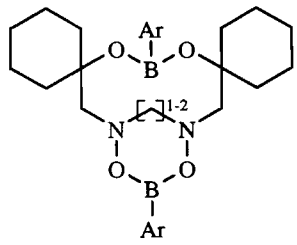

17

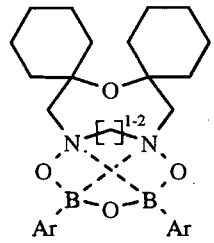

18

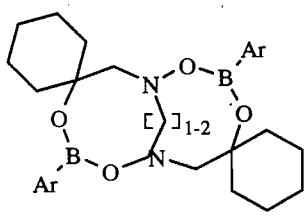

19

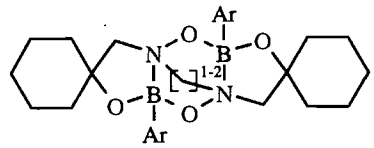

20

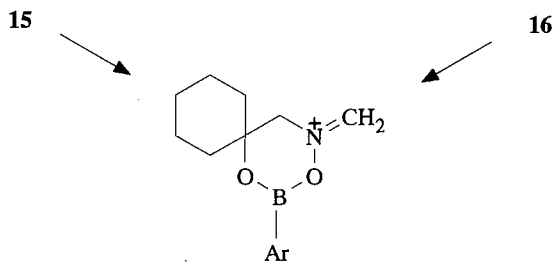

FIG. 1. Mass spectral fragmentation pattern of **15** and **16**.

easy dissociation of a C—N aminal bond in the case of **15**,[3] and of the C—C ethylene bond connecting the two BONCCO rings in **16**. To provide additional structural certainty, especially for the pyroboronate type **15** (with a relatively labile aminal function), an X-ray crystallographic analysis of **15***a*, which formed good crystals as a 1:1 benzene solvate, was carried out.

Experimental

N-*Benzylidene-3-hydroxy-2-methyl-2-butanamine* N-*oxide* (**1**,R^1 = H, $R^2 = R^3 = R^4 = CH_3$, $R^5 = C_6H_5$)

3-Hydroxyamino-3-methyl-2-butanol (5) (0.24 g, 2 mmol) and benzaldehyde (0.21 g, 2 mmol) are reacted as described previously (5). Yield: 0.34 g (82%) of colorless crystals. Mp 67°C (from benzene/petroleum ether), Infrared (KBr): 3220 (O—H), 1585 cm^{-1} (C=N). ^1H nmr (90 MHz, $CDCl_3$/TMS): δ (ppm) = 1.19 (d, J = 7 Hz, O—C—CH_3), 1.54 and 1.61 (s and s, $C(CH_3)_2$), 3.89 (q, J = 7 Hz, O—CH), 4.58 (s, broad, exchangeable, OH), 7.17–7.37 (m, 4 aromatic H and N=CH), 8.05–8.02 (m, 2 aromatic H). Anal. calcd. for $C_{12}H_{17}NO_2$: C 69.54, H 8.27, N 6.76; found: C 69.39, H 8.29, N 6.76.

N-*(2-Hydroxyethylidene)methanamine* N-*oxide* (**2**a, $R = CH_3$, $R^1 = R^2 = H$)

Glycolaldehyde (1.20 g, 20 mmol) and *N*-methylhydroxylamine hydrochloride (1.67 g, 20 mmol) are dissolved in 20 mL of ethanol (96%). A solution of K_2CO_3 (1.38 g, 10 mmol) in 5 mL of water is added under stirring. After 48 h the precipitated KCl is filtered off and the solvent removed in vacuo. The residue is taken up in 50 mL of absolute ethanol, and after filtration the ethanol is distilled off. The remaining oil is not purified further and is used in subsequent reactions as a crude product (see below). ^1H nmr (90 MHz, $CDCl_3$/TMS): δ (ppm) = 3.65 (s, NCH_3), 4.15 (s, broad, exchangeable, OH), 4.35 (d, J = 4 Hz, CH_2O), 6.92 (t, J = 4 Hz, N=CH).

N-*(2-Hydroxyethylidene)cyclohexanamine* N-*oxide* (**2**b, $R = C_6H_{11}$, $R^1 = R^2 = H$)

Glycolaldehyde (0.60 g, 10 mmol) and *N*-cyclohexylhydroxylamine (1.14 g, 10 mmol) are dissolved in 50 mL of absolute ethanol and refluxed for 1 h. After removal of solvent in vacuo, the oily residue is taken up in a small amount of ethanol and ether and stored 24 h at −18°C. Yield: 0.76 g (49%) colorless needles. Mp 127°C (from ethanol/ether). Infrared (KBr): 3280 (O—H), 1615 cm^{-1} (C=N). ^1H nmr (90 MHz, $CDCl_3$): δ (ppm) = 1.03–2.22 (m, $(CH_2)_5$), 3.44–3.84 (m, =N—CH), 4.39 (d, J = 4 Hz, O—CH_2), 4.89 (s, broad, exchangeable, OH), 6.98 (t, J = 4 Hz, N=CH). Anal. calcd. for $C_8H_{15}NO_2$: C 61.12, H 9.62, N 8.91; found: C 61.02, H 9.84, N 8.67.

N-*(2-Hydroxypropylidene)cyclohexanamine* N-*oxide* (**2**c, $R = C_6H_{11}$, $R^1 = H$, $R^2 = CH_3$)

2-Hydroxypropanal (6) (2.22 g, 30 mmol) and *N*-cyclohexylhydroxylamine (3.45 g, 30 mmol) are dissolved in 30 mL of absolute ethanol and stirred at room temperature for 48 h. The solvent is removed in vacuo, and the residue recrystallized from ethanol. Yield: 4.42 g (86%) of colorless needles. Mp 129°C (from absolute ethanol). Infrared (KBr): 3210 (O—H), 1605 cm^{-1} (C=N). ^1H nmr (90 MHz, $CDCl_3$/TMS): δ (ppm) = 1.04–2.02 (m, $(CH_2)_5$), 1.39 (d, J = 7 Hz, O—C—CH_3), 3.64 (m, =N—CH), 4.71 (m, O—CH), 5.61 (s, exchangeable,

[3]The relatively high stability of the methyleniminium cation and the dissociation of the aminal **15** is reminiscent of the dissociation pattern of the corresponding *N,N'*-dihydroxyaminals **12** (see footnote 2) and also the mass spectral fragments of aminal-derived pyroboronates (4):

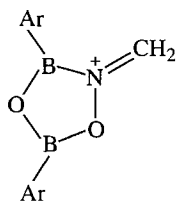

OH), 6.85 (d, J = 5 Hz, N=CH). Anal. calcd. for $C_9H_{17}NO_2$: C 63.13, H 10.01, N 8.18; found: C 63.09, H 10.15, N 7.97.

N-*(2-Hydroxyethylidene)phenylmethanamine* N-*oxide* (**2**d, R = $CH_2C_6H_5$, $R^1 = R^2 = H$)

Glycolaldehyde (1.20 g, 20 mmol) and *N*-benzylhydroxylamine hydrochloride (1.38 g, 10 mmol) are reacted as described for **2***a*, and the remaining residue is recrystallized from absolute ethanol and ether. Yield: 2.30 g (70%) of colorless platelets. Mp 82–84°C (from ethanol/ether). Infrared (KBr): 3300, 3170 (broad, O—H), 1610 cm^{-1} (C=N). ^1H nmr (90 MHz, $CDCl_3$/TMS): δ (ppm) = 4.15 (s, very broad, exchangeable, OH), 4.35 (d, J = 5 Hz, O—CH_2), 4.83 (s, N—CH_2), 6.88 (t, J = 5 Hz, N=CH), 7.37 (s, 5 aromatic H). Anal. calcd. for $C_9H_{11}NO_2$: C 65.44, H 6.71, N 8.48; found: C 65.41, H 6.71, N 8.57.

N-*(2-Hydroxypropylidene)diphenylmethanamine* N-*oxide* (**2**e, R = $CH(C_6H_5)_2$, $R^1 = H$, $R^2 = CH_3$)

2-Hydroxypropanal (1.48 g, 20 mmol) and *N*-benzhydrylhydroxylamine (7) (3.98 g, 20 mmol) are reacted as described for **2***c*. Yield: 4.21 g (82%) of colorless crystals. Mp 110–111°C (from ethanol/ether). Infrared (KBr): 3290 (O—H), 1590 cm^{-1} (C=N). ^1H nmr (90 MHz, $CDCl_3$/TMS): δ (ppm) = 1.34 (d, J = 7 Hz, CH_3), 4.71 (m, O—CH), 5.47 (s, broad, exchangeable, 2 OH), 6.15 (s, N—CH), 6.82 (d, J = 5 Hz, N=CH), 7.32 (s, 10 aromatic H). Anal. calcd. for $C_{16}H_{17}NO_2$: C 75.27, H 6.71, N 5.49; found: C 75.47, H 6.71, N 5.64.

*1-(*N-*Cyclohexyl*-N-*hydroxyamino)-2-propanol* (**3**a)

To a solution of **2***c* (1.71 g, 10 mmol) in 60 mL of methanol a solution of KBH_4 (1.08 g, 20 mmol) in 15 mL of water is added dropwise over a period of 30 min. After 24 h the excess KBH_4 is decomposed with tartaric acid, the methanol distilled off in vacuo, and the remaining aqueous solution brought to pH 9–10 using aqueous Na_2CO_3, solution. After extraction with 3 × 70 mL of dichloromethane, the collected dichloromethane solutions are dried with $MgSO_4$ and evaporated in vacuo. The residue is crystallized from benzene/petroleum ether. Yield: 1.56 g (90%). Mp 79°C. Infrared (KBr): 3250 cm^{-1} (O—H). ^1H nmr (90 MHz, $CDCl_3$/TMS): δ (ppm) = 1.03–2.17 (m, —$(CH_2)_5$—), 1.18 (d, J = 7 Hz, CH_3), 2.62 (m, N—CH_2C and N—CH(C,C)), 4.05 (m, O—CH), 5.28 (s, broad, exchangeable, OH). Anal. calcd. for $C_9H_{19}NO_2$: C 62.39, H 11.05, N 8.08; found: C 62.36, H 11.18, N 7.96.

*2-(*N-*Benzyl*-N-*hydroxyamino)ethanol(***3**b)

2*d* (0.66 g, 4 mmol) and KBH_4 (0.54 g, 10 mmol) are reacted as described for **3***a* (see above). The oily residue is not purified further and is used as crude product in subsequent reactions. ^1H nmr (90 MHz, $CDCl_3$/TMS): δ (ppm) = 2.75 (t, J = 5 Hz, N—CH_2CO), 3.62 (t, J = 5 Hz, O—CH_2), 3.69 (s, N—CH_2(Ph)), 4.40 (s, very broad, exchangeable, 2 OH), 7.17 (s, 5 aromatic H).

*2-(*N-*Benzyl*-N-*hydroxyamino)-1-propanol* (**3**c)

N-Benzylidene-1-hydroxy-2-propanamine *N*-oxide (**1**, $R^1 = R^2 = R^3 = H$, $R^4 = CH_3$, $R^5 = C_6H_5$) (5) (2.15 g, 12 mmol) and KBH_4 (3.24 g, 60 mmol) are reacted as described for **3***a*. The oily residue is analytically pure. Yield: 2.05 g (94%) of a colorless oil. Infrared (film): 3100–3600 cm^{-1} (broad, O—H). ^1H nmr (90 MHz, $CDCl_3$/TMS): δ (ppm) = 1.05 (d, J = 6 Hz, CH_3), 2.91 (m, J = 6 Hz, O—CH), 3.49 (d, J = 6 Hz, CH_2CO), 3.65 and 3.96 (d and d, J = 12 Hz, N—CH_2 (Ph)), 4.53 (s, very broad, exchangeable, 2 OH), 7.30 (s, 5 aromatic H). Anal. calcd. for $C_{10}H_{15}NO_2$: C 66.27, H 8.34, N 7.73; found: C 66.34, H 8.19, N 7.43.

*2-(*N-*Hydroxy*-N-*methylamino)ethanol* (**3**d)

2*a* (crude product, 0.9 g, 10 mmol) and KBH_4) (1.08 g, 20 mmol) are reacted as described for **3***a*. The oily residue is not further purified and is used as crude product in subsequent reactions. ^1H nmr (90 MHz, $CDCl_3$/TMS): δ (ppm) = 2.4 (m_c, N—CH_3 and N—CH_2C), 3.5 (m_c, O—CH_2 and 2 OH).

*1-(*N-*Hydroxy*-N-*methylaminomethyl)cyclohexanol* (**3**e)

3-Hydroxy-5,5-pentamethylene-1,3-oxazolidine[4] (9) (1.57 g, 10 mmol) and KBH_4 (1.08 g, 20 mmol) are reacted as described for **3***a*. The oily residue is used as crude product in further reactions.

*1-(*N-*Ethyl*-N-*hydroxyaminomethyl)cyclohexanol* (**3**f)

N-Ethylidene-(1-hydroxycyclohexyl)methanamine *N*-oxide (**1**, $R^1 + R^2$ = —$(CH_2)_5$—, $R^3 = R^4 = H$, $R^5 = CH_3$) (8) (1.71 g, 10 mmol) and KBH_4 (1.08 g, 20 mmol) are reacted as described for **3***a*. The oily residue is used as crude product in further reactions.

*2-(*N-*Cyclohexyl*-N-*hydroxyamino)ethanol* (**3**g)

2*b* (3.14 g, 20 mmol) and $LiAlH_4$ (0.76, 20 mmol) are suspended in 150 mL of dry ether. After refluxing for 5 h, hydrolysis is carried out with water under cooling with ice, and subsequent acidification with 6N HCl. The mixture is neutralized with $NaHCO_3$, the ether layer separated, and the aqueous phase extracted with an additional 3 × 40 mL of ether. The combined ether solutions are dried over Na_2SO_4 and evaporated in vacuo. The reside is crystallized from benzene/petroleum ether. Yield: 2.04 g (65%) of colorless crystals. Mp 60–62°C. Infrared (KBr): 3500–2600 cm^{-1} (broad, O—H). ^1H nmr (90 MHz, $CDCl_3$/TMS): δ (ppm) = 0.71–2.17 (m, —$(CH_2)_5$—), 2.32–2.70 (m, N—CH(C,C)), 2.87 (t, J = 5 Hz, N—CH_2), 3.79 (t, J = 5 Hz, O—CH_2), 6.11 (s, exchangeable, 2 OH). Anal. calcd. for $C_8H_{17}NO_2$: C 60.35, H 10.76, N 8.80; found: C 60.52, H 11.17, N 8.60.

*1-(*N-*Cyclohexylmethyl*-N-*hydroxyaminomethyl)cyclohexanol* (**3**h)

N-Cyclohexylmethylene-(1-hydroxycyclohexyl)methanamine *N*-oxide (**1**, $R^1 + R^2$ = —$(CH_2)_5$—, $R^3 = R^4 = H$, $R^5 = C_6H_{11}$) (8) (1.20 g, 5 mmol) and KBH_4 (0.54 g, 10 mmol) are reacted as described for **3***a*. The residue is crystallized from absolute ethanol. Yield: 0.91 g (75%) of colorless crystals. Mp 74°C. Infrared (KBr): 3410, 3250 cm^{-1} (O—H). ^1H nmr (90 MHz, $CDCl_3$/TMS): δ (ppm) = 0.66–1.98 (m, —$(CH_2)_5$— and C_6H_{11}), 2.52 (d, J = 6 Hz, N—$CH_2C_6H_{11}$), 2.71 (s, N—CH_2CO), 3.31 and 5.70 (s and s, broad, exchangeable, 2 OH). Anal. calcd. for $C_{14}H_{27}NO_2$: C 69.67, H 11.28, N 5.80; found: C 69.67, H 11.35, N 5.71.

*2-(*N-*Benzyl*-N-*hydroxyamino)-2-methylpropanol* (**3**i)

N-Benzylidene-1-hydroxy-2-methyl-2-propanamine *N*-oxide (**1**, $R^1 = R^2 = H$, $R^3 = R^4 = CH_3$, $R^5 = C_6H_5$) (5) (0.97 g, 5 mmol) and KBH_4 (1.08 g, 20 mmol) are reacted as described for **3***a*. The residue is crystallized from benzene/petroleum ether. Yield: 0.90 g (92%) of colorless crystals. Mp 107°C. Infrared (KBr): 3460, 3360 cm^{-1} (O—H). ^1H nmr (90 MHz, $CDCl_3$/TMS): δ (ppm) = 1.12 (s, 2 CH_3), 3.12 (s, very broad, exchangeable, OH), 3.38 (s, OCH_2) 3.70 (s, NCH_2), 4.88 (s, very broad, exchangeable, OH), 7.26 (s, 5 aromatic H). Anal. calcd. for $C_{11}H_{17}NO_2$: C 67.66, H 8.78, N 7.17; found: C 67.72, H 8.82, N 6.97.

*3-(*N-*Benzyl*-N-*hydroxyamino)-3-methyl-2-butanol* (**3**j)

N-Benzylidene-3-hydroxy-2-methyl-2-butanamine *N*-oxide (**1**, $R^1 = H$, $R^2 = R^3 = R^4 = CH_3$, $R^5 = C_6H_5$) (this work, see above) (1.04 g, 5 mmol) and KBH_4 (1.08 g, 20 mmol) are reacted as described for **3***a*. The residue is crystallized from benzene/petroleum ether. Yield: 0.72 g (69%) of colorless crystals. Mp 86°C. Infrared (KBr): 3460, 3360 cm^{-1} (O—H). ^1H nmr (90 MHz, $CDCl_3$/TMS): δ (ppm) = 1.09 (s, 2 CH_3), 1.10 (d, J = 6 Hz, $OCCH_3$), 3.37 (s, very broad, exchangeable, OH), 3.78 (q, J = 6 Hz, OCH), 3.79 (s, NCH_2), 5.10 (s, very broad, exchangeable, OH) 7.30 (s, 5, aromatic H). Anal. calcd. for $C_{12}H_{19}NO_2$: C 68.87, H 9.15, N 6.69; found: C 68.90, H 9.17, N 6.55.

*1-(*N-*Benzyl*-N-*hydroxyaminomethyl)cyclohexanol* (**3**k)

N-Benzylidene-(1-hydroxycyclohexyl)methanamine *N*-oxide (**1**, $R^1 + R^2$ = —$(CH_2)_5$—, $R^3 = R^4 = H$, $R^5 = C_6H_5$) (5) (1.16 g, 5 mmol)

[4]This is the ring tautomer of *N*-methylene-(1-hydroxycyclohexyl)-methanamine *N*-oxide (**1**, $R^1 + R^2$ = —$(CH_2)_5$—, $R^3 = R^4 = R^5 = H$). The ring/chain tautomerism of other aliphatic aldonitrones of this type has already been reported (8).

Can. J. Chem. Downloaded from www.nrcresearchpress.com by 85.192.166.187 on 09/08/12
For personal use only.

Can. J. Chem. Downloaded from www.nrcresearchpress.com by 85.192.166.187 on 09/08/12
For personal use only.

and KBH_4 (0.54 g, 10 mmol) are reacted as described for **3***a*. The residue is crystallized from benzene/petroleum ether. Yield: 0.76 g (66%) of colorless platelets. Mp 85–86°C. Infrared (KBr): 3470, 3210 cm^{-1} (O—H). ^1H nmr (90 MHz, $CDCl_3$/TMS): δ (ppm) = 1.03–1.88 (m, —$(CH_2)_5$—), 2.71 (s, NCH_2CO), 3.40 (s, broad, exchangeable, OH), 3.82 (s, $NCH_2C_6H_5$), 6.02 (s, broad, exchangeable, OH), 7.11–7.40 (m, 5 aromatic H). Anal. calcd. for $C_{14}H_{21}NO_2$: C 71.45, H 8.99, N 5.95; found: C 71.40, H 9.15, N 5.74.

*1-[*N*-(4-Chlorophenylmethyl)-*N*-hydroxyaminomethyl]cyclohexanol (**3**l)*

N - (4 - Chlorophenylmethylene) - (1 - hydroxycyclohexyl)methanamine *N*-oxide (**1**, $R^1 + R^2$ = —$(CH_2)_5$—, $R^3 = R^4$ = H, R^5 = 4-ClC_6H_4) (5) (1.34 g, 5 mmol) and KBH_4 (0.54 g, 10 mmol) are reacted as described for **3***a*. The residue is crystallized from benzene. Yield: 1.00 g (74%) of colorless small needles. Mp 113°C. Infrared (KBr): 3390, 3180 cm^{-1} (O—H). ^1H nmr (90 MHz, $CDCl_3$/TMS): δ (ppm) = 1.07–1.83 (m, —$(CH_2)_5$—), 2.17 (s, NCH_2CO), 3.04 (s, broad, exchangeable, OH), 3.78 (s, $CH_2C_6H_4Cl$), 5.64 (s, very broad, exchangeable, OH), 7.21 (s, 4 aromatic H). Anal. calcd. for $C_{14}H_{20}ClNO_2$: C 62.33, H 7.47, N 5.19; found: C 62.17, H 7.49, N 5.00.

*2-[*N*-Hydroxy-N-(4-nitrophenylmethyl)amino]-2-methylpropanol (**3**m)*

1-Hydroxy-2-methyl-*N*-(4-nitrophenylmethylene)-2-propanamine *N*-oxide (**1**, $R^1 = R^2$ = H, $R^3 = R^4 = CH_3$, R^5 = 4-$NO_2C_6H_4$) (5) (2.38 g, 10 mmol) and KBH_4 (1.08 g, 20 mmol) are reacted as described for **3***a*. The residue is crystallized from benzene. Yield: 1.17 g (49%) of yellowish crystals. Mp 113–114°C. Infrared (KBr): 3600–3200 (broad, O—H), 1525 cm^{-1} (NO_2). ^1H nmr (90 MHz, $CDCl_3$/TMS): δ (ppm) = 1.12 (s, 2 CH_3), 2.70 (s, broad, exchangeable, OH), 3.43 (s, NCH_2), 3.83 (s, OCH_2), 5.30 (s, broad, exchangeable, OH), 7.45 and 8.07 (d and d, *J* = 8 Hz, AA′BB′ system, 4 aromatic H). Anal. calcd. for $C_{11}H_{16}N_2O_4$: C 54.99, H 6.71, N 11.66; found: C 55.58, H 6.87, N 11.36.

*1-[*N*-Hydroxy-N-(4-nitrophenylmethyl)aminomethyl]cyclohexanol (**3**n)*

(1-Hydroxycyclohexyl)-*N*-(4-nitrophenylmethylene)methanamine *N*-oxide (**1**, $R^1 + R^2$ = —$(CH_2)_5$—, $R^3 = R^4 = CH_3$, R^5 = 4-$NO_2C_6H_4$) (5) (1.39 g, 5 mmol) and KBH_4 (1.08 g, 20 mmol) are reacted as described for **3***a*. The residue is crystallized from benzene. Yield: 1.13 g (81%) of yellow needles. Mp 125–126°C. Infrared (KBr): 3380, 3140 (O—H), 1510 cm^{-1} (NO_2). ^1H nmr (90 MHz, $CDCl_3$/TMS): δ (ppm) = 1.08–1.86 (m, —$(CH_2)_5$—), 2.81 (s, NCH_2CO), 2.96 (s, broad, exchangeable, OH), 3.95 (s, $NCH_2C_6H_4NO_2$), 5.83 (s, broad, exchangeable, OH), 7.51 and 8.14 (d and d, *J* = 8 Hz, AA′BB′ system, 4 aromatic H). Anal. calcd. for $C_{14}H_{20}N_2O_4$: C 59.99, H 7.19, N 9.99; found: C 60.01, H 7.29, N 9.87.

*1-[*N*-(4-Dimethylaminophenylmethyl)-N-hydroxyaminomethyl]cyclohexanol (**3**o)*

N-(4-Dimethylaminophenylmethylene)-(1-hydroxycyclohexyl)methanamine N-oxide (**1**, $R^1 + R^2$ = —$(CH_2)_5$—, $R^3 = R^4 = CH_3$, R^5 = 4-$(CH_3)_2NC_6H_4$) (5) (1.38 g, 5 mmol) and KBH_4 (1.62 g, 30 mmol) are reacted as described for **3***a*. The residue is crystallized from benzene/petroleum ether. Yield: 0.75 g (54%) of colorless crystals. Mp 69–70°C. Infrared (KBr): 3370, 3250 cm^{-1} (O—H). ^1H nmr (90 MHz, $CDCl_3$/TMS): δ (ppm) = 1.19–1.77 (m, —$(CH_2)_5$—), 2.72 (s, NCH_2CO), 2.94 (s, $N(CH_3)_2$), 3.75 (s, $NCH_2C_6H_4N(CH_3)_2$), 6.67 and 7.17 (d and d, *J* = 9 Hz, AA′BB′ system, 4 aromatic H); OH signals not observed.

*1-(*N*-Benzhydryl-N-hydroxyamino)-2-propanol (**3**p)*

2*e* (1.53 g, 6 mmol) and KBH_4 (0.65 g, 12 mmol) are reacted as described for **3***a*. The residue is crystallized from benzene. Yield: 1.35 g (87%) of colorless crystals. Mp 137–138°C. Infrared (KBr): 3430, 3300 cm^{-1} (O—H). ^1H nmr (90 MHz, $CDCl_3$/TMS): δ (ppm) = 1.09 (d, *J* = 6 Hz, CH_3), 2.62 (d, *J* = 5 Hz, NCH_2), 3.14 (s, broad, exchangeable, OH), 4.07 (m, OCH), 4.37 (s, $NCHPh_2$), 5.26 (s, broad, exchangeable, OH), 7.08–7.51 (m, 10 aromatic H). Anal. calcd. for $C_{16}H_{19}NO_2$: C 74.68, H 7.44, N 5.44; found: C 74.70, H 7.44, N 5.45.

*1-Cyclohexyl-7-methyl-3,5-diphenyl-2,4,6-trioxa-1-azonia-3-bora-5-boratabicyclo[3.3.0]octane (**4**a)*

3*a* (0.51 g, 3 mmol) and phenylboronic acid 0.73 g, 6 mmol) are dissolved in 20–30 mL of benzene and refluxed for 1 h with continuous removal of water using a Dean Stark trap. After evaporation in vacuo the residue is crystallized from benzene/petroleum ether. Yield: 0.85 g (78%) of colorless needles. Mp 130°C. Infrared (KBr): 1605 cm^{-1} (phenyl C=C). ^1H nmr (90 MHz, $CDCl_3$/TMS): δ (ppm) = 0.74–2.10 (m, —$(CH_2)_5$—), 1.42 (d, *J* = 6 Hz, CH_3), 2.67 (m, NCH and 1 H of NCH_2), 3.32 and 3.45 (d and d, 1 H of NCH_2), 4.27 (m, OCH), 7.18–7.53 (m, 6 aromatic H), 7.57–7.77 (m, 2 aromatic H), 7.81–8.01 (m, 2 aromatic H). ^{11}B nmr (64.2 MHz, $CDCl_3/Et_2OBF_3$): δ (ppm) = 29.2 ($w_{1/2}$ = 640 Hz) and 14.5 ($w_{1/2}$ = 300 Hz); ratio of peak areas: 1:1. Anal. calcd. for $C_{21}H_{27}B_2NO_3$: C 69.47, H 7.50, B 5.96, N 3.86; found: C 69.36, H 7.50, B 6.19, N 4.01.

*1-Benzyl-3,5-diphenyl-2,4,6-trioxa-1-azonia-3-bora-5-boratabicyclo[3.30]octane (**4**b)*

3*b* (crude product, 0.50 g, 3 mmol) and phenylboronic acid (0.73 g, 6 mmol) are reacted as described for **4***a*. Yield: 0.91 g (85%) of colorless crystals. Mp 128–129°C (from benzene/petroleum ether). Infrared (KBr): 1600 cm^{-1} (phenyl C=C). ^1H nmr (90 MHz, $CDCl_3$/TMS): δ (ppm) = 3.04 (m, NCH_2CO), 3.44 and 3.94 (d and d, *J* = 15 Hz, AB system, NCH_2Ph), 4.07 (m, OCH_2), 7.17–7.53 (m, 11 aromatic H), 7.61 – 7.78 (m, 2 aromatic H), 7.80–7.98 (m, 2 aromatic H). ^{11}B nmr (64.2 MHz, $CDCl_3/Et_2OBF_3$): δ (ppm) = 29.2 ($w_{1/2}$ = 640 Hz) and 14.7 ($w_{1/2}$ = 340 Hz); ratio of peak areas: 1:1. Anal. calcd. for $C_{21}H_{21}B_2NO_3$: C 70.65, H 5.93, N 3.92; found: C 70.64, H 5.94, N 3.94.

*1-Benzyl-8-methyl-3,5-diphenyl-2,4,6-trioxa-1-azonia-3-bora-5-boratabicyclo[3.3.0] octane (**4**c)*

3*c* (0.72 g, 4 mmol) and phenylboronic acid (0.98 g, 8 mmol) are reacted as described for **4***a*. Yield: 1.18 g (80%) of colorless crystals. Mp 126°C (from benzene/petroleum ether). Infrared (KBr): 1600 cm^{-1} (phenyl C=C). ^1H nmr (90 MHz), $CDCl_3$/TMS): δ (ppm) = 0.68 (d, *J* = 6 Hz, CH_3), 3.16–4.15 (m, CH_2CHN), 3.54 and 3.88 (d and d, *J* = 14 Hz, AB system, NCH_2Ph), 7.11–7.50 (m, 11 aromatic H), 7.56–7.72 (m, 2 aromatic H), 7.81–8.00 (m, 2 aromatic H). ^{11}B nmr (64.2 MHz, $CDCl_3/Et_2OBF_3$): δ (ppm) = 28.6 ($w_{1/2}$ = 640 Hz) and 15.1 ($w_{1/2}$ = 340 Hz); ratio of peak areas: 1:1. Anal. calcd. for $C_{22}H_{23}B_2NO_3$: C 71.21, H 6.25, N 3.78; found: C 71.23, H 6.25, N 3.85.

*4-Methyl-2-phenyl-1,3-dioxa-4-aza-2-boracyclohexane (**5**d)*[5]

3*d* (0.27 g, 3 mmol) and phenylboronic acid (0.37 g, 3 mmol) are reacted as described for **4***a*. The residue was crystallized from absolute ethanol. Yield: 0.25 g (47%) of colorless thin needles. Mp 126°C. ^1H nmr (90 MHz, $CDCl_3$/TMS): δ (ppm) = 2.87 (s, CH_3), 3.00 (t, *J* = 4 Hz, NCH_2C), 4.24 (t, *J* = 4 Hz, OCH_2), 7.15–7.40 (m, 3 aromatic H), 7.57–7.77 (m, 2 aromatic H). Anal. calcd. for $C_9H_{12}BNO_2$: C 61.07, H 6.83, N 7.91; found: C 61.06, H 6.93, N 7.80.

*4-Methyl-6,6-pentamethylene-2-phenyl-1,3-dioxa-4-aza-2-boracyclohexane (**5**e)*

3*e* (0.48 g, 3 mmol) and phenylboronic acid (0.37 g, 3 mmol) are reacted as described for **4***a*. Yield: 0.57 g (78%) of colorless oil, the crystallization of which could not be induced. Infrared (film): 1600

[5]The solid state infrared spectrum (KBr pellet) of **5***d*, which lacks the ν_{16} band, and the X-ray crystallographic analysis of a homologous compound that has a comparable infrared spectrum (1) suggest that **5***d* should also exist as a dimer of the type **8** in the crystalline state and should be named: *1,6-dimethyl-2,7-diphenyl-3,8,11,12-tetraoxa-1,6-diazonia-2,7-diboratatricyclo[5.3.1.1^{2,6}]dodecane.*

Can. J. Chem. Downloaded from www.nrcresearchpress.com by 85.192.166.187 on 09/08/12
For personal use only.

cm^{-1} (phenyl C=C). ^1H nmr (90 MHz, $CDCl_3$/TMS): δ (ppm) = 1.17–2.05 (m, —$(CH_2)_5$—), 2.74 (s, CH_3), 2.78 (s, NCH_2CO), 7.03–7.32 (m, 3 aromatic H), 7.50–7.73 (m, 2 aromatic H). Anal. calcd. for $C_{14}H_{20}BNO_2$: C 68.60, H 8.22, N 5.71; found: C 68.86, H 8.25, N 5.38.

*4-Ethyl-6,6-pentamethylene-2-phenyl-1,3-dioxa-4-aza-2-boracyclohexane (5*f)

3*f* (0.52 g, 3 mmol) and phenylboronic acid (0.37 g, 3 mmol) are reacted as described for **4***a*. The residue was crystallized from absolute ethanol. Yield: 0.49 g (63%) of colorless crystals. Mp 36°C. Infrared (KBr): 1600 cm^{-1} (phenyl C=C). ^1H nmr (90 MHz, $CDCl_3$/TMS): δ (ppm) = 1.10–2.02 (m, —$(CH_2)_5$—), 1.27 (t, J = 7 Hz, CH_3), 2.78 (s, NCH_2CO), 2.89 (q, J = Hz, NCH_2CH_3), 7.13–7.38 (m, 3 aromatic H), 7.63–7.81 (m, 2 aromatic H). Anal. calcd. for $C_{15}H_{22}BNO_2$: C 69.52, H 8.56, B 4.17, N 5.40; found: C 69.49, H 8.60, B 4.16, N 5.31.

*4-Cyclohexyl-2-phenyl-1,3-dioxa-4-aza-2-boracyclohexane (5*g)

3*g* (0.80 g, 5 mmol) and phenylboronic acid (0.61 g, 5 mmol) are reacted as described for **4***a*. The residue was crystallized from absolute ethanol. Yield: 0.82 g (67%) of colorless crystals. Mp 73°C. Infrared (KBr): 1605 cm^{-1} (phenyl C=C). ^1H nmr (90 MHz, $CDCl_3$/TMS): δ (ppm) = 0.92–2.32 (m, —$(CH_2)_5$—), 2.45–2.82 (m, NCH(C,C)), 3.02 (t, J = 4 Hz, NCH_2), 4.13 (t, J = 4 Hz, OCH_2), 7.10–7.38 (m, 3 aromatic H), 7.57–7.71 (m, 2 aromatic H). Anal. calcd. for $C_{14}H_{20}BNO_2$: C 68.60, H 8.22, N 5.71; found: C 68.63, H 8.37, N 5.78.

*4-Cyclohexylmethyl-6,6-pentamethylene-2-phenyl-1,3-dioxa-4-aza-2-boracyclohexane (5*h)

3*h* (0.72 g, 3 mmol) and phenylboronic acid (0.37 g, 3 mmol) are reacted as described for **4***a*. The residue was crystallized from absolute ethanol. Yield: 0.69 g (70%) of colorless crystals. Mp 81°C. Infrared (KBr): 1600 cm^{-1} (phenyl C=C). ^1H nmr (90 MHz, $CDCl_3$/TMS): δ (ppm) = 0.79–2.03 (m, C_6H_{11} and —$(CH_2)_5$—), 2.63 (d, J = 7 Hz, $NCH_2C_6H_{11}$), 2.75 (s, NCH_2CO), 7.17–7.37 (m, 3 aromatic H), 7.60–7.81 (m, 2 aromatic H). ^{11}B nmr (64.2 MHz, $CDCl_3/Et_2OBF_3$): δ (ppm) = 27.5 ($w_{1/2}$ = 420 Hz). Anal. calcd. for $C_{20}H_{30}BNO_2$: C 73.40, H 9.24, N 4.28; found: C 73.45, H 9.31, N 4.49.

*4-Benzyl-5,5-dimethyl-2-phenyl-1,3-dioxa-4-aza-2-boracyclohexane (5*i)

3*i* (0.20 g, 1 mmol) and phenylboronic acid (0.12 g, 1 mmol) are reacted as described for **4***a*. The residue was crystallized from absolute ethanol. Yield: 0.20 g (71%) of colorless platelets. Mp 86–87°C. Infrared (KBr): 1600 cm^{-1} (phenyl C=C). ^1H nmr (90 MHz, $CDCl_3$/TMS): δ (ppm) = 1.26 (s, 2 CH_3), 3.88 (s, NCH_2CH_2O), 7.19–7.45 (m, 8 aromatic H), 7.53–7.71 (m, 2 aromatic H). ^{11}B nmr (64.2 MHz, $CDCl_3/Et_2OBF_3$): δ (ppm) = 27.5 ($w_{1/2}$ = 360 Hz). Anal. calcd. for $C_{17}H_{20}BNO_2$: C 72.62, H 7.17, N 4.98; found: C 72.61, H 7.21, N 4.99.

*4-Benzyl-5,5,6-trimethyl-2-phenyl-1,3-dioxa-4-aza-2-boracyclohexane (5*j)

3*j* (0.21 g, 1 mmol) and phenylboronic acid (0.12 g, 1 mmol) are reacted as described for **4***a*. The residue was crystallized from absolute ethanol. Yield: 0.25 g (85%) of colorless crystals. Mp 97°C. Infrared (KBr): 1600 cm^{-1} (phenyl C=C). ^1H nmr (90 MHz, $CDCl_3$/TMS): δ (ppm) = 1.15 and 1.25 (s and s, $C(CH_3)_2$), 1.36 (d, J = 6 Hz, CH_3CO), 3.92 (s, NCH_2), 4.11 (q, J = 6 Hz, OCH), 7.13–7.46 (m, 8 aromatic H), 7.52–7.72 (m, 2 aromatic H). Anal. calcd. for $C_{18}H_{22}BNO_2$: C 73.24, H 7.51, N 4.75; found: C 73.30, H 7.51, N 4.80.

*4-Benzyl-6,6-pentamethylene-2-phenyl-1,3-dioxa-4-aza-2-boracyclohexane (5*k)

3*k* (0.54 g, 2 mmol) and phenylboronic acid (0.24 g, 2 mmol) are reacted as described for **4***a*. The residue was crystallized from benzene/petroleum ether. Yield: 0.59 g (92%) of colorless crystals. Mp 76–78°C. Infrared (KBr): 1600 cm^{-1} (phenyl C=C). ^1H nmr (90 MHz, $CDCl_3$/TMS): δ (ppm) = 1.01–2.04 (m, —$(CH_2)_5$—), 2.78 (s, NCH_2CO), 4.04 (s, NCH_2Ph), 7.12–7.47 (m, 8 aromatic H), 7.62–7.81 (m, 2 aromatic H). ^{11}B nmr (64.2 MHz, $CDCl_3/Et_2OBF_3$): δ (ppm) = 27.5 ($w_{1/2}$ = 380 Hz). Anal. calcd. for $C_{20}H_{24}BNO_2$: C 74.78, H 7.53, N 4.26; found: C 74.75, H 7.61, N 4.26.

*4-(4-Chlorophenylmethyl)-6,6-pentamethylene-2-phenyl-1,3-dioxa-4-aza-2-boracyclohexane (5*l)

3*l* (0.27 g, 1 mmol) and phenylboronic acid (0.12 g, 1 mmol) are reacted as described for **4***a*. The residue was crystallized from absolute ethanol/ether. Yield: 0.33 g (92%) of colorless crystals. Mp 86°C. Infrared (KBr): 1600 cm^{-1} (phenyl C=C). ^1H nmr (90 MHz, $CDCl_3$/TMS): δ (ppm) = 1.04–2.05 (m, —$(CH_2)_5$—), 2.76 (s, NCH_2CO), 4.00 (s, $CH_2C_6H_4Cl$), 7.11–7.38 (m, 7 aromatic H), 7.57–7.78 (m, 2 aromatic H). ^{11}B nmr (64.2 MHz, $CDCl_3/Et_2OBF_3$): δ (ppm) = 28.3 ($w_{1/2}$ = 430 Hz). Anal. calcd. for $C_{20}H_{23}BClNO_2$: C 67.54, H 6.52, B 3.04, Cl 9.97, N 3.94; found: C 67.37, H 6.63, B 3.18, Cl 9.88, N 3.82. Crystals suitable for X-ray analysis were obtained by slow recrystallization from ethanol (99.5%).

*4-(4-Nitrophenylmethyl)-5,5-dimethyl-2-phenyl-1,3-dioxa-4-aza-2-boracyclohexane (5*m)

3*m* (0.24 g, 1 mmol) and phenylboronic acid (0.12 g, 1 mmol) are reacted as described for **4***a*. The residue was crystallized from absolute ethanol. Yield: 0.26 g (79%) of yellowish crystals. Mp 94°C. Infrared (KBr): 1605, 1600 (aryl C=C), 1515 cm^{-1} (NO_2). ^1H nmr (400 MHz, $CDCl_3$/TMS): δ (ppm) = 1.22 (s, $C(CH_3)_2$), 3.90 (s, OCH_2), 4.01 (s, NCH_2), 7.18–7.40 (m, 3 aromatic H), 7.56–7.61 (m, 2 aromatic H), 7.64 and 8.25 (d, and d, J = 9 Hz, AA′BB′ system, $C_6H_4NO_2$). ^{11}B nmr (64.2 MHz, $CDCl_3/Et_2OBF_3$): δ (ppm) = 27.6 ($w_{1/2}$ = 380 Hz). EI mass spectrum (70 eV): m/z = 326 (58%, M^+), 311 (100%, $M^+ - CH_3$), 240 (5%), 191 (26%), 136 (62%, $CH_2C_6H_4NO_2$), 120 (64%), 106 (16%), 90 (14%), 78 (22%).

*4-(4-Nitrophenylmethyl)-6,6-pentamethylene-2-phenyl-1,3-dioxa-4-aza-2-boracyclohexane (5*n)

3*n* (0.56 g, 2 mmol) and phenylboronic acid (0.24 g, 2 mmol) are reacted as described for **4***a*. The residue was crystallized from absolute ethanol. Yield: 0.59 g (80%) of yellowish crystals. Mp 116°C. Infrared (KBr): 1605, 1600 (aryl C=C), 1515 cm^{-1} (NO_2). ^1H nmr (90 MHz, $CDCl_3$/TMS): δ (ppm) = 1.21–2.08 (m, —$(CH_2)_5$—), 2.87 (s, NCH_2CO), 4.09 (s, $NCH_2C_6H_4NO_2$), 7.11–7.35 (m, 3 aromatic H), 7.45–7.68 (m, 2 aromatic H), 7.56 and 8.16 (d and d, J = 9 Hz, AA′BB′ system, $C_6H_4NO_2$). ^{11}B nmr (64.2 MHz, $CDCl_3/Et_2OBF_3$): δ (ppm) = 27.9 ($w_{1/2}$ = 390 Hz). Anal. calcd. for $C_{20}H_{23}BN_2O_4$: C 65.59, H 6.33, B 2.95, N 7.65; found: C 65.61, H 6.43, B 3.06, N 7.61.

*4-(4-Dimethylaminophenylmethyl)-6,6-pentamethylene-2-phenyl-1,3-dioxa-4-aza-2-boracyclohexane (5*o)

3*o* (0.28 g, 1 mmol) and phenylboronic acid (0.12 g, 1 mmol) are reacted as described for **4***a*. The residue was crystallized from absolute ethanol. Yield: 0.30 g (82%) of colorless crystals. Mp 92°C. Infrared (KBr): 1610, 1600 cm^{-1} (aryl C=C). ^1H nmr (90 MHz, $CDCl_3$/TMS): δ (ppm) = 1.22–2.01 (m, —$(CH_2)_5$—), 2.75 (s, NCH_2CO), 2.95 (s, $N(CH_3)_2$), 4.01 (s, $NCH_2C_6H_4NMe_2$), 6.69 (d, J = 9 Hz, AA′BB′ system, 2 aromatic H), 7.17–7.42 (m, 5 aromatic H), 7.69–7.86 (m, 2 aromatic H). Anal. calcd. for $C_{22}H_{29}BN_2O_2$: C 72.53, H 8.02, N 7.69; found: C 72.53, H 8.09, N 7.69.

*4-Benzhydryl-6-methyl-2-phenyl-1,3-dioxa-4-aza-2-boracyclohexane (5*p)

3*p* (0.51 g, 2 mmol) and phenylboronic acid (0.24 g, 2 mmol) are reacted as described for **4***a*. The residue was crystallized from absolute benzene. Yield: 0.51 g (74%) of colorless crystals. Mp 185–186°C. Infrared (KBr): 1600, 1595 cm^{-1} (shoulder, aryl C=C). ^1H nmr (90 MHz, $CDCl_3$/TMS): δ (ppm) = 1.30 (d, J = 6 Hz, CH_3), 2.50/2.64 and 3.02/3.15 (d/d and d/d, J = 12/8 Hz, NCH_2), 4.44 (m, OCH), 4.80 (s, $NCHPh_2$), 7.09–7.54 (m, 15 aromatic H). Anal. calcd. for $C_{22}H_{22}BNO_2$: C 76.99, H 6.46, N 4.08; found: C 77.02, H 6.48, N 4.15.

N,N′-*Ethanediylidenebis[1-hydroxycyclohexyl)methylamine]* N,N′-*dioxide (11)*

1-(*N*-Hydroxyaminomethyl)cyclohexanol **10** (5) (1.45 g, 10 mmol)

Can. J. Chem. Downloaded from www.nrcresearchpress.com by 85.192.166.187 on 09/08/12
For personal use only.

and glyoxal monohydrate (0.38 g, 5 mmol) are dissolved in 20 mL of ethanol. After 1 day at room temperature the solution is partially evaporated in vacuo and cooled down for crystallization which is complete after a few days. Yield: 1.56 g (100%) of colorless crystals. Mp 188–189°C. Infrared (KBr): 3370 (O—H), 1530 cm^{-1} (C—N). ^1H nmr (60 MHz, d_6-DMSO/TMS): δ (ppm) = 1.40 (m_c, 2 —$(CH_2)_5$—), 3.86 (s, 2 NCH_2), 4.70 (s, exchangeable, 2 OH), 7.80 (s, N=CH). EI mass spectrum (70 eV, 240°C): *m/z* = 312 (3%, M^+), 197 (38%), 156 (19%), 140 (16%), 99 (100% $C_6H_{11}O$), 95 (41%) 81 (63%). Anal. calcd. for $C_{16}H_{28}N_2O_4$: C 61.51, H 9.03, N 8.96; found: C 61.19, H 9.02, N 8.93.

N,N′-*Dihydroxy*-N,N′-*bis(1-hydroxycyclohexylmethyl)methanediamine (**12**)*

1-*N*-Hydroxyaminomethyl)cyclohexanol **10** (5) (0.28 g, 2 mmol) and formaldehyde (0.1 g 35% aqueous solution, 1 mmol) are dissolved in 20 mL ethanol and stored at room temperature for 1 day. After evaporation in vacuo the residue is crystallized from benzene. Yield: 0.28 g (93%) of colorless crystals. Mp 104–105C. ^1H nmr (100 MHz, $CDCl_3$/TMS)[6]: δ (ppm) = 1.2–2.9 (m, 2 —$(CH_2)_5$—), 2.75 (s, 44% of NCH_2CO of **12**), 2.94 (s, 56% of NCH_2 of **10**), 3.63 (s, 44% of NCH_2N of **12**), 3.76 (s, 56% of NCH_2CO of the formaldehyde nitrone of **10**; cf. footnote 2), 4.3–4.9 (m, broad, exchangeable, 4 OH), 6.41 (q, AB system, 56% of N=CH_2 of the formaldehyde nitrone of **10**). EI mass spectrum (70 eV, 120C): *m/z* = 157 (100%, H_2C=N(O)CH_2C(OH)$(CH_2)_5$=formaldehyde nitrone of **10**), 140 (41%), 139 (55%), 127 (67%), 114 (39%), 112 (49%), 99 (73%, $C_6H_{11}O$), 95 (82%), 81 (95%). Molecular mass (cryoscopic determination in $CHCl_3$): 157 (formaldehyde nitrone of **10**, see footnote 2). Anal. calcd. for $C_{15}H_{30}N_2O_4$: C 59.57, H 9.99, N 9.26; found: C 59.17, H 9.90, N 9.10. Determination of the formaldehyde content (gravimetrically with dimedone (10)), after hydrolysis: calcd. for **12**: 10%; found: 12%.

N,N′-*Dihydroxy*-N,N′-*bis(1-hydroxycyclohexylmethyl)-1,2-ethanediamine (**13**)*

11 (3.12 g, 10 mmol) and $LiAlH_4$ (0.76 g, 20 mmol) are suspended in 100 mL of dry ether and refluxed for 6 h. After 24 h stirring at room temperature the reaction mixture is hydrolyzed with water and ice-cooling, and subsequently mixed with 6N HCl until the $Al(OH)_3$ precipitate redissolves. The mixture is brought to pH 7–8 using $NaHCO_3$ and the solid product that forms in the layer between the two phases is separated. The ether phase is dried over Na_2SO_4 and evaporated in vacuo. The residue is combined with the previously separated product. Yield: 1.77 g (56%) of colorless crystals. Mp 153°C (from absolute ethanol). Infrared (KBr): 3460, 3160 cm^{-1} (O—H). ^1H nmr (90 MHz, d_6-DMSO/TMS): δ (ppm) = 1.50 (m, 2 —$(CH_2)_5$—), 2.60 (s, 2, NCH_2CO), 2.81 (s, NCH_2CH_2N), 3.89 (s, exchangeable, 2 OH), 7.77 (s, exchangeable, 2 OH). Anal. calcd. for $C_{16}H_{32}N_2O_4$: C 60.73, H 10.19, N 8.85; found: C 60.47, H 10.39, N 8.61.

*4,4′-Methylenebis(6,6-pentamethylene-2-phenyl-1,3-dioxa-4-aza-2-boracyclohexane) (**15**a)*

12 (0.60 g, 2 mmol) and phenylboronic acid (0.49 g, 4 mmol) are dissolved in 20 mL of benzene and refluxed for 1 h with continuous removal of water using a Dean-Stark trap. The solvent is partially (about 1/2 of the volume) distilled off, and after the addition of petroleum ether the solution is stored at −18°C. The crystallization (after a few days) yields 0.52 g (55%) of colorless crystals which are recrystallized from ethanol. Mp 78–81°C. Infrared (KBr): 1600 cm^{-1} (phenyl C=C). ^1H nmr (90 MHz, $CDCl_3$/TMS): δ (ppm) = 1.14–2.04 (m, 2 —$(CH_2)_5$—), 3.12 (s, 2 NCH_2CO), 4.17 (s, NCH_2N), 7.18–7.42 (m, 6 aromatic H), 7.62–7.81 (m, 4 aromatic H). ^{11}B nmr (64.2 MHz, $CDCl_3$/Et_2OBF_3): δ (ppm) = 27.5 ($w_{1/2}$ = 640 Hz). EI mass spectrum (70 eV, 150°C); *m/z* = 474 (0.7%, M^+), 244 (100%, M^+ − PhB[$ONCH_2C(CH_2)_5O$]) 140 (2%), 105 (3%, PhBOH), 95 (6%), 81 (3%). Anal. calcd. for $C_{27}H_{36}B_2N_2O_4$: C 68.39, H 7.65, N 5.91; found: C 68.50, H 7.74, N 6.04

Crystals suitable for X-ray analysis were obtained by recrystallization from benzene/petroleum ether, and contain 1 mol of benzene. Mp 55–56°C. The ^1H nmr spectrum of **15***a*·C_6H_6 in $CDCl_3$ (TMS) shows an additional signal: δ (ppm) = 7.31 (s, 6 aromatic H). Anal. calcd. for $C_{27}H_{36}B_2N_2O_4$+C_6H_6: C 71.76, H 7.67, B 3.91, N 5.07; found: C 71.47, H 7.78, B 3.83, N 4.99.

*4,4′-Methylenebis[2-(4-methoxyphenyl)-6,6-pentamethylene-1,3-dioxa-4-aza-2-boracyclohexane] (**15**b)*

12 (0.30 g, 1 mmol) and 4-methoxyphenylboronic acid (0.30 g, 2 mmol) are reacted as described for **15***a*. Yield: 0.45 g (84%) of colorless crystals. Mp 134–135°C (from benzene/petroleum ether). Infrared (KBr): 1600 cm^{-1} (slightly broadened, aryl C=C). ^1H nmr (90 MHz, $CDCl_3$/TMS): δ (ppm) = 1.15–2.03 (m, 2 —$(CH_2)_5$—), 3.10 (s, 2 NCH_2CO), 3.78 (s, 2 OCH_3), 4.15 (s, NCH_2N), 6.82 and 7.65 (d, and d, *J* = 8 Hz, AA′BB′ system, 8 aromatic H), EI mass spectrum (70 eV, 125°C): *m/z* = 534 (0.2%, M^+), 274 (100%, M^+ − 4-$MeOC_6H_4$-$BOCH_2C(CH_2)_5O$), 134 (8%, 4-$MeOC_6H_4BO$), 124 (6%), 95 (16%), 81 (4%). Anal. calcd. for $C_{29}H_{40}B_2N_2O_6$: C 65.20, H 7.55, N 5.24, found: C 65.25, H 7.67, N 5.30.

*4,4′-Ethylenebis(6,6-pentamethylene-2-phenyl-1,3-dioxa-4-aza-2-boracyclohexane) (**16**a)*

13 (0.32 g, 1 mmol) and phenylboronic acid (0.24 g, 2 mmol) are dissolved in 50 mL of benzene and refluxed for 10 min. Crystallization commences in the boiling solution and is complete after cooling down to room temperature. The precipitate is separated and recrystallized. Yield: 0.46 g (94%) of colorless crystals. Mp 169°C (from $CHCl_3$/petroleum ether). Infrared (KBr): 1600 cm^{-1} (phenyl C=C). ^1H nmr (90 MHz, $CDCl_3$/TMS): δ (ppm) = 1.14–2.11 (m, 2 —$(CH_2)_5$—), 2.92 (s, 2 NCH_2CO), 3.29 (s, NCH_2CH_2N), 7.13–7.41 (m, 6 aromatic H), 7.63–7.82 (m, 4 aromatic H). ^{11}B nmr (64.2 MHz, $CDCl_3$/Et_2OBF_3): δ (ppm) = 28.9 ($w_{1/2}$ = 640 Hz). EI mass spectrum (70 eV, 125°C): *m/z* = 488 (0.1%, M^+), 411 (14%, M^+ − C_6H_5), 393 (7%), 285 (4%), 258 (6%), 244 (100%, 1/2 M^+), 228 (4%), 168 (6%), 140 (8%), 105 (5%, PhBOH), 95 (18%) 81 (4%). Anal. calcd. for $C_{28}H_{38}B_2N_2O_4$: C 68.88, H 7.85, B 4.43, N 5.74; found: C 68.71, H 7.95, B 4.60, N 5.62.

*4,4′-Ethylenebis[2-(2-methylphenyl)-6,6-pentamethylene-1,3-dioxa-4-aza-2-boracyclohexane] (**16**b)*

13 (0.32 g, 1 mmol) and 2-methylphenylboronic acid (0.27 g, 2 mmol) are reacted as described for **16***a*. Yield: 0.47 g (86%) of colorless small needles. Mp 145–146°C (from $CHCl_3$/petroleum ether). Infrared (KBr): 1600 cm^{-1} (aryl C=C). ^1H nmr (90 MHz, $CDCl_3$/TMS): δ (ppm) = 1.07–2.08 (m, 2 —$(CH_2)_5$—), 2.53 (s, 2 CH_3), 2.92 (s, 2 NCH_2CO), 3.27 (s, NCH_2CH_2N), 6.89–7.32 (m, 6 aromatic H), 7.61–7.78 (m, 2 aromatic H). ^{11}B nmr (64.2 MHz, $CDCl_3$/Et_2OBF_3): δ (ppm) = 28.1 ($w_{1/2}$ = 640 Hz). Anal. calcd. for $C_{30}H_{42}B_2N_2O_4$: C 69.79, H 8.20, B 4.19, N 5.43; found: C 69.79, H 8.40, B 4.24, N 5.33.

*4,4′-Ethylenebis[2-(1-naphthyl)-6,6-pentamethylene-1,3-dioxa-4-aza-2-boracyclohexane] (**16**c)*

13 (0.32 g, 1 mmol) and 1-naphthylboronic acid (0.35 g, 2 mmol) are reacted as described for **16***a*. Yield: 0.58 g (91%) of colorless crystals. Mp 189–200°C (from $CHCl_3$/petroleum ether). Infrared (KBr): 1595, 1580 cm^{-1} (weak, strong, aryl C=C). ^1H nmr (90 MHz, $CDCl_3$/TMS): δ (ppm) = 1.01–2.12 (m, 2 —$(CH_2)_5$—), 3.02 (s, 2 NCH_2CO), 3.37 (s, NCH_2CH_2N), 7.22–7.52 (m, 6 aromatic H), 7.63–8.04 (m, 6 aromatic H), 8.56–8.80 (m, 2 aromatic H). ^{11}B nmr (64.2 MHz, $CDCl_3$/Et_2OBF_3): δ (ppm) = 27.7 ($w_{1/2}$ = 640 Hz). Anal. calcd. for $C_{36}H_{42}B_2N_2O_4$: C 73.49, H 4.76, B 3.67, N 4.76; found: C 73.56, H 7.49, B 3.65, N 4.84.

*X-ray crystallographic analysis of **5**l and **15**a·C_6H_6*

Crystallographic data appear in Table 1. The final unit-cell parameters were obtained by least-squares on the setting angles for 25 reflections with 2θ = 36.1–38.9° for **5***l* and 56.6–82.3° for **15***a*. The

[6]In solution ($CDCl_3$) the aminal **12** dissociates into the hydroxylamine **10** and the formaldehyde nitrone of **10** (see footnote 2).

Can. J. Chem. Downloaded from www.nrcresearchpress.com by 85.192.166.187 on 09/08/12
For personal use only.

TABLE 1. Crystallographic data[a]

Compound	**5***l*	**15***a*·C_6H_6
Formula	$C_{20}H_{23}BClNO_2$	$C_{33}H_{42}B_2N_2O_4$
fw	355.67	552.33
Crystal system	Triclinic	Monoclinic
Space group	$P\bar{1}$	$C2/c$
a, Å	11.540(2)	22.690(1)
b, Å	10.402(3)	16.867(1)
c, Å	8.440(2)	8.4783(9)
α, deg	108.86(2)	90
β, deg	97.62(2)	104.912(8)
γ, deg	89.36(2)	90
V, Å^3	949.8(4)	3135.6(4)
Z	2	4
ρ_{calc}, g/cm^3	1.244	1.170
$F(000)$	376	1184
Radiation	Mo-K_α	Cu-K_α
μ, cm^{-1}	2.13	5.59
Crystal size, mm	0.30 × 0.45 × 0.50	0.30 × 0.30 × 0.35
Transmission factors (relative)	0.89–1.00	0.95–1.00
Scan type	ω–2θ	ω–2θ
Scan range, deg in ω	1.30 + 0.35 tan θ	1.00 + 0.20 tan θ
Scan speed, deg/min	32	32
Data collected	$\pm h$, $+k$, $\pm l$,	$+h$, $+k$, $\pm l$
$2\theta_{max}$, deg	60	155
Crystal decay, %	2.6	2.8
Total reflections	5821	3536
Total unique reflections	5529	3450
R_{merge}	0.019	0.018
Reflections with $I \geq 3\sigma(I)$	3190	2084
No. of variables	318	215
R	0.037	0.035
R_w	0.035	0.044
gof	2.70	1.64
Maximum Δ/σ (final cycle)	0.0003	0.09
Residual density e/Å^3	−0.29 to 0.17	−0.10 to 0.17

[a]Temperature 294 K, Rigaku AFC6S diffractometer, Mo-K_α (λ = 0.71069 Å) or Cu-K_α (λ = 1.54178 Å) radiation, graphite monochromator, takeoff angle 6.0°, aperture 6.0 × 6.0 mm at a distance of 285 mm from the crystal, stationary background counts at each end of the scan (scan/background time ratio 2:1, up to 8 rescans), $\sigma^2(F^2) = [S^2(C + 4B)]/Lp^2$ (S = scan rate, C = scan count, B = normalized background count), function minimized $\Sigma w(|F_o| - |F_c|)^2$ where $w = 4F_o^2/\sigma^2(F_o^2)$, $R = \Sigma||F_o| - |F_c||/\Sigma|F_o|$, $R_w = (\Sigma w(|F_o| - |F_c|)^2/\Sigma w|F_o|^2)^{1/2}$, and gof = $[\Sigma w(|F_o| - |F_c|)^2/(m - n)]^{1/2}$. Values given for R, R_w, and gof are based on those reflections with $I \geq 3\sigma(F^2)$.

intensities of three standard reflections, measured every 200 reflections throughout the data collections, decayed linearly by 2.6% and 2.8% for **5***l* and **15***a*, respectively. The data were processed,[7] corrected for Lorentz and polarization effects, decay and absorption (empirical, based on azimuthal scans for three reflections).

The structures were solved by direct methods, the coordinates of the non-hydrogen atoms being determined from an E-map or from subsequent difference Fourier syntheses. The structure analysis of **15***a*·C_6H_6 was initiated in the centrosymmetric space group $C2/c$ on the basis of the E-statistics. This choice was confirmed by the subsequent successful solution and refinement of the structure. The **15***a* molecule has exact C_2 symmetry. The benzene solvate molecule in **15***a*·C_6H_6 is two-fold disordered about a crystallographic C_2 axis. A split-atom anisotropic model was employed, the site occupancy factors being adjusted as the refinement progressed to result in approximately equal thermal parameters for the two components of the disorder. Non-hydrogen atoms were refined with anisotropic thermal parameters. The hydrogen atoms of **5***l* were refined with isotropic thermal parameters and those of **15***a*·C_6H_6 were fixed in idealized positions (C—H = 0.98 Å, B_H = $1.2B_{bonded\ atom}$). A correction for secondary extinction was applied for **15***a*·C_6H_6, the final value of the extinction coefficient being 6.13(6) × 10^{-6}. Neutral atom scattering factors for all atoms (11*a*) and anomalous dispersion corrections for the non-hydrogen atoms (11*b*) were taken from the International tables for X-ray crystallography. Final atomic coordinates and equivalent isotropic thermal parameters, bond lengths, bond angles, and intra-annular torsion angles appear in Tables 2–5, respectively. Stereoviews of the **5***l* and **15***a* molecules are shown in Figs. 2 and 3, respectively. Hydrogen atom parameters, anisotropic thermal parameters, torsion angles, intermolecular contacts, and least-squares planes are included as supplementary material.[8] Measured and calculated structure factor amplitudes are available from the authors.

[7]*teXsan*: Crystal structure analysis package. Molecular Structure Corp. The Woodlands, TX. 1985 & 1992.

[8]Supplementary material mentioned in the text may be purchased from the Depository of Unpublished Data, Document Delivery, CISTI, National Research Council Canada, Ottawa, ON K1A 0S2, Canada.

Tables of hydrogen atom coordinates and bond lengths and angles involving hydrogen atoms have also been deposited with the Cambridge Crystallographic Data Centre and can be obtained on request from The Director, Cambridge Crystallographic Data Centre, University Chemical Laboratory, 12 Union Road, Cambridge CB2 1EZ, UK.

TABLE 2. Final atomic coordinates (fractional) and B_{eq} (Å^2)[a]

Atom	x	y	z	B_{eq}	Occupancy
			5*l*		
Cl(1)	−0.11091(5)	−0.36876(5)	0.19633(7)	5.91(2)	
O(1)	0.26241(10)	0.17706(10)	0.42123(13)	4.04(4)	
O(2)	0.32724(9)	0.41041(9)	0.55526(12)	3.47(4)	
N(1)	0.18641(11)	0.21676(12)	0.2932(2)	3.71(5)	
C(1)	0.2497(2)	0.3242(2)	0.2604(2)	3.88(6)	
C(2)	0.26699(13)	0.45020(14)	0.4165(2)	3.34(5)	
C(3)	0.15170(15)	0.5109(2)	0.4673(2)	4.15(6)	
C(4)	0.1687(2)	0.6412(2)	0.6176(3)	4.87(8)	
C(5)	0.2431(2)	0.7458(2)	0.5832(3)	5.07(8)	
C(6)	0.3605(2)	0.6880(2)	0.5366(3)	4.51(7)	
C(7)	0.3455(2)	0.5555(2)	0.3892(2)	4.00(7)	
C(8)	0.1740(2)	0.0932(2)	0.1461(2)	4.27(7)	
C(9)	0.10617(14)	−0.0201(2)	0.1701(2)	3.70(6)	
C(10)	0.0168(2)	0.0025(2)	0.2688(2)	4.21(6)	
C(11)	−0.0492(2)	−0.1028(2)	0.2800(2)	4.34(7)	
C(12)	−0.0262(2)	−0.2341(2)	0.1895(2)	4.03(6)	
C(13)	0.0625(2)	−0.2603(2)	0.0921(3)	5.43(8)	
C(14)	0.1283(2)	−0.1530(2)	0.0833(3)	5.12(8)	
C(15)	0.39793(13)	0.23310(15)	0.6895(2)	3.34(5)	
C(16)	0.4171(2)	0.0966(2)	0.6663(2)	4.54(7)	
C(17)	0.4861(2)	0.0554(2)	0.7862(3)	5.49(8)	
C(18)	0.5366(2)	0.1489(2)	0.9323(3)	5.15(8)	
C(19)	0.5176(2)	0.2840(2)	0.9613(3)	5.89(9)	
C(20)	0.4498(2)	0.3251(2)	0.8393(2)	5.08(8)	
B(1)	0.3246(2)	0.2787(2)	0.5492(2)	3.34(6)	
			15*a*·C_6H_6		
O(1)	0.06953(5)	0.15335(6)	0.50190(11)	4.56(4)	
O(2)	0.14930(4)	0.25083(6)	0.57213(11)	4.11(4)	
N(1)	0.04100(6)	0.20244(7)	0.36261(14)	4.18(5)	
C(1)	0	0.14930(13)	1/4	4.9(1)	0.50
C(2)	0.08913(7)	0.23397(9)	0.2963(2)	4.46(7)	
C(3)	0.12768(7)	0.29180(9)	0.4168(2)	3.91(6)	
C(4)	0.09083(7)	0.36352(9)	0.4441(2)	4.28(6)	
C(5)	0.12992(8)	0.42369(9)	0.5588(2)	4.83(7)	
C(6)	0.18379(8)	0.45017(10)	0.4962(2)	5.49(8)	
C(7)	0.22171(7)	0.37926(11)	0.4721(2)	5.32(8)	
C(8)	0.18344(7)	0.31746(10)	0.3617(2)	4.80(7)	
C(9)	0.14368(7)	0.14208(8)	0.7731(2)	3.87(6)	
C(10)	0.11015(8)	0.08161(9)	0.8196(2)	4.92(7)	
C(11)	0.12929(9)	0.04439(10)	0.9695(2)	5.92(9)	
C(12)	0.18281(10)	0.06747(11)	1.0765(2)	5.94(9)	
C(13)	0.21714(8)	0.12649(11)	1.0343(2)	5.69(8)	
C(14)	0.19775(7)	0.16351(10)	0.8837(2)	4.82(7)	
B(1)	0.12007(8)	0.18557(10)	0.6063(2)	3.85(7)	
C(15)	1/2	0.2360(13)	1.2500	7.0(5)	0.335
C(16)	0.4508(5)	0.2012(9)	1.1510(13)	6.5(3)	0.67
C(17)	0.4529(3)	0.1167(3)	1.1517(10)	7.5(5)	0.67
C(18)	1/2	0.0785(11)	1.2500	12(2)	0.335
C(15a)	0.4755(14)	0.216(2)	1.202(4)	16(3)	0.33
C(16a)	0.4483(8)	0.1534(7)	1.141(2)	7.6(8)	0.33
C(17a)	0.4808(10)	0.0778(13)	1.185(3)	6.3(7)	0.33

[a] $B_{eq} = (8/3)\pi^2\Sigma\Sigma U_{ij}a_i^*a_j^*(\mathbf{a}_i\cdot\mathbf{a}_j)$.

Results and discussion

The X-ray analyses of **5*l*** and **15*a*** both confirm the presence of six-membered cycloboronate ring systems (Figs. 2 and 3). In each case a trigonal planar sp^2-hybridized boron atom forms part of the planar portion of the six-membered heterocycle that has a "sofa" (semiplanar) conformation, typical for this type of cyclic boronic ester. This 1,3-dioxa-4-aza-2-boracyclohexane ring type has so far only been found for *N-un*substituted derivatives having bulky enough (e.g. mesityl) *B*-aryl groups (3), or for *N*-acyl derivatives (2). Thus, **5*l*** and **15*a*** are the first examples of *N*-alkyl derivatives of this type of boron heterocycle to be characterized in the solid state by X-ray crystallography.

The other *N*-alkyl derivatives of the types **5**, **15**, and **16** can generally be assumed to possess similar cycloboronate moieties with trivalent sp^2 boron atoms. The *N*-methyl derivative **5*d***, however, appears to have a dimeric structure **8** with twofold

Can. J. Chem. Downloaded from www.nrcresearchpress.com by 85.192.166.187 on 09/08/12
For personal use only.

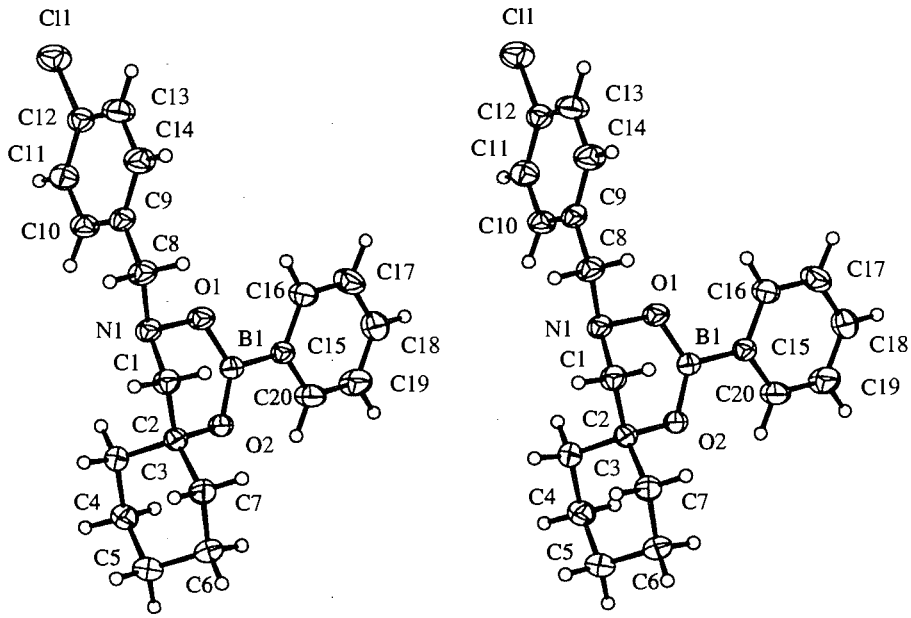

FIG. 2. Stereoview of **5***l*; 33% probability thermal ellipsoids are shown for the non-hydrogen atoms.

TABLE 3. Bond lengths (Å) with estimated standard deviations[a]

Atoms	Distance	Atoms	Distance
		5l	
Cl(1)—C(12)	1.738(2)	C(8)—C(9)	1.503(2)
O(1)—N(1)	1.462(2)	C(9)—C(10)	1.382(2)
O(1)—B(1)	1.369(2)	C(9)—C(14)	1.379(2)
O(2)—C(2)	1.456(2)	C(10)—C(11)	1.375(2)
O(2)—B(1)	1.354(2)	C(11)—C(12)	1.375(2)
N(1)—C(1)	1.460(2)	C(12)—C(13)	1.367(3)
N(1)—C(8)	1.463(2)	C(13)—C(14)	1.384(3)
C(1)—C(2)	1.521(2)	C(15)—C(16)	1.388(2)
C(2)—C(3)	1.520(2)	C(15)—C(20)	1.379(2)
C(2)—C(7)	1.521(2)	C(15)—B(1)	1.560(2)
C(3)—C(4)	1.521(3)	C(16)—C(17)	1.379(2)
C(4)—C(5)	1.516(3)	C(17)—C(18)	1.361(3)
C(5)—C(6)	1.524(3)	C(18)—C(19)	1.367(3)
C(6)—C(7)	1.522(2)	C(19)—C(20)	1.385(2)
		***15a*·C_6H_6**	
O(1)—N(1)	1.451(1)	C(9)—C(14)	1.387(2)
O(1)—B(1)	1.368(2)	C(9)—B(1)	1.561(2)
O(2)—C(3)	1.456(2)	C(10)—C(11)	1.384(2)
O(2)—B(1)	1.354(2)	C(11)—C(12)	1.372(2)
N(1)—C(1)	1.457(2)	C(12)—C(13)	1.368(2)
N(1)—C(2)	1.452(2)	C(13)—C(14)	1.387(2)
C(2)—C(3)	1.517(2)	C(15)—C(16)	1.35(1)
C(3)—C(4)	1.522(2)	C(16)—C(17)	1.43(2)
C(3)—C(8)	1.520(2)	C(17)—C(18)	1.34(1)
C(4)—C(5)	1.523(2)	C(15a)—C(15a)″	1.20(6)
C(5)—C(6)	1.520(2)	C(15a)—C(16a)	1.27(4)
C(6)—C(7)	1.518(2)	C(16a)—C(17a)	1.47(3)
C(7)—C(8)	1.516(2)	C(17a)—C(17a)″	1.22(6)
C(9)—C(10)	1.389(2)		

[a]Primes and double primes refer (here and elsewhere) to symmetry operations: $-x, -y, 1-z$ and double primes: $1-x, -y, 2-z$.

N→B coordination like that reported for the homologue **8** (R = $R^1 = CH_3$, $R^2 = R^3 = R^4 = H$) (1), at least for the solid state (cf. footnote 5). The other *N*-methyl compound, **5***e*, could not be obtained in crystalline form. Nevertheless, it seems that a small *N*-substituent, such as the methyl group in **5***d* or in its previously reported homologue (1), and at least one ring C—H group (R^1 and/or $R^2 = H$) are necessary for the formation of the dimer **8**, stabilized by a pair of transannular C—H···O interactions in the solid state (1).

Some of the *N*-alkylhydroxylaminoalkanols **3** were observed to react preferentially with 2 mol of phenylboronic acid to give the bicyclic pyroboronates **4**, no matter what molar ratio of **3** and phenylboronic acid was applied (1). As already mentioned (1), it is not yet understood which competitive factors control of formation of the crystalline product, either **4** or **5**, out of the reaction equilibrium during the condensation of **3** and phenylboronic acid.

The six-membered BONCCO rings in **5***l* and **15***a* have slightly distorted "sofa" conformations (see Table 5) with C(1) and C(2) on the flaps, respectively. The five-atom BONCCO ring segments (excluding the carbon atoms on the flaps) are planar to within 0.071(2) Å for **5***l* and 0.091(2) Å for **15***a*. Both compounds display a minor deviation from co-planarity of the *B*-phenyl ring and the planar O—B—O ring segment of the BONCCO heterocycle (the angles between normals to the boron coordination group and phenyl ring mean planes are 13.1° for **5***l* and 7.7° for **15***a*). The B—C(phenyl) bond lengths of 1.560(2) Å for **5***l* and 1.561(2) Å for **15***a* are similar to those observed for other related phenylboronates. The boron coordination group is planar within experimental error in **15***a*, while that in **5***l* shows a small (but statistically significant) deviation from planarity (maximum displacement 0.012(2) Å for B, $\chi^2 = 51.0$ for CBO_2).

The N—O bonds in both compounds (**5***l*: 1.462(2) Å, **15***a*: 1.451(1) Å) are comparable to those in the *N*-unsubstituted mesitylboronate (3) (1.46(1) and 1.469(9) Å) that has a similar BONCCO ring system, but are considerably longer than those in the *N*-acyl derivatives (2) (1.402(3) and 1.401(1) Å). This difference between the N—O bond lengths is clearly a consequence of the *N*-alkyl substitution in contrast to the electron-withdrawing *N*-acyl substitution. The remaining geometric parameters of the BONCCO ring systems in **5***l* and **15***a* are in

Can. J. Chem. Downloaded from www.nrcresearchpress.com by 85.192.166.187 on 09/08/12
For personal use only.

TABLE 4. Bond angles (deg) with estimated standard deviations

Atoms	Angle	Atoms	Angle
		5l	
N(1)—O(1)—B(1)	117.1(1)	C(10)—C(9)—C(14)	117.6(2)
C(2)—O(2)—B(1)	120.4(1)	C(9)—C(10)—C(11)	121.8(2)
O(1)—N(1)—C(1)	106.7(1)	C(10)—C(11)—C(12)	119.1(2)
O(1)—N(1)—C(8)	103.5(1)	Cl(1)—C(12)—C(11)	120.2(1)
C(1)—N(1)—C(8)	110.9(1)	Cl(1)—C(12)—C(13)	119.2(1)
N(1)—C(1)—C(2)	110.6(1)	C(11)—C(12)—C(13)	120.6(2)
O(2)—C(2)—C(1)	107.8(1)	C(12)—C(13)—C(14)	119.4(2)
O(2)—C(2)—C(3)	108.1(1)	C(9)—C(14)—C(13)	121.4(2)
O(2)—C(2)—C(7)	107.2(1)	C(16)—C(15)—C(20)	116.8(2)
C(1)—C(2)—C(3)	112.4(1)	C(16)—C(15)—B(1)	121.0(1)
C(1)—C(2)—C(7)	110.5(1)	C(20)—C(15)—B(1)	122.2(1)
C(3)—C(2)—C(7)	110.8(1)	C(15)—C(16)—C(17)	121.5(2)
C(2)—C(3)—C(4)	112.5(1)	C(16)—C(17)—C(18)	120.3(2)
C(3)—C(4)—C(5)	111.2(2)	C(17)—C(18)—C(19)	119.9(2)
C(4)—C(5)—C(6)	110.6(2)	C(18)—C(19)—C(20)	119.7(2)
C(5)—C(6)—C(7)	111.8(2)	C(15)—C(20)—C(19)	121.9(2)
C(2)—C(7)—C(6)	113.2(1)	O(1)—B(1)—O(2)	123.8(1)
N(1)—C(8)—C(9)	113.4(1)	O(1)—B(1)—C(15)	115.4(1)
C(8)—C(9)—C(10)	122.9(1)	O(2)—B(1)—C(15)	120.7(1)
C(8)—C(9)—C(14)	119.4(2)		
		15a $\cdot C_6H_6$	
N(1)—O(1)—B(1)	115.1(1)	C(10)—C(9)—C(14)	117.0(1)
C(3)—O(2)—B(1)	120.6(1)	C(10)—C(9)—B(1)	121.1(1)
O(1)—N(1)—C(1)	105.0(1)	C(14)—C(9)—B(1)	121.9(1)
O(1)—N(1)—C(2)	107.5(1)	C(9)—C(10)—C(11)	121.9(2)
C(1)—N(1)—C(2)	112.9(1)	C(10)—C(11)—C(12)	119.6(2)
N(1)—C(1)—N(1)′	104.1(2)	C(11)—C(12)—C(13)	120.0(2)
N(1)—C(2)—C(3)	109.6(1)	C(12)—C(13)—C(14)	120.1(2)
O(2)—C(3)—C(2)	107.8(1)	C(9)—C(14)—C(13)	121.4(2)
O(2)—C(3)—C(4)	108.1(1)	O(1)—B(1)—O(2)	124.0(1)
O(2)—C(3)—C(8)	107.4(1)	O(1)—B(1)—C(9)	115.8(1)
C(2)—C(3)—C(4)	111.7(1)	O(2)—B(1)—C(9)	120.2(1)
C(2)—C(3)—C(8)	111.0(1)	C(16)—C(15)—C(16)″	128(2)
C(4)—C(3)—C(8)	110.7(1)	C(15)—C(16)—C(17)	114(2)
C(3)—C(4)—C(5)	112.0(1)	C(16)—C(17)—C(18)	120(1)
C(4)—C(5)—C(6)	111.2(1)	C(17)—C(18)—C(17)″	122(1)
C(5)—C(6)—C(7)	110.5(1)	C(15a)″—C(15a)—C(16a)	123(1)
C(6)—C(7)—C(8)	111.7(1)	C(15a)—C(16a)—C(17a)	118(2)
C(3)—C(8)—C(7)	113.3(1)	C(16a)—C(17a)—C(17a)″	115(1)

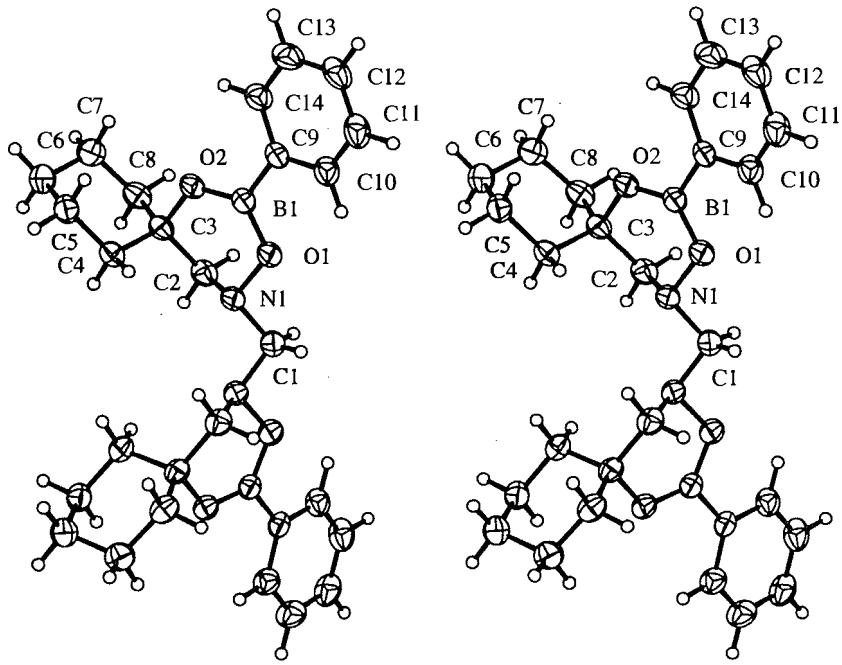

FIG. 3. Stereoview of **15***a* molecule; 33% probability thermal ellipsoids are shown for the non-hydrogen atoms.

Can. J. Chem. Downloaded from www.nrcresearchpress.com by 85.192.166.187 on 09/08/12
For personal use only.

TABLE 5. Intra-annular torsion angles (deg) with estimated standard deviations[a]

Atom	Angle	
	5*l*	**15*a***
B(1)—O(1)—N(1)—C(a)	38.6(2)	44.9(2)
O(1)—N(1)—C(a)—C(b)	−65.4(2)	−67.6(1)
N(1)—C(a)—C(b)—O(2)	56.3(2)	55.0(1)
C(a)—C(b)—O(2)—B(1)	−21.1(2)	−21.1(2)
C(b)—O(2)—B(1)—O(1)	−3.5(2)	0.1(2)
O(2)—B(1)—O(1)—N(1)	−5.9(2)	−11.8(2)
C(g)—C(b)—C(c)—C(d)	−52.9(2)	−53.1(2)
C(b)—C(c)—C(d)—C(e)	56.2(2)	56.4(2)
C(c)—C(d)—C(e)—C(f)	−56.3(2)	−56.6(2)
C(d)—C(e)—C(f)—C(g)	54.7(2)	54.9(2)
C(e)—C(f)—C(g)—C(b)	−53.0(2)	−53.3(2)
C(f)—C(g)—C(b)—C(c)	51.3(2)	51.8(2)

[a]C(a–g) correspond, respectively, to C(1–7) for **5*l***, and to C(2–8) for **15*a***.

good agreement. In both compounds the oxygen substituent, O(2), is situated at an axial position of the spiro-connected cyclohexane ring. The cyclohexane rings in the two compounds have virtually identical, slightly distorted chair conformations (see Table 5).

The **15*a*** molecule has exact C_2 symmetry in the solid state, the twofold axis passing through the central aminal carbon atom C(1). The C—N bonds of the N—C—N (aminal) grouping in **15*a*** (1.457(2) Å) are not significantly different from those reported for the *N*,*N*′-dihydroxyaminal derived from *N*-methylhydroxylamine that has the same (C,O)N—C—N(C,O) moiety as **15*a*** (N—C = 1.452(3) Å) (12). The N—C—N angle in **15*a***, however, is somewhat compressed (to 104.1(2)°), presumably as a result of crystal packing effects.

The crystal structure of **5*l*** consists of discrete molecules separated by normal van der Waals distances, the shortest intermolecular distance between non-hydrogen atoms being Cl(1)···B(1)($-x$, $-y$, $1-z$) = 3.409(2) Å. Compound **15*a*** crystallizes as a 1:1 benzene solvate with the benzene molecules disordered about a twofold axis (see Experimental). The packing in **15*a***·C_6H_6 is also dominated by van der Waals forces; the shortest distance between non-hydrogen atoms of the structural moieties involves a molecule of **15*a*** and a benzene molecule: B(1)···C(15a) ($1/2-x$, $1/2-y$, $2-z$) = 3.45(3) Å.

Acknowledgements

We thank the Natural Sciences and Engineering Research Council of Canada and the Fonds der Chemischen Industrie, Frankfurt am Main, for financial support. We are grateful to the nmr and mass spectrometry laboratories of the Chemische Institute der Technischen Universität, Braunschweig, for running the ^{11}B nmr and mass spectra.

1. W. Kliegel, G. Lubkowitz, S.J. Rettig, and J. Trotter. Can. J. Chem. **70**, 2809 (1992).
2. W. Kliegel, L. Preu, U. Schumacher, S.J. Rettig, and J. Trotter. Can. J. Chem. **70**, 1176 (1992).
3. W. Kliegel, G. Lubkowitz, S.J. Rettig, and J. Trotter. Can. J. Chem. **72**, 1154 (1994).
4. W. Kliegel. J. Organomet. Chem. **253**, 9 (1983).
5. W. Kliegel and H. Becker. Chem. Ber. **110**, 2067 (1977).
6. L. Hough and J.K.N. Jones. J. Chem. Soc. 4052 (1952).
7. W. Kliegel, G. Zinner, and R. Vollrath. Liebigs Ann. Chem. **736**, 173 (1970).
8. W. Kliegel and H. Becker. Chem. Ber. **110**, 2090 (1977).
9. H. Becker. Dissertation, Braunschweig. 1975.
10. E. Heuser. *In* Houben-Weyl, Methoden der organischen Chemie. Vol. 2. Thieme Verlag, Stuttgart. 1953. p. 456.
11. (*a*) International tables for X-ray crystallography. Vol. IV. Kynoch Press, Birmingham, England. 1974. pp. 99–102; (*b*) International tables for X-ray crystallography. Vol. C. Kluwer Academic Publishers, Boston. 1992. pp. 200–206.
12. W. Kliegel, S.J. Rettig, and J. Trotter. Can. J. Chem. **67**, 1959 (1989).
13. W. Kliegel, G. Lubkowitz, U. Reibe, S.J. Rettig, and J. Trotter. Can. J. Chem. **72**, 1735 (1994).

Can. J. Chem. Downloaded from www.nrcresearchpress.com by 85.192.166.187 on 09/08/12
For personal use only.

Practical synthesis of 4-aryl- and 4-heteroarylazetidin-2-ones: applications in the synthesis of the Taxol® side chain[1]

ALLAN W. REY,[2] ROBERT DROGHINI, AND JAMES L. DOUGLAS
Bristol-Myers Squibb, Pharmaceutical Research Institute, Candiac, QC J5R 1J1, Canada

AND

PURUSHOTHAM VEMISHETTI, SUSAN D. BOETTGER, SAIBABA RACHA, AND JOHN L. DILLON
Bristol-Myers Squibb, Bio/Chem Division, Syracuse, NY 13221-4755, U.S.A.

Received April 4, 1994

ALLAN W. REY, ROBERT DROGHINI, JAMES L. DOUGLAS, PURUSHOTHAM VEMISHETTI, SUSAN D. BOETTGER, SAIBABA RACHA, and JOHN L. DILLON. Can. J. Chem. **72**, 2131 (1994).

A convenient, high-yielding procedure has been developed for the kilogram-scale synthesis of (±)-*cis*-3-acetoxy-4-phenylazetidin-2-one (**3**), a β-lactam that has been used in the semi-synthesis of Taxol®. The Staudinger reaction between hydrobenzamide (**5**) and acetoxyacetyl chloride in the presence of a base provided the α-benzylideneiminotoluene protected β-lactam **8**. Without isolation of the intermediate β-lactam, the protecting group was removed under various reductive or hydrolytic conditions. The overall yields were about 80%. The synthesis of other (±)-*cis*-4-aryl- and 4-heteroarylazetidin-2-ones by this methodology has also been accomplished. These compounds are of value for the synthesis of 3′-Taxol® side-chain analogs and their preparation demonstrates the generality of this approach.

ALLAN W. REY, ROBERT DROGHINI, JAMES L. DOUGLAS, PURUSHOTHAM VEMISHETTI, SUSAN D. BOETTGER, SAIBABA RACHA et JOHN L. DILLON. Can. J. Chem. **72**, 2131 (1994).

On a mis au point une méthode donnant d'excellents rendements et appropriée pour la synthèse de kilogrammes de la (±)-*cis*-3-acétoxy-4-phénylazétidin-2-one (**3**), un β-lactame qui peut être utilisé dans la semi-synthèse du Taxol®. La réaction de Staudinger entre l'hydrobenzamide (**5**) et le chlorure d'acétoxyacétyle, en présence d'une base, conduit au β-lactame **8** protégé par un α-benzylidèneiminotoluène. Sans procéder à l'isolement du β-lactame intermédiaire, on a enlevé le groupe protecteur sous diverses conditions de réduction ou d'hydrolyse. Les rendements globaux sont d'environ 80%. Utilisant cette méthodologie, on a aussi réalisé la synthèse d'autres (±)-*cis*-4-aryl- et 4-hétéroarylazétidin-2-ones. Ces composés sont utiles pour la synthèse d'analogues du 3′-Taxol® portant des chaînes latérales différentes et leur préparation démontre la généralité de cette approche.

[Traduit par la rédaction]

Introduction

Taxol® (paclitaxel, **1**), a potent antineoplastic agent isolated from the bark of the Pacific yew tree (*Taxus brevifolia*), has proven to be very effective for the treatment of various cancers (for recent reviews, see ref. 1). The labour-intensive extraction/purification procedure required and the limited supply of yew trees have motivated extensive research into obtaining paclitaxel from alternative sources. An early solution was supplied by Greene and Guéritte-Voegelein (2) who prepared paclitaxel semi-synthetically by coupling the hydroxyl at the C-13 position of appropriately protected 10-deacetylbaccatin III (**2**) with a derivative of *N*-benzoyl-(2*R*,3*S*)-3-phenylisoserine. The needles of the ornamental bush *T. baccata* provide a renewable and relatively abundant source (1 g/kg) of the diterpenoid **2**. More recently, Holton (3) patented a method for the semi-synthesis of paclitaxel by acylating protected baccatin III with a derivative of *cis*-3-hydroxy-4-phenylazetidin-2-one. A semi-synthetic route of this type is expected to be the source of most paclitaxel by 1994 (4). A key intermediate in syntheses of the paclitaxel side chain by Holton (3) and others (5) was (±)-*cis*-3-acetoxy-4-phenylazetidin-2-one (**3**). Many other workers have used β-lactams as paclitaxel side-chain synthons (6).

The procedure used by Holton (3) for the preparation of **3** is depicted in Scheme 1. On laboratory scales (i.e., <100 g), this procedure is acceptable. However, for production purposes (i.e., kilogram-scale), the ceric ammonium nitrate (CAN) oxidative removal of the *para*-methoxyphenyl (PMP) group on **4** becomes problematic due to the large quantities of CAN required for the reaction.[3] Other more cost-effective and convenient approaches to **3** were examined. Also, paclitaxel's unique biological profile (8) combined with its unusual chemical architecture make it an important lead for a new series of chemotherapeutic agents. Thus, a route to **3** that could be generalized to allow the synthesis of side-chain analogs of **1** would be desirable.

Results and discussion

The use of hydrobenzamide (**5**) as the imine precursor in the Staudinger reaction (for a recent review, see ref. 9) was reported in 1969 by Wells and Lee (10). Thus, the [2 + 2] cycloaddition reaction between hydrobenzamide and the ketene derived from azidoacetyl chloride furnished, after deprotection, (±)-*cis*-3-azido-4-phenylazetidin-2-one (**7**, Scheme 2). Using a slightly modified Staudinger reaction but identical deprotection conditions, Manhas et al. (11) prepared the same compound in 1981. Both groups employed 10% HCl (aq) for the deprotection and isolated the intermediate hydrochloride salt (**6**).

Applying similar methodology to the preparation of (±)-*cis*-3-acetoxy-4-phenylazetidin-2-one (i.e., using acetoxyacetyl

[1]A subject patent application on this process was filed with the U.S.A. Patent Office, April 23rd, 1993 (*N*-Substituted 2-Azetidinones, USSN No. 08/052,434). An addendum was filed on December 13th, 1993 (USSN No. 08/165,610).

[2]Author to whom correspondence may be addressed. Tel.: (514) 444-4113; Fax.: (514) 676-8244; E-mail: "Rey@bms.com".

[3]It is pertinent to note that, for *N*-dearylations of this type (7), the yields are often modest (~60%).

Can. J. Chem. Downloaded from www.nrcresearchpress.com by 85.192.166.187 on 09/08/12
For personal use only.

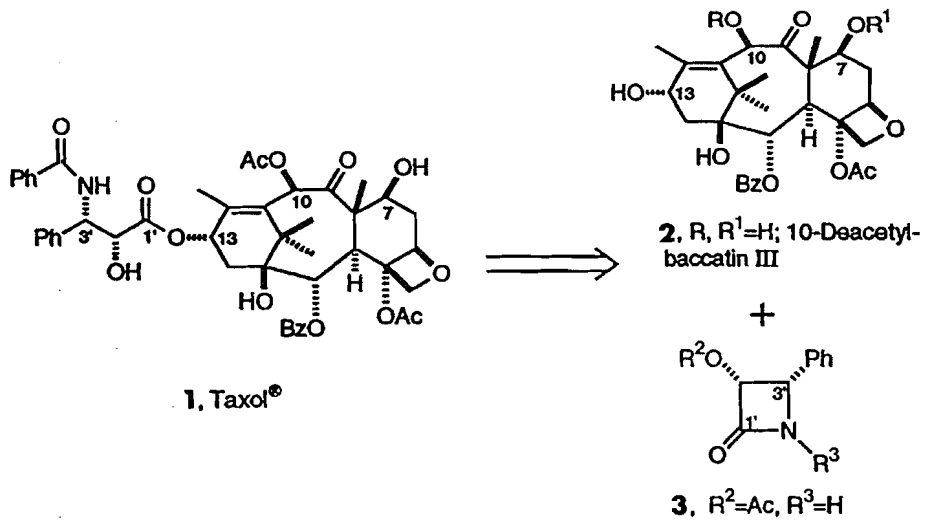

FIG. 1

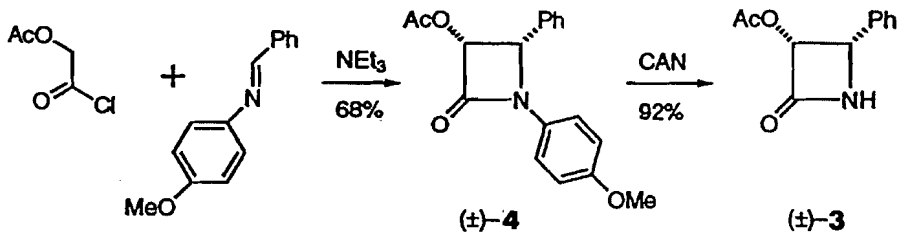

SCHEME 1

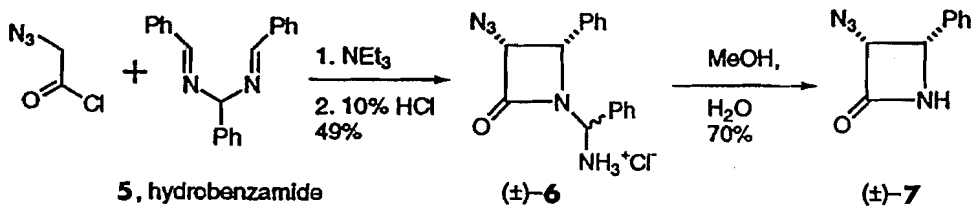

SCHEME 2

chloride instead of azidoacetyl chloride) gave low yields of product (13%), presumably due to the instability of the β-lactam ring and the 3-acetoxy group to aqueous HCl. However, it was noted that the intermediate α-benzylideneiminotoluene-(BIT) protected azetidin-2-one **8** (Scheme 3) could be isolated in acceptable quantities. An investigation was undertaken to find better methods for BIT-group deprotection, relative to the one employed previously (10, 11). Other objectives included the optimization of the Staudinger reaction and the development of a telescoped method that would avoid isolation of the intermediate BIT-lactam.

Synthesis of BIT-lactam 8

The starting material, hydrobenzamide, is commercially available (Lancaster). For this work, it was readily prepared in 250-g batches by condensing benzaldehyde with 30% ammonium hydroxide in 2-propanol (20°C, 3 d, 97%). The product was then collected by filtration. This method is a modification of a preparation described by Nicholson and Portez (12).

The reaction between hydrobenzamide and acetoxyacetyl chloride in the presence of triethylamine afforded, after an aqueous extractive work-up, predominantly the BIT-protected azetidin-2-one **8** as a mixture of diastereomers (^{1}H nmr; 85% by hplc) (Scheme 3). No (±)-*trans*-3,4-azetidin-2-one was detected by hplc and ^{1}H nmr comparison with the authentic compound (6*c*). The only other clearly identifiable side-products were the *bis*-lactam **9**[4] (~9%, hplc) together with small amounts of free azetidin-2-one **3** and benzaldehyde.

By optimizing the amount of acetoxyacetyl chloride (AAC), the rate of addition of AAC, and the reaction temperature, it was possible to minimize the amount of *bis*-lactam **9** formed to <1.5% (hplc) and to maximize the amount of BIT-lactam (91%) (see experimental section for optimized reaction conditions). Suitable solvents were dichloromethane, toluene, and ethyl acetate. Both triethylamine and *N,N*-diisopropylethylamine (Hünig's base) were acceptable as bases; however, Hünig's base allowed the Staudinger reaction to be accomplished at lower temperatures (−20°C vs. 5°C) and in shorter reaction times (5 h vs. 18 h).

Deprotection of BIT-lactam 8

As mentioned, 10% HCl (aq) has been used (10, 11) for deprotection of the adduct formed between azidoacetyl chloride

[4]The *bis*-lactam **9** was formed by reaction of 2 equivalents of acetoxyacetyl chloride with 1 equivalent of hydrobenzamide. The methods that were used to convert **8** into **3** failed to convert **9** into **3**.

Can. J. Chem. Downloaded from www.nrcresearchpress.com by 85.192.166.187 on 09/08/12
For personal use only.

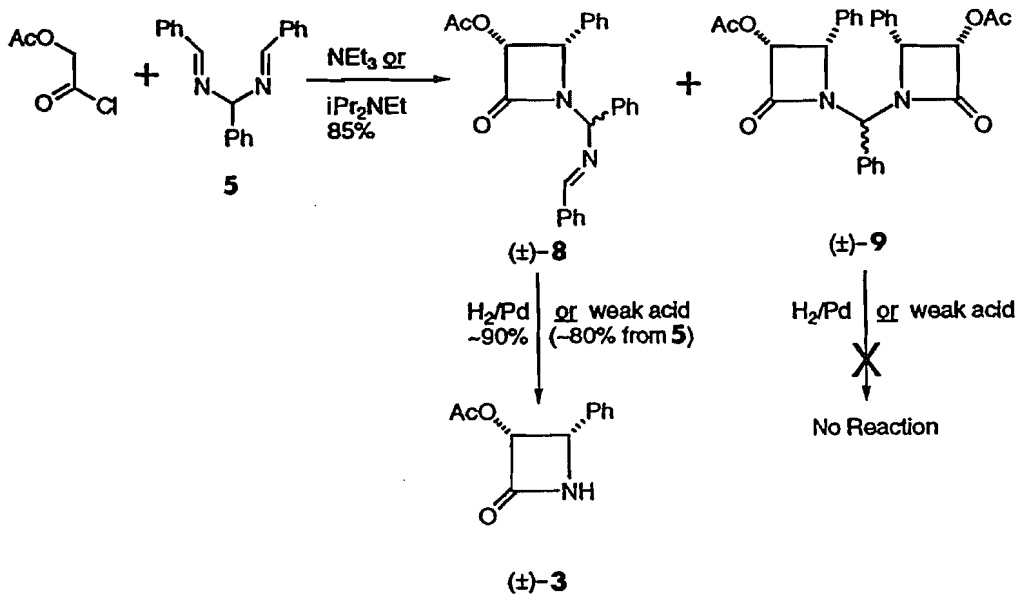

SCHEME 3

and hydrobenzamide. Deprotection of **8** using similar conditions (1% and 10% HCl) provided low yields of product. The ^{1}H nmr spectrum of the crude reaction mixture indicated a mixture of open-chain acids with and without the acetoxy moiety.

Initial attempts to purify the BIT-lactam **8** by silica gel chromatography gave mainly the deprotected azetidin-2-one **3**.[5] The lability of the BIT group to silica gel suggested that other higher yielding methods of deprotection might be available. Indeed, various reagents were found to be significantly more effective than aqueous HCl and are described in the experimental section. The deprotection protocols that were most amenable to scale-up were catalytic hydrogenation (e.g., Pd/C or $Pd(OH)_2$, Method 1), weak-acid hydrolysis (e.g., 75% aqueous acetic acid, Method 2), or 30% aqueous sodium bisulfite (Method 3). Reductive deprotection using sodium cyanoborohydride in methanol (23°C, 1 h) gave equivalent results on smaller scales. The overall isolated yields using the optimized deprotection conditions were in the 70–80% range.

This versatility in terms of deprotection is a valuable feature of the BIT group. It should, for example, be amenable to the synthesis of 3-substituted azetidin-2-ones, which may be sensitive to either acid hydrolysis or catalytic hydrogenation conditions.

Telescoping the sequence

In terms of operational simplicity, a telescoped procedure that would not require isolation of the BIT-lactam **8** was desirable. Thus, after the Staudinger reaction and aqueous extractive processing were complete, the organic layer was submitted to the deprotection conditions described above. For instance, when using the hydrogenation-mediated deprotection method (Method 1), the Staudinger reaction was performed in ethyl acetate. After the aqueous washings, the catalyst was added and the mixture hydrogenated using a Parr apparatus.[6] The catalyst was removed by filtration and the organic layer was washed with 1 *N* HCl to remove the dibenzylamine by-product as its hydrochloride salt. Subsequent concentration of the organic layer precipitated the desired azetidin-2-one **3**.

For the telescoped, weak-acid-mediated hydrolysis, the best option found was to perform the Staudinger reaction in dichloromethane followed by addition of an aqueous mixture of the desired acid (Method 2). Complete BIT-group removal was effected by warming the reaction mixture to ~40°C. The aqueous layer was then neutralized by addition of aqueous NaOH and, after phase separation, the product was precipitated out of the organic layer using heptane.

The Staudinger reaction was accomplished in ethyl acetate for the bisulfite-mediated deprotection (Method 3). After aqueous work-up, the organic layer was treated with aqueous sodium bisulfite at 50°C. Separation and concentration of the organic phase provided **3**.

In all cases, (±)-*cis*-3-acetoxy-4-phenylazetidin-2-one was obtained as a white crystalline product of excellent purity (>99%, hplc). All of these reactions were performed on scales of at least 100 g of starting hydrobenzamide. For the acetic acid mediated hydrolysis, the telescoped sequence was performed on kilogram-scale without having an adverse effect on the yield or purity of **3** obtained.

The separation of the racemic intermediate **3** to give the enantiomeric side-chain precursor of paclitaxel (2′*R*,3′*S*) has been described by Holton (3) using optical resolution of the diastereomeric Mosher's esters of (±)-*cis*-3-hydroxy-4-phenylazetidin-2-one (formed at the 3-position after saponification of the acetoxy moiety). In addition, the kinetic resolution of **3** and derivatives of **3** using highly enantioselective and practical chemoenzymatic methods has been described by Sih et al. (5*a*) and Patel et al. (5*b*).

Analogs of the paclitaxel side chain

To demonstrate the generality of this hydrobenzamide methodology for construction of synthetically useful β-lactams (e.g., refs. 6*g*, 13) and the synthesis of potentially therapeutically useful 3′-paclitaxel side-chain analogs (refs. 6*j*, 6*k*, and 6*l*), a series of analogs of **3** were prepared (Table 1).

The requisite hydroanisamide, hydrofuramide, hydrothien-

[5]BIT-lactam **8** has since been purified by Florisil® chromatography.

[6]Other experiments have demonstrated that these hydrogenations may be performed using a H_2-filled balloon although the deprotection reaction was slower (reaction time ~2 d).

Can. J. Chem. Downloaded from www.nrcresearchpress.com by 85.192.166.187 on 09/08/12
For personal use only.

TABLE 1. 4-Analogs of (±)-*cis*-3-acetoxy-4-phenylazetidin-2-one (**3**) prepared by the hydrobenzamide method

Compound	Overall yield (%)	Method of deprotection
(±)-*cis*-3-Acetoxy-4-*p*-methoxyphenylazetidin-2-one, **10**	75	Hydrogenation
(±)-*cis*-3-Acetoxy-4-(2′-furanyl)azetidin-2-one, **11**	61	Hydrogenation
(±)-*cis*-3-Acetoxy-4-(2′-thienyl)azetidin-2-one, **12**	75	Acetic acid
(±)-*cis*-3-Acetoxy-4-*p*-methylphenylazetidin-2-one, **13**	70	Bisulfite

amide, and hydrotoluamide were readily prepared in a manner similar to that described for hydrobenzamide (12). Acetoxyacetyl chloride was used as the ketene equivalent and the reactions were performed with inputs of at least 10 mmol of the starting imine.

Conclusions

A practical procedure that is suitable for the preparation of kilogram quantities of (±)-*cis*-3-acetoxy-4-phenylazetidin-2-one (**3**) was developed. This compound has been used in the semi-synthesis of paclitaxel (3, 5). The key step was the Staudinger reaction between hydrobenzamide and acetoxyacetyl chloride. Subsequent removal of the BIT-protecting group was achieved by hydrogenation, and hydrolytic or reductive protocols.

In terms of many process aspects (processing volumes, cost of reagents, yields, etc.), this methodology is superior to the CAN oxidative removal of the PMP group used previously for the preparation of (±)-*cis*-3-acetoxy-4-phenylazetidin-2-one (3).

The generality of this protocol was demonstrated by the synthesis of several (±)-*cis*-3,4-substituted azetidin-2-ones. These compounds are of use for the synthesis of paclitaxel side-chain analogs. As well, hydrobenzamide methodology may be of general use for the improved synthesis of 4-aryl- or 4-heteroaryl-substituted β-lactams.

Experimental

Melting points were determined on a Büchi 510 melting point apparatus and are not corrected. The ^{1}H nuclear magnetic resonance (^{1}H nmr) spectra were taken on a Bruker AC200SY instrument operating at 200 MHz. Chemical shifts are expressed in parts per million (ppm) downfield from internal tetramethylsilane. The ^{13}C nmr spectra were recorded on a Bruker AMX 400 instrument operating at 100.6 MHz. The carbon chemical shifts are quoted in parts per million (ppm) with reference to $CDCl_3$ (77.0 ppm) or $(CD_3)_2SO$ (39.6 ppm). Mass spectra (ms) were recorded on a Fisons VG Quattro Fast Ion Bombardment mass spectrometer. The infrared spectra (ir) were recorded on a Perkin–Elmer 781 infrared spectrophotometer. Ultraviolet (uv) spectra were recorded on a Hewlett–Packard 8451A diode array spectrophotometer. Elemental analyses were performed by Bristol-Myers Squibb Pharmaceutical Research Institute, Analytical R&D, Syracuse. Solvents and reagents used were reagent grade. High-performance liquid chromatography (hplc) was performed on a Hewlett–Packard 1090 Series 2 system with a diode array detector at 220 nm. A 30 cm × 3.9 mm 10 μ-Bondapack C_{18} column was used. The eluent was 40:60 CH_3CN:0.01M KH_2PO_4 (pH 7.4). Karl-Fischer titrations were performed using a Metrohm 655 Dosimat – Karl-Fischer Automat titrator.

*Telescoped preparations of (±)-*cis*-3-acetoxy-4-phenylazetidin-2-one (3)*

Method 1. Hydrogenation over Pd/C with isolation of intermediate BIT-lactam 8

*A. (±)-*cis*-3-Acetoxy-1-[(phenyl)(phenylmethyleneimino)methyl]-4-phenylazetidin-2-one (8).* Triethylamine (16.8 mL, 121 mmol) was added to a solution of hydrobenzamide (**5**) (30.00 g, 101 mmol) in ethyl acetate (150 mL). With stirring and under a blanket of argon, this mixture was cooled to 5°C and a solution of acetoxyacetyl chloride (12.5 mL, 116 mmol) in ethyl acetate (300 mL) was added dropwise over 1.5 h. After 16 h at 5°C, the reaction mixture was allowed to warm to 20°C (1.5 h). The organic layer was washed successively with saturated aqueous NH_4Cl (2 × 120 mL), saturated aqueous $NaHCO_3$ (120 mL), and brine (120 mL). The BIT-lactam **8** was isolated at this stage by drying the organic phase over $MgSO_4$, filtering, and removing the solvent in vacuo. This provided the crude protected β-lactam **8** in quantitative yield as a red glassy solid; hplc purity (area): 87.9% (1:1 mixture of diastereomers). For purposes of characterization, this compound was purified by Florisil® chromatography (ethyl acetate – hexane (1:4)) and recrystallized from ethyl acetate – hexane to yield **8** as a white solid; hplc purity (area): 98.3%; ir ν_{max} (KBr): 1763 (C=O), 1641 (C=N), cm^{-1}; UV λ_{max} (methanol): 216, 252 nm; ^{1}H nmr ($CDCl_3$) δ: 8.45 (s, 1H, N=CH), 7.80–7.85 (m, 1H, Ph), 7.60–7.65 (m, 1H, Ph), 7.26–7.50 (m, 9H, Ph), 7.00–7.10 (m, 4H, Ph), 6.28 (s, 0.5H, NCHN), 6.23 (s, 0.5H, NCHN), 5.81 (d, J = 4.8 Hz, 0.5 H, H-3), 5.76 (d, J = 4.8 Hz, 0.5 H, H-3), 5.30 (d, J = 4.8 Hz, 0.5 H, H-4), 4.75 (d, J = 4.8 Hz, 0.5 H, H-4), 1.63 (s, 3H, CH_3CO); ms (FAB), *m/z*: 399 (M^+ + H, 4%), 294 (M^+ − PhCHN, 17%).

*B. (±)-*cis*-3-Acetoxy-4-phenylazetidin-2-one (3).* The crude BIT-lactam **8** from above was redissolved in ethyl acetate (500 mL) and carefully transferred, under a stream of argon, to a Parr flask containing 10% palladium on activated carbon[7] (6.00 g). This mixture was treated with hydrogen (4 atm; 1 atm = 101.3 kPa) for 20 h at which point the catalyst was removed by filtration through a pad of Celite®. The filter cake was slurried in ethyl acetate (200 mL), stirred (10 min), filtered, and rinsed with ethyl acetate (100 mL). The filtrates were combined and the organic layer was washed with 10% HCl (300 mL). Both layers were filtered to remove the white precipitate (dibenzylamine·HCl), which was rinsed with ethyl acetate (100 mL). The phases were separated and the organic layer was washed with another portion of 10% HCl (200 mL). The combined 10% HCl washes were re-extracted with ethyl acetate (200 mL) and the combined organic layers were washed with saturated aqueous $NaHCO_3$ (300 mL) and brine (250 mL). The organic layer was dried over $MgSO_4$, filtered, and concentrated in vacuo to a volume of 75 mL. This mixture was cooled to 4°C and the precipitated product isolated by filtration. The filter cake was washed with hexane (200 mL) to provide 16.1 g (78% overall yield from hydrobenzamide) of β-lactam **3** as white needles, mp 150–151°C; hplc purity (area): 99.8%; ir ν_{max} (KBr): 3210 (N-H), 1755, 1720 (C=O) cm^{-1}; UV λ_{max} (methanol): 218, 260 nm; ^{1}H nmr ($CDCl_3$) δ: 7.30–7.38 (m, 5H, Ph), 6.54 (br s, D_2O exchangeable, 1H, NH), 5.87 (dd, J = 2.7, 4.7 Hz, 1H, H-3), 5.04 (d, J = 4.7 Hz, 1H, H-4), 1.67 (s, 3H, CH_3CO); ^{13}C nmr (DMSO-d_6) δ: 168.6, 165.0, 135.9, 128.0, 127.9, 127.3, 78.0, 56.0, 19.7; moisture content (by KF): 0.17%. Anal. calcd. for $C_{11}H_{11}NO_3$: C 64.38, H 5.40, N 6.83; found: C 64.07, H 5.34, N 6.77.

Method 2. Hydrolysis with 75% acetic acid

To hydrobenzamide (100.0 g, 335 mmol) in dichloromethane (335

[7]Wet 10% Pd/C (50% water content) was used as catalyst with identical results.

Can. J. Chem. Downloaded from www.nrcresearchpress.com by 85.192.166.187 on 09/08/12
For personal use only.

Can. J. Chem. Downloaded from www.nrcresearchpress.com by 85.192.166.187 on 09/08/12
For personal use only.

mL) was added *N,N*-diisopropylethylamine (67.1 mL, 385 mmol). This mixture was cooled to −20°C under N_2 and a solution of acetoxyacetyl chloride (39.6 mL, 368 mmol) in dichloromethane (185 mL) was added dropwise over 5 h. After the reaction was complete (<5% hydrobenzamide by hplc), water (330 mL) was added in one portion and the temperature was increased to 5°C. The phases were separated and the aqueous layer was washed with another 100 mL of dichloromethane. The combined organic layers were treated with acetic acid (150 mL, 2.62 mol) and water (50 mL). The reaction mixture was stirred and warmed to reflux (~40°C). After about 4 h, the hydrolysis was judged complete (<2% **8** by hplc) and the reaction mixture was cooled to 15°C. The pH was adjusted to 6.9 by the addition of 3.75 *N* NaOH (705 mL) over 2 h, keeping the temperature between 10 and 20°C. The mixture was warmed to 25°C to redissolve partially precipitated **3** and the phases separated. The aqueous phase was washed with a portion of dichloromethane (100 mL) and the organic layers combined (~850 mL). The organic layer was then cooled to −5°C–0°C and heptane (850 mL) was added over 1 h with stirring. The resulting slurry was stirred for an additional 1 h at this temperature at which point the solid was collected by filtration. The filter cake was washed with cold 10% dichloromethane in heptane (200 mL). This provided 54.4 g (79% yield from hydrobenzamide) of β-lactam **3** as off-white needles; hplc purity (area): 100%.

Method 3. Hydrolysis with 30% sodium bisulfite

To hydrobenzamide (50.00 g, 167 mmol) in ethyl acetate (500 mL) and under an atmosphere of argon was added triethylamine (26.9 mL, 193 mmol). This mixture was cooled to 5°C and a solution of acetoxyacetyl chloride (18.9 mL, 176 mmol) in ethyl acetate (200 mL) was added dropwise over 1.5 h with stirring. After another 2 h, the stirring was discontinued and the reaction mixture was maintained at 5°C for 17 h. The mixture was diluted with water (250 mL) and the layers separated. The aqueous phase was washed with another portion of ethyl acetate (100 mL) and the organic phases combined and treated with sodium bisulfite (75.0 g) in water (250 mL). The resulting biphasic solution was vigorously stirred (overhead stirrer) at 50 ± 2°C until the hydrolysis was judged complete by tlc (~4 h). The phases were separated and the organic layer was washed with water (150 mL) and then dried over $MgSO_4$, filtered, and concentrated in vacuo to a volume of 100 mL. This mixture was cooled to ~4°C and stirred for 2 h. The precipitated product was isolated by filtration. The filter cake was washed with cold ethyl acetate (25 mL) to provide 20.6 g (60% overall yield from hydrobenzamide) of β-lactam **3** as white needles; hplc purity (area): 99.3%.

*(±)-*cis*-3-Acetoxy-4-*p*-methoxyphenylazetidin-2-one (**10**) by Method 1*

The β-lactam **10** was prepared according to Method 1, except that hydroanisamide (14) was used instead of hydrobenzamide. Thus, hydroanisamide (5.00 g, 12.9 mmol), triethylamine (2.15 mL, 15.4 mmol), and acetoxyacetyl chloride (1.59 mL, 14.8 mmol) gave a solution of the protected β-lactam in ethyl acetate (80 mL). This solution was treated with H_2 (4 atm) over 10% palladium on activated carbon (1.00 g). Standard processing and removal of the solvent in vacuo furnished 4.28 g of a crude solid. A portion (300 mg) was purified by preparative tlc (20 cm × 20 cm × 2 mm silica gel; ethyl acetate – hexane (1:1)) and recrystallized from dichloromethane–hexane to provide 160 mg (75% overall yield from hydroanisamide) of the 4-(*p*-methoxyphenyl) β-lactam **10** as white crystals, mp 110–111°C; hplc purity (area): 99.7%; ir ν_{max} (KBr): 3218 (N-H), 1751, 1728 (C═O) cm^{-1}; UV λ_{max} (methanol): 208, 230, 276 nm; ^1H nmr ($CDCl_3$) δ: 7.24 (d, J = 9.0 Hz, 2H, Ar), 6.89 (d, J = 8.7 Hz, 2H, Ar), 6.23 (br s, D_2O exchangeable, 1H, NH), 5.83 (dd, J = 2.7, 4.6 Hz, 1H, H-3), 4.99 (d, J = 4.6 Hz, 1H, H-4), 3.81 (s, 3H, $ArOCH_3$), 1.73 (s, 3H, CH_3CO). Anal. calcd. for $C_{12}H_{13}NO_4$: C 61.27, H 5.57, N 5.95; found: C 61.04, H 5.49, N 5.88.

*(±)-*cis*-3-Acetoxy-4-(2′-furanyl)azetidin-2-one (**11**) by Method 1*

The β-lactam **11** was prepared according to Method 1 except that hydrofuramide (15) was used instead of hydrobenzamide. Thus, hydrofuramide (80.48 g, 300 mmol), triethylamine (50.2 mL, 360 mmol), and acetoxyacetyl chloride (37.0 mL, 344 mmol) gave a solution of the protected β-lactam in ethyl acetate (1.5 L). This solution was treated with H_2 (4 atm) over 10% palladium on activated carbon (12.0 g). The catalyst was removed by filtration through Celite® and the reaction mixture treated with decolourizing charcoal (30 g, Norit®). After the standard aqueous processing, the organic layer was concentrated to a volume of 160 mL. This mixture was cooled to 4°C and the precipitated product was isolated by filtration. The filter cake was rinsed with diethyl ether and hexane (100 mL of each) to provide 36.0 g (61% overall yield from hydrofuramide) of the 4-(2′-furanyl) β-lactam **11** as white needles, mp 118–119°C; hplc purity (area): 99.4%; ir ν_{max} (KBr): 3203 (N-H), 1756, 1726 (C═O) cm^{-1}; UV λ_{max} (methanol): 222 nm; ^1H nmr ($CDCl_3$) δ: 7.44 (t, J = 1.3 Hz, 2H, furyl), 6.39 (d, J = 1.3 Hz, 1H, furyl), 6.21 (br s, D_2O exchangeable, 1H, NH), 5.88 (dd, J = 2.2, 4.6 Hz, 1H, H-3), 5.05 (d, J = 4.6 Hz, 1H, H-4), 1.92 (s, 3H, CH_3CO). Anal. calcd. for $C_9H_9NO_4$: C 55.39, H 4.65, N 7.18; found: C 55.76, H 4.64, N 6.95.

*(±)-*cis*-3-Acetoxy-4-(2′-thienyl)azetidin-2-one (**12**) by Method 2*

The β-lactam **12** was prepared according to Method 2 for the preparation of **3** except that hydrothienamide was used instead of hydrobenzamide. Thus, hydrothienamide (30.0 g, 94.8 mmol), triethylamine (15.9 mL, 114 mmol), and acetoxyacetyl chloride (11.6 mL, 109 mmol) gave a solution of the protected β-lactam in ethyl acetate. In this case, the ethyl acetate was removed in vacuo to provide the crude intermediate protected β-lactam as a viscous oil. A portion of this oil (0.431 g, 1.03 mmol) was redissolved in dichloromethane (2.93 mL) and treated with acetic acid (0.35 mL, 6.1 mmol) and water (0.15 mL). After 2.5 h at reflux, the reaction mixture was diluted with dichloromethane (50 mL) and washed with saturated aqueous $NaHCO_3$ (2 × 75 mL) and brine (50 mL). The organic layer was concentrated in vacuo to a brown oil, which was purified by silica gel chromatography (ethyl acetate – hexane (1:10 to 3:2)) to give 0.154 g (75% overall yield from hydrothienamide) of the 4-(2′-thienyl) β-lactam **12** as a white solid, mp 101.4–103.3°C; ir ν_{max} (KBr): 3216 (N-H), 1752, 1724 (C═O) cm^{-1}; ^1H nmr ($CDCl_3$) δ: 7.32 (dd, J = 1.5, 4.7 Hz, 1H, thienyl), 7.03 (m, 2H, thienyl), 6.75 (br s, D_2O exchangeable, 1H, NH), 5.86 (dd, J = 2.7, 4.6 Hz, 1H, H-3), 5.27 (d, J = 5.3 Hz, 1H, H-4), 1.83 (s, 3H, CH_3CO); ^{13}C nmr ($CDCl_3$) δ: 169.3, 165.5, 138.4, 127.1, 127.07, 126.2, 78.3, 54.0, 20.0. Anal. calcd. for $C_9H_9NO_3S$: C 51.17, H 4.29, N 6.63; found: C 51.17, H 4.31, N 6.48.

*(±)-*cis*-3-Acetoxy-4-*p*-methylphenylazetidin-2-one (**13**) by Method 3*

The β-lactam **13** was prepared according to Method 3 except that hydrotoluamide (15) was used instead of hydrobenzamide. Thus, hydrotoluamide (10.00 g, 29.4 mmol), triethylamine (4.91 mL, 35.2 mmol), and acetoxyacetyl chloride (3.63 mL, 33.8 mmol) gave a solution of the protected β-lactam in ethyl acetate (150 mL). This solution was treated with water (50 mL) and sodium bisulfite (15 g). This biphasic mixture was vigorously stirred at 50°C for 15 h and the organic and aqueous layers were separated. The organic layer was washed with water (50 mL) and brine (50 mL), dried over $MgSO_4$, and concentrated in vacuo to 20 mL. The mixture was cooled to 5°C and the precipitated product was isolated by filtration and rinsed with cold ethyl acetate (10 mL) and hexane (20 mL) to provide 2.59 g of **13**. Subsequent evaporation of the filtrate and recrystallization from ethyl acetate yielded another two crops of material (1.27 and 0.65 g) to furnish a total of 4.51 g (70% overall yield from hydrotoluamide) of the β-lactam **13** as white needles, mp 130–131°C; hplc purity (area): 99.8%; ir ν_{max} (KBr): 3192 (N-H), 1778, 1752 (C═O) cm^{-1}; UV λ_{max} (methanol): 222, 266 nm; ^1H nmr ($CDCl_3$) δ: 7.13–7.22 (m, 4H, Ar), 6.29 (br s, D_2O exchangeable, 1H, NH), 5.85 (dd, J = 2.6, 4.7 Hz, 1H, H-3), 5.00 (d, J = 4.7 Hz, 1H, H-4), 2.35 (s, 3H, $ArCH_3$), 1.70 (s, 3H, CH_3CO). Anal. calcd. for $C_{12}H_{13}NO_3$: C 65.74, H 5.98, N 6.39; found: C 65.85, H 5.91, N 6.40.

Acknowledgements

We would like to thank Mr. J. Lajeunesse, Mr. P. Sirard (Bris-

tol-Myers Squibb, Candiac), and Dr. J.F. Kadow (BMS, Wallingford) for technical assistance and Mr. G. Lacasse (BMS, Candiac) for analytical support. The authors also wish to thank Dr. R.A. Partyka (BMS, New Brunswick) for his interest and encouragement and Drs. E.H. Ruediger and V.S. Rao (BMS, Candiac) for helpful discussion.

1. (*a*) K.C. Nicolaou, W.-M. Dai, and R.K. Guy. Angew. Chem. Int. Ed. Engl. **33**, 15 (1994); (*b*) M. Suffness. Annu. Rep. Med. Chem. **28**, 305 (1993).
2. J.-N. Denis, A.E. Greene, D. Guénard, F. Guéritte-Voegelein, L. Mangatal, and P. Potier. J. Am. Chem. Soc. **110**, 5917 (1988).
3. (*a*) R.A. Holton. Method for preparation of Taxol. Eur. Pat. Appl. 0400971 A2, pp. 1–18 (1990); (*b*) Chem. Abstr. **114**, 164568q (1991).
4. M.D. DeFuria and Z. Horovitz. J. Natl. Cancer Inst. Monographs, No. 15, 195 (1993).
5. (*a*) R. Brieva, J.Z. Crich, and C.J. Sih. J. Org. Chem. **58**, 1068 (1993); (*b*) R.N. Patel, L.J. Szarka, and R.A. Partyka. Enzymatic processes for resolution of enantiomeric mixtures of compounds useful as intermediates in the preparation of taxanes. Eur. Pat. App. 0552041 A2, pp. 1–32 (1993).
6. β-Lactams prepared by the Staudinger reaction and used for the synthesis of paclitaxel and (or) analogs of paclitaxel: (*a*) J. Kant, S. Huang, H. Wong, C. Fairchild, D. Vyas, and V. Farina. Bioorg. Med. Lett. **3**, 2471 (1993); (*b*) R.A. Holton and J.H. Liu. Bioorg. Med. Lett. **3**, 2475 (1993); (*c*) M. Endo R. Droghini. Bioorg. Med. Lett. **3**, 2483 (1993); (*d*) J.D. Bourzat and A. Commerçon. Tetrahedron Lett. **34**, 6049 (1993); (*e*) G.I. Georg, E. Akgün, P.M. Mashava, M. Milstead, H. Ping, Z. Wu, D. Vander Velde, and F. Takusagawa. Tetrahedron Lett. **33**, 2111 (1992); (*f*) V. Farina, S.I. Hauck, and D.G. Walker. Synlett, 761 (1992); (*g*) C. Palomo, A. Arrieta, F.P. Cossio, J.M. Aizpurua, A. Mielgo, and N. Aurrekoetxea. Tetrahedron Lett. **31**, 6429 (1990). β-Lactams prepared by enolate chemistry and used for the synthesis of paclitaxel and (or) analogs of paclitaxel: (*h*) G.I. Georg, Z.S. Cheruvallath, G.C.B. Harriman, M. Hepperle, and H. Park. Bioorg. Med. Lett. **3**, 2467 (1993); (*i*) I. Ojima, M. Zucco, O. Duclos, S.D. Kuduk, C.M. Sun, and Y.H. Park. Bioorg. Med. Lett. **3**, 2479 (1993); (*j*) I. Ojima, I. Habus, M. Zhao, M. Zucco, Y.H. Park, C.M. Sun, and T. Brigaud. Tetrahedron, **48**, 6985 (1992); (*k*) G.I. Georg, Z.S. Cheruvallath, R.H. Himes, M.R. Mejillano, and C.T. Burke. J. Med. Chem. **35**, 4230 (1992); (*l*) G.I. Georg, Z.S. Cheruvallath, R.H. Himes, and M.R. Mejillano. Bioorg. Med. Lett. **2**, 295 (1992); (*m*) I. Ojima, I. Habus, M. Zhao, G.I. Georg, and L.R. Jayasinghe. J. Org. Chem. **56**, 1681 (1991).
7. D.R. Kronenthal, C.Y. Han, and M.K. Taylor. J. Org. Chem. **47**, 2765 (1982).
8. P.B. Schiff, J. Fant, and S.B. Horwitz. Nature, **277**, 665 (1979).
9. G.I. Georg and V.T. Ravikumar. *In* The organic chemistry of β-lactams. *Edited by* G.I. Georg. VCH Publishers, Inc., New York. 1993. pp. 295–368.
10. J.N. Wells and R.E. Lee. J. Org. Chem. **34**, 1477 (1969).
11. M.S. Manhas, A.K. Bose, and M.S. Khajavi. Synthesis, 209 (1981).
12. I. Nicholson and R. Portez. J. Chem. Soc. 3067 (1965).
13. J.E. Lynch, I. Shinkai, W.L. Laswell, and R.P. Volante. Nitrogen deprotected 4-acyloxyazetidin-2-ones. Eur. Pat. Appl. 0404586 A2, pp. 1–14 (1990).
14. L.B. Howard, G.E. Hilbert, R. Wiebe, and V.L. Gaddy. J. Am. Chem. Soc. **54**, 3628 (1932).
15. D.H. Hunter and S.K. Sim. Can. J. Chem. **50**, 669 (1972).

Can. J. Chem. Downloaded from www.nrcresearchpress.com by 85.192.166.187 on 09/08/12
For personal use only.

Spruce budworm (*Choristoneura fumiferana*) antifeedants 4. Synthesis of specionin and biological studies

ANMAR K. MOHAMMAD-ALI AND T.H. CHAN[1]
Department of Chemistry, McGill University, Montreal, QC H3A 2K6, Canada

AND

A.W. THOMAS, B. JEWETT, AND G.M. STRUNZ
Forestry Canada – Maritimes Region, Fredericton, NB E3B 5P7 Canada

Received April 25, 1994

ANMAR K. MOHAMMAD-ALI, T.H. CHAN, A.W. THOMAS, B. JEWETT, and G.M. STRUNZ. Can. J. Chem. **72**, 2137 (1994).

Specionin (**1**) was synthesized in seven steps from aucubin (**2**), an abundant iridoid form *aucuba japonica*. In a "no-choice" bioassay, specionin and several of its derivatives showed only modest antifeedant activity against the spruce budworm, while other derivatives were devoid of activity.

ANMAR K. MOHAMMAD-ALI, T.H. CHAN, A.W. THOMAS, B. JEWETT et G.M. STRUNZ. Can. J. Chem. **72**, 2137 (1994).

On a synthétisé la spécionine (**1**) en sept étapes à partir de l'aucubine (**2**), un iridoïde abondant de l'*aucuba japonica*. Dans un essai biologique sans choix, la spécionine et plusieurs de ses dérivés n'ont montré qu'une activité modeste comme antiappétent contre la tordeuse des bourgeons de l'épinette alors que d'autres dérivés n'ont aucune activité.

[Traduit par la rédaction]

Introduction

Because of problems associated with the widespread use of synthetic broad-spectrum pesticides, alternative strategies in the management of insect pests in forestry and agriculture are required. The spruce budworm, *Choristoneura fumiferana*, inflicts severe damage to the forest resource in Canada (1). A strategy that has been considered for the control of spruce budworm is to employ antifeedants to interfere with larval feeding behaviour (2–4). The approach offers the potential advantage that antifeedants could protect current year foliage while leading indirectly to budworm mortality without being generally toxic (5).

In screening programs using various insects, a number of natural products have been found to have antifeedant activity (6). Of particular interest to the spruce budworm problem is the report by Chang and Nakanishi that an active antifeedant compound, specionin (**1**), had been isolated from the leaves of *Catalpa speciosa* Warder (Bignoniaceae) (7, 8). Specionin was reported to be active at 50–100 ppm. Several chemical syntheses of **1** have since been reported (8–11) but without further biological studies. As part of our ongoing program in the chemical and biological studies of spruce budworm antifeedants (2–4, 12), we have undertaken the synthesis of specionin.

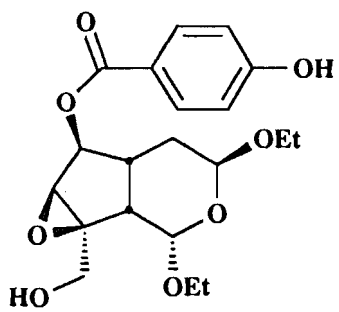

1

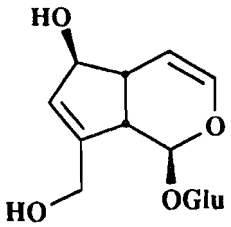

2

[1]Author to whom correspondence may be addressed.

Chemical synthesis

Most previous syntheses of specionin have been designed to construct the iridoid skeleton through the oxidative cleavage of fused cyclopentenes (13), or retro-aldol cleavage of a 2 + 2 cycloadduct (14) or the Norrish type I cleavage of a norbornanone (8). Curran et al. (11), on the other hand, took advantage of an intramolecular cycloaddition of nitrile oxide onto a dihydropyran. All these were lengthy multistep syntheses and give low overall yield of the final, optically active, product. Alternatively, specionin could be synthesized from the iridoid natural product catapol (8).

We previously proposed (2) the use of the natural iridoid glycoside, aucubin (**2**), for the synthesis of specionin. Aucubin is present to the extent of about 1% of fresh plant weight in the leaves of *Aucuba japonica* (15) and can be extracted and purified in large quantities. It had been used as starting material for the synthesis of prostaglandins (16). However, aucubin is degraded extensively under the acidic conditions usually required for removal of the glycosidic linkage. Under the mildest ethanolysis conditions reported by us previously, aucubin rearranged to give **3** with migration of the double bond (2).

Recently, Falck and co-workers reported on the unique ability of triphenylphosphine hydrobromide (TPHB) to promote the addition of oxygen nucleophiles to glucals to give the corresponding acetals without the double bond rearrangement (Ferrier reaction) (17). On the basis of this report, we became interested in using TPHB for the ethanolysis of aucubin. Aucubin was first peracetylated with acetic anhydride in pyridine and dimethylaminopyridine (DMAP) to give **4** (Scheme 1). Ethanolysis of **4** with 20 mol% of TPHB in dichloromethane gave the bis-ethoxy acetal **5** in 60% yield. ^{1}H NMR showed clearly the removal of the sugar moiety and the addition of two ethoxy groups. However, ^{13}C NMR indicated the presence of four diastereomers arising from all possible configurations of the ethoxy groups. At this stage, we did not separate these isomers and proceeded with the synthesis using the mixture. Attempted epoxidation of **5** with *m*-chloroperbenzoic acid (mCPBA) was not successful. Accordingly, the acetate groups were cleaved with NaOMe to give a mixture of the monoacetates **6** and **7** and

Can. J. Chem. Downloaded from www.nrcresearchpress.com by 85.192.166.187 on 09/08/12
For personal use only.

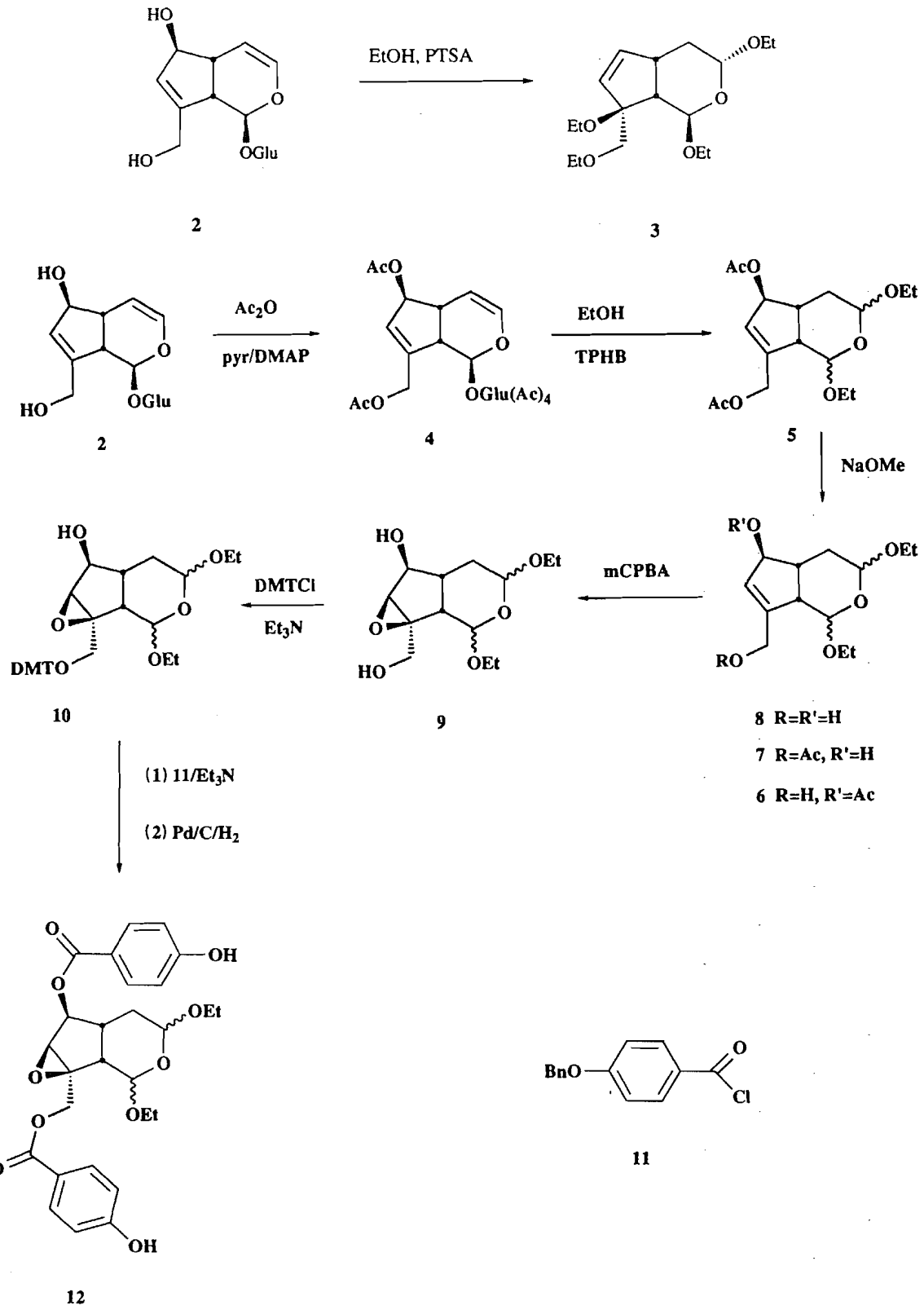

SCHEME 1

the diol **8**, the ratio of which depended on reaction time. The three compounds could be separated by flash column chromatography. Allowing the reaction to proceed for sufficient time, the diol **8** was obtained as the major product in 69% yield. Epoxidation now of **8** with mCPBA afforded the β-epoxide **9** in 60% yield. The ^{1}H NMR spectral data of **9** were compared with those reported in the literature (8). This comparison indicated that in the mixture of stereoisomers constituting **9**, the second most abundant isomer had the same stereochemistry as that of (−)-specionin.

Before benzoylation of the C-6 hydroxyl group, the primary hydroxyl group had to be protected. The use of silicon protect-

Can. J. Chem. Downloaded from www.nrcresearchpress.com by 85.192.166.187 on 09/08/12
For personal use only.

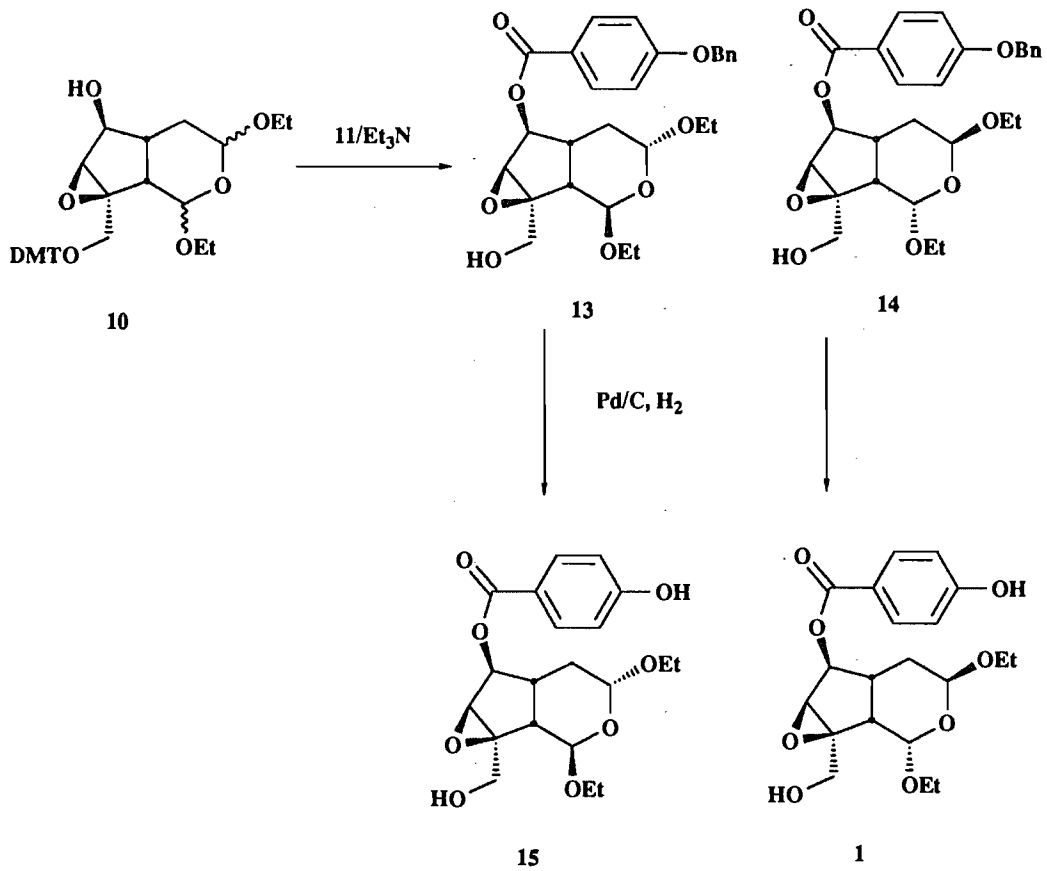

10 13 14 15 1

SCHEME 2

ing groups for this purpose has been reported but gave both the mono- and di-silylated compounds (8). We selectively protected the primary hydroxyl as its 4,4′-dimethoxytrityl (DMT) ether by reacting **9** with DMT chloride and triethylamine. The mono-DMT ether **10** was obtained in 75% yield. The coupling of **10** with an excess (4 equivalents) of *p*-benzyloxybenzoyl chloride (**11**) in the presence of triethylamine gave a product that, without purification, was treated with palladium hydroxide on carbon and cyclohexene to effect deprotection. To our surprise, the deprotected product, obtained in 60% yield, was clearly not specionin or any of its isomers. The material obtained was identified as the diester **12** (as a mixture of isomers) on the basis of ^{1}H and ^{13}C NMR and a HMQC experiment which indicated the coupling of the C-10 methylene protons with a carbonyl carbon. To explain the formation of **12**, it was assumed that the triethylamine hydrochloride formed was sufficiently acidic to remove the DMT protecting group. The unmasked primary hydroxy function was then benzoylated by the acid chloride.

The reaction was then repeated using less of the acid chloride **11** and for a shorter reaction time. Under these conditions, **13** and **14** were formed in a ratio of 3:1 in a combined yield of 55% (Scheme 2). The two diastereomers could be separated by column chromatography and were assigned the indicated stereochemistry. The minor isomer **14** was debenzylated over palladium on carbon with hydrogen to give pure (−)-specionin after silica gel column chromatography. Its proton NMR data were identical to the literature values (8). Similar debenzylation of the major isomer **13** gave the isomer of specionin, **15**, whose proton NMR was also identical with those reported in the literature (8).

Some comments need to be made regarding the difference in

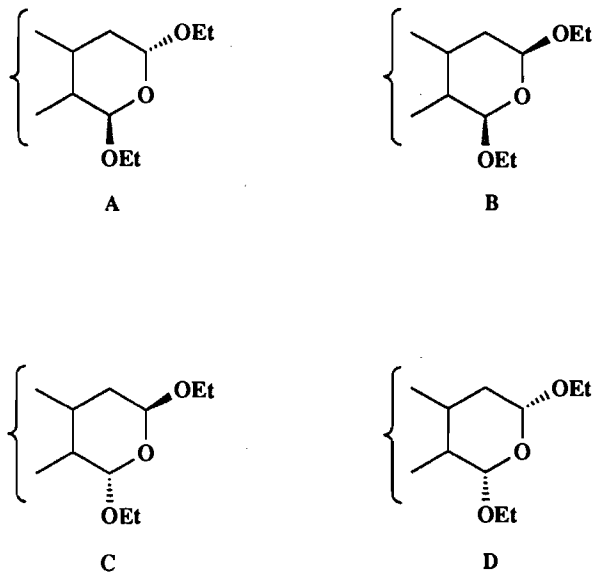

SCHEME 3

stereoselectivity in the various syntheses of specionin reported in the literature. Obviously, the bis-ethoxy acetal structure can lead to four possible stereoisomers A, B, C, and D (Scheme 3). Structure C has the relative configuration corresponding to specionin. Previous syntheses of specionin that used *p*-toluenesulfonic acid (PTSA) for the ethanolysis step gave different diastereomeric mixtures. Vandewalle and co-workers reported a ratio of 4:4:1:1 for A, B, C, and D, respectively (8). In Hussain and Leonard's synthesis, A, B, and C were initially formed in

Can. J. Chem. Downloaded from www.nrcresearchpress.com by 85.192.166.187 on 09/08/12
For personal use only.

Can. J. Chem. Downloaded from www.nrcresearchpress.com by 85.192.166.187 on 09/08/12
For personal use only.

the ratio of 10:10:1, respectively, and D was not reported (9). Whitesell and Allen reported that only the C isomer was formed (10). Finally, Vandewalle, Leonard, and co-workers (8, 9) and Curran et al. (11) all reported that when the mixture of isomers of specionin was subjected to equilibration conditions ($BF_3.OEt_2$ or PTSA in EtOH), the ratio was changed in favour of specionin. The results of these equilibration reactions suggest that the stereochemistry of the bis-acetal in specionin is the thermodynamically stable arrangement. Nevertheless, it remains difficult to reconcile the different ratios of isomers produced under different reaction conditions. We suggest that the different ratios of diastereomeric mixtures reported could be due to the presence of different functionalities on the cyclopentane ring, particularly at the C-6 position. With intermediates where the cyclopentane (ene) ring has no substituent at C-6, as in Vandewalle's synthesis, or a hydroxy group at C-6, as in our synthesis, a mixture of all four diastereomers resulted, with the C arrangement being the minor isomer. In cases where the cyclopentane ring has the bulky *p*-hydroxy- or *p*-benzyloxybenzoate group present at C-6, then the specionin structure C predominated in the equilibration step, as in Leonard's, Whitesell's, or Curran's syntheses. A similar conclusion was recently drawn by Leonard and Hussain (9*b*). In our synthesis, even though specionin was obtained as the minor isomer, it is clear that the major isomer **15** could be equilibrated into specionin. Our synthesis represents therefore a seven-step sequence for the conversion of the readily available aucubin into specionin.

Biological studies

Many experimental designs have been devised to assess the antifeedant effect of a compound. These experiments generally fall into two broad classes, namely "choice" or "no-choice" assays. The occasional disparity between results reported for the efficacy of a given antifeedant compound, using different criteria and methodology, highlights the necessity to use care in designing a bioassay that will yield the most appropriate information for the system under investigation (18). A "choice" type of bioassay is appropriate for polyphagous insects that have access to several plant species. A "no-choice" test was preferred for spruce budworm larvae in the present study, as these larvae are oligophagous and alternate food sources are not usually available in the forest.

Diet containing between 0.023 and 0.60% wet weight of the test compounds was prepared by treating lyophilized artificial diet (19) with a solution of the compound, usually in methylene chloride, and then removing the solvent completely at 30°C on a rotatory evaporator. The residual powder was rehydrated to 80% water content with 0.4% aqueous potassium sorbate solution (fungicide). Control diets were treated as above with solvent alone, or were untreated. Newly emerged 2nd-instar larvae were reared individually on the diets (19) at 24°C, 17-h photoperiod, 25 replicates per test compound and control. After 17 days, the larvae were sacrificed and their mean development stage (i.e., mean instar) determined.

Specionin and a number of its derivatives were tested for antifeedant activity against the spruce budworm (Table 1). The result for each compound tested should be compared with that for the corresponding control. The biological assay showed that the development of larvae reared from 2nd instar on specionin (with 10% of **15** present) at 230 ppm was not significantly retarded from the control. Moreover, all the derivatives tested at 1500 ppm were found to be essentially inactive. Compounds **9** and **10** were moderately active when tested at 3000 ppm, and compound **8** was also moderately active when tested at 6000 ppm. These observations are in contrast to reported activity of specionin at 50 ppm (7). We must only attribute the difference to the type of bioassays used or to the possible presence of another active component in the leaf extract studied by Nakanishi.

These results should also be compared with the potent biological activity of azadirachtin (**16**) against spruce budworm

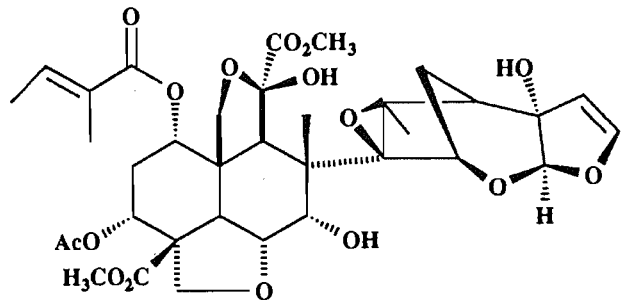

16

Azadirachtin

larvae. In a similar "no-choice" bioassay, but starting with 3rd instars instead of 2nd instars, a concentration of 1.2 ppm of azadirachtin (in the form of 0.3% azadirachtin in Margosan-O, a commercial preparation of neem oil) stopped development (12). Future studies on the use of antifeedants for the control of spruce budworm should be directed at azadirachtin and related compounds (20).

Experimental

General

For all moisture-sensitive reactions, glassware was oven-dried at 200°C and cooled in a desiccator. All reactions were run under an argon atmosphere, dried by being passed through a column of indicating Drierite and potassium hydroxide, unless otherwise noted. Materials were obtained from commercial suppliers unless noted otherwise. Temperatures of reactions refer to bath temperatures. Solvents were dried as follows: tetrahydrofuran distilled from Na/benzophenone; hexane, pyridine, ethyl acetate, dichloromethane distilled from calcium hydride; methanol distilled from magnesium methoxide; triethylamine stored over sodium hydroxide pellets. Solvents were evaporated under reduced pressure using a Buchi rotary evaporator. Melting points (mp) were determined on a Gallenkamp block and were uncorrected. Flash column chromatography was performed using BDH Silica Gel 60 (230–400 mesh ASTM). Thin-layer chromatography was performed on commercial Merck silica gel 60 F_{254} precoated plates supplied by Merck Co. Visualization was effected by ultraviolet fluorescence (UV) or by spraying the plates with an anisaldehyde – sulfuric acid spray. Proton nuclear magnetic resonance (^1H NMR) spectra were taken on Varian XL-200, XL-300, XL-500, and JEOL 270 instruments. The data are reported in parts per million (ppm) relative to the TMS reference line with the multiplicity (s, singlet; d, doublet; t, triplet; q, quartet; m, multiplet; b, broad), coupling constants in hertz, and the number of protons also given for the major isomer in the cases of stereoisomeric mixtures. Carbon-13 nuclear magnetic resonance (^{13}C NMR) spectra were recorded on Varian XL-300 (75.4 MHz) or JEOL-270 (67.8 MHz) instruments. Infrared (IR) spectra were obtained on an Analect AQS-18 FT-IR instrument and are reported in reciprocal centimeters (cm^{-1}). Solution spectra were obtained using sodium chloride cells of 0.2 mm thickness. Low- and high-resolution ammonia chemical ionization (CI) mass spectra were recorded on Hewlett–Packard 5980A and ZAB 2F HS instruments, respectively. Aucubin was generously provided by Dr. J.T. Edward of McGill University (15*b*).

TABLE 1. Biological assays of specionin and derivatives

(a)

Compound tested	Mean instar at concentrations 0.023%	0.30%
CH_2Cl_2 control	← 4.64 →	
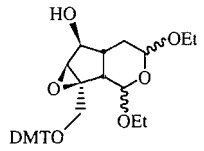 **10**		3.20[a]
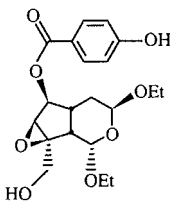 Specionin	4.24	

(b)

Compound tested	Mean instar at concentrations 0.15%	0.30%	0.60%
Nontreated control	← 5.28 →		
CH_2Cl_2 control	← 5.34 →		
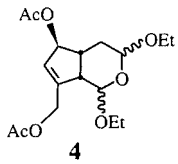 **4**	5.24	4.96	
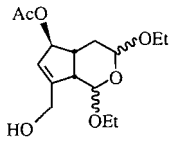 **6**	5.00		
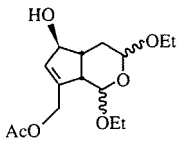 **7**	5.26		
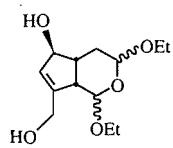 **8**	5.20	4.68	4.08[a]
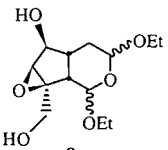 **9**	4.81	4.17[a]	
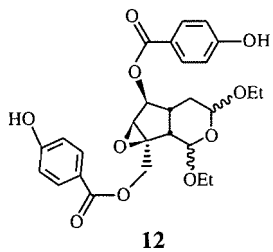 **12**	5.12	5.15	

[a]Means significantly different from controls, $P < 0.05$.

Compound 4

To a suspension of aucubin (1.02 g, 3.0 mmol) in THF (20 mL), pyridine (1.5 mL, 18 mmol) was added. Acetic anhydride (1.6 mL, 18 mmol) was then added followed by the addition of a few crystals of 4-dimethylaminopyridine. The reaction mixture was stirred for 4 h at ambient temperature. The solution was diluted with ether and washed 3 times with 5% aqueous HCl solution, dried with magnesium sulfate, filtered, and evaporated under reduced pressure. The residue was then purified by flash column chromatography using hexane – ethyl acetate mixture, 1:1 ratio, to give **4** as a solid (1.56 g), mp 112–112.5°C, in 87% yield. FTIR ($CHCl_3$): 2960, 2259, 1755, 1660, 1432, 1371, 1231, 1045, 969, 911; ^{1}H NMR ($CDCl_3$): 6.16 (dd, J = 1.9 and 6.2 Hz, 1 H), 5.85 (bs, 1 H), 5.29 (bs, 1 H), 5.24 (t, J = 9.5 Hz, 1 H), 5.16 (d, J = 4.0 Hz, 1 H), 5.10 (t, J = 9.8 Hz, 1 H), 5.02 (dd, J = 8.1 and 9.6 Hz, 1 H), 4.91 (dd, J = 3.2 and 6.3 Hz, 1 H), 4.85 (d, J = 8.0 Hz, 1 H), 4.74 (bs, 2 H), 4.28 (dd, J = 4.5 and 12.3 Hz, 1 H), 4.15 (dd, J = 2.1 and 12.5 Hz, 1 H), 3.72 (ddd, J = 2.3, 2.4, and 9.9 Hz, 1 H), 3.19 (m, 1 H), 2.82 (m, 1 H), 2.1 (s, 3 H), 2.09 (s, 3 H), 2.04 (s, 3 H), 2.03 (s, 3 H), 2.027 (s, 3 H), 2.01 (s, 3 H); ^{13}C NMR ($CDCl_3$): 170.6, 170.4, 170.2, 170.00, 169.2, 169.0, 144.3, 139.6, 127.1, 103.9, 95.8, 93.4, 82.3, 72.3, 71.9, 70.4, 68.1, 61.5, 61.1, 46.6, 39.00, 20.9, 20.6, 20.4; MS (CI): 616 (100, M + NH_4^+); HRMS calcd. for $C_{27}H_{38}N_1O_{15}$: 616.2241; found: 616.2244.

Compound 5

Triphenylphosphine hydrobromide (TPHB) (0.012 g, 0.037 mmol) was added to a dichloromethane solution of acetylated aucubin **4** (0.119 g, 0.185 mmol) and absolute ethanol (0.027 mL, 0.444 mmol). The mixture was refluxed overnight, then excess solvent was evaporated. The residue was redissolved in ether. The organic layer was washed with saturated aqueous sodium bicarbonate and brine, dried with magnesium sulfate, filtered, and evaporated under reduced pressure. The residue was then subjected to flash column chromatography using hexane – ethyl acetate (2:1) as the eluent to give **5** (anomeric mixture, 38 mg, 60% yield). FTIR ($CDCl_3$): 2979, 2932, 2362, 2263, 1733, 1450, 1376, 1242, 1106, 1022; ^{1}H NMR ($CDCl_3$): 5.80 (s, 1 H), 5.77 (s), 5.74 (s), 5.58 (m), 5.36 (bs, 1 H), 5.26 (bs), 4.95 (dd, J = 5.1 and 5.5 Hz, 1 H), 4.79 (dd, J = 4.9 and 4.7 Hz), 4.65 (bs, 2 H), 4.63 (d, J = 8.1 Hz, 1 H), 4.47 (d, J = 5.6 Hz), 4.2 (dd, J = 3.5 and 3.9 Hz), 3.84 (dq, J = 7.2 and 9.5 Hz, 2 H), 3.49 (dq, J = 7.2 and 9.5 Hz, 2 H), 3.23 (m), 3.16 (d, J = 9.0 Hz), 2.89 (t, J = 7.7 Hz, 1 H), 2.82 (t, J = 7 Hz), 2.65 (m), 2.56 (dd, J = 5.8 and 5.8 Hz), 2.46 (m, 1 H), 2.09 (s, 3 H), 2.02 (s, 3 H), 1.81 (m, 1 H), 1.52 (ddd, J = 6.8, 3.6, and 6.8 Hz, 1 H), 1.19 (dt, J = 7.0 Hz, 6 H); ^{13}C NMR ($CDCl_3$): 15.1, 20.8, 21.2, 29.5, 29.6, 29.7, 30.6, 38.9, 39.8, 40.4, 41.0, 48.0, 48.1, 48.3, 49.2, 61.7, 61.9, 61.9, 62.5, 63.1, 63.2, 63.7, 63.8, 63.8, 64.4, 65.5, 82.4, 83.0, 84.0, 84.7, 95.3, 96.21, 96.8, 96.9, 97.4, 97.2, 97.5, 100.2, 125.5, 126.0, 127.2, 128.0, 128.8, 130.9, 143.2, 144.5, 145.0, 145.3, 170.4, 170.5, 170.5, 171.0, 171.0, 171.2; MS (CI): 360 (4, M + NH_4^+), 177 (35), 180 (35), 209 (58), 226 (73), 237 (100).

Compounds 6, 7, and 8

Sodium methoxide (0.07 g, 1.29 mmol) was added to a solution of **5** (0.20 g, 0.59 mmol) in dry methanol (5 mL). The mixture was stirred for 3 h at room temperature. The solution was filtered and evaporated under reduced pressure. The material was then subjected to flash column chromatography using hexane and ethyl acetate (3:1) as eluent to separate compounds **6**, **7**, and **8**. Compound **8** (anomeric mixture) was obtained as a colorless oil (0.10 g, 69% yield). FTIR ($CDCl_3$): 3470, 2978, 2929, 2244, 1710, 1438, 1418, 1361, 1223, 1117, 1092, 1038, 1007, 964, 940; ^{1}H NMR ($CDCl_3$): 5.78 (d, J = 1.0 Hz, 1 H), 5.74 (s),

Can. J. Chem. Downloaded from www.nrcresearchpress.com by 85.192.166.187 on 09/08/12
For personal use only.

Can. J. Chem. Downloaded from www.nrcresearchpress.com by 85.192.166.187 on 09/08/12
For personal use only.

5.29 (s), 5.01, (d, J = 4.9 Hz), 4.99 (dd, J = 4.9 and 5.5 Hz, 1 H), 4.74 (dd, J = 3.2 and 8.3 Hz), 4.66 (s, 1 H), 4.62 (d, J = 8.1 Hz, 1 H), 4.37 (d, J = 7.3 Hz), 4.21 (bs, 2 H), 3.94 (dq, J = 7.1 and 9.5 Hz, 1 H), 3.81 (dq, J = 7.1 and 9.6 Hz, 1 H), 3.50 (dq, J = 7.1 and 9.5 Hz, 2 H), 3.19 (m), 2.89 (t, J = 7.9 Hz, 1 H), 2.75 (t, J = 7.6 Hz), 2.44 (m), 2.33 (m, 1 H), 1.98 (m, 1 H), 1.81 (m, 2 H), 1.62 (dddd, J = 5.5, 5.6, and 5.6 Hz, 1 H), 1.23 (t, J = 7.1 Hz), 1.22 (t, J = 7.1 Hz, 6 H), 1.20 (t, J = 7.0 Hz); ^{13}C NMR ($CDCl_3$): 15.0, 15.1, 29.1, 29.6, 29.8, 44.1, 44.6, 46.4, 48.1, 48.6, 48.8, 60.9, 61.21, 61.5, 63.1, 64.0, 64.1, 64.4, 64.5, 80.2, 80.6, 81.28, 95.36, 97.09, 97.54, 97.64, 97.77, 101.36, 129.6, 130.5, 131.4, 146.5, 147.0, 147.2; MS (CI): 230 (16, M − C_2H_4), 167 (32), 184 (100), 195 (38), 213 (16).

Compound ***6*** (anomeric mixture). ^{1}H NMR ($CDCl_3$): 1.20 (t, J = 7.0 Hz, 3 H), 1.63 (dddd, J = 5.4, 5.6, 5.8, and 5.2 Hz), 1.8–2.0 (m, 2 H), 2.07 (s), 2.08 (s), 2.09 (s, 3 H), 2.29–2.41 (m, 1 H), 2.75 (t, J = 6.4 Hz), 2.81 (t, J = 7.7 Hz, 1 H), 3.09–3.10 (m), 3.25–3.20 (m), 3.43–3.53 (m, 2 H), 3.77–3.92 (m, 2 H), 4.40 (d, J = 6.1 Hz), 4.58 (d, J = 7.7 Hz), 4.65 (bs, 2 H), 4.67 (bs, 1 H), 4.99–4.93 (m, 2 H), 5.73 (s), 5.79 (s, 1 H); ^{13}C NMR ($CDCl_3$): 15.1, 20.8, 29.4, 29.5, 31.1, 42.0, 43.8, 44.6, 45.6, 47.9, 48.0, 48.3, 48.64, 62.1, 62.8, 63.1, 63.8, 64.0, 64.5, 80.2, 80.4, 81.8, 82.5, 95.6, 96.3, 97.2, 97.6, 100.8, 129.9, 130.5, 131.2, 132.3, 141.1, 142.5, 142.8, 170.6, 170.7.

Compound ***7*** (anomeric mixture). ^{1}H NMR ($CDCl_3$): 1.20 (t, J = 7.1 Hz, 3 H), 1.25 (t, J = 7.2 Hz, 3 H), 1.50 (dddd, J = 7.1, 2.9, 2.9, and 7.1 Hz, 1 H), 1.85–1.76 (m, 1 H), 2.01 (s, 3 H), 2.02 (s), 2.04 (s), 2.16–2.07 (m), 2.66–2.40 (m), 2.85 (t, J = 7.0 Hz), 2.99 (t, J = 8.0 Hz, 1 H), 3.23 (m), 3.57–3.46 (m, 2 H), 3.95–3.80 (m, 2 H), 4.22 (bs, 2 H), 4.44 (d, J = 6.8 Hz), 4.67 (d, J = 8.0 Hz, 1 H), 4.97 (m, 1 H), 5.34 (bs, 1 H), 5.49 (m), 5.59 (m), 5.72 (s), 5.75 (s, 1 H); ^{13}C NMR ($CDCl_3$): 15.0, 15.1, 21.2, 29.2, 29.9, 30.6, 39.5, 40.4, 41.6, 48.1, 48.3, 49.2, 54.9, 60.7, 61.1, 61.3, 63.1, 63.3, 63.8, 64.0, 64.3, 64.5, 82.5, 83.2, 83.6, 84.1, 95.2, 97.0, 97.3, 100.8, 124.8, 125.2, 126.4, 127.2, 148.9, 149.3, 149.9, 150.3, 171.0, 171.2.

Compound ***9***

mCPBA (0.18 g, 1.03 mmol) was added to a dichloromethane solution of **8** (0.13 g, 0.519 mmol). After 1 h at ambient temperature, an additional portion of mCPBA was added to the reaction mixture and stirring was maintained for 1 h at room temperature. Saturated aqueous sodium bicarbonate was added and the mixture was stirred for 30 min. The mixture was evaporated under vacuum and the material was then subjected to flash column chromatography, using hexane and ethyl acetate (1:3) as the solvent system to give **9** (anomeric mixture) as a colorless oil (0.082 g) in 58% yield. FTIR ($CDCl_3$): 3588, 2979, 2932, 2264, 1440, 1381, 1343, 1118, 1074, 1031, 970; ^{1}H NMR ($CDCl_3$): 4.99 (d, J = 3.9 Hz, 1 H), 4.96 (d, J = 3.2 Hz), 4.81 (dd, J = 2.7 and 7.0 Hz), 4.73 (dd, J = 3.5 and 9.0 Hz), 4.59 (d, J = 9.2 Hz, 1 H), 4.45 (dd, J = 8.5 and 1.0 Hz, 1 H), 4.13 (dd, J = 1.0 and 7.5 Hz), 4.04 (d, J = 13.4 Hz, 1 H), 4.00 (dd, J = 7.1 and 9.3 Hz), 3.95 (d, J = 12.6 Hz, 1 H), 3.82 (dq, J = 7.1 and 9.3 Hz, 1 H), 3.70 (dq, J = 7.1 and 9.6 Hz, 1 H), 3.68 (d, J = 12.5 Hz), 3.51 (d, J = 1.2 Hz), 3.47 (dq, J = 7.1 and 9.5 Hz, 1 H), 3.468 (d, J = 1.5 Hz, 1 H), 3.46 (dq, J = 7.1 and 9.5 Hz, 1 H), 2.69 (dd, J = 4.2 and 7.4 Hz, 1 H), 2.60 (dd, J = 3.3 and 8.5 Hz), 2.36 (dd, J = 7.0 and 9.0 Hz, 1 H), 1.97 (m, 3 H), 1.86 (m, 1 H), 1.27 (t, J = 7.1 Hz), 1.20 (t, J = 7.1 Hz, 3 H), 1.20 (t, J = 7.0 Hz), 1.18 (t, J = 7.0 Hz, 3 H); ^{13}C NMR ($CDCl_3$): 98.2, 96.3, 93.8, 93.5, 77.1, 75.1, 72.2, 69.5, 66.4, 65.4, 64.5, 63.7, 63.2, 63.1, 62.7, 61.0, 60.6, 60.4, 53.7, 41.5, 40.1, 36.3, 36.2, 31.6, 29.1, 28.7, 26.3, 15.1, 15.0; MS (CI): 292 (10, M + NH_4^+), 229 (60), 246 (72), 279 (100).

Compound ***10***

4,4′-Dimethoxytrityl chloride (0.080 g, 0.23 mmol) was added to a solution of **9** (0.043 g, 0.15 mmol) in dichloromethane (3 mL). Excess triethylamine (0.15 mL) was added to the reaction mixture, which was then stirred overnight at room temperature. Toluene was added and the mixture was evaporated to dryness under reduced pressure. The material was then redissolved in ethyl acetate, washed with brine, dried with magnesium sulfate, filtered, and evaporated under reduced pressure. The product was then subjected to flash column chromatography using hexane – ethyl acetate in a ratio of 2:1, respectively, to give **10** (anomeric mixture) as a colorless oil (68.3 mg) in 75% yield. FTIR ($CDCl_3$): 3595, 2976, 2933, 2840, 2362, 2252, 1703, 1608, 1580, 1463, 1382, 1343, 1300, 1151, 1006, 974, 938, 898; ^{1}H NMR ($CDCl_3$): 0.81 (t, J = 7.1 Hz), 0.88 (t, J = 7.1 Hz), 1.17 (t, J = 7.1 Hz, 3 H), 1.21 (t, J = 7.1 Hz, 3 H), 1.22 (t, J = 7.1 Hz), 1.28 (t, J = 7.1 Hz), 1.72 (m, 1 H), 1.84 (m, 1 H), 1.95 (m, 1 H), 2.22 (t, J = 8.4 Hz, 1 H), 2.37 (dd, J = 7.5 and 9.2 Hz), 2.80 (m), 2.93 (m), 3.15 (d, J = 10.7 Hz), 3.25 (d, J = 11.8 Hz, 1 H), 3.32 (d, J = 7.5 Hz), 3.46 (m, 2 H), 3.63 (d, J = 11.5 Hz, 1 H), 3.69 (m, 2 H), 3.78 (s, 6 H), 3.79 (s), 3.82 (s), 3.85 (s, 1 H), 4.01 (m), 4.34 (d, J = 8.8 Hz, 1 H), 4.47 (bs, 1 H), 4.60 (d, J = 9.2 Hz), 4.68 (d, J = 4.1 Hz), 4.74 (dd, J = 2.3 and 7.8 Hz), 4.93 (d, J = 3.6 Hz, 1 H), 5.00 (d, J = 3.7 Hz), 6.83 (d, J = 8.9 Hz, 4H), 7.31 (m, 9H); ^{13}C NMR ($CDCl_3$): 158.5, 158.5, 144.9, 144.5, 136.24, 136.0, 136.0, 135.6, 130.1, 130.0, 128.2, 128.1, 127.8, 127.8, 126.8, 126.7, 113.2, 113.1, 113.1, 97.9, 96.9, 93.8, 93.2, 85.9, 85.7, 76.8, 75.6, 69.5, 65.1, 65.0, 63.9, 63.2, 62.6, 62.3, 62.1, 61.2, 60.4, 55.2, 53.8, 42.6, 40.1, 37.0, 36.6, 31.7, 29.3, 28.87, 26.6, 15.3, 15.1, 14.9, 14.8, 14.74; MS, FAB (glycerol) calcd. for $C_{34}H_{41}O_8$: 577.2801; found: 577.2804.

p-*Benzyloxybenzoyl chloride (****11****)*

To a stirred mixture of 4-benzyloxybenzaldehyde (1.14 g, 5.3 mmol) and magnesium sulfate (1.14 g) in acetone (30 mL) was added potassium permanganate (1.08 g, 2.1 mmol) over 2 h. The mixture was stirred at room temperature for an additional 30 min. The solvent was evaporated under reduced pressure and the solid residue was treated with 3 × 50 mL of hot water and filtered. The cold aqueous solution was washed with chloroform, then acidified with hydrochloric acid and extracted with chloroform. The organic layer was dried over magnesium sulfate, filtered, and evaporated under reduced pressure, to give 1.06 g of *p*-benzyloxybenzoic acid as white solid material, 88% yield, mp 167–168°C. FTIR ($CHCl_3$): 3073, 1690, 1605, 1254, 1240, 1168. MS (CI): 246(100, M + NH_4^+), 229(90, MH^+), 228(48, M + NH_4^+ − H_2O), 211(48). To a cold solution (0°C) of *p*-benzyloxybenzoic acid (0.13 g, 0.58 mmol) and oxalyl chloride (0.065 mL, 0.75 mmol) in dichloromethane (10 mL), a few drops of DMF were added and the solution was stirred for 2 h. The reaction mixture was evaporated under reduced pressure to give **11** (0.158 g) as white solid, mp 166–167°C (98% yield). FTIR ($CHCl_3$): 2263, 2240, 2226, 1771, 1739, 1601, 1262, 1210, 1165, 941. ^{1}H NMR ($CDCl_3$): 5.15 (s, 2 H), 7.03 (d, J = 9.0 Hz, 2 H), 7.40 (m, 5H), 8.08 (d, J = 9.0 Hz, 2 H); MS (CI): 248(19), 246(58, M + NH_4^+), 211(100).

Compound ***12***

To a solution of **10** (10 mg, 0.017 mmol) in dichoromethane (3 mL) was added triethylamine (0.009 mL, 0.068 mmol) and *p*-benzyloxybenzoyl chloride (**11**, 0.008 g, 0.034 mmol). After 48 h stirring at room temperature, a further equal amount of triethylamine and the acid chloride was added and the mixture was stirred for 24 h. A few drops of ethanol were then added and the mixture was diluted with diethyl ether, washed with saturated aqueous sodium bicarbonate and brine, dried with magnesium sulfate, filtered, and evaporated under reduced pressure. The product **12** (7.1 mg, 0.014 mmol) was then dissolved in ethanol (0.11 mL) and cyclohexene (0.057 mL), 20% palladium hydroxide on carbon (0.7 mg, 1:10 catalyst:substrate by weight) was added, and the suspension was stirred under reflux for 2 h. The catalyst was removed by filtration and the filtrate was evaporated to dryness. The resulting material was then subjected to flash column chromatography using hexane – ethyl acetate (4:1) as the eluent to give **12** (anomeric mixture) as an oil in 60% yield. ^{1}H NMR ($CDCl_3$): 7.96 (d, J = 8.5 Hz, 2 H), 7.93 (d, J = 9.0 Hz, 2 H), 6.85 (d, J = 8.5 Hz, 2 H), 6.83 (d, J = 9.0 Hz, 2 H), 5.84 (bs, 2 H), 5.65 (d, J = 9.0 Hz, 1 H), 5.02 (d, J = 4.0 Hz, 1 H), 4.77 (d, J = 9.0 Hz, 1 H), 4.76 (d, J = 12.5 Hz, 1 H), 4.44 (d, J = 12.5 Hz, 1 H), 4.00–3.94 (dq, J = 7.0 and 9.0 Hz, 1 H), 3.88 (s, 1 H), 3.77–3.72 (dq, J = 7.0 and 9.0 Hz, 1 H), 3.55–3.45 (m, 2 H), 2.52 (d, J = 9.0 Hz, 1 H), 2.47 (dt, J = 7.0 Hz, 1 H), 1.88–1.78 (m, 2 H), 1.24 (t, J = 7.0 Hz, 3 H), 1.19 (t, J = 7.0 Hz, 3 H); ^{13}C NMR ($CDCl_3$): 15.01, 15.03, 26.5, 32.9, 41.6, 58.7, 62.1, 63.3, 64.6, 77.4, 93.7, 97.9, 115.2, 115.3, 122.30, 122.32, 132.0, 132.2, 160.0, 160.1, 165.8, 166.5.

Can. J. Chem. Downloaded from www.nrcresearchpress.com by 85.192.166.187 on 09/08/12
For personal use only.

Compounds 13 and 14

To a solution of **10** (84 mg, 0.146 mmol) in dichloromethane (10 mL) was added triethylamine (0.082 mL, 0.58 mmol) and *p*-benzyloxybenzoyl chloride (0.072 g, 0.29 mmol). The mixture was stirred for 24 h. A few drops of ethanol were then added, the mixture was diluted with diethyl ether and washed with saturated aqueous sodium bicarbonate and brine, dried with magnesium sulfate, filtered, and evaporated under reduced pressure. The residue was then subjected to flash column chromatography using hexane – ethyl acetate (40:1) as eluent to give separately compounds **13** and **14** in a ratio of 3:1 in a combined yield of 55% (0.031 g).

Compound 13. ^{1}H NMR ($CDCl_3$): 8.01 (d, J = 9.0 Hz, 2 H), 7.41 (m, 5H), 6.99 (d, J = 9.0 Hz, 2 H), 5.57 (dd, J = 8.9 and 1.2 Hz, 1 H), 5.12 (s, 2 H), 5.01 (dd, J = 3.8 and 1.6 Hz, 1 H), 4.73 (d, J = 8.7 Hz, 1 H), 4.10 (d, J = 13.4 Hz, 1 H), 4.05 (dq, J = 7.1 and 9.3 Hz, 1 H), 3.77 (d, J = 1.2 Hz, 1 H), 3.74 (dq, J = 7.1 and 9.8 Hz, 1 H), 3.62 (d, J = 13.4 Hz, 1 H), 3.55 (dq, J = 7.1 and 9.3 Hz, 1 H), 3.48 (dq, J = 7.1 and 9.7 Hz, 1 H), 2.45 (m, 2 H), 1.82 (m, 2 H), 1.62 (bs, 1 H), 1.390 (t, J = 7.1 Hz, 3 H), 1.23 (t, J = 7.1 Hz, 3 H).

Compound 14. ^{1}H NMR ($CDCl_3$): 1.22 (t, J = 7.1 Hz, 3 H), 1.23 (t, J = 7.1 Hz, 3 H), 1.80 (m, 1 H), 2.0 (m, 1 H), 2.43 (d, J = 8.0 Hz, 1 H), 2.77 (dd, J = 8.5 and 3.9 Hz, 1 H), 3.46 (m, 1 H), 3.49 (m, 1 H), 3.70 (d, J = 1.3 Hz, 1 H), 3.74 (d, J = 12.3 Hz, 1 H), 3.82 (m, 1 H), 3.85 (m, 1 H), 3.98 (d, J = 12.3 Hz, 1 H), 4.71 (d, J = 9.2 Hz), 4.86 (dd, J = 2.6 and 6.5 Hz, 1 H), 4.94 (d, J = 4.6 Hz), 4.99 (d, J = 1.9 Hz), 5.03 (d, J = 3.9 Hz, 1 H), 5.11 (s, 2 H), 5.24 (m), 5.34 (dd, J = 1.3 and 7.9 Hz, 1 H), 5.55 (dd, J = 1.3 and 9.1 Hz), 6.97 (d, J = 9.2 Hz, 2 H), 7.40 (m, 5 H), 8.00 (d, J = 9.2 Hz, 2 H).

Compound 15

A mixture of **13** (7.0 mg; 0.014 mmol) and 10% palladium on carbon (5 mg) in ethanol (2 mL) was stirred under a hydrogen atmosphere for 3 h. The mixture was diluted with ethyl acetate, and filtered through Celite. The product was then subjected to flash column chromatography using ethyl acetate and hexane (4:6) as eluent to give **15** as a colorless oil (4.3 mg) in 78% yield. ^{1}H NMR ($CDCl_3$): 7.98 (d, J = 9.0 Hz, 2 H), 6.85 (d, J = 9.0 Hz, 2 H), 5.58 (dd, J = 1.0 and 8.7 Hz, 1 H), 5.30 (b, 1 H), 5.02 (dd, J = 1.5 and 4.5 Hz, 1 H), 4.73 (d, J = 8.5 Hz, 1 H), 4.10 (dd, J = 3.2 and 13.5 Hz, 1 H), 4.05 (dq, J = 7.0 and 9.0 Hz, 1 H), 3.78 (d, J = 1.0 Hz, 1 H), 3.74 (dq, J = 7.0 and 9.5 Hz, 1 H), 3.62 (dd, J = 11.0 and 13.5 Hz, 1 H), 3.55 (dq, J = 7.0 and 9.0 Hz, 1 H), 3.48 (dq, J = 7.0 and 9.5 Hz, 1 H), 2.52 (dd, J = 3.5 and 11.5 Hz, 1 H), 2.48–2.41 (m, 2 H), 1.85 (ddd, J = 3.5, 5.5, and 14.5 Hz, 1 H), 1.82 (dt, J = 1.5 and 14.5 Hz, 1 H), 1.30 (t, J = 7.0 Hz, 3 H), 1.23 (t, J = 7.0 Hz, 3 H); ^{13}H NMR ($CDCl_3$): 14.8, 14.9, 26.3, 32.6, 40.7, 58.0, 61.2, 63.2, 64.6, 65.2, 77.1, 93.6, 97.8, 115.0, 121.3, 132.0, 160.1, 166.1.

Specionin (1)

A mixture of **14** (3.0 mg, 0.006 mmol) and 10% palladium on carbon (2 mg) in ethanol (2 mL) was stirred under a hydrogen atmosphere for 3 h. The mixture was diluted with ethyl acetate, and filtered through Celite. The material was then subjected to flash column chromatography using ethyl acetate and hexane (4:6) as eluent to give **1** as a colorless oil (1.8 mg) in 79% yield. ^{1}H NMR ($CDCl_3$): 7.98 (d, J = 9.0 Hz, 2 H), 6.86 (d, J = 9.0 Hz, 2 H), 5.36 (dd, J = 8.5 and 1.5 Hz, 1 H), 5.06 (d, J = 4.0 Hz, 1 H), 4.88 (dd, J = 7.0 and 2.5 Hz, 1 H), 3.99 (d, J = 12.5 Hz, 1 H), 3.83 (m, 2 H), 3.77 (s, 1 H), 3.75 (d, J = 1.5 Hz, 1 H), 3.72 (d, J = 12.5 Hz, 1 H), 3.48 (m, 2 H), 2.78 (dd, J = 4.0 and 8.0 Hz, 1 H), 2.42 (m, J = 5.3, 8.0, and 8.5 Hz, 1 H), 1.99 (ddd, J = 2.5, 5.3, and 13.8 Hz, 1 H), 1.83 (dt, J = 7.0 and 13.8 Hz, 1 H), 1.24 (t, J = 7.0 Hz, 3 H), 1.20 (t, J = 7.0 Hz, 3 H).

Acknowledgement

Financial support from the Natural Sciences and Engineering Research Council of Canada (NSERC) and "le Fonds pour la formation de chercheurs et l'aide à la recherche (Québec)" (FCAR) is gratefully acknowledged.

1. D.M. Schmitt, D.G. Grimble, and J.L. Searcy. Managing the spruce budworm in eastern North America. USDA Agriculture Handbook 620. 1984.
2. T.H. Chan, Y.J. Zhang, F. Saurial, A.W. Thomas, and G.M. Strunz. Can. J. Chem. **65**, 1853 (1987).
3. T.H. Chan, K.R. Guertin, C.V.C. Prasad, A.W. Thomas, G.M. Strunz, and A. Salonius. Can. J. Chem. **68**, 1170 (1990).
4. A.E. Schwerdtfeger, T.H. Chan, A.W. Thomas, G.M. Strunz, A. Salonius, and M. Chiasson. Can. J. Chem. **71**, 1184 (1993).
5. K. Munakata. *In* Control of insect behaviour by natural products. *Edited by* D.L. Wood, R.M. Silverstein, and M. Nakajima. Academic Press, New York. 1970.
6. H.B. Broughton, S.V. Ley, A.M.A. Alawin, D.J. Williams, and E.D. Morgan. J. Chem. Soc. Chem. Commun. 46 (1986); D.H.R. Barton, H.T. Cheung, A.D. Cross, L.M. Jackman, and M. Martin-Smith. J. Chem. Soc. 5061 (1961); M.J. Begley, L. Cromie, P.J. Ham, and D.A. Whiting. J. Chem. Soc. Perkin Trans. 1, **296**, 304 (1976).
7. C.C. Chang and K. Nakanishi. J. Chem. Soc. Chem. Commun. 605 (1983).
8. E. Van der Eycken, J. Van der Eycken, and M. Vandewalle. J. Chem. Soc. Chem. Commun. 1719 (1985); E. Van der Eycken, A. DeBruyn, J. Van der Eycken, P. Callant, and M. Vandewalle. Tetrahedron, **42**, 5385 (1986); E. Van der Eycken, A. Janssens, and M. Vandewalle. Tetrahedron Lett. **28**, 3519 (1987).
9. (*a*) N. Hussain and J. Leonard. Tetrahedron Lett. **28**, 4871 (1987); (*b*) J. Leonard and N. Hussain. J. Chem. Soc. Perkin Trans. 1, 61 (1994).
10. J.K. Whitesell and D.E. Allen. J. Am. Chem. Soc. **110**, 3585 (1988).
11. D.P. Curran, P.B. Jacobs, R.L. Elliott, and B.H. Kim. J. Am. Chem. Soc. **109**, 5280 (1987); B.H. Kim, P.B. Jacobs, R.L. Elliott, and D.P. Curran. Tetrahedron, **44**, 3079 (1988).
12. A.W. Thomas, G.M. Strunz, M. Chiasson, and T.H. Chan. Entomol. Exp. Appl. **62**, 37 (1992).
13. G. Buchi, B. Gulder, R.S. Schneider, and I. Wilde. J. Am. Chem. Soc. **89**, 2776 (1967).
14. G. Buchi, J.A. Carlson, J.E. Powell, Jr., and L.F. Tietze. J. Am. Chem. Soc. **92**, 2165 (1970).
15. (*a*) W.F. Berkowitz, I. Sasson, P.S. Sampathkuman, J. Hrabie, S. Chondhry, and D. Pierce. Tetrahedron Lett. 1641 (1979); (*b*) W.H. Lunn, D.W. Edward, and J.T. Edward. Can. J. Chem. **40**, 104 (1962).
16. M. Maruto, K. Ohno, N. Naruse, and H. Takeuchi. Tetrahedron Lett. 251 (1979).
17. V. Bolitt, C. Mioskowski, S.G. Lee, and J.R. Falck. J. Org. Chem. **55**, 5812 (1990).
18. G.M. Strunz, P. Giguere, and A.W. Thomas. J. Chem. Ecol. **12**, 251 (1986); L.M. Schoonhoven. Entomol. Exp. Appl. **31**, 57 (1982).
19. A. McMorran. Can. Entomol. **97**, 58 (1965).
20. J.C. Anderson and S.V. Ley. Tetrahedron Lett. **31**, 431 (1990); S.V. Ley, A.A. Denholm, and A. Wood. Nat. Prod. Rep. **10**, 109 (1993).

Crystal chemistry of tetraradial species. Part 6. *Embarras de richesses*: lithium cation coordinated by eight O—H...phenyl bonds[1]

PRADIP K. BAKSHI,[2] SERGEY V. SEREDA, AND OSVALD KNOP[3]
Department of Chemistry, Dalhousie University, Halifax, NS B3H 4J3, Canada

AND

MICHAEL FALK
Institute for Marine Biosciences, National Research Council of Canada,[4] Halifax, NS B3H 3Z1, Canada

Received May 10, 1994

This paper is dedicated to Professor David B. MacLean

PRADIP K. BAKSHI, SERGEY V. SEREDA, OSVALD KNOP, and MICHAEL FALK. Can. J. Chem. **72**, 2144 (1994).

Lithium tetraphenylborate tetrahydrate, $[Li(OH_2)_4]BPh_4$ (LiTBw; tetragonal, $I4_1/a$, $a = 27.566(2)$ Å, $c = 12.228(2)$ Å, $Z = 16$) is remarkable in that the four H_2O molecules coordinating the Li^+ ion all form O—H...π hydrogen bonds to the phenyl groups of the anion. LiTBw thus appears to be the first reported example of such an exhaustive O—H...π coordination and can be described as a 3-dimensional, completely H-bonded polymer in which all the H_2O hydrogens are bonded to phenyl groups and all the phenyl groups are involved in O—H...phenyl bonds. Six of the O—H...phenyl bonds are essentially normal and two are highly bent, possibly bifurcated. The existence of the H-bonds has been corroborated from variable-temperature FT-ir spectra of weakly deuterated LiTBw. The O—Li—O angles in the LiO_4 coordination tetrahedron (of symmetry C_1) exhibit large departures from the tetrahedral angle, two of the angles bisected by a quasi-S_4 axis being 118.3° and 122.5°, respectively. An *ab initio* (6-31G*) investigation of the $Li(OH_2)_4^+$ and $Be(OH_2)_4^{2+}$ cations has shown that such large O—M—O angles are to be expected even in the free ions and are thus not necessarily the result of packing effects. A detailed comparison with several $Li(OH_2)_4^+$ and $Be(OH_2)_4^{2+}$ salts provides a rationale for the observed $M(OH_2)_4^{n+}$ (M = Li, Be) geometries.

PRADIP K. BAKSHI, SERGEY V. SEREDA, OSVALD KNOP et MICHAEL FALK. Can. J. Chem. **72**, 2144 (1994).

Le tétrahydrate du tétraphénylborate de lithium, $[Li(OH_2)_4]BPh_4$ (LiTBw; tétragonal, $I4_1/a$, $a = 27,566(2)$ et $c = 12,228(2)$ Å et $Z = 16$) est remarquable par le fait que les quatre molécules d'eau qui se coordonnent à l'ion Li^+ forment toutes des liaisons hydrogène O—H...π avec les groupes phényles de l'anion. Le LiTBw semble donc être le premier exemple à avoir été rapporté d'une coordination O—H...π aussi extensive; on peut le décrire comme un polymère tridimensionnel à liaisons hydrogène dans lequel toutes les molécules d'eau sont liées aux groupes phényles et tous les groupes phényles sont impliqués dans des liaisons O—H...phényle. Six des liaisons O—H...phényle sont essentiellement normales et deux sont fortement recoudées et possiblement bifurquées. L'existence de liaisons hydrogène a été corroboré par des spectres FT-ir à température variable de LiTBw faiblement deutéré. Les angles O—Li—O du tétraèdre de coordination du LiO_4 (de symétrie C_1) présentent des différences importantes par rapport aux angles tétraédriques; deux de ces angles sont bissectés par un axe quasi-S_4 de respectivement 118,3 et 122,5°. Une étude *ab initio* (6-31G*) des cations $Li(OH_2)_4^+$ et $Be(OH_2)_4^{2+}$ montre que l'on peut s'attendre à de tels grands angles O—M—O même dans les ions libres et qu'ils ne résultent pas nécessairement d'un effet d'empilement. Une comparaison détaillée des plusieurs sels $Li(OH_2)_4^+$ et $Be(OH_2)_4^{2+}$ fournit une explication pour les géométries observées pour le $M(OH_2)_4^{n+}$ (M = Li, Be).

[Traduit par la rédaction]

The study and demonstration of hydrogen bonding to aromatic π systems in crystals is a relatively new field of enquiry (for a brief historical review see ref. 2). Reported examples of such bonding have been so sporadic and uncommon that even simple situations involving one or two X—H...π(aromatic) bonds have received prominent exposure (3–6). The crystal-structure determination of the hitherto unreported lithium tetraphenylborate tetrahydrate, $[Li(OH_2)_4]BPh_4$ (LiTBw for short), has now shown that the X—H...π bonding can be much more extensive: in this crystal the Li^+ cation is completely coordinated by *eight* O—H...phenyl bonds, and all the phenyl groups are H-bonded. LiTBw is thus the first example of such maximum O—H...π engagement.

The crystallography of LiTBw (see below) has been supplemented by examination of the ir spectrum of the isotopically decoupled water molecules in this crystal between 10 K and room temperature, and by an *ab initio* treatment of the free $Li(OH_2)_4^+$ cation. The Li—$4H_2O$ coordination in LiTBw is also compared with that in $[Li(OH_2)_4](UO_2)AsO_4$ (= LiUAw) (7) and also with its nearest formal analog, Be—$4H_2O$, in $[Be(OH_2)_4]SO_4$ (= BeSw) (8, 9) and $[Be(OH_2)_4](NO_3)_2$ (= BeNw) (10).

Crystal structure

The crystal data of LiTBw are listed in Experimental. The atom positions and the interatomic distances and bond angles are given in Tables 1 and 2. The positions and isotropic temperature factors of the hydrogens (Table A), the anisotropic thermal parameters of the nonhydrogen atoms (Table B), and the deviations of the C and B atoms from the best planes through the phenyl-ring skeletons (Table C) have been deposited.[5]

LiTBw has a large centrosymmetric tetragonal unit cell: $a = 27.566(2)$ Å, $c = 12.228(2)$ Å, $Z = 16$. Systematic absences detected by the data reduction procedure were consistent with space group symmetry $I4_1/a$. However, the positional parame-

[1]For Part 5, see ref. 1.

[2]Holder of a graduate scholarship, Canadian Commonwealth Scholarship and Fellowship Plan, and of a Killam Graduate Scholarship.

[3]To whom correspondence may be addressed (tel. (902) 494-3317 or 494-3305, facsimile (902) 494-1310).

[4]NRCC No. 38053.

[5]This material may be purchased from the Depository of Unpublished Data, Document Delivery, CISTI, National Research Council of Canada, Ottawa, ON K1A 0S2, Canada.

Can. J. Chem. Downloaded from www.nrcresearchpress.com by 85.192.166.187 on 09/08/12
For personal use only.

TABLE 1. Positional parameters ($\times 10^4$) of nonhydrogen atoms in LiTBw[a]

Atom	x	y	z	Atom	x	y	z
B	6140(3)	4000(3)	1284(9)	C(33)	7294(3)	3737(3)	3137(7)
C(11)	6178(3)	3524(3)	0474(5)	C(34)	7354(3)	4172(3)	3680(7)
C(12)	6603(3)	3440(3)	−0127(6)	C(35)	7052(3)	4555(3)	3442(6)
C(13)	6653(3)	3058(3)	−0870(7)	C(36)	6683(3)	4497(3)	2662(6)
C(14)	6261(4)	2748(3)	−1060(7)	C(41)	5667(2)	3969(3)	2123(5)
C(15)	5831(3)	2829(3)	−0512(7)	C(42)	5411(3)	4388(3)	2460(6)
C(16)	5791(3)	3214(3)	0226(6)	C(43)	5021(3)	4363(3)	3183(7)
C(21)	6085(3)	4461(3)	0438(5)	C(44)	4873(3)	3927(4)	3621(7)
C(22)	6482(3)	4721(3)	0060(7)	C(45)	5130(3)	3513(3)	3362(7)
C(23)	6446(3)	5078(3)	−0751(7)	C(46)	5521(3)	3536(3)	2631(6)
C(24)	6001(3)	5186(3)	−1209(7)	Li	1311(5)	1598(5)	3750(10)
C(25)	5599(3)	4935(3)	−0856(6)	O(1)	1546(2)	1328(2)	5119(5)
C(26)	5644(2)	4584(3)	−0056(6)	O(2)	1475(2)	1324(2)	2355(5)
C(31)	6608(3)	4064(3)	2098(5)	O(3)	0616(2)	1546(3)	3865(5)
C(32)	6929(3)	3680(3)	2355(7)	O(4)	1595(3)	2242(2)	3677(5)

[a]Space group $I4_1/a$, origin choice 2.

TABLE 2. Interatomic distances (Å) and bond angles (deg) in LiTBw[a]

	Distance		Angle
Atoms	Uncorr./Corr.	Atoms	Uncorr./Corr.
B—C(11)	1.647(11)	C(11)—B—C(21)	104.1(7)
B—C(21)	1.647(11)	C(31)—B—C(41)	104.4(7)
B—C(31)	1.640(11)	**Mean**	**104.3(2)**
B—C(41)	1.661(11)	C(11)—B—C(31)	113.8(6)
Mean	**1.649(8)**	C(11)—B—C(41)	112.4(6)
Li—O(1)	1.938(15)/1.960	C(21)—B—C(31)	111.5(6)
Li—O(2)	1.924(15)/1.941	C(21)—B—C(41)	110.9(6)
Li—O(3)	1.928(16)/1.962	**Mean**	**112.2(11)**
Li—O(4)	1.941(16)/1.976	C(12)—C(11)–C(16)	115.0(7)
Mean	**1.933(7)/1.960(12)**	C(22)—C(21)—C(26)	114.9(7)
O(1)...O(2)	3.386(8)	C(32)—C(31)—C(36)	115.9(7)
O(3)...O(4)	3.321(10)	C(42)—C(41)—C(46)	114.8(7)
Mean	**3.354(33)**	**Mean**	**115.2(4)**
O(1)...O(3)	3.047(9)	O(1)—Li—O(2)	122.5(8)/121.9
O(1)...O(4)	3.078(9)	O(3)—Li—O(4)	118.3(8)/118.1
O(2)...O(3)	3.064(9)	**Mean**	**120.4(21)/120.0(19)**
O(2)...O(4)	3.020(9)	O(1)—Li—O(3)	104.0(8)/104.4
Mean	**3.052(22)**	O(1)—Li—O(4)	105.0(8)/105.0
O(1)...π_c(2b)	3.27	O(2)—Li—O(3)	105.4(8)/105.3
O(1)...π_c(1b)	3.57	O(2)—Li—O(4)	102.8(7)/103.1
O(2)...π_c(3a)	3.30	**Mean**	**104.3(10)/104.5(8)**
O(2)...π_c(4a)	3.46	π_c(1b)...O(1)...π_c(2b)	86
O(3)...π_c(4c)	3.53	π_c(3a)...O(2)...π_c(4a)	90
O(3)...π_c(1b)	4.13	π_c(1b)...O(3)...π_c(4c)	123
O(4)...π_c(1d)	3.34	π_c(1c)...O(3)...π_c(4c)	67
O(4)...π_c(4a)	4.03	π_c(1d)...O(4)...π_c(4a)	125
		π_c(1d)...O(4)...π_c(4d)	56

Symmetry code: a $-1/4 + y$, $3/4 - x$, $-1/4 + z$
b $-1/4 + y$, $3/4 - x$, $3/4 + z$
c $1/2 - x$, $1/2 - y$, $1/2 - z$
d $-1/2 + x$, y, $1/2 - z$

[a]The numbers in parentheses quoted with the means are standard deviations of the sample means; they do not include the esd's of the component values. The corrected distances and angles are from a TLS analysis of the cation (see text).

ters z(B) and z(Li) turned out to be remarkably close to multiples of 1/8, and even the corresponding x and y values were not far from multiples of 1/8. Since fractional atom coordinates equal to $n/8$ are characteristic of tetragonal subgroups of the cubic space groups $Fd\bar{3}m$, $Fd\bar{3}c$, and $Ia\bar{3}d$, the indices of the observed reflections were carefully examined for possible consistency with the maximal subgroups of these cubic groups, $I4_1/amd \subset Fd\bar{3}m$ and $I4_1/acd \subset Fd\bar{3}c$, $Ia\bar{3}d$, both of which contain $I4_1/a$ as a maximal subgroup of index two. The examination, however, confirmed the $I4_1/a$ symmetry assignment. A signifi-

Can. J. Chem. Downloaded from www.nrcresearchpress.com by 85.192.166.187 on 09/08/12
For personal use only.

Can. J. Chem. Downloaded from www.nrcresearchpress.com by 85.192.166.187 on 09/08/12
For personal use only.

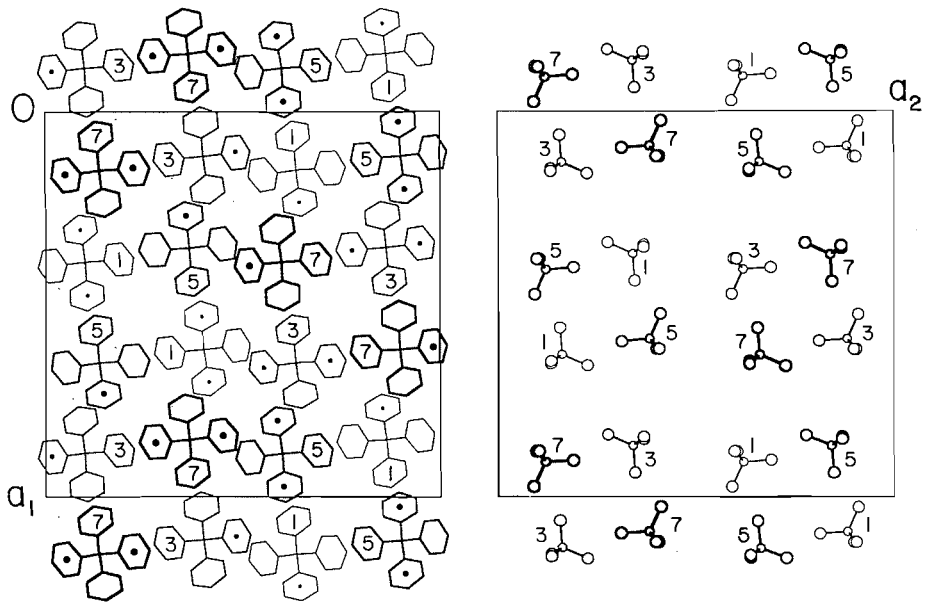

FIG. 1. Projection of the LiTBw unit cell on (001) (origin at centre of symmetry). (*Left*) Packing of anions. The number n identifies ring 1 (cf. Table 1) and indicates the approximate z(B) expressed as $n/8$. Phenyl rings pointing upward from the page are marked with a dot. (*Right*) A matching projection of the cation packing. The number n indicates the approximate z(Li) = $n/8$ fractional coordinate.

cant number of large F_o's had indices incompatible with either of the two space groups, and the corresponding $R_{merg} \sim 60\%$ values calculated for the latter were clearly unacceptable. The departures of the B and Li positions from multiples of 1/8 are therefore genuine and the ion packing in LiTBw may thus be regarded as the result of a frustrated though nearly successful attempt to achieve a higher symmetry.

Each Li atom is tetrahedrally coordinated by four water molecules. The geometry of the LiO_4 coordination tetrahedron approximates D_{2d} symmetry, with the quasi-S_4 axis almost parallel to [$\bar{3}$40] for the Li position listed in Table 1. The mean Li—O distance uncorrected for thermal motion, 1.933(7) Å (Table 2), is comparable to the corresponding uncorrected distance in the LiO_4 tetrahedron of LiUAw, 1.955(4) Å, and to the uncorrected mean Li^{iv}—O distance in $LiB(OH)_4$ (11), 1.967(35) Å.

The O—Li—O angles α bisected by the quasi-S_4 axis of the LiO_4 tetrahedron, 118.3 and 122.5°, depart substantially from the tetrahedral angle. From geometrical considerations for an S_4 tetrahedron[6] the mean associated O—Li—O angle $\bar{\alpha}'$, 104.3(10)° (Table 2), should correspond to $\bar{\alpha}$ = 120.4°. This value is the same as the observed mean, α = 120.4(21)°, which indicates that the LiO_4 tetrahedron is close to S_4 symmetry, but it does not explain why the observed α are so large. This matter is considered in more detail below.

The tetraphenylborate (TB) anion (Table 2), although of crystallographic symmetry C_1, is dimensionally not far from D_{2d}. The geometry of its $BC(\alpha)_4$ core is, within the statistics, indistinguishable from the corresponding mean geometry (based on many TB anions) reported in ref. 2. The planarity of the phenyl rings is satisfactory (Table C).

The overall organization of the LiTBw structure is presented in Fig. 1. The structure can be thought of as consisting of cation + anion columns ||c with $\bar{4}$ as the column axis (projecting to x, y = (0, ± ¼) and (½, ± ¼) in the figure). In each column the B and Li atoms are arranged at the alternate corners of B_4Li_4 cuboids, which are easily identifiable on superposing the left and right parts of Fig. 1. Neighbouring columns are related by centres of symmetry between the columns (projecting to x, y = (0, 0), (½, 0) etc. in the figure).

[6]In a tetrahedron of symmetry S_4 the angles α and α′ are related by $\tan^2(\alpha'/2) = 1 + 2\tan^{-2}(\alpha/2)$.

Thermal motion

The anisotropic thermal parameters of the nonhydrogen atoms are reasonable, with the exception of U_{22}[O(1)] = 0.128 and in particular U_{22}[O(3)] = 0.240 and U_{11}[O(4)] = 0.210 Å^2 (Table B). The orientations and magnitudes of the thermal ellipsoids on these oxygens are displayed in the lower-left half of Fig. 2, where a portion of the structure is projected on (001) to provide a favourable view.

To see whether these large U_{ii} values are accidental or arising from correlated motions we tested the LiO_4 tetrahedron for rigid-body behaviour. The TLS analysis resulted in $R(U_{ij})$ = 6.7%, $R_w(U_{ij})$ = 5.9%, and rms(U_{ij}) = 0.0048 as against rms[esd(U_{ij})] = 0.0063 Å^2, i.e. the LiO_4 motion is reasonably consistent with the rigid-body-motion model, and the above three largest U_{ii} values are satisfactorily explained as resulting mainly from a large-amplitude libration about the principal libration axis L_3 practically ||c (Fig. 2, upper right). The mean amplitudes about the three principal axes of libration are L_1, 3.4°; L_2, 5.6°; and L_3, 10.1°.

The Li—O distances and O—Li—O angles corrected on the rigid-body-motion model are listed in Table 2.

Hydrogen bonding

The $Li(OH_2)_4^+$ cation is coordinated by four pairs of phenyl groups, each pair from a different anion (Fig. 3*A*). The geometry of this environment is strongly suggestive of O—H...π bonding. Difference Fourier maps showed evidence of two hydrogen atoms each between two of the oxygens and their nearest phenyl rings, and of one hydrogen each between the other two oxygens and their nearest phenyl rings, but their positions could not be ascertained with complete confidence. Unlike in the case of N—H...π bonds in tetraphenylborates of

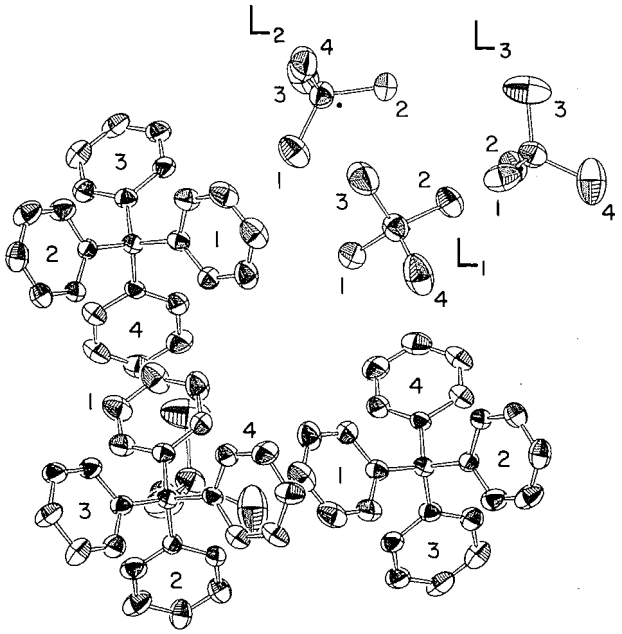

FIG. 2. Projection of a portion of the LiTBw structure on (001). Orientation as in Fig. 1; *xyz* of Li as in Table 1; 50% probability thermal ellipsoids. The phenyl rings are numbered 1–4. Note the large ellipsoids of O(3) (under ring 1) and O(4) (under ring 4) in the LiO_4 tetrahedron. *Upper right*: projections of the LiO_4 tetrahedron down its principal axes of libration L_1–L_3 (rigid-body-motion model, see text). The numbers refer to the oxygen atoms; the black dots indicate the position of the LiO_4 centroid. The projection down L_3 is to be compared with the projection of LiO_4 (from the structure refinement) down in the main figure; the two scales approximately match.

secondary and tertiary organic ammonium cations (2, 12), the H atoms of a water molecule cannot be placed geometrically, and the results of refining some of the H_2O molecules as rigid bodies (using the information from the difference maps) were not sufficiently conclusive. Without unambiguous location of the H(O) atoms the present *crystallographic* evidence of O—H...π bonding in LiTBw is therefore indirect but (as shown below) no less compelling.

The problem with defining the length and direction of an H...phenyl bond is discussed in detail in ref. 2 where, *faute de mieux*, the centre π_c of the phenyl ring is used as an "anchor" point of the bond, and the mean O...C distance and its standard deviation serve to describe the geometric relation (distance and attitude) of the H_2O molecule to the phenyl ring. This usage is adopted in the following.

The distances from an oxygen atom to the centre of the nearest phenyl ring range from 3.27 to 4.13 Å and the π_c...O...π_c angles, from 86° to 125° (Table 2, Fig. 3). With the exception of the two longest distances, 4.03 and 4.13 Å, this O...π_c range coincides with that for the corresponding distances in Table 5 of ref. 2, 3.12 to 3.54 Å. The two exceptions involve the oxygen atoms O(3) and O(4), each having one very large U_{ii} value (cf. above). Significantly, while the pair of phenyl rings nearest O(1) belongs to one anion, and ditto for O(2), the two rings nearest O(3) belong each to a different anion, and similarly for O(4). Further, the corresponding π_c...O...π_c angles at O(1) and O(2) are 86° and 90°, respectively, but those at O(3) and O(4) are 123° and 125°, pointing to the existence of strongly bent or bifurcated O—H...π bonds.

Conforming to the principle (which to our knowledge has no known exceptions, cf. ref. 13) that *all* H_2O hydrogens in a crystalline salt hydrate are always engaged in H-bonding, LiTBw is a three-dimensional, completely H-bonded polymer in which all the H_2O hydrogens are bonded to phenyl groups and all the phenyl groups are involved in O—H...phenyl bonds. In this respect LiTBw resembles BeSw (8, 9) and $[C(CH_2NH_3)_4]^{4+}(SO_4^{2-})_2$ (14), both of which also contain complete three-dimensional systems of H-bonds. However, while the Li and Be compounds dissolve readily in water, the high ion charges in the tetrakis(ammoniomethyl) sulfate conspire to make it very insoluble. The effects of ion charge in LiTBw and BeSw are compared below.

TABLE 3. Oxygen to ring centre and mean oxygen to carbon distances (Å) in LiTBw[a]

Distance	d(O...π_c)	$\bar{d}$(O...C)[b]	Δ[c]
O(1)...R1	3.57(9)	3.82(26)	0.73(13)
O(1)...R2	3.27(10)	3.55(7)	0.18(13)
O(2)...R3	3.30(11)	3.58(17)	0.43(17)
O(2)...R4	3.46(11)	3.73(16)	0.45(13)
O(3)...R1	4.13(10)	4.20(59)	1.78(14)
O(3)...R4	3.53(12)	3.79(26)	0.73(13)
O(4)...R1	3.34(10)	3.61(18)	0.50(13)
O(4)...R4	4.03(11)	4.22(62)	1.77(14)

[a]For coordinates of equivalent atom positions see Table 2.
[b]The standard deviation (in parentheses) of the mean does not include the esd's.
[c]$\Delta = d_{max}$(O...C) – d_{min}(O...C) for a phenyl ring.

The involvement of the phenyl groups in the H-bonding is not uniform (Fig. 3*B*). Rings 1 and 4 are each bonded from *both* sides, while rings 2 and 3 are bonded from one side only. The O...π_c distances to the latter are also the shortest O...π_c distances in the crystal, 3.27 and 3.30 Å, respectively, consistent with the unbalanced H...phenyl interaction.

The d(O...π_c) and the mean oxygen-to-ring-carbon d(O...C) distances are compared in Table 3. The standard deviations of the mean O...C distances (which do not include the esd's) can be taken as a measure of the inclination of the O...π_c vector to the ring plane (Fig. 4*A*).

The differences Δ between the longest and the shortest O...C distances in a ring vary quasi-linearly with d(O...π_c) ($r^2 = 0.97$, $\sigma = 0.11$ Å; Fig. 4*B*). The d(O...π_c) in this crystal are larger than the mean for normal (i.e. essentially straight) O—H...π bonds in ref. 2, but they fall within the corresponding range for bifurcated N—H...2π bonds and are entirely within the range for the two trifucated N—H...3π bonds reported there (cf. Fig. 4*B* and discussion in ref. 2).

Infrared spectrum of HDO and H_2O in LiTBw

Since the positions of the H_2O hydrogens could not be established with complete confidence and a suitable neutron-diffraction experiment could not be easily arranged, it seemed worthwhile to corroborate the existence of H-bonding in LiTBw by noncrystallographic means. This could in principle be accomplished by examining the ir spectrum of H_2O in the crystal for ν(OH) frequency lowering were it not for the well-known complications encountered with standard ir spectra of H_2O in hydrates, viz. the extensive vibrational coupling and Fermi resonance in the ν(OH) region which preclude satisfactory resolution of absorptions originating in the individual O—H groups. A technique developed to circumvent these difficul-

Can. J. Chem. Downloaded from www.nrcresearchpress.com by 85.192.166.187 on 09/08/12
For personal use only.

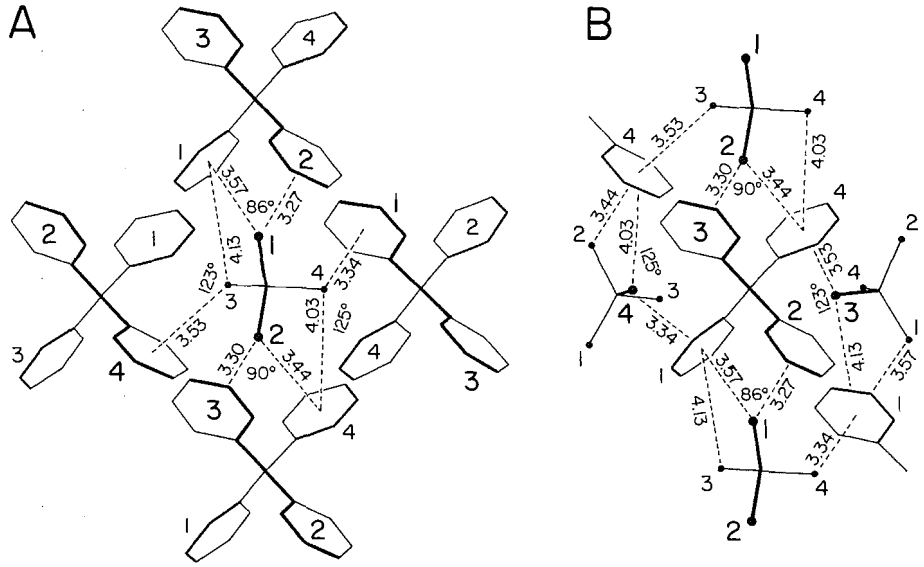

FIG. 3. The hydrogen-bonding system in LiTBw as represented by the O...π_c vectors (broken lines; lengths in Å). (*A*) Cation environment. (*B*) Anion environment. Black circles, oxygen atoms. Projection angle chosen such as to minimize overlap.

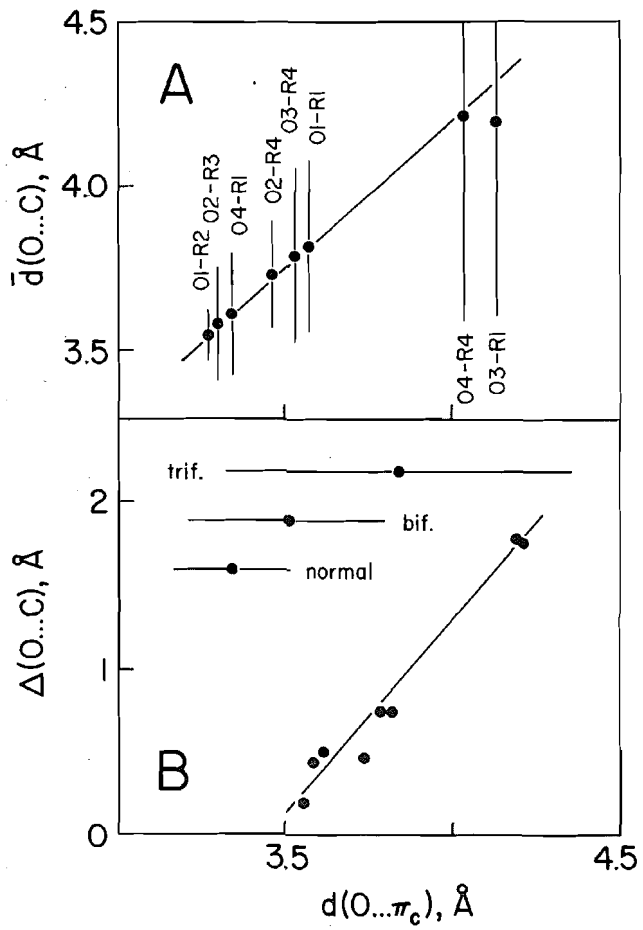

FIG. 4. (*A*) Correlation of the mean oxygen to ring-carbon distance d(O...C) with the oxygen to ring-centre distance d(O...π_c) in LiTBw. O1—R2 stands for O(1)...ring 2 etc. The standard deviation of d(O...C) (vertical bar) is a measure of the inclination of the O...π_c vector to the ring plane. (*B*) Correlation of Δ(O...C) with d(O...π_c); Δ(O...C) is the difference between the longest and the shortest O...C distance for the associated phenyl ring. The horizontal bars indicate the d(O...π_c) means for normal O—H...π bonds and the d(N...π_c) means for bifurcated and trifurcated N—H...π bonds from ref. 2.

ties (13, 15, 16) and employed here uses a weakly deuterated sample, thereby replacing a suitably small proportion of the H_2O molecules in the crystal by isotopically isolated (decoupled) HDO molecules. LiTBw was thought to offer a particularly challenging test of the power of this technique, given the eight distinct but very similar O—H groups weakly bonded to the phenyl groups: the four HDO molecules corresponding to the four asymmetric H_2O molecules should give rise to eight ν(OD) absorptions, all of them with frequencies lowered with respect to a non-H-bonded standard, and to four δ(HOD) absorptions. In addition, the temperature dependence of the ν(OD) frequency should provide information on the *type* of H-bond (17).

In the following we present only the ν(OD) of HDO and the δ(HOD) of H_2O regions of the FT-ir spectrum of a LiTBw sample with an estimated 3% of the H_2O hydrogen replaced by deuterium (figs. 5–8). The δ(HOD) absorptions were too weak to be observed.

The HOH bending region of the 10 K spectrum (Fig. 5) contained two resolved doublets with frequencies between 1594 and 1617 cm^{-1}. These four absorptions of comparable intensity are consistent with the presence of four nonequivalent sets of H_2O molecules in the crystal. With increasing temperature the four bands underwent shifts to higher frequencies, but there was no obvious indication of a thermally-induced phase transition in the δ(HOH) vs. T plot (Fig. 6). The doublet at the higher frequency (1611.7 and 1616.5 cm^{-1}, respectively) may correspond to H_2O molecules with stronger H-bonding than the doublet at the lower frequency (1594.1 and 1598.0 cm^{-1}). This would be consistent with the normal O(1)—H...phenyl and O(2)—H...phenyl bonds, and with one normal and one bifurcated O—H...phenyl bonds each for O(3) and O(4) (Fig. 3*A*).

In the ν(OD) region of the 10 K spectrum there were five resolved absorptions instead of the expected eight (Fig. 7). Four of these were closely-spaced peaks of equal weight, at 2619.6, 2623.4, 2626.3, and 2631.1 cm^{-1}. The fifth, at 2643.9 cm^{-1}, had an approximately fourfold weight but showed no sign of incipient splitting. However, with increasing temperature this band split into several components. Without a reliable analytic deconvolution (not attempted here) of the composite band the

Can. J. Chem. Downloaded from www.nrcresearchpress.com by 85.192.166.187 on 09/08/12
For personal use only.

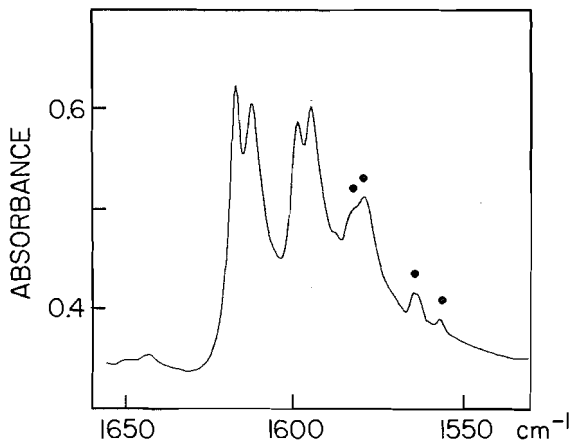

FIG. 5. FT-ir spectrum of H_2O in LiTBw in the HOH bending region at 10 K. Black dots indicate tetraphenylborate absorptions.

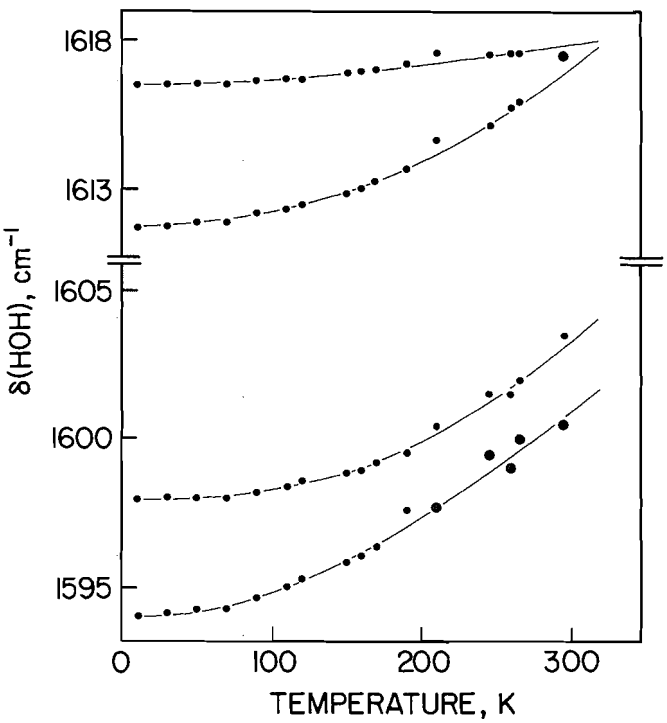

FIG. 6. Variation of the δ(HOH) bending frequency of H_2O in weakly *O*-deuterated LiTBw (see text) with temperature. The lines are intended to guide the eye only.

number of the components could not be established with certitude, but it was at least three and probably four (Fig. 8).

The temperature coefficient $d\nu/dT$ of the ν(OD) frequency was positive for three of the four bands in the lower-frequency quartet but negative for the fourth. For the bands in the higher-frequency group, it was positive for one and negative for the other outer band, and probably positive (or at least not negative) for the inner components. Since $d\nu/dT > 0$ is associated with normal and $d\nu/dT < 0$ with highly bent or branched H-bonds (17), at least five of the eight O—H...phenyl bonds are normal (i.e. essentially straight) and two are highly bent or branched. This is consistent with the crystallographic finding. However, a detailed 1:1 correlation is not possible, partly because the H atoms have not been located with sufficient confidence, partly

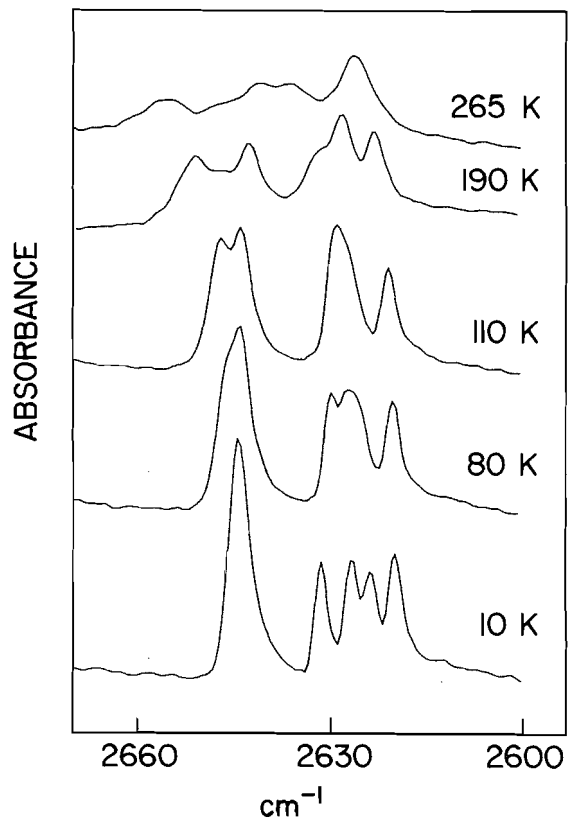

FIG. 7. FT-ir spectrum of HDO in weakly deuterated LiTBw (see text) in the OD stretching region at different temperatures.

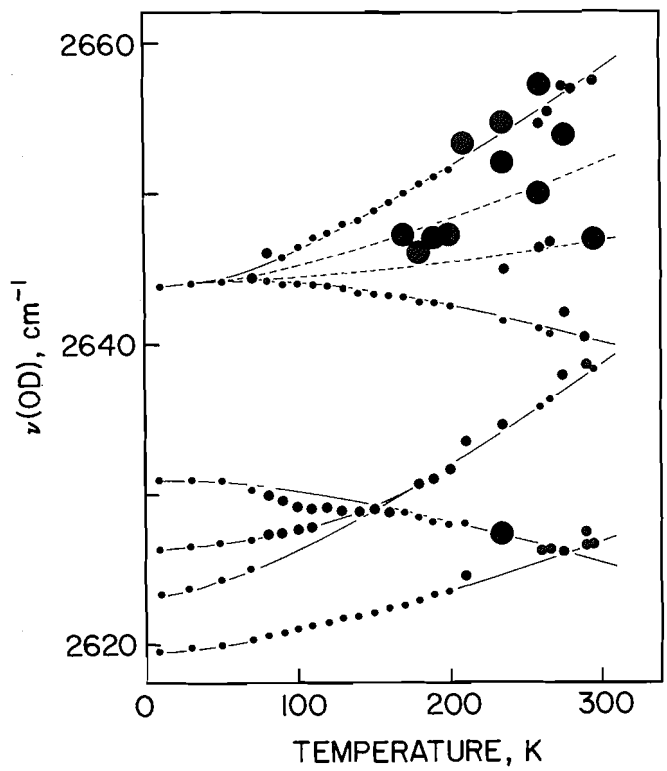

FIG. 8. Variation of the ν(OD) frequency of HDO in weakly deuterated LiTBw (see text) with temperature. The uncertainty of the visual peak-frequency estimate increases with the size of the black circle. The lines are intended to guide the eye only.

Can. J. Chem. Downloaded from www.nrcresearchpress.com by 85.192.166.187 on 09/08/12
For personal use only.

TABLE 4. *Ab initio* optimized molecular parameters of $Li(OH_2)_4^+$ and $Be(OH_2)_4^{2+}$ species in D_{2d} symmetry[a]

Parameter	$Li(OH_2)_4^+$ STO-3G	$Li(OH_2)_4^+$ 6-31G	$Li(OH_2)_4^+$ 6-31G*	$Be(OH_2)_4^{2+}$ 6-31G*
E, au	−307.40192	−311.40045	−311.48113	−318.30180
x(O), Å	−1.4962	−1.6443	−1.6905	−1.3970
y(O), Å	0	0	0	0
z(O), Å	0.9714	1.0368	1.0050	0.8656
x(H), Å	−1.9185	−2.0396	−2.0380	−1.7609
y(H), Å	−0.7675	−0.7869	−0.7577	−0.7713
z(H), Å	1.4021	1.3947	1.4531	1.2954
M—O, Å	1.784	1.944	1.967	1.643
O...O′, Å	2.873	3.116	3.123	2.627
O...O″, Å	2.992	3.289	3.381	2.794
O—H, Å	0.976	0.951	0.946	0.955
H...H′, Å	1.535	1.574	1.515	1.543
H...H″, Å	3.242	3.306	3.424	2.945
O—M—O″ = α	114.01°	115.54°	118.54°	116.43°
O—M—O′ = α′	107.25°	106.53°	105.14°	106.11°
M—O—H	127.09°	123.57°	123.89°	124.12°
H—O—H′	103.68°	111.68°	106.38°	107.73°
ε_M(M), e	0.185	0.726	0.586	0.982
ε_M(O), e	−0.305	−0.863	−0.878	−0.827
ε_M(H), e	0.255	0.466	0.489	0.541
ε_L(M), e	−0.329	0.229	−0.379	−0.458
ε_L(O), e	−0.075	−0.494	−0.532	−0.337
ε_L(H), e	0.203	0.343	0.439	0.476

[a]*E*, total electronic energy; *x*, *y*, *z*, Cartesian coordinates; M = Li or Be; *x*(M) = *y*(M) = *z*(M) = 0. O′: $x' = 0$, $y' = x$, $z' = -z$. O″: $x'' = -x$, $y'' = -y$, $z'' = z$. H′: $x' = x$, $y' = -y$, $z' = z$. H″: $x'' = y$, $y'' = x$, $z'' = -z$. ε_M, net charge (Mulliken); ε_L, net charge (Löwdin).

because of the progressive loss of definition of the ν(OD) spectrum as the temperature approaches ambient. The reason for the coalescence of the higher-frequency absorptions at 10 K is not understood in structural terms at present. A low-temperature structure determination of LiTBw to match at least some of the low-temperature spectra is planned for a later date.

The above ν(OD) stretching frequencies are among the highest reported for crystalline salt hydrates (13) (the gas-phase ν(OD) of HDO is 2727 cm^{-1}). While direct comparisons cannot be made, it may be noted that the isotopically decoupled ν(ND) stretching and δ(HND) bending frequencies in NH_4BPh_4 (18, 19) which correspond to N—H...phenyl interactions are, respectively, $\nu_1(NH_3D^+)$ = 2363.6(3) amd $\nu_{4bc}(NH_3D^+)$ = 1232.3(3) cm^{-1} at 10 K, and 2362.0(6) and 1234.3(6) cm^{-1} (extrapolated) at 293 K, i.e. close to the estimated "nonbonded" frequencies obtained by extrapolation for the NH_3D^+ in crystals (18).

Ab initio calculations

As pointed out above, the LiO_4 coordination tetrahedron in LiTBw is almost of $S_4 \subset D_{2d}$ symmetry, with the two O—Li—O "valence" angles α equal to 118.3° and 122.5°. The question arises, are these large departures from the tetrahedral angle fortuitous, caused by packing and H-bonding exigencies, or are they essentially intrinsic to the $Li(OH_2)_4^+$ cation and thus to be expected? Further, to what extent can $Li(OH_2)_4^+$ be regarded as a chemical rather than crystallographic entity, i.e. can the Li—O interaction be described as a chemical bond?

To shed some light on these questions, the equilibrium geometry of the $Li(OH_2)_4^+$ ion was optimized at the RHF/STO-3G, 6-31G, and 6-31G* levels (Table 4) . The Li—O distance and the angle α are both seen to increase with the size of the basis set, and their 6-31G* values are comparable to those observed in the crystal (Table 5): the 6-31G* Li—O distance is indistinguishable from the corrected Li—O distance in LiTBw, and the calculated α is equal to the smaller of the two observed α angles, 118.3°. Since 6-31G* optimization usually yields reasonably realistic equilibrium molecular geometries, this agreement between calculation and experiment suggests that the reason for the large α values in the crystal resides in the ion itself.

This finding contrasts strongly with the significant angular distortion of the LiO_4 tetrahedron (of symmetry S_4) in the tetragonal LiUAw (7). Here the distortion is *in the opposite direction:* the O—Li—O angle α bisected by the S_4 axis is *smaller* than the associated O—Li—O angle α′, while the Li—O distance, 1.955(4) Å, is comparable to that in LiTBw: α = 105.1(2)°, α′ = 111.7(2)°. The departure of this α from the tetrahedral angle is −4.4°, but the difference between α(6-31G*) of $Li(OH_2)_4^+$ and the α in LiUAw amounts to +13.4°.

Differences in the angular distortion of this magnitude cannot be glossed over. To strengthen our confidence in the *ab initio* result for $Li(OH_2)_4^+$ we therefore optimized the geometry of the nearest analog of this cation, $Be(OH_2)_4^{2+}$, for which two reliable crystal-structure determinations are available, viz. those of BeSw (8, 9) and BeNw (10). In both salts the symmetry at Be is S_4: in BeSw (neutron diffraction) the H...H vector in the H_2O molecule is inclined by only ~2° to (001), i.e. the cation symmetry is practically D_{2d}. The 6-31G* optimization in D_{2d} symmetry (Table 4) resulted in *d*(Be—O) = 1.643 Å, α = 116.4°, α′ = 106.1°. The uncorrected *d*(Be—O) is 1.618(4) Å in BeSw and 1.616(5) Å in BeNw. the α and α′ angles in BeSw are

Can. J. Chem. Downloaded from www.nrcresearchpress.com by 85.192.166.187 on 09/08/12
For personal use only.

TABLE 5. Comparison of interatomic distances (Å) and bond angles (deg) in LiTBw and BeSw crystals at room temperature and in $Li(OH_2)_4^+$ and $Be(OH_2)_4^{2+}$ with 6-31G* optimized D_{2d} equilibrium molecular geometries[a]

	$Li(OH_2)_4^+$			$Be(OH_2)_4^{2+}$	
Parameter	Uncorr.	Corr.	6-31G*	Uncorr.[b]	6-31G*
M—O	1.933(7)	1.960(12)	1.967	1.618 [1.610]	1.643
O...O′	3.052(22)		3.123	2.582 [2.566]	2.627
O...O″	3.354(33)		3.381	2.760 [2.753]	2.794
O—H			0.946	0.969(2)	0.955
H...H′			1.515	1.614	1.543
H...H″			3.424	2.819	2.945
O—M—O″ = α	120.4(21)	120.0(19)	118.5	117.0 [117.5]	116.4
O—M—O′ = α′	104.3(10)	104.5(18)	105.1	105.8 [105.6]	106.1
M—O—H M—O—H′			123.9	118.2 126.2	124.1
H—O—H′			106.4	112.7	107.7
Σ(—O—)[c]			354.2	357.1(11)	355.9

[a]Uncorr., uncorrected mean value in crystal at room temperature; corr., corrected mean value (see text). Numbers in parentheses: standard deviations of means, esd's not included. O′: $x' = -y$, $y' = x$, $z' = -z$. O″: $x'' = -x$, $y'' = -y$, $z'' = z$. H′: $x' = x$, $y' = -y$, $z' = z$. H″: $x'' = y$, $y'' = x$, $z'' = -z$.

[b]First number, neutron diffraction (9); number in brackets, X-ray diffraction (8).

[c]Σ(—O—) = M—O—H + M—O—H′ + H—O—H′. For M...OH_2 to be coplanar (i.e. for the M...O line to bisect the angle between the two lone electron pairs on the oxygen), Σ(—O—) = 360°.

117.0(2)° and 105.8(2)°, respectively (Table 5), and 111.5(2)° and 108.5(2)° in BeNw. The anticipated correction for thermal motion would be of the order of 0.02–0.03 Å for the distance and 0.2° for the angle. This would bring the experimental d(Be—O) values in both salts, and the α in BeSw, in good agreement with the 6-31G* value. In BeNw, however, α is considerably smaller than the 6-31G* value.

Closer examination of the LiUAw structure reveals the likely, crystallographic reason for the large distortion. The LiO_4 and AsO_4 tetrahedra are arranged in columns ∥c. In each column the Li and As atoms, on a common S_4 axis, alternate, so that each LiO_4 tetrahedron is sandwiched between two AsO_4^{3-} ions. The water hydrogens are oriented in such a way that one forms a H-bond to an anion oxygen *within* the column, at an O_w..O_w distance of 2.783(5) Å (H(2)...O_{As} = 1.860(4) Å) and an O_w—H(2)—O_{As} angle of 167.5(4)°, while the other forms an O_w—H(1)...O_{As} bond *between* columns, at O_w..O_w = 2.953(6) Å (H(1)...O_w = 1.979(6) Å) and an O_w—H(1)...O_w angle of 161.8(5)°. The O_w—H(1)...O_w bonds are situated in layers ∥(001); the U_{22} of H(1) is large, ~0.15 Å^2. The LiO_4 tetrahedron is thus attached to its two, highly-charged AsO_4^{3-} neighbours by four O_w—H(2)...O_{As} bonds, two of which engage the upper and two the lower anion. These H-bonds are stronger than the lateral, intercolumn O_w—H(1)...O_w bonds. The O_{As}...O_{As} edge of the anion which faces the Li atom is 2.65 Å long, compared to the matching O_w..O_w separation of 3.10 Å. This disparity in length and the skewing of the AsO_4 tetrahedron about S_4 relative to the LiO_4 tetrahedron thus force the H_2O molecules to adopt a compromise orientation which satisfies neither the intra- nor the inter-column H-bonding properly (witness the O—H...O angles and the large U_{22} of H(1)) and which in addition tends to close up the angle α.[7] This situation is thus substantially different from that in LiTBw, where the single charge on the anion is diffuse and the phenyl groups exert only weak additional influence on the H-bonds.

[7]The angular distortion of the AsO_4 tetrahedron is practically the same as that of LiO_4: α = 105.2(1)°, α′ = 111.6(1)°.

In the tetragonal BeSw the Be and S atoms are segregated on different S_4 axes, so that the O_w—H...O_S bonds (O_w—H...O_S ~ 172°) are *between* columns, i.e. lateral. Each H_2O molecule (H—O—H = 112.7°) forms two H-bonds to O_S oxygens. These O_S have the same z but are from two different anion neighbours. Every O_S atom participates in two H-bonds, with the result that the BeSw crystal is completely and three-dimensionally H-bonded. Although the anion is compact and carries a double charge, the overall arrangement in the structure is such that it minimizes, by adjustment of the c/a ratio and of the angle of rotation of the BeO_4 and SO_4 tetrahedra about their respective S_4 axes, the angular distortion of BeO_4 from its "free-ion" geometry in $Be(OH_2)_4^{2+}$. The SO_4 tetrahedron is only slightly distorted.

In BeNw, which too is tetragonal, the O—Be—O angle α is reduced from the free-ion geometry value of 116.4° to 111.5°. This reduction appears to be connected with the layer-type arrangement of the planar NO_3^- ions in sheets ∥(001), at average vertical heights of $n/8$, $n = \pm(1, 5)$, with the Be atoms at $z = 0, \frac{1}{2}$. The O_w—H...O_N bonds are in part in the NO_3^- layers, in part cross-linking them, whereby they connect, laterally, the columns of the cations with the columns of the nitrate ions, again in an exhaustive H-bonding manner.

It would seem that where the H-bonding interaction is weak and not strongly reinforced by ion-charge interaction, and especially when the acceptors are mostly in neighbouring ion columns, the angular distortion of the MO_4 tetrahedron of the $M(OH_2)_4^{n+}$ cation from its free-ion geometry is not severe. This is the case in LiTBw, where the H-bonding and Coulombic interactions are weak, and also in BeSw, for the reasons suggested above. In LiUAw, however, the $Li(OH_2)_4^+$ cation is constrained, by its two AsO_4^{3-} H-bonding partners in the same column, to undergo an angular distortion which not only is significant with respect to the tetrahedral angle but very large with respect to the *ab initio* geometry of the cation. In providing a rationale for the existence of the angular deviations of the LiO_4 and BeO_4 tetrahedra in their respective $M(OH_2)_4^{n+}$ cations in crystals, the above examination of the observed ion geometries reconciles theory with experiment and vindicates the essential

Can. J. Chem. Downloaded from www.nrcresearchpress.com by 85.192.166.187 on 09/08/12
For personal use only.

correctness of the *ab initio* stereochemistry. The agreement of the observed and calculated Li—O and Be—O distances supports the view that the M—OH_2 interaction in the two tetrahydrated M^{n+} ions is chemical in nature and not the result of packing exigencies in the crystal (for the structure and dynamics of these cations in solution see ref. 20).

Experimental

Preparation

The NaCl precipitate that formed on combining acetone solutions of LiCl and $NaBPh_4$ was filtered off. The filtrate was evaporated almost to dryness, the solid was redissolved in acetone and the NaCl residue was filtered off again. This step was repeated twice. The final evaporate was dissolved in water and allowed to crystallize by slow evaporation at room temperature.

X-ray diffraction

Data acquisition

Rigaku AFC5R single-crystal diffractometer, Mo $K\alpha$, λ = 0.71069 Å (graphite monochromator); $T \sim 18$°C. Crystal size, 0.3 × 0.35 × 0.4 mm^3; θ-range, 2–23° (cell dimensions and orientation matrices from 24 reflections); $\mu_{Mo} = 0.70\ cm^{-1}$. Total reflections measured, 3586; unique total, 3422; unique used, 1176 ($I > 3\sigma(I)$), $R_{merg} = 3.9\%$. Like most tetraphenylborates, LiTBw is a weak scatterer (cf. ref. 1).

Crystal data

$BC_{24}H_{28}LiO_4$, fw 398.2. Tetragonal, a = 27.566(2) Å, c = 12.228(2) Å, V = 9291(3) $Å^3$, Z = 16. $F(000)$ = 3392 e, ρ_c = 1.139(1) g/cm^3. Space group, $I4_1/a$ (no. 88). Systematic absences: hkl, $h + k + l$ odd; $hk0$, h, k odd; $0kl$, $k + l$ odd; hhl, l odd; $00l$, $l \neq 4n$; $h00$, h odd; $h\bar{h}0$, h odd.

Structure solution and refinement

Direct methods; programs used, refs. 21–23. Function minimized, $w(|F_o| - |F_c|)^2$; unit weights; d/p = 4.3. Temperature factor, $\exp[-2\pi^2(U_{11}h^2a^{*2} + U_{22}k^2b^{*2} + U_{33}l^2c^{*2} + 2U_{23}klb^*c^* + 2U_{13}hla^*c^* + 2U_{12}hka^*b^*)]$. H(C) atoms placed geometrically and not refined (C—H, 1.08 Å, $U_{iso}(H) = 1.2B_{eq}(C)$); H(O) atoms, see text. $R = 4.7\%$, $R_w = 5.0\%$, G.O.F. = 3.21. Max/min residual electron density in final difference map, $-0.25/0.18\ e^{-3}$.

Tables A (positional parameters and U_{iso} of the H atoms), B (anisotropic thermal parameters of the nonhydrogen atoms), and C (deviations of the C and B atoms from the best planes through the phenyl-ring skeletons and angles between the best planes) have been deposited.[5]

Infrared spectrum

The sample used was authenticated shortly before use by X-ray diffraction. It was then dissolved in 3% D_2O, evaporated to dryness, and mulled in fluorolube. The mull was supported on CaF_2 plates. The spectra, at 2 cm^{-1} resolution, between 10 K and room temperature were obtained using a Bomem DA3.02 FT-ir spectrometer fitted with a closed-cycle He refrigerator.

Ab initio calculations

These were performed using the GAMESS (24) system. When the optimizations of $Li(OH_2)_4^+$ were started in S_4 symmetry, they invariably converged to D_{2d} symmetry. The $S_4 \rightarrow D_{2d}$ convergence was confirmed by a separate optimization directly in D_{2d} symmetry. This was therefore the symmetry adopted from the outset for $Be(OH_2)_4^{2+}$. For previous calculations on $Be(OH_2)_4^{2+}$ see refs. 20, 25, and 26; on hydrated Li^+ species, ref. 27.

Acknowledgements

We wish to thank Mr. Ping Seto for obtaining the FT-ir spectra. This investigation was supported by a Natural Sciences and Engineering Research Council of Canada (NSERC) research grant to O.K.

1. O. Knop, T.S. Cameron, P.K. Bakshi, A. Linden, and S.P. Roe. Can. J. Chem. **72**, 1870 (1994).
2. P.K. Bakshi, A. Linden, B.R. Vincent, S.P. Roe, D. Adhikesavalu, T.S. Cameron, and O. Knop. Can. J. Chem. **72**, 1273 (1994).
3. J.L. Atwood, F. Hamada, K.D. Robinson, G.W. Orr, and R.L. Vincent. Nature (London), **349**, 683 (1991).
4. H.S. Rzepa, M.L. Webb, A.M.Z. Slawin, and D.J. Williams. J. Chem. Soc. Chem. Commun. 765 (1991).
5. J.L. Atwood, S.G. Bott, C. Jones, and C.L. Raston. J. Chem. Soc. Chem. Commun. 1349 (1992).
6. L.R. Hanton, C.A. Hunter, and D.H. Purvis. J. Chem. Soc. Chem. Commun. 1134 (1992).
7. A.N. Fitch, B.E.F. Fender, and A.F. Wright. Acta Crystallogr. Sect. B, **38**, 1108 (1982).
8. I.G. Dance and H.C. Freeman. Acta Crystallogr. Sect. B, **25**, 304 (1969).
9. S.K. Sikka and R. Chidambaram. Acta Crystallogr. Sect. B. **25**, 310 (1969).
10. V. Divjaković, A. Edenharter, W. Nowacki, and B. Ribár. Z. Kristallogr. **114**, 314 (1976).
11. E. Höhne. Z. Anorg. Allg. Chem. **342**, 188 (1966).
12. O. Knop, T.S. Cameron, P.K. Bakshi, W. Kwiatkowski, S.C. Choi, and D. Adhikesavalu. Can. J. Chem. **71**, 1495 (1993).
13. M. Falk and O. Knop. *In* Water: a comprehensive treatise. Vol. 2. *Edited by* F. Franks. Plenum Press, New York. 1973. Chapt. 2.
14. T.S. Cameron, W.J. Chute, and O. Knop. Can. J. Chem. **63**, 586 (1985).
15. V. Seidl, O. Knop, and M. Falk. Can. J. Chem. **47**, 1361 (1969).
16. I.A. Oxton, O. Knop, and M. Falk. J. Phys. Chem. **80**, 1212 (1976).
17. O. Knop, W.J. Westerhaus, and M. Falk. Can. J. Chem. **58**, 867 (1980).
18. O. Knop, I.A. Oxton, and M. Falk. Can. J. Chem. **57**, 404 (1979); (errata) **57**, 2003 (1979).
19. W.J. Westerhaus, O. Knop, and M. Falk. Can. J. Chem. **58**, 1355 (1980).
20. H. Ohtaki and T. Radnai. Chem. Rev. **93**, 1157 (1993).
21. G.M. Sheldrick. SHELXS-86. *In* Crystallographic computing. *Edited by* G.M. Sheldrick, C. Kruger, and R. Goddard. Oxford University Press, Oxford, U.K. 1985.
22. TEXSAN-TEXRAY single crystal structure analysis package. Molecular Structure Corporation, The Woodlands, Tex. 1989.
23. J.R. Carruthers and D.L. Watkin. CRYSTALS, issue 5. Chemical Crystallography Laboratory, Oxford, U.K. 1981.
24. M.W. Schmidt, K.K. Baldridge, J.A. Boatz, J.H. Jensen, S. Koseki, M.S. Gordon, K.A. Nguyen, T.L. Windus, and S.T. Elbert. QCPE Bull. **10**, 52 (1990).
25. M.M. Probst, J.P. Limtrakul, and B.M. Rode. Chem. Phys. Lett. **132**, 370 (1986).
26. K. Hashimoto, N. Yoda, and S. Iwata. Chem. Phys. **116**, 193 (1987).
27. K. Hermansson. Acta Crystallogr. Sect. B, **41**, 161 (1985).

Can. J. Chem. Downloaded from www.nrcresearchpress.com by 85.192.166.187 on 09/08/12
For personal use only.

Conformationally induced and conjugatively amplified doubly degenerate uneven sulfuranes

ELIZABETH A. INNES AND IMRE G. CSIZMADIA
Department of Chemistry, University of Toronto, Toronto, ON M5S 1A1, Canada

JEAN-LOUIS RIVAIL AND MICHEL LOOS
Laboratoire de Chimie Théorique, U.A. 510 CNRS, Université de Nancy-I, BP 239, F-54506 Vandœuvre-les-Nancy, Cedex, France

AND

ÁRPÁD KUCSMAN
Department of Organic Chemistry, Eötvös University, Pázmány Péter sétány 2, Budapest XI, Hungary 1117

Received May 5, 1994

ELIZABETH A. INNES, IMRE G. CSIZMADIA, JEAN-LOUIS RIVAIL, MICHEL LOOS, and ÁRPÁD KUCSMAN. Can. J. Chem. **72**, 2153 (1994).

Sulfuranes, containing hypervalent or 10 valence electron central sulfur atoms of the type $CH_3(H)SCl_2$ (**I**), $H_2N(H)SCl_2$ (**II**), $HO(H)SCl_2$ (**III**), $(H_2N)_2SCl_2$ (**IV**), and $(HO)_2SCl_2$ (**V**) have been studied by *ab initio* MO computations. All sulfuranes exhibited pseudo trigonal bipyramide structure as appropriate 5 valence electron pairs. The two chlorine atoms were in apical positions and the other two ligands were in equatorial position. The fifth electron pair was a lone pair, also located in an equatorial position. The lone pair "pushed away" the S—Cl bonds from the ideal axis of the trigonal bipyramide and therefore the ClSCl bond angle was always less than 180°. With the changing conformations of the equatorial groups the axial bond lengths are varied. Even though the compounds had constitutionally identical S—Cl bonds at certain torsional angles of the equatory ligands the two S—Cl bond lengths became unequal. The difference between the two bond lengths was used as a measure of the extent of unevenness of the sulfurane structures. This led to the creation and annihilation of certain critical points on the conformational Potential Energy Surfaces.

ELIZABETH A. INNES, IMRE G. CSIZMADIA, JEAN-LOUIS RIVAIL, MICHEL LOOS et ÁRPÁD KUCSMAN. Can. J. Chem. **72**, 2153 (1994).

Utilisant des calculs d'OM *ab initio*, on a étudié des sulfuranes contenant des atomes de soufre nucléaires hypervalents ou à 10 électrons du type $CH_3(H)SCl_2$ (**I**), $H_2N(H)SCl_2$ (**II**), $HO(H)SCl_2$ (**III**), $(H_2N)_2SCl_2$ (**IV**) et $(HO)_2SCl_2$ (**V**). Tous les sulfuranes présentent des structures pseudo-trigonales bipyramidales, comme on peut s'y attendre pour des produits comportant cinq paires d'électrons de valence. Les deux atomes de chlore sont toujours dans les positions apicales et les deux autres coordinats sont dans des positions équatoriales. La cinquième paire d'électrons est une paire libre qui est aussi placée dans une position équatoriale. La paire libre d'électrons déforme les liaisons S—Cl par rapport à l'axe idéal de la bipyramide trigonale; l'angle de la liaison ClSCl est donc toujours inférieur à 180°. Avec les changements dans les conformations des groupes équatoriaux, les longueurs des liaisons axials varient. Même si les composés comportent des liaisons S—Cl qui sont constitutionnellement indentiques, les longueurs des deux liaisons S—Cl deviennent inégales à certains angles de torsion des cooordinats équatoriaux. On a utilisé les différences entre les longueurs des deux liaisons comme mesure des disparités dans les structures des sulfuranes. Ces mesures ont conduit à la création et à l'annihilation de certains points critiques sur les surfaces d'énergie potentielle des conformations.
[Traduit par la rédaction]

Introduction

We have previously introduced (1) the principle of conformationally induced double degenerate unevenness in sulfuranes using simple model compounds such as HS—SH_2—SH. The unevenness of these constitutionally symmetric sulfuranes is manifested in the two nonequivalent apical bond lengths, shown below, computed at the Hartree–Hock (HF) and Møller–Plesset (MP) levels of theory:

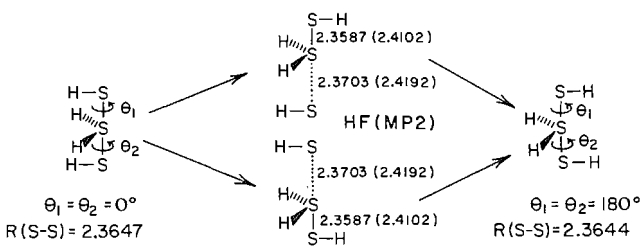

In the above figure, bond lengths (Å) without parentheses are those obtained by HF at a 4-31G* level of theory; bond lengths (Å) in parenthesis are the MP2 results obtained at the same basis set level. (The left- hand side, the central and right-hand side structures are labelled in ref. 1 as **IV**(0_2), **IV**(0_1), and **IV**(0_0) respectively.)

When the *apical* SH groups are replaced by Cl, conformational induction disappears. Replacing the *equatorial* hydrogens by CH_3 or F groups and maintaining the two chlorine atoms in the apical positions resulted in no anomalies (2) as illustrated by the structures below:

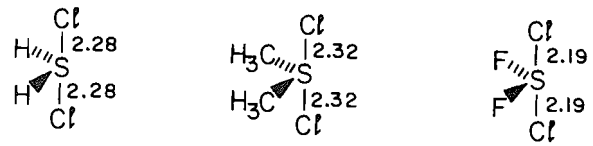

The above figure represents gradient optimized geometries for R_2SCl_2 (where R = H, CH_3, and F) obtained (2) at a 3-21G* basis set level. The two S—Cl bond lengths are identical even though no C_{2v} symmetry has been enforced.

However, when NH_2 or OH groups are introduced at the two equatorial positions the preliminary gradient optimized geome-

Can. J. Chem. Downloaded from www.nrcresearchpress.com by 85.192.166.187 on 09/08/12
For personal use only.

tries (2) showed the existence of doubly degenerate uneven sulfuranes.[1] The extent of unevenness may be measured by the difference of the two apical (S—Cl) bond lengths: $\Delta R = [R(S—Cl^1)] - [R(S—Cl^2)]$.

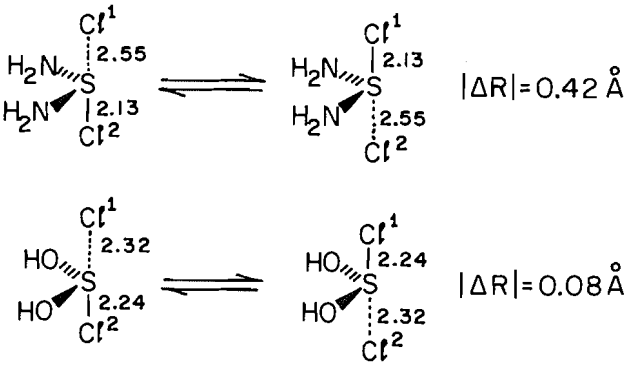

Results and discussions

These somewhat surprising preliminary results (2) discussed in the introduction, namely, that constitutionally symmetric $(H_2N)_2SCl_2$ and $(HO)_2SCl_2$ have different bond lengths, immediately posed four questions which formed the basis of the present paper. (*1*) Would the same effect emerge if only one equatorial NH_2 (or OH) group were present in the molecule with a rotational angle (χ) about the N—S or O—S bond?[2] (*2*) What is the stereoelectronic basis for the very existence of such uneven structures for constitutionally symmetric molecules? (*3*) Is the effect of equatorial CH_3 groups fundamentally different from those of equatorial NH_2 and OH groups? (*4*) In the case of two equatorial NH_2 (or OH) groups what features does the conformational potential energy surface (PES), such as $E = E(\chi_1, \chi_2)$, have? Note that χ_1 and χ_2 are the two S—N (or S—O) rotational angles.

The first three questions can be answered by studying the following compounds:

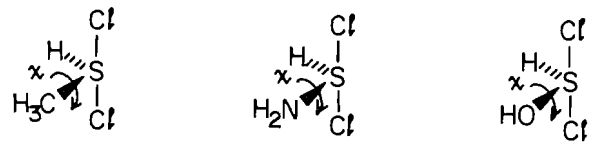

Typical conformations of **I**, **II**, and **III** with varying χ values are shown in Scheme 1 below. (Note that in the case of **III** only the "hybridized" lone pair with directionality is shown. The other, orthogonal, canonical lone pair, analogous to the unhybridized 2*p* on oxygen is not shown.)

The variation of the total molecular energy (*E*), typical bond lengths, and bond orders (BO) (3) with the rotational angle (χ) about the C—S, N—S or O—S bonds are shown in Fig. 1 for $H_3C(H)SCl_2$ (**I**), $H_2N(H)SCl_2$ (**II**), and $HO(H)SCl_2$ (**III**) having two chlorine atoms in the apical positions. This figure clearly illustrates the following variation in average equatorial bond orders: BO(C—S) < BO(N—S) ≈ BO(O—S). Furthermore, in the case of **II** and **III**, at certain χ values the BO of the two apical S—Cl bonds were computed to be quite different, while in the case of **I** these two S—Cl BO values remained very close to each other. Thus the conformational induction effect of the CH_3 group is present but it is not so pronounced. For the N—S and O—S bonds, however, the larger BO corresponds to a conjugative amplification of this effect. The principal geometrical parameters of **I**, **II**, and **III** as functions of rotation about the S—CH_3, S—NH_2, and S—OH bonds are listed in Tables 1, 2, and 3, respectively. It should perhaps be emphasized that the ClSCl bond angle is changing with conformational change but is always smaller than 180°. In view of the above results we may answer the first three questions.

(*1*) The effect is present even if only one heteroatom (N or O) is located in an equatorial position. However, in the case of one NH_2, the unevenness ($|\Delta R| > 0$) does not occur at the minimum energy conformation.

(*2*) At certain χ values in **II** and **III** the two chlorine atoms

TABLE 1. Bond lengths and ClSCl angles for different structures of $ClS(CH_3)HCl$

Structure	Bond length Cl_aS	Bond length Cl_bS	Angle Cl_aSCl_b
$CH_3(0)$	2.297	2.304	171.329
$CH_3(30)$	2.297	2.304	171.233
$CH_3(60)$	2.302	2.302	172.415
$CH_3(90)$	2.305	2.296	171.189
$CH_3(120)$	2.301	2.300	169.986
$CH_3(150)$	2.297	2.304	171.329
$CH_3(180)$	2.304	2.301	172.455

TABLE 2. Bond lengths and ClSCl angles for different structures of $ClS(NH_2)HCl$

Structure	Bond length Cl_aS	Bond length Cl_bS	Angle Cl_aSCl_b
$NH_2(0)$	2.285	2.285	172.192
$NH_2(100)$	2.266	2.304	172.005
$NH_2(120)$	2.214	2.368	171.542
$NH_2(150)$	2.166	2.449	169.864
$NH_2(180)$	2.333	2.333	163.208
$NH_2(210)$	2.448	2.167	169.822
$NH_2(300)$	2.252	2.329	172.404
$NH_2(330)$	2.243	2.401	166.535

TABLE 3. Bond lengths and ClSCl angles for different structures of ClS(OH)HCl

Structure	Bond length Cl_aS	Bond length Cl_bS	Angle Cl_aSCl_b
OH(0)	2.275	2.275	172.405
OH(60)	2.466	2.098	173.595
OH(90)	2.476	2.093	171.347
OH(120)	2.409	2.141	169.946
OH(180)	2.273	2.276	168.147

[1]Preliminary gradient optimized geometries for X_2SCl_2 (where X = NH_2 or OH) obtained by HF at a 3-21G* basis set level. Each constitutionally identical pairs show the double degeneracy of the sulfurane structure as defined in ref. 1.

[2]The rotational angles were defined analogously to the torsional angles specified in the IUPAC convention but not with respect to the XSX (X = C, N, O) planes. Rather it was defined with respect to the bisecting plane of the ClSCl bond angle. Thus our rotational angles are related to the conventional torsional angles and they are identical at 0°, ±90°, ±180° but differ slightly at the in-between regions.

Can. J. Chem. Downloaded from www.nrcresearchpress.com by 85.192.166.187 on 09/08/12
For personal use only.

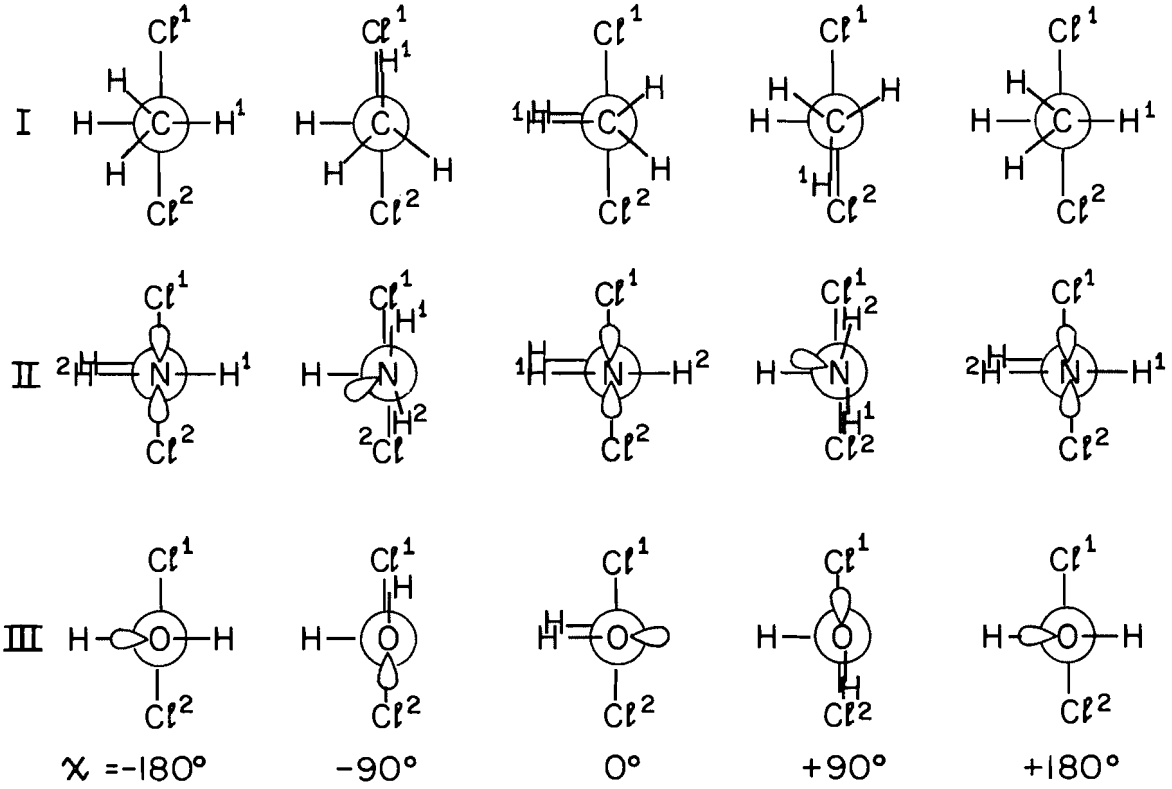

SCHEME 1

become nonequivalent. If such conformations also favour a stereoelectronic effect, i.e. the formation of a partial double bond between N—S or O—S, then this bond strengthening in the equatorial plane amplifies the S—Cl bond stretch along a nearly orthogonal direction. (*a*) In the case of oxygen (**III**) the partial double bond formation and coupled S—Cl bond stretch occurs when the minimum energy conformation is reached. In this particular conformation one of the oxygen lone pairs is in alignment with the σ* S—Cl orbital for a favourable stereoelectronic interaction. Consequently, at this conformation ($\chi \approx 90°$) the BO for the C—S bond, one of the S—Cl bonds, is shorter with a maximum BO while the other S—Cl bond is longer with a minimum BO. (*b*) The changing pyramidality of nitrogen with the varying rotational angle (χ) makes the situation more complicated for **II**. At the minimum energy conformation ($\chi \approx 90°$) the N—S BO is minimum. This may be expected since the lone pair of the slightly pyramidal N is nearly orthogonal to Cl—S—Cl line, thus there is no chance for partial double bond formation. However, at the rotational angle $\chi = 180°$ the N becomes fully planar and its lone pair is evenly distributed towards the top and bottom apical S—Cl bonds. Consequently, the two S—Cl bonds become identical, with a modest stretch, since partial double bond formation is now possible.

(*3*) The equatorial CH_3 group is able to carry out conformational induction but this induction is not amplified further conjugatively because this ligand cannot form a partial C—S double bond. Consequently, the overall effect is very small amounting to nothing more than hyperconjugation (ΔR = 0.0093 Å at $\chi = -90°$ for **I**, however for **III** the ΔR value is about 40 times larger: ΔR = 0.3871 Å at $\chi = -96.35°$).

In order to answer the last question the PES, $E = E(\chi_1, \chi_2)$, had to be explored. Considering the PES of $(H_2N)_2SCl_2$ (**IV**) and $(HO)_2SCl_2$ (**V**) it is prudent to start with a prediction of the ideal surface with the aid of multidimensional conformational analysis or MDCA (4) as it has also been applied in a previous article concerning uneven sulfuranes (1). The indices of the critical points for **IV** and **V** are given in the central column and at the top of Fig. 2.

Since the topological periodicities of the component model potential energy curves for NH_2 and OH were 2 (which may be inferred from Fig. 2 as 1–0–1–0–1) the idealized surface for each case had $2 \times 2 = 4$ minima. Consequently, the number of minima (N_0), the number of saddle points (N_1) and the number of maxima (N_2) obeyed the following alternating sum rule:

$$N_0 - N_1 + N_2 = 0$$
$$4 - 8 + 4 = 0$$

However, due to the excessive interaction between the geminal NH_2 (or geminal OH) groups the idealized surfaces are substantially modified. In the case of **IV** each minimum (labelled as 0) is split up to two minima and a saddle point (labelled as 1) in between. In the case of **V** two saddle points and a minimum collapsed into one saddle point according to the previously recognized (5) selection rules. Consequently, the alternating sum rule for the computed PES assumed the following form:

	$N_0 - N_1 + N_2 = 0$
$(H_2N)_2SCl_2$	$8 - 12 + 4 = 0$
$(HO)_2SCl_2$	$2 - 6 + 4 = 0$

The computed surfaces for the two compounds (shown at the right hand side column of Fig. 2) clearly indicate eight degen-

Can. J. Chem. Downloaded from www.nrcresearchpress.com by 85.192.166.187 on 09/08/12
For personal use only.

Can. J. Chem. Downloaded from www.nrcresearchpress.com by 85.192.166.187 on 09/08/12
For personal use only.

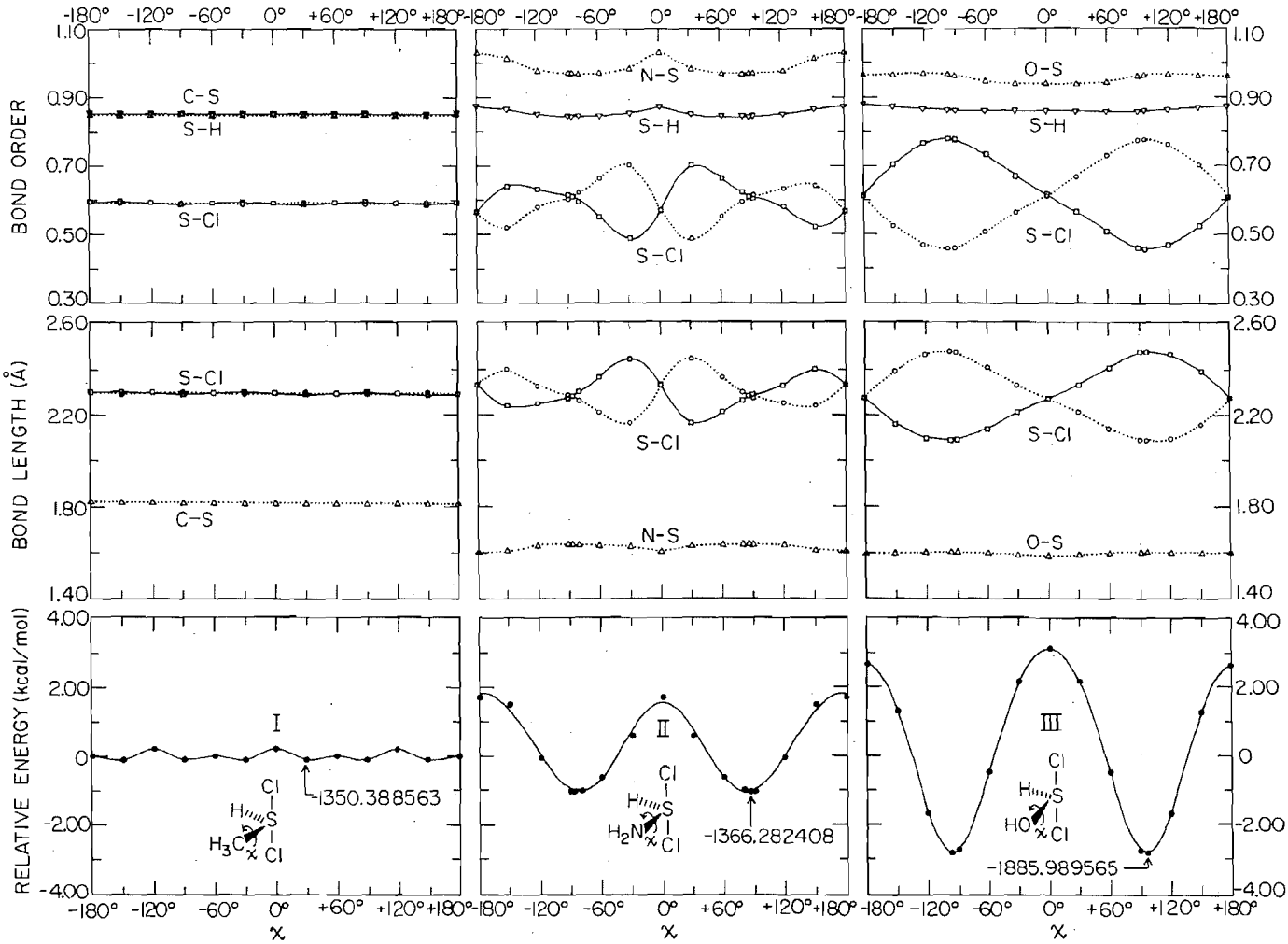

FIG. 1. The variation of the total molecular energy (E), various bond lengths (R) and Mayer type (7) bond orders (BO), with rotational angle χ computed for $H_3C(H)SCl_2$ (**I**), $H_2N(H)SCl_2$ (**II**), and $HO(H)SCl_2$ (**III**) within the SCF framework at a 3-21G* basis set level.

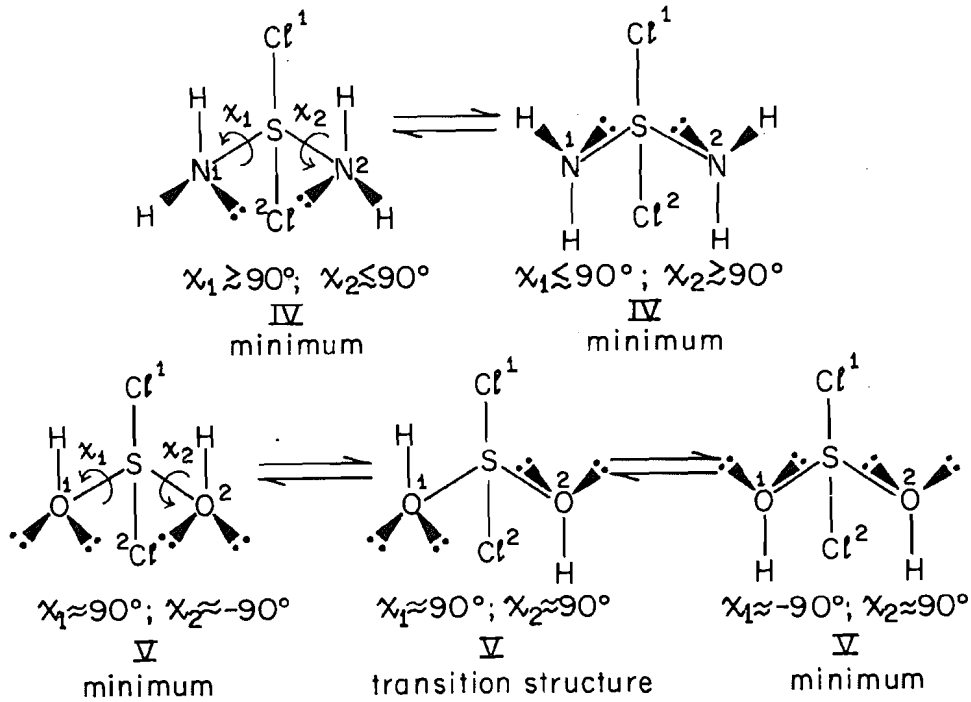

SCHEME 2

Can. J. Chem. Downloaded from www.nrcresearchpress.com by 85.192.166.187 on 09/08/12
For personal use only.

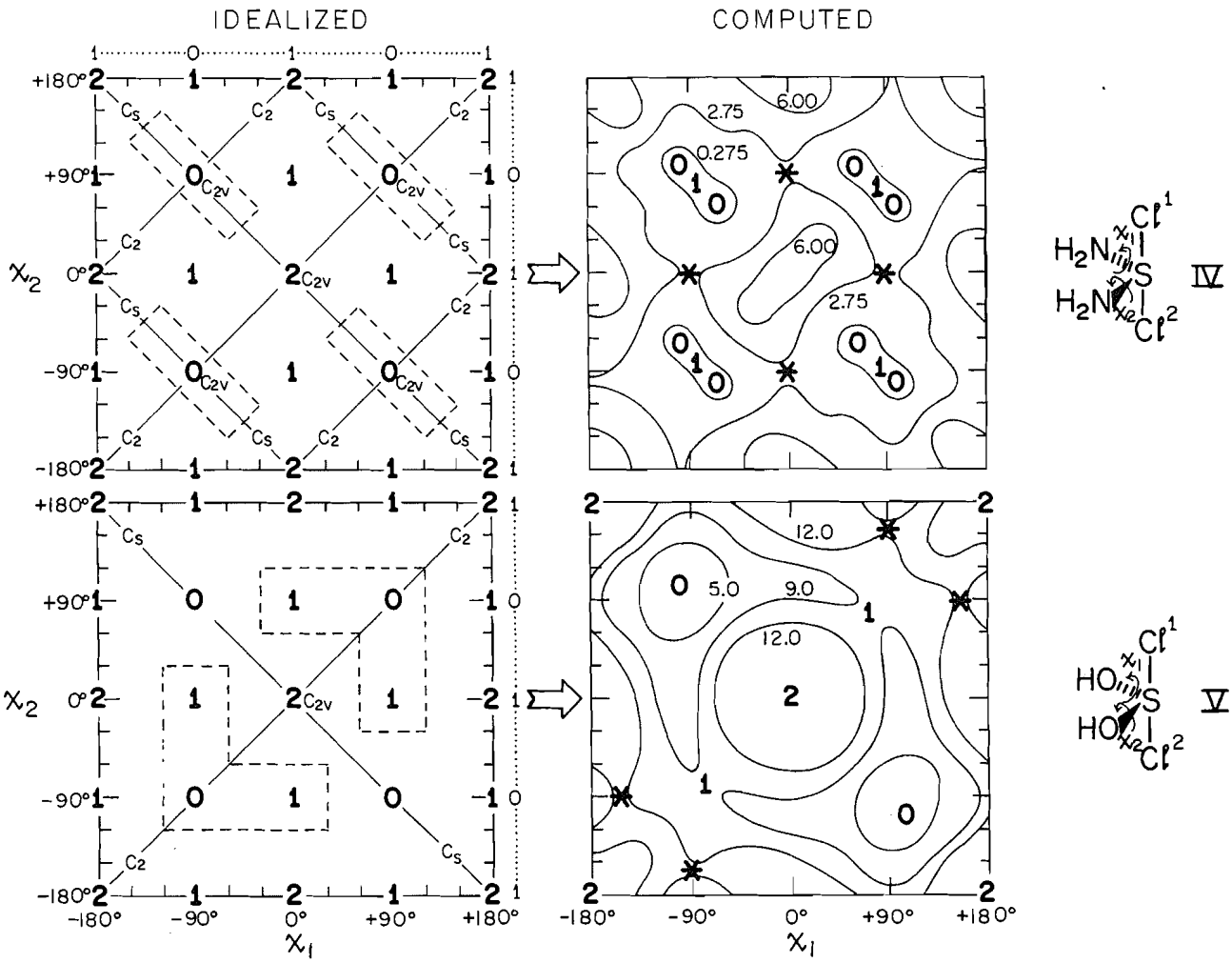

FIG. 2. Topology of the conformational PES, $E = E(\chi_1, \chi_2)$, of $(H_2N)_2SCl_2$ (**IV**) and $(HO)_2SCl_2$ (**V**). At the left hand side the idealized surfaces are given as predicted from the component potential energy curves, $E = E(\chi)$, presented in the lower part of Fig. 1. At the left hand side the location of the critical points, predicted by MDCA, are specified by the index of the critical points (**0** for minima, **1**, for saddle points, and **2** for maxima). At the right hand side, the location of only those critical points that have been determined by gradient optimization are indicated by their index. (An * marks the anticipated location of each of those saddle points that were not gradient optimized.)

TABLE 4. Main geometric parameters for the energy optimized structures of compounds **I–V** of the type $(X^1X^2)SCl_2$

	Value				
Parameter	**I** (CH_3; H)	**II** (NH_2; H)	**III** (OH; H)	**IV** (NH_2; NH_2)	**V** (OH; OH)
R(S—Cl^1)	2.2968	2.2847	2.0910	2.1295	1.9908
R(S—Cl^2)	2.3040	2.2847	2.4781	2.5385	2.7377
ΔR	0.0072	0.000	0.3871	0.4090	0.7469
R(S—X^1)	1.8216	1.6340	1.599	1.6212	1.5660
R(S—X^2)				1.6212	1.5660
χ_1	−143.95 −25.85	−87.2 87.2	−96.35	−94.2 70.0	83.77
χ_2	95.89 —	—	—	−70.0 94.2	−83.77

TABLE 5. The change of four idealized minima at $\chi_1 = \pm 90°$ and $\chi_2 = \pm 90°$ to eight minima on the potential energy hypersurface of $(H_2N)_2SCl_2$

χ_1	χ_2
−(90 + 4.2) = −94.2	(90 + 4.2) = +94.2
−(90 − 20.0) = −70.0	−(90 − 20.0) = −70.0
−(90 + 4.2) = −94.2	−(90 − 20.0) = −70.0
−(90 − 20.0) = −70.0	−(90 + 4.2) = −94.2
+(90 − 20.0) = +70.0	+(90 + 4.2) = +94.2
+(90 + 4.2) = +94.2	+(90 − 20.0) = +70.0
+(90 − 20.0) = +70.0	−(90 − 20.0) = −70.0
+(90 + 4.2) = +94.2	−(90 + 4.2) = −94.2

TABLE 6. The change of four idealized minima at $\chi_1 = \pm 90°$ and $\chi_2 = \pm 90°$ to two minima on the potential energy hypersurface of $(HO)_2SCl_2$

χ_1	χ_2
−(90 − 6.23) = −83.77	(90 − 6.23) = 83.77
(90 − 6.23) = +83.77	−(90 − 6.23) = −83.77

erate catchment regions (6) for **IV** and two degenerate catchment regions (6) for **V**. Typical conformations of **IV** and **V** with varying χ_1 and χ_2 values are shown in Scheme 2 and the main geometrical parameters for compounds **I** and **V** are summarized in Table 4.

It is interesting to note that there is constant shift in geometry, away from the idealized minimum energy conformations. Although this can be seen qualitatively in Fig. 2, it is summarized quantitatively in Tables 5 and 6.

In closing, it should be mentioned that several uneven structures of constitutionally symmetric sulfuranes have been reported (cf. ref. 7). However, as pointed out by Volatron and Eisenstein (8) these observations have been attributed to the anisotropy of crystal packing.

Can. J. Chem. Downloaded from www.nrcresearchpress.com by 85.192.166.187 on 09/08/12
For personal use only.

Acknowledgements

The *ab-initio* computations were carried at the University of Toronto and at CIRCE (Orsay, France). The authors thank IBM-France and CNRS for the generous allocation of computer time within the framework of the GS (Groupement Scientifique) "Modelisation Moléculaire". Thanks are also due to the IBM "Academic Initiative" in Hungary.

The continued financial support of the Natural Sciences and Engineering Research Council of Canada is gratefully acknowledged.

This research was also supported in part by the Hungarian Scientific Research Foundations (OTKA n° 2244) Budapest, Hungary.

1. M. Loos, J.-L. Rivail, A. Kucsman, and I.G. Csizmadia. J. Mol. Struct. Theochem, 230, 143 (1991).
2. E.A. Innes. Ph.D. Thesis. University of Toronto, Toronto, Ont. 1991.
3. I. Mayer. Chem. Phys. Lett. **97**, 270 (1983).
4. (*a*) I.G. Csizmadia. General and theoretical aspects of the thiol group. *In* The chemistry of the thiol group. *Edited by* Saul Patai. John Wiley and Sons, New York. 1974. pp. 1–109 (cf. particularly pp. 36–41 including Figs. 23 and 24, Table 20); (*b*) I.G. Csizmadia. Multidimensional theoretical stereochemistry and conformational potential energy surface topology. *In* New theoretical concept for understanding organic reactions. *Edited by* J. Bertrán. D. Reidel Publishing Co., Dordrecht. 1989. pp. 1–31.
5. J.G. Angyan, R. Daudel, A. Kucsman, and I.G. Csizmadia. 1989. Chem. Phys. Lett. **136**, 1 (1987).
6. P.G. Mezey. Potential energy hypersurfaces. Elsevier Science Publishers. 1987. p. 227.
7. A. Kucsman. Non-bonded sulfur–oxygen interaction in organic sulfur compounds. *In* Organic sulfur chemistry, theoretical and experimental advances. *Edited by* F. Bernardi, I.G. Csizmadia, and A. Mangini. Elsevier, Amsterdam. 1985. Chap. 4, pp. 191–245.
8. F. Volatron and O. Eisenstein. Chem. Commun. 301 (1986).

Rate constants for reactions of horseradish peroxidase compounds I and II with 4-substituted arylboronic acids

WEIMEI SUN
Department of Chemistry, University of Alberta, Edmonton, AB T6G 2G2, Canada

XIAOYING JI AND LARRY J. KRICKA
Department of Pathology and Laboratory Medicine, University of Pennsylvania, Philadelphia, PA 19104, U.S.A.

AND

H. BRIAN DUNFORD[1]
Department of Chemistry, University of Alberta, Edmonton, AB T6G 2G2, Canada

Received May 13, 1994

WEIMEI SUN, XIAOYING JI, LARRY J. KRICKA, and H. BRIAN DUNFORD. Can. J. Chem. **72**, 2159 (1994).

The rate constants for the reactions of horseradish peroxidase compound I (k_1) and compound II (k_2) with three 4-substituted arylboronic acids, which enhance chemiluminescence in the horseradish peroxidase catalyzed oxidation of luminol by hydrogen peroxide, were determined at pH 8.6, total ionic strength 0.11 M, using stopped-flow kinetic measurements. For comparison, the rate constants of the reactions of 4-iodophenol with compounds I and II were also determined under the same experimental conditions. The three arylboronic acid derivatives and their rate constants are: 4-biphenylboronic acid, $k_1 = (1.21 \pm 0.08) \times 10^6\ M^{-1}\ s^{-1}$, $k_2 = (4.6 \pm 0.2) \times 10^5\ M^{-1}\ s^{-1}$; 4-bromophenylboronic acid, $k_1 = (5.5 \pm 0.2) \times 10^4\ M^{-1}\ s^{-1}$, $k_2 = (3.6 \pm 0.2) \times 10^4\ M^{-1}\ s^{-1}$; and 4-iodophenylboronic acid, $k_1 = (1.1 \pm 0.2) \times 10^5\ M^{-1}\ s^{-1}$, $k_2 = (1.3 \pm 0.1) \times 10^4\ M^{-1}\ s^{-1}$. 4-Biphenylboronic acid, which shows comparable luminescent enhancement to 4-iodophenol, has the highest reactivity in the reduction of both compounds I and II among the three arylboronic acid derivatives tested.

WEIMEI SUN, XIAOYING JI, LARRY J. KRICKA et H. BRIAN DUNFORD. Can. J. Chem. **72**, 2159 (1994).

Opérant à un pH de 8,6 et un force ionique totale de 0, 11 M et faisant appel à des techniques de mesures cinétiques à flux stoppé, on a déterminé les constantes de vitesse des réactions des composés I (k_1) et II (k_2) de la peroxydase du raifort avec trois acides arylboroniques substitués en position 4 qui augmentent la chimiluminescence de l'oxydation, catalysée par la peroxydase du raifort, du luminol par le peroxyde d'hydrogène. Pour fins de comparaison, on a aussi déterminé les constantes de vitesse des réactions du 4-iodophénol avec les composés I et II dans les mêmes conditions expérimentales. Les trois dérivés d'acides arylboroniques et leurs constantes de vitesse sont : acide 4-biphénylboronique, $k_1 = (1{,}21 \pm 0{,}08) \times 10^6\ M^{-1}\ s^{-1}$, $k_2 = (4{,}6 \pm 0{,}2) \times 10^5\ M^{-1}\ s^{-1}$, acide 4-bromophénylboronique, $k_1 = (5{,}5 \pm 0{,}2) \times 10^4\ M^{-1}\ s^{-1}$, $k_2 = (3{,}6 \pm 0{,}2) \times 10^4\ M^{-1}\ s^{-1}$ et acide 4-iodophénylboronique, $k_1 = (1{,}1 \pm 0{,}2) \times 10^5\ M^{-1}\ s^{-1}$, $k_2 = (1{,}3 \pm 0{,}1) \times 10^4\ M^{-1}\ s^{-1}$. Parmi les trois dérivés de l'acide arylboronique qui ont été examinés, l'acide 4-biphénylboronique, qui présente une augmentation de la luminescence comparable à celle du 4-iodophénol, est le plus réactif dans la réduction des composés I et II.

[Traduit par la rédaction]

Introduction

Recently, certain arylboronic acid derivatives have been shown to function as enhancers in the chemiluminescent horseradish peroxidase (HRP) catalyzed oxidation of luminol (1). The most potent enhancers are 4-bromo-, 4-iodo-, and 4-biphenylboronic acids. The structures of the biphenyl and phenyl compounds are as follows:

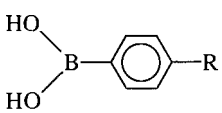

where R = Br, I, or phenyl. These compounds increase the light emission in the HRP-catalyzed reaction of luminol by >10-fold and also reduce the background light emission from the luminol–peroxide assay reagent. The light emission increases rapidly during a 1–5 min period depending upon the enhancer used, and then decays slowly over a 30–60 min period. Previously other compounds that are enhancers have been discovered and these include substituted phenols, naphthols, aromatic amines, and benzothiazoles (2–7). The phenolic enhancers have been most extensively studied and a mechanism for the enhancement proposed (8). It involves a preferential and rapid reaction of the phenol with compound I and compound II to form phenoxyl radicals. These then react with luminol to form luminol radicals, which react further in a light-generating reaction.

The rate constants for the reaction of luminol and a series of enhancers with compound I (k_1) and compound II (k_2) have been measured and, in accordance with the proposed mechanism, the rate constants for the enhancers are higher than the rate constants for luminol (e.g., luminol, $k_1 = 2.3 \times 10^6\ M^{-1}\ s^{-1}$ and $k_2 = 7.2 \times 10^4\ M^{-1}\ s^{-1}$; 4-iodophenol, $k_1 = 5.5 \times 10^6\ M^{-1}\ s^{-1}$ and $k_2 = 4.0 \times 10^6\ M^{-1}\ s^{-1}$) (9–11).

In this study we have determined the rate constants for selected 4-substituted arylboronic acids with HRP compounds I and II in order to determine if the mechanism of enhancement is similar to that with phenols.

Experimental

Horseradish peroxidase (type VI-A) was obtained from Sigma Chemical Co. The concentration of the enzyme solution was determined spectrophotometrically at 403 nm using a molar absorptivity of $1.02 \times 10^5\ M^{-1}\ cm^{-1}$ (12). The purity number (A_{403nm}/A_{280nm}) of the enzyme solution was 3.1. The concentration of H_2O_2, obtained from BDH Chemicals, was determined after appropriate dilution using the horseradish peroxidase assay (13). *p*-Cresol was obtained from J.T. Baker Chemical Co. and its concentration was determined by weight.

[1]Author to whom correspondence may be addressed. Telephone: (403) 492-3818. Fax: (403) 492-8231. e-mail: brian_dunford@dept.chem.ualberta.ca

Can. J. Chem. Downloaded from www.nrcresearchpress.com by 85.192.166.187 on 09/08/12
For personal use only.

TABLE 1. The apparent second-order rate constants for the reactions of HRP-I and HRP-II at pH 8.6, total ionic strength 0.11 M

Substrate	HRP-I (M^{-1} s^{-1})	HRP-II (M^{-1} s^{-1})
4-Iodophenol	$(5.6 \pm 0.3) \times 10^6$	$(1.78 \pm 0.09) \times 10^6$
4-Biphenylboronic acid	$(1.21 \pm 0.08) \times 10^6$	$(4.6 \pm 0.2) \times 10^5$
4-Bromophenylboronic acid	$(5.5 \pm 0.2) \times 10^4$	$(3.6 \pm 0.2) \times 10^4$
4-Iodophenylboronic acid	$(1.1 \pm 0.2) \times 10^5$	$(1.3 \pm 0.1) \times 10^4$
Luminol	2.3×10^6 (at pH 8.0)[a]	7.2×10^4 (at pH 8.0)[a]

[a]See ref. 10.

4-Biphenylboronic acid was from Aldrich, and 4-bromophenylboronic acid was from Lancaster. 4-Iodophenylboronic acid was synthesized by Cookson Chemicals Ltd., Southampton.

For each substrate, a stock solution of around 2.5 mM concentration was prepared by dissolving a weighed amount of the compound in a small amount of dimethyl sulfoxide (DMSO, < 200 μL) and then in a certain volume of deionized water. All substrate solutions were stored in dark brown bottles to prevent photochemical reactions. The substrate solution for each experiment was then made by diluting the stock solution to the desired concentration with Tris–HCl buffer, ph 8.6, just before the measurement.

0.1 M Tris(hydroxymethyl)methylamine–HCl buffer at pH 8.6 and 0.01 M tris(hydroxymethyl)methylamine–HCl buffer at pH 9.1 were prepared. The ionic strengths of the buffers were 0.01 M and 0.001 M, respectively. Analytical grade reagent K_2SO_4, obtained from AnalaR, was used to keep the total ionic strength of the solutions at 0.11 M. A Fisher Scientific Accumet pH meter 25 was used for pH measurements.

All solutions were prepared using water purified by a Milli-Q water purification system from Millipore.

HRP-I, stable for 6 min, was prepared by the addition of 1 equivalent of H_2O_2 to the native enzyme in deionized water of ionic strength 0.11 M by adding K_2SO_4 as an inert salt. HRP-II, stable for at least 10 min, was prepared in 0.01 M Tris-HCl buffer of pH 9.1 by adding 1 equivalent of H_2O_2 and 0.5 molar equivalent of *p*-cresol to the native enzyme solution. Optical spectra of native enzyme, HRP-I, and HRP-II were recorded on a Beckman DU 650 spectrophotometer. The stability of the HRP-I and HRP-II solutions was confirmed each day before the stopped-flow experiments.

The stopped-flow measurements were made using a Photal Rapid Reaction Analyzer model RA-601 equipped with a 1-cm observation cell. Experimental curves were recorded and stored in the computer interfaced to the rapid reaction analyzer. A pH-jump method was used for all stopped-flow experiments to attain the final pH of 8.6.

For measurement of rate constants involving HRP-I, one cuvette contained stable HRP-I in deionized water, pH 5.7, ionic strength 0.11 M by adding K_2SO_4; the other cuvette contained substrate in 0.1 M Tris–HCl buffer, pH 8.6, total ionic strength 0.11 M. After the two solutions were mixed, the final pH was 8.6. The HRP-I reactions were monitored at 412 nm, the isosbestic point between native enzyme and HRP-II (14).

For measurement of rate constants involving HRP-II, one cuvette contained stable HRP-II in 0.01 M Tris–HCl buffer, pH 9.1, total ionic strength 0.11 M; the other cuvette contained substrate in 0.1 M Tris–HCl buffer, pH 8.6, total ionic strength 0.11 M. After the mixing of the two solutions, the final pH was 8.6. The HRP-II reactions were monitored at 430 nm, the isosbestic point between native enzyme and HRP-I (14).

The enzyme concentration for all kinetic measurements was 1 μM. At least at 10-fold excess of substrate was used to maintain pseudo-first-order conditions. Six to eight traces were collected for each substrate concentration. Measurements of relative absorbance at regular time intervals from the recorded exponential traces followed by a nonlinear least-squares analysis gave the observed pseudo-first-order rate constants (k_{obs}). The mean value of k_{obs} obtained from the recorded traces was taken. The linear slope of the plot of k_{obs} versus substrate concentration gives the apparent second-order rate constant (k_{app}).

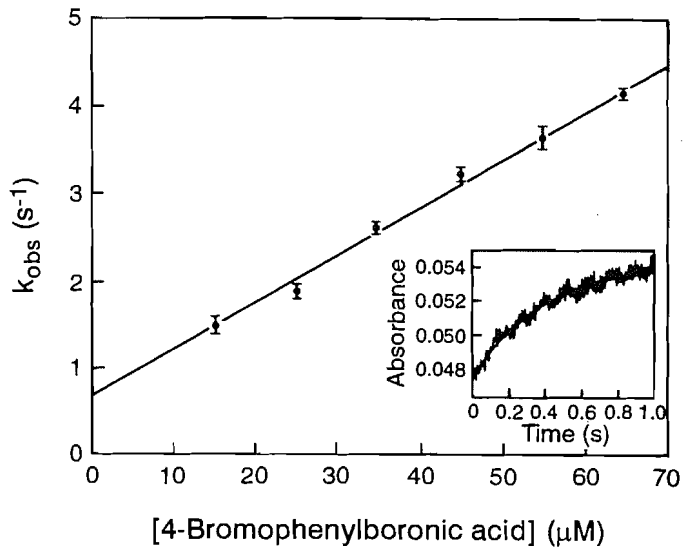

FIG 1. Plot of k_{obs} versus 4-bromophenylboronic acid concentration for the oxidation of 4-bromophenylboronic acid by horseradish peroxidase compound I. The reactions were carried out in Tris–HCl buffer, pH 8.6, ionic strength 0.11 M; [HRP-I], 1.0 μM. The inset shows an example of first-order exponential trace monitored at 412 nm (35 μM 4-bromophenylboronic acid) followed by a nonlinear least-squares analysis from which k_{obs} was obtained.

The pH dependence of light emission of the 4-biphenylboronic acid enhanced chemiluminescent oxidation of luminol catalyzed by horseradish peroxidase was determined as follows. Luminol–hydrogen peroxide reagents were prepared in different Tris buffer (0.1 M, pH 7.58, 8.10, 8.58, 9.12, 9.26). Sodium luminol (12.5 mg) was dissolved in 50 mL of the buffer, 15.5 μL of hydrogen peroxide (30% w/v) was mixed with 0.5 mL of the same buffer, and these two solutions were combined and protected from light. Stock solutions of 4-biphenylboronic acid (20 mM in DMSO) and HRP (1 mg/mL in 0.1 M Tris buffer) were diluted in Tris buffer (0.1 M, pH 8.58). The luminol–hydrogen peroxide reagent (100 μL), 4-biphenylboronic acid (10 μL, 1 mM), and HRP (10 μL, 20 ng/mL) were mixed in a microwell and light emission intensity was measured in a mL-3000 luminometer (Dynatech Laboratories Inc, Chantilly, Va).

Results

Determination of the rate constants of the reactions involving HRP-I

With substrate in excess of HRP-I, pseudo-first-order kinetics was observed. An example is shown in the inset of Fig. 1. The corresponding differential expression is

$$[1] \quad -d[\text{HRP-I}]/dt = k_{obs}[\text{HRP-I}]$$

where k_{obs} is the observed pseudo-first-order rate constant. The

Can. J. Chem. Downloaded from www.nrcresearchpress.com by 85.192.166.187 on 09/08/12
For personal use only.

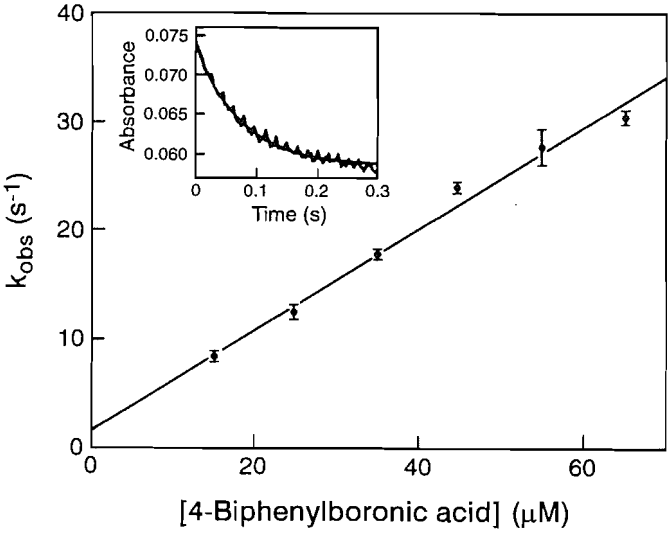

FIG 2. Plot of k_{obs} versus 4-biphenylboronic acid concentration for the oxidation of 4-biphenylboronic acid by horseradish peroxidase compound II. The reactions were carried out in Tris–HCl buffer, pH 8.6, ionic strength 0.11 M; [HRP-II], 1.0 μM. The inset shows an example of first-order exponential trace monitored at 430 nm (25 μM 4-biphenylboronic acid) followed by a nonlinear least-squares analysis from which k_{obs} was obtained.

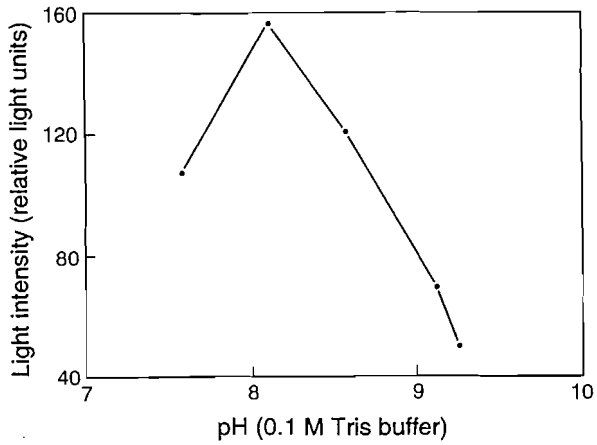

FIG 3. pH dependence of light emission of the 4-biphenylboronic acid enhanced chemiluminescent oxidation of luminol catalyzed by horseradish peroxidase. Luminol–hydrogen peroxide reagents were prepared in different Tris buffers (0.1 M, pH 7.58, 8.10, 8.58, 9.12, 9.26) by mixing two solutions of 12.5 mg of sodium luminol in 50 mL of the buffer and 15.5 μL of 30% (w/v) hydrogen peroxide in 0.5 mL of the same buffer. Stock solutions of 4-biphenylboronic acid and HRP were diluted in Tris buffer (0.1 M, pH 8.58). After mixing 100 μL of the luminol–hydrogen peroxide reagent with 10 μL of 1 mM 4-biphenylboronic acid and 10 μL of 20 ng/mL HRP in a microwell, the light emission intensity was measured.

apparent second-order rate constant, k_{app}, is related to k_{obs} by the equation

[2] $k_{obs} = k_{app}[\text{substrate}]$

Values of k_{app} were obtained from the slopes of plots of k_{obs} versus substrate concentration, as shown by an example in Fig. 1. The intercept in Fig. 1 is zero, within experimental error. The apparent second-order rate constants for the reactions of HRP-I with 4-biphenylboronic acid, 4-bromophenylboronic acid, 4-iodophenylboronic acid, and 4-iodophenol are listed in Table 1.

Determination of the rate constants of the reactions involving HRP-II

One example is shown in the inset of Fig. 2. The corresponding differential rate expression is

[3] $-\text{d[HRP-II]} / \text{d}t = k_{obs}[\text{HRP-II}]$

and the apparent second-order rate constant, k_{app}, is related to k_{obs} by eq. [2]. Values of k_{app} were then obtained from the slopes of plots of k_{obs} versus substrate concentration, as shown by an example in Fig. 2. The intercept in Fig. 2 is zero, within experimental error. The apparent second-order rate constants for the reactions of HRP-II with 4-biphenylboronic acid, 4-bromophenylboronic acid, 4-iodophenylboronic acid, and 4-iodophenol are collected in Table 1.

The pH dependence of light emission intensity from the 4-biphenylboronic acid enhanced reaction is shown in Fig. 3.

Discussion

It was observed that the light emission in the HRP-catalyzed reaction of luminol was at its maximum at pH 8.6 in the presence of certain phenols and therefore this pH was chosen for the comparison with the arylboronic acid derivatives (1). The rate constants of the reactions of three 4-substituted arylboronic acids with HRP-I and HRP-II were therefore measured at this pH.

The rate constants of the reactions of HRP-I and HRP-II with 4-iodophenol were determined previously by Hodgson and Jones (9), and are $k_1 = 5.5 \times 10^6\ M^{-1}\ s^{-1}$ and $k_2 = 4.0 \times 10^6\ M^{-1}\ s^{-1}$ at pH 7.0, ionic strength 0.11 M. The effect of pH on the rate constants was also measured (9). The HRP-I reaction rate with 4-iodophenol shows a pH-independent phase in the pH range of 7.0–8.7 followed by a decrease at pH higher than 8.7, whereas the log of the rate constant for the HRP-II reaction, plotted versus pH, has a slope of –1 in the pH range of 7–10. In the present study, we determine values of the rate constants at pH 8.6 as follows: $k_1 = 5.6 \times 10^6\ M^{-1}1\ s^{-1}$, which is the same within experimental error as that at pH 7.0, and $k_2 = 1.8 \times 10^6\ M^{-1}\ s^{-1}$, which is smaller, as expected, than the value at pH 7.0. Our data for 4-iodophenol thus are in accord with the data previously reported (9).

The rate constant for the reaction of 4-biphenylboronic acid with HRP-I is of the same order of magnitude as that for 4-iodophenol, whereas the bromo and iodo derivatives have lower reactivities. All three boronic acids have lower reactivities towards HRP-II than 4-iodophenol, again with the bromo and iodo derivatives slower than biphenylboronic acid (Table 1).

The pK_a value of 4-iodophenol is 9.22 (15). Therefore, the percentage of 4-iodophenol in its ionized form is 19.4% at pH 8.6. The pK_a values of 4-biphenylboronic acid (in 50% EtOH) and 4-bromophenylboronic acid (in 52% EtOH) are 10.80 and 9.14, respectively (16, 17). According to these pK_a values, the approximate percentage of the compounds in their ionized forms at pH 8.6 is about 0.63% for 4-biphenylboronic acid and 22.4% for 4-bromophenylboronic acid.

The data at pH 8.6 would appear to indicate that if the arylboronic acid is unionized there is greater enhancement. However, at lower pH there is a smaller percentage of ionization of the arylboronic acids and luminescence enhancement is

Can. J. Chem. Downloaded from www.nrcresearchpress.com by 85.192.166.187 on 09/08/12
For personal use only.

reduced (Fig. 3). An explanation for the pH dependence of the HRP-catalyzed luminescent reactions can be found in a pulse radiolysis study of aqueous luminol reactions (18) and in the numerous pH-dependent studies of HRP-II reactions (19).

Several key rate constants in the luminol reactions leading to light emission were measured in the pulse radiolysis study of Lind et al. (18). The pH dependence of the formation of a hydroperoxide intermediate from the luminol diazasemiquinone radical roughly parallels the pH dependence of light emission, which reaches a plateau value at ~pH 10. Thus the radiation-induced luminescence is strongest at high pH. HRP-II reactions are dependent upon a key acid–base group in the active site which has a pK_a value of 8.6 (19). If this group is protonated HRP-II is reactive; if it is deprotonated HRP-II is totally unreactive. Thus for the HRP-catalyzed reaction, at low pH luminescence intensity is low because of the luminol chemistry, and at very high pH it is low because the enzyme cycle is blocked by the accumulation of unreactive HRP-II. In the vicinity of pH 8.6 conditions are optimal because HRP-II is reactive and there is sufficient accumulation of diazasemiquinone radicals.

Thus although the pH dependence of the HRP–luminol reaction can be explained, the mechanistic details of the effect of arylboronic acid enhancers is less clear. Hodgson and Jones (9) noted that the best phenolic luminescent enhancer in the HRP-catalyzed light-emitting reaction, 4-iodophenol, reacts more rapidly than predicted by the Hammett $\rho\sigma$ correlation for phenols (20–23) and also exhibits a nontypical pH–rate profile. They suggest that because of the enhanced reactivity of 4-iodophenol, free radicals formed from it attack unreacted luminol, enhancing the production of luminol semiquinone radicals and thus enhancing chemiluminescence. On the other hand, Vlasenko et al. examine the possibility that the enhancer facilitates a higher steady concentration of HRP-I that in turn facilitates greater reactivity of luminol (11). They conclude that the latter possibility does not lead to a large enough enhancement.

4-Biphenylboronic acid causes a greater luminescence enhancement than that of 4-iodophenol, yet the rate constant for the reaction of 4-biphenylboronic acid with HRP-I is smaller than that for 4-iodophenol; and with HRP-II it is much smaller. Unlike 4-iodophenol, the rate constants for the arylboronic acid type enhancers are not much higher than the rate constants for luminol (Table 1). Therefore, it appears that the arylboronic acid derivatives may have a different mechanism of enhancement from that for phenolic enhancers.

Acknowledgement

The financial support of the British Technology Group (NRDC) is gratefully acknowledged. This work is the subject of patent applications assigned to the British Technology Group.

1. L.J. Kricka. Chemiluminescent enhancers. WO Patent Appl 93/16/95 (1993).
2. G.H.G. Thorpe and L.J. Kricka. Methods Enzymol. **133**, 331 (1986).
3. G.H.G. Thorpe, L.J. Kricka, E. Gillespie, S. Moseley, R. Amess, N. Baggett, and T.P. Whitehead. Anal. Biochem. **145**, 96 (1985).
4. G.H.G. Thorpe, S.B. Moseley, L.J. Kricka, R.A. Stott, and T.P. Whitehead. Anal. Chim. Acta, **170**, 101 (1985).
5. G.H.G. Thorpe, L.J. Kricka, S.B. Moseley, and T.P. Whitehead. Clin. Chem. **31**, 1335 (1985).
6. G.H.G. Thorpe, L.J. Kricka, and T.P. Whitehead. Clin. Chem. **31**, 913 (1985).
7. L.J. Kricka, A. M. O'Toole, G.H.G. Thorpe, and T.P. Whitehead. Enhanced luminescent or luminometric assay. U.S. Patent 4/729/950 (1988).
8. G.H.G. Thorpe and L.J. Kricka. *In* Bioluminescence and chemiluminescence: new perspectives. *Edited by* J. Scholmerich, R. Andreesen, A. Kapp, M. Ernst, and W.G. Wood. Wiley, Chichester. 1987. p. 199.
9. M. Hodgson and P. Jones. J. Biolumin. Chemilumin. **3**, 21 (1989).
10. M.J. Cormier and P.M. Pritchard. J. Biol. Chem. **243**, 4706 (1968).
11. S.B. Vlasenko, A.A. Arefyev, A.D. Klimov, B.B. Kim, A.P. Osipov, E.M. Gavrilova, and A.M. Yegorov. J. Biolumin. Chemilumin. **4**, 164 (1989).
12. P.-I. Ohlsson and K.-G. Paul. Acta Chem. Scand Ser B: **B30**, 373 (1976).
13. M.L. Cotton and H.B. Dunford, Can. J. Chem. **51**, 582 (1973).
14. H.B. Dunford. Adv. Inorg. Biochem. **4**, 41 (1982).
15. W. Simon, A. Morikofer, and E. Heilbronner. Helv. Chim. Acta, **40**, 1918 (1957).
16. B. Bettman, G.E.K. Branch, and D.L. Yabroff. J. Am. Chem. Soc. **56**, 1865 (1934).
17. D.L. Yabroff, G.E.K. Branch, and B. Bettman. J. Am. Chem. Soc. **56**, 1850 (1934).
18. J. Lind, G. Merényi, and T.E. Eriksen. J. Am. Chem. Soc. **105**, 7655 (1983).
19. H.B. Dunford and J.S. Stillman. Coord. Chem. Rev. **19**, 187 (1976).
20. D. Job and H.B. Dunford, Eur. J. Biochem. **66**, 607 (1976).
21. H.B. Dunford and A.J. Adeniran. Arch. Biochem. Biophys. **251**, 536 (1986).
22. J. Sakurada, R. Sekiguchi, K. Sato and T. Hosoya. Biochemistry, **29**, 4093 (1990).
23. H. Zhang and H.B. Dunford. Can. J. Chem. **71**, 1990 (1993).

Can. J. Chem. Downloaded from www.nrcresearchpress.com by 85.192.166.187 on 09/08/12
For personal use only.

Lewis acid catalyzed Diels–Alder reactions of two useful dienyl phosphate esters[1]

HSING-JANG LIU, WAISENG MARTIN FENG, JEUNG BEA KIM, AND ERIC N.C. BROWNE[2]

Department of Chemistry, The University of Alberta, Edmonton, AB T6G 2G2, Canada

Received June 1, 1994

HSING-JANG LIU, WAISENG MARTIN FENG, JEUNG BEA KIM, and ERIC N.C. BROWNE. Can. J. Chem. **72**, 2163 (1994).

The Lewis acid catalyzed Diels–Alder reactions of dienyl phosphate esters **1** and **2** were examined. 2-Diethylphosphoryloxy-1,3-butadiene (**1**) was found to react with a variety of α,β-unsaturated carbonyl compounds under Lewis acid catalysis with excellent regioselectivity to give synthetically useful cyclohexene derivatives. The adducts were produced in accordance with the normal rules governing the Diels–Alder addition. In the presence of stannic chloride acyclic α,β-unsaturated ketones such as ethyl vinyl ketone and methyl vinyl ketone reacted rapidly with diene phosphate **1** to give exclusively the *para*-addition products **8** and **9** in excellent yields. When diene **1** was treated with the complex cyclic enone ester **14** in the presence of ferric chloride the single *para*-rule adduct **15** was obtained in good yield. The stannic chloride catalyzed Diels–Alder reactions of *trans*-2-diethylphosphoryloxy-1,3-pentadiene (**2**) were also studied. Diene phosphate **2** reacted efficiently with a number of acyclic α,β-unsaturated ketones such as methyl vinyl ketone, ethyl vinyl ketone, and *trans*-3-penten-2-one with complete regio- and stereoselectivity to give single cyclohexene derivatives **38**, **39**, and **40**.

HSING-JANG LIU, WAISENG MARTIN FENG, JEUNG BEA KIM et ERIC N.C. BROWNE. Can. J. Chem. **72**, 2163 (1994).

On a étudié les réactions de Diels–Alder catalysées par les acides de Lewis des esters **1** et **2**, phosphates de diényle. On a trouvé que, sous catalyse par les acides de Lewis, le 2-diéthylphosphoryloxybuta-1,3-diène (**1**) réagit avec une variété de composés carbonylés α,β-insaturés avec une excellent régiosélectivité pour conduire à des dérivés du cyclohexène qui sont utiles en synthèse. Les adduits se produisent selon les règles normales gouvernant les additions de Diels–Alder. En présence de chlorure stannique, les cétones α,β-insaturées, telles que l'éthyl vinyl cétone et la méthyl vinyl cétone, réagissent rapidement avec le phosphate diénique **1** pour donner exclusivement les produits d'addition *para*, **8** et **9**, avec d'excellents rendements. Lorsqu'on traite le diène **1** avec l'ester cyclohexénonique complexe **14**, en présence de chlorure ferrique, seul l'adduit *para*, **15**, a été obtenu avec un bon rendement. On a aussi étudié les réactions de Diels–Alder catalysées par le chlorure stannique du *trans*-2-diéthylphosphoryloxybuta-1,3-diène (**2**). Le phosphate diénique **2** réagit d'une façon efficace avec un certain nombre de cétones α,β-insaturées, telles que la méthyl vinyl cétone, l'éthyl vinyl cétone et la *trans*-pent-3-én-2-one, avec des régio- et stéréosélectivités complètes pour donner uniquement les dérivés cyclohexéniques **38**, **39** et **40**.

[Traduit par la rédaction]

Introduction

In the past decade Diels–Alder reactions of heterosubstituted 1,3-dienes with dienophiles have increasingly been developed as valuable methods for the synthesis of highly functionalized ring systems. Recent advances in the comprehension of electronic and steric effects governing this reaction[3] have been accompanied by the use of new specifically functionalized dienes and dienophiles to produce hitherto unattainable substitution patterns both regioselectively and stereoselectively.[4] The introduction of one or more hetero substituents on the diene invariably has an effect on the regiochemistry of the cycloaddition and permits further transformations of the adducts that take advantage of the relationship between the hetero substituents and the newly formed carbon–carbon double bonds. For example silyloxy-substituted butadienes (13–15) have come into widespread use in natural product syntheses. Unfortunately, these types of dienes and the cycloaddition products derived from them are rather labile under acidic or basic conditions, or even in polar solvents.

In a practical sense, the instability of these compounds is sometimes a serious problem in the Diels–Alder reaction as well as in further transformations of the adducts. On the other hand, enol phosphates are significantly more stable while retaining a high degree of synthetic versatility. 2-Diethylphosphoryloxy-1,3-butadiene (**1**) has been found (28, 29) to be an oxygen-substituted diene of unusual stability. Liu and Ngooi have used the analogue *trans*-2-diethylphosphoryloxy-1,3-pentadiene (**2**) to add to 2-carbomethoxy-2-cyclohexen-1-one (**3**) with excellent stereoselectivity in the synthesis (30, 31) of petasitolone (**4**) *via* adduct **5**. In the same study they also found that the addition of *trans*-2-trimethylsilyloxy-1,3-pentadiene (**6**) to the dienone ester **3** gave the corresponding adduct as a mixture of degradation products, the two epimeric diketones **7**, in much poorer yield (31, 32). The diketones **7** apparently result from hydrolysis of the expected Diels–Alder adducts under the reaction conditions.

Dienyl phosphates such as **1** and **2** represent attractive intermediates to serve as the diene component in Diels–Alder reactions. The previous brief study of dienyl phosphate **1** as a diene in the Diels–Alder reaction examined only thermal conditions (28, 29). The potential utility of dienyl phosphates in diene synthesis coupled with the observed stability of these compounds towards acidic conditions led us to undertake a study of the synthetic utility of **1** and **2** in Lewis acid catalyzed Diels–Alder reactions, which are characteristically faster (33–35), more stereoselective (36), and more regioselective (37–39) than the corresponding uncatalyzed cycloadditions. The details of this investigation are described.

Results and discussion[5]

The previously reported (28, 29, 42, 43) 2-diethylphosphoryloxy-1,3-butadiene (**1**) was conveniently prepared in our

[1]Taken in part from the M.Sc. thesis of W.M. Feng, the University of Alberta, 1986

[2]Present address: Wyeth-Ayerst Laboratories, 1025 Laurentian Blvd., St. Laurent, QC H4R 1J6, Canada.

[3]For example, see refs. 1–12 and references therein.

[4]For example, see refs. 13–27 and references therein.

[5]These results have been briefly described in preliminary communications (40, 41).

Can. J. Chem. Downloaded from www.nrcresearchpress.com by 85.192.166.187 on 09/08/12
For personal use only.

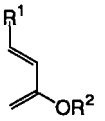

1 $R^1 = H$; $R^2 = PO(OEt)_2$
2 $R^1 = Me$; $R^2 = PO(OEt)_2$
6 $R^1 = Me$; $R^2 = SiMe_3$

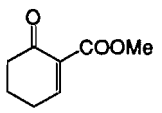

3

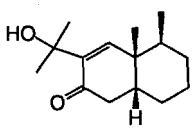

4

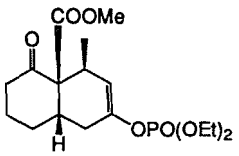

5

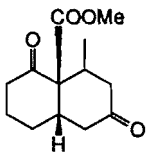

7

laboratories by a modification of the method of Ireland and Pfister (44) by treatment of methyl vinyl ketone with lithium diisopropylamide in tetrahydrofuran at −78°C followed by trapping of the resulting enolate ion with diethyl chlorophosphate. Diene **1** was obtained as a colorless oil in 75% yield. Dienyl phosphate **1** can be stored at 0°C over a long period of time without apparent decomposition. *trans*-2-Diethylphosphoryloxy-1,3-pentadiene (**2**) was obtained (30, 31) in a similar manner from *trans*-3-penten-2-one and diethyl chlorophosphate, which gave diene **2** as a stable (0°C) colorless oil in 41% yield (31).

The Diels–Alder reactions of dienes **1** and **2** with a variety of dienophiles were carried out under Lewis acid catalysis. The various adducts were identified by their spectral characteristics, especially by ^1H nmr decoupling and nOe experiments, and by chemical modification where necessary. A brief study of the effect of changing the catalyst on the products of the additions of diene **1** was conducted. The results of the cycloadditions, structural assignments, and catalyst study are discussed.

1. Diels–Alder reactions of 2-diethylphosphoryloxy-1,3-butadiene (1)

Diene **1** was subjected to reaction with a variety of α,β-unsaturated carbonyl compounds in methylene chloride solution at 0°C, using stannic chloride as the catalyst. In general the Diels–Alder additions of **1** proceeded rapidly and in excellent yield with very small excesses of the diene. In most cases the recovery of intact unreacted diene **1** rendered the incorporation of that intermediate nearly quantitative. Unfortunately the yields of addition to simple cyclic enones were disappointing.[6] The usual rules of Diels–Alder addition (45, 48–51) were followed. The results are summarized in Table 1. Although structural assignments relied heavily on ^1H nmr, ^{13}C nmr, and nOe experiments, several of the adducts of **1** required further chemical modification in order to unambiguously establish their structures. These conversions are summarized in Scheme 1. The details of the Diels–Alder additions and the corresponding structural assignments will be discussed in sequence.

Cycloadditions and structural assignments

It is known that the Diels–Alder reaction with a 2-substituted diene can lead to a mixture of regioisomers (49), and complete orientational reversal in violation of the *para* rule has been observed (51, 52). We wished to prove conclusively that the addition of dienyl phosphate **1** to ethyl vinyl ketone (Entry 1) gave *para*-addition product **8** and not regioisomer **30**. Accordingly, the Diels–Alder adduct **8** was treated with sodium hydroxide in refluxing methanol. Two compounds were obtained, in 44 and 12% yields. The minor product, obtained as a yellow oil, was positively identified as diketone **20** since, due to symmetry, it showed only seven signals in the ^{13}C nmr spectrum. The major compound was obtained as a white solid that was identified as hydroxy ketone **21**. Compound **21** was clearly derived from **20** by intramolecular aldol condensation. The isolation of compound **20** confirmed that adduct must possess the regiochemistry depicted in structure **8**, arising from addition according to the *para* rule.

Diels–Alder addition of **1** to methyl vinyl ketone (Entry 2) also followed the normal *para* rule. The spectral data were consistent with assignment of structure **9** to the adduct. To establish the regiochemistry conclusively the Diels–Alder adduct was treated with sodium hydroxide in refluxing methanol and gave a diketone in 27% yield. As in the case of degradation product **20**, the ^{13}C nmr spectrum indicated that the diketone had symmetrical structure **22** (four non-carbonyl signals) and not unsymmetrical structure **31** (six non-carbonyl signals). It followed that the Diels–Alder product must possess the regiochemistry depicted in structure **9**.

Several noteworthy features were observed for the stannic chloride catalyzed reaction of methyl vinyl ketone and diene phosphate **1**; the fast reaction rate, the excellent yield, and the complete regioselectivity. In contrast, the thermal addition of methyl vinyl ketone to 2-dimethylphosphoryloxy-1,3-butadiene (29) produced two inseparable regioisomers in a 2:1 ratio.

Preliminary analysis of the spectral data for the single adduct of **1** with *trans*-3-penten-2-one (Entry 3) did not distinguish between structure **10** resulting from normal *para* addition and the regioisomeric structure **32** resulting from anti-*para* addition. The observation of two large *trans*-1,2-diaxial coupling constants of 10 Hz each for the methine proton adjacent to the ketone at δ2.42 in the ^1H nmr spectrum confirmed the *trans* configuration of the two methine protons predicted by the *cis* principle of Diels–Alder addition. It remained to determine the regiochemistry of the adduct. A conclusive proof was achieved by aromatization of the adduct, a technique that has been developed and used with considerable success by this group (31, 51, 52). The adduct was treated with *N*-bromosuccinimide in refluxing carbon tetrachloride. The reaction gave a rather complex mixture of products from which aryl ketone **23** was isolated in 19% yield. The ^1H nmr spectrum of this derivative showed one aromatic proton adjacent to the acyl group as a relatively deshielded doublet at δ7.78 with a coupling constant of 8.5 Hz. The spectral data, particularly the coupling pattern of

[6]This result is typical of the characteristic difficulty in achieving Diels–Alder additions to simple cyclic enones (32, 45–47, and references therein).

Can. J. Chem. Downloaded from www.nrcresearchpress.com by 85.192.166.187 on 09/08/12
For personal use only.

TABLE 1. Stannic chloride catalyzed Diels–Alder reactions of diene **1**[a]

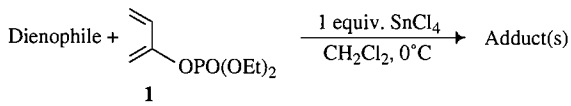

1

Entry	Dienophile	Diene **1** (equiv.)	Time (h)	Yield[b]	Product(s) (ratio)[c]
1		1.3	1	94%	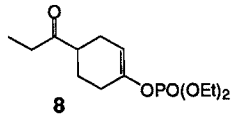 **8**
2		1.3	1.5	100%	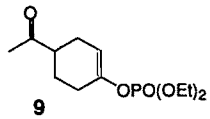 **9**
3		1.3	40	90%	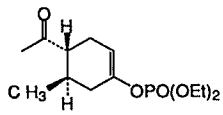 **10**
4		1.3	18	81%	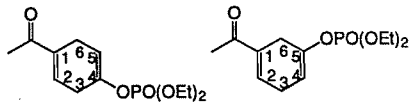 **11** (8:1) **12**
5	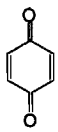	1.3	5	93%	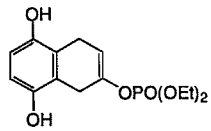 **13**
6	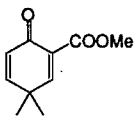 **14**	1.3	65	23%[d]	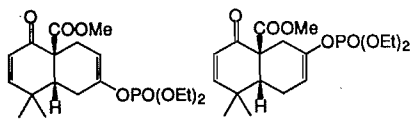 **15** (9:2) **16**
7		3	54	12%[e]	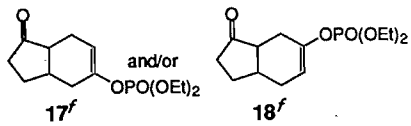 **17**[f] **18**[f]
8[g]		4	34	34%[e]	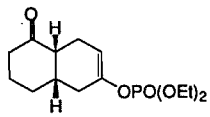 **19**

[a]Reactions were run using 1 equivalent of stannic chloride in methylene chloride at 0°C and under an atmosphere of nitrogen or argon.

[b]The yields are reported from the respective dienophile used.

[c]Ratios were determined by ^{1}H nmr integration.

[d]The yield was 72% based on the consumed starting dienophile **14**.

[e]Compound **9** was also obtained as a by-product.

[f]The complete regiochemical and stereochemical assignment of the product was not made.

[g]This reaction was run at room temperature instead of 0°C. The solvent system for the reaction was a 1:1 mixture of dichloromethane and diethyl ether.

Can. J. Chem. Downloaded from www.nrcresearchpress.com by 85.192.166.187 on 09/08/12
For personal use only.

Can. J. Chem. Downloaded from www.nrcresearchpress.com by 85.192.166.187 on 09/08/12
For personal use only.

Adduct(s) (ratio)[a]	Conditions	Product(s) yield (ratio)[a]
8	NaOH/MeOH, reflux, 5 h	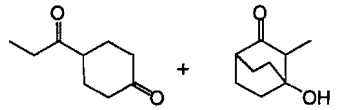 **20** 12% + **21** 44%
9	NaOH/MeOH, reflux, 3.5 h	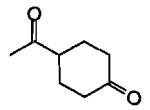 **22** 27%
10	NBS/CCl_4, reflux, 1 h	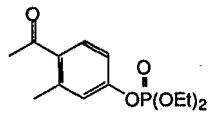 **23** 19%
11 + 12 (8:1)	DDQ/φH, reflux, 2 h	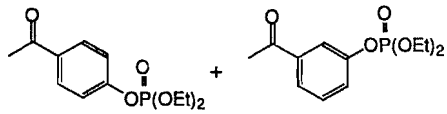 **24** + **25** 79% (11:1)
15	$LiI \cdot 2H_2O$, γ-collidine, reflux 2.5 h	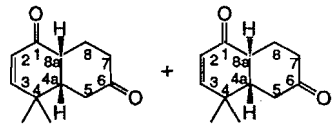 **26** + **27** 70% (1:6) → $H_2SO_4/H_2O/EtOH$, 3 h, reflux (87% yield)
19	Na_2CO_3, H_2O/MeOH, 20 h	No reaction
19	NaOH/MeOH, 23 h	No reaction
19	NaOH/H_2O/MeOH, 20 h	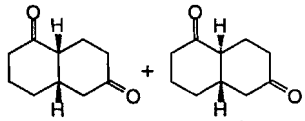 **28** + **29** 87% (1:11)

[a]Ratios were determined by ^1H nmr integration.

SCHEME 1. Derivatization of adducts of **1**.

the *peri*-deshielded aromatic proton, agreed only with the assignment of structure **23** to the aryl ketone. Thus the regiochemistry of the Diels–Alder adduct was as defined by structure **10.**

Diene **1** reacted with 3-butyn-2-one (Entry 4) to give an inseparable 8:1 mixture of two regioisomeric enol phosphates tentatively identified as **11** and **12**. The *para* rule predicts (45, 48, 49) that adduct **11** would be the major component in the

TABLE 2. The ^{13}C nmr chemical shifts (δ) for adducts **11** and **12**[a]

	Carbon									
	1	2	3	4	5	6	7	8	9,10	11,12
11	135.4	134.6	28.8[b]	142.6[b]	107.1[b]	24.0	196.6	24.3	63.4[b]	15.2[b]
12	135.3	135.7	26.9	104.8[b]	145.0[b]	26.2[b]	196.4	24.3	63.4[b]	15.2[b]

[a]The distinct sets of signals in the spectrum of the mixture were separable on the basis of their relative peak areas (8:1).

[b]Because of carbon–phosphorus coupling, a doublet was observed for each of these carbons.

product mixture and this was supported by the ^{13}C nmr spectrum of the mixture, which showed two distinct sets of signals listed in Table 2. The signal due to C-3 of **11**, which is linked to a relatively more electron deficient sp^2 carbon (C-2), should appear at lower field than the signal due to C-6, which is attached to an sp^2 carbon (C-1) that is relatively less electron deficient. Furthermore, C-3 of **11** should appear as a doublet due to carbon–phosphorus coupling while a singlet should be observed for C-6. Similarly the signal assigned to C-3 of **12** should appear at lower field than that of C-6 while a doublet should appear for the C-6 signal due to carbon–phosphorus coupling. The ^{13}C nmr spectrum (Table 2) showed that the major set of signals was consistent with these expectations for structure **11** while the minor set of signals agreed with structure **12**.

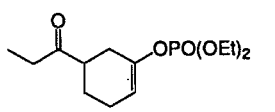

30

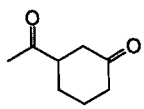

31

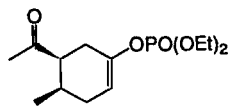

32

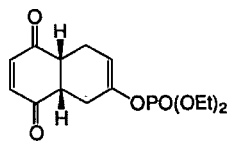

33

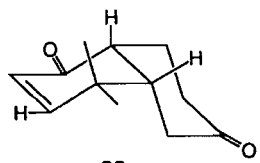

26*a*

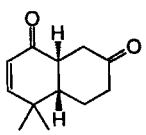

34

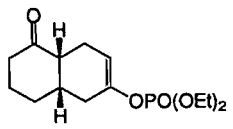

35

Rigorous proof of the regiochemistry of adducts **11** and **12** was achieved by aromatization. The 8:1 mixture of Diels–Alder adducts was treated with 2,3-dichloro-5,6-dicyano-1,4-benzoquinone in refluxing benzene. An inseparable 11:1 mixture of two isomeric aryl ketones was obtained in 79% yield. The major set of ^1H nmr signals for the mixture showed aryl doublets at δ7.79 and 7.32 typical of *para*-substituted benzenes. The minor set consisted of two multiplets at δ7.78 and 7.47 attributable to a *meta*-substituted benzene ring. These data established that aryl ketone **24** was the major component and **25** the minor component of the derivative mixture and consequently the assignments of structure **11** to the major Diels–Alder adduct and **12** to the minor adduct were confirmed.

The infrared spectrum of the Diels–Alder cycloaddition product of **1** with *p*-benzoquinone (Entry 5) clearly indicated that the initially formed adduct **33** had undergone subsequent aromatization, as expected via bis-enolization under the influence of the acidic reaction conditions, to produce the aromatic enol phosphate **13**. This structural assignment was confirmed by the ^{13}C nmr spectrum, which indicated the presence of eight sp^2 carbons.

When the dienone ester **14** (51–53) was treated with diene **1** in the presence of stannic chloride at 0°C (Entry 6) the cycloaddition reaction proceeded slowly. After 65 h it gave an inseparable 9:2 mixture of two isomeric adducts in 23% yield. The starting dienophile **14** was obtained in 68% recovery. On the basis of the spectral data and the *cis* principle the structures **15** and **16** were tentatively assigned to the two adducts. Identification of compound **15** as the major adduct and, by inference, **16** as the minor one followed from analysis of pure **15** obtained in subsequent catalyst studies detailed below.

The determination of the regiochemistry of the pure isolated adduct **15** was achieved by the decarbomethoxylation approach previously developed (51, 52) for adducts of **14**. The adduct **15** was treated with lithium iodide dihydrate (54) in refluxing 2,4,6-collidine to give a mixture of two chromatographically separable epimeric diketones **26** and **27** (1:6, in 70% yield) resulting from concomitant decarbomethoxylation and cleavage of the enol phosphate ester. The *cis* ring junction of the minor diketone **26** was confirmed by the ^1H nmr spectrum, which showed a long-range W-coupling of 2 Hz in the signal (δ6.56) due to the proton at C-3. Conformational analysis showed that the protons on C-3 and C-4a can assume a W configuration only when the two rings are *cis*-fused as shown in formula **26*a***. In accord with the assigned *cis* fusion, treatment of **26** with aqueous sulfuric acid in refluxing ethanol gave complete epimerization to the *trans* isomer **27** in 87% yield.

The regiochemistry of the *trans*-diketone **27** was determined by a study of the ^1H nmr spectrum including a nuclear Overhauser enhancement (nOe) experiment. Saturation of the *gem*-dimethyl singlet at δ1.12 caused substantial enhancement of signals corresponding to protons on C-4a (18%), C-5 axial (13%), C-5 equatorial, and C-8a (total 22%). This experiment allowed the complete solution of the coupling patterns of the axial and equatorial protons at C-5. The C-5 axial proton was a doublet of doublets with two large couplings of 13 Hz each while the C-5 equatorial was also a doublet of doublets with a large germinal coupling constant of 13 Hz and a small vicinal coupling constant of 4 Hz. This indicated that the group at C-6 must be the saturated ketone carbonyl as in structure **27** and not a methylene group as in **34**. With the regiochemistry of **27** and, by inference, **26** clearly established, the assignment of structure **15** to their precursor was confirmed.

The addition of **1** to 2-cyclopenten-1-one (Entry 7) gave

Can. J. Chem. Downloaded from www.nrcresearchpress.com by 85.192.166.187 on 09/08/12
For personal use only.

Can. J. Chem. Downloaded from www.nrcresearchpress.com by 85.192.166.187 on 09/08/12
For personal use only.

problematic results. The major component of the product mixture was identical with ketone phosphate **9** representing 75% of the mixture by ^{1}H nmr integration. Based on 75% of **9** and 25% of **17** and (or) **18**, the carbon and hydrogen contents of the mixture should be 52.67 and 7.59%, respectively. The microanalytical results were consistent with this calculation showing 52.42% carbon and 7.58% hydrogen. The isolation in 57% yield of aryl ketone **24**, on treatment of the mixture with *N*-bromosuccinimide in refluxing carbon tetrachloride, provided additional proof for the identity of by-product **9**.

Compound **9** could have been derived from the Diels–Alder reaction between diene phosphate **1** and methyl vinyl ketone, arising from acid-catalyzed cleavage of the former during the relatively long reaction time. However, when diene phosphate **1** was treated with stannic chloride in ether at room temperature for 44 h compound **9** was formed only in a comparatively small quantity. Similarly no by-product **9** was isolated after the relatively long reaction time used in the addition of **1** to **14** (Entry 6). Apparently the presence of 2-cyclopentenone facilitated the cleavage of the diene phosphate **1** to methyl vinyl ketone. Rigorous structural assignment of the minor adducts **17/18** was not carried out.

Addition of 2-cyclohexen-1-one (Entry 8) to diene **1** in the presence of stannic chloride gave a chromatographically separable mixture of a single adduct and by-product **9**. With a view to determining the ring junction stereochemistry, the pure adduct was treated with sodium carbonate in aqueous methanol at room temperature for 20 h and also with aqueous sodium hydroxide in methanol at room temperature for 23 h. In both cases the starting material was recovered unchanged. Since the compound was not affected under conditions that are expected to induce epimerization, we presume that the originally formed *cis* adduct **35** had undergone epimerization[7] to give the more stable *trans* isomer **19** during the reaction or purification.

To verify its regiochemistry the Diels–Alder adduct **19** was treated with sodium hydroxide in aqueous methanol giving two separable products (11:1) in 87% yield. The minor and major products were shown to be identical with *cis*- and *trans*-diketones **28** and **29**, respectively, confirming the regiochemistry of the adduct **19**.

Authentic *cis*- and *trans*-diketones **28** and **29** were easily prepared from 1,6-dihydroxynaphthalene (**36**) by the route summarized in Scheme 2. Compound **36** was hydrogenated using 5% rhodium on alumina in acetic acid and ethanol to give diol **37**. The transformation of diol **37** to *cis*-diketone **28** was achieved in 77% yield by treatment with pyridinium chlorochromate (55) in methylene chloride. By treatment with sodium hydroxide in aqueous methanol, *cis*-diketone **28** was isomerized to *trans*-diketone **29** in 87% yield.

Catalyst studies on additions of ***1***

The Diels–Alder reaction of dienone ester **14** and diene **1** was found to be highly dependent on the particular Lewis acid used. The results of a study of the Diels–Alder reactions of diene **1** with dienone ester **14** using different Lewis acid catalysts are summarized in Table 3. When this cycloaddition was run in the presence of boron trifluoride etherate at room temperature the reaction occurred more rapidly than with stannic chloride to give a single adduct in 48% yield that was identical with the

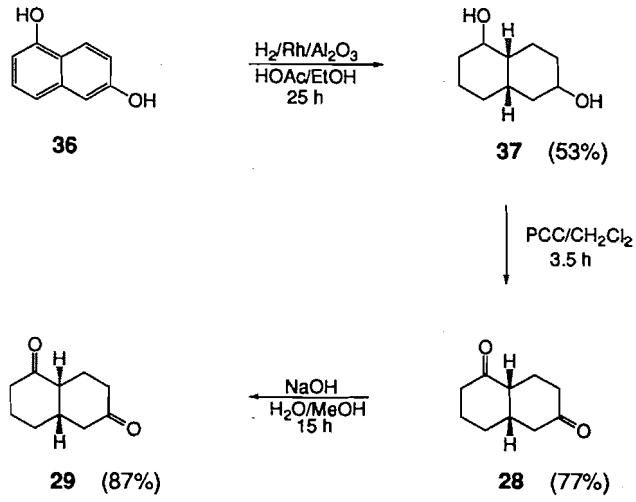

SCHEME 2. Preparation of authentic diketones **28** and **29**.

major product **15** obtained previously from the stannic chloride catalyzed reaction. The use of ferric chloride as a catalyst in the addition of **1** to **14** was also examined.[8] At room temperature adduct **15** was obtained as the sole product in 61% yield. The yield was improved to 71% when the reaction temperature was reduced to 0°C. Clearly ferric chloride is the catalyst of choice for the preparation of this particular Diels–Alder adduct.

In an attempt to improve the Diels–Alder reaction of **1** to cyclohexenone several other Lewis acids such as ferric chloride, aluminum chloride, zinc chloride, and boron trifluoride etherate were briefly examined. Unfortunately all of these catalysts gave results inferior to those obtained with stannic chloride. With ferric chloride, aluminum chloride, and zinc chloride no detectable amount of product was formed even over an extended reaction time. With boron trifluoride etherate the reaction did occur but the yield of the adduct was found to be considerably poorer than with stannic chloride.

2. Diels–Alder reactions of trans*-2-diethylphosphoryloxy-1,3-pentadiene (2)*

Diene phosphate **2** was subjected to Diels–Alder reaction with several α,β-unsaturated ketones using stannic chloride as the catalyst in ether or methylene chloride and at temperatures ranging from 0°C to −30°C. In general the Diels–Alder additions of **2** proceeded in good to excellent yield with small excesses of the diene. As with **1** the usual orientational and stereochemical rules (45, 48, 49), particularly the *para* rule (51, 52) and *endo* rule (32, 51, 57), were followed with a very high degree of selectivity. The structures of the adducts of **2** were unambiguously assigned on the basis of their spectral data including ^{1}H nmr decoupling experiments. The results are summarized in Table 4. The details of the additions and structural assignments will be discussed below.

Cycloadditions and structural assignments

In the presence of 1 equivalent of stannic chloride, ethyl vinyl ketone (Entry 9) reacted rapidly with diene phosphate **2** in methylene chloride at 0°C to give a single adduct in 61% yield. The spectral data allowed the assignment of structure **38** to the

[7]The epimerization of the initially formed products under Lewis acid catalyzed conditions is sometimes observed. See for example ref. 47.

[8]A profound catalytic effect of ferric chloride in Diels–Alder additions to **14** was previously observed and exploited (51, 56).

TABLE 3. Effect of catalyst on addition of **1** to **14**

Catalyst (1.0 equiv.)	Dienophile **14** (equiv.)	Diene **1** (equiv.)	Temp. (°C)	Solvent	Time (h)	Product(s) (ratio)[a]	Yield (%)
						15 + 16	
$SnCl_4$	1.0	1.3	0	CH_2Cl_2	65	(9:2)	23
$BF_3{\cdot}Et_2O$	1.0	2.0	25	Et_2O	24	**15**	48
$FeCl_3$	1.0	2.0	25	Et_2O	24	**15**	61
$FeCl_3$	1.0	2.0	0	Et_2O	72	**15**	71

[a]Ratio was determined by ^1H nmr integration.

TABLE 4. Stannic chloride catalyzed Diels–Alder reactions of diene phosphate **2**[a]

Entry	Dienophile	$SnCl_4$ (equiv.)	Solvent	Time (h)	Temp. (°C)	Yield[b]	Adduct (ratio)[c]
9		1	CH_2Cl_2	0.25	0	61%	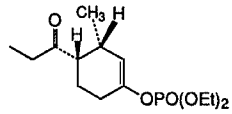 **38**
		0.5	Et_2O	24	-30	81%	
10		1	Et_2O	0.09	-30	72%	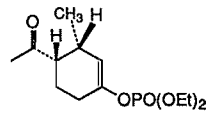 **39**
		0.5	Et_2O	14	-30	79%	
11		1	Et_2O	11	0	72%	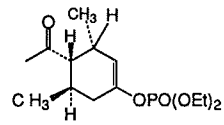 **40**
12	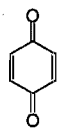	1	CH_2Cl_2	0.5	0	52%	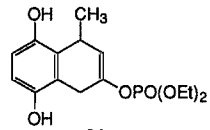 **41**
		1	CH_2Cl_2	6.5	-20	60%	
13	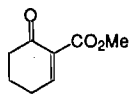 **3**	0.5	Et_2O	6	-30	66%	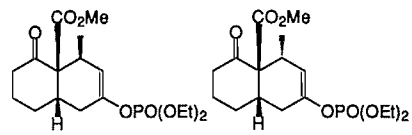 **5** **42** (6:1)

[a]All the reactions were carried out under a nitrogen or argon atmosphere with 1.5 equivalents of diene **2**.
[b]The yields were calculated based on the amounts of the dienophiles used.
[c]Ratio was determined by ^1H nmr integration.

adduct and ^1H nmr decoupling experiments confirmed the regiochemical and stereochemical assignments. A one-proton signal appeared as a doublet of doublets of doublets ($J = 13$, $J' = 7$, $J'' = 4$ Hz) at δ2.72, which was assigned to the methine proton adjacent to the ketone carbonyl. This signal was coupled to a one-proton multiplet at δ2.83 assigned to the allylic methine proton. Irradiation of the signal at δ2.83 caused a change in the signal at δ2.72 to a doublet of doublets ($J = 13$, $J' = 7$ Hz). This irradiation also led to a collapse of the vinylic proton signal at δ5.53 from a multiplet to a broad singlet and the methyl doublet (δ0.81) collapsed to a singlet. This demonstrated proximity of the keto methine and allylic methine protons confirmed the regiochemistry of the adduct **38**. The coupling constant of 13 Hz observed for the methine proton adjacent to the ketone indicated that this proton must possess an axial orientation. Its established coupling with the allylic methine proton (4 Hz) indicated an equatorial orientation for the latter proton and thus a *cis* relationship for these two protons in **38** was confirmed.

The Diels–Alder reaction of ethyl vinyl ketone with **2** was also run at −30°C in ether using 0.5 equivalent of stannic chloride. Although the reaction was much slower under these conditions, a substantially improved yield (81%) was obtained for the adduct **38**.

Under stannic chloride catalysis (1 equiv.) diene phosphate **2**

Can. J. Chem. Downloaded from www.nrcresearchpress.com by 85.192.166.187 on 09/08/12
For personal use only.

Can. J. Chem. Downloaded from www.nrcresearchpress.com by 85.192.166.187 on 09/08/12
For personal use only.

reacted very rapidly with methyl vinyl ketone (Entry 10) in ether at −30°C to give a single adduct, **39**, in 72% yield. In the ^{1}H nmr spectrum a one-proton doublet of doublets of doublets (J = 10, J' = J'' = 5 Hz) at δ2.71 was assigned to the methine proton adjacent to the ketone carbonyl group. By decoupling experiments this proton was shown to be coupled with a proton at δ2.86 with a small coupling constant of 5 Hz. The latter was further coupled with the methyl protons at δ0.87 and the vinyl proton at δ5.56. On the basis of these results, as was found for **38**, the stereochemistry and regiochemistry of structure **39** were assigned to the Diels–Alder adduct.

When a smaller amount of stannic chloride (0.5 equiv.) was used the reaction of methyl vinyl ketone with dienyl phosphate **2** was much slower but the yield of adduct **39** was improved (79%).

Addition of **2** to *trans*-3-penten-2-one (Entry 11) under stannic chloride catalysis in ether at 0°C gave a single adduct **40** in 72% yield. The regiochemistry was indicated by the ^{1}H nmr spectrum. The signal due to the proton at C-4 (δ2.61) was a distinct doublet of doublets with coupling constants of 11 and 5 Hz, indicating that the proton had only two neighboring protons. When the multiplet at δ2.75 (C-3 proton) was irradiated the C-4 proton signal collapsed to a doublet with a coupling constant of 11 Hz. At the same time the methyl doublet at δ0.86 changed to a singlet and the multiplet at δ5.55 due to the vinylic proton sharpened to give a broad singlet. This confirmed the position of the allylic methine adjacent to the keto methine proton of **40**. The stereochemistry of the adduct was demonstrated by the splitting pattern of the doublet of doublets at δ2.61 due to the C-4 proton. The presence of a large coupling constant of 11 Hz and a small one of 5 Hz indicated that this proton was axial and further coupled to an axial proton (C-5 proton, J = 11 Hz) and an equatorial proton (C-3 proton, J = 5 Hz).

Under stannic chloride catalysis, diene phosphate **2** reacted rapidly with 1,4-benzoquinone (Entry 12) in methylene chloride at 0°C to give an aromatic compound in 52% yield. The spectral data showed that, as had occurred with **33**, the initially formed Diels–Alder adduct **43** had aromatized via bis-enolization to give compound **41** during the reaction or isolation.

In an attempt to improve the yield of adduct **41** the Diels–Alder reaction was run in ether at −30°C for 36 h. Interestingly, in addition to the desired product **41** (24% yield), the unexpected oxidation product **44** was formed in 24% yield. A more successful preparation of **41** was achieved (60% yield) when the reaction was carried out in methylene chloride at −20°C using 3 equivalents of the diene **2**.

The addition of **2** to enone ester **3** (Entry 13) to give adducts **5** and **42** has already been described in detail (32, 46) and was used in the total synthesis of petasitolone (**4**) (31).

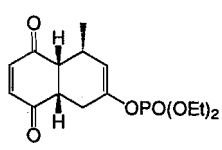

43

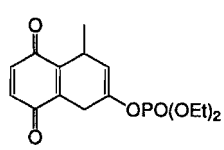

44

Conclusion

In conclusion, diene phosphates **1** and **2** have been shown to be useful substrates in Diels–Alder reactions under Lewis acid catalysis. They react with a variety of α,β-unsaturated ketones in good to excellent yields, with efficient conversions of the dienes and with high regio- and stereoselectivity to give synthetically useful cyclohexene derivatives. The dienes and products are found to be unusually stable towards acidic conditions compared to other oxygen-substituted dienes such as silyloxy and alkoxy dienes. The application of Lewis acids to the Diels–Alder reactions of diene phosphates is, therefore, more successful and potentially useful than other oxygen-substituted dienes.

Experimental

General

Melting points were determined on a Kofler hot stage apparatus and are uncorrected. Elemental analyses were performed by the microanalytical laboratory of this department. Infrared (ir) spectra were recorded on a Perkin–Elmer model 457 or Nicolet 7-199 FT-IR spectrophotometer and, except where otherwise stated, were obtained on solutions in chloroform. Proton nuclear magnetic resonance (^{1}H nmr) spectra were recorded on a Varian HA-100, HA-100/Digilab, Bruker WH-200, or WH-400 spectrometer and, except where otherwise stated, were obtained on solutions in deuterochloroform with tetramethylsilane as internal reference. The ^{13}C nmr spectra were recorded on a Bruker HFX-90/Nicolet 1085, Bruker WH-200, or WH-400 system and were obtained on solutions in deuterochloroform using tetramethylsilane as internal reference. The following abbreviations are used: s = singlet, d = doublet, t = triplet, q = quartet, and m = multiplet. Mass spectra (ms) were recorded using an A.E.I. model MS9, MS12, or MS50 mass spectrometer. Anhydrous magnesium sulfate was used for drying organic solutions. Crystalline samples were recrystallized before submitting for elemental analysis. Flash chromatography (58) was used routinely for purification and separation of product mixtures.

Materials

Ether and benzene were freshly distilled over lithium aluminum hydride. Dichloromethane was freshly distilled over phosphorus pentoxide. Anhydrous stannic chloride was purchased from Fluka Chemical Corp. and was used without further purification. Nitrogen and argon were passed through a purification train of Fieser's solution (59), saturated aqueous lead acetate, concentrated sulfuric acid, and potassium hydroxide pellets. Diene **2** was prepared according to the published procedure (31). Lithium iodide dihydrate – collidine reagent was prepared as previously reported (51). Dienone ester **14** was prepared according to the published procedure (52, 53). *trans*-3-Penten-2-one was prepared according to the method of Odom and Pinder (60). 1,6-Dihydroxynaphthalene **37** was commercially available. Enone ester **3** was prepared according to the published procedure (32, 61).

2-Diethylphosphoryloxy-1,3-butadiene (1)

To a solution of diisopropylamine (4.1 g, 40.3 mmol) in tetrahydrofuran (50 mL) at 78°C and under an atmosphere of argon, was added a 1.6 M solution of *n*-butyllithium in hexane (25.2 mL, 40.3 mmol) with stirring. After 10 min, a solution of methyl vinyl ketone (2.59 g, 37.0 mmol) in tetrahydrofuran (20 mL) was added dropwise over 10 min. After another 10 min, diethyl chlorophosphate (13.8 g, 80 mmol) was added. The reaction mixture was allowed to warm up to room temperature. Ice-cold water (200 mL) was then added and the resulting mixture was extracted with a solution of ether and *n*-hexane (1:1; 4 × 200 mL). The extracts were washed with water, dried, combined, filtered, and concentrated. Flash chromatography of the residue on silica gel, eluting with a 20% solution of ethyl acetate in hexane, gave a yellow oil that was further purified by bulb-to-bulb distillation at 83–85°C/1.5 Torr (1 Torr = 133.3 Pa) to give diene **1** (5.70 g, 75% yield) as a colorless oil: ir ($CDCl_3$ cast): 1643, 1594 (C=C), 1274, 1022, and 1002 (phosphate) cm^{-1}; ^{1}H nmr δ: 6.17 (ddd, 1H, J = 3 Hz, J' = 10 Hz, J'' = 17 Hz, CH_2=C*H*-), 5.57 (d, 1H, J = 17 Hz, C*H*H=CH-), 5.20 (d, J = 10 Hz, CH*H*=CH-), 5.08 (dd, 1H, J = 4 Hz, J' = 2 Hz, C*H*H=C-O-), 4.74 (dd, 1H, J = J' = 2 Hz, CH*H*=C-O-), 4.18 (qd, 4H, J = J' = 7 Hz, 2 × -OCH_2-), and 1.35 (dt, 6H, J = 1 Hz,

Can. J. Chem. Downloaded from www.nrcresearchpress.com by 85.192.166.187 on 09/08/12
For personal use only.

J' = 7 Hz, 2 × -OCH_2CH_3); ^{13}C nmr δ: 151.3 (d),[9] 131.4 (d), 116.0, 101.3 (d), 64.4 (d), and 16.1 (d); ms M^+: 206.0704 (calcd. for $C_8H_{15}PO_4$: 206.0708). Anal. calcd. for $C_8H_{15}PO_4$: C 46.60, H 7.33; found: C 46.39, H 7.28.

1-Diethylphosphoryloxy-4-(1-oxopropyl)-1-cyclohexene (8)

Diene **1** (773 mg, 3.75 mmol) was dissolved in dichloromethane (2 mL) under an atmosphere of nitrogen. The solution was cooled to 0°C and anhydrous stannic chloride (753 mg, 2.89 mmol) was added dropwise to the stirred solution over 2 min followed by addition of ethyl vinyl ketone (243 mg, 2.89 mmol). After stirring at 0°C for 1 h the reaction mixture was diluted with dichloromethane. Then 5% aqueous sodium bicarbonate was added and the resulting emulsion was filtered with suction. The filtrate was extracted with dichloromethane and the extracts were combined, dried, filtered, and concentrated. Flash chromatography of the residue on silica gel, eluting with 25% acetone in petroleum ether, gave diene **1** (144 mg, 19% recovery). Continued elution gave enol phosphate **8** (787 mg, 94% yield) as a light yellow oil: ir: 1710 (ketone C=O), 1680 (enol phosphate C=C), 1277 and 1035 (phosphate) cm^{-1}; ^{1}H nmr δ: 5.52 (br s, 1H, -CH=C-), 4.17 (m, 4H, 2 × -OCH_2-), 2.53 (m, 2H, -CH_2CO-), 1.38 (m, 6H, 2 × -OCH_2CH_3), and 1.08 (t, 3H, J = 7 Hz, CH_3CH_2CO-); ^{13}C nmr δ: 212.7, 147.0 (d), 108.8 (d), 64.0 (d), 45.2, 33.8, 26.9 (d), 25.4, 24.6, 15.9 (d), and 7.5; ms M^+: 290.1278 (calcd. for $C_{13}H_{23}PO_5$: 290.1283). Anal. calcd. for $C_{13}H_{23}PO_5$: C 53.78, H 8.00; found: C 53.87, H 7.96.

4-(1-Oxopropyl)-1-cyclohexanone (20) and 4-hydroxy-3-methylbicyclo[2.2.2]octan-2-one (21)

Enol phosphate **8** (251 mg, 0.87 mmol) was dissolved in methanol (14 mL) and aqueous 0.5 N sodium hydroxide (14 mL) was added with stirring. The reaction mixture was heated at reflux under an atmosphere of argon. After 5 h the mixture was cooled to 0°C, poured into cold aqueous 10% hydrochloric acid, and extracted with methylene chloride and then with ethyl acetate. The combined extracts were washed with water, dried, filtered, and concentrated. Flash chromatography of the residue on silica gel, eluting with acetone and ether in petroleum ether (1:3:6), gave diketone **20** (16 mg, 12% yield) as a yellow oil: ir: 1711 (ketone C=O) cm^{-1}; ^{1}H nmr δ: 2.82 (tt, 1H, J = 10 Hz, J' = 4 Hz, -COCH-), 2.58 (q, 2H, J = 7 Hz, CH_3CH_2CO-), and 1.10 (t, 3H, J = 7 Hz, -CH_3); ^{13}C nmr δ: 212.2, 209.8, 47.6, 39.8, 34.0, 28.1, and 7.7; ms M^+: 154.1000 (calcd. for $C_9H_{14}O_2$: 154.0994). Continued elution gave hydroxy ketone **21** as a white solid (59 mg, 44% yield): mp 123–127°C; ir: 3420 (-OH) and 1710 (ketone C=O) cm^{-1}; ^{1}H nmr δ: 2.58 (br s, 1H, D_2O exchangeable, -OH), 2.25 (m, 2H, -CHCOCH-), and 1.16 (d, 3H, J = 7 Hz, CH_3); ^{13}C nmr δ: 216.7, 71.7, 53.1, 41.3, 34.3, 27.4, 22.9, 21.8, and 9.3; ms M^+: 154.1002 (calcd. for $C_9H_{14}O_2$: 154.0993).

1-Diethylphosphoryloxy-4-(1-oxoethyl)-1-cyclohexene (9)

Diene **1** (783 mg, 3.80 mmol) was dissolved in methylene chloride (2 mL) and the solution was cooled to 0°C under an atmosphere of nitrogen. Anhydrous stannic chloride (753 mg, 2.89 mmol) was added dropwise to the stirred solution over 2 min, followed by methyl vinyl ketone (203 mg, 2.90 mmol). After stirring at 0°C for 1.5 h the reaction mixture was diluted with methylene chloride. Then aqueous 5% sodium bicarbonate was added and the resulting emulsion was filtered with suction. The filtrate was extracted with methylene chloride and then with ethyl acetate, and the combined extracts were dried, filtered, and concentrated. Flash chromatography of the residue on silica gel, eluting with acetone and ether in petroleum ether (1:3:6), gave the diene **1** (119 mg, 15% recovery). Continued elution gave pure Diels–Alder adduct **9** (797 mg, 100% yield) as a colorless oil: ir (film): 1710 (ketone C=O), 1685 (enol phosphate C=C), 1276 and 1035 (phosphate) cm^{-1}; ^{1}H nmr δ: 5.53 (br s, 1H, -CH=C-), 4.18 (m, 4H, 2 × -OCH_2-), 2.20 (s, 3H, CH_3CO-), and 1.38 (m, 6H, 2 × -OCH_2CH_3); ^{13}C nmr δ: 209.8, 147.1 (d), 108.7 (d), 64.0 (d), 46.2, 27.8, 26.9 (d), 25.2, 24.5, and 15.9 (d); ms M^+: 276.1125 (calcd. for $C_{12}H_{21}PO_5$: 276.1127). Anal. calcd. for $C_{12}H_{21}PO_5$: C 52.17, H, 7.66; found: C 52.42, H 7.70.

4-(1-Oxoethyl)-1-cyclohexanone (22)

Adduct **9** (200 mg, 0.72 mmol) was dissolved in methanol (11 mL) and aqueous 0.5 N sodium hydroxide (11.6 mL) was added with stirring. The reaction mixture was heated at reflux under an atmosphere of argon. After 3.5 h the reaction mixture was cooled to 0°C and cold aqueous 5% hydrochloric acid was added. The resulting mixture was extracted with methylene chloride and then with ethyl acetate. The combined extracts were dried, filtered, and concentrated. Flash chromatography of the residue on silica gel, eluting with acetone and ether in petroleum ether (1:3:6), gave diketone **22** (27 mg, 27% yield) as a yellow oil: ir: 1710 (ketone C=O) cm^{-1}; ^{1}H nmr δ: 2.80 (tt, 1H, J = 10 Hz, J' = 4 Hz, -COCH-), and 2.24 (s, 1H, CH_3CO-); ^{13}C nmr δ: 48.5, 39.7, 28.0, and 27.8 (two carbonyl carbons did not appear); ms M^+: 140.0844 (calcd. for $C_8H_{12}O_2$: 140.0837).

1-Diethylphosphoryloxy-5β-methyl-4α-(1-oxoethyl)-1-cyclohexene (10)[10]

To a solution of diene **1** (729 mg, 3.54 mmol) in dichloromethane (2 mL) at 0°C and under an atmosphere of nitrogen, anhydrous stannic chloride (709 mg, 2.72 mmol) was added followed by *trans*-3-penten-2-one (228 mg, 2.71 mmol). After stirring for 40 h the reaction mixture was diluted with dichloromethane and aqueous 5% sodium bicarbonate was added. The resulting mixture was extracted with dichloromethane. The extracts were combined, dried, filtered, and concentrated. Flash chromatography of the residue on silica gel, eluting with acetone and ether in petroleum ether (1:1:3), gave diene **1** (150 mg, 21% recovery). Continued elution gave pure enol phosphate **10** (706 mg, 90% yield) as a pale yellow oil: ir: 1711 (ketone C=O), 1275 and 1036 (phosphate) cm^{-1}; ^{1}H nmr δ: 5.48 (br s, 1H, -CH=C-), 4.16 (m, 4H, 2 × -OCH_2-), 2.42 (ddd, 1H, J = J' = 10 Hz, J'' = 5.5 Hz, -COCH-), 2.10 (s, 3H, CH_3CO-), 1.36 (m, 6H, 2 × -OCH_2CH_3), and 0.98 (d, 3H, J = 6 Hz, CH_3CH-); ^{13}C nmr δ: 210.6, 146.4 (d), 108.0 (d), 63.9 (d), 53.0, 34.9 (d), 30.5, 29.1, 26.1, 19.2, and 15.8 (d); ms M^+: 290.1284 (calcd. for $C_{13}H_{23}PO_5$: 290.1284). Anal. calcd. for $C_{13}H_{23}PO_5$: C 53.79, H 7.98; found: C 54.05, H 7.98.

1-Diethylphosphoryloxy-3-methyl-4-(1-oxoethyl)benzene (23)

To a solution of adduct **10** (101 mg, 0.35 mmol) in carbon tetrachloride (5 mL), *N*-bromosuccinimide (124 mg, 0.70 mmol) was added with stirring under an atmosphere of nitrogen. The reaction mixture was heated at reflux for 1 h, then the mixture was cooled to room temperature, filtered, and concentrated. Flash chromatography of the residue on silica gel, eluting with 20% acetone in petroleum ether, gave impure aryl ketone **23**. Further purification by Kuhgelrohr distillation at 110°C under 1.0 Torr pressure, followed by preparative thin-layer chromatography on silica gel developed twice with 2% acetone in ether, gave pure aryl ketone **23** (19 mg, 19% yield) as a light yellow oil: ir (film): 3060 (aryl C-H), 1684 (ketone C=O), 1610 and 1580, (aryl C=C), 1278, and 1031 (phosphate) cm^{-1}; ^{1}H, nmr δ: 7.78 (d, 1H, J = 8.5 Hz, C-5 Ar-H), 7.18 (dd, 1H, J = 8.5 Hz, J' = 2.5 Hz, C-6 Ar-H), 7.14 (d, 1H, J = 2.5 Hz, C-2 Ar-H), 4.27 (m, 4H, 2 × -OCH_2-), 2.59 (s, 3H, CH_3Ar or CH_3CO-), 2.56 (s, 3H, CH_3Ar or CH_3CO-), and 1.38 (m, 6H, 2 × -OCH_2CH_3); ms M^+: 286.0974 (calcd. for $C_{13}H_{19}PO_5$: 286.0970).

1-Diethylphosphoryloxy-4-(1-oxoethyl)-1,4-cyclohexadiene (11) and 1-diethylphosphoryloxy-5-(1-oxoethyl)-1,4-cyclohexadiene (12)

To a solution of diene **1** (942 mg, 4.57 mL) in methylene chloride (3 mL) at 0°C and under an atmosphere of nitrogen, anhydrous stannic chloride (886 mg, 3.40 mmol) was added followed by 3-butyn-2-one

[9] ^{13}C nmr signals indicated by (d) appeared as ^{13}C–^{31}P coupled doublets in the broadband decoupled spectrum.

[10] The stereochemical designations used in this and all other chemical names used in this section denote relative stereochemistry. All compounds used and obtained were racemic.

Can. J. Chem. Downloaded from www.nrcresearchpress.com by 85.192.166.187 on 09/08/12
For personal use only.

(230 mg, 3.38 mmol). After stirring for 18 h the mixture was diluted with methylene chloride. Aqueous 5% sodium bicarbonate was added and the resulting emulsion was filtered. The filtrate was extracted with methylene chloride and the extracts were combined, dried, filtered, and concentrated. Flash chromatography of the residue on silica gel, eluting with acetone and ether in petroleum ether (2:3:5), gave diene **1** (225 mg, 24% recovery). Continued elution gave a mixture of enol phosphates **11** and **12** (747 mg, 81% yield) as a pale yellow oil. The ^{1}H nmr spectrum of the mixture showed two sets of signals in an integral ratio of 8:1. The major set, assigned to **11**, showed signals at δ: 6.82 (m, 1H, -CO-C=CH-), 5.58 (m, 1H, -CH=C-O-), 4.18 (m, 4H, 2 × -OCH_2-), 3.16 (m, 2H, -CH_2-), 3.03 (m, 2H, -CH_2-), 2.23 (s, 3H, CH_3CO-), and 1.36 (m, 6H, 2 × -OCH_2CH_3). The other set, assigned to **12**, showed signals at δ: 6.86 (m, 1H, -CO-C=CH-), 5.52 (m, 1H, -CH=C-O-), 4.18 (m, 4H, 2 × -OCH_2-), 3.16 (m, 2H, -CH_2-), 3.03 (m, 2H, -CH_2-), 2.34 (s, 3H, CH_3CO-), and 1.36 (m, 6H, 2 × -OCH_2CH_3). The ^{13}C nmr spectrum of the mixture also showed two sets of signals. The major set, assigned to **11**, showed signals at δ: 196.6, 142.6 (d), 135.4, 134.6, 107.1 (d), 63.4 (d), 28.8 (d), 24.3, 24.0, and 15.2 (d). The minor set, assigned to **12**, showed signals at δ: 196.4, 145.0 (d), 135.7, 135.3, 104.8 (d), 63.4 (d), 26.9, 26.2 (d), 24.3, and 15.2 (d). The mixture also showed the following data: ir: 1705 (enol phosphate), 1670 (ketone C=O), 1277 and 1031 (phosphate) cm^{-1}; ms M$^+$: 274.0968 (calcd. for $C_{12}H_{19}PO_5$: 274.0970). Anal. calcd. for $C_{12}H_{19}PO_5$: C 52.55, H 6.93; found: C 52.25, H 6.91.

*1-Diethylphosphoryloxy-4-(1-oxoethyl)benzene (**24**) and 1-diethylphosphoryloxy-3-(1-oxoethyl)benzene (**25**)*

An 8:1 mixture of Diels–Alder adducts **11** and **12** (157 mg, 0.57 mmol) was dissolved in benzene (2 mL). 2,3-Dichloro-5,6-dicyano-1,4-benzoquinone (145 mg, 0.64 mmol) was added and the reaction mixture was then heated at reflux under an atmosphere of nitrogen. After 2 h the reaction mixture was cooled to room temperature, filtered, and concentrated. Flash chromatography of the residue on silica gel, eluting with acetone and ether in petroleum ether (2:3:5), gave a mixture of aryl ketones **24** and **25** (118 mg, 79% yield). The ^{1}H nmr spectrum of the mixture showed two sets of signals in an integral ratio of 11:1. The major set, assigned to **24**, showed signals at δ: 7.79 (d, 2H, J = 9 Hz, 2 × -CO-C=CH-), 7.32 (dd, 2H, J = 9 Hz, J' = 1 Hz, 2 × -HC=C-O-), 4.24 (m, 4H, 2 × -OCH_2-), 2.58 (s, 3H, CH_3CO-), and 1.36 (m, 6H, 2 × -OCH_2CH_3). The other set, assigned to **25**, showed signals at δ: 7.78 (m, 2H, 2 × -CO-C=CH-), 7.47 (m, 2H, 2 × Ar-H), 4.24 (m, 4H, 2 × -OCH_2-), 2.60 (s, 3H, CH_3CO-), and 1.36 (m, 6H, 2 × -OCH_2CH_3). The mixture also showed the following data: ir: 3060 (aryl C-H), 1686 (ketone C=O), 1600 and 1505 (aryl C=C), 1267, and 1035 (phosphate) cm^{-1}; ms M$^+$: 272.0816 (calcd. for $C_{12}H_{17}PO_3$: 272.0813). Anal. calcd. for $C_{12}H_{17}PO_5$: C 52.93, H 6.31; found: C 53.01, H 6.20.

*2-Diethylphosphoryloxy-5,8-dihydroxy-1,4-dihydronaphthalene (**13**)*

Diene phosphate **1** (505 mg, 2.45 mmol) was dissolved in methylene chloride (2 mL) and the solution was cooled to 0°C. Anhydrous stannic chloride (487 mg, 1.87 mmol) was added under an atmosphere of nitrogen, followed by *p*-benzoquinone (198 mg, 1.83 mmol). After stirring for 5 h the viscous solution was diluted with methylene chloride and water was added. The resulting emulsion was filtered by suction and the filtrate was extracted with methylene chloride. The extracts were combined, dried, filtered, and concentrated. Flash chromatography of the residue on silica gel, eluting with acetone and ether in petroleum ether (1:3:6), gave traces of diene **1**. Continued elution gave adduct **13** (532 mg, 93% yield). Recrystallization from acetone–ether gave bright white needles, soluble in methanol or hot acetone but insoluble in ether: mp 124.5–126.5°C; ir (KBr): 3320 (-OH), 3010 (aryl C-H), 1705 (enol phosphate C=C), 1615 and 1491 (aryl C=C), 1287, and 1038 (phosphate) cm^{-1}; ^{1}H nmr (CD_3OD) δ: 6.50 (s, 2H, 2 × Ar-H), 5.64 (m, 1H, -CH=C-O-), 4.18 (m, 4H, 2 × -OCH_2-), 3.36 (slightly broad s, 4H, 2 × -C=C-CH_2-), and 1.36 (m, 6H, 2 × -OCH_2CH_3); ^{13}C nmr (CD_3OD) δ: 148.5, 146.5 (d), 122.0, 121.7, 113.5, 113.4, 109.1 (d), 65.9 (d), 28.2 (d), 25.9, and 16.3 (d); ms M$^+$: 314.0921 (calcd. for $C_{14}H_{19}PO_6$: 314.0919). Anal. calcd. for $C_{14}H_{19}PO_6$: C 53.50, H 6.11; found: C 53.71, H 6.15.

*8aβ-Carbomethoxy-6-diethylphosphoryloxy-4,4-dimethyl-4aβ,5,8,8a-tetrahydro-1(4H)-naphthalenone (**15**) and 8aβ-carbomethoxy-7-diethylphosphoryloxy-4,4-dimethyl-4aβ,5,8,8a-tetrahydro-1(4H)-naphthalenone (**16**)*

*A. Adduct **15** from $FeCl_3$ catalysis*

To a solution of dienone ester **14** (306 mg, 1.69 mmol) and diene phosphate **1** (691 mg, 3.35 mmol) in ether (2.5 mL) at 0°C and under an atmosphere of nitrogen, anhydrous ferric chloride (270 mg, 1.66 mmol) was added. After stirring for 72 h water was added and the resulting mixture was extracted with dichloromethane. The extracts were combined, washed with water, dried, filtered, and concentrated. Flash chromatography of the residue on silica gel, eluting with acetone and ether in petroleum ether (1:3:6), gave diene **1** (326 mg, 47% recovery). Continued elution gave enone phosphate **15** (462 mg, 71% yield) as a pale yellow oil: ir: 1747, 1731 (ester C=O), 1675 (ketone C=O), 1275, and 1029 (phosphate) cm^{-1}; ^{1}H nmr δ: 6.60 (d, 1H, J = 10 Hz, -CO-CH=C*H*-), 5.90 (d, 1H, J = 10 Hz, -CO-C*H*=CH-), 5.50 (br s, 1H, -CH=C-O-), 4.15 (m, 4H, 2 × -OCH_2-), 3.74 (s, 3H, -OCH_3), 1.35 (m, 6H, 2 × -OCH_2CH_3), 1.22 and 1.15 (both s, 6H, -$C(CH_3)_2$); ^{13}C nmr δ: 196.4, 172.0, 157.7, 145.7 (d), 123.7, 108.3 (d), 64.2 (d), 56.1, 52.5, 41.8, 36.0, 30.1, 27.8, 26.5 (d), 23.1, and 15.9 (d); ms M$^+$: 386.1498 (calcd. for $C_{18}H_{27}PO_7$: 386.1494). Anal. calcd. for $C_{18}H_{27}PO_7$: C 55.94, H 7.06; found: C 55.85, H 7.11.

*B. Adduct mixture **15** and **16** from $SnCl_4$ catalysis*

To a solution of dienone ester **14** (428 mg, 2.38 mmol) and diene phosphate **1** (641 mg, 3.11 mmol) in methylene chloride (4 mL) at 0°C and under an atmosphere of argon, was added anhydrous stannic chloride (619 mg, 2.38 mmol). After stirring for 65 h, the reaction mixture was diluted with methylene chloride and a 5% aqueous sodium bicarbonate solution (20 mL) was added. The resulting mixture was filtered and the filtrate was extracted with methylene chloride. The extracts were combined, dried, filtered, and concentrated. The residue was subjected to flash chromatography on silica gel. Elution with 30% ethyl acetate in hexane gave diene phosphate **1** (142 mg, 22% recovery) and dienone ester **14** (291 mg, 68% recovery). Continued elution gave an inseparable mixture of adducts **15** and **16** (9:2, 206 mg, 23% yield). The ^{1}H nmr spectrum of the mixture showed two sets of signals in an integral ratio of 9:2. The major set was due to adduct **15** (see above) and the minor set was assigned to adduct **16** with signals at δ: 6.67 (d, 1H, J = 10 Hz, -CO-CH=C*H*-), 5.93 (d, 1H, J = 10 Hz, -CO-C*H*=CH-), 5.54 (br s, 1H, -CH=C-C-O-), 4.15 (m, 4H, 2 × -OCH_2-), 3.74 (s, 3H, -OCH_3), 1.35 (m, 6H, 2 × -OCH_2CH_3), 1.20 and 1.12 (both s, 6H, -$C(CH_3)_2$). The mixture also showed the following spectra data: ir ($CDCl_3$ cast): 1745, 1735 (ester C=O), 1675 (ketone C=O), 1272, and 1027 (phosphate) cm^{-1}; ms M$^+$: 386.1500 (calcd. for $C_{18}H_{27}PO_7$: 386.1494).

*4,4-Dimethyl-4,4aβ,5,7,8,8aβ-hexahydro-1,6-naphthalenedione (**26**) and 4,4-dimethyl-4,4aβ,5,7,8,8aα-hexahydro-1,6-naphthalenedione (**27**) from enone phosphate **15***

Enone phosphate **15** (355 mg, 0.92 mmol) was dissolved in lithium iodide dihydrate – collidine reagent (3.19 mL, 3.83 mmol) and heated at reflux with stirring. After 2.5 h the mixture was cooled to room temperature, poured into cold aqueous 5% hydrochloric acid, and extracted with methylene chloride. The extracts were washed with water, dried, filtered, and concentrated. Flash chromatography of the residue on silica gel, eluting with 10% ether in methylene chloride, gave pure diketones **26** and **27** (124 mg, 70% yield) in an ^{1}H nmr integral ratio of 1:6. Pure **26** was separated from **27** by a second flash chromatography on silica gel. Elution with acetone and ether in petroleum ether (1:3:6) gave diketone **26**: ir: 1714 (ketone C=O), and 1677 (ketone C=O) cm^{-1}; ^{1}H nmr δ: 6.56 (dd, 1H, J = 10 Hz, J' = 2 Hz, -CO-CH=C*H*-), 6.00 (d, 1H, J = 10 Hz, -CO-C*H*=CH-), 1.36 and 1.11 (both s, 6H, -$C(CH_3)_2$); ms M$^+$: 192.1150 (calcd. for $C_{12}H_{16}O_2$:

Can. J. Chem. Downloaded from www.nrcresearchpress.com by 85.192.166.187 on 09/08/12
For personal use only.

192.1150). Continued elution gave diketone **27**: ir: 1711 (ketone C=O) and 1678 (ketone C=O) cm^{-1}; ^1H nmr δ: 6.71 (d, 1H, J = 10 Hz, -CO-CH=C*H*-), 5.91 (d, 1H, J = 10 Hz, -CO-C*H*=CH-), 2.09 (ddd, 1H, J = J' = 13 Hz, J'' = 4 Hz, C-4a *H*), and 1.12 (s, 6H, $-C(CH_3)_2$); ^{13}C nmr δ: 210.0, 198.7, 160.0, 126.1, 48.0, 44.1, 41.8, 40.3, 36.0, 27.2, 26.2, and 20.4; ms M^+: 192.1156 (calcd. for $C_{12}H_{16}O_2$: 192.1151).

4,4-Dimethyl-4,4aβ,5,7,8,8aα-hexahydro-1,6-naphthalenedione (27) from diketone 26

Diketone **26** (5.68 mg) was dissolved in ethanol (0.5 mL) and aqueous 10% sulfuric acid (0.5 mL) was added with stirring. The reaction mixture was then heated at reflux. After 3 h the mixture was cooled to room temperature, diluted with water, and extracted with methylene chloride. The extracts were washed with water, dried, filtered, and concentrated. Flash chromatography of the residue on silica gel, eluting with 10% ether in methylene chloride, gave a diketone (4.92 mg, 87% yield) that was identical in ^1H nmr and ir spectra, as well as silica gel thin-layer chromatographic behaviour, to the *trans*-diketone **27** obtained directly from **15**.

3-Diethylphosphoryloxybicylo[4.3.0]non-3-en-7-one (17) and (or) 4-diethylphosphoryloxybicyclo[4.3.0]non-3-en-7-one (18)

To a solution of diene phosphate **1** (748 mg, 3.63 mmol) in methylene chloride (5 mL) at 0°C and under an atmosphere of argon, were added anhydrous stannic chloride (316 mg, 1.21 mmol) and 2-cyclopenten-1-one (100 mg, 1.21 mmol). After stirring for 54 h, the reaction mixture was diluted with methylene chloride. Aqueous 5% sodium bicarbonate was added. The resulting emulsion was filtered and the filtrate was extracted with methylene chloride. The extracts were combined, washed with water, dried, and concentrated. Flash chromatography of the residue on silica gel, eluting with 50% ethyl acetate in hexane, gave diene **1** (336 mg, 45% recovery). Continued elution gave a mixture (162 mg) consisting of 75% of ketone **9** and 25% of adduct(s) **17** and (or) **18** (12% yield) as indicated by the ^1H nmr, which displayed two sets of signals in an integral ratio of 3:1. The major signals were identical to those of ketone **9**. The minor signals were attributed to **17** and (or) **18**: δ: 5.50 (br s, 1H, -CH=C-O-), 4.10 (m, 4H, 2 × $-OCH_2-$), and 1.32 (m, 6H, 2 × $-OCH_2CH_3$). The mixture also showed the following spectral data: ir ($CDCl_3$ cast): 1741 (ketone C=O, **17/18**), 1709 (ketone C=O, **9**), 1682 (enol phosphate C=C), 1275, and 1034 (phosphate) cm^{-1}; ms M^+: 288.1124 (**17/18**, calcd. for $C_{13}H_{21}PO_5$: 288.1127) and 276.1126 (**9**, calcd. for $C_{12}H_{21}PO_5$: 276.1127).

6-Diethylphosphoryloxy-3,4,4aβ,5,8,8aβ-1(2H)-naphthalenone (19)

To a solution of diene **1** (1.206 g, 5.85 mmol) in ether (1.5 mL) and methylene chloride (1.5 mL) at 0°C and under an atmosphere of nitrogen, anhydrous stannic chloride (399 mg, 1.53 mmol) was added followed by 2-cyclohexen-1-one (141 mg, 1.47 mmol). After stirring at room temperature for 34 h the reaction mixture was diluted with methylene chloride. Aqueous 5% sodium bicarbonate was added. The resulting emulsion was filtered by suction and the filtrate was extracted with methylene chloride. The extracts were combined, washed with water, dried, and concentrated. Flash chromatography of the residue on silica gel, eluting with acetone and ether in petroleum ether (2:3:5), gave diene phosphate **1** (779 mg, 65% recovery). Continued elution gave a mixture of adducts **19** and **9** (224 mg). The adduct **19** (151 mg, 34% yield) was separated from **9** by extensive column chromatography on silica gel. Pure **19** showed the following data: ir: 1710 (ketone C=O) cm^{-1}; ^1H nmr δ: 5.50 (br s, 1H, -CH=C-O-), 4.18 (m, 4H, 2 × $-OCH_2-$), and 1.36 (m, 6H, 2 × $-OCH_2CH_3$); ^{13}C nmr δ: 210.7, 145.6 (d), 109.4 (d), 64.1 (d), 49.4, 41.8, 40.2, 35.2 (d), 32.2, 25.9, 23.0, and 16.0 (d); ms M^+: 302.1273 (calcd. for $C_{14}H_{23}PO_5$: 302.1274). Anal. calcd. for $C_{14}H_{23}PO_5$: C 55.65, H 7.67; found: C 55.72, H 7.66.

2,3,4,4aβ,5,7,8,8aβ-Octahydro-1,6-naphthalenedione (28) and 2,3,4,4aβ,5,7,8,8aα-octahydro-1,6-naphthalenedione (29)

A. From adduct 19

Enone phosphate **19** (200 mg, 0.66 mmol) was dissolved in methanol (1 mL) and cooled by an ice bath. Then aqueous 5 N sodium hydroxide (1.5 mL) was added. After stirring at room temperature for 20 h, the mixture was acidified with aqueous 5% hydrochloric acid and extracted with ether. The extracts were washed with water, dried, filtered, and concentrated. Flash chromatography of the residue on silica gel, eluting with 30% ethyl acetate in hexane, gave diketones **28** and **29** (1:11, total 95 mg, 87% yield).

B. From 1,6-dihydroxynaphthalene (36)

(a) Hydrogenation of 36. A mixture of diol **36** (4.01 g, 25 mmol), 5% rhodium on alumina (2.3 g), and acetic acid (0.8 mL) in ethanol (20 mL) was placed in a Parr hydrogenation apparatus. The reaction mixture was shaken under 50 psi (1 psi = 6.9 kPa) of hydrogen at room temperature for 25 h. Filtration and concentration, followed by flash chromatography of the residue on silica gel, eluting with 30% ethyl acetate in hexane, gave diol **37** (2.5 g, 53% yield): ir ($CDCl_3$ cast): 3347 and 3268 (OH) cm^{-1}; ^1H nmr ($CDCl_3$–$(CD_3)_2SO$) δ: 3.90 (br s, 2H, 2 × -OH) and 3.54 (m, 2H, 2 × -C*H*-OH); ^{13}C nmr δ: 72.1, 66.3, 56.7, 42.0, 37.2, 34.4, 32.4, 29.5, 27.4, and 17.8; ms M^+: 170.1308 (calcd. for $C_{10}H_{18}O_2$: 170.1307).

(b) Oxidation of diol 37. To a solution of pyridinium chlorochromate (586 mg, 2.73 mmol) in methylene chloride (5 mL) at room temperature under an atmosphere of argon was added diol **37** (150 mg, 0.89 mmol) with stirring. After 3.5 h, the reaction mixture was diluted with ether, filtered, and concentrated. Flash chromatography of the residue on silica gel, eluting with 30% ethyl acetate in hexane, gave *cis*-diketone **28** (114 mg, 77% yield): ir ($CDCl_3$ cast): 1709 (ketone C=O) cm^{-1}; ^1H nmr δ: 1.5–2.8 (complex, 14H); ^{13}C nmr δ: 211.5, 210.9, 48.7, 44.1, 41.1, 40.7, 38.2, 29.0, 25.0, and 22.9; ms M^+: 166.0993 (calcd. for $C_{10}H_{14}O_2$: 166.0994).

(c) Epimerization of cis*-diketone 28.* Diketone **28** (90 mg, 0.54 mmol) was dissolved in methanol (1 mL). Then 1.5 N aqueous sodium hydroxide (1 mL) was added. The reaction mixture was stirred at room temperature under an atmosphere of argon for 15 h. The resulting solution was extracted with ether. The extracts were washed with water, dried, filtered, and concentrated. Flash chromatography of the residue on silica gel, eluting with 30% ethyl acetate in hexane, gave *trans*-diketone **29** (78 mg, 87% yield): ir ($CDCl_3$ cast): 1693 (ketone C=O) cm^{-1}; ^1H nmr δ: 1.5–2.5 (complex 14H); ^{13}C nmr δ: 209.9, 209.3, 52.9, 48.1, 45.5, 41.5, 40.2, 33.0, 26.1, and 25.1; ms M^+: 166.0990 (calcd. for $C_{10}H_{14}O_2$: 166.0994).

1-Diethylphosphoryloxy-3β-methyl-4β-[1-oxopropyl]-1-cyclohexene (38)

To a solution of diene phosphate **2** (834 mg, 3.79 mmol) and ethyl vinyl ketone (240 mg, 2.85 mmol) in ether (2 mL) at −30°C and under an atmosphere of nitrogen, anhydrous stannic chloride (377 mg, 1.45 mmol) was added. After stirring for 24 h the reaction mixture was diluted with ether. Aqueous 5% sodium bicarbonate was added and the resulting emulsion was filtered by suction. The filtrate was extracted with methylene chloride and the extracts were combined, washed with water, dried, filtered, and concentrated. Flash chromatography of the residue on silica gel, eluting with acetone and ether in petroleum ether (2:3:5), gave the diene **2** (157 mg, 19% recovery). Further elution gave pure enol phosphate **38** (703 mg, 81% yield) as a pale yellow oil: ir: 1710 (ketone C=O), 1680 (enol phosphate C=C), 1273, and 1033 (phosphate) cm^{-1}; ^1H nmr δ: 5.53 (m, 1H, -CH=C-O-), 4.16 (m, 4H, 2 × $-OCH_2-$), 2.83 (m, 1H, -C*H*CH_3), 2.72 (ddd, 1H, J = 13 Hz, J' = 7 Hz, J'' = 4 Hz, -COCH-), 1.33 (m, 6H, 2 × $-OCH_2CH_3$), 1.02 (t, 3H, J = 7 Hz, CH_3CH_2-CO-), and 0.81 (d, 3H, J = 6.5 Hz, -CHC*H*$_3$); ^{13}C nmr δ: 211.6, 146.8 (d), 114.6 (d), 63.6 (d), 48.6, 33.7, 29.6, 26.7 (d), 18.0, 15.8, 15.5 (d), and 7.0; ms M^+: 304.1432 (calcd. for $C_{14}H_{25}PO_5$: 304.1439). Anal. calcd. for $C_{14}H_{25}PO_5$: C 55.24, H 8.30; found: C 55.27, H 8.06.

1-Diethylphosphoryloxy-3β-methyl-4β-(1-oxoethyl)-1-cyclohexene (39)

To a solution of diene phosphate **2** (801 mg, 3.64 mmol) and methyl vinyl ketone (196 mg, 2.80 mmol) in ether (2 mL) at −30°C and under

Can. J. Chem. Downloaded from www.nrcresearchpress.com by 85.192.166.187 on 09/08/12
For personal use only.

an atmosphere of nitrogen, anhydrous stannic chloride (731 mg, 2.81 mmol) was added. After stirring for 5 min the reaction mixture was diluted with ether. Aqueous 5% sodium bicarbonate was added and the resulting emulsion was filtered by suction. The filtrate was extracted with dichloromethane and the extracts were washed with water, dried, filtered, and concentrated. Flash chromatography of the residue on silica gel, eluting with acetone and ether in petroleum ether (2:3:5), gave diene **2** (205 mg, 26% recovery). Continued elution gave pure enol phosphate **39** (586 mg, 72% yield) as a pale yellow oil: ir (neat): 1709 (ketone C=O), 1678 (enol phosphate C=C), 1273, and 1027 (phosphate) cm^{-1}; ^1H nmr δ: 5.56 (m, 1H, -CH=C-O-), 4.18 (m, 4H, 2 × -OCH_2-), 2.86 (m, 1H, -C*H*CH_3), 2.71 (ddd, 1H, J = 10 Hz, J' = J'' = 5 Hz, -COCH-), 2.17 (s, 3H, CH_3CO-), 1.35 (t, 6H, J = 7 Hz, 2 × -OCH_2CH_3), and 0.87 (d, 3H, J = 7 Hz, -$CHCH_3$); ^{13}C nmr δ: 209.5, 147.3 (d), 114.9 (d), 64.0 (d), 50.2, 29.7, 28.3, 27.0 (d), 18.2, 15.8, and 15.9 (d); ms M^+: 290.1283 (calcd. for $C_{13}H_{23}PO_5$: 290.1283). Anal. calcd. for $C_{13}H_{23}PO_5$: C 53.77, H 8.00; found: C 54.05, H 7.94.

*1-Diethylphosphoryloxy-3α,5β-dimethyl-4α-(1-oxoethyl)-1-cyclohexene (**40**)*

To a solution of diene **2** (783 mg, 3.56 mmol) and *trans*-3-penten-2-one (204 mg, 2.43 mmol) in ether (2 mL) at 0°C and under an atmosphere of argon, anhydrous stannic chloride (620 mg, 2.38 mmol) was added. After stirring for 11 h the reaction mixture was diluted with ether. Aqueous 5% sodium bicarbonate was added and the resulting emulsion was filtered by suction. The filtrate was extracted with dichloromethane and the extracts were combined, dried, filtered, and concentrated. Flash chromatography of the residue on silica gel, eluting with acetone and ether in petroleum ether (2:3:5), gave pure adduct **40** (529 mg, 72% yield, no diene **2** recovery) as a light yellow oil: ir: 1710 (ketone C=O), 1658 (enol phosphate C=C), 1270, and 1033 (phosphate) cm^{-1}; ^1H nmr δ: 5.55 (m, 1H, -CH=C-O-), 4.19 (m, 4H, 2 × -OCH_2-), 2.75 (m, 1H, -C*H*-CH=), 2.61 (dd, 1H, J = 11 Hz, J' = 5 Hz, -COCH-), 2.17 (s, 3H, CH_3CO-), 1.36 (t, 6H, J = 7 Hz, 2 × -OCH_2CH_3), 0.96 (d, 3H, J = 6 Hz, CH_3CHCH_2-), and 0.86 (d, 3H, J = 7 Hz, CH_3CHCH=); ^{13}C nmr δ: 209.2, 145.9 (d), 114.4 (d), 63.8 (d), 56.3, 35.1 (d), 30.3, 30.0, 24.6, 19.3, 16.7, and 15.7 (d); ms M^+: 304.1445 (calcd. for $C_{14}H_{25}PO_5$: 304.1440). Anal. calcd. for $C_{14}H_{25}PO_5$: C 55.24, H 8.30; found: C 55.16, H 8.18.

*2-Diethylphosphoryloxy-5,8-dihydroxy-4-methyl-1,4-dihydronaphthalene (**41**)*

To a solution of diene **2** (598 mg, 2.72 mmol) and *p*-benzoquinone (195 mg, 1.80 mmol) in dichloromethane (2 mL) at 0°C and under an atmosphere of nitrogen, anhydrous stannic chloride (465 mg, 1.79 mmol) was added. After stirring for 30 min water was added and the resulting emulsion was filtered with suction. The filtrate was extracted with dichloromethane and the extracts were combined, dried, filtered, and concentrated. Flash chromatography of the residue on silica gel, eluting with acetone and ether in petroleum ether (2:3:5), gave aromatic enol phosphate **41** (308 mg, 52% yield, no diene **2** recovery), which was recrystallized from acetone – petroleum ether to give light yellow crystals: mp 130.5–132.0°C; ir: 3304 (-OH), 1700 (enol phosphate C=C), 1492 (aromatic C=C), 1247 and 1035 (phosphate) cm^{-1}; ^1H nmr (acetone-d_6) δ: 7.86 (br s, 2H, D_2O exchangeable, 2 × -OH), 6.60 and 6.59 (both s, 1H each, 2H, 2 × Ar-H), 5.72 (m, 1H, -CH=C-O-), 4.20 (m, 4H, 2 × -OCH_2-), 1.33 (m, 6H, 2 × -OCH_2CH_3), and 1.27 (d, 3H, J = 7 Hz, -$CHCH_3$); ^{13}C nmr (acetone-d_6) δ: 148.2, 145.9 (d), 127.3, 121.5, 115.2 (d), 113.8, 113.2, 64.9 (d), 31.4, 28.1 (d), 22.6, and 16.4 (d); ms M^+: 328.1075 (calcd. for $C_{15}H_{21}PO_6$: 328.1075). Anal. calcd. for $C_{15}H_{21}PO_6$: C 54.86, H 6.46; found: C 54.84, H 6.46.

Acknowledgements

We are grateful to the Natural Sciences and Engineering Research Council of Canada and the University of Alberta for financial support.

1. K.N. Houk, Y.T. Lin, and F.K. Brown. J. Am. Chem. Soc. **108**, 554 (1986).
2. M.J.S. Dewar, S. Olievella, and J.J.P. Stewart. J. Am. Chem. Soc. **108**, 5771 (1986).
3. S.D. Kahn, C.F. Pau, L.E. Overman, and W.J. Hehre. J. Am. Chem. Soc. **108**, 7381 (1986).
4. R. Gleiter and M.C. Bohm. Pure Appl. Chem. **55**, 237 (1983).
5. R.B. Woodward and R. Hoffmann. Angew. Chem. Int. Ed. Engl. **8**, 781 (1969).
6. I. Flemming. Frontier orbitals and organic chemical reactions. Wiley, London. 1978.
7. K.N. Houk. Acc. Chem. Res. **8**, 361 (1975).
8. J. Sauer and R. Sustmann. Angew. Chem. Int. Ed. Engl. **19**, 779 (1980).
9. K.N. Houk. *In* Pericyclic reactions. Vol. 2. *Edited by* A.P. Marchand and R.E. Lehr. Academic Press, New York. 1977.
10. M. Kakushima. Can. J. Chem. **57**, 2564 (1979).
11. D. Ginsburg. Tetrahedron, **39**, 2095 (1983).
12. N.T. Anh, E. Canadell, and O. Eisenstein. Tetrahedron, **34**, 2283 (1978).
13. M. Petrzilka and J.I. Grayson. Synthesis, 753 (1981).
14. S. Danishefsky. Acc. Chem. Res. **14**, 400 (1981).
15. S.J. Danishefsky. Aldrichimica Acta, **19**, 59 (1986).
16. S.M. Weinreb and J.I. Levin. Heterocycles, **12**, 949 (1979).
17. W. Oppolzer. Angew. Chem. Int. Ed. Engl. **23**, B76 (1984).
18. D.L. Boger. Tetrahedron, **39**, 2869 (1983).
19. E. Ciganek. Org. React. **32**, 1 (1984).
20. S.M. Weinreb and R.R. Staib. Tetrahedron, **38**, 3087 (1982).
21. D.L. Boger. Chem. Rev. **86**, 781 (1986).
22. A.G. Fallis. Can. J. Chem. **62**, 183 (1984).
23. G. Brieger and J.N. Bennett. Chem. Rev. **80**, 63 (1980).
24. T. Wagner-Jauregg. Synthesis, 165 (1980).
25. T. Wagner-Jauregg. Synthesis, 769 (1980).
26. T. Wagner-Jauregg. Synthesis, 349 (1976).
27. G. Desimone and G. Tacconi. Chem. Rev. **75**, 651 (1975).
28. K.F. Burri, F. Kienzle, and P. Rosen. United States Pat. US 3,933,948 (20 Jan. 1976) to Hoffmann-La Roche Inc.; Chem. Abstr. **84**, 121130k (1976).
29. F. Kienzle and P. Rosen. Helv. Chim. Acta, **62**, 442 (1979).
30. T.K. Ngooi. Ph.D. Dissertation, The University of Alberta, 1984.
31. H.J. Liu and T.K. Ngooi. Can. J. Chem. **62**, 2676 (1984).
32. H.J. Liu, T.K. Ngooi, and E.N.C. Browne. Can. J. Chem. **66**, 3143 (1988).
33. P. Yates and P. Eaton. J. Am. Chem. Soc. **82**, 4436 (1960).
34. G.I. Fray and R. Robinson. J. Am. Chem. Soc. **83**, 249 (1961).
35. T. Inukai and M. Kasai. J. Org. Chem. **30**, 3567 (1965).
36. T. Inukai and T. Kojima. J. Org. Chem. **31**, 2032 (1966).
37. E.F. Lutz and G.M. Bailey. J. Am. Chem. Soc. **86**, 3899 (1964).
38. T. Inukai and T. Kojima. J. Org. Chem. **31**, 1121 (1966).
39. T. Inukai and T. Kojima. J. Org. Chem. **32**, 869 (1967).
40. H.J. Liu and W.M. Feng. Synth. Commun. **16**, 1485 (1986).
41. H.J. Liu and W.M. Feng. Synth. Commun. **17**, 1777 (1987).
42. A. Claesson, A. Quader, and C. Sahlberg. Tetrahedron Lett. **24**, 1297 (1983).
43. C. Sahlberg, A. Quader, and A. Claesson. Tetrahedron Lett. **24**, 5137 (1983).
44. R.E. Ireland and G. Pfister. Tetrahedron Lett. 2145 (1969).
45. J.G. Martin and R.I. Hill. Chem. Rev. **61**, 537 (1961).
46. H.J. Liu and T.K. Ngooi. Synth. Commun. **12**, 715 (1982).
47. F. Fringuelli, F. Pizzo, A. Taticchi, T.D.J. Halls, and E. Wenkert. J. Org. Chem. **47**, 5056 (1982).
48. K. Alder and G. Stein. Angew. Chem. **50**, 510 (1937).
49. A.S. Onishchenko. Diene synthesis. Israel Program for Scientific Translation, Jerusalem. 1964.
50. J. Sauer. Angew. Chem. Int. Ed. Engl. **6**, 16 (1967).
51. H.J. Liu and E.N.C. Browne. Can. J. Chem. **65**, 1262 (1987).
52. H.J. Liu and E.N.C. Browne. Can. J. Chem. **59**, 601 (1981).
53. H.J. Liu and E.N.C. Browne. Tetrahedron Lett. 2919 (1977).
54. F. Elsinger. Org. Synth. **45**, 7 (1965).

55. E.J. Corey and J.W. Suggs. Tetrahedron Lett. **31**, 2647 (1975).
56. E.N.C. Browne. Ph.D. Dissertation, The University of Alberta, 1980.
57. H.J. Liu, E.N.C. Browne, and S.Y. Chew. Can. J. Chem. **66**, 2345 (1988).
58. W.C. Still, M. Kahn, and A. Mitra. J. Org. Chem. **43**, 2923 (1978).
59. L.F. Fieser and M. Fieser. Reagents for organic synthesis. Vol. 1. Wiley and Sons, Inc., New York. 1967.
60. H.C. Odom and A.R. Pinder. Org. Synth. **51**, 115 (1971).
61. D. Liotta, C. Barnum, R. Puleo, G. Zima, C. Bayer, and H.S. Kezar. J. Org. Chem. **46**, 2970 (1981).

Can. J. Chem. Downloaded from www.nrcresearchpress.com by 85.192.166.187 on 09/08/12
For personal use only.

Electron inductive perturbation(s) of heteronuclear metal–metal bonds. Isocyanide and indenyl derivatives of the mixed metal dimers $[(\eta^5\text{–}C_5H_5)Fe(CO)_2Re(CO)_5]$ and $[MnRe(CO)_{10}]$

PIERRE D. HARVEY[1]

Département de chimie, Université de Sherbrooke, Sherbrooke, QC J1K 2R1, Canada

AND

PETER JOHNSTON AND NEIL J. COVILLE[1]

Department of Chemistry, University of the Witwatersrand, Johannesburg, 1 Jan Smuts Avenue, PO Wits 2050, South Africa

Received June 17, 1994

PIERRE D. HARVEY, PETER JOHNSTON, and NEIL J. COVILLE. Can. J. Chem. **72**, 2176 (1994).

The properties of the heteronuclear metal–metal bonds in the unbridged $[\eta^5\text{–}C_5H_5)Fe(CO)_2Re(CO)_{5-n}(CNR)_n]$ and $[(\eta^5\text{–}C_9H_7)Fe(CO)_2Re(CO)_{5-n}(CNR)_n]$ complexes ($n = 0, 1, 2$; R = *tert*-butyl (*t*Bu) and 2,6-dimethylphenyl (Xy)) and the two equatorially substituted isomers of $[MnRe(CO)_8(CN\text{-}tBu)_2]$ have been investigated theoretically by Extended Hückel Molecular Orbital calculations (EHMO) and experimentally by UV–visible spectroscopy, electrochemistry, and by microRaman or FT-Raman spectroscopy. The expected $d\sigma^*$ orbital is the lowest unoccupied molecular orbital (LUMO), mainly fabricated by interactions of the metal d_{z^2} orbital, but the $d\pi^*$ and $d\sigma$ orbitals are the highest occupied molecular orbital (HOMO) and HOMO-1, respectively, as demonstrated experimentally from the UV–visible spectra. The EHMO computations demonstrate the mixing between these two $d\pi^*$ (and $d\delta$) and $d\sigma$ MO orbitals. The influence of substituent effects on the spectroscopic and electrochemical properties is complicated and is interpreted in terms of inductive effects and relative destabilisation of the $d\sigma$, $d\pi^*$, and $d\sigma^*$ molecular orbitals. Finally, the metal–metal stretching frequencies for four mixed metal dimers (MnRe and FeRe) are reported.

PIERRE D. HARVEY, PETER JOHNSTON et NEIL J. COVILLE. Can. J. Chem. **72**, 2176 (1994).

Utilisant des calculs théoriques d'orbitales moléculaires de Hückel étendues et des méthodes expérimentales incluant de la spectroscopie UV–visible, de l'électrochimie et des spectroscopies microRaman et Raman par transformation de Fourier, on a étudié les propriétés des liaisons métal–métal hétéronucléaires des complexes non pontés $[\eta^5\text{–}C_5H_5)Fe(CO)_2Re(CO)_{5-n}(CNR)_n]$ et $[(\eta^5\text{–}C_9H_7)Fe(CO)_2Re(CO)_{5-n}(CNR)_n]$ ($n = 0, 1, 2$; R = *tert*-butyl (*t*Bu) et 2,6-diméthylphényle (Xy)) ainsi que de deux isomères substitués d'une façon équatoriales des isomères $[MnRe(CO)_8(CN\text{-}tBu)_2]$. L'orbitale $d\sigma^*$ attendue est l'orbitale moléculaire basse vacante (BV), obtenue principalement par les interactions de l'orbitale d_{z^2} du métal; toutefois, tel que démontré expérimentalement par les spectres UV–visible, les orbitales $d\pi^*$ et $d\sigma$ sont respectivement orbitales moléculaires hautes occupées HOMO et HOMO-1. Des calculs EHMO démontre l'existence d'un mélange entre ces deux orbitales moléculaires $d\pi^*$ (et $d\delta$) et $d\sigma$. L'influence des effets des substituants sur les propriétés spectroscopiques et électrochimiques est complexe et on l'interprète en fonction d'effets inductifs et de déstabilisation relative des orbitales moléculaires $d\sigma$, $d\pi^*$ et $d\sigma^*$. Enfin, on rapporte les valeurs des fréquences d'élongation métal–métal des quatre dimères métalliques (MnRe et FeRe).

[Traduit par la rédaction]

Introduction

The nature of covalent (1) and dative (2) heteronculear metal–metal bonds is of current interest. These dimers appear to be polar, and chemical and physical properties often differ between heteronuclear binuclear complexes and the homonuclear dimers (1). In this paper we will describe the heteronuclear metal–metal bond from the extended Hückel molecular orbital theoretical point of view, in particular for the complex $(\eta^5\text{–}C_5H_5)Fe(CO)_2Re(CO)_5$, in an attempt to rationalize those differences. We also report the influence of substitution effects on such metal–metal bond properties as the $d\sigma \rightarrow d\sigma^*$ and $d\pi^* \rightarrow d\sigma^*$ transition energies (UV–visible), oxidation potential (cyclic voltametry), and $\nu(MM')$ (Raman spectra). It will be shown that unusual properties with respect to the homonuclear systems are often observed.

Experimental Section

Materials

The bimetallic compounds were synthesized according to literature methods (3–7). 2-Methyltetrahydrofuran (2MeTHF; Aldrich Chemical Co) was purified by refluxing over sodium/benzophenone, and fractional distillation.

Instruments

The UV–visible spectra were recorded on a Cary model 17 spectrometer. The experimental procedure used was the same as previously outlined in ref. 8. The uncertainties in the measured λ_{max} for the glass solutions at 77 K was at most 0.5 nm. The microcrystalline samples were sealed in Pyrex capillaries for the Raman measurements, which were made on an Instruments S.A. Raman spectrometer equipped with a U-1000 Jobin–Yvon 1.0-m double monochromator employed at the 514.5-nm green line of a Spectra Physics model 164 argon ion laser (typically 10–20 mW at the samples) for excitation. The spectra were calibrated against the emission lines of a standard neon lamp, and the peak positions are considered to be accurate to ± 0.2 cm^{-1}. The FT-Raman spectra for the solid samples were obtained on a Bruker IFS 66/CS FT-IR spectrometer coupled with an FRA106 FT-Raman module using a Nd: YAG laser (1064 nm excitation) and a Notch filter (cutoff ~ 70 cm^{-1}).

Electrochemistry

Electrochemical measurements were made on argon degassed CH_3CN (Aldrich Chemical Co.; refluxed and distilled over CaH_2) solutions containing 0.1 M TBA(PF_6) (tetra-*n*-butylammonium hexafluorophosphate; Aldrich Chemical Co.; recrystallized three times from EtOH) as the supporting electrolyte. Cyclic voltammetric measurements were performed with a PAR 173 potentiostat and a PAR 175 universal programmer. Pt disk electrodes were polished with alumina for 5 min with 1:1 CH_3OH/H_2O before use. Coulometry measurements were

[1]Authors to whom correspondence may be addressed.

Can. J. Chem. Downloaded from www.nrcresearchpress.com by 85.192.166.187 on 09/08/12
For personal use only.

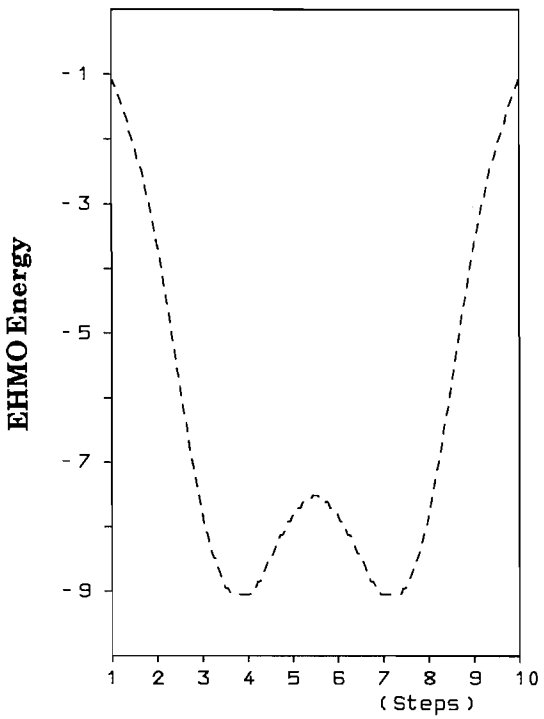

FIG. 1. Plot of the total EHMO energy as a function of the (η^5–C_5H_5)—Fe—Re$(CO)_{eq}$ dihedral angle. Each step represents 10° going from 0° (step 1) to 90° (step 10). The energy difference between the maximum and minimum values is 0.019 eV (i.e., each division on the "y" axis is 0.002 375 eV). The ReFe distance was set at 2.888 Å.

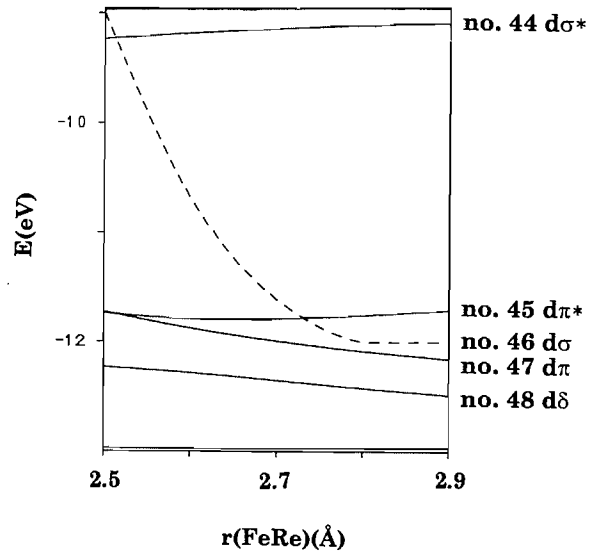

FIG. 2. MO diagram for (η^5–C_5H_5)Fe$(CO)_2$Re$(CO)_5$ (where the dihedral angle is 45°) as a function of the Fe—Re distance. The dotted line is the total EHMO energy of the molecule. Each step represents 0.10 Å going from 2.5 to 2.9 Å.

performed with a H-cell with Pt-gauze working and auxillary electrodes. All potentials are versus SSCE.

Computational details

All MO calculations were of the extended Hückel type (EHMO) using a modified version of the Wolsberg–Helmholz formula (9). The atomic parameters used for C, O, and H are taken from refs. 10–12. For Fe and Re, the atomic parameters used were from refs. 13 and 14, respectively. All distances (C═O, M—C, C═C, and C—H) and angles were taken from the X-ray crystallographic data for (η^5–C_5H_5)Fe$(CO)_2$Re$(CO)_5$ (4). The geometry has been kept intact during the computations, as reported for the X-ray crystal structure (4) (except for the (η^5–C_5H_5)Fe—Re$(CO)_{eq}$ twist angle (45°)). The distance Fe—Re was varied from 2.50 to 2.90 Å (see discussion in the text). A detailed description of the graphic programs used in this work can be found in ref. 15.

Results and discussion

1. *Molecular orbital analysis*

To assess the role of orbital interactions on the heteronuclear metal–metal bonded complexes (η^5–C_5H_5)Fe$(CO)_2$Re$(CO)_5$), it is important to establish the appropriate geometry of the molecule to be used in EHMO calculations. Initially a (η^5–C_5H_5)—M′—M$(CO)_{eq}$ dihedral angle of 16°, corresponding to that observed in the crystal structure analysis (4), was used. However, this resulted in anomalous results in that the $d_{Fe—Re}$ bond length was predicted to be much less than that observed in the structural analysis.

Further investigations have revealed the source of the problem. A plot of the total EHMO energy as a function of the (η^5–C_5H_5)-Fe-Re$(CO)_{eq}$ dihedral angle is shown in Fig. 1. This clearly indicates two minima at ~28° and ~62° with a maximum at 45°. The barrier between the two minima is very small (~30 cm^{-1}, in vacuo) and is presumed to arise from steric interactions between the C_5H_5 and CO ligands on the respective metal atoms. In solution, exchange between these two conformers should be facile and should lead to an average dihedral angle of 45°. For computational purposes, this configuration (C_s point group) was assumed.

Based upon the earlier theoretical and experimental work by Gray *et al.* (16, 17) and more recently by Nakatsuji et al. (2) on the covalently σ-bonded metal–metal $M_2(CO)_{10}$ dimers (M = Mn, Re), one can unambiguously predict that the metal–metal bond in the d^7–d^7 system will be formed using the d_{z^2}–d_{z^2} metal–metal interaction, and that the lowest energy electronic transitions will be either $d\sigma \rightarrow d\sigma^*$ (M = Re) or $d\pi^* \rightarrow d\sigma^*$ (M = Mn). However, mixing between the $d\pi^*$ (or $d\pi$) and $d\sigma$ molecular orbitals is not expected to be extensive.

Before detailed analysis of the dimer, one should state that for the Re$(CO)_5$ fragment (referred to as the Re fragment in the text below), the computed ordering for the *d* orbitals is as follows: $d_{x^2-y^2} > d_{z^2} > d_{xz} = d_{yz} > d_{xy}$, which is in agreement with previous *ab initio* molecular orbital calculations (2). These metal orbitals generate the $d\delta$, $d\sigma$, $d\pi = d\pi$, and $d\delta$ molecular orbitals, respectively, in the homonuclear dimers. For the (η^5–C_5H_5)Fe$(CO)_2$ fragment (referred to as the Fe fragment in the text below), the computed molecular orbital ordering is $d\sigma$, $d\delta$, $d\pi$, $d\delta$, $d\pi$ (nomenclature adopted from ref. 16). This ordering is the same as previously reported for the (η^5–C_5H_5)Mo$(CO)_3$ fragment (16). Importantly, the d_{z^2} orbital of the Fe fragment is located ~0.5 eV above the d_{z^2} orbital of the Re fragment, indicating evidence of a covalent polarity in the metal–metal bond. This difference is not great enough to invoke the possibility of a dative metal–metal bond. Nakatsuji et al. (2) computed the d_{z^2} orbital energies for mixed metal dimers known to exhibit a dative metal–metal bond; the differences between the two fragments in $OsW(CO)_{10}$ and $OsCr(CO)_{10}$ are of the order of 4.0–6.5 eV, according to the *ab initio* results.

The MO analysis of the (η^5–C_5H_5)Fe$(CO)_2$Re$(CO)_5$ complex turned out to be more interesting than anticipated. The computed total energy as a function of the metal–metal distance 2.5–2.9 Å (Fig. 2) shows a flat minimum ranging from 2.8 to

Can. J. Chem. Downloaded from www.nrcresearchpress.com by 85.192.166.187 on 09/08/12
For personal use only.

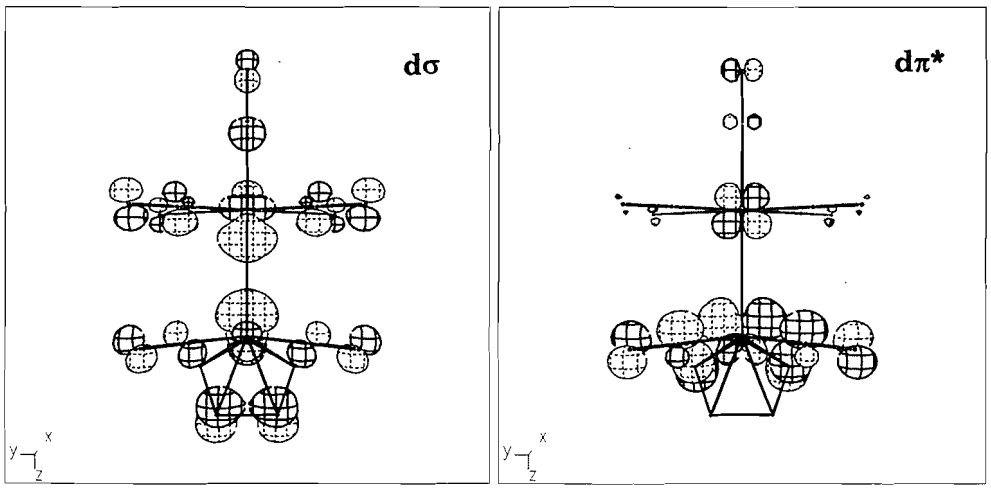

FIG. 3. The MO picture for the HOMO ($d\pi^*$) and HOMO-1 ($d\sigma$) for the $(\eta^5\text{–}C_5H_5)Fe(CO)_2Re(CO)_5$ complex. Note that the $d\sigma^*$ orbital is identical in shape to the $d\sigma$ one with the exception that the dz^2 orbital of the Re atom is inverted in sign to promote antibonding Re–Fe interactions. The dihedral angle is 45°, and the Re—Fe distance is 2.88 Å in this plot.

2.9 Å. These values compare particularly well with experiment (2.888 Å). The energy difference between the maximum energy distance (2.5 Å) and the minimum one (2.8–2.9 Å) is 0.655 eV (i.e., 5.28×10^3 cm^{-1}), and is mostly due to electronic factors. This is indeed observed via the stabilization of the MO no. 45 and no. 47, which are the $d\sigma$ and $d\pi$ MO's, respectively (Fig. 2). These MO's are now briefly described with respect to the atomic contributions.

The LUMO (MO no. 44 = $d\sigma^*$) and the HOMO-1 (no. 46 = $d\sigma^*$) are composed of p_z(CO) and metal d_{z^2} orbitals (Fe and Re) as expected, but also include some M *s* and p_z characteristics. The addition of these later orbitals has the effect of modifying the shape of the orbital located at the M atom in order to increase the lobe size located along "z" axis, hence promoting Fe–Re interactions. A picture of the HOMO-1 (MO no. 46) is shown in Fig. 3. In addition, the Fe fragment also provides a weak but non-negligible CO(p_y), Fe(d_{xy}), and Fe(d_{yz}) contribution, due to the close proximity in energy of the $d\pi$ and $d\delta$ orbitals of the Fe fragment to the $d\sigma$(Fe–Re) MO. The HOMO is the $d\pi^*$ (MO no. 45) as shown in Fig. 3, and is composed of Re(d_{yz}) and Fe(d_{yz}) orbitals (generating the $d\pi$ Fe–Re interactions), and some amount of Fe d_{xy}, d_{xy} and Re d_{xz} orbitals as well as some CO ligand orbitals. Again mixing is also noted. The HOMO-2 (no. 47) is the $d\pi$ orbital, also exhibiting some mixing similar to that of the $d\pi^*$ orbital. These computations clearly indicate that the $d\pi^*$ MO lies above the $d\sigma$ orbital, as experimentally observed. The EHMO $d\pi^* \rightarrow d\sigma^*$ and $d\sigma \rightarrow d\sigma^*$ transition energies at r(FeRe) = 2.9 Å (~2.6 eV (20 970 cm^{-1}) and ~3.1 eV (25 000 cm^{-1}), respectively, compare favourably with the UV–visible data below (i.e, 22 300 and 27 700 cm^{-1}, respectively).

2. *Electrochemistry*

The cyclic voltammetric properties have also been investigated to address the effect of substitution on the heteronuclear metal–metal bond. In all complexes investigated, the oxidation waves are irreversible and are associated with a return wave in the reduction region of the cyclic voltammogram. Coulometric measurements suggest that the redox processes involve two electrons. No other reduction wave is observed in the –2.0–0.0 V range. A typical cyclic voltammogram is shown in Fig. 4 and the peak potentials for the oxidation process $E^{+/0}$ are reported in Table 1. The results in each instance are consistent with an

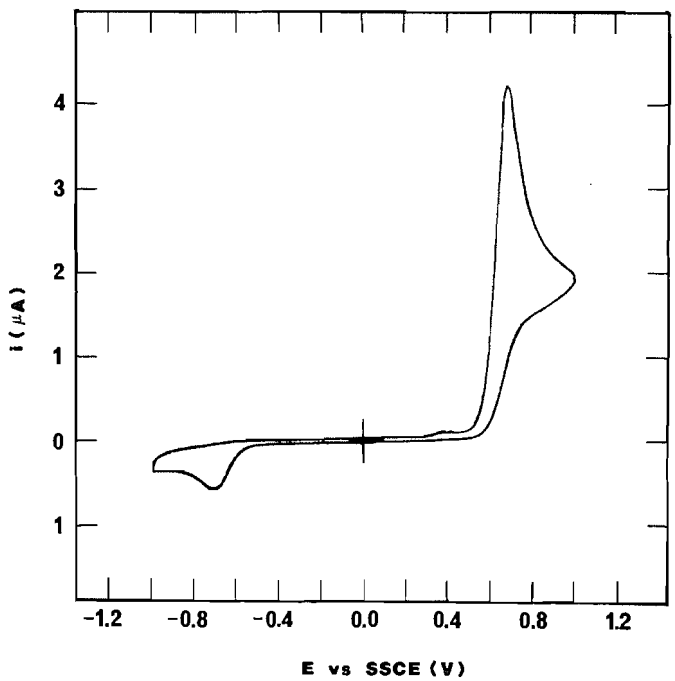

FIG. 4. Cyclic voltammogram for the oxidation of $[(\eta^5\text{–}C_5H_5)Fe(CO)_2Re(CO)_5]$ in CH_3CN containing 0.1 M TBA(PF_6) at room temperature. Scan rate 500 mV s^{-1}.

TABLE 1. Cyclic voltammetric data for the oxidation of some isocyanide and indenyl derivatives of $[(\eta^5\text{-}C_5H_5)Fe(CO)_2Re(CO)_5]$ in CH_3CN – 0.1 M TBA (PF_6) with a scan rate of 500 mV s^{-1}[a]

Compounds	$E^{+/0}$[b] (±0.02 V)	No. of electrons
$[(\eta^5\text{-}C_5H_5)Fe(CO)_2Re(CO)_5]$	0.68	2
$[(\eta^5\text{-}C_5H_5)Fe(CO)_2Re(CO)_4(CNXy)]$	0.54	2
$[(\eta^5\text{-}C_9H_7)Fe(CO)_2Re(CO)_4(CNXy)]$	0.44	2
$[(\eta^5\text{-}C_9H_7)Fe(CO)_2Re(CO)_3(CN\text{-}t\text{Bu})_2]$	0.36	2

[a]Room temperature data.
[b]Peak potentials of irreversible waves, vs. SSCE.

Can. J. Chem. Downloaded from www.nrcresearchpress.com by 85.192.166.187 on 09/08/12
For personal use only.

Can. J. Chem. Downloaded from www.nrcresearchpress.com by 85.192.166.187 on 09/08/12
For personal use only.

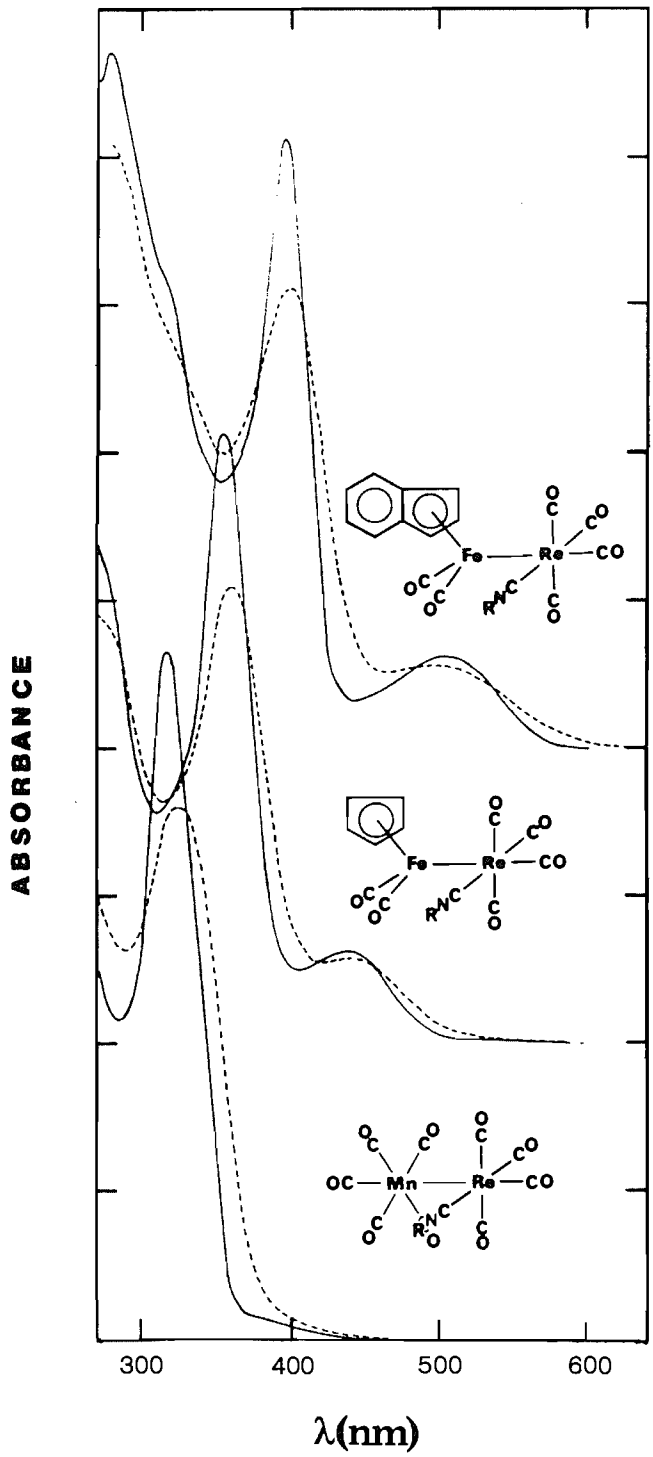

FIG. 5. Comparison of the absorption of the $[(\eta^5\text{–}C_5H_5)Fe(CO)_2Re(CO)_{5-n}(CNR)_n]$ complexes; $n = 0$–2; R = *t*Bu, in 2MeTHF at 293 (...) and 77 K (...). Corrected for the base line and glass contraction.

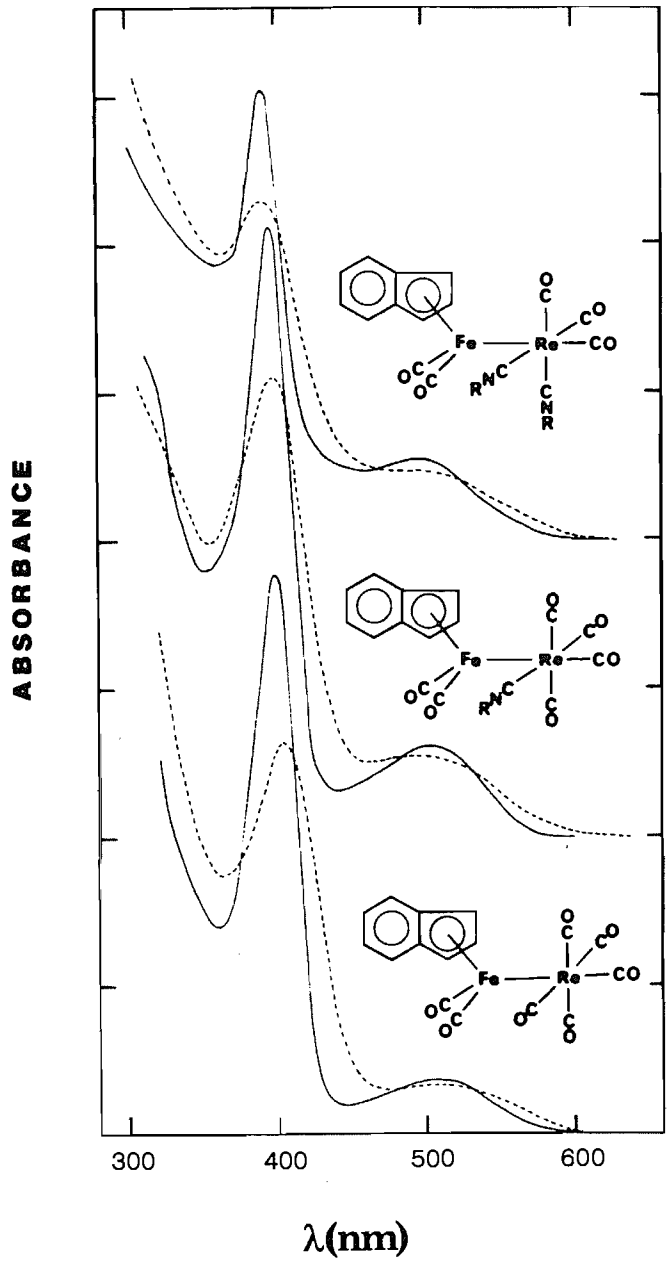

FIG. 6. Comparison of the absorption spectra of the $[X\text{-}Re(CO)_4(CN\text{-}t\text{Bu})]$ complexes: X = $Mn(CO)_5$, $(\eta^5\text{–}C_5H_5)Fe(CO)_2$, $(\eta^5\text{–}C_9H_7)Fe(CO)_2$, in 2MeTHF at 293 (...) and 77 K (...). Corrected for the base line and glass contraction.

increase in electronic density around the M–M bond when substitution of CO and (or) $\eta^5\text{–}C_5H_5$ is made regardless of the site of substitution! This is also consistent with the published IR data (3–7). Indeed red shifts of the ν(CO) peaks are observed upon the replacement of CO by CNR and $\eta^5\text{–}C_5H_5$ by $\eta^5\text{–}C_9H_7$.

3. *Electronic spectra of the FeRe complex*

Typical room temperature and 77 K UV–visible spectra (Table 2) of the complexes in 2MeTHF are shown in Figs. 5 and 6. The spectra are similar to other heterobimetallic d^7–d^7 single-bonded complexes (18, 19) and show a strong absorption in the 320–450 nm range ($\epsilon \sim 26\,000 \pm 300\ M^{-1}\ cm^{-1}$; room temperature) and a weaker band ($\epsilon \sim 4500 \pm 800\ M^{-1}\ cm^{-1}$; room temperature) in the 450–520 nm region. Upon cooling to 77 K, the intense bands sharpen and blue-shift slightly. No new band that could be associated with a bridged species appears at low temperature. Based upon their absorptivities, transition energies, and their temperature dependence, the electronic bands are confidently assigned to $d\sigma \rightarrow d\sigma^*$ and $d\pi^* \rightarrow d\sigma^*$ transitions for their intense and weak features, respectively.

Upon substitution of CO by CN-*t*Bu in the $[(ring)Fe(CO)_2Re(CO)_5]$ complexes, small *blue* shifts of the electronic

TABLE 2. Electronic spectral data of mixed-metal dimers[a]

Compounds	λ_{max}/nm	$\bar{\nu}_{max}$/cm^{-1} [b]	ε/M^{-1} cm^{-1} [c]	Assignment
$[(\eta^5\text{-}C_5H_5)Fe(CO)_2Re(CO)_5]$	363	27 700	24 600	$d\sigma^* \leftarrow d\sigma$
	448	22 300	3 800	$d\sigma^* \leftarrow d\pi$
$[(\eta^5\text{-}C_5H_5)Fe(CO)_2Re(CO)_4(CN\text{-}t\text{Bu})]$	361	27 500	25 400	$d\sigma^* \leftarrow d\sigma$
	445	22 500	5 100	$d\sigma^* \leftarrow d\pi$
$[(\eta^5\text{-}C_5H_5)Fe(CO)_2Re(CO)_4(CNXy)]$	365	27 400	28 600	$d\sigma^* \leftarrow d\sigma$
	450	22 200	5 400	$d\sigma^* \leftarrow d\pi$
$[(\eta^5\text{-}C_9H_7)Fe(CO)_2Re(CO)_5]$	403	24 800	25 600	$d\sigma^* \leftarrow d\sigma$
	510	19 600	3 700	$d\sigma^* \leftarrow d\pi$
$[(\eta^5\text{-}C_9H_7)Fe(CO)_2Re(CO)_4(CN\text{-}t\text{Bu})]$	398	25 100	22 800	$d\sigma^* \leftarrow d\sigma$
	508	19 700	4 000	$d\sigma^* \leftarrow d\pi$
$[(\eta^5\text{-}C_9H_7)Fe(CO)_2Re(CO)_4(CNXy)]$	405	24 700	26 600	$d\sigma^* \leftarrow d\sigma$
	512	19 500	3 900	$d\sigma^* \leftarrow d\pi$
$[(\eta^5\text{-}C_9H_7)Fe(CO)_2Re(CO)_3(CN\text{-}t\text{Bu})_2]$	392	25 500	29 400	$d\sigma^* \leftarrow d\sigma$
	505	19 800	5 300	$d\sigma^* \leftarrow d\pi$

[a]In 2MeTHF solutions at room temperature.
[b]±50 cm^{-1}.
[c]±5%.

Can. J. Chem. Downloaded from www.nrcresearchpress.com by 85.192.166.187 on 09/08/12
For personal use only.

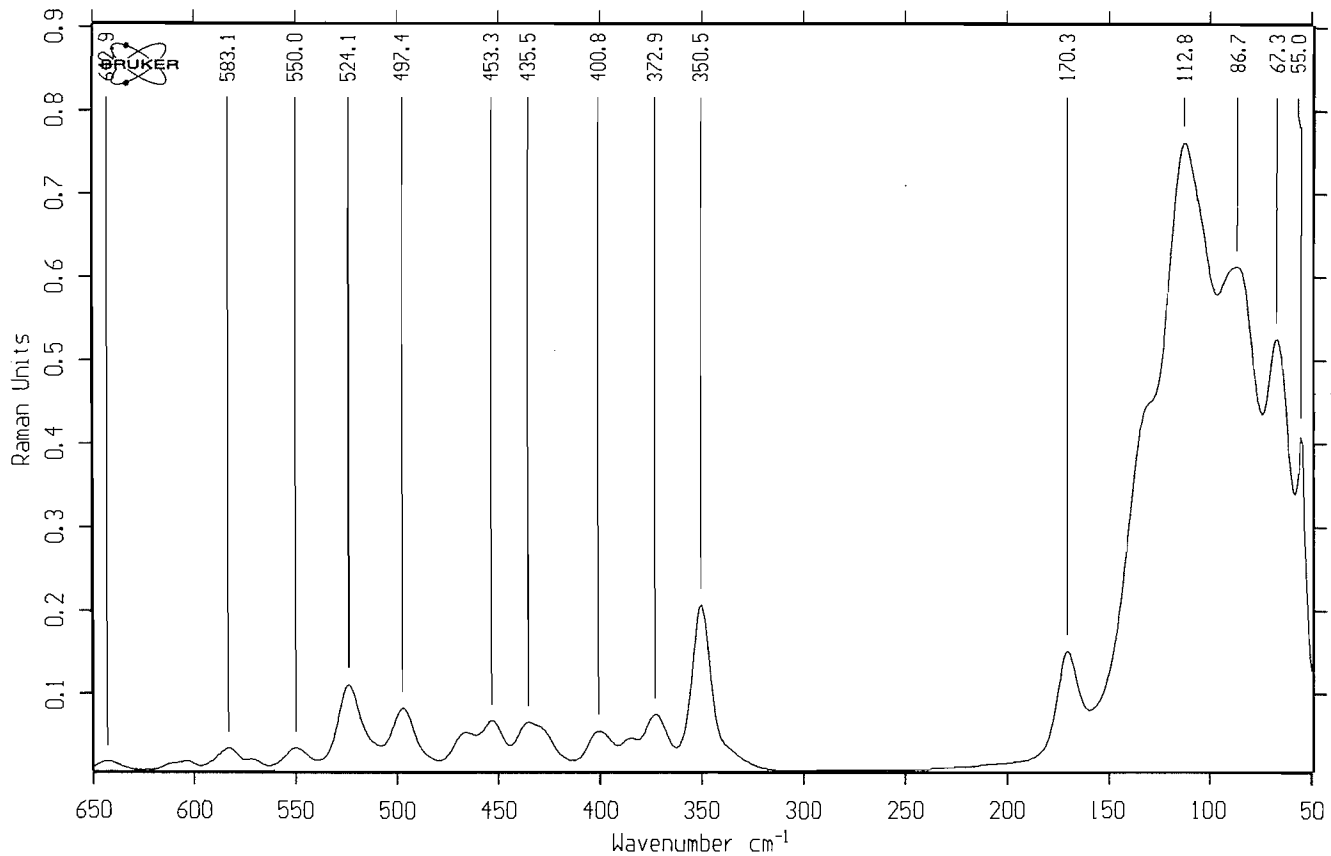

FIG. 7. FT-Raman spectrum of solid $(\eta^5\text{-}C_5H_5)Fe(CO)_2Re(CO)_4(CN\text{-}t\text{Bu})$ at 293 K. Experimental conditions: 200 scans, 4 cm^{-1} resolutions, corrected for the Notch filter, 75 mW laser power. The 170 cm^{-1} is the peak of interest in this work ν(FeRe).

bands are observed (see Fig. 7): ~3–4 nm (~350 cm^{-1} for each CO ligand replaced) for the $d\sigma \rightarrow d\sigma^*$ and ~3 nm (~100 cm^{-1} for each CO ligand replaced) for the $d\pi^* \rightarrow d\sigma^*$ bands. For the $[Re_2(CO)_{10-n}(CNR)_n]$ complexes (n = 0–4; R = *t*Bu, Me, $CH_2C_6H_5$), a regular *red* shift of 800 cm^{-1} for each CO ligand replaced was observed and was associated with the better σ-donor and poorer π-acceptor capacity of the CNR ligand relative to the CO ligand (8). To our knowledge, the blue shift observed in the $[(ring)Fe(CO)_2\text{–}Re(CO)_{5-n}(CN\text{-}t\text{Bu})_n]$ compounds (ring = $\eta^5\text{–}C_5H_5$, $\eta^5\text{–}C_9H_7$) on increasing n is unprecedented.

Replacement of CO by CNXy at the Re atom in the [(ring)

TABLE 3. Spectroscopic and structural properties of some selected M (M = Mn, Re) homo- and heteronuclear complexes

	$d\sigma^* \rightarrow d\sigma$/cm^{-1} (77 K)	r(MM′)/Å	ν(M–M′)/cm^{-1}
$Mn(CO)_5$–X			
-$Re(CO)_5$	31 950[a]	2.909(1)[b]	155[c]
-$Re(CO)_4$(CN-*t*Bu)	31 550	2.963(3)[d]	157[c] (This work)
-$Mn(CO)_5$	29 240[a]	2.895(1)[f]	160[c]
-$W(\eta^5\text{-}C_5H_5)(CO)_3$	27 940[a]	3.16(1)[g]	
-$Mo(\eta^5\text{-}C_5H_5)(CO)_3$	26 810[a]	3.083(8)[d]	
-$Fe(\eta^5\text{-}C_5H_5)(CO)_2$	25 970[e]	2.843(4)[h]	
$Re(CO)_5$–X			
-$Re(CO)_5$	32 300[a]	3.041(1)[f]	121[k]
-$Re(CO)_4$(CN-*t*Bu)	31 350[i]	3.048(1)[j]	122[k]
-$Mn(CO)_5$	31 950[a]	2.909(1)[b]	155[c]
-$Mn(CO)_4$(CN-*t*Bu)	31 850		159 (This work)
-$W(\eta^5\text{-}C_5H_5)(CO)_3$	28 800[a]		
-$Mo(\eta^5\text{-}C_5H_5)(CO)_3$	28 500[a]	3.12(1)[g]	
-$Fe(\eta^5\text{-}C_5H_5)(CO)_2$	27 950	2.888(1)[l]	170[m] R 175 IR weak (This work)
-$Fe(\eta^5\text{-}C_9H_7)(CO)_2$	25 150	2.881(1)[l]	191[m] (This work)

[a]From ref. 19.
[b]From ref. 23.
[c]From ref. 22.
[d]From refs. 1 and 24.
[e]From ref. 17.
[f]From ref. 25.
[g]From ref. 26.
[h]From ref. 27.
[i]From ref. 8.
[j]From ref. 28.
[k]From ref. 21.
[l]From ref. 4.
[m]For $(\eta^5\text{-}C_5H_5)Fe(CO)_2Re(CO)_4$(CN-*t*Bu) and for $(\eta^5\text{-}C_9H_7)Fe(CO)_2Re(CO)_4$(CNXy) assuming that r(MM′) is little affected by the CNR substitution.

$Fe(CO)_2Re(CO)_5$] complexes (ring = η^5–C_5H_5, η^5–C_9H_7) produces unusually small red shifts (2 nm or ~100 cm^{-1} for each CO ligand replaced) for both electronic $d\sigma \rightarrow d\sigma^*$ and $d\pi^* \rightarrow d\sigma^*$ bands. In the [$Re(CO)_{10-n}(CNXy)_n$] complexes (n = 0–4), the red shift of these electronic bands was much larger upon substitution of CO by CNXy (~1600 cm^{-1} per CO ligand replaced) and was associated with a strong inductive electron-withdrawing effect due to the presence of the phenyl group (8). By replacing the η^5–C_5H_5 group in [$(\eta^5\text{–}C_5H_5)Fe(CO)_2$-$Re(CO)_{5-n}(CNR)_n$] complexes ($n$ = 0–2; R = *t*Bu, Xy) with a η^5–C_9H_7 group, large red shifts of ~40 nm and ~60 nm (~2700 cm^{-1}) for the $d\sigma \rightarrow d\sigma^*$ and $d\pi^* \rightarrow d\sigma^*$ bands, respectively, are observed (see Fig. 6).

The $MnRe(CO)_{10}$ dimer can also be considered as a polar molecule since the $d\sigma$ orbital of the $Mn(CO)_5$ fragment lies above the $Re(CO)_5$ fragment by ~1.2 eV according to recent *ab initio* calculations (2). The UV–visible spectra of [$MnRe(CO)_{10}$] and both isomers [$MnRe(CO)_9$(CN-*t*Bu)] are similar, and the electronic spectra of the [$Mn(CO)_5Re(CO)_4$(CN-*t*Bu)] complex in 2MeTHF at room temperature and at 77 K are shown in Fig. 6 as an example. The complexes [$MnRe(CO)_{10}$], [$Mn(CO)_4$(CN-*t*Bu)$Re(CO)_5$], and [$Mn(CO)_5Re(CO)_4$(CN-*t*Bu)] have $d\sigma \rightarrow d\sigma^*$ bands (77 K) at 313, 314, and 317 nm, respectively. The red shift induced by the substitution at the Mn atom (~1 nm or ~100 cm^{-1}) is smaller than the red shift induced by substitution at the Re atom (4 nm or ~400 cm^{-1}).

The "take home" lesson from the UV–visible measurements is that the red shifts of the $d\sigma \rightarrow d\sigma^*$ (and $d\pi \rightarrow d\sigma^*$) bands upon CO substitution (by CNR) are not as extensive in the heteronuclear complexes as in the homonuclear dimers. On some occasions even blue shifts are observed. In these cases, one has to conclude that the anti-bonding $d\sigma^*$ MO orbital is also *destabilized* (during the substitution), and the degree of destabilization depends upon the nature of the fragments and the entering ligand.

4. *Bond lengths and stretching frequencies*

The spectroscopic data and metal–metal bond distances for several d^7–d^7 $M(CO)_5$–X complexes (M = Mn, Re, X = organometallic fragment) are presented in Table 3. The assignment for ν(M–M′) (metal–metal stretching frequency) were made on the basis of comparison with well-known binuclear compounds (20, 21). In the case of the mixed Re–Fe dimers, only two spectra were successfully recorded as the compounds were very sensitive to laser degradation. A typical spectrum is presented in Fig. 7. According to the literature, the ν(FeM) values should range between 150 and 200 cm^{-1} (20) for singly bonded dimers or trimers. For $(\eta^5\text{–}C_5H_5)Fe(CO)_2$–$Re(CO)_4$ (CN-*t*Bu), only one peak was found in this range and was hence assigned to ν(FeRe). The peaks below 120 cm^{-1} are due to lattice modes and are generally intense. To support this assignment, the far-IR spectrum was also acquired using the polarity of the molecule to induce some IR activity. Indeed, a weak peak was found at ~175 cm^{-1}. No Raman polarization study was successfully

Can. J. Chem. Downloaded from www.nrcresearchpress.com by 85.192.166.187 on 09/08/12
For personal use only.

undertaken due to the accelerated laser-induced decomposition of the compounds in solutions. For the $(\eta^5\text{–}C_9H_7)Fe(CO)_2\text{-}Re(CO)_4$ (CNXy) dimer, two peaks were observed in the expected range (191 cm^{-1}, medium; 203 cm^{-1}, weak). An IR peak of medium intensity was located at 203 cm^{-1}. We also noticed that this 203 cm^{-1} peak is often present in the CNR complexes. There was no sign of the 191 cm^{-1} peak in the IR spectrum: presumably it was hidden by the 203 cm^{-1} peak. Based upon the relative intensity argument and the 203 cm^{-1} peak activity in the IR spectrum (for CNR complexes), the assignment for ν(FeRe) at 191 cm^{-1} is preferred.

For the substituted $MnRe(CO)_{10}$ species, the micro-Raman spectra were easy to interpret since the strong and sharp peak associated with ν(MnRe) was readily found at around 155 cm^{-1}. This is the position predicted by the literature (22). While it is well established that CO ligand substitution by a phosphine or an isocyanide group leads to a slight decrease in the r(MM′) (1), we find that ν(MM′) slightly increased in this study (see Table 3 for details). The reverse should have been observed. There is no easy explanation for this behaviour and, tentatively, one can only suggest that low-frequency vibrational mode mixing may be at the origin of this unusual result.

It is also interesting to note that the FeRe dimers exhibit the smallest $d\sigma \rightarrow d\sigma^*$ transition energies, the shortest metal–metal bond distances, and the largest ν(MM′) values. A large part of the reason for these observations is that (*i*) the $(\eta^5\text{–}C_5H_5)Fe(CO)_2$ fragment is energetically different from the $Re(CO)_5$ fragment, (*ii*) third-row elements generally exhibit smaller covalent radii than do fourth- and fifth-row elements, and (*iii*) the lower Fe mass generates higher ν(MM′) values (cf. $\nu = 2\pi C)^{-1}(F/\mu)^{1/2}$).

Acknowledgements

P.D.H. thanks the Natural Sciences and Engineering Research Council of Canada (NSERC), le Fonds pour la formation de chercheurs et l'aide à la recherche (FCAR), and the Université de Sherbrooke for financial support. N.J.C. and P.J. wish to acknowledge the financial assistance of the University of the Witwatersrand and the FRD (CSIR).

1. A.E. Leins, D.G. Billing, D.C. Levendis, J. du Toit, and N.J. Coville. Inorg. Chem. **31**, 4756 (1992), and references therein.
2. H. Nakatsuji, M. Hada and A. Kawashinma. Inorg. Chem. **31**, 1740 (1992), and references therein.
3. P. Johnston, G.J. Hutchings, L. Denner, J.C.A. Boeyens, and N.J. Coville. Organometallics, **6**, 1992 (1987).
4. P. Johnston, C.A. Dickson, A.J. Markell, L. Denner, J.C.A. Boeyens, and N.J. Coville. Inorg. Chim. Acta, **144**, 185 (1988).
5. P. Johnston, G.J. Hutchings, and N.J. Coville. Inorg. Chim. Acta, **117**, L11 (1986).
6. D.J. Robinson, E.A. Darling, and N.J. Coville. J. Organomet. Chem. **310**, 203 (1986).
7. M. Bojurik, B.T. Heaton, A. Johnson, C.A. Ghilardi, and A. Orlandini. J. Organomet. Chem. **341**, 473 (1988), and references therein.
8. P.D. Harvey, I.S. Butler, W.G. Harris, M.C. Barreto, and N.J. Coville. Inorg. Chem. **27**, 639 (1988).
9. J.H. Ammeter, H.B. Burgi, J.C. Thibeault, and R. Hoffmann. J. Am. Chem. Soc. **100**, 3686 (1978).
10. R. Hoffman and W.N. Lipscomb. J. Chem. Phys. **36**, 2179 (1962).
11. R. Hoffman and W.N. Lipscomb. J. Chem. Phys. **37**, 2873 (1972).
12. R. Hoffman. J. Chem. Phys. **39**, 1397 (1963).
13. J.Y. Saillard and R. Hoffmann. J. Am. Chem. Soc. **106**, 2006 (1984).
14. A. Dedieu, T.A. Albright, and R. Hoffmann. J. Am. Chem. Soc. **101**, 3141 (1979).
15. C. Mealli and D.M. Proserpio. J. Chem. Educ. **67**, 399 (1990).
16. E.D. Jemmis, A.R. Pinhas, and R. Hoffmann. J. Am. Chem. Soc. **102**, 2576 (1980).
17. K.R. Pope and M.S. Wrighton. J. Am. Chem. Soc. **109**, 4545 (1987).
18. T.J. Oyer and M.S. Wrighton. Inorg. Chem. **27**, 3691 (1988).
19. G.L. Geoffroy and M.S. Wrighton. Organometallic photochemistry. Academic Press, New York. 1979, and references therein.
20. K. Nakamoto. Infrared and Raman spectra of inorganic and coordination compounds. 3rd ed. Wiley & Sons, New York. 1986, and references therein.
21. P.H. Harvey, I.S. Butler, W.G. Harris, and N.J. Coville. Inorg. Chem. **25**, 3608 (1986), and references therein.
22. H.J. Svec and G.A. Junk. J. Am. Chem. Soc. **89**, 2836 (1967).
23. A.L. Rheingold, W.K. Meckstroth, and D.P. Ridge. Inorg. Chem. **25**, 3700 (1986); W.K. Meckstroth and D.P. Ridge. J. Am. Chem. Soc. **107**, 2281 (1985).
24. W.L. Ingham, D.G. Billing. D.C. Levendis, and N.J. Coville. Inorg. Chim. Acta, **187**, 17 (1991).
25. M.R. Churchill, K.N. Amoh, and H.J. Wasserman. Inorg. Chem. **20**, 1609 (1981).
26. Yu. T. Struchkov, K.N. Anisimov, O.P. Osipova, N.E. Kolobova, and A.N. Nesmeyanov. Dokl. Akad Nauk SSR, **172**, 102 (1967).
27. P.J. Hansen and R.A. Jacobson. J. Organomet. Chem. **6**, 389 (1966).
28. M.D. Abers and N.J. Coville. S. Afr. J. Chem. **35**, 139 (1982).

Can. J. Chem. Downloaded from www.nrcresearchpress.com by 85.192.166.187 on 09/08/12
For personal use only.

Molecular and crystal structure of a mixed-phosphine ligand Tc(II) complex, $Tc(PMe_2Ph)_2(DMPE)Cl_2$

FERNANDE D. ROCHON,[1] ROBERT MELANSON, AND PI-CHANG KONG

Département de chimie, Université du Québec à Montréal, C.P 8888, Succ. Centre-ville, Montréal, QC H3C 3P8, Canada

Received February 14, 1994

FERNANDE D. ROCHON, ROBERT MELANSON, and PI-CHANG KONG. Can. J. Chem. **72**, 2183 (1994).

The reaction of $Tc(PMe_2Ph)_3Cl_3$ with an excess of bis(dimethylphosphino)ethane (DMPE) in ethanol solution produced a yellow compound, which was identified by X-ray diffraction methods as a mixed-ligand Tc(II) complex, $Tc(PMe_2Ph)_2(DMPE)Cl_2$. The compound crystallizes in the $P2_1/c$ space group with a = 12.899(6), b = 13.142(8), c = 19.088(9) Å, β = 121.13(3)°, V = 2770(2) Å^3, Z = 4, R = 0.061, and R_w = 0.051. The geometry around the Tc atom is octahedral with the chloro ligands *trans* to each other, while the two PMe_2Ph ligands are in *cis* positions. The Tc—Cl bond distances are 2.431(5) and 2.431(5) Å while the Tc—P bond lengths are 2.434(4) and 2.435(4) Å for PMe_2Ph and 2.400(4) and 2.398(4) Å for the bidentate DMPE ligand. An increase of multiple bonding of the Tc—P bond, as the oxidation state of Tc decreases, is suggested.

FERNANDE D. ROCHON, ROBERT MELANSON et PI-CHANG KONG. Can. J. Chem. **72**, 2183 (1994).

La réaction du $Tc(PMe_2Ph)_3Cl_3$ avec un excès de bis(diméthylphosphino)éthane (DMPE), en solution dans l'éthanol fournit un composé jaune que l'on a identifié par des méthodes de diffraction des rayons X comme un complexe à coordinats mixtes du Tc(II), le $Tc(PMe_2Ph)_2(DMPE)Cl_2$. Le composé cristallise dans le groupe d'espace $P2_1/c$ avec a = 12,899(6), b = 13,142(8), et c = 19,088(9) Å, β = 121,13(3)°, V = 2770(2) Å^3, Z = 4, R = 0,061, and R_w = 0,051. La géométrie autour de l'atome de Tc est octaédrique, avec deux coordinats chloro en *trans* l'un par rapport à l'autre alors que les deux ligands PMe_2Ph sont en positions *cis*. Les longueurs des liaisons Tc—Cl sont de 2,431(5) et 2,431(5) Å alors que celles des liaisons Tc—P sont de 2,434(4) et 2,435(4) Å pour le ligand PMe_2Ph et 2,400(4) et 2,398(4) Å pour le ligand bidentate DMPE. Les résultats suggèrent l'existence d'une augmentation du caractère multiple de la liaison Tc—P avec une diminution de l'état d'oxydation du Tc.

[Traduit par la rédaction]

Introduction

The chemistry of technetium has recently become very important, especially because of the use of the isotope ^{99m}Tc in nuclear medicine. For several years, it was used for bone scanning and recently it has been used to study the heart, the brain, the kidneys, the liver, and other organs and also tumor tissue. A good review on medical diagnostic imaging with complexes of ^{99m}Tc was published in 1987 by Clarke and Podbielski (1). Recent advances in this area have been published in a book edited by Nicolini, Bandoli, and Mazzi (2).

We recently started a research project on the synthesis of mixed-ligand Tc complexes with ligands that could be of some interest to the radiopharmaceutical industry. Few mixed-ligand Tc complexes have been reported in the literature. To be useful in the radiopharmaceutical industry, the methods must be simple and adaptable to the use of industrial kits. One type of ligands under study in our laboratory is phosphine derivatives, both monodentate and bidentate. It has been shown that $[Tc(DMPE)_2Cl_2]^+$ (DMPE = bis(dimethylphosphino)ethane) accumulates in the heart of animals (3,4). In humans, the retention time in the heart is too short, probably due to a reduction of the complex to a neutral Tc(II) species that washes out of the heart (5,6). Neutral *trans*-$^{99m}Tc(DMPE)_2X_2$ was found to cross the blood–brain barrier in rats and thus might provide the basis for brain-perfusion imaging agents (7).

Phosphines react with metals in high oxidation states not only as complexing agents but also as reductants. The reaction of NH_4TcO_4 with PR_3 in acidic ethanol solution produces, depending on the conditions, $Tc(PR_3)_2Cl_4$ or (except if R = Ph) $Tc(PR_3)_3Cl_3$ (8). In these reactions, no other reducing agent is used. We recently prepared and characterized several such complexes. These compounds were used as starting material for the preparation of mixed-ligand complexes with Tc in low oxidation states. One such reaction with DMPE produced an interesting Tc(II) compound, which was characterized by X-ray diffraction. The results of this study are described below.

[1]Author to whom correspondence may be addressed. Telephone: (514) 987-4896. Fax: (514) 987-4054. e-mail: rochon.fernande@uqam.ca

Experimental section

Ammonium pertechnetate ($NH_4{}^{99}TcO_4$) was obtained from Oak Ridge National Laboratory. It was recrystallized in nitric acid (**caution**: ammonium pertechnetate in acid medium will produce some radioactive volatile compound) and dissolved in water. A 0.286 M solution was prepared. All manipulations were made in a laboratory approved for low-level radioactive material (^{99}Tc is a β emitter with a particle energy of 0.292 MeV and a half-life of 2.13×10^5 years). Dimethylphenylphosphine and DMPE were bought from Aldrich.

$Tc(PMe_2Ph)_3Cl_3$ was synthesized according to the method published by Mazzi et al. (8).

$[Tc(PMe_2Ph)_2(DMPE)Cl_2$

$Tc(PMe_2Ph)_3Cl_3$ (0.19 g) was added to a solution containing 1 g of DMPE in 20 mL of ethanol. The solution was left at room temperature until most of the solvent had evaporated. The oily residue was washed with ether, and then dissolved in ethanol. Slow evaporation of the solvent produced crystals suitable for X-ray diffraction methods.

Crystallographic measurements and structure resolution

The yellow crystal was selected after examination for homogeneity under a polarizing microscope. The unit cell parameters were obtained by least-squares refinement of the angles 2θ(16–25°), ω, and χ for 15 well-centred reflections on a Syntex $P\bar{1}$ diffractometer using graphite-monochromatized MoKα radiation. Scan rates and data treatment have already been described (9). Corrections were made for Lorentz-polarization effects, and the anomalous dispersion terms of Tc, P, and Cl were included in the calculations (10).

The coordinates of the Tc atom were determined from the three-dimensional Patterson map and the positions of all the other non-hydrogen atoms were found by the usual Fourier methods. The refinement of the structure was done by full-matrix least-squares analysis

Can. J. Chem. Downloaded from www.nrcresearchpress.com by 85.192.166.187 on 09/08/12
For personal use only.

Can. J. Chem. Downloaded from www.nrcresearchpress.com by 85.192.166.187 on 09/08/12
For personal use only.

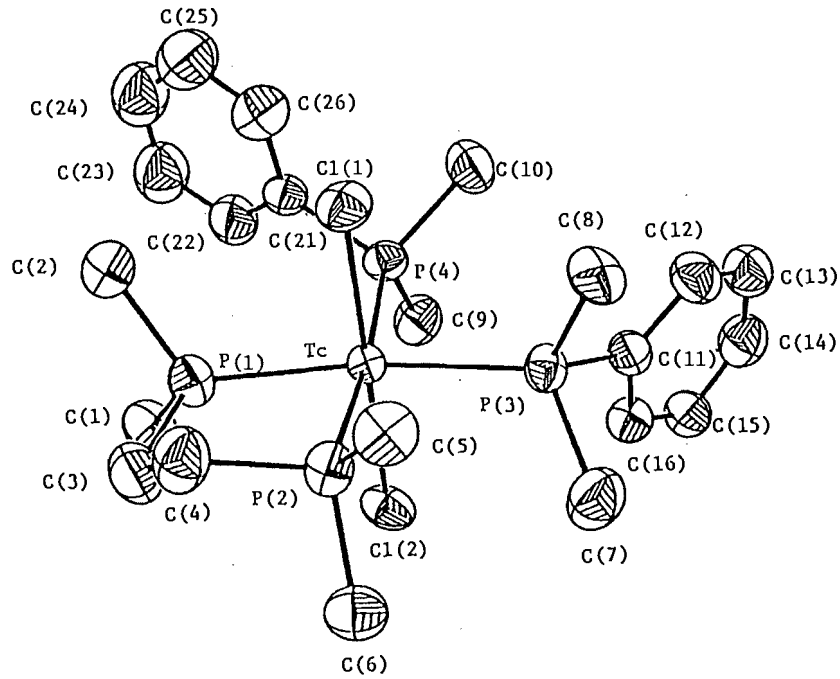

FIG. 1. Labelled diagram of $Tc(PMe_2Ph)_2(DMPE)Cl_2$.

TABLE 1. Positional parameters ($\times 10^4$) with their esd's and temperature factors (10^3). $U_{eq} = 1/3\ \Sigma_i\Sigma_j U_{ij} a_i^* a_j^* a_i \cdot a_j$

Atom	x	y	z	U_{eq}(Å^2)
Tc	2 344(1)	7 048(1)	5 111(1)	21
Cl(1)	508(3)	6 888(3)	5 164(2)	45
Cl(2)	4 179(3)	7 227(3)	5 059(2)	36
P(1)	1 820(4)	5 583(3)	4 241(2)	36
P(2)	3 247(3)	5 736(3)	6 127(2)	32
P(3)	3 105(3)	8 369(3)	6 155(2)	34
P(4)	1 258(3)	8 262(3)	4 001(2)	29
C(1)	2 197(16)	5 536(12)	3 452(8)	57
C(2)	260(14)	5 157(13)	3 687(9)	62
C(3)	2 570(16)	4 459(10)	4 866(10)	54
C(4)	2 603(15)	4 487(11)	5 650(8)	49
C(5)	3 016(14)	5 672(12)	7 003(8)	47
C(6)	4 860(13)	5 512(13)	6 596(9)	46
C(7)	4 635(13)	8 110(13)	7 018(8)	60
C(8)	2 221(15)	8 531(12)	6 671(10)	66
C(9)	2 138(12)	8 911(11)	3 643(8)	45
C(10)	519(15)	9 326(11)	4 189(9)	53
C(11)	3 363(12)	9 701(10)	5 952(7)	34
C(12)	2 767(14)	10 532(12)	6 037(9)	52
C(13)	2 951(15)	11 518(11)	5 851(10)	55
C(14)	3 845(14)	11 665(10)	5 680(9)	47
C(15)	4 497(12)	10 866(11)	5 631(8)	46
C(16)	4 248(12)	9 887(10)	5 771(8)	38
C(21)	−12(11)	7 764(10)	3 058(7)	33
C(22)	46(14)	7 559(11)	2 357(9)	45
C(23)	−921(16)	7 160(15)	1 647(9)	77
C(24)	−1 975(17)	7 017(16)	1 622(10)	95
C(25)	−2 080(12)	7 245(16)	2 297(11)	76
C(26)	−1 097(12)	7 595(13)	3 004(9)	61

minimizing $\Sigma w(|F_o| - |F_c|)^2$. Most H atoms could be located, but they were fixed at their calculated positions with a $U_{eq} = 0.076$ Å^2. For the methyl H atoms, at least one H was obtained from a difference Fourier map and the positions of the remaining atoms were calculated. Individual weights $w = 1/\sigma^2(F)$ were applied. An isotropic secondary-extinction correction (11) was included in the calculations. The refinement of the scale factor, coordinates, and anisotropic temperature factors of all the non-hydrogen atoms converged to $R = 0.061$ and $R_w = 0.051$. There were a few residual peaks (<0.38 e Å^{-3}) in the close environment of the Tc atom.

The scattering curves of Cromer and Waber (12) were used except for the hydrogen atoms (13). The calculations were done on a Cyber 830 with programs already described (9).

Crystal data and experimental details of the X-ray diffraction study

Compound: $Tc(PMe_2Ph)_2(DMPE)Cl_2 \cdot C_{22}H_{38}Cl_2P_4Tc$; Fw, 596.26; space group: $P2_1/c$; $a = 12.899(6)$, $b = 13.142(8)$, $c = 19.088(9)$ Å, $\beta = 121.13(3)°$, $V = 2770(2)$ Å^3, $Z = 4$, $F(000) = 1228$, $\lambda(MoK\alpha) = 0.710\ 69$ Å, $\rho_{calcd} = 1.429$ Mg m^{-3}, $\mu(MoK\alpha)$ 0.93 mm^{-1}, 2θ max. 55°, octants: $h, k, \pm l, h, 0 \rightarrow 15, k, 0 \rightarrow 17, l, -24 \rightarrow 21$; scan technique and speed; $2\theta/\theta$, 2°–24°/min; standard reflections: 4 0 –4, 0 2 –6, 1 4 –3; no. of independent reflections: 6228, no. of observed reflections: 1925; $I_{net} > 3.0\sigma$; $R = \Sigma||F_o| - |F_c|| / \Sigma|F_o| = 0.061$; $R_w = [\Sigma w(|F_o| - |F_c|)^2 / \Sigma|F_o|^2]^{1/2} = 0.051$; $\Delta/\sigma(\max) = 0.45$; $S = [\Sigma w(|F_o| - |F_c|)^2/(m-n)]^{1/2} = 1.50$.

Results and discussion

Complexes of the types $Tc(PR_3)_2Cl_4$ and $Tc(PR_3)_3Cl$ are good starting material for the synthesis of low oxidation state Tc compounds. In an attempt to synthesize mixed-ligand complexes, we studied the reaction of $Tc(PMe_2Ph)_3Cl_3$ with a bidentate ligand, bis(dimethylphosphino)ethane in ethanol. We obtained yellow crystals, which were studied by X-ray diffraction methods. The results have shown that the compound is a neutral Tc(II) mixed-ligand complex, $Tc(PMe_2Ph)_2(DMPE)Cl_2$.

The refined atomic parameters of the structure are listed in Table 1. A labelled diagram of the molecule is shown in Fig. 1. The bond distances and angles are shown in Table 2. The geometry around the Tc atom is octahedral with the two Cl ligands located in *trans* position to each other and the two monodentate phosphines in *cis* position to each other. The angles around the Tc atom are close to 90° and 180°, but there are some distortions caused by the presence of the bidentate ligand. The chelate angle P(1)—Tc—P(2) is only 80.1(1)°, as was observed in other Tc-bidentate phosphine complexes (14–20).

TABLE 2. Selected bond distances (Å) and angles (°)

Tc—Cl(1)	2.431(5)	Tc—Cl(2)	2.431(5)
Tc—P(1)	2.400(4)	Tc—P(2)	2.398(4)
Tc—P(3)	2.435(4)	Tc—P(4)	2.434(4)
P(1)—C(1)	1.81(2)	P(1)—C(2)	1.81(2)
P(1)—C(3)	1.83(1)	P(2)—C(4)	1.85(1)
P(2)—C(5)	1.85(2)	P)2)—C(6)	1.82(2)
P(3)—C(7)	1.83(2)	P(3)—C(8)	1.86(2)
P(3)—C(11)	1.86(1)	P(4)—C(21)	1.82(1)
P(4)—C(9)	1.81(2)	P(4)—C(10)	1.83(2)
C(3)—C(4)	1.48(2)	C—C (avg. Ph1)	1.38(2)
C—C (avg. Ph2)	1.38(2)		
Cl(1)—Tc—Cl(2)	1794(1)	Cl(1)—Tc—P(1)	91.6(1)
Cl(1)—Tc—P(2)	88.9(1)	Cl(1)—Tc—P(3)	91.0(1)
Cl(1)—Tc—P(4)	87.6(1)	Cl(2)—Tc—P(1)	88.9(1)
Cl(2)—Tc—P(2)	91.5(1)	Cl(2)—Tc—P(3)	88.6(1)
Cl(2)—Tc—P(4)	92.0(1)	P(1)—Tc—P(2)	80.1(1)
P(1)—Tc—P(3)	171.4(1)	P(1)—Tc—P(4)	95.4(1)
P(2)—Tc—P(3)	91.7(1)	P(2)—Tc—P(4)	174.2(1)
P(3)—Tc—P(4)	93.0(1)	Tc—P(1)—C(1)	120.2(6)
Tc—P(1)—C(2)	118.9(6)	Tc—P(1)—C(3)	109.4(6)
Tc—P(2)—C(4)	109.5(5)	Tc—P(2)—C(5)	121.8(6)
Tc—P(2)—C(6)	118.0(6)	Tc—P(3)—C(7)	113.2(5)
Tc—P(3)—C(8)	114.6(6)	Tc—P(3)—C(11)	122.7(5)
Tc—P(4)—C(9)	116.5(5)	Tc—P(4)—C(10)	117.0(6)
Tc—P(4)—C(21)	116.4(5)	C(1)—P(1)—C(2)	101.5(8)
C(1)—P(1)—C(3)	103.6(8)	C(2)—P(1)—C(3)	100.7(8)
C(4)—P(2)—C(5)	99.4(8)	C(4)—P(2)—C(6)	102.0(8)
C(5)—P(2)—C(6)	103.1(8)	C(7)—P(3)—C(8)	102.4(8)
C(7)—P(3)—C(11)	97.8(7)	C(8)—P(3)—C(11)	103.1(7)
C(9)—P(4)—C(10)	101.9(7)	C(9)—P(4)—C(21)	102.4(7)
C(10)—P(4)—C(21)	100.1(7)	P(1)—C(3)—C(4)	112(1)
P(2)—C(4)—C(3)	107(1)	P(3)—C(11)—C(12)	123(1)
P(3)—C(11)—C(16)	119(1)	P(4)—C(21)—C(22)	123(1)
P(4)—C(21)—C(26)	120(1)	C—C—C (avg.)	120(1)

TABLE 3. Average and range of reported Tc—Cl (*trans* to Cl) and Tc—P (*trans* to P, for monodentate (first value) and bidentate) bond distances in octahedral related complexes

Configuration	Tc—Cl	No. of structures	References	Tc—P	No. of structures	Reference
Tc(II), d^5	2.423 2.410(1)–2.438(1)	3	16, 21, this work	2.409 2.391(2)–2.435(4)	4	21, 35, this work
				2.415 2.385(2)–2.473(6)	7	14, 16, 20, 33, 34, this work
Tc(III), d^4	2.335 2.319(1)–2.353(2)	11	16, 18, 22–28	2.478 2.430(2)–2.525(2)	9	22–27, 36
				2.456 2.397(2)–2.513(1)	7	15–18, 24, 39
Tc(IV), d^3	2.337 2.32(1)–2.379(2)	8	23, 29–32	2.518 2.44(1)–2.556(1)	4	30, 32, 40
				2.500(9)	1	41 (tetradentate)
Tc(V), d^2	2.410(2)	1	38	2.489 2.480(2)–2.517(2)	3	38, 42, 43
				2.461 2.443(3)–2.480(1)	2	18, 44

The two bond distances Tc—Cl are 2.431(5) Å, very similar to those reported for the Tc(II) compounds, *trans*-$Tc(DPPE)_2Cl_2$, (2.410(1) and 2.438(1), DPPE = bis(diphenylphosphino)ethane (16)) and *trans*-$Tc(PPh(OEt)_2)_4Cl_2$ (2.41(1) and 2.42(1), (21)). A brief survey (Table 3) of several related Tc(III) (16, 18, 22–28) and Tc(IV) (23, 29–32) octahedral structures containing Cl ligands located in *trans* position to each other has shown that the observed Tc(II)—Cl bond distances are larger than those observed for Tc(III) (d^4 configuration with two unpaired electrons) and Tc(IV) (d^3, with three unpaired electrons) complexes (ave. 2.335 and 2.337 Å, respectively). It seems that the addition of a fourth electron does not

Can. J. Chem. Downloaded from www.nrcresearchpress.com by 85.192.166.187 on 09/08/12
For personal use only.

Can. J. Chem. Downloaded from www.nrcresearchpress.com by 85.192.166.187 on 09/08/12
For personal use only.

change the radius of the Tc atom, probably because it is paired in the low energy, t_{2g} orbital. But the addition of a fifth electron (Tc(II) has a d^5 configuration) in the lower energy orbitals (t_{2g} in an octahedral field with only one unpaired electron) seems to increase the Tc—Cl bond distances significantly, as expected.

The Tc—P bond distances are 2.400(4) and 2.398(4) Å for the bidentate DMPE ligand. The reported values for Tc(II)-bidentate phosphine ligands vary from 2.39 to 2.47 Å (14, 16, 20, 33, 34) with an average value of 2.42 Å. For the monodentate ligands, the Tc—P bonds are slightly longer, 2.434(4) and 2.435(4) Å. Values ranging from 2.39 to 2.42 (21, 35) have been reported for Tc—P (monodentate, *trans* to P). A survey of 40 related octahedral structures containing Tc—P bonds in *trans* position to a P atom was made for monodentate and bidentate phosphines. The results show that for all oxidation states, except Tc(II) (few Tc(II) structures were reported with monodentate phosphines), the Tc—P bonds are longer by about 0.02 Å for monodentate ligands. This trend is attributed mainly to steric interactions. It was shown that the Tc—P bond distance increases in the order $PMe_2Ph < PEtPh_2 < PPh_3$ (36). Furthermore, the aromatic R groups on the phosphine ligands decrease the σ donor properties, thus weaker bonds are formed. For example, the Tc—P bonds in *trans*-$Tc(PR_3)_2Cl_4$ are 2.524(2), 2.541(1), and 2.556(1) Å for PMe_3, PEt_3, and $PMePh_2$, respectively (30, 32). For bidentate phosphines, a similar trend has been observed. For *trans*-$[Tc(DMPE)_2Cl_2]^+$, the average Tc—P is 2.435(2) Å (18), while it is 2.501(1) Å for *trans*-$[Tc(DPPE)_2Cl_2]^+$ (16) and *trans*-$[Tc(DPPE)_2Br_2]^+$ (15).

A comparison of the reported Tc(II)—P bond distances (in *trans* position to another P), including our values, with those observed for Tc(III) and Tc(IV) compounds, has shown that Tc(II) bonds are significantly shorter. The average values are 2.478 Å (monodentate) and 2.456 Å (bidentate) for Tc(III) and 2.518 (monodentate) and 2.500 Å (tetradentate) for Tc(IV). It has been suggested that the oxidation state of Tc has little effect on its bond length (37). Since bond lengths vary with several factors, including geometry and the ligand located in *trans* position, we have surveyed only octahedral structures and looked at Tc—Cl bonds in *trans* position to Cl and Tc—P bonds in *trans* position to P. The results are shown in Table 3. More data are needed to make definite conclusions on these bond distances, but the data can be useful for future data search. The observed bond ranges are fairly large but it can be suggested that the values are not completely independent of the number of *d* electrons. Several factors must be considered in order to understand the variations: the bulkiness and aromaticity of the ligands (already discussed), the configuration of the metallic center, the charge on the complex, and the possibility of π back-donation to the ligand. Cl is usually not classified as a π-acceptor. Therefore the main factor affecting the Tc—Cl bond should be the number and arrangement of the electrons, which has already been discussed.

Phosphines can accept π-electron density from the metal. Tc in a low oxidation state (≤ 3) is a soft metal and should form π bonds with phosphines. Examination of the Tc—P values in Table 3 shows that the Tc(IV) bonds (2.50–2.52 Å) are longer than the Tc(V) bonds (2.46–2.49 Å), which can be ascribed to an increased number of unpaired electrons (three vs. two). Tc(IV) and Tc(V) are hard metallic centers and no π bonds are expected. For the Tc(III) compounds, the distances are reduced to average values of 2.46 and 2.48 Å. Since the Tc(III)—Cl and Tc(IV)—Cl bonds are identical, the shorter Tc(III)—P bonds compared to Tc(IV)—P bonds cannot be ascribed only to the pairing of the fourth electron. We suggest that the presence of π bonds in Tc(III) compounds is mostly responsible for the decrease. The hypothesis is further confirmed by the Tc(II)—P bond distances, which are significantly shorter, contrary to the Tc(II)—Cl values.

All these data indicate that the configuration of Tc and the number of unpaired electrons are not sufficient to account for these observations, especially when we compared the Tc—P values with the Tc—Cl bonds. We suggest that the decrease of the Tc—P bond distance as the number of electrons increases is due to an increase of multiple bonding of the bond as the oxidation state of Tc decreases.

The average P—C distance is 1.83(2) Å. The angles around the P atom in DMPE are close to the tetrahedral value for the Tc—P—C(ethane) angles (avg. 109.5(7)°), but are larger for Tc—P—CH_3 (avg. 119.7(6)°) angles. The internal angles around C(3) and C(4) are normal (avg. 109(1)°). For the PMe_2Ph ligands, the Tc—P—CH_3 angles (avg. 115.3(5)° are smaller than the Tc—P—C(phenyl) angles (avg. 119.6(5)°) due to the bulkiness of the phenyl groups. All the C—P—C bond angles are smaller than the tetrahedral value, with an average angle of 101.5(8)°. The average C—C bond distance in the phenyl groups is 1.38(2) Å, with an average C—C—C angle of 120(1)°.

A drawing of the packing of the ions inside the unit cell is included in the supplementary material.[2] No hydrogen bonding is expected in this compound. The packing consists of layers of molecules centered at $z = \sim 0$ and ~ 0.5, parallel to the *ab* plane. The molecules are held together only by van der Waals forces.

Acknowledgement

The authors are grateful to the Medical Research Council of Canada for financial support.

1. M.J. Clarke and L. Podbielski. Coord. Chem Rev. **78**, 253 (1987).
2. M. Nicolini, G. Bandoli, and U. Mazzi (*Editors*). Technetium and rhenium in chemistry and nuclear medicine. Raven Press, New York. 1990.
3. V.J. Sodd, K.L. Scholz, L.W. Grossman, D.L. Fortman, P.J. Robbins, E. Deutsch, H. Nishiyama, R.J. Adolph, and K. Libson. J. Nucl. Med. **23**, P87 (1982).
4. E. Deutsch, W. Bushong, K.A. Glavan, R.C. Elder, V.J. Sodd, K.L. Scholtz, D.L. Fortman, and S.J. Lukes. Science, **214**, 85 (1981).
5. J.L. Vanderheyden, M.J. Heeg, and E. Deutsch. Inorg. Chem. **24**, 1666 (1985).
6. E. Deutsch, K. Libson, J.L. Vanderheyden, A.R. Ketring, and H.R. Maxon. Nucl. Med. Biol. **13**, 465 (1986).
7. M. Neves, K. Libson, and E. Deutsch. Nucl. Med. Biol. **14**, 503 (1987).
8. U. Mazzi, G. De Paoli, P. Di Bernado, and L. Magnon. J. Inorg. Nucl. Chem. **38**, 721 (1976).

[2]The supplementary material includes Fig. 2 (packing diagram) and lists of anisotropic temperature factors (Table S1), hydrogen coordinates (Table S2), and bond distances and angles (Table S3), and can be purchased from: The Depository of Unpublished Data, Document Delivery, CISTI, National Research Council Canada, Ottawa, ON K1A 0S2, Canada.

Figure 2 and Tables S2 and S3 have also been deposited with the Cambridge Crystallographic Data Centre, and can be obtained on request from The Director, Cambridge Crystallographic Data Centre, University Chemical Laboratory, 12 Union Road, Cambridge, CB2 1EZ, U.K.

Structure factor amplitudes are no longer being deposited and may be obtained directly from the author.

9. R. Melanson and F.D. Rochon. Can. J. Chem. **53**, 2371 (1975).
10. D.T. Cromer. Acta Crystallogr. **18**, 17 (1965).
11. P. Coppens and W. Hamilton. Acta. Crystallogr. Sect. A: Cryst. Phys. Diffr. Theor. Gen. Crystallogr. **A26**, 71 (1970).
12. W.T. Cromer and J.T. Waber. Acta Crystallogr. **18**, 104 (1965).
13. R.F. Stewart, E.R. Davidson, and W.T. Simpson. J. Chem. Phys. **42**, 3175 (1965).
14. F.D. Rochon, R. Melanson, and P.C. Kong. Inorg. Chim. Acta, **194**, 43 (1992).
15. K. Libson, L. Barnett, and E. Deutsch. Inorg. Chem. **22**, 1695 (1983).
16. K. Libson, M.N. Doyle, R.W. Thomas, T. Nelesnik, M. Woods, J.C. Sullivan, R.C. Elder, and E. Deutsch. Inorg. Chem. **27**, 3614 (1988).
17. T. Konno, M.J. Heeg, and E. Deutsch. Inorg. Chem. **27**, 4113 (1988).
18. J.L. Vanderheyden, A.R. Ketring, K. Libson, M.J. Heeg, L. Roeker, P. Motz, R. Whittle, R.C. Elder, and E. Deutsch. Inorg. Chem. **23**, 3184 (1984).
19. V.Y. Struchkov and A.S. Bazanov. Z. Anorg. Allg. Chem. **494**, 91 (1982).
20. G. Bandoli, U. Mazzi, A. Ichimura, K. Libson, W.R. Heineman, and E. Deutsch. Inorg. Chem. **23**, 2808 (1984).
21. U. Mazzi, D.A. Clemente, G. Bandoli, L. Magon, and A.A. Orio. Inorg. Chem. **16**, **5**, 1042 (1977).
22. G. Bandoli, D.A. Clemento, and U. Mazzi. J. Chem. Soc. Dalton Trans. 125 (1976).
23. F.D. Rochon, R. Melanson, and P.C. Kong. Can. J. Chem. **69**, 3397 (1991).
24. C.M. Archer, J.R. Dilworth, J.D. Kelly, and M. McPartlin. Polyhedron, **8**, 1879 (1989); C.M. Archer, J.R. Dilworth, R.M. Thompson, M. McPartlin, D.C. Povey, and J.D. Kelly. *In* Technetium and rhenium in chemistry and nuclear medicine. *Edited by* M. Nicolini, G. Bandoli, and U. Mazzi. Raven Press, New York. 1990. pp. 201–206; J. Chem. Soc. Dalton Trans. 461 (1993).
25. P.L. Watson, J.A. Albanese, J.C. Calabrese, D.W. Ovenall, and R.G. Smith. Inorg. Chem. **30**, 4638 (1991).
26. R.M. Pearlstein, W.M. Davis, A.G. Jones, and A. Davison. Inorg. Chem. **28**, 3332 (1989).
27. J. Lu, A. Yamano, and M.J. Clarke, Inorg. Chem. **29**, 3483 (1990).
28. B. Lorenz, K. Schmidt, W. Hiller, U. Abram, and R. Hubener. Inorg. Chim. Acta, **208** 195 (1993).
29. J. Baldas, J. Bonnyman, D. Samuels, and G.A. Williams. Acta Crystallogr. Sect. C: Cryst. Struct. Commun. **C40**, 1343 (1984).
30. F.D. Rochon. and R. Melanson. Acta. Crystallogr. Sect. C: Cryst. Struct. Commun. **C49**, 1259 (1993).
31. G. Bandoli, D.A. Clemente, U. Mazzi, and E. Roncari. J. Chem. Soc. Dalton Trans. 1381 (1982).
32. F.D. Rochon, R. Melanson, and P.C. Kong. Acta Crystallogr. Sect. C: Cryst. Struct. Commun. **C47**, 732 (1991).
33. T. Konno, M.J. Heeg, and E. Deutsch. Inorg. Chem. **28**, 1694 (1989).
34. S. Seifert, R. Muenze, P. Leibnitz, G. Reck, and J. Stach. Inorg. Chim. Acta, **193**, 167 (1992).
35. B.E. Wilcox, D.M. Ho, and E. Deutsch. Inorg. Chem. **28**, 3917 (1989).
36. B.E. Wilcox, D.M. Ho, and E. Deutsch. Inorg. Chem. **28**, 1743 (1989).
37. Yi Wei, B. Liu, and X. Wang. He Huaxue Yu Fangshe Huaxue, **12**, 203 (1990).
38. T. Nicholson, A. Davidson, and A.G. Jones. Inorg. Chim. Acta, **187**, 51 (1991).
39. R. Muenze, U. Abram, J. Stach, and W. Hiller. Inorg. Chim. Acta, **186**, 151, (1991).
40. F. Tisato, F. Refosco, U. Mazzi, G. Bandoli, and M. Nicolini. Inorg. Chim. Acta, **157**, 227, 1989.
41. F. Refosco, G. Bandoli, U. Mazzi, F. Tisato, A. Dolmella, and M. Nicolini. Inorg. Chem. **29**, 2179 (1990).
42. M.J. Abrams, S.K. Larsen, S.N. Shaikh, and J. Zubieta. Inorg. Chim. Acta, **185**, 7 1991. M.J. Abrams, S.K. Larsen, and J. Zubieta. Inorg. Chim. Acta, **173**, 133 (1990).
43. A.S. Batsanov, Yu T. Struchkov, B. Lorenz, and B. Olk. Z. Anorg. Allg. Chem. **564**, 129 (1988).
44. C.M. Archer, J.R. Dilworth, D.V. Griffiths, M. McPartlin, and J.D. Kelly. J. Chem. Soc. Dalton Trans. 183 (1992).

Can. J. Chem. Downloaded from www.nrcresearchpress.com by 85.192.166.187 on 09/08/12
For personal use only.

Variable-pressure dynamic NMR studies: effects of paramagnetic metal ions on NMR parameters in nonexchanging systems

HIDEO D. TAKAGI, KAYOKO MATSUDA, SEN-ICHI AIZAWA, AND SHIGENOBU FUNAHASHI[1]
Department of Chemistry, Nagoya University, Chikusa-ku, Nagoya 464-01, Japan

STEPHEN D. KINRADE
Department of Chemistry, Lakehead University, Thunder Bay, ON P7B 5E1, Canada

AND

THOMAS W. SWADDLE[1]
Department of Chemistry, University of Calgary, Calgary, AB T2N 1N4, Canada

Received April 11, 1994

Can. J. Chem. Downloaded from www.nrcresearchpress.com by 85.192.166.187 on 09/08/12
For personal use only.

HIDEO D. TAKAGI, KAYOKO MATSUDA, SEN-ICHI AIZAWA, SHIGENOBU FUNAHASHI, STEPHEN D. KINRADE, and THOMAS W. SWADDLE. Can. J. Chem. **72**, 2188 (1994).

The possible effects of paramagnetic relaxation on the apparent volumes of activation for exchange reactions in solution, as measured by NMR at high pressures, are considered. Two model paramagnetic systems that do not undergo ligand exchange on the NMR time scale were examined: tri(acetylacetonato)chromium(III) in various perdeuterated solvents, and tris(ethylenediamine)nickel(II) ion in ethylenediamine solvent. No pressure dependence was discernible up to 200 MPa for the chemical shifts of ^{1}H (exemplifying nuclei of spin 1/2) in the Cr(III) complex, or of solvent ^{14}N (representing quadrupolar nuclei) in the Ni(II)–ethylenediamine case. The line widths $\Delta\nu_{1/2}$, however, were significantly dependent on pressure. For ^{1}H in the Cr complex, the increase of $\Delta\nu_{1/2}$ with pressure was less than expected from the theory of scalar interactions, and was small enough to imply that any contribution from this source to the observed volume of activation in exchanging systems may be neglected. For ^{14}N in liquid ethylenediamine, the increase of $\Delta\nu_{1/2}$ with pressure was significantly greater when a paramagnetic solute was present. Thus, before the observed $\Delta\nu_{1/2}$ at a pressure P (in MPa) measured by the NMR of a quadrupolar nucleus can be used to obtain a chemical exchange rate for a paramagnetic solute, it should be reduced by an amount $\Delta\nu_{1/2}{}^0 \exp\{\theta(P - 0.1)(\Delta V_V{}^{\ddagger}/RT + \kappa)\}$, where $\Delta V_V{}^{\ddagger}$ is the activation volume for viscous flow and κ the compressibility of the solvent, $\Delta\nu_{1/2}{}^0$ is the linewidth at 0.1 MPa in the absence of chemical exchange, and θ is a scaling factor between 0 and 1. The factors $\Delta\nu_{1/2}{}^0$ and $\theta(\Delta V_V{}^{\ddagger}/RT + \kappa)$ are obtainable from measurements with a chemically equivalent, nonexchanging, paramagnetic solute.

HIDEO D. TAKAGI, KAYOKO MATSUDA, SEN-ICHI AIZAWA, SHIGENOBU FUNAHASHI, STEPHEN D. KINRADE et THOMAS W. SWADDLE. Can. J. Chem. **72**, 2188 (1994).

On considère les effets possibles de la relaxation paramagnétique sur les volumes apparents d'activation des réactions d'échange en solution, tels que mesurés par la RMN à pressions élevées. On a examiné deux systèmes paramagnétiques modèles qui ne subissent pas d'échange de coordinat à l'échelle de temps de la RMN : le tri(acétylacétonato)chrome(III) dans divers solvants perdeutérés et l'ion tris(éthylènediamine)nickel(II) dans l'éthylènediamine comme solvant. Pour les déplacements chimiques du ^{1}H (représentant le spin 1/2) du complexe de chrome(III) ou du ^{14}N (représentant les noyaux quadripolaires) présents dans le cas du nickel(II)–éthylènediamine, on n'a pas pu décelé de relation avec la pression jusqu'à 200 MPa. Toutefois, les largueurs des raies, $\Delta\nu_{1/2}$, varient beaucoup avec la pression. Pour le ^{1}H du complexe de chrome, l'augmentation du $\Delta\nu_{1/2}$ avec la pression est moins importante que celle prévue par la théorie des interactions scalaires et elle est suffisamment faible pour impliquer que toute contribution de cette source au volume d'activation observé dans les systèmes subissant un échange peut être négligée. Pour le ^{14}N dans l'éthylènediamine liquide, l'augmentation du $\Delta\nu_{1/2}$ avec la pression est beaucoup plus importante lorsqu'un soluté paramagnétique est présent. Donc, un $\Delta\nu_{1/2}$ d'un noyau quadripolaire obtenu à une pression donnée P (en MPa) par une mesure de RMN doit, avant d'être utilisé pour obtenir une vitesse d'échange chimique d'un soluté paramagnétique, être réduit par une quantité égale à $\Delta\nu_{1/2}{}^0 \exp\{\theta(P - 0{,}1)(\Delta V_V{}^{\ddagger}/RT + \kappa)\}$ dans laquelle $\Delta V_V{}^{\ddagger}$ est le volume d'activation pour un écoulement visqueux et κ est la compressibilité du solvant, $\Delta\nu_{1/2}{}^0$ est la largueur de la raie à 0,1 MPa en l'absence d'échange chimique et θ est un facteur scalaire entre 0 et 1. On peut obtenir les facteurs $\Delta\nu_{1/2}{}^0$ et $\theta(\Delta V_V{}^{\ddagger}/RT + \kappa)$ en faisant de mesures à l'aide d'un soluté paramagnétique chimiquement équivalent qui ne s'échange pas.

[Traduit par la rédaction]

Introduction

The volume of activation $\Delta V^{\ddagger}$ (= $-RT(\partial \ln k/\partial P)_T$, where k is a rate constant at pressure P and temperature T) is frequently used in the elucidation of mechanisms of ligand substitution and electron transfer reactions in solution (1, 2). In particular, analysis based on the high-pressure NMR technique has provided a significant amount of mechanistic information (2). The estimation of exchange rate constants by the NMR technique is usually carried out by a line-shape analysis based on the Swift–Connick equation (3) or the slow- or fast-exchange approximations (2). However, relatively little attention has been paid to the effect of pressure on the relevant NMR parameters (4–6). It is well known that natural line widths of solvent signals without chemical exchange are influenced significantly by the presence of paramagnetic molecules (7). As the nuclear spin relaxation depends strongly on the mobility of the molecules and (or) the electric field gradient around the observed nuclei, the possibility arises that the relaxation time and chemical shift may be significantly influenced by the applied pressure in the presence of paramagnetic molecules.

In this article, we examine the pressure dependence of ^{1}H and ^{14}N signals, representing spin-1/2 and quadrupolar nuclei, respectively, in the presence of paramagnetic nuclei. The results

[1]Authors to whom enquiries may be addressed. Corresponding author: T.W. Swaddle. Telephone: (403) 220-5358. Fax: (403) 289-9488. E-mail: swaddle@acs.ucalgary.ca

TABLE 1. Pressure dependences of the chemical shifts $\Delta\nu$ and line widths $\Delta\nu_{1/2}$ of methyl protons in $Cr(acac)_3$ in various solvents[a]

Solvent	Pressure/MPa	$\Delta\nu$/Hz[b]	$\Delta\nu_{1/2}$/Hz[b]
$(CD_3)_2CO$	0.1	3630 ± 80	890 ± 50
	71.9 ± 0.1	3680 ± 100	1030 ± 40
	123.9 ± 0.1	3630 ± 100	1100 ± 50
	167.5 ± 0.1	3650 ± 100	1190 ± 50
	202.0 ± 0.1	3650 ± 100	1260 ± 80
CD_3CN	0.1	3670 ± 100	920 ± 60
	60.0 ± 0.1	3650 ± 100	1030 ± 60
	118.0 ± 0.1	3660 ± 80	1120 ± 60
	148.4 ± 0.2	3650 ± 80	1200 ± 50
	191.5 ± 0.1	3660 ± 100	1250 ± 80
CD_3OD	0.1	3630 ± 80	1070 ± 50
	55.5 ± 0.1	3690 ± 80	1130 ± 50
	136.0 ± 0.1	3710 ± 100	1250 ± 50
	161.5 ± 0.3	3630 ± 100	1300 ± 80
	198.8 ± 0.2	3630 ± 100	1360 ± 80
$CDCl_3$	0.1	3800 ± 100	1280 ± 50
	33.0 ± 0.1	3750 ± 100	1360 ± 50
	74.0 ± 0.1	3760 ± 100	1400 ± 50
	139.5 ± 0.2	3700 ± 100	1500 ± 50
	192.5 ± 0.3	3760 ± 100	1530 ± 60

[a]Chemical shift relative to benzene; T = 24.9°C.
[b]^{1}H frequency 90.02 MHz.

are discussed on the basis of the extended Solomon–Bloembergen–Morgan (SBM) theory (8).

Experimental

Tri(acetylacetonato)chromium(III) (acetylacetone = 2,4-pentanedione, "Hacac") and tris(ethylenediamine)nickel(II) trifluoromethanesulfonate (ethylenediamine = 1,2-diaminoethane, "en") were synthesized by the literature methods (9, 10). Acetonitrile-d_3 (MSD Isotopes) was distilled twice from phosphorus pentoxide in a vacuum line before use. Other perdeuterated solvents, also from MSD Isotopes, were used without further purification. Ethylenediamine (Wako Pure Chemical Co. Ltd.) was purified by vacuum distillation after treatment with sodium (10, 11).

NMR measurements were carried out by using specially designed high-pressure probeheads with Bruker WH-90 (12) and JEOL GX-270 (13) NMR spectrometers for the ^{1}H and ^{14}N observations, respectively. The temperature of the sample solutions was controlled by passing either thermostated water or air through the jackets of the respective probeheads. Perfluorohexane was used as a pressurizing fluid for the observation of ^{1}H, and Daifloil no. 1 (Daikin Kogyo Co.) for ^{14}N measurements.

Results

The pressure dependences of the chemical shift ($\Delta\nu$) and line width ($\Delta\nu_{1/2}$) of methyl protons in coordinated acetylacetone on tri(acetylacetonato)chromium(III) ion (0.03–1.0 mol kg^{-1}) were observed at 90.02 MHz in various perdeuterated solvents. The results are listed in Table 1. The chemical shift of the methyl proton signal relative to that of the internal benzene signal as a reference was not affected by the applied pressure up to 200 MPa. Benzene was chosen as a reference material as little or no interaction with $Cr(acac)_3$ was found in previous studies (12).

The line width $\Delta\nu_{1/2}$ of the proton signal was, however, obviously dependent on pressure (Table 1). Plots of $\ln(\pi\Delta\nu_{1/2})$ (i.e., $\ln T_2^{-1}$, where T_2 is the nuclear transverse relaxation time) vs. pressure for the methyl proton signals on the coordinated acetylacetone were linear, as shown in Fig. 1. As $Cr(acac)_3$ is substitution-inert, the line-width change caused by the applied pressure is attributable to the variation in T_2 of protons through

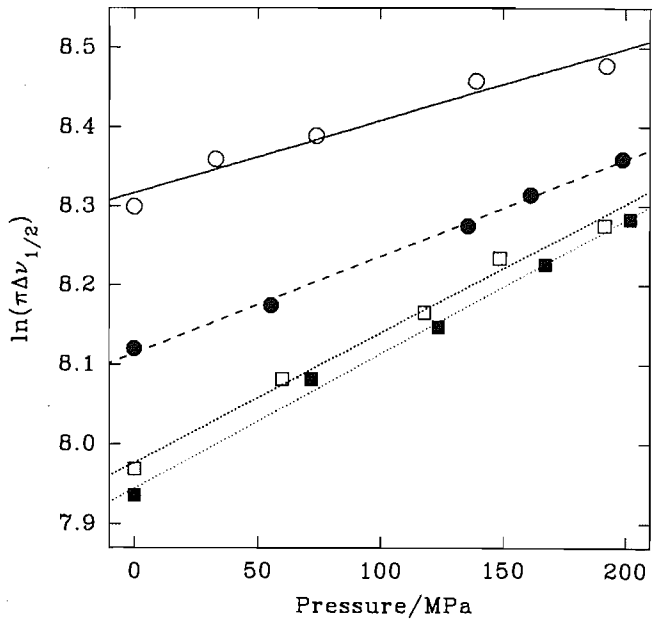

FIG. 1. Pressure dependence of the line widths of the methyl protons on tri(acetylacetonato)chromium(III) (0.1 mol kg^{-1}) in selected solvents at 24.9°C. Filled squares and dotted line: acetone-d_6. Open squares and short-dashed line: acetonitrile-d_3. Filled circles and long-dashed line: methanol-d_4. Open circles and solid line: chloroform-d_3.

the change in the rotational correlation time τ_R of molecular tumbling. As the relaxation of nuclei on the coordinated ligand occurs essentially through the scalar interaction, the correlation time for this process should be directly related to the electron spin relaxation time τ_e of the central paramagnetic metal ion.

It was not possible to observe the line width of ^{14}N in coordinated ethylenediamine in $Ni(en)_3^{2+}$ because of the very strong electronic interaction between coordinated nitrogen atoms and the central paramagnetic metal ion, together with the intrinsically broad line width characteristic of quadrupolar nuclei. Instead, the pressure dependence of the ^{14}N line width of *bulk* ethylenediamine was measured with and without the presence of the $Ni(en)_3^{2+}$ ion and results are listed in Table 2. Errors in $\Delta\nu_{1/2}$ were less than ±1%. No pressure dependence of the chemical shift was observable. Semi-logarithmic plots of $\pi\Delta\nu_{1/2}$ (= T_2^{-1}) against pressure, with and without the presence of 0.1145 mol kg^{-1} $Ni(en)_3^{2+}$, are shown in Fig. 2. Both plots are linear, but both the $\pi\Delta\nu_{1/2}$ values and the slope ($(2.73 \pm 0.08) \times 10^{-3}$ vs. $(2.00 \pm 0.06) \times 10^{-3}$ MPa^{-1}) are larger for $Ni(en)_3^{2+}$/en than for pure ethylenediamine, which implies the operation of an extra relaxation process in the presence of Ni(II). Figure 3 shows that the ^{14}N line-broadening due to the presence of Ni(II) is quite strongly dependent on pressure: the slope of the semi-logarithmic plot is $(5.3 \pm 0.4) \times 10^{-3}$ MPa^{-1}, corresponding in volume terms to 13 cm^3 mol^{-1}. Thus, the practice in exchange studies of subtracting the natural line width of the solvent from the exchange-broadened $\Delta\nu_{1/2}$ at various pressures may yield erroneous values of k and $\Delta V^{\ddagger}$ for the exchange process at paramagnetic centres.

Discussion

Proton NMR

The fractional chemical shift $\Delta\nu/\nu$ caused by the presence of paramagnetic species is generally expressed by the following two equations, corresponding to the Fermi contact (FCS) and

Can. J. Chem. Downloaded from www.nrcresearchpress.com by 85.192.166.187 on 09/08/12
For personal use only.

TABLE 2. Pressure dependence of line width $\Delta\nu_{1/2}$ of ^{14}N in ethylenediamine

Pressure/MPa[a]	$\Delta\nu_{1/2}$/Hz, pure ethylenediamine[b]	Pressure/MPa[a]	$\Delta\nu_{1/2}$/Hz, en with added Ni(II)[b,c]
0.2	260	0.1	308
19.4	278	0.1	316
26.5	277	2.8	323
33.1	282	24.1	342
45.6	283	34.5	347
64.3	297	63.7	377
79.7	312	80.2	403
84.2	306	82.9	398
98.4	321	102.9	424
118.5	334	126.7	449
131.5	341	148.4	466
139.6	351		
150.4	352		

[a]±0.2 MPa; T = 24.2°C.
[b]Precision ±1%.
[c]0.1154 mol kg^{-1} $[Ni(en)_3](CF_3SO_3)_2$.

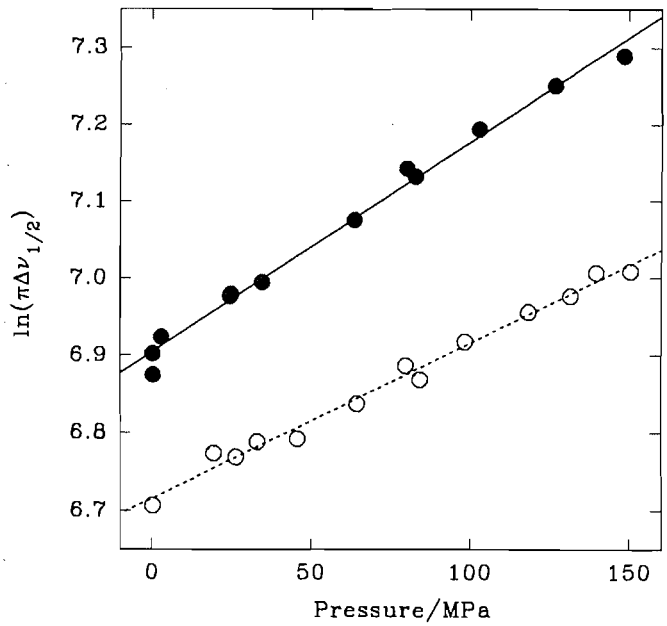

FIG. 2. Pressure dependence of the ^{14}N line width of pure ethylenediamine (open circles, dashed line) and ethylenediamine containing 0.1154 mol kg^{-1} $Ni(en)_3^{2+}$ (filled circles, solid line) at 24.2°C.

the pseudo-contact (or dipolar) (PCS) terms, respectively (14, 15):

$$[1]\quad \Delta\nu/\nu = -A_c(\gamma_e/\gamma_N)g_e\beta_e S(S+1)/3k_BT\ (\text{FCS})$$

$$[2]\quad \Delta\nu/\nu = -(3\cos^2\phi - 1)(g_\parallel^2 - g_\perp^2)\beta_e^2 S \times (S+1)/9k_BTr^3\ (\text{PCS})$$

Here, A_c is the Fermi contact coupling constant, g_e is the electronic Landé splitting factor, γ_e and γ_N are the magnetogyric ratios of the electron and the nucleus, respectively, β_e is the Bohr magneton, S is the electronic spin quantum number, k_B is Boltzmann's constant, T is the temperature, r is the distance from the paramagnetic centre to the observed nucleus, ϕ is the angle between r and the principal symmetry axis of the molecule, and $g_\parallel$ and $g_\perp$ are, respectively, the components of g_e parallel and perpendicular to this axis. As the terms that appear in the isotropic FCS interaction are not pressure sensitive, the Fermi contact term is not pressure dependent, as Nielson et al. (4) have verified experimentally. The pseudo-contact term, however, might be expected to show some pressure dependence, as the interaction distance r in eq. [2] is dependent on pressure. The pressure dependence of the anisotropic PCS interaction is expressed by eq. [3], in which κ_i is the compressibility of the complex ion, P is the pressure in MPa, and r_0 is the value of r at atmospheric pressure:

$$[3]\quad \{\partial(\Delta\nu/\nu)/\partial P\}_T = (\text{constant}/T)\exp\{\kappa_i(P - 0.1) - 3\ln r_0\}$$

For complexes of first-row transition metals, however, κ_i is on the order of 10^{-5} MPa^{-1} (16), so that the pressure dependence of the chemical shift should be negligible over the usual range of pressures (0.1–200 MPa), as was indeed observed in our ^1H NMR experiments on $Cr(acac)_3$ in four different solvents (Table 1) and in those of Newman et al. (6) on $Ni(CH_3CN)_6^{2+}$ in CH_3CN.

Unlike the chemical shift, however, the ^1H line width $\Delta\nu_{1/2}$ did exhibit a degree of pressure dependence (Table 1 and Fig. 1). Intramolecular scalar interactions between ^1H and unpaired electrons control the rate of transverse relaxation (15) and hence $\Delta\nu_{1/2}$:

$$[4]\quad T_{2sc}^{-1} = [A_c^2 S(S+1)/3][\tau_e + \tau_e/\{1 + (\omega^2 - \omega_I^2)\tau_e^2\}]$$

where T_{2sc}^{-1} ($\approx \pi\Delta\nu_{1/2}$) is the rate of transverse relaxation by unpaired electrons, ω_s and ω_I are the Larmor frequencies of the electron and nuclear spins, respectively, and τ_e is the electron spin relaxation time. Usually, $\omega_s^2\tau_e^2$ is very large, so that the term $\tau_e/\{1 + (\omega_s^2 - \omega_I^2)\tau_e^2\}$ can be neglected and T_{2sc}^{-1} is effectively proportional to τ_e. For small ions in solution, τ_e may be taken to be proportional to the solution viscosity η (17). On the

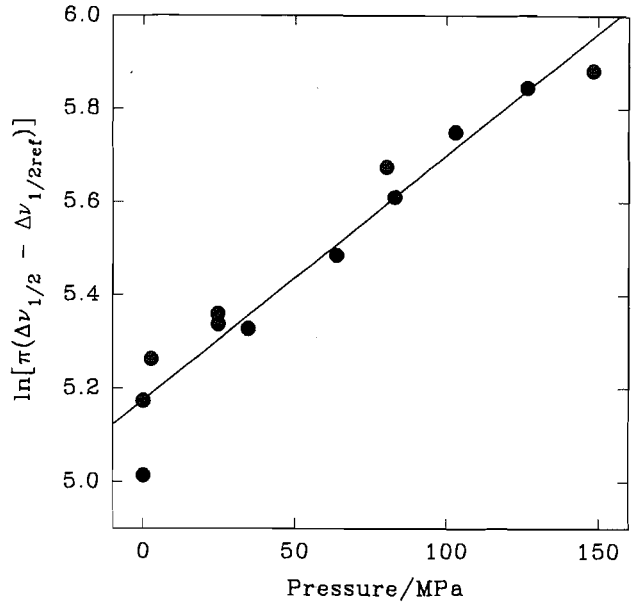

FIG. 3. Pressure dependence of the excess ^{14}N line width of ethylenediamine due to the presence of 0.1154 mol kg^{-1} $Ni(en)_3^{2+}$ at 24.3°C; $\Delta\nu_{1/2ref}$ is the ^{14}N line width of pure ethylenediamine interpolated from the data of Table 2.

Can. J. Chem. Downloaded from www.nrcresearchpress.com by 85.192.166.187 on 09/08/12
For personal use only.

TABLE 3. Pressure derivatives of ln $\Delta\nu_{1/2}$ for the methyl protons of $Cr(acac)_3$ in various solvents, and solvent compressibilities and volumes of activation for viscous flow

Solvent	$(\partial \ln \Delta\nu_{1/2}/\partial P)_T/10^{-3}$ MPa^{-1} [a,b]	$\Delta V_V^{\ddagger}/cm^3$ mol^{-1}	$\kappa/10^{-3}$ MPa^{-1} [b,c]	θ [d]
Acetone	1.69 ± 0.07	14.7 [e,f]	1.26	0.23_5
Acetonitrile	1.63 ± 0.09	5.5 [c,f]	1.11	0.49
Methanol	1.22 ± 0.04	8.3 [e,f]	1.15	0.27
Chloroform	0.91 ± 0.11	—	0.99	—

[a]Slopes of plots in Fig. 1.
[b]25°C.
[c]Reference 19.
[d]Ratio of experimental $(\partial \ln \Delta\nu_{1/2}/\partial P)_T$ to $(\Delta V_V^{\ddagger}/RT + \kappa)$.
[e]Reference 18.
[f]30°C.

other hand, the outer sphere relaxation time for the proton, T_{2os}, is related to the dipole–dipole interactions expressed by eq. [5] (14):

$$[5] \quad T_{2os}^{-1} = 8\pi\gamma_I^2\gamma_S^2 S(S+1)N\eta/5k_BT$$

where N denotes the concentration of the paramagnetic species.

Thus, the pressure dependence of T_2^{-1} $(= T_{2sc}^{-1} + T_{2os}^{-1})$ is, in principle, determined by the pressure dependence of the viscosity, and this in turn can be presented in terms of the Stearn–Eyring volume of activation for viscous flow $\Delta V_V^{\ddagger} = RT[(\partial \ln \eta/\partial P)_T - \kappa]$, where κ is the isothermal compressibility of the solvent (18).[2] For normal liquids, over relatively low ranges of P (here, 0.1–200 MPa), $(\partial \ln \eta/\partial P)_T$ is sensibly constant, and we might therefore anticipate that a plot of ln $\pi\Delta\nu_{1/2}$ vs. P would give a straight line of slope $[(\Delta V_V^{\ddagger}/RT) + \kappa]$. Although these plots are indeed linear for ^1H in $Cr(acac)_3$ in various solvents (Fig. 1), their slopes are only a fraction θ of the theoretical value (Table 3):

$$[6] \quad T_{2(P)}^{-1} = T_{2(0)}^{-1} \exp[\theta(\Delta V_V^{\ddagger}/RT + \kappa)(P - 0.1)]$$

where $T_{2(P)}$ and $T_{(0)}$ are the values of T_2 at pressures P and 0.1 MPa, respectively.

This result echoes the findings of several authors (20–26) that the pressure dependences of the longitudinal relaxation times T_1 of protons in many liquids are smaller than expected from those of the corresponding bulk viscosities. The essence of the generally accepted explanation, first advanced by Benedek and Purcell (20), is that an increase in pressure restricts translational motion more severely than it restricts molecular rotation (24). Accordingly, following the approach of McClung and Kivelson (27), the Stokes–Einstein–Debye expression for the rotational correlation time τ_R,

$$[7] \quad \tau_R = V\eta/k_BT$$

where V is the molecular volume, can be modified by introduction of parameters f_{stick}, which is a pressure-independent function of molecular shape, and C, which is a measure of the rotational–translational coupling (26), such that generally $0 < f_{stick}C \leq 1$:

$$[8] \quad \tau_R = V\eta f_{stick}C/k_BT + \tau_O$$

[2]In effect, $\Delta V_V^{\ddagger}/RT$ is the pressure derivative of the logarithm of the *kinematic* viscosity (18*b*).

In the present context, the zero-viscosity correlation time τ_O can be disregarded, and it may be assumed that T_2 depends on τ_R in the same way as does T_1. The key point is that C generally diminishes with increasing pressure, partially offsetting the increase in η. It follows that $0 < \theta \leq 1$.

The following formalism is therefore proposed to distinguish exchange broadening from that of, for example, paramagnetic relaxation and probehead distortion:

$$[9] \quad \Delta\nu_{1/2(obs)} = \Delta\nu_{1/2(exch)} + \Delta\nu_{1/2}{}^0 \exp[\theta(P - 0.1)(\Delta V_V^{\ddagger}/RT + \kappa)]$$

Here, $\Delta\nu_{1/2(obs)}$ is the observed line width at half maximum, $\Delta\nu_{1/2(exch)}$ is the contribution of chemical exchange, and $\Delta\nu_{1/2}{}^0$ is the line width measured at 0.1 MPa in the absence of chemical exchange. The parameter $[\theta(\Delta V_V^{\ddagger}/RT + \kappa)]$ can be obtained experimentally from measurements on chemically similar nonexchanging systems, and so the correction of pressure effects on line widths for paramagnetic effects becomes possible.

Nitrogen-14 NMR

For quadrupolar nuclei, Merbach et al. suggested that the scalar interaction is also the dominant relaxation process for the nuclei on the coordinated ligand (5). Therefore, eq. [6] may again be applicable to the estimation of the extra broadening of line widths of quadrupolar nuclei on the ligand directly coordinated to paramagnetic metal ions. However, for the outer-sphere interactions it is well known that quadrupolar relaxation is usually the dominant relaxation pathway for nuclei with spins greater than 1/2. For such nuclei in a molecule in solution, the quadrupolar relaxation time, T_{2q}, in the motional narrowing limit may be expressed by the following equation:

$$[10] \quad T_{2q}^{-1} \approx T_{1q}^{-1} = (3\pi^2/10)[(2I+3)/I^2(2I-1)] \times (e^2qQ/h)^2(1 + \xi^2/3)\tau_R$$

in which e^2qQ/h is the nuclear quadrupolar coupling constant, I is the nuclear spin quantum number (= 1 for ^{14}N), and ξ represents the deviation of the electric field gradient from axial symmetry (28). As τ_R is related to the solvent viscosity, the pressure dependence of T_{2q} may again be expected to be partly related to the volume of activation $\Delta V_V^{\ddagger}$ of viscous flow of the solvent. For neat liquid ethylenediamine, neither $\Delta V_V^{\ddagger}$ nor the compressibility κ are known; however, ln T_2^{-1} for ^{14}N is a linear function of pressure (Fig. 2) with slope $(2.00 \pm 0.06) \times 10^{-3}$ MPa^{-1}, which corresponds to a volume of activation $\Delta V_R^{\ddagger}$ of

Can. J. Chem. Downloaded from www.nrcresearchpress.com by 85.192.166.187 on 09/08/12
For personal use only.

Can. J. Chem. Downloaded from www.nrcresearchpress.com by 85.192.166.187 on 09/08/12
For personal use only.

4.9 ± 0.2 cm^3 mol^{-1} for rotational diffusion. This may be compared with $\Delta V_R^{\ddagger} = 6.3$ cm^3 mol^{-1} for diffusion of acetonitrile by rotation perpendicular to the C_{3v} axis, obtained from the pressure dependence of the ^{14}N line width of liquid CH_3CN (29).

The additional broadening caused by the addition of $Ni(en)_3^{2+}$ ion to ethylenediamine, together with the steep slope of the plot in Fig. 3, implies the existence of strong outer-sphere interactions between ^{14}N of the bulk solvent and paramagnetic $Ni(en)_3^{2+}$. One of the authors has reported, on the basis of the Swift–Connick plot, that outer-sphere relaxation characterized by the relaxation time T_{os} is indeed the dominant process for the Ni(II)–ethylenediamine solvent exchange system under the conditions used in this experiment (10). These outer-sphere interactions may again be expected to correlate with τ_R, as discussed above. As the plots shown in Figs. 2 and 3 are linear within the experimental uncertainty, the dependence of line width on the applied pressure may reasonably be expressed by an equation similar to eq. [3], and the relatively large correction to $\Delta\nu_{1/2(obs)}$ for the paramagnetic contribution may again be made through eq. [9].

Conclusion

In this article, we report the pressure dependence of the chemical shifts and line widths of ^{1}H in a coordinated ligand, and of ^{14}N in a bulk solvent, under the influence of paramagnetic metal ions. The chemical shifts of ^{1}H and ^{14}N were independent of pressure up to at least 200 MPa. The line width of the proton signal in $Cr(acac)_3$, however, showed a small but measurable dependence on pressure. As the pressure effect on the proton line widths was smaller than that expected from the theory of scalar interactions, a scaling factor θ, representing the pressure dependence of the rotational–translational coupling, was introduced in eq. [6]. Since θ is substantially less than 1, a conservative upper limit to the paramagnetic correction to the pressure effect on ^{1}H relaxation can be calculated from the pressure dependence of solvent viscosity, where this is known. In practice, the paramagnetic correction to pressure effects on ^{1}H line widths will be much less than this. For the quadrupolar nucleus ^{14}N, the pressure dependence of the line width was significant even in the absence of a paramagnetic solute. In the presence of paramagnetic molecules in solution, a relatively large pressure effect on the ^{14}N line width was observed even when chemical exchange was not significant.

Thus, activation volumes for exchange reactions, obtained from line-broadening measurements using ^{1}H or other spin-1/2 nuclei, may be reliable within experimental accuracy even without correction for the extra broadening caused by the outer-sphere interactions between the observing nucleus and a paramagnetic solute, which is consistent with experience in previous studies (2, 6, 12). On the other hand, when quadrupolar nuclei are used for the observation of exchange kinetics, volumes of activation obtained by high-pressure NMR methods may not be valid without corrections for the pressure dependence of the natural line widths using the method described here. For water, the factor $(\Delta V_V^{\ddagger}/RT + \kappa)$ at near-ambient temperatures is only about 5×10^{-4} MPa^{-1}, so that paramagnetic corrections to $\Delta V^{\ddagger}$ for exchange reactions will generally be less than the experimental uncertainty even for measurements using quadrupole nuclei. For many commonly used nonaqueous solvents including ethylenediamine, $\Delta V_V^{\ddagger}$ or κ values are not available at present, but quantitative correction of $\Delta V^{\ddagger}$ is still possible through NMR measurements on chemically similar nonexchanging systems using eq. [9].

Acknowledgement

H.D.T. and T.W.S. wish to express their thanks to the Natural Sciences and Engineering Research Council of Canada for financial support. This joint research was also supported by Grants-in-Aid for Scientific Research (Grant Nos. 05453042 and 04403011) from the Ministry of Education, Science, and Culture of Japan and by the Research Foundation for the Electrotechnology of Chubu.

1. R. van Eldik, T. Asano, and W.J. Le Noble. Chem. Rev. **89**, 549 (1989).
2. H. Doine and T.W. Swaddle. Inorg. Chem. **27**, 665 (1988); H.D. Takagi and T.W. Swaddle. Inorg. Chem. **31**, 4669 (1992); A.D. Hugi, L. Helm, and A.E. Merbach. Inorg. Chem. **26**, 1763 (1987); A.E. Merbach. Pure Appl. Chem. **54**, 1479 (1982).
3. T.J. Swift and R.E. Connick. J. Chem. Phys. **37**, 307 (1962).
4. R.M. Nielson, H.W. Dodgen, J.P. Hunt, and S.E. Wherland. Inorg. Chem. **25**, 582 (1986).
5. K. Micskei, L. Helm, E. Brucher, and A.E. Merbach. Inorg. Chem. **32**, 3844 (1993).
6. K.E. Newman, K. Meyer, and A.E. Merbach. J. Am. Chem. Soc. **101**, 1470 (1979).
7. I. Bertini and C. Luchinat. NMR of paramagnetic molecules in biological systems. Benjamin–Cummings Publ. Co. Inc., New York. 1986.
8. R.B. Lauffer. Chem. Rev. **87**, 901 (1987).
9. W.C. Fernelius and J.E. Blanch. Inorg. Synth. **5**, 130 (1957).
10. S. Soyama, M. Ishii, S. Funahashi, and M. Tanaka. Inorg. Chem. **31**, 536 (1992).
11. J.A. Riddick, W.B. Bunger, and T.K. Sakano. Organic solvents. John Wiley & Sons, New York. 1986.
12. H. Doine and T.W. Swaddle. Can. J. Chem. **66**, 2763 (1988), and references therein.
13. M. Ishii, S. Funahashi, K. Ishihara, and M. Tanaka. Bull. Chem. Soc. Jpn. **62**, 1852 (1989).
14. A. Abragam. The principles of nuclear magnetism. Oxford University Press, London. 1961. Chap. 8.
15. D.R. Eaton and W.D. Phillips. Adv. Magn. Reson. **1**, 103 (1965).
16. D.R. Stranks. Pure Appl. Chem. **38**, 303 (1974).
17. G.E. Pake and T.R. Tuttle. Phys. Rev. Lett. **3**, 423 (1959).
18. (*a*) N.S. Isaacs. Liquid phase high pressure chemistry. John Wiley & Sons, Chichester. 1981; (*b*) A.E. Stearn and H. Eyring. Chem. Rev. **29**, 509 (1941).
19. T.W. Swaddle. Inorg. Chem. **29**, 5017 (1990).
20. G.B. Benedek and E.M. Purcell. J. Chem. Phys. **22**, 2003 (1954).
21. T.E. Bull and J. Jonas. J. Chem. Phys. **52**, 2779 (1970).
22. R.A. Assink, J. DeZwaan, and J. Jonas. J. Chem. Phys. **56**, 4976 (1972).
23. D.L. VanderHart. J. Chem. Phys. **60**, 1858 (1974).
24. J. Jonas. Annu. Rev. Phys. Chem. **26**, 167 (1975).
25. J. Jonas and J.A. Akai. J. Chem. Phys. **66**, 4946 (1977).
26. D.G. Gillies, S.J. Matthews, and L.H. Sutcliffe. Magn. Reson. Chem. **29**, 823 (1991), and references cited.
27. R.E.D. McClung and D. Kivelson. J. Chem. Phys. **49**, 3380 (1968).
28. R.G. Kidd. *In* NMR of newly accessible nuclei. Vol. 1. *Edited by* P. Laszlo. Academic Press, New York. 1983. Chap. 5.
29. Y. Yano, M.T. Fairhurst, and T.W. Swaddle. Inorg. Chem. **19**, 3267 (1980).

1994 Syntex Award Lecture
Anionic electrophiles, protein modification, and artificial blood[1]

RONALD KLUGER[2]

Lash Miller Laboratories, Department of Chemistry, University of Toronto, Toronto, ON M5S 1A1, Canada

Received June 16, 1994

RONALD KLUGER. Can. J. Chem. **72**, 2193 (1994).

Monomethyl esters of acyl phosphates (mixed anhydrides of carboxylic and phosphoric acids) are being developed as site-directed acylating agents for amino growps in proteins. In an illustrative application, these anionic materials are shown to bind to a positively charged region of hemoglobin where they convert amino groups to amides. Bifunctional acyl methyl phosphates cross-link hemoglobin to give a variety of products, some of which have the oxygen-binding properties anticipated for materials that can serve as an alternative to red cells in transfusions. Higher yields of desired products result from the use of a trifunctional analogue. Kinetic patterns of the reactions of a series of alkyl amines and methyl aroyl phosphates indicate that the transition state for formation of the amide involves almost complete development of positive charge on nitrogen.

RONALD KLUGER. Can. J. Chem. **72**, 2193 (1994).

On a développé des méthodes permettant d'utiliser les esters monométhylés des phosphates d'acyles (anhydrides mixtes des acides carboxylique et phosphorique) comme agents d'acylation orientées vers les sites de groupes aminés des protéines. Dans une application typique, on a montré que ces matériaux anioniques se lient à une région chargée positivement de l'hémoglobine et qu'ils transforment alors les groupes aminés en amides. Les phosphates bifonctionnels acyle méthyle provoquent une réticulation de l'hémoglobine conduisant à une variété de produits dont quelques-uns possèdent les propriétés de liaison à oxygène recherchées pour des matériaux pouvant servir comme alternative aux globules rouges lors de transfusions. On obtient de meilleurs rendements des produits désirés lorsqu'on utilise un analogue trifonctionnel. Les patrons de la cinétique des réactions d'une séries d'alkylamines et de phosphates de méthyle et d'aroyle indiquent que l'état de transition de la formation de l'amide implique un développement pratiquement complet de la charge positive sur l'azote.

[Traduit par la rédaction]

We have been developing methyl acyl phosphates as a new type of highly specific reagent for the modification of proteins (1–4). We have found convenient routes for preparing a variety of acyl derivatives and have demonstrated the utility of these compounds in specifically cross-linking human hemoglobin so that the modified protein can be used in medical applications, such as carrying oxygen in a transfusion medium (5–8).

Methyl acetyl phosphate

When we began our study, we were aware of no specific attempt to use acyl phosphate monoesters as reagents for protein modification. However, there were a number of studies that indicated that they would be worth trying. We had been studying enzymes that catalyze reactions of acetoacetate and found that 3-ketophosphonate monoesters, such as methyl acetonylphosphonate, are competitive inhibitors (9).

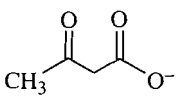

Acetoacetate

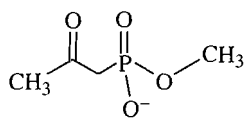

Methyl acetonylphosphonate

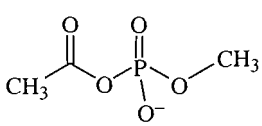

Methyl acetyl phosphate

Extending the analogy, methyl acetyl phosphate might bind and also react with nucleophiles. Di Sabato and Jencks reported in 1961 that phenyl acetyl phosphate monoanion is stable in nuetral solution (half-life of about 100 h) and reacts rapidly with amines to produce amides (10, 11). Based on this reaction pattern, acyl phosphate monoesters, such as methyl acetyl phosphate, might be especially useful for the selective modification of proteins. If they associate with the protein, then they could acylate amino groups of the protein with minimal competing hydrolysis. Since they are negatively charged, they would bind at sites that attract anions (12).

A major obstacle to testing this hypothesis was the lack of a practical route to methyl acetyl phosphate. While acetyl phosphate can be made from acetic anhydride and potassium phosphate (13), the reaction of methyl phosphate and acetic anhydride does not give methyl acetyl phosphate in useful, isolable quantities. However, we had already prepared dimethyl acetyl phosphate (14) and had also used sodium iodide in acetone to monodemethylate a very reactive phosphate triester (15). While dimethyl acetyl phosphate is a very reactive and unselective acylating agent, reaction with sodium iodide in dry acetone quantitatively converts the diester to the monoester sodium salt, leaving the anhydride intact (1).

We found that methyl acetyl phosphate binds competitively with acetoacetate to D-3-hydroxybutyrate dehydrogenase at high pH and inactivates the enzyme in a few minutes (1, 2). Methyl acetyl phosphate is very stable in neutral water at 25°C with a half-life of 160 h (1). Our report of these results led Manning to recognize that the molecule might be an alternative to cyanate for the selective modification of hemoglobin.

The treatment of sickle cell disease with chemicals has been a significant medicinal target. Cerami, Manning, and co-workers showed that cyanate selectively carbamylates amino groups in a positively charged central cavity of hemoglobin, the site to which 2,3-diphosphoglycerate (DPG) binds (16). The alteration

[1]This Syntex Award Lecture was delivered by Professor Kluger at the Annual Conference of the Canadian Society for Chemistry, Winnipeg, Manitoba, May 30, 1994.

[2]Internet: rkluger@alchemy.chem.utoronto.ca Telephone: 416-978-3582. Fax: 416-978-8775.

Can. J. Chem. Downloaded from www.nrcresearchpress.com by 85.192.166.187 on 09/08/12
For personal use only.

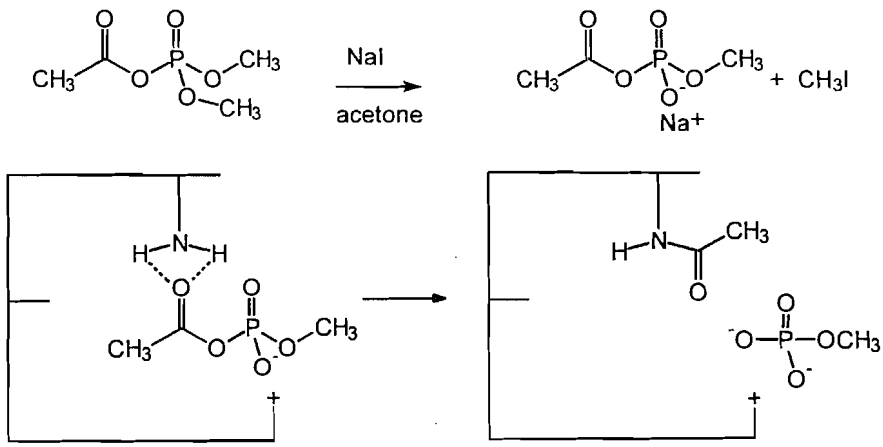

of hemoglobin's oxygen affinity by modification of this site reduces the tendency of sickle cell hemoglobin to undergo sickling (the condition blocks circulation of the red cells). When cyanate proved to be unsuitable for further development for the treatment of sickle cell disease (due to its causing peripheral neuropathy), other anionic acylating agents were examined. Klotz et al. prepared and studied a variety of substituted salicylates, some of which proved to react selectively with amino groups in the region to which DPG binds (17).

Methyl acetyl phosphate and hemoglobin

Manning suggested that we jointly investigate the utility of methyl phosphate. The work in Manning's laboratory with Pospischil and Ueno established that methyl acetyle phosphate preferentially acetylates amino groups in the DPG-binding site of human hemoglobin, making it a potentially less toxic alternative to cyanate (16). The reagent is highly selective, reacting mainly with two of the 24 amino groups per αβ dimer, the ϵ-amino group of β-lys-82, and the α-amino group of the β-N-terminal valine (3, 18). Further work from Manning and coworkers indicated that methyl acetyl phosphate is an effective anti-sickling agent and can also be used as a general acetylating agent for identifying sites that bind anions (19, 20).

Since methyl acetyl phosphate is highly selective in its reactions with hemoglobin, it appeared that acyl phosphate monoesters in general might be useful in site-directed protein modification. As anions, the reagents would be attracted to positively charged regions and, as anionic electrophiles, they should react with uncharged nucleophiles in preference to anions. Thus, they would react with amino groups in the regions that were associated with other positively charged groups. However, our synthesis of methyl acetyl phosphate could not be easily extended to many other acyl derivatives since the acid chloride serves as the solvent for the reaction.

Chemicals that selectively modify hemoglobin are also an important resource in the development of hemoglobin-based oxygen carriers, replacements for red cells in transfusions. Red cells are the key component in a blood transfusion, being the material that gives blood the ability to carry adequate amounts of oxygen to tissues and organs via the circulatory system. The membranes of the red cells are subject to viral infection and their antigenic properties are the basis for the human blood type groups. Hemoglobin is the predominant protein within the red cell, reversibly and cooperatively binding oxygen (four molecules of oxygen per hemoglobin tetrarner.) Outside the red cell, native hemoglobin is not a satisfactory oxygen-carrying material. The tetramer dissociates into dimers that are passed through the kidney and into the urine. As well, 2,3-diphosphoglycerate (DPG) in the red cell promotes release of oxygen from hemoglobin. In free circulation, where DPG concentration is low, native hemoglobin does not release oxygen to a useful extent (21).

Difunctional acyl phosphate methyl esters and cross-linking hemoglobin

The problems with native hemoglobin as a substitute for hemoglobin in red cells might be overcome by appropriate chemical modification of hemoglobin. The tetramer can be held together by covalently connecting one dimer to another by a chemical cross-link (22). If the cross-link also reduces the oxygen affinity in analogy to the effect of DPG, then both major problems would be overcome. Since methyl acetyl phosphate reacts at the site to which DPG binds, it is possible that such a reaction might also lead to an appropriate decrease in oxygen affinity of the modified hemoglobin. A cross-linker that is directed to the DPG site could combine the needed properties. Therefore, a general synthesis of acyl phosphate monoesters, including difunctional materials, became desirable on several counts. Klotz's pioneering work with dibromosalicylate esters of dicarboxylic acids had shown that cross-linking can be made to occur with some degree of selectivity.

First of all, the reaction of acetyl chloride and trimethyl phosphate to produce dimethyl acetyl phosphate, the precursor to methyl acetyl phosphate, is very slow and inefficient, requiring days of heating. Andrew Grant in our laboratory found that the simple expedient of using the more reactive acetyl bromide in place of acetyl chloride makes the reaction occur more rapidly and efficiently. However, the method did not extend to diacid bromides, potential precursors of cross-linkers, since these tended to form anhydrides. An efficient alternative was devised by Grant in collaboration with Stephen Bearne. They found that sodium dimethyl phosphate reacts efficiently with acid chlorides and diacid chlorides to produce the corresponding dimethyl acyl phosphate or bis(dimethyl phosphate) in tetrahydrofuran. To encourage reaction by increasing solubility, crown ethers were added. However, we found that the yield increased with decreasing amounts of crown ether. The reaction was most efficient in the absence of crown ethers (4).

The product could be converted to the corresponding methyl acyl phosphate or bis(methyl phosphate) by reaction with sodium iodide in acetone. Thus, we converted a number of diacid chlorides to diacyl bis(methyl phosphates). The method

Can. J. Chem. Downloaded from www.nrcresearchpress.com by 85.192.166.187 on 09/08/12
For personal use only.

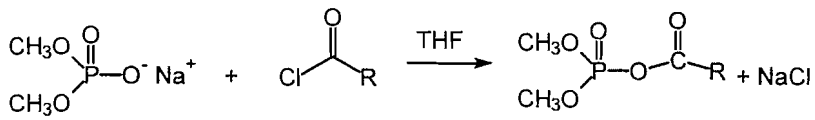

also permitted us to make methyl benzoyl phosphate and aromatic-substituted derivatives. The latter compounds served as the basis for physical organic studies of the reactivity of methyl acyl phosphates.

We then began an ongoing collaboration with Richard T. Jones of Oregon Health Sciences University. Jones had done extensive research that had focused on the determination of structures of mutant and modified hemoglobins. Reaction of the bis(dimethyl) diacyl phosphates with hemoglobin gave a variety of products whose structures were analyzed in Oregon. The method involves HPLC separations and analysis of the products of proteolytic digestion. With Jones' help we also began to do structural analyses in our laboratory. Daniel T.-b. Shih, also of Oregon Health Sciences University, joined this collaboration based on his interest in the oxygen-binding properties of modified hemoglobins.

In consultation with Jones and Shih we decided to prepare potential cross-linkers in which the span between the two acyl functions was relatively rigid so that we could develop an understanding of the effects of length and site of the cross-link. The derivatives were from the following relatively rigid dicarboxylic acids: fumaric, isophthalic, terephthalic, *trans*-stilbene-3,3′-dicarboxylic, and *trans*-stilbene-4,4′-dicarboxylic. The approximate distances between cross-linked amino groups with these reagents are 6.1, 7.3, 7.5, 13.2, and 16 Å, respectively. Human hemoglobin A was reacted with about 1.5 equivalents each of bis(methyl acyl phosphates) and the products separated on an AX-300 anion exchange column. The individual modified hemoglobins were collected and their oxygen-binding properties determined. The hemoglobins were also separated into ferrohemes and globin chains on a C-4 reverse-phase HPLC column. Since amino acid sequences of the tryptic peptides of hemoglobin are known, the site of an acylated amino residue is easily localized because the adjacent peptide is no longer susceptible to cleavage by trypsin, a digestive enzyme that is specific for peptides adjacent to basic amino acids. Acid hydrolysis and amino acid analysis of the peptides is used to confirm the contents of the peptides.

The products of the reaction of hemoglobin and the methyl acyl phosphates reflected our expectation that reaction in the DPG site at residues lys-82 and val-1 of the β chains would be predominant. Different product patterns appear when hemoglobin is reacted after being deoxygenated compared to when the hemes are occupied by CO (or dioxygen). In deoxyhemoglobin, most cross-links were between val-1 of one β subunit and lys-82 of the other β subunit. With carbonmonoxy-hemoglobin the cross-links form mainly between the ϵ-amino groups of the two lys-82 residues of the β subunits (8).

Properties of cross-linked hemoglobins

All the cross-linked hemoglobins we produced show a high degree of cooperativity in their binding of oxygen. The Hill coefficient at 50% saturation (n_{50}) is a common empirical indicator of the extent of cooperativity in the binding of oxygen to hemoglobin and is related to the slope of a tangent to a curve measuring oxygen bound as a function of oxygen pressure at half saturation. With four ligands, as in hemoglobin, $1 < n_{50} < 4$. Noncooperative binding gives $n_{50} = 1$. In the red cell, binding of

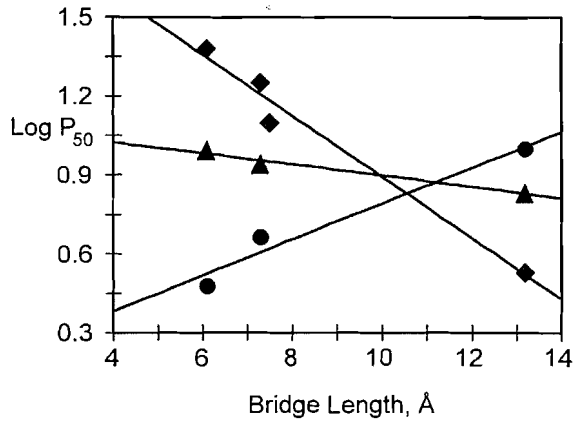

FIG. 1. Variation of oxygen affinity of cross-linked human hemoglobin as a function of site and structure of cross-link: (◆) β-lys-82 (ϵ-amino) to β′-val-1 (α-amino); (●) β-lys-82 (ϵ-amino) to β′-lys-82 (ϵ-amino); (▲) β-lys-82 (ϵ-amino), not cross-linked.

oxygen is highly cooperative and n_{50} is ~3. In all the cross-linked hemoglobins in our studies n_{50} is >2.

There is a considerable variation in affinities of the cross-linked hemoglobins for oxygen. In the case of those cross-linked from val-1 to lys-82, there appears to be a systematic and approximately linear variation between the length of the cross-link and log P_{50}. (P_{50} is the oxygen pressure necessary to cause the hemoglobin oxygen-binding sites to be 50% occupied. Since this is related to the free energy of binding, correlation is logical between a property and the log P_{50}.)

The relationship indicates that for hemoglobin cross-linked from β-val-1 to β′-lys-82, the shorter the cross-link, the lower the oxygen affinity. For materials linked between the two β-lys-82 residues, the relationship has a smaller slope with opposite sign: the longer the cross-link, the lower the oxygen affinity (8). The physical basis of these relationships and tests with further examples are the subjects of ongoing research.

The Monod model for hemoglobin's oxygen affinity assumes the existence of two states, R ("relaxed") and T ("tense"), with high and low oxygen affinities, respectively. If deoxy-hemoglobin is cross-linked in the T state, then relaxation of the protein to the R state upon oxygen binding (axial movement of αβ dimers with respect to one another) is reduced. The shorter the cross-link, the less movement is possible toward the conformation of the R state. On the other hand, if CO hemoglobin, in which the protein is in the R form, is cross-linked, then the shorter the cross-link, the more difficult it will be for the protein to move to the T conformation of the deoxygenated state (21).

Based on the oxygen-binding curves of the derivatives and the typical oxygen pressures in arterial and venous blood, the isophthalyl (or benzene-1,3-dicarboxyl) derivative (cross-linked between residues β-val-1 and β′-lys-82) appears to be the most suitable to be tried as a red cell substitute. However, this is only one component of the mixture that results from the reaction. The reagent also links residues val-1 and lys-82 of the same subunit and produces a significant amount of material linking the lys-82 residues of the two β subunits. In addition, some derivatives are not cross-linked but instead involve sin-

Can. J. Chem. Downloaded from www.nrcresearchpress.com by 85.192.166.187 on 09/08/12
For personal use only.

Can. J. Chem. Downloaded from www.nrcresearchpress.com by 85.192.166.187 on 09/08/12
For personal use only.

gle-chain modifications. For a modified hemoglobin to be produced on a useful scale, there has to be more of the desired product.

Trifunctional reagents for efficient cross-linking

There are two logical approaches to this problem. The first is to change conditions to favor the desired product. The results we had did not indicate that any particular conditions would do this. Variation in pH, temperature, mode of addition, ionic strength, and buffer were considered and some were tested with and without modest success. The second approach involves changing the reagent. Acyl phosphate monoesters were probably the most likely type of compound to give the desired product. The span of the isophthalyl geometry was what we were seeking, so that could not be changed. The operational problem is that if an undesired cross-link is produced, there is no further reaction possible since the reagent has two reaction sites. If the reagent has more reaction sites, then the possibility of having further reactions produce useful cross-links occurs even if an undesired cross-link has been formed. This should be a suitable solution if the desired cross-link requires holding the protein in a conformation that is less relaxed. A survey of known tricarboxylic acids led to trimesic acid, benzene-1,3,5-tricarboxylic acid. The reagent trimesoyl tris(methyl phosphate), TMMP, should produce cross-links with the isophthalyl geometry. To the extent that undesirable products result from consumption of the reagent by undesired reactions, the third reaction site gives the reagent a "second chance" at making the proper connection. On the other hand, if the desired val-1 to lys-82 linkage between chains occurs as the initial reaction, it is likely that an additional cross-link would not be undesirable. Jolanta Wodzinska found that preparation of the trifunctional reagent required gentler conditions than for the bifunctional reagents. Dealkylation at three sites with sodium iodide had not previously been attempted but conditions were found that led to a successful procedure (7).

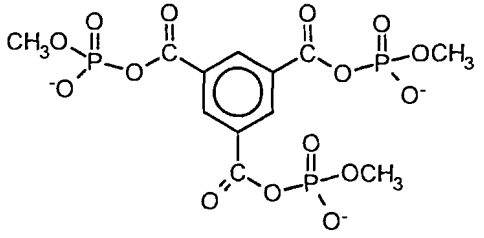

TMMP

When TMMP was reacted with deoxyhemoglobin, chromatography revealed many fewer products than are formed with the isophthalyl reagent. Analysis of the globin chains and proteolytic digests showed that the major products are hemoglobins in which cross-links between val-1 and lys-82 of the β subunits are the predominant products. In particular, about 30% was triply cross-linked between both lys-82 ϵ-amino groups and the amino group of one N-terminal valine. The second major product was cross-linked from one β-lys-82 ϵ-amino group of one subunit and one β-N-terminal valine of the other dimer. In this case, the third functional group of the reagent did not react. Thus, TMMP produces a significant change in product distribution in the positive direction (7).

Analysis of products as a function of time reveals that the various products form in parallel. Therefore, the compound with two links is not a precursor to the one with three. Based on this result, we proposed that there must be structural variations that lead to the different products since in principle the triply linked species must be preceded by a doubly linked species. If there were two isomeric doubly linked species, the results could be understood. Because an amide bond at the β-val-1 amino group is created in the reaction, it is possible that the two cases differ by being *E* or *Z* at this pseudo-double bond. Structural studies of these compounds by X-ray crystallography are dealing with this issue. Interestingly, X-ray crystallographic structure determination by Richard Brennan at Oregon Health Sciences University revealed that the isophthalyl 1-82 cross-linked species is a mixture of *E* and *Z* stereoisomers.

The oxygen-binding properties of the hemoglobins cross-linked by TMMP and containing val-1 to lys-82 cross-links were measured by Shih and shown to be the same as those of the isophthalyl cross-linked material. Earlier workers had proposed that additional negative charges in the DPG site would affect oxygen affinity (23). This work shows that for the case of the isophthalyl distance at least, the only significant consideration in controlling oxygen affinity of modified hemoglobins is the site and size of the cross-link, supporting the validity of the correlation (8).

Further work with TMMP and hemoglobin has been undertaken at Hemosol, Inc., under the direction of Diana Pliura and Gordon Adamson in collaboration with our group. They have found convenient ways to produce large of amounts of usefully cross-linked hemoglobin.

Reaction patterns of methyl acyl phosphates

To understand the basis of the reagents' selectivity, it is necessary to have a reasonable idea of transition states and intermediates in the reaction mechanism. The use of Brönsted plots for a series of amine nucleophiles gives a measure of charge development in the transition state and other details (24).

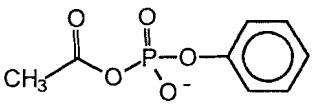

As in all reactions involving amines as nucleophiles, the rate of reaction of amines with acyl phosphate monoesters depends on the concentration of the unprotonated amine and of the electrophile:

$$v = k\,[\text{amine}][\text{AcP}]$$

$$\log v = \log k + \log [\text{amine}] + \log [\text{AcP}]$$

Since log [amine] will depend on pH with a slope of 1.0, at a lower pH, each pH decreases lowers free amine concentration about tenfold. For an amine of p*K* 10, at pH 7 only about one molecule in 1000 will be unprotonated, i.e., the rate is lowered by a factor of 1000. In addition, we found that β_{nuc} for the reaction is 0.91. Thus the Brönsted-like expression for β_{nuc} is

$$\log k = \beta_{nuc}(pK_a) + c$$

$$\log k_1 - \log k_2 = \beta_{nuc}(pK_{a1} - pK_{a2})$$

$$\log k_1/k_2 = 0.91\ (\Delta\ pK_a)$$

Therefore the less basic nucleophile will undergo the faster

reaction in neutral solutions. In the case of proteins, the α-amino group of the N-terminus is less basic than the ϵ-amino group of a lysine residue. In the modification of hemoglobin with methyl acyl phosphates, this factor will favor reaction at the N-terminal valine of the β chain over reaction of the ϵ-amino group of β-82-lys. On the other hand, if the reagent has a preferred orientation upon binding to the protein, then the effect is minimal.

A general mechanism for the reaction of benzoyl methyl phosphate with an amine is shown below (Scheme 1). Formation of a high-energy tetrahedral addition intermediate is followed by rate-determining breakdown of the intermediate.

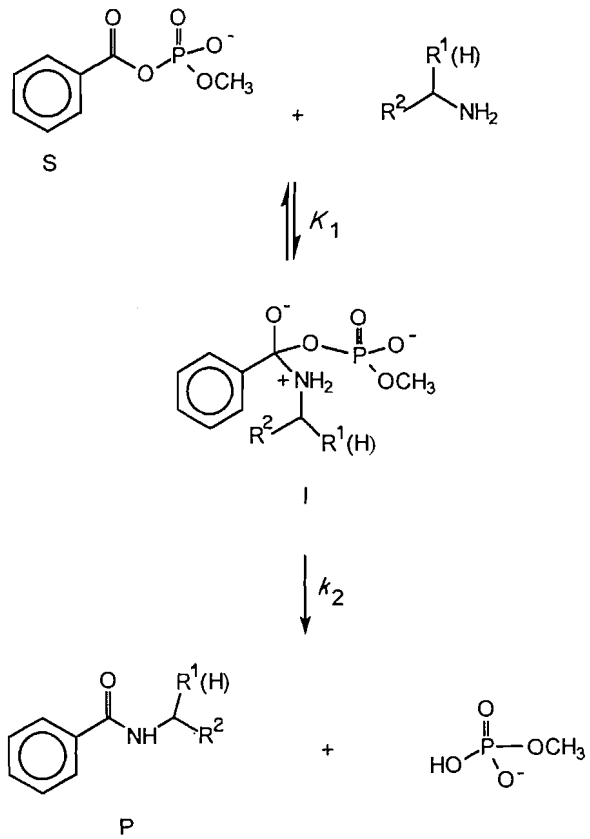

SCHEME 1

With the second step rate determining, the observed second-order rate coefficient (k, corrected for the concentration of free amine) is equal to the product of the equilibrium constant (K_1) for the addition of the amine to the substrate and the rate constant for the decomposition of the intermediate ($k2$) (24).

$$v = k_{obs}[BMP][RNH_2] = K_1k_2[BMP][RNH_2]$$

$$k_{obs} = K_1k_2$$

The slope of the plot of log k_{obs} vs. pK_a of RNH_3^+ gives β_{nuc}:

$$\beta_{nuc} = \delta \log k_{obs}/\delta\ pK_a$$

$$\beta_{nuc} = \delta \log K_1/\delta\ pK_a + \delta \log k_2/\delta\ pK_a$$

The observed value for β_{nuc} of 0.91 implies the retention of about 90% of a positive charge on the amino group in the rate-determining transition state. The first term in the sum of the expression for β_{nuc} is 1.0 since the addition of amines to the carbonyl group generates a series of protonated amines. The observed value for β_{Nuc} is 0.9, making $\delta \log k_2/\delta\ pK_a = 0.1$. This means that the rate of the decomposition of the tetrahedral intermediate depends very little on the basicity of the amine and the transition state is early on the reaction coordinate. On the other hand, the extent of formation of the intermediate is very sensitive to the basicity of the amine. In the process of protein modification, the reversibility of the initial step provides an additional opportunity for selectivity.

Additional work in our group has diversified these results by using other cross-linkers and by taking advantage of products that retain a reactive center after the cross-link has formed. The retained functional group permits the addition of nucleophilic materials, which could be delivered as a hemoglobin conjugate in circulation (25, 26).

Acknowledgements

I appreciate the support of the Natural Sciences and Engineering Research Council of Canada (NSERC) through the operating and strategic grants programs, as well as general support from Hemosol, Inc. I thank the Canadian Society for Chemistry and Syntex Canada Inc. for the Syntex Award.

1. R. Kluger and W.-C. Tsui. J. Org. Chem. **45**, 2723 (1980).
2. R. Kluger and W.-C. Tsui. Biochem. Cell Biol. **64**, 434 (1985).
3. H. Ueno, M.A. Pospischil, R. Kluger, and J.M. Manning. Arch. Biochem. Biophys. **244**, 795 (1986).
4. R. Kluger, A.S. Grant, S.L. Bearne, and M.R. Trachsel. J. Org. Chem. **55**, 2864 (1990).
5. R. Kluger. Chem. Rev. **87**, 863 (1987).
6. K.D. Vandegriff and R.M. Winslow. Chem. Ind. (London), 497 (1991).
7. R. Kluger, J. Wodzinska, R.T. Jones, C. Head, T.S. Fujita, and D.T. Shih. Biochemistry, **31**, 7551 (1992).
8. R.T. Jones, C.G. Head, T.S. Fujita, D.T. Shih, J. Wodzinska, and R. Kluger. Biochemistry, **32**, 215 (1993).
9. R. Kluger and W.-C. Tsui. Can. J. Biochem. **59**, 810 (1981).
10. G. Di Sabato and W.P. Jencks. J. Am. Chem. Soc. **83**, 4393 (1961).
11. G. Di Sabato and W.P. Jencks. J. Am. Chem. Soc. **83**, 4400 (1961).
12. A. Warshel. Proc. Natl. Acad. Sci. U.S.A. **75**, 5250 (1978).
13. A.W.D. Avison. J. Chem. Soc. 732 (1955).
14. R. Kluger and P. Wasserstein. Biochemistry, **11**, 1544 (1972).
15. R. Kluger and P. Wasserstein. Tetrahedron Lett. 3451 (1974).
16. J.M. Manning. Adv. Enzymol. **64**, 55 (1991).
17. I.M. Klotz, D.N. Haney, and L.C. King. Science (Washington D.C.), **213**, 724 (1981).
18. H. Ueno, M.A. Pospischil, R. Kluger, and J.M. Manning. J. Chromatogr. **359**, 193 (1986).
19. H. Ueno, L.J. Benjamin, M.A. Pospischil, and J.M. Manning. Biochemistry, **26**, 3125 (1987).
20. H. Ueno, M.A. Pospischil, and J.M. Manning. J. Biol. Chem. **264**, 12344 (1989).
21. R.E. Dickerson and I. Geis. Hemoglobin: structure, function, evolution, and pathology. The Benjamin/Cummings Publishing Co., Menlo Park, Calif. 1983.
22. S.R. Snyder, E.V. Welty, R.Y. Walder, L.A. Williams, and J.A. Walder. Proc. Natl. Acad. Sci. U.S.A. **84**, 7280 (1987).
23. A. Arnone, R.E. Benesch, and R. Benesch. J. Mol. Biol. **115**, 627 (1977).
24. J.L. Wodzinska. Ph.D. Thesis, University of Toronto, 1994.
25. R. Kluger, Y. Song, J. Wodzinska, C. Head, T.S. Fujita, and R.T. Jones. J. Am. Chem. Soc. **114**, 9275 (1992).
26. R. Kluger and Y. Song. J. Org. Chem. **59**, 733 (1994).

Can. J. Chem. Downloaded from www.nrcresearchpress.com by 85.192.166.187 on 09/08/12
For personal use only.

Acid-catalyzed reactions of six- and seven-membered cyclic hemiperacetals and peracetals and of related bicyclic ozonides

KARL GRIESBAUM,[1] GILBERT KIESEL, HENRI MERTENS, AND PETRA KRIEGER-BECK
Engler-Bunte-Institut, Bereich Petrochemie, Universität Karlsruhe (TH), 76128 Karlsruhe, Germany

AND

HENNING HENKE
Institut für Anorganische Chemie, Universität Karlsruhe (TH), 76128 Karlsruhe, Germany

Received May 13, 1994

KARL GRIESBAUM, GILBERT KIESEL, HENRI MERTENS, PETRA KRIEGER-BECK, and HENNING HENKE. Can. J. Chem. **72**, 2198 (1994).

HCl-catalyzed reactions of the hemiperacetals 3-methoxy-3-methyl-7-hydroxy-1,2-dioxepane (**1***a*) and 3-methoxy-3-methyl-6-hydroxy-1,2-dioxane (**1***b*) and of the related ozonides 1-methyl-6,7,8-trioxabicyclo[3.2.1]octane (**2***a*) and 1-methyl-5,6,7-trioxabicyclo[2.2.1]heptane (**2***b*) gave peroxidic monocyclic (**11**—**13**), bicyclic (**14**), and (or) tricyclic (**15**) products. By contrast, reactions of the peracetals corresponding to **1***a* and **1***b*, viz., 3-methyl-3,7-dimethoxy-1,2-dioxepane (**13***a*) and 3-methyl-3,6-dimethoxy-1,2-dioxane (**13***b*) gave only non-peroxidic products. Reactions of the persubstituted peracetals 3,6-dimethoxy-3,6-dimethyl-1,2-dioxane (**25**) and 3,6-dimethoxy-3-isopropyl-6-methyl-1,2-dioxane (**27**) also gave non-peroxidic products, which resulted from fragmentation of the carbon skeletons.

KARL GRIESBAUM, GILBERT KIESEL, HENRI MERTENS, PETRA KRIEGER-BECK et HENNING HENKE. Can. J. Chem. **72**, 2198 (1994).

Les réactions catalysées par le HCl des hémiperacétals 3-méthoxy-3-méthyl-7-hydroxy-1,2-dioxépane (**1***a*) et 3-méthoxy-3-méthyl-6-hydroxy-1,2-dioxane (**1***b*) et des ozonides apparentés 1-méthyl-6,7,8-trioxabicyclo[3.2.1]octane (**2***a*) et 1-méthyl-5,6,7-trioxabicyclo[2.2.1]heptane (**2***b*) conduisent respectivement aux produits peroxydés monocycliques (**11**–**13**) et bicyclique (**14**) et (ou) tricyclique (**15**). Par opposition, les réactions des peracétals correspondants à **1***a* et **1***b*, les 3-méthyl-3,7-diméthoxy-1,2-dioxépane (**13***a*) et 3-méthyl-3,6-diméthoxy-1,2-dioxane (**13***b*) ne donnent que des produits non peroxydés. Les réactions des peracétals persubstitués 3,6-diméthoxy-3,6-diméthyl-1,2-dioxane (**25**) et 3,6-diméthoxy-3-isopropyl-6-méthyl-1,2-dioxane (**27**) fournissent aussi des produits non peroxydés qui résultent de la fragmentation des squelettes carbonés.

[Traduit par la rédaction]

Introduction

Ozonolyses of a number of unsaturated cyclic compounds in methanol have been reported to give cyclic hemiperacetals (1–4). In line with this, we found that ozonolysis of 1-methylcyclopentene in methanol gave **1***a*, **8***a*, and **11***a* in a molar ratio of 90:8:2 (5). By contrast, ozonolysis of the same substrate in 1 N HCl – methanol gave 9% of a mixture of **5***a* and **6***a*, 75% of **7***a*, and a number of minor by-products (6). The non-peroxidic products **5***a*, **6***a*, and **7***a* were most likely formed via **1***a* as an intermediate, as reaction of isolated **1***a* in 1 N HCl – methanol afforded 8% of **5***a* + **6***a*, and 67% of **7***a* (6). When we followed the latter reaction by ^{1}H nmr spectroscopy and by thin-layer chromatography, we observed that a series of peroxidic intermediates were formed on the way from **1***a* to **5***a*, **6***a*, and **7***a*, as evidenced by the transient appearance of ^{1}H nmr signals and of spots of peroxidic compounds in the chromatograms. In an attempt to identify such intermediates, we have now treated **1***a* and, based on the questions raised by the ensuing results, the related peroxidic compounds **2***a*, **1***b*, **2***b*, **13**a, **13***b*, **25**, and **27** under less acidic conditions in the presence and absence of methanol.

Results and discussion

Reactions of cyclic hemiperacetals **1**a, **1**b, *and of ozonides* **2**a, **2**b

Reaction of **1***a* with HCl–methanol at room temperature gave **2***a*, **5***a*, **7***a*, **8***a*, **11***a*, **12***a*, and **13***a* in the proportions reported in Table 1. By chromatographic separation we have isolated **2***a*, a mixture consisting of **5***a*, **7***a*, **8***a*, *cis*-**11***a*, and *trans*-**11***a*, and the individual compounds *cis*-**12***a*, *trans*-**12***a*, *cis*-**13***a*, and *trans*-**13***a*. The structures of the known compounds **2***a* (7), **5***a* (6), **7***a* (6), **8***a* (5), *cis*-**11***a* (5), and *trans*-**11***a* (5) were assigned based on the identity of their ^{1}H nmr data with those of authentic samples. The structures of the hitherto unknown peroxidic products *cis*-**12***a*, *trans*-**12***a*, and *cis*-**13***a* and *trans*-**13***a*[2] have been assigned based on their ^{1}H nmr and mass spectra and by reductions with triphenylphosphine to give **6***a*, or **5***a* after further treatment of **6***a* with HCl–methanol. The stereochemical assignments of the isomers of **12***a* and of **13***a* are based on the assumption that the *cis*-isomers exhibit higher chromatographic R_f values. Additional evidence for the structure of **12***a* was accrued from the following facts: reduction of **12***a* with dimethyl sulfide gave 2 molar equivalents of dimethyl sulfoxide, and the ^{1}H nmr signals for the CH_3(C) groups of *cis*-**12***a* and of *trans*-**12***a* appeared 0.15 ppm downfield from those of *cis*- and *trans*-**13***a*, whereas the CH signals for **12***a* and for **13***a* had nearly the same chemical shift values. This indicates that the CH_3O group in **12***a* is attached to the CH moiety and, hence, the a priori also conceivable, isomeric structure of 7-hydroperoxy-3-methoxy-3-methyl-1,2-dioxepane is ruled out. A particular feature of peroxide **13***a* is the fact that it is not reduced by dimethyl sulfide at room temperature within 24 h.

For the acid-catalyzed conversion of **1***a* to give the products listed in Table 1, there are apparently three initial steps, viz. (*i*) loss of OCH_3 followed by ring closure with OH to give ozonide **2***a*, (*ii*) exchange of OH for OCH_3 to give **13***a*, and (*iii*) acid-catalyzed ring opening of **1***a* to give **3***a*, which, in turn, undergoes the following sequence of subsequent reactions: hydrolysis of **3***a* to give **6***a*, addition of the coproduced hydrogen peroxide

[1]Author to whom correspondence may be addressed.

[2]Compound **13***a* had been reported previously, but the isomers were not separated (8).

Can. J. Chem. Downloaded from www.nrcresearchpress.com by 85.192.166.187 on 09/08/12
For personal use only.

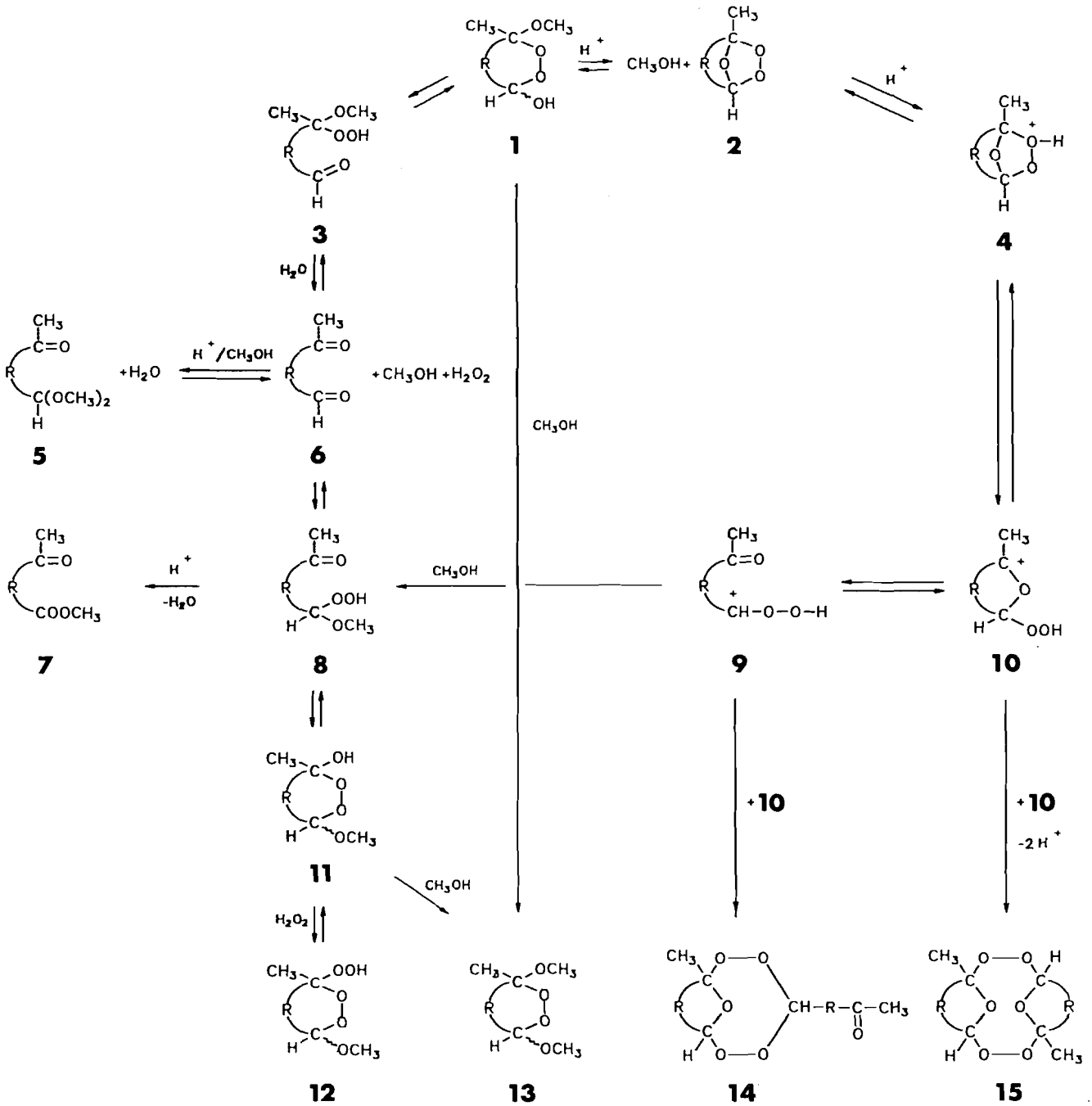

SCHEME 1

and methanol to the aldehyde group of **6***a* to give **8***a*, cyclization of **8***a* to give **11***a*, and reaction of **11***a* with hydrogen peroxide or with methanol to give **12***a* and **13***a*, respectively.

The low yield in the acid-catalyzed conversion of **1***a* into ozonide **2***a* is presumed to be due to the instability of **2***a* in HCl–methanol. Indeed, **2***a* underwent a fast reaction in HCl–methanol at room temperature to give the same products in similar proportions as were obtained starting from **1***a* (Table 1). This can be rationalized by acid-catalyzed cleavage of the C—O bond of the ether bridge in **2***a* to give **1***a* or by sequential cleavage of the C—O bond of the peroxide bridge, and of the ether bridge in **2***a* to give **8***a* via **4***a*, **10***a*, and **9***a*.

In line with the reasoning that the presence of methanol lowers the yield of ozonide **2***a* obtained from **1***a*, the reaction of **1***a* in HCl–$CDCl_3$, i.e., in the absence of added methanol, gave a higher yield (16%) of **2***a* than the reaction in HCl–methanol (1%). Additional products from the reaction of **1***a*, in HCl–$CDCl_3$ were 23% of **12***a*, 24% of **13***a*, 5% of **14***a*, and 5% of **15***a*. The formation of **14***a* and of **15***a* is explained by considering **2***a* as the key intermediate. In agreement with this, reaction of **2***a* in HCl–$CDCl_3$ gave **14***a* and **15***a* as the major products, albeit at low conversion of **2***a*.

The structure of **14***a* has been confirmed by comparison of the ^{13}C nmr data obtained from our material with those from an

Can. J. Chem. Downloaded from www.nrcresearchpress.com by 85.192.166.187 on 09/08/12
For personal use only.

TABLE 1. Products from the reactions of **1***a*, **1***b*, **2***a*, and **2***b* in HCl–methanol

Substrate	Reaction time (h)	Product distribution (mol%) 2	5	7	8 + 11	12	13	15
1*a*	1	1	18	17	12	14	38	—
2*a*	2	2	22	11	17	17	31	—
1*b*	5	—	12	—	6	—	60	22
2*b*	30	—	24	—	13	—	38	10[a]

[a]In addition, ca. 15% of **1***b* was present in the product mixture.

authentic sample (9). The structural assignment of **15***a* is based on its ^{1}H nmr and mass spectral data and, as well, on single-crystal X-ray diffraction. The latter analysis demonstrates that the centrosymmetric molecule **15***a* is closely related to a C_{16} fragment of the diamond structure (Fig. 1). In analogy with a variety of cyclodecane derivatives, in which some of the hydrogen atoms are very close (10), the increased angle of 119.2° at the ether bridge and especially the torsional angle of the C-O-O-C unit of 158.4° instead of 180° as in diamond, are attributed to repulsive interactions between the oxygen lone pairs. This view is supported by the fact that, in the carbocyclic rings, precisely those CH_2 groups are involved in short transannular contacts that in **15***a* are replaced by oxygen atoms, and therefore it is not surprising that the results of minimum-energy calculations for 10-membered cycloalkanes (10, 11) compare well with the observed angle pattern of **15***a* (see Table 3). The O—O distance of 1.476 Å for the peroxide bond is the expected length (12, 13).

For the formation of **14***a* and of **15***a* we assume a common path from **2***a* via **4***a* to **10***a*, and from thereon the separate routes **10***a* → **9***a* → **14***a* and **10***a* → **15***a*. The essential features of this reaction course are similar to those proposed for the $SbCl_5$- or $ClSO_3H$-catalyzed reaction of **2***a*, which gave **14***a* but not **15***a* (9). There is, however, precedence for the formation of other dimeric ozonides of type **15**, though only starting from monomeric ozonides that are unsaturated in the ozonide ring. Hence, such educts are more reactive (15, 16).

Reaction of **1***b* with HCl–methanol at room temperature gave **5***b*, **8***b*, **11***b*, **13***b*, and **15***b*, yet no detectable amounts of **2***b*, **12***b*, and **14***b* (Table 1). Reaction of **2***b* with HCl-methanol gave the same products and, in addition, **1***b* (Table 1). Similar results were obtained when **1***b* was treated with *p*-toluenesulfonic acid in $CDCl_3$. From the crude product of the latter reaction, a mixture of **8***b*, *cis*-**11***b*, and *trans*-**11***b*, a mixture of *cis*-**13***b* and *trans*-**13***b*, and pure **15***b* were isolated. For the formation of these products we assume the pertinent reaction paths outlined in Scheme 1.

The structures of the previously known compounds **5***b* (17), **6***b* (5), **7***b* (18), **8***b* (5), *cis*-**11***b* (5), and *trans*-**11***b* (5) were assigned based on the identity of their ^{1}H nmr data, and in the case of **5***b*, **6***b*, and **7***b* also of their gc retention times, with those of authentic samples prepared according to literature procedures. The structures of the hitherto unknown peroxidic products *cis*-**13***b*, *trans*-**13***b*, and **15***b* were assigned based on the identity of their ^{1}H nmr data with those of independently prepared authentic samples. *cis*- and *trans*-**13***b* were prepared by the previously reported ozonolysis of 5-hexene-2-one in methanol (5), followed by acid treatment of the crude ozonolysis product. The stereochemical assignments of *cis*-**13***b* and of *trans*-**13***b* are based on the assumption that the *cis*-isomer has the higher gc retention time.

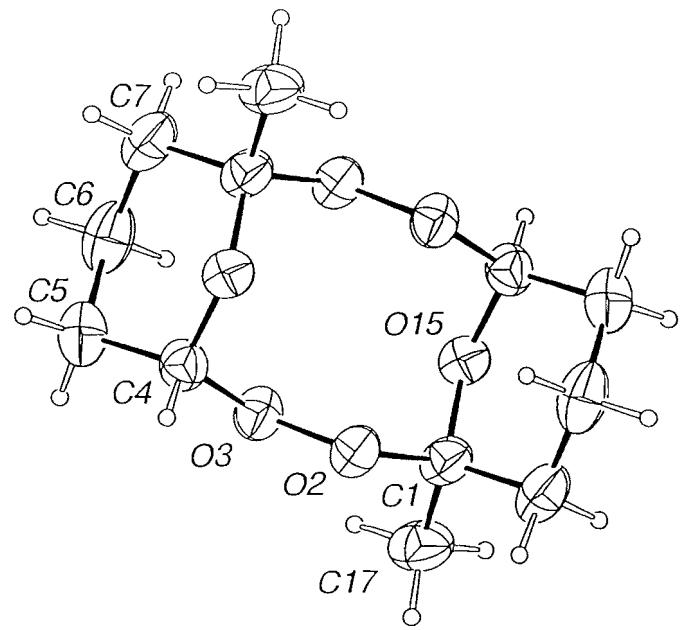

FIG. 1. ORTEP view (14) of the centrosymmetric molecule of **15***a* as found in the crystal. All thermal ellipsoids are drawn at the 50% probability density level. Hydrogen atoms are represented as open circles of arbitrary size.

*Reactions of cyclic peracetals 13*a, *13*b, *25, and 27*

Reactions of **13***a* and of **13***b* with anhydrous HCl in $CDCl_3$ differed considerably from those of the corresponding hemiperacetals **1***a* and **1***b* in two ways: they occurred quickly, within minutes even at 0°C, and they afforded exclusively non-peroxidic products. Reaction of **13***a* with HCl gave **7***a*, **19**, and **20** in relative proportions of 53:25:22, along with methanol and minute amounts of methyl acetate and methyl formate. This result can be rationalized by protonation of the peroxide bond in **13***a* to give **16***A* and **16***B*. Opening of C—O bond of the peroxide moiety in **16***A* provides **17**, which reacts further with water to give hydroperoxide **8***a*, in line with reported acid-catalyzed hydrolysis reactions of peracetals (19). Finally, acid-catalyzed dehydration of **8***a* yields **7***a*. Opening of the C—O bond of the peroxide moiety in **16***B* provides **18**, which reacts further with water to give methanol, H_2O_2, and **6***a*. Intramolecular aldol condensation (20) of **6***a* provides **19**, which by addition of HCl gives **20**. Since steps **8***a* → **7***a* and **6***a* → **19** result in the coproduction of water, adventitious amounts of water at the outset of the reaction are sufficient to effect these reaction sequences.

Reaction of **13***b* with anhydrous HCl gave **7***b* and **24** in relative proportions of 59:41, along with methyl formate and methanol. For the formation of these products we assume **21** as the

Can. J. Chem. Downloaded from www.nrcresearchpress.com by 85.192.166.187 on 09/08/12
For personal use only.

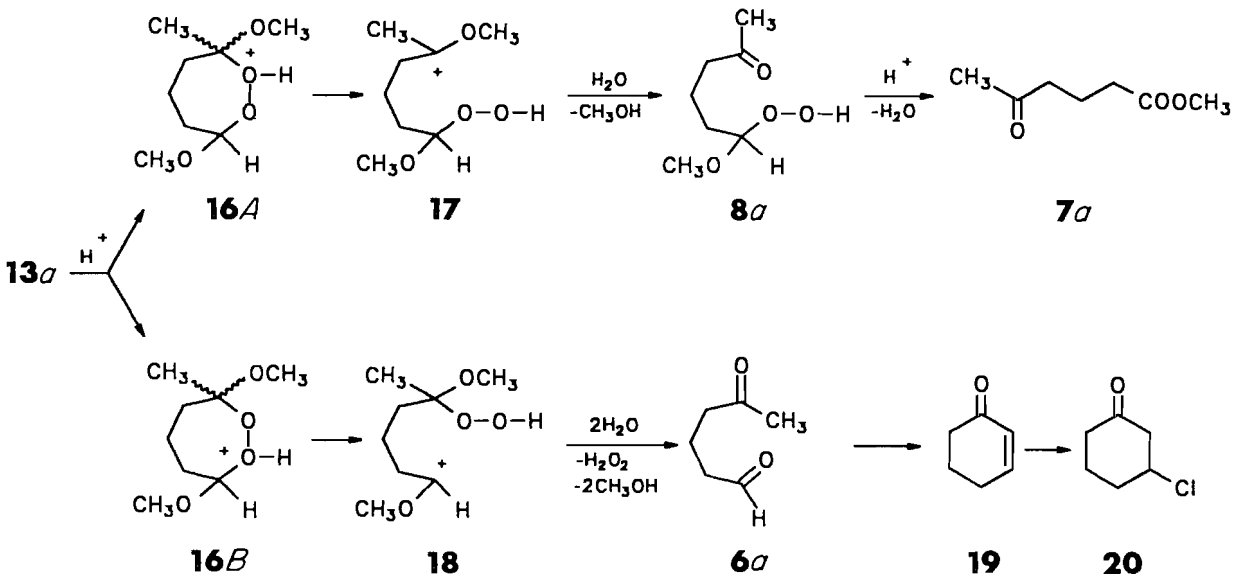

SCHEME 2

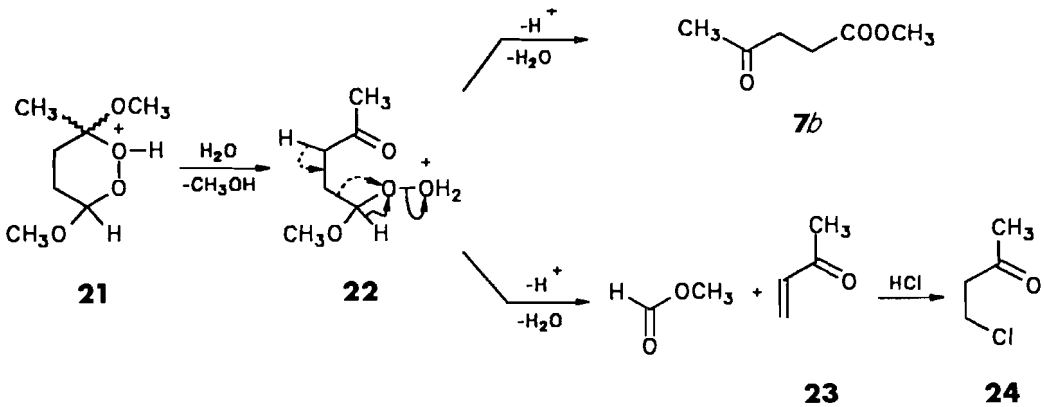

SCHEME 3

central intermediate, which gives **22** by rupture of the C—O bond and subsequent reaction of the ensuing carbenium ion with water, followed by loss of methanol. Fragmentation of **22** in the sense indicated by the solid arrows affords **7*b***, whereas fragmentation of **22** in the sense of the dotted arrows yields methyl formate and **23**, which in turn reacts with HCl to give **24**. The latter fragmentation step of **22** is probably favored by the fact that the ensuing double bond is in conjugation to the carbonyl group in **23**. This reasoning would explain why no fragmentation product was observed in the acid catalyzed reaction of the homologous peracetal **13*a***, since the expected unsaturated ketone would not be conjugated.

The fact that fragmentation of **13*b*** occurred only in one direction, viz., by elimination of methyl formate yet not by elimination of methyl acetate, raised the question whether 3,6-dialkyl-substituted 3,6-dimethoxy-1,2-dioxanes do not undergo HCl-catalyzed fragmentations. To examine this, we treated **25** and **27** with anhydrous HCl in $CDCl_3$ at 0°C. In both cases a rapid reaction, which was terminated within a few minutes, occurred. From **25** we obtained **26** and **24** in a molar ratio of 1:1, along with methanol. From **27** we obtained **24** and **29** in a molar ratio of ca. 1:7, along with **26**, **28**, and methanol. This shows that 3,6-dialkyl-substituted 3,6-dimethoxy-1,2-dioxanes undergo fragmentation as the single major HCl-catalyzed reaction, as opposed to the monoalkyl-substituted 3,6-dimethoxy-1,2-dioxane **13*b***, which underwent fragmentation and γ-keto-ester formation in a ratio of ca. 2:3.

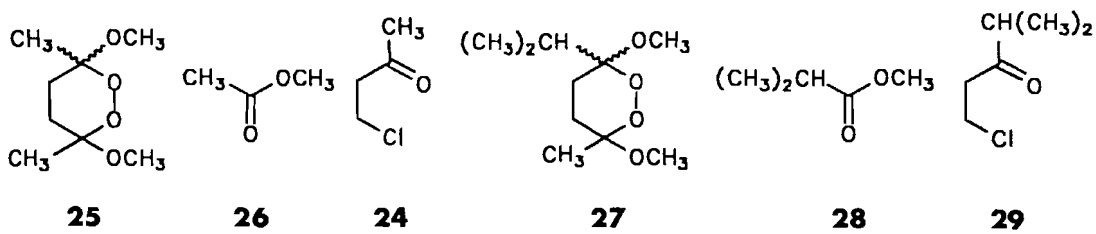

Can. J. Chem. Downloaded from www.nrcresearchpress.com by 85.192.166.187 on 09/08/12
For personal use only.

Can. J. Chem. Downloaded from www.nrcresearchpress.com by 85.192.166.187 on 09/08/12
For personal use only.

Experimental section

*Reaction of **1**a in HCl–methanol*

A solution of 1.50 g (9.3 mmol) of **1***a* (5) in 5.0 mL of 0.35 N HCl – methanol was stirred at room temperature for 1 h, neutralized with solid $NaHCO_3$, and concentrated by evaporation of ca. 3 mL of methanol at room temperature and 15 Torr. (1 Torr = 133.3 Pa) Flash chromatography (21) (column 2.2 × 136 cm, 226 g of silica gel; pentane: diethyl ether, 7:3 (1 L), 1:1 (0.5 L), then pentane) of the liquid residue (3.70 g) gave 2 mg (<1%) of **2***a*, 400 mg of a mixture of **5***a*, **7***a*, **8***a*, *cis*-**11***a*, and *trans*-**11***a*, 40 mg (2%) of *cis*-**12***a*, 90 mg (5%) of *trans*-**12***a*, 180 mg (11%) of *cis*-**13***a*, and 180 mg (11%) of *trans*-**13***a*.

*Reaction of **2**a in HCl–methanol*

In a similar manner, a solution of 1.0 g (7.7 mmol) of **2***a* (7) in 10.0 mL of 0.35 N HCl – methanol was stirred at room temperature for 2 h, neutralized, and concentrated by removal of ca. 6 mL of methanol. Flash chromatography (conditions as above) of the liquid residue (4.80 g) gave 305 mg (25%) of a mixture of **5***a* and **7***a*, 190 mg (15%) of a mixture of **8***a*, *cis*-**11***a*, and *trans*-**11***a*, 75 mg (5%) of *cis*-**12***a*, 97 mg (7%) of *trans*-**12***a*, 95 mg (7%) of *cis*-**13***a*, and 105 mg (8%) of *trans*-**13***a*.

*1-Methyl-6,7,8-trioxabicyclo[3.2.1]octane (**2**a):* ^{1}H nmr ($CDCl_3$, TMS) δ: 1.51 (s, 3 H), 1.60–1.97 (m, 6H), 5.78 (s, 1 H); ^{13}C nmr ($CDCl_3$, TMS) δ: 15.88, 21.12, 29.03, 33.72, 103.10, 107.97.

*1,1-Dimethoxy-5-oxo-hexane (**5**a):* ^{1}H nmr ($CDCl_3$, TMS) δ: 1.46–1.73 (m, 4H), 2.14 (s, 3H), 2.33–2.60 (m, 2H), 3.32 (s, 6H), 4.36 (m, 1H); ^{13}C nmr ($CDCl_3$, TMS) δ: 18.20, 29.32, 31.33, 42.65, 52.20, 104.94, 208.20.

*Methyl-5-oxo-hexanoate (**7**a):* ^{1}H nmr ($CDCl_3$, TMS) δ: 1.76–2.00 (m, 2H), 2.14 (s, 3H), 2.24–2.51 (m, 4H), 3.67 (s, 3H).

*1-Hydroperoxy-1-methoxy-5-oxo-hexane (**8**a) (5):* ^{1}H nmr ($CDCl_3$, TMS) δ: 1.51–1.78 (m, 4H), 2.15 (s, 3H), 2.35–2.65 (m, 2H), 3.50 (s, 3H), 4.53–5.85 (m, 1H), 8.78 (s, 1H).

cis- *and* trans-*7-Methoxy-3-methyl-1,2-dioxepane-3-ol (**11**a):* ^{1}H nmr ($CDCl_3$, TMS) δ: 1.37 (s, 3H), 1.39 (s, 3H), 3.48 (s, 3H), 3.53 (s, 3H), 4.70 (m, 2H).

cis-*3-Hydroperoxy-3-methyl-7-methoxy-1,2-dioxepane* (cis-***12**a*): colorless liquid; ^{1}H nmr ($CDCl_3$, TMS) δ: 1.44 (s, 3H), 1.50–2.13 (m, 6H), 3.49 (s, 3H), 4.80 (t, J = 5.8 Hz, 1H), 8.19 (s, 1H); Cl-MS *m/e* (%): 179 (5) $[M + 1]^+$, 145 (18) $[M - OOH]^+$, 113 (50) $[M - OOH - CH_3OH]^+$, 85 (100) $[C_5H_9O]^+$. Anal. calcd. for $C_7H_{14}O_5$: C 47.19, H 7.92; found: C47.36, H 7.77.

trans-*3-Hydroperoxy-3-methyl-7-methoxy-1,2-dioxepane* (trans-***12**a*): colorless solid, mp 67°C (dec.); ^{1}H nmr ($CDCl_3$, TMS) δ: 1.42 (s, 3H), 1.42–2.06 (m, 6H), 3.54 (s, 3H), 4.87–4.91 (dd, J = 2.8 Hz, 1H), 8.40 (s, 1H); Cl-MS *m/e* (%): 179 (5) $[M + 1]^+$, 145 (4) $[M - OOH]^+$, 113 (11) $[M - OOH - CH_3OH]^+$, 85 (100) $[C_5H_9O]^+$. Anal. calcd. for $C_7H_{14}O_5$: C 47.19, H 7.92; found: C 47.38, H 7.92.

*Reductions of compounds **12**a with DMS*

Solutions containing 15 mg (0.084 mmol) of *cis*-**12***a* or of *trans*-**12***a* in 0.3 mL of $CDCl_3$ were admixed with 0.168 mmol of dimethyl sulfide and kept at room temperature. After 20 min, ^{1}H nmr analysis showed the signals of **8***a* (δ 2.15), of *cis*-**11***a* (δ 3.48), and of *trans*-**11***a* (δ 3.53). After several days, small samples were removed, concentrated by evaporation, and analyzed by glc (50-m capillary column, 5% phenylmethyl silicone SE 54, 50–180°C at 7°C/min) to show **6***a* (t_R: 9.06 min) as the major product. Then, the remaining major parts of the reaction mixtures were treated with 1 N HCl – methanol at room temperature for several hours, neutralized with solid $NaHCO_3$, and concentrated by evaporation. Analysis of the residue by ^{1}H nmr showed the presence of **5***a* (δ: 1.46 – 173 (m, 4H), 2.14 (s, 3H), 2.33 – 2.60 (m, 2H), 3.32 (s, 6H), 4.36 (m, 1H) and of dimethyl sulfoxide (δ: 2.62 (s, 6H) in a molar ratio of 1:2.

cis-*3-Methyl-3,7-dimethoxy-1,2-dioxepane* (cis-***13**a*): colorless liquid; ^{1}H nmr ($CDCl_3$, TMS) δ: 1.29 (s, 3H) 1.40–2.07 (m, 6H), 3.38 (s, 3H), 3.48 (s, 3H), 4.77 (t, J = 5.2 Hz, 1H); ^{13}C nmr ($CDCl_3$, TMS) δ: 18.35, 20.15, 33.82, 40.29, 49.10, 55.32, 106.95, 107.22; Cl-MS *m/e* (%): 176 (52) $[M]^+$, 145 (72) $[M - OCH_3]^+$, 101 (84) $[M - HCOOCH_3 - CH_3]^+$, 85 (100) $[M - HCOOCH_3 - OCH_3]^+$. Anal. calcd. for $C_8H_{16}O_4$: C 54.53, H 9.15; found: C 54.37, H 8.98.

trans-*3-Methyl-3,7-dimethoxy-1,2-dioxepane* (trans-***13**a*): colorless liquid; ^{1}H nmr ($CDCl_3$, TMS) δ: 1.27 (s, 3H), 1.36–2.10 (m, 6H), 3.36 (s, 3H), 3.53 (s, 3H), 4.84 (t, J = 3.3 Hz, 1H); ^{13}C nmr ($CDCl_3$, TMS) δ: 18.56, 19.23, 35.38, 38.48, 48.98, 56.96, 107.77, 109.77; Cl-MS *m/e* (%): 176 (23) $[M]^+$, 145 (27) $[M - OCH_3]^+$, 101 (49) $[M - HCOOCH_3 - CH_3]^+$, 85 (100) $[M - HCOOCH_3 - OCH_3]^+$. Anal. calcd. for $C_8H_{16}O_4$: C 54.53, H 9.15; found: C 54.38, H 8.95.

*Reductions of compounds **13**a with triphenylphosphine*

Solutions containing 8.8 mg of *cis*-**13***a* and 24.6 mg of *trans*-**13***a*, respectively, in ca. 0.4 mL of $CDCl_3$ were admixed with 1.5 molar equivalents of triphenylphosphine and with 5 molar equivalents of CH_3OD and kept at room temperature for 22 h. Analysis by ^{1}H nmr showed the presence of **5***a*, which was formed in yields of 85 and 96%, respectively, as determined with the help of 1,1,2,2-tetrachloroethane as internal standard.

*Reactions of **1**a in HCl–$CDCl_3$*

A solution of 0.20 g (1.23 mmol) of **1***a* in 4 mL of $CDCl_3$ was admixed with one drop of $CDCl_3$, which was saturated with gaseous HCl, and the mixture was stirred for 24 h at room temperature in a sealed flask. The mixture was neutralized with solid $NaHCO_3$, the solvent was removed by vacuum evaporation at room temperature, and the residue was separated by flash chromatography (column 2 × 60 cm, 85 g of silica gel; pentane:diethyl ether, 2:1) to give 25 mg (16%) of **2***a*, 50 mg (23%) of *cis*-**12***a* and *trans*-**12***a*, 45 mg (24%) of a mixture containing **2***a*, *cis*-**13***a*, and *trans*-**13***a*, 8 mg (5%) of **14***a*, and 8 mg (5%) of **15***a*.

*1-Methyl-2,3,5,6,11-pentaoxa-4-(4-oxopentyl)-bicyclo[5.3.1]undecane (**14**a):* ^{13}C nmr ($CDCl_3$, TMS) δ: 14.09, 19.10, 24.74, 25.32, 28.01, 29.82, 31.05, 42.93, 98.00, 102.19, 108.85, 207.71.

*1,8-Dimethyl-2,3,9,10,15,16-hexaoxatricyclo[9.3.1.1^{4,8}]hexadecane (**15**a):* colorless solid, mp 181°C (dec.); ^{1}H nmr ($CDCl_3$, TMS) δ: 1.50 (s, 6H), 1.59–2.09 (m, 12 H), 5.25–5.37 (m, 2H); Cl-MS *m/e* (%): 261 (92) $[M + 1]^+$. Anal. calcd. for $C_{12}H_{20}O_6$: C 55.37, H 7.75; found: C 55.53, H 8.08.

*Reduction of **15**a with DMS*

A solution of **15**a and excess DMS in $CDCl_3$ was kept at room temperature for 1 week. Analysis by ^{1}H nmr showed that no reaction had occurred. Upon addition of trace amounts of water, however, reduction occurred, and ^{1}H nmr analysis after 10 h showed the presence of ca. 30% of **6**a.

*Reaction of **2**a in HCl–$CDCl_3$*

A solution of 90 mg (0.7 mmol) of **2***a* in 4 mL of $CDCl_3$ was treated for 4 days as described above for **1***a*. Separation of the residue by flash chromatography (column 1.5 × 30 cm, 20 g of silica gel, pentane:diethyl ether, 1.5:1) gave 40 mg (44%) of recovered **2***a*, 30 mg (18%) of **14***a*, and 13 mg (7%) of **15***a*.

*Reaction of **1**b in HCl–methanol*

A solution of 32 mg (0.21 mmol) of **1**b (5) in 0.3 mL of $CDCl_3$ was admixed with 3 mL of 0.35 N HCl – methanol and left at room temperature for 5 h. Analysis by ^{1}H nmr showed the presence of **5**b, **8**b, **11**b, **13**b, and **15**b in the proportions reported in Table 1.

*Reaction of **2**b in HCl–methanol*

A solution of 13.8 mg (0.12 mmol) of **2***b* (5), 0.3 mL of $CDCl_3$, and 0.3 mL of 0.3 N HCl – methanol was stirred at room temperature for 30 h. Analysis by ^{1}H nmr showed the presence of **5***b*, **8***b*, **11***b*, **13***b*, **15***b* in the proportions reported in Table 1, and also ca. 15% of **1***b*.

*Reaction of **1**b in p-toluenesulfonic acid $CDCl_3$–methanol*

A solution consisting of 300 mg (2.0 mmol) of **1***b* (5), 1 mg of *p*-tol-

Can. J. Chem. Downloaded from www.nrcresearchpress.com by 85.192.166.187 on 09/08/12
For personal use only.

uenesulfonic acid, 3 mL of $CDCl_3$, and 5 μL of methanol was stirred at room temperature for 4 days, neutralized with solid $NaHCO_3$, and concentrated by distillation at room temperature and 15 Torr. Flash chromatography (column 1 × 60 cm, 30 g silica gel; pentane:diethyl ether, 7:3) of the liquid residue (1.5 mL) gave 30 mg (10%) of a mixture of **8***b*, *cis*-**11***b*, and *trans*-**11***b*, 25 mg (8%) of a mixture of *cis*-**13***b* and *trans*-**13***b*, and 37 mg (16%) of **15***b*.

Independent preparation of cis-***13***b *and* trans-***13***b

A solution of 3.2 g (32.6 mmol) of 5-hexene-2-one in 20 mL of methanol was ozonized to exhaustion at –75°C. The cold solution was purged with nitrogen, admixed with ca. 50 mg of *p*-toluenesulfonic acid, and stirred for 24 h at room temperature. It was neutralized with solid $NaHCO_3$ and evaporated at room temperature and 15 Torr. Flash chromatography (column 2.2 × 140 cm, 226 g of silica gel; pentane:diethyl ether, 6:1) of the residue (6.2 g) gave 1.30 g (25%) of a mixture of *cis*-**13***b* and *trans*-**13***b*, and 138 mg (0.2%) of *cis*-**13***b*. From 200 mg of the above mixture of *cis*- and *trans*-**13***b*, 40 mg of *trans*-**13***b* was obtained by hplc separation (column 32 × 120 mm, Li Chrosorb Si-60; pentane:diethyl ether, 6:1).

cis-*3-Methyl-3,6-dimethoxy-1,2-dioxane* (cis-***13***b)*:* colorless liquid; ^{1}H nmr ($CDCl_3$, TMS) δ: 1.31 (s, 3H), 1.52–2.17 (m, 4H), 3.36 (s, 3H), 3.47 (s, 3H), 4.80–4.84 (m, 1H); El-MS *m/e* (%): 162 (0.1) $[M]^+$; gc,t_R: 10.67 min (50-m capillary column SE 54, 50–180°C at 7°C/min). Anal. calcd. for $C_7H_{14}O_4$:C 51.84, H 8.70; found: C 51.83, H 8.59.

trans-*3-Methyl-3,6-dimethoxy-1,2-dioxane* (trans-***13***b)*:* colorless liquid; ^{1}H nmr ($CDCl_3$, TMS) δ: 1.31 (s, 3H), 1.69–2.05 (m, 4H), 3.35 (s, 3H), 3.56 (s, 3H), 4.83–4.87 (m, 1H); gc,t_R: 11.21 min (conditions as above). Anal. calcd. for $C_7H_{14}O_6$: C 51.84, H 8.70; found: C 51.91; H 8.58.

Independent preparation of ***15***b

A solution of 2.94 g of natural rubber in a mixture of 70 mL of tetrachloromethane, 130 mL of pentane, and 11 mL of methanol was prepared, ozonized, and worked up as described previously (5). Of the remaining residue, 2.0 g was dissolved in 15 mL of trichloromethane, admixed with a solution of 50 mg of *p*-toluenesulfonic acid in 50 μL of methanol, and stirred for 7 h at room temperature. The solution was neutralized with solid $NaHCO_3$ and then evaporated at room temperature at 15 Torr. From the residue (3 mL), 200 mg of **15***b* was obtained by flash chromatography (column 2.2 × 120 cm, 220 g of silica gel; pentane:diethyl ether, 2.5:1). It was sublimated at room temperature and 10^{-3} Torr.

*1,7 - Dimethyl - 2,3,8,9,13,14 - hexaoxatricyclo[8.2.1.1^{4,7}]tetradecane (**15**b):* colorless solid, mp 120°C (dec.); ^{1}H nmr ($CDCl_3$, TMS) δ: 1.46 (s, 6H), 1.71–2.72 (m, 8H), 5.50–5.63 (m, 2H); Cl-MS *m/e* (%): 233 (6) $[M + 1]^+$. Anal. calcd. for $C_{10}H_{16}O_6$: C 51.75, H 6.94; found: C 51.78, H 6.87.

Reaction of ***13***a *in HCl–$CDCl_3$*

A solution of 25 mg (0.14 mmol) of **13***a* in 0.8 mL of $CDCl_3$ was flushed with gaseous HCl at 0°C; ^{1}H nmr analysis showed that after 8 min **13***a* was completely consumed. Gas–liquid chromatography and gc–ms analysis (50-m capillary column, 5% phenylmethyl silicone SE 54, 50–180°C at 7°C/min) showed the presence of **7***a* (t_R: 14.34 min; *m/e* 144), **19** (t_R: 10.75 min; *m/e*: 96), and **20** (t_R: 14.27 min; *m/e*: 134, 132) in relative proportions of 53:25:22, along with 5% of methanol (t_R: 5.71 min), 2% of methyl acetate (t_R: 7.16 min), and 1% of methyl formate (t_R: 5.98 min). The mixture was neutralized with solid $NaHCO_3$ and separated by flash chromatography (column 1.5 × 30 cm, 15 g silica gel; pentane:diethyl ether, 3:2 (300 mL), diethyl ether) to give 7 mg (29%) of **7***a*, 4 mg (14%) of **19**, and 3 mg (12%) of **20**.

*5-Oxo-methylhexanoate (**7**a):* ^{1}H nmr ($CDCl_3$, TMS) δ: 1.89 (quint., J = 7.1 Hz, 2H), 2.15 (s, 3H), 2.35 (t, J = 7.1 Hz, 2H), 2.52 (t, J = 7.1 Hz, 2H), 3.68 (s, 3H).

*Cyclohexene-3-one (**19**):* ^{1}H nmr ($CDCl_3$, TMS) δ: 1.97–2.08 (m, 2H), 2.33–2.46 (m, 4H), 6.01 (dt, J = 10.0 and 2.0 Hz, 1H), 6.98–7.05 (m, 1H).

*3-Chlorocyclohexanone (**20**):* ^{1}H nmr ($CDCl_3$, TMS) δ: 1.72–1.91 (m, 1H), 2.02–2.12 (m, 1H), 2.17–2.32 (m, 2H), 2.39–2.48 (m, 2H), 2.59–2.72 (m, 1H), 2.82–2.92 (m, 1H), 4.38–4.48 (m, 1H).

Reaction of ***13***b *in HCl–$CDCl_3$*

A solution of 37 mg (0.23 mmol) of **13***b* in 0.6 mL of $CDCl_3$ was flushed with gaseous HCl at 0°C. Analysis by ^{1}H nmr showed that after 4 min **13***b* was consumed and that **7***b* (δ 3.68, s) and **24** (δ 2.20, s) were present in relative proportions of 59:41, along with methyl formate (δ 8.06) and methanol (δ 3.49). Analysis by glc and gc–ms (column 0.3 × 300 cm, 5% Nitrilesiliconoil on Chromosorb G; 60–160°C at 4°C/min) with the help of authentic samples confirmed the identity of **7***b* (t_R: 20.41 min; *m/e*: 130), of **24** (t_R: 13.63 min; *m/e*: 108, 106), and of the other components.

Reaction of ***25*** *in HCl–$CDCl_3$*

A solution of 73 mg (0.41 mmol) of **25** (22) in 0.8 mL of $CDCl_3$ was flushed with gaseous HCl at 0°C. Analysis by ^{1}H nmr showed that after 2 min **25** was consumed and that **26** (δ 2.06, s) and **24** (δ 2.22, s) were present in a molar ratio of 1:1, along with methanol (δ 3.50, s). Analysis by glc and gc–ms (conditions as above) with the help of authentic samples confirmed the identity of **26** (t_R: 3.31 min; *m/e*: 74), **24** (t_R: 13.59 min; *m/e*: 108, 106), and methanol (δ 3.50, s).

Reaction of ***27*** *in HCl–$CDCl_3$*

A solution of 35 mg (0.17 mmol) of **27** (22) in 0.7 mL of $CDCl_3$ was flushed with gaseous HCl at 0°C. Analysis by ^{1}H nmr showed that after 2 min **27** was consumed and that **24** (δ 2.20, s) and **29** (δ 1.12, d) were present in a molar ratio of 1:7, along with **26** (δ 2.06, s), **28** (δ 1.07, d), and methanol (δ 3.48, s). Analysis by glc and gc–ms (conditions as above) with the help of authentic samples confirmed the identity of **24** (t_R: 13.61 min; *m/e*: 108, 106), **26** (t_R: 3.34 min; *m/e*: 74), **28** (t_R: 4.23 min; *m/e* 102), **29** (t_R: 13.61 min; *m/e*: 136, 134), and methanol.

X-ray structure analysis of ***15***a

Single crystals were grown from n-pentane:ether (65:35) solution. A suitable little block bounded by the faces (011), (100), (01$\bar{1}$) and the corresponding counterfaces, of dimensions 0.50 × 0.56 × 0.70 mm^3, was cut from a larger specimen and enclosed in a glass capillary. Crystal data: $C_{12}H_{20}O_6$, fw = 260.3, monoclinic, $P2_1/c$, a = 6.550(2), b = 10.414(3), c = 9.840(3) Å, β = 108.29(2)° at room temperature, V = 637.3 Å^3, Z = 2, D_{calc} = 1.356 mg mm^{-3}, μ_{lin} = 0.101 mm^{-1} for MoKα radiation.

Data collection was done on a Siemens–Stoe diffractometer equipped with a pyrolytic graphite monochromator; all 3989 reflections *h*, ±k, ±l with 2θ ≤ 60° were measured and finally merged into 1857 independent intensity data. Scan mode: 40 steps with Δω = Δ2θ = 0.03°, extra steps for α_1/α_2 dispersion, background determined from 6 points each at the beginning and at the end of a reflection profile, counting time between 0.5 and 1.5 s per step depending on $I/\sigma(I)$. Three standard reflections were recorded at regular intervals for scaling purposes; the overall loss of intensity was less than 1.3%. Corrections were made for background intensity and Lorentz and polarization effects.

The structure was solved with the aid of MULTAN (23). Parameter refinement with CRYLSQ (24) included anisotropic temperature factors and an isotropic extinction correction (r^* = 1089(9)) according to Larson (25) with individual path lengths calculated from the shape of the crystal. The quantity minimized was $\Sigma w(|F_o| - |F_c|)^2$ with weights *w* derived from counting statistics. All hydrogen atoms appeared in a difference Fourier synthesis (24). Their positions were refined with the thermal *B* values kept at a fixed level. The final $R = \Sigma||F_o| - |F_c||\Sigma|F_o|$ was 0.034 (113 free parameters, full-matrix refinement, 1410 reflections above the significance level of $I > 3\sigma(I)$; R = 0.046 for all 1857 independent reflections). A plot of the molecule is shown in Fig. 1. Distances and angles as

TABLE 2. Fractional crystallographic coordinates for all non-hydrogen atoms of the asymmetric unit of **15***a*. The numbering scheme refers to Fig. 1. Equivalent *B* values (26) as calculated from the anisotropic thermal parameters

Atom	*x*	*y*	*z*	*B* (Å^2)
C(1)	0.318 58(2)	−0.116 32(1)	0.319 51(1)	3.17(1)
O(2)	0.275 24(1)	−0.088 47(1)	0.450 04(1)	3.15(1)
O(3)	0.253 63(1)	0.052 41(1)	0.455 03(1)	3.23(1)
C(4)	0.292 35(2)	0.084 00(1)	0.600 55(1)	3.11(1)
C(5)	0.254 34(2)	0.227 66(1)	0.599 32(1)	4.00(1)
C(6)	0.434 31(2)	0.299 63(1)	0.566 27(1)	4.38(1)
C(7)	0.647 52(2)	0.261 59(1)	0.673 14(1)	4.09(1)
O(15)	0.501 14(1)	−0.048 20(1)	0.309 84(1)	2.93(1)
C(17)	0.134 59(2)	−0.072 89(1)	0.191 02(1)	4.27(1)

TABLE 3. Interatomic distances (Å), valency angles (°), and selected torsional angles (°) of **15***a*. Primes refer to a center of symmetry in $\frac{1}{2}$, 0, $\frac{1}{2}$. Probably the standard deviations calculated by BONDLA (24) are underestimated: distance values ±0.0005 Å, valency angles ±0.02°

C(1)—O(2)	1.429	O(3)—C(4)	1,412
C(1)—C(7′)	1.527	C(4)—C(5)	1.516
C(1)—O(15)	1.419	C(4)—O(15′)	1.413
C(1)—C(17)	1.516	C(5)—C(6)	1.516
O(2)—O(3)	1.476	C(6)—C(7)	1.514
O(2)...O(3′)	2.954		
O(2)...O(2′)	3.349		
O(3)...O(3′)	3.256		
O(2)—C(1)—C(7)	103.0	O(3)—C(4)—C(5)	104.2
O(2)—C(1)—O(15)	111.6	O(3)—C(4)—O(15′)	113.8
O(2)—C(1)—C(17)	111.0	C(5)—C(4)—O(15′)	112.8
C(7)—C(1)—O(15)	112.7	C(4)—C(5)—C(6)	110.7
C(7)—C(1)—C(17)	113.6	C(5)—C(6)—C(7)	109.4
O(15)—C(1)—C(17)	105.1	C(1′)—C(7)—C(6)	112.4
C(1)—O(2)—O(3)	106.2	C(1)—O(15)—C(4)	119.2
O(2)—O(3)—C(4)	106.1		
C(4′)—O(15)—C(1)—O(2)	+70.9		
O(15)—C(1)—O(2)—O(3)	+55.5		
C(1)—O(2)—O(3)—C(4)	−158.4		
O(2)—O(3)—C(4)—O(15′)	+60.3		
O(3)—C(4)—O(15′)—C(1′)	+70.9		

calculated from the atomic coordinates of Table 2 are listed in Table 3.[3]

[3]Tables of anisotropic temperature factors, hydrogen atom coordinates, and interatomic distances and angles involving hydrogen atoms can be purchased from: The Depository of Unpublished Data, Document Delivery, CISTI, National Research Council Canada, Ottawa, ON K1A 0S2, Canada.

Tables of hydrogen atom coordinates, interatomic distances, and angles have also been deposited with the Cambridge Crystallographic Data Centre, and can be obtained on request from The Director, Cambridge Crystallographic Data Centre, University Chemical Laboratory, 12 Union Road, Cambridge, CB2 1EZ, U.K.

Structure factor amplitudes are no longer being deposited and may be obtained directly from the author.

1. R.H. Callighan, M.F. Tarker, and M.H. Wilt. J. Org. Chem. **26**, 1379 (1961).
2. J.E. Franz, W.S. Knowles, and C. Osuch. J. Org. Chem. **30**, 4328 (1965).
3. S. Fliszár, C. Belzecki, and J.B. Chylinska. Can. J. Chem. **45**, 221 (1967).
4. K. Schank and S. Moschel. Phosphorus, Sulfur Silicon Relat. Elem. **74**, 419 (1993).
5. K. Griesbaum and G. Kiesel. Chem. Ber. **122**, 145 (1989).
6. K. Griesbaum and G. Kiesel. Erdöl Kohle, Erdgas, Petrochem. **42**, 19 (1989).
7. R. Criegee, G. Blust, and G. Lohaus. Liebigs Ann. Chem. **583**, 2 (1953).
8. M. Miura, M. Nojima, and S.J. Kusabayashi. J. Chem. Soc. Perkin Trans. 1, 2909 (1980).
9. M. Miura and M. Nojima. J. Am. Chem. Soc. **102**, 288 (1980).
10. O. Ermer, J.D. Dunitz, and I. Bernal. I. Acta Crystallogr. Sect. B: Struct. Crystallogr. Cryst. Chem. **B29**, 2278 (1973).
11. J. Dale. Acta Chem. Scand. **27**, 1115 (1973).
12. H. Henke and H. Keul. Cryst. Struct. Commun. **4**, 451 (1975).
13. K. Griesbaum, P. Krieger-Beck, and J. Beck. Chem. Ber. **124**, 391 (1991).
14. C.A. Johnson. ORTEP-II. A Fortran thermal-ellipsoid plot program for crystal structure illustrations. ORNL-3794. 2nd rev. with supplemental instructions, Oak Ridge National Laboratory, Oak Ridge, Tenn.
15. G. Rio and M.J. Rio. J. Chem. Soc. Chem. Commun. 72 (1982).
16. K. Gollnick and A. Griesbeck. Angew. Chem. **95**, 751 (1983); Angew. Chem. Int. Ed. Engl. **22**, 726 (1983).
17. D.S.P. Eftax and A.P. Dunlop. J. Org. Chem. **30**, 1317 (1965).
18. L.F. Tietze and T. Eicher. Reaktionen und Synthesen. Georg Thieme Verlag, Stuttgart. 1981. p. 114.
19. P. Dussault and A. Sahli. J. Org. Chem. **57**, 1009 (1992).
20. C. Chapuis, R. Brauchli, and W. Thommen. Helv. Chim. Acta, **76**, 535 (1993).
21. W.C. Still, M. Kahn, and A. Mitra. J. Org. Chem. **43**, 2923 (1978).
22. K. Griesbaum, H. Mertens, and I.C. Jung. Can. J. Chem. **68**, 1369 (1990).
23. P. Main, S.J. Fiske, S.E. Hull, L. Lessinger, G. Germain, J.-P. Declercq, and M.M. Woolfson. MULTAN 80. A system for computer programs for the automatic solution of crystal structures from X-ray diffraction Data. University of York, England.
24. J.M. Stewart, P.A. Machin, C. Dickinson, H.L. Ammon, H. Heck, and H. Flack. The XRAY system. Techn. Report TR-446, Computer Science Center, University of Maryland, College Park, Md. 1976.
25. A.C. Larson. Crystallographic computing. Munksgaard, Kopenhagen. 1970. p. 291.
26. W.C. Hamilton. Acta Crystallogr. **12**, 609 (1959).

Can. J. Chem. Downloaded from www.nrcresearchpress.com by 85.192.166.187 on 09/08/12
For personal use only.

An energy-resolved study of the fragmentation reactions of alkyl ammonium ions[1]

NANCY L. BOSMA AND ALEX. G. HARRISON[2]

Department of Chemistry, University of Toronto, Toronto, ON M5S 1A1, Canada

Received May 31, 1994

NANCY L. BOSMA and ALEX. G. HARRISON. Can. J. Chem. **72**, 2205 (1994).

The unimolecular metastable ion and low-energy collision-induced fragmentation reactions of alkyl ammonium ions $R_nH_{4-n}N^+$ ($n = 2$ to 4, R = n-C_3H_7 and n-C_4H_9) have been studied and breakdown graphs expressing the % fragment ion abundances as a function of the centre-of-mass collision energy have been established. The dialkyl and trialkyl ammonium ions fragment primarily by olefin ([R − H]) elimination or by formation of the alkyl ion R^+ (with rearrangement to the more stable secondary structure). By contrast the tetraalkyl ammonium ions show both elimination of [R − H] and elimination of an alkane, which is C_5H_{12} for the propyl compound C_7H_{16} for the butyl compound. The results are interpreted in terms of competition between heterolytic bond cleavage to form a $[R^+{---}NH_{4-n}R_{n-1}]$ complex and homolytic bond cleavage to form a $[R_{n-1}H_{4-n}N^{+\cdot}{---}{}^{\cdot}R]$ complex. The former complex fragments either to form R^+ or undergoes internal proton transfer to form $R_{n-1}H_{4-n}NH^+ + [R - H]$, while the latter complex fragments by alkane elimination resulting from attack of R˙ on the α-CC bond of the alkyl group. For the propyl ammonium ions plausible potential energy profiles are established which show that the former complex is favoured for $n = 2$, 3 while the two complexes have similar energies for $n = 4$.

NANCY L. BOSMA et ALEX. G. HARRISON. Can. J. Chem. **72**, 2205 (1994).

On a étudié l'ion unimoléculaire métastable et les réactions de fragmentation induites par des collisions de base énergie des ions alkylammonium $R^nH_{4-n}N^+$ ($n = 2$ à 4, R = n-C_3H_7 et n-C_4H_9) et on a déterminé les graphiques de bris en pourcentage des abondances ioniques des fragments en fonction de l'énergie de collision du centre de masse. Les ions ammonium di- et tri-alkylés se fragmentent principalement par l'élimination d'une oléfine [R − H] ou par la formation de l'ion alkyle R^+ (avec une transposition vers la structure secondaire qui est plus stable). Par ailleurs, les ions ammonium tétraalkylés donnent aussi bien l'élimination d'un alcéne [R − H] que celle d'un alcane qui est le C_5H_{12} pour le composé propylé et C_7H_{16} pour le composé butylé. On interprète les résultats en fonction d'une compétition entre des bris hétérolytique (conduisant à un complexe $[R^+{---}NH_{4-n}R_{n-1}]$) et homolytique (conduisant à un complexe $[R_{n-1}H_{4-n}N^{+\cdot}{---}{}^{\cdot}R]$). Le premier complexe se fragmente soit pour former du R^+ ou pour subir un transfer interne de proton conduisant à $R_{n-1}.H_{4-n}NH^+ + [R - H]$, alors que le dernier se fragmente par une élimination d'alcane provenant d'une attaque de R˙ sur la liaison α-CC du groupe alkyle. Pour les ions ammonium, on a déterminé les profils plausible d'énergie potentielle et ils démontrent que le premier complexe est favorisé pour $n = 2$ et 3 alors que les deux complexes ont des énergies semblables lorsque $n = 4$.

[Traduit par la rédaction]

Introduction

The low energy fragmentation reactions of simple protonated alkyl amines ($R_1(R_2)_2NH^+$, R_2 = H or CH_3), prepared by Brønsted acid chemical ionization, have been extensively studied in this laboratory (1, 2). When the alkyl group R_1 is propyl or larger, the dominant fragmentation reactions on the metastable ion time scale lead to formation of the alkyl ion R_1^+ or to elimination of an alkene (R_1 − H) to form a protonated amine of lower carbon number. These results have been rationalized (2) in terms of a fragmentation mechanism involving the initial formation of a $[R_1^+{---}NH(R_2)_2]$ ion/dipole complex which either may separate to form R_1^+ (accompanied by H-migration to form a secondary or tertiary carbenium ion) or may undergo internal proton transfer resulting in olefin elimination and formation of a protonated amine. The alkyl ion and protonated amine products also dominate the low energy collision-induced dissociation (CID) mass spectra (3); however, the high energy CID mass spectra show (3–5) significant fragmentation by way of alkane elimination.

In contrast to the protonated amines, tetraalkyl ammonium ions, R_4N^+, show very abundant elimination of alkanes in metastable ion fragmentation reactions and in both low energy and high energy CID studies (6–11). The nominal alkanes eliminated correspond to RH and to (R˙ + [R − CH_2]˙), the latter either as an alkane or as two alkyl radicals. The mechanisms for alkane elimination have not been clearly established nor has it been clearly delineated why the dominant fragmentation reactions of protonated amines differ from the fragmentation reactions of tetraalkyl ammonium ions. It appeared that a study of both the unimolecular fragmentation reactions and the energy-resolved (ERMS) (12–14) collision-induced fragmentation reactions of $R_nH_{4-n}N^+$ ($n = 2$–4) ions might provide insight into these questions. The present work reports such a study for the n-propyl and n-butyl systems. The results obtained are interpreted in terms of a mechanism for fragmentation of the ions in which there is a competition between heterolytic and homolytic cleavage of the $R_nH_{4-n}N^+$ ion with the former leading to alkene elimination and alkyl ion formation while the latter leads to alkane elimination. Plausible potential energy profiles are presented to rationalize the reaction competition observed.

Experimental

All experimental work was carried out using a VG Analytical ZAB-2FQ mass spectrometer which has been described in detail previously (15). Briefly, the instrument is a reversed-geometry (BE) double-focussing mass spectrometer which is followed by a third stage consisting of a deceleration lens systems, a radio-frequency (rf)-only quadrupole collision cell and a quadrupole mass analyzer.

In the unimolecular metastable ion fragmentation studies the appropriate ion beam was mass selected by the magnetic sector and underwent unimolecular fragmentation in the field-free region between the magnetic and electric sectors, with the fragment ions being analyzed according to their kinetic energy by scanning the voltage applied to the electric sector, the so-called MIKES technique (16). In addition, the appropriate ion beam was mass-selected by the BE double-focussing mass spectrometer, decelerated to 50 eV kinetic energy and underwent

[1]Taken, in part, from the M.Sc. Thesis of N.L. Bosma, University of Toronto, 1994.

[2]To whom correspondence should be addressed. Tel: (416) 978-3577, fax: (416) 978-8775.

Can. J. Chem. Downloaded from www.nrcresearchpress.com by 85.192.166.187 on 09/08/12
For personal use only.

Can. J. Chem. Downloaded from www.nrcresearchpress.com by 85.192.166.187 on 09/08/12
For personal use only.

TABLE 1. Mestastable fragmentation of propyl ammonium ions

	% of base peak		
Fragmentation	Dipropyl	Tripropyl	Tetrapropyl
$-C_3H_6$	100	100	84
$-C_3H_8$	3	6	38
$-C_5H_{12}$			100
$C_3H_7^+$	10	12	7

TABLE 2. Mestastable fragmentation of butyl ammonium ions

	% of base peak		
Fragmentation	Dibutyl	Tributyl	Tetrabutyl
$-C_4H_8$	100	100	100
$-C_4H_{10}$	2	6	37
$-C_7H_{16}$			87
$C_4H_9^+$	32	29	8

unimolecular fragmentation in the rf-only quadrupole cell in the absence of collision gas. The fragment ions were detected by scanning the final mass-analyzing quadrupole.

In the low energy collisional activation studies the ion beam was again mass-selected by the BE instrument at 6 keV ion energy, decelerated to the appropriate collision energy (2.5 to 60 eV, laboratory scale) and introduced into the quadrupole collision cell containing N_2 at a pressure of 3×10^{-7} torr (1 torr = 133.3 Pa) as indicated by the ionization gauge attached to the pumping line for the region. The results are presented in the following as graphs of the percentage fragment ion abundance versus the centre-of-mass collision energy. In both the unimolecular and CID studies 20–50 2 s scans were accumulated on a Tracor Northern multichannel analyzer.

The alkyl ammonium ions were prepared by fast atom bombardment (FAB) ionization using an Ar atom beam of 7–8 keV kinetic energy. For the tetraalkyl ammonium ions the appropriate tetraalkyl ammonium bromide was dissolved in a glycerol matrix and subjected to atom bombardment while for the dialkyl and trialkyl ammonium ions the appropriate amine was dissolved in a thioglycerol/2,2′-dithioethanol (saturated with oxalic acid) matrix and subjected to atom bombardment. All chemicals were obtained from Aldrich Chemical Co., Milwaukee.

Results and discussion

The relative fragment ion abundances observed for unimolecular fragmentation of the *n*-propyl ammonium ions in the quadrupole cell in the absence of collision gas are presented in Table 1. For the dipropyl and tripropyl ammonium ions the dominant metastable ion fragmentation results in the elimination of neutral propene, i.e.,

$$[1] \quad (C_3H_7)_nH_{4-n}H^+ \rightarrow (C_3H_7)_{n-1}H_{4-n}NH^+ + C_3H_6$$

with possible minor fragmentation to form $C_3H_7^+$ and by elimination of C_3H_8. However, it should be noted that the alkyl ammonium ions appear to have large cross-sections for collision-induced dissociation and we cannot preclude the possibility of minor contributions from CID processes. In contrast to the dipropyl and tripropyl systems, the tetrapropyl ammonium ion shows elimination of C_5H_{12} as the base peak in the metastable ion spectrum with significant elimination of C_3H_6 and C_3H_8 also being observed. These metastable ion fragmentation reactions of the tetrapropyl ammonium ion have been reported previously by Ohashi et al. (8); they also reported observation of loss of C_3H_7 in metastable ion fragmentation of the tetrapropyl ion, a reaction which we do not observe. Alkyl radical loss from tetraalkyl ammonium ions is commonly observed in high energy CID (8, 9, 11) but is not observed in low energy CID in this work nor in the work of Mesdach et al. (10); this implies that alkyl radical loss has a high onset energy which is not achieved in low energy CID.

The metastable ion fragmentation reactions of the *n*-butyl ammonium ions (Table 2) parallel those of the propyl ammonium ions. Thus, the dibutyl and tributyl ammonium ions show

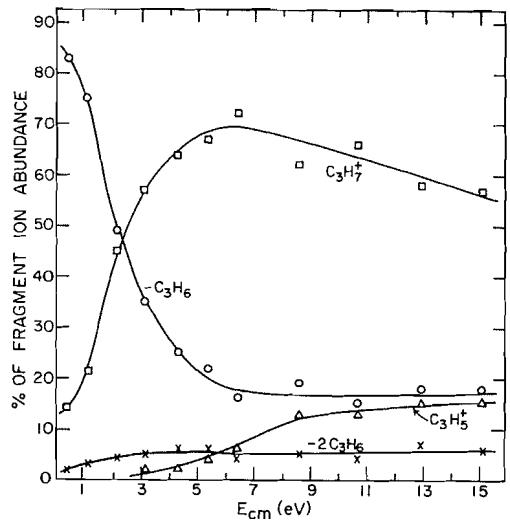

FIG. 1. Breakdown graph for $(n\text{-}C_3H_7)_2H_2N^+$.

predominant elimination of butene (C_4H_8) with minor formation of $C_4H_9^+$, while the tetrabutyl ammonium ion shows significant elimination of C_7H_{16} in competition with elimination of C_4H_8 and C_4H_{10} in metastable ion fragmentation reactions. We also recorded the unimolecular fragmentation reactions occurring in the drift region between the magnetic and electric sectors; the results obtained were in good agreement with the data reported in Tables 1 and 2. The fragmentation reaction resulting in nominal elimination of C_7H_{16} from $(C_4H_9)_4N^+$ has been proposed earlier (8–10) to involve sequential elimination of $C_4H_9^{\cdot}$ and $C_3H_7^{\cdot}$, viz

$$[2] \quad (C_4H_9)_4N^+ \xrightarrow{-C_4H_9} (C_4H_9)_3N^{+\cdot} \xrightarrow{-C_3H_7} (C_4H_9)_2NCH_2^+$$

rather than direct elimination of C_7H_{16} (reaction [3]).

$$[3] \quad (C_4H_9)_4N^+ \rightarrow (C_4H_9)_2NCH_2^+ + C_7H_{16}$$

Reaction [2] would be ca. 87 kcal mol^{-1} more energy demanding than reaction [3] and would not be expected to compete with the alternative of elimination of C_4H_8 (for a more complete discussion of the energetics see below); hence we conclude that the observation of nominal elimination of C_7H_{16} in metastable ion fragmentation reactions implies direct elimination of the species as a stable neutral rather than as two radicals. A similar conclusion has been reached by Beranová and Wesdemiotis (11) with respect to C_3H_8 elimination from $(C_2H_5)_4N^+$.

The low energy CID data for the propyl ammonium ions are shown in Figs. 1 to 3 as plots of the % fragment ion abundance as a function of the centre-of-mass collision energy. The similar data for the butyl amonium ions are presented in Figs. 4 to 6.

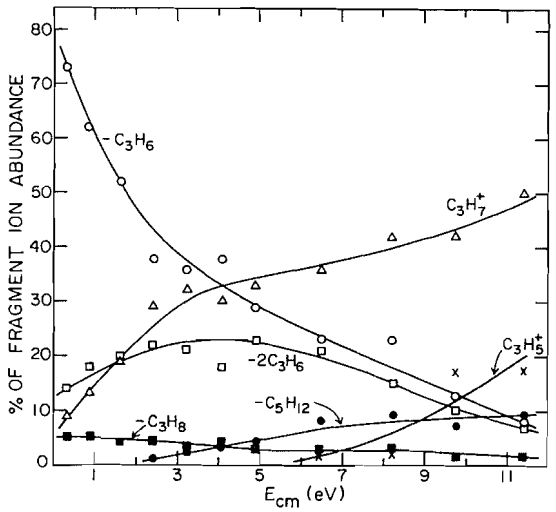

FIG. 2. Breakdown graph for $(n\text{-}C_3H_7)_3HN^+$.

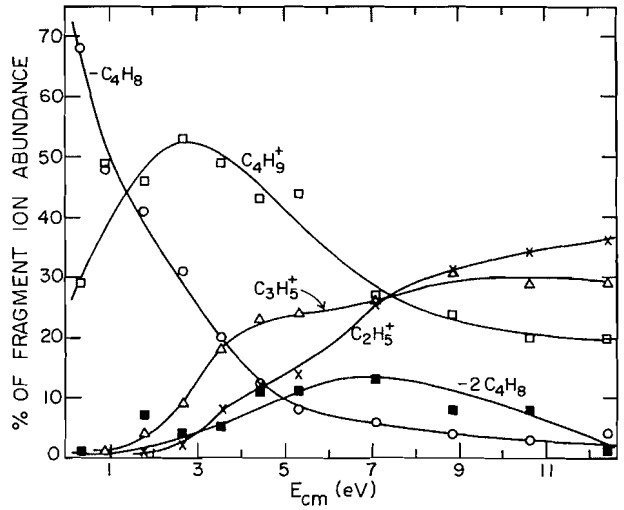

FIG. 4. Breakdown graph for $(n\text{-}C_4H_9)_2H_2N^+$.

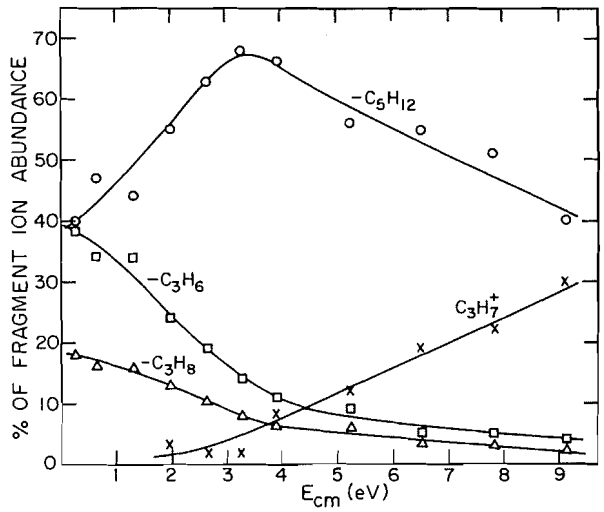

FIG. 3. Breakdown graph for $(n\text{-}C_3H_7)_4N^+$.

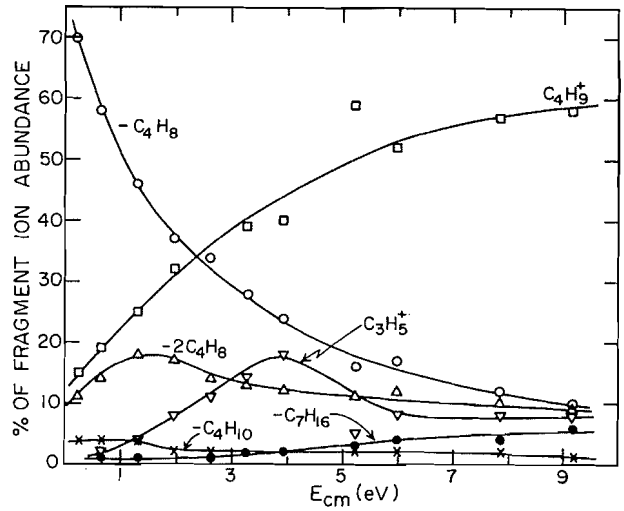

FIG. 5. Breakdown graph for $(n\text{-}C_4H_9)_3HN^+$.

The relative ion signals at the lowest collision energies are in essential agreement with the metastable ion data of Tables 1 and 2.

The breakdown graph for $(C_3H_7)_2H_2N^+$ (Fig. 1) shows that elimination of propene is the dominant low energy fragmentation reaction with formation of $C_3H_7^+$ increasing rapidly in importance with increasing collision energy. The breakdown graph is in good agreement with that reported earlier by Reiner et al. (3) for $(C_3H_7)_2H_2N^+$ ions produced by Brønsted acid chemical ionization of dipropyl amine. The breakdown graph for $(C_3H_7)_3HN^+$ (Fig. 2) is very similar in also showing dominant elimination of propene at the lowest collision energies with $C_3H_7^+$ increasing in importance at higher collision energies. In addition, elimination of two molecules of propene to form $C_3H_7NH_3^+$ is observed at the lowest collision energies as well as minor elimination of C_3H_8. However, elimination of C_5H_{12} from $(C_3H_7)_3HN^+$ obviously is a higher energy process and is observed only at higher centre-of-mass collision energies.

In contrast to the dipropyl and tripropyl ammonium ions, CID of the tetrapropyl ammonium ion (Fig. 3) leads to almost equal elimination of C_3H_6 and C_5H_{12} at the lowest collision energies with a more minor elimination of C_3H_8. With increasing collision energy the C_5H_{12} elimination channel increases in importance at the expense of the other two primary fragmentation channels. The $C_3H_7^+$ ion is formed only at higher collision energies and its increase appears to correlate with the decrease in the abundance of the $(C_3H_7)_2NCH_2^+$ product formed by C_5H_{12} elimination, suggesting that it may arise by further fragmentation of the latter ion. In this regard, it is interesting to note that elimination of C_3H_6 from $(C_3H_7)_2NCH_2^+$ is proposed (17, 18) to proceed through a $[C_3H_7^+\text{----}CH_2{=}NC_3H_7]$ complex, which may, under collisional activation conditions, fragment to yield $C_3H_7^+$.

The butyl ammonium ions show (Figs. 4 to 6) a behaviour similar to the propyl ammonium ions in their fragmentation following collisional activation. For $(C_4H_9)_2H_2N^+$ the primary fragmentation reactions involve elimination of C_4H_8 and formation of $C_4H_9^+$, with the former being favoured at lower collision energies. At higher collision energies $C_4H_9^+$ and its fragmentation products, $C_3H_5^+$ and $C_2H_5^+$, are favoured. Similarly, for $(C_4H_9)_3HN^+$ elimination of C_4H_8 and formation of $C_4H_9^+$ are the dominant fragmentation processes, although elimination of two C_4H_8 molecules and elimination of C_4H_{10} are observed as minor low energy fragmentation routes. Note that elimination of C_7H_{16} is observed as a minor fragmentation process at higher collision energies. The lowest energy CID

Can. J. Chem. Downloaded from www.nrcresearchpress.com by 85.192.166.187 on 09/08/12
For personal use only.

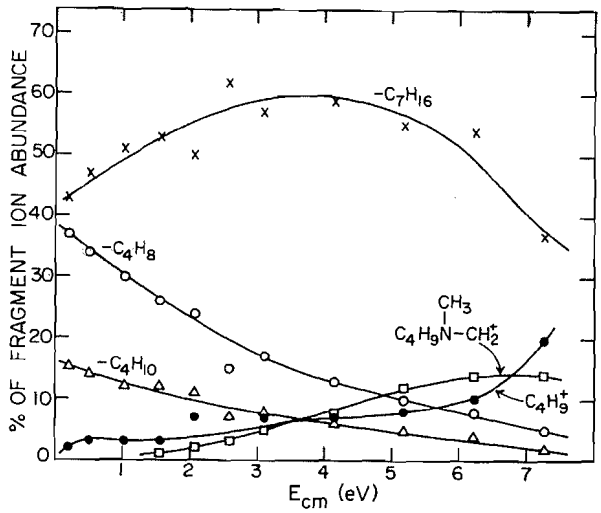

FIG. 6. Breakdown graph for $(n\text{-}C_4H_9)_4N^+$.

processes for $(C_4H_9)_4N^+$ correspond to elimination of C_4H_8, elimination of C_4H_{10} and elimination of C_7H_{16}; the latter reaction (eq. [3]) is analogous to the elimination of C_5H_{12} for the tetrapropyl ammonium ion. The $(C_4H_9)_2NCH_2^+$ (*m/z* 142) ion formed in reaction [3] has been shown (19) to fragment further by elimination of propene (reaction [4])

[4] $(C_4H_9)_2NCH_2^+ \rightarrow (C_4H_9)CH_3NCH_2^+$ (*m/z* 100) + C_3H_6

and, in agreement, we see *m/z* 100 as a significant product at higher collision energies. Rolando and co-workers (10) have provided evidence that $C_4H_9^+$ is a secondary fragmentation product rather than a primary product for the tetrabutyl ammonium ion; the results of Fig. 6 suggest that this is largely so although the mechanism by which $C_4H_9^+$ is formed is not clear.

Mechanistic and energetic considerations

The fragmentation of alkyl and dialkyl ammonium ions formed by Brønsted acid CI has been considered (2, 3) to proceed by formation of a $[R^+\text{----}NH_2R']$ ion/dipole complex;[3] this complex may fragment either by H^+ transfer from R^+ to the amine to form $R'NH_3^+$ or by simple cleavage to form R^+. In contrast, the fragmentation of tetraalkyl ammonium ions has been considered (7–11) to proceed by homolytic cleavage of the C—N bond to form a complex[3] $[R^{\cdot}\text{---}^{\cdot+}NR_3]$ which may fragment to form $R_3N^{+\cdot}$ or may fragment by alkane elimination proceeding by way of H atom or alkyl group abstraction by $R^{\cdot}$ in the complex. As a logical merging of these separate mechanisms, we propose that these two routes for the fragmentation of alkyl ammonium ions are in competition as outlined in the generalized Scheme 1 and that the relative energetics will determine which fragmentation route predominates.

Figures 7 to 9 present plausible potential energy profiles for fragmentation of the three *n*-propyl ammonium ions studied in this work; the relevant thermochemical data used to derive these profiles are summarized in the Appendix. In drawing these profiles we have assumed, in line with previous work (20), that the

[3]Although these species are described as complexes, it is not clear, in the absence of high level theoretical calculations, whether they exist in potential wells (true complexes) or whether they represent only saddle points on the potential energy curve and, thus, should be identified as transition states.

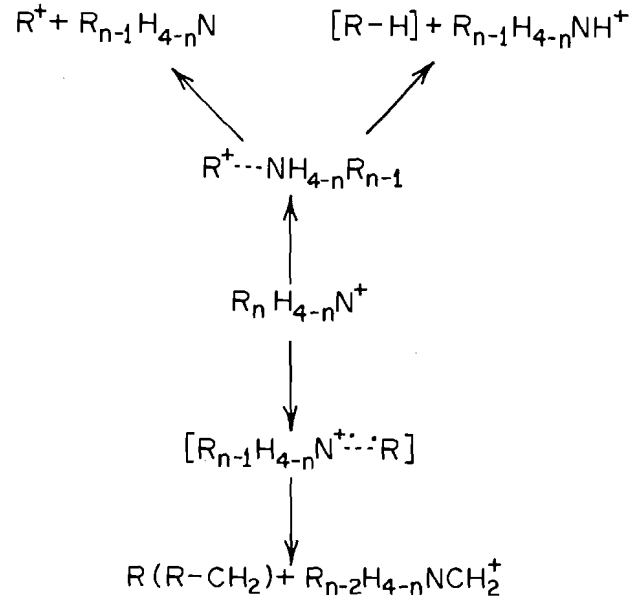

SCHEME 1

incipient *n*-propyl ion rearranges to the *i*-propyl structure during heterolytic bond cleavage and a plausible energy barrier for this process is included. We also have estimated a binding energy of 20 kcal mol^{-1} for the $[i\text{-}C_3H_7^+\text{----}NH_{4-n}(C_3H_7)_{n-1}]$ ion/dipole complex in line with previous estimates (20, 21). The binding energy in the $[R_{n-1}H_{4-n}N^{+\cdot}\text{----}^{\cdot}R]$ complex is unknown. We have assumed a value of 15 kcal mol^{-1}, in line with the lower dipole moment of $R^{\cdot}$, although this value may be subject to considerable error.

The potential energy profile of Fig. 7 clearly shows that fragmentation of the dipropyl ammonium ion by way of the $[i\text{-}C_3H_7^+\text{---}NH_2C_3H_7]$ complex is favoured energetically by a substantial amount and, experimentally, this is the fragmentation channel observed (Fig. 1). For the tripropyl ammonium ion the potential energy profile of Fig. 8 shows that heterolytic bond cleavage still is favoured, although the energy difference between the two complexes is less. In line with this potential energy profile we observe elimination of propene and formation of $i\text{-}C_3H_7^+$ at low collision energies with minor elimination of C_5H_{12} at higher collision energies (Fig. 2). As Fig. 9 shows the two possible fragmentation routes of $(C_3H_7)_4N^+$ are very similar in energy requirements and, in agreement with this potential energy profile we observe (Fig. 3) that elimination of C_3H_6 and elimination of C_5H_{12} are in competition with each other at the lowest collision energies and also in the metastable ion fragmentation reactions (Table 1).

We have not included in Figs. 7 to 9 the fragmentation channel which results in elimination of C_3H_8 since the heats of formation of the product ions, $(C_3H_7)_{n-2}H_{4-n}NCH^+CH_2CH_3$, are difficult to estimate. However, if this reaction also proceeds by way of the intermediate $[(C_3H_7)_{n-1}H_{4-n}N^{+\cdot}\text{---}^{\cdot}C_3H_7]$ one might anticipate that the dependence of the fragment ion intensity on collision energy would be similar to that of the C_5H_{12}-loss fragment. This is not so; indeed, for $(C_3H_7)_3HN^+$, the C_3H_8-loss channel is observed as a minor route even at the lowest collision energies. This raises the possibility that C_3H_8 elimination occurs, at least in part, by a direct 1,2-elimination without the intermediacy of the $[(C_3H_7)_{n-1}H_{4-n}N^{+\cdot}\text{---}^{\cdot}C_3H_7]$ complex.

Thermochemical data are not available to derive potential energy profiles for the butyl ammonium ions. However, it is

Can. J. Chem. Downloaded from www.nrcresearchpress.com by 85.192.166.187 on 09/08/12
For personal use only.

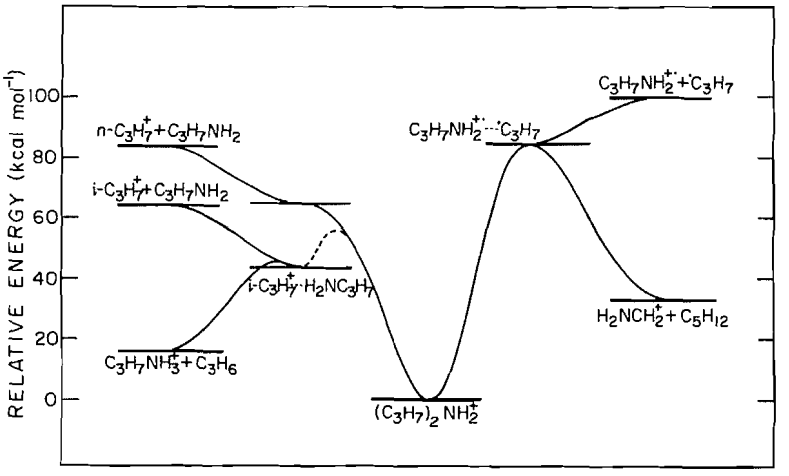

FIG. 7. Potential energy surface for fragmentation of $(n\text{-}C_3H_7)_2H_2N^+$.

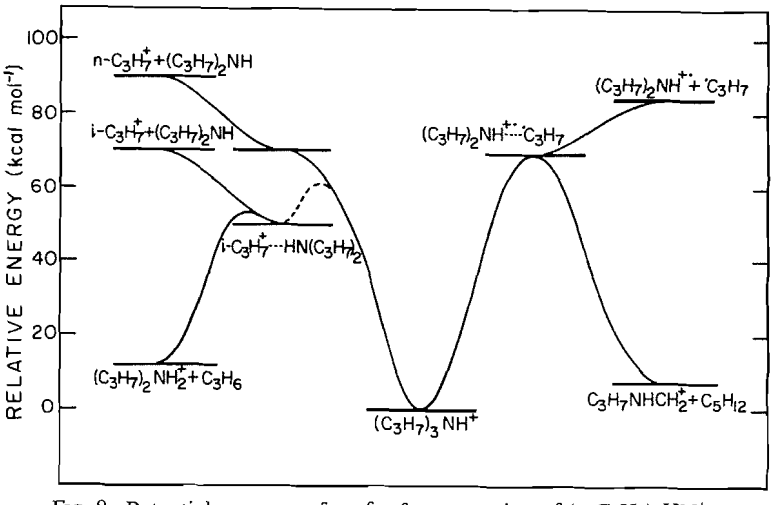

FIG. 8. Potential energy surface for fragmentation of $(n\text{-}C_3H_7)_3HN^+$.

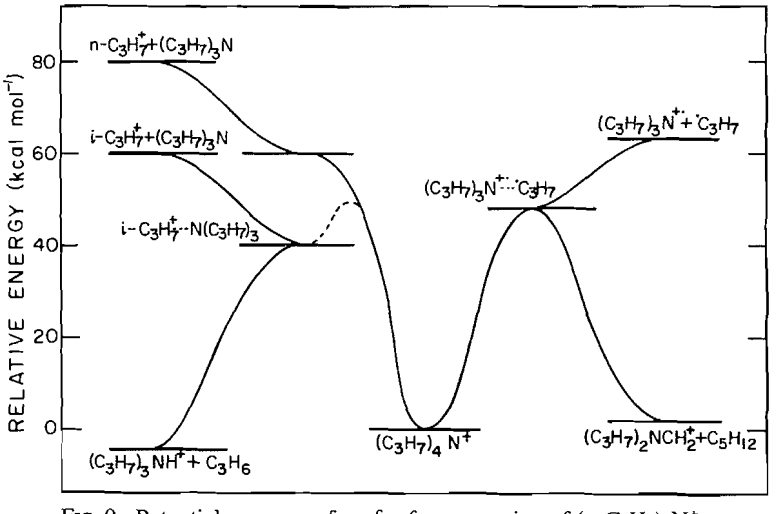

FIG. 9. Potential energy surface for fragmentation of $(n\text{-}C_3H_7)_4N^+$.

likely that these potential energy surfaces would be very similar to those for the propyl ammonium ions. Certainly the experimental breakdown graphs are very similar for ammonium ions with the same degree of alkyl substitution.

Beranová and Wesdemiotis (11) have suggested that the competition between the two reaction channels is determined by the relative ionization energies of $R_{n-1}H_{4-n}N$ and $R^{\cdot}$. That this might be so is seen from the thermochemical pathways indicated in Scheme 2 where $RE(R_nH_{4-n}N^+)$ is the recombination energy of the ion and an electron. Thus, for the competing reactions

[5] $R_nH_{4-n}N^+ \rightarrow R^+ + R_{n-1}H_{4-n}N$

[6] $\rightarrow R^{\cdot} + R_{n-1}H_{4-n}N^{+\cdot}$

Can. J. Chem. Downloaded from www.nrcresearchpress.com by 85.192.166.187 on 09/08/12
For personal use only.

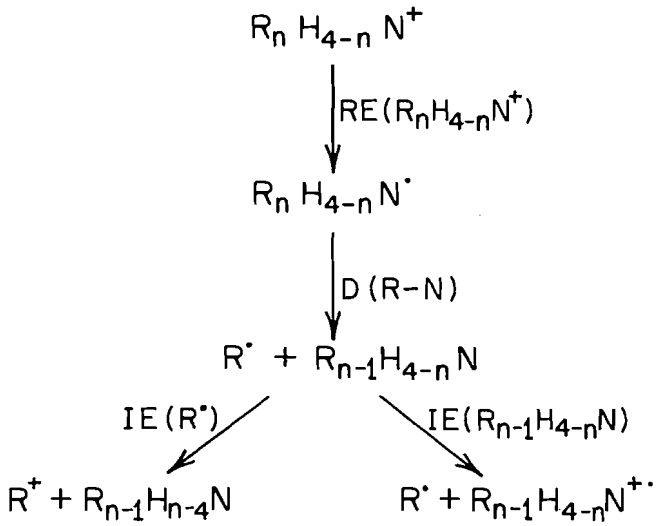

SCHEME 2

TABLE 3. Ionization energies in eV[a]

Species	Ionization energy
$C_2H_5^{\cdot}$	8.13
n-$C_3H_7^{\cdot}$	8.09
i-$C_3H_7^{\cdot}$	7.36
n-$C_4H_9^{\cdot}$	8.02
s-$C_4H_9^{\cdot}$	7.25
$(C_2H_5)H_2N$	8.86
$(C_2H_5)HN$	8.01
$(C_2H_5)_3N$	7.5
$(n$-$C_3H_7)H_2N$	8.78
$(n$-$C_3H_7)_2HN$	7.84
$(n$-$C_3H_7)_3N$	~7.4
$(n$-$C_4H_9)H_2N$	8.71
$(n$-$C_4H_9)_2HN$	7.69
$(n$-$C_4H_9)_3N$	~7.4

[a]From Lias et al. (22).

it follows that

[7] $\Delta H_5 - \Delta H_6 = IE(R^{\cdot}) - IE(R_{n-1}H_{4-n}N)$

Table 3 records ionization energies, taken from Lias et al. [22], relevant to the ethyl, propyl and butyl ammonium ion systems. For the tetraethyl ammonium ion the relative ionization energies suggest dominant fragmentation by way of the $[(C_2H_5)_3N^{+\cdot}\text{---}{}^{\cdot}C_2H_5]$ complex as has been observed by Beranová and Wesdemiotis (11). For the triethyl ammonium ion system the relevant ionization energies are very similar. Experimentally, unimolecular fragmentation of $(C_2H_5)_3HN^+$ on the metastable ion time scale results entirely in elimination of C_2H_4 (23) and C_2H_4 elimination is the dominant CID reaction at low collision energies although elimination of C_3H_8 becomes the dominant reaction as the collision energy is increased (3). These results imply that the $[C_2H_5^+\text{---}NH(C_2H_5)_2]$ complex is slightly lower in energy that the $[(C_2H_5)_2HN^{+\cdot}\text{---}{}^{\cdot}C_2H_5]$ complex. The comparison of ionization energies gives the relative energies of the separated species not the relevant ion/neutral complexes.

For the propyl and butyl ammonium ions the conclusions derived from a comparison of ionization energies are in agreement with the experimental observations only if we assume that IE(R˙) refers to the secondary alkyl radical not the primary alkyl radical. For example, the comparison of IE(n-$C_4H_9^{\cdot}$) = 8.02 eV with IE((n-$C_4H_9)_2NH$) = 7.69 eV would suggest that C_7H_{16} elimination should be observed as a prominent, if not the dominant, fragmentation reaction of the tributyl ammonium ion, contrary to the experimental observations. However, comparison of IE(s-$C_4H_9^{\cdot}$) = 7.25 eV with IE((n-$C_4H_9)_2HN$) = 7.69 eV predicts elimination of C_4H_8 and formation of $C_4H_9^+$ as the dominant fragmentation reactions, in agreement with the experimental observations. Of course, rearrangement to the secondary structure for the incipient alkyl ion is what we have assumed in deriving the potential energy surfaces of Figs. 7 to 9.

In conclusion, the present work has shown that the fragmentation of alkyl ammonium ions, regardless of the extent of alkyl substitution, can be rationalized in terms of competitive homolytic and heterolytic bond cleavages to form ion/neutral complexes, which display specific fragmentation modes. Homolytic bond cleavage, which eventually results in alkane elimination, is favoured by extensive alkyl substitution which lowers the ionization energy of the alkyl amine in the complex. With decreasing alkyl substitution heterolytic bond cleavage, resulting eventually in alkene elimination and alkyl ion formation, becomes the energetically favoured fragmentation route.

Acknowledgements

We are indebted to the Natural Sciences and Engineering Research Council (Canada) for financial support and to Fisons Instruments, Inc. for a loan of the FAB source and fast atom gun.

1. E.J. Reiner, R.A. Poirier, M.R. Peterson, I.G. Csizmadia, and A.G. Harrison. Can. J. Chem. **64**, 1652 (1986).
2. R.D. Bowen, A.G. Harrison, and E.J. Reiner. J. Chem. Soc. Perkin Trans. 2, 1009 (1988).
3. E.J. Reiner, A.G. Harrison, and R.D. Bowen. Can. J. Chem. **67**, 2081 (1989).
4. M.L. Sigsby, R.J. Day, and R.G. Cooks. Org. Mass Spectrom. **14**, 556 (1979).
5. W. Wagner, H. Heimbach, and K. Levsen. Int. J. Mass Spectrom. Ion Phys. **36**, 125 (1980).
6. H.H. Gierlich, F.W. Röllgen, F. Borchers, and K. Levsen. Org. Mass Spectrom. **12**, 367 (1977).
7. M. Fischer and H.-J. Veith. Helv. Chim. Acta, **61**, 3038 (1978).
8. M. Ohashi, R.P. Barrow, and W.R. Benson. J. Am. Chem. Soc. **103**, 3943 (1981).
9. H.J. Veith. Org. Mass Spectrom. **18**, 154 (1983).
10. H. Mestdagh, N. Morin, and C. Rolando. Org. Mass Spectrom. **23**, 246 (1988).
11. Š. Beranová and C. Wesdemiotis. Int. J. Mass Spectrom. Ion Processes. **134**, 83 (1994).
12. S.A. McLuckey, G.L. Glish, and R.G. Cooks. Int. J. Mass Spectrom. Ion Phys. **39**, 219 (1981).
13. D.D. Fetterolf and R.A. Yost. Int. J. Mass Spectrom. Ion Phys. **44**, 37 (1982).
14. S.A. McLuckey and R.G. Cooks. *In* Tandem mass spectrometry. *Edited by* F.W. McLafferty. Wiley, New York. 1983.
15. A.G. Harrison, R.S. Mercer, E.J. Reiner, A.B. Young, R.K. Boyd, R.E. March, and C.J. Porter. Int. J. Mass Spectrom. Ion Processes, **76**, 13 (1986).
16. R.G. Cooks, J.H. Beynon, R.M. Caprioli, and G.R. Lester. Metastable ions. Elsevier, New York. 1973.
17. H.J. Veith and J.H. Gross. Org. Mass Spectrom. **26**, 1097 (1991).
18. R.D. Bowen, A.W. Colburn, and P.J. Derrick. J. Chem. Soc. Perkin Trans. 2, 2363 (1993).
19. H. Budzikiewicz and P. Bold. Org. Mass Spectrom. **26**, 709 (1991).

Can. J. Chem. Downloaded from www.nrcresearchpress.com by 85.192.166.187 on 09/08/12
For personal use only.

TABLE 4. Thermochemical data[a]

Species M	ΔH_f^0(M)	ΔH_f^0(M$^+$)	ΔH_f^0(MH$^+$)
n-$C_3H_7NH_3$	−17	186	131
$(n$-$C_3H_7)_2NH$	−28	153	110
$(n$-$C_3H_7)_3N$	−38	132	93
$(n$-$C_3H_7)_4N$		93[b]	
n-$C_3H_7^{\cdot}$	24	211	
i-$C_3H_7^{\cdot}$		191	
$C_2H_5^{\cdot}$	28		
C_3H_6	−5		
C_5H_{12}	−35		
$C_3H_7NHCH_2^{\cdot}$		135[c]	
$(C_3H_7)_2NCH_2^{\cdot}$		130[c]	

[a]In kcal mol^{-1}, from ref. 22 unless noted.
[b]Estimated, see text.
[c]Estimated by comparison with ΔH_f^0 ($CH_3NHCH_2^+$) = 166 kcal mol^{-1} and ΔH_f^0($C_2H_5NHCH_2^+$) = 156 kcal mol^{-1} (24).

20. R.D. Bowen. Org. Mass Spectrom. **28**, 1577 (1993).
21. M. Moet-Ner (Mautner). J. Am. Chem. Soc. **114**, 3312 (1992).
22. S.G. Lias, J.E. Bartmess, J.F. Liebman, J.L. Holmes, R.D. Levin, and W.G. Mallard. J. Phys. Chem. Ref. Data, 17, (1988). Suppl. 1.
23. E.J. Reiner. Ph.D. Thesis, University of Toronto, Toronto, Ont. 1986.
24. F.P. Lossing, Y.-T. Lam, and A. Maccoll. Can. J. Chem. **59**, 2228 (1981).

Appendix

The thermochemical data used to derive the potential energy surfaces of Figs. 7 to 9 are summarized in Table 4. Unless otherwise noted these data are taken from Lias et al. (22).

$\Delta H_f^0((n$-$C_3H_7)_4N^+)$ = 93 kcal mol^{-1} has been estimated by assuming ΔH^0 = −80 kcal mol^{-1} for the reaction

[A1] n-$C_3H_7^+ + (n$-$C_3H_7)_3N \rightarrow (n$-$C_3H_7)_4N^+$

in line with standard enthalpy changes of −84 kcal mol^{-1} and −90 kcal mol^{-1}, respectively, for the reactions

[A2] n-$C_3H_7^+ + n$-$C_3H_7NH_2 \rightarrow (n$-$C_3H_7)_2NH_2^+$

[A3] n-$C_3H_7^+ + (n$-$C_3H_7)_2NH \rightarrow (n$-$C_3H_7)_3NH^+$

The absolute value of $\Delta H_f^0((n$-$C_3H_7)_4N^+)$ is not essential to the arguments based on Fig. 9 since formation of either complex from the ammonium ion is substantially endothermic.

$\Delta H_f^0(C_3H_7NHCH_2^+)$ and $\Delta H_f^0((C_3H_7)_2NCH_2^+)$ also have been estimated. However, again the absolute values are not essential since elimination of C_5H_{12} from $[(CD_3H_7)_{n-1}H_{4-n}N^{+\cdot}$---$^{\cdot}C_3H_7]$ is very exothermic in all cases. Note, however, that elimination of $C_3H_7^{\cdot}$ + $C_2H_5^{\cdot}$ from this complex would be substantially endothermic (ΔH^0 = 35 kcal mol^{-1}) and, if the two radicals were eliminated, fragmentation to $C_3H_7^{\cdot}$ + $(C_3H_7)_{n-1}H_{4-n}N^{+\cdot}$ would be more likely (ΔH^0 = 15 kcal mol^{-1}). Thus, we conclude that the nominal alkane elimination does correspond to elimination of the alkane rather than two alkyl radicals. Similar considerations apply to the elimination of C_7H_{16} from the butyl ammonium ions.

Can. J. Chem. Downloaded from www.nrcresearchpress.com by 85.192.166.187 on 09/08/12
For personal use only.

Isotherme 75°C, du système quaternaire réciproque H_3PO_4–K_2SO_4–H_2SO_4–K_3PO_4–H_2O. Étude des nappes du liquidus

NÉJI BOURGUIBA ET TAHAR JOUINI[1]

Département de chimie, Faculté des sciences de Tunis, Campus Universitaire, 1060 Tunis, Tunisie

Reçu le 11 mars 1994

NÉJI BOURGUIBA et TAHAR JOUINI. Can. J. Chem. **72**, 2212 (1994).

Les nappes du liquidus de l'isotherme isobare (75°C, 1 atm) du système considéré ont fait l'objet d'une étude systématique permettant de tracer les lignes de niveau d'eau constant du système. Leur investigation a été menée au moyen de coupes isopléthiques judicieusement situées. Leurs positions ont été choisies de manière à compléter l'information sur les nappes déduites des systèmes ternaires limitant le quaternaire et des lignes à double saturation établis au cours de travaux antérieurs. Les mesures de solubilité ont été effectuées par conductimétrie. Quatre coupes isopléthiques : K_2SO_4–KH_2PO_4, K_2SO_4–K_2HPO_4, $KHSO_4$–K_2HPO_4 et $KHSO_4$–KH_2PO_4 ont été déterminées en totalité. Les deux premières sont des sections quasi-ternaires du système. Neuf portions de coupes ont été, également, établies pour préciser notre connaissance du liquidus. Les nappes limitant respectivement le domaine de $KHSO_4$ et de $K_8(H_2PO_4)_{1+X}(HSO_4)_{7-X}$ présentent une allure tournante qui révèle un phénomène de solubilité rétrograde en fonction de la teneur en eau.

NÉJI BOURGUIBA and TAHAR JOUINI. Can. J. Chem. **72**, 2212 (1994).

The liquidus curves at 75°C, 1 atm, of the system under consideration have been studied systematically by means of solubilities determined conductimetrically, and lines of constant water content have been deduced. The study used isoplethic sections chosen to complete data on previous measurements of limiting ternary systems and lines of double saturation. Four isoplethic sections: K_2SO_4–KH_2PO_4, K_2SO_4–K_2HPO_4, $KHSO_4$–K_2HPO_4, and $KHSO_4$–KH_2PO_4 were determined, the first two of which are quasi-ternary systems. A total of nine portions of the curves were measured to extend knowledge of the liquidus. The limiting curves in the field of $KHSO_4$ and $K_8(H_2PO_4)_{1+X}(HSO_4)_{7-X}$ show curvature, which reveals retrograde solubility as a function of water content.

Introduction

L'étude du système H_3PO_4–K_2SO_4–H_2SO_4–K_3PO_4–H_2O à 75°C et 1 atm (= 101,3 kPa), a été abordée lors d'étapes antérieures par l'établissement des systèmes ternaires limites (1) puis des lignes limites de domaines de cristallisation (2). En outre une phase solide a été caractérisée par détermination structurale aux rayons X (3).

Le présent travail complète l'établissement de cette isotherme par l'investigation des nappes du liquidus et le tracé des lignes de niveau d'eau constant.

L'intérêt pour ce système s'explique par son exploitation potentielle dans la fabrication d'engrais phosphopotassiques, comme nous l'avons justifié dans une publication antérieure (1).

Techniques expérimentales

Elles ont été précédemment décrites (1, 2). Nous nous limitons ici à rappeler le système de coordonnées de Jänecke, utilisé pour la représentation du quaternaire. Dans ce mode, le repère est un prisme droit à base carrée. Le point représentatif d'un mélange situé à l'intérieur du prisme est défini par les variables X, Y et Z.

L'abscisse X et l'ordonnée Y sont respectivement les pourcentages de moles d'équivalents d'ions phosphates et de protons :

$$X = \frac{3 \times 10^2 n\mathrm{PO_4}^{3-}}{N} \qquad Y = \frac{10^2 n\mathrm{H}^+}{N}$$

où n représente le nombre de moles de l'entité concernée et N la neutralité électrique du milieu.

$$N = n\mathrm{H}^+ + n\mathrm{K}^+ = 2n\mathrm{SO_4}^{2-} + 3n\mathrm{PO_4}^{3-}$$

La cote Z, portée par les arêtes verticales du prisme, exprime le nombre de mole d'eau correspondants à 100 moles d'équivalents de sels :

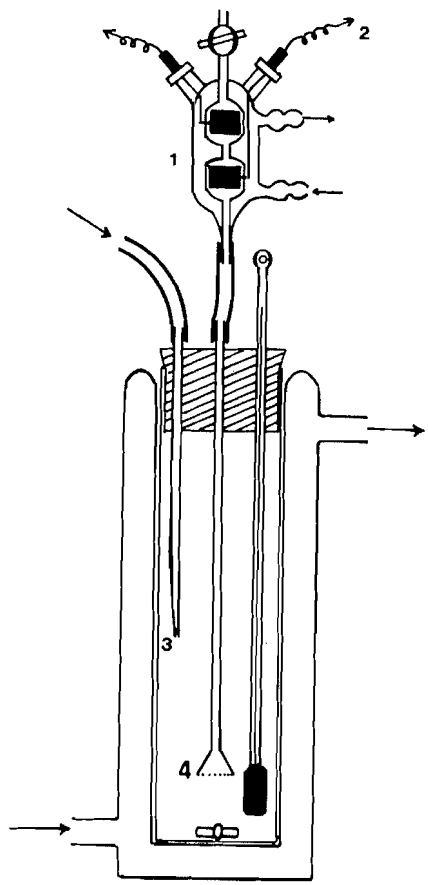

FIG. 1. Dispositif de mesures conductimétriques. 1 : Cellule conductimétrique. 2 : Liaison avec le pont de Wheatstone. 3 : Tube relié à une pipette graduée permettant l'addition d'eau au mélange. 4 : Filtre plongeur permettant de séparer la solution saturée de ses cristaux lors de la mesure.

[1]Auteur à qui adresser toute correspondence. Tel : 512600 poste : 215; Téléx : FACSIT 13162 TN; Téléfax : 885-008.

Can. J. Chem. Downloaded from www.nrcresearchpress.com by 85.192.166.187 on 09/08/12
For personal use only.

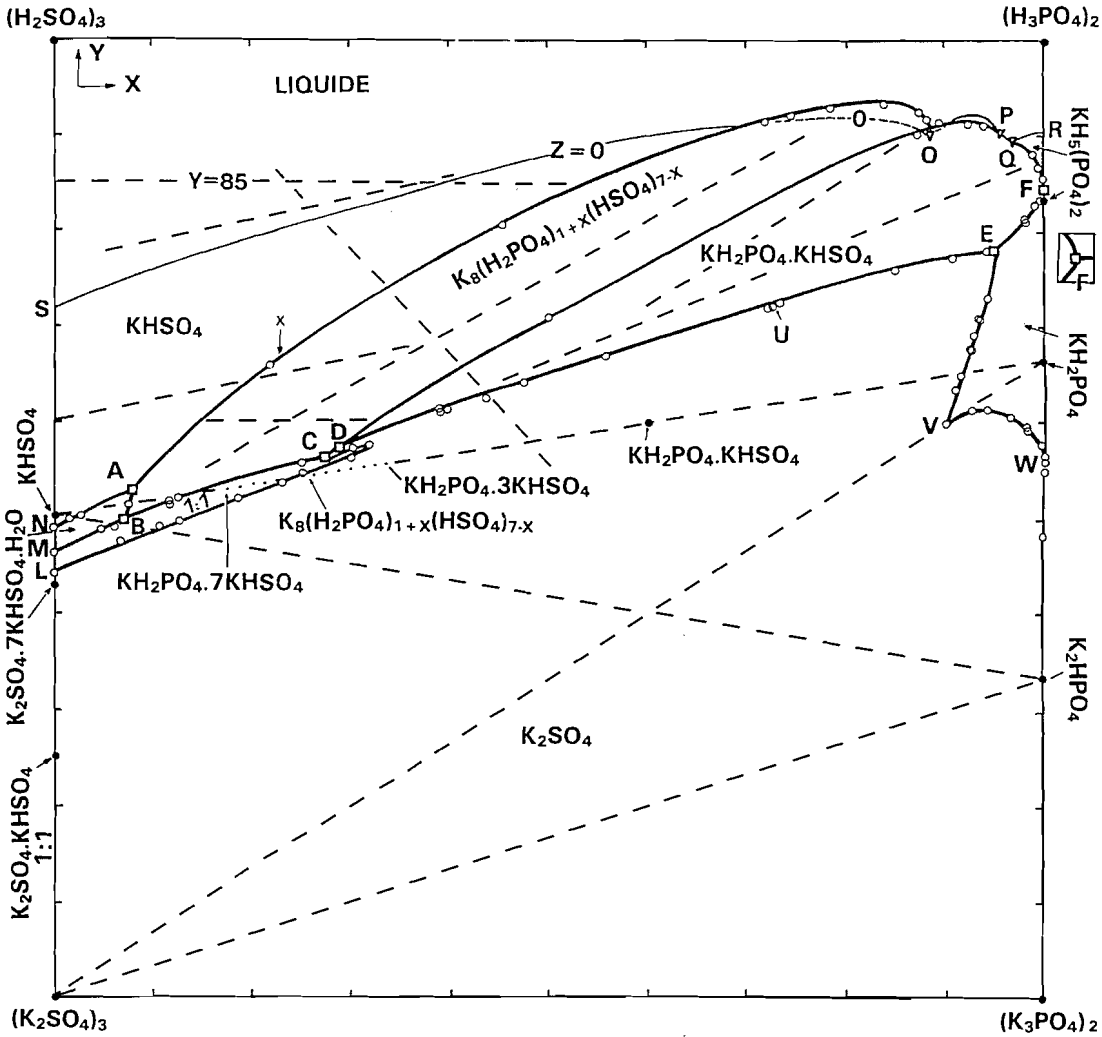

FIG. 2. Représentation des traces des coupes isopléthiques étudiées en projection sur le carré de base (– – –) ainsi que des lignes de deux sels (O—O—) établies précédemment (2).

$$Z = \frac{10^2 n\mathrm{H_2O}}{N}$$

Le point représentatif de l'eau pure est ainsi rejeté à l'infini (N tendant vers 0).

L'établissement des nappes du liquidus a été effectuée par conductimétrie (4–6) au moyen de coupes perpendiculaires au carré de base du prisme de Jänecke. Elles sont caractérisées par une relation linéaire entre X et Y et appelées coupes isopléthiques.

Dans cette méthode nous partons d'un mélange hétérogène de composition connue, appartenant au plan de la coupe étudiée. Ce mélange est soumis à l'agitation dans un vase à double enveloppe thermostaté (figure 1) jusqu'à établissement de l'équilibre, vérifié de la manière suivante. Une petite quantité de la solution est aspirée dans une cellule conductimétrique, également thermostatée et reliée à un pont de Wheatstone. Aprés mesure de la résistance R la solution est refoulée dans l'ensemble de départ. Cette opération est repétée jusqu'à obtention d'une valeur constante. On procède alors à la measure de solubilité, par ajouts successifs de quantités connues d'eau distillée et mesures de R, selon le protocole précédent.

Le tracé de la courbe donnant la résistance en fonction du volume d'eau présente une brisure à chaque changement de variance du système, en particulier la dernière correspond à la quantité d'eau, complémentaire, nécessiare pour dissoudre tout le solide présent. C'est-à-dire pour amener le point représentaitif du mélange de départ à percer la nappe du liquidus. On en déduit la cote Z du point de cette nappe ayant les mêmes coordonnées X et Y que le mélange étudié.

La cellule conductimétrique utilisée, de constante 106 cm^{-1}, est de type Metrohm 660 (figure 1) et le pont de Wheatstone est de marque General-Radio de type impédance bridge B-1650.

Résultats expérimentaux

Les coupes à étudier ont été choisies de manière à compléter l'information sur les nappes de solubilité déduites des systèmes ternaires limitant le quaternaire (1) et des lignes à double saturation (2) établies précédemment. Elles sont représentées à la figure 2 qui comporte également les traces des coupes étudiées.

Les coordonnées des points caractéristiques appartenant aux systèmes ternairs limites déterminées dans un mémoire antérieur (1) et utilisées dans le présent travail sont rappelées au tableau 1.

Étude des coupes isopléthiques

1. Coupe isopléthique K_2SO_4–KH_2PO_4

Les résultats obtenus sont donnés à la figure 3 et au tableau 2.

Cette section ($Y = 2X/3$) constitue une coupe quasi-ternaire du système, en effet, elle ne traverse aucun domaine de sel étranger au plan considéré. Les seules phases solides observées sont les composés de départ.

Les coordonnées du point invariant **b** ont été déterminées par analyse de la solution en équilibre avec K_2SO_4 et KH_2PO_4.

Can. J. Chem. Downloaded from www.nrcresearchpress.com by 85.192.166.187 on 09/08/12
For personal use only.

TABLEAU 1. Coordonnées de points caractéristiques appartenant aux systèmes ternaires limitant le système quaternaire réciproque : H^+, K^+, PO_4^{3-}, SO_4^{2-}, H_2O à 75°C d'après la référence 1

(*a*) Système ternaire : H_2SO_4–H_3PO_4–K_2SO_4–K_3PO_4

Points caractéristiques	Solutions saturées: Coordonnées de Jänecke *X*	*Y*	Composition pondérale %K_2O	%SO_3	%P_2O_5	%H_2O	Phases solides en équilibre
S	0,00	70,95	22,78	66,59	0,00	10,63	$KHSO_4$
O	88,24	90,07	12,19	12,26	54,42	21,13	$KHSO_4$ + $KH_2PO_4{\cdot}7KHSO_4$
P	95,74	90,51	12,09	04,61	61,27	22,03	$KH_2PO_4{\cdot}3KHSO_4$ + $KH_2PO_4{\cdot}KHSO_4$
Q	96,37	98,27	13,53	03,89	61,07	21,51	$KH_2PO_4{\cdot}KHSO_4$ + $KH_5(PO_4)_2$
R	100	90,50	12,33	0,00	65,22	22,45	$KH_5(PO_4)_2$

(*b*) Système ternaire : K_2SO_4–H_2SO_4–H_2O

Points caractéristiques	Solutions saturées: Coordonnées de Jänecke *Y*	*Z*	Composition pondérale %K_2O	%SO_3	%H_2O	Phases solides en équilibre
N	48,78	166,5	24,50	40,61	34,89	$KHSO_4$ + $K_2SO_4{\cdot}7KHSO_4{\cdot}H_2O$
M	46,25	171,4	25,24	39,89	34,89	$K_2SO_4{\cdot}7KHSO_4{\cdot}H_2O$ + $K_2SO_4{\cdot}KHSO_4$
L	44,00	260,0	22,52	34,15	43,33	$K_2SO_4{\cdot}KHSO_4$ + K_2SO_4
S	70,95	0,00	22,78	66,59	10,63	$KHSO_4$

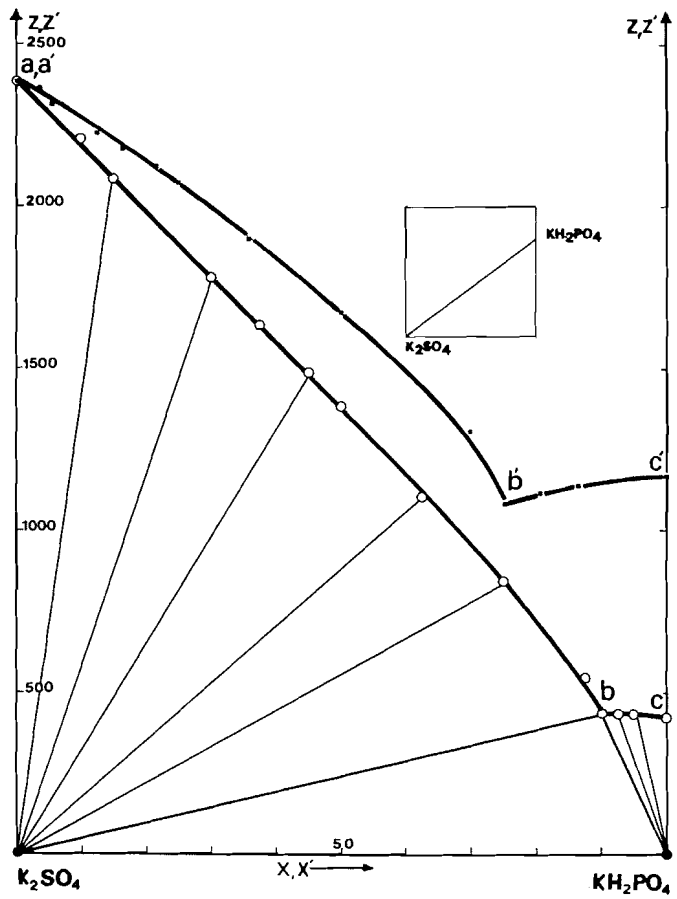

FIG. 3. Coupe isopléthique K_2SO_4–KH_2PO_4. La trace de la coupe est représentée dans le carré. ○—○— courbe (*Z*, *X*), ■—■— courbe (*Z'*, *X'*).

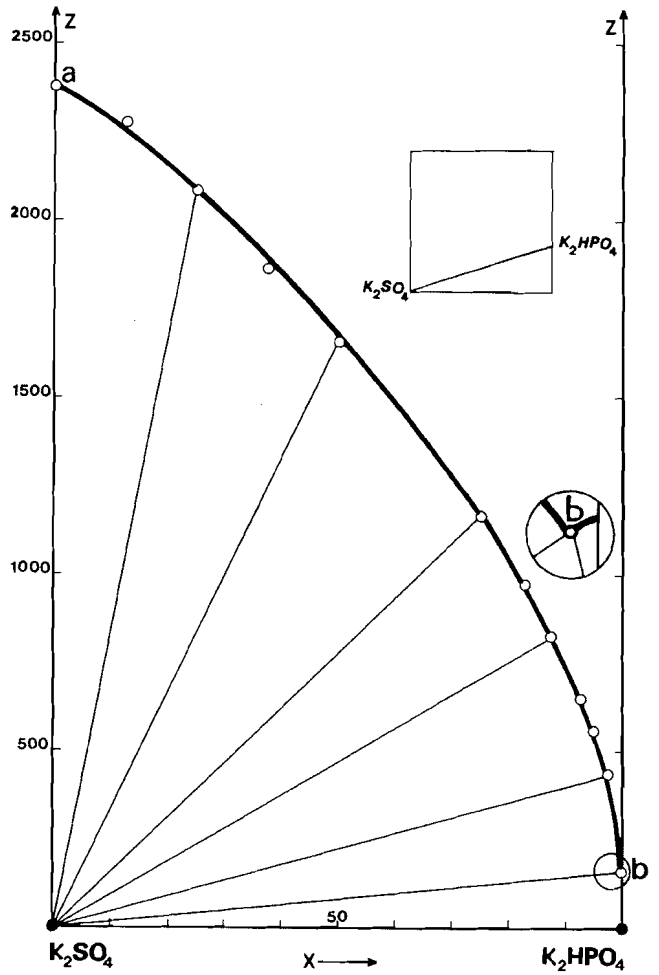

FIG. 4. Coupe isopléthique K_2SO_4–K_2HPO_4. La trace de la coupe est représentée dans le carré.

Can. J. Chem. Downloaded from www.nrcresearchpress.com by 85.192.166.187 on 09/08/12
For personal use only.

TABLEAU 2. Coupe isopléthique : K_2SO_4–KH_2PO_4

Solutions saturées						
	Coordonnées de Jänecke[a]			Nouvelles coordonnées[b]		
Points	X	Z	Points	X'	Z'	Phases solides en équilibre
a	0	2380	**a'**	0	2380	K_2SO_4
	10	2207,4		3,55	2365,3	K_2SO_4
	15	2083,3		5,55	2314,6	K_2SO_4
	30	1780		12,52	2224,7	K_2SO_4
	37,5	1635,5		16,67	2181,4	K_2SO_4
	45	1489		21,43	2126,8	K_2SO_4
	50	1385		25	2077	K_2SO_4
	59,05	1135		32,47	1872,4	K_2SO_4
	62,5	1105,5		35,70	1895	K_2SO_4
	75	839		50,01	1678	K_2SO_4
	87,5	546,3		70,01	1311,4	K_2SO_4
b	90	435	**b'**	75	1087,3	K_2SO_4 + KH_2PO_4
	92,5	430,5		80,42	1123	KH_2PO_4
	95	420		86,36	1145,6	KH_2PO_4
c	100	389,4	**c'**	100	1168	KH_2PO_4

[a]Les coordonnées X et Z sont définies dans les techniques expérimentales.

[b]$X' = \dfrac{10^2\, n\mathrm{H_2PO_4^-}}{N'}$ et $Z' = \dfrac{10^2\, n\mathrm{H_2O}}{N'}$ avec $N' = n\mathrm{K^+} = 2\, n\mathrm{SO_4^{2-}} + n\mathrm{H_2PO_4^-}$.

Can. J. Chem. Downloaded from www.nrcresearchpress.com by 85.192.166.187 on 09/08/12
For personal use only.

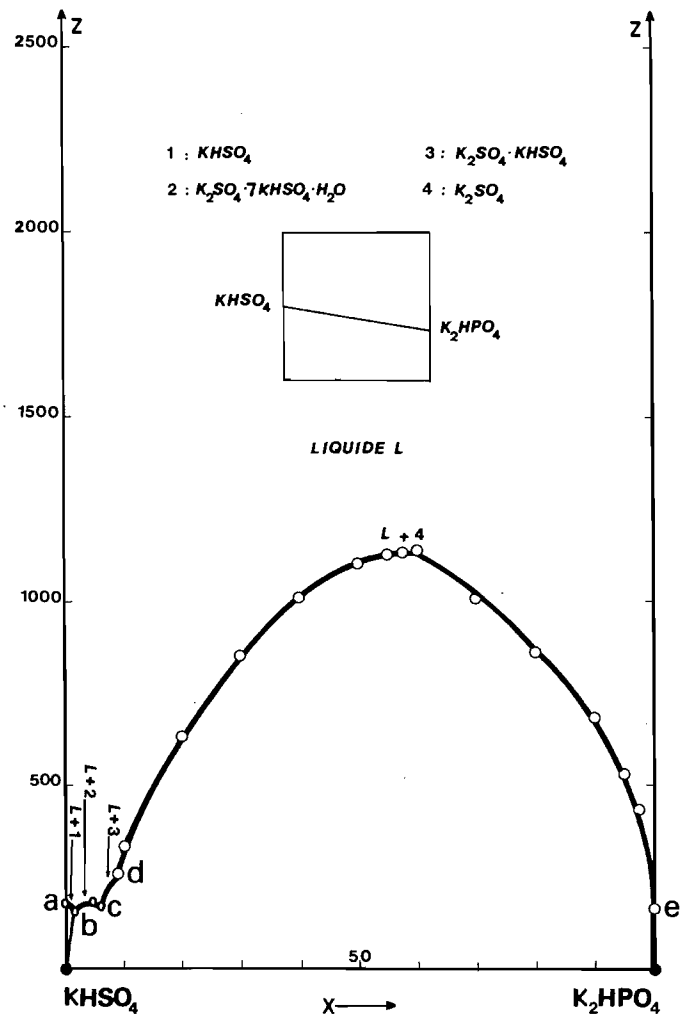

FIG. 5. Coupe isopléthique $KHSO_4$–K_2HPO_4. La trace de la coupe est représentée dans le carré.

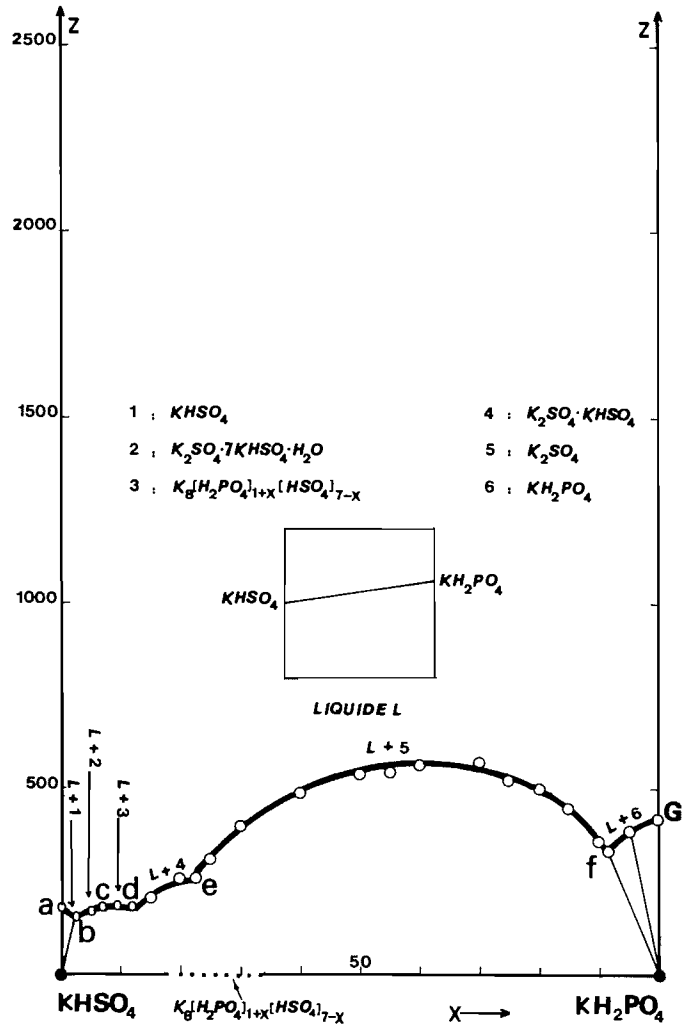

FIG. 6. Coupe isopléthique $KHSO_4$–KH_2PO_4. La trace de la coupe est représentée dans le carré.

TABLEAU 3. Coordonnées des points caractéristiques dans les coupes isopléthique du système quaternaire réciproque : H^+, K^+, PO_4^{3-}, SO_4^{2-}, H_2O à 75°C

(*a*) Coupe isopléthique : K_2SO_4–KH_2PO_4 ($Y = 2\ X/3$)

Point invariant	Solutions saturées: Coordonnées de Jänecke *X*	*Y*	*Z*	Composition pondérale %K_2O	%SO_3	%P_2O_5	%H_2O	Phases solides en équilibre
b	90	60	435	14,74	3,13	16,66	65,47	$K_2SO_4 + KH_2PO_4$

(*b*) Coupe isopléthique : K_2SO_4–K_2HPO_4 ($Y = X/3$)

Point invariant	Solutions saturées: Coordonnées de Jänecke *X*	*Y*	*Z*	Composition pondérale %K_2O	%SO_3	%P_2O_5	%H_2O	Phases solides en équilibre
b	100	33,33	166	35,70	0,00	26,91	37,39	$K_2SO_4 + K_2HPO_4$

(*c*) Coupe isopléthique : $KHSO_4$–K_2HPO_4 ($Y + X/6 = 50$)

Points caractéristiques	Solutions saturées: Coordonnées de Jänecke *X*	*Y*	*Z*	Composition pondérale %K_2O	%SO_3	%P_2O_5	%H_2O	Phases solides en équilibre
b	1,5	49,75	160	24,48	40,74	0,37	34,41	$KHSO_4 + K_2SO_4{\cdot}7KHSO_4{\cdot}H_2O$
c	6	49,00	170	24,50	38,35	1,45	35,71	$K_2SO_4{\cdot}7KHSO_4{\cdot}H_2O + K_2SO_4{\cdot}KHSO_4$
d	9	48,50	260	21,29	31,94	1,87	44,90	$K_2SO_4 + K_2SO_4{\cdot}KHSO_4$
e	100	33,33	166	35,70	0,00	26,91	37,39	$K_2SO_4 + K_2HPO_4$

(*d*) Coupe isopléthique : $KHSO_4$–KH_2PO_4 ($Y - X/6 = 50$)

Points caractéristiques	Solutions saturées: Coordonnées de Jänecke *X*	*Y*	*Z*	Composition pondérale %K_2O	%SO_3	%P_2O_5	%H_2O	Phases solides en équilibre
b	2,5	50,42	160	24,25	40,51	0,61	34,63	$KHSO_4 + K_2SO_4{\cdot}7KHSO_4{\cdot}H_2O$
c	7,5	51,25	180	23,25	37,47	1,80	37,48	$K_2SO_4{\cdot}7KHSO_4{\cdot}H_2O + KH_2PO_4{\cdot}7KHSO_4$
d	12,5	52,08	185	22,91	35,53	3,00	38,56	$K_2SO_4{\cdot}KHSO_4 + K_8(H_2PO_4)_{1+x}(HSO_4)_{7-x}$
e	22,5	53,75	260	19,85	28,25	4,85	47,05	$K_2SO_4 + K_2SO_4{\cdot}KHSO_4$
f	91,5	65,25	335	15,21	3,16	20,13	61,50	$K_2SO_4 + KH_2PO_4$

Signalons que la courbe de solubilité **cb** est croissante de **c** vers **b**. Cette allure peu courante s'explique dans ce cas par la définition de la cote *Z* qui fait intervenir les ions H^+ et PO_4^{3-} n'existant pratiquement pas en solution à pH ≈ 5. En effet, le composé KH_2PO_4 se dissocie pour donner, dans ce domaine de pH, essentiellement K^+ et $H_2PO_4^-$.

Un calcul tenant compte de ces dernières espèces ioniques a été effectué. Les résultats présentés au tableau 2 et à la figure 3 revèlent une décroissance de *Z'* de **c'** vers **b'**, comme attendu. Mais pour une raison d'homogéneité nous devons garder la même définition de *X* et *Z* dans tout le diagramme.

Can. J. Chem. Downloaded from www.nrcresearchpress.com by 85.192.166.187 on 09/08/12
For personal use only.

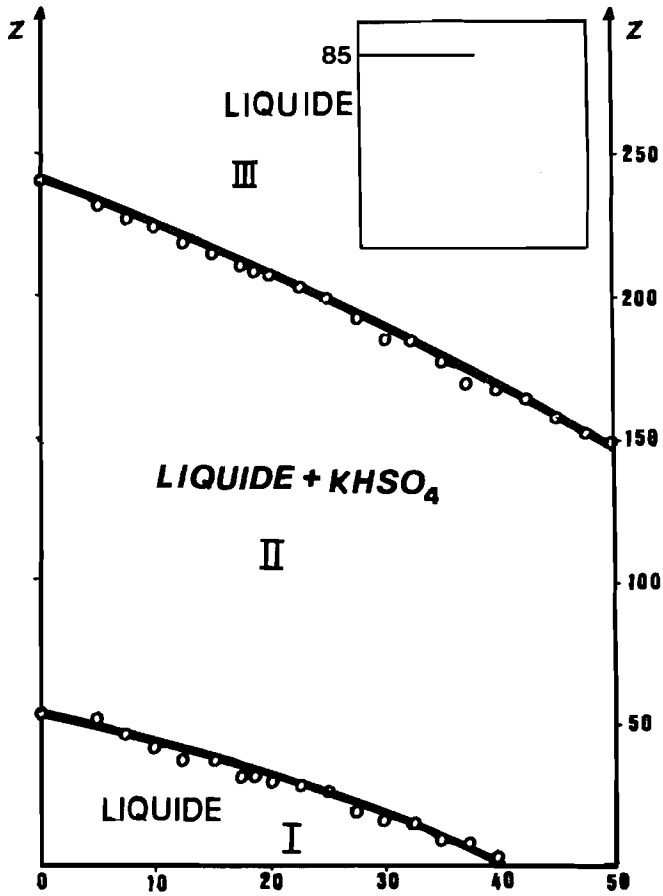

FIG. 7. Coupe isopléthique $Y = 85$. Double intersection avec la nappe de $KHSO_4$ révèlant l'allure tournante de cette dernière. La trace de la coupe est représentée dans le carré.

Cependant un liquidus peut présenter une allure croissante pour un composé à solubilité congruente (7).

Une approche thermodynamique de cette question est en cours d'étude.

2. Coupe isopléthique K_2SO_4–K_2HPO_4

La section K_2SO_4–K_2HPO_4 ($Y = X/3$) constitue également une coupe quasi-ternaire du système (figure 4, tableau 3). Les sels qui s'y manifestent sont les composés de départ. Cependant, le domaine de K_2SO_4 englobe presque tout le diagramme. Il en résulte que le point invariant **b** est pratiquement collé à l'axe représentant le système binaire K_2HPO_4–H_2O. Le point **b** a été localisé par analyse de la solution invariante où coexistent K_2SO_4 et K_2HPO_4.

3. Coupe isopléthique $KHSO_4$–K_2HPO_4 ($Y + X/6 = 50$)

Les résultats obtenus sont rassemblés à la figure 5 et au tableau 3.

Les domaines traversés par cette coupe correspondent aux phases solides suivantes : $KHSO_4$, $K_2SO_4 \cdot 7KHSO_4 \cdot H_2O$, $K_2SO_4 \cdot KHSO_4$, K_2SO_4 et K_2HPO_4.

Les points caractéristiques **b**, **c** et **d** sont situés à l'intersection du plan de la coupe étudiée avec les lignes monovariantes précédemment établies (2).

4. Coupe isopléthique $KHSO_4$–KH_2PO_4 ($Y - X/6 = 50$)

Dans cette section (figure 6, tableau 3), les phases solides observées sont : $KHSO_4$, $K_2SO_4 \cdot 7KHSO_4 \cdot H_2O$, la solution solide $K_8(H_2PO_4)_{1+x}(HSO_4)_{7-x}$, $K_2SO_4 \cdot KHSO_4$, K_2SO_4 et KH_2PO_4.

La remarque du paragraphe précédent concernant la localisation des points caractéristiques reste valable.

5. Coupe isopléthique $Y = 85$

L'étude de cette section limitée à l'intervalle $0 \leq X \leq 55$ a été entreprise dans le but de mettre en évidence l'allure du liquidus de la nappe de cristallisation de $KHSO_4$.

Les résultats sont présentés à la figure 7. Ils révèlent que l'intersection du plan de cette coupe avec la nappe relative à $KHSO_4$ s'effectue suivant deux courbes distinctes. On en déduit l'allure tournante de la nappe de $KHSO_4$ qui rencontre deux fois la section $Y = 85$. Il en résulte un phénomène de solubilité rétrograde en fonction de la teneur en eau : partant d'un mélange liquide situé dans le domaine I, l'addition d'eau provoque la précipitation de $KHSO_4$, lorsque le point représentatif du mélange pénètre dans le domaine II. En poursuivant l'addition d'eau le sel se redissout lorsque le mélange entre dans le domaine III.

6. Autres coupes

Dans le but de compléter notre connaissance du liquidus, différentes portions de coupes ont été établies. Leurs projections, sur le carré de base, sont données à la figure 2.

Seule les intersections de ces coupes avec la partie supérieure du liquidus ont été déterminées dans les régions où se manifeste le phénomène de solubilité rétrograde en fonction de la teneur en eau.

Lignes de niveau d'eau constant du système

En utilisant les informations déduites des études précédentes : systèmes ternaires limites (1), lignes à double saturation (2) et celles déduites des coupes isopléthiques établies au cours de ce travail, nous avons tracé sur la figure 8*A* les courbes de niveau d'eau constant du système. Elle comporte également les projections, sur les plans horizontal et frontal, des lignes de deux sels, établies précédemment (2).

Les agrandissements de deux parties de la figure 8*A* sont représentés dans les figures 8*B* et 8*C*.

On observe que certaines lignes de niveau d'eau constant coupent en projection d'autres représentées en pointillé. Ce phénomène se manifeste dans une partie du domaine de $KHSO_4$ et dans une mesure moindre pour la solution solide $K_8(H_2PO_4)_{1+x}(HSO_4)_{7-x}$. Il est dû à l'allure tournante du liquidus. Dans ces régions, les normales au plan percent les nappes deux fois. Il en résulte le phénomène de solubilité rétrograde en fonction de la teneur en eau, mis en évidence dans la coupe décrite au paragraphe 5.

Pour visualiser la rotation de la nappe de $KHSO_4$ nous en donnons à la figure 9 une vue en perspective cavalière.

Ce travail complète notre connaissance de l'isotherme 75°C du système quaternaire réciproque H_3PO_4–K_2SO_4–H_2SO_4–K_3PO_4–H_2O. Ces résultats joints à ceux obtenus pour l'isotherme 25°C du même système (8–10) peuvent être exploités par les intéressés pour l'optimisation des procédés de fabrication d'engrais phosphopotassiques.

Un travail envisageant différentes situations est en cours d'étude.

Can. J. Chem. Downloaded from www.nrcresearchpress.com by 85.192.166.187 on 09/08/12
For personal use only.

Can. J. Chem. Downloaded from www.nrcresearchpress.com by 85.192.166.187 on 09/08/12
For personal use only.

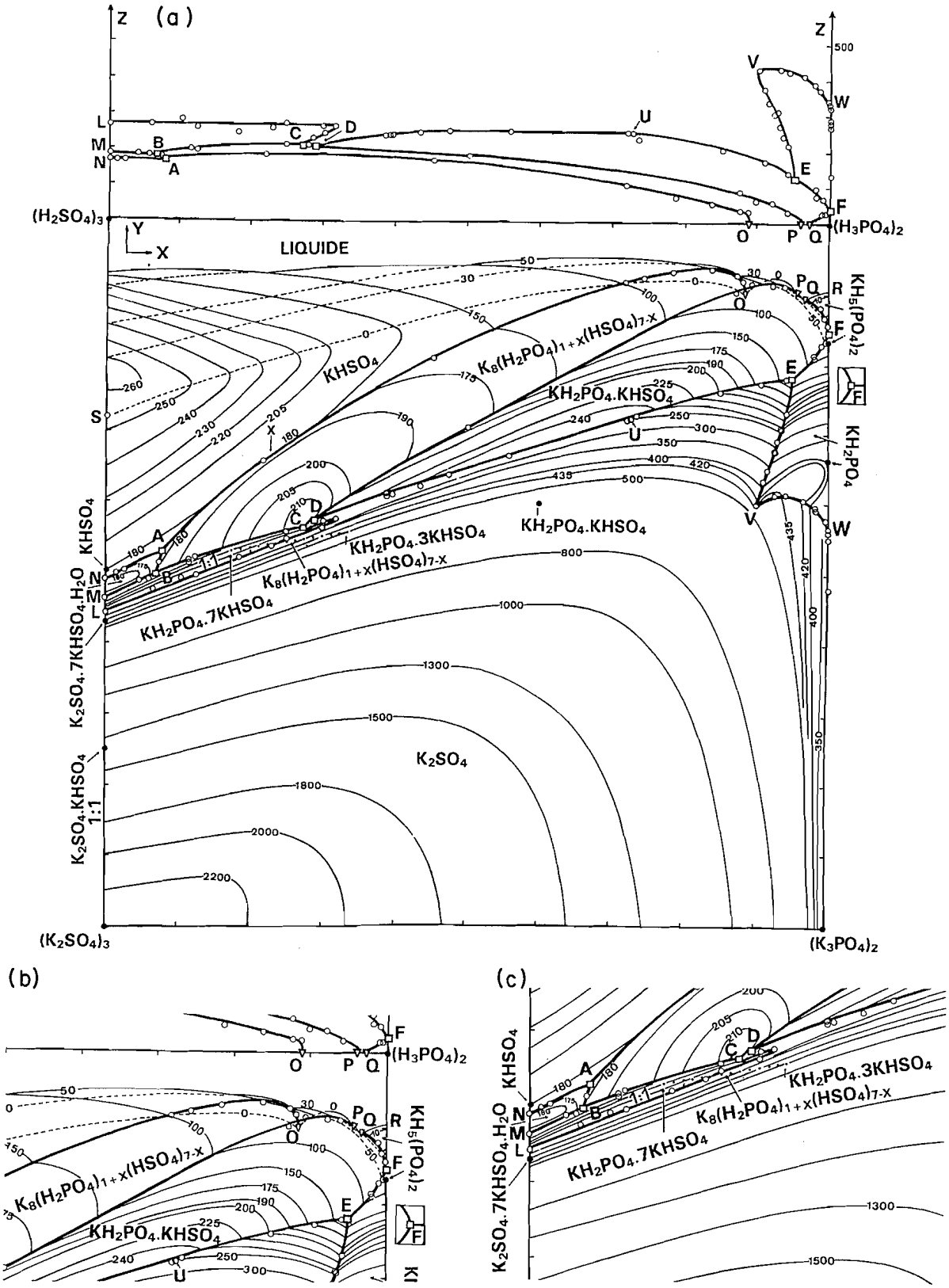

FIG. 8. (*a*) Tracé des lignes de niveau d'eau constant de l'isotherme 75°C du quaternaire réciproque H_3PO_4–K_2SO_4–H_2SO_4–K_3PO_4–H_2O, ainsi que des lignes de deux sels d'après la référence 2. (*b*) Agrandissement de la région acide de l'isotherme 75°C du quaternaire réciproque H_3PO_4–K_2SO_4–H_2SO_4–K_3PO_4–H_2O. (*c*) Agrandissement d'une région de l'isotherme 75°C du quaternaire réciproque H_3PO_4–K_2SO_4–H_2SO_4–K_3PO_4–H_2O.

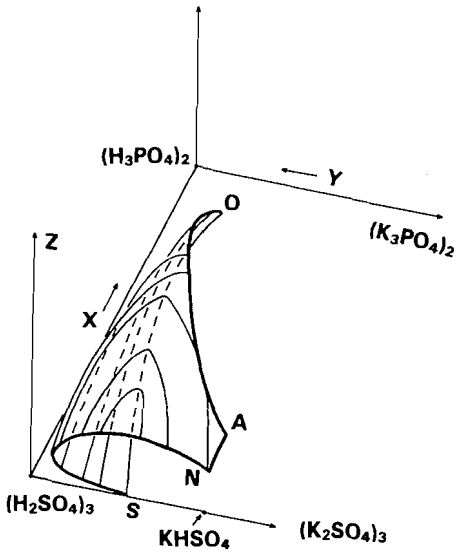

FIG. 9. Représentation de la nappe de $KHSO_4$ en perspective cavalière

1. N. Bourguiba et T. Jouini. Can. J. Chem. **70**, 2197 (1992).
2. N. Bourguiba et T. Jouini. Can. J. Chem. **71**, 1816 (1993).
3. N. Bourguiba et T. Jouini. C.R. Acad. Sci. Paris, Sér. 2, **309**, 1643 (1989).
4. O. Sackur et E. Fritzman. Z. Electrochem. **15**, 842 (1909).
5. J. Nyvlt. Solid–liquid phase equilibria. Elsevier Scientific Publishing Company, Amsterdam. 1977. p. 98.
6. M. Bouchacourt, M.T. Saugier et R. Cohen-Adad. Bull. Soc. Chim. Fr. **9–10**, 842 (1977).
7. F. Carrillo et J. Said. Douzièmes Journées d'Études des Équilibres entre Phases, Bordeaux. Mars 1986. pp. 15–19.
8. N. Bourguiba et T. Jouini. Thermochim. Acta, **237**, 187 (1994).
9. N. Bourguiba et T. Jouini. Thermochim. Acta. Sous presse.
10. N. Bourguiba et T. Jouini. Thermochim. Acta. Sous presse.

Can. J. Chem. Downloaded from www.nrcresearchpress.com by 85.192.166.187 on 09/08/12
For personal use only.

Nuclear magnetic resonance study of complexes formed between conjugated Schiff bases and carboxylic acids

H. LE-THANH AND D. VOCELLE[1]

Département de Chimie, Université du Québec à Montréal. C.P. 8888, Succ. A, Montréal, PQ, H3C 3P8, Canada

Received July 5, 1993[2]

H. LE-THANH and D. VOCELLE. Can. J. Chem. **72**, 2220 (1994).

The NMR spectra of the proton located in a N^+---H---^-O bond formed in the reaction of a conjugated Schiff base (SB) with a carboxylic acid (HA) in a non-polar solvent indicate that this proton is rapidly exchanging with other protons present in the system. For this study, two SB were used: all-*trans*-retinylidene *tert*-butylamine (RBA) and *trans,trans*-2,4-heptadienylidene *tert*-butylamine (HBA), and five carboxylic acids having pK_a's between 0.66 and 4.87.

^{1}H NMR spectra were taken at 293 and 233 K in $CDCl_3$ of systems of SB:HA using different ratios of acid to SB. Results indicate that the rapid proton exchanges are temperature and concentration dependent. Finally, the results are related to the natural pigments rhodopsin and bacteriorhodopsin.

H. LE-THANH et D. VOCELLE. Can. J. Chem. **72**, 2220 (1994).

Des spectres de RMN du proton localisé dans une liaison N^+---H---^-O formée à partir d'une réaction d'une base conjuguée (SB) et d'un acide carboxylique (HA) dans un solvant non polaire indiquent que ce proton s'échange rapidement avec d'autres protons présents dans le système. Pour cette étude, deux SB ont été utilisées : la toute *trans*-rétinylidène *tert*-butylamine (RBA) et la *trans,trans*-2,4-heptadiénylidène *tert*-butylamine (HBA) et cinq acides carboxyliques ayant des pK_a variant de 0,66 à 4,87. Les spectres de ^{1}H RMN ont été pris à 293 et 233 K dans le $CDCl_3$ à différents ratios de SB et HA. Les résultats montrent que les échanges de proton sont sensibles à la température et aux ratios d'acides utilisés. Finalement, les résultats sont discutés en rapport avec deux pigments naturels, la rhodopsine et la bactériorhodopsine.

Introduction

The formation of Schiff base:carboxylic acid complexes (abbreviated SB:HA) has not been studied extensively and yet the interest for these structures could well be quite important since in two photosensitive pigments — rhodopsin and bacteriorhodopsin — these complexes could be present. For example, some years ago, several groups have submitted the idea that, in the visual pigment rhodopsin, the retinylidene chromophore could be protonated via a proton relay transfer mechanism involving possibly many carboxylic acids, phenols, or water molecules (1–5). Recently, Khorana and his collaborators (6*a*–*g*) have shown that in bacteriorhodopsin, three amino acids participated in the protonation of the retinylidene chromophore while with rhodopsin, Glu-113 with the possible help of Glu-122 was the protonating agent of the chromophore. Other groups arrived at similar conclusions (7–9). However, Nathans (10) has shown that when the Schiff base chromophore is deprotonated (as when Glu-113 is changed to Gln-113), reprotonation could reappear in the presence of small anions such as iodide.

The existence of a proton relay transfer in model systems of rhodopsin has been used by us to explain the results obtained on models studied by different spectroscopic techniques (11–13). Such a mechanism requires the high mobility of the protons engaged in this process and it is the goal of this work to show that such mobility is present in the SB:HA systems. Recently, we were able to demonstrate the existence of complexes between simple unconjugated Schiff bases and carboxylic acids (14) by studying the NMR behaviour of the proton located in the N^+---H---^-O bond in such complexes. Scheme 1 presents the results obtained in this study.

The present work extends the previous study to conjugated Schiff bases and more particularly to all-*trans* retinylidene Schiff base, a good model for the chromophore of rhodopsin. Thus, it is the purpose of this research to discuss what possible role proton exchanges could play in systems where proton translocations are present.

Two Schiff bases are used in this work: *trans,trans*-2,4-heptadienylidene *tert*-butylamine (HBA) and all-*trans*-retinylidene *tert*-butylamine (RBA). We picked the first base because it is a conjugated Schiff base whose NMR spectra are easy to investigate and the second because of its relevance with rhodopsin or bacteriorhodopsin. To study the behaviour of the "acidic" proton (that is N^+---H---^-O), several different carboxylic acids were used: a strong acid, trichloroacetic acid (TCA); a moderately strong acid, monochloroacetic acid (MCA); a still weaker acid, propionic acid (PRO) with a pK_a in the same range as the second carboxylic group in glutamic acid or aspartic acid; and finally with both aspartic and glutamic acids protected by BOC for the amino group and benzyl ester for the α acid group (abbreviated GBE and ABE).

Experimental

HBA and RBA were prepared by using *trans,trans*-2,4-heptadienal (Aldrich Co.) and all-*trans*-retinal (Aldrich Co.) and *tert*-butylamine according to a method already described elsewhere (15). The structures of these two Schiff bases are shown below.

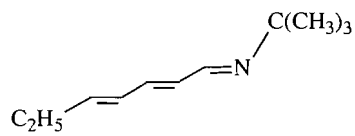

E,E-2,4-heptadienylidene *tert*-butylamine (HBA)

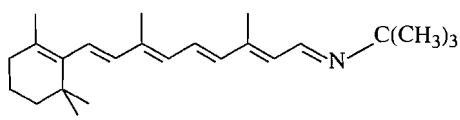

all-*trans*-retinylidene *tert*-butylamine (RBA)

[1]To whom correspondence should be addressed.

[2]Revision received June 22, 1994.

Can. J. Chem. Downloaded from www.nrcresearchpress.com by 85.192.166.187 on 09/08/12
For personal use only.

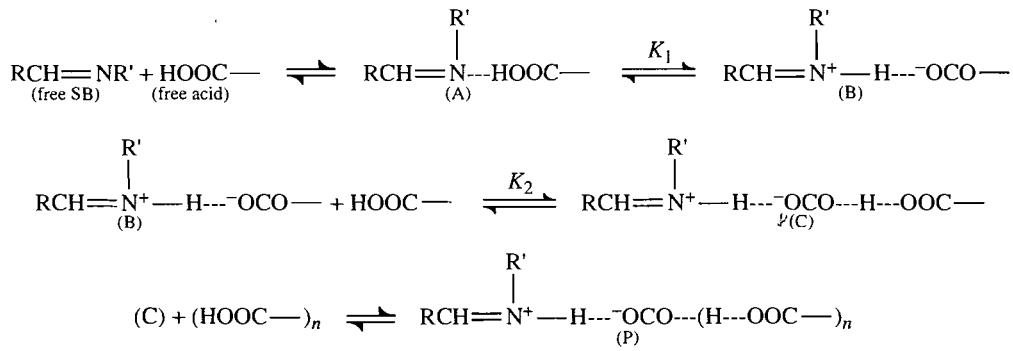

SCHEME 1

Since these Schiff bases are rather unstable, they were always freshly prepared or distilled before use. All acids (Aldrich Co; the protected amino acids ABE and GBE were obtained from Sigma), except PRO which was dried over activated molecular sieve (3Å), were kept under vacuum in a desiccator and in the presence of P_2O_5. No hydrolysis was noted under these conditions (in the NMR spectra the aldehydic proton would show if hydrolysis had occurred). Deuterated chloroform (Merck, Sharp & Dohme) was used as received and was quite satisfactory. To prove the absence of HCl or DCl in this solvent, a UV spectrum of RBA (10^{-5} M) in $CDCl_3$ was taken. No trace of absorption was observed in the 440 nm region, indicating the absence of any protonated SB. One could always argue that these precautions were not enough and that the model systems could contain trace amounts of water and of HCl. First of all, if some water molecules were indeed present, the protonated SB would immediately hydrolyze, producing all-*trans* retinal and the primary amine and this would be seen in the NMR spectra. Secondly, no trace of HCl (or DCl) could be detected in $CDCl_3$. But to insure that point and following the comments of one of the referees, we undertook two parallel NMR studies using in one case $CDCl_3$ kept over some molecular sieves, the other using $CDCl_3$ eluted twice on a basic alumina column and then kept over molecular sieves. With a strong acid like TCA or with a weaker one like MCA, at 233 K, the NMR spectra of RBA taken in both solvents were almost identical.

The concentration of the imines was 0.1 M for all spectra. All operations concerning the preparation of the samples were carried out under a dry nitrogen atmosphere (in a glovebox) and the spectra were recorded immediately after. A Bruker WH-400/DS (400 MHz) spectrometer was used for the study. Since the chemical shifts of the N^+---H---$^-$O proton vary with the concentrations of the acid, the spectra of the acids alone in $CDCl_3$ were always taken at the same concentrations as the ones used in conjunction with the SB.

Results and discussion

First, it is necessary to label the three kinds of "acidic" protons that are present in our system. H_{NO} will refer to the proton located between a protonated Schiff base (hereafter, PSB) and its counterion (v.g. N^+---H---$^-$O). H_{OO} will represent the proton between two carboxylic groups (v.g. O---H---O) in structures encompassing PSB and at least two carboxylic acids and finally, H_a is the proton between two carboxylic acids existing in a dimeric or polymeric forms. This can be visualized in Fig. 1. It must be remembered that carboxylic acids usually exist as dimers in nonpolar solvents (16).

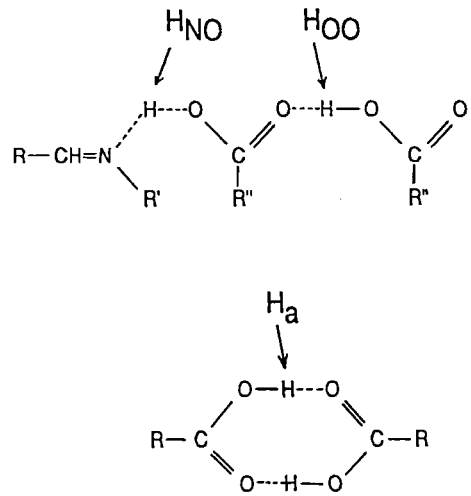

FIG. 1. Structure of a 1:2 complex showing two labile protons and structure of the dimeric form of an acid.

Depending on the conditions used, the "acidic" protons are expected to appear as a sharp or a broad singlet or a doublet. If there is rapid exchanges between the "acidic" protons, a sharp singlet should be observed. If the speed of the exchange is slower some peak broadening is expected. Finally, when the H_{NO} proton, for all practical purposes, stops to exchange with the other protons, a doublet will be formed since H_{NO} will couple with the azomethine proton (that is, the proton at C_{15} for RBA).

In proton exchange studies it is important to check for the presence of water and acid molecules since these will promote the exchanges. As indicated in the Experimental, all the data were collected in stringent anhydrous conditions and no trace amount of acid (like HCl) was observed. This means that the proton exchanges present in our study are due solely to the "acidic" protons of HA.

Table 1 presents the chemical shifts for H_{NO}, H_{OO}, and H_a for the systems consisting of RBA and five acids: TCA, MCA, PRO, ABE, and GBE in deuterated chloroform at 293 and 233 K while Fig. 2 shows a portion of the NMR spectra in the region above 10 ppm for the system of RBA with different molar ratios of TCA and at two different temperatures. Figure 2*a* shows that a rather broad peak at 14.72 ppm (J = 16 Hz) is present for a system consisting of an equimolar mixture of RBA and TCA at 293 K, whereas in Fig. 2*b* a doublet appears at 14.47 ppm for the same system at 233 K. In the first case, the

Can. J. Chem. Downloaded from www.nrcresearchpress.com by 85.192.166.187 on 09/08/12
For personal use only.

TABLE 1. Chemical shifts for H_{NO}, H_{OO}, and H_a for the imine RBA and five acids: TCA, MCA, PRO, ABE and GBE in $CDCl_3$

	Chemical shift[b]					
	H_{NO}		H_{OO}		H_a	
Systems[a]	293 K	233 K	293 K	233 K	293 K	233 K
TCA 1:0.5	10.94	11.61	—	—	10.41	12.04
1:1	14.72	14.47d	—	—	10.87	12.29
1:2	12.80d	12.50d	13.43	14.42	11.47	12.58
1:5	11.28d	11.03d	12.66	13.40	11.82	12.68
MCA 1:0.5	15.20	16.07	—	—	10.32	11.59
1:1	15.24	15.51	—	—	11.06	12.05
1:2	14.07[c]	13.49d	14.07[c]	15.10	11.57	12.40
1:5	12.52[c]	12.12d	12.52[c]	13.12	11.90	12.55
PRO 1:0.5	10.29	14.12	—	—	10.61	11.80
1:1	11.35	14.87	—	—	11.19	12.13
1:2	12.07[c]	14.72[c]	12.07[c]	14.72[c]	11.94	12.52
1:5	12.39[c]	13.55[c]	12.39[c]	13.55[c]	12.10	12.55
1:10	12.39[c]	13.01[c]	12.39[c]	13.01[c]	12.10	12.54
ABE 1:1	13.95	16.06	—	—	10.53	11.43
1:2	14.10[c]	15.02[c]	14.10[c]	15.02[c]	11.04	11.76
1:5	12.30[c]	13.66[c]	12.49[c]	13.12[c]	11.35	11.98
GBE 1:1	13.74	15.44	—	—	11.08	12.18
1:1	13.44[c]	14.67[c]	13.44[c]	14.67[c]	11.31	12.25
1:3	13.15[c]	13.84[c]	13.15[c]	13.84[c]	11.44	12.23
1:5	12.83[c]	13.57[c]	12.83[c]	13.57[c]	11.35	12.16
1:10	12.63[c]	13.31[c]	12.63[c]	13.31[c]	11.61	12.31

[a]Expressed in molar ratios of RBA:acids.
[b]d = doublet, otherwise a singlet.
[c]Unresolved peaks.

peak is assigned to H_{NO} since under the same concentration, H_a has a chemical shift of 10.87 and 12.29 ppm at 293 and 233 K, respectively. The broadness of the 14.72 ppm peak means that, at 293 K, the proton is rapidly exchanging with other "acidic" protons. At 233 K, the presence of a doublet for H_{NO} at 14.47 ppm signifies that the rate of proton exchange has slowed down considerably and that its coupling with the aldimine proton can now be observed. Thus at 233 K, the fact that H_{NO} is a doublet means that this proton must stay on the nitrogen atom long enough (compared to the time scale of NMR) to be coupled with the aldimine proton. The effect of lowering the temperature has been seen and discussed before, notably by Al-Dilaimi et al. (17).

Figure 2*c* shows the NMR spectrum of RBA and TCA in a 1:2 ratio at 293 K. Two peaks are observed. The rather slender peak at 13.43 ppm is assigned to H_{OO} and the doublet, as before, must belong to H_{NO}. That the peak at 13.43 ppm is H_{OO} rather than H_a is easily explained by the fact that at the same concentration, the proton of the pure TCA appears at 11.47 ppm. The fact that H_{NO} appears as a not too well resolved doublet means that the rate of exchange of this proton with the other "acidic" protons of the system has slowed down by adding an excess of TCA.

With a larger excess of TCA (ratio of 1:5) and at the two specified temperatures, H_{NO} appears as a doublet (see Table 1) as it would be expected, whereas all the H_{OO} (integration of four protons) appear as a singlet located at 12.66 ppm (at 293 K) and 13.40 ppm (at 233 K). The fact that a unique singlet is obtained here means that H_{OO} is exchanging rapidly with all the other "acidic" protons in the milieu with the exception of H_{NO} which is strongly held by the positive nitrogen atom of the SB. This is not surprising since H_{NO} is structurally different from H_{OO} or H_a while all the H_{OO} protons are similar between themselves and their differences with H_a become small (as seen by the convergence of their chemical shift values).

When an excess of the SB is used instead of the acid (v.g. 1:0.5 in Table 1), H_{NO} appears as a broad peak at 10.94 and 11.61 ppm when the spectra are taken at 293 and 233 K, respectively. Under these conditions proton exchanges are again present.

With MCA, H_{NO} appears as a doublet only at 233 K and with a ratio of SB:acid of 1:2 and 1:5. This result is expected since MCA, being a weaker acid than TCA, would require stronger conditions in order to allow the protonated SB to hold tightly to its proton. As indicated in Table 1, the differentiation between H_{NO} and H_{OO} cannot be made at 293 K, whatever the SB:HA ratios, since both have the same chemical shifts. However, at 233 K, H_{NO} and H_{OO} do appear at different chemical shifts but this difference is much less than with TCA (compared values of more than 2 ppm for TCA and values of 1.0–1.6 ppm for MCA). Proton exchanges are here the rule rather than the exception.

When PRO, a much weaker acid than MCA or TCA, is used at room temperature, as Table 1 indicates, almost no PSB can be seen since the chemical shifts of the "acidic" protons fall closely to the values of H_a. At 233 K, some protonation is observed (more highly deshielded peaks) but even with a very large excess of acid (v.g. 1:10), no doublet can be detected. These results mean that at 293 K, the SB is largely unprotonated whereas at 233 K some PSB is present as well as proton exchanges.

Can. J. Chem. Downloaded from www.nrcresearchpress.com by 85.192.166.187 on 09/08/12
For personal use only.

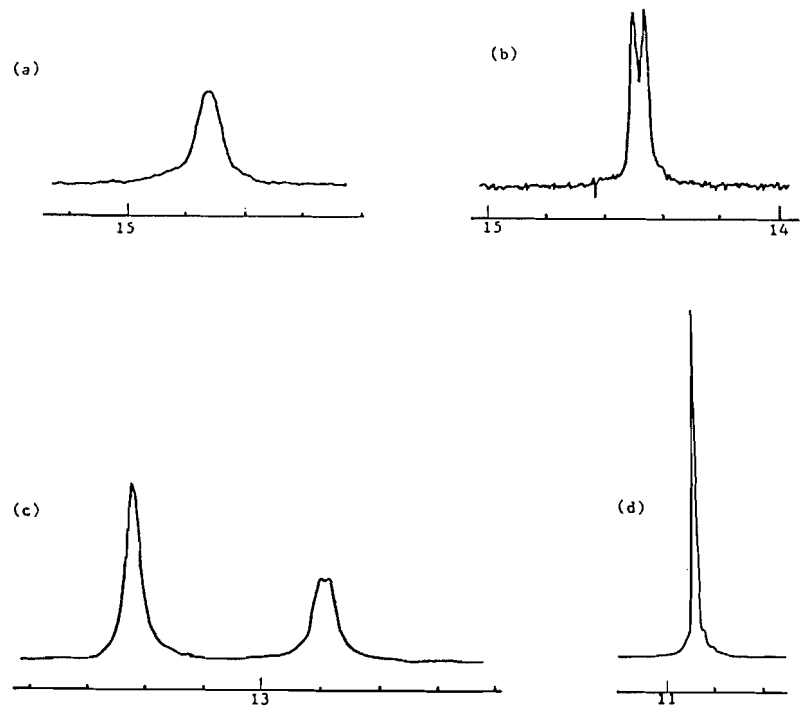

FIG. 2. NMR spectra of H_{NO}, H_{OO}, and H_a for (*a*) RBA:TCA, 1:1 at 293 K; (*b*) RBA:TCA, 1:1 at 233 K; (*c*) RBA:TCA, 1:2 at 293 K; (*d*) TCA alone, 0.1 M in $CDCl_3$, at 293 K

TABLE 2. Chemical shifts of H_{NO}, H_{OO}, and H_a for the imine HBA interacting with TCA, MCA, and PRO in $CDCl_3$

	Chemical shift[b]					
	H_{NO}		H_{OO}		H_a	
Systems[a]	293 K	233 K	293 K	233 K	293 K	233 K
TCA 1:0.5	14.38	14.14	—	—	10.41	12.04
1:1	15.09	14.75d	—	—	10.87	12.29
1:2	13.08	12.71d	14.49	15.29	11.47	12.58
1:5	11.80	11.47d	12.81	13.55	11.82	12.68
MCA 1:0.5	16.39	16.72	—	—	10.32	11.59
1:1	16.12	16.56	—	—	11.06	12.05
1:2	14.82[c]	14.57	14.82[c]	15.66	11.57	12.40
1:5	13.01[c]	12.86d	13.01[c]	13.57	11.90	12.55
PRO 1:0.5	10.88	13.82	—	—	10.61	11.80
1:1	11.83	14.87	—	—	11.19	12.13
1:2	12.37[c]	14.84[c]	12.37[c]	14.84[c]	11.94	12.52
1:10	12.49[c]	13.15[c]	12.49[c]	13.15[c]	12.10	12.54

[a]Expressed in molar ratios of HBA:acids.
[b]d = doublet, otherwise a singlet.
[c]Unresolved peaks.

The results obtained with GBE are similar to those of PRO which is not surprising since both acids have nearly the same pK_a's. However, the deshielding values of H_{NO} and H_{OO} is somewhat higher with GBE than with PRO, indicating that protonation could be somewhat higher. With ABE, which is slightly more acidic than GBE, differences in chemical shifts are seen for H_{NO} and H_{OO} only when the molar ratio of RBA:ABE reaches 1:5. Characteristically, H_{NO} still appears as a singlet thus indicating that the rate of proton exchange is still too fast compared to the time scale of NMR.

Similar data for HBA and three acids (TCA, MCA, and PRO) are shown in Table 2. For the three acids, the ratios of the SB to the acid varied from 1:0.5 to 1:5. Unless otherwise indicated, and as before, the chemical shift values are for singlets.

At 293 K, the data shown in Table 2 indicate that with HBA, H_{NO} is always a singlet whatever the acid used. With an excess of the carboxylic acid, for MCA and PRO, H_{NO} cannot be differentiated from H_{OO} since both have identical chemical shifts (indicated in Table 2 as unresolved peaks). However, for TCA at 233 K and at ratios of 1:2 and 1:5, H_{NO} appears as a doublet like in the previous case for RBA; thus here, both HBA and RBA behave similarly and the difference in conjugation does not seem to play a major role. With a ratio of 1:5 in TCA, data in Table 2 show that all the H_{OO} are exchanging rapidly between

Can. J. Chem. Downloaded from www.nrcresearchpress.com by 85.192.166.187 on 09/08/12
For personal use only.

themselves and the chemical shifts of these protons tend towards the values of H_a as it was also the case for RBA.

All these results can be used to gain some insight about the behaviour of the proton located in a N^+---H---^-O bond in systems where protonated Schiff bases are rapidly exchanging protons with the milieu.

First, depending on the protonating agent, the SB can be fully or partially protonated. Even when fully protonated as in the case with the strong acid TCA, the proton in the N^+---H---^-O bond is exchanging rapidly with other "acidic" protons. Only when excess acid or low temperature is used does the proton appear as a doublet, meaning that the rate of exchange has slowed down and that the coupling of H_{NO} with the aldimine proton can be seen. With weaker acids like PRO, GBE, and ABE that mimic aspartic and glutamic acids present in the natural pigments, the exchange rate is always very fast in a nonpolar solvent.

The results obtained in this study do not contradict those found for unconjugated systems (14). For conjugated SB, the main point here is that the N^+---H---^-O bond, being highly polarizable (18^{e-g}), also has a highly mobile proton that can exchange quite easily with other "acidic" protons. Extrapolated to the pigments these results suggest that the protonated retinal Schiff base has an "acidic" proton which is not tightly held by the positive nitrogen atom in the salt bridge (as in structure B in Scheme 1). This could explain, in part, why proton translocation in both rhodopsin and bacteriorhodopsin occurs so readily.

Acknowledgements

The NMR spectra were obtained at the Centre régional de RMN de haut champ of Université de Montréal. This study was made possible by grants received from the National Research Council (AO-943) and the Fonds pour la formation de chercheurs et l'aide à la recherche (FCAR) of Québec.

1. V.L. Khristoforov, E.N. Zvonkova, and R.P. Evstigneeva. Zh. Obshch. Khim. **44**, 909 (1974).
2. G.S. Denisov and N.S. Golubev. J. Mol. Struct. **75**, 311 (1981).
3. J.P. Rosenbusch. Bull. Inst. Pasteur, **83**, 207 (1985).
4. G. Zundel and H. Merz. *In* Information and energy transduction in biological membranes. Alan R. Liss, New York. 1984. p. 153.
5. C. Sandorfy and D. Vocelle. *In* Molecules in physics, chemistry and biology. Vol. 4. Kluwer Academic Publishers, Norwell, Mass., USA. 1989. p. 195.
6. (*a*) T. Marti, H. Otto, S.J. Rösselet, M.P. Heyn, and H.G. Khorana. J. Biol. Chem. **267**, 16992 (1992); (*b*) T.P. Sakmar, R.R. Franke, and H.G. Khorana. Proc. Natl. Acad. Sci. USA, **86**, 8309 (1989); (*c*) H. Otto, T. Marti, M. Holz, T. Mogi, M. Lindau, H.G. Khorana, and M.P. Heyn. Proc. Natl. Acad. Sci. USA, **86**, 9229 (1989); (*d*) H. Otto, T. Marti, M. Holz, T. Mogi, L.J. Stern, F. Engel, H.G. Khorana, and M.P. Heny. Proc. Natl. Acad. Sci. USA, **87**, 1018 (1990); (*e*) S. Subramaniam, T. Marti, and H.G. Khorana. Proc. Natl. Acad. Sci. USA, **87**, 1013 (1990); (*f*) T.P. Sakmar, R.R. Franke, and H.G. Khorana. Proc. Natl. Acad. Sci. USA, **88**, 3079 (1991); (*g*) T. Marti, S.J. Rösselet, H. Otto, M.P. Heyn, and H.G. Khorana. J. Biol. Chem. **266**, 18674 (1991).
7. E.A. Zhukorsky and D.D. Oprian. Science, **246**, 928 (1989).
8. H.J.M. de Groot, G.S. Harbison, J. Herzfeld, and R.G. Griffin. Biochemistry, **28**, 3346 (1989).
9. R. Needleman, M. Chang, B. Ni, G. Varo, J. Fornés, S.H. White, and J.K. Lanyi. J. Biol. Chem. **266**, 11478 (1991).
10. J. Nathans. Biochemistry, **31**, 4923 (1992) and references therein.
11. D. Larouche, A. Gélinas, H. Le-Thanh, C. Sandorfy, and D. Vocelle. Photochem. Photobiol. **53**, 153 (1991).
12. C. Rhofir, D. Vocelle, and C. Sandorfy. Res. Chem. Intermed. **12**, 131 (1989).
13. L.S. Lussier, C. Sandorfy, H. Le-Thanh, and D. Vocelle. J. Phys. Chem. **91**, 2282 (1987).
14. H. Le-Thanh and D. Vocelle. Can. J. Chem. **68**, 1909 (1990).
15. L.S. Lussier, A. Dion, C. Sandorfy, H. Le-Thanh, and D. Vocelle. Photochem. Photobiol. **44**, 629 (1986).
16. J.T. Bulmer and H.F. Shurwell. J. Phys. Chem. **77**, 256 (1973).
17. S.K. Al-Dilaimi, J.C. Aumiller, R.H. Johson, and P.E. Blatz. Photochem. Photobiol. **46**, 403 (1987).
18. (*a*) G. Zundel. *In* The hydrogen bond. Vol. 1. *Edited by* P. Schuster, G. Zundel, and C. Sandorfy. North-Holland, Amsterdam. 1976. p. 683; (*b*) E.G. Weidemann and G. Zundel. Z. Naturforsch. **25a**, 627 (1970); (*c*) R. Janoschek, E.G. Weidemann, H. Pfeiffer, and G. Zundel. J. Am. Chem. Soc. **94**, 3287 (1972); (*d*) B. Brzezinski and G. Zundel. Chem. Phys. Lett. **115**, 212 (1985); (*e*) H. Merz and G. Zundel. Biochem. Biophys. Res. Commun. **101**, 540 (1981); (*f*) G. Zundel and B. Brzezinski. *In* Proton transfer in hydrogen-bonded systems. *Edited by* T. Bountis. Plenum Press, New York. 1992. p. 153; (*g*) J. Olejnik, B. Brzezinski, and G. Zundel. J. Mol. Struct. **271**, 157 (1992).

Can. J. Chem. Downloaded from www.nrcresearchpress.com by 85.192.166.187 on 09/08/12
For personal use only.

Differential reactivity of carbohydrate hydroxyls in glycosylations. II.[1] The likely role of intramolecular hydrogen bonding on glycosylation reactions. Galactosylation of nucleoside 5′-hydroxyls for the syntheses of novel potential anticancer agents

DENNIS M. WHITFIELD AND STEPHEN P. DOUGLAS

Department of Molecular and Medical Genetics, and Carbohydrate Research Centre, Protein Engineering Network of Centres and Excellence (PENCE), University of Toronto, Toronto, ON M5S 1A8, Canada

TING-HUA TANG

Protein Engineering Network of Centres of Excellence (PENCE) and Department of Chemistry, University of Toronto, Toronto, ON M5S 1A8, Canada

IMRE G. CSIZMADIA

Department of Chemistry, University of Toronto, Toronto, ON M5S 1A8, Canada

HENRIANNA Y.S. PANG

Department of Molecular and Medical Genetics, and Carbohydrate Research Centre, University of Toronto, Toronto, ON M5S 1A8, Canada

FREDERICK L. MOOLTEN

Edith Nourse Rogers Memorial Veterans Hospital, Bedford, MA 01730, U.S.A. and Department of Microbiology, Boston University, Boston, MA 02215, U.S.A.

AND

JIRI J. KREPINSKY[2]

Department of Molecular and Medical Genetics, and Carbohydrate Research Centre, Protein Engineering Network of Centres of Excellence (PENCE), University of Toronto, Toronto, ON M5S 1A8, Canada

Received June 25, 1993[3]

DENNIS M. WHITFIELD, STEPHEN P. DOUGLAS, TING-HUA TANG, IMRE G. CSIZMADIA, HENRIANNA Y.S. PANG, FREDERICK L. MOOLTEN, and JIRI J. KREPINSKY. Can. J. Chem. **72**, 2225 (1994).

Contrary to expectations, many primary hydroxy groups are completely unreactive in glycosylation reactions, or give the desired glycosides in very low yields accompanied by products of many side reactions. Hydrogens of such primary hydroxyls are shown to be intramolecularly hydrogen bonded. Intermediates formed by nucleophilic attack by these hydroxyls on activated glycosylating agents may resist hydrogen abstraction. This resistance to proton loss is postulated to be the origin of the observed unreactivity. It is shown that successful glycosylations take place under acidic conditions under which such hydrogen bonds cease to exist. Accordingly, direct galactosylations of the normally unreactive 5′-hydroxyls of nucleosides were accomplished for the first time with a galactose trichloroacetimidate donor in chloroform under silver triflate promotion. It is noted that such galactosylated anticancer nucleosides may have improved biological specificity.

DENNIS M. WHITFIELD, STEPHEN P. DOUGLAS, TING-HUA TANG, IMRE G. CSIZMADIA, HENRIANNA Y.S. PANG, FREDERICK L. MOOLTEN et JIRI J. KREPINSKY. Can. J. Chem. **72**, 2225 (1994).

Contrairement à ce que l'on peut prévoir, plusieurs groupes hydroxyles primaires ne réagissent pas du tout au cours des réactions de glycosylation ou avec seulement de faibles rendements accompagnés de plusieurs sous-produits. On a démontré que les hydrogènes de ces hydroxyles primaires sont impliqués dans des liaisons hydrogènes. Les intermédiaires qui se forment par attaque nucléophile de ces hydroxyles sur des agents activés de glycosylation peuvent résister à la réaction d'enlèvement de l'hydrogène. Cette résistance à la perte d'un proton se produit en milieu acide alors que de telles liaisons hydrogènes cessent d'exister. On a réalisé pour la première fois des galactosylations directes des hydroxyles normalement non réactifs en 5′ des nucléosides en utilisant comme donneur un trichloroacétimidate de galactose dans le chloroforme sous promotion par le triflate d'argent. Il a été suggéré que de tels nucléosides anticancéreux galactosylés pourraient avoir une spécificité biologique améliorée.

[Traduit par la rédaction]

Introduction

Glycosylation of carbohydrate primary hydroxyls usually proceeds smoothly and many examples of glycosylations of OH-6 of hexopyranosides,[4] using Koenigs–Knorr, Helferich, and related procedures, have been described (3). However, we have observed surprisingly unreactive primary hydroxyl groups with certain acceptors. In our experience with difficult glycosylations, these acceptors often contained benzyl or allyl protecting groups (4). Similar observations have been made in other laboratories as well (e.g., P. Sinaÿ, V.V. Bencomo, personal communications). The common-sense explanation is that steric hindrance renders the primary hydroxyl groups inaccessible to the glycosylating agent. We were intrigued by reports of surprising difficulties (5) in the glycosylation of the primary O-5′ H of nucleosides (6, 7). Not only are orthoesters (8) formed when using an ester protective group at C-2 under common Koenigs–Knorr reaction conditions, but even this

[1]For article I in this series, see ref. 1.

[2]Author to whom correspondence may be addressed.

[3]Revision received July 18, 1994.

[4]There has been little interest in the syntheses of oligosaccharides through the OH-5 of pentofuranoses; this is perhaps because the 1–5 linkage is very rare among naturally occurring oligosaccharides.

Can. J. Chem. Downloaded from www.nrcresearchpress.com by 85.192.166.187 on 09/08/12
For personal use only.

Can. J. Chem. Downloaded from www.nrcresearchpress.com by 85.192.166.187 on 09/08/12
For personal use only.

reaction is sluggish and low yielding (9). To invoke steric effects of bulky protective groups resulting in inaccessibility of reactive sites did not seem quite correct in the case of nucleosides since no large protective groups were present in the reported cases. Consequently, we wondered whether intramolecular interactions such as hydrogen bonding between the hydroxyl and a lone pair or a π-electron system may be responsible for this unreactivity.

The success, although very limited, of the Bredereck modification of the Koenigs–Knorr reaction involving 2-deoxynucleosides such as thymidine (**T1**) indicated that these effects may indeed be of importance. In the Bredereck reaction, the primary hydroxyl is protected with a trityl group and glycosylations are performed under acidic conditions (10). Obviously, since the hydrogen atom of the 5′-hydroxy group is not present, it cannot participate in hydrogen bonding. This observation supports our hypothesis that glycosylations should be successful in the absence of the hydrogen bonding. In addition, glycosylations should occur if the hydrogen bond breaks under the reaction conditions.

To control effectively the outcome of glycosylations, the factors limiting reactivity should be determined. Because of our long-standing interest in a polymer-supported design (11) for synthesis of oligosaccharides in which such control is essential, we have undertaken a program investigating the origins of the low reactivity of such primary hydroxyls. We are also exploring a novel concept of cancer therapy based on the assumption that, under certain conditions, 5′-galactosylation yields nucleoside

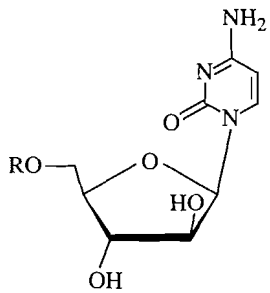

Ar1
Ar2

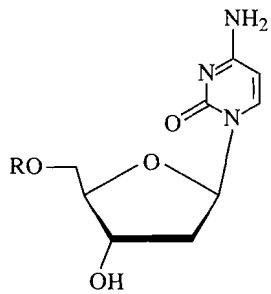

C1
C2

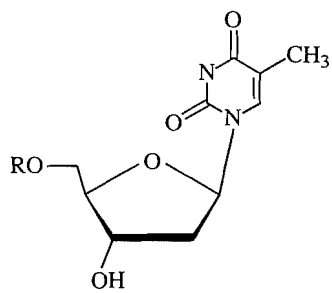

T1
T2

1, R = H

2, R =

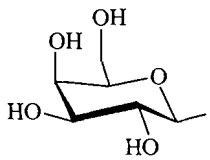

Ar, derivatives of arabinocytosine; **C,** derivatives of cytidine; **T,** derivatives of thymidine

anticancer drugs that can be specifically targeted against neoplastic cells (see Appendix I). We have already demonstrated (1) through ab initio mechanical calculations the existence of non-covalent interactions in nucleosides and of the potential for hydrogen bonding between the O5′-H and the nucleoside base in low-polarity solvents (12). To the best of our knowledge, direct glycosylation of nucleoside 5′-hydroxyl groups has not yet been reported. Consequently, we had to develop methodologies, capable of overcoming this hydrogen bonding, for the preparation of 5′-galactosylated nucleosides araC (**Ar2**), 2-deoxycytidine (**C2**), and thymidine (**T2**).

Results

Conformation of acceptor nucleosides

To determine the origins of the unusual unreactivity of primary hydroxyls of aglycons such as **Ar3**, **C3**, and **T3** (intermediates for the synthesis of **Ar2**, **C2**, and **T2**, see Scheme 1), and considering the hypothesis that such hydroxyls may be involved in intramolecular hydrogen bonding, their conformations in dry CD_2Cl_2 (to mimic the glycosylation conditions) were determined by NMR spectrometry. Infrared spectrometry was also used to probe the presence of internal hydrogen bonding in these substances.

*Deoxycytidine derivative **C3***

A. Nuclear magnetic resonance spectrometry

The data for deoxycytidine derivative **C3** in CD_2Cl_2 solution (cf. also ref. 1) have shown that **C3** exists in one overall predominant conformation. It is the *syn* conformation (cf. Fig. 1 for definition (13)) about the glycosidic linkage, as indicated by a large NOE between the anomeric proton H-1′ and the base H-6 and the *gauche-gauche* ($\gamma = 60°$) conformation for the hydroxymethylene group (based on the small values of the coupling constants $J_{4',5'}$ and $J_{4',5''}$, 2.7 and 2.9 Hz, see Table 3). Such a general conformation allows for a hydrogen bond between O-5′ H and the base carbonyl O-2. In the more acidic deuterated chloroform, the NOE between the H-1′ and H-6 diminished (8.1% → 5.1%), consequently the distance may have increased between O-5′ H and the base carbonyl O-2.

B. Infrared spectrometry

Stretching vibrations of a free OH group are normally absorbing in the frequency range 3610–3645 cm^{-1}, and the intra- and intermolecular hydrogen bonds give rise to an absorption in the frequency range 3200–3600 cm^{-1}. The two hydrogen bondings can be distinguished since the intermolecular hydro-

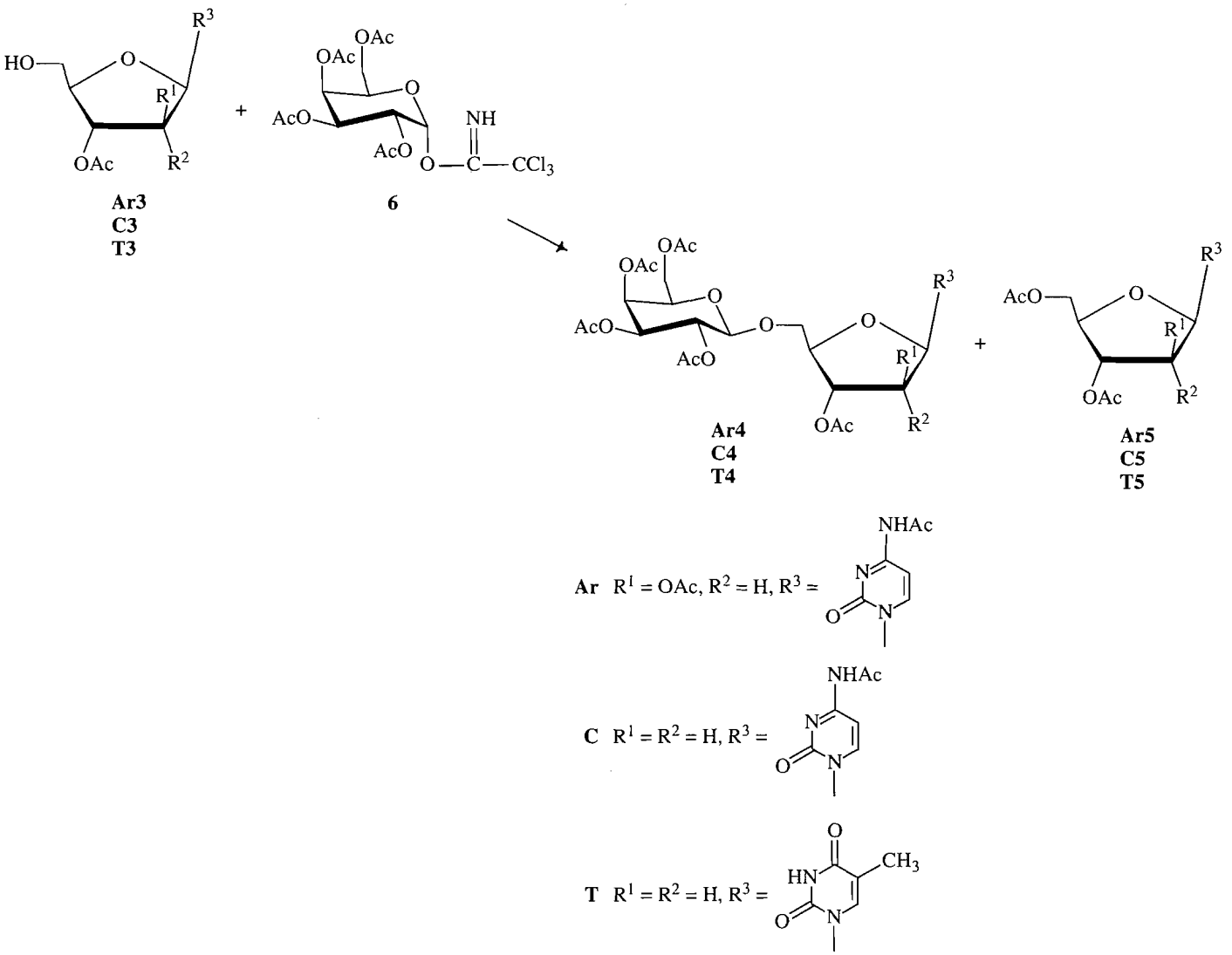

SCHEME 1. Galactosylation of nucleosidic O-5′H.

gen bonding diminishes with increased dilution of the sample, and consequently the absorption band disappears, while in the case of the intramolecular hydrogen bonding the absorption band remains unchanged. Intermolecular hydrogen bonding is not expected to occur at concentrations below 0.5 molar (14). If an NH group is present in the molecule, N–H stretching vibrations interfere since they give rise to a broad absorption between 3000 and 3500 cm^{-1}, thus overlapping with the absorption due to the OH vibrations.

To mimic the glycosylation conditions, the IR measurements have to be done in CH_2Cl_2, in which **C3** is not very soluble. At the highest concentration possible (1.3 mM), OH stretching vibrations in **C3** are found as a shoulder at 3620 cm^{-1} (free OH) of 3404 cm^{-1} (superimposed OH intramolecular bonding and NH). These absorptions did not change on further dilution until the sample became too dilute to record the spectrum.

Arabinocytidine derivative ***Ar3***

A. Nuclear magnetic resonance spectrometry

The arabinosylcytosine derivative **Ar3** exists in an *anti-syn* equilibrium with the *anti* conformation predominating, since the presence of the O-2′ acetate disfavours the *syn* conformation (15); cf. Fig. 1*a* for the definition of *syn* and *anti*, and the variations of the angle χ within the definition. The small NOE (cf. Fig. 2) between H-1′ and H-6 indicates that for **Ar3** the *anti* conformation, $\chi = 180°$,[5] most likely predominates over the *syn* conformation (16). The conformation around the hydroxymethylene moiety is indicated by the small (3.7 Hz) and medium (5.1 Hz) H-4′–H-5′ and H-4′–H-5″ couplings (see Table 1), nearly identical before and after D_2O exchange (cf. Fig. 3). Such couplings are consistent with an equilibrium between the *gauche-gauche* ($\gamma = 60°$) and the *gauche-trans* ($\gamma = 180°$) rotamers about C-4′–C-5′ (17). Further evidence of such an equilibrium is obtained from NOE measurements after irradiation of H-5′ or H-5″. In both cases a moderate intensity NOE was observed to H-3′ as well as to H-4′. In the *gauche-gauche* conformation only H-5″ (proR) is close enough to H-3′ to expect an observable NOE, while in the *gauche-trans* conformation H-5″ comes close to H-4′.

Another hydrogen bond is possible between O-5′ H and O-2′ in the *gauche-gauche* conformation. Such a hydrogen bond would be best accommodated in the C-2′ *endo* conformation of

[5]The *anti* conformation has been recognized as the predominant conformation for most nucleosides (ref. 43); the parent compound Ara C, **Ar1**, adopts the *anti* conformation in the crystalline state (44). Cf. also ref. 18.

Can. J. Chem. Downloaded from www.nrcresearchpress.com by 85.192.166.187 on 09/08/12
For personal use only.

Can. J. Chem. Downloaded from www.nrcresearchpress.com by 85.192.166.187 on 09/08/12
For personal use only.

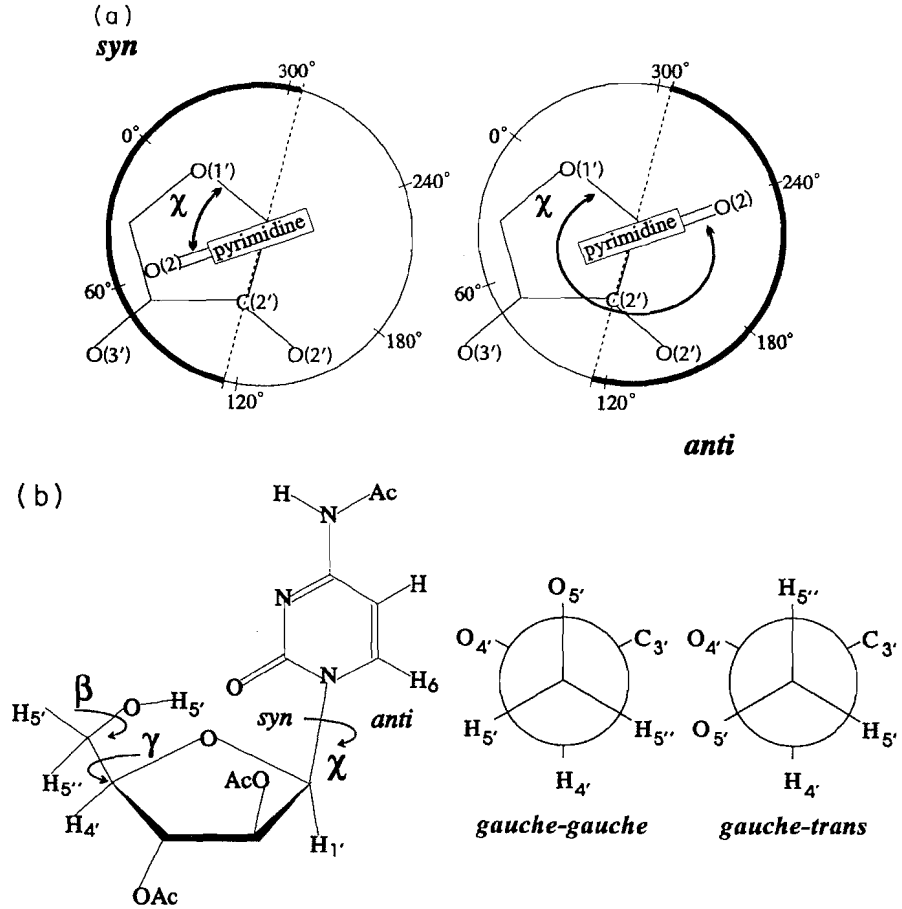

FIG. 1. Definitions of conformational parameters of nucleosides. Part (*a*) is reproduced from Saenger (13), with permission.

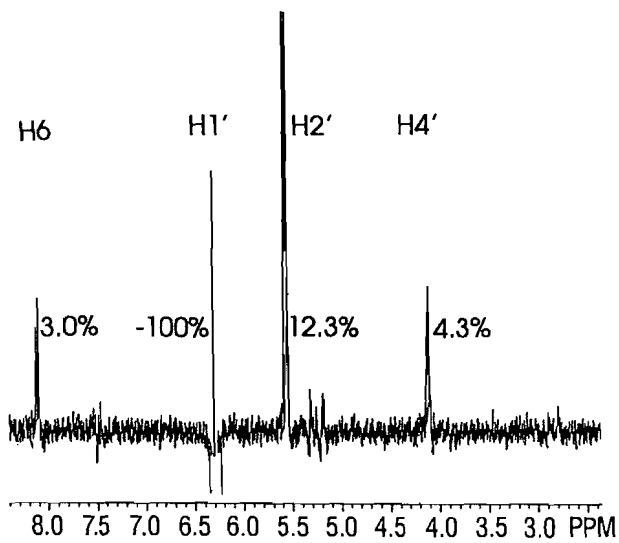

FIG. 2. Partial 500 MHz ^{1}H NMR spectrum of **Ar3** in CD_2Cl_2 solution. Difference 500 MHz ^{1}H NMR nuclear Overhauser effect spectrum of **Ar3** in CD_2Cl_2 solution after irradiation of anomeric H-1′ showing a small NOE to H-6.

the furanoside ring. This ring conformation is deduced from the small values of $J_{3',4'}$ (see Table 1). However, the small values of $J_{1',2'}$ and $J_{2',3'}$ are consistent with a mixture of conformers C-2′ *endo* and C-3′ *endo* (18).

B. Infrared spectrometry

The infrared spectrum of **Ar3** at a concentration of 7.2 mmol (the maximal concentration of freely soluble **Ar3**) displays two broad absorption bands for OH and NH stretching vibrations at 3482 cm^{-1} that did not change on dilution. No free OH absorption could be identified in the spectrum (cf. also Wechter, ref. 19). The absence of the absorption for free OH from the spectra of **Ar3** may seem somewhat puzzling since it appears to suggest that the hydrogen-bonded (O-5′ H...O-2) conformation predominates, while the NMR spectrometry would at first glance indicate that only a certain percentage of **ArC** in the conformational equilibrium is in a hydrogen-bonded *syn* conformation. However, hydrogen bonding from the O-5′ H can be directed to other acceptors than O-2 (18).

*Thymidine derivative **T3***

The thymidine derivative **T3** was not investigated in detail since key resonances overlapped. However, the small $J_{4',5'}$ and $J_{4',5''}$ coupling constants suggest that this derivative resembles the intramolecularly hydrogen-bonded conformation of **C3**.

Thus it is very likely that the deoxycytidine and thymidine derivatives having a free 5′-hydroxyl exist predominantly in an intramolecularly hydrogen-bonded conformation, O-5′ H...O-2. This hydrogen-bonded conformation may also be a significant component of the conformational equilibrium of the arabinosylcytosine derivatives, in addition to other hydrogen bondings.

TABLE 1. 500-MHz ^{1}H NMR data for arabinosylcytidine derivatives **Ar3**, **Ar5**, **Ar4**, and **Ar2**. Chemical shifts are in ppm and coupling constants are in Hz

Resonance	**Ar3**; CD_2Cl_2[a]	**Ar5**; $CDCl_3$	**Ar4**; $CDCl_3$	**Ar2**; D_2O
H5 ($J_{5,6}$)	7.49 (7.5)	7.49 (7.5)	7.51 (7.6)	6.06 (7.5)
H6	8.12	7.92	8.09	7.84
H1′ ($J_{1',2'}$)	6.30 (4.2)	6.36 (3.6)	6.40 (4.9)	6.22 (4.9)
H2′ ($J_{2',3'}$)	5.55 (2.5)	5.55 (<0.5)	5.58 (3.0)	4.42 (4.3)
H3′ ($J_{3',4'}$)	5.20 (3.3)	5.08 (2.6)	5.21 (3.0)	4.17 (4.4)
H4′ ($J_{4',5'}$)	4.12 (3.7)	4.25 (6.6)	4.11 (2.7)	4.16 (1.2)
H5′ ($J_{4',5''}$)	3.94 (5.1)	4.44 (4.4)	3.79 (4.1)	4.25 (3.4)
H5″ ($J_{5',5''}$)	3.87 (−12.2)	4.42 (−11.9)	4.24 (−10.9)	3.94 (−11.3)
NH	9.56	9.60	9.39	—
OH5′ ($J_{OH,5'}$) ($J_{OH,5''}$)	2.82 (4.3) (5.1)	—	—	—
GH1 ($J_{1,2}$)	—	—	4.58 (7.9)	4.49 (7.7)
GH2 ($J_{2,3}$)	—	—	5.22 (10.5)	3.57 (9.7)
GH3 ($J_{3,4}$)	—	—	5.06 (3.4)	3.67 (3.5)
GH4 ($J_{4,5}$)	—	—	5.43 (<0.5)	3.94 (<0.5)
GH5 ($J_{5,6}$)	—	—	3.95 (6.5)	3.69 (4.1)
GH6 ($J_{5,6'}$)	—	—	4.22 (6.9)	3.81 (7.9)
GH6′ ($J_{6,6'}$)	—	—	4.15 (−11.2)	3.77 (−11.7)
CH_3CO	2.24, 2.13, 1.91	2.28, 2.15, 2.14, 1.98	2.27, 2.20, 2.12, 2.06, 2.06, 2.00, 1.98	—

[a]Comparable to partial NMR data in ref. 16.

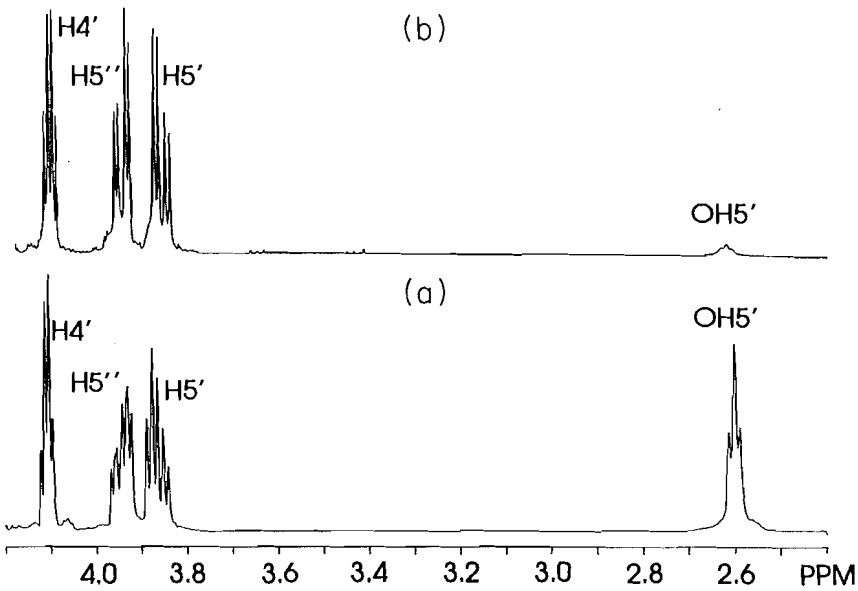

FIG. 3. Partial 500 MHz ^{1}H NMR spectrum of **Ar3** in CD_2Cl_2 solution. Figure 3(*a*) (lower tracing): a portion of the spectrum exhibiting signals of the H-4′, H-5′, H-5″, and OH-5′ protons; Figure 3(*b*) (upper tracing): the same area of the spectrum after exchange with D_2O showing that the signal for OH-5′ disappeared and one coupling was removed from both H-5′ and H-5″ resonances.

Synthesis of 5′-galactosylated nucleosides

The known acetylated nucleosides **Ar3** (19), **C3** (20), and **T3**,[6] having a free 5′-hydroxyl, were prepared as follows: N-acetylation of the free amino group (when present), temporary regioselective protection of the 5′-hydroxyl with the dimethoxytrityl (DMT) group, acetylation of the secondary hydroxyls, and removal of the DMT group. Attempts to selectively react the 5′-hydroxyl with DMT chloride without prior N-acetylation led to considerable substitution with DMT at the amino group. Even mild conditions for the removal of the DMT group with 1% dichloroacetic acid in CH_2Cl_2 led to some unavoidable nucleoside glycosidic bond cleavage necessitating a chromatographic purification.

These derivatives with a free 5′-hydroxyl did not give the desired galactosylated nucleosides with acetobromogalactose under standard Koenigs–Knorr conditions. However, they could all be galactosylated with 2,3,4,6 tetra-*O*-acetyl α-D-galactopyranosyl trichloracetimidate **6** (21) in CH_2Cl_2 promoted by

[6]Also commercially available (e.g., from Sigma, St. Louis, Mo.).

Can. J. Chem. Downloaded from www.nrcresearchpress.com by 85.192.166.187 on 09/08/12
For personal use only.

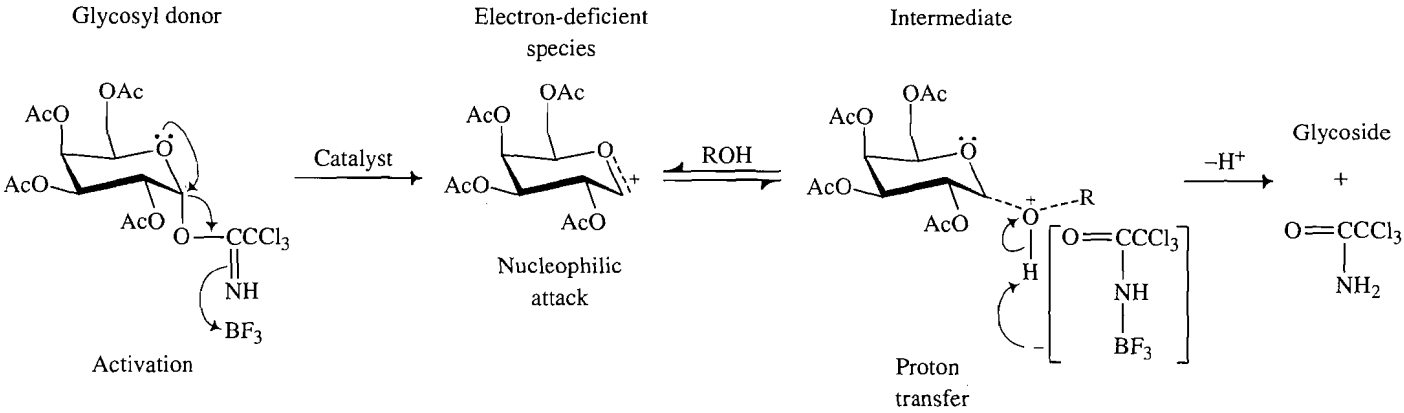

SCHEME 2. Simplified mechanism of the glycosylation reaction showing three principal stages of the reaction: activation, nucleophilic attack, and hydrogen loss. A protonated intermediate is formed in the second step of this reaction sequence. This intermediate must lose the proton to give the desired glycoside. In most cases the deprotonation is facile; it may become difficult if the hydrogen present in the intermediate is stabilized by an intramolecular hydrogen bond.

$BF_3{\cdot}Et_2O$ (22) to give the desired galactosides **Ar4**, **C4**, and **T4**. In all cases galactosylation was accompanied by significant acetate transfer from O-2 of the galactosyl imidate to the 5′-hydroxyl, giving the known nucleoside peracetates **Ar5** (23), **C5** (24), and **T5** (25) in ratios 1.25:1 (**Ar4**:**Ar5**), 0.23:1 (**C4**:**C5**), and 0.36:1 (**T4**:**T5**). No other nucleoside-containing products were observed. Imidate **6** and $BF_3{\cdot}Et_2O$ were used in equimolar quantities; when $BF_3{\cdot}Et_2O$ was used in catalytic amounts, acetate transfer predominated, and the overall yields were low. Variations in the temperature or the rate of addition of the $BF_3{\cdot}Et_2O$ had little effect and $BF_3{\cdot}Et_2O$ had to be added to a mixture of the imidate and the acceptor (26). Some nucleoside (base–sugar) cleavage occurred when reaction times exceeded 1 h.

Acetate transfer is not uncommon and has often been reported to compete with glycosylation reactions (27). To suppress this transfer, other Lewis acids were examined. $ZnBr_2$, although reported to eliminate acetate transfer (28), gave only complex mixtures. Triethylsilyl triflate (TESOTf) (29) gave results similar to those obtained with $BF_3{\cdot}Et_2O$. Silver triflate, recently described as a promoter of glycosylation reactions with trichloroacetimidates (30) in CH_2Cl_2, *significantly suppressed* acetate transfer, raising the ratio of glycosylation to transfer from 0.23:1 to 1.67:1 (**C4**:**C5**).

Further suppression of the acetate transfer reaction was achieved by changing the solvent from CH_2Cl_2 to the more acidic $CHCl_3$; using $BF_3{\cdot}Et_2O$ improved the ratio from 0.23:1 to 0.5:1 (**C4**:**C5**) in favour of the glycoside, and using silver triflate improved the ratio even further to 3.33:1 (**C4**:**C5**). The ratio for **Ar4**:**Ar5** improved to 20:1 from 1.25:1 using AgOTf in $CHCl_3$.

The peracetylated galactosylated nucleosides and the products of the acetate transfer reaction (peracetylated nucleosides) were separated by chromatography on silica gel followed by size-exclusion chromatography on Sephadex LH-20. During the silica gel chromatography a major by-product, the peracetylated disaccharide Galβ1,2GalαNHCOCCl$_3$ (**7***a*), was isolated. Its structure was determined by NMR and mass spectrometries; in particular, a strong ^{1}H NMR NOE between the β-Gal H-1 and the H-2 of the α-Gal residue established the β1–2 interglycosidic linkage. The α-NHCOCCl$_3$ anomer **7***a* was accompanied by a variable small amount of the β-anomer **7***b*. Both **7***a* and its anomer arise from the galactosylation of the monosaccharide formed after transfer of the acetate from O-2 of **6**, and imidate rearrangement of **6** (31).

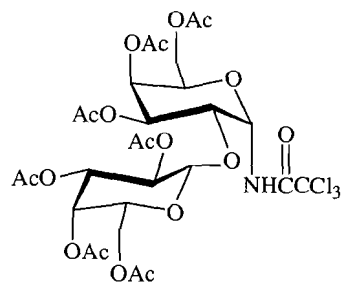

7*a*

The desired glycosylated nucleosides were finally obtained by removing both O- and N-acetate protective groups with DBU-catalysed transesterefication.

Preliminary biological assays

The galactosylated compounds exhibited the increased specificity in toxicity for cell types expressing the lacZ gene while they were nontoxic to other cells. This is the basic requirement for one approach to overcoming the low-selectivity problem associated with cancer chemotherapeutics (see Appendix II).

Discussion

The understanding of glycosylation reactions has been greatly advanced during the last two decades through the efforts of many chemists, and particularly through the pioneering insights into anomeric effects by R.U. Lemieux and his colleagues (32). It is clear that currently most common methods for the formation of glycosidic linkages proceed via nucleophilic substitution at the electron-deficient anomeric carbon as shown in Scheme 2. Details of the mechanism are less clear and apparently vary among different experimental designs. Despite these possible variations, it would be intuitively anticipated that primary hydroxyl groups (e.g., O-5H in pentofuranoses or O-6H in hexopyranoses) should always be reasonably reactive nucleophilic partners in glycosylation reactions. It is not, however, the case for nucleosides.

The results reported in this article suggest that 2′-deoxycytidine derivative **C3** assumes a conformation indicative of a hydrogen bond from the 5′-hydroxyl to the 2-carbonyl group and ab initio calculations and topological bond-path determinations confirm this conclusion (1). The NMR and infrared data demonstrate that analogous derivatives of thymidine, **T3**, and

Can. J. Chem. Downloaded from www.nrcresearchpress.com by 85.192.166.187 on 09/08/12
For personal use only.

Can. J. Chem. Downloaded from www.nrcresearchpress.com by 85.192.166.187 on 09/08/12
For personal use only.

arabinofuranosyl cytosine, **Ars**, also exist in such hydrogen-bonded conformations, at least to some extent. The O-5′ H of **Ar3** may be engaged in other hydrogen bonding (18).

The hydroxyl groups acting as hydrogen bond donors should have increased electron density at the oxygen (33), and this increase in the electron density should in turn make this oxygen a better (more reactive) nucleophile. Thus such a hydroxyl should be more reactive in a glycosylation reaction than the same hydroxyl would be, if not engaged in hydrogen bonding. Eventually the glycosylating agent becomes bound in a protonated intermediate that is still intramolecularly hydrogen bonded as portrayed in Scheme 2. To obtain the desired glycoside from the reaction, *this hydrogen must be abstracted.* Until this happens, the protonated intermediate remains in equilibrium with other species and therefore can become involved in competing reactions. For instance, the newly formed glycosidic bond can break, thus recreating the electron-deficient species, which may be diverted into other reaction pathways as illustrated in Scheme 3. These pathways, which involve the loss of the 2-O-acetyl and result in acetyl transfer to the aglyconic hydroxyl a well as in 1,2 disaccharides, can effectively compete (cf. the formation of the disaccharides **7***a*, *b*).

It is also important to appreciate that for donors like trichloroacetimidates, once the electron-deficient species is formed, it cannot form the original donor again because the imidate is transformed into an amide after activation. This amide or its complex with a Lewis acid can also act as a nucleophile. Lewis acids such as $BF_3{\cdot}Et_2O$ or silver triflate can also bind to nucleosides; this explains the requirements for larger than equimolar amounts of such acids in successful glycosylations. By such binding the Lewis acids may break up the intramolecular hydrogen bonding: it was shown in the previous communication (1) that complexation at the N-3 of the nucleoside by BF_3 markedly destabilized the hydrogen-bonded conformer. The intramolecular hydrogen bond can be further destabilized by solvent effects; for instance, successful 5′-galactosylations in chloroform (see also footnote 7) are described in this article.

Concluding remarks

We have attempted in this article to explain the origins of the low reactivity of primary hydroxyls acting as acceptors of glycosylating agents. We formulated a hypothesis that such unreactive primary hydroxyls are involved in intramolecular hydrogen bonding. Led by this hypothesis, we devised conditions in which this unreactivity can, at least to some extent, be overcome. Although we developed the argument using nucleosides as examples, it is equally applicable to glycosylations of any substrate, including oligosaccharides, in which the hydroxyl is involved in an intramolecular hydrogen bond. Clearly, more work, using suitably designed experimental strategy, is necessary to provide additional evidence for this hypothesis.

It is also worth noting that the aromatic ring of protecting groups, so commonly used in oligosaccharide synthesis (e.g., benzyls), can be the acceptor in hydrogen bonds as is well known from conformational studies of proteins. π-Type hydrogen-bonded complexes between benzene with acceptors HA or H_nA (including H_2O) have been described both experimentally (34) and theoretically (35). One of the possible ways (both a single or a bifurcated hydrogen bond is possible) to form this type of bonding in $C_6H_6{\cdot}H_2O$ is shown in Fig. 4. Assuming that such a hydrogen bond is sufficiently strong (typically 2–4 kcal mol^{-1}), the reaction mechanism portrayed in Scheme 2 applies to glycosylations of such hydroxyls as well. Examples from this laboratory of such glycosylations will be published in due course.

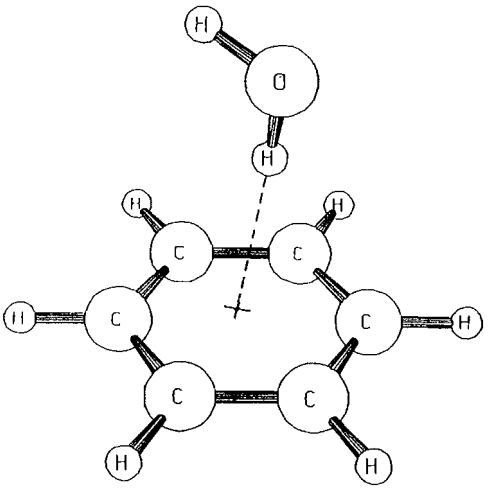

FIG. 4. One of the possible ways to form π-type hydrogen-bonded $C_6H_6{\cdot}H_2O$ complexes. One hydrogen atom of the water molecule is above the centre of the benzene ring and the O—H bond is almost perpendicular to the plane of the benzene ring. One minimum is found using the semiempirical Parametric Method 3 (PM3) method (41), the hydrogen bonding energy ΔE (PM3) = −1.39 kcal mol^{-1}. It has been shown that a similar intramolecular π-type hydrogen bonding in which an aromatic ring is the acceptor is not uncommon (42) and that such bonds are one of the stabilization forces of protein conformations.

Experimental

General methods

Thin-layer chromatography (TLC) was performed on silica gel $60F_{254}$ (Merck) plates and visualized by spraying with 50% aqueous sulfuric acid and heating at 200°C. Silica gel (230–400 mesh, Toronto Research Chemicals) was used for flash chromatography. All starting materials were dried overnight in vacuo (10^{-3} Torr; 1 Torr = 133.3 Pa) over KOH or P_2O_5 prior to use, and the solvents were distilled from appropriate drying agents. Solutions were concentrated at 1 Torr pressure in a rotary evaporator.

All compounds were characterized by ^1H (Tables 1, 3, and 5) and ^{13}C NMR (Tables 2, 4, and 6). To the best of our knowledge, the complete NMR spectra of the known compounds **AR3**, **AR5**, **C3**, **C5**, **T3**, and **T5** have not yet been reported. ^1H NMR assignments were made by standard decoupling techniques and all coupling constants were determined by first-order analysis of peak separations where possible. In the case of the fully deprotected compounds in D_2O solutions, the methylene protons were analyzed using inversion–recovery experiments with short delays (0.2−0.4 s) after the 180° pulse. With optimum delays, the short T_1's of the methylene hydrogens allowed the signals for these protons to be observed, whereas all other signals were either nulled or inverted (longer T_1's). ^{13}C NMR spectra of the title compounds were assigned by ^{13}C–^1H correlation, and of protected compounds by comparison to the literature (36, 37). All spectra are consistent with the proposed structures.

H and ^{13}C NMR spectra were recorded at 500 (125, ^{13}C) MHz with a Bruker AM 500 spectrometer or at 300 (75.5, ^{13}C) MHz with a Bruker AM 300 spectrometer, both at the NMR Spectrometry Laboratory of the Carbohydrate Research Centre, University of Toronto. Spectra were obtained either in $CDCl_3$ containing a trace of TMS (0 ppm, ^1H and ^{13}C) as the internal standard or in D_2O (99.98%, Ald-

[7]Another example is silver triflate promoted galactosylation (by trichloroacetimidate, **6**) of a 5-fluorouridine derivative in chloroform at elevated temperature (45).

Can. J. Chem. Downloaded from www.nrcresearchpress.com by 85.192.166.187 on 09/08/12
For personal use only.

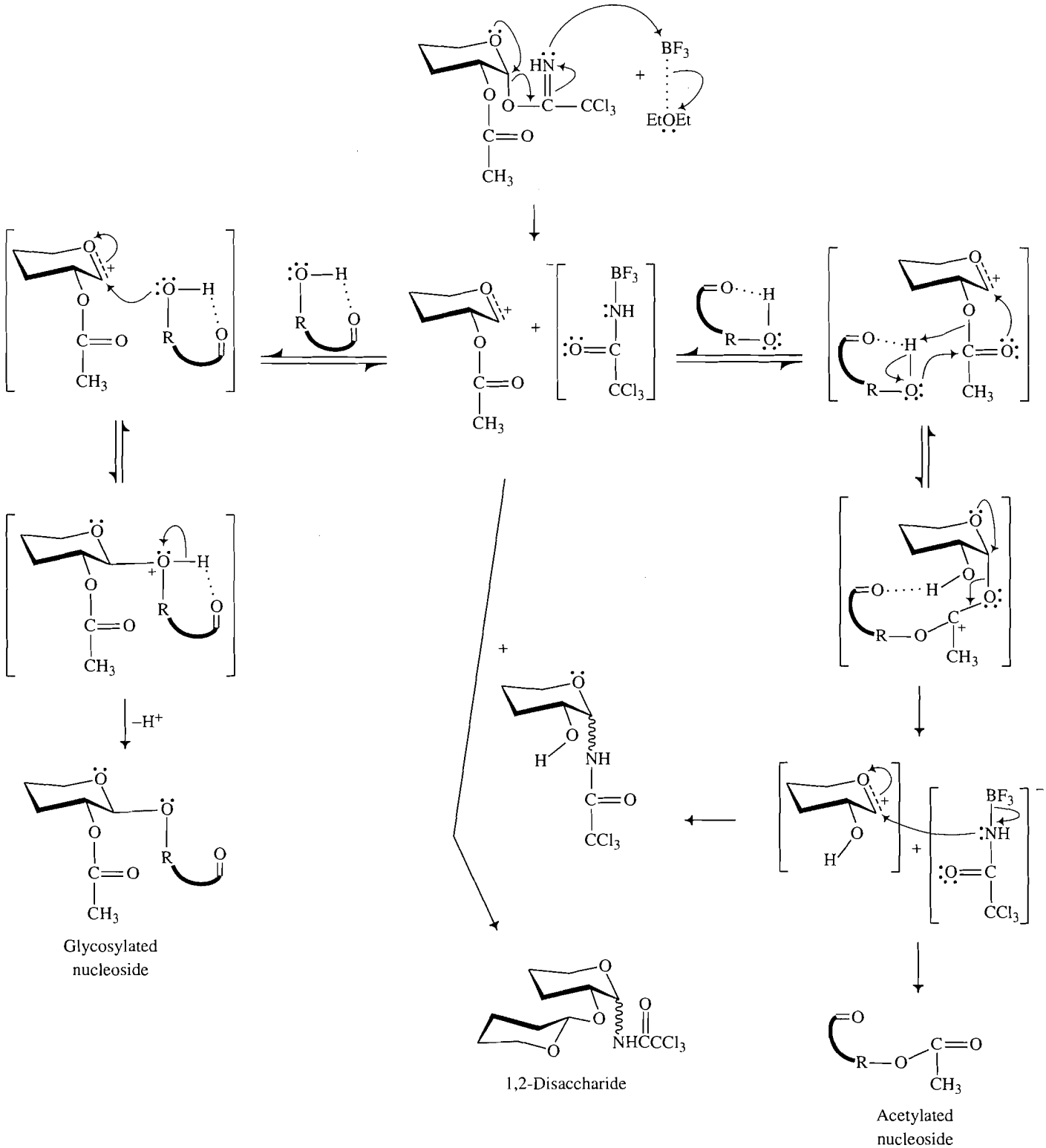

SCHEME 3. The glycosylation reaction is diverted from yielding the desired glycoside to a formation of by-products. The + and − signs represent electron deficiency or excess rather than true charges. The pyran ring represents properly protected pyranosides, BF_3 is used as an example of a promoter or catalyst.

rich) containing a trace of acetone (2.225 ppm relative to internal DSS, ^1H, and 30.5 ppm, ^{13}C) as the internal standard using the δ(ppm) scale. Spectra in CD_2Cl_2 were referenced to the residual $CHDCl_2$ (5.32 ppm) for ^1H spectra or to the ^{13}C resonance (53.6 ppm). Samples in CD_2Cl_2 had activated powdered 4 Å molecular sieves added directly to the NMR tube to ensure the complete removal of any residual water. For D_2O exchange, 1 drop of D_2O was added to the NMR tube, mixed vigorously, and then left to equilibrate with added molecular sieves before the spectra were obtained. NOE spectra were obtained in the 1D difference mode using an internal reference; the solutions were not de-

TABLE 2. 75.5 MHz ^{13}C NMR data for arabinosylcytidine derivatives **Ar3**, **Ar5**, **Ar4**, and **Ar2**. Chemical Shifts are in ppm

Resonance	**Ar3**; CD_2Cl_2	**Ar5**; $CDCl_3$	**Ar4**; $CDCl_3$	**Ar2**; D_2O
C2	155.1	154.7	154.7	157.0
C4	163.3	163.7	163.3	166.0
C5	96.3	95.9	96.3	95.5
C6	146.0	145.1	145.9	143.3
C1′	85.7	84.6	84.7	82.1
C2′	76.3[a]	75.2[b]	75.4[c]	75.5[d]
C3′	74.7[a]	74.1[b]	74.6[c]	75.7[d]
C4′	83.6	81.3	80.8	86.5
C5′	62.1	62.7	67.6	69.0
G1	—	—	101.3	103.4
G2	—	—	68.6[c]	71.1
G3	—	—	70.8[c]	73.0
G4	—	—	67.0[c]	68.9
G5	—	—	70.9[c]	75.7[d]
G6	—	—	61.2	61.3
COCH_3	171.0, 170.6, 169.0	170.4, 170.3, 170.2, 168.8	171.1, 170.2, 170.1(2), 169.7, 169.5, 168.7	—
NHCO*CH*$_3$	25.2	24.9	24.8	—
OCO*CH*$_3$	21.0, 20.6 20.37	20.5 (2), 20.43, 20.4	20.6(4), 20.5	—

[a]Assignments of these resonances may be interchanged.
[b]Assignments of these resonances may be interchanged.
[c]Assignments of these resonances may be interchanged.
[d]Assignments of these resonances may be interchanged.

TABLE 3. 500 MHz ^1H nmr data for 2′-deoxycytidine derivatives **C3**, **C5**, **C4**, and **C2**. Chemical shifts are in ppm and coupling constants are in Hz

Resonance	**C3**; CD_2Cl_2	**C5**; $CDCl_3$[a]	**C4**; $CDCl_3$	**C2**; D_2O
H5 ($J_{5,6}$)	7.43 (7.5)	7.47 (7.5)	7.48 (7.5)	7.91 (7.5)
H6	8.21	7.99	8.30	6.05
H1′ ($J_{1',2'}$)	6.23 (6.0)	6.25 (5.7)	6.46 (5.8)	6.29 (6.4)
H2′ ($J_{1',2''}$)	2.66 (7.4)	2.81 (7.2)	2.63 (8.3)	2.44 (6.9)
H2″ ($J_{2',3'}$)	2.39 (7.7)	2.09 (1.9)	2.13 (<1.0)	2.32 (4.4)
($J_{2',2''}$)	(−14.1)	(−14.4)	(−14.2)	(−14.2)
H3′ ($J_{2'',3'}$)	5.36 (6.6)	5.22 (4.4)	5.18 (6.3)	4.52 (6.7)
H4′ ($J_{3',4'}$)	4.18 (3.3)	4.37[b]	3.79[b]	4.22 (3.1)
H5′ ($J_{4',5'}$)	3.97 (2.7)	4.37[b]	4.22[b]	4.20 (3.6)
H5″ ($J_{4',5''}$)	3.91 (2.9)	4.37[b]	4.22[b]	3.83 (6.2)
($J_{5',5''}$)	(−11.1)	[b]	[b]	(−12.1)
NH	8.55	9.44	9.20	—
OH5′ ($J_{OH,5'}$)	2.87 (3.3)	—	—	—
($J_{OH,5''}$)	(5.9)			
GH1 ($J_{1,2}$)	—	—	4.52 (7.9)	4.45 (7.8)
GH2 ($J_{2,3}$)	—	—	5.13 (10.6)	3.56 (9.9)
GH3 ($J_{3,4}$)	—	—	5.05 (3.4)	3.66 (3.4)
GH4 ($J_{4,5}$)	—	—	5.44 (<0.5)	3.94 (<0.5)
GH5 ($J_{5,6}$)	—	—	3.94 (6.6)	3.69 (7.8)
GH6 ($J_{5,6'}$)	—	—	4.25 (6.8)	3.81 (4.2)
GH6′ ($J_{6,6'}$)	—	—	4.15 (−11.4)	3.76 (−11.5)
CH_3CO	2.23, 2.11	2.28, 2.11, 2.10	2.22, 2.21, 2.08, 2.06, 2.05, 1.09	—

[a]Comparable to partial NMR data in ref. 21.
[b]Resonances are not 1st order due to chemical shift overlap and so accurate coupling constants could not be determined.

Can. J. Chem. Downloaded from www.nrcresearchpress.com by 85.192.166.187 on 09/08/12
For personal use only.

Can. J. Chem. Downloaded from www.nrcresearchpress.com by 85.192.166.187 on 09/08/12
For personal use only.

TABLE 4. 75.5 MHz ^{13}C NMR data for 2′-deoxycytidine derivatives **C3**, **C5**, **C4**, and **C2**. Chemical shifts are in ppm

Resonance	**C3**; $CDCl_3$	**C5**; $CDCl_3$	**C4**; $CDCl_3$	**C2**; D_2O
C2	155.4	155.0	155.2	157.6
C4	162.6	162.4	162.7	166.3
C5	97.0	96.4	96.7	96.3
C6	145.3	143.4	145.0	141.9
C1′	86.1	83.0	84.1	85.5
C2′	38.7	39.1	38.6	39.5
C3′	74.9	74.1	68.8[a]	70.9
C4′	88.0	87.4	86.9	86.5
C5′	62.3	63.6	69.1	69.3
G1	—	—	100.8	103.1
G2	—	—	70.4[a]	71.1
G3	—	—	71.0[a]	72.9
G4	—	—	66.8[a]	68.8
G5	—	—	75.2	75.3
G6	—	—	61.2	61.2
COCH_3	170.83, 170.75	170.3, 170.2	170.6, 170.5,	—
			170.4, 170.2,	—
			170.0, 169.5	—
NHCO*CH*$_3$	24.9	25.0	25.0	—
OCO*CH*$_3$	21.0	20.9, 20.8	20.9, 20.7,	—
			20.6(2), 20.5	—

[a]Resonance assignments may be interchanged.

TABLE 5. 500 MHz ^1H NMR data for 2′-deoxythymidine derivatives **T4** and **T2**. Chemical shifts are in ppm and coupling constants are in Hz

Resonance	**T4**; $CDCl_3$	**T2**; D_2O
H6	7.67	7.64
H1′ ($J_{1',2'}$)	6.47 (5.7)	6.31 (11.4)
H2′ ($J_{1',2''}$)	2.32 (9.3)	2.40 (11.4)
H2″ ($J_{2',3'}$)	2.18 (<0.5)	2.40 (3.7)
($J_{2',2''}$)	(−14.3)	[a]
H3′ ($J_{2'',3'}$)	5.17 (6.1)	4.55 (6.7)
H4′ ($J_{3',4'}$)	4.17 (<0.5)	4.17 (3.3)
H5′ ($J_{4',5'}$)	4.28 (<0.5)	4.19 (3.3)
H5″ ($J_{4',5''}$)	3.73 (<0.5)	3.84 (4.6)
($J_{5',5''}$)	(−9.8)	(−10.8)
NH	8.53	—
GH1 ($J_{1,2}$)	4.51 (7.9)	4.46 (7.8)
GH2 ($J_{2,3}$)	5.20 (10.6)	3.57 (9.9)
GH3 ($J_{3,4}$)	5.09 (3.5)	3.66 (3.3)
GH4 ($J_{4,5}$)	5.45 (<0.5)	3.93 (<0.5)
GH5 ($J_{5,6}$)	3.97 (6.6)	3.70 (7.9)
GH6 ($J_{5,6'}$)	4.19 (6.8)	3.81 (4.2)
GH6′ ($J_{6,6'}$)	4.14 (−11,3)	3.75 (−11.7)
CH_3C	2.01	1.91
CH_3CO	2.12, 2.11	—
	2.09, 2.05(2)	

[a]The H2′ and H2″ resonances are overlapped and so this coupling constant could not be determined. The remaining coupling constants involving these two resonances were determined from the H1′ and H3′ multiplet patterns.

TABLE 6. 75.5 MHz ^{13}C NMR data for 2′-deoxythymidine derivatives **T4** and **T2**. Chemical shifts are in ppm

Resonance	**T4**; $CDCl_3$	**T2**; D_2O
C2	150.4	152.0
C4	163.6	166.9
C5	111.4	111.8
C6	135.9	137.7
C1′	84.6[a]	85.4[a]
C2′	37.0	38.6
C3′	68.8[b]	68.9
C4′	83.4[a]	85.6[a]
C5′	70.1	69.7
G1	101.3	103.5
G2	70.3[b]	73.1
G3	71.1[b]	71.18
G4	66.9[b]	71.13
G5	75.4[b]	75.5
G6	61.0	61.3
CH_3C	12.5	11.9
CHCH_3	170.7, 170.3,	—
	169.92(2), 169.85	
OCO*CH*$_3$	20.9, 20.63,	—
	20.58, 20.4,	
	20.0	

[a]Assignments for C4′ and C1′ may be interchanged.
[b]Assignments for these resonances may be interchanged.

gassed.[8] Inversion–recovery experiments used the standard Bruker software for T_1 determinations.

UV spectra were recorded with a Cary 20 UV–VIS spectrophotometer. Infrared spectra of compounds in saturated CH_2Cl_2 solutions were recorded with a Nicolet FTIR 5DX instrument. These solutions were subjected to stepwise dilutions to halve the previous concentration, and recorded again.

[8]A referee has suggested that traces of oxygen in solutions may significantly influence the quantitation of the NOE measurements. Although the specimens were not purged free of air, a possible experimental error would not exceed 15% as can be seen from the comparison of T_1's in $CDCl_3$ for **Ar3** before and after purging (data after purging are in parentheses): NH, 0.70 (0.71); H5, 1.55 (1.79); H6, 1.20 (1.32); H1′, 1.17 (1.46); H2′, 1.31 (1.46); H3′, 1.35 (1.53); H4′, 1.14 (1.24); H5′ + H5″, 0.41 (0.46); O5′H, 0.84 (0.82).

TABLE 7. Summary of EI mass spectral data for nucleoside intermediates. Relative intensities (%) of the fragment ions are shown in parentheses

Compound	M^b	Sugar	Hexose	Base (BH; B + 2H)	Others
Ar3	369(1.97)	217(38)	—	154(50) 112(80);	193(100); B + 41 (ref. 21)
Ar4	699(0.8)	547(4)	331(37)	154(50)	81(100)
					193(48); B + 41
					352(62); M – Hex[a]
C3	311(3.4)	159(15)	—	112(30)	69(100)
				154(60)	
C4	641(0.2)	489(0.2)	331(8.6)	152(15)	81(100)
				153(10)	294(2.6); M – Hex[a]
				154(10)	
T4	614(0.5)	489(2.8)	331(29)	126(10)	81(100)
				127(20)	
A5	411(4.5)	259(45.7)	—	154(40)	193(100); B + 41
C5	353(5)	201(8)	—	154(95)	81(100)

[a]Hex = hexose.
[b]For molecular formulae, see Experimental.

All mass spectra were recorded with a VG Analytical ZAB-SE mass spectrometer at the Mass Spectrometry Laboratory of the Carbohydrate Research Centre, University of Toronto. For Fast Atom Bombardment (FAB) the samples dissolved in methanol were loaded onto a target that contained 1–2 μL of glycerol and thioglycerol (3:1) and were bombarded by neutral xenon atoms (8 keV and 1 mA anode current) generated by an Ion-Tech Saddle Field ion gun. The spectra were recorded using the multichannel analyzing mode with a VG 11-250 data system. For low-resolution FAB-MS, the resolution was set at 1000 and the instrument was calibrated with CsI. For high-resolution FAB-MS measurements, i.e., 10 000 resolution (10% valley definition), 2% polyethylene glycol (avg. mol. wt. 300 or 600) was added to the matrix as internal calibrant and a narrow mass range was scanned using the accelerating voltage.

Electron-impact mass spectra (EI) were recorded using the direct insertion probe, and the source conditions were 200°C, 70 eV, and the electron trap current 100 μA. Resolution was approximately 1000 for low-resolution spectra and 10 000 for high-resolution spectra. Perfluoroalkane used as internal calibrant was introduced into the ion source via the septum inlet and the high-resolution spectra were acquired by scanning the magnet.

All derivatives of sufficient volatility, i.e., protected nucleosides, were characterized by electron ionization mass spectrometry, EIMS, and the title galactosylated nucleosides by fast-atom-bombardment mass spectrometry, FAB-MS. All new compounds purified by chromatography gave satisfactory elemental composition as determined by high-resolution MS spectra. The mass spectra of the peracetylated nucleosides exhibit facile elimination of ketene or acetic acid from the original molecules or fragment ions but otherwise the fragment ions are very similar to those reported for the trimethylsilyl derivatives (38, 39). Ions characteristic of the carbohydrate and base moieties are summarized in Table 7. In the case of the compounds **Ar3** and **C3**, the free hydroxyl group was also blocked by the trimethylsilyl group to confirm the presence of the free hydroxyl group at the 5′-position by observing the *m/z* 103 ion in the derivatized compounds (35, 36).

N^4-*Acetyl-1-[2′,3′-di*-O-*acetyl*-β-D-*arabinofuranosyl] cytosine* (***Ar3***)

1-[β-D-Arabinosyl]cytosine (**Ar1**, 3.0 g, 12.3 mmol) was dissolved in dry methanol (300 mL) and acetic anhydride (3.0 mL) and refluxed under argon. Additional portions of acetic anhydride were added after 1 h and, again, after 2 h (40). After heating for a total of 3 h, the mixture was concentrated to about 10 mL, cooled on ice, and diethyl ether (100 mL) was added. The resulting white precipitate was isolated by filtration with suction. The dried solid was dissolved in dry pyridine (60 mL) containing 4-dimethylaminopyridine (20 mg) under argon, dimethoxytrityl chloride (6.27 g; 18.5 mmol) was added, and the mixture was stirred at room temperature for 24 h. Another portion (0.9 g) of dimethoxytrityl chloride was added and stirring was continued for another 8 h. At this time TLC (1% CH_3OH:CH_2Cl_2) indicated that the reaction was complete, and the flask was cooled in an ice-bath, acetic anhydride (18 mL) was added dropwise by a syringe, and the mixture was stirred overnight in the ice-bath. After warming up to room temperature, the volatiles were removed by evaporation in high vacuum, and the residue was subjected to chromatography on a column of silica gel eluted sequentially with 500 mL CH_2Cl_2, 1% CH_3OH:CH_2Cl_2, 3% CH_3OH:CH_2Cl_2, and 5% CH_3OH:CH_2Cl_2, to yield slightly impure solid peracetylated 5′-dimethoxytritylated compound (6.0 g). After drying, the solid was dissolved in CH_2Cl_2 (150 mL) and a 1% solution of $CHCl_2COOH$ in CH_2Cl_2 (1.5 mL; 18.3 mL) was added dropwise under argon. After stirring was continued for another 5 min, solid $NaHCO_3$ (1.6 g; 20 mmol) was added and the reaction mixture was stirred for another 10 min. The solids were filtered off, rinsed with $CHCl_3$, and the combined filtrates were evaporated to dryness. The residue was at once subjected to chromatography on a column of silica gel and eluted sequentially with 1% CH_3OH:CH_2Cl_2, 3% CH_3OH:CH_2Cl_2, 5% CH_3OH:CH_2Cl_2, and 10% CH_3OH:CH_2Cl_2 to yield slightly impure **Ar3** (3.5 g; 77%). After repeated chromatography on silica gel with 5% CH_3OH:CH_2Cl_2, a pure specimen of **Ar3** ($C_{15}H_{19}N_3O_8$) was obtained: $[\alpha]_D$ +96.3 (*c* 0.30, CH_3OH:CH_2Cl_2 1:15); UV: 304, 245 nm (CH_2Cl_2) (lit. (16) UV 299, 249 nm); IR: 3482, 3295, 1754, 1727, 1674, 1655 (sh), 1628 cm^{-1} (CH_2Cl_2) (lit. (19) IR 3400, 3280, 3240, 1750, 1710, 1655 cm^{-1}).

N^4-*Acetyl-1-[3′*-O-*acetyl-2′-deoxy*-β-D-*ribofuranosyl] cytosine* (***C3***)

Compound **C3** ($C_{15}H_{19}N_3O_7$) was prepared in a manner analogous to that described for **Ar3**; yield 40%; $[\alpha]_D$ +54.9 (c 0.36, CH_3OH:CH_2Cl_2 1:15); UV: 302, 245 nm (CH_2Cl_2) (lit. (20) UV 296, 247 nm); IR: 3620, 3404, 1739, 1727, 1662, 1632 cm^{-1} (CH_2Cl_2).

N^4-*Acetyl-1-[2′,3′-di*-O-*acetyl-5′-(2,3,4,6-tetra*-O-*acetyl*-β-D-*galactopyranosyl)*-β-D-*arabinofuranosyl] cytosine* (***Ar4***)

Procedure A

To a solution of **Ar3** (300 mg, 0.81 mmol) in CH_2Cl_2 (20 mL) containing activated powdered 4 Å molecular sieves (500 mg) was added a solution of trichloroacetimidate **6** (520 mg; 1.22 mmol) in CH_2Cl_2 (36.6 mL) at 5°C, followed by $BF_3{\cdot}Et_2O$ (150 μL; 1.22 mmol). After stirring for 40 min, solid NH_4HCO_3 (100 mg) was added and stirring was continued for another 10 min. The solids were filtered off, rinsed with CH_2Cl_2, and the combined filtrates were evaporated to dryness. The residue was subjected to flash chromatography on silica gel, which on elution with 3% CH_3OH:CH_2Cl_2, followed by 5% CH_3OH:CH_2Cl_2, yielded fractions containing **6**, decomposition products of **6**, disaccharide **7** (see below), and a mixture of galactosylated

Can. J. Chem. Downloaded from www.nrcresearchpress.com by 85.192.166.187 on 09/08/12
For personal use only.

Can. J. Chem. Downloaded from www.nrcresearchpress.com by 85.192.166.187 on 09/08/12
For personal use only.

nucleoside **Ar4** and peracetylated nucleoside **Ar5** (total 296 mg). This mixture was further chromatographed on Sephadex LH-20 in CH_3OH:$CHCl_3$ (4:3) to give **Ar4** (174 mg, 20%) and a fraction containing **Ar5** contaminated with **Ar4**. The latter fraction, after a repeated chromatography on LH-20, yielded an additional small amount of **Ar4** and pure N^4-*acetyl-1-[2',3',5'-tri*-O-*acetyl*-β-D-arabinofuranosyl] cystosine (**Ar5**) ($C_{17}H_{21}N_3O_{17}$, $[\alpha]_D$ +118.2 (*c* 4.25, CH_2Cl_2) (lit. (footnote 6) $[\alpha]_D$ +87); UV: 304, 245 nm (CH_2Cl_2)). The fractions containing **Ar4** were further purified by flash chromatography on silica gel in 4% CH_3OH:$CHCl_3$ to yield pure **Ar4** ($C_{29}H_{37}N_3O_{17}$; 120 mg, 14%), $[\alpha]_D$ +52.0 (*c* 0.59, CH_2Cl_2); UV: 303, 244 nm (CH_2Cl_2). FAB-MS showed *m/z*: 700 (MH^+), 658 ($MH^+ - CH_2CO$), 370 (MH^+ − hexose − H_2O), and 331 (hexose). The observed Exact Mass value of MH^+ is 700.2215 (calcd. 700.2201).

Procedure B

Alcohol **Ar3** (500 mg, 1.37 mmol), trichloracetimidate **6** (945 mg, 1.92 mmol), and silver triflate (458 mg, 1.8 mmol) were dried together at high vacuum overnight. Chloroform (5 mL), freshly distilled from CaH_2, was added to this mixture of solids under an atmosphere of argon at room temperature. The reaction mixture was stirred for 24 h and then diisopropylethylamine (5 drops) was added, the solids were filtered off and rinsed with dichloromethane (2 × 23 mL), and the combined filtrate plus washings were washed with cold 0.05 M HCl (3 × 50 mL) and cold saturated aqueous bicarbonate (1 × 50 mL). The organic layer was dried with $MgSO_4$, filtered, and evaporated to dryness. The residue was purified by sequential chromatography on silica gel and Sephadex LH20 (cf. procedure A) to yield 394 mg, 41% of **Ar4**.

N-*[2-O-(2,3,4,6-Tetra*-O-*acetyl*-β-D-*galactopyranosyl)-3,4,6-tri*-O-*acetyl*-α-D-*galactopyranosyl] trichloroacetamide* (*7a*)

The fractions containing **7***a*, *b* (cf. the preparation of **Ar4**) were subjected to another chromatography on silica gel using ethyl acetate:hexane (3:2) as eluent, yielding **7***a* contaminated with *N*-[2-*O*-(2,3,4,6 tetra-*O*-acetyl-β-D-galactopyranosyl)-3,4,6-tri-*O*-acetyl-β-D-galactopyranosyl] trichloroacetamide (**7***b*). ^{1}H NMR: 7.33 (d, $J_{1,NH}$ 5.0, NH), 5.77 (t, $J_{1,2}$ 5.4, $J_{1,NH}$ 5.0, αGal H1), 5.38 (m, *J* 1.9, αGal H4), 5.35 (brd, $J_{3,4}$ 3.4, $J_{4,5} < 0.5$, βGal H4), 5.11 (dd, $J_{1,2}$ 7.5, $J_{2,3}$ 9.6, βGal H2), 5.11 (dd, $J_{2,3}$ 9.6, $J_{3,4}$ 3.6, αGal H3), 4.98 ($J_{2,3}$ 9.6, $J_{3,4}$ 3.4, βGal H3), 4.62 (d, $J_{1,2}$ 7.5, βGal H1), 4.18 (dd, $J_{1,2}$ 5.4, $J_{2,3}$ 9.6, αGal H2), 4.16 (m, αGal H6 and H6'), 4.13 (m, αGal H5), 4.11 (dd, $J_{6,6'}$ −11.3, $J_{5,6}$ 6.6, βGal H6), 4.08 (dd, $J_{6,6'}$ −11.3, $J_{5,6'}$ 6.2, βGal H6'), 3.93 (brdd, $J_{5,6}$ 6.6, $J_{5,6'}$ 6.2, βGal H5), 2.16, 2.12, 2.08, 2.06, 2.04, 2.03, 1.97 (7 × s, CH_3CO); ^{13}C NMR: 170.4 (2), 170.0 (2) 169.9, 169.5, 169.0 (CH_3COO), 162.5 CON, 101.7 βGal C1, 92.2 CCl_3, 78.0 αGal C1, 72.7, 71.0, 70.4, 68.9, 68.7, 67.9, 66.9, 66.7 (αGal and βGal C2, C3, C4 and C5), 61.1 and 60.8 (αGal and βGal C6), 20.62(4), 20.58(2), 20.5 (CH_3CO). FAB-MS exhibited fragments at *m/z* 780 (MH^+), 619 (peracetylated hexose − hexose), and 331 (peracetylated hexose). Exact Mass: calcd. for $C_{28}H_{37}NO_{18}Cl_3$: 780.1076; found: 780.1074.

N^4-*Acetyl-1-[2'-deoxy-2',3'-di*-O-*acetyl-5'-(2,3,4,6-tetra*-O-*acetyl*-β-D-*glactopyranosyl)*-β-D-*ribofuranosyl] cytosine* (***C4***)

Compound **C4** ($C_{27}H_{35}N_3O_{15}$, $[\alpha]_D$ +6.93 (*c* 0.37, CH_2Cl_2); UV: 303, 243 nm (CH_2Cl_2)) was prepared as described for **Ar4**. Yield 9% (procedure A) and 35% (procedure B). FAB-MS exhibited ions at *m/z* 642 (MH^+), 600 ($MH - CH_2CO$)$^+$, and 331 (peracetylated hexose). Exact Mass calcd. for $C_{27}H_{35}N_3O_{15}$: 642.2146; found: 642.2128. Compound **C4** was accompanied by N^4-*acetyl-1-[2'-deoxy-3',5'-di*-O-*acetyl*-β-D-ribofuranosyl] cytosine (**C5**), ($C_{15}H_{19}N_3O_7$, $[\alpha]_D$ +71.4 (*c* 12.4, CH_2Cl_2); UV: 304, 244 nm (CH_2Cl_2), (lit. (21) UV 307, 239 nm). The compounds **C4** and **C5** were separated by chromatography on silica gel and Sephadex LH20.

1-[3'-O-*Acetyl-2' deoxy-5'-(2,3,4,6-tetra*-O-*acetyl*-β-D-*galactopyranosyl)*-β-D-*ribofuranosyl] thymine* (***T4***)

Compound **T4** ($C_{26}H_{34}N_2O_{15}$, $[\alpha]_D$ −13.2 (*c* 0.67, CH_2Cl_2); UV: 262 nm (CH_2Cl_2)) was prepared as described for **Ar4**. Yield 24% (procedure A). FAB-MS exhibited ions at *m/z* 637(MNa^+), 615 (MH^+), 573 ($MH - CH_2CO$)$^+$, and 331 (peracetylated hexose). Exact Mass calcd. for $C_{26}H_{34}N_2O_{15}$: 615.2037; found: 615.2040. Compound **T4** was accompanied by *1-[2'-deoxy-3',5'-di*-O-*acetyl*-β-D-ribofuranosyl] thymine (**T5**).

1-[5'-β-D-*Galactopyranosyl*-β-D-*arabinofuranosyl] cytosine* (***Ar2***)

Peracetylated galactosylated nucleoside **Ar4** (120 mg) was dissolved in CH_3OH (20 mL) under argon, DBU (5 drops) was added, and the mixture was stirred overnight. After an addition of toluene (15 mL), the reaction mixture was concentrated using a rotary evaporator until a precipitate appeared. The solid was filtered off, rinsed with toluene and CH_2Cl_2, and then redissolved in CH_3OH and subjected to chromatography on LH-20 using $CHCl_3$:CH_3OH 4:3. Pure **Ar2** (62 mg, 89%) ($C_{15}H_{22}N_3O_{10}$, $[\alpha]_D$ +93.0 (*c* 0.13, CH_3OH); UV: 273, 230 nm (CH_3OH)) was obtained. FAB-MS exhibited ions at *m/z* 406 (MH^+), 244 (MH^+ − hexose), and 112 (base + 2H). Exact Mass calcd. for $C_{15}H_{22}N_3O_{10}$: 406.1462; found: 406.1469.

1-[2'-Deoxy-5'-β-D-*galactopyranosyl*-β-D-*ribofuranosyl] cytosine* (***C2***)

Compound **C2**; yield 71% ($C_{15}H_{22}N_3O_9$, $[\alpha]_D$ +51.3 (*c* 0.37, CH_3OH); UV: 273, 230 nm (CH_3OH)) was prepared as described for **Ar2**. FAB-MS exhibited ions at *m/z* 390 (MH^+), 228(MH^+ − hexose), and 112 (base + 2H). Exact Mass calcd. for $C_{15}H_{22}N_3O_9$: 390.1512; found: 390.1502.

1-[2'-Deoxy-5'-β-D-*galactopyranosyl*-β-D-*ribofuranosyl] thymine* (***T2***)

Compound **T2** ($C_{16}H_{24}N_2O_{10}$, $[\alpha]_D$ +11.2 (*c* 0.42, CH_3OH:H_2O 3:2); UV: 264, 202 nm (CH_3OH)) was prepared as described for **Ar2**. Yield 96%; FAB-MS exhibited ions at *m/z* 427 (MNa^+), 405 (MH^+), 243 (MH^+ − hexose), and 127 (base + 2H). Exact Mass calcd. for $C_{16}H_{24}N_2O_{10}$: 405.1509; found: 405.1544.

Acknowledgements

This work was supported through the Protein Engineering Network of Centres of Excellence (Canada), the Natural Sciences and Engineering Research Council of Canada, and the Department of Veteran Affairs (USA). The Carbohydrate Research Centre is a Faculty of Medicine (University of Toronto) facility partially supported by a maintenance grant from the Medical Research Council of Canada (MT-6499). Our thanks are due to Mr. Richard Crombie for obtaining the mass spectra. The skilful technical assistance of Mr. Raymond Ngan and Mr. Minh D. To is appreciated with thanks.

1. T.H. Tang, D.M. Whitfield, S.P. Douglas, J.J. Krepinsky, and I.G. Csizmadia. Can. J. Chem. **70**, 2434 (1992).
2. F.L. Moolten. CRC Crit. Rev. Immunol. **10**, 203 (1990).
3. H. Paulsen. Angew. Chem. Int. Ed. Engl. **21**, 155 (1982); **29**, 823 (1990).
4. S.P. Douglas, D.M. Whitfield, and J.J. Krepinsky. Abstracts, Fuji '90 Post-Symposium: Recent progress of synthetic methods in carbohydrates and their applications to synthetic chemistry. Susono City, Shizuoka, Japan. 1990; The Fuji Training Institute, Shizuoka.
5. F.W. Lichtenthaler, Y. Sanemitsu, and T. Nohara. Angew. Chem. Int. Ed. Engl. **17**, 772 (1978).
6. N.D. Chkanikov and M.N. Preobrazhenskaya. (*a*) Bioorg. Khim. **6**, 67 (1980); *b*) J. Carbohydr. Nucleosides Nucleotides, **8**, 391 (1981).
7. N.B. Hanna, R.K. Robins, and G.R. Revankar. Carbohydr. Res. **165**, 267 (1987).
8. N.K. Kochetkov and A.F. Bochkov. *In* Recent developments in the

chemistry of natural carbon compounds. *Edited by* A. Bognár, V. Bruckner, and Cs. Szántay. Akademiai Kiadó, Budapest. 1971.
9. N.D. Chkanikov, V.N. Tolkachev, and M.N. Preobrazhenskaya. Bioorg. Khim. **4**, 1620 (1978).
10. H. Bredereck, A. Wagner, G. Faber, H. Ott, and J. Rauther. Chem. Ber. **92**, 1135 (1959).
11. S.P. Douglas, D.M. Whitfield, and J.J. Krepinsky. J. Am. Chem. Soc. **113**, 5095 (1991).
12. E. Bosch, M. Moreno, and J.M. Leuch. Can. J. Chem. **70**, 1640 (1992).
13. W. Saenger. Angew. Chem. **85**, 680 (1973); K.H. Scheit. Nucleotide analogs. Wiley–Interscience, New York. 1980. p. 3.
14. L.P. Kuhn. J. Am. Chem. Soc. **74**, 2492 (1952).
15. J.G. Dalton, A.L. George, F.E. Hruska, T.N. McGaig, K.K. Ogilvie, J. Feeling, and D.J. Wood. Biochim. Biophys. Acta, **478**, 261 (1978).
16. A. Saran, B. Pullman, and D. Perahia. Biochim. Biophys. Acta, **349**, 189 (1974).
17. F.E. Hruska, D.J. Wood, T.N. McCaig, A.A. Smith, and A. Holy. Can. J. Chem. **52**, 497 (1974).
18. G.I. Birnbaum and D. Shugar. Top. Nucleic Acid Struct. Part 3. *Edited by* S. Neidle. Macmillan Press, London. 1987. p. 1.
19. W.J. Wechter. J. Med. Chem. **10**, 762 (1967).
20. A.M. Michelson and A.R. Todd. J. Chem. Soc. 34 (1954).
21. P. Zimmermann, R. Bommer, T. Bär, and R.R. Schmidt. J. Carbohydr. Chem. **7**, 435 (1988).
22. R.R. Schmidt. Angew. Chem. Int. Ed. Engl. **25**, 212 (1986).
23. A.P. Martinez, W.W. Lee, and L. Goodman. J. Med. Chem. **9**, 268 (1966).
24. M.J. Robins, M. MacCoss, S.R. Naik, and G. Ramani. J. Am. Chem. Soc. **98**, 7381 (1976).
25. A.M. Michelson and A.R. Todd. J. Chem. Soc. 816 (1955).
26. R. Bommer, W. Kinzy, and R.R. Schmidt. Liebigs Ann. Chem. 425 (1991).
27. (*a*) P.J. Garegg, P. Konradsson, I. Kvarnström, T. Norberg, S.C.T. Svensson, and B. Wigilius. Acta Chem. Scand. B, **39**, 569 (1985); (*b*) T. Ziegler, P. Kováč, and C.P.J. Glaudemans. Ann. Chem. 613 (1990); (*c*) N.I. Uvarova, G.I. Oshitok, and G.B. Elyakov. Carbohydr. Res. **27**, 79 (1973); (*d*) A. Ya. Khorlin, V.A. Nesmeyanov, and S.E. Zurabyan. Carbohydr. Res. **43**, 69 (1975); (*e*) R.U. Lemieux. Chem. Can. **16**, 14 (1964); (*f*) J. Banoub and D.R. Bundle. Can. J. Chem. **57**, 2091 (1979); (*g*) G. Wulff, and G. Röhle. Angew. Chem. Int. Ed. Engl. **13**, 157 (1974).
28. F.J. Urban, B.S. Moore, and R. Breitenbach. Tetrahedron Lett. **31**, 4421 (1990).
29. Y.D. Vankar, P.S. Vankar, M. Behrendt, and R.R. Schmidt. Tetrahedron, **47**, 9985 (1991).
30. S.P. Douglas, D.M. Whitfield, and J.J. Krepinsky. J. Carbohydr. Chem. **12**, 131 (1993).
31. (*a*) S. Nilsson, H. Lönn, and T. Norberg. Glycoconjugate J. **8**, 9 (1991); (*b*) C.W. Yue, J. Thierry, and P. Potier. Tetrahedron Lett. **34**, 323 (1993).
32. A.J. Kirby. The anomeric effect and related stereoelectronic effects at oxygen. Springer, Berlin and New York. 1983.
33. (*a*) K. Kefurt, J. Staněk, Jr., Z. Kefurtová, and J. Jarý. Collect. Czech. Chem. Commun. **70**, 1640 (1992); (*b*) G.J.F. Chittenden and J.G. Buchanan. Carbohydr. Res. **11**, 379 (1969); (*c*) G.J.F. Chittenden. Carbohydr. Res. **43**, 366 (1975); (*d*) D.M. Whitfield, J.P. Carver, and J.J. Krepinsky. J. Carbohydr. Chem. **4**, 369 (1985).
34. (*a*) A. Engdahl and B. Nelander. J. Phys. Chem. **89**, 2860 (1985); (*b*) J. Wanna, J.A. Menapace, and E.R. Bernstein. J. Phys. Chem. **91**, 2533 (1987); (*c*) F.A. Baiocchi, J.H. Williams, and J. Klemperer. J. Phys. Chem. **87**, 2079 (1983); (*d*) L. Andrews, G.L. Johnson, and S.R. Davis. J. Phys. Chem. **89**, 1706 (1985); (*e*) S. Suzuki, P.G. Green, R.E. Bumgarner, S. Dasgupta, W.A. Goddard III, and G.A. Blake. Science, **257**, 942 (1992); (*f*) J.L. Atwood, F. Hamada, K.D. Robinson, G.W. Orr, and R.L. Vincent. Nature, **349**, 683 (1991).
35. (*a*) J.L. Bredas and G.B. Street. J. Chem. Phys. **90**, 7291 (1989); (*b*) T.-H. Tang, W.-J. Hu, D.-Y. Yan, and Y.-P. Cui. J. Mol. Struct. (THEOCHEM), **207**, 319 (1990); (*c*) B.V. Cheney, M.W. Schulz, J. Cheney, and W.G. Richards. J. Am. Chem. Soc. **110**, 4195 (1988).
36. E. Breitmeier and W. Voelter. Monogr. Mod. Chem. **5**, 270 (1978).
37. D.B. Davies. Prog. NMR Spectrosc. **12**, 135 (1978).
38. J.A. McCloskey. Methods Enzymol. **93**, 825 (1990), and references therein.
39. H. Pang, K.H. Schram, D.L. Smith, S.P. Gupta, L.B. Townsend, and J.A. McCloskey. J. Org. Chem. **47**, 3823 (1982).
40. K.A. Watanabe and J.J. Fox. Angew. Chem. Int. Ed. Engl. **5**, 579 (1966).
41. (*a*) J.J.P. Stewart. J. Comput. Chem. **10**, 209 (1989); **10**, 221 (1989); (*b*) J. Comput. Chem. **12**, 320 (1991).
42. E.A. Gallo and S.H. Gellman. Tetrahedron Lett. **33**, 7485 (1992); (*b*) S.K. Burley and G.A. Petsko. Adv. Protein Chem. **39**, 125 (1988).
43. D.B. Davies, P. Rajani, and H.J. Sadikot. J. Chem. Soc. Perkin Trans. 2, 279 (1985).
44. J.S. Sherfinski and R.E. Marsh. Acta Crystallogr. **52**, 497 (1974).
45. J.J. Krepinsky, D.M. Whitfield, S.P. Douglas, N. Lupescu, D. Pulleyblank, F.L. Moolten. Methods Enzymol. **247**, 144 (1994).

Appendix I

Many cancer chemotherapeutic agents are capable of eradicating cancer cells. Practical clinical problems arise from the low selectivity of these agents: they kill normal healthy cells along with the cancerous ones, albeit at a slower rate. A significant increase in selectivity would dramatically enhance the curative potential of such drugs. For instance, if the cytotoxicity of β-D-arabinofuranosylcytosine, Ara C (**Ar1**), clinically used for treatment of leukemias, can be abolished by glycosylation of the drug, and if a suitable glycosidase is present only in the neoplastic cells, then this glycosylation would bring about the desired increase in the selectivity. One of us has been investigating such a scenario for future cancer chemotherapies (cf. ref. 2 for a review). The glycosidase employed is β-galactosidase, the product of the *Escherichia coli* β-galactosidase (lacZ) gene, inserted artificially into cancer cells. Galactosylation of Ara C then masks the toxicity of the nucleoside until the masking β-galactoside is removed inside such a cell, and Ara C is activated. Galactosylation of an Ara C antagonist, i.e., 2-deoxy-β-D-ribofuranosylcytosine (**C1**), would result in analogous deactivation of this nucleoside. To permit direct testing of this hypothesis, galactosylated nucleosides 5′-β-galactosyl β-D-arabinofuranosylcytosine (**Ar2**) and 5′-β-galactosyl 2-deoxy-β-D-ribofuranosylcytosine (**C2**) were required.

Appendix II

Galactosylation presumably turns the active compounds into proactive ones: e.g., toxic Ara C (**Ar1**) is turned into nontoxic Gal-Ara C (**Ar2**), which should become toxic again after the hydrolysis of the galactose–arabinose linkage using β-galactosidase. Two cell lines were used: (1) mouse fibroblasts *psi-2* capable of packaging retroviral genetic

Can. J. Chem. Downloaded from www.nrcresearchpress.com by 85.192.166.187 on 09/08/12
For personal use only.

information into infectious viral particles that can transfer the information to new cells, and its subline *psi-2 BAG* α containing retroviral information that includes β-galactosidase (lacZ) gene from *Escherichia coli*; and (2) murine sarcoma cell line *K3T3* from which a subline *K3T3 lacZ+* was created by exposing *K3T3* cells to *lacZ*-bearing virus released from *psi-2 BAG* α. As expected, Ara C (**Ar1**), added to the growth medium, was equally toxic to all the above cell lines and sublines. When Gal-Ara C (**Ar2**) was used, it was toxic to the sublines expressing lacZ gene, i.e., to *psi-2 BAG* α and *K3T3 lacZ+* cells, albeit about two orders of magnitude less than Ara C (**Ar1**), while non-toxic to the lines without lacZ gene (*psi-2* and *K3T3*).

Galactosylated compounds **C2** and **T2** were also used to examine rescue effects of deoxycytidine and thymidine. For instance, when cells are grown in the presence of Ara C (**Ar1**), they can be saved from death by an addition into the medium of deoxycytidine that acts as an antidote to the toxicity of **Ar1**. When such an experiment has been performed with *K3T3* and *K3T3 lacZ+* cells and galactosylated deoxycytidine (**C2**), only the line containing lacZ gene showed a slight rescue effect. A similar small rescue effect was observed when *psi-2 BAG* α cells (but not *psi-2* cells) were exposed to a "HAT" (hypoxanthin–aminopterin–thymidine) regimen in which galactosylated thymidine (**T2**) was substituted for thymidine as an antidote to aminopterin toxicity.

The low level of activity of galactosylated compounds in lacZ-containing cell lines may reflect, at least in part, two possible causes: first, the galactosylated compound **Ar2** is inefficiently taken up by the cells or, second, the rate of release of toxic **Ar1** in the cells is slow. The latter may happen since the enzyme is originally targeted for the Galβ1-4Gal linkage and so it may be less active for the Galβ1-5Ara linkage. Studies to clarify these issues and remedy the situation are underway.

Can. J. Chem. Downloaded from www.nrcresearchpress.com by 85.192.166.187 on 09/08/12
For personal use only.

Photophysics of some substituted 3*H*-indole probe molecules and their charged species

MICHEL BELLETÊTE, RANJIT S. SARPAL, AND GILLES DUROCHER[1]

Département de Chimie, Université de Montréal, C.P. 6128, Succ. Centre-ville, Montréal, QC H3C 3J7, Canada

Received June 3, 1994

MICHEL BELLETÊTE, RANJIT S. SARPAL, and GILLES DUROCHER[1]. Can. J. Chem. **72**, 2239 (1994).

The spectroscopic and photophysical parameters of neutral and cationic species of the following molecules have been discussed: 2-phenyl-3,3-dimethyl-3*H*-indole (**1**), 2-[(*p*-amino)phenyl]-3,3-dimethyl-3*H*-indole (**2**), 2-[(*p*-dimethylamino)phenyl]-3,3-dimethyl-3*H*-indole (**3**), 2-[(*p*-amino)phenyl]-3,3-dimethyl-5-carboethoxy-3*H*-indole (**4**), 2-[(*p*-methylamino)phenyl]-3,3-dimethyl-5-carboethoxy-3*H*-indole (**5**), 2-[(*p*-dimethylamino)phenyl]-3,3-dimethyl-5-carboethoxy-3*H*-indole (**6**). Solvatochromic shifts have been interpreted in terms of the nature of the substituent groups and the state of solute–solvent interactions and complexation. The theoretical radiative decay rate constant (k_F^t) along with the bandwidth of the absorption profile of the different species involved have been used to discuss the geometrical changes from one species to the other in the ground state. The mirror-image relationship between absorption and fluorescence spectra has proven to be a good tool to discuss any geometrical changes occurring in the excited state. A radiationless torsional mechanism takes place in the excited state relaxation of the various species. The protonation of the ring nitrogen atom generates a highly planar cationic species which retains its conformation in the relaxed excited state. The very effective quenching of the monocation fluorescence is interpreted by the formation of a non-emissive TICT state.

MICHEL BELLETÊTE, RANJIT S. SARPAL et GILLES DUROCHER[1]. Can. J. Chem. **72**, 2239 (1994).

On discute des paramètres spectroscopiques et photophysiques des espèces neutres et cationiques suivantes: 2-phényl-3,3-diméthyl-3*H*-indole (**1**), 2-[(*p*-amino)phényl]-3,3-diméthyl-3*H*-indole (**2**), 2-[(*p*-diméthylamino)phényl]-3,3-diméthyl-3*H*-indole (**3**), 2-[(*p*-amino)phényl]-3,3-diméthyl-5-carboéthoxy-3*H*-indole (**4**), 2-[(*p*-méthylamino)phényl]-3,3-diméthyl-5-carboéthoxy-3*H*-indole (**5**) et 2-[(*p*-diméthylamino)phényl]-3,3-diméthyl-3*H*-indole (**6**). On interprète les déplacements solvatochromiques en fonction de la nature des substituants et de l'état des interactions et de la complexation soluté–solvant. On a utilisé les constantes théoriques de vitesse de la dégénérescence radiative (k_F^t) de concert avec la largeur de bande du profile d'absorption des différentes espèces impliquées pour discuter des changements de géométrie se produisant d'une espèce à l'autre dans l'état fondamental. On a prouvé que la relation d'image dans un miroir entre les spectres d'absorption et de fluorescence est un bon outil pour discuter de tout changement géométrique se produisant dans l'état excité. Un mécanisme de torsion sans radiation se produit dans la relaxation de l'état excité des diverses espèces. La protonation de l'atome d'azote dy cycle génère une espèce cationique très plane qui retient sa conformation dans l'état excité relaxé. On interprète la désactivation très efficace de la fluorescence du monocation par la formation d'un état TICT qui ne donne pas d'émission.

[Traduit par la rédaction]

1. Introduction

The photophysical and photochemical properties of a molecule are determined by the nature and energy of its electronically excited states. Solvatochromism has proven to be a sensitive function of the dipole moment as well as any geometrical changes of the molecules in the excited state. In other words, solvatochromic shifts can be taken as experimental evidence in support of these changes (1–4).

Since natural photosynthesis involves charge separation on a molecular level, there has been widespread interest in designing model systems in order to mimic these processes occurring in nature. Bichromophoric molecules with donor (D) and acceptor (A) substituents form a special class of such molecules (5–7). The prime function for these molecules is to ensure a charge separation via fast electron transfer and then subsequently stabilize the resulting charged species. The main action is the interplay between the strength of donor and acceptor moieties. Marcus theory has been the most successful and also the most documented in explaining these processes (8, 9). Testing of the Marcus theory has become nowadays a usual practice in the field (10). Grabowski et al. (11) and Rettig (12) have identified another class of molecules in which the D and A moieties involved in charge separation are orbitally decoupled and in a perpendicular configuration. This class of excited states has been named the twisted intramolecular charge transfer (TICT) state (11, 12).

In an attempt to investigate the phenomenon of solvatochromism and electron transfer and to identify their usefulness in probing microheterogeneous media, we have synthesized molecules **1** to **6** whose structures have been described in our recent paper (13) and are reproduced in Fig. 1. The donor properties of the amino group are altered by the substituent methyl groups. Similarly, the acceptor properties of the indole moiety are enhanced by substituting an ethyl ester group at the position *para to* the amino substituents. During the course of our work (14–18), we have observed that the first electronic transition is always of $\pi\pi^*$ nature in both the absorption and fluorescence processes. Changes in the spectral shifts have been used to evaluate the dipole moments of the ground and first singlet excited states, which compared favorably with the results of INDO-S calculations (15). The first excited singlet state is more polar by a factor of two in all cases studied (16, 17). AMPAC and INDO-S calculations have also shown that the phenyl moiety is not coplanar with the rest of the molecule and is allowed to librate within the kT energy barrier. This torsional movement is responsible for the geometrical changes happening in the ground and excited states and also provides an important deactivation pathway for the S_1 state in nonpolar media.

The identification of the various species present in water has been recently described (13). The acid–base chemistry has resulted in four species in molecules **2** and **3**, whereas the ester-substituted **4**, **5**, and **6** molecules give rise to an additional anion due to ester hydrolysis. The various species observed in molecules **2** and **3** are as follows: neutral form, monocation due to

[1]Author to whom correspondence should be addressed.

Can. J. Chem. Downloaded from www.nrcresearchpress.com by 85.192.166.187 on 09/08/12
For personal use only.

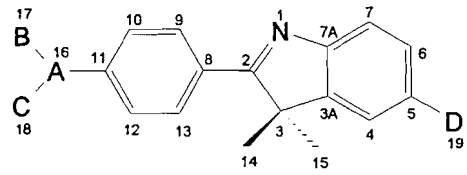

	A	B	C	D
1	H	-	-	H
2	N	H	H	H
3	N	CH_3	CH_3	H
4	N	H	H	CO_2Et
5	N	H	CH_3	CO_2Et
6	N	CH_3	CH_3	CO_2Et

FIG. 1. Molecular structure of the 3H-indole substituted chromophores.

ring nitrogen protonation, and dication due to the protonation of terminal amino as well as ring nitrogen group. The anion formed in **2** is due to amino group deprotonation, whereas in **1** it is due to the ring carbon deprotonation. In molecules **4**, **5**, and **6**, the order of protonation and the resulting species produced are the same as in **2** and **3** except for the fact that the ester hydrolysis leads to the formation of an additional anion (13).

As a continuation of our studies, this paper reports on the spectroscopic and photophysical properties of molecules **1** to **6** (see Fig. 1) in water as a function of pH since such species can be used as probes for microheterogeneous media (19). It is shown that the main deactivation pathway of the relaxed excited state of the neutral 3*H*-indoles in nonpolar media occurs via a torsional movement involving the amino group and/or the phenyl ring. Protonation of the indole ring greatly enhances the ground state planarity of these molecules. Nevertheless, fluorescence emissions of the cations are very weak, this is interpreted as due to the possible occurrence of a non-emissive TICT (twisted internal charge transfer) channel in the decay mechanism.

2. Experimental section

Synthesis, purification, absorption spectroscopy and methodology have already been described (13). The modified Hammett's acidity scale and Yagil's basicity scale used here to fix the pH values and the method for preparing the solutions have also been described (13). Fluorescence quantum yields of all the mentioned species were measured using molecules **3** as a standard in ethanol (ϕ_F = 0.33). The theoretical radiative decay rate constants (k_F^t) have been calculated from the Strickler and Berg relationship (18, 20). Fluorescence lifetime values larger than 0.2 ns were obtained from a multiplexed time-correlated single photon counting fluorimeter (Edinburg Instruments, Model 299T), as described in ref. 21. The short lifetimes (<0.2 ns) were measured on a time-correlated single photon-counting system which uses a synchronously pumped cavity dumped, rhodamine 6G-dye laser pumped by a mode-lacked argon ion laser as an excitation source. Details are given in ref. 16.

3. Results and discussion

3.1 Neutral species

The absorption and fluorescence spectral characteristics of **1** to **6**, and their dependency on acidity, have been studied in ref. 13. It was observed that the neutral species is present in water at pH = 9. Spectral characteristics of the neutral species in water and some of the representative solvents at 300 K are listed in Table 1. Table 2 reports on the photophysical parameters obtained in the same solvents. All molecular fluorescence decay curves could be fitted to a single exponential function except for molecules **4**, **5**, and **6** in water, where only multiple exponential functions can accurately describe the fluorescence decays. The corresponding preexponential factors and lifetimes for these three molecules in aqueous medium are **4** (A_1 = 0.59, τ_1 = 126 ps; A_2 = 0.015, τ_2 = 1060 ps), **5** (A_1 = 0.81, τ_1 = 73 ps; A_2 = 0.009, τ_2 = 700 ps; A_3 = 0.002, τ_3 = 1800 ps), and **6** (A_1 = 0.63, τ_1 = 82 ps; A_2 = 0.009; τ_2 = 1030 ps; A_3 = 0.001, τ_3 = 2030 ps). For each molecule the first component is mainly responsible for the overall fluorescence spectrum ($A_1\tau_1/\Sigma_i A_i\tau_i > 0.8$) and thus Table 2 reports on the shortest lifetimes of **4**, **5**, and **6** in water.

In the present set of molecules, it is well-known that the lowest energy transition is of the $\pi\pi^*$ type is polarized along the long molecular axis (14–17, 22). Table 1 shows that the energy of the absorption spectrum of these molecules in *n*-heptane decreases from **1** to **3** and from **4** to **6**. This strongly supports the fact that the electronic delocalization from the terminal nitrogen atom toward the indole ring increases with the electron donor and acceptor properties of the amino and ester groups. INDO/S calculations also corroborated this (15, 16, 22). As electronic delocalization along the long molecular axis is more favoured, the oscillator strength of the first electronic transition increases. Indeed, the oscillator strengths calculated by INDO/S equal to 0.41 (22), 1.08 (15), 1.12, 1.23, and 1.29 (16) for molecules **1** and **3** to **6** respectively.

The theoretical radiative transition probability in this work is obtained from the absorption and fluorescence spectra via the Strickler and Berg relationship (18, 20):

$$[1]\quad k_F^t = 2.88 \times 10^{-9} n^2 \langle \bar{\nu}_F^{-3} \rangle_{av}^{-1} \int \frac{\epsilon(\bar{\nu})}{\bar{\nu}}\, d\bar{\nu}$$

where

$$\langle \bar{\nu}_F^{-3} \rangle_{av}^{-1} = \frac{\int I_F(\bar{\nu}) d\bar{\nu}}{\int \bar{\nu}^{-3} I_F(\bar{\nu}) d\bar{\nu}}$$

By dividing k_F^t by A ($= n^2 \langle \bar{\nu}_F^{-3} \rangle_{av}^{-1}$), one obtains an expression which is proportional to the Einstein coefficient for the absorption process or to the square of the transition moments, that are independent of both the refractive index of the solvents and the spectral shift in the various solvents. These corrected k_F^t and k_F values are reported in Table 3. One can see that the k_F^t/A values in *n*-heptane follow the trend of the oscillator strength calculated from INDO/S except for the unsubstituted molecule **1**.

We have shown recently that these molecules are not rigid and that the phenyl ring can librate to a certain extent within the kT energy barrier (14–17, 22). The freedom of this motion should be reduced when the electronic delocalization throughout the molecule is increased. As a result, a sharpening of the absorption band is expected together with an increase in the

Can. J. Chem. Downloaded from www.nrcresearchpress.com by 85.192.166.187 on 09/08/12
For personal use only.

TABLE 1. Spectral characteristics of the neutral species in some of the representative solvents at 300 K

Molecule	Solvent	$\bar{\nu}_{CM}$[a] (Abs)	ϵ_{max} (M^{-1} cm^{-1})	FWHM[b] absorption (cm^{-1})	$\bar{\nu}_{CM}$[a] (Flu)	FWHM[b] fluorescence (cm^{-1})	Stokes shift (cm^{-1})
1	Heptane	33 300	17 600	6 300	25 300	6 300	8 000
	Acetonitrile	33 300	16 200	6 600	24 700	5 600	8 600
	Methanol	33 300	16 500	6 900	24 200	5 400	9 100
	Water (pH = 9)	33 400	14 600	7 200	23 500	5 200	9 900
2	Heptane	30 900	27 000	5 200	23 100	5 200	7 800
	Acetronitrile	29 800	31 300	5 200	22 400	4 400	7 400
	Methanol	28 900	30 100	5 200	21 800	4 100	7 100
	Water (pH = 9)	29 600	23 300	6 200	21 800	3 900	7 800
3	Heptane	28 900	28 400	4 400	22 700	4 500	6 200
	Acetronitrile	28 100	31 500	4 500	22 000	4 300	6 100
	Methanol	27 400	30 700	4 500	21 600	3 900	5 800
	Water (pH = 9)	27 500	24 700	5 500	21 300	3 400	6 200
4	Heptane	29 300	30 100	4 800	22 100	4 900	7 200
	Acetronitrile	27 900	30 500	4 900	21 000	4 200	6 900
	Methanol	27 100	34 100	5 100	20 700	3 900	6 400
	Water (pH = 9)	27 900	32 700	5 700	20 700	3 300	7 200
5	Heptane	28 300	33 000	4 800	22 000	4 900	6 300
	Acetronitrile	26 900	32 500	4 600	20 700	4 100	6 200
	Methanol	26 100	34 900	4 600	20 400	3 800	5 700
	Water (pH = 9)	26 500	30 200	5 400	20 300	3 200	6 200
6	Heptane	27 400	41 700	4 100	21 900	4 700	5 500
	Acetronitrile	26 300	41 100	4 400	20 300	3 900	6 000
	Methanol	25 800	44 100	4 500	20 200	3 800	5 600
	Water (pH = 9)	25 600	32 500	5 200	19 900	3 300	5 700

[a]Wavenumbers at the center of mass.
[b]Full width at half maximum.

transition moment. Indeed, going from **1** to **6** in *n*-heptane, the FWHM of the absorption band decreases, reaching its smallest value for **6** where the electronic delocalization is the highest. Table 2 shows that the k_{nr} values of these molecules in *n*-heptane also decrease with a decrease in the fluorescence transition energy and a concomitant increase in the electronic delocalization throughout the molecule. This supports the assumption that the main radiationless deactivation pathway is the motion of the Ph_C ring (14–17, 22). As the electronic delocalization increases, the molecule becomes less flexible, consequently k_{nr} is reduced. The increase in the rigidity of the molecule in the relaxed excited singlet state is also reflected by the sharpening of the fluorescence spectra going from **1** to **6**.

We have recently shown with the help of INDO/S calculations that the dipole moments of these molecules in their ground and first singlet excited states are relatively high (15, 16). Consequently dipole–dipole interactions are expected to lower the energy of the absorption as well as the fluorescence band. Table 1 reports on the Stokes shift of all the molecules in nonpolar, polar aprotic, and protic solvents. The Stokes shift increases for molecule **1** going from *n*-heptane to water. However, for all other molecules the Stokes shift is always larger in *n*-heptane than in polar solvents. These results are in contrast with those obtained for similar kind of polar molecules like *N*-substituted anilines (2, 3) and 4-aminophthalimide (3) which show larger Stokes shifts in polar solvents. This is interpreted in terms of specific interactions (complexation) with the solvents involved in the solvation process. The present set of molecules possesses three polar and/or hydrogen bond accepting sites which are the lone pairs of the terminal nitrogen, the tertiary ring nitrogen and the carbonyl oxygen (for molecules **4** to **6**) whereas the terminal amino group in molecules **2**, **4**, and **5** is a hydrogen bond donor site. The carbonyl and the tertiary ring nitrogens have rather localized electron lone pairs whereas in the terminal amino group, electron migration occurs toward the indole ring. Thus in these molecules a combination of all these effects is expected and their magnitude depends upon the preference of the complexation sites.

One can see in Table 1 that the absorption bands in molecules **2** to **5** are blue shifted going form methanol to water. This suggests that stronger specific interactions occur at the terminal nitrogen atom in the case of water. Since water and methanol have similar polarity function ($f(D) = 2(D - 1)/(2D + 1)$, this suggests that water is acting as a better hydrogen bond donor to the lone pair of the terminal amino group in the ground electronic state. Previous workers (2, 3) have also observed this effect in aniline, *N*-methylaniline, and *N*,*N*-dimethylaniline. These chromophores represent the donor part of the molecules studied here. The interaction of the amino lone pair with water via hydrogen bonding is also highlighted in the FWHM and ϵ values. The former property increases much more in going from methanol to water, for molecules **2** to **6** compared to molecule **1** where water interacts with the tertiary nitrogen lone pair alone. This suggests that the hydrogen bonding interactions involving the lone pair of the terminal nitrogen atom reduce the conjugation of the amino group with the rest of the molecule and thus are responsible for the blue shifting and for the decrease in the ϵ values observed in water. As a result, the freedom of motion of the phenyl moiety is increased causing a broadening of the absorption band due to the existence of more conformers within

Can. J. Chem. Downloaded from www.nrcresearchpress.com by 85.192.166.187 on 09/08/12
For personal use only.

TABLE 2. Various photophysical parameters of the neutral species in some representative solvents at 300 K

Molecule	Solvent	ϕ_F	τ_F (ps)	$k_F^t \times 10^{-8}$ (s^{-1})	$(k_F^t/A)10^6$ ($cm^3\ s^{-1}$)	$k_F \times 10^{-8}$[a] (s^{-1})	$(k_F/A)10^6$ ($cm^3\ s^{-1}$)	$k_{nr} \times 10^{-10}$[b] (s^{-1})
1	Heptane	0.00046	1.6[c]	2.9	9.3			63[d]
	Acetonitrile	0.00051	2.0[c]	2.6	9.3			51[d]
	Methanol	0.00063	2.5[c]	2.5	9.9			40[d]
	Water (pH = 9)	0.0011	5.2[c]	2.1	9.3			19[d]
2	Heptane	0.0014	4.4[c]	3.2	13.8			23[d]
	Acetonitrile	0.019	130	3.1	15.1	1.5	7.4	0.77
	Methanol	0.064	430	2.8	15.4	1.5	8.2	0.22
	Water (pH = 9)	0.17	920	2.3	12.5	1.8	9.6	0.088
3	Heptane	0.020	50	3.2	14.5	4.0	17.9	2.2
	Acetonitrile	0.28	1 170	4.0	20.7	2.4	12.2	0.062
	Methanol	0.24	1 430	2.8	15.9	1.7	9.5	0.053
	Water (pH = 9)	0.21	1 130	2.3	13.5	1.9	11.4	0.071
4	Heptane	0.016	63	3.1	14.8	2.5	12.0	1.6
	Acetonitrile	0.29	1 740	2.7	16.2	1.7	10.2	0.042
	Methanol	0.28	1 820	2.7	16.9	1.5	9.6	0.040
	Water (pH = 9)	0.022	126	3.0	19.2	1.8	11.3	0.80
5	Heptane	0.072	190	3.3	16.0	3.8	18.8	0.49
	Acetonitrile	0.31	1 940	2.7	16.9	1.6	9.9	0.036
	Methanol	0.25	1 750	2.6	17.7	1.4	9.3	0.042
	Water (pH = 9)	0.013	73	2.7	17.9	1.8	12.0	1.4
6	Heptane	0.24	680	3.3	16.2	3.5	17.1	0.11
	Acetonitrile	0.30	1 980	2.6	16.7	1.5	9.9	0.035
	Methanol	0.26	1 900	2.7	18.2	1.4	9.6	0.040
	Water (pH = 9)	0.012	82	2.7	19.0	1.5	10.7	1.2

[a] $k_F = \phi_F/\tau_F$.
[b] $k_{nr} = (1 - \phi_F)k_F/\phi_F$.
[c] Values calculated from $\tau_f = \phi_F/k_f^{(t)}$.
[d] Values calculated from $k_{nr} = k_f^{(t)}\phi_f^{-1}(1 - \phi_f)$.

the kT energy barrier. In contrast to the ground state behavior, it can be seen in Table 1 that the FWHM value of the fluorescence bands decreases going from *n*-heptane to water, which is consistent with the regular observed red shift. This suggests that these molecules in their first relaxed singlet excited states are more planar in polar and/or hydrogen bonding environments. This could occur via solute–solvent specific interactions (complexation) formed mostly at the ring nitrogen atom (23–26). This process would favour the electronic delocalization toward the indole part of the molecule and increase the planarity of the complex. In solvent mixtures of methylcyclohexane (MCH) and acetonitrile, dipole–dipole interactions were proposed to stabilize the ground state complex and the exciplex (excited state complex) of these kinds of solutes whereas in mixtures of MCH/ethanol or dioxane/water, hydrogen bonding interactions are involved (23–26). Since water is a much better proton donor than methanol, it is not surprising to observe that the fluorescence bands measured in pure water are sharper than those obtained in pure methanol.

The existence of specific interactions at the indole nitrogen ring is also emphasized by the reported values of k_{nr} in polar aprotic and protic solvents; these values are much smaller than those obtained in *n*-heptane with the notable exceptions of **4** to **6** in water (Table 2). The abnormally high values of k_{nr} for the ester derivatives in water will be discussed in the next section. The existence of these hydrogen bonding interactions might be the reason why the fluorescence decay curves of molecules **4**, **5**, and **6** in water can be fitted only with multiple exponential functions. Since fluorescence decay curves for **2** and **3** are accurately described with single exponential functions, hydrogen bonding at the terminal nitrogen atom does not seem to be involved in the multiexponential decays. Thus the second and third small components in the multiexponential decay curves could originate mainly via hydrogen bonding interactions at the carbonyl site and/or from various conformational hydrogen bonding complexes involving the nitrogen ring atom. Proton donation to water from the amino group is also excluded since the triexponential decay is also obtained for molecule **6**.

To get more insight about conformational changes involved in the relaxation of the Franck–Condon state, the mirror-image relationship between the absorption and fluorescence spectra can be verified. Recently, we have shown that for the ester derivatives, the mirror-symmetry is well respected in nonpolar solvents (16). The modified absorption spectrum $(\epsilon(\bar{\nu})/\bar{\nu}$, the modified fluorescence spectrum $F(\bar{\nu})/\bar{\nu}^3$, and its reflection $F(2\bar{\nu}_0 - \bar{\nu})/(2\bar{\nu}_0 - \bar{\nu})^3$ about $\bar{\nu}_0$ plotted as a function of ν are displayed in Fig. 2*B* for molecule **6** as well as its monocation in water. It could be noticed that the mirror-symmetry is not effective for the neutral form of **6** in water (Fig. 2*B*). The absorption profile is much broader than the fluorescence profile. This means that the ground state complex geometry differs from the relaxed excited state complex geometry in pure polar protic and/or aprotic solvents. The same conclusions were previously obtained in mixed solvents (24–26). This is further supported by comparing the k_F and k_F^t values. In *n*-heptane where the mirror-symmetry is respected, the k_F^t values are approximately equal to the k_F values for all molecules. On the other hand, in polar protic and aprotic solvents, $k_F < k_F^t$, reflecting the differ-

Can. J. Chem. Downloaded from www.nrcresearchpress.com by 85.192.166.187 on 09/08/12
For personal use only.

Can. J. Chem. Downloaded from www.nrcresearchpress.com by 85.192.166.187 on 09/08/12
For personal use only.

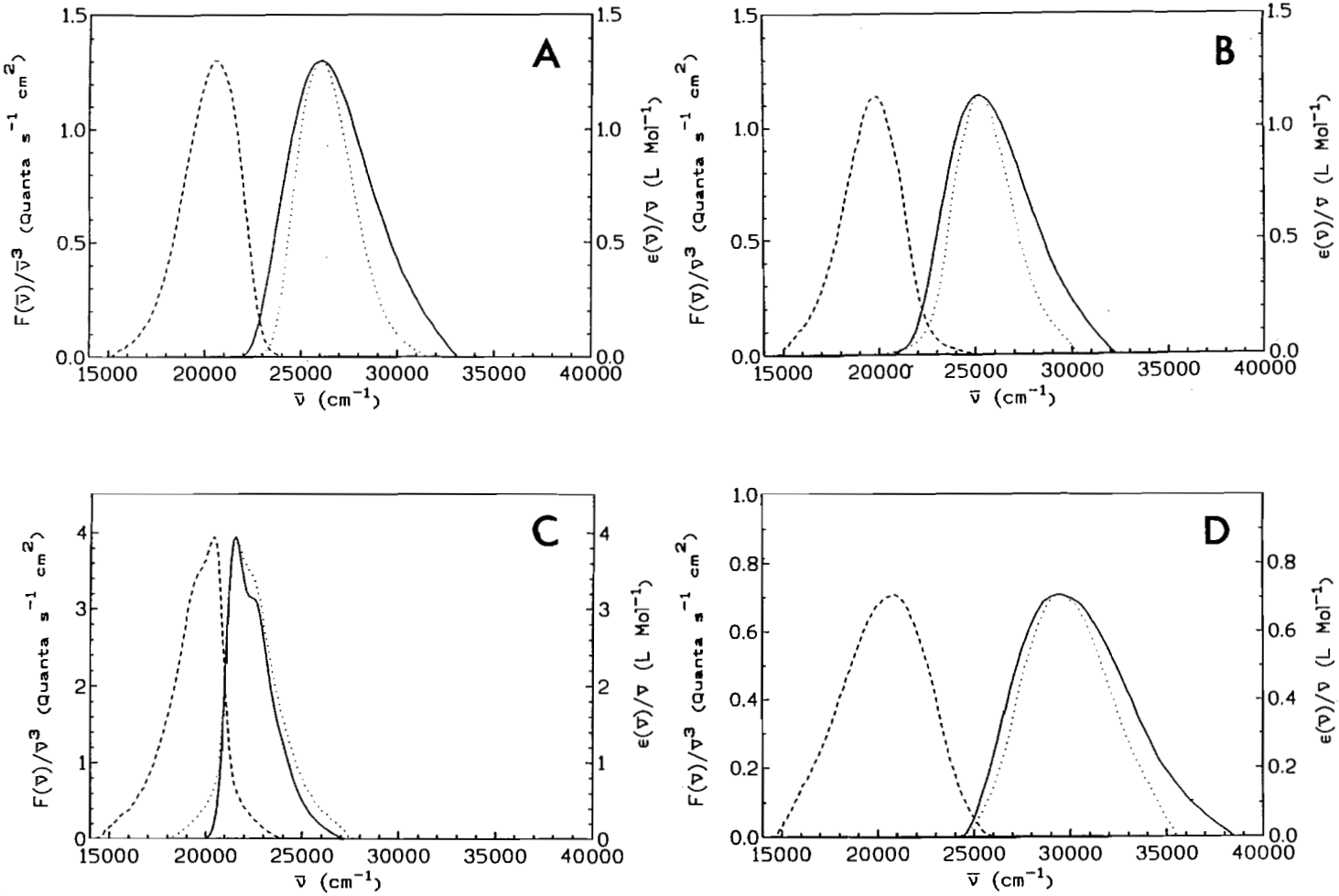

FIG. 2. Modified absorption spectra $\epsilon(\bar{\nu})/\bar{\nu}$ (right hand solid curves, modified fluorescence spectra $F(\bar{\nu})/\bar{\nu}^3$ (left hand broken curve) and their reflections $F(2\bar{\nu}_0 - \bar{\nu})/(2\bar{\nu}_0 - \bar{\nu})^3$ (right hand dotted curves) for the monoanion or carboxylate (*A*), neutral (*B*), monocation (*C*) and dication (*D*) of molecule **VI** in water. The proposed structures of these species have been described elsewhere (13).

Can. J. Chem. Downloaded from www.nrcresearchpress.com by 85.192.166.187 on 09/08/12
For personal use only.

ence in the charge delocalization in both complexes. These geometrical changes between the ground and relaxed excited singlet states of these complexes in polar aprotic and protic solvents are thus responsible for the anomaly observed in the Stokes shifts of the molecules in these environments.

3.2. Charged species

The various spectroscopic and photophysical parameters of the cationic species in water are reproduced in Tables 3 and 4 along with those of the neutral species. The selected pH values in these tables were determined from the absorption and fluorescence spectral dependence upon acidity (13).

3.2.1 Molecules 2 and 3

A. Monocation

Since protonation is an extreme case of hydrogen bonding by a solvent with the basic centers, its effect on spectral and photophysical characteristics forms an essential part of this work. Highly intense, large red-shifted and structured absorption bands have been obtained. They are explained as follows: once the tertiary ring nitrogen atom is protonated it becomes a better acceptor and pulls the electron density away from the terminal amino group. Consequently, the electronic delocalization is increased (13), thus reducing the freedom of the torsional movement of the phenyl moiety. This effect is well reflected in the bandwidth (FWHM) which is highly narrowed as compared to that of the neutral species. High k_F^t values also support the notion of an increased planarity. It is well known that the ground state geometry is responsible for the electronic transition dipole moments in the absorption process and is characterized by k_F^t. All the above-mentioned parameters support an increased planarity that follows the order **3** > **2** > **1**, which means that a better donor group increases the planarity of the ground state monocation.

Contrary to the absorption spectral characteristics, the position of the fluorescence maxima of the monocations were not significantly shifted with respect to the neutral species (13). Moreover, the mirror-symmetry relationship for the monocations was found to be well respected in both **2** and **3** (similar as in Fig. 2*C*). This shows that geometrical changes, if any, in the monocation during the relaxation of the FC state are minor. This is interpreted in terms of the formation of a highly planar rigid structure C (Scheme 1) (13) in the ground state itself. Very small Stokes shifts compared to that of the neutral species also support the formation of the rigid structure C. A similar kind of rigid structure was not observed in the monocation of molecule **1**. This shows that the presence of a donor group on the Ph_C ring is an essential requirement to impart extra rigidity to these monocations.

On the other hand, the k_{nr} values of the monocations of molecules **2** and **3** are drastically higher compared to those of the neutral species. Since the protonation of molecule **1** does not really affect the k_{nr} value, an increase in k_{nr} upon protonation is also primarily related to the donor properties of the terminal amino group. The dimethylamino substituent is a better electron donor than the amino group and it is not surprising to observe that an increase in k_{nr} caused by the protonation of the ring nitrogen atom. Thus k_{nr} is larger for **3** than it is for **2**. To see the effect of the relaxation of the Franck–Condon excited state on the photophysics of neutral and monocation species in water, the excitation and fluorescence spectra as well as the fluorescence lifetimes have been measured in ice at 77 K (Table 5). From these results, one can see that, at 77 K, the excitation spectra of both species of **2** are red shifted compared to the room temperature spectra whereas the fluorescence spectra are much less affected. Since there is no relaxation of the Franck–Condon excited state at 77 K, it implies that the planar ground state geometry is also responsible for the fluorescence emission observed in aqueous solutions for the monocation. The strong quenching of the fluorescence emission following protonation in an aqueous solution can then be ascribed to a radiationless channel involving the rotation of the dimethylamino or dimethylanilino groups. This channel is effectively eliminated in rigid matrices and the fluorescence lifetimes reach their maximum (2.6 ns) for both the neutral and the cationic species. The fluorescence quantum yields measured in *n*-heptane are very instructive in this regard. They show that in an aprotic solvent, protonation increases the planarity in the relaxed excited state of cation **2** compared to the neutral species. The same conclusion can also be applied for species **1** even though the effect is smaller for the unsubstituted chromophore.

Grabowski and other researchers have defined a new class of excited states commonly known as twisted intramolecular charge transfer state (TICT), which involves a 90° rotation of the donor group and a complete charge separation on the perpendicular donor and acceptor moieties (11, 12). These TICT states are considerably stabilized in polar solvents but their fluoresence is generally weak because of the small k_F values (11). The monocations of **1** to **3** also show weak fluorescence bands. To check if these bands originate from a TICT state, the fluorescence of these species has been measured in *n*-heptane; characteristics for **1** and **2** are reported in Table 5. It can be noted that the positions of the fluorescence bands are not very much altered by the hydrogen bonding ability of the solvent i.e., going from *n*-heptane to water. Thus these bands do not arise form TICT fluorescence. We have recently suggested with the help of INDO/S calculations that the quenching of the monocation fluorescence could arise from the formation of a non-emissive TICT state involving the rotation of the dimethylamino group (13). Many molecules have been reported to deactivate via the formation of non-fluorescent TICT states (27–29). Their ϕ_F and τ_F values have been shown to decrease with the polarity of the environment but are restored in highly viscous media. For example, substituted benzopyrylium dyes, which are structurally similar to the monocations of **2** and **3**, have been described in terms of non-fluorescent TICT state formation (27, 28). Coumarin dyes are other examples in which a fluorescence intramolecular charge transfer structure (ICT), quite similar to the C structure in our molecules, is first formed and then relaxes to a TICT state (29).

B. Dication

The spectral characteristics of the dications are similar to those of the monocation of **1**. An indication that electron delocalization from the terminal amino group to the indole ring is hindered is reflected in the high energy of the absorption bands (13). This is confirmed by the low k_F^t and k_F values which indicate that the dications are even more twisted than the molecules in their neutral forms. This allows more freedom of motion for the phenyl moiety and consequently the dication's absorption and fluorescence bands are broader than those observed for the neutral species (Table 3). This is in agreement with the fact that the k_{nr} values of the dications are higher by an order of magnitude compared to those reported for the neutral species in water (Table 3).

TABLE 3. Spectroscopic and photophysical parameters of some of the species at 300 K in water

Molecule	Species	$\bar{\nu}_A$[a] (cm^{-1})	FWHM absorption (cm^{-1})	$\bar{\nu}_F$[a] (cm^{-1})	FWHM fluorescence (cm^{-1})	Stokes shift (cm^{-1})	ϕ_F	$k_F \times 10^{-8}$ (s^{-1})	$k_F^t \times 10^{-8}$ (s^{-1})	τ_F (ps)	$k_{nr} \times 10^{-10}$ (s^{-1})
1	Neutral (pH = 9)	33 400	7 200	23 500	5 200	9 900	0.0011	—	2.1	5.2[b]	19[c]
	Monocation (pH = 1.5)	29 800	6 900	20 700	4 700	9 100	0.0011	—	1.6	6.9[b]	15[c]
2	Neutral (pH = 9)	29 600	6 200	21 800	3 900	7 900	0.17	1.8	2.3	920	0.088
	Monocation (pH = 2)	24 600	3 700	21 300	2 900	3 300	0.0031	—	2.8	11[b]	9.0[c]
	Dication ($H_0 = -8$)	29 600	7 500	20 500	5 000	9 100	0.0056	0.40	1.4	140	0.71
3	Neutral (pH = 9)	27 500	5 500	21 300	3 400	6 200	0.21	1.9	2.3	1130	0.071
	Monocation (pH = 2)	22 900	3 100	20 400	2 400	2 500	0.0012	—	2.9	4.1[b]	24[c]
	Dication ($H_0 = -8$)	29 400	7 400	20 500	4 800	8 900	0.0071	0.43	1.2	165	0.60

[a]Wavenumbers at the center of mass of the bands.
[b]Values calculated from $\tau_F = \phi_F/k_F^t$.
[c]Values calculated from $k_{nr} = k_F^t\phi_F^{-1}(1 - \phi_F)$.

TABLE 4. Spectroscopic and photophysical parameters of some of the species at 300 K in water

Molecule	Species	$\bar{\nu}_A$[a] (cm^{-1})	FWHM absorption (s^{-1})	$\bar{\nu}_F$[a] (cm^{-1})	FWHM fluorescence (s^{-1})	Stokes shift (ps)	ϕ_F	$k_F \times 10^{-8}$ (s^{-1})	$k_F^t \times 10^{-8}$ (cm^{-1})	τ_F	$k_{nr} \times 10^{-10}$ (cm^{-1})
4	Monoanion (pH = 12)	28 200	5 600	21 200	3 900	7 000	0.17	1.3	3.2	1 230	0.066
	Neutral (pH = 9)	27 900	5 700	20 700	3 300	7 200	0.022	1.8	3.0	126	0.80
	Monocation (pH = 2)	23 800	3 300	21 100	2 300	2 700	0.0018	—	3.8	4.7[b]	21[c]
	Dication ($H_0 = -8$)	29 700	6 900	20 800	4 900	8 900	0.045	1.0	1.8	440	0.21
5	Monoanion (pH = 13)	26 700	5 600	20 900	3 200	5 800	0.13	1.5	3.1	890	0.078
	Neutral (pH = 9)	26 500	5 400	20 300	3 200	6 200	0.013	1.8	2.7	73	1.4
	Monocation (pH = 2)	22 800	2 700	20 500	2 200	2 300	0.0010	—	3.5	2.9[b]	35[c]
	Dication ($H_0 = -8$)	29 900	7 100	20 800	4 900	9 100	0.049	1.0	1.9	492	0.19
6	Monocation (pH = 13)	26 400	5 400	20 600	3 100	5 800	0.16	1.6	3.0	1 000	0.084
	Neutral (pH = 9)	25 600	5 200	19 900	3 300	5 700	0.012	1.5	2.7	82	1.2
	Monocation (pH = 2)	22 200	2 500	19 900	2 300	2 300	0.0094	—	4.1	2.4[b]	41[c]
	Dication ($H_0 = -8$)	29 900	7 400	20 800	4 400	9 100	0.055	1.0	2.2	535	0.17

[a]Values at the center of mass of the bands.
[b]Values calculated from $\tau_F = \phi_F/k_F^\tau$.
[c]Values calculated from $k_{nr} = k_F^\tau\phi_F^{-1}(1 - \phi_F)$.

3.2.2 Ester-substituted molecules

A. Monoanion

These molecules are in their neutral forms from pH 7 to 9. At pH 9, a new species starts to appear and its formation is complete at pH ≈ 12. This species has been assigned to a monoanion (MA) formed following the hydrolysis of the ester group (13). The geometry of this species is not much altered compared to that of the neutral species. Indeed, Table 4 shows that the bandwidth of the absorption and fluorescence bands (FWHM) as well as k_F^t and k_F are similar for both species. However, judging by the FWHM values of the absorption and fluo-

Can. J. Chem. Downloaded from www.nrcresearchpress.com by 85.192.166.187 on 09/08/12
For personal use only.

Can. J. Chem. Downloaded from www.nrcresearchpress.com by 85.192.166.187 on 09/08/12
For personal use only.

rescence bands it is clear that the torsional movement of the molecule in the anionic form is hindered in the relaxed excited state.

It is important to point out here that the k_{nr} values for the anion are one order of magnitude lower than those for the neutral molecule. This is because once the hydrolysis has taken place, the negative charge generated is delocalized on the ester group and indole moiety, negating its electron acceptor properties. This supports, as argued in the previous sections, that k_{nr} is mainly related to the donor–acceptor properties of the substituent groups and the occurrence of a possible non-radiative TICT state in the neutral and cationic species.

B. Monocation

The effect of protonation on the ring nitrogen of ester derivatives is similar to that described for **2** and **3** above. However, since an ester substituent is present as an acceptor group, the electronic delocalization becomes more effective. Indeed, the absorption and fluorescence bandwidths of **4** and **6** are smaller than those of **2** and **3** (Tables 3 and 4). The fact that k_F^l values of **4** and **6** are higher than those of **2** and **3** supports that assumption. This shows that the presence of an ester group at the *para* position of the 3*H*-indoles makes the whole indole moiety a better acceptor. This helps in attaining more planarity in the ground and excited states by delocalizing the charge density of the terminal amino group.

In our previous paper (13), we show that the excited state pK_a value (pK_a^*) evaluated by the Förster cycle method using absorption spectral data for all molecules were considerably higher for the ring nitrogen protonation equilibrium. The pK_a^* value for the same equilibrium has been reported for 2-(*p*-aminophenyl) benzimidazole (30), which is structurally similar to **2** to certain extent. The difference between pK_a and pK_a^* (abs) for 2-(*p*-aminophenyl) benzimidazole is ~6 units, which is small compared to the difference in **2** (~10 units). A higher value for **2** and as a matter of fact in all the molecules may be due to the fact that the freedom of the torsional movement in these systems is restricted upon ring nitrogen atom protonation. That would imply that the geometry of the molecule changes from one species to another in the different equilibria involving the ring protonation.

The mirror-image relationship for the monocation of **6** is shown in Fig. 2*C*. It can be seen that the mirror-symmetry is well respected, confirming the formation of a highly planar structure as observed for **2** and **3**. Like these molecules, the ester derivatives have very high k_{nr} values that shows strong dependence over the donor properties of the *N*-alkyl amino substituents. This justifies the fact that the charge transfer properties are highly dependent upon the donor and acceptor capabilities of the attached moieties. This will be the topic of a forthcoming paper.

As suggested for the fluorescence quenching of **2** and **3** monocations, one might expect that the excited state relaxation of the ester derivatives in their cationic forms might involve the formation of a TICT non-emissive state. The protonation of the ring nitrogen favours the charge transfer process from the terminal amino group toward the indole ring. The presence of the ester group favours this mechanism, e.g., k_{nr} (**4**) > k_{nr}(**2**) and k_{nr}(**6**) > k_{nr} (**3**) for the molecules in their cationic form. Moreover, as mentioned in the first part of this paper, the fluorescence of molecules **4**, **5**, and **6** are quenched even in their neutral forms in water (see Table 2). This strongly suggests that the TICT formation mechanism is plausible for the ester-substituted neutral molecules in water but not in methanol. This TICT formation process would require protonation or strong hydrogen bonding interactions at the ring nitrogen site to occur. Methanol does not seem to form hydrogen bonds strong enough to favour the charge transfer process toward the indole ring. If one compares the k_{nr} values in methanol and water for neutral **2** and **3**, the fluorescence of **2** is enhanced in water whereas the fluorescence of **3** is quenched in aqueous medium. Thus, on the one hand, an amino group is not a good enough electron donor to produce efficient charge transfer; on the other hand, a weak charge transfer process may occur for the molecule having only a dimethylamino group as the terminal donor group. However, the combined effects of an amino group and an ester substituent favour the charge transfer process to a great extent.

C. Dication

A Decrease in planarity upon terminal amino group protonation of the ester-substituted molecules is evident from the various spectroscopic parameters reported in Table 4. All the photophysical parameters were affected similarly to molecules **2** and **3**, hence similar explanations hold. However, the FWHM of the absorption and fluorescence bands as well as the k_F^l and k_F values indicate that the ester derivatives in their dicationic forms are more rigid than the dications of molecules **2** and **3** (Tables 3 and 4). This is supported by the k_{nr} values which are lower for molecules **4** to **6**.

3.3 Is a TICT state involved in these systems?

No direct experimental proof exists to support the TICT assumption since the *A* (TICT) state, if exists, is not an emitting state.

What we know is that the neutral molecules are involved in ground state complexes in polar protic or aprotic solvents. Studies of molecule **3** in solvent mixtures of *n*-alkanes/ethanol or *p*-dioxane/ethanol or water have shown complexes of 1:1 stoïchiometry with well-defined isosbestic points in the absorption spectra (24–26). In pure polar solvents, as is the case in this paper, one can think about ground state complexes stabilized by dipole–dipole interactions (acetonitrile) or by hydrogen-bonding interactions (methanol, water) that involve the indole ring nitrogen electron lone pair. Water brings about another hydrogen bonding site at the terminal amino group nitrogen in the electronic ground state of these molecules. We have no evidence for the complexation of the ester carbonyl group.

As far as the excited state is concerned, when polar protic or aprotic molecules are added to a non-polar solvent containing molecule **3**, an isosbestic point is obtained and both the fluorescence lifetime and quantum yield increases considerably (25, 26). These results have been demonstrated to fit an over all kinetics where the ground state complexes are not emissive but an excited-state complex (exciplex) less polar than the ground state complex is formed with a rate that is diffusion-controlled (24–26). The rationale for complexes of different nature involved in the ground and excited relaxed singlet states is based on the following data (26):

(*1*) Weak bathochromic shifts are observed in fluorescence compared to the absorption with polar solvent addition to a non-polar solvent. (*2*) The fluorescence bandwidths get smaller and smaller with further addition of polar solvents. (*3*) The quenching of the fluorescence band assigned to molecule **3** in the non-polar solvent is diffusion-controlled. (*4*) When molecule **3** is studied in a mixture of ethanol–isopentane–ether 2:5:5 (EPA) from room temperature to 77 K, a red shift is observed in the

TABLE 5. Spectroscopic and photophysical parameters of molecules **1** and **2** at 300 and 77 K

Molecule	Solvent	Species	$\bar{\nu}_{CM}$(Exc) (cm^{-1})	$\bar{\nu}_{CM}$(Flu) (cm^{-1})	ϕ_F	τ_F (ps)
1	Heptane	Neutral				
		300 K	33 300	25 300	0.00046	1.6[a]
		Monocation[b]				
		300 K	30 300	21 000	0.0012	6.9[a]
	Water	Neutral				
		300 K	33 400	23 500	0.0011	5.2[a]
		77 K (ice)	32 800	24 600	—	3420
		Monocation				
		300 K	29 800	20 700	0.0011	6.9[a]
		77 K (ice)	30 400	21 900	—	4350
2	Heptane	Neutral				
		300 K	30 900	23 300	0.0014	4.4[a]
		Monocation[b]				
		300 K	24 400	20 900	0.015	51[a]
	Water	Neutral				
		300 K	29 600	21 800	0.17	920
		77 K (ice)	28 100	22 000	—	2600
		Monocation				
		300 K	24 600	21 300	0.0031	11[a]
		77 K (ice)	24 100	21 600	—	2680

[a]Values calculated from $\tau_f = \phi_F/k_f^l$.
[b]Generated using trifluoroacetic acid (0.2% v/v) (19).

absorption but a blue shift is observed in the fluorescence, indicating that there is a different geometry between the two complexes.

Tables 1, 2, and 5 show that all the 3*H*-indole molecules studied here in pure solvents conform to points 1 to 4 such that one can ascertain that complexes of different nature (more polar and less planar in the ground state than in the relaxed excited state) are responsible for the absorption and fluorescence spectra. This is also confirmed by the different values of the radiative decay rate constants (k_F^l and k_F). In other words, the free molecules exists only in *n*-heptane where the geometry of the ground and relaxed excited states is approximately the same ($k_F^l = k_F$ and an excellent mirror-image relationship). The main deactivation channel in this environment has been shown to be the Ph_C ring torsion which is hindered by increasing the viscosity of the medium (15) (see Table 5).

This work shows clearly that complexation is another way of hindering the torsional movement in all these molecules. Methanol and acetonitrile behave approximately the same way in that they both reduce the Ph_C ring libration when compared to a nonpolar medium (same k_{nr}). Moreover, this phenomenon is independent of the electron donor–acceptor properties of the molecules. But water, which is a strong proton donor, behaves totally differently. A new excited state deactivation channel is created, causing a marked increase in the radiationless decay. This new channel is promoted by increasing the electron donor property of the anilino moiety and/or the electron-acceptor property of the indole ring. Protonation at the indole nitrogen (monocation) strongly favors this deactivation channel, protonation at the amino nitrogen (dications) inhibits it, and in monoanions the channel completely disappears. Since neutral molecules are complexed at both sites in the ground electronic states in water, it is then not surprising that there is no fast deactivation by this channel.

What we also know from the semiempirical INDO/S molecular orbital calculations based on uncomplexed neutral molecules and monocations to which we have added the dipole–dipole interaction energy components in water, is that the TICT state occurring from the rotation of the dimethylamino group in **3** is both energetically and kinetically feasible in these systems (13, 31). Examples are known in the literature of TICT state formation favored by ground state hydrogen bonding formation on 4-(dialkylamino) pyrimidines (32–34). Both **a** and **b** fluorescence appeared and was influenced by the proton-donating ability of the *n*-alcohols. However, the corresponding monocations did not show any trace of luminescence at room temperature. Both fluorescences coming from the LE (*b*) and TICT (*a*) states are totally quenched. The decay of the higher energy fluorescence **b** in the neutral species is a multiexponential function reflecting the diversity of complexes giving rise to this band. Because the long-wave emission **a** has a very fast rise and a mono-exponential decay, the authors concluded that only one of the hydrogen-bonded species is able to form the TICT state, and tentatively suggested that that species was hydrogen-bonded at the N1 atom. These results are rather similar to ours except that in our case we do not have access to the TICT **a** band but we have access to the **b** fluorescence in both neutral and cationic species.

Concluding remarks

The main deactivation pathway of the relaxed excited state of the neutral 3*H*-indoles in nonpolar media as well as the anions and dications in water occurs via a torsional movement involving the amino group and/or phenyl ring. When this motion is reduced by the viscosity and/or by the complexation to the solvent or by weak hydrogen bonding, the radiationless decay rate constant decreases. The hindrance of torsion in these molecules in the ground and relaxed excited states is reflected by a sharpening of the absorption and fluorescence bands. This mechanism is highly dependent on the donor/acceptor proper-

Can. J. Chem. Downloaded from www.nrcresearchpress.com by 85.192.166.187 on 09/08/12
For personal use only.

ties of the substituent in the *para* positions, these properties affect the extent of electronic delocalization over the whole molecule.

Protonation of the indole ring greatly enhances the ground state planarity of the molecule. The planarity of the molecule is retained in the relaxed excited state as judged by the excellent mirror-symmetry relationship observed between the absorption and fluorescence spectra in the monocations. Nevertheless, the fluorescence intensities of the cations are very weak. We have interpreted this phenomenon by a plausible formation of a non-emissive TICT state involving the rotation of the amino group and/or the aniline moiety. This mechanism could also be responsible for the fluorescence quenching observed for neutral molecules **3** to **6** in water via hydrogen bonding interactions at the ring nitrogen.

Acknowledgments

The financial assistance of the Natural Sciences and Engineering Research Council of Canada and the "Fonds FCAR" (Québec) is gratefully acknowledged. We would also like to thank Mr. Adrian Popowicz for the synthesis and purification of the substituted 3*H*-indoles.

1. R.S. Meech, D.V. O'Connor, and D. Philips. J. Chem. Soc. Faraday Trans. 2, **79**, 1563 (1983).
2. G. Köhler. J. Photochem. **38**, 217 (1987).
3. P. Suppan. J. Photochem. Photobiol. A: Chem. **50**, 293 (1990).
4. H. Halloway, R. Neauman, and J. Wharton. J. Phys. Chem. **72**, 4468 (1968).
5. J.R. Bolton, N. Mataga, and G. McClendon (*Editors*). *In* Electron transfer in inorganic, organic and biological systems. Adv. Chem. Ser. 228, CSC Ottawa (1991).
6. J.R. Miller, L.T. Calcaterra, and G.L. Closs. J. Am. Chem. Soc. **106**, 3047 (1984).
7. A. Masad, O. Huppert, and E.M. Kosower. Chem. Phys. **144**, 391 (1990).
8. R.A. Marcus. J. Chem. Phys. **24**, 966 (1956).
9. R.A. Marcus. Faraday Dissus. Chem. Soc. **74**, 7 (1982).
10. T. Ganguly, D.K. Sharma, S. Gauthier, D. Gravel, and G. Durocher. J. Phys. Chem. **96**, 3757 (1992).
11. Z.R. Grabowski, K. Rotkiewicz, A. Siemiarczuk, J.D. Cowley, and W. Baumann. Nouv. J. Chim. **3**, 443 (1976).
12. W. Rettig. Angew. Chem. Int. Ed. Engl. **25**, 971 (1986).
13. R.S. Sarpal, M. Belletête, and G. Durocher. Can. J. Chem. **71**, 1570 (1993).
14. M. Belletête and G. Durocher. J. Phys. Chem. **93**, 1793 (1989).
15. M. Lachapelle, M. Belletête, M. Poulin, N. Godbout, F. LeGrand, A. Héroux, F. Brisse, and G. Durocher. J. Phys. Chem. **95**, 9764 (1991).
16. M. Belletête and G. Durocher. J. Phys. Chem. **96**, 9183 (1992).
17. M. Belletête, R.S. Sarpal, and G. Durocher. Chem. Phys. Lett. **201**, 145 (1993).
18. M. Belletête and G. Durocher. J. Photochem. **21**, 251 (1983).
19. R.S. Sarpal, M. Belletête, G. Durocher. (*a*) J. Phys. Chem. **97**, 5007 (1993); (*b*) Chem. Phys. Lett. **221**, 1 (1994).
20. S.J. Strickler and R.A. Berg. J. Chem. Phys. **37**, 814 (1962).
21. B. Zelent, T. Ganguly, L. Farmer, D. Gravel, and G. Durocher. J. Photochem. Photobiol. A: Chem. **56**, 165 (1991); T. Ganguly, L. Farmer, D. Gravel. J. Photochem. Photobiol. A: Chem. **60**, 63 (1991).
22. M. Belletête, F. Brisse, G. Durocher, D. Gravel, A. Héroux, and A. Popowicz. J. Mol. Struct. **297**, 63 (1993).
23. M. Belletête, G. Lessard, and G. Durocher. Can. J. Spectrosc. **31**, 89 (1986).
24. J. Richer, G. Lessard, M. Belletête, and G. Durocher. Int. J. Chem. Kinet. **18**, 1163 (1986).
25. M. Belletête, G. Lessard, and G. Durocher. J. Luminesc. **42**, 337 (1989).
26. M. Belletête and G. Durocher. J. Photochem. Photobiol. **44**, 275 (1988).
27. M. Vogel, W. Rettig, R. Sens, and K.H. Drenhage. Chem. Phys. Lett. **147**, 452 (1988).
28. W. Rettig, W. Majena, R. Lepouyade, and G. Haucke. J. Photochem. Photobiol. A: Chem. **62**, 415 (1982).
29. G. Jones II, W.R. Jackson, C. Choi, and W.R. Bergmark. J. Phys. Chem. **89**, 294 (1985).
30. A.K. Mishra and S.K. Dogra. Bull. Chem. Soc. Jpn. **58**, 3587 (1985).
31. M. Belletête and G. Durocher. J. Phys. Chem. To be published.
32. J. Herbich, Z.R. Grabowski, H. Wojtowicz, and K. Golankiewicz. J. Phys. Chem. **93**, 3439 (1989).
33. J. Herbich, J. Karpiuk, Z.R. Grabowski, N. Tamai, K. Yoshihara. J. Luminesc. **54**, 165 (1992).
34. Z.R. Grabowski. Pure Appl. Chem. **65**, 1751 (1993).

Can. J. Chem. Downloaded from www.nrcresearchpress.com by 85.192.166.187 on 09/08/12
For personal use only.

Oxygen transfer reactions. 2. A comparison of the reactions of ruthenium tetroxide, chromyl chloride, and permanganate with thianthrene 5-oxide[1]

BONNIE L. MAY, HENRY YEE, AND DONALD G. LEE[2]
Department of Chemistry, University of Regina, Regina, SK S4S 0A2, Canada

Received May 27, 1994

BONNIE L. MAY, HENRY YEE, and DONALD G. LEE. Can. J. Chem. **72**, 2249 (1994).

Products obtained from the oxidation of thianthrene 5-oxide, **SSO**, have been used to compare oxygen transfer mechanisms for three high-valent transition metals. Oxidation of **SSO** by benzyltriethylammonium permanganate in methylene chloride gives the corresponding sulfone, thianthrene 5,5-dioxide (**SSO_2**), as the exclusive product. Oxidation of **SSO** by ruthenium tetroxide also gives **SSO_2** as the predominant product along with minor amounts of the disulfoxide, thianthrene 5,10-dioxide (**SOSO**). However, the converse is observed when chromyl chloride is used as the oxidant; **SOSO** is the major product. It is suggested that oxygen transfers from permanganate and ruthenium tetroxide are initiated by complexation between the central metal atom and the oxygen end of the S=O dipole, while oxidation by chromyl chloride is likely initiated by an alternative mechanism, possibly a single electron transfer.

BONNIE L. MAY, HENRY YEE et DONALD G. LEE. Can. J. Chem. **72**, 2249 (1994).

On a utilisé les produits obtenus lors de l'oxydation du thianthrène 5-oxyde, **SSO**, pour comparer les mécanismes de transfert d'oxygène de trois métaux de transition de valence élevée. L'oxydation du **SSO** par le permanganate de benzyltriéthylammonium dans le chlorure de méthylène conduit à la sulfone correspondante, le thianthrène 5,5-dioxyde (**SSO_2**), comme seul produit. L'oxydation du **SSO** par le tétroxyde de ruthénium fournit aussi le **SSO_2** comme produit prépondérant aux côtés de quantités mineures du disulfoxyde, le thianthrène 5,10-dioxyde (**SOSO**). Toutefois, on a observé l'inverse lors d'oxydations avec le chlorure de chromyle; le **SOSO** est alors le produit majeur. On suggère que les transferts d'oxygène à partir du permanganate et du tétroxyde de ruthénium sont initiés par une complexation de l'atome métallique central et le portion oxygénée du dipôle S=O alors que l'oxydation par le chlorure de chromyle est vraisemblablement initiée par un autre mécanisme, possiblement un transfert unique d'électron.

[Traduit par la rédaction]

Introduction

Oxygen tranfers from transition metals to nonmetals are useful for organic synthesis (1) and essential for human life (2). The latter reactions usually involve porphyrin-complexed transition metals such as those found in hemoglobin (3) whereas the oxidants commonly used in organic synthesis are often high-valent transition metals with oxygen or halogen ligands (4). Although the oxidants may exist as neutral molecules, oxyanions, or complexes, most contain a common structural element, the metal–oxo bond, M=O (5). Despite the importance of these reactions, a detailed understanding of the way in which oxygen is transferred has not been achieved (4, 5).

Many oxygen transfers employed in organic synthesis are accompanied by significant bond transformation in the reductant. For example, the oxidation of alkanes to ketones by iron(V) compounds involves the cleavage of two carbon–hydrogen bonds as well as an oxygen transfer (6), while the asymmetric dihydroxylation of terminal alkenes by osmium tetroxide involves the cleavage of a carbon–carbon π-bond as well as the formation of two C—O and two H—O bonds (7). However, when the reductants are sulfides ($L_nMO + R_2S \rightarrow L_nM + R_2SO$) direct transfers not involving the cleavage or formation of other bonds occur (8, 9). Because these reactions are free of complications associated with the cleavage and (or) formation of other bonds, they provide a good vehicle for the study of oxygen transfers.

In this paper we wish to compare results that were obtained from a study of oxygen transfers to thianthrene 5-oxide (**SSO**) by ruthenium tetroxide, chromyl chloride, and permanganate ion. Thianthrene 5-oxide was chosen as the reductant because it contains sulfur atoms in two different oxidation states and can be used to quantify the selectivity of various reagents with respect to the oxidation of sulfides and sulfoxides (10–12). Oxidation of **SSO** by an oxidant with a high selectivity for sulfoxides results in formation of the corresponding sulfone, **SSO_2**, while the disulfoxide, **SOSO**, is obtained when the oxidant is selective for sulfides. Further oxidation of either of these two products results in the formation of thianthrene 5,5,10-trioxide, **$SOSO_2$**, as illustrated in Scheme 1.

The parameter, X_{SO}, defined in eq. 1, has been used as a quantitative measure of an oxidant's selectivity for sulfoxide oxidation (10–12). Under conditions where little or no **$SOSO_2$** is produced, X_{SO} is simply the mole fraction of **SSO_2** in the product.

$$[1] \quad X_{SO} = \frac{N_{SSO_2} + N_{SOSO_2}}{N_{SSO_2} + N_{SOSO} + 2N_{SOSO_2}}$$

The two sulfurs present in thianthrene 5-oxide are expected to have substantially different electron densities as illustrated by the resonance structures for **SSO** depicted in eq. [2]. Because of this, the magnitude of X_{SO} has been interpreted theoretically to be an indication of the electronic nature of oxygen transfer reagents. Those oxidants that preferentially oxidize sulfoxide sulfur and thereby produce X_{SO} values close to unity are considered to be nucleophiles; i.e., they react more readily with an electron-deficient sulfur. Conversely, those oxidants that selectively oxidize the sulfide sulfur, and produce small X_{SO} values, are considered to be electrophiles. X_{SO} has thus been used as a scale of nucleophilicity or electrophilicity to guide mechanistic predictions, although complexation prior to

[1]For part 1 see ref 8.

[2]Author to whom correspondence may be addressed. Telephone: (306) 585-4246. FAX: (306) 585-4894.

Can. J. Chem. Downloaded from www.nrcresearchpress.com by 85.192.166.187 on 09/08/12
For personal use only.

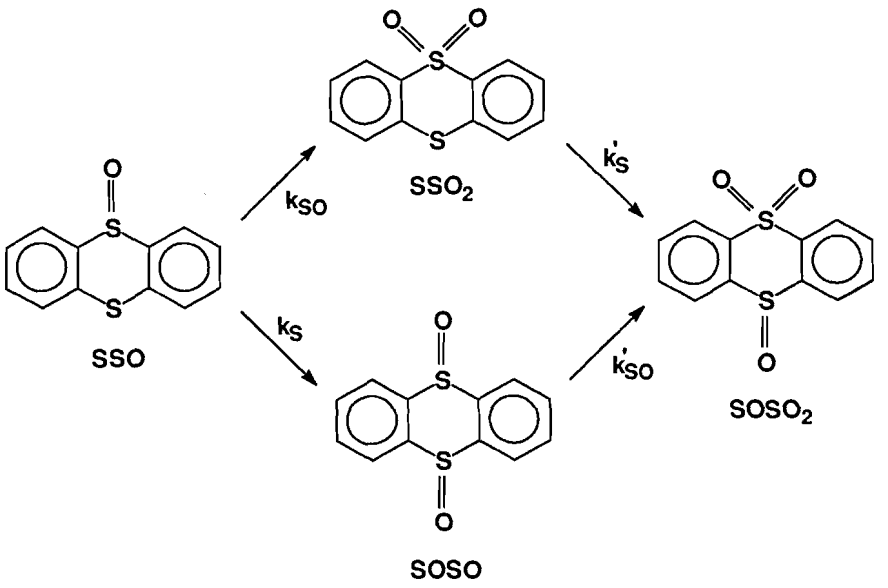

SCHEME 1. The oxidation of thianthrene 5-oxide.

oxygen transfer can reduce the effectiveness of its application in this way (10).

[2] 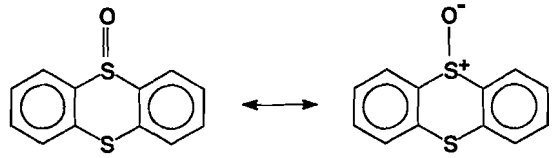

Experimental

Materials

Thianthrene 5-oxide, **SSO**, was prepared according to the procedure reported by Gilman and Swayampati (13): Thianthrene, **SS**, (5.0 g, 23 mmol) was stirred and refluxed in 81 mL of glacial acetic acid. Dilute HNO_3 (2.9 mL of conc. HNO_3 plus 6.3 mL of water) was added dropwise. The solution turned yellow and a brown gas, presumably N_2O_4, was released. After refluxing for an additional 15 min, the solution was poured into 300 mL of ice water. The white solid that precipitated was suction filtered, washed with water, and vacuum dried. Purification by flash chromatography followed by recrystallization from cyclohexane gave white, needle-like crystals, mp 148.5–149.5°C (lit. (14) mp 143.0–143.5°C). ^{1}H NMR ($CDCl_3$) δ: 7.35 (td, J = 7.5 and 2, 2H), 7.50 (td, J = 7.5 and 1.5, 2H), 7.55 (dd, J = 7.5 and 2, 2H), 7.90 (dd, J = 7.0 and 2, 2H). Anal. calcd. for $C_{12}H_8S_2O$: C 62.04, H 3.47; found: C 61.98, H 3.20. GC–MS analysis of this product indicated that it contained 1.4% unoxidized thianthrene that could not be removed by column chromatography or repeated recrystallization.

Benzyltriethylammonium permanganate was prepared by adding a saturated aqueous solution of $KMnO_4$ (4.16 g, 0.0264 mol) dropwise to a stirred solution of benzyltriethylammonium chloride (6.00 g, 0.0264 mol) in 100 mL of water (15). The dark purple precipitate that formed was collected under suction and vacuum dried over phosphorus pentoxide. It was recrystallized by dissolving in a minimum of hot methylene chloride, adding an equal amount of carbon tetrachloride, and cooling, mp 125–127.5°C (lit. (15) mp 114°C (dec.)). ^{1}H NMR ($CDCl_3$) δ: 1.6 (t, J = 7, 9H), 3.5 (q, J = 7, 6H), 4.7 (s, 2H), 7.6 (m, 5H). The UV–VIS spectrum exhibited four peaks between 500 and 575 nm that are characteristic of permanganate ion (16).

Ruthenium tetroxide was prepared by oxidation of ruthenium dioxide hydrate (0.4 g) with $NaIO_4$ (3.2 g, 0.015 mol) in a stirred heterogeneous solution of water (50 mL) and carbon tetrachloride (50 mL) at 0°C for 30 min (17). The carbon tetrachloride layer, now bright yellow, was separated and stored at 5°C over a few crystals of $NaIO_4$. Concentration was determined spectrophotometrically using known extinction coefficients (18).

Chromyl chloride was obtained commercially (Alfa Inorganics) and used without further purification.

Methylene chloride, the solvent used in these reactions, was carefully distilled from solid $KMnO_4$ before use.

Oxidations

Benzyltriethylammonium permanganate (0.1–0.2 g), dissolved in methylene chloride (50–100 mL), was added dropwise to a stirred solution of **SSO** (0.20 g, 0.86 mmol) in methylene chloride (20 mL). When the reaction was complete, MnO_2 was removed by suction filtration through a short column of alumina or silica and the products were eluted with acetone. The solvents were removed by rotary evaporation and the products vacuum dried (1 Torr (= 133.3 Pa)).

Ruthenium tetroxide (0.2–0.5 mmol) dissolved in carbon tetrachloride was added dropwise to a stirred solution of **SSO** (0.20 g, 0.86 mmol) in methylene chloride (20 mL). When the reaction was complete, RuO_2 was removed by suction filtration through 5 mm of Celite and the Celite washed with acetone to remove all products. After removal of the solvents by rotary evaporation, the products were vacuum dried.

Chromyl chloride (0.15–0.51 mmol), dissolved in methylene chloride (40 mL), was added dropwise to a stirred solution of **SSO** (0.20 g, 0.86 mmol) in methylene chloride (20 mL). The final solution was reddish-brown. 2-Propanol (3 mL) was added to reduce any excess oxidant. The solution was filtered through a short column of silcia gel (0.5 cm TLC grade silica and 3 cm 200–400 mesh silica gel) to remove the brown color. The column was eluted with acetone to recover all products. The solution was concentrated to about 40 mL and added to a similar volume of dilute aqueous NaCl. The products were extracted with 2 × 30 mL of CH_2Cl_2. Insoluble material at the interface was not collected because TLC showed it to contain no products. The extracts were filtered through silica once more to remove residual brown coloration and rotary evaporated to dryness.

Characterization of products

Thin-layer chromatography using 20:80 = 2-propanol:petroleum ether as the mobile phase indicated from four to six compounds present in the product mixture obtained from each reaction. These were separated using dry flash chromatography and characterized by gas chromatography (mass selective detector) and ^{1}H NMR (200 mHz). Thianthrene, **SS**: R_f = 0.87. ^{1}H NMR ($CDCl_3$) δ: 7.15 (dd, J = 6 and 3, 4H), 7.40 (dd, J = 6 and 3, 4H). Thianthrene 5-oxide, **SSO**: R_f = 0.71. ^{1}H NMR ($CDCl_3$) δ: 7.36 (td, J = 7.5 and 2, 2H), 7.50 (td, J = 7.5 and

Can. J. Chem. Downloaded from www.nrcresearchpress.com by 85.192.166.187 on 09/08/12
For personal use only.

TABLE 1. Products obtained from the oxidation of thianthrene 5-oxide by benzyltriethylammonium permanganate ($QMnO_4$)

$QMnO_4$ (mmol)[a]	Products	A (cm^2)[b]	Conc. (M)	Mass (mmol)	X_{SO}
0.618	**SSO_2**	1.92	2.1×10^{-4}	5.3×10^{-1}	1.0
	SOSO	0	0	0	
	$SOSO_2$	0	0	0	
0.289	**SSO_2**	1.89	2.06×10^{-4}	5.16×10^{-3}	1.0
	SOSO	0	0	0	
	$SOSO_2$	0	0	0	
0.351	**SSO_2**	>2[c]	$>2.2 \times 10^{-4}$	$>5.5 \times 10^{-3}$	1.0
	SOSO	0	0	0	
	$SOSO_2$	0	0	0	

[a]$QMnO_4$ was reacted with 0.86 mmol of **SSO**. The products were collected and dried, and a portion dissolved in sufficient solvent (60% hexane, 15% 2-propanol, 25% methylene chloride) to give a concentration appropriate for HPLC analysis.
[b]Peak area.
[c]The concentration, made deliberately high to search for trace amounts of **SOSO** and **$SOSO_2$**, gave a peak that went off scale.

TABLE 2. Products obtained from the oxidation of thianthrene 5-oxide by ruthenium tetroxide

RuO_4 (mmol)[a]	Products	A (cm^2)[b]	Conc. (M)	Mass (mmol)	X_{SO}
0.257	**SSO_2**	2.90	3.35×10^{-4}	8.37×10^{-3}	0.78
	SOSO	1.80	5.12×10^{-5}	1.28×10^{-3}	
	$SOSO_2$	1.16	5.91×10^{-5}	1.48×10^{-3}	
0.259	**SSO_2**	4.23	5.04×10^{-4}	1.26×10^{-2}	0.78
	SOSO	2.75	7.99×10^{-5}	2.00×10^{-3}	
	$SOSO_2$	1.71	9.12×10^{-5}	2.28×10^{-3}	
0.514	**SSO_2**	1.67	1.8×10^{-4}	8.9×10^{-3}	0.79
	SOSO	0.96	2.6×10^{-5}	1.3×10^{-3}	
	$SOSO_2$	0.65	3.0×10^{-5}	1.5×10^{-3}	

[a]RuO_4 was reacted with 0.86 mmol of **SSO**. The products were collected and dried, and a portion dissolved in sufficient solvent (60% hexane, 15% 2-propanol, 25% methylene chloride) to give a concentration appropriate for HPLC analysis.
[b]Peak area.

1.5, 2H), 7.58 (dd, J = 7.5 and 1.5, 2H), 7.89 (dd, J = 7.0 and 2.0, 2H). Thianthrene 5,5-dioxide, **SSO_2**: R_f = 0.59. ^{1}H NMR ($CDCl_3$) δ: 7.45 (m, 4H), 7.60 (td, J = 6.5 and 2.5, 2H), 8.15 (dd, J = 6.0 and 2.0). Thianthrene 5,5,10-trioxide, **$SOSO_2$**: R_f = 0.43. ^{1}H NMR ($CDCl_3$) δ: 7.70 (m, 4H), 8.07 (dd, J = 7.5 and 1.5, 4H). Thianthrene 5,10-dioxide, **SOSO**: R_f = 0.13. ^{1}H NMR ($CDCl_3$) δ: 7.60 (dd, J = 6.0 and 2.0, 4H), 8.03 (dd, J = 6.0 and 2.0, 4H). Thianthrene 5,5,10,10-tetroxide, **SO_2SO_2**: R_f = 0. ^{1}H NMR (DMSO-d_6) δ: 8.05 (dd, J = 6.0 and 2.5, 4H), 8.33 (dd, J = 6.0 and 2.0, 4H).

Disproportionation of thianthrene 5-oxide

As noted above, thianthrene 5-oxide used in these experiments contained 1.4% thianthrene, **SS**, that could not be removed by column chromatography or repeated recrystallization. When oxidized by permanganate or chromyl chloride, the amount of **SS** present in the product decreased, presumably because it had been oxidized to **SSO**. When the oxidant was ruthenium tetroxide, however, the amount of **SS** in the product was always greater than 1.4%. This additional **SS** appears to have come from the disproportionation of **SSO** (to **SS** and **SOSO** or **SSO_2**). A similar reaction was observed to occur when a solution of RuO_2 and **SSO** was stirred for a few hours. No reaction was observed, however, when **SSO** was stirred with MnO_2.

Results

The products were analyzed by HPLC. Chromatograms were obtained using a Dionex Series 4000i liquid chromatograph fitted with an Alltech, Econosphere, 250-mm silica (5 μm) column and a Perkin Elmer UV detector operated at 258 nm. Integration was performed manually. The flow rate was 2.0 mL/min and the solvent protocol was 80% hexane, 20% 2-propanol (1.0–3.5 min), gradient (3.5–7.0 min), 35% hexane, 65% 2-propanol (3.5–10.5 min). Injection was started at 1.0 min and stopped at 1.5 min.

Using pure compounds, standard curves of concentration vs. peak area were prepared for **SS**, **SSO**, **SOSO**, **SSO_2**, **$SOSO_2$**, and **SO_2SO_2** under these conditions. The results obtained from triplicate experiments with each oxidant are summarized in Tables 1–3. The estimated uncertainties are ±2% in individual concentration measurements and ±10% in the X_{SO} values.

Discussion

The results summarized in Tables 1–3 clearly indicate that there is a substantial difference in selectivity for the three high-valent transition metal oxidants under consideration, with permanganate showing the greatest selectivity for oxygen transfer to a sulfoxide sulfur. This result is consistent with the work of Ogura et al. (19) who found that methyl (methylthio)methyl sulfoxide, **1**, was oxidized by permanganate to methyl (methylthio)methyl sulfone, **2**, in 97% yield. It also explains why monosulfones, and not disulfoxides, are the usual products

Can. J. Chem. Downloaded from www.nrcresearchpress.com by 85.192.166.187 on 09/08/12
For personal use only.

TABLE 3. Products obtained from the oxidation of thianthrene 5-oxide by chromyl chloride

CrO_2Cl_2 (mmol)[a]	Products	A (cm^2)[b]	Conc. (M)	Mass (mmol)	X_{SO}
0.245	**SSO_2**	0.56	3.73×10^{-5}	1.86×10^{-3}	0.25
	SOSO	5.30	2.11×10^{-4}	1.05×10^{-2}	
	$SOSO_2$	0.95	4.73×10^{-5}	2.36×10^{-3}	
0.484	**SSO_2**	0.57	3.85×10^{-5}	9.63×10^{-4}	0.17
	SOSO	8.30	3.30×10^{-4}	8.25×10^{-3}	
	$SOSO_2$	0.80	3.84×10^{-5}	9.58×10^{-4}	
0.646	**SSO_2**	0.57	3.85×10^{-5}	9.63×10^{-4}	0.15
	SOSO	10.05	4.00×10^{-4}	9.99×10^{-3}	
	$SOSO_2$	0.80	3.84×10^{-5}	9.58×10^{-4}	

[a]CrO_2Cl_2 was reacted with 0.86 mmol of **SSO**. The products were collected and dried, and a portion dissolved in sufficient solvent (60% hexane, 15% 2-propanol, 25% methylene chloride) to give a concentration appropriate for HPLC analysis.
[b]Peak area.

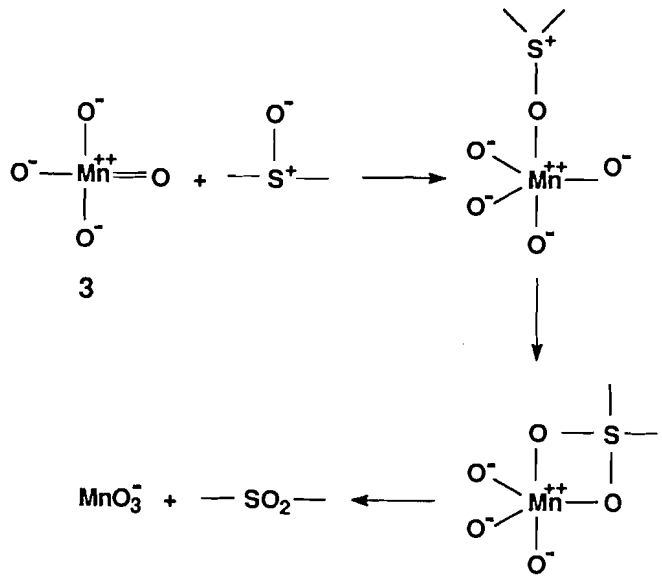

SCHEME 2. The oxidation of a sulfoxide by permanganate.

obtained from the oxidation of *gem*-disulfides by permanganate (20).

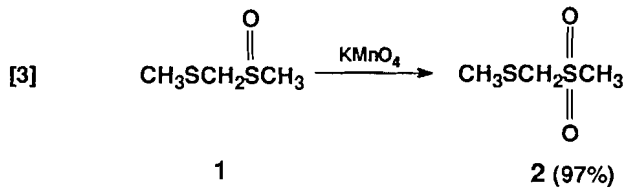

From a comparison with other permanganate oxidations, it seems likely that oxygen transfer is preceded by complexation between the oxidant and the reductant (21). It is known that the manganese atom in permanganate is approximately dipositive with the oxygen atoms bearing corresponding negative charges as depicted in structure 3 (22). It therefore seems likely, on the basis of electrostatic considerations, that complex formation would involve interaction between the manganese atom and the oxygen end of the sulfoxide dipole as in Scheme 2. Oxygen transfer could then occur as indicated. The product, manganate(V) ion, also suggested as an intermediate in other permanganate oxidations (23), would likely be reduced very rapidly to manganese(IV) by electron capture from the solvent.

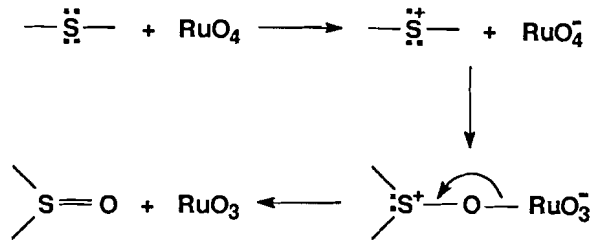

SCHEME 3. The oxidation of a sulfide by RuO_4.

A similar mechanism would account for the oxidation of **SSO** to **SSO_2** by ruthenium tetroxide. However, the observation of some **SOSO** in the products of this reaction indicates that the sulfide sulfur is also oxidized by RuO_4, although at a substantially slower rate. Such an oxidation may be initiated by electron transfer to give perruthenate and a radical cation as in Scheme 3. Since the medium is nonpolar, it is unlikely, as envisaged in Scheme 3, that these ions would diffuse out of the solvent cage prior to oxygen transfer.

It is also possible that the small amount of **SOSO** observed in the product when **SSO** is oxidized by RuO_4 could be due to the reactions of RuO_3, which is a by-product of these reactions.

The observation that transfer of oxygen to the sulfide sulfur is the main reaction when **SSO** is oxidized by chromyl chloride indicates that an alternative reaction mechanism must pertain. By analogy with the preceding discussion, a single electron transfer mechanism may be considered as a possibility for the reactions of this oxidant. This suggestion is also consistent with other known chemical properties of chromyl chloride. Recent results, described by Cook and Mayer (24), provide strong evidence for the intermediacy of cyclohexyl radicals during the oxidation of cyclohexane by chromyl chloride, and free radical intermediates have also been suggested for the Etard reaction (Cl_2CrO_2 + $ArCH_3$), which ultimately yields arylaldehydes (25).

A tentative mechanism involving electron transfer as the initial reaction has been outlined in Scheme 4.

The difference between chromyl chloride and other transition metal oxides or oxyanions may be associated with different modes of polarization of the M=O and M—Cl bonds. Polarization of the metal oxo bond (M=O ↔ M—O$^-$) places a greater positive charge on the metal while the converse would be true for metal–chlorine bonds (M—Cl: ↔ M=Cl) (26). Permanganate could therefore be considered as a resonance hybrid of the

Can. J. Chem. Downloaded from www.nrcresearchpress.com by 85.192.166.187 on 09/08/12
For personal use only.

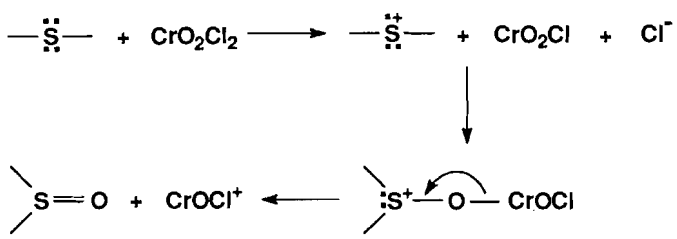

SCHEME 4. The oxidation of sulfide by CrO_2Cl_2.

structures depicted in eq. [4] (22), while the corresponding structures for chromyl chloride would be those in eq. [5]. A reduction of the positive charge on chromium as compared to manganese, suggested by these resonance structures, and the presence of an electron-deficient chlorine ligand could promote an electrostatic interaction between the ligand and the nonbonding electrons of sulfur that would initiate an alternative reaction such as a single electron transfer.

In any event it is clear from these results that there is a fundamental difference between the oxygen transfer reactions of

[4] 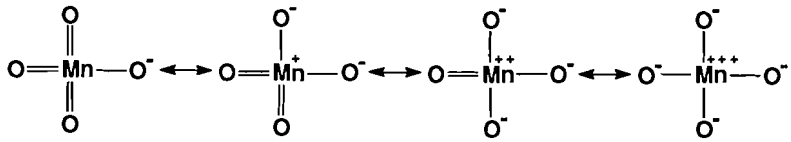

[5] 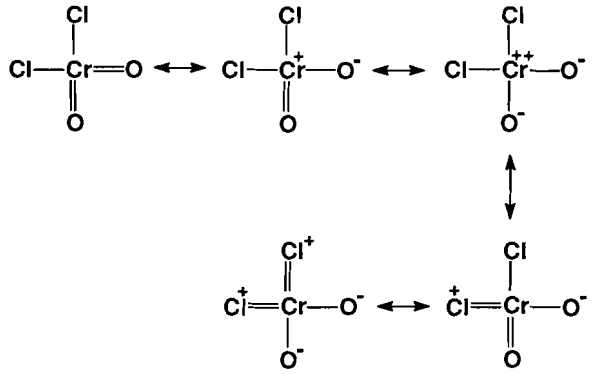

chromyl chloride and the other two oxidants considered in this study. For this reason the extensive experimental and theoretical information currently available for chromyl chloride oxidations (24, 27) may not be directly applicable to an understanding of other high-valent transition metal oxidants.

Acknowledgments

Financial assistance from the Natural Sciences and Engineering Research Council of Canada (NSERC) is gratefully acknowledged. B.L.M. also acknowledges support from NSERC in the form of two Undergraduate Research Awards during the completion of this work.

1. M. Hudlicky. Oxidations in organic chemistry. ACS Monograph 186, Washington, D.C. 1990; M.B. Smith. Organic synthesis. McGraw–Hill, New York. 1994. Chap. 3.
2. L.A. Moran, K.G. Scrimgeour, H.R. Horton, R.S. Ochs, and J.D. Rawn. Biochemistry. 2nd ed. Prentice Hall, Englewood Cliffs, N.J. 1994. Chap. 5.
3. S. Ozawa, Y. Watanabe, S. Nakashima, T. Kitagawa, and I. Morishima. J. Am. Chem. Soc. **116**, 634 (1994); C.T. Choma, J.D. Lear, M.J. Nelson, P.L. Dutton, D.E. Robertson, and W.F. DeGrado. J. Am. Chem. Soc. **116**, 856 (1994); R.E. Dickerson and I. Geis. Hemoglobin: structure, function, evolution and pathology. Benjamin/Cummings, Menlo Park, Calif. 1983; C. Ho, W.A. Eaton, J.P. Collman, Q.H. Gibson, J.S. Leigh, E. Margoliash, K. Moffat, and W.R. Scheidt. Hemoglobin and oxygen binding. Elsevier Biomedical, New York. 1982; A.B.P. Lever and H.B. Gray. Iron porphyrins. Parts 1 and 2. Addison–Wesley, London. 1983.
4. S.V. Ley and A. Madin. *In* Comprehensive organic synthesis. Vol. 7. *Edited by* B.M. Trost. Pergamon, New York. 1991. p. 251; F. Freeman. *In* Organic syntheses by oxidation with metal compounds. *Edited by* W.J. Mijs and C.R.H.I. de Jonge. Plenum, New York. 1986. Chaps. 1 and 2; J.L. Courtney. *In* Organic syntheses by oxidation with metal compounds. *Edited by* W.J. Mijs and C.R.H.I. de Jonge. Plenum, New York. 1986. Chap. 8; W.P. Griffith and S.V. Ley. Aldrichimica Acta, **23**, 13 (1990).
5. W.A. Nugent and J.M. Mayer. Metal–ligand multiple bonds. Wiley, New York. 1988; R.H. Holm. Chem. Rev. **87**, 1401 (1987); C-M. Che and V. W-W. Yam. Adv. Inorg. Chem. **39**, 233 (1992); R.H. Holm. Coord. Chem. Rev. **100**, 183 (1990).
6. D.H.R. Barton and D. Doller. Acc. Chem. Res. **25**, 504 (1992); D.H.R. Barton, S.D. Beviere, W. Chavasiri, E. Csuhai, D. Doller, and W-G. Liu. J. Am. Chem. Soc. **114**, 2147 (1992); D.H.R. Barton, E. Csuhai, and N. Ozbalik. Tetrahedron, **46**, 3743 (1990).
7. H.C. Kolb, P.G. Andersson, and K.B. Sharpless. J. Am. Chem. Soc. **116**, 1278 (1994).
8. D.G. Lee and T. Chen. J. Org. Chem. **56**, 5346 (1991).
9. J.H. Acquaye, J.G. Muller, and K.J. Takeuchi. Inorg. Chem. **32**, 160 (1993); K.R. Guertin and A.S. Kende. Tetrahedron Lett. **34**, 5369 (1993); C.M. Rodriguez, J.M. Ode, J.M. Palazon, and V.S. Martin. Tetrahedron, **48**, 3571 (1992); K.K. Banerji. Tetrahedron, **44**, 2969 (1988); M.E. Marmion, R.A. Leising, and K.J. Takeuchi. J. Coord. Chem. **19**, 1 (1988); L. Roecker, J.C. Dobson, W.J. Vining, and T.J. Meyer. Inorg. Chem. **26**, 779 (1987).
10. W. Adam, W. Haas, and B.B. Lohray. J. Am. Chem. Soc. **113**, 6202 (1991); W. Adam, H. Durr, W. Haas, and B.B. Lohray. Angew. Chem. Int. Ed. Engl. **25**, 101 (1986); **25**, 188 (1986).
11. M. Matsui, Y. Miyamoto, K. Shibata, and Y. Takase. Bull. Chem. Soc. Jpn. **57**, 2526 (1984); S. Oae, T. Takata, and Y.H. Kim. Bull. Chem. Soc. Jpn. **54**, 2712 (1981); S. Oae, Y. Ohnishi, S. Kozuka, and W. Tagaki. Bull. Chem. Soc. Jpn. **39**, 364 (1966).
12. M. Hamamoto, K. Nakayama, Y. Nishiyama, and Y. Ishii. J. Org. Chem. **58**, 6421 (1993); F.P. Ballistreri, G.A. Tomaselli, R.M. Toscano, V. Conte, and F. Di Furia. J. Am. Chem. Soc. **113**, 6209

Can. J. Chem. Downloaded from www.nrcresearchpress.com by 85.192.166.187 on 09/08/12
For personal use only.

(1991); A.J. Bloodworth, T. Melvin, and J.C. Mitchell. J. Org. Chem. **53**, 1078 (1988).
13. H. Gilman and D.R. Swayampati. J. Am. Chem. Soc. **77**, 3387 (1955).
14. H.J. Shine and L. Piette. J. Am. Chem. Soc. **84**, 4798 (1962).
15. H. Karaman, R.J. Barton, B.E. Robertson, and D.G. Lee. J. Org. Chem. **49**, 4509 (1984).
16. R. Stewart. *In* Oxidation in organic chemistry. Part A. *Edited by* K.B. Wiberg. Academic Press, New York. 1965. p. 14.
17. L.F. Fieser and M. Fieser. Reagents for organic synthesis. Vol. 1. Wiley, New York. 1967. p. 986.
18. D.G. Lee and M. van den Engh. *In* Oxidation in organic chemistry. Part B. *Edited by* W.S. Trahanovsky. Academic Press, New York. 1973. p. 177.
19. K. Ogura, M. Suzuki, and G. Tsuchihashi. Bull. Chem. Soc. Jpn. **53**, 1414 (1980).
20. M. Poje and K. Balenovic. Tetrahedron Lett. 1231 (1978).
21. T. Gobel and K.B. Sharpless. Angew. Chem. Int. Ed. Engl. **32**, 1329 (1993); D.G. Lee, K.C. Brown, and H. Karaman. Can. J. Chem. **64**, 1054 (1986).
22. T. Ziegler, A. Rauk, and E. Baerends. Chem. Phys. **16**, 209 (1976).
23. R. Stewart. Oxidation mechanisms. Benjamin, New York. 1964. p. 62; D. Arndt. Manganese compounds as oxidizing agents in organic chemistry. Open Court, Peru, Ill. 1981. p. 186; A.J. Fatiadi. Synthesis, 85 (1987).
24. G.K. Cook and J.M. Mayer. J. Am. Chem. Soc. **116**, 1855 (1994).
25. J. March. Advanced organic chemistry. 4th ed. Wiley, New York. 1992. pp. 1190–1191.
26. W.A. Howard and G. Parkin. J. Am. Chem. Soc. **116**, 606 (1994); K.B. Sharpless, A.Y. Teranishi, and J-E. Backvall. J. Am. Chem. Soc. **99**, 3120 (1977).
27. A.K. Rappe and W.A. Goddard. J. Am. Chem. Soc. **104**, 3287 (1982).

Can. J. Chem. Downloaded from www.nrcresearchpress.com by 85.192.166.187 on 09/08/12
For personal use only.

Spin diffusion in a triblock thermoplastic elastomer

GYUNGGOO CHO AND ALMERIA NATANSOHN[1]
Department of Chemistry, Queen's University, Kingston, ON K7L 3N6, Canada

Received June 14, 1994

GYUNGGOO CHO and ALMERIA NATANSOHN. Can. J. Chem. **72**, 2255 (1994).

A triblock copolymer thermoplastic elastomer (SEBS) consisting of an ethylene–butylene random-copolymer rubbery domain flanked by rigid polystyrene short blocks has been analyzed using novel solid-state NMR techniques. ^{13}C NMR relaxation measurements suggest that at the $T_1(H)$ level (minimum observable phase size of about 18 nm) the material appears homogeneous, but at the $T_{1\rho}(H)$ level (minimum observable phase size of about 3 nm) the expected two distinct phases are noted. Two-dimensional WISE spectra (high-resolution ^{13}C – broadline ^1H) show the different mobility in the two phases. A broad component associated with the highly mobile rubbery phase indicates the presence of an interface. The mobile phase is selected using a dipolar filter pulse sequence and the magnetization is allowed to transfer to the rigid polystyrene phase during a period called "mixing time." From the growth of the polystyrene magnetization during the mixing period, the size of the dispersed polystyrene phase can be calculated to be 16 ± 2 nm.

GYUNGGOO CHO et ALMERIA NATANSOHN. Can. J. Chem. **72**, 2255 (1994).

Faisant appel aux nouvelles techniques de la RMN de l'état solide, on a analysé un élastomère thermoplastique, un copolymère à trois blocs (SEBS) formé du domaine caoutchouté d'un copolymère aléatoire d'éthylène–butylène flanqué de petits blocs de polystyrène rigide. Les mesures de relaxation de la RMN du ^{13}C suggèrent que, au niveau $T_1(H)$ (taille minimale de la phase observable d'environ 18 nm), le produit semble homogène, mais que au niveau $T_{1\rho}(H)$ (taille minimale de la phase observable d'environ 3 nm), on peut noter les deux phases distinctes attendues. Le spectre WISE bidimensionel (^{13}C à haute résolution et ^1H avec des raies larges) montre la mobilité différente dans les deux phases. Une composante importante associée à la phase caoutchouté très mobile indique la présence d'une interface. On choisit la phase mobile en utilisant un filtre dipolaire à séquence pulsée et on permet à la magnétisation de se transférer à la phase polystyrène rigide au cours d'une période que l'on appelle «temps de mélange». En se basant sur la croissance de la magnétisation du polystyrène durant le période de mélange, on a calculé que la taille de la phase polystyrène dispersée est de 16 ± 2 nm.

[Traduit par la rédaction]

Introduction

Phase-separated materials have proven to be quite useful due to their enhanced mechanical properties. Probably the best known example of such a material is high-impact polystyrene, which consists of a polystyrene matrix with a dispersed rubber phase. As the name says, this material has better impact properties than polystyrene itself. In fact, most polymer materials are being mixed with other polymers or fillers or other materials, to improve some of the properties and (or) lower costs. The degree of mixing in a multiphasic material is crucial for the properties exhibited by that material. The dispersion of the minor phase as well as the nature and thickness of the interface separating the two components are the most important parameters.

One method to analyze mixing in polymer materials makes use of ^{13}C CPMAS NMR spectroscopy. High-resolution spectra are obtained in the solid state on materials as they are being used. Selective excitation of one of the components (based on mobility differences) followed by spin diffusion to the other phase was proposed in 1966 by Goldman and Shen (1) as a procedure to determine domain sizes. Since then, various similar techniques have been proposed (2–7). One of those is the "dipolar filter" proposed by Spiess and co-workers (8) and subsequently applied to some soft–hard polymer pairs (9–12).

Thermoplastic elastomers are such phase-separated polymer systems consisting of a dominant rubbery phase and a dispersed rigid phase. The dispersed rigid phase acts as a physical crosslink, replacing the usual chemical crosslink in commercial rubber. Its advantage is that the products can be reprocessed at temperatures exceeding the softening temperature of the hard

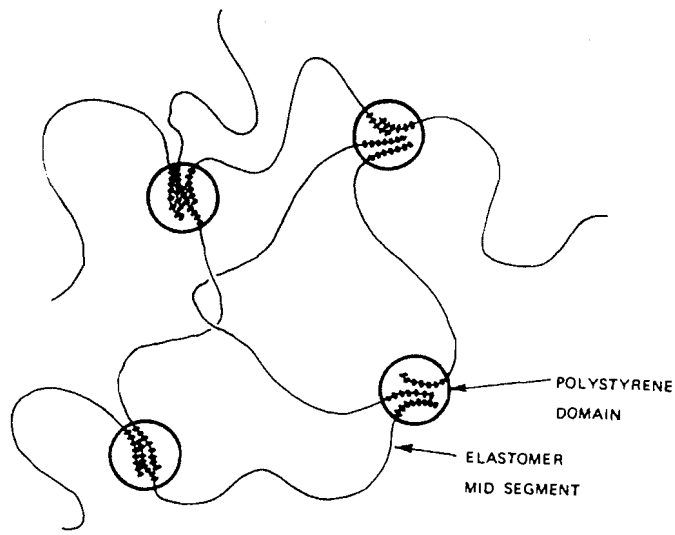

SCHEME 1 (ref. 13)

domains. For this reason there is considerable interest in thermoplastic elastomers. One class of thermoplastic elastomers are triblock copolymers of the type hard–soft–hard. The molecular weight of the hard segments is much lower than that of the soft segment, thus making the rubbery phase the dominant one. The typical morphology of a thermoplastic elastomer is represented in Scheme 1. We have chosen SEBS, a triblock copolymer of styrene–(ethylene-*co*-butylene)–styrene to investigate its phase structure using various available solid-state NMR techniques.

Experimental

The thermoplastic elastomer sample was obtained from Shell Labo-

[1]Author to whom correspondence may be addressed. Telephone: 613-545-2008. Fax: 613-545-6669. e-mail: natansoh@qucdn.queensu.ca

Can. J. Chem. Downloaded from www.nrcresearchpress.com by 85.192.166.187 on 09/08/12
For personal use only.

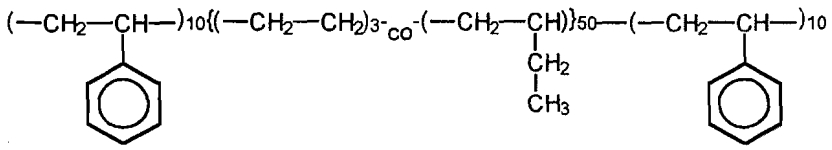

SCHEME 2

ratories (Houston, Tex.) and used without modification. The degree of polymerization of the styrene blocks was 10 and the degree of polymerization of the ethylene-*co*-butylene block was 50 (13). The molar ratio of ethylene to butylene units in the rubber segment was determined by solution ^{1}H NMR to be 3:1. The formula of the SEBS sample is shown in Scheme 2.

Proton-decoupled solid-state ^{13}C NMR spectra were obtained on a Bruker ASX-200 spectrometer operating at 50.29 MHz (200 MHz proton resonance). All spectra were obtained at room temperature with spinning of 5.5 kHz (chosen to produce spinning side-bands outside of the region of interest in the spectra). No spinning side-bands suppression was necessary. The proton $\pi/2$ pulse was 3.6 μs, the cross-polarization time was 1.5 ms, and the delay between pulses was 5 s.

Proton spin-lattice relaxation times in the rotating frame ($T_{1\rho}$(H)) were measured using carbon detection in a pulse sequence with increasing proton spin locking times (14). The two-dimensional WISE (WISE = WIdeline SEparation) and the dipolar filter pulse sequences are shown schematically in Fig. 1 (8). For the WISE experiment (Fig. 1*a*) 512 complex points were used in the carbon domain and 64 points in the proton domain with an increment of 4 μs. The dipolar filter pulse sequence (Fig. 1*b*) was used in two ways. One procedure involved complete saturation of the whole NMR spectrum, using 300-μs delays between pulses in the dipolar filter and 5 repetitions of the filter. Then the magnetization was allowed to recover during the mixing time in order to measure T_1(H) for all the carbon peaks. The phase cycling pulse (PC in Fig. 1*b*) was not used for the T_1(H) measurements. In the second procedure, selection of the mobile phase was achieved with cycles of 12 $\pi/2$ proton pulses repeated 9 times and with spacings of 7 μs between them. For the dipolar filter, the PC pulse was used to eliminate the T_1(H) effect in spin diffusion.

Results and discussion

Dynamic mechanical measurements of this SEBS sample indicate two glass transition regions, one for the rubbery phase at about –40°C and the other one for the polystyrene domains at about 110°C (13). Glass transitions are usually visible when the phases have dimensions greater than about 10 nm. To confirm the presence of the two phases, proton spin-lattice relaxation times can be used. The ^{13}C CPMAS NMR spectrum of SEBS is shown in Fig. 2. Some assignments are straightforward; for example, the peaks at about 130 ppm and at about 150 ppm belong to the protonated aromatic carbons and to the *ipso* aromatic carbon of the polystyrene, respectively. In the aliphatic region, assignments can be made using a dipolar dephasing procedure (15). Due to the relatively high mobility of the rubbery phase, a longer dipolar dephasing time is required to eliminate its carbon signals in the spectrum. Thus, at 50 μs most of the signals around 40 ppm are dephased, thus they can be assigned to the methylene and methine carbons of the polystyrene. The most intense signals between 30 and 40 ppm are assigned to the methylene carbons in the rubbery phase. The methine carbons of the rubber resonate in the signal centered at 40 ppm, while the methyl appears at about 13 ppm.

It is well known that the proton spin-lattice relaxation is related to spin diffusion among the abundant spins and that it can be used as a probe for the phase structure of polymer blends (16). T_1(H) is usually smaller than a second and $T_{1\rho}$(H) is around 10 ms in polymer materials. Thus each of these parameters will

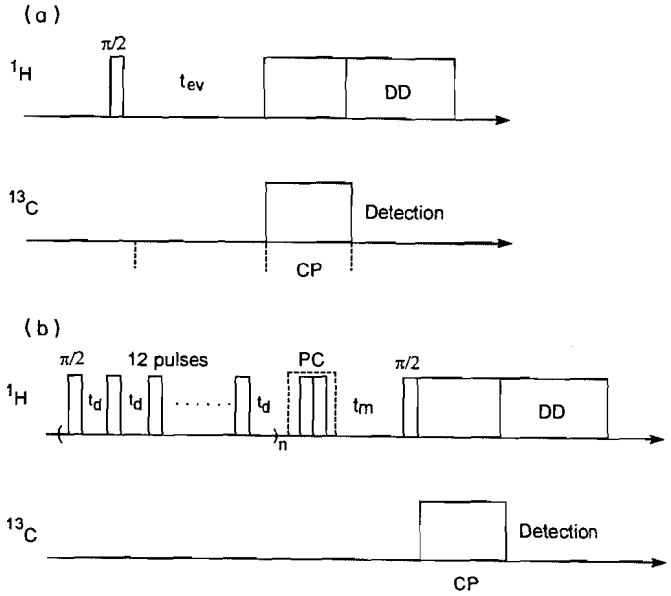

FIG. 1. Pulse sequences for: (*a*) WISE; (*b*) dipolar filter and T_1(H) measurements.

give information about phase structure at a different level. One can estimate the minimum size of various phases from the spin traveling distance obtained with eq. [1]:

$$[1] \quad \langle x \rangle = \frac{4}{3} Dt$$

where D is the diffusion coefficient and t is the timescale represented by the relaxation measurement (17). The proton spin-lattice relaxation time constants for the two phases were measured using the signals at 130 ppm (polystyrene) and 32 ppm (rubber). T_1(H) is the same for all carbons in the material (310 ± 20 ms), while $T_{1\rho}$(H) is different for the polystyrene phase (7.0 ms) and for the rubber (2.6 ms). Using eq. [1] and the spin diffusion coefficient of polystyrene of (0.8 ± 0.2) × 10^{-15} m^2/s (8), one can estimate the phase sizes from the relaxation parameters. The polystyrene is the dispersed phase, hence its size will have to be smaller. A spin traveling distance of 18.2 nm is obtained from T_1(H). At this level, the material appears homogeneous (a single relaxation parameter). From $T_{1\rho}$(H) a minimum phase size of 2.7 nm is obtained for polystyrene. This means that the dispersed polystyrene phase dimension has to be greater than 2.7 nm and smaller than 18.2 nm in order to exhibit a two-phase behaviour for $T_{1\rho}$(H) and a monophasic behaviour for T_1(H). This agrees with the preliminary estimate from the dynamic mechanical measurements (13) that the phases have to be greater than about 10 nm.

To confirm the very different mobility of the two phases, a 2D-WISE spectrum was run and Fig. 3 shows the result. The projection on the carbon axis is shown as the carbon spectrum. There is a clear difference in the widths of the proton spectra for the two components, and Fig. 4 shows the two slices taken at 32 ppm and at 130 ppm. The aromatic protons show a half-height

Can. J. Chem. Downloaded from www.nrcresearchpress.com by 85.192.166.187 on 09/08/12
For personal use only.

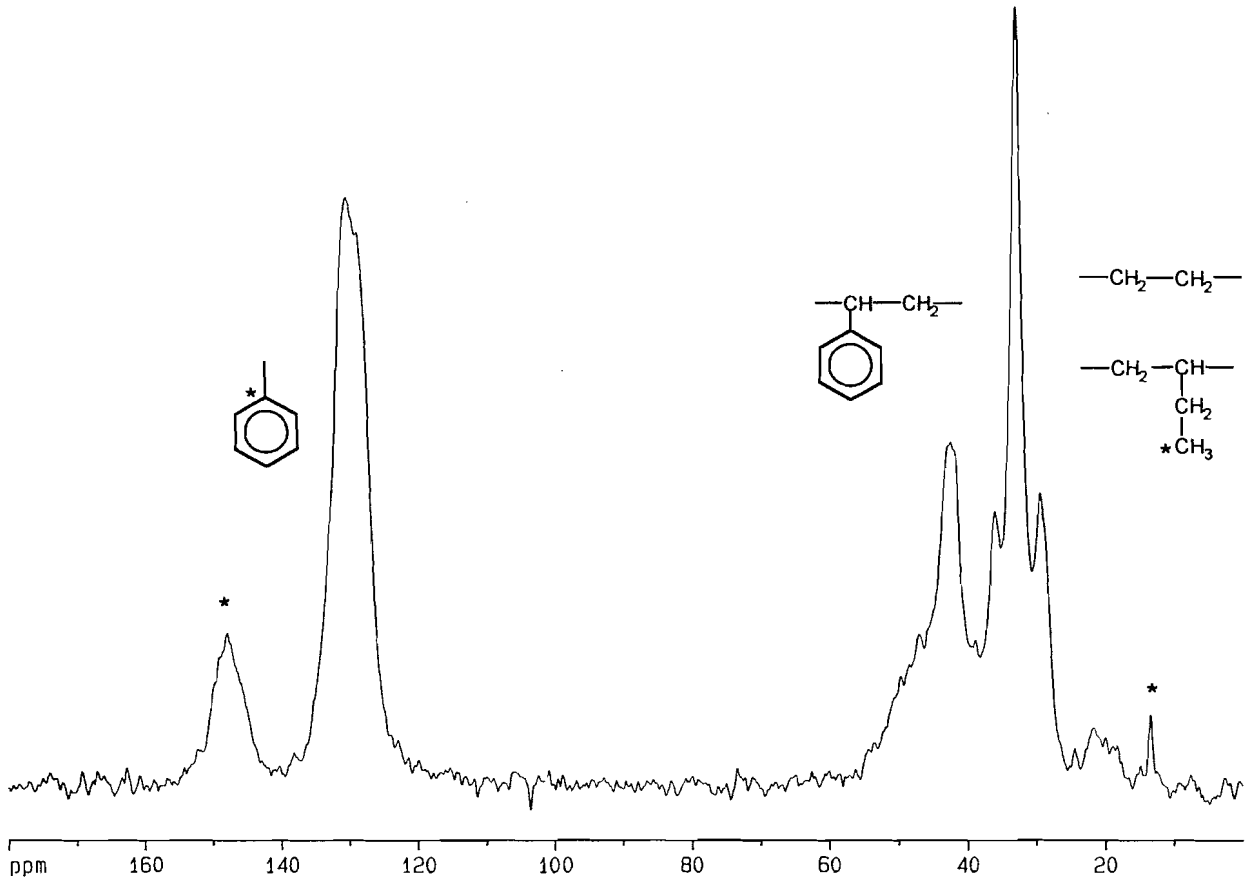

FIG. 2. ^{13}C CPMAS NMR spectrum of SEBS. The assignments are given on the spectrum. A weak spinning side-band can be seen at about 20 ppm.

linewidth of 60.5 kHz, while at 32 ppm there seem to be two superimposed broadline proton spectra. The narrow spectrum belongs to the rubber phase and has a half-height linewidth of 12 kHz. The presence of a broader component in the rubber signal may suggest that a small part of the rubber has a restricted kind of motion and it is fairly reasonable to assume that the rubber surrounding the polystyrene domains may be less mobile than the bulk of the rubbery phase. In fact, the presence of such a broad component in a two-phase system has been previously explained as being part of the interface (11). Due to the difference in linewidth between the rubber and the polystyrene and to the fact that the rubber is the dominant phase, most of the signal intensity in the 2D spectrum in Fig. 3 is concentrated in the aliphatic region. The polystyrene signal may sometimes be lost in the noise, as is the case with the *ipso* carbon. The WISE spectrum demonstrates that there is a significant difference in mobility between the rubbery phase and the polystyrene rigid phase.

The dipolar filter sequence in Fig. 1*b* contains a very important part: the phase cycling pulse applied previous to the mixing time. If this pulse is omitted, all signals grow in intensity as a function of mixing time, due to the spin-lattice relaxation. When this pulse is present, however, a loss of absolute intensity is detected in the spectra and a correction factor of $\exp(t_m/T_1)$ has to be applied to the measured intensities (8), where t_m is the mixing time shown in Fig. 1*b*. Figure 5 shows the spectra obtained with the dipolar filter sequence at various mixing times. The selection is sampled at 50 μs mixing time, and already at 10 ms the polystyrene signals are very visible, which is an indication of fairly fast spin diffusion. The equilibrium (a

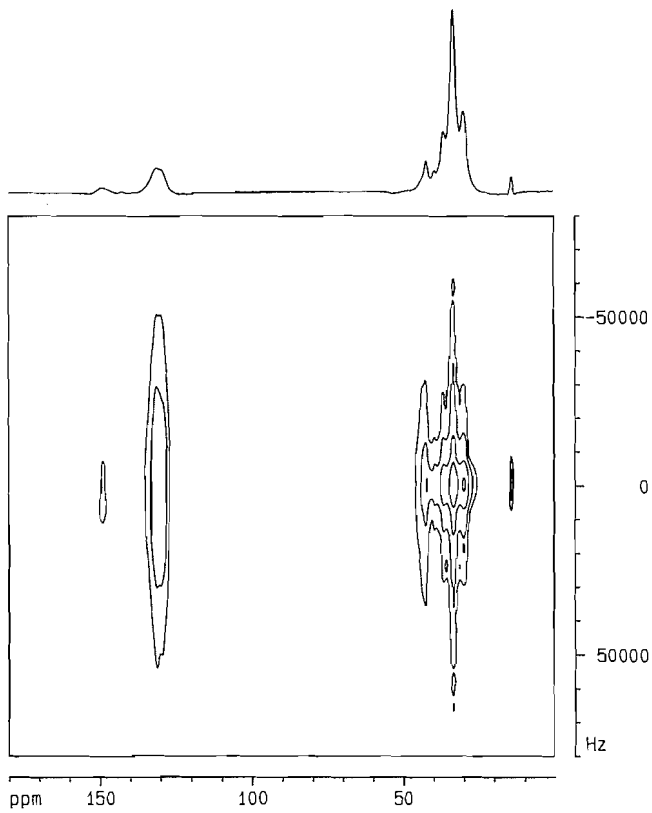

FIG. 3. The WISE spectrum of SEBS.

Can. J. Chem. Downloaded from www.nrcresearchpress.com by 85.192.166.187 on 09/08/12
For personal use only.

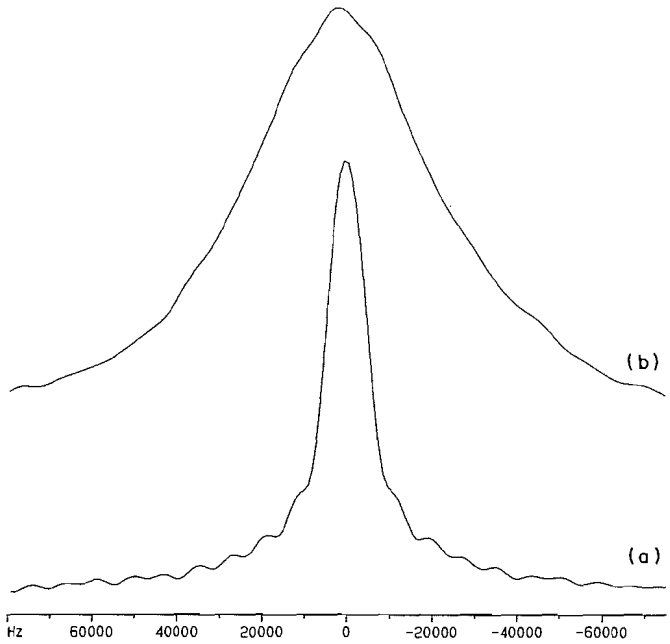

FIG. 4. Two slices taken from the WISE spectrum shown in Fig. 3:(*a*) 32 ppm; (*b*) 130 ppm.

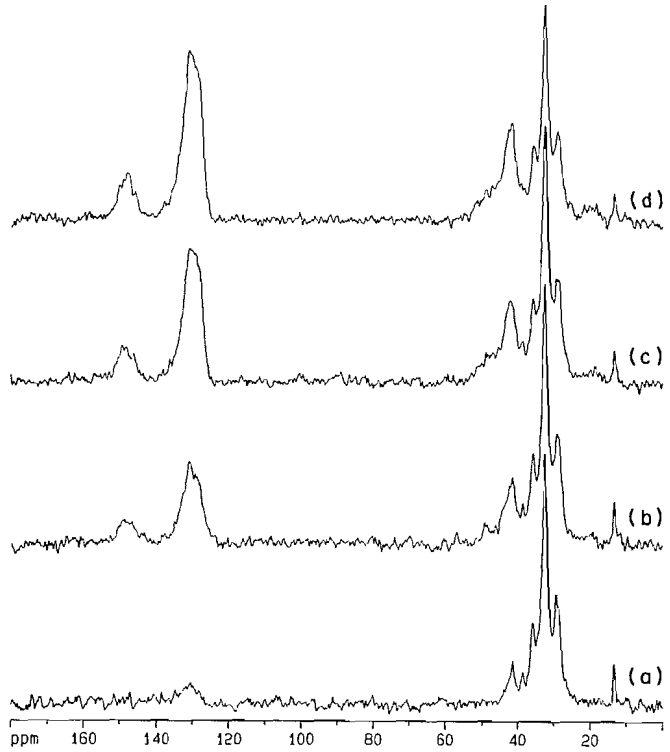

FIG. 5. Spectra of SEBS obtained after the dipolar filter selection at various mixing times (*a*) 50 μs; (*b*) 10 ms; (*c*) 30 ms; (*d*) 50 ms.

spectrum with its components in the same ratio as a spectrum obtained without selection) is obtained at about 300 ms. One would normally expect that as the polystyrene signals increase, some decrease should be noted for the rubber signals, because the selection–transfer procedure eliminates the polystyrene magnetization and the whole source of magnetization in the spectrum comes from the rubber signals. This decrease is not very noticeable, and the reason is that the rubber is the main component and each of its structural units has 4.5 times more protons than the structural unit of the polystyrene. This is a very "rich" source for magnetization and its decrease is insignificant compared to the increase in magnetization of the polystyrene.

Equation [2] describes how the size of the dispersed domains can be determined as a function of the proton density of each phase (ρ_{HA}, ρ_{HB}), the volume fraction of each phase (ϕ_A, ϕ_B, one of which, the polystyrene in this case, is ϕ_{dis}, the volume fraction of the dispersed phase), the dimensionality (ϵ), the diffusion coefficients for each phase (D_A, D_B), and $(t_m^*)^{1/2}$ (8). In a similar manner, the long distance can be calculated using the size of the dispersed domains and the formula in eq. [3].

$$[2] \qquad d_{dis} = \left(\frac{\rho_{HA}\phi_A + \rho_{HB}\phi_B}{\phi_A\phi_B}\right) \times \frac{4\epsilon\phi_{dis}\sqrt{D_A D_B}}{\sqrt{\pi}\left(\sqrt{D_A}\rho_{HA} + \sqrt{D_B}\rho_{HB}\right)} \sqrt{t_m^*}$$

$$[3] \qquad d = \frac{d_{dis}}{\sqrt[\epsilon]{\phi_{dis}}}$$

Both equations [2] and [3] have been derived for the general case of a blend composed of two polymers, which may be bound (as in this case of triblock copolymers) or mixed together. The equations have also been shown to be valid for a random distribution of two types of structural units (8).

Most of the parameters in eq. [2] are known or can be approximated. From the composition of the terpolymer and the densities of polystyrene and of polyethylene (low density, similarly branched) the volume fraction of each phase can be calculated. The proton densities are similary calculated using the proton fractions in each component. The spin diffusion coefficient of polystyrene has been reported (8), while the spin diffusion coefficient of the rubber block can be approximated with that of polybutadiene ($(0.05 \pm 0.015) \times 10^{-15}$ m^2/s) (12), mainly because it is obtained by hydrogenation of the polybutadiene blocks. The dimensionality of this block terpolymer is 2, i.e., the morphology is cylindrical (13). The square root of t_m^* can be found from extrapolating the straight line of initial magnetization growth as shown in Fig. 6.

Using the parameters discussed above, a domain size of 16 ± 2 nm is obtained for the dispersed polystyrene and a long period of 31 ± 5 nm is obtained for the combination of the dispersed and major phase. The error was estimated by introducing the lower values of the diffusion coefficients for the two components to obtain the smallest estimate of the dispersed size (13.8 nm) and then the higher values for the largest estimate (17.7 nm). The calculated median value (15.6 nm) was taken as the average domain size.

If the average size of the polystyrene domains is indeed about 16 nm, then the results obtained for the relaxation parameters are easy to explain. T_1(H) is about 0.3 s, reflecting domain sizes of about 18 nm. By measuring T_1(H), the polystyrene phases are just small enough to be undetectable. $T_{1\rho}$(H) detects phases down to 2.7 nm. As the polystyrene phase is greater than that, the $T_{1\rho}$(H) measurements show the presence of two phases. As for the dynamic mechanical results, the polystyrene phase is greater than the 10 nm believed necessary to show the glass transition.

Regarding the interface in this triblock copolymer, the data

Can. J. Chem. Downloaded from www.nrcresearchpress.com by 85.192.166.187 on 09/08/12
For personal use only.

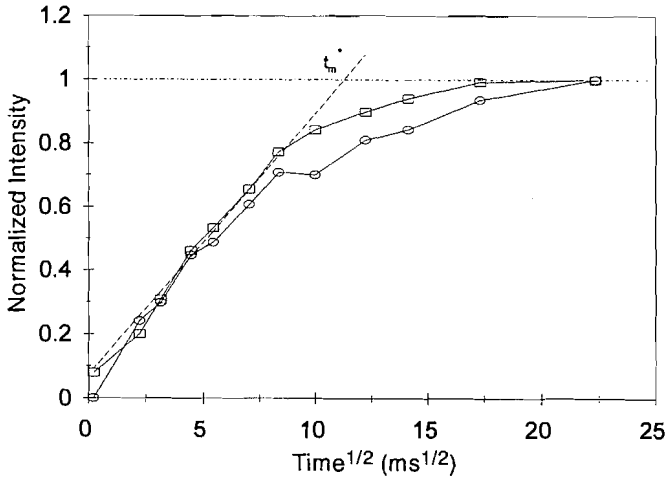

FIG. 6. Magnetization growth for two polystyrene signals at 150 and 130 ppm. The open circles represent the 150 ppm signal.

here could be modeled assuming such an interface exists. In fact the presence of the broader background on the relatively narrow proton slice of the rubber (Fig. 4) is indicative of an interface, according to the literature (11). We believe that more theoretical background is necessary to calculate such an interfacial thickness.

Finally, this triblock copolymer fits fairly well the developed models for magnetization transfer presented in the literature for other block copolymers (8, 11, 12), i.e., the two phases of all these systems are chemically bonded to each other. In most of the "real life" phase-separated systems, the two phases have no chemical bond and sometimes not even a physical interaction. The model for magnetization transfer in such systems has to be different; some of them may even have fairly good dispersion but no magnetization transfer due to the physical barrier between phases.

Conclusions

Solid-state NMR techniques can be used to obtain information about the phase structure and dimensions in a triblock thermoplastic elastomer. In the case of SEBS, the size of the polystyrene dispersed phase has been determined to be of the order of 16 nm with a cylindrical morphology.

Can. J. Chem. Downloaded from www.nrcresearchpress.com by 85.192.166.187 on 09/08/12
For personal use only.

Acknowledgements

We thank the Natural Sciences and Engineering Research Council of Canada (NSERC) for a strategic grant on phase structure of polymer blends, mixtures, and composites, which included the purchase of the NMR spectrometer. Acknowledgement is also made to the donors of the Petroleum Research Fund, administered by the American Chemical Society, for partial support of this research.

1. M. Goldman and L. Shen. Phys. Rev. **144**, 321 (1966).
2. P. Caravatti, P. Neuenschwander, and R.R. Ernst. Macromolecules, **18**, 119 (1985).
3. P. Caravatti, P. Neuenschwander, and R.R. Ernst. Macromolecules, **19**, 1880 (1986).
4. P. Caravatti, M.H. Levitt, and R.R. Ernst. J. Magn. Reson. **68**, 323 (1986).
5. K. Schmidt-Rohr, J. Clauss, B. Blumich, and H.W. Spiess. Magn. Reson. Chem. **28**, S3 (1990).
6. G.C. Campbell and D.L. VanderHart. J. Magn. Reson. **96**, 69 (1992).
7. D.L. VanderHart. Macromolecules, **27**, 2837 (1994).
8. J. Clauss, K. Schmidt-Rohr, and H.W. Spiess. Acta Polym. **44**, 1 (1993).
9. J. Clauss, K. Schmidt-Rohr, A. Adam, C. Boeffel, and H.W. Spiess. Macromolecules, **25**, 5208 (1992).
10. N. Egger, K. Schmidt-Rohr, B. Blumich, W.D. Domke, and B. Stapp. J. Appl. Polym. Sci. **44**, 289 (1992).
11. W.Z. Cai, K. Schmidt-Rohr, N. Egger, B. Gerharz, and H.W. Spiess. Polymer, **34**, 267 (1993).
12. S. Spiegel, K. Schmidt-Rohr, C. Boeffel, and H.W. Spies. Polymer, **34** 4566 (1993).
13. W.P. Gergen, R.G. Lutz, and S. Davison. *In* Thermoplastic elastomers. A comprehensive review. *Edited by* N.R. Legge, G. Holden, and H.E. Schroeder. Hanser Publishers, Munich, Vienna, New York. 1987. pp. 508–540.
14. E.O. Stejskal, J. Schaefer, M.D. Sefcik, and R.A. McKay. Macromolecules, **14**, 275 (1981).
15. S.J. Opella and M.H. Frey. J. Am. Chem. Soc. **101**, 5854 (1979).
16. V.J. McBrierty, D.C. Douglass, and T.K. Kwei. Macromolecules, **11**, 1265 (1978).
17. J.R. Havens and D.L. VanderHart. Macromolecules, **18**, 1663 (1985).

Antineoplastic agents 285.[1] Isolation and structures of cephalostatins 14 and 15

GEORGE R. PETTIT,[2] JUNPING XU, YOSHITATSU ICHIHARA, AND MICHAEL D. WILLIAMS

Cancer Research Institute and Department of Chemistry, Arizona State University, Tempe, AZ 85287-1604, U.S.A.

AND

MICHAEL R. BOYD

Laboratory of Drug Discovery Research and Development, Developmental Therapeutics Program, Division of Cancer Treatment, National Cancer Institute, Frederick Cancer Research and Development Center, Frederick, MD 21702-1201, U.S.A.

Received March 16, 1994

GEORGE R. PETTIT, JUNPING XU, YOSHITATSU ICHIHARA, MICHAEL D. WILLIAMS, and MICHAEL R. BOYD. Can. J. Chem. **72**, 2260 (1994).

The tube-inhabiting marine worm, *Cephalodiscus gilchristi* has been found to produce a series of cytotoxic and antineoplastic disteroidal alkaloids. A substantial study concerned with discovery of new cell growth inhibitory constituents of this marine animal has led to isolation of cephalostatins 14 (**5***a*) and 15 (**5***b*). The structures were determined by interpretation of spectral data, principally high-field (400 and 500 MHz) NMR and HRFABMS combined with NMR spectral relationships to cephalostatin 1 (**4**) where the structure was previously assigned by X-ray crystal structure analysis. The stereochemical assignments were established employing the ROESY NMR technique. Both new cephalostatins significantly inhibited growth of the P388 lymphocytic leukemia and a selection of human cancer cell lines. The two new cephalostatins further enhance knowledge of structure–activity parameters for these potentially important steroidal alkaloids.

GEORGE R. PETTIT, JUNPING XU, YOSHITATSU ICHIHARA, MICHAEL D. WILLIAMS et MICHAEL R. BOYD. Can. J. Chem. **72**, 2260 (1994).

On a trouvé que le ver marin habitant un tube, *Cephalodiscus gilchristi*, produit une série d'alcaloïdes distéroïdaux cytotoxiques et antinéoplastiques. Une étude importante relative à la découverte de nouveaux constituants de cet animal marin inhibants la croissance de nouvelles cellules a conduit à l'isolement des céphalostatines 14 (**5***a*) et 15 (**5***b*). On a déterminé le structures par l'interprétation des données spectrales obtenues principalement par RMN à champ élevé (400 et 500 MHz) et par HRFABMS combiné avec des relations spectrales avec la céphalostatine 1 (**4**) dont la structure a été attribuée antérieurement par diffraction des rayons X. Les attributions stéréochimiques ont été faites par la technique REOSY de la RMN. Les deux nouvelles céphalostatines inhibent fortement la croissance de la leucémie lymphocytaire P388 ainsi qu'une sélection de cellules humaines cancéreuses. Les deux nouvelles céphalostatines augmentent nos connaissances sur les paramètres structure–activité de ces alcaloïdes stéroïdaux potentiellement importants.

[Traduit par la rédaction]

Can. J. Chem. Downloaded from www.nrcresearchpress.com by 85.192.166.187 on 09/08/12
For personal use only.

Introduction

Considerable research effort is currently being focused on discovery of new marine animal antineoplastic and (or) cytotoxic constituents based on nitrogen, oxygen, and (or) sulfur heterocyclic systems (2–15). Among the nitrogen heterocyclic compounds, dolastatins 10 (16) (**1**) and 15 (17) (**2**), ecteinascidin 729 (9) (**3**), and cephalostatin 1 (**4**) (18) are especially noteworthy. All are at various stages of preclinical or clinical development. To increase the supply of cephalostatin 1 and expand knowledge of structure–activity relationships in the important cephalostatin series (18–22) we have been utilizing a large-scale (450 kg wet wt., includes coenecium) recollection of the relatively small (~5 mm long) Southwest Indian Ocean marine worm *Cephalodiscus gilchristi* (Pterobranchia, Hemichordata Phylum). Previously we described the isolation and structural elucidation of cephalostatins 1–13 (1, 18–22), disteroidal alkaloids that are powerful human cancer cell line and murine P388 lymphocytic leukemia (PS system) cell growth inhibitors (ED_{50} 10^{-7}–10^{-9} μg/mL). Further investigation of the antineoplastic and (or) cytotoxic constituents of this marine worm have now resulted in discovery of two new disteroidal alkaloids, cephalostatins 14 (**5***a*) and 15 (**5***b*), with potent activity against a diverse group of human solid tumor types (in vitro) in the U.S. National Cancer Institute's (NCI) disease-oriented anticancer screen. We describe here the isolation and structure determination of these two novel alkaloids as well as their significant cancer cell growth inhibitory activity.

Results and discussion

The most recent scaled-up acquisition of *Cephalodiscus gilchristi* (450 kg wet wt.) was conducted in 1990 in the Indian Ocean off southeast Africa and was initially stored in methanol. Preliminary solvent partition separations of the methanol extract were performed as recently summarized (19) to yield a PS-active methylene chloride fraction (ED_{50} 0.044 μg/mL) that was chromatographed repeatedly on Sephadex LH-20 (eluents: methylene chloride – methanol 3:2, hexane–toluene–methanol 3:1:1, hexane–2–propanol–methanol 8:1:1, and hexane – methylene chloride – methanol 5:1:1) to afford several principal fractions. Final purification by reversed phase HPLC on C-8 silica gel columns using 10:10:12 acetonitrile–methanol–water as eluent furnished cephalostatin 14 (**5***a*) (32 mg, 7.1×10^{-6}% yield) and 15 (**5***b*) (5.1 mg, 1.2×10^{-6}% yield). Cephalostatins 14 and 15 caused significant inhibition of the murine leukemia (PS ED_{50} 4.1×10^{-3} μg/mL and 2.5×10^{-2} μg/mL, respectively) cell line.

Cephalostatin 14 (**5***a*) was obtained as a colorless powder and found to have molecular formula $C_{54}H_{72}N_2O_{12}$ by HRFABMS data (*m/z* 963.4974 $[M + Na]^+$, Δ −0.9 mmu). The UV absorption maxima at 305 (shoulder) and 288 nm (log ε 3.96) implied the presence of the same pyrazine chromophore as that of ceph-

[1]Advance 284 refers to ref. 1.

[2]Author to whom correspondence may be addressed.

Can. J. Chem. Downloaded from www.nrcresearchpress.com by 85.192.166.187 on 09/08/12
For personal use only.

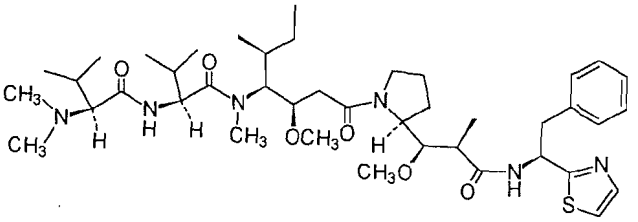

1, Dolastatin 10

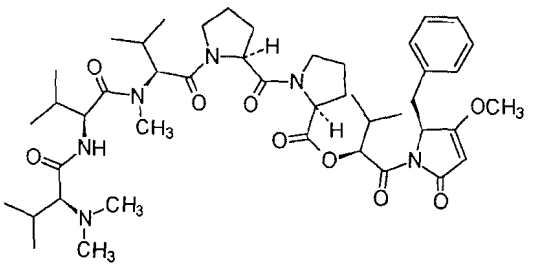

2, Dolastatin 15

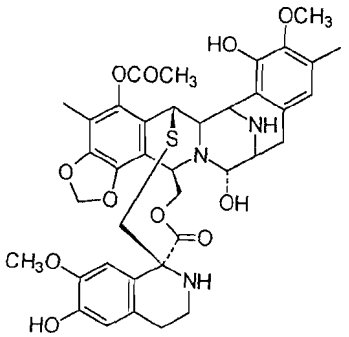

3, Ecteinascidin 729

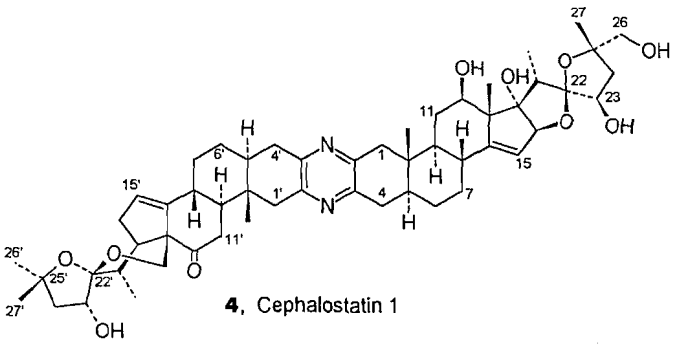

4, Cephalostatin 1

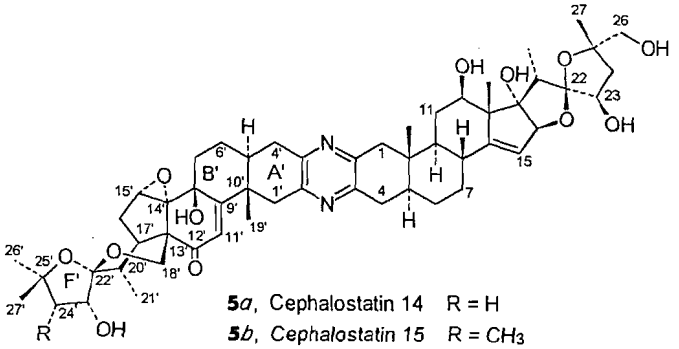

5*a*, Cephalostatin 14 R = H
5*b*, Cephalostatin 15 R = CH_3

alostatins 1–13. All signals of the ^1H and ^{13}C NMR were rigorously assigned by analyses of the APT, ^1H,^1H-COSY, ^{13}C,^1H-COSY, TOCSY, and HMBC spectra. From these NMR results combined with high-resolution, fast-atom-bombardment mass spectra (HRFABMS) and UV data, cephalostatin 14 (**5*a***) was established as a new member of the series. By comparing the 1D and 2D NMR data of cephalostatin 14 (**5*a***) with those earlier assigned to cephalostatin 1 (**4**, by X-ray crystal structure) it became apparent that all the NMR signals attributed to the right-side steroid unit of alkaloid **4** also appeared in the spectra of cephalostatin 14 (**5*a***). The HMBC analysis helped confirm this conclusion. Furthermore, it was found that the A′, E′, and F′ rings in the left-side unit corresponded to those of cephalostatin 1. Two carbon signals belonging to a double bond (δ 123.6 d and 165.77 s) and a carbonyl signal were observed in the left-side unit of steroid **5*a***. The ^{13}C chemical shift of the carbonyl group in cephalostatin 14 was found shifted upfield about 10 ppm by comparison with that of steroid **4**. In turn, this indicated that the carbonyl group was conjugated with a double bond, which was supported by UV absorption at 230 nm.

From ^1H,^1H-COSY and TOCSY results, it was concluded that the carbonyl group should be at C-12′ with the double bond between C-9′ and C-11′. Meanwhile, HMBC correlations were found between the hydrogen atom at C-11′ (δ 6.47) and the carbon atoms at C-10′ (δ 39.66 s), C-9′ (δ 165.78 s), and C-13′ (δ 52.1 s). By following the coupling network from the C-21′–CH_3 (δ 1.38 d, 14.84 q) using ^1H,^1H-COSY, TOCSY, and HMBC correlations, it was found that C-15′ (δ 3.75 brs, 57.56 d) must share an epoxy group with C-14′ (δ 71.58 s). Further-

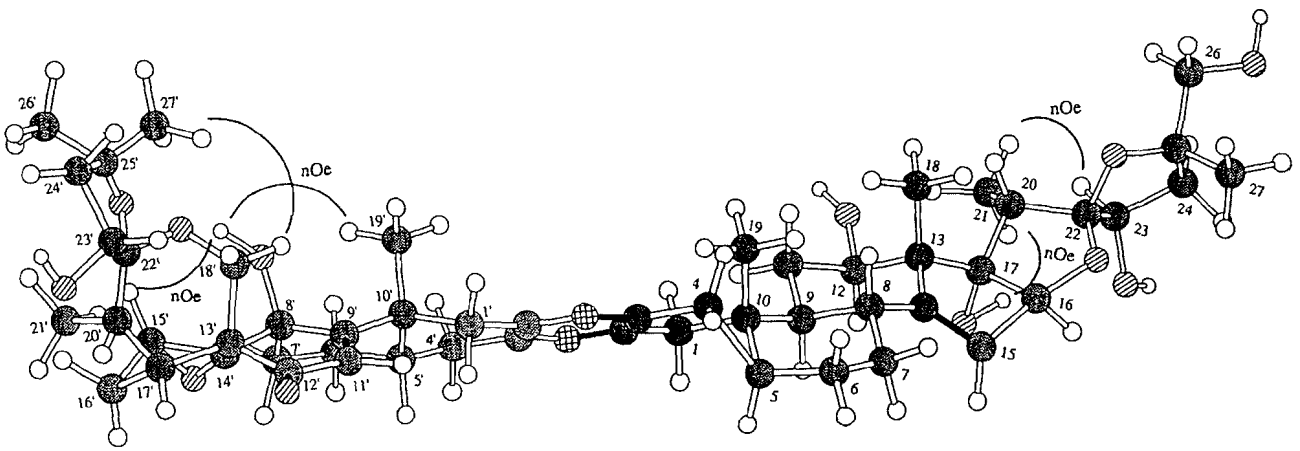

FIG. 1. Computer-drawn stereochemical structure of cephalostatin 14 (**5*a***) and pertinent nOe correlations.

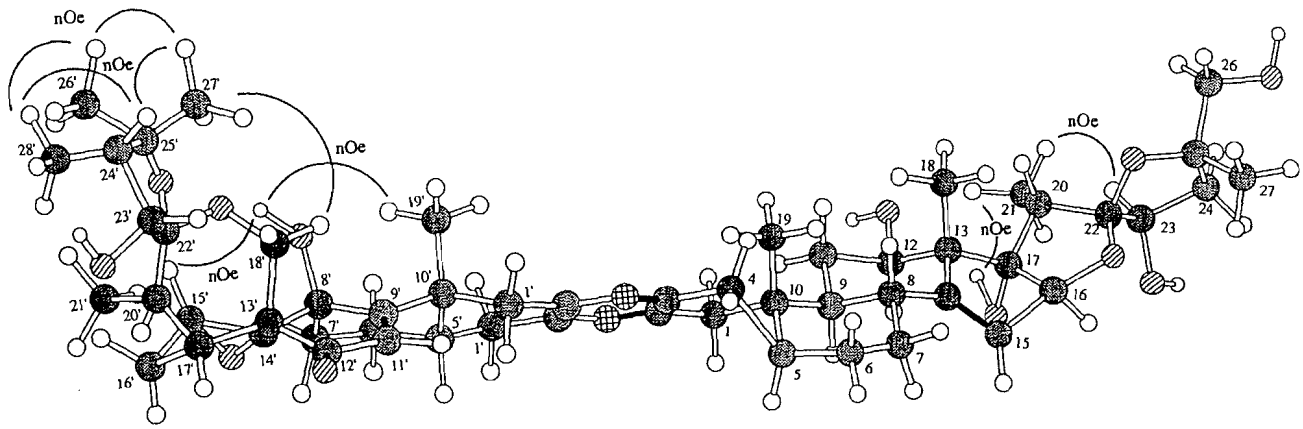

FIG. 2. Computer-drawn stereochemical structure of cephalostatin 15 (**5*b***) and pertinent nOe correlations.

TABLE 1. The high field (500 MHz) ^{1}H and ^{13}C NMR spectral data in cephalostatin 14 (**5*a***) and assignments in pyridine-d_5 solution

Left side					Right side				
Position no.	^{13}C (ppm)	^{1}H (ppm)	*J* (Hz)	HMBC (H to C)	Position no.	^{13}C (ppm)	^{1}H (ppm)	*J* (Hz)	HMBC (H to C)
1′	45.13 t	3.36 d	16.4	2′	1	45.65 d	2.66 m		2
							3.11 m		
2′	152.01 s				2	148.65 s			
3′	147.67 s				3	148.66 s			
4′	36.19 t	2.73 m		3′	4	35.48 t	2.76 m		3, 5
		3.06 dd	17.0, 6.0	3′			2.96 m		3, 5
5′	34.23 d	1.90 m			5	41.44 d	1.62 m		9
6′	28.12 t	1.57 m		10′	6	27.92 t	1.32 m		
		2.18 m		10′			1.55 m		
7′	24.56 t	1.82 m		5′, 8′, 9′, 14′	7	28.40 t	1.45 m		
		2.02 m		5′, 8′, 9′, 14′			1.72 m		
8′	70.23 s				8	33.49 d	2.08 m		14
9′	165.78 s				9	51.92 d	0.92 dt	11.5, 4.0	
10′	39.66 s				10	35.96 s			
11′	123.60 d	6.47 s		8′, 9′, 10′, 13′	11	28.74 t	1.78 m		12
							2.07 m		12
12′	201.34 s				12	75.30 d	4.07 dd	11.0, 4.5	
13′	52.10 s				13	55.09 s			
14′	71.68 s				14	152.42 s			
15′	57.56 d	3.75 brs		13′, 14′, 16′, 17	15	121.99 d	5.66 brs		8, 13, 14, 16, 17
16′	28.32 t	2.17 m		17′	16	92.85 d	5.28 brs		15, 22
		2.38 m		17′					
17′	36.02 d	2.56 m		16′	17	91.36 s			
18′	64.43 t	4.68 dd	13.0	12′, 13′, 17′, 22′	18	12.29 q	1.36 s		
19′	20.54 q	1.43 s		1′, 5′, 10′	19	11.46 q	0.78 s		1, 9, 10
20′	32.29 d	3.24 dq	13.0, 6.0	17′, 21′, 22′	20	44.21 d	2.80 m		13, 17
21′	14.84 q	1.38 d	6.6	17′, 20′	21	8.71 q	1.36 d	6.8	17, 20, 22
22′	109.52 s				22	116.16 s			
23′	81.28 d	4.88 t	7.0	22′, 24′, 25′	23	71.21 d	4.82 dd	10.2, 8.4	24
24′	47.08 t	1.95 m		22′, 23′, 25′	24	39.19 t	2.40 m		22, 23, 26
		2.35 m		22′, 23′, 25′			2.75 m		22, 23, 26
25′	81.13 s				25	82.52 s			
26′	29.41 q	1.44 s		24′, 25′, 27′	26	68.97 t	3.77 d	11.0	25, 27
							3.72 d	11.0	25, 27
27′	28.93 q	1.33 s		24′, 25′, 26′	27	26.12 q	1.67 s		25, 26
8′-OH		6.92 s		7′, 8′, 9′	17-OH		6.26 s		13, 17
					12-OH		4.70 s		12

more, a tertiary hydroxyl group was deduced, by elimination, to be located at C-8′. The HMBC correlations from the hydrogen atom of C-11′ to carbon C-8′ (δ 70.23 s) and from the hydroxyl hydrogen of C-8′ (δ 6.92 s) to carbons C-9′, C-8′, and C-7′ (δ 24.56 t) also supported this assignment. Consequently, the structure of cephalostatin 14 was established as **5*a***.

Cephalostatin 15 (**5*b***) was also obtained as a colorless non-crystalline powder. The UV and ^{1}H and ^{13}C NMR spectra data were found to be very similar to those of steroid **5*a*** except for the addition of one methyl signal. HRFABMS suggested molec-

Can. J. Chem. Downloaded from www.nrcresearchpress.com by 85.192.166.187 on 09/08/12
For personal use only.

TABLE 2. The nOe effects exhibited by cephalostatin 14 (**5***a*) from ROESY (500 MHz, in C_5D_5N) spectra

Left side			Right side		
No.	δ	nOe	No.	δ	nOe
H-1α	3.12	H-11α, H-5α	H-1α	2.66	H-5α, H-9α
H-1β	3.36	CH_3-19, H-11α	H-1β	3.11	CH_3-19, H-11α, H-8β
H-4α	3.06	H-6α, H-5α	H-4α	2.96	H-6α, H-5α
H-4β	2.73	CH_3-19, H-6β	H-4β	2.76	H-6β, CH_3-19
H-5α	1.90	H-1α, H-4α, H-6α	H-5α	1.62	H-1α, H-9α, H-4α
H-6α	1.57	H-4α, H-5α, H-7α	H-6α	1.55	H-4α
H-6β	2.18	H-7β, CH_3-19	H-6β	1.32	H-6β, H-7β, H-8P, CH_3-19
			H-7α	1.45	H-15
H-7β	1.82	H-15P, 8-OH	H-7β	1.72	H-15, H-6α, H-8β
8-OH	6.92	H-18, CH_3-19, H-15β	H-8β	2.08	H-11β, H-7β, CH_3-18, CH_3-19
		H-6β, H-7β	H-9α	0.92	H-1α, H-12α, H-11α, H-5α
H-11α	6.47	CH_3-19, H-1α, H-1β	H-11α	2.07	H-9α, H-1β
			H-11β	1.78	CH_3-18, CH_3-19, H-8β
			H-12α	4.07	17-OH, 12-OH, H-11α, H-9α
			12-OH	4.70	CH_3-18, H-12α, H-11α, H-11β
H-15β	3.75	H-7β, H-16β, 8-OH	H-15	5.66	H-7β
H-16α	2.17	H-17α	H-16α	5.28	23-OH, 17-OH
H-16β	2.38	H-18, H-15β			
H-17α	2.56	H-16α, H-20, CH_3-21	17-OH	6.26	CH_3-21, H-16α, H-12α H-23α, 12-OH
H-18	4.68	CH_3-27, 8-OH, H-16β	CH_3-18	1.36	
CH_3-19	1.43	8-OH, H-4β	CH_3-19	0.78	
H-20	3.24	H-17α, CH_3-21	H-20	2.80	CH_3-18
CH_3-21	1.38	H-16α, H-17α, H-20	CH_3-21	1.36	H-23α
H-23β	4.88	23-OH, H-24β	H-23α	4.82	17-OH, 23-OH, H-24α, CH_3-21
H-24α	1.95	CH_3-26	H-24α	2.75	H-23α
H-24β	2.35	CH_3-27, CH_3-28	H-24β	2.40	CH_3-27
CH_3-26	1.44	H-24α	H-26	3.77	CH_3-27
CH_3-27	1.33	H-18, H-24β	CH_3-27	1.67	H-26, H-24β

ular formula $C_{55}H_{74}N_2O_{12}$ ($[M + H]^+$ 955.5318, Δ −0.2 mmu), which supported the presence of an additional methyl group. Assignments using APT, ^1H,^1H-COSY, ^{13}C,^1H-COSY, TOCSY, and HMBC spectra showed that cephalostatins **5***a* and **5***b* shared the same right-side steroidal unit. Cephalostatin 15 was also found to possess a carbonyl group at C-12′ (δ 201.67 s), a double bond between C-11′ and C-9′ (δ 123.9 and 165.92 s), an epoxy group between C-14′ and C-15′ (δ 77.99 s and 58.02 d), and a tertiary hydroxyl group at C-8′ (δ 70.96 s) in the left-side steroidal unit. Based on the proton–proton coupling system around the F′ ring and the HMBC correlations between the extra methyl proton signals (28′-CH_3, δ 1.08 d) and C-23′ (δ 86.87 d), C-24′ (δ 51.55 d), and C-25′ (δ 81.28 s), the methyl group (28′-CH_3) was confirmed to be at C-24′. From observed nOe correlations involving the atom pairs C-26′–CH_3 (δ 1.18 s) and C-28′–CH_3 (δ 1.08 d), C-27′–CH_3 (δ 1.26 s) and C-24′–βH (δ 2.03 m), the C-28′–CH_3 was assigned to the α face of the F′ ring as with the α-OH at C-23′. Therefore, the structure of cephalostatin 15 was determined to be **5***b*.

Analyses of the ROESY spectra obtained for cephalostatins 14 and 15 revealed cross peaks that showed the relative stereochemistry of the right-side unit to be identical with that of cephalostatin 1 (**4**). Some interesting nOe interactions were detected that showed effects between the C-8′ β-OH (**5***a*, 6.92 ppm and **5***b*, 6.88 ppm), C-7′ β-H (**5***a*, 1.82 ppm and **5***b*, 1.82 ppm), and C-15′–H (**5***a*, 3.75 ppm and **5***b*, 3.68 ppm), and C-18′–H_2 (**5***a*, 4.68 ppm and **5***b*, 4.72 ppm), C-19′–CH_3 (**5***a*, 1.43 ppm and **5***b*, 1.36 ppm), and C-8′ β-OH in both left-side units of cephalostatins **5***a* and **5***b* (Tables 2 and 4 and Figs. 1 and 2). The results clearly indicated that the configuration of the proton at C-15′ must be β and the epoxy group must be below the face of the D′ ring in the α configuration.

Cephalostatins 14 (**5***a*) and 15 (**5***b*) were comparatively evaluated, along with cephalostatin 1 (**4**), in the U.S. National Cancer Institute's human tumor disease-oriented in vitro primary screen (23–26). Each compound was tested in quadruplicate at each of three different concentration ranges (10^{-6}, 10^{-7}, and 10^{-8} M upper limits; five $\log_{10}$-spaced concentrations in each range) against the entire group of 60 cell lines making up the screening panel. The standard (**4**) yielded the expected overall panel GI_{50} value of approximately 1 nM, and produced the distinctive mean-graph "fingerprint" of differential cellular response (23) that is typical of all members of the cephalostatin series heretofore studied (e.g., see ref. 19). In the present investigation, **5***a* and **5***b* also produced the characteristic cytotoxicity profile, as confirmed by comparing (23, 25) pattern-recognition analyses; the TGI-based correlation coefficients were 0.75 and 0.80 for **5***a* and **5***b*, respectively, against the standard (**4**). Although the latter analyses implied that the cytotoxic mechanism(s) of these newest cephalostatins did not diverge substantially from the rest of the series, the overall panel-averaged cytotoxic potencies were somewhat less (e.g., 100 nM and 68 nM for **5***a* and **5***b*, respectively) compared to the benchmark compound (**4**).

Results of the study of human cancer cell growth inhibition clearly emphasized that modification of the "left-side" moiety by introduction of the 8β-hydroxy-11-ene-12-one and (or) the 14, 15α-epoxy system served to reduce in vitro activity. Pre-

Can. J. Chem. Downloaded from www.nrcresearchpress.com by 85.192.166.187 on 09/08/12
For personal use only.

TABLE 3. Cephalostatin 15 (**5b**) ^1H and ^{13}C NMR spectral data and assignments (500 MHz, in C_5D_5N)

Left side					Right side				
Position no.	^{13}C (ppm)	^1H (ppm)	J (Hz)	HMBC (H to C)	Position no.	^{13}C (ppm)	^1H (ppm)	J (Hz)	HMBC (H to C)
1′	45.42 t	3.08 m		2′, 3′, 5′, 10′, 19′	1	45.96 t	2.62 m		2, 3, 5, 10, 19
		3.33 d	16.5	2′, 3′, 5′, 10′, 19′			3.07 m		2, 3, 5, 10, 19
2′	148.89 s				2	149.18 s			
3′	148.13 s				3	148.23 s			
4′	35.78 t	2.88 m		5′, 10′	4	35.64 t	2.68 m		5, 10
		3.02 m		5′, 10′			2.92 m		5, 10
5′	41.15 d	1.90 m			5	41.73 d	1.62 m		
6′	23.72 t	1.53 m			6	28.20 t	1.54 m		
		2.15 m							
7′	24.35 t	1.82 m		8′, 9′, 14′	7	28.92 t	2.12 m		
8′	70.96 s				8	33.77 d	2.03 m		
9′	165.92 s				9	53.19 d	0.89 m		
10′	39.94 s				10	36.31 s			
11′	123.90 d	6.46 s		8′, 10′, 13′	11	28.67 t	1.77 m		12
							2.05 m		
12′	201.67 s				12	75.57 d	4.06 dd	11.0, 4.0	11
13′	52.24 s				13	55.37 s			
14′	77.99 s				14	152.71 s			
15′	58.02 d	3.68 brs		16′, 17′	15	122.27 d	5.64 brs		8, 13, 14, 17
16′	28.52 t	2.02 m		13′, 14′, 15′, 17′	16	93.15 d	5.24 brs		22
17′	36.05 d	2.60 m			17	91.64 s			
18′	63.45 t	4.72 dd	11.0	12′, 17′, 22′	18	12.61 q	1,34 s		12, 13, 14, 17
19′	20.76 q	1.36 s		1′, 5′, 9′, 10′	19	11.74 q	0.76 s		1, 5, 9, 10
20′	32.35 d	3.22 m		16′, 17′, 21′, 22′	20	44.49 d	2.88 m		13, 17, 22, 23
21′	14.89 q	1.24 d	6.8	16′, 17′, 20′, 22′	21	9.00 q	1.35 d	6.4	17, 20
22′	108.03 s				22	117.16 s			
23′	86.87 d	4.37 d	10.0	22′, 28′	23	71.51 d	4.80 m		
24′	51.55 t	2.03 m		22′, 25′, 26′, 27′	24	39.49 t	2.35 m		23, 25, 26, 27
							2.78 m		23, 25, 26, 27
25′	81.28 s				25	82.81 s			
26′	23.72 q	1.18 s		24′, 25′, 28′	26	69.26 t	3.81 d	11.2	25, 27
							3.71 d	11.2	25, 27
27′	28.05 q	1.32 s		24′, 25′, 26′	27	26.41 q	1.65 s		25, 26
28′	12.61 q	1.08 d	6.7	23′, 24′, 25′	17-OH		6.24 s		13, 17
8′-OH		6.88 s		8′, 9′	12-OH		4.70 s		

sumably, the α orientation of the epoxide was primarily responsible for this effect. In our early studies of steroidal bufadienolides against the P388 cell line, the 14, 15β-epoxides were found more potent. Further useful structure–activity information should be obtained by discovery and evaluation of new cephalostatins, and research toward those objectives is in progress.

Experimental

General procedures

Solvents used for column chromatography were freshly distilled. Sephadex LH-20, particle size 25–100 μm, used in gel permeation and partition column chromatographic separations, was obtained from Pharmacia Fine Chemicals AB, Uppsala, Sweden. The TLC plates were viewed under shortwave UV light and then developed by 20% sulfuric acid or 3% ceric sulfate – 3 N sulfuric acid spray reagent followed by heating at approximately 150°C. Uncorrected melting points were observed with a Kofler-type mp apparatus. Optical rotations were determined employing a Perkin–Elmer model 241 polarimeter. UV spectra were obtained by using a Hewlett–Packard 8450 UV–VIS spectrometer. For high-pressure liquid chromatography separations, Phenomenex Prepex (particle size 5–20 μm, diameter 10.0 mm × length 25 cm, C8) was used in the reversed phase mode with Altex (model 110A) solvent metering pumps and Gilson HM UV detection at 288 nm. The ^1H and ^{13}C NMR, APT, ^1H,^1H-COSY, and ^{13}C,^1H-COSY spectra were recorded with a Bruker AM-400 instrument equipped with an ASPECT-3000 computer. The TOCSY (mixing times of 45 and 60 ms), HMQC (optimized for $^1J_{H-C}$ = 140 Hz), HMBC (optimized for $^nJ_{H-C}$ = 8.2 Hz), and ROESY (mixing times of 100 and 150 ms) (27) data were recorded using a Varian 500 NMR spectrometer. HRFAB mass spectra were obtained employing a Kratos MS-50 spectrometer.

Animal extraction and solvent partition sequence

Approximately 450 kg (wet wt.) of *Cephalodiscus gilchristi* was recollected in the summer of 1990 in the Indian Ocean off Southeast Africa by SCUBA (ca. −20 m). The total marine worm collection was extracted with 70% methanol (3×) and the extract was subjected to the solvent partition sequence (19, 28, 29) previously described to yield an active (97 g, PS ED_{50} 0.044 μg/mL) dichloromethane fraction.

*Isolation of cephalostatins 14 (**5a**) and 15 (**5b**)*

The P388 cell line was utilized for bioassay-guided separation (cf. Scheme 1) of the active dichloromethane fraction (97 g). Six fractions (A–F) were obtained from this fraction by Sephadex LH-20 chromatography with methanol as eluent. Active fraction D (PS ED_{50} 1.4×10^{-2} μg/mL) was chromatographed on a column of Sephadex LH-20 with dichloromethane–methanol (3:2) as eluent to give three main fractions G, H, and I. The most active material (H, PS ED_{50} 0.0032 μg/mL) was separated on a Sephadex LH-20 column employing hexane–

Can. J. Chem. Downloaded from www.nrcresearchpress.com by 85.192.166.187 on 09/08/12
For personal use only.

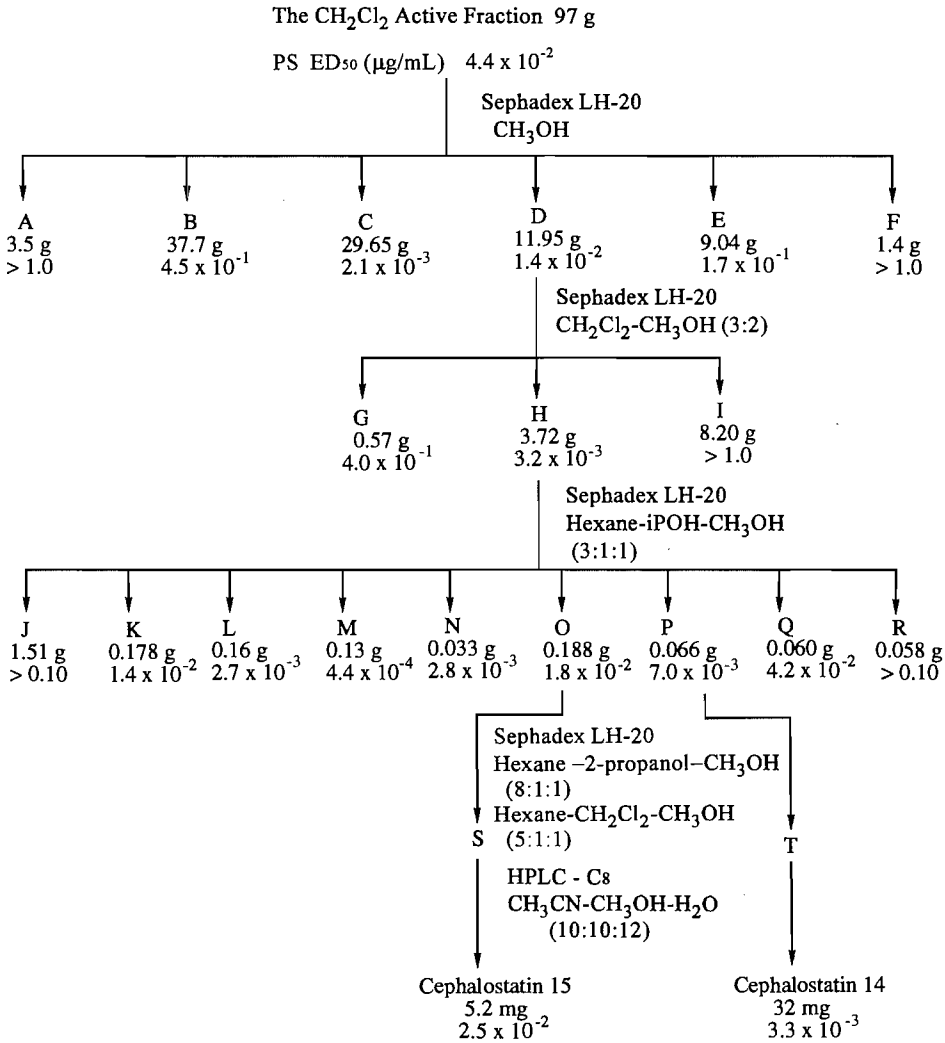

SCHEME 1

TABLE 4. The nOe effects exhibited by cephalostatin 15 (**5***b*) from ROESY (500 MHz, in C_5D_5N) spectra

Left side			Right side		
No.	δ	nOe	No.	δ	nOe
H-1α	3.08	H-11α, H-5α	H-1α	2.62	H-5α, H-9α
H-1β	3.33	CH_3-19, H-11α	H-1β	3.07	CH_3-19, H-11α, H-8β
H-4α	3.02	H-6α, H-5α	H-4α	2.92	H-6α, H-5α
H-4β	2.88	CH_3-19, H-6β	H-4β	2.68	H-6β, CH_3-19
H-5α	1.90	H-1α, H-4α, H-6α	H-5α	1.62	H-1α, H-9α, H-4α
H-6α	1.53	H-4α, H-5α	H-6α	1.54	H-4α
H-6β	2.15	H-7β, CH_3-19	H-6β	1.32	
8-OH	6.88	H-18, CH_3-19, H-15β, H-6β, H-7β	H-8β	2.03	H-1β, CH_3-18, CH_3-19
			H-9β	0.89	H-1α, H-12α, H-11α, H-5α
H-11α	6.46	CH_3-19, H-1α, H-1β	H-11α	2.05	H-9α, H-1β
			H-11β	1.77	CH_3-18, CH_3-19
			H-12α	4.06	12-OH, H-11α, H-9α
			12-OH	4.70	CH_3-18, H-12α, H-11α, H-11β
H-15β	3.68	H-7β, 8-OH	H-15	5.64	H-16α
H-16α	2.02	H-17α, CH_3-21	H-16α	5.24	23-OH, 17-OH
H-17α	2.60	H-16α, H-20, CH_3-21	17-OH	6.24	CH_3-21, H-16α, H-12α, H-23α, 12-OH
H-18	4.72	CH_3-27, 8-OH	CH_3-18	1.34	H-8β, H-11β
CH_3-19	1.36	8-OH, H-4β, H-6β, H-11β, H-1β	CH_3-19	0.76	H-1β, H-4β, H-6β, H-11β

Can. J. Chem. Downloaded from www.nrcresearchpress.com by 85.192.166.187 on 09/08/12
For personal use only.

TABLE 4 (*Concluded*)

Left side			Right side		
No.	δ	nOe	No.	δ	nOe
H-20	3.22	H-17α, CH_3-21	H-20	2.88	CH_3-18
CH_3-21	1.24	H-17α, H-20	CH_3-21	1.35	17-OH, H-23α
H-23β	4.37	H-24β	H-23α	4.80	17-OH, 23-OH, CH_3-21
			H-24α	2.78	H-23α
H-24β	2.03	H-23β, CH_3-27, CH_3-28	H-24β	2.35	CH_3-27
CH_3-26	1.18	CH_3-27, CH_3-28	H-26	3.71	CH_3-27, H-24α
CH_3-27	1.32		CH_3-27	1.65	H-24β
CH_3-28	1.08	CH_3-26			

toluene–methanol (3:1:1) to provide the next nine principal fractions (J–R). Active fraction P (PS ED_{50} 0.007 μg/mL) and fraction O (PS ED_{50} 0.018 μg/mL) were subjected to partition column chromatographic steps using Sephadex LH-20 with hexane–2-propanol–methanol (8:1:1) followed by hexane–dichloromethane–methanol (5:1:1) as eluents to yield fractions S and T. Final separation and purification of cephalostatins 14 (**5***a*) and 15 (**5***b*) was achieved by reversed phased HPLC (C8) with methanol–acetonitrile–water (5:5:6) as the mobile phase. By this means the two pure, and PS cytostatic, substances cephalostatins 14 (**5***a*) and 15 (**5***b*) were isolated from fractions T and S, respectively. *Cephalostatin 14* (**5***a*) (32 mg, 7.1×10^{-6}% yield, ED_{50} 0.0041 μg/mL): mp >300°C, $[\alpha]_D$ +80.9 (*c* 0.11, CH_3OH); TLC: R_f 0.12 (SiO_2, solvent: hexane–$CHCl_3$–CH_3OH, 11:9:2); UV (CH_3OH log ε) λ: 305 (shoulder), 288 (3.96), 230 (3.69) nm; IR (KBr) *ν*: 3418, 2928, 1674, 1449, 1400, 1233, 1101, 1057, 995, 949, 901 cm^{-1}; and HRFABMS, *m/z* $[M + Na]^+$, calcd. for $C_{54}H_{72}N_2O_{12}Na$: 963.4983; found: 963.4974. *Cephalostatin 15* (**5***b*) (5.2 mg, 1.2×10^{-6}% yield, ED_{50} 0.025 μg/mL): mp >300°C; $[\alpha]_D$ +71.5 (*c* 0.34, CH_3OH); TLC: R_f 0.15 (SiO_2, solvent: hexane–$CHCl_3$–CH_3OH, 11:9:2); UV (CH_3OH log ε) λ: 305 (shoulder), 288 (3.96), 228 (shoulder), 202 (4.25) nm; IR (KBr) *ν*: 3439, 2924, 1674, 1451, 1400, 1171, 1101, 1049, 941, 889 cm^{-1}; HRFABMS, *m/z* $[M + H]^+$, calcd. for $C_{55}H_{75}N_2O_{12}$: 955.5320; found: 955.5318. The ^1H and ^{13}C NMR assignments and the ^1H–^{13}C long-range correlations from the HMBC experiments have been recorded in Tables 1 and 3 (2). The nOe correlations from the ROESY experiments are shown in Tables 2 and 4.

Acknowledgments

For financial assistance our appreciation is extended to the Arizona Disease Control Research Commission, OIG Grant CA44344-01A1-05 awarded by the Division of Cancer Treatment, NCI, DHHS, Eleanor W. Libby, Virginia Piper, the Robert B. Dalton Endowment, and the Fraternal Order of Eagles Art Ehrmann Cancer Fund. Also, we are pleased to thank Drs. F. Hogan, Jean M. Schmidt, Mrs. Kim M. Weiss, Mr. Lee Williams, the National Science Foundation for equipment Grants CHE-8409644 and BBS-88-04992, and the NSF Regional Instrumentation Facility in Nebraska (Grant CHE-8620177).

1. G.R. Pettit, Y. Ichihara, J. Xu, M.R. Boyd, and M.D. Williams. J. BioMed Chem. Lett. **4**, 1507 (1994).
2. G.R. Pettit, Z.A. Cichacz, F. Gao, C.L. Herald, M.R. Boyd, and J.M. Schmidt. J. Org. Chem. **58**, 1302 (1993).
3. G.R. Pettit, R. Tan, F. Gao, M.D. Williams, D.L. Doubek, M.R. Boyd, J.M. Schmidt, J.-C. Chapuis, E. Hamel, R. Bai, J.N.A. Hooper, and L. Tackett. J. Org. Chem. **58**, 2538 (1993).
4. G.R. Pettit, F. Gao, D.L. Doubek, M.R. Boyd, E. Hamel, R. Bai, J.M. Schmidt, L.P. Tackett, and K. Rützler. Gazz. Chim. Ital. **123**, 371, (1993).
5. G.R. Pettit, C.L. Herald, M.R. Boyd, J.E. Leet, C. Dufresne, D.L. Doubek, J.M. Schmidt, R.L. Cerny, J.N.A. Hooper, and K.C. Rützler. J. Med. Chem. **34**, 3339 (1991).
6. G.R. Pettit, J.K. Srirangam, D.L. Herald, K.L. Erickson, D.L. Doubek, J.M. Schmidt, L.P. Tackett, and G.J. Bakus. J. Org. Chem. **57**, 7217 (1992).
7. G.R. Pettit, J.C. Collins, D.L. Herald, D.L. Doubek, M.R. Boyd, J.M. Schmidt, J.N.A. Hooper, and L.P. Tackett. Can. J. Chem. **70**, 1170 (1992).
8. G.R. Pettit, P.J. Clewlow, C. Dufresne, D.L. Doubek, R. Cerny, and L. Rützler. Can. J. Chem. **68**, 708 (1990).
9. R. Sakai, K.L. Rinehart, Y. Guan, and A.H.J. Wang. Proc. Natl. Acad. Sci. U.S.A. **89**, 11456 (1992).
10. J. Kobayashi, M. Tsuda, A. Tanabe, M. Ischibashi, J.-F. Cheng, S. Yamamura, and T. Sasaki. J. Nat. Prod. **54**, 1634 (1991).
11. M.R. Prinsep, J.W. Blunt, and M.H.G. Munro. J. Nat. Prod. **54**, 1068 (1991).
12. S. Matsunaga, N. Fusetani, Y. Kato, and H. Hirota. Chem. Pharm. Bull. **40**, 766 (1992).
13. K. Ishida, M. Ishibashi, H. Shigemori, T. Sasaki, and J. Kobayashi. Chem. Pharm. Bull. **40**, 766 (1992).
14. M.F. Raub, J.H. Cardellina, M.I. Choudhary, C.-Z. Ni, J. Clardy, and M.C. Alley. J. Am. Chem. Soc. **113**, 3178 (1991).
15. B.R. Copp, C.M. Ireland, and L.R. Barrows. J. Nat. Prod. **55**, 822 (1992).
16. G.R. Pettit, Y. Kamano, C.L. Herald, Y. Fujii, H. Kizu, M.R. Boyd, F.E. Boettner, D.L. Doubek, J.M. Schmidt, J.-C. Chapuis, and C. Michal. Tetrahedron, **49**, 9151 (1993).
17. G.R. Pettit, D.L. Herald, S.B. Singh, T.J. Thornton, and J.T. Mullaney. J. Am. Chem. Soc. **113**, 6692 (1991).
18. G.R. Pettit, M. Inoue, Y. Kamano, D.L. Herald, C. Arm, C. Dufresne, N.D. Christie, J.M. Schmidt, D.L. Doubek, and T.S. Krupa. J. Am. Chem. Soc. **110**, 2006 (1988).
19. G.R. Pettit, J.P. Xu, M.D. Williams, N.D. Christie, D.L. Doubek, J.M. Schmidt, and M.R. Boyd. J. Nat. Prod. **57**, 52 (1994).
20. G.R. Pettit, Y. Kamano, M. Inoue, C. Dufresne, M.R. Boyd, C.L. Herald, J.M. Schmidt, D.L. Doubek, and N.D. Christie. J. Org. Chem. **57**, 429 (1992).
21. G.R. Pettit, M. Inoue, Y. Kamano, C. Dufresne, N.D. Christie, M.L. Niven, and D.L. Herald. J. Chem. Soc. Chem. Commun. 865 (1988).
22. G.R. Pettit, Y. Kamano, C. Dufresne, M. Inoue, N. Christie, J.M. Schmidt, and D.L. Doubek. Can. J. Chem. **67**, 1509 (1989).
23. M.R. Boyd, K.D. Paull, and L.R. Rubinstein. Data display and analysis strategies from the NCI disease-oriented in vitro antitumor drug screen, *In* Antitumor drug discovery and development. *Edited by* F.A. Valeriote, T. Corbette, and L. Baker. Kluwer Academic Press, Amsterdam. 1992. pp. 11–34.
24. M.R. Boyd. Status of the NCI preclinical antitumor drug discovery screen *In* Principles and practices of oncology update. *Edited by* V.T. DeVita, Jr., S. Hellman, and S.A. Rosenberg. Lippincott, Philadelphia. 1989. pp. 1–12.
25. K.D. Paull, R.H. Shoemaker, L. Hodes, A. Monks, D.A. Scudiero, L. Rubinstein, J. Plowman, and M.R. Boyd. J. Natl. Cancer Inst. **81**, 1088 (1989).
26. A. Monks, D.A. Scudiero, P. Skehan, R.H. Shoemaker, K.D. Paull,

Can. J. Chem. Downloaded from www.nrcresearchpress.com by 85.192.166.187 on 09/08/12
For personal use only.

D. Vistica, C. Hose, N. Langley, P. Cronise, A. Vaigro-Wolff, Gray-Goodrich, H. Campbell, and M.R. Boyd. J. Natl. Cancer Inst. **84**, 757 (1989).
27. H. Kessler, C. Griesinger, R. Kerssebaum, K. Wagner, and R.R. Erust. J. Am. Chem. Soc. **109**, 607 (1987).
28. G.R. Pettit, Y. Kamano, R. Aoyagi, C.L. Herald, D.L. Doubek, J.M. Schmidt, and J.J. Rudloe. Tetrahedron, **41**, 985 (1985).
29. E.O. Arene, G.R. Pettit, and R.H. Ode. Lloydia, **41**, 186 (1987).

Can. J. Chem. Downloaded from www.nrcresearchpress.com by 85.192.166.187 on 09/08/12
For personal use only.

A comparison of nickel boride and Raney nickel electrode activity in the electrocatalytic hydrogenation of phenanthrene

BEHZAD MAHDAVI, PRZEMYSLAW LOS, MARIE JOSÉE LESSARD, AND JEAN LESSARD[1]

Centre de recherche en électrochimie et électrocatalyse, Département de chimie, Université de Sherbrooke, Sherbrooke, QC J1K 2R1, Canada

Received July 14, 1994

BEHZAD MAHDAVI, PRZEMYSLAW LOS, MARIE JOSÉE LESSARD, and JEAN LESSARD. Can. J. Chem. **72**, 2268 (1994).

The electrocatalytic activity of nickel boride in the electrocatalytic hydrogenation (ECH) of phenanthrene in ethylene glycol – water at 80°C has been compared to that of Raney nickel and fractal nickel. The intrinsic activity of the electrode material (*real electrode activity*) is the same for nickel boride and Raney nickel electrodes and is lower for fractal nickel electrodes. The *apparent electrode activity* of nickel boride pressed powder electrodes (Ni_2B electrodes) is less than that of codeposited Raney nickel (RaNi) electrodes and pressed powder fractal nickel/Raney nickel (Ni/RaNi = 50/50 to 0/100) electrodes. The apparent activity of Ni_2B electrodes is improved by adding sodium chloride to the powder and dissolving it after pressing (Ni_2B–NaCl electrodes). The Ni_2B–NaCl electrodes have the same apparent activity as codeposited RaNi and pressed powder Ni/RaNi (20/80 to 0/100) electrodes. The apparent and real electrode activity of Ni/RaNi electrodes increases with the RaNi content up to a 20/80 ratio. The Tafel and alternating current (ac) impedance parameters were determined for the hydrogen evolution reaction (HER) in 1 M aqueous sodium hydroxide at 25°C at nickel boride and at codeposited RaNi electrodes. The intrinsic electrocatalytic activity for HER, expressed by the ratio of the exchange current density over the roughness factor (I_0/R), is similar for Ni_2B, Ni_2B–NaCl, and codeposited RaNi electrodes. Surface characterization of Ni_2B and Ni_2B–NaCl electrodes was carried out by BET, ac impedance, scanning electron microscopy, and mercury porosimetry. No direct relation between the apparent electrode activity in ECH and the surface measured by BET and ac impedance was found. The ac impedance measurements were also carried out in the presence of sodium *trans*-cinnamate.

BEHZAD MAHDAVI, PRZEMYSLAW LOS, MARIE JOSÉE LESSARD et JEAN LESSARD. Can. J. Chem. **72**, 2268 (1994).

L'activité électrocatalytique du borure de nickel est comparée à celle du nickel de Raney et du nickel fractal pour l'hydrogénation électrocatalytique (HEC) du phénanthrène dans le glycol d'éthylène – eau à 80°C. L'activité intrinsèque du matériau d'électrode (*activité réelle de l'électrode*) est la même pour le borure de nickel et le nickel de Raney et moindre pour le nickel fractal. *L'activité apparente* (activité de l'électrode) des électrodes de poudre de borure de nickel pressée (électrodes Ni_2B) est moindre que celle des électrodes de nickel de Raney (RaNi) codeposé et des électrodes de poudres de nickel fractal/nickel de Raney (Ni/RaNi = 50/50 à 0/100) pressées. L'activité apparente des électrodes Ni_2B est accrue par addition de chlorure de sodium à la poudre métallique puis dissolution de ce dernier après pressage (électrodes Ni_2B–NaCl). Les électrodes Ni_2B–NaCl ont la même activité apparente que les électrodes RaNi codéposé et les électrodes de poudre Ni/RaNi (20/80 à 0/100) pressées. L'activité apparente et l'activité réelle des électrodes Ni/RaNi croît avec la proportion de RaNi jusqu'à un rapport de 20/80. On a obtenu les paramètres de Tafel et d'impédance ac pour la réaction du dégagement d'hydrogène (RDH) en milieu hydroxyde de sodium aqueux 1 M à 25°C sur les électrodes de borure de nickel et les électrodes RaNi codeposé. L'activité électrocatalytique intrinsèque pour la RDH, exprimée par le rapport du courant d'échange sur le facteur de rugosité (I_0/R), est sensiblement la même pour les électrodes Ni_2B, Ni_2B–NaCl et RaNi codeposé. La surface des électrodes Ni_2B et Ni_2B–NaCl est caractérisée par BET, impédance ac, microscopie électronique à balayage et porosimétrie au mercure. Il n'y a pas de relations directes entre l'activité apparente en HEC et la surface mesurée par BET et impédance ac. Les mesures d'impédance ont aussi été effectuées en présence de *trans*-cinnamate de sodium.

Introduction

The electrocatalytic hydrogenation (ECH) of an unsaturated organic molecule in aqueous or mixed aqueous–organic media involves the mechanism described by reactions [1]–[4] where M represents the metallic surface, (H)M chemisorbed hydrogen, and (Y = Z)M the adsorbed organic substrate (1). The first step is the electroreduction of water (or hydronium ions) with the formation of adsorbed hydrogen on the electrode surface (Volmer reaction [1]), followed by reaction of the adsorbed substrate (Y = Z)M with chemisorbed hydrogen (reaction [3]). There is a competition between hydrogenation (reaction [3]) and the desorption of hydrogen by an electrochemical (Heyrovský reaction [5]) and (or) chemical (Tafel reaction [6]) pathway.

[1] $2H_2O(H_3O^+) + 2e^- + M \rightarrow 2\,(H)M + 2OH^-(H_2O)$

[2] $Y = Z + M \rightarrow (Y = Z)M$

[3] $(Y = Z)M + 2(H)M \rightarrow (YH\text{–}ZH)M$

[4] $(YH\text{–}ZH)M \rightarrow YH\text{–}ZH + M$

[5] $(H)M + H_2O + e^- \rightarrow H_2 + M + OH^-$

[6] $(H)M + (H)M \rightarrow H_2 + M$

The competition between ECH and the HER may also be represented as in Scheme 1. Since, in the ECH of organic substrates, the sole processes occurring are hydrogenation and hydrogen evolution (1), the current efficiency is a measure of the competition between the two reactions. This competition depends on a number of factors such as the substrate, the reaction conditions, and the electrode (1). For a given substrate and given reaction conditions, the current efficiency for the ECH becomes, therefore, a measure of the electrode activity.

Using the ECH of phenanthrene (**1**) under given electrolysis conditions (see below), we have compared the activity of nickel

[1]Author to whom correspondence may be addressed. Telephone: (819) 821-7091. Fax: (819) 821-8017.

Can. J. Chem. Downloaded from www.nrcresearchpress.com by 85.192.166.187 on 09/08/12
For personal use only.

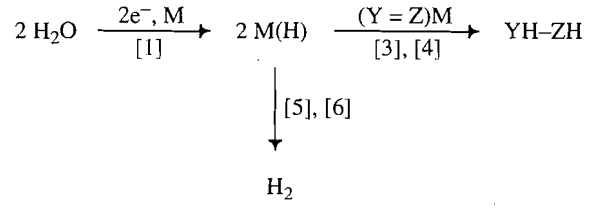

SCHEME 1

electrodes made of different nickel material (P-1 nickel boride, Raney nickel, and fractal nickel), and compared the activity of electrodes made of the same material but differing by the surface structure and surface area: unmodified (Ni_2B) and modified (Ni_2B–NaCl) nickel boride electrodes made of pressed P-1 nickel boride powder (NaCl being dissolved after pressing), codeposited Raney nickel (RaNi) electrodes (1), and pressed RaNi powder electrodes. The effect of varying the relative proportion of the fractal nickel (Ni) and RaNi on the activity of pressed Ni/RaNi electrodes was also investigated. The results reported in this paper show that the current efficiency and the conversion rate reflect the *apparent activity* of the electrode for the ECH of **1** in the specified electrolysis conditions and that the apparent activity depends on the electrode material and, for a given material, on the surface structure and surface area of the electrode as determined by mercury porosimetry, BET, and ac impedance measurements. The results also show that the ratio of the yield of the most highly hydrogenated products, octahydrophenanthrenes (octa-as **4** + octa-s **5** = Σ octahydrophenanthrenes) to the conversion rate, defined as coefficient β_{oct}, represents the intrinsic or *real activity* of the electrode material for the ECH of **1** under the specified electrolysis conditions. The intrinsic electrocatalytic activity of Ni_2B, Ni_2B–NaCl, and codeposited RaNi electrodes in the hydrogen evolution reaction (HER) in 1 M aqueous sodium hydroxide at 25°C, as expressed by the ratio I_0/R of the exchange current density I_0 (obtained from Tafel curves) to the roughness factor R (obtained by ac impedance measurements), was also determined, together with the influence of sodium *trans*-cinnamate, a water-soluble unsaturated organic substrate, which is electrohydrogenated by ECH, on the double layer capacity of these electrodes.

Experimental

Electrolyses

A two-compartment glass H-cell with a jacketed cathodic compartment (volume of each compartment 25 mL) having a Nafion-324 (E.I. du Pont de Nemours & Co) membrane (1.8 cm^2) as separator was connected to a Haake D8 constant temperature circulating bath filled with ethylene glycol. The counter electrode was a glassy carbon plate (≈12 cm^2) and the electrolyses were carried out with a 410 potentiostatic controller, 640 digital coulometer, and 2830 digital multimeter (Electrosynthesis Company). Phenanthrene (224 μmol, 9 mM solution) was dissolved in a stock solution (25 mL) of sodium chloride (0.1 M) and boric acid (0.1 M) in ethylene glycol – water (24:1 v/v) by stirring and heating slightly on a hot plate. The solution was then poured into the cathodic compartment. The anodic compartment was filled with the above stock solution (25 mL) of sodium chloride and boric acid. The cathodic compartment was heated to 80°C while deaerated (N_2), the cathode and the counter electrode were immersed and a constant current of 16 mM (J = 250 mA/dm^2) was applied. The cathodic solution was stirred magnetically. Aliquots (0.2 mL) were extracted with ether after the addition of a saturated NaCl solution (1 mL) and analyzed by vapour phase chromatography (vpc). The products were identified by comparison of retention times with those of authentic samples. The same system and method were used for the ECH of *trans*-cinnamic acid (448 μmol, 18 mM solution) in 25 mL of a 1 M aqueous solution of sodium hydroxide at room temperature. Aliquots were acidified before extraction with ether.

Electrodes

P-1 nickel boride (Ni_2B) was obtained by reduction of nickel acetate with sodium borohydride in an aqueous solution containing sodium hydroxide. It was prepared by following, with slight modifications, a procedure already described (2): 300 mL of an aqueous solution of sodium borohydride and sodium hydroxide was added to 1000 mL of the nickel acetate solution over a 3 h period. The product of the reaction (a black porous precipitate) was filtered on a fritted glass funnel with suction (water pump), washed with absolute ethanol, and dried at 50°C. The X-ray diffraction spectrum was identical to that reported for amorphous Ni_2B (2, 3–6). The particles had a spherical shape with an average diameter approximately equal to 0.5 μm according to scanning electron microscopy (SEM). The electrodes were obtained by pressing the particles at p = 800 or 400 MPa at room temperature. Nickel boride – sodium chloride (Ni_2B–NaCl) electrodes were prepared in two ways. One was to first put 0.3 g of NaCl in the mold, add 1.7 or 3 g of nickel boride powder, and then put 0.3 g of NaCl on top of the nickel boride powder. The other way was to first mix 3 g of nickel boride powder with 4.5–7 g of crystalline NaCl (BDH Company), then add 0.3 g of NaCl in the mold, add the mixture of nickel boride and NaCl, and add 0.3 g of NaCl on top. The mixing of nickel boride with NaCl was made in two ways: (*i*) mechanical mixing of the nickel boride particles with NaCl crystals (Ni_2B–NaCl(b-solid/s)); (*ii*) nickel boride particles suspended in an aqueous solution of NaCl and evaporation of the water under reduced pressure (Ni_2B–NaCl(b-solution/s)). After pressing, the Ni_2B–NaCl precursory electrode was immersed for 10 min in water to completely dissolve the sodium chloride at the surface and partly dissolve (2–2.5 g) the sodium chloride within the electrode disc. The geometric surface area of the electrodes was 2π cm^2 according to the diameter of the pressed fixed piston (2 cm). The codeposited Raney nickel electrodes consisted of Raney Ni particles dispersed in a nickel matrix, had a geometric area of 6.4 cm^2, and were prepared according to the previously described method (1). The nickel/Raney nickel pressed powder (Ni/RaNi) electrodes were prepared by pressing a mixture of fractal powder with Raney nickel alloy powder (Aldrich Company) at p = 800 MPa and room temperature. The pressed powder electrodes containing RaNi were activated by leaching in 10% aqueous NaOH for 3 h at 50°C.

Alternating current impedance measurements

Tafel and ac impedance measurements were carried out using systems and procedures analogous to those used in refs. 4 and 7–12, and using an ac amplitude of 5 mV peak-to-peak in 1 M aqueous sodium hydroxide in the absence and in the presence of *trans*-cinnamic acid, its concentration ranging from 9 to 90 mM.

Results and discussion

The ECH of phenanthrene (**1**) at unmodified (Ni_2B) and modified (Ni_2B–NaCl) pressed nickel boride powder electrodes (see below), at codeposited Raney nickel (RaNi) electrodes, and at pressed fractal nickel/Raney nickel (Ni/RaNi) electrodes was carried out on 9 mM solutions under conditions reported by Robin et al. (1) to be the best for the ECH of **1** at codeposited RaNi electrodes: ethylene glycol containing 4% of water as solvent, a slightly acidic medium containing boric acid (0.1 M) as buffer, and sodium chloride (0.1 M) as supporting electrolyte, 80°C. Two types of nickel boride electrodes were investigated: unmodified electrodes made of pressed nickel boride powder (Ni_2B electrodes), and modified electrodes made of nickel boride powder pressed with sodium chloride followed by total or partial dissolution of the sodium chloride (Ni_2B–NaCl electrodes). Electrolyses were performed under steady current control (dc) and the charge passed was 300 C (14 moles of electrons

Can. J. Chem. Downloaded from www.nrcresearchpress.com by 85.192.166.187 on 09/08/12
For personal use only.

TABLE 1. ECH of phenanthrene at nickel boride and Raney nickel electrodes at J = 250 mA/dm^2 [a]

Entry	Electrode[b] Ni_2B (g)	Electrode[b] NaCl[d] (g)	Conversion[c] (%)	Yield of products[c] (%) Di (2)	Tetra (3)	Octa (4 + 5)	Current efficiency (%)	β_{oct}[e]
1	1.7	0	35	4	11	20	15	0.57
2	3	0(p = 400 MPa)	33	4	12	17	14	0.52
3[f]	3	0	32–36	3–4	11–13	18–19	14–15	0.53–0.56
4[f]	3[d]	0.6	53–56	6	16–17	31–33	24–25	0.58–0.59
5[f]	3[d]	7(Solid) + 0.6	78–84	7–9	24–29	46–47	35–36	0.54–0.6
6	2[d]	5(Solid) + 0.6	81	8	25	49	37	0.6
7[f]	3[d]	7(Solution) + 0.6	68–71	8	22–24	38–39	30–31	0.55–0.56
8[f]	Codeposited RaNi electrodes[g]		78–85	4–6	25–35	41–49	35–37	0.51–0.62
9	Pressed RaNi electrodes[h]		84–86	7	29–35	42–50	35–38	0.5–0.59

[a]Electrolysis conditions: 224 μmol of phenanthrene (9 mM solution); 0.1 M NaCl; 0.1 M H_3BO_3; T = 80°C; charged passed (Q) = 300 C (14 moles of electrons per mole of phenanthrene).

[b]The nickel boride electrodes were prepared by pressing the Ni_2B or Ni_2B–NaCl powder at p = 800 MPa (except for entry 2).

[c]The conversion rate and yield of products were determined by vpc analysis. The yields are based on converted phenanthrene (material balance >99%).

[d]For all Ni_2B–NaCl electrodes, NaCl was added both at the bottom (0.3 g) and at the top (0.3 g) of the powder layer before pressing and was dissolved afterwards by immersing electrodes in water. In entries 4, 5, and 6 the amount of NaCl mixed intimately into the Ni_2B powder is indicated. "Solid" means that the Ni_2B powder was mixed with crystalline NaCl. "Solution" means that the Ni_2B powder was suspended in an aqueous solution of NaCl followed by the evaporation of water under reduced pressure.

[e]β_{oct} = (**4** + **5**)/conversion rate.

[f]Three electrolyses were performed using three different electrodes prepared in the same way and the range of values obtained for the conversion rate, yield of products, current efficiency, and β_{oct} is indicated.

[g]See ref. 1. Geometric area: 6.4 cm^2; 0.27–0.49 g of precursory alloy (48–66% in the nickel matrix).

[h]Prepared by pressing the Raney alloy powder at p = 800 MPa, followed by leaching in 10% aqueous NaOH for 3 h at 50°C.

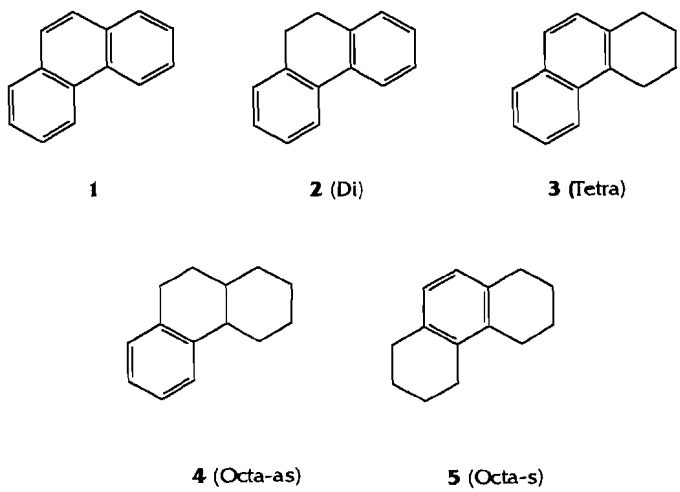

FIG. 1. The hydrogenated products of ECH of phenanthrene (**1**).

per mole of phenanthrene). The products formed were 9,10-dihydrophenanthrene (**2**), tetrahydrophenanthrene (**3**), and the octahydrophenanthrenes (octa-as **4** and octa-s **5**) (Fig. 1). The octahydrophenanthrenes are not electrohydrogenated under the above conditions (1) and therefore the maximum current efficiency for a charge corresponding to 14 moles of electrons per mole of **1** is 57%.

Nickel boride electrodes

The results of entries 2 and 3 of Table 1 show that Ni_2B electrodes pressed at 400 MPa (entry 2) have the same activity as electrodes pressed at 800 MPa (entry 3). A comparison of the results of entry 1 with those of entries 2 and 3 demonstrates clearly that increasing the amount of Ni_2B in a Ni_2B electrode by a factor 1.8 has no effect on the conversion rate and the current efficiency. This shows that the electrocatalytic hydrogenation takes place only at the surface of the electrode disc. With the aim of increasing the active surface area of the electrode, Ni_2B–NaCl electrodes were prepared by adding sodium chloride to the Ni_2B powder before pressing, then removing NaCl totally or partly from the precursory electrode disc to obtain the actual electrodes (see the Experimental). Two types of Ni_2B–NaCl electrodes were used: Ni_2B–NaCl(s) electrodes for which NaCl was present only at the surface of the precursory electrode (see entry 4); Ni_2B–NaCl(bs) electrodes for which NaCl was present both within the bulk and at the surface of the precursory electrode (see entries 5–7). It is clear from a comparison of the results of entries 4–7 with those of entries 1 and 3 that the activity of the Ni_2B–NaCl electrodes is higher than that of the Ni_2B electrodes, as shown by the higher conversion rates and better current efficiencies in entries 4–7. Furthermore, the activity of a Ni_2B–NaCl(bs) electrode is better than that of a Ni_2B–NaCl(s) electrode: higher conversion rates (78–84%) and better current efficiencies (35–37%) in entries 5 and 6 than in entry 4 (53–56% and 24–25%, respectively). However, Ni_2B–NaCl(bs) electrodes are mechanically less stable than Ni_2B–NaCl(s) electrodes. It was noticed that the Ni_2B–NaCl(b-solution/s) electrodes prepared by suspending the Ni_2B powder in a NaCl solution and evaporating water (entry 7) had a better mechanical stability than Ni_2B–NaCl(b-solid/s) electrodes prepared by mixing the Ni_2B powder with crystalline NaCl (entries 5 and 6), but the activity of the latter was slightly higher. Therefore, for the same amount of catalytic material and for the same geometric surface area, it is possible to increase the conversion rate and current efficiency (*apparent activity* of the electrode) with a simple modification in electrode design: adding sodium chloride before pressing the nickel boride powder and dissolving it afterwards. Clearly, this modification in electrode design has led to a change in surface area and (or) in surface structure that favors the ECH process over the HER. As can be seen from Table 1, the coefficient β_{oct} (ratio of the yield of octahydrophenanthrenes (**4** + **5**) to the conversion rate) determined at a

Can. J. Chem. Downloaded from www.nrcresearchpress.com by 85.192.166.187 on 09/08/12
For personal use only.

TABLE 2. ECH of phenanthrene at pressed fractal nickel/Raney Ni electrodes at J = 250 mA/dm^2 [a]

Entry	Electrode[b] Ni/NiRa (%)	Conversion[c] (%)	Yield of products[c] (%) Di (2)	Tetra (3)	Octa (4 + 5)	Current efficiency (%)	β_{oct}[d]
1	100/0	6–10	1	4–5	1–3	2–3	0.2–0.3
2	80/20	30	4	13	12	11	0.4
3	50/50	48–51	6	21–22	22–23	19–20	0.46
4	20/80	81	7–8	27–30	40–44	32–35	0.52–0.54
5	10/90	78–81	5	26–28	47	35–36	0.58–0.6
6	5/95	77	6	30	42	34	0.54
7[e]	0/100	84–86	7	29–35	42–50	35–38	0.5–0.59

[a]See footnote *a* of Table 1.
[b]Prepared by pressing fractal nickel and Raney alloy powders at p = 800 MPa, then leaching in 10% aqueous NaOH for 3 h at 50°C. The Ni/RaNi ratio refers to the weight ratio of fractal nickel and Raney alloy before leaching.
[c]See footnote *c* of Table 1.
[d]See footnote *e* of Table 1.
[e]Taken from Table 1.

charge of 300 C (14 moles of electrons per mole of phenanthrene) is constant from entry 1 to entry 7 and equal to about 0.56. This ratio in thus independent of the surface area and surface structure. It depends only on the nature of the catalytic material and represents the intrinsic activity of P-1 nickel boride for the ECH of phenanthrene under the electrolysis conditions used. It can therefore be utilized to evaluate the *real activity* of any electrode material for the ECH of phenanthrene under given conditions.

Raney nickel electrodes

The results of the ECH of phenanthrene (**1**) at codeposited RaNi electrodes and at pressed powder RaNi electrodes presented in entries 8 and 9 of Table 1 show that the two types of Raney nickel electrodes have the same apparent activity. This means that they have very similar active surface requirements (see below) for the ECH of phenanthrene even though the leaching conditions are quite different. For the codeposited RaNi electrodes, leaching of the Raney alloy particles embedded in the nickel matrix was carried out in 30% aqueous NaOH for 7 h at 80°C (1) and, for the pressed powder RaNi electrodes, the pressed Raney alloy precursory electrodes were leached in 10% aqueous NaOH for 3 h at 50°C. In the pressed electrodes, it was necessary to use much milder leaching conditions in order to leach only the top layers of the disc and prevent the pressed particles from falling apart. X-ray fluorescence shows that the amount of aluminium left in the top layers of a pressed electrode is about 6% compared to 1% in a codeposited RaNi electrode. As expected, the two types of electrodes made of the same material, Raney nickel, have the same real activity, as seen from the β_{oct} value (average value 0.55–0.57). Interestingly, P-1 nickel boride and Raney nickel have the same intrinsic (real) activity for the ECH of phenanthrene under the electrolysis conditions used (same average β_{oct} value of 0.56, compare entries 1–7 with entries 8 and 9, respectively). The apparent activity of the Raney nickel electrodes (entries 8 and 9) is the same as that of Ni_2B–NaCl(b-solid/s) electrodes (entries 5 and 6) for which NaCl crystals were both intimately mixed within the nickel boride powder and present at the surface of the disc before its dissolution (see the Experimental). From the results of Table 1, it is clear that the apparent electrode activity for the ECH process does not depend only on the intrinsic activity of the electrode material and, therefore, a direct evaluation of the intrinsic activity of different electrode materials for the ECH of organic substrates cannot always be made from the apparent electrode activity. For instance, the nickel boride electrodes of entries 1–3 (Ni_2B unmodified electrodes) are clearly less active than Raney nickel electrodes (entries 8 and 9) for the ECH of phenanthrene although both P-1 nickel boride and Raney nickel have the same intrinsic activity.

Table 2 reports on the comparison of the apparent and real activity, for the ECH of phenanthrene, of pressed fractal nickel electrodes (entry 1) and pressed Raney nickel electrodes (entry 7), and on the effect of mixing fractal nickel particles with Raney particles in various proportions on these activities (entries 2–6). Clearly, fractal nickel (β_{oct} = 0.25, entry 1) is a less active electrode material (real electrode activity) than Raney nickel (β_{oct} = 0.55, entry 7). As a result, the apparent activity of fractal nickel electrodes is much lower (much smaller conversion rates and current efficiencies) than that of Raney nickel electrodes. For the Ni/RaNi electrodes (entries 2–6), as the proportion of Raney nickel is increased (decreasing Ni/RaNi ratio), the real activity and thus the apparent activity increase until the proportion of RaNi reaches 80% (entry 4). At this point, the Ni/RaNi (20/80) electrodes have the same activity (real and apparent) as the 100% RaNi electrodes (entry 7). The activity for ECH is related to the competition between hydrogenation (eq. [3]) and hydrogen evolution (eq. [4] and (or) [5]), as already mentioned (see Scheme 1 also), and for a Ni/RaNi ratio of 20/80 the influence of Ni is too small to be detected within the experimental error. The ECH of phenanthrene on Ni/RaNi electrodes confirms that β_{oct} does reflect the activity of the catalytic material, since the β_{oct} value varies between that of a 100% fractal Ni electrode and that of a 100% RaNi electrode as the Ni/RaNi ratio decreases.

Tafel and alternating current impedance parameters for the HER in alkaline medium

To characterize further the pressed nickel boride powder and codeposited Raney nickel electrodes used above in the ECH of

Can. J. Chem. Downloaded from www.nrcresearchpress.com by 85.192.166.187 on 09/08/12
For personal use only.

Can. J. Chem. Downloaded from www.nrcresearchpress.com by 85.192.166.187 on 09/08/12
For personal use only.

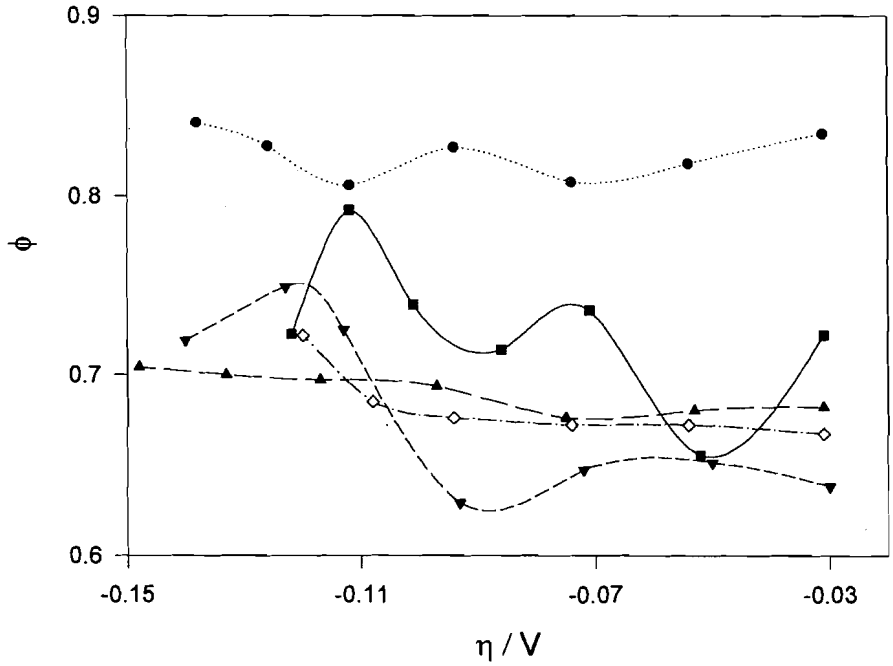

FIG. 2. Constant phase angle as a function of the overpotential for pressed nickel boride powder electrodes in 1 M NaOH at 25°C:(●) Ni_2B; (■) Ni_2B–NaCl(s); (▼) Ni_2B–NaCl(b-solid/s): (▲) Ni_2B–NaCl(b-solution/s); (◇) Ni_2B (p = 400 MPa).

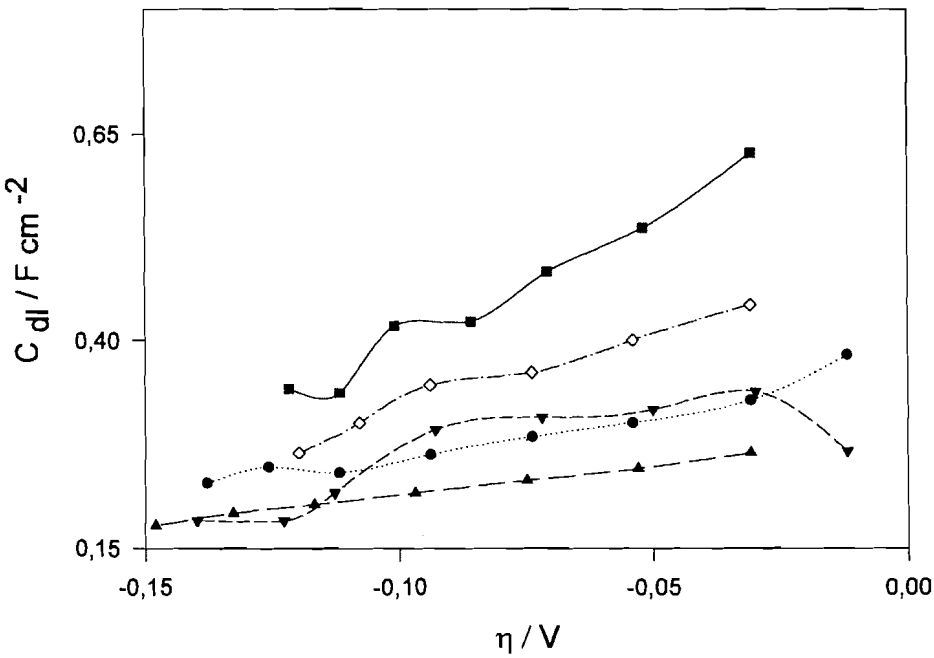

FIG. 3. Double layer capacities as a function of the overpotential for pressed nickel boride powder electrodes in 1 M NaOH at 25°C: (●) Ni_2B; (■) Ni_2B–NaCl(s); (▼) Ni_2B–NaCl(b-solid/s); (▲) Ni_2B–NaCl(b-solution/s); (◇) Ni_2B (p = 400 MPa).

phenanthrene, we determined their intrinsic activity and their real surface for the HER in 1 M NaOH at 25°C using Tafel plots and ac impedance measurements (4, 7–12). Such studies could not be carried out on the pressed RaNi electrodes because of the continuous leaching of the Raney alloy particles inside the disc during the experiments, causing the particles to fall apart. For the determination of the double layer capacity (C_{dl}) by ac impedance, the CPE model was used (eqs. [7] and [8] (13) where ω is the angular frequency of the ac signal, T is a constant, ϕ is the phase angle related to the surface roughness, R_s is the solution resistance, and parameter A is equal to $1/R_{ct}$ where R_{ct} is the charge transfer resistance (4, 7–12, 14)). For an ideally flat electrode, ϕ is equal to 1 and thus T is equal to C_{dl}. The roughness factor R was estimated from the experimental values of the capacity of the double layer divided by 27.9 $\mu F/cm^2$, the capacity of a platinum smooth surface (15).

$$[7] \quad Z_{CPE} = 1/T(j\omega)^{\phi}$$

$$[8] \quad T = C_{dl}^{\phi}(R_s^{-1} + A)^{(1-\phi)}$$

Figure 2 shows the dependency of ϕ on the overpotential (η)

TABLE 3. Tafel parameters, roughness factors, and real current densities for the HER in 1 M NaOH at 25°C

Entry	Electrode[a] (3 g of Ni_2B) NaCl[b] (g)	I_0 (mA cm^{-1})	b (mV)	o.c.p.[c] (mV)	r^2	η_{150} (mV)	C_{dl}[d] (F cm^{-2})	R	I_0/R[e] (A cm^{-2})
1	0	2.8	106	−30	0.999	183	0.28	10 000	2.8×10^{-7}
2	0 (p = 400 MPa)	3.4	108	−30	0.997	182	0.25	9 000	3.8×10^{-7}
3	0.6	3.7	102	−30	0.996	165	0.48	17 400	2.1×10^{-7}
4	7(Solid) + 0.6	3.4	127	0	0.995	205	0.25	9 000	3.8×10^{-7}
5	7(Solution) + 0.6	2.6	118	0	0.998	207	0.22	7 900	3.3×10^{-7}
6	Codeposited RaNi electrodes	7.3	123	0	0.992	175	0.55	20 000	3.7×10^{-7}

[a]The nickel boride electrodes were prepared by pressing the Ni_2B or Ni_2B–NaCl powder at p = 800 MPa (except in entry 2).
[b]See footnote *d* of Table 1.
[c]Open circuit potential obtained from extrapolation of the low-current part of the Tafel curves to zero current.
[d]Mean values obtained from the experimental C_{dl} values measured at different overpotentials (see Fig. 3).
[e]Real current density.

for different nickel boride electrodes. The ϕ value is the highest (0.83) for an electrode of Ni_2B powder pressed at 800 MPa. It is smaller for an electrode of Ni_2B powder pressed at 400 MPa (ϕ = 0.68) and also for the Ni_2B–NaCl electrodes (ϕ = 0.65–0.75). Thus, the latter electrodes behave more like the limiting case of a true porous electrode for which ϕ is equal to 0.5 (11). The mean ϕ value for a codeposited RaNi electrode is 0.75. In Fig. 3, the decrease of C_{dl} with η for the various nickel boride electrodes used in Table 1 is shown. For the codeposited RaNi electrodes C_{dl} also decreases with η (16). This decrease is due to hydrogen bubbles formed on the surface (17). The roughness factors R presented in Table 3 were estimated from the mean value of the experimental C_{dl} values measured at the different overpotentials (see Fig. 3). The codeposited RaNi electrodes have the highest R value and the various nickel boride electrodes have different R values. This will be discussed below (see *Surface studies*).

Based on the overpotential at 150 mA/cm^2 (η_{150}), the electrocatalytic activity of the nickel boride and codeposited RaNi electrodes for the HER in 1 M aqueous NaOH at 25°C decreases in the order: Ni_2B–NaCl(s) (η_{150} = 165 mV, entry 3) > codeposited RaNi (η_{150} = 175 mV, entry 6) > Ni_2B (unmodified) (η_{150} = 182–183 mV, entries 1 and 2) > Ni_2B–NaCl(bs) (η_{150} = 203–207 mV, entries 4 and 5). The decreasing order of apparent activity of these same electrodes for the ECH of phenanthrene in ethylene glycol at 80°C and pH 3–6 (see discussion above and Table 1) is as follows: codeposited RaNi (entry 8) ~ Ni_2B–NaCl(b-solid/s) (entries 5 and 6) > Ni_2B–NaCl(b-solution/s) (entry 7) > Ni_2B-NaCl(s) (entry 4) > Ni_2B (unmodified) (entries 1–3). Therefore there is no direct relation between the electrode activity in the ECH of phenanthrene under the conditions used and the electrode activity for the HER in aqueous alkali. It was likewise found that for RaNi and RaNiXY (XY = CoCr, CrMo, CrTi, CuCr, CuTi, and CrTi) electrodes, there was no direct relation between the activity of the electrodes in the two electrolytic processes: the most active electrode for the ECH of phenanthrene was the RaNi electrode, which was less active than the RaNiXY electrodes for the HER in alkaline solution.[2] Interestingly, the intrinsic electrocatalytic activity for the HER, expressed by the ratio of the exchange current density over the roughness factor (I_0/R), is of a similar order of magnitude ((2–4) $\times 10^{-7}$) for all the electrodes of Table 3 just as the real electrode activity of these same electrodes for the ECH of phenanthrene was the same (average β_{oct} value of 0.55–0.57, Table 1). This shows that the intrinsic activity for the HER is determined by the electrode material and not by the surface structure and the real surface area, as is the real activity in the ECH of phenanthrene (see above). It is coincidental that two different electrode materials, nickel boride and Raney nickel, give the same real electrode activity for the ECH of phenanthrene. For instance, RaNiXY electrodes have a lower real activity for the ECH of phenanthrene than RaNi electrodes.[2]

[2]J.M. Chapuzet, J. Depo, G.A. Capuano, and J. Lessard. Unpublished results.

TABLE 4. Specific surface area and diameter of pores for selected nickel boride electrodes

Entry	Electrode[a] (3 g of Ni_2B) NaCl[b] (g)	Specific surface area[c] (m^2/g)	R[d]	Pore diameter[e] (μm)
1	0	10.7	10 000	0.012
2	0.6	9.7	17 400	0.012
3	7(Solid) + 0.6	9	9 000	8

[a]See footnote *b* of Table 1.
[b]See footnote *d* of Table 1.
[c]Obtained from BET measurements and based on the mass of Ni_2B for Ni_2B–NaCl electrodes.
[d]Taken from Table 3, entries 1, 3, and 4.
[e]Obtained from mercury porosimetry measurements.

Two of the electrodes of Table 3, the Ni_2B (unmodified) (entries 1 and 2) and Ni_2B–NaCl(s) (entry 3) electrodes, have a negative (−30 mV) open circuit potential (o.c.p.) (obtained by extrapolating the low-current part of the Tafel curve to zero current) while the three others (entries 4–6) have an o.c.p. of 0 mV. A negative o.c.p. has been attributed to hydrogen absorption to form metal hydrides (4, 18).

Electrocatalytic activity and surface of nickel boride electrodes

We have shown above (see *Nickel boride electrodes*) that modifying the nickel boride electrodes made of pressed powder, by adding NaCl before pressing and dissolving it afterwards, caused an increase of the apparent activity for the ECH of phenanthrene (Table 1), and suggested that their improved activity was related to a change in surface area and (or) structure. To clarify this point, surface studies were carried out on nickel boride electrodes having different apparent activities for the ECH of phenanthrene by determination of the specific surface area using the BET method, by scanning electron microscopy (SEM), and by pore size measurements using mercury

Can. J. Chem. Downloaded from www.nrcresearchpress.com by 85.192.166.187 on 09/08/12
For personal use only.

Can. J. Chem. Downloaded from www.nrcresearchpress.com by 85.192.166.187 on 09/08/12
For personal use only.

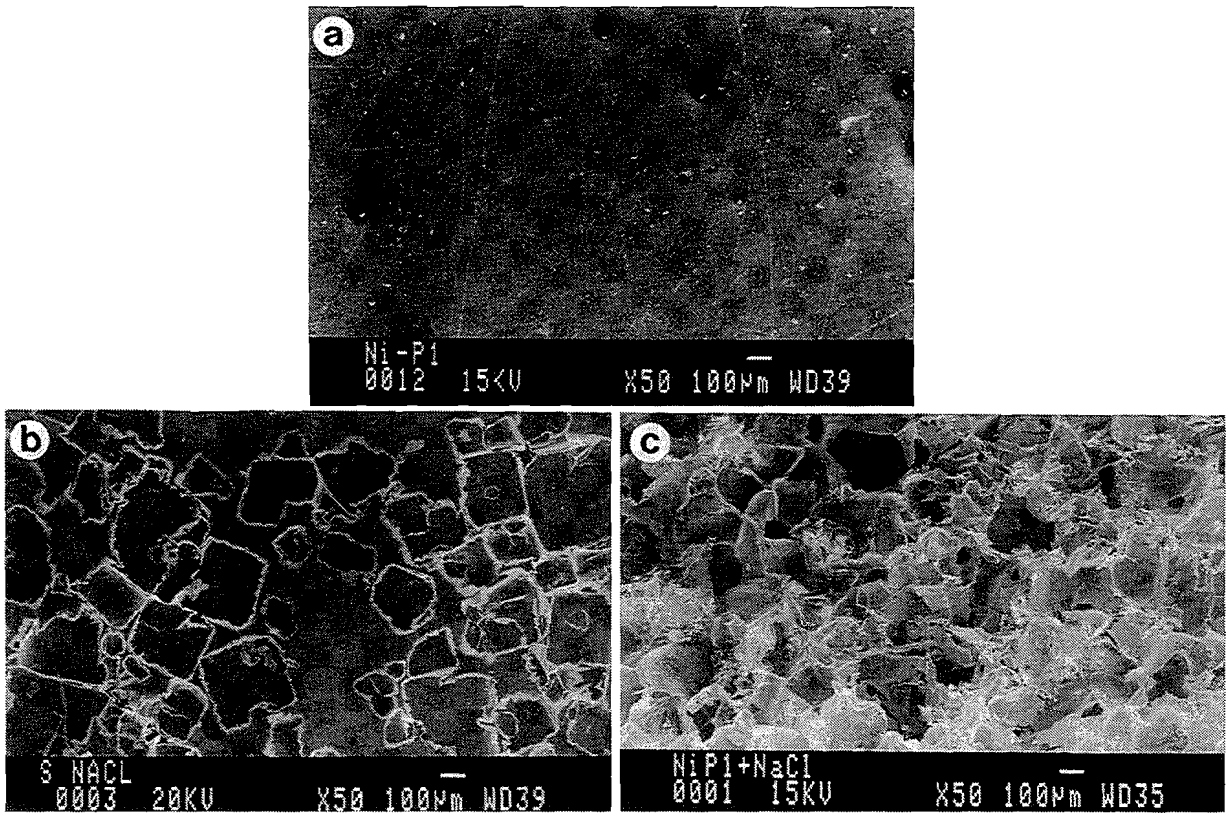

FIG. 4. SEM pictures of pressed nickel boride powder electrodes after removing NaCl: (*a*) Ni_2B; (*b*) Ni_2B–NaCl(s); (*c*) Ni_2B–NaCl(b-solid/s).

porosimetry. The data for Ni_2B, Ni_2B–NaCl(s), and Ni_2B–NaCl(b-solid/s) electrodes (order of increasing apparent activity) are collected in Table 4 (entries 1–3, respectively) together with the roughness factor (*R*) for the HER in alkaline medium. The SEM pictures are shown in Fig. 4.

The specific surface area of the pressed Ni_2B powder (entry 1) is exactly the same as that of the free powder (10 m^2/g), which means that pressing did not remove any site accessible to the nitrogen molecules. The specific surface area decreases slightly from the least active Ni_2B electrode (entry 1) to the most active Ni_2B–NaCl(b-solid/s) electrode (entry 3). So there is no direct correlation between the permeability to nitrogen molecules and the apparent activity for the ECH of phenanthrene. There is no direct correlation between the specific surface area and either the roughness factor or the electrocatalytic activity based on η_{150} for the HER in alkaline medium: the Ni_2B electrode with the largest specific surface area (entry 1) does not have the largest roughness factor and the highest electrocatalytic activity. One possible cause for the lack of correlation between the specific surface area and the activity in the electrocatalytic processes studied could be the difference in the nature of the interface: a gas–solid interface in the BET measurements and a solution–solid interface in the ECH process and the HER. Furthermore, the solid is polarized in the electrochemical processes. When comparing the two electrocatalytic processes, there is no direct correlation between the apparent electrode activity for the ECH process and the electrode activity for the HER, as already pointed out. The latter activity refers to the overpotential for the HER in aqueous alkali and the overpotential is determined by the rate of the slow step, which is the electrochemical desorption of chemisorbed hydrogen (Heyrovský step [5]) on nickel boride electrodes (4). The apparent activity for the ECH process refers to the competition between the hydrogenation step [3] and desorption of chemisorbed hydrogen (eqs. [5] and (or) [6]), that is, on the relative rates of reaction [3] and reactions [5] and (or) [6]. Since the hydrogenation step involves the reaction between the adsorbed organic substrate and chemisorbed hydrogen, accessibility of the sites for the adsorption of the former (mass transfer to the active sites) is bound to play a role in the ECH reaction (see below). Thus the surface requirements for the ECH reaction are expected to differ from those of the HER in which only chemisorbed hydrogen is involved. Therefore the most active electrode in the ECH process (the Ni_2B–NaCl(s-solid/s) electrode in this case) does not necessarily have to be the most active electrode in the HER under different electrolysis conditions, as experimentally found (the Ni_2B–NaCl(s) electrode is the most active in the HER).

There is good agreement between the SEM pictures (Fig. 4) and the size of the pores determined by mercury porosimetry. The Ni_2B and Ni_2B–NaCl(s) electrodes have pores of the same size (diameter of 0.012 µm, Table 4, entries 1 and 2) and appear to have the same compactness on the SEM pictures (Figs. 4*a* and 4*b*, respectively). In Fig. 4*b*, the prints left by the NaCl crystals after their dissolution are clearly seen and the surface in contact with solution should be larger in the case of the Ni_2B–NaCl(s) electrodes, and, indeed, the roughness factor of the latter electrode is larger (17 400 in entry 2 compared to 10 000 in entry 1 for the Ni_2B electrode). As result, the Ni_2B–NaCl(s) electrode is more active both for the ECH of phenanthrene (compare entry 4 with entries 1–3 of Table 1) and the HER in alkaline medium (lower η_{150} in entry 3 than in entries 1 and 2 of Table 3). The Ni_2B–NaCl(b-solid/s) electrodes resulting from intimate mixing of NaCl crystals within the nickel boride pow-

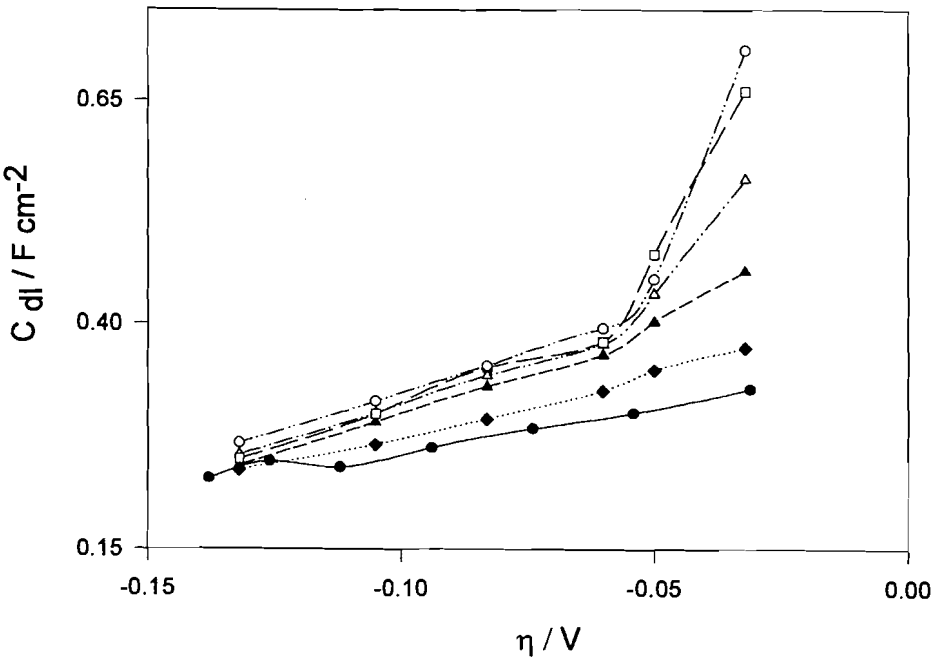

FIG. 5. Double layer capacities as a function of the overpotential and the *trans*-cinnamic acid concentration for a Ni_2B electrode in 1 M NaOH at 25°C: (●) C = 0 mM; (◆) C = 9 mM; (▲) C = 27 mM; (△) C = 45 mM; (□) C = 72 mM; (○) C = 90 mM.

der plus the addition of NaCl at the surface have much larger pores (Table 4, entry 3) than the two other electrodes (entries 1 and 2) and also appear quite different (much rougher) on the SEM picture (compare Fig. 4*c* with Figs. 4*a* and 4*b*). Surprisingly, the Ni_2B–NaCl(b-solid/s) electrode has also the same roughness factor (R = 9000) as a Ni_2B electrode (R = 9000–10 000) and is the least active (has the highest η_{150}) of the three electrodes of Table 3 for the HER. Thus, the solution–solid interface and the number of sites for the chemisorption of hydrogen are not increased in the less closely packed structure of a Ni_2B–NaCl(b-solid/s) electrode. However, the Ni_2B–NaCl(b-solid/s) electrode has the highest apparent activity of the three electrodes of Table 3 for the ECH of phenanthrene and this could be explained by a larger number of readily accessible sites for the adsorption of phenanthrene (ECH active sites) due to the larger pores. For probing the existence of more readily accessible adsorption sites for the organic substrate in the Ni_2B–NaCl(b-solid/s) electrode, we carried out ac impedance measurements on Ni_2B and Ni_2B–NaCl(b-solid/s) electrodes in the presence of sodium *trans*-cinnamate in 1 M NaOH at 25°C, after the work of Kam Cheong et al. (16). They found that C_{dl} of codeposited Raney electrodes in 1 M KOH at 25°C is increased in the presence of potassium *trans*-cinnamate, a water-soluble substrate that is electrohydrogenated by ECH, and attributed this increase to its adsorption on the electrode. According to their hypothesis, for a given concentration of sodium *trans*-cinnamate, the increase of C_{dl} should be more pronounced for an electrode having sites that are more readily accessible for the adsorption and hydrogenation of the organic substrate. And in agreement with this hypothesis, the maximum C_{dl} value at low overpotential (> −0.05 V, close to the o.c.p. obtained from the Tafel curves) (see Figs. 5 and 6) is reached at a lower concentration of sodium *trans*-cinnamate (C = 27 mM, Fig. 6) on a less closely packed Ni_2B–NaCl(b-solid/s) electrode, which should have more readily accessible sites for adsorption and hydrogenation of the organic substrate, than on a Ni_2B electrode (C = 90 mM, Fig. 5). The higher apparent activity of the former electrode would then be related to the accessibility of the ECH active sites and thus to the efficiency of the mass transfer of the organic substrate to these sites. It is interesting to note in Figs. 5 and 6 that the increase of C_{dl} with the concentration of sodium *trans*-cinnamate occurs only at low overpotentials. At these low overpotentials, the current density is about the same as that used for the ECH electrolyses. At higher overpotentials (η < −0.1 V), the HER predominates and bubbles of hydrogen cover the surface of the electrode; the presence and concentration of *trans*-cinnamate have little effect on C_{dl}. This suggests that at these potentials there is little adsorption of the organic substrate on the electrode surface because an effective mass transfer to the active sites is prevented by the bubbles of hydrogen covering the surface and (or) because at more cathodic potentials there is desorption of sodium *trans*-cinnamate. We emphasize the fact that a Ni_2B–NaCl(b-solid/s) electrode, which is more active than a Ni_2B electrode for the ECH of phenanthrene in ethylene glycol – water containing H_3BO_3 at 80°C (see Table 1), is also more active for the ECH of sodium *trans*-cinnamate in 1 M aqueous NaOH at 25°C as shown by the higher current efficiency and conversion rate in entry 2 of Table 5 than those in entry 1. Thus the electrodes show the same behaviour in these two ECH reactions despite the different conditions.

Conclusion

We have shown in this paper that the apparent electrode activity for the ECH of phenanthrene (as measured by the conversion rate, the yield of octahydrophenanthrenes, and the current efficiency) of nickel boride electrodes is increased by pressing the P-1 nickel boride powder with NaCl and dissolving it afterwards. This increase of activity does not correspond to an increase in the specific surface area measured by the BET method and does not correlate directly either with the roughness factor (obtained from ac impedance measurements on the HER in aqueous alkaline medium) or with the electrocatalytic activity for the HER in aqueous alkaline medium (based on the η_{150} value determined from Tafel curves). The fact that the increase of C_{dl} with the concentration of sodium *trans*-cinnamate, which is electrohydrogenated to sodium 3-phenylpropaonate in aque-

Can. J. Chem. Downloaded from www.nrcresearchpress.com by 85.192.166.187 on 09/08/12
For personal use only.

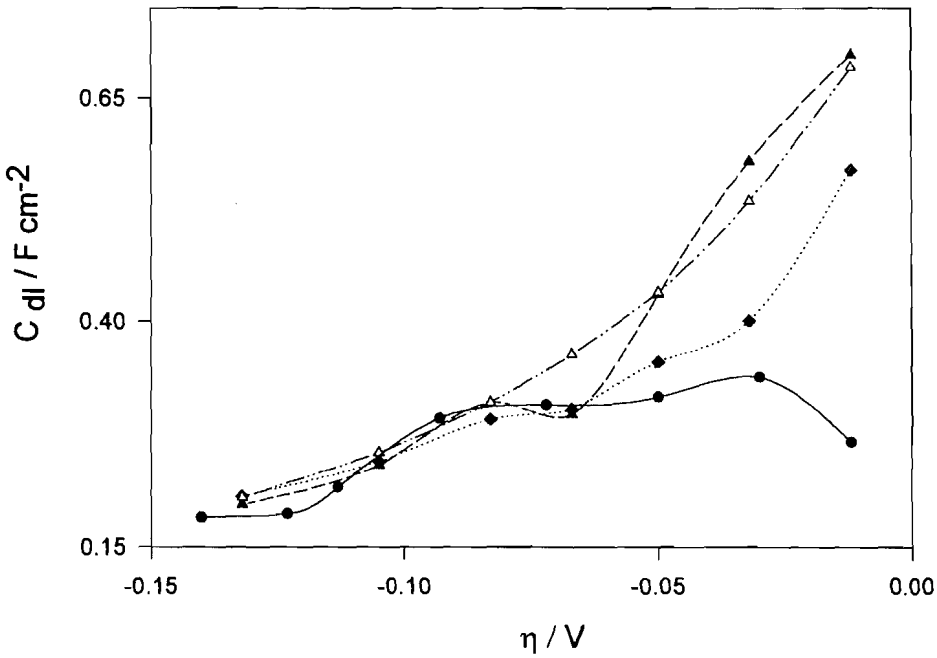

FIG. 6. Double layer capacities as a function of the overpotential and the *trans*-cinnamic acid concentration for a Ni_2B–NaCl(b-solid/s) electrode in 1 M NaOH at 25°C: (●) $C = 0$ mM; (◆) $C = 9$ mM; (△) $C = 27$ mM; (▲) $C = 72$ mM.

TABLE 5. ECH of *trans*-cinnamic acid at nickel boride electrodes at $J = 250$ mA/dm^2[a]

Entry	Electrode[b] (3 g of Ni_2B) NaCl[d] (g)	Yield of hydrocinnamic acid[c] (%)	Current efficiency (%)
1	0	21	21
2	7(Solid) + 0.6	42	42

[a]Electrolysis conditions: 448 μmol of *trans*-cinnamic acid (18 mM solution); 1 M NaOH; T = 25°C; charged passed (Q) = 88 C (2 moles of electrons per mole of *trans*-cinnamic acid).
[b]See footnote *b* of Table 1.
[c]The yield of product and conversion rate were similar (material balance >96%) and were determined by vpc analysis.
[d]See footnote *d* of Table 1.

ous alkaline medium, was steeper (maximum C_{dl} reached at lower concentrations of cinnamate) for a more active electrode together with the pore size effect (larger pore diameter for the most active electrode as determined by mercury porosimetry and as confirmed by SEM) led to the conclusion that the apparent activity for the ECH of phenanthrene depends not only on the true area of the solution–solid interface but also the accessibility of the active sites, that is, on the mass transfer of the organic substrate to the active sites.

The ratio of the yield of octahydrophenanthrenes to the conversion rate (defined as β_{ocl}) was found to be independent of the true area of the solution–solid interface and the accessibility of the active sites since it is the same for all the nickel boride electrodes (modified and unmodified) investigated. It depends only on the electrode material and thus must represent the true or real electrode activity for the ECH of phenanthrene under given conditions. Similarly, the intrinsic activity for the HER in alkaline medium as measured by the ratio of exchange current density to the roughness factor (I_0/R) is the same for all nickel boride electrodes studied. It is noteworthy that nickel boride and Raney nickel electrodes have the same real activity for the ECH of phenanthrene and the same intrinsic activity for the HER in basic aqueous medium. Fractal nickel is much less active than Raney nickel as electrode material (real activity and apparent activity) for the ECH of phenanthrene and the activity of Ni/RaNi electrodes increases with the RaNi content up to a 20/80 ratio. With 20% of less fractal nickel, its influence on the activity of Ni/RaNi electrodes is not detected within the experimental errors.

Acknowledgements

Financial support from the Natural Sciences and Engineering Research Council of Canada, the "Fonds pour la formation de chercheurs et l'aide à la recherche du Québec", and the "Ministère de l'énergie et des ressources du Québec" is gratefully acknowledged. We thank Sylvain Roy for mercury porosimetry measurements.

1. D. Robin, M. Comtois, A. Martel, R. Lemieux, A. Kam Cheong, G. Belot, and J. Lessard. Can. J. Chem. **68**, 1218 (1990).
2. C.A. Brown. J. Org. Chem. **35**, 1900 (1970).
3. J. Saida, A. Inone, and T. Masumoto. Metall. Trans. A: 22, 2125 (1992).
4. P. Los and A. Lasia. J. Electroanal. Chem. **333**, 115 (1992).
5. J. van Wonterghem, S. Morup, Ch.J. Koch, S.W. Charles, and S. Wells. Nature, **322**, 622 (1986).
6. M.L. Trudeau, J.Y. Huot, R. Schulz, D. Dussault, A. van Neste, and G. L'Esperance. Phys. Rev. B, **45**, 4626 (1992).
7. E. Potvin, A. Lasia, H. Ménard, and L. Brossard. J. Electrochem. Soc. **138**, 900 (1991).
8. L. Chen and A. Lasia. J. Electrochem. Soc. **138**, 3321 (1991).
9. Y. Choquette, L. Brossard, A. Lasia, and H. Ménard. Electrochim. Acta, **35**, 1251 (1990).
10. P. Los, A. Rami and A. Lasia. J. Appl. Electrochem. **23**, 135 (1993).
11. P. Los, A. Lasia, L. Brossard, and H. Ménard. J. Electroanal. Chem. **360**, 101 (1993).

Can. J. Chem. Downloaded from www.nrcresearchpress.com by 85.192.166.187 on 09/08/12
For personal use only.

12. P. Los, L. Brossard, H. Dumont, A. Lasia, J. Lessard, and H. Ménard. Proceedings of the 5th Canadian Hydrogen Workshop, Ottawa, February 1992. p. 39.
13. G.J. Brug, A.L.G. van den Eeden, M. Sluyters-Rehbach, and J.H. Sluyters. J. Electroanal. Chem. **176**, 275 (1984).
14. D.A. Harrington and B.E. Conway. Electrochim. Acta, **32**, 1703 (1987).
15. L. Bai, L. Goa, and B.E. Conway. J. Chem. Soc. Faraday Trans. **89**, 235 (1993).
16. A. Kam Cheong, A. Lasia, and J. Lessard. J. Electrochem. Soc. **141**, 975 (1994).
17. A. Rami and A. Lasia. J. Appl. Electrochem. **22**, 376 (1992).
18. D.M. Soares, O. Teschke, and I. Torriani. J. Electrochem. Soc. **139**, 98 (1992).

Can. J. Chem. Downloaded from www.nrcresearchpress.com by 85.192.166.187 on 09/08/12
For personal use only.

Silver nitrate in aqueous solution and as molten salt: A molecular dynamics simulation and NMR relaxation study

AATTO LAAKSONEN[1]
Department of Chemistry, Dalhousie University, Halifax, NS B3H 4J3 Canada

AND

HELENA KOVACS
Laboratorium für Physikalische Chemie, ETH Zentrum, CH-8092 Zürich, Switzerland

Received June 10, 1994

AATTO LAAKSONEN AND HELENA KOVACS. Can. J. Chem. **72**, 2278 (1994).

Using molecular dynamics simulations, the motion and intermolecular interactions of the ions of silver nitrate are studied in aqueous solution and compared to the results obtained from simulations of molten $AgNO_3$. The particularly interesting and experimentally frequently studied modes of reorientational motion (*in-plane* and *end-over-end*) of the planar nitrate ion have been determined from the simulation results. In accordance with earlier experimental results, the correlation times for the *end-over-end* rotation in aqueous solution are longer than those for the *in-plane* rotation, while the opposite is found to hold in the melt. In addition, the rotational motion of the nitrate ion in aqueous solution is experimentally studied using ^{14}N relaxation measurements. Good agreement is found between the reorientational correlation times obtained from MD simulations and from NMR relaxation measurements.

AATTO LAAKSONEN ET HELENA KOVACS. Can. J. Chem. **72**, 2278 (1994).

Utilisant des simulations de dynamique moléculaire, on a étudié le mouvement et les interactions intermoléculaires des ions du nitrate d'argent en solution aqueuse et on a comparé les résultats à ceux obtenus à partir de simulations de $AgHO_3$ fondu. Sur la base des résultats de simulation, on a déterminé les modes particulièrement intéressants et les plus fréquemment étudiés expérimentalement du mouvement de réorientation (*dans le plan* et *bout sur bout*) de l'ion de nitrate d'argent. En accord avec les résultats expérimentaux antérieurs, les temps de corrélation de la rotation *bout sur bout* en solution aqueuse sont plus longs que ceux de la rotation *dans le plan* alors que l'on observe l'inverse dans le sel fondu. De plus, faisant appel à de mesures de relaxation du ^{14}N, on a étudié expérimentalement le mouvement de rotation de l'ion nitrate en solution aqueuse. On a trouvé un bon accord entre les temps de corrélation de réorientation obtenus à partir de simulations de dynamique moléculaire et des mesures de relaxation en RMN.

[Traduit par la rédaction]

1. Introduction

Anion solvation is very different from cation solvation, particularly in the case of molecular anions. Ionic motion and interactions in aqueous nitrate solutions have attracted the interest of several spectroscopic groups since the late sixties. These studies include IR, Raman, depolarized Rayleigh scattering and NMR techniques (1–17). In the earlier works the main concern was to find the origin of the behaviour of the $\nu_3(E')$ mode, which appears as a broad doublet in Raman and IR spectra (1–4). The unperturbed nitrate ion is trigonal planar with D_{3h} symmetry. Raman studies, even carried out at relatively low concentrations of nitrate ions, showed rather clear evidence of a perturbation ($D_{3h} \rightarrow C_{2v}$), which was observed when the $E'(D_{3h})$ mode showed a tendency to split into A_1 and B_1 components (2). Because the Raman and IR spectra were not identical, it was first assumed that the nitrates were rotating in a cage of water molecules, giving rise to the perturbation. Lockwood later showed (3) through calculations of the spectra that the primary cause of the splitting of the ν_3 band were not the rotations, but rather the interactions with the local environments. This was also the conclusion of Findlay and Symons (4) who suggested that one or two hydrogen bonds between the nitrate and the water molecules were likely to cause the lowering of the symmetry. At higher salt concentrations, possible contact or solvent separated ion pairing between the nitrate and the cation could contribute to the perturbing effect. Apparently the nitrate ion is very sensitive to variations in solution environment and is therefore an ideal agent to study molecular ionic solutions.

In aqueous nitrate solution, strong hydrogen bonds are involved in vibrational and rotational–reorientational relaxation processes, which are responsible to the line broadening of the solution–state spectra (5–17). In addition, large effects are brought about by varying the temperature or the ion concentration. In general, vibrational correlation times decrease upon increasing ion concentration, while the opposite is true for the rotational correlation times. Particularly large effects are observed by varying the cation species. Highly polarizing cations with small ionic radii, such as, Li^+, Be^+, Be^{2+} or Mg^{2+} have a very large impact on the reorientational motion when the ion concentration is increased, while the effect is small, for example, for ammonium ion, because it can easily replace the water molecules while leaving the hydrogen bonding network intact.

Polarized Raman spectra can be used to obtain both the vibrational and reorientational contributions to the relaxation processes of polyatomic molecules in the liquid state. The isotropic line shape contains the pure vibrational motion of the molecule and its Fourier transform gives the vibrational correlation. The origin of the vibrational line broadening processes can be described either in terms of vibrational dephasing or energy relaxation between the vibrational states. The anisotropic spectra is a product of both vibrational and reorientational motion and it has to be first deconvoluted in order to separate the reorientational motion from the vibrational motion. This procedure is valid under assumption that cross-correlations between the reorientational and vibrational motions are negligible. In other

[1]Permanent address: Division of Physical Chemistry, Arrhenius Laboratory, Stockholm University, S-106 91 Stockholm, Sweden.

Can. J. Chem. Downloaded from www.nrcresearchpress.com by 85.192.166.187 on 09/08/12
For personal use only.

Can. J. Chem. Downloaded from www.nrcresearchpress.com by 85.192.166.187 on 09/08/12
For personal use only.

words the time scales of these motions should be sufficiently well separated.

NMR studies of rotational-reorientational motion, on the other hand, are free from cross-correlation effects. Also, because of the sensitivity of the method, it is possible to study more diluted solutions by using NMR, than by using IR or Raman spectroscopy (11, 13). However, the NMR method mainly gives the long time behaviour of the correlation functions, while the short time behaviour can be studied by Raman techniques through band analysis. Therefore, a combination of the Raman and NMR techniques should be a very powerful experimental method in studies of molecular motions in pure liquids and solutions.

In studying the reorientations of nitrates, two types of rotations are of particular interest: the *end-over-end* rotation of the three-fold symmetry axis (assuming the unperturbed nitrate) and the *in-plane* rotation of the vector perpendicular to the C_3-axis. The tumbling, *end-over-end* rotation (or the perpendicular mode) can be probed by Raman or ^{14}N NMR spin–lattice (T_1) measurements and the spinning, *in-plane* rotation around the C_3-axis (or the parallel mode) by ^{17}O NMR T_1 measurements. In general, the correlation time τ_2 for the perpendicular reorientational motion of planar symmetric molecules, of which benzene is one of the most thoroughly studied case (18–20), is observed to be longer than that for the parallel motion. This means that the rotation around the symmetry axis is less hindered than the rotation of the symmetry axis itself, since in the latter case the rotation involves displacement of the molecules in the solvation sphere. For the nitrates in aqueous solution, the opposite behaviour has been observed in previous studies. The *in-plane* rotations are found (11, 13) to be more hindered than the *end-over-end* rotations at any concentration (10). The strong hydrogen bonds between the nitrate oxygens and the water hydrogens are assumed be an important cause to this unusual behaviour (11, 13).

The pure inorganic nitrates form highly conducting liquids in melts. Many nitrates melt at sufficiently low temperatures so they can rather easily be used in spectroscopic studies. Fused nitrate salts have been extensively studied using spectroscopic techniques (21–42), X-ray and neutron diffraction measurements (43–46) and computer simulations (46–48). There are many similarities in the behaviour of nitrates in liquids (or even in crystals) and in solution and it is therefore useful to correlate results from both the liquid and solution state studies.

Silver nitrate is a particularly interesting molecule. As a solid, $AgNO_3$ is a colourless crystal which melts at 212°C. It is highly soluble in water and in many organic solvents. The crystal structure (49, 50) is found to be rather unusual with six nitrates forming a cavity for two silver atoms. The silver atoms are above the nitrate plane, off the C_3-axis. It has even been suggested that silver ions are found in molten salt (27) in the same locations as they are in concentrated aqueous solutions (51).

In the present work, we have carried out molecular dynamics (MD) computer simulations to study the motion and intermolecular interactions of the hydrated ions of $AgNO_3$ in aqueous solution. The main objective of our work is to investigate the rotational-reorientational motion of the planar anionic nitrate in some detail and especially investigate the role of hydrogen bonds to the rotational motion. We also carried out MD simulations of molten silver nitrate to correlate the behaviour of the ions in the melt with that in aqueous solution and to study the rotational motion without hydrogen bonds. The results from the simulation of molten salt provide a reference for a possible occurrence of ion-pairs in aqueous nitrate solution. The MD simulations of aqueous solution were combined with ^{14}N NMR relaxation measurements to obtain corresponding experimental information about the rotational correlation times. A similar study of $AgNO_3$ in acetonitrile and in water/acetonitrile mixture is in progress.

TABLE 1. Physical specification of the simulated systems

Parameter	Value		
	Run I	Run II	Run III
N (H_2O)	256	—	248
N (Ag^+)	—	128	4
N (NO_3^-)	—	128	4
T (K)	300	595	315
Time step (fs)	1.0	1.0	1.0
Density (g cm^{-3})	1.0	4.35	1.05

2. NMR measurements

Nitrogen-14 relaxation measurements were performed at 9.4 T on a Jeol GX 400 MHz NMR spectrometer at the concentration used in the MD simulation (see next section). The transverse relaxation rate for ^{14}N in NO_3^- was determined manually from the linewidths through the relationship: $T_2^{-1} = \pi\Delta\nu_{1/2}$. Assuming extremely narrowing conditions, the correlation time, τ_2, was calculated by using the following equation.

$$[1]\quad \frac{1}{T_1^Q} = \frac{1}{T_2^Q} = \frac{3}{10}\pi^2\frac{2I+3}{I^2(2I-1)}\chi^2\tau_2$$

Quadrupolar coupling constant, χ = 745 kHz was used for $^{14}NO_3^-$, which is a solid state value for $NaNO_3$ (52). Two measurements were recorded and the relaxation rate is taken as an average. The experimental uncertainty is estimated to 10%.

3. Physical models and computational methods

Constant volume (NVE) molecular dynamics simulations were carried out for $AgNO_3$ dissolved in water in 4:252 proportions. Also, both components, $AgNO_3$ and H_2O, were simulated as pure liquids to be used as references in the anlaysis of the results. A summary of the physical states and characteristic simulation parameters is given in Table 1. The pure water simulation is denoted by **I**, the $AgNO_3(l)$ simulation by **II**, and the mixture simulation by **III**.

Both molecular species, i.e. water and nitrate were kept rigid throughout the simulations and the equations of motions were solved using fifth order Nordsieck–Gear predictor–corrector integration scheme (53, 54). The rotational motion was treated using the second order quaternion scheme by Sonnenschein (55). The pair potentials of site–site (1–6–12) type are given in standard Lennard–Jones plus electrostatic form. The potential parameters for water (SPC) were taken from Berendsen et al. (56). For $AgNO_3$, we used standard epsilon values of ϵ(Ag) = 300 K, ϵ(N) = 37 K and ϵ(O) = 37 K, and sigmas σ(Ag) = 2.10 Å, σ(N) = 3.10 Å and σ(O) = 3.00 Å. The charge in units of $|e|$ are q(Ag) = 1.0, q(N) = 1.31, and q(O) = −0.77. The cross-interaction terms were constructed using the so-called Lorentz–Berthelot combination rules (57, 58). The long-range electrostatic interactions were treated using the Ewald summation techniques and the minimum image convention was used together with the periodic boundary conditions to maintain constant density and to prevent condensation at walls of the simulation cell (59). The simulations were extended to 70 ps for the

TABLE 2. Interaction energies (in J/mol) see text for details

	Interaction energy					
	Lennard-Jones:			Electrostatic		
System	Run I	Run II	Run III	Run I	Run II	Run III
H_2O-H_2O	1873	—	2016	−12711	—	−11590
H_2O-Ag^+	—	—	105	—	—	−1518
H_2O-NO_3^-	—	—	131	—	—	−1583
Ag^+-Ag^+	—	−148	0	—	23829	10
Ag^+-NO_3^-	—	3178	0	—	−109634	−112
NO_3^--NO_3^-	—	−1520	0	—	34859	5

pure liquids (water and molten $AgNO_3$) and to 100 ps for the mixture. All simulations were performed using a modified version of McMoldyn package (60) on a Convex C220 computer.

4. Static and structural properties

4.1 Pair interaction energies

The pairwise interaction energies of the simulated systems are reported in Table 2. In get more information, the short-range Lennard-Jones and the long-range electrostatic contributions are separated. The total water–water interaction energies are −42.3 kJ/mol for pure water at 300 K. The corresponding value reported by Jorgensen et al. (61) is 42.6 kJ/mol for SPC water in their comparison of different water models at 25°C. The total potential energy for water in the mixture is −37.4 kJ/mol, which is considerably higher than for pure water. The water–Ag^+ and water–NO_3^- energies are of same magnitude, the electrostatic contributions being completely dominant. These are, in fact, an order of magnitude larger than the corresponding Lennard–Jones energies. The total ion–ion energy in the melt is −193.1 kJ/mol. In solution, the ion–ion interaction energies are vanishingly small, an indication of the ions being well dissolved and hydrated by water molecules. No ion-pairing effects or clustering is observed in the simulation of the aqueous solution.

4.2 Structural results

The solvent structure is disturbed by the presence of the solute particles. It is of particular interest to study how the hydrogen bonding network of liquid water is affected after dissolving salt into it. In our analysis, we have not differentiated between bulk and hydration water, Instead, we used pure water as reference. The ion concentration is high enough that most water molecules are involved in the hydration of Ag^+ and NO_3^- ions, making the differentiation meaningless.

Radial distribution functions (RDF) are convenient presentations of the simulated liquid structure. Water–water radial distribution functions are given in Fig. 1*a–c* of the pairs O–O, O–H, and H–H for pure water and for water in a mixture. Water in a mixture seemed more structured than pure water. Many monatomic ions tend to break the structure of the water surrounding them, thus are called structure breakers. Hydrophobic solutes tend to enhance the water structure exerting a structure-making effects on water. In the case of a mixture of silver cations and polyatomic nitrate anions, the solvation mechanism is an interplay of many different types of interactions; it is therefore difficult to rationalize in simple terms.

Figures 2*a* and *b* display the RDFs between the ion sites and water sites. Hydration number for Ag^+ is estimated to be between 0.3 to 4.0 (62, 63), depending on the method used in the estimation. Due to fast solvent exchanges at Ag^+, the signals from hydration and bulk water cannot be separated in the ^{17}O spectrum and no estimates of $n(Ag^+)$ are reported. The first, very sharp, peak of the simulated $g(r_{Ow—Ag})$, shown in Fig. 2*a*, contains 5.4 water-oxygens when integrated to the first minimum at 3.25 Å. The radial distribution function between the water-oxygen and the nitrate-nitrogen shows a maximum at 3.5 Å, indicating that water molecules do not closely coordinate to the nitrogen but rather to the oxygen. From the RDF curve we can calculate up to eight water molecules in the first hydration shell around the nitrate by integrating to the first minimum at 4.1 Å. Figure 2*b* shows the corresponding radial distribution functions between the water-hydrogen and the ion-atoms. Both water-hydrogens are found within the first maximum at 3.0 Å around the silver ion. The $g(r_{H—O})$ curve shows a very strong hydrogen bond structure with the first maximum at 1.75 Å followed by a broader second maximum due to the second water hydrogen, not involved in the hydrogen bond with the nitrate. The second maximum also contains a weaker subsidiary peak, corresponding to a pair between the hydrogen-bonded water hydrogen (responsible to the first maximum) and both the nearest neighbouring nitrate oxygens.

Figures 3*a–c* show the radial distribution functions for Ag–Ag, Ag–N, and Ag–O pairs, respectively, between the ions. Each figure contains the RDF curves for both the melt and the solution in a direct comparison. The small number of ions in the solution, however, gives rise to some statistical noise. It is immediately evident that there are no direct contacts between the bare ions in the simulated solution, as the first peaks found in the molten salts are absent in the solution. However, there is an evidence for weaker contacts for $Ag^+(aq)$–$Ag^+(aq)$ pairs (Fig. 3*a*) and $Ag^+(aq)$ with the oxygen sites in NO_3^- (Fig. 3*c*).

In the melt, the first peak for $g(r_{Ag—O})$ is found at 2.4 Å which is the same distance at that found by Yamaguchi et al. (45) from neutron diffraction of molten $AgNO_3$. The X-ray diffraction work by Holmberg and Johansson (44) for $AgNO_3(l)$ gives a Ag–O distance of 2.45 Å. It can be deduced from the radial distribution functions between the nitrate and silver ions that there are five Ag^+ ions around the nitrate in the first coordination sphere with a radius of 2.4–4.2 Å. Two of the Ag^+ ions give the first peak of $g(r_{Ag—N})$ curve in Fig. 3*b* at a distance of 3.7 Å, which can be assigned to the silver ions, one above and one below the plane. The remaining three are found at a distance of 2.4 Å from the nitrate oxygens (Fig 3*c*). The second maximum at 4.1 Å in $g(r_{Ag—O})$ is at the distance to the other oxygens in the same nitrate or to an oxygen in a neighbouring nitrate.

Can. J. Chem. Downloaded from www.nrcresearchpress.com by 85.192.166.187 on 09/08/12
For personal use only.

Can. J. Chem. Downloaded from www.nrcresearchpress.com by 85.192.166.187 on 09/08/12
For personal use only.

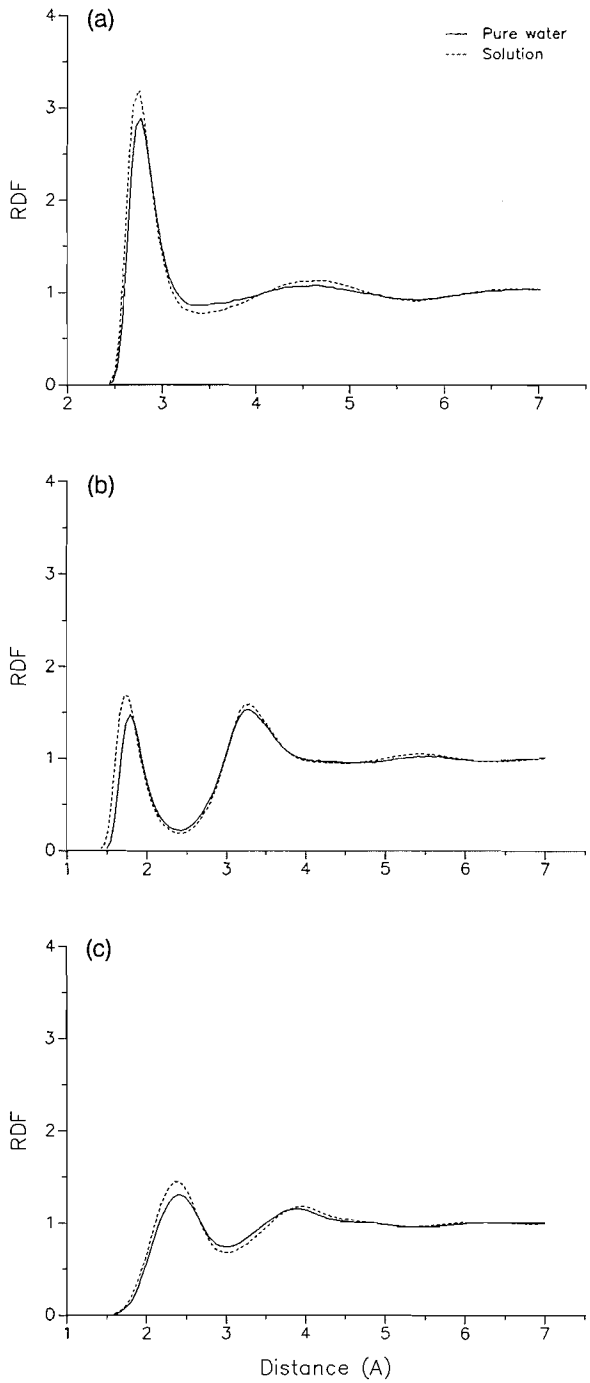

FIG. 1. Radial distribution functions for pure water and water in $AgNO_3$ solution. Oxygen–oxygen (*a*), oxygen–hydrogen (*b*) and hydrogen–hydrogen (*c*).

Figures 4*a–c* correspondingly show the structural pair correlations between the nitrate sites N—N, N—O, and O—O, respectively. In the solution there is hardly any structure to be observed between the nitrate sites, since they are strongly hydrated by the water. In the melt, all three figures show qualitatively the same features, the first peak being found between 3 and 4 Å. All the simulated ionic pair distribution functions in Figs 3 and 4 for the $AgNO_3$ melt are very similar to the ones obtained by Adya et al. (46) in their MD and X-ray work for $NaNO_3$(*k*).

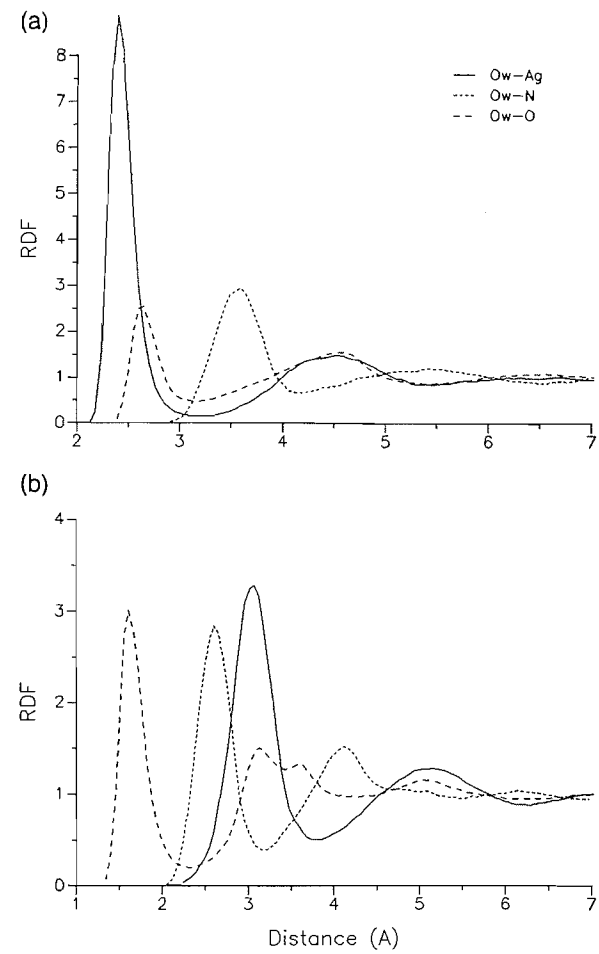

FIG. 2. Radial distribution functions between water oxygen (*a*)/ water hydrogen (*b*) and Ag, N, and O atoms, respectively.

5. Dynamic properties

5.1 Translational motion

The simulated translational diffusion coefficients for water and ions are given in Table 3. Diffusion coefficients are calculated from the translational velocity correlation times as:

$$[2] \quad D_v = \frac{kT}{M}\int_0^\infty \frac{\langle v(t)\ v(0)\rangle}{\langle v(0)\ v(0)\rangle}\,dt$$

The diffusion coefficient for pure water, 4.35×10^{-9} m^2 s^{-1}, obtained from the simulation, is close to the value of 4.4×10^{-9} m^2 s^{-1}, obtained by Teleman et al. (64) using the same water model. This value, however, is a factor of two larger than the experimental diffusion coefficient for pure water at room temperature, which is known to be a property of the SPC model.

In the presence of $AgNO_3$, the translational motion for water molecules is reduced by 20%. There is also a difference of 15° between the two simulations, the mixture simulated being carried out at the higher temperature of 315 K, thus the actual reduction should be more. According to the simulation results, both ions are more mobile in solution than in the melt, where the motion of the ions is hindered by the strong interionic interactions. In solution, the strongly hydrated Ag^+ ions (see Fig. 2) clearly follow water dynamics. At the same time, the mass effect of the hydrated ions slows down the average diffusion

Can. J. Chem. Downloaded from www.nrcresearchpress.com by 85.192.166.187 on 09/08/12
For personal use only.

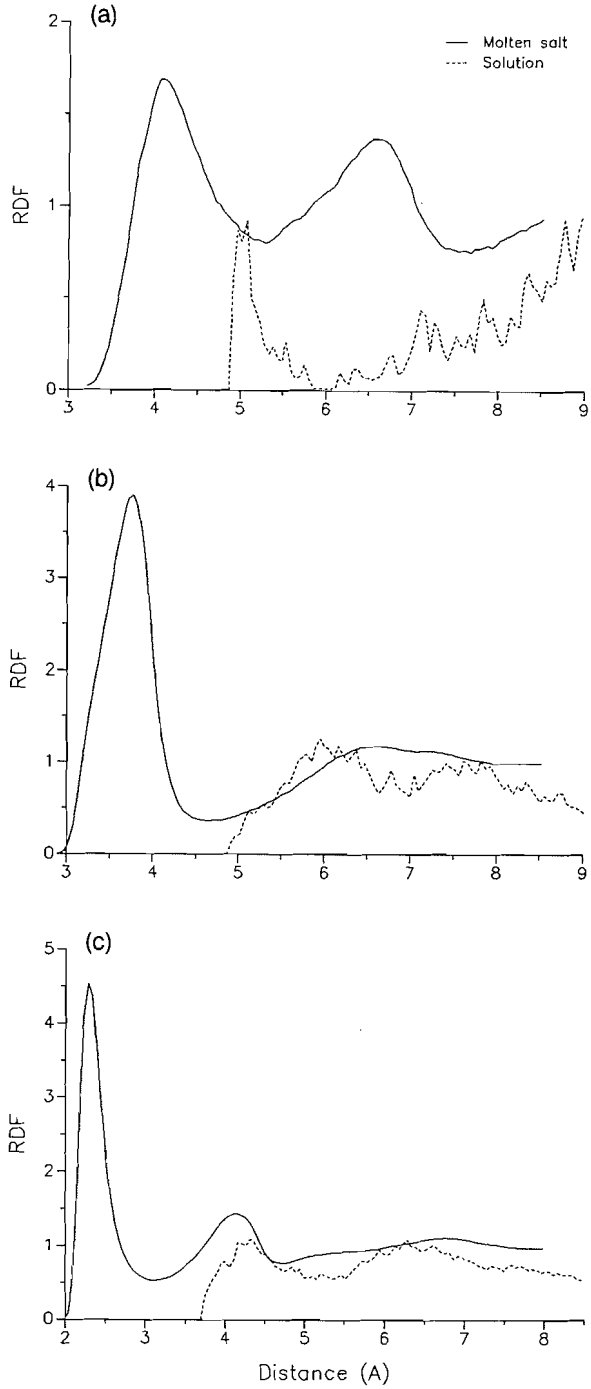

FIG. 3. Radial distribution functions $g(r_{Ag-X})$: X = Ag (*a*), X = N (middle) and X = O (*b*) in molten salt and in water solution.

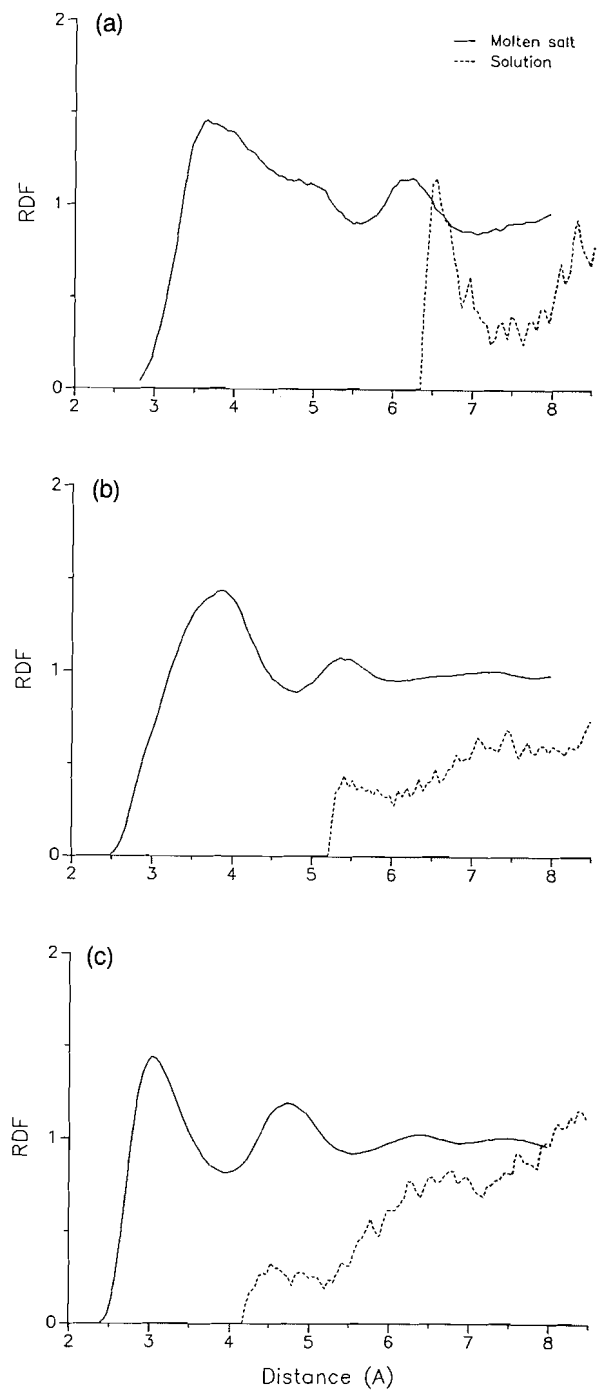

FIG. 4. Radial distribution functions: $g(r_{N-N})$ (*a*), $g(r_{N-O})$ (*b*), and $g(r_{O-O})$ (*c*) in molten salt and in water solution.

rate of the water. In the same way, the nitrate ions also follow the water dynamics, having approximately the same diffusion rate as the silver ions. The nitrates are hydrated by strong, long-living hydrogen bonds (see Fig. 2). The experimental values for the nitrate diffusion in the melt of $NaNO_3$ (1.48×10^{-9} m^2/s at 623 K) and for $LiNO_3$ (1.15×10^{-9} m^2/s at 620 K) are quoted in ref. 46 and 47, respectively. Our simulated result is 0.70×10^{-9} m^2/s at 595 K.

The velocity autocorrelation functions for (VACF) show very deep negative portions in the molten salt for both Ag^+ (Fig. 5) and NO_3^- (Figs 6*a* and *b*), which are missing in the solution curves. The anticorrelation in the VACF curves is an effect due to strong intermolecular interactions an ion or a molecule experiences in the solvation shell, making it bounce back and forth inside the cage. In solution the VACF curves show a distinct change in the decay rate after approximately 0.1 ps for the both ions, indicating a breakup of the water cage.

5.2 Rotational–reorientational motion

To study the reorientational motion of the molecules, we have placed a unit vector along the dipole axis of the water molecule and perpendicular to the molecular plane of the nitrate ion

TABLE 3. Diffusion coefficients (in 10^{-9} m^2 s^{-1})

Species	Diffusion coefficient		
	Run I	Run II	Run III
H_2O	4.35	—	3.5
Ag^+	—	0.7	2.4
NO_3^-	—	0.7	2.5

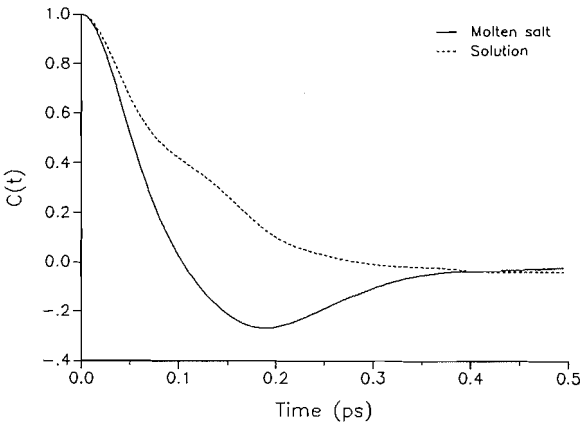

FIG. 5. Velocity autocorrelation functions for Ag^+ in molten salt and in water solution.

TABLE 4. Reorientational correlation times (in ps)

Parameter		Value		
		Run I	Run II	Run III
H_2O	τ_{10}	2.44	—	4.08
	τ_{20}	0.80	—	1.59
NO_3^- (*end-over-end*)	τ_{10}	—	15.5	6.15
	τ_{11}	—	14.5	8.50
	τ_{20}	—	5.15	1.85
	τ_{21}	—	5.00	2.10
	τ_{22}	—	5.00	3.00
NO^{3-} (*in-plane*)	τ_{10}	—	14.5	6.6
	τ_{20}	—	5.04	2.72

and calculated the normalized time correlation functions over the spherical harmonics:

$$[3] \quad C_{lm}(t) = \frac{\langle Y_{lm}(t)\ Y_{lm}(0)\rangle}{\langle Y_{lm}(0)\ Y_{lm}(0)\rangle}$$

The calculated correlation times, τ_{1m} and τ_{2m}, obtained after integrating over the area under the time correlation function $C_{lm}(t)$ in eq. [3], are gathered in Table 4.

Water: The reorientational motion of the water molecules is very much affected after dissolving the nitrate into the solution. The reorientational correlation times for water are nearly doubled, compared to the corresponding values for pure water. This is because a large part of the water molecules are involved in hydration, the rotational motion of these waters become more hindered. The reorientational motion in pure water appears to be more diffusional than in the solution. This can be seen from the ratio τ_1/τ_2, which is close to 3 in pure water while it deviates considerably from the diffusional behaviour in the solution.

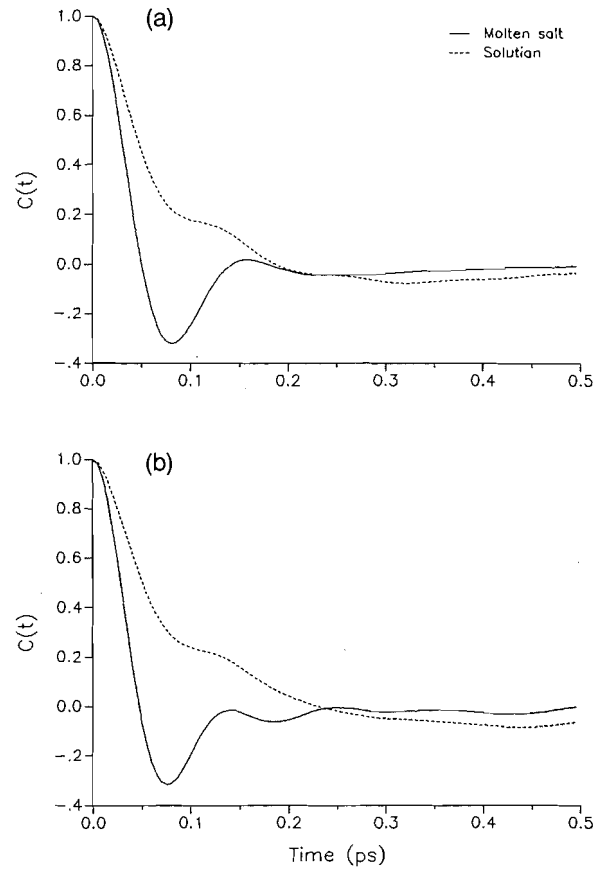

FIG. 6. Velocity autocorrelation functions for the nitrate ion in molten salt and in water solution. Parallel motion (*a*), perpendicular motion (*b*).

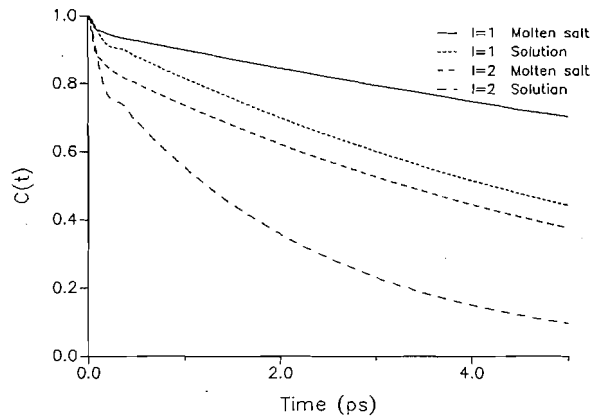

FIG. 7. Reorientational time correlation functions $C_{10}(t)$ and $C_{20}(t)$ for the nitrate ion in molten salt and in water solution.

Nitrate: The unit vector along the C_3-axis allows us to study the *end-over-end* orientations. In Fig. 7 are given normalized reorientational time correlation functions $C_{10}(t)$ and $C_{20}(t)$ for the tumbling motion of the symmetry axis both in solution and in liquid. The curves calculated from the solution data are characterized by the same behaviour typically observed in reorientational correlation functions for water. After a fast initial decay, and the rate always to indicate a pronounced librational motion because of extended hydrogen bonding. Note that this is not found in the corresponding curves from molten salt data. Fur-

Can. J. Chem. Downloaded from www.nrcresearchpress.com by 85.192.166.187 on 09/08/12
For personal use only.

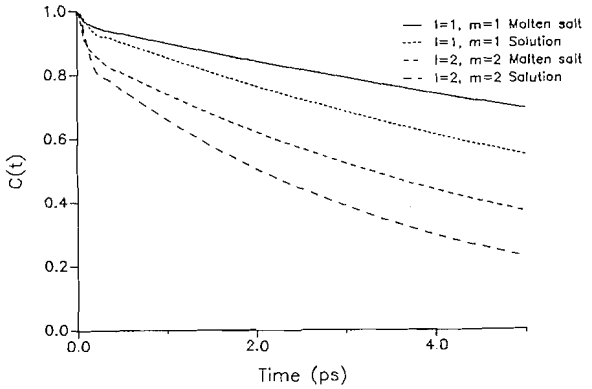

FIG. 8. Reorientational time correlation functions $C_{11}(t)$ and $C_{22}(t)$ for the nitrate ion in molten salt and in water solution.

thermore, the decay change appears at 0.1–0.2 ps, approximately the same time as the decay change for water, indicating that the librational motions of the nitrogens and the water molecules are coupled. Coupled rotation between water and nitrate in aqueous solutions in terms of a "cogwheel effect" has already been discussed by Whittle and Clarke (7) in their depolarized light scattering study of NO_3^- in water solutions. Kato et al. (6) have discussed the appearance and life time of the Gaussian initial decay in the rotational time correlation function, which was obtained from Fourier transformed Raman spectra for the reorientational motion of the symmetry axis. The initial short time behaviour ($t < 0.15$ ps) corresponds to jumps of about 17° on average. The effective moment of inertia for NO_3^- was found to be more than three times larger compared to that for a free nitrate, indicating strong water–nitrate interactions.

The nitrate ion is a symmetric top molecule. We can therefore obtain the $\tau^{(i)}10$ and $\tau^{(i)}20$ correlation times for the *in-plane* rotations using *end-over-end* correlation times τ_{1m} and the relationship (20):

$$[4] \quad \tau^{(i)}10 = \tau_{11} \text{ and } \tau^{(i)}20 = 0.25\tau_{20} + 0.75\tau_{22}$$

The reorientational time correlation functions $C_{11}(t)$ and $C_{22}(t)$ are calculated using eq. [3] and are given in Fig. 8. They have the same general behaviour as the curves in Fig. 7. The time correlation functions in Figs 7 and 8 are shown only to 5 ps, although they have been calculated up to 10 ps in the simulations.

While Raman spectra provide information on the perpendicular motion, the perpendicular mode can be studied by ^{14}N NMR and the parallel mode by ^{17}O relaxation. It can be mentioned that Nicholas and Wasylishen have reported a useful correlation between the ^{14}N and ^{17}O NMR relaxation data for the nitrate in aqueous solution (13). The reorientational motion of the nitrates and the anisotropy between the parallel and perpendicular motions have been observed to be very much dependent on the counterions present in the solution and the ion concentration (13, 14), but not so much dependent on the temperature (13). Nicholas and Wasylishen obtained a correlation time 0.94 ps for the perpendicular motion of a free nitrate (11, 13). Whittle and Clarke (7) reported a correlation time of 2.4 ps as the limiting value for the nitrate ion in aqueous solution from depolarized light scattering. Adachi et al. (15) have measured the limiting, cation-independent values by combining Raman and NMR techniques to be 1.25 and 1.9 ps for perpendicular and parallel motions, respectively, measured at 298 K in H_2O. In a subsequent study on solvent isotopic effects, the same authors report the corresponding values measured in D_2O to be 1.42 and 2.17 ps (16). Our corresponding simulated values obtained at 315 K are 1.85 and 2.72 ps. Our ^{14}N relaxation measurement for the perpendicular (*end-over-end*) motion at 315 K gives a correlation time of 1.61 ps, which is close to the simulated value. In solution or melt, the tumbling motion is more diffusive than the spinning motion, in accordance with the experimental findings based on the Lorentzian line shape obtained from Raman studies for the perpendicular mode. At high concentrations the line shape is found to become non-Lorentzian (7), an effect due to cation–anion interactions. In the melt the simulated *in-plane* correlation time is slightly shorter than the *end-over-end* correlation time. This is in agreement with the observation by Kato et al. (48) in their MD simulations of molten $LiNO_3$. For the *end-over-end* motion of nitrate ion in liquid $AgNO_3$, Kato and Takenaka reported a correlation time of 3.1 ps using Raman. Our corresponding simulated value is 5.15 ps.

Shen et al. (65) have recently calculated optimized hydrogen bond structures between a nitrate ion and a single water molecule at the SCF level using DZ + P basis sets. They found one C_{2v} complex in which one single water molecule has two simultaneous, rather bent hydrogen bonds, the energy of which was 2.6 kcal/mol lower than that in the conventional hydrogen bond. The simulated radial distribution functions (Fig. 2) do not show evidence of double hydrogen bonds. It should be remembered that the quantum mechanical calculations correspond to vacuum or low density gaseous conditions at 0 K. In aqueous solutions at room temperature the water molecule hydrogen bonded to the nitrate experiences concurrence from other water molecules in the close neighbourhood to form H bonds. Moreover, the thermal motion at finite temperature effectively decreases the lifetimes of the hydrogen bonds. In the calculations of Shen et al. (65), the water molecule in the double hydrogen bond had its HOH angle reduced to 99.3°. In the simulation, an equilibrium water geometry was used, where the HOH bond angle 104.5°. However, double hydrogen bonds are observed experimentally in several dimers and complexes and the calculations of Shen et al. clearly show how strong hydrogen bonds are between nitrate and water. Consequently the strong hydrogen bond coupling to water has a strong impact on the rotational motion of the nitrate and its unusual reversed anisotropy. More experimental and theoretical studies are needed to resolve the mechanism in detail.

Acknowledgements

This work has been supported by the Swedish Natural Science Council (NFR). AL wants to thank Professor R.E. Wasylishen for valuable discussions.

1. D.E. Irish and A.R. Davis. Can. J. Chem. **46**, 943 (1968).
2. D.E. Irish. *In* Structure of water and aqueous solutions. *Edited by* W.A.P. Luck. Verlag Chemie, Weinheim. 1974.
3. D.J. Lockwood, J. Chem. Soc. Faraday Trans. II, **71**, 1440 (1975).
4. T.J. Findley and M.C.R. Symons, J. Chem. Soc. Faraday Trans. II, **72**, 820 (1976).
5. D.W. James and R.L. Frost. Faraday Discuss. Chem. Soc. **64**, 48 (1977).
6. T. Kato, J. Umemura, and T. Takenaka. Mol. Phys. **36**, 621 (1978).
7. M. Whittle and J.H.R. Clarke. Mol. Phys. **44**, 1435 (1981).
8. R.L. Frost and D.W. James. J. Chem. Faraday Trans. II, **78**, 3223 (1982).
9. D.W. James and R.L. Frost. Aust. J. Chem. **35**, 1793 (1982).

Can. J. Chem. Downloaded from www.nrcresearchpress.com by 85.192.166.187 on 09/08/12
For personal use only.

10. M. Perrot, F. Guillame, and W.G. Rotschild. J. Phys. Chem. **87**, 5193 (1983).
11. A.M. de P. Nicholas and R.E. Wasylishen. J. Phys. Chem. **89**, 5446 (1985).
12. T. Noguchi, A. Tanaka, K. Suzuki, and Y. Taniguchi. Physica, **139&140B**, 508 (1986).
13. A.M. de P. Nicholas and R.E. Wasylishen. Can J. Chem. **65**, 951 (1987).
14. B. Rosi and M.P. Fontana. J. Chem. Phys. **87**, 6406 (1987).
15. A. Adachi, H. Kiyoyama, M. Nakahara, Y. Masuda, A. Shimizu, and Y. Taniguchi. J. Chem. Phys. **90**, 392 (1989).
16. M. Nakahara, A. Adachi, H. Kiyoyama, A. Shimizu, Y. Taniguchi, and Y. Masuda. J. Phys. Chem. **94**, 6179 (1990).
17. M. Nakahara and K. Emi. J. Chem. Phys. **99**, 5418 (1993).
18. K.T. Gillen and J.E. Griffiths. Chem. Phys. Lett. **53**, 801 (1970).
19. D.R. Bauer, G.R. Alms, J.I. Brauman, and R. Pecora. J. Chem. Phys. **61**, 2255 (1974).
20. W.A. Steele. Adv. Chem. Phys. **34**, 1 (1976).
21. G.J. Janz and D.W. James. J. Chem. Phys. **35**, 739 (1961).
22. J.K. Wilmhurst and S. Senderoff. J. Chem. Phys. **35**, 1078 (1961).
23. G.J. Janz and T.R. Kozlowski. J. Chem. Phys. **40**, 1699 (1963).
24. G.E. Walrafen and D.E. Irish. J. Chem. Phys. **41**, 911 (1964).
25. S.C. Wait Jr. and A.T. Ward. J. Chem. Phys. **44**, 448 (1966).
26. J.P. Devlin, K. Williamson, and G. Austin. J. Chem. Phys. **44**, 2203 (1966).
27. S.C. Wait Jr., A.T. Ward, and G.J. Janz. J. Chem. Phys. **45**, 133 (1966).
28. P. Li and J.P. Devlin. J. Chem. Phys. **49**, 1441 (1968).
29. D.W. James and W.H. Leong. J. Chem. Phys. **51**, 646 (1969).
30. C.A. Angell, J. Wong, and W.F. Edgell. J. Chem. Phys. **51**, 4519 (1969).
31. D.W. James and W.H. Leong. J. Chem. Faraday Trans. II, **66**, 1948 (1970).
32. J.P. Devlin, Ritzhaupt, and T. Hudson. J. Chem. Phys. **58**, 817 (1972).
33. E. Eluard, K. Balasubrahmaniam, and G.J. Janz. J. Chem. Phys. **59**, 133 (1973).
34. C.H. Huang and M.H. Brooker. Spectrochim. Acta, **32A**, 1715 (1976).
35. T. Kato, J. Umemura and T. Takenaka, Mol. Phys., **36**, 621 (1978).
36. S.A. Kirillov and W. Horlbeck. Z. Phys. Chem. **260**, 931 (1979).
37. T. Kato and T. Takenaka. Chem. Phys. Lett. **62**, 77 (1979).
38. T. Kato. Mol. Phys. **39**, 559 (1980).
39. R.E. Wasylishen. Spectrochem. Acta, **40A**, 115 (1984).
40. T. Kato and T. Takenaka. Mol. Phys. **54**, 1393 (1985).
41. R.E. Wasylishen. Can J. Chem. **64**, 115 (1984).
42. H. Ohno and K. Furukawa. J. Chem. Soc. Faraday Trans. I, **74**, 297 (1978).
43. K. Suzuki and Y. Fukushima. Z. Naturforsch. **32**A, 1438 (1977).
44. B. Holmberg and G. Johansson. Acta Chem. Scand. **A37**, 367 (1983).
45. T. Yamaguchi, T. Tamura, I. Okada, H. Ohtaki, M. Misawa, and N. Watanabe. Z. Naturforsch. **40***a*, 490 (1985).
46. A.K. Adya, R. Takagi, K. Kawamura, and M. Mikami. Mol. Phys. **62**, 227 (1987).
47. T. Kato, K. Machida, M. Oobatake, and S. Hayashi. J. Chem. Phys. **89**, 3211 (1988).
48. T. Kato, K. Machida, M. Oobatake, and S. Hayashi. J. Chem. Phys. **89**, 7471 (1988).
49. P.F. Lindley and P. Woodward. J. Chem. Soc. A, 123 (1966).
50. C.S. Gibbons and J. Trotter. J. Chem. Soc. A, 2058 (1971).
51. T.G. Chang and D.E. Irish. J. Solution Chem. **3**, 161 (1974).
52. J.E. Huheey. Inorganic chemistry. 3rd ed. Harper New York. 1983. Chap. 7.
53. A. Nordsieck. Math. Comput. **16**, 22 (1962).
54. C.W. Gear. *In* Numerical initial value problems in ordinary differential equations.' Prentice Hall, Princeton, N.J. 1971.
55. R. Sonnenschein. J. Comput. Phys. **59**, 347 (1985).
56. H.J.C. Berendsen, J.P.M. Postma, W.F. van Gunsteren, and J. Hermans. *In* Intermolecular forces. *Edited by* B. Pullman. Reidel, Dordrecht, Holland, 1981. p. 331.
57. H.A. Lorentz. Ann. Phys. **12**, 127 (1881).
58. D. Berthelot. C.R.Hebd. Seances Acad. Sci. Paris, 1703 (1898).
59. M.P. Allen and D.J. Tildesley. Computer simulations of liquids. Clarendon Press. 1987.
60. A. Laaksonen. Comput. Phys. Commun. **42**, 271 (1986).
61. W.L. Jorgensen, J. Chandrasekhar, J.D. Madura, R.W. Impey, and M.L. Klein. J. Chem. Phys. **79**, 926 (1983).
62. J. Burgess. Metal ions in solution. Wiley, New York. 1978.
63. J.C. Bailar, H.J. Emeleus, R. Nyholm, and A.F. Trotman-Dickenson. (*Editors*). Comprehensive inorganic chemistry. Vol. 3. Pergamon Press, New York. 1973. p. 104.
64. O. Teleman, B. Jönsson, and S. Engström. Mol. Phys. **60**, 193 (1987).
65. M. Shen, X. Yaoming, H.F. Schaefer III, and A.A. Deakyne. J. Chem. Phys. **93**, 3379 (1990).

Can. J. Chem. Downloaded from www.nrcresearchpress.com by 85.192.166.187 on 09/08/12
For personal use only.

Mixed alkali effect in $0.2[xKNO_3 + (1 - x)NaNO_3] + 0.8$glycerol systems

SEKH MAHIUDDIN[1]

Department of Chemistry, North Eastern Hill University, Bijni Complex, Laitumkhrah, Shillong-793003, India

Received October 25, 1993

SEKH MAHIUDDIN. Can. J. Chem. **72**, 2286 (1994).

Density, electrical conductivity, and fluidity of $0.2[xKNO_3 + (1 - x)NaNO_3] + 0.8$glycerol systems were measured as functions of temperature (363.15 to 428.15 K) and composition (0.0 to 1.0 mole fraction). Densities were linear functions of temperature. The temperature dependence of conductivity and fluidity has been analysed by using the Vogel–Tammann–Fulcher (VTF) equation. Deviation from additivity has been observed in the electrical conductivity, fluidity isotherms to a lesser extent, and in electrical conductivity under isofluidity condition. The onset of the mixed alkali effect (MAE) in the present system has been explained by the anion polarization model.

SEKH MAHIUDDIN. Can. J. Chem. **72**, 2286 (1994).

On a mesuré les densités, les conductivités électriques et les fluidités des systèmes contenant $0,2[xKNO_3 + (1 - x)NaNO_3] +$ 0,8glycérol en fonction de la température (de 363,15 à 428,15 K) et des fractions molaires (de 0,0 à 1,0). Les densités varient d'une façon linéaire avec la température. On a analysé la relation entre la température et les conductivités et les fluidités en faisant appel à l'équation de Vogel–Tammann–Fulcher (VTF). On a observé une déviation de l'additivité avec la conductivité électrique et, à un degré moindre, avec les isothermes de fluidité ainsi qu'avec la conductivité dans les conditions d'isofluidité. On explique le début de l'effet des métaux alcalins mixtes observé dans ce système en faisant appel au modèle de polarisation de l'anion.

[Traduit par la rédaction]

Introduction

When one alkali ion is replaced by another in an oxide glass and ionic melt several properties (preferably dynamic) vary as a function of composition in a highly non-additive fashion, a phenomenon usually referred to as mixed alkali effect (MAE). This phenomenon has been well documented by several authors (1–12) and is more pronounced in ionic and mass transport properties (2).

To date very few studies on the MAE using hydrate melt (6–12) as solvent have been made. Moynihan (6), in his studies using $xNaNO_3 + (0.2 - x)KNO_3 + 0.8Ca(NO_3)_2.4.09H_2O$ system failed to observe MAE in conductivity in the temperature range −5 to 70°C. But Ingram et al. (13) observed deviation in viscosity and conductivity while studying $xK_2SiO_3 + (1 - x)Na_2SiO_3 + 7H_2O$ systems in the temperature range −70 to 20°C. The observed shallow minima in conductivity and viscosity isotherms was considered an evidence for the onset of MAE. In earlier systems (9–12) containing hydrate melt as medium the MAE in fluidity and/or viscosity has been detected but to a lesser extent (ca. 4%). In all these systems MAE was found to depend on the temperature range of the study and the total alkali metal ion concentration. Moynihan (6) suggested that MAE may only be observed in systems with high viscosity and conductivity. On the other hand, based on their studies Easteal and Emson (7) suggested that MAE becomes significant when the total alkali metal ion concentration in the system is high.

Therefore, in this study we have made an attempt to find MAE by measuring the density, viscosity, and electrical conductivity of $0.2[xKNO_3 + (1 - x)NaNO_3] + 0.8$glycerol systems due to the fact that glycerol is having inherent glass-forming tendency and high viscosity.

Experimental section

Both KNO_3 and $NaNO_3$ (BDH, LR grade) were recrystallized twice from distilled water and dried over P_2O_5 in a vacuum desiccator. Glycerol (EM, reagent grade) was used as solvent. Maximum water content in glycerol was found to be <1% when the observed density value was compared with the reported value (14) at 20°C.

KNO_3 was found to be soluble up to 20 mol% at about 100°C and the composition of the system in this study was chosen to be $0.2[xKNO_3 + (1 - x)NaNO_3] + 0.8$glycerol. Accordingly six samples were prepared, keeping the total alkali ion concentration at 0.2 mole fraction. The densities of the systems were measured accurate to 0.01% by using a precalibrated single stem pyknometer. A suspended level Cannon–Ubbelhode viscometer of viscometer constant 1.243×10^{-6} $m^2 s^{-2}$ was used to measure the viscosity. Conductivity measurements (at 1 kHz) of all solutions were made by using a Philips PR9500 conductivity bridge and a dip-type cell of cell constant 198 m^{-1}. Viscosity and conductivity data were found to be reproducible to within ±1%. Density, viscosity, and electrical conductivity were measured as functions of temperature (363.15 to 428.15 K) and composition, $x = 0.0$ to 1.0 mole fraction. All measurements were made in a thermostated oil bath (Ultra Thermostat type NBE) that maintained the temperature to ±0.02 K.

Results and discussion

Measured density data (ρ) of $0.2[xKNO_3 + (1 - x)NaNO_3] +$ 0.8glycerol systems are found to be linear functions of temperature and are presented in Table 1. Composition dependence of density isotherms at four temperatures are illustrated in Fig. 1. Density data were least-squares fitted to the polynomial equation in composition up to second degree and the maximum% deviation of ρ_{obs} from ρ_{cal} was found to be 0.56%. The interesting point to note from Fig. 1 is the deviation from additivity (≃0.8%) at lower temperature (298.15 K) in the ρ vs. x plot (Fig. 1) and decreases at higher temperature and the density isotherm becomes linear at 398.15 K. Similar positive deviation from additivity (≃0.7%) in density isotherm was found in the $(1 - x)K_2O + xLi_2O + 2SiO_2$ glass systems (2) at 293.15 K.

The measured values of conductivity (κ) and fluidity ($\phi = 1/\eta$) of the systems under study are presented in Table 2 and Fig. 2 in the form of an Arrhenius plot. From Fig. 2 it is apparent that both κ and ϕ show a slight non-Arrhenius temperature dependence. Such a temperature dependence of transport properties (κ, ϕ) is an inherent nature of the concentrated electrolyte and

[1]Present address: Material Science Division, Regional Research Laboratory, Jorhat-785006, Assam, India.

[2]Revision received July 20, 1994.

Can. J. Chem. Downloaded from www.nrcresearchpress.com by 85.192.166.187 on 09/08/12
For personal use only.

TABLE 1. Least-squares fitted values of the density equation, $\rho = a - b(T - 273.15)$ for $0.2[x\mathrm{KNO_3} + (1 - x)\mathrm{NaNO_3}]$ + 0.8glycerol systems

x	$a/10^3$ kg m^{-3}	b/kg m^{-3} K^{-1}	Std. dev. in ρ
0.0	1.3750	0.6251	0.0006
0.2	1.3967	0.7688	0.0001
0.4	1.3834	0.6301	0.0001
0.6	1.3973	0.7221	0.0002
0.8	1.3865	0.6425	0.0001
1.0	1.3845	0.5520	0.0002

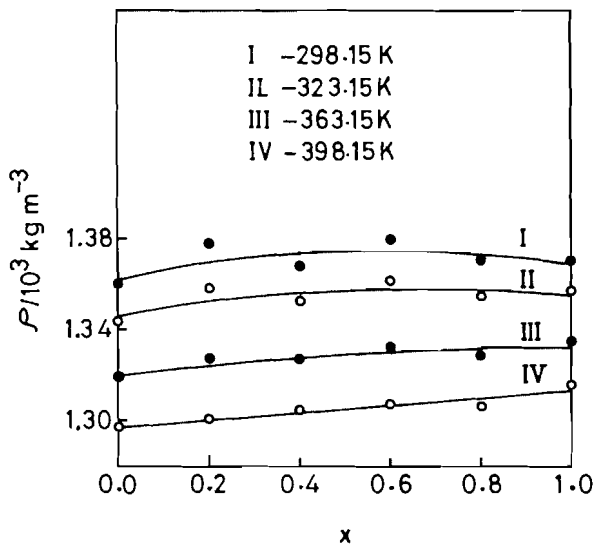

FIG. 1. Variation of density versus composition for $0.2[x\mathrm{KNO_3} + (1 - x)\mathrm{NaNO_3}]$ + 0.8glycerol systems under isothermal condition (open and closed circles represent observed values and solid curves represent values calculated (from polynomial equation up to second degree), respectively).

ionic melt systems. The conductivity and fluidity values were, therefore, least-squares fitted to the Vogel–Tammann–Fulcher (VTF) equation of the form considering the insignificant contribution of the preexponential temperature term

$$[1] \quad Y(\kappa, \phi) = A_y \exp[-B_y/(T - T_{0y})]$$

where Y refers to either conductivity or fluidity, A_y and B_y are the adjustable parameters, and T_0 is the ideal glass transition temperature. The least-squares fitted values of A_y, B_y, and T_{0y} are presented in Table 3.

A relatively high T_{0y} value has been obtained for the present system. Similarly a high value for T_0 was observed by Sangma et al. (9) and Ingram et al. (13) while investigating MAE in ternary systems. On the other hand, similar high value for T_0 was also found for binary hydrate melts (15–17).

The presence of MAE in our system has been examined by plotting T_{0y}, A_y, and B_y versus x, $x = \mathrm{K^+/(K^+ + Na^+)}$ in Fig. 3. From Fig. 3 it is evident that the T_0 values for both κ and ϕ vary non-linearly. Such a positive deviation from additivity in T_0 vs. x (Fig. 3) may be attributed to the onset of MAE in the present system.

Although non-linear variations (generally negative deviation) in experimental glass transition temperature, T_g, and in ideal glass transition temperature, T_0, with alkali ion concentration were reported for mixed alkali systems containing hydrate

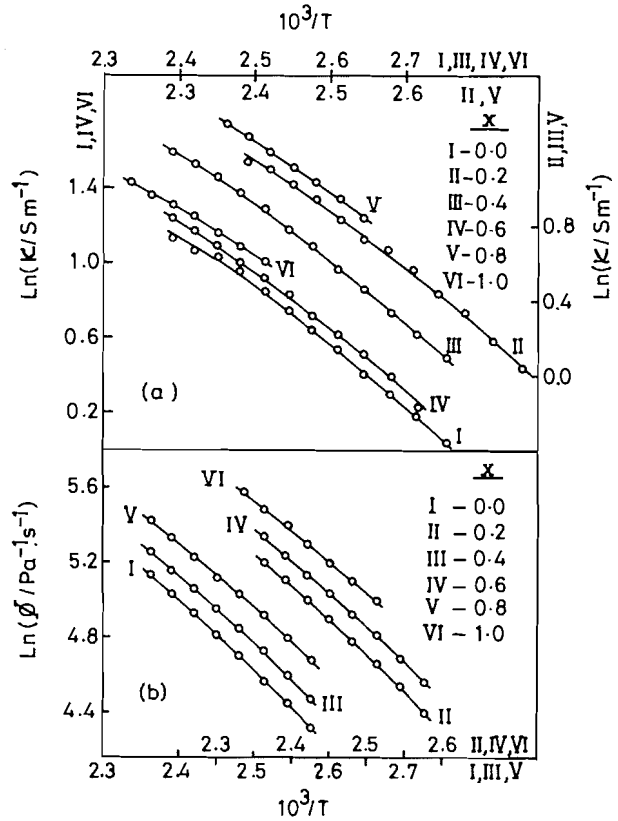

FIG. 2. Arrhenius plots for (*a*) conductivity and (*b*) fluidity of $0.2[x\mathrm{KNO_3} + (1 - x)\mathrm{NaNO_3}]$ + 0.8glycerol systems.

(6, 7, 10, 12) and anhydrous (18, 19) melts, to date no report on positive deviation in T_0 with composition in mixed alkali system has been made. On the other hand, T_0 was also reported to vary linearly with alkali ion fraction in $0.2[x\mathrm{NaNO_3} + (1 - x)\mathrm{KNO_3}] + 0.8\mathrm{Ca(NO_3)_2.4.09H_2O}$ (6), $0.3[x\mathrm{KSCN} + (1 - x)\mathrm{NaSCN}] + 0.7\mathrm{Ca(NO_3)_2.4.06H_2O}$ (9), and in $x\mathrm{K_2SiO_3} + (1 - x)\mathrm{Na_2SiO_3} + 7\mathrm{H_2O}$ (13) systems. In general, an irregular trend in T_0 vs. composition are reported for binary (15, 16) as well as ternary (9, 10) melts containing hydrated salts and in all such cases an alternative method suggested by Moynihan et al. (16) was normally adopted for data analysis. In our system, as a consequence, the positive deviation in the T_0 vs. x plot in Fig. 3 could be illusory. One of the reasons may be pointed out that in the temperature ranges of the study the conductivity and fluidity data in the present system vary by factors of 1.5 to 3 and the computed values of T_0 parameter may not be precise.

The composition dependence of A_y and B_y parameters are illustrated in Fig. 3. From Fig. 3 it is apparent that both A_y and B_y parameters vary non-linearly with negative deviation. Similar negative deviation in A vs. x plot was found in $0.3[x\mathrm{KSCN} + (1 - x)\mathrm{NaSCN}] + 0.7\mathrm{Na_2S_2O_3.5.1H_2O}$ system (11). However, we observed that the variations of the VTF parameters (A_y, B_y, and T_{0y}) with composition (9–11) are interrelated.

In mixed alkali metal ion systems in hydrate melt medium an interdependence between the three VTF parameters was recently observed (12), as represented by empirical relationships of the type

$$[2] \quad \ln A_y = A_{1y} + A_{2y}[B_y/T_{0y}]$$

$$[3] \quad 1/B_y = B_{1y} + B_{2y}T_{0y}$$

Can. J. Chem. Downloaded from www.nrcresearchpress.com by 85.192.166.187 on 09/08/12
For personal use only.

Can. J. Chem. Downloaded from www.nrcresearchpress.com by 85.192.166.187 on 09/08/12
For personal use only.

TABLE 2. Electrical conductivity and fluidity[a] data for $0.2[xKNO_3 + (1 - x)NaNO_3] + 0.8$glycerol systems

	κ/S m^{-1} and ϕ/Pa^{-1} s^{-1}					
T/K	$x = 0.0$	$x = 0.2$	$x = 0.4$	$x = 0.6$	$x = 0.8$	$x = 1.0$
363.15	1.02	1.05	1.10			
368.15	1.20	1.21	1.25	1.25		
373.15	1.36	1.40	1.40	1.48		
378.15	1.51	1.55	1.59	1.68		
383.15	1.72	1.76	1.78	1.86		
388.15	1.91	1.95	2.00	2.05		
	(75.1)	(81.8)	(87.6)	(96.2)	(108.2)	
393.15	2.10	2.08	2.18	2.30	2.32	
	(85.7)	(93.8)	(99.7)	(108.9)	(122.2)	
398.15	2.33	2.30	2.40	2.50	2.58	2.75
	(96.4)	(106.1)	(113.1)	(123.2)	(137.1)	(148.6)
403.15	2.60	2.55	2.64	2.74	2.82	2.98
	(110.3)	(119.5)	(126.9)	(137.7)	(153.4)	(164.2)
408.15	2.80	2.78	2.89	2.98	3.05	3.20
	(123.3)	(134.3)	(142.2)	(153.8)	(170.3)	(180.9)
413.15	2.90	3.00	3.10	3.22	3.31	3.50
	(138.1)	(149.3)	(157.5)	(169.9)	(187.8)	(200.4)
418.15	3.08	3.12	3.30	3.45	3.59	3.72
	(153.1)	(165.9)	(174.7)	(188.1)	(207.3)	(220.5)
423.15					3.82	4.00
	(169.6)	(182.4)	(192.8)	(207.8)	(227.0)	(241.3)
428.15						4.20
						(265.8)

[a]Fluidity data in parentheses.

TABLE 3. Least-squares fitted values of the parameters of eq [1] for conductivity (S m^{-1}) and fluidity (Pa^{-1} s^{-1}) for $0.2[xKNO_3 + (1 - x)NaNO_3] + 0.8$glycerol systems[a]

x	$A_\kappa/10^2$ S m^{-1} $A_\phi/10^3$ Pa^{-1} s^{-1}	B_y/K	T_{0y}/K	Std. dev. in ln Y
0.0	0.5951 ± 0.48	725.7 ± 140	180.4 ± 9	0.089
	(25.59 ± 3.2)	(1252.9 ± 340)	(173.4 ± 7)	(0.004)
0.2	0.3142 ± 0.08	389.2 ± 40	248.6 ± 8	0.013
	(9.92 ± 1.4)	(836.1 ± 191)	(213.9 ± 9)	(0.001)
0.4	0.3890 ± 0.1	387.4 ± 38	250.0 ± 8	0.012
	(12.97 ± 1.4)	(935.1 ± 203)	(201.1 ± 9)	(0.002)
0.6	0.2994 ± 0.04	342.3 ± 30	259.9 ± 5	0.009
	(20.43 ± 2.4)	(1121.5 ± 349)	(178.9 ± 9)	(0.002)
0.8	0.2887 ± 0.1	408.8 ± 70	224.4 ± 9	0.049
	(13.93 ± 1.4)	(944.7 ± 151)	(193.7 ± 7)	(0.001)
1.0	0.3088 ± 0.15	512.4 ± 80	170.8 ± 9	0.094
	(32.35 ± 8.9)	(1337.3 ± 470)	(150.0 ± 8)	(0.005)

[a]Value of parameter for fluidity in parentheses.

where A_{1y}, A_{2y}, B_{1y}, and B_{2y} are all empirical constants. The above empirical relationships between A_y, B_y, and T_{0y} are found to hold reasonably well in the present system as is evident from Fig. 4. The validity of such empirical relationships actually indicates that the composition dependence of the T_{0y} parameter alone can fully govern the composition dependence of transport properties of mixed alkali metal ion system in a hydrate melt medium.

An attempt has been made to describe the observed nature of the composition dependence of both κ and ϕ on x (Fig. 5) by least-squares fitting the κ and ϕ data for the present system to an empirical equation of the form

$$[4] \quad Y(\kappa, \phi) = a_y \exp(b_y x + c_y x^2)$$

where a_y, b_y, and c_y are empirical constants. Equation [4] was successfully used by Sangma et al. (9) to explain the composition dependence of observed conductivity and/or fluidity data for $0.3[xKSCN + (1 - x)NaSCN] + 0.7Ca(NO_3)_2.4.06H_2O$, and the reported data for $xK_2O + (1 - x)Na_2O + 3SiO_2$ (6) and $0.45[xLiNO_3 + (1 - x)KNO_3] + 0.55Ca(NO_3)_2.4.09H_2O$ (8) systems and a reasonably good fit was obtained. The least-squares fitted values of the parameters of eq. [4] for the conductivity and fluidity for the present system are given in Table 4. A reasonably good fit has been obtained as is apparent from Fig.

Can. J. Chem. Downloaded from www.nrcresearchpress.com by 85.192.166.187 on 09/08/12
For personal use only.

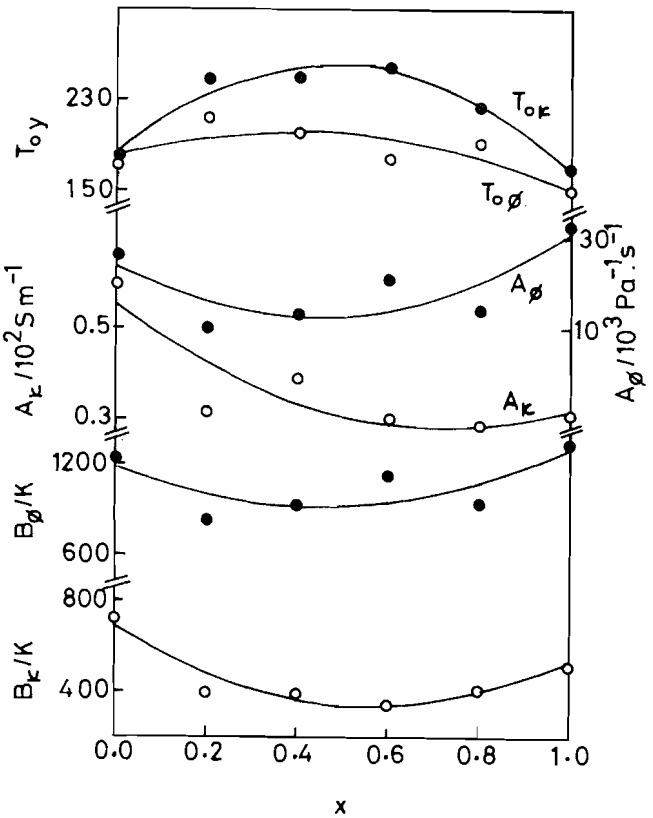

FIG. 3. Variation of T_{0y}, A_y, and B_y with composition for $0.2[x\mathrm{KNO_3} + (1 - x)\mathrm{NaNO_3}] + 0.8$glycerol systems.

TABLE 4. Least-squares fitted values of the parameters of eq. [4] for conductivity (S m^{-1}) and fluidity (Pa^{-1} s^{-1}) of $0.2[x\mathrm{KNO_3} + (1 - x)\mathrm{NaNO_3}] + 0.8$glycerol systems[a]

T/K	ln a_y	b_y	c_y	Std. dev. in ln Y
398.15	0.8385	0.0218	0.1516	0.011
	(4.5729)	(0.3886)	(0.0426)	(0.010)
408.15	1.0236	0.0442	0.0953	0.009
	(4.8170)	(0.3628)	(0.0239)	(0.011)
418.15	1.1167	0.1798	0.0215	0.010
	(5.0341)	(0.3268)	(0.0398)	(0.010)

[a]Parameters for fluidity in parentheses.

5. It is evident form Fig. 5 that in the temperature range of the study κ exhibits negative deviation from additivity whereas ϕ shows slightly narrow deviation from additivity. The maximum deviation from additivity was estimated to be ≃4% for conductivity and ≃3.5% in the case of fluidity at 398.15 K which is more than the uncertainty involved in the measured data. The deviation from additivity both in κ and ϕ isotherms decreases at higher temperatures.

In mixed alkali systems containing Na^+ and K^+ ions in hydrate melt medium the maximum negative deviation was found to be ≃4% (9, 12) at 328 K. On the other hand, about 11% negative deviation from additivity was reported in the similar mixed alkali system containing Li^+ and K^+ ions (8). One of the key parameters for the significant MAE may be attributable to the large difference in the radii of the alkali ions in addition to the low temperature study and the higher alkali ion concentration in the mixed alkali systems. The small amount of MAE in

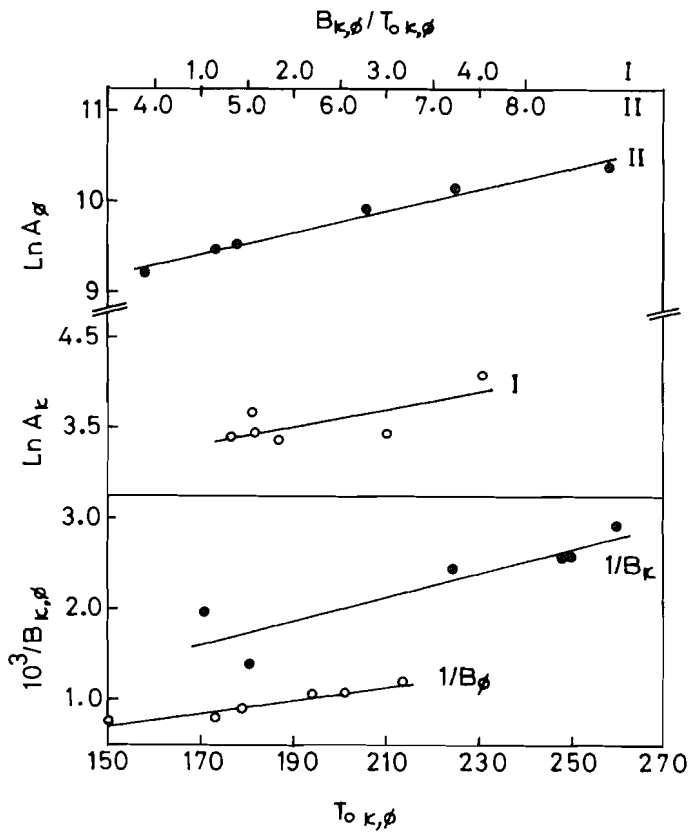

FIG. 4. Plots of ln $A_{\kappa,\phi}$ vs. $B_{\kappa,\phi}/T_{0\kappa,\phi}$ and $1/B_{\kappa,\phi}$ vs. $T_{0\kappa,\phi}$ for $0.2[x\mathrm{KNO_3} + (1 - x)\mathrm{NaNO_3}] + 0.8$glycerol systems (open and closed circles represent observed values and solid lines represent values calculated (from eqs. [2] and [3]), respectively).

the present systems (≃4% negative deviation in κ and ϕ isotherms) may be due to the type of alkali ions (Na^+–K^+) present with $\Delta F = 0.04$ (ΔF is the difference in field strength) (20) in comparison to $\Delta F = 0.10$–0.14 for Li^+–K^+ ion (where maximum deviation of 11% was found (8)) resulted in non-rigid type structure in the present system.

According to the idea of solid-like conduction mechanism proposed by Moynihan (6) the structure of the mixed alkali system must be fixed. Therefore, based on the above argument isofluidity condition may be one of the important criteria to detect MAE in the electrical conductivity. Variation of κ with composition at different fluidity values are illustrated in Fig. 6. Electrical conductivity values at constant fluidity both within and outside the experimental ranges of fluidity required were calculated using eq. [1] and the least-squares fitted values of A_y, B_y, and T_{0y} parameters (Table 3). From Fig. 6 it is apparent that the percentage deviation from additivity in conductivity at low fluidity is higher, decreasing in value at higher fluidities, and becoming almost linear at $\phi = 100$ Pa^{-1} s^{-1}. Moynihan (6) suggested that the largest apparent deviation from linearity under low fluidity condition is due to the long time scale for the rearrangement of the local structure compared to that required for local diffusion of alkali cations from site to site. Similar explanation may also be used on the present system.

Several theories and model (21–24) have been proposed to account for the onset of MAE in ternary oxide glass and hydrate melt. The cation interaction theory seems to be more appropriate for the system not having such a rigid-network type structure. The anion polarization model (APM) proposed by

Can. J. Chem. Downloaded from www.nrcresearchpress.com by 85.192.166.187 on 09/08/12
For personal use only.

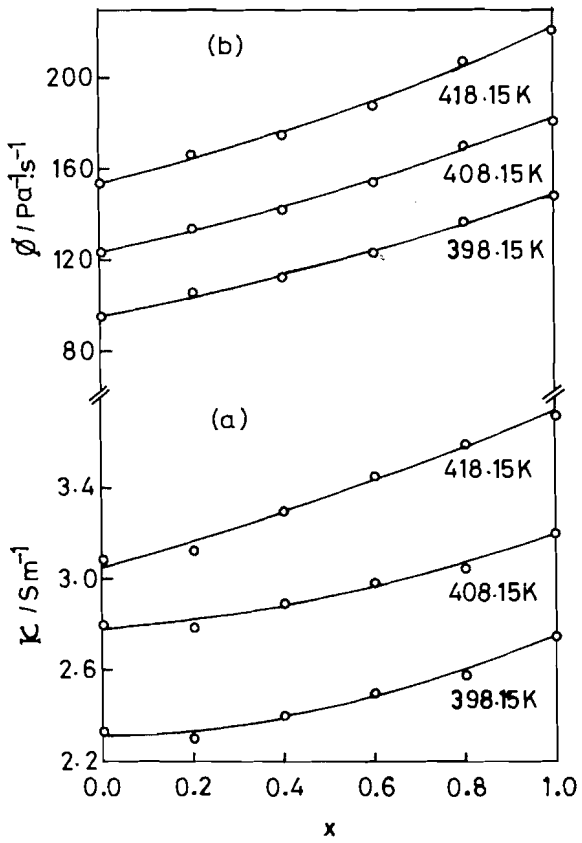

FIG. 5. Plots of (*a*) conductivity and (*b*) fluidity versus composition for $0.2[xKNO_3 + (1 - x)NaNO_3] + 0.8$glycerol systems under isothermal condition (open circles and solid curves represent observed and calculated values (from eq. [4], Table 4), respectively).

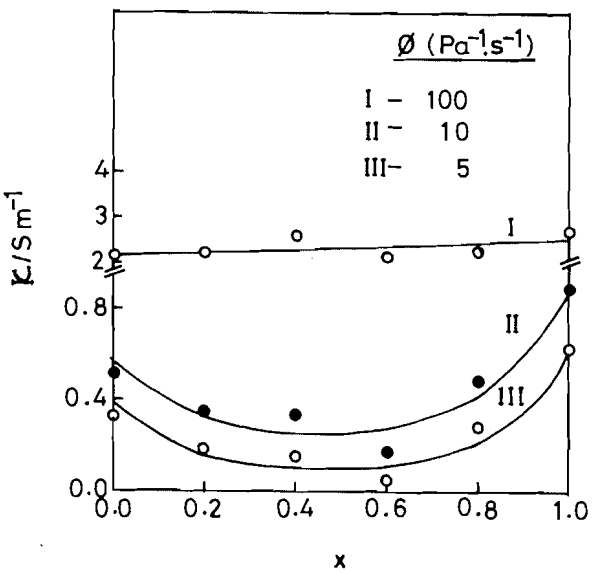

FIG. 6. Plots of conductivity versus composition under isofluidity condition (open and closed circles represent observed values and solid lines represent values calculated (from eq. [4]), respectively).

Moynihan and Laity (22, 25) is one such cation interaction theory. The APM has been used earlier to explain MAE on the electrical conductivity in hydrate melt medium (8, 10). The APM may, therefore, also be used to explain MAE in electrical conductivity and fluidity in a glycerol medium. According to this model, the NO_3^- ion experiences an average symmetrical field when the glycerol medium contains either $NaNO_3$ or KNO_3. On the other hand, when the medium contains both Na^+ and K^+ ions, some of the NO_3^+ ions find themselves between electrical fields of differing intensities. This results in a competitive polarization of the anion and generates an asymmetric electrical field around NO_3^-, causing the NO_3^- ion to be more polarized towards the Na^+ ion. As a result, the internal mobilities of Na^+ and K^+ ions are affected, thereby causing a net deviation from additivity.

Acknowledgements

The financial assistance from North Eastern Hill University, Shillong, India, is gratefully acknowledged. The author also thanks Dr. K. Ismail, Department of Chemistry, NEHU, Shillong and RRL, Jorhat, India for providing the necessary experimental and computational facilities.

1. J.O. Isard. J. Non-Cryst. Solids, **1**, 295 (1969).
2. D.E. Day. J. Non-Cryst. Solids, **21**, 343 (1976) and references therein.
3. R.M. Hakim and D.R. Uhlmann. Phys. Chem. Glasses, **8**, 174 (1976).
4. H.M. van Ass and J.N. Stevels. J. Non-Cryst. Solids, **14**, 131 (1974); **15**, 215 (1974); **16**, 46 (1974).
5. A.K. Varshneya. J. Am. Ceram. Soc. **57**, 37 (1974).
6. C.T. Moynihan. J. Electrochem. Soc. **126**, 2144 (1979).
7. A.J. Easteal and M.C. Emson. J. Phys. Chem. **84**, 3330 (1980).
8. A.J. Easteal. Aust. J. Chem. **34**, 1853 (1981).
9. P. Sangma, S. Mahiuddin, and K. Ismail. J. Phys. Chem. **88**, 2378 (1984).
10. S.S. Islam and K. Ismail. Can. J. Chem. **66**, 242 (1988).
11. S.S. Islam and K. Ismail. J. Chem. Eng. Data, **33**, 472 (1988).
12. S.S. Islam and K. Ismail. J. Chem. Eng. Data, **35**, 348 (1990).
13. M.D. Ingram, K. King, D. Kranbuehl, and M. Adel-Hadadi. J. Phys. Chem. **85**, 289 (1981).
14. J.A. Dean. Lange's handbook of chemistry. 13th ed. *Edited by* J.A. Dean. McGraw Hill, New York. 1985. pp. 10–97.
15. N. Islam and K. Ismail. J. Phys. Chem. **79**, 2180 (1975).
16. C.T. Moynihan, C.R. Smalley, C.A. Angell, and E.J. Sare. J. Phys. Chem. **73**, 2287 (1969).
17. K.V. Ramana, R.C. Sharma, and H.C. Gaur. J. Chem. Eng. Data, **35**, 293 (1990).
18. C.T. Moynihan, A.J. Easteal, D.C. Tran, J.A. Wilder, and E.P. Donovan. J. Am. Ceram. Soc. **59**, 137 (1976).
19. C.M. Kuppinger and J.E. Shelby. J. Am. Ceram. Soc. **68**, 463 (1985).
20. A.H. Dietzel. Phys. Chem. Glasses, **24**, 172 (1983).
21. C.T. Moynihan, N.S. Saad, D.C. Tran, and A.V. Lesikar. J. Am. Ceram. Soc. **63**, 458 (1980).
22. C.T. Moynihan and R.W. Laity. J. Phys. Chem. **68**, 3312 (1964).
23. O.V. Mazurin. *In* Structure of glass. Vol. 4. *Edited by* O.V. Mazurin. Consultants Bureau, New York. 1965. pp. 5–55.
24. J.R. Hendrickson and P.J. Bray. Phys. Chem. Glasses, **13**, 43 (1972).
25. C.T. Moynihan. *In* Ionic interactions. Vol. 1. *Edited by* S. Petrucci. Academic Press, New York. 1971. p. 261.

Photochemical nucleophile–olefin combination, aromatic substitution (photo-NOCAS) reaction. Part 7: methanol, conjugated dienes, and 1,4-dicyanobenzene[1]

KIMBERLY A. MCMANUS AND DONALD R. ARNOLD[2]

Department of Chemistry, Dalhousie University, Halifax, NS B3H 4J3, Canada

Received May 24, 1994

KIMBERLY A. MCMANUS and DONALD R. ARNOLD. Can. J. Chem. **72**, 2291 (1994).

The scope of the photochemical nucleophile–olefin combination, aromatic substitution (photo-NOCAS) reaction has been extended to include conjugated dienes: 1,3-butadiene (**9**), 2-methyl-1,3-butadiene (**10**), 2,3-dimethyl-1,3-butadiene (**11**), and 2,5-dimethyl-2,4-hexadiene (**12**). Acetonitrile–methanol solutions of the dienes **9**, **10**, and **11**, and 1,4-dicyanobenzene (**1**), with and without codonor (biphenyl (**5**)), were irradiated with a medium-pressure mercury vapour lamp through Pyrex. Both 1,2- and 1,4-addition products were formed in approximately equal amounts (combined yields of photo-NOCAS products, 50–65%). In marked contrast, when an acetonitrile–methanol solution of 2,5-dimethyl-2,4-hexadiene (**12**), **1**, and **5** was irradiated, only the 1,4-addition product, *trans*-2-(4-cyanophenyl)-5-methoxy-2,5-dimethyl-3-hexene (**22**, 82%), was obtained. This photolysate also contained a small amount of another 1,4-addition product, that which had incorporated cyanide ion instead of methanol, *trans*-2-(4-cyanophenyl)-2,2,5-trimethyl-3-hexenenitrile (**23**, 2%). Irradiation of an acetonitrile solution (no methanol) of **12**, **1**, and **5** gave **23** in good yield (68%). An excellent yield (80%) of **23** was obtained upon irradiation of an acetonitrile solution of **1**, **12**, **5**, potassium cyanide, and 18-crown-6. Addition of 2,4,6-trimethylpyridine (collidine, **25**), a mild, non-nucleophilic base, to the reaction mixture diverts the reaction involving **12** from photo-NOCAS products to 1:1 substitution products; 3-(4-cyanophenyl)-2,5-dimethyl-1,4-hexadiene (**26**), *trans*-5-(4-cyanophenyl)-2,5-dimethyl-1,3-hexadiene (**27**), (*Z*)-1-(4-cyanophenyl)-2,5-dimethyl-2,4-hexadiene (**28**), and (*E*)-1-(4-cyanophenyl-2,5-dimethyl-2,4-hexadiene (**29**) were formed. The mechanisms of these reactions are discussed and an explanation for the observed regio- and stereoselectivity is given.

KIMBERLY A. MCMANUS et DONALD R. ARNOLD. Can. J. Chem. **72**, 2291 (1994).

On a élargi le domaine d'application de la combinaison photochimique nucléophile–oléfine, la réaction de substitution aromatique photo-NOCAS, de façon à inclure les dienes conjugués suivants : buta-1,3-diène (**9**), 2-méthylbuta-1,3-diène (**10**), 2,3-diméthylbuta-1,3-diène (**11**) et 2,5-diméthylbuta-1,3-diène (**12**). On a soumis des solutions acétonitrile–méthanol des dienes **9**, **10** et **11** avec le 1,4-dicyanobenzène (**1**), avec ou sans codonneur (biphényle **5**), avec une lampe à vapeur de mercure à pression moyenne à travers du Pyrex. Les produits d'additions 1,2 et 1,4 se forment en quantités approximativement égales (rendements combinés des produits de photo-NOCAS, 50–65%). Par ailleurs, lorsqu'on irradie une solution acétonitrile–méthanol du 2,5-diméthylbuta-1,3-diène (**12**) avec les composés **1** et **5**, il ne se forme que du produit d'addition 1,4, le *trans*-2-(4-cyanophényl)-5-méthoxy-2,5-diméthylhex-3-ène (**22**, 82%). Ce photolysat contenait aussi une faible quantité d'un autre produit d'addition 1,4, celui qui incorpore un ion cyanure à la place du méthanol, le *trans*-2-(4-cyanophényl)-2,2,5-triméthylhex-3-ènenitrile (**23**, 2%). Une irradiation d'une solution des composés **12**, **1** et **5** dans l'acétonitrile (sans méthanol) fournit le produit **23** avec un bon rendement (68%). On obtient un excellent rendement (80%) du produit **23** par irradiation d'une solution dans l'acétonitrile des composés **1**, **12**, **5**, avec du cyanure de potassium et de la 18-couronne-6. L'addition au mélange réactionnel de 2,4,6-triméthylpyridine (collidine, **25**), une base non nucléophile douce, empêche la réaction du composé **12** pour donner des produits de photo-NOCAS et provoque plutôt la formation des produits de substitution 1 : 1 suivants : 3-(4-cyanophényl)2,5-diméthylhexa-1,4-diène (**26**), *trans*-5-(4-cyanophényl)-2,5-diméthylhexa-1,3-diène (**27**), (*Z*)-1-(4-cyanophényl)-2,5-diméthylhexa-2,4-diène (**28**) et (*E*)-1-(4-cyanophényl)-2,5-diméthylhexa-2,4-diène (**29**). On discute des mécanismes de ces réactions et on propose une explication pour les régio- et stéréo-sélectivités observées.

[Traduit par la rédaction]

Introduction

Among the first examples of the photochemical nucleophile–olefine combination, aromatic substitution (photo-NOCAS) reaction were the combination of methanol, 2,3-dimethyl-2-butene (**2**), and 1,4-dicyanobenzene (1) (reaction [1]); and the combination of methanol, 2-methylpropene (**6**), and 1,4-dicyanobenzene (**1**) (reaction [2]) (3*a*, 3*b*). These are synthetically useful processes that provide a single-step pathway to alkylation of an aromatic, with formation of a difunctional molecule.

A mechanism for the photo-NOCAS reaction has been proposed and supported (Scheme 1) (1, 3). The reaction is initiated by photo-induced single electron transfer to the singlet excited state of 1,4-dicyanobenzene (**1**) from the olefin (Scheme 1; steps 1 and 2). The resulting olefin radical cation is attacked by methanol, giving a β-alkoxy alkyl radical (step 3). This radical can either couple with the 1,4-dicyanobenzene radical anion ($\mathbf{1}^{-\cdot}$) at the *ipso* position (step 4) or the radical may be reduced to the anion by the radical anion (step 4a). Subsequent protonation of the anion leads to ethers. Formation of ethers by this mechanism is the usual result with phenyl-substituted olefins (3*c*, 3*d*). Phenyl substitution lowers the reduction potential of the radical so that reduction by the radical anion ($\mathbf{1}^{-\cdot}$) is favourable. Ethers may also result from disproportionation of the β-alkoxy alkyl radical.

Addition of an electron transfer photosensitizer (e.g., phenanthrene (**4**)) or a codonor (e.g., biphenyl (**5**)) has been shown to increase the efficiency of the reaction (Scheme 1; steps 6 and 7) (1, 3). Addition of a photosensitizer (electron transfer) to the reaction mixture can increase the efficiency of the reaction simply by absorbing more light. The excited singlet state of the photosensitizer (electron transfer), phenanthrene (**4**), can donate an electron to 1,4-dicyanobenzene (**1**) to give the photosensitizer radical cation and 1,4-dicyanobenzene radical anion. The photosensitizer radical cation may then oxidize the olefin (steps 6b, 6c, and 7). The explanation we favour for the

[1]This is also Part 33 of the series Radical Ions in Photochemistry; see refs. 1 and 2 for preceding parts of these series.

[2]Author to whom correspondence may be addressed. Telephone: (902) 494-3714. Fax: (902) 494-1310. e-mail: arnold@ac.dal.ca

Can. J. Chem. Downloaded from www.nrcresearchpress.com by 85.192.166.187 on 09/08/12
For personal use only.

Can. J. Chem. Downloaded from www.nrcresearchpress.com by 85.192.166.187 on 09/08/12
For personal use only.

Reaction [1] (3)

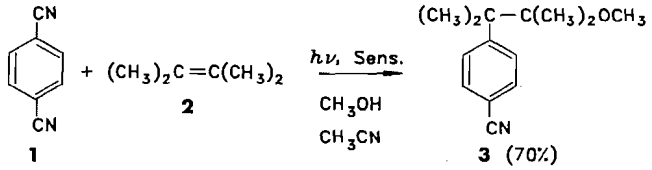

Sens. (photosensitizer) = phenanthrene (**4**)

Reaction [2] (3)

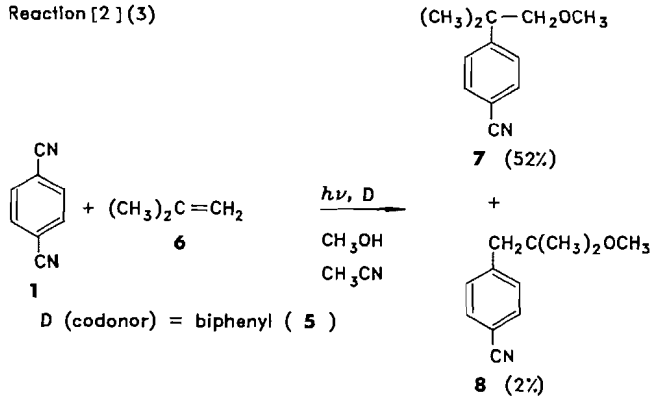

D (codonor) = biphenyl (**5**)

Mechanism for formation of photo-NOCAS products

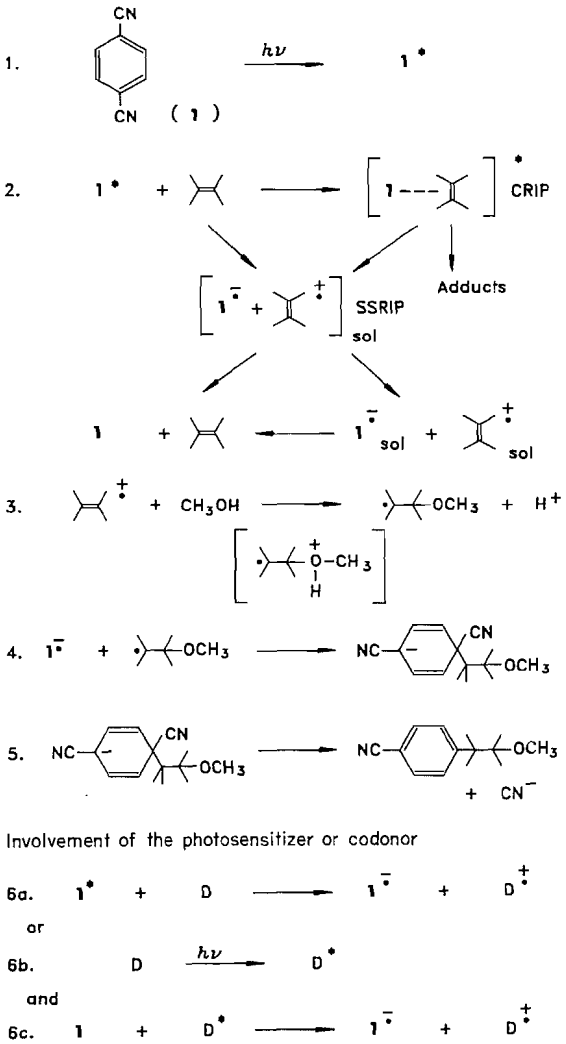

Involvement of the photosensitizer or codonor

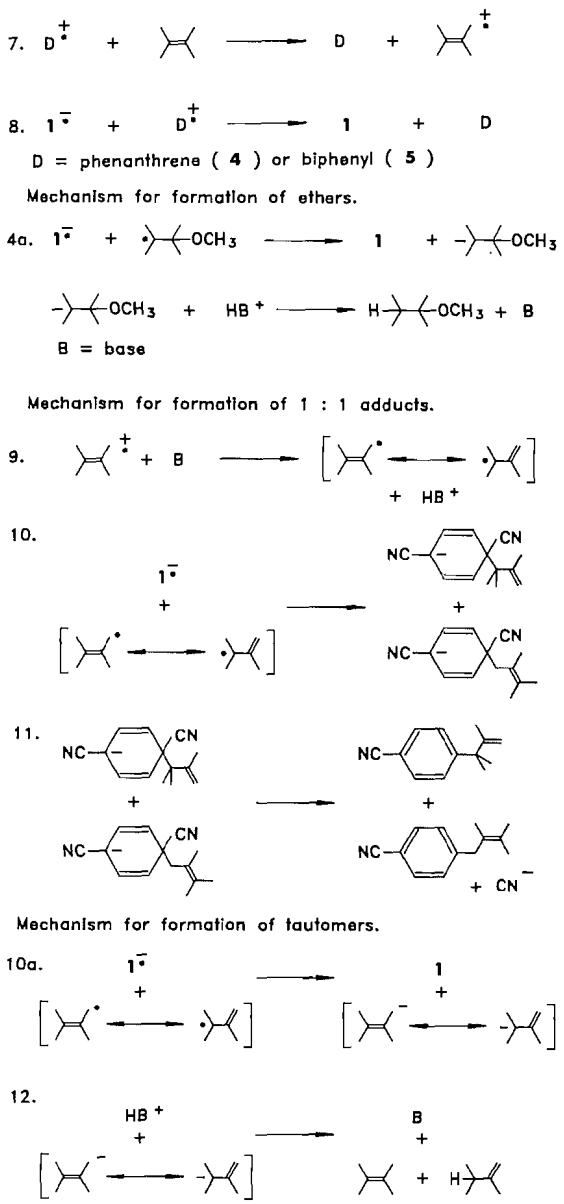

SCHEME 1

effect of added codonor involves differences in the efficiency of radical ion pair escape for the olefin–1,4-dicyanobenzene radical ion pair compared to the codonor–1,4-dicyanobenzene radical ion pair. The reorganization energy is thought to be larger for the olefin–1,4-dicyanobenzene radical ion pair than for the codonor–1,4-dicyanobenzene radical ion pair. The smaller reorganization energy leads to a decrease in the rate of back electron transfer and, thus, greater escape from the solvent cage and a consequent increase in the efficiency of the reaction (Scheme 1; steps 2 and 8) (4).

Deprotonation of the radical cation of the olefin may compete with reaction with nucleophile (Scheme 1, step 9) (3). Deprotonation may in fact dominate in the absence of nucleophile (methanol) (3). The resulting allylic radical may then couple with the 1,4-dicyanobenzene (**1**) radical anion at the *ipso* position (step 10), followed by loss of the cyanide anion, to give the 1:1 (olefin:aromatic) substitution product(s) (step 11). If, however, the reduction potential of the allylic radical is less (i.e., less negative) than that of 1,4-dicyanobenzene, the radical

Can. J. Chem. Downloaded from www.nrcresearchpress.com by 85.192.166.187 on 09/08/12
For personal use only.

may be reduced (step 10a); subsequent protonation of the ambident anion will then give the tautomer (step 12) (*3e*, *3f*).

Several olefins have been examined under these varying reaction conditions and the regio- and stereoselectivity of the photo-NOCAS reaction has been defined (1, 3). Recent studies, which have focused on the reactivity of nonconjugated dienes, have provided additional insight into the mechanism (*1a*). The scope of the photo-NOCAS reaction has now been extended to include conjugated dienes, providing a simple procedure for the direct allylic alkylation of the aromatic. The proposed mechanism has been confirmed and expanded. There have been few reports of the reactivity of the radical cations of these dienes (5–9). This work has provided additional insight into the regio- and stereoselectivity of these reactions.

Results

The conjugated dienes chosen for study were the 1,3-butadiene homologues: 1,3-butadiene (**9**), 2-methyl-1,3-butadiene (**10**), 2,3-dimethyl-1,3-butadiene (**11**), and 2,5-dimethyl-2,4-hexadiene (**12**). Acetonitrile–methanol (3:1) solutions of 1,4-dicyanobenzene (**1**) and the conjugated diene were irradiated with a medium-pressure mercury vapour lamp through Pyrex. The products were 1:1:1 (methanol:diene:**1**) photo-NOCAS adducts.

The progress of the reaction was monitored by capillary column gas chromatography with a flame ionization detector (gc/fid). The first indication of the structure of the products was obtained from a gas chromatograph equipped with a mass selective detector (gc/ms). The photo-NOCAS products were generally isolated by medium-pressure liquid chromatography (mplc). The yields were based upon 1,4-dicyanobenzene (**1**) as the limiting reagent; the diene was generally present in excess. In cases where the photo-NOCAS adducts were difficult to separate, a total weight of the combined products was obtained, and the ratio(s) of the isomers was determined by gc/fid. Usually the ratio of products was not dependent upon the extent of conversion, these ratios remaining constant during the irradiation. The exception was reaction [6] where the ratio of products was dependent upon irradiation time. Yields and product ratios, shown in the illustrations, are for reactions taken to complete conversion of **1**. Structural assignments of the products were based primarily upon detailed analysis of ^{1}H and ^{13}C nmr spectra.

An acetontrile–methanol (3:1) solution of 1,3-butadiene (**9**), 1,4-dicyanobenzene (**1**), and biphenyl (**5**) was irradiated; 3-(4-cyanophenyl)-4-methoxy-1-butene (**13**, 35%) and *trans*-1-(4-cyanophenyl)-4-methoxy-2-butene (**14**, 30%) were isolated (reaction [3]). Compound **13** is a 1,2-addition product, whereas compound **14** results from 1,4-addition. The *cis* isomer of **14** was not detected.

Four photo-NOCAS adducts were produced upon irradiation of a solution of 2-methyl-1,3-butadiene (**10**), **1**, and **5** in acetonitrile–methanol (3:1). The structures and yields of these products were as follows: 3-(4-cyanophenyl)-4-methoxy-3-methyl-1-butene (**15**, 20%), 3-(4-cyanophenyl)-4-methoxy-2-methyl-1-butene (**16**, 6%), (*E*)-4-(4-cyanophenyl)-1-methoxy-2-methyl-2-butene (**17**, 26%), and (*Z*)-4-(4-cyanophenyl)-1-methoxy-2-methyl-2-butene (**18**, 3%) (reaction [4]). Isomers **15** and **16** are 1,2-addition products. Isomers **17** and **18** are the result of 1,4 addition and their combined yield makes this the major mode of addition. The *E* isomer, **17**, is dominant. Both

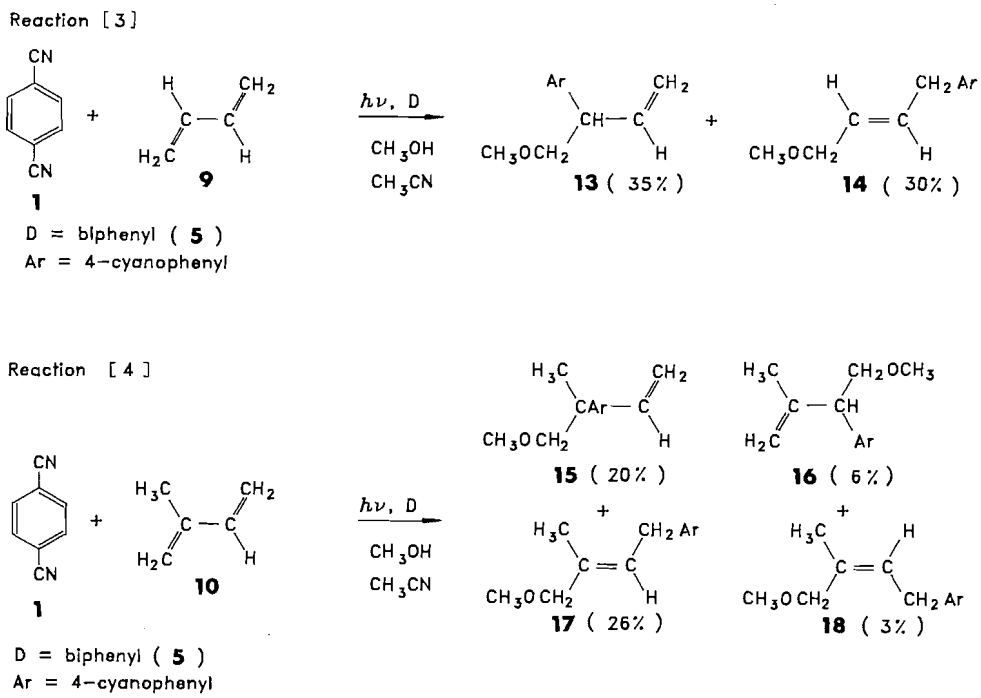

major products, **15** and **17**, are the result of initial addition of the nucleophile (methanol) to the terminal end of the more highly substituted double bond.

A solution of 2,3-dimethyl-1,3-butadiene (**11**), **1**, and **5** in acetonitrile–methanol (3:1) was irradiated. Three major photo-NOCAS adducts were formed: (3-(4-cyanophenyl)-4-methoxy-2,3-dimethyl-1-butene (**19**, 30%), (*E*)-1-(4-cyanophenyl)-4-methoxy-2,3-dimethyl-2-butene (**20**, 15%), and (*Z*)-1-(4-cyanophenyl)-4-methoxy-2,3-dimethyl-2-butene (**21**, 8%) (reaction [5]). In this case the 1,2-addition product (**19**) was the major adduct; 1,2 addition (30%) is favoured over 1,4 addition (23%).

An acetonitrile–methanol (3:1) solution of 2,5-dimethyl-2,4-hexadiene (**12**), **1**, and **5** was irradiated to give two photo-

Can. J. Chem. Downloaded from www.nrcresearchpress.com by 85.192.166.187 on 09/08/12
For personal use only.

Reaction [5]

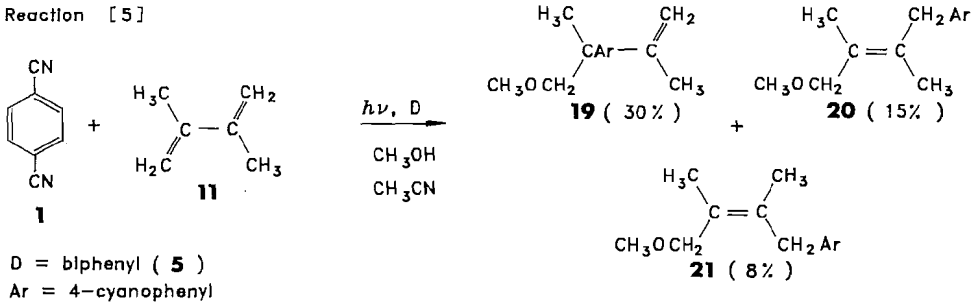

D = biphenyl (**5**)
Ar = 4-cyanophenyl

Reaction [6]

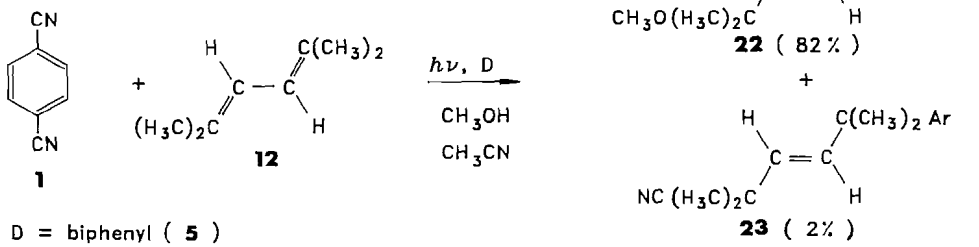

D = biphenyl (**5**)
Ar = 4-cyanophenyl

NOCAS adducts: *trans*-2-(4-cyanophenyl)-5-methoxy-2,5-dimethyl-3-hexene (**22**, 82%) and *trans*-5-(4-cyanophenyl)-2,2,5-trimethyl-3-hexenenitrile (**23**, 2%) (reaction [6]; yields are based on essentially complete conversion of **1**). The major product, **22**, was the expected 1,4-addition product. The minor product, **23**, was not the typical photo-NOCAS product involving methanol, diene, and **1**, but, instead, it results from the combination of cyanide ion, diene, and **1**. The ratio of **22/23** changes during the irradiation; increasing irradiation time, ratio **22/23** decreases. The ratio of **22/23** = 40 when the irradiation was continued until almost complete consumption of **1**. Biphenyl (**5**) had little effect on this reaction; a slight increase in the efficiency was observed but no effect on the product ratio. There was no cyano adduct (**23**) formed when lithium perchlorate (0.1 M) was added to the photolysis mixture. A similar irradiation involving **12**, **1**, and **5** in an acetonitrile solution, without added methanol, gave a 68% yield of **23**, this yield was also based on essentially complete conversion of **1**.

No analogous cyano adducts were detected in the reactions described above with conjugated dienes **9**, **10**, and **11**. Furthermore, when these irradiations were carried out in acetonitrile alone (without added methanol), no cyano adducts were produced.

Several experiments were performed in an attempt to determine the mechanism of the reaction leading to formation of **23**. A photochemically initiated free radical chain mechanism was ruled out; no adducts were formed in a thermal reaction (110°C) to which the free radical chain initiator di-*tert*-butyl peroxide had been added.

Another possible mechanism for the formation of **23** would involve reaction of the contact radical ion pair (CRIP) formed upon irradiation of a charge transfer complex (CTC) between **1** and **12**. A CTC does form between **1** and **12**. The uv-absorption spectra of acetonitrile solutions with a constant concentration of **1** and varying concentrations of **12** were recorded. Figure 1 illustrates the uv-absorption spectrum, in the long-wavelength region, of an acetonitrile solution of **1** (0.06 M) as a function of diene concentration ([**12**]). Figure 2 is a plot (Benesi–Hildebrand) of the absorption due to the CTC (320 nm). The associ-

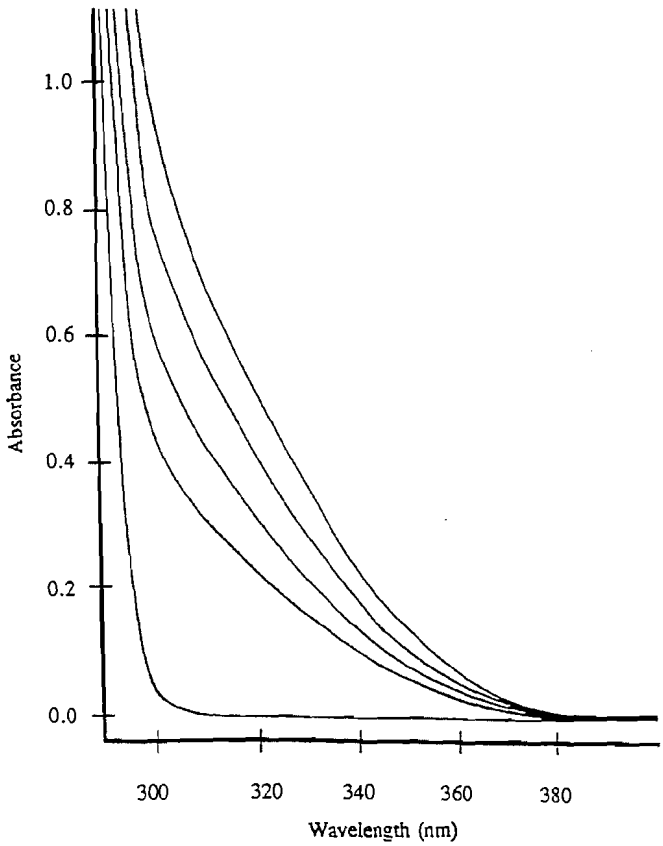

FIG. 1. The uv-absorption spectrum of 1,4-dicyanobenzene (**1**) (0.06 M), in acetonitrile, as a function of varying concentrations of 2,5-dimethyl-2,4-hexadiene (**12**) (see Fig. 2 for concentrations).

Can. J. Chem. Downloaded from www.nrcresearchpress.com by 85.192.166.187 on 09/08/12
For personal use only.

ation constant, calculated from the slope of the line, is $K_a = 2.0$ M^{-1}. The product ratio, **22/23**, was determined upon selective excitation of the charge transfer transition. This experiment was carried out using standard acetonitrile–methanol solutions of **1** and **12**, placed in a Pyrex tube with an outer Pyrex vessel. The outer vessel was filled with a solution filter consisting of varying concentrations of **1** (0.0–0.1 M) in acetonitrile–methanol. The rate of formation of the photo-NOCAS adducts decreased significantly with increasing concentration of **1** in the filter solution; however, the ratio of adducts (**22/23**) followed the same pattern as in the reaction without filter solution. The ratio (**22/23**) decreases from an initial maximum >55 to <30 at complete conversion of **1**.

Formation of the photo-NOCAS adducts, **22** and **23**, can be photosensitized (electron transfer). An acetonitrile–methanol solution of **1**, **12**, and a photosensitizer (electron transfer), anthracene (**24**), was irradiated through a glass filter that absorbed light of wavelengths shorter than 330 nm. Under these conditions only **24** absorbs light; no reaction occurred upon irradiation of an acetonitrile–methanol solution of **1** and **12**, without added **24**, through this filter. The ratio of methanol and cyanide ion incorporated products, at complete consumption of **1**, was essentially the same (**22/23** = 40).

In another relevant experiment, the possibility of incorporating added cyanide ion was tested. An acetonitrile–methanol solution of **1**, **12**, and added $K^{13}CN$ (2×10^{-2} M) was irradiated. The ratio of photo-NOCAS adducts was greatly decreased (**22/23** = 1) and there was a >80% increase in the relative intensity of the $(M + 1)^{+\cdot}$ peak, for the molecular ion, in the mass spectrum of **23** formed at low conversion. Irradiation of an acetonitrile solution of **1**, **12**, **5**, KCN, and crown ether (18-crown-6) gave an excellent yield (80%) of **23** (reaction [7]).

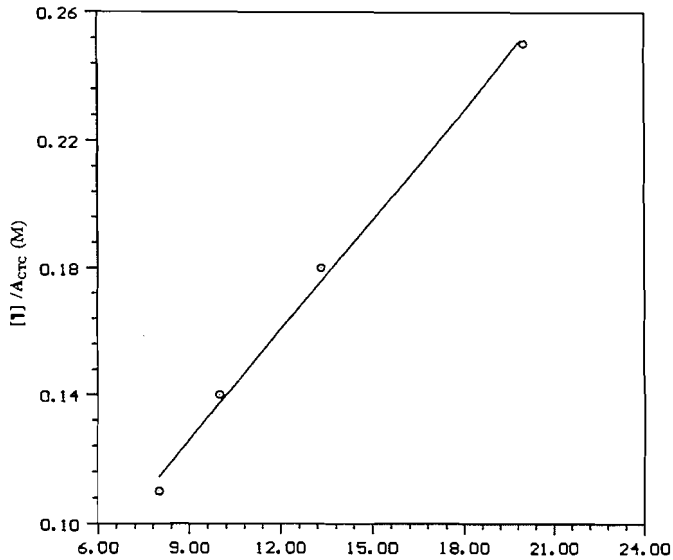

[12]	A_{CTC}	[1]/A_{CTC}	1/[12]
0.050	0.24	0.25	20.0
0.075	0.33	0.18	13.3
0.100	0.43	0.14	10.0
0.125	0.54	0.11	8.0

FIG. 2. A Benesi–Hildebrand plot of [**1**]/A_{CTC} against 1/[**12**] for a series of acetonitrile solutions of 1,4-dicyanobenzene (**1**) with varying concentrations of 2,5-dimethyl-2,4-hexadiene (**12**) (ref. 24).

Reaction [7]

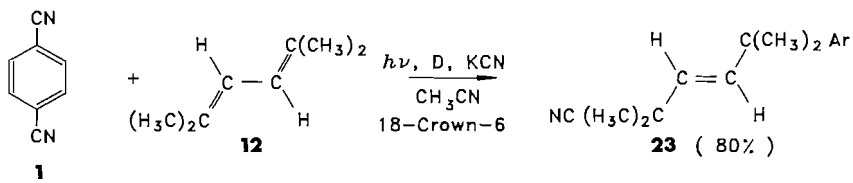

D = biphenyl (**5**)
Ar = 4-cyanophenyl

An acetonitrile solution of 2,5-dimethyl-2,4-hexadiene (**12**), **1**, **5**, and 2,4,6-trimethylpyridine (collidine, **25**) was irradiated to give 1:1 substitution products: 3-(4-cyanophenyl)-2,5-dimethyl-1,4-hexadiene (**26**, 7%), *trans*-5-(4-cyanophenyl)-2,5-dimethyl-1,3-hexadiene (**27**, 27%), (*Z*)-1-(4-cyanophenyl)-2,5-dimethyl-2,4-hexadiene (**28**, 10%), and (*E*)-1-(4-cyanophenyl)-2,5-dimethyl-2,4-hexadiene (**29**, 14%) (reaction [8]). The tautomer of 2,5-dimethyl-2,4-hexadiene (**12**), 2,5-dimethyl-1,4-hexadiene (**30**), was also formed. The structure of **30** was confirmed by comparison (retention time and mass spectrum) with an authentic sample (1*a*, 10). The 1:1 substitution products (**26–29**) were minor products in reactions [6] and [7], and a small amount of the cyanide adduct (**23**) was observed in reaction [8].

Structural assignments

The products were generally isolated from the crude photolysate by medium-pressure liquid chromatography (mplc) on silica gel. Structural assignments were based primarily upon analysis of the ^1H and ^{13}C nmr spectra. Mass and infrared spectra and elemental analyses were also useful. In one case, **28**, the structure was determined by X-ray crystallography.

The photo-NOCAS adducts, 3-(4-cyanophenyl)-4-methoxy-1-butene (**13**) and *trans*-1-(4-cyanophenyl)-4-methoxy-2-butene (**14**), were isolated from the irradiation of an acetonitrile–methanol (3:1) solution of 1,3-butadiene (**9**), 1,4-dicyanobenzene (**1**), and biphenyl (**5**) (reaction [3]). The ^1H and ^{13}C nmr spectra provide good evidence for the structure of **13** as the *anti*-Markovnikov 1,2-adduct. The low-field singlet (3.33 ppm) in the ^1H nmr spectrum is indicative of the methoxy methyl group. The multiplet (3.70 ppm) is an ABC second-order pattern for the protons of the methylene group next to an oxygen and that of the benzylic/allylic methine group. A terminal alkene is supported by two doublets and the multiplet (5.10, 5.19, and 5.96 ppm) in the vinyl proton region. A multiplet for the vinyl proton on carbon-2 exhibits *trans*, *cis*, and vicinal coupling (17.2, 10.4, and 6.6 Hz, respectively). The typical AA′XX′ pattern in the aromatic region of the ^1H nmr spectrum is indicative of the 4-cyanophenyl group.

Even though the signal, in the ^1H nmr spectrum, due to the

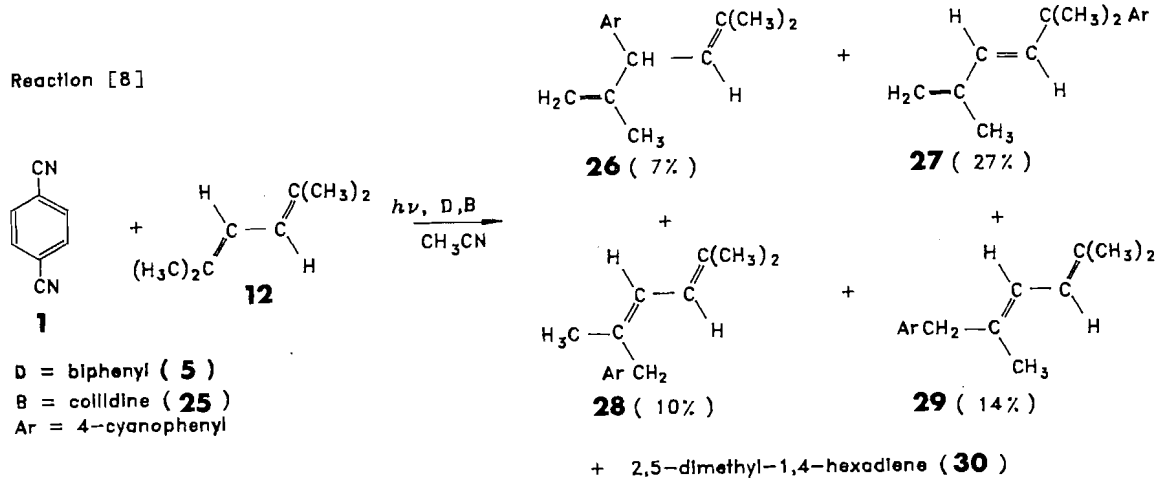

methylene and methine hydrogens could not be rigorously analyzed, the presence of these groups was evident from the observed coupling in the ^{13}C nmr spectrum. The methine carbon appears as a low-field doublet (49.63 ppm) shifted by allylic and aryl substitution. The methylene carbon appears as a triplet (75.40 ppm) indicative of a methoxy-substituted methylene. The signals due to a carbon adjacent to an oxygen generally occur at lower field (72–94 ppm), compared to those adjacent to the 4-cyanophenyl group (37–55 ppm) (1, 3). The terminal alkene is further supported by methylene and methine carbon signals appearing in the vinyl region of the ^{13}C nmr spectrum.

Compound **14** was identified as *trans*-1-(4-cyanophenyl)-4-methoxy-2-butene. The ^{1}H nmr spectrum exhibits a singlet (3.33 ppm) indicative of a methoxy methyl group. Two doublets (3.45 and 3.90 ppm) represent methylene groups, aryl and methoxy substituted, respectively. Protons adjacent to oxygen generally occur at lower field (3.2–3.7 ppm) than those adjacent to the 4-cyanophenyl group (2.4–3.0 ppm) (1, 3). Two doublets of triplets appear in the vinyl region of the ^{1}H nmr spectrum, each representing a vinyl proton adjacent to a methylene group. The coupling constant (15.4 Hz) between the vinyl protons is indicative of the *trans* configuration. The infrared spectrum shows a C–H bending frequency at 953 cm^{-1}, further supporting a *trans* alkene. An AA'XX' pattern in the aromatic region of the ^{1}H nmr is indicative of a 4-cyanophenyl group.

In the ^{13}C nmr spectrum of **14**, there is a triplet (38.68 ppm), which indicates a methylene group substituted by the 4-cyanophenyl group. There is a lower field quartet (58.00 ppm), which is consistent with the methyl of the methoxy group, and a triplet (76.62 ppm), which indicates a methylene carbon bonded to the methoxy group. Two vinyl methine groups are present (129.05 ppm and 132.20 ppm).

An acetonitrile–methanol solution of 2-methyl-1,3-butadiene (**10**), **1**, and **5** was irradiated and the resulting photolysate gave four photo-NOCAS adducts: **15**, **16**, **17**, and **18**. Adduct **15** was identified as 3-(4-cyanophenyl)-4-methoxy-3-methyl-1-butene. The ^{1}H nmr of **15** is very similar to compound **13**. The ABC multiplet for **13** has now been simplified to an AB pattern, indicating a methylene group adjacent to a quaternary stereogenic centre. In the ^{13}C nmr spectrum, an aryl-substituted quaternary carbon is observed (46.11 ppm).

Compound **16** was identified as the 1,2-addition product resulting from attack at the less substituted end of the diene; this product is 3-(4-cyanophenyl)-4-methoxy-2-methyl-1-butene. Again, the ^{1}H nmr of **16** is very similar to that of compound **13**. A less complex AMX pattern is observed due to the substitution of a methyl group on carbon-2 of the double bond. The vinyl region shows two singlets representing the geminal protons on carbon-1. The ^{13}C nmr spectrum exhibits a triplet (112.59 ppm) for the terminal vinyl methylene and the quaternary vinyl carbon shows up as a singlet (144.02 ppm).

Compound **18** was identified as the 1,4-addition product having the *Z* configuration, (*Z*)-4-(4-cyanophenyl)-1-methoxy-2-methyl-2-butene. The aliphatic region of the ^{1}H nmr spectrum exhibits a singlet corresponding to a methyl group and a singlet at higher frequency for the methoxy methyl group. A doublet appears at 3.48 ppm, representing a methylene group substituted by both aryl and vinyl groups, and a singlet appears at 3.99 ppm, representing a methoxy-substituted methylene group. The distinction between these methylene groups, assigned on the basis of chemical shift, establishes the regiochemistry of the adduct (1, 3).

A vinyl proton appears as a triplet (5.50 ppm, J = 7.4 Hz) resulting from coupling to the higher field methylene group (3.48 ppm). Therefore, the aryl-substituted methylene group is vicinal to the vinyl proton. Since only one vinyl proton is present, the methyl group and methoxy-substituted methylene group must be the other substituents on the double bond.

The ^{13}C nmr spectrum provides further evidence for structure **18**. A triplet at 34.04 ppm indicates an aryl-substituted methylene group, a triplet at 70.96 ppm shows a methoxy-substituted methylene group, a vinyl methine group is observed at 125.72 ppm, and a vinyl quaternary carbon at 134.74 ppm.

The decision in favour of the *Z* configuration for **18** was based upon the results of a double irradiation experiment leading to a nuclear Overhauser effect (nOe). The methylene groups were irradiated and the nOe recorded. When the methoxy-substituted methylene group was irradiated, an enhanced signal was observed for the methyl group, methoxy methyl group, and for the aryl-substituted methylene group. This shows the methoxy-substituted methylene group is *syn* to the aryl-substituted methylene group. Further proof of the *Z* configuration was provided by irradiating the aryl-substituted methylene group. An nOe was seen for the methoxy-substituted methylene group, the vinyl proton, and the aryl protons.

Compound **17** is the configurational isomer of **18**; (*E*)-4-(4-cyanophenyl)-1-methoxy-2-methyl-2-butene. The ^{1}H and ^{13}C nmr spectra show characteristic patterns similar to those of compound **18**. The *E* configuration was assigned on the basis of

Can. J. Chem. Downloaded from www.nrcresearchpress.com by 85.192.166.187 on 09/08/12
For personal use only.

Can. J. Chem. Downloaded from www.nrcresearchpress.com by 85.192.166.187 on 09/08/12
For personal use only.

the observed nOe. When the methoxy-substituted methylene group was irradiated, an enhancement was observed for the signal due to the methyl and the methoxy methyl groups. When the aryl-substituted methylene group was irradiated, an nOe was seen for the methyl group and the aryl hydrogens. These observations support the *E* configuration and confirm the regiochemical assignment for **17**.

When an acetonitrile–methanol solution of 2,3-dimethyl-1,3-butadiene (**11**), **1**, and **5** was irradiated, compounds **19**, **20**, and **21** were produced (reaction [5]). Compound **19** was identified as an *anti*-Markovnikov 1,2-addition product, 3-(4-cyanophenyl)-4-methoxy-2,3-dimethyl-1-butene. The ^{1}H and ^{13}C nmr spectra were similar to those of compound **15**. Unlike **15**, there are only two vinyl protons, instead of three, and they appear as slightly broadened singlets in the vinyl region of the ^{1}H nmr spectrum, indicative of a terminal, disubstituted double bond. In the ^{13}C nmr spectrum, there are signals due to a vinyl carbon with no bonded protons (148.13 ppm) and a vinyl methylene (112.19 ppm).

Compound **20** was identified as the 1,4-addition product having the *E* configuration, (*E*)-1-(4-cyanophenyl)-4-methoxy-2,3-dimethyl-2-butene. The ^{1}H and ^{13}C nmr spectra are similar to those of compound **17**. The main difference is one additional methyl group, which shows up as a singlet in the ^{1}H nmr spectrum and a quartet in the ^{13}C nmr spectrum. The ^{1}H nmr spectrum, also, exhibits no vinyl protons but two vinyl quaternary carbons are identified in the ^{13}C nmr spectrum. The *E* configuration was assigned by nOe. The methoxy-substituted methylene group was irradiated and an nOe was observed for two methyl groups and the methoxy methyl group. When the aryl-substituted methylene group was irradiated, an nOe was observed for two methyl groups. This information supports a *trans* configuration of the methylene groups; thus, **20** has an *E* configuration.

Compound **21** was identified as a 1,4-addition product with *Z* configuration: (*Z*)-1-(4-cyanophenyl)-4-methoxy-2,3-dimethyl-2-butene. The ^{1}H and ^{13}C nmr spectra exhibit similar characteristic patterns to those of compound **20**. The observed nuclear Overhauser effect (nOe) was used to determine the *Z* configuration of **21**. The methoxy-substituted methylene group was irradiated and an enhanced signal was observed for one methyl group and the aryl-substituted methylene group. The aryl-substituted methylene group was irradiated and an nOe was observed for the other methyl group and the methoxy-substituted methylene group. This information confirms that the methylene groups are *syn* to one another and that **21** has a *Z* configuration.

Irradiation of an acetonitrile–methanol solution of **1**, **5**, and 2,5-dimethyl-2,4-hexadiene (**12**) yields two 1,4-adducts, **22**, and **23** (reaction [6]). The major product, **22**, was identified as *trans*-2-(4-cyanophenyl)-5-methoxy-2,5-dimethyl-3-hexene. The structural proof of compound **22** comes neatly from the ^{1}H nmr, ^{13}C nmr, and infrared spectra. There are two singlets in the aliphatic region of the ^{1}H nmr spectrum; each represents two chemically equivalent methyl groups. A low-field singlet (3.16 ppm) indicates the presence of a methoxy methyl group and an AA′XX′ pattern in the aromatic region indicates the 4-cyanophenyl group. Two doublets appear in the vinyl region, each with a coupling (16 Hz) typical of a *trans* configuration. The infrared spectrum shows a C–H bending frequency at 970 cm^{-1}, further supporting the *trans* configuration for this alkene.

In the ^{13}C nmr spectrum of **22**, there is a singlet (40.73 ppm) supporting a quaternary carbon substituted by a 4-cyanophenyl group and a quartet (50.29 ppm) representing a methoxy methyl group. The methoxy group is bonded to a quaternary carbon, which shows up as a singlet (74.73 ppm).

Compound **23** was identified as *trans*-5-(4-cyanophenyl)-2,2,5-trimethyl-3-hexenenitrile. The nmr spectra of **23** are very similar to those of compound **22**. The main differences in the spectra of the two compounds is that in **23** there is no methoxy group; and the ^{13}C nmr spectrum shows that there are two cyano groups present in the molecule (singlets at 118.90 and 123.52 ppm). Both cyano groups are affixed to quaternary centres, one singlet (34.56 ppm) representing an alkyl quaternary carbon, and another singlet (109.99 ppm) representing an aryl carbon.

An acetonitrile–collidine solution (without added methanol) of **12**, **1**, and **5** was irradiated and gave four 1:1 substitution products: **26**, **27**, **28**, and **29** (reaction [8]). Compound **26** was identified as 3-(4-cyanophenyl)-2,5-dimethyl-1,4-hexadiene. The aliphatic region of the ^{1}H nmr spectrum exhibits three singlets assigned to the methyl groups. A methine proton on carbon-3 is a doublet (4.20 ppm, J = 9.2 Hz), which is indicative of an allylic and benzylic methine group. A doublet in the vinyl region indicates one vinyl proton coupled to a vicinal proton. The presence of a terminal disubstituted olefin is supported by two singlets in the vinylic region. The typical AA′XX′ pattern in the aromatic region of the ^{1}H nmr spectrum supports the presence of the 4-cyanophenyl group.

In the ^{13}C nmr spectrum of **26**, there is a doublet (51.47 ppm), which is consistent with an aryl substituted methine group, there is a triplet (112.54 ppm), which is consistent with a methylene group of a terminal double bond, and there is a doublet (124.38 ppm), which supports a vinyl methine group. There are also two singlets for vinyl carbons.

Compound **27** was identified as *trans*-5-(4-cyanophenyl)-2,5-dimethyl-1,3-hexadiene. The aliphatic region of the ^{1}H nmr exhibits two singlets; the signal at 1.45 ppm represents two chemically equivalent methyl groups, while the signal at 1.84 ppm represents the other methyl group. The presence of a terminal disubstituted olefin is supported by two singlets in the vinylic region. Two doublets appear in the vinyl region of the ^{1}H spectrum, each representing a vinyl proton adjacent to an allylic quaternary carbon. The coupling constant (16.0 Hz) between the vinyl protons is indicative of the *trans* configuration. The infrared spectrum shows a C–H bending frequency of 951 cm^{-1}, further supporting a *trans* configuration. An AA′XX′ pattern in the aromatic region of the ^{1}H nmr spectrum is indicative of a 4-cyanophenyl group.

The ^{13}C nmr spectrum of **27** exhibits a singlet (40.95 ppm), which is consistent with an aryl-substituted quaternary carbon. There is a triplet (116.04 ppm), which is indicative of the terminal vinyl methylene group; two doublets (130.14 and 138.25 ppm) and a singlet in the vinyl region of the ^{13}C nmr spectrum indicate two vinyl methine groups and a vinyl-disubstituted carbon.

Compound **28** was identified as (*Z*)-1-(4-cyanophenyl)-2,5-dimethyl-2,4-hexadiene. The ^{1}H nmr exhibits three singlets in the aliphatic region, indicative of three methyl groups. A low-field singlet (3.52 ppm) shows a methylene group substituted with an aryl group. In the vinyl region there are two doublets (J = 11.3 Hz) indicative of the two adjacent methine groups. An AA′XX′ pattern in the aromatic region of the ^{1}H nmr spectrum is indicative of a 4-cyanophenyl group. The ^{13}C nmr spectrum of **28** indicates a methylene group substituted by a 4-

Can. J. Chem. Downloaded from www.nrcresearchpress.com by 85.192.166.187 on 09/08/12
For personal use only.

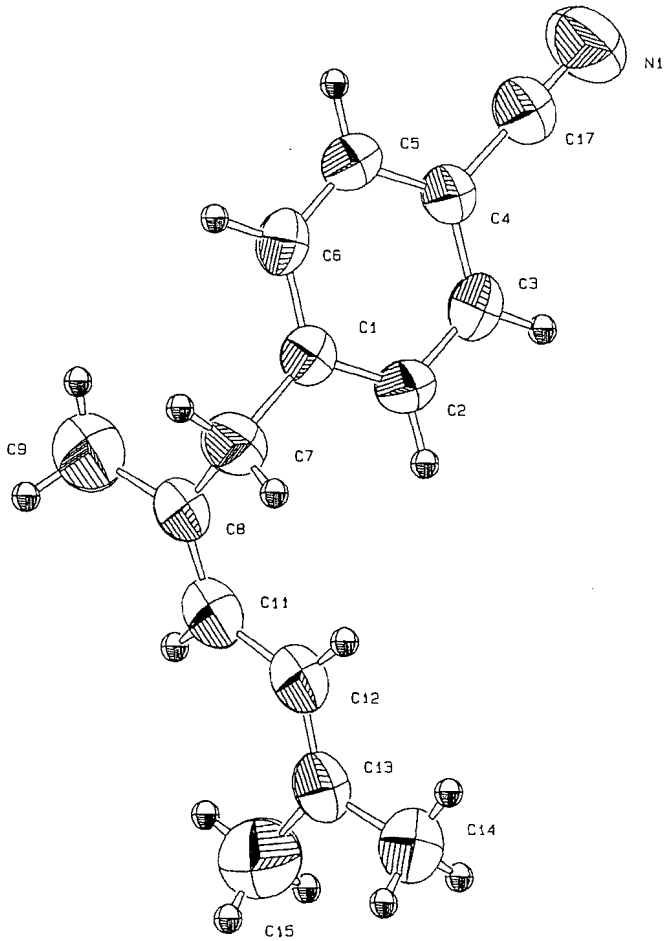

FIG. 3. X-ray crystallographic structure of (*Z*)-1-(4-cyanophenyl)-2,5-dimethyl-2,4-hexadiene (**28**).

cyanophenyl group (38.12 ppm), two doublets (120.40 and 124.02 ppm) for two vinyl methine groups, and two singlets (132.20 and 135.02 ppm) for the other two vinyl carbons. The *Z* configuration, as well as the overall structure of **28**, was firmly established by X-ray analysis of a single crystal (Fig. 3).[3]

Compound **29** was identified as the configurational isomer of **28**, (*E*)-1-(4-cyanophenyl)-2,5-dimethyl-2,4-hexadiene. The ^1H and ^{13}C nmr are very similar to those of the *Z* isomer.

Discussion

These results (reactions [3]–[8]) can be accounted for by the extended mechanism shown in Scheme 1. Initial excitation of 1,4-dicyanobenzene (**1**) (step 1) is achieved by irradiation with a medium-pressure mercury vapour lamp through Pyrex. The dienes, **9–12**, do not absorb light transmitted through Pyrex (>280 nm). Single electron transfer from the diene to the singlet excited state of **1** and formation of the solvent-separated radical ion pair (SSRIP) is thermodynamically favourable. The ΔG_{et} for this process, calculated by the Weller equation (eq. [9]) is exergonic by more than 20 kJ mol^{-1} (Table 1); therefore, the singlet excited state of **1** should be quenched, by the single electron transfer mechanism, at the diffusion-controlled rate in every case (11).

TABLE 1. The oxidation potentials of the dienes **9–12** and the calculated free energy change (ΔG) for the electron transfer process from the diene to the electronic excited singlet state of 1,4-dicyanobenzene (**1**)

Diene	$E_{1/2}^{ox}$ (V)	ΔG_{et} (kJ/mol)[a]
1,3-Butadiene (**9**)	2.37[c]	−25.0
2-Methyl-1,3-butadiene (**10**)	2.25[b]	−36.6
2,3-Dimethyl-1,3-butadiene (**11**)	2.16[b]	−45.3
2,5-Dimethyl-2,4-hexadiene (**12**)	1.24[b]	−134

[a]Based upon the Weller equation (reaction [9]) (11); $E_{0,0}$(**1**) 408.4 kJ/mol, $E_{1/2}^{red}$(**1**) −1.66 V; the Coulombic attraction term was taken to be 5.40 kJ/mol (3*a*).

[b]Oxidation potentials were measured at a platinum electrode relative to the saturated calomel electrode (SCE) using tetraethylammonium perchlorate (0.1 M TEAP) as the electrolyte in acetonitrile. The anodic wave was irreversible, the half-wave potential was estimated by substracting 0.028 V from the peak potential (12).

[c]This potential was reported by Neikam and Desmond (13), versus the silver/silver ion (Ag/0.1 N Ag^+) reference electrode; it as relating to the SCE by adding 0.34 V.

[9] $\Delta G_{et} = F[E_{1/2}^{ox}(D) - E_{1/2}^{red}(A) - e/\epsilon\alpha] - E_{0,0}(A)$

Photo-NOCAS adducts were obtained upon irradiation of acetonitrile–methanol solutions of **1** and the dienes. Addition of photosensitizer (electron transfer) or codonor to the irradiation mixture generally increases the efficiency of the reaction and the yield of adducts (steps 6–8).

Step 3 determines the regiochemistry of adduct formation. In every case, initial attack of the nucleophile (methanol or cyanide ion) occurs at a terminal position of the diene. This is consistent with previous results involving addition to monoalkenes where formation of *anti*-Markovnikov adducts is favoured (1, 3). The initial intermediate, formed upon attack of methanol on the diene radical cation, is the distonic radical cation. This intermediate may be bridged (3).

The addition of nucleophile (methanol) to the radical cation of 2-methyl-1,3-butadiene (**10**$^{+\cdot}$) occurs at the more heavily substituted double bond (carbon-1); the combined yield of adducts **15**, **17**, and **18** (49%) is significantly greater than the yield of **16** (6%). Attack at this position, the end of the more heavily substituted double bond, leads to formation of the more stable allylic radical. In addition, the more heavily substituted double bond bears the greater proportion of positive charge. Both of these factors contribute to the regiochemistry of the reaction.

The next step in the proposed mechanism involves coupling of the allylic radical with the radical anion, **1**$^{-\cdot}$, at the *ipso* position, a position of high spin density. Attack at the alternative ends of the ambident allylic radical leads to 1,2 and 1,4 addition. Reactions [3], [4], and [5] show little regioselectivity. In reaction [3], with the allylic radical from **9** where the alternative positions are secondary (1,2) or primary (1,4), 1,2 addition is slightly favoured. In reaction [4], with the allylic radical from **10** where the alternative positions are tertiary (1,2) or primary (1,4) addition is slightly favoured. In reaction [5], with the allylic radical from **11** where the alternative positions are ter-

[3]These data may be purchased from: The Depository of Unpublished Data, Document Delivery, CISTI, National Research Council Canada, Ottawa, Canada K1A 0S2.

Details of data collection, structural analysis and refinement, and tables of interatomic distances and bond angles have also been deposited with the Cambridge Crystallographic Data Centre and may be obtained on request from the Director, Cambridge Crystallographic Data Centre, University Chemical Laboratory, 12 Union Road, Cambridge, CB2 1EZ, U.K.

Can. J. Chem. Downloaded from www.nrcresearchpress.com by 85.192.166.187 on 09/08/12
For personal use only.

tiary (1,2) or primary (1,4), 1,2 addition is favoured. In marked contrast, in reaction [6], where the alternative positions are secondary (1,2) or tertiary (1,4), 1,4 addition is the exclusive reaction. A tentative explanation for these observations is preferential attack at the centre of higher spin density, moderated by steric interactions.

The results from reaction [6] were particularly interesting, firstly, because of the specific formation of one regio- and stereoisomer (**22**) in high yield, and secondly, because of the competitive formation of the cyanide adduct (**23**) in low yield. Related cyanide ion adducts were not detected in reactions [3], [4], or [5]. However, incorporation of cyanide ion in photo-NOCAS products has been observed before. The nitrile is a minor product in the photo-NOCAS reaction of methanol, 2,3-dimethyl-2-butene (**2**), and 1,4-dicyanobenzene (**1**) (reaction [1]) (3). The concentration of cyanide ion during the course of reaction [6] must be very low (initially, $[CN^-] = 0$). This competitive formation of nitrile can be inhibited by the addition of lithium perchlorate, which presumably coordinates with the cyanide ion.

Clearly, the radical cation $\mathbf{12}^{+\cdot}$ is the most stable of the diene radical cations studied; the oxidation potential of **12** is relatively low (Table 1). This increased radical cation stability leads to greater selectivity toward reaction with nucleophile (14). Under these conditions, the relative reactivity of alternative nucleophiles will become evident. Cyanide ion is significantly more reactive as a nucleophile than is methanol. The nucleophilicity of cyanide ion in methanol, for the S_N2 reaction with methyl iodide, is greater than that of methanol by more than 10^6 (15)! Measured (flash photolysis) rates of reaction of the radical cations of substituted styrenes toward methanol and cyanide ion reflect this difference. The second-order rate constant for the nucleophilic attack of cyanide ion on the radical cation of 4-methoxystyrene in acetonitrile–water (1:4) was measured to be 1.0×10^8 M^{-1} s^{-1}; with methanol as the nucleophile the rate constant is 3.0×10^4 M^{-1} s^{-1} (14*a*).

When the irradiation of **1**, **12**, and **5** is carried out in acetonitrile, without added methanol, the nitrile adduct **23** is formed in high yield. The only source of cyanide ion in this reaction is that from the 1,4-dicyanobenzene (**1**), presumably lost in the rearomatization step (step 5). The initial concentration of cyanide may be generated in step 5, following the addition of water to the diene radical cation. A small amount of adventitious water is, no doubt, present in the (dried) acetonitrile. Added cyanide ion is efficiently incorporated (reaction [7]).

The possibility that the nitrile adduct was formed by reaction of the contact radical ion pair (CRIP) resulting from excitation of the charge transfer complex, was effectively ruled out by the observation that the product ratio (**22**/**23**) is essentially the same when the charge transfer transition is selectively excited. Furthermore, this ratio is the same when the reaction is photosensitized (electron transfer). Under these conditions, the radical anion, $\mathbf{1}^{-\cdot}$, and the radical cation, $\mathbf{12}^{+\cdot}$, are certainly formed separately solvated.

The stereoselectivity for the formation of *cis* and *trans* 1,4-addition products reflects the equilibrium ratio of s-*cis* to s-*trans* conformations of the starting material. The diene radical cation prefers to be planar and thus maintain its conformation. The intermediate allylic radical also prefers to be planar (16). Consequently, the initial conformation of the starting diene is maintained in the final photo-NOCAS adducts (16). There is good evidence that the s-*trans* conformation of these dienes (**9**–**12**) is preferred (17). Differences in the energy of the s-*trans*–s-*cis* conformations can be calculated by molecular mechanics (MM3), Table 2 (18). The observed ratios of s-*trans* to s-*cis* configuration of the photo-NOCAS adducts are in good agreement with these calculated energy differences: from **9**, 100% (calculated composition at 10°C, 92% s-*trans*); from **10**, 90% (89%); from **11**, 65% (66%); and from **12**, 100% (99%), *trans*-1,4-addition.

TABLE 2. Calculated relative steric energies and s-dihedral angles for the s-*trans*–s-*cis* conformations of the dienes **9**–**12**

Diene		ΔE (kJ/mol)[a]	∠1234 (°)
1,3-Butadiene (**9**)	s-*trans*	0	180.0
	s-*cis*	5.90 (9.75)[b]	0.0
2-Methyl-1,3-butadiene (**10**)	s-*trans*	0	180.0
	s-*cis*	4.88 (4.85)[b]	0.1
2,3-Dimethyl-1,3-butadiene (**11**)	s-*trans*	0	180.0
	s-*cis*	1.61 (3.26)[c]	0.0
2,5-Dimethyl-2,4-hexadiene (**12**)	s-*trans*	0	180.0
	s-*cis*	11.65	61.8

[a]Using the MMP3 (1992) force field (18*c*). Steric energy s-*cis* − s-*trans*.
[b]Reported value, using the MMP2 (1977) force field (18*b*).
[c]Reported value, using the MMP1 (1973) force field (18*a*).

The photo-NOCAS reaction involving **1** and **12** can be diverted to 1:1 (diene:aromatic) substitution products by the addition of a non-nucleophilic base, 2,4,6-trimethylpyridine (collidine, **25**) (reaction [8]). The radical cation $\mathbf{12}^{+\cdot}$ is acidic (19). Deprotonation leads to the 2,4-dienyl radical, which can react at all three ambident positions. Coupling with the 1,4-dicyanobenzene anion radical, at the *ipso* position, occurs preferentially at the end of the allylic radical, to give the conjugated diene products, **27**–**29**.

Reduction of the alkyl-substituted 2,4-pentadienyl radical by the anion radical is now competitive with coupling. The reduction potential of the 2,4-dienyl radical is low enough that the 1,4-dicyanobenzene radical anion ($\mathbf{1}^{-\cdot}$) can reduce the radical to the anion, which, upon protonation, yields the tautomer (**30**) (steps 10a and 12). Alkenyl methyl ethers were not formed in reactions [3]–[7]. The reduction potentials of alkyl-substituted 2-propenyl radicals are greater (more negative) than that of 1,4-dicyanobenzene (**1**) (−1.66 V, SCE) (20).

Conclusions

1. The scope of the photo-NOCAS reaction has been extended to include conjugated dienes. Yields can be high (reactions [6] (82%) and [7] (80%)). This process has synthetic utility.

2. The extended mechanism (Scheme 1) can account for all the observations.

3. The regiochemistry is consistent with initial attack of nucleophile (methanol) at that terminal position of the diene radical cation which leads to formation of the more stable allylic radical. Subsequently, both 1,2 and 1,4 adducts can result. Coupling of the allylic radical with the radical anion occurs at the position of higher spin density.

4. The more heavily substituted, and therefore more stable, radical cations show significant selectivity toward reaction with nucleophile; the rate of reaction with cyanide ion is appreciably greater than with methanol.

5. Competitive formation of the nitrile, by attack by cyanide ion released in the rearomatization step, can be prevented by addition of lithium perchlorate to the irradiation mixture.

Can. J. Chem. Downloaded from www.nrcresearchpress.com by 85.192.166.187 on 09/08/12
For personal use only.

6. The stereochemistry of 1,4-adduct formation reflects the equilibrium conformation of the initial diene.

7. In the presence of non-nucleophilic base, deprotonation of the diene radical cation gives the allylic radical, which subsequently leads to formation of 1:1 (diene:aromatic) adducts.

Experimental

General information

^1H and ^{13}C nmr spectra were obtained from Bruker 250, 300, and 400 spectrometers or from a Nicolet 360 NB nmr spectrometer. Spectra were recorded in parts per million and frequencies are relative to tetramethylsilane. Infrared spectra (ir) were recorded on an air-purged Perkin–Elmer 180 grating spectrometer and are reported in wave numbers (cm^{-1}) relative to the 1601.4 cm^{-1} absorption band of polystyrene film. Elemental analyses were performed by Canadian Microanalytical Service Ltd., B.C. Exact mass determinations were obtained using a ZAB-E spectrometer. Melting points were determined using a Cybron Corporation Thermolyne apparatus with a digital thermocouple and are corrected. Ultraviolet (uv) absorbance spectra were recorded using a Cary Varian 219 spectrometer and are reported in nanometres (nm). Product yields were determined using a Hewlett–Packard (HP) 5890 gas chromatograph with a DB-1701 fused silica WCOT column (20 m × 0.25 mm, 0.4-μm film thickness) and a calibrated flame ionization detector (gc/fid) and are based upon 1,4-dicyanobenzene (**1**) as the limiting reagent. An HP 3392A integrator was interfaced with the gc/fid to obtain peak areas. An HP 5890 gas chromatograph with a 5% phenyl methyl silicone fused silica WCOT column (25 m × 0.20 mm, 0.33-μm film thickness) interfaced with an HP 5970 mass selective detector (gc/ms) was also used for product analyses. Mass spectra are reported as *m/z* (relative intensity). Separation of product mixtures was generally carried out using preparative medium-pressure liquid chromatography (mplc) (*3b*). The mplc consists of a 2.5 cm × 1 m column packed with thin-layer chromatography (tlc) grade silica gel (without binder, 7747 Merck) at a pressure of 15 psi using helium (1 psi = 6.9 kPa). Connected to the mplc was a uv spectrophotometer – fraction collector that collects ca. 10-mL fractions. Dry column flash chromatography (dc/fc) was also used (21). The column was packed with thin-layer chromatography grade silica gel (without binder, 7747 Merck). Fraction sizes were ca. 5 mL. Preparative-GC (prep/gc) was carried out using a Varian Aerograph A700 or 920.

Materials

Acetronitrile (Fisher ACS grade) was distilled twice, first from sodium hydride and then from phosphorous pentoxide. It was then passed through a column of basic alumina, refluxed over calcium hydride for 24 h (under a nitrogen atmosphere), fractionally distilled (under nitrogen), and stored over molecular sieves (3 Å) (22). Methanol was distilled and then stored over molecular sieves (4 Å). 1,4-Dicyanobenzene (**1**) (Aldrich) was purified by treatment with activated carbon in methylene chloride, followed by recrystallization from 95% ethanol. Tetraethylammonium perchlorate (TEAP) (Aldrich) was recrystallized three times from water and then dried in a vacuum oven for 15 h, 70°C, 0.25 Torr (1 Torr = 133.3 Pa). 1,3-Butadiene, 99% (**9**), 2-methyl-1,3-butadiene, 99% (**10**), 2,3-dimethyl-1,3-butadiene, 98% (**11**), and 2,5-dimethyl-2,4-hexadiene, 99% (**12**) were obtained from the Aldrich Chemical Co. Biphenyl (**5**) (Eastman Kodak Co.) was recrystallized from methanol. 2,4,6-Trimethylpyridine (collidine, **25**) (BDH) was purified by distillation.

Irradiations

Irradiations were generally carried out on solutions of acetonitrile–methanol (3:1) with 1,4-dicyanobenzene, the diene, and with or without a codonor. Solutions were irradiated in either 2 cm i.d. Pyrex tubes or 5 mm Pyrex nmr tubes, which were degassed by nitrogen ebullition. These samples were irradiated at 10°C using a CGE 1-kW or a Hanovia 450-W medium-pressure mercury vapour lamp contained in a water-cooled Pyrex and quartz immersion well, respectively, unless otherwise noted.

Cyclic voltammetric measurements

Cyclic voltammetry was used to obtain the oxidation potential of the dienes. The apparatus has been described (23). The working electrode was a platinum sphere (1 mm diameter) and the counter electrode was a platinum wire. The reference electrode was a saturated calomel electrode (SCE), which was connected to the solution (TEAP 0.1 M, acetonitrile) through a Luggin capillary. The dienes were purified by prep/gc using a 0.95 cm × 350 cm aluminum column packed with 40% SE-30 on Chromosorb W 60/80 NAW. The diene concentration was ca. 0.005 M. The anodic wave was irreversible; the half-wave potential was taken as 0.028 V before the anodic peak potential (12).

*Formation of the methanol, 1,3-butadiene (**9**), and 1,4-dicyanobenzene (**1**) photo-NOCAS adducts **13** and **14** (reaction [3])*

A solution of 1,3-butadiene (**9**) (1.2 g, 0.022 mol), 1,4-dicyanobenzene (**1**) (1.0 g, 0.0078 mol), and biphenyl (**5**) (1.2 g, 0.0078 mol) in acetonitrile–methanol (3:1, 60 mL) was degassed by nitrogen ebullition for 5 min and irradiated for 98 h using a 450-W lamp at 10°C. The solvent was removed to yield a crude photolysate. Unreacted 1,4-dicyanobenzene (**1**), precipitated from the photolysate by the addition of a mixture of hexanes and ethyl acetate, was removed by filtration. The crude photolysate was separated by dc/fc (diameter: 50 mm) eluting with 10% ethyl acetate in hexanes. The products eluted in the order **13** followed by **14**.

*3-(4-Cyanophenyl)-4-methoxy-1-butene (**13**)*

The yield was 35%: infrared (PE-180) ν: 3081(w), 2981(m), 2931(m), 2881(m), 2829(m), 2239(s), 1636(w), 1606(m), 1503(m), 1476(w), 1456(w), 1411(w), 1377(w), 1181(m), 1111(s), 991(w), 971(w), 946(w), 903(m), 821(m); ^1H nmr (361.08 MHz, $CDCl_3$) δ_{TMS}: 3.33 (s, 3H, OCH_3), 3.70 (m, 3H, H of methylene and methine groups), 5.10 (d, 1H, $^3J_{1trans-2}$ = 17.2 Hz, vinyl H (1*trans*-H)), 5.19 (d, 1H, $^3J_{1cis-2}$ = 10.4 Hz, vinyl H (1*cis*-H)), 5.96 (m, 1H, $^3J_{1trans-2}$ = 17.2 Hz, $^3J_{1cis-2}$ = 10.4 Hz, $^3J_{2-3}$ = 6.6 Hz, vinyl H (2-H)), 7.35 (d, 2H, $^3J_{2'-3'}$ = 8.3 Hz, $^3J_{5'-6'}$ = 8.3 Hz, H's adjacent to alkyl-substituted aryl carbon (2′-H, 6′-H)), 7.60 (d, 2H, $^3J_{2'-3'}$ = 8.3 Hz, $^3J_{5'-6'}$ = 8.3 Hz, H's adjacent to cyano-substituted aryl carbon ((3′-H, 5′-H)); ^{13}C nmr (90.80 MHz, $CDCl_3$) δ: 49.63 (d, 129.8 Hz, CH, aryl substituted), 58.95 (q, 141.4 Hz, OCH_3), 75.40 (t, 141.9 Hz, OCH_2), 110.39 (s, quaternary aryl carbon, cyano substituted), 117.08 (t, 157.6 Hz, terminal vinyl CH_2), 118.87 (s, CN), 128.79 (d, 160.1 Hz, aromatic CH adjacent to alkyl-substituted aryl carbon), 132.18 (d, 165.4 Hz, aromatic CH adjacent to cyano-substituted aryl carbon), 137.26 (d, 155.2 Hz, vinyl CH), 146.98 (s, quaternary aryl carbon, alkyl substituted); ms *m/z*: 51(51), 62(25), 63(52), 75(42), 89(66), 114(30), 115(96), 116(82), 127(25), 140(77), 141(25), 142(47), 156(45), 157(100), 187(19). Exact Mass calcd. for $C_{12}H_{13}NO$: 187.0997; found: 187.0992.

trans-*1-(4-Cyanophenyl)-4-methoxy-2-butene (**14**)*

The yield of **14** was 30%: infrared (PE-180) ν: 2978(w), 2928(m), 2898(m), 2803(m), 2223(s), 1603(m), 1503(m), 1448(w), 1413(w), 1381(w), 1193(w), 1173(w), 1113(s), 953(m), 893(w), 828(w), 803(m); ^1H nmr (361.08 MHz, $CDCl_3$) δ_{TMS}: 3.33 (s, 3H, OCH_3), 3.45 (d, 2H, $^3J_{3-4}$ = 6.7 Hz, CH_2, aryl-substituted (4-H)), 3.90 (d, 2H, $^3J_{1-2}$ = 5.5 Hz, CH_2, methoxy-substituted (1-H)), 5.64 (m, 1H, $^3J_{2-3}$ = 15.4 Hz, $^3J_{1-2}$ = 5.5 Hz, vinyl H (2-H)), 5.83 (m, 1H, $^3J_{2-3}$ = 15.4 Hz, $^3J_{3-4}$ = 6.7 Hz, vinyl H (3-H)), 7.30 (d, 2H, $^3J_{2'-3'}$ = 8.1 Hz, $^3J_{5'-6'}$ = 8.1 Hz, H's adjacent to alkyl-substituted aryl carbon (2′-H, 6′-H)), 7.57 (d, 2H, $^3J_{2'-3'}$ = 8.1 Hz, $^3J_{55'-6'}$ = 8.1 Hz, H's adjacent to cyano-substituted aryl carbon (3′-H, 5′-H)); ^{13}C nmr (90.80 MHz, $CDCl_3$) δ: 38.68 (t, 128.7 Hz, CH_2, aryl substituted), 58.00 (q, 140.2 Hz, OCH_3), 76.62 (t, 139.2 Hz, OCH_2), 110.00 (s, quaternary aryl carbon, cyano substituted), 118.93 (s, CN), 129.05 (d, 157.1 Hz, vinyl CH), 129.31 (d, 160.9 Hz, aromatic CH adjacent to alkyl-substituted aryl carbon), 130.69 (d, 163.8 Hz, aromatic CH adjacent to cyano-substituted aryl carbon), 132.20 (d, 150.6 Hz, vinyl CH), 145.55 (s, quaternary aryl carbon, alkyl substituted); ms *m/z*: 51(38), 58(24), 63(33), 71(100), 72(22), 75(22), 76(20), 89(48), 115(40), 116(49), 127(25), 128(24),

Can. J. Chem. Downloaded from www.nrcresearchpress.com by 85.192.166.187 on 09/08/12
For personal use only.

129(24), 140(25), 154(25), 155(20), 187(1). Anal. calcd. for $C_{12}H_{13}NO$: C 76.97, H 7.00, N 7.48; found: C 76.70, H 7.09, N 7.45.

*Formation of the methanol, 2-methyl-1,3-butadiene (**10**) and 1,4-dicyanobenzene (**1**) photo-NOCAS adducts **15–18** (reaction [4])*

A solution of 2-methyl-1,3-butadiene (**10**) (2.6 g, 0.04 mol) (the stabilizer, hydroquinone, was removed by distillation at atmospheric pressure), 1,4-dicyanobenzene (**1**) (2.5 g, 0.02 mol), and biphenyl (**5**) (6.0 g, 0.04 mol) in acetonitrile–methanol (3:1, 160 mL) was degassed by nitrogen ebullition for 5 min and irradiated for 136 h using a 450-W lamp. The crude photolysate was separated by mplc using a linear solvent gradient of hexanes – dichloromethane. Products were eluted in the order **15**, **16**, **18**, and **17**. Several fractions were combined and rechromatographed by dc/fc and mplc to achieve purity of the four photo-NOCAS products.

*3-(4-Cyanophenyl)-4-methoxy-3-methyl-1-butene (**15**)*

The yield of **15** was 20%: infrared (PE-180) ν: 3087(w), 2977(m), 2927(m), 2877(m), 2827(m), 2232(s), 1602(w), 1603(m), 1502(m), 1477(w), 1452(w), 1412(w), 1382(w), 1362(w), 1272(w), 1192(w), 1180(w), 1107(s), 1012(w), 982(w), 962(w), 902(m), 820(m); ^{1}H nmr (361.08 MHz, $CDCl_3$) δ_{TMS}: 1.40 (s, 3H, CH_3), 3.31 (s, 3H, OCH_3), 3.53 (d, 1H, $^2J_{4-4'}$ = 9.1 Hz, H of methylene group (4-H)), 3.57 (d, 1H, $^2J_{4-4'}$ = 9.1 Hz, H of methylene group (4′-H)), 5.08 (d, 1H, $^3J_{1trans-2}$ = 17.6 Hz, terminal vinyl H (1*trans*-H), 5.20 (d, 1H, $^3J_{1cis-2}$ = 10.8 Hz, terminal vinyl H (1*cis*-H)), 6.02 (dd, 1H, $^3J_{1trans-2}$ = 17.6 Hz, $^3J_{1cis-2}$ = 10.8 Hz, vinyl H (2-H)), 7.45 (d, 2H, $^3J_{2'-3'}$ = 8.2 Hz, $^3J_{5'-6'}$ = 8.2 Hz, H's adjacent to alkyl-substituted aryl carbon (2′-H, 6′-H)), 7.57 (d, 2H, $^3J_{2'-3'}$ = 8.2 Hz, $^3J_{5'-6'}$ = 8.2 Hz, H's adjacent to cyano-substituted aryl carbon (3′-H, 5′-H)); ^{13}C nmr (90.80 MHz, $CDCl_3$) δ: 23.06 (q, 128.0 Hz, CH_3) 46.11 (s, quaternary carbon, aryl substituted), 59.29 (q, 141.1 Hz, OCH_3), 79.68 (t, 142.3 Hz, OCH_2), 109.89 (s, quaternary aryl carbon, cyano substituted), 114.27 (t, 156.7 Hz, terminal vinyl CH_2), 118.99 (s, CN), 127.79 (dd, 161.6 Hz, 5.0 Hz, aromatic CH adjacent to alkyl-substituted aryl carbon), 131.83 (dd, 165.4 Hz, 4.2 Hz, aromatic CH adjacent to cyano-substituted aryl carbon), 142.83 (d, 154.6 Hz, vinyl CH), 150.88 (s, quaternary aryl carbon, alkyl substituted); ms *m/z*; 51(55), 53(27), 63(42), 75(33), 76(28), 77(42), 89(44), 115(45), 116(100), 127(49), 128(54), 129(89), 140(55), 141(27), 154(36), 156(89), 170(42), 171(55), 201(13). Anal. calcd. for $C_{13}H_{15}NO$: C 77.58, H 7.51, N 6.96; found: C 77.82, H 7.65, N 7.04.

*3-(4-Cyanophenyl)-4-methoxy-2-methyl-1-butene (**16**)*

The yield was 6%: infrared (PE-180) ν: 3090(w), 2980(m), 2920(m), 2890(m), 2830(m), 2210(s), 1648(m), 1610(s), 1505(m), 1450(m), 1411(w), 1374(m), 1230(w), 1190(m), 1175(w), 1115(s), 1020(w), 955(w), 940(w), 884(m), 820(m); ^{1}H nmr (361.08 MHz, $CDCl_3$) δ_{TMS}: 1.62 (s, 3H, CH_3), 3.34 (s, 3H, OCH_3), 3.59 (dd, 1H, $^3J_{3-4}$ = 7.6 Hz, $^3J_{3-4'}$ = 6.4 Hz, H of methine group (3-H)), 3.67 (dd, 1H, $^2J_{4-4'}$ = 9.1 Hz, $^3J_{3-4}$ = 7.6 Hz, H of methylene group (4-H)), 3.76 (dd, 1H, $^2J_{4-4'}$ = 9.1 Hz, $^3J_{3-4'}$ = 6.4 Hz, H of methylene group (4′-H)), 4.88 (s, terminal vinyl H), 4.98 (s, terminal vinyl H), 7.35 (d, 2H, $^3J_{2'-3'}$ = 8.2 Hz, $^3J_{5'-6'}$ = 8.2 Hz, H's adjacent to alkyl-substituted aryl carbon (2′-H, 6′-H)), 7.60 (d, 2H, $^3J_{2'-3'}$ = 8.2 Hz, $^3J_{5'-6'}$ = 8.2 Hz, H's adjacent to cyano-substituted aryl carbon (3′-H, 5′-H)); ^{13}C nmr (90.80 MHz, $CDCl_3$) δ: 21.80 (q, 125.9 Hz, CH_3), 52.39 (d, 129.1 Hz, CH, aryl substituted), 59.00 (q, 140.9 Hz, OCH_3), 74.14 (t, 142.6 Hz, OCH_2), 110. 49 (s, quaternary aryl carbon, cyano substituted), 112.59 (t, 155.8 Hz, terminal vinyl CH_2), 118.94 (s, CN), 128.91 (d, 160.3 Hz, aromatic CH adjacent to alkyl-substituted aryl carbon), 132.12 (d, 164.4 Hz, aromatic CH adjacent to cyano-substituted aryl carbon), 144.02 (s, vinyl quaternary carbon), 146.72 (s, quaternary aryl carbon, alkyl substituted); ms *m/z*: 51(53), 63(49), 77(32), 89(59), 116(100), 127(49), 128(53), 129(64), 140(64), 154(43), 156(33), 170(57), 171(58), 201(49). Anal. calcd. for $C_{13}H_{15}NO$: C 77.58, H 7.51, N 6.96; found: C 77.50, H 7.59, N 6.91.

*(E)-4-(4-Cyanophenyl)-1-methoxy-2-methyl-2-butene (**17**)*

The yield was 26%: infrared (PE-180) ν: 2990(m), 2930(s), 2825(m), 2231(s), 1606(m), 1505(m), 1449(m), 1415(w), 1377(w), 1192(m), 1110(s), 1090(s), 1020(w), 939(w), 900(w), 855(w), 809(m); ^{1}H nmr (361.08 MHz, $CDCl_3$) δ_{TMS}: 1.74 (s, 3H, CH_3), 3.31 (s, 3H, OCH_3), 3.46 (d, 2H, $^3J_{3-4}$ = 7.3 Hz, CH_2 group, aryl substituted (4-H)), 3.84 (s, 2H, CH_2 group, methoxy substituted), 5.56 (t, 1H, $^3J_{3-4}$ = 7.3 Hz, vinyl H (3-H)), 7.28 (d, 2H, $^3J_{2'-3'}$ = 8.1 Hz, $^3J_{5'-6'}$ = 8.1 Hz, H's adjacent to alkyl-substituted aryl carbon (2′-H, 6′-H)), 7.57 (d, 2H, $^3J_{2'-3'}$ = 8.1 Hz, $^3J_{5'-6'}$ = 8.1 Hz, H's adjacent to cyano-substituted aryl carbon (3′-H, 5′-H)). The nOe experiment: The methylene group (methoxy substituted) was irradiated. A 4% nOe on the methyl group and 2% on the methoxy group signals was observed; no nOe was observed for the vinyl hydrogen or the methylene group (aryl substituted). The methylene group (aryl substituted) was irradiated. An 11% nOe on the methyl group and 10% on aryl hydrogens signals was observed, ^{13}C nmr (90.80 MHz, $CDCl_3$) δ: 14.05 (q, 126.0 Hz, CH_3), 34.05 (t, 126.9 Hz, CH_2, aryl substituted), 57.75 (q, 140.4 Hz, OCH_3), 78.04 (t, 143.0 Hx, OCH_2), 109.87 (s, quaternary aryl carbon, cyano substituted), 118.98 (s, CN), 124.08 (d, 158.2 Hz, vinyl CH), 129.09 (d, 158.3 Hz, aromatic CH adjacent to alkyl-substituted aryl carbon), 132.22 (d, 163.8 Hz, aromatic CH adjacent to cyano-substituted aryl carbon), 134.79 (s, vinyl quaternary carbon), 146.59 (s, quaternary aryl carbon, alkyl substituted); ms *m/z*: 51(11), 55(48), 63(11), 72(12), 85(100), 89(19), 116(24), 127(19), 129(12), 153(10), 154(42), 169(11), 201(2). Exact Mass calcd. for $C_{13}H_{15}NO$: 201.1153; found: 201.1158.

*(Z)-4-(4-Cyanophenyl)-1-methoxy-2-methyl-2-butene (**18**)*

The yield of **18** was 3%: infrared (PE-180) ν: 2978(m), 2926(s), 2830(m), 2231(s), 1606(m), 1506(m), 1451(m), 1413(w), 1378(w), 1191(m), 1176(w), 1100(s), 1021(w), 946(m), 896(w), 851(w), 812(m); ^{1}H nmr (361.08 MHz, $CDCl_3$) δ_{TMS}: 1.82 (s, 3H, CH_3), 3.33 (s, 3H, OCH_3), 3.48 (d, 2H, $^3J_{3-4}$ = 7.4 Hz, CH_2 group, aryl substituted (4-H)), 3.99 (s, 2H, CH_2 group, methoxy substituted), 5.50 (t, 1H, $^3J_{3-4}$ = 7.4 Hz, vinyl H (3-H)), 7.28 (d, 2H, $^3J_{2'-3'}$ = 8.1 Hz, $^3J_{5'-6'}$ = 8.1 Hz, H's adjacent to alkyl-substituted aryl carbon (2′-H, 6′-H)), 7.57 (d, 2H, $^3J_{2'-3'}$ = 8.1 Hz, $^3J_{5'-6'}$ = 8.1 Hz, H's adjacent to cyano-substituted aryl carbon (3′-H, 5′-H)). The nOe experiment: The methylene group (methoxy substituted) was irradiated. A 2% nOe on the methyl group, 2% on the methoxy group, and 3% on the methylene group (aryl substituted) signals was observed; no nOe was observed for the vinyl hydrogen. The methylene group (aryl substituted) was irradiated. A 4% nOe on the methylene group (methoxy substituted), 3% on aryl hydrogens, and 4% on the vinyl hydrogen was observed; ^{13}C nmr (90.80 MHz, $CDCl_3$) δ: 21.80 (q, 125.8 Hz, CH_3), 34.04 (t, 126.8 Hz, CH_2, aryl substituted), 58.06 (q, 140.7 Hz, OCH_3), 70.96 (t, 139.2 Hz, OCH_2), 109.82 (s, quaternary aryl carbon, cyano substituted), 119.03 (s, CN), 125.72 (d, 149.9 Hz, vinyl CH), 129.11 (d, 160.5 Hz, aromatic CH adjacent to alkyl-substituted aryl carbon), 132.23 (d, 164.0 Hz, aromatic CH adjacent to cyano-substituted aryl carbon), 134.74 (s, vinyl quaternary carbon), 146.59 (s, quaternary aryl carbon, alkyl substituted); ms *m/z*: 51(20), 75(23), 76(12), 77(14), 101(27), 102(14), 128(77), 129(10), 156(100), 157(14), 170(24), 171(38). Exact Mass calcd. for $C_{13}H_{15}NO$: 201.1153; found: 201.1148.

*Formation of the methanol, 2,3-dimethyl-1,3-butadiene (**11**), and 1,4-dicyanobenzene (**1**) photo-NOCAS adducts **19–21** (reaction [5])*

A solution of 2,3-dimethyl-1,3-butadiene (**11**) (1.2 g, 0.02 mol) (the stabilizer, hydroquinone, was removed by distillation at atmospheric pressure), 1,4-dicyanobenzene (**1**) (1.9 g, 0.02 mol), and biphenyl (**5**) (1.1 g, 0.01 mol) in acetonitrile–methanol (3:1, 120 mL) was degassed by nitrogen ebullition for 5 min and irradiated for 144 h using a 450-W lamp at 3°C. The crude photolysate was separated by mplc using a linear gradient of hexanes – (50% dichloromethane, 50% hexanes). Products were eluted in the order **19**, **21**, and **20**. Further separation of **20** and **21** was achieved by dc/fc (diameter: 50 mm; eluent: 10% ethyl acetate – 90% hexanes).

*3-(4-Cyanophenyl)-4-methoxy-2,3-dimethyl-1-butene (**19**)*

The yield of **19** was 30%: infrared (PE-180) ν: 2979(m), 2929(m),

Can. J. Chem. Downloaded from www.nrcresearchpress.com by 85.192.166.187 on 09/08/12
For personal use only.

2889(m), 2919(m), 2237(s), 1643(w), 1609(m), 1507(m), 1454(m), 1405(w), 1379(m), 1197(m), 1163(w), 1108(s), 1071(w), 1029(w), 967(w), 944(w), 886(m), 828(m); ^{1}H nmr (361.08 MHz, $CDCl_3$) δ_{TMS}: 1.46 (s, 3H, CH_3), 1.51 (s, 3H, CH_3), 3.31 (s, 3H, OCH_3), 3.59 (d, 1H, $^2J_{4-4'}$ = 8.9 Hz, H of methylene group (4-H)), 3.63 (d, 1H, $^2J_{4-4'}$ = 8.9 Hz, H of methylene group (4′-H)), 4.93 (s, 1H, terminal vinyl H), 5.01 (s, 1H, terminal vinyl H), 7.40 (d, 2H, $^3J_{2'-3'}$ = 8.3 Hz, $^3J_{5'-6'}$ = 8.3 Hz, H's adjacent to alkyl-substituted aryl carbon (2′-H, 6′-H)), 7.56 (d, 2H, $^3J_{2'-3'}$ = 8.3 Hz, $^3J_{5'-6'}$ = 8.3 Hz, H's adjacent to cyano-substituted aryl carbon (3′-H, 5′-H)); ^{13}C nmr (90.80 MHz, $CDCl_3$) δ: 21.63 (q, 127.9 Hz, CH_3), 23.05 (q, 128.4 Hz, CH_3), 48.70 (s, quaternary carbon, aryl substituted), 59.33 (q, 141.0 Hz, OCH_3), 79.13 (t, 141.9 Hz, OCH_2), 109.87 (s, quaternary aryl carbon, cyano substituted), 112.19 (t, 154.6 Hz, terminal vinyl CH_2), 119.02 (s, CN), 127.70 (dd, 159.3 Hz, 4.9 Hz, aromatic CH adjacent to alkyl-substituted aryl carbon), 131.85 (dd, 165.5 Hz, 4.2 Hz, aromatic CH adjacent to cyano-substituted aryl carbon), 148.13 (s, quaternary vinyl carbon), 150.90 (s, quaternary aryl carbon, alkyl substituted); ms *m/z*: 51(23), 77(23), 89(23), 115(38), 116(46), 127(28), 128(33), 130(22), 140(28), 142(92), 143(38), 153(28), 154(46), 155(27), 168(46), 169(21), 170(100), 184(43), 215(27). Anal. calcd. for $C_{14}H_{17}NO$: C 78.10, H 7.96, N 6.51; found: C 77.83, H 7.85, N 6.54.

*(E)-1-(4-Cyanophenyl)-4-methoxy-2,3-dimethyl-2-butene (**20**)*

The yield of **20** was 15%: infrared (PE-180) ν: 2983(m), 2928(s), 2819(m), 2236(s), 1606(m), 1503(m), 1445(m), 1421(w), 1373(m), 1183(w), 1093(s), 1018(w), 923(w), 883(w), 828(w), 801(m); ^{1}H nmr (361.08 MHz, $CDCl_3$) δ_{TMS}: 1.65 (s, 3H, CH_3), 1.82 (s, 3H, CH_3), 3.32 (s, 3H, OCH_3), 3.48 (s, 2H, CH_2 group, aryl substituted), 3.97 (s, 2H, CH_2 group, methoxy substituted), 7.25 (d, 2H, $^3J_{2'-3'}$ = 7.9 Hz, $^3J_{5'-6'}$ = 7.9 Hz, H's adjacent to alkyl-substituted aryl carbon (2′-H, 6′-H)), 7.55 (d, 2H, $^3J_{2'-3'}$ = 7.9 Hz, $^3J_{5'-6'}$ = 7.9 Hz, H's adjacent to cyano-substituted aryl carbon (3′-H, 5′-H)). The nOe experiment: The methylene group (methoxy substituted) was irradiated. A 4% nOe on one methyl group, 2% on the other methyl group, and 1% on the methoxy group were observed. The methylene group (aryl substituted) was irradiated. A 3% nOe on one methyl group and 5% on the other methyl group were observed; ^{13}C nmr (90.80 MHz, $CDCl_3$) δ: 16.83 (q, 125.6 Hz, CH_3), 18.12 (q, 122.0 Hz, CH_3), 40.65 (t, 126.7 Hz, CH_2, aryl substituted), 57.80 (q, 140.4 Hz, OCH_3), 73.15 (t, 140.2 Hz, OCH_2), 110.07 (s, quaternary aryl carbon, cyano substituted), 118.89 (s, CN), 128.94 (s, quaternary vinyl carbon), 129.18 (d, 162.2 Hz, aromatic CH adjacent to alkyl-substituted aryl carbon), 130.55 (s, quaternary vinyl carbon), 132.18 (d, 164.8 Hz, aromatic CH adjacent to cyano-substituted aryl carbon), 145.86 (s, quaternary aryl carbon, alkyl substituted); ms *m/z*: 51(4), 53(4), 65(5), 67(12), 69(8), 89(12), 99(100), 100(7), 115(7), 116(15), 128(4), 140(8), 141(8), 142(11), 143(4), 153(9), 154(14), 166(4), 168(53), 169(7), 182(7), 183(25), 184(4), 215(1). Exact Mass calcd. for $C_{14}H_{17}NO$: 215.1310; found: 215.1291.

*(Z)-1-(4-Cyanophenyl)-4-methoxy-2,3-dimethyl-2-butene (**21**)*

The yield was 8%: infrared (PE-180) ν: 2980(m), 2820(m), 2230(s), 1608(m), 1505(m), 1450(m), 1413(w), 1385(m), 1190(m), 1145(w), 1090(s), 1020(w), 925(w), 830(w), 801(m); ^{1}H nmr (361.08 MHz, $CDCl_3$) δ_{TMS}: 1.60 (s, 3H, CH_3), 1.81 (s, 3H, CH_3), 3.33 (s, 3H, OCH_3), 3.52 (s, 2H, CH_2 group, aryl substituted), 3.98 (s, 2H, CH_2 group, methoxy substituted), 7.25 (d, 2H, $^3J_{2'-3'}$ = 7.6 Hz, $^3J_{5'-6'}$ = 7.6 Hz, H's adjacent to alkyl-substituted aryl carbon (2′-H, 6′-H)), 7.56 (d, 2H, $^3J_{2'-3'}$ = 7.6 Hz, $^3J_{5'-6'}$ = 7.6 Hz, H's adjacent to cyano-substituted aryl carbon (3′-H, 5′-H)). The nOe experiment: The methylene group (methoxy substituted) was irradiated. A 2% nOe on one methyl group and 4% on the methylene group (aryl substituted) signal was observed. The methylene group (aryl substituted) was irradiated. A 2% nOe on one methyl group and 3% on the methylene group (methoxy substituted) signal was observed; ^{13}C nmr (90.80 MHz, $CDCl_3$) δ: 17.19 (q, 129.1 Hz, CH_3), 18.74 (q, 128.4 Hz, CH_3), 40.01 (t, 128.2 Hz, CH_2, aryl substituted), 58.11 (q, 140.0 Hz, OCH_3), 73.35 (t, 144.1 Hz, OCH_2), 110.00 (s, quaternary aryl carbon, cyano substituted), 118.98 (s, CN), 128.95 (s, quaternary vinyl carbon), 129.32 (d, 161.9 Hz, aromatic CH adjacent to alkyl-substituted aryl carbon), 130.80 (s, quaternary vinyl carbon), 132.16 (d, 163.3 Hz, aromatic CH adjacent to cyano-substituted aryl carbon), 146.11 (s, quaternary aryl carbon, alkyl substituted); ms *m/z*: 51(5), 53(6), 63(6), 67(9), 69(9), 89(12), 99(37), 115(7), 116(14), 127(5), 140(8), 141(9), 142(8), 143(5), 153(11), 154(8), 166(5), 168(100), 169(12), 183(30), 184(5). Exact Mass calcd. for $C_{14}H_{17}NO$: 215.1310; found: 215.1285.

*Formation of the methanol, 2,5-dimethyl-2,4-hexadiene (**12**), and 1,4-dicyanobenzene (**1**) photo-NOCAS adducts **22** and **23** (reaction [6])*

A solution of 2,5-dimethyl-2,4-hexadiene (**12**) (4.9 g, 0.04 mol), 1,4-dicyanobenzene (**1**) (2.8 g, 0.02 mol), and biphenyl (**5**) (6.7 g, 0.04 mol) in acetonitrile-methanol (3:1, 180 mL) (freshly distilled) was degassed by nitrogen ebullition for 15 min and irradiated for 123 h using a 450-W lamp (irradiation time is only 18 h using a 1-kW lamp equipped with a quartz immersion vessel). The yield of the crude mixture was 12.8 g. This crude mixture was partially separated by mplc using a linear solvent gradient of hexanes–dichloromethane. Products were eluted in the order **22**, **23**, followed by unreacted **1**. Unreacted **1** was recovered by adding hexanes to the mixture; **1** precipitated and was then removed by filtration. Fractions containing mixtures were combined and rechromatographed (dc/fc; dimensions 50 mm × 65 mm) eluting with 10% diethyl ether/90% hexanes. Fractions containing pure **23** were dissolved in methanol; **23** crystallizes upon cooling. The crystals were repeatedly washed with methanol and dried in vacuo.

trans-*2-(4-Cyanophenyl)-5-methoxy-2,5-dimethyl-3-hexene (**22**)*

The yield of **22** was 82% (based on almost complete conversion of **1**): the melting point was 44.6–45.6°C; infrared (PE-180) ν: 2970(s), 2930(m), 2821(w), 2230(s), 1608(m), 1501(m), 1465(m), 1401(w), 1379(m), 1362(m), 1292(w), 1255(w), 1170(m), 1160(w), 1072(s), 1020(w), 1000(w), 970(m), 825(s), 750(w), 725(w); ^{1}H nmr (361.08 MHz, $CDCl_3$) δ_{TMS}: 1.28 (s, 6H, two CH_3 groups), 1.42 (s, 6H, two CH_3 groups), 3.16 (s, 3H, OCH_3), 5.48 (d, 1H, $^3J_{3-4}$ = 16.2 Hz, vinyl H), 5.72 (d, 1H, $^3J_{3-4}$ = 16.2 Hz, vinyl H), 7.43 (d, 2H, $^3J_{2'-3'}$ = 8.4 Hz, $^3J_{5'-6'}$ = 8.4 Hz, H's adjacent to alkyl-substituted aryl carbon (2′-H, 6′-H)), 7.59 (d, 2H, $^3J_{2'-3'}$ = 8.4 Hz, $^3J_{5'-6'}$ = 8.4 Hz, H's adjacent to cyano-substituted aryl carbon (3′-H, 5′-H)); ^{13}H nmr (90.80 MHz, $CDCl_3$) δ: 25.90 (q, 126.2 Hz, CH_3), 28.57 (q, 126.7 Hz, CH_3), 40.73 (s, quaternary carbon, aryl substituted), 50.29 (q, 140.2 Hz, OCH_3), 74.73 (s, quaternary carbon, methoxy substituted), 109.64 (s, quaternary aryl carbon, cyano substituted), 119.01 (s, CN), 126.94 (dd, 158.6 Hz, 5.2 Hz, aromatic CH adjacent to alkyl-substituted aryl carbon), 131.99 (dd, 165.5 Hz, 4.8 Hz, aromatic CH adjacent to cyano-substituted aryl carbon), 132.87 (d, 146.9 Hz, vinyl CH), 138.03 (d, 148.9 Hz, vinyl CH), 154.39 (s, quaternary aryl carbon, alkyl substituted); ms *m/z*: 55(23), 73(53), 77(26), 99(96), 116(53), 154(31), 168(58), 170(27), 181(31), 196(71), 228(100). Anal. calcd. for $C_{16}H_{21}NO$: C 78.97, H 8.70, N 5.76; found: C 78.88, H 8.76, N 5.79.

trans-*5-(4-Cyanophenyl)-2,2,5-trimethyl-3-hexenenitrile (**23**)*

The yield of **23** was 2% (based on almost complete conversion of **1**): the melting point was 84.2–85.0°C; infrared (PE-180) ν: 2970(w), 2917(w), 2892(s), 2846(s), 2982(m), 2226(s), 1604(s), 1522(w), 1500(s), 1467(s), 1446(m), 1388(m), 1371(m), 1360(m), 1300(m), 1247(m), 1228(m), 1216(m), 1203(w), 1180(w), 1136(m), 1110(w), 1090(s), 1014(m), 1010(w), 987(w), 964(s), 934(m), 911(w), 852(m), 828(s), 813(s), 722(w); ^{1}H nmr (361.08 MHz, $CDCl_3$) δ_{TMS}: 1.43 (s, 6H, two CH_3 groups), 1.46 (s, 6H, two CH_3 groups), 5.34 (d, 1H, $^3J_{3-4}$ = 15.8 Hz, vinyl H), 6.01 (d, 1H, $^3J_{3-4}$ = 15.8 Hz, vinyl H), 7.41 (d, 2H, $^3J_{2'-3'}$ = 8.7 Hz, $^3J_{5'-6'}$ = 8.7 Hz, H's adjacent to alkyl-substituted aryl carbon (2′-H, 6′-H)), 7.60 (d, 2H, $^3J_{2'-3'}$ = 8.7 Hz, $^3J_{5'-6'}$ = 8.7 Hz, H's adjacent to cyano-substituted aryl carbon (3′-H, 5′-H)); ^{13}C nmr (90.80 MHz, $CDCl_3$) δ: 27.70 (q, 131.2 Hz, CH_3), 28.01 (q, 127.9 Hz, CH_3), 34.56 (s, quaternary carbon, cyano substituted), 40.64 (s, quaternary carbon, aryl substituted), 109.99 (s, quaternary aryl carbon, cyano substituted), 118.90 (s, CN), 123.52 (s, CN), 126.88 (d, 161.3

Can. J. Chem. Downloaded from www.nrcresearchpress.com by 85.192.166.187 on 09/08/12
For personal use only.

Hz, aromatic CH adjacent to alkyl-substituted aryl carbon), 129.08 (d, 149.5 Hz, vinyl CH), 132.12 (d, 169.8 Hz, aromatic CH adjacent to cyano-substituted aryl carbon), 138.90 (d, 152.1 Hz, vinyl CH), 153.38 (s, quaternary aryl carbon, alkyl substituted); ms *m/z*: 51(7), 77(8), 89(6), 115(7), 116(16), 127(8), 128(8), 140(8), 142(20), 143(8), 153(8), 154(15), 155(12), 168(8), 170(100), 171(12), 181(9), 196(29), 238(1). Anal. calcd. for $C_{16}H_{18}N_2$: C 80.63, H 7.61, N 11.76; found: C 80.41, H 7.78, N 11.57.

*Formation of the 2,5-dimethyl-2,4-hexadiene (**12**) photo-NOCAS adduct **23**, using acetonitrile as solvent and added KCN, 18-crown-6 (reaction [7])*

A solution of 2,5-dimethyl-2,4-hexadiene (**12**) (1.9 g, 0.017 mol), 1,4-dicyanobenzene (**1**) (0.6 g, 0.005 mol), biphenyl (**5**) (1.3 g, 0.0084 mol), KCN (0.45 g, 0.0069 mol), and 18-crown-6 (0.10 g, 0.38 mmol) in 40 mL of acetonitrile (freshly distilled) was degassed by nitrogen ebullition for 5 min and irradiated for 24 h using a 1-kW lamp equipped with a quartz immersion vessel. The crude photolysate was separated by mplc, eluting with a hexanes – (50% ether, 50% hexanes) solvent gradient. The yield of *trans*-5-(4-cyanophenyl)-2,2,5-trimethyl-3-hexanenitrile (**23**) was 80% (based on almost complete conversion of **1**).

*Formation of the 2,5-dimethyl-2,4-hexadiene (**12**), 1,4-dicyanobenzene (**1**) 1:1-adducts **26**, **27**, **28**, and **29**, by irradiation of an acetonitrile–2,4,6-trimethylpyridine (**25**, collidine) solution (reaction [8])*

A solution of 2,5-dimethyl-2,4-hexadiene (**12**) (4.3 g, 0.04 mol), 1,4-dicyanobenzene (**1**) (2.6 g, 0.02 mol), and biphenyl (**5**) (1.5 g, 0.01 mol) in 160 mL of acetonitrile and 2.4 mL of collidine (**25**) was degassed by nitrogen ebullition for 15 min and irradiated for 100 h using a 1-kW lamp. The solvent was removed and the crude photolysate was separated (mplc) with hexanes as the eluent. The products eluted in the order: **26**, **27**, **28**, followed by **29**.

*3-(4-Cyanophenyl)-2,5-dimethyl-1,4-hexadiene (**26**)*

The yield of **26** was 7%: infrared (PE-180) ν: 2977(s), 2927(s), 2857(m), 2237(s), 1647(w), 1607(m), 1503(m), 1442(m), 1377(m), 1174(w), 1112(w), 1022(w), 880(m), 847(w), 827(m), 797(m), 722(w); ^{1}H nmr (361.08 MHz, $CDCl_3$) δ_{TMS}: 1.62 (s, 3H, CH_3), 1.66 (s, 3H, CH_3), 1.78 (s, 3H, CH_3), 4.20 (d, 1H, $^3J_{3-4}$ = 9.2 Hz, H of methine group (3-H)), 4.83 (s, 1H, terminal vinyl H), 4.91 (s, 1H, terminal vinyl H), 5.36 (d, 1H, $^3J_{3-4}$ = 9.2 Hz, vinyl H (4-H)), 7.32 (d, 2H, $^3J_{2'-3'}$ = 8.2 Hz, $^3J_{5'-6'}$ = 8.2 Hz, H's adjacent to alkyl-substituted aryl carbon (2'-H, 6'-H)), 7.58 (d, 2H, $^3J_{2'-3'}$ = 8.2 Hz, $^3J_{5'-6'}$ = 8.2 Hz, H's adjacent to cyano-substituted aryl carbon (3'-H, 5'-H)); ^{13}C nmr (90.80 MHz, $CDCl_3$) δ: 18.03 (q, 127.3 Hz, CH_3), 21.07 (q, 126.5 Hz, CH_3), 25.95 (q, 127.1 Hz, CH_3), 51.47 (d, 126.8 Hz, CH, aryl substituted), 109.82 (s, quaternary aryl carbon, cyano substituted), 112.54 (t, 156.0 Hz, terminal vinyl CH_2), 119.11 (s, CN), 124.38 (d, 156.0 Hz, vinyl CH), 128.69 (d, 159.9 Hz, aromatic CH adjacent to alkyl-substituted aryl carbon), 132.15 (d, 163.3 Hz, aromatic CH adjacent to cyano-substituted aryl carbon), 134.19 (s, vinyl quaternary carbon), 146.37 (s, quaternary carbon), 149.32 (s, quaternary carbon); ms *m/z*: 55(11), 77(16), 116(46), 127(26), 140(23), 142(28), 153(23), 154(47), 168(100), 170(28), 196(87), 211(23). Exact Mass calcd. for $C_{15}H_{17}N$: 211.1361; found: 211.1368.

trans-*5-(4-Cyanophenyl)-2,5-dimethyl-1,3-hexadiene (**27**)*

The yield of **27** was 27%: infrared (PE-180) ν: 2966(m), 2928(s), 2871(m), 2236(m), 1609(m), 1506(m), 1466(m), 1376(w), 1091(w), 1018(w), 951(m), 871(w) 821(m); ^{1}H nmr (361.08 MHz, $CDCl_3$) δ_{TMS}: 1.45 (s, 6H, two CH_3 groups), 1.84 (s, 3H, CH_3), 4.96 (s, 1H, terminal vinyl H), 4.97 (s, 1H, terminal vinyl H), 5.77 (d, 1H, $^3J_{3-4}$ = 16.0 Hz, vinyl H (3-H)), 6.17 (d, 1H, $^3J_{3-4}$ = 16.0 Hz, vinyl H (4-H)), 7.44 (d, 2H, $^3J_{2'-3'}$ = 8.6 Hz, $^3J_{5'-6'}$ = 8.6 Hz, H's adjacent to alkyl-substituted aryl carbon (2'-H, 6'-H)), 7.58 (d, 2H, $^3J_{2'-3'}$ = 8.6 Hz, $^3J_{5'-6'}$ = 8.6 Hz, H's adjacent to cyano-substituted aryl carbon (3'-H, 5'-H)); ^{13}C nmr (90.80 MHz, $CDCl_3$) δ: 18.70 (q, 127.2 Hz, vinyl CH_3), 28.54 (q, 127.0 Hz, two CH_3 groups), 40.95 (s, quaternary carbon, aryl substituted), 110.00 (s, quaternary aryl carbon, cyano substituted), 116.04 (t, 155.5 Hz, terminal vinyl CH_2), 119.04 (s, CN), 127.05 (d, 161.3 Hz, aromatic CH adjacent to alkyl-substituted aryl carbon), 130.14 (d, 158.5 Hz, vinyl CH), 131.98 (d, 166.0 Hz, aromatic CH adjacent to cyano-substituted aryl carbon), 138.25 (d, 150.9 Hz, vinyl CH), 141.64 (s, quaternary carbon), 154.52 (s, quaternary carbon); ms *m/z*: 51(22), 53(16), 55(14), 67(13), 77(25), 89(13), 115(14), 116(50), 127(16), 128(13), 140(19), 141(14), 153(25), 154(33), 166(16), 167(28), 168(100), 169(25), 181(19), 182(31), 196(66), 211(17). Exact Mass calcd. for $C_{15}H_{17}N$: 211.1361; found: 211.1372.

*(Z)-1-(4-Cyanophenyl)-2,5-dimethyl-2,4-hexadiene (**28**)*

The yield of **28** was 10%: infrared (PE-180) ν: 2970(m), 2930(s), 2870(m), 2250(s), 1740(m), 1685(m), 1620(s), 1510(m), 1450(m), 1420(w), 1380(m), 1270(w), 1180(w), 1150(w), 970(w), 840(w); ^{1}H nmr (250.13 MHz, $CDCl_3$) δ_{TMS}: 1.68 (s, 3H, CH_3), 1.79 (s, 3H, CH_3), 1.81 (s, 3H, CH_3), 3.52 (s, 2H, CH_2 group, aryl substituted), 6.06 (d, 1H, $^3J_{3-4}$ = 11.3 Hz, vinyl H (3-H)), 6.20 (d, 1H, $^3J_{3-4}$ = 11.3 Hz, vinyl H (4-H)), 7.27 (d, 2H, $^3J_{2'-3'}$ = 8.2 Hz, $^3J_{5'-6'}$ = 8.2 Hz, H's adjacent to alkyl-substituted aryl carbon (2'-H, 6'-H)), 7.56 (d, 2H, $^3J_{2'-3'}$ = 8.2 Hz, $^3J_{5'-6'}$ = 8.2 Hz, H's adjacent to cyano-substituted aryl carbon (3'-H, 5'-H)); ^{13}C nmr (62.90 MHz, $CDCl_3$) δ: 18.27 (q, 123.4 Hz, CH_3), 23.74 (q, 125.1 Hz, CH_3), 26.45 (q, 131.6 Hz, CH_3), 38.12 (t, 127.9, CH_2), 109.78 (s, quaternary aryl carbon, cyano substituted), 119.13 (s, CN), 120.40 (d, 151.0 Hz, vinyl CH), 124.02 (d, 151.3 Hz, vinyl CH), 129.30 (d, 161.0 Hz, aromatic CH adjacent to alkyl-substituted aryl carbon), 132.17 (d, 164.4 Hz, aromatic CH adjacent to cyano-substituted aryl carbon), 132.20 (s, vinyl quaternary carbon), 135.02 (s, vinyl quaternary carbon), 145.95 (s, quaternary aryl carbon, alkyl substituted); ms *m/z*: 53(21), 55(27), 67(32), 77(27), 89(25), 95(27), 116(50), 154(32), 168(100), 196(53), 211(58). X-ray data: see footnote 3.

*(E)-1-(4-Cyanophenyl)-2,5-dimethyl-2,4-hexadiene (**29**)*

The yield of **29** was 14%: infrared (PE-180) ν: 2965(m), 2915(s), 2855(w), 2235(s), 1608(s), 1505(m), 1435(m), 1405(m), 1385(m), 1175(w), 1105(w), 1045(w), 1015(w), 835(m), 805(m), 785(m); ^{1}H nmr (361.08 MHz, $CDCl_3$) δ_{TMS}: 1.64 (s, 3H, CH_3), 1.75 (s, 3H, CH_3), 1.82 (s, 3H, CH_3), 3.42 (s, 2H, CH_2 group, aryl substituted), 5.99 (d, 1H, $^3J_{3-4}$ = 11.3 Hz, vinyl H (3-H)), 6.10 (d, 1H, $^3J_{3-4}$ = 11.3 Hz, vinyl H (4-H)), 7.27 (d, 2H, $^3J_{2'-3'}$ = 8.1 Hz, $^3J_{5'-6'}$ = 8.1 Hz, H's adjacent to alkyl-substituted aryl carbon (2'-H, 6'H)), 7.56 (d, 2H, $^3J_{2'-3'}$ = 8.1 Hz, $^3J_{5'-6'}$ = 8.1 Hz, H's adjacent to cyano-substituted aryl carbon (3'-H, 5'-H)); ^{13}C nmr (90.80 MHz, $CDCl_3$) δ: 16.24 (q, 125.9 Hz, CH_3), 18.27 (q, 124.2 Hz, CH_3), 26.39 (q, 125.0 Hz, CH_3), 46.66 (t, 126.6, CH_2), 110.75 (s, quaternary aryl carbon, cyano substituted), 119.10 (s, CN), 120.76 (d, 152.0 Hz, vinyl CH), 123.86 (d, 149.4 Hz, vinyl CH), 129.58 (d, 161.3 Hz, aromatic CH adjacent to alkyl-substituted aryl carbon), 132.09 (d, 163.2 Hz, aromatic CH adjacent to cyano-substituted aryl carbon), 132.77 (s, vinyl quaternary carbon), 134.87 (s, vinyl quaternary carbon), 145.97 (s, quaternary aryl carbon, alkyl substituted); ms *m/z*: 53(25), 55(33), 67(43), 77(38), 79(21), 89(31), 95(37), 116(76), 140(20), 154(46), 167(22), 168(100), 169(24), 182(24), 196(66), 211(80). Exact Mass calcd. for $C_{15}H_{17}N$: 211.1361; found: 211.1370.

*Photosensitized (electron transfer) irradiation of **1** and **12***

A solution of **1** (31 mg, 2.4×10^{-4} mol), **12** (0.07 mL, 4.9×10^{-4} mol), and the photosensitizer (electron transfer), anthracene (**24**) (18 mg, 9.9×10^{-5} mol), in 4 mL of acetonitrile–methanol (3:1), was irradiating using a 1-kW lamp in a quartz immersion vessel. The light was passed through a glass filter, which absorbs light of wavelengths shorter than 330 nm. After 3 h, analysis (gc/fid) of an aliquot showed the ratio of **22/23** = 40. No reaction occurred when a solution of **1** and **12** was irradiated, without added **24**, under identical conditions.

Acknowledgements

This work was supported by a grant from the Natural Sciences and Engineering Research Council of Canada. We

thank Dr. D.L. Hooper at the Atlantic Regional Magnetic Resonance Centre at Dalhousie University for the high-field NMR spectra and for help in the preparation of the manuscript. Exact mass determinations were carried out by Mr. D. Embree at the Institute for Marine Biosciences, Halifax. We thank Dr. T.S. Cameron at Dalhousie for the X-ray analysis of **28**.

1. (*a*) D.R. Arnold, K.A. McManus, and X. Du. Can. J. Chem. **72**, 415 (1994); (*b*) D.R. Arnold and X. Du. Can. J. Chem. **72**, 403 (1994); (*c*) K. McMahon and D.R. Arnold. Can. J. Chem. **71**, 450 (1993); (*d*) D.R. Arnold and X. Du. J. Am. Chem. Soc. **111**, 7666 (1989).
2. (*a*) A.L. Perrott and D.R. Arnold. Can. J. Chem. **70**, 272 (1992); (*b*) R. Popielarz and D.R. Arnold. J. Am. Chem. Soc. **112**, 3068 (1990).
3. (*a*) R.M. Borg, D.R. Arnold, and T.S. Cameron. Can. J. Chem. **62**, 1785 (1984); (*b*) D.R. Arnold and M.S. Snow. Can. J. Chem. **66**, 3012 (1988); (*c*) Y. Shigemitsu and D.R. Arnold. J. Chem. Soc. Chem. Commun. 407 (1975); (*d*) R.A. Neunteufel and D.R. Arnold. J. Am. Chem. Soc. **95**, 4080 (1973); (*e*) D.R. Arnold and S.A. Mines. Can. J. Chem. **67**, 689 (1989); (*f*) Can. J. Chem. **65**, 2312 (1987).
4. (*a*) I.R. Gould, D. Ege, J.E. Moser, and S. Farid. J. Am. Chem. Soc. **112**, 4290 (1990); (*b*) P. Suppan. Top. Curr. Chem. **163**, 95 (1992).
5. K. Mizuno, C. Pac, and H. Sakurai. J. Am. Chem. Soc. **96**, 2993 (1974).
6. (*a*) T. Shono and A. Ikeda. Chem. Lett. 311 (1976); (*b*) T. Shono, K. Tsubata, and Y. Nakamura. Nippon Kagaku Kaishi, 1794 (1984).
7. J.H.H. Meurs and W. Eilenberg. Tetrahedron, **47**, 705 (1991).
8. Y. Kubo, M. Mihara, and T. Araki. Bull. Chem. Soc. Jpn. **60**, 241 (1987).
9. (*a*) D.J. Bellville and N.L. Bauld. J. Am. Chem. Soc. **104**, 2665 (1982); (*b*) D.J. Bellville, D.D. Wirth, and N.L. Bauld. J. Am. Chem. Soc. **103**, 718 (1981); (*c*) N.L. Bauld and R. Pabon. J. Am. Chem. Soc. **105**, 633 (1983).
10. (*a*) N.C Yang and M.J. Jorgenson. Tetrahedron Lett. **19**, 1203 (1964); (*b*) H.J. Bestmann. Angew. Chem. Int. Ed. Engl. **4**, 583 (1965); (*c*) R.S. Bly and R.T. Swindell. J. Org. Chem. **30**, 10 (1965).
11. D. Rehm and A. Weller. Isr. J. Chem. **8**, 259 (1970).
12. (*a*) R.S. Nicholson and I. Shain. Anal. Chem. **36**, 706 (1964); (*b*) Anal. Chem. **37**, 178 (1965).
13. W.C. Neikam and M.M. Desmond. J. Am. Chem. Soc. **86**, 4811 (1964).
14. (*a*) L.J. Johnston and N.P. Schepp. J. Am. Chem. Soc. **115**, 6564 (1993); (*b*) S.L. Mattes and S. Farid. J. Am. Chem. Soc. **108**, 7356 (1986).
15. (*a*) R.G. Pearson and J. Songstad. J. Am. Chem. Soc. **89**, 1827 (1967); (*b*) R.G. Pearson, H. Sobel, and J. Songstad. J. Am. Chem. Soc. **90**, 319 (1968); (*c*) P.L. Bock and G.M. Whitesides. J. Am. Chem. Soc. **96**, 2826 (1974).
16. (*a*) J.K. Kochi and P.J. Krusic. J. Am. Chem. Soc. **90**, 7157 (1968); (*b*) D.M. Golden, N.A. Gac, and S.W. Benson. J. Am. Chem. Soc. **91**, 2136 (1969); (*c*) P.J. Gorton and R. Walsh. Chem. Commun. 783 (1972); (*d*) E.S. Huyser, F.W. Siegert, and H. Wynberg. Tetrahedron Lett. 2569 (1965).
17. (*a*) D.A.C. Compton, W.O. George, and W.F. Maddams. J. Chem. Soc. Perkin Trans. 2, 1399 (1972); (*b*) D.J. Marais, N. Sheppard, and B.P. Stoicheff. Tetrahedron, **17**, 163 (1962); (*c*) P.W. Mui and E. Grunwald. J. Am. Chem. Soc. **104**, 6562 (1982); (*d*) J. Phys. Chem. **88**, 6340 (1984); (*e*) M.E. Squillacote, T.C. Semple, and P.W. Mui. J. Am. Chem. Soc. **107**, 6842 (1985).
18. (*a*) J.C. Tai and N.L. Allinger. J. Am. Chem. Soc. **98**, 7928 (1976); (*b*) Tetrahedron, **37**, 2755 (1981); (*c*) N.L. Allinger, Y.H. Yuh, and J.-H. Lii. J. Am. Chem. Soc. **111**, 8551 (1989).
19. A.M. de P. Nicholas and D.R. Arnold. Can. J. Chem. **60**, 2165 (1982).
20. (*a*) B. Jaun, J. Schwarz, and R. Breslow. J. Am. Chem. Soc. **102**, 5741 (1980); (*b*) D.D.M. Wayner and D. Griller. *In* From atoms to polymers: isoelectronic analogies. *Edited by* J.F. Leibman and A. Greenberg. VCH Publishers, Inc., New York. 1989.
21. (*a*) W.C. Still, M. Kahn, and A. Mitra. J. Org. Chem. **43**, 2923 (1978); (*b*) L.M. Harwood. Aldrichimica Acta, **18**, 25 (1985).
22. A. Okamoto, M.S. Snow, and D.R. Arnold. Tetrahedron, **42**, 6175 (1986).
23. D.R. Arnold and D.D.M. Wayner. Can. J. Chem. **64**, 100 (1986).
24. H.A. Benesi and J.H. Hildebrand. J. Am. Chem. Soc. **71**, 2703 (1949).

Can. J. Chem. Downloaded from www.nrcresearchpress.com by 85.192.166.187 on 09/08/12
For personal use only.

Study of the reaction between conjugated azoalkenes and α-unsubstituted- or α-substituted-β-dicarboxylate derivatives: an improved preparation of unknown polyfunctionalized 1-amino-1*H*-pyrrol-2(3*H*)-ones[1]

ORAZIO A. ATTANASI, LUCIA DE CRESCENTINI, AND FRANCO SERRA-ZANETTI[2]

Istituto di Chimica Organica della Facoltà di Scienze, Università di Urbino, Piazza della Repubblica 13, 61029 Urbino, Italy

AND

ELISABETTA FORESTI

Dipartimento di Chimica "G. Ciamician," Università di Bologna, Via Selmi 2, 40126 Bologna, Italy

Received October 27, 1993[3]

ORAZIO A. ATTANASI, LUCIA DE CRESCENTINI, FRANCO SERRA-ZANETTI, and ELISABETTA FORESTI. Can. J. Chem. **72**, 2305 (1994).

In the presence of sodium methoxide in catalytic amounts, conjugated azoalkenes easily react with α-unsubstituted-or α-substituted-β-dicarboxylate derivatives to give at first hydrazonic derivatives, by 1,4-conjugate addition, and, by increasing sodium methoxide up to stoichiometric amounts, new polyfunctionalized 1-amino-1*H*-pyrrol-2(3*H*)-ones.

ORAZIO A. ATTANASI, LUCIA DE CRESCENTINI, FRANCO SERRA-ZANETTI et ELISABETTA FORESTI. Can. J. Chem. **72**, 2305 (1994).

En présence de quantités catalytiques de méthylate de sodium, les azoalcènes conjugués réagissent avec les dérivés β-dicarboxylates, substitués ou non en α, pour donner en premier lieu des dérivés hydrazoniques, par addition-1,4 conjuguée. Lorsqu'on augmente les quantités de méthylate de sodium pour arriver à des proportions stoechiométrique, il y a formation de nouvelles 1-amino-1*H*-pyrrol-2(3*H*)-ones polyfonctionnalisées.

[Traduit par la rédaction]

Introduction

It is recognized that the synthesis of new heterocycles represents an important area of research of immense academic and industrial importance (1).

Conjugated azoalkenes have attracted increasing attention because of their potential use in the synthesis of heterocycles and a great deal of effort has been directed by our group towards the development of a convenient strategy for the synthesis of a variety of widely substituted new 1-aminopyrrole derivatives.

The reaction of conjugated azoalkenes with many compounds containing active methine and methylene groups gives polyfunctionalized 1-aminopyrrole derivatives via a preliminary 1,4-conjugate addition, followed by subsequent intramolecular cyclization of the hydrazonic intermediates first obtained (2).

In the course of our previous investigations, cyano or ketonic carbonyl groups had frequently been observed to be effective in the internal heterocyclization processes of the 1,4-adduct intermediates, but several other activating groups exhibited no efficiency in the ring-closure processes (3, 4). We also studied in detail the reactions, in different molar ratios, of conjugated azoalkenes with alkylcyanoacetates $RO_2C\text{-}CH_2\text{-}CN$, in which we always observed ring closure on the cyano group and never on the ester group (3).

It was noteworthy therefore, that in the reactions of conjugated azoalkenes with ethylphenylcyanoacetate Ph-CH(CN)-COOEt, the 1,4-adducts did not behave in the same way, and intramolecular heterocyclization was effective on the ester group with loss of an alcohol molecule to yield previously unknown 1-amino-3-cyano-3-phenyl-1*H*-pyrrol-2(3*H*)-ones in good to excellent yields (5). In this latter case, in fact, the ring closure on the ester group appeared to be favoured, probably because the final products 1-amino-1*H*-pyrrol-2(3*H*)-ones are more stable than the 2-iminopyrrolines arising from the heterocyclization on the cyano group.

This occurrence prompted us to turn our attention to a possible general procedure for the synthesis of new classes of pyrrolin-2-ones from the reaction between conjugated azoalkenes and β-dicarboxylate derivatives possessing one or two active hydrogen atoms (i.e., α-substituted- or α-unsubstituted-β-diesters).

We examined the possibility of carrying out a straightforward synthesis of pyrrolin-2-ones in a stable form in view of the biological activity associated with a variety of pyrrole derivatives (6, 7), especially as building blocks in the construction of antiviral and antitumour DNA antibiotics (8).

The ability to prepare the desired polyfunctionalized compounds by a simple and efficient procedure seemed to us particularly attractive.

Results and discussion

The reaction of conjugated azoalkenes **1***a–f* with an equimolecular amount of diethyl methylmalonate (**2***a*) or diethyl phenylmalonate (**2***b*) proceeded easily at room temperature and produced the pertinent hydrazonic derivatives **3***a–l* in the presence of sodium methoxide in catalytic amounts. These products can be isolated in good yields by chromatography on a silica gel column, crystallized, and characterized. When they were subsequently treated with a stoichiometric amount of sodium methoxide in tetrahydrofuran (THF), the related 1-amino-1*H*-pyrrol-2(3*H*)-ones (**4***a–l*) were isolated in good yields by column chromatography, crystallized, and characterized (Scheme 1).

More conveniently, the synthesis of 1-amino-1*H*-pyrrol-2(3*H*)-ones **4***a–l* may be directly achieved in one pot by treating conjugated azoalkenes **1***a–f* with diethyl methylmalonate (**2***a*) or diethyl phenylmalonate (**2***b*). At the beginning, the reaction can be carried out in the presence of a catalytic amount of sodium methoxide to afford hydrazonic intermediates **3***a–l* with complete disappearance of the azoalkene (monitored by TLC).

[1]Part XVII of the series on conjugated azoalkenes.

[2]Author to whom correspondence may be addressed. Telephone and Fax: 0722/2907.

[3]Revision received August 18, 1994.

Can. J. Chem. Downloaded from www.nrcresearchpress.com by 85.192.166.187 on 09/08/12
For personal use only.

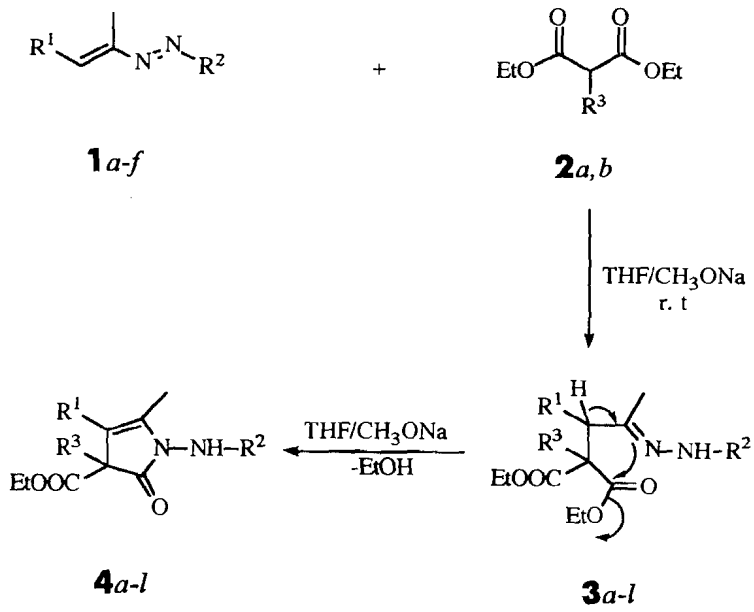

SCHEME 1

TABLE 1. Yield of hydrazones (**3***a–l*) and 1-amino-1*H*-pyrrol-2(3*H*)-ones (**4***a–l*) from conjugated azoalkenes (**1***a–f*) and diethylmethylmalonate (**2***a*) or diethylphenylmalonate (**2***b*)[a]

Reactants					Products		Yields[b] (%)	
1	**2**	R^1	R^2	R^3	**3**	**4**	**3**	**4**
a	*a*	CO_2Me	$CONH_2$	Me	*a*	*a*	64	69
b	*a*	CO_2Et	$CONH_2$	Me	*b*	*b*	82	91
c	*a*	CO_2Me	CONHPh	Me	*c*	*c*	60	80
d	*a*	CO_2Et	CONHPh	Me	*d*	*d*	57	86
e	*a*	CO_2Me	CO_2Me	Me	*e*	*e*	87	67
f	*a*	CO_2Et	CO_2t-Bu	Me	*f*	*f*	72	89
a	*b*	CO_2Me	$CONH_2$	Ph	*g*	*g*	89	61
b	*b*	CO_2Et	$CONH_2$	Ph	*h*	*h*	89	82
c	*b*	CO_2Me	CONHPh	Ph	*i*	*i*	48	89
d	*b*	CO_2Et	CONHPh	Ph	*j*	*j*	54	75
e	*b*	CO_2Me	CO_2Me	Ph	*k*	*k*	87	77
f	*b*	CO_2Et	CO_2t-Bu	Ph	*l*	*l*	71	89

[a]All reaction times were 0.1 h.
[b]Yields of pure isolated products.

TABLE 2. Yield of hydrazones (**5***a–i*) and 1-amino-1*H*-pyrrol-2(3*H*)-ones (**6***a–i*) from conjugated azoalkenes (**1***a–f*) and dimethylmalonate (**2***c*) or dibenzylmalonate (**2***d*)[a]

Reactants					Products		Yields[b] (%)	
1	**2**	R^1	R^2	R^3	**5**	**6**	**5**	**6**
a	*c*	CO_2Me	$CONH_2$	Me	*a*	*a*	95	98
b	*c*	CO_2Et	$CONH_2$	Me	*b*	*b*	93	94
c	*c*	CO_2Me	CONHPh	Me	*c*	*c*	91	95
d	*c*	CO_2Et	CONHPh	Me	*d*	*d*	90	97
e	*c*	CO_2Me	CO_2Me	Me	*e*	*e*	94	64
f	*c*	CO_2Et	CO_2t-Bu	Me	*f*	*f*	89	74
a	*d*	CO_2Me	$CONH_2$	CH_2Ph	*g*	*g*	74	90
c	*d*	CO_2Me	CONHPh	CH_2Ph	*h*	*h*	93	98
e	*d*	CO_2Me	CO_2Me	CH_2Ph	*i*	*i*	83	99

[a]All reaction times were 0.1 h.
[b]Yields of pure isolated products.

At this point, a further addition in situ of sodium methoxide, up to the stoichiometric amount, induces the ready cyclization of the hydrazonic intermediates **3***a–l* into 1-amino-1*H*-pyrrol-2(3*H*)-ones **4***a–l*. Yields of hydrazones **3***a–l* and 1-amino-1*H*-pyrrol-2(3*H*)-ones **4***a–l* are given in Table 1.

Presumably, the reaction takes place by a base-catalyzed nucleophilic attack from the active methine group of α-substituted-β-diesters containing one active hydrogen atom to the azo-ene system of conjugated azoalkene, resulting in the 1,4-addition (Michael-type) of the diester residue to the azoalkene molecule to provide the preliminary formation of the hydrazonic compound. In the presence of sodium methoxide in stoichiometric amounts, this compound undergoes ring closure by means of internal nucleophilic attack from the C=N nitrogen atom on the ester carboxyl group, with consequential loss of an alcohol molecule. Under these conditions, the reaction stops and gives 1-amino-1*H*-pyrrol-2(3*H*)-one.

Also the reactions of conjugated azoalkenes **1***a–f* (Scheme 2) at room temperature with an equimolecular amount of dimethyl malonate (**2***c*) or dibenzyl malonate (**2***d*) readily led to the related hydrazonic derivatives **5***a–i* in the presence of sodium methoxide in catalytic amounts. These products (**5***a–i*) were crystallized in good yield and utilized for the smooth preparation, by addition of the stoichiometric amount of sodium methoxide in THF and subsequent treatment by strongly acid cation exchanger, of pertinent 1-amino-1*H*-pyrrol-2(3*H*)-ones **6***a–i*, bearing a hydrogen atom in position 3 and probably susceptible to tautomeric equilibrium (Scheme 2) (6, 9, 10).

More conveniently, the synthesis of 1-amino-1*H*-pyrrol-2(3*H*)-ones **6***a–i* from conjugated azoalkenes **1***a–f* by treatment with dimethyl malonate (**2***c*) or dibenzyl malonate (**2***d*) may be directly achieved in one pot in the same way as broadly described above for the synthesis of products **4**. Yields of the hydrazones **5***a–i* and 1-amino-1*H*-pyrrol-2(3*H*)-ones **6***a–i* are listed in Table 2.

The first and the second step of this reaction follow the same pathway as previously discussed in detail. In this case, however, the 1,4-adducts contain, in position α to a carbonyl group,

Can. J. Chem. Downloaded from www.nrcresearchpress.com by 85.192.166.187 on 09/08/12
For personal use only.

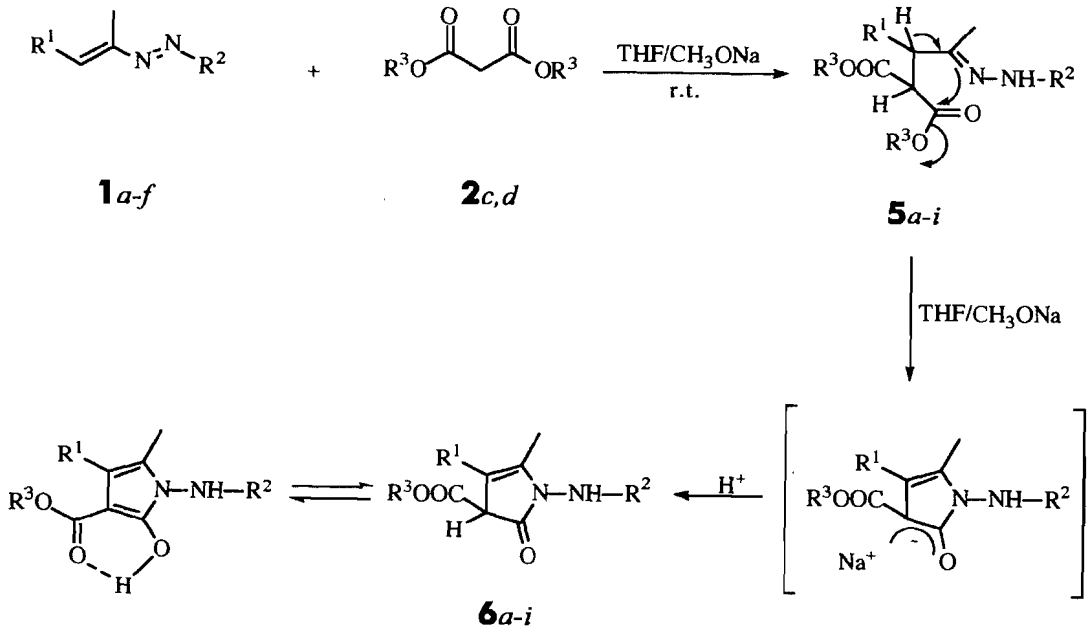

1*a-f* **2***c,d* **5***a-i* **6***a-i*

SCHEME 2

a further hydrogen atom probably able to tautomerize (Scheme 2).

When conjugated azoalkenes **1***a–f* reacted with dibenzyl malonate (**2***d*) to produce related 1-amino-1*H*-pyrrol-2(3*H*) ones **6***g–i*, the loss of the alcohol molecule was demonstrated by isolation of benzyl alcohol in quantitative yield from the residual solution after filtration of solid reaction products. Benzyl alcohol was detected by TLC, isolated, and characterized by comparison with an authentic specimen. This result supports the reaction mechanism pictured in Scheme 2.

Furthermore, in early experiments, we studied the reactions between conjugated azoalkenes with nitriles containing active methylene groups (i.e., malononitrile, β-cyanoesters, β-cyanoamides) in the ratio 2:1. Double conjugated additions afforded bis-1,4 adducts that underwent double ring closure on the cyano group to give pyrrol[2,3-*b*]pyrroles (3, 4).

From these findings we went on to explore the reactions between conjugated azoalkenes **1***a–f* and dimethyl malonate (**2***c*) or dibenzyl malonate (**2***d*) in the ratio 2:1, but very poor yields of bis adducts were obtained, reactions did not go to completion, and reaction times were very slow.

To tentatively improve the yields of bis adducts, we also tried the 1,4-conjugate addition of the hydrazonic intermediates **5***a–i* to the heterodienic system of the azoalkenes **1***a–f* in the presence of sodium methoxide. All attempts were unsuccessful, because a preferential cyclization to the 1-amino-1*H*-pyrrol-2(3*H*)-ones prevented the conjugated addition to a further molecule of azoalkene.

In conclusion, this simple procedure really represents a useful entry to a new class of pyrrole derivatives not obtainable by other methods (11). In fact, all the pyrrole ring positions may be simultaneously functionalized with different substituents that are very difficult to introduce separately. These substituents may be selected in advance by varying the functionalization both on the starting conjugated azoalkenes (2) and β-diester derivatives. Moreover, some of these functional groups appear to be suitable for further structural modifications.

In former studies on the simple monocyclic pyrrolinones (or 2-hydroxypyrroles) as terminal rings of the bile pigments, Fischer and Plieninger formulated the products as 2-hydroxypyrroles (9), but more recently it was reported, based on NMR studies, that 2-hydroxypyrroles exist predominantly in the tautomeric pyrrolin-2-one form (10).[4] However, spectroscopic evidence indicates the considerable presence of the enol form, in solution. Further investigations are presently in progress to better clarify the nature of this tautomeric equilibrium.

Experimental section

General

Products **1***a–d*(12) and **1***e–f*(13) were prepared as described previously. Products **2***a–d* were commercial materials and were used without further purification. All melting points were recorded on a capillary melting point apparatus and are uncorrected. IR spectra were obtained as Nujol mulls, and ^{1}H NMR spectra were measured in DMSO-d_6 solution. Chemical shifts (δ) are reported in ppm, downfield from Me_4Si as internal standard. Machery–Nagel precoated silica gel SIL G-25 UV_{254} plates (0.25 mm) were employed for analytical thin-layer chromatography (TLC), Baker silica gel (0.063-0.200 mm) for column chromatography, and Merck I strongly acid cation exchanger for Na^+/H^+ exchange.

Preparation of hydrazones 3a–l and 5a–i

To a stirred solution of azoalkene (**1***a–f*) (1 mmol) in THF (3 mL) was added dropwise a solution of β-diester (**2***a–d*) (1 mmol) and sodium methoxide (0.1 mmol) in THF (3 mL). The mixture was magnetically stirred at room temperature (~5 min) until the reaction was completed (monitored by TLC). Products **3***a–l* were purified by chromatography on a silica gel column (elution with cyclohexane – ethyl acetate mixtures) and then crystallized from THF–*n*-pentane. Products **5***a–i* were crystallized by partial evaporation of the reaction solvent and by addition of *n*–pentane to this crude reaction.

[4]To unambiguously confirm the structure of these compounds, an X-ray diffraction study of methyl 4-benzyl-oxycarbonyl-2-methyl-5-oxo-1-(*N'*-phenylureido)-1,4-dihydropyrrole-3-carboxylate (**6***h*) was carried out. Structure determination confirmed that, in the solid state, the pyrrole derivatives reported here exist in the keto form, but a final unsatisfactory all-data agreement index $R = 0.3924$ prevented us from publishing these results in the text.

Can. J. Chem. Downloaded from www.nrcresearchpress.com by 85.192.166.187 on 09/08/12
For personal use only.

Can. J. Chem. Downloaded from www.nrcresearchpress.com by 85.192.166.187 on 09/08/12
For personal use only.

Ethyl 4-(carbamoylhydrazono)-2-(ethoxycarbonyl)-3-(methoxycarbonyl)-2-methylpentanoate (**3**a): mp 154–156°C; crystallized from THF–*n*-pentane; IR: 3460 (NH), 3300, 3220, 3170 (NH, NH_2 overlap), 1735 (C=O), 1690 (C=O), 1645 (C=O), and 1590 (C=O) cm^{-1}; ^1H NMR: 1.00–1.20 (6H, m, 2 × CO_2CH_2*Me*), 1.45 (3H, s, Me), 1.82 (3H, s, Me), 3.61 (3H, s, CO_2Me), 3.84 (1H, s, CH), 4.02–4.16 (4H, m, 2 × CO_2*CH_2*Me), 6.09 (2H, br s, NH_2, D_2O-exch.), and 9.33 (1H, s, NH, D_2O-exch.). Anal. calcd. for $C_{14}H_{23}N_3O_7$: C 48.69, H 6.71, N 12.17; found: C 48.85, H 6.52, N 12.29.

Ethyl 4-(carbamoylhydrazono)-2,3-(diethoxycarbonyl)-2-(methylpentanoate) (**3**b): mp 110–112°C; crystallized from THF–*n*-pentane; IR: 3450 (NH), 3300, 3220, 3170 (NH, NH_2 overlap), 1740 (C=O), 1690 (C=O), 1650 (C=O), and 1585 (C=O) cm^{-1}; ^1H NMR: 1.09–1.19 (9H, m, 3 × CO_2CH_2*Me*), 1.44 (3H, s, Me), 1.81 (3H, s, Me), 4.03–4.09 (7H, m, CH and 3 × CO_2*CH_2*Me), 6.06 (2H, br, s, NH_2, D_2O-exch.), and 9.30 (1H, s, NH, D_2O-exch.). Anal. calcd. for $C_{15}H_{25}N_3O_7$: C 50.13, H 7.01, N 11.69; found: C 50.29, H 6.81, N 11.87.

Ethyl 2-(ethoxycarbonyl)-3-(methoxycarbonyl)-2-(methyl-4-(N′-phenylcarbamoylhydrazono)pentanoate (**3**c): mp 119–122°C; crystallized from THF–*n*-pentane; IR: 3340 (NH), 3190 (NH), 3090 (NH, 1740 (C=O), 1710 (C=O), 1675 (C=O), and 1590 (C=O) cm^{-1}; ^1H NMR: 1.08–1.20 (6H, m, 2 × CO_2CH_2*Me*), 1.51 (3H, s, Me), 1.90 (3H, s, Me), 3.63 (3H, s, CO_2Me), 4.07–4.18 (5H, m, CH and 2 × CO_2*CH_2*Me), 7.00–7.63 (5H, m, Ph), 8.15 (1H, s, NH, D_2O-exch.), and 9.85 (1H, s, NH, D_2O-exch.). Anal. calcd. for $C_{20}H_{27}N_3O_7$: C 57.0, H. 6.46, N 9.97; found: C 57.12, H 6.31, N 9.88.

Ethyl 2,3-(diethoxycarbonyl)-2-methyl-4-(N′-phenylcarbamoylhydrazono)pentanoate (**3**d): mp 128–130°C; crystallized from THF–*n*-pentane; IR: 3340 (NH), 3190 (NH), 3090 (NH), 1745 (C=O), 1730 (C=O), 1675 (C=O), and 1595 (C=O) cm^{-1}; ^1H NMR: 1.10–1.22 (9H, m, 3 × CO_2CH_2*Me*), 1.53 (3H, s, Me), 1.92 (3H, s, Me), 4.06–4.18 (7H, m, CH and 3 × CO_2*CH_2*Me), 7.00–7.65 (5H, m, Ph), 8.17 (1H, s, NH, D_2O-exch.), and 9.87 (1H, s, NH, D_2O-exch.). Anal. calcd. for $C_{21}H_{29}N_3O_7$: C 57.92, H 6.71, N 9.65; found: C 58.02, H 6.61, N 9.81.

Ethyl 2-(ethoxycarbonyl)-3-(methoxycarbonyl)-4-(methoxycarbonylhydrazono)-2-methylpentanoate (**3**e): mp 88–91°C; crystallized from THF–*n*-pentane; IR: 3250 (NH), 1740 (C=O), 1725 (C=O), 1690 (C=O), and 1630 (C=O) cm^{-1}; ^1H NMR: 1.11–1.19 (6H, m, 2 × CO_2CH_2*Me*), 1.44 (3H, s, Me), 1.79 (3H, s, Me), 360 (3H, s, CO_2Me), 3.63 (3H, s, CO_2Me), 4.04–4.11 (5H, m, CH and 2 × CO_2*CH_2*Me), and 9.97 (1H, s, NH, D_2O-exch.). Anal. calcd. for $C_{15}H_{24}N_2O_8$: C 50.0, H 6.71, N 7.77; found: C 50.15, H 6.57, N 7.69.

Ethyl 4-(tert-*butoxycarbonylhydrazono)-2,3-(diethoxycarbonyl)-2-methylpentanoate* (**3**f): mp 60–62°C; crystallized from THF–*n*-pentane; IR: 3250 (NH), 1765 (C=O), 1730 (C=O), 1685 (C=O), and 1640 (C=O) cm^{-1}; ^1H NMR: 1.15 (9H, t, J = 7 Hz, 3 × CO_2CH_2*Me*), 1.43 (9H, s, *t*-Bu), 1.46 (3H, s, Me), 1.78 (3H, s, Me), 4.03–4.16 (7H, m, CH and 3 × CO_2*CH_2*Me), and 9.62 (1H, s, NH, D_2O-exch.). Anal. calcd. for $C_{19}H_{32}N_2O_8$: C 54.8, H 7.74, N 6.73; found: C 54.61, H 7.63, N 6.64.

Ethyl 4-(carbamoylhydrazono)-2-(ethoxycarbonyl)-3-(methoxycarbonyl)-2-phenylpentanoate (**3**g): mp 153–160°C; crystallized from THF–*n*-pentane; IR: 3440 (NH), 3290, 3170 (NH, NH_2 overlap), 1735 (C=O), 1705 (C=O), 1695 (C=O), and 1590 (C=O) cm^{-1}; ^1H NMR: 1.10–1.22 (6H, m, 2 × CO_2*CH_2*Me), 1.96 (3H, s, Me), 3.67 (3H, s, CO_2Me), 4.08–4.18 (4H, m, 2 × CO_2*CH_2*Me), 4.69 (1H, s, CH), 5.43 and 6.25 (2H, 2 br s, NH_2, D_2O-exch.), 7.28–7.33 (5H, m, Ph), and 9.21 (1H, s, NH, D_2O-exch.). Anal. calcd. for $C_{19}H_{25}N_3O_7$: C 56.01, H. 6.18, N 10.31; found: C 56.15, H 6.18, N 10.31.

Ethyl 4-(carbamoylhydrazono)-2,3-(diethoxycarbonyl)-2-(phenylpentanoate (**3**h): mp 161–164°C; crystallized from THF–*n*-pentane; IR: 3430 (NH), 3270, 3150 (NH, NH_2 overlap), 1720 (C=O), 1700 (C=O), 1685 (C=O), and 1585 (C=O) cm^{-1}; ^1H NMR: 1.02–1.16 (9H, m, 3 × CO_2CH_2*Me*), 1.89 (3H, s, Me), 4.02–4.12 (6H, m, 3 × CO_2*CH_2*Me), 4.60 (1H, s, CH), 5.34 and 6.16 (2H, 2 br s, NH_2, D_2O-exch.), 7.19–7.27 (5H, m, Ph), and 9.14 (1H, s, NH, D_2O-exch.). Anal. calcd. for $C_{20}H_{27}N_3O_7$: C 57.0, H. 6.46, N 9.97; found: C 57.19, H 6.35, N 10.06.

Ethyl 2-(ethoxycarbonyl)-3-(methoxycarbonyl)-2-(phenyl-4-(N′-phenylcarbamoylhydrazono)pentanoate (**3**i): mp 178–180°C; crystallized from THF–*n*-pentane; IR: 3350 (NH), 3200 (NH), 3080 (NH), 1745 (C=O), 1725 (C=O), 1680 (C=O), and 1595 (C=O) cm^{-1}; ^1H NMR: 1.05–1.12 (6H, m, 2 × CO_2CH_2*Me*), 2.03 (3H, s, Me), 3.64 (3H, s, CO_2Me), 4.07–4.12 (4H, m, 2 × CO_2*CH_2*Me), 4.82 (1H, s, CH), 6.90–7.44 (10H, m, 2 × Ph), 7.70 (1H, s, NH, D_2O-exch.), and 9.74 (1H, s, NH, D_2O-exch.). Anal. calcd. for $C_{25}H_{29}N_3O_7$: C 62.10, H 6.05, N 8.69; found: C 61.98, H 6.21, N 8.86.

Ethyl 2,3-(diethoxycarbonyl)-2-phenyl-4-(N′-phenylcarbamoylhydrazono)pentanoate (**3**j): mp 138–141°C; crystallized from THF–*n*-pentane; IR: 3340 (NH), 3190 (NH), 3060 (NH), 1750 (C=O), 1725 (C=O), 1675 (C=O), and 1590 (C=O) cm^{-1}; ^1H NMR: 1.03–1.16 (9H, m, 3 × CO_2CH_2*Me*), 2.03 (3H, s, Me), 4.02–4.14 (6H, m, 3 × CO_2*CH_2*Me), 4.80 (1H, s, CH), 6.93–7.48 (10H, m, 2 × Ph), 7.72 (1H, s, NH, D_2O-exch.), and 9.75 (1H, s, NH, D_2O-exch.). Anal. calcd. for $C_{26}H_{31}N_3O_7$: C 62.76, H 6.28, N 8.45; found: C 62.67, H 6.39, N 8.36.

Ethyl 2-(ethoxycarbonyl)-3-(methoxycarbonyl)-4-(methoxycarbonylhydrazono)-2-phenylpentanoate (**3**k): mp 139–141°C; crystallized from THF–*n*-pentane; IR: 3310 (NH), 1750 (C=O), 1730 (C=O), and 1695 (C=O) cm^{-1}; ^1H NMR: 1.08–1.17 (6H, m, 2 × CO_2CH_2*Me*), 1.67 (3H, s, Me), 3.58 (6H, s, 2 × CO_2Me), 4.10–4.21 (4H, m, 2 × CO_2*CH_2*Me), 4.49 (1H, s, CH), 7.27 (5H, s, Ph), and 9.79 (1H, s, NH, D_2O-exch.). Anal. calcd. for $C_{20}H_{26}N_2O_8$: C 56.87, H. 6.20, N 6.63; found: C 57.06, H 6.11, N 6.81.

*Ethyl 4-*tert-*butoxycarbonylhydrazono)-2,3-(diethoxycarbonyl)-2-phenylpentanoate* (**3**l): mp 90–93°C; crystallized from THF–*n*-pentane; IR: 3250 (NH), 1780 (C=O), 1730 (C=O), and 1690 (C=O) cm^{-1}; ^1H NMR: 1.08–1.17 (9H, m, 3 × COX_2CH_2*Me*), 1.40 (9H, s, *t*-Bu), 1.61 (3H, s, Me), 4.00–4.21 (6H, m, 3 × CO_2*CH_2*Me), 4.44 (1H, s, CH), 7.27 (5H, s, Ph), and 9.38 (1H, s, NH, D_2O-exch.). Anal. calcd. for $C_{24}H_{34}N_2O_8$: C 60.39, H. 7.16, N 5.85; found: C 60.39, H 7.33, N 5.74.

Methyl 4-carbamoylhydrazono)-2,3-(dimethoxycarbonyl)pentanoate (**5**a): mp 138–140°C; crystallized from THF–*n*-pentane; IR: 3450 (NH), 3440 (NH), 3300 (NH_2), 3190 (NH_2), 1730 (C=O), 1695 (C=O), 1665 (C=O), and 1640 (C=O) cm^{-1}; ^1H NMR: 1.86 (3H, s, Me), 3.60–3.65 (9H, m, 3 × CO_2*CH_2*Me), 3.91 (1H, d, J = 10 Hz, CH), 4.23 (1H, d, J = 10 Hz, CH), 6.25 (2H, br s, NH_2, D_2O-exch.), and 9.33 (1H, s, NH, D_2O-exch.). Anal. calcd. for $C_{11}H_{17}N_3O_7$: C 43.57, H. 5.65, N 13.86; found: C 43.49, H 5.79, N 13.98.

Methyl 4-carbamoylhydrazono)-3-(ethoxycarbonyl)-2-(methoxycarbonyl)pentanoate (**5**b): mp 119–122°C; crystallized from THF–*n*-pentane; IR: 3530 (NH), 3400 (NH), 3200 (NH_2), 1750 (C=O), 1730 (C=O), 1690 (C=O), and 1640 (C=O) cm^{-1}; ^1H NMR: 1.16 (3H, t, J = 7 Hz, CO_2CH_2*Me*), 1.86 (3H, s, Me), 3.61 (3H, s, CO_2Me), 3.65 (3H, s, CO_2Me), 3.88 (1H, d, J = 10 Hz, CH), 4.10 (2H, q, J = 7 Hz, CO_2*CH_2*Me), 4.21 (1H, d, J = 10 Hz, CH), 6.20 (2H, br s, NH_2, D_2O-exch.), and 9.32 (1H, s, NH, D_2O-exch.). Anal. calcd. for $C_{12}H_{19}N_3O_7$: C 45.42, H. 6.04, N 13.24; found: C 45.35, H 6.21, N 13.16.

Methyl 2,3-(dimethoxycarbonyl)-4-(N′-phenylcarbamoylhydrazono)pentanoate (**5**c): mp 145–147°C; crystallized from THF–*n*-pentane; IR: 3380 (NH), 3200 (NH), 3090 (NH), 1740 (C=O), 1720 (C=O), 1700 (C=O), and 1600 (C=O) cm^{-1}; ^1H NMR: 1.94 (3H, s, Me), 3.58 (3H, s, CO_2Me), 3.66 (6H, s, 2 × CO_2Me), 4.03 (1H, d, J = 10 Hz, CH), 4.48 (1H, d, J = 10 Hz, CH), 7.00–7.61 (5H, m, Ph), 8.48 (1H, s, NH, D_2O-exch.), and 9.86 (1H, s, NH, D_2O-exch.). Anal. calcd. for $C_{17}H_{21}N_3O_7$: C 53.82, H 5.58, N 11.08; found: C 53.99, H 5.39, N 11.15.

Methyl 3-(ethoxycarbonyl)-2-(methoxycarbonyl)-4-(N′-phenylcarbamoylhydrazono)pentanoate (**5**d): mp 130–132°C; crystallized from THF–*n*-pentane; IR: 3370 (NH), 3210 (NH), 3100 (NH), 1745 (C=O), 1730 (C=O), 1700 (C=O), and 1605 (C=O) cm^{-1}; ^1H NMR: 1.18 (3H, t, J = 7 Hz, CO_2CH_2*Me*), 1.95 (3H, s, Me), 3.59 (3H, s, CO_2Me), 3.66 (3H, s, CO_2Me), 4.01 (1H, d, J = 10 Hz, CH), 4.13 (2H, q, J = 7 Hz, CO_2*CH_2*Me), 4.46 (1H, d, J = 10 Hz, CH), 7.00–7.61 (5H, m, Ph), 8.46 (1H, s, NH, D_2O-exch.), and 9.85 (1H, s, NH, D_2O-exch.). Anal. calcd. for $C_{18}H_{23}N_3O_7$: C 54.96, H 5.89, N 10.68; found; C 55.13, H 5.75, N 10.74.

Can. J. Chem. Downloaded from www.nrcresearchpress.com by 85.192.166.187 on 09/08/12
For personal use only.

*Methyl 2,3-(dimethoxycarbonyl)-4-(methoxycarbonylhydrazono)-pentanoate (**5**e)*: mp 127–129°C; crystallized from THF–*n*-pentane; IR: 3230 (NH), 3150 (NH), 1730, 1710 (C=O overlap), and 1640 (C=O) cm^{-1}; ^1H NMR: 1.87 (3H, s, Me), 3.61–3.66 (12H, m, 4 × CO_2Me), 3.88 (1H, d, J = 10 Hz, CH), 4.08 (1H, d, J = 10 Hz, CH), and 10.03 (1H, s, NH, D_2O-exch.). Anal. calcd. for $C_{12}H_{18}N_2O_8$: C 45.28, H 5.70, N 8.80; found: C 45.16, H 5.82, N 8.96.

*Methyl 4-(*tert*-butoxycarbonylhydrazono)-3-(ethoxycarbonyl)-2-(methoxycarbonyl)pentanoate (**5**f)*: mp 90–93°C; crystallized from THF–*n*-pentane; IR: 3230 (NH), 3150 (NH), 1745, (C=O), 1730 (C=O), 1720 (C=O), 1690 (C=O), and 1640 (C=O) cm^{-1}; ^1H NMR: 1.15 (3H, t, J = 7 Hz, CO_2CH_2*Me*), 1.43 (9H, s, *t*-Bu), 1.86 (3H, s, Me), 3.61 (3H, s, CO_2Me), 3.66 (3H, s, CO_2Me), 3.84 (1H, d, J = 10 Hz, CH), 4.05–4.11 (3H, m, CH and CO_2CH_2Me), and 9.71 (1H, s, NH, D_2O-exch.). Anal. calcd. for $C_{16}H_{26}N_2O_8$: C 51.33, H 7.0, N 7.48; found: C 51.21, H 7.17, N 7.39.

*Benzyl 2-(benzyloxycarbonyl)-4-(carbamoylhydrazono)-3-(methoxycarbonyl)pentanoate (**5**g)*: mp 110–112°C; crystallized from THF–*n*-pentane; IR: 3520 (NH), 3400 (NH), 3180 (NH_2), 1745, (C=O), 1720 (C=O), 1685 (C=O), and 1630 (C=O) cm^{-1}; ^1H NMR: 1.85 (3H, s, Me), 3.56 (3H, s, CO_2Me), 3.94 (1H, d, J = 10 Hz, CH), 4.43 (1H, d, J = 10 Hz, CH), 5.04–5.20 (4H, m, 2 × CO_2CH_2Ph), 6.27 (2H, br s, NH_2, D_2O-exch.), 7.27–7.34 (10H, m, 2 × CO_2CH2*Ph*), and 9.33 (1H, s, NH, D_2O-exch.). Anal. calcd. for $C_{23}H_{25}N_3O_7$: C 60.65, H 5.53, N 9.23; found: C 60.51, H 5.71, N 9.09.

*Benzyl 2-(benzyloxycarbonyl)-3-(methoxycarbonyl)-4-(N′-phenylcarbamoylhydrazono)pentanoate (**5**h)*: mp 152–154°C; crystallized from THF–*n*-pentane; IR: 3360 (NH), 3190 (NH), 1755, (C=O), 1730 (C=O), 1680 (C=O), and 1640 (C=O) cm^{-1}; ^1H NMR: 1.91 (3H, s, Me), 3.57 (3H, s, CO_2Me), 4.07 (1H, d, J = 10 Hz, CH), 4.84 (1H, d, J = 10 Hz, CH), 5.14–5.20 (4H, m, 2 × CO_2CH_2Ph), 7.00–7.58 (15H, m, Ph and 2 × CO_2CH_2*Ph*), 8.47 (1H, s, NH, D_2O-exch.) and 9.80 (1H, s, NH, D_2O-exch.). Anal. calcd. for $C_{29}H_{29}N_3O_7$: C 65.53, H. 5.50, N 7.90; found: C 65.39, H 5.41, N 7.75.

*Benzyl 2-(benzyloxycarbonyl)-3-(methoxycarbonyl)-4-(methoxycarbonylhydrazono)pentanoate (**5**i)*: mp 118–120°C; crystallized from THF–*n*-pentane; IR: 3230 (NH), 1735, and 1700 (C=O overlap) cm^{-1}; ^1H NMR: 1.86 (3H, s, Me), 3.56 (3H, s, CO_2Me), 3.64 (3H, s, CO_2Me), 3.93 (1H, d, J = 10 Hz, CH), 4.24 (1H, d, J = 10 Hz, CH), 5.08–5.15 (4H, m, 2 × CO_2CH_2Ph), 7.31–7.34 (10H, m, 2 × CO_2CH_2*Ph*), and 10.07 (1H, s, NH, D_2O-exch.). Anal. calcd. for: $C_{24}H_{26}N_2O_8$: C 61.27, H 5.57, N 5.95; found: C 61.27, H 5.73, N 6.09.

*Conversion of hydrazones **3**a–l into 1-amino-1*H*-pyrrol-2(3*H*)-ones **4**a–l*

To a stirred solution of hydrazone (**3***a–l*) in THF (3 mL) was added a solution of sodium methoxide (1 mmol) in methanol (1 mL). The conversion to give products **4***a–l* occurred rapidly, under magnetic stirring at room temperature (~5 min), and was monitored by TLC. The reaction mixture was concentrated to a small volume under reduced pressure, the residue was dissolved in ethyl acetate, and the solution extracted with aqueous sulphuric acid (1%). The organic phase was separated, washed with water, dried with magnesium sulphate, and concentrated under reduced pressure. Products **4***a–l* were purified by chromatography on a silica gel column (elution with cyclohexane – ethyl acetate mixtures), and then crystallized from ethyl ether – light petroleum, bp 30–60°C, or dichloromethane – light petroleum, bp 30–60°C.

*Direct preparation of 1-amino-1*H*-pyrrol-2(3*H*)-ones **4**a–l*

To a stirred solution of azoalkene (**1***a–f*) (1 mmol) in THF (3 mL) was added dropwise a solution of β-diester (**2***a, b*) (1 mmol) and sodium methoxide (0.1 mmol) in THF (3 mL). When the reaction at room temperature was completed, affording hydrazones (**3***a–l*) (monitored by TLC), a solution of sodium methoxide (1 mmol) in methanol (1 mL) was added directly to the reaction. The conversion to afford products **4***a–l* occurred rapidly, under magnetic stirring at room temperature (~5 min), and was monitored by TLC. The reaction mixture was then treated as described in detail above for the isolation of the same products **4***a–l*.

*Methyl 4-ethoxycarbonyl-2,4-dimethyl-5-oxo-1-ureido-1,4-dihydropyrrole-3-carboxylate (**4**a)*: mp 138–140°C; crystallized from dichloromethane – light petroleum, bp 30–60°C; IR: 3440 (NH), 3290, 3250, 3190 (NH, NH_2 overlap), 1750 (C=O), 1705 (C=O), 1645 (C=O), and 1615 (C=O) cm^{-1}; ^1H NMR: 1.07 (3H, t, J = 7 Hz, CO_2CH_2*Me*), 1.44 (3H, s, Me), 2.25 (3H, s, Me), 3.63 (3H, s, CO_2Me), 4.06 (2H, q, J = 7 Hz, CO_2CH_2Me), 6.33 and 6.39 (2H, 2 s, NH_2, D_2O-exch.), and 8.65 and 8.96 (1H, 2 s, NH, D_2O-exch.), Anal. calcd. for: $C_{12}H_{17}N_3O_6$: C 48.16, H 5.73, N 14.04; found: C 48.05, H 5.65, N 14.15.

*Ethyl 4-ethoxycarbonyl-2,4-dimethyl-5-oxo-1-ureido-1,4-dihydropyrrole-3-carboxylate (**4**b)*: mp 102–106°C; crystallized from dichloromethane – light petroleum, bp 30–60°C; IR: 3435 (NH), 3290, 3250, 3190 (NH, NH_2 overlap), 1745 (C=O), 1705 (C=O), 1640 (C=O), and 1615 (C=O) cm^{-1}; ^1H NMR: 1.05–1.21 (6H, m, 2 × CO_2CH_2*Me*), 1.45 (3H, s, Me), 2.26 (3H, s, Me), 4.00–4.15 (4H, m, 2 × CO_2CH_2Me), 6.29 and 6.36 (2H, 2 s, NH_2, D_2O-exch.), and 8.62 and 8.93 (1H, 2 s, NH, D_2O-exch.). Anal. calcd. for $C_{13}H_{19}N_3O_6$: C 49.84, H 6.11, N 13.41; found: C 49.75, H 6.26, N 13.32.

*Methyl 4-ethoxycarbonyl-2,4-dimethyl-5-oxo-1-(N′-phenylureido-1,4-dihydropyrrole-3-carboxylate (**4**c)*: mp 149–151°C; crystallized from ethyl ether – light petroleum, bp 30–60°C; IR: 3300 (NH), 3210 (NH), 1760 (C=O), 1710 (C=O), 1650 (C=O), and 1605 (C=O) cm^{-1}; ^1H NMR: 1.10 (3H, t, J = 7 Hz, CO_2CH_2Me), 1.49 (3H, s, Me), 2.31 (3H, s, Me), 3.66 (3H, s, CO_2Me), 4.10 (2H, q, J = 7 Hz, CO_2CH_2Me), 6.95–7.46 (5H, m, Ph), 9.19 (1H, s, NH, D_2O-exch.), and 9.37 (1H, s, NH, D_2O-exch.). Anal. calcd. for $C_{18}H_{21}N_3O_6$: C 57.59, H 5.64, N 11.19; found: C 57.44, H 5.73, N 11.38.

*Ethyl 4-ethoxycarbonyl-2,4-dimethyl-5-oxo-1-(N′-phenylureido-1,4-dihydropyrrole-3-carboxylate (**4**d)*: mp 236–239°C; crystallized from ethyl ether – light petroleum, bp 30–60°C; IR: 3310 (NH), 3200 (NH), 1760 (C=O), 1720 (C=O), 1675 (C=O), and 1615 (C=O) cm^{-1}; ^1H NMR: 1.08–1.23 (6H, m, 2 × CO_2CH_2*Me*), 1.51 (3H, s, Me), 2.32 (3H, s, Me), 4.05–4.18 (4H, m, 2 × CO_2CH_2Me), 6.96–7.48 (5H, m, Ph), 8.19 (1H, s, NH, D_2O-exch.), and 9.59 (1H, s, NH, D_2O-exch.). Anal. calcd. for $C_{19}H_{23}N_3O_6$: C 58.60, H 5.95, N 10.79; found: C 58.78, H 5.81, N 10.93.

*Methyl 4-ethoxycarbonyl-1-(methoxycarbonylamino)-2,4-dimethyl-5-oxo-1,4-dihydro-pyrrole-3-carboxylate (**4**e)*: mp 109–111°C; crystallized from ethyl ether – light petroleum, bp 30–60°C; IR: 3240 (NH), 1770 (C=O), 1750 (C=O), 1730 (C=O), 1675 (C=O), and 1635 (C=O) cm^{-1}; ^1H NMR: 1.08 (3H, t, J = 7 Hz, CO_2CH_2*Me*), 1.45 (3H, s, Me), 2.28 (3H, s, Me), 3.67 (3H, s, CO_2Me), 3.88 (3H, s, CO_2Me), 4.05 (2H, q, J = 7 Hz, CO_2CH_2Me), and 10.35 (1H, br s, NH, D_2O-exch.). Anal. calcd. for $C_{13}H_{18}N_2O_7$: C 49.68, H 5.77, N 8.91; found: C 49.53, H 5.95, N 8.83.

*Ethyl 1-(*tert*-butoxycarbonylamino)-4-ethoxycarbonyl-2,4-dimethyl-5-oxo-1,4-dihydropyrrole-3-carboxylate (**4**f)*: mp 72–75°C; crystallized from ethyl ether – light petroleum, bp 30–60°C; IR: 3245 (NH), 1765 (C=O), 1740 (C=O). 1730 (C=O), 1680 (C=O), and 1635 (C=O) cm^{-1}; ^1H NMR: 1.05–1.21 (6H, m, 2 × CO_2CH_2*Me*), 1.42 (9H, s, *t*-Bu), 1.45 (3H, s, Me), 2.26 (3H, s, Me), 3.97–4.18 (4H, m, 2 × CO_2CH_2Me), and 10.01 (1H, br s, NH, D_2O-exch.). Anal. calcd. for $C_{17}H_{26}N_2O_7$: C 55.13, H 7.08, N 7.56; found: C 55.02, H 7.22, N 7.47.

*Methyl 4-ethoxycarbonyl-2-methyl-5-oxo-4-phenyl-1-ureido-1,4-dihydropyrrole-3-carboxylate (**4**g)*: mp 207–209°C; crystallized from dichloromethane – light petroleum, bp 30–60°C; IR: 3400 (NH), 3320, 3250, 3180 (NH, NH_2 overlap), 1760 (C=O), 1735 (C=O), 1670 (C=O), and 1635 (C=O) cm^{-1}; ^1H NMR: 1.09–1.16 (3H, m, CO_2CH_2*Me*), 2.33 and 2.35 (3H, 2 s, Me), 3.57 and 3.60 (3H, 2 s, CO_2Me), 4.10–4.16 (2H, m, CO_2CH_2Me), 6.35 (2H, s, NH_2, D_2O-exch.), 7.28–7.43 (5H, m, Ph), and 8.76 and 9.06 (1H, 2 s, NH, D_2O-exch.). Anal. calcd. for $C_{17}H_{19}N_3O_6$: C 56.51, H 5.30, N 11.63; found: C 56.65, H 5.21, N 11.77.

*Ethyl 4-ethoxycarbonyl-2-methyl-5-oxo-4-phenyl-1-ureido-1,4-dihydropyrrole-3-carboxylate (**4**h)*: mp 214–216°C; crystallized from dichloromethane – light petroleum, bp 30–60°C; IR: 3420 (NH), 3320, 3260, 3210 (NH, NH_2 overlap), 1765 (C=O), 1740 (C=O), 1675 (C=O), and 1640 (C=O) cm^{-1}; ^1H NMR: 1.07–1.17 (6H, m, 2 ×

Can. J. Chem. Downloaded from www.nrcresearchpress.com by 85.192.166.187 on 09/08/12
For personal use only.

CO_2CH_2*Me*), 2.35 and 2.37 (3H, 2 s, Me), 4.02–4.15 (4H, m, 2 × CO_2CH_2Me), 6.34 (2H, s, NH_2, D_2O-exch.), 7.29–7.45 (5H, m, Ph), and 8.75 and 9.05 (1H, 2 s, NH, D_2O-exch.). Anal. calcd. for $C_{18}H_{21}N_3O_6$: C 57.59, H 5.64, N 11.19; found: C 57.54, H 5.53, N 11.37.

*Methyl 4-ethoxycarbonyl-2-methyl-5-oxo-4-phenyl-1-(*N′*-phenylureido-1,4-dihydropyrrole-3-carboxylate (***4i***)*: mp 162–164°C; crystallized from dichloromethane – light petroleum, bp 30–60°C; IR: 3340 (NH), 3300 (NH), 1725 (C=O), 1710 (C=O), 1650 (C=O), and 1600 (C=O) cm^{-1}; ^1H NMR: 1.12–1.19 (3H, m, CO_2CH_2*Me*), 2.40 (3H, s, Me), 3.60 and 3.62 (3H, 2 s, CO_2Me), 4.12–4.18 (2H, m, CO_2CH_2Me), 6.98–7.48 (10H, m, 2 × Ph), 8.96 and 9.33 (1H, 2 s, NH, D_2O-exch.), and 9.36 and 9.43 (1H, 2 s, NH, D_2O-exch.). Anal. calcd. for $C_{23}H_{23}N_3O_6$: C 63.15, H 5.30, N 9.61; found: C 63.31, H 5.24, N 9.72.

*Ethyl 4-ethoxycarbonyl-2-methyl-5-oxo-4-phenyl-1-(*N′*-phenylureido)-1,4-dihydropyrrole-3-carboxylate (***4j***)*: mp 169–173°C; crystallized from dichloromethane – light petroleum, bp 30–60°C; IR: 3360 (NH), 3290 (NH), 1755 (C=O), 1715 (C=O), 1695 (C=O), and 1650 (C=O) cm^{-1}; ^1H NMR: 1.08–1.20 (6H, m, 2 × CO_2CH_2*Me*), 2.39 (3H, s, Me), 4.04–4.26 (4H, m, 2 × CO_2CH_2Me), 6.98–7.48 (10H, m, 2 × Ph), 8.93 and 9.28 (1H, 2 s, NH, D_2O-exch.), and 9.39 and 9.43 (1H, 2 s, NH, D_2O-exch.). Anal. calcd. for $C_{24}H_{25}N_3O_6$: C 63.85, H 5.58, N 9.31; found: C 63.78, H 5.74, N 9.42.

*Methyl 4-ethoxycarbonyl-1-(methoxycarbonylamino)-2-methyl-5-oxo-4-phenyl-1,4-dihydropyrrole-3-carboxylate (***4k***)*: mp 143–146°C; crystallized from ethyl ether – light petroleum, bp 30–60°C; IR: 3320 (NH), 1765 (C=O), 1725 (C=O), 1690 (C=O), and 1635 (C=O) cm^{-1}; ^1H NMR: 1.09–1.24 (3H, m, CO_2CH_2*Me*), 2.36 (3H, s, Me), 3.60 and 3.62 (3H, 2 s, CO_2Me), 3.67 and 3.70 (3H, 2 s, CO_2Me), 4.04–4.24 (2H, m, CO_2CH_2Me), 7.32–7.43 (5H, m, Ph), and 10.13 and 10.46 (1H, 2 s, NH, D_2O-exch.). Anal. calcd. for $C_{18}H_{20}N_2O_7$: C 57.44, H 5.36, N 7.44; found: C 57.64, H 5.45, N 7.28.

*Ethyl 1-(*tert*-butoxycarbonylamino)-4-ethoxycarbonyl-2-methyl-5-oxo-4-phenyl-1,4-dihydropyrrole-3-carboxylate (***4l***)*: mp 120–125°C; crystallized from ethyl ether – light petroleum, bp 30–60°C; IR: 3280 (NH), 1765 (C=O), 1735 (C=O), 1710 (C=O), 1675 (C=O), and 1640 (C=O) cm^{-1}; ^1H NMR: 1.06–1.65 (6H, m, 2 × CO_2CH_2*Me*), 1.41 and 1.44 (9H, 2 s, *t*-Bu), 2.35 (3H, s, Me), 4.04–4.25 (4H, m, 2 × CO_2CH_2Me), 7.32–7.37 (5H, m, Ph), and 10.12 and 10.45 (1H, 2 s, NH, D_2O-exch.). Anal. calcd. for $C_{22}H_{28}N_2O_7$: C 61.10, H 6.53, N 6.48; found: C 60.95, H 6.36, N 6.66.

Conversion of hydrazones **5**a–i *into 1-amino-1*H*-pyrrol-2(3*H*)-ones* **6**a–i

To a stirred solution of hydrazone (**5***a–i*) (1 mmol) in THF (3 mL) was added a solution of sodium methoxide (1 mmol) in methanol (1 mL). The conversion to give products **6***a–i* occurred rapidly, under magnetic stirring at room temperature (~5 min), and was monitored by TLC. Products **6***a–i*, after partial evaporation of the reaction solvent, were crystallized by addition of ethyl ether to the crude reaction, dissolved in water and treated by the strongly acid cation exchanger. The aqueous solution was extracted with ethyl acetate and the organic phase was separated, dried with magnesium sulphate, and concentrated under reduced pressure. After this treatment, products **6** crystallized as follows: **6***a*, **6***b* from tetrahydrofuran – *n*-pentane, **6***c*, **6***d*, and **6***h* from ethyl acetate, **6***g* from dichloromethane – light petroleum, bp 30–60°C, while products **6***e*, **6***f*, and **6***i* are oils.

*Direct preparation of 1-amino-1*H*-pyrrol-2(3*H*)-ones* **6**a–i

To a stirred solution of azoalkene (**1***a–f*) (1 mmol) in THF (3 mL) was added dropwise a solution of β-diester (**2***c*, *d*) (1 mmol) and sodium methoxide (0.1 mmol) in THF (3 mL). When the reaction was completed, affording hydrazones **5***a–i* (monitored by TLC), a solution of sodium methoxide (1 mmol) in methanol (1 mL) was added directly to the reaction. The conversion to afford products **6***a–i* occurred rapidly, under magnetic stirring at room temperature (~5 min), and was monitored by TLC. The reaction mixture was then treated as described in detail above for the isolation of the same products **6***a–i*.

*Methyl 4-methoxycarbonyl-2-methyl-5-oxo-1-ureido-1,4-dihydropyrrole-3-carboxylate (***6a***)*: mp 166–168°C; crystallized from tetrahydrofuran – *n*-pentane; IR: 3440 (NH), 3330, 3190 (NH_2 overlap), 1760, 1680, 1640, and 1610 (C=O overlap) cm^{-1}; ^1H NMR: 2.26 (3H, s, Me), 3.65 (6H, s, 2 × CO_2Me), 4.37 and 4.44 (1H, 2 s, CH, D_2O-exch.), 6.28 and 6.40 (2H, 2 s, NH_2, D_2O-exch.), and 8.68 and 8.76 (1H, 2 s, NH, D_2O-exch.). Anal. calcd. for $C_{10}H_{13}N_3O_6$: C 44.14, H 4.83, N 15.49; found: C 44.14, H 4.74, N 15.35.

*Ethyl 4-methoxycarbonyl-2-methyl-5-oxo-1-ureido-1,4-dihydropyrrole-3-carboxylate (***6b***)*: mp 80–82°C; crystallized from tetrahydrofuran – *n*-pentane; IR: 3440 (NH), 3330, 3190 (NH_2 overlap), 1760, 1690, 1645, and 1600 (C=O overlap) cm^{-1}; ^1H NMR: 1.17 (3H, t, J = 7 Hz, CO_2CH_2*Me*), 2.26 (3H, s, Me), 3.66 (3H, s, CO_2Me), 4.14 (2H, q, J = 7 Hz, CO_2CH_2Me), 4.36 and 4.43 (1H, 2 s, CH, D_2O-exch.). 6.30 and 6.42 (2H, 2 s, NH_2, D_2O-exch.), and 8.70 and 8.77 (1H, 2 s, NH, D_2O-exch.), Anal. calcd. for $C_{11}H_{15}N_3O_6$: C 46.32, H 5.30, N 14.73; found: C 46.46, H 5.21, N 14.91.

*Methyl 4-methoxycarbonyl-2-methyl-5-oxo-1-(*N′*-phenylureido)-1,4-dihydropyrrole-3-carboxylate (***6c***)*: mp 174–177°C; crystallized from ethyl acetate; IR: 3340 (NH), 3200, 3140 (NH overlap), 1760 (C=O), 1715 (C=O), 1690 (C=O), 1650 (C=O), and 1600 (C=O) cm^{-1}; ^1H NMR: 2.31 (3H, s, Me) 3.67 (3H, s, CO_2Me), 3.68 (3H, s, CO_2Me), 4.51 (1H, s, CH, D_2O-exch.), 6.99–7.46 (5H, m, Ph), 8.89 and 9.06 (1H, 2 s, NH, D_2O-exch.), and 9.30 (1H, s, NH, D_2O-exch.). Anal. calcd. for $C_{16}H_{17}N_3O_6$: C 55.33, H 4.93, N 12.10; found: C 55.21, H 5.01, N 12.27.

*Ethyl 4-methoxycarbonyl-2-methyl-5-oxo-1-(*N′*-phenylureido)-1,4-dihydropyrrole-3-carboxylate (***6d***)*: mp 188–190°C; crystallized from ethyl acetate; IR: 3340 (NH), 3190, 3120 (NH overlap), 1760 (C=O), 1710 (C=O), 1680 (C=O, 1650 (C=O), and 1600 (C=O) cm^{-1}; ^1H NMR: 1.19 (3H, t, J = 7 Hz, CO_2CH_2*Me*) 2.31 (3H, s, Me), 3.68 (3H, s, CO_2Me), 4.12 (2H, q, J = 7 Hz, CO_2CH_2Me), 4.48 (1H, s, CH, D_2O-exch.), 6.99–7.46 (5H, m, Ph), 8.87 and 9.04 (1H, 2 s, NH, D_2O-exch.), and 9.28 (1H, s, NH, D_2O-exch.). Anal. calcd. for $C_{17}H_{19}N_3O_6$: C 56.51, H 5.22, N 11.63; found: C 56.71, H 5.22, N 11.77.

*Methyl 2-methyl-4-methoxycarbonyl-1-(methoxycarbonylamino)-5-oxo-1,4-dihydropyrrole-3-carboxylate (***6e***)*: oil; IR: 3480, 3280 (NH overlap), 1770, 1730, 1710 (C=O overlap), and 1640 (C=O) cm^{-1}; ^1H NMR: 2.27 (3H, s, Me), 3.66 (9H, s, 3 × CO_2Me), 4.58 (1H, s, CH, D_2O-exch.), and 10.19 and 10.25 (1H, 2 s, NH, D_2O-exch.). Anal. calcd. for $C_{11}H_{14}N_2O_7$: C 46.16, H 4.93, N 9.79; found: C 46.31, H 4.77, N 9.88.

*Ethyl 1-(*tert*-butoxycarbonylamino)-4-(methoxycarbonyl-2-methyl-5-oxo-1,4-dihydropyrrole-3-carboxylate (***6f***)*: oil; IR: 3480, 3290 (NH overlap), 1765, 1735, 1710 (C=O overlap), and 1645 (C=O) cm^{-1}; ^1H NMR: 1.20 (3H, q, J = 7 Hz, CO_2CH_2*Me*), 1.43 (9H, s, t-Bu), 2.30 (3H, s, Me), 4.18 (2H, t, J = 7 Hz, CO_2CH_2Me), 4.58 (1H, s, CH, D_2O-exch.), and 9.91 and 9.93 (1H, 2 s, NH, D_2O-exch.). Anal. calcd. for $C_{15}H_{22}N_2O_7$: C 52.63, H 6.48, N 8.18; found: C 52.78, H 6.59, N 8.03.

*Methyl 4-benzyloxycarbonyl-2-methyl-5-oxo-1-ureido-1,4-dihydropyrrole-3-carboxylate (***6g***)*: mp 88–92°C; crystallized from dichloromethane – light petroleum, bp 30–60°C; IR: 3440 (NH), 3330, 3180 (NH_2 overlap), 1760, 1710, 1680, 1640, and 1610 (C=O overlap) cm^{-1}; ^1H NMR: 2.25 (3H, s, Me), 3.55 (3H, s, CO_2Me), 4.43 and 4.49 (1H, 2 s, CH, D_2O-exch.), 5.17 (2H, s, CO_2CH_2Ph), 6.29 and 6.39 (2H, 2 s, NH_2, D_2O-exch.), 7.35 (5H, s, CO_2CH_2*Ph*), and 8.69 and 8.76 (1H, 2 s, NH, D_2O-exch.). Anal. calcd. for $C_{16}H_{17}N_3O_6$: C 55.33, H 4.93, N 12.10; found: C 55.27, H 5.07, N 11.96.

*Methyl 4-benzyloxycarbonyl-2-methyl-5-oxo-1-(*N′*-phenylureido)-1,4-dihydropyrrole-3-carboxylate (***6h***)*: mp 118–120°C; crystallized from ethyl acetate; IR: 3320 (NH), 3210, 3140 (NH overlap), 1750 (C=O), 1690 (C=O overlap), 1640 (C=O), and 1600 (C=O) cm^{-1}; ^1H NMR: 2.32 (3H, s, Me), 3.57 (3H, s, CO_2Me), 4.58 (1H, s, CH, D_2O-exch.), 5.21 (2H, s, CO_2CH_2Ph), 8.96–7.48 (10H, m, Ph and CO_2CH_2*Ph*), 8.92 and 9.09 (1H, 2 s, NH, D_2O-exch.), and 9.34 (1H, s, NH, D_2O-exch.). Anal. calcd. for $C_{22}H_{21}N_3O_6$: C 62.41, H 5.0, N 9.92; found: C 62.53, H 4.86, N 10.05.

*Methyl 4-benzyloxycarbonyl-1-(methoxycarbonylamino)-2-methyl-5-oxo-1,4-dihydropyrrole-3-carboxylate (***6i***)*: oil; IR: 3490, 3280 (NH

overlap), 1760, 1740, 1710 (C=O overlap), 1640 (C=O) cm^{-1}; ^1H NMR: 2.28 (3H, s, Me), 3.65 (6H, s, 2 × CO_2Me), 4.58 (1H, s, CH, D_2O-exch.), 5.19 (2H, s, CO_2CH_2Ph), 7.36 (5H, s, CO_2CH_2Ph), and 10.06 and 10.10 (1H, 2 s, NH, D_2O-exch.). Anal. calcd. for $C_{17}H_{18}N_2O_7$: C 56.35, H 5.01, N 7.73; found: C 56.49, H 5.15, N 7.65.

Acknowledgement

This work was supported by financial assistance from the Ministero dell'Università e della Ricerca Scientifica e Tecnologica (MURST-Roma) and the Consiglio Nazionale delle Ricerche (CNR-Roma).

1. A.R. Katritzky. Chem. Heterocycl. Compd. (Engl. Transl.), **28**, 291 (1992).
2. O. Attanasi and L. Caglioti. Org. Prep. Proced. Int. **18**, 299 (1986).
3. O. Attanasi, S. Santeusanio, F. Serra-Zanetti, E. Foresti, and A. McKillop. J. Chem. Soc. Perkin Trans. 1, 1669 (1990).
4. O. Attanasi, L. De Crescentini, S. Santeusanio, F. Serra-Zanetti, A. McKillop, and Z. Liao. J. Chem. Soc. Perkin Trans. 1, 1009 (1992).
5. O. Attanasi, L. De Crescentini, A. McKillop, S. Santeusanio, and F. Serra-Zanetti. J. Chem. Soc. Perkin Trans. 1, 3099 (1992).
6. J.H. Atkinson, R.S. Atkinson, and A.W. Johnson, J. Chem. Soc. 5999 (1964).
7. R. Di Santo, S. Massa, and M. Artico. Farmaco, **48**, 209 (1993).
8. J. Parrick and M. Porssa. Tetrahedron Lett. **34**, 5011 (1993); F. Arcamone. Farmaco, **48**, 143 (1993).
9. H. Fischer and H. Plieninger. Z. Physiol. Chem **274**, 231 (1949).
10. H. Plieninger, H. Bauer, and A.R. Katritzky. Justus Liebigs Ann. Chem. **654**, 165 (1962).
11. H. Suschitzky and O. Meth-Cohn (*Editors*). Heterocyclic chemistry. Vols. 1–4. Royal Society of Chemistry, London. 1978–1985; H. Suschitzky and E.F.V. Scriven (*Editors*). Progress in heterocyclic chemistry. Vols. 1–4. Pergamon Press, Oxford. 1985–1991; E.A.A. Hafez, N.N. Abed, M. Rifaat, H. Elmoghayer, and A.G.A. El-Agamey. Heterocycles, **22**, 1821 (1984). A.R. Katritzky and C.W. Rees (*Editors*). Comprehensive heterocyclic chemistry. Pergamon Press, Oxford. 1984; R.A. Jones and G.P. Bean. The chemistry of pyrroles. Academic Press, New York. 1977; J.M. Patterson. Synthesis, 281 (1976); A. Gossauer. Die Chemie der Pyrrole. Springer Verlag, Berlin. 1974.
12. O.A. Attanasi, P. Filippone, A. Mei, and S. Santeusanio. Synthesis, 873 (1984).
13. O.A. Attanasi, P. Filippone, A. Mei, and S. Santeusanio. Synthesis, 671 (1984).

Can. J. Chem. Downloaded from www.nrcresearchpress.com by 85.192.166.187 on 09/08/12
For personal use only.

Chemoenzymatic enantioselective synthesis of baclofen

ROBERT CHÊNEVERT[1] AND MICHEL DESJARDINS

Département de chimie, Faculté des sciences et de génie, Université Laval, Québec, QC G1K 7P4, Canada

Received June 17, 1994

ROBERT CHÊNEVERT and MICHEL DESJARDINS. Can. J. Chem. **72**, 2312 (1994).

We report two different chemoenzymatic enantioselective syntheses of baclofen based on the distinction between enantiotopic ester groups in compounds bearing a prochiral centre. In the first approach, the key step is the highly stereoselective enzymatic hydrolysis of dimethyl 3-(4-chlorophenyl)glutarate by chymotrypsin in an aqueous medium. In the second approach, the key step is the enzyme-catalyzed esterification of 2-(4-chlorophenyl)-1,3-propanediol by acetic anhydride in the presence of a lipase in an organic medium.

ROBERT CHÊNEVERT et MICHEL DESJARDINS. Can. J. Chem. **72**, 2312 (1994).

Nous décrivons deux synthèses chimio-enzymatiques des énantiomères du baclofen basées sur une distinction de groupements ester énantiotopiques dans des composés comportant un centre prochiral. Dans la première approche, l'étape-clé est une hydrolyse stéréosélective du 3-(4-chlorophényl)glutarate de diméthyle par la chymotrypsine en milieu aqueux. Dans la seconde approche, l'étape-clé est une estérification enzymatique du 2-(4-chlorophényl)-1,3-propanediol par l'anhydride acétique en présence d'une lipase en milieu organique.

Introduction

The neutral amino acid γ-aminobutyric acid (GABA) is an inhibitory neurotransmitter related to the control of neuronal activity in the central nervous system and to the regulation of several physiological mechanisms (1). GABA has been shown to act through at least two different receptor sites with different binding properties ($GABA_A$ and $GABA_B$ receptors) (1, 2). Baclofen or 4-amino-3-(4-chlorophenyl)butanoic acid is an analog of GABA but, unlike GABA, it can cross the blood–brain barrier. Baclofen is the reference selective agonist for the $GABA_B$ receptor, and racemic baclofen is widely used as an antispastic agent (1). The enantiomers of this compound differ in their pharmacodynamic and toxicological properties; the (–) enantiomer is much more active but also more toxic than the (+) enantiomer (3–5). The *R* configuration was assigned to the more active enantiomer on the basis of X-ray crystallography (6). Enantiomers of baclofen have been obtained by resolution of racemates (5) and (*R*)-baclofen has been prepared from (*S*)-pyroglutamic acid (7). Also, a synthesis of (*R*)-baclofen using the Evans' oxazolidinone chiral auxiliaries has been reported (8). We report here two different chemoenzymatic syntheses of optically active baclofen based on the distinction between enantiotopic ester groups in compounds bearing a prochiral centre (9, 10).

Results and discussion

The first approach to the synthesis of both enantiomers of baclofen is based on the enzyme-catalyzed enantioselective hydrolysis of dimethyl 3-(4-chlorophenyl) glutarate (**4**) in an aqueous medium. The reaction sequence is shown in Scheme 1. Esterification of 4-chlorocinnamic acid **1** with methanol in the presence of an acidic resin as a catalyst gave ester **2**. The base-catalyzed (sodium methoxide) Michael-type reaction of dimethyl malonate with **2** gave the triester **3**. The demethoxycarboxylation of **3** on heating in aqueous dimethyl sulfoxide containing sodium chloride (11) led to the diester **4**. A screening for the enantioselective hydrolysis of **4** was started using a variety of commercially available hydrolytic enzymes. Among the tested enzymes, only α-chymotrypsin and pig liver esterase (PLE) could recognize **4** as substrate. Thus, when compound **4** was hydrolyzed in aqueous buffer (pH 7.7) under the catalysis of chymotrypsin, chiral mono-ester (***R***)-**5** was obtained in 85% yield and with a high enantiomeric excess (ee ≥ 98%). The enzymatic reaction was indicated by a decrease of pH, which was maintained at its initial value by the addition of aqueous sodium hydroxide. The reaction was monitored by the consumption of base, and the reaction stopped completely when 1 equivalent of base was consumed. Hydrolysis of **4** in the presence of pig liver esterase (PLE) in aqueous DMSO (40%) gave the other enantiomer in a lower enantiomeric yield (ee = 80%). The optical purity of compound **5** was determined by ^{1}H NMR (300 MHz) analysis and further confirmed by HPLC analysis of the diastereomeric amides, obtained by reaction of mono-ester **5** with (*R*)-1-(phenyl)ethylamine in the presence of 1-(3-dimethylaminopropyl)-3-ethylcarbodiimide hydrochloride (EDC).

The carboxyl group of **5** was converted to an amino group with retention of configuration through a Curtius rearrangement. Thus, the mono-ester was treated with ethyl chloroformate at 0°C in acetone and then with sodium azide. Acetone was replaced by toluene; the solution was heated to 100°C and the resulting isocyanate was hydrolyzed with aqueous HCl to give (*R*)-(–)-baclofen hydrochloride (***R***)-**6**. The *S* enantiomer of baclofen was also obtained from the same mono-ester (***R***)-**5**. Ammonolysis of **5** under pressure produced the corresponding amide **7**, which was submitted to a Hoffmann rearrangement with bis(trifluoroacetoxy)iodobenzene (12), then acidification to give (*S*)-(+)-baclofen hydrochloride (***S***)-**6**. Both enantiomers were purified by ion exchange chromatography.

The second approach was based on the enzyme-catalyzed esterification of 2-(4-chlorophenyl)-1,3-propanediol (**11**) by acetic anhydride in the presence of a lipase in an organic medium. The synthesis is illustrated in Scheme 2. Esterification of *p*-chlorophenylacetic acid (**8**) with ethanol in the presence of an acidic resin gave ester **9**. The reaction of ethyl *p*-chlorophenylacetate **9** with diethyl carbonate in the presence of sodium hydride gave diester **10**. This diester was reduced to the diol **11** by lithium aluminium hydride. Esterification of 2-(4-chlorophenyl)-1,3-propanediol (**11**) by acetic anhydride (13) in benzene, in the presence of porcine pancreatic lipase (PPL), gave the hemi-ester (***S***)-**12** in high enantiomeric yield (ee ≥ 96%). The enantiomeric purity was determined by ^{1}H NMR analysis in the presence of tris[(heptafluoropropylhydroxymethylene)-*d*-cam-

[1]Author to whom correspondence may be addressed. Telephone: (418) 656-3283. Fax: (418) 656-7916.

Can. J. Chem. Downloaded from www.nrcresearchpress.com by 85.192.166.187 on 09/08/12
For personal use only.

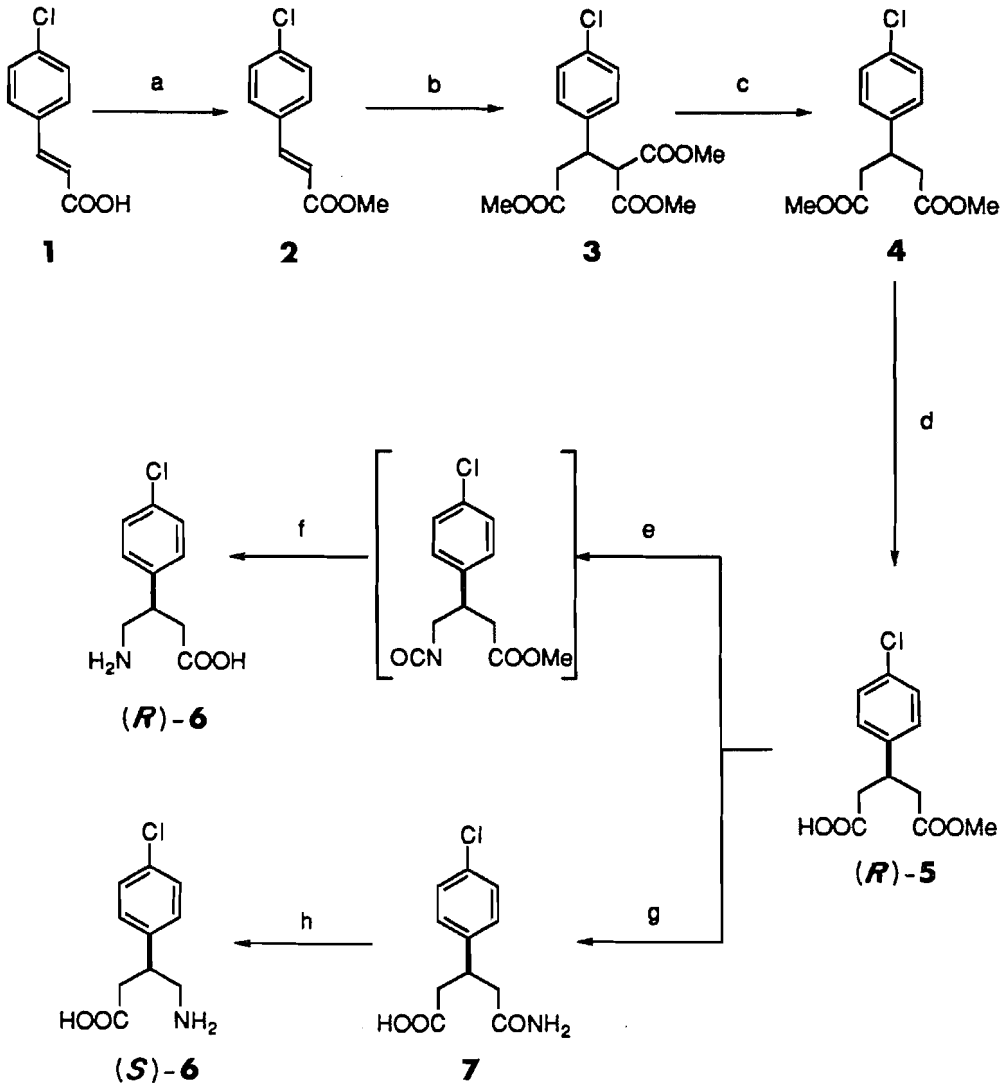

(a) MeOH, resin H^+, 95%; (b) $CH_2(COOMe)_2$, MeONa, MeOH, 85%; (c) NaCl, H_2O, DMSO, 79%; (d) α-chymotrypsin, phosphate buffer pH 7.7, Triton-X, 85%; (e) (*i*) $ClCO_2Et$, Et_3N, acetone, (*ii*) NaN_3, H_2O, acetone, (*iii*) Δ, toluene; (f) HCl, H_2O, 30% (for e and f); (g) $NH_{3(g)}$, MeOH, 40°C; (h) bis(trifluoroacetoxy)iodobenzene, H_2O, DMF, 36% (for g and h).

SCHEME 1

phorato]Europium III as a chiral shift reagent. Hemi-ester **12** was treated with mesyl chloride in the presence of triethylamine to give **13**. Displacement of the mesylate with cyanide afforded **14**. The ester **14** was then hydrolyzed, and the product **15** was converted to the mesylate **16**. The enantiomeric purity (ee ≥ 97%) of **16** was determined by ^{19}F NMR analysis of the corresponding (*S*)-MTPA derivative (Mosher ester). Displacement of this mesylate with sodium azide gave azido-nitrile **17**. The azido group was reduced by triphenylphosphine in water–THF to the corresponding amine, and the nitrile was hydrolyzed in acidic water in a one-pot reaction to give (*R*)-baclofen (***R***)-**6**.

Guanti et al. (14) found that the hydrolysis of diacetate **18** by PPL gave the hemi-ester (***R***)-**12** (Scheme 3). Therefore the two procedures (acylation and hydrolysis by PPL) can be considered complementary for the final product configuration, and consequently both enantiomers of baclofen are accessible from the same diol **11**, using PPL as the catalyst.

The present report represents another example of the versatility and the usefulness of the chemoenzymatic approach to the synthesis of both enantiomers of bioactive compounds.

Experimental

Melting points were recorded on a Thomas–Hoover apparatus and uncorrected. Infrared spectra were recorded using a Beckman IR-4250 spectrometer. ^1H NMR (300 MHz) and ^{13}C NMR (75.5 MHz) spectra were recorded on a Bruker AC-300 instrument. Optical rotations were measured using a JASCO DIP-360 polarimeter (sodium light, cell length = 10 cm, *c* = g/100 mL). Mass spectra were determined on a Hewlett–Packard 5989-A instrument using an ionization energy of 70 eV. Chymotrypsin (EC 3.4.21.1, type II, from bovine pancreas), PLE (EC 3.1.1.1, porcine liver esterase), and PPL (EC 3.1.1.3, type II, from porcine pancreas) were purchased from Sigma Chemical Co.

Methyl p-chlorocinnamate (2)

To a solution of *p*-chlorocinnamic acid **1** (18.22 g, 99.8 mmol) in methanol (150 mL) was added 2,2-dimethoxypropane (12.47 g, 119.7 mmol) and 2 g of an acidic ion exchange resin (Dowex-WX4). The mixture was refluxed overnight, cooled to room temperature, filtered,

Can. J. Chem. Downloaded from www.nrcresearchpress.com by 85.192.166.187 on 09/08/12
For personal use only.

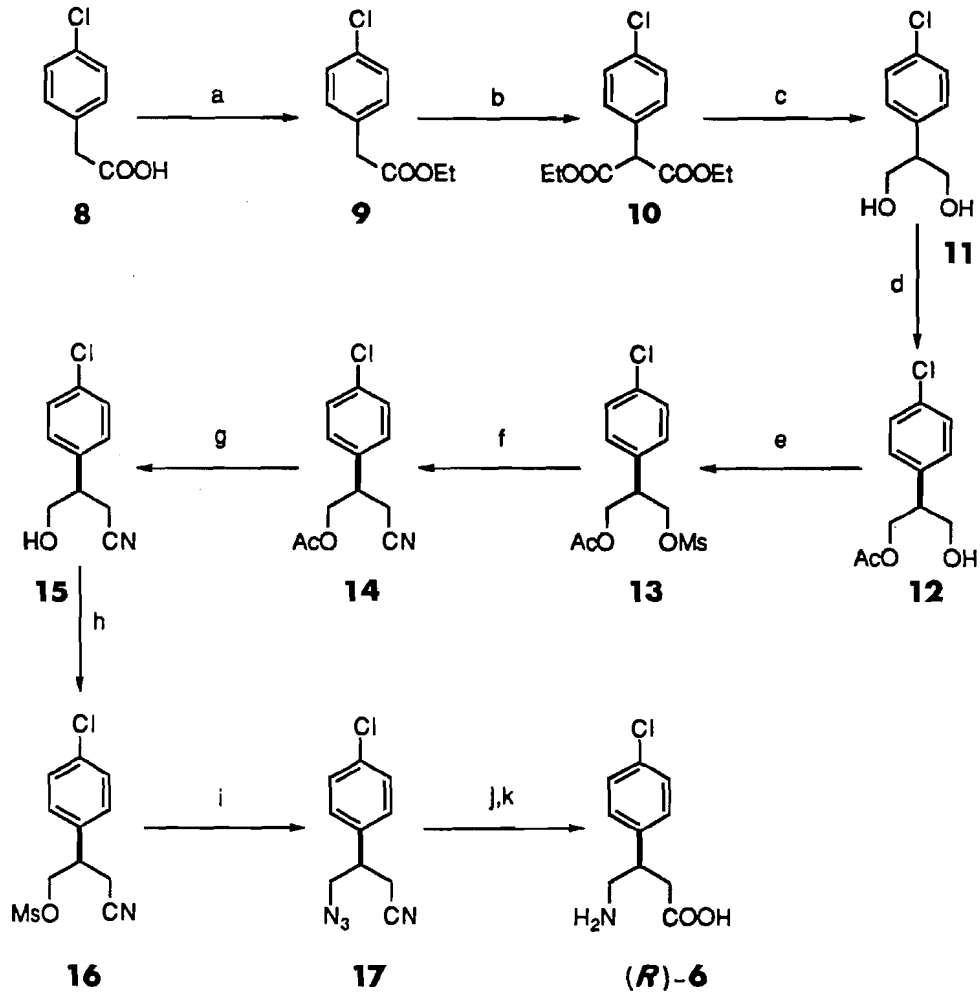

(a) EtOH, resin H^+, 94%; (b) $(EtO)_2CO$, NaH, THF, 71%; (c) $LiAlH_4$, ether, 97%; (d) PPL, Ac_2O, Celite, benzene, 93%; (e) MsCl, Et_3N, ether, 93%; (f) KCN, DMSO, 84%; (g) NaOH 0.1 M, THF–MeOH 9:1, 77%; (h) MsCl, Et_3N, THF, 91%; (i) NaN_3, DMF, 82%; (j) PPh_3, H_2O, THF; (k) HCl, H_2O, 46% (for j and k).

SCHEME 2

and the solvent was evaporated. The crude product was taken up in ether and this organic phase was washed with brine, dried ($MgSO_4$), and evaporated. The product was recrystallized in methanol–water to yield **2** (18.64 g, 95%); mp 74–75°C. IR (KBr) ν_{max}: 3030, 2900–3000, 1910, 1700, 1630, 1590, 1490 cm^{-1}. ^1H NMR ($CDCl_3$) δ: 7.64 (d, J = 16.0 Hz, 1H), 7.45 (m, J_1 = 9.0 Hz, 2H), 7.36 (m, J_1 = 9.0 Hz, 2H), 6.41 (d, J = 16.0 Hz, 1H), 3.81 (s, 3H). ^{13}C NMR ($CDCl_3$) δ: 166.97, 143.25, 136.06, 132.74, 129.10, 129.02, 118.29, 51.77 MS *m/z* (relative intensity): 198 (M^+, ^{37}Cl, 12), 196 (M^+, ^{35}Cl, 43), 167 (29), 165 (100), 139 (32), 137 (13).

Dimethyl 3-(p-chlorophenyl)-2-methoxycarbonylglutarate (3)

Clean sodium (690 mg, 30 mmol) cut in small pieces was added to anhydrous methanol (20 mL) under dry atmosphere. After all the sodium was dissolved, the solution was cooled to 0°C. A solution of methyl *p*-chlorocinnamate (5.063 g, 25.7 mmol) and dimethyl malonate (3.964 g, 30 mmol) in anhydrous THF (15 mL) was added dropwise. The mixture was then refluxed for 1.5 h. The solvent was evaporated and water (50 mL) was added to the crude oil. The product was taken up in ether and this organic phase was dried ($MgSO_4$) and evaporated. The crude product was recrystallized from hexane to yield triester **3** (7.202 g, 85%); mp 85–86°C. IR (neat) ν_{max}: 2840–2950, 1730, 1490, 1370, 830, 700 cm^{-1}. ^1H NMR ($CDCl_3$) δ: 7.24 (m, 2H), 7.16 (m, 2H), 3.87 (m, 1H), 3.72 (d, J = 10.0 Hz, 1H), 3.71 (s, 3H), 3.51 (s, 3H), 3.48 (s, 3H), 2.86 (dd, J_1 = 5.0 Hz, J_2 = 15.0 Hz, 1H), 2.66 (dd, J_1 = 9.0 Hz, J_2 = 15.0 Hz, 1H). ^{13}C NMR ($CDCl_3$) δ: 171.03, 167.88, 167.42, 138.17, 132.95, 129.22, 128.48, 56.63, 52.66, 52.39, 51.37, 40.71, 38.02. MS *m/z* (relative intensity): 330 (M^+, ^{37}Cl, 4), 328 (M^+, ^{35}Cl, 14), 211 (36), 209 (100), 167 (13), 165 (39), 157 (19), 155 (56).

Dimethyl 3-(p-chlorophenyl)glutarate (4)

A solution of ester (2.513 g, 7.64 mmol), water (0.275 g, 15.2 mmol), and sodium chloride (0.447 g, 7.64 mmol) in DMSO (15 mL) was refluxed for 4 h. The solvent was evaporated and the residue was taken up in ether. The organic phase was washed three times with brine, dried ($MgSO_4$), and evaporated. The crude product was recrystallized in ether – petroleum ether to yield **4** (1.629 g, 79%); mp 61–62°C. IR (neat) ν_{max}: 2995, 2940, 2840, 1730, 1490, 1430, 1090, 1010, 820 cm^{-1}. ^1H NMR ($CDCl_3$) δ: 7.25 (m, 2H), 7.14 (m, 2H), 3.61 (m, 1H), 3.57 (s, 6H), 2.71 (dd, J_1 = 7 Hz, J_2 = 16.0 Hz), 2.59 (dd, J_1 = 8.0 Hz, J_2 = 16.0 Hz). ^{13}C NMR ($CDCl_3$) δ: 171.57, 140.93, 132.54, 128.61, 128.49, 51.46, 40.08, 37.53. MS m/z (relative intensity): 272 (M^+, ^{37}Cl, 6), 270 (M^+, ^{35}Cl, 18), 212 (100), 210 (31), 165 (21), 154 (19), 152 (59), 138 (19).

Enzymatic hydrolysis of diester 4

The diester **4** (247 mg, 0.91 mmol) was suspended in a phosphate buffer (0.05 M, pH 7.70) and a drop of surfactant Triton X-100 was added to the mixture. Chymotrypsin (300 mg) was added and the pH of the solution was maintained at its initial value by addition of 0.1 M

Can. J. Chem. Downloaded from www.nrcresearchpress.com by 85.192.166.187 on 09/08/12
For personal use only.

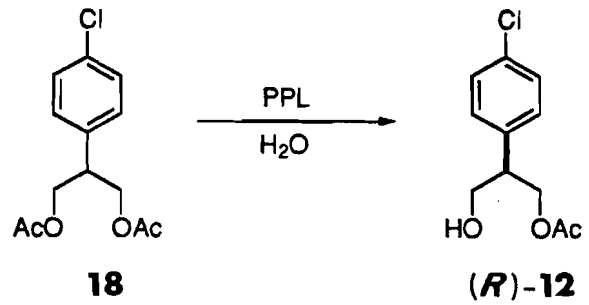

SCHEME 3

aqueous NaOH. After the addition of 1 equivalent of base (30 h), the enzyme was eliminated by ultrafiltration. The pH of the aqueous solution was raised to 9 and the aqueous phase was extracted with ether to remove unchanged diester. The aqueous phase was then acidified to pH 2.0 with cold 2 M aqueous HCl and was extracted with ether. Combined organic extracts were washed with brine, dried ($MgSO_4$), and concentrated to yield **5** (190 mg, 85%). $[\alpha]_D^{25}$ +4.1 (*c* 2.6, $CHCl_3$). IR (neat) ν_{max}: 2800–3650, 1690–1730, 1490, 1090, 1010, 820 cm^{-1}. ^1H NMR ($CDCl_3$) δ: 7.26 (d, *J* = 8.5 Hz, 2H), 7.14 (d, *J* = 8.5 Hz, 2H), 3.6 (m, 1H), 3.57 (s, 3H), 2.63 (m, 4H). ^{13}C NMR ($CDCl_3$) δ: 177.16, 171.66, 140.61, 132.66, 128.70, 128.52, 53.15, 51.73, 40.27, 37.38. MS *m/z* (relative intensity): 258 (M^+, ^{37}Cl, 9), 256 (M^+, ^{35}Cl, 16), 227 (7), 225 (22), 198 (11), 196 (47), 154 (16), 152 (56).

*(R)-Baclofen [(**R**)-6]*

A solution of acid **5** (492 mg, 1.92 mmol) in dry acetone (10 mL) was cooled to 0°C and triethylamine (400 μL) was added, followed by the dropwise addition of ethyl chloroformate (275 μL, 2.9 mmol). The solution was stirred at 0°C for 15 min and then at 25°C for 40 min. The solution was cooled to 0°C and sodium azide (152 mg, 2.34 mmol) in water (3 mL) was added dropwise. The mixture was stirred for 2 h at 0°C, poured into ice water (100 mL), and extracted with ether. The ether extracts were dried ($MgSO_4$), and the ether was evaporated. The crude acylazide was dissolved in toluene (10 mL) and the solution was refluxed for 8 h. The solvent was evaporated to leave an oil, which was dissolved in cold 6 N HCl. The solution was refluxed for 2 h, cooled to room temperature, washed with ether, and evaporated. The crude product was dissolved in a 1 N HCl solution (2 mL), and the solution was applied to an ion exchange resin (Dowex 50X2-200). The chlorides were eliminated by washing the column with distilled water; then the amino acid was eluted with a solution of triethylamine 10% in water. The ninhydrin-positive fractions were collected, evaporated, and the crude product was recrystallized (water–ethanol) to yield (*R*)-baclofen (124 mg, 30%). $[\alpha]_D^{25}$ –1.5 (*c* 0.2, H_2O) (lit. (8) $[\alpha]_D$ –1.7 (*c* 0.2, H_2O)). IR (KBr) ν_{max}: 3500–2200, 1630, 1570, 1400, 1160, 1100, 830, 730 cm^{-1}. ^1H NMR (D_2O + NaOD) δ: 7.15 (d, *J* = 8.0 Hz, 2H), 7.04 (d, *J* = 8.0 Hz, 2H), 2.84 (m, 1H), 2.63 (dd, J_1 = 6.0 Hz, J_2 = 15.0 Hz, 1H), 2.52 (dd, J_1 = 10.0 Hz, J_2 = 15.0 Hz, 1H), 2.33 (dd, J_1 = 7.0 Hz, J_2 = 15.0 Hz, 1H), 2.18 (dd, J_1 = 9.0 Hz, J_2 = 15.0 Hz, 1H). ^{13}C NMR (D_2O + NaOD) δ: 181.03, 141.46, 131.47, 129.34, 128.46, 46.10, 45.17, 42.19.

3-(p-Chlorophenyl)glutaramide 7

To a cooled (–30°C, CCl_4 – Dry Ice) solution of hemi-ester **5** (641 mg, 2.50 mmol) in methanol (5 mL) placed in a pressure tube was added an excess of liquid ammonia. The reaction mixture was kept at 40°C for 48 h, then the tube was cooled to –30°C and opened carefully to allow the excess ammonia to evaporate. The solvent was evaporated and the crude product was purified by flash chromatography (ether 90% – methanol 10%) to yield amide **7** (516 mg, 85%). $[\alpha]_D^{25}$ –6.5 (*c* 1.2, MeOH). IR (neat) ν_{max}: 3420, 3400, 2920, 1700, 1590, 1200, 1100, 1090, 1010, 820 cm^{-1}. ^1H NMR (methanol-d_4) δ: 7.27 (s, 4H), 3.60 (m, 1H), 2.59 (m, 4H). ^{13}C NMR (methanol-d_4) δ: 176.54, 175.61, 143.09, 133.38, 130.22, 129.44, 42.76, 41.49, 39.65. MS *m/z* (relative intensity): 241 (M^+, ^{35}Cl, 9), 225 (27), 197 (20), 196 (9), 152 (26), 138 (100), 140 (34).

*S-Baclofen [(**S**)-6]*

A solution of amide **7** (188 mg, 0.78 mmol) in water–acetonitrile (1:1, v/v, 5 mL) was treated with [bis(trifluoroacetoxy)iodo]benzene (442 mg, 1.03 mmol) and the mixture was stirred at room temperature for 24 h. The reaction mixture was diluted with water and extracted with ether to remove starting materials and iodobenzene. The aqueous phase was concentrated (2 mL), and the product was purified by ion exchange chromatography as described above to yield (*S*)-baclofen (71 mg, 42%). $[\alpha]_D^{25}$ +1.4 (*c* 0.2, H_2O) (lit. (5) $[\alpha]_D^{25}$ +1.4 (*c* 1, H_2O).

*Ethyl p-chlorophenylacetate (**9**)*

4-Chlorophenylacetic acid **8** (19.42 g, 114 mmol) was dissolved in anhydrous ethanol (150 mL). 2,2-Dimethoxypropane (14.24 g, 137 mmol) and Dowex-WX4 ion exchange resin (2 g) were added, and the mixture was refluxed overnight. The resin was filtered, the solvent was evaporated in vacuo, and the residue was taken up in ether. The organic phase was washed twice with brine, dried on $MgSO_4$, and evaporated to yield ester (21.28 g, 94%); mp 33–34°C; bp 78°C (0.3 Torr. 1 Torr = 133.3 Pa). IR (KBr) ν_{max}: 2990, 1730, 1595, 1490, 1370, 1090, 1015, 800 cm^{-1}. ^1H NMR ($CDCl_3$) δ: 7.24 (m, 4H), 4.14 (q, *J* = 7.0 Hz, 2H), 3.57 (s, 2H), 1.24 (t, *J* = 7.0 Hz, 3H). ^{13}C NMR ($CDCl_3$) δ: 170.88, 132.79, 132.41, 130.44, 128.48, 60.90, 40.62, 14.14. MS *m/z* (relative intensity): 200 (M^+, ^{37}Cl, 10), 198 (M^+, ^{35}Cl, 29), 127 (66), 125 (100), 89 (21).

*Diethyl p-chlorophenylmalonate (**10**)*

To a mixture of sodium hydride (0.66 g, 13 mmol) and diethyl carbonate (3.80 mL, 31 mmol) in anhydrous tetrahydrofuran (15 mL) was added dropwise a solution of ester **9** (1.24 g, 6.2 mmol) in anhydrous tetrahydrofuran (5 mL). The mixture was refluxed for 2 h, cooled, neutralized with a saturated aqueous solution of ammonium chloride (30 mL), and extracted with ether. The combined organic phases were washed with saturated $NaHCO_3$ and brine, and dried over sodium sulfate. After evaporation of solvent, the residue was purified by vacuum distillation to yield diester **10** (1.20 g, 71%); bp 116–118°C (0.3 Torr). IR (neat) ν_{max}: 2980, 2940, 2900, 1740, 1595, 1490, 1410, 1320, 1090, 1030, 860 cm^{-1}. ^1H NMR ($CDCl_3$) δ: 7.33 (s, 4H), 4.57 (s, 1H), 4.20 (q, *J* = 7.0 Hz, 4H), 1.24 (t, *J* = 7.0 Hz, 6H). ^{13}C NMR ($CDCl_3$) δ: 167.55, 134.10, 131.13, 130.52, 128.59, 61.88, 57.19, 14.99. MS *m/z* (relative intensity): 272 (M^+, ^{37}Cl, 18), 270 (M^+, ^{35}Cl, 59), 199 (37), 197 (100), 169 (66), 152 (69), 127 (32), 125 (97).

*2-(p-Chlorophenyl)-1,3-propanediol (**11**)*

Lithium aluminum hydride (5.0 g, 125 mmol) was suspended in anhydrous ether (125 mL) at 0°C under a dry N_2 atmosphere. Diester **10** (16.72 g, 61.8 mmol) was added dropwise and the reaction mixture was stirred at 25°C for 12 h. The mixture was acidified with 10% HCl (200 mL) and extracted with ether. The combined extracts were washed with brine, dried over sodium sulfate, and concentrated. The crude product was purified by flash chromatography (silica gel, ether – petroleum ether, 4:1) to yield diol **11** (11.188 g, 97%); mp 51–52°C. IR (KBr) ν_{max}: 3100–3600, 2920, 2880, 1590, 1490, 1200, 1060, 950, 820 cm^{-1}. ^1H NMR ($CDCl_3$) δ: 7.21 (m, 4H), 3.96 (dd, J_1 = 11.0 Hz, J_2 = 7.0 Hz, 2H), 3.88 (dd, J_1 = 11.0 Hz, J_2 = 7.0 Hz, 2H), 3.04 (m, *J* = 7.0 Hz, 1H), 2.26 (br s, 2H). ^{13}C NMR ($CDCl_3$) δ: 137.86, 132.57, 129.17, 128.57, 64.83. (MS *m/z* (relative intensity): 188 (M^+, ^{37}Cl, 2), 186 (M^+, ^{35}Cl, 6), 157 (4), 155 (10), 140 (31), 138 (100), 91 (24).

*Lipase-catalyzed acylation of **11***

To a stirred solution of diol **11** (205 mg, 1.10 mmol) was added porcine pancreatic lipase (200 mg) supported on Celite (13) and acetic anhydride (105 μL, 1.11 mmol). The reaction was monitored by TLC and was complete after 4 h. The solid enzyme preparation was filtered off and the solvent was evaporated in vacuo. The crude product was purified by flash chromatography on silica gel (ether – petroleum ether, 3:2) to yield monoester **12** (234 mg, 93%). $[\alpha]_D^{25}$ +15.3 (*c* 0.98, $CHCl_3$). IR (neat) ν_{max}: 3100–3700, 2860–2960, 1730, 1495, 1250, 1095, 1040, 1015, 825 cm^{-1}. ^1H NMR ($CDCl_3$) δ: 7.28 (d, *J* = 8.5 Hz, 2H), 7.16 (d, *J* = 8.5 Hz, 2H), 4.31 (d, *J* = 6.5 Hz, 2H), 3.77 (d, *J* = 6.0 Hz, 2H), 3.08

Can. J. Chem. Downloaded from www.nrcresearchpress.com by 85.192.166.187 on 09/08/12
For personal use only.

Can. J. Chem. Downloaded from www.nrcresearchpress.com by 85.192.166.187 on 09/08/12
For personal use only.

(m, J = 6.5 Hz, 1H), 2.33 (br s, 1H), 2.00 (s, 3H). ^{13}C NMR ($CDCl_3$) δ: 171.23, 137.59, 132.83, 129.35, 128.64, 64.64, 63.29, 46.43, 20.70. MS *m/z* (relative intensity): 228 (M^+, 0.2), 170 (27), 168 (8), 140 (33), 138 (100).

*1-Acetoxy-2-(*p*-chlorophenyl)-3-mesyloxypropane (**13**)*

A solution of **12** (1.423 g, 6.22 mmol) in anhydrous THF (65 mL) was prepared under nitrogen. The solution was cooled to 0°C and triethylamine (0.92 mL, 6.60 mmol) was added first, and then methanesulfonyl chloride (0.76 mL, 9.81 mmol) was added dropwise. The solution was stirred for 3 h while the temperature was increased to 25°C. The solvent was evaporated and the residue was taken up in ether (200 mL). The organic phase was washed with a 1 N HCl solution, with a saturated $NaHCO_3$ solution (three times), dried and concentrated. The crude product was purified by flash chromatography (silica gel, elution with ether – petroleum ether, 3:2) to yield **13** (2.051 g, 93%). $[\alpha]_D^{25}$ +6.8 (c 3.8, $CHCl_3$). IR (neat) ν_{max}: 3020, 2900–2980, 1730, 1590, 1490, 1350, 1165, 1090 cm^{-1}. ^{1}H NMR ($CDCl_3$) δ: 7.27 (m, 4H), 4.44 (d, J = 6.5 Hz, 2H), 4.34 (m, 2H), 3.39 (m, J = 6.5 Hz, 1H), 2.91 (s, 3H), 2.05 (s, 3H). ^{13}C NMR ($CDCl_3$) δ: 170.57, 135.47, 133.73, 129.30, 129.02, 69.13, 63.69, 43.54, 37.33, 20.73.

*4-Acetoxy-3-(*p*-chlorophenyl)propionitrile (**14**)*

To a solution of mesylate **13** (126 mg, 0.41 mmol) in anhydrous DMSO (5 mL) was added finely pulverized sodium cyanide (26 mg, 0.53 mmol). The solution was stirred at 45°C for 12 h. The solvent was evaporated in vacuo and the residue was taken up in ether (100 mL). The organic phase was washed several times with water, dried over magnesium sulfate, and evaporated. The crude product was purified by flash chromatography (silica gel, elution with ether – petroleum ether, 1:1) to yield nitrile **14** (82 mg, 84%). $[\alpha]_D^{25}$ +130 (c 1.1, $CHCl_3$). IR (neat) ν_{max}: 2950, 2240, 1735, 1595, 1490, 1360, 1230, 1090, 1010, 820 cm^{-1}. ^{1}H NMR ($CDCl_3$) δ: 7.24 (d, J = 6.5 Hz, 2H), 7.19 (d, J = 8.5 Hz, 2H), 4.33 (dd, J_1 = 6.0 Hz, J_2 = 11.0 Hz, 1H), 4.21 (dd, J_1 = 8.0 Hz, J_2 = Hz, 1H), 3.32 (m, J = 6.0 Hz, 1H), 2.79 (dd, J_1 = 7.0 Hz, J_2 = 18.0 Hz, 1H), 2.66 (dd, J_1 = 9.0 Hz, J_2 = 18.0 Hz, 1H), 2.05 (s, 3H). ^{13}C NMR ($CDCl_3$) δ: 170.21, 136.19, 133.83, 129.08, 128.57, 117.42, 65.70, 40.57, 21.21, 20.70. MS *m/z* (relative intensity): 239 (M^+, ^{37}Cl, 0.1), 237 (M^+, ^{35}Cl, 0.3), 235 (0.3), 179 (31), 177 (100), 139 (11), 137 (30).

*4-Hydroxy-3-(*p*-chlorophenyl)propionitrile (**15**)*

To a solution of **14** (27 mg, 0.11 mmol) in THF and methanol (4 mL, ratio 10:1) was added a 0.1 N NaOH solution (600 μL) and the solution was stirred at room temperature for 30 min. The solution was poured into ethyl acetate and the organic phase was decanted, washed with a saturated $NaHCO_3$ solution and with brine, dried over magnesium sulfate, and evaporated. The crude product was purified by flash chromatography on silica gel (elution with ether – petroleum ether, 70:30) to yield **15** (17 mg, 77%). $[\alpha]_D^{25}$ +27.5 (c 1.3, $CHCl_3$). IR (neat) ν_{max}: 3200–3600, 2920, 2870, 2240, 1595, 1490 cm^{-1}. ^{1}H NMR ($CDCl_3$) δ: 7.30 (d, J = 8.5 Hz, 2H), 7.15 (d, J = 8.5 Hz, 2H), 3.78 (dd, J_1 = 5.5 Hz, J_2 = 11.0 Hz, 1H), 3.68 (dd, J_1 = 7.0 Hz, J_2 = 11.0 Hz, 1H), 3.08 (m, J = 7.0 Hz, 1H), 2.78 (dd, J_1 = 17.0 Hz, J_2 = 6.0 Hz, 1H), 2.62 (dd, J_1 = 17.0 Hz, J_2 = 8.0 Hz, 1H), 2.20 (br s, 1H). ^{13}C NMR ($CDCl_3$) δ: 137.17, 133.34, 128.84, 128.68, 118.31, 64.52, 43.46, 20.34. MS *m/z* (relative intensity): 197 (M^+, ^{37}Cl, 3), 195 (M^+, ^{35}Cl, 6), 166 (4), 164 (12), 140 (31), 138 (100).

*4-Mesyloxy-3-(*p*-chlorophenyl)propionitrile (**16**)*

To a cold (0°C), stirred solution of **15** (610 mg, 3.12 mmol) in dry THF (35 mL) under a N_2 atmosphere was added triethylamine (0.5 mL, 3.6 mmol), followed by dropwise addition of methanesulfonyl chloride (0.30 mL, 3.6 mmol). The solution was stirred for 2 h while the temperature raised to 25°C. The solvent was evaporated and the residue was taken up in dichloromethane. The organic phase was washed with a 1 N HCl solution, a saturated $NaHCO_3$ solution, dried ($MgSO_4$), and evaporated. The crude product was purified by flash chromatography on silica gel (elution with dichloromethane – ethyl acetate, 97:3) to yield **16** (776 mg, 91%). $[\alpha]_D^{25}$ +14.1 (c 1.5, $CHCl_3$). IR (neat) ν_{max}: 3015, 2940, 2240, 1595, 1495, 1420, 1350, 1275, 1095, 920–980 cm^{-1}. ^{1}H NMR ($CDCl_3$) δ: 7.38 (d, J = 8.5 Hz, 2H), 7.22 (d, J = 8.5 Hz, 2H), 4.46 (dd, J_1 = 10.5 Hz, J_2 = 5.5 Hz, 1H), 4.36 (dd, J_1 = 10.5 Hz, J_2 = 7.5 Hz, 1H), 3.43 (m, J = 7.0 Hz, 1H), 3.01 (s, 3H), 2.87 (dd, J_1 = 17.0 Hz, J_2 = 7.0 Hz, 1H), 2.75 (dd, J_1 = 17.0 Hz, J_2 = 7.5 Hz, 1H). ^{13}C NMR ($CDCl_3$) δ: 135.02, 134.29, 129.29, 128.75, 117.22, 70.10, 40.69, 37.29, 20.60. MS *m/z* (relative intensity): 275 (M^+, ^{37}Cl, 1), 273 (M^+, ^{35}Cl, 3), 235 (1), 233 (2), 179 (36), 177 (100), 166 (19), 164 (58).

*4-Azido-3-(*p*-chlorophenyl)butyronitrile (**17**)*

To a solution of mesylate **16** (772 mg, 2.82 mmol) in dry DMF (27 mL) was added finely pulverized sodium azide (229 mg, 3.52 mmol). The solution was stirred overnight at 40°C under a N_2 atmosphere, then stirred at 80°C for 2 h. The solvent was evaporated in vacuo and the residue was taken up in ether. The organic phase was washed with a saturated $NaHCO_3$ solution, with brine, dried ($MgSO_4$), and concentrated. The crude product was purified by flash chromatography on silica gel (elution with ether – petroleum ether, 30:70) to yield **17** (508 mg, 82%). $[\alpha]_D^{25}$ –1.4 (c 1.5, $CHCl_3$). IR (neat) ν_{max}: 2910, 2860, 2080, 1490, 1445, 1410, 1085 cm^{-1}. ^{1}H NMR ($CDCl_3$) δ: 7.34 (d, J = 8.5 Hz, 2H), 7.18 (d, J = 8.5 Hz, 2H), 3.66 (dd, J_1 = 12.5 Hz, J_2 = 6.5 Hz, 1H), 3.56 (dd, J_1 = 12.5 Hz, J_2 = 7.0 Hz, 1H), 3.16 (m, J = 7.0 Hz, 1H), 2.76 (dd, J_1 = 9.0 Hz, J_2 = 6.0 Hz, 1H), 2.64 (dd, J_1 = 9.0 Hz, J_2 = 7.0 Hz, 1H). ^{13}C NMR ($CDCl_3$) δ: 136.62, 133.78, 129.03, 128.50, 117.39, 54.27, 40.90, 21.18. MS *m/z* (relative intensity): 192 (15), 166 (39), 164 (100), 140 (24), 138 (62), 130 (9), 128 (45).

*(R)-Baclofen [(**R**)-6]*

To a solution of **17** (218 mg, 0.99 mmol) in dry THF (5 mL) under a N_2 atmosphere was added triphenylphosphine (285 mg, 1.09 mmol) and the mixture was stirred at room temperature for 3 h. Water (20 μL) was added and the solution was stirred for 3 h, then poured into ether. The amine product was extracted from the organic phase with a 1 N HCl solution. The aqueous phase was washed with ether and its pH was fixed at 9 by addition of NaOH. This basic aqueous solution was extracted three times with ether. The combined organic phases were dried over Na_2CO_3 and concentrated. The solid product was dissolved in a 6 N HCl solution (2 mL) and the solution was stirred at room temperature for 18 h, and then refluxed 1 h. Water was evaporated in vacuo to yield a white solid, which was dissolved in a 1 N HCl solution (2 mL) and purified by ion exchange chromatography as described above to yield (*R*)-baclofen (97 mg, 46%). $[\alpha]_D^{25}$ –1.7 (c 0.2, H_2O) (lit. (7) $[\alpha]_D^{20}$ –2 (c 0.2, H_2O); lit. (8) $[\alpha]_D$ –1.7 (c 0.2, H_2O)).

Acknowledgement

We acknowledge the financial support of this work by the Natural Sciences and Engineering Research Council of Canada.

1. C. Hansch, P.G. Sammes, and J.B. Taylor (*Editors*). Comprehensive medicinal chemistry. Pergamon Press, New York. 1990.
2. N.G. Bowery, G.D. Pratt, and C. Knott. *In* $GABA_B$ receptors in mammalian function. *Edited by* N.G. Bowery, M. Bittiger, and H.R. Olpe. Wiley, Chichester. 1990. p. 3.
3. E. Falch, A. Hedegaard, L. Nielsen, B.R. Jensen, H. Hjeds, and P. Krogsgaard-Larsen. J. Neurochem. **47**, 898 (1986).
4. N.G. Bowery, D.R. Hill, A.L. Hudson, A. Doble, D.N. Middlemiss, J. Shaw, and M. Turnbull. Nature, **283**, 92 (1980).
5. H.R. Olpe, H. Demiéville, V. Baltzer, W.L. Bencze, W.P. Koella, P. Wolf, and H.L. Haas. Eur. J. Pharmacol. **52**, 133 (1978).
6. C.H. Chang, D.S.C. Yang, C.Y. Chung, W. Bi-Cheng, J. Pletcher, M. Sax, and C.F. Terrence. Acta Crystallogr. Sect. B: Struct. Crystallogr. Cryst. Chem. **B38**, 2065 (1982).
7. C. Herdeis and H.P. Hubmann. Tetrahedron: Asymmetry, **3**, 1213 (1992).
8. A. Schoenfelder, A. Mann, and S. Le Coz. Synlett, 63 (1993).
9. S. Servi (*Editor*). Proceedings: Microbial reagents in organic synthesis. Kluwer Academic Publishers, Dordrecht. 1992. Presented,

in part, at a NATO Advanced Research Workshop, Sestri Levante, Italy, March 23–27, 1992.
10. R. Chênevert and M. Desjardins. Tetrahedron Lett. **32**, 4249 (1991).
11. A.P. Krapcho. Synthesis, 805 (1982).
12. A.S. Radhakrishna, M.E. Parham, R.M. Riggs, and G.M. Loudon. J. Org. Chem. **44**, 1746 (1979).
13. D. Bianchi, P. Cesti, and E. Battistel. J. Org. Chem. **53**, 5531 (1988).
14. G. Guanti, E. Narisano, T. Podgorski, S. Thea, and A. Williams. Tetrahedron, **46**, 7081 (1990).

Can. J. Chem. Downloaded from www.nrcresearchpress.com by 85.192.166.187 on 09/08/12
For personal use only.

Structural and conformational analysis of six-, seven-, and eight-membered cycloalkanes in tris(5-acetyl-3-thienyl)methane inclusion compounds

LI PANG AND FRANÇOIS BRISSE[1]

Département de chimie, Université de Montréal, C.P. 6128, Succ. A, Montréal, QC H3C 3J7, Canada

Received October 26, 1993[2]

LI PANG and FRANÇOIS BRISSE. Can. J. Chem. **72**, 2318 (1994).

Tris(5-acetyl-3-thienyl)methane (TATM) forms inclusion compounds with cyclohexane, -heptane, and -octane in a host/guest ratio of 2:1. The clathrate compounds have been studied by X-ray crystallography. The inclusion compound with cyclohexane crystallizes in two distinct triclinic unit cells of space group $P\bar{1}$: in the **A** form, the unit cell dimensions are a = 8.622(2), b = 10.194(2), c = 12.795(2) Å, α = 79.09(1)°, β = 72.74(1)°, γ = 84.89(1)°, V = 1053.9(4) Å^3 (220 K); for the **B** form, a = 11.668(4), b = 13.729(3), c = 14.227(4) Å, α = 89.40(3)°, β = 77.20(4)°, γ = 76.24(4)°, V = 2157(1) Å^3 (room temperature). In the **A** form the cavity is of the channel type but the guest molecule is located on a centre of inversion while in the **B** form the cavity is also of the channel type but the guest molecule is in a general position. The inclusion compounds of cycloheptane and cyclooctane crystallize only in the **B** form. The guest molecules in the **B** form are disordered. Conformational analyses of the guest molecules have also been performed by a combination of molecular dynamics and energy minimization.

LI PANG et FRANÇOIS BRISSE. Can. J. Chem. **72**, 2318 (1994).

Le tris(5-acétyl-3-thiényl)méthane (TATM) forme des composés d'inclusion avec les cyclohexane, -heptane et -octane avec un rapport hôte/invité de 2 : 1. On a étudié ces clathrates par diffraction des rayons X. Le composé d'inclusion avec le cyclohexane cristallise dans deux mailles tricliniques distinctes du groupe d'espace $P\bar{1}$: dans la forme **A**, a = 8,622(2), b = 10,194(2) et c = 12,795(2) Å, α = 79,09(1)°, β - 72,74(1)° et γ = 84,89(1)°, V = 1053,9(4) Å^3 (220 K) alors que, dans la forme **B**, a = 11,668(4), b = 13,729(3) et c = 14,227(4) Å, α = 89,40(3)°, β = 77,20(4)° et γ = 76,24(4)°, V = 2157(1) Å^3 (température ambiante). Dans la forme **A**, la cavité est du type canal dans lequel la molécule invitée se trouve sur un centre d'inversion alors que, dans la forme **B**, la cavité est du type canal dans lequel la molécule invitée se trouve en une position générale. Les composés d'inclusion des cycloheptane et cyclooctane ne cristallisent que dans la forme **B**. Les molécules invitées dans la forme **B** sont désordonnées. On a réalisé une analyse conformationnelle des molécules invitées par une combinaison de dynamique moléculaire et de minimisation d'énergie.

[Traduit par la rédaction]

Introduction

Tris(5-acetyl-3-thienyl)methane (TATM) has been found to form inclusion compounds with a large number of organic molecules (1). The crystal and molecular structures of a few TATM inclusion compounds, with ethyl acetate, benzene, *n*-hexane, ethanol, cyclononanone, and carbon tetrachloride, have been published in recent years (2–7). From these X-ray determinations, it was shown that the crystals of the TATM inclusion compounds are usually triclinic except for the cyclononanone clathrate, which belongs to the monoclinic system (6). Furthermore, the guest molecules always have higher thermal parameters than the TATM host molecules, which is evidence for a statistical or dynamic disorder effect. To analyze the order–disorder effect and the molecular conformation of the guest molecules in the TATM inclusion compounds, we have performed an X-ray study of the TATM clathrates with six- (**1′** and **1**), seven- (**2**) and eight-membered cycloalkanes (**3**), respectively, at room temperature or at 220 K, as well as some molecular dynamics simulations of the TATM clathrates **2** and **3**.

Experimental

Preparations

The host TATM molecule was synthesized according to the method described by Yakubov et al. (8) and was characterized by ^{1}H nmr ($CDCl_3$/TMS): δ (ppm) = 2.49, 2.77 (s, 2H, thiophene), 4.41 (s, 1H, CH), 7.49 (s, 9H, $-CH_3$); MS: 388; and melting point 125–128°C (recrystallized from $CHCl_3$). The crystals of the inclusion compounds were obtained by a slow recrystallization of the TATM host molecule from cyclohexane, cycloheptane, and cyclooctane solvents, respectively. The crystals of the **A** and **B** forms were obtained using different recrystallization conditions. Thus, the **A** form resulted from a slow cooling of the TATM–cyclohexane solution (5°C/day) whereas the **B** form was obtained by a relatively quick cooling of the solutions (1°C/h). The host/guest ratios of 2:1 were determined by crystal density measurements (flotation in KI/H_2O).

*X-ray crystallographic analysis of **1′**, **1**, **2**, and **3***

Single crystals were selected and mounted on the tip of a glass fibre. The structures were determined on an Enraf–Nonius CAD4 single crystal diffractometer. Lattice constants were determined by least-squares refinement using 25 well-centered reflections in the range 20° < θ < 25°. The crystals of **1′**, **2**, and **3** were measured at low temperature (220 K) and that of **1** at room temperature. Intensity data were collected using Cu $K\alpha$ graphite monochromatized radiation in the ω–2θ scan mode with a scan width defined by $\Delta\omega$ = (0.80 + 0.14 tan θ)° and a scan rate of 16.48° min^{-1}. The structures were solved by direct methods using the MULTAN80 program (9) for **1′** and the SHELXS86 program (10) for **1**, **2**, and **3**. The structures were refined through full-matrix least-squares calculations based on F's by using the NRCVAX program (11) for **1′** and the SHELX76 program (12) for **1**, **2**, and **3**.

All the non-hydrogen atoms of the TATM molecule were refined with anisotropic thermal parameters. The positions of the hydrogen atoms were calculated,[3] and their isotropic thermal parameters were refined.

The guest molecules in the **A** form are ordered, while in the **B** form they are always disordered. The models of the disordered structures were established from difference Fourier syntheses and refined by constraining the C—C bond distances to 1.54 ± 2 Å and the nonbonded distances to 2.56 ± 5 Å (for **1**) or to 2.95 ± 2 Å (for **2** and **3**). The non-hydrogen atoms of the guest molecule in **1′** and only those of the major structure of the guest molecules in **2** and **3** were refined anisotropically. Occupancy factors of 0.40, 0.35, and 0.25 were fixed in **1**, while those

[1]Author to whom correspondence may be addressed.

[2]Revision received August 2, 1994.

[3]One hydrogen atom of each CH_3 group of the TATM molecule was found from the difference Fourier syntheses and refined. The two remaining hydrogen atoms were calculated.

Can. J. Chem. Downloaded from www.nrcresearchpress.com by 85.192.166.187 on 09/08/12
For personal use only.

Can. J. Chem. Downloaded from www.nrcresearchpress.com by 85.192.166.187 on 09/08/12
For personal use only.

TABLE 1. Crystallographic data of interest and summary of X-ray data collections and structure refinements

Compound	**1′**	**1**	**2**	**3**
Formula	$2(C_{19}H_{16}O_3S_3)\cdot C_6H_{12}$	$2(C_{19}H_{16}O_3S_3)\cdot C_6H_{12}$	$2(C_{19}H_{16}O_3S_3)\cdot C_7H_{14}$	$2(C_{19}H_{16}O_3S_3)\cdot C_8H_{16}$
Host:guest ratio	2:1	2:1	2:1	2:1
fw	430.59	861.19	875.22	889.24
Temperature, K	220	295	220	220
Crystal system	Triclinic	Triclinic	Triclinic	Triclinic
Space group	$P\bar{1}$	$P\bar{1}$	$P\bar{1}$	$P\bar{1}$
a, Å	8.622(2)	11.668(4)	11.721(5)	11.914(1)
b, Å	10.194(2)	13.729(3)	13.734(6)	14.013(2)
c, Å	12.795(2)	14.227(4)	14.177(6)	13.986(2)
α, deg	79.09(1)	89.40(3)	89.22(4)	89.46(1)
β, deg	72.74(1)	77.15(4)	76.84(4)	77.15(1)
γ, deg	84.89(1)	76.24(4)	76.01(3)	75.22(1)
V, Å^3	1053.9(4)	2157(1)	2154(2)	2198.4(4)
Z	1	2	2	2
$F(000)$	452	904	920	936
Radiation	Cu	Cu	Cu	Cu
d_x, g cm^{-3}	1.36	1.33	1.35	1.34
d_m	1.32	1.30	1.30	1.32
μ, mm^{-1}	3.33	3.25	3.26	3.20
Crystal size, mm	0.62 × 0.26 × 0.08	0.17 × 0.12 × 0.09	0.52 × 0.14 × 0.09	0.40 × 0.20 × 0.08
Color	Pale yellow	Pale yellow	Pale yellow	Pale yellow
$2\theta_{max}$, deg	140	140	140	140
Crystal decay, %	1.8	3.6	5.8	2.5
h	−10, 10	−14, 14	−14, 14	−14, 14
k	0, 12	−16, 16	−16, 16	−17, 17
l	−15, 15	−17, 17	−17, 17	−17, 17
R_{int}	0.020	0.042	0.052	0.035
Number of measured reflections	7856	16081	15805	16367
Number of unique reflections	3996	8085	8096	8316
Reflections with $I > 1.96\sigma(I)$	3590	3960	5985	6008
g	0.0001	0.00015	0.00015	0.00015
R	0.047	0.087	0.070	0.065
R_w	0.054	0.071	0.076	0.066
S	2.76	1.77	2.22	1.93
Number of refined parameters	342	609	621	638
Final Δρ, (e Å^{-3})	0.62, −0.33	0.57, −0.51	0.59, −0.77	0.43, −0.45
Final (Δ/σ)max	0.03	0.40	0.32	0.60

of 0.709(4) and 0.291(4) in **2** and 0.763(3) and 0.237(3) in **3** were refined. The positions of the hydrogen atoms of the guest molecules were calculated (d(C—H) = 0.95 Å, θ(C-C-H) = 109.5°). The scattering factors were taken from ref. 13. The function minimized was $\Sigma w(|F_o| - |F_c|)^2$, $R = \Sigma||F_o| - |F_c||/\Sigma|F_o|$, $R_w = [\Sigma w(|F_o| - |F_c|)^2/\Sigma w|F_o|^2]^{1/2}$, where $w^{-1} = \sigma^2(F_o) + g(F_o)^2$, and $S = [\Sigma(|F_o| - |F_c|)^2/(m - n)]^{1/2}$.

A summary of the crystal data, intensity measurements, and refinement results is presented in Table 1. Atomic coordinates[4] are given in Table 2 while the molecular structure of **1′** and the atomic numbering scheme adopted are shown in Fig. 1.

Conformational analyses of 2 and 3

The conformational behaviour of cycloheptane and cyclooctane in **2** and **3** has been studied by a combination of energy minimization and molecular dynamics simulation in the solid state at different temperatures. The calculations were performed using the HyperChem™ Release 2 package[5] running on a 80486-50Hz IBM compatible personal computer.

Since the crystallographic structures of the TATM host molecules are always well defined, the geometry of the TATM molecules was fixed during the calculation and only the conformational energy of the two guest molecules in the unit cells was minimized. Consequently, 32 TATM molecules, whose geometries were taken directly from the crystallographic work, were chosen to build the host cavities inside the unit cells of **2** and **3**. The initial structures of the cycloheptane and the cyclooctane guest molecules were taken from the two models determined in this X-ray study.

The conformational search of the guest molecules in **2** and **3** was carried out using the quenched molecular dynamics method.[6] Thus, two guest molecules inside the host cavity were subjected to molecular dynamics simulation at different temperatures in order to cross over the energy barriers and to obtain possible conformations in a local minimum. Following the molecular dynamics simulation at a given temper-

[4]Lists of the atomic coordinates, bond lengths and angles, torsion angles, anisotropic thermal parameters, and least-squares planes data may be purchased from: The Depository of Unpublished Data Document Delivery, CISTI, National Research Council Canada, Ottawa ON K1A 0S2, Canada.

Tables of atomic coordinates and bond lengths and angles have also been deposited with the Cambridge Crystallographic Data Centre, and can be obtained on request from The Director, Cambridge Crystallographic Data Centre, University Chemical Laboratory, 12 Union Road, Cambridge, CB2 1EZ, U.K.

Structure factor amplitudes are no longer being deposited and may be obtained directly from the author.

[5]HyperChem™ program, AutoDesk Inc., Scientific Modeling Division, 2320 Marinship Way, Sausalito, CA 94965-9910, U.S.A.

[6]Quenched dynamics is a combination of high-temperature molecular dynamics and energy minimization. This process can determine a conformation in a relatively deep local minimum in reasonable time space. See HyperChem's manual, Computational Chemistry, Autodesk, Inc., Publication 100033-02, assy no. 100210, 1992.

Can. J. Chem. Downloaded from www.nrcresearchpress.com by 85.192.166.187 on 09/08/12
For personal use only.

TABLE 2. Atomic coordinates and equivalent isotropic thermal parameters for TATM–cyclohexane clathrates **1′** and **1** with estimated standard deviation in parentheses

Atom	*x*	*y*	*z*	$B_{iso}{}^{a}/U_{eq}{}^{b}$
		1′, **A** form		
Host molecule				
S(1)	0.99779(9)	0.27894(8)	0.46565(5)	3.57(3)
S(2)	1.21799(8)	0.05128(6)	0.01288(5)	2.94(2)
S(3)	0.45394(8)	0.31390(6)	0.15531(6)	3.13(3)
O(1)	0.8366(3)	0.0702(2)	0.6502(2)	4.87(11)
O(2)	1.2813(2)	0.0648(2)	−0.2318(2)	4.15(9)
O(3)	0.2472(2)	0.5576(2)	0.1364(2)	4.19(9)
C(1)	0.9168(3)	0.3292(2)	0.1660(2)	2.5(1)
C(11)	0.9210(3)	0.2868(2)	0.2853(2)	2.7(1)
C(12)	1.0136(3)	0.3484(3)	0.3310(2)	3.2(1)
C(13)	0.8628(3)	0.1639(2)	0.4647(2)	2.9(1)
C(14)	0.8346(3)	0.1794(2)	0.3634(2)	2.9(1)
C(15)	0.7948(3)	0.0703(3)	0.5676(2)	3.4(1)
C(16)	0.6673(4)	−0.0211(3)	0.5688(3)	4.6(1)
C(21)	1.0151(3)	0.2334(2)	0.0913(2)	2.5(1)
C(22)	1.1129(3)	0.1288(2)	0.1217(2)	2.9(1)
C(23)	1.1317(3)	0.1584(2)	−0.0775(2)	2.6(1)
C(24)	1.0249(3)	0.2490(2)	−0.0225(2)	2.5(1)
C(25)	1.1759(3)	0.1458(2)	−0.1945(2)	3.0(1)
C(26)	1.0899(4)	0.2361(3)	−0.2676(2)	4.4(1)
C(31)	0.7432(3)	0.3522(2)	0.1582(2)	2.5(1)
C(32)	0.6423(3)	0.2542(2)	0.1613(2)	2.9(1)
C(33)	0.5052(3)	0.4758(2)	0.1468(2)	2.7(1)
C(34)	0.6643(3)	0.4820(2)	0.1490(2)	2.6(1)
C(35)	0.3819(3)	0.5834(3)	0.1394(2)	3.3(1)
C(36)	0.4235(4)	0.7238(3)	0.1386(3)	4.5(1)
Guest molecule				
CG(1)	0.3706(4)	0.5025(4)	0.4481(3)	5.4(2)
CG(2)	0.4585(5)	0.3730(3)	0.4802(3)	5.4(2)
CG(3)	0.5220(4)	0.3801(3)	0.5767(3)	5.2(2)
		1, **B** form		
Host molecule I				
S(1)	0.5804(2)	0.4019(2)	0.2905(2)	0.048(1)
S(2)	0.0159(2)	0.2801(2)	0.3580(2)	0.078(1)
S(3)	0.3769(2)	0.1292(2)	0.6294(2)	0.054(1)
O(1)	0.4973(6)	0.6077(5)	0.3841(5)	0.075(3)
O(2)	0.1037(7)	0.2278(6)	0.0808(5)	0.094(3)
O(3)	0.3167(6)	−0.0598(4)	0.7023(4)	0.067(3)
C(1)	0.3721(7)	0.2019(5)	0.3527(5)	0.038(3)
C(11)	0.4283(7)	0.2921(6)	0.3403(5)	0.034(3)
C(12)	0.5393(7)	0.2902(6)	0.2854(5)	0.040(3)
C(13)	0.4451(7)	0.4551(6)	0.3682(6)	0.041(3)
C(14)	0.3726(7)	0.3871(6)	0.3899(5)	0.037(3)
C(15)	0.4195(8)	0.5615(6)	0.4066(6)	0.045(3)
C(16)	0.2991(8)	0.6046(7)	0.4696(7)	0.070(3)
C(21)	0.2477(7)	0.2246(5)	0.3325(6)	0.039(3)
C(22)	0.1424(8)	0.2570(6)	0.4003(7)	0.056(3)
C(23)	0.1031(9)	0.2483(6)	0.2419(6)	0.049(3)
C(24)	0.2287(6)	0.2171(5)	0.2332(6)	0.027(2)
C(25)	0.0427(10)	0.2511(8)	0.1611(8)	0.070(3)
C(26)	−0.0928(10)	0.2849(9)	0.1759(9)	0.106(4)
C(31)	0.3708(7)	0.1567(6)	0.4510(6)	0.037(3)
C(32)	0.3935(7)	0.2001(6)	0.5292(6)	0.047(3)
C(33)	0.3418(7)	0.0371(6)	0.5671(6)	0.039(3)
C(34)	0.3425(7)	0.0622(6)	0.4735(6)	0.040(3)
C(35)	0.3133(8)	−0.0514(6)	0.6187(7)	0.048(3)
C(36)	0.2816(9)	−0.1280(7)	0.5621(7)	0.070(3)

TABLE 2. (*Concluded*)

Atom	*x*	*y*	*z*	$B_{iso}{}^{a}/U_{eq}{}^{b}$
Host molecule II				
S(1′)	0.5676(2)	0.0594(2)	0.8114(2)	0.066(1)
S(2′)	0.3694(2)	0.4206(2)	1.1307(2)	0.053(1)
S(3′)	0.0132(2)	0.4297(2)	0.8527(2)	0.066(1)
O(1′)	0.4632(7)	−0.1101(5)	0.8894(5)	0.089(3)
O(2′)	0.3117(6)	0.6374(4)	1.1946(4)	0.066(2)
O(3′)	0.1238(6)	0.4344(5)	0.5732(4)	0.068(2)
C(1′)	0.3686(7)	0.3467(5)	0.8558(6)	0.039(3)
C(11′)	0.4179(7)	0.2329(6)	0.8485(5)	0.036(3)
C(12′)	0.5342(8)	0.1876(6)	0.8044(6)	0.051(3)
C(13′)	0.4210(8)	0.0655(6)	0.8749(6)	0.046(3)
C(14′)	0.3526(8)	0.1625(6)	0.8891(6)	0.044(3)
C(15′)	0.3874(10)	−0.0302(7)	0.9041(7)	0.064(3)
C(16′)	0.2574(10)	−0.0215(7)	0.9511(8)	0.095(4)
C(21′)	0.3667(7)	0.3928(6)	0.9529(6)	0.035(3)
C(22′)	0.3848(7)	0.3427(6)	1.0339(6)	0.045(3)
C(23′)	0.3371(7)	0.5254(6)	1.0648(6)	0.036(3)
C(24′)	0.3389(7)	0.4990(6)	0.9725(6)	0.039(3)
C(25′)	0.3115(7)	0.6257(6)	1.1100(7)	0.044(3)
C(26′)	0.2821(9)	0.7149(7)	1.0509(7)	0.070(3)
C(31′)	0.2449(7)	0.3784(5)	0.8334(6)	0.037(3)
C(32′)	0.1357(7)	0.3958(6)	0.9001(6)	0.053(3)
C(33′)	0.1057(7)	0.4222(6)	0.7382(6)	0.040(3)
C(34′)	0.2278(7)	0.3944(5)	0.7359(6)	0.030(2)
C(35′)	0.0551(8)	0.4426(6)	0.6513(6)	0.044(3)
C(36′)	−0.0774(8)	0.4724(7)	0.6610(7)	0.067(3)
Guest molecule I (Occupancy factor 0.4)				
CG(11)	−0.018(2)	0.830(2)	0.248(2)	0.042(5)
CG(12)	0.001(3)	0.924(2)	0.195(2)	0.162(6)
CG(13)	0.100(2)	0.965(2)	0.221(1)	0.037(4)
CG(14)	0.107(3)	0.964(2)	0.326(2)	0.084(6)
CG(15)	0.092(3)	0.862(2)	0.370(2)	0.149(6)
CG(16)	−0.026(2)	0.843(2)	0.357(2)	0.088(6)
Guest molecule II (Occupancy factor 0.35)				
CG(21)	0.060(2)	1.002(2)	0.278(2)	0.058(5)
CG(22)	0.109(3)	0.942(2)	0.357(2)	0.154(7)
CG(23)	0.026(3)	0.871(2)	0.403(2)	0.068(6)
CG(24)	0.024(3)	0.809(2)	0.315(2)	0.106(6)
CG(25)	−0.038(3)	0.866(2)	0.239(2)	0.071(6)
CG(26)	0.048(3)	0.935(2)	0.198(2)	0.153(7)
Guest molecule III (Occupancy factor 0.25)				
CG(31)	0.018(3)	0.974(2)	0.217(2)	0.078(6)
CG(32)	0.122(2)	0.963(2)	0.268(2)	0.026(5)
CG(33)	0.085(4)	0.929(3)	0.371(2)	0.175(7)
CG(34)	0.050(3)	0.829(2)	0.373(3)	0.072(6)
CG(35)	−0.042(3)	0.826(2)	0.312(2)	0.049(6)
CG(36)	−0.023(4)	0.874(3)	0.215(2)	0.079(7)

[a] B_{iso} is the mean of the principal axes of the thermal ellipsoid.
[b] $U_{eq} = \frac{1}{3}$ of the trace of the orthogonalized U_{ij} tensor.

ature, the structures of the guest molecules were minimized through a molecular mechanics force field (14) using the MM+ force field.[7] The molecular dynamics simulations were performed using a constant temperature bath at 300, 400, 500, 600, 700, 800, 900 and 1000 K, respec-

[7] The MM+ force field is an extension of MM2. Its bond and angle terms can contain higher-order terms than the standard quadratic. See HyperChem's manual, Computational Chemistry, Autodesk, Inc., Publication 100033-02, assy no. 100210, 1992.

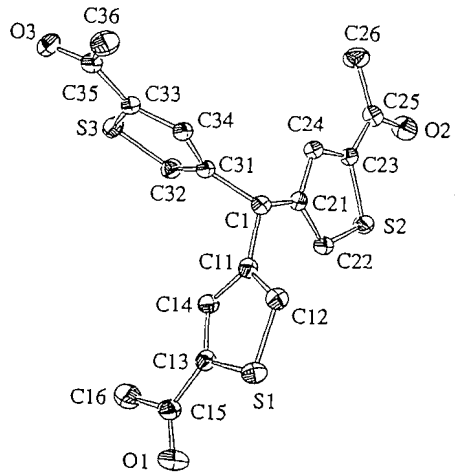

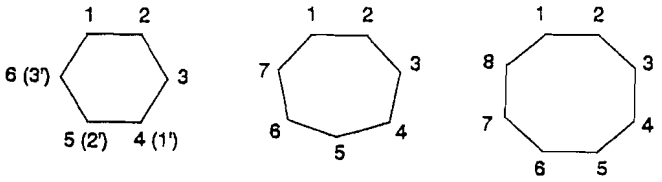

FIG. 1. Structure of the TATM molecule of **1′** and schematic diagrams of the six-, seven-, and eight-membered cycloalkanes and their atomic numbering.

tively. The molecules were allowed to equilibrate for a period of 1 ps. A time step of 0.001 ps and a relaxation time of 0.1 ps were used in the integration algorithm. The energy minimization employed the Polak–Ribiere conjugate gradient technique. The minimization was concluded after the maximum derivative of all atoms was less than 0.005 kcal mol^{-1} $Å^{-1}$. Atoms outside a cut-off sphere centered at 1/2 1/2 1/2 with a 12 Å radius were not considered in the calculation.

Results and discussion

The crystal data of interest for the TATM inclusion compounds under investigation are presented in Table 1. The cyclohexane inclusion compounds **1′** and **1** crystallize in two distinct triclinic forms. The crystal of the **A** form contains two TATM molecules and one guest molecule whereas there are four TATM molecules and two cyclohexane molecules in the unit cell of the **B** form. The volume of the unit cell of the **B** form is about twice that of the **A** form. No phase transition was observed between these two forms in the range 220–295 K so that these phases are independently stable and depend only upon the recrystallization procedure. The guest molecules in the **B** form are always disordered due to a slightly larger cavity. The following occupancy factors were evaluated: 40/35/25, 71/29, and 76/24 for the guest molecules in **1**, **2**, and **3**, respectively.

Structure of tris(5-acetyl-3-thienyl)methane (TATM)

The molecular structures of the TATM molecule in the **A** and **B** crystal forms are very similar (Fig. 1) and close to those of previously published work (2–7). Selected bond lengths and angles of the TATM molecules in **1′** and **1–3** are compared in Table 3. The acetyl groups are nearly coplanar with the thienyl rings, since the oxygen atoms and the methyl groups deviate

TABLE 3. (*a*) Average bond lengths (Å) and (*b*) bond angles (deg) for TATM molecules in **1′**, **1**, **2**, and **3** (n = 1, 2, and 3, the number of the thienyl ring)

		1		**2**		**3**	
Bond	**1′**	Molecule 1	Molecule 2	Molecule 1	Molecule 2	Molecule 1	Molecule 2
(*a*)							
S(n)—C(n2)	1.705	1.702	1.697	1.707	1.707	1.703	1.709
S(n)—C(n3)	1.724	1.723	1.724	1.728	1.726	1.726	1.725
O(n)—C(n5)	1.217	1.206	1.213	1.232	1.224	1.218	1.219
C(1)—C(n1)	1.520	1.514	1.516	1.513	1.522	1.518	1.521
C(n1)—C(n2)	1.370	1.360	1.366	1.375	1.369	1.371	1.368
C(n1)—C(n4)	1.425	1.428	1.429	1.436	1.425	1.420	1.432
C(n3)—C(n4)	1.378	1.386	1.367	1.384	1.367	1.372	1.387
C(n3)—C(n5)	1.465	1.483	1.474	1.461	1.468	1.463	1.465
C(n5)—C(n6)	1.499	1.487	1.483	1.498	1.497	1.499	1.503
(*b*)							
C(n2)—S(n)—C(n3)	91.7	90.9	90.9	91.6	91.3	91.5	91.5
C(n1)—C(1)—C(n1)	112.1	112.1	111.8	112.0	111.6	111.8	111.4
C(1)—C(n1)—C(n2)	124.5	125.0	125.2	124.7	124.8	124.8	124.6
C(1)—C(n1)—C(n4)	123.9	122.9	123.6	123.6	123.6	123.8	123.5
C(n2)—C(n1)—C(n4)	111.5	112.0	111.2	111.6	111.6	111.3	111.9
S(n)—C(n2)—C(n1)	112.9	113.7	113.6	113.0	112.8	112.6	113.0
S(n)—C(n3)—C(n4)	111.2	112.8	112.2	111.8	111.6	111.1	111.6
S(n)—C(n3)—C(n5)	119.1	119.5	120.1	120.1	120.0	120.3	120.4
C(n4)—C(n3)—C(n5)	129.8	127.7	127.7	128.1	128.3	128.6	128.0
C(n1)—C(n4)—C(n3)	112.8	110.6	112.0	112.3	112.6	113.1	112.0
O(n)—C(n5)—C(n3)	120.7	119.6	120.4	120.4	120.6	120.7	120.4
O(n)—C(n5)—C(n6)	121.2	121.8	121.4	120.9	121.4	121.4	121.8
C(n3)—C(n5)—C(n6)	118.2	118.6	118.2	118.7	118.0	118.0	117.9

Can. J. Chem. Downloaded from www.nrcresearchpress.com by 85.192.166.187 on 09/08/12
For personal use only.

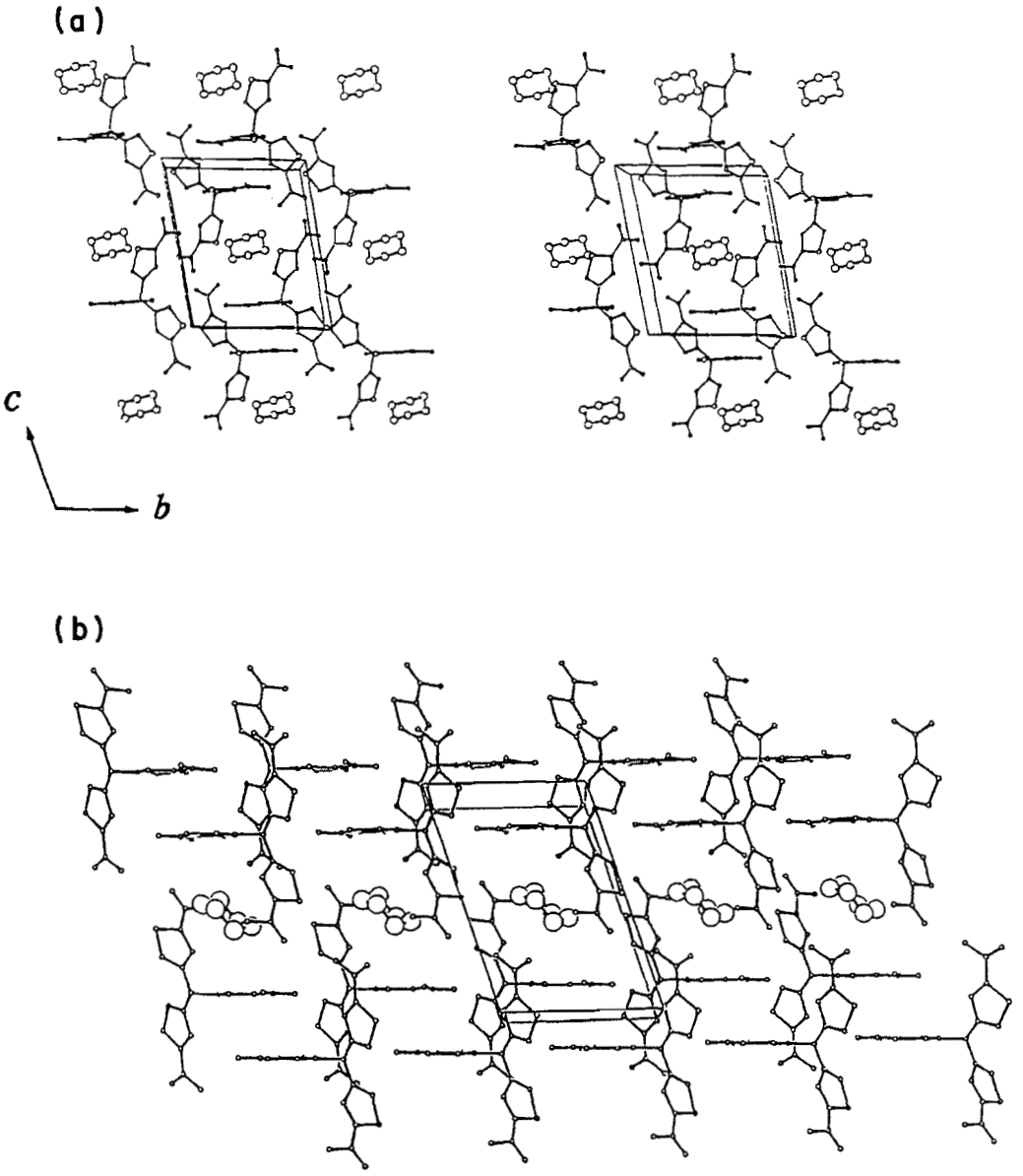

FIG. 2. The unit cell content of the TATM–cyclohexane clathrate in the **A** form (*a*) Stereo pair showing the channel cross section down the *a* axis; (*b*) side view (the *a* axis is horizontal).

from the thienyl ring by an average value of 0.06(2) and 0.08(2) Å. The hydrogen atoms of the methyl groups have a fair amount of disorder as indicated by their high thermal parameters. The dihedral angles formed between the three thienyl rings are in the range 68°–81°.

*Description of the cavities in the **A** and **B** forms*

Since the TATM molecule has a relatively rigid structure, the different crystal structures and the cavity type depend upon the size and the shape of the guest molecule and the resulting molecular packing.

The two views in Fig. 2 clearly show that there is a channel-like cavity in the unit cell of the **A** form. Thus, two of the three thienyl rings of one molecule and the acetyl group of another TATM molecule contribute to the formation of the channel. The axis of the channel, parallel to *a*, passes through the crystallographic centres of symmetry at 0 1/2 1/2, 1/2 1/2 1/2, etc. The cyclohexane guest molecules are located on these centres of inversion and are ordered.

The situation in the **B** form is slightly different. It can be seen from Fig. 3 that the cavity is also of the channel type. However, the molecules in the channel of the **B** form adopt a zigzag disposition rather than the linear one of the **A** form. The molecular packing of the TATM molecules in the **B** form is slightly different from that in the **A** form. Thus, the TATM molecules are arranged in such a way that one of the thienyl rings is almost parallel to the *bc* face of the unit cell, while the remaining two thienyl rings form the sides of the channels. The comparison of the *b* and *c* parameters of the **A** form with the *a* and *b* parameters of the **B** form, which are a measure of the channel cross section, reveals that the channels in the **B** are slightly larger than in the **A** form. This increase in the channel section could explain the disorder of the guest molecules. These results confirm some previously published work (3, 7).

Can. J. Chem. Downloaded from www.nrcresearchpress.com by 85.192.166.187 on 09/08/12
For personal use only.

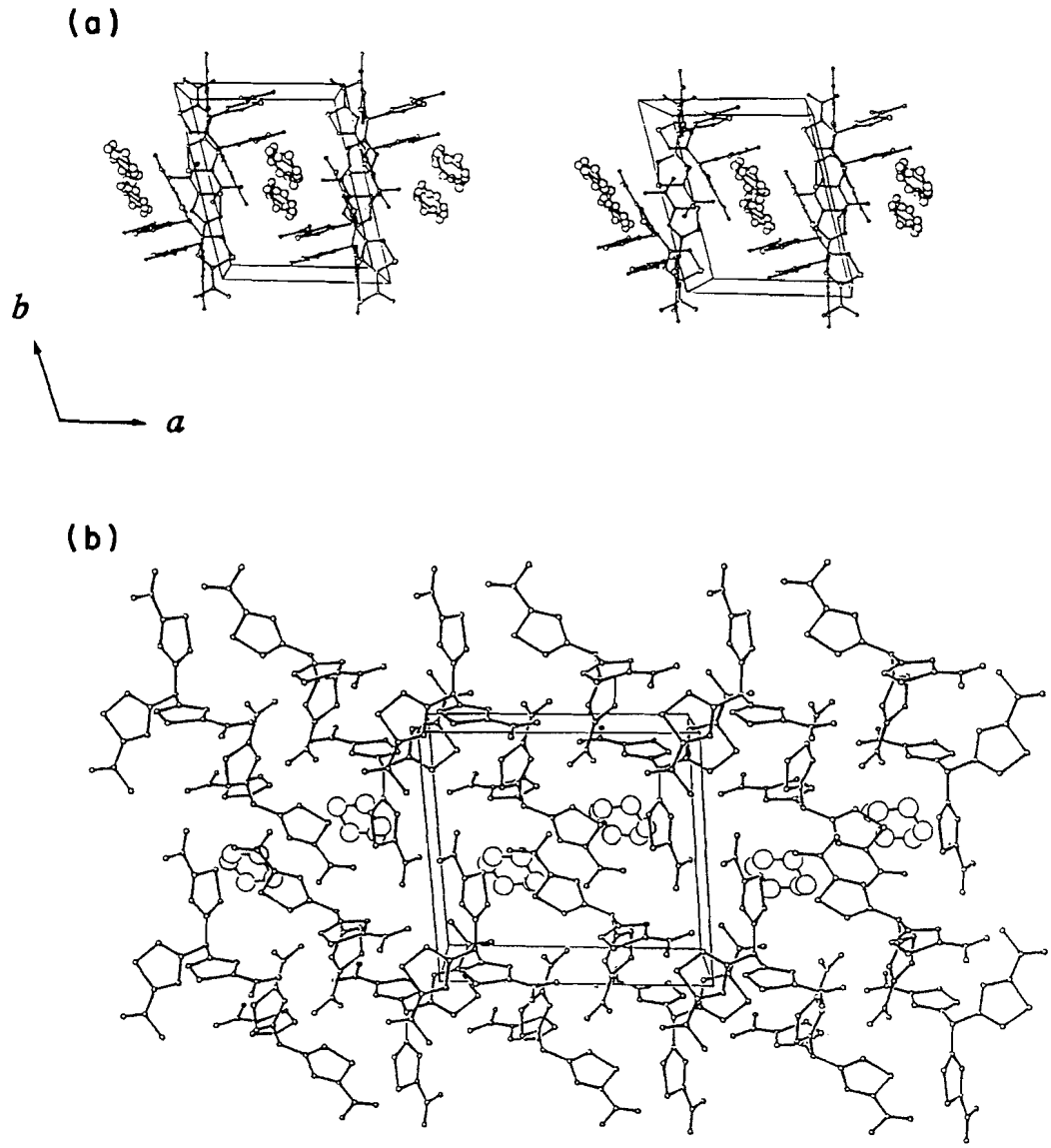

FIG. 3. The unit cell content of the TATM–cyclohexane clathrate in the **B** form. (*a*) Stereo pair showing the channel cross section down the *a* axis; (*b*) side view showing the length of the channel (the *c* axis is horizontal).

TABLE 4. Torsion angles (deg) of the guest molecules with estimated standard deviation in parentheses

		1			2		3	
	1′	Molecule 1	Molecule 2	Molecule 3	Molecule 1	Molecule 2	Molecule 1	Molecule 2
-CG(1)-CG(2)	55.6(3)	64(3)	56(3)	60(4)	−54(1)	−83(3)	88(1)	101(2)
-CG(2)-CG(3)-	−55.7(3)	−61(3)	−65(3)	−50(4)	83(1)	87(3)	−37(2)	−91(2)
-CG(3)-CG(4)-		48(3)	66(3)	41(4)	−98(1)	−98(3)	34(2)	102(2)
-CG(4)-CG(5)-		−41(3)	−58(3)	−40(4)	46(1)	67(3)	−82(1)	−110(2)
-CG(5)-CG(6)-		44(3)	59(3)	48(4)	30(1)	19(3)	43(1)	35(2)
-CG(6)-CG(7)-					−72(1)	−64(3)	70(1)	71(2)
-CG(7)-CG(8)-							−65(1)	−67(2)
-CG(1)-/CG(6)/CG(7)/ -CG(8)/CG(3′)-	−55.9(3)	−56(3)	−58(3)	−58(4)	62(1)	66(3)	−46(1)	−36(2)

Conformation of the cycloalkane guest molecules

The most significant difference between the **A** and **B** forms resides in the structure of the guest molecule. Thus, in the **A** form, the cyclohexane molecule is located on a crystallographic centre of symmetry and is ordered. However, in the **B** form, the cyclohexane molecule is in a general position and has three molecular orientations. These orientations have an occupation factor of 40/35/25 and thus produce a statistical disorder. The cyclohexane guest molecule in both the **A** and **B** forms always has the *chair* conformation, so that the disordered structures in

Can. J. Chem. Downloaded from www.nrcresearchpress.com by 85.192.166.187 on 09/08/12
For personal use only.

Can. J. Chem. Downloaded from www.nrcresearchpress.com by 85.192.166.187 on 09/08/12
For personal use only.

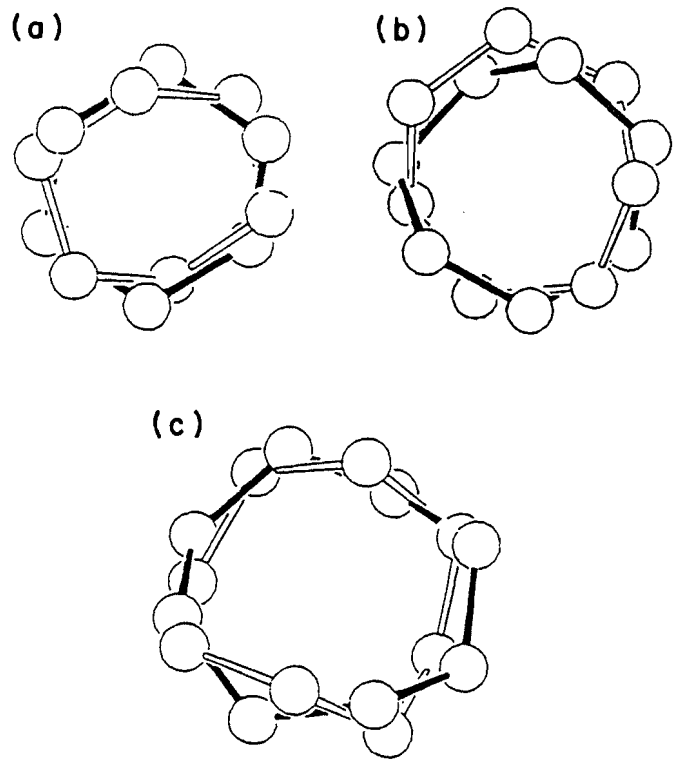

FIG. 4. Molecular orientations of (*a*) cyclohexane; (*b*) cycloheptane; (*c*) cyclooctane.

the **B** form are of the orientational type. Figure 4(*a*) shows the disordered structure for the cyclohexane molecule.

The inclusion compounds of cycloheptane and cyclooctane crystallize only in the **B** form. This may be understood by the fact that these guest molecules are slightly larger and do not fit in the cage of the **A** form, which would result in shorter intermolecular contacts and thus a higher potential energy. In the **B** form, these guest molecules are disordered. The cycloheptane molecule was found in two orientations with respective occupancy factors of 0.709(4) and 0.291(4). The molecules have the same conformation ($g^-gg^-ggg^-g$) so that the disorder is only of an orientational type.

A similar result was obtained for the cyclooctane inclusion compound. Thus, two orientations of the molecule in the same conformation ($gg^-gg^-ggg^-g^-$) were found with occupancy factors of 0.763(3) and 0.237(3), respectively. Figures 4(*b*) and 4(*c*) show the orientational disorder for cycloheptane and cyclooctane in the TATM inclusion compounds. The bond lengths and angles for the six-, seven-, and eight-membered cycloalkane molecules are given in Table 3, while in Table 4 are reported the torsion angles of the guest molecules.

From a crystallographic point of view, the difficulty of refining disordered structures lies in the fact that the electron density map, derived from a difference Fourier synthesis, reflects many possible molecular orientations or conformations within several potential minima. It is thus useful to carry out some molecular dynamics simulations to determine the low-energy orientations, or conformations, which will be useful in confirming or predicting the actual structure.

The results of a molecular dynamics simulation for the cycloheptane and cyclooctane guest molecules in the TATM cavities are shown in Fig. 5. The calculations were started using the molecular conformations α ($g^-gg^-ggg^-g$) and β ($ggg^-ggg^-g^-$)

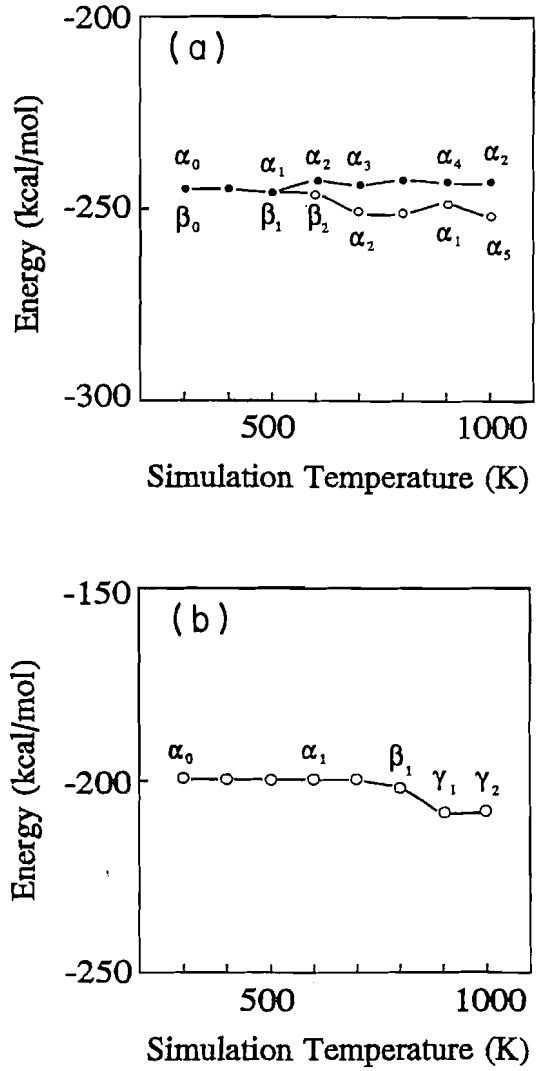

FIG. 5. Molecular dynamics simulation results of (*a*) cycloheptane; (*b*) cyclooctane.

for cycloheptane and the conformation α ($ggg^-g^-ggg^-g^-$) for cyclooctane.

These calculations reveal that the cycloheptane molecule could exist in two conformations, α and β. The molecule in the α conformations takes a number of orientations within the cavity, α_1, α_2, ... etc. The energy barrier to reorientation is about 1 kcal/mol. The situation is different for the molecule in the β conformation. Besides reorienting itself, the molecule undergoes a conformational transformation at 700 K, which brings it into the more energetically stable α conformation. The energy barrier of this is about 2 kcal/mol.

For the cyclooctane molecule, there are three molecular conformations. When the molecule is in the α conformation ($ggg^-g^-ggg^-g^-$), it goes through two conformational transformations at 800 and 900 K, respectively, to arrive at the energetically more stable β ($gg^-gg^-g^-ggg^-$) and γ ($gg^-gg^-ggg^-g^-$) conformations. It is the latter that was observed in the X-ray work.

In conclusion, the X-ray crystal structure determination of the **B** form of the TATM clathrates with six-, seven-, and eight-membered cycloalkanes indicates that all guest molecules have an orientational disorder. Only the energetically stable conformations, the *chair* for the cyclohexane, the α for the cycloheptane, and the γ for cyclooctane, are observed. However, the

molecular dynamics simulation displays more conformations for the more flexible cycloheptane and cyclooctane molecules.

Acknowledgements

The Natural Sciences and Engineering Research Council of Canada supported this work. We thank Dr. M. Simard and Mme F. Bélanger-Gariépy for their assistance in the crystallographic work.

1. L.B. Din and O. Meth-Cohn. J. Chem. Soc. Chem. Commun. 741 (1977).
2. J.L.M. Dillen and H.M. Roos. Acta Crystallogr. Sect. C: Cryst. Struct. Commun. **C48**, 2229 (1992).
3. H.M. Roos and J.L.M. Dillen. Acta Crystallogr. Sect. C: Cryst. Struct. Commun. **C48**, 1882 (1992).
4. P.H. Van Rooyen and H.M. Roos. Acta Crystallogr. Sect. C: Cryst. Struct. Commun. **C47**, 2468 (1991).
5. P.H. Van Rooyen and H.M. Roos. Acta Crystallogr. Sect. C: Cryst. Struct. Commun. **C47**, 2718 (1991).
6. L. Pang, R.C. Hynes, and M.A. Whitehead. Acta Crystallogr. Sect. C: Cryst. Struct. Commun. **C50**, 615 (1994).
7. L. Pang and F. Brisse. Acta Crystallogr. Sect. C: Cryst. Struct. Commun. **C50** (1994). In press.
8. A.P. Yakubov, Y.K. Sudarushkin, L.I. Belenkiin, and Y.L. Gold'farb. J. Org. Chem. (U.S.S.R.), **9**, 1549 (1973).
9. P. Main, S.J. Fiske, S.E. Hull, L. Lessinger, G. Germain, J.-P. Declercq and M.M. Woolfson. MULTAN80. A system of computer programs for the automatic solution of crystal structures from X-ray diffraction data. Universities of York, England, and Louvain, Belgium. 1980.
10. G.M. Sheldrick. SHELXS86. Program for the solution of crystal structures. Univ. of Göttingen, Germany. 1985.
11. E.J. Gabe, Y. Le Page, J.-P. Charland, F.L. Lee, and P.S. White. J. Appl. Crystallogr. **22**, 384 (1989).
12. G.M. Sheldrick. SHELX76. A program for crystal structure determination. Cambridge Univ., England. 1976.
13. International tables for X-ray crystallography. Vol. IV. Kynoch Press, Birmingham, England. 1974.
14. U. Berkert and N.L. Allinger. Molecular mechanics. American Chemical Society Monograph **177**, Washington, D.C. 1982.

Can. J. Chem. Downloaded from www.nrcresearchpress.com by 85.192.166.187 on 09/08/12
For personal use only.

Phomalone, an antifungal metabolite of *Phoma etheridgei*

WILLIAM A. AYER AND LUIS DIEGO JIMENEZ
Department of Chemistry, University of Alberta, Edmonton, AB T6G 2G2, Canada

Received June 23, 1994

WILLIAM A. AYER and LUIS DIEGO JIMENEZ. Can. J. Chem. **72**, 2326 (1994).

The metabolites produced by liquid cultures of *Phoma etheridgei*, a new fungus isolated from black galls of aspen, have been examined. This fungus is antagonistic to the aspen decay fungus *Phellinus tremulae*. The compound responsible for this antagonism has been isolated and its structure elucidated. Phomalone (**1**) is a previously undescribed natural product that possesses the same carbon skeleton as the *Phoma pigmentivora* metabolite LL-D253α. The structure was determined by physical methods, mainly ^{1}H and ^{13}C NMR. INAPT experiments played an important role. Some chemical transformations of phomalone (**1**) are described and it is shown by ^{13}C-labelling experiments to be derived from six acetate units. Phomalone is active against *Phellinus tremulae*. Compounds **4**, **6**, **7**, and **8** are also new natural products produced by *P. etheridgei*.

WILLIAM A. AYER et LUIS DIEGO JIMENEZ. Can. J. Chem. **72**, 2326 (1994).

On a étudié les métabolites produits par des cultures liquides du *Phoma etheridgei*, un nouveau champignon isolé des galles noires de peuplier. Ce champignon est un antagoniste pour le champignon *Phellinus tremulae* qui provoque la détérioration du peuplier. On a isolé le composé responsable de cet antagonisme et on a élucidé sa structure. La phomalone (**1**) est un produit naturel qui n'a pas été décrit antérieurement et qui possède le même squelette carboné que le métabolite LL-D253α du *Phoma pigmentivora*. On a déterminé la structure par des méthodes physiques, principalement le RMN du ^{1}H et du ^{13}C. Des expériences INAPT en joué un rôle important. On décrit quelques transformations chimiques de la phomalone (**1**) et, sur la base d'expériences de marquage au ^{13}C, on démontre qu'elle est obtenue à partir de six unités acétate. La phomalone est active contre le *Phellinus tremulae*. Les composés **4**, **6**, **7** et **8** sont aussi de nouveaux produits naturels produits par le *P. etheridgei*.

[Traduit par la rédaction]

Introduction

Trembling aspen (*Populus tremuloides* Michx.) is the most widely distributed tree species in North America (1). It is a fast-growing pioneer species, intolerant of shade, which thrives in areas disturbed by logging, fire, and other natural disruptions. In Canada, aspen represents more than one half of the net merchantable hardwood timber and 11% of the entire timber resource (2).

The commercial utilization of aspen has increased tremendously in the past decade. In Alberta, aspen accounted for only 2.4% of the total timber harvest in 1980; however, by 1992 this had increased to 18% (3). The reasons for this change include an increasing scarcity of economically accessible softwood timber in Canada and the introduction of new technologies to use this resource more efficiently. The development of oriented strand board (OSB) in the early 1980s contributed substantially to the increased use of this hitherto neglected resource. In the manufacture of OSB, large, thin strands of aspen are bonded together with resins under heat and pressure. Aspen's low density is an advantage in this process, since moderate pressure serves to create a board with good strength. Because of its low lignin and high cellulose content, aspen is also being utilized more in the pulp and paper industry, especially in the chlorine-free chemothermomechanical pulping (CTMP) process (1). Its natural light weight and lack of color, taste, and odor make it deal for chopsticks and popsicle sticks (4).

The greatest limitation on the utilization of aspen is that it is very susceptible to wood decay and straining fungi. Heartwood decay, especially by *Phellinus tremulae*, is often present in a majority of the trees in a mature stand (5). Stored logs and chips of aspen are very susceptible to blue stain fungi (6). Recently it has been found that certain types of black galls occurring as stem deformities on aspen appear to confer protection against decay and stain-causing fungi (7). As part of a collaborative project investigating the nature of this black gall protective effect, we have examined the metabolites of several fungi associated with the black galls (8–11). We report herein on the metabolites of a newly described fungus (12), *Phoma etheridgei*, isolated from the surface of the galls, which has been shown to be antagonistic to the aspen decay fungus *Phellinus tremulae*.

Results and discussion

Phoma etheridgei sp. nov. Hutchison and Hiratsuka is a previously undescribed species of fungus that frequently occurs on the surface of black galls of aspen in central Alberta (12). This fungus shows antagonistic activity in agar culture and on aspen chips against the aspen decay fungus *Phellinus tremulae* and the blue strain fungus *Ophiostoma crassivaginata*. After considerable experimentation it was possible to obtain liquid cultures that consistently produced metabolites that show antifungal activity against *P. tremulae*. The production of active metabolites is very dependent on the inoculum used for the liquid cultures. The use of mycelium from Petri dish agar cultures gave inconsistent results: at times activity was observed, at other times the extracts were inactive. Spore (pycnidia) suspensions of the fungus were found to give more consistent results. *Phoma etheridgei* products pycnidia in Phytone yeast extract agar (PYEA) and malt extract agar (MEA) when grown at 25–30°C under light (λ <360 nm) for 2–4 weeks. Shake cultures in malt extract or Phytone yeast extract liquid media at room temperature for 12–16 days provide bioactive extracts. Activity was determined by bioassay against *P. tremulae* (see Experimental). The activity of the extracts diminished when the growth period was extended beyond 16 days.[1] To facilitate the isolation of the active compounds we found it convenient to add DIAION HP-20 resin (a polystyrene–divinylbenzene copolymer) to the culture medium (14). After fermentation, the resin and adhering mycelium were separated from the broth and the metabolites were eluted from the resin-mycelium with ethyl acetate. When the resin was not used, the mycelium was separated by filtration

[1]Full details of the fermentation studies are provided in ref. 13.

Can. J. Chem. Downloaded from www.nrcresearchpress.com by 85.192.166.187 on 09/08/12
For personal use only.

Can. J. Chem. Downloaded from www.nrcresearchpress.com by 85.192.166.187 on 09/08/12
For personal use only.

through cheesecloth, and the broth was concentrated and extracted with ethyl acetate. The mycelium was extracted separately but did not yield an appreciable quantity of active metabolites. The resin method provided about 0.25 g/L of metabolites while the extraction method provided approximately 0.1 g/L. TLC analysis indicated that both procedures provided essentially the same mixture of metabolites.

Bioassay (against *P. tremulae*) guided separation of the crude metabolites by flash chromatography over silica gel, followed by high-performance medium-pressure liquid chromatography (HPMPLC) over reverse-phase (C-18) silica gel, gave a crystalline compound, $C_{13}H_{18}O_5$, mp 126–127°C, which we have named phomalone. This compound is responsible for the antifungal activity against *P. tremulae* as described in more detail below.

The structure of phomalone (**1**) was deduced as follows. The molecular formula $C_{13}H_{18}O_5$ was determined by high-resolution electron impact mass spectrometry (HERIMS) and the molecular weight (254 amu) confirmed by chemical ionization mass spectrometry (CIMS). The IR spectrum shows hydroxyl (3200 cm^{-1}) and low-frequency carbonyl (1618 cm^{-1}) absorption. The ^1H NMR spectrum shows a chelated phenolic hydroxyl proton (δ 14.50), a single aromatic hydrogen (δ 6.01), an aromatic methoxyl (δ 3.85), and signals for a 2-hydroxyethyl group (two proton triplets at δ 3.70 and δ 2.74) and a propyl group (triplet (2H) at δ 2.80, quarter (3H) at δ 0.95, tq (2H) at δ 1.66). Acetylation of phomalone gave a triacetyl derivative (**2***a*), confirming the presence of three hydroxyl groups in phomalone. The ketonic carbonyl in triacetylphomalone appears at 1699 cm^{-1} in the IR spectrum. The ^{13}C NMR spectrum of phomalone (acetone-d_6) confirms the presence of a carbonyl group (δ 206.4), three oxygenated aromatic carbons (δ 165.9, 164.3, 162.7), two substituted aromatic carbons (δ 106.9, 105.5), and an upfield unsubstituted aromatic carbon (δ 92.1). The oxygenated methylene carbon appears at δ 62.9, and the methoxyl carbon at δ 55.9. The C-methyl signal appears at δ 14.2, and the remaining methylene carbons at δ 46.3 (C-2), 26.3 (benzylic), and 16.9 (C-3). These data indicate that phomalone is a pentasubstituted benzene bearing two hydroxyls, a methoxyl, a 2-hydroxyethyl, and a 1-butanoyl group. Nuclear Overhauser enhancement (NOE) experiments reveal that the aromatic hydrogen is *ortho* to the methoxyl group, but apparently not *ortho* to the hydroxyethyl group. The chelated carbonyl requires an *ortho* relationship between the butanoyl group and a phenolic hydroxyl, and the very high field position (δ 92.1) of the unsubstituted aromatic carbon and the aromatic hydrogen (δ 6.01) suggests that the aromatic oxygen functions are all *ortho* and *para* to this position. Simpson and co-workers have shown that the *Phoma pigmentivora* metabolite LL-D253α possesses the closely related structure **3** (15). In the ^{13}C NMR spectrum of **3** the aromatic carbon and hydrogen appear at δ 92.7 and δ 6.13, respectively. The absorption for the *unchelated* carbonyl group of **3** is at 1652 cm^{-1} in the IR spectrum.

To define unambiguously the substitution pattern in phomalone we turned to Insensitive Nuclei Assigned by Polarization Transfer (INAPT) (16) experiments. These experiments, carried out in DMSO-d_6 solution, show that the benzylic methylene hydrogens of the hydroxyethyl side chain are correlated with two oxygenated aromatic carbons (δ 164.4 and δ 163.5) as well as the aromatic carbon at δ 104.5 and the oxygenated methylene carbon (δ 59.8). The hydrogens of the methoxyl methyl show correlation with the aromatic carbon at δ 161.0. Thus, the

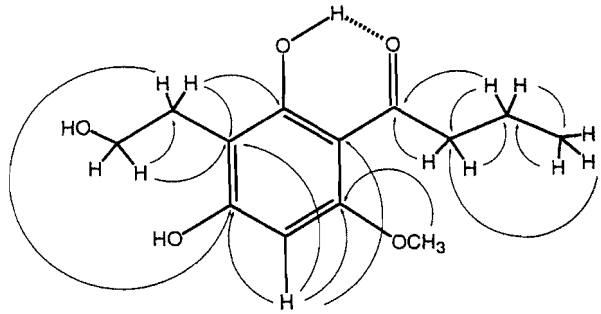

SCHEME 1

hydroxyethyl group is situated on a carbon *between* two phenolic hydroxyl-bearing carbons. The aromatic hydrogen correlates with the carbon bearing the methoxyl group (δ 161.0), one of the phenolic carbon (δ 163.5), and the two quaternary aromatic carbons. All of the correlations observed are summarized in Scheme 1. These serve to locate the positions of the various substituents on the aromatic ring and establish structure **1** for phomalone.

Treatment of phomalone with *p*-toluenesulfonic acid in refluxing benzene gave a mixture of the two anhydro derivatives **4** and **5**. The formation of these two cyclization products further confirms the location of the hydroxyethyl group. Compound **4** shows carbonyl absorption at 1650 cm^{-1} in the IR, and a chelated phenolic OH proton at δ 14.5 in its NMR spectrum. The ^1H and ^{13}C NMR spectra of **4** are very similar to those of phomalone (**1**), except that the signal for the oxygenated methylene hydrogens is shifted downfield to δ 4.50 (δ 3.70 in **1**). The isomeric compound **5** also shows carbonyl absorption at 1650 cm^{-1}, but now the phenolic OH proton is not chelated and appears at δ 9.5 in the ^1H NMR spectrum. The fact that the carbonyl absorption appears at about the same frequency in both **4** and **5** is not unusual, since both *ortho* and *para* hydroxyl groups in acetophenones cause shifts to lower frequency due to electron-donating effects rather than H-bonding effects (15). Phomalone, with both an *ortho* and a *para* hydroxyl, absorbs at 1618 cm^{-1}. The dihydrobenzofuran **4** also occurs as one of the minor metabolites of *P. etheridgei* (see below).

Acetylation of phomalone with a limited amount of acetic anhydride–triethylamine in CH_2Cl_2 at room temperature affords a mixture of the triacetyl derivative **2***a* and the diacetyl derivative **2***b*. A large excess of the acetylating agent provides only the triacetyl derivative **2***a*. The location of the free hydroxyl group in the diacetate **2***b* is apparent from its ^1H NMR spectrum, which shows a chelated OH signal at δ 14.05. The IR spectra of the acetylated derivatives illustrate nicely the electron-donating effects mentioned above. The ketonic carbonyl appears at 1699 cm^{-1} in **2***a*, 1651 cm^{-1} in **2***b*, and at 1618 cm^{-1} in phomalone (**1**). Irradiation of the aromatic hydrogen in **2***a* causes a 3.6% NOE enhancement of the signal for the methoxyl hydrogens at δ 3.82. The reverse experiment causes 2.9% enhancement of the aromatic hydrogen signal (δ 6.13). INAPT experiments on the triacetate confirmed the atomic connectivity as in phomalone (**1**) itself.

During the course of the separation of phomalone (**1**), several other metabolites of the fungus were isolated and identified. One of these, the dihydrobenzofuran **4**, has already been discussed. Another compound that eluted with **4** on flash chromatography was separated from **4** by preparative TLC. This compound, which we call deoxyphomalone, has the molecular formula $C_{13}H_{18}O_4$ and possesses structure **6**. It is obtained as a

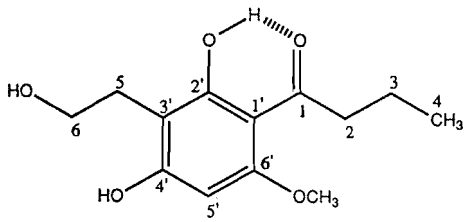

1

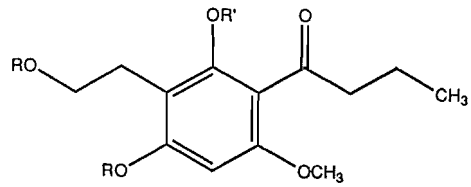

2*a* R = R' = Ac
2*b* R = Ac, R' = H

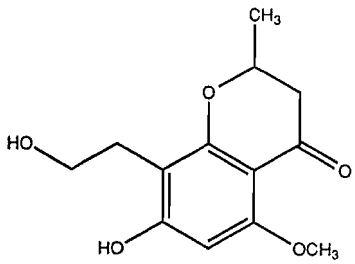

3

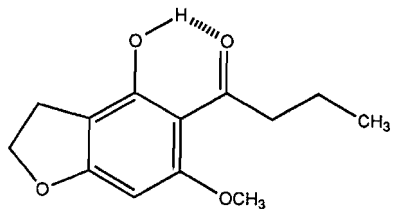

4

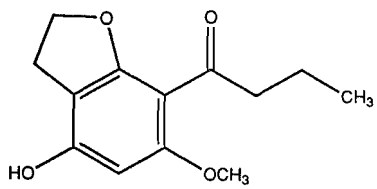

5

Can. J. Chem. Downloaded from www.nrcresearchpress.com by 85.192.166.187 on 09/08/12
For personal use only.

crystalline solid that gives a positive ferric chloride reaction. The spectroscopic properties are very similar to those of phomalone except that the hydroxymethylene proton signal at δ 3.70 is replaced by a methyl triplet at δ 1.12. The benzylic methylene group in **6** appears as a quartet at δ 2.59. Structure **6** is consistent with the data accumulated for this compound.

The next compound eluted also possesses an ethyl group as indicated by ^{1}H NMR. It has the molecular formula $C_{12}H_{14}O_4$ and has structure **7**. It shows hydroxyl and low-frequency carbonyl (1631 cm^{-1}) absorption in its IR spectrum. It is positive to ferric chloride. The ^{1}H NMR spectrum shows two methyl signals, a triplet at δ 1.09 and a doublet at δ 1.40, and two exchangeable phenolic hydrogens, one chelated (δ 12.50). The oxygenated sp^3 carbon appears at δ 73.5 in the ^{13}C NMR spectrum. The compound does not possess a methoxyl group. The remaining hydrogen and carbon signals are similar to those in **6**. Based on the presumed relationship of **7** with phomalone (**1**) and deoxyphomalone (**6**), structure **7** (8-ethyl-5,7-dihydroxy-2-methylchroman-4-one) is proposed for this compound.

The fraction eluting after phomalone (**1**) in the initial flash chromatography gave material that could not be purified satisfactorily by further chromatography. However, acetylation (Ac_2O–NEt_3–CH_2Cl_2) and preparative TLC provided a colorless oil that shows NMR properties similar to those of triacetylphomalone (**2***a*) except that the signals for the butanoyl side chain are replaced by signals at δ 6.75 (1H) and δ 6.34 (1H), and δ 1.92 (3H), consistent with a 2-butenoyl side chain. The ketonic carbonyl absorbs at 1660 cm^{-1} in the IR spectrum, and the H–H coupling constant for the alkenic hydrogens is 16.5 Hz. This compound is thus the α,β-unsaturated analog **8** of triacetylphomalone (**2***a*), and presumably occurs in the unacetylated form **8***a*.

Bioassays of phomalone (**1**) using the multiwell method (5) show that it completely inhibits the growth of *Phellinus tremulae* at a concentration of 1×10^{-3} mol/L, but has no effect at 1×10^{-4} mol/L. Intermediate concentrations show partial inhibition. It thus appears unlikely that phomalone is responsible for the "black gall effect" described above.

Simpson et al. have shown (17) that compound LL-D253α (**3**) results from the combination of two ketide units (possibly triketide + triketide, but tetra + di, and penta + mono are not excluded). ^{13}C-Labelling experiments using [1,2-$^{13}C_2$]-acetate reveal that phomalone (**1**) also is formed from six acetate units. When [1-^{13}C]-sodium acetate is added to the culture medium, carbons 1, 3, 2′, 4′, and 6′ are labelled, and *both* carbons of the hydroxyethyl are enriched (see Table 1). When [2-^{13}C]-acetate

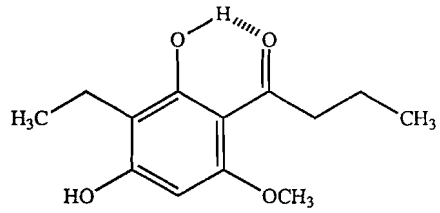

6

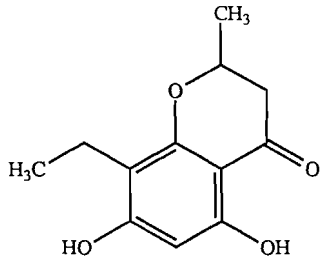

7

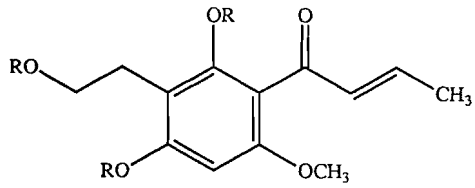

8 R = Ac
8*a* R = H

is added, C-2, C-4, C-1′, C-3′, and C-5′ are enriched, as are both carbons of the hydroxyethyl side chain (Table 1). In the case of the [1-^{13}C] label, the benzylic carbon carries more label than the carbinol carbon. The reverse is true in the [2-^{13}C]-acetate case. These results are consistent with the biosynthetic pathway illustrated in Scheme 2, similar to that proposed for LL-D253α (**3**) (17), in which at least a portion of the phomalone (**1**) is formed via the symmetrical cyclopropyl intermediate A shown, accounting for the labelling of both C-5 and C-6. Scheme 2 uses the triketide pathway for illustrative purposes only; the 4+2 and the 5+1 pathways are also possible. We do not wish to imply that it is necessarily the *p*-hydroxyl group that is involved in the formation of the cyclopropyl intermediate.

Phomalone (**1**) and compounds **4**, **6**, **7**, and **8** have not been described previously as natural products.

Experimental

General

Melting points were determined on a Fisher–Johns melting point apparatus and are uncorrected. Infrared spectra (IR) were obtained using the following spectrophotometers: Nicolet 7199 FTIR, Nicolet MX-1 FTIR, and Nicolet 750 FTIR. Electron impact mass spectra (EIMS) were obtained using a Kratos AE1 MS50 high-resolution mass spectrometer and a Kratos AE1 MS12 low-resolution mass spectrometer. Chemical ionization mass spectra (CIMS) were recorded on an Kratos AE1 MS-12 mass spectrometer with ammonia as the reagent gas. Ultraviolet (UV) spectra were recorded on a Hewlett Packard 8450A diode array spectrophotometer. Hydrogen nuclear magnetic resonance spectra (^{1}H NMR) were obtained using the following spectrometers: Bruker WH-200 (200 MHz), Bruker AM-400 (400 MHz), and Varian Unity-500 (500 MHz). Carbon-13 nuclear magnetic resonance spectra (^{13}C NMR) were obtained on Bruker AM-300 (75 MHz) and Bruker AM-400 (100.6 MHz) spectrometers. Carbon-13 multiplicities were determined using spin echo *J*-modulated experiments (APT or Attached Proton Test). Nuclear Overhauser Enhancement (NOE) experiments were determined in the difference mode. Homonuclear decoupling experiments were performed by using the Bruker DISNMR software package. Insensitive Nuclei Assigned by Polarization Transfer (INAPT) experiments were performed using the Varian Unity-500 spectrometer. Carbon-13 nuclear magnetic resonance spectra (^{13}C NMR) of labeled material were obtained on a Bruker AM-400 (100.6 MHz) spectrometer. Carbon-13 experiments on labeled material were performed using the Bruker DISNMR software package. A relaxation delay of 4 s was used. High-performance medium-pressure liquid chromatography (HPMPLC) was carried out on ACE Glass Inc. Michel–Miller equipment using a Fluid Metering Inc. model RP-SY solvent pump. High-pressure liquid chromatography (HPLC) analyses were performed on a Waters 600E system controller equipped with a 490E programmable multiwavelength UV detector and a M730 data module. *Phoma etheridgei* spores were counted with a hemacytometer (graduated surface normally used to count blood cells) under a microscope.

Flash chromatography was performed using 230–400 mesh silica gel. DIAION HP 20 was obtained from TCI America, Portland, Oreg.

TABLE 1. Results of [1-^{13}C]- and [2-^{13}C]-sodium acetate labelling experiments[a]

Carbon	δ	% Enrichment [1-^{13}C]-acetate	% Enrichment [2-^{13}C]-acetate
1	202.6	3.5	—
2	45.8	—	6.7
3	17.8	3.2	—
4	13.7	—	7.9
5	24.1	4.9	1.3
6	62.6	1.1	4.6
1′	115.9	—	8.8
2′	156.3	2.7	—
3′	122.6	—	4.2
4′	151.3	2.7	—
5′	104.2	—	5.8
6′	147.6	1.7	—

[a]The spectra of the triacetyl derivative **2***a* were determined in $CDCl_3$ at 100.6 MHz. Normalization of the ^{13}C NMR enrichment was carried out by using the signals for the introduced acetoxyl methyls as the measure of natural abundance. The % enrichment was calculated as described in ref. 18.

Fermentation methods

Liquid cultures

Inocula for liquid cultures were obtained from malt extract agar plates of *P. etheridgei*. After 30 days growth the spores were counted using a hemacytometer. The agar culture was blended with 200 mL of sterile water and the volume of the resulting aqueous suspension was adjusted to contain 10 000 –20 000 spores/mL. A 3 mL aliquot of this spore suspension was used as inoculum for 1 L of liquid media (20 g malt extract, 20 g glucose, 1 g bactopeptone/L). After inoculation, the liquid cultures were shaken at room temperature for 12 days.

Liquid cultures with DIAION HP-20 resin

Liquid cultures were prepared in 10-L batches. A 3-mL aliquot of the aqueous suspension containing 10 000–20 000 spores/mL was used to inoculate 10 1-L portions of sterile malt extract liquid medium in 2-L Erlenmeyer flasks. DIAION HP-20 resin (20 g/L) was added to the liquid medium. After inoculation, the liquid cultures were shaken at room temperature for 12 days.

Labelling experiments

Liquid cultures (2 L) were prepared using spore suspensions as

Can. J. Chem. Downloaded from www.nrcresearchpress.com by 85.192.166.187 on 09/08/12
For personal use only.

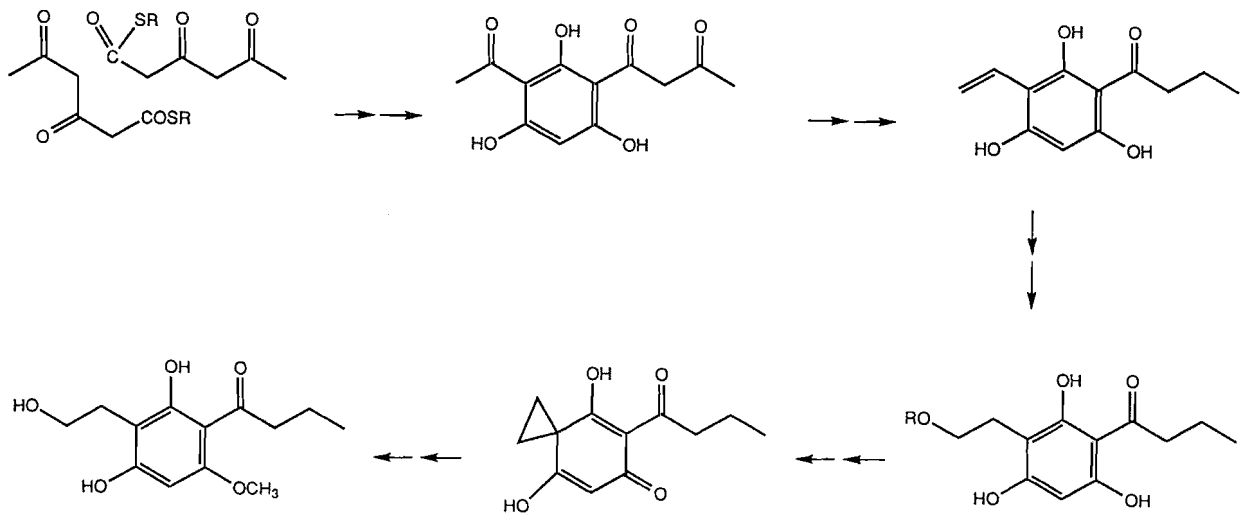

SCHEME 2

above. A 3-mL aliquot of the aqueous suspension containing 10 000–20 000 spores/mL was used to inoculate 2 1-L portions of sterile malt extract liquid medium in 4-L Erlenmeyer flasks. DIAION HP-20 ion exchange resin (20 g/L) was added. The liquid cultures were shaken at room temperature. After 3 days, a solution of [1-^{13}C]-sodium acetate (15 mL, 0.2 mol/L) was added under sterile conditions. Two similar additions were made on the fifth and seventh day. The *P. etheridgei* culture was kept under shake conditions for a total of 13 days. The same procedure was followed using [2-^{13}C]-sodium acetate and [1,2-$^{13}C_2$]-sodium acetate.

Isolation of metabolites

The floating HP-20 ion exchange resin was decanted from the liquid culture (2 L, 12 days). The remaining resin, which adhered to the mycelium, was separated by vacuum filtration through Whatman filter paper No. 1. The resin and the mixture of resin and mycelium were transferred to a sintered glass filter (porosity D, ASTM 10–20 μm) and extracted with ethyl acetate (1.6 L). The ethyl acetate extract was dried over anhydrous sodium sulfate and concentrated under reduced pressure to give a crude extract (0.457 g). Flash chromatography of the resin extract (10% ethyl acetate in methylene chloride) gave 60 fractions (10 mL each), which were combined, according to TLC analysis, as follows: 1–5 (fraction 1, 6 mg), 6–9 (fraction 2, 14 mg), 10–15 (fraction 3, 9 mg), 15–25 (fraction 4, 23 mg), 26–41 (fraction 5, 0.1 g). Further separation of these fractions afforded five major compounds: 4-hydroxy-6-methoxy-5-(1′-oxobutyl)benzo[*b*]dihydrofuran (**4**); 3-ethyl-2,4-dihydroxy-6-methoxybutyrophenone (**6**); 8-ethyl-5,7-dihydroxy-2-methylchroman-4-one (**7**); phomalone (**1**).

4-Hydroxy-6-methoxy-5-(1′-oxobutyl)benzo[b]dihydrofuran (4)

Flash chromatography of fraction 1 (10% ethyl acetate in methylene chloride) gave 4-hydroxy-6-methoxy-5-(1′-oxobutyl)benzo[*b*]dihydrofuran (**4**) as a white solid (4 mg): R_f 0.30(2% ethyl acetate in methylene chloride); IR ($CHCl_3$, cast): 3250 (OH), 1650 (ketone C=O cm^{-1}); ^{1}H NMR (400 MHz, $CDCl_3$) δ: 14.50 (s, 1H, Ar-O*H*), 5.90 (s, 1H, Ar-*H*), 4.5 (t, 2H, J = 7.0 Hz, -O-CH_2-CH_2-), 3.8 (s, 3H, -OCH_3), 3.2 (t, 2H, J = 7.0 Hz, -CH_2-CH_2-Ar), 2.80 (t, 2H, J = 7.0 Hz, O=C-CH_2-), 1.60 (tq, 2H, $J = J'$ = 7.0 Hz, -CH_2-CH_2-CH_3), and 0.98 (t, 3H, J = 7.0 Hz, -CH_2-CH_3); ^{13}C NMR (100.6 MHz, acetone-d_6) δ: 206.4 (s), 165.9 (s), 164.3 (s), 162.7 (s), 142.6 (s), 132.9 (s), 92.4 (d), 62.9 (t), 55.9 (q), 46.6 (t), 26.4 (t), 18.9 (t), and 14.2 (q); HREIMS, *m/z*: 236.1055 (M$^+$, calcd. for $C_{13}H_{16}O_4$: 236.1062), 193.0501 (100), 149.0241 (30).

3-Ethyl-2,4-dihydroxy-6-methoxybutyrophenone (6)

Flash chromatography of fraction 2 (10% ethyl acetate in methylene chloride) followed by prep-TLC (30% ethyl acetate in hexanes) gave 3-ethyl-2,4-dihydroxy-6-methoxybutyrophenone as a white solid (6 mg); IR ($CHCl_3$, cast): 3200 (OH), 1618 (ketone C=O cm^{-1}); ^{1}H NMR (400 MHz, $CDCl_3$) δ: 14.35 (s, 1H, Ar-O*H*), 5.90 (s, 1H, Ar-*H*), 3.52 (s, 3H, -OCH_3), 2.98 (t, 2H, J = 7.0 Hz, O=C-CH_2), 2.59 (q, 2H, J = 7.0 Hz, -CH_2-CH_3), 1.70 (tq, 2H, $J = J'$ = 7.0 Hz, -CH_2-CH_2-CH_3), 1.12 (t, 3H, J = 7.0 Hz, CH_2-CH_3), and 0.98 (t, 3H, J = 7.0 Hz, CH_2-CH_3); ^{13}C NMR (100.6 MHz, $CDCl_3$) δ: 202.3 (s), 164.9 (s), 161.5 (s), 159.6 (s), 109.5 (s), 105.7 (s), 90.1 (d), 55.4 (q), 46.3 (t), 22.3 (t), 18.2 (t), 14.0 (q), 13.4 (q). HREIMS, *m/z*: 238.1207 (M$^+$, calcd. for $C_{13}H_{18}O_4$: 238.1209), 195.0661 (100).

8-Ethyl-5,7-dihydroxy-2-methylchroman-4-one (7)

Flash chromatography of fraction 3 (20% ethyl acetate in methylene chloride) followed by HPMPLC (NP, Si60, 2% ethyl acetate in methylene chloride) and prep. TLC (2% ethyl acetate in methylene chloride) gave 8-ethyl-5,7-dihydroxy-2-methylchroman-4-one as a white solid (1.3 mg): IR ($CHCl_3$, cast): 3133 (-OH), 1631 (ketone C=O), and 1467, 1451 (Ar-H) cm^{-1}. ^{1}H NMR (400 MHz, acetone-*d*6) δ: 12.50 (s, 1H, Ar-O*H*), 9.50 (s, 1H, Ar-O*H*), 6.10 (s, 1H, Ar-*H*), 4.50 (m, 1H, -C*H*), 2.60 (m, 4H, -CH_2-), 1.4 (d, 3H, -CH-CH_3, J = 7.0 Hz), and 1.09 (t, 3H, CH_2-CH_3, J = 7.0 Hz). ^{13}C NMR (acetone-d_6, 100.6 MHz) δ: 191.7 (s), 161.5 (s), 154.5 (s), 155.0 (s), 109.6 (s), 104.2 (s), 90.9 (d), 73.5 (d), 45.9 (t), 22.3 (t), 20.3 (q), 13.4 (q); HREIMS, *m/z*: 222.08944 (M$^+$, calcd. for $C_{12}H_{14}O_4$: 222.0892), 207.0668 (100), 165.0192 (50).

(E)-2,4-Acetoxy-3-(2-acetoxyethyl)-6-methoxy-2′-en-butyrophenone (8a)

Acetylation of fraction 4 gave a brown oil (22 mg). Preparative TLC of this material (10% ethyl acetate in methylene chloride) afforded (*E*)-2,4-acetoxy-3-(2-acetoxyethyl)-6-methoxy-2′-en-butyrophenone as a colorless liquid (2 mg): IR ($CHCl_3$, cast): 1771 (C=O ester), 1738 (C=O ester), 1660 (C=O ketone), 1617 (C=C), 968 (-CH=CH-) cm^{-1}; ^{1}H NMR (400 MHz, $CDCl_3$) δ: 6.64 (s, 1H, Ar-*H*), 6.75 (dq, 1H, J = 16.5 Hz, J' = 7.0 Hz, O=C-CH=C*H*-), 6.34 (dq, 1H, J = 16.5 Hz, J' = 2.0 Hz, -C*H*=CH-CH_3), 4.11 (t, 3H, J = 7.5 Hz, -CH_2-CH_2-OAc), 3.77 (s, 3H, -O-CH_3), 2.71 (t, 2H, J = 7.5 Hz, Ar-CH_2-CH_2-), 2.38 (s, 3H, -O-C=O-CH_3), 2.23 (s, 3H, -O-C=O-CH_3), 2.03 (s, 3H, -O-C=O-CH_3), and 1.92 (dd, 1H, J = 7.0 Hz, J' = 2.0 Hz, =CH-CH_3); ^{13}C NMR ($CHCl_3$, 100.6 MHz) δ: 202.7 (s), 170.9 (s), 169.1 (s), 168.9 (s), 156.3 (s), 151.3 (s), 147.6 (s), 146.9 (d), 132.5 (d), 120.9 (s), 115.9 (s), 104.3 (d), 62.6 (t), 56.0 (q), 23.9 (t), 21.0 (q), 20.9 (q), and 17.2 (q).

Isolation of phomalone (2,4-dihydroxy-3-(2-hydroxyethyl)-6-methoxybutyrophenone) (1)

HPMPLC on fraction 4 (NP-Si60, 10% ethyl acetate in methylene chloride) followed by HPMPLC (RP-18, 30% water in methanol)

Can. J. Chem. Downloaded from www.nrcresearchpress.com by 85.192.166.187 on 09/08/12
For personal use only.

afforded phomalone, 2,4-dihydroxy-3-(2-hydroxyethyl)-6-methoxybutyrophenone (75 mg): mp 126–127°C; R_f 0.25 (10% ethyl acetate in methylene chloride); IR ($CHCl_3$, cast): 3200 (OH), 1618 (ketone C=O) cm^{-1}; UV (EtOH): 205, 211, and 293 nm; ^1H NMR (400 MHz, acetone-d_6) δ: 14.50 (s, 1H, Ar-O*H*), 6.01 (s, 1H, Ar-*H*), 3.85 (s, 3H, -OCH_3), 3.70 (t, 2H, J = 7.0 Hz, -CH_2-CH_2OH), 2.80 (t, 2H, J = 7.0 Hz, O=C-CH_2-), 2.74 (t, 2H, J = 7.0 Hz, Ar-CH_2-), 1.66 (tq, 2H, $J = J'$ = 7.0 Hz, -CH_2-CH_2-CH_3), and 0.95 (t, 3H, J = 7.0 Hz, -CH_3); ^{13}C NMR (100.6 MHz, acetone-d_6) δ: 206.4 (s), 165.9 (s), 164.3 (s), 162.7 (s), 106.9 (s), 105.6 (s), 92.1 (d), 62.9 (t), 55.9 (q), 46.6 (t), 26.3 (t), 16.9 (t), and 14.2 (q). HREIMS, *m/z*: 254.1154 (M^+, calcd. for $C_{13}H_{18}O_5$: 254.1158), 223.2343 (100, 211.2345 (93), 193.1111 (63).

Derivatives of phomalone

O,O-Diacetylphomalone (2b)

Triethylamine (0.2 mL) and acetic anhydride (0.2 mL) were added to a solution of phomalone (11 mg) in methylene chloride (2 mL). After stirring for 2 h at room temperature the solution was concentrated under reduced pressure and the residue was dissolved in chloroform (3 mL). Prep-TLC (10% ethyl acetate in methylene chloride) gave phomalone diacetate (**2b**) (11 mg) and phomalone triacetate (mp 82–83°C, 3.5 mg). Diacetylphomalone: IR ($CHCl_3$, cast): 2961 (OH), 1760 (ester C=O), 1734 (ester C=O), 1651 (ketone C=O) cm^{-1}; ^1H NMR (400 MHz, $CDCl_3$) δ: 14.05 (s, 1H, Ar-O*H*), 6.15 (s, 1H, Ar-*H*), 4.18 (t, 2H, J = 7.0 Hz, -CH_2-O-), 3.87 (s, 3H, -OCH_3), 3.01 (t, 2H, J = 7.0 Hz, Ar-CH_2-), 2.86 (t, 2H, J = 7.0 Hz, O=C-CH_2), 2.36 (s, 3H, O=C-CH_3), 2.05 (s, 3H, O=C-CH_3), 1.71 (tq, 2H, $J = J'$ = 7.0 Hz, -CH_2-CH_2-CH_3), and 0.99 (t, 3H, J = 7.0 Hz, -CH_2-CH_3); ^{13}C NMR (100.6 MHz, $CDCl_3$) δ: 207.2 (s), 166.9 (s), 155.0 (s), 111.1 (s), 109.1 (s), 103.4 (s), 96.3 (s), 90.9 (d), 62.8 (t), 55.7 (q), 46.6 (t), 22.7 (t), 21.0 (q), 20.9 (q), 17.8 (t), 13.9 (q); HREIMS, *m/z*: 338.13607 (M^+, calcd. for $C_{17}H_{22}O_7$: 338.13657), 278.11542 (56), 236.10486 (64), 193.04978 (100).

Triacetylphomalone (2a)

Triethylamine (0.3 mL) and acetic anhydride (0.3 mL) were added to a solution of phomalone (7.8 mg) in methylene chloride (2 mL). After stirring the mixture for 2 h at room temperature, the solution was concentrated under reduced pressure and the residue was dissolved in chloroform (3 mL). Prep-TLC (10% ethyl acetate in methylene chloride) gave triacetylphomalone (10.5 mg); IR ($CHCl_3$, cast): 1772, 1739 (ester -O-C=O), 1699 (ketone C=O) cm^{-1}; ^1H NMR (400 MHz, $CDCl_3$) δ: 6.13 (s, 1H, Ar-*H*), 4.10 (t, 2H, J = 7.0 Hz, -CH_2-CH_2-), 3.82 (s, 3H, -OCH_3), 2.79 (t, 2H, J = 7.0 Hz, Ar-CH_2-), 2.72 (t, 2H, O=C-CH_2-), 2.40 (s, 3H, O=C-CH_3), 2.27 (s, 3H, O=C-CH_3), 2.05 (s, 3H, -O-C=O-CH_3), 1.66 (tq, 2H, $J = J'$ = 7.0 Hz, -CH_2-CH_2-CH_3), and 0.95 (t, 3H, J = 7.0 Hz, -CH_2-CH_3); ^{13}C NMR (100.6 MHz, $CDCl_3$) δ: 202.7 (s), 170.9 (s), 169.9 (s), 169.1 (s), 156.3 (s), 151.4 (s), 147.5 (s), 122.6 (s), 116.0 (s), 104.3 (d), 62.7 (t), 56.1 (q), 45.9 (t), 24.2 (t), 20.9 (q), 20.6 (q), 17.3 (t), 13.7 (q). HREIMS, *m/z*: 380.1468 (M^+, calcd. for $C_{19}H_{24}O_8$: 380.1461), 278.1154 (98), 236.1046 (39).

4-Hydroxy-6-methoxy-5-(1′-oxobutyl)benzo[b]dihydrofuran (4) and 4-hydroxy-6-methoxy-7-(1′-oxobutyl)benzo[b]dihydrofuran (5)

p-*Toluenesulfonic acid method*: *p*-Toluenesulfonic acid monohydrate (5.3 mg) was added to a solution of phomalone (7.5 mg) in benzene (5 mL). After stirring at room temperature for 1.5 h, more (10.6 mg) acid was added and a the mixture was refluxed for 4.5 h with continuous removal of water (Dean–Stark). The solvent was then evaporated under pressure and the residue was dissolved in chloroform (3 mL). Prep-TLC (10% ethyl acetate in methylene chloride) gave **4** and **5** in a 2:1 ratio. Compound **4** (2.2 mg); IR ($CHCl_3$, cast): 3250 (OH), 1650 (ketone C=O), 1450, 1497 (Ar-H) cm^{-1}; ^1H NMR (400 MHz, $CDCl_3$) δ: 9.50 (s, 1H, Ar-O*H*), 5.90 (s, 1H, Ar-*H*), 4.5 (t, 2H, J = 7.0 Hz, -O-CH_2-CH_2-), 3.8 (s, 3H, -OCH_3), 3.2 (t, 2H, J = 7.0 Hz, -CH_2-CH_2-Ar), 2.80 (t, 2H, J = 7.0 Hz, O=C-CH_2-), 1.60 (qt, 2H, $J = J'$ = 7.0 Hz, -CH_2-CH_2-CH_3), and 0.98 (t, 3H, J = 7.0 Hz, -O-CH_2-CH_3); HREIMS: *m/z*: 236.1055 (M^+, calcd. for $C_{13}H_{16}O_4$: 236.1062), 193.0501 (100), 149.0241 (30). Compound **5** (1.4 mg); IR ($CHCl_3$, cast): 3250 (OH), 1650 (ketone C=O), 1450, 1497 (Ar-H) cm^{-1}; ^1H NMR (400 MHz, $CDCl_3$) δ: 14.50 (s, 1H, Ar-O*H*), 5.90 (s, 1H, Ar-*H*), 4.5 (t, 2H, J = 7.0 Hz, -O-CH_2-CH_2-), 3.8 (s, 3H, -OCH_3), 3.2 (t, 2H, J = 7.0 Hz, -CH_2-CH_2-Ar), 2.80 (t, 2H, J = 7.0 Hz, O=C-CH_2-), 1.60 (qt, 2H, $J = J'$ = 7.0 Hz, -CH_2-CH_2-CH_3), and 0.98 (t, 3H, J = 7.0 Hz, -O-CH_2-CH_3); ^{13}C NMR (100.6 MHz, $CDCl_3$) δ: 206.4 (s), 165.9, (s), 164.3 (s), 162.7 (s), 142.6 (s), 132.9 (s), 92.4 (d), 62.9 (t), 55.9 (q), 46.6 (t), 26.4 (t), 18.9 (t), and 14.2 (q). HREIMS, *m/z*: 236,1055 M^+, calcd. for $C_{13}H_{16}O_4$: 236.1062), 193.0501 (100), 149.0241 (30).

p-*Toluenesulfonyl chloride method*: *p*-Toluenesulfonyl chloride (45 mg) was added to a solution of phomalone (10 mg) in benzene (15 mL). The mixture was refluxed for 4.5 h. The solvent was then evaporated under reduced pressure and the residue was dissolved in chloroform (3 mL). Prep-TLC (10% ethyl acetate in methylene chloride) gave **4** (5 mg) and **5** (2.5 g).

^{13}C-Labeled phomalone

Isolation of ^{13}C-labelled phomalone

Liquid cultures (2 L, 13 days shaking) were prepared as described above. The floating HP-20 ion exchange resin was decanted from the broth. The remaining resin, which adhered to the mycelium, was separated by vacuum filtration through Whatman paper No. 1. The resin and the resin-mycelium mixture were transferred to a sintered glass filter (porosity D, ASTRM 10–20 μm) and extracted with ethyl acetate (1.6 L). The extract was dried over anhydrous sodium sulfate and concentrated under reduced pressure to give a crude extract (548 mg, after the experiment with [1-^{13}C]-sodium acetate). Flash chromatography of this resin extract (10% ethyl acetate in methylene chloride) followed by HPMPLC (NP-Si60, 10% ethyl acetate in methylene chloride) and HPLC (Waters, μBondapak C-18; gradient: 40% water in methanol to 100% methanol) gave ^{13}C-labelled phomalone (6 mg). The same procedure was repeated with [2-^{13}C]- and [1,2-$^{13}C_2$]-sodium acetate. Triacetylphomalone was prepared as described above.

Bioassay method

Chromatography fractions. The sample was sterilized by filtration through a 0.22-μm Nylon membrane. A 200-μL aliquot was applied directly to the well of the multiwell plate (24-well, flat bottom, Falcon 3047) using a micropipette. The solvent was evaporated in a sterile fumehood for 3 h. The inoculum was obtained from the growing edge of a colony of *Phellinus tremulae* in MEA Petri dishes. After 10 days of growth at room temperature, a plug (7 mm diameter) cut from this culture was placed in each well of the multiwell plate. Four replicates of each sample and a solvent control were evaluated in each multiwell plate. This procedure was repeated for each chromatographic fraction. Inhibition in the radial growth of a colony of *P. tremulae* relative to the control constitutes a positive result.

Pure compounds. The sample was sterilized by filtration through a 0.22-μm Nylon membrane. A 0.25-mL aliquot of a standard solution was applied directly to the well of the multiwell plate (6-well, flat bottom, Falcon 3046) using a micropipette. The solvent was evaporated in a sterile fumehood for 3 h. The inoculum was obtained from the growing edge of a colony of *P. tremulae* in MEA Petri dishes. After 10 days of growth at room temperature, a plug (7 mm diameter) cut from this culture was placed in each well of the multiwell plate. Three replicas of each sample and the solvent control were evaluated for each multiwell plate. This procedure was repeated for seven different concentrations: 4×10^{-3}, 2×10^{-3}, 1×10^{-3}, 4×10^{-4}, 2×10^{-4}, 1×10^{-4}, and 4×10^{-5} mol/L. The bioassay was evaluated by the amount of growth of *P. tremulae*, relative to control, in each well. The radial growth was measured 8, 14, and 30 days after inoculation.

Acknowledgements

We wish to acknowledge with thanks the financial support of

Can. J. Chem. Downloaded from www.nrcresearchpress.com by 85.192.166.187 on 09/08/12
For personal use only.

the Natural Sciences and Engineering Research Council of Canada. We thank Dr. Y. Hiratsuka of the Northern Forestry Centre, Canadian Forest Service, Edmonton, and L. Sigler, University of Alberta Microfungus Herbarium, for cultures of *P. etheridgei* and for valuable discussion.

1. E.B. Peterson and N.M. Peterson. Ecology, management, and use of aspen and balsam poplar in the prairie provinces, Canada. For. Can. Northwest Reg. North. For. Cent., Edmonton, Alta. Spec. Rep. 1. 1992.
2. K. Hunt, J.T. Bashan, and J.A. Kemperman. Can. J. For. Res. **8**, 181 (1978).
3. P.E. Crane. M. Sc. Thesis, University of Alberta, Edmonton. 1993. p. 3.
4. W.J. Ondro. Utilization and market potential of poplars in Alberta. Can. For Serv. North. For. Cent. Rep. NOR-X-305. 1989. p. 64.
5. L.S. Trifonov, P. Chakravarty, Y. Hiratsuka, and W.A. Ayer. Eur. J. For. Pathol. **22**, 441 (1992).
6. Y. Hiratsuka, P. Chakravarty, S. Miao, and W.A. Ayer. Can. J. For. Res. **24**, 174 (1994).
7. P.E. Crane, P.V. Blenis, and Y. Hiratsuka. Can. J. For. Res. In press.
8. W.A. Ayer and L.S. Trifonov. J. Nat. Prod. **55**, 1454 (1992).
9. W.A. Ayer and S. Miao. Can. J. Chem. **71**, 487 (1993).
10. W.A. Ayer and S. Miao. J. Nat. Prod. **56**, 2046 (1993).
11. W.A. Ayer and A.Q. Khan. Heterocycles. In press.
12. L.J. Hutchison, P. Chakravarty, L.M. Kawchuk, and Y. Hiratsuka. Can. J. Bot. **72**, 1424 (1994).
13. L.D. Jimenez. M. Sc. Thesis, University of Alberta, Edmonton. 1994. pp. 13–17.
14. W.A. Ayer and E.R. Cruz. J. Org. Chem. **58**, 7529 (1993).
15. I.M. Chandler, C.R. McIntyre, and T.J. Simpson. J. Chem. Soc. Perkin Trans. 1, 2271 (1992).
16. A. Bax. J. Magn. Reson. **57**, 314 (1984).
17. T.J. Simpson, I.M. Chandler, and C.R. McIntyre. J. Chem. Soc. Perkin Trans. 1, 2285 (1992).
18. T.J. Simpson. Chem. Soc. Rev. **4**, 497 (1975).

Can. J. Chem. Downloaded from www.nrcresearchpress.com by 85.192.166.187 on 09/08/12
For personal use only.

Hydration equilibria of 9-acridinecarboxaldehyde

ROBERT A. MCCLELLAND[1] AND PRATIMA SUKHAI
Department of Chemistry, University of Toronto, Toronto, ON M5S 1A1, Canada
AND
KAREN M. ENGELL AND POUL E. SORENSEN
Chemistry Department A. The Technical University of Denmark, DK-2800 Lyngby, Denmark
Received June 8, 1994

ROBERT A. MCCLELLAND, PRATIMA SUKHAI, KAREN M. ENGELL, and POUL E. SORENSEN. Can. J. Chem. **72**, 2333 (1994).

Hydration rate constants and equilibrium constants have been obtained for 9-acridinecarboxaldehyde in aqueous solution. Under acidic conditions where the acridine is protonated, signals for the hydrate and free aldehyde forms can be observed as separate species in the ^{1}H NMR spectrum. Integration provides the hydration equilibrium constant K_{h^+} = [hydrate]/[aldehyde] = 2.5. Using an apparent acidity constant obtained from a spectroscopic titration curve, the rate–pH profile was fitted to provide the hydration constant for the equilibration of the neutral acridines, K_H = 0.07. This analysis also provides the acidity constants for the two acridinium ions, the aldehyde with pK = 3.78 and the hydrate with pK = 5.36. A comparison with the 4-pyridinecarboxaldehdye system reveals that the K_{h^+}: K_h ratios for the acridine and pyridine are the same within experimental error, but that the acridine and acridinium aldehydes are 20-fold less hydrated than their pyridine analogs. A comparison with benzaldehydes reveals that, in their reactivities, the two heterocyclic aldehydes behave in a similar manner. Thus, for example, plots of log k_H for the acid-catalyzed dehydration and hydrations versus log K_h for the equilibrium hydration show single correlation lines including the points for the benzaldehydes and heterocyclic aldehydes (but not the aliphatic aldehydes).

ROBERT A. MCCLELLAND, PRATIMA SUKHAI, KAREN M. ENGELL et POUL E. SORENSEN. Can. J. Chem. **72**, 2333 (1994).

On a mesuré les constantes de vitesse d'hydratation et les constantes d'équilibre de l'acridine-9-carboxaldéhyde en solution aqueuse. En milieu acide, alors que l'acridine peut être protonée, les spectres RMN du ^{1}H permettent d'observer séparément les signaux des formes aldéhydiques et hydratées. L'intégration fournit la constante d'équilibre d'hydratation, K_{h^+} = [hydrate]/[aldéhyde] = 2,5. Utilisant une constante d'acidité apparente obtenue à partir d'une courbe de titrage spectroscopique, on a ajusté le profil vitesse–pH pour déduire la constante d'hydratation pour l'équilibre des acridines neutres, K_H = 0,07. Cette analyse fournit aussi les constantes d'acidité des deux ions acridinium; pour l'aldéhyde, le pK = 3,78 alors que, pour l'hydrate, le pK = 5,36. Une comparaison avec le système pyridine-4-carboxaldéhyde révèle que les rapports K_{h^+} : K_h pour l'acridine et la pyridine sont essentiellement les mêmes, aux erreurs expérimentales près, mais que les aldéhydes de l'acridine et de l'acridinium sont 20 fois moins hydratés que leurs analogues de la série pyridinique. Une comparaison avec les benzaldéhydes révèle que, pour leurs réactivités, les deux aldéhydes hétérocycliques se comportent de manières similaires. Ainsi, par exemple, les courbes des log k_H de la déshydratation ou des hydratations acidocatalysées en fonction du log K_h pour l'équilibre d'hydratation présentent des droites de corrélation unique comportant les points des benzaldéhydes et des aldéhydes hétérocycliques (mais pas des aldéhydes aliphatiques).

[Traduit par la rédaction]

The anticonvulsant drug carbamazepine (5*H*-dibenz[*b*,*f*]-azepine-5-carboxamide) is associated with a significant incidence of idiosyncratic reactions including agranulocytosis. It has been found that many of the drugs that are associated with agranulocytosis are metabolized to reactive species by activated neutrophils (1). The major neutrophil enzyme involved in such oxidations is myeloperoxidase. This enzyme has, as its usual substrate, chloride, which undergoes a two-electron oxidation producing either hypochlorite or an activated chlorine bound to the enzyme that mimics hypochlorite in its behavior. Carbamazepine is indeed oxidized by neutrophils, resulting in covalent binding of radiolabelled drug to the neutrophil (2). The major metabolite in both these and model studies involving hypochlorite is 9-acridinecarboxaldehyde (3). This product can be envisaged to arise from electrophilic chlorination of the C_1=C_2 double bond, followed by ring contraction and replacement of chlorine with oxygen. This aldehyde provides an electrophilic site for reaction with biological nucleophiles, and experiments with labelled material result in a 100-fold greater binding to cells (2).

[1]Author to whom correspondence may be addressed. Telephone: (416) 978-3592; Fax: (416) 978-1631; e-mail: rmcclell@alchemy.chem.utoronto.ca

There were indications that this aldehyde, like its analog 4-pyridinecarboxaldehyde (4), is significantly hydrated in aqueous solution. As part of our studies into the chemical reactivity of 9-acridinecarboxaldehyde, we have therefore carried out a detailed examination of the hydration equilibrium.

Experimental section

9-Acridinecarboxaldehyde

(The following procedure offers a considerable improvement over a literature method, which involves reaction of *m*-chloroperbenzoic acid with iminostilbene, and produces the aldehyde in only a 20–30% yield after chromatography (5).) Carbamazepine (2.1 g, 8.9 mmol) was added to 5 L of water and the mixture was heated to about 80°C to bring the solid into solution. To this was added NaCl (100 g), Na_2HPO_4 (4.5 g, 31.7 mmol), and $NaH_2PO_4 \cdot H_2O$ (51 g, 370 mmol), to form a solution buffered at pH 8. The reaction flask was then allowed to cool. When the temperature reached ~50°C (below which the carbamazepine precipitates), 25 mL of 0.60 *M* sodium hypochlorite in water was added all at once. This corresponds to about 1.5 equivalents of hypochlorite per equivalent of carbamazepine, a ratio which appears to be optimal. The reaction flask was wrapped in aluminum foil (to prevent photochemical degradation of the product), and the mixture stirred at 5–10°C overnight. Filtration provided a reasonably pure brown solid. One recrystallization from CCl_4 provided 1.1 g (60%) of pure material: mp 135–136°C (lit. (5) mp 138–140°C).

Can. J. Chem. Downloaded from www.nrcresearchpress.com by 85.192.166.187 on 09/08/12
For personal use only.

^{1}H NMR (200 MHz, DMSO-d_6) δ: 7.79 (t), 7.94 (t), 8.25 (d), 8.7 (d), 11.50 (s).

UV–visible spectra were recorded with a Varian 2200 spectrophotometer, by injecting 10 μL of a stock solution of the aldehyde (0.1 M) in acetonitrile into a 10-mL volumetric flask and filling to the mark with the appropriate solution.

Kinetic experiments were carried out with a Hi-Tech stopped-flow apparatus. In one set of experiments, a solution of the aldehyde (0.0002 M) in 0.002 M HCl was placed in one syringe of the apparatus, and this was mixed with acetate (pH 4.4–5.5), phosphate (pH 5.5–8.0), and borate (pH 8–9) buffers containing 0.002 M NaOH. In a second set of experiments, the aldehyde (0.0001 M) was dissolved in a 1:1 Na_2HPO_4:NaH_2PO_4 solution (0.001 M) and this was mixed with HCl solutions and acetate buffers (pH 3.6–4.3). The pH of the mixed solutions was measured. Sodium chloride was employed to maintain an ionic strength after mixing of 0.1 M. The stopped-flow experiments were carried out at 25°C and 355 nm. The absorbance–time data were digitized, and first-order rate constants were obtained by nonlinear least-squares fitting to the exponential equation

$$\text{absorbance} = A_0 \exp(-k_{obs}t) + \text{base}$$

Replicate kinetic runs agreed to ±2%.

Results and discussion

Scheme 1 summarizes the equilibria that can occur with 9-acridinecarboxaldehyde in aqueous solutions, ignoring strongly basic solutions where ionization of the OH group of the hydrate can also take place.

In acids, protonation of the acridine makes the substrate sufficiently soluble that NMR spectra can be recorded in highly aqueous solutions. With conditions of 0.005 M acridinecarboxaldehyde in D_2O containing 0.02 M DCl plus 10% CD_3CN, a 400 MHz ^{1}H NMR spectrum showed the presence of both the free aldehyde and hydrate forms **AH$^+$** and **BH$^+$**. The most characteristic signals were two singlets, one at 11.4 ppm for the CHO proton and one at 7.5 ppm for the corresponding proton in the hydrate. The ratio of these two was 1:2.5. This was unchanged within experimental error in similar solutions with 20 and 30% CD_3CN. As will be apparent from the analysis of the protonation equilibria, the acid concentration employed in these experiments is sufficient to ensure complete protonation of both the aldehyde and hydrate forms. In consequence, this analysis measures the hydration equilibrium constant K_{h^+}, the value of which is 2.5. This ignores the solvent isotope effect, which would be small and probably not outside the experimental error associated with NMR integration.

A corresponding experiment to determine K_h could not be carried out since solubility problems prevented the recording of NMR spectra in solutions containing enough water for a meaningful result. As illustrated in Fig. 1 (*a*), the UV spectrum of the aldehyde in neutral aqueous solution is similar to one recorded in acetonitrile, where there can be no hydrate. Moreover, both spectra are different from that of acridine, whose chromophore would serve as a model for the hydrate. From these observations we conclude that the equilibrium under neutral conditions favors the free aldehyde, i.e., that K_h is significantly smaller than unity. It can also be noted that, in acids, the spectra of the aldehyde and parent acridine are more similar (Fig. 1(*b*)), consistent with the NMR result showing that the hydrate is the major species under these conditions.

We also determined a spectroscopic acidity constant from the variation in the OD at 355 nm in a series of solutions with pH ranging from 1 to 10 and containing the same concentration of aldehyde (1.0×10^{-4} M). This produced a standard titration

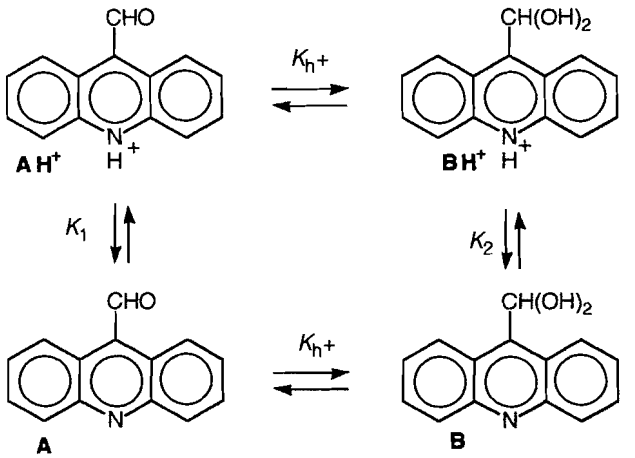

SCHEME 1

curve that was fitted to the appropriate equation to provide an acidity constant of 4.30 ± 0.05. In terms of Scheme 1, this is an apparent acidity constant, as given by the following equation.

$$[1] \qquad K_a(\text{app}) = \frac{K_1 + K_2K_{h^+}}{1 + K_{h^+}}$$

Rate constants for the interconversion of the aldehyde and hydrate forms were obtained in a manner similar to that employed previously for pyridinecarboxaldehydes (4), by taking advantage of the different equilibrium positions in acidic and neutral solutions. Thus, a jump from low to high pH, or vice versa, results initially in a solution where the forms are not at equilibrium. The kinetics of the approach to equilibrium can then be monitored through changes in the UV–visible spectrum. For our experiments we employed a stopped-flow apparatus to carry out the pH jumps, with detection at 355 nm. Experiments were carried out in the two directions, with substrate in dilute acid (0.002 M HCl) being mixed to give solutions with a final pH of 4.4 or greater, and substrate in dilute (0.001 M) pH 7 phosphate buffer being mixed to give solutions with a pH of 4.2 or smaller. Measurements in more acidic solutions (pH <2.4) involved HCl; in all other cases buffers were employed. In these cases catalysis by the buffer was observed, and rate constants were extrapolated to zero buffer concentration. Table 1 lists the rate constants at zero buffer concentration as a function of pH.

In terms of the kinetic analysis for an approach to an equilibrium,

$$[2] \qquad k_{obs} = k_f\left(\frac{[A]}{[A]+[AH^+]}\right) + k_{f^+}\left(\frac{[AH^+]}{[A]+[AH^+]}\right) + k_r\left(\frac{[B]}{[B]+[BH^+]}\right) + k_{r^+}\left(\frac{[BH^+]}{[B]+[BH^+]}\right)$$

where k_f and k_r are the first-order rate constants at a given pH for the reactions of the neutral species in the forward and reverse direction, k_{f^+} and k_{r^+} refer to the forward and reverse processes involving the protonated species, and the terms in parentheses are the fraction of that particular species in the appropriate acid–base equilibrium. Recognizing that $K_h = k_f/k_r$, $K_{h^+} = k_{f^+}/k_{r^+}$, and $K_hK_1 = K_{h^+}K_2$, this can be rewritten as

$$[3] \qquad k_{obs} = (k_rK_2 + k_{r^+}[H^+])\left(\frac{K_{h^+}}{[H^+]+K_1} + \frac{1}{[H^+]+K_2}\right)$$

Can. J. Chem. Downloaded from www.nrcresearchpress.com by 85.192.166.187 on 09/08/12
For personal use only.

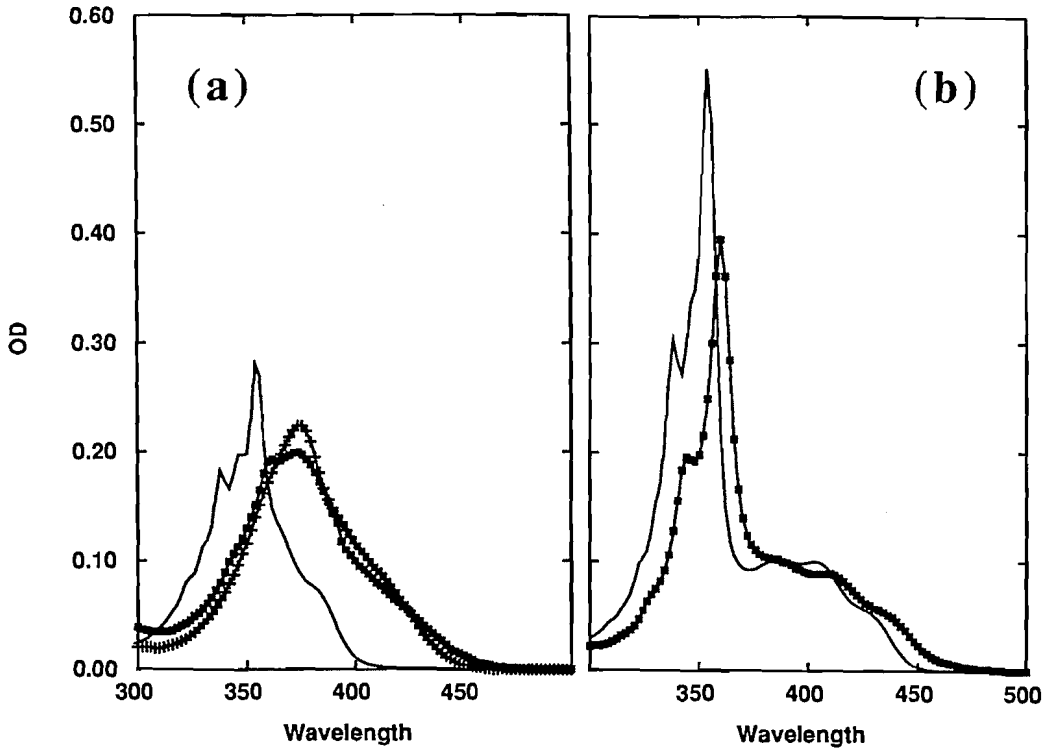

FIG. 1. UV–visible spectra. (*a*) 9-Acridinecarboxaldehyde in (+) acetonitrile and (■) aqueous solution, pH 8, and acridine in (—) aqueous solution, pH 8. (*b*) 9-Acridinecarboxaldehyde (+) and acridine (—) in 1 M HCl. Concentrations in all cases were 1×10^{-4} M.

TABLE 1. Rate constants (25°C, ionic strength = 0.1) for the interconversion of aldehyde and hydrate forms of 9-acridinecarboxaldehyde. Values in solutions with pH >3 were obtained by extrapolation to zero buffer concentration

pH	k_{obs}, s^{-1}	pH	k_{obs}, s^{-1}
1.12	0.929	6.05	0.0665
1.21	0.822	6.07	0.0682
1.24	0.798	6.20	0.0606
1.36	0.650	6.27	0.0643
1.49	0.601	6.59	0.0735
1.67	0.530	6.63	0.0854
1.97	0.457	7.20	0.166
2.16	0.430	7.48	0.345
2.39	0.410	7.70	0.501
3.01	0.364	7.83	0.633
3.60	0.271	8.16	1.205
4.19	0.198	8.30	1.67
4.45	0.158	8.38	2.00
4.62	0.141	8.51	2.68
4.92	0.121	8.77	5.33
5.26	0.0980	8.95	8.00
5.90	0.0645	9.15	12.3

Each dehydration can occur with H^+, OH^-, and no catalysis (or water catalysis),

$$[4] \qquad k_r = k_H[H^+] + k_0 + k_{OH}[OH^-]$$

$$[5] \qquad k_{r^+} = k_{H^+}[H^+] + k_{0^+} + k_{OH^+}[OH^-]$$

resulting in the following expression for k_{obs}:

$$[6] \qquad k_{obs} = \left\{k_{H^+}[H^+]^2 + (k_H K_2 + k_{0^+})[H^+] + (k_0 K_2 + k_{OH^+} K_w) + \left(\frac{k_{OH} K_2 K_w}{[H^+]}\right)\right\} \times \left(\frac{K_{h^+}}{[H^+] + K_1} + \frac{1}{[H^+] + K_2}\right)$$

It can be noted that the reactions involving H^+ catalysis on the neutral equilibration and water catalysis on the cationic equilibration are kinetically equivalent and have the same rate–pH dependence, as do the reactions involving water catalysis on the neutral and hydroxide ion catalysis on the cationic equilibration.

Under strongly acidic solutions, $[H^+] > 0.01$, only the terms in $[H^+]^2$ and $[H^+]$ should be important, and $[H^+]$ should be greater than K_1, K_2, so that eq. [6] simplifies to

$$[7] \qquad k_{obs} = k_{H^+}(K_{h^+} + 1)[H^+] + (k_H K_2 + k_{0^+})(K_{h^+} + 1)$$

This predicts a linear relation between k_{obs} and $[H^+]$, and this is observed. Least-squares fitting (for data in solutions with pH <2) gives a slope $= k_{H^+}(K_{h^+} + 1) = (7.2 \pm 0.4)$ M^{-1} s^{-1}, and an intercept $= (k_H K_2 + k_{0^+})(K_{h^+} + 1) = (0.39 \pm 0.02)$ s^{-1}. From the known value of K_{h^+}, this provides values for k_{H^+} of 2.05 M^{-1} s^{-1} and $(k_H K_2 + k_{0^+})$ of 0.111 s^{-1}.

For solutions with pH >7, the last two terms in the first part of the rate law are expected to be important and $[H^+] < K_1$, K_2, so that

$$[8] \qquad k_{obs} = (k_0 K_2 + k_{OH^+} K_w)\left(\frac{K_{h^+}}{K_1} + \frac{1}{K_2}\right) + k_{OH}(K_h + 1)[OH^-]$$

Can. J. Chem. Downloaded from www.nrcresearchpress.com by 85.192.166.187 on 09/08/12
For personal use only.

Can. J. Chem. Downloaded from www.nrcresearchpress.com by 85.192.166.187 on 09/08/12
For personal use only.

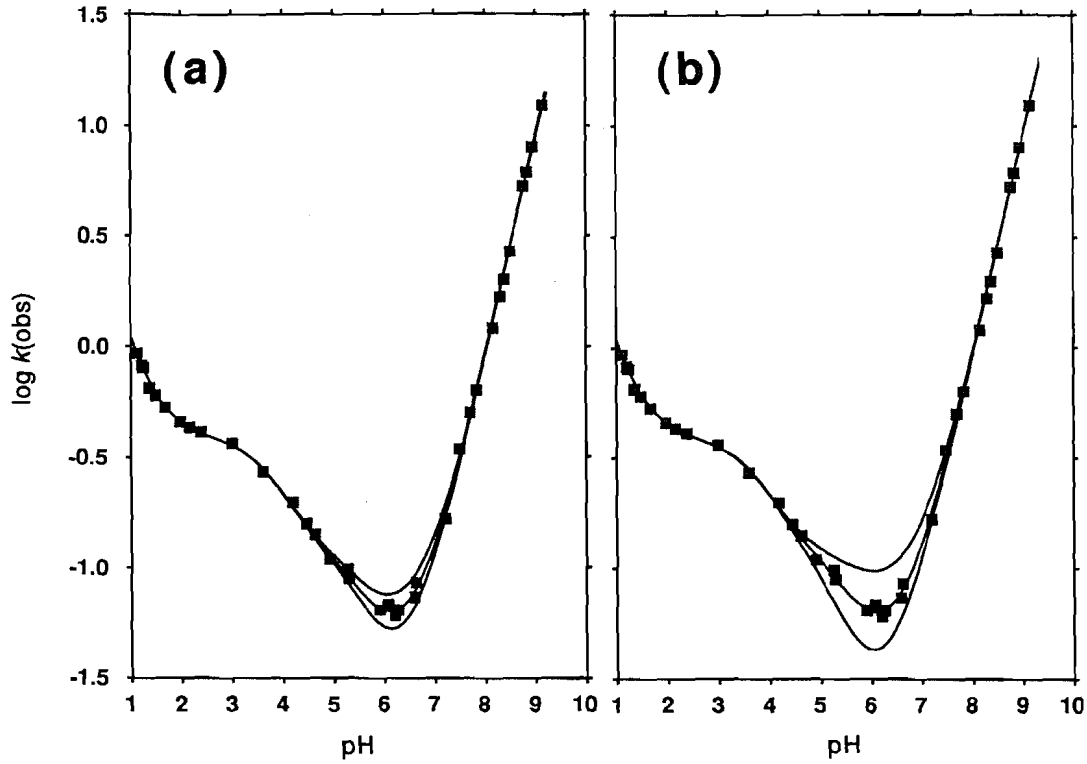

FIG. 2. Rate–pH profile for the equilibrium of the aldehyde and hydrate forms of 9-acridinecarboxaldehyde. The points are experimental, the curves have been calculated according to eq. [6]. The middle curve in each figure represents the best fit, obtained as described in the text, with $k_{H^+} = 2.05$, $(k_H K_2 + k_{0^+}) = 0.111$, $(k_0 K_2 + k_{OH^+} K_w) = 1.71 \times 10^{-7}$, $k_{OH}(K_h + 1) = 8.8 \times 10^5$, $K_{h^+} = 2.5$, $pK_1 = 3.784$, $pK_2 = 5.357$, and $K_h = 0.067$. The other two curves in Fig. 2(*a*) illustrate the result of different values of $(k_0 K_2 + k_{OH^+} K_w)$, 2.3×10^{-7} (top curve) and 1.2×10^{-7} (bottom). In Fig. 2(*b*), pK_1 is varied: $pK_1 = 3.77$, $pK_2 = 5.65$, $K_h = 0.033$ (top), and $pK_1 = 3.81$, $pK_2 = 5.09$, $K_h = 0.133$ (bottom).

This predicts a linear relation in hydroxide ion concentration, and this is also observed. The slope, $k_{OH}(K_h + 1)$, is equal to $(8.8 \pm 0.7) \times 10^5$. The intercept, for data with pH >7, is not statistically relevant.

This analysis of the regions at the pH extremes leaves one rate constant term in eq. [6] unknown, $(k_0 K_2 + k_{OH^+} K_w)$. With respect to the equilibrium constants, there is also only one independent variable. We arbitrarily chose this as K_1, and, with K_{h^+} known and K_a(app) known, calculate the remaining equilibrium constants as follows.

$$[9] \qquad K_2 = \frac{K_a(\text{app})(1 + K_{h^+}) - K_1}{K_{h^+}}$$

$$[10] \qquad K_h = \frac{K_2 K_{h^+}}{K_1}$$

Employing a spread-sheet program, values of the two unknowns were then varied, until a minimum in $[k_{obs}(\text{experimental}) - k_{obs}(\text{calculated eq. [6]})]^2$ was reached. The best fit had $(k_0 K_2 + k_{OH^+} K_w) = 1.71 \times 10^{-7}$, $pK_1 = 3.784$ (and, from this, $pK_2 = 5.357$ and $K_h = 0.067$). The experimental and calculated rate–pH profiles are compared in Fig. 2. As also illustrated, the fitting was sensitive to the value of pK_1, but less sensitive to $(k_0 K_2 + K_{OH^+} K_w)$.

With these various constants now available, the question of the relative importance of the kinetically equivalent mechanisms can be addressed. The quantity $(k_H K_2 + k_{0^+})$, 0.111 s^{-1}, represents a pH-independent rate constant for the equilibration under acidic conditions where both acid–base equilibriums are shifted predominantly to the conjugate acid side ($[H^+] > K_1$, K_2). For $k_H K_2$ to make a 10% contribution to this rate constant, $(k_H K_2 = 0.011)$, k_H is required to be 2.5×10^3 M^{-1} s^{-1}. This is three orders of magnitude larger than k_{H^+}, which is determined unambiguously. This, however, is not the best comparison since the H^+-catalyzed dehydration of the neutral species should be faster than that of the protonated one. As will be domonstrated later, the hydrates of *p*-chloro- or *m*-chlorobenzaldehyde offer better comparisons, since these are not only neutral, but have hydration equilibrium constants similar to the neutral acridine. These benzaldehyde hydrates have $k_H = 1.23 \times 10^3$ M^{-1} s^{-1} (4-Cl) and 4.9×10^2 M^{-1} s^{-1} (3-Cl), from which we conclude that k_H for the neutral acridine is unlikely to be greater than 10^3 M^{-1} s^{-1}. This corresponds to at most a 5% contribution of $k_H K_2$ in the $(k_H K_2 + k_{0^+})$ term. Thus the predominant reaction of this kinetically equivalent pair is the pH-independent equilibration of the protonated species, and $k_{0^+} \sim 0.11$ s^{-1}.

The situation with respect to the other pair of kinetically equivalent reactions is less clear. With $(k_0 K_2 + k_{OH^+} K_w)$ deter-

TABLE 2. Equilibrium constants for hydration and protonation reactions of aromatic aldehydes

Aldehyde	K_h	K_{h^+}	pK_1	pK_2
9-Acridinecarboxaldehyde	0.07	2.5	3.78	5.36
4-Pyridinecarboxaldehyde[a]	1.53	52	3.20	4.74

[a]Reference 4.

TABLE 3. Rate constants for dehydration[a] of hydrates of aromatic aldehydes (25°C)

Aldehyde	K_h	k_H, M^{-1} s^{-1}	k_0, s^{-1}	k_{OH}, M^{-1} s^{-1}
9-Acridine-CHO	0.07	—[b]	0.02–0.04[c]	8.2×10^5
9-Acridinium-CHO	2.5	2.1×10^0	0.11	$1–8 \times 10^6$[c]
4-Pyridine-CHO[d]	1.53	—[b]	0.023	1.9×10^5
4-Pyridinium-CHO[d]	52	2.8×10^{-1}	0.044	—[b]
4-ClC_6H_4CHO[e]	0.016[f]	1.2×10^3	0.021	2.0×10^5
3,5-$(NO_2)_2C_6H_3CHO$[e]	2.1	3.9×10^0	0.048	7.7×10^5

[a]Rate constants in the hydration direction can be calculated from the relation $k_{hyd} = k_{deh} \times K_H$.
[b]Rate constant could not be obtained because of dominance of a second kinetically equivalent mechanism.
[c]Kinetically equivalent mechanisms. The rate constant k_0 is 0.04 s^{-1} if $k_{OH} < 1 \times 10^6$ M^{-1} s^{-1} so that the k_{OH} process makes less than a 10% contribution. If $k_{OH} = 8 \times 10^6$ s^{-1} (50% contribution), $k_0 = 0.02$ s^{-1}.
[d]Reference 4.
[e]Reference 6.
[f]Reference 7.

mined to be 1.71×10^{-7}, a 10% contribution from $k_{OH^+}K_w$ requires k_{OH^+} to be 1.7×10^6 M^{-1} s^{-1}. This is only twofold larger than k_{OH}, the rate constant for the OH^--catalyzed dehydration of the neutral hydrate. This difference is in the correct direction since, at least with benzaldehyde hydrates, electron-withdrawing substituents increase k_{OH}, with $\rho = +0.5$ (6). On the other hand, a 100% contribution from $k_{OH^+}K_w$ requires $k_{OH^+} = 1.7 \times 10^7$ M^{-1} s^{-1}, and this seems too large. This latter situation would also mean that k_0 would be less than 0.01 s^{-1}, which, in comparison with other hydrates, seems unlikely (see later). Our conclusion is that both reactions likely contribute to the $(k_0K_2 + k_{OH^+}K_w)$ term, and we are unable to unambiguously assign definite values to either k_0 or k_{OH^+}.

It is interesting that with 4-pyridinecarboxaldehyde the $k_{OH^+}K_w$ term is relatively unimportant. This had been assumed in the original kinetic analysis with this system (4), and our analysis of the data shows that this is reasonable. With this aldehyde, $(k_0K_2 + k_{OH^+}K_w)$ is 4.2×10^7, so that for $k_{OH^+}K_w$ to make a 10% contribution, k_{OH^+} must be 4.2×10^6 M^{-1} s^{-1}. This value is 20-fold larger than the value of k_{OH} for the neutral species, and thus it is likely an upper limit. There are two differences that result in the decreased importance of the OH^--catalyzed reaction of the protonated form. The first is that hydroxide ion catalysis seems to be less efficient in the pyridine system. The second is that the pyridinium ions are more acidic, so that under conditions where the hydroxide ion catalyzed processes become important, there is a lower concentration of the protonated pyridine.

Equilibrium constants for the 9-acridinecarboxaldehyde system are given in Table 2, along with those for the analog 4-pyridinecarboxaldehyde. Both aldehydes show significantly more hydration in their protonated forms, with $K_{h^+}/K_h = 37$ (acridine) and 35 (pyridine), numbers that are not statistically different. In each case the acridinealdehydes are 20-fold less hydrated. This is likely a consequence of steric crowding in the hydrate form of this system, associated with interactions of the 9-substituent and the hydrogen atoms at C1 and C8. The similarities in the K_{h^+}/K_h ratio provide confidence in the derivations employed to obtain these numbers. It can be noted that in the pyridine case, the measurable hydration constant was K_h, with K_{h^+} being determined through the analysis of the rate–pH profile. Further consistency is also seen in the 0.6 pK differences between the analogous pyridinium and acridinium

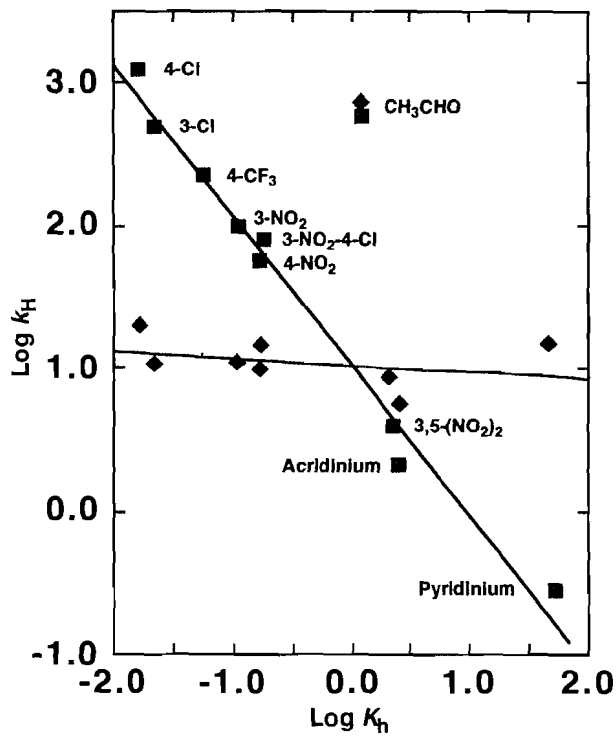

FIG. 3. Correlation of log k_H and log K_h for hydration of aromatic aldehydes. (■) $-k_H$ in dehydration direction. (◆) $-k_H$ in hydration direction. The identity of the substrates for the latter points is the same as that of the vertically related squares. Data for benzaldehydes from ref. 6, for 4-pyridiniumcarboxaldehyde from ref. 4, and for acetaldehyde from ref. 9. Slopes of the lines are −1.04 for the dehydration (correlation coefficient 0.989) and −0.04 for the hydration.

ions, since this is typical of differences for such a comparison (8).

Table 3 summarizes rate constants for the dehydration of the hydrates of the 9-acridine and 4-pyridinecarboxaldehydes, along with two representative benzaldehydes. The conclusion from these data is that the heterocyclic aldehydes behave in a manner similar to the benzaldehydes. Thus the values for k_{OH} for the dehydration all lie in the 10^5–10^6 M^{-1} s^{-1} range while

Can. J. Chem. Downloaded from www.nrcresearchpress.com by 85.192.166.187 on 09/08/12
For personal use only.

the k_0 values range from 0.02–0.1 s^{-1}. As shown in Fig. 3, for the acid-catalyzed equilibration, the heterocyclic aldehydes fit rate–equilibrium correlations for the benzaldehyde system. That is, despite their positive charge, the acridinium and pyridinium points in the log k_H–log K_h correlation fall on the same line as the benzaldehydes. Interestingly, changes in the hydration equilibrium constant have by far a larger effect on the dehydration rate constant for H^+ catalysis. It also noteworthy that the points for aliphatic aldehydes do not lie on the same line, as illustrated in Fig. 3 for acetaldehyde.

Acknowledgements

We thank the Natural Sciences and Engineering Research Council of Canada for a research grant, the Danmarks Forskerakademi for a travel grant, and NATO for a NATO Collaborative Research Grant (CRG 900990). We thank Dr. J. Uetrecht for useful discussions.

1. J.P. Uetrecht. CRC Crit. Rev. Toxicol. **20**, 213 (1990).
2. S.M. Furst. Ph. D. Thesis, University of Toronto, 1993.
3. S.M. Furst and J.P. Uetrecht. Biochem. Pharmacol. **45**, 1267 (1993).
4. S. Cabani, P. Giann, and E. Matteoli. J. Phys. Chem. **76**, 2959 (1972).
5. K. Kwashima and T. Isiguro. Chem. Pharm. Bull. **26**, 951 (1978).
6. R.A. McClelland and M. Coe. J. Am. Chem. Soc. **105**, 2719 (1983).
7. E.G. Sander and W.P. Jencks. J. Am. Chem. Soc. **90**, 6154 (1968).
8. A. Albert. *In* Physical methods in heterocyclic chemistry. Vol. 1 *Edited by* A.R. Katritzky. Academic Press, New York. 1963.
9. P.E. Sorensen and W.P. Jencks. J. Am. Chem. Soc. **109**, 4675 (1987).

Can. J. Chem. Downloaded from www.nrcresearchpress.com by 85.192.166.187 on 09/08/12
For personal use only.

Preparation and characterization of azaindolyl-azaindole and structure of its halogen-free dicationic cluster containing the μ_4-oxotetracopper(II) core

JACQUES POITRAS AND ANDRÉ L. BEAUCHAMP[1]

Département de chimie, Université de Montréal, C.P. 6128, Succ. centre-ville, Montréal, QC H3C 3J7, Canada

Received March 7, 1994

JACQUES POITRAS and ANDRÉ L. BEAUCHAMP. Can. J. Chem. **72**, 2339 (1994).

Refluxing $NbCl_5$ and excess 7-azaindole (Haza) in benzene yielded a solid mixture containing $NbCl_5$(Haza), $NbCl_4(Haza)_2$, the azaindolium ion $(H_2aza)^+$, and the azaindolyl-azaindolium ion $(H_2aza\text{-}aza)^+$. The neutral (Haza-aza) molecule was obtained from the hydrolysed mixture and shown by X-ray diffraction (monoclinic, $P2_1/c$, a = 10.025, b = 13.758, c = 8.416 Å, β = 102.89°, Z = 4, R = 0.035) to result from the coupling of two azaindole units via N7—C6′. This compound was the only oxidation product detected, but concurrent formation of other niobium- and (or) azaindole-containing products keeps the yield of Haza-aza low. Dark green crystals of $[Cu_4O(aza\text{-}aza)_4]Cl_2\cdot 6.5H_2O$ were obtained from (Haza-aza) and $CuCl_2$ in wet methanol. The crystal structure (monoclinic, $C2/c$, a = 17.704, b = 25.240, c = 14.457 Å, β = 116.14°, Z = 4, R = 0.051) shows the presence of a tetranuclear dicationic cluster consisting of a μ_4-oxide ion surrounded by a tetrahedron of Cu(II) atoms. A distorted square-planar coordination is achieved about each copper atom by $(aza\text{-}aza)^-$ ligands each bridging two copper atoms and providing a third nitrogen donor to one of them. For each such cation, the unit cell also includes two chloride ions and 6.5 disordered lattice water molecules. The ^1H NMR and infrared spectroscopy data are discussed.

JACQUES POITRAS et ANDRÉ L. BEAUCHAMP. Can. J. Chem. **72**, 2339 (1994).

Le reflux de $NbCl_5$ et de 7-azaindole (Haza) en excès dans le benzène a conduit à un mélange solide contenant $NbCl_5$(Haza), $NbCl_4(Haza)_2$, l'ion azaindolium $(H_2aza)^+$ et l'ion azaindolyl-azaindolium $(H_2aza\text{-}aza)^+$. Le composé neutre (Haza-aza) a été obtenu à partir du mélange hydrolysé et la diffraction des rayons X (monoclinique, $P2_1/c$, a = 10,025, b = 13,758, c = 8,416 Å, β = 102,89°, Z = 4, R = 0,035) a montré qu'il comporte deux motifs azaindole couplés par N7—C6′. Ce composé est le seul produit d'oxydation décelé, mais la formation concurrente d'autres produits contenant du niobium et (ou) de l'azaindole contribue à garder le rendement en Haza-aza faible. Des cristaux vert foncé de $[Cu_4O(aza\text{-}aza)_4]Cl_2\cdot 6{,}5H_2O$ ont été obtenus par addition de (Haza-aza) à $CuCl_2$ dans le méthanol humide. La structure cristalline (monoclinique, $C2/c$, a = 17,704, b = 25,240, c = 14,457 Å, β = 116,14°, Z = 4, R = 0,051) a révélé la présence d'un agrégat tétranucléaire dicationique contenant un ion μ_4-oxyde entouré d'un tétraèdre d'atomes de Cu(II). Une coordination plane carrée déformée autour de chaque atome de cuivre est complétée au moyen de ligands $(aza\text{-}aza)^-$ qui pontent deux atomes de cuivre et fournissent un troisième azote à l'un d'entre eux. Pour chaque cation complexe, la maille élémentaire renferme en outre deux ions de chlorure et 6,5 molécules d'eau désordonnées non liées au métal. Les données des spectroscopies RMN ^1H et infrarouge sont aussi discutées.

Can. J. Chem. Downloaded from www.nrcresearchpress.com by 85.192.166.187 on 09/08/12
For personal use only.

Introduction

In a previous paper (1), we reported on the reactions of niobium and tantalum pentachlorides with 7-azaindole (Haza, structure **I**).[2] Although this ligand can act as a binucleating agent (2–4), the complexes obtained were monomeric and contained unidentate azaindole in the non-deprotonated N7-coordinated form also found for other metals (5–11). With niobium, besides the expected $NbCl_5$(Haza) adduct, the reduced $NbCl_4(Haza)_2$ complex formed, whereas an oxidized species, the unusual azaindolyl-azaindolium ion $(H_2aza\text{-}aza)^+$ (structure **II**),[3] was observed as the counterion in the crystal structures of the $[NbOCl_5]^{2-}$ and $[NbOCl_4(Haza)]^-$ salts. Reduction of $NbCl_5$ to the Nb(IV) state was reported to occur under relatively mild conditions (12), but the oxidation products are usually unknown. The only exception is the NbX_5–pyridine systems (X = Cl, Br) studied by McCarley et al. (13), where oxidation has been shown to lead to the 4-pyridyl-pyridinium cation.

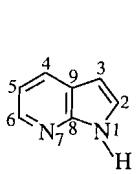

I

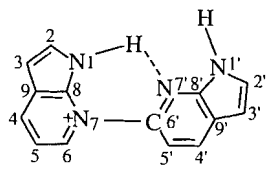

II

The present work was undertaken to better understand the redox process and determine whether $(H_2aza\text{-}aza)^+$ is the only oxidation product formed in the $NbCl_5$–Haza system. On the other hand, this coupled species is a promising ligand and its coordinating ability was tested with $CuCl_2$. In a previous work (9), this salt had been found to react well with azaindole and to generate unusual structural patterns. Furthermore, Cu(II) is known to form di- and polynuclear assemblies where the Cu–Cu separations are consistent with the anticipated "bite" of the donor atoms in Haza-aza. Crystallographic work on the material so obtained revealed tridentate coordination of the $(aza\text{-}aza)^-$ ion and provided the first crystal structure on a halogen-free μ_4-OCu_4 cluster.

Experimental

Reactants and techniques

Anhydrous $CuCl_2$ (K & K), $NbCl_5$ (Aldrich, stored in glove box), and 7-azaindole (Aldrich) were used as received. The reactions involving $NbCl_5$ were carried out in standard Schlenk glassware under dry argon. Benzene was dried by distillation over Na and vigorously outgassed immediately before use. The remaining reactions were run in open air in aqueous solutions or in reagent grade solvents.

[1]Author to whom correspondence may be addressed. Telephone: (514) 343-6446. FAX: (514) 343-7586. E-mail: beauchmp@ere.umontreal.ca

[2]1*H*-Pyrrolo[2,3-*b*]pyridine. Haza = neutral molecule, H_2aza^+ = N7-protonated cation.

[3]$(H_2aza\text{-}aza)^+$ cation (IUPAC name: 7-(1*H*-pyrrolo[2,3-*b*]pyridin-6-yl)-1*H*-pyrrolo[2,3-*b*]pyridin-7-ium); neutral (Haza-aza) (IUPAC name: 7-(1*H*-pyrrolo[2,3-*b*]pyridin-6-yl)-1*H*-pyrrolo[2,3-*b*]pyridin-7-ium-1-ide); $(aza\text{-}aza)^-$ anion (IUPAC name: 7-(1*H*-pyrrolo[2,3-*b*]pyridin-6-yl-1-ide)-1*H*-pyrrolo[2,3-*b*]pyridin-7-ium-1-ide).

Can. J. Chem. Downloaded from www.nrcresearchpress.com by 85.192.166.187 on 09/08/12
For personal use only.

TABLE 1. Crystal data and conditions for data collection

	(Haza-aza)	$[Cu_4O(aza\text{-}aza)_4]Cl_2 \cdot 6.5H_2O$
Formula	$C_{11}H_{10}N_4$	$C_{56}H_{49}Cu_4Cl_2N_{16}O_{7.5}$
Formula weight	234.26	1391.20
Crystal system	Monoclinic	Monoclinic
Space group	$P2_1/c$	$C2/c$
a, Å	10.0247(4)	17.704(10)
b, Å	13.7577(7)	25.240(15)
c, Å	8.4155(3)	14.457(8)
α, deg	90	90
β, deg	102.890(3)	116.14(5)
γ, deg	90	90
V, Å^3	1131.4	5799.4
D_{calc}, g cm^{-3}	1.375	1.593
Z	4	4
Radiation, λ (Å)	CuKᾱ, 1.54178	MoKᾱ, 0.71069
Scan technique	ω	ω/2θ
Scan range, Δω (deg)	0.80° + 0.14 tan θ	0.80° + 0.35 tan θ
Scan speed, deg (ω) min^{-1}	16.5	3.1
F(000)	488	2828
μ, cm^{-1}	6.6	16.2
Crystal size, mm (faces)	0.15 (110–1$\bar{1}$0)	0.14 (20$\bar{1}$–$\bar{2}$01)
	0.23 (100–$\bar{1}$00)	0.61 (010–0$\bar{1}$0)
	0.49 (001–00$\bar{1}$)	0.30 (0$\bar{2}\bar{1}$–021)
Transmission range		0.49–0.81
$2\theta_{max}$, deg	140	50
No. reflections measured	4923	11626
No. unique reflections measured	2217	5106
R_{av}	0.036	0.054
No. observed reflections	1932	2176
Rejection criterion, $I/\sigma(I)$ <	3.0	3.0
T, K	293	223
R^a	0.035	0.051
$R_w{}^a$	0.042	0.052
Goodness-of-fit	3.69	1.42

$^aR = \Sigma||F_o| - |F_c||/\Sigma|F_o|$, $R_w = [\Sigma w(|F_o| - |F_c|)^2/\Sigma w|F_o|^2]^{1/2}$.

Samples of $(H_2aza\text{-}aza)_2[NbOCl_5]$ for quantitative analysis or physical measurements were prepared in the glove box. For analysis, they were hydrolysed with 1 M NH_4OH and the mixture was acidified to pH 1 with 1.5 M HNO_3. Chlorine was then determined as AgCl by potentiometric titration with $AgNO_3$. For Nb analysis, the hydrolysed mixture was heated to dryness on a hot plate, then heated in an oven at 1000°C for 24 h (14, 15), and weighed as Nb_2O_5.

The IR spectra (4000–220 cm^{-1}) were recorded with a Perkin–Elmer 783 spectrophotometer on KBr pellets. ^{1}H NMR spectra were taken in $(CD_3)_2SO$ (CIL) with a Varian VXR-300 spectrometer. They were referenced to the residual solvent signal (δ = 2.50 ppm) and converted to the TMS scale.

Preparative work

$(H_2aza\text{-}aza)_2[NbOCl_5]$

This salt precipitated from acetonitrile when this solvent (i.e., acetonitrile) was used to wash the solid produced by refluxing a 2.4:1 Haza:$NbCl_5$ mixture in benzene, as described earlier (1). Scaling up the reaction gave larger samples, which were characterized by elemental analysis, and infrared and NMR spectroscopies. Anal. calcd. for $NbOCl_5C_{28}H_{22}N_8$: Nb 12.3, Cl 23.4; found: Nb 12.1, Cl 22.9. The IR spectrum was identical with the one obtained with the homogeneous crystalline sample used for X-ray work.

When the same reaction was run with a 2:1 Haza:$NbCl_5$ mixture without heating, the colourless crystals precipitated from acetonitrile were much more moisture sensitive than the material originally isolated. By X-ray diffraction work, the composition was determined to be the same, although the unit cell was different (triclinic, $P\bar{1}$, a = 7.705, b = 9.960, c = 10.729 Å, α = 110.93°, β = 96.67°, γ = 104.69°). The structure of this second polymorph will be described elsewhere.[4]

(Haza-aza)

Benzene (35 mL) was added to a mixture of 1.98 g (7.33 mmol) of $NbCl_5$ and 3.02 g (25.6 mmol) of azaindole both weighed in a dry box. The brown suspension was refluxed for 78 h. The resulting orange-brown precipitate was filtered from the colourless solution and dried in vacuo. At this point, this homogeneous solid contained $NbCl_5$(Haza), $NbCl_4(Haza)_2$, $(H_2aza)^+$, and $(H_2aza\text{-}aza)^+$ (see below). This mixture was suspended in 200 mL of 1 M HCl for 24 h, filtered to removed the precipitated Nb_2O_5, and treated with concentrated NaOH to raise the pH to 10. The emulsion was extracted with four 100-mL portions of CCl_4. On each extraction, a yellow precipitate formed at the phase interface and was removed by filtration. The combined solid fractions were washed with 20 mL CCl_4, dried under vacuum, and identified as neutral (Haza-aza). Yield: 0.34 g. This compound was absent from the CCl_4 solution, which contained only Haza. Yellow crystals of (Haza-aza) were obtained by recrystallization in ethanol and the structure was determined by X-ray diffraction (see below). This reaction was rerun several times with similar yields.

The compound can be obtained as the hydrochloride by adding 1 drop of concentrated HCl to (Haza-aza) (0.03 g) suspended in 20 mL of water. The resulting solution is evaporated to dryness, yielding a light yellow precipitate of $(H_2aza\text{-}aza)Cl$.

[4] J. Poitras and A.L. Beauchamp. Manuscript in preparation.

Can. J. Chem. Downloaded from www.nrcresearchpress.com by 85.192.166.187 on 09/08/12
For personal use only.

$[Cu_4O(aza\text{-}aza)_4]Cl_2 \cdot 6.5H_2O$

A solution of (Haza-aza) (0.198 g; 0.85 mmol) in methanol (25 mL) was added to a solution of $CuCl_2$ (0.064 g; 0.48 mmol) dissolved in wet methanol (10 mL). A small amount of an unidentified light green precipitate formed immediately and was filtered. The clear green solution darkened and dark green crystals (0.035 g) appeared. The same crystals were obtained when the same reaction was run on a smaller scale to obtain larger specimens for the X-ray diffraction study described below.

Crystallographic measurements

The crystallographic work on both compounds was carried out on an Enraf–Nonius CAD-4 diffractometer. For (Haza-aza), monoclinic Laue symmetry and systematic absence ($h0l$, $l \neq 2n$; $0k0$, $k \neq 2n$) uniquely defined $P2_1/c$ as the space group. For $[Cu_4O(aza\text{-}aza)_4]Cl_2 \cdot 6.5H_2O$, the Niggli matrix indicated a C-centred monoclinic cell, which was checked with axial photographs. The systematic absences (hkl, $h + k \neq 2n$; $h0l$, $l \neq 2n$) were consistent with space groups $C2/c$ and Cc. The structure was solved and refined in the centric $C2/c$ space group.

Crystal data are given in Table 1. The intensities were measured as described earlier (16). The raw data were corrected for the effects of Lorentz and polarization for both compounds and for absorption (Gaussian integration) in the case of $[Cu_4O(aza\text{-}aza)_4]Cl_2 \cdot 6.5H_2O$.

For both structures, full-matrix least-squares procedures were used to refine the non-hydrogen atoms anisotropically. The function minimized was $\Sigma w(|F_o| - |F_c|)^2$, with individual weights w based on counting statistics. The scattering curves were from standard sources (17, 18). The anomalous dispersion terms of Cu and Cl were taken from Cromer (19). The calculations were done with NRCVAX (20), SHELX-76 (21), SHELX-86 (22), and local utility programs (23).

Structure resolution and refinement of (Haza-aza)

The structure was solved by the direct methods of SHELX-76 (21). Clear features for 15 non-hydrogen atoms were visible in the E-map. The remaining atoms, including hydrogens, were found from structure factor calculations and ΔF syntheses. All hydrogen atoms were refined isotropically. Residual electron densities in the final ΔF map were between +0.12 and −0.16 e Å^{-3}.

Structure resolution and refinement of $[Cu_4O(aza\text{-}aza)_4]Cl_2 \cdot 6.5H_2O$

The two independent Cu atoms were located by the direct method of SHELX-86 (22). The remaining non-hydrogen atoms, except those of water molecules, were located from subsequent ΔF maps. After refining this model ($R = 0.101$), the ΔF map showed seven residuals (1.4–3.4 e Å^{-3}) between the Cl^- ions. On the basis of separations and heights, it was concluded that these site were partially occupied by disordered uncoordinated water molecules. These water positions were initially assigned occupancies between 0.2 and 1.0, proportional to peak heights. A common isotropic temperature factor was defined for all uncoordinated atoms, namely Cl(1), Cl(2), and water positions O(2)–O(8). This temperature factor was allowed to refine, together with individual occupancies and coordinates. Three chains of two or three water molecules joining two Cl^- ions could be assembled.

(*a*) Cl(2)]-O(2)-O-5-O(2)-[Cl(2), always present, O(5) disordered over two symmetry equivalent sites;

(*b*) Cl(2)]-O(2)-O(3)-O(4)-[Cl(1), not disordered, but present only half of the time;

(*c*) Cl(2)]-O(6)-O(7)-O(8)-[Cl(1), present half of the time and disordered over two orientations. The following idealized occupancy factors, obtained by averaging and normalizing the refined values, were used for the rest of the refinement: O(2) = 1.00; O(3), O(4), O(5) = 0.50; O(6), O(7), O(8) = 0.25. Except for O(3)–O(8), which were refined isotropically, all non-hydrogen atoms were refined anisotropically. The hydrogen atoms in the complex were fixed at idealized positions and recalculated after each cycle. At a late stage, their isotropic temperature factors were refined for two cycles and fixed for the final cycles. Those of water molecules were not located. The general background in the final ΔF map was below ±0.35 e Å^{-3}, except for a few peaks in the range ±|0.5–0.6| eÅ^{-3} near the water molecules and a 0.7 e Å^{-3} residual near Cu(1).

TABLE 2. Refined coordinates (× 10^5) and equivalent isotropic temperature factors (Å^2 × 10^3) for (Haza-aza)

Atom	x	y	z	U_{eq}
N(1)	72 644(10)	−14 286(7)	−11 574(13)	44
C(2)	64 207(14)	−16 485(10)	−26 585(18)	52
C(3)	55 135(13)	−9 245(11)	−32 687(17)	52
C(4)	53 036(13)	7 675(10)	−19 600(17)	51
C(5)	59 299(15)	13 207(10)	−6 167(18)	54
C(6)	69 801(14)	9 500(9)	5 474(16)	47
N(7)	74 464(10)	296(7)	4 562(12)	38
C(8)	68 737(11)	−5 392(8)	−8 517(14)	38
C(9)	57 785(11)	−1 623(9)	−21 094(15)	43
N(1′)	94 141(10)	−22 178(8)	45 852(13)	45
C(2′)	107 183(13)	−23 235(10)	55 185(16)	48
C(3′)	115 421(12)	−16 011(10)	51 984(16)	46
C(4′)	109 093(12)	−1 539(9)	31 527(15)	43
C(5′)	98 160(13)	1 817(9)	19 831(15)	42
C(6′)	85 816(11)	−3 229(8)	17 147(14)	37
N(7′)	83 198(9)	−11 081(7)	25 020(12)	39
C(8′)	94 013(11)	−14 181(8)	36 224(14)	37
C(9′)	107 251(11)	−9 948(9)	39 914(14)	38

The refined coordinates for the two structures are listed in Tables 2 and 3, respectively.[5]

Results and discussion

$NbCl_5$–azaindole reaction

$NbCl_5$ and excess Haza in refluxing benzene have been shown to give a red-brown insoluble mixture in which $NbCl_5$(Haza), $NbCl_4$(Haza)$_2$, and $(H_2aza)^+$ could be identified (1). When the mixture was washed with acetonitrile, two compounds eventually crystallized from this solvent and they were shown by X-ray diffraction to contain the $(H_2aza\text{-}aza)^+$ cation, thereby identifying this species as an oxidation product. However, with the very small samples available, it could not be established whether this N7—C6′ coupled molecule was the only oxidation product.

The same reaction was first repeated several times on a larger scale and, from the aged filtrates, sizable crystalline samples of the $(H_2aza\text{-}aza)_2[NbOCl_5]$ salt were isolated. A single crystal from each batch was mounted on the diffractometer for unit cell determination and it was generally found to be identical with those described earlier (1). However, when a 2:1 Haza:$NbCl_5$ ratio was reacted without heating, more moisture-sensitive crystals with a different unit cell were obtained. These new crystals were found to correspond to a second polymorph, containing the same $(H_2aza\text{-}aza)^+$ and $[NbOCl_5]^{2-}$ ions differently

[5]The supplementary material includes tables of refined temperature factors, hydrogen coordinates, least-squares plane calculations for both structures, distances and angles for the ligands and the hydrogen bonds in the $[Cu_4O(aza\text{-}aza)_4]^{2+}$ ion, stereoview of packing for Haza-aza, and infrared data. Copies of material on deposit may be purchased from: The Depository of Unpublished Data, Document Delivery, CISTI, National Research Council Canada, Ottawa, Canada K1A 0S2.

Tables of hydrogen coordinates and distances and angles for the $[Cu_4O(aza\text{-}aza)_4]^{2+}$ ion have also been deposited with the Cambridge Crystallographic Data Centre and can be obtained on request from The Director, Cambridge Crystallographic Data Centre, University Chemical Laboratory, 12 Union Road, Cambridge, CB2 1EZ, U.K.

Structure factor amplitudes are no longer being deposited and may be obtained directly from the author.

Can. J. Chem. Downloaded from www.nrcresearchpress.com by 85.192.166.187 on 09/08/12
For personal use only.

TABLE 3. Refined coordinates (10^4, Cu, $\times 10^5$) and equivalent isotropic temperature factors ($Å^2 \times 10^3$) for $[Cu_4O(aza\text{-}aza)_4]Cl_2 \cdot 6.5H_2O$

Atom	x	y	z	U_{eq}
Cu(1)	55 692(8)	12 172(5)	17 629(10)	15
Cu(2)	40 512(8)	18 116(5)	13 679(10)	16
Cl(1)	0	383(2)	7500	148
Cl(2)	0	3463(2)	2500	110
N(11)[a]	6447(5)	842(3)	1617(7)	35
C(12)	7219(6)	1053(4)	1741(8)	35
C(13)	7836(7)	672(4)	2037(8)	37
C(14)	7713(7)	−308(5)	2425(9)	41
C(15)	7133(8)	−670(5)	2465(9)	49
C(16)	6305(8)	−542(4)	2147(9)	42
N(17)	6023(5)	−42(3)	1810(6)	28
C(18)	6593(7)	332(4)	1848(9)	33
C(19)	7447(7)	196(4)	2135(9)	37
N(11′)	3654(5)	1104(3)	908(7)	34
C(12′)	2786(6)	990(4)	448(8)	36
C(13′)	2633(7)	466(4)	263(9)	42
C(14′)	3728(7)	−290(4)	546(8)	32
C(15′)	4571(7)	−368(4)	933(8)	35
C(16′)	5116(7)	46(4)	1342(8)	30
N(17′)	4880(5)	557(3)	1357(6)	27
C(18′)	4033(7)	623(4)	963(8)	29
C(19′)	3431(7)	213(4)	587(8)	31
N(21)	3476(5)	2184(4)	95(7)	40
C(22)	3245(7)	1979(5)	−899(8)	39
C(23)	3306(8)	2341(5)	−1547(9)	50
C(24)	3858(7)	3314(5)	−1083(11)	54
C(25)	4165(7)	3663(5)	−314(10)	45
C(26)	4208(6)	3548(4)	615(10)	37
N(27)	3933(5)	3063(3)	791(7)	34
C(28)	3691(7)	2695(5)	26(10)	39
C(29)	3596(7)	2813(5)	−978(10)	48
N(21′)	4203(5)	1924(3)	3563(7)	33
C(22′)	4236(6)	2044(4)	4530(9)	37
C(23′)	4125(7)	2582(5)	4616(9)	41
C(24′)	3868(7)	3334(4)	3276(9)	38
C(25′)	3829(6)	3398(5)	2306(10)	41
C(26′)	3940(6)	2980(4)	1772(9)	34
N(27′)	4055(5)	2470(3)	2120(7)	30
C(28′)	4077(6)	2395(4)	3086(9)	27
C(29′)	4018(7)	2819(5)	3693(9)	38
O(1)	5000	1522(4)	2500	27
O(2)[b]	1987(7)	3361(4)	4073(8)	99
O(3)[b]	1493(9)	983(5)	4983(10)	42
O(4)[b]	522(11)	96(7)	4637(18)	89
O(5)[b]	2228(13)	2279(9)	4237(18)	111
O(6)[b]	221(15)	935(13)	2975(23)	47
O(7)[b]	930(22)	1656(14)	3338(28)	91
O(8)[b]	293(18)	2308(11)	2685(28)	62

[a]The first digit in the atomic symbols corresponds to ligand number (1 or 2), the second to position in the ring as defined in structure **II**.

[b]Disordered water molecules. Occupancies are: O(2) = 1.00; O(3), O(4), O(5) = 0.50; O(6), O(7), O(8) = 0.25 (see text).

packed in the cell.[4] Both polymorphs showed the same IR and ^1H NMR spectra, to be discussed below.

In a second step, the raw reaction product was examined for other azaindole-derived products. To this end, after refluxing the $NbCl_5$–azaindole mixture, the solvent was completely removed under vacuum. The solid phase was stirred in dilute aqueous HCl in open air, whereupon all niobium species were quantitatively oxidized and (or) hydrolysed to Nb_2O_5. The insoluble oxide precipitate, which contained no organic matter, was removed by filtration, whereas azaindole and any derived compounds remained as protonated cations in the aqueous phase. Evaporation of this water solution to dryness led to a light yellow solid, whose ^1H NMR spectrum in $(CD_3)_2SO$ showed signals for only two compounds: the strongest set originated from the $(H_2aza)^+$ cation, whereas the remaining peaks were those observed above for the $(H_2aza\text{-}aza)^+$ ion. It was then concluded that the N7—C6′ coupled species is the only oxidation product formed.

Finally, by raising the pH of the above aqueous phase to 10 with NaOH, the cationic species deprotonated and an emulsion of neutral Haza and (Haza-aza) formed. By extraction with CCl_4, Haza was transferred into the organic phase, leaving a light yellow layer of solid (Haza-aza), which was isolated and recrystallized in ethanol. The X-ray structure (see below) confirms that it is the deprotonated form of the $(H_2aza\text{-}aza)^+$ cation described earlier (1).

Although pure (Haza-aza) can be obtained, the reaction is very inefficient in terms of both the ligand and $NbCl_5$. This was anticipated to some extent from the studies of McCarley et al. with neat pyridine (13). These authors indeed found that 30% of the $NbCl_5$ ended up are unreduced $NbCl_5(py)$ (eq. [1]), whereas the redox pathway (70%) required four ligands to form two reduced $NbCl_4(py)_2$ molecules for each pyridyl-pyridinium species obtained (eq. [2]). The coupling process liberated a proton that was quenched by the coupled product itself, becoming a $(Hpy\text{-}py)^{2+}$ cation. For the $NbCl_5$–Haza reaction, a solvent (benzene) had to be used, in which the products were all insoluble. The $(H_2aza)^+$ ion was identified as a major component of the raw product, suggesting that the proton liberated in the coupling process was quenched by an extra Haza molecule instead of the $(H_2aza\text{-}aza)^+$ ion (eq. [3]). The subsequent tests were run using a 7:2 Haza:$NbCl_5$ ratio and special care was taken to isolate all the (Haza-aza) formed, in order to determine the % $NbCl_5$ having been reduced. A series of reactions gave a range of 26–40%, that is, much below the 70% value observed with pyridine.

[1] $NbCl_5 + L \rightarrow NbCl_5(L)\downarrow$

[2] $2\ NbCl_5 + 6\ py \rightarrow 2\ NbCl_4(py)_2\downarrow + (Hpy\text{-}py)Cl_2$

[3] $2\ NbCl_5 + 7\ Haza \rightarrow 2\ NbCl_4(Haza)_2\downarrow + (H_2aza\text{-}aza)^+ + (H_2aza)^+ + 2\ Cl^-$

Since the $NbCl_5(Haza)$ adduct precipitates quantitatively as soon as $NbCl_5$ and Haza are mixed, its very low solubility was first considered as a possible reason for this poor reduction efficiency. However, this explanation was not retained since longer refluxing time produced no detectable improvement. A more likely possibility is that some $NbCl_5$ is used to quench the Cl^- ions liberated in reaction [3] by forming $[NbCl_6]^-$, which would then act as the counterion for the cationic species present. Two qualitative observations support this assumption: $(H_2aza)[NbCl_6]$ is very insoluble in benzene, whereas $(H_2aza\text{-}aza)^+$ is undoubtedly extracted as the $[NbCl_6]^-$ salt when the raw reaction product is washed with acetonitrile, since the precipitate eventually appearing in this solvent is the slightly hydrolyzed $(H_2aza\text{-}aza)_2[NbOCl_5]$ compound. Therefore, the redox pathway is probably better represented by reaction [4], where half of the $NbCl_5$ is wasted in forming $[NbCl_6]^-$ counterions. If this equation applies, the redox pathway would represent 52–80% of the reaction with azaindole, that is, a range close to the

TABLE 4. (*a*) Distances (Å) and (*b*) angles (°) for (Haza-aza)

(*a*) Distances

Atoms	Distance (Å)	Atoms	Distance (Å)
N(1)—C(2)	1.388(2)	N(1′)—C(2′)	1.375(2)
N(1)—C(8)	1.327(2)	N(1′)—C(8′)	1.365(2)
C(2)—C(3)	1.369(2)	C(2′)—C(3′)	1.357(2)
C(3)—C(9)	1.416(2)	C(3′)—C(9′)	1.424(2)
C(4)—C(5)	1.391(2)	C(4′)—C(5′)	1.379(2)
C(4)—C(9)	1.380(2)	C(4′)—C(9′)	1.388(2)
C(5)—C(6)	1.367(2)	C(5′)—C(6′)	1.393(3)
C(6)—N(7)	1.358(2)	C(6′)—N(7′)	1.324(3)
N(7)—C(8)	1.368(2)	N(7′)—C(8′)	1.338(3)
C(8)—C(9)	1.441(2)	C(8′)—C(9′)	1.419(3)
N(7)—C(6′)	1.454(2)	N(1)[a]···H(1′)	1.859(9)
N(1′)···N(1)[a]	2.811(2)		

(*b*) Angles

Atoms	Angle (°)	Atoms	Angle (°)
C(2)—N(1)—C(8)	103.36(10)	C(2′)—N(1′)—C(8′)	107.83(10)
N(1)—C(2)—C(3)	113.69(12)	N(1′)—C(2′)—C(3′)	110.64(12)
C(2)—C(3)—C(9)	105.87(12)	C(2′)—C(3′)—C(9′)	106.98(11)
C(5)—C(4)—C(9)	118.61(13)	C(5′)—C(4′)—C(9′)	117.84(11)
C(4)—C(5)—C(6)	120.94(13)	C(4′)—C(5′)—C(6′)	119.00(11)
N(7)—C(6)—C(5)	121.83(12)	N(7)—C(6′)—N(7′)	115.24(10)
C(6)—N(7)—C(8)	119.40(10)	N(7)—C(6′)—C(5′)	118.33(10)
C(6)—N(7)—C(6′)	119.56(10)	N(7′)—C(6′)—C(5′)	126.43(11)
C(8)—N(7)—C(6′)	121.00(10)	C(6′)—N(7′)—C(8′)	113.13(10)
N(1)—C(8)—N(7)	126.46(10)	N(1′)—C(8′)—N(7′)	125.04(10)
N(1)—C(8)—C(9)	113.51(10)	N(1′)—C(8′)—C(9′)	108.45(10)
N(7)—C(8)—C(9)	119.96(10)	N(7′)—C(8′)—C(9′)	126.49(10)
C(3)—C(9)—C(4)	137.16(12)	C(3′)—C(9′)—C(4′)	136.89(12)
C(3)—C(9)—C(8)	103.57(11)	C(3′)—C(9′)—C(8′)	106.07(10)
C(4)—C(9)—C(8)	119.23(11)	C(4′)—C(9′)—C(8′)	117.04(11)
		N(1′)—H(1′)···N(1)[a]	167.5(8)

[a] $x, -1/2 - y, 1/2 + z$.

70% value reported for pyridine. Nevertheless, if the reaction takes place by attack on the coordinated ligand in the $NbCl_5(L)$ adduct, as suggested by McCarley et al. (13), the reason for the redox process not going to completion with either pyridine or azaindole is still unclear, since in both cases a large excess of free ligand is still available.

[4] $4\ NbCl_5 + 7\ Haza \rightarrow 2\ NbCl_4(Haza)_2\downarrow + (H_2aza\text{-}aza)[NbCl_6]\downarrow + (H_2aza)[NbCl_6]\downarrow$

Crystal structure of (Haza-aza)

The molecule (Fig. 1) contains two azaindole units coupled via N(7)—C(6′), as reported for $(H_2aza\text{-}aza)^+$. Distances and angles are listed in Table 4. For the cationic form, various structural modifications with respect to azaindole, especially in the azaindolium ring, were pointed out (1). Besides these modifications, changes due to deprotonation are noted here for the neutral form, mainly on the angles in the five-membered ring: at the deprotonation site, the C(2)—N(1)—C(8) angle is reduced by 5.2°, whereas those at C(8), C(9), and C(2) undergo changes of +5.3°, −2.3°, and +3.0°, respectively, keeping the ring planar. Some distortion is transmitted to the six-membered ring via C(8), resulting in variations of −2.0° at C(8) and +2.5° at N(7). As the H(1) proton of $(H_2aza\text{-}aza)^+$ has been removed, no intramolecular N(1)—H(1)···N(7′) bond can form here and the

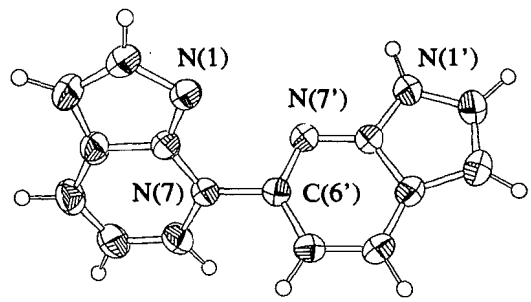

FIG. 1. ORTEP drawing of the (Haza-aza) molecule. Numbering sequence around the rings is the same as in structure **II**. Ellipsoids correspond to 50% probability. Hydrogens are shown as spheres of arbitrary size.

two azaindole halves are not longer coplanar (dihedral angle ~61°) (Table S-3).[5] Differences of ~2° on the angles around C(6′) are likely related to the conformational difference: any strain due to ring coplanarity in $(H_2aza\text{-}aza)^+$ is removed in the neutral molecule, whereas distortion could result from constraints imposed by packing of the two non-coplanar units in (Haza-aza).

Distances to the weighted least-squares planes are given in Table S-3.[5] In both units, most of the distortion can be regarded

Can. J. Chem. Downloaded from www.nrcresearchpress.com by 85.192.166.187 on 09/08/12
For personal use only.

TABLE 5. ^{1}H NMR data[a]

	Haza	$(H_2aza\text{-}aza)[NbOCl_5]$[b]	$(H_2aza\text{-}aza)Cl$	(Haza-aza)
H1	11.65	12.72	13.16 (+1.54)	
H1′		12.41	12.33 (+0.69)	12.04 (+0.40)
H2	7.462	7.88	7.871 (+0.41)	7.689 (+0.23)
H2′		7.82	7.821 (+0.36)	7.665 (+0.20)
H3	6.443	7.08	7.072 (+0.63)	6.668 (+0.22)
H3′		6.74	6.736 (+0.29)	6.631 (+0.19)
H4	7.943	8.94	8.936 (+0.99)	8.349 (+0.41)
H4′		8.44	8.443 (+0.50)	8.252 (+0.31)
H5	7.031	7.80	7.793 (+0.76)	7.142 (+0.11)
H5′		7.70	7.691 (+0.66)	8.054 (+1.02)
H6	8.218	8.98	8.961 (+0.74)	8.500 (+0.28)
^3J(H2–H3)	3.24	2.8	3.5	2.4
^3J(H2′–H3′)		3.3	3.3	3.0
^3J(H2–H1)	2.44	2.8	2.2	
^3J(H2′–H1′)		—[c]	—[c]	1.0
^4J(H3–H1)	1.12	—[c]	1.2	
^4J(H3′–H1′)		1.6	1.8	1.8
^3J(H4–H5)	7.92	7.8	7.8	7.3
^3J(H4′–H5′)		8.2	8.3	8.4
^4J(H4–H6)	1.53	—[c]	0.9	—[c]
^3J(H5–H6)	4.80	6.2	6.3	6.5

[a]In $(CD_3)_2SO$, 300 MHz, δ in ppm (vs. TMS), J in Hz, Δδ values from free Haza within parentheses.
[b]90 MHz.
[c]Not completely resolved.

as a slight bend of the two rings about the common bond, by 2.1° for the azaindolyl and 3.2° for the azaindolium unit.

Packing in the unit cell (Fig. S-1)[5] is controlled to a large extent by ring stacking and an intermolecular N(1′)—H(1′)···N(1) hydrogen bond.

Infrared and ^{1}H nuclear magnetic resonance data

A list of infrared frequencies and tentative assignments for $(H_2aza\text{-}aza)_2[NbOCl_5]$, $(H_2aza\text{-}aza)Cl$, and (Haza-aza) are provided as supplementary material.[5]

For the $[NbOCl_5]^{2-}$ salt, a strong and sharp band, missing in the spectrum of the chloride, is observed at 919 cm^{-1} for Nb═O stretching. Between 250 and 350 cm^{-1}, where the organic part makes no contribution, the spectrum contains two very strong ν(Nb—Cl) peaks at 300 and 315 cm^{-1}. Similar frequencies have been reported for these modes in the Cs^+ salt (24). Except for these bands, the spectra of $(H_2aza\text{-}aza)_2[NbOCl_5]$ and $(H_2aza\text{-}aza)Cl$ are essentially superimposable.

The $[H_2aza\text{-}aza]^+$ ion shows features similar to those of azaindole itself (3, 6), but the presence of two nonequivalent units leads to band splitting or broadening throughout the spectrum, as well as small shifts that will not be discussed here. In earlier studies (1, 9, 10), the 350–500 cm^{-1} region, where azaindole itself exhibits well-defined out-of-plane ring vibrations at 428 and 419 cm^{-1}, was found to be sensitive to complexation and useful for identification purposes. The present coupled cation shows five components (near 505, 480, 447, 431, and 349 cm^{-1}, respectively), including these two modes for each type of azaindole unit and probably a new vibration involving the connecting N7—C6′ bond.

In (Haza-aza), the very broad ν(N—H) band of $(H_2aza\text{-}aza)^+$ at ~3200 cm^{-1} is replaced by seven sharper peaks between 2765 and 3115 cm^{-1}, including ν(C—H) components near 3100 cm^{-1}, the ν(N—H) mode near 2900 cm^{-1}, and combinations or overtones. This neutral form can be identified from the five fingerprint components at 520, 478, 440, 420, and 362 cm^{-1}, respectively, and from other small shifts with respect to $(H_2aza\text{-}aza)^+$ (Table S-12).[5]

The ^{1}H NMR data for Haza-aza and the $(H_2aza\text{-}aza)^+$ salts are compared with those of 7-azaindole in Table 5. Doublets of doublets for the mutually coupled H4, H5, and H6 protons in the azaindolium part are assigned on the basis of their relative positions and coupling constants (6, 25). In the other unit, the absence of H6′ leads to doublets for H4′ and H5′. When the five-membered ring is N-protonated, the already coupled C—H protons appear as doublets of doublets because of extra coupling to N—H. Thus, for (Haza-aza), H2′ and H3′ can be differentiated from H2 and H3, respectively, since the latter belong to the deprotonated unit and appear as simple doublets. In the case of $(H_2aza\text{-}aza)^+$, where both units are protonated, the lower-field signal is assumed to originate for the azaindolium part, since this is the trend noted for the six-membered rings.

Can. J. Chem. Downloaded from www.nrcresearchpress.com by 85.192.166.187 on 09/08/12
For personal use only.

TABLE 6. (*a*) Interatomic distances and (*b*) bond angles in $[Cu_4O(aza\text{-}aza)_4]Cl_2 \cdot 6.5H_2O$

(*a*) Distances

Atoms	Distance (Å)	Atoms	Distance (Å)
Cu(1)—N(11)	1.909(10)	Cu(2)–N(11′)	1.927(9)
Cu(1)—N(17′)	1.995(9)	Cu(2)—N(21)	1.912(9)
Cu(1)—N(21′)[a]	1.932(9)	Cu(2)—N(27′)	1.984(9)
Cu(1)—O(1)	1.921(4)	Cu(2)—O(1)	1.901(4)

(*b*) Angles (°)

Atoms	Angle (°)	Atoms	Angle (°)
N(11)—Cu(1)—N(17′)	88.6(4)	N(21)—Cu(2)—N(27′)[a]	89.3(4)
N(11)—Cu(1)—N(21′)	99.4(4)	N(21)—Cu(2)—N(11′)	99.5(4)
N(17′)—Cu(1)—N(21′)	150.0(4)	N(11′)—Cu(2)—N(27′)[a]	151.4(4)
N(11)—Cu(1)—O(1)	155.7(3)	N(21)—Cu(2)—O(1)	155.8(3)
N(17′)—Cu(1)—O(1)	95.5(3)	N(27′)[a]—Cu(2)—O(1)	93.6(3)
N(21′)—Cu(1)—O(1)	90.0(3)	N(11′)—Cu(2)—O(1)	89.5(3)
Cu(1)—O(1)—Cu(2)	99.0(3)	Cu(1)—O(1)—Cu(2)[a]	98.7(3)
Cu(1)—O(1)—Cu(1)[a]	132.8(3)	Cu(2)—O(1)—Cu(2)[a]	134.8(3)

[a] 1 − *x*, *y*, 1/2 + *z*.

The positive charge on $(H_2aza\text{-}aza)^+$ brings all signals downfield from those of free azaindole. Since this charge is carried mainly by the azaindolium part, the displacements are larger in this unit than in the other (Table 5). The shifts follow a pattern similar to those observed when azaindole is N7-methylated (25) or N7-coordinated to CH_3Hg^+ (6) or $NbCl_5$ (1), but they are ~50% greater. The charge also increases the acidity of the N—H protons, which exhibit individual signals shifted downfield by ~0.8 (azaindolyl) and ~1.3 ppm (azaindolium) with respect to azaindole.

On the basis of the X-ray work on (Haza-aza), the proton lost by $(H_2aza\text{-}aza)^+$ is removed from the azaindolium part. The molecule likely adopts the same structure in solution, since most of the azaindolium protons occur ~0.5 ppm upfield, whereas the effect is generally small (~0.15 ppm) in the other unit. However, H5′ behaves differently, being displaced 0.35 ppm *downfield*: it is not clear whether this reflects a charge redistribution or the conformational difference between (Haza-aza) and $(H_2aza\text{-}aza)^+$. As expected, the N—H proton left in (Haza-aza) is less acidic than it was in $(H_2aza\text{-}aza)^+$, as evidenced from the ~0.3 ppm upfield shift.

(Haza-aza) as ligand

Interesting coordinating capabilities are anticipated for the anion derived from (Haza-aza). The N(1′) and N(7′) sites in the azaindolyl unit are well positioned to bridge a pair of metal atoms, as observed for azaindole itself. With the conformation shown in Fig. 1, the other unit would mainly produce steric hindrance, but further coordination via N(1) would become possible by rotation about the N(7)—C(6′) bond to bring the two units roughly coplanar, as they are in $(H_2aza\text{-}aza)_2[NbOCl_5]$. A test was run with $CuCl_2$ in methanol under the conditions used for earlier studies on the $CuCl_2$–Haza system (9). Dark-green crystals were obtained, whose composition was found to be $[Cu_4O(aza\text{-}aza)_4]Cl_2 \cdot 6.5H_2O$ from X-ray diffraction work.

The $[Cu_4O(aza\text{-}aza)_4]^{2+}$ cation (Fig. 2) contains a μ_4-OCu_4 unit surrounded by four tridentate $(aza\text{-}aza)^-$ ligands. Unlike most compounds containing this core, the cluster is halide-free and Cl^- simply acts as the counterion. Selected distances and angles are listed in Table 6.

For a series of $Cu_4OCl_6L_4$ compounds, Norman et al. (26) noticed that the Cu_4O tetrahedra retain a relatively constant geometry (Cu-O-Cu angle in the 105–113° range). The particular donor arrangement in $(aza\text{-}aza)^-$ and the steric requirements of the large rings result here in a large distortion of the tetrahedron: the Cu-O-Cu angles range from 99.0(3)° to 134.8(3)° (mean 116.3(3)°). However, the Cu—O bond lengths seem to be rather insensitive to distortion: our values (1.921(4) and 1.901(4) Å) agree with those found in $Cu_4OCl_6(Haza)_4$ (mean 1.918 Å) (9) and relates systems from the literature (1.869–1.939 Å, mean 1.908 Å) (26).

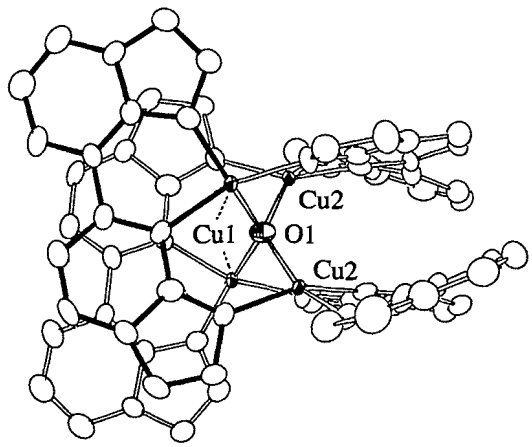

FIG. 2. ORTEP drawing of the $[Cu_4O(aza\text{-}aza)_4]^{2+}$ cation. The central oxygen atom lies on a crystallographic twofold axis running horizontally in the plane of the figure. Two symmetry-equivalent ligands of type 1 (first digit in atomic symbol, one shown with black bonds) lie on the left-hand side, ligands of type 2 are seen approximately edgewise on the right-hand side. Individual atoms are labelled as in structure **II**. Ellipsoids correspond to 50% probability. Hydrogens are omitted for simplicity.

The coordination sphere of copper is best described as a tetrahedrally distorted square plane with *trans* angles between 150.0(4)° and 155.7(3)°. The distortion is further reflected by distances of 0.24–0.61 Å between the N donors and the least-squares planes through $CuON_3$ (Table S-9).[5] The Cu—N distances to the pyridine-type N(17′) and N(27′) atoms (mean 1.990 Å) compare well with those involving the corresponding

Can. J. Chem. Downloaded from www.nrcresearchpress.com by 85.192.166.187 on 09/08/12
For personal use only.

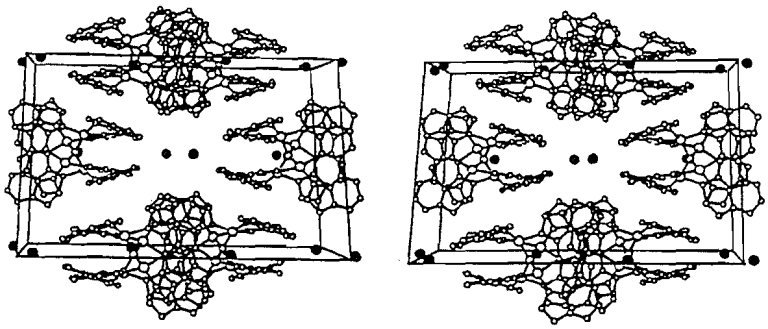

FIG. 3. Stereoview of the unit cell of $[Cu_4O(aza\text{-}aza)_4]Cl_2 \cdot 6.5H_2O$ down the *c* axis (*a* vertical and *b* horizontal). Cl^- ions are shown as black spheres. The disordered water molecules are not shown.

donor atom in $Cu_4OCl_6(Haza)_4$ (mean 1.998 Å) (9), but they are appreciably longer than those to the pyrrole N(11), N(11′), N(21), N(21′) atoms (mean 1.920 Å). This is consistent with the pyridine rings having a greater steric demand than the pyrrole rings, as suggested by the difference found between complexes with pyridines (mean 1.98 Å) (27, 28) and with imidazoles (mean 1.94 Å) (26, 29).

Distances and angles in the coordinated tridentate ligands are listed in Table S-7.[5] Any effect of coordination on bond lengths is obscured by the relatively high esd's (0.01–0.02 Å). Deprotonation of the azaindolyl units reduces the C(*n*2′)-N(*n*1′)-C(*n*8′) angles by 3.4° and produces an equivalent increase of the adjacent N(*n*1′)-C(*n*8′)-C(*n*9′) angles. Variations of ~3° with respect to (Haza-aza) are also noted around C(*n*6′) and N(*n*7), at the junction of the two units, where steric strain imposed by coordination can be absorbed. The two units make a dihedral angle of ~25° in ligand 1 and ~29° in ligand 2 (Table S-8).[5] Each of these units can be regarded as individually planar five- and six-membered rings with a slight bend of 2°–4° about the common C(*n*8)—C(*n*9) or C(*n*8′)—C(*n*9′) bonds (Table S-9).[5]

In the packing diagram (Fig. 3), the $[Cu_4O(aza\text{-}aza)_4]^{2+}$ ions are so oriented that rings in adjacent cations are parallel. There are two types of Cl^- ions, both lying on crystallographic twofold axes: Cl(1) occupies channels parallel to *c* through the origin and the middle of the *ab* face, whereas Cl(2) is nested between consecutive complex ions along *c*. These anions are connected by disordered chains of two or three water molecules (not shown in Fig. 4, data in Table S-10[5]).

In the infrared spectrum of $[Cu_4O(aza\text{-}aza)_4]Cl_2 \cdot 6.5H_2O$,[5] a new strong band is found at 557 cm^{-1} for Cu—O stretching in the Cu_4O core (9, 27, 30, 31). Four components at 330, 310, 300, and 290 cm^{-1} are assigned to Cu–N stretching, a strong band at ~290 cm^{-1} being present for $[CuL_4]^{2+}$ complexes with pyridines (32) and imidazoles (32–37). Since the ligands are deprotonated, the high-frequency region contains no ν(N—H) bands: the strong and broad feature at 3320 cm^{-1} is due to ν(O—H) of the hydrogen-bonded water molecules. Other changes due to ligand deprotonation and coordination are found throughout the spectrum. The five fingerprint bands occur at 510, 475, 446, 430, and 352 cm^{-1}, respectively.

Concluding remarks

Although the N7—C6′-coupled (Haza-aza) molecule is the only oxidized species generated by the redox reaction between $NbCl_5$ and 7-azaindole, the formation of other niobium- and azaindole-containing products renders the conversion inefficient. Efforts are being made to circumvent this problem and devise more practical routes to this ligand, whose potential as assembling ligand is well illustrated by the unusual oxotetracopper cluster stabilized here. These coordinating abilities are being examined for other metal centres and the reactivity of $NbCl_5$ with various N-heterocycles is underway to better understand the coupling mechanism.

Acknowledgments

We wish to thank M. Simard and F. Bélanger-Gariépy for their assistance in solving the X-ray structures. The support of the Natural Sciences and Engineering Research Council of Canada is gratefully acknowledged.

1. J. Poitras and A.L. Beauchamp. Can. J. Chem. **72**, 1675 (1994).
2. S.M. Peng and Y.N. Lin. Acta Crystallogr. Sect. C: Cryst. Struct. Commun. **C42**, 1725 (1986); S.M. Peng and C.H. Lai. J. Chin. Chem. Soc. (Taipei), **35**, 325 (1988).
3. F. Allaire and A.L. Beauchamp. Inorg. Chim. Acta, **156**, 241 (1989).
4. J.J.H. Edema, S. Gambarotta, A. Meetsma, F. Van Bolhuis, A.L. Spek, and W.J.J. Smeets. Inorg. Chem. **29**, 2147 (1990); L.A. Oro, M.A. Ciriano, B.E. Villaroya, A. Tiripicchio, and F.J. Lahoz. J. Chem. Soc. Dalton Trans. 1891 (1985); F.A. Cotton, D.G. Lay, and M. Millar. Inorg. Chem. **17**, 186 (1978).
5. P. Dufour, Y. Dartiguenave, M. Dartigeunave, N. Dufour, A.M. Lebuis, F. Bélanger-Gariépy, and A.L. Beauchamp. Can. J. Chem. **68**, 193 (1990).
6. N. Dufour, A.M. Lebuis, M.C. Corbeil, A.L. Beauchamp, P. Dufour, Y. Dartiguenave, and M. Dartiguenave. Can. J. Chem. **70**, 2914 (1992).
7. F.A. Cotton and T.R. Felthouse. Inorg. Chem. **20**, 600 (1981).
8. F. Allaire. Ph.D. Thesis, Université de Montréal, Montréal, Canada. 1987.
9. J. Poitras and A.L. Beauchamp. Can. J. Chem. **70**, 2846 (1992).
10. A.M. Lebuis and A.L. Beauchamp. Can. J. Chem. **71**, 2060 (1993); Acta Crystallogr. Sect. C: Cryst. Struct. Commun. **C50**, 882 (1994).
11. W.S. Sheldrick. Z. Naturforsch. B: Chem. Sci. **37**, 653 (1982).
12. L.G. Hubert-Pfalzgraf, M. Postel, and J.G. Riess. *In* Comprehensive coordination chemistry. *Edited by* G. Wilkinson, R.D. Gillard, and J.A. McCleverty. Pergamon Press, New York. 1987. Chap. 34.
13. R.E. McCarley, B.G. Hughes, J.C. Boatman, and B.A. Torp. Adv. Chem. Ser. **37**, 243 (1963).
14. G.W.A. Fowles, D.J. Tidmarsh, and R.A. Walton. Inorg. Chem. **8**, 631 (1969).
15. N. Vuletic and C. Djordjevic. J. Chem. Soc. Dalton Trans. 550 (1973).
16. F. Bélanger-Gariépy and A.L. Beauchamp. J. Am. Chem. Soc. **102**, 3461 (1980).
17. International tables for X-ray crystallography. Vol. III. Kynoch Press, Birmingham, England. 1968.
18. D.T. Cromer and J.T. Waber. Acta Crystallogr. **18**, 104 (1965); R.F.

Can. J. Chem. Downloaded from www.nrcresearchpress.com by 85.192.166.187 on 09/08/12
For personal use only.

Stewart, E.R. Davidson, and W.T. Simpson. J. Chem. Phys. **42**, 3175 (1965).
19. D.T. Cromer. Acta Crystallogr. **18**, 17 (1965).
20. E.J. Gabe, Y. Le Page, J.P. Charland, and F.L. Lee. J. Appl. Crystallogr. **22**, 384 (1989).
21. G. Sheldrick. SHELX-76, Crystallographic program system. Cambridge University, U.K. 1976.
22. G. Sheldrick, SHELX-86, Crystallographic program system. Institute für Anorganische Chemie der Universität Gottingen, Gottingen, Germany. 1986.
23. M. Authier-Martin and A.L. Beauchamp. Can. J. Chem. **55**, 1213 (1977).
24. D. Brown. J. Chem. Soc. **5**, 4944 (1964).
25. R.H. Cox and S. Sankar. Org. Magn. Reson. **14**, 150 (1980).
26. R.E. Norman, N.J. Rose, and R.E. Stenkamp. Acta Crystallogr. Sect. C: Cryst. Struct. Commun. **C45**, 1707 (1989).
27. N.S. Gill and M. Sterns. Inorg. Chem. **9**, 1619 (1970).
28. B.T. Kilbourn and J.D. Dunitz. Inorg. Chim. Acta, **1**, 209 (1967).
29. A. Erdonmez, J.H. van Diemen, R.A.G. de Graaff, and J. Reedijk. Acta Crystallogr. Sect. C: Cryst. Struct. Commun. **C46**, 402 (1990).
30. R.C. Dickinson, F.T. Helm, W.A. Baker, Jr., T.D. Black, and W.H. Watson, Jr. Inorg. Chem. **16**, 1530 (1977).
31. R. Belford, D.E. Fenton, and M.R. Truter. J. Chem. Soc. Dalton Trans. 2345 (1972).
32. J. Reedijk. Recl. Trav. Chim. Pays-Bas, **88**, 1451 (1969).
33. D.M.L. Goodgame, M. Goodgame, P.J. Hayward, and G.W. Rayner-Canham. Inorg. Chem. **7**, 2447 (1968).
34. D.M.L. Goodgame, M. Goodgame, and G.W. Raymer-Canham. Inorg. Chim. Acta, **3**, 399 (1969); **3**, 406 (1969).
35. W.J. Eilbeck, F. Holmes, C.E. Taylor, and A.E. Underhill. J. Chem. Soc. A, 128 (1968).
36. B.C. Cornilsen and K. Nakamoto. J. Inorg. Nucl. Chem. **36**, 2467 (1974).
37. J.B. Hodgson, G.C. Percy, and D.A. Thornton. J. Mol. Struct. **66**, 81 (1980).

Can. J. Chem. Downloaded from www.nrcresearchpress.com by 85.192.166.187 on 09/08/12
For personal use only.

AM1 calculational and experimental evidence that a β-nitroxyl group significantly enhances the thermodynamic and kinetic acidities of ketones

NICK HENRY WERSTIUK[1] AND CHANDRA DEO ROY

Department of Chemistry, McMaster University, Hamilton, ON L8S 4M1, Canada

Received June 24, 1994

NICK HENRY WERSTIUK and CHANDRA DEO ROY. Can. J. Chem. **72**, 2348 (1994).

The kinetics of NaOD-catalysed H/D exchange of 3,3,5,5-tetramethylcyclohexanone (**1**), 1-hydroxy-4-oxo-2,2,6,6-tetramethylpiperidine (**2**), 4-oxo-2,2,6,6-tetramethylpiperidine-1-oxyl (**3**), 9-hydroxynorpseudopelletierine (**4**), and norpseudopelletierine-9-oxyl (**5**) have been studied in 60:40 dioxane–D_2O (v/v) at 25.0°C. The second-order rate constants are 9.20×10^{-3}, 6.39×10^{-2}, 1.59, 2.20×10^{-2}, and 5.67×10^{-1} L mol^{-1} s^{-1} for **1**, **2**, **3**, **4**, and **5**, respectively. Gas-phase enthalpies of ionization (the values are 363.0, 359.4, 352.0, 360.7, and 354.1 kcal mol^{-1} for **1**, **2**, **3**, **4**, and **5**, respectively) calculated with AM1 correlate with the relative rates of enolization. Thus replacement of the β-hydroxylamino groups of **2** and **4** with a nitroxyl group produces sizable increases in the kinetic and thermodynamic acidities of the hydrogens α to the carbonyl group.

NICK HENRY WERSTIUK et CHANDRA DEO ROY. Can. J. Chem. **72**, 2348 (1994).

Opérant à 25°C, dans un mélange 60 : 40 de dioxane–D_2O (v/v), on a étudié la cinétique de l'échange H/D, catalysé par le NaOH, des 3,3,5,5-tétraméthylcyclohexanone (**1**), 1-hydroxy-4-oxo-2,2,6,6-tétraméthylpipéridine (**2**), 4-oxo-2,2,6,6-tétraméthylpipéridine-1-oxyl (**3**), 9-hydroxynorpseudopelletiérine (**4**) et norpseudopelletiérine (**5**). Les constantes de vitesse du deuxième ordre sont $9{,}20 \times 10^{-3}$, $6{,}39 \times 10^{-2}$, 1,59, $2{,}20 \times 10^{-2}$ et $5{,}67 \times 10^{-1}$ L mol^{-1} s^{-1} respectivement pour les composés **1**, **2**, **3**, **4** et **5**. Les enthalpies d'ionisation en phase gazeuse (les valeurs sont de 363,0, 359,4, 352,0, 360,7 et 354,1 kcal mol^{-1} respectivement pour les composés **1**, **2**, **3**, **4** et **5**) calculées par la méthode AM1 permettent d'établir une bonne corrélation avec les vitesses relatives d'énolisation. Ainsi, le remplacement des groups β-hydroxylamino des composés **2** et **4** par une groupe nitroxyle provoque une augmentation importante des acidités cinétiques et thermodynamiques des hydrogènes en α du groupe carbonyle.

[Traduit par la rédaction]

Introduction

While a great deal of research work has been carried out to define the factors, e.g., orbital alignment, steric, torsional, and polar effects, that determine the rates of base-catalyzed α enolization of ketones (1–4), there have been no reports detailing the effect of remote heteroatom-centered radicals on the kinetic and thermodynamic acidities of carbonyl compounds. Our longstanding interest in establishing how remote polar substituents enhance the rates of α and β(homoenolization) enolization of ketones and in using semiempirical calculations to predict and understand variations in the thermodynamic acidities of carbon and oxygen acids (5, 6) motivated us to undertake a calculational and kinetic study of the base-catalysed enolization of five ketones. The group included 3,3,5,5-tetramethylcyclohexanone (**1**), 1-hydroxy-4-oxo-2,2,6,6-tetramethylpiperidine (**2**), 4-oxo-2,2,6,6-tetramethylpiperidine-1-oxyl (**3**), 9-hydroxynorpseudopelletierine (**4**), and norpseudopelletierine-9-oxyl (**5**), of which two, **3** and **5**, have a polar nitroxyl group R_2N-O· located β to the enolizable centers.[2] That the nitroxyl group is electron withdrawing is well documented in the literature (7). We chose to study these compounds because the enthalpies of ionization (ΔH_i's) calculated with AM1 (8) indicated that **3** and **5** should enolize much more quickly than **1**, **2**, and **4**. In this communication we report and discuss the results of calculational and experimental studies on **1**–**5**.

The enthalpies of ionization (Table 1) were obtained from the calculated heats of formation of **1**–**5** and their corresponding enolates.[3] The geometrical structures of the optimized geometries of 1-hydroxy-4-oxo-2,2,6,6-tetramethylpiperidine (**2**), 4-oxo-2,2,6,6-tetramethylpiperidine-1-oxyl (**3**), 9-hydroxynorpseudopelletierine (**4**), and norpseudopelletierine-9-oxyl (**5**) (**2c**, **3tb**, **4cc**, and **5cc**) and their enolates (**2c-enolate**, **3tb-enolate**, **4cc-enolate**, and **5cc-enolate**) are given in Fig. 1. It is seen that the nitroxyl nitrogens of the ketones and enolates are nearly triangular planar. While chair conformations are found to be the most stable geometrical structures of **1** and **2**, the twist-boat conformer **3tb** of the piperidinoxyl radical is 0.29 kcal mol^{-1} lower in energy than the chair conformer **3c**, in accord with the results of gas-phase electron diffraction studies carried out by Nakken and co-workers on **2** and **3** (10, 11). In the case of 9-

[1] Author to whom correspondence may be addressed.

[2] In principle, a β-nitroxyl group can stabilize a carbanion via a polar effect, through bond and through space, and a hyperconjugative interaction involving a σ* orbital of a C—N bond. It is also possible that the polarity of the nitroxyl group increases upon deprotonation at a β carbon, giving rise to a reflex polar stabilization of the enolate. In terms of resonance theory, the dipolar canonical form written for the nitroxyl group is a more important contributor for the enolate than the ketone.

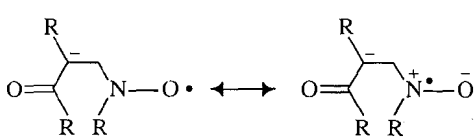

Support for such a reflex polar stabilization by a nitroxyl group is found in the fact that the AM1 calculations show that there is a differential increase in negative charge on the oxygens of the nitroxyl groups of **3tb** and **5cc** relative to the oxygens of the hydroxyl groups of **2c** and **4cc** upon enolate formation: **2c**, –0.270, **2c-enolate**, –0.291; **3tb**, –0.319, **3tb-enolate**, –0.404; **4cc** –0.271, **4cc-enolate**, –0.306; **5cc**, –0.306, **5cc-enolate**, –0.401.

[3] PCMODEL (9) was used to generate input geometries for the AM1 calculations, which were carried out with the keyword PRECISE to tighten the convergence criteria. UHF calculations were carried out for the hydroxy compounds, the nitroxyl radicals, and their enolates.

Can. J. Chem. Downloaded from www.nrcresearchpress.com by 85.192.166.187 on 09/08/12
For personal use only.

Can. J. Chem. Downloaded from www.nrcresearchpress.com by 85.192.166.187 on 09/08/12
For personal use only.

TABLE 1. Calculated enthalpies of formation and ionization

Ketone	ΔH_f Ketone[a]	ΔH_f Enolate	ΔH_i[b]	$\Delta\Delta H_i$
1	−74.99	−77.40	363.0	0.0
2c	−59.81	−65.82	359.4	−3.6
2tb	−58.88			
3c	−44.91			
3tb	−45.24	−58.74	351.9	−11.1
4cb	−56.65(*syn*)[c]	−67.04(*syn*)		
	−57.39(*anti*)	−61.76(*anti*)	361.3	−1.7
4cc	−60.56(*syn*)	−70.04(*syn*)	355.9	−7.1
	−60.44(*anti*)	−64.72(*anti*)	360.7	−2.3
5cb	−40.73(*syn*)	−52.11(*syn*)	353.5	−9.5
	−40.88(*anti*)	−52.55(*anti*)		
5cc	−43.63(*syn*)	−54.90)(*syn*)	354.1	−8.9
	−43.74(*anti*)	−55.50(*anti*)	353.6	−9.4

[a]In kcal mol^{-1}.

[b]ΔH_i = [ΔH_f (enolate) − ΔH_f (ketone)] − $\Delta H_f(H^+)$; $\Delta H_f(H^+)$ taken as 365.4 kcal mol^{-1}.

[c]The values for the -OH group *syn* and *anti* to the carbonyl and enolate groups, respectively.

TABLE 2. Second-order rate constants and relative rates of H/D exchange of ketones

Ketone[a]	k(L mol^{-1} s^{-1})[b]	Relative rate	Calculated $\Delta\Delta H_i$
1	0.92×10^{-2}[c]	1	0.0
2	6.39×10^{-2}[c]	6.9	−3.6
3	1.59[c,d]	173.1	−11.1
4	2.20×10^{-2}[c]	2.4	−7.1(OH *syn*), −2.3(*anti*)
5	5.67×10^{-1}[c,d]	61.7	−8.9(OH *syn*), −9.4(*anti*)

[a]Substrates **2**, **4**, and **5** were synthesized using procedures reported in the literature (11–14).

[b]In 60:40 dioxane–D_2O(v/v). Ketone concentrations ranged from 0.10 to 0.12 M. Second-order rate constants were obtained by dividing the measured pseudo-first-order rate constant by the base concentration, which was in the range of 0.005–0.04 M. Rates were reproducible with a maximum deviation of <±5% except for **1** where the deviation was ±7.5%.

[c]The uptake of deuterium was monitored with ^{1}H nmr spectroscopy by integrating the appropriate resonances. The signals of the C4 methylene hydrogens of **1** and methyl hydrogens of **2** were used as internal standards. For bicyclic compounds **4** and **5**, the resonances of the bridgehead hydrogens or the equatorial hydrogens α to the carbonyl group (the equatorial hydrogens of **5** exchange at least 100 times more slowly than the axial hydrogens) were used as the internal standards. The radicals were catalytically hydrogenated (PtO_2 in ethanol) to **2** and **4**, which were analysed with ^{1}H nmr spectroscopy.

[d]The H/D exchange of radicals **3** and **5** was extremely fast. The pseudo-first-order rate constants obtained from one-point kinetic runs were divided by the base concentration to calculate the second-order rate constants. The first-order rate constants exhibited a linear relationship with base concentration.

hydroxynorpseudopelletierine, the chair-chair conformation **4cc** is 3.10 kcal mol^{-1} lower in energy than the chair-boat conformation **4cb**, and the isomer with the -OH group *syn* to the carbonyl was found to be only marginally lower in energy than the *anti* diastereomer. But the orientation of the N-OH group has a dramatic effect on the stability of the gas-phase enolates derived from **4cb** and **4cc**; the *syn* enolates (the -OH group is *syn* to the enolate) are 5–6 kcal mol^{-1} lower in energy than the *anti* diastereomers, indicating that a gas-phase enolate ion is stabilized markedly by a single intramolecular hydrogen bond that is aligned perpendicular to the plane of the enolate anion. Even so, we expected that **4** would not exhibit an enhanced acidity in

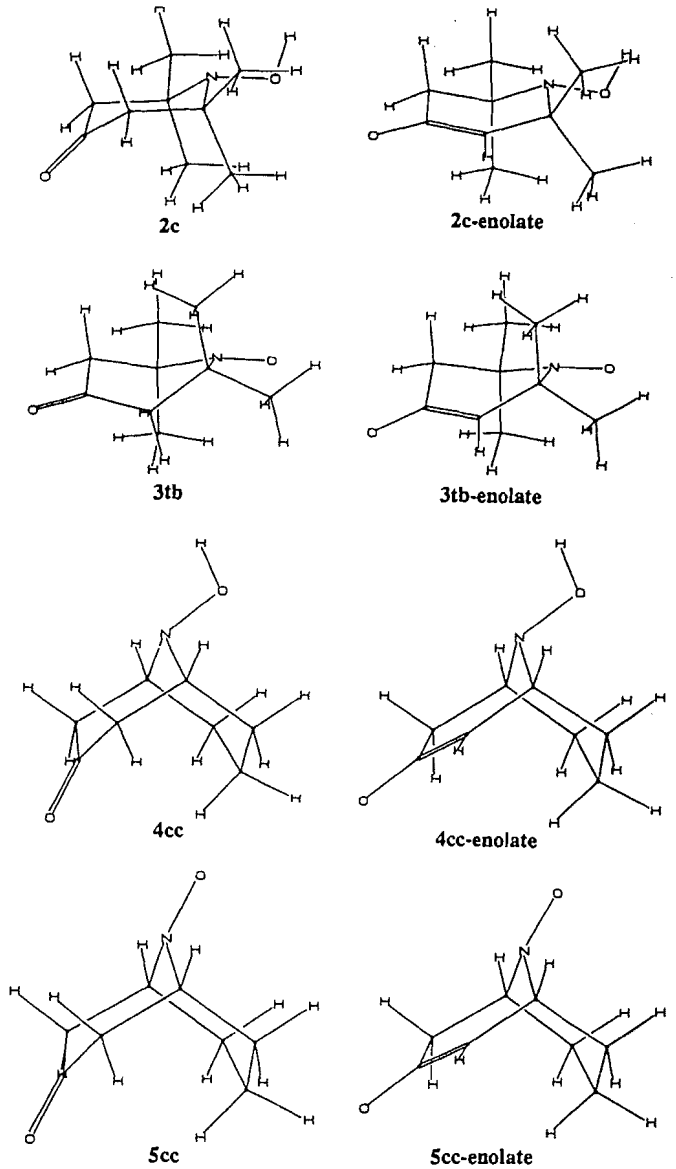

FIG. 1. Geometrical structures of the AM1 optimized geometries of **2c**, **3tb**, **4cc**, **5cc**, and their enolates.

aqueous solution[4] because enolates are solvated intermolecularly by solvent, and axial approach by OH^- at C2 should hinder formation of an intramolecular hydrogen bond to the incipient enolate. In the case of norpseudopelletierine-9-oxyl, the chair-chair conformation **5cc** is 2.86 kcal mol^{-1} lower in energy than the chair-boat conformation **5cb** and the orientation of the nitroxyl oxygen has little effect on the stability of enolates. Because the $\Delta\Delta H_i$'s of **3tb** and **5** were found to be nearly three times the values calculated for **2** and **4**, we expected the nitroxyl compounds to enolize much more quickly than **2** and **4**, and **2** to be more reactive than **1**.

The second-order rate constants for H/D exchange in NaOD/D_2O 60:40 dioxane–D_2O along with the relative rates and the $\Delta\Delta H_i$'s are given in Table 2. It is seen that the relative rates of

[4]We are modelling polycyclic cage compounds bearing hydrophobic cavities calculationally with AM1 to design substrates that will be useful for probing the stabilization of enolates by intramolecular hydrogen bonding in solution.

enolization correlate with the calculational gas-phase ΔH_i's and, as predicted, piperidine-1-oxyl **3** is more reactive than pelletierine-9-oxyl **5**; 1-hydroxypiperidine **2** is slightly more reactive than **4** and both compounds are substantially less reactive than **3** and **5**. As expected, the kinetic acidity of **4** correlates with the calculational ΔH_i of the *anti* diastereomer and not with the ΔH_i of the *syn* isomer. Because there are no σ substituent constants for the nitroxyl and hydroxylamino groups, it will be difficult to assess the relative importances of the polar (inductive and field) and hyperconjugation effects. Even so, the group electronegativities (χ values) calculated by Boyd and Boyd (15) on the basis of a bond critical point model indicate that through-bond electron-withdrawing effects of the nitroxyl and hydroxylamino groups are virtually identical.[5] Because the calculated N-C$(CH_3)_2$-CH=C (34.9°) and N-C$(R)_2$-CH=C (30.2°) torsional angles of **3tb-enolate** and **5cc-enolate** are far from the optimal angle of 90°, hyperconjugation with an adjacent C—N bond plays a minor role in stabilizing the enolates.

Acknowledgements

We thank the Natural Sciences and Engineering Research Council of Canada for financial support.

[5]We thank Professor Susan Boyd of Mount St. Vincent University, Halifax, Nova Scotia, for providing the χ values of the nitroxyl (χ = 3.18) and hydroxylamino (χ = 3.17) groups evaluated with calculations on $CH_3NHO^{\cdot}$ and CH_3NHOH.

1. E. Buncel. *In* Carbanions: mechanistic and isotopic aspects. Monograph 9. *Edited by* C. Eaborn and N.B. Chapman. Elsevier, Amsterdam. 1975. pp. 69–93.
2. J. Toullec. *In* Advances in physical organic chemistry. Vol. 18. *Edited by* V. Gold and D. Bethell. Academic Press, London. 1982. pp. 1–77.
3. N.H. Werstiuk and P. Andrews. Can. J. Chem. **56**, 2605 (1978).
4. N.H. Werstiuk, R. Taillefer, and S. Banerjee. Can. J. Chem. **56**, 1140 (1978).
5. N.H. Werstiuk. Can. J. Chem. **66**, 2958 (1988).
6. N.H. Werstiuk and R. Taillefer. Can. J. Chem. **48**, 3966 (1970).
7. A.R. Forrester, J.M. Hay, and R.H. Thomson. *In* Organic chemistry of stable radicals. Academic Press, London and New York. 1968. Chap. 5, p. 191.
8. Dewar Research Group and J.J.P. Stewart. Austin model 1. Package 1.0. QCPE 506. QCPE Bull. **6**, 2 (1986).
9. PCMODEL. Version 4. Serena Software, Box 3076, Bloomington, Ind.
10. P. Anderson, E.E. Astrup, P.S. Frederichsen, and K.F. Nakken. Acta Chem. Scand. **28**, 671 (1974).
11. P. Anderson, E.E. Astrup, P.S. Frederichsen, and K.F. Nakken. Acta Chem. Scand. **28**, 675 (1974).
12. R.-M. Dupeyre and A. Rassat. J. Am. Chem. Soc. **88**, 3180 (1966).
13. E.W. Garbisch, Jr. J. Org. Chem. **30**, 2109 (1965).
14. Y. Kashman and E. Benary. J. Org. Chem. **37**, 3778 (1972).
15. R.J. Boyd and S.L. Boyd. J. Am. Chem. Soc. **114**, 1653 (1992).

Can. J. Chem. Downloaded from www.nrcresearchpress.com by 85.192.166.187 on 09/08/12
For personal use only.

Shinichi Sasaki and Gordon R. Freeman. Molecular shape effects on electron and ion behavior in dielectric liquids: *cis*- and *trans*-butene-2 between the freezing and critical points. Can. J. Chem. **72**, 1625 (1994).

On page 1625, the first author's last name should read Sasaki (instead of Sasakaki).

Can. J. Chem. Downloaded from www.nrcresearchpress.com by 85.192.166.187 on 09/08/12
For personal use only.

Influence of oxidative treatment of copper grid electrodes on the efficiency of conversion to aniline in the electroreduction of nitrobenzene and azobenzene in basic aqueous methanol

ANNA MARTEL, AMOY KAM CHEONG, AND JEAN LESSARD[1]

Centre de recherche en électrochimie et électrocatalyse, Département de chimie, Université de Sherbrooke, Sherbrooke, (QC) J1K 2R1, Canada

AND

LOUIS BROSSARD

Institut de recherche d'Hydro-Québec, 1800, Montée Ste-Julie, Varennes, (QC) J3X 1S1, Canada

Received March 26, 1994

ANNA MARTEL, AMOY KAM CHEONG, JEAN LESSARD, and LOUIS BROSSARD. Can. J. Chem. **72**, 2353 (1994).

The influence of preoxidizing the surface of polycrystalline copper electrodes on the efficiency of the controlled potential electrochemical reduction of nitrobenzene and azobenzene to aniline in basic aqueous methanol has been investigated. Electrodes electrochemically preoxidized to $Cu(OH)_2$ or to Cu_2O gave high yields of aniline (90–100%) with high current efficiencies (88–99%) for the electrohydrogenation of nitrobenzene compared to electrodes preoxidized by air (7–29% of aniline, 64–74% current efficiency). For the electrohydrogenation of azobenzene, copper electrodes preoxidized to Cu_2O were found to be more active (average yield of aniline of 28%, average current efficiency of 55%) than electrodes preoxidized to $Cu(OH)_2$ (3–11% of aniline, 42–53% current efficiency), and electrodes preoxidized by air were inactive (the electrohydrogenation stopped at hydrazobenzene). The improvement of activity induced by preoxidation of the copper surface is linked to the increase of the surface area.

ANNA MARTEL, AMOY KAM CHEONG, JEAN LESSARD et LOUIS BROSSARD. Can. J. Chem. **72**, 2353 (1994).

Nous avons étudié l'influence de l'oxydation préalable d'électrodes de cuivre polycristalline sur l'efficacité de la réduction électrochimique du nitrobenzene et de l'azobenzène en aniline en milieu basique méthanol–eau. Les électrodes préalablement oxydées pour former du $Cu(OH)_2$ ou du Cu_2O ont donné d'excellents rendements en aniline (90–100%) et des efficacités de courant élevées (88–99%) en comparison aux électrodes oxydées à l'air (7–29% d'aniline, efficacité de courant de 64 à 74%) pour l'électrohydrogénation du nitrobenzène. Dans le cas de l'électrohydrogénation de l'azobenzène, les électrodes préoxydées en CuO_2 se sont avérées plus actives (rendement moyen de 28% en aniline, efficacité de courant moyenne de 55%) que les électrodes oxydées en $Cu(OH)_2$ (3–11% d'aniline, efficacité de courant de 42 à 53%) alors que les électrodes oxydées à l'air étaient inactives (arrêt à l'hydrazobenzène). L'augmentation de l'activité est reliée à un accroissement de la surface de l'électrode.

Introduction

The voltammetric reduction of nitrobenzene in basic aqueous or mixed aqueous organic solutions at various electrode materials is a four-electron process (eq. [1])

[1] $PhNO_2 + 4e^- + 3H_2O \rightarrow PhNHOH + 4OH^-$

whereas preparative electrochemical reduction usually gives condensation products resulting mainly from a chemical reaction between phenylhydroxylamine and nitrosobenzene: azoxy, azo, and hydrazobenzene (ref. 1, and references in ref. 2). At the beginning of the century, Löb and Moore (3) reported the formation of aniline in 33% yield, in addition to azoxybenzene (60% yield), in the preparative electrolysis of a suspension of nitrobenzene in 2% aqueous NaOH at a copper cathode, the yield of aniline being increased to 53% in the presence of copper powder (41% yield of azoxybenzene). Stutts et al. (4) reported a 25% yield of aniline for the constant current (80 mA/cm^2) reduction of nitrobenzene in 1 N NaOH (methanol added for solubility) at polycrystalline copper after a charge corresponding to 6 F/mol of nitrobenzene. The yield of aniline was practically the same (28%) at a charge corresponding to 7.5 F/mol of substrate. Cyr et al. (2) obtained substantial yields of aniline in the controlled potential reduction of nitrobenzene at polycrystalline copper in basic (0.14 M KOH) aqueous methanol (45% at −1.0 V vs. SCE and up to 87% at −1.2 V); the other product was phenylhydroxylamine (50% and 8% yield, respectively), the formation of condensation products during the electrolysis being negligible (0–3%).

Clearly, the copper electrode is capable of reducing the unprotonated hydroxylamine. One mechanistic possibility would be a reduction via chemisorbed hydrogen (eq. [3]) generated by the reduction of water (eq. [2]) as proposed for the efficient electrochemical reduction of nitroaromatic compounds to anilines on Devarda copper (5–7). Another mechanistic possibility would be a classical electronation–protonation path (eq. [4]), the reducibility of phenylhydroxylamine on copper being due to its adsorption and to the existence of specific interactions with the metal (8). That adsorption phenomena and specific interactions are operative has been confirmed by voltammetric studies at a Cu microelectrode showing hysteresis phenomena in alkaline media, for phenylhydroxylamine as well as for nitrobenzene, and by particular features of the voltammetric curves for nitrobenzene when compared to those obtained on carbon and mercury (8). A third mechanistic possibility has been proposed (4) and it would involve an electrocatalytic reduction in which an active form of copper generated by the reduction of surface copper oxides and (or) hydroxides (ca. eq. [5]) would reduce nitrobenzene and phenylhydroxylamine with regeneration of the surface copper oxides and (or) hydroxides (ca. eq. [6]). Huang (9) has shown that copper oxides and (or) hydroxides are always present on the surface of copper electrodes, even after careful polishing treatments carried out in the presence of air.

[1]Author to whom correspondence may be addressed. Telephone: 819-821-7091. Fax: 819-821-8017.

Can. J. Chem. Downloaded from www.nrcresearchpress.com by 65.111.164.53 on 09/08/12
For personal use only.

[2] $2H_2O + 2e^- + Cu \rightarrow 2(H)Cu + 2OH^-$

[3] $2(H)Cu + PhNHOH \rightarrow PhNH_2 + H_2O + Cu$

[4] $(PhNHOH)Cu + 2e^- + H_2O \rightarrow PhNH_2 + 2OH^-$

[5] $Cu(OH)_2 + 2e^- \rightarrow Cu^0 + 2OH^-$

[6] $PhNHOH + Cu^0 + H_2O \rightarrow PhNH_2 + Cu(OH)_2$

In the course of investigations on the electrochemical reduction of nitrobenzene at copper electrodes, we noticed variations in the yields of aniline and phenylhydroxylamine with the same electrode as well as with different electrodes. This led us to believe that these variations were caused by variations in the amount and (or) the nature of the oxides/hydroxides present on the surface of the copper electrodes.

In this paper, we report a study of the electrochemical reduction of nitrobenzene and azobenzene in basic aqueous methanol at polycrystalline copper electrodes that have been submitted to an oxidative treatment prior to their use in preparative electrolyses. We describe the various types of oxidative treatment applied and compared the morphology of the surface of the resulting electrodes and their activity (and efficiency) for the conversion of nitrobenzene and azoxybenzene to aniline.

Experimental

The controlled potential preparative electrolyses were carried out with an Electrosynthesis Company (ECS) 410 potentiostat connected in series with an ECS 640 digital coulometer and a Dynascon Corporation 2830 digital ammeter. A two-compartment glass H-cell (the volume of each compartment was 125 mL) having a Nafion-324 (E.I. du Pont de Nemours and Co.) membrane as separator was used. The counter electrode was a platinum grid cylinder (4 cm long and 6 cm in diameter). The reference electrode, a Cole Parmer saturated calomel electrode (SCE), was connected to the catholyte through a fritted glass disc close to the surface of the working electrode facing the counter electrode.

The polycrystalline bulk copper electrodes (grid 3×4 cm, 60 mesh) were made of pure metal (99.9%) purchased from Greening Donald Ltd. Before electrolysis, the copper electrodes were treated by one of the methods A–G described below. For the treatments involving electrochemical oxidations and reductions as well as for the voltammetric curve of Fig. 1, a Princeton Applied Research (PAR) potentiostat, model 173, with a PAR universal programmer, model 175, coupled to a PAR XY recorder, model RE0089, was used.

Treatment A

Cleaning in 50% nitric acid and thorough rinsing.

Treatment B

Cleaning according to the method used by Kyriacou et al. (10). The copper grid was washed with warm dichloromethane and then immersed in concentrated hydrochloric acid for 1 h for degreasing and removal of metallic surface impurities. It was then anodized in 85% w/w phosphoric acid at a current density of 500 mA/cm^2 for 2 min, after which a smooth shiny surface was obtained. It was then washed several times in deionized water.

Treatment C

Cleaning using method A followed by cleaning as described by Shoesmith et al. (11), by applying a reducing pontential of -1.2 V vs. SCE in a 1 M LiOH solution (prepared from anhydrous AR LiOH purchased from Fisher Scientific Co.) in the cell described above until the current decreased to zero. Then the electrode was oxidized as described in ref. 11. An oxidation potential (-0.22 to -0.20 V) corresponding to the formation of $Cu(OH)_2$ (Fig. 1) was applied. When the oxidation current dropped to zero, one redox cycle was completed. The redox cycle (reduction at -1.2 V, then oxidation) was repeated a number of times if required (until the desired amount of charge at the oxidation potential was passed). The electrode was then thoroughly rinsed.

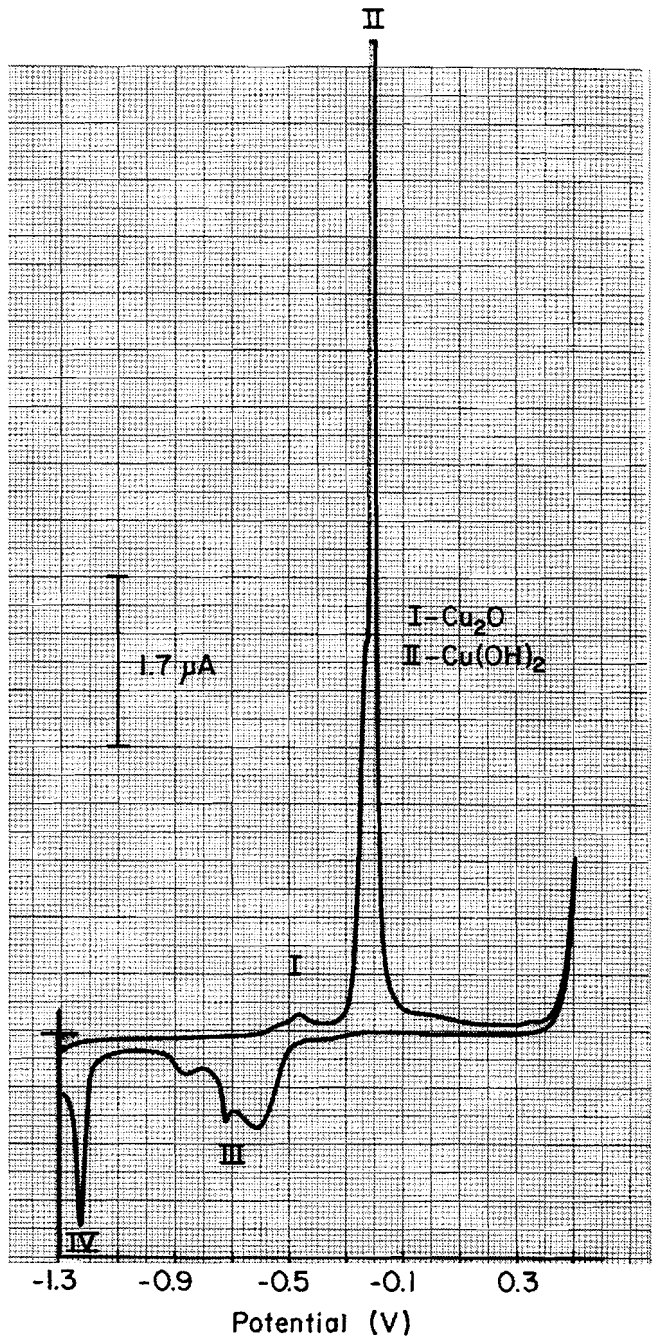

FIG. 1. Cyclic voltammogram of a copper electrode in 1 M aqueous LiOH at 21°C. Scan rate: 2 mV/s; potential (V) vs. SCE.

Treatment D

Same as treatment C except that the oxidation potential (-0.29 to -0.33 V) did correspond to the formation of Cu_2O (Fig. 1).

Treatment E

Cleaning as in treatment C followed by potential pulses at -1.2 and -0.3 V at a period of 1 s until a total charge of 86 C at -0.3 V was passed. Then an oxidation potential of -0.3 V was applied until the current dropped to zero: 336 C.

Treatment F

Cleaning as in treatment C followed by cycling the potential

Can. J. Chem. Downloaded from www.nrcresearchpress.com by 65.111.164.53 on 09/08/12
For personal use only.

TABLE 1. Electrohydrogenation of $PhNO_2$ (0.01 M) in basic (0.14 M KOH) methanol–water (93:7 w/w) solutions at copper electrodes at −1.0 V vs. SCE[a]

Entry	Working electrode pretreatment[b]	C_{dl}[c] (μF/cm²)	Unreacted $PhNO_2$[d] (%)	Yield of products[d] (%)			Material balance[d] (%)	Current efficiency (%)
				$PhNH_2$	PhNHOH	PhNHNHPh		
1	A	41[e]	4–5[f]	7–17[f]	39–53[f]	28–36[f]	93–96[f]	69–74[f]
2	B	86[e]	0	29	19	36	84	64
3	C(−0.22 V, 20 C)	400	0	90–97[g]	0	3–7[g]	97–100[g]	89–97[g]
4	D(−0.33 V, 7 C)	—	0	94–100[g]	0	1–5[g]	99–100[g]	88–99[g]

[a]The electrolysis was stopped after a charge corresponding to 6–7 moles of electrons per mole of substrate.
[b]A: Cleaning in nitric acid; B: cleaning according to the Kyriacou method (10) followed by reduction at −1.2 V; C: oxidation to $Cu(OH)_2$ (11); D: oxidation to Cu_2O(11). For C and D the oxidation potential and the charge passed for the oxidation are indicated between parentheses.
[c]Double layer capacity determined by ac impedance in aqueous 1 M KOH at 25°C.
[d]By glc.
[e]Mean value from two determinations.
[f]Range obtained from two electrolyses, the same electrode being reused after cleaning in nitric acid.
[g]Range obtained from three electrolyses using three different electrodes.

between −1.3 and +0.1 V at a scan rate of 100 mV/s until the peak corresponding to the oxidation to $Cu(OH)_2$ at −0.22 V stopped increasing.

Treatment G

Same as treatment F but cycling the potential between −1.3 and −0.21 V at a scan rate of 1 mV/s.

Solutions of KOH (0.14 M) in methanol–water 93:7 w/w were prepared from ACS methanol, distilled water, and KOH purchased from BDH. Nitrobenzene and azobenzene were purchased from BDH, aniline from Anachemia, and azoxybenzene from Lancaster Synthesis.

The electrolysis procedure was as follows. After treating the copper electrode as described above (see treatments A–G), it was placed in the cathodic compartment containing the supporting electrolyte solution, then polarized for 30 min at a potential (−0.55 to −1.0 V) generating a current density of 0.2 mA/cm² while bubbling nitrogen through the solution. The current density was then suddenly increased to 3.3 mA/cm² (potential of −1.4 to −1.7 V) for 30 min, during which time reduction of surface oxides occurred as well as hydrogen evolution. The potential was then increased to −1.0 V. A residual current density of 0.2 mA/cm² resulted. The organic substrate was then added, causing an increase of the current. For the reduction of nitrobenzene, the electrolysis was stopped when the current dropped to almost zero. For the reduction of azobenzene, the potential was also initially increased to −1.0 V. At this potential, the electrohydrogenation of azobenzene to hydrazobenzene was fast (large initial currents) and was complete. After a charge corresponding to about 2 mol of electrons (2 F) per mole of substrate, the current dropped almost to the background value so the potential was further decreased to −1.2 V in order to speed up the electrolysis (to increase the current). The electrolysis was stopped after a charge corresponding to 4–5 F/mol of azobenzene and (or) after the current dropped to the background value.

The progress of the electrolyses was followed by gas–liquid chromatography (glc) on a Hewlett Packard (HP) 5790A or 5840A chromatograph equipped with a FID detector and a HP 3390A integrator, using a 30 m long DB-5 fused silica capillary column with the following temperature programming: 80°C for 5 min, increase to 200°C at 10°C/min, and 200°C for 5 min. Products were identified by comparison of retention times with those of authentic samples. Yields and mass balances were determined by the internal standard method. The yield of phenylhydroxylamine was determined after its complete oxidation by air to azoxybenzene and nitrobenzene (2) and the yield of hydrazobenzene was determined after complete air oxidation to azobenzene (2).

The characterization of the electrode surfaces was carried out by scanning electron microscopy (SEM) on a JEOL GSM 840A apparatus. X-ray diffraction analyses were performed with a Rigaku D/MaxB diffractomter. The specific surface areas were determined by the BET method, with nitrogen adsorption, using a Quanta Chrome Quanta Sorb QS-10 apparatus. The double layer capacities were measured by the ac impedance technique, using a PAR potentiostat, model 273, monitored by a Commodore PC2 computer, with a GPIB PC2A interface, and connected to a PAR 5208 lock-in amplifier; the measurements were carried out in 1 M KOH aqueous solutions.

Results and discussion

The potentiodynamic trace of Fig. 1 corresponds to that reported by Shoesmith et al. (11) and displays two oxidation peaks: peak I is ascribed to the formation of Cu_2O, the formation of $Cu(OH)_2$ starts at the shoulder of peak II (the shoulder being located on the cathodic side of the latter), and peak II itself is linked to the formation of $Cu(OH)_2$ only. On the reverse sweep, region III corresponds to the reduction of a Cu(II) solid species and peak IV to the reduction of Cu_2O. Since the nature and amount of the predominant phases are largely dependent on the applied potential where the oxidation is carried out in the region of peak II (11), the copper grid was potentiostatically preoxidized at two different potentials, i.e., −0.3 and −0.2 V, to generate two different oxides as shown by X-ray diffraction analysis (Fig. 2): Cu_2O at −0.30 V (Fig. 2*a*) and $Cu(OH)_2$ at −0.20 V (Fig. 2*b*).

The electrohydrogenation of nitrobenzene at polycrystalline copper electrodes cleaned in nitric acid (treatment A) or polished electrochemically (treatment B) was compared to the electrohydrogenation at copper electrodes electrochemically preoxidized to form $Cu(OH)_2$ (treatment C) or to form Cu_2O (treatment D) at the copper surface. The results are summarized in Table 1. In all cases, the material balance is high. The current efficiencies are higher with electrochemically preoxidized copper electrodes (entries 3 and 4) than the electrodes not electrochemically preoxidized (entries 1 and 2). The most striking feature of Table 1 is the much greater activity of the electrochemically preoxidized copper electrodes for the formation of aniline: yields of aniline of 90–100% in entries 3 and 4 compared to yields of 7–29% in entries 1 and 2. In fact, the yields of aniline and the current efficiencies obtained with electrochemically preoxidized copper electrodes are comparable to those obtained with Devarda copper electrodes under the same conditions: 99% yield, 95% current efficiency (5). With the copper electrodes not electrochemically preoxidized (entries 1 and 2), the amount of hydrazobenzene is relatively important (28–36%). These results differ from those reported by Cyr et al. (2) for electrohydrogenation on a copper plate under the same conditions 0–3% of hydrazobenzene. The hydrazobenzene comes from the reduction of the azoxybenzene resulting from the reaction between nitrosobenzene and phenylhydroxylamine in the bulk of the solution during the electrolysis. Darchen and Moinet (12) have indeed shown that the nitro group is first reduced to

Can. J. Chem. Downloaded from www.nrcresearchpress.com by 65.111.164.53 on 09/08/12
For personal use only.

Can. J. Chem. Downloaded from www.nrcresearchpress.com by 65.111.164.53 on 09/08/12
For personal use only.

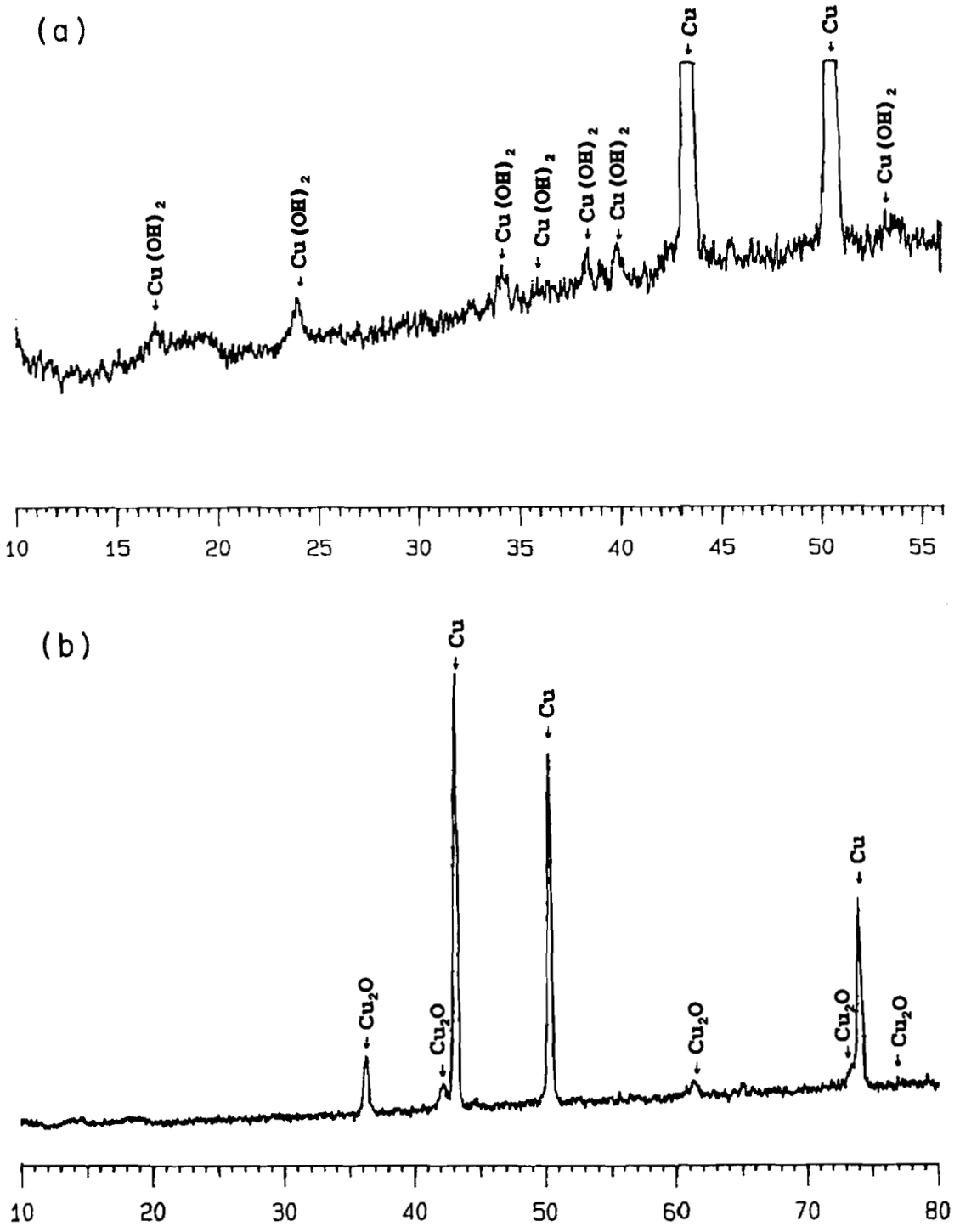

FIG. 2. X-ray diffraction analysis of copper electrodes oxidized in a 1 M aqueous LiOH solution : (*a*) oxidation at −0.30 V vs. SCE; (*b*) at −0.20 V (see the Experimental).

the dihydroxylamine, which is then dehydrated to the nitroso derivative. If dehydration occurs at the surface of the electrode, the nitroso derivative is immediately reduced to the hydroxylamine, whereas if dehydration occurs in solution, the nitroso derivative has a high probability of reacting with the hydroxylamine to give the azoxy derivative (12). It is quite possible then that the intermediate dihydroxylaminobenzene could move away from the electrode surface at a faster rate in the case of a copper grid (this work) than in the case of a copper plate (ref. 2).

A comparison of entries 3 and 4 of Table 1 shows that the activity of the electrochemically preoxidized electrodes for the electrohydrogenation of nitrobenzene does not depend on the nature of the oxide formed at the surface, i.e., $Cu(OH)_2$ (entry 3) or Cu_2O (entry 4). For the electrodes not electrochemically preoxidized, an electrode that has been polished electrochemically prior to the electrohydrogenation (10) (entry 2) is more active than an electrode cleaned in nitric acid (entry 1). This could reflect a greater extent of oxidation by air (larger amount of surface oxides) when the copper grid is polished electrochemically than when it is cleaned in nitric acid. The difference in yields of

TABLE 2. Electrohydrogenation of PhNNPh (0.01 M) in basic (0.14 M KOH) methanol–water (93:7 w/w) solutions at copper electrodes at −1.2 V vs. SCE

Entry	Working electrode pretreatment[a]	C_{dl}[b] ($\mu F/cm^2$)	Mol of e^- per mol of AB[c]	Yield of products[d] (%)		Material balance[d] (%)	Current efficiency (%)
				$PhNH_2$	PhNHNHPh		
1	A	41	2.7	0	97	97	73
2	C(−0.22 V, 20 C)	400	2.7	4	96	100	76
3	C(−0.22 V, 40 C)	—	4.4	3	85	88	42
4	C(−0.2 V, 70 C)	490	4.2	11	89	100	53
5	D(−0.3 V, 7 C)	—	4.1	10	84	94	51
6	D(−0.3 V, 12 C)	—	5.5	31	66	97	46
7	D(−0.3 V, 20 C)	1330	4.1	26	72	98	61
8	D(−0.3 V, 45 C)	2000	4.2	40	50	90	62
9	D(−0.3 V, 60 C)	1830	4.2	25	72	97	58
10	D(−0.3 V, 66 C)	—	4.3	19	76	95	53
11	D(−0.3 V, 100 C)	2430	4.2	27	63	90	55
12	E(−0.3 V, 1 s, 86 C; then −0.3 V, 336 C)	2550	4.4	41	56	97	63
13	F(−1.3 V to +0.1 V; 77 C)	264	3.5	18	65	83	58
14	G(−1.3 V to −0.21 V; 133 C)	760	4.8	26	68	93	50

[a]A, C, D: same as in Table 1; E: the potential was pulsed between −1.2 and −0.3 V at a period of 1 s followed by oxidation at −0.3 V. F: the potential was cycled between −1.3 and 0.1 V at 100 mV/s; G: the potential was cycled between −1.3 and −0.21 V at 1 mV/s. The oxidation potential(s) and the charge for oxidation are indicated between parentheses.

[b]Double layer capacity determined by ac impedance in aqueous 1 M KOH at 25°C.

[c]In entries 1, 2, and 13, the electrolysis was stopped when the current dropped to the background value.

[d]By glc; there was 100% conversion of azobenzene in all case.

aniline obtained in the two electrolyses of entry 1 with an electrode cleaned in nitric acid shows that using the same electrode and cleaning it the same way before each use does not reproduce exactly the same activity, that is, the same amount of surface oxides by air oxidation.

Cyr et al. (2) have reported that the electrohydrogenation of azobenzene at polycrystalline copper stopped at hydrazobenzene in basic (0.14 M KOH) methanol–water (93:7 w/w); aniline was not detected. On the other hand, at Devarda copper and under the same conditions, the hydrogenolysis of hydrazobenzene was found to be quite efficient (5). Since the copper grid electrochemically preoxidized appeared to be almost as efficient as a Devarda copper electrode for the electrohydrogenation of nitrobenzene to aniline (hydrogenolysis of phenylhydroxylamine), it was of interest to also determine their activity for the hydrogenolysis of hydrazobenzene to aniline. So we studied the electrohydrogenation of azobenzene. The results are recorded in Table 2.

On a copper electrode cleaned in nitric acid (treatment A, entry 1), the current dropped to the background value after a charge corresponding to 2.7 mol of electrons (2.7 F) per mol of azobenzene and no aniline was detected. So there was no hydrogenolysis of hydrazobenzene, as already reported (2). Copper electrodes that had been preoxidized to $Cu(OH)_2$ (treatment C, entries 2–4) were slightly more active since there was some hydrogenolysis of hydrazobenzene (3–11% of aniline). The current in excess of a charge corresponding to 2 F/mol of azobenzene (reduction to hydrazobenzene) was used mainly for hydrogen evolution as shown by the low (≤50%) current efficiencies of entries 3 and 4. Since the conversion rate and current efficiency for the conversion of azobenzene to hydrazobenzene (after 2 F/mol of azobenzene) are close to 100%, a yield of about 10% of aniline and a current efficiency of about 50% for the overall reaction (after 4 F/mole of azobenzene) means that only 10% of the current was effectively used for the hydrogenolysis of hydrazobenzene to aniline (90% for hydrogen evolution). With one redox cycle (reduction at −1.2 V until a zero current was reached, with a subsequent oxidation at −0.2 V until a zero current (11) was reached again, see treatment C of the experimental), it was not possible to go beyond a charge of 40 C for the formation of $Cu(OH)_2$. With three successive redox cycles, it was possible to increase the amount of $Cu(OH)_2$ formed on the electrode surface up to a charge of 70 C (entry 4). This led to a slight improvement of the activity (11% of aniline compared to 3–4% in entries 2 and 3).

The electrodes preoxidized to Cu_2O were found to be more active than those preoxidized to $Cu(OH)_2$, as shown by the higher yields of aniline obtained with the former electrodes (see Table 2, entries 5–11). The charge used to form Cu_2O was varied from 7 C (entry 5) to 100 C (entry 11). There was an increase in the yield of aniline from 10% (entry 5) to 31% (entry 6) upon increasing the preoxidation charge from 7 to 12 C. Increasing the charge from 12 to 100 C (entries 6–11) did not cause any real increase of the yield of aniline (31% yield in entry 6 compared to 27% in entry 11; yields varying from 20 to 40% in entries 6–11 with an average yield of 28%). Therefore, practically only the Cu_2O formed at the surface leads, after reduction, to a surface that is active for the hydrogenolysis of hydrazobenzene. Overall current efficiencies of 60% for an average yield of aniline of 28% (after a charge corresponding to 4 F/mol of azobenzene) corresponds to a current efficiency of about 30% for the hydrogenolysis of hydrazobenzene to aniline (see above).

As in the case of preoxidation to $Cu(OH)_2$, the oxidation to Cu_2O using one reduction (−1.2 V) – preoxidation (−0.3 V) cycle stopped after an oxidation charge of 40 C (treatment D). With four successive reduction–oxidation cycles, a charge of 60 C could be reached and, with six cycles, a charge of 100 C. By first pulsating the potential between −1.2 and −0.3 V at a period of 1 s until a total charge at −0.3 V (oxidation) of 86 C and then applying a potential of −0.3 V, it was possible to reach a charge of 336 C (treatment E, see entry 12). Despite the sig-

Can. J. Chem. Downloaded from www.nrcresearchpress.com by 65.111.164.53 on 09/08/12
For personal use only.

Can. J. Chem. Downloaded from www.nrcresearchpress.com by 65.111.164.53 on 09/08/12
For personal use only.

nificant increase of the amount of Cu_2O formed in treatment E, there was no improvement of the activity for the hydrogenolysis of hydrazobenzene (41% yield of aniline in entry 12 compared to 40% in entry 8). Other types of treatment, such as submitting the electrode to voltammetric cycles between −1.3 and 0.1 V at 100 mV/s (treatment F, entry 13) or between −1.3 and −0.21 V at 1 mV/s (treatment G, entry 14), until the Cu_2O reduction peak at −0.21 V stopped increasing, did not lead to any improvement of the activity (18% yield of aniline in entry 13, 26% yield in entry 14) when compared to treatment D (entries 6–11, average yield of aniline 28%).

The simplest explanation for the increase of activity of copper electrodes for the hydrogenolysis of N—O and N—N bonds when preoxidizing the surface to $Cu(OH)_2$ or to Cu_2O, which are then reduced in situ, is an increase of the surface area. Indeed, as shown in Tables 1 and 2, the double layer capacity (C_{dl}) for the hydrogen evolution reaction (HER) in aqueous alkali measured by ac impedance and, hence, the roughness of the surface[2] are larger for electrodes that have been electrochemically preoxidized (entry 3 of Table 1; entries 2, 4, 7–9, and 11–14 of Table 2) than for electrodes cleaned in nitric acid and oxidized by air (treatment A, entry 1 of Tables 1 and 2) or electrochemically polished in nitric acid and oxidized by air (treatment B, entry 2 of Table 1), and the former electrodes are more active (higher yields of aniline). Furthermore, electrodes preoxidized to Cu_2O (treatment D, entries 6–11 of Table 2) are more active (20–40% yield of aniline) and have a larger C_{dl} (1330–2430 $\mu F/cm^2$) than electrodes preoxidized to $Cu(OH)_2$ (treatment C, entries 2–4 of Table 2: 3–11% yield of aniline; C_{dl} = 400–490 $\mu F/cm^2$).[2] That the more active electrodes have generally the larger C_{dl} (and hence the larger surface area) is clearly seen from Fig. 3, where the yield of aniline in the electrohydrogenation of azobenzene is correlated to C_{dl}. As expected, the electrodes preoxidized to Cu_2O (treatment D) have a larger specific area measured by BET (1.6–1.7 m^2/g) than electrodes polished by immersion in nitric acid and oxidized by air (treatment A, 0.84 m^2/g). The SEM pictures of some copper electrodes are illustrated in Fig. 4. For Fig. 4*a*, the copper electrode was not electrochemically preoxidized; for Fig. 4*b*, the copper electrode was preoxidized to Cu_2O at −0.33 V up to a charge of oxidation of 40 C and, for Fig. 4*c*, Cu_2O was further reduced to metallic copper. The formation of a dense network of microcracks is noticed in Fig. 4*c*. Consequently, it is deduced that the increase of C_{dl} noticed after formation (treatment D) and reduction of Cu_2O on the copper grid surface (Table 2 and Fig. 3) is induced by morphological changes at the electrode surface. Furthermore, reduction of the oxide (Fig. 4*c*) appears to make the electrode surface still more porous.

The activity of the electrode referred to above (evaluated by the yield of aniline and current efficiency) reflects the competition between the electrohydrogenolysis of phenylhydroxylamine or hydrazobenzene to aniline (eq. [7], where YH-ZH = PhNH-OH or PhNH-NHPh, YH_2 = $PhNH_2$ and ZH_2 = $PhNH_2$ or

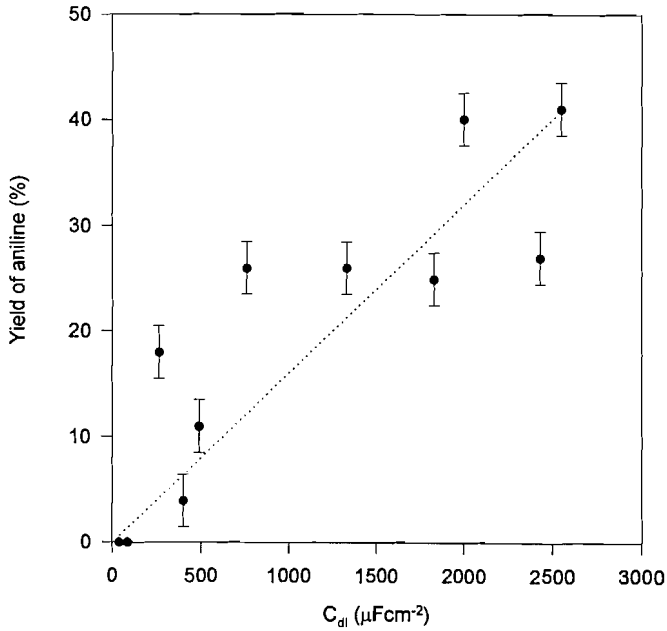

FIG. 3. Correlation between the yield of aniline and the double layer capacity (C_{dl}) of copper electrodes in the electrohydrogenation of azobenzene in basic (0.14 M KOH) methanol–water (93:7 w/w) solution at −1.0 to −1.2 V vs. SCE at room temperature.

H_2O) and the HER (eq. [8]). If reaction [7] was as fast as reaction [8], the yield of aniline from azobenzene, for instance,

[7] $YH - ZH + 2e^- + 2H_2O \rightarrow YH_2 + ZH_2 + 2OH^-$

[8] $2H_2O + 2e^- + 2e^- \rightarrow H_2 + 2OH^-$

would be less than 50% and the current efficiency less than 67%[3] because of a decrease of the rate of reaction [7] due to a diminution of the concentration of YH-ZH as the electrohydrogenolysis proceeds, while the rate of reaction [8] remains more or less constant, water being present in large excess. This is nearly the case for the electrohydrogenation of azobenzene on copper electrochemically preoxidized to Cu_2O (Table 2, entries 7–12) with an average yield of aniline of 30% and an average current efficiency of 59%. When reaction [7] is faster than reaction [8], high yields of aniline and high current efficiencies are obtained, as in the electrohydrogenation of nitrobenzene on electrochemically preoxidized copper electrodes (Table 1, entries 3 and 4; yield of aniline ≥90%, current efficiency ≥88%). The electrohydrogenation of Table 2, entry 1 (on copper electrodes not electrochemically preoxidized), represents the limiting case of reaction [7] being much slower than reaction [8] so that no hydrogenolysis occurred and only the HER was observed (see also Table 2 of ref. 2). Clearly, for a given substrate, the surface area of the electrode has an influence on the competition between reactions [7] and [8]: an increase of the surface area favors reaction [7] over reaction [8] and hence leads to an increase of electrode activity. This can be readily

[2]The C_{dl} of a smooth nickel surface is 20 mF/cm^2 (13) so the surface of copper electrodes not electrochemically preoxidized (treatments A and B, entries 1 and 2 of Table 1) is about two to four times rougher (roughness factor $R = C_{dl}/20$ = 2.1–4.3) than the surface of smooth nickel. The surface resulting from electrochemical preoxidation to $Cu(OH)_2$ (treatment C, entries 2 and 4 of Table 2) is then about 20 times rougher (R = 20–24.5) and the surface resulting form preoxidation to Cu_2O (treatment D, entries 5–11 of Table 2) is between 65 and 122 times rougher (R = 66.5–121.5).

[3]The electrohydrogenation of azobenzene to hydrazobenzene is quantitative and proceeds with 100% current efficiency. For a 50% conversion of hydrazobenzene to aniline with a 50% current efficiency, the overall current efficiency would be 66.6%. In the case of nitrobenzene, assuming a 100% current efficiency for the electrohydrogenation to phenylhydroxylamine, a 50% conversion with a 50% current efficiency for the phenylhydroxylamine to aniline hydrogenation, the overall current efficiency would be 75%.

Can. J. Chem. Downloaded from www.nrcresearchpress.com by 65.111.164.53 on 09/08/12
For personal use only.

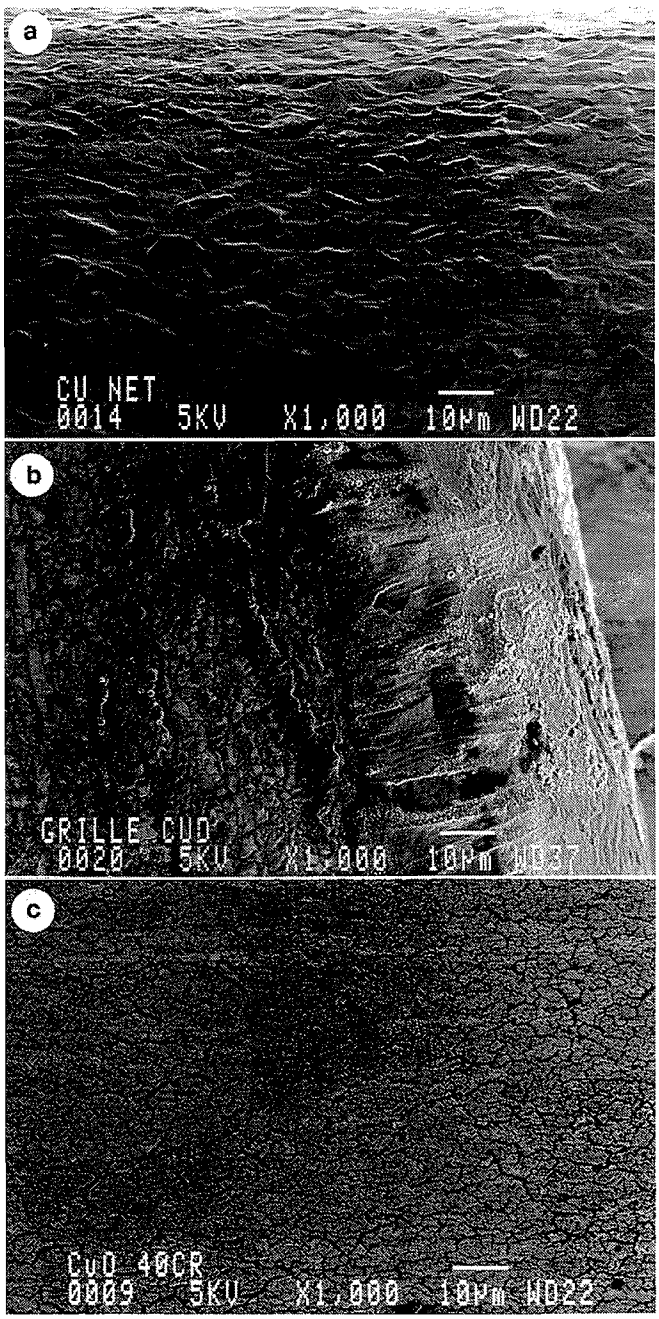

FIG. 4. Scanning electron microscopy pictures of copper electrodes: (*a*) cleaned in nitric acid and further oxidized in air (treatment A); (*b*) oxidized to Cu_2O (treatment D); (*c*) oxidized to Cu_2O (treatment D), which was then reduced at −1.0 V vs. SCE.

explained by an electrocatalytic hydrogenation mechanism (see eqs. [2] and [3]) in which the reaction of phenylhydroxylamine or hydrazobenzene with chemisorbed hydrogen (eq. [9]) competes with the formation of molecular hydrogen from chemisorbed hydrogen (eq. [10]). An increase of the surface area

[9] $2Cu(H) + YH - ZH \rightarrow YH_2 + ZH_2 + Cu$

[10] $2Cu(H) \rightarrow H_2 + Cu$

would then augment the number but also make more readily accessible the sites for the adsorption of the organic substrate (active sites for hydrogenation) and thus increase the mass transfer to these sites as found in the electrocatalytic hydrogenation of phenanthrene on porous nickel electrodes (14). The increase of copper electrode activity upon increasing the surface area can also be accounted for by the two other possible mechanisms of the electrohydrogenation of phenylhydroxylamine and hydrazobenzene if hydrazobenzene behaves as phenylhydroxylamine: by an increase of the number of accessibility of adsorption sites for YH-ZH for the classical electron–protonation mechanism (8) (see eq. [4]) or of active reducing copper sites in the electrocatalytic mechanism described by eqs. [5] and [6] (4).

Conclusion

The activity of polycrystalline copper electrodes for the hydrogenolysis of N—O and N—N bonds can be increased by electrochemically preoxidizing their surface to $Cu(OH)_2$ or to Cu_2O. These electrodes are very active for the electrohydrogenation of nitrobenzene to aniline in alkaline medium (yields of 90–100%, current efficiencies of 88–99%). The hydrogenolysis of hydrazobenzene being more difficult than that of phenylhydroxylamine, the yields of aniline and current efficiencies are much lower than those obtained for the electrohydrogenation of nitrobenzene, but they show clearly that electrodes preoxidized to Cu_2O are more active (an average of 28% for the yield of aniline and 55% for the current efficiency) than electrodes preoxidized to $Cu(OH)_2$ (yield of aniline of 3–11% and current efficiency of 42–53%). The larger activity is related to the increase of active surface area, as evidenced by an increase of the double layer capacity for the HER in alkaline medium from 40 $\mu F/cm^2$ for a non-preoxidized copper electrode to about 400 $\mu F/cm^2$ for an electrode preoxidized to $Cu(OH)_2$ and to about 2000 $\mu F/cm^2$ for an electrode preoxidized to Cu_2O. Devarda copper electrodes are still more active (93% aniline from azobenzene with a current efficiency of 96% (14)) and, indeed, their active surface area is still larger ($C_{dl} > 10^4$ $\mu F/cm^2$).[4] The three mechanisms considered in the introduction would be consistent with an increase of activity due to an increase of the number of active sites for a given geometric area.

Acknowledgements

Financial support from the Natural Sciences and Engineering Research Council of Canada, the "Fonds pour la formation des chercheurs at l'aide à la recherche (FCAR) du Québec" and the "Ministère de l'Énergie et des Ressources du Québec" is gratefully acknowledged. We thank Mr. Pierre Magny for the SEM measurements.

1. H. Lund. *In* Organic electrochemistry. *Edited by* H. Lund and M.M. Baizer. Marcel Dekker, Inc., New York. 1991. pp. 411–417.
2. A. Cyr, P. Huot, J.-F. Marcoux, G. Belot, E. Laviron, and J. Lessard. Electrochim. Acta, **34**, 439 (1989).
3. W. Löb and R.W. Moore. Z. Phys. Chem. **47**, 418 (1904).
4. K.J. Stutts, C.L. Scortichini, and C.M. Repucci. J. Org. Chem. **54**, 3740 (1989).
5. A. Cyr, P. Huot, G. Belot, and J. Lessard. Electrochim. Acta, **35**, 147 (1990).
6. A. Vélin-Prikidanovics and J. Lessard. J. Appl. Electrochem. **20**, 527 (1990).
7. J. Lessard, G. Belot, Y. Couture, S. Desjardins, and C. Roy. Int. J. Hydrogen Energy, **18**, 681 (1993).

[4]A. Martel, B. Behzadian, D.L. Piron, and J. Lessard. Unpublished results

8. A. Cyr, E. Laviron, and J. Lessard. J. Electroanal. Chem. **263**, 69 (1989).
9. Y. Huang. Ph.D. Thesis, Université de Sherbrooke (1992).
10. G. Kiryakou and A. Anagnostopoulos. J. Electroanal. Chem. **322**, 233 (1992).
11. D.W. Shoesmith, T.E. Rummery, D. Owen, and W. Lee. J. Electrochem. Soc. **123**, 790 (1976).
12. A. Darchen and C. Moinet. J. Electroanal. Chem. **61**, 373 (1969); **68**, 173 (1976); **78**, 81 (1977).
13. S. Trasatti and O.A. Petrii. Pure Appl. Chem. **63**, 711 (1991).
14. B. Mahadavi, P. Los, M.J. Lessard, and J. Lessard. Can. J. Chem. **72**, 2268 (1994).

Can. J. Chem. Downloaded from www.nrcresearchpress.com by 65.111.164.53 on 09/08/12
For personal use only.

Synthèse et études structurales de nouveaux complexes polyhydroxamiques du fer(III) potentiellement utilisables en imagerie par résonance magnétique nucléaire. Deuxième partie : Études des complexes formés in situ à partir d'acides hydroxamiques. Relaxivité du complexe Fe(III) – *N,N'*-bis(acétylhydroxyamino-3' propyl)-(amino-4'' butyloxy)-4 pyridine-2,6 dicarboxamide

FRÉDÉRIC CHAUBET, KIEM NGUYEN VAN DUONG,[1] JACQUES COURTIEU ET ALAIN GAUDEMER[1]

Institut de chimie moléculaire d'Orsay, Unité de recherche associée au Centre national de la recherche scientifique n° 1384, Université de Paris Sud, 91405 Orsay, France

AURORE GREF

Institut de chimie moléculaire d'Orsay, Unité de recherche associée au Centre national de la recherche n° 255, Université de Paris Sud, 91405 Orsay, France

ET

ALVIN L. CRUMBLISS ET MATTHEW T. CAUDLE

Paul M. Gross Laboratory, Department of Chemistry, Duke University, Durham, NC 27706, U.S.A.

Reçu le 3 juin 1994

FRÉDÉRIC CHAUBET, KIEM NGUYEN VAN DUONG, JACQUES COURTIEU, ALAIN GAUDEMER, AURORE GREF, ALVIN L. CRUMBLISS et MATTHEW T. CAUDLE. Can. J. Chem. **72**, 2361 (1994).

Après avoir préparé plusieurs dihydroxamates analogues de l'acide rhodotorulique, nous avons étudié leur mode de complexation du fer(III) et la stabilité des complexes obtenus en fonction du pH, par comparaison avec la ferrioxamine B et le complexe acide acétohydroxamique – fer(III). Cette étude révèle une stoechiométrie des complexes 2 : 3 à pH 7 et 1 : 1 à pH 2 ainsi qu'un comportement électrochimique très différent suivant le pH malgré une complexation totale. La très forte constante de formation ($\log \beta_{110} = 21{,}3$) obtenue à pH 1 avec le ligand *N,N'*-bis(acétylhydroxyamino-3' propyl)-pentyloxy-4 pyridine-2,6 dicarboxamide confirme le fort pouvoir de complexation du fer(III) par ces composés. La relaxivité élevée du complexe fer(III) – *N,N'*-bis(acétylhydroxyamino-3' propyl)-(amino-4'' butyloxy)-4-pyridine-2,6 dicarboxamide permet de considérer ce produit comme un agent de constraste potentiel pour l'imagerie par résonance magnétique.

FRÉDÉRIC CHAUBET, KIEM NGUYEN VAN DUONG, JACQUES COURTIEU, ALAIN GAUDEMER, AURORE GREF, ALVIN L. CRUMBLISS, and MATTHEW T. CAUDLE. Can. J. Chem. **72**, 2361 (1994).

Numerous analogous dihydroxamates of rhodotorulic acid have been prepared, and their mode of complexation of iron(III) and the stability of these complexes studied as a function of pH, for comparison with ferrioxamine B and the complex of acetohydroxamic acid with iron(III). This study has shown that the stoichiometry of the complexes is 2:3 (at a pH of 7) and 1:1 (at a pH of 2), and that, in spite of a complete complexation, their electrochemical behaviour varies greatly with pH. The very strong complexation constant observed ($\log \beta_{110} = 21.3$) at a pH of 1 with the ligand *N,N'*-bis(acetylhydroxamino-3' propyl)-pentyloxy-4 pyridine-2,6-dicarboxamide confirms the strong complexation capacity of iron(III) by these complexes. The high relaxivity of the complex of iron(III) with the *N,N'*-bis(acetylhydroxyamino-3'-propyl)-(amino-4''-butyloxy)-4-pyridine-2,6-dicarboxamide suggests that this product could be a useful contrasting agent for nuclear magnetic imaging.

[Journal translation]

Introduction

Dans la première partie de ce travail nous avons présenté la synthèse d'acides dihydroxamiques **1***a–d* susceptibles de conduire par complexation avec le fer(III) à de nouveaux agents de contraste pour l'imagerie de résonance magnétique (1, 2). Nous présentons maintenant les résultats des études physicochimiques réalisées sur les complexes qu'ils forment en solution avec l'ion ferrique. Les sidérophores polyhydroxamiques forment avec le fer(III) des complexes très stables dans lesquels l'ion ferrique haut spin se trouve dans un environnement octaédrique (3–5). La coexistence en solution de plusieurs isomères géométriques rend difficile l'obtention d'un composé cristallisé analysable par rayons X. L'essentiel des informations structurales sur ces composés provient donc de l'analyse des espèces en solution (6, 7) en particulier en utilisant la spectrophotométrie visible entre 350 et 550 nm, la RPE et la voltamétrie cyclique. La première de ces techniques permet en particulier de différencier les trois types de complexes mono-, di- et trihydroxamates avec le fer(III) car ils présentent des longueurs d'onde d'absorption maximum très différentes et indépendantes du reste de la structure du ligand (8). Dans le cas du complexe fer(III) – acide rhodotorulique, qui présente un nombre élevé d'isomères en solution (6), on a ainsi pu proposer une stoechiométrie Fe_2L_3 (fig. 1). Nous avons étudié dans les mêmes conditions de solvant les complexes formés par le fer(III) avec l'acide acétohydroxamique **2** et la déferriferrioxamine B **3** afin de pouvoir comparer valablement leurs propriétés de complexation déjà bien connues avec celles des ligands **1** dans les mêmes conditions expérimentales. Enfin, nous avons mesuré la relaxivité du complexe fer(III)-**1***d* in vitro, et nous l'avons comparé à la relaxivité du complexe Gd(DTPA) déterminée dans les mêmes conditions.

Materiels et methodes

Les spectres UV–visible ont été enregistrés sur un spectromètre Perkin–Elmer Lambda 5 pour les déterminations des points isosbestiques. Les spectres RPE ont été enregistrés sur un spectromètre Bruker ER 200E fonctionnant en bande X avec une fréquence de 9,4 GHz.

1. Auteurs à qui doit être adressée toute correspondance. Tel. : 69-41-70-19. FAX : 69-41-29-60.

Can. J. Chem. Downloaded from www.nrcresearchpress.com by 85.192.166.187 on 09/08/12
For personal use only.

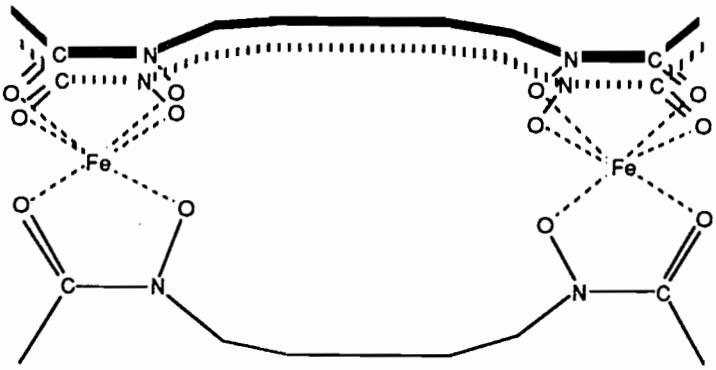

FIG. 1. Structure schématique du complexe Fe_2(acide rhodotorulique)$_3$ en solution.

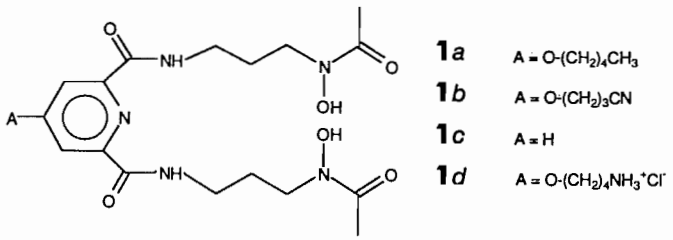

1

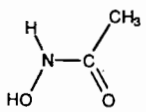

2

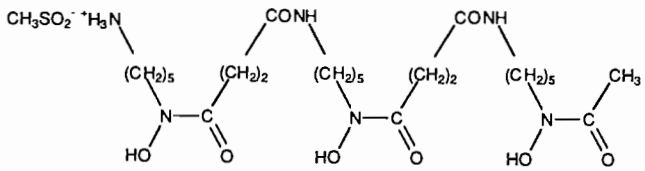

3

Les valeurs du pH ont été mesurées avec une microélectrode Tacussel raccordée à un pH mètre Tacussel Minisis 5000. Une courbe de calibration de la microélectrode combinée a été réalisée afin de pourvoir corréler le pH mesuré dans le mélange méthanol–eau au pH mesuré dans l'eau. L'électrolyte de la microélectrode était une solution saturée de LiCl dans le mélange méthanol–eau employé. Les titrations potentiométriques ont été effectuées dans une cellule thermostatée à 25,0 ± 0,2°C et sous atmosphère inerte. Les additions de KOH ont été effectuées à l'aide d'une burette automatique Schott ou d'une microburette de précision Gilmont de même que les solutions de fer(III). Chaque courbe de titration a été tracée à partir de 60 points expérimentaux enregistrés avec un pHmètre Corning model 250 raccordé à une électrode combinée à jonction échangeable. Une courbe de calibration de l'électrode a été réalisée suivant la méthode de May et al. (9).

Les mesures spectrophotométriques ont été effectuées à l'aide d'un spectrophotomètre UV–visible Beckman Acta III équipé d'un compartiment de measure thermostaté à 25,0 ± 0,2°C.

Les voltamogrammes ont été enregistrés en utilisant un circuit à trois électrodes : électrode de mesure à carbone vitreux, électrode de référence SCE, contre-électrode de platine. Nous avons utilisé un potentiostat Princeton Applied Research (PAR) 273 comme générateur de signaux électriques et une table traçante X, Y Ifelec 3700. La cellule employée avait une capacité de 2 mL.

Les mesures des temps de relaxation ont été effectuées avec un appareil Bruker AM 250MHz à température ambiante.

Les solvants ont été distillés et l'eau a été ultrafiltrée sur cartouches Millipore. La solution de Gd(DTPA) 0,40 M (Ca-méglumine 0,40 M) dans l'eau a été fournie gracieusement par ORIS bioindustries. La déterriferrioxamine B était un produit Sigma. L'acide acétohydroxamique a été fourni par le professeur Crumbliss.

Spectrophotométrie visible

Les six solutions suivantes ont été préparées : (A) $6{,}9 \times 10^{-3}$ M de chaque ligand dans le méthanol; (B) $Fe(NO_3)_3$ $7{,}25 \times 10^{-2}$ M, HNO_3 0,10 M, $NaNO_3$ 0,10 M dans le mélange méthanol–eau (70 : 30), (C) $NaHCO_3$ $3{,}0 \times 10^{-2}$ M, $NaNO_3$ 10^{-2} M dans le mélange méthanol–eau (70 : 30); (D) $NaNO_3$ $3{,}3 \times 10^{-2}$ M dans l'eau; (E) $NaNO_3$ 10^{-2} M dans le mélange méthanol–eau (70 : 30); (F) HNO_3 $3{,}0 \times 10^{-2}$ M, $NaNO_3$ 10^{-2} M dans le mélange méthanol–eau (70 : 30).

À pH 7

Chaque échantillon comprenait 2,1 mL de la solution (A), un volume de la solution (B) déterminé en fonction du rapport $[Fe^{3+}]/[L]$ choisi, et 0,9 mL de la solution (D). Le mélange a été soniqué pendant 3 min puis le pH a été ajusté entre 6,9 et 7,1 avec la solution (C). Le volume de l'échantillon à été complèté à 5 mL avec la solution (E) dans une fiole jaugée.

À pH 2

La méthode était la même que ci-dessus, mais l'adjustement de la valeur du pH a été effectuée avec la solution (F).

Détermination du point isosbestique

La méthode était la même que ci-dessus, mais le pH a été ajusté à différentes valeurs comprises entre 2,5 et 7,2 à l'aide des solutions (C) et (F).

Dans tous les cas les spectres d'absorption visible ont été enregistrés entre 350 et 550 nm.

Voltamétrie cyclique

Toutes les solutions utilisées ont été préparées à partir d'une solution de $NaNO_3$ 0,10 M dans le mélange méthanol–eau (70 : 30).

Pour les complexes fer(III)–**2** et fer(III)–**3**, une solution stock de $Fe(NO_3)_3$ 10^{-2} M et une solution de ligand 0,10 M toutes deux dans le mélange méthanol–eau (70 : 30) ont été utilisées pour l'étude des complexes en milieu acide (pH <1). La concentration désirée (1–5 mM) a été obtenue par dilution. Pour les complexes préparés avec les ligands synthétisés la quantité nécessaire de ligand a été ajoutée à l'état solide directement dans la cellule à une quantité stoechiométrique de $Fe(NO_3)_3$ 10^{-3} M. Le volume a été complété à 2 mL. Le pH à été ajusté entre 1 et 7 avec $NaHCO_3$ solide ou en solution concentrée dans le mélange méthanol–eau (70 : 30). Les potentiels ont été mesurés par rapport à l'électrode standard au calomel.

Can. J. Chem. Downloaded from www.nrcresearchpress.com by 85.192.166.187 on 09/08/12
For personal use only.

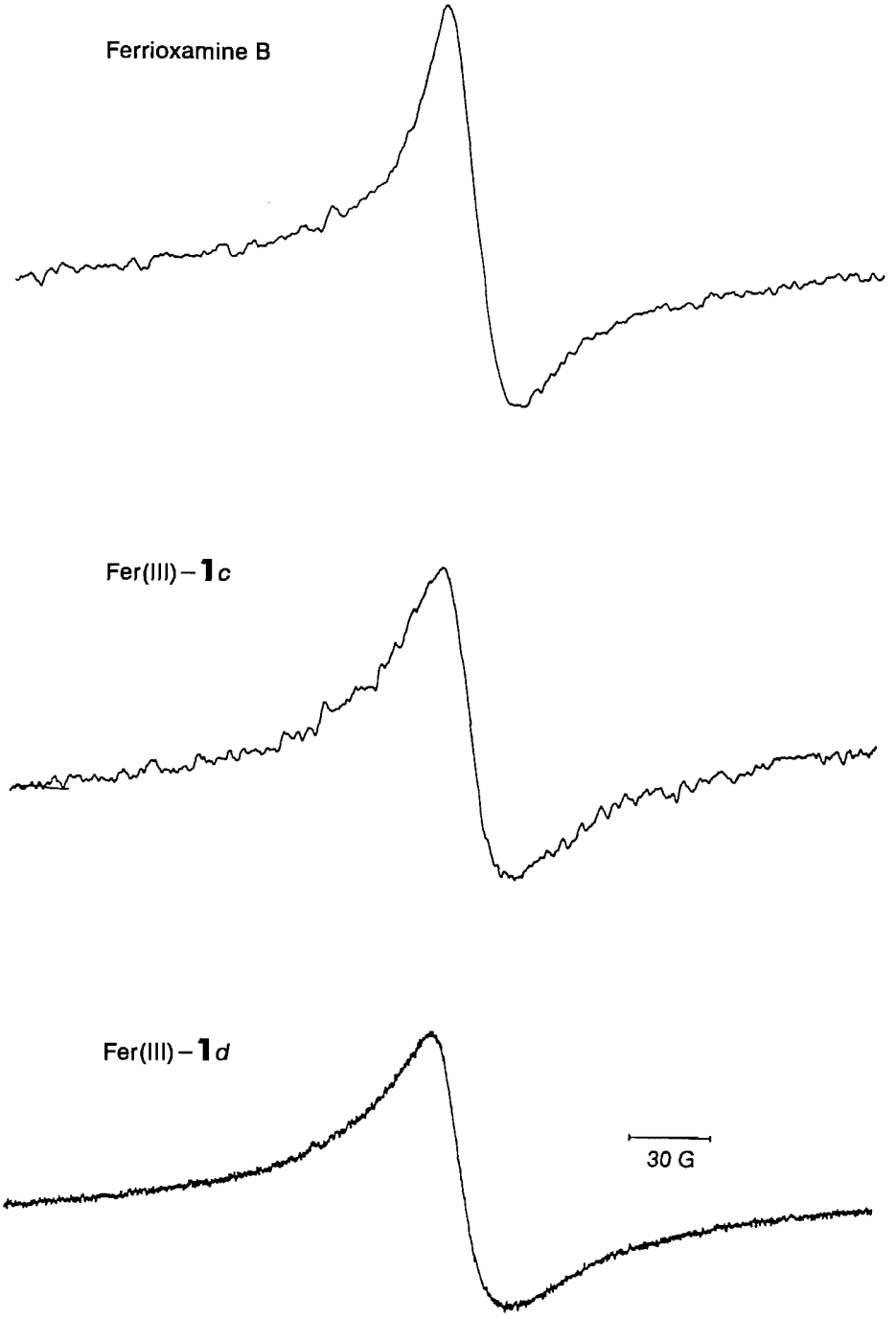

FIG. 2. Spectres RPE dans l'eau des complexes ferrioxamine B (fer(III)–**3**, fer(III)–**1***c* et fer(III)–**1***d*). [fer(III)] = 10^{-3} M, 0,16 M $NaNO_3$, pH 7.

RPE

Les complexes de fer(III) ont été préparés dans l'eau à partir de solutions de $Fe(NO_3)_3$ 10^{-3} M et de ligands $1{,}05 \times 10^{-3}$ M. Le pH a été ajusté à l'aide de $NaHCO_3$ solide et contrôlé au papier pH. Les spectres ont été enregistrés à 110 K.

Constantes d'équilibre

Les solutions de titrage (KOH) ont été préparées par la méthode d'échange d'ion avec l'hydroxyde de baryum (10) et maintenues sous azote débarrassé de O_2 et CO_2 par barbotage dans une solution de Fieser. Le nitrate de potassium a été recristallisé juste avant son utilisation. Le nitrate terrique a été préparé par dissolution de fer métallique dans HNO_3 concentré. $Fe(NO_3)_3{,}9H_2O$ précipité a été recristallisé une fois dans HNO_3 concentré. Toutes les solutions ont été préparées dans le mélange méthanol–eau (30 : 70). La concentration de fer(III) a été établie par réduction en fer(II) et titration du fer(II) par une solution standard de dichromate de potassium. La concentration d'acide dans les solutions de fer a été déterminée par élution sur une colonne échangeuse de cations (Dowex 50W-X8) suivie d'une titration de l'acide libéré par la phénolphtaléine. Les solutions de KOH ont été titrées par l'hydrogènophtalate de potassium. Les valeurs de pK_a ont été obtenues à partir de solutions de ligands 0,10 M dans KNO_3 0,10 M.

La constante de stabilité du complexe FeL^+ a été établie à partir des données spectrophotométriques de complexation par une méthode de moindres carrés non linéaire (11). Un programme appelé MRATIO11 a été développé dans ce but.

Can. J. Chem. Downloaded from www.nrcresearchpress.com by 85.192.166.187 on 09/08/12
For personal use only.

TABLEAU 1. Valeurs des coefficients d'absorption molaire par centre métallique et stoechiométrie des complexes formés

Paramètre	Complexe fer(III)–**1***a*	Complexe fer(III)–**1***b*	Complexe fer(III)–**1***c*	Complexe fer(III) – acide rhodotorulique[a]
ε_M (420) pH 7 (M^{-1} cm^{-1})	2640	2720	2460	2700 (425 nm)
ε_M (470) pH 2 (M^{-1} cm^{-1})	1720	1790	1670	1670 (480 nm)
Stoechiométrie pH 7	2:3	2:3	2:3	2:3
Stoechiométrie pH 1	1:1	1:1	1:1	1:1 (pH 2)

[a]Valeurs déterminées dans l'eau par Raymond et coll. à 425 nm (pH 7) et 480 nm (pH 2) (19).

Relaxométrie

Pour le complexe fer(III)–**1***d* : nous avons préparé les solutions suivantes : (A) $Fe(NO_3)_3$ 0,10 M, HNO_3 0,10 M dans l'eau; (B) ligand **1***d* $3,9 \times 10^{-2}$ M dans l'éthanol absolu; (C) $NaNO_3$ 1,0 M dans l'eau; (D) $NaNO_3$ 0,15 M dans le mélange éthanol–eau (40 : 60) contenant 10% de D_2O.

À 800 μL de la solution (B) ont été ajoutés 200 μL de la solution (A) et 240 μL de la solution (C). La solution obtenue a été neutralisée avec 1 équivalent de $NaHCO_3$ (22,0 mg) et le pH a été ajusté à 7 avec $NaHCO_3$ 0,10 M. D_2O (200 μL) a été ajouté et le volume complété à 2 mL dans une fiole jaugée avec de l'eau bidistillée. La solution a été soniquée 3 min. Le titre de cette solution était 0,010 M en fer(III), à pH 7, 0,15 M de $NaNO_3$, dans le mélange éthanol–eau (40 : 60). À l'aide de la solution (D), nous avons préparé six échantillons de concentrations 0,010; 0,008; 0,006; 0,004; 0,002; 0,001 M en fer(III) pour un volume final de 600 μL par échantillon. Pour le complexe Gd(DTPA), six solutions de même titre et de même volume que pour le fer(III) ont été préparées à partir d'une solution mère commerciale de Gd (DTPA) 0,40 M (Ca-méglumine 0,40 M) dans l'eau.

Résultats

Spectres de RPE de la ferrioxamine B et des complexes formés avec le fer(III) à partir des ligands **1***c et* **1***d*

La figure 2 représente les spectres RPE des complexes formés par les ligands **1***c* et **1***d* avec le fer(III) et de la ferrioxamine B enregistrés dans les mêmes conditions. Dans les trois cas le signal unique était à $g = 4,3$. Cette valeur, commune à tous les complexes polyhydroxamiques du fer(III), est caractéristique d'un environnement octaédrique haut spin de l'ion ferrique (6).

Détermination de la stoechiométrie des complexes fer(III)–hydroxamates dans le mélange méthanol–eau (70 : 30)

La proportion méthanol–eau (70 : 30) a été choisie afin d'assurer une bonne solubilisation des ligands et de leurs complexes avec le fer aux concentrations utilisées. La stoechiométrie des complexes formés par le fer(III) et les ligands a été déterminée par la méthode de Job (12) dans ce mélange à pH 2 et pH 7 en maintenant une concentration constante de ligand. Le fer(III) a été utilisé sous forme de $Fe(NO_3)_3$ et conservé en milieu acide fort (HNO_3 10^{-2} M) afin d'éviter la formation d'hydroxydes de fer (13). Le rapport $[Fe(NO_3)_3]/[\text{ligand}]$ n'a jamais été supérieur à deux fois la stoechiométrie car l'absorption entre 350 et 450 nm du nitrate de fer excédentaire augmentait beaucoup l'absorbance totale et pertubait la détermination des coefficients d'absorption molaire.

Nous avons déterminé ainsi la stoechiométrie des complexes formés par les ligands **1***a*, **1***b* et **1***c* avec le fer(III). L'ensemble des résultats est présenté dans le tableau 1. Les figures 3 et 4 représentent les courbes Absorbance = $f([\text{fer(III)}]/[\text{ligand}])$ à pH 2 et pH 7. Le maximum d'absorption, situé à 420 nm à pH 7, s'est déplacé à 470 nm à pH 2. Cette variation s'est accompagnée d'un changement de couleur des solutions qui de jaune orangé sont devenues rouge pâle. L'analyse des courbes a révélé une stoechiométrie 2 : 3 à pH 7 et 1 : 1 à pH 2 dans tous les cas. Les résultats sont résumés dans le tableau 1. L'étude de la variation de l'absorbance en fonction du pH a montré l'existence de points isosbestiques à 450–460 nm.

Étude par voltamétrie cyclique

Les complexes fer(III)–hydroxamates ont fait l'objet de très nombreuses études électrochimiques (14–17) visant à mieux comprendre les mécanismes de transport du fer dans les microorganismes producteurs de sidérophores. Ces études ont montré que dans ces complexes l'ion fer(III) était réduit à des valeurs de potentiel assez fortement négatives conduisant à des complexes de fer(II) beaucoup moins stables. La plupart de ces études ayant été réalisées en utilisant l'eau comme solvant, il nous a paru indispensable, compte tenu de l'insolubilité des ligands **1** dans ce solvant, d'effectuer une étude électrochimique préalable des complexes du fer(III) avec les ligands **2** et **3** dans le mélange méthanol–eau (70 : 30) et de comparer les caractéristiques de ces complexes avec celles des complexes fer(III) – ligands **1** dans les mêmes conditions (solvant, pH, force ionique). Les résultats sont rassemblés dans le tableau 2.

Dans le solvant utilisé et en milieu acide fort (HNO_3 0,10 M), la réduction du fer(III) en fer(II) est irréversible avec des potentiels cathodiques et anodiques respectivement de +0,26 et +0,90 volt ($E_{p1/2}$ = +0,60 V).

Avec l'acide acétohydroxamique **2**, l'étude a été menée à pH 6,9 et pH 2 pour des rapports fer(III)/**2** variable (fig. 5). À pH 6,9, le voltammogramme présente pour un rapport supérieur ou égal à 3 une vague quasi réversible à $E_{1/2} = -0,62$ V correspondant à la réduction du complexe fer(III)–$(\mathbf{2})_3$. À pH 2, quelques soient les valeurs du rapport fer(III)/**2**, on observe la présence de complexes fer(III)–$(\mathbf{2})_3$ et fer(III)–$(\mathbf{2})_3^+$, la réduction de ces deux complexes se manifestant par deux vagues irréversibles quelque soit la vitesse de balayage.

Le comportement de la déferriferrioxamine **3** est différent dans la mesure où l'on n'observe qu'une seule espèce réductible entre pH 1,5 et 7 caractérisée par une vague quasi réversible ($E_{1/2} = -0,70$ V) à cette dernière valeur de pH (fig. 6). Les

Can. J. Chem. Downloaded from www.nrcresearchpress.com by 85.192.166.187 on 09/08/12
For personal use only.

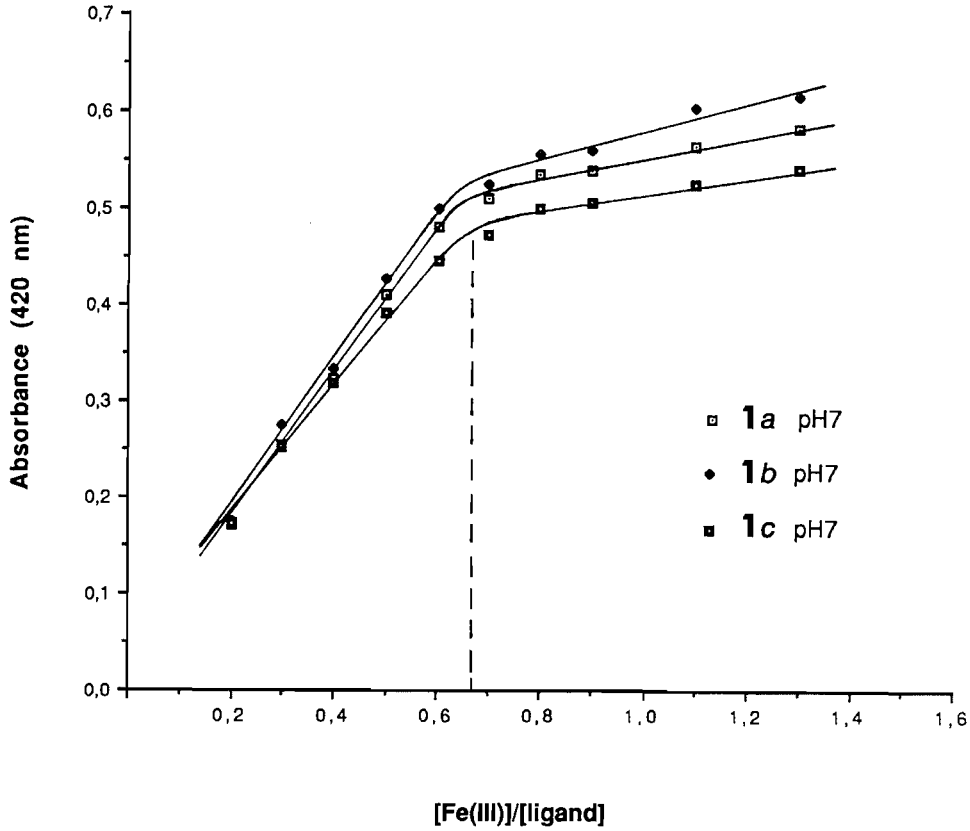

FIG. 3. Détermination de la stoechiométrie en solution des complexes fer(III)–**1***a*, fer(III)–**1***b*, fer(III)–**1***c*. Absorbance à 420 nm = *f*([fer(III)]/[ligand]). [Ligand] = $2{,}9 \times 10^{-4}$ M, pH 7, $NaNO_3$ 0,010 M, méthanol–eau (70 : 30).

TABLEAU 2. Valeurs des potentiels électrochimiques (V) des complexes fer(III)–**1**, fer(III)–**2** et fer(II)–**3** en fonction du pH

		Ligands					
		2	**3**	**1***a*	**1***b*	**1***c*	**1***d*
pH 1–2	red.	−0,26 / −0,60	−0,73	−0,18 / −0,58	−0,36 / −0,75	—	−0,30
	ox	—	—	—	—	—	−0,75
		Irréversible	Irréversible	Irréversible	Irréversible	Adsorption sur électrode	Irréversible
pH 7	red	−0,67	−0,77	−0,75 / −0,63	−0,72 / −0,60	−0,72 / −0,54	−0,75
	ox	−0,58	−0,65	−0,34	−0,30	−0,36	—
	$E_{1/2}$	−0,62	−0,70				
		Quasi réversible	Quasi réversible	Quasi réversible	Quasi réversible	Quasi réversible	Irréversible

valeurs de $E_{1/2}$ observées pour les complexes de fer(III) avec les ligands **2** et **3** sont pratiquement identiques dans le mélange méthanol–eau (70 : 30) et dans l'eau (14, 15, 18) à pH 7–7,5.

Les voltammogrammes des complexes **1***a–d* avec le fer(III) ont été enregistrés dans les mêmes conditions que ci-dessus en utilisant une concentration de $5{,}0 \times 10^{-3}$ M en fer(III) et $7{,}5 \times 10^{-3}$ M en ligand (fig. 7). À pH 7, on observe pour les complexes avec **1***a–d* une seule vague quasi réversibles vers −0,70 V attribuable aux complexes de stoechiométrie $Fe_2(\mathbf{1})_3$. Cette valeur est très proche de celle mesurée pour le complexe avec l'acide rhodotorulique (−0,65 V) (19). À pH 2, on observe avec les ligands **1***a*, **1***b* et **1***d* deux espèces réductibles entre 0 et −0,70 V. Il s'agit sans doute des complexes fer(III)–L^+ et fer$(III)_2$–L_3 en équilibre. Avec **1***c*, un important courant de réduction apparait dès −0,4 V qui ne peut être attribué à la réduction d'un complexe de fer(III) : dans ce cas il y a sans doute un phénomène d'adsorption sur l'électrode dû peut-être à la présence dans ce ligand d'un noyau pyridine non substitué.

Détermination de la constante de formation des complexes fer(III)–ligand dihydroxamique

La stabilité des complexes fer(III)–dihydroxamate a pu être exprimée à l'aide des constantes β_{110} et β_{230} correspondant aux équilibres suivants :

$$Fe^{3+} + L^{2-} \rightleftharpoons FeL^{+}$$

$$\beta_{110} = \frac{[FeL^{+}]}{[Fe^{3+}][L^{2-}]}$$

$$2Fe^{3+} + 3L^{2-} \rightleftharpoons Fe_2L_3$$

$$\beta_{230} = \frac{[Fe_2L_3]}{[Fe^{3+}]^2[L^{2-}]^3}$$

Toutefois, ces constantes ne caractérisent qu'imparfaitement les équilibres de formation des complexes. Ceux-ci sont en effet

Can. J. Chem. Downloaded from www.nrcresearchpress.com by 85.192.166.187 on 09/08/12
For personal use only.

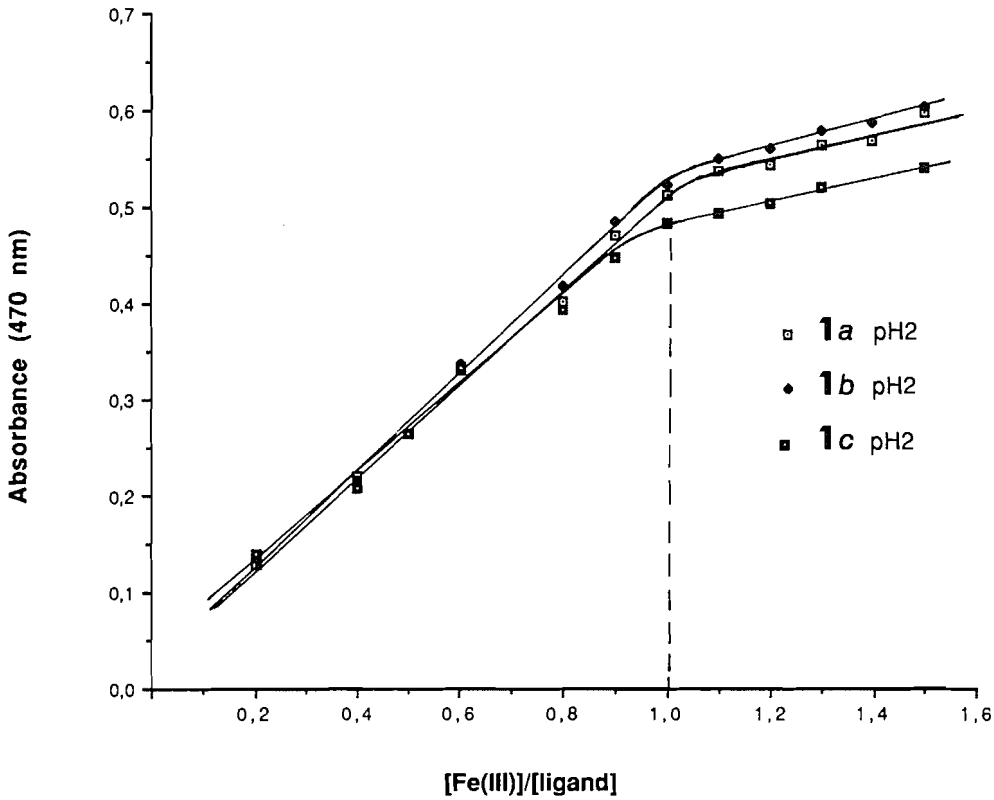

FIG. 4. Détermination de la stoechiométrie en solution des complexes fer(III)–**1***a*, fer(III)–**1***b*, fer(III)–**1***c*. Absorbance à 470 nm = *f*([fer(III)]/[ligand]). [Ligand] = $2{,}9 \times 10^{-4}$ M, pH 2, $NaNO_3$ 0,010 M, méthanol–eau (70 : 30).

dépendants du pH puisque, pour des pH inférieurs à 7, les acides hydroxamiques, de pK_a voisins de 9, sont en grande partie non dissociés et que l'ion Fe^{3+} est hydrolysé. Les équilibres tenant compte de l'influence du pH sont :

$$Fe^{3+} + H_2L \rightleftharpoons FeL^+ + 2H^+$$

$$2Fe^{3+} + 3H_2L \rightleftharpoons Fe_2L_3 + 6H^+$$

La constante d'équilibre effective K_{eff} pour le premier équilibre s'écrit (12) :

$$\log K_{eff} = \log \beta_{FeL} - n \log \alpha_L{}^{-1}$$

avec

$$\alpha_L = (1 + \beta_{011}[H^+] + \beta_{012}[H^+]^2 + \ldots)^{-1}$$

où

$$\beta_{01n} = \frac{[LH_n]^{n+}}{[H^+]^n[L]}$$

sont les constantes d'acidité globales du ligand.

La détermination des constantes de stabilité des complexes fer(III)–dihydroxamate nécessitant une quantité de ligands assez importante, seule la constante du complexe FeL^+ avec le ligand **1***a* a pu être déterminée. Pour l'obtenir, les valeurs des pK_a des groupements hydroxamiques du ligand **1***a* ont été déterminées par titration potentiométrique dans le mélange méthanol–eau (30 : 70). Pour comparaison, le pK_a de **2** a été déterminé dans les mêmes conditions de solvant et dans l'eau pure. Les valeurs de pK_a sont rassemblées dans le tableau 3. On constate

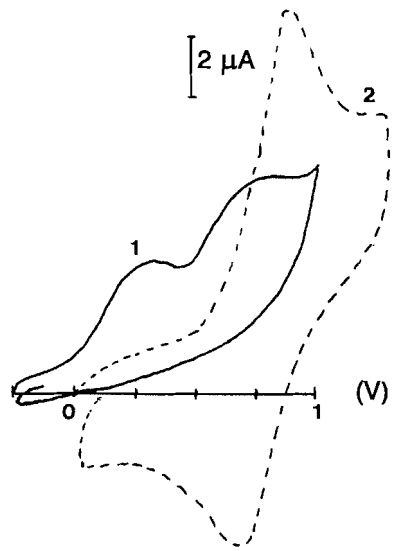

FIG. 5. [Acide acétohydroxamique] = 10 mM, [fer(III)] = 1,0 mM dans le mélange méthanol–eau (70 : 30); électrode de carbone vitreux vs. SCE, 100 mV/s. 1: pH 2; 2: pH 6,9.

que les valeurs sont un peu plus élevées (0,2 à 0,5 unités de pK_a) dans le mélange méthanol–eau (30 : 70) que dans l'eau pure.

La constante d'équilibre pour la réaction : $Fe^{3+} + H_2L \rightleftharpoons FeL^+ + 2H^+$ a été déterminée à pH 1, pour lequel le complexe FeL^+ était seul présent, en mesurant l'absorption entre 350 et 600 nm d'une solution $3{,}0 \times 10^{-4}$ M du ligand **1***a*, en présence de quantités croissantes de Fe^{3+} et en utilisant la valeur ϵ_{470} pour le complexe FeL^+. La constante K_{eff} ainsi obtenue (log K_{eff} = 2,32) à été utilisée pour déterminer log β_{110} = 21,3, à pH 1, con-

Can. J. Chem. Downloaded from www.nrcresearchpress.com by 85.192.166.187 on 09/08/12
For personal use only.

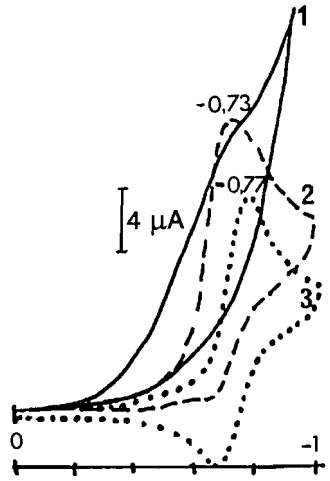

FIG. 6. [3] = 3,0 mM, [fer(III)] = 1,0 mM dans le mélange méthanol–eau (70 : 30); électrode de carbone vitreux vs. SCE, 100 mV/s. 1: pH 1,5; 2: pH 4,4; 3: pH 7.

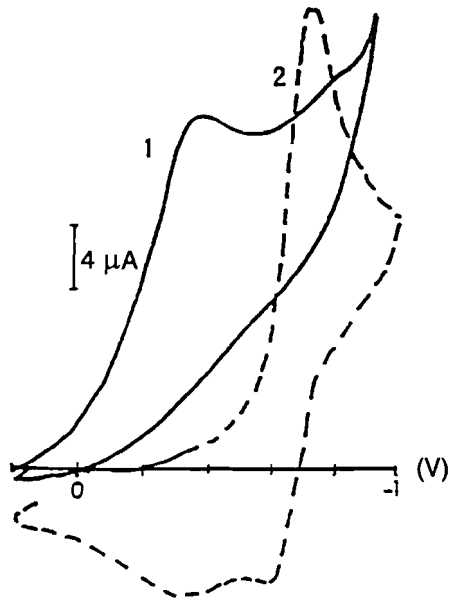

FIG. 7. [1*b*] = 7,5 mM, [fer(III)] = 5,0 mM dans le mélange méthanol–eau (70 : 30); électrode de carbone vitreux vs. SCE, 100 mV/s. 1: pH 1,6; 2: pH 7,1.

naisant log β_H (avec = $\beta_H = [H_2L]/[H^+][L^{2-}]$). Cette valeur, en accord avec les données obtenues avec d'autres dihydroxamates (19), est un peu plus faible que les valeurs de log β_{110} mesurées par Raymond et coll. (20) pour les complexes FeL^+ où L sont des dihydroxamates de formule générale :

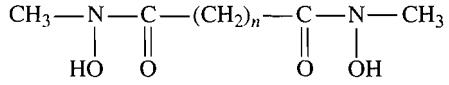

Cette stabilité un peu plus faible du complexe fer(III) – ligand **1***a* est peut être due à des effets stériques provenant de la rigidité du cycle pyridinique et des liaisons amides dans ce complexe.

Nous n'avons pu déterminer la constante log β_{230} pour ce complexe en raison de sa valeur trop élevée.

TABLEAU 3. Valeurs des pK_a de l'acide hydroxamique (AH) et du ligand **1***a* mesurées dans l'eau pure et dans le mélange méthanol–eau (30 : 70)

Ligand	pK_a Mélange H_2O–MeOH	pK_a H_2O
AH[a]	9,95	9,36
	9,16	8,60
1*a*	9,95	9,36
	8,90	8,34

[a]AH = $CH_3N(OH)C(O)(CH_2)_8C(O)N(OH)CH_3$.

Détermination et comparaison de la relaxivité des complexes fer(III)–1d et Gd(DTPA)

En présence d'une espèce paramagnétique, les vitesses de relaxation du spin nucléaire $1/T_1$ et $1/T_2$ se décomposent en la somme d'une contribution diamagnétique du solvant (mouvements moléculaires et échanges chimiques) et d'une contribution de l'espèce paramagnétique (21). In vivo, la contribution diamagnétique en $1/T_1$ est beaucoup plus faible que celle en $1/T_2$. Les contributions paramagnétiques étant équivalentes, l'addition d'un agent paramagnétique a une influence beaucoup plus grande sur le temps de relaxation spin-réseau T_1 que sur le temps de relaxation spin–spin T_2 (22). Nous n'avons donc considéré que l'effet des agents paramagnétiques sur le temps de relaxation T_1, en négligeant les effets sur le temps T_2.

En solution aqueuse, la vitesse de relaxation des noyaux d'hydrogène de l'eau dépend de la concentration c de l'espèce paramagnétique selon la relation expérimentale : $v = v_0 + Rc$ où v_0 est la vitesse de relaxation en absence d'agent paramagnétique et R la relaxivité (mol^{-1} L s^{-1}). R est une fonction complexe des distances et des interactions entre l'espèce paramagnétique et l'eau. Après transformée de Fourier du signal des noyaux d'hydrogène de l'eau, nous avons mesuré l'aimantation de l'échantillon $M_z(t)$ dont la loi d'évolution est : $M_z(t) = A + B \exp(-t/T_1)$ où A et B sont des paramètres tenant compte de la réponse du spectromètre et de l'efficacité de l'impulsion de 180°. Les données ont été traitées par une méthode de moindres carrés non linéaire pour ajuster les paramètres A, B et T_1.

Les deux ions ferriques du complexe $Fe_2(\mathbf{1}d)_3$ étant indépendants, nous avons déterminé les relaxivités par rapport aux concentrations en ion métallique dans chaque cas. La figure 8 représente les droites $1/T_1 = f([\text{Ligand}])$ dont les pentes sont égales à la relaxivité. Les vitesses de relaxation d'un ion fer(III) dans la structure dimère créée en solution avec le ligand **1***d*, dans le domaine de concentration étudié, sont 5 fois plus faibles que celles du complexe Gd(DTPA) dans les mêmes conditions. Ceci se traduit par des valeurs de relaxivité de $4{,}9 \times 10^{-3}$ M^{-1} s^{-1} et $26{,}0 \times 10^{-3}$ M^{-1} s^{-1} respectivement.

Conclusion

L'étude rapportée ci-dessus montre que les ligands **1***a–d* se comportent en solution vis-à-vis du fer(III) de manière très comparable à l'acide rhodotorulique, que ce soit pour la stoechiométrie des complexes, leurs propriétés électrochimiques et la constante de dissociation mesurée avec le ligand **1***a* à pH 1. Ces similitudes suggèrent que le noyau pyridine et les fonctions amides présents dans ces ligands n'entrent pas en compétition avec les groupements hydroxamates pour la com-

Can. J. Chem. Downloaded from www.nrcresearchpress.com by 85.192.166.187 on 09/08/12
For personal use only.

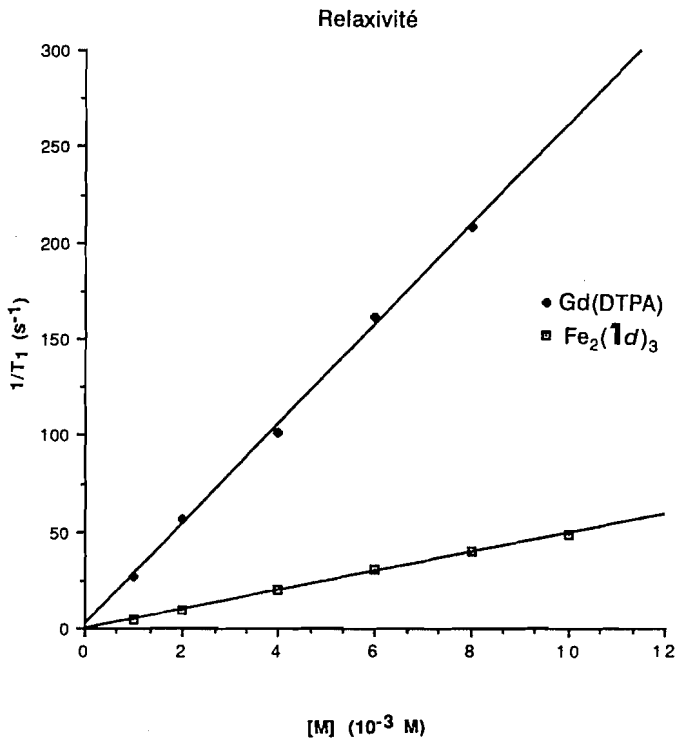

FIG. 8. Courbes $1/T_1 = f([M])$ pour les complexes $Fe_2(\mathbf{1}d)_3$ et Gd(DTPA).

plexation du fer(III). On a pu constater aussi qu'il n'y avait pas de variations sensibles de ces propriétés en remplaçant l'eau comme solvant par un mélange méthanol–eau. La stabilité élevée et la forte relaxivité de ces complexes en font des produits de contraste pour l'IRM potentiellement intéressants. Leur trop faible solubilité dans l'eau constitue toutefois un handicap important qui ne pourra être surmonté qu'en rendant les ligands eux mêmes plus hydrosolubles par l'introduction de substituants chargés positivement ou négativement.

Remerciements

Alvin L. Crumbliss remercie l'American Chemical Society Petroleum Research Fund, pour une aide financière. F. Chaubet remercie la Ligue Nationale Française contre le Cancer pour son soutien financier.

1. F. Chaubet, M. Nguyen van Duong, J. Courtieu, A. Gaudemer, A. Gref et A.L. Crumbliss. Tetrahedron Lett. 5729 (1990).
2. F. Chaubet, M. Nguyen van Duong, J. Courtieu, A. Gaudemer, A. Gref et A.L. Crumbliss. Can. J. Chem. **69**, 1107 (1991).
3. J.B. Neilands. *Dans* Microbial iron metabolism. *Édité par* J.B. Neilands. Academic Press, New York. 1974.
4. K.N. Raymond. Adv. Chem. Ser. **162**, 98 (1977).
5. K.N. Raymond et C.J. Carrano. Acc. Chem. Res. **12**. 183 (1979).
6. B.F. Matzanke, G. Muller-Matzanke et K.N. Raymond. Iron carriers and iron proteins Phys. Bioinorg. Chem. Ser. Vol. 4. V.C.H., Cambridge. 1989. Chap. 21.
7. A.L. Crumbliss. *Dans* CRC handbook of microbial iron chelates. *Édité par* G. Winkelmann. CRC Press, Boca Raton, Fla. 1991. p. 177.
8. J.B. Neilands. Struct. Bonding (Berlin), **1**, 59 (1966).
9. P.M. May, D.R. Williams, P.W. Linder et R.G. Torrington. Talanta, **20**, 249 (1982).
10. M. Melloun, J. Havel et E. Hogfeldt. Computation of solution equilibria. John Wiley and Sons, New York. 1988. p. 14.
11. J. Havel et M. Meloun. *Dans* Computational methods for the determination of formation constants. Plenum Press, New York. 1985. p. 252.
12. F.J.C. Rossotti et H. Rossotti. The determination of stability constants. McGraw–Hill, New York. 1961.
13. A.E. Martell et R.M. Smith. Critical stability constants. Vols. 1–5. Plenum Press, New York. 1974–1977.
14. K. Abu-Dari, S.R. Cooper et K.N. Raymond. Inorg. Chem. **17**, 3394 (1978).
15. S.R. Cooper, J.V. McArdle et K.N. Raymond. Proc. Natl. Acad. Sci. U.S.A. **75**, 3551 (1978).
16. D.J. Brockway, K.S. Murray et P.J. Newman. J. Chem. Soc. Dalton Trans. 1112 (1980).
17. T. Emery. Biochemistry, **10**, 1483 (1971).
18. H. Bickel, G.E. Hall, W. Keller-Schierlein, V. Prelog, E. Wischer et A. Wettstein. Helv. Chim. Acta, **18**, 2129 (1980).
19. C.J. Carrano, S.R. Cooper et K.N. Raymond. J. Am. Chem. Soc. **101**, 599 (1979).
20. S.J. Barclay, B.H. Huynh et K.N. Raymond. Inorg. Chem. **23**, 2011 (1984).
21. R.B. Lauffer. Chem. Rev. **87**, 901 (1987).
22. J.D. Lovin, G.E. Wesbey, B.L. Engelstadt, G. Sosnovsky, M. Moseley, D.L. Tuck et R.C. Brasch. Magn. Reson. Imaging, **3**, 73 (1985).

Can. J. Chem. Downloaded from www.nrcresearchpress.com by 85.192.166.187 on 09/08/12
For personal use only.

Reverse pulse voltammetry and polarography: a general analytical solution

LUIS CAMACHO[1] AND JUAN JOSÉ RUIZ
Departamento de Química Física y Termodinámica Aplicada, Facultad de Ciencias, Universidad de Córdoba, c) San Alberto Magno s/n E-14004 Córdoba, Spain
AND
CARMEN SERNA[1], ANGELA MOLINA, AND FRANCISCO MARTÍNEZ-ORTIZ
Departamento de Química Física, Facultad de Química, Universidad de Murcia, Campus de Espinardo, E-30100 Murcia, Spain
Received February 4, 1994

LUIS CAMACHO, JUAN JOSÉ RUIZ, CARMEN SERNA, ANGELA MOLINA, and FRANCISCO MARTÍNEZ-ORTIZ. Can. J. Chem. **72**, 2369 (1994).

A rigorous analytical solution to reverse pulse techniques for a plane electrode expanding with an arbitrary power of time is presented. Our results include the plane approximation for SMDE as well as the expanding plane electrode model for DME. In the case of SMDE, our results have been contrasted with those obtained by numerical solution of the problem, obtaining identical results. Finally, we have compared our treatment with previous solutions in literature.

LUIS CAMACHO, JUAN JOSÉ RUIZ, CARMEN SERNA, ANGELA MOLINA et FRANCISCO MARTÍNEZ-ORTIZ. Can. J. Chem. **72**, 2369 (1994).

On présente une solution analytique rigoureuse pour renverser les techniques de pulsation d'une électrode plane en expansion avec une puissance arbitraire du temps. Nos résultats incluent l'approximation plane de la SMDE ainsi que le modèle de l'électrode plane en expansion de la SME. Dans le cas de la SMDE, on a comparé nos résultats avec ceux obtenus par la solution numérique du problème et les résultats obtenus sont les mêmes. Enfin, on a comparé notre traitement avec les solutions proposées antérieurement dans la littérature.

[Traduit par la rédaction]

Can. J. Chem. Downloaded from www.nrcresearchpress.com by 85.192.166.187 on 09/08/12
For personal use only.

Introduction

Many authors have studied the problem of the *i–t* Faradaic response of a slow charge transfer reaction to a second potential pulse for several electrode models (1–8). Their solutions can be used in Reverse Pulse (RP) techniques: Reverse Pulse Voltametry (RPV, stationary plane electrode) or Reverse Pulse Polarography (RPP, expanding plane electrode). This application has been explicitly carried out in certain papers (1, 8), while in others the obtained solutions were used only in Differential Pulse (DP) techniques (2–7).

Among double pulse techniques, RP is the least complex and, without doubt, the most powerful in kinetic applications. Up-to-date RP has been applied to the analysis of limiting currents (9–11) yielding qualitative information on the degree of reversibility of the electrode process; this information is similar to that obtained from cyclic voltametry (12). However, the complexity in the resulting analytical solutions and, more importantly, the controversy over the rigor of these solutions, have limited their kinetic applications in practice.

As far as we know, only the equations derived by Matsuda (1); Aoki et al. (3) (expanding plane electrode), and Lovric and Osteryoung (2) and Aoki and Osteryoung (4) (stationary plane electrode) are mathematically rigorous for a slow charge transfer reaction; however, the analytical response deduced by these authors is given by complex integral equations which should be solved numerically in each particular case. The authors of other papers claim to have obtained a rigorous analytical solution to the problem; however, in most of these papers some kind of approximation was used (5-8). These approximations are, in general, very interesting but sometimes not explicitly assumed in the paper. One of the more frequently used approximation is the analytical expression of surface concentrations and concentration gradient of the first pulse remain unaltered during the second pulse, that is to say, the bases of the superposition principle have been applied under conditions in which this principle is not applicable. The applicability of superposition principle to yield rigorous results is restricted to reversible systems, it depends on electrode geometry and on the values of diffusion coefficients of the electroactive couple (2, 13–17).

This paper is to present a rigorous and closed analytical solution to a plane electrode expanding with an arbitrary power of time under conditions relevant to RP techniques, i.e., when the boundary conditions selected for the application of the second pulse correspond to a first step controlled by diffusion. Our results, which used plane approximation for SMDE and expanding plane electrode model for DME, are in excellent agreement with the results obtained by numerical solutions (18, 19). In certain cases, we have also reproduced our solutions using Laplace Transforms.

Theory

Let us consider the following charge-transfer reaction

$$[1] \qquad A + ne^- \underset{k_b}{\overset{k_f}{\rightleftharpoons}} B$$

and assume that the area of the plane electrode $q(t) = q_0 t^z$, increases with any power $z \geq 0$ of time t($z = 2/3$ for a DME and $z = 0$ for the planar approximation of a SMDE). Operator $\hat{D}_i$ is given by (20)

$$[2] \qquad \hat{D}_i = \frac{\partial}{\partial t} - D_i \frac{\partial^2}{\partial x^2} - \frac{zx}{t} \frac{\partial}{\partial x} \qquad i = \text{A or B}$$

We shall denote by E_1, E_2, and t_1, t_2, the potential and

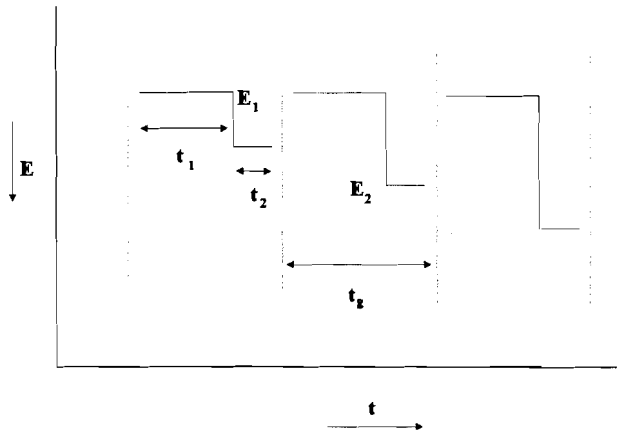

FIG. 1. Potential–time waveform corresponding to the RP technique.

time durations of each pulse, respectively. Likewise, we shall assume these potentials to be superimposed to a linear ramp of potential, which is only effective in successive drops of life time t_d (see Fig. 1). In the RP technique E_1 is always constant and corresponds to a potential at which the reduction process is controlled by diffusion, whereas E_2 shifts to anodic potentials. However, these potential conditions will be applied later. The corresponding currents for each pulse will be called i_1 and i_2, respectively. The signal used in the RP technique is given by $i_2 = i_{RP}$

The experimental time may be divided into two periods. In the first period ($0 \leq t \leq t_1$) the potential is maintained at value E_1. Under these conditions the concentration profiles $C_A^1(x,t)$ and $C_B^1(x,t)$ and the current–time response are given by (21)

$$[3] \qquad \frac{C_A^1(x,t)}{C_A^*} = \frac{C_A^1(s1_A,\chi)}{C_A^*} = 1 + \frac{1}{1+\gamma K_1} \times \sum_{j=1} \frac{(-1)^j \psi_j^z(s1_A)}{\prod_{k=1}^{j} p_k(z)} \chi^j$$

$$[4] \qquad \frac{C_B^1(x,t)}{C_A^*} = \frac{C_B^1(s1_B,\chi)}{C_A^*} = -\frac{\gamma}{1+\gamma K_1} \times \sum_{j=1} \frac{(-1)^j \psi_j^z(s1_B)}{\prod_{k=1}^{j} p_k(z)} \chi^j$$

$$[5] \qquad i_1(t) = nFq_0 t^z \sqrt{\frac{(2z+1)D_A}{\pi t}} \frac{F_z(\chi)}{1+\gamma K_1} C_A^*$$

where

$$[6] \qquad \psi_j^z(s1_i) \equiv \psi_{j/(2z+1)}(s1_i)$$

are the Koutecky functions (22)

$$[7] \qquad \begin{cases} s1_i = \sqrt{\dfrac{(2z+1)}{4tD_i}}\, x \\ \chi = \sqrt{\dfrac{4t}{(2z+1)D_A}} \dfrac{1+\gamma K_1}{K_1^\alpha} k_s \end{cases}$$

$$[8] \qquad K_i = \exp \frac{nF}{RT}(E_i - E^0)$$

and $p_k(z)$ and $F_z(\chi)$ are given in Appendix A.

From $t \geq t_1$ the potential is maintained at E_2. Thus during the second period $0 \leq \tau_2 \leq t_2$ with $t = t_1 + \tau_2$ and the operator $\hat{D}_i$ becomes

$$[9] \qquad \hat{D}_i = \frac{\partial}{\partial \tau_2} - D_i \frac{\partial^2}{\partial x^2} - \frac{zx}{(t_1+\tau_2)} \frac{\partial}{\partial x}$$

the boundary value is now given by

$$[10] \qquad \hat{D}_A C_A = \hat{D}_B C_B = 0$$

$$[11] \qquad \left.\begin{array}{l} \tau_2 = 0,\ x \geq 0 \\ \tau_2 \geq 0,\ x \to \infty \end{array}\right\} \begin{array}{l} C_A^2(x,t) = C_A^1(x,t) \\ C_B^2(x,t) = C_B^1(x,t) \end{array}$$

At $\tau_2 > 0$, $x = 0$

$$[12] \qquad D_A \left(\frac{\partial C_A^2(x,t)}{\partial x}\right)_{x=0} = -D_B \left(\frac{\partial C_B^2(x,t)}{\partial x}\right)_{x=0} = \frac{i_2}{nFq(t)}$$

$$[13] \qquad \frac{i_2}{nFq(t)} = \frac{k_s}{K_2^\alpha}\left(C_A^2(x=0,t) - K_2 C_B^2(x=0,t)\right)$$

As differential equations [10] are linear (see eq. [2] or [9]), any linear combination of solutions is also a solution. Thus, we will suppose that $C_A^2(x,t)$ and $C_B^2(x,t)$ have the form

$$[14] \qquad \begin{array}{l} C_A^2(x,t) = C_A^1(x,t) + \tilde{C}_A(x,t) \\ C_B^2(x,t) = C_B^1(x,t) + \tilde{C}_B(x,t) \end{array}$$

where the superscripts of C_A^i and C_B^i ($i = 1$ or 2) refer to first and second pulse, respectively.

The new unknown functions $\tilde{C}_A(x,t)$ and $\tilde{C}_B(x,t)$ have the advantage that they are solutions for the problem with null initial conditions (see eq. [11]).

When using dimensionless parameters, it is appropriate to assume that $\tilde{C}_A(x,t)$ and $\tilde{C}_B(x,t)$ have the form (22, 23)

$$[15] \qquad \begin{cases} \tilde{C}_A(x,t) = \sum_{j,m} \phi_{j,m}(s2_A)\beta^{j/2} y^m \\ \tilde{C}_B(x,t) = \sum_{j,m} \delta_{j,m}(s2_B)\beta^{j/2} y^m \end{cases}$$

with

$$[16] \qquad s2_i = \frac{x}{2\sqrt{D_i \tau_2}}$$

$$[17] \qquad \beta = \frac{\tau_2}{t_1 + \tau_2}$$

$$[18] \qquad y = \sqrt{\frac{4\tau_2}{D_A}}\, k_s \frac{1+\gamma K_2}{K_2^\alpha}$$

Inserting eqs. [15]–[18] in [10], we obtain

$$[19] \qquad \phi''_{j,m}(s2_A) + 2s2_A \phi'_{j,m}(s2_A) - 2(j+m)\phi_{j,m}(s2_A) = -4zs2_A \phi'_{j-2,m}(s2_A) - 2(j-2)\phi_{j-2m}(s2_A)$$

Can. J. Chem. Downloaded from www.nrcresearchpress.com by 85.192.166.187 on 09/08/12
For personal use only.

Can. J. Chem. Downloaded from www.nrcresearchpress.com by 85.192.166.187 on 09/08/12
For personal use only.

[20] $$\delta''_{j,m}(s2_B) + 2s2_B\delta'_{j,m}(s2_B) - 2(j+m)\delta_{j,m}(s2_B) = -4zs2_B\delta'_{j-2,m}(s2_B) - 2(j-2)\delta_{j-2m}(s2_B)$$

when $E_1 \rightarrow -\infty(\chi \rightarrow \infty)$ from eqs. [3]–[4] we deduce

[21] $$C_A^1(s1_A = 0,\ \chi \rightarrow \infty) = 0$$

[22] $$C_B^1(s1_B = 0,\ \chi \rightarrow \infty) = \gamma C_A^*$$

[23] $$\gamma\left(\frac{\partial C_A^1(s1_A, \infty)}{\partial s1_A}\right)_{s1_A=0} = -\left(\frac{\partial C_B^1(s1_B, \infty)}{\partial s1_B}\right)_{s1_B=0} = \frac{2\gamma C_A^*}{\sqrt{\pi}}$$

[24] $$i_1(t) = i_{1d}(t) = nFq_0t^z\sqrt{\frac{(2z+1)D_A}{\pi t}}\,C_A^*$$

Therefore, for $\tau_2 \geq 0$, eq. [14] at the surface of electrode takes the form

[25] $$C_A^2(x=0,\ t) = \sum_{j,m}\phi_{j,m}(s2_A = 0)\beta^{j/2}y^m$$

[26] $$C_B^2(x=0,\ t) = \gamma C_A^* + \sum_{j,m}\delta_{j,m}(s2_B = 0)\beta^{j/2}y^m$$

and the surface concentration gradients of species A and B

[27] $$\left(\frac{\partial C_A^2(x,\ t)}{\partial x}\right)_{x=0} = \underbrace{\frac{\sqrt{2z+1}}{2\sqrt{D_At}}\left(\frac{2}{\sqrt{\pi}}\,C_A^*\right)}_{\text{First pulse component}} + \underbrace{\frac{1}{2\sqrt{D_A\tau_2}}\sum_{j,m}\phi'_{j,m}(s2_B = 0)\beta^{j/2}y^m}_{\text{Second pulse component}}$$

[28] $$\left(\frac{\partial C_B^2(x,\ t)}{\partial x}\right)_{x=0} = \underbrace{\frac{\sqrt{2z+1}}{\sqrt{2}D_Bt}\left(\frac{-2\gamma}{\sqrt{\pi}}\,C_A^*\right)}_{\text{First pulse component}} + \underbrace{\frac{1}{2\sqrt{D_B\tau_2}}\sum_{j,m}\delta'_{j,m}(s2_B = 0)\beta^{j/2}y^m}_{\text{Second pulse component}}$$

by substituting eqs. [14], [15] in eq. [11] we deduce that for $s_{2i} \rightarrow \infty$

[29] $$\delta_{j,m}(s2_B) = \phi_{j,m}(s2_A) = 0$$

from eq. [12] with eqs. [27] and [28], it is clear that for $s_{2i} = 0$

[30] $$\gamma\phi'_{j,m}(s2_A = 0) = -\delta'_{j,m}(s2_B = 0)$$

and from eqs. [13], [21], [22], [25]–[27] we obtain

[31] $$\sum_{j,m}\phi'_{j,m}(s2_A = 0)\beta^{j/2}y^m = -\frac{\gamma K_2}{1+\gamma K_2}\,C_A^*y + \frac{y}{1+\gamma K_2}\sum_{k,l}\left(\phi_{k,l}(s2_A = 0) - K_2\delta_{k,l}(s2_B = 0)\right)\beta^{k/2}y^l - 2\sqrt{\frac{2z+1}{\pi}}\,\beta^{1/2}C_A^*$$

In RP, the surface concentrations obtained by the application of first pulse are constant (see eqs. [21], [22]), as a consequence of the condition $E_1 \rightarrow -\infty$. However, it is clear that the first pulse component in the surface concentration gradient (eq. [27] or [28]) always depends on time. Therefore, when the second pulse is applied, the analytical expression of this gradient component changes. This variation is reflected in the last term or the right hand side of eq. [31]. Consequently, our treatment is strictly rigorous.

From eqs. [19], [20], [30], and [31], we deduce the following limiting conditions for the $\phi_{j,m}$ functions
As $s2_i \rightarrow 0$

[32] $$\phi'_{0,1} = -\frac{\gamma K_2}{1+\gamma K_2}\,C_A^*$$

[33] $$\phi'_{1,0} = -2\sqrt{\frac{2z+1}{\pi}}\,C_A^*$$

[34] $$\phi'_{j,m} = \phi_{j,m-1} \quad m \geq 1$$

[35] $$\phi'_{j,0} = 0 \quad \text{unless } j = 1$$

Following the procedure referenced in (23), we solve for the $\phi_{j,m}(s2_A)$ and $\delta_{j,m}(s2_B)$ functions and, therefore, the concentration profiles (which are given in eqs. [A4] and [A5] in Appendix A).

Inserting the $\phi_{j,m}(s2_A)$ function is eq. [13] leads to the following expression for i_{RP}

[36] $$i_{RP}(t) = i_{1d}(t) + nFq_0t^z\sqrt{\frac{D_A}{t_2}}\,C_A^*\{ZG_z(\beta, y) + \mu_dH_z(\beta, y)\}$$

[37] $$Z = -\frac{\gamma K_2}{(1+\gamma)K_2}$$

[38] $$\mu_d = -\frac{2}{y}\sqrt{\frac{(2z+1)\beta}{\pi}}$$

In eq. [36] the G_z series (which is given in Appendix A and refs. 8 and 23) is multiplied by Z. Taking into account that Z can also be written as (eqs. [13], [21], [22], [31])

[39] $$Z = \frac{C_A^1(s1_A = 0,\ \chi \rightarrow \infty) - K_2C_B^1(s1_B = 0,\ \chi \rightarrow \infty)}{C_A^*(1+\gamma K_2)}$$

In the second pulse, the G_z series multiplies the constant component of first pulse (see eqs. [39], [21], [22]). On the other hand, the series H_z (given in Appendix A) is multiplied

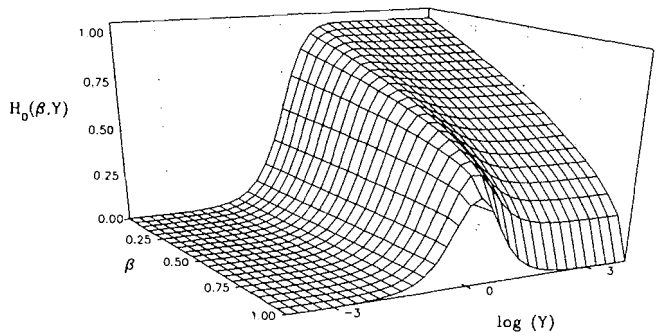

FIG. 2. 3D plot of $H_0(\beta, y)$ vs. β and log y.

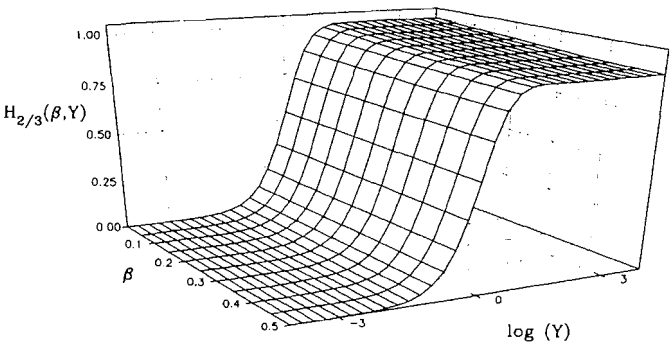

FIG. 3. 3D plot of $H_{2/3}(\beta, y)$ vs. β and log y.

by μ_d and appears as a consequence of the consideration of the disturbance suffered by the first pulse concentration gradient component due to the second pulse application.

i_{RP} was also deduced by making $E_1 \rightarrow -\infty (K_1 \rightarrow 0)$ in eq. [7] in ref. 23. However, eq. [36] differs from eq. [32] in ref. 8, due to the fact that in the deduction of this last equation, the disturbance of the surface gradient of species A originated by the second pulse application is not taken into account. For this reason, in ref. 8 only the G_z series appears.

Results and discussion

Previous to this study, we performed a careful analysis of the properties of the $H_z(\beta, y)$ function (see appendix A). A 3D plot of $H_0(\beta, y)$ is shown in Fig. 2. For $\beta \rightarrow 0$, $H_z(0, y) = G_z(0, y) = F_0(y)$. As β increases and approaches unity, the absolute value of the H_0-function decreases, showing a maximum for y values close to 5.

An analogous plot for $H_{2/3}(\beta, y)$ (Fig. 3) shows a shape similar to Fig. 2. In order to guarantee high accuracy, only the values of $H_{2/3}$ corresponding to $\beta \leq 0.5$ have been presented in Fig. 3. The function $H_{2/3}$ has been evaluated with only five terms of the sum in β, since the general term of this series could not be obtained because of its mathematical complexity (see comments in appendix A). As can be observed, these curves are less dependent on β than those in Fig. 2.

The behavior of eq. [36] has been exhaustively studied and has been compared with the solution given in ref. 8, as well as with the numerical solution obtained in Appendix B (see eqs. [B13]–[B15]). In Fig. 4 the plot of i_{RP}/i_{DC} vs. $E_2 - E^0$ ($i_{DC} = nFq_0t^z\sqrt{D_A/(\pi t_2)}\,C_A^*$) is shown for $k_s = 10^{-4}$ cm/s, $t_1 = 1$ s, $t_2 = 0.4$ s, and $z = 0$. As can be observed, the three solutions almost coincide in the potential range studied. This behavior indicates that, from a practical point of view,

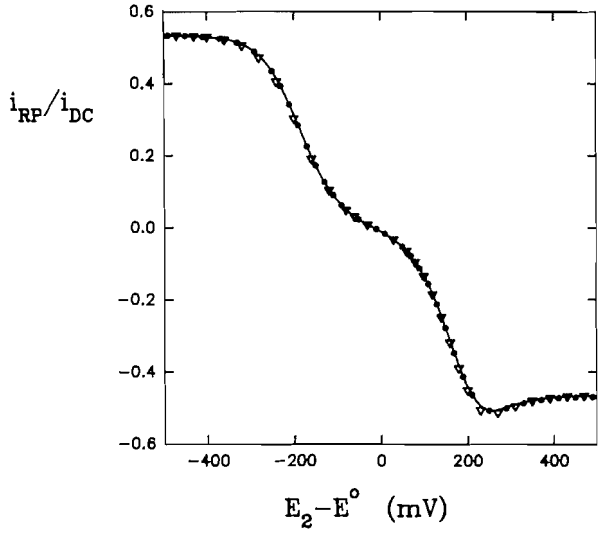

FIG. 4. Plot of i_{RP}/i_{DC} vs. $E_2 - E^0$ for $k_s = 10^{-4}$ cm s^{-1}, $t_1 = 1$ s, $t_2 = 0.4$ s, $n = 1$, $\alpha = 0.5$, $D_A = 10^{-5}$ cm^2 s^{-1}, $\gamma = 1$, and $z = 0$. Solid line corresponds to the predictions of eq. [36]. Triangles correspond to the solution given in ref. 8. Circles correspond to the numerical solution given in Appendix B (eq. [B13] with $r = 160$).

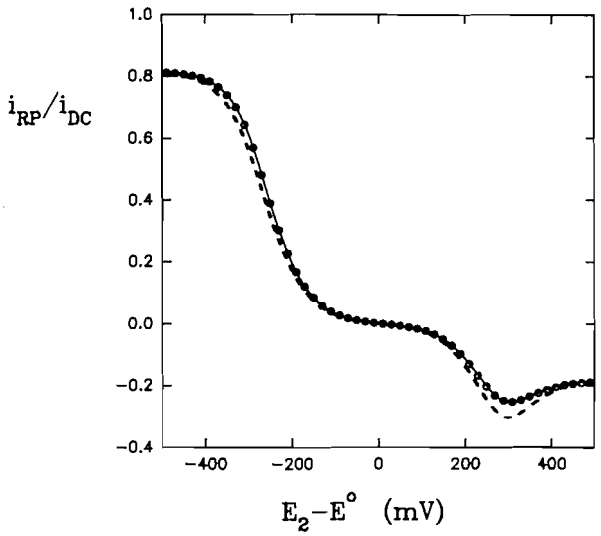

FIG. 5. Plot of i_{RP}/i_{DC} vs. $E_2 - E^0$ for $k_s = 10^{-5}$ cm s^{-1}, $t_1 = 1$ s, $t_2 = 2$ s, $n = 1$, $\alpha = 0.5$, $D_A = 10^{-5}$ cm^2 s^{-1}, $\gamma = 1$, and $z = 0$. Solid line corresponds to the predictions of eq. [36]. Dashed line corresponds to the solution given in ref. 8. Circles correspond to the numerical solution given in Appendix B (eq. [B13] with $r = 160$).

the three analyzed solutions are numerically indistinguishable, even for relatively high values of β in a typical experimental record such as that in Fig. 4 ($\beta = 0.4/1.4 = 0.285$). For $z = 2/3$ the behavior (not shown) is similar.

For larger values of β some deviations are observed in the solution given in ref. 8 with respect to that obtained from eq. [36] and [B15]. In Fig. 5 we have plotted i_{RP}/i_{DC} vs. $E_2 - E^0$ for $k_s = 10^{-5}$ cm/s, $\beta = 2/3$, and $z = 0$. The results obtained from eq. [36] and from the numerical solution of Appendix B are in total agreement. This concordance is maintained for all of our calculations indicating the rigorous character of our treatment (eq. [36]). In Fig. 5, one can also observe how the variation of i_{RP} obtained from the solution given in ref. 8 (dashed line) is different. This discrepancy is only evident in

Can. J. Chem. Downloaded from www.nrcresearchpress.com by 85.192.166.187 on 09/08/12
For personal use only.

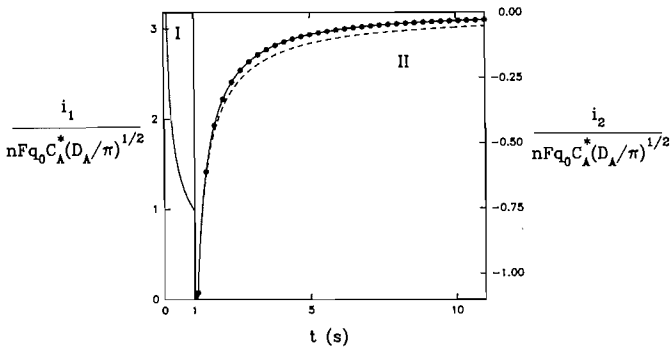

FIG. 6. Plot of $i_j/[nFq_0C_A^*(D_A/\pi)^{1/2}]$ vs t. Part I corresponds to the variation of i_1 (eq. [24]) for $t_1 \leq 1$ s. Part II corresponds to the variation of $i_2 = i_{RP}$ for $t \leq 10$ s and $E_2 - E^0 = 300$ mV. Other conditions as in Fig. 4.

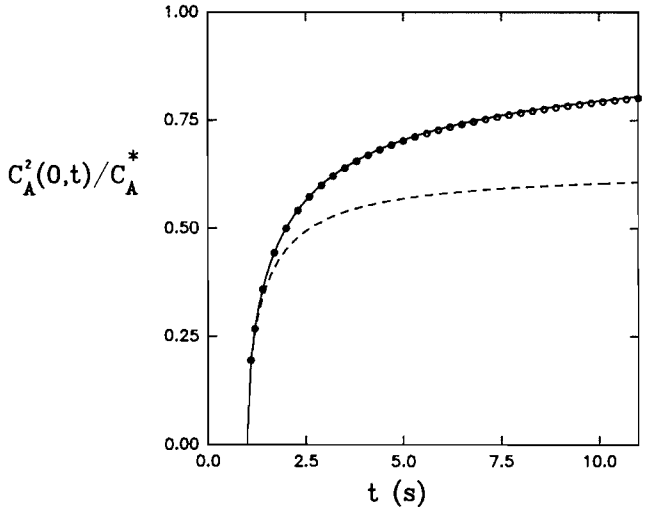

FIG. 7. Plot of $C_A^2(0,t)/C_A^*$ vs t. Solid line corresponds to eq. [40] and dashed line to eq. [45], in both cases with $z = 0$, $k_s \ll 1$ cm s^{-1} and $E_2 \simeq E^0$. Circles corresponds to eq. [B16] with $k_s = 10^{-7}$ cm s^{-1}, $E_2 - E^0 = 0$, and $r = 160$. $t_1 = 1$ s, $t_2 = 10$ s. Other conditions as in Fig. 4.

the extreme conditions under which Fig. 5 has been obtained. The deviations are more prominent at the potential region near the peak, where the error amounts to 18%. To appreciate the magnitude of the deviations at this potential, we have plotted as Fig. 6 a theoretical i–t curve for the same conditions as those of Fig. 5, for $E_2 - E^0 = 300$ mV. Part I of Fig. 6 represents the current (i_1) due to the application of first pulse ($t \leq t_1 = 1$ s and $E_1 - E^0 \longrightarrow -\infty$, eq. [24]), while part II corresponds to the current ($i_2 - i_{RP}$) during the application of second pulse ($t > t_1, t_2 = 10$ s and $E_2 - E^0 = 300$ mV). Again, a total concordance between numerical solution and eq. [36] is observed, while the results obtained from the solution given in ref. 8 only agree for small values of t. For $t - t_1 > 0.5$ s some deviations are observed. For $t_2 = 5$ s the error amounts to 30%.

The solutions from ref. 8 leads to a reasonable agreement with the rigorous solution for i_{RP} (eq. [36]), provided β is small. In general, $\beta = 0.33$ may be considered a limit for the correct use of the solution in ref. 8, as the error is always less than 10%.

Experimentally, deviations from the rigorous solution can

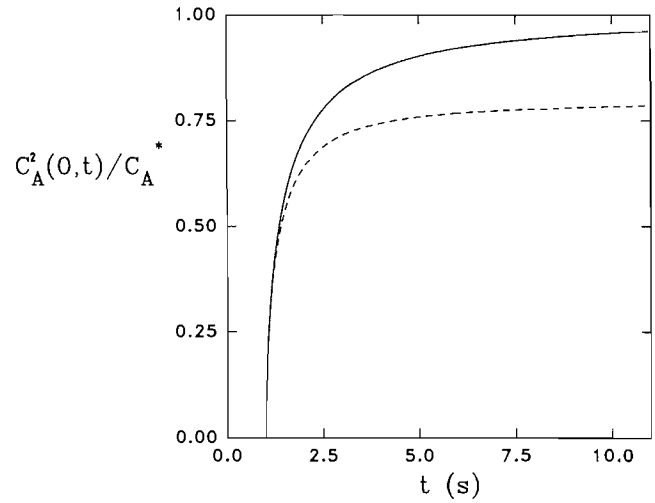

FIG. 8. Plot of $C_A^2(0,t)/C_A^*$ vs t. Solid line corresponds to eq. [40] and dashed line to eq. [45], in both cases with $z = 2/3$, $k_s \ll 1$ cm s^{-1}, $E_2 \simeq E^0$, $t_1 = 1$ s, $t_2 = 10$ s. Other conditions as in Fig. 4.

be observed in careful experiments similar to those described in Figs. 5 and 6.

There is no mention in the literature about the problems inherent to the solution in ref. 8 analyzed in this paper. The reason being experimentally, the RP technique has so far been used for $\beta \leq 0.1$, and therefore the wrong behavior of the solution in ref. 8 cannot be observed.

The final analysis of the three solutions compares the time dependence of surface concentration of reactant, $C_A^2(0,t)$. For this purpose, we have used eq. [A5], corresponding to the prediction made in this paper, eq. [A7] corresponding to the solution given in ref. 8 and eq. [B16], corresponding to the numerical solution to the problem.

Figures 7 and 8 show theoretical curves of $C_A^2(0,t)$ vs. t for $t_1 = 1$ s and $t_2 = 10$ s for $z = 0$ (Fig. 7) and for $z = 2/3$ (Fig. 8). When $t < t_1$ the surface concentration of reactant is zero as a consequence of the large negative potential applied ($E_1 - E^0 \longrightarrow -\infty$). When $t > t_1$ a total agreement between our treatment (eq. [A5]) and our numerical solution (eq. [B16]) is observed, while the values of $C_A^2(0,t)$ obtained from eq. [A7] differ notably from the others. The conditions imposed in Figs. 7 and 8 correspond to a limiting reduction process, selected to quarantee that there is no anodic or cathodic current so that $i_{RP} \longrightarrow 0$. Moreover, under these conditions $\mu_d \gg Z$ (eqs. [37], [38]). Physically, the situation is such that, as a consequence of the absence of any Faradaic current, the surface concentration of species A must return to its initial value: $C_A^2(0, t_2 \longrightarrow \infty) \longrightarrow C_A^*$.

If the conditions of Fig. 7 ($y \ll 1$) are applied to eq. [A5], the following expression is obtained

$$[40] \qquad \frac{C_A^2(0,t)}{C_A^*} = \frac{2}{\pi}\sqrt{(2z+1)\beta}\, h_z(\beta)$$

where

$$[41] \qquad h_0(\beta) = 1 + \sum_{k=1}^{\infty} \frac{(2k-1)!\beta^k}{2^{2k-1}k!(k-1)!(2k+1)}$$

$$[42] \qquad h_{2/3}(\beta) = 1 + \frac{\beta}{18} + \frac{\beta^2}{1080} - \frac{7\beta^2}{1296} - \frac{461\beta^4}{93312} - \cdots$$

Can. J. Chem. Downloaded from www.nrcresearchpress.com by 85.192.166.187 on 09/08/12
For personal use only.

We have also solved this problem using Laplace Transform on eq. [B11], and found a solution identical to eq. [40], but in a more compact general form:

$$[43] \qquad \frac{C_A^2(0,t)}{C_A^*} = \frac{2}{\pi} \text{ arc tang } \sqrt{\frac{1}{(1-\beta)^{2z+1}} - 1}$$

where

$$[44] \qquad \sqrt{(2z+1)\beta}\, h_z(\beta) = \text{arc tang } \sqrt{\frac{1}{(1-\beta)^{2z+1}} - 1}$$

The condition $t_2 \longrightarrow \infty$ is equivalent to $\beta \longrightarrow 1$, and, therefore, $C_A^2(0,t)/C_A^* = 1$, for any value of z, which is in accordance with the previous reasoning; the process is very slow, but takes places at infinitely large time. However, the application of the same conditions to eq. [A7] leads to the following result

$$[45] \qquad \frac{C_A^2(0,t)}{C_A^*} = \frac{2}{\pi} \sqrt{\beta(2z+1)}\, g_z(\beta)$$

$$[46] \qquad g_0(\beta) = 1$$

$$[47] \qquad g_{2/3}(\beta) = 1 - \frac{1}{9}\beta - \frac{11}{270}\beta^2 - \frac{10}{567}\beta^3 - \frac{3087}{367416}\beta^4 \ldots$$

If $\beta = 1$, the prediction of eq. [45] is $C_A^2(0,t)/C_A^* = 2/\pi = 0.6366$ (for $z = 0$) and $C_A^2(0,t)/C_A^* = 0.7995$ (for $z = 2/3$), that is to say, eq. [45] is unable to predict the return to initial conditions in the pulse sequence applied in the ideal experiment of Figs. 7 and 8.

It may be surprising that the method applied in ref. 8 allows us to calculate i_{RP} very close to the correct values (even for moderately large β) but it is unable to obtain accurate values of the surface concentrations. The reason of this apparent paradox must be sought in the very structure of eqs. [36] and [A5], as well as in the analysis of the conditions under which these equations coincide with that deduced in ref. 8. When the electrode process is reversible ($k_s \longrightarrow \infty$) or diffusion conditions are applied ($E_2 - E^0 \longrightarrow \pm\infty$), the treatment developed in ref. 8 and our own treatment are the same (conditions under which the superposition principle is applicable). In short, the function $H_z(\beta, y)$ is operative only when the process is not at equilibrium or when y does not increase towards infinity.

If we analyze the expression for the current i_{RP} (eq. [36]), one sees that as the value of y decreases, the importance of the product $\mu_d H_z(\beta, y)$, i.e., of $H_z(\beta, y)/y$ (see eq. [38]) increases while the current i_{RP} simultaneously decreases. For this reason, the difference between eq. [36] and eq. [32] in ref. 8 is not very great in absolute value. Moreover, it should be added that the functions $H_z(\beta, y)$ and $G_z(\beta, y)$ are more similar as y becomes smaller.

The expressions for surface concentration depend on the product $\mu_d H_z(\beta, y)/y = H_z(\beta, y)/y^2$, which also increases as y decreases but $C_A^2(0,1)_{y \ll 1} \neq 0$. For example, while $C_A^2(0,t)$ is strongly dependent on $H_z(\beta, y)$, i_{RP} can be represented approximately by eq. [32] in ref. 8. However, this does not mean the method in ref. 8 can be used indiscriminately. For example, these results should not be used to obtain the current–time response corresponding to posterior pulses, as in the technique called Reverse Differential Normal Pulse (16, 23, 24), or in the Double Differential Pulse Voltammetry technique (25). In these cases the current is obtained from surface concentrations and surface concentration gradients deduced for second pulse, and the use of eq. [A7] leads to inadequate results.

Acknowledgements

The authors wish to express their gratitude to the Junta de Andalucía, DREUCA de la Región de Murcia (Project PB91/025), and DGICyT (Projects PB91-0834 and PB90-0307) for financial assistance.

1. H. Matsuda. Bull. Chem. Soc. Jpn. **53**, 3439 (1980).
2. M. Lovric and J. Osteryoung. Electrochim. Acta, **27**, 963 (1982).
3. K. Aoki, J. Osteryoung, and R.A. Osteryoung. J. Electroanal. Chem. **110**, 1 (1980).
4. K. Aoki and J. Osteryoung. J. Electroanal. Chem. **110**, 19 (1980).
5. G.J.M. Heijne and W.E. Van der Linden. Anal Chim. Acta, **82**, 231 (1976); **99**, 183 (1978).
6. I. Ruzic and M. Sluyters-Rehbach. Anal. Chim. Acta, **99**, 177 (1978).
7. R.L. Birke, M.H. Kim, and M. Strassfeld. Anal. Chem. **53**, 852 (1981).
8. J. Gálvez, J. Zapata, and C. Serna. J. Electroanal. Chem. **205**, 21 (1986).
9. J. Osteryoung and E. Kirowa-Eisner. Anal. Chem. **52**, 62 (1980).
10. T. Brumleve and J. Osteryoung. J. Phys. Chem. **86**, 1794 (1982).
11. L. Sinru, J. Osteryoung, J. O'Dea, and R.A. Osteryoung. Anal. Chem. **60**, 1135 (1988).
12. J. Osteryoung and M.M. Murphy. *In* Microelectrodes: theory and applications. *Edited by* M.I. Montenegro et al. Kluwer Academic Publisher, Netherlands. 1991. pp. 123–138.
13. A.J. Bard and L.R. Faulkner. *In* Electrochemical methods. Wiley, New York. 1980. pp. 176–183.
14. J. Osteryoung and M.M. Schreiner. CRC Crit. Rev. Anal. Chem. **19**, S1 (1988).
15. R. Danielsson, P. Baecklund, and A. Källström. Anal. Chim. Acta, **158**, 305 (1984).
16. L. Camacho, J.J. Ruiz, A. Molina, C. Serna, and F. Martinez-Ortiz. To be published.
17. J. Kambara. Bull Chem. Soc. Jpn. **27**, 523 (1954).
18. R.S. Nicholson and I. Shain. Anal. Chem. **36**, 706 (1964).
19. R. Seralathan, R.A. Osteryoung, and J. Osteryoung. J. Electroanal. Chem. **222**, 69 (1987).
20. K.B. Oldham. Anal. Chem. **41**, 936 (1969).
21. J. Gálvez and S.M. Park. J. Electroanal. Chem. **259**, 21 (1989).
22. J. Koutecky. Czech. J. Phys. **2**, 50 (1953).
23. C. Serna, A. Molina, L. Camacho, and J.J. Ruiz. Anal. Chem., **65**, 215 (1993).
24. T.R. Brumleve, R.A. Osteryoung, and J. Osteryoung. Anal. Chem. **54**, 782 (1982).
25. L. Camacho, J.J. Ruiz, A. Molina, and C. Serna. J. Electroanal. Chem. **365**, 97 (1994).
26. J. Gálvez and A. Serna. J. Electroanal. Chem. **69**, 145 (1976).
27. M. Sánchez-Maestre, E. Muñoz, J.L. Avila, and L. Camacho. Electrochim. Acta, **37**, 1129 (1992).

Can. J. Chem. Downloaded from www.nrcresearchpress.com by 85.192.166.187 on 09/08/12
For personal use only.

Can. J. Chem. Downloaded from www.nrcresearchpress.com by 85.192.166.187 on 09/08/12
For personal use only.

Appendix A

$F_z(\chi)$ is the Koutecky Function. For $z = 0$ (planar approximation of SMDE) and for $z = 2/3$ (planar approximation of DME)

$$[A1] \qquad F_z(\chi) = \sum_{j=0}^{\infty} \frac{(-1)^j \chi^{j+1}}{\prod_{k=0}^{j} p_k(z)}$$

$G_z(\chi)$ is the Galvez Function (8, 26)

$$[A2] \qquad G_z(\beta, \chi) = \sum_{j=0}^{\infty} \frac{(-1)^j \chi^{j+1}}{\prod_{k=0}^{j} p_k(z)} \left\{ 1 - \frac{j\beta}{3(j+2)} - \frac{j(2j+9)}{18(j+2)(j+4)} \cdot \beta^2 \cdot - \cdots \right\}$$

$$[A3] \qquad p_k(z) = p_{k/(2z+1)} = \frac{2\Gamma\left(1 + \frac{k}{4z+2}\right)}{\Gamma\left(\frac{1}{2} + \frac{k}{4z+2}\right)}$$

$$[A4] \qquad p_k p_{k-1} = 2k$$

The surface concentrations of species A and B for $\tau_2 > 0$ are given by

$$[A5] \qquad \frac{C_A^2(0, t)}{C_A^*} = Z\left(\frac{2}{\sqrt{\pi}} \frac{C_z(\beta, y)}{y} - 1\right) + \mu_d\left(\frac{2}{\sqrt{\pi}} \frac{H_z(\beta, y)}{y} - 1\right)$$

$$[A6] \qquad \frac{C_B^2(0, t)}{C_A^*} = \gamma\left(1 - \frac{C_A^2(0, t)}{C_A^*}\right)$$

However, from eq. [16] in ref. 8 with $E_1 \longrightarrow -\infty$, we deduce

$$[A7] \qquad \left(\frac{C_A^2(0, t)}{C_A^*}\right)_{\text{ref. 8}} = (Z + \mu_d)\left(\frac{2}{\sqrt{\pi}} \frac{G_z(\beta, y)}{y} - 1\right)$$

H_z function which appears in eq. [35] is given for $y < 10$ by ($z = 0$)

$$[A8] \qquad H_0(\beta, y) = \sum_{m=0}^{\infty} \frac{(-1)^m y^{m+1}}{\prod_{i=0}^{m} p_i(0)} \left\{ 1 + \sum_{k=1}^{\infty} \frac{(2k-1)!m\beta^k}{2^{2k-1}k!(k-1)!(m+2k)} \right\} = \sum_{m=0}^{\infty} \frac{(-1)^m y^{m+1}}{\prod_{i=0}^{m} p_i(0)} \cdot \text{Hg2}F1[1/2, m/2, 1 + m/2, \beta]$$

where Hg2$F1[a, b, c, z]$ is the hypergeometric function ${}_2F_1(a, b, c, z)$ and for $y > 10$

$$[A9] \qquad H_0(\beta, y) = \sqrt{1-\beta} + \sqrt{\pi} \sum_{k=1}^{\infty} \frac{(-1)^{k-1}(2k-1)!\beta^k}{(k-1)!y^{2k-1}} + \sum_{m=1}^{\infty} \frac{(-1)^m 2(2m-1)!}{(m-1)!y^{2m}} \left(1 - \sum_{k=1}^{\infty} \frac{(2k-1)!(2m+1)\beta^k 2^{1-2k}}{k!(k-1)!(2k-2m-1)}\right)$$

$$= \sqrt{1-\beta} + \sqrt{\pi} \sum_{k=1}^{\infty} \frac{(-1)^{k-1}(2k-1)!\beta^k}{(k-1)!y^{2k-1}} + \sum_{m=1}^{\infty} \frac{(-1)^m 2(2m-1)!}{(m-1)!y^{2m}} \text{Hg2}F1[1/2, -(m+1/2), 1/2 - m, \beta]$$

The function $H_0(\beta, y)$ is defined for $0 \leq \beta \leq 1$, and can be obtained with the desired precision in this interval. The value $\beta = 1$ corresponds to two extreme situations, as are $t_1 = 0$, that is to say, the first pulse does not exists (this situation is physically meaningless, since H is only obtained if the departure point is a perturbed system) or $t_2 \longrightarrow \infty$.

The general term of the sum in β in the above equations has been obtained taking into account the relationship between the coefficients of the series depending on β in the H_0 function and the following expression

$$[A10] \qquad (1-\beta)^{-1/2} = 1 + \sum_{k=1}^{\infty} \frac{(2k-1)!\beta^k}{2^{k-1}k!(k-1)!}$$

For $z = 2/3$ and for $y < 10$ we find

$$[A11]\quad H_{2/3}(\beta, y) = \sum_{m=1}^{\infty} \frac{(-1)^m y^{m+1}}{\prod_{i=0}^{\infty} p_i} \left\{ 1 + \frac{m}{6(m+2)}\beta + \frac{m(7m-6)}{72(m+2)(m+4)}\beta^2 + \frac{7m(13m-34)}{1296(m+2)(m+6)}\beta^3 + \frac{m(1729m^3+9828m^2-23284m-133488)}{31104(m+2)(m+4)(m+6)(m+8)}\beta^4 + \cdots \right\}$$

and for $y > 10$

$$[A12]\quad H_{2/3}(\beta, y) = \sum_{m=1}^{\infty} (-1)^{m+1} y^{-m+1} \left(\frac{\prod_{i=1}^{m} p_{-i}}{p_{-m}} \right) \left\{ 1 + \frac{m}{6(m-2)} + \frac{m(7m+6)}{72(m-2)(m-4)}\beta^2 + \frac{7m(13m+34)}{1296(m-2)(m-6)}\beta^3 + \frac{m(1729m^3-9828m^2-23284m+133488)}{31104(m-2)(m-4)(m-6)(m-8)}\beta^4 + \cdots \right\} = 1 - \frac{1}{6}\beta + \frac{13}{216}\beta^2 + \frac{329}{6480}\beta^3 + \frac{2269}{72576}\beta^4 + \cdots + \frac{1}{3}p_1\beta\left(1 - \frac{5}{6}\beta - \frac{35}{72}\beta^2 - \frac{20}{81}\beta^3 \cdots\right) y^{-1} - \left(2 + \beta - \frac{9}{4}\beta^2 - \frac{511}{648}\beta^3 - \frac{7289}{25920}\beta^4 \cdots\right) y^{-2} - p_1\beta^2\left(\frac{34}{9} - \frac{65}{324}\beta^2 \cdots\right) y^{-3} + 2\left(12 + \frac{10}{3}\beta + \frac{205}{18}\beta^2 - \frac{385}{36}\beta^3 - \frac{20845}{3888}\beta^4 \cdots\right) y^{-4}$$

Equation [A11] suggests us the grouping of β into the expression

$$[A13]\quad (1-\beta)^{-1/6} = 1 + \frac{\beta}{6} + \frac{7\beta^2}{72} + \frac{91\beta^3}{1296} + \frac{1729\beta^4}{31104} + \cdots$$

However, because of its complexity, we can not find a general expression for [A11].
We have also used the relationship

$$[A14]\quad \lim_{k \to m} (m-k) = \pm\frac{p_{-1}}{p_1}$$

in which the upper sign relates to direct treatment and the lower sign to the asymptotic one.

Appendix B

For a stationary plane electrode ($z = 0$), the Faradaic current corresponding to process [1], can be expressed by a Volterra integral of the form (1)

$$[B1]\quad \phi = k - \frac{\lambda}{\sqrt{\pi}} \int_0^t \frac{\phi \mathrm{d}u}{\sqrt{t-u}}$$

where

$$[B2]\quad k = k_s K^{-\alpha}$$

$$[B3]\quad \lambda = \frac{k(1+\gamma K)}{\sqrt{D_A}}$$

$$[B4]\quad \phi = \frac{i}{nFq_0 C_A^*}$$

In double pulse conditions eq. [B1] can written as (1)

$$[B5]\quad \phi_2 = k_2 - \frac{\lambda_2}{\sqrt{\pi}} \left(\int_0^{t_1} \frac{\phi_1 \mathrm{d}u}{\sqrt{t_1+t_2-u}} + \int_{t_1}^{t_1+t_2} \frac{\phi_2 \mathrm{d}u}{\sqrt{t_1+t_2-u}} \right)$$

Can. J. Chem. Downloaded from www.nrcresearchpress.com by 85.192.166.187 on 09/08/12
For personal use only.

where the subscripts 1 and 2 indicate, respectively, the conditions corresponding to first pulse, E_1 of length t_1 and current i_1 and those corresponding to the second pulse E_2 of length t_2 and current i_2.

Taking into account eq. [B1], eq. [B5] can be rearranged as (27)

$$[B6] \quad \phi_2 - \phi_1 = \left(k_2 - k_1 \frac{\lambda_2}{\lambda_1}\right) - \phi_1 \left(\frac{\lambda_2}{\lambda_1} - 1\right) - \frac{\lambda_2}{\sqrt{\pi}} \int_0^{t_2} \frac{(\phi_2 - \phi_1)\mathrm{d}u}{\sqrt{t_2 - u}}$$

Let us define

$$[B7] \quad \psi = \phi_2 - \phi_1$$

In the conditions of RP, $E_1 - E^0 \longrightarrow -\infty$, therefore $K_1 \longrightarrow 0$, $k_1 \longrightarrow \infty$ and $(k_1/\lambda_1) = (D_A)^{1/2}$, consequently

$$[B8] \quad k_2 - k_1 \frac{\lambda_2}{\lambda_1} \simeq -\gamma K_2 k_2 = -\gamma k_s K_2^{(1-\alpha)} = k_{-2}$$

$$[B9] \quad \frac{\lambda_2}{\lambda_1} - 1 \simeq -1$$

$$[B10] \quad \phi_1(t) = \sqrt{\frac{D_A}{\pi t}}$$

which allows us to rewrite eq. [B6] as follows

$$[B11] \quad \psi = -k_{-2} - \sqrt{\frac{D_A}{\pi(t_1 + t_2)}} - \frac{\lambda_2}{\sqrt{\pi}} \int_0^{t_2} \frac{\psi \mathrm{d}u}{\sqrt{t_2 - u}}$$

The numerical method that followed to solve this integral equation has been previously described in literature (18, 19). In accordance with this method, the integral in eq. [B11] is substituted by

$$[B12] \quad \int_0^{t_2} \frac{\psi \mathrm{d}u}{\sqrt{t_2 - u}} \simeq 2\sqrt{(t_2/r)} \left(\psi_r + \sum_{i=1}^{r-1} \psi_i(\sqrt{r+1-i} - \sqrt{r-i})\right)$$

where r is the number of steps in which t_2 is divided, in such a way that $\Delta t = t_2/r$. Thus ψ_i's evaluated from

$$[B13] \quad \psi_1 = \frac{-k_{-2} - \sqrt{\frac{D_A}{\pi(t_1 + i\Delta t)}} - 2\lambda_2 \sqrt{\frac{\Delta t}{\pi}} \sum_{j=1}^{i-1} \psi_j(\sqrt{i+1-j} - \sqrt{i-j})}{1 + 2\lambda_2 \sqrt{\frac{\Delta t}{\pi}}}$$

where

$$[B14] \quad \psi_1 = \frac{-k_{-2} - \sqrt{\frac{D_A}{\pi(t_1 + \Delta t)}}}{1 + 2\lambda_2 \sqrt{\frac{\Delta t}{\pi}}}$$

The current $i_2 = i_{RP}$ is determined from

$$[B15] \quad \phi_2 = \psi_r + \phi_1 = \psi_r + \sqrt{\frac{D_A}{\pi(t_1 + t_2)}} = \frac{i_{RP}}{nFq_0 C_A^*}$$

Finally, $C_A^2(0, t)$ can be evaluated from

$$[B16] \quad \frac{C_A^2(0, t)}{C_A^*} = \frac{\phi_2/k_2 + \gamma K_2}{1 + \gamma K_2}$$

All the calculations have been carried out with $r = 160$. In all cases, the difference observed in i_{RP} or in $C_A^2(0, t)$ with respect to the predictions of eqs. [36] and [A5], respectively, are always less than 1%.

Can. J. Chem. Downloaded from www.nrcresearchpress.com by 85.192.166.187 on 09/08/12
For personal use only.

General analytical solution for a reversible *i/t* response to a double potential step at spherical electrodes in the absence/presence of amalgamation effects

A. MOLINA,[1] C. SERNA, AND R. CHICÓN

Departamento de Química Física, Facultad de Ciencias Químicas, Universidad de Murcia, Campus de Espinardo, E-30100 Murcia, Spain

AND

L. CAMACHO[1] AND J.J. RUIZ

Departamento de Química Física y Termodinámica Aplicada, Facultad de Ciencias, Universidad de Córdoba, c) San Alberto Magno s/n, E-14004 Córdoba, Spain

Received February 4, 1994

A. MOLINA, C. SERNA, R. CHICÓN, L. CAMACHO, and J.J. RUIZ. Can. J. Chem. **72**, 2378 (1994).

The general rigorous theory corresponding to double potential step chronoamperometry for a reversible charge transfer reaction in a spherical electrode whose area increases with t^z, where $z \geq 0$, is presented. The static mercury drop electrode ($z = 0$) and the dropping mercury electrode ($z = 2/3$) are addressed specifically. The explicit equations for the current versus time response assuming unequal diffusion coefficients for the oxidized and reduced species are valid when the product is soluble in both the electrolytic solution and the electrode. Comparisons with previous general treatments in the literature are made. The theory is applied to the detection of amalgamation in RP and DNP techniques.

Moreover, in this work we show the origin of errors appearing in some general treatments in the literature, these errors lead to physically meaningless results when amalgamation takes place.

A. MOLINA, C. SERNA, R. CHICÓN, L. CAMACHO et J.J. RUIZ. Can. J. Chem. **72**, 2378 (1994).

On présente la théorie générale rigoureuse correspondant à la chronoampérométrie avec une étape à double potentiel d'une réaction réversible de transfert de charge dans une électrode sphérique dont la superficie augmente comme t^z, où $z \geq 0$. On examine d'une façon spécifique les cas des électrodes avec goutte de mercure statique ($z = 0$) et avec goutte de mercure tombante ($z = 2/3$). Les équations explicites pour le courant en fonction du temps de réponse, en supposant des coefficients de diffusions différents pour les espèces oxydées et réduites, sont valides lorsque le produit est soluble dans le solution électrolytique ainsi que dans l'électrode. On présente des comparaisons avec les traitements généraux rapportés antérieurement dans la littérature. On applique la théorie à la détection d'amalgamation dans les techniques de RP et de DNP.

De plus, dans ce travail, on montre l'origine des erreurs qui apparaissent des quelques traîtements généraux rapportés dans la littérature et qui, lorsqu'une amalgamation se produit, rendent les résultats physiquement sans signification.

[Traduit par la rédaction]

Introduction

In this paper we study the application of a double potential pulse to a reversible charge transfer process at stationary and nonstationary spherical electrodes. We consider the general case when the diffusion coefficients of the oxidized and reduced species are different, and the reduced species can dissolve in the electrolytic solution as well as in the electrode. In order to obtain an exact expression for the response corresponding to the second potential pulse, it is essential to consider the perturbation of the second pulse on the concentration profiles generated by the first potential pulse. Previous investigators (1, 2) have neglected this perturbation.

The difficulties in the calculation of the response to the second potential step for a spherical electrode arise from surface concentrations which are dependent on potential, diffusion coefficients, and time (3–5). Birke et al. (6) first reported that it was necessary to account for the variation of the concentration profiles obtained with the first pulse during the application of the second pulse. They found that this variation can be neglected only when both species are soluble and have equal diffusion coefficients.

The Koutecky approximation has been used when amalgamation is present (7), and the mathematical procedure developed in this work shows clearly that this approximation is valid for any value of the time of application of the second pulse. This can be easily verified from the analytic expressions obtained in this work for a Static Mercury Drop Electrode (SMDE) and a Dropping Mercury Electrode (DME). In the case of SMDE, the expression for i_2 is simple enough to permit direct match of the theoretical and experimental results.

We have applied our equations to the study of double potential step chronoamperometry, and we have analyzed the influence of the electrode sphericity and amalgamation on the *i–t* response. The same considerations have been made for reverse pulse and differential normal pulse techniques. For reverse pulse techniques we have proposed a condition for the formation of amalgam based on measurements of the cathodic and anodic diffusion currents. Brumleve et al. (8) have used the reverse pulse technique to study the influence of spherical diffusion at a SMDE, for processes with and without amalgamation. They used numerical methods to obtain a complicated analytical solution for only the limiting current. Goodisman (5) solved the problem for a SMDE alone did not give explicit solutions that are directly applicable to double pulse techniques. The effect of amalgamation in differential pulse techniques has been studied experimentally for a DME (9) and a SMDE (10). These works clearly demonstrate the lack of a suitable theory that accounts quantitatively for the effect of amalgamation in double pulse techniques.

The equations derived in this paper are applied to double potential step chronoamperometry, reverse pulse (RP) and

[1]To whom correspondence should be addressed.

Can. J. Chem. Downloaded from www.nrcresearchpress.com by 85.192.166.187 on 09/08/12
For personal use only.

Can. J. Chem. Downloaded from www.nrcresearchpress.com by 85.192.166.187 on 09/08/12
For personal use only.

differential normal pulse (DNP) techniques to analyze the influence of electrode sphericity and amalgamation on the i–t response. In RP, a criterion for the formation of amalgam based on the measurements of cathodic and anodic currents is proposed. Single pulse techniques including normal pulse (NP), dc voltammetry, or polarography are also considered. Our results do not differ from those previously reported (1, 3, 4, 11) because single pulse techniques do not suffer from the concentration perturbations that must be considered in double pulse methods.

Theory

Consider the following charge-transfer.

[1] $\quad A + ne^- \rightleftharpoons B$

Let us consider a spherical electrode with its area increasing as a power of time, $q(t) = q_0 t^z$ ($z = 0$ for a SMDE and $z = 2/3$ for a DME), and a reversible charge transfer such that the potential is set at the value E_1 in the interval $0 \leq t \leq t_1$ and stepped from E_1 to E_2 at the time $t \geq t_1$ (see Fig. 1). The current for each pulse will be called i_1 and i_2 respectively. See footnote 2 for notations.

The concentration profiles in the interval $0 \leq t \leq t_1$ are given in ref. 1*a*.

[2] $\quad C_A^1(r, t) = C_A^1(s1_A, \xi 1_A) = \rho_0(s1_A) + \xi 1_A \rho_1(s1_A)$

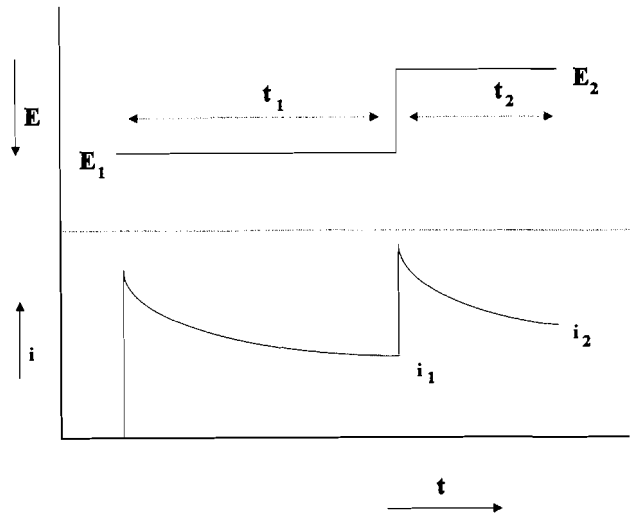

FIG. 1. Potential–time waveform and current–time response to a double potential step.

[3] $\quad C_B^1(r, t) = C_B^1(s1_B, \xi 1_B) = \phi_0(s1_B) + \xi 1_B \phi_1(s1_B)$

with

[4] $\quad s1_i = \sqrt{\dfrac{2z+1}{4D_i t}}(r - r_0)$

[5] $\quad \xi 1_i = \sqrt{\dfrac{4D_i t}{2z+1}}\,\dfrac{1}{r_0}$

[6] $\quad r_0 = \sqrt{\dfrac{A_0}{4\pi}}\,t^{z/2}$

and where $\rho_0(s1_A)$, $\rho_1(s1_A)$, $\phi_0(s1_B)$ and $\phi_0(s1_B)$ are given in ref. 1*a* (eqs. [9]–[17]).

The concentration on the surface of the electrode are

[7] $\quad C_A^1(r_0, t) = A_1 + B_1 \xi 1_A$

[8] $\quad C_B^1(r_0, t) = C_A^1(r_0, t)/K_1$

where we have taken

[9] $\quad A_1 = \dfrac{C_A^* K_1 \gamma}{1 + \gamma K_1}$

[10] $\quad B_1 = \dfrac{4(2z+1)(\gamma \mp 1) C_A^* K_1}{(5z+4)(1+\gamma K_1)^2 \sqrt{\pi}}$

[11] $\quad K_i = \exp[nF(E_i - E_0)/RT]$

If only the first order spherical correction is considered, the current has the expression (1*a*, 4)

[12] $\quad i_1(t) = nFq(t)\sqrt{\dfrac{(2z+1)D_A}{\pi t}}\,C_A^*\,\dfrac{1 + \theta_z \Omega_1 \xi 1_A}{1 + \gamma K_1}$

with

[13] $\quad \theta_z = \dfrac{2(2z+1)P_z}{(5z+4)}$

---

[2]Notation:

$q(t) = q_0 t^z$	time-dependent electrode area ($z = 0$ for a SMDE and $z = 2/3$ for a DME)
$c_i^m(r, t)$	concentration profile of species i (i = A or B) when the first ($m = 1$) or second ($m = 2$) potential pulse is applied
r_0	constant electrode radius for a SMDE. $= at^{1/3}$ for a DME
$a = \left(\dfrac{3m_{Hg}}{4\pi d}\right)^{1/3}$	
m_{Hg}, d	rate of flow and density of mercury
$\xi 1_i = \xi 1_i^0 t^{(1-z)/2}$	(or eq. [5])
$\xi 1_i^0 = 4\sqrt{\dfrac{\pi D_i}{(2z+1)A_0}}$	
$\beta = \dfrac{\tau_2}{t_1 + \tau_2}$	
$\xi 2_i = \xi 1_i \sqrt{(2z+1)\beta}$	
t_1	time elapsed between the application of the first and second pulse
τ_2	time elapsed between the second pulse application and the measurement of the current
$t = t_1 + \tau_2$	
$\gamma = \sqrt{\dfrac{D_A}{D_B}}$	
$K_j = \exp[nF(E_j - E^0)/RT]$	
$i_{DC} = nFq_0 C_A^* \sqrt{\dfrac{D_A}{\pi t_2}}$	
$i_0 = i_{DC}\sqrt{t_2}$	

When two signs appear, the upper sign refers to a solution soluble product and the lower sign to amalgam formation. Other definitions are conventional.

Can. J. Chem. Downloaded from www.nrcresearchpress.com by 85.192.166.187 on 09/08/12
For personal use only.

$$[14] \quad P_z \equiv P_{(1-Z)/(2Z+1)} = \frac{2\Gamma\left(1+\frac{1-z}{4z+2}\right)}{\Gamma\left(\frac{1}{2}+\frac{1-z}{4z+2}\right)}$$

$$[15] \quad \Omega_1 = \frac{1 \pm K_1}{1+\gamma K_1}$$

$$[16] \quad \gamma = \sqrt{\frac{D_A}{D_B}}$$

Throughout this paper the upper sign in any equation refers to a reaction product which is soluble in the electrolytic solution whilst the lower sign refers to a product soluble in the electrode (amalgam formation).

The theoretical analysis presented in this paper has been also carried out by taking into account the second order spherical correction. This highly increases the mathematical complexity, without significantly improving the results of the current in the second pulse of the potential, at least when $\xi 1_A^0 \leq 0.35$ (see footnote 2 for notation). Therefore, to make our conclusions as clear as possible without invoking mathematical complexity, we only present our analysis on first order spherical correction.

It is important to note that the surface concentrations of species A and B were dependent on time (see eqs. [7], [8]). However, when $\gamma = 1$ and both species are soluble in the electrolytic solution the surface concentrations depend only on the applied potential E_1 (eqs. [7] and [10]) with upper sign), as is the case for plane electrodes (4, 5).

With $t = t_1 + \tau_2$ the boundary values in the interval $0 \leq \tau_2 \leq t_2$ take the form

$$[17] \quad \hat{D}_A C_A^2(r, t) = \hat{D}_B C_B^2(r, t) = 0$$

$$[18] \quad \tau_2 = 0;\ r = r_0 \begin{cases} C_A^2(r, t) = C_A^1(r, t) \\ C_B^2(r, t) = C_B^1(r, t) \end{cases}$$

$$[19] \quad \tau_2 > 0;\ r \to \pm\infty: \quad C_B^2(r, t) = C_B^1(r, t) = 0$$

$$[20] \quad \tau_2 > 0;\ r = r_0: \quad C_A^2(r_0, t) = K_2 C_B^2(r_0, t)$$

$$[21] \quad \frac{i_2}{nFq(t)} = D_A\left(\frac{\partial C_A^2}{\partial r}\right)_{r=r_0} = \mp D_B\left(\frac{\partial C_B^2}{\partial r}\right)_{r=r_0}$$

where the linear differential operator $\hat{D}_i$ (i = A, B) is given by

$$[22] \quad \hat{D}_1 = \frac{\partial}{\partial \tau_2} - D_1\left(\frac{\partial^2}{\partial r^2} + \frac{2}{r}\frac{\partial}{\partial r}\right) + \frac{z r_0^3}{2r^2(t_1+\tau_2)}\frac{\partial}{\partial r}$$

The linearity of the differential equations involved means that we can search for a solution of the form

$$[23] \quad C_A^2(r, t) = C_A^1(r, t) + \tilde{C}_A(r, \tau_2)$$

$$[24] \quad C_B^2(r, t) = C_B^1(r, t) + \tilde{C}_B(r, \tau_2)$$

where the new functions $\tilde{C}_A(r, \tau_2)$ and $\tilde{C}_B(r, \tau_2)$ are solutions of eq. [17] with null initial conditions (at $\tau_2 = 0$) as it is immediately seen from eq. [18].

We seek a solution for the power series

$$[25] \quad \tilde{C}_A(r, \tau_2) = \sum_{i,j} \sigma_{i,j}^{(-)}(s2_A)\xi 2_A^i \beta^{(j-1)/2}$$

$$[26] \quad \tilde{C}_B(r, \tau_2) = \sum_{i,j} \delta_{i,j}^{(\mp)}(s2_B)\xi 2_B^i \beta^{(j-1)/2}$$

where

$$[27] \quad s2_i = \frac{(r - r_0)}{2\sqrt{D_i \tau_2}}$$

$$[28] \quad \xi 2_i = \frac{2\sqrt{D_i \tau_2}}{r_0}$$

$$[29] \quad \beta = \frac{\tau_2}{(t_1 + \tau_2)}$$

Introducing these expressions into eq. [17] leads to the following set of ordinary differential equations for the coefficients $\sigma_{i,j}(s2_A)$ and $\delta_{i,j}(s2_B)$

$$[30] \quad \sigma''_{i,j}(s2_A) + 2s2_A\sigma'_{i,j}(s2_A) - 2(i+j-1)\sigma_{i,j}(s2_A) = -\sum_{m+l+1=i} c_m \sigma'_{i,j}(s2_A) - \sum_{r+p=i} d_r \sigma'_{p,j-2}(s2_A) - 2z\left(i + \frac{j-3}{z}\right)\sigma_{i,j-2}(s2_A)$$

$$[31] \quad \delta''_{i,j}(s2_B) + 2s2_B\delta'_{i,j}(s2_B) - 2(i+j-1)\delta_{i,j}(s2_B) = -\sum_{m+l+1=i} c_m \delta'_{i,j}(s2_B) - \sum_{r+p=i} d_r \delta'_{p,j-2}(s2_B) - 2z\left(i + \frac{j-3}{z}\right)\delta_{i,j-2}(s2_A)$$

where

$$[32] \quad c_m = 2(-1)^m (s2_i)^m$$
$$c_m = 0 \text{ for planar electrodes}$$

$$[33] \quad d_r = 2z(-1)^r (r+2)(s2_i)^{r+1}$$

A rigorous treatment of the problem is complicated since the dimensionless parameters $\xi 1_1$ and $\xi 2_1$ (connected to the electrode sphericity during the first and second pulses, respectively) are not independent. In fact, they are linked as follows:

$$[34] \quad \frac{\xi 2_i}{\xi 1_i} = \sqrt{(2z+1)\beta}$$

The appropriate boundary conditions for $\sigma_{i,j}(s2_A)$ and $\delta_{i,j}(s2_B)$ functions can be deduced from the initial conditions given in eq. [18], the boundary condition in eqs. [19]–[21] and also eq. [34]. Thus when $s2_A, s2_B \to \infty$:

$$[35] \quad \sigma_{i,j} = \delta_{i,j} = 0 \qquad \forall i, j$$

when $s2_A = s2_B = 0$

$$[36] \quad \gamma^{i+1}\sigma'_{i,j} = \mp\delta'_{i,j} \qquad \forall i, j$$

Can. J. Chem. Downloaded from www.nrcresearchpress.com by 85.192.166.187 on 09/08/12
For personal use only.

[37] $$\sigma_{0,1} = -C_A^* Z_2(1+\gamma K_2) + K_2\delta_{0,1}$$

[38] $$\gamma\sigma_{1,0} = -C_A^* Z_2 N_z(1+\gamma K_2) + K_2\delta_{1,0}$$

[39] $$\gamma^i\sigma_{i,j} = K_2\delta_{i,j} \text{ unless } i=1,\ j=0 \text{ and } i=0,\ j=1$$

[40] $$Z_2 = \frac{1}{1+\gamma K_2} - \frac{1}{1+\gamma K_1}$$

[41] $$N_z = \frac{4\sqrt{2z+1}\,(\gamma \mp 1)}{(5z+4)(1+\gamma K_1)\sqrt{\pi}}$$

The expressions for $\sigma_{i,j}(s2_A)$ and $\delta_{i,j}(s2_B)$ are then obtained by the procedure developed in ref. 12, and are given in Appendix (eqs. [A3]–[A8], [A11]–[A22], and [A25]–[A33]).

The surface concentration of both species A and B during the second pulse, for an expanding spherical electrode, can now be found by substituting $r = r_0$ and eq. [A23] in eqs. [23] and [24]. Then we obtain

[42] $$C_A^2(r_0,t) = \frac{C_A^* K_2}{1+\gamma K_2}\left\{\gamma + \frac{4(2z+1)(\gamma \mp 1)}{(5z+4)(1+\gamma K_1)\sqrt{\pi}}\,\xi 1_A\right\} + C_A^* Z_2 \frac{K_2(\gamma \mp 1)}{(1+\gamma K_2)\sqrt{\pi}}\,Q_z(\beta)\xi 2_A$$

[43] $$C_B^2(r_0,t) = C_A^2(r_0,t)/K_2$$

where

[44] $$Q_z(\beta) = 1 - \frac{z(5z+2)}{48}\beta^2 + \frac{z(3z^2-20z-8)}{240}\beta^3\cdots$$

It is worth noting that if $\gamma = 1$ (i.e., $D_A = D_B$) and both species are soluble in the electrolytic solution (upper sign), $C_A^2(r_0,t)$ and $C_B^2(r_0,t)$ depend only on the applied potential E_2, for any type of electrode ($z \geq 0$).

The current time response can also be immediately obtained from eqs. [21], [A9], and [A24].

[45] $$i_2 = i_1(t) + nFq(t)\sqrt{\frac{D_A}{\pi t_2}}\,C_A^* Z_2\left\{f_z(\beta) + \frac{4(2z+1)(\gamma \mp 1)}{(5z+4)(1+\gamma K_1)\gamma\sqrt{\pi}}\,g_z(\beta)\xi 1_A + \frac{\sqrt{\pi}}{2}\,\Omega_2 h_z(\beta)\xi 2_A\right\}$$

where

[46] $$\Omega_2 = \frac{1 \pm K_2}{1+\gamma K_2}$$

[47] $$f_z(\beta) = \sqrt{\frac{(2z+1)\beta}{1-(1-\beta)^{(2z+1)}}}$$

[48] $$g_z(\beta) = 1 + \frac{1}{2}\beta + \frac{2z^2+2z+1}{24}\beta^2 + \frac{2z^2+2z+1}{80}\beta^3\cdots$$

[49] $$h_z(\beta) = 1 - \frac{3z(7z+2)}{128}\beta^2 + \frac{z(z-4)(7z+2)}{256}\beta^3\cdots$$

$f_z(\beta)$ and the series $h_z(\beta)$, in the particular case when $z = 0$ and $z = 2/3$, are coincident with the series $h_0(z,\tau)$ and $h_1(z,\tau)$ given by eqs. [42] and [43] in ref. 1*a* respectively ($\tau \equiv \beta$). On the other hand, the series $g_z(\beta)$ is a new series. It came about as a result of the disturbance on the surface concentrations deduced for the first pulse ($C_A^1(r_0,t)$ and $(C_B^1(r_0,t))$ due to the application of the second pulse. Therefore, eq. [45] in this work does not coincide in general with eq. [41] in ref. 1*a*. Nevertheless, in the special case when $\gamma = 1$ and both species are soluble in the electrolytic solution, eq. [41] in ref. 1*a* (or eq. [36] in ref. 2) and our eq. [45] are the same; because in this particular case the surface concentrations of the electroactive couple are time-independent. On the other hand, if $D_A \neq D_B$ or there is amalgam formation one should use our eq. [45] instead of the equations deduced in refs. 1*a* and 2.

The results expressed by eq. [45] simplify in the following cases:

(*a*) $z = 2/3$ (DME)

[50] $$i_2 = i_1(t) + nFA_0 t^{2/3}\sqrt{\frac{D_A}{\pi t_2}}\,C_A^* Z_2\left\{f_{2/3}(\beta) + \frac{14(\gamma \mp 1)}{11(1+\gamma K_1)\gamma\sqrt{\pi}}\,g_{2/3}(\beta)\xi 1_A + \frac{\sqrt{\pi}}{2}\,\Omega_2 h_{2/3}(\beta)\xi 2_A\right\}$$

where (13)

[51] $$f_{2/3}(\beta) = \sqrt{\frac{7\beta}{3(1-(1-\beta)^{7/3})}}$$

[52] $$g_{2/3}(\beta) = 1 + \frac{1}{2}\beta + \frac{29}{216}\beta^2 + \frac{29}{720}\beta^3 + \cdots$$

[53] $$h_{2/3}(\beta) = 1 - \frac{5}{48}\beta^2 - \frac{25}{432}\beta^3\cdots$$

(*b*) $z = 0$ (SMDE)

[54] $$i_2 = i_1(t) + nFA_0\sqrt{\frac{D_A}{\pi t_2}}\,C_A^* Z_2 \times \left\{1 + \frac{(\gamma \mp 1)}{\sqrt{\pi}\gamma(1+\gamma K_1)}\,g_0(\beta)\xi 1_A + \frac{\sqrt{\pi}}{2}\,\Omega_2\xi 2_A\right\}$$

The expression for $g_0(\beta)$ is given by (14).

[55] $$g_0(\beta) = 1 + \sum_{k=1}^{\infty}\frac{\beta^k(2k-1)!}{k!2^{2k-1}(k-1)!(2k-1)^2} = \sqrt{\beta}\arcsin(\sqrt{\beta}) + \sqrt{1-\beta}$$

[56] $$f_0(\beta) = h_0(\beta) = 1$$

and eq. [54] takes the simpler form

[57] $$i_2 = i_1 + nFA_0 C_A^*\sqrt{\frac{D_A}{\pi}}\left(\frac{1}{1+\gamma K_2} - \frac{1}{1+\gamma K_1}\right) \times \left\{\frac{1}{\sqrt{t_2}} + \frac{\gamma \mp 1}{\gamma(1+\gamma K_1)}\sqrt{\frac{D_A}{\pi}}\,\frac{2}{r_0}\left(\sqrt{\frac{1-\beta}{\beta}} + \arcsin(\sqrt{\beta})\right) + \frac{\sqrt{\pi D_A}}{r_0}\,\frac{1 \pm K_2}{1+\gamma K_2}\right\}$$

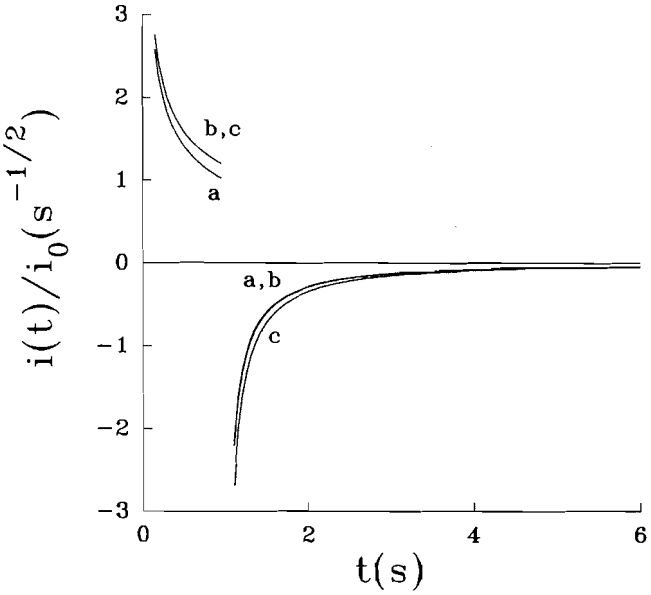

FIG. 2. Influence of the amalgamation on $i/i_0 - t$ recording for a double potential step at a SMDE (eq. [12] with $E_1 \rightarrow -\infty$ and [63]). $\xi 1^0_A = 0.2\ s^{-1/2}$, $t_1 = 1$ s, $n = 1$, and $\gamma = 0.8$. (*a*) Planar electrode, (*b*) solution-soluble product, (*c*) amalgam formation.

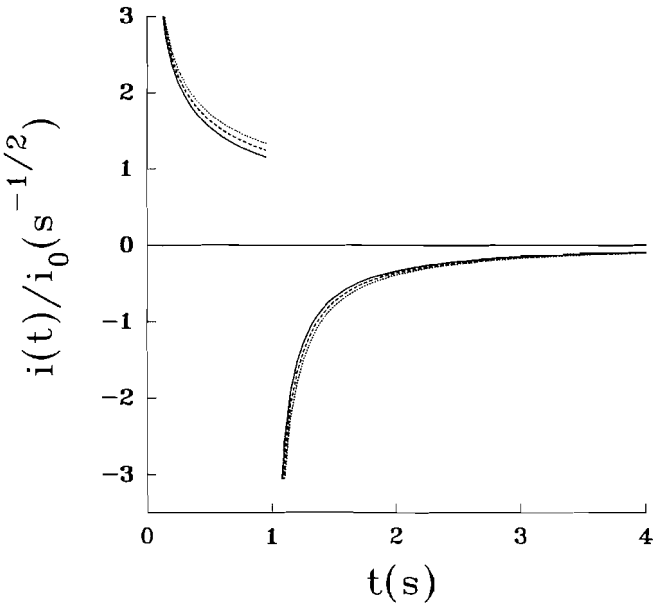

FIG. 3. Influence of sphericity on $i/i_0 - t$ recording for a double potential step when the amalgamation takes place in a SMDE. The values of $\xi 1^0_A$ in $s^{-1/2}$ are (—) 0.15, (– – –) 0.25, (···) 0.35. Other conditions as in Fig. 2.

(*c*) $\xi 1_i = \xi 2_i = 0$ (expanding plane electrode)

$$[58] \qquad i_2 = i_1(t) + nFq(t)\sqrt{\frac{D_A}{\pi t_2}}\, C^*_A Z_2 f_z(\beta)$$

(*d*) $\gamma = 1$ and the reduced species B soluble in the electrolytic solution (upper sign)

$$[59] \qquad i_2 = i_1(t) + nFq(t)\sqrt{\frac{D_A}{\pi t_2}}\, C^*_A Z_2 \left\{ f_z(\beta) + \frac{\sqrt{\pi}}{2}\, \xi 2_A h_z(\beta) \right\}$$

Results and discussion

(A) i–t curves

The i–t response to a single pulse E_2 (normal pulse voltametry or polarography) is directly obtained from eq. [45] by making $E_1 \rightarrow \infty$. In this case we have $K_1 \rightarrow \infty$, $i_1 \rightarrow 0$ and $Z_2 = 1/(1 + \gamma K_2)$, and therefore

$$[60] \qquad i_2 = i_{NP} = nFq(t)\sqrt{\frac{D_A}{\pi t_2}}\, \frac{C^*_A}{1 + \gamma K_2} \times \left\{ f_z(\beta) + \frac{\sqrt{\pi}}{2}\, \Omega_2 \xi 2_A h_z(\beta) \right\}$$

If now we substitute $E_2 \equiv E_1$ (i.e. $\Omega_2 \equiv \Omega_1$), $t_1 \rightarrow 0$ (i.e. $\beta = 1$) and $\xi 2_A = \sqrt{2z+1}\,\xi 1_A$ in eq. [60], it reduces to a dc response, as can be seen from eq. [12]. The following equations are therefore valid:

$$[61] \qquad f_z(\beta = 1) = \sqrt{2z+1} \begin{cases} 1 & (z = 0) \\ \sqrt{7/3} & (z = 2/3) \end{cases}$$

$$[62] \qquad h_z(\beta = 1) = \frac{2}{\sqrt{\pi}}\, \theta_z \begin{cases} 1 & (z = 0) \\ 0.8878 & (z = 2/3) \end{cases}$$

The i_1–t and i_2–t curves obtained under conditions of control by diffusion for both pulses, i.e. $E_1 \rightarrow -\infty$ ($i_1 \equiv i_{D1}$) and $E_2 \rightarrow +\infty$ ($i_2 \equiv i_{D2}$), are shown in Figs. 2 and 3 for a SMDE, and Figs. 4 and 5 for a DME. They allow us to analyze the effects of sphericity and amalgam formation. Under these conditions eq. [45] leads to the following expression for a second pulse current:

$$[63] \qquad -\frac{i_{D2}}{i_0} = \frac{t^z}{\sqrt{t_2}} f_z(\beta) - \sqrt{2z+1}\, t^{z-1/2} + \frac{2t^z\sqrt{D_A}}{r_0} \times \left\{ M_z \frac{(\gamma \mp 1) g_z(\beta)}{\gamma\sqrt{\beta}} \pm \frac{\sqrt{\pi}}{2\gamma} h_z(\beta) - \theta_z \right\}$$

$$[64] \qquad M_z = \frac{4\sqrt{2z+1}}{(5z+4)\sqrt{\pi}}$$

$$[65] \qquad i_0 = nFA_0 C^*_A \sqrt{D_A/\pi}$$

The behaviour of the i_1–t and i_2–t curves is very similar to that shown in Figs. 2–5 when $E_1 - E_0 \leq -2RT/nF$ and $E_2 - E_0 \geq 2RT/nF$.

Since the current i_{D2} is due to the oxidization of species B, which initially is not present in the solution, it is clear that

$$[66] \qquad i_{D2} \rightarrow 0 \text{ when } t_2 \rightarrow +\infty$$

and this condition is verified both when B is soluble in the solution and when it produces amalgamation.

When $t_2 \rightarrow +\infty$ we have $\beta \rightarrow 1$, and therefore, by introducing eqs. [61] and [62] into eq. [63] we obtain (see also eqs. [52] and [55])

$$[67] \qquad g_z(\beta = 1) = \frac{\theta_z}{M_z} \begin{cases} \pi/2 & (z = 0) \\ 1.674 & (z = 2/3) \end{cases}$$

These results can also be obtained from eqs. [52] and [55].

Can. J. Chem. Downloaded from www.nrcresearchpress.com by 85.192.166.187 on 09/08/12
For personal use only.

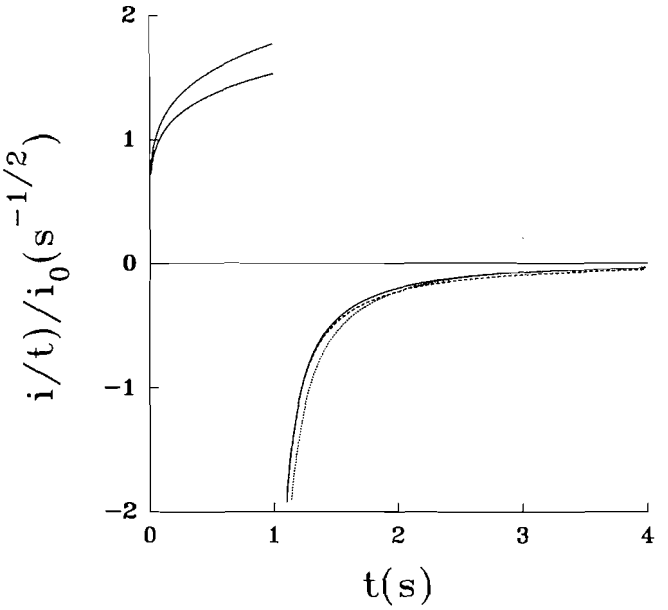

FIG. 4. Influence of the amalgamation on $i/i_0 - t$ recording for a double potential step in a DME (eq. [12] with $E_1 \rightarrow -\infty$ and [63]). $\xi 1^0_A = 0.2\ s^{-1/6}$. (—) Planar electrode, (– – –) solution-soluble product, (···) amalgam formation. Other conditions as in Fig. 2.

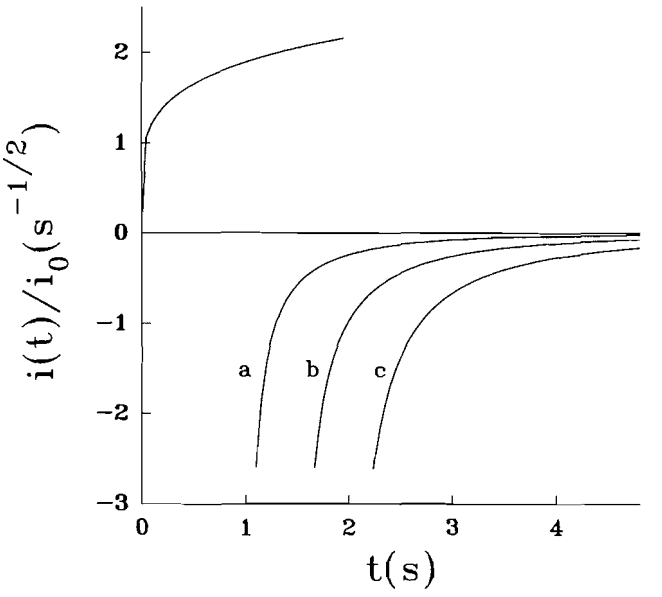

FIG. 5. Influence of the first pulse duration on $i/i_0 - t$ recorder for a double potential step in a DME. $\gamma = 1.3$, $\xi 1^0_A = 0.3\ s^{-1/6}$. The values of t_1 in s are (*a*) 1.0, (*b*) 1.5, (*c*) 2.0. Other conditions as in Fig. 3.

The Koutecky approximation (7) that we introduced in eq. [19] for amalgam formation works very well; this becomes apparent as in all cases:

[68] $\quad i_{D2} \leq 0$ for $0 < t_2 < +\infty$

However, in refs. 1 and 2 condition [68] is not fulfilled when the amalgamation takes place. This becomes clear in Figs. 3 and 4 (curves *b*) in ref. 1*a*, where i_2 suffers a change in sign for $t_2 > t_1$.

As shown in Figs. 2 and 4 SMDE and DME, respectively, the current i_2 is lower when amalgamation is present than

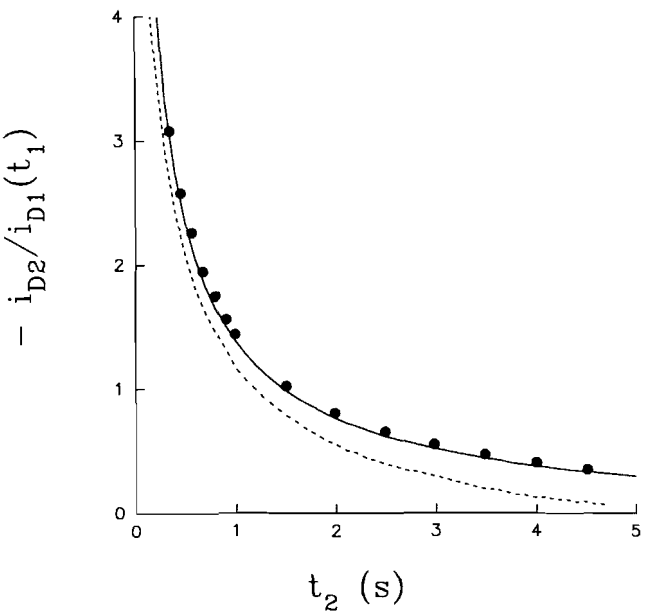

FIG. 6. Amalgam-forming systems: current–time response (●) for the second step in double-potential-step chronoamperometry at an SMDE (Pb(II)/Pb(Hg) system: $C_{Pb(II)} = 0.5$ mM; $[KNO_3] = 0.2$ M) with $E_1 = -0.7$ V, $E_2 = -0.2$ V, $t_1 = 5$ s, and $r_0 = 0.0413$ cm. (—) Current–time curve computed using eqs. [63] and [12]. (– – –) Current–time curve computed using eqs. [65] and [67] in ref. (1*a*).

when both species are soluble in the solution or for a plane electrode.

The effect of sphericity or a SMDE and the effect of the length of the first pulse, t_1, or a DME when species B amalgamates with the electrode are shown in Figs. 3 and 5, respectively.

Equation [63] has been used to explain the behaviour of the system Pb(II)/Pb(Hg) at a SMDE ($z = 0$). The applicability of eq. [63] corresponds to an experimental situation with $E_1 \ll E_0$ ($i_1 = i_{D1}$ cathodic current) and $E_2 \gg E_0$ ($i_2 = i_{D2}$ anodic current). Under these conditions the system Pb(II)/Pb(Hg) has been studied by double potential step chronoamperometry (1*b*). The experimental results from the literature (see Fig. 5 in ref. 1*b*) are shown in Fig. 6 (circles). Other experimental conditions are given in the caption of Fig. 6. The continuous line in Fig. 6 corresponds to the results obtained from eq. [63] with $D_A = 8.1 \times 10^{-6}$ cm^2/s ($D_{Pb(II)}$) and $D_B = 1.33 \times 10^{-5}$ cm^2/s ($D_{Pb(Hg)}$) (1*a*).

Following the procedure in ref. 1*b*, we have plotted $-i_{D2}/-i_{D1}(t_1)$, where $i_{D1}(t_1)$, is the solution of eq. [12] for $E_1 \ll E_0$ and $t = t_1$. As it can be noticed, there is an excellent agreement between experimental and the results obtained from eq. [63].

It has been also included in Fig. 6 the theoretical predictions of the model presented in ref. 1*a* (dashed line). As is observed and stated in ref. 1*b*, that model leads to wrong results for electrode processes with amalgam formation. The reason is that the model does not take into account the perturbation of the second pulse on the concentration profiles generated by the first potential pulse.

(B) Reverse pulse techniques

Reverse pulse techniques (1, 2, 3, 8–10) are based on the choice $E_1 \rightarrow -\infty$ ($K_1 \rightarrow 0$) and a variable potential E_2. The current $I_{RP} = -i_2/i_{DC}$ can then be easily evaluated from eq.

Can. J. Chem. Downloaded from www.nrcresearchpress.com by 85.192.166.187 on 09/08/12
For personal use only.

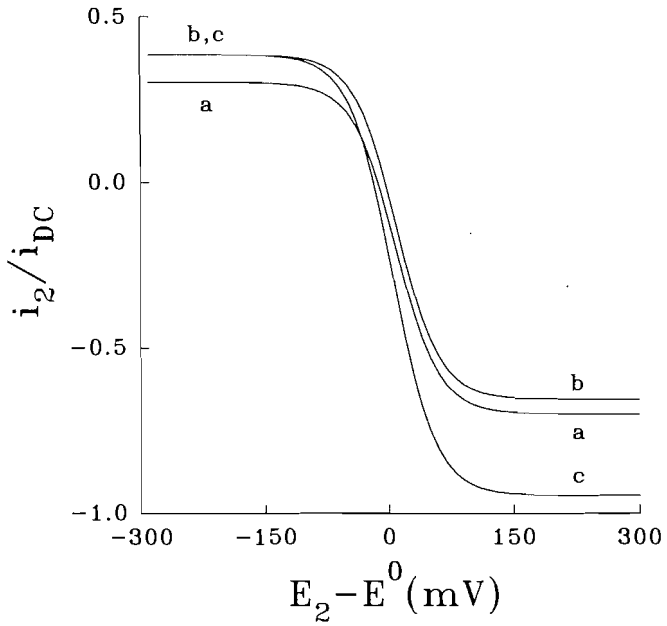

FIG. 7. Reverse pulse voltammograms computed by eq. [45] with $z = 0$ and $E_1 \rightarrow -\infty$. $\xi 1^0_A = 0.3\ s^{-1/2}$, $\gamma = 0.7$, $n = 1$, $T = 298$ K, $\beta = 0.091$. (*a*) Planar electrode, (*b*) solution soluble product, (*c*) amalgam formation.

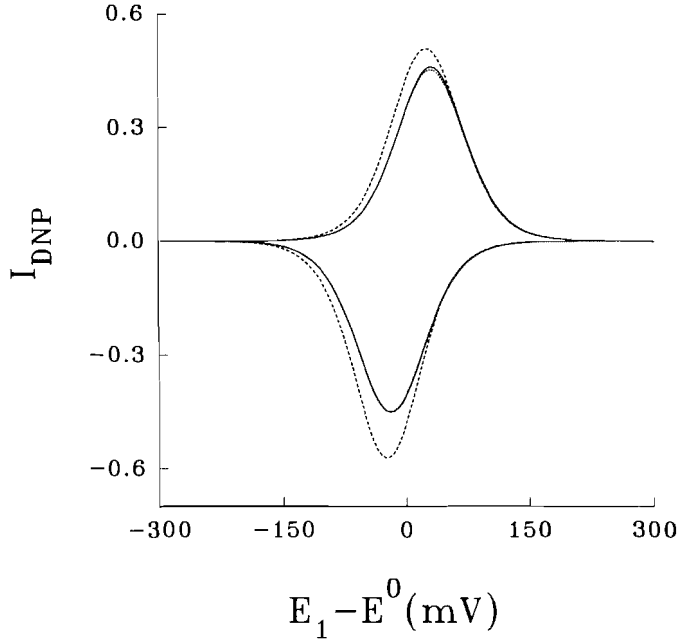

FIG. 8. Influence of amalgam formation in Differential Pulse Voltametry (eq. [76] with $z = 0$). $n = 1$, $\gamma = 0.8$, $\beta = 0.01$, $|\Delta E| = 50$ mV; (—) Solution-soluble product, (– – –) amalgam formation, (· · ·) planar electrode. Other conditions as in Fig. 7.

[45]. An example of application of this technique is shown in Fig. 7. It can be seen that the effect of sphericity is quite remarkable, whether the reaction product is soluble in the electrolytic solution or if it amalgamates.

A criterion to determine if amalgamation occurs in a spherical electrode can be found by analyzing the limiting values of the cathodic, i_{D1}, and anodic, i_{D2}, currents. For the sake of simplicity we consider a SMDE ($z = 0$), and from eq. [12] with $K_1 = 0$ we have

$$[69] \qquad \frac{i_{D1}}{i_{DC}} = \sqrt{\beta}\left(1 + \frac{\sqrt{\pi D_A t}}{r_0}\right)$$

where

$$[70] \qquad i_{DC} = nFA_0C^*_A\sqrt{\frac{D_A}{\pi t_2}}$$

Furthermore, from eqs. [63], [69], and [70]

$$[71] \qquad -\frac{i_{D2} - i_{D1}}{i_{DC}} = 1 + \frac{\sqrt{\pi D_A t_2}}{r_0} \times \left\{1 + \left(\frac{2g_0(\beta)}{\pi\sqrt{\beta}} - 1\right)\left(\frac{\gamma \mp 1}{\gamma}\right)\right\}$$

this equation can also be written as

$$[72] \qquad R = -\frac{i_{D2} - i^P_{D2}}{i_{D1} - i^P_{D1}} = \left(\frac{2g_0(\beta)}{\pi\sqrt{\beta}} - 1\right)\frac{(\gamma \mp 1)}{\gamma}$$

where i^P_{D1} and i^P_{D2} are the limiting values of i_{D1} and i_{D2} when $r_0 \rightarrow \infty$ (planar electrode), respectively, given by (eqs. [69] and [63] with $r_0 \rightarrow \infty$)

$$[73] \qquad i^P_{D1} = i_{DC}\sqrt{\beta}$$

$$[74] \qquad i^P_{D2} = i_{DC}(\sqrt{\beta} - 1)$$

Therefore, eq. [72] gives the ratio between the contributions of sphericity to the first and second pulses. Since the bracket in eq. [74] fulfills the condition

$$[75] \qquad 0 \leq \left(\frac{2g_0(\beta)}{\pi\sqrt{\beta}} - 1\right) \leq \infty \quad \text{for } 1 \geq \beta \geq 0$$

we can make the following classification: (*a*) If $0 \leq R < (2g_0(\beta)/\pi\sqrt{\beta} - 1)$, B is soluble in solution and $\gamma \geq 1$; (*b*) If $R < 0$, B is again soluble, and $\gamma < 1$; (*c*) If $R > (2g_0(\beta)/\pi\sqrt{\beta} - 1)$, then amalgamation is present.

(C) Differential pulse techniques

These techniques are characterized because $\Delta E = E_2 - E_1$ is kept constant. A cathodic record is obtained if $\Delta E < 0$, and an anodic record if $\Delta E > 0$. The response is $I_{DNP} = (i_2 - i_1)/i_{DC}$, which is positive if $\Delta E < 0$ and negative if $\Delta E > 0$, respectively. From eq. [45] we deduce

$$[76] \qquad I_{DNP} = \frac{\sqrt{2z+1}}{1+\gamma K_1}\left\{t^z\sqrt{\beta}[1 + \theta_z\Omega_1\xi 1_A(t)] - t_1^z\sqrt{\beta/(1-\beta)}[1 + \theta_z\Omega_1\xi 1_A(t_1)]\right\} + t^z Z_2\left\{f_z(\beta) + \frac{4(2z+1)(\gamma \mp 1)}{(5z+4)(1+\gamma K_1)\gamma\sqrt{\pi}} \times g_z(\beta)\xi 1_A + \frac{\sqrt{\pi}}{2}\Omega_2 h_z(\beta)\xi 2_A\right\}$$

A criterion for the analysis of electrode processes has been proposed by Birke et al. (6) on the basis of the ratio between

Can. J. Chem. Downloaded from www.nrcresearchpress.com by 85.192.166.187 on 09/08/12
For personal use only.

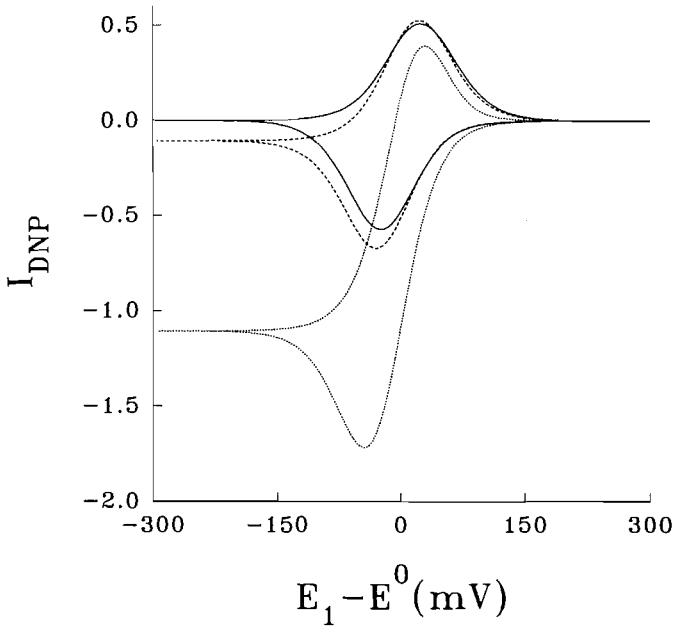

FIG. 9. Differential normal pulse voltagrams (eq. [76] with $z = 0$) when the amalgamation takes place. The values of β are (—) 0.01, (— — —) 0.3, (· · ·) 0.8. Other conditions as in Fig. 8.

the current peaks corresponding to two records with opposite values of ΔE. In this way the same peaks of current in absolute value are obtained in the cathodic and anodic records for a reversible charge transfer in a planar electrode with $\gamma = 1$. On the other hand, for a spherical electrode with amalgam formation the anodic record increases strongly with respect to the cathodic record (see Fig. 8).

The influence of β on the records obtained is shown in Fig. 9. In general, it can be said that amalgam formation increases the current peaks, and also that they are shifted to more positive values of potential.

Acknowledgement

The authors wish to express their gratitude to the Junta de Andalucia and to the DGICYT (Projects PB91-0834 and PB90-0307) for financial help granted.

1. J. Gálvez, M.L. Alcaraz, Y.B. Shim, and S.M. Park. J. Electroanal. Chem. (*a*) **341**, 15 (1992); (*b*) **341**, 209 (1992).
2. J. Gálvez. Anal. Chem. **57**, 585 (1985).
3. J.R. Delmastro and D.E. Smith. J. Phys. Chem. **71**, 2138 (1967).
4. A.M. Bond and K.B. Oldham. J. Electroanal. Chem. **158**, 193 (1983).
5. J. Goodisman. J. Electroanal. Chem. **144**, 33 (1983).
6. R.L. Birke, M.H. Kim, and M. Strassfeld. Anal. Chem. **53**, 852 (1981).
7. J. Koutecky. Czech. J. Phys. **2**, 50 (1953).
8. T.R. Brumleve and J. Osteryoung. Anal. Chem. **86**, 1794 (1982).
9. A.M. Bond, B.S. Grabaric, and N.W. Rumble. J. Electroanal. Chem. **106**, 85 (1980).
10. L. Nyholm and G. Wikmark. Anal. Chem. **59**, 2383 (1987).
11. J.E. Anderson, A.M. Bond, and K.B. Oldham. J. Electroanal. Chem. **218**, 1 (1987).
12. A. Molina, C. Serna, and M. López-Tenés. J. Electroanal. Chem. **284**, 21 (1990).
13. L. Camacho, J.J. Ruiz, C. Serna, A. Molina, and F. Martinez-Ortíz. To be published.
14. Mathematica 2.2. Wolfram Research Inc., Champaing, IL, USA, 1993.

Appendix

The differential equations [30] and [31] for $i = 0$ are simplified to

[A1] $$\sigma_{0,j}^{(-)''}(s2_A) + 2s2_A\sigma_{0,j}^{(-)'}(s2_A) - 2(j-1)\sigma_{0,j}^{(-)}(s2_A) = -4zs2_A\sigma_{0,j-2}^{(-)'}(s2_A) - 2(j-3)\sigma_{0,j-2}^{(-)}(s2_A)$$

[A2] $$\delta_{0,j}^{(\mp)''}(s2_B) + 2s2_B\delta_{0,j}^{(\mp)'}(s2_B) - 2(j-1)\delta_{0,j}^{(\mp)}(s2_B) = -4zs2_A\delta_{0,j-2}^{(\mp)'}(s2_B) - 2(j-3)\delta_{0,j-2}^{(\mp)}$$

The solutions of these equations (corresponding to an expanding plane electrode of area $q(t) = q_0 t^z$) with the boundary value problem given by eqs. [36], [37], and [39] with $i = 0$, are

[A3] $$\sigma_{0,2n}^{(-)}(s2_A) = 0 \qquad n = 0,\ 1,\ 2\ldots$$

[A4] $$\sigma_{0,1}^{(-)}(s2_A) = -\Psi_0^{(-)}(s2_A)C_A^*Z_2$$

[A5] $$\sigma_{0,3}^{(-)}(s2_A) = \frac{z}{\sqrt{\pi}}\, s2_A e^{-(s2_A)^2} C_A^* Z_2$$

[A6] $$\sigma_{0,5}^{(-)}(s2_A) = \frac{z}{2\sqrt{\pi}}\left\{\frac{z+4}{6} - z(s2_A)^2\right\} s2_A e^{-(s2_A)^2} C_A^* Z_2$$

[A7] $$\sigma_{0,7}^{(-)}(s2_A) = \frac{z}{6\sqrt{\pi}}\left\{\frac{4-z^2}{4} - z(z+2)(s2_A)^2 + z^2(s2_A)^4\right\} s2_A e^{-(s2_A)^2} C_A^* Z_2$$

Can. J. Chem. Downloaded from www.nrcresearchpress.com by 85.192.166.187 on 09/08/12
For personal use only.

[A8] $$\sigma_{0,9}^{(-)}(s2_A) = \frac{z}{24\sqrt{\pi}}\left\{\frac{96-32z-56z^2-3z^3}{40} - \frac{z(8-z)(5z+8)}{12}(s2_A)^2 + \frac{z^2(5z+8)}{2}(s2_A)^4 - z^3(s2_A)^6\right\} s2_A e^{-(s2_A)^2} C_A^* Z_2$$

These functions hold

[A9] $$\sum_{n=0} \sigma_{0,2n+1}^{(-)'}(0)\beta^n = \frac{2C_A^* Z_2}{\sqrt{\pi}} f_z(\beta)$$

where

[A10] $$f_z(\beta) = 1 + \frac{z}{2}\beta + \frac{z(z+4)}{24}\beta^2 + \frac{z(2+z)(2-z)}{48}\beta^3 + \frac{z(96-32z-56z^2-3z^3)}{1920}\beta^4$$

This is equivalent to eq. [47] (13). Moreover

[A11] $$\delta_{0,2n+1}^{(\mp)}(s2_B) = \mp\gamma\sigma_{0,2n+1}^{(\mp)}(s2_B) \quad \text{unless } n = 0$$

[A12] $$\delta_{0,1}^{(\mp)}(s2_B) = -\gamma\sigma_{0,1}^{(\mp)}(s2_B)$$

For $i = 1$ (first order spherical correction) eqs. [30] and [31] become

[A13] $$\sigma_{1,j}^{(-)''}(s2_A) + 2s2_A\sigma_{1,j}^{(-)'}(s2_A) - 2j\sigma_{1,j}^{(-)}(s2_A) = -2\sigma_{0,j}^{(-)'}(s2_A) - 4zs2_A\sigma_{1,j-2}^{(-)'}(s2_A) + 6z(s2_A)^2\sigma_{0,j-2}^{(-)'}(s2_A) - 2(z+j-3)\sigma_{1,j-2}^{(-)}(s2_A)$$

[A14] $$\delta_{1,j}^{(\mp)''}(s2_B) + 2s2_B\delta_{1,j}^{(\mp)'}(s2_B) - 2j\delta_{1,j}^{(\mp)}(s2_B) = -2\delta_{0,j}^{(\mp)'}(s2_B) - 4zs2_B\delta_{1,j-2}^{(\mp)'}(s2_B) + 6z(s2_B)^2\delta_{0,j-2}^{(\mp)'}(s2_B) - 2(z+j-3)\delta_{1,j-2}^{(\mp)}(s2_B)$$

and the solutions are

[A15] $$\sigma_{1,0}^{(-)}(s2_A) = -\frac{C_A^* Z_2 N_z}{\gamma}\Psi_0^{(-)}(s2_A)$$

[A16] $$\sigma_{1,1}^{(-)}(s2_A) = \frac{1}{\sqrt{\pi}}\{e^{-(s2_A)^2} - \Omega_2\Psi_1^{(-)}(s2_A)\}C_A^* Z_2$$

[A17] $$\sigma_{1,2}^{(-)}(s2_A) = \left\{\frac{z}{\sqrt{\pi}} s2_A e^{-(s2_A)^2} - \frac{z-1}{2}[\Psi_0^{(-)}(s2_A) - \Psi_2^{(-)}(s2_A)]\right\}\frac{C_A^* Z_2 N_z}{\gamma}$$

[A18] $$\sigma_{1,3}^{(-)}(s2_A) = \frac{z}{2\sqrt{\pi}}\left\{[\Omega_2 - 4(s2_A)^2]e^{-(s2_A)^2} - \Omega_2[3\Psi_1^{(-)}(s2_A) - 2\Psi_3^{(-)}(s2_A)]\right\}$$

[A19] $$\sigma_{1,4}^{(-)}(s2_A) = \left\{\left(\frac{7z-2}{6} - z(s2_A)^2\right)\frac{z}{2\sqrt{\pi}} s2_A e^{-(s2_A)^2} - \frac{(z-1)(5z+1)}{8}[\Psi_0^{(-)}(s2_A) - 2\Psi_2^{(-)}(s2_A) + \Psi_4^{(-)}(s2_A)]\right\}\frac{C_A^* Z_2 N_z}{\gamma}$$

[A20] $$\sigma_{1,5}^{(-)}(s2_A) = \frac{z}{2\sqrt{\pi}}\left\{\left(\frac{2(13z+4)\Omega_2 - 5z - 2}{24} - \frac{17z+14+6z\Omega_2}{12}(s2_A)^2 + 3z(s2_A)^4\right)e^{-(s2_A)^2} - \frac{(7z+2)\Omega_2}{8}[6\Psi_1^{(-)}(s2_A) - 8\Psi_3^{(-)}(s2_A) + 3\Psi_5^{(-)}(s2_A)]\right\}C_A^* Z_2$$

[A21] $$\sigma_{1,6}^{(-)}(s2_A) = \left\{\left(\frac{3z^2-z-1}{4} - \frac{z(5z+1)}{6}(s2_A)^2 + \frac{z^2}{3}(s2_A)^4\right)\frac{z}{2\sqrt{\pi}} s2_A e^{-(s2_A)^2} - \frac{(z-1)(5z+1)(3z+1)}{16}[\Psi_0^{(-)}(s2_A) - 3\Psi_2^{(-)}(s2_A) + 3\Psi_4^{(-)}(s2_A) + \Psi_6^{(-)}(s2_A)]\right\}\frac{C_A^* Z_2 N_z}{\gamma}$$

Can. J. Chem. Downloaded from www.nrcresearchpress.com by 85.192.166.187 on 09/08/12
For personal use only.

Can. J. Chem. Downloaded from www.nrcresearchpress.com by 85.192.166.187 on 09/08/12
For personal use only.

[A22] $$\sigma_{1,7}^{(-)}(s2_A) = \frac{z}{8\sqrt{\pi}}\left\{\left(\frac{3z^2-20z-8+5(33z^2+22z+4)\Omega_2}{30}+\frac{59z^2-50z-64-2z(35z+20)\Omega_2}{30}(s2_A)^2\right.\right.$$
$$\left.+\frac{z(25z+22)+2z^2\Omega_2}{3}(s2_A)^4-\frac{16z^2}{3}(s2_A)^6\right)e^{-(s2_A)^2}-\frac{(7z+2)(11z+4)\Omega_2}{4}$$
$$\left.\times\left(2\Psi_1^{(-)}(s2_A)-\frac{43z+16}{11z+4}\Psi_3^{(-)}(s2_A)+3\Psi_5^{(-)}(s2_A)-\frac{4}{5}\Psi_7^{(-)}(s2_A)\right)\right\}C_A^*Z_2$$

These functions have the following relationships:

[A23] $$\begin{cases}\displaystyle\sum_{n=0}\sigma_{1,2n}^{(-)}(0)\beta^{(2n-1)/2} = -\frac{C_A^*Z_2N_z}{\gamma\sqrt{\beta}}\\ \displaystyle\sum_{n=0}\sigma_{1,2n+1}^{(-)}(0)\beta^n = \frac{(1-\Omega_2)C_A^*Z_2}{\sqrt{\pi}}Q_z(\beta)\end{cases}$$

[A24] $$\begin{cases}\displaystyle\sum_{n=0}\sigma_{1,2n}^{(-)'}(0)\beta^{(2n-1)/2} = \frac{2C_A^*Z_2N_z}{\gamma\sqrt{\pi\beta}}g_z(\beta)\\ \displaystyle\sum_{n=0}\sigma_{1,2n+1}^{(-)'}(0)\beta^n = C_A^*Z_2\Omega_2h_z(\beta)\end{cases}$$

where $g_z(\beta)$ and $h_z(\beta)$ are given by eqs. [48] and [49], respectively, Moreover

[A25] $$\delta_{1,j}^{(-)}(s2_B) = -\gamma^2\sigma_{1,j}^{(-)}(s2_B)$$

[A26] $$\delta_{1,0}^{(+)}(s2_B) = \gamma C_A^*Z_2N_z\Psi_0^{(+)}(s2_B)$$

[A27] $$\delta_{1,1}^{(+)}(s2_B) = \frac{1}{\sqrt{\pi}}\left\{e^{-(s2_B)^2}+\gamma\Omega_2\Psi_1^{(+)}(s2_B)\right\}\gamma C_A^*Z_2$$

[A28] $$\delta_{1,2}^{(+)}(s2_B) = \left\{\frac{z}{\sqrt{\pi}}s2_Be^{-(s2_B)^2}+\frac{z-1}{2}[\Psi_0^{(+)}(s2_B)-\Psi_2^{(+)}(s2_B)]\right\}\gamma C_A^*Z_2N$$

[A29] $$\delta_{1,3}^{(+)}(s2_B) = \frac{z}{2\sqrt{\pi}}\left\{-[\gamma\Omega_2+4(s2_B)^2]e^{-(s2_B)^2}+\gamma\Omega_2[3\Psi_1^{(+)}(s2_B-2\Psi_3^{(+)}(s2_B)]\right\}\gamma C_A^*Z_2$$

[A30] $$\delta_{1,4}^{(+)}(s2_B) = \left\{\left(\frac{7z-2}{6}-z(s2_B)^2\right)\frac{z}{2\sqrt{\pi}}s2_Be^{-(s2_B)^2}+\frac{(z-1)(5z+1)}{8}[\Psi_0^{(+)}(s2_B)-2\Psi_2^{(+)}(s2_B)+\Psi_4^{(+)}(s2_B)]\right\}\gamma C_A^*Z_2N_z$$

[A31] $$\delta_{1,5}^{(+)}(s2_B) = \frac{z}{2\sqrt{\pi}}\left\{\left(-\frac{2(13z+4)\gamma\Omega_2+5z+2}{24}-\frac{17z+14-6z\gamma\Omega_2}{12}(s2_B)^2+3z(s2_B)^4\right)e^{-(s2_B)^2}+\frac{(7z+2)\gamma\Omega_2}{8}[6\Psi_1^{(+)}(s2_B)\right.$$
$$\left.-8\Psi_3^{(+)}(s2_B)+3\Psi_5^{(+)}(s2_B)]\right\}\gamma C_A^*Z_2$$

[A32] $$\delta_{1,6}^{(+)}(s2_B) = \left\{\left(\frac{3z^2-z-1}{4}-\frac{z(5z+1)}{6}(s2_B)^2+\frac{z^2}{3}(s2_B)^2\right)\frac{z}{2\sqrt{\pi}}s2_Be^{-(s2_B)^2}+\frac{(z-1)(5z+1)(3z+1)}{16}[\Psi_0^{(+)}(s2_B)\right.$$
$$\left.-3\Psi_2^{(+)}(s2_B)+3\Psi_4^{(+)}(s2_B)+\Psi_6^{(+)}(s2_B)]\right\}\gamma C_A^*Z_2N_z$$

[A33] $$\delta_{1,7}^{(+)}(s2_B) = \frac{z}{8\sqrt{\pi}}\left\{\left(\frac{3z^2-20z-8-5(33z^2+22z+4)\gamma\Omega_2}{30}+\frac{59z^2-50z-64+2z(35z+20)\gamma\Omega_2}{30}s2_{AB}^2\right.\right.$$
$$\left.+\frac{z(25z+22)-2z^2\gamma\Omega_2}{3}s2_{AB}^4-\frac{16z^2}{3}(s2_B)^6\right)e^{-(s2_B)^2}+\frac{(7z+2)(11z+4)\gamma\Omega_2}{4}$$
$$\left.\times\left(2\Psi_1^{(+)}(s2_B)-\frac{43z+16}{11z+4}\Psi_3^{(+)}(s2_B)+3\Psi_5^{(+)}(s2_B)-\frac{4}{5}\Psi_7^{(+)}(s2_B)\right)\right\}\gamma C_A^*Z_2$$

Enhanced basicity of 1,3-dialkoxy-substituted benzenes: cyclophane derivatives

GUANGZHONG ZHANG, YIJIAN SHI, RENÉE MOSI, THAO HO, AND PETER WAN[1]

Department of Chemistry, Box 3055, University of Victoria, Victoria, BC V8W 3P6, Canada

Received May 28, 1994

GUANGZHONG ZHANG, YIJIAN SHI, RENÉE MOSI, THAO HO, and PETER WAN. Can. J. Chem. **72**, 2388 (1994).

The photoprotonation of four dialkoxy-substituted benzenes in their excited singlet states has been studied. The parent systems **4** and **5** are regioselectively photoprotonated at the 2-position, with significant quantum efficiencies for deuterium incorporation at acidities greater than pH 2. The structurally related cyclophane derivatives **6** and **7** did not show any deuterium exchange over the same acidity range but fluorescence quenching by proton (in aqueous solution) and laser flash photolysis studies (in 1,1,1,3,3,3-hexafluoro-2-propanol) indicate that photoprotonation does take place with these compounds. Due to structural constraints imposed by the most stable conformation adopted by these molecules (**6** and **7**), the attacking proton (deuteron) is also the proton (deuteron) that is deprotonated from the cyclohexadienyl cation (2,6-dialkoxybenzenonium ion) intermediate, resulting in the absence of incorporation of deuterium.

GUANGZHONG ZHANG, YIJIAN SHI, RENÉE MOSI, THAO HO et PETER WAN. Can. J. Chem. **72**, 2388 (1994).

On a étudié la photoprotonation de quatre benzènes substitués par deux groupes alkoxyles, dans leurs états singulets excités. Les systèmes fondamentaux **4** et **5** sont photoprotonés régiosélectivement en position 2, avec des efficacités quantiques importantes pour l'incorporation du deutérium à des acidités plus grandes qu'un pH de 2. À des degrés d'acidité semblable, les dérivés cyclophanes structuralement apparentés **6** et **7** ne présentent pas d'échange du deutérium; toutefois, des études de désactivation de la fluorescence par les protons (en solution aqueuse) et de photolyse éclair au laser (dans le 1,1,1,3,3,3-hexafluoropropan-2-ol) indiquent qu'il se produit bien un photodéprotonation de ces composés. À cause des contraintes de structure imposées par la conformation stable adoptée par ces molécules (**6** et **7**), le proton (deutéron) qui attaque est aussi le proton (deutéron) qui est déprotoné à partir du cation cyclohexadiényle (ion 2,6-dialkoxybenzénonium) intermédiare; il en résulte donc qu'il n'y a pas d'incorporation de deutérium.

[Traduit par la rédaction]

Introduction

Deuterium exchange of aromatic rings most often proceeds via initial electrophilic attack of the aromatic ring by proton (deuteron) and therefore represents the simplest of all electrophilic aromatic substitution reactions (1, 2). In general, relatively strong acids are required to effect observable reaction rates in the thermal process. We have shown in recent studies (3–6) that dimethoxy-substituted benzenes are particularly prone to undergo deuterium exchange when photolyzed (via the S_1 state) in dilute aqueous D_2SO_4, under conditions where the thermal rate for exchange is not measurable or is negligible. Moreover, we found (4) that 1,3-dimethoxybenzene (**1**) undergoes deuterium exchange primarily at the 2-position, and to a much lesser extent at the 5-position. In contrast, thermal exchanges take place primarily at the 4-position, and to a lesser extent at the 2-position. The difference in sites of protonation between the S_0 and S_1 states of **1** may be readily rationalized by simple HMO theory (4–6), by considering the change in MO coefficients on the benzene ring on promoting an electron from the HOMO to the LUMO. With respect to mechanism, evidence for formation of the expected cyclohexadienyl cation intermediate **2** (2,6-dimethoxybenzenonium ion) (eq. [1]) and derivatives

[1] 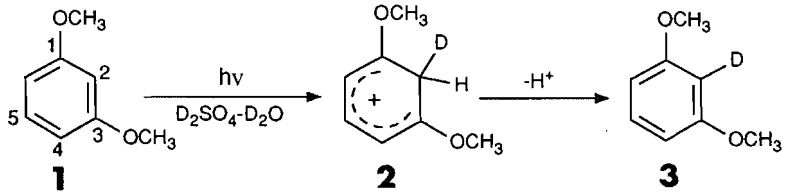

1 **2** **3**

is available from laser flash photolysis (LFP) studies carried out in 1,1,1,3,3,3-hexafluoro-2-propanol (HFP) by McClelland and co-workers (7).

The finding that the 2-position of **1** is a very basic site in S_1 that can be protonated in mild acid naturally invites the investigation of related compounds. In principle, these systems offer a general method for the study of cyclohexadienyl cations under conditions where they could not be generated under thermal (equilibrium) conditions. To this end, Lew and McClelland (8) recently reported the photochemical generation of β-silyl-substituted-1,3-dimethoxycyclohexadienyl cations in HFP. In this paper, we address two structural effects on the excited state photoprotonation process: (*a*) the effect of using two larger alkoxy groups (compared to methoxy) as represented by compounds **4** and **5**; and (*b*) the effect of tethering the two alkoxy groups in two different ways, as represented by cyclophanes **6** and **7**, as probes for a stereoelectronic requirement for proton exchange. We report[2] that both **4** and **5** react with similar efficiency to **1** whereas neither **6** nor **7** undergo measurable deuterium ex-change. However, fluorescence and LFP studies in HFP indicate that cyclophane **7** is photoprotonated almost as efficiently as **4** or **5**, with **6** less efficiently so. The lack of observed deuterium exchange in **6** and **7**

[1]Author to whom correspondence may be addressed.

[2]Full details of the photochemical exchange of **4** and **5** are reported, along with those of several other more closely related systems, in a separate paper (14) concerned with the generality of the reaction for simpler systems.

Can. J. Chem. Downloaded from www.nrcresearchpress.com by 65.111.164.53 on 09/08/12
For personal use only.

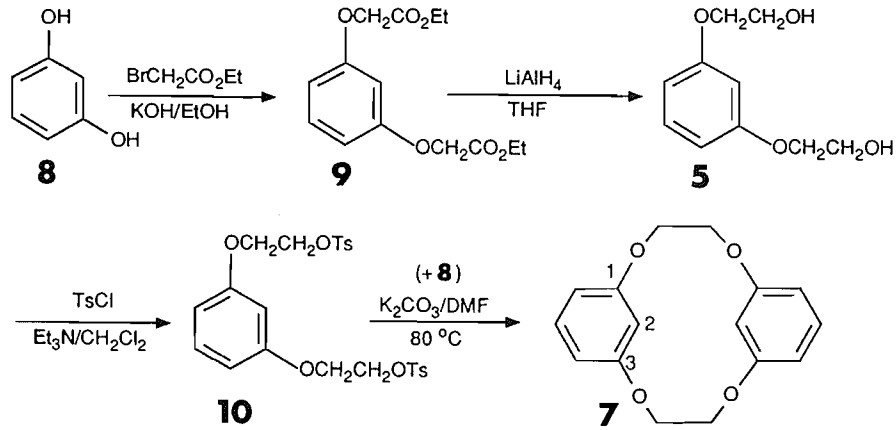

SCHEME 1

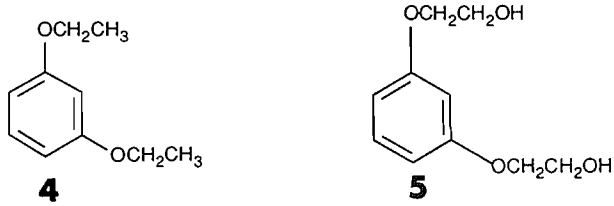

is attributed to the structural constraints imposed by these systems that permit only the attacking proton (deuteron) to be deprotonated from the intermediate cyclohexadienyl cations.

Results and discussion

Materials

Compound **4** was made by alkylation of resorcinol (**8**) with iodoethane. Diol **5** was made from $LiAlH_4$ reduction of diester **9**, which was readily available from the reaction of resorcinol (**8**) with ethyl bromoacetate (Scheme 1). Cyclophane **6** was made from a modified published procedure (9, 10), involving the reaction of resorcinol (**8**) with 1,8-dibromooctane (eq. [2]).

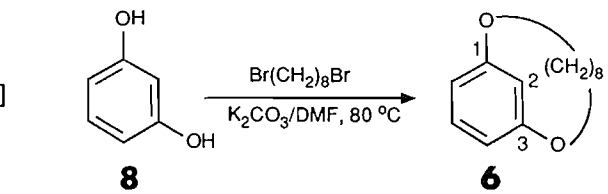

It has been shown (9) that an eight-carbon methylene chain is probably the shortest chain that can successfully tether the 1,3-positions of resorcinol (**8**). Therefore, this eight-carbon chain is expected to impart severe steric interactions with the π-system of the benzene ring of **6**. We were unable to obtain crystals of sufficient quality for an X-ray structure determination. However, a minimized PCMODEL structure shows (Fig. 1) that there are severe steric interactions on one side of the benzene ring, especially in the vicinity of the 2-position. Space filling displays show this congestion even more convincingly. Photoprotonation at the 2-position from the other side would result in pushing the 2-hydrogen into the methylene chain as C2 changes hybridization from sp^2 to sp^3. Based on this analysis, the photoprotonation rate of **6** should be attenuated significantly if not prevented altogether.

Cyclophane **7** was made via the reaction sequence shown in Scheme 1 with an overall yield of ≈2% from resorcinol (**8**).

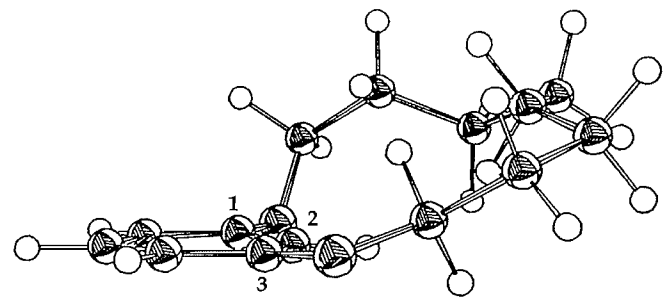

FIG. 1. Minimized structure of **6** from a PCMODEL calculation. Spacing filling presentation shows severe steric congestion on the top face of the benzene ring around and near the 2-position.

TABLE 1. Summary of X-ray crystallographic data for **7**

Formula	$C_{16}H_{16}O_4$
Mol. Wt.	272.3
Crystal system	Monoclinic
Space group	$P2_1/c$
Cell dimensions	
a, Å	7.759(2)
b, Å	11.000(3)
c, Å	15.409(6)
α, deg	90
β, deg	93.97(3)
γ, deg	90
V, Å^3	1311.8
Z	4
T	20°C
λ	Mo (0.71069)
ρ_{obsd}, g cm^{-1}	1.376
ρ_{calcd}, g cm^{-1}	1.379
μ, cm^{-1}	1.06
$R(F_o)$	0.0538
$R_w(F_o)$	0.0534
$R_g(F_o)$	0.0624

Molecular mechanics calculations (PCMODEL) predict that the *anti* conformation will be of lowest energy. This was confirmed by its crystal structure (Table 1 and Fig. 2). Steric interactions around the 2-position (C2) are less severe than is the situation for **6**. As in the case of **6**, the photoprotonation can only take place from one face of the benzene ring. Because the tethering ring is large, the change in hybridization at C2 on protonation can be readily accommodated. This may result in a faster protonation rate than for **6**.

Can. J. Chem. Downloaded from www.nrcresearchpress.com by 65.111.164.53 on 09/08/12
For personal use only.

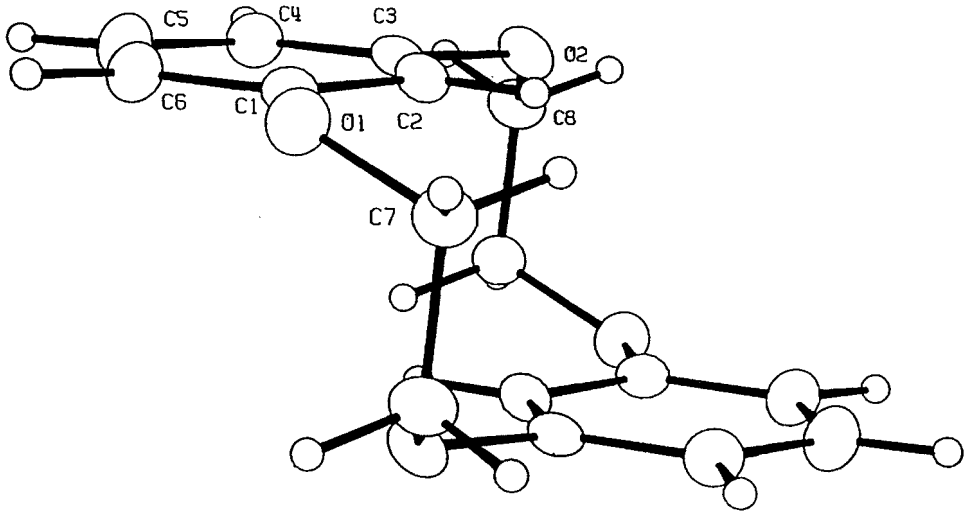

FIG. 2. ORTEP Drawing of crystal structure of **7**.

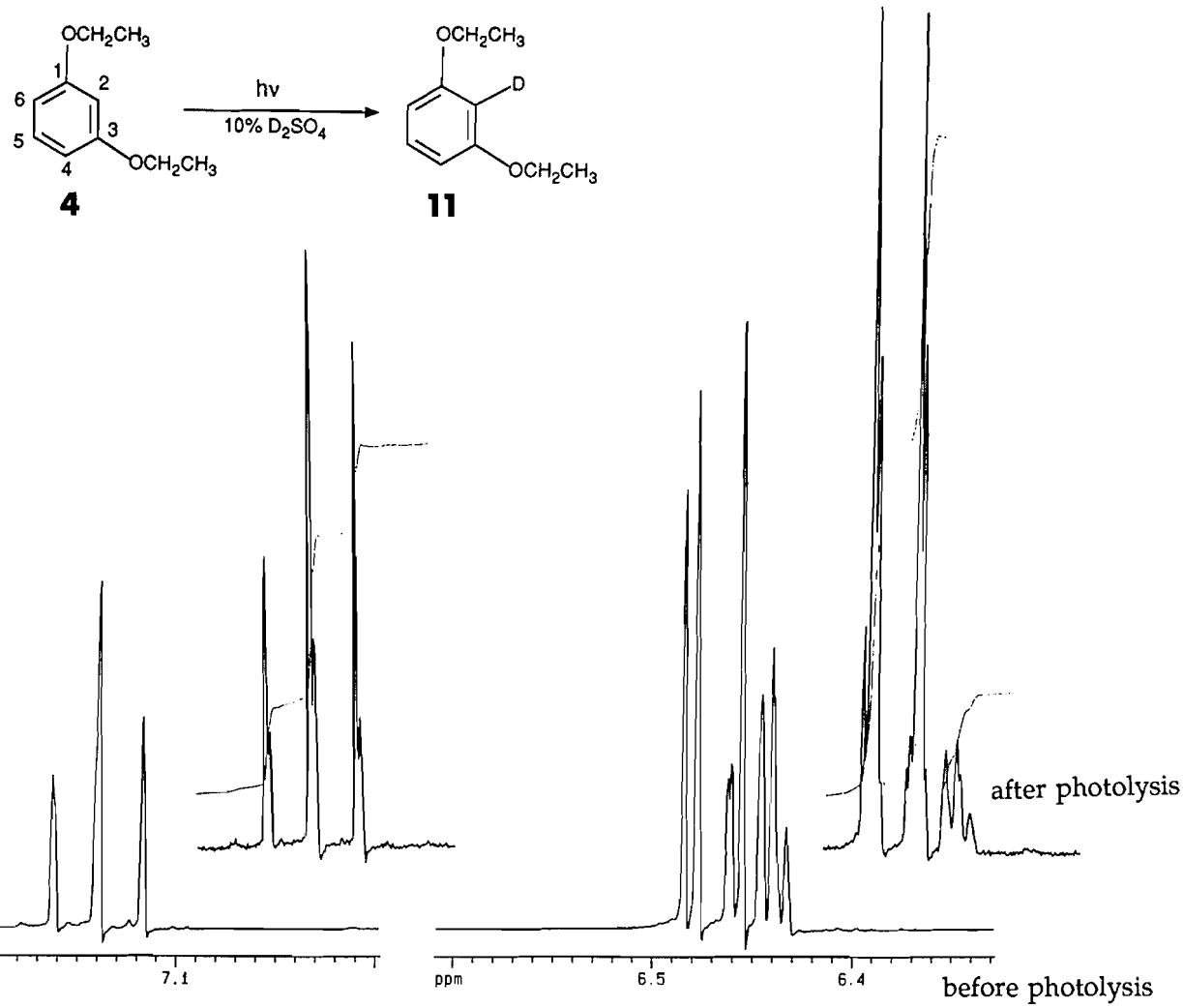

FIG. 3. ^{1}H NMR (360 MHz) spectra (aromatic portion only) of deuterium incorporation for **4** on photolysis in 2:1 10% D_2SO_4 – CH_3CN (60 min). Lower spectrum is unreacted starting material. Upper spectrum is recovered material after photolysis.

Deuterium exchange studies

Photolysis of $\approx 10^{-3}$ M solutions of **4** and **5** in 2:1 aqueous D_2SO_4 – CH_3CN (Rayonet RPR 100 photochemical reactor; 10–60 min; 254-nm lamps; argon purged; ≈15°C) resulted in clean deuterium incorporation into the 2-positions of these compounds when pD ≤ 2. The exchange can be followed readily by 360 MHz ^{1}H NMR, as shown in Fig. 3 for reaction of **4**. On photolysis, the triplet of H2 (δ 6.44, J = 2 Hz) of unre-

Can. J. Chem. Downloaded from www.nrcresearchpress.com by 65.111.164.53 on 09/08/12
For personal use only.

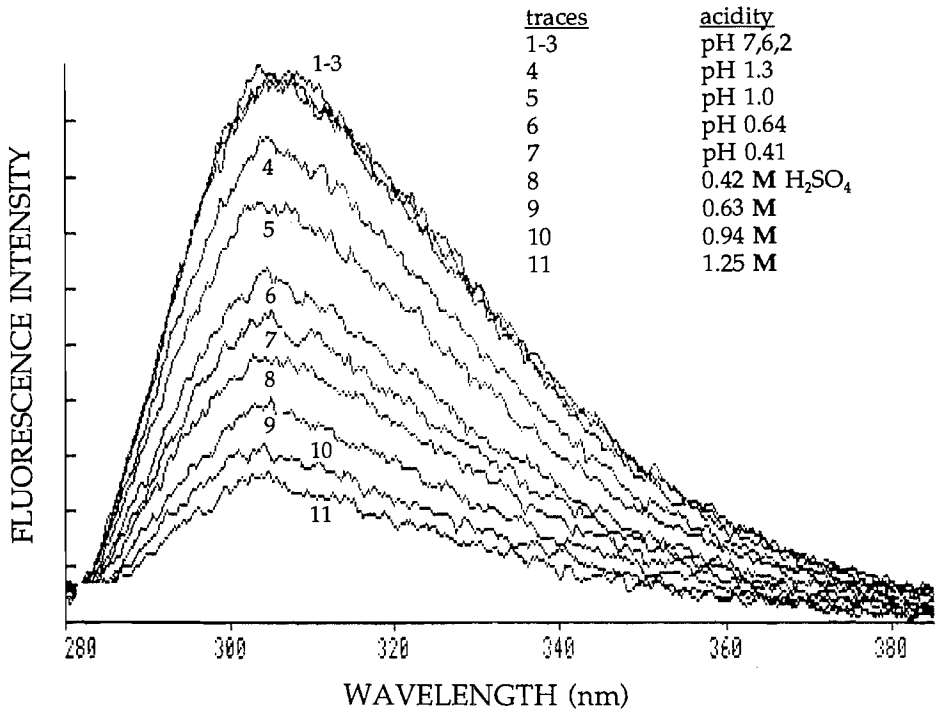

FIG. 4. Fluorescence quenching by protons observed for **7** carried out in 9:1 H_2O–CH_3CN (λ_{ex} = 265 nm).

acted **4** decreased in intensity while a doublet (J = 8 Hz) grows in at δ 6.47, which is attributed to H4 of the exchanged product **11** since coupling to deuterium at the 2-position is not resolvable. In addition, the triplet (J = 8 Hz) of H5 of **11** is slightly further upfield than H5 of unreacted **4** (at δ 7.14). NMR integration of this run gave ≈70% exchange of H2. In general, mass spectra (GC–MS) gave percent deuterium content in close agreement with the values calculated by NMR integration. Similar results were observed for **5**. Thermal exchange was not observed or was insignificant in the range of acidity studied (pD 7–10% (w/w) D_2SO_4). In stronger acids (e.g., 30% D_2SO_4), thermal exchange takes place predominantly at C4 of these compounds (4, 5).

Photolysis of **6** or **7** under the above conditions (or with longer photolysis times, up to 2 h) resulted in complete recovery of unreacted substrate; no deuterium incorporation was observed by NMR or GC–MS. The complete lack of deuterium incorporation is consistent with expectation based on the stereoelectronic requirements for exchange. However, it is not clear at this point whether **6** or **7** is photoprotonated at all. Fluorescence and LFP studies (*vide infra*) were used to address this.

Quantum yields

Quantum yields (Φ) for formation of the corresponding 2-deuterio products from **4** and **5** were measured as a function of medium acidity (8:2 aqueous $D_2SO_4(H_2SO_4)$ – CH_3CN; λ_{ex} = 254 nm) in 3.0-mL quartz cells using GC–MS for analysis. Conversions were kept below 20% to avoid dideuteration. The results are shown in Table 2. Quantum yields (Φ) for exchange were measurable at acidities greater than pD 2, increasing rapidly with increasing acidity in this acidity region. The values are similar to those reported for **1** in our previous study (4). The presence of the extra hydroxyl groups in **5** results in a significant reduction in Φ that can be completely attributed to a reduction in the photoprotonation rate for this compound (*vide infra*).

TABLE 2. Quantum yields (Φ) for deuterium incorporation of **4** and **5**

	Φ[a]	
Acidity (pD or % D_2SO_4)[b]	**4**	**5**
pD = 6.9	0.0	0.0
pD = 2.0	0.011	0.015
pD = 1.5	0.037	0.037
pD = 1.2	0.063	0.042
pD = 1.0	0.12	0.072
pD = 0.79	0.14	0.078
pD = 0.48	0.24	0.13
5%	0.33	0.14
10%	0.34	0.23

[a]Calculated by GC–MS. Estimated error, ±10% of quoted value.
[b]Solvent system: 8:2 aqueous D_2SO_4–CH_3CN; quoted pD is of the aqueous portion.

Steady-state and transient fluorescence studies

Fluorescence emission spectra of **4**–**7** were measured as a function of medium acidity, in wholly aqueous medium for **4**–**6** and with 10% CH_3CN for **7**, the latter being less soluble. Fluorescence emissions from all of **4**–**7** were quenched on increasing acidity, as shown in Fig. 4 for **7**. Stern–Volmer plots of fluorescence quenching were linear, as shown in Fig. 5 for both cyclophanes **6** and **7**. Absolute fluorescence quantum yields were measured in 8:2 H_2O-CH_3CN (water portion at pH 7) using 1,3-dimethoxybenzene (**1**) as reference (Φ_f = 0.14 ± 0.02) (4) and are shown in Table 3. Fluorescence lifetimes were measured at pH 7 using single photon counting and are given in Table 3.

Laser flash photolysis studies

LFP studies (YAG laser; 266 nm; <20 mJ) of **1** and **4**–**7** in 1:1

Can. J. Chem. Downloaded from www.nrcresearchpress.com by 65.111.164.53 on 09/08/12
For personal use only.

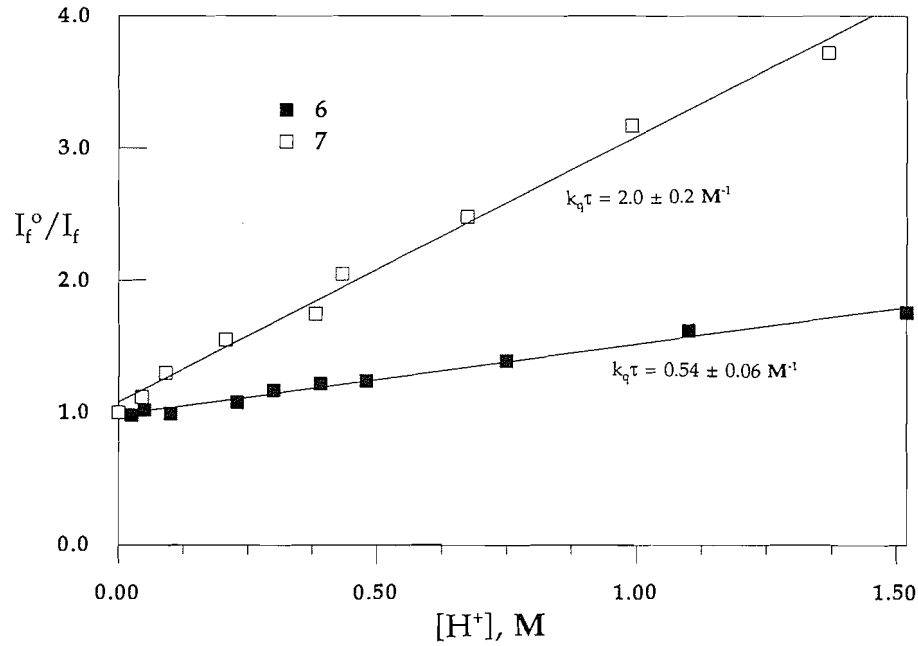

FIG. 5. Linear Stern–Volmer plots of fluorescence quenching by protons for **6** and **7**. Compound **6** measurements were carried out in wholly aqueous solution while 9:1 H_2O–CH_3CN was used for **7** due to its lower solubility.

TABLE 3. Fluorescence parameters and quenching rate constants for **4-7**

Substrate	τ^a (ns)	Φ_f^b	k_q^c (M^{-1} s^{-1})
1[d]	1.5 ± 0.1	0.14 ± 0.02	(2.2 ± 0.2) × 10^9
4	1.4 ± 0.1	0.14 ± 0.02	(2.6 ± 0.2) × 10^9
5	2.1 ± 0.1	0.14 ± 0.02	(1.4 ± 0.1) × 10^9
6	0.94 ± 0.1	0.045 ± 0.004	(5.7 ± 1) × 10^8
7	1.5 ± 0.1[e]	0.062 ± 0.005	(1.3 ± 0.1) × 10^9

[a]Fluorescence lifetime from single photon counting, in wholly aqueous solution (pH 7) unless otherwise noted.
[b]Fluorescence quantum yield in 8:2 H_2O–CH_3CN (pH 7) using 1,3-dimethoxybenzene (**1**) as reference (Φ_f = 0.14 ± 0.02) (4).
[c]Quenching rate constant by proton from Stern–Volmer analysis. Equatable to photoprotonation rate constant (k_H).
[d]Data from ref. 4.
[e]Lifetime measured in 9:1 H_2O–CH_3CN (pH 7) due to poor solubility.

H_2O–CH_3CN (pH 7; 5 and 10% H_2SO_4) in a flow cell (oxygen purged) gave a weak ($\Delta OD \leq 0.01$) transient at 460 nm. The initial intensity and the first-order decay of this signal were not significantly affected by the acidity of the medium ($k_{decay} = 1 \times 10^5$ s^{-1} at pH 7). In addition, since none of **1** and **4–7** photoexchange in neutral aqueous solution (**6** and **7** do not exchange even in acid), the transient at 460 nm cannot be a cyclohexadienyl cation. Moreover, McClelland and co-workers (7) have reported LFP results for **1** (and related compounds) in HFP in which the *strongly absorbing* ($\Delta OD \approx 0.1$) photogenerated cation **2** had λ_{max} = 410 nm ($k_{decay} = 4.2 \times 10^3$ s^{-1} at 20°C). Although the 50 nm difference in λ_{max} might be attributable to a solvent shift, the large difference in initial absorbance cannot be readily accounted for unless the quantum yield for photoprotonation (i.e., generation of cyclohexadienyl cation) is much lower in H_2SO_4–CH_3CN than in HFP. To examine this possibility, relative quantum yields for photochemical exchange of **3** (Φ_e) were carried out in HFP and in 5% H_2SO_4 (20% CH_3CN in both solutions) and analysis was carried out by NMR. We reported $\Phi_e = 0.10$ for **3** in 5% H_2SO_4 (4). We found that Φ_e was about a factor of two lower in HFP ($\Phi_e \approx 0.05$), indicating that cation **2** is generated *more* efficiently in aqueous acid (5% H_2SO_4) than in HFP, assuming that the primary isotope effect for loss of proton (deuteron) is similar in the two solvent systems. All of these observations strongly indicate that the 460-nm transient observed in aqueous solution is not due to the cyclohexadienyl cation. It is assigned to the corresponding radical cation since several thermally generated dimethoxybenzene radical cations have λ_{max} near 450 nm (11, 12). Interestingly, the radical cations in our study are probably formed via a one-photon process in aqueous solution (1:1 H_2O–CH_3CN) since a plot of ΔOD vs. laser power (5–33 mJ; intercept of plot went through the origin) for **1** gave good linear plots whereas plotting ΔOD versus the square of the laser power gave curved plots. The conclusion from LFP studies in aqueous solution is that cyclohexadienyl cations of the general type **3** are too short-lived in aqueous solution, even in 10% H_2SO_4, and a picosecond laser system would be required to detect these transients in this medium.

Fluorescence quenching by protons in aqueous medium observed for each of **4–7** (Table 3) indicated that they are all photoprotonated, although with different rates. This implies that cyclohexadienyl cations are formed in aqueous acid in all cases. Because these cations are apparently too short-lived in this medium, we carried out additional LFP studies of **4–7** in HFP, to confirm that all of **4–7** are indeed photoprotonated to give the corresponding cyclohexadienyl cations. Since neither **6** nor **7** undergo exchange, fluorescence quenching results alone for these two compounds are not sufficiently compelling to warrant the conclusion that they are also photoprotonated. LFP of **4–7** in HFP (oxygen-purged samples) gave much stronger transients than those observed in H_2O–CH_3CN. These transients have λ_{max} in the region 415–450 nm with decays unaffected by oxygen but very sensitive to the presence of water and added MeOH. These transients are assigned as the corresponding 1,3-dialkoxybenzenonium ions

Can. J. Chem. Downloaded from www.nrcresearchpress.com by 65.111.164.53 on 09/08/12
For personal use only.

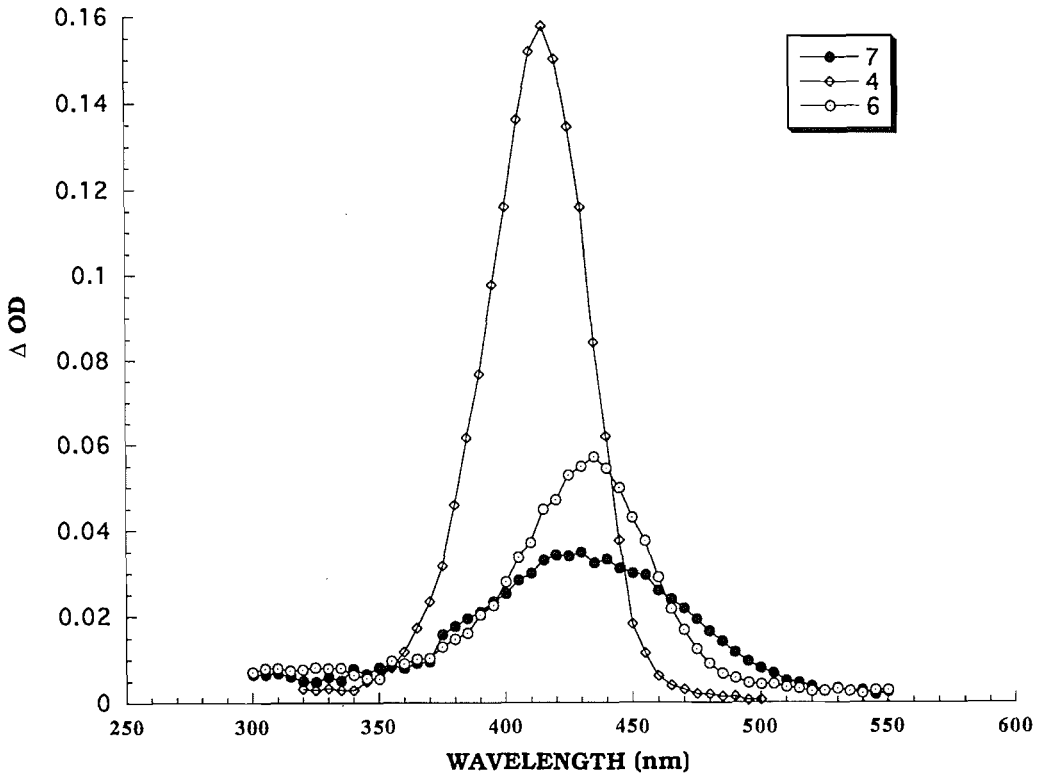

FIG. 6. Overlay of transient spectra observed from LFP studies of **4**, **6**, and **7** in HFP ≈0.5 μs after the laser pulse.

(Fig. 6), generated via photoprotonation in HFP. The transient spectra observed for **4** and **5** are essentially identical to that reported for 1,3-dimethoxybenzenonium ion in HFP (7) with $\lambda_{max} = 415$ nm ($k_{decay} = 2.1 \times 10^4$ s^{-1} and 6.9×10^4 s^{-1} for **4** and **5**, respectively). The initial ΔOD observed for **5** was ≈0.6, a factor of about 2.5 lower than for **4**. This is consistent with the difference in photoprotonation rates (k_q) (Table 3) and quantum yields of exchange (Table 2) measured for these two compounds in aqueous acid. The 1,3-benzenonium ion for **6** is red-shifted ($\lambda_{max} = 485$ nm) with $k_{decay} = 2.8 \times 10^5$ s^{-1}. Similarly, the 1,3-benzenonium ion for **7** is also red-shifted with a broader envelope (λ_{max} = 415–450 nm). Moreover, whereas the transient decays observed for all of **4**–**6** were good first order and independent of wavelength, decays for the transient observed for **7** could not be fitted to a single exponential decay. They could be fitted to the sum of two first-order exponentials, although fitting to higher-order sums was not investigated. Rate constants derived from biphasic fits were dependent on the monitoring wavelength. For example, monitoring the decay at 430 nm gave two components with 1.0 and 4.4 μs lifetimes while monitoring at 480 nm gave 1.2 and 3.9 μs lifetimes. These differences in lifetimes are well above the experimental error normally expected on the LFP system and fitting program used, which are typically <10%. These observations are consistent with our view that the transient observed for **7** is a composite of a variety of 1,3-benzenonium ions. This is reasonable since **7** is conformationally the most flexible system and several very close lower energy conformations are available for either **7** itself or its corresponding 1,3-benzenonium ion. Thus, the results are consistent with photoprotonating several different conformers or the initially photoprotonated single isomer can exist as several relatively stable conformers, or a combination of the two situations.

Conclusions

This study has shown that the 2-position of a variety of 1,3-dialkoxybenzenes is kinetically as basic (as measured by fluorescence quenching rates) as that of the parent 1,3-dimethoxybenzene and that it is possible to design systems in which the attacking proton is the proton that is also deprotonated. Replacement of an ethoxy group (**4**) for methoxy (**1**) resulted in no observable changes in reactivity. The fluorescence parameters for these compounds are essentially the same (Table 3) and LFP studies in HFP show essentially identical spectra for the two 1,3-benzenonium ions. The lower Φ for deuterium exchange observed for **5** compared to that for **4** is due to a lower rate for photoprotonation (k_q) (Table 3). This may be due to the increased solvent congestion present in **5**, due to hydrogen bonding of the hydroxyl groups with solvent water, which retards the rate of protonation. The resulting 1,3-benzenonium ion for **5** was essentially identical to that observed for **4** except that it was it was formed 50% less efficiently (based on initial ΔOD's), consistent with the difference in k_q's (Table 3) and Φ's (Table 2). The main finding in this work is that cyclophanes **6** and **7** are photoprotonated at substantial rates, giving rise to their respective 1,3-benzenonium ions. Steric constraints built into these systems require that only the attacking proton can be deprotonated from the intermediate 1,3-benzenonium ions, resulting in lack of proton exchange for these compounds. Protonation (deuteration) takes place from the more open side as shown in **12** for

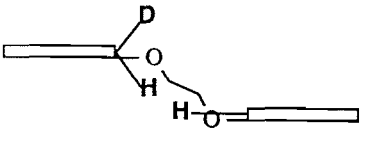

12

Can. J. Chem. Downloaded from www.nrcresearchpress.com by 65.111.164.53 on 09/08/12
For personal use only.

Can. J. Chem. Downloaded from www.nrcresearchpress.com by 65.111.164.53 on 09/08/12
For personal use only.

7. Since the deuteron is much more exposed than the original proton, it is selectively lost in the re-aromatization step, resulting in lack of deuterium incorporation. Additional studies are in progress that are aimed at learning about controlling these photochemical reactions by appropriate design of substrate structure.

Experimental

General

^{1}H NMR spectra were recorded on Perkin–Elmer R32, Bruker WM 250, or Bruker AM 360 instruments, in $CDCl_3$ (TMS internal standard). Mass spectra were taken on Finnigan 3300 (CI) or Kratos Concept H (EI) instruments. Melting points were obtained on a Koefler hot stage microscope and are uncorrected. Preparative photolyses were carried out in Suprasil quartz cuvettes, 25- or 100-mL quartz tubes using a Rayonet RPR 100 photochemical reactor with 16 × 254 nm lamps. Chemical analysis was performed by Canadian Microanalytical Service, Delta, B.C.

Materials

Resorcinol (**8**), iodoethane, 1,8-dibromooctane, triethylamine, *p*-toluenesulfonyl chloride, and ethyl bromoacetate were purchased from Aldrich and used as received.

*Resorcinol octamethylene ether (**6**)*

To a mechanically stirred solution of K_2CO_3 (15.1 g, 0.11 mol) in 2 L DMF in a 4-L round-bottom flask was added a mixture of resorcinol (3.0 g, 0.027 mol) and 1,8-dibromooctane (7.4 g, 0.027 mol) in 500 mL DMF over the course of 4 days using a slow-addition funnel. During the course of addition, the reaction mixture was kept at ~80°C under N_2. After addition, the mixture was stirred at 80°C overnight and filtered. The filtrate was diluted with an equal amount of CH_2Cl_2 and washed with saturated NaCl solution (5 times) followed by 1 M NaOH solution (3 times). The organic layer was dried over $MgSO_4$. Removal of the solvent gave a brown sticky solid, which was subjected to column chromatography (silica, CH_2Cl_2–hexanes) to give a white solid. Recrystallization from hexane gave 120 mg (2% yield) of white needles, mp 104–105°C (lit. (9) mp 99–100.5°C); ^{1}H NMR (250 MHz), δ: 1.24–1.53 (m, 8H), 1.85–1.93 (m, 4H), 4.09–4.16 (m, 4H), 6.49 (dd, J = 8 Hz and 2 Hz, 2H), 6.61 (t, J = 2 Hz, 1H), 7.10 (t, J = 8 Hz, 1 H); mass spectrum (CI) (*m/z*): 221 ($M^+ + 1$).

*1,3-Diethoxybenzene (**4**)*

To a stirred solution of **8** (15 g, 0.14 mol) in 100 mL acetone was added 25 mL (0.21 mol) iodoethane and 43.2 g (0.31 mol) anhydrous K_2CO_3 with stirring. The mixture was gently refluxed for 8 h. It was then diluted with H_2O (500 mL) and extracted with 3 × 50 mL ether. Evaporation of the ether followed by bulb-to-bulb distillation gave 13.6 g (60%) of **4** as a clear oil. ^{1}H NMR (90 MHz); δ: 1.40 (t, J = 8 Hz, 6H, CH_3), 4.00 (q, J = 8 Hz, 4H, $ArOCH_2$), 6.45 (t, J = 2.4 Hz, 1H, H2), 6.51 (d, J = 8 Hz, 2H, H4), 7.15 (t, J = 8 Hz, 1H, H5).

*Diester **9***

Resorcinol (30.0 g, 0.27 mol) and ethyl bromoacetate (136.5 g, 0.82 mol) were dissolved in 900 mL EtOH, transferred to a 4-L round-bottom flask equipped with a mechanical stirrer (under N_2), and brought to reflux. Excess KOH (45.9 g, 0.82 mol) in EtOH was added dropwise to the refluxing mixture. After addition, the mixture was mechanically stirred and refluxed for 3 days. After cooling, 1 L H_2O was added and the resulting solution extracted with diethyl ether and back-washed with 0.1 M ice-cold NaOH. The extract was dried over $MgSO_4$ and the solvent evaporated. Subsequent bulb-to-bulb distillation afforded 36 g (47%) of **9** as a viscous colourless oil. ^{1}H NMR (90 MHz); δ: 1.3 (t, 6H, J = 6 Hz), 4.2 (q, 4H, J = 6 Hz), 4.6 (s, 4H), 6.5–7.3 (m, 4H).

*1,3-Bis(2′-hydroxyethoxy)benzene (**5**)*

Diester **9** (20 g, 0.07 mol) was dissolved in 250 mL dry THF and excess $LiAlH_4$ (4.0 g, 0.11 mol) was added in portions, after which the reaction mixture was refluxed for 3 h. The solution was allowed to cool and 100 mL of NaCl-saturated H_2O was added. The solution was then acidified with 10% HCl and extracted with several portions of Et_2O. Removal of the solvent gave 11.4 g (81%) of **5** as a white solid, on standing. ^{1}H NMR (360 MHz); δ: 2.04 (t, J = 6 Hz, 2H), 3.92–4.06 (m, 8H), 6.49 (t, J = 2 Hz, 1H) 6.52 (dd, J = 8 Hz and 2 Hz, 2H), 7.17 (t, J = 8 Hz, 1H).

*Ditosylate **10***

Diol **5** (2.0 g, 0.01 mol) was dissolved in 250 mL of CH_2Cl_2 and transferred to a 500-mL round-bottom flask and cooled in an ice bath (~ –5°C). Triethylamine (2.2 g, 21.2 mmol) was added dropwise. A slight excess of *p*-toluenesulfonyl chloride (4.0 g, 20.7 mmol) was then added in portions to the above solution, keeping the temperature no higher than 0°C. After 1 h at 0°C, the stirred reaction mixture was allowed to reach room temperature and was stirred for 4 days. The solution was then washed with H_2O, 1 M HCl, and $NaHCO_3$ and the organic layer dried over $MgSO_4$. Removal of the solvent gave a yellow viscous liquid, which was washed several times with 100% EtOH to remove unreacted *p*-toluenesulfonyl chloride. This material turned into a white solid (2.9 g, 60%), on standing, which was used without further purification in the next step. ^{1}H NMR (90 MHz); δ: 2.4 (s, 6H), 4.1 (t, 4H, J = 6 Hz), 4.3 (t, 4H, J = 6 Hz), 6.25 (t, 1H, J = 2 Hz), 6.4 (dd, 2H, J = 8 Hz and 2 Hz), 7.1 (t, 1H, J = 8 Hz), 7.35 (d, 4H, J = 8 Hz), 7.8 (d, 4H, J = 8 Hz).

*Bis(1,3-phenylene)-14-crown-4 (**7**)*

To our knowledge, this compound has not been reported in the literature although the 1,2 isomer is well known. A mixture of resorcinol (3.8 g, 34.6 mmol) and **10** (7.5 g, 15.7 mmol) dissolved in 300 mL of DMF was slowly added to a solution of 8.7 g (62.9 mmol) of K_2CO_3 in 200 mL DMF kept at 80°C over the course of 4 days. After addition, the mixture was stirred at 80°C overnight and then filtered. An equal volume of CH_2Cl_2 was added to the filtrate, which was then washed several times with brine and 1 M NaOH. The resulting organic layer was dried over $MgSO_4$. Removal of the solvent gave a brown solid, which was subjected to column chromatography (silica; benzene) and prep. TLC. The band at R_f 0.4 was found to be the required adduct **7**. Final recrystallization from 95% EtOH gave 0.15 g (4%) of white crystals, mp 173–174°C. ^{1}H NMR (360 MHz); δ: 4.31 (s, 8H), 6.23 (t, 2H, J = 2 Hz), 6.57 (dd, 4H, J = 8 Hz, 2 Hz), 7.18 (t, 2H, J = 8 Hz); mass spectrum (CI) *m/z*: 273 ($M^+ + 1$). Anal. calcd. for $C_{16}H_{16}O_4$: C 70.58%, H 5.92%; found: C 70.23%, H 5.87%.

Crystal structure analysis

Suitable crystals of **7** were grown from 95% EtOH. The experimental details are listed in Table 1. A Picker diffractometer using a θ/2θ scan was used to collect the data. A total of 2300 reflections were used and 2002 ($I > 1.0\sigma(I)$) were used in the structure refinement. The structure was solved using SHELX-S direct methods (13).[3]

Deuterium exchange studies and quantum yield measurements

Deuterium exchange experiments and quantum yield measurements were carried out as described in a previous study (4). Relative quantum yields of exchange of **3** in HFP and in 5% H_2SO_4 (20% CH_3CN cosolvent) were carried out using 15-mg samples of **3** dissolved in a total of 10 mL solvent. The samples were transferred to 20-mL quartz vessels, purged with argon, and sealed. Photolysis was carried out at 254 nm for 20 min using a merry-go-round assembly. The extent of exchange was calculated by NMR integration of the aromatic protons as described in ref. 4.

[3]Tables of supplementary X-ray data have been deposited and can be purchased from: The Depository of Unpublished Data, Document Delivery, CISTI, National Research Council Canada, Ottawa, ON K1A 0S2, Canada.

These tables have also been deposited with the Cambridge Crystallographic Data Centre, and can be obtained on request from The Director, Cambridge Crystallographic Data Centre, University Chemical Laboratory, 12 Union Road, Cambridge, CB2 1EZ, U.K.

Fluorescence measurements

Fluorescence spectra were taken on a Perkin–Elmer MPF 66 spectrofluorimeter at ambient temperature (22 ± 2°C) and were uncorrected. Samples were prepared in 3.0 mL Suprasil quartz cuvettes by injecting into the appropriate solvent a determined amount of substrate in CH_3CN (20–50 μL). Spectra run after purging with argon were identical to those run without prior purging. Fluorescence lifetimes were measured using time-correlated single photon counting on a PTI LS-1 instrument and analyses were carried out using standard software supplied by PTI. Samples were prepared as described for fluorescence spectra. All fluorescence decays were good first order.

Laser flash photolysis studies

These experiments were carried out at the University of Victoria LFP Facility at 20 ± 2°C. A Spectra Physics GCR 12 YAG laser at 266 nm (<20 mJ) was used for excitation and signals were digitized with a Tektronix TDS 520 recorder. Samples of OD ≈ 0.3 at 266 nm (10^{-4} M) were prepared in 7-mm quartz cells and purged with oxygen prior to measurement. A flow system was used for runs in H_2O–CH_3CN solutions. Due to the cost of HFP, a flow system was not used in this solvent. Negligible deterioration of signals was observed in HFP if the samples were not excessively irradiated. Rate constants for decay are the average of several runs.

Acknowledgments

The authors thank the Natural Sciences and Engineering Research Council of Canada for support of this research.

1. R.O.C. Norman and R. Taylor. Electrophilic substitution in benzenoid compounds. Elsevier, New York. 1965. Chap. 5.
2. J. March. Advanced organic chemistry. 3rd ed. Wiley, New York. 1985. Chap. 11.
3. P. Wan and P. Wu. J. Chem. Soc. Chem. Commun. 822 (1990).
4. R. Pollard, S. Wu, G. Zhang, and P. Wan. J. Org. Chem. **58**, 2605 (1993).
5. G. Zhang and P. Wan. Res. Chem. Intermed. **19**, 119 (1993).
6. P. Wan and D. Shukla. Chem. Rev. **93**, 571 (1993).
7. N. Mathivanan, F. Cozens, R.A. McClelland, and S. Steenken. J. Am. Chem. Soc. **114**, 2198 (1992).
8. C.S.Q. Lew and R.A. McClelland. J. Am. Chem. Soc. **115**, 11516 (1993).
9. A. Dalla Cort, L. Mandolini, and B. Masci. J. Org. Chem. **45**, 3929 (1980).
10. L. Mandolini, B. Masci, and S. Roelens. J. Org. Chem. **42**, 3733 (1977).
11. J. Scaiano (*Editor*). CRC handbook of organic photochemistry. Vol. II. CRC Press, Boca Raton, Fla. 1989. p. 26.
12. T. Shida. Electronic absorption spectra of radical ions. Elsevier, Amsterdam. 1988. pp. 256–257.
13. P. Main. Programs for crystal structure solution. Anorganisch-Chemisches Institut der Universitat Gottingen, Gottingen, Germany. 1986.
14. R. Mosi, G. Zhang, and P. Wan. J. Org. Chem. In press.

Can. J. Chem. Downloaded from www.nrcresearchpress.com by 65.111.164.53 on 09/08/12
For personal use only.

Control of regioselectivity in reactions of dialkylstannylene acetals. Part I. A dramatic reversal of regioselectivity in mono-*p*-toluenesulfonation reactions[1]

XIANQI KONG[2] AND T. BRUCE GRINDLEY[3]

Department of Chemistry, Dalhousie University, Halifax, NS B3H 4J3, Canada

Received May 10, 1994

XIANQI KONG and T. BRUCE GRINDLEY. Can. J. Chem. **72**, 2396 (1994).

The regioselectivities of *p*-toluenesulfonation reactions of dialkylstannylene acetals obtained from a number of carbohydrate-derived terminal 1,2-diols in the absence of added nucleophiles have been explored as functions of the carbohydrate structure, the nature of the alkyl group on tin, the solvent, and the reaction temperature. Virtually all dibutylstannylene acetals react preferentially on the primary oxygen atom, sometimes with excellent regioselectivity. Increasing the steric bulk of the alkyl substituents on tin increases the preference for reaction at the secondary oxygen atom, but at the expense of increased reaction times. Hexamethylenestannylene acetals react at about the same rate as dibutylstannylene acetals; in almost all cases, they react preferentially on the secondary oxygen atom, sometimes with excellent regioselectivity.

XIANQI KONG et T. BRUCE GRINDLEY. Can. J. Chem. **72**, 2396 (1994).

On an examiné l'influence de la structure de l'hydrate de carbone, de la nature du solvant ou des groupes alkyles attachés à l'étain ainsi que de la température réactionnelle sur les régiosélectivités des réactions de *p*-toluènesulfonation des acétals des dialkylstannylènes, obtenus à partir d'un certain nombre de 1,2-diols dérivés d'hydrates de carbone. Pratiquement tous les acétals du dibutylstannylène réagissent d'une façon préférentielle avec l'atome d'oxygène primaire, quelquefois avec d'excellentes régiosélectivités. Une augmentation de l'encombrement stérique des substituants alkyles présents sur l'étain augmente la préférence pour la réaction au niveau de l'atome d'oxygène secondaire; cette sélectivité se fait avec une augmentation du temps de réaction. Les acétals de l'hexaméthylènestannylène réagissent approximativement à la même vitesse que les acétals du dibutylstannylène; dans pratiquement tous les cas, ils réagissent préférentiellement sur l'atome d'oxygène secondaire, quelquefois avec une excellent régiosélectivité.

[Traduit par la rédaction]

Can. J. Chem. Downloaded from www.nrcresearchpress.com by 85.192.166.187 on 09/08/12
For personal use only.

Introduction

Selective functionalization and chemical manipulation of diols and polyols have been subjects of much interest to organic chemists. This is particularly the case in the field of carbohydrate chemistry. Dibutylstannylene acetals have been shown to be especially useful for this purpose. They were first used by Moffat and co-workers (3) and by David (4) as intermediates that enhanced the nucleophilicity of hydroxyl oxygen atoms and induced regioselective reactions. During the last two decades, dibutylstannylene acetals derived from a wide range of diols and polyols have been observed to react with many types of electrophiles to give predominantly monosubstituted products (5–8). Regioselectivity of monosubstitution ranges from poor to excellent depending on the structure of the substrate, the reaction conditions, and the nature of the electrophile. For particular classes of substrates with common reaction conditions, regioselectivity has become predictable (8). Thus, the dibutylstannylene acetal reaction has become one of the standard methods employed to differentiate among hydroxyl groups in diols and polyols.

For *trans*-1,2-diols on pyranose rings, reaction regioselectivity of the derived dibutylstannylene acetals was related to the dimeric structures assumed by these compounds in solution (9). For stannylene acetals obtained from diols in which the oxygen atoms are diastereotopic, three dimers are possible. Figure 1 illustrates the dimeric structures possible for the dibutylstannylene acetal obtained from 3-*O*-benzyl-1,2-*O*-isopropylidene-α-D-glucofuranose (**1**). The nature of the dimeric mixtures present in solution has been shown to be controlled mainly by steric effects (9). The most populated dimer has the tricoordinate oxygen atoms as far away as possible from the side of the diol that has the most bulky substituents. Dicoordinate oxygen atoms in the dimer are more nucleophilic than tricoordinate oxygen atoms (9). Dibutylstannylene acetals from *trans*-1,2-diols that exist as single symmetric dimers gave highly regioselective reactions on the dicoordinate oxygen atoms in the dimers.

Terminal 1,2-diols in carbohydrates have one large substituent attached to the carbon bearing the secondary oxygen atom. Thus, it was thought that the most populated dimer in the derived dialkylstannylene acetal would have the oxygen atom remote from this substituent, the primary oxygen atom, tricoordinate. Regioselective reactions should then occur on the secondary dicoordinate oxygen atom in the preferred dimer, i.e., for **1**, at O-5 of the 6,6-dimer.

It is well known that primary hydroxyl groups are more reactive than secondary hydroxyl groups in reactions with electrophiles (10). As a result, it is usually possible to perform regioselective acylation reactions on a primary hydroxyl group in a diol or polyol unit. It has been shown that dibutylstannylene acetals of carbohydrate-derived primary–secondary diols react with benzoyl chloride or *p*-toluenesulfonyl chloride in the presence of added nucleophiles or in polar solvents to give higher regioselectivity for reaction at the primary oxygen atoms than direct reactions of the parent diols (11–14). It is thought that the reaction intermediate in the presence of added nucleophiles is the coordinated monomer (8, 15). Alkylating agents also react with stannylene acetals in the presence of added nucleophiles to give excellent yields of the primary monosubstituted products (16–21).

Reversal of regioselectivity to direct reaction at secondary

[1]Part of this work has appeared in a preliminary communication (1). For Part II, see the following publication (2).

[2]Present address: Department of Chemistry, Queen's University, Kingston, ON K7L 3N6, Canada.

[3]Author to whom correspondence may be addressed; email address: GRINDLEY@AC.DAL.CA

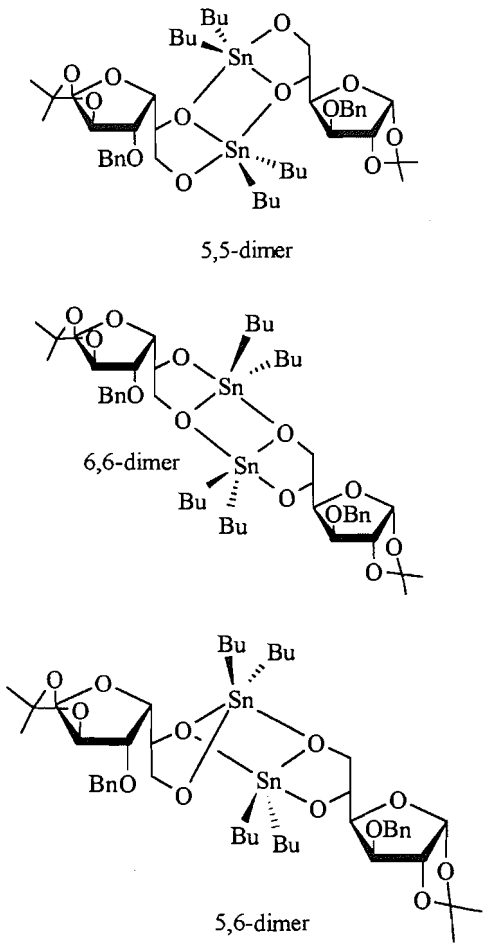

FIG. 1. Structures of dimers possible for the dibutylstannylene acetal of **1**. Dimer nomenclature is based on the numbers of the tricoordinate oxygen atoms (9).

hydroxyl oxygen atoms in the presence of primary hydroxyls is often highly desirable. Oxidation of dibutylstannylene acetals (22, 23) and related tributylstannyl ethers of terminal 1,2-diols with bromine (24–26) or with *N*-bromosuccinimide (27) occurs on the secondary centres. The only acylation reaction for which reversal of regioselectivity was accomplished was benzoylation, performed by Reginato et al. (28). Reactions were performed on simple 1,2-diols not bearing additional electronegative substituents, using dibutystannylene acetals as intermediates in chloroform without added nucleophiles. We have not been able to repeat this work with the regioselectivity reported and others have also reported that this reaction is "troublesome" (29). With dibutylstannylene acetals obtained from carbohydrate-derived terminal 1,2-diols, the initial benzoylation reaction occurs at about the same rate as rearrangement of the initial secondary product to the more stable primary derivative (vide infra), making selective substitution at the secondary centre impossible.

This publication outlines a study of reactions of dialkystannylene acetals from a variety of terminal 1,2-diols with *p*-toluenesulfonyl chloride. The products of these reactions do not rearrange under the reaction conditions. Based on the considerations outlined above, it was thought that *p*-toluenesulfonation reactions, if conducted on dibutylstannylene acetals in the absence of added nucleophiles, would give predominantly secondary substitution. When this proved not to be the case, the reactions of a variety of dialkylstannylene acetals were investigated. Hexamethylenestannylene acetals have been found to give excellent reversed regiochemistry in *p*-toluenesulfonation reactions. In addition, the results of this study have led to a more complete understanding of the source of the regioselectivity obtained in reactions of dialkylstannylene acetals in general that is described in Part II of this series (2).

Results and discussion

The diols used in this study were primary–secondary 1,2-diols derived from monosaccharides, including D-glucose derivatives **1**, **2**, and **3**, D-allose derivatives **4**, **5**, and **6**, a 3-deoxy-D-*ribo*-hexose derivative **7**, a D-mannose derivative **8**, and D-mannitol derivatives **9** and **10**. Dialkyltin oxides prepared for use in this study include diisobutyltin oxide (**12**), diisopropyltin oxide (**13**), dineopentyltin oxide (**14**), dineohexyltin oxide (**15**), dicyclohexyltin oxide (**16**), hexamethylenetin oxide (**17**), dihexyltin oxide (**18**), and di-*tert*-butyltin oxide (**19**). Except for dibutyltin oxide (**11**) and compound **19**, neither the oxide nor an easily accessible precursor was available, and it was necessary to develop a new synthetic approach in order to obtain these dialkyltin oxides in a pure form (30). The dialkylstannylene acetals derived from the dialkyltin oxide are numbered as shown for the D-glucose derivatives, i.e., dibutylstannylene acetals are always indicated by the number of the precursor sugar followed by the designation **sa**.

For all reactions, dialkylstannylene acetals were prepared from diols and dialkyltin oxides (1 mol-equivalent) by reflux in benzene or in toluene with azeotropic removal of water. The dialkylstannylene acetals thus obtained were used directly, without separation or purification, for subsequent reactions.

Reginato et al. reported that benzoylation of simple primary-secondary 1,2-diols (such as propane-1,2-diol) via their dibutylstannylene acetals in chloroform gave highly reversed regioselectivity (28). In initial experiments here, benzoylation reactions were performed on dibutylstannylene acetals **1sa**, and **3sa**, and benzyl 5,6-*O*-dibutylstannylene-2,3-*O*-isopropylidene-α-D-mannofuranoside with benzoyl chloride (1 equiv.) in benzene. Compound **1sa** gave mainly primary benzoate (77%), with some secondary benzoate (15%). This result was very similar to that obtained from benzoylation of **2sa**, the methyl analog of **1sa**, by David et al., where a lower overall yield was reported (46%), but the ratio of primary benzoate to secondary benzoate products (5:1) was identical (11, 22). The other two starting materials also gave predominantly primary benzoates here.

As noted in the introduction, migration of benzoyl groups from the products formed first was observed to occur while the reaction was in progress. Benzoylation of **1sa** in benzene was followed by TLC. At low product conversion, the major product was the secondary benzoate but as the reaction proceeded the apparent product ratio reversed to favour the primary benzoate. Thus, it was concluded that the rate of migration was only slightly slower than that of benzoylation for **1sa**.

An effort was made to repeat the work of Reginato et al. (28) on propane-1,2-diol in which the initial products were trapped with phenyldimethylsilyl chloride. In our hands, the secondary product was favoured (2:1), but not with the good regiochemistry reported (85:15) (28). For the carbohydrate-derived stannylene acetals, it appears that the additional electronegative oxygen atoms present slow the rate of the benzoylation reaction but do not affect the rate of the rearrangement reaction as much.

As a result of the difficulties with rearrangements, *p*-toluenesulfonation was selected as the reaction to study instead of

Can. J. Chem. Downloaded from www.nrcresearchpress.com by 85.192.166.187 on 09/08/12
For personal use only.

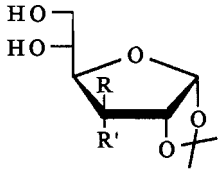

1 R = OBn R' = H
2 R = OMe R' = H
3 R = OH R' = H
4 R = H R' = OMe
5 R = H R' = OTs
6 R = H R' = OH
7 R = R' = H

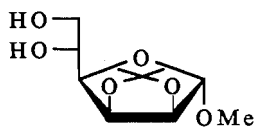

8

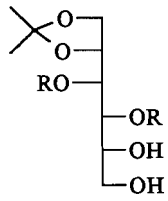

9 2R = CMe_2
10 R = Bn

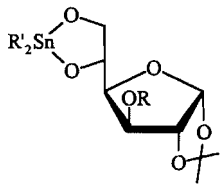

1sa R = Bn, R' = Bu
1sb R = Bn, R' = iBu
1sc R = Bn, R' = iPr
1sd R = Bn, R' = hexamethylene
1se R = Bn, R' = neohexyl
1sf R = Bn, R' = cyclohexyl
1sg R = Bn, R' = hexyl
1si R = Bn, R' = *tert*-butyl
3sa R = H, R' = Bu

2sa R = Me, R' = Bu
2sb R = Me, R' = iBu
2sc R = Me, R' = iPr
2sd R = Me, R' = hexamethylene
2se R = Me, R' = neohexyl
2sf R = Me, R' = cyclohexyl
2sg R = Me, R' = hexyl
2sh R = Me, R' = neopentyl
2si R = Me, R' = *tert*-butyl

benzoylation. *p*-Toluenesulfonyl groups do not rearrange under the conditions used for reaction.

A typical example of the reaction sequence used for *p*-toluenesulfonation is outlined in Scheme 1. 3-*O*-Benzyl-1,2-*O*-isopropylidene-α-D-glucofuranose (**1**) was refluxed with one equivalent of dibutyltin oxide in toluene to form the corresponding dibutylstannylene acetal **1sa**. Dry chloroform was added after toluene had been removed on a vacuum line. To the chloroform solution of **1sa** was added 1 equivalent of *p*-toluenesulfonyl chloride. The reaction mixture was kept at room temperature for 20 h and then poured directly onto a column for separation of the mono-*O*-substituted products, 3-*O*-benzyl-1,2-*O*-isopropylidene-6-*O*-*p*-toluenesulfonyl-α-D-glucofuranose (**1a**) and 3-*O*-benzyl-1,2-*O*-isopropylidene-5-*O*-*p*-toluenesulfonyl-α-D-glucofuranose (**1b**). For other reactions, the primary *p*-toluenesulfonate is also numbered by using the number of the parent diol followed by **a** while the secondary product is indicated by **b**.

Structural assignments of products were made primarily from their ^1H and ^{13}C NMR spectra. For instance, for **1a** and **1b**, integrations of the signals of the aromatic protons and aryl methyl protons versus those of the anomeric proton and the isopropylidene methyl groups indicated that both were mono-*O*-*p*-toluenesulfonyl derivatives. The most obvious indication of structure was the appearance of the signal for the OH proton of **1a**; it was a sharp doublet, which could only arise from ^3J coupling to one proton, H-5 of **1a**. The OH signal for **1b** was a broadened signal without obvious coupling. In addition, expected deshieldings were observed for the protons on the carbons bearing the OTs groups. The signals of H-6 and H-6′ moved from

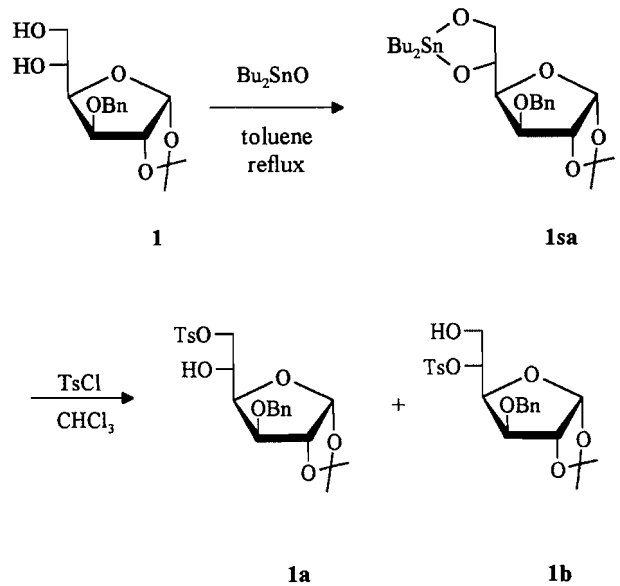

SCHEME 1

3.68 and 3.80 ppm in the spectrum of **1** to between 4.05 and 5.15 ppm in the spectrum of **1a**. The signal of H-5 moved from 4.03 ppm in the spectrum of **1** to 5.04 ppm in the spectrum of **1b**. Similar effects were noted for the corresponding signals in the ^{13}C NMR spectra. In addition, many products could be characterized by comparison with literature data.

Table 1 outlines the results of *p*-toluenesulfonation reactions on all substrates.

Can. J. Chem. Downloaded from www.nrcresearchpress.com by 85.192.166.187 on 09/08/12
For personal use only.

TABLE 1. Results of *p*-toluenesulfonation of dialkylstannylene acetals of terminal 1,2-diols

Entry	Acetal	Reaction conditions			Selectivity (%)		Yield[a] (%)
		Solvent	Temp. (°C)	Time	**a**[b]	**b**[c]	
Glucose derivatives							
1	**1sa**	Toluene	20	48 h	69	31	99
2	**1sa**	$CHCl_3$	20	20 h	45	55	95
3	**1sa**	CH_2Cl_2	20	12 h	57	43	95
4	**1sa**	CH_3CN	20	20 h	71	29	93
5	**1sb**	Toluene	20	48 h	42	58	67
6	**1sb**	$CHCl_3$	20	48 h	31	69	97
7	**1sc**	Toluene	20	48 h	37	63	98
8	**1sc**	$CHCl_3$	20	48 h	31	69	88
9	**1sc**	$CHCl_3$	5	14 d	20	80	94
10	**1sc**	CH_2Cl_2	20	12 h	32	68	95
11	**1sc**	CH_2Cl_2	5	48 h	28	72	87
12	**1sc**	CH_3CN	20	20 h	71	29	93
13	**1sd**	$CHCl_3$	20	20 h	4	96	99
14	**1se**	$CHCl_3$	20	10 h	57	43	98
15	**1sf**	$CHCl_3$	20	36 h	48	52	96
16	**1sg**	$CHCl_3$	20	12 h	45	55	96
17	**1si**	$CHCl_3$	20	5 d	86	14	29
18	**2sa**	Toluene	20	48 h	80	20	97
19	**2sa**	$CHCl_3$	20	12 h	60	40	98
20	**2sb**	Toluene	20	48 h	40	60	77
21	**2sc**	Toluene	20	24 h	40	60	80
22	**2sc**	$CHCl_3$	5	14 d	25	75	96
23	**2sc**	CH_2Cl_2	5	48 h	35	65	80
24	**2sd**	$CHCl_3$	20	12 h	5	95	94
25	**2se**	$CHCl_3$	20	12 h	70	30	98
26	**2sf**	$CHCl_3$	20	36 h	44	56	85
27	**2sg**	$CHCl_3$	20	12 h	58	42	98
28	**2sh**	$CHCl_3$	20	14 d	30	70	65
29	**3sa**	Toluene	20	4 d	76	24	51
Allose derivatives							
30	**4sa**	$CHCl_3$	20	12 h	100	0	98
31	**4sc**	$CHCl_3$	20	12 h	67	33	67
32	**4si**	$CHCl_3$	20	14 d	90	10	36
33	**5sa**	$CHCl_3$	20	12 h	92	8	97
34	**5sc**	$CHCl_3$	20	12 h	64	36	88
35	**6sa**	$CHCl_3$	20	8 h	100	0	90
36	**6sd**	$CHCl_3$	20	12 h	92	8	99
3-Deoxy-ribo-*hexose derivatives*							
37	**7sa**	$CHCl_3$	20	12 h	95	5	99
38	**7sb**	$CHCl_3$	20	20 h	79	21	90
39	**7sc**	$CHCl_3$	20	20 h	78	22	90
40	**7sd**	$CHCl_3$	20	20 h	48	52	99
Mannose derivatives							
41	**8sa**	Toluene	20	12 h	100	0	98
42	**8sa**	$CHCl_3$	20	5 h	100	0	98
43	**8sc**	Toluene	20	60 h	67	33	98
44[d]	**8sc**	Toluene	20	2 h	68	32	99
45	**8sc**	$CHCl_3$	20	12 h	62	38	91
46	**8sd**	$CHCl_3$	20	12 h	30	70	92
Mannitol derivatives							
47	**9sa**	$CHCl_3$	20	24 h	98	2	98
48	**9sd**	$CHCl_3$	20	24 h	40	60	96
49	**10sa**	$CHCl_3$	20	24 h	87	13	92
50	**10sd**	$CHCl_3$	20	24 h	22	78	77

[a]Total combined yield of isolated mono-*p*-toluenesulfonates.
[b]Primary *p*-toluenesulfonate.
[c]Secondary *p*-toluenesulfonate; in the cases of triols (entries 14, 33, and 34), **b** indicates the 5-*O*-*p*-toluenesulfonate.
[d]This reaction was carried out with 12 equivalents of TsCl.

Can. J. Chem. Downloaded from www.nrcresearchpress.com by 85.192.166.187 on 09/08/12
For personal use only.

Can. J. Chem. Downloaded from www.nrcresearchpress.com by 85.192.166.187 on 09/08/12
For personal use only.

The effect of changing the reaction solvent was evaluated using dibutylstannylene acetal **1sa**, which gave mono-*O*-*p*-toluenesulfonates **1a** and **1b** on reaction with 1 equivalent of *p*-toluenesulfonyl chloride at 20°C. The ratios of **1b** to **1a** were 29:71 in acetonitrile, 31:69 in toluene, 43:57 in dichloromethane, and 55:45 in chloroform (entries 1–4). Thus, regioselectivity for reaction at the secondary position was best in chloroform and worst in acetonitrile and toluene, the solvents commonly used in reactions of stannylene acetals. Other stannylene acetals, in particular, **1sc** and **2sc**, showed similar trends in solvent effects on regioselectivity.

The lower selectivity obtained in acetonitrile was probably due to its nucleophilicity. It seems likely that acetonitrile acts as a nucleophile towards the stannylene acetal dimers and releases coordinated monomers so that at least part of the reaction in acetonitrile occurs through these monomeric intermediates. In DMF (17, 20), pyridine (11, 22) or 4-dimethylaminopyridine (14), amines (12, 13), and methanol (12, 13), all of which are more nucleophilic than acetonitrile as measured by, for instance, Gutmann's donor number (31), greater regioselectivity is obtained for reaction at the primary centre.

The lower selectivity obtained in toluene is probably related to the slower reaction rates in this solvent. This point will be discussed in Part II (2).

Lowering the reaction temperature improved regioselectivity somewhat but slowed reaction rates considerably. For instance, *p*-toluenesulfonation of stannylene acetal **1sc** in chloroform at 20°C gave an 88% yield of mono-*O*-substitution products in 48 h with the ratio of **1b** to **1a** being 7:3 (entry 8). The same reaction conducted at 5°C resulted in mono-*O*-substitution products with a yield of 94%. The ratio of **1b** to **1a** increased to 8:2 (entry 9). Similarly, good selectivity at the secondary position for compound **2sc** was also obtained when the reaction was performed at 5°C (**2b** to **2a**, 3:1, entry 22). However, reactions at the lower temperature were very slow, taking 14 d to reach complete conversion of starting material.

Very different regioselectivities were observed from different diols. Comparisons of reactions performed on dibutylstannylene acetals in chloroform at 20°C show that the glucofuranose derivatives gave a slight preference for reaction with the secondary oxygen atom (entries 2 and 19), whereas all the other terminal 1,2-diols (entries 30, 33, 35, 37, 42, 47, and 49) showed a very strong preference for reaction with the primary oxygen atom. These differences in selectivity are probably related to the relative populations of the most populated stannylene acetal dimer with respect to the next most populated dimer and will be further discussed in Part II (2).

Changing the alkyl groups on tin had the largest effect on the regioselectivity of the reaction. These effects were studied in a systematic manner for *p*-toluenesulfonation reactions of the dialkylstannylene acetals of **1** and **2**.

Making the alkyl group longer, for instance, changing from butyl to hexyl, had little effect on the regioselectivity. Compare entries 2 and 16 and also 19 and 27. Branching far from the point of attachment to tin, as for the 3,3-dimethylbutyl (neohexyl) group, also had only slight effects on reaction selectivity. Compare entries 2 and 14 and also 19 and 25.

Branching on the carbon attached to tin and also on the next carbon had substantial effects on both reaction regioselectivity and rate. Replacement of primary butyl groups by secondary isopropyl groups improved the secondary/primary ratio from 55:45 to 69:31 for compound **1** at the expense of a fourfold increase in the time required to complete the reaction. Cyclohexyl groups did not have as large an effect. Introduction of branching on the β-carbon, as in the isobutyl group, had almost the same effect on both selectivity and reaction rate as did changing to an isopropyl group.

Further increases in steric bulk of the alkyl group gave mixed results. The *p*-toluenesulfonation reactions of di-*tert*-butylstannylene acetals were extremely slow and the products were mainly primary *p*-toluenesulfonates. One reaction was conducted on a dineopentylstannylene acetal, entry 28. Here good selectivity was obtained, slightly better than that for the diisopropylstannylene acetal, but the reaction was so slow as to make it impractical.

The trend of increased selectivity for reaction on the secondary oxygen atom as steric bulk increased was only broken for the *tert*-butyl group. This observation suggests that reactions of di-*tert*-butylstannylene acetals proceed through a different intermediate than those of the other dialkylstannylene acetals. A monomer would be expected to react at the more reactive primary oxygen atom. Monomers constitute a larger proportion of the species present in solution as the bulk of the groups around tin is increased both for noncyclic (32) and cyclic[4] dialkoxydialkyltin(IV) derivatives.

In contrast to the relatively minor improvements in regioselectivity obtained when the bulk of the acyclic alkyl groups was increased, use of the cyclic hexamethylenestannylene acetal gave major improvements without the increase in reaction time associated with the larger alkyl groups. Regioselective reactions were obtained at the secondary oxygen atoms for all substrates except for compound **6**, a triol. The reversal in regioselectivity in comparison to the dibutylstannylene acetals is striking: from 45:55 to 4:96 for **1**; from 60:40 to 5:95 for **2**; from 95:5 to 48:52 for **7**; from 100:0 to 30:70 for **8**; from 98:2 to 40:60 for **9**; and from 87:13 to 22:78 for **10**. Reaction times for hexamethylenestannylene acetals are identical for some substrates or slightly longer for others in comparison with dibutylstannylene acetals. The causes of these changes will be discussed in the following paper (2).

Applications of the reactions of hexamethylenestannylene acetals to other types of diols and polyols are currently being investigated.

Experimental

Melting points were determined using a Fisher–Johns melting point apparatus and are uncorrected. Specific rotations were determined with a Perkin–Elmer 141 polarimeter. Flash column chromatography was performed using TLC grade silica gel (60 PF-254, Merck). NMR spectra were recorded on Bruker AC 250F or AMX 400 spectrometers at 20°C for solutions in $CDCl_3$ unless otherwise specified; ^1H NMR spectra were referenced to internal tetramethylsilane (TMS), ^{13}C NMR spectra to internal TMS or to chloroform-*d* as 77.0 ppm, ^{119}Sn NMR spectra to external tetramethyltin as 0.0 ppm. AA′BB′ ^1H NMR patterns were analyzed using the iterative fitting program, LAME8 (33). Mass spectra were measured on a Dupont-CEC 21-104 mass spectrometer at 70 eV ionization and a source temperature of 105°C, using a glass, direct-insertion probe. Accurate masses were measured on a Dupont-CEC 21-110B mass spectrometer at 70 eV ionization and a source temperature of 100°C, using a silica, direct-insertion probe. Microanalyses were performed by Canadian Microanalytical Service Ltd., Vancouver, B.C. Assignments of ^1H NMR spectra were made by first-order analysis using COSY experiments to confirm assignments where necessary; ^{13}C NMR spectra were assigned by HETCOR experiments.

[4]R. Thangarasa and T.B. Grindley. Unpublished results.

Can. J. Chem. Downloaded from www.nrcresearchpress.com by 85.192.166.187 on 09/08/12
For personal use only.

Starting materials

Most compounds were prepared by literature methods: 3-*O*-benzyl-1,2-*O*-isopropylidene-α-D-glucofuranose (**1**) (34, 35), a syrup, $[\alpha]_D^{21}$ −47.3 (*c* 1.0, chloroform) (lit. (36) $[\alpha]_D$ −48.4); 3-*O*-methyl-1,2-*O*-isopropylidene-α-D-glucofuranose (**2**) (37), a syrup, $[\alpha]_D^{21}$ −52.5 (*c* 1.4, chloroform) (lit. (38) $[\alpha]_D$ −54); 1,2-*O*-isopropylidene-α-D-glucofuranose (**3**) (37), colourless crystals, mp 162–163°C, $[\alpha]_D^{23}$ −12.7 (*c* 1.0, water) (lit. (37) mp 161–162°C; $[\alpha]_D^{20}$ −11.4); 1,2-*O*-isopropylidene-3-*O*-methyl-α-D-allofuranose (**4**) (39), colourless crystals, mp 116–118°C, $[\alpha]_D^{23}$ +105 (*c* 1.0, water) (lit. (39) mp 120–121°C, $[\alpha]_D^{20}$ +108.8); 1,2-*O*-isopropylidene-3-*O*-*p*-toluenesulfonyl-α-D-allofuranose (**5**) (40), colourless crystals, mp 151–153°C (from ethyl acetate), $[\alpha]_D^{23}$ 48.3 (*c* 1.0, acetone) (lit. (40) mp 130°C (from ethanol), $[\alpha]_D^{24}$ +50); ^{1}H NMR (DMSO-d_6) δ: 7.82 (d, 2H, *J* = 8.0 Hz, 2Ar-H), 7.48 (d, 2H, 2Ar-H), 5.69 (br, 1H, H-1), 4.99 (m, 1H, H-2), 4.78 (m, 1H, H-3), 4.60, 4.51 (2m, 2H, H-6, H-6′), 4.07 (m, 1H, H-4), 3.57 (m, 1H, H-5), 1.41, 1.20 (2s, 6H, $2CH_3$); ^{13}C NMR (DMSO-d_6) δ: 145.1 (s, C_{arom}), 132.5 (s, $C_{arom\text{-}para}$), 129.9 (d, $2C_{arom\text{-}ortho}$), 127.9 (d, $2C_{arom\text{-}meta}$), 112.2 (s, C_{acetal}), 103.5 (d, C-1), 77.8 (d, C-2), 75.8 (d, C-3), 77.5 (d, C-4), 70.0 (d, C-5), 61.6 (t, C-6), 26.6, 26.4 (2q, $2CH_3$), 21.2 (q, $ArCH_3$); 1,2-*O*-isopropylidene-α-D-allofuranose (**6**) (41), colourless crystals, mp 131–133°C, $[\alpha]_D^{23}$ +44.4 (*c* 1.0, water) (lit. (39) mp 129–130°C, $[\alpha]_D^{20}$ +47.8); 3-deoxy-1,2-*O*-isopropylidene-α-D-*ribo*-hexofuranose (**7**) (42), colourless crystals, mp 83–84°C (lit. (42) mp 82–83°C); methyl 2,3-*O*-isopropylidene-α-D-mannofuranoside (**8**) (43) was a syrup; 1,2:3,4-di-*O*-isopropylidene-D-mannitol (**9**) (44), colourless crystals, mp 36–37°C, $[\alpha]_D^{23}$ +5.6 (*c* 1.0, chloroform) (lit. (44) mp 37°C); ^{1}H NMR (D_2O) δ: 4.21 (m, 1H, H-2), 4.1–4.0 (m, 2H, H-1, H-1′), 3.91 (m, 1H, H-3), 3.8–3.6 (m, 4H, H-4, H-5, H-6, H-6′), 1.39 (s, 3H, CH_3), 1.38 (s, 9H, $3CH_3$); ^{13}C NMR (D_2O) δ: 110.3, 109.6 (2s, $2C_{acetal}$), 80.6 (d, C-3, C-4), 76.4 (d, C-2), 72.3 (d, C-5), 67.9 (t, C-1), 63.8 (t, C-6), 26.8 (q, $2CH_3$), 26.3, 25.0 (2q, $2CH_3$).

*3,4-Di-*O*-benzyl-1,2-*O*-isopropylidene-D-mannitol (**10**)*

3,4-Di-*O*-benzyl-1,2:5,6-di-*O*-isopropylidene-D-mannitol (20 g), a syrup, prepared according to Gurjar's method (45), $[\alpha]_D^{23}$ +37.2 (*c* 1.0, chloroform) (lit. (45) $[\alpha]_D$ +29.6 and lit. (46) $[\alpha]_D$ +36) was dissolved in 70% ethanol–water (40 mL). Concentrated hydrochloric acid (1.5 mL) was added and the mixture was kept at 40°C for 2.5 h, then cooled to room temperature. Barium carbonate was added to the stirred reaction mixture until it was slightly basic. The solid materials were removed by filtration and the filtrate was concentrated to dryness. The residue was extracted with acetone (200 mL). The combined extracts were dried (K_2CO_3) and the solvent was removed on a rotary evaporator. This residue was stirred with hexane (300 mL) for 1 h at room temperature. The hexane layer was decanted and concentrated to dryness to give starting material (7.04 g). The residue was separated by flash column chromatography with hexane – ethyl acetate as eluant. The first fraction was title compound (**10**), 5.5 g, 47% yield based on consumed starting material, a syrup: $[\alpha]_D^{23}$ +25.8 (*c* 1.0, chloroform); ^{1}H NMR δ: 7.31 (m, 10H, 10Ar-H), 4.76 (d, 1H, *J* = 11.3 Hz, $ArCH_a$), 4.71 (d, 1H, $ArCH'_a$), 4.66 (d, 1H, *J* = 11.3 Hz, $ArCH_b$), 4.61 (d, 1H, $ArCH'_b$), 4.31 (m, 1H, H-2), 4.07 (dd, 1H, $J_{1,1'}$ = 8.24 Hz, $J_{1,2}$ = 6.4 Hz, H-1), 3.97 (dd, 1H, $J_{2,3\text{ or }3,4}$ = 3.4 Hz, $J_{3,4\text{ or }2,3}$ = 5.5 Hz, H-3), 3.95 (dd, 1H, $J_{1',2}$ = 4.9 Hz, H-1′), 3.79 (m, 1H, H-5), 3.75–3.60 (m, 3H, H-6, H-4, H-6′), 2.91 (d, 1H, $J_{OH,5}$ = 5.5 Hz, OH), 2.05 (m, 1H, OH), 1.45 (s, H, CH_3), 1.36 (s, H, CH_3); ^{13}C NMR δ: 137.9, 137.8 (2s, $2C_{arom}$), 128.7, 128.6, 128.5, 128.2, 128.1, 158.0 (6d, $8C_{arom}$), 108.6 (s, C_{acetal}), 79.2 (d, C-3), 78.6 (d, C-4), 76.0 (d, C-2), 74.5, 73.9 (2t, $2C_{benzyl}$), 71.1 (d, C-5), 66.5 (t, C-1), 63.6 (t, C-6), 26.6 (q, CH_3), 25.2 (q, CH_3); mass spectrum: 402, (M^+ 1.7%), 311 ($M^+ - CH_2Ph$, 4.4%), 253 (311 − CH_3COCH_3, 3.4%), 91 ($C_7H_7^+$, 100%). Anal. calcd. for $C_{23}H_{30}O_6$: C 68.64, H 7.51; found: C 68.17, H 7.47.

The second fraction, which crystallized after being kept under toluene, was 3,4-di-*O*-benzyl-D-mannitol, 5.1 g, 48% yield based on consumed starting material; mp 73–75°C; ^{1}H NMR δ: 7.3 (m, 10H, 10Ar-H), 4.65 (m, 4H, 4ArCH), 4.15 (br, 2H, 2OH), 3.90 (br, 2H, H-2, H-5), 3.8–3.6 (m, 6H, H-1, H-1′, H-3, H-4, H-6, H-6′), 3.32 (br, 2H, 2OH); ^{13}C NMR δ: 137.5 (s, $2C_{arom}$), 128.6, 128.3, 128.1 (3d, $8C_{arom}$), 77.8 (d, C-3, C-4), 73.8 (t, $2C_{benzyl}$), 71.5 (d, C-2, C-5), 63.4 (t, C-1, C-6); MS, *m/z*: 91 (100%, $PhCH_2^+$), 163 (5.7%, $M^+/2 - H_2O$), 181 (3.4%, $M^+/2$), 271 (5.3%, M^+ − Bn). Exact Mass calcd. for $C_{13}H_{19}O_6$: 271.118; found: 271.118.

General method for preparation of dialkylstannylene acetals

A 1,2-diol or triol (1 mmol) derived from a monosaccharide was refluxed with 1 equivalent of dialkyltin oxide overnight in benzene (20 mL) or toluene with continuous removal of water in a Dean–Stark apparatus. The solvent was removed on a vacuum line and the stannylene acetal residue was kept under vacuum for an additional half hour. To this residue was added a dry solvent (usually 10 mL), which was used for *p*-toluenesulfonation reaction. The solvent used will be specified for each reaction.

General method for p-*toluenesulfonation reactions*

To the stannylene acetal, prepared as above (1.00 mmol) in a specified solvent (Table 1) was added *p*-toluenesulfonyl chloride (0.191 g, 1.00 mmol) at a specified temperature (Table 1) and the reaction mixture was stirred a specified time (Table 1) until the starting material had disappeared as determined by TLC. Unless specified, the reaction was stopped by adding water and diluting with methylene chloride as follows. To the reaction mixture (1 mmol stannylene acetal and 1 mmol electrophile in benzene (20 mL) or toluene (20 mL), or in chloroform (5 mL), methylene chloride (5 mL), or acetonitrile (5 mL)) was added water (5 mL) and the mixture was stirred for 2 h at room temperature. The mixture was filtered and the filtrate was diluted with methylene chloride (25 mL) and washed with water (15 mL × 2). The organic layer was separated and dried over potassium carbonate. The solvent was removed on a rotary evaporator. The residue thus obtained was separated or purified by means of dry column flash chromatography with hexane – ethyl acetate as the eluent (usually performed in gradient manner). Only information on the characterization of the products is provided below. Yields and selectivities obtained for individual stannylene acetals are listed in Table 1.

*3-*O*-Benzyl-1,2-*O*-isopropylidene-6-*O*-*p*-toluenesulfonyl-α-D-glucofuranose (**1a**)*

The first fraction eluted from the column was the title compound (**1a**), a syrup: $[\alpha]_D^{23}$ −8.0 (*c* 1.0, CH_3OH) (lit. (47) $[\alpha]_D^{20}$ −7.24, $[\alpha]_D^{23}$ −23.7 (*c* 1.1, chloroform); lit. (48) $[\alpha]_D^{20}$ −39.2); ^{1}H NMR δ: 7.27–7.81 (m, 9H, Ar-H), 5.90 (d, 1H, $J_{1,2}$ = 3.7 Hz, H-1), 4.71 (d, 1H, *J* = 11.7 Hz, ArCH), 4.62 (d, 1H, H-2), 4.58 (d, 1H, ArCH′), 4.28 (dd, 1H, $J_{5,6}$ = 2.7 Hz, $J_{6,6'}$ = 10.0 Hz, H-6), 4.23 (m, 1H, H-5), 4.19–4.22 (m, 3H, H-3, H-4, H-6′), 2.68 (d, 1H, $J_{OH,5}$ = 5.8 Hz, OH), 2.46 (s, 3H, CH_3-Ar), 1.48 (s, 3H, CH_3), 1.35 (s, 3H, CH_3); ^{13}C NMR δ: 127–145 (12C, Ar-C), 112.0 (s, q-C), 105.2 (d, C-1), 82.18 (d, C-2), 81.93 (d, C-3), 78.3 (d, C-4), 72.3 (t, 2C, $ArCH_2$-C and C-6), 67.4 (d, C-5), 26.8 (q, CH_3), 26.3 (q, CH_3), 21.61 (q, CH_3-Ar).

*3-*O*-Benzyl-1,2-*O*-isopropylidene-5-*O*-*p*-toluenesulfonyl-α-D-glucofuranose (**1b**)*

The second fraction, compound **1b**, was also a syrup: $[\alpha]_D^{23}$ −16.3 (*c* 1.2, chloroform); ^{1}H NMR δ: 7.20–7.76 (m, 9H, Ar-H), 5.85 (d, 1H, $J_{1,2}$ = 3.5 Hz, H-1), 5.04 (m, 1H, H-5), 4.57 (d, 1H, *J* = 11.0 Hz, ArCH), 4.56 (d, 1H, H-2), 4.54 (d, 1H, ArCH′), 4.36 (dd, 1H, $J_{3,4}$ = 2.8 Hz, $J_{4,5}$ = 7.7 Hz, H-4), 4.00 (d, 1H, H-3), 3.92 (m, 1H, H-6), 3.80 (m, 1H, H-6′), 2.40 (s, 3H, CH_3-Ar), 2.26 (br, 1H, OH), 1.46 (s, 3H, CH_3), 1.29 (s, 3H, CH_3); ^{13}C NMR δ: 127–145 (12C, Ar-C), 112.2 (s, q-C), 105.1 (d, C-1), 81.5, 81.3 (2d, C-2 and C-3), 78.8, 78.5 (2d, C-4 and C-5), 72.1 (t, $ArCH_2$-C), 62.3 (t, C-6), 26.8 (q, CH_3), 26.3 (q, CH_3), 21.6 (q, CH_3-Ar).

Compound **1b** was further characterized by conversion to its 6-*O*-benzoate (**1d**); compound **1b** (0.300 g, 0.65 mmol) was dissolved in pyridine (1 mL) and a solution of benzoyl chloride (0.5 mL) in methylene chloride (3 mL) was added in three portions over 20 min with intermittent shaking. After standing for 1 h, the reaction mixture was diluted with methylene chloride (20 mL). The resulting solution was washed with water (10 mL × 2) and the organic layer was dried

Can. J. Chem. Downloaded from www.nrcresearchpress.com by 85.192.166.187 on 09/08/12
For personal use only.

(K_2CO_3). After solvent was removed, column purification of the residue afforded compound **1d**, 0.310 g, 86%; mp 68–69°C, $[\alpha]_D^{23}$ −0.7 (*c* 1.35, chloroform) (lit. (49) mp 64–67°C, $[\alpha]_D$ −2.2).

*1,2-O-Isopropylidene-3-O-methyl-6-O-p-toluenesulfonyl-α-D-glucofuranose (**2a**), 1,2-O-isopropylidene-3-O-methyl-5-O-p-toluenesulfonyl-α-D-glucofuranose (**2b**), and 1,2-O-isopropylidene-3-O-methyl-5,6-di-O-p-toluenesulfonyl-α-D-glucofuranose (**2c**)*

The isomer mixture from the reaction with *p*-toluenesulfonyl chloride could not be separated by flash column chromatography in this case. For each reaction, the ratio of 5-*O*-*p*-toluenesulfonate to 6-*O*-*p*-toluenesulfonate was obtained from the average values of the ratios of integrals of several well-separated signals in the ^{1}H NMR spectrum.

Information that was used to confirm the ^{1}H NMR signal assignments used for integration was obtained by *p*-toluenesulfonation of the above reaction mixture as follows. The mixture of isomers (0.384 g, 1 mmol; 5-*O*-*p*-toluenesulfonate to 6-*O*-*p*-toluenesulfonate, 2:8) was dissolved in dichloromethane (5 mL) and pyridine (2 mL) and treated with *p*-toluenesulfonyl chloride (0.96 g, 0.5 mmol) at room temperature for 24 h. Solvents were removed under vacuum. The residue was separated into two components by flash chromatography with hexane – ethyl acetate as eluent. The first fraction (0.1 g) contained 5,6-di-*O*-*p*-toluenesulfonyl-1,2-*O*-isopropylidene-3-*O*-methyl-α-D-glucofuranose (**2c**). The more polar fraction (0.3 g) contained the 6-*O*-*p*-toluenesulfonate, which was pure according to TLC and NMR analyses. Data for characterization of the three compounds are given below.

Compound **2a** was a syrup: $[\alpha]_D^{23}$ −26.8 (*c* 1.2, chloroform) (lit. (50) $[\alpha]_D$ −24); ^{1}H NMR δ: 7.27–7.84 (m, 4H, Ar-H), 5.85 (d, 1H, $J_{1,2}$ = 3.4 Hz, H-1), 4.56 (d, 1H, H-2), 4.26 (dd, 1H, $J_{3,4}$ = 2.8 Hz, $J_{4,5}$ = 8.0 Hz, H-4), 3.79–4.20 (m, 3H, H-5, H-6, H-6′), 3.88 (d, 1H, H-3), 3.43 (s, 3H, OCH_3), 2.94 (d, 1H, $J_{OH,5}$ = 6.0 Hz, OH), 2.45 (s, 3H, CH_3-Ar), 1.46 (s, 3H, CH_3), 1.31 (s, 3H, CH_3); ^{13}C NMR δ: 145.0 (s, C_{arom}), 132.4 (s, $C_{arom\text{-}para}$), 129.9 (d, $2C_{arom\text{-}ortho}$), 128.0 (d, $2C_{arom\text{-}meta}$), 111.86 (s, C_{acetal}), 104.98 (d, C-1), 84.17 (d, C-3), 81.31 (d, C-2), 78.95 (d, C-4), 72.23 (t, C-6), 67.39 (d, C-5), 57.94 (q, OCH_3), 26.76 (q, CH_3), 26.19 (q, CH_3), 21.68 (q, CH_3-Ar).

NMR data could be obtained for compound **2b** by subtraction of the data for compound **2a** from that of the mixture; ^{1}H NMR δ: 7.83 (d, 2H, *J* = 7.7 Hz, $2Ar\text{-}H_{ortho}$), 7.35 (d, 2H, $2Ar\text{-}H_{meta}$), 5.84 (d, 1H, $J_{1,2}$ = 3.7 Hz, H-1), 4.93 (m, 1H, H-5), 4.56 (d, 1H, H-2), 4.32 (dd, 1H, $J_{3,4}$ = 3.0 Hz, $J_{4,5}$ = 7.9 Hz, H-4), 3.94–3.75 (m, 2H, H-6, H-6′b), 3.70 (d, 1H, H-3), 3.27 (s, 3H, OCH_3) 2.44 (s, 3H, CH_3-Ar), 2.20 (br, 1H, OH), 1.46, 1.31 (2s, 2 × 3H, $C(CH_3)_2$); ^{13}C NMR δ: 145.0 (s, C_{arom}), 134.0 (s, $C_{arom\text{-}para}$), 129.9 (d, $C_{arom\text{-}ortho}$), 127.9 (d, $C_{arom\text{-}meta}$), 112.2 (s, C_{acetal}), 105.1 (d, C-1), 82.6 (d, C-3), 80.7 (d, C-2), 78.3 (d, C-5), 78.2 (d, C-4), 62.3 (t, C-6), 57.4 (q, OCH_3), 26.7, 26.2 (2q, $C(CH_3)_2$), 21.7 (q, $ArCH_3$).

Compound **2c** was a colourless powder: mp 50–54°C, $[\alpha]_D^{23}$ −21.1 (*c* 1.0, chloroform) (lit. (51) mp 90–93°C, $[\alpha]_D^{22}$ −20); ^{1}H NMR δ: 7.81–7.63 (m, 4H, $4Ar\text{-}H_{ortho}$), 7.36–7.27 (m, 4H, $4Ar\text{-}H_{meta}$), 5.76 (d, 1H, $J_{1,2}$ = 3.6 Hz, H-1), 5.07 (ddd, 1H, $J_{4,5}$ = 7.3 Hz, $J_{5,6}$ = 2.0 Hz, $J_{5,6'}$ = 6.2 Hz, H-5), 4.53 (d, 1H, H-2), 4.33 (dd, $J_{6,6'}$ = 11.2 Hz, H-6), 4.27 (dd, $J_{3,4}$ = 3.1 Hz, 1H, H-4), 4.04 (dd, 1H, H-6′), 3.79 (d, 1H, H-3), 3.34 (s, 3H, OCH_3), 2.45, 2.43 (2s, 2 × 3H, $2ArCH_3$), 1.44, 1.30 (2s, 2 × 3H, $C(CH_3)_2$); ^{13}C NMR δ: 145.1, 144.9 (2s, $2C_{arom}$), 133.7, 132.4 (2s, $2C_{arom\text{-}para}$), 129.8 (d, $4C_{arom\text{-}ortho}$), 128.1, 128.0 (2d, 2 × $2C_{arom\text{-}meta}$), 112.3 (s, $C_{accetal}$), 105.2 (d, C-1), 82.6 (d, C-3), 80.7 (d, C-2), 78.1 (d, C-4), 74.8 (d, C-5), 68.6 (t, C-6), 56.7 (q, OCH_3), 26.8, 26.3 (2q, $C(CH_3)_2$), 21.7 (q, $2ArCH_3$).

*1,2-O-Isopropylidene-5-O-p-toluenesulfonyl-α-D-glucofuranose (**3b**)*

The title compound (**3b**) eluted first from the column and was obtained as colourless crystals: mp 121–122°C, $[\alpha]_D^{23}$ +6.5 (*c* 1.0, chloroform) (lit. (52) mp 122–124°C, $[\alpha]_D^{22}$ +6); ^{1}H NMR δ: 7.27–7.84 (m, 4H, Ar-H), 5.90 (d, 1H, $J_{1,2}$ = 3.6 Hz, H-1), 4.83 (m, 1H, H-5), 4.58 (d, 1H, H-2), 4.36 (br, 1H, H-3), 4.27 (dd, 1H, $J_{3,4}$ = 2.4 Hz, $J_{4,5}$ = 9.3 Hz, H-4), 3.72–3.76 (m, 2H, H-6, H-6′), 3.31 (d, 1H, $J_{OH,3}$ = 4.4 Hz, C_3-OH), 2.47 (s, 3H, $ArCH_3$), 2.05 (br, 1H, C_6-OH), 1.47 (s, 3H, CH_3), 1.31 (s, 3H, CH_3).

*1,2-O-Isopropylidene-6-O-p-toluenesulfonyl-α-D-glucofuranose (**3a**)*

Compound **3a** eluted second from the column and was also obtained as colourless crystals: mp 99–100°C, $[\alpha]_D^{23}$ −5.7 (*c* 1.1, chloroform) (lit. (53) mp 100–101°C, $[\alpha]_D^{23}$ −6); ^{1}H NMR δ: 7.34–7.80 (m, 4H, Ar-H), 5.90 (d, 1H, $J_{1,2}$ = 3.6 Hz, H-1), 4.51 (d, 1H, H-2), 4.35 (br, 1H, H-3), 4.28 (dd, 1H, $J_{5,6}$ = 2.5 Hz, $J_{6,6'}$ = 10.2 Hz, H-6), 4.18 (br, 1H, H-5), 4.10 (dd, 1H, $J_{5,6'}$ = 6.8 Hz, H-6′), 4.01 (dd, 1H, $J_{3,4}$ = 2.7 Hz, $J_{4,5}$ = 7.8 Hz, H-4), 3.73 (br, 1H, OH), 3.50 (br, 1H, OH), 2.45 (s, 3H, $ArCH_3$), 1.45 (s, 3H, CH_3), 1.29 (s, 3H, CH_3).

*1,2-O-Isopropylidene-3-O-methyl-6-O-p-toluenesulfonyl-α-D-allofuranose (**4a**)*

^{1}H NMR δ: 7.79 (d, 2H, *J* = 8.2 Hz, $2Ar\text{-}H_{ortho}$), 7.34 (d, 2H, $2Ar\text{-}H_{meta}$), 5.74 (d, 1H, $J_{1,2}$ = 3.5 Hz, H-1), 4.68 (dd, $J_{2,3}$ = 4.1 Hz, H-2), 4.18–4.09 (m, 2H, H-5, H-6), 4.03 (dd, $J_{5,6'}$ = 8.0 Hz, $J_{6,6'}$ = 10.4 Hz, H-6′), 3.92 (dd, 1H, $J_{3,4}$ = 8.7 Hz, $J_{4,5}$ = 3.5 Hz, H-4), 3.76 (dd, 1H, H-3), 3.42 (s, 3H, OCH_3), 2.79 (d, 1H, $J_{OH,5}$ = 1.7 Hz, OH), 2.45 (s, 3H, $ArCH_3$), 1.55, 1.35 (2s, 2 × 3H, $2CH_3$); ^{13}C NMR δ: 145.0 (s, C_{arom}), 132.6 (s, $C_{arom\text{-}para}$), 129.9 (d, $2C_{arom\text{-}ortho}$), 128.0 (d, $2C_{arom\text{-}meta}$), 113.3 (s, C_{acetal}), 104.2 (d, C-1), 79.6 (d, C-4), 77.4 (d, C-3), 76.9 (d, C-2), 70.5 (t, C-6), 69.1 (d, C-5), 57.9 (q, OCH_3), 26.8, 26.4 (2q, $2CH_3$), 21.6 (q, $ArCH_3$).

*1,2-O-Isopropylidene-3-O-methyl-5-O-p-toluenesulfonyl-α-D-allofuranose (**4b**)*

^{1}H NMR δ: 7.79 (m, 2H, 2Ar-H), 7.34 (m, 2H, 2Ar-H), 5.38 (d, 1H, $J_{1,2}$ = 3.7 Hz, H-1), 4.84 (m, 1H, H-5), 4.58 (dd, $J_{2,3}$ = 4.2 Hz, H-2), 3.44 (s, 3H, OCH_3), 2.76 (m, 1H, OH), 2.44 (s, 3H, $ArCH_3$), 1.51, 1.32 (2s, 2 × 3H, $2CH_3$); ^{13}C NMR δ: 144.8 (s, C_{arom}), 133.8 (s, $C_{arom\text{-}para}$), 129.6 (d, $2C_{arom\text{-}ortho}$), 128.0 (d, $2C_{arom\text{-}meta}$), 113.4 (s, C_{acetal}), 103.9 (d, C-1), 81.1 (d, C-5), 79.2 (d, C-4), 77.5 (d, C-3), 76.7 (d, C-2), 61.6 (t, C-6), 57.9 (q, OCH_3), 26.8, 26.5 (2q, $2CH_3$), 21.6 (q, $ArCH_3$).

*1,2-O-Isopropylidene-3,6-di-O-p-toluenesulfonyl-α-D-allofuranose (**5a**)*

The first fraction to elute was the title compound, **5a**, which crystallized and was recrystallized from ethyl acetate and hexane to give colourless crystals: mp 118–119°C (lit. (40) mp 117–118°C); ^{1}H NMR δ: 7.85–7.76 (m, 4H, $4Ar\text{-}H_{ortho}$), 7.35 (m, 4H, $4Ar\text{-}H_{meta}$), 5.69 (d, 1H, $J_{1,2}$ = 3.5 Hz, H-1), 4.69 (dd, $J_{2,3}$ = 4.6 Hz, $J_{3,4}$ = 8.0 Hz, H-3), 4.55 (dd, 1H, H-2), 4.11–4.01 (m, 2H, H-4, H-5), 3.99 (dd, $J_{5,6}$ = 2.5 Hz, H-6), 3.87 (dd, 1H, $J_{5,6'}$ = 7.9 Hz, $J_{6,6'}$ = 10.2 Hz, H-6′), 2.57 (d, 1H, $J_{OH,5}$ = 3.7 Hz, OH), 2.46 (s, 6H, $2ArCH_3$), 1.49, 1.28 (2s, 2 × 3H, $2CH_3$).

*1,2-O-Isopropylidene-3,5-di-O-p-toluenesulfonyl-α-D-allofuranose (**5b**)*

The second fraction, compound **5b**, decomposed quickly: ^{1}H NMR δ: 7.85–7.76 (m, 4H, $4Ar\text{-}H_{ortho}$), 7.38–7.32 (m, 4H, $4Ar\text{-}H_{meta}$), 5.42 (d, 1H, $J_{1,2}$ = 3.4 Hz, H-1), 4.77 (m, 1H, H-5), 4.67 (dd, $J_{2,3}$ = 4.6 Hz, $J_{3,4}$ = 8.6 Hz, H-3), 4.47 (dd, 1H, H-2), 4.17 (dd, 1H, $J_{4,5}$ = 1.6 Hz, H-4), 3.59 (m, 2H, H-6, H-6′), 2.47, 2.45 (2s, 2 × 3H, $2ArCH_3$), 2.10 (t, 1H, $J_{OH,6}$ = 6.6 Hz, OH), 1.43, 1.24 (2s, 2 × 3H, $2CH_3$).

*1,2-O-Isopropylidene-6-O-p-toluenesulfonyl-α-D-allofuranose (**6a**)*

Compound **6a** was obtained as colourless crystals: mp 115–117°C, $[\alpha]_D^{23}$ +30.2 (*c* 1.0, chloroform) (lit. (54) mp 117–119°C, $[\alpha]_D^{23}$ +31.2); ^{1}H NMR δ: 7.77 (m, 2H, $Ar\text{-}H_{ortho}$), 7.35 (m, 2H, $2Ar\text{-}H_{meta}$), 5.74 (d, 1H, $J_{1,2}$ = 3.7 Hz, H-1), 4.56 (dd, 1H, $J_{2,3}$ = 5.0 Hz, H-2), 4.24–4.02 (m, 4H, H-3, H-5, H-6, H-6′), 3.73 (dd, 1H, $J_{3,4}$ = 8.5 Hz, $J_{4,5}$ = 4.8 Hz, H-4), 2.99 (d, $J_{OH,3\text{ or }5}$ = 7.5 Hz, OH), 2.72 (d, 1H, $J_{OH,5\text{ or }3}$ = 9.1 Hz, OH), 2.57 (d, 1H, $J_{OH,5}$ = 3.7 Hz, OH), 2.43 (s, 3H, $ArCH_3$), 1.52, 1.34 (2s, 2 × 3H, $2CH_3$), ^{13}C NMR δ: 145, 132 (2s, $2C_{arom}$), 129.9, 127.9 (2d, 2 × $2C_{arom}$), 113.0 (s, C_{acetal}), 103.9 (d, C-1), 78.8 (d, C-2), 78.7 (d, C-4), 72.0 (d, C-3), 70.6 (t, C-6), 69.7 (d, C-5), 26.5 (q, $2CH_3$), 21.6 (q, $ArCH_3$).

*1,2-O-Isopropylidene-5-O-p-toluenesulfonyl-α-D-allofuranose (**6b**)*

This compound was also obtained as colourless crystals: mp 175–

Can. J. Chem. Downloaded from www.nrcresearchpress.com by 85.192.166.187 on 09/08/12
For personal use only.

177°C, $[\alpha]_D^{23}$ +83.8 (*c* 1.0, chloroform) (lit. (54) mp 178–179°C, $[\alpha]_D^{23}$ +85.8 (*c* 0.88, acetone)).

*3-Deoxy-1,2-*O*-isopropylidene-6-*O*-*p*-toluenesulfonyl-α-D-*ribo*-hexofuranose (**7a**) and 3-deoxy-1,2-*O*-isopropylidene-5-*O*-*p*-toluenesulfonyl-α-D-*ribo*-hexofuranose (**7b**)*

The mixture of the 6-*O*-toluenesulfonate and 5-*O*-toluenesulfonate could not be separated. The percentage of each product was obtained from integration of well-separated signals in the ^{1}H NMR spectrum: for compound **7a**, δ 5.73 (d, 1H, $J_{1,2}$ = 3.7 Hz, H-1); for compound **7b**, δ 5.49 (d, 1H, $J_{1,2}$ = 3.5 Hz, H-1), 4.27 (m, 1H, H-5).

*Methyl 2,3-*O*-isopropylidene-6-*O*-*p*-toluenesulfonyl-α-D-mannofuranoside (**8a**)*

Treatment of the syrupy product mixture from the reaction of **8sa** with diethyl ether – hexane gave compound **8a** as colourless crystals: mp 95–96°C, $[\alpha]_D^{23}$ +4.1 (*c* 1.0, chloroform) (lit. (55) mp 94–95°C, $[\alpha]_D^{26}$ +4.5); ^{1}H NMR δ: 7.2–7.8 (m, 5H, Ar-H), 4.86 (s, 1H, H-1), 4.79 (dd, 1H, $J_{2,3}$ = 5.8 Hz, $J_{3,4}$ = 3.3 Hz, H-3), 4.55 (d, 1H, H-2), 4.30 (dd, 1H, $J_{6,6'}$ = 10.1 Hz, $J_{5,6}$ = 3.0 Hz, H-6), 4.18 (dd, 1H, $J_{5,6'}$ = 5.9 Hz, H-6′), 4.13 (m, 1H, H-5), 3.90 (dd, 1H, $J_{4,5}$ = 7.8 Hz, H-4), 3.26 (s, 3H, OCH_3), 2.75 (br, 1H, OH), 2.45 (s, 3H, Ar-CH_3), 1.43 (s, 3H, CH_3), 1.31 (s, 3H, CH_3); ^{13}C NMR δ: 144.9 (s, $C_{arom\text{-}para}$), 129.8 (s, C_{arom}), 129.5 (d, $C_{arom\text{-}ortho}$), 127.9 (d, $C_{arom\text{-}meta}$), 112.7 (s, C_{acetal}), 107.0 (d, C-1), 84.6 (d, C-2), 79.6 (d, C-3), 78.0 (d, C-4), 71.5 (t, C-6), 68.0 (d, C-5), 54.6 (q, CH_3O), 25.8 (q, CH_3), 24.5 (q, CH_3), 21.6 (q, CH_3-Ar).

In the ^{1}H NMR spectra of the initial product mixtures, the following signals could be assigned to methyl 2,3-*O*-isopropylidene-5-*O*-*p*-toluenesulfonyl-α-D-mannofuranoside (**8b**), δ: 4.82 (s H-1), 2.40 (t, OH), 3.28 (s, OCH_3), 1.27 and 1.12 (2s, CMe_2). Integrals of the signals of the methoxy groups were used to obtain the isomer ratios reported in Table 1.

*1,2:3,4-Di-*O*-isopropylidene-6-*O*-*p*-toluenesulfonyl-D-mannitol (**9a**)*

The first fraction was the title compound **9a**, a syrup: $[\alpha]_D^{23}$ 19.8 (*c* 1.3, chloroform); ^{1}H NMR δ: 7.80 (m, 2H, Ar-H), 7.32 (m, 2H, Ar-H), 4.29 (dd, 1H, $J_{5,6}$ = 1.6 Hz, $J_{6,6'}$ = 10.3 Hz, H-6), 4.17 (dd, 1H, $J_{1,1'}$ = 8.0 Hz, $J_{1,2}$ = 2.3 Hz, H-1), 4.17 (dd, 1H, $J_{5,6'}$ = 5.3 Hz, H-6′), 4.07–3.94 (m, 2H, H-2, H-1′), 3.82–3.65 (m, 4H, H-5, H-3, H-4, OH), 2.40 (s, 3H, CH_3-Ar), 1.40 (s, 3H, CH_3), 1.33 (s, 3H, CH_3), 1.30 (s, 6H, $2CH_3$); ^{13}C NMR δ: 144.7 (s, $C_{arom\text{-}para}$), 133.0 (s, C_{arom}), 129.8 (d, $2C_{arom\text{-}ortho}$), 128.0 (d, $2C_{arom\text{-}meta}$), 110.3 (s, C_{acetal}), 109.9 (s, C_{acetal}), 80.9 (d, C-4), 79.2 (d, C-3), 76.1 (d, C-2), 71.3 (t, C-6), 70.7 (d, C-5), 67.7 (t, C-1), 26.8 (q, $2CH_3$), 26.3 (q, CH_3), 25.0 (q, CH_3), 21.6 (q, CH_3-Ar). Anal. calcd. for $C_{19}H_{28}O_8S$: C 54.79, H 6.78; found: C 54.48, H 6.77.

*1,2:3,4-Di-*O*-isopropylidene-5-*O*-*p*-toluenesulfonyl-D-mannitol (**9b**)*

The second fraction, compound **9b**, was also a syrup: $[\alpha]_D^{23}$ 10.8 (*c* 0.86, chloroform); ^{1}H NMR δ: 7.82 (m, 2H, Ar-H), 7.33 (m, 2H, Ar-H), 4.78 (m, 1H, H-5), 4.19 (dd, 1H, $J_{3,4\text{ or }4,5}$ = 3.6 Hz, $J_{4,5\text{ or }3,4}$ = 6.4 Hz, H-4), 4.10 (dd, 1H, $J_{1,1'}$ = 8.2 Hz, $J_{1,2}$ = 5.8 Hz, H-1), 4.03–3.73 (m, 5H, H-2, H-1′, H-3, H-6, H-6′), 2.73 (t, $J_{OH,6}$ = 7.0 Hz, OH), 2.43 (s, 3H, CH_3-Ar), 1.37 (s, 3H, CH_3), 1.32 (s, 3H, CH_3), 1.30 (s, 3H, CH_3), 1.27 (s, 3H, CH_3); ^{13}C NMR δ: 145.1 (s, $C_{arom\text{-}para}$), 133.5 (s, C_{arom}), 130.1 (d, $2C_{arom\text{-}ortho}$), 128.1 (d, $2C_{arom\text{-}meta}$), 110.5 (s, C_{acetal}), 110.1 (s, C_{acetal}), 80.8 (d, C-5), 79.1 (d, C-4), 77.6 (d, C-3), 77.0 (d, C-2), 67.6 (t, C-1), 61.3 (t, C-6), 27.2 (q, CH_3), 27.0 (q, CH_3), 26.3 (q, CH_3), 25.2 (q, CH_3), 21.7 (q, CH_3). Anal. calcd. for $C_{19}H_{28}O_8S$: C 54.79, H 6.78; found: C 54.48, H 6.74.

*3,4-Di-*O*-benzyl-1,2-*O*-isopropylidene-6-*O*-*p*-toluenesulfonyl-D-mannitol (**10a**)*

Separation of the two *p*-toluenesulfonates was accomplished with difficulty. The first fraction, compound **10a**, was a syrup: $[\alpha]_D^{24}$ 27.2 (*c* 0.90, chloroform); ^{1}H NMR δ: 7.76 (m, 2H, Ar-H), 7.4–7.2 (m, 12H, Ar-H), 4.69 (d, 1H, *J* = 11.6 Hz, $ArCH_a$), 4.65 (d, 1H, $ArCH_a'$), 4.60 (d, 1H, *J* = 11.3 Hz, $ArCH_b$), 4.49 (d, 1H, $ArCH_b'$), 4.24 (m, 1H, H-2), 4.17 (dd, $J_{5,6}$ = 6.4 Hz, $J_{6,6'}$ = 10.2 Hz, H-6), 4.08 (dd, 1H, $J_{5,6'}$ = 5.2 Hz, H-6′), 4.03 (dd, 1H, $J_{1,1'}$ = 8.7 Hz, $J_{1,2}$ = 6.4 Hz, H-1), 3.99 (m, 1H, H-5), 3.89 (dd, $J_{2,3}$ = 6.1 Hz, $J_{3,4}$ = 2.8 Hz, H-3), 3.85 (dd, $J_{1',2}$ = 6.4 Hz, H-1′), 3.66 (dd, 1H, $J_{4,5}$ = 7.6 Hz, H-4), 2.48 (br, 1H, OH), 2.42 (s, 3H, CH_3-Ar), 1.42 (s, 3H, CH_3), 1.33 (s, 3H, CH_3); ^{13}C NMR δ: 145.0, 137.7, 137.4, 132.4, (4s, $4C_{arom}$), 130.0, 128.5, 128.4, 128.22, 128.20, 128.0, 127.97 (7d, $14C_{arom}$), 108.7 (s, C_{acetal}), 78.9 (d, C-3), 78.1 (d, C-4), 76.0 (d, C-2), 74.5 (t, CH_2Ar), 74.0 (t, CH_2Ar), 71.6 (t, C-6), 69.2 (d, C-5), 67.7 (t, C-1), 26.6 (q, CH_3), 25.1 (q, CH_3), 21.7 (q, CH_3-Ar). Anal. calcd. for $C_{30}H_{36}O_8S$: C 64.73, H 6.52; found: C 64.38, H 6.58.

*3,4-Di-*O*-benzyl-1,2-*O*-isopropylidene-5-*O*-*p*-toluenesulfonyl-D-mannitol (**10b**)*

The second fraction, compound **10b**, was also a syrup: $[\alpha]_D^{24}$ 19.3 (*c* 0.90, chloroform); ^{1}H NMR δ: 7.78 (m, 2H, Ar-H), 7.4–7.2 (m, 12H, Ar-H), 4.84 (m, 1H, H-5), 4.74 (d, 1H, *J* = 11.3 Hz, $ArCH_a$), 4.65 (s, 2H, $ArCH_2$-b), 4.63 (d, 1H, $ArCH'_a$), 4.08 (m, 1H, H-2), 3.99 (dd, $J_{1,1'}$ = 8.3 Hz, $J_{1,2}$ = 6.1 Hz, H-1), 3.96–3.91 (m, 2H, H-6, H-4), 3.87 (dd, 1H, $J_{1,2}$ = 6.1 Hz, H-1′), 3.83 (m, 1H, H-6′), 3.68 (dd, 1H, $J_{3,4}$ = 4.3 Hz, $J_{2,3}$ = 6.1 Hz, H-3), 2.24 (t, $J_{OH,6}$ = 6.4 Hz, OH), 2.43 (s, 3H, CH_3-Ar), 1.38 (s, 3H, CH_3), 1.30 (s, 3H, CH_3); ^{13}C NMR δ: 145.2, 137.8, 137.5, (4s, $4C_{arom}$), 130.0, 128.5, 128.4, 128.2, 128.1, 128.0, 127.9 (7d, $14C_{arom}$), 108.9 (s, C_{acetal}), 83.2 (d, C-5), 80.4 (d, C-4), 79.3 (d, C-3), 76.2 (d, C-2), 75.0 (t, CH_2Ar), 74.7 (t, CH_2Ar), 66.7 (t, C-1), 61.3 (t, C-6), 26.5 (q, CH_3), 25.2 (q, CH_3), 21.7 (q, CH_3). Anal. calcd. for $C_{30}H_{36}O_8S$: C 64.73, H 6.52; found: C 63.72, H 6.49.

*Benzoylation of 3-*O*-benzyl-1,2-*O*-isopropylidene-α-D-glucofuranose (**1**)*

To a solution of **1sa** (1 mmol) in benzene was added powdered 4Å molecular sieves (1 g). A solution of freshly distilled benzoyl chloride (0.15 g, 1 mmol) in benzene (12 mL) was added dropwise over 20 min and the mixture was stirred for 4 h. The molecular sieves were removed by filtration and the resulting solution was worked up in the standard way. Chromatographic separation afforded first 6-*O*-benzoyl-3-*O*-benzyl-1,2-*O*-isopropylidene-α-D-glucofuranose (**1e**) as a syrup: 0.320 g, 77%; ^{1}H NMR δ: 7.30–8.10 (m, 10H, Ar-H), 5.97 (d, 1H, $J_{1,2}$ = 3.7 Hz, H-1), 4.73 (d, 1H, *J* = 11.7 Hz, ArCH), 4.65 (d, 1H, H-2), 4.63 (dd, 1H, $J_{5,6}$ = 2.8 Hz, $J_{6,6'}$ = 11.7 Hz, H-6), 4.58 (d, 1H, ArCH′), 4.42 (dd, 1H, $J_{5,6'}$ = 6.0 Hz, H-6′), 4.33 (m, 1H, H-5), 4.24 (dd, 1H, $J_{3,4}$ = 3.1 Hz, $J_{4,5}$ = 5.0 Hz, H-4), 4.15 (d, 1H, H-3), 3.2 (br, 1H, OH), 1.48 (s, 3H, CH_3), 1.32 (s, 3H, CH_3); and then 5-*O*-benzoyl-3-*O*-benzyl-1,2-*O*-isopropylidene-α-D-glucofuranose (**1f**), also as a syrup: 0.062 g, 15%; ^{1}H NMR δ: 7.1–8.0 (m, 10H, Ar-H), 5.95 (d, 1H, $J_{1,2}$ = 3.7 Hz, H-1), 5.45 (m, 1H, H-5), 4.63 (d, 1H, H-2), 4.56 (d, 1H, $J_{ArCH,ArCH'}$ = 11.3 Hz, ArCH), 4.54 (dd, 1H, $J_{3,4}$ = 3.2 Hz, $J_{4,5}$ = 6.0 Hz, H-4), 4.37 (d, 1H, ArCH′), 4.08 (dd, 1H, $J_{5,6}$ = 3.0 Hz, $J_{6,6'}$ = 12.5 Hz, H-6), 4.02 (d, 1H, H-3), 3.96 (dd, 1H, $J_{5,6'}$ = 4.2 Hz, H-6′), 2.5 (br, 1H, OH), 1.53 (s, 3H, CH_3), 1.33 (s, 3H, CH_3).

*6-*O*-Benzoyl-1,2-*O*-isopropylidene-α-D-glucofuranose (**3e**)*

To a solution of compound **3sa** (1 mmol) in toluene (20 mL) was added a solution of benzoyl chloride (0.15 g, 1.05 mmol) in chloroform (7 mL) at −5°C with vigorous magnetic stirring. The cold bath was removed after 30 min and the mixture was kept at room temperature for 3 h. After work-up, recrystallization of the residue from ethyl acetate afforded the title compound as colourless crystals: 0.20 g, 75%; mp 194–195°C (lit. (56) mp 196°C); ^{1}H NMR (DMSO-d_6) δ: 7.51–8.03 (m, 5H, Ar-H), 5.82 (d, 1H, $J_{1,2}$ = 3.6, H-1), 5.32 (d, 1H, *J* = 5.0, OH), 5.23 (d, 1H, *J* = 5.7, OH), 4.47 (dd, 1H, $J_{5,6}$ = 1.9 Hz, $J_{6,6'}$ = 11.3 Hz, H-6), 4.42 (d, 1H, H-2), 4.20 (dd, 1H, $J_{5,6'}$ = 5.4 Hz, H-6′), 4.09 (dd, 1H, $J_{3,4}$ = 2.3 Hz, $J_{4,5}$ = 4.9 Hz, H-4), 4.04 (m, 1H, H-5), 4.02 (d, 1H, H-3), 1.37 (s, 3H, CH_3), 1.27 (s, 3H, CH_3).

*Benzyl 6-*O*-benzoyl-2,3-*O*-isopropylidene-α-D-mannofuranoside (**8e**)*

Benzyl 2,3-*O*-isopropylidene-α-D-mannofuranoside (0.31 g, 1 mmol) and dibutyltin oxide (0.274 g, 1.1 mmol) were refluxed overnight in benzene (20 mL) with azeotropic removal of water. The solution was cooled to room temperature and a solution of benzoyl chloride (0.191 g, 1 mmol) in benzene (6 mL) was added. After the reaction

mixture had been stirred for 30 min, standard work-up yielded a colourless solid that was recrystallized from ethyl acetate and hexane to give the title compound (**8e**) as colourless crystals: 0.290 g, 70%; mp 116–118°C, ^{1}H NMR δ: 7.25–8.08 (m, 10H, Ar-H), 5.14 (s, 1H, H-1), 4.91 (dd, 1H, $J_{2,3}$ = 5.9 Hz, $J_{3,4}$ = 3.6 Hz, H-3), 4.68 (d, 1H, H-2), 4.63 (dd, 1H, $J_{5,6}$ = 2.9 Hz, $J_{6,6'}$ = 11.7 Hz, H-6$_a$), 4.62 (d, 1H, J = 11.7 Hz, ArCH), 4.90 (dd, 1H, $J_{5,6'}$ = 6.6 Hz, H-6′), 4.46 (d, 1H, ArCH′), 4.32 (m, 1H, H-5), 4.06 (dd, 1H, H-4), 3.01 (d, 1H, $J_{OH,H-5}$ = 5.7 Hz, OH), 1.50 (s, 3H, CH_3), 1.34 (s, 3H, CH_3).

*Benzylation of 3-*O*-benzyl-1,2-*O*-isopropylidene-α-D-glucofuranose (1)*

To a solution of compound **1sa** (1 mmol) in benzene (20 mL) was added powdered 4 Å molecular sieves (1.5 g), tetrabutylammonium iodide (0.406 g, 1.1 equiv.) and benzyl chloride (0.140 g, 1.1 mmol). The mixture was refluxed for 3 d. Insoluble material was removed by filtration, then standard work-up followed by flash chromatography yielded 3,6-di-*O*-benzyl-1,2-*O*-isopropylidene-α-D-glucofuranose (**1g**) as a syrup: 0.24 g, 60%, $[\alpha]_D^{23}$ −20.6 (*c* 1.1, chloroform) (lit. (57) $[\alpha]_D^{25}$ −25.9 and lit. (58) $[\alpha]_D^{23}$ −14.5), ^{1}H NMR δ: 7.30–7.35 (m, 10H, Ar-H), 5.92 (d, 1H, $J_{1,2}$ = 3.7 Hz, H-1), 4.66 (d, 1H, J = 12.6 Hz, ArCH), 4.59 (d, 1H, H-2), 4.51–4.60 (m, 3H, 3 ArCH), 4.1–4.2 (m, 3H, H-3, H-4, H-5), 3.73 (dd, 1H, $J_{5,6}$ = 2.8 Hz, $J_{6,6'}$ = 9.7 Hz, H-6$_a$), 3.60 (dd, 1H, $J_{5,6'}$ = 5.6 Hz, H-6′), 2.72 (br, 1H, d, OH), 1.48 (s, 3H, CH_3), 1.31 (s, 3H, CH_3) and 3,5-di-*O*-benzyl-1,2-*O*-isopropylidene-α-D-glucofuranose (**1h**), also as a syrup: 0.041 g, 10%, ^{1}H NMR δ: 7.25–7.31 (m, 10H, Ar-H), 5.91 (d, 1H, $J_{1,2}$ = 3.7 Hz, H-1), 4.67 (d, 1H, J = 11.6 Hz, ArCH$_a$), 4.63 (d, 1H, J = 11.2 Hz, ArCH$_b$), 4.62 (d, 1H, H-2), 4.48 (d, 1H, ArCH$_a$), 4.47 (d, 1H, ArCH$_b$′), 4.30 (dd, 1H, $J_{3,4}$ = 3.1 Hz, $J_{4,5}$ = 8.6 Hz, H-4), 4.11 (d, 1H, H-3), 3.77–3.95 (m, 3H, H-5, H-6, H-6′), 1.80 (br, 1H, OH), 1.49 (s, 3H, CH_3), 1.31 (s, 3H, CH_3).

Acknowledgements

We thank the Natural Sciences and Engineering Research Council of Canada (NSERC) for continuing support. X.K. thanks the Killam Trust for a Killam Graduate Scholarship. NMR spectra were recorded at the Atlantic Region Magnetic Resonance Centre (ARMRC). We thank Dr. L.R. Ramaley for the accurate mass determination.

1. T.B. Grindley and X. Kong. Tetrahedron Lett. **34**, 5231 (1993).
2. X. Kong and T.B. Grindley. Can. J. Chem. **72**, 2405 (1994).
3. D. Wagner, J. Verheyden, and J.G. Moffat. J. Org. Chem. **39**, 24 (1974).
4. S. David. C.R Acad. Sci. Ser. C, **278**, 1051 (1974).
5. S. David and S. Hanessian. Tetrahedron, **41**, 643 (1985).
6. M. Pereyre, J.P. Quintard, and A. Rahm. *In* Tin in organic synthesis. Butterworths, London. 1987. Chap. 11. pp. 261–323.
7. S.J. Blunden, P.A. Cusack, and P.J. Smith. J. Organomet. Chem. **325**, 141 (1987).
8. T.B. Grindley. *In* Synthetic oligosaccharides: Indispensable probes for the life sciences. *Edited by* P. Kováč. ACS, Washington. 1994. pp. 51–76.
9. T.B. Grindley and R. Thangarasa. Can. J. Chem. **68**, 1007 (1990).
10. A.H. Haines. Adv. Carbohydr. Chem. Biochem. **33**, 11 (1976).
11. S. David and G. de Sennyey. Carbohydr. Res. **77**, 79 (1979).
12. J. Thiem and H.-P. Wessel. Liebigs Ann. Chem. 2173 (1983).
13. M.H. Kim, J.W. Yang, B.J. Lee, H.O. Kim, and M.W. Chun. Soul Taehakkyo Yakhak Nonmunjip, **11**, 71 (1986).
14. Y. Tsuda, M. Nishimura, T. Kobayashi, Y. Sato, and K. Kanemitsu. Chem. Pharm. Bull. Jpn. **39**, 2883 (1991).
15. R. Thangarasa. Ph.D. Thesis, Dalhousie University, Halifax. 1990.
16. N. Nagashima and M. Ohno. Chem. Pharm. Bull. Jpn. **39**, 1972 (1991).
17. T. Ogawa and T. Horisaki. Carbohydr. Res. **123**, C1 (1983).
18. M. Marzi and D. Misiti. Tetrahedron Lett. **30**, 6075 (1989).
19. F.-I. Auzanneau, D. Charon, and L. Szabó. J. Chem. Soc. Perkin Trans. 1, 509 (1991).
20. F. Bauer, K.-P. Ruess, and M. Liefländer. Liebigs Ann. Chem. 765 (1991).
21. A. Duréault, M. Portal, and J.C. Depezay. Synlett, 225 (1991).
22. S. David and A. Thiéffry. J. Chem. Soc. Perkin Trans. 1, 1568 (1979).
23. A.B. Reitz and E.W. Baxter. Tetrahedron Lett. **31**, 6777 (1990).
24. J.L. Marco-Contelles, C. Fernández, N. Martin-León, and B. Fraser-Reid. Synlett, 167 (1990).
25. Y. Tsuda, Y. Okuno, and K. Kanemitsu. Heterocycles, **27**, 63 (1988).
26. Y. Tsuda, M. Hanajima, N. Matsuhira, Y. Okuno, and K. Kanemitsu. Chem. Pharm. Bull. Jpn. **37**, 2344 (1989).
27. X. Kong and T.B. Grindley. J. Carbohydr. Chem. **12**, 557 (1993).
28. G. Reginato, A. Ricci, S. Roelens, and S. Scapecchi. J. Org. Chem. **55**, 5132 (1990).
29. I. Mancini, G. Guella, and F. Pietra. Helv. Chim. Acta, **74**, 941 (1991).
30. X. Kong and T.B. Grindley. Organometallics, **12**, 4881 (1993).
31. V. Gutmann. Coord. Chem. Rev. **18**, 225 (1976).
32. P.J. Smith, R.F.M. White, and L. Smith. J. Organomet. Chem. **40**, 341 (1972).
33. C.W. Haigh. Annu. Rep. NMR Spectrosc. **4**, 311 (1974).
34. H.G. Fletcher, Jr. Methods Carbohydr. Chem. **2**, 166 (1963).
35. R.L. Whistler and W.C. Lake. Methods Carbohydr. Chem. **8**, 286 (1972).
36. R.E. Gramera, R.M. Bruce, S. Hirase, and R.L. Whistler. J. Org. Chem. **28**, 1401 (1963).
37. O. Th. Schmidt. Methods Carbohydr. Chem. **2**, 318 (1963).
38. R.B. Duff and E.G.V. Percival. J. Chem. Soc. 1675 (1947).
39. M. Haga, M. Takano, and S. Tejima. Carbohydr. Res. **21**, 440 (1972).
40. J.M. Heap and L.N. Owen. J. Chem. Soc. C, 707 (1970).
41. R.R. Schmidt and A. Gohl. Chem. Ber. **112**, 1689 (1979).
42. D.H.R. Barton and S.W. McCombie. J. Chem. Soc. Perkin Trans. 1, 1574 (1975).
43. M.E. Evans and F.W. Parrish. Methods Carbohydr. Chem. **8**, 173 (1980).
44. L.F. Wiggins. J. Chem. Soc. 13 (1946).
45. M.K. Gurjar and S.M. Pawar. Indian J. Chem. **26B**, 55 (1987).
46. J. Jurczak, T. Bauer, and M. Chemielewski. Carbohydr. Res. **164**, 493 (1987).
47. H. Redlich, J.B. Lenfers, and W. Bruns. Liebigs Ann. Chem. 1570 (1985).
48. H. Weidmann and H. Schwarz. Monatsh. Chem. **103**, 218 (1972).
49. A.S. Mayer and T. Reischstein. Helv. Chim. Acta, **29**, 152 (1946).
50. Y.A. Zhdanov and V.A. Polenov. Carbohydr. Res. **16**, 466 (1971).
51. N. Baggett and R.W. Jeanloz. J. Org. Chem. **28**, 1845 (1963).
52. M. Blanc-Muesser and J. Defaye. Synthesis, 568 (1977).
53. S. Valaerde, A. Fernandez, B. Herradon, R.M. Rabanal, and M. Martin-Lomas. Tetrahedron, **43**, 3499 (1987).
54. J. Jary, Z. Kefurtova, and J. Kovar. Collect. Czech. Chem. Commun. **34**, 1452 (1969).
55. A. Dmytraczenko, W.A. Szarek, and J.K.N. Jones. Carbohydr. Res. **26**, 297 (1973).
56. L. Vargha. Ber. Dtsch. Chem. Ges. **66**, 704 (1933).
57. H. Yamamoto, C. Hosoyamada, H. Kawamoto, and S. Inokawa. Carbohydr. Res. **102**, 159 (1982).
58. H. Hori, Y. Nishida, H. Ohrui, and H. Meguro. J. Org. Chem. **54**, 1346 (1989).

Can. J. Chem. Downloaded from www.nrcresearchpress.com by 85.192.166.187 on 09/08/12
For personal use only.

Control of regioselectivity in reactions of dialkylstannylene acetals. Part II. NMR results and mechanistic analysis[1]

XIANQI KONG[2] AND T. BRUCE GRINDLEY[3]

Department of Chemistry, Dalhousie University, Halifax, NS B3H 4J3, Canada

Received May 10, 1994

XIANQI KONG and T. BRUCE GRINDLEY. Can. J. Chem. **72**, 2405 (1994).

The ^{119}Sn NMR spectra of dialkylstannylene acetals derived from a number of carbohydrate-based terminal 1,2-diols have been recorded. The spectra of chloroform-*d* solutions at room temperature of most of these dialkylstannylene acetals were consistent with the presence of single symmetric dimers only although some did contain small proportions of higher oligomers. A general mechanistic scheme is presented that explains the regioselectivity of *p*-toluenesulfonation reactions of dialkylstannylene acetals presented in the preceding paper. In the scheme, the reaction intermediates are the dialkylstannylene acetal dimers. For *p*-toluenesulfonation reactions, equilibration between the three possible dimers is faster than reaction with *p*-toluenesulfonyl chloride. Reaction regioselectivity depends both on the position of the dimer equilibrium and on the rates of reaction of individual dicoordinate oxygen atoms in the dimers. The general scheme was also used to explain the regioselectivity obtained for the very fast oxidation reactions of dialkylstannylene acetals with bromine or *N*-bromosuccinimide. In these kinetically controlled reactions, regiochemistry is determined by the initial reaction of dicoordinate oxygen atoms in the most populated dimer(s) with the electrophilic oxidizing reagent.

XIANQI KONG et T. BRUCE GRINDLEY. Can. J. Chem. **72**, 2405 (1994).

On a déterminé les spectres RMN du ^{119}Sn d'acétals de dialkylstannylènes obtenus à partir d'un certain nombre de 1,2-diols dérivés d'hydrates de carbone. Les spectres de la plupart de ces acétals de dialkylstannylène, obtenus à la température ambiante, pour des solutions dans le chloroforme-*d*, sont en accord avec la présence de dimères symétriques uniques, même si certains contiennent de faibles proportions d'oligomères de masses plus élevées. On propose un schéma mécanistique général pour expliquer la régiosélectivité des réactions de *p*-toluènesulfonation des acétals de dialkylstannylènes présentées dans la communication précédente. Dans ce schéma, les intermédiaires réactionnels sont les acétals de dialkylstannylènes dimères. Pour les réactions de *p*-toluènesulfonation, l'équilibre entre les trois dimères possibles est plus rapide que la réaction avec le chlorure de *p*-toluènesulfonyle. La régiosélectivité de la réaction dépend à la fois de la position de l'équilibre du dimère et des vitesses de réaction des atomes d'oxygène dicoordinés individuels dans les dimères. On a aussi utilisé le schéma général pour expliquer la régiosélectivité observée lors de réactions d'oxydation très rapides des acétals de dialkylstannylènes par le brome ou par la *N*-bromosuccinimide. Dans ces réactions sous contrôle cinétique, la régiochimie est déterminée par la réaction initiale des atomes d'oxygène dicoordinés dans le(s) dimère(s) le(s) plus populeux avec le réactif oxydant électrophile.

[Traduit par la rédaction]

Introduction

Dialkylstannylene acetals have become important intermediates for the regioselective substitution of diols and polyols by electrophiles (3). Despite the considerable interest in their applications, a full understanding of the causes of the remarkable regioselectivity observed in their reactions has not been achieved. The preceding paper outlines the large effects of changing the alkyl groups in dialkylstannylene acetals on the regioselectivity obtained in reactions on dialkylstannylene derivatives of carbohydrate-derived terminal 1,2-diols with *p*-toluenesulfonyl chloride (2). In a previous publication, we related the regioselectivity obtained in reactions on dibutylstannylene acetals of *trans*-1,2-diols to the species present in solution (4). The current results demonstrate that the previous conclusions were oversimplified; this publication outlines a more complete description of the causes of the regioselectivity obtained in reactions of dialkylstannylene acetals.

The system used for numbering compounds in the previous paper (2) is also employed here for compounds up to compound **10**; other compounds in this paper are numbered starting with compound **11**.

X-ray diffraction studies of crystalline dibutylstannylene acetals obtained from ethylene glycol, 2,2-dibutyl-1,3,2-dioxastannolane (**11**) (5), and from 1,3-propanediol, 2,2-dibutyl-1,3,2-dioxastannane (**12**) (6), have shown that these compounds are polymers in the solid state. More highly substituted stannylene acetals are mostly present as dimers in the solid state (7–9), although one has been found to be a pentamer (10). In solution, compounds **11** and **12** exist as highly temperature dependent mixtures of dimers and oligomers that shift towards the less aggregated species as the temperature is raised (6, 11). More substituted compounds, such as carbohydrate-derived stannylene acetals, have been found to be present in solution mainly as dimers (4, 9). When the two hydroxyl oxygen atoms in the parent diol are diastereotopic, three dimeric structures are possible (see Fig. 1 in the preceding paper (2)). The major factor determining which of the three dimers is most populated has been shown to be steric effects between the two monomeric sections of each dimer molecule (4).

Tin-119 NMR spectroscopy is the best method available to study the composition of solutions of dibutylstannylene acetals (4, 6, 11). The region of the NMR spectrum where absorption occurs is related to the coordination status of the tin atoms; tetracoordinate tin atoms in dialkoxydialkyltin compounds absorb at chemical shifts greater than −40 ppm, pentacoordinate tin atoms absorb between −80 and −190 ppm, and hexacoordinate tin atoms have shifts less than −200 ppm. Since tetracoordinate tin atoms are only present in monomers, only pentacoordinate tin atoms are present in dimers, and only trimers and higher oligomers contain hexacoordinate tin atoms, the nature of the species present can be established easily from chemical shifts. The

[1]Part of this work has appeared in a preliminary communication (1). For Part I, see the preceding publication (2).

[2]Present address: Department of Chemistry, Queen's University, Kingston, ON K7L 3N6, Canada.

[3]Author to whom correspondence may be addressed; e-mail address: GRINDLEY@AC.DAL.CA

Can. J. Chem. Downloaded from www.nrcresearchpress.com by 85.192.166.187 on 09/08/12
For personal use only.

TABLE 1. Tin-119 NMR spectral data of the dialkylstannylene acetals[a]

Compound	Solvent	Temp. (°C)	Conc. (M)	Chemical shift (δ)	$J_{Sn\text{-}119,Sn\text{-}117}$[b]
1sa	C_7D_8	19	0.2	−119.6	
	$CDCl_3$	26	0.2	−118.3	146.3
	$CDCl_3$	−60	0.2	−118.9	152.6
1sb	$CDCl_3$	19	0.33	−120.1	
	$CDCl_3$	−60	0.33	−120.8	
1sc	$CDCl_3$	19	0.33	−170.1	
	$CDCl_3$	−60	0.33	−167.8	
1sd	$CDCl_3$	20	0.3	−99.2	
2sa	$CDCl_3$	26	0.5	−118.9	143.2
	$CDCl_3$	26	0.2	−118.8	148.5
	$CDCl_3$	−60	0.2	−119.7	
2sb	$CDCl_3$	19	0.33	−120.1	
	$CDCl_3$	−60	0.33	−123.8	
2sc	$CDCl_3$	19	0.33	−171.3	
	$CDCl_3$	−60	0.33	−169.8	
2sd	$CDCl_3$	20	0.3	−98.9	142
2se	$CDCl_3$	20	0.3	−114.5	137
2sf	$CDCl_3$	20	0.3	−186.4	
2sh	$CDCl_3$	20	0.3	−120.2	134
4sa	$CDCl_3$	19	0.33	−119.3	
4sc	$CDCl_3$	19	0.33	−169.0	
6sc	$CDCl_3$	19	0.33	−121.8 (−130.8)[c]	
8sa	$CDCl_3$	19	0.33	−118.9	
8sc	$CDCl_3$	19	0.33	−168.9	
8sd	$CDCl_3$	20	0.3	−92.8	152.4
9sa	$CDCl_3$	20	0.3	−116.7	
9sd	$CDCl_3$	20	0.3	−93.5	149.2
10sa	$CDCl_3$	20	0.3	−118.9	131.0
10sd	$CDCl_3$	20	0.3	−97.2	140.2

[a]Spectra were recorded in $CDCl_3$ solution in sealed tubes at 20°C, chemical shifts are in ppm from external tetramethyltin at 20°C.

[b]Coupling constants are in Hz; no entry indicates that the coupling constant could not be measured (see text).

[c]The minor peak.

numbers of signals present in the pentacoordinate regions are employed here to study dimerization and thus to evaluate the contribution of the populations of particular dimers in determining the degree of regioselectivity of dialkylstannylene acetals in mono-*O*-substitution reactions.

In addition, a kinetic analysis of the mechanism of the reactions of stannylene acetals with electrophiles in the absence of added nucleophiles is developed that comprehensively explains, for the first time, the causes of the regioselectivity observed in the reactions of these compounds.

Results and discussion

Tin-119 NMR spectra

The NMR spectra of most dialkylstannylene acetals described in Part I (2) were recorded as a function of temperature. All NMR samples were prepared carefully on a vacuum line to avoid atmospheric moisture, then sealed. Tin-119 NMR chemical shifts are listed in Table 1. The ^{119}Sn NMR spectra of most dialkylstannylene acetals contained a single sharp peak at room temperature with a chemical shift typical of pentacoordinate tin atoms (4, 11). If tin atoms are only present in pentacoordinate environments, the only species present are dimers. The line widths varied considerably due to exchange processes for some compounds and other factors (see later). When the lines were very narrow, additional small ^{117}Sn satellite signals were observed in the ^{119}Sn NMR spectra due to ^2J coupling to ^{117}Sn atoms in the 7.5% of the ^{119}Sn-containing molecules that also contained ^{117}Sn atoms. As previously noted (12), observation of such coupling confirms that these compounds contained two or more tin atoms, consistent only with dimers or higher oligomers.

The major effect on the chemical shifts of the tin atoms in the dimeric dialkylstannylene acetals studied here was the nature of the alkyl substituents on tin. The shifts fall into three groups according to the nature of the alkyl groups as follows: (*i*) stannylene acetals that have two primary alkyl groups attached to tin; (*ii*) stannylene acetals with two secondary alkyl groups attached to tin; (*iii*) hexamethylenestannylene acetals. The first type gives chemical shifts (−115 to −124 ppm) typical of those observed for pentacoordinate tin atoms in dimeric 2,2-dibutyl-1,3,2-dioxastannolanes, regardless of the structure of the alkyl group attached to tin. For instance, the signals of the tin atoms in compounds **2sa** and **2sh** have very similar chemical shifts, −118.8 ppm for those in **2sa**, and −120.2 ppm for those in **2sh**, even though the former compound possesses two *n*-butyl groups and the latter has two sterically hindered neopentyl groups. A single sharp peak in each ^{119}Sn NMR spectrum at room temperature suggests that only one of the three possible dimers is being observed. In previous work, ^{119}Sn NMR spectra of stannylene acetals that contained more than one species at room temperature were either broad or contained more than one line (4, 11). The ^{13}C NMR spectra of the type (*i*) compounds are also consistent with single dimeric species because only single sets of peaks were observed.

The tin atoms in the diisopropylstannylene acetals **1sc**, **2sc**,

Can. J. Chem. Downloaded from www.nrcresearchpress.com by 85.192.166.187 on 09/08/12
For personal use only.

5

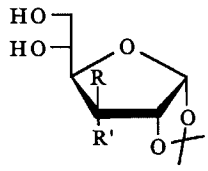

1 R = OBn R' = H
2 R = OMe R' = H
3 R = OH R' = H
4 R = H R' = OMe
5 R = H R' = OTs
6 R = H R' = OH
7 R = R' = H

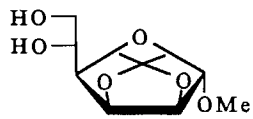

8

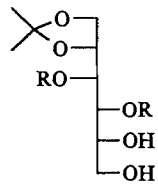

9 2R = CMe_2
10 R = Bn

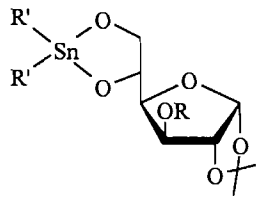

1sa R = Bn, R' = Bu
1sb R = Bn, R' = iBu
1sc R = Bn, R' = iPr
1sd R = Bn, R' = hexamethylene
1se R = Bn, R' = neohexyl
1sf R = Bn, R' = cyclohexyl
1sg R = Bn, R' = hexyl
1si R = Bn, R' = *tert*-butyl
3sa R = H, R' = Bu

2sa R = Me, R' = Bu
2sb R = Me, R' = iBu
2sc R = Me, R' = iPr
2sd R = Me, R' = hexamethylene
2se R = Me, R' = neohexyl
2sf R = Me, R' = cyclohexyl
2sg R = Me, R' = hexyl
2sh R = Me, R' = neopentyl
2si R = Me, R' = *tert*-butyl

4sc, and **8sc** and dicyclohexylstannylene acetal **2sf** absorb at lower frequencies, −169 to −186 ppm. Only single lines were observed for all compounds. These chemical shift values are halfway between those of the first type and that of a di-*tert*-alkylstannylene acetal, 2,2-di-*tert*-butyl-1,3,2-dioxastannolane, −225 ppm (9). This latter compound was shown to exist as a dimer both in the solid state and in solution (9, 13). Thus, di-*sec*-alkylstannylene acetals also exist in solution as single symmetric dimers to the level of detection by ^{119}Sn NMR spectroscopy.

The tin atoms in the five hexamethylenestannylene acetals absorbed in a narrow chemical shift range, −93 to −100 ppm. The substantial differences in shifts of signals from tin atoms in five- and six-membered rings (14) has been attributed to bond-angle changes and it seems likely that a similar effect causes the shift to higher frequencies for these hexamethylene derivatives. C-Sn-C bond angles in hexamethylenestannylene acetals are slightly smaller than those in most acyclic dialkylstannylene acetals (see later).

Variable temperature spectra

Low-temperature ^{119}Sn NMR spectra of a number of dialkylstannylene acetals were recorded in chloroform-*d* and a few were also recorded in toluene-d_8. The glucofuranose derivatives will be considered first. In chloroform-*d*, all derivatives showed single lines at all temperatures, consistent with the presence of single dimers. These results are summarized in Table 1.

The ^{119}Sn NMR spectra of compound **2sa** were recorded at 134.6 MHz for a 0.20 M solution in toluene-d_8. It had previously been noted (4) that stannylene acetals are more aggregated in toluene than in chloroform, and this was also observed here. At room temperature, one peak was present at −119.0 ppm with a line width of 115 Hz. As the temperature was lowered, this signal broadened, and then split. By −20°C, three sharp equal-intensity signals at −112.9, −115.7, and −287.6 ppm had emerged from the main peak, which had broadened and moved to a lower frequency. The three sharp equal-intensity signals can only be assigned to a trimer, since one signal (at −287.6 ppm) is in the hexacoordinate tin region. By −40°C, the major peak was ca. 35 ppm wide and centred at −127.0 ppm. As the temperature was lowered further, the main peak sharpened and moved to more positive frequencies, being 25 ppm wide at −123.0 ppm at −50°C, 12 ppm wide at −122.0 ppm at −60°C, 7 ppm wide at −120.0 ppm at −70°C, 7 ppm wide at −119.5 ppm at −80°C, and 7 ppm wide at −119.3 ppm at −90°C. The trimer peaks gradually decreased in relative intensity, and were negligible at −90°C.

The outcome of this process was the observation of two peaks at the lowest temperature studied (−90°C), one at −269.2 ppm, and another, two to three times larger, at −119.3 ppm. It seems likely that the coalescence process was for a dimer–tetramer equilibrium. The tetramer has to have C_2 symmetry to give only one peak in each of the pentacoordinate and hexacoordinate regions of the spectrum. It was observed

Can. J. Chem. Downloaded from www.nrcresearchpress.com by 85.192.166.187 on 09/08/12
For personal use only.

Can. J. Chem. Downloaded from www.nrcresearchpress.com by 85.192.166.187 on 09/08/12
For personal use only.

previously that hexacoordinate peaks in tetramers are less shielded than those in trimers (13). The dimer peak and the pentacoordinate tin tetramer peak occurred at the same chemical shift for **2sa** in toluene-d_8.

Rates of interconversion and activation barriers can be obtained from coalescence processes. In the current situation, increasing the rate of dimer–tetramer exchange caused the dimer signal at −119.0 ppm to coalesce with the two tetramer signals at −119.3 ppm (pentacoordinate tin) and at −269.6 ppm (hexacoordinate tin). The populations of the species present were changing rapidly as a function of temperature, and also the chemical shifts were changing somewhat as a function of temperature, particularly that of the signal at −269.6 ppm. The main factor that influences the magnitude of $\Delta G^{\ddagger}$ is the temperature of coalescence, not the rate constant at coalescence. Coalescence of the two signals that are farthest apart causes most of the line broadening (15, 16). A coalescence temperature of −45 ± 5°C and a chemical shift difference of 2.0×10^4 Hz yield $k = 4.5 \times 10^4$ s^{-1} and $\Delta G^{\ddagger} = 8.4 \pm 0.2$ kcal mol^{-1}, using the equation for the coalescence of equally populated singlets, $k = \pi\Delta\nu/\sqrt{2}$ (15). If the amount of broadening at coalescence is used to estimate the population of the minor exchanging partner using equations developed by Okazawa and Sorenson (16), a line broadening of 40 ppm at coalescence gives a population of the minor partner of 25%. Using equations developed in the same paper, $k = 2.7 \times 10^4$ and $\Delta G^{\ddagger} = 8.6 \pm 0.2$ kcal mol^{-1}. The dimer–trimer barrier is more difficult to estimate but a T_c of −5°C and a $\Delta\nu$ of 10 000 Hz gives $\Delta G^{\ddagger}$ of 10.3 kcal mol^{-1} using the coalescence equation (15).

The spectra of benzyl 5,6-*O*-dibutylstannylene-2,3-*O*-isopropylidene-α-D-mannofuranoside were slightly more complex. At room temperature in chloroform-*d*, a single peak was at −114.8 ppm for a 0.40 M sample and at −114.3 ppm for a 0.15 M sample, with a $J_{\text{Sn-119,Sn-117}}$ value of 140.5 Hz. The ^{119}Sn NMR spectrum of the 0.15 M sample contained no additional signals at low temperature but the spectrum of the 0.40 M sample contained small amounts of trimer peaks at −111.6, −117.1, and −274.9 ppm. From peak heights, the ratio [trimer]/[dimer] was 0.072 at −60°C. A 0.15 M sample of the same compound in toluene-d_8 precipitated at low temperature but at 25°C contained a broad peak (half-height line width, 3 ppm at 134.6 MHz) at −120.1 ppm plus a much smaller broad peak at about −112 ppm. The small broad peak probably contained the signals of the pentacoordinate tin atoms in the trimer that were starting to coalesce. The analogous methyl glycoside showed similar behaviour.

The spectra of the allofuranose derivatives were still more complicated. Figure 1 shows variable temperature spectra of a 0.33 M solution of compound **4sa** in chloroform-*d*. At room temperature, a slightly broadened peak at −119.5 ppm was accompanied by a small broad peak on the positive frequency side. By −20°C, in addition to the main peak at −117.9 ppm, small peaks were clearly visible at −112.8, −119.6, −123.9, and −277.4 ppm. The peak at −277.4 ppm increased in intensity as the temperature was lowered, as did that at −119.6 ppm, and these two peaks were about the same size at −60°C. The signal at −277.4 ppm must be assigned to the hexacoordinate tin atom in a trimer; a signal at −119.6 ppm was due to the same trimer; a third signal is still needed. The only possibility is that the third signal overlapped with the major peak. The two other small signals present at −20°C in the pentacoordinate region could be due to either dimers or trimers. The very small signal that appeared at about −295 ppm in the −60°C spectrum must

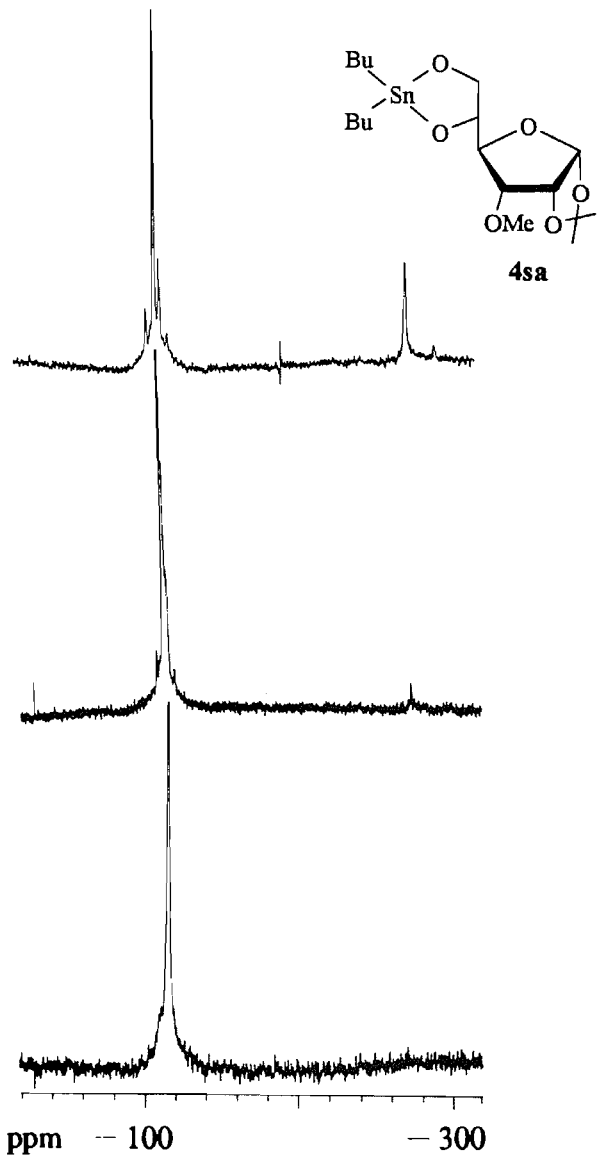

FIG. 1. 134.6 MHz ^{119}Sn NMR spectra of a 0.33 M solution of 5,6-*O*-dibutylstannylene-1,2-*O*-isopropylidene-3-*O*-methyl-α-D-allofuranose (**4sa**) in chloroform-*d* at, from the top, −60°C, −20°C, 20°C. The top 25% of the major peak has been cut off in each case.

be assigned to a second trimer, because the ^{119}Sn NMR spectrum of a tetramer would contain a signal that was less shielded than that of the trimer at −277 ppm (13).

The stannylene acetals with the most complicated behaviour in solution were the derivatives of 1,2-*O*-isopropylidene-α-D-allofuranose (7). The ^{119}Sn NMR spectra of a 0.30 M solution of compound **7sa** in chloroform-*d* at 20°C contained one large peak at −121.8 ppm plus a much smaller one at −130.8 ppm. When the temperature was raised the minor signal broadened and coalesced with the major signal at about 60°C, then reappeared when the temperature was lowered, proving that it was not an impurity. The minor signal is probably due to a second 5,6-*O*-dibutylstannylene dimer. It cannot be due to a 3,5-dimer because tin atoms in six-membered-ring stannylene acetals absorb at very different ^{119}Sn NMR chemical shifts, approximately 60 ppm more shielded (6). Cooling the sample to 0°C produced a new signal at −332.4 ppm, plus another new signal at −138.1 ppm. These latter signals continued to grow as the

TABLE 2. Comparison of ^{13}C NMR chemical shifts of the dialkylstannylene acetals with those of their precursors

Compound	Chemical shifts[a] C-1	C-2	C-3	C-4	C-5	C-6
1	105.1	82.1	82.0	80.0	69.2	64.4
1sa	105.1 (0.0)	82.9 (+0.8)	81.6 (−0.4)	84.2 (+4.2)	68.6 (−0.6)	65.0 (+0.6)
1sc	105.1(0.0)	82.9 (+0.8)	81.6 (−0.4)	84.1 (+4.1)	68.7 (−0.5)	67.0 (+2.6)
1sd	105.1 (0.0)	83.0 (+0.9)	81.4 (−0.6)	83.2 (+3.2)	68.6 (−0.6)	65.3 (+0.9)
2	105.0	81.4	84.5	79.8	69.4	64.4
2sa	105.1 (+0.1)	81.9 (+0.5)	83.6 (−0.9)	83.4 (+3.6)	68.5 (−0.9)	64.7 (+0.3)
2sc	105.0 (0.0)	82.0 (+0.6)	83.7 (−0.8)	83.4 (+3.6)	68.6 (−0.8)	69.9 (+5.5)
2sd	101.1 (+0.1)	82.1 (+0.7)	83.7 (−0.8)	82.3 (+2.5)	68.6 (−0.8)	64.8 (+0.4)
2se	105.1 (+0.1)	81.9 (+0.5)	83.6 (−0.9)	83.4 (+3.6)	68.7 (−0.7)	65.3 (+0.9)
2sf	105.2 (+0.2)	82.0 (+0.6)	83.9 (−0.6)	83.7 (+3.9)	68.8 (−0.6)	67.0 (+2.6)
2sh	105.3 (+0.3)	81.9 (+0.5)	84.5 (0.0)	83.8 (+4.0)	68.1 (−1.3)	64.9 (+0.5)
8	107.2	84.8	79.8	80.1	70.4	64.5
8sa	107.3 (+0.1)	84.7 (−0.1)	79.9 (+0.1)	81.8 (+1.7)	69.4 (−1.0)	64.2 (−0.3)
8sc	107.4 (+0.2)	84.7 (−0.1)	80.0 (+0.2)	82.2 (+2.1)	69.3 (−1.1)	66.0 (+1.5)
8sd	107.4 (+0.2)	84.9 (+0.1)	80.0 (+0.2)	80.4 (+0.3)	68.9 (−1.5)	63.8 (−0.7)
9	67.9	76.4	80.6	80.6	72.3	63.8
9sa	65.4 (−2.5)	76.4 (0.0)	79.8 (−0.8)	81.6 (−1.0)	73.8 (+1.6)	64.0 (+0.2)
9sd	65.9 (−2.0)	76.5 (+0.1)	79.9 (−0.7)	81.6 (+1.0)	72.7 (+0.4)	63.3 (−0.5)
10	66.5	76.0	79.2	78.6	71.1	63.6
10sa	67.3 (+0.8)	75.4 (−0.6)	79.4 (+0.2)	83.4 (+4.8)	71.8 (+0.7)	65.5 (+1.9)
10sd	67.7 (+1.2)	75.2 (−0.8)	79.8 (+0.6)	82.3 (+3.7)	70.9 (−0.2)	64.6 (+1.0)

[a]The numbers in parentheses are the chemical shift increments, $\Delta\delta = \delta_{\text{stannylene acetal}} - \delta_{\text{diol}}$.

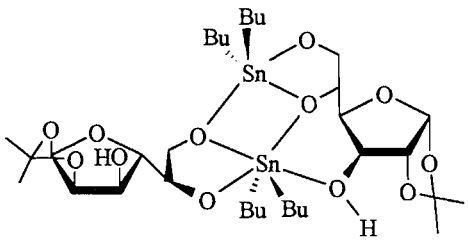

FIG. 2. The probable structure of the major species present in chloroform solutions of 5,6-*O*-dibutylstannylene-1,2-*O*-isopropylidene-α-D-allofuranose (**6sa**) below 0°C: a 5,6-dimer with additional coordination from O-3.

temperature was lowered, until by −50°C the ratio of intensities was 6:6:1:1 for the peaks at −137.4, −331.9, −129.2, and −120.9 ppm, respectively. The ratio of signal intensities of the −137.4 and −331.9 ppm signals was also 1:1 at intermediate temperatures. The position of the hexacoordinate tin signal is about the same as that (−346.1 ppm) of the hexacoordinate peak in trimeric 2,2-dibutyl-1,3,2-dioxastannane, in which the tin atom is in a six-membered ring (6). The signals of hexacoordinate tin atoms in five-membered 2,2-dibutyl-1,3,2-dioxastannolane rings always appear at positions less shielded than −300 ppm. The most likely structure for this species is an unsymmetrical dimer in which O-3 of the monomer unit having O-5 tricoordinate coordinates with the tin atom of the other monomer unit (see Fig. 2).

In summary, oligomerization of dialkylstannylene acetals depends on the structure of their precursors. For the dialkylstannylene acetals of glucofuranose derivatives, only single symmetric dimers were observed in chloroform-*d* at all temperatures. The stannylene acetals of allofuranose derivatives were present as dimers at room temperature. At lower temperatures higher oligomers were also observed. For one compound, the dibutylstannylene acetal of 1,2-*O*-isopropylidene-α-D-allofuranose, a second dimer was present as a minor species even at room temperature.

There are known to be large temperature effects on dimer–oligomer equilibria (4, 11). Even for compounds in which oligomers are dominant at −100°C, dimers constitute the majority of the species present at room temperature.

Dimer structure

The three possible dimeric structures of dialkylstannylene acetals derived from primary–secondary 1,2-diols (a primary,primary dimer, a primary,secondary dimer, and a secondary,secondary dimer) are illustrated in Fig. 3. It has been shown that steric effects are the major factor in determining dimer populations (4, 11). On this basis, the stability of the three dimers decreases in the order: primary,primary dimer (p,p dimer) to primary,secondary dimer (p,s dimer) to secondary,secondary dimer (s,s dimer). In the secondary,secondary dimer, there are steric interactions between the R groups on each monomer unit and the R′ groups on the tin atoms of the other monomer unit, causing significant destabilization. Only in primary,primary dimers can this steric interaction be fully avoided (see Fig. 3). Therefore, if only a single ^{119}Sn NMR signal is observed in the pentacoordinate region, the single symmetric dialkylstannylene acetal dimer present must be a primary,primary dimer.

Carbon-13 NMR chemical shifts provided useful information about the structures of the dimers for dibutylstannylene acetals derived from *trans*-diols (4). The formation of a dibutylstannylene acetal had only a slight effect on the chemical shift of most carbon atoms but caused the signal of the carbon atom attached to the dicoordinate oxygen atom to be significantly deshielded (by 3.5–4.4 ppm) and that of the carbon adjacent to the latter carbon but outside the stannylene acetal ring to be somewhat deshielded (by 1.6–3.3 ppm).

The data obtained from stannylene acetals are compared with their precursors in Table 2. In contrast to the earlier result (4),

Can. J. Chem. Downloaded from www.nrcresearchpress.com by 85.192.166.187 on 09/08/12
For personal use only.

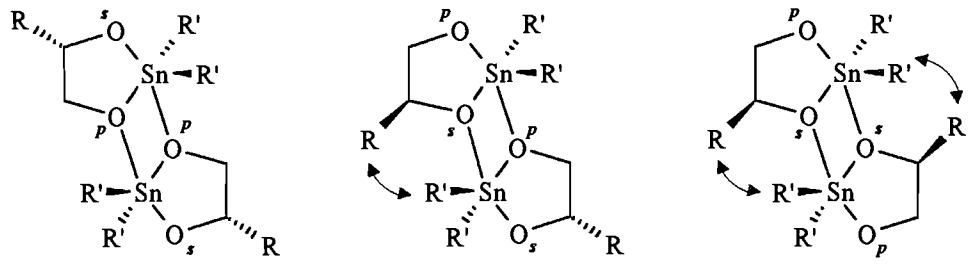

FIG. 3. Dimeric structures of dialkylstannylene acetals derived from primary–secondary 1,2-diols. Dimer nomenclature is based on the types of the tricoordinate oxygen atoms.

Can. J. Chem. Downloaded from www.nrcresearchpress.com by 85.192.166.187 on 09/08/12
For personal use only.

the chemical shift changes for the signals of the carbons inside the stannylene acetal rings, i.e., C-5 and C-6, were generally quite small, except when the alkyl group on tin was secondary. In this case, the signal of C-6 was deshielded by variable amounts (1.5–5.5 ppm). A relatively constant feature was that the signal of the carbon atom next to the stannylene acetal ring, i.e., C-4, was deshielded on stannylene acetal formation (by 0.3–4.8 ppm, avg. 3.0 ± 1.3 ppm). Perhaps this latter observation is related to the modest deshielding previously observed (4) for the carbon outside the stannylene acetal ring but adjacent to the carbon bearing the dicoordinate oxygen atom. In any case, it is clear that the chemical shifts of the carbons inside the stannylene ring are not strongly affected by ring formation, consistent with only slight changes in charge density on ring formation. This observation is in contrast to previous assumptions (17), but is consistent with conclusions drawn earlier in this laboratory (4).

Mechanistic discussion

Although only a single sharp line corresponding to a primary,primary dimer was observed in the ^{119}Sn NMR spectra of most dialkylstannylene acetals at temperatures from −60°C to +60°C in chloroform-*d*, other dimers or higher oligomers must be present at concentrations that are below the level of detection by NMR spectroscopy. Based on previous experience in this laboratory (4), it was expected that reaction would take place on the dicoordinate oxygen atoms of the dimers that were predominant in solution. This process would lead only to secondary substitution, contrary to observation (2). Several possible explanations for this difference from expectation were considered but only that outlined below fits the effects of substitution on regioselectivity.

Primary oxygen atoms are inherently much more reactive than secondary oxygen atoms. In stannylene acetal dimers, dicoordinate oxygen atoms are much more reactive than the tricoordinate oxygen atoms. If all products are formed through stannylene acetal dimers and only dicoordinate oxygen atoms react, the primary *p*-toluenesulfonate (**P**) is obtained from the secondary,secondary dimer (s,s dimer) and the primary,secondary dimer (p,s dimer), and the secondary *p*-toluenesulfonate (**S**) is formed from the primary,primary dimer (p,p dimer) and the p,s dimer.

A comprehensive mechanistic scheme is shown in Scheme 1. More elaborate schemes involving oligomers and (or) monomers can be ruled out as follows. Oligomers will not be reactive intermediates because they are much less populated than dimers and the segments that contain the reactive dicoordinate oxygen atoms, the terminal units, would have about the same reactivity as similar segments in dimers. On electronic grounds, monomers should be less reactive than dimers because the oxygen atoms in monomers are not activated by being bonded to an electron-rich pentacoordinate tin atom. In support of this statement, tributylstannyl ethers, which normally exist as monomers with tetracoordinate tin, are much activated for reaction when an adjacent oxygen atom has the correct orientation to form an intermediate with a pentacoordinate tin atom (18). In addition, monomers are very much less populated than dimers. It is also assumed that only dicoordinate oxygen atoms react.

Another possible complication may be the chloride ions released as the *p*-toluenesulfonation reaction proceeds. These could act as added nucleophiles and produce additional intermediates. However, as noted in the preceding paper (2), in the presence of added nucleophiles, substitution occurs mainly on the primary oxygen atom. If this effect was important here, reaction regioselectivity should shift towards the primary product as the reaction proceeds and the concentration of the chloride ion increases. No such shift was observed and excellent regioselectivity for reaction on the secondary oxygen atoms was observed for many substrates. Therefore, this factor was not included in the mechanistic scheme.

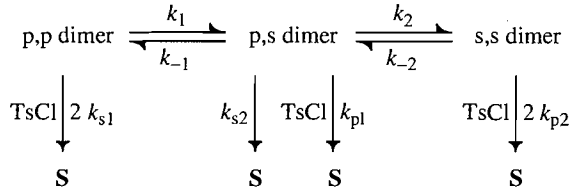

SCHEME 1. p,p: primary,primary; p,s: primary,secondary; s,s: secondary,secondary; **P**: primary *p*-toluenesulfonate; **S**: secondary *p*-toluenesulfonate; k_{s1}, k_{s2}: rate constants for reaction at secondary dicoordinate oxygen atoms; k_{p1}, k_{p2}: rate constants for reaction at primary dicoordinate oxygen atoms; k_1, k_{-1}, k_2, k_{-2}: rate constants for dimer interconversion.

The following equations can be derived from the reaction pathway outlined in Scheme 1,

[1] $$d[\mathbf{S}]/dt = 2\,k_{s1}[p,p][TsCl] + k_{s2}[p,s][TsCl]$$

[2] $$d[\mathbf{P}]/dt = k_{p1}[p,s][TsCl] + 2\,k_{p2}[s,s][TsCl]$$

$$K_1 = k_1/k_{-1}$$

and

$$K_2 = k_2/k_{-2}$$

Can. J. Chem. Downloaded from www.nrcresearchpress.com by 85.192.166.187 on 09/08/12
For personal use only.

where [p,p] is the concentration of the p,p dimer, [p,s] is the concentration of the p,s dimer, [s,s] is the concentration of the s,s dimer, K_1 and K_2 are dimer equilibrium constants, and the other terms are defined in the scheme.

The environments of the dicoordinate secondary oxygen atoms in the p,p dimer and in the p,s dimer are very similar and the environments of the dicoordinate primary oxygen atoms in the p,s dimer and in the s,s dimer are almost the same. On this basis, it will be assumed that $k_{s1} = k_{s2} = k_s$, $k_{p1} = k_{p2} = k_p$, and $K_1 = K_2 = K = k_1/k_{-1}$, where k_s and k_p are rate constants for reaction at secondary and primary dicoordinate oxygen atoms in dimers and K is the dimer equilibrium constant.

From the ^{119}Sn NMR spectral measurements, it was shown that [p,p] $\gg$ [p,s] for all compounds. For the same reasons that make the p,p dimer more stable than the p,s dimer, [p,s] $\gg$ [s,s]. Therefore, it can be concluded that k_{s1}[p,p] $\gg$ k_{s2}[p,s] and k_{p1}[p,s] $\gg$ k_{p2}[s,s].
Thus, eqs. [1] and [2] simplify to

[3] $d[\mathbf{S}]/dt = 2\,k_s[p,p][TsCl]$

[4] $d[\mathbf{P}]/dt = k_p[p,s][TsCl]$

The ratio of the increment of the product at the secondary oxygen atom to that at the primary oxygen atom can be expressed as follows:

[5] $d[\mathbf{S}]/d[\mathbf{P}] = (2\,k_s/k_p)([p,p]/[p,s])$

Two limiting kinetic situations can be considered with respect to the p,s dimer; either it is in equilibrium with the major p,p dimer or it is at a steady-state concentration. When $k_p \ll k_{-1}$, the p,p dimer and the p,s dimer are in equilibrium and [p,p]/[p,s] = $1/K$, which leads to

[6] $d[\mathbf{S}]/d[\mathbf{P}] = (2\,k_s/k_p)(1/K)$

Thus, the regioselectivity of the *p*-toluenesulfonation reaction, or the ratio of the increment of the product at the secondary oxygen atom to that at the primary oxygen atom, depends only on the relative reactivity of the dicoordinate secondary and primary oxygen atoms and the relative populations of the p,p dimer and the p,s dimer.

When k_p is larger than k_{-1}, the concentration of the p,s dimer can be assumed to be in a steady state. Under these conditions, the concentrations of p,p dimer and p,s dimer are related by the following:

$$k_1[p,p] = k_{-1}[p,s] + k_p[p,s][TsCl]$$

$$[p,p]/[p,s] = (k_{-1} + k_p[TsCl])/k_1$$

Thus, eq. [5] becomes

[7] $d[\mathbf{S}]/d[\mathbf{P}] = (2\,k_s/k_p)\{(k_{-1} + k_p[TsCl])/k_1\}$

Since under normal reactions conditions [TsCl] is $\geq$1 M, if $k_p \gg k_{-1}$ k_p[TsCl] > k_{-1}, and therefore

[8] $d[\mathbf{S}]/d[\mathbf{P}] = 2\,k_s[TsCl]/k_1$

Therefore, the ratio of the amount of reaction at the secondary hydroxyl oxygen atom to that at the primary hydroxyl oxygen atom would increase with the increase of the concentration of TsCl used for the reaction, if indeed $k_{-1} < k_p$[TsCl]. The tosylation reaction is quite slow. Thus, k_p[TsCl] is expected to be less than k_{-1}. Not surprisingly, reaction on **8sc** at concentrations of *p*-toluenesulfonyl chloride of 0.10 and 1.2 M gave identical product ratios within experimental error. Therefore, it can be concluded that *p*-toluenesulfonation reactions occur under conditions in which dimer equilibration is much faster than reaction.

When the dimers are in equilibrium, eq. [6] applies. Regioselectivity for reaction on the secondary oxygen atom is determined by the product of two factors, the inverse of the dimer equilibrium constant, $1/K$, and the ratio of the relative reactivities of the dicoordinate secondary oxygen atoms to that of the dicoordinate primary oxygen atoms, k_s/k_p. For a given starting diol, increasing the bulk of the alkyl groups on tin will increase the intermonomer steric effects about the tricoordinate secondary oxygen atom. The already small population of the minor p,s dimer will decrease further. Thus, K will decrease and $1/K$ will increase, causing the relative amount of secondary product to increase. Altering alkyl groups on the tin atom in its dialkylstannylene acetals will also change k_s/k_p, but the differential effect is probably not large. In fact, increasing the bulk of the alkyl groups would be expected to decrease the reactivity of the dicoordinate oxygen atoms on secondary positions more than that on primary positions because the former are already sterically hindered. As outlined in the preceding paper (2), the introduction of sterically hindered alkyl groups on tin increases the selectivity for reaction at the secondary position. Thus, changing the alkyl groups on tin has a larger effect on the equilibrium constant between the p,p and p,s dimers than on the rate constants for reaction at the two types of oxygen atoms.

Introducing a cyclic hexamethylene group on tin causes by far the largest effect on the regioselectivity of the reaction. The most reasonable explanation of this change is that replacement of the two butyl groups on tin by a hexamethylene group has a larger effect on K than does replacement by sterically hindered acyclic groups. A cyclic group on tin will be considerably restricted in its motion and will be unable to adopt very different orientations to escape the steric interactions present when a secondary oxygen atom is tricoordinate.

Another factor that may be important in causing the improved regioselectivity of reactions of hexamethylenestannylene acetals is the somewhat different geometry about tin in these compounds. In the one crystal structure available for a dimeric dibutylstannylene acetal (7, 8), the dicoordinate oxygen atom is apical in a very distorted trigonal bipyramid at tin. All bond angles to tin in stannylene acetals derived from 1,2-diols are approximately fixed by the fact that the oxygen and tin atoms are in fused four- and five-membered rings. The equatorial butyl groups have C-Sn-C bond angles of 133.2(5)° and 128.4(4)°. The C-Sn-C bond angle in hexamethylenetin(IV) bischloroacetate is 122.2(3)°(19). Thus, the hexamethylenestannylene acetal C-Sn-C bond angle required by ring formation is likely to impose strain on the acetal that could result in more reactive apical oxygen atoms. This would be particularly true if, in the reaction mechanism, cleavage of the apical tin–oxygen bond occurs as the apical oxygen atom is forming a bond to the electrophile. This factor would increase the rate of reaction and, by raising the energy of the starting materials, decrease the difference in rates of reaction of dicoordinate primary and secondary oxygen atoms. In addition, the dicoordinate oxygen atoms in hexamethylenestannylene acetals may be

Can. J. Chem. Downloaded from www.nrcresearchpress.com by 85.192.166.187 on 09/08/12
For personal use only.

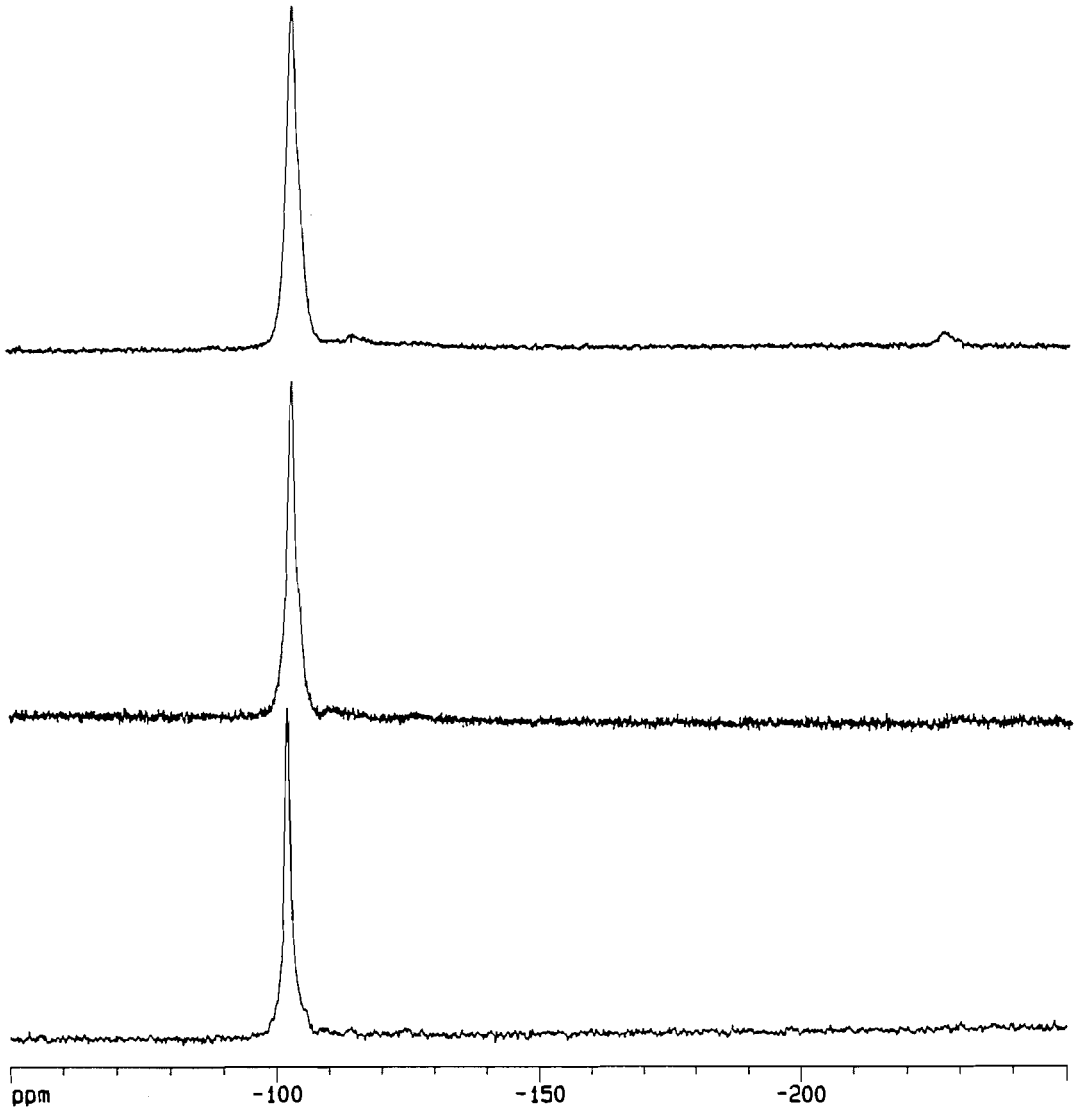

FIG. 4. 149.2 MHz ^{119}Sn NMR spectra of a 0.30 M solution of the hexamethylenestannylene acetal of ethane-1,2-diol (**13**) in chloroform-*d* at, from the top, −60°C, −20°C, 0°C.

electrophiles than those in dibutylstannylene acetals because the very mobile butyl groups (7, 8) will populate some conformations that hinder approach to the dicoordinate oxygen atoms by electrophiles.

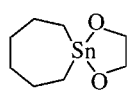

13

Supporting evidence about changes in geometry of hexamethylenestannylene acetals with respect to that of dibutylstannylene acetals was obtained from a study of the equilibrium mixtures present in solutions of the hexamethylenestannylene acetal of ethane-1,2-diol, spiro[4.6]1,4-dioxa-5-stannaundecane (**13**). Figure 4 shows ^{119}Sn NMR spectra of a 0.30 M solution of **13** in chloroform-*d* at 0°C, −40°C, and −60°C. The mole fraction of dimer was calculated from integrals of the areas of the large pentacoordinate tin peak and the hexacoordinate tin peak with the following assumptions. The hexacoordinate tin peak is due to trimer, but the trimer pentacoordinate tin peak is coincident with the pentacoordinate tin peak of the dimer. On this basis, the mole fraction of dimer of the hexamethylenestannylene acetal of ethylene glycol was 0.90 at −60°C. In comparison, the mole fraction of dimer for a much more dilute solution of the dibutylstannylene acetal of ethylene glycol at −73°C was 0.14 (4, 11). Evidentially, hexamethylenestannylene acetals favour dimers over higher oligomers much more than do acyclic dialkylstannylene acetals bearing alkyl groups of comparable bulk.

One cause of the difference between the two types of stannylene acetals is the steric restriction of C-Sn-C angles by ring formation in the hexamethylenestannylene acetal. In pentacoordinate tin sites of dibutylstannylene acetals, C-Sn-C bond angles average 127.8 ± 5.1°, whereas in structures where the tin atom is hexacoordinate the bond angles are larger, averaging 138.1 ± 3.0° (6). Stannacycloheptane rings are unable to accommodate the larger bond angles required in higher oligomers as easily and thus their formation is disfavoured. Additional support for this point comes from the fact that the C-Sn-C bond angle in hexamethylenetin bischloroacetate (122.3°) is

TABLE 3. One-bond ^{119}Sn–^{13}C coupling constants and calculated C-Sn-C angles of dialkylstannylene acetals

Compound	Coupling constant (Hz)[a] $^1J_{Sn\text{-}119,C\text{-}13}$		$^1J_{Sn\text{-}119,C\text{-}13}$ used for calculation[b]	Calcd. C-Sn-C bond angle (°)[c]
1sa	585.8	584.2	585.0	133.2
1sb	575.0		575.0	132.2
1sd	557.4	561.9	559.7	130.7
2sb	574.1	574.7	574.4	132.2
2sc	584.1		584.1	133.2
2sd	556.2	560.7	558.5	130.6
2se	588.2	582.0	585.1	133.2
2sf	562.6		562.6	131.0
2sh	575.8	554.4	565.1	131.2
8sd	559.1	552.6	555.9	130.3
9sa	603.5		603.5	135.1
9sd	566.5	546.8	556.7	130.4
10sa	588.0	577.9	583.0	133.0
10sd	561.9	551.7	556.8	130.4

[a]The two carbon atoms attached to tin are not equivalent in the dimer.
[b]When two different coupling constants are observed, the number used for calculation is the average.
[c]Calculated using eq. [9] (20).

much smaller than those in acyclic dialkyltin dicarboxylates (136 ± 5°) (19).

The magnitudes of one-bond tin–carbon coupling constants ($^1J_{Sn\text{-}119,C\text{-}13}$) in butyltin derivatives have been related to the sizes of C-Sn-C bond angles (θ) by eq. [9] (20) and a very similar relationship has been developed for methyltin derivatives (21). Therefore, it is likely that this relationship will give reasonable values of bond angles for most organotin derivatives.

$$[9] \quad {}^1J_{Sn\text{-}119,C\text{-}13} = (9.99 \pm 0.73)\theta - (746 \pm 100)$$

Table 3 lists $^1J_{Sn\text{-}119,C\text{-}13}$ values and bond angles calculated with eq. [9]. The C-Sn-C bond angles for the hexamethylenestannylene acetals calculated in this way are somewhat smaller than those of acyclic dialkylstannylene acetals, in agreement with the above discussion, and it is clear that further expansion of a bond angle as required for hexacoordination at tin would cause strain.

Application to literature problems

The regiochemistry obtained in oxidation reactions of stannylene acetals with bromine or *N*-bromosuccinimide is often the reverse of that obtained from other reactions of stannylene acetals with electrophiles (3,22–24). This reversal can be explained by means of the above mechanistic considerations. Oxidation of dibutylstannylene acetals derived from primary–secondary 1,2-diols yields α-hydroxyketones with very high regioselectivity (22, 24). Oxidation with bromine is complete almost instantaneously at room temperature and with *N*-bromosuccinimide is complete between 1 and 20 min (24). Formation of *p*-toluenesulfonate esters from dialkystannylene acetals is much slower, taking between 12 h and 2 d to go to completion with one equivalent of *p*-toluenesulfonyl chloride at room temperature if the alkyl group is not large.

A pathway for the oxidation reaction that is consistent with the results presented here is outlined in Figure 5.

The first step in the oxidation reaction is the same as in all other reactions of stannylene acetals, an electrophilic addition to the dicoordinate oxygen atom. It is followed by elimination of hydrogen bromide to give the carbonyl group. Both steps are very fast at room temperature but the overall reaction slows if base is not present to remove the hydrogen bromide (22, 25).

The products obtained in oxidation reactions of terminal 1,2-diols are consistent with control by the relative populations of dibutylstannylene acetal dimers present in solution. As discussed above, the only detectable species of a dibutylstannylene acetal of a carbohydrate-derived primary–secondary 1,2-diol by ^{119}Sn NMR spectroscopy in solution is the p,p dimer. If the oxidation reaction occurs as shown in Fig. 5, initiated by electrophilic attack at the dicoordinate oxygen atom, the secondary oxygen atom in the p,p dimer, the corresponding α-hydroxyketone results (22, 24). Thus, the second kinetic situation, in which the population of the minor dimer is in a steady state, applies.

Under these conditions the product ratio can be predicted from eq. 8, adapted to the oxidation reaction under steady-state conditions as eq. [10],

$$[10] \quad d[\mathbf{S}]/d[\mathbf{P}] = 2\,(k_s/k_1)[O]$$

where [O] is the concentration of oxidizing reagent. The product ratio is determined by the relative rates at which the major dimer goes to product or to minor dimer. Product formation is undoubtedly considerably faster than dimer interconversion for bromine oxidation and, most probably, is also faster for NBS oxidation.

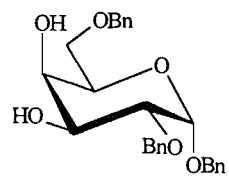

14

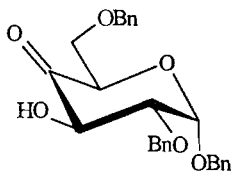

15

This conclusion also explains many results in the literature where the regioselectivity obtained in oxidation by bromine was different from that obtained in other reactions. For example, bromine oxidation of the dibutylstannylene acetal of benzyl 2,6-di-*O*-benzyl-α-D-galactopyranoside (**14**) in benzene gave only the 4-keto product (**15**) in a yield of 69% at room temperature, whereas benzoylation of this dibutylstannylene acetal under the same conditions as used for oxidation resulted in a 74% yield of 3-*O*-benzoyl derivative after 24 h (22). The only experimental evidence available about the structures of the dimers present for stannylene acetals derived from *cis*-1,2-diols on pyranose rings comes from the X-ray structure of methyl 4,6-*O*-benzylidene-2,3-dibutylstannylene-α-D-mannopyranoside, where the terminal units of the pentamer in the crystal have the axial oxygen atoms dicoordinate (10). Examination of models suggests that having the axial oxygen atom tricoordinate would bring one of the butyl groups on tin over the pyranose ring, causing severe steric destabilization. Both of these considerations indicate that dimers having the equatorial oxygen atoms tricoordinate are considerably favoured, i.e., the 3,3-dimer for the stannylene acetal of **14**. Oxidation will then trap the 3,3-dimer by reaction at the axial dicoordinate oxygen atom, O-4. All the other reactions of stannylene acetals are slower, which allows dimer equilibration to take place so that

Can. J. Chem. Downloaded from www.nrcresearchpress.com by 85.192.166.187 on 09/08/12
For personal use only.

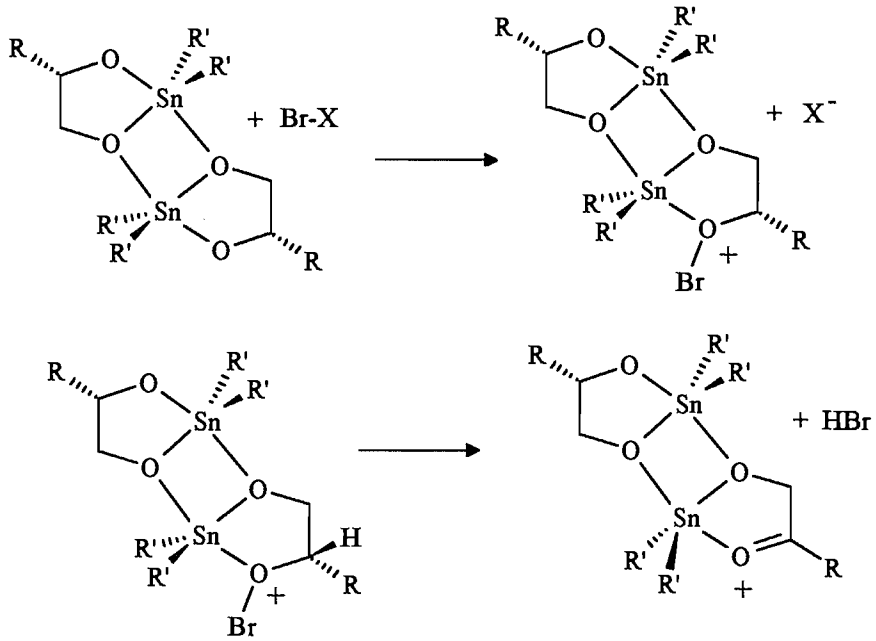

FIG. 5. A pathway for the oxidation of stannylene acetals.

the much more reactive equatorial oxygen atom, O-3, in the less populated 3,4-dimer reacts preferentially.

Conclusions

Dialkylstannylene acetals derived from primary,secondary 1,2-diols are present in solution predominantly as dimers. Steric effects are most important in determining which of the three possible dimers are most populated. The symmetrical dimer with the secondary oxygen atoms dicoordinate is favoured and the preference increases with both the size of the substituent on the secondary centre and the size of the alkyl groups on tin.

A mechanistic scheme has been developed that explains the regioselectivity observed in reactions of the above stannylene acetals with electrophiles in the absence of added nucleophiles. The key factor is the equilibrium between the major symmetrical dimer, which only reacts at the secondary oxygen atom, and the minor nonsymmetrical dimer, which reacts at the more reactive primary oxygen atom. For slow reactions, such as *p*-toluenesulfonylation, regioselectivity is determined by the product of the ratio of the rate constants for reaction at the two sites and the inverse of the dimer equilibrium constant, that is, by competition between the position of the equilibrium and the relative reactivity of the two oxygen atoms. For fast reactions, primarily oxidation, regioselectivity is determined by the position of the equilibrium.

Experimental

NMR spectra were recorded on Bruker AC 250F or AMX 400 or Nicolet NT-360 NB spectrometers; ^{13}C NMR spectra were referenced to internal tetramethylsilane (TMS) or to chloroform-*d* as a secondary reference at 77.0 ppm; ^{119}Sn NMR spectra were referenced to external tetramethyltin at 20°C. The variable temperature ^{119}Sn NMR spectra of dibutylstannylene acetals were recorded at 134.6 MHz on the Nicolet NMR spectrometer, those of the other stannylene acetals at 149.2 MHz on the Bruker AMX spectrometer.

Preparation of dialkylstannylene acetal samples for NMR spectroscopy

The mixture of a carbohydrate-derived diol (1 mmol) and dialkyltin oxide (1 mmol) was refluxed overnight in toluene (20 mL) with azeotropic removal of water. The solvent was removed under reduced pressure and the residue was dried under vacuum for 1 h. Dry chloroform-*d* or toluene-d_8 (3 mL) was distilled through a vacuum line onto the residual stannylene acetal. The solution was filtered, transferred under vacuum through a bridge into a pre-connected NMR tube, and then the tube was sealed. Tin-119 and carbon-13 NMR data for dialkylstannylene acetals are listed in Tables 1–3.

Acknowledgements

We thank the Natural Sciences and Engineering Research Council of Canada (NSERC) for continuing support. X.K. thanks the Killam Trust for a Killam Graduate Scholarship. NMR spectra were recorded at the Atlantic Region Magnetic Resonance Centre (ARMRC).

1. T.B. Grindley and X. Kong. Tetrahedron Lett. **34**, 5231 (1993).
2. X. Kong and T.B. Grindley. Can. J. Chem. **72**, 2396 (1994).
3. S. David and S. Hanessian. Tetrahedron, **41**, 643 (1985); M. Pereyre, J.P. Quintard, and A. Rahm. *In* Tin in organic synthesis. Butterworths, London. 1987. Chap. 11. pp. 261–323; S.J. Blunden, P.A. Cusack, and P.J. Smith. J. Organomet. Chem. **325**, 141 (1987); T.B. Grindley. *In* Synthetic oligosaccharides: indispensable probes for the life sciences. *Edited by* P. Kováč. ACS, Washington. 1994. pp. 51–76.
4. T.B. Grindley and R. Thangarasa. Can. J. Chem. **68**, 1007 (1990).
5. A.G. Davies, A.J. Price, H. M. Dawes, and M.B. Hursthouse. J. Chem. Soc. Dalton Trans. 297 (1987).
6. T.B. Grindley, R. Thangarasa, P.K. Bakshi, and T.S. Cameron. Can. J. Chem. **70**, 197 (1992).
7. T.S. Cameron, P.K. Bakshi, R. Thangarasa, and T.B. Grindley. Can. J. Chem. **70**, 1623 (1992).
8. S. David, C. Pascard, and M. Cesario. Nouv. J. Chim. **3**, 63 (1979).
9. P.A. Bates, M.B. Hursthouse, A.G. Davies, and S.D. Slater. J. Organomet. Chem. **363**, 45 (1989).
10. C.W. Holzapfel, J.M. Koekomoer, C.F. Marais, G.J. Kruger, and J.A. Pretorius. S. Afr. J. Chem. **35**, 80 (1982).
11. T.B. Grindley and R. Thangarasa. J. Am. Chem. Soc. **112**, 1364 (1990).
12. S. David, A. Thiéffry, and A. Forchioni. Tetrahedron Lett. **22**, 2647 (1981).
13. T.B. Grindley, R.E. Wasylishen, R. Thangarasa, W.P. Power, and R.E. Curtis. Can. J. Chem. **70**, 205 (1992).

Can. J. Chem. Downloaded from www.nrcresearchpress.com by 85.192.166.187 on 09/08/12
For personal use only.

14. J.D. Kennedy and W. MacFarlane. *In* Multinuclear NMR. *Edited by* J. Mason. Pergamon Press, London. 1988. pp. 311–312.
15. M.L. Martin, G.J. Martin, and J.J. Delpuech. *In* Practical NMR spectroscopy. Heyden, London. 1980. pp. 300 and 340.
16. N. Okazawa and T.S. Sorenson. Can. J. Chem. **56**, 2737 (1978).
17. S.J. Blunden, P.J. Smith, P.J. Beynon, and D.G. Gillies. Carbohydr. Res. **88**, 9 (1981).
18. T. Ogawa and M. Matsui. Tetrahedron, **37**, 2363 (1981).
19. X. Kong and T.B. Grindley. Organometallics, **12**, 4881 (1993).
20. J. Holeček and A. Lyčka. Inorg. Chim. Acta, **118**, L17 (1986); J. Holeček, K. Nádvorník, K. Handlíř, and A. Lyčka. J. Organomet. Chem. **315**, 299 (1986).
21. T.P. Lockhart and W.F. Manders. J. Am. Chem. Soc. **109**, 7015 (1987).
22. S. David and A. Thiéffry. J. Chem. Soc. Perkin Trans. 1, 1568 (1979).
23. Y. Tsuda, M. Hanajima, N. Matsuhira, Y. Okuno, and K. Kanemitsu. Chem. Pharm. Bull. Jpn. **37**, 2344 (1989); H.-M. Liu, Y. Sato, and Y. Tsuda. Chem. Pharm. Bull. Jpn. **41**, 491 (1993).
24. X. Kong and T.B. Grindley. J. Carbohydr. Chem. **12**, 557 (1993).
25. A. Fernandez-Mayoralas, M. Bernabe, and M. Martín-Lomas. Tetrahedron, **44**, 4877 (1988).

Can. J. Chem. Downloaded from www.nrcresearchpress.com by 85.192.166.187 on 09/08/12
For personal use only.

An intermolecular Diels–Alder approach to (±)-isoacanthodoral

HSING-JANG LIU,[1] GERARDO ULIBARRI, AND LLOYD A.K. NELSON
Department of Chemistry, The University of Alberta, Edmonton, AB T6G 2G2, Canada

Received July 7, 1994

HSING-JANG LIU, GERARDO ULIBARRI, and LLOYD A.K. NELSON. Can. J. Chem. **72**, 2416 (1994).

The total synthesis of marine sesquiterpenoid isoacanthodoral (**3**), in racemic form, has been accomplished, using the boron trifluoride catalyzed Diels–Alder reaction of dienone ester **4** and isoprene as the key step.

HSING-JANG LIU, GERARDO ULIBARRI et LLOYD A.K. NELSON. Can. J. Chem. **72**, 2416 (1994).

On a effectué la synthèse total du sesquiterpénoïde marin, isoacanthodoral (**3**) racémique, impliquant comme étape clé une réaction de Diels–Alder, catalysée par le trifluorure de bore, de la diénone ester **4** et de l'isoprène.

[Traduit par la rédaction]

Can. J. Chem. Downloaded from www.nrcresearchpress.com by 85.192.166.187 on 09/08/12
For personal use only.

Introduction

Acanthodoris nanaimoensis is a colorful nudibranch found in the shallow intertidal zone of British Columbia's coast line. It is one of the nudibranchs characterized by the fruity odor. The odoriferous principle of this nudibranch could be extracted with methanol and the sweet smelling oil residue, which was obtained in small quantities, was shown to possess antibacterial activity against *Bacillus subtilis* and *Staphylococcus aureus*, and antifungal activity against *Phythiam ultimum* and *Rhyzoctonia solani* (1).

The odor of the oily residue was later found to be due to a mixture of aldehydes. Three major components were subsequently identified as nanaimoal (**1**), acanthodoral (**2**), and isoacanthodoral (**3**) (2–4).

Herein we wish to report the details of the total synthesis,[2] in racemic form, of isoacanthodoral, which confirms the structural assignment of this structurally novel natural product.[3]

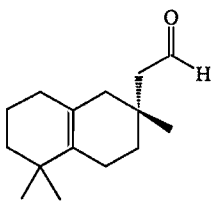

1

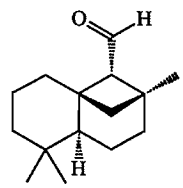

2

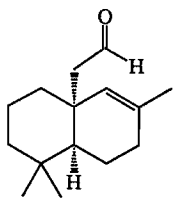

3

Results and discussion

During the course of our synthetic studies on himachalenes (6), the Diels–Alder reaction of 2-carbomethoxy-4,4-dimethyl-2,5-cyclohexadienone (**4**)[4] and isoprene was investigated. Interestingly, under boron trifluoride catalysis, the cycloaddition gave mainly the abnormal *anti-para* adduct **7** (64% yield) along with a small amount (28% yield) of the expected *para* adduct **8**.

Adduct **7** is an attractive starting substrate that has almost the complete carbon skeleton for the synthesis of isoacanthodoral (**3**). Complete reduction of the α,β-unsaturated ketone moiety, modification of the carbomethoxy group to an acetaldehyde unit, and isomerization of the isolated double bond are all that is required to furnish compound **3**. These transformations were experimentally realized as follows.

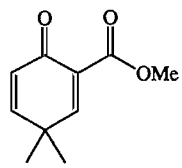

4

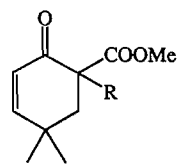

5 R=H
6 R=Br

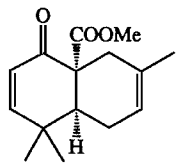

7

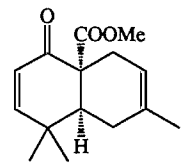

8

To reduce the enone moiety, compound **7** was treated with triethylsilane in the presence of tris(triphenylphosphine)rhodium(I) chloride (Wilkinson's catalyst) (6, 7). The silyl enol ether **9** thus obtained in 97% yield was subsequently hydrolyzed with aqueous potassium bicarbonate in methanol to give crystalline keto ester **10** (mp 41–42°C) in quantitative yield. For the

[1]Author to whom correspondence may be addressed. Telephone: (403) 492-3477. Fax: (403) 492-8231. Bitnet: USERHJL2@UALTAMTS

[2]For preliminary communication, see ref. 5.

[3]Isoacanthodoral could not be isolated in pure form. Its structural assignment was carried out on the corresponding 2,4-dinitrophenylhydrazone (4).

[4]This compound was previously prepared from keto ester **5** via selenium dioxide oxidation (6). An improved procedure has since been developed, involving bromination of **5** with *N*-bromosuccinimide followed by dehydrobromination of the resulting bromide **6** with 1,8-diazabicyclo[5.4.0]undec-7-ene.

Can. J. Chem. Downloaded from www.nrcresearchpress.com by 85.192.166.187 on 09/08/12
For personal use only.

removal of the ketone carbonyl, keto ester **10** was subjected to thioketalization with 1,2-ethanedithiol in the presence of boron trifluoride etherate to generate the thioketal **11**.

Upon Raney nickel reduction, compounds **12** and **13** were obtained in a 1:1 ratio and an overall yield of 80%. This means that the desired ester **12** was produced in only 40% yield.

An improved route to compound **12** employed the stepwise reduction of the ketone carbonyl, first to the alcohol level and then deoxygenation. Thus, keto ester **10** was dissolved in methanol and cooled to –40°C. Slow addition of sodium borohydride to the solution and a short reaction time (15 min) gave 95% of a mixture of epimeric alcohols **14** and **15** in 5:1 ratio. The stereochemistry of these alcohols at C-2 was proven by the following NOE experiments. Irradiation of the proton at C-2 (δ 3.90) in the major isomer **14** gave an 8% enhancement of the signal at δ 1.93, attributed to the proton at C-6. On the other hand, irradiation of the C-2 proton (δ 3.60) in the minor isomer **15** gave no enhancement of the signal at δ 2.15–2.30 for the C-6 proton and two others.

It is noteworthy that in the reduction of **10**, higher temperature or longer reaction time led to the production of the over-reduced product **16**. The reduction of the ester moiety is thought

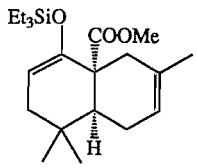

9

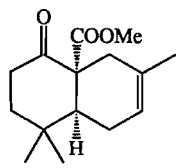

10

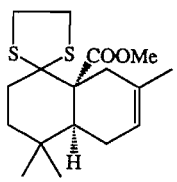

11

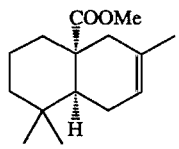

12

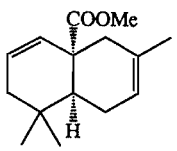

13

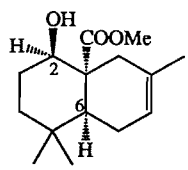

14

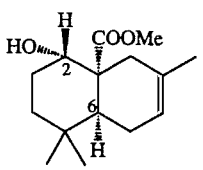

15

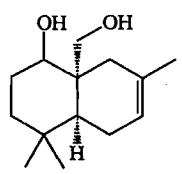

16

to proceed through a four-membered ring lactone, formed after the initial reduction of the ketone carbonyl, or through an intramolecular hydride transfer from the boron-C-2 oxygen complex formed after the initial reduction.

To remove the hydroxy group present in compounds **14** and **15** the corresponding xanthates were prepared. Each of the hydroxy esters **14** and **15** was treated with sodium hydride in 1,2-dimethoxyethane to give the corresponding sodium alkoxide, followed by reaction with carbon disulfide to generate the sodium xanthate. The salt was alkylated in situ with methyl iodide to produce the corresponding methyl xanthate in quantitative yield. The reduction of xanthates **17** and **18** in pure form or as a mixture with tri-*n*-butyltin hydride in the presence of a catalytic amount of azobisisobutyronitrile (8) afforded ester **12** in virtually quantitative yield.

Having successfully removed the unnecessary functionalities from "ring A", it remained to carry out the following transformations in order to complete the synthesis of isoacanthodoral. The ester group in compound **12** must be converted to an acetaldehyde unit and the double bond must be moved to the adjacent position. We chose to modify the ester group first.

Homologation by one carbon unit can be carried out in a number of ways (9–14). A frequently used procedure involves the Wittig reaction (13, 14) of an aldehyde with methoxymethylenetriphenylphosphorane, followed by hydrolysis of the resulting enol ethers.

Several attempts were made to reduce ester **12** directly to aldehyde **19**. When ester **12** was treated with diisobutylaluminum hydride (15) in toluene at –78°C, reduction did not take place. When the reaction was carried out at room temperature, only a 20% yield of the desired aldehyde was obtained. This aldehyde was produced more effectively by a two-step sequence as follows.

Treatment of ester **12** with lithium aluminum hydride in dry ether gave the alcohol **20** as a crystalline solid in 96% yield. When alcohol **20** was subjected to Swern oxidation (16), aldehyde **19** was formed in 80% yield. Unfortunately, compound **19** proved to be quite volatile, making its isolation rather difficult.

Another good method for the conversion of alcohols to the corresponding aldehydes involves the use of pyridinium chlorochromate on alumina (17). This method is especially useful when the product is unstable or volatile. Treatment of alcohol **20** with pyridinium chlorochromate on alumina in dichloromethane at room temperature for 2 h gave an 88% yield of aldehyde **19**, which did not require further purification.

Addition of aldehyde **19** to a deep red benzene solution of methoxymethylenetriphenylphosphorane gave a 1:1 mixture of *cis* and *trans* enol ethers **21** in 98% yield. However, attempts to hydrolyze **21** under a variety of acidic conditions led invariably to decomposition of the material. The desired aldehyde was not detected. Several demethylating agents such as chlorotrimethylsilane and sodium iodide in acetonitrile (18), phenyl dichlorophosphate and sodium iodide (19), and sodium ethylthiolate (20) were also examined. In all cases, the starting material was recovered intact. A vinyl ether exchange reaction catalyzed by mercury(II) salts (21, 22) was also attempted. Mercury(II) nitrate was added to a solution of enol ethers **21** in acetonitrile–water (5:1). After 2 h at room temperature, the starting material was completely consumed. Unfortunately, no identifiable products were isolated.

In reassessing the synthetic strategy it was deemed appropriate to move the existing endocyclic double bond first, since most of the difficulties encountered were likely due to this double bond. Direct isomerization of the double bond was attempted. α,β-Unsaturated keto ester **7** was dissolved in carbon tetrachloride and refluxed overnight in the presence of trifluoroacetic acid. Only starting material was recovered. Under the same conditions, keto ester **10** was also recovered intact. At this point, it seemed unlikely that a clean direct isomerization of the double bond could be achieved. Therefore, a functional

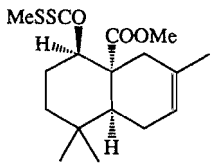

17

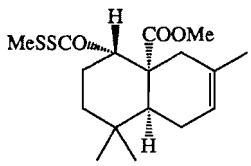

18

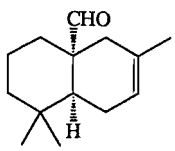

19

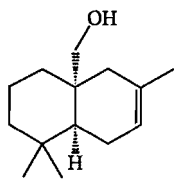

20

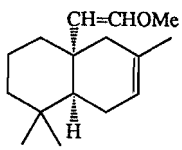

21

group must be introduced to the disubstituted end of the double bond followed by elimination.

Ester **12** has only two functional groups, making it a good candidate for the introduction of the required functional group. Treatment of ester **12** in hexane saturated with hydrogen bromide or hydrogen chloride gas at room temperature gave a crystalline product that did not contain any halogen atoms. Apparently hydrohalogenation had not taken place. A strong absorption at 1753 cm^{-1} in the infrared spectrum, the absence of the ester group and the double bond in the ^1H nmr spectrum, and the molecular ion peak corresponding to $C_{14}H_{22}O_2$ in the mass spectrum indicated the formation of lactone **22**. When ester **12** was treated with *p*-toluenesulfonic acid in refluxing benzene, lactone **22** was also obtained in 90% yield.

Compound **22** would arise if the double bond of compound **22** is protonated and the incipient tertiary carbocation is attacked intramolecularly by the carbonyl oxygen rather than by the external nucleophile (halogen). Although it was not possible to introduce a halogen to the double bond, an oxygen atom was efficiently incorporated. This would, hopefully, allow for the subsequent regeneration of a double bond at the required position. To accomplish this, it was necessary to convert the lactone ring to a hydroxy ester. The combinations of sodium methoxide – methanol, sodium ethoxide – ethanol, and sodium isopropoxide – isopropyl alcohol were used in attempts to cleave the lactone ring in compound **22**. Examination of the reaction in each case, by thin-layer chromatography, showed that, even though the starting material was consumed, the lactone was regenerated upon work-up.

Another alternative was to reduce the lactone completely to a diol. Thus, **22** was treated with lithium aluminum hydride in ether and diol **23** was formed in 97% yield.

At this point, it was necessary to decide whether to introduce the double bond or to extend the side chain first. In an unsuccessful attempt to extend the angular chain, the primary alcohol was oxidized with pyridinium chlorochromate on alumina. The unstable hydroxy aldehyde thus obtained was immediately subjected to a Wittig reaction with methoxymethylenetriphenylphosphorane. Complete decomposition of the starting aldehyde occurred without apparent formation of the desired product. These results prompted us to examine the approach of regenerating the double bond before extension of the angular chain.

To avoid problems during the dehydration reaction, it was deemed necessary to protect the primary alcohol first. Selective protection was readily achieved as follows. Freshly distilled acetic anhydride was added to a solution of diol **23** in dry pyridine. After overnight at room temperature, hydroxy acetate **24** was isolated in 90% yield.

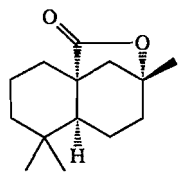

22

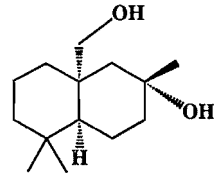

23

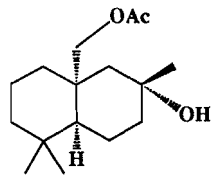

24

Several methods for the dehydration of hydroxy acetate **24** were examined, including the use of copper(II) sulfate on silica gel (23), thionyl chloride in pyridine (24), and phosphorus oxychloride in pyridine (25). A mixture of isomeric olefins was always obtained. The results are given in Table 1.

As can be seen from Table 1, the dehydration reaction with copper(II) sulfate impregnated on silica gel in refluxing benzene (Entry 1) gave predominantly the undesirable acetate **26**. No change in the product ratio was observed when benzene was replaced with toluene. When xylenes were used, complete decomposition occurred. In contrast, when the dehydration was carried out in refluxing ether, no reaction took place.

Thionyl chloride in pyridine gave a mixture of olefins **25** and **26** in equal amounts, when the reaction was carried out at room temperature (Entry 2). When the temperature was decreased to 5°C (Entry 3), the rate of reaction decreased as expected but the product ratio remained the same.

Similar results were obtained with phosphorus oxychloride in pyridine at a temperature range of –30°C to 20°C (Entries 4–6). With the aid of 4-dimethylaminopyridine (DMAP), however, the formation of the desired isomer **25** was enhanced at the expense of **26**. It appears that preferential formation of **25** is highly dependent upon the ratio of the reagents and the reaction temperature (Entries 7–12). The best results were obtained when the reaction was carried out at –40°C in pyridine using 10 equivalents of phosphorous oxychloride and 5 equivalents of DMAP (Entry 12). Under these conditions a 3:1 mixture of acetates **25** and **26** was obtained in virtually quantitative yield.

It is noteworthy that in virtually all the cases examined a very small amount (<4% by ^1H nmr, showing a pair of broad doublets at δ 4.69 and 4.57 (J = 1 Hz each)) of the exocyclic olefin **27** was also produced. However, all attempts to isolate this

Can. J. Chem. Downloaded from www.nrcresearchpress.com by 85.192.166.187 on 09/08/12
For personal use only.

TABLE 1. Dehydration of hydroxy acetate **24**

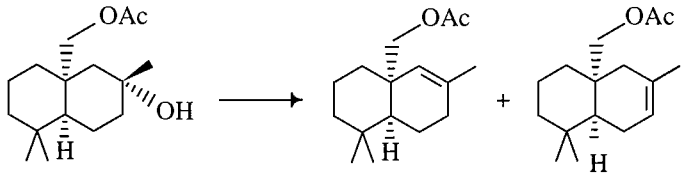

24 **25** **26**

Entry	Reagent (equiv.)	Solv.	DMAP (equiv.)	Temp. (°C)	Time (h)	Yield (%)	Ratio **25**:**26**
1	$CuSO_4$ (1)	PhH	—	78	0.5	94	1.0:9.0
2	$SOCl_2$ (20)	Py	—	20	1	88	1.0:1.0
3	$SOCl_2$ (20)	Py	—	5	4	80	1.0:1.0
4	$POCl_3$ (2)	Py	—	20	12	—	1.0:0.8
5	$POCl_3$ (2)	Py	—	5	24	81	1.0:1.0
6	$POCl_3$ (10	Py	—	−30	72	86	1.1:1.0
7	$POCl_3$ (10)	Py	1	0	21	74	0.9:1.0
8	$POCl_3$ (10)	Py	2	−15	39	98	1.1:1.0
9	$POCl_3$ (10)	Py	2.7	−30	72	99	1.5:1.0
10	$POCl_3$ (10)	Py	10	−52	24	96	1.4:1.0
11	$POCl_3$ (20)	Py	10	−62	16	97	1.4:1.0
12	$POCl_3$ (10)	Py	5	−40	12	95	3.0:1.0

compound by chromatography were unsuccessful, probably due to isomerization of the double bond to the more stable endocyclic position on silica gel.

Isomeric olefins **25** and **26** were found to be inseparable. For characterization purposes, compound **26** was produced via a different route. Alcohol **20** was acetylated with acetic anhydride in pyridine to give pure **26**.

The mixture of acetates **25** and **26** was hydrolyzed with an aqueous solution of potassium carbonate in methanol. After refluxing for 2.5 h a mixture of hydroxy olefins was obtained in 98% yield. Separation of alcohols **20** (20%) and **28** (70%) was achieved by flash chromatography on silica gel.

The studies on the dehydration of hydroxy acetate **24** depleted our stock of this material. It was necessary to prepare more Diels–Alder adducts, to separate isomer **7** required for the synthesis, and then to repeat the reaction sequence leading to alcohol **28**. It has been reported that ionic hydrogenation can be performed using trialkylsilanes and a strong acid or boron trifluoride (26–30). Under these conditions, an α,β-unsaturated ketone can be reduced to the saturated ketone or alcohol, depending on the quantities of the acid and the reducing agent used. Therefore, ionic hydrogenation presented itself as a good option for the reduction of the α,β-unsaturated ketone group in compound **7**. Compounds **7** and **8** were used to study the selective reduction of the enone system to the saturated ketone using the ionic hydrogenation conditions described by Kurzanov et al. (28). When a mixture of **7** and **8** was treated with triethylsilane and trifluoroacetic acid, in a ratio of 1:1:10, respectively, in refluxing carbon tetrachloride only partial reduction was observed. A variety of reduction products was obtained along with unreacted starting material. The reaction was repeated several times using different temperatures and reaction times. Invariably, a complex mixture was formed. Kurzanov also reported (28) the direct reduction of an α,β-unsaturated ketone to the corresponding alcohol by the use of a higher concentration of triethylsilane. When a mixture of keto esters **7** and **8** was treated with 3 equivalents of triethylsilane and 10 equivalents of trifluoroacetic acid in refluxing carbon tetrachloride, the starting material was consumed in 9 h and a mixture of products was obtained. Complete separation of these products proved to be difficult. Nevertheless, a combination of crystallization and flash chromatography allowed for the separation of four major compounds **29–32**. Lactone **29** (65%) and ether **31** (29%) were produced in 94% yield from keto ester **7**, while lactone **30** (30%) and ether **32** (36%) were obtained in 66% yield from keto ester **8**. There was a small fluctuation of the ratio of each pair of the products in different experiments. However, the total yield of each pair was rather reproducible.

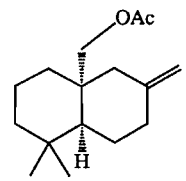

27

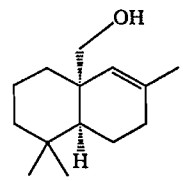

28

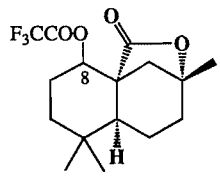

29

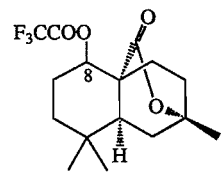

30

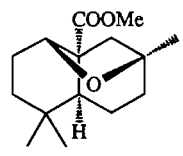

31

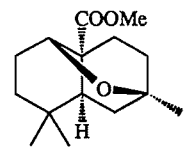

32

Lactone **29** could be purified directly by crystallization from

Can. J. Chem. Downloaded from www.nrcresearchpress.com by 85.192.166.187 on 09/08/12
For personal use only.

Can. J. Chem. Downloaded from www.nrcresearchpress.com by 85.192.166.187 on 09/08/12
For personal use only.

a petroleum ether solution of the products mixture. Recrystallization from the same solvent gave a white solid with a melting point of 132–133°C. Lactone **30** sometimes crystallized from the products mixture together with the isomeric lactone **29**. At other times it remained in the mother liquor until the separation by flash chromatography was carried out. The stereochemistry at C-8 in lactones **29** and **30** could not be unambiguously assigned. An NOE experiment on **29** including irradiation of the C-8 hydrogen did not produce any conclusive evidence.

Of the four compounds **29–32**, **29** and **31** are potentially useful for the current studies. In practice, attempted cleavage of the ether ring present in the minor compound **31** under acidic conditions failed to give any desired hydroxy lactone **33**. The conversion of trifluoroacetate lactone **29** to lactone **22**, prepared previously via a different route, requires the cleavage of a carbon–oxygen bond. The cleavage of a sterically hindered ester group has been demonstrated by Barton et al. (31) by the use of metallic lithium in ethylamine at –78°C. When lactone **29** was subjected to reduction under these conditions for 1 h the only product obtained in 56% yield was hydroxy lactone **33**.

Pète and co-workers (32) have reported that carboxylic esters are readily reduced to the hydrocarbon level in hexamethylphosphorous triamide – water (95:5) upon irradiation with 254-nm UV light. In our case irradiation of **29** with a 12-W low-pressure mercury lamp for 3 h gave again the hydroxy lactone **33** as the only product in approximately 50% yield.

In a successful indirect procedure, trifluoroacetate **29** was hydrolyzed with 10% aqueous potassium carbonate in methanol at room temperature to give hydroxy lactone **33** in almost quantitative yield after 24 h. Similar results were obtained by the use of sodium methoxide in methanol at room temperature. As expected, the reaction proceeded more rapidly and the starting material was completely consumed after 10 h. Recrystallization of **33** from ether afforded white crystals that start subliming at 105°C and have a melting point of 120°C.

Reaction of hydroxy lactone **33** with sodium hydride in 1,2-dimethoxyethane followed by addition of carbon disulfide gave the corresponding sodium xanthate, which was trapped with methyl iodide to form methyl xanthate **34** in 61% yield. The modest yield is probably due to the sterically hindered hydroxy group. Reduction of the xanthate **34** was carried out under the conditions used previously for the conversion of compounds **17** and **18** to ester **12**. Refluxing a toluene solution of xanthate **34** with tri-*n*-butyltin hydride, in the presence of a catalytic amount of azobisisobutyronitrile, gave a 71% of lactone **22** identical in all respects with the lactone obtained previously by the acid-catalyzed cyclization of ester **12**.

Application of the same reaction sequence (**29**→**33**→**34**→**22**) to the mixture of trifluoroacetate lactones **29** and **30** gave isomeric lactones **22** and **35**. The two isomeric lactones were readily separated by flash chromatography on silica gel. Based on these findings, a practical route that allowed the preparation of compound **22** in large quantity was developed as follows. An equimolar mixture of isomeric keto esters **7** and **8** was converted to esters **12** and **36** using the route developed earlier for the transformation of pure keto ester **7** to compound **12**, via hydrosilylation, sodium borohydride reduction, xanthate formation, and tri-*n*-butyltin hydride reduction. The mixture of **12** and **36** was treated with *p*-toluenesulfonic acid in benzene. Purification by flash chromatography on silica gel gave lactone **22** (41% yield) and its isomer **35** (42% yield). By the use of this synthetic sequence a large quantity of **22** was readily obtained in five simple operations with one chromatographic separation. This compound was subsequently reduced to diol **23**, which was converted to alcohol **28** via hydroxy acetate **24** and olefin **25** according to the procedure described earlier.

The conversion of alcohol **28** to the target molecule **3** requires the modification of the angular substituent. This was achieved in the following manner. Alcohol **28** was oxidized with pyridinium chlorochromate on alumina in dichloromethane. Filtration followed by careful concentration of the filtrate gave the volatile aldehyde **37** in 94% yield. Aldehyde **37** underwent a Wittig reaction with methoxymethylenetriphenylphosphorane in benzene – dimethyl sulfoxide. A 1:1 mixture of enol ethers **38** and **39** was obtained in 93% yield. Flash chromatography on silica gel pretreated with 1% triethylamine in petroleum ether and eluting with the same solvent system resulted in the separation of these isomers. The use of triethylamine was found to be crucial in order to avoid the hydrolysis of the enol ether functional group during the chromatography. The ^{1}H nmr spectrum of the faster moving isomer displays signals for the vinylic hydrogens of the enol ether moiety at δ 5.64 and 4.27. Each signal appears as a doublet with a small coupling constant of 7 Hz indicating the presence of a *Z* double bond. Accordingly, structure **38** was assigned to this compound. The protons attached to the enol ether double bond are displayed at δ 6.11 and 4.71 in the ^{1}H nmr spectrum of the more polar isomer **39**. The *E* configuration of this double bond is apparent from the large coupling constant of 13 Hz.

To complete the synthesis of isoacanthodoral it remained to hydrolyze the enol ethers **38** and **39**. During the purification of these compounds by flash chromatography on silica gel, it was observed that substantial hydrolysis occurred, apparently due to the acidity of the adsorbent. It was necessary to use triethylamine in order to circumvent this problem. However, for the conversion of enol ether moiety to the aldehyde, one would take advantage of the ability of silica gel to induce the hydrolysis for the desired conversion. To enhance the acidity of the silica gel, it was washed with glacial acetic acid and then petroleum ether. A flash chromatography of enol ethers **38** and **39** was carried out using this material with ether – petroleum ether elution. Hydrolysis indeed occurred and the desired aldehyde was formed. However, a substantial amount of the starting enol ethers was also recovered. In another experiment, silica gel was prewashed with 70% perchloric acid and then petroleum ether, and flash chromatography was carried out. In this case a greater amount of aldehyde was obtained along with the recovery of a small quantity of the enol ethers. However, a substantial loss of material also took place. In a more successful experiment, the mixture of enol ethers was applied to a column containing acetic acid-washed silica gel and the elution with 0–5% ether – petroleum ether was carried out after 24 h. In this manner, complete hydrolysis occurred and a virtually quantitative yield of the desired aldehyde was obtained. The synthetic isoacanthodoral **3** thus obtained in racemic form shows characteristic aldehyde absorptions at 2845, 2720, and 1720 cm^{-1} in the infrared spectrum. Its ^{1}H nmr spectrum shows a diagnostic aldehyde signal at δ 9.73 as a doublet of doublets (J = J' = 3 Hz) due to the coupling with the adjacent methylenic protons at δ 2.71 (dd, J = 15, J' = 3 Hz) and 2.13 (dd, J = 15, J' = 3 Hz). A slightly broad doublet (J = 1 Hz) at δ 5.23 could be readily assigned to the vinylic hydrogen. Three methyl signals are displayed at δ 1.65 (vinylic), 1.00, and 0.91 (*gem*-dimethyl), each as a singlet. A ^{13}C nmr Distortionless Enhancement by Polarization Transfer (DEPT) experi-

Can. J. Chem. Downloaded from www.nrcresearchpress.com by 85.192.166.187 on 09/08/12
For personal use only.

ment was employed to determine the multiplicity of each carbon in the molecule. On the basis of this experiment the following assignments were made: δ 204.8 (-*C*=O), 135.5 (-CH=*C*-), 129.9 (-*C*H=*C*-), 57.2 (-CH_2CHO), 46.3 (C-6), 40.1 (-CH_2-), 38.5 (-CH_2-), 38.2 (C-1), 34.2 (C-7), 32.4 (=C(CH_3)), 28.9 ((-CH_2-), 26.4 (-CH_3), 23.5 (-CH_3), 19.9 (-CH_2-), and 19.2 (-CH_2-). A molecular peak at *m/z* 220.1821 in the high-resolution mass spectrum was consistent with the molecular formula $C_{15}H_{24}O$.

A comparison of the ^{1}H nmr, ^{13}C nmr, and mass spectral data of the synthetic material with those reported (3) for the natural isoacanthodoral readily establishes that they are identical. Naturally occurring isoacanthodoral was isolated in very small quantities, sufficient only to obtain spectroscopic data (^{1}H nmr, ^{13}C nmr, and ms) (3). The complete structural assignment was carried out by means of X-ray crystallography on the 2,4-dinitrophenylhydrazone derivative (4).

To further confirm the identity of our synthetic (±)-isoacanthodoral, it was converted to the 2,4-dinitrophenylhydrazone derivative by treatment with 2,4-dinitrophenylhydrazone (3% in ethanol – water – H_2SO_4 (2:2:1)) at room temperature for 3 h. Flash chromatography of the crude product on silica gel (0–5% ether in petroleum ether), followed by recrystallization from ether – petroleum ether, gave orange needles with a melting point of 144–146°C. The spectral data of this material were found to be in good agreement with those described for the 2,4-dinitrophenylhydrazone derivative (**40**) of the natural material.

In conclusion, the marine natural product isoacanthodoral (**3**) has been synthesized in racemic form from 2-carbomethoxy-4,4-dimethyl-2,5-cyclohexadien-1-one in ca. 38% overall yield, using an intermolecular Diels–Alder approach.

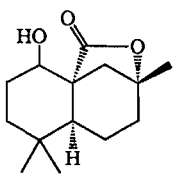

33

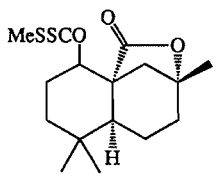

34

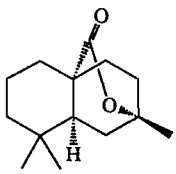

35

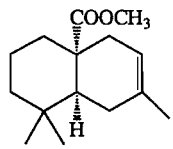

36

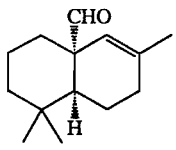

37

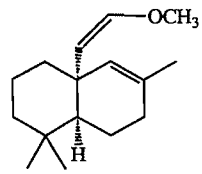

38

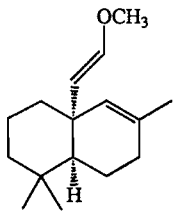

39

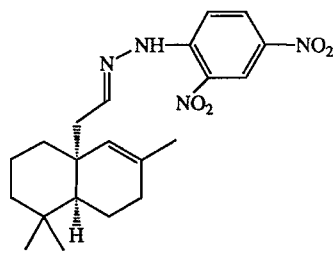

40

Experimental

General

Melting points were measured on a Köfler hot stage apparatus and are uncorrected. Elemental analyses were carried out using a Perkin Elmer 240-B for C, H, N detection. Infrared spectra (ir) were obtained on a Nicolet 7199 FTIR spectrophotometer. Mass spectra (ms) were determined using a AEI Kratos MS-50 high-resolution mass spectrometer attached to a Data General Nova 2 with Kratos DS-55 software. Proton nuclear magnetic resonance spectra (^{1}H nmr) were obtained using one of the following spectrometers: Bruker WH-200 (200 MHz), Bruker AM-300 (300 MHz), or Bruker AM-400 (400 MHz). Coupling constants are recorded to within ± 0.5 Hz. Carbon-13 nuclear magnetic resonance spectra (^{13}C nmr) were run on a Bruker AM-300 (75 MHz) or a Bruker AM-400 (100.6 MHz). Two methods were used to determine the carbon-13 multiplicities: the distortionless enhancement by polarization transfer (DEPT) experiment with proton decoupling using a Bruker software microprogram (DEPT.AUR) and the attached proton test (APT). Peaks in antiphase (a) with deuteriochloroform were assigned as methyls or methines, while peaks in phase (p) correspond to methylenes or quaternary carbons. Aldehydic carbonyls appear in antiphase with $CDCl_3$ and other carbonyls in phase with the deuteriochloroform signal. Nuclear Overhauser Enhancement (NOE) experiments were obtained after computer subtraction of the off-resonance irradiated spectrum from the irradiated spectrum. Positive enhancements are defined as signals in antiphase with the irradiated signal. Immediately before the experiment each sample was deoxygenated by passing helium gas through the solution for 10 min. Reaction yields are quoted with a degree of purity better than 95% as determined by nmr spectroscopy.

Materials

Products were purified either by flash chromatography using silica gel 60 (230–400 mesh), distillation using a Kugelrohr apparatus, or by fractional crystallization. Reactions were monitored by thin-layer chromatography using Merck aluminum-backed plates precoated with silica gel 60 GF_{254}. Solvents were dried and distilled prior to use as follows: ether and 1,2-dimethoxyethane from a blue–purple solution of sodium benzophenone ketyl under an argon atmosphere; toluene, benzene, pyridine, dichloromethane, and dimethyl sufloxide from calcium hydride or lithium hydride.

6-Bromo-6-carbomethoxy-4,4-dimethyl-2-cyclohexen-1-one (6)

6-Carbomethoxy-4,4-dimethyl-2-cyclohexen-1-one (**5**) (5.12 g, 28.12 mmol) was dissolved in carbon tetrachloride (25 mL) and the reaction vessel was protected from light. *N*-Bromosuccinimide (10.00 g, 56.24 mmol) was added to the solution. After 10 h at room temperature, the suspension was filtered and the filtrate was concentrated. The residue was distilled using a Kugelrohr apparatus (100°C/0.8 Torr; 1 Torr = 133.3 Pa) to yield **6** (6.82 g, 93%) as a pale yellow oil: ir ($CHCl_3$ cast): 1734 (ester) and 1698 (α,β-unsaturated ketone) cm^{-1}; ^{1}H nmr (200 MHz, $CDCl_3$) δ: 6.68 (dd, 1H, J = 10, J' = 2 Hz, -C*H*=CHCO), 6.05 (d, 1H, J = 10 Hz, -CH=C*H*CO), 3.82 (s, 3 H, -OCH_3), 3.03 (dd, 1 H, J = 14, J' = 2 Hz, -C*H*HCBr), 2.53 (d, J = 14 Hz, -CH*H*CBr), 1.28 (s, 3 H, -CH_3), and 1.13 (s, 3 H, -CH_3); ^{13}C nmr APT (75 MHz, $CDCl_3$) δ: 187.7 (p), 169.0 (p), 158.5 (a), 124.1 (a), 61.9 (p), 53.7 (a), 48.8 (p), 35.2 (p), 30.1 (a), and 27.6 (a); ms M^+: 260.0048 (calcd. for $C_{10}H_{13}O_3Br$: 260.0049).

2-Carbomethoxy-4,4-dimethyl-2,5-cyclohexadien-1-one (4)

Bromide **6** (6.80 g, 26.0 mmol) was dissolved in benzene (30 mL) and 1,8-diazabicyclo[5.4.0]undec-7-ene (5.8 mL, 39 mmol) was added dropwise at room temperature with stirring. After 2 h the solid, which had formed during the reaction, was removed by filtration using a sintered glass funnel packed with Florisil as filter-acid. The filtrate was extracted with ether (3 × 20 mL). The combined

Can. J. Chem. Downloaded from www.nrcresearchpress.com by 85.192.166.187 on 09/08/12
For personal use only.

organic extracts were washed successively with 5% HCl solution (2 × 20 mL), water (1 × 20 mL), saturated sodium bicarbonate solution (1 × 20 mL), and brine (1 × 20 mL). The organic solution was then dried ($MgSO_4$), filtered, and concentrated. Bulb-to-bulb distillation (100°C/0.5 Torr) of the concentrate gave 3.70 g (78%) of **4** (6) as a colorless oil.

(1R, 6S*)-1-Carbomethoxy-5,5,9-trimethylbicyclo[4.4.0]deca-3,8-dien-2-one (7) and (1R*, 6S*)-1-carbomethoxy-5,5,8-trimethylbicyclo[4.4.0]deca-3,8-dien-2-one (8)*

2-Carbomethoxy-4,4-dimethyl-2,5-cyclohexadien-1-one (**4**) (8.75 g, 48.6 mmol) was dissolved in dry ether (350 mL) and the solution cooled with an ice–water bath. Isoprene (97 mL, 0.97 mol) was added. Then boron trifluoride etherate (3 mL, 11.7 mmol) was slowly introduced into the reaction flask by means of a syringe. The reaction mixture was stirred at room temperature for 96 h. Aqueous saturated sodium bicarbonate (75 mL) was carefully added to the reaction mixture. The organic layer was separated and the aqueous layer extracted with ether (3 × 50 mL). The organic extracts were combined, washed with water (2 × 20 mL) followed by brine (1 × 20 mL), dried ($MgSO_4$), filtered, and concentrated to afford a colorless oil. Purification by flash chromatography on silica gel (0–10% ether in petroleum ether) gave a mixture of Diels–Alder adducts (11.60 g, 96%) **7** and **8** in a 7:3 ratio. The major isomer was isolated by fractional crystallization by seeding the ether solution of the mixture of the adducts with pure crystals of compound **7**, which were obtained by preparative high-pressure liquid chromatography of the mixture using a Waters Associates Prep LC/System 500 instrument charged with a silica gel cartridge, using a solution of 5% ethyl acetate in *n*-hexane as eluent. Repeated crystallization with seeding (×3) yielded 4.00 g (35%) of compound **7** (6) as white crystals: mp 97–98°C; ir ($CHCl_3$ cast): 1739 (ester) and 1667 (α,β-unsaturated ketone) cm^{-1}; ^1H nmr (400 MHz, $CDCl_3$) δ: 6.54 (d, 1 H, J = 10 Hz, -C*H*=CHCO), 5.86 (d, 1 H, J = 10 Hz, -CH=C*H*CO), 5.32 (br s, 1 H, -C(CH_3)=C*H*-), 3.72 (s, 3 H, -COOCH_3), 2.66 (ddd, 1 H, J = 6, J' = 4, J'' = 1, -C(CH_3)$_2$C*H*CH_2-), 2.49 (d, 1 H, J = 17 Hz, -C*H*HC(CH_3)=), 2.12 (d, 1 H, J = 17 Hz, -CH*H*C(CH_3)=), 2.10–2.00 (complex, 2 H, -CH_2CH=C(CH_3)-), 1.64 (s, 3 H, -C(CH_3)=CH-), 1.14 (s, 3 H, -C(CH_3)$_2$), and 0.99 (s, 3 H, -C(CH_3)$_2$); ^{13}C nmr APT (100.6 MHz, $CDCl_3$) δ: 197.3 (p), 173.1 (p), 157.8 (a), 131.3 (p), 124.1 (a), 119.3 (a), 57.6 (p), 52.4 (a), 40.6 (a), 36.1 (p), 33.3 (p), 30.5 (a), 24.4 (p), 23.8 (a), and 23.1 (a); ms M^+: 248.1418 (calcd. for $C_{15}H_{20}O_3$: 248.1412). Anal. calcd. for $C_{15}H_{20}O_3$: C 72.54, H 8.12; found: C 72.36, H 8.04. The mother liquor was found to consist of adducts **7** and **8** in nearly equal amount.

(1R, 6S*)-1-Carbomethoxy-5,5,9-trimethyl-2-triethylsiloxybicyclo-[4.4.0]deca-2,8-diene (9)*

A dichloromethane solution of keto ester **7** (3.50 g, 14 mmol) was allowed to evaporate to dryness slowly in order to produce very fine crystals. These were suspended in triethylsilane (4.5 mL, 28 mmol), and tris(triphenylphosphine)rhodium(I) chloride (64 mg, 0.07 mmol) was added. The slurry was stirred for 5 h at room temperature, then additional triethylsilane (4.5 mL, 28 mmol) was added. The reaction mixture was stirred overnight, after which time all the solid keto ester dissolved. The reaction mixture was diluted with petroleum ether, filtered through Florisil contained in a sintered glass funnel, and concentrated under reduced pressure. Purification of the residue by flash chromatography on silica gel (0–10% ether in petroleum ether) gave silyl enol ether **9** (4.95 g, 97%) as a colorless oil: ir ($CHCl_3$ cast): 1742, 1729 (ester) and 1670 (olefin) cm^{-1}; ^1H nmr (400 MHz, $CDCl_3$) δ: 5.35 (br s, 1 H, -C=C*H*-), 4.67 (dd, 1 H, J = 6, J' = 2 Hz, -SiO-C=C*H*-), 3.65 (s, 3 H, -COOCH_3), 2.66 (br, d, 1 H, J = 17 Hz, -SiOC=CHC*H*H-), 2.25–1.90 (complex, 5 H), 1.79 (dd, 1 H, J = 17, J' = 6 Hz, -SiOC=CHCH*H*-), 1.67 (br s, 3 H, =CCH_3), 0.97 (complex, 15 H, -C(CH_3)$_2$ and -Si(CH_2CH_3)$_3$, and 0.66 (q, 6 H, J = 7 Hz, -Si(CH_2CH_3)$_3$); ^{13}C nmr APT (100.6 MHz, $CDCl_3$) δ: 176.3 (p), 151.0 (p), 131.9 (p), 118.8 (a), 99.1 (a), 51.9 (a), 51.5 (p), 42.1 (a), 39.7 (p), 35.1 (p), 32.3 (p), 31.0 (a), 23.5 (p), 23.3 (a), 22.6 (a), 6.7 (a), and 5.1 (p); ms M^+: 364.2440 (calcd. for $C_{21}H_{36}O_3Si$: 364.2434).

(1R, 6S*)-1-Carbomethoxy-5,5,9-trimethylbicyclo[4.4.0]deca-8-en-2-one (10)*

Silyl enol ether **9** (1.00 g, 2.75 mmol) was dissolved in methanol and a 10% aqueous solution of potassium bicarbonate (50 mL) was added. The mixture was stirred at room temperature for 10 h, then poured into water. The water layer was extracted with dichloromethane (3 × 10 mL). The combined organic extracts were washed successively with water (2 × 10 mL) and brine solution (1 × 10 mL), then dried ($MgSO_4$), filtered, and concentrated. Purification of the residue by flash chromatography on silica gel (0–5% ethyl acetate in petroleum ether) gave a quantitative yield of keto ester **10** (0.69 g) as white crystals: mp 41–42°C; ir (neat): 1743, 1731 (ester) and 1711 (ketone) cm^{-1}; ^1H nmr (300 MHz, $CDCl_3$) δ: 5.32 (br s, 1 H, -C=C*H*-), 3.70 (s, 3 H -COOCH_3), 2.60–2.45 (complex, 3 H), 2.37 (br s, 2H), 2.10 (complex d, 1 H, J = 18 Hz, -C*H*HCH=C(CH_3)-), 1.90 (complex d, 1 H, J = 18 Hz, -CH*H*CH=C(CH_3)-), 1.82 (dd, 1 H, J = 7, J' = 6 Hz), 1.72 (dd, 1H, J = 9, J' = 6 Hz), 1.68 (s, 3 H, -C(CH_3)=CH-), 1.10 (s, 3 H, -CH_3), and 1.02 (s, 3 H, -CH_3); ^{13}C nmr APT (75.5 MHz, $CDCl_3$) δ: 207.3 (p), 172.9 (p), 129.8 (p), 118.4 (a), 59.6 (p), 51.6 (a), 43.4 (a), 37.5 (p), 34.9 (p), 33.0 (p), 32.6 (p), 29.8 (a), 23.6 (p), 23.5 (a), and 22.4 (p); ms M^+: 250.1578 (calcd. for $C_{15}H_{22}O_3$: 250.1569). Anal. calcd. for $C_{15}H_{22}O_3$: C 71.95, H 8.86; found: C 71.64, H 8.78.

(1R, 2R*, 6S*)-1-Carbomethoxy-5,5,9-trimethylbicyclo[4.4.0]dec-8-en-2-ol (14), (1R*, 2S*, 6S*)-1-carbomethoxy-5,5,9-trimethylbicyclo[4.4.0]dec-8-en-2-ol (15) and (1R*, 6S*)-1-hydroxymethyl-5,5,9-trimethylbicyclo[4.4.0]dec-8-en-2-ol (16)*

Sodium borohydride (0.46 g, 12.2 mmol) was slowly added during 30 min to a stirred, cooled (–40°C) solution of keto ester **10** (1.80 g, 7.2 mmol) in methanol (15 mL). The reaction mixture was left to react for 15 min, a saturated aqueous solution of ammonium chloride (1 mL) was added and the resulting mixture allowed to warm to room temperature. The mixture was extracted with dichloromethane (2 × 10 mL). The combined organic extracts were washed with water (2 × 5 mL) and brine (1 × 5 mL), dried ($MgSO_4$), filtered, and concentrated. Purification of the concentrate by flash chromatography on silica gel (0–30% ethyl acetate in petroleum ether) led to the isolation of two epimeric alcohols **14** and **15** (1.70 g, 95%) in a ratio of 5:1. The major alcohol (**14**) was obtained as a colorless oil: ir ($CHCl_3$ cast): 3470 (alcohol) and 1737 (ester) cm^{-1}; ^1H nmr (400 MHz, $CDCl_3$) δ: 5.27 (br s, 1 H, -C(CH_3)=C*H*-), 3.90 (ddd, 1 H, J = 9, J' = 7, J'' = 4 Hz, -C*H*OH), 3.72 (s, 3 H, -OCH_3), 2.45 (d, 1 H, J = 16 Hz, -C*H*HC(CH_3)=), 2.12 (d, 1 H, J = 16 Hz, -CH*H*C(CH_3)=), 2.05 (m, 2 H, -CH_2CH=), 1.93 (dd, 1 H, J = 7, J' = 1.5 Hz, -C(CH_3)$_2$C*H*CH_2-), 1.88 (d, 1 H, J = 4 Hz, -O*H*), 1.73 (dd, 1 H, J = 4, J' = 2 Hz, -C*H*HCHOH), 1.70 (dd, 1 H, J = 7, J' = 4 Hz, -CH*H*CHOH), 1.68 (s, 3 H, -C(CH_3)=CH-), 1.47 (ddd, 1 H, J = 13.5, J' = 3.5, J'' = 3.5 Hz, -C*H*HC(CH_3)$_2$-), 1.40 (ddd, 1 H, J = 13.5, J' = 10, J'' = 7 Hz, -CH*H*C(CH_3)$_2$-), 0.94 (s, 3 H, -CH_3), and 0.83 (s, 3 H, -CH_3); ^{13}C nmr APT (75.5 MHz, $CDCl_3$) δ: 177.6 (p), 131.8 (p), 119.7 (a), 75.4 (a), 52.4 (p), 52.2 (a), 41.9 (a), 39.3 (p), 33.1 (p), 32.8 (a), 28.5 (p), 27.2 (p), 24.4 (p), 23.5 (a), and 21.7 (a); ms M^+: 252.1729 (calcd. for $C_{15}H_{24}O_3$: 252.1726). The minor alcohol **15** was obtained as white needles: mp 42–44°C; ir ($CHCl_3$ cast): 3529 (alcohol) and 1739 (ester) cm^{-1}; ^1H nmr (400 MHz, $CDCl_3$) δ 5.35 (br s, 1 H, -C(CH_3)=C*H*-), 3.70 (s, 3 H, -OCH_3), 3.60 (ddd, 1 H, J = 10, J' = 7, J'' = 7 Hz, -C*H*OH), 3.06 (br s, 1 H, -O*H*), 2.49 (d, 1 H, J = 17 Hz, -C*H*HC (CH_3)=CH-), 2.30–2.15 (complex, 3 H, -CH*H*C(CH_3)=CH-, -C(CH_3)$_2$C*H*CH_2- and -CH*H*CH=C(CH_3)-), 2.00 (m, 1 H, -C*H*H-CH=), 1.87 (dd, 2 H, J = 13, J' = 7 Hz, -CH_2CHOH), 1.66 (br s, 3 H, -C(CH_3)=CH-), 1.54 (ddd, 1 H, J = 14, J' = 14, J'' = 7 Hz, -CH*H*C(CH_3)$_2$-), 1.40 (ddd, 1 H, J = 14, J' = 5.5, J'' = 5 Hz, -C*H*HC(CH_3)$_2$-), 0.96 (s, 3 H, -CH_3), and 0.89 (s, 3 H, -CH_3); ^{13}C nmr APT (75.5 MHz, $CDCl_3$) δ: 178.8 (p), 129.6 (p), 119.8 (a), 69.7 (a), 51.4 (a), 49.7 (p), 40.4 (a), 35.3 (p), 33.7 (p), 33.5 (p), 29.5 (a), 27.8 (p), 24.7 (p), and 23.1 (a); Further elution gave diol **16** in 3–5% yield. Recrystallization from acetone gave white needles, which started subliming at 150°C: ir (Nujol): 3290 (alcohol) cm^{-1}; ^1H nmr (400 MHz, CD_3OD) δ: 5.22 (br s, 1 H, -C(CH_3)=CH-), 4.51 (br s, 1 H, -O*H*), 3.65 (dd, 1 H, J = 12, J' = 4 Hz, -C*H*OH), 3.53 (d, 1 H, J = 10 Hz,

Can. J. Chem. Downloaded from www.nrcresearchpress.com by 85.192.166.187 on 09/08/12
For personal use only.

-C*H*HOH), 3.26 (d, 1 H, J = 10 Hz, -CH*H*OH), 3.22 (br d, 1 H, J = 1 Hz, -O*H*), 2.00–1.30 (complex, 9 H), 1.54 (s, 3 H, -C(C*H*$_3$)=CH-), 0.82 (s, 3 H, -C*H*$_3$), and 0.75 (s, 3 H, -CH$_3$); ^{13}C nmr (100.6 MHz, CD_3OD) δ: 132.5, 121.2, 121.0, 74.7, 67.4, 43.1, 40.9, 34.5, 33.4, 30.5, 27.7, 24.2, 24.0, and 22.4; ms M$^+$: 224.1774 (calcd. for $C_{14}H_{24}O_2$: 224.1777).

(1R, 2R*, 6S*)-1-Carbomethoxy-3,7,7-trimethyl-10-(methylmercaptothiocarbonyloxy)bicyclo[4.4.0]dec-3-ene (**17**), and (1R*, 6S*, 10S*)-1-carbomethoxy-3,7,7-trimethyl-10-(methylmercaptothiocarbonyloxy)bicyclo[4.4.0]dec-3-ene (**18**)*

Sodium hydride (80% dispersion in mineral oil, 0.95 g, 32 mmol) was slowly added to a cooled (0°C) solution of hydroxy ester **14** or **15** (or the mixture of both) (2.00 g, 7.94 mmol) in 1,2-dimethoxyethane (34 mL). After 20 min carbon disulfide (1.8 mL, 29.8 mmol) was introduced to the reaction vessel, followed by methyl iodide (6.2 mL, 100 mmol). The reaction mixture was then allowed to warm up to room temperature. After 10 h of stirring the solution was poured into ice-water. The aqueous layer was extracted with ether (3 × 15 mL). The combined ether extracts were washed with water (1 × 15 mL) and brine (1 × 15 mL), dried ($MgSO_4$), filtered, and concentrated. Purification of the concentrate by flash chromatography on silica gel (0–10% ether in petroleum ether) gave a quantitative yield of the xanthate **17** or **18** (or the epimeric mixture) (2.70 g). Compound **17** was isolated as a yellow oil: ir ($CHCl_3$ cast): 1737 (ester) and 1240 (xanthate) cm^{-1}; ^{1}H nmr (400 MHz, $CDCl_3$) δ: 5.96 (dd, 1 H, J = 11.5, J' = 4.5 Hz, -C*H*OCSSCH$_3$), 5.26 (br s, 1 H, -C(CH$_3$)=C*H*-), 3.62 (s, 3 H, -OC*H*$_3$), 2.54 (d, 1 H, J = 18 Hz, -CH*H*C(CH$_3$)=CH-), 2.52 (s, 3 H, -SCH$_3$), 2.28 (d, 1 H, J = 18 Hz, -C*H*HC(CH$_3$)=CH-), 1.98–2.06 (complex, 4 H, -C(CH$_3$)$_2$C*H*CH$_2$-, -CHC*H*$_2$CH=, and -C*H*HCHO), 1.79 (dddd, 1 H, J = 12, J' = 12, J'' = 8.5, J''' = 8.5 Hz, -CH*H*CHO), 1.69 (s, 3 H, -C(C*H*$_3$)=CH-), 1.52 (dd, 2 H, J = 8.5 J' = 3.5 Hz, -C*H*$_2$C(CH$_3$)$_2$CH-), 0.96 (s, 3 H, -C*H*$_3$), and 0.87 (s, 3 H, -C*H*$_3$); ^{13}C nmr APT (75.5 MHz, $CDCl_3$) δ: 214.9 (p), 175.5 (p), 131.9 (p), 119.3 (a), 86.8 (a), 52.5 (a), 51.1 (p), 42.6 (a), 38.9 (p), 33.1 (p), 32.6 (a), 29.8 (p), 24.1 (p), 23.6 (a), 23.4 (p), 21.9 (a), and 18.8 (a); ms M$^+$: 342.1315 (calcd. for $C_{17}H_{26}O_3S_2$: 342.1338). Compound **18** was isolated as a red oil: ir ($CHCl_3$ cast): 1738 (ester) and 1232 (xanthate) cm^{-1}; ^{1}H nmr (400 MHz, $CDCl_3$) δ: 5.74 (dd, 1 H, J = J' = 3 Hz, -C*H*OCSSCH$_3$), 52.8 (br s, 1 H, -C(CH$_3$)=C*H*-), 3.55 (s, 3 H, -OC*H*$_3$), 2.55–2.45 (m, 1 H, -C*H*HCHO-), 2.50 (s, 3 H, -SC*H*$_3$), 2.34 (d, 1 H, J = 18 Hz, -C*H*HC(CH$_3$)=), 2.26 (d, 1 H, J = 8 Hz, -CH*H*CHO-), 2.13 (d, 1 H, J = 18 Hz, -CH*H*C(CH$_3$)=), 2.06 (br s, 1 H, -C(CH$_3$)$_2$C*H*CH$_2$-), 2.00 (ddd, 1 H, J = 15, J' = 7, J'' = 4 Hz, -CHC*H*HCH=), 1.88 (ddd, 1 H, J = 14, J' = 4, J'' = 2 Hz, -CHCH*H*CH=), 1.54 (s, 3 H, -CH$_2$C(C*H*$_3$)=CH-), 1.46 (ddd, 1 H, J = 14, J' = 13, J'' = 4 Hz, -C*H*HC(CH$_3$)$_2$-), 1.23 (ddd, 1 H, J = 14, J' = 4, J'' = 4 Hz, -CH*H*C(CH$_3$)$_2$-), 0.96 (s, 3 H, -C*H*$_3$), and 0.81 (s, 3 H, -CH$_3$); ^{13}C nmr APT (75.5 MHz, $CDCl_3$) δ: 213.9 (p), 174.6 (p), 129.3 (p), 121.7 (a), 84.1 (a), 52.0 (a), 50.2 (p), 37.8 (a), 34.9 (p), 34.0 (p), 33.3 (p), 32.9 (a), 24.3 (p), 23.5 (a), 22.2 (p), 21.5 (a), and 18.4 (a).

(1R, 6S*)-1-Carbomethoxy-3,7,7-trimethylbicyclo[4.4.0]dec-3-ene (**12**)*

Argon was bubbled for 30 min through a solution of xanthate **17** or **18** (or the mixture) (2.60 g, 7.7 mmol) in dry toluene (100 mL), then tri-*n*-butyltin hydride (3.10 mL, 11.5 mmol) was added followed by a catalytic amount of azobisisobutyronitrile (54 mg, 0.33 mmol). The solution was refluxed for 10 h, cooled down, and concentrated under reduced pressure. Purification of the residue by flash chromatography on silica gel (0–5% ether in petroleum ether) gave ester **12** (1.73 g, 95% yield) as a colorless oil: ir (neat): 1730 (ester) cm^{-1}; ^{1}H nmr (400 MHz, $CDCl_3$) δ: 5.30 (br s, 1 H, -C(CH$_3$)=C*H*-), 3.68 (s, 3 H, -OC*H*$_3$), 2.32 (d, 1 H, J = 18 Hz), 2.20–2.00 (complex, 3 H), 1.64 (s, 3 H, -CH$_2$C(C*H*$_3$)=), 1.60–1.50 (complex, 4 H), 1.45 (m, 1 H), 1.36 (dddd, 1 H, J = 15, J' = 15, J'' = 7, J''' = 2 Hz), 1.24 (m, 1 H), 0.96 (s, 3 H, -C*H*$_3$), and 0.88 (s, 3 H, -C*H*$_3$); ^{13}C nmr APT (100.6 MHz, $CDCl_3$) δ: 178.8 (p), 131.2 (p), 119.8 (a), 51.6 (a), 46.2 (p), 41.3 (a), 39.2 (p), 36.4 (p), 33.5 (p), 31.7 (a), 24.7 (p), 24.1 (a), 23.3 (a), and 18.9 (p); ms M$^+$: 236.1780 (calcd. for $C_{15}H_{24}O_2$: 236.1776).

(1R, 6S*)-1-Hydroxymethyl-3,7,7-trimethylbicyclo[4.4.0]dec-3-ene (**20**)*

Lithium aluminum hydride (0.20 g, 5.27 mmol) was slowly added to a cooled (ice-water) ether solution (8 mL) of ester **12** (0.24 g, 1.03 mmol). The solution was stirred for 3 h at room temperature before it was poured into a saturated aqueous ammonium chloride solution (5 mL). The organic layer was separated and the aqueous layer extracted with dichloromethane (3 × 5 mL). The combined organic extracts were washed with water (2 × 5 mL) and brine (2 × 5 mL), dried ($MgSO_4$), filtered, and concentrated. Purification of the concentrate by flash column chromatography (0–15% ether in petroleum ether) gave alcohol **20** (0.21 g, 96%) as a crystalline solid: mp 67–68°C; ir ($CHCl_3$ cast) 3280 cm^{-1} (alcohol); ^{1}H nmr (400 MHz, $CDCl_3$) δ: 5.29 (ddd, 1 H, J = 7, J' = 3, J'' = 1.5 Hz, -C(CH$_3$)=C*H*-), 3.39 (d, 1 H, J = 10 Hz, -C*H*HOH), 3.27 (d, 1 H, J = 10 Hz, -CH*H*OH), 2.16–2.00 (complex, 3 H), 1.62 (s, 3 H, -C(C*H*$_3$)=CH-), 1.50–1.10 (complex, 9 H), 0.94 (s, 3 H, -C*H*$_3$), and 0.84 (s, 3 H, -C*H*$_3$); ^{13}C nmr APT (100.6 MHz, $CDCl_3$) δ: 131.6 (p), 119.7 (a), 71.4 (p), 42.4 (p), 41.2 (a), 37.4 (p), 34.4 (p), 34.3 (p), 33.7 (p), 33.3 (a), 23.6 (a), 23.5 (p), 21.8 (a), and 18.3 (p); ms M$^+$: 208.1833 (calcd. for $C_{14}H_{24}O$: 208.1827). Anal. calcd. for $C_{14}H_{24}O$: C 80.70, H 11.62; found: C 80.87, H 11.65.

(1R, 6S*)-1-Formyl-3,7,7-trimethylbicyclo[4.4.0]dec-3-ene (**19**)*

Pyridinium chlorochromate impregnated on alumina (1.19 g, 0.93 mmol/g) was added to a solution of alcohol **20** (114 mg, 0.55 mmol) in dry dichloromethane (7 mL). The reaction mixture was stirred at room temperature for 2 h, and filtered through Florisil using a sintered-glass filter. The reaction mixture was washed with dichloromethane (10 mL). Concentration of the dichloromethane solution, using a rotary evaporator under slightly reduced pressure (the compound is rather volatile), afforded a colorless oil, which was pure as demonstrated by nmr analysis (99 mg, 88%); ir (neat): 2840, 2700 and 1724 (aldehyde) cm^{-1}; ^{1}H nmr (400 MHz, $CDCl_3$) δ: 9.32 (s, 1 H, -C*H*O), 5.32 (br s, 1 H, -C(CH$_3$)=C*H*-), 2.10–1.90 (complex, 4H), 1.67 (s, 3 H, -C(C*H*$_3$)=CH-), 1.70–1.44 (complex, 5 H), 1.35 (m, 1 H), 1.24 (m, 1 H), 0.96 (s, 3 H, -C*H*$_3$), and 0.86 (s, 3 H, -C*H*$_3$); ^{13}C nmr APT (75.5 MHz, $CDCl_3$) δ: 205.6 (a), 130.7 (p), 120.5 (a), 49.1 (p), 40.6 (a), 39.4 (p), 33.3 (p), 31.7 (a), 29.8 (p), 24.2 (a), 23.9 (a), 23.5 (p), and 18.2 (p); ms M$^+$: 206.1673 (calcd. for $C_{14}H_{22}O$: 206.1670). Anal. calcd. for $C_{14}H_{22}O$: C 81.48, H 10.75; found: C 81.62, H 10.70.

(1R, 6S*)-1-(2-Methoxyethenyl)-3,7,7-trimethylbicyclo[4.4.0]dec-3-ene (**21**)*

Potassium hydride (35% oil dispersion, 0.105 g, 1.04 mmol) was washed with ether (3 × 1 mL), and the washings were discarded. The dry potassium hydride was covered with benzene (1 mL), then dimethyl sulfoxide (0.55 mL) was added at room temperature. After all of the solid had dissolved, a solution of (methoxymethyl)triphenylphosphonium chloride (374 mg, 1.09 mmol) in benzene (0.5 mL) was added and the resulting mixture allowed to react until a deep red-burgundy color solution developed (about 30 min). Aldehyde **19** (41 mg, 0.2 mmol) in benzene (0.5 mL) was added slowly and the reaction mixture was stirred for 10 h. The reaction mixture was poured into ice-water and extracted with ether (4 × 2 mL). The organic extracts were combined, washed with water (1 × 2 mL) and brine (1 × 2 mL), dried ($MgSO_4$), filtered, and concentrated to yield a colorless oil. Purification of the oil by bulb-to-bulb distillation (100°C/1 Torr) gave 45.5 mg (98%) of a 1:1 mixture of enol ethers **21**; ir (neat): 1651 (olefin) and 1205 (ether) cm^{-1}; ^{1}H nmr (400 MHz, $CDCl_3$) δ: 6.18, 5.63 (d, 1 H, J = 13 Hz; d, 1 H, J = 7.5 Hz, -CH=C*H*OCH$_3$), 5.32 (br s, 2 H, -C(CH$_3$)=C*H*-), 4.77, 4.17 (d, 1 H, J = 13 Hz; d, 1 H, J = 7.5 Hz, -CH=C*H*OCH$_3$), 3.52, 3.48 (both s, 3 H each, -CH=CHOC*H*$_3$), 2.32–2.12 (complex, 4 H), 2.05 (br d, 2 H, J = 18 Hz), 1.85 (br d, 1 H, J = 16.5 Hz), 1.61 (br s, 6 H, -C(C*H*$_3$)=CH-), 1.70–1.05 (complex, 15 H), 0.92, 0.90, 0.83, and 0.81 (all s, 3 H each, 4 × -C*H*$_3$); ^{13}C nmr (100.6 MHz, $CDCl_3$) δ: 145.1, 144.6, 132.4, 131.3, 120.7 120.2, 118.6, 116.0, 59.6, 55.9, 47.0, 44.7, 42.2, 41.6, 39.2, 38.1, 37.8, 36.9, 36.6, 36.2, 34.0, 33.9, 33.6, 24.4, 24.2, 23.9, 23.6, 22.5, 22.3, 19.2, and 18.8; ms M$^+$: 234.1984 (calcd. for $C_{16}H_{26}O$: 234.1984).

Can. J. Chem. Downloaded from www.nrcresearchpress.com by 85.192.166.187 on 09/08/12
For personal use only.

(1R, 4S*, 9R*)-1,5,5-Trimethyl-11-oxa-tricyclo[7.2.1.0^{4,9}]dodecan-10-one (**22**)*

*A. From ester **12***

p-Toluensulfonic acid monohydrate (450 mg, 2.40 mmol) was added to a solution of ester **12** (0.23 g, 0.96 mmol) in benzene (5 mL). The reaction mixture was refluxed for 3 h with removal of water by means of a Dean–Stark trap. The solution was cooled, washed successively with saturated sodium bicarbonate solution (1 × 3 mL), water (2 × 3 mL), and brine (1 × 3 mL), dried ($MgSO_4$), filtered, and concentrated. Purification by recrystallization from petroleum ether or by flash chromatography on silica gel (0–3% ether in petroleum ether) gave lactone **22** (177 mg, 90%) as white needles: mp 87–88°C; ir (CH_2Cl_2 cast): 1753 (lactone) cm^{-1}; ^{1}H nmr (400 MHz, $CDCl_3$) δ: 2.38 (d, 1 H, J = 12 Hz, -CC*H*HC(CH_3)O-), 1.90–1.70 (complex, 4 H), 1.62 (complex, 2 H), 1.60–1.46 (complex, 3 H), 1.45 (s, 3 H, -CH_2C(CH_3)O-), 1.40–1.20 (complex, 3 H), 1.01 (s, 3 H, -CH_3), and 0.95 (s, 3 H, -CH_3); ^{13}C nmr APT (75.5 MHz, $CDCl_3$) δ: 181.0 (p), 82.8 (p), 49.5 (p), 43.6 (p), 42.8 (a), 40.8 (p), 34.6 (p), 33.2 (p), 33.1 (a), 32.8 (p), 25.3 (a), 22.7 (a), 19.5 (p), and 19.2 (p); ms M$^+$: 222.1619 (calcd. for $C_{14}H_{22}O_2$: 222.1619). Anal. calcd. for $C_{14}H_{22}O_2$: C 75.62, H 9.98; found: C 75.64, H 9.95.

*B. From xanthate **34***

Tri-*n*-butyltin hydride (75 mg, 0.25 mmol) and a catalytic amount of azoisobutyronitrile (~10 mg) were added to a solution of xanthate **34** (56 mg, 0.17 mmol) in toluene. Argon was bubbled through the solution for 20 min, then the reaction mixture was refluxed for 10h. Concentration of the solution in vacuo and purification of the product by flash chromatography on silica gel (0–15% ether in petroleum ether) gave lactone **22** (27 mg, 71%).

(1R, 3R*, 6S*)-1-Hydroxymethyl-3,7,7-trimethylbicyclo[4.4.0]-decan-3-ol (**23**)*

A solution of lactone **22** (1.84 g, 8.3 mmol) in ether (60 mL) was cooled in an ice-water bath. After 10 min, lithium aluminum hydride (1.55 g, 40.8 mmol) was carefully added and the resulting mixture allowed to warm to room temperature. After 1 h the reaction mixture was cooled with an ice-water bath. After an addition 1 h, water (10 mL) was slowly added, followed by aqueous 10% sodium hydroxide (10 mL) and then water again (10 mL). The resulting mixture was filtered. The water layer was extracted with ethyl acetate (3 × 15 mL). The organic layers were combined, washed with water (2 × 5 mL) and brine (1 × 5 mL), dried ($MgSO_4$), filtered, and concentrated. Crystallization of the concentrate from petroleum ether gave diol **23** (1.82 g, 97%) as a crystalline solid: ir ($CHCl_3$ cast): 3349 (alcohol) cm^{-1}; ^{1}H nmr (300 MHz, $CDCl_3$) δ: 3.98 (d, 1 H, J = 11 Hz, -C*H*HOH), 3.14 (d, 1 H, J = 11 Hz, -CH*H*OH), 1.97 (m, 2 H, -CH_2C(CH_3)OH), 1.80–1.30 (complex, 10 H), 1.23 (s, 3 H, -C(CH_3)OH), 1.20–1.10 (br d, 1 H, J = 6 Hz), 0.98 (s, 3 H, -CH_3), and 0.95 (s, 3 H, -CH_3); ^{13}C nmr APT (75.5 MHz, $CDCl_3$) δ: 74.1 (p), 70.6 (p), 43.0 (p), 42.6 (a), 40.5 (p), 38.7 (p), 37.9 (p), 36.2 (p), 34.3 (p), 33.4 (a), 33.2 (a), 26.8 (a), 19.3 (p), and 18.2 (p); ms M$^+$: 226.1924 (calcd. for $C_{14}H_{26}O_2$: 226.1933). Anal. calcd. for $C_{14}H_{26}O_2$: C 74.27, H 11.58; found: C 73.87, H 11.43.

(1R, 3R*, 6S*)-1-Acetoxymethyl-3,7,7-trimethylbicyclo[4.4.0]-decan-3-ol (**24**)*

Diol **23** (1.80 g, 8.05 mmol) was dissolved in pyridine (10 mL) at room temperature. Acetic anhydride (7.6 mL, 80.5 mmol) was added and the reaction mixture stirred overnight. Methanol (4 mL) was added and the resulting mixture was stirred for an additional 3 h before water (10 mL) was added. The mixture was extracted with ether (3 × 10 mL). The organic extracts were combined and washed successively with aqueous 5% HCl solution (2 × 10 mL), water (2 × 10 mL), and brine (1 × 5 mL), dried ($MgSO_4$), filtered, and concentrated. The oily residue was purified by flash chromatography on silica gel (0–10% ethyl acetate in petroleum ether) to afford hydroxy acetate **24** as a colorless oil (1.95 g, 90%): ir ($CHCl_3$ cast): 3480 (alcohol), 1737 and 1720 (acetate) cm^{-1}; ^{1}H nmr (300 MHz, $CDCl_3$) δ: 4.31 (d, 1 H, J = 11 Hz, -C*H*HOAc), 4.14 (d, 1H, J = 11 Hz, -CH*H*OAc), 2.07 (s, 3 H, -COCH_3), 2.00–1.80 (m, 1H), 1.73 (dd, 1 H, J = 14, J' = 4 Hz), 1.67 (dd, 1 H, J = 6, J' = 4 Hz), 1.50–1.28 (complex, 7 H), 1.22 (s, 3 H, -C(CH_3)OH), 1.27 –1.10 (complex, 3 H), 0.98 (s, 3 H, -CH_3), and 0.97 (s, 3 H, -CH_3); ^{13}C nmr APT (75.5 MHz, $CDCl_3$) δ: 171.4 (p), 73.1 (p), 70.2 (p), 42.5 (p), 42.3 (a), 42.1 (p), 37.1 (p), 36.3 (p), 35.9 (p), 34.3 (p), 33.2 (a), 33.1 (a), 27.3 (a), 21.2 (a), 19.4 (p), and 18.1 (p); ms M$^+$: 268.2033 (calcd. for $C_{16}H_{28}O_3$: 268.2039).

(1R, 6R*)-1-Acetoxymethyl-3,7,7-trimethylbicyclo[4.4.0]dec-2-ene (**25**) and (1R*, 6S*)-1-acetoxymethyl-3,7,7-trimethylbicyclo-[4.4.0]dec-3-ene (**26**)*

Hydroxy acetate **24** (1.39 g, 5.18 mmol) and 4-dimethylaminopyridine (3.16 g, 25.9 mmol) were dissolved in a solution of dry pyridine (55 mL). After cooling the solution to –40°C, phosphorus oxychloride (4.80 mL, 51.8 mmol) was added and the mixture allowed to react at –40°C for 12 h. The reaction was quenched with water (5 mL). The resulting solution was allowed to warm to room temperature and extracted with dichloromethane (3 × 15 mL). The extracts were combined, washed successively with aqueous 5% HCl solution (3 × 20 mL), water (2 × 10 mL), and brine (1 × 10 mL), dried ($MgSO_4$), filtered, and concentrated. A colorless oil, which did not require further purification, was obtained (1.25 g, 97%). It consisted of separable acetate **25** and **26** in a ratio of 3:1 (ratio obtained by ^{1}H nmr area integration); ir ($CHCl_3$ cast): 1742 and 1735 (acetate) cm^{-1}; ^{1}H nmr (300 MHz, $CDCl_3$), major isomer **25**: δ: 5.05 (br s, 1 H, -C*H*=C(CH_3)-), 3.96 (d, 1 H, J = 10.5 Hz, -C*H*HOAc), 3.75 (d, 1 H, J = 10.5 Hz, -CH*H*OAc), 2.22 (br s, 1 H, -C*H*HC(CH_3)=), 2.16 (br s, 1 H, -CH*H*C(CH_3)=), 2.05 (s, 3 H, -COCH_3), 1.62 (d, 3 H, J = 1 Hz, -C(CH_3)=CH-), 1.50–1.00 (complex, 9 H), 0.96 (s, 3 H, -CH_3), and 0.92 (s, 3 H, -CH_3); minor isomer **26**: δ: 5.28 (br s, 1 H, -C(CH_3)=C*H*-), 3.87 (d, 1 H, J = 10.5 Hz, -C*H*HOAc), 3.78 (d, 1 H, J = 10.5 Hz, -CH*H*OAc), 2.24 (br s, 1 H, -C*H*HC(CH_3)=), 2.18 (s, 1 H, -CH*H*C(CH_3)=), 2.08 (s, 3 H, -COCH_3), 1.60 (d, 3 H, J = 1 Hz, -CH=C(CH_3)-), 0.92 (s, 3 H, -CH_3), and 0.83 (s, 3 H, -CH_3), other peaks were overlapped with those of the major isomer; ^{13}C nmr APT (75.5 MHz, $CDCl_3$), major isomer **25**; δ: 171.3 (p), 137.0 (p), 120.5 (a), 71.4 (p), 41.6 (p), 41.5 (a), 35.4 (p), 34.7 (p), 34.3 (p), 33.9 (p), 32.6 (a), 23.5 (a), 23.4 (p), 21.7 (a), 21.0 (a), and 18.2 (p); minor isomer **26**: δ: 171.4 (p), 131.2 (p), 119.9 (a), 72.2 (p), 42.2 (p), 36.1 (p), 33.8 (p), 33.4 (a), 23.6 (a), and 18.2 (p), other peaks were overlapped with those of the major isomer; ms M$^+$: 250.1930 (calcd. for $C_{16}H_{26}O_2$: 250.1933).

(1R, 6S*)-1-Hydroxymethyl-3,7,7-trimethylbicyclo[4.4.0]dec-2-ene (**28**) and (1R*, 6S*)-1-hydroxymethyl-3,7,7-trimethylbicyclo-[4.4.0]dec-3-ene (**20**)*

The mixture of acetates **25** and **26** (1.43 g, 5.7 mmol) was dissolved in methanol (15 mL) at room temperature and a saturated aqueous solution of potassium carbonate (15 mL) was added. The mixture was refluxed for 2.5 h and then cooled. Methanol was removed under reduced pressure and the remaining aqueous solution was extracted with ethyl acetate (3 × 10 mL). The combined extracts were washed with water (2 × 10 mL) and brine (1 × 5 mL), dried ($MgSO_4$), filtered, and concentrated. Purification of the concentrate by flash chromatography on silica gel (0–3% ether and 1% of 2-propanol in petroleum ether) gave alcohol **20** (270 mg, 22%) as a crystalline solid. Further elution gave alcohol **28** (835 mg, 70%) as a colorless oil; ir ($CHCl_3$ cast): 3256 (alcohol) cm^{-1}; ^{1}H nmr (300 MHz, $CDCl_3$) δ: 5.01 (br s, 1 H, -C*H*=C(CH_3)-), 3.43 (d, 1 H, J = 11 Hz, -C*H*HOH), 3.27 (d, 1 H, J = 11 Hz, -CH*H*OH), 1.94 (complex, 3 H), 1.80–1.70 (m, 1 H), 1.75 (s, 3 H, -CH=C(CH_3)-), 1.55–1.10 (complex, 8 H), 1.00 (s, 3 H, -CH_3), and 0.91 (s, 3 H, -CH_3); ^{13}C nmr APT (75.5 MHz, $CDCl_3$) δ: 137.6 (p), 128.3 (a), 71.5 (p), 41.8 (a), 40.9 (p), 40.7 (p), 35.0 (p), 33.7 (p), 32.2 (a), 29.0 (p), 25.7 (a), 23.6 (a), 19.8 (p), and 19.2 (p); ms M$^+$: 208.1827 (calcd. for $C_{14}H_{24}O$: 208.1828).

(1R, 4S*, 9R*)-8-Trifluoroacetyl-1,5,5-trimethyl-11-oxatricyclo-[7.2.1.0^{4,9}]dodecan-10-one (**29**), (1S*, 3S*, 8R*)-7-trifluoroacetyl-1,4,4-trimethyl-10-oxatricyclo[6.2.2.0^{3,8}]dodecan-9-one (**30**),*

Can. J. Chem. Downloaded from www.nrcresearchpress.com by 85.192.166.187 on 09/08/12
For personal use only.

(1S, 4S*, 8R*, 9R*)-9-carbomethoxy-1,5,5-trimethyl-11-oxatricyclo[6,2,1,$0^{4,9}$]undecane (**31**), and (1S*, 3S*, 7R*, 8R*)-8-carbomethoxy-1,4,4-trimethyl-11-oxatricyclo[5.3.1.$0^{3,8}$]-undecane (**32**)*

A mixture of isomeric keto esters **7** and **8** (1:1.75) (0.45 g, 1.8 mmol) was dissolved in CCl_4 (2 mL). Triethylsilane (0.86 mL, 5.42 mmol) and trifluoroacetic acid (1.39 mL, 18 mmol) were added, and the reaction mixture was refluxed for 9 h. The solution was cooled to room temperature, washed with water (3 × 2 mL) and brine (1 × 2 mL), dried ($MgSO_4$), filtered, and concentrated. Purification of the concentrate by flash chromatography on silica gel (0–5% ether petroleum ether) gave, in the following order, compounds **31** (85 mg, 29%), **32** (106 mg, 36%), **29** (100 mg, 65%), and **30** (84 mg, 30%). Yields are calculated from the original nmr ratio of the respective keto esters. Spectroscopic data obtained for these compounds are as follows. Compound **31**, a colorless oil: ir (neat): 1730 (ester) and 1250 (-C-O-) cm^{-1}; ^1H nmr (400 MHz, $CDCl_3$) δ: 4.43 (dd, 1 H, $J = J' = 2$ Hz, -C*H*O-), 3.66 (s, 3 H, -COOCH_3), 2.24 (dd, 1 H, $J = 2$, $J' = 1$ Hz), 1.90–1.40 (complex, 10 H), 1.30 (s, 3 H, -OCCH_3), 0.90 (s, 3 H, -CH_3), and 0.82 (s, 3 H, -CH_3); ^{13}C nmr APT (75 MHz, $CDCl_3$) δ: 176.1 (p), 78.5 (p), 76.7 (a), 51.8 (a), 51.7 (p), 48.4 (p), 41.8 (a), 37.9 (p), 34.1 (p), 29.8 (a), 27.9 (p), 26.7 (a), 26.2 (a), 23.6 (p), and 20.2 (p); ms M^+: 252.1725 (calcd. for $C_{15}H_{24}O_3$: 252.1726). Compound **32**, a colorless oil: ir (neat): 1729 (ester) and 1250 (ether) cm^{-1}; ^1H nmr (400 MHz, $CDCl_3$) δ: 4.42 (br s, 1 H, -C*H*O-), 3.68 (s, 3 H, -OCH_3), 2.28 (dd, 1 H, $J = 9$, $J' = 7$ Hz), 2.00–1.50 (complex, 9 H), 1.29 (s, 3 H, -C(CH_3)O-), 0.95 (dd, 1 H, $J = 14$, $J' = 5$ Hz), 0.89 (s, 3 H, -CH_3), and 0.82 (s, 3 H, -CH_3); ^{13}C nmr APT (75.5 MHz, $CDCl_3$) δ: 176.0 (p), 74.8 (p), 76.6 (a), 51.8 (p), 51.6 (a), 48.3 (p), 41.8 (a), 37.9 (p), 34.0 (p), 29.8 (a), 27.8 (p), 26.6 (a), 26.1 (a), 23.5 (p), and 20.1 (a); ms M^+: 252.1727 (calcd. for $C_{15}H_{24}O_3$: 252.1726). Compound **29**, white crystals: mp 132–133°C (petroleum ether); ir ($CHCl_3$ cast): 1789 (ester) and 1770 (lactone) cm^{-1}; ^1H nmr (400 MHz, $CDCl_3$) δ: 5.22 (dd, 1 H, $J = 11$, $J' = 4$ Hz, -C*H*OOCCF$_3$), 2.24 (d, 1 H, $J = 11$ Hz, -CC*H*HC(CH$_3$)O-), 2.11 (d, 1 H, $J = 11$ Hz, -CCH*H*C(CH$_3$)O-), 2.03 (m, 1 H, -C*H*HCHOOCF$_3$), 1.92–1.75 (complex, 3 H), 1.52 (s, 3 H, -C(CH_3)O-), 1.68–1.43 (complex, 5 H), 1.07 (s, 3 H, -CH_3), and 0.98 (s, 3 H, -CH_3); ^{13}C nmr (100.6 MHz, $CDCl_3$) δ: 177.1, 118.7, 82.9, 76.9, 53.5, 42.8, 38.1, 36.8, 34.2, 33.5, 32.3, 25.2, 24.6, 22.7, and 19.5; ms M^+: 334.1390 (calcd. for $C_{16}H_{21}F_3O_4$: 334.1386). Anal. calcd. for $C_{16}H_{21}F_3O_4$: C 57.46, H 6.33; found: C 57.77, H 6.51. Compound **30**, a colorless oil: ir ($CHCl_3$ cast): 1784 (ester) and 1739 (lactone) cm^{-1}; ^1H nmr (300 MHz, $CDCl_3$) δ 5.42 (dd, 1 H, $J = 12$, $J' = 5$ Hz, -C*H*OOCCF$_3$), 2.40–1.20 (complex, 11 H), 1.44 (s, 3 H, -C(CH_3)O-), 1.09 (s, 3 H, -CH_3), and 0.89 (s, 3 H, -CH_3); ^{13}C nmr APT (75.5 MHz, $CDCl_3$) δ: 175.1 (p), 116.5 (p), 112.7 (p), 80.9 (p), 76.6 (a), 44.1 (p), 43.7 (a), 37.9 (p), 34.1 (p), 33.4 (p), 31.6 (a), 31.3 (p), 25.6 (a), 23.2 (p), 20.5 (a), and 18.4 (p); ms M^+: 334.1390 (calcd. for $C_{16}H_{21}F_3O_4$: 334.1386).

(1R, 4S*, 9R*)-8-Hydroxy-1,5,5-trimethyl-11-oxatricyclo[7.2.1.^{4,9}]-dodecan-10-one (**33**)*

Trifluoroacetate ester **29** (500 mg, 1.5 mmol) was dissolved in methanol (5 mL). Sodium methoxide (122 mg, 2.25 mmol) was added and the mixture stirred at room temperature overnight. After quenching the reaction with water, the solution was extracted with ethyl acetate (3 × 3 mL). The extracts were combined and washed successively with aqueous 5% HCl (1 × 3 mL), water (1 × 3 mL), and brine (1 × 2 mL). The organic solution was dried ($MgSO_4$), filtered, and concentrated. Upon crystallization from ether, white crystals of **33** (350 mg, 98%) were obtained: mp 120°C (it starts subliming at ~105°C); ir ($CHCl_3$ cast): 3470 (-OH), 1773 and 1757 (lactone) cm^{-1}; ^1H nmr (300 MHz, $CDCl_3$) δ: 3.79 (dd, 1 H, $J = 11$, $J' = 4$ Hz, -C*H*OH), 2.96 (br s, 1 H, -O*H*), 2.11 (d, 1 H, $J = 11$ Hz, -CC*H*HC(CH$_3$)O-), 1.92 (d, 1 H, $J = 11$ Hz, -CCH*H*C(CH$_3$)O-), 1.80–1.10 (complex, 9 H), 1.37 (s, 3 H, -C(CH_3)O-), 0.90 (s, 3 H, -CH_3), and 0.82 (s, 3 H, -CH_3); ^{13}C nmr APT (75.5 MHz, $CDCl_3$) δ: 180.1 (p), 83.2 (p), 70.2 (a), 55.9 (p), 42.6 (a), 38.8 (p), 35.6 (p), 34.1 (p), 33.8 (p), 32.6 (a), 27.8 (p), 25.2 (a), 22.8 (a), and 19.7 (p); ms M^+: 238.1571 (calcd. for $C_{14}H_{22}O_3$: 238.1563). Anal. calcd. for $C_{14}H_{22}O_3$: C 70.54, H 9.31; found: C 70.64, H 9.48.

(1R, 4S*, 9R*)-8-(Methylmercaptothiocarbonyloxy)-1,5,5-trimethyl-11-oxatricyclo[7.2.1.$0^{4,9}$]dodecan-10-one (**34**)*

Hydroxy lactone **33** (205 mg, 0.8 mmol) was dissolved in 1,2-dimethoxyethane under an argon atmosphere. Sodium hydride (130 mg of an 80% dispersion in mineral oil, 4.3 mmol) was added slowly with stirring. After 20 min, carbon disulfide (0.52 mL, 8.6 mmol) and methyl iodide (0.27 mL, 4.3 mmol) were added. The solution was stirred for 10 h, then the reaction mixture was poured into ice-water. The aqueous layer was extracted with ether (3 × 3 mL). The organic layers were combined, washed successively with aqueous 10% NaOH (1 × 2 mL), bleach (2 × 2 mL), water (1 × 2 mL), and brine (1 × 2 mL), dried ($MgSO_4$), filtered, and concentrated to give **34** (173 mg, 61%) as a colorless oil. After crystallization from ethyl acetate – petroleum ether, white crystals were obtained: mp 180–181°C; ir ($CHCl_3$ cast): 1775 (lactone), 1224 and 1062 (xanthate) cm^{-1}; ^1H nmr (300 MHz, $CDCl_3$) δ: 5.77 (dd, 1 H, $J = 9$, $J' = 4$ Hz, -C*H*OCSSCH$_3$), 2.52 (s, 3 H, -SCH_3), 2.32–2.10 (complex, 3 H), 1.90–1.70 (complex, 3 H), 1.70–1.30 (complex, 5 H), 1.50 (s, 3 H, -C(CH_3)O-), 1.06 (s, 3 H, -CH_3), and 0.97 (s, 3 H, -CH_3); ^{13}C nmr (75.5 MHz, $CDCl_3$) δ: 214.5, 177.6, 82.9, 81.3, 53.9, 42.9, 38.1, 37.7, 34.3, 33.6, 32.3, 25.3, 24.1, 22.7, 19.6, and 19.0; ms M^+: 328.1169 (calcd. for $C_{16}H_{24}O_3S_2$: 328.1159). Anal. calcd. for $C_{16}H_{24}O_3S_2$: C 58.51, H 7.37; found: C 58.38, H 7.47.

(1R, 4S*, 9R*)-1,5,5-Trimethyl-11-oxatricyclo[7.2.1.$0^{4,9}$]dodecan-10-one (**22**) and (1R*, 3S*, 8R*)-1,4,4-trimethyl-10-oxatricyclo-[6.2.2.$0^{3,8}$]dodecan-9-one (**35**)*

A mixture of isomeric keto esters **12** and **36** (1:1, 27 mg, 0.96 mmol) was dissolved in benzene. *p*-Toluenesulfonic acid monohydrate (500 mg, 2.6 mmol) was added and the reaction flask connected to a Dean–Stark apparatus for water removal. The solution was refluxed for 3 h and then cooled down to room temperature. The organic layer was washed successively with water (2 × 2 mL), saturated aqueous sodium bicarbonate solution (2 × 3 mL), water (1 × 2 mL), and brine (1 × 2 mL), dried ($MgSO_4$), filtered, and concentrated. Purification of the concentrate by flash chromatography on silica gel (0–15% ether in petroleum ether) gave white crystals of lactone **22** (87 mg, 41%) identical with an authentic sample obtained previously from pure ester **12**. Further elution gave lactone **35** (89 mg, 42%) as a colorless oil: ir ($CHCl_3$ cast): 1734 (lactone) cm^{-1}; ^1H nmr (400 MHz, $CDCl_3$) δ 2.38 (ddd, 1 H, $J = 14$, $J' = 12.5$, $J'' = 4$ Hz), 1.95–1.30 (complex, 11 H), 1.42 (s, 3 H, -C(CH_3)O-), 1.16 (ddd, 1 H, $J = 13$, $J' = J'' = 5$ Hz), 1.04 (s, 3 H, -CH_3), and 0.86 (s, 3 H, -CH_3); ^{13}C nmr APT (75.5 MHz, $CDCl_3$) δ: 178.9 (p), 80.5 (p), 43.5 (a), 40.6 (p), 40.5 (p), 34.2 (p), 33.9 (p), 32.5 (a), 32.1 (p), 30.6 (p), 25.6 (a), 24.5 (p), 20.7 (a), and 17.9 (p); ms M^+: 222.1616 (calcd. for $C_{14}H_{22}O_2$: 222.1619).

(1R, 6S*)-1-Formyl-3,7,7-trimethylbicyclo[4.4.0]dec-2-ene (**37**)*

Pyridinium chlorochromate impregnated on alumina (0.9 mmol/g, 14.10 g, 12.7 mmol) was added to a solution of alcohol **28** (530 mg, 2.55 mmol) in dry dichloromethane (30 mL). The suspension was stirred at room temperature for 5 h. The mixture was filtered, concentrated, and the residue was purified by flash chromatography on Florisil (eluting with dichloromethane) to afford aldehyde **37** as a colorless oil (495 mg, 94%): ir ($CHCl_3$ cast): 2795, 2740 and 1719 (CHO) cm^{-1}; ^1H nmr (300 MHz, $CDCl_3$) δ: 9.27 (d, 1 H, $J = 2$ Hz, -C*H*O), 4.65 (br s, 1 H, -C*H*=C(CH$_3$)-), 2.15–1.95 (complex, 3 H), 1.86 (ddt, 1 H, $J = 12$, $J' = 5$, $J'' = 2$ Hz), 1.68 (s, 3 H, -CH=C(CH_3)-), 1.60–1.00 (complex, 7 H), 0.95 (s, 3 H, -CH_3), and 0.86 (s, 3 H, -CH_3); ^{13}C nmr APT (75.5 MHz, $CDCl_3$) δ: 204.4 (a), 139.5 (p), 121.9 (a), 53.7 (p), 44.6 (a), 34.6 (p), 33.4 (p), 31.3 (p), 30.2 (a), 28.2 (a), 27.8 (p), 23.7 (a), 20.0 (p), and 19.0 (p); ms M^+: 206.1665 (calcd. for $C_{14}H_{22}O$: 206.1670).

(1R, 6S*)-1-((Z)-2-Methoxyethenyl)-3,7,7-trimethylbicyclo[4.4.0]-dec-2-ene (**38**) and (1R*, 6S*)-1-((E)-2-methoxyethenyl)-3,7,7-trimethylbicyclo[4.4.0]dec-2-ene (**39**)*

Potassium hydride (35% dispersion in oil, 1.00 g, 8.78 mmol) was washed with ether (3 × 5 mL) under an argon atmosphere and then suspended in benzene (40 mL) at room temperature. Dimethyl sulfoxide

Can. J. Chem. Downloaded from www.nrcresearchpress.com by 85.192.166.187 on 09/08/12
For personal use only.

(10 mL) was slowly added. When all the potassium hydride had reacted and the evolution of hydrogen had ceased, (methoxymethyl)triphenylphosphonium chloride (3.50 g, 10.2 mmol) was added. After 2 h of stirring, the solution developed a deep red–burgundy color. At this point aldehyde **37** (424 mg, 2.06 mmol) in a small amount of benzene was added. The reaction mixture was stirred for an additional 2 h and then quenched with water (10 mL). The aqueous layer was extracted with ether (3 × 10 mL). The combined organic layers were washed with water (1 × 5 mL) and brine (1 × 5 mL), dried ($MgSO_4$), filtered, and concentrated. Bulb-to-bulb distillation (70°C/2.5 Torr) of the concentrate gave a colorless oil (452 mg, 93%) consisting of a 1:1 mixture of enol ethers **38** and **39** as determined by nmr analysis. Purification by flash chromatography on silica gel (1% triethylamine in petroleum ether) afforded *cis*-enol ether **38** as a colorless oil (205 mg): ir ($CHCl_3$ cast): 1654 (C=C) and 1109 (C-OCH_3) cm^{-1}; ^1H nmr (300 MHz, $CDCl_3$) δ: 5.64 (d, 1 H, J = 7 Hz, =C*H*OCH_3), 5.12 (br s, 1 H, -C*H*=$C(CH_3)$-), 4.27 (d, 1 H, J = 7 Hz, -C*H*=$CHOCH_3$), 3.52 (s, 3 H, -OCH_3), 2.10–1.80 (complex, 3 H), 1.75 (ddd, 1 H, J = 13, J' = 6, J'' = 3 Hz), 1.62 (s, 3 H, -CH=$C(CH_3)$-), 1.56–1.20 (complex, 7 H), 1.11 (s, 3 H, -CH_3), and 0.89 (s, 3 H, -CH_3); ^{13}C nmr APT (75.5 MHz, $CDCl_3$) δ: 143.9 (a), 131.6 (a), 129.9 (p), 118.2 (a), 59.6 (a), 48.3 (a), 40.7 (p), 36.5 (p), 34.0 (p), 33.5 (p), 31.0 (p), 30.9 (a), 30.8 (a), 23.4 (a), 21.3 (p), and 19.8 (p); ms M^+: 234.1989 (calcd. for $C_{16}H_{26}O$: 234.1984). Continued elution gave *trans*-enol ether **39** as a colorless oil (195 mg): ir ($CHCl_3$ cast): 1644 (C=C) and 1209 (C-OCH_3) cm^{-1}; ^1H nmr (300 MHz, $CDCl_3$) δ: 6,11 (d, 1 H, J = 13 Hz, -CH=C*H*OCH_3), 4.92 (br d, 1 H, J = 1.5 Hz, -C*H*=$C(CH_3)$-), 4.71 (d, 1 H, J = 13 Hz, -C*H*=$CHOCH_3$), 3.48 (s, 3 H, -OCH_3), 1.90–1.78 (m, 1 H), 1.62 (s, 3 H, -CH=$C(CH_3)$-), 1.60–1.05 (complex, 8 H), 1.02 (s, 3 H, -CH_3), and 0.89 (s, 3 H, -CH_3); ^{13}C nmr APT (75.5 MHz, $CDCl_3$) δ: 146.1 (a), 132.7 (p), 131.4 (a) 116.3 (a), 56.0 (a), 49.3 (a), 38.9 (p), 36.4 (p), 34.0 (p), 31.9 (a), 29.9 (p), 28.2 (a), 23.4 (a), 20.5 (p), and 19.3 (p); ms M^+: 234.1985 (calcd. for $C_{16}H_{26}O$: 234.1984).

(1R, 6S*)-1-(2-Oxoethyl)-3,7,7-trimethylbicyclo[4.4.0]dec-2-ene ((±)-isoacanthodoral) (3)*

A column containing silica gel was eluted with a petroleum ether solution containing 1% acetic acid and 1% water. A mixture of enol ethers **38** and **39** (25 mg, 0.107 mmol) was placed in the column and eluted slightly. The column was allowed to stand for 24 h. Elution with 0–5% ether in petroleum ether afforded (±)-isoacanthodoral (**3**) (23 mg, 97%) as a colorless fragrant oil: ir ($CHCl_3$ cast): 2845, 2720, and 1720 (CHO) cm^{-1}; ^1H nmr (400 MHz, $CDCl_3$) δ: 9.73 (dd, 1 H, J = J' = 3 Hz, -C*H*O), 5.23 (d, 1 H, J = 1 Hz, -C*H*=$C(CH_3)$-), 2.71 (dd, 1 H, J = 15, J' = 3 Hz, -C*H*HCHO), 2.13 (dd, 1 H, J = 15, J' = 3 Hz, -CH*H*CHO), 2.00–1.70 (complex, 4 H), 1.65 (s, 3 H, -CH=$C(CH_3)$-), 1.50–1.11 (complex, 7 H), 1.00 (s, 3 H, -CH_3), and 0.91 (s, 3 H, -CH_3); ^{13}C nmr DEPT (75.5 MHz, $CDCl_3$) δ: 204.8 (d), 135.5 (s), 129.9 (d), 57.2 (t), 46.3 (d), 40.1 (t), 38.5 (t), 38.2 (s), 34.2 (s), 32.4 (q), 28.9 (t), 26.4 (q), 23.5 (q), 19.9 (t), and 19.2 (t); ms M^+: 220.1821 (calcd. for $C_{15}H_{24}O$: 220.1827).

(1R, 6S*)-1-(2-Oxoethyl)-3,7,7-trimethylbicyclo[4.4.0]dec-2-ene 2,4-dinitrophenylhydrazone (40)*

Aldehyde **3** (20 mg, 0.09 mmol) was dissolved in ethanol (0.5 mL). A 3% solution of 2,4-dinitrophenylhydrazine (1 mL, 0.15 mmol) in water, ethanol, and H_2SO_4 (2:7:2) was added and the resulting mixture was stirred for 3 h. After addition of H_2O (2 mL), the reaction mixture was extracted with dichloromethane (3 × 3 mL). The organic extracts were washed with H_2O (2 × 1 mL) and brine (1 × 1 mL), dried ($MgSO_4$), filtered, and concentrated under reduced pressure. The orange residue was redissolved in dichloromethane, and petroleum ether added to precipitate a red solid. The precipitate was filtered off and the filtrate passed through Florisil with petroleum ether elution. The solution was concentrated to give an oil, which was purified by flash chromatography on silica gel (0–5% ether in petroleum ether). Recrystallization from ether – petroleum ether gives 2,4-DNP derivative **40** (28.8 mg, 80%) as orange needles. The following physical properties of this compound were found to be identical with those reported for the 2,4-DNP derivative of the naturally occurring isoacanthodoral: mp 144–146°C; ir ($CHCl_3$ cast): 3302 (NH), 1618 (C=N), and 1516 (NO_2) cm^{-1}; ^1H nmr (300 MHz, $CDCl_3$) δ: 11.02 (br, s, 1 H, -CH=N-N*H*-), 9.12 (d, 1 H, J = 2.5 Hz), 8.29 (ddd, 1 H, J = 9.5, J' = 2.5, J'' = 1 Hz), 7.93 (d, 1 H, J = 9.5 Hz), 7.46 (dd, 1 H, J = J' = 6 Hz), 5.14 (br, s, 1 H, -CH=$C(CH_3)$-), 2.79 (dd, 1 H, J = 14, J' = 6 Hz), 2.24 (dd, 1 H, J = 14, J' = 6 Hz), 1.95 (m, 3 H), 1.75 (m, 1 H), 1.67 (s, 3 H), 1.60–1.10 (complex, 7 H), 1.04 (s, 3 H, -CH_3), and 0.91 (s, 3 H, -CH_3); ^{13}C nmr APT (75.5 MHz, $CDCl_3$) δ: 152.1 (a), 145.2 (p), 137.8 (p), 135.5 (p), 130.3 (a), 130.0 (a), 128.8 (p), 123.6 (a), 116.6 (a), 46.5 (p), 45.8 (a), 40.2 (p), 38.9 (p), 38.2 (p), 34.3 (p), 32.3 (a), 28.9 (p), 26.5 (a), 23.5 (a), 19.9 (p), and 19.2 (p); ms M^+: 400.2116 (calcd. for $C_{21}H_{28}N_4O_4$: 400.2110). Anal. calcd. for $C_{21}H_{28}N_4O_4$: C 62.79, H 7.05, N 14.00; found: C 62.38, H 7.05, N 13.65.

Acknowledgements

We are grateful to the Natural Sciences and Engineering Research Council of Canada and the University of Alberta for financial support, and Drs. R.J. Andersen and S.W. Ayer for discussion and information.

1. J. Hellou. M.Sc. Thesis, The University of British Columbia, 1980.
2. R.J. Andersen, S.W. Ayer, J. Hellou, and M. Tischler. Tetrahedron Lett. **25**, 141 (1984).
3. S.W. Ayer. Ph.D. Thesis, The University of British Columbia, 1985.
4. R.J. Andersen, S.W. Ayer, H.C. Heng, and J. Clardy. J. Org. Chem. **49**, 2653 (1984).
5. H.J. Liu, G. Ulibarri, and L.A.K. Nelson. J. Chem. Soc. Chem. Commun. 1419 (1990).
6. H.J. Liu and E.N.C. Browne. Can. J. Chem. **59**, 601 (1981).
7. I. Ojima, M. Nihonyanagi, T. Kogure, M. Kumagai, S. Horiuchi, K. Nakatsugawa, and Y. Nagai. J. Organomet. Chem. **94**, 449 (1975).
8. D.H.R. Barton and S.W. McCombie. J. Chem. Soc. Perkin Trans. 1, 1574 (1975).
9. C.D. Gutsche. Org. React. **8**, 364 (1954).
10. D. Peterson. J. Org. Chem. **33**, 780 (1968).
11. P. Magnus and G. Roy. Organometallics, **1**, 553 (1982).
12. P. Magnus and G. Roy. J. Chem. Soc. Chem. Commun. 822 (1979).
13. G. Wittig, W. Böll, and K.H. Krück. Chem. Ber. **95**, 2514 (1962).
14. G. Wittig and M. Schlosser. Chem. Ber. **94**, 1373 (1961).
15. L.I. Zakharkin and I.M. Khorlina. Tetrahedron Lett. 619 (1962).
16. D. Swern, A.J. Mancuso, and S.L. Huang. J. Org. Chem. **43**, 2480 (1978).
17. Y.S. Cheng, W.L. Liu, and S.H. Chen. Synthesis, 223 (1980).
18. G.A. Olah, S.C. Narang, B.G.B. Gupta, and R. Malhotra. J. Org. Chem. **44**, 1247 (1979).
19. H.J. Liu and V. Wiszniewski. Synth. Commun. **18**, 119 (1988).
20. G.I. Feutrill and R.N. Mirrington. Tetrahedron Lett. 1327 (1970).
21. D.H.R. Barton, A.G.M. Barrett, H.J. V.d.O. Baptista, M. Girijavallabhan, R.C. Jennings, J. Kelly, V.J. Papadimitrieu, J.V. Turner, and N.A. Usher. J. Chem. Soc. Perkin Trans. 1, 1485 (1977).
22. H. Yuki, K. Hatada, and K. Nagata. Bull. Chem. Soc. Jpn. **43** 1817 (1970).
23. R.V. Hoffman, R.D. Bishop, P.M. Fitch, and R. Hardenstein. J. Org. Chem. **45**, 917 (1980).
24. S. Berstein and W.S. Allen. J. Am. Chem. Soc. **77**, 1028 (1955).
25. K.L. Rinehart and E.G. Perkins. Org. Synth. Coll. Vol. IV, 444 (1963).
26. M.P. Doyle, C.T. West, S.J. Donnelly, and D.A. Kooistra. J. Org. Chem. **38**, 2675 (1973).
27. D.N. Kursanov and Z.N. Parnes. Russ. Chem. Rev. **38**, 812 (1969).
28. D.N. Kursanov, N.M. Loim, V.A. Baranova, L.V. Moiseeva, L.P. Zalukaev, and Z.N. Parnes. Synthesis, 420 (1973).

29. Z.N. Parnes, N.M. Loim, V.A. Baranova, and D.N. Kursanov. Zh. Org. Khim. **7**, 2145 (1971).
30. J.L. Fry, M. Orfanopoulos, M.G. Adlington, W.R. Dittman, and S.B. Silverman. J. Org. Chem. **43**, 374 (1978).
31. D.H.R. Barton, A.G.M. Barrett, P.A. Prokopiou, R.B. Boar, L. Joukhadar, J.F. McGhie, and S.C. Misra. J. Chem. Soc. Chem. Commun. **68** (1978).
32. H. Deshayes, J.P. Pète, and C. Portella. Tetrahedron Lett. 2019 (1976).

Can. J. Chem. Downloaded from www.nrcresearchpress.com by 85.192.166.187 on 09/08/12
For personal use only.

X-ray structures of triphenylphosphine and 1,2,5-triphenylphosphole products with dimethyl acetylenedicarboxylate tetramer[1]

MARTIN B. HOCKING[2] AND FRANCES W. VAN DER VOORT MAARSCHALK
Department of Chemistry, University of Victoria, Victoria, BC V8W 3P6, Canada

Received March 21, 1994

MARTIN B. HOCKING and FRANCES W. VAN DER VOORT MAARSCHALK. Can. J. Chem. **72**, 2428 (1994).

A tetramer of dimethyl acetylenedicarboxylate, tetramethyl 4-methoxy-5-[1,2,3-tris(methoxycarbonyl)-2-cyclopropen-1-yl]-7-oxabicyclo[2.2.1]hepta-2,5-diene-1,2,3,6-tetracarboxylate **3**, was recovered from old stocks of the monomer, and was also prepared thermally from the monomer by a variation of a previous method. NMR data and an X-ray crystal structure were determined for a red 1:1 adduct of this ester with triphenylphosphine. This red adduct, tetramethyl 4-methoxy-5-[1,2,3-tris(carbomethoxy)-3-triphenylphosphoranylidenepropen-1-yl]-7-oxabicyclo[2.2.1]hepta-2,5-diene-1,2,3,6-tetracarboxylate **5**, crystallized in the triclinic space group $P\bar{1}$ (No. 2) with two molecules in the unit cell (a = 12.315(2) Å, b = 12.321(2) Å, c = 14.652(2) Å, α = 110.60(1)°, β = 90.62 (1)°, and γ = 103.22(1)°). Refinement converged at R = 0.0694 (R_w = 0.0986) for 542 parameters using 4714 reflections with $I > 2\sigma(I)$. Triphenylphosphine oxide did not react with tetramer **3**. Reaction of the tetramer of dimethyl acetylenedicarboxylate **3** with 1,2,5-triphenylphosphole gave an orange product with concomitant loss of a furan triester. NMR data confirmed that this was not a simple adduct, and examination of a crystal by X-ray established the structure as the dichloromethane complex of tetramethyl 1,9,10-triphenyl-1-phospha(V)tricyclo[5,2,1,$0^{5,10}$] deca-1,3,5,8-tetraene-2,3,4,6-tetracarboxylate **10**. This orange product crystallized in the monoclinic space group $P2_1/c$ (No. 14) with four molecules in the unit cell (a = 10.056(2) Å, b = 14.280(1) Å, c = 23.892(3)Å, α = 90.0°, β = 94.15(1)°, and γ = 90.0°). Refinement converged at R = 0.0683 (R_w = 0.0710) for 540 parameters using 3180 independent reflections with $I > 3\sigma(I)$. The tetramer **3** did not react with 1,2,5-triphenylphosphole-1-oxide quickly, but after 9 months gave a white, probably polymeric, product.

MARTIN B. HOCKING et FRANCES W. VAN DER VOORT MAARSCHALK. Can. J. Chem. **72**, 2428 (1994).

On a isolé un tétramère de l'acétylènedicarboxylate de diméthyle, le 4-méthoxy-5-[1,2,3-tris(méthoxycarbonyl)-2-cyclopropèn-1-yl]-7-oxabicyclo[2.2.1]hepta-2,5-diène-1,2,3,6-tétracarboxylate de tétraméthyle (**3**), à partir de vieux stocks du monomère et on l'a aussi préparé thermiquement à partir du monomère, par une variation d'une méthode antérieure. On a déterminé les données de la RMN et, faisant appel à la diffraction des rayons X, on a déterminé la structure d'un adduit 1 : 1 de cet ester avec la triphénylphosphine. Cet adduit rouge, le 4-méthoxy-5-[1,2,3-tris(carbométhoxy)-3-triphénylphosphoranylydènepropèn-1-yl]-7-oxaboicyclo[2.2.1]hepta-2,5-diène-1,2,3,6-tétracarboxylate de tétraméthyle (**5**), cristallise dans le groupe d'espace triclinique $P\bar{1}$ (No. 2) avec deux molécules par motif et a = 12,315(2), b = 12,321(2) et c = 14,652(2) Å, α = 110,60(1)°, β = 90,62 (1)° et γ = 103,22(1)°). L'affinement converge à R = 0,0694 (R_w = 0,0986) pour 542 paramètres utilisant 4714 réflexions avec $I > 2\sigma(I)$. L'oxyde de triphénylphosphine ne réagit pas avec le tétramère **3**. La réaction du tétramère de l'acétylènedicarboxylate de diméthyl avec le 1,2,5-triphénylphosphole fournit un produit orange avec la perte concomitante d'un triester de furane. Les données de RMN confirment qu'il ne s'agit pas d'un adduit simple et une étude par diffraction des rayons X a permis d'en établir la structure; il s'agit du complexe du 1,9,10-triphényl-1-phospha(V)tricyclo[5.2.1,$0^{5,10}$]déca-1,3,5,8-tétraène-2,3,4,6-tétracarboxylate de tétraméthyle (**10**) avec du dichlorométhane. Ce produit orange cristallise dans le group d'espace $P2_1/c$ (No. 14) avec quatre molécules par motif et a = 10,056(2), b = 14,280(1) et c = 23,892(3) Å, α = 90,0°, β = 94,151(1)° et γ = 90,0°. L'affinement converge à R = 0,0683 (R_w = 0,0710) pour 540 paramètres utilisant 3180 réflexions avec $I > 3\sigma(I)$. Le tétramère **3** ne réagit pas rapidement avec le 1-oxyde de 1,2,5-triphénylphosphole; après 9 mois, il fournit un produit blanc, probablement un polymère.

[Traduit par la rédaction]

Introduction

A thermally produced condensation trimer and a tetramer of dimethyl acetylenedicarboxylate apparently were first described and partially characterized by Thayer, who also examined the dienophilic character of the cyclopropene ring component of the tetramer (1). Hexamethyl mellitate and structure **1** were considered for the trimer, and rejected. Subsequently two groups examined the physical and chemical properties of trimethyl 2-methoxyfurantricarboxylate **2**, a dimeric product less a carbon derived from the monomeric acetylene ester, and devised plausible pathways for its formation (2, 3). A third laboratory reacted supposed furan **2**, which has some similar properties to the dimethyl acetylenedicarboxylate (DMADC) tetramer **3**, with triphenylphosphine and obtained a red product formulated as the zwitterion **4** (4). This adduct has a very similar elemental analysis and physical properties to those of the reaction product from the DMADC tetramer with triphenylphosphine, and therefore it was probably the same material (5).

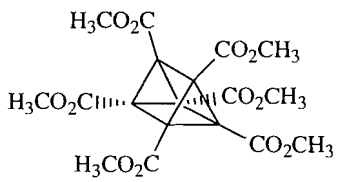

1

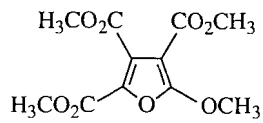

2

The structures of both the DMADC tetramer as **3** and the triphenylphosphine adduct as 5 were better established by the subsequent combined contributions of Kauer and Simmons, LeGoff and LaCount, and Gericke and Winterfeldt (5–7). Gericke and Winterfeldt also provided the well-supported structure **6** for the trimer originally described by Thayer.

We were interested in confirming the rather unusual structure of the tetramer of dimethyl acetylenedicarboxylate via an X-ray

[1]Presented at the 49th Northwest Regional Meeting of the American Chemical Society, University of Alaska Anchorage, June 16–18, 1994.

[2]Author to whom correspondence may be addressed. Fax: (604) 721-7147. Telephone (604) 721-7152.

Can. J. Chem. Downloaded from www.nrcresearchpress.com by 85.192.166.187 on 09/08/12
For personal use only.

TABLE 1. ^{1}H NMR spectra of isomers of tetramer **3** in deuteriochloroform[a]

Isomer mixture		High-field isomer				Low-field isomer	
		At +28°C		At +10°C (resolved)			
Shift, ppm	Relative intensity	Shift, ppm	Relative intensity	Shift, ppm	Relative intensity	Shift, ppm	Relative intensity
3.88	7.4					3.88	12.6
3.86	12.6	3.86	5.5	3.86	5.8	3.865	17.0
						3.859	16.9
3.85	11.0					3.85	13.5
3.84	18.0			3.84	5.8		
		3.83	6.0	3.83	6.0		
3.82	9.2	3.82	5.7	3.82	5.8		
3.75	7.1					3.76	10.4
3.73	9.2	3.73	5.5	3.73	5.5		
3.71	6.6					3.71	10.2
3.69	8.5	3.68	5.5	3.68	5.3		
3.64	6.9						
3.62	9.2	3.61	4.7	3.61	5.5		
3.57	6.8					3.58	9.5
3.55	9.3	3.55	4.6	3.55	5.5	3.47	1.4

[a]At room temperature, ca. 28°C, unless otherwise stated. Shifts are reported relative to tetramethylsilane and relative intensities are given in arbitrary units. Shift of traces of $CHCl_3$ in the deuteriochloroform was assigned the value 7.2399 ± 2 ppm, throughout.

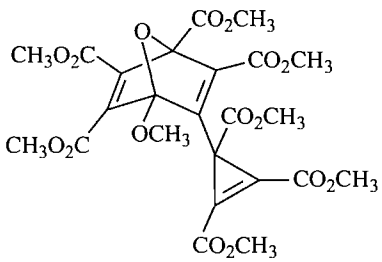

3

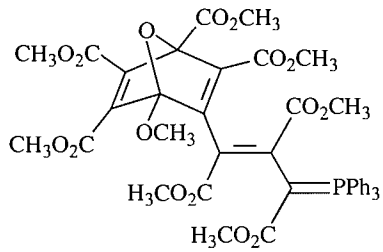

5

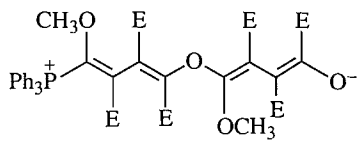

E = $-CO_2CH_3$

4

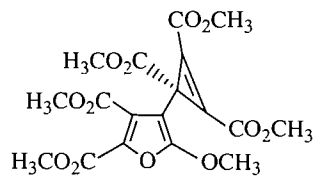

6

structure of a crystal of either the compound itself or of a derivative of the tetramer in which the bulk of the skeleton of the tetramer remained intact, such as the triphenylphosphine adduct. It was also intended to test restricted rotational features that were previously reported for certain ester-stabilized phosphoranes (8) and were likely to be observable for several of the target compounds synthesized for the structural study. If feasible, evaluation of the rotational energy barriers of the target molecule(s) could also be made via NMR coalescence temperatures to probe molecular features giving rise to the restricted rotation.

Results and discussion

Isolation and preparation of tetramer 3

The first samples of tetramer isolated from 17-year-old bottle of almost completely crystalline dimethyl acetylenedicarboxylate (DMADC) gave 13 methyl singlets (10 well resolved, 3 with evidence of overlapping) with 4 closely spaced pairs in the 3.75–3.55 ppm shift range in the 250 MHz ^{1}H NMR spectrum (Table 1). Since only eight (or fewer) resonances were expected for the tetramer this multiplicity was taken as suggestive of the existence in this sample of two very similar tetramer isomers, not noticed by the previous workers perhaps because of the lower-frequency spectrometers used. It was not the photochemically produced isomer **7**, since this has only two types of ester methyls, which give ^{1}H NMR resonances at 3.74 (6H) and 3.79 ppm (18H) (6).

To explain the very similar NMR spectra observed it was thought possible, for example, that the methoxyl and the cyclopropene moieties could be on opposite sides rather than on the same side of the oxanorbornadiene ring in the postulated two isomers, **3** and **9**. Examination of a possible pathway from the DMADC monomer to the tetramer showed that it would be difficult to perceive mechanistically how this particular possibility could occur directly (Scheme 1). However, this could be envisaged by a reverse Diels–Alder reaction of the tetramer **3** to the

Can. J. Chem. Downloaded from www.nrcresearchpress.com by 85.192.166.187 on 09/08/12
For personal use only.

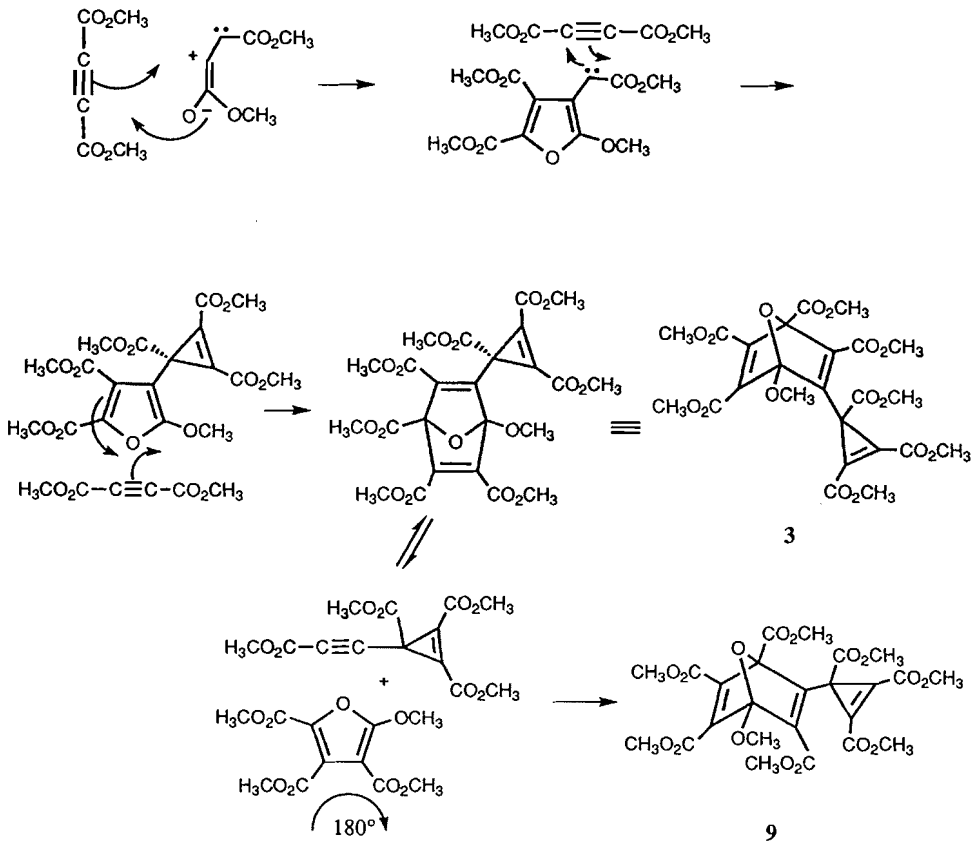

SCHEME 1. A possible pathway to the dimethyl acetylenedicarboxylate tetramer **3** and its postulated isomer **9** (extended from ref. 6).

TABLE 2. Results of thermal equilibration experiments with the tetramer of dimethyl acetylenedicarboxylate **3** in nitrogen atmosphere

Temperature, °C[a]	Time, h	Composition by 250 MHz ^{1}H NMR
111	0.3	No change
111	3	Ca. 90% original tetramer, + 10% possible isomer
111	18	No tetramer; seven new compounds (TLC)
111	20	Extensive decomposition
137	2.3	No tetramer; six new compounds
137	24	Severe decomposition.

[a]Runs at 111°C contained added hydroquinone and were heated by the vapours of boiling toluene. Runs at 137°C (performed first) had no hydroquinone present, and were heated by the condensed vapour of boiling of mixed xylenes.

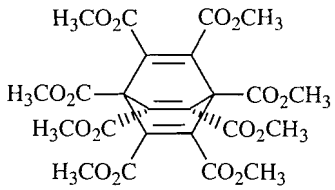

7

cyclopropenyl acetylene **8** and furan **2** followed by a 180° rotation of either product, and a forward Diels–Alder recyclization could conceivably give this result. This possibility is supported by the earlier 18% recovery of **6** from a vacuum pyrolysis of the methanol addition product of the tetramer **3** by Gericke and Winterfeldt (7). Significant attention therefore was directed towards resolution of the supposed isomeric mixture, both from old, spontaneously formed, tetramer samples present in old DMADC monomer as well as by examination of fresh, thermally prepared, tetramer, to try to answer this question.

Tetramer recoveries from spontaneously tetramerized monomer ranged from about 80% from a 17-year-old, almost completely crystallized, sample of DMADC to about 20% for recovery from viscous but noncrystalline samples of less old DMADC and for fresh, thermally prepared, tetramer samples. Use of a nitrogen atmosphere did not significantly alter our yields of thermally produced tetramer from the 20–25% previously reported (5). None of the samples isolated from spontaneously produced material, nor those from subsequent thermal preparation, showed the same near doubling of ester methyl proton NMR resonances observed in the initially isolated sample. Attempts to observe formation of the second "isomer" by thermal equilibration of isolated tetramer under a nitrogen atmosphere, either with or without radical inhibitor present, were also unsuccessful (Table 2).

Can. J. Chem. Downloaded from www.nrcresearchpress.com by 85.192.166.187 on 09/08/12
For personal use only.

TABLE 3. Comparison of the mass spectrum of an isomeric mixture of tetramers **3** with that of the low-field isomer of tetramer **3** of dimethyl acetylenedicarboxylate

	Relative intensities		
m/z	Tetramer mixture	Low-field isomer	Relative intensity differences, %[a]
105	7	15	114
111	1.8	1.7	−5.5
121	0	13	—
133	3.9	3.3	−15
143	3	6	100
157	7	11	57
171	6	14	133
213	4.6	7.6	65
465	4	9	125
479	4	3.6	−10
481	13	26	100
493	9	16	78
509	42	76	81
525	100	100	0
527	4	0	−100
537	74	57	−23
568 M^+	6	3	−50
569 M + 1	23	11	−52
570	2	0	−100
597 M + 29	26	18	−31
609 M + 41	3	4.6	53

[a][(Relative intensity of low field isomer) − (relative intensity of isomer mixture)]/[relative intensity of isomer mixture] × 100.

Chemical ionization mass spectra of the originally isolated tetramer mixture relative to more recent, thermally prepared, tetramer gave significantly different fragmentation susceptibilities (Table 3). Therefore, a few small-scale experiments were conducted to reveal any differential reactivity of the tetramer isomer towards triphenylphosphine or 1,2,5-triphenylphosphole. These also failed to give any conclusive answers. Further experiments to confirm the formation of isomer(s) of tetramer **3** were therefore abandoned.

Several attempts were made to deoxygenate the tetramer using triiron dodecacarbonyl and triiron nonacarbonyl under mild conditions. These experiments were directed towards confirmation of both the structures of the tetramer and whether our interpretation of the isomers present under some conditions, i.e., **3** and **9**, was correct from the nature of the aromatic product(s) **10** that would result. It was also possible that the observed second "isomer" was spontaneously deoxygenated tetramer **3**. Although examination of the chromatographed reaction mixture under the best conditions demonstrated conversion of the starting material to two compounds, neither corresponded to the structure **10**.

Adduct of tetramer 3 with triphenylphosphine

Since the thermal ellipsoids determined from an X-ray crystal structure of the low melting point tetramer were likely to be large, it was decided to first obtain a crystal structure for the tetramer–triphenylphosphine adduct **5**. Only in the event of an unexpected structure for this adduct would it be necessary to attempt a crystal structure of the tetramer itself.

The yield of the crude red tetramer–triphenylphosphine adduct prepared in ether was nearly 90% and after one recrystallization gave material melting at 212–214°C, the same as previously recorded (5). Electron impact and MALDI (matrix assisted laser desorption ionization) mass spectra confirmed the required molecular weight of 831. While the adduct is thermally stable at temperatures up to the melting point, observation of major fragment ions at *m/z* 558.3 and 262.1 in the electron impact mass spectrum indicates loss of the furan **2** or the equivalent, and triphenylphosphine (*m/z* 830.7 − 272.2, and 262.3, respectively), as significant components of either its thermal or electron impact fragmentation pathways. The ester methyl/methoxyl region of the 360 MHz ^1H NMR adduct shows 14 peaks in the shift range 3.91–2.89 ppm.

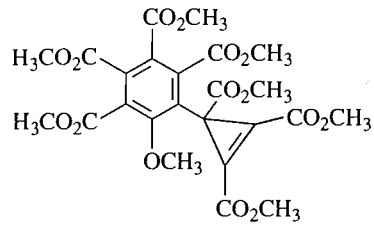

10*a*

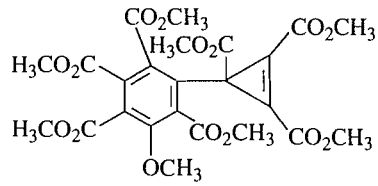

10*b*

X-ray quality crystals of a 1:1 complex of the tetramer–triphenylphosphine adduct **5** with dichloromethane were obtained by recrystallization of the crude product from a mixture of dichloromethane and ether. Figure 1 gives an ORTEP representation of the molecular structure excluding hydrogen atoms, which were not sought (Tables 4–7). This endorses structure **5** for the adduct, as first proposed by Kauer and Simmons (5). It also strongly supports the structure **3** originally put forward by LeGoff and LaCount for the DMADC tetramer itself (6).

A gross feature of interest from this crystal structure, from intersecting plane dihedral angle calculations, is that the oxygen bridge of the oxanorbornadiene moiety remains approximately equally spaced between the triphenylphosphine substituent side and the two-ester substituent side of the bridged ring, despite the steric bulk of the former (Fig. 2). Bond angle and torsion angle calculations also give quite even spacing between the A, B, and C phenyls on the phosphorus of 106°, 107°, and 108°, respectively. Also each phenyl is tilted to a similar angle of somewhat more than 90° away from the P1—C1 axis to the extent of 107°, 113°, and 115°, as would be expected. This "tilt" is the reason that the angles between the phenyls do not total 360°, and can be likened to a propellor in which the blades (phenyls) lie outside the plane of rotation. An interesting feature of this analogy, emerging from torsion calculations, is the wide differences found for the angle of "pitch" of the phenyl "blades" expressed relative to the plane of rotation of 42.14(4)°, 137.(4)°, and 75.9(4)°, respectively. The B ring shows a relatively fine pitch whereas the C ring is almost feathered (with respect to the *axis* of rotation).

Detailed examination reveals a P1—C1 bond distance of 1.748(3) Å, close to the 1.728 Å reported by Kennard et al. (9) for a P=C double bond in a cyclopentylidene phosphorane and significantly shorter than the 1.87 Å normally expected for a

Can. J. Chem. Downloaded from www.nrcresearchpress.com by 85.192.166.187 on 09/08/12
For personal use only.

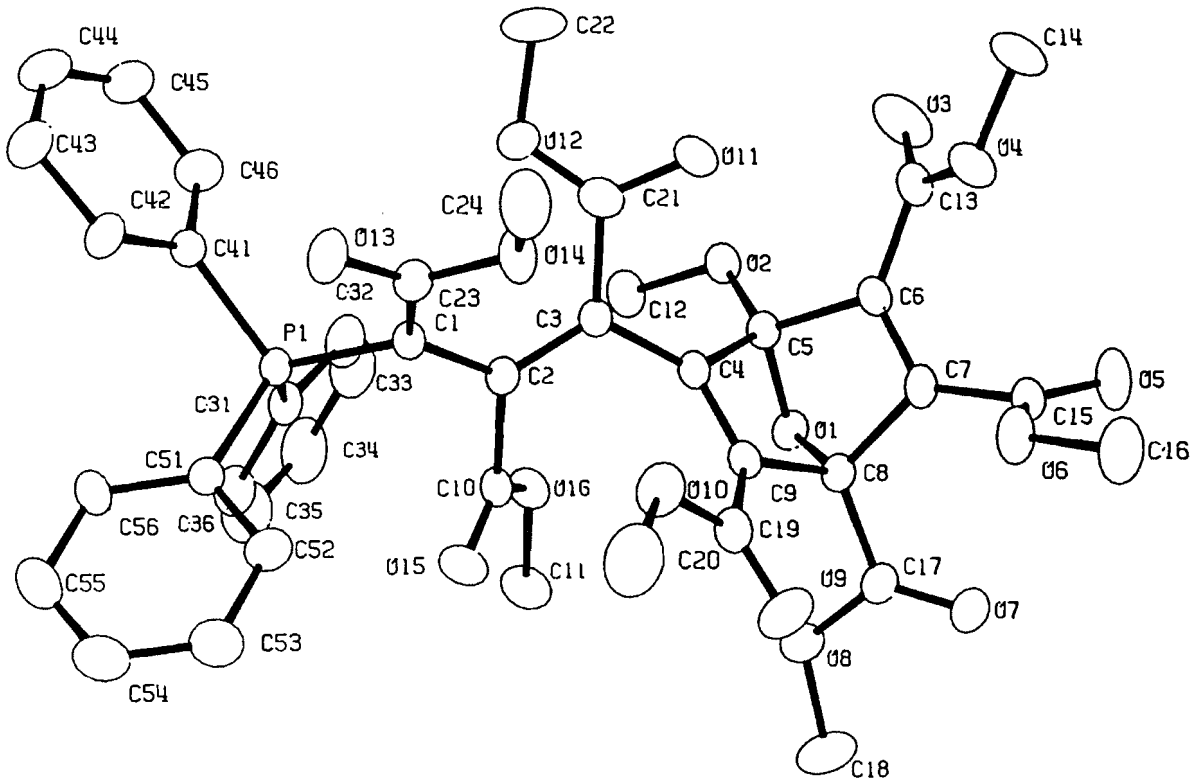

FIG. 1. ORTEP representation of the crystal structure of the adduct of tetramer **3** with triphenylphosphine, compound **5**.

TABLE 4. Experimental crystallographic data measured at 20°C

	Red triphenylphosphine adduct, **5**	Orange phosphole product, **11**
Crystal dimensions, mm	0.73 × 0.61 × 0.37	0.9 × 0.7 × 0.4
Molecular formula	$C_{42}H_{39}O_{16}P$	$C_{36}H_{31}O_8PCl_2$ (includes molecule of CH_2Cl_2)
Method used	-EI mass spectrometry	-MALDI mass spectrometry
Molecular weight	830.4	610 (w/o CH_2Cl_2)
Asymmetric unit	1 molecule	1 molecule
Crystal system	Triclinic	Monoclinic
Space group	$P\bar{1}$ (No. 2)	$P2_1/c$ (No. 14)
Unit cell: *a*, Å	12.315(2)	10.056(2)
b, Å	12.321(2)	14.280(1)
c, Å	14.652(2)	23.892(3)
α, deg	110.60(1)	90.0
β, deg	90.62(1)	94.15(1)
γ, deg	103.22(1)	90.0
Cell volume: Å^3	2015.7	3421.9
Z, molecules/cell	2	4
Density:		
Measured (flot'n), g cm^{-3}	1.346	1.329
Calculated, g cm^{-3}	1.368	1.346
Diffractometer	Nonius + PDP11	Nonius + PDP11
Radiation	Ni-filtered Cu Kα	Ni-filtered Cu Kα
	λ = 1.542 Å	λ = 1.542 Å
Intensity measurements	2θ = 0°–120°	2θ = 0°–130°
Number observed	4714, $I > 2\sigma(I)$	3180, $I > 3\sigma(I)$
Number collected	5668	5344
Solution method	SHELX-76, direct	SHELX, Patterson
Refinement method	SHELX-76, least squares	SHELX-76, least squares
Final *R* value	0.0694	0.0683
Final R_w	0.0986	0.0710

Can. J. Chem. Downloaded from www.nrcresearchpress.com by 85.192.166.187 on 09/08/12
For personal use only.

Can. J. Chem. Downloaded from www.nrcresearchpress.com by 85.192.166.187 on 09/08/12
For personal use only.

TABLE 5. Fractional atomic coordinates and temperature parameters for all non-hydrogen atoms of the red 1:1 adduct **5**

Atom	*x/a*	*y/b*	*z/c*	U_{eq}
P(1)	−43951(8)	−21687(8)	21580(7)	396(4)
O(1)	10(2)	1675(2)	1577(2)	45(1)
O(2)	−1091(2)	1740(2)	731(2)	48(1)
O(3)	−889(4)	4366(3)	1304(3)	107(2)
O(4)	−570(3)	5203(3)	2917(2)	67(1)
O(5)	2034(3)	5439(3)	3424(3)	82(2)
O(6)	1213(3)	4589(3)	4445(2)	67(1)
O(7)	2770(3)	2828(3)	3260(3)	73(2)
O(8)	1939(3)	890(3)	2544(3)	80(2)
O(9)	739(3)	1667(4)	4425(3)	89(2)
O(10)	−1131(3)	1268(3)	4285(2)	70(2)
O(11)	−2674(3)	2688(3)	2382(3)	66(1)
O(12)	−4007(3)	998(3)	1702(3)	72(2)
O(13)	−5169(2)	−423(3)	3634(2)	59(1)
O(14)	−3787(3)	1200(2)	3822(2)	59(1)
O(15)	−1611(3)	−1434(3)	2856(3)	66(2)
O(16)	−1210(2)	−1018(3)	1520(2)	54(1)
C(1)	−3680(3)	−658(3)	2669(3)	41(2)
C(2)	−2594(3)	−185(3)	2420(3)	39(1)
C(3)	−2249(3)	904(3)	2321(3)	39(1)
C(4)	−1074(3)	1483(3)	2382(3)	39(1)
C(5)	−536(3)	2038(3)	1623(3)	41(2)
C(6)	−82(3)	3407(3)	2178(3)	44(2)
C(7)	769(3)	3512(4)	2796(3)	46(2)
C(8)	842(3)	2230(3)	2613(3)	42(2)
C(9)	−201(3)	1646(3)	3017(3)	41(2)
C(10)	−1758(3)	−938(3)	2312(3)	43(2)
C(11)	−384(4)	−1722(5)	1356(4)	75(3)
C(12)	−1481(4)	463(4)	149(3)	63(2)
C(13)	−570(4)	4346(4)	2057(4)	54(2)
C(14)	−1021(5)	6190(5)	2885(5)	92(3)
C(15)	1423(4)	4629(4)	3575(3)	49(2)
C(16)	1765(5)	5649(5)	5298(4)	87(3)
C(17)	1971(4)	2037(4)	2854(3)	51(2)
C(18)	2938(5)	551(6)	2801(6)	114(4)
C(19)	−128(4)	1519(4)	3965(3)	54(2)
C(20)	−1172(6)	1040(7)	5196(4)	109(4)
C(21)	−3046(4)	1547(4)	2125(3)	55(2)
C(22)	−4714(10)	1743(15)	1595(13)	112(10)
C(22′)	−3489(10)	3264(9)	2137(10)	84(6)
C(23)	−4287(3)	30(4)	3398(3)	45(2)
C(24)	−4326(5)	1861(5)	4648(4)	86(3)
C(31)	−3747(3)	−2830(3)	1066(3)	49(2)
C(32)	−3553(4)	−2242(4)	398(3)	65(2)
C(33)	−3047(5)	−2737(5)	−463(4)	86(3)
C(34)	−2746(6)	−3788(6)	−628(5)	99(3)
C(35)	−2936(5)	−4373(5)	29(5)	103(3)
C(36)	−3446(4)	−3910(4)	878(4)	71(2)
C(41)	−5860(3)	−2405(3)	1759(3)	44(2)
C(42)	−6706(3)	−2762(4)	2290(3)	58(2)
C(43)	−7837(4)	−3029(4)	1919(4)	70(2)
C(44)	−8098(4)	−2909(5)	1046(4)	76(2)
C(45)	−7277(5)	−2515(5)	549(4)	80(3)
C(46)	−6149(4)	−2266(5)	902(4)	69(2)
C(51)	−4349(3)	−3007(3)	2938(3)	46(2)
C(52)	−3571(4)	−2502(4)	3771(3)	55(2)
C(53)	−3480(4)	−3145(5)	4378(4)	72(3)
C(54)	−4190(5)	−4262(6)	4167(5)	84(3)
C(55)	−4981(5)	−4765(5)	3365(5)	89(3)
C(56)	−5059(4)	−4146(4)	2723(4)	68(2)

Estimated standard deviations are given in parentheses. Coordinates × 10^n where n = 5, 4, 4, 4 for P, O , N, C. Temperature parameters × 10^n where n = 4, 3, 3, 3 for P, O, N, C. U_{eq} = the equivalent isotropic temperature parameter. $U_{eq} = 1/3\ \Sigma_i\Sigma_j U^{ij} a^i{*} a_j{*}(a_i \cdot a_j)$. $T = \exp(-8\pi^2 U_{iso} \sin^2\theta/\lambda^2)$. Anisotropic temperature factors for nonhydrogen atoms have been deposited (see footnote 3).

TABLE 6. Interatomic distances for all skeletal atoms of the red adduct **5** (Å)[a]

Atoms	Distance	Atoms	Distance
C(1)—P(1)	1.748(3)	C(4)—C(3)	1.447(5)
C(31)—P(1)	1.807(4)	C(21)—C(3)	1.477(7)
C(41)—P(1)	1.816(4)	C(5)—C(4)	1.576(6)
C(51)—P(1)	1.797(5)	C(9)—C(4)	1.346(6)
C(5)—O(1)	1.451(5)	C(6)—C(5)	1.553(5)
C(8)—O(1)	1.438(4)	C(7)—C(6)	1.331(6)
C(5)—O(2)	1.357(5)	C(13)—C(6)	1.480(7)
C(12)—O(2)	1.461(5)	C(8)—C(7)	1.530(6)
C(2)—C(1)	1.438(5)	C(15)—C(7)	1.488(5)
C(23)—C(1)	1.444(6)	C(9)—C(8)	1.552(6)
C(3)—C(2)	1.370(6)	C(17)—C(8)	1.521(7)
C(10)—C(2)	1.511(6)	C(19)—C(9)	1.455(7)

[a]Estimated standard deviations are given in parentheses. Phenyl and ester bond distances, which were all normal, have been deposited (see footnote 3).

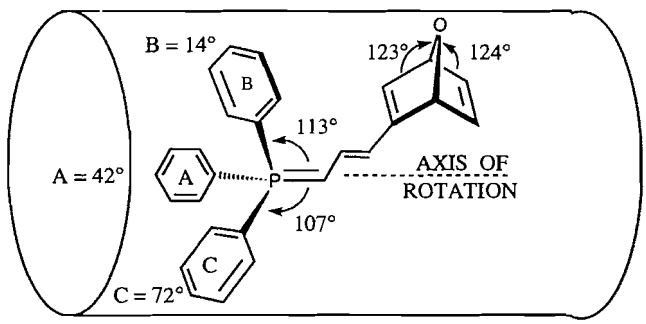

FIG. 2. Three-dimensional illustration of the dihedral angles, and of the pitch of the phenyl groups in the red triphenylphosphine–tetramer adduct **5**, omitting ester and ether groups for clarity.

phosphorus–carbon single bond (10). This establishes the existence and position of the phosphorane P=C double bond. While carbon–carbon single and double bonds in the chain are apparently about 0.1 Å shorter and 0.03 Å longer, respectively, than expected, these differences are of a similar magnitude to their estimated standard deviations. This indicates that there is little or no measurable electron delocalization along the chain. The *trans* and *transoid* orientations of ester groups on the chain were as expected. The chain ester group (C21, C22) adjacent to the oxanorbornadiene moiety was found to have a small disorder problem concerning the approximately 180° rotation of the ester group. This was resolved by using two sites for C22, with complementary occupation factors of 0.48 and 0.52. Figure 1 has been drawn with C22 attached to O12. The rest of the structure is unexceptional.

A likely pathway for the formation of this adduct is given in Scheme 2. This proposal suggests an initial electrophilic attack of the cyclopropene by triphenylphosphine that may proceed in two discrete steps or as a concerted process, as shown. This is followed by ketonization of the resulting enol to give the observed product. Two of the four possible resonance-stabilized forms are shown.

An attempt to react the tetramer **3** with triphenylphosphine oxide in ether at room temperature resulted in recovered starting materials, as expected.

TABLE 7. Bond angles for all skeletal atoms of red adduct **5** (deg)

Atoms	Angle	Atoms	Angle
C(31)—P(1)—C(1)	106.9(2)	C(4)—C(5)—O(1)	98.8(3)
C(41)—P(1)—C(1)	113.4(2)	C(4)—C(5)—O(2)	120.5(3)
C(41)—P(1)—C(31)	106.1(2)	C(6)—C(5)—O(1)	99.5(3)
C(51)—P(1)—C(1)	114.8(2)	C(6)—C(5)—O(2)	114.0(4)
C(51)—P(1)—C(31)	108.0(2)	C(6)—C(5)—C(4)	107.7(3)
C(51)—P(1)—C(41)	107.2(2)	C(7)—C(6)—C(5)	104.8(4)
C(8)—O(1)—C(5)	95.3(3)	C(13)—C(6)—C(5)	125.6(3)
C(12)—O(2)—C(5)	116.6(4)	C(13)—C(6)—C(7)	129.5(3)
C(14)—O(4)—C(13)	115.8(5)	C(8)—C(7)—C(6)	105.4(3)
C(16)—O(6)—C(15)	116.6(4)	C(15)—C(7)—C(6)	127.0(4)
C(18)—O(8)—C(17)	117.4(4)	C(15)—C(7)—C(8)	127.3(4)
C(20)—O(10)—C(19)	117.7(5)	C(7)—C(8)—O(1)	100.7(4)
C(22')—O(11)—C(21)	113.2(5)	C(9)—C(8)—O(1)	100.6(3)
C(22)—O(12)—C(21)	115.4(6)	C(9)—C(8)—C(7)	106.4(3)
C(24)—O(14)—C(23)	114.9(3)	C(17)—C(8)—O(1)	110.5(3)
C(2)—C(1)—P(1)	123.3(3)	C(17)—C(8)—C(7)	118.0(3)
C(23)—C(1)—P(1)	111.9(3)	C(17)—C(8)—C(9)	118.0(4)
C(23)—C(1)—C(2)	124.7(3)	C(8)—C(9)—C(4)	104.9(4)
C(3)—C(2)—C(1)	125.4(4)	C(19)—C(9)—C(4)	132.7(4)
C(10)—C(2)—C(1)	116.2(4)	C(19)—C(9)—C(8)	121.8(3)
C(10)—C(2)—C(3)	118.3(3)	C(2)—C(10)—O(15)	124.6(4)
C(4)—C(3)—C(2)	121.7(4)	C(2)—C(10)—O(16)	112.3(4)
C(21)—C(3)—C(2)	122.5(4)	C(32)—C(31)—P(1)	118.8(3)
C(21)—C(3)—C(4)	115.8(4)	C(36)—C(31)—P(1)	121.3(4)
C(5)—C(4)—C(3)	124.4(4)	C(42)—C(41)—P(1)	121.0(4)
C(9)—C(4)—C(3)	131.3(4)	C(46)—C(41)—P(1)	120.0(3)
C(9)—C(4)—C(5)	104.2(3)	C(52)—C(51)—P(1)	118.6(3)
O(2)—C(5)—O(1)	113.5(3)	C(56)—C(51)—P(1)	121.5(4)

[a]Estimated standard deviations are given in parentheses. Phenyl and ester bond angles, which were all normal, have been deposited (see footnote 3).

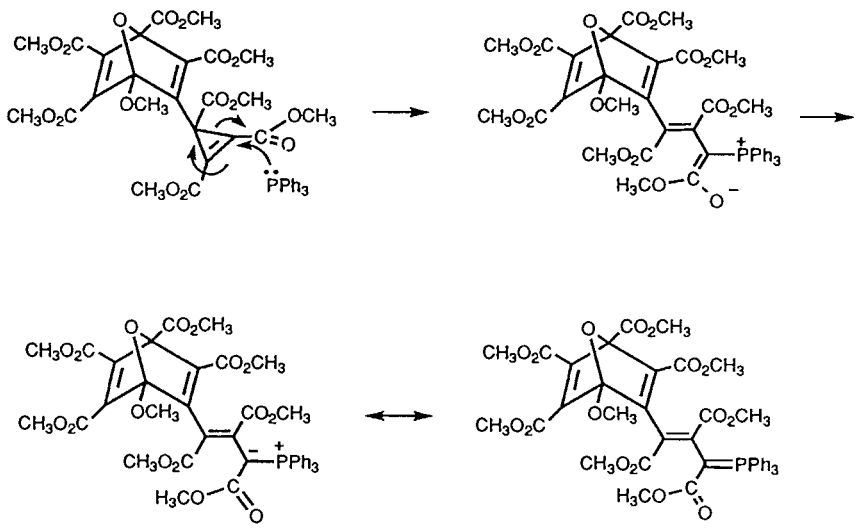

5

SCHEME 2. A possible pathway for the formation of the red triphenylphosphine–DMADC tetramer adduct **5**.

*The reaction of tetramer **3** with 1,2,5,-triphenylphosphole*

The reaction of excess tetramer with 1,2,5-triphenylphosphole at room temperature was much slower than with triphenylphosphine, and incomplete. However, if afforded the same orange crystalline product as obtained in 61% yield by short-term heating of a solution of equivalents amounts of the two reactants. An analogous product to that obtained with the tetramer and triphenylphosphine was anticipated for this reaction. However, an ^{1}H NMR spectrum of the product showed only four ester methyls, rather than the eight expected. Also the MALDI mass spectrum gave an M + 1 of 610 rather than the 882 value required for the analog expected. Hence the product was not a simple adduct of the component reagents.

Apart from the four chemically different ester methyls, the

Can. J. Chem. Downloaded from www.nrcresearchpress.com by 85.192.166.187 on 09/08/12
For personal use only.

Can. J. Chem. Downloaded from www.nrcresearchpress.com by 85.192.166.187 on 09/08/12
For personal use only.

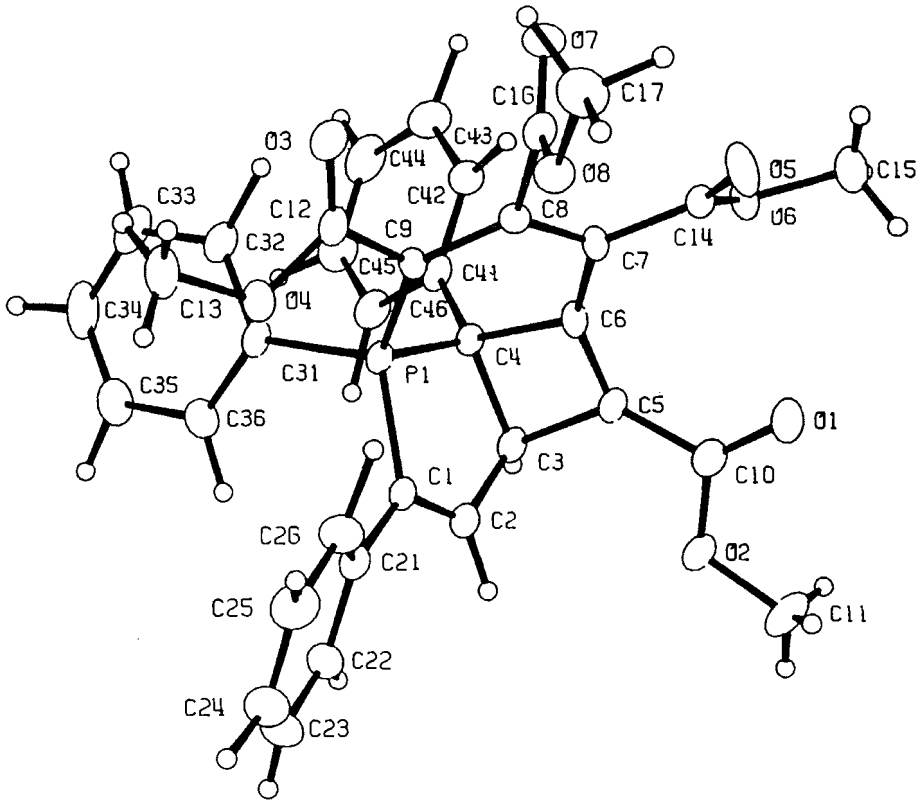

FIG. 3. ORTEP representation of the crystal structure of the orange product **11**, prepared from DMADC tetramer **3** plus 1,2,5-triphenylphosphole.

^{1}H NMR spectrum of the phosphole product demonstrated the presence of one methine hydrogen coupled to one olefinic hydrogen, with the latter also subject to a large coupling to phosphorus. This information had to be accommodated by the structure of the product. Consideration of earlier vacuum pyrolysis results of Gericke and Winterfeldt with the DMADC tetramer itself (7) and our own experience with other acetylenic adducts of the phosphole (11) led to the postulation of **11** as a possible structure. The signal for one of the ester methyls in the ^{1}H NMR spectrum was broadened, perhaps by the proximity to phosphorus (12), which is provided for by this structure. The red colour, too, is supported by the presence of the P=C chromophore conjugated to the multiple double-bonded system of this proposal.

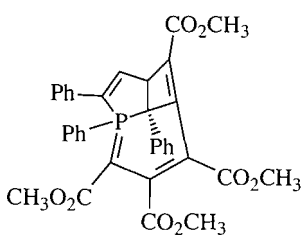

11

The three-fused-ring structure **11** originally deducted from the available NMR information for this new compound was confirmed by an X-ray structure determination of a single crystal selected from material recrystallized from a dichloromethane–hexane mixture. Figure 3 gives an ORTEP representation of the molecular structure, including hydrogen atoms that were resolved (Tables 8–10). The fusion of the cyclobutene, phosphacyclopentene, and phosphacyclohexadiene rings obtained in this product is evident in this representation. Cocrystallized dichloromethane was also observed in this crystal but the thermal values of the atoms of the solvent molecule were higher and thus obscured several of the atoms of the molecule of interest. For this reason the solvent was excluded from the structure shown although the fractional atomic coordinates, interatomic distances, and bond angles are included in Table 8 and Supplementary Tables S.5 and S.6.[3]

Mean plane and dihedral angle calculations allow further broad stereochemical interpretations. The four carbons of the phosphacyclopentene are approximately coplanar with a χ^2 of 37 for the displacements from the best mean plane. The χ^2's reported are calculated by squaring the perpendicular deviations from the best mean plane, of each of the atoms specified, and then summing these. C1 and C4 are 0.054 and 0.034 Å below the plane, C2 and C3 are 0.041 and 0.009 Å above, while the phosphorus lies virtually in the best mean plane at +0.003 Å. The dihedral angle between the mean plane of this four-carbon fragment and the plane defined by the C1-P1-C4 atoms in the phosphacyclopentene is 5.0°. This is a slightly flat-

[3]Tables of bond lengths and angles and anisotropic temperature parameters for both crystals **5** and **11** are available as supplementary material (Tables S1–S11) and can be purchased from: The Depository of Unpublished Data, Document Delivery, CISTI, National Research Council of Canada, Ottawa, ON K1A 0S2, Canada.

Tables of bond lengths and angles have also been deposited with the Cambridge Crystallographic Data Centre, and can be obtained on request from The Director, Cambridge Crystallographic Data Centre, University Chemical Laboratory, 12 Union Road, Cambridge, CB2 1EZ, U.K.

Structure factor amplitudes are no longer being deposited and may be obtained directly from the author.

Can. J. Chem. Downloaded from www.nrcresearchpress.com by 85.192.166.187 on 09/08/12
For personal use only.

TABLE 8. Fractional atomic coordinates and temperature parameters for the orange compound **11**

Atom	*x/a*	*y/b*	*z/c*	U_{eq}
P(1)	16415(16)	18616(11)	12903(6)	344(5)
C(1)	23(6)	1478(4)	971(2)	37(1)
C(2)	−721(6)	2223(5)	842(2)	41(2)
C(3)	−149(6)	3183(4)	897(2)	40(2)
C(4)	1340(5)	3098(4)	1166(2)	35(1)
O(1)	485(5)	3940(4)	−599(2)	74(2)
O(2)	−1421(4)	3567(4)	−208(2)	56(1)
O(3)	5166(4)	782(3)	1216(2)	56(1)
O(4)	3172(4)	216(3)	1427(2)	50(1)
O(5)	4257(5)	3286(4)	−438(2)	67(1)
O(6)	3183(4)	4495(3)	−77(2)	48(1)
O(7)	6025(4)	2462(3)	525(2)	51(1)
O(8)	4892(4)	1332(3)	30(2)	46(1)
C(5)	507(6)	3505(4)	365(2)	39(2)
C(6)	1768(6)	3312(4)	569(2)	36(2)
C(7)	3035(6)	3075(4)	373(2)	37(1)
C(8)	3658(5)	2286(4)	603(2)	33(1)
C(9)	3161(5)	1665(4)	1009(2)	32(1)
C(10)	−111(7)	3708(5)	−197(3)	46(2)
C(11)	−2161(8)	3708(7)	−741(3)	76(2)
C(12)	3963(7)	874(4)	1215(2)	41(2)
C(13)	3807(9)	−547(6)	1734(4)	75(2)
C(14)	3555(6)	3601(5)	−90(2)	43(2)
C(15)	3516(8)	5070(6)	−554(3)	67(2)
C(16)	5019(7)	2054(4)	384(2)	42(2)
C(17)	6121(8)	1058(6)	−213(3)	66(2)
H(21)	−167(3)	222(3)	66(2)	5(0)′
H(31)	−66(3)	355(3)	104(2)	5(0)′
H(111)	−186(3)	329(3)	−104(2)	6(0)′
H(112)	−308(4)	363(3)	−72(2)	7(0)′
H(113)	−221(3)	438(3)	−75(2)	5(0)′
H(131)	426(4)	−25(3)	208(2)	7(0)′
H(132)	323(4)	−103(3)	163(2)	6(0)′
H(133)	459(4)	−80(3)	153(2)	7(0)′
H(151)	277(3)	497(3)	−89(2)	6(0)′
H(152)	428(4)	493(3)	−61(2)	6(0)′
H(153)	321(4)	569(3)	−43(2)	7(0)′
H(171)	593(3)	64(3)	−53(2)	6(0)′
H(172)	646(3)	165(3)	−45(2)	6(0)′
H(173)	703(4)	111(3)	9(2)	7(0)′
C(21)	−381(6)	492(4)	895(2)	41(2)
C(22)	−1711(7)	230(5)	975(3)	52(2)
C(23)	−2100(8)	−683(6)	883(3)	66(2)
C(24)	−1253(9)	−1349(6)	702(3)	70(2)
C(25)	48(8)	−1104(6)	630(3)	69(2)
C(26)	485(7)	−182(5)	716(3)	55(2)
C(31)	1731(6)	1612(4)	2027(2)	41(2)
C(32)	2891(7)	1803(5)	2357(2)	56(2)
C(33)	2898(9)	1728(6)	2942(3)	72(2)
C(34)	1755(10)	1463(6)	3185(3)	78(2)
C(35)	625(9)	1265(7)	2867(3)	75(2)
C(36)	584(7)	1336(5)	2286(3)	55(2)
C(41)	1823(6)	3732(4)	1635(2)	40(2)
C(42)	3022(7)	4200(5)	1633(3)	49(2)
C(43)	3497(8)	4726(6)	2092(3)	69(2)
C(44)	2740(9)	4780(6)	2559(3)	73(2)
C(45)	1534(8)	4327(5)	2566(3)	63(2)
C(46)	1066(7)	3803(5)	2103(3)	52(2)
Cl(1)	71593(30)	39031(24)	18597(11)	1221(11)
Cl(2)	67377(43)	22353(21)	24935(16)	1658(14)
C(0)	6386(12)	2814(9)	1872(4)	135(2)
H(221)	−236(3)	75(3)	112(2)	6(0)′
H(231)	−291(3)	−81(3)	90(2)	5(0)′
H(241)	−149(3)	−202(3)	66(2)	5(0)′
H(251)	71(4)	−149(3)	47(2)	7(0)′
H(261)	158(3)	1(3)	62(2)	6(0)′
H(321)	393(3)	200(3)	217(2)	6(0)′
H(331)	374(4)	202(3)	315(2)	7(0)′
H(341)	172(3)	135(3)	362(2)	6(0)′
H(351)	−24(4)	105(3)	296(2)	7(0)′
H(361)	−31(3)	119(3)	206(2)	6(0)′
H(421)	363(3)	408(3)	133(2)	6(0)′
H(431)	448(4)	508(3)	205(2)	7(0)′
H(441)	307(3)	520(3)	291(2)	7(0)′
H(451)	89(3)	434(3)	299(2)	7(0)′
H(461)	4(3)	346(3)	209(2)	5(0)′

Estimated standard deviations are given in parentheses. Coordinates × 10^n where n = 5, 5, 4, 4, 4, 3 for Cl, P, O, N, C, H. Temperature parameters × 10^n where n = 4, 4, 3, 3, 3, 2 for Cl, P, O, N, C, H. U_{eq} = the equivalent isotropic temperature parameter. U_{eq} = 1/3 $\Sigma_i\Sigma_j U_{ij} a_i^* a_j^* (a_i \cdot a_j)$. Primed values indicate that U_{iso} is given. T = exp-($8\pi U_{iso} \sin^2 \theta/\lambda U2$). Hydrogen atom bond distances and angles and anisotropic temperature factors for nonhydrogen atoms have been deposited (see footnote 3).

TABLE 9. Interatomic distances for all skeletal atolms of the orange compound **11** (Å)[a]

Atoms	Distance	Atoms	Distance
C(1)—P(1)	1.830(6)	C(6)—C(4)	1.549(7)
C(4)—P(1)	1.812(6)	C(41)—C(4)	1.496(8)
C(9)—P(1)	1.736(6)	C(6)—C(5)	1.353(8)
C(31)—P(1)	1.792(5)	C(10)—C(5)	1.467(8)
C(2)—C(1)	1.325(9)	C(7)—C(6)	1.429(8)
C(21)—C(1)	1.474(9)	C(8)—C(7)	1.383(8)
C(3)—C(2)	1.489(9)	C(14)—C(7)	1.466(8)
C(4)—C(3)	1.590(8)	C(9)—C(8)	1.431(8)
C(5)—C(3)	1.545(8)	C(16)—C(8)	1.536(9)
		C(12)—C(9)	1.453(8)

[a]Estimated standard deviations are given in parentheses. Phenyl, ester, and hydrogen bond distances, which were all normal, have been deposited (see footnote 3).

ter ring than the equivalent angle calculated from the mean plane deviations reported for the atoms of the parent phosphole itself (13), which is 6.2°. The cyclobutene has a pronounced twist to it with C4 and C5 deviating 0.042 and 0.054 Å to one side of the mean plane and C3 and C6 deviating to about the same extent on the other (χ^2 = 263). Excluding C4, the atoms of the phosphacyclohexadiene are also nearly coplanar, with individual deviations of 0.008 Å or less and a χ^2 of 5.1. C4 is substantially below this mean plane by 0.649 ± 0.005 Å.

Dihedral angle calculations for the three-component central rings clearly demonstrate the cage-like core to this molecule. The angles for the intersecting mean planes at ring junctions P1—C4, C4—C6, and C3—C4 come out to be 57°, 42°, and 73°, respectively. A rotated ORTEP representation omitting hydrogen atoms illustrates more clearly the effect of this core semi-cage on the overall shape of the molecule (Fig. 4). Also evident from this representation is the near-orthogonal alignment to the mean plane of the phosphacyclohexadiene taken up by the three phenyls, minimizing steric interactions. The P—C9 distance, with a bond length of 1.736 Å, is 0.13 Å shorter than the normal P—C single bond, and quite similar to the 1.728 Å previously reported for a P═C double bond (9). Hence this

TABLE 10. Bond angles for all skeletal atoms of orange compound **11** (deg)[a]

Atoms	Angle	Atoms	Angle
C(4)—P(1)—C(1)	95.2(3)	C(17)—O(8)—C(16)	114.6(5)
C(9)—P(1)—C(1)	124.9(3)	C(6)—C(5)—C(3)	95.1(4)
C(9)—P(1)—C(4)	103.6(3)	C(10)—C(5)—C(3)	129.4(5)
C(31)—P(1)—C(1)	109.2(3)	C(10)—C(5)—C(6)	133.9(6)
C(31)—P(1)—C(4)	110.6(3)	C(5)—C(6)—C(4)	93.2(5)
C(31)—P(1)—C(9)	111.4(3)	C(7)—C(6)—C(4)	124.6(5)
C(2)—C(1)—P(1)	109.1(5)	C(7)—C(6)—C(5)	139.9(5)
C(21)—C(1)—P(1)	124.5(4)	C(8)—C(7)—C(6)	116.9(5)
C(21)—C(1)—C(2)	126.3(5)	C(14)—C(7)—C(6)	120.0(5)
C(3)—C(2)—C(1)	120.7(5)	C(14)—C(7)—C(8)	122.7(5)
C(4)—C(3)—C(2)	108.2(5)	C(9)—C(8)—C(7)	127.1(5)
C(5)—C(3)—C(2)	112.7(5)	C(16)—C(8)—C(7)	115.4(5)
C(5)—C(3)—C(4)	84.8(4)	C(16)—C(8)—C(9)	117.5(5)
C(3)—C(4)—P(1)	106.4(4)	C(8)—C(9)—P(1)	121.5(4)
C(6)—C(4)—P(1)	106.8(4)	C(12)—C(9)—P(1)	118.5(4)
C(6)—C(4)—C(3)	86.0(4)	C(12)—C(9)—C(8)	119.9(5)
C(41)—C(4)—P(1)	115.2(4)	C(22)—C(21)—C(1)	119.3(6)
C(41)—C(4)—C(3)	120.0(5)	C(26)—C(21)—C(1)	121.8(6)
C(41)—C(4)—C(6)	118.3(5)	C(32)—C(31)—P(1)	119.9(5)
C(11)—O(2)—C(10)	116.4(5)	C(36)—C(31)—P(1)	120.3(5)
C(13)—O(4)—C(12)	117.8(6)	C(42)—C(41)—C(4)	121.8(5)
C(15)—O(6)—C(14)	116.0(5)	C(46)—C(41)—C(4)	118.5(5)

[a]Estimated standard deviations are given in parentheses. Phenyl, ester, and hydrogen bond angles, which were all normal, have been deposited (see footnote 3).

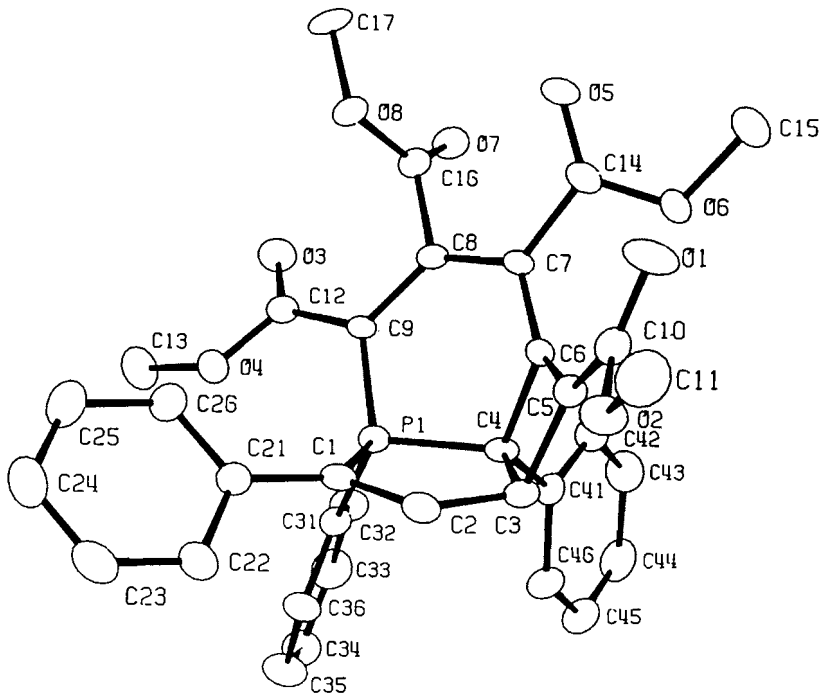

FIG. 4. ORTEP representation of the orange compound **11** without hydrogen atoms, rotated to illustrate the core semi-cage structure.

establishes the position of the phosphorane linkage. A possible indication of some charge delocalization from the positively charged phosphorus atom to the P-phenyl is indicated by a P—C31 bond length of 1.792 Å, 0.08 Å shorter than the normal. All other bond lengths to phosphorus and the olefinic and saturated linkages of the rest of the molecule are normal. The bond angles of the cyclobutene are all 90 ± 5°.

A possible pathway to the orange product **11** is given in Scheme 3. Nucleophilic attack of the cyclopropene of the tetramer by the phosphorus of the phosphole initially gives the same type of intermediate as the final product with triphenylphosphine. This process might proceed in two discrete steps, or in a concerted process as illustrated. A 2+2 intramolecular cycloaddition of a relatively reactive residual olefinic double bond in the phosphole component of this intermediate then follows, together with a reverse Diels–Alder reaction releasing furan **2** from the oxanorbornadiene component of the initial unstable adduct. Ketonization of the initially formed enol then

Can. J. Chem. Downloaded from www.nrcresearchpress.com by 85.192.166.187 on 09/08/12
For personal use only.

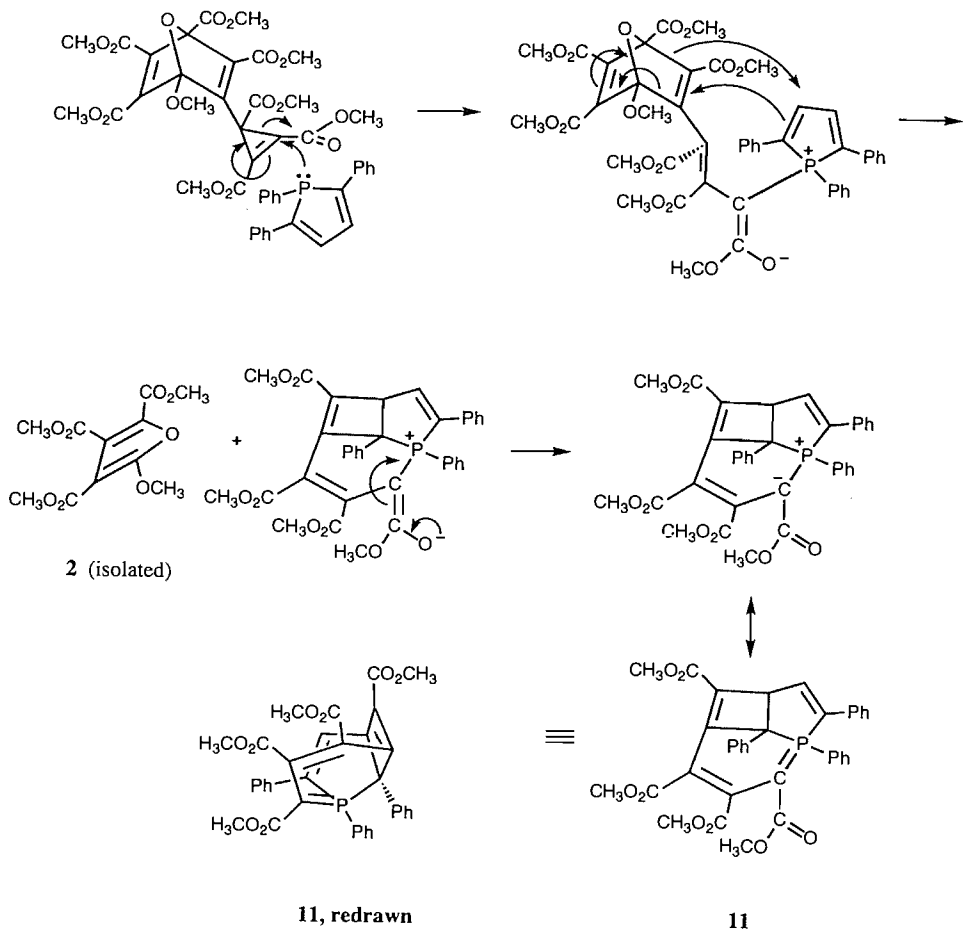

SCHEME 3. A possible pathway to the orange semi-cage product **11** from the reaction of the DMADC tetramer **3** with 1,2,5-triphenylphosphole.

gives the observed product. Two of the four possible resonance-stabilized forms are shown.

Support for the proposed pathway would be obtained if furan **2** could be observed among the products during the reaction of the tetramer **3** with 1,2,5-triphenylphosphole. The physical properties of the furan **2** are known from previous preparations by others via vacuum pyrolysis of the tetramer (7), and by thermal or other treatment of the acetylene ester itself (2,3). Accordingly, a reaction between the tetramer and phosphole specifically designed to detect the presence of the furan **2**, if formed, was carried out. The total partially isolated furan obtained from this experiment by solvent chromatography represented the equivalent of about 830 mg, or 84% of that theoretically expected from the starting amount of tetramer. The furan recovery was confirmed by isolation, from a portion of this material, of 225 mg of crystalline material of the correct melting point and ^{1}H NMR spectrum. This outcome, while it does not exclude other possible pathways to the orange product, is consistent with the pathway given.

Conclusions

We have duplicated and added refinements to earlier methods of isolation of an interesting tetramer of dimethyl acetylenedicarboxylate. With access to high-frequency NMR it has been possible to provide evidence of the presence of two, probably very similar, isomeric forms of this tetramer. Despite additional evidence of this isomeric interpretation of the NMR spectra, it has not been possible to conclusively confirm this by chemical or physical means.

Confirmation of the structure and stereochemistry of the acetylenic tetramer was obtained from an X-ray crystal structure of the triphenylphosphine adduct. Reacting 1,2,5-triphenylphosphole with the tetramer gave a new phosphorus-containing heterocycle of fused 4-, 5-, and 6-membered rings with concomitant loss of a substituted furan. Structural confirmation of this novel semi-cage product was obtained through a further X-ray crystal structure determination.

Experimental

Infrared spectra were recorded on KBr pellets using a Perkin-Elmer model 1130 instrument. Ultraviolet spectra were obtained on a Philips PU 8740 UV–VIS spectrophotometer in solvents as specified. Bruker WM 250 or Bruker AMX 360 spectrometers were used to collect magnetic resonance data at the appropriate frequency for nuclei of interest, as specified. Spectra were obtained at ambient temperature on samples dissolved in deuteriochloroform, unless otherwise specified. Shift and coupling assignments were aided by decoupling and COSY experiments, when necessary. Mass spectra were determined using a Finnegan 3300 GC–MS system, a Kratos Concept H (high field) instrument, or a Kratos MALDI (Matrix Assisted Laser Desorption Ion) time-of-flight spectrometer. For spectra from the latter instrument an ionizing matrix of 2,5-dihydroxybenzoic acid (DHB) – fucose containing a trace of trifluoroacetic acid (placed using acetonitrile) was used, first in the normal mode for rapid scanning and finally in Reflectron mode for optional resolution. Gramicidin S (Gram.SH$^+$ = m/z 1142) was used to calibrate the MALDI instrument. Melting points were carried out on a Reichert 7905 hot-stage microscope or on a Gallenkamp MF-370 Kofler aluminum block apparatus, and are uncorrected. Commercially prepared sheets (Polygram silica gel G, 254 μm UV indicator) visual-

Can. J. Chem. Downloaded from www.nrcresearchpress.com by 85.192.166.187 on 09/08/12
For personal use only.

Can. J. Chem. Downloaded from www.nrcresearchpress.com by 85.192.166.187 on 09/08/12
For personal use only.

ized by daylight, and by medium (365 μm) and short wave (254 μm) UV illumination, were used for thin-layer chromatography (TLC) for reaction monitoring or solvent chromatography screening tests. A Varian model 5000 liquid chromatograph was used for high-pressure chromatographic separations.

*Tetramer **3** of dimethyl acetylenedicarboxylate (DMADC)*

Isolation from 17-year-old sample

A small sample of the solids removed from a 17-year-old, half-used bottle of almost fully crystallized "DMADC" was triturated with 100% ethanol, and the resulting slurry was suction filtered. The filter cake of white crystals was rinsed with fresh solvent and dried, 5.6 g(ca. 80% recovery), mp 94–96°C. The tetramer mixture mass spectrum is given in Table 3. ^{1}H NMR of isomer mixture (250 MHz): 3.88 ppm (7.4 rel. intensity), 3.86 (12.6), 3.85 (11.0), 3.84 (18.0), 3.82 (9.2), 12.3H; 3.75 (7.1), 3.73 (9.2), 3.2H; 3.71 (6.6) 3.69 (8.5), 3.1H; 3.64 (6.9), 3.62 (9.1), 2.9H; 3.57 (6.8), 3.55 (9.3), 2.6H.

A 2.4 g portion of the crystalline sample above was recrystallized from 95% ethanol. First crop, 21 mg; ^{1}H NMR (250 MHz): 3.89 ppm (8.6 rel. intensity), 3.87 (12.7), 3.85 (10.8), 3.76 (8.4), 3.72 (8.9). A small portion of the mother liquor from this crystallization examined by thin-layer chromatography (TLC; developer 28:72 v/v acetone: toluene) showed four discrete spots, R_f values 0.075 (streak), 0.261, 0.36, 0.44 (streak). Tetramer blank R_f was 0.522. ^{1}H NMR (250 MHz) of a further portion of this material showed that it consisted of a complex mixture of compounds, probably contributed to by partial hydrolysis.

Samples of crystalline material dissolved in 100% ethanol, ethanol–methanol mixtures, and cyclohexane–dichloromethane mixtures were put through a high-pressure liquid chromatograph using a C_{18} reverse phase column (CSC-S, ODS2 10 μm, 25 cm × 0.46 mm), using a UV detector set at 215 nm. No isomer resolution was obtained.

*Isolation of tetramer **3** from 16-year-old DMADC*

A 1.01 g sample from a less old bottle of partially used viscous yellow (but non-crystalline) DMADC in a round-bottomed flask was heated by a silicone oil bath at 60°C under reduced pressure (1 Torr = 133.3 Pa) for 4 h and at 75°C for 4.5 h. TLC (20:80 acetone:toluene v/v) on the 0.707 g residue demonstrated the presence of the tetramer **3**, plus four other compounds, R_f values 0.0, 0.069, 0.118, 0.24, 0.32 (tetramer). Removal of DMADC monomer from another sample of old DMADC under reduced pressure (1 Torr) for 24 h at room temperature gave a 28% weight loss plus a similar residue composition.

A total of 1.195 g of combined viscous residues from which most of the monomeric ester had been removed was column chromatographed on silica gel (Baker Ltd., 60–200 mesh; packed column, 56 × 3.5 cm diam) eluting ca. 200 mL fractions 1–6 with ethyl acetate:ether (10:90 v/v). DMADC monomer (by ^{1}H NMR; 89 mg) was recovered from fraction 2. Fraction 3 (113 mg, pale yellow glass) was mostly the tetramer **3** (^{1}H NMR), which was also present together with other compounds in fraction 4 (135 mg, pale yellow glass). Fractions 5 and 6 (30 and 5 mg) were mixtures, without tetramer present. A further seven fractions (two using ethyl acetate:ether, 20:80 v/v; and five using 100% acetone) yielded a total of about 400 mg of brown gums.

Similar treatment of a further 10-year-old partially crystalline sample of dimethyl acetylene dicarboxylate showed the presence of only the low-field isomer of the tetramer, both on initial examination and from the NMR spectra of differentiated fractions.

*Preparation of **3** from fresh dimethyl acetylenedicarboxylate*

Aldrich DMADC (49.71 g; 43.0 mL) in a 250 mL round-bottomed flask was thoroughly flushed with nitrogen and, still under nitrogen, was heated by a stirred silicone oil bath at 85°C. In this inert-atmosphere modification of the method of Kauer and Simmons (5), small aliquots of the liquid were removed via syringe through a serum cap at 7–8 day intervals and examined by ^{1}H NMR for the extent of conversion to DMADC tetramer **3** (Table 1). After 23 days the viscous amber liquid, now about 61% by weight or 28 mol% tetramer, was poured into a crystallization dish and covered for 3 days. The oily crystalline mass obtained was triturated with ether, and the resulting slurry suction-filtered to give 5.94 g of clear crystals of the tetramer **3**, mp 97–100°C. ^{1}H NMR spectra all showed the presence of only the low-field isomer in all fractions (details, Table 1). Slow evaporation of the ether enabled recovery of a further 3.47 g of the tetramer in three crops, mp 96–100°C, 98–101°C, and 97–100°C, respectively. ^{13}C NMR (250 MHz): carbonyl carbons, 168.7 ppm (1.6 rel. intensity), 164.4 (1.6), 163.5 (1.5), 161.3 (1.3), 160.8 (1.5), 159.3 (1.3), 156.8 (1.7), 156.7 (1.8), 156.1 (1.4); unassigned carbons, 145.2 (1.3), 143.9 (1.2), 116.6 (1.1), 113.6 (1.8), 112.8 (2.1), 86.0 (0.4), 55.7 (6.7), 53.3 (10.7), 53.2 (14.2), 52.9 (9.2), 52.7 (8.9), 52.4 (8.3), 52.1 (7.5); ether methyl, 33.5 (0.54). Total tetramer recovery by recrystallization was 9.41 g (18.9%).

Examination of the residue left after evaporation of the solvent from the mother liquor by TLC (acetone:toluene, 30:70 v/v) gave five spots, R_f values 0.283, 0.434, 0.509, 0.547 (tetramer), and 0.604. This, and ^{1}H and ^{13}C NMR spectra, indicated that several compounds were present. A 0.924 g portion of this tetramerization residue was column-chromatographed on silica gel (Baker Ltd., 60–200 mesh; column 200 × 20 mm diameter) eluting fractions 1–3 with acetone:ether 25:75 v/v and 4 with acetone:ether, 50:50 v/v. Recoveries from fractions 2 and 3 indicated, by TLC (acetone:toluene, 15:85) and ^{1}H NMR, that mixtures were obtained. Fraction 2:four compounds; R_f values of 0.14, 0.24, 0.35, and 0.55; NMR, 30 peaks in 3.44–4.07 ppm range. Fraction 3: three compounds; R_f values 0.0, 0.13, 0.26; NMR, 32 peaks in 2.60–3.91 ppm range.

*Attempted isomerizations of the tetramer **3***

A small sample (0.10–0.52 g) of crystalline tetramer alone, or usually with 10–15% by weight of added hydroquinone, was placed in a test tube, sealed with a serum cap, and then flushed with nitrogen for several minutes. While keeping the test tube and contents under a positive pressure of nitrogen, the sample was heated by boiling solvent and vapour using toluene, bp 111°C, for the lower temperature experiments, and mixed xylenes, bp 137–144°C. for the higher temperatures. After the intended heating period the tetramer sample was allowed to cool to room temperature and the contents examined by TLC, or ^{1}H NMR, or a combination of both methods (summary, Table 2).

A tetramer sample heated at 140°C for 24 h without added hydroquinone had no residual tetramer and TLC indicated that five new compounds had formed. Development by acetone:toluene 50:50 v/v gave R_f values of 0.02, 0.30, 0.46, 0.57 (blue fluorescence), and 0.65 for these compounds. The R_f value for the tetramer spot under these conditions was also 0.57 but this showed no fluorescence.

A tetramer sample heated at 111°C for 3 h appeared by ^{1}H NMR to be ca. 90% unchanged tetramer plus ca. 10% of two or three similar compounds. TLC (acetone:toluene 10:90 v/v) gave four compounds, R_f values 0.04, 0.08, 0.21 (streak), 0.30. The R_f value of the tetramer under these conditions was 0.18. All other heating experiments except the shortest gave results intermediate between these extremes.

*Attempted deoxygenation of tetramer **3** with iron carbonyls*

Modifications of the methods of Best et al. (14) were employed. To nitrogen-flushed solutions of about 220 mg of the tetramer **3** in 20–30 mL of benzene was added a solution of exactly 1 equivalent of the iron carbonyl compound ($Fe_3(CO)_{12}$, or $Fe_3(CO)_9$) in benzene, still under nitrogen. After 3 h at 45–50°C or 7 h at room temperature, monitored by thin-layer chromatography, the solvent was removed under reduced pressure. The residue was taken up in solvent and chromatographed on Merck Kieselgel using methylene chloride, or ethyl acetate. No discrete, fully aromatic compounds were resolved on checking the various chromatography fractions by 250 MHz ^{1}H NMR.

*Reaction of the DMADC tetramer **3** and triphenylphosphine*

Tetramer **3** (635 mg), prepared by the last method described, was dissolved in 200 mL of ether at room temperature and a solution of triphenylphosphine (644 mg) in 20 mL of ether was added with stirring. During ca. 5 min the solution changed from colourless to a deep red. After suction filtration of the reaction solution and slow evaporation of the filtrate, red prisms formed, and were filtered; yield 574 mg,

Can. J. Chem. Downloaded from www.nrcresearchpress.com by 85.192.166.187 on 09/08/12
For personal use only.

mp 206–209°C. A further 253 mg was recovered in two crops, mp 207–210°C and 210–213°C, giving a total product recovery of 827 mg (89% on DMADC). A portion of this material (781 mg) was recrystallized twice more from dichloromethane–ether (ca. 5 mL) to give 640 mg of pure red crystals of the adduct **5** mp 212–214°C (lit. (5) mp 213–214°C), that were suitable for X-ray crystal structure determination. ^{1}H NMR (360 MHz): aromatic protons, 7.82 ppm, quartet, J_{PH} 7.9, J_{HH} 2.3 Hz; and 7.71 ppm, quartet, J_{PH} 7.9, J_{HH} 4.0 Hz, total 6H; aromatic multiplet, 7.50–7.36 ppm, (total 9 H); ester methyl, and methoxyl protons (no evidence of ^{31}P coupling, from decoupling experiments), 3.91, 3.84, 3.83, 3.78, 3.76, 3.74, (10.2H); 3.64, 3.63, (5.5H); 3.54 (2.1H); 3.43, 3.41, 3.32, (3.0H); 2.94 and 2.89 ppm, (3.2H). ^{31}P NMR (360 MHz) ^{1}H decoupled): 20.36 ppm (rel. intensity 4.07), 18.37 (8.00). ^{13}C NMR (360 MHz): carbonyl carbons (some coupled to ^{31}P), 171.0 ppm (rel. intensity 0.48), 170.4 (0.35), 168.6 (0.28), 168.5 (0.32), 167.1 (0.54), 166.7 (0.39), 165.5 (0.44), 165.3 (0.95), 164.5 (1.48), 163.3 (0.43), 162.5 (0.59), 161.2 (0.54), 160.9 (1.00); aromatic and olefinic carbons (some coupled to ^{31}P), 144.9 ppm (rel. intensity 0.24), 143.2 (0.51), 137.7 (0.57), 134.6 (1.8), 134.5 (1.7), 134.1 (10.7), 134.0 (10.9), 131.8 (5.3), 131.8 (3.8), 128.6 (14.9), 128.4 (14.8), 128.3 (3.5), 126.5 (1.4), 125.5 (1.3), 116.5 (0.27); ester methyl and methoxyl carbons, 55.4 ppm (rel. intensity 2.4), 53.1 (1.7), 53.0 (2.2), 52.4 (4.5), 52.0 (3.4), 51.8 (1.5), 51.6 (4.1), 51.4 (3.7), 50.9 (0.67), 50.1 (1.8), 50.2 (2.3); quaternary carbons, 52.2 ppm (intensity 0.29), 15.17 (0.93). Mass spectra of this purified material after removal of the solvent (32 h, 80°C, 1 Torr): Kratos MALDI, M + 1: 831; calcd. for $C_{42}H_{40}O_6P$, MH^+: 831.8; Kratos Concept H EI spectrum, M^+: 830.4; ^{13}C isotopic peaks (% of M^+): 831.4 (47), 832.4 (15), 833.4 (3.5); calcd. for $C_{42}H_{39}O_6P^+$: 830.8, 831.8 (47), 832.8 (22), 833.8 (10); major fragment ions at *m/z* 183.0, 262.1, 313.3 (small), 368.4, 499.2, 558.3, 771.4, 815.4.

*Reaction of tetramer **3** with triphenylphosphine in nonpolar solvent*

DMADC tetramer (2.09 g) was added, with stirring, to excess triphenylphosphine (1.5 g) dissolved in benzene. The solution instantaneously changed from colourless to deep red. It was then reduced in volume, cold ethanol was added, and the solution was allowed to crystallize. Filtration gave 2.84 g (96% on tetramer) of deep red crystals.

A small sample of the red crystals was recrystallized twice from acetone, yielding material melting at 203–207°C. UV (95% EtOH), nm (log ϵ): 202 (4.72), 223.3 (4.43), 254.5 (3.91), 458.1 (3.57); ($CHCl_3$), (log ϵ): 241 (4.17), 262.4 (3.80), 268.9 (3.77), 275.5 (3.70), 301.6 (3.45), 471.3 (3.91). IR (KBr) cm^{-1}: 2960w, 2922w, 2860w, 1740m, 1690m, 1630m, 1490w, 1430w, 1260m, 1140w, 1100w, 1030w, 720w, 700w. ^{1}H NMR (250 MHz): aromatic protons, 7.30–7.89 ppm; ester methyl protons, 3.91, 3.88, 3.83, 3.78, 3.76, 3.74, 3.63, 3.55, 3.44, 3.41, 3.33, 2.94, 2.90 ppm; ^{31}P relative to external phosphoric acid, 20.76, 18.79 ppm. ^{13}C NMR: carbonyl carbons, 165.3, 164.45, 162.5, 160.9 ppm; aromatic and olefinic carbons, 137–125 ppm; ester methyl and methoxyl carbons, 55.4–50.1 ppm (details given above).

*Attempted reaction of tetramer **3** and triphenylphosphine oxide*

Triphenylphosphine oxide (153 mg; 0.58 mmol) was dissolved with stirring into a solution of the tetramer **3** (231 mg; 0.41 mmol), previously dissolved in 5 mL of diethyl ether and held at room temperature for 5 days. TLC chromatograms indicated little or no change during this period. Evaporation of the ether and trituration of the residue gave 211 mg of colourless crystals, mp 98–102°C, and an IR spectrum identical to that of an authentic sample of the tetramer.

Colourless crystals (180 mg) were obtained from the concentrated mother liquor, mp 155–158°C. An IR spectrum indicated, by comparison with that of an authentic sample, that this was slightly impure triphenylphosphine oxide.

*Reaction of tetramer **3** with 1,2,5-triphenylphosphole at room temperature*

Finely ground phosphole (0.527 g; 1.69 mmol) was added with stirring to a solution of the finely ground tetramer (1.315 g; 2.31 mmol) in 100 mL of benzene at room temperature. The solution was stirred at room temperature for 4 days and then reduced in volume and allowed to crystallize.

The first crop of yellow crystals (198 mg) was unreacted phosphole, as indicated by ^{1}H NMR (60 MHz). A second crop of colourless crystals was unreacted tetramer (507 mg), identified by ^{1}H NMR (250 MHz) by singlets at 3.88, 3.86, 3.86, 3.84, 3.76, 3.71, 3.60, and 3.58 ppm. Crude orange crystals (354 mg; 34%, 56% with recovered phosphole) were then obtained in two crops. The best portion of this was recrystallized from 95% ethanol to give pure product **11**, mp 165–171°C. UV (95% EtOH), nm (log ϵ): 205 (4.87), 227 sh (4.59), 309.5 (4.27), 448.6 (3.83). IR (KBr) cm^{-1}: 3015w, 2995w, 2940w, 1740m, 1720m, 1700m, 1680m, 1620w, 1460m, 1440m, 1430m, 1365m, 1220s, 1200s, 1190s, 1120w, 1090w, 700w, 695w, 680w. ^{1}H NMR (360 MHz): vinylic proton, quartet, 7.91 ppm, J_{HH} 3.46, J_{PH} 38.7 Hz; aromatic protons, 6.89–7.58; methine proton, doublet, 4.52 ppm, J_{HH} 3.16 Hz; methoxy protons, 3.99, 3.73, 3.71, and 3.13 ppm; decoupled ^{31}P relative to external 85% phosphoric acid, 25.48 ppm. ^{13}C NMR (250 MHz): carbonyl carbons, 165.2, 165.1, 164.8, 161.9 ppm; aromatic and olefinic carbons, 153–122 ppm; ester methyls, 52.6, 52.0, 51.3, 50.1 ppm; methine carbon, doublet, 57.7 ppm, J_{PC} 6.31 Hz.

*Reaction of tetramer **3** with 1,2,5-triphenylphosphole with heating*

The tetramer (1.28 g; 2.25 mmol) was added with stirring to a solution of the phosphole (0.68 g; 2.17 mmol) dissolved in 100 mL toluene at room temperature, and then heated to 70–80°C for 4 h. The solution slowly changed colour from yellow to orange and thin-layer chromatography (toluene:ethanol, 95:5 v/v) at intervals indicated that only the product obtained at room temperature was being formed. On allowing the solution to cool, orange crystals of **11**, 0.803 g (61%), were produced, mp 164–170°C. Recrystallization from 210 mL of warm toluene gave pure material, 0.476 g (36%), mp 168–171°C (dec.).

*X-ray quality crystals of the phosphole product **11***

Slow recrystallization of 592 mg of the orange crystalline product **11**, from 300 mL diethyl ether plus 1% dichloromethane, yielded 51 mg of orange crystals, mp 157–159°C. These became opaque and powdery after a standing at room temperature for a short period of time. Crystallization of 274 mg of the orange compound from a dichloromethane: hexane mixture (2:3 v/v, ca. 10 mL) gave a recovery of 250 mg of suitable crystals of a 1:1 dichloromethane:compound **11** complex, mp 160–162°C (dec.). ^{1}H NMR (360 MHz): olefinic proton; 7.97 ppm, dd, J_{HH} 3.4 J_{PH} 41.8 Hz, (1 H); aromatic protons, 7.52 ppm, d, J_{HH} 5.1 Hz, (2 H); multiplet, 7.369 ppm (rel. intensity 0.37), 7.366 ppm (0.38), 7.363 (0.38), 7.359 (0.25), 7.35 (1.00), 7.343 (0.93), 7.339 (0.58), 7.335 (0.68), 7.33 (1.34), 7.32 (4.47), 7.317 (4.15), 7.31 (1.50), 7.30 (2.37), 7.290 (0.79), 7.288 (0.81), 7.285 (0.78), 7.280 (0.61), 7.275 (0.71), 7.24 (1.09), total area 5.74; double triplet, 7.15 ppm, J_{PH} 3.6, J_{HH} 7.56 Hz (meta protons of phenyl on P), area 1.87; aromatic multiplet, 7.02 ppm (rel. intensity 2.13), 7.01 (2.94), 7.00 (2.85) total area 2.85; 6.93 (1.33), 6.92 (1.23), 6.91 (0.87), total area 1.87; methine proton, 4.50 ppm, d, J_{HH} 3.4 Hz, (1 H); ester methyl protons, 3.97, 3.71, 3.69, and 3.12 ppm (each 3H). ^{13}C NMR (360 MHz): carbonyl carbons (some split or broadened by coupling to ^{31}P), 165.2 ppm (intensity 0.42), 165.1 (0.44), 164.78 (0.46), 161.79 (1.45), 161.76 (1.33); aromatic and olefinic carbons (some coupled to ^{31}P), 153.5 (0.83), 153.4 (1.03), 153.2 (0.83), 143.8 (0.33), 135.7 (1.12), 135.0 (1.02), 133.3 (1.35), 133.0 (0.73), 132.9 (0.81), 132.81 (3.93), 132.78 (4.42), 131.7 (6.19), 131.6 (5.81), 129.3 (6.39), 128.7 (8.72), 128.5 (12.12), 128.4 (16.00), 128.21 (8.61), 128.16 (8.14), 127.50 (7.65), 127.46 (7.84), 127.4 (4.81), 127.3 (3.97), 123.5 (1.70), 122.5 (1.50), 98.6 (0.53); quaternary carbon α to phosphorus, 60.3 ppm, d, J_{CP} 104.8 Hz; methine carbon β to phosphorus; 57.6 ppm, d, J_{CP} 7.0 Hz; ester methyl carbons, 52.6 ppm (rel. intensity 0.81), 51.9 (7.16), 51.3 (5.20), 50.0 (4.76). ^{31}P NMR (360 MHz): ^{1}H decoupled; 25.5 ppm (rel. intensity 11.00), 24.9 (4.40); this coalesced to a single peak at 313 K (40°C) at 25.42 ppm shift; coupled ^{31}P; overlapping dd (apparent triplet) 25.1 ppm (9.2, 11.0, 4.7), J_{H1P} ca. 40, JJ_{H2P} ca. 60 Hz. Mass spectrum: Kratos MALDI, M + 1: 610; also reproducibly 612, 614, 616 (M + 3, M + 5, M + 7); calcd. for $C_{35}H_{29}PO_8H^+$: 609.6.

Can. J. Chem. Downloaded from www.nrcresearchpress.com by 85.192.166.187 on 09/08/12
For personal use only.

*Reaction of tetramer **3** with 1,2,5-triphenylphosphole for associated products*

Tetramer (2.037 g, 3.58 mmol), was added to a solution of 1,2,5-triphenylphosphole (1.035 g; 3.31 mmol) in 250 mL of toluene and the flask and contents thoroughly flushed with nitrogen. The solution was heated at 80–100°C under nitrogen for 20 h after which time the volume was reduced to 50 mL and allowed to crystallized with slow evaporation. The resulting orange crystals were separated by filtration, and rinsed with toluene, 770 mg (38%; 49% with recovered phosphole), mp 158–162°C (dec.). The volume of the mother liquor was reduced to 10 mL and then allowed to crystallize, to recover 0.235 g of yellow needles, mp 180–183°C, identified as the starting phosphole.

For detailed examination of coproducts, a 1.765 g portion of the residual evaporated mother liquor, 1.974 g, was preadsorbed on 2.9 g of silica gel and loaded onto a silica gel column (Baker Ltd, 60–200 mesh, 53 cm × 3.5 cm diameter). The first seven fractions were eluted with 20% acetone – 80% diethyl ether, v/v, and the solvent removed, redissolved in deuteriochloroform, and examined for composition by 250 MHz ^{1}H NMR. Fractions 1 (225 mL) and 2 (100 mL) eluted nothing. Fraction 3 (100 mL) eluted 81 mg of a yellow, partially crystalline, glass that was ca. 80% furan **2**, by integration; resonances at 4.19 ppm (rel. intensity 17.4), 3.92 (17.1), 3.82 (17.0), 3.77 (14.9). The remainder of this fraction appeared to be starting phosphole, or its oxide. Fraction 4 (50 mL) gave 481 mg of a pale yellow glass that was a mixture of the starting phosphole or its oxide, the furan **2** and the tetramer **3** (approx. 9, 69, and 22 mol% respectively), by integration. This furan sample gave resonances at 4.19 ppm (rel. intensity 15.2), 3.90 (16.7), 3.83 (11.6), 3.74 (10.2), and the tetramer **3** at 3.87 (10.9), 3.85 (13.3), 3.81 (17.1), 3.75 (16.6), 3.69 (9.3), 3.62 (8.4), 3.56 (7.5). Fraction 5 (100 mL) eluted 680 mg of an orange glass that was a mixture of several compounds, unreacted tetramer being the only identifiable and largest component (51 mol%, by integration). Fractions 6–10 (100–225 mL each) gave unpromising mixtures that were not examined further.

Rechromatography of combined fractions 3 and 4 on silica gel and elution with 20% ethyl acetate – 80% toluene enabled isolation of a total of 225 mg of colourless crystals of the furan **2**, mp 115–120°C (lit. (2) mp 117–118°C; (5) mp 118–119.2°C; (3) mp 121°C) from the two middle fractions. ^{1}H NMR (250 MHz); δ: 4.22 (3.0), 3.93 (3.9), 3.84 (4.3), and 3.78 ppm (3.4 relative intensity).

*Reaction of tetramer **3** with 1,2,5-triphenylphosphole-1-oxide*

Short term

The oxide (214 mg; 0.652 mmol) was added with stirring to 407 mg (715 mmol) of the tetramer dissolved in 20 mL of dry benzene. The solution was refluxed for 5 h with no visible change, confirmed by TLC. The solution was held at room temperature for a further 7 days, and then concentrated and allowed to crystallize. The first crop was 202 mg of recovered phosphole oxide, mp 235–239°C, confirmed by IR. The second crop was 297 mg of colourless crystals, mp 98–101°C, which was unreacted tetramer **3** (IR).

Long term

The oxide (134 mg; 0.4 mmol) was added to 231 mg (0.406 mmol) of DMADC tetramer dissolved in 30 mL of benzene and allowed to stand for 9 months. The yellow colour of the phosphole oxide gradually dissipated to become nearly colourless, with accompanying deposition of an amorphous white powder. The solvent was then removed and the solid residue was triturated with acetone. The residual insoluble white powder (231 mg) was dried at room temperature, mp 320°C (dec.). This solid was insoluble in all common solvents. A mass spectrum (CI) could not be obtained. IR (KBr) cm^{-1}: 3050m, 3010m, 2930w, 1588m, 1485m, 1427m, 1295w, 1250w, 1190m, 1162s, 1100s, 1055w, 1027w, 915w, 750s, 715m, 687s, 645w, 585w, 500m.

X-ray crystallography

The experimental parameters and crystal data for both compounds are given in Table 4. In both cases data were collected at 20°C, and scattering factors for uncharged atoms were used (15). The unit cell and matrix for the red triphenylphosphine adduct **5** were refined using 25 2θ measurements in the range 50°–63°, each measured in both the positive and negative directions. Intensity measurements were made in the 2θ range 0.1°–120° from *h,k,l* 0,–13,–15 to 13,13,15. Three standard orientation reflections –4,6,0; 0,4,4; and 5,2,3 were measured every 3600 seconds of X-ray exposure time. The measurements were corrected for absorption using an empirical absorption correction on the Nonius ($\mu = 12.13$ cm^{-1}), then the EMPABS program[4] was run on the mainframe computer. The phase problem was solved and refined by SHELX-76[5] using direct methods. All non-hydrogen atoms were found for the main molecule. A small disorder problem was noted for C22, which had a site occupation factor of 0.48 where placed and (1–0.48) for C22′ for the equivalent position bonded to O11. The refinements converged with a maximum shift/esd of 0.069. The final difference map had a maximum of 0.49 e Å^{-3}, indicating that nothing had been missed. The final residuals were $R = 0.0694$, and $R_w = 0.0986$ for 542 parameters and 4714 independent reflections ($I > 2\sigma(I)$). Results are given in Tables 5–7.

The unit cell and matrix for the orange phosphole product **11** were refined using 25 2θ measurements in the range 34°–95°, again measured in both the positive and negative directions. Intensity measurements were made in the 2θ range 0.1°–130° from *h,k,l* –11,0,0 to 11,16,27. Three standard orientation reflections –4,2,6; 0,2,11; and 4,7,6, were measured every 3600 seconds of X-ray exposure time. The measurements were corrected for absorption using an empirical absorption correction on the Nonius ($\mu = 25.98$ cm^{-1}), then the EMPABS program was run on the mainframe computer. The phase problem was solved by SHELXS[6] Patterson methods and refined by SHELX-76. All atoms, including hydrogens, were found and refined. The refinements converged with a maximum shift/esd of 0.04 for hydrogens and 0.02 for non-hydrogens. The final difference map had a maximum of 0.4 e Å^{-3}, which indicated that nothing had been missed. The final residuals were $R = 0.0683$, and $R_w = 0.0710$ for 540 parameters and 3180 independent reflections ($I > 3\sigma(I)$). Results are given in Tables 8–10.

Acknowledgements

The authors thank Arthur Perlin, McGill University, for a sample of old, partially tetramerized, dimethyl acetylenedicarboxylate, K. Beveridge for the X-ray crystal structures, and Colin Moore, of Kratos Analytical, for the MALDI spectra. The Government of British Columbia and the University of Victoria are thanked for financial support of this work.

1. G.L. Thayer, Jr. Ph.D. Thesis, Cornell University, 1965; Diss. Abstr. **26** 104 (1965).
2. C.F. Huebner, E. Donoghue, L. Dorfman, F.A. Stuber, N. Danieli, and E. Wenkert. Tetrahedron Lett. 1185 (1966).
3. E. Winterfeldt and G. Giesler. Angew. Chem. Int. Ed. Engl. **5**, 579 (1966).
4. A.N. Hughes and M. Woods. Tetrahedron, **23**, 2973 (1967).
5. J.C. Kauer and H.E. Simmons. J. Org. Chem. **33**, 2721 (1968).
6. E. LeGoff and R.B. LaCount. Tetrahedron Lett. 2333 (1967).
7. R. Gericke and E. Winterfeldt. Tetrahedron, **27**, 4109 (1971).
8. H.J. Bestmann, G. Joachim, I. Lengyel, J.F.M. Oth. R. Merényi, and H. Weitkamp. Tetrahedron Lett. 3355 (1966).

[4]An empirical absorption correction program for the Nonius diffractometer written by G.W. Bushnell of this department. This is based on the ENRAF–Nonius program. The absorption correction is measured as a function of ψ for a conveniently placed reflection, and the experimental curve is used to correct other reflections. For details see ref. 16 and the Nonius CAD4 manual.

[5]G.M. Sheldrick. A program for crystal structure determination. Anorganisch-Chemisches Institut der Universitat Gottingen, Tammannstrasse 4, Göttingen, Germany.

[6]G.M. Sheldrick and E. Egert. A program for crystal structure determination. Anorganisch-Chemisches Institut der Universitat Gottingen, Tammannstrasse 4, 3400 Gottingen, Germany.

9. O. Kennard, W.D.S. Motherwell, and J.C. Coppola. J. Chem. Soc. (C), 2461 (1971).
10. R.C. Weast (*Editor*). Handbook of chemistry and physics. 56th ed. CRC Press Ltd., Cleveland, Ohio. 1975. p. F-211.
11. M.B. Hocking and F.W. van der Voort Maarschalk. Can. J. Chem. **71**, 1873 (1993).
12. N.E. Waite, J.C. Tebby, R.S. Ward, and D.H. Williams. J. Chem. Soc. (C), 1100 (1969).
13. W.P. Ozbirn, R.A. Jacobsen, and J.C. Clardy. Chem. Commun. 1062 (1971).
14. W.M. Best, P.A. Collins, R.K. McCulloch, and D. Wege. Aust. J. Chem. **35**, 843 (1982).
15. D.T. Cromer and J.T. Waber. *In* International tables for X-ray crystallography. Vol. IV. *Edited by* J.A. Ibers and W.C. Hamilton. Kynoch Press, Birmingham. 1974.
16. A.C.T. North, D.C. Phillips, and F.S. Mathews. Acta Crystallogr. Sect. A: Cryst. Phys. Diffr. Theor. Gen. Crystallogr. **A24**, 351 (1968); and the Nonius CAD4 Manual.

Can. J. Chem. Downloaded from www.nrcresearchpress.com by 85.192.166.187 on 09/08/12
For personal use only.

Micellar catalysis in mixed anionic/cationic surfactant systems

YVETTE L. FAVARO AND VINCENT C. REINSBOROUGH
Department of Chemistry, Mount Allison University, Sackville, NB E0A 3C0, Canada

Received July 27, 1994

YVETTE L. FAVARO and VINCENT C. REINSBOROUGH. Can. J. Chem. **72**, 2443 (1994).

Dye solubility and stopped-flow kinetic studies were conducted in sodium dodecylsulfate/dodecyltrimethylammonium bromide and sodium dodecylsulfate/decyltrimethylammonium bromide micellar solutions with excess anionic surfactant. The enhanced rate in the presence of anionic micelles of the $Ni^{2+}_{(aq)}$/pyridine-2-azo-*p*-dimethylaniline (PADA) complexation reaction was used as a probe of the mixed micellar situation. PADA solubilities and the kinetic parameters derived through the Robinson model for micellar catalysis were consistent with a complete incorporation of the cationic surfactant into the sodium dodecylsulfate micelles.

YVETTE L. FAVARO et VINCENT C. REINSBOROUGH. Can. J. Chem. **72**, 2443 (1994).

On a effectué des études de solubilité de colorant et de cinétique à flux stoppé dans des solutions micellaires de dodécylsulfate de sodium/bromure de dodécyltriméthylammonium et de dodécysulfate de sodium/bromure de décyltriméthylammonium dans lesquelles l'agent tensioactif est en excès. On a utilisé l'augmentation de la vitesse de la réaction de complexation $Ni^{2+}_{(aq)}$/pyridine-2-azo-*p*-diméthylaniline (PADA) en présence de micelles anioniques comme sonde d'une situation micellaire mixte. Les solubilités du PADA et les paramètres cinétiques obtenus à l'aide du modèle de Robinson pour les catalyses micellaires sont en accord avec une incorporation complète de l'agent de surface cationique dans les micelles de dodécylsulfate de sodium.
[Traduit par la rédaction]

Can. J. Chem. Downloaded from www.nrcresearchpress.com by 85.192.166.187 on 09/08/12
For personal use only.

Introduction

From both the industrial and theoretical points of view, surfactant mixtures are currently of much interest because, for reasons not quite clear, they are more efficient than single surfactants in a wide variety of applications. Anionic/cationic surfactant mixtures are an especially intriguing subset because the opposite charges must give rise to unusual solution aggregates of "pseudononionic" character (1). As if by way of confirmation, their limited miscibility ranges point to contentious forces at work that find early resolution in phase separation or liquid crystal formation, sometimes preceded by vesicle formation (2). Yet, the form and composition of the "micelles" present in solution are problematic. To this end, solubility and rate enhancement studies have been undertaken in the anionic-rich side of the phase diagram for solutions of sodium dodecylsulfate (SDS) with added dodecyltrimethylammonium bromide (DTAB) (X = 0.10, 0.20 and 0.30) or decyltrimethylammonium bromide (DeTAB) (X = 0.10 and 0.20). Both techniques have been shown in this laboratory to be informative of and sensitive to structural micellar adaptations resulting from additives (3), solubilizates (4) and surfactant mixtures (5–8). The chosen concentration ranges mirror the complete miscibility ranges in SDS-rich solutions. Beyond these mole fractions in DTAB or DeTAB at room temperature, the solutions are cloudy or give rise to precipitates.

Experimental

Solubilities of the hydrophobic dye, pyridine-2-azo-p-dimethylaniline (PADA), were obtained spectrophotometrically in mixed surfactant systems at 25.0°C as described previously (8, 9). Kinetic data on the $Ni^{2+}_{(aq)}$/PADA complexation reaction were obtained at the same temperature by mixing $NiNO_3$ and PADA solutions in a Cantech stopped-flow apparatus under pseudo-first-order conditions (10^{-3} mol dm^{-3} Ni^{2+} and 10^{-5} mol dm^{-3} PADA) at pH 7.2 ± 0.1. Surfactants and other reagents were the best available commercially.

Results and discussion

(a) Solubilities

The solubility of PADA in SDS solutions increases in proportion to the surfactant concentration beyond the critical micelle concentration (CMC) until at 0.18 mol dm^{-3} SDS (Fig.1), it is approximately a thousand times greater than its value in water (1.5×10^{-4} mol dm^{-3} (10)). At SDS concentrations lower than the CMC (8.5 mmol dm^{-3} SDS), the solubility of PADA shows little change from its pure water value. Similarly micellar DTAB increases the solubility of PADA about 500 times at 0.18 mol dm^{-3} DTAB. When the CMC of DTAB, which is twice as large in value, is taken into account (0.0153 mol dm^{-3} DTAB from the break in the solubility curve; agreed with literature values (11)), PADA is seen to be equally well solubilized by DTAB as by SDS. Despite their differences in charges either micelle

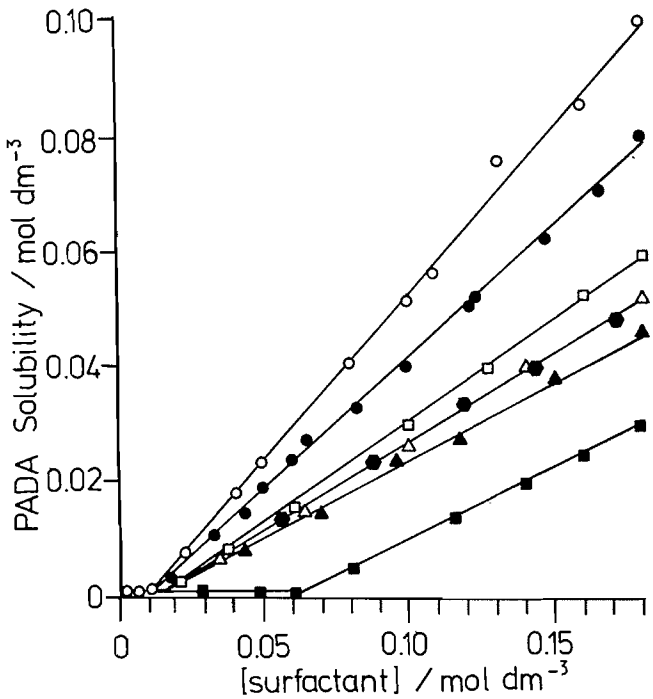

FIG. 1. Solubility of PADA as a function of total surfactant concentration: ○ SDS, □ DTAB, ■ DeTAB, ● SDS-DTAB (X_{DTAB} = 0.10) and SDS–DeTAB (X_{DeTAB} = 0.10), △ SDS–DTAB (X_{DTAB} = 0.20), ⬣ SDS–DeTAB (X_{DeTAB} = 0.20), ▲ SDS–DTAB (X_{DTAB} = 0.30).

TABLE 1. Binding constants, CMC, reaction volumes, and R_{MAX} values for SDS-rich mixtures with DTAB and DeTAB.

System	K_{PADA} (dm^3 mol^{-1})	CMC[a] (mmol dm^{-1})	K_{Ni} (dm^3 mol^{-1})	V (dm^3 mol^{-1})	R_{MAX}
SDS	2400	8.5	220	0.91	ca.170
SDS(X = 0.90) – DTAB	1650	6.9	150	0.81	ca.120
SDS(X = 0.80) – DTAB	1150	6.6	30	0.30	75
SDS(X = 0.70) – DTAB	870	6.5	—	—	55
SDS(X = 0.90) – DeTAB	1200	6.0	80	0.53	ca.130
SDS(X = 0.80) – DeTAB	1450	6.7	30	0.34	80
DTAB	1400	15.3	—	—	—
DeTAB	850	61	—	—	—

[a]From PADA solubilities

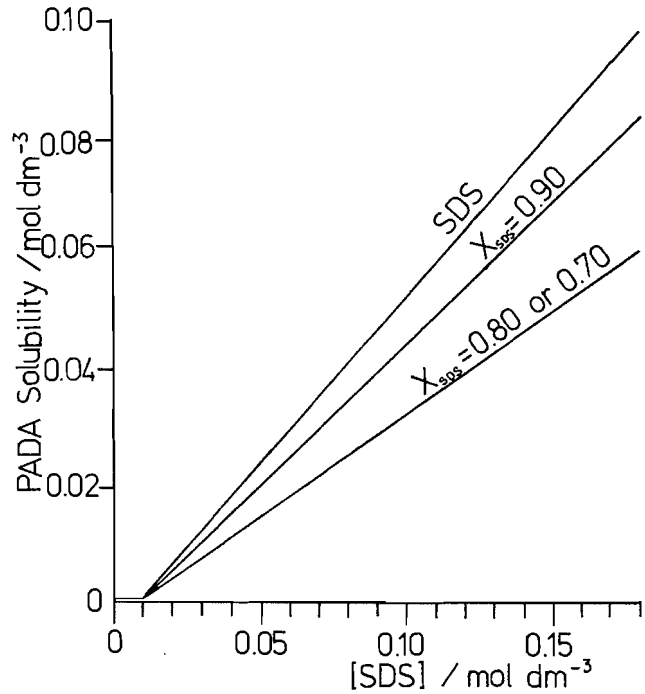

FIG. 2. Solubility of PADA as a function of SDS concentration in mixed micelles containing DTAB and DeTAB. (cf. Fig. 1 for an explanation of data points).

must present a similarly favorable hydrophobic interior environment to PADA.

When DTAB is added to SDS micellar solutions, the solubility of PADA is still enhanced but not as markedly (Fig. 1). In fact, in the X_{DTAB} = 0.30 system, the solubility of PADA per total surfactant is less than what it is in pure DTAB. Comparing solubilities on a total surfactant basis may not be the correct yardstick because it presumes that SDS and DTAB are in such a form as to be both promoting PADA solubilization in a similar manner. If, on the other hand, in SDS-rich solutions, the solubilizing agents are SDS micelles into which DTAB and PADA have been simply assimilated (9, 12), a more informative approach might be to plot solubility against SDS concentration. When this is done (Fig. 2), DTAB is still is seen as working adversely against PADA solubilization but for the X_{DTAB} = 0.20 and X_{DTAB} = 0.30 systems the depressant effect is the same.

DeTAB has a much greater CMC (0.061 mol dm^{-3} DeTAB from solubility measurements; again in ageement with the literature (11)) as befits its shorter chain length and at 0.18 mol dm^{-3} DeTAB solubilizes PADA about 200 times better than does pure water (Fig. 2). In SDS mixes to X_{DeTAB} = 0.20 beyond which concentration the solutions become cloudy, DeTAB acts roughly in the same fashion and to the same extent as DTAB in modifying PADA solubility despite the fact that it has greater disparity acting as a surfactants between DeTAB and SDS than that between DTAB and SDS. These data support the view that DeTAB and DTAB become totally absorbed into SDS micelles in the clear, SDS-rich part of the phase diagrams. The two cationic surfactants are assimilated as in the case of any hydrophobic molecule, without causing any great change in the SDS micelle size or shape (2).

The CMC values of the mixtures as revealed by PADA solubility data are listed in Table 1. The remarkable constancy among the values reinforces the notion that DTAB and DeTAB act interchangebly in determining the properties of the SDS micelles which act as their host.

One method by which the solubilization power of surfactants on solutes such as PADA can be compared quantitatively is through the association constant K_{PADA}, defined as $(S - S_0)/(C_T - CMC)S_0$ where S and S_0 are the solubilities of PADA in the micellar solution and in pure water respectively and C_T – CMC is the surfactant concentration in micellar form (C_T is the total surfactant concentration) (9). K_{PADA} values emerge as the slopes of the linear plots of $(S - S_0)/S_0$ against $(C_T - CMC)$ and are listed in Table 1 for the systems investigated.

(b) Rate enhancements

An extremely sensitive, indirect method of monitoring anionic micellar change is through rate enhancements that the micelles exert on the $Ni^{2+}_{(aq)}$/PADA complexation reaction (3–7). Below the CMC, the observed rate constant is simply the pure water value but the onset of micellization is heralded by a dramatic increase in the forward reaction. This occurs when oppositely charged $Ni^{2+}_{(aq)}$ ions and hydrophobic PADA are attracted to the anionic micelles for different reasons. As the micelles multiply with increasing surfactant concentration, the rate enhancements diminish as the reactants become effectively diluted in the concentrated micelle region. The measure of this rate enhancement is conveniently expressed as R, the ratio of k_{obs} in micellar solution ($^{m}k_{obs}$) to k_{obs} in water alone. Figure 3 depicts the R values for the SDS–DTAB system when X_{DTAB} = 0, 0.10, 0.20, and 0.30 and Fig. 4 for the SDS-DeTAB system when X_{DeTAB} = 0, 0.10 and 0.20.

If cationic surfactants are incorporated into the anionic micelles in some form, the effectiveness of the anionic micelles to act as catalysts for the probe reaction will decrease since the electrostatic attraction between $Ni^{2+}_{(aq)}$ and the mixed micelle is decreased. The PADA solubility treatment above shows that

Can. J. Chem. Downloaded from www.nrcresearchpress.com by 85.192.166.187 on 09/08/12
For personal use only.

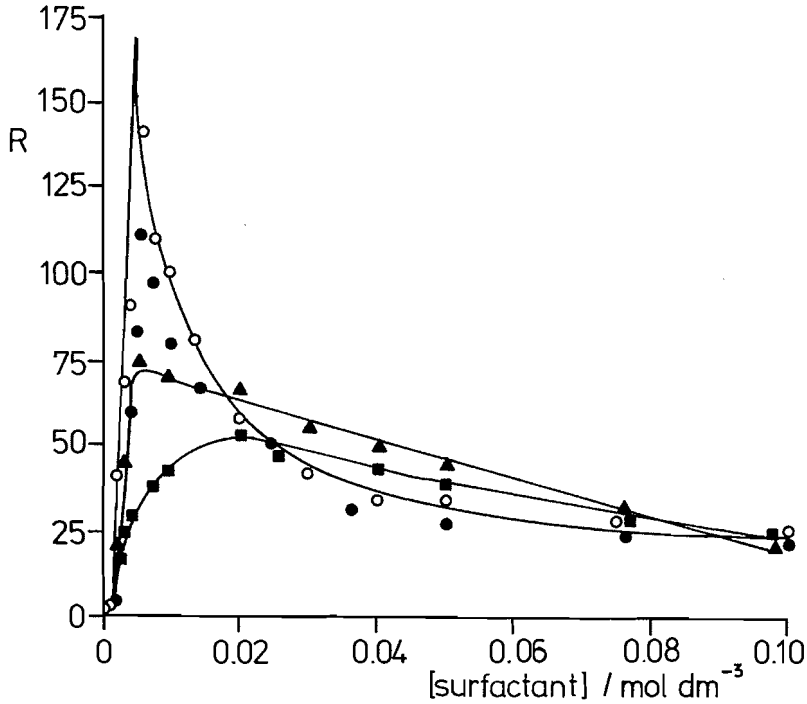

FIG. 3. Rate enhancements (R) of Ni^{2+}/PADA complexation in mixed SDS–DTAB systems: ○ SDS, ● SDS–DTAB (X_{DTAB} = 0.10), ▲ SDS–DTAB (X_{DTAB} = 0.20), ■ SDS–DTAB (X_{DTAB} = 0.30). To avoid confusion, the best-fit curve is omitted for the X_{DTAB} = 0.10 system.

PADA is slightly less attracted to mixed micelles than to pure SDS micelles and this will also lead to a slight reduction in R when switching from the SDS–DTAB system to the SDS–DeTAB system. Figures 3 and 4 confirm this conclusion. The Robinson model for the probe reaction occurring in both the bulk of the solution and in the micelles gives the following relationship for $^{m}k_{obs}$ (9, 10):

$$^{m}k_{obs} = {}^{m}k_f[Ni^{2+}]/\{CV[1 + (CK_{Ni})^{-1}][1 + (CK_{PADA})^{-1}]\}$$

where $^{m}k_f$ is the second-order rate constant in micellar solution which can be reasonably assumed to equate its value in aqueous solution (1.2×10^3 dm^3 mol^{-1} s^{-1}), C is the micellar surfactant concentration, i.e., the total surfactant concentration less the CMC, and V is the molar reaction volume of the surfactant. For mixed systems, the total concentration includes both surfactants. The parameter V usually is approximately the same as the molar volume of the surfactant. K_{Ni} is defined analogously to K_{PADA}, i.e., $K_{Ni} = [Ni^{2+}]_m/C[Ni^{2+}]_b$ where subscripts m and b denote the micellar surface and bulk solution pseudophases respectively. Curve-fitting of the kinetic data to the above expression yields K_{Ni} and V parametrically while K_{PADA} is obtained from solubility measurements as outlined previously. Table 1 lists the best fit values for K_{Ni} and V and estimates of the maximum value of R (R_{MAX}) for each investigated surfactant system. The system SDS–DTAB (X_{DTAB} = 0.30) was not included in this analysis since the fitted results were erratic, as might be expected on approaching a phase transition. Cationic surfactants inhibit the probe reaction so that the kinetically derived parameters could not be obtained for DTAB and DeTAB.

The first simple micellar model to explain the solubility and kinetic data for the mixtures would have the anionic and cationic micelles form independently, i.e., with no intermingling of monomeric surfactant ions. Thus, in the mixtures, SDS micelles would form first as the concentration of total surfactant was increased. The formation of the cationic micelles would occur at much higher concentrations (extreme right of Figs. 3 and 4), and this would have a catastrophic effect on the observed rate enhancements as PADA but not $Ni^{2+}_{(aq)}$ would be extracted from the solution. No abrupt quenching of the rate enhancement was observed. Also, the R_{MAX} values and the shape of the R curve, among other quantities, would not be as drastically changed as Figs. 3 and 4 indicate they were, if the cationic surfactant was simply a spectator ion. Even given the fact that the present analysis neglects ionic strength and excluded volume considerations, it is clear that this scenario of two "pure" micelles is not supported by the kinetic and solubility data for the systems at hand.

A more likely picture is that SDS micelles are formed which then solubilize the cationic surfactant monomers. The percent of DTAB or DeTAB solubilization is open to question but Kamenka et al. (2) have reported that their tracer self-diffusion and specific electrode potentiometry results signify that all the DTAB is accommodated by SDS micelles without any appreciable increase in size. Our work concurs with this assessment. A total incorporation of oppositely charged DTAB or DeTAB into the SDS micelles would have to occur to explain the precipitous decline of K_{Ni} from 220 to 30 when 20 mol% of cationic surfactant is present. On being assimilated within the SDS micelles, the cationic monomers displace the Na^+ counterions leading to a lower effective micellar charge (2). At 30 mol% DTAB, the kinetic analysis according to the Robinson equation by which the values of K_{Ni} and V might be obtained proved intractable, signifying a breakdown in the modelling situation. Indeed, Kamenka et al. (2) had found evidence of vesicle formation beyond 30 mol% in this same system and, in an allied system involving SDS, Marques et al. (13) reported vesicles in even dilute surfactant solutions. Spontaneous vesicle formation is commonplace with catanionic surfactants that are essentially 1:1 combinations of anionic and cationic surfactants but with the counterions removed (14). Catanionic "micelles" represent a

Can. J. Chem. Downloaded from www.nrcresearchpress.com by 85.192.166.187 on 09/08/12
For personal use only.

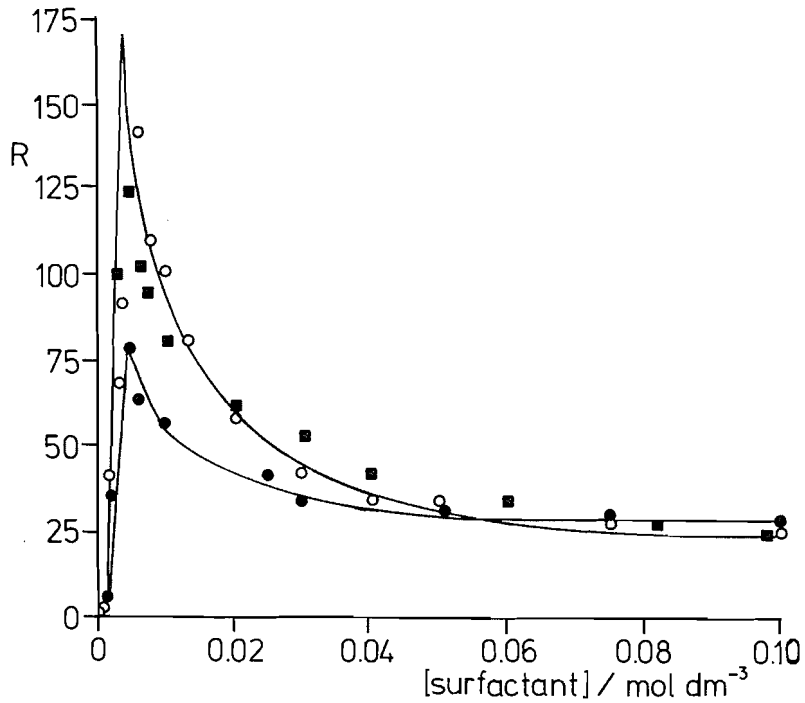

FIG. 4. Rate enhancements (R) of Ni^{2+}/PADA complexation in mixed SDS–DeTAB systems: ○ SDS, ■ SDS–DeTAB (X_{DETAB} = 0.10), ● SDS–DeTAB (X_{DeTAB} = 0.20). To avoid confusion, the best-fit curve is omitted for the X_{DeTAB} = 0.10 system.

no-charge situation but even at 30 mol% DTAB the electrostatic attraction experienced by $Ni^{2+}_{(aq)}$ with the mixed micelle or vesicle must be greatly reduced.

Another telling parameter that emerges from the Robinson model is the reaction volume which for either DTAB or DeTAB at $X = 0.20$ is reduced roughly to a third of the value found in pure SDS micelles (Table 1). To account for this dramatic reduction in V for a micelle that has not undergone a change in size, only about one in every three SDS monomers can be effective in attracting $Ni^{2+}_{(aq)}$ to the mixed micelle (PADA is equally well incorporated into cationic or anionic micelle when the surfactant chain lengths are comparable). If ion-pairing between oppositely charged monomers were occurring, then it might be expected that in a 20 mol% DTAB or DeTAB system three of every four SDS monomers would be available as micellar binding sites for $Ni^{2+}_{(aq)}$. This would lead to about a 30% reduction in V, which is much less than what is actually observed. Clearly, the incorporation of the oppositely charged surfactant monomer into the micelle is more seriously disruptive to the SDS micelle in its role in promoting the Ni^{2+}/PADA complexation reaction.

Rather than forming a distinctive ion-pair with an SDS monomer, a DTAB or DeTAB monomer might simply find itself in the mixed micelle with SDS monomers as the next nearest neighbours. This would be a region of the micelle to which $Ni^{2+}_{(aq)}$ would be minimally attracted and thus a large fraction of nominally "free" SDS monomers would be eliminated as possible $Ni^{2+}_{(aq)}$ micellar binding sites. An argument in this vein makes the observed 70% reduction in reaction volume in SDS micellar systems containing 20 mol% DTAB or DeTAB more reasonable. Mixed micellar systems of this type clearly do not admit yet of comprehensive solutions but their study is worth pursuing because of the valuable insight their interesting properties must provide for micellization phenomena in general.

Acknowledgement

We are grateful to the Natural Sciences and Engineering Council of Canada for providing funding for this project and an Undergraduate Research Scholarship to Y.L.F.

1. A. Mehreteab and F.J. Loprest. J. Colloid Interface Sci. **125**, 602 (1988).
2. N. Kamenka, M. Chorro, Y. Talmon, and R. Zana. Colloids Surf. **67**, 213 (1992).
3. J.R. Hicks and V.C. Reinsborough. Can. J. Chem. **62**, 990 (1984).
4. J.R. Hicks and V.C. Reinsborough. *In* Surfactants in solution. Vol. 2. *Edited by* K.L. Mittal and B. Lindman. Plenum Press, New York. 1984. p. 1207.
5. P.D.I. Fletcher, J.R. Hicks, and V.C. Reinsborough. Can. J. Chem. **61**, 1594 (1983).
6. V.C. Reinsborough, T.D.M. Stultz, and X. Xiang. Aust. J. Chem. **43**, 11 (1990).
7. T.J. Connolly and V.C. Reinsborough. Can. J. Chem. **70**, 1581 (1992).
8. T.J. Connolly, V.C. Reinsborough, and X. Xiang. Aust. J. Chem. **45**, 769 (1992).
9. V.C. Reinsborough and B.H. Robinson. J.Chem. Soc. Faraday Trans. 1. **75**, 2395 (1979).
10. P.D.I. Fletcher and B.H. Robinson. J. Chem. Soc. Faraday Trans. **80**, 2417 (1984).
11. P. Mukerjee and K.J. Mysels. *In* Critical micelle concentrations of aqueous surfactant systems. NSRDS-NBS 36. U.S. Government Printing Office, Washington. 1971.
12. M. Chorro and N. Kamenka. J. Chim. Phys. **88**, 515 (1991).
13. E. Marquest, A. Khan, M. Migueli, and B. Lindman. J. Phys. Chem. **97**, 4729 (1993).
14. B. Jonsson, P. Jokela, A. Khan, B. Lindman, and A. Sadaghiani. Langmuir **7**, 889 (1991).

Can. J. Chem. Downloaded from www.nrcresearchpress.com by 85.192.166.187 on 09/08/12
For personal use only.

Porphyrin chemistry pertaining to the design of anti-cancer drugs; part 2, the synthesis and *in vitro* tests of water-soluble porphyrins containing, in the *meso* positions, the functional groups: 4-methylpyridinium, or 4-sulfonatophenyl, in combination with phenyl, 4-pyridyl, 4-nitrophenyl, or 4-aminophenyl

GUANGZHEN G. MENG AND BRIAN R. JAMES[1]

Department of Chemistry, University of British Columbia, Vancouver, BC V6T 1Z1, Canada

AND

KIRSTEN A. SKOV AND MLADEN KORBELIK

BC Cancer Research Centre, Vancouver, BC V5Z 1L3, Canada

Received July 7, 1994

GUANGZHEN G. MENG, BRIAN R. JAMES, KIRSTEN A. SKOV, and MLADEN KORBELIK. Can. J. Chem. **72**, 2447 (1994).

Water-soluble, *meso*-substituted porphyrins are synthesized by sulfonation or methylation of the phenyl or pyridyl groups, respectively, of some non-water-soluble functionalized porphyrins that we have recently synthesized (Can. J. Chem. **72**, 1894 (1994)). Twelve anionic sulfonated and seven cationic methylpyridinium porphyrins, usually containing other functional groups (phenyl, pyridyl, nitro- and amino-phenyl), are reported on. Twelve of these porphyrins are new, and all nineteen porphyrins are characterized by ^{1}H NMR. UV–VIS data are presented for the isolated porphyrins, while mass spectral data are noted for selected compounds. Partition coefficients of the porphyrins in octanol–water, and the accumulation of the porphyrins in HT-29 cells of a human-cancer tumor, were measured and both were inversely related to the charges of the porphyrins. The 11 porphyrins soluble in biological buffer solutions are basically nontoxic to Chinese hamster ovary (CHO) cells in oxic or hypoxic conditions or to aerobic HT-29 cells at the 100 μM concentration used (which is sometimes limited by solubility). No significant X-ray radiosensitization was observed for selected porphyrins toward CHO cells at the 100 μM concentrations used, but some photosensitized cell kill (using 630 nm light) was observed using the disodium salt of 5,10-bis(4-pyridyl)-15,20-bis(4-sulfonatophenyl)porphyrin (**24**).

GUANGZHEN G. MENG, BRIAN R. JAMES, KIRSTEN A. SKOV et MLADEN KORBELIK. Can. J. Chem. **72**, 2447 (1994).

On a synthétisé des porphyrines hydrosolubles, substituées en *méso*, en procédant à la méthylation ou à la sulfonation respectivement des groupes phényles ou pyridyles de quelques porphyrines fonctionnalisées, non solubles dans l'eau, qui ont été synthétisées récemment (Can. J. Chem. **72**, 1894 (1994)). On présente des données relatives à 12 porphyrines anioniques sulfonées et à 7 porphyrines méthylpyridinium cationiques, qui contiennent généralement d'autres groupes fonctionnels (phényle, pyridyle, nitro- et amino-phényle). Douze de ces porphyrines sont nouvelles et on a caractérisé les dix-neuf par RMN du ^{1}H. On présente des données d'UV–visible pour les porphyrines isolées et on rapporte de données de spectres de masse pour certains composés. On a mesuré les coefficients de partition des porphyrines dans un mélange octanol–eau ainsi que leur accumulation dans les cellules tumorales HT-29 du cancer humain; les deux ensembles de données présentent une relation inversée avec les charges des porphyrines. Les onze porphyrines solubles dans des solutions de tampon biologique sont essentiellement non toxique pour les cellules des ovaires du hamster chinois (OHC), dans des conditions oxiques ou hypoxiques, ou pour les cellules aérobiques HT-29, à la concentration de 100 μM utilisée (qui est quelquefois limitée par la solubilité). On n'a pas observé de radiosensibilisation marquée aux rayons X des porphyrines aux cellules OHC aux concentrations de 100 μM utilisées; toutefois, on a observé que quelques cellules ont été tuées par photosensibilisation (utilisant de la lumière à 630 nm) lorsqu'on a utilisé de sel disodique de la 5,10-bis(4-pyridyl)-15,20-bis(4-sulfonatophényl)porphyrine (**24**).

[Traduit par la rédaction]

Introduction

Synthetic water-soluble porphyrins have been reported to accumulate in tumors (1), and such compounds containing pyridinium, sulfonato, or carboxylato substituents, and their metal complexes, have also been briefly noted to be effective radiosensitizers, although no experimental details were given for the synthetic work (2). In a search for more effective radiosensitizers, modified water-soluble porphyrins and their metallated derivatives became of interest to us (3) because of their potential to accumulate in tumors, their potential to act as radiosensitizers during irradiation of cells, and their ease of testing in aqueous buffers.

The well-known anionic porphyrin, 5,10,15,20-tetra(4-sulfonatophenyl)porphyrin, abbreviated as Tet(SPh)P (**21**) in this work (Fig. 1), also labelled TSPP or $TPPS_4$ by others (4), has four negative charges and this may prevent easy diffusion of this porphyrin through highly hydrophobic, biological bilayers. Less highly charged anionic porphyrins, including $TPPS_3$ (5-phenyl-10,15,20-tris(4-sulfonatophenyl)porphyrin) (5–7), *cis*- and *trans*-$TPPS_2$ (5,10-diphenyl-15,20-bis(4-sulfonatophenyl)-porphyrin and (5,15-diphenyl-10,20-bis(4-sulfonatophenyl)-porphyrin) (6, 7), $TPPS_1$ (5,10,15-triphenyl-20-(4-sulfonatophenyl)porphyrin) (6, 7), and (APh)T(SPh)P (5-(4-aminophenyl)-10,15,20-tris(4-sulfonato-phenyl)porphyrin) (**17**) (8), have also been addressed in the literature for medicinal interests, and the results encouraged further investigations by us on similar compounds containing a larger variety of functional substituents. A few cationic porphyrins, including Tet(MPy)P (**30**), T(MPy)PhP (**32**), *cis*- and *trans*-B(MPy)DPhP (**35** and **36**), have been reported in connection with their DNA binding properties (9), their photosensitizing abilities in photodynamic therapy (PDT) (10), and aspects of their solution chemistry (11). Some of these reports appeared during the course of our studies (3).

[1]Author to whom correspondence may be addressed. Telephone: (604)-822-6645. Fax: (604)-822-2847

Can. J. Chem. Downloaded from www.nrcresearchpress.com by 85.192.166.187 on 09/08/12
For personal use only.

Can. J. Chem. Downloaded from www.nrcresearchpress.com by 85.192.166.187 on 09/08/12
For personal use only.

In the present work, the synthesis, characterization, and results from some *in vitro* studies of certain designed water-soluble porphyrins are presented. The structures of the new porphyrins (**19**, **20**, **22**, **24–29**, **31**, **33**, and **34**) are included in Fig. 1. The porphyrins with nonionic substituents, which served as synthetic precursors in the present work, have been reported elsewhere (*3a*). An example of the basic synthesis is shown in Fig. 2: a nitro group is introduced into the porphyrin structure in order to increase the reduction potential (*3a*), which is believed to be important for radiosensitizers containing this group (12), followed by introduction of two sulfonate groups to increase aqueous solubility. The remaining anionic porphyrins are synthesized similarly; the amino group is incorporated by reduction of the nitro group prior to, or sometimes during, the sulfonation. The cationic porphyrins are synthesized by methylation of the pyridyl groups of prefunctionalized porphyrins, some of which also contain nitro substituents. All the sulfonated porphyrins are isolated as sodium salts, and all the cationic porphyrins are finally isolated as chloride salts. The counterions (Na^+ for anionic porphyrins and Cl^- for cationic porphyrins, unless otherwise specified) are omitted in the names and abbreviations (Fig. 1), when the emphasis is on the porphyrin structure, for clarity of presentation.

Experimental

General methods and materials

The precursor porphyrins **1–16** were synthesized according to our recently published procedures (*3a*). Other chemicals used, including alumina (activities I–III) and silica gel, were as described previously (*3a*), as was instrumentation for NMR and UV–VIS; ^1H references were TMS (in DMSO-d_6) (s = singlet, d = doublet, q = quartet, m = multiplet, b = broad). Mass spectroscopy (EI and FAB techniques) and microanalyses were performed in service laboratories in this department. An anion (Cl^-) exchange resin (Amberlite, IRA-402) was a BDH product. A sample of Photofrin II, a clinically used photosensitizer drug, was obtained from Quadralogic Technologies, Inc.

Dialysis was carried out in a 1.0 L beaker. A 10 × 3 cm piece of molecular porous membrane tubing (1000 Mol. Wt. cutoff, Spectra/Por) was rinsed with distilled water, and then one end was closed with string. The porphyrin sample was dissolved in a minimum amount of distilled water (2–10 mL), and the resultant solution was transferred into the tubing; the other end of the tubing was then closed with string. This dialysis "bag" was put into the beaker containing distilled water (~800 mL), and the contents were stirred for 2 h. The solution outside the dialysis bag was replaced by distilled water and dialysis continued for another 2 h, after which the solution in the bag was evaporated to dryness. Acetone (10 mL) was then added to the residue, the suspension was filtered, and the solid was collected and air-dried.

For biological tests, stock solutions (1.0 mM) of the compounds were made by dissolving the compounds in double-distilled water. The so-called "drug solutions", made by dilution of the stock solutions using the appropriate medium, were sterilized by filtering using 10 mL disposable syringes and Nalgene 0.22 μm filter units.

A centrifuge (Sorvall RC-3) was operated at 600 RPM at 4°C for separating cells from solution. The cell concentration was determined using a Coulter cell counter (Coulter Electronic Inc.). Media containing: no serum and no $NaHCO_3$, 10% bovine serum (Gilco) and no $NaHCO_3$, and 10% serum and 0.2% $NaHCO_3$, are labelled –/–, +/–, and +/+, respectively.

The cells used in the toxicity and radiosensitization assays were obtained from a CHO (Chinese hamster ovary) cell line. The cells were routinely grown in a spinner culture flask in α+/+ medium (Gilco), and the cell solutions were maintained at 37°C in an "Incu-cover" incubator (Associated Biomedic Systems) under an atmosphere of 95% air and 5% CO_2 (Canadian Liquid Air Co.). The cell cultures were diluted daily to maintain exponential growth (doubling time was approximately 13 h).

Drug accumulation and photosensitization assays were performed using cells from an HT-29 (human-cancer tumor) cell line, which was maintained as a monolayer in tissue flasks (Falcon) in RPMI+/+ medium (Gilco) at 37°C under an atmosphere of 95% air and 5% CO_2. The cultures were trypsinized (0.1% trypsin solution) twice a week (doubling time was approximately 24 h).

Porphyrin synthesis

The precursor porphyrins used in the various syntheses are included in Table 1.

Sulfonation reactions were performed using a modified literature procedure (4). The synthesis procedure for each of the porphyrins was about the same, and is described generally as follows:

The precursor porphyrin (~0.50 g) was mixed well with concentrated H_2SO_4 (10 mL) in a 50 mL round-bottom flask. The flask was stoppered and heated in an oil bath at 100–110°C for 4–12 h (see below). The mixture was then cooled to room temperature, and ice-cold water (50 mL) was added slowly. The mixture was carefully neutralized with concentrated NaOH and dilute Na_2CO_3 to pH = 8–9, while being cooled in an ice bath. After being concentrated by evaporation to about 20 mL, the solution was cooled in an ice bath, when a precipitate of inorganic salts (mainly Na_2SO_4) formed; this was filtered off and washed with MeOH (50 mL). To the aqueous MeOH filtrate was added 100 mL MeOH, when more inorganic salt precipitated. This mixture again was filtered and then the filtrate was evaporated to dryness on a Rotovap. The purple residue, a mixture of porphyrin product and inorganic salts, was washed with MeOH until only a light yellow solid remained; if the purple colour of the residue could not be washed out by MeOH, then the residue was dissolved in minimum hot water, reprecipitated with MeOH, and then filtered. The purple MeOH solution (typically 100–200 mL) was evaporated to dryness, and the purple residue was collected and dried under vacuum at 100°C overnight to give the crude product.

For Na_4Tet(SPh)P (**21**), made from precursor **1**, the crude product was redissolved in MeOH (100 mL) and the solution was filtered to remove some insoluble impurity. The filtrate volume was reduced to ~20 mL by evaporation, and then acetone (~200 mL) was added with stirring; the resulting brown precipitate was collected by filtration. This MeOH–acetone reprecipitation procedure was repeated three more times, and the final brown, very hygroscopic, product was dried at 100°C under vacuum. Another form of the product was made by evaporating to dryness aqueous solutions of the brown material. The resulting bright purple flakes were collected and dried at room temperature under vacuum; this material (60% yield) was not hygroscopic.

For the other isolated sulfonated porphyrins (**17**, **19**, **20**, and **22–25**), the crude products were generally either purified by dialysis or (and) by repetitive MeOH–acetone reprecipitation (3 times). Products purified by dialysis were collected by evaporation of aqueous solutions, were dried under vacuum, and were not hygroscopic, while products purified by reprecipitation were hygroscopic and thus, for elemental analysis, were handled under N_2. The actual purification method used for each of these porphyrins is indicated in Table 1 together with elemental analyses and reaction times used, the overall yields being 70–80%.

The crude product from the sulfonation of *cis*-(NPh)DPhPyP (**10**) was dissolved in MeOH (~30 mL), loaded on a column of silica gel (3 × 30 cm), and the column was eluted by a mixture of CH_2Cl_2 and CH_3OH (1:3). The major band was identified by ^1H NMR as *cis*-(NPh)PyB(SPh)P (**22**) (Table 2). The MeOH solution of the crude product (13%) from the sulfonation (100°C, 0.5 h) of the mixture of *cis*- and *trans*-B(NPh)DPhP (**8** and **9**) was loaded on a column of silica gel and, after elution by 1:1 MeOH/CH_2Cl_2, three products were separated; these were identified by ^1H NMR as B(NPh)B(SPh)P (mixture of **26** and **27**), (APh) (NPh)B(SPh)P (mixture of **28** and **29**), and B(APh)B(SPh)P (mixture of **19** and **20**) (see Results and discussion section).

The methylation of TetPyP (**6**) to give **30** was carried out according to the literature procedure (6), when the pyridinium porphyrins are first isolated as tosylate salts. Briefly, TetPyP (0.50 g) was mixed with 50

Can. J. Chem. Downloaded from www.nrcresearchpress.com by 85.192.166.187 on 09/08/12
For personal use only.

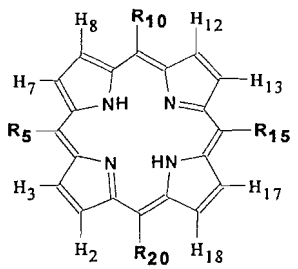

Ph=phenyl

APh=4-aminophenyl

NPh=4-nitrophenyl

SPh=4-sulfonatophenyl

Py=4-pyridyl

MPy=4-methylpyridinium

$R_5=R_{10}=R_{15}=R_{20}$=Ph	TetPhP [5,10,15,20-tetraphenylporphyrin]	1
$R_5=R_{10}=R_{15}$=Ph, R_{20}=Py	TPhPyP [5,10,15-triphenyl-20-(4-pyridyl)porphyrin]	2
$R_5=R_{10}$=Ph, $R_{15}=R_{20}$=Py	*cis*-DPhBPyP [5,10-diphenyl-15,20-bis(4-pyridyl)porphyrin]	3
$R_5=R_{15}$=Ph, $R_{10}=R_{20}$=Py	*trans*-DPhBPyP [5,15-diphenyl-10,20-bis(4-pyridyl)porphyrin]	4
R_5=Ph, $R_{10}=R_{15}=R_{20}$=Py	PhTPyP [5-phenyl-10,15,20-tris(4-pyridyl)porphyrin]	5
$R_5=R_{10}=R_{15}=R_{20}$=Py	TetPyP [5,10,15,20-tetrakis(4-pyridyl)porphyrin]	6
R_5=NPh, $R_{10}=R_{15}=R_{20}$=Ph	(NPh)TPhP [5-(4-nitrophenyl)-10,15,20-triphenylporphyrin]	7
$R_5=R_{10}$=NPh, $R_{15}=R_{20}$=Ph	*cis*-B(NPh)DPhP [5,10-bis(4-nitrophenyl)-15,20-diphenylporphyrin]	8
$R_5=R_{15}$=NPh, $R_{10}=R_{20}$=Ph	*trans*-B(NPh)DPhP [5,15-bis(4-nitrophenyl)-10,20-diphenylporphyrin]	9
R_5=NPh, $R_{10}=R_{15}$=Ph, R_{20}=Py	*cis*-(NPh)DPhPyP [5-(4-nitrophenyl)-10,15-diphenyl-20-(4-pyridyl)porpbyrin]	10
$R_5=R_{10}$=NPh, $R_{15}=R_{20}$=Py	*cis*-B(NPh)BPyP [5,10-bis(4-nitrophenyl)-15,20-bis(4-pyridyl)porphyrin]	11
$R_5=R_{15}$=NPh, $R_{10}=R_{20}$=Py	*trans*-B(NPh)BPyP [5,15-bis(4-nitrophenyl)-10,20-bis(4-pyridyl)porphyrin]	12
R_5=NPh, $R_{10}=R_{15}=R_{20}$=Py	(NPh)TPyP [5-(4-nitrophenyl)-10,15,20-tris(4-pyridyl)porphyrin]	13
R_5=APh, $R_{10}=R_{15}=R_{20}$=Ph	(APh)TPhP [5-(4-aminophenyl)-10,15,20-triphenylporphyrin]	14
$R_5=R_{10}$=APh, $R_{15}=R_{20}$=Ph	*cis*-B(APh)DPhP [5,10-bis(4-aminophenyl)-15,20-diphenylporphyrin]	15
$R_5=R_{15}$=APh, $R_{10}=R_{20}$=Ph	*trans*-B(APh)DPhP [5,15-bis(4-aminophenyl)-10,20-diphenylporphyrin]	16
R_5=APh, $R_{10}=R_{15}=R_{20}$=SPh	(APh)T(SPh)P [5-(4-aminophenyl)-10,15,20-tris(4-sulfonatophenyl)porphyrin]	17
R_5=NPh, $R_{10}=R_{15}=R_{20}$=SPh	(NPh)T(SPh)P [5-(4-nitrophenyl)-10,15,20-tris(4-sulfonatophenyl)porphyrin]	18
$R_5=R_{10}$=APh, $R_{15}=R_{20}$=SPh	*cis*-B(APh)B(SPh)P [5,10-bis(4-aminophenyl)-15,20-bis(4-sulfonatophenyl)porphyrin]	19
$R_5=R_{15}$=APh, $R_{10}=R_{20}$=SPh	*trans*-B(APh)B(SPh)P [5,15-bis(4-aminophenyl)-10,20-bis(4-sulfonatophenyl)porphyrin]	20
$R_5=R_{10}=R_{15}=R_{20}$=SPh	Tet(SPh)P [5,10,15,20-tetrakis(4-sulfonatophenyl)porphyrin]	21
R_5=NPh, R_{10}=Py, $R_{15}=R_{20}$=SPh	*cis*-(NPh)PyB(SPh)P [5-(4-nitrophenyl)-10-(4-pyridyl)-15,20-bis(4-sulfonatophenyl)porphyrin]	22
R_5=Py, $R_{10}=R_{15}=R_{20}$=SPh	PyT(SPh)P [5-(4-pyridyl)-10,15,20-tris(4-sulfonatophenyl)porphyrin]	23
$R_5=R_{10}$=Py, $R_{15}=R_{20}$=SPh	*cis*-BPyB(SPh)P [5,10-bis(4-pyridyl)-15,20-(4-sulfonatophenyl)porphyrin]	24
$R_5=R_{15}$=Py, $R_{10}=R_{20}$=SPh	*trans*-BPyB(SPh)P [5,15-bis(4-pyridyl)-10,20-(4-sulfonatophenyl)porphyrin]	25
$R_5=R_{10}$=NPh, $R_{15}=R_{20}$=SPh	*cis*-B(NPh)B(SPh)P [5,10-bis(4-nitrophenyl)-15,20-bis(4-sulfonatophenyl)porphyrin]	26
$R_5=R_{15}$=NPh, $R_{10}=R_{20}$=SPh	*trans*-B(NPh)B(SPh)P [5,15-bis(4-nitrophenyl)-10,20-bis(4-sulfonatophenyl)porphyrin]	27
R_5=APh, R_{10}=NPh, $R_{15}=R_{20}$=SPh	*cis*-(APh)(NPh)B(SPh)P [5-(4-aminophenyl)-10-(4-nitrophenyl)-15,20-bis(4-sulfonatophenyl)-porphyrin]	28
R_5=APh, R_{15}=NPh, $R_{10}=R_{20}$=SPh	*trans*-(APh)(NPh)B(SPh)P [5-(4-aminophenyl)-15-(4-nitrophenyl)-10,20-bis(4-sulfonatophenyl)porphyrin]	29
$R_5=R_{10}=R_{15}=R_{20}$=MPy	Tet(MPy)P [5,10,15,20-tetrakis(4-methylpyridinium)porphyrin]	30
$R_5=R_{10}=R_{15}$=MPy, R_{20}=NPh	T(MPy)(NPhP)P [5,10,15-tris(4-methylpyridinium)-20-(4-nitrophenyl)porphyrin]	31
$R_5=R_{10}=R_{15}$=MPy, R_{20}=Ph	T(MPy)PhP [5,10,15-tris(4-methylpyridinium)-20-(4-phenyl)porphyrin]	32
$R_5=R_{10}$=MPy, $R_{15}=R_{20}$=NPh	*cis*-B(MPy)B(NPh)P [5,10-bis(4-methylpyridinium)-15,20-bis(4-nitrophenyl)porphyrin]	33
$R_5=R_{15}$=MPy, $R_{10}=R_{20}$=NPh	*trans*-B(MPy)B(NPh)P [5,15-bis(4-methylpyridinium)-10,20-bis(4-nitrophenyl)-porphyrin]	34
$R_5=R_{10}$=MPy, $R_{15}=R_{20}$=Ph	*cis*-B(MPy)DPhP [5,10-bis(4-methylpyridinium)-15,20-diphenylporphyrin]	35
$R_5=R_{15}$=MPy, $R_{10}=R_{20}$=Ph	*trans*-B(MPy)DPhP [5,15-bis(4-methylpyridinium)-10,20-diphenylporphyrin]	36

FIG. 1. Porphyrin structures and abbreviations; B = bis, D = di, T = tri(s), Tet = tetra(kis), P = porphyrin.

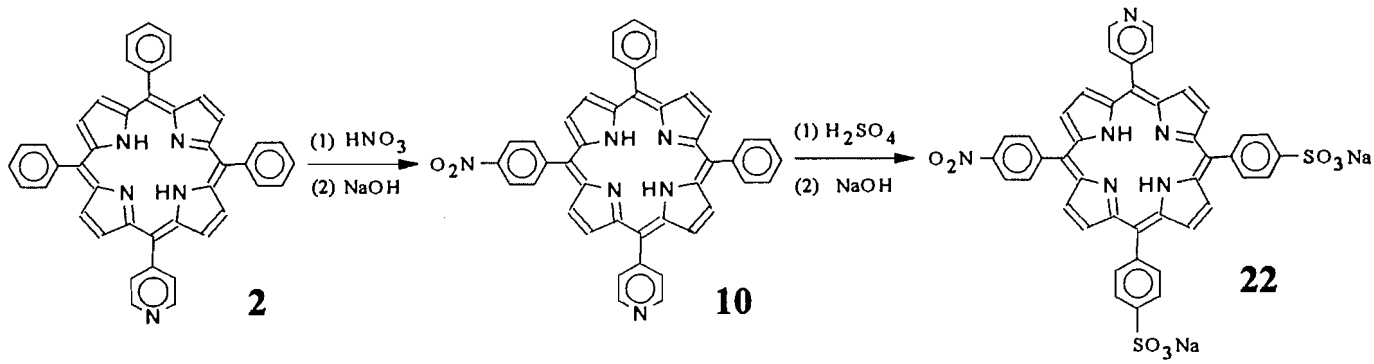

FIG. 2. A typical scheme for nitration and subsequent sulfonation of TPhPyP (**2**).

TABLE 1. Elemental analyses for the porphyrins[a]

	Porphyrin product	C %	H %	N %	Precursor (Reaction time)
17	Na_3[(APh)T(SPh)P]·$2H_2O$[b]	54.51(54.31)	3.06(3.30)	7.40(7.20)	**14** (4 h) or **5** (0.5 h)
19	Na_2[*cis*-B(APh)B(SPh)P]·$2H_2O$[b,f]	59.87(59.73)	3.85(4.10)	9.50(9.41)	**15** (4 h)
20	Na_2[*trans*-B(APh)B(SPh)P]·$3H_2O$[b,f]	59.13(58.93)	4.31(4.02)	9.43(9.38)	**16** (4 h)
21	Na_4[Tet(SPh)P]·$10H_2O$[c]	43.65(43.93)	3.70(3.83)	4.39(4.66)	**1** (4 h)
22	Na_2[*cis*-(NPh)PyB(SPh)P]·$4H_2O$[d]	55.60(55.31)	3.95(3.64)	8.76(9.00)	**10** (6 h)
23	Na_3[PyT(SPh)P]·$2H_2O$[b]	53.84(53.91)	3.36(3.13)	7.20(7.31)	**2** (4 h)
23	Na_3[PyT(SPh)P]·$11H_2O$[d]	46.63(46.87)	4.21(4.36)	6.23(6.36)	**2** (4 h)
23	Na_3[PyT(SPh)P]·$2H_2O$[d,e,f]	53.91(53.91)	2.92(3.13)	7.22(7.31)	**2** (4 h)
24	Na_2[*cis*-BPyB(SPh)P]·$10H_2O$[d,f,g]	50.04(50.40)	4.45(4.60)	8.41(8.40)	**3** (12 h)
25	Na_2[*trans*-BPyB(SPh)P]·$7H_2O$[d,f,g]	53.45(53.28)	4.25(4.23)	8.66(8.88)	**4** (12 h)
30	[Tet(MPy)P]Cl_4·$4H_2O$[g]	59.52(59.21)	5.36(5.16)	12.55(12.56)	**6**
31	[T(MPy)(NPh)P]Cl_3·$4H_2O$[g]	59.72(59.63)	5.00(4.86)	12.47(12.65)	**13**
32	[T(MPy)PhP]Cl_3·$4H_2O$[g]	63.15(62.82)	5.23(5.23)	11.66(11.86)	**5**
33	[*cis*-B(MPy)B(NPh)P]Cl_2·$4H_2O$[d,g]	59.86(60.07)	4.80(4.55)	12.50(12.74)	**11**
34	[*trans*-B(MPy)B(NPh)P]Cl_2·xH_2O		See footnote[h]		**12**
35	[*cis*-B(MPy)DPhP]Cl_2·$5.5H_2O$[d,g]	64.91(64.73)	5.32(5.52)	10.14(10.30)	**3**
36	[*trans*-B(MPy)DPhP]Cl_2·$4.5H_2O$[d]	66.21(66.17)	5.22(5.38)	10.55(10.52)	**4**

[a]Found (calculated).
[b]Sample collected from MeOH–acetone precipitations.
[c]Sample purified by MeOH–acetone precipitations; then collected from evaporation of an aqueous solution of the purified sample, and dried at room temperature under vacuum.
[d]Sample purified by dialysis and collected from evaporation of aqueous solutions.
[e]Sample dried at 100°C under vacuum overnight, and analyzed after being stored and weighed under N_2.
[f]Analyses for sulfur: **23**, 10.03 (10.10); **24**, 6.40 (6.70); **25**, 6.77 (6.65).
[g]Anionic FAB mass spectra, *m/z*, assignment (major peak in each spectrum noted with *). For **19**: 825* [M – Na]$^-$, 803 (M – 2Na + H]$^-$. For **20**: 825* [M – Na]$^-$, 803 [M – 2Na + H]$^-$. For **22**: 841 [M – Na]$^-$, 819* [M – 2Na + H]$^-$. For **24**: 797* [M – Na]$^-$, 775 [M – 2Na + H]$^-$. Cationic FAB mass spectra, *m/z*, assignment (major peak in each spectrum is noted with *). For **30**: 713 [M – 3Cl]$^+$, 694, 678* [M – 4Cl]$^+$, 663 [M – 4Cl – CH_3]$^+$, 648 [M – 4Cl – $2CH_3$]$^+$, 633 [M – 4Cl – $3CH_3$]$^+$. For **31**: 723, 707* [M – 3Cl]$^+$, 692 [M – 3Cl – CH_3]$^+$, 677 [M – 3Cl – $2CH_3$]$^+$. For **32**: 697 [M – 2Cl]$^+$, 662* [M – 3Cl]$^+$, 646. For **33**: 752, 736* [M – 2Cl]$^+$, 721 [M – 2Cl – CH_3]$^+$. For **35**: 661, 646* [M – 2Cl]$^+$, 631 [M – 2Cl – CH_3]$^+$.
[h]Satistactory elemental analysis was not obtained; for example with x = 4, C 53.50 (60.07), H 5.22 (4.55), N 10.18 (12.74).

mL DMF in a 100 mL round-bottom flask, and the mixture was heated with stirring almost to boiling to dissolve the porphyrin; methyl *p*-toluenesulfonate (~2 mL) was added and the solution was then refluxed for 4 h. The methylated pyridiniumporphyrin tetra(tosylate) (cf. **30**) formed as a precipitate when this solution was cooled at ~0°C; this precipitate was filtered off, washed with acetone, and air-dried.

cis- and *trans*-DPhBPyP (**3**, **4**), PhTPyP (**5**), *cis*- and *trans*-B(NPh)BPyP (**11**, **12**), and (NPh)TPyP (**13**), were methylated under conditions similar to those described above (0.20 g porphyrin, 20 mL DMF, 1 mL methyl *p*-toluenesulfonate, 4 h), but the tosylate salts of the methylated porphyrins (**35** and **36**, **32**, **33** and **34**, and **31**, respectively) did not precipitate from the cooled reaction solutions. These were thus reduced in volume by evaporation to ~10 mL; acetone (~100 mL) was then added with stirring, and the resulting mixtures were filtered. The precipitated purple tosylate salts of the methylated porphyrin were then washed with acetone (~20 mL) and dried under vacuum at room temperature. The methylated products **34–36** were further washed with cold water (~20 mL), and then dried under vacuum at room temperature.

The tosylate salts were converted to the corresponding chloride salts by passing an aqueous solution of the porphyrin through an anion exchange column (Cl^-). The aqueous solutions of the tosylate salts of Tet(MPy)P (**30**), (NPh)T(MPy)P (**31**), and T(MPy)PhP (**32**) were obtained by stirring the products in hot water (~20 mL for 0.2 g porphyrin). The tosylate salts of *cis*- and *trans*-B(MPy)B(NPh)P (**33**, **34**), and *cis*- and *trans*-B(MPy)DPhP (**35**, **36**) were dissolved by stirring these materials (0.2 g) with the exchange resin (~2 mL) in hot water (40 mL). The purple aqueous solutions from the anion exchange resin were evaporated to dryness, and acetone (~10 mL) was added to the residues; the suspensions were filtered, and the collected materials dried under vacuum at 100°C. The overall yields of methylation followed by anion conversion were ~90%.

The chloride salts of *cis*- and *trans*-B(MPy)B(NPh)P (**33**, **34**), and *cis* and *trans*-B(MPy)DPhP (**35**, **36**), were further purified by dialysis in attempts to obtain better elemental analyses. These attempts were successful except in the case of **34**, where a satisfactory analysis was not obtained; an observed low solubility of **34** leads to difficulties in purification.

Can. J. Chem. Downloaded from www.nrcresearchpress.com by 85.192.166.187 on 09/08/12
For personal use only.

TABLE 2. ^{1}H NMR data for the sulfonatoporphyrins[a]

	Porphyrin	Pyrrole	2,6-SPh 3,5-SPh	3,5-Py 2,6-Py	2,6-APh 3,5-APh	-NH_2	*N*-Pyrrole
17	(APh)T(SPh)P	8.99 d(2) 8.85 b s(6)	8.18 d(6) 8.06 d(6)	—	7.90 d(2) 7.04 d(2)	5.61 s(2)	–2.80 s(2)
19	*cis*-B(APh)B(SPh)P	8.92 m(4) 8.79 m(4)	8.17 d(4) 8.05 d(4)	—	7.87 d(4) 7.00 d(4)	5.55 s(4)	–2.78 s(2)
20	*trans*-B(APh)B(SPh)P	8.94 d(4) 8.79 d(4)	8.17 d(4) 8.03 d(4)	—	7.86 d(4) 7.00 d(4)	5.57 s(4)	–2.78 s(2)
21	Tet(SPh)P	8.84 s(8)	8.18 d(8) 8.04 d(8)	—	—	—	–2.95 s(2)
22	*cis*-(NPh)PyB(SPh)P	8.87 b s(8)	8.16 d(4) 8.03 d(4)	9.02 d(2) 8.25 d(2)	8.66 d(2)[b] 8.49 d(2)[b]	—	–3.01 s(2)
23	PyT(SPh)P	8.86 m(8)	8.19 m(6) 8.07 d(6)	9.03 d(2) 8.27 m(2)	—	—	–2.97 s(2)
24	*cis*-BPyB(SPh)P	8.89 m(8)	8.18 m(4) 8.05 m(4)	9.04 d(4) 8.28 d(4)	—	—	–2.98 s(2)
25	*trans*-BPyB(SPh)P	8.89 m(8)	8.18 d(4) 8.05 d(4)	9.04 d(4) 8.29 d(4)	—	—	–2.98 s(2)
26 and **27**	*cis*- and *trans*-B(NPh)B(SPh)P	8.88 m(8)	8.19 d(4) 8.07 d(4)	8.68 d(4)[b] 8.52 d(4)[b]	—	—	–2.91 s(2)
28 and **29**	*cis*- and *trans*-(APh)(NPh)B(SPh)P	8.98 m(2) 8.83 m(6)	8.17 m(4) 8.06 m(4)	8.67 d(2)[b] 8.51 d(2)[b]	7.87 d(2) 7.02 d(2)	—	–2.84 s(2)

[a]In DMSO-d_6 at ~20°C; δ signal pattern (number of protons).
[b]Signals for 3,5-nitrophenyl and 2,6-nitrophenyl protons, respectively.

TABLE 3. ^{1}H NMR data for the methylpyridiniumporphyrins[a]

	Porphyrin	Pyrrole	3,5-NPh 2,6-NPh	3,5-MPy 2,6-MPy	2,6-Ph 3,4,5-Ph	-CH_3	*N*-Pyrrole
30	[Tet(MPy)P]Cl_4	9.2 s(8)	—	9.55 d(8) 9.00 d(8)	—	4.77 s(12)	–3.10 s(2)
31	[T(MPy)(NPh)P]Cl_3	9.1 m(8)	8.74 d(2) 8.52 d(2)	9.51 d(6) 9.00 d(6)	—	4.74 s(9)	–3.06 s(2)
32	[T(MPy)PhP]Cl_3	9.00 q(4) 9.20 s(4)	—	9.50 d(2) 9.03 m(2)	8.23 d(2) 7.90 m(3)	4.71 s(9)	–3.04 s(2)
33	[*cis*-B(MPy)B(NPh)P]Cl_2	9.0 m(8)	8.71 d(4) 8.51 d(4)	9.49 d(4) 9.00 d(4)	—	4.72 s(6)	–3.02 s(2)
34	[*trans*-B(MPy)B(NPh)P]Cl_2	9.0 m(8)[b]	8.72 d(4) 8.50 d(4)	9.46 d(4) 9.0 m(4)[b]	—	4.70 s(6)	–3.02 s(2)
35	[*cis*-B(MPy)DPhP]Cl_2	9.12 s(2) 9.00 m(4) 8.91 s(2)	—	9.46 d(4) 9.00 d(4)	8.21 d(4) 7.89 m(6)	4.73 s(6)	–2.95 s(2)
36	[*trans*-B(MPy)DPhP]Cl_2	9.0 m(8)	—	9.48 d(4) 9.03 d(4)	8.23 d(4) 7.90 m(6)	4.72 s(6)	–2.99 s(2)

[a]In DMSO-d_6 at ~20°C; δ signal pattern (number of protons).
[b]Signals for the pyrrole and 2,6-methylpyridinium protons overlap.

FAB mass spectral data for selected porphyrins are noted in footnote *g* of Table 1. The ^{1}H NMR data of all the anionic and cationic porphyrins are given in Tables 2 and 3, respectively; the spectra recorded in DMSO-d_6 were independent of concentration from 0.002 to 0.02 M, and we assume aggregation phenomena are not important in this solvent (3*b*, 3*c*). The UV–VIS spectra of the water-soluble porphyrins in aqueous solution are complicated because of aggregation phenomena, which is more fully discussed elsewhere (3*b*, 3*c*). Table 4 presents such spectral data at one concentration (1.0×10^{-5} M) in distilled water.

Partition coefficients

The porphyrin free bases (as sodium or chloride salts) were dissolved in distilled water saturated with *n*-octanol (10 mL) to make 5×10^{-6} M solutions which were convenient for absorbance measurements (A_e values) at the Soret-band maximum. Each solution (5.00 mL) was then mixed with *n*-octanol saturated with water (5.00 mL), shaken for 1 h, and centrifuged (600 RPM, 5 min) in order to separate the layers. The absorbances of the aqueous fractions (A_f) were then remeasured at the Soret maximum. Partition coefficient (P) values were then calculated as $(A_e - A_f)/A_f$, and are listed in Table 4. The method follows a standard procedure (13).

Accumulation in cells

Accumulation of the porphyrins by human cancer cells was determined using a fluorometric assay (14). The HT-29 cells (1×10^6) were seeded into 10 cm Petri dishes with 15 mL RPMI+/+ medium and incubated at 37°C for 2 d to form subconfluent monolayers. The drug solutions (17 mL) at 100 μM were made from each of the drug stock solutions by dilution in RPMI–/+ medium. The Petri dishes with subconfluent monolayers were rinsed with phosphate buffer saline solution (PBS) three times to remove traces of serum in the medium and thus avoid interactions between the drugs and serum; then the drug solution (5 mL) was added to each of three Petri dishes, which were wrapped immediately in Al foil to avoid possible photosensitization, and then incubated for 1 h. Thereafter, the drug solutions were decanted, and the dishes rinsed with PBS solution three times. The

Can. J. Chem. Downloaded from www.nrcresearchpress.com by 85.192.166.187 on 09/08/12
For personal use only.

TABLE 4. UV–VIS data and partition coefficients for the porphyrins[a]

Porphyrin[b]	Soret	Visible IV	Visible III	Visible II	Visible I	P^c (species charge)
17	412.6 (314)	516 (12.7)	555 (8.4)	577 (7.1)	635 (5.7)	0 (–3)
19	415 (98.8)	—	—	—	665 (13.9)	0.71 (–2)
20	413 (61.7)	491 (65.9)	—	—	700 (23.0)	0.71 (–2)
21	411.0 (464)	513 (15.5)	549 (7.0)	577 (6.5)	630 (3.9)	0 (–4)
22	416.0 (177)	515 (10.7)	552 (6.5)	578 (4.6)	640 (2.1)	0.82 (–2)
23	410.6 (417)	513 (15.3)	555 (6.8)	577 (6.4)	632 (3.2)	0 (–3)
24	409.3 (282)	514 (11.7)	550 (5.2)	579 (4.4)	636 (2.0)	0.23 (–2)
25	409.3 (263)	514 (11.7)	550 (4.6)	579 (3.8)	636 (1.5)	0.16 (–2)
30	420.0 (250)	516 (14.3)	550 (6.7)	580 (6.2)	636 (1.4)	0.44 (+4)
31	419.0 (276)	516 (15.3)	552 (6.5)	580 (6.7)	636 (1.7)	1.2 (+3)
32	419.0 (292)	516 (15.2)	553 (7.5)	580 (7.2)	637 (2.2)	0.88 (+3)
33	417.0 (241)	518 (13.4)	555 (7.6)	578 (7.2)	635 (2.4)	2.8 (+2)
34[d]	417.0 (159)	516 (10.9)	552 (6.7)	582 (5.2)	637 (2.3)	3.0 (+2)
35	416.5 (211)	517 (12.1)	555 (6.6)	578 (6.5)	636 (2.2)	17 (+2)
36	415.5 (178)	516 (8.0)	555 (6.3)	578 (4.7)	637 (2.7)	13 (+2)

[a]In H_2O, ~20°C, at 1×10^{-5} M; λ_{max} in nm (extinction coefficient ($\varepsilon \times 10^{-3}$, M^{-1} cm^{-1})).
[b]For porphyrin formula, see Table 1; the sample used for **23** was the unidecahydrate.
[c]*P* values <0.01 are presented as 0.
[d]Minimum ε values, because the compound is impure (see text).

cells were harvested using a rubber policeman instead of trypsinization to avoid possible interactions with the drugs, and were resuspended into 10 mL PBS solution by vortexing (for another wash) in dilution tubes. Controls were also done with identical experiments, but without the drug treatment. Cells in two such controls were also harvested and counted, the average giving the number of cells per Petri dish.

Cells in the PBS solution were centrifuged, and the PBS solution was poured off. ScintiGest solution (from Fisher Scientific, 10%, 5.00 mL) was added to each of the dilution tubes, which were then wrapped in Al foil to prevent possible photo-destruction of the drugs. The solutions were kept at 37°C for at least 24 h to digest the cells. Standard solutions at 0.10–5 μM, made by diluting 100 μM drug solution with 10% ScintiGest, were also wrapped in foil and treated similarly at 37°C.

The concentrations of the drugs in the digested solutions were measured by fluorescence using a Farrent Optical System 3 scanning spectrometer at the maxima for excitation (scanned from 380 to 500 nm) and emission (scanned from 600 to 700 nm). Results were calibrated by using standard solutions of each drug. At least two or three experiments were performed for each porphyrin. Some samples were too concentrated for the measurements, and so were diluted 10–50 times; the diluted samples were again wrapped in foil and kept at 37°C for at least another 12 h to assure reproducible results.

Toxicity

The toxicities of the compounds were measured by incubating CHO cells with the 100 μM drug solutions for various time intervals (to a maximum of 3 h) under 1 atm (101.3 kPa) of either air (oxic conditions) or N_2 (hypoxic conditions), as described in the literature (15).

Toxicity was also assessed with subconfluent monolayers of HT-29 cells for some selected porphyrins. The experiments were performed as in the "cell accumulation" experiments except that two Petri dishes were treated with each drug solution, one being incubated in the dark at 37°C for 1 h, and the other for 2 h. The drug solutions were then poured off, and the cells were rinsed with PBS, trypsinized, and added into dilution tubes containing 10 mL of PBS solution. The cell concentrations were counted, and ~2×10^5 cells were taken from each tube and added to another dilution tube containing 10 mL of RPMI+/– medium; these cells were washed again, counted, and plated. The colonies were stained (methylene blue, Gilco) and counted 13 d later. The plate efficiency (PE) values were calculated as (number of colonies)/(number of cells plated).

Radiosensitization in hypoxic conditions

A published procedure was followed for the radiosensitization assays (15, 16). Irradiation was performed using an X-ray source (Philips, 250 kV, 0.5 mm Cu). A suspension of CHO cells in a drug solution of α–/– or α+/– medium, stirred under N_2 at 37°C for 1 h to produce hypoxic conditions, was chilled at 0°C at least for 5 min before irradiation. After irradiation, the cells were washed, counted, and plated; colonies were counted 7 d later. The surviving fraction (SF) was calculated as (PE with irradiation)/(PE without irradiation). The survival curves were obtained by plotting log SF vs. radiation dose (17). The sensitization enhancement ratio (SER) was calculated at 1% survival, which is commonly chosen for comparison (17), as (dose without drug)/(dose with drug).

Photosensitization

These experiments were carried out following an established procedure (18) with minor changes. HT-29 cells (1×10^6) were seeded into tissue culture flasks 2 d before experiments. The subconfluent monolayers were then treated with 30 or 50 μM drug solutions (5 mL) as described in the cell accumulation experiments except that cells were harvested by trypsinization (6 min). Cells were counted, and 2×10^6 cells were taken and washed with 10 mL of PBS solution, resuspended in 1 mL of cold PBS solution, and chilled in ice.

A tunable light source (Photo Technology International Inc., model 500) was adjusted to 630 ± 10 nm. To a Petri dish, placed on ice that had been covered with a black cloth, was added 120 μL of cell solution, and the sample was then irradiated to a certain dose; 100 μL of solution was recovered and added to a dilution tube containing 9.9 mL of RPMI–/+ medium. The doses used under aerobic conditions were typically 0, 0.25, 0.50, 0.75, 1.0, 1.5, 2.0 J/cm^2 (maximum exposure being ~1 min) and a new Petri dish was used for each sample. The diluted samples were then washed with RPMI–/+ medium, counted, and plated. Colonies were stained and counted 13 d later; PE values were calculated as in toxicity experiments.

Results and discussion

Synthesis and characterization of the porphyrins

There are several literature reports on the sulfonation of TetPhP (**1**) to synthesize Tet(SPh)P (**21**) (4, 7, 19–22); the sulfonation procedures reported here are essentially the same as a literature one (4) except that shorter reaction times are employed. Preliminary studies on the reaction time for different types of porphyrins were also carried out. Samples were taken of the reaction mixture at different reaction times, and the porphyrin samples were then isolated (as described in the synthesis procedure), and their ^1H NMR spectra recorded. The degree of sulfonation was

Can. J. Chem. Downloaded from www.nrcresearchpress.com by 85.192.166.187 on 09/08/12
For personal use only.

Can. J. Chem. Downloaded from www.nrcresearchpress.com by 85.192.166.187 on 09/08/12
For personal use only.

calculated by the integration ratio of the peaks for the sulfonatophenyl and the phenyl protons, which are readily distinguished (Table 2 and ref. 3*a*). The more pyridyl groups present, the longer the reaction time needed. For instance, sulfonation of (NPh)TPhP (**7**) to give **17** is complete in 0.5 h; for *cis*-(NPh)DPhPyP (**10**) to give **22** requires 6 h reaction time; and sulfonation time for *cis*- or *trans*-DPhBPyP (**3** or **4**, 12 h) to give **24** or **25**, respectively, is longer than that required for TetPhP (**1**, 4 h). A pyridyl substituent, which would be protonated in the acidic conditions, was never sulfonated, as expected under these conditions.

Major differences have been reported (4, 7, 19–22) for purification of the sulfonated porphyrin Tet(SPh)P (**21**). Following studies in 1962 by Winkelman (20) on the localization of sulfonated TetPhP in tumors, Fleischer et al. (19) developed a synthetic method using six precipitations of the ammonium salt of **21** from MeOH by addition of acetone. Srivastava and Tsutsui (4) later used lime to precipitate the excess acid as calcium sulfate and then isolated **21** as the sodium salt following recrystallization from aqueous EtOH. Busby et al. (21) pointed out problems with these procedures, and reported a dialysis method to purify Na_4(Tet(SPh)P). Celite and Sephadex G-10 have also been used to chromatographically purify ammonium salts of (**21**) (22), and (APh)T(SPh)P (**17**) (8), respectively. Most recently, Sutter et al. (7) used *o*-phenanthroline to separate **21** from an aqueous acid solution.

We found that the "neutralization by lime" method (4) gave **21** contaminated by Ca salts, while use of $Ba(OH)_2$ gave coprecipitation of the sulfonated barium porphyrin. Use of a Sephadex G-10 chromatography column gave a low yield because of absorption of the porphyrin by the stationary phase. Dialysis was shown to be a good purification method for all the sulfonated porphyrins, although **21** tended to diffuse through the membrane, resulting in a low yield. Related to the effectiveness of the dialysis process are probably the different aggregation properties of the various sulfonated porphyrins, which are discussed elsewhere (3*b*, 3*c*).

Solvation of ionic porphyrins by water molecules (hydration) is a well-known phenomenon that gives rise to difficulties in determining elemental analyses. Taking Tet(SPh)P compounds (**21**) as an example, our Na_4 salt dried at 100°C analyzed well for a decahydrate and the ^{1}H NMR spectra in DMSO-d_6 showed free water to the amount of 10 ± 2 molecules per porphyrin; Srivastava and Tsutsui (4) reported only N and S analyses for the Na_4 salt, also dried at 100°C, a dodecahydrate being formulated, while more vigorous drying (at 150°C) gave a compound formulated as anhydrous and again only percent N and S were given (21). No analysis was given for the phenanthrolinium salt (7). The C, H, and N analyses reported for the $(NH_4)_4$ salt corresponded to a nonahydrate (19, 22). All of the porphyrins synthesized are hydrated, as evidenced by ^{1}H NMR data, which support at least semi-quantitatively the formulations given in Table 1. The ^{1}H data (Tables 2 and 3) reveal the presence in all cases, except for some geometrical isomers (see below), of just a single porphyrin species. We did not attempt to remove hydrated water completely because handling of hygroscopic samples for biological experiments is inconvenient and inappropriate.

The ^{1}H NMR spectra of Na_4Tet(SPh)P (**21**) in D_2O and in DMSO-d_6 have been reported before (4, 21, 23), and the data obtained here (Table 2) agree with the literature data. The assignments of the resonances are discussed below.

Sulfonation of the nitro precursor (NPh)TPhP (**7**) for 30 min gave the amino product Na_3(APh)T(SPh)P (**17**) instead of the expected nitro product Na_3(NPh)T(SPh)P (**18**); the yield was ~40%, relatively low compared to the 80% yield of **17** formed from sulfonation of (APh)TPhP (**14**). The reducing species is probably an intermediate formed by destruction of the porphyrin. Longer reaction times decrease the yield of the amino species (e.g., 13% after 4 h), but do not give a sulfonated nitro porphyrin. The characteristic signals for an aminophenyl substituent are readily seen in a ^{1}H NMR spectrum, and are easily distinguished from those of a nitrophenyl substituent (Table 2, cf. **17** and **22**).

Porphyrin **17** as the trisodium salt was prepared previously by Kruper et al. via sulfonation of **14** (8). Elemental analysis data were not reported, but the ^{1}H NMR data in DMSO-d_6 match closely those we give in Table 2; the UV–VIS spectrum of the tris(ammonium) salt in 0.1 M $(NH_4)_2CO_3$ was reported as λ_{max} ($\epsilon \times 10^{-3}$, M^{-1} cm^{-1}): 415(295), 529(12.3), 562(10.0), and 643(4.1), but the concentration used was not quoted and thus comparison with our data (Table 4) is not very meaningful. The other six isolated, analyzed sulfonated porphyrins (**19**, **20**, **22**–**25**), and those characterized just by ^{1}H NMR data (**26**–**29**), were not reported on previously, although data on a Ni(II) complex of **23** have appeared (24).

Sulfonation of pure *cis*- and *trans*-B(APh)DPhP (**15** and **16**, respectively) gives the expected bisaminophenyl, bis(sulfonated)phenyl compounds **19** and **20**, respectively.

Some nitro-reduction is again observed during sulfonation of the mixture of *cis*- and *trans*-B(NPh)DPhP (**8** and **9**). The ^{1}H NMR spectra of the three products isolated after a column separation are shown in Fig. 3 and Table 2, and are consistent with each product being a mixture of *cis* and *trans* isomers. In spectrum A, the two doublets (8H) in the δ 8.5–8.7 region correspond to two NPh substituents; in spectrum B, the intensity of these two doublets is reduced to 4H, while two doublets (4H) at δ 7.02 and 7.87 appear, corresponding to one APh; in spectrum C, only the peaks (8H) for APh are observed. The products, corresponding to spectra A, B, and C, are thus identified as a mixture of *cis*- and *trans*-B(NPh)B(SPh)P (**26** and **27**), a mixture of *cis*- and *trans*-(APh)(NPh)B(SPh)P (**28** and **29**), and a mixture of *cis*- and *trans*-B(APh)B(SPh)P (**19** and **20**), respectively. The patterns of the pyrrole signals of various porphyrin structures have been discussed in our recent paper (3a); for a *cis* isomer with two different *meso* substituents, e.g., **19**, the pyrrole protons are expected to give two singlets and two doublets, while for a *trans* isomer, e.g. **20**, two doublets are expected. In the spectrum of pure **19**, synthesized by sulfonation of **15**, each of the two expected pyrrole singlets overlaps with one of the two expected pyrrole doublets in the δ 8.7–9.0 region. The expected two doublets for the pyrrole protons of the pure *trans* isomer (**20**) appear at essentially the same frequencies as the other two doublets (or singlets) of the *cis* isomer, so that the spectrum of the isomer mixture looks similar in this region to the spectrum of the *cis* isomer. Attempted separation of each of the *cis*- and *trans*-isomer mixtures using silica gel failed, and the mixtures were only isolated in sufficient amounts for recording NMR spectra. The trend in the singlets for the *N*-pyrrole protons, at δ –2.91, –2.84, and –2.78 for the bis(nitro), mono(amino)–mono(nitro), and the bis(amino) species, respectively, can be rationalized in terms of electronic effects of the substituents (see below).

Sulfonation of *cis*-(NPh)DPhPyP (**10**) in a 6 h reaction time gives the unreduced nitroporphyrin *cis*-(NPh)PyB(SPh)P (**22**) as the major product, although a minor contaminant, an amino-

Can. J. Chem. Downloaded from www.nrcresearchpress.com by 85.192.166.187 on 09/08/12
For personal use only.

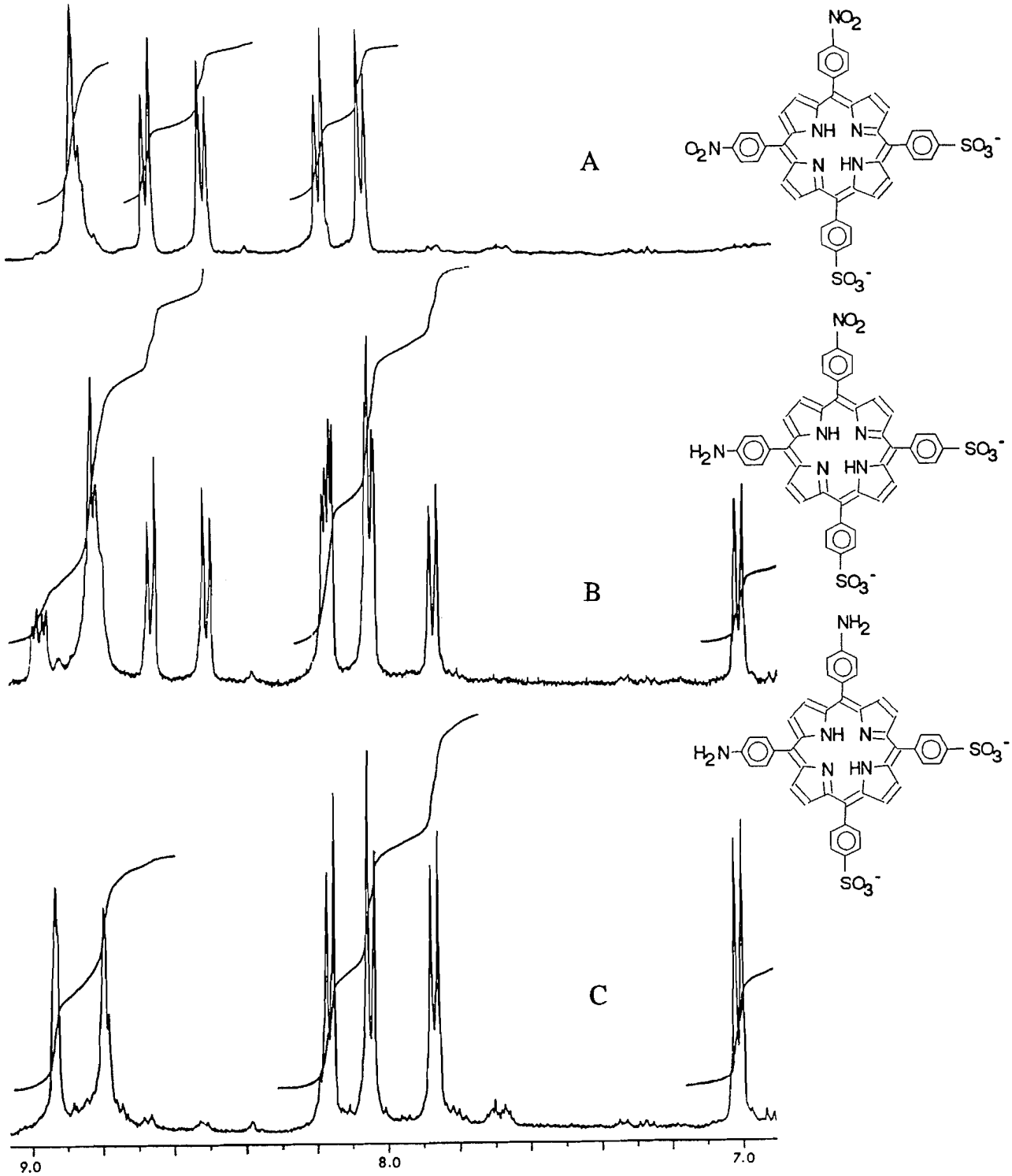

FIG. 3. ^{1}H NMR spectra of **26** and **27** (*A*), **28** and **29** (*B*), and **19** and **20** (*C*) in DMSO-d_6; the structures drawn are for the *cis* isomers, but the spectra refer to *cis/trans* mixtures.

substituted product, as evidenced by ^{1}H NMR, was removed using column chromatography. Compared to the (NPh)TPhP (**5**) system, the presence of the protonated pyridyl in **10** in acidic solution might stabilize this porphyrin structure against electrophilic attack and perhaps limit the formation of an intermediate reducing species. The ^{1}H NMR spectra of samples taken at different reaction times show that a reaction time of 6 h was optimal, because more amino porphyrin was formed with longer reaction times, and incomplete sulfonation was evident with shorter reaction times.

Methylation of pyridyl moieties on a porphyrin was easily performed with methyl 4-toluenesulfonate in DMF with a high yield, as described in the literature (6), although we found that a reaction time of 4 h was adequate instead of overnight as reported; prolonged reaction times caused complications in isolation of the product. The tosylate salts of the dicationic porphy-

Can. J. Chem. Downloaded from www.nrcresearchpress.com by 85.192.166.187 on 09/08/12
For personal use only.

rins **33–36** are insoluble in cold water or acetone, but are soluble in a mixture of these two solvents, presumably because organic solvents including acetone break up the aggregation of such porphyrins (25) and therefore increase their solubility in water. Some water-soluble impurities in these dicationic products were washed off using cold water.

The perchlorate salt of the diacid of Tet(MPy)P (**30**) (26), and the tetra(tosylate)salt of the free base porphyrin (6) have been synthesized previously, but characterized only by elemental analysis and UV-VIS spectra in aqueous solution. The tetrachloride salt has been noted in later literature (2, 27), but NMR data for this salt were reported only recently (28) along with those for the chlorides of T(MPy)PhP (**32**), and *cis*- and *trans*-B(MPy)DPhP (**35** and **36**), while our studies were in progress. However, elemental analyses for the chlorides were not reported, while the ^{1}H NMR spectra were reported in D_2O, CD_3OD, or CD_3OD–CD_2Cl_2 without specific reference to the solvent used for each compound, and the UV–VIS spectra in aqueous solutions were reported without mention of concentration (28). The literature ^{1}H NMR data for **30**, **32**, **35** and **36** (28) appear to be somewhat less well resolved than ours (Table 3); there is general agreement, and differences of up to 0.7 ppm that are noted for certain resonances probably reflect differences in solvent. The reported UV–VIS data are in reasonable agreement with ours (Table 4), but our λ_{max} values are consistently lower (by 2–5 nm) than those reported.

Dialysis was also attempted for final purification of all the methylpyridinium-porphyrin chlorides, but a major loss of product was observed during dialysis of Tet(MPy)PCl_4 (**30**), this probably reflecting different aggregation properties of this compound in comparison to those of the other cationic porphyrins (3*b*, 3*c*).

Methylpyridinium porphyrins containing nitrophenyl moieties (**31**, **33** and **34**) have not been reported previously.

Assignments of ^{1}H NMR resonances

The resonances given in Tables 2 and 3 for the NPh, Py, and APh protons of the anionic porphyrins, and for the NPh and Ph protons of the cationic porphyrins, were assigned using the shielding parameters method that we discussed recently (3*a*). The H–H coupling characteristics of these substituents were also discussed in the same report (3*a*). To similarly assign SPh proton resonances (two doublets, J_{HH} = 8.0 Hz) for the anionic porphyrins requires the NMR data for TetPhP (**1**) in DMSO-d_6, which are not available because of low solubility of **1** in DMSO, and the shielding parameters (29) for the sulfonato substituent on a phenyl ring, which have also not been reported. However, the two doublets of the SPh protons in the spectrum of Tet(SPh)P (**21**) in DMSO-d_6 were assigned unambiguously by using partial deuteration at the 2,6-positions (23), and our assignments in Table 2 have been made accordingly: the resonances at δ ~8.18 and ~8.05 are attributed to the 2,6- and 3,5-SPh protons, respectively. The ^{1}H NMR spectra of the phenyl-containing porphyrins **32**, **35**, and **36** (Table 3) show the 2,6- and 3,4,5-phenyl protons at δ ~8.22 and ~7.90, respectively, and thus substitution of the 4-phenyl proton by sulfonato (an electron-withdrawing group) is expected to give an increase in both δ values, i.e., positive shielding parameters are expected for a sulfonato substituent (29). Our data yield a plausible shielding parameter value of ~ +0.15 ppm for the *ortho* (3,5) positions, but a rather surprising value of ~ –0.04 for the *meta* (2,6) positions. By considering the data for PyT(SPh)P (**23**) in Table 2, and that the introduction of a methyl group onto a pyridyl should result in a positive shielding parameter for both *meta* and *ortho* protons, the peaks of the MPy protons (which appear as two doublets with J_{HH} = 6.0 Hz) of cationic porphyrins can be assigned, with the 3,5-MPy protons at δ 9.46–9.55 and the 2,6-MPy protons at δ 9.00–9.03 (Table 3). Our assignments agree with those in literature reports (28, 30), although the studies involve different solvents.

The pyrrole proton signals in the spectra of the water-soluble porphyrins are broad and (or) overlap each other except in the spectra of the aminophenyl-sulfonatophenyl porphyrins, **17**, **19**, and **20** (Tables 2 and 3). Using the method that we discussed recently (3*a*), and considering that APh and SPh are electron-donating and electron-withdrawing groups, respectively, some of the pyrrole resonances can then be assigned. For example, the doublet at δ 8.99 (J = 4.3 Hz) for (APh)T(SPh)P (**17**) is assigned to H_3 and H_7 (see Fig. 1 for the numbering system), and the broad singlet at δ 8.85 (6H) comprises an overlapping doublet (2H, H_2 and H_8) and singlet (4H, H_{12}, H_{13}, H_{17}, and H_{18}) Similarly for *cis*-B(APh)B(SPh)P (**19**), the δ 8.92 signal is an overlapping singlet (H_7 and H_8) and doublet (H_3 and H_{12}), and the δ 8.79 signal is an overlapping singlet (H_{17} and H_{18}) and doublet (H_2 and H_{13}). In the spectrum of *trans*-B(APh)B(SPh)P (**20**), the doublet at δ 8.94 is assigned to H_3, H_7, H_{13}, and H_{17}, and the doublet at δ 8.79 to H_2, H_8, H_{12}, and H_{18}.

A singlet corresponding to the *N*-pyrrole protons (2H) always appears at δ –2.8 to –3.1 ppm. With the presence of an electron-donating group, e.g., APh, this signal appears at relatively lower field, while the reverse is seen for an electron-withdrawing group, e.g., SPh and MPy. Thus, the *N*-pyrrole protons of **17** (one APh, three SPh) resonate at δ –2.80, while those of **21** (four SPh) resonate at δ –2.95, and those of **30** (four MPy) resonate at even higher field, δ –3.10. If this trend is a more general one, the data for the *N*-pyrrole protons (see Tables 2 and 3, and data in ref. 3*a*), imply electron-withdrawing strengths in the order: MPy > NPh > Py > SPh > Ph > APh. Some of the relative electron-withdrawing strengths are well established (NPh > SPh > Ph > APh) (31), while others are not so well known (e.g., MPy > NPh > Py > SPh) and may, at least partly, be specific to porphyrin systems.

Mass spectral and partition coefficient data

As noted in footnote *g* of Table 1, the major peaks for selected anionic porphyrins in the anionic FAB spectra (3-nitrobenzyl alcohol matrix) are $(M - Na)^-$ or $(M - 2Na + H)^-$. The EI mass spectrum of (Tet(MPy)P)Cl_4 (**30**) was also recorded; 678 ($(M - 4Cl)^+$, 100%), 679 (52%), 680 (52%), and 681 (27%) were the main peaks detected. The main peaks in an EI spectrum of (T(MPy)PhP)Cl_3 (**32**) were at 618 ($(M - 3Cl - 3CH_3)^+$, 100%) and 619 (43%). The data from cationic FAB spectra (3-nitrobenzyl alcohol matrix) of selected cationic porphyrins are also noted in footnote *g*, and the major peaks are those of the porphyrin fragments without the counterions. Sari et al. (28) have reported FAB mass spectral data for **30**, **32**, and **35**, but in different matrices; in contrast to our data, major peaks corresponded to species with complete loss of methyl groups.

A partition coefficient value (P) is one factor that determines the ability of a drug to diffuse through biomembranes (32), and such values determined here are presented in Table 4. It should be noted that their determination depends on the validity of Beer's law for the porphyrins in aqueous solutions, while deviation from this are commonly found because of aggregation of the porphyrins (3*b*, 3*c*). Nevertheless, the measurements pro-

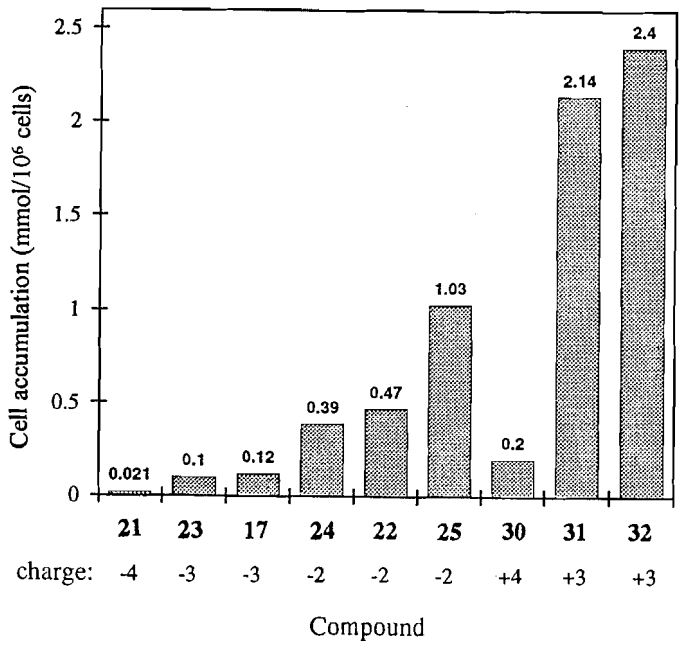

FIG. 4. Drug accumulation in HT-29 cells; data for the dicationic porphyrins, **33** and **35**, were in the 12–25 mmol/10^6 cells range.

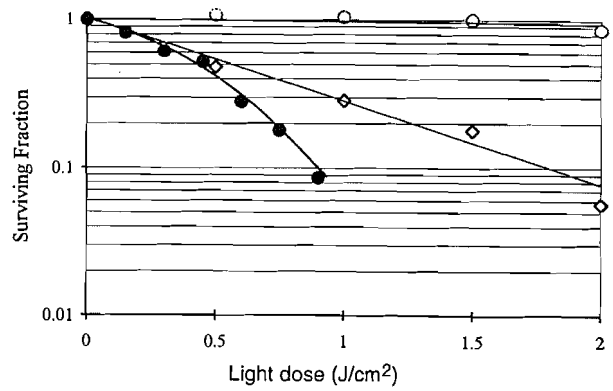

FIG. 5. Photosensitization using 630 nm radiation by compounds **30** (30 μM) ○, **24** (50 M) ◇, and Photofrin II (25 μg/mL) ●, with HT-29 cells.

vide a good approximation of the trends of the *P* values with structure; the error in *P* values is estimated to be 10–25%.

The anionic porphyrins with charges of –3 or –4 (**17**, **21**, **23**) are, not surprisingly, very lipophobic ($P < 0.01$), but those with a charge of –2 (**19**, **20**, **22**, **24**, **25**) are relatively lipophilic (P = 0.16–0.82). Cationic porphyrins are seen to be more lipophilic than anionic porphyrins with equivalent charges, and indeed some of the cationic porphyrins are highly lipophilic (P = 13, 17 for **36** and **35**, respectively) (P values of 0.1, 1.0, and 10 imply 10, 50, and 90% extraction, respectively, into the *n*-octanol). Of note, replacement of a phenyl by the more polar nitrophenyl (**33** and **34** vs. **35** and **36**) gives a significant decrease in *P* values, and a similar but less marked trend is seen on replacing an aminophenyl by pyridyl (**24** and **25** vs. **19** and **20**). The effect of charge distribution, as reflected in *cis* vs. *trans* isomers (**19/20**, **24/25**, **33/34**, **35/36**) is not significant. The effects of structural changes on the partition coefficients are of importance for the design of porphyrin drugs.

In vitro *activities*

All the porphyrins or porphyrin mixtures listed in Tables 2 and 3 are soluble in water. However, the solubilities of the porphyrins **19**, **20**, **34**, and **36** in water are low (<0.1 mM), and in the biological media are even lower; thus, these compounds were not tested in *in vitro* experiments.

The accumulation of porphyrins (**17**, **21–25**, **30–33**, and **35**) in HT-29 cells was studied, and some results are shown in Fig. 4. The data for the dicationic species **33** and **35** were variable and in the range 12–25 mmol/10^6 cells (i.e., 5–10 times the values for **31** or **32**). In general, the accumulation values increase with decreasing charge within both the anionic and cationic series; the cationic species have accumulation values typically an order of magnitude greater than an anionic species of the same charge, which is consistent with the fact that cell membranes are negatively charged. The net charge seems the dominant factor, incorporation of the nitro (**22**), amino (**17**) or pyridyl group(s) (**22–25**) having little effect; the charge distribution also seems significant (*trans*-(**25**) > *cis* (**24**)), this possibly reflecting difference in the mode of interaction of the porphyrins with cell membranes.

Rationalization of the accumulation data is clouded by possible aggregation of the porphyrins which affects the size of the solution species and is governed by the nature, charge, and position of the substituents (3*b*, 3*c*); the degree of aggregation, which could also possibly affect spectral measurements used for the concentration values, could depend on experimental conditions, particularly on the concentration of the cells and particles from cell digestion that could vary in the experiments. The degree of aggregation for anionic species increases with charge as determined within the series **21** < **23** ≈ **17** < **25** (3*b*, 3*c*), which correlates with the accumulation trend, suggesting aggregation could be an important factor.

Some selected water-soluble porphyrins (**17**, **21–25**, and **30**) at 100 μM were nontoxic toward CHO cells for incubation up to 3 h under oxic or hypoxic conditions. Tests on **31** and **32** gave highly irreproducible data, for example, giving SF values of 0–0.7 for "identical" conditions, which were conventional and included exposure to background light; photosensitization processes with background light could be involved, although **31** and **32** were not toxic toward HT-29 cells with 630 nm light in photosensitization studies. Porphyrins **31** and **32** (and **33** and **35**) were nontoxic toward HT-29 cells under oxic conditions in the dark.

The photosensitization studies used an established *in vitro* assay (18) with HT-29 cells using red light. Of porphyrins **23–25** and **30–32**, only **24** shows photosensitization activity and this porphyrin required about twice the light dose of a Photofrin II sample to obtain the same cell kill under corresponding conditions (Fig. 5). Tet(SPh)P (**21**), under certain conditions, is reported to have photosensitizing properties superior to those of Photofrin II (1, 33). The quantum yield of singlet oxygen and the DNA damage produced by light, in the presence of **21** and Tet(MPy)P, have also been studied by others from the interest of PDT (10, 34).

The porphyrin free bases **17**, **21–23**, and **30–33** have very weak, if any, radiosensitization effects, with SER values being in the range 0.92–1.04 either in a medium with or without added serum under hypoxic conditions; both sets of conditions were employed because the presence of serum was reported (35) to result in lower accumulation of Photofrin II, which is a mixture of hematoporphyrin derivatives. Contrary to expectation (see

Can. J. Chem. Downloaded from www.nrcresearchpress.com by 85.192.166.187 on 09/08/12
For personal use only.

Introduction), the presence of nitro groups within **22**, **31**, and **33** did not generate effective radiosensitizers; indeed, the SER values of 0.92–0.94 for these porphyrins imply slight radioprotection. Of note, cobalt(III) complexes of some of the porphyrins do show radiosensitizer ability under corresponding conditions, the most effective being a complex of **33** with SER = 1.22 (*3b*). O'Hara et al. (2) noted that **21** and **30** are ineffective as radiosensitizers, while some cobalt and copper derivatives of these porphyrins, whose characterization was not discussed, were reported to be effective with SER values up to 2.4. The synthesis, characterization, and biochemical studies (including radiosensitization data) on metallo derivatives of porphyrins (of Co, Cu, Zn, and Pt) described in this paper are discussed elsewhere (*3b*, *3c*).

Although the *in vitro* studies reveal disappointing results regarding the potential of the synthesized porphyrins for activity as cytotoxins, and photo- or radiosensitizers, the data from partition coefficient and cell accumulation experiments do assist in designing structures of potential drugs. In any case, the data are very preliminary and further investigations, including variations in drug concentration, cell line, and light wavelength, are ongoing.

Acknowledgments

We thank the Natural Sciences and Engineering Research Council and the Medical Research Council of Canada for financial support, and H. Adomat, H. Zhou, and G. Krosl for technical support.

1. J.W. Winkelman. *In* Methods in porphyrin photosensitization. *Edited by* D. Kessel. Plenum Press, New York. 1985. p. 91.
2. J.A. O'Hara, E.B. Douple, M.J. Abrams, D.J. Picker, C.M. Giandomenico, and J.F. Vollano. Int. J. Radiat. Oncol. Biol. Phys. **16**, 1049 (1989).
3. (*a*) G. Meng, B.R. James and K.A. Skov. Can. J. Chem. **72**, 1894 (1994); (*b*) G. Meng. Ph. D. dissertation, University of British Columbia, Vancouver. 1993; (*c*) G. Meng, B.R. James, and K.A. Skov. To be published.
4. T.S. Srivastava and M. Tsutsui. J. Org. Chem. **38**, 2103 (1973).
5. R.F. Pasternack, P.R. Huber, P. Boyd, G. Engasser, L. Francesconi, E. Gibbs, P. Fasella, G.C. Venturo, and L. deC. Hinds. J. Am. Chem. Soc. **94**, 4511 (1972), and references therein.
6. D. Kessel, P. Thompson, K. Saatio, and K.D. Nantwi. Photochem. Photobiol. **45**, 787 (1987).
7. T.P.G. Sutter, R. Rahimi, P. Hambright, J.C. Bommer, M. Kumar, and P. Neta. J. Chem. Soc. Faraday Trans. **89**, 495 (1993).
8. W.J. Kruper, Jr., T.A. Chamberlin, and M. Kochanny. J. Org. Chem. **54**, 2753 (1989).
9. R.F. Pasternack, C. Bustamante, P.J. Collings, A. Giannetto, and E.J. Gibbs. J. Am. Chem. Soc. **115**, 5392 (1990); R.J. Fiel. J. Biomol. Struct. & Dyn. **6**, 1259 (1989); R.F. Pasternack and E.J. Gibbs. *In* Metal–DNA chemistry. *Edited by* T.D. Tullins. Am. Chem. Soc. Washington D.C. 1989. p. 59.
10. B.R. Munson and R.J. Fiel. Nucleic Acids Res. **20**, 1315 (1992); S.J. Milder, L. Ding, G. Etemad-Moghadam, B. Meunier, and N. Paillous. J. Chem. Soc. Chem. Commun. 1131 **1990**; J.B. Verlhac and A. Gaudemer. Nouv. J. Chim. **8**, 402 (1984).
11. K. Kano, T. Nakajima, M. Takei, and S. Hashimoto. Bull. Chem. Soc. Jpn. **60**, 1281 (1987); R.F. Pasternack, E.J. Gibbs, A. Gaudemer, A. Antebi, S. Bassner, L. De Poy, D.H. Turner, A. Williams, F. Laplace, M. H. Lansard, C. Merienne, and M. Perre-Fauvet. J. Am. Chem. Soc. **107**, 8179 (1985); R.L. Brookfield, H. Ellul, and A. Harriman. J. Photochem. **31**, 97 (1985).
12. G.E. Adams, E.D. Clarke, I.R. Flockhart, R.S. Jacobs, D.S. Sehmi, I.J. Stratford, P. Wardman, M.E. Watts, J. Parrick, R.G. Wallace, and C.E. Smithen. Int. J. Radiat. Biol. **35**, 133 (1979); K.E. Linder, Y. Chan, J.E. Cyr, M.F. Malley, D.P. Nowotnik, and A.D. Nunn. J. Med. Chem. **37**, 9 (1994), and references therein.
13. T. Fujita, J. Iwasa, and C. Harsch. J. Am. Chem. Soc. **86**, 5175 (1964).
14. M. Korbelik and J. Hung. Photochem. Photobiol. **53**, 501 (1991); M. Korbelik, G. Krosl, H Adomat, and K.A. Akov. Photchem. Photobiol. **58**, 670 (1993).
15. B.A. Moore, B. Palcic, and L.D. Skarsgard. Radiat. Res. **67**, 459 (1976).
16. L. Parker, L.D. Skarsgard, and P.T. Emmerson. Radiat. Res. **38**, 493 (1969).
17. B. Palcic, J. Brosing, and L.D. Skarsgard. Br. J. Cancer, **46**, 980 (1982).
18. M. Korbelik, G. Krosl, H. Adomat, and K.A.Skov. Photochem. Photobiol. **55** Suppl. 54S (1992).
19. E.G. Fleischer, J.M. Palmer, T.S. Srivastava, and A. Chatterjee. J. Am. Chem. Soc. **93**, 3162 (1971).
20. J.W. Winkelman. Cancer Res. **22**, 589 (1962).
21. C.A. Busby, R.K. DiNello, and D. Dolphin. Can. J. Chem. **53**, 1554 (1975).
22. A. Harriman and G. Porter. J. Chem. Soc. Faraday Trans. 2, **75**, 1532 (1979).
23. A. Corsini and O. Harrman. Talanta, **33**, 335 (1986).
24. G.S. Nahor, P. Neta, P. Hambright, L.R. Robinson, and A. Harriman. J. Phys. Chem. **94**, 6659 (1990).
25. K.E. Keller and N. Foster. Inorg. Chem. **31**, 1353 (1992); G. Doughty and R.F. Pasternack. Inorg. Chim. Acta, **195**, 95 (1992).
26. P. Hambright and E. B. Fleischer. Inorg. Chem. **9**, 1757 (1970).
27. E.J. Gibbs, I. Tinoco, M.F. Maestre, P.A. Ellinas, and R.F. Pasternack. Biochem. Biophys. Res. Commun. **157**, 350 (1988).
28. M.A. Sari, J.P. Battioni, D. Mansuy, and J.B. Le Pecq. Biochemistry, **29**, 4205 (1990).
29. M. Zanger. Org. Magn. Reson. **4**, 1 (1972).
30. L. Ding, C. Casas, G. Etemad-Moghadam, and B. Meunier. New J. Chem. **14**, 421 (1990).
31. D.D. Perrin, B. Dempsey, and E.P. Serjeant. pK_a prediction for organic acids and bases. Chapman and Hall, London. 1981. Chap. 4.
32. S.H. Curry. Drug disposition and pharmacokinetics. Blackwell, Oxford. 1977.
33. M.D. Berenbaum, S.L. Akande, R. Bonnett, H. Kaur, S. Ioannou, R.D. White, and U.J. Winfield. Br. J. Cancer, **54**, 717 (1986).
34. R.J. Fiel, N. Datta-Gupta, E.H. Mark, and J.C. Howard. Cancer Res. **41** 3543 (1981).
35. M. Korbelik. Photochem. Photobiol. **56**, 391 (1992).

Can. J. Chem. Downloaded from www.nrcresearchpress.com by 85.192.166.187 on 09/08/12
For personal use only.

Évolution thermique et photochimique des triazolines résultant de l'addition des diazocomposés aux esters d'oximino-malonodinitriles, oximino-cyanoacétates et oximino-malonates de méthyle

JACQUES PERROCHEAU ET ROBERT CARRIÉ[1]

Université de Rennes I, Groupe de physicochimie structural, Centre national de la recherche scentifique, Unité de recherche associée n° 704, Avenue du Général Leclerc, F 35042 Rennes Cedex, France

ET

JEAN-PIERRE FLEURY

École Nationale Supérieure de Chimie de Mulhouse, 3, rue A. Werner, F 68093 Mulhouse Cedex, France

Reçu le 23 avril 1994

JACQUES PERROCHEAU, ROBERT CARRIÉ et JEAN-PIERRE FLEURY. Can. J. Chem. **72**, 2458 (1994).

La thermolyse des 1,2,3-triazolines **4**, **5**, **6** permet l'obtention des aziridines correspondantes seulement lorsque X = Y = CO_2Me et encore avec une faible rendement. Par contre la photolyse ou l'évolution en présence d'acide trifluoroacétique donne de bons résultats à condition d'opérer à une température suffisamment basse. L'étude de la thermolyse de **4**–**6** montre un nouveau mode d'évolution des 1,2,3-triazolines non encore signalé dans la littérature. La grande facilité d'élimination du groupement paratoluènesulfonate ou benzoate est certainement le facteur déterminant dans le comportement de ces composés.

JACQUES PERROCHEAU, ROBERT CARRIÉ, and JEAN-PIERRE FLEURY. Can. J. Chem. **72**, 2458 (1994).

Thermolysis of 1,2,3-triazolines **4**, **5**, **6** leads to the corresponding aziridines only when X = Y = CO_2Me, and then with a very low yield. However, photolysis or evolution in the presence of trifluoroacetic acid gives good results when carried out at sufficiently low temperature. The thermolysis study of **4**–**6** shows a new route to 1,2,3-triazoline decomposition that has not yet been mentioned in the literature. The easy elimination of the paratoluenesulfonate or benzoate group explains this particular behaviour.

Can. J. Chem. Downloaded from www.nrcresearchpress.com by 85.192.166.187 on 09/08/12
For personal use only.

Description des résultats

Dans un travail antérieur (1), nous avons montré que les esters d'oximes **1**, **2** et **3** réagissent avec divers diazocomposés pour conduire aux 1,2,3-triazolines **4**–**6** (Fig. 1).

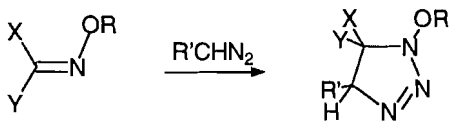

1 : R = Ts — **4**
2 : R = $COC_6H_4(pZ)$, (Z = H, NO_2) — **5**
3 : R = COMe — **6**

a : X = CN, Y = CO_2Me
b : X = Y = CO_2Me

A : R' = H
B : R' = $(MeO)_2CH$
C : R' = Me
D : R' = Ph

FIG. 1

L'évolution thermique et photochimique de ces adduits fait l'objet de ce mémoire. L'étude de la photolyse et le comportement des triazolines marquées à l'azote 15 a facilité l'analyse du comportement thermique relativement complexe de ces composés.

I. Photolyse de quelques 1,2,3-triazolines O-tosylées

La photolyse permet d'obtenir facilement les aziridines. L'identification de celles-ci dans les produits de thermolyse en a été ainsi facilitée.

Seule la photolyse des triazolines **4** (R = Ts) a été étudiée. La thermolyse de ces triazolines ne permet pas l'obtention des aziridines correspondantes sauf lorsque X = Y = CO_2Me, où elles sont obtenues avec des rendements de 30–40%.

Par contre, la photolyse en solution dans le dichlorométhane à −40°C conduit aux aziridines de façon pratiquement quantitative. La photolyse de **4aA** (X = CN, Y = CO_2Me, R' = H) donne le mélange des deux aziridines diastéréoisomères **7aA'** et **7aA"** (proportions relatives 70/30) (Fig. 2).

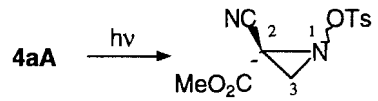

4aA —hν→ **7aA'** et **7aA"**

FIG. 2

Pour la triazoline **4aB** (deux diastéréoisomères **4aB'** et **4aB"** dont les stéréochimies ne sont pas attribuées) la formation des quatre aziridines diastéréoisomères **7aB** est observée (Fig. 3).

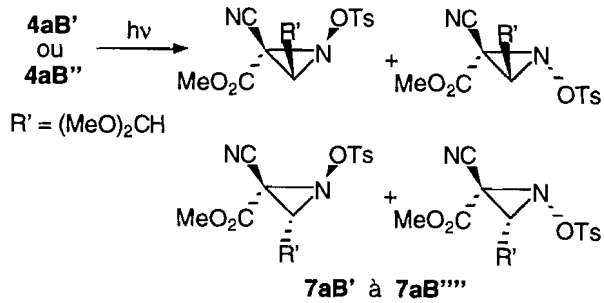

4aB' ou **4aB"** —hν→ **7aB'** à **7aB""**

R' = $(MeO)_2CH$

FIG. 3

Pour chaque triazoline, les proportions relatives de ces quatre aziridines sont précisées dans le tableau 1.

1. Auteur à qui adresser toute correspondance. Téléphone : (33) 99 28 63 74. Fax : (33) 99 28 67 38.

TABLEAU 1. Caractéristiques de rmn ^1H (δ, J) ($CDCl_3$) et physiques des aziridines **7**

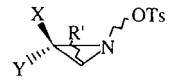

Composé	X	Y	R'	*H* cyclique (CH_3) δ	*H* cyclique (CH_3) $^2J_{AB}$ ($^3J_{AX}$)	CO_2CH_3	$(CH_3O)_2C$	$(MeO)_2CH$ δ	$(MeO)_2CH$ ^3J	% relatif		*F* (°C)	Rdt[a] (%)
7aA′ ou 7aA″	CN	CO_2Me	H	3,14 3,06	3,8	3,81	—	—	—	70		136	87
7aA″ ou 7aA′	CN	CO_2Me	H	3,43 2,97	3,9	3,87	—	—	—	30		118	
7aB′	CN	CO_2Me	$(MeO)_2CH$	[b]		3,81	3,28 3,25	4,35	7,0	8[c]	6[d]		
7aB″	CN	CO_2Me	$(MeO)_2CH$	3,28	(7,3)	3,81	3,50	4,70	7,3	≈5	41	119–122[c] 118–120[d]	70[c] 77[d]
7aB‴	CN	CO_2Me	$(MeO)_2CH$	[b]		3,78	3,48 3,46	5,06	7,8	≈3	10		
7aB⁗	CN	CO_2Me	$(MeO)_2CH$	3,15	(6,9)	3,87	3,42 3,41	5,27	6,9	84	43		
7bA	CO_2Me	CO_2Me	H	3,15 2,15	(3,9)	3,81 3,73	—	—	—			90–92	82[e]
7bB′ ou 7bB″	CO_2Me	CO_2Me	$(MeO)_2CH$	2,89	(7,4)	3,80 3,70	3,45 3,33	4,85	7,4	70		[f] 84–88	90
7bB″ ou 7bB′	CO_2Me	CO_2Me	$(MeO)_2CH$	3,54	(5,0)	3,75 3,70	3,22 3,10	4,19	5,0	30		[f]	
7bC′ ou 7bC″	CO_2Me	CO_2Me	Me	2,83 (1,51)	(6,1)	3,78 3,70	—	—	—	78[g]		90–92	77
7bC″ ou 7bC′	CO_2Me	CO_2Me	Me	3,40 (1,12)	(6,2)	3,78 3,74	—	—	—	15[g]		[b]	
7bD′ ou 7bD″	CO_2Me	CO_2Me	Ph	3,86		3,77 3,74	—	—	—	70		[h]	
7bD″ ou 7bD′	CO_2Me	CO_2Me	Ph	4,52		3,92 3,48	—	—	—	30		[h]	

[a]Rendement en produit isolé cristallisé.
[b]Sur le spectre du mélange des diastéréoisomères, il est impossible de préciser les déplacements des hydrogènes cycliques.
[c]Photolyse de **4aB′**.
[d]Photolyse de **4aB″**.
[e]Littérature (2) : F = 90–91°C, Rdt = 73%, rmn ^1H ($CDCl_3$), δ : 3,77 et 3,64 (2s, CO_2CH_3); 3,09 et 2,59 (système AB, H cycliques).
[f]Aziridines non séparées.
[g]Avec 7% de produit non identifié.
[h]Aziridines instables (J. Perrocheau et R. Carrié. Résultats non publiés).

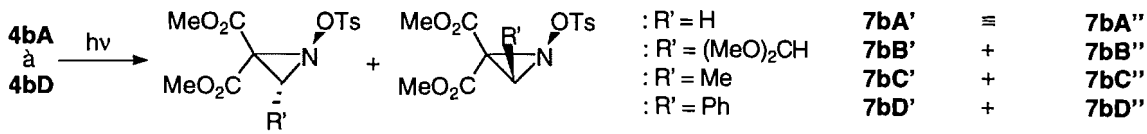

FIG. 4

De même les triazolines **4bA–4bD** donnent les aziridines **7bA–7bD** (Fig. 4).

Lorsque X = CN et Y = CO_2Me, il est nécessaire d'opérer à la température la plus basse possible pour éviter la cycloréversion du diazométhane.

Avec la triazoline **4bA**, à −40°C, on observe dans le produit brut de la réaction 5% d'oxime **8bA** (Schéma 1), composé principalement formé lors de la thermolyse. Ces observations peuvent expliquer les résultats Kostyanovsky et al. (3) : lors de la photolyse de l'ester diéthylique correspondant à **4bA** à −10°C, ils obtiennent à côté de l'aziridine une proportion importante de produits de thermolyse (19% d'oxime de départ, 44% d'oxime correspondant à **8bA**) (Fig. 5).

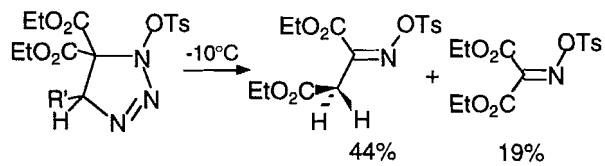

FIG. 5

Can. J. Chem. Downloaded from www.nrcresearchpress.com by 85.192.166.187 on 09/08/12
For personal use only.

Can. J. Chem. Downloaded from www.nrcresearchpress.com by 85.192.166.187 on 09/08/12
For personal use only.

Les caractéristiques de rmn ^1H confirment la structure des aziridines **7** obtenues. Elles figurent dans le tableau 1. Lorsque X = Y = CO_2Me avec R′ = H, la non-équivalence des protons cycliques et des groupements esters est la conséquence de la haute barrière d'inversion de l'azote. Kostyanovsky et al. (3) ont montré que dans ce type de composés, les groupements précédents restent non équivalents même si le spectre est enregistré dans le diphényléther ou l'α-bromonaphtalène à 200°C.

Remarques : (*i*) L'attribution d'une stéréochimie aux différentes aziridines diastéréoisomères obtenues n'a pas été faite. (*ii*) Certaines aziridines ne sont pas très stables. Par exemple, on constate pour **7bD′** et **7bD″** une évolution totale de l'isomère majoritaire en 45 min après sa dissolution dans le chloroforme à température ambiante.

*II. Thermolyse des 1,2,3 triazolines **4**, **5**, et **6***

Les triazolines **4**, **5** et **6** sont des composés thermiquement peu stables. En solution dans le benzène ou le chloroforme, leur décomposition est totale à température ambiante (6 h – 5 jours suivant la substitution).

Le schéma 1 résume les évolutions thermiques possibles pour les triazolines et propose une interprétation mécanistique de ces évolutions (les composés isolés sont encadrés). Cette tentative de rationalisation du comportement thermique des 1,2,3-triazolines est susceptible d'expliquer les résultats expérimentaux obtenus. Il subsiste toutefois des incertitudes puisqu'un certain nombre d'intermédiaires ne sont pas mis en évidence.

II.1. Triazolines diesters (X = Y = CO_2Me)

Avec les triazolines diesters (X = Y = CO_2Me), la cycloréversion est observée uniquement lorsque R′ = H et 8% de tosylate de méthyle **15** sont mis en évidence à l'aide de la rmn dans le produit brut de thermolyse de la triazoline **4bA**. Comme nous le verrons dans la suite, ce tosylate ne peut résulter que de l'action de l'acide paratoluènesulfonique sur le diazométhane libéré par cycloréversion. Dans tous les autres cas (R′ ≠ H), les oximes **8**, **9** et **10** (55–65%) et les aziridines **7**, **11** et **12** (45–35%) sont exclusivement obtenues. Ces composés sont caractérisés à l'aide de la rmn (voir partie expérimentale, les caractéristiques des aziridines tosylées **7** sont données dans le tableau 1).

Kostyanovsky et al. (3) ont déjà signalé la formation des composés **8** et proposé pour la formation de ces derniers, soit le processus synchrone 2s + 2s + 2s **23** soit le réarrangement du biradical singulet **24** (Fig. 6).

23 **24**

FIG. 6

Les migrations radicalaires de groupements esters n'étant à notre connaissance jamais observées, la première proposition parait plus vraisemblable.

La formation des aziridines **7**, **11**, et **12** peut résulter de la cyclisation du biradical **24** (voie **c**) ou de la substitution nucléophile intramoléculaire de **13** (voie **f**) qui provient de la rupture hétérolytique de la liaison N1—N2 des triazolines diesters (voie **b**).

II.2. Triazolines ester nitriles (X = CN, Y = CO_2Me)

II.2.1. Cycloréversion en diazocomposés et esters d'oximes. L'évolution la plus importante est la cycloréversion (≈50% R′ = H à ≈80% R′ = $(MeO)_2CH$)). Cette rétrocycloaddition peut être concertée (voie **a**) ou s'effectuer en deux étapes (voie **b** puis voie **e**). L'oxime O-substituée est identifiée dans tous les cas dans le produit brut de la réaction à l'aide de la rmn par comparaison avec un échantillon authentique.

Le diazoacétal $(MeO)_2CHCHN_2$ est mis en évidence par identification avec un échantillon authentique, lors du suivi de la thermolyse de **4aB** (mélange des deux isomères **4aB′** et **4aB″**) à l'aide de la rmn. La cycloréversion du diazométhane a été vérifiée de deux manières dans le cas plus particulièrement étudié de la triazoline **4aA**.

1. La thermolyse en présence d'acide benzoïque entraîne la formation de benzoate de méthyle identifié à l'aide de la chromatographie de partage gaz–liquide par comparaison avec un échantillon authentique.

2. Si la décomposition est effectuée après addition de propiolate de méthyle, on peut caractériser les pyrazoles **25** et **26** (proportion relative 55/45) ainsi que l'oxime **1a** (62%) à l'aide de la rmn (Fig. 7).

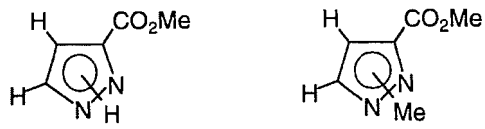

25 **26**

FIG. 7

Remarque : L'addition du diazométhane au propiolate de méthyle donne préférentiellement **25** qui est méthylé pour donner **26** si la réaction est effectuée en présence d'acide paratoluènesulfonique. Les diazocomposés (R′ = H et CH_3) réagissent sur l'acide paratoluènesulfonique (triazolines issues de **1a**, **1b**), les acides benzoïque ou (pNO_2)benzoïque (triazolines issues de **2a**) ou l'acide acétique (triazoline issue de **3a**) pour donner les paratoluènesulfonates, benzoates ou acétates de méthyle ou d'éthyle **15–17** identifiés en rmn ^1H et en chromatographie de partage gaz–liquide par comparaison avec des échantillons authentiques.

II.2.2. Évolution avec perte d'azote. Avec les triazolines **4aC** et **5aC** (R′ = Me) et **4aD** (R′ = Ph), les oxazoles **21** ou **22** sont obtenus, ce qui implique une étape dans laquelle il y a rupture de la liaison entre les deux carbones cycliques des triazolines. Ceci conduit à l'hypothèse suivante : l'azirine **18** résultant de la cyclisation de **14** (R′ ≠ H) peut être protonée sur l'azote par l'acide ROH présent dans le milieu selon un mécanisme mentionné par Taniguchi et collaborateurs (4). L'entité **19** par un réarrangement concerté du type $2\pi s + 2\sigma a$ peut donner **20** puis **21** (ou **22**) en libérant un proton de sorte que le processus est catalytique du point de vue de l'acide.

En partant de l'oxime **1a** marquée à l'azote 15 (52%), on obtient l'oxazole **21** (R = Me) marqué à 52%. Le mécanisme proposé rend compte de cette observation.

Lorsque R′ = H, à côté des oximes **1** ou **2** provenant de la cycloréversion et des esters **15** ou **16**, la réaction conduit à des composés pâteux amorphes, sans doute des polymères présentant en rmn un massif large entre 3,4 et 3,9 ppm (C_6D_6). Il est connu (5) que les azirines correspondantes sont peu stables et polymérisent facilement.

Can. J. Chem. Downloaded from www.nrcresearchpress.com by 85.192.166.187 on 09/08/12
For personal use only.

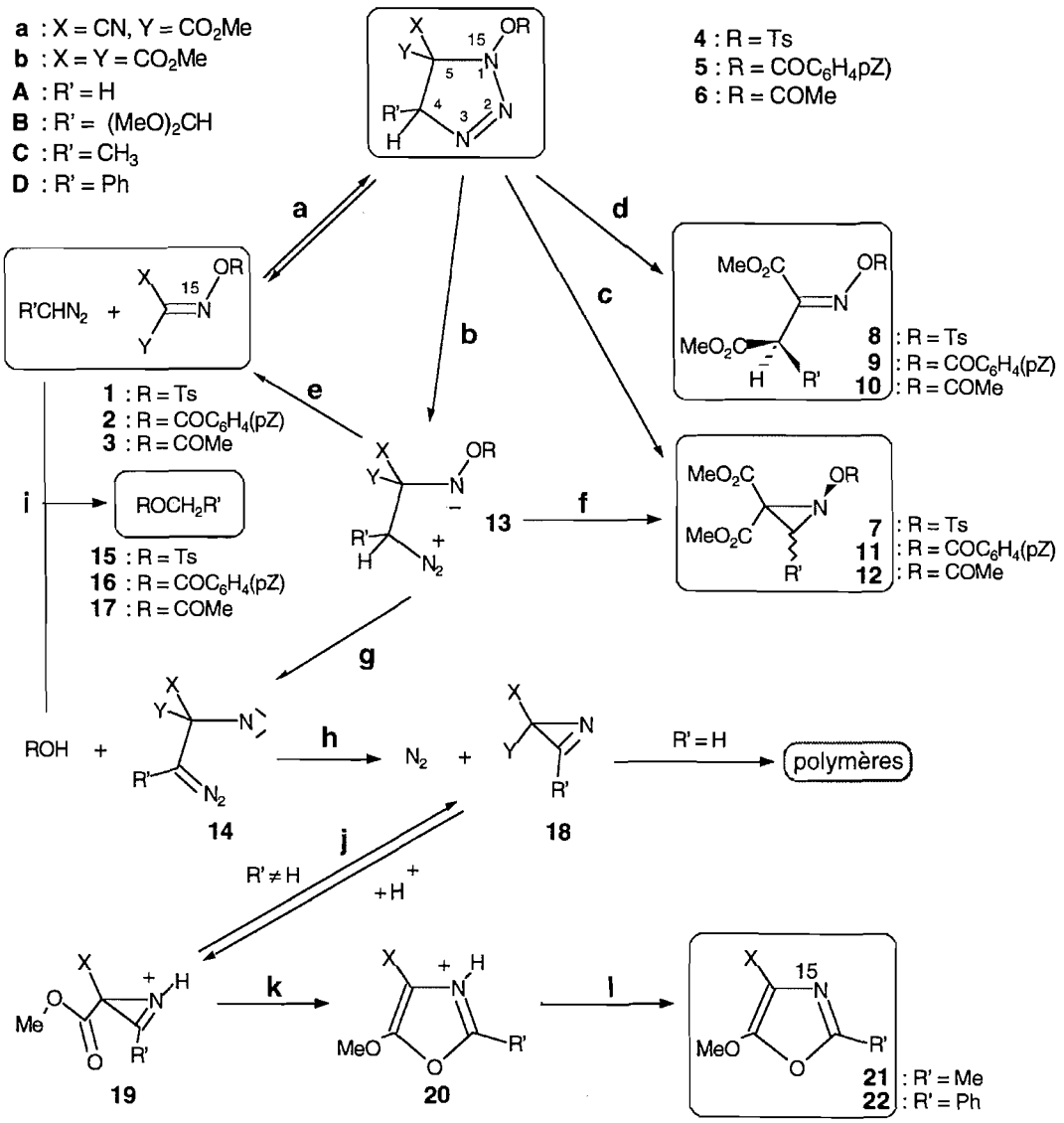

SCHÉMA 1

Enfin les aziridines **7bA′** et **7bA″** (X = CN, Y = CO_2Me, R = Ts, R′ = H), qui peuvent être obtenues par photolyse, n'évoluent pas dans le milieu réactionnel. Ces aziridines ne sont donc pas des intermédiaires dans la formation des oxazoles **21** ou **22**.

Le mécanisme d'évolution des triazolines avec perte d'azote implique donc une rupture hétérolytique entre les atomes N1 et N2 conduisant à **13**. Un tel comportement est signalé dans la littérature (6). L'évolution de **13** est explicitée dans le schéma 1. Le composé **13** donne **14** avec élimination du composé ROH qui est susceptible de réagir avec les diazocomposés libérés dans la cycloréversion.

Remarques : Les essais de préparation de 1,2,3-triazolines disubstituées en 4, intéressantes pour étudier l'évolution des entités analogues à **13**, ont échoué. La faible réactivité du diphényldiazométhane, l'instabilité du diazopropane ne permettent pas d'isoler les triazolines correspondantes.

II.2.3. Structure des oxazoles 21 et 22. En ce qui concerne **21** l'infrarouge, la spectrométrie de masse, la rmn ^1H et ^{13}C sont en accord avec la structure proposée mais ne permettent pas de distinguer **21** de son isomère isoxazole **27** qui pourrait résulter du réarrangement de **19** (Fig. 8).

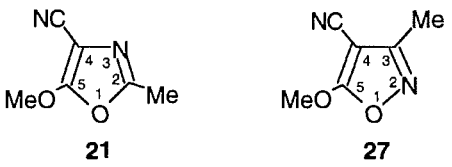

FIG. 8

L'enregistrement du spectre de rmn ^{13}C du dérivé **21** marqué à l'azote 15 (marquage à 52%) apporte un argument décisif. Le carbone du groupement nitrile (δ = 112,4 ppm) est couplé avec l'azote 15. La valeur de la constante observée (7,8 Hz) est caractéristique d'un couplage $^2J_{^{13}C^{15}N}$ lorsque le noyau est en *cis* de la paire libre. Elle est incompatible avec un couplage ^3J et donc avec la structure **27** (7). Dans la mesure où l'on compare deux carbones de même hybridation, il semble bien établi que la proximité de la paire libre est le facteur prépondérant contribuant à la valeur de la constante $^2J_{^{13}C^{15}N}$ (8, 9).

On remarquera que pour X = CN, Y = CO_2Me et R′ = CH_3, l'oxazole obtenu est le même quelle que soit la nature de R. L'analogie des déplacements chimiques des carbones cycliques

Can. J. Chem. Downloaded from www.nrcresearchpress.com by 85.192.166.187 on 09/08/12
For personal use only.

de **21** et du composé phénylé correspondant conduit à attribuer à ce dernier la structure **22**.

II.3 Conclusion

En ce qui concerne l'évolution thermique des triazolines **4**, **5** et **6**, les points suivants doivent être soulignés :

1. Le remplacement d'un groupement nitrile par un groupement ester (X = Y = CO_2Me) augmente la stabilité thermique des triazolines. Cette observation est valable quels que soient R et R′ (R = Ts, PhCO, Ac; R′ = H, Me, Ph, $(MeO)_2CH$).

2. De même, le remplacement d'un groupement tosyle par un groupement benzoyle augmente la stabilité thermique. Un groupement acétyle la renforce davantage.

3. L'ordre de stabilité croissante en fonction de R′ est le suivant : $(MeOH)_2CH$ > H > Me, Ph. Si X = Y = CO_2Me, on isole dans tous les cas les adduits primaires. Avec X = CN, Y = CO_2Me, ces derniers ne sont pas mis en évidence lorsque R′ = Me ou Ph.

La cycloréversion est une voie d'évolution importante lorsque X = CN, Y = CO_2Me. Dans un premier temps elle a pu faire croire à l'absence de réactivité des esters d'oxime **1a** lorsque les essais d'addition sont effectués à la température ambiante.

*III. Évolution des triazolines **4aA** et **4bA** en présence d'acide trifluoroacétique*

L'action de l'acide trifluoroacétique sur la triazoline **4bA** a déjà été étudiée par Kostyanovsky et al. (3). Il est ainsi possible d'obtenir dans de bonnes conditions l'aziridine correspondante.

Nous avons repris cette étude à −20°C en solution dans le chloroforme, température où les triazolines **4aA** et **4bA** sont stables. L'acide trifluoroacétique en quantité stœchiométrique conduit avec d'excellents rendements aux aziridines **7aA′**, **7aA″** d'une part et **7bA** d'autre part. Les caractéristiques de ces composés ont été données précédemment lors de l'étude de la photolyse des triazolines. **7aA′** et **7aA″** sont obtenues dans les mêmes proportions (70/30) que lors de la photolyse de la triazoline correspondante.

La protonation de la triazoline facilite la rupture de la liaison N1—N2 conduisant à l'entité **13** protonée qui évolue de façon spécifique vers l'aziridine correspondante.

*IV. Réaction des oximinomalodinitriles **28** et **29** avec le diazométhane et le diazoéthane*

Les composés **28** et **29** sont préparés selon le schéma de réaction suivant, variante au mode opératoire décrit par Fleury et al. (9) (Fig. 9).

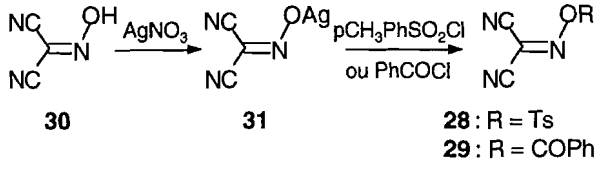

FIG. 9

Avec **28**, l'addition du diazométhane aussi réalisée par Fleury et collaborateurs (10) conduit, lorsqu'elle est effectuée à −20°C, au composé **32′** (52%) accompagné de son isomère **32″** (16%) et du tosylate de méthyle (22%) (intégration des signaux N-Me des différents composés par rapport aux signaux des méthyles des groupements tosyles) (Fig. 10).

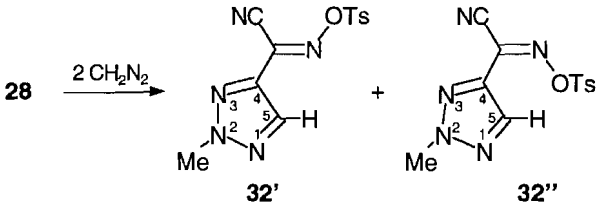

FIG. 10

L'addition du diazométhane à **29** donne le mélange des triazoles **33** (38%) et **34** (ou **35**) (31%). La formation du benzoate de méthyle (21%) et d'un produit non identifié (10%), qui présente un signal attribuable par rmn à un méthyle lié à l'azote, est observé (évaluation rmn) (Fig. 11).

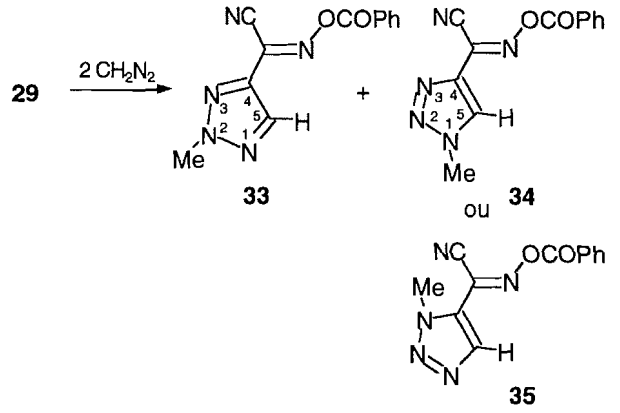

FIG. 11

Les structures de **32′** et de **32″** ont déjà été établies sans ambiguïté par Fleury et collaborateurs (9). De plus, ces auteurs ont montré que **32′** s'isomérise en **32″** en milieu chlorhydrique.

Étant donné l'analogie des caractéristiques de rmn ^{13}C entre **32″** et le produit prépondérant obtenu à partir de **29**, la structure **33** est attribuée à ce dernier. Contrairement à ce qui est observé avec **28**, le second produit ne semble pas être l'isomère géométrique de **33** et la structure **34** (ou **35**) lui est attribuée à l'aide de la rmn ^{13}C. Les déplacements chimiques des carbones des groupements nitriles de **33** et de **34** (ou **35**) sont pratiquement identiques (107,8 et 107,6 ppm). S'il s'agissait d'une isomérie *syn-anti* du motif oxime, les données de la littérature (11) laisserait prévoir une différence notable entre ces deux déplacements chimiques comme il est observé pour **32′** (106,7 ppm) et **32″** (110,9 ppm, $\Delta\delta_{C\equiv N}$ = 4,2 ppm).

Remarque : Contrairement à ce qui est observé avec **32′**, le traitement de **33** en milieu acide dans le méthanol ne conduit pas à l'isomère géométrique attendu mais à l'oxime **36** (Fig. 12), caractérisé à l'aide de la rmn et de la spectroscopie de masse, et au benzoate de méthyle (rmn ^1H).

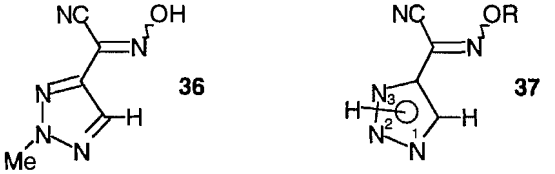

FIG. 12

Can. J. Chem. Downloaded from www.nrcresearchpress.com by 85.192.166.187 on 09/08/12
For personal use only.

Discussion et conclusion

1. Les composés **32′**, **32″**, **33** et **34** (ou **35**) résultent de l'addition préférentielle sur la triple liaison C≡N en *anti* par rapport au groupement OR de l'oxime. L'addition s'effectue préférentiellement sur le groupement nitrile le moins encombré stériquement. De telles additions sur des groupements nitriles activés ont déjà été signalées dans la littérature (12); c'est en particulier le cas des cyano-2 coumarines (13) et de l'α-fluorocinnamonitrile (14).

2. Dans un premier temps, la cycloaddition du diazométhane conduit au triazole tautomère **37** pour lesquels la méthylation par une seconde molécule de diazocomposé peut s'effectuer sur l'un ou l'autre des trois azotes cycliques (azote 1, 2 ou 3) (15). Elle est plus ou moins facile selon la substitution. La méthylation des cycloadduits primaires est facilitée dans notre cas par des traces d'acide paratoluènesulfonique ou benzoïque présentes dans le milieu.

3. La formation de tosylate ou de benzoate de méthyle ne peut s'expliquer que par une cycloaddition compétitive sur la double liaison C=N de l'oxime. La 1,2,3-triazoline correspondante, produit cinétique de la réaction, évolue alors selon le schéma 1. Avec le diazoéthane l'addition sur la double liaison C=N de **28** est exclusivement observée. Seule l'oxime tosylée de départ et le tosylate d'éthyle, résultant respectivement de la cycloréversion et de l'évolution de l'adduit primaire, sont mis en évidence.

Partie expérimentale

L'appareillage de rmn suivant a été utilisé :

Appareil à onde continue JEOL MH100 (100 MHz). Appareil à onde continue Bruker WP 80 CW (80 MHz). Appareil à transformée de Fourier Bruker WP 80 DS (80 MHz pour le proton et 20 MHz pour le carbone 13) du Centre Régional de Mesures Physiques de l'Ouest (C.R.M.P.O.). Appareil à transformée de Fourier Bruker AC 300 P (300 MHz pour le proton et 75 MHz pour le carbone 13) commun aux U.R.A. n° 704 et 415. Le solvant utilisé pour l'enregistrement des spectres de RMN ^1H et ^{13}C est $CDCl_3$ sauf indication contraire. Les déplacements chimiques (δ) sont exprimés en parties par million (ppm) par rapport au tétraméthylsilane (TMS) utilisé comme référence interne. Les constantes de couplage sont exprimées en hertz. Les notations suivantes sont utilisées : s : singulet; d : doublet; t : triplet; q : quadruplet; m : multiplet ou massif non analysable; dq : double quadruplet; tt: triple triplet; tm : triple multiplet; etc.... Les caractéristiques de rmn concernant les protons aromatiques ne sont pas données.

Les spectres de masse sont enregistrés à l'aide d'un spectromètre Varian MAT 311 du C.R.M.P.O. L'énergie du faisceau électronique est de 70 eV, l'intensité du courant d'émission 300 μA et la tension d'accélération des ions 3 kV.

Les analyses élémentaires sont effectuées au Laboratoire Central de Microanalyse du C.N.R.S. de Lyon.

Les points de fusion sont déterminés sur un banc chauffant Kofler et ne sont pas corrigés.

La préparation des oximes **1**, **2**, **3** et des triazolines **4**, **5** et **6** a été décrite dans un mémoire antérieur (1).

I. Photolyse des 1,2,3-triazolines ***4***

Mode opératoire général

Les photolyses à basse température (−40 à −50°C) sont effectuées dans un réacteur refroidi dans un cryostat. La réfrigération de la double enveloppe en Pyrex entourant la lampe est assurée par une circulation d'éther de pétrole à −50°C. Les triazolines sont dissoutes sous atmosphère d'azote dans 250 cm^{-3} de dichlorométhane anhydre préalablement refroidi. La solution est dégazée par barbotage d'azote puis irradiée à l'aide d'une lampe Philips HPK 125 W.

I.1. Photolyse de la triazoline ***4aA***. La photolyse de 1,00 g de triazoline **4aA** demande 20 h. Le spectre de rmn ^1H du résidu après distillation du solvant montre la formation des deux aziridines **7aA′** et **7aA″**. Le résidu repris à l'éther abandonne 0,8 g de cristaux (F = 102–108°C, mélange 70/30 des deux isomères (analyse rmn)) (Rdt = 87%).

Les deux isomères sont séparés à l'aide de la chromatographie sur colonne de silice (25 g, éluant : éther/éther de pétrole 50/50). On sépare ainsi successivement : (*i*) 0,05 g de l'aziridine minoritaire (F = 118°C); (*ii*) 0,13 g d'un mélange 60 : 40 (majoritaire/minoritaire); (*iii*) 0,23 g de l'aziridine majoritaire (F = 136°C). **7aA′** (ou **7aA″**), isomère majoritaire 70%; rmn ^{13}C, δ : 37,6 (dd, aspect de triplet, $^2J_{CH} \approx {}^2J'_{CH}$ = 3, C2); 44,8 (dd, $^1J_{CH}$ = 177 et 184, C3); 111,5 (dd, $^3J_{CH}$ = 3 et 5, *C*≡N); 162,1 (s, *C*O_2Me). **7aA″** (ou **7aA′**), isomère minoritaire 30%; rmn ^{13}C, δ : 38,1 (dd, aspect de triplet, $^2J_{CH} = {}^2J'_{CH}$ = 3, C2); 43,0 (dd, $^1J_{CH} \approx {}^1J'_{CH}$ = 181, C_3); 113,6 (dd, aspect de triplet, $^3J_{CH} \approx {}^3J'_{CH}$ = 4, *C*≡N); 159,1 (s, *C*O_2Me). **7aA′** et **7aA″**, analyse : $C_{12}H_{12}N_2O_5S$, calc. % : C 48,64; H 4,08; N 9,45. Mélange (60/40) : tr. : C 48,43; H 4,02; N 9,45. Isomère majoritaire : tr : C 48,66; H 4,02; N 9,31.

I.2. Photolyse de la triazoline ***4aB′***. La photolyse de 950 mg du dérivé **4aB′** (Déc. 120–125°C) demande 12 h pour être totale. Après analyse à l'aide de la rmn (tableau 1), le résidu (800 mg sous forme d'huile) est purifié par filtration sur 10 g de silice (éluant : éther/éther de pétrole 50/50). On obtient ainsi 640 mg de cristaux, mélange des aziridines **7aB** diastéréoisomères (Rdt = 70%; F = 119–122°C). **7aB**, analyse : $C_{15}H_{18}N_2O_7S$ (mélange d'isomèrs dont la composition est donnée dans le tableau 1), calc. % : C 48,64; H 4,90; N 7,56; tr. : C 48,89; H 4,96; N 7,67.

I.3 Photolyse de la triazoline ***4aB″***. La solution de 900 mg de triazoline **4aB″** (Déc. 90–95°C) est irradiée pendant 11 h. Après analyse à l'aide de la rmn (tableau 1), l'huile résiduelle (800 mg) est purifiée par filtration sur 15 g de silice. On obtient 650 mg de cristaux, mélange des aziridines dont la composition est donnée dans le tableau 1 (F = 118–120°C; Rdt = 77%).

I.4. Photolyse de la triazoline ***4bA***. La photolyse de 700 mg de triazoline **4bA** est totale en 10 h. Après élimination du solvant l'aziridine **7bA** cristallise. Elle est essorée et lavée à l'éther. On obtient 525 mg de cristaux (F = 90–92°C; Rdt = 82%) (litt. (3), F = 90–91°C; Rdt = 73%). **7bA**, rmn ^{13}C, δ : 41,4 (dd, $^1J_{CH}$ = 176 et 181, C_3); 49,8 (signal partiellement masqué par ceux des groupements méthoxyles, C2); 53,3 et 53,7 (q, $^1J_{CH}$ = 148 et 148, CO_2CH_3); 161,9 et 164, 8 (2s, *C*O_2Me).

I.5. Photolyse de la triazoline ***4bB***. La photolyse est effectuée sur 1,23 g de triazoline. Après 7 h d'irradiation à −40°C, la réaction est totale. L'analyse rmn du produit brut montre la formation exclusive des aziridines **7bB′** et **7bB″** (proportions relatives 70/30). Après distillation du solvant, l'huile brute reprise à l'éthanol abandonne 1,10 g de cristaux (mélange des deux isomères). Une recristallisation dans l'éthanol fournit un premier jet (0,80 g) de cristaux (F = 82–84°C). Les eaux mères sont évaporées, le résidu après filtration sur silice (éluant : éther/éther de pétrole 50/50) donne 250 mg de cristaux. On obtient ainsi 1,05 g du mélange 70/30 des deux isomères **7bB′** et **7bB″** (Rdt global = 90%, F = 84–88°C). **7bB″** ou **7bB″**, isomère majoritaire, rmn ^{13}C, δ : 50,7 (dd, $^1J_{CH}$ = 178, $^2J_{CH} \approx$ 2, C3); 53,5 (d, $^2J_{CH}$ = 3, C2); 53,4 et 53,8 (q, $^1J_{CH}$ = 149 et 148, CO_2CH_3); 55,5 (qd, $^1J_{CH}$ = 143, $^3J_{CH}$ = 5, (CH_3O_2CH); 98,3 (dqd, $^1J_{CH}$ = 171, $^3J_{CH}$ = 9, $^2J_{CH}$ = 4, $(CH_3O)_2CH$); 161,3 et 164,8 (qd aspect de quintuplet, $^3J \approx {}^3J'$ = 4, *C*O_2Me). Spectre enregistré sur le mélange des isomères **7bB′** et **7bB″**. **7bB′** et **7bB″** mélange (70/30), analyse : $C_{16}H_{21}NO_9S$, calc. % : C 47,64; H 5,25; N 3,47; tr. : C 47,54; H 5,16; N 3,42.

I.6. Photolyse de la triazoline ***4bC***. La photolyse de 2,00 g de triazoline **4bC** demande 3 h pour être totale. L'analyse rmn montre la formation, à côté des deux aziridines **7bC′** (78%) et **7bC″** (15%), d'un troisième produit (7%) qui n'a pas été identifié. Ce dernier présente un doublet à 1,37 ppm attribuable à un groupement méthyle couplé avec un hydrogène.

Après élimination du solvant le résidu cristallise (1,70 g). Une recristallisation dans l'éthanol permet d'obtenir dans un premier jet, 1,20 g de l'isomère majoritaire (F = 90–92°C) et dans un deuxième jet 0,18 g d'un mélange 50/50 des deux isomères (analyse rmn) (rendement global = 77%). **7bC′**, isomère majoritaire, rmn ^{13}C, δ : 8,4 (q, $^1J_{CH}$ = 131, CH_3-C); 47,4 (dq, $^1J_{CH}$ = 174, $^2J_{CH}$ = 5, C3); 51,1 (d, $^2J_{CH}$ = 4, C2); 53,0 et 53,3 (q, $^1J_{CH}$ = 148, CO_2CH_3); 161,7 et 165,6 (qd

Can. J. Chem. Downloaded from www.nrcresearchpress.com by 85.192.166.187 on 09/08/12
For personal use only.

aspect de quintuplet, $^3J \approx {}^3J' = 4$, CO_2Me). **7bC′** et **7bC″** (mélange 70/30), analyse : $C_{14}H_{17}NO_7S$, calc. % : C 48,97; H 4,99; N 4,08. Isomère maj. F = 90–92°C : tr. : C 49,01; H 5,06; N 4,08. Mélange 50/50 des isomères : tr. : C 49,19; H 4,91; N 4,17.

*I.7. Photolyse de la triazoline **4bD**.* La photolyse de 2,30 g de triazoline **4dD** est conduite dans les conditions décrites précédemment. Après 10 h 30 min d'irradiation, l'analyse rmn montre la disparition complète de la triazoline et la formation des aziridines **7bD′** et **7dD″**. Celles-ci évoluent à température ambiante, elles sont caractérisées uniquement à l'aide de la rmn.

*II. Évolution thermique des triazolines **4**, **5**, **6***

II.1. Triazolines diesters (X = Y = CO_2Me)

*II.1.1. Triazolines **4bA**.* La décomposition est totale en 16 h à température ambiante (solutions benzéniques). L'analyse en rmn ^1H des produits bruts montre la formation des oximes **8bA** (58%), de l'aziridine **7bA** (29%) et du tosylate de méthyle (12%). Kostyanovsky et al. (3) opérants dans des conditions différentes n'observent pas les mêmes proportions de ces composés.

Nous avons déjà précisé les caractéristiques rmn de **7bA** (tableau 1). **8bA**, rmn ^1H, δ : 2,45 (s, CH_3-Ph); 3,66 et 3,85 (2s, 3H, CO_2CH_3); 3,78 (s, 2H, CH_2-CO_2-CH_3).

*II.1.2. Triazoline **4bC**.* En solution benzénique (10 cm^{-3}) à température ambiante, la triazoline **4bC** (1,20 g) est totalement décomposée en 5 h. Le spectre de rmn ^1H du produit brut montre la formation de l'oxime **8bC** (62%) et des deux aziridines **7bC′** et **7bC″**. Après distillation sous pression réduite du benzène, le résidu (1,15 g) est chromatographié sur colonne de silice (90 g, éluant : éther/éther de pétrole : 50/50) on recueille, successivement, 240 cm^{-3} de solution ne contenant aucun produit, et 180 cm^{-3} de solution de **8bC** pur, soit 0,56 g de cristaux qui après recristallisation à froid dans le mélange éther/éther de pétrole fondent à 72–73°C (0,50 g). **8bC**, rmn ^1H, δ : 1,37 (t, J = 7,0, $CHCH_3$); 2,47 (s, CH_3-Ph); 3,66 et 3,85 (2s, CO_2CH_3); 4,11 (q, J = 7,0, CH_3CH). **8bC**, rmn ^{13}C, δ : 13,4 (dq, $^1J_{CH}$ = 131, $^2J_{CH}$ = 6, $CHCH_3$); 21,8 (qt, ^1J = 127, ^3J = 4, CH_3Ph); 38,1 (dq, ^1J = 131, ^2J = 4, CH_3CH); 52,6 (q, ^1J = 148, CH_3O); 53,4 (q, ^1J = 149, CH_3O); 157,9 (dq, ^2J = 8, ^3J = 4, C=N-O); 161,8 (dq aspect de quintuplet, $^3J \approx {}^3J' \approx 4$, =C-$CO_2CH_3$); 170,1 (m, CH-$CO_2CH_3$). Les attributions sont confirmées par des irradiations sélectives à 1,37 et 3,85 ppm. **8bC**, analyse : $C_{14}H_{18}NO_7S$, calc. % : C 48,83; H 5,27; N 4,07; tr. : C 48,80; H 5,06; N 4,12.

Les autres fractions (170 mg et 150 mg) sont constituées de mélanges de **8bC** et des aziridines **7bC′** et **7bC″** qui n'ont pu être séparées. Les aziridines sont caractérisées par comparaison avec des échantillons authentiques obtenus lors de la photolyse de la triazoline correspondante.

*II.1.3. Triazoline **5bA** (Z = H).* La décomposition est totale en 4 jours à température ambiante (solution chloroformique). L'analyse en rmn ^1H des produits bruts montre la formation de l'oxime **9bA** (60%) et de l'aziridine **11bA** (40%). **9bA**, rmn ^1H, δ : 3,70 et 3,96 (2s, CO_2CH_3); 3,84 (s, CH_2-CO_2CH_3). **11bA**, rmn ^1H, δ : 2,94 et 3,24 (système AB, ^2J = 3,2, H cycliques); 3,77 et 3,90 (2s, CO_2CH_3).

*II.1.4. Triazoline **6bA**.* À 1,8 g d'oxime **3b** (0,9 × 10^{-2} mol) partiellement dissous dans 5 cm^3 d'éther sec refroidis à −50°C, on ajoute en une seule fois 45 cm^{-3} d'une solution de diazométhane (1,8 × 10^{-2} mol) également refroidie à −50°C. La solution est abandonnée 1 nuit à −20°C. Les cristaux formés sont essorés et lavés à l'éther de pétrole. On obtient 1,8 g de triazoline **6bA** (Rdt = 83%) fondant à 74°C avec décomposition.

Un échantillon dissous dans $CDCl_3$ du produit ainsi obtenu est abandonné à température ambiante. Après 11 jours la décomposition est totale. L'analyse à l'aide de la rmn ^1H montre la formation des composés **10bA** (34%) et **12bA** (66%). **10bA**, rmn ^1H, δ : 2,26 (s, CH_3CO); 3,72 et 3,92 (2s, CO_2CH_3); 3,80 (s, CH_2-CO_2CH_3). **12bA**, rmn ^1H, δ: 2,20 (s, CH_3CO); 2,80 et 3,04 (système AB, ^2J = 3,3, H cycliques); 3,78 et 3,84 (2s, CO_2CH_3).

*II.1.5. Triazoline **6bC**.* À une suspension, maintenue dans un bain réfrigérant à −50°C, de 1,0 g d'oxime **3b** (4,9 × 10^{-3} mol) dans 1 cm^{-3} d'éther sec, on ajoute en une seule fois 17 cm^{-3} d'une solution éthérée de diazoéthane (9,8 × 10^{-3} mol) (solution maintenue au préalable sur KOH à −20°C pendant 1 heure avant utilisation). L'ensemble est abandonné pendant 1 nuit à −20°C. Les cristaux formés sont essorés puis lavés à l'éther de pétrole froid. On obtient ainsi 1,2 g de **6bC** (Rdt = 95%) fondant avec décomposition à 72°C.

L'évolution thermique est sommairement étudiée à l'aide de la rmn sur un échantillon de **6bC** dissous dans $CDCl_3$. La transformation est totale après 5 jours à la température ambiante. La rmn ^1H met en évidence la formation de l'oxime homologuée **10bC** (54%) et des aziridines **12bC′** (24%) et **12bC″** (22%). **10bC**, rmn ^1H, δ : 1,43 (d, ^3J = 7,0, $CHCH_3$); 2,23 (s, CH_3-Ph); 3,66 et 3,89 (2s, CO_2CH_3); 4,16 (q, ^3J = 7,0, $CHCH_3$). **12bC′** et **12bC″**, isomère majoritaire (24%), rmn ^1H, δ : 1,33 (d, ^3J = 6,0, $CHCH_3$); 3,30 (q, ^3J = 6,0, $CHCH_3$); 3,89 et 3,95 (2s, CO_2CH_3); isomère minoritaire (22%), rmn ^1H, δ : 1,51 (d, ^3J = 6,0, $CHCH_3$); 3,01 (q, ^3J = 6,0, $CHCH_3$); 3,83 et 3,89 (2s, CO_2CH_3).

II.2. Triazolines ester nitrile (X = CN, Y = CO_2Me)

*II.2.1. Triazoline **4aA**.* En solution dans le benzène ou le chloroforme (0,5–0,9 mol/L), la décomposition est totale après 6–8 h à la température ambiante. L'oxime **1a** (50%) et le tosylate de méthyle **15** (50%) sont mis en évidence à l'aide de la rmn ^1H (la décomposition est effectuée dans le tube de rmn en solution dans C_6D_6). De plus, le tosylate de méthyle est caractérisé par couplage chromatographie de partage gaz–liquide – spectrométrie de masse.

Exemple de tentative de séparation des différents composés à l'aide de la chromatographie sur couche mince, séparation effectuée (éluant dichlorométhane) sur le produit résultant de la thermolyse de 310 mg de triazoline dans le benzène. On récupère une première fraction (151 mg) R_f = 0,7 qui est un mélange d'oxime **1a** et de tosylate de méthyle. Les autres constituants du mélange ne migrent pas. On récupère ainsi 51 mg d'une poudre brune (pas de fusion définie) n'ayant pas migré et qui ne présente en rmn (C_6D_6) aucun signal à part un massif non résolu entre 3,4 et 3,9 ppm (polymères provenant de l'évolution de **18**).

II.2.2. Mise en évidence de la formation de diazométhane

II.2.2.1. Piégeage avec l'acide benzoïque. Dans un tube on introduit 50 mg (1,5 × 10^{-4} mol) de triazoline **4aA**, 20 mg d'acide benzoïque (1,6 × 10^{-4} mol) et 0,4 cm^{-3} de benzène deutérié. On abandonne pendant 6 h à température ambiante le tube fermé par un septum. La chromatographie de partage gaz–liquide (colonnes DOW 11 et QF 1) et la rmn ^1H permettent d'identifier le benzoate de méthyle formé (comparaison avec un échantillon authentique).

II.2.2.2. Piégeage avec le propiolate de méthyle. Dans un tube pour échantillon de rmn, on introduit une solution de 100 mg de triazoline **4aA** (3,1 × 10^{-4} mol) et de 52 mg de propiolate de méthyle (6,2 × 10^{-4} mol) dans 0,4 cm^{-3} de benzène deutérié. Le tube est fermé par un septum. L'enemble est abandonné 48 h à température ambiante. L'enregistrement du spectre de rmn montre la présence de l'oxime tosylée **1a** et des pyrazoles **25** et **26** (proportions relatives 55/45). **25**, rmn ^1H, (C_6D_6), δ : 3,58 (s, CO_2CH_3); 6,78 (d, ^3J = 2,2); 7,68 (d, ^3J = 2,2). **26**, rmn ^1H, (C_6D_6), δ : 3,42 et 3,90 (2s, N-CH_3 et CO_2-CH_3); 6,76 (d, ^3J = 2,5); 7,41 (d, ^3J = 2,5).

II.2.3. Addition du diazométhane au propiolate de méthyle. À 300 mg (3,6 × 10^{-3} mol) de propiolate de méthyle dissous dans 25 cm^3 d'éther refroidi à −20°C, on ajoute par fractions 6 cm^{-3} d'une solution de diazométhane (3,4 × 10^{-3} mol) dans l'éther. Après 1 nuit à −20°C le pyrazole majoritaire **25** qui cristallise est essoré (300 mg; F = 138–139°C). Le solvant du filtrat est éliminé par distillation. On obtient ainsi 145 mg d'une huile incolore analysée à l'aide de la rmn. Elle est essentiellement constituée des pyrazoles **25** (77%) et **38** (23%). La formation de ce dernier n'est pas signalée dans la littérature (16) (Fig. 13). **38**, rmn ^1H : (C_6D_6), δ : 3,57 (s, CO_2CH_3); 7,24 et 8,07 (2s, H cycliques).

À une solution de 100 mg (7,9 × 10^{-4} mol) de pyrazole **25** en solution dans 5 cm^{-3} de dichlorométhane, on ajoute 15 mg d'acide paratoluènesulfonique (≈7,9 × 10^{-5} mol) monohydraté (F = 105°C). Ce dernier se dissout très progressivement. On abandonne le mélange 1

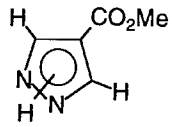

38

FIG. 13

demi-heure à −20°C puis on ajoute 2 cm^{-3} de solution éthérée de diazométhane (2 équivalents). Après 1 nuit à −20°C, le solvant est distillé, le résidu est repris avec 40 cm^{-3} dichlorométhane. La phase organique est lavée à l'eau et séchée sur Na_2SO_4. Après distillation du solvant l'analyse rmn du résidu montre que l'huile obtenue contient un mélange de pyrazole méthylé **26** (71%), de pyrazole non transformé (17%) et de tosylate de méthyle (12%).

*II.2.4. Triazoline **4aC**.* On dissout 2,50 g (9×10^{-3} mol) d'oxime **1a** dans 10 cm^{-3} de THF (ou 2,00 g dans 5 cm^{-3} de dichlorométhane). Après refroidissement à −50°C, on ajoute par fractions 65 cm^{-3} d'une solution éthérée de diazoéthane ($1{,}8 \times 10^{-2}$ mol). L'ensemble est abandonné 1 nuit à −20°C (on constate au bout de 2 heures la décoloration complète de la solution). Le solvant est distillé sous pression réduite (1–2 Torr; 1 Torr = 133,3 Pa) en dessous de −10°C. Le spectre de rmn enregistré immédiatement montre l'existence de tosylate d'éthyle (50%) et de l'oxazole **21** (50%). La triazoline n'est pas mise en évidence.

La séparation des composés formés est réalisée sur colonne d'alumine neutre (Merck 90, activité I) que l'on désactive au préalable à l'aide d'un mélange éther/éther de pétrole (20/80) réalisé avec de l'éther ordinaire non séché. On utilise 25 g d'alumine pour 0,40 g d'huile, l'éluant étant le mélange éther anhydre/éther de pétrole (20/80). On recueille successivement, 50 cm^{-3} de solution ne contenant pas **21** puis 175 cm^{-3} d'une solution contenant 150 mg d'oxazole **21** pur. **21**, ir (nujol) ν : 2228 (-C≡N lié au noyau aromatique), absence d'absorption attribuable à aun groupement ester; rmn ^{1}H, δ : 2,38 (s, CH_3C); 4,22 (s, CH_3O); rmn ^{13}C, δ : 13,8 (q, ^1J = 131, CH_3-C); 59,9 (q, ^1J = 149, CH_3O-); 87,4 (s, =*C*-CN); 112,9 (s, -*C*≡N); 152,3 (q, ^2J = 7, N=*C*-CH_3); 164,7 (q, ^3J = 4, =*C*-OCH_3); spectrométrie de masse : Masse calculée pour $C_6H_6N_2O_2$, $M^{\cdot+}$: 138,043; trouvée : 138,043.

L'identification à l'aide de la chromatographie de partage gaz–liquide (phase stationnaire DOW 11) et à l'aide de la rmn ^{1}H du tosylate d'éthyle est effectuée sur le produit brut (comparaison avec un échantillon authentique, F = 35°C (17)).

Remarque : L'addition du diazoéthane sur l'oxime **1a** marquée à l'azote 15 à 52% (dosage isotopique à l'aide de la spectrométrie de masse) est effectuée dans les mêmes conditions que précédemment : 16 cm^{-3} de solution éthérée de diazoéthane ($3{,}8 \times 10^{-2}$ mol) sont ajoutés à une solution dans le dichlorométhane (≈1 cm^{-3}) refroidie à −50°C de 0,45 g d'oxime **1a** ($1{,}6 \times 10^{-3}$ mol). On obtient après évaporation des solvants 0,67 g d'huile colorée.

En raison de la difficulté de séparation de l'oxazole et du tosylate d'éthyle, les données spectroscopiques sont enregistrées sur le mélange après filtration de l'huile brute (mélange 50/50 d'oxazole **21** et de tosylate d'éthyle) sur 10 g de silice (élution par 100 cm^{-3} de mélange 50/50 d'éther/éther de pétrole).

Les caractéristiques de l'oxazole **21** marqué à l'azote 15 sont les suivantes. **21**, rmn ^{13}C : spectre totalement découplé, δ : 13,3 (d, $^2J_{^{12}C^{15}N}$ = 5,9, CH_3-C=); 59,9 (q, ^1J = 149, CH_3O-); 87,6 (=*C*-C≡N)[2]; 112,4 (d, $^2J_{^{12}C^{15}N}$ = 7,8, -*C*≡N); 152,1 (N=*C*-CH_3)[2]; 164,7 (s, =*C*-OCH_3).

L'analyse isotopique est effectuée à l'aide de la spectrométrie de masse. Conditions d'enregistrement : température de la source : 130°C, température de la canne d'introduction directe 80°C et 25°C respectivement pour **1a** et **21**.

Les mesures de l'intensité des pics $M^{\cdot+}$ et $M+1^{\cdot+}$ permettent après correction des contributions isotopiques naturelles, le pourcentage relatif de l'espèce marquée et non marquée pour l'oxime **1a** et pour l'oxazole **21** :

	Ion	Formule	%	Masse trouvée	Masse calculée
1a	$M^{\cdot+}$	$C_{11}H_{10}N_2O_5S$	48	282,031	282,031
	$(M+1)^{\cdot+}$	$C_{11}H_{10}{}^{15}N^{14}NO_5S$	52	283,028	283,028
21	$M^{\cdot+}$	$C_6H_6N_2O_2$	48	138,043	138,043
	$(M+1)^{\cdot+}$	$C_6H_6{}^{15}N^{14}NO_2$	52	139,040	139,040

*II.2.5. Triazoline **4aD**.* À une solution de 1,60 g d'oxime **1a** ($5{,}7 \times 10^{-3}$ mol) dissous dans 9 cm^{-3} de dichlorométhane refroidie à −50°C, on ajoute en une seule fois 1,20 g de phényldiazométhane (1×10^{-2} mol) en solution dans 14 cm^{-3} d'éther. L'ensemble est abandonné à −20°C pendant 4 jours. Le précipité formé est essoré. On obtient ainsi 0,40 g de cristaux (F = 107–109°C) d'oxazole **22**, Rdt = 28%. Une recristallisation dans le méthanol fournit 0,20 g de produit fondant à 109°C. **22**, rmn ^{1}H, δ : 4.27 (s, CH_3O); rmn ^{13}C, δ : 60,1 (q, ^1J = 149, CH_3O); 113,0 (s, -*C*≡N); 89,0 (s, =*C*-CN); 152,3 (t, ^3J = 5, N=*C*-Ph); 164,7 (q, ^3J = 5, =*C*-OCH_3). Analyse : $C_{11}H_8N_2O_2$, calc. % : C 66,00; H 4,03; N 13,99; tr. : C 66,10; H 3,97; N 13,99.

Le filtrat initial est conservé encore 2 jours à −20°C. On n'observe pas la formation d'autres précipités. Les solvants sont éliminés à la température ambiante. Un essai de distillation sous pression réduite (100–120°C/4×10^{-3} Torr) du résidu (2,2 g) n'a pas permis de séparer le tosylate de benzyle (signaux en rmn ^{1}H à 3,70 ppm, 2H et 2,40 ppm, 3H) des produits de décomposition du phényldiazométhane.

*II.2.6. Triazoline **5aA** (Z = H).* Le produit brut résultant de l'addition du diazométhane sur l'oxime **2a** (Z = H) après distillation de l'éther à basse température est abandonné dans le chloroforme à température ambiante une journée. La formation du benzoate de méthyle est mise en évidence à l'aide de la chromatographie de partage gaz–liquide (phase stationnaire DOW 11, comparaison avec un échantillon authentique).

*II.2.7. Triazoline **5aA** ($Z = NO_2$).* La décomposition du produit brut résultant de la réaction du diazométhane sur l'oxime **2a** ($Z = NO_2$) est totale en 8 h en solution benzénique à température ambiante. L'enregistrement du spectre rmn ^{1}H du produit brut montre uniquement la formation de l'oxime **2a** (60%) et de *p*-nitrobenzoate de méthyle (30%). Ceux-ci sont caractérisés par comparaison avec des échantillons authentiques (rmn ^{1}H pour **2a**, rmn et chromatographie pour le *p*-nitrobenzoate de méthyle **16** ($Z = NO_2$, $R' = H$).

*II.2.8. Triazoline **5aC** ($Z = NO_2$).* L'oxime **2a** ($Z = NO_2$) (2,0 g; $6{,}8 \times 10^{-3}$ mol) est dissoute dans 10 cm^{-3} de THF ou de dichlorométhane. À cette solution refroidie à −50°C, on ajoute par fractions 50 cm^{-3} de solution éthérée de diazoéthane ($1{,}4 \times 10^{-2}$ mol). On note l'apparition immédiate d'une coloration rouge. La solution est alors abandonnée 12 h à −20°C (elle est complètement décolorée après 2 h). Le solvant est distillé sous pression réduite sans dépasser −10°C. Le spectre de rmn ^{1}H est alors immédiatement enregistré. L'oxazole **21** (25%) et le paranitrobenzoate d'éthyle (43%) ont été caractérisés à l'aide de la rmn ^{1}H. À côté, deux autres composés qui n'ont pas été identifiés (25% et 7%, intégration des signaux méthoxycarbonyle) sont mis en évidence. Les caractéristiques de rmn ^{1}H de **21** ont été donné lors de l'étude de la triazoline **4aC**. p-$NO_2C_6H_4CO_2Et$, rmn ^{1}H, δ : 1,43 (t, ^3J = 7, OCH_2CH_3); 4,48 (q, ^3J = 7, OCH_2CH_3).

*II.2.9. Triazoline **6aA**.* La triazoline **6aA** est obtenue lors de la réaction de **3a** avec le diazométhane. Étant donné la difficulté d'obtention de cette triazoline (Rdt = 10%), l'étude systématique de son évolution thermique n'a pas été effectuée.

En solution benzénique la décomposition est totale en 20 h à température ambiante. L'analyse à l'aide de la rmn ^{1}H du produit brut montre la formation d'oxime acétylée **3a** (53%), d'acétate de méthyle (28%) et de trois produits minoritaires (9%, 7%, 8%) dont les structures n'ont pas été déterminées.

*II.2.10. Évolution des triazolines **4aA** et **4bA** en présence d'acide trifluoroacétique.* Dans un tube muni d'une tubulure latérale et contenant 2 cm^3 de chloroforme anhydre refroidi à −50°C, on introduit sous

2. Constante de couplage $^1J_{^{13}C^{15}N}$ non mesurable, doublets masqués par le signal du produit non marqué, ^1J < 2 Hz.

Can. J. Chem. Downloaded from www.nrcresearchpress.com by 85.192.166.187 on 09/08/12
For personal use only.

Can. J. Chem. Downloaded from www.nrcresearchpress.com by 85.192.166.187 on 09/08/12
For personal use only.

courant d'azote sec 300 mg de triazoline **4aA**. Une quantité stœchiométrique (774 mg) d'acide trifluoroacétique anhydre est additionnée goutte à goutte à l'aide d'une seringue au travers d'un septum. L'ensemble est abandonné à −20°C pendant 1 nuit. Après distillation du chloroforme et de l'acide trifluoroacétique, la rmn montre la formation prépondérante (90%) des aziridines **7aA′** et **7aA″** (70/30). Ces produits sont identifiés après comparaison avec les aziridines obtenues par photolyse de la triazoline correspondante. La structure du produit minoritaire (10%) n'a pas été déterminée. Il présente en rmn ^{1}H un signal à 4,04 ppm attribuable à un groupement méthoxyle.

L'action de l'acide trifluoroacétique sur **4bA** est étudié dans les mêmes conditions que pour **4aA** en solution dans 0,3 cm^{-3} de chloroform deutérié (0,1 g de **4bA**). L'analyse rmn après 1 nuit à −20°C montre la formation exclusive de l'aziridine **7bA** identifiée par comparaison avec le composé obtenu lors de la photolyse de **4bA**.

*II.3. Réaction des dicyanooximes **28** et **29** avec les diazométhane et éthane*

*II.3.1. Préparation du sel d'argent **31**.* La technique de Longo (18) est utilisée. Au mélange de 3,3 g de malonodinitrile (5×10^{-2} mol) et de 6,0 g (1×10^{-1} mol) d'acide acétique glacial refroidi par un bain de glace, on ajoute lentement (0,5 h) et sous agitation 6,9 g de nitrite de sodium (1×10^{-1} mol) en solution dans le minimum d'eau (environ 10 cm^{-3}). On laisse réagir pendant 4 h puis on dilue avec 200 cm^{-3} d'eau et on ajoute une solution de 3,5 g (5×10^{-2} mol) de nitrate d'argent dans 100 cm^{-3} d'eau. Le sel d'argent qui précipite sous forme de cristaux jaune, est essoré puis séché au dessiccateur à potasse. On obtient 9,8 g de cristaux (Rdt = 97%), $F \geq 270$°C avec décomposition.

*II.3.2. Préparation de **28**.* À une solution de 2,9 g ($1,5 \times 10^{-2}$ mol) de chlorure de paratoluènesulfonyle dans 100 cm^{-3} de benzène, on additionne sous azote 3,1 g ($1,5 \times 10^{-2}$ mol) du sel d'argent de l'oxime. Deux gouttes de pyridine sont ajoutées à la suspension précédente. Après 5 min, le solide présent dans la solution est blanc (AgCl). On agite pendant 10 min à 40–50°C. On filtre AgCl qui est lavé au benzène. L'addition d'éther de pétrole au filtrat permet d'obtenir 2,4 g de produit solide. Après concentration de la solution un deuxième jet (0,3 g) est isolé. La recristallisation des deux jets précédents, à froid dans le mélange CH_2Cl_2/éther de pétrole, donne 2,6 g de **28**, (F = 114–115°C; Rdt = 68%) (lit. (12) F = 114°C).

*II.3.3. Préparation de **29**.* Sous azote et agitation 2,0 g (1×10^{-2} mol) du sel d'argent de l'oxime sont mis en suspension dans 15 cm^{-3} de benzène anhydre. Toujours sous agitation, 1,6 g ($1,1 \times 10^{-2}$ mol) de chlorure de benzoyle sont ajoutés en une seule fois. L'addition d'une goutte de pyridine permet de faire démarrer la réaction (disparition du sel d'argent de couleur jaune au profit d'un autre précipité blanc (AgCl)). Après 30 min d'agitation, AgCl est essoré, lavé au benzène. L'addition d'éther de pétrole au filtrat après concentration à l'évaporateur rotatif permet la cristallisation du produit. On obtient ainsi 1,8 g de cristaux de **29** (F = 110°C; Rdt = 90%) (litt. (9) F = 104–106°C).

*II.3.4. Réaction du diazométhane avec l'oxime tosylée **28**.* L'oxime tosylée **28** (1,0 g; $4,0 \times 10^{-3}$ mol) est dissous dans un mélange de 100 cm^{-3} d'éther et 30 cm^{-3} de THF. Après refroidissement de l'ensemble à −20°C, on ajoute 50 cm^{-3} d'une solution éthérée de diazométhane ($1,7 \times 10^{-2}$ mol). L'addition effectuée par fractions provoque l'apparition immédiate d'une coloration rouge. L'ensemble est abandonné 4 jours à température ambiante. Le spectre de rmn ^{1}H du produit brut de la réaction est enregistré après élimination des solvants à température ambiante. Il est ainsi possible de mettre en évidence les composés **32′** (52%), **32″** (16%) et le tosylate de méthyle (22%). Les pourcentages relatifs sont évalués en intégrant les signaux du groupement méthyle lié au noyau aromatique. Après ébullition dans le benzène (10 cm^{-3}), la composition du mélange obtenu n'est pratiquement pas modifiée. Le benzène est distillé, l'addition d'un peu d'éthanol à 95°C provoque la cristallisation du triazole **32′** qui fond à 139–140°C (litt (9) F = 138–139°C) après recristallisation dans l'éthanol à 95°C.

Un mélange de triazole **32′** (40 mg), de méthanol (1 cm^{-3}) et d'acide chlorhydrique concentré (0,26 cm^{-3} d'HCl à 27–29%) est maintenu à reflux pendant 14 h (10). Après distillation des solvants, le composé **32″** (80%) est caractérisé à l'aide dc la rmn. Il reste 20% de triazole **32′**.

Le composé **32″** n'a pas été purifié. Les travaux de Fleury et collaborateurs (9) indiquent que ce composé fond à 165°C. Ces mêmes auteurs ont donné et discuté les caractéristiques de rmn ^{13}C des composés **32′** et **32″**.

*II.3.5. Réaction du diazoéthane avec l'oxime **28**.* À la solution de 1,0 g ($4,0 \times 10^{-3}$ mol) de **28** dans 10 cm^{-3} de dichlorométhane refroidie à −30°C, on ajoute par fractions 20 cm^{-3} de solution éthérée de diazoéthane ($\approx 8 \times 10^{-3}$ mol). L'ensemble est abandonné à −20°C pendant 1 nuit. Après distillation des solvants à basse température (−10 à 0°C), l'analyse du produit brut à l'aide de la rmn montre exclusivement l'oxime tosylée **28** (35%) et le tosylate d'éthyle **15**, R′ = CH_3 (65%).

L'huile obtenue (1,1 g) est chromatographiée sur colonne de silice (30 g) (éluant : éther/éther de pétrole 50/50). On recueille successivement : (*i*) 50 cm^{-3} d'une solution d'oxime **28** (F = 114°C après recristallisation dans le mélange CH_2Cl_2/éther de pétrole), identifiée à l'aide de la rmn ^{1}H par comparaison avec un échantillon authentique; (*ii*) 100 cm^{-3} d'un mélange de tosylate d'éthyle et d'oxime **28**; (*iii*) 50 cm^{-3} d'une solution de tosylate d'éthyle. Celui-ci est caractérisé en rmn ^{1}H par comparaison avec un échantillon authentique (F = 35°C).

*II.3.6. Réaction du diazométhane avec l'oxime **29**.* L'oxime benzoylée (1,00 g; 5×10^{-3} mol) est dissoute dans 20 cm^{-3} de dichlorométhane. À cette solution refroidie à −30°C, on ajoute par fractions 35 cm^{-3} d'une solution éthérée de diazométhane ($1,5 \times 10^{-3}$ mol). L'ensemble est abandonné à −20°C pendant 1 nuit. Le précipité formé est essoré, on obtient 0,67 g de cristaux. Leur analyse à l'aide de la rmn montre qu'il s'agit d'un mélange des triazoles **33** (41%) et **34** (ou **35**) (44%) et de **36** (15%). Après distillation à basse température (−10 à 0°C) des solvants, l'huile obtenue, reprise au méthanol, abandonne 0,37 g de cristaux (F = 115–120°C), mélange (70/30) des triazoles **33** et **34** ou **35** (analyse rmn). Une recristallisation dans le méthanol ne permet pas d'isoler un isomère pur.

Les triazoles ont été séparés par chromatographie sur couche mince à partir de 650 mg d'un mélange de **33** et **34** (ou **35**) (SiO_2, éluant CH_2Cl_2/C_6H_6 : 67/33) R_f (**33**) = 0,34 (180 mg), R_f (**34** ou **35**)) = 0,14 (400 mg). Cette chromatographie permet d'isoler en petite quantité (20 mg) le triazole **36** (F = 228°C). **33**, F = 134°C, rmn ^{1}H, δ : 4,22 (s, N-C*H*$_3$); 8,19 (s, H cyclique); rmn ^{13}C, δ : 42,6 (q, $^1J_{CH}$ = 143, N-*C*H$_3$); 107,8 (s, C≡N); 131,9 (s, *C*=N-O); 133,9 (d, $^1J_{CH}$ = 199, C5); 138,1 (d, $^2J_{CH}$ = 11, C4); **34** (ou **35**), F = 152°C (méthanol), rmn ^{1}H, δ : 4,43 (s, N-C*H*$_3$); 8,22 (s, H cyclique); rmn ^{13}C, δ : 39,1 (q, $^1J_{CH}$ = 144, N-*C*H$_3$); 107,6 (s, C≡N); 126,9 (d, $^2J_{CH}$ = 10, C4); 128,1 (s, *C*=N-O); 138,7 (d, $^1J_{CH}$ = 199, C5). **33** et **34** (ou **35**), analyse : $C_{12}H_9N_5O_2$, calc. % : C 56,47; H 3,55; N 27,44. **33**, tr. % : C 56,35; H 3,54; N 27,23. Mélange **33** + **34** (ou **35**) (70/30), tr. % : C 56,44; H 3,47; N 27,30. **36**, F = 228°C, rmn ^{1}H δ : 4,26 (s, N-C*H*$_3$); 7,89 (s, H cyclique), absence de signaux attribuables aux protons aromatiques; spectrométrie de masse: Masse calculée $C_5H_5N_5O$ (M^+) : 151,049; trouvée : 151,049.

Une quantité (0,32 g) du mélange des triazoles **33** et **34** (ou **35**) (70/30) dissoute dans 5 cm^{-3} de méthanol et additionné de 2 cm^{-3} d'acide chlorhydrique concentré est maintenu au reflux pendant 24 h. L'analyse du produit brut de la réaction à l'aide de la rmn ^{1}H ne permet l'identification que du benzoate de méthyle (comparaison avec un échantillon authentique).

1. J. Perrocheau et R. Carrié. Bull. Soc. Chim. Belg. **102**, 749 (1993).
2. R.G. Kostyanovsky, A.V. Prosyanik, A.I. Mishenko, G.V. Shustov, I.I. Chervin, N.L. Zaïchenko, A.P. Pheshkova, P.N. Belov et V.I. Markov. Izv. Akad. Nauk SSSR, Ser. Khim. 1780 (1979).
3. R.G. Kostyanovsky, G.K. Kadorkina, G.V. Shustov et K.S. Zakharov. Dokl. Akad. Nauk SSSR, **221**, 370 (1975).
4. K. Isomura, Y. Hyrose, H. Shuyama, S. Abe, G.I. Ayabe et H. Taniguchi. Heterocycles, **9**, 1207 (1978).
5. K. Isomura, M. Okada et H. Taniguchi. Tetrahedron Lett. 4073 (1969).
6. G. L'abbé. Chem. Rev. **69**, 345 (1969).
7. R.L. Lichter, D.E. Dorman et R. Wasylishen. J. Am. Chem. Soc. **96**, 930 (1974).
8. G.L. Levy et R.L. Lichter. *Dans* ^{15}N nuclear magnetic resonance spectroscopy. J. Wiley & Sons, New York. 1979. p. 122.

9. J.P. Fleury, J.P. Schœni, D. Clerin et H. Fritz. Bull. Soc. Chim. Fr. 1831 (1976).
10. J.M. Biehler, J. Perchais et J.P. Fleury. Bull. Soc. Chim. Fr. 2711 (1971).
11. R.G. Kostyanovsky, A.I. Mishenko, A.V. Prosyanik et N.L. Zaichenko. Izv. Akad. Nauk SSSR, 1572 (1983).
12. M. Regitz et H. Heydt. *Dans* 1,3-Dipolar cycloaddition chemistry. Vol. 1. *Édité par* A. Padwa. John Wiley & Sons, New York. 1984. p. 362.
13. F.M. Dean et R.S. Johnson. J. Chem. Soc. Perkin Trans. 1, 224 (1981).
14. Y.M. Saunier. Thèse de 3ème cycle, Rennes. 1976.
15. G. Keller, J.P. Fleury, W. Anschutz et M. Regitz. Bull. Soc. Chim. Fr. 1219 (1975).
16. J. Bastide, J. Hamelin, F. Texier et Y. Vo Quang. Bull. Soc. Chim. Fr. 2555 (1973); K.V. Auwers et O. Ungemach. Chem. Ber. **66**, 1205 (1933).
17. V.C. Sekera et C.S. Marvel. J. Am. Chem. Soc. **55**, 346 (1933); V.C. Sekera. J. Am. Chem. Soc. **55**, 421 (1933); F. Brakowzal et O. Klumann. Monatsh. Chem. **82**, 460 (1951).
18. G. Longo. Gazz. Chim. Ital. **61**, 578 (1931).

Can. J. Chem. Downloaded from www.nrcresearchpress.com by 85.192.166.187 on 09/08/12
For personal use only.

Palladium(0)-catalyzed addition of $Me_3SnSnMe_3$ to alkyl 2-alkynoates and *N,N*-dimethyl-2-alkynamides. Facile preparation of alkyl (*Z*)- and (*E*)-2,3-bis(trimethylstannyl)-2-alkenoates and (*E*)-*N,N*-dimethyl-2,3-bis(trimethylstannyl)-2-alkenamides

EDWARD PIERS[1] AND RENATO T. SKERLJ

Department of Chemistry, University of British Columbia, 2036 Main Mall, University Campus, Vancouver, BC V6T 1Z1, Canada

Received July 5, 1994

EDWARD PIERS and RENATO T. SKERLJ. Can. J. Chem. **72**, 2468 (1994).

Treatment (tetrahydrofuran (THF), room temperature or reflux) of the alkyl 2-alkynoates **9–26** with $(Me_3Sn)_2$ in the presence of a Pd(0) catalyst ($(Ph_3P)_4Pd$) provides good to excellent yields of the corresponding alkyl (*Z*)-2,3-bis(trimethylstannyl)-2-alkenoates **47–64**. The latter substances are thermally labile and, as demonstrated by a number of examples, are transformed upon heating (75–95°C) into the thermodynamically more stable *E* isomers. The Pd(0)-catalyzed addition of $(Me_3Sn)_2$ to *N,N*-dimethyl-2-alkynamides **44–46** is quite slow and the initially formed products ((*Z*)-*N,N*-dimethyl-2,3-bis(trimethylstannyl)-2-alkenamides) rearrange to the corresponding *E* isomers at room temperature.

EDWARD PIERS et RENATO T. SKERLJ. Can. J. Chem. **72**, 2468 (1994).

La réaction des alk-2-ynoates d'alkyles **9–26** avec le $(Me_3Sn)_2$, en présence du catalyseur Pd(0) ($(Ph_3P)_4Pd$) à la température ambiante, dans du tétrahydrofurane fournit d'excellent rendements des (*Z*)-2,3-bis(triméthylstannyl)alcén-2-oates d'alkyles correspondants **47–64**. Ces dernières substances sont thermolabiles et, tel que démontré par une série d'exemples, elles sont transformées par chauffage (75–95°C) en isomères *E* thermodynamiquement plus stables. L'addition, catalysée par le Pd(0), du $(Me_3Sn)_2$ sur les *N,N*-diméthylalk-2-ynamides **44–46** sont très lentes et les produits qui se forment initialement, les (*Z*)-*N,N*-diméthyl-2,3-bis(triméthylstannyl)alc-2-énamides) se réarrangent en isomères *E* correspondants à la température ambiante.

[Traduit par la rédaction]

Introduction

It has been shown (1, 2) that the palladium(0)-catalyzed addition of hexamethyldistannane to 1-alkynes **1** produces, stereoselectively, (*Z*)-1,2-bis(trimethylstannyl)-1-alkenes **2** in fair to excellent yields (eq. [1]).[2] The analogous process does not work well when non-terminal alkynes are used as substrates (2) or when hexabutyldistannane is employed as the reagent (ref. 2; see, however, ref. 5). The products **2** have been shown to be of use for the preparation of functionalized 2-trimethylstannyl-1-alkenes (6).

In connection with our continuing interest in the use of bifunctional compounds for organic synthesis and our desire to develop a new general method to prepare configurationally defined tetrasubstituted alkenes, we describe in this paper the details of an investigation (7) that showed that reaction of α,β-acetylenic esters with $(Me_3Sn)_2$ in the presence of a catalytic amount of $(Ph_3P)_4Pd$ provides, cleanly and efficiently, alkyl (*Z*)-2,3-bis(trimethylstannyl)-2-alkenoates **4** (eq. [4]). Furthermore, it was found that substances **4** are thermally unstable and, when warmed to 75–95°C, rearrange smoothly to the corresponding *E* isomers **5** (eq. [3]). Finally, we report that Pd(0)-catalyzed additions of $(Me_3Sn)_2$ to *N,N*-dimethyl-2-alkynamides **6** are also achievable processes, although, in these cases, the initially formed *Z* addition products **7** generally isomerize to the *E* isomers **8** under the conditions necessary to effect the original addition (eq. [4]).

Results and discussion

Preparation of alkyl 2-alkynoates and N,N-*dimethyl-2-alkynamides*

The α,β-acetylenic esters employed in this study are listed in Chart 1. Compound **9** is commercially available, while many of the other substrates have been reported previously.[3] The esters **15** and **26** were prepared as shown in Scheme 1. Sequential treatment of 1,5-hexadiyne (**27**) with MeLi and methyl chloroformate in THF gave a mixture of the monoester **29** (36%) and the diester **31** (40%), which were separated by chromatography on silica gel. In similar fashion, substances **30** and **32** were derived from 1,7-octadiyne (**28**). Hydrogenation of **29** in hexane provided methyl 6-hepten-2-ynoate (**15**) while reaction of **30** with *B*-bromo-9-borabicyclo[3.3.1]nonane (*B*-Br-9-BBN) in dichloromethane (11) afforded methyl 8-bromo-8-nonen-2-ynoate (**26**).

Ethyl 5-chloro-2-pentynoate (**18**) and the corresponding bromide **19** were obtained as follows. Treatment of 3-butyn-1-ol (**33**) with PCl_3 in *N,N*-dimethylformamide (DMF) (12) gave the

[1] Author to whom correspondence may be addressed. Telephone: (604) 822-3219. Fax: (604) 822-2847. Bitnet:EPIER@UNIXG.UBC.CA

[2] For the palladium(0)-catalyzed addition of $(Me_3Sn)_2$ to allenes, see refs. 3 and 4.

[3] Compound **10**: ref. 8; compounds **11–14**, **16**, **17**, **21–23**: ref. 9; compound **20**: ref. 10.

Can. J. Chem. Downloaded from www.nrcresearchpress.com by 85.192.166.187 on 09/08/12
For personal use only.

Can. J. Chem. Downloaded from www.nrcresearchpress.com by 85.192.166.187 on 09/08/12
For personal use only.

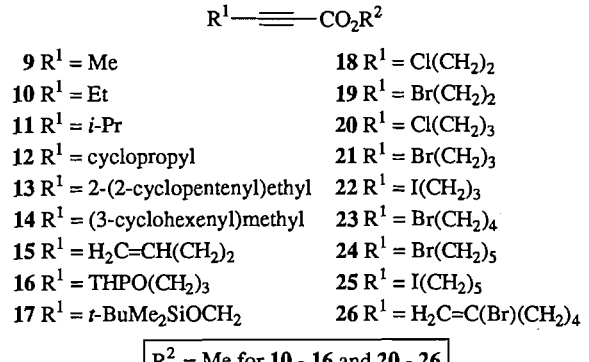

CHART 1

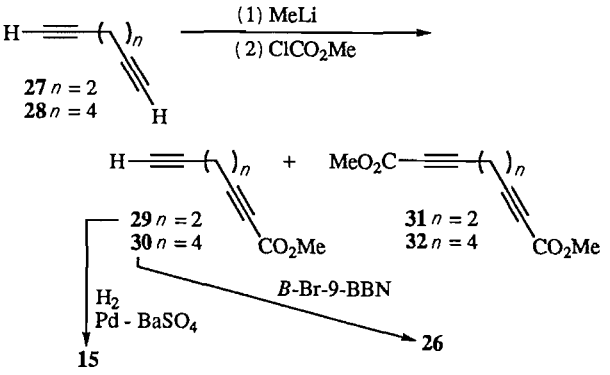

SCHEME 1

chloride **34**, which was readily transformed into the ethyl ester **18** (eq. [5]). On the other hand, conversion (*p*-toluenesulfonyl chloride (*p*-TsCl), 4-(*N*,*N*-dimethylamino)pyridine (DMAP), pyridine) of ethyl 5-hydroxy-2-pentynoate (**35**)[4] into the *p*-toluenesulfonate **36**, followed by reaction of **36** with NaBr in DMF, produced the bromide **19** (eq. [6]).

Treatment of 1,6-hexanediol (**37**) with 48% aqueous HBr in refluxing benzene gave the bromo alcohol **38** (see Scheme 2). Oxidation (pyridinium chlorochromate (PCC), CH_2Cl_2) of the latter material provided the bromo aldehyde **39**, which, upon reaction with (dibromomethylene)triphenylphosphorane (prepared from Ph_3P and CBr_4 in the presence of zinc dust (13)), gave the tribromoalkene **40**. Sequential treatment of **40** with BuLi (2.5 equiv.) and methyl chloroformate (13) in THF afforded the ester substrate **24**. Upon reaction with excess NaI in acetone, **24** was transformed into the corresponding iodide **25**.

The *N*,*N*-dimethyl-2-alkynamides **44–46** used in this investigation were prepared by sequential treatment of the corresponding 1-alkynes **41–43** with MeLi and *N*,*N*-dimethylcarbamyl chloride in THF (eq. [7]). The preparation of the functionalized 1-pentyne **43** has been reported (14).

Conversion of alkyl 2-alkynoates into alkyl (Z)-2,3-bis(trimethylstannyl)-2-alkenoates

Initial experimentation, using substrate **9**, quickly disclosed that the Pd(0)-catalyzed addition of $(Me_3Sn)_2$ to the triple bond of α,β-acetylenic esters is a clean, efficient process. After a solution of **9** in THF containing $(Me_3Sn)_2$ (1 equiv.) and

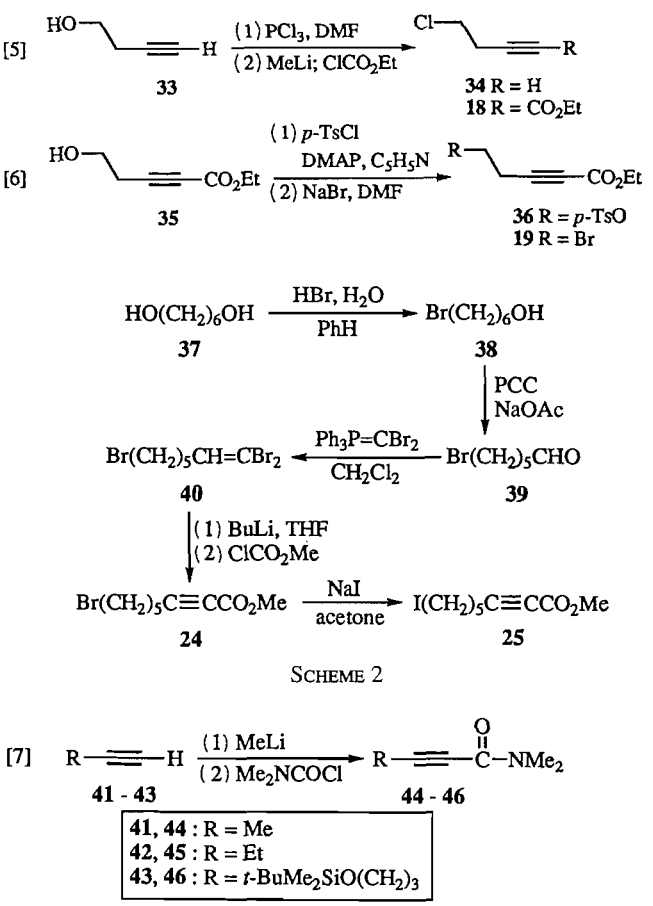

SCHEME 2

41, 44 : R = Me
42, 45 : R = Et
43, 46 : R = *t*-BuMe$_2$SiO(CH$_2$)$_3$

$(Ph_3P)_4Pd$ (~0.01 equiv.) had been stirred at room temperature for 14 h, analysis (thin-layer chromatography (tlc)) of the mixture indicated that the starting material **9** has been transformed into a single product. Isolation of the latter material provided ethyl (*Z*)-2,3-bis(trimethylstannyl)-2-butenoate **47** in 95% yield (see Table 1, entry 1).

The generality of this addition reaction was demonstrated by the conversion of the α,β-acetylenic esters **10–26** into the corresponding bis(trimethylstannyl)-2-alkenoates **48–64**. The results are summarized in Table 1.

Collectively, the substrates **9–26** contain a diverse array of functionality, including carbon–carbon double bonds (Table 1, entries 5–7), a tetrahydropyranyl ether (entry 8), a silyl ether (entry 9), primary halides (Cl, Br, I) (entries 10–17), and an alkenyl bromide (entry 18). Thus, the addition process can be effected successfully in the presence of a variety of functional groups. In nearly all of the cases studied, the reactions were clean and, although not optimized, the yields are consistently good to excellent.

Initially, the additions were carried out at room temperature (entries 1–4, 8). However, under these conditions the conversions were found to be quite sluggish when the size of R^1 in the substrate was more bulky than methyl or primary alkyl (see entries 3 and 4). Fortunately, when the reactions were performed at elevated temperatures (normally in refluxing THF), the times required to complete the additions dropped significantly.

Analysis (tlc) of aliquots of the reaction mixture involving ethyl 5-bromo-2-pentynoate (**19**) as substrate (entry 11) showed that, as the reaction progressed, the formation of the product **57** was accompanied by the production of a number of minor uni-

[4]We thank Dr. John Wai for a sample of this compound.

TABLE 1. Conversion of alkyl 2-alkynoates **9–26** into alkyl (*Z*)-2,3-bis(trimethylstannyl)-2-alkenoates **47–64**

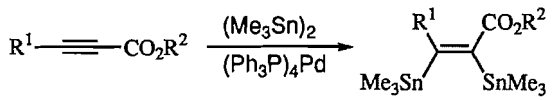

Entry	Substrate	R^1	R^2	Reaction conditions[a]	Reaction time (h)	Product (yield, %)[b]
1	**9**	Me	Et	A	14	**47** (95)
2	**10**	Et	Me	A	18	**48** (88)
3	**11**	i-Pr	Me	A	36	**49** (90)
4	**12**	Cyclopropyl	Me	A	28	**50** (83)
5	**13**	2-(2-Cyclopentenyl)ethyl	Me	B	6	**51** (73)
6	**14**	(3-Cyclohexenyl)methyl	Me	B	3	**52** (74)
7	**15**	$H_2C{=}CH(CH_2)_2$	Me	B	4	**53** (85)
8	**16**	$THPO(CH_2)_3$	Me	A	15	**54** (83)
9	**17**	t-$BuMe_2SiOCH_2$	Et	B[c]	4	**55** (83)
10	**18**	$Cl(CH_2)_2$	Et	B	6	**56** (89)
11	**19**	$Br(CH_2)_2$	Et	B	8	**57** (66)
12	**20**	$Cl(CH_2)_3$	Me	B	5	**58** (86)
13	**21**	$Br(CH_2)_3$	Me	B	6	**59** (84)
14	**22**	$I(CH_2)_3$	Me	B	6	**60** (79)
15	**23**	$Br(CH_2)_4$	Me	B	5	**61** (78)
16	**24**	$Br(CH_2)_5$	Me	B	15	**62** (83)
17	**25**	$I(CH_2)_5$	Me	B	6	**63** (76)
18	**26**	$H_2C{=}C(Br)(CH_2)_4$	Me	B[d]	2	**64** (64)

[a]The reactions were performed using ~1 equiv. of $(Me_3Sn)_2$ and ~0.01–0.02 equiv. of $(Ph_3P)_4Pd$ in THF at room temperature (A) or under reflux (B). Any changes from these conditions are noted.
[b]Yield of chromatographically purified product.
[c]The reaction mixture was heated at 55–60°C.
[d]The Pd(0) catalyst was prepared from $Pd(OAc)_2$ and Ph_3P and the reaction was carried out at 60°C in the presence of Et_3N.

dentified substances. Nevertheless, work-up of the reaction mixture when most of the starting material had been consumed, followed by chromatography of the crude material on silica gel, gave **57** in 66% yield.

The experiment summarized in entry 18, Table 1, also requires brief comment. At the outset, it was recognized that, under the reaction conditions, the initially formed product **64** derived from addition of $(Me_3Sn)_2$ to the substrate **26** could undergo intramolecular Pd(0)-catalyzed cross-coupling (15–17) to give the diene **65**. However, for unknown reasons, treatment (THF, room temperature, 20 h) of **26** with $(Me_3Sn)_2$ in the presence of $(Ph_3P)_4Pd$ gave back mainly starting material. When the reaction was carried out in refluxing THF, a number of unidentified products were produced (tlc analyses). Use of other solvents (MeCN, PhH, or 1,2-dimethoxyethane) did not lead to significant improvement. On the other hand, use of THF as solvent and a Pd(0) catalyst formed from $Pd(OAc)_2$, Ph_3P, and Et_3N (18) produced the "normal" addition product **64** in 64% yield (entry 18). Interestingly, under these conditions, **64** was not converted into the diene **65**.

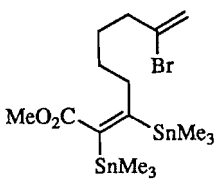

64

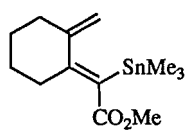

65

During the course of the studies described above, it became apparent that the (*Z*)-2,3-bis(trimethylstannyl)-2-alkenoate products **47–64** are thermally unstable. Although the relatively volatile product **47** was found to be stable to distillation (70–75°C/0.1 Torr (1 Torr = 133.3 Pa)), attempted distillation of other products with greater molecular masses led to rearrangement. For example, when methyl (*Z*)-6-chloro-2,3-bis(trimethylstannyl)-2-hexenoate (**58**) was distilled (90–95°C/0.01 Torr), the acquired liquid was shown to consist of **58** and another substance, in a ratio of ~2:1, respectively. Chromatographic separation of the two substances, along with appropriate spectral analyses, showed that the minor component in the distillate was methyl (*E*)-6-chloro-2,3-bis(trimethylstannyl)-2-hexenoate. Thus, during the distillation process, the primary *Z* product **58** had undergone partial isomerization to the corresponding *E* isomer.[5] In view of these and other similar observations, the products listed in Table 1 were generally not distilled. In each case, last traces of solvent were removed from the chromatographically purified product by subjecting the material to reduced pressure (vacuum pump, ~0.05 Torr) for a period of 1–2 h.

A possible pathway for the Pd(0)-catalyzed addition of $(Me_3Sn)_2$ to α,β-acetylenic esters **3** is shown in Scheme 3.[6] Oxidative addition of the palladium catalyst to the Sn–Sn bond of the distannane would give the palladium(II) species **66**. Coordination of **66** with the substrate **3** to provide **67**, followed by insertion of the triple bond into one of the tin–palladium bonds,

[5]The facile, thermally induced rearrangement of alkyl (*Z*)-2,3-bis(trimethylstannyl)-2-alkenoates into the corresponding *E* isomers will be discussed in the next section of this paper (vide infra).

[6]A similar pathway has been evoked to account for the *Z* configuration of products derived from the Pd(0)-catalyzed addition of disilanes to 1-alkynes (19).

Can. J. Chem. Downloaded from www.nrcresearchpress.com by 85.192.166.187 on 09/08/12
For personal use only.

TABLE 2. Conversion of alkyl (*Z*)-2,3-bis(trimethylstannyl)-2-alkenoates **47–55**, **58**, **61**, **62**, and **64** into alkyl (*E*)-2,3-bis(trimethylstannyl)-2-alkenoates **69–81**

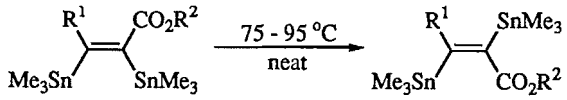

Entry	Substrate	R^1	R^2	Temperature (°C), time (h)	Product (yield, %)[a]
1	**47**	Me	Et	79, 30	**69** (82)
2	**48**	Et	Me	85, 18	**70** (82)
3	**49**	i-Pr	Me	80, 6	**71** (98)
4	**50**	Cyclopropyl	Me	85, 7	**72** (83)
5	**51**	2-(2-Cyclopentenyl)ethyl	Me	80, 8	**73** (81)
6	**52**	(3-Cyclohexenyl)methyl	Me	88, 48	**74** (88)
7	**53**	$H_2C{=}CH(CH_2)_2$	Me	80, 14	**75** (81)
8	**54**	$THPO(CH_2)_3$	Me	80, 6	**76** (93)
9	**55**	t-$BuMe_2SiOCH_2$	Et	81, 12	**77** (86)
10	**58**	$Cl(CH_2)_3$	Me	75, 24	**78** (96)
11	**61**	$Br(CH_2)_4$	Me	85, 40	**79** (80)
12	**62**	$Br(CH_2)_5$	Me	86, 21	**80** (88)
13	**64**	$H_2C{=}C(Br)(CH_2)_4$	Me	83, 36	**81** (66)

[a]Yield of distilled product.

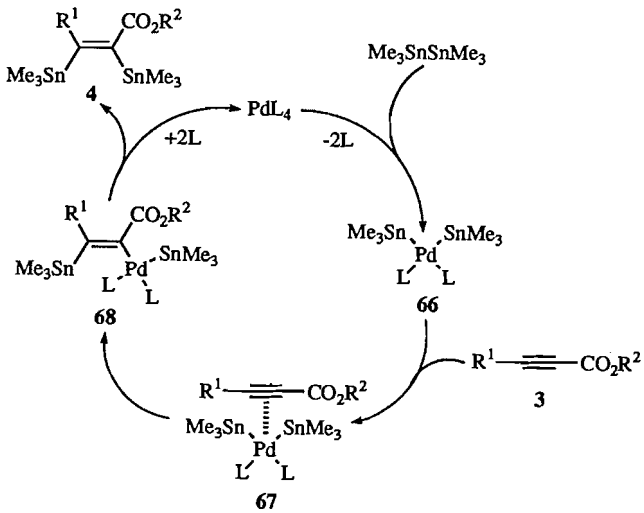

SCHEME 3

would afford **68**. Finally, reductive elimination would produce the observed product **4** and regenerate the Pd(0) catalyst.

Conversion of alkyl (Z)-2,3-bis(trimethylstannyl)-2-alkenoates into alkyl (E)-2,3-bis(trimethylstannyl)-2-alkenoates

As mentioned above, alkyl (*Z*)-2,3-bis(trimethylstannyl)-2-alkenoates are thermally labile. To investigate this phenomenon more thoroughly, a stirred, neat sample of the enoate **58** was heated at approximately 75°C. After a period of 24 h, analysis (tlc) indicated the absence of starting material and the clean production of another substance. Distillation (~105°C/0.1 Torr) of the pale yellow oil afforded the *E* isomer **78** in 96% yield (eq. [8]).

[8]

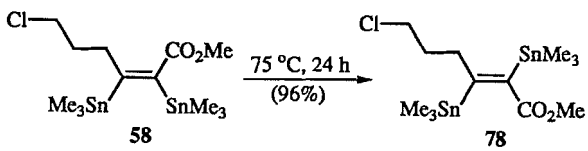

To demonstrate the generality of this isomerization process, a number of (*Z*)-2,3-bis(trimethylstannyl)-2-alkenoates were subjected to thermolysis. The results of these experiments are summarized in Table 2. As can been seen from the tabulated data, the rearrangement process is compatible with the presence of a variety of functional groups and the yields of the *E* products are generally good to excellent. Only the thermolysis of **64** (Table 2, entry 13) did not produce a clean product. Analysis (tlc) of the material derived from heating **64** showed that the production of **81** was accompanied by the formation of minor amounts of other substances. Furthermore, a small amount of an unidentified, insoluble solid was also produced. Nevertheless, chromatography of the crude mixture after complete disappearance of starting material provided **81** in 66% yield.

It is also pertinent to point out that the (*Z*)-2,3-bis(trimethylstannyl)-2-alkenoates are not completely stable to storage for long periods of time. For example, the *Z* compounds **47–50** and **55**, when stored at 5°C for several months, slowly became pale yellow and were shown to contain minor amounts of the corresponding *E* isomers (**69–72**, **77**). Furthermore, in each case, a small amount of insoluble solid material was formed.

It appears reasonable to propose that the facile rearrangement of **4** into **5** proceeds via a trimethylstannyl allenoate intermediate **82** (Scheme 4). Thus, reversible, thermally induced migration of the α-trimethylstannyl group[7] from carbon to the ester carbonyl oxygen would produce **82**. A second migration of the Me_3Sn moiety back to the α carbon, but to the side of the molecule opposite to the β-Me_3Sn group, would give the *E* isomer **5**. Presumably, the relief of steric repulsion between the two as

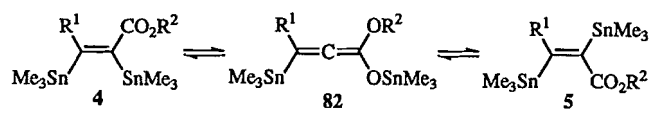

SCHEME 4

[7]The labile nature of the carbon–tin bond associated with the α-Me_3Sn function has been demonstrated by the facility with which this group undergoes transmetallation (MeLi, THF, −98°C) (20).

Can. J. Chem. Downloaded from www.nrcresearchpress.com by 85.192.166.187 on 09/08/12
For personal use only.

Can. J. Chem. Downloaded from www.nrcresearchpress.com by 85.192.166.187 on 09/08/12
For personal use only.

Me_3Sn groups in **4** is primarily responsible for the observation that the equilibrium between **4** and **5** favors the latter substances.

Configurational considerations

On the basis of literature precedents concerning the stereochemical outcome of Pd(0)-catalyzed additions of $(Me_3Sn)_2$ to 1-alkynes (1, 2), it seemed entirely reasonable to conclude that the products derived from similar reactions involving α,β-acetylenic ester substrates would possess the *Z* configuration. Furthermore, the fact that the addition products, upon thermolysis, are cleanly transformed into the corresponding geometric isomers, along with the reasonable prediction that the *E* isomers would be more stable than the *Z* substances, provides further support for the conclusions regarding product stereochemistry. Nevertheless, explicit evidence for the configurational assignments was obtained by use of ^1H nmr spectroscopy. For example, the configuration of each of the diastereomers **58** and **78** (see eq. [8]) was confirmed by nuclear Overhauser enhancement (nOe) difference experiments. In the spectrum of **58**, irradiation at δ 3.70 (OMe signal) caused enhancement of the resonance due to *one* of the 9-proton Me_3Sn singlets (δ 0.25). On the other hand, irradiation at δ 3.71 (OMe) in the spectrum of **78** increased the intensity of *both* of the Me_3Sn singlets (δ 0.17, 0.26). These results, along with those of similar experiments involving other geometrically isomeric pairs, clearly show that the configuration of each of the primary products derived from Pd(0)-catalyzed addition of $(Me_3Sn)_2$ to 2-alkynoates is *Z*, while the configuration of substances obtained from thermolysis of these products is *E*.

Spectral data derived from alkyl (Z)- and (E)-2,3-bis(trimethylstannyl)-2-alkenoates

The ^1H nmr spectroscopic data derived from alkyl (*Z*)-2,3-bis(trimethylstannyl)-2-alkenoates **47**–**64** and from the *E* isomers **69**–**81** are summarized in Table 3. These data show that the difference (Δδ) between the chemical shifts of the two 9-proton Me_3Sn signals in a given substance is related to its geometric configuration. In each of the *Z* isomers (general formula **4**, Chart 2) the two Me_3Sn resonances have very similar chemical shifts (Δδ = 0–0.03 ppm). On the other hand, the corresponding Δδ values for the *E* isomers (formula **5**, Chart 2) vary from 0.03 to 0.11 ppm, but, with the exception of compound **71** (Table 3, entry 6), are in the range 0.08–0.11 ppm. Thus, these Δδ values may be employed as a diagnostic tool in assigning the configuration of alkyl 2,3-bis(trimethylstannyl)-2-alkenoates.

Interestingly, the ^1H nmr spectroscopic signals due to the C-4 (γ) proton(s) in the (*Z*)-2,3-bis(trimethylstannyl)-2-alkenoates are commonly found at *higher* field than the corresponding resonances for the *E* isomers (Table 3, entries 1–4, 7, 8, 11–18, 21, 22, 25–28, 30, 31).[8] This finding is unusual. Generally, in α,β-unsaturated esters, γ protons *cis* to the ester function resonate at lower field than γ protons in the corresponding geometric isomers. This is certainly the case in a fairly large number of alkyl (*E*)- and (*Z*)-3-trimethylstannyl-2-alkenoates (general formulas **83**, **84**, Chart 2) that have been prepared in our laboratories (9, 10, 14, 21). The C-4 proton(s) in the *E* compounds **83** consistently resonate at lower field than the C-4 proton(s) of the corresponding *Z* isomers **84**.

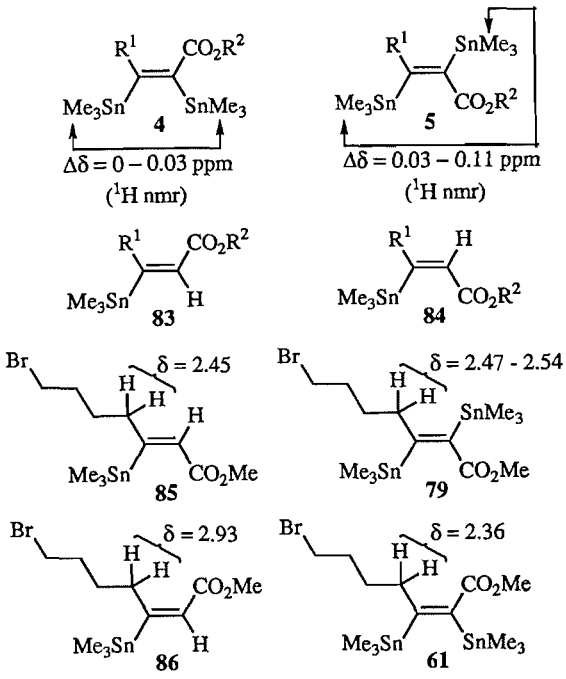

CHART 2

An examination of available data (9, 10, 14, 21, present work) indicates that, in general, the chemical shifts of the γ protons of a given pair of substances of general structures **5** and **84** (Chart 2) are quite similar. In contrast, replacement of the C-2 hydrogen of **83** with a $SnMe_3$ function (to give **4**) results in a significant *upfield* shift of the resonance due to the C-4 proton(s). This phenomenon is illustrated by the ^1H nmr chemical shift data shown in conjunction with the set of compounds **85**, **79**, **86**, and **61** (Chart 2). Similar trends are exhibited by other sets of substances structurally related to those shown in Chart 2. Thus, it appears that the "anomalous" (relative) chemical shifts of the γ protons in the nmr spectra of **4** and **5** are related to the presence of the C-2 Me_3Sn function in the *Z* isomers **4**. Although the reason(s) underlying this phenomenon is (are) obscure, it is evident that these observations can also be of assistance in assigning the geometry of substances of general structure **4** and **5**.

Table 4 contains a summary of the ^{13}C nmr chemical shift data derived from a selected number of alkyl (*Z*)- and (*E*)-2,3-bis(trimethylstannyl)-2-alkenoates. It is apparent from these data that, irrespective of molecular constitution or geometric configuration, the carbonyl carbons of these materials resonate at nearly the same position (δ ~172). More interesting and informative are the patterns observed for the chemical shifts of the olefinic carbons (C-2, C-3). For each pair of geometric isomers, C-2 of the *Z* isomer resonates at *lower* field than that of the *E* compound. In contrast, the signal for C-3 of the *Z* substance appears at *higher* field than the corresponding resonance of the *E* isomer. For the α carbons (C-2) the chemical shift differences (Δδ values) for the various isomeric pairs are quite small, ranging from ~2 ppm (substances **55**, **77**, Table 4, entries 11, 12) to nearly 6 ppm (compounds **47**, **69**, entries 1, 2). On the other hand, the Δδ values for the β carbons (C-3) are considerably larger and range from about 11 ppm (**55**, **77**, entries 11, 12) to approximately 21 ppm (**47**, **69**, entries 1, 2).

[8]The only exception to this generalization involves the pair of geometric isomers **49** and **71** (Table 3, entries 5, 6). In these two substances, the C-4 protons have similar chemical shifts (Δδ = 0.11 ppm), but the γ proton of the *Z* isomer **49** gives rise to a signal *downfield* from that of the *E* isomer **71**.

TABLE 3. The ^{1}H nmr spectral data of alkyl (*Z*)- and (*E*)-2,3-bis(trimethylstannyl)-2-alkenoates[a]

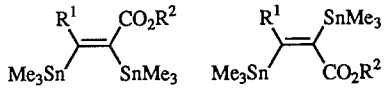

Entry	R^1	R^2	Compound number (configuration)	Chemical shifts[b] (number of protons, multiplicity,[c] coupling constant(s), *J*, in Hz)			
				High-field Me_3Sn[d]	Low-field Me_3Sn[d]	C-4 (γ) proton(s)	Other signals
1	Me	Et	**47** (*Z*)	0.22	0.25	2.07 (3, s)	1.27 (3, t, 7), 4.15 (2, q, 7)
2			**69** (*E*)	0.14	0.25	2.22 (3, s)	1.28 (3, t, 7), 4.17 (2, q, 7)
3	Et	Me	**48** (*Z*)	0.21	0.22	2.35 (2, q, 7)	1.00 (3, t, 7), 3.69 (3, s)
4			**70** (*E*)	0.18	0.26	2.49 (2, q, 7)	0.98 (3, t, 7), 3.70 (3, s)
5	i-Pr	Me	**49** (*Z*)	0.25	0.28	2.77 (1, septet, 6.5)	1.04 (6, d, 6.5), 3.68 (3, s)
6			**71** (*E*)	0.20	0.23	2.66 (1, septet, 7)	1.10 (6, d, 7), 3.68 (3, s)
7	Cyclopropyl	Me	**50** (*Z*)	0.23	0.23	1.73 (1, m)	0.40–0.48 (2, m), 0.66–0.76 (2, m), 3.70 (3, s)
8			**72** (*E*)	0.17	0.26	1.78 (1, m)	0.53–0.59 (2, m), 0.83–0.91 (2, m), 3.68 (3, s)
9	2-(2-Cyclopentenyl)ethyl	Me	**51** (*Z*)	0.23	0.24	Not assigned	1.29–1.50 (3, m), 1.97–2.08 (1, m), 2.20–2.40 (4, m), 2.59–2.69 (1, m), 3.70 (3, s), 5.63–5.68 (1, m), 5.70–5.75 (1, m)
10			**73** (*E*)	0.15	0.25	Not assigned	1.24–1.40 (2, m), 1.40–1.51 (1, m), 2.00–2.11 (1, m), 2.22–2.41 (2, m), 2.46–2.56 (2, m), 2.74–2.83 (1, m), 3.70 (3, s), 5.65–5.70 (1, m), 5.72–5.78 (1, m)
11	(3-Cyclohexenyl)methyl	Me	**52** (*Z*)	0.18	0.20	2.21–2.37 (2, m)	1.07–1.19 (1, m), 1.51–1.72 (3, m), 1.88–2.06 (3, m), 3.63 (3, s), 5.58–5.62 (2, m)
12			**74** (*E*)	0.10	0.20	2.36–2.53 (2, m)	1.07–1.20 (1, m), 1.58–1.71 (3, m), 1.90–2.05 (3, m), 3.65 (3, s), 5.55–5.65 (2, m)
13	$H_2C{=}CH(CH_2)_2$	Me	**53** (*Z*)	0.24	0.245	2.38–2.45 (2, m)	2.11 (2, qt, 7, 1.5), 3.69 (3, s), 4.95 (1, ddt, 10, 2, 1.5), 5.01 (1, ddt, 17, 2, 1.5), 5.80 (1, ddt, 17, 10, 7)
14			**75** (*E*)	0.16	0.26	2.53–2.61 (2, m)	2.05 (2, qt, 7, 1.5), 3.70 (3, s), 5.00 (1, ddt, 10, 2, 1.5), 5.04 (1, ddt, 17, 2, 1.5), 5.69 (1, ddt, 17, 10, 7)
15	$THPO(CH_2)_3$	Me	**54** (*Z*)	0.25	0.26	2.35–2.47 (2, m)	1.47–1.74 (7, m), 1.77–1.89 (1, m), 3.38 (1, dt, 10, 6.5), 3.46–3.53 (1, m), 3.66–3.74 (1, m), 3.70 (3, s), 3.82–3.89 (1, m), 4.58 (1, t, 3)
16			**76** (*E*)	0.17	0.25	2.51–2.62 (2, m)	1.48–1.65 (6, m), 1.67–1.76 (1, m), 1.79–1.90 (1, m) 3.41 (1, dt, 10, 7), 3.47–3.55 (1, m), 3.70 (3, s), (3, s), 3.75 (1, dt, 10, 7), 3.82–3.90 (1, m), 4.60 (1, t, 4)
17	t-$BuMe_2SiOCH_2$	Et	**55** (*Z*)	0.20	0.23	4.34 (2, s)	0.03 (6, s), 0.87 (9, s), 1.26 (3, t, 7), 4.10 (2, q, 7)
18			**77** (*E*)	0.15	0.24	4.37 (2, s)	0.06 (6, s), 0.89 (9, s), 1.26 (3, t, 7), 4.11 (2, q, 7)
19	$Cl(CH_2)_2$	Et	**56** (*Z*)	0.27	0.28	2.79 (2, t, 8)	1.31 (3, t, 7), 3.52 (2, t, 8), 4.19 (2, q, 7)
20	$Br(CH_2)_2$	Et	**57** (*Z*)	0.26	0.28	2.84 (2, t, 8)	1.28 (3, t, 7), 3.32 (2, t, 8), 4.15 (2, q, 7)
21	$Cl(CH_2)_3$	Me	**58** (*Z*)	0.25	0.26	2.44–2.51 (2, m)	1.85 (2, quintet, 8), 3.51 (2, t, 8), 3.70 (3, s)
22			**78** (*E*)	0.17	0.26	2.60–2.66 (2, m)	1.73–1.82 (2, m), 3.55 (2, t, 7), 3.71 (3, s)
23	$Br(CH_2)_3$	Me	**59** (*Z*)	0.25	0.26	2.43–2.50 (2, m)	1.93 (2 quintet, 7.5), 3.38 (2, t, 7.5), 3.71 (3, s)

Can. J. Chem. Downloaded from www.nrcresearchpress.com by 85.192.166.187 on 09/08/12
For personal use only.

TABLE 3. (*Concluded*)

Entry	R^1	R^2	Compound number (configuration)	Chemical shifts[b] (number of protons, multiplicity,[c] coupling constant(s), J, in Hz) High-field Me_3Sn[d]	Low-field Me_3Sn[d]	C-4 (γ) proton(s)	Other signals
24	$I(CH_2)_3$	Me	**60** (*Z*)	0.245	0.25	2.40–2.47 (2, m)	1.91 (2, quintet, 8), 3.15 (2, t, 8), 3.71 (3, s)
25	$Br(CH_2)_4$	Me	**61** (*Z*)	0.25	0.25	2.34–2.40 (2, m)	1.48–1.57 (2, m), 1.86 (2, quintet, 7), 3.40 (2, t, 7), 3.70 (3, s)
26			**79** (*E*)	0.17	0.26	2.47–2.54 (2, m)	1.42–1.52 (2, m), 1.91 (2, quintet, 7), 3.42 (2, t, 7), 3.71 (3, s)
27	$Br(CH_2)_5$	Me	**62** (*Z*)	0.24	0.25	2.32–2.38 (2, m)	1.34–1.49 (4, m), 1.85 (2, quintet, 7.5), 3.40 (2, t, 7.5), 3.70 (3, s)
28			**80** (*E*)	0.15	0.25	2.46–2.52 (2, m)	1.32 (2, quintet, 7), 1.49 (2, quintet, 7), 1.88 (2, quintet, 7), 3.41 (2, t, 7), 3.70 (3, s)
29	$I(CH_2)_5$	Me	**63** (*Z*)	0.23	0.24	2.30–2.37 (2, m)	1.32–1.45 (4, m), 1.82 (2, quintet, 7), 3.18 (2, t, 7), 3.69 (3, s)
30	$H_2C{=}C(Br)(CH_2)_4$	Me	**64** (*Z*)	0.23	0.25	2.32–2.39 (2, m)	1.22–1.32 (2, m), 1.55 (2, quintet, 8), 2.42 (2, t, 8), 3.70 (3, s), 5.39 (1, d, 2), 5.56 (1, d, 2)
31			**81** (*E*)	0.17	0.27	Not assigned	1.26–1.37 (2, m), 1.60 (2, quintet, 8), 2.39–2.53 (4, m), 3.70 (s, 3), 5.41 (1, d, 1.5), 5.57 (1, d, 1.5)

[a]All spectra were run at 400 MHz, except those of entries 1 and 2 (80 MHz), entries 3, 7, 17, 18, and 20 (270 MHz), and entry 6 (300 MHz).
[b]Chemical shifts (δ values) were measured relative to the signal for $CHCl_3$ (δ 7.25).
[c]Singlet = s; doublet = d; triplet = t; quartet = q; multiplet = m.
[d]The $^2J_{Sn-H}$ values associated with the Me_3Sn signals are in the range 50–56 Hz.

The ^{13}C nmr chemical shift assignments for carbons 1, 2, and 3, as outlined in Table 4, were confirmed by suitable nmr correlation experiments. An example is given in Table 5, which summarizes HMQC (22, 23) and HMBC (24, 25) data for the geometrically isomeric pair of substances **58** and **78**.[9] These data clearly show that the ^{13}C nmr signals at δ 172.1 and 172.0 for **58** and **78**, which exhibit no correlations, are due to the carbonyl carbons. On the other hand, the HMBC correlations associated with the pairs of resonances at δ 150.8 and 163.2 (isomer **58**) and at δ 145.5 and 182.3 (isomer **78**) allow unambiguous assignment of the ^{13}C nmr signals of the olefinic carbons as well.

On the basis of the data given in Tables 4 and 5, as discussed above, it is evident that ^{13}C nmr spectroscopy can be very helpful in determining the configuration of alkyl 2,3-bis(trimethylstannyl)-2-alkenoates.

A summary of selected $^{119}Sn-^{13}C$ coupling constants obtained from the ^{13}C nmr spectra of a number of alkyl 2,3-bis(trimethylstannyl)-2-alkenoates is given in Table 6. It can be seen that the $^2J_{Sn-C}$ values related to coupling between ^{119}Sn of the C-3 Me_3Sn group and ^{13}C of the C-4 allylic carbon (column A in Table 6) are, for each isomeric pair, nearly equal. The only exception to this generalization relates to the isomers **55** and **77**, which contain an electronegative oxygen function on the allylic (C-4) carbon. For these substances, the $^2J_{Sn-C}$ value in question is 6 Hz larger in the *E* isomer than in the *Z* compound (Table 6, entries 11, 12).

In contrast to the data given in column A, Table 6, the $^{119}Sn-^{13}C$ coupling constants related to coupling between ^{119}Sn of the C-2 Me_3Sn function and ^{13}C of the allylic carbon ($^3J_{Sn-C}$, column B, Table 6) do provide diagnostic information regarding double bond configuration. For a given pair of geometric isomers, the magnitude of this coupling constant for the *Z* isomer is consistently larger than that derived from the corresponding *E* compound. For the isomeric pairs shown in Table 6, the difference in $^3J_{Sn-C}$ values varies from 6 Hz (compounds **49**, **71**; entries 5, 6) to 15 Hz (substances **55**, **77**; entries 11, 12).

The ^{119}Sn nmr spectroscopy of alkyl 2,3-bis(trimethylstannyl)-2-alkenoates has also been studied briefly. The acquired data are given in Table 7. In nearly all of the *E* isomers that were investigated, the chemical shifts of the ^{119}Sn signals of the two $SnMe_3$ groups are very similar and show up at about −50 ppm. An exception to this generalization is exhibited by substance **71** (Table 7, entry 2), in which the two ^{119}Sn resonances have quite different chemical shifts (δ −60.2, −44.5). In the spectra of the two *Z* isomers that were recorded, the δ values for the two ^{119}Sn signals were again quite similar (~ −36 ppm), but were found to be ~14 ppm to higher field that the corresponding resonances for the *E* isomers (Table 7, entries 6–9).

A striking feature of the data given in Table 7 is the difference in the $^3J_{Sn-Sn}$ values for the *Z* and *E* isomers. The coupling constants for the *E* substances are consistently greater than 500 Hz, while, as shown by entries 6 and 8, the corresponding *J* values for the *Z* isomers are smaller by more than 200 Hz (see also ref. 2). These observations, along with those related to ^{119}Sn chemical shifts (vide supra), provide yet another method for determining the double bond configuration of alkyl 2,3-bis(trimethylstannyl)-2-alkenoates.

Conversion of N,N-*dimethyl-2-alkynamides into* (E)-N,N-*dimethyl-2,3-bis(trimethylstannyl)-2-alkenamides*

The investigations described above showed, inter alia, that

[9]We thank Mr. Todd Schindeler for carrying out these correlation experiments.

Can. J. Chem. Downloaded from www.nrcresearchpress.com by 85.192.166.187 on 09/08/12
For personal use only.

TABLE 4. The ^{13}C nmr chemical shift data of selected alkyl (*Z*)- and (*E*)-2,3-bis(trimethylstannyl)-2-alkenoates[a]

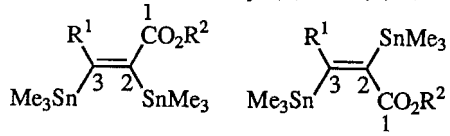

Entry	R^1	R^2	Compound number (configuration)	Chemical shifts[b] Me_3Sn groups[c]	Carbon 1(C=O)	Carbon 2	Carbon 3	Carbon 4[d]	Other signals
1	Me	Et	**47** (*Z*)	−7.2, −6.8	171.7	149.9	159.8	26.4	14.5, 60.1
2			**69** (*E*)	−6.7, −5.9	171.6	144.2	180.9	28.2	14.3, 60.8
3	Et	Me	**48** (*Z*)	−6.8, −6.7	172.3	148.2	166.8	34.0	14.7, 51.0
4			**70** (*E*)	−6.6, −6.1	172.3	143.4	185.6	34.5	14.8, 51.7
5	i-Pr	Me	**49** (*Z*)	−6.3, −4.5	172.8	146.6	170.9	40.3	22.7, 50.9
6			**71** (*E*)	−6.2, −4.4	172.7	143.7	184.2	43.1	22.1, 51.5
7	(3-Cyclohexenyl)methyl	Me	**52** (*Z*)	−6.6, −6.5	172.4	149.9	163.7	47.7	25.4, 28.3, 31.5, 33.9, 50.9, 126.5, 126.8
8			**74** (*E*)	−6.2, −5.5	171.7	144.7	184.2	47.8	25.4, 28.4, 31.7, 34.2, 51.7, 126.3, 127.1
9	$H_2C{=}CH(CH_2)_2$	Me	**53** (*Z*)	−6.8, −6.7	172.1	149.6	164.5	40.3	34.3, 50.9, 114.7, 137.6
10			**75** (*E*)	−6.5, −6.0	172.1	144.6	183.7	40.8	34.4, 51.8, 115.0, 137.0
11	*t*-$BuMe_2SiOCH_2$	Et	**55** (*Z*)	−6.5, −5.8	171.6	147.1	166.1	68.0	−5.3, 14.5, 18.4, 26.0, 60.1
12			**77** (*E*)	−6.1, −6.0	171.9	144.9	177.4	69.9	−5.1, 14.2, 18.2, 26.0, 60.8
13	$Cl(CH_2)_3$	Me	**58** (*Z*)	−6.74, −6.70	172.1	150.8	163.2	38.2	32.8, 44.4, 51.1
14			**78** (*E*)	−6.4, −6.0	172.0	145.5	182.3	39.0	33.0, 44.3, 51.8
15	$Br(CH_2)_4$	Me	**61** (*Z*)	−6.8, −6.7	172.1	149.7	164.4	39.8	28.3, 32.3, 33.6, 51.0
16			**79** (*E*)	−6.5, −6.0	172.0	144.6	183.5	40.7	28.9, 32.7, 33.3, 51.8
17	$Br(CH_2)_5$	Me	**62** (*Z*)	−6.8, −6.7	172.1	149.2	164.8	40.6	27.8, 29.1, 32.5, 33.6, 51.0
18			**80** (*E*)	−6.5, −6.0	172.1	144.1	183.9	41.4	28.2, 29.6, 32.6, 33.5, 51.8
19	$H_2C{=}C(Br)(CH_2)_4$	Me	**64** (*Z*)	−6.75, −6.65	172.2	149.2	164.9	40.6	27.6, 28.8, 41.1, 51.0, 116.5, 134.2
20			**81** (*E*)	−6.5, −6.0	172.1	144.2	183.8	41.3	27.8, 29.2, 41.2, 51.7, 116.7, 134.2

[a]All spectra were recorded at 75.6 MHz, using $CDCl_3$ as solvent.
[b]The chemical shifts were measured relative to that of $CDCl_3$ (δ 77.0).
[c]The carbon–tin coupling constants ($^1J_{Sn-C}$) associated with these signals are in the range 326–346 Hz.
[d]Carbon 4 is the allylic carbon attached to carbon 3.

TABLE 5. Selected nmr data from compounds **58** and **78**[a]

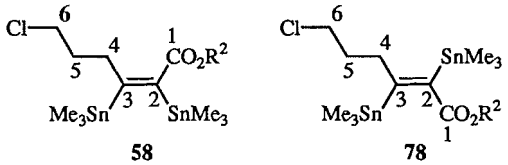

Carbon number	δ: ^{13}C **58**	δ: ^{13}C **78**	δ: ^1H **58**	δ: ^1H **78**	HMQC correlations[b]	HMBC correlations[b]
1	172.1	172.0				
2	150.8	145.5				H4
3	163.2	182.3				H4, H5
4	38.2	39.0	2.44–2.51	2.60–2.66	H4	H5, H6
5	32.8	33.0	1.85	1.73–1.82	H5	H4, H6
6	44.4	44.3	3.51	3.55	H6	H4, H5

[a]^{13}C nmr: 100.6 MHz; ^1H nmr: 400 MHz; HMQC and HMBC: 400 MHz.
[b]Correlated to carbon resonances in δ: ^{13}C columns. The correlations for the two isomers (**58**, **78**) are identical.

Pd(0)-catalyzed addition of $(Me_3Sn)_2$ across the triple bond of α,β-acetylenic esters in a facile, highly stereoselective process. To determine whether this process would work as well with other, structurally similar substrates, we carried out a brief study employing the *N*,*N*-dimethyl-2-alkynamides **44**–**46** as starting materials. These substances were prepared as described previously (see eq. [7]).

Compared to the reaction of ethyl 2-butynoate (**9**) with

Can. J. Chem. Downloaded from www.nrcresearchpress.com by 85.192.166.187 on 09/08/12
For personal use only.

TABLE 6. The ^{119}Sn–^{13}C coupling constants derived from ^{13}C nmr spectra of selected alkyl (*Z*)- and (*E*)-2,3-bis(trimethylstannyl)-2-alkenoates

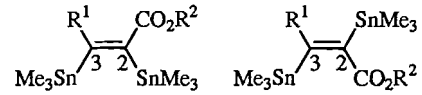

Entry	R^1	R^2	Compound number (configuration)	Coupling constants, J_{Sn-C} (Hz) A[a]	B[b]	C[c]
1	Me	Et	**47** (*Z*)	62	71	—
2			**69** (*E*)	62	62	—
3	Et	Me	**48** (*Z*)	57	68	9
4			**70** (*E*)	57	57	8
5	i-Pr	Me	**49** (*Z*)	52	65	13
6			**71** (*E*)	51	59	13
7	(3-Cyclohexenyl)methyl	Me	**52** (*Z*)	53	65	7
8			**74** (*E*)	52	52	7
9	$H_2C{=}CH(CH_2)_2$	Me	**53** (*Z*)	55	66	8
10			**75** (*E*)	55	55	8
11	t-$BuMe_2SiOCH_2$	Et	**55** (*Z*)	35	76	—
12			**77** (*E*)	41	61	—
13	$Cl(CH_2)_3$	Me	**58** (*Z*)	55	66	7
14			**78** (*E*)	55	55	8
15	$Br(CH_2)_4$	Me	**61** (*Z*)	55	66	8
16			**79** (*E*)	54	54	7
17	$Br(CH_2)_5$	Me	**62** (*Z*)	54	66	8
18			**80** (*E*)	54	54	8
19	$H_2C{=}C(Br)(CH_2)_4$	Me	**64** (*Z*)	55	66	8
20			**81** (*E*)	55	55	7

[a]A: $^2J_{Sn-C}$ for the coupling between ^{119}Sn of the C-3 $SnMe_3$ function and ^{13}C of the allylic carbon (C-4) in R^1.
[b]B: $^3J_{Sn-C}$ for the coupling between ^{119}Sn of the C-2 $SnMe_3$ group and ^{13}C of the allylic carbon (C-4) in R^1.
[c]C: $^3J_{Sn-C}$ for the coupling between ^{119}Sn of the C-3 $SnMe_3$ group and ^{13}C of the homoallylic carbon (C-5) in R^1.

TABLE 7. The ^{119}Sn nmr data derived from selected alkyl (*Z*)- and (*E*)-2,3-bis(trimethylstannyl)-2-alkenoates[a]

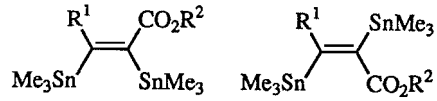

Entry	R^1	R^2	Compound number (configuration)	^{119}Sn chemical shifts[b] (Me_3Sn groups)	$^3J_{Sn-Sn}$[c]
1	Et	Me	**70** (*E*)	−51.1, −50.7	562
2	i-Pr	Me	**71** (*E*)	−60.2, −44.5	548
3	2-(2-Cyclopentenyl)ethyl	Me	**73** (*E*)	−51.8, −50.2	564
4	$H_2C{=}CH(CH_2)_2$	Me	**75** (*E*)	−51.6, −51.0	551
5	t-$BuMe_2SiOCH_2$	Et	**77** (*E*)	−48.8, −47.1	510
6	$Cl(CH_2)_3$	Me	**58** (*Z*)	−35.5, −35.3	317
7			**78** (*E*)	−50.2, −49.3	527
8	$Br(CH_2)_5$	Me	**62** (*Z*)	−36.9, −36.0	330
9			**80** (*E*)	−51.5, −50.5	558

[a]All spectra were recorded at 111.8 MHz, using $CDCl_3$ as solvent.
[b]Chemical shifts (δ, in ppm) were measured relative to the signal for Me_4Sn (δ = 0).
[c]Coupling constants are given in Hz and represent coupling between the two ^{119}Sn isotopes.

$(Me_3Sn)_2$ in the presence of $(Ph_3P)_4Pd$ in THF at room temperature (Table 1, entry 1), the corresponding process employing *N*,*N*-dimethyl-2-butynamide (**44**) as starting material was quite sluggish. Nevertheless, analysis (tlc) of the reaction mixture after a reaction time of 44 h showed the absence of the starting material **44** (see Scheme 5). However, tlc analysis of the crude material derived from the reaction mixture showed the presence of two products, which were separated by chromatography on silica gel. The major and minor products (isolated in yields of 50 and 13%) proved to be (*Z*)-*N*,*N*-dimethyl-2,3-bis(trimethyl-

Can. J. Chem. Downloaded from www.nrcresearchpress.com by 85.192.166.187 on 09/08/12
For personal use only.

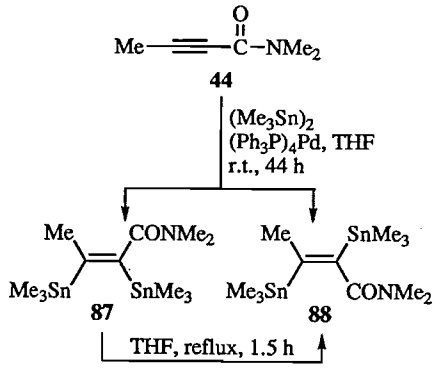

SCHEME 5

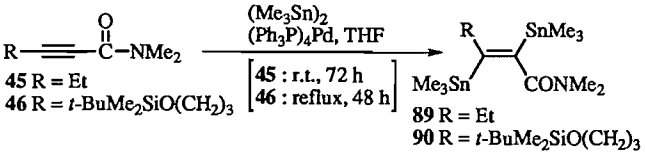

SCHEME 6

stannyl)-2-butenamide (**87**) and the corresponding *E* isomer **88**, respectively. When a solution of **87** in THF was refluxed for 1.5 h, it was transformed cleanly into **88**.

Subjection of the acetylenic amides **45** and **46** to the reaction conditions shown in Scheme 6 provided the *E* alkenamides **89** and **90** in isolated yields of 48 and 63%, respectively. The crude materials derived from these reactions did not show the presence of the corresponding *Z* alkenamides and thus it is presumed that, under the reaction conditions, the primary *Z* products rearranged to the *E* isomers.

This brief study revealed that the Pd(0)-catalyzed addition of $(Me_3Sn)_2$ to *N,N*-dimethyl-2-alkynamides is much slower than the corresponding reaction involving alkyl 2-alkynoates as substrates. Furthermore, it is evident that (*Z*)-*N,N*-dimethyl-2,3-bis(trimethylstannyl)-2-alkenamides are notably less stable than alkyl (*Z*)-2,3-bis(trimethylstannyl)-2-alkenoates. Although thermal rearrangement of the latter substances to the corresponding *E* isomers is quite slow even at elevated temperatures (see Table 2), the reactions summarized in Schemes 5 and 6 show that (*Z*)-*N,N*-dimethyl-2,3-bis(trimethylstannyl)-2-alkenoates are transformed into the corresponding *E* isomers under relatively mild conditions.

Conclusion

The investigations described in this paper showed that alkyl (*Z*)-2,3-bis(trimethylstannyl)-2-alkenoates (**4**) are readily prepared by reaction of α,β-acetylenic esters **3** with $(Me_3Sn)_2$ in the presence of a catalytic amount of $(Ph_3P)_4Pd$. The conversions are generally clean and efficient and the presence of various functional groups in the R^1 group of the substrates **3** does not interfere with the addition process. The products **4** were found to be thermally unstable and, upon heating, are cleanly converted into the thermodynamically more stable *E* isomers **5**.

The Pd(0)-catalyzed addition of $(Me_3Sn)_2$ to *N,N*-dimethyl-2-alkynamides (**6**) can also be carried out, although this process is considerably slower than the conversion of **3** into **4**. Furthermore, the primary products derived from **6** (*Z*)-*N,N*-dimethyl-2,3-bis(trimethylstannyl)-2-alkenamides (**7**), are much less stable than the analogous esters **4** and rearrange to the corresponding *E* isomers **8** even at room temperature.

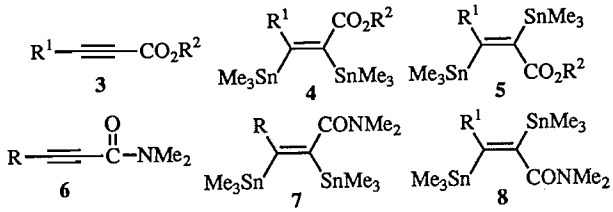

The use of substances of general structures **4**, **5**, and **8** as intermediates for organic synthesis will be the subject of future reports.

Experimental

General information

Distillation temperatures, which refer to short-path (Kugelrohr) distillations, and melting points are uncorrected. Proton (^1H), carbon (^{13}C), and tin (^{119}Sn) nuclear magnetic resonance (nmr) spectra were recorded using $CDCl_3$ solutions. Signal positions in ^1H nmr spectra were measured relative to the signals for Me_4Si (δ 0) (internal standard) or $CHCl_3$ (δ 7.25), while resonances in ^{13}C and ^{119}Sn nmr spectra were measured relative to the signals for $CDCl_3$ (δ 77.0) and Me_4Sn (δ 0) (internal standard), respectively. In ^{13}C nmr spectra, multiplicity was determined from attached proton test (APT) experiments. Tin–hydrogen and tin–carbon coupling constants (J_{Sn-H}, J_{Sn-C}) are given as the average of the ^{117}Sn and ^{119}Sn values, unless otherwise stated. Tin–tin coupling constants (J_{Sn-Sn}) are given as ^{119}Sn values. Molecular mass determinations (high-resolution mass spectrometry) for substances containing Me_3Sn groups are based on ^{120}Sn (unless stated otherwise) and were made on the ($M^+ - Me$) peak (26). Flash chromatography (27) and conventional column chromatography were carried out with 230–400 and 70–230 mesh silica gel (E. Merck), respectively. Thin-layer chromatography (tlc) was accomplished with commercial aluminum- or plastic-backed plates (E Merck, Type 5554 or 5735, respectively). Gas–liquid chromatography (glc) was performed on instruments equipped with flame ionization detectors and 25 m × 0.21 mm fused silica columns coated with cross-linked SE-54. Commercial $(Me_3Sn)_2$ (Organometallics Inc.) was stored under an inert atmosphere in a glove box and was generally distilled (water aspirator pressure) just prior to use. $(Ph_3P)_4Pd$ was obtained from the Aldrich Chemical Company, was stored and weighed under an inert atmosphere (glove box), and was used without further purification. Other reagents and solvents were purified and dried using standard methods. Aqueous NH_4Cl–NH_4OH (pH 8) refers to a solution prepared by addition of aqueous ammonia (58%, ~50 mL) to saturated aqueous NH_4Cl (~950 mL).

Note: Unless otherwise stated, all reactions were carried out under an atmosphere of dry argon in flame-dried glassware.

Note: All compounds for which high-resolution mass measurements are given exhibited clean ^1H nmr spectra and showed one spot on tlc analyses.

*Methyl 2,6-heptadiynoate (**29**) and dimethyl 2,6-octadiyndioate (**31**)*

To a cold (−78°C), stirred solution of 1,5-hexadiyne (**27**) (1.72 g, 22 mmol) in 120 mL of dry THF was added a solution of MeLi (29 mmol) in Et_2O and the mixture was stirred at −78°C for 15 min and at −20°C for 1 h. Methyl chloroformate (31 mmol) was added and the solution was stirred at −20°C for 1 h and at room temperature for 1 h. Saturated aqueous $NaHCO_3$ and Et_2O were added and the phases were separated. The aqueous phase was extracted with Et_2O. The combined organic extracts were washed (saturated aqueous $NaHCO_3$, brine), dried ($MgSO_4$), and concentrated. Column chromatography (90 g silica gel, 2:3 petroleum ether – Et_2O) of the residual material, followed by distillation (90–93°C/20 Torr; 110–115°C/0.05 Torr (1 Torr = 133.3 Pa)) of the oils obtained, gave 1.07 g (36%) of the monoester **29** (a colorless oil) and 1.71 g (40%) of the diester **31** (a colorless solid).

Compound **29** displayed ir (neat): 3295, 2333, 1713, 1435, 1338–1100 (br), 1078 cm^{-1}; ^1H nmr (300 MHz) δ: 2.08 (t, 1H, J = 2 Hz),

Can. J. Chem. Downloaded from www.nrcresearchpress.com by 85.192.166.187 on 09/08/12
For personal use only.

Can. J. Chem. Downloaded from www.nrcresearchpress.com by 85.192.166.187 on 09/08/12
For personal use only.

2.44–2.52 (m, 2H), 2.55–2.62 (m, 2H), 3.78 (s, 3H). Exact Mass calcd. for $C_8H_7O_2$ ($M^+ - H$): 135.0446; found: 135.0448.

Compound **31** showed mp 63–64°C (from MeOH–H_2O); ir (CCl_4): 2237, 1733, 1435, 1300–1200 (br), 1077 cm^{-1}; ^1H nmr (300 MHz) δ: 2.64 (s, 4H), 3.79 (s, 6H). Exact Mass calcd. for $C_{10}H_{10}O_4$: 194.0579; found: 194.0574.

*Methyl 6-hepten-2-ynoate (**15**)*

To a stirred solution of the monoester **29** (1.06 g, 7.83 mmol) in 50 mL of hexane was added 106 mg of 10% palladium-on-barium sulfate and the reaction mixture was stirred under an atmosphere of hydrogen at room temperature. After 2.15 h, analysis of an aliquot by glc indicated that the starting material had been consumed. Removal of the solvent, column chromatography (20 g silica gel, 17:1 petroleum ether – Et_2O) of the residual material, and distillation (85–95°C/20 Torr) of the acquired oil afforded 790 mg (73%) of the heptenynoate **15**, a colorless oil that showed ir (neat): 3081, 2332, 1718, 1643, 1258, 921 cm^{-1}; ^1H nmr (300 MHz) δ: 2.28–2.48 (m, 4H), 3.73 (s, 3H), 5.06 (dd, 1H, J = 10, 2 Hz), 5.10 (dd, 1H, J = 17, 2 Hz), 5.83 (ddt, 1H, J = 17, 10, 6 Hz). Exact Mass calcd. for C_7H_7O (M^+ –OMe): 107.0497; found: 107.0504.

*Ethyl 5-chloro-2-pentynoate (**18**)*

To stirred, dry *N*,*N*-dimethylformamide (50 mL) was added, dropwise, PCl_3 (2.5 mL) and the mixture was stirred at room temperature for 90 min. To the resultant yellow slurry was added 3-butyn-1-ol (**33**) (6.7 mL) and stirring was continued for 40 min. The crude product was distilled (70–110°C) from the reaction mixture. The colorless distillate was then fractionally distilled to afford 7 g (42%) of 4-chloro-1-butyne (**34**), bp 80–85°C, which exhibited ^1H nmr (80 MHz) δ: 2.11 (t, 1H, J = 2.5 Hz), 2.68 (dt, 2H, J = 2.5, 7 Hz), 3.63 (t, 2H, J = 7 Hz).

To a cold (−78°C), stirred solution of the chloride **34** (4.4 g, 50 mmol) in dry THF (100 mL) was added a solution of MeLi (55 mmol) in Et_2O. After the mixture had been stirred at −78°C for 10 min and at −20°C for 1 h, ethyl chloroformate (5.7 mL, 60 mmol) was added and stirring was continued for 1 h at −20°C and 1 h at room temperature. The mixture was diluted with Et_2O and the resultant solution was washed (twice with aqueous sodium bicarbonate and twice with brine), dried ($MgSO_4$), and concentrated. Flash chromatography (300 g silica gel, 9:1 petroleum ether – Et_2O) of the crude product and distillation (80–82°C/0.02 Torr) of the acquired oil gave 5.0 g (63%) of the chloro pentynoate **18**, a colorless oil that was homogeneous by glc analyses and exhibited ir (film): 2235, 1710, 1258, 1090, 760 cm^{-1}; ^1H nmr (80 MHz) δ: 1.32 (t, 3H, J = 7 Hz), 2.83 (t, 2H, J = 7 Hz), 3.65 (t, 2H, J = 7 Hz), 4.20 (q, 2H, J = 7 Hz). Exact Mass calcd. for $C_5H_4{}^{35}ClO$ (M^+ –OEt): 114.9950; found: 114.9950.

*Ethyl 5-bromo-2-pentynoate (**19**)*

To a stirred solution of ethyl 5-hydroxy-2-pentynoate (**35**)[4] (563 mg, 4.26 mmol) in 25 mL of dry CH_2Cl_2 was added *p*-toluenesulfonyl chloride (1.21 g, 6.34 mmol), dry pyridine (0.69 mL, 8.53 mmol), and 4-(*N*,*N*-dimethylamino)pyridine (0.5 g, 4.1 mmol). After the mixture had been stirred at room temperature for 30 h, it was concentrated under reduced pressure. Petroleum ether (50 mL) was added to the residual material and the resultant solution was washed (10% hydrochloric acid, 20 mL; saturated aqueous $NaHCO_3$, 20 mL; water, 20 mL), dried ($MgSO_4$), and concentrated. Flash chromatography (20 g silica gel, 1:1 petroleum ether – EtOAc) of the crude product, followed by distillation (80°C/0.05 Torr) of the acquired oil, provided 600 mg (47%) of the *p*-toluenesulfonate **36**, a colorless oil that displayed ^1H nmr (80 MHz) δ: 1.32 (t, 3H, J = 7 Hz), 2.50 (s, 3H), 2.75 (t, 2H, J = 7 Hz), 4.17 (t, 2H, J = 7 Hz), 4.22 (q, 2H, J = 7 Hz), 7.37, 7.72 (d, d, 2H each, J = 8 Hz).

To a stirred solution of the ester **36** (570 mg, 1.93 mmol) in 10 mL of dry *N*,*N*-dimethylformamide was added NaBr (0.6 g, 7.7 mmol) and the solution was stirred at room temperature for 3 days. Water (10 mL) and petroleum ether (20 mL) were added and the aqueous phase was washed (3 × 15 mL) with petroleum ether. The combined organic solutions were washed (water, 20 mL), dried ($MgSO_4$), and concentrated. Distillation (80°C/0.05 Torr) of the residual oil produced 365 mg (90%) of the bromo ester **19**, a colorless oil that displayed ir (neat): 2241, 1713, 1256, 1075 cm^{-1}; ^1H nmr (80 MHz) δ: 1.30 (t, 3H, J = 7 Hz), 2.75–3.02 (m, 2H), 3.30–3.57 (m, 2H), 4.20 (q, 2H, J = 7 Hz). Exact Mass calcd. for $C_5H_4{}^{81}BrO$ (M^+ –OEt): 158.9446; found: 158.9443.

*6-Bromo-1-hexanol (**38**)*

To a stirred solution of 1,6-hexanediol (**37**) (5.0 g, 42.3 mmol) in 100 mL of dry benzene was added 6.76 mL (84.6 mmol) of 48% aqueous HBr. A Dean–Stark water trap was attached to the reaction flask and the mixture was refluxed for 23 h. The cooled solution was washed (6 N aqueous NaOH, 50 mL; 10% hydrochloric acid, 50 mL; brine, 100 mL), dried ($MgSO_4$), and concentrated. Analysis (glc) of the crude product showed that it consisted of a mixture of the desired bromo alcohol **38** and the corresponding dibromide. Column chromatography (20 g silica gel, elution with petroleum ether and then with Et_2O) and distillation (58–60°C/0.05 Torr) afforded 5.84 g (70%) of the bromo alcohol **38**, a colorless oil that showed ir (neat): 3300 (br), 1450, 1060 cm^{-1}; ^1H nmr (270 MHz) δ: 1.33–1.52 (m, 3H), 1.59 (quintet, 2H, J = 7 Hz), 1.89 (quintet, 2H, J = 7 Hz), 3.42 (t, 2H, J = 7 Hz), 3.65 (t, 2H, J = 7 Hz). Exact Mass calcd. for $C_6H_{11}{}^{81}Br$ ($M^+ - H_2O$): 164.0025; found: 164.0021.

*6-Bromohexanal (**39**)*

To a stirred solution of PCC (6.1 g, 28.3 mmol) and NaOAc (0.58 g, 7.1 mmol) in 25 mL of dry CH_2Cl_2 was added a solution of the alcohol **38** (2.58 g, 14.2 mmol) in 55 mL of dry CH_2Cl_2. The brown mixture was stirred for 1.5 h at room temperature and then was poured into 300 mL of Et_2O. The mixture was passed through a short column of Florisil (20 g, elution with Et_2O). Concentration of the combined eluate, followed by distillation (55–60°C/0.05 Torr) of the remaining oil, provided 1.76 g (69%) of the aldehyde **39**, a colorless oil that displayed ir (neat): 2700, 1708, 1450, 1280 cm^{-1}, ^1H nmr (270 MHz) δ: 1.39–1.55 (m, 2H), 1.58–1.72 (m, 2H), 1.87 (quintet, 2H, J = 7 Hz), 2.40 (td, 2H, J = 7, 1 Hz), 3.49 (t, 2H, J = 7 Hz), 9.75 (t, 1H, J = 1 Hz). Exact Mass calc. for $C_6H_{10}{}^{79}BrO$: 176.9916; found: 176.9919.

*1,1,7-Tribromo-1-heptene (**40**)*

To a stirred solution–suspension of Ph_3P (5.13 g, 19.5 mmol) in 100 mL of dry CH_2Cl_2 was added CBr_4 (19.5 mmol) and zinc dust (19.5 mmol). After the reaction mixture had been stirred at room temperature for 23 h, a solution of 6-bromohexanal (**39**) (1.76 g, 9.77 mmol) in 20 mL of dry CH_2Cl_2 was added dropwise over a period of 20 min. The resulting mixture was stirred for 2 h. Petroleum ether (350 mL) was added, and the supernatant solution was decanted from the heavy oil. The oil was dissolved in CH_2Cl_2 (70 mL). Petroleum ether (350 mL) was added to the solution and, again, the supernatant solution was decanted. Concentration of the combined petroleum ether solutions, followed by distillation (80°C/0.05 Torr) of the remaining oil, afforded 3.15 g (96%) of the tribromide **40**, a colorless oil that showed ir (neat): 1620, 1450, 800 cm^{-1}; ^1H nmr (270 MHz) δ: 1.41–1.56 (m, 4H), 1.81–1.95 (m, 2H), 2.08–2.19 (m, 2H), 3.41 (t, 2H, J = 7 Hz), 6.40 (t, 1H, J = 7 Hz). Exact Mass calcd. for $C_7H_{11}{}^{81}Br_3$: 337.8354; found: 337.8354.

*Methyl 8-bromo-2-octynoate (**24**)*

To a cold (−78°C), stirred solution of 1,1,7-tribromo-1-heptene (**40**) (3.15 g, 9.32 mmol) in 120 mL of dry THF was added a solution of BuLi (23.3 mmol) in hexane. The mixture was stirred at −78°C for 1 h, at room temperature for 1 h, and then was recooled to −20°C. Methyl chloroformate (10.25 mmol) was added and the solution was stirred at −20°C for 1 h and at room temperature for 1 h. Saturated aqueous $NaHCO_3$ and Et_2O were added and the organic phase was washed (saturated aqueous $NaHCO_3$, brine), dried ($MgSO_4$), and concentrated. Distillation (90°C/0.05 Torr) of the crude product provided 1.95 g (89%) of the bromo ester **24**, a colorless oil that showed ir (neat): 2200, 1700, 1430, 1078 cm^{-1}; ^1H nmr (270 MHz) δ: 1.54–1.68 (m, 4H), 1.89 (quintet, 2H, J = 7 Hz), 2.38 (t, 2H, J = 7 Hz), 3.41 (t, 2H, J = 7 Hz), 3.77 (s, 3H). Exact Mass calcd. for $C_8H_{10}{}^{81}BrO$ (M^+ –OMe): 202.9896; found: 202.9896.

Can. J. Chem. Downloaded from www.nrcresearchpress.com by 85.192.166.187 on 09/08/12
For personal use only.

*Methyl 8-iodo-2-octynoate (**25**)*

Sodium iodide (2.48 g, 16.5 mmol) was added to a stirred solution of methyl 8-bromo-2-octynoate (**24**) (970 mg, 4.13 mmol) in 40 mL of dry acetone. The mixture was refluxed for 7.5 h and then was cooled and concentrated. Petroleum ether (40 mL) and water (20 mL) were added to the residual material. The organic phase was washed twice with water (15 mL) and then was dried ($MgSO_4$) and concentrated. Distillation (80–85°C/0.05 Torr) of the crude product gave 1.08 g (93%) of the iodo ester **25**, a colorless oil that showed ir (neat): 2236, 1714, 1256 cm^{-1}; ^1H nmr (300 MHz) δ: 1.50–1.70 (m, 4H), 1.88 (quintet, 2H, J = 7.5 Hz), 2.49 (t, 2H, J = 7.5 Hz), 3.22 (t, 2H, J = 7.5 Hz), 3.80 (s, 3H). Exact Mass calcd. for $C_9H_{13}IO_2$: 279.9962; found: 279.9965.

*Methyl 2,8-nonadiynoate (**30**) and dimethyl 2,8-decadiyndioate (**32**)*

A solution of MeLi (31.2 mmol) in Et_2O was added to a cold (−78°C), stirred solution of 1,7-octadiyne (**28**) (2.54 g, 24.0 mmol) in 70 mL of dry THF and the mixture was stirred at −78°C for 10 min and at −20°C for 1 h. Methyl chloroformate (33.5 mmol) was added and stirring was continued at −20°C for 1 h and at room temperature for 1 h. Saturated aqueous $NaHCO_3$ and Et_2O were added. The organic phase was separated, washed (saturated aqueous $NaHCO_3$, brine), dried ($MgSO_4$), and concentrated. Column chromatography (100 g silica gel, 2:3 petroleum ether – Et_2O) of the crude product provided two oils. Distillation (100°C/0.05 Torr; 160°C/0.05 Torr) of these materials gave 1.58 g (40%) and 1.71 g (32%) of the monoester **30** and the diester **32**, respectively.

Compound **30**, a colorless oil, displayed ir (neat): 3296, 2238, 1718, 1436, 1260, 1080 cm^{-1}; ^1H nmr (300 MHz) δ: 1.60–1.81 (m, 4H), 1.98 (t, 1H, J = 2 Hz), 2.23 (dt, 2H, J = 2, 7 Hz), 2.39 (t, 2H, J = 7 Hz), 3.76 (s, 3H). Exact Mass calcd. for $C_{10}H_{11}O_2$ (M^+ −H): 163.0759; found: 163.0757.

Compound **32**, a solid, exhibited mp 34°C (from MeOH–H_2O); ir (CCl_4): 2245, 1733, 1456, 1279, 1084 cm^{-1}; ^1H nmr (300 MHz) δ: 1.68–1.80 (m, 4H), 2.32–2.48 (m, 4H), 3.78 (s, 6H). Exact Mass calcd. for $C_{11}H_{11}O_3$ (M^+ −OMe): 191.0708; found: 191.0714.

*Methyl 8-bromo-8-nonen-2-ynoate (**26**)*

To a cold (0°C), stirred solution of *B*-bromo-9-borabicyclo[3.3.1]nonane (4.02 mmol) in 5 mL of dry CH_2Cl_2 was added dropwise, over a period of 10 min, a solution of methyl 2,8-nonadiynoate (**30**) (300 mg, 1.83 mmol) in 5 mL of dry CH_2Cl_2. The mixture was stirred at 0°C for 3 h, 1 mL of HOAc was added, and stirring was continued at 0°C for 1 h. Aqueous NaOH (3 M, 12 mL) and aqueous H_2O_2 (30%, 2 mL) were added and the mixture was stirred at room temperature for 30 min. The mixture was extracted with petroleum ether (3 × 20 mL). The combined extracts were washed (water, 15 mL; saturated aqueous $NaHCO_3$, 15 mL; water, 15 mL), dried ($MgSO_4$), and concentrated. Column chromatography (15 g silica gel, 4:1 petroleum ether – Et_2O) of the crude product and distillation (130°C/0.05 Torr) of the acquired oil afforded 388 mg (87%) of the ester **26**, a colorless oil that showed ir (neat): 2238, 1718, 1631, 1435, 1261, 1079 cm^{-1}; ^1H nmr (270 MHz) δ: 1.54–1.72 (m, 4H), 2.36 (t, 2H, J = 7 Hz), 2.44 (t, 2H, J = 7 Hz), 3.76 (s, 3H), 5.41 (d, 1H, J = 1.5 Hz), 5.58 (d, 1H, J = 1.5 Hz). Exact Mass calcd. for $C_9H_{10}{}^{81}BrO$ (M^+ −OMe): 214.9896; found: 214.9894.

General procedure 1. Conversion of 1-alkynes into N,N*-dimethyl-2-alkyamides*

To a cold (−78°C), stirred solution of the 1-alkyne in dry THF (~2 mL per mmol of alkyne) was added a solution of MeLi (1 equiv.) in Et_2O. The mixture was stirred at −78°C for 30 min and at −20°C for 1 h. *N,N*-Dimethylcarbamyl chloride (1.1 equiv.) was added and the mixture was stirred at −20°C for 1 h and at room temperature for 2 h. Saturated aqueous $NaHCO_3$ (~0.25 mL per mmol of starting material used) was added, the mixture was stirred at room temperature for 2 h, and then was diluted with Et_2O. The phases were separated and the aqueous phase was thoroughly extracted with Et_2O. The combined extracts were washed (saturated aqueous $NaHCO_3$), dried ($MgSO_4$), and concentrated. Distillation of the remaining liquid produced the amide product.

The following compounds were prepared via this method.

N,N-*Dimethyl-2-butynamide (**44**)*

The crude product derived from 50 mmol of propyne (**41**) was distilled (100°C/20 Torr; lit. (28) bp 98–102°C/17–18 Torr) to give 4.51 g (81%) of **44**, a colorless oil that displayed ir (neat): 2240, 2210, 1630, 1400 cm^{-1}; ^1H nmr (80 MHz) δ: 2.02 (s, 3H), 2.98, 3.22 (s, s, 3H each).

N,N-*Dimethyl-2-pentynamide (**45**)*

Distillation (125–130°C/12 Torr) of the crude product obtained from 50 mmol of 1-butyne (**42**) afforded 5.32 g (85%) of the amide **45**, a colorless oil that showed ir (neat): 2230, 2200, 1630, 1400, 1190 cm^{-1}; ^1H nmr (100 MHz) δ: 1.06 (t, 3H, J = 7.5 Hz), 2.23 (q, 2H, J = 7.5 Hz), 2.82, 3.06 (s, s, 3H each). Exact Mass calcd. for $C_7H_{11}NO$: 125.0841; found: 125.0843.

N,N-*Dimethyl-6-*tert*-butyldimethylsiloxy-2-hexynamide (**46**)*

Distillation (140–145°C/0.8 Torr) of the crude product acquired from 1.88 g (9.5 mmol) of 5-*tert*-butyldimethylsiloxy-1-pentyne (**43**) (14) provided 2.34 g (92%) of the amide **46**, a colorless oil that displayed ir (neat): 2210, 1630, 1390, 1110, 840 cm^{-1}; ^1H nmr (80 MHz) δ: 0.02 (s, 6H), 0.86 (s, 9H), 1.77 (m, 2H), 2.45 (t, 2H, J = 7 Hz), 2.97, 3.19 (s, s, 3H each), 3.70 (t, 2H, J = 6 Hz). Exact Mass calcd. for $C_{13}H_{24}NO_2Si$ (M^+ −Me): 254.1576; found: 254.1576.

General procedure 2. Conversion of alkyl 2-alkynoates into alkyl (Z)-2,3-bis(trimethylstannyl)-2-alkenoates

To a stirred solution of the alkyl 2-alkynoate (1 equiv.) in dry THF (~15 mL per mmol of substrate) was added $(Me_3Sn)_2$ (1 equiv.) and $(Ph_3P)_4Pd$ (0.009–0.02 equiv.) and the mixture was stirred at room temperature or at reflux temperature for the time specified in Table 1. Concentration of the reaction mixture afforded a dark oil that was purified by column chromatography on silica gel. Since the products (colorless oils) are thermally unstable and, therefore, were not distilled, last traces of solvent were removed by subjection of each product to reduced pressure (vacuum pump, 0.05 Torr) for 1–2 h at room temperature.

General procedure 3. Conversion of alkyl (Z)-2,3-bis(trimethylstannyl)-2-alkenoates into alkyl (E)-2,3-bis(trimethylstannyl)-2-alkenoates

A stirred sample of the (Z) substrate in a round-bottomed flask was heated (neat) at the temperature and for the time specified in Table 2. The acquired yellow oil was purified by direct distillation (receiving bulb cooled to −10°C) or by flash chromatography (silica gel, elution with petroleum ether – Et_2O) prior to distillation. Each alkyl (*E*)-2,3-bis(trimethylstannyl)-2-alkenoate was obtained as a colorless oil.

The following compounds were prepared by means of general procedures 2 and 3. The nmr spectroscopic data derived from all or a selected number of these substances are shown in Tables 3–7.

*Ethyl (Z)- and (E)-2,3-bis-(trimethylstannyl)-2-butenoates (**47** and **69**)*

Column chromatography (30 g silica gel, 19:1 petroleum ether – Et_2O) of the crude product obtained from ethyl 2-butynoate (**9**) (344 mg, 3.07 mmol) and $(Me_3Sn)_2$ (3.07 mmol) in the presence of $(Ph_3P)_4Pd$ (0.043 mmol) gave 1.29 g (95%) of **47**, which exhibited ir (neat): 1702, 1200, 1040, 775 cm^{-1}. Exact Mass calcd. for $C_{11}H_{23}O_2Sn_2$ (M^+ −Me): 426.9743; found: 426.9743.

Flash chromatography (5 g silica gel, 17:1 petroleum ether – Et_2O) of the yellow oil obtained from heating **47** (78 mg), followed by distillation (70–75°C/0.1 Torr) of the acquired oil gave 64 mg (82%) of the *E*-isomer **69**, which exhibited ir (neat): 1685, 1230, 775 cm^{-1}. Exact Mass calcd. for $C_{11}H_{23}O_2Sn_2$ (M^+ − Me): 426.9743; found: 426.9743.

*Methyl (Z)- and (E)-2,3-bis(trimethylstannyl)-2-pentenoates (**48** and **70**)*

Reaction of methyl 2-pentynoate (**10**) (8) (1.13 g, 9.94 mmol) with

Can. J. Chem. Downloaded from www.nrcresearchpress.com by 85.192.166.187 on 09/08/12
For personal use only.

$(Me_3Sn)_2$ (9.94 mmol) in the presence of $(Ph_3P)_4Pd$ (0.113 mmol), followed by column chromatography (40 g silica gel, 19:1 petroleum ether – Et_2O) of the crude product, provided 3.88 g (88%) of the *Z* isomer **48**, which displayed ir (neat): 1708, 1191, 771 cm^{-1}. Exact Mass calcd. for $C_{11}H_{23}O_2Sn_2$ (M^+ − Me): 426.9743; found: 426.9747.

Heating of the *Z* substance **48** (71 mg), followed by purification of the yellow oil by flash chromatography (5 g silica gel, 17:1 petroleum ether – Et_2O) and distillation (90–95°C/0.05 Torr), produced 58 mg (82%) of the *E* isomer **70**, which showed ir (neat): 1693, 1224, 772 cm^{-1}. Exact Mass calcd. for $C_{11}H_{23}O_2Sn_2$ (M^+ − Me): 426.9743; found: 426.9741.

*Methyl (Z)- and (E)-4-methyl-2,3-bis(trimethylstannyl)-2-pentenoate (**49** and **71**)*

Treatment of methyl 4-methyl-2-pentynoate (**11**) (9) (856 mg, 6.85 mmol) with $(Me_3Sn)_2$ (6.85 mmol) and $(Ph_3P)_4Pd$ (0.068 mmol) and column chromatography (35 g silica gel, 9:1 petroleum ether – Et_2O) of the crude product afforded 2.82 g (90%) of the *Z* product **49**, which displayed ir (neat): 1705, 1190, 770 cm^{-1}. Exact Mass calcd. for $C_{12}H_{25}O_2Sn_2$ (M^+ −Me): 440.9899; found: 440.9909.

Distillation (90–95°C/0.05 Torr) of the yellow oil obtained from heating a sample of **49** (417 mg) gave 407 mg (98%) of the *E* isomer **71**, which showed ir (neat): 1688, 1220, 775 cm^{-1}. Exact Mass calcd. for $C_{12}H_{25}O_2Sn_2$ (M^+ − Me): 440.9899; found: 440.9896.

*Methyl (Z)- and (E)-3-cyclopropyl-2,3-bis(trimethylstannyl)-propenoate (**50** and **72**)*

Column chromatography (20 g silica gel, 9:1 petroleum ether – Et_2O) of the crude product derived from reaction of methyl 3-cyclopropylpropynoate (**12**) (9) (304 mg, 2.45 mmol) with $(Me_3Sn)_2$ (2.45 mmol) in the presence of $(Ph_3P)_4Pd$ (0.043 mmol) afforded 916 mg (83%) of the *Z* ester **50**, which exhibited ir (neat): 1703, 1200, 770 cm^{-1}. Exact Mass calcd. for $C_{12}H_{23}O_2Sn_2$ (M^+ −Me): 438.9742; found: 438.9743.

Distillation (~100°C/0.05 Torr) of the yellow oil obtained from heating **50** (412 mg) produced 344 mg (83%) of the *E* isomer **72**, which displayed ir (neat): 1685, 1220, 775 cm^{-1}. Exact Mass calcd. for $C_{12}H_{23}O_2Sn_2$ (M^+ − Me): 438.9742; found: 438.9745.

*Methyl (Z)- and (E)-5-(2-cyclopentenyl)-2,3-bis(trimethylstannyl)-2-pentenoate (**51** and **73**)*

Reaction of methyl 5-(2-cyclopentenyl)-2-pentynoate (**13**) (9) (122 mg, 0.68 mmol) with $(Me_3Sn)_2$ (0.68 mmol) in the presence of $(Ph_3P)_4Pd$ (0.007 mmol), followed by column chromatography (5 g silica gel, 17:3 petroleum ether – Et_2O) of the crude product, afforded 255 mg (73%) of the *Z* product **51**, which showed ir (neat): 1700, 1200, 770 cm^{-1}. Exact Mass calcd. for $C_{16}H_{29}O_2Sn_2$ (M^+ −Me): 493.0212; found: 493.0216.

Distillation (~130°C/0.05 Torr) of the liquid derived from heating a sample of the *Z* substance **51** (158 mg) gave 128 mg (81%) of the *E* isomer **73**, which showed ir (neat): 1685, 1225, 775 cm^{-1}. Exact Mass calcd. for $C_{16}H_{29}O_2Sn_2$ (M^+ − Me): 493.0212; found: 493.0218.

*Methyl (Z)- and (E)-4-(3-cyclohexenyl)-2,3-bis(trimethylstannyl)-2-butenoate (**52** and **74**)*

Column chromatography (5 g silica gel, 17:3 petroleum ether – Et_2O) of the crude material acquired from treatment of methyl 4-(3-cyclohexenyl)-2-butynoate (**14**) (9) (89 mg, 0.5 mmol) with $(Me_3Sn)_2$ (0.5 mmol) in the presence of $(Ph_3P)_4Pd$ (0.007 mmol) afforded 188 mg (74%) of the *Z* ester **52**, which exhibited ir (neat): 1703, 1640, 1190, 780 cm^{-1}. Exact Mass calcd. for $C_{16}H_{29}O_2Sn_2$ (M^+ − Me): 493.0212; found: 493.0209.

Distillation (~150°C/0.05 Torr) of the yellow oil acquired from heating a sample of **52** (170 mg) produced 150 mg (88%) of the *E* isomer **74**, which showed ir (neat): 1685, 1640, 1220, 775 cm^{-1}. Exact Mass calcd. for $C_{16}H_{29}O_2Sn_2$ (M^+ − Me): 493.0212; found: 493.0206.

*Methyl (Z)- and (E)-2,3-bis(trimethylstannyl)-2,6-heptadienoate (**53** and **75**)*

Column chromatography (20 g silica gel, 17:3 petroleum ether – Et_2O) of the dark oil acquired from reaction of methyl 6-hepten-2-ynoate (**15**) (350 mg, 2.53 mmol) with $(Me_3Sn)_2$ (2.53 mmol) in the presence of $(Ph_3P)_4Pd$ (0.045 mmol) produced 1.0 g (85%) of the *Z* ester **53**, which displayed ir (neat): 1708, 1641, 1191, 770 cm^{-1}. Exact Mass calcd. for $C_{13}H_{25}O_2Sn_2$ (M^+ − Me): 452.9898; found: 452.9896.

Flash chromatography (5 g silica gel, 17:3 petroleum ether – Et_2O) of the yellow oil derived from heating a sample of **53** (155 mg), followed by distillation (95–100°C/0.05 Torr) of the acquired oil, afforded 125 mg (81%) of the *E* ester **75**, which showed ir (neat): 1692, 1641, 1229, 770 cm^{-1}. Exact Mass calcd. for $C_{13}H_{25}O_2Sn_2$ (M^+ − Me): 452.9898; found: 452.9907.

*Methyl (Z)- and (E)-6-(tetrahydropyranyloxy)-2,3-bis(trimethylstannyl)-2-hexenoate (**54** and **76**)*

Treatment of methyl 6-(tetrahydropyranyloxy)-2-hexynoate (**16**) (9) (365 mg, 1.6 mmol) with $(Me_3Sn)_2$ (1.6 mmol) in the presence of $(Ph_3P)_4Pd$ (0.015 mmol), followed by column chromatography (20 g silica gel, 1:1 petroleum ether – Et_2O) of the crude brown oil, produced 734 mg (83%) of the *Z* ester **54**, which exhibited ir (neat): 1700, 1190, 1030, 730 cm^{-1}. Exact Mass calcd. for $C_{17}H_{33}O_4Sn_2$ (M^+ − Me): 541.0423; found: 541.0425.

Distillation (~155°C/0.05 Torr) of the yellow oil obtained from heating a sample of **54** (705 mg) gave 652 mg (93%) of the *E* ester **76**, which displayed ir (neat): 1686, 1190, 1030, 780 cm^{-1}. Exact Mass calcd. for $C_{17}H_{33}O_4Sn_2$ (M^+ − Me): 541.0423; found: 541.0426.

*Ethyl (Z)- and (E)-4-(*tert*-butyldimethylsiloxy)-2,3-bis(trimethylstannyl)-2-butenoate (**55** and **77**)*

Column chromatography (10 g silica gel, 9:1 petroleum ether – Et_2O) of the crude brown oil acquired from reaction of ethyl 4-(*tert*-butyldimethylsiloxy)-2-butynoate (**17**) (9) (205 mg, 0.85 mmol) with $(Me_3Sn)_2$ (0.85 mmol) in the presence of $(Ph_3P)_4Pd$ (0.011 mmol) provided 403 mg (83%) of the *Z* ester **55**, which showed ir (neat): 1698, 1170, 1060, 840, 770 cm^{-1}. Exact Mass calcd. for $C_{17}H_{37}O_3SiSn_2$ (M^+ − Me): 557.0556; found: 557.0549.

Flash chromatography (10 g silica gel, 97:3 petroleum ether – Et_2O) of the yellow oil obtained from heating a sample of **55** (162 mg), followed by distillation (~135°C/0.05 Torr) of the acquired oil, gave 140 mg (86%) of the *E* ester **77**, a colorless oil that displayed ir (neat): 1698, 1640, 1230, 845, 780 cm^{-1}. Exact Mass calcd. for $C_{17}H_{37}O_3SiSn_2$ (M^+ −Me): 557.0556; found: 557.0556.

*Ethyl (Z)-5-chloro-2,3-bis(trimethylstannyl)-2-pentenoate (**56**)*

Column chromatography (35 g silica gel, 23:2 petroleum ether – Et_2O) of the crude product derived from reaction of ethyl 5-chloro-2-pentynoate (**18**) (742 mg, 4.64 mmol) with $(Me_3Sn)_2$ (4.64 mmol) in the presence of $(Ph_3P)_4Pd$ (0.056 mmol) provided 2.02 g (89%) of the *Z* ester **56**, a colorless oil that displayed ir (neat): 1702, 1186, 773 cm^{-1}. Exact Mass calcd. for $C_{12}H_{24}{}^{35}ClO_2Sn_2$ (M^+ − Me): 474.9509; found: 474.9503.

*Ethyl (Z)-5-bromo-2,3-bis(trimethylstannyl)-2-pentenoate (**57**)*

Reaction of ethyl 5-bromo-2-pentynoate (**19**) (347 mg, 1.69 mmol) with $(Me_3Sn)_2$ (1.69 mmol) in the presence of $(Ph_3P)_4Pd$ (0.034 mmol), followed by column chromatography (20 g silica gel, 9:1 petroleum ether – Et_2O) of the crude product (dark oil), gave 600 mg (66%) of the *Z* ester **57**, a colorless oil that showed ir (neat): 1698, 1186, 770 cm^{-1}. Exact Mass calcd. for $C_{12}H_{24}{}^{81}BrO_2Sn_2$ (M^+ − Me): 520.8985; found: 520.8982.

*Methyl (Z)- and (E)-6-chloro-2,3-bis(trimethylstannyl)-2-hexenoate (**58** and **78**)*

Column chromatography (40 g silica gel, 19:1 petroleum ether – Et_2O) of the crude dark oil derived from reaction of methyl 6-chloro-2-hexynoate (**20**) (10) (1.0 g, 6.25 mmol) with $(Me_3Sn)_2$ (6.25 mmol) in the presence of $(Ph_3P)_4Pd$ (0.062 mmol) afforded 2.62 g (86%) of the *Z* ester **58**, a colorless oil that displayed ir (neat): 1698, 1195, 770 cm^{-1}. Exact Mass calcd. for $C_{12}H_{24}{}^{35}ClO_2Sn_2$ (M^+ − Me): 474.9509; found: 474.9518.

Can. J. Chem. Downloaded from www.nrcresearchpress.com by 85.192.166.187 on 09/08/12
For personal use only.

Distillation (~105°C/0.1 Torr) of the pale yellow oil acquired from heating a sample of the *Z* ester **58** (477 mg) produced 457 mg (96%) of the *E* ester **78**, a colorless oil that crystallized on standing: mp 30–31°C; ir (KBr): 1691, 1227, 771 cm^{-1}. Exact Mass calcd. for $C_{12}H_{24}{}^{35}ClO_2Sn_2$ (M^+ − Me): 474.9509; found: 474.9510.

*Methyl (Z)-6-bromo-2,3-bis(trimethylstannyl)-2-hexenoate (**59**)*

Column chromatography (30 g silica gel, 19:1 petroleum ether – Et_2O) of the crude product acquired from reaction of methyl 6-bromo-2-hexynoate (**21**) (9) (644 mg, 3.14 mmol) with $(Me_3Sn)_2$ (3.14 mmol) in the presence of $(Ph_3P)_4Pd$ (0.043 mmol) gave 1.41 g (84%) of the *Z* ester **59**, a colorless oil that showed ir (neat): 1700, 1200, 780 cm^{-1}. Exact Mass calcd. for $C_{12}H_{24}{}^{81}BrO_2Sn_2$ (M^+ −Me): 520.8985; found: 520.8988.

*Methyl (Z)-6-iodo-2,3-bis(trimethylstannyl)-2-hexenoate (**60**)*

Reaction of methyl 6-iodo-2-hexynoate (**22**) (9) (756 mg, 3.0 mmol) with $(Me_3Sn)_2$ (3.0 mmol) in the presence of $(Ph_3P)_4Pd$ (0.06 mmol), followed by column chromatography (50 g silica gel, 23:2 petroleum ether – Et_2O) of the acquired dark oil, provided 1.37 g (79%) of the *Z* ester **60**, a colorless oil that displayed ir (neat): 1705, 1190, 771 cm^{-1}. Exact Mass calcd. for $C_{12}H_{24}IO_2Sn_2$ (M^+ − Me): 566.8867; found: 566.8882.

*Methyl (Z)- and (E)-7-bromo-2,3-bis(trimethylstannyl)-2-heptenoate (**61** and **79**)*

Reaction of methyl 7-bromo-2-heptynoate (**23**) (9) (600 mg, 2.74 mmol) with $(Me_3Sn)_2$ (2.74 mmol) in the presence of $(Ph_3P)_4Pd$ (0.043 mmol), followed by column chromatography (45 g silica gel, 19:1 petroleum ether – Et_2O) of the crude product, afforded 1.17 g (78%) of the *Z* ester **61**, a colorless oil that showed ir (neat): 1698, 1290, 770 cm^{-1}. Exact Mass calcd. for $C_{13}H_{26}{}^{81}BrO_2Sn_2$ (M^+ − Me): 534.9141; found: 534.9148.

Flash chromatography (10 g silica gel, 17:1 petroleum ether – Et_2O) of the pale yellow oil derived from heating a sample of the *Z* ester **61** (101 mg), followed by distillation (~130°C/0.05 Torr) of the acquired liquid, gave 81 mg (80%) of the *E* ester **79**, a colorless oil that exhibited ir (neat): 1692, 1224, 770 cm^{-1}. Exact Mass calcd. for $C_{13}H_{26}{}^{79}BrO_2Sn_2$ (M^+ − Me): 532.9161; found: 532.9164.

*Methyl (Z)- and (E)-8-bromo-2,3-bis(trimethylstannyl)-2-octenoate (**62** and **80**)*

Column chromatography (30 g silica gel, 9:1 petroleum ether – Et_2O) of the dark oil derived from reaction of methyl 8-bromo-2-octynoate (**24**) (930 mg, 3.98 mmol) with $(Me_3Sn)_2$ (3.98 mmol) in the presence of $(Ph_3P)_4Pd$ (0.063 mmol) afforded 1.85 g (83%) of the *Z* ester **62**, a colorless oil that exhibited ir (neat): 1707, 1191, 771 cm^{-1}. Exact Mass calcd. for $C_{14}H_{28}{}^{79}BrO_2Sn_2$ (M^+ −Me): 546.9317; found: 546.9321.

Flash chromatography (10 g silica gel, 9:1 petroleum ether – Et_2O) of the pale yellow oil obtained from heating a sample of the *Z* ester **62** (120 mg), followed by distillation (~130°C/0.05 Torr) of the acquired oil, gave 106 mg (88%) of the *E* ester **80**, a colorless oil that displayed ir (neat): 1691, 1230, 772 cm^{-1}. Exact Mass calcd. for $C_{14}H_{28}{}^{79}BrO_2Sn_2$ (M^+ − Me): 546.9317; found: 546.9321.

*Methyl (Z)-8-iodo-2,3-bis(trimethylstannyl)-2-octenoate (**63**)*

Column chromatography (40 g silica gel, 93:3 petroleum ether – Et_2O) of the dark oil derived from reaction of methyl 8-iodo-2-octynoate (**25**) (1.07 g, 3.82 mmol) with $(Me_3Sn)_2$ (3.82 mmol) in the presence of $(Ph_3P)_4Pd$ (0.048 mmol) gave 1.77 g (76%) of the *Z* ester **63**, a colorless oil that displayed ir (neat): 1707, 1191, 770 cm^{-1}. Exact Mass calcd. for $C_{14}H_{28}IO_2{}^{118}Sn^{120}Sn$ (M^+ − Me): 592.9174; found: 592.9170.

*Methyl (Z)- and (E)-8-bromo-2,3-bis(trimethylstannyl)-2,8-nonadienoate (**64** and **81**)*

To a stirred solution of $Pd(OAc)_2$ (2.7 mg) in 1 mL of dry THF was added Ph_3P (6.4 mg) and dry Et_3N (114 μL). After the mixture had been stirred at 60°C for 1 h, $(Me_3Sn)_2$ (0.41 mmol) and a solution of methyl 8-bromo-8-nonen-2-ynoate (**26**) (100 mg, 0.41 mmol) in 1 mL of dry THF were added. The resulting yellow solution was refluxed for 2 h. Removal of the solvent, column chromatography (10 g silica gel, 9:1 petroleum ether – Et_2O) of the remaining dark liquid, and subjection of the acquired colorless oil to reduced pressure (vacuum pump, 0.05 Torr, 1.5 h) afforded 149 mg (64%) of the *Z* ester **64**, which exhibited ir (neat): 1708, 1630, 1191, 770 cm^{-1}. Exact Mass calcd. for $C_{15}H_{28}{}^{79}BrO_2Sn_2$ (M^+ − Me): 558.9317; found: 558.9312.

Flash chromatography (10 g of silica gel, 9:1 petroleum ether – Et_2O) of the yellow liquid derived from heating a sample of the *Z* ester **64** (80 mg), followed by distillation (~145°C/0.05 Torr) of the acquired oil, gave 53 mg (66%) of the *E* ester **81**, a colorless oil that showed ir (neat): 1691, 1630, 1226, 770 cm^{-1}. Exact Mass calcd. for $C_{15}H_{28}{}^{81}BrO_2Sn_2$ (M^+ − Me): 560.9298; found: 560.9306.

General procedure 4. Conversion of N,N*-dimethyl-2-alkynamides into (E)-*N,N*-dimethyl-2,3-bis(trimethylstannyl)-2-alkenamides*

To a stirred solution of the *N,N*-dimethyl-2-alkynamide (1 equiv.) in dry THF was added $(Me_3Sn)_2$ (1 equiv.) and $(Ph_3P)_4Pd$ (~0.01 equiv.) and the mixture was stirred at room temperature (substrates **44**, **45**) or at reflux temperature (substrate **46**) for the times specified in Schemes 5 and 6. Concentration of the reaction mixture, followed by purification of the crude product by chromatography and distillation (receiving bulb cooled to −10°C), provided the product.

*(Z)- and (E)-*N,N*-Dimethyl-2,3-bis(trimethylstannyl)-2-butenamide (**87** and **88**)*

Reaction of *N,N*-dimethyl-2-butynamide (**44**) (269 mg, 2.43 mmol) with $(Me_3Sn)_2$ (2.43 mmol) in the presence of $(Ph_3P)_4Pd$ (0.023 mmol) in dry THF (20 mL), followed by flash chromatography (25 g silica gel, 1:1 petroleum ether – EtOAc), gave two products, in a ratio of about 4:1. Distillation (~105°C/0.1 Torr) of the minor product produced 140 mg (13%) of the *E* amide **88**, while subjection of the major product to reduced pressure (vacuum pump, 0.1 Torr, 1.5 h) provided 540 mg (50%) of the *Z* amide **87**. When a solution of the latter substance in dry THF was refluxed for 1.5 h, it was cleanly converted into the *E* isomer **88**.

The *Z* amide **87**, a colorless oil, displayed ir (neat): 1620, 1390, 1160, 770 cm^{-1}; ^1H nmr (270 MHz) δ: 0.20, 0.22 (s, s, 9H each, $^2J_{Sn-H}$ = 54 Hz in each case), 1.94 (s, 3H, $^3J_{Sn-H}$ = 45 Hz, $^4J_{Sn-H}$ = 11 Hz), 2.91 (s, 3H), 2.95 (s, 3H). Exact Mass calcd. for $C_{11}H_{24}NOSn_2$ (M^+ − Me): 425.9902; found: 425.9909.

The *E* amide **88** exhibited ir (neat): 1620, 1390, 1170, 770 cm^{-1}; ^1H nmr (80 MHz) δ: 0.12, 0.25 (s, s, 9H each, $^2J_{Sn-H}$ = 53 Hz in each case), 2.05 (s, 3H, $^3J_{Sn-H}$ = 46 Hz, $^4J_{Sn-H}$ = 11 Hz), 2.92 (s, 6H). Exact Mass calcd. for $C_{11}H_{24}NOSn_2$ (M^+ − Me): 425.9902; found: 425.9906.

*(E)-*N,N*-Dimethyl-2,3-bis(trimethylstannyl)-2-pentenamide (**89**)*

Column chromatography (30 g silica gel, 1:1 petroleum ether – Et_2O) of the crude product obtained from reaction of *N,N*-dimethyl-2-pentynamide (**45**) (565 mg, 4.42 mmol) with $(Me_3Sn)_2$ (4.42 mmol) and $(Ph_3P)_4Pd$ (0.045 mmol) in dry THF (70 mL), followed by distillation (105–108°C/0.1 Torr) of the acquired liquid, gave 960 mg (48%) of the *E* amide **89**, a colorless oil that displayed ir (neat): 1620, 1385, 1160, 775 cm^{-1}; ^1H nmr (80 MHz) δ: 0.15 (s, 9H, $^2J_{Sn-H}$ = 53 Hz), 0.25 (s, 9H, $^2J_{Sn-H}$ = 54 Hz), 1.00 (t, 3H, *J* = 7 Hz), 2.32 (q, 2H, *J* = 7 Hz), 2.92 (s, 6H); ^{13}C nmr (75.4 MHz) δ: −8.0 (q, $^1J_{Sn-C}$ = 319 Hz), −7.6 (q, $^1J_{Sn-C}$ = 327 Hz), 14.6 (q, $^3J_{Sn-C}$ = 8 Hz), 34.0 (q), 36.0 (t, $^2J_{Sn-C}$ = $^3J_{Sn-C}$ = 65 Hz), 38.0 (q), 151.4 (s), 162.0 (s), 173.4 (s); ^{119}Sn nmr (111.8 MHz) δ: −47.8; −50.5 (s, s, $^3J_{Sn-Sn}$ = 644 Hz). Exact Mass calcd. for $C_{12}H_{26}NOSn_2$ (M^+ − Me): 440.0058; found: 440.0052.

*(E)-*N,N*-Dimethyl-6-(*tert*-butyldimethylsiloxy)-2,3-bis(trimethylstannyl)-2-hexenamide (**90**)*

Reaction of *N,N*-dimethyl-6-(*tert*-butyldimethylsiloxy)-2-hexynamide (**46**) (159 mg, 0.59 mmol) with $(Me_3Sn)_2$ (0.59 mmol) and $(Ph_3P)_4Pd$ (0.008 mmol) in dry THF (20 mL), followed by column chromatography (20 g silica gel, 4:1 petroleum ether – EtOAc) of the

crude product and distillation (~170°C/0.1 Torr) of the acquired liquid, afforded 222 mg (63%) of the *E* amide **90**, a colorless oil that showed ir (neat): 1620, 1380, 1100, 840, 780 cm^{-1}; ^1H nmr (400 MHz) δ: 0.06 (s, 6H), 0.16, 0.25 (s, s, 9H each, $^2J_{Sn-H}$ = 54 Hz in each case), 0.91 (s, 9H), 1.57 (quintet, 2H, J = 6 Hz), 2.33–2.42 (m, 2H), 2.92 (s, 3H), 2.94 (s, 3H), 3.64 (t, 2H, J = 6 Hz); ^{13}C nmr (75.4 MHz) δ: −8.0 (q, $^1J_{Sn-C}$ = 327 Hz), −7.6 (q, $^1J_{Sn-C}$ = 328 Hz), −5.7 (q), 18.3 (s), 25.9 (q), 33.5 (t), 34.2 (q), 38.3 (q), 40.3 (t, $^2J_{Sn-C} = {}^3J_{Sn-C}$ = 63 Hz), 63.0 (t), 152.5 (s), 160.5 (s), 173.7 (s). Exact Mass calcd. for $C_{19}H_{42}NO_2SiSn_2$ (M^+ − Me): 584.1029; found: 584.1031.

Acknowledgements

We are grateful to the Natural Sciences and Engineering Research Council of Canada and to Merck Frosst Canada Inc. for generous financial support.

1. T.N. Mitchell, A. Amamria, H. Killing, and D. Rutschow. J. Organomet. Chem. **241**, C45 (1983).
2. T.N. Mitchell, A. Amamria, H. Killing, and D. Rutschow. J. Organomet. Chem. **304**, 257 (1986).
3. H. Killing and T.N. Mitchell. Organometallics, **3**, 1318 (1984).
4. T.N. Mitchell and U. Schneider. J. Organomet. Chem. **407**, 319 (1991).
5. I. Beaudet, J.-L. Parrain, and J.-P. Quintard. Tetrahedron Lett. **32**, 6333 (1991).
6. T.N. Mitchell, K. Kwetkat, D. Rutschow, and U. Schneider. Tetrahedron, **45**, 969 (1989).
7. E. Piers and R.T. Skerlj. J. Chem. Soc. Chem. Commun. 626 (1986).
8. R.M. Moriarty, R.K. Vaid, V.T. Ravikumar, T.E. Hopkins, and P. Farid. Tetrahedron, **45**, 1605 (1989).
9. E. Piers, J.M. Chong, and H.E. Morton. Tetrahedron, **45**, 363 (1989).
10. E. Piers, R.W. Friesen, and S.J. Rettig. Can. J. Chem. **70**, 1385 (1992).
11. S. Hara, H. Dojo, S. Takinami, and A. Suzuki. Tetrahedron Lett. **24**, 731 (1983).
12. A.G. Anderson, Jr., N.E.T. Owen, F.J. Freenor, and D. Erickson. Synthesis, 398 (1976).
13. E.J. Corey and P.L. Fuchs. Tetrahedron Lett. **36**, 3769 (1972).
14. E. Piers, T. Wong, and K.A. Ellis. Can. J. Chem. **70**, 2058 (1992).
15. J.K. Stille. Angew. Chem. Int. Ed. Engl. **25**, 508 (1986).
16. E. Piers and Y.-F. Lu. J. Org. Chem. **53**, 926 (1988).
17. E. Piers and K.A. Ellis. Tetrahedron Lett. **34**, 1875 (1993).
18. S. Cacchi, E. Morera, and G. Ortar. Tetrahedron Lett. **26**, 1109 (1985).
19. H. Watanabe, M. Kobayashi, K. Higuchi, and Y. Nagai. J. Organomet. Chem. **186**, 51 (1980).
20. E. Piers and R.T. Skerlj. J. Org. Chem. **52**, 4421 (1987).
21. E. Piers and A.V. Gavai. J. Org. Chem. **55**, 2374 (1990).
22. A. Bax, R.H. Griffey, and B.L. Hawkins. J. Magn. Reson. **55**, 301 (1983).
23. A. Bax and S. Subramanian. J. Magn. Reson. **67**, 565 (1986).
24. M.F. Summers, L.G. Marzilli, and A. Bax. J. Am. Chem. Soc. **108**, 4285 (1986).
25. A. Bax and M.F. Summers. J. Am. Chem. Soc. **108**, 2093 (1986).
26. H.G. Kuivila, K.-H. Tsai, and D.G.I. Kingston. J. Organomet. Chem. **23**, 129 (1970).
27. W.C. Still, M. Kahn, and A. Mitra. J. Org. Chem. **43**, 2923 (1978).
28. S.L. Spassov, V.S. Dimitrov, M. Agova, I. Kantschovska-Dimicoli, and R. Todorova-Momcheva. Org. Magn. Reson. **6**, 508 (1974).

Can. J. Chem. Downloaded from www.nrcresearchpress.com by 85.192.166.187 on 09/08/12
For personal use only.

Nouvelle méthode de synthèse de pyrroles sous micro-ondes

BOUALEM OUSSAID ET BERNARD GARRIGUES[1]

Laboratoire AMPERES-EP-52, Université Paul Sabatier, 118 Route de Narbonne, 31062 Toulouse Cedex, France

ET

MOHAMMED SOUFIAOUI

Université Mohammed V, Faculté des Sciences, Rabat, Avenue Ibn Batouta, Rabat, Maroc

Reçu le 20 mars 1994

BOUALEM OUSSAID, BERNARD GARRIGUES et MOHAMMED SOUFIAOUI. Can. J. Chem. **72**, 2483 (1994).

La déshydrogénation de pyrrolidines effectuée en présence de dioxyde de manganèse, sous irradiation micro-ondes, permet de préparer dans des conditions douces, des pyrroles substitués.

BOUALEM OUSSAID, BERNARD GARRIGUES, and MOHAMMED SOUFIAOUI. Can. J. Chem. **72**, 2483 (1994).

The dehydrogenation of pyrrolidines by manganese dioxide, under microwave irradiation, provides a mild method for the preparation of substituted pyrroles.

Can. J. Chem. Downloaded from www.nrcresearchpress.com by 85.192.166.187 on 09/08/12
For personal use only.

Introduction

Depuis leur découverte, les dérivés pyrroliques ont pris une grande extension. Ces molécules présentent des propriétés phytosanitaires (1–3) ou pharmacologiques (4–7) importantes. Le noyau pyrrole se trouve incorporé à de nombreux produits naturels très importants, tels que les pigments biliaires (8) ou les porphyrines (9).

De nombreuses méthodes de synthèse de dérivés pyrroliques sont décrites dans la littérature. On retiendra, parmi les plus connues, les méthodes de Hantzsch (10, 11), de Knorr (12, 13), de Paal-Knorr (14, 15), ou celles faisant intervenir des ylures de nitriles (16), des acétyléniques (17), des vinylazirines (18), des furanes (19). Les dérivés pyrroliques disubstitués, uniquement en positions 3 et 4, sont d'un accès difficile. On peut les préparer à partir du succinate d'éthyle (20–22), du tosylmethyl isonitrile (23–25) ou enfin par retro Diels–Alder (26–28).

La synthèse de pyrrole à partir de pyrrolidine n'a été étudiée que dans deux cas dans la littérature. La photolyse de pyrrolidines en présence de benzophénone, comme accepteur d'hydrogène, conduit au pyrrole correspondant (29). Le 1,2,5-triphenylpyrrole a pu être obtenu par déshydrogénation de la pyrrolidine de départ, au reflux du *p*-cymène, et en présence de chloranil (30). Nous proposons dans cette étude une nouvelle méthode de synthèse de composés pyrroliques, par oxydation avec du dioxyde de manganèse, sous irradiation micro-ondes.

Partie Expérimentale

Généralités

Points du fusion, non corrigés en capillaires (appareil Tottoli, Büchi). Spectres IR : en suspension dans le Nujol ou sous forme de film, entre lames CaF_2, enregistrés sur un spectromètre Perkin–Elmer 257. Spectres de RMN ^1H : déplacements chimiques en ppm par rapport au TMS; constantes de couplage en Hz; appareil Bruker AC 250. Les analyses élémentaires ont été effectuées par le service de microanalyse de l'École Nationale Supérieure de Chimie de Toulouse. En outre, les chromatographies analytiques sont effectuées sur plaque de silice Riedel-de-Haen réf. 37333.

Au cours de ce travail, nous avons utilisé comme four domestique à micro-ondes (multimode) le Brandt ME 210 B à la puissance maximum de 850 W; utilisation du plateau tournant et de petits Erlenmeyers de Pyrex de 25 mL.

Composés **1**a–**1**j

Les pyrrolidines **1***a* et **1***b* sont des produits commerciaux; **1***c* et **1***d* ont été préparés par débenzylation (31) de la pyrrolidine obtenue d'après la littérature (32, 33); **1***e* par réduction par $LiAlH_4$ de **1***c*; **1***f* par traitement à la soude (26) de **1***c*; **1***g* après méthylation (34) de **1***c*; **1***h* après débenzylation (31) puis méthylation (34) de la pyrrolidine préparée d'après la référence 32; **1***i* d'après la littérature (33) et enfin **1***j* par action du ditosylate sur **1***e*.

Composés **2***a*–**2***j*

Méthode générale : 0,01 mol de **1***a*–**1***j* est solubilisée dans 20 mL de dichlorométhane. On rajoute à cette solution 0,05 mol de dioxyde de manganèse et 3 g de silice. La suspension est évaporée à sec, puis, irradiée sous micro-ondes; le produit recherché est obtenue après trois lavages avec 100 mL de dichlorométhane après avoir été soniqué chaque fois 5 min au bac à ultrasons. Après filtration, le solvant est évaporé et le produit isolé après séparation sur une colonne de silice avec un rendement de 58–96% (tableau 1).

2*a* : Paramètres comparables au produit commercial (F = 62°C (35)).

2*b* : IR (entre lames) : 1703 (C═O) cm^{-1}. RMN ^1H comparable aux données de la littérature (36).

2*c* : F = 143°C (litt. (22) F 151–152°C). RMN ^1H comparable aux données de la littérature (22). IR (KBr) : 3160 cm^{-1} (NH), 1740 (C═O) cm^{-1}.

2*d* : F = 247°C (litt. (23) F 243–245°C). RMN ^1H ($CDCl_3$) : 7,34 (s, 2H, pyr.); 3,69 (s, 6H, CH_3). IR (KBr) : 3148 cm^{-1} (NH), 1732 (C═O) cm^{-1}.

2*e* : F = 50–52°C. RMN ^1H ($CDCl_3$) : 6,51 (s, 2H, CH); 4,48 (s, 4H, CH_2); 3,54 (s, 3H, CH_3); 3,40 (s, 2H, OH). Analyses $C_7H_{11}NO_2$, MM = 141,08. Calc. : C 59,59; H 7,79; N 9,92; tr. : C 60,19; H 7,91; N 10,17.

2*f*: F > 300 (litt. (25) F > 300). IR (KBr) : 3172 cm^{-1} (NH); 1589 (C═O) cm^{-1}. RMN ^1H ($CDCl_3$) : 12,13 (s, 1H, NH); 7,60 (d, 2H, ^3J = 2,9, CH).

2*g* : F : 43°C. IR (KBr) : 1736 (C═O) cm^{-1}. RMN ^1H ($CDCl_3$) : 7,13 (s, 2H, CH); 4,25 (q, 4H, ^3J = 7,2, CH_2); 3,63 (s, 3H, CH_3N); 1,30 (t, 6H, ^3J = 7,2, CH_3). Analyses $C_{11}H_{15}NO_4$, MM = 225,23. Calc. : C 58,65; H 6,71; N 6,21; tr. : C 58,49; H 6,51; N 6,40.

2*h* : F : 79°C. IR (KBr) : 1728 (C═O) cm^{-1}. RMN ^1H ($CDCl_3$) : 7,57–7,50 (m, 2H, Ar); 7,20–7,40 (m, 4H, Ar); 6,65 (d, 1H, ^4J = 2,3, CH-Ph); 3,78 (s, 3H, CH_3O); 3,65 (s, 3H, CH_3N). Analyses $C_{13}H_{13}NO_2$, MM = 215,23. Calc. : C 72,53; H 6,08; N 6,50; tr. : C 72,61; H 6,24; N 6,66.

2*i* : F : 84°C. IR (KBr) : 1658 (C═O) cm^{-1}. RMN ^1H ($CDCl_3$) : 7,50–7,20 (m, 11H); 6,65 (d, 1H, ^4J = 2,7, CH-Ph); 5,13 (s, 2H, CH_2); 2,27 (s, 3H, CH_3). Analyses $C_{19}H_{17}NO$, MM = 275,33. Calc. : C 82,87; H 6,22; N 5,08; tr. : C 82,67; H 6,43; N 5,27.

2*j* : IR (entre lames) : 1640 (C═O) cm^{-1}. RMN ^1H ($CDCl_3$) : 6,54 (s, 2H, CH); 4,25 (s, 4H, CH_2); 3,68–3,53 (m, 15H, CH_3 et CH_2). RMN

1. Auteur à qui adresser toute correspondance.

TABLEAU 1. Pyrroles préparés

Composé	R^1	R^2	R^3	R^4	Rdt (%)	Durée d'irradiation (puissance 850 W) en minutes
2*a*	Ph	H	H	H	96	3
2*b*	CH_2Ph	CO_2Et	H	H	87	5
2*c*	H	H	CO_2Et	CO_2Et	71	6
2*d*	H	H	CO_2Me	CO_2Me	83	5
2*e*	Me	H	CH_2OH	CH_2OH	62	3
2*f*	H	H	CO_2H	CO_2H	75	5
2*g*	Me	H	CO_2Et	CO_2Et	82	6
2*h*	Me	H	CO_2Me	Ph	86	7
2*i*	CH_2Ph	H	COMe	Ph	58	5
2*j*	CH_3	H	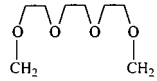		65	7

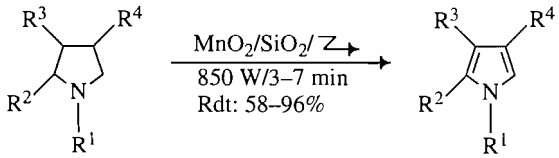

SCHÉMA 1

^{13}C {^1H} : 157,0 (s, C=N); 125,3 (s, C2, C5, pyr.); 120,7 (s, C3, C4, pyr.); 70,4 (s, CH_2); 69,5 (s, CH_2); 60,6 (s, CH_2); 35,9 (s, CH_3). Spectrographie de masse (Ionisation chimique / NH_3) : [MH^+] = 250 (100 %). Analyses $C_{13}H_{19}N_3O_2$, MM = 249,30. Calc. : C 62,22; H 7,68; N 16,85; tr. : C 62,52; H 7,58; N 16,71.

Résultats

Nous avons été amenés à réaliser la synthèse des composés pyrroliques **2***a*–**2***j* à partir des pyrrolidines **1***a*–**1***j* (Schéma 1, Tableau 1). Les produits de départ sont, soit des produits commerciaux, soit des produits déjà décrits dans la littérature, ou obtenus par débenzylation (31) suivie dans certains cas d'une méthylation (34).

Depuis environ 8 ans de nombreuses publications sont consacrées à l'utilisation de fours micro-ondes en chimie, et les fours domestiques sont en passe de devenir un outil courant de laboratoire. On retiendra les cinq mises au point (37–41). L'utilisation des micro-ondes a été étendue également à la chimie hétérocyclique (42–44).

Nous avons pu accéder en quelques minutes (3–7), dans un four à micro-ondes commercial, aux dérivés pyrroliques attendus. Après imprégnation de la pyrrolidine de départ sur un support de silice, par déshydrogénation effectuée en présence de cinq équivalents de dioxyde de manganèse, on obtient les composés pyrroliques **2***a*–**2***j*. La structure des composés obtenus a été confirmée par RMN, IR, analyse élémentaire ou spectrographie de masse pour **2***j*.

Sauf dans le cas de **2***b*, les composés obtenus ne présentent pas de substituants sur les carbones en α de l'azote. De telles molécules sont susceptibles de se polymériser par voie électrochimique.[2]

Le macrocycle **2***j* est le premier exemple de macrocycle pyrrolique disubstitué en positions 3 et 4.

Les composés ont pu être obtenus avec un excellent rendement (58–96%) bien supérieur à celui existant dans la littérature et qui fait appel à la photodeshydrogénation de pyrrolidines (30–50%).

La réaction d'oxydation par MnO_2 peut être réalisée par chauffage classique au reflux du toluène. Dans le cas de **2***a* la réaction est terminée après 5 h de chauffage avec un rendement de 71% alors que sous micro-ondes il est de 96% après seulement 3 min d'irradiation.

Cette augmentation du rendement sous micro-ondes résulte du moindre séjour des produits à haute température, mais aussi de l'absence de surchauffe évitant les phénomènes de décomposition locale.

En conclusion, nous présentons dans ce travail une nouvelle méthode de synthèse de pyrroles qui sont obtenus par action du dioxyde de manganèse sur les pyrrolidines. L'activation sous micro-ondes dans un four domestique implique un bref chauffage, évite l'utilisation de solvant et conduit à de bons rendements.

Remerciement

Nous remercions A. Colomer pour l'enregistrement des spectres IR.

1. H. Hasegawa, K. Mogi, N. Shioiri, S. Sato et T. Katori. Eur. Pat. Appl. EP 337, 277 (1990); Chem. Abstr. **112**, 198117 (1990).
2. E. Differding, W. Frick, R.W. Lang, P. Martin, C. Schmit, S. Veenstra et H. Greuter. Bull. Soc. Chim. Belg. **99**, 647 (1990).
3. D. Wollweber et W. Brandes. Eur. Pat. Appl. EP 318, 704 (1989); Chem. Abstr. **112**, 7360 (1990).
4. G. Martinez, D. Hirschfeld, P. Maloney et D. Yand. J. Med. Chem. **32**, 890 (1989).
5. J. Liebscher, A. Knoll, A. Uschmajew, A. Rolfs, D. Lohmann, G. Faust, E. Margenstern et P. Scharfenbert. Eur. Pat. Appl. EP 431, 371 (1989); Chem. Abstr. **115**, 92063 (1991).
6. G. Dannhardt, L. Sterndl et M. Lehr. Eur. Pat. Appl. EP 397, 175, (1990); Chem. Abstr. **114**, 163999 (1991).
7. B. Bray, P.H. Mathies, R. Naef, D.R. Solas, T. Tidwell, D.R. Artis et J.M. Muchowski. J. Org. Chem. **55**, 6317 (1990).
8. R.A. Jones et G.P. Bean. The chemistry of pyrroles. Academic Press, London. 1977.
9. R.J. Sundberg. *Dans* Comprehensive heterocyclic chemistry. Vol. 4. *Édité par* A.R. Katritsky et C.W. Rees. Pergamon Press, Oxford. 1984.
10. A. Hantzch. Ber. Dtsch. Chem. Ges. **23**, 1474 (1890).
11. M.W. Roomi et S.F. MacDonald. Can. J. Chem. **48**, 1689 (1970).
12. L. Knorr et H. Lange. Ber. Dtsch. Chem. Ges. **35**, 2998 (1902).

2. F. Soulet, P.L. Fabre, P. Castan, B. Oussaid et B. Garriques. À paraître.

Can. J. Chem. Downloaded from www.nrcresearchpress.com by 85.192.166.187 on 09/08/12
For personal use only.

13. H. Fisher et F. Fink. Z. Physiol. Chem. **280**, 123 (1944).
14. W. Keller-Schierlein, M.L. Mihailovic et V. Prelog. Helv. Chim. Acta, **41**, 220 (1958).
15. H.S. Broadbent, S. Burnham, R.K. Olsen et R.M. Shelley. J. Heterocycl. Chem. **5**, 757 (1968).
16. K.E. Schulte, J. Reisch et H. Walker. Chem. Ber. **98**, 98 (1965).
17. B.S. Thyagarajan et P.E. Glaspy. J. Chem. Soc. Chem. Commun. 515 (1979).
18. F. Bellamy. J. Chem. Soc. Chem. Commun. 998 (1978).
19. J.K. Zurjew. Zh. Obshch. Khim. **8**, 1934 (1938).
20. E.C. Kornfeld et R.G. Jones. J. Org. Chem. **19**, 1671 (1954).
21. R. Olsen et H.R. Snyder. J. Org. Chem. **30**, 184 (1965).
22. E. Legoff et R.W. Kaesler. J. Org. Chem. **48**, 4399 (1983).
23. A.M. van Leusen, H. Siderius, B.E. Hoogenboom et D. van Leusen. Tetrahedron Lett. 5337 (1972).
24. J. Leroy. J. Fluorine Chem. **53**, 61 (1991).
25. D.P. Arnold, L.J. Nitschinsk, C.H. Kennard et G. Smith. Aust. J. Chem. **44**, 323 (1991).
26. J.K. Groves, N. Cundasawmy et M.J. Anderson. Can. J. Chem. **51**, 1089 (1973).
27. J. Leroy, D. Cantacuzene et C. Wakselman. Synthesis, 313 (1982).
28. R.W. Kaesler et E. Legoff. J. Org. Chem. **47**, 4779 (1982).
29. J. Cossy et J.P. Pete. Tetrahedron Lett. 4941 (1978).
30. P.L. Southwick, D.I. Sapper et L.A. Pursglove. J. Am. Chem. Soc. **72**, 4940 (1950).
31. R.J. Bergeron, P.S. Burton, K.A. McGovern et S.J. Kline. Synthesis, 732 (1981).
32. Y. Terao, H. Kokati et N. Imai. Chem. Pharm. Bull. **33**, 2762 (1985).
33. A. Padwa, Y.Y. Chen, W. Dent et H.J. Nimmesgen. J. Org. Chem. **50**, 4006 (1985).
34. J.A. de Groot, R. van der Steen et J. Lugtenburg. Recl. Trav. Chim. Pays-Bas, **102**, 347 (1983).
35. N. Elming et N. Clauson-Kaas. Acta Chem. Scand. **6**, 867 (1952).
36. G.H. Walizei et E. Breitmaier. Synthesis, 337 (1989).
37. R.G. Giguere. *Dans* Organic synthesis: theory and applications. Vol. 1. *Édité par* T. Hudlicky. JAI Press, London. pp. 153–172. 1989.
38. D.M. Mingos et D.R. Baghurst. Chem. Soc. Rev. **20**, 1 (1991).
39. R.A. Abramovitch. Org. Prep. Proced. Int. **23**, 685 (1991).
40. G. Bram, A. Loupy et D. Villemin. Solid supports and catalysts in organic synthesis. Prentice Hall, London. 1992. Chap. XII. p. 302.
41. D.M. Mingos. Res. Chem. Intermed. **20**, 85 (1994).
42. D. Villemin et A. Ben Alloum. Synth. Commun. **22**, 1351 (1992).
43. D. Villemin, B. Martin et B. Garrigues. Synth. Commun. **23**, 2251 (1993).
44. A. Molina, J.J. Vaquero, J.L. Garcia-Navio et J. Alvarez-Builla. Tetrahedron Lett. **34**, 2673 (1993).

Can. J. Chem. Downloaded from www.nrcresearchpress.com by 85.192.166.187 on 09/08/12
For personal use only.

Speed of sound, viscosity, and refractive index of multicomponent systems: analysis of experimental data from the Bertrand–Acree–Burchfield equation

J.D. PANDEY,[1] P. JAIN, AND V. VYAS
Department of Chemistry, University of Allahabad, Allahabad – 211 002, U.P., India
Received February 22, 1994

J.D. PANDEY,[1] P. JAIN, and V. VYAS. Can. J. Chem. **72**, 2486 (1994).

The speed of sound in and the viscosity and refractive index of two ternary mixtures (I) toluene + *n*-heptane + *n*-hexane and (II) cyclohexane + *n*-heptane + *n*-hexane, and six binary combinations of these constituents have been measured experimentally. The excess values of these properties are calculated and the results are analysed using the Bertrand–Acree–Burchfield (BAB) model. All the experimental and theoretical values are in fairly reasonable agreement.

J.D. PANDEY,[1] P. JAIN, et V. VYAS. Can. J. Chem. **72**, 2486 (1994).

On a déterminé expérimentalement la vitesse du son dans ainsi que la viscosité et l'indice de réfraction de deux mélanges tertiaires ((I) toluène + *n*-heptane + *n*-hexane et (II) cyclohexane + *n*-heptane + *n*-hexane) ainsi que de six des mélanges binaires qui y contribuent. On a calculé les valeurs en excès et on a analysé les résultats à la lumière du modèle théorique de Bertrand–Acree–Burchfield (BAB). On a trouvé que l'accord entre les valeurs expérimentales et théoriques de toutes les propriétés en excès est raisonnable.

[Traduit par la rédaction]

Can. J. Chem. Downloaded from www.nrcresearchpress.com by 65.111.164.53 on 09/08/12
For personal use only.

Introduction

A thorough knowledge of thermodynamic and transport properties of multicomponent liquid systems is essential in many industrial applications such as design calculation, heat transfer, mass transfer, and fluid flow etc. Various empirical, semi-empirical, and group contribution methods for computing the thermodynamic properties of multicomponent systems have been thoroughly reviewed by Acree (1), Singh et al. (2–4) used the graphical–theoretical approach to analyse the experimental data on molar excess volume and molar excess enthalpies of ternary non-electrolyte solutions. Flory's statistical mechanical theory (5) in combination with the method used by Patterson and Rastogi (6), has been successfully used to evaluate activity coefficient (7), heat of mixing (7), surface tension (8–10), sound velocity (11–13), excess volume (14, 15), and viscosity (16) of various multicomponent liquid systems. In all these methods, properties of multicomponent systems have been calculated using properties of the pure components. However, a more promising approach to predict the thermodynamic and physical properties of multicomponent liquid systems using binary combinations of their constituents has been developed by Bertrand, Acree, and Burchfield (1, 17, 18). There are a number of equations (1) to compute excess enthalpy, excess free energy, and other excess thermodynamic properties of multicomponent systems from the excess properties of these binary combinations, provided the composition of the binary combinations is similar to the ternary combinations. Bertrand et al. modified this approach by considering binary systems with components at the same molar ratio as in the ternary systems and evaluated excess enthalpy, excess Gibbs free energy, and excess volume for the ternary systems. The Bertrand–Acree–Burchfield method has not been applied to transport properties. Many important properties such as sound velocity, isothermal compressibility, internal pressure, surface tension etc. have not been estimated using this approach. Recently Acree and Teng (19) tested the applicability and limitations of a newly derived semi-empirical relationship (20) that includes contributions from both two-body and three-body interactions.

This work is to determine density, sound velocity, viscosity, and refractive index of two ternary non-electrolyte solutions (I) toluene + *n*-heptane + *n*-hexane and (II) cyclohexane + *n*-heptane + *n*-hexane. To use the Bertrand–Acree–Burchfield method to estimate sound velocity, refractive index, and viscosity of these ternary systems, we measured the same properties in the respective binary mixtures. The theoretical sound velocity, refractive index, and viscosity values obtained from the Bertrand–Acree–Burchfield method were compared to the experimental values. A slight modification in the Bertrand–Acree–Burchfield method was adopted.

Experimental

AnalaR grade toluene, *n*-heptane, *n*-hexane, and cyclohexane were obtained from M/S BDH Chemicals Ltd., Poole, England. These were purified by double distillation and dried in accordance with the usual procedure. All measurements were carried out while using a thermostatically-controlled water-bath where temperature had been set and maintained by a Beckmann thermometer, which was calibrated against a platinum resistance thermometer. The variation in the temperature was not allowed to exceed ±0.01°C during the measurements.

The speed of sound (c) in all liquid systems was measured using an ultrasonic interferometer. To determine the velocity of sound a single crystal-controlled variable path ultrasonic interferometer having a frequency of 2.0 MHz has been used. This method has been described in earlier papers (21, 22), and the estimated error is found to be ±0.07%.

Viscosities (η) of the various liquid systems were determined using a pre-calibrated Ubbelhode-type viscometer. This method is based on the measurement of the time in which a constant volume of liquid flows through a capillary. Uncertainty in the viscosity measurement has been found to be ±0.01%.

The refractive indices of various liquid systems have been measured using Abbe's refractometer. The temperature was kept constant by maintaining a constant flow of water from a thermostat through the outer jacket of the cell. Measured refractive indices were found to be accurate to ±0.0002 units. Other experimental details have been discussed in an earlier paper (17).

Theoretical

A number of equations have been proposed (1–19) to predict the thermodynamic excess properties of multicomponent systems. These methods have been critically reviewed by Acree

[1]Author to whom correspondence may be addressed.

Can. J. Chem. Downloaded from www.nrcresearchpress.com by 65.111.164.53 on 09/08/12
For personal use only.

(1). However, the most accurate method to estimate the physical and thermodynamic excess properties was developed by Bertrand, Acree, and Burchfield (17–19). They have developed an equation based on a model ternary system to study the thermodynamic properties of solute in simple binary solvents. This equation obeys the general mixing equation,

$$[1]\qquad \Delta Z^{ex}_{123} = (n_1\gamma_1 + n_2\gamma_2 + n_3\gamma_3)^{-1}(n_1\gamma_1 n_2\gamma_2 A_{12} + n_1\gamma_1 n_3\gamma_3 A_{13} + n_2\gamma_2 n_3\gamma_3 A_{23})$$

where Z_{ij} represents any extensive thermodynamic property described in terms of interaction parameters A_{ij} and weighting factor γ_i. By suitable manipulations, eq. [1] can be rearranged to

$$[2]\qquad \Delta Z^{ex}_{123} = \frac{\{(n_1+n_2)(f_1+f_2)x_1^*x_2^*\gamma_1\gamma_2 A_{12}\}}{(x_1^*\gamma_1 + x_2^*\gamma_2)} + \{\frac{(n_1+n_3)(f_1+f_3)x_1^*x_3^*\gamma_1\gamma_3 A_{13}\}}{(x_1^*\gamma_1 + x_3^*\gamma_3)} + \{\frac{(n_2+n_3)(f_2+f_3)x_2^*x_3^*\gamma_2\gamma_3 A_{23}\}}{(x_2^*\gamma_2 + x_3^*\gamma_3)}$$

where

$$[3]\qquad f_i = \frac{x_i\gamma_i}{(x_1\gamma_1 + x_2\gamma_2 + x_3\gamma_3)}$$

and the subscript * represents the composition of a binary system which would be formed if all the third components were removed, so that for an i–j system,

$$[4]\qquad x_i^* = (1 - x_j) = \frac{x_i}{(x_i + x_j)}$$

Review of eq. [2] shows that for the systems obeying this equation, the properties of contributing binary systems would obey (per mole of ternary solution) the following equation:

$$[5]\qquad \Delta\bar{Z}^{ex}_{ij} = \frac{x_i^*x_j^*\gamma_i\gamma_j A_{ij}}{(x_i^*\gamma_i + x_j\gamma_j)}$$

For one mole of ternary solution eq. [2] can be rearranged to

$$[6]\qquad \Delta\bar{Z}^{ex}_{123} = (x_1+x_2)(f_1+f_2)(\Delta\bar{Z}^{ex}_{12})^* + (x_1+x_3)(f_1+f_3)(\Delta\bar{Z}^{ex}_{13})^* + (x_2+x_3)(f_2+f_3)(\Delta\bar{Z}^{ex}_{23})^*$$

or in general, for multicomponent systems,

$$[7]\qquad \Delta\bar{Z}^{ex}_{123....N} = \sum_{i=1}^{N}\sum_{j>i}(x_i+x_j)(f_i+f_j)(\Delta\bar{Z}^{ex}_{ij})^*$$

A number of methods have been suggested for the evaluation of weighting factors which are a rough measure of the skew of the binary excess mixing property from a symmetric curve with an extremum at the equimolar composition. A method for the calculation of the ratio of raw weighting factors has been given by Bertrand et al. (15).

$$[8]\qquad \gamma_i = (100N)\Big/\left[\frac{\gamma_1^{raw}}{\gamma_i^{raw}} + \frac{\gamma_2^{raw}}{\gamma_i^{raw}} + \frac{\gamma_3^{raw}}{\gamma_i^{raw}} + \ldots + \frac{\gamma_N^{raw}}{\gamma_i^{raw}}\right]$$

In a reasonable modified approach volume fraction can be used in place of weighted mole fractions and the equation takes the following form:

$$[9]\qquad \Delta Z^{E}_{12....N} = \sum_{i=1}^{N}\sum_{j>i}(x_i+x_j)(\phi_i+\phi_j)(\Delta Z^{E}_{ij})$$

where x_i and x_j are the mole fractions of multicomponent systems; and ϕ_i and ϕ_j are their respective volume fractions and ΔZ^{E}_{ij} can be more appropriately taken as the experimental excess property of the constituent binary combinations at the same molar ratio of the components as in a multicomponent system.

In subsequent studies eq. [9] has been used to determine the excess ultrasonic velocity, excess viscosity, and excess refractive indices of two ternary systems for which eq. [9] takes the form,

$$[10]\qquad (\Delta c^{E}_{123}) = \sum_{i=1}^{2}\sum_{j>i}(x_i+x_j)(\phi_i+\phi_j)(\Delta c^{E}_{ij})$$

$$[11]\qquad (\Delta\eta^{E}_{123}) = \sum_{i=1}^{2}\sum_{j>i}(x_i+x_j)(\phi_i+\phi_j)(\Delta\eta^{E}_{ij})$$

$$[12]\qquad (\Delta n^{E}_{123}) = \sum_{i=1}^{2}\sum_{j>i}(x_i+x_j)(\phi_i+\phi_j)(\Delta n^{E}_{ij})$$

Values of the sound velocity, viscosity, and refractive index are then calculated using the following equations:

$$[13]\qquad c = c_{id} + (\Delta c^{E}_{123})$$

$$[14]\qquad \eta = \eta_{id} + (\Delta\eta^{E}_{123})$$

$$[15]\qquad n = n_{id} + (\Delta n^{E}_{123})$$

where

$$[16]\qquad c_{id} = x_1c_1 + x_2c_2 + x_3c_3$$

$$[17]\qquad \eta_{id} = x_1\eta_1 + x_2\eta_2 + x_3\eta_3$$

$$[18]\qquad n_{id} = x_1n_1 + x_2n_2 + x_3n_3$$

The results so obtained were compared with the experimental findings and with the results of those theories which utilise the properties of single components to predict the thermodynamic properties of multicomponent liquid mixtures.

Finally, the theoretically predicted results were examined in the light of average percentage deviations (σ) and standard error (δ) calculated from the expressions:

$$[19]\qquad \sigma = \frac{1}{N}\sum_{i=1}^{N}[(Z_{i_{expt}} - Z_{i_{calc}})/Z_{i_{expt}}] \times 100$$

and

$$[20]\qquad \delta = \frac{1}{N}\sum_{i=1}^{N}[(Z_{i_{expt}} - Z_{i_{calc}}) \times 100/Z_{i_{expt}}]^2$$

where Z is any measured and theoretically computed property and N is the total number of sets.

Results and discussion

Sound velocity, viscosity, and refractive index of two ternary liquid mixtures — toluene + *n*-heptane + *n*-hexane (I) and cyclohexane + *n*-heptane + *n*-hexane (II) have been predicted using the respective experimental excess properties of their constituent binary liquid mixtures. In this paper a modified Bertrand–Acree–Burchfield approach has been utilized, where weighted mole fractions have been replaced by volume fractions and values of the experimental excess properties for constituent binary liquid systems have been used at the same molar ratio as these are in the ternary liquid mixtures. The values of sound velocity (c), viscosity (η), and refractive index (n) are presented in Table 1.

Mole fractions of the constituent binary mixtures were calculated to ensure that they are in the same molar ratio as in the ternary liquid mixture. The values of c, η, and n at the new mole fractions were determined graphically from the experimental values. Using these values the excess properties of binary liquid mixtures were evaluated. These values, compiled in Tables 2*b*, 2*c*, 2*d* and 3*b*, 3*c*, 3*d* were then used to predict Δc^E_{123}, $\Delta\eta^E_{123}$, and Δn^E_{123} for systems I and II using eqs. [10] to [12]. Respective values of sound velocity, viscosity, and refractive index of mixtures were then calculated using eqs. [13] to [15]. These values are compiled in Tables 2*a* and 3*a* for systems I and II respectively, and their percentage deviations were recorded in Tables 4 and 5. A close look at Tables 4 and 5 reveals that the percentage deviations in the computation of sound velocity is 1.92 and 0.70 respectively for

TABLE 1. Parameters of the pure components at 298.15 K

Component	Ultrasonic velocity (m s^{-1})	Viscosity × 10^3 (N s m^{-2})	Refractive index
Toluene	1304.0	0.6036	1.4961
Cyclohexane	1253.3	0.8950	1.4266
n-Heptane	1131.0	0.3860	1.3852
n-Hexane	1076.0	0.2940	1.3723

TABLE 2.

(*a*) Computed ultrasonic velocity, viscosity, and refractive index of the ternary system — toluene (x_1) + *n*-heptane (x_2) + *n*-hexane (x_3) at 298.15 K

x_1	x_2	Δc^E (m s^{-1})	c_{calcd} (m s^{-1})	$\Delta\eta^E \times 10^3$ (N s M^{-2})	$\eta_{calcd} \times 10^3$ (N s m^{-2})	Δn^E	n_{calcd}
0.1210	0.1838	8.0	1111.6	—	—	−0.0153	1.3744
0.1459	0.2011	−0.6	1108.4	−0.0243	0.3302	−0.0147	1.3784
0.1698	0.2170	−5.8	1108.7	−0.0284	0.3344	−0.0145	1.3816
0.1929	0.2358	−10.9	1108.8	−0.0314	0.3399	−0.0140	1.3855
0.2160	0.2544	−4.9	1109.4	−0.0324	0.3472	−0.0141	1.3884
0.2390	0.2726	−20.0	1111.2	−0.0378	0.3501	−0.0146	1.3910
0.3641	0.2875	−24.8	1112.5	−0.0405	0.3560	−0.0147	1.3942
0.2849	0.3060	−28.1	1114.9	−0.0405	0.3637	−0.0140	1.3977
0.3088	0.3222	−31.7	1117.4	−0.0405	0.3690	−0.0144	1.4005
0.3330	0.3391	−33.2	1122.2	−0.0436	0.3765	−0.0142	1.4039
0.3559	0.3553	−33.3	1128.9	−0.0446	0.3846	−0.0132	1.4080
0.3760	0.3735	−31.0	1137.2	−0.0446	0.3931	−0.0120	1.4119
0.3983	0.3908	−26.9	1148.1	−0.0405	0.4042	−0.0102	1.4166
0.4204	0.3974	−22.8	1158.0	−0.0375	0.4142	−0.0087	1.4211
0.4433	0.4045	−18.6	1168.5	−0.0344	0.4245	−0.0108	1.4219

(*b*) Excess sound velocity, excess viscosity, and excess refractive index of the binary system — *n*-heptane (x_1) + toluene (x_2) at different molar ratios

x_1	c_{exptl} (m s^{-1})	Δc^E_{ij} (m s^{-1})	$\eta_{exptl} \times 10^3$ (N s m^{-2})	$\Delta\eta^E_{ij} \times 10^3$ (N s m^{-2})	n_{exptl}	Δn^E_{ij}
0.6030	1195.5	−4.2	0.4535	−0.0110	1.4170	−0.0125
0.5790	1199.0	−4.7	0.4580	−0.0100	1.4190	−0.0131
0.5610	1201.5	−5.4	0.4615	−0.0110	1.4215	−0.0127
0.5500	1203.0	−5.9	0.4640	−0.0100	1.4225	−0.0129
0.5408	1204.5	−5.9	0.4655	−0.0110	1.4235	−0.0129
0.5328	1206.0	−5.8	0.4670	−0.0110	1.4240	−0.0133
0.5212	1207.5	−6.3	0.4690	−0.0110	1.4255	−0.0131
0.5179	1208.0	−6.4	0.4700	−0.0100	1.4260	−0.0130
0.5106	1209.0	−6.7	0.4710	−0.0110	1.4265	−0.0133
0.5045	1210.0	−6.7	0.4720	−0.0110	1.4270	−0.0135
0.4996	1211.0	−6.6	0.4730	−0.0110	1.4280	−0.0130
0.4983	1211.5	−6.3	0.4735	−0.0110	1.4280	−0.0132
0.4953	1212.0	−6.3	0.4740	−0.0110	1.4280	−0.0135
0.4859	1213.5	−6.4	0.4760	−0.0110	1.4290	−0.0136
0.4771	1215.0	−6.5	0.4775	−0.0110	1.4300	−0.0136

Can. J. Chem. Downloaded from www.nrcresearchpress.com by 65.111.164.53 on 09/08/12
For personal use only.

TABLE 2. (*Concluded*)

(*c*) Excess sound velocity, excess viscosity, and excess refractive index of the binary system — *n*-heptane (x_1) + *n*-hexane (x_2) at different molar ratios

x_1	c_{exptl} (m s^{-1})	Δc^E_{ij} (m s^{-1})	$\eta_{exptl} \times 10^3$ (N s m^{-2})	$\Delta\eta^E_{ij} \times 10^3$ (N s m^{-2})	$n_{exptl.}$	Δn^E_{ij}
0.2091	1086.8	−1.3	0.3150	0.0020	1.3745	−0.0005
0.2355	1087.6	−1.8	0.3160	0.0000	1.3750	−0.0003
0.2614	1088.4	−2.4	0.3170	−0.0010	1.3755	−0.0002
0.2921	1089.6	−2.9	0.3190	−0.0020	1.3760	−0.0001
0.3245	1090.9	−3.4	0.3205	−0.0040	1.3770	0.0005
0.3582	1092.1	−4.0	0.3230	−0.0040	1.3780	0.0011
0.3907	1093.6	−4.3	0.3250	−0.0050	1.3785	0.0012
0.4279	1095.5	−4.4	0.3280	−0.0050	1.3795	0.0017
0.4662	1097.6	−4.4	0.3310	−0.0060	1.3805	0.0022
0.5084	1100.4	−3.9	0.3345	−0.0060	1.3815	0.0026
0.5516	1103.5	−3.1	0.3390	−0.0060	1.3825	0.0031
0.5986	1107.0	−2.2	0.3440	−0.0050	1.3835	0.0035
0.6496	1111.0	−0.9	0.3500	−0.0040	1.3850	0.0043
0.6856	1114.0	0.1	0.3545	−0.0020	1.3855	0.0044
0.7266	1117.2	1.1	0.3595	−0.0010	1.3870	0.0053

(*d*) Excess sound velocity, excess viscosity, and excess refractive index of the binary system — toluene (x_1) + *n*-hexane (x_2) at different molar ratios

x_1	c_{exptl} (m s^{-1})	Δc^E_{ij} (m s^{-1})	$\eta_{exptl} \times 10^3$ (N s m^{-2})	$\Delta\eta^E_{ij} \times 10^3$ (N s m^{-2})	$n_{exptl.}$	Δn^E_{ij}
0.1483	1120.0	9.7	0.3210	−0.0120	1.3900	−0.0008
0.1826	1124.0	5.9	0.3330	−0.0140	1.3940	−0.0010
0.2169	1128.0	2.1	0.3400	−0.0160	1.3980	−0.0013
0.2524	1132.0	−2.0	0.3480	−0.0190	1.4030	−0.0007
0.2897	1136.0	−6.5	0.3600	−0.0170	1.4070	−0.0014
0.3286	1141.0	−10.3	0.3660	−0.0230	1.4110	−0.0024
0.3707	1147.0	−13.9	0.3770	−0.0240	1.4160	−0.0035
0.4105	1143.0	−16.9	0.3865	−0.0250	1.4210	−0.0024
0.4556	1160.0	−20.2	0.3985	−0.0260	1.4260	−0.0030
0.5039	1169.0	−22.2	0.4115	−0.0270	1.4320	−0.0030
0.5520	1179.0	−23.1	0.4260	−0.0270	1.4380	−0.0030
0.6002	1191.0	−22.1	0.4400	−0.0270	1.4450	0.0020
0.6539	1206.0	−19.3	0.4570	−0.0250	1.4530	−0.0007
0.6976	1219.0	−16.2	0.4710	−0.0240	1.4600	0.0008
0.7444	1245.9	−12.9	0.4860	−0.0220	1.4680	0.0030

TABLE 3.

(*a*) Computed ultrasonic velocity, viscosity, and refractive index of the ternary system — cyclohexane (x_1) + *n*-heptane (x_2) + *n*-hexane (x_3) at 298.15 K

x_1	x_2	Δc^E (m s^{-1})	c_{calcd} (m s^{-1})	$\Delta\eta^E \times 10^3$ (N s M^{-2})	$\eta_{calcd} \times 10^3$ (N s m^{-2})	Δn^E	n_{calcd}
0.1189	0.1823	−8.6	1091.9	0.0185	0.3897	−0.0012	1.3799
0.1440	0.2012	−12.1	1093.2	0.0131	0.4109	−0.0015	1.3812
0.1650	0.2202	−8.9	1100.7	0.0113	0.4233	0.0010	1.3851
0.1879	0.2379	−9.0	1105.2	0.0095	0.4367	−0.0018	1.3837
0.2062	0.2484	−9.8	1107.9	0.0079	0.4469	−0.0021	1.3846
0.2346	0.2729	−8.9	1114.8	0.0056	0.4636	−0.0023	1.3862
0.2564	0.2903	−9.0	1119.3	0.0006	0.4732	−0.0027	1.3872
0.2799	0.3073	−7.6	1125.7	−0.0004	0.4876	−0.0047	1.3867
0.3031	0.3266	−6.1	1132.4	−0.0012	0.5023	−0.0032	1.3897
0.3249	0.3424	−4.2	1139.1	−0.0002	0.5177	−0.0026	1.3917
0.3487	0.3599	−3.0	1145.7	−0.0014	0.5322	−0.0021	1.3937
0.3700	0.3776	−1.9	1151.8	0.0004	0.5483	−0.0017	1.3955
0.3933	0.3948	−2.3	1156.8	0.0017	0.5649	−0.0005	1.3982
0.4143	0.4030	−1.8	1161.8	0.0032	0.5796	−0.0001	1.3998
0.4364	0.4103	−1.2	1167.1	0.0051	0.5953	0.0014	1.4036

Can. J. Chem. Downloaded from www.nrcresearchpress.com by 65.111.164.53 on 09/08/12
For personal use only.

TABLE 3. (*Concluded*)

(*b*) Excess sound velocity, excess viscosity, and excess refractive index of the binary system — cyclohexane (x_1) + *n*-heptane (x_2) at different molar ratios

x_1	c_{exptl} (m s^{-1})	Δc^E_{ij} (m s^{-1})	$\eta_{exptl} \times 10^3$ (N s m^{-2})	$\Delta\eta^E_{ij} \times 10^3$ (N s m^{-2})	n_{exptl}	Δn^E_{ij}
0.3947	1176.0	−2.8	0.5880	0.0050	1.3970	−0.0045
0.4171	1178.0	−3.5	0.5980	0.0034	1.3978	−0.0046
0.4283	1179.0	−3.8	0.6040	0.0038	1.3982	−0.0046
0.4413	1181.0	−3.4	0.6120	0.0053	1.3988	−0.0046
0.4536	1182.0	−3.9	0.6180	0.0051	1.3992	−0.0047
0.4623	1183.0	−3.9	0.6220	0.0048	1.3996	−0.0046
0.4690	1184.0	−3.7	0.6260	0.0054	1.3999	−0.0046
0.4767	1185.0	−3.7	0.6290	0.0046	1.4002	−0.0046
0.4813	1186.0	−3.2	0.6310	0.0043	1.4004	−0.0046
0.4869	1187.0	−2.9	0.6340	0.0054	1.4006	−0.0047
0.4921	1187.0	−3.5	0.6360	0.0039	1.4008	−0.0047
0.4949	1188.0	−2.9	0.6380	0.0045	1.4010	−0.0046
0.4990	1188.0	−3.4	0.6400	0.0044	1.4011	−0.0047
0.5069	1189.0	−3.4	0.6440	0.0044	1.4015	−0.0046
0.5154	1190.0	−3.4	0.6480	0.0042	1.4018	−0.0046

(*c*) Excess sound velocity, excess viscosity, and excess refractive index of the binary system — *n*-heptane (x_1) + *n*-hexane (x_2) at different molar ratios

x_1	c_{exptl} (m s^{-1})	Δc^E_{ij} (m s^{-1})	$\eta_{exptl} \times 10^3$ (N s m^{-2})	$\Delta\eta^E_{ij} \times 10^3$ (N s m^{-2})	n_{exptl}	Δn^E_{ij}
0.2069	1086.8	−0.4	0.3145	0.0015	1.3745	−0.0005
0.2351	1087.6	−1.2	0.3160	0.0004	1.3750	−0.0003
0.2637	1088.5	−1.9	0.3170	−0.0013	1.3755	−0.0002
0.2929	1089.6	−2.4	0.3190	−0.0019	1.3765	0.0004
0.3129	1090.4	−2.7	0.3200	−0.0028	1.3770	0.0007
0.3665	1092.1	−3.4	0.3245	−0.0023	1.3780	0.0011
0.3904	1093.0	−3.8	0.3250	−0.0049	1.3785	0.0012
0.4267	1095.5	−3.9	0.3275	−0.0058	1.3785	0.0007
0.4687	1097.9	−3.8	0.3310	−0.0061	1.3805	0.0022
0.5072	1100.4	−3.4	0.3345	−0.0062	1.3815	0.0027
0.5526	1103.6	−2.7	0.3380	−0.0068	1.3825	0.0031
0.5994	1105.5	−3.4	0.3440	−0.0052	1.3835	0.0035
0.6507	1107.1	−4.6	0.3500	−0.0039	1.3850	0.0043
0.6881	1116.0	−5.4	0.3550	−0.0023	1.3855	0.0043
0.7280	1110.4	−5.6	0.3600	−0.0010	1.3870	0.0053

(*d*) Excess sound velocity, excess viscosity, and excess refractive index of the binary system — cyclohexane (x_1) + *n*-hexane (x_2) at different molar ratios

x_1	c_{exptl} (m s^{-1})	Δc^E_{ij} (m s^{-1})	$\eta_{exptl} \times 10^3$ (N s m^{-2})	$\Delta\eta^E_{ij} \times 10^3$ (N s m^{-2})	n_{exptl}	Δn^E_{ij}
0.1454	1096.0	−5.4	0.3920	0.0119	1.3840	0.0038
0.1803	1100.3	−7.3	0.4100	0.0092	1.3855	0.0034
0.2116	1110.0	−3.1	0.4280	0.0087	1.3865	0.0028
0.2465	1116.0	−3.2	0.4460	0.0060	1.3880	0.0024
0.2744	1121.0	−3.1	0.4620	0.0055	1.3890	0.0019
0.3226	1131.0	−1.6	0.4880	0.0030	1.3910	0.0012
0.3613	1138.0	−1.5	0.5080	0.0000	1.3925	0.0007
0.4041	1147.0	0.0	0.5349	0.0007	1.3935	−0.0007
0.4501	1156.0	0.9	0.5610	0.0005	1.3960	−0.0007
0.4941	1165.0	2.1	0.5880	0.0014	0.0014	−0.0005
0.5448	1175.0	3.2	0.6180	0.0014	1.4010	−0.0008
0.5945	1165.0	4.4	0.6470	0.0009	1.4040	−0.0005
0.6499	1196.0	5.7	0.6800	0.0011	1.4075	0.0000
0.6940	1205.0	6.9	0.7060	0.0010	1.4100	0.0002
0.7400	1214.0	7.8	0.7340	0.0018	1.4130	0.0007

Can. J. Chem. Downloaded from www.nrcresearchpress.com by 65.111.164.53 on 09/08/12
For personal use only.

TABLE 4. Mean percentage deviation and standard percentage error in the computation of ultrasonic velocity, viscosity, and refractive index of the ternary system — toluene (x_1) + n-heptane (x_2) + n-hexane (x_3) at 298.15 K

					Δ%		
x_1	x_2	c_{exptl} (m s^{-1})	$\eta_{exptl} \times 10^3$	n_{exptl}	c	η	n
0.1210	0.1838	1106.2	0.3354	1.3810	0.5	2.9	0.5
0.1459	0.2011	1112.1	0.3405	1.3830	0.3	3.0	0.3
0.1698	0.2170	1116.9	0.3458	1.3850	0.7	3.3	0.2
0.1929	0.2358	1122.0	0.3528	1.3890	1.2	3.7	0.3
0.2160	0.2544	1128.3	0.3589	1.3930	1.7	3.3	0.3
0.2390	0.2726	1133.8	0.3656	1.3950	1.9	4.2	0.3
0.2641	0.2875	1139.9	0.3723	1.3980	2.4	4.4	0.3
0.2849	0.3060	1145.3	0.3786	1.4000	2.7	3.9	0.2
0.3088	0.3222	1151.5	0.3844	1.4030	2.9	4.0	0.3
0.3330	0.3391	1158.0	0.3926	1.4050	3.1	4.1	0.2
0.3559	0.3553	1164.4	0.3996	1.4090	3.1	3.8	0.1
0.3760	0.3735	1170.3	0.4063	1.4110	2.8	3.3	−0.1
0.3983	0.3908	1177.2	0.4146	1.4120	2.5	2.5	−0.2
0.4204	0.3974	1183.0	0.4233	1.4170	2.1	2.2	−0.3
0.4433	0.4045	1189.6	0.4415	1.4190	1.8	3.9	−0.2
	Mean percentage deviation (σ)				1.92	3.53	0.12
	Standard percentage error (δ)				2.17	3.58	0.26

TABLE 5. Mean percentage deviation and standard percentage error in the computation of ultrasonic velocity, viscosity, and refractive index of the ternary system — cyclohexane (x_1) + n-heptane (x_2) + n-hexane (x_3) at 298.15 K

					Δ%		
x_1	x_2	c_{exptl} (m s^{-1})	$\eta_{exptl} \times 10^3$ (N s m^{-2})	n_{exptl}	c	η	n
0.1189	0.1823	1101.8	0.4872	1.3940	0.9	−1.84	1.0
0.1440	0.2012	1107.1	0.4199	1.3960	1.3	−2.14	1.1
0.1650	0.2202	1111.3	0.4293	1.3970	0.9	1.40	0.9
0.1879	0.2379	1115.0	0.4407	1.3980	0.9	0.91	1.0
0.2062	0.2484	1119.0	0.4528	1.3990	1.0	1.19	1.0
0.2346	0.2729	1126.1	0.4686	1.4000	1.0	1.07	1.0
0.2564	0.2903	1129.5	0.4796	1.4020	0.9	0.31	1.1
0.2799	0.3073	1135.1	0.4909	1.4030	0.8	0.67	1.2
0.3031	0.3266	1140.2	0.5086	1.4040	0.7	1.24	1.0
0.3249	0.3424	1144.7	0.5288	1.4050	0.5	1.16	1.0
0.3487	0.3599	1150.6	0.5896	1.4070	0.4	1.37	1.0
0.3700	0.3776	1155.5	0.5573	1.4070	0.3	1.61	0.8
0.3933	0.3948	1161.9	0.5682	1.4090	0.4	0.58	0.8
0.4143	0.4030	1164.8	0.5876	1.4100	0.3	−1.36	0.7
0.4364	0.4103	1169.2	0.6053	1.4100	0.2	−1.65	0.6
	Mean percentage deviation (σ)				0.70	−1.23	0.93
	Standard percentage error (δ)				0.77	1.51	0.95

systems I and II. This shows that the results are in excellent agreement with the experimental findings, and are much better than those obtained when computed using the Flory–Patterson approach by Pandey et al. (11–16). This method yields better results because the predictions are made using the thermodynamic properties of pure components and excess velocities of constituent binary liquid mixtures. Here, all possible binary interactions are considered and are easily accountable by using the experimental excess velocities. More encouraging results were obtained while predicting the viscosity and refractive index of ternary systems. The standard error in computing viscosity was found to be 3.58 and 1.51 for systems I and II. Viscosity of the same ternary liquid mixtures was predicted using empirical, semi-empirical, and statistical approaches and the standard error in most cases was found to be more than 5%. Thus, this approach has an advantage over other methods to predict the viscosity of the multicomponent systems using data of the pure components. The deviations may be due to the polarity and size effects of the components. In systems I and II, an increase in η with increasing concentration of the

Can. J. Chem. Downloaded from www.nrcresearchpress.com by 65.111.164.53 on 09/08/12
For personal use only.

first and second component contributes to the filling up of the third component into the empty sites afforded by the first and second components. For refractive index, the standard errors were found to be 0.12 and 0.93 for systems I and II, respectively, indicating an excellent agreement with the experimental results. Hence, this approach can be used to predict refractive indices more accurately.

The most important feature of this type of equation is that it is applicable to both integral and differential mixing properties and is independent of the manner in which the binary mixing data are represented. It provides reasonably accurate predictions. The excess properties of the multicomponent systems containing more than three liquids can also be successfully expressed in terms of the contributing ternary solutions as

$$\Delta\bar{Z}^{ex}_{123\ldots N} = (N-2)^{-1}\sum_{i=1}\sum_{j>i}\sum_{k>j}^{N}(x_i + x_j + x_k)(\phi_i + \phi_j + \phi_k)(\Delta\bar{Z}^{ex}_{ijk})$$

However, this equation is not expected to be as useful as eq. [9] due to the scarcity of ternary data and tediousness of obtaining the same molar ratios in the ternary liquid mixture as is present in multicomponent liquid systems. We conclude, therefore, that the modified Bertrand–Acree–Burchfield approach can be successfully applied to predict various excess thermodynamical parameters in the case of multicomponent liquid systems.

1. W.E. Acree. *In* Thermodynamic properties of non-electrolyte solutions. Academic Press, New York. 1984. pp. 62–171.
2. P.P. Singh and V.K. Sharma. Can. J. Chem. **61**, 2321 (1983).
3. P.P. Singh, H.P. Dahiya, and S. Dagar. Fluid Phase Equil. **43**, 341 (1988).
4. P.P. Singh, S. Maken, and M. Bhatia. Indian J. Chem. **29** A, 108 (1990).
5. P.J. Flory. J. Am. Chem. Soc. **87**, 1833 (1965).
6. D. Patterson and A.K. Rastogi. J. Phys. Chem. **74**, 1067 (1970).
7. W. Brostow and J.S. Sochanski. J. Mater. Sci. **10**, 2134 (1975).
8. J.D. Pandey and N. Pant. J. Am. Chem. Soc. **104**, 3299 (1982).
9. J.D. Pandey, R.K. Shukla, and R.D. Rai. J. Chem. Soc. Faraday Trans. I, **85**, 331 (1989).
10. M.S. Khanwalkar. Indian J. Pure Appl. Phys. **29**, 616 (1991).
11. J.D. Pandey, V.N.P. Srivastava, (Mrs.) V. Vyas, and N. Pant. Indian J. Pure Appl. Phys. **25**, 467 (1987).
12. J.D. Pandey, N. Pant, (Mrs.) N. Agrawal, and (Mrs.) Shikha. Acustica, **68**, 225 (1989).
13. J.D. Pandey, A.K. Shukla, R.K. Shukla, and R.D. Rai. J. Chem. Thermodyn. **21**, 125 (1989).
14. J.D. Pandey, R.K. Shukla, A.K. Shukla, and R.D. Rai. J. Chem. Soc. Faraday Trans. I, **84**, 1853 (1988).
15. J.D. Pandey, R.D. Rai, A.K. Shukla, and R.K. Shukla. J. Phys. Chem. **91**, 4627 (1989).
16. J.D. Pandey, R.D. Rai, A.K. Shukla, R.K. Shukla, and (Mrs.) N. Mishra. Indian J. Pure Appl. Phys. **31**, 54 (1993).
17. G.L. Bertrand, W.E. Acree (Jr.), and T.E. Burchfield. J. Soln. Chem. **12**, 327 (1987).
18. W.E. Acree and G.L. Bertrand. J. Soln. Chem. **12**, 755 (1983).
19. I.L. Ten and W.E. Acree (Jr.). Phys. Chem. Liq. **25**, 101 (1993).
20. G.A. Mansoori, K.R. Hall, J.C. Holste, and C.A. Hwang. Fluid Phase Equil. **62**, 173 (1991).
21. J.D. Pandey, A.K. Puri, and K. Misra. Thermochim. Acta, **74**, 313 (1984).
22. J.D. Pandey, K. Misra, A.K. Shukla, and R.D. Rai. Can. J. Chem. **65**, 303 (1987).

Can. J. Chem. Downloaded from www.nrcresearchpress.com by 65.111.164.53 on 09/08/12
For personal use only.

An AM1 calculational study of the Diels–Alder addition of maleic anhydride to C5-substituted pentamethylcyclopentadienes and 2,5-dimethylthiophene oxide. An attempt to ascertain the factors controlling the π-facial selectivities and relative reactivities

NICK HENRY WERSTIUK AND JIANGONG MA

Department of Chemistry, McMaster University, Hamilton, ON L8S 4M1, Canada

Received February 28, 1994

NICK HENRY WERSTIUK and JIANGONG MA. Can. J. Chem. **72**, 2493 (1994).

The Diels–Alder reactions of maleic anhydride (**1**) with a group of C5-substituted cyclopentadienes and 2,5-dimethylthiophene oxide (**5**) have been studied with the semi-empirical method AM1. We find that the facial selectivities and relative reactivities found experimentally for six dienes (**2***a*–**2***f*) are accurately reproduced at this level of theory. The results of the calculational study provide no concrete support for the proposal that σ–σ* hyperconjugation in the transition state – an interaction between a σ bond at C5 of the cyclopentadiene and the incipient σ bonds *anti* to it (the Cieplak effect) — is the major source of the *syn* facial selectivity observed for **2***a*–**2***d*. In addition, the relative reactivities and facial selectivities are predicted for a number of cyclopentadienes which will be synthesized and studied experimentally.

NICK HENRY WERSTIUK et JIANGONG MA. Can. J. Chem. **72**, 2493 (1994).

Faisant appel à la méthode semi-empirique AM1, on a étudié les réactions de Diels-Alder de l'anhydride maléique (**1**) avec un certain nombre de cyclopentadiènes substitués en position 5 et avec l'oxyde du 2,5-diméthylthiophène (**5**). On a trouvé que, à ce niveau de la théorie, il est possible de reproduire fidèlement les sélectivités faciales et les réactivités relatives observées expérimentalement pour les six diènes (**2***a*–**2***f*). Les résultats de l'étude par calculs ne fournit aucun support concret pour la proposition qui a été faite selon laquelle de l'hyperconjugaison σ–σ* dans l'état de transition – une interaction entre une liaison σ au niveau C5 du cyclopentadiène et les liaisons σ qui se forment *anti* par rapport à elles (effet Cieplak) – serait la cause principale de la sélectivité faciale *syn* observée avec les composés **2***a*–**2***d*. De plus, on a prédit les réactivités relatives et les sélectivités faciales d'un certain nombre de cyclopentadiènes qui seront synthétisés et étudiés expérimentalement.

[Traduit par la rédaction]

Introduction

The synthetic utility of the Diels–Alder reaction is well established although the ability to control the facial selectivity which would render the reaction enantioselective with asymmetric planar 1,3-dienes and potentially generate five or more chiral centres in one operation, is limited in the absence of chiral auxiliaries. In the reaction of C5-substituted cyclopentadienes where π-facial diastereoselectivity has been observed in the absence of chiral auxiliaires, the origin of the selectivity is still imperfectly understood even though a wide range of substrates have been studied experimentally (1–16) and computationally (17–25). These investigations revealed that a number of factors are important and various suggestions have been advanced as possible sources of the pattern observed. These include steric effects, complexation between diene and dienophile, secondary orbital interactions, polarizability, electrostatic interactions, orbital mixing, and transition state hyperconjugation. This latter interpretation proposed by Cieplak for reactions of cyclohexanones is based on the concept of transition state stabilisation by σ donation from an adjacent σ bond into the vacant σ* orbital associated with the incipient bond (26, 27). This explanation was used to account for the *syn* approach of 2,3-dimethylbutadiene to C5-fluoroadamantane-2-thione (28) and rationalize the preference observed for addition *anti* to the antiperiplanar σ bond that is the better donor in the reactions of dienophiles with C5-substituted pentamethylcyclopentadienes (29, 30) and 2,5-dimethylthiophene oxide (15). Clearly, it is desirable to continue research in this area to gain a complete understanding of the factors which affect the π-facial selectivity so that the stereochemistry of D–A reactions of C5-substituted cyclopentadienes can be predicted with certainty and the adducts utilized for the total synthesis of complex molecules. In fact, we showed by means of a calculational and ultraviolet photoelectron spectroscopic study of C5-substituted pentamethylcyclopentadienes (**2***a*, **2***c*, **2***d*, **2***e*, **2***f*, and **2***h*) that n–π orbital mixing (the orbital mixing rule (17, 25)) in the HOMO of **2***a*, **2***c*, and **2***d* is not the source of the *syn* facial selectivity observed in reactions of these dienes with maleic anhydride and *N*-phenylmaleimide (31).

TABLE 1. Facial selectivities and relative rates of Diels–Alder reactions of C5-substituted pentamethylcyclopentadienes with maleic anhydride

Diene	Reaction[a] time	Addition ratio[b] *syn*	Addition ratio[b] *anti*
2*a*	3.5 h[c]	10	0
2*b*	3.5 h	10	0
2*c*	<30 s	10	0
2*d*	<10 min	10	0
2*e*	27.5 h	1	9
2*f*	<30 s	8[d]	2

[a]Taken from ref. 13.
[b]Determined by integration of ^{1}H nmr spectra of the total reaction mixture.
[c]The dienophile was *N*-phenylmaleimide.
[d]Addition *syn* to C—H.

In this paper we document the results of an AM1 (32) calculational study of the Diels–Alder (D–A) reactions of maleic anhydride (**1**) with C5-substituted pentamethylcyclopentadienes(**2***a*–**2***k*), 2,3,4,5-tetramethylcyclopentadienes (**3***a* and **3***b*) mono-substituted cyclopentadienes (**4***a* and **4***b*) and 2,5-dimethylthiophenoxide (**5**). The objectives of the study were (*a*) to determine whether the facial selectivities and relative reactivities found experimentally (Table 1) are accurately calculated with AM1, (*b*) to ascertain, by studying SiR_3-substituted ana-

Can. J. Chem. Downloaded from www.nrcresearchpress.com by 85.192.166.187 on 09/08/12
For personal use only.

Can. J. Chem. Downloaded from www.nrcresearchpress.com by 85.192.166.187 on 09/08/12
For personal use only.

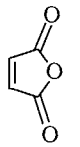

1

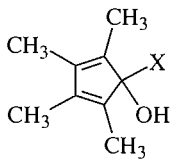

2

a, X = NH_2
b, X = $NHCOCH_3$
c, X = OH
d, X = OCH_3
e, X = SCH_3
f, X = H
g, X = SiH_3
h, X = CH_3
i, X = $Si(CH)_3$
j, X = CF_3
k, X = NH_3^+

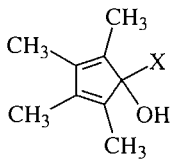

3

a, X = H
b, X = SiH_3

4

a, X = OH
b, X = $OCOCH_3$

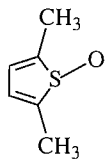

5

logues and analyzing the changes in the C5—X and C5—R bond lengths and the charges (X, C5, and R) whether a hyperconjugative interaction — the frontier MOs were to be examined as well — between the incipient C—C bonds and the best σ donor is the source of the π-facial selectivities and relative reactivities of cyclopentadienes and, (*c*) to predict facial selectivities which could be verified experimentally.

Results and discussion

Calculations

Reaction coordinate potentials and transition structures for *syn* and *anti* addition of maleic anhydride (**1**) to the group of substituted cyclopentadienes (**2***a*–**2***k*, **3***a*, **3***b*, **4***a*, and **4***b*) and **5** were calculated with AM1 using version 2.1 of AMPAC (32). In one series of calculations, the geometry of the D–A product was optimized, then the incipient bonds (icbs) were lengthened in one step to 1.9 Å; the optimized 1.9 Å geometry was used as the starting point to complete the *retro* Diels–Alder reaction by stretching the icbs to 3.5 or 3.8 Å in 0.1 Å increments. In a second series of calculations, the 2.8 Å geometry of each complex was optimized first, then the D–A addition was completed by shortening the icibs to 1.9 Å. The 1.9 Å geometry was used as the input to compute the optimized geometry of the final product. MMX-optimized input geometries generated with PCMODEL (33) were used as starting points for the AM1 calculations and the icbs were forced to be equal through the use of the keyword SYMMETRY because this was the only convenient way to calculate the energy profiles. The keyword PRECISE was use to tighten the convergence criteria. A two-step approach was to locate the transition structures (TSs). First, the optimized geometry near the maximum of the potential energy profile was calculated with the icbs fixed at 2.15 Å, then the TS was obtained by refining the 2.15 Å geometry with a SIGMA or NLLSQ calculation.[1] In the case of **2***a*, **2***b*, **2***c*, **2***d*, **2***e*, **3***a*, **4***a*, and **4***b*, the forced equivalence of the icbs did not yield symmetrical TSs of C_s symmetry because the substituents bearing lone pairs adopted the lowest energy conformation with respect to the CH_3 (and SiH_3) group or hydrogen or C5. That is, the CH_3—C5—X—H(CH_3) torsional angles were not 0 or 180°. The incipient bond lengths (icbls) of the TSs located in this way are given in Table 2. The icbls fall in the region of 2.15 Å, in accordance with the results of calculational studies on other cyclopentadienes (34). FORCE calculations were carried out to ensure that transition structures located had one imaginary frequency, and this was found to be the case. That these vibrations involve motions of the atoms of the incipient bonds which could lead to the product formation was clearly seen with PC-VIBRATE (35), computer software which animates normal modes of vibration calculated with semi-empirical and *ab initio* quantum chemistry programs. Calculations were also carried out on **2***c* and **2***e* by stepping across the potential energy surface from the transition structures to the 1.9 Å and 3.8 Å complexes in 0.1 Å increments. The potentials were identical to those calculated with the 1.9 Å and 2.8 Å complexes as the starting

TABLE 2. Calculational incipient bond lengths of transition structures

Transition structure	Incipient bond lengths/Å
2*a-syn*	2.159 (2.153) (2.167)[c]
2*a-anti*	2.164 (2.186) (2.142)
2*b-syn*	2.161
2*b-anti*	2.158
2*c-syn*	2.144 (2.139) (2.151)[c]
2*c-anti*	2.157 (2.181) (2.141)
2*d-syn*	2.148
2*d-anti*	2.163
2*e-syn*[a]	2.149
2*e-anti*[a]	2.150
2*e-syn*[b]	2.150 (2.151) (2.153)[c]
2*e-anti*[b]	2.150 (2.154) (2.151)
2*f-syn*	2.151
2*f-anti*	2.140
2*g-syn*	2.159
2*g-anti*	2.138
2*h*	2.157
2*i-syn*	2.165 (2.179, 2.151)
2*i-anti*	2.134 (2.135, 2.134)
2*j-syn*	2.158 (2.159, 2.159)
2*j-anti*	2.151 (2.151, 2.151)
2*k-syn*	2.152
2*k-anti*	2.159
3*b-syn*	2.143 (2.142, 2.142)
3*b-anti*	2.147 (2.147, 2.147)
5-*syn*[a]	2.114 (2.113, 2.113)
5-*anti*[a]	2.120 (2.122, 2.120)
5-*syn*[b]	2.138
5-*anti*[b]	2.132

[a]Computed with full AM1 parameters.
[b]Computed with mixed parameters (C, H, O AM1; S MNDO).
[c]Computed without the constraint that the incipient bonds be equal.

[1]The keyword SIGMA envokes the McIver–Komornicki gradient norm minimisation routines. The keyword NLLSQ envokes Bartel's nonlinear least squares gradient norm minimisation method.

TABLE 3. Calculational thermochemical data for Diels–Alder reactions

Diene and facial approach	ΔH_f diene + **1**[c]	ΔH_f final product	ΔH_f transition structure	$\Delta H^{\ddagger}$	$\Delta\Delta H^{\ddagger}$ (*syn* – *anti*)
2*a-syn*	−68.22	−92.42	−37.09 (−37.09)[d]	31.13	−3.76
2*a-anti*		−92.24	−33.33 (−33.36)	34.89	
2*b-syn*	−103.97	−127.27	−72.17	31.80	−3.82
2*b-anti*		−127.74	−68.35	35.62	
2*c-syn*	−113.75	−139.63	−84.85 (−84.85)	28.90	−5.28
2*c-anti*		−136.70	−79.57 (−79.59)	34.18	
2*d-syn*	−106.07	−132.50	−77.19	28.88	−4.58
2*d-anti*		−129.22	−72.61	33.46	
2*e-syn*[a]	−66.47	−88.55	−34.63	31.84	+1.06
2*e-anti*[a]		−86.81	−33.57	32.90	
2*e-syn*[b]	−64.19	−85.35	−30.36 (−30.36)	34.13	+0.40
2*e-anti*[b]		−84.01	−30.76 (−30.77)	33.73	
2*f-syn*[e]	−75.99	−99.07	−46.94	29.05	−2.03
2*f-anti*		−99.12	−44.91	31.08	
2*g-syn*[f]	−69.63	−83.69	−30.37	39.26	+6.14
2*g-anti*		−85.18	−36.51	33.12	
2*h*	−77.79	−99.18	−44.73	33.06	—
2*i-syn*[g]	−109.29	−123.14	−68.67 (−68.58)	40.62	+8.49
2*i-anti*		−124.43	−77.16 (−77.15)	32.13	
2*j-syn*[b]	−226.64	−245.33	−188.57 (−188.57)	38.07	+0.82
2*j-anti*		−243.42	−189.39 (−189.39)	37.25	
2*k-syn*	75.71	65.06	121.47	45.76	−0.24
2*k-anti*		61.11	121.71	46.00	

[a]Computed with full AM1 parameters.
[b]Computed with mixed parameters (C, H, O AM1; S MNDO).
[c]The ΔH_f of **1** is −76.35 kcal/mol.
[d]The value in parentheses corresponds to the ΔH_f of the transition structure obtained without the constraint that the incipient bonds be equal.
[e]Addition *syn* to C—H.
[f]Addition *syn* to C—SiH_3.
[g]Addition *syn* to C—$Si(CH_3)_3$.
[h]Addition *syn* to C—CF_3.

TABLE 4. Calculational thermochemical data for Diels–Alder reactions

Diene and facial approach	ΔH_f diene + **1**[c]	ΔH_f final product	ΔH_f transition structure	$\Delta H^{\ddagger}$	$\Delta\Delta H^{\ddagger}$ (*syn* – *anti*)
3*a-syn*	−114.68	−138.33	−83.61 (−83.61)	31.07	+1.02
3*a-anti*		−140.27	−84.63 (−84.63)	30.05	
3*b-syn*	−106.02	−124.92	−75.35	30.67	−8.71
3*b-anti*		−124.56	−66.64	39.38	
4*a-syn*	−81.33	−55.12	−55.12 (−55.12)	26.21	−0.44
4*a-anti*		−54.68	−54.68 (−54.68)	26.65	
4*b-syn*	−116.03	−111.13	−91.03 (−91.03)	25.00	−1.59
4*b-anti*		−110.51	−89.44 (−89.44)	26.59	
5-*syn*[a]	−79.33	−104.36	−46.74 (−46.74)	32.59	−3.45
5-*anti*[a]		−100.21	−43.29 (−43.28)	36.04	
5-*syn*[b]	−27.83	−57.14	3.81	31.64	−3.69
5-*anti*[b]		−52.50	8.51	35.33	

[a]Computed with full AM1 parameters.
[b]Computed with mixed parameters (C, H, O AM1; S MNDO).

points. To ensure that the calculations with the forced equivalence of the icbls gave realistic TSs, SIGMA/NLLSQ calculations were carried out on the *syn* and *anti* TSs of **2***a*, **2***c*, **2***e*, **2***i*, **2***j*, **3***a*, **3***b*, **4***a*, **4***b*, and **5** — the geometries of the TSs with equal icbls were used as the input — without the equivalence constraint. The results for **2***a*, **2***c*, **2***e*, **2***i*, **2***j*, **3***b*, and **5** are given in parentheses in Table 2. It is seen that the icbls differ slightly from those obtained with the equivalence constraint with the largest differences being found in the case of the *anti* TSs, except in the case of **2***i*. Similar results were obtained for **3***a*, **4***a*, and **4***b*. Even so, the ΔH_fs of the TSs (the values are given in parentheses in Tables 3 and 4) remain virtually unchanged. FORCE calculations on these TSs yielded imaginary frequencies which were virtually identical to the frequencies calculated

Can. J. Chem. Downloaded from www.nrcresearchpress.com by 85.192.166.187 on 09/08/12
For personal use only.

TABLE 5. Selected calculational bond lengths of Diels–Alder complexes, transition structures, and products

Diene and facial approach	Bond type	Bond lengths/Å			
		Diene	2.8 Å complex	Transition structure	Final product
2*a-syn*	C5—NH_2	1.456	1.451	1.444	1.443
	C5—CH_3	1.533	1.542	1.548	1.527
2*a-anti*	C5—NH_2	1.456	1.466	1.471	1.467
	C5—CH_3	1.533	1.526	1.524	1.524
2*b-syn*	C5—$NHCOCH_3$	1.448	1.447	1.440	1.444
	C5—CH_3	1.533	1.541	1.546	1.526
2*b-anti*	C5—$NHCOCH_3$	1.448	1.458	1.464	1.445
	C5—CH_3	1.533	1.528	1.525	1.523
2*c-syn*	C5—OH	1.420	1.418	1.414	1.414
	C5—CH_3	1.521	1.524	1.526	1.509
2*c-anti*	C5—OH	1.420	1.430	1.435	1.414
	C5—CH_3	1.521	1.516	1.514	1.512
2*d-syn*	C5—OCH_3	1.427	1.421	1.421	1.420
	C5—CH_3	1.518	1.521	1.524	1.507
2*d-anti*	C5—OCH_3	1.427	1.438	1.443	1.420
	C5—CH_3	1.518	1.516	1.512	1.509
2*e-syn*[a]	C5—SCH_3	1.749	1.792	1.785	1.788
	C5—CH_3	1.507	1.514	1.517	1.500
2*e-anti*[a]	C5—SH_3	1.749	1.811	1.822	1.788
	C5—CH_3	1.507	1.501	1.500	1.499
2*e-syn*[b]	C5—SCH_3	1.760	1.753	1.751	1.752
	C5—CH_3	1.512	1.520	1.523	1.505
2*e-anti*[b]	C5—SCH_3	1.760	1.811	1.785	1.756
	C5—CH_3	1.512	1.501	1.504	1.504
2*f-syn*	C5—H	1.125	1.122	1.120	1.118
	C5—CH_3	1.508	1.511	1.513	1.499
2*f-anti*	C5—H	1.125	1.132	1.135	1.120
	C5—CH_3	1.508	1.503	1.501	1.498
2*g-syn*[c]	C5—SiH_3	1.843	1.835	1.853	1.864
	C5—CH_3	1.504	1.521	1.528	1.505
2*g-anti*	C5—SiH_3	1.843	1.867	1.886	1.861
	C5—CH_3	1.504	1.500	1.502	1.503
2*h*[d]	C5—CH_3	1.517	1.512	1.510	1.510
	C5—CH_3	1.517	1.528	1.540	1.513
2*i-syn*[e]	C5—$Si(CH_3)_3$	1.891	1.902	1.934	1.944
	C5—CH_3	1.503	1.526	1.531	1.509
2*i-anti*	C5—$Si(CH_3)_3$	1.891	1.930	1.965	1.935
	C5—CH_3	1.503	1.498	1.500	1.503
2*j-syn*	C5—CF_3	1.568	1.561	1.565	1.567
	C5—CH_3	1.515	1.530	1.538	1.515
2*j-anti*	C5—CF_3	1.568	1.582	1.592	1.570
	C5—CH_3	1.515	1.510	1.511	1.513
2*k-syn*	C5—NH_3^+	1.513	1.506	1.501	1.504
	C5—CH_3	1.521	1.531	1.537	1.520
2*k-anti*	C5—NH_3^+	1.513	1.527	1.534	1.506
	C5—CH_3	1.521	1.516	1.515	1.515

for the TSs in which the icbls were forced to be equal. The ΔH_fs of **1**, the cyclopentadienes, and **5** were calculated and summed to give the enthalpy of each D–A reaction at infinite separation of the reactants. These data along with the ΔH_fs of the final products, the TSs and the activation enthalpies are given in Tables 3 and 4. The C5—X and C5—R (R = CH_3, SiH_3, $Si(CH_3)_3$, or H) and S—O bond lengths of the starting dienes, the 2.8 Å complexes, the TSs and the final products are given in Tables 5 and 6. Displays of the potentials for *syn* (closed circles) and *anti* (open circles) addition of **1** to a selected group of cyclopentadienes are given in Figs. 1 to 5. The sum of the heats of formation of **1** and the diene corresponding to the enthalpy of the reaction with the reactants at an infinite separation is plotted as a data point (■) at 3.9 Å.

Calculational facial selectivities and relative reactivities

The TS for *syn* addition of **1** to **2***a* was found to be lower in energy than the *anti* diastereomer in accord with the high *syn* facial selectivity found experimentally (Table 1). It is seen in Fig. 1 that the increases in the ΔH_fs of the *syn* and *anti* complexes of **1** and **2***a* are virtually identical up to icbls of 3.5 Å, then the values diverge. Based on the geometrical structures of the 3.6 Å- and 3.4 Å-icbl *anti* complexes of **2***a* (structural formulas not shown), it appears that the differential increase in the

Can. J. Chem. Downloaded from www.nrcresearchpress.com by 85.192.166.187 on 09/08/12
For personal use only.

TABLE 6. Selected calculational bond lengths of Diels–Alder complexes, transition structures, and products

Diene and facial approach	Bond type	Bond lengths/Å			
		Diene	2.8 Å complex	Transition structure	Final product
3*b*-*syn*	C5—OH	1.408	1.405	1.402	1.403
	C5—SiH_3	1.866	1.885	1.915	1.913
3*b*-*anti*	C5—OH	1.408	1.422	1.426	1.405
	C5—SiH_3	1.866	1.875	1.902	1.917
5-*syn*[a]	S—O	1.478	1.481	1.474	1.475
5-*anti*[a]	S—O	1.478	1.478	1.471	1.469
5-*syn*[b]	S—O	1.592	1.593	1.584	1.575
5-*anti*[b]	S—O	1.592	1.591	1.583	1.569

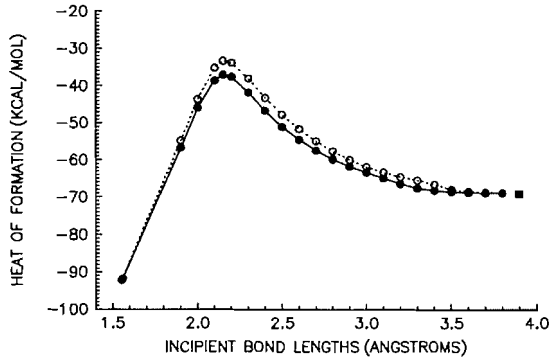

FIG. 1. Displays of the potentials for *syn* (filled circles) and *anti* (open circles) addition of **1** to 5-aminopentamethylcyclopentadiene (**2***a*).

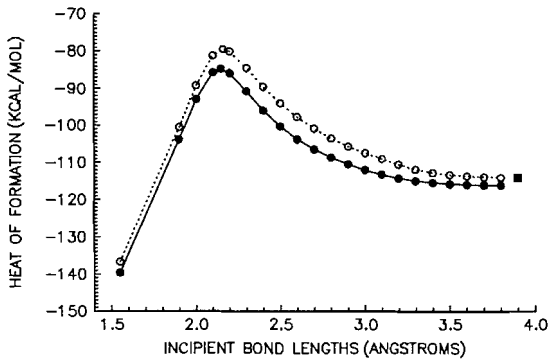

FIG. 2. Displays of the potentials for *syn* (filled circles) and *anti* (open circles) addition of **1** to 5-hydroxypentamethylcyclopentadiene (**2***c*).

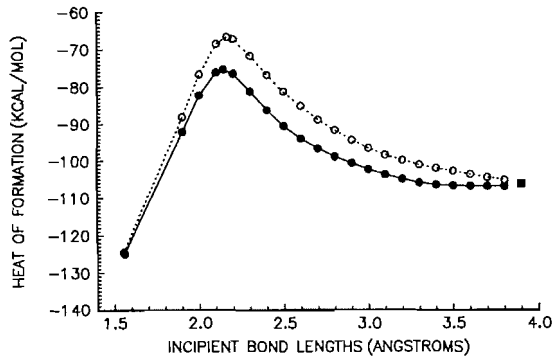

FIG. 3. Displays of the potentials for *syn* (filled circles) and *anti* (open circles) addition of **1** to 5-hydroxy-5-silamethyl-1,2,3,4-tetramethylcyclopentadiene (**3***b*).

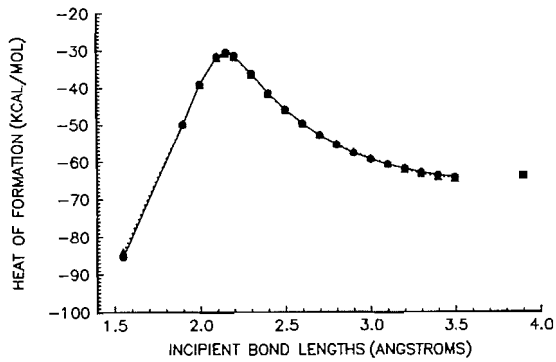

FIG. 4. Displays of the potentials for *syn* (filled circles) and *anti* (filled triangles) addition of **1** to 5-methylthiopentamethylcyclopentadiene (**2***e*).

energy of the *anti* complex at icbls of 3.6 Å occurs as **1** reorientates to maximize overlap of the π systems and initiate C—C bond formation. This effect undoubtedly derives from a steric interaction between the methyl group and the vinyl hydrogens of **1**. In the case of the *syn* complex, a reorientation of **1** occurs when the icbls are between 3.3 and 3.1 Å (structural formulas not shown), leading to a barely perceptible inflection in the potential. It appears that a differential steric interaction is one of factors responsible for the addition of **1** *syn* to the amino group of **2***a*. The data point (■) at 3.9 Å corresponds to the sum of the ΔH_fs of **1** and **2***a*.

As was the case for **2***a*, the *syn* TS of acetamide **2***b* was found to be lower in energy than the *anti* diastereomer (plots not shown) in accord with the experimental results (Table 1). The ΔH_fs also diverge at 3.4 Å as found for **2***a*. At icbls of 3.8 Å, the heats of formation of the *syn* and *anti* complexes are −103.99 and −104.58 kcal/mol, respectively, close to the sum of the ΔH_fs of **1** and **2***b* (−103.97 kcal/mol).

Displays of the potentials of *syn* and *anti* addition of **1** to hydroxy compound **2***c* are given in Fig. 2. The data at 3.9 Å is the sum of the ΔH_fs (−113.75 kcal) of **1** and **2***c*. The calculational ΔH_fs of the *syn* and *anti* complexes with icbls of 3.8 Å are −116.10 and −114.10 kcal, respectively. As was computed for **2***a* and **2***b*, addition of **1** *syn* to the methyl group leads to a discernible increase in the energy of the complex when the icbls approach 3.3 Å. As found in the case of **2***a* and **2***b*, this occurs

Can. J. Chem. Downloaded from www.nrcresearchpress.com by 85.192.166.187 on 09/08/12
For personal use only.

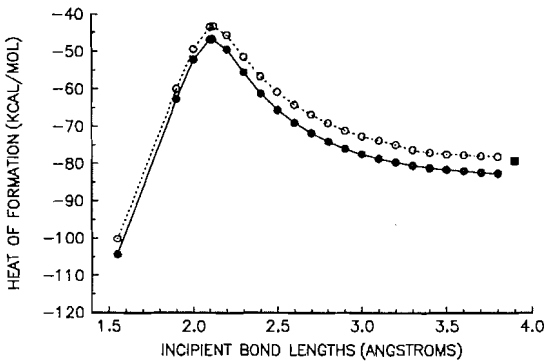

FIG. 5. Displays of the potentials for *syn* (filled circles *syn* to S—O) and *anti* (open circles) addition of **1** to 2,5-dimethylthiophene oxide (**5**).

when **1** reorientates to maximize overlap of the π systems and to initiate bond formation. That the *syn* complex with icbls of 3.8 Å is lower in energy than the reactants at infinite separation suggests that an additional differential stabilising interaction develops early for *syn* addition but not in the *anti* case. This means that it may be possible to use the $\Delta\Delta H_f$s when the icbls are in the region of 3.8 Å or less to identify cases where long-range effects come into play to stabilise or destabilise the D–A complexes. And the *syn* D–A product by calculation is 2.93 kcal/mol lower in energy than the *anti* isomer. Additional calculation studies on the *syn* and *anti* products — the HO—C5 and CH_3—C5 dihedral angles were driven 180° in 15° increments — did not establish the source of this difference. It appears that a combination of a stabilising complexation interaction, a steric effect, and a difference in product stabilities can account for the stereoselectivity observed for the addition of **1** to **2***c*. While it would be useful to establish experimentally whether the *syn* adduct is thermodynamically more stable than the *anti* isomer, it may not be easy to achieve this goal. To obtain a sufficient amount of the *anti* adduct and to carry out equilibration studies will be difficult.

To gain additional information on the role of the methyl groups in determining the facial selectivity and relative reactivities of cyclopentadienes, the additions of **1** to 5-hydroxy-1,2,3,4-tetramethylcyclopentadiene (**3***a*), 5-hydroxycyclopentadiene (**4***a*), and 5-acetoxycyclopentadiene (**4***b*) were also studied with AM1. Given that addition *syn* to the OH group is preferred for **2***c*, it is surprising that *anti* attack is the low energy pathway in the case of **3***a*. Because *syn* facial selectivities (to the OH and OAc groups) are calculated for the addition of **1** to **4***a* and **4***b* (Table 4), the opposite facial selectivities calculated for **2***c* and **3***a* do not result from differential steric effects between the C—H and C—OH groups. Although the addition of **1** to **3***a* has not been studied experimentally, the *syn* selectivities calculated for **4***a* and **4***b* are supported by the fact that ethene adds *syn* to the OAc group of **4***b* (1). According to the results from calculation, the *anti* D–A product of **3***a* is 1.99 kcal/mol lower in energy than the *syn* isomer and this could be the primary reason for the preferred *anti* addition of **1** to this diene. It would be worthwhile to prepare **3***a* and experimentally determine the facial selectivity and its reactivity relative to **2***c* (35). Given that from calculation, $\Delta H^{\ddagger}$ for **3***a* is larger (30.05 kcal/mol) than $\Delta H^{\ddagger}$ for **2***c* (28.90 kcal/mol), **3***a* should be less reactive than **2***c*.

The effect of replacing the C5—CH_3 bond with a better σ donor on the facial selectivity and reactivity was probed through a study of 5-hydroxy-5-silamethylpentamethylcyclopentadiene (**3***b*). Displays of the potentials for the *syn* and *anti* additions of **1** to **3***b* are given in Fig. 3. Although the difference in the energies of the *syn* and *anti* TSs is greater than in the case of **2***c*, from calculation, the activation enthalpy for addition *syn* to the OH group of **3***b* is 1.82 kcal/mol higher than the enthalpy of activation for *syn* addition to **2***c*. Because a Si—C bond is a better σ donor than a CH_3—C bond, this result suggests that transition state hyperconjugation in the transition state is not the major factor controlling π-facial selectivity in the D–A reactions of C5-substituted pentamethylcyclopentadienes. It would certainly be of interest to synthesize **3***b* or its 5-(1-silaethyl) analogue and test the AM1 results from calculations (36).

As was seen in the case of **2***c*, the difference in the $\Delta H^{\ddagger}$s of the *syn* and *anti* complexes of **2***d* develops early and the *syn* transition structure was found to be lower in energy than the *anti* one in keeping with the experimental results (Table 3) (potentials not shown). The factors which control the facial selectivity and reactivity of **2***c* also prevail in **2***d*.

When AM1 parameters for C, H, and S were used in the calculations on **2***e*, *syn* addition was found to be the low energy pathway, a result which is not in keeping with the 9:1 *anti* selectivity found experimentally (Table 1). On the other hand, when mixed parameters were used (C and H, AM1; S, MNDO), the *anti* TS was calculated to be 0.40 kcal/mol lower in energy than the *syn* TS in accord with the *anti* facial selectivity found experimentally. The potentials are displayed in Fig. 4 (*syn* addition, filled circles; *anti* addition, filled triangles). Prior to the development of the AM1 sulfur parameters, calculations with mixed AM1/MNDO parameters were considered to be acceptable, but not ideal (37). While we recognise that calculations of this type should be avoided in general, we view the mixed parameter computations as test calculations. We have found two additional cases where the results of mixed-parameter calculations on low-valent sulfur compounds — the interaction between sulfur lone pairs and the cyclopentadiene π system (31) and the potential for twisting about the Ph—SCH_3 bond of substituted thioanisoles (38) — appear to correlate better with experimental results than full AM1 calculations.

That addition of **1** *syn* to C5—H of pentamethylcyclopentadiene (**2***f*) is the low energy process (Table 3) is in keeping with the facial selectivity found experimentally. Four additional cyclopentadienes — 5-silamethylpentamethylcyclopentadiene (**2***g*), hexamethylcyclopentadiene (**2***h*), 5-trimethylsilyl-1,2,3,4,5-pentamethylcyclopentadiene (**2***i*) and 5-trifluoromethylpentamethylcyclopentadiene (**2***j*) — were studied as well. According to calculations, **1** is expected to add selectively *anti* to the SiH_3 group of **2***g*, the $(CH_3)_3Si$ group of **2***i*, and the CF_3 group of **2***j*. For **2***g*, a difference in the energy between the *syn* and *anti* complexes develops early at 3.8 Å when **1** reorientates to maximized the overlap of the π systems, then the gap increases further at 3.3 Å (potentials not shown). This is a consequence of the fact that a SiH_3 group is bulkier (the Si—H bond lengths are 1.46 Å) than a methyl group (the C—H bond lengths are 1.10 Å). Even so, given the fact that the Si—C bond is a better σ donor than a C—O bond, it is surprising that the enthalpy of activation for *anti* addition to **2***g* is virtually identical ($\Delta H^{\ddagger}$ = 33.12 kcal/mol) to the enthalpy of activation for addition of **1** to **2***h* ($\Delta H^{\ddagger}$ = 33.06 kcal/mol) (Table 3). Because the trimethylsilyl group is bulkier than a methyl group, in calculation, preference for addition *anti* to this group is not surprising. However, that the calculational enthalpy for **2***i* is nearly identical (32.12 kcal/mol) to the activation enthalpy of **2***h* (33.06 kcal/mol) is unexpected. That addition *anti* to the CF_3

Can. J. Chem. Downloaded from www.nrcresearchpress.com by 85.192.166.187 on 09/08/12
For personal use only.

TABLE 7. Calculational and experimental data for Diels–Alder reactions of pentamethylcyclopentadienes with maleic anhydride

		syn		*anti*		
Diene	Reaction time[b]	$\Delta H^{\ddagger}$[c]	Relative yield	$\Delta H^{\ddagger}$[c]	Relative yield	$\Delta\Delta H^{\ddagger}$ (*syn-anti*)
2*a*[a]	3.5 h	—[d]	10	—[d]	0	—[d]
2*a*	—[e]	31.13	—[e]	34.89	—[e]	−3.76
2*b*	3.5 h	31.80	10	35.62	0	−3.82
2*c*	<30 s	28.90	10	34.18	0	−5.28
2*d*	<10 min	28.88	10	33.46	0	−4.58
2*e*	27.5 h	34.13	1	33.73	9	+0.40
2*f*	<30 s	29.05[f]	8	31.08	2	−2.03

[a]The dienophile was *N*-phenylmaleimide.
[b]Reactions carried out at 22°C (13).
[c]In kcal/mol.
[d]Not studied computationally.
[e]Not determined experimentally.
[f]Addition *syn* to C—H.

group is preferred in the case of **2***j* is also surprising and suggests that the differential steric effect of a trifluoromethyl group outweighs the differential electron-donating ability of a CH_3—C bond. These calculational results also suggest that the Cieplak effect is probably not the major factor responsible for variation in rates and facial selectivities found in the additions of maleic anhydride and *N*-phenylmaleimide to C5-substituted cyclopentadienes. It would be instructive to synthesize **2***i* and **2***j* and establish whether the predictions made on the basis the AM1 calculations are borne out by experimental studies (36).

To establish the effect of protonating the amino group of **2***a*, the addition of **1** to **2***k* was studied as well. Unlike the case the **2***a*, the *anti* complex is lower in energy (2.3 kcal/mol) than the *syn* complex when the icbls are 3.5 Å, but a crossover in the relative energies occurs when the icbs are shortened to 2.5 Å leading to the *syn* TS being marginally lower in energy (0.24 kcal) than the *anti* diastereomer (Table 3). This means that a much lower *syn* facial selectivity is expected for **2***k* than is found for **2***a*, not what would be expected if transition state hyperconjugation is the major factor determining the stereoselectivity of the D–A addition. Furthermore, based on the calculated $\Delta H^{\ddagger}$s, **2***k*, and of course **2***j*, will be inert relative to the other compounds of the series.

Figure 5 displays the potentials for the *syn* and *anti* addition of **1** to **5** calculated with AM1. The *syn* TS is 3.69 kcal/mol lower in energy than the *anti* TS (Table 4). As found for **2***c*, the difference in energy develops early and is maintained through to the transition structures. Noteworthy is the fact that the *syn* D–A adduct is calculated to be substantially lower in energy (4.15 kcal/mol) than the *anti* adduct. It appears that this is another case where the thermodynamic stability of the final product plays a role in determining the facial selectivity. As in the case of **2***c*, it may be a difficult task to establish the relative stabilities of the *syn* and *anti* D–A products experimentally. Even so, it has been established that **1** adds to **5** and yields a single adduct, but crystals suitable for X-ray analysis were not obtained. Because *p*-quinone adds *syn* to the S—O bond of **5** (15, 16), it is certain to be the *syn* adduct as predicted with AM1.

If $\Delta\Delta S^{\ddagger} \approx 0$ for the series of dienes studied with AM1 — this is a reasonable assumption because the dienes are very similar structurally — then the $\Delta\Delta H^{\ddagger}$s calculated for **2***a*, **2***b*, **2***c*, and **2***d* (−3.76 to −5.28 kcal/mol (Table 3) correlate well with high *syn* facial selectivities found for the addition of **1** to these dienes (Table 1). And the $\Delta\Delta H^{+}$(*syn* − *anti*) of 0.40 kcal/mol calculated for **2***e* correlates with the *anti* selectivity of 9:1 observed experimentally. In the case of pentamethylcyclopentadiene the computed $\Delta\Delta H^{+}$(*syn* − *anti*) (−2.03 kcal/mol) is larger than expected on the basis of the 4:1 *syn* selectivity observed experimentally. This result suggests that AM1 overestimates the differential steric interaction between the *syn* methyl group at C5 and the vinyl hydrogens of the incoming dieneophile relative to a hydrogen at C5 by about 1.5 kcal/mol. Even if the differences in the *syn/anti* TS energies of **2***a*, **2***b*, **2***c*, and **2***d* are reduced by 1.5 kcal/mol, the adjusted $\Delta\Delta H^{+}$s which range between −2.25 and −3.84 kcal/mol still correlate well with the facial selectivites found for **2***a*–**2***d*. Table 7 shows the calculated transition structure enthalpies, the facial selectivites, and relative reactivities found experimentally. From these data is seen that AM1 also accurately predicts the relative reactivities of the cyclopentadienes with **2***c* and **2***f* being the most reactive compounds. According to the AM1 calculations, **2***j* and **2***k* should be inert under the conditions used to carry out the cycloadditions to the other cyclopentadienes. On the basis of the calculated ΔH^{+}s, we expect that thiophene oxide **5** will be less reactive than **2***c*, yet it should exhibit the same reactivity as **2***a* and **2***b*.

Transition structure geometries

As is seen in the geometrical structures (see Figs. 6(*a*) and 6(*b*)), there is a distinct pyramidalisation of the C2 and C3 carbons of the TSs for addition to **2***c*. This pyramidalisation which bends the methyl groups towards the incoming dieneophile is not related to the factor(s) determining the *syn* facial selectivity because it occurs in *syn* and *anti* TSs and in the case of **2***e* which exhibits an *anti* preference. The same deviation from planarity — the hydrogens at C3 and C4 bend towards **1** — is seen in TSs for *syn* and *anti* addition of **1** to 2,5-dimethylthiopheneoxide (**5**). It is possible that this pyramidalisation which may arise from the fact that sp^2 hybridization is not maintained at these carbons during the addition — the C1—C2 and C2—C3 bond lengths are 1.42 Å for the addition of **1** to **2***c* and the other pentamethylcyclopentadienes — and there is relief of torsional strain is a general feature of the D–A reactions of substituted cyclopentadienes. Regardless of its source, this pyramidalisation may be important in determining the rates and stereochem-

Can. J. Chem. Downloaded from www.nrcresearchpress.com by 85.192.166.187 on 09/08/12
For personal use only.

Can. J. Chem. Downloaded from www.nrcresearchpress.com by 85.192.166.187 on 09/08/12
For personal use only.

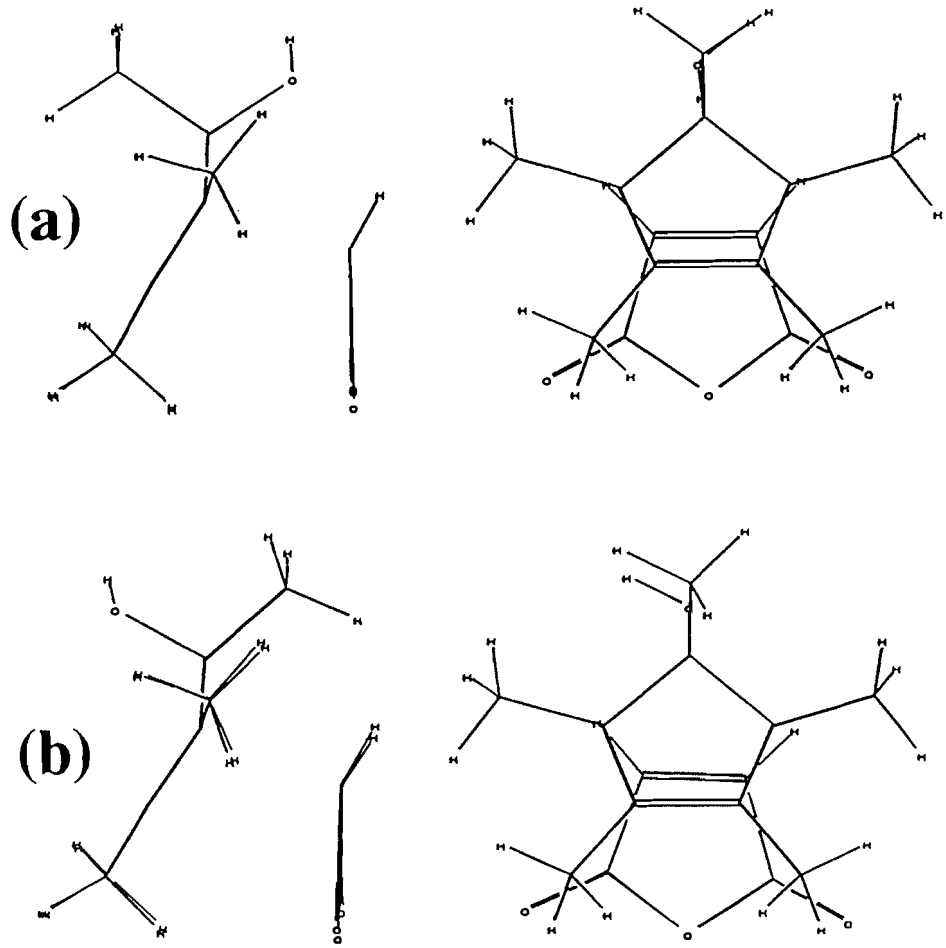

FIG. 6. (*a*): Displays of the geometrical structure of the TS for *syn* addition of **1** to **2***c*. (*b*): Displays of the geometrical structure of the TS for *anti* addition of **1** to **2***c*.

istry of Diels–Alder reactions of dienes and dieneophiles bearing bulky groups. It is interesting to note that this pyramidalisation is evident in the complexes with icbls of 2.8 Å (geometrical structures not shown) even though bonding at the bridgehead carbons C1 and C4 is not greatly advanced.

Analysis of changes in C5—X and C5—CH_3 bond lengths

In the case of additions to **2***a*–**2***d*, the CH_3—C5 bonds of the *syn* TSs are marginally longer than the CH_3—C5 bonds of the *anti* structures (Table 5). For hydroxy compound **2***c*, one of the most reactive compounds in the series, the CH_3—C5 bond *anti* to the incipient bonds of the *syn* TS is 0.012 Å longer than the CH_3—C5 bond of the *anti* diastereomer. A lengthening of the $Si(R)_3$—C5 bonds is also found for silyl compounds **2***g*, **2***i*, and **3***b* when addition occurs *anti* to the $Si(R)_3$ groups. While these results are in accord with the hyperconjugation model, it is unlikely that the differences are related to the major factor(s) responsible for the *syn* π-facial selectivity. This is so because the difference in the HO—C5 bond lengths is found to be larger — the HO—C5 bond of the *anti* transition structure is 0.021 Å longer than the HO—C5 bond of the *syn* transition structure — than the difference computed for the CH_3—C5 bonds. The same results were obtained for **2***d* and **3***b* (Table 6) and the mono-substituted dienes **4***a* and **4***b* (data not shown). An added complication in interpreting the differences in the *syn* and *anti* bond lengths at C5 and relating the results to the major factor controlling the facial selectivity is the fact that, in general, the X—C5 and CH_3—C5 bonds are shorter in the final product than in the starting diene (Tables 5 and 6). For **2***e* the C5—SCH_3 bond is longer in the *anti* transition structure than in the *syn* analogue; in the case of the silyl-substituted compounds, the Si—C bonds in of the final products are longer than the Si—C bonds of the dienes. To establish how small a change the CH_3—C5 bond length affects the energy of the TS, the CH_3—C5 bond length of the *syn* TS of **2***c* (originally 1.526 Å) was set to the bond length of the *anti* TS (1.514 Å) and an optimized geometry of the hypothetical TS was computed with a SIGMA calculation. That this geometrical structure was only 0.06 kcal/mol higher in energy than the fully optimized transition structure shows that the energy of the transition structure is relatively insensitive to small changes in the bond lengths at C5 at AM1 level of theory. Yet the facial selectivities and the relative reactivities for the D–A reactions of a group of cyclic dienes are calculated with good accuracy. While Coxon and McDonald (34) concluded on the basis of an AM1 study of the D–A addition of ethene to 5,5-disubstituted cyclopentadienes that transition state hyperconjunction was important in determining the facial selectivity, on the basis of our calculations on pentamethylcyclopentadienes, it is not possible to connect the small changes in the CH_3—C5 and X—C5 bond lengths to the major factor determining the *syn* facial selectivities found for **2***a*, **2***c*, and **2***d* with any degree of certainty.

TABLE 8. Calculational charges on selected atoms of transition structures

Transition structure	X	C5	S of CH_3—C5 Si of SiR_5—C5
2*a-syn*	−0.3320(−0.3138)[a]	0.0587(0.0683)	−0.1468(−0.1864)
2*a-anti*	−0.3191	0.0566	−0.1989
2*b-syn*	−0.3775(−0.3608)	0.1259(0.1401)	−0.2147(−0.2041)
2*b-anti*	−0.3677	0.1270	−0.2079
2*c-syn*	−0.3058(−0.3021)	0.1071(0.1273)	−0.2300(−0.2218)
2*c-anti*	−0.3058	0.1114	−0.2315
2*d-syn*	−0.2626(−0.2522)	0.1124(0.1305)	−0.2269(−0.2218)7
2*d-anti*	−0.2597	0.1159	−0.2306
2*e-syn*[b]	0.1059(0.1000)	−0.1344(−0.0990)	−0.2023(−0.1884)
2*e-anti*[b]	0.0927	−0.1111	−0.2076
2*e-syn*[c]	0.1277(0.1367)	−0.1309(−0.1049)	−0.2108(−0.1978)
2*e-anti*[c]	0.1378	−0.1202	−0.2130
2*f-syn*	0.1143(0.1146)	−0.0779(−0.0591)	−0.1985(−0.1878)
2*f-anti*	0.1271	−0.0775	−0.2005
2*g-anti*	−0.2022(−0.1759)	−0.3130(−0.2808)	0.8360(0.8410)
2*g-syn*	−0.2013	−0.2949	0.8226
2*h*	−0.1983[d](−0.1866)	−0.0222(−0.0040)	−0.1973[e](0.1866)
2*i-syn*	−0.2065(−0.1719)	−0.3291(−0.3107)	1.2429(1.2593)
2*i-anti*	−0.1995	−0.3229	1.2524
2*j-syn*	0.4344(0.4320)	−0.0564(−0.0245)	−0.2129(−0.1996)
2*j-anti*	0.4209	−0.0373	−0.2192
2*k-syn*	−0.0593(−0.0548)	−0.0051(0.0388)	−0.2371(−0.2290)
2*k-anti*	−0.07131	−0.0351	−0.2450

[a]The values in parentheses correspond to the charges of the corresponding cyclopentadiene.
[b]Computed with full AM1 parameters.
[c]Computed with mixed parameters (H, C, O; AM1: S; MNDO).
[d]The carbon of the *syn* CH_3 group.
[e]The carbon of the *anti* CH_3 group.

TABLE 9. Calculational charges on selected atoms of transition structures

Transition structure	X (OH or O)	C5 or S	Si of SiH_3
3*b-syn*	−0.2978(−0.2902)[d]	−0.1581(−0.1477)	0.8752(0.8777)
3*b-anti*	−0.3080	−0.1600	0.8826
5-*syn*[b]	−0.7410(−0.7497)	1.4328(1.4821)	
5-*anti*[b]	−0.7532	1.4417	
5-*syn*[c]	0.7028	1.0084	
5-*anti*[c]	−0.6873(−0.6981)	1.0108(1.0251)	

[a]The OH group is syn to **1**.
[b]Computed with full AM1 parameters.
[c]Computed with mixed parameters (H, C, O; AM1: S; MNDO).
[d]The values in parentheses are the charges for the diene.

Analysis of charges on atoms

The charges on the atoms X, C5, and the carbon of the methyl group attached to C5 of the *syn* and *anti* transition structures are given in Tables 8 and 9. If there is differential hyperconjugative interaction with the CH_3—C5 bond in the *syn* and *anti* transition structures then the C atom of the C5 methyl should be more positive in the *syn* transition structure than the *anti* one. Although this is the case — the differences range between 0.015 and 0.037 units of charge — similar differences are computed for the nitrogen and oxygen atoms of the *anti* TSs of **2***a*, **2***c*, and **2***d*. The situation is reversed for the *anti* and *syn* methyl groups in the *syn* and *anti* additions to acetamide **2***b*. With mixed AM1 parameters, the positive charge on the sulfur of the *anti* transition structure of **2***e* was computed to be larger than the charge on the sulfur of the *syn* analogue. Calculations with full AM1 parameters gave the opposite result. That the N atom of the *anti* transition structures of **2***k* is more negative than the N atom of the *syn* structure suggests the incipient bonds *release electrons hyperconjugatively to the polar C5—X bonds.* We recognise that the magnitudes of the atom charges calculated at the semiempirical level of theory on the whole are inaccurate, and if any interpretation/analysis of the values is attempted at all, it should be on the basis of trends. For the group of structurally similar cyclopentadienes examined in this study, we find no trends in the changes in the atom charges which could provide support for the hyperconjugation model.

Analysis of frontier molecular orbitals

The FMOs of the *syn* transition structure of **2***c* obtained with AM1 and PSI88 (39) are given in Fig. 7. Of the six frontier MOs displayed, only HOMO-3 (two spacial orientations of this MO are displayed) exhibits an involvement of the σ framework including the C5—CH_3 bond. But there is no marked interaction of σ framework (orbitals) with the π system of the dieneophile **1**. The plots of HOMO-3 and HOMO-4 suggest that the oxygen lone pairs are involved in bonding

Can. J. Chem. Downloaded from www.nrcresearchpress.com by 85.192.166.187 on 09/08/12
For personal use only.

Can. J. Chem. Downloaded from www.nrcresearchpress.com by 85.192.166.187 on 09/08/12
For personal use only.

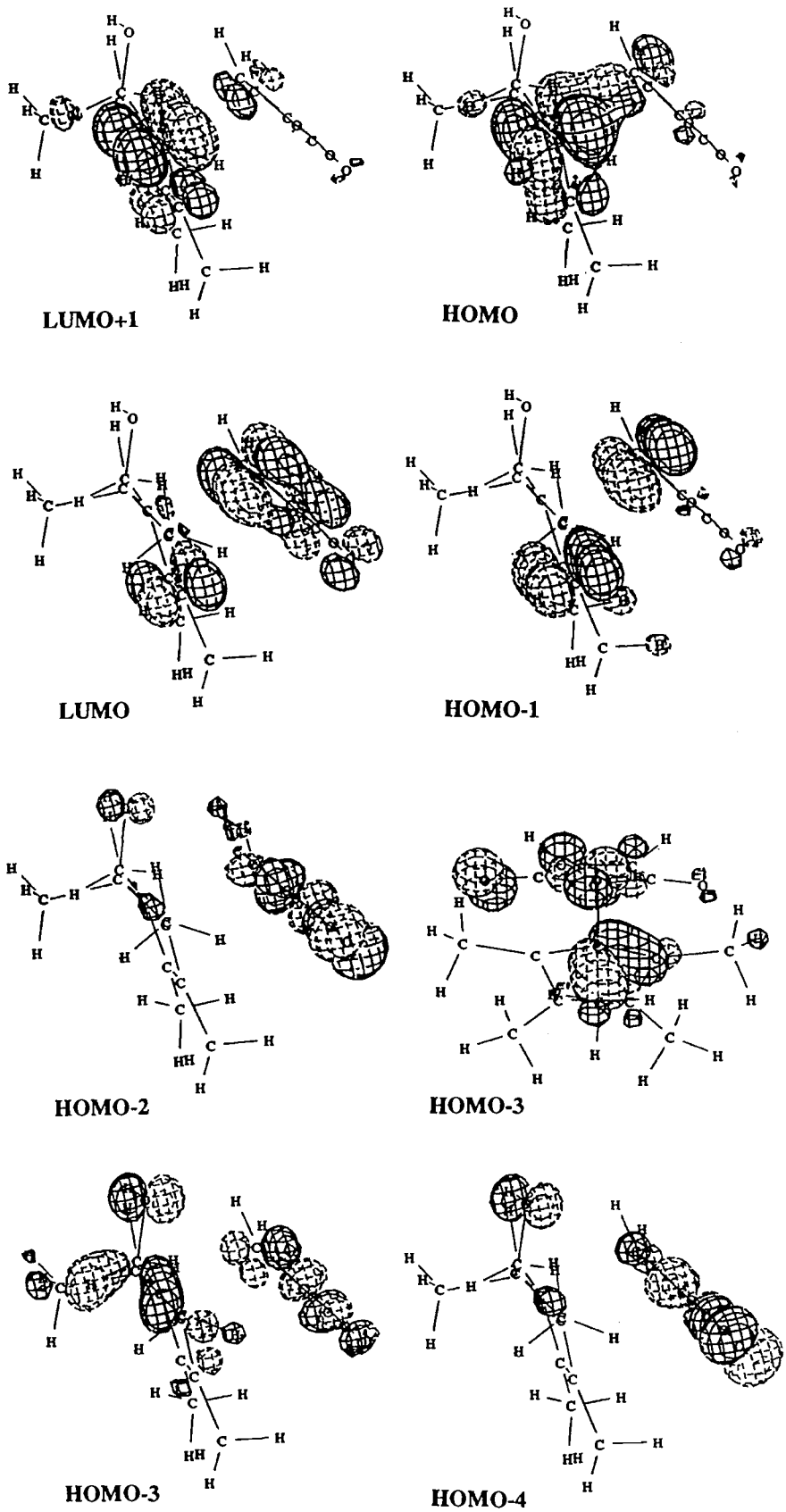

FIG. 7. Displays of the MO orbital contours (0.075 au) of selected frontier MOs of the *syn* TS of **2***c*.

Can. J. Chem. Downloaded from www.nrcresearchpress.com by 85.192.166.187 on 09/08/12
For personal use only.

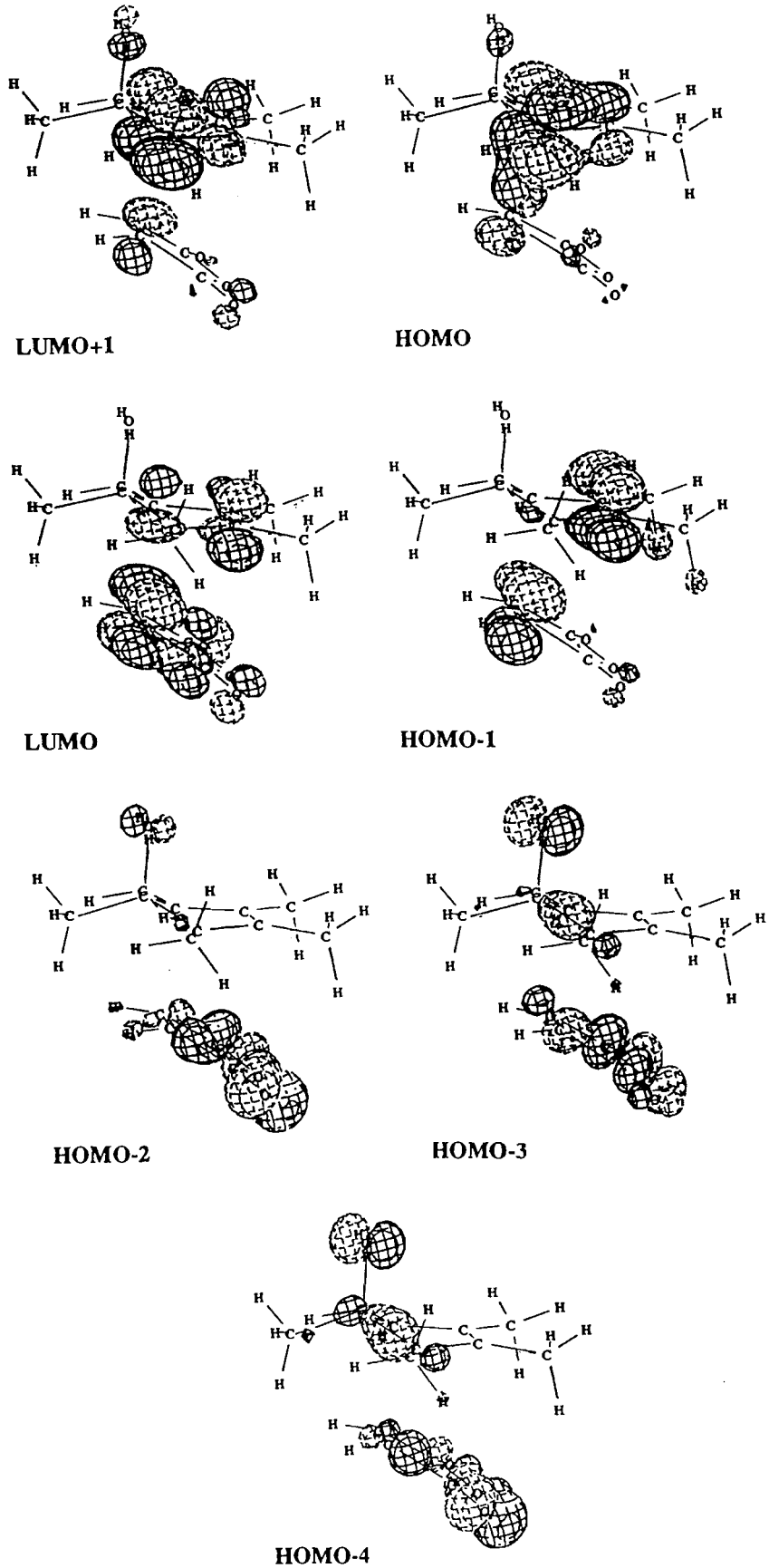

FIG. 8. Displays of the MO orbital contours (0.075 au) of selected frontier MOs of the *anti* TS of **2***c*.

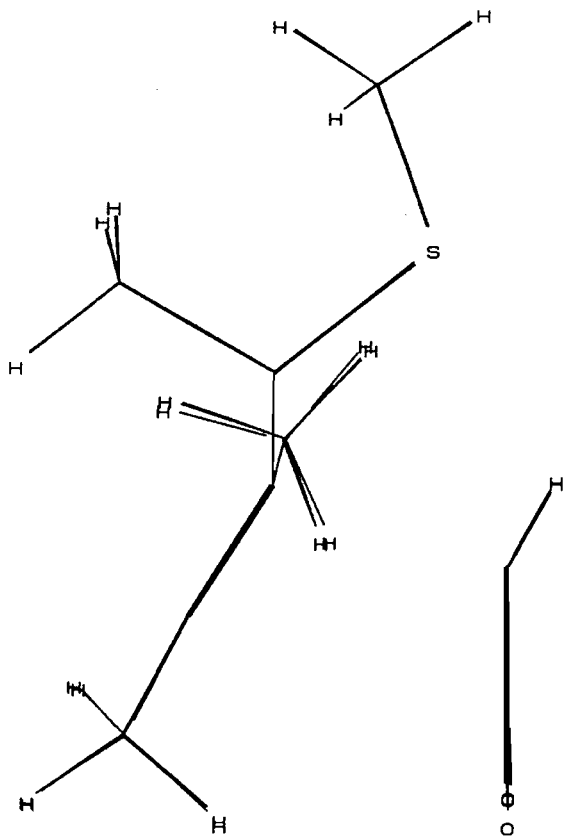

FIG. 9. Display of the geometrical structure of the TS for *syn* addition of **1** to **2***e*.

interactions; in HOMO-3 there appears to be an interaction between the lone pair on oxygen and the π system of the dieneophile in accord with Anh's proposal (16). The point here is that no MO or combination of MOs corresponds to the array of orbitals written to describe hyperconjugative interactions in terms of the Cieplak effect (29). Six frontier MOs of the *anti* transition structure are given in Fig. 8. HOMO-3 and HOMO-4 also indicate the involvement of the oxygen *lps* in bonding interactions. While care should be exercised in interpreting orbital coefficients obtained at the semiempirical level of theory, we are confident that the FMO analysis presented here is valid because we showed in an earlier study (31) that the AM1 FMOs calculated for **2***c* and **2***e* were virtually identical to *ab initio* FMOs obtained at the HF/4-31G**//HF/4-31G level of theory. In the case of **2***e* which exhibits an *anti* selectivity, HOMO-2 (MO displays not shown) shows that there is an interaction between the sulfur *lps* and one of the incipient C—C bonds. HOMO-3 exhibits an interaction between the C5—SCH_3 σ bond and the π system of **1**. The reason that the sulfur *lps* of the methylthio group do not interact with the dienophile is seen in the *syn* TS (Fig. 9); the C5—SCH_3 bond length of 1.8 Å makes overlap with the π system of the dienophile impossible.

Conclusions

AM1 accurately reproduces the π-facial selectivities and relative reactivities — differential steric and complexation effects and differences in the thermodynamic stabilities of the final products rather than transition state hyperconjugation appear to be the controlling factors — of a group of C5-substituted cyclopentadienes. This indicates that semi-empirical calculations will be useful for predicting the relative rates and facial selectivities of D–A reactions of cyclopentadienes.

Acknowledgement

We thank the Natural Sciences and Engineering Research Council of Canada for financial support.

1. S. Winstein, M. Shatavsky, C. Norton, and R.B. Woodward. J. Am. Chem. Soc. **77**, 4183 (1955).
2. D.W. Jones. J. Chem. Soc. Chem. Commun. 739 (1980).
3. K.L. Williamson, Y.L. Hsu, R. Lacko, and C.H. Young. J. Am. Chem. Soc. **91**, 6129 (1969).
4. K.L. Williamson and Y.L. Hsu. J. Am. Chem. Soc. **92**, 7385 (1970).
5. G. Bianchi, C. De Micheli, A. Gamba, and R. Gandolfi. J. Chem. Soc. Perkin Trans. **1**, 137 (1974).
6. R. Breslow and J.M. Hoffman, Jr. J. Am. Chem. Soc. **94**, 2110 (1972).
7. R. Breslow, J.M. Hoffman, Jr., and C. Perchonock. Tetrahedron Lett. 3723 (1973).
8. M. Franck-Neumann and M. Sedrati. Tetrahedron Lett. 1391 (1983).
9. D.J. Burnell and Z. Valenta. J. Chem. Soc. Chem. Commun. 1247 (1985).
10. F.K. Brown, K.N. Houk, D.J. Burnell, and A. Valenta. J. Org. Chem. **52**, 3050 (1987).
11. E.J. Corey, N.M. Weinshenker, T.K. Schaat, and W. Huber. J. Am. Chem. Soc. **91**, 5675 (1969).
12. L.A. Paquette, C. Vanucci, and R.D. Rogers. J. Am. Chem. Soc. **111**, 5792 (1989).
13. J.B. Macaulay and A.G. Fallis. J. Am. Chem. Soc. **110**, 4074 (1988).
14. M. Ishida, T. Aoyama, and S. Kato. Chem. Lett. 663 (1989).
15. A.G. Fallis and Y-F. Lu. Adv. Cycloadditions. JAI Press. Greenwich, Conn. 1993. Vol. 3, pp. 1–16.
16. A.M. Naperstkow. M.Sc. Thesis, Memorial University of Newfoundland, St. John's, Nfld. 1990.
17. N.T. Anh. Tetrahedron, **29**, 3227 (1973).
18. S. Inagaki, H. Fujimoto, and K. Fukui. J. Am. Chem. Soc. **98**, 4054 (1976).
19. R. Gleiter and L.A. Paquette. Acc. Chem. Res. **16**, 328 (1983).
20. F.K. Brown and K.M. Houk. J. Am. Chem. Soc. **107**, 1971 (1985).
21. M.H. Padden-Row, N.G. Rondan, and K.N. Houk. J. Am. Chem. Soc. **104**, 7162 (1982).
22. S.D. Kahn and W.J. Hehre. J. Am. Chem. Soc. **109**, 663 (1987).
23. S.D. Kahn and W.J. Hehre. J. Org. Chem. **53**, 301 (1988).
24. N. Kaila, R.W. Frank, and J.J. Dannenberg. J. Org. Chem. **54**, 4206 (1989).
25. M. Ishida, Y. Beniya, S. Inagaki, and S. Kato. J. Am. Chem. Soc. **112**, 8980 (1990).
26. A.S. Cieplak. J. Am. Chem. Soc. **103**, 4540 (1981).
27. A.S. Cieplak, B.D. Tait, and C.R. Johnson. J. Am. Chem. Soc. **111**, 8447 (1989).
28. W.-S. Chung, N.J. Turro, S. Srivastava, H. Li, and W.J. le Noble. J. Am. Chem. Soc. **110**, 7882 (1988).
29. A.M. Naperstkow, J.B. Macaulay, M.J. Newlands, and A.G.N. Fallis. Tetrahedron Lett. 5077 (1989).
30. J.B. Macaulay and A.G. Fallis. J. Am. Chem. Soc. **112**, 1136 (1990).
31. N.H. Werstiuk, J. Ma, J.B. Macaulay and A.G. Fallis. Can. J. Chem. **70**, 2798 (1992).
32. Dewar Research Group and J.J.P. Stewart. Austin Method I, Package 1.0. QCPE 506, QCPE Bulletin. 6, 2 (1986).
33. PCMODEL Version 4.0. A molecular mechanics package including MM2 (Allinger-QCPE 395), MMP1 Pi (Allinger-QCPE 318), and MODEL parameters (Still) plus more atoms and constants by K.E. Gilberta and J.J. Gajewski, Indiana University. Available

Can. J. Chem. Downloaded from www.nrcresearchpress.com by 85.192.166.187 on 09/08/12
For personal use only.

from Dr. K.E. Gilbert, Serena Software, P.O. Box 3096, Bloomington, IN, 47402-3076.
34. J.M. Coxon and D.Q. McDonald. Tetrahedron, **48**, 3353 (1992).
35. PC-VIBRATE. Available from Serena Software, P.O. Box 3096, Bloomington, IN, 47402-3076.
36. I. Brizna and A.G. Fallis. To be published.
37. J.J.P. Stewart. *In* Reviews in computational chemistry. *Edited by* K.B. Lipkowitz and D.B. Boyd. VCH Publishers, New York. 1990. Chapt. 2, p. 68.
38. D. Chmielewski, N.H. Werstiuk, and T.A. Wildman. Can. J. Chem. **71**, 1741 (1993).
39. W.L. Jorgensen and D.L. Severence. Department of Chemistry, Yale University, New Haven, Conn. PSI/88, Version 1.0

Can. J. Chem. Downloaded from www.nrcresearchpress.com by 85.192.166.187 on 09/08/12
For personal use only.

Studies on the interaction of selenite and selenium with sulphur donors. Part 2. A kinetic study of the reaction with 2-mercaptoethanol

WIMAL AMARATUNGA[1] AND JOHN MILNE

Ottawa–Carleton Chemistry Institute, Department of Chemistry, University of Ottawa, Ottawa, ON K1N 6N5, Canada

Received July 18, 1994

WIMAL AMARATUNGA and JOHN MILNE. Can. J. Chem. **72**, 2506 (1994).

Selenous acid is reduced by 2-mercaptoethanol in water to elemental selenium in two stages.

$$H_2SeO_3 + 4HOC_2H_4SH \rightarrow HOC_2H_4SSeSC_2H_4OH + HOC_2H_4SSC_2H_4OH + 3H_2O$$

$$HOC_2H_4SSeSC_2H_4OH \rightarrow Se + HOC_2H_4SSC_2H_4OH$$

The reactions have been followed by spectrophotometry and by proton and ^{77}Se NMR spectroscopy. The mechanism of the first stage parallels that proposed for butyl thiols in 60% dioxane but nucleophilic attack by RS^- rather than RSH on the Se(IV) intermediate, $RSSeO_2^-$, is of greater significance for 2-mercaptoethanol than for *n*-butylthiol. The signals of three intermediates are observed in the Se-77 NMR spectra of a mixture undergoing the first reaction stage. These arise from $HOC_2H_4SSeO_2^-$, $(HOC_2H_4S)_2SeO$, and an asymmetric intermediate that chemical shift evidence suggests is the sulfinic acid ester, $HOC_2H_4S(O)SeSC_2H_4OH$. The second stage involves coordination of the bis(thio)selenide by thiolate followed by decomposition to disulfide and selenium. Evidence is presented to support a reaction mechanism involving nucleophilic attack exclusively at Se(II) and not at S(II) as suggested in previous work. This stage is strongly accelerated at basic pH and, at pH 8.3 and above, both the first and second stages can take place simultaneously.

WIMAL AMARATUNGA et JOHN MILNE. Can. J. Chem. **72**, 2506 (1994).

L'acide sélénieux est réduit par le 2-mercaptoéthanol dans l'eau pour conduire au sélénium élémentaire, en deux étapes.

$$H_2SeO_3 + 4HOC_2H_4SH \rightarrow HOC_2H_4SSeC_2H_4OH + HOC_2H_4SSC_2H_4OH + 3H_2O$$

$$HOC_2H_4SSeC_2H_4OH \rightarrow Se + HOC_2H_4SC_2H_4OH$$

On a suivi les réactions par spectrophotométrie et par spectroscopie RMN du ^1H et du ^{77}Se. Le mécanisme de la première étape est parallèle à celui proposé pour les butylthiols, dans le dioxane à 60%; toutefois l'attaque nucléophile par le RS^- plutôt que celle du RSH sur l'intermédiaire Se(IV), $RSSeO_2^-$, est plus importante que celle du 2-mercaptoéthanol sur le *n*-butylthiol. On peut observer les signaux de trois intermédiaires en RMN du ^{77}Se d'un mélange dans la première étape de la réaction. Ils proviennent du $HOC_2H_4SSeO_2^-$, du $(HOC_2H_4S)_2SeO$ et d'un intermédiaire asymétrique pour lequel une structure d'ester sulfinique, $HOC_2H_4S(O)SeSC_2H_4OH$, est suggérée par le déplacement chimique. La deuxième étape implique une coordination du bis(thio)sélénure par le thiolate suivie par la décomposition en disulfure et en sélénium. On présente des données qui supportent un mécanisme réactionnel impliquant une attaque nucléophile exclusivement au niveau du Se(II) et non pas au niveau du S(II) tel que suggéré dans un travail antérieur. Cette étape est fortement accélérée en milieu basique; à des pH de 8,3 et plus, les deux premières étapes peuvent se produire simultanément.

[Traduit par la rédaction]

Introduction

The antioxidant and cancer-inhibiting properties of selenium in biological systems have stimulated great interest in its biochemistry (1, 2). It is generally accepted (3, 4) that selenium(IV) undergoes reduction to a bis(alkylthio)selenide, RSSeSR, in living systems, according to a reaction first demonstrated to take place by Ganther (5),

[1] $$4\,RSH + H_2SeO_3 \rightarrow RSSeSR + RSSR + 3\,H_2O$$

Some thiosulfinate is also produced in the case of bulky thiols (6). It has been shown (5) that the bis(thio)selenides are readily decomposed to elemental selenium and the disulfide in the presence of excess thiolate under basic conditions.

[2] $$RSSeSR \xrightarrow[RSH]{} Se + RSSR$$

This is the basis of a turbidimetric method of analysis for Se(IV), using 2-mercaptoethanol as the reducing agent (7). The reduction of selenite by 2-mercaptoethanol at neutral to basic pH in the presence of excess HOC_2H_4SH is a two-stage process. There is an initial stage during which the solution remains clear, followed by a stage when the solution becomes turbid due to the formation of elemental selenium. For selenium analysis this method is complicated by the dissolution of selenium by excess thiolate, which has been shown to be a result of selenothiolate formation (8).

[3] $$Se + RS^- \rightleftharpoons RSSe^-$$

Kice et al. have studied the kinetics of reactions [1] (6) and [2] (9) for butyl thiols in 60% aqueous dioxane solutions. Their proposed mechanism for reaction [1] proceeds by formation of the bis(alkylthio)selenoxide, $(RS)_2SeO$, which, after rearrangement to RSOSeSR, undergoes further attack by 2 moles of RSH to form RSSeSR and RSSR. Peracetic acid oxidation of *t*-BuSSeSBu-*t* in $CDCl_3$ has provided evidence for the formation of the RSOSeSR intermediate (10). The Se-77 NMR chemical shift of this intermediate suggests that it is an oxygen-bridged species but it may also be a sulfinic acid ester, RS(O)SeSR. Evi-

[1]Chemical Industries (Colombo) Ltd., P. O. Box 352, Colombo, Sri Lanka.

[2]Author to whom correspondence may be addressed.

Can. J. Chem. Downloaded from www.nrcresearchpress.com by 85.192.166.187 on 09/08/12
For personal use only.

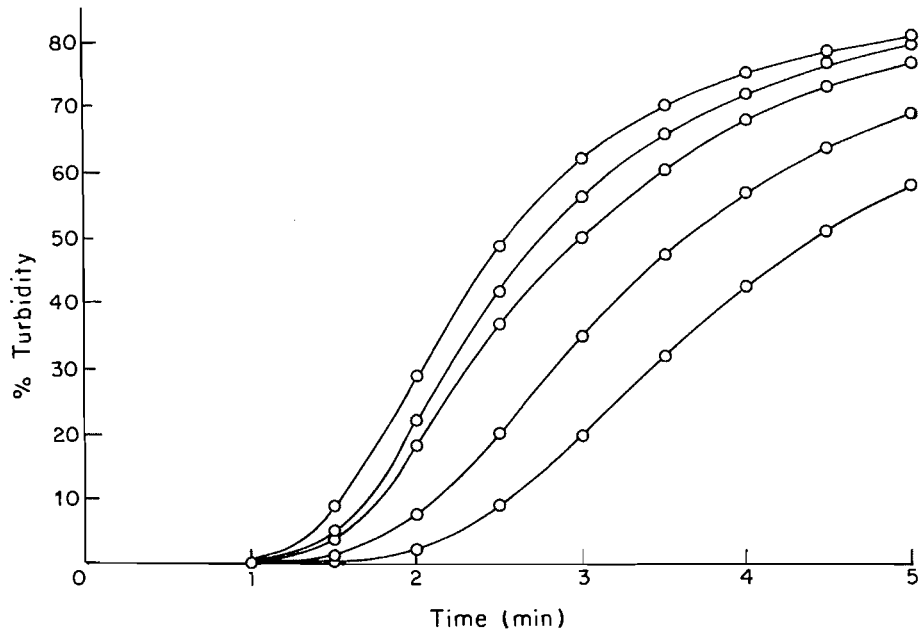

FIG. 1. Turbidity plots at 600 nm for $c(H_2SeO_3) = 5.0 \times 10^{-4}$ mol L^{-1} and $c_i(HOC_2H_4SH) = 6.0 \times 10^{-3}$, 5.4×10^{-3}, 4.8×10^{-3}, 4.2×10^{-3}, and 3.6×10^{-3} mol L^{-1}.

dence for the formation of this intermediate in the reduction of Se(IV) (reaction [1]) is, however, lacking.

The mechanism for reaction [2] is thought to proceed by bimolecular nucleophilic attack of RS^- in RSSeSR at sulphur.

[4] $RS^- + RSSeSR \rightarrow RSSR + SeSR^-$

This would then proceed to give elemental selenium by the reverse of equilibrium [3] (8).

Our interest in the course of the metabolism of selenite in bacterial systems and the stability of Se(II) in such systems (11) led us to explore the chemistry of the Se(IV)–thiol interaction. As a model thiol we chose 2-mercaptoethanol, which is a relatively simple molecule, is readily available, and has the advantage of being water soluble.

Experimental section

Kinetics

The rates of the two steps of the first stage of the reduction of selenous acid by 2-mercaptoethanol (reaction [1]) were followed by spectrophotometry at 310 nm. The solutions became pale yellow during this stage. The second stage (reaction [2]) was followed by transmission turbidimetry at 600 nm. During this stage, the solutions became orange-red turbid. The rate for the first stage could also be monitored at 600 nm through the length of the induction period before the solutions became turbid. Solutions of SeO_2 (Aldrich) and 2-mercaptoethanol (Aldrich) in the millimolar range were made up in 0.050 M potassium phosphate buffer in the pH range 6.85–8.40, and in acetate buffer at pH 5.5. All solutions were made up with distilled water purged of oxygen. The change in absorbance with time was followed in a water-jacketed 1 cm pathlength silica cell at 25.0 ± 0.1°C in a Varian DMS 90 or Varian/Cary 1E spectrophotometer.

The first stage of the reduction was followed initially via the induction period before the solutions became turbid. The induction period was determined by extrapolation of the turbidity curve at its steepest slope to zero absorbance. The rate was taken as selenous acid concentration ($c(H_2SeO_3)$) divided by induction period. The first stage was also followed by monitoring the rate of increase in absorbance at 310 nm due to the formation of $HOC_2H_4SSeO_2H$ (reaction [5], pH 5.5) and $(HOC_2H_4S)_2Se$ (reactions [6], [7], and [8], pH 6.85). This wavelength was chosen to avoid any absorbance by selenite, thiol, or buffer. For reactions [5] and [6] (first stage), the change in concentration over time was taken as the rate for the mean concentrations of the reacting species.

The second stage of the reduction was followed by turbidimetry. The rate was determined from the slope of absorbance vs. time plots at the point of half-reaction ($t_{1/2}$: $[HOC_2H_4SSeSC_2H_4OH] = 1/2\ c_i(HOC_2H_4SSeSC_2H_4OH)$). This procedure was felt to be more accurate than that of Apak and co-workers (7), because of the uncertainty in the initial slopes.

NMR spectra

The Se-77 NMR spectra were measured with a Bruker AMX 500 spectrometer operating at 95.48 MHz. A 90° tip angle and 2 s pulse delay were used. The samples were contained in 10 mm diameter precision NMR tubes. The mixtures were made up at 0°C from deoxygenated aqueous solutions of HOC_2H_4SH and SeO_2 (4:1 mole ratio) and placed immediately in the spectrometer probe held at 0°C. All chemical shifts were measured by sample replacement with respect to saturated selenous acid in water at 22°C (12). The chemical shifts are all listed relative to $\delta(Me_2Se) = 0.0$ ppm ($\delta(Me_2Se) = \delta(H_2SeO_3) + 1300$ ppm (12)).

The proton NMR spectra were measured using a Varian FT300 spectrometer. The chemical shifts were measured relative to the known $\delta(Me_4Si)$ of HOC_2H_4SH and $HOC_2H_4SSC_2H_4OH$ in D_2O solution (8). The chemical shifts measured at 9°C are referred to Me_4Si at 20°C. The temperature coefficient for these signals was found to be 0.02 ppm/°C.

Results and discussion

Under most of the conditions used in this work (pH > 6.5, millimolar $c(HOC_2H_4SH)$ and $c(Se(IV))$, the two stages of the reduction were readily observed, as shown in Fig. 1. Any interference from reaction [3] is negligible under these conditions, as indicated by a consideration of the dissociation constant for HOC_2H_4SH (2.5×10^{-10} mol L^{-1} (13)) and the equilibrium constant for reaction [3] (0.33 (8)). The two stages represented by reactions [1] and [2] will be considered.

Induction period; reaction [1]

In general, without excess RSH ($c(RSH)/c(H_2SeO_3) \leq 4.0$) and at acid pH, RSSeSR is produced according to reaction [1] (5, 8) and subsequent reduction by reaction [2] is slow. A

Can. J. Chem. Downloaded from www.nrcresearchpress.com by 85.192.166.187 on 09/08/12
For personal use only.

TABLE 1. Dependence of rate of reaction [1] on $c(HOC_2H_4SH)$ at pH = 6.85 ($c_i(H_2SeO_3) = 5 \times 10^{-4}$ M)

10^4 $[HOC_2H_4SSeO_2H]^b$ (mol L^{-1})	10^3 $[HOC_2H_4SH]^b$ (mol L^{-1})	10^3 $c_i(HOC_2H_4SH)$ (mol L^{-1})	10^6 Rate[a] (mol L^{-1} s^{-1})	k_1 (L mol^{-1} s^{-1})
2.5	4.8	6.0	6.3	5.3
2.5	4.2	5.4	5.6	5.3
2.5	3.6	4.8	5.3	5.9
2.5	3.0	4.2	4.5	6.0
2.5	2.4	3.6	3.8	6.3

[a]Determined from the induction period.
[b]Concentrations at half-reaction; $[HOC_2H_4SH] = c_i(HOC_2H_4SH) - (5/2)c_i(H_2SeO_3)$.

kinetic study of this stage has been made for *t*-BuSH and *n*-BuSH in 60% aqueous dioxane (6) and a mechanism has been proposed consisting of two kinetically distinguishable steps, an initial equilibrium,

$$[5] \quad H_2SeO_3 + RSH \underset{k_r}{\overset{k_f}{\rightleftharpoons}} RSSeO_2H + H_2O$$

followed by the slow step,

$$[6] \quad RSSeO_2H + RSH \xrightarrow[k_1]{\text{slow}} (RS)_2SeO + H_2O$$

This reaction is followed by several rapid steps to produce RSSeSR and RSSR.

$$[7] \quad (RS)_2SeO \xrightarrow{\text{rapid}} RSOSeSR$$

$$[8] \quad RSOSeSR + RSH \xrightarrow{\text{rapid}} RSSeSR + RSOH$$

$$[9] \quad RSOH + RSH \xrightarrow{\text{rapid}} RSSR + H_2O$$

Rates for the reaction of HOC_2H_4SH and H_2SeO_3 (4:1 mole ratio; pH = 6.85) determined from the induction period, assuming complete reaction to $(HOC_2H_4S)_2Se$ before any Se turbidity occurs, are given in Table 1 for constant $c_i(H_2SeO_3)$ ($= 5 \times 10^{-4}$ mol L^{-1}) and varying $c(HOC_2H_4SH)$. As shown in previous work (6) and demonstrated below for HOC_2H_4SH, the equilibrium constant for reaction [5] is large and formation of $HOC_2H_4SSeO_2H$ is essentially complete. The induction period is then determined principally by reaction [6], which has been shown to be second order (See Tables 1 and 3). The rate calculated from the induction period will be lower than the true rate for the starting concentration and better corresponds to the concentrations at half-reaction. An estimate of the rate constant for [6], k_1, may be calculated from the rates and the half-reaction concentrations assuming reaction [5] is complete, and these are given in Table 1 ($k_1 = 5.8 \pm 0.4$ L mol^{-1} s^{-1}).

The steps represented by reactions [5] and [6] may be studied separately. At pH 5.5, reaction [5] proceeds at a conveniently slow rate and may be distinguished from reaction [6], which is much slower at this pH. The rates of these individual steps were studied by spectrophotometry. The spectral changes for the various steps are shown in Fig. 2. Individually, selenite, 2-mercaptoethanol, and buffer exhibit weak absorbances below 250 nm, which are not significant relative to the absorbance of the Se(IV) species formed and are ignored. As reaction [5] proceeds, the spectra show an increase in absorbance at 260 nm with the production of $HOC_2H_4SSeO_2H$. At pH 6.85 and above, reaction [5] is rapid and is followed by a decrease in the absorbance of this peak accompanied by an increase in absorbance at 225 and 300 nm. The absorbance at 300 nm arises from a broad peak centred at 263 nm. Two isosbestic points at 242 and 273 nm are observed, consistent with the presence of two species, one of which has two peaks in this region of the spectrum. These changes are due to the formation of $(HOC_2H_4S)_2Se$, according to reaction [6], followed by reactions [7] and [8], which are rapid. The decrease in the 260 nm peak is not as large as might be expected because the $(HOC_2H_4S)_2Se$ and the disulfide, $HOC_2H_4SSC_2H_4OH$, formed in subsequent reactions, also absorb in this region.

The first step of this stage, reaction [5], is governed by the differential rate law,

$$[10] \quad \text{Rate} = k_f[H_2SeO_3][HOC_2H_4SH] - k_r[HOC_2H_4SSeO_2H]$$

The absorbance data at 310 nm, which are free of interferences from acetate buffer, HOC_2H_4SH, and H_2SeO_3, are readily fit to this rate law for an extinction coefficient, $\epsilon_{310}(HOC_2H_4SSeO_2H)$ of 500 L mol^{-1} cm^{-1}, $k_f = 5.6$ L mol^{-1} s^{-1}, and $k_r = 1.6 \times 10^{-3}$ s^{-1}, as shown in Table 2. The equilibrium constant for reaction [5] is then 3500 L mol^{-1} at pH 5.5, which is to be compared with 300 L mol^{-1} for *t*-BuSH and a much larger value for *n*-BuSH in 60% dioxane at comparable pH (6).

At pH = 6.85, reaction [5] goes rapidly to completion (<15 s) and the peak at 260 nm, due to $HOC_2H_4SSeO_2H$, begins to decrease in intensity, while the absorbance at 225 and 300 nm increases, due to the formation of $(HOC_2H_4S)_2Se$, which is rapidly formed from $(HOC_2H_4S)_2SeO$ via reactions [7] and [8]. The rate constant, k_1, for the second-order rate law,

$$[11] \quad \text{Rate} = k_1[HOC_2H_4SSeO_2H][HOC_2H_4SH]$$

was calculated from the absorbances given in Table 3. The extinction coefficients used were $\epsilon_{310}(HOC_2H_4SSeO_2H) = 480$ L mol^{-1} cm^{-1}, which is slightly smaller than the value determined at pH 5.5, and $\epsilon_{310}((HOC_2H_4S)_2Se) = 645$ L mol^{-1} cm^{-1}, which was measured for a 4:1 HOC_2H_4SH/H_2SeO_3 molar mixture in unbuffered water ($c(HOC_2H_4S)_2Se) = 1.0 \times 10^{-3}$ mol L^{-1}) after complete reaction, according to eq. [1]. This gave $k_1 = 6 \pm 1$ L mol^{-1} s^{-1}, which compares well with the initial value of k_1 estimated from the induction period at pH 6.85.

The induction period, during which reactions [5] and [6] of the first stage of the reduction are rate determining, decreases with increasing pH. The rates for this stage, at $c_i(H_2SeO_3) = 5.0 \times 10^{-4}$ mol L^{-1} and $c_i(HOC_2H_4SH) = 2.0 \times 10^{-3}$, are plotted against pH in Fig. 3. At pH = 6.85, the rate of the first step (k_f) is

Can. J. Chem. Downloaded from www.nrcresearchpress.com by 85.192.166.187 on 09/08/12
For personal use only.

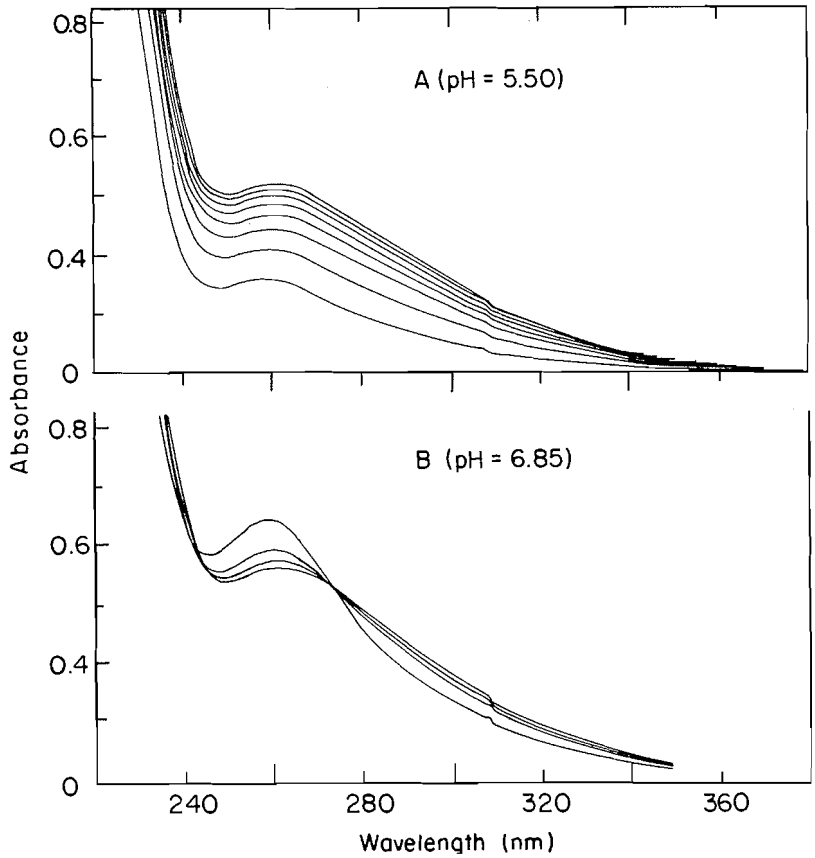

FIG. 2. Spectral changes with time for reactions [5] and [6] of the reduction of H_2SeO_3. Trace A: Formation of $HOC_2H_4SSeO_2H$ at pH = 5.5. Trace B: Formation of $(HOC_2H_4S)_2Se$ at pH = 6.85.

TABLE 2. Evaluation of the forward, k_f, and reverse, k_r, rate constants for step 1 of the first stage (reaction [5]) at pH = 5.5 from absorbance data at 310 nm. Initial $c(H_2SeO_3) = 5 \times 10^{-4}$ mol L^{-1}; initial $c(HOC_2H_4SH) = 2 \times 10^{-3}$ mol L^{-1}

Time (s)	A_{310}	10^4 [a] $c(HOC_2H_4SSeO_2H)$	10^6 Obsd. rate (mol L^{-1} s^{-1})	10^{6b} Calcd. rate (mol L^{-1} s^{-1})
25	0.060	1.20	4.8	4.7
63	0.116	2.32	2.9	3.0
101	0.150	3.00	1.8	1.9
139	0.172	3.44	1.2	1.2
177	0.187	3.74	0.8	0.7

[a]Calculated, using $\epsilon_{310}(HOC_2H_4SSeO_2H) = 500$ L mol^{-1} cm^{-1}.
[b]Calculated for $k_f = 5.6$ L mol^{-1} s^{-1}, $k_r = 1.6 \times 10^{-3}$ s^{-1}.

TABLE 3. Evaluation of the rate constant, k_1, for step 2 (reaction [6]) of the first stage at pH = 6.85 from absorbance data at 310 nm. Initial $c(HOC_2H_4SSeO_2H) = 5 \times 10^{-4}$ mol L^{-1}; initial $c(HOC_2H_4SH) = 2 \times 10^{-3}$ mol L^{-1}

Time (s)	A_{310}	10^4 $[HOC_2H_4SSeO_2H]$ (mol L^{-1})	10^3 $[HOC_2H_4SH]$ (mol L^{-1})	10^6 Obsd. rate (mol L^{-1} s^{-1})	k_1[a] (mol L^{-1} s^{-1})
38	0.244	4.8	1.43	8.3	6.9
76	0.263	3.6	1.09	3.0	5.6
114	0.277	2.8	0.84	2.2	7.3
190	0.290	2.0	0.59	1.1	6.3

[a]Calculated from $\epsilon_{310}(HOC_2H_4SSeO_2H) = 480$ L mol^{-1} cm^{-1} and $\epsilon_{310}((HOC_2H_4S)_2Se) = 645$ L mol^{-1} cm^{-1}.

Can. J. Chem. Downloaded from www.nrcresearchpress.com by 85.192.166.187 on 09/08/12
For personal use only.

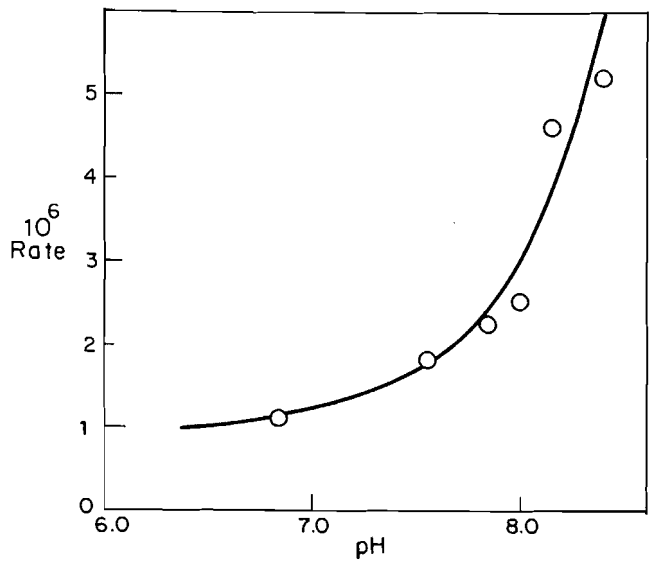

FIG. 3. Variation in the rate of reaction [6] with pH as determined from the induction period.

too rapid for measurement by normal methods and the pH effect illustrated in Fig. 3 must arise in the second step. Many pathways contribute to reaction [6] (6) that are dependent upon the ionic dissociation equilibria of $HOC_2H_4SSeO_2H$ and HOC_2H_4SH and the rates of the reactions between the various thiol and thioselenous acid species formed. For purposes of fitting the rate curve in Fig. 3 over the range of pH studied (6.85–8.40), the contribution of the $HOC_2H_4SSeO_2H_2^+$ ion was ignored and only the equilibria,

$$[12]\quad HOC_2H_4SSeO_2H \overset{K_a}{\rightleftharpoons} H^+ + HOC_2H_4SSeO_2^-$$

$$[13]\quad HOC_2H_4SH \overset{K_s}{\rightleftharpoons} H^+ + HOC_2H_4S^-$$

and the rates of the reactions,

$$[14]\quad HOC_2H_4SSeO_2H + HOC_2H_4SH \xrightarrow{k_{RSH}} (HOC_2H_4S)_2SeO + H_2O$$

$$[15]\quad HOC_2H_4SSeO_2H + HOC_2H_4S \xrightarrow{k_{RS^-}} (HOC_2H_4S)_2SeO + OH^-$$

$$[16]\quad HOC_2H_4SSeO_2^- + HOC_2H_4SH \xrightarrow{k^-_{RSH}} (HOC_2H_4S)_2SeO + OH^-$$

$$[17]\quad HOC_2H_4SSeO_2^- + HOC_2H_4S^- \xrightarrow[H_2O]{k^-_{RS^-}} (HOC_2H_4S)_2SeO + 2\ OH^-$$

were considered. The equilibrium and rate expressions for [12]–[17] and the mass balance for selenium species may be used to derive the expression,

$$[18]\quad \frac{d[(HOC_2H_4S)_2SeO]}{dt} = c_{Se}[HOC_2H_4SH] \times \frac{k_{RSH}[H^+] + k_{RS^-}K_s + k^-_{RSH}K_a + k^-_{RS^-}K_aK_s/[H^+]}{[H^+] + K_a}$$

where c_{Se} represents total Se species concentration. Using the dissociation constant for HOC_2H_4SH (13), the observed variation in rate with pH in Fig. 3 could be best reproduced by choosing $k_{RSH} = 5 \times 10^{-3}$ L mol^{-1} s^{-1}, $K_a = 1.2 \times 10^{-4}$ mol L^{-1}, $(k_{RS^-}K_s + k^-_{RSH}K_a) = 5 \times 10^{-4}$ s^{-1}, and $k^-_{RS^-} = 1.2 \times 10^2$. Unlike the previous work with *n*-BuSH and *t*-BuSH, which extended only up to pH 7.0, it was not possible to produce the strong increase in rate with increasing pH without inclusion of reactions [16] and [17]. Since the rate-determining step may be considered in general as a nucleophilic attack on Se(IV), it is to be expected that the rate constants for reactions involving $HOC_2H_4S^-$, reactions [15] and [17], will be large relative to those involving HOC_2H_4SH and that the rate will increase significantly with increasing pH. It should be noted that $k^-_{RS^-}$ is much greater than k_{RSH} in spite of the unfavourable combination of two anions, $HOC_2H_4SSeO_2^-$ and $HOC_2H_4S^-$, in reaction [17].

NMR spectra, reaction [1]

The Se-77 NMR spectrum of a solution 0.30 mol L^{-1} in SeO_2 and 0.60 mol L^{-1} in HOC_2H_4SH at 0°C shows two signals at δ = 1296 and 671 ppm with intensities 1.0 and 1.8, respectively. When the solution is warmed to 20°C, two equally intense signals are observed at 1298 and 681 ppm. The signal at 1298 ppm, which is shifted to lower frequency at the lower temperature, is due to unreacted H_2SeO_3 (12). The reported temperature coefficient for H_2SeO_3 is 0.094 ppm/K (12), which accounts well for the shift with temperature observed here. The 681 ppm signal is due to $(HOC_2H_4S)_2Se$, which has δ = 684 ppm for a saturated solution in pure water (8). The 1:1 intensity ratio of the room temperature spectrum corresponds to complete reaction according to eq. [1], which for a 2:1 HOC_2H_4SH/H_2SeO_3 mole ratio solution would result in a 1:1 $(HOC_2H_4S)_2Se/H_2SeO_3$ mole ratio mixture. The reported temperature coefficients for Se species, 0.025–0.094 ppm/K (12, 14), do not account for the chemical shift from 671 to 681 ppm when the temperature is raised to 20°C. This, and the nearly 2:1 intensity ratio of the 671 and 1296 ppm peaks at 0°C, shows that this shift is not due to the bis(thio)selenide but is probably a result of the initial formation of $HOC_2H_4SSeO_2H$ or $(HOC_2H_4S)_2SeO$ in the solution.

The Se-77 NMR spectra of a solution of 0.20 mol L^{-1} H_2SeO_3 and 0.80 mol L^{-1} HOC_2H_4SH at 0°C, studied over an 80 min time period, are shown in Fig. 4. No signal for selenous acid is observed in the spectra of any of these 4:1 HOC_2H_4SH/H_2SeO_3 solutions, showing that step 1 takes place rapidly at neutral pH even at 0°C. At 20 min, the spectrum consists of a strong signal at 667 ppm with a weak signal at 683 ppm due to trace formation of $(HOC_2H_4S)_2Se$. The formation of trace amounts of $(HOC_2H_4S)_2Se$ was unavoidable in spite of cooling, due to the difficulty in efficient mixing of the reactant solutions in the NMR tube with these 4:1 solutions and the favourable conditions for reaction [2] in the presence of excess HOC_2H_4SH (vide infra). At 40 min, the 667 ppm signal has fallen in intensity and new signals at 670 and 685 ppm appear. At 60 min both of the signals at lower chemical shift have disappeared and only the signal at 685 ppm and a new signal at 683 ppm, due to the final product, $(HOC_2H_4S)_2Se$, are observed. Finally at 80 min only the signal due to the bis(hydroxyethylthio)selenide is observed. This signal is broadened ($w_{1/2} \sim$ 0.75 ppm) due to the presence of some insoluble bis(hydroxyethylthio)selenide (8). The sequence of changes is readily interpreted in terms of the various species formed in the mechanism proposed by Kice et al. (6). The first signal observed after 20

Can. J. Chem. Downloaded from www.nrcresearchpress.com by 85.192.166.187 on 09/08/12
For personal use only.

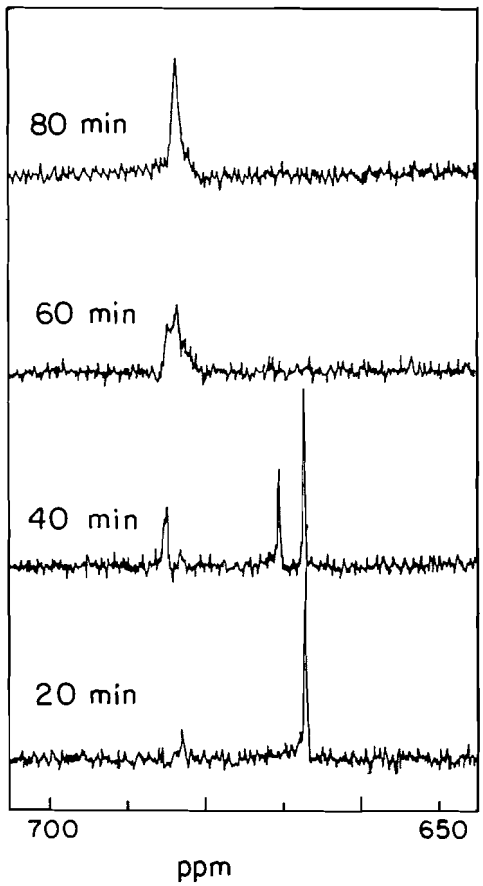

FIG. 4. ^{77}Se NMR spectra of a HOC_2H_4SH/H_2SeO_3 mixture ($c(HOC_2H_4SH)$ = 0.80 mol L^{-1}; $c(H_2SeO_3)$ = 0.20 mol L^{-1}; unbuffered, 0°C), taken at various times.

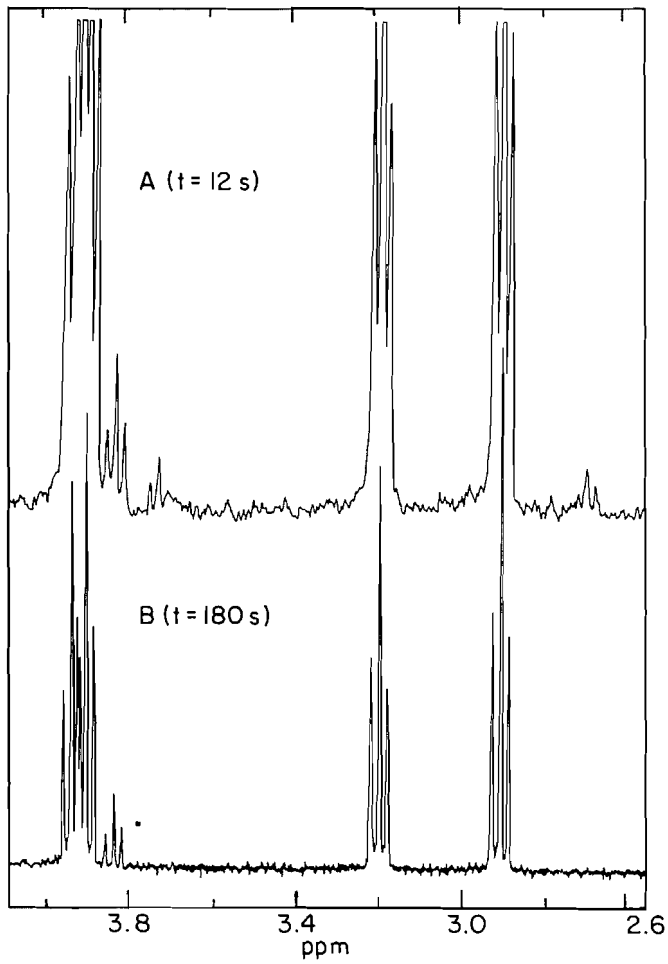

FIG. 5. Proton NMR spectra of a HOC_2H_4SH/H_2SeO_3 mixture ($c(HOC_2H_4SH)$ = 0.21 mol L^{-1}; $c(H_2SeO_3)$ = 0.054 mol L^{-1}, unbuffered, 9°C), taken at (*A*) 12 s; (*B*) 180 s.

min, at 667 ppm, is assigned to $HOC_2H_4SSeO_2H$, which is relatively rapidly formed in solution in reaction [5]. Excess HOC_2H_4SH in solution then causes the slower reaction [6] to proceed, with the formation of $(HOC_2H_4S)_2SeO$, for which δ = 670 ppm. This species rapidly rearranges to a third intermediate, which may be $HOC_2H_4OSSeSC_2H_4OH$ or $HOC_2H_4S(O)SeSC_2H_4OH$ by reaction [7], producing the signal at 685 ppm. Subsequent reactions with excess thiol via eqs. [8] and [9] then give the final product, $(HOC_2H_4S)_2Se$, with δ = 683 ppm.

The Se-77 signals for $HOC_2H_4SSeO_2H$ and $(HOC_2H_4S)_2SeO$ at 667 and 670 ppm are the lowest observed for Se(IV) species (15). The Se-77 chemical shifts for Se(IV) species range from 738 to 1479 ppm (16). No examples of Se-77 NMR spectra of Se(IV) species with Se—S bonds have been reported but, on the basis of the comparable electronegativities of carbon and sulphur, Se(IV) species with bonded sulphur would be expected to have shifts near those of selenoxides, which lie at the low-frequency end of the reported range. The chemical shift of the asymmetric *t*-BuSOSeSBu-*t* intermediate in the oxidation of $(t\text{-BuS})_2Se$ with peracetic acid has a Se-77 chemical shift at 854 ppm (10). A weaker signal at 845 ppm was also observed by these authors and this may be due to the selenoxide, $(t\text{-BuS})_2SeO$, on the basis of the present work, where the shift of the selenoxide, $(HOC_2H_4S)_2SeO$, lies 15 ppm to lower frequency from the signal for the asymmetric intermediate.

The intermediate, formed by the rearrangement of $(HOC_2H_4S)_2SeO$, is a Se(II) species and has an asymmetric structure. The structure is confirmed by the ^1H NMR spectrum given in Fig. 5 for a 0.054 M H_2SeO_3 and 0.21 M HOC_2H_4SH solution in D_2O at 9°C. It was not possible to prepare a 4:1 molar ratio HOC_2H_4SH/H_2SeO_3 solution even at temperatures just above the freezing point (4°C) in a 5 mm diameter NMR tube without causing some formation of elemental selenium. To prevent such precipitation, a slight stoichiometric excess of H_2SeO_3 (<5%) was necessary. Because of inefficient mixing and the slightly higher temperature of the experiment, the ^1H spectra show the progress of the reaction at a later period relative to the ^{77}Se spectra. The spectrum at 12 s (trace A) shows two overlapped triplets centred near 3.9 ppm, due to methylene protons bound to carbon next to oxygen, and two separated triplets of approximately equal intensity at 2.92 and 3.21 ppm, due to methylene protons on carbon next to sulphur, in $HOC_2H_4SSC_2H_4OH$ and $HOC_2H_4SSeSC_2H_4OH$, respectively (8). In addition, there is a triplet at 3.85 ppm and two broad weak triplets of equal intensity at 2.71 and 3.74 ppm. At 180 s (trace B) these two latter signals are no longer observed and are assigned, for this reason, to the short-lived symmetric $(HOC_2H_4S)_2SeO$ intermediate, perhaps undergoing rapid exchange with $HOC_2H_4SSeO_2H$. The asymmetric intermediate, which lies kinetically between $(HOC_2H_4S)_2SeO$ and the final products of the first stage, may be the oxygen-bridged compound, $HOC_2H_4SOSeSC_2H_4OH$, or the sulfinate, $HOC_2H_4S(O)SeSC_2H_4OH$, either of which will give a spectrum

Can. J. Chem. Downloaded from www.nrcresearchpress.com by 85.192.166.187 on 09/08/12
For personal use only.

Can. J. Chem. Downloaded from www.nrcresearchpress.com by 85.192.166.187 on 09/08/12
For personal use only.

consisting of four triplets of equal intensity. The triplet at 3.85 ppm is assigned to the methylene protons on carbon, next to sulphur(II) bound to oxygen or next to sulphur(IV). These protons are expected to have a chemical shift that differs, to the greatest extent, from the signals of the other methylene protons. The remaining protons bound to carbon next to sulphur in this asymmetric intermediate lie under the triplet due to the similar protons in $HOC_2H_4SSC_2H_4OH$ at 2.92 ppm, as judged by the increased intensity of this peak relative to that of $(HOC_2H_4S)_2Se$ at 3.21 ppm. The remaining four methylene protons on carbon bound to the OH group lie under the overlapped triplets at 3.9 ppm. The higher frequency triplet of the overlapped triplets at 3.93 ppm (^3J = 6.0 Hz) arises from $(HOC_2H_4S)_2Se$, and the lower frequency signal at 3.90 ppm (^3J = 5.7 Hz) from the $HOC_2H_4SSC_2H_4OH$, based on δ and ^3J reported in previous work (8). The signal of the methylene protons on carbon bound to the OH group in the asymmetric species lies under this latter triplet. This assignment of the ^1H NMR spectrum of the asymmetric intermediate is confirmed quantitatively by the signal intensities. The sum of the areas under the signals at 2.92 and 3.21 ppm is less than that of the overlapped triplets at 3.9 ppm by the area of the triplet at 3.85 ppm, confirming that this triplet is due to methylene protons on carbon bound to sulphur and not those on carbon bound to a hydroxyl group. Moreover, the difference in intensity of the signals at 2.92 and 3.21 ppm equals the intensity of the peak at 3.85 ppm, which verifies the assignment of the methylene protons on the carbon bound to sulphur(II) next to selenium in the asymmetric intermediate at 2.92 ppm.

Similar observations have been made for solutions of 4:1 HOC_2H_4SH/H_2SeO_3 mole ratio without excess H_2SeO_3 but, in the spectra of these solutions, the ratio of the signals of the disulfide to those of the bis(thio)selenide are much greater than 1:1 due to decomposition of the selenide via reaction [2], which may take place if thiol is available for further reduction (vide infra). In these experiments, the signals of the asymmetric intermediate disappear on warming as reactions [8] and [9] go to completion.

The asymmetric intermediate may be the oxygen-bridged species, $HOC_2H_4SOSeSC_2H_4OH$, or the sulfinate, $HOC_2H_4S(O)SeSC_2H_4OH$. The significant deshielding of the methylene protons on carbon bound to sulphur linked to oxygen relative to the those on carbon bound to sulphur in the bis(thio)selenide (–0.63 ppm) supports binding to S(IV) just as convincingly as binding to S(II). The two possibilities cannot be differentiated on the basis of ^1H NMR. Some comment may, however, be made about the structure of the asymmetric intermediate from the Se-77 chemical shift. Kice et al. (10) have presented Se-77 NMR chemical shift evidence to support the formation of the oxygen-bridged species as the product formed by peracetic acid oxidation of *t*-BuSSeSBu-*t* in $CDCl_3$. In their work, the shift of the asymmetric oxidation product (854 ppm) lies ca. 300 ppm to higher frequency from the bis(*tert*-butylthio)selenide, *t*-BuSSeSBu-*t* (565 ppm), which is unexpected, if a sulfinate is formed, in view of the similar shifts of selenium(II) in the related selenoselinates and diselenides (10, 16). For this reason, it was suggested (6, 10) that the asymmetric intermediate is an oxygen-bridged species rather than a sulfinate. In the present work the shift of the asymmetric intermediate (685 ppm) lies 2 ppm to higher frequency of the shift of the bis(thio)selenide (683 ppm), which suggests that the asymmetric intermediate is a sulfinate. We favour the sulfinate for two additional reasons: (*a*) we have been unable to find any precedent for the formation of an oxygen link between divalent chalcogens (S and Se at least), and (*b*) in the chemistry of organosulphur compounds, -SOC- linkages normally rearrange to sulfoxide, -S(O)C-, structures (17). Until definitive evidence is forthcoming, however, which asymmetric intermediate is formed remains unanswered and, indeed, both possibilities may exist, depending upon the reaction conditions and direction (oxidation or reduction) chosen. It is interesting to note that the sulfinate would be favourably stabilized by the formation of a six-membered ring, $HOCH_2CH_2S(O)SeSCH_2CH_2OH$, in the case of 2-mercaptoethanol while such stabilization would not be possible for butyl thiols, and this may account for the different asymmetric intermediates.

Reduction to elemental selenium, reaction [2]

In the presence of excess HOC_2H_4SH, the bis(thio)selenide is further reduced to Se and $HOC_2H_4SSC_2H_4OH$, according to reaction [2]. In earlier studies of the reactions of nucleophiles with bis(alkylthio)selenides, little evidence for the formation of elemental selenium was reported (9). Under the conditions used (pH > 10, considerable excess of nucleophile, 60% aqueous dioxane), equilibria like [3] would keep selenium in solution. For all of the nucleophilic anions used, soluble selenoanions may be formed ($BuSSe^-$, $SeCN^-$, $SeSO_3^{2-}$, $SePh^-$). In our studies, which were carried out at near neutral pH and with a low concentration of excess thiol, elemental selenium was formed. The rates were measured by determining the slope of plots of percent turbidity against time (Fig. 1) at the point of 50% reduction to Se ($t_{1/2}$). This procedure minimizes interference from reaction [6] of the first stage. The data given in Table 4 show that the rate is first order in HOC_2H_4SH and $(HOC_2H_4S)_2Se$ and the rate law is given by,

$$[19] \quad \text{Rate} = k_2[(HOC_2H_4S)_2Se][HOC_2H_4SH]$$

It was reported previously (7) that this rate was second order in initial $c(HOC_2H_4SH)$ but allowance for the thiol consumed in reaction [1] shows reaction [2] to be first order in the excess thiol. Overall second-order kinetics have also been observed for the reaction of bis(butylthio)selenides with nucleophiles in 60% dioxane and nonaqueous media (9). Earlier work (7) showed that the rate of reaction [2] increases with pH. The results in Table 4 show that, at pH = 7.35, k_2 is 22 ± 2 L mol^{-1} s^{-1}, while, at pH = 6.85, k_2 is 4.2 ± 0.3 L mol^{-1} s^{-1}. The increased rate at higher pH is due to increased concentration of the thiolate anion, $HOC_2H_4S^-$, which is a stronger nucleophile than the thiol. Previous work with butyl thiols has provided evidence that nucleophilic attack on bis(butylthio)selenides takes place both at sulphur and selenium (9). The evidence that two independent mechanisms are involved is based on steric arguments and analogy with other nucleophilic substitutions, particularly by phenyllithium, on bis(butylthio)selenides. The polarity of the SeS bond favours nucleophilic attack at Se and an alternate mechanism for reaction [2] may proceed via a preequilibrium step.

$$[20] \quad HOC_2H_4S^- + (HOC_2H_4S)_2Se \overset{K}{\rightleftharpoons} (HOC_2H_4S)_3Se^-$$

followed by decomposition of the complex anion,

$$[21] \quad (HOC_2H_4S)_3Se^- \xrightarrow{k_2'} HOC_2H_4SSC_2H_4OH + SeSC_2H_4OH^-$$

and dissociation of the thioselenide (8),

TABLE 4. Dependence of rate of reaction [2] on $c_i((HOC_2H_4S)_2Se)$ and $c(HOC_2H_4SH)$ (excess) at pH = 7.35 and 6.85

10^4 $c_i((HOC_2H_4S)_2Se)^a$ (mol L^{-1})	10^4 $c(HOC_2H_4SH)^b$ (mol L^{-1})	10^6 Rate[c] (mol L^{-1} s^{-1})	$k_2{}^d$ (L mol^{-1} s^{-1})	Kk_2' (L mol^{-1} s^{-1})	pH
5.0	40	3.96	4.0	2.3×10^3	
5.0	34	3.26	3.8	2.2×10^3	
5.0	28	2.70	3.9	2.2×10^3	6.85
5.0	22	2.45	4.4	2.6×10^3	
5.0	16	1.92	4.8	2.8×10^3	
5.0	5.0	2.4	19	3.5×10^3	
3.6	3.6	1.4	21	4.0×10^3	
3.3	3.3	1.2	22	4.0×10^3	7.35
2.9	2.9	1.1	26	4.8×10^3	
2.6	2.6	0.81	23	4.4×10^3	

[a] $c_i((HOC_2H_4S)_2Se) = c(H_2SeO_3)$ at the point of completion of stage 1.
[b] Excess $c(HOC_2H_4SH)$ after completion of stage 1 (reaction [1]).
[c] Determined from the slope of the turbidity vs. time plot at the point of half reaction ($t_{1/2}$).
[d] Calculated at half-reaction, $[(HOC_2H_4S)_2Se] = c_i((HOC_2H_4S)_2Se)/2$.

[22] $SeSC_2H_4OH^- \underset{(23°C)}{\overset{K=3.0}{\rightleftharpoons}} SC_2H_4OH^- + Se$

At the concentrations and pH's employed in this work, dissociation via reaction [22] would be virtually complete. Thus, the thiolate acts as a catalyst for the decomposition of the bis(thio)selenide. According to this mechanism, overall second-order kinetics would be observed and k_2 in reaction [19] then becomes $Kk_2'K_s/[H^+]$, where K_s is the acid dissociation constant for 2-mercaptoethanol (7, 13). Values of Kk_2' at the two pH's are listed in Table 4 and, while the agreement between the two mean values ($(2.4 \pm 0.2) \times 10^3$ M^{-1} s^{-1} (pH = 6.85) and $(4.1 \pm 0.4) \times 10^3$ M^{-1} s^{-1} (pH = 7.35)) is better than that for k_2, the variation is greater than that caused by the uncertainty in the pH measurement. The faster rate at higher pH may be, in part, due to a parallel reaction mechanism involving direct nucleophilic attack by OH^-.

[23] $(HOC_2H_4S)_2Se + OH^- \rightarrow (HOC_2H_4S)_2SeOH^-$

[24] $(HOC_2H_4S)_2SeOH^- \rightarrow HOC_2H_4SS_2H_4OH + SeOH^-$

[25] $SeOH^- \rightleftharpoons Se + OH^-$

Further studies will be needed to confirm this.

Even for solutions with HOC_2H_4SH/H_2SeO_3 stoichiometric ratios of 4:1 and less, where no excess HOC_2H_4SH is available for reaction [2], Se turbidity is observed. Previous studies (7) have shown that the rate of increase in percent turbidity with time increases with pH (7.62–9.28) for solutions with 4:1 HOC_2H_4SH/H_2SeO_3 mole ratio ($c(H_2SeO_3) = 5 \times 10^{-4}$ M). We have confirmed this observation for the pH range 7.85–8.40. At the 4:1 stoichiometric ratio, sufficient thiol is present for the completion of reaction [1] and, indeed, only the bis(thio)-selenide is formed under more acid conditions, provided that any excess of thiol is avoided. However, under more basic conditions, reaction [2] is sufficiently accelerated (see Table 4) that, before reaction [1] is complete and all free thiol is consumed, reaction [2] may proceed to give elemental Se. The limiting amount of Se produced will depend upon the relative rates of reactions [1] and [2] and, thus, upon the pH. For this reason differing plateaus of constant turbidity would be expected at constant $c(H_2SeO_3)$ with different pH's and this is exactly what is observed (7). The maximum percent turbidity observed at 4:1 HOC_2H_4SH/H_2SeO_3 increases with pH. From Fig. 3, it is seen that the rate of reaction [1] increases by 35% when the pH is increased from 6.85 to 7.35 but that of reaction [2] increases over 400% for the same pH range, as seen from Table 4.

NMR spectra, reaction [2]

An attempt was made to observe the ^1H NMR signal of the complex anion, $(HOC_2H_4S)_3Se^-$, by measuring the spectrum of a 0.013 mol L^{-1} solution of $(HOC_2H_4S)_2Se$ (and $HOC_2H_4SSC_2H_4OH$), containing 0.003 mol L^{-1} HOC_2H_4SH in D_2O at 9°C. The initial trace, taken 15 s after mixing, exhibited the spectrum shown in Fig. 6. The spectrum consists of the two triplets at 2.92 and 3.88 ppm, due to $HOC_2H_4SSC_2H_4OH$, two broad peaks at 3.22 and 3.96 ppm, due to $(HOC_2H_4S)_2Se$, and two weak broad signals at 2.74 and 3.86 ppm, due to HOC_2H_4SH. The HOC_2H_4SH and $(HOC_2H_4S)_2Se$ are undergoing intermolecular exchange via equilibria [13] and [20]. In addition, the complex ion, which has a T-shaped structure according to Valence Shell Electron Pair Repulsion (VSEPR) theory, may undergo an intramolecular exchange of axial and equatorial (HOC_2H_4S) groups. These exchange processes will broaden the individual members of the methylene triplets and lead to the signals observed. The signals, due to $(HOC_2H_4S)_2Se$, still show some vestige of proton–proton coupling, especially the signal at 3.96 ppm, which is expected to show the effect of the exchange to a lesser extent, since this signal arises from methylene protons more distant from the site of exchange. A slight turbidity was noted at this stage but the signal intensities for $(HOC_2H_4S)_2Se$ and $HOC_2H_4SSC_2H_4OH$ are equal within the error in measurement, indicating that reduction to Se had just begun to take place. The spectrum of the solution at 120 s exhibits the sharp triplets due to the disulfide, very weak signals due to HOC_2H_4SH, and broad but distinct triplets due to $(HOC_2H_4S)_2Se$. The intensity of these latter peaks at 3.21 and 3.95 ppm is much less at this point than those due to the disulfide, showing that significant reduction via reaction [2] has occurred. After 15 h at room temperature the bis(thio)selenide peaks are barely perceptible, no thiol peaks are observed, but the disulfide triplets are still strong. Inasmuch as the thiol acts as a catalyst for reaction [2] and is not consumed in the reaction,

Can. J. Chem. Downloaded from www.nrcresearchpress.com by 85.192.166.187 on 09/08/12
For personal use only.

Can. J. Chem. Downloaded from www.nrcresearchpress.com by 85.192.166.187 on 09/08/12
For personal use only.

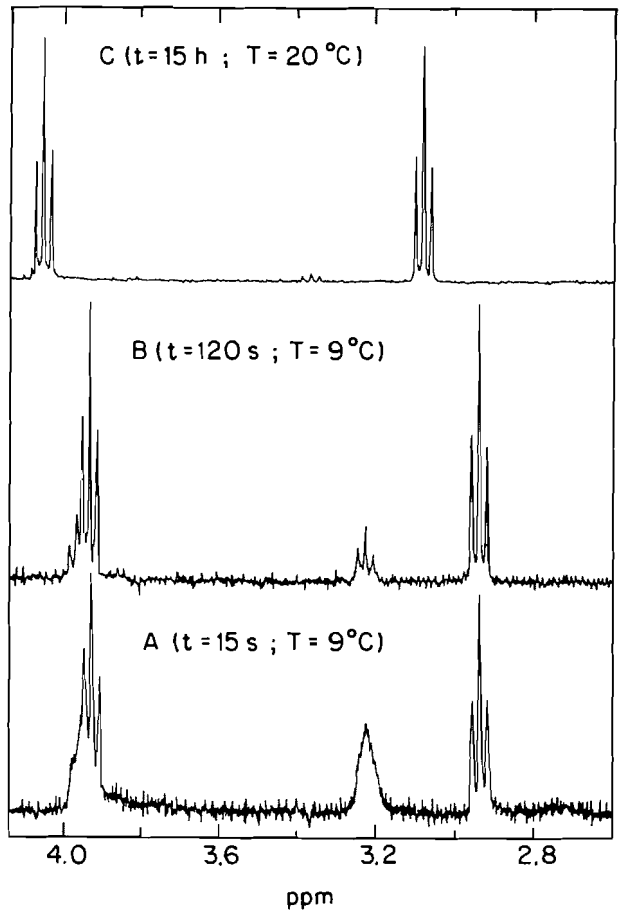

FIG. 6. Proton NMR spectra of a $(HOC_2H_4S)_2Se/HOC_2H_4SH$ mixture ($c((HOC_2H_4S)_2Se) = 0.013$ mol L^{-1}; $c(HOC_2H_4SH) = 0.003$ mol L^{-1}, unbuffered at (*A*) 15 s, (*B*) 120 s (9°C), and (*C*) 15 h (20°C)

its disappearance requires explanation. Thiols are subject to oxidation by oxygen (18) and the reaction is catalyzed by elemental selenium.[3]

$$[26] \quad 4\,RSH + O_2 \xrightarrow[Se]{} 2\,RSSR + 2\,H_2O$$

Thus, the generation of Se by reaction [2] accelerates the oxidation of the catalyst for the second stage, HOC_2H_4SH, by the ambient oxygen in the NMR tube over the course of several hours at room temperature. This also accounts for the presence of a trace of bis(hydroxyethylthio)selenide at the end of the experiment, because the catalyst is consumed by reaction [26] before reaction [2] is complete. The increasing resolution of the triplets with time, due to the bis(hydroxyethylthio)-selenide, is a result of the decreasing rate of exchange with decreasing concentration of bis(hydroxyethylthio)selenide and thiol.

The enthalpy and entropy of activation for reaction [2] were determined from data listed in Table 5 and found to be $\Delta H^{\ddagger} = 82 \pm 4$ kJ mol^{-1} and $\Delta S^{\ddagger} = 172 \pm 4$ J K^{-1} mol^{-1}. The large positive entropy of activation is not consistent with a bimolecular mechanism and supports a pre-equilibrium step, reaction [20], followed by a unimolecular dissociation, reaction [21]. In 60% dioxane the reaction of *t*-BuSH with *t*-BUSSeSBu-*t* gives $\Delta H^{\ddagger} = 64 \pm 4$ kJ mol^{-1} and $\Delta S^{\ddagger} = -75 \pm 12$ J K^{-1} mol^{-1} (9). In this case the measured $\Delta S^{\ddagger}$ supports an associative mechanism.

[3]W. Amaratunga and J. Milne. Manuscript in preparation.

TABLE 5. Rates for reaction [2] determined from slopes at various temperatures ($c_i(H_2SeO_3) = 5 \times 10^{-4}$ M; $c_i(HOC_2H_4SH) = 2.5 \times 10^{-3}$ M)

T (K)	10^6 Rate[a] (mol L^{-1} s^{-1})	k_2 (L mol^{-1} s^{-1})
292	0.41	3.2
296	0.58	4.3
299	0.89	7.1
302	1.14	9.1
305	1.57	12.6

[a]Determined from the slope of the turbidity vs. time plot at the point of half-reaction.

Conclusion

The reduction of H_2SeO_3 by HOC_2H_4SH in aqueous solution takes place in two distinct stages, each involving more than one step and similar to the mechanism proposed by Kice et al. (6, 9, 10) for butyl thiols in 60% dioxane. The first stage involves two slow steps. There is an initial formation of 2-hydroxyethylthioselenous acid, $HOC_2H_4SSeO_2H$, in a process akin to the formation of $XSeO_2H$ (X = Cl, Br) by equilibria known for solutions of H_2SeO_3 in aqueous HCl (19) and HBr (20). This step (reaction [5]) proceeds very rapidly at pH 6.85 with a rate comparable to that observed for *n*-BuSH in 60% dioxane (6). However, at this pH, the rate of the forward reaction of [5] for butylthiols decreases with increasing pH while that for HOC_2H_4SH increases. These opposing trends are the result of the different degrees of dissociation of the two thiols. For *n*-butyl thiol in the pH range 0.2–8.0, the rate is dominated by nucleophilic attack of undissociated *n*-BuSH ($pK_a = 10.65$ (21)) on H_2SeO_3 and $HSeO_3^-$ (6) but for HOC_2H_4SH ($pK_a = 9.6$ (13)) at this pH, the thiolate ion is the most important nucleophile in determining the rate and its concentration increases with pH. The second step of the first stage (reaction [6]) proceeds more slowly than the first and involves coordination of another molecule of thiol to form $(HOC_2H_4S)_2SeO$, parallel to the formation of X_2SeO in HX (X = Cl, Br) solutions from $XSeO_2H$ (19, 20). This rate-determining step of the first stage is more rapid for HOC_2H_4SH in water than for *n*-BuSH or *t*-BuSH in 60% dioxane, due also to the greater degree of dissociation of HOC_2H_4SH, compared to *n*-BuSH, as well as the change of solvent. Several rapid steps complete this stage with the formation of bis(hydroxyethylthio)selenide. In the second stage this selenide undergoes further thiolate coordination at Se parallel to the related SeX_2 compounds (X = Cl, Br), which form SeX_3^- and SeX_4^{2-} anions (22, 23), and the complex undergoes further reaction to give disulfide and $HOC_2H_4SSe^-$ ion, which rapidly dissociates to thiolate and elemental selenium (8). The positive $\Delta S^{\ddagger}$ measured for this stage favours a dissociative rate-controlling step rather than the nucleophilic attack at sulphur.

Acknowledgement

The Natural Sciences and Engineering Research Council of Canada is thanked for financial support. Dr. G. Facey and R. Capoor are thanked for obtaining the NMR spectra.

1. L. Flohe. *In* Glutathione, chemical, biochemical and medical aspects. Part A. *Edited by* D. Dolphin, O. Avramovic, and R. Poulson. Wiley, New York. 1989. p. 643.

2. B. Jansson. *In* Metal ions in biological systems. Vol. 10. *Edited by* H. Sigel. Marcel Dekker, New York. 1980. Chap. 9. p. 281.
3. D.L. Rabenstein and K.-S. Tan. Magn. Reson. Chem. **26**, 1079 (1988)
4. J.L. Kice. *In* Selenium in biology and medicine. *Edited by* J.E. Spallholz, J.L. Martin, and H.E. Ganther. AVI Publishing Co. Inc., Westport, Conn. 1981. p. 17.
5. (*a*) H.E. Ganther. Biochemistry, **7**, 2898 (1968); (*b*) Biochemistry, **10**, 4089 (1971).
6. J.L. Kice, T.W.S. Lee, and S.-t. Pan. J. Am. Chem. Soc. **102**, 4448 (1980).
7. H. Afsar, I. Tor, and R. Apak. Analyst, **114**, 1315 (1989).
8. W. Amaratunga, O. Chaudry, and J. Milne. Can. J. Chem. **72**, 1165 (1994).
9. J.L. Kice and H. Slebocka-Tilk. Am. Chem. Soc. **104**, 7123 (1982).
10. J.L. Kice, D. M. Wilson, and J.M. Espinola. J. Org. Chem. **56**, 3520 (1991).
11. R.L. Charlebois, W. Lear, L. Lorusso, and J. Milne. Proc. 5th Int. Symp. on the Uses of Selenium and Tellurium, May 8–10, 1994, Brussels. *Edited by* Y. Palmieri. Selenium and Tellurium Development Assoc., Grimbergen, Belgium.
12. J. Milne. Magn. Reson. Chem. **31**, 652 (1993).
13. J.M. Wilson, R.J. Bayer, and D.J. Hupe. J. Am. Chem. Soc. **99**, 7922 (1977).
14. N.P. Luthra, R.B. Dunlap, and J.D. Odom. J. Magn. Reson. **52**, 318 (1983).
15. H.C.E. McFarlane and W. McFarlane. *In* NMR of newly accessible nuclei. Vol. 2. *Edited by* P. Laszlo. Academic Press, New York. 1983. Chap. 10.
16. H.J. Reich, C.A. Hoeger, and W.W. Willis. J. Am. Chem. Soc. **104**, 2936 (1982).
17. S. Braverman. *In* The chemistry of sulfones and sulfoxides. *Edited by* S. Patai and Z. Rappoport. J. Wiley, Chichester. 1988. p. 718.
18. G. Capozzi and G. Modena. *In* The chemistry of the thiol group. *Edited by* S. Patai. John Wiley, London. 1974. p. 818.
19. J. Milne and P. Lahaie. Inorg. Chem. **24**, 840 (1985).
20. J. Milne. Can. J. Chem. **65**, 316 (1987).
21. M.R. Crampton. *In* The chemistry of the thiol group. *Edited by* S. Patai. J. Wiley, London. 1974. p. 398.
22. K.J. Wynne and J. Golen. Inorg. Chem. **13**, 185 (1974).
23. J.B. Milne. Polyhedron, **6**, 849 (1987).

Can. J. Chem. Downloaded from www.nrcresearchpress.com by 85.192.166.187 on 09/08/12
For personal use only.

Absolute rate constant measurements for the reaction of atomic hydrogen with acetone, 2-butanone, propionaldehyde, and butyraldehyde in aqueous solution[1]

STEPHEN P. MEZYK[2]

Research Chemistry Branch, AECL Research, Whiteshell Laboratories, Pinawa, MB R0E 1L0, Canada

AND

DAVID M. BARTELS

Chemistry Division, Argonne National Laboratory, Argonne, IL 60439, U.S.A.

Received April 14, 1994

STEPHEN P. MEZYK and DAVID M. BARTELS. Can. J. Chem. **72**, 2516 (1994).

Arrhenius parameters for the reaction of hydrogen atoms with acetone, 2-butanone, propionaldehyde, and butyraldehyde in aqueous solution have been directly measured by electron paramagnetic resonance free induction decay (FID) attenuation measurements. For these compounds, absolute scavenging rate constants at 25°C of $(1.97 \pm 0.10) \times 10^6$, $(3.82 \pm 0.32) \times 10^7$, $(8.11 \pm 0.47) \times 10^7$, and $(1.14 \pm 0.07) \times 10^8$ dm^3 mol^{-1} s^{-1}, with corresponding activation energies of 30.7 ± 1.3 (7.5–52.8°C), 40.1 ± 0.7 (8.1–74.5°C), 22.2 ± 0.9 (8.0–39.0°C) and 23.8 ± 0.8 (5.4–67.7°C) kJ mol^{-1} were measured, respectively. Competition kinetic measurements have established that greater than 95% of ·H atom reaction with 2-butanone is by abstraction.

STEPHEN P. MEZYK et DAVID M. BARTELS. Can. J. Chem. **72**, 2516 (1994).

Faisant appel à des mesures d'atténuation de la décroissance par induction libre (FID) de la résonance paramagnétique électronique, on a déterminé directement les paramètres d'Arrhenius de la réaction des atomes d'hydrogène avec l'acétone, la butan-2-one, le propionaldéhyde et le butyraldéhyde en solutions aqueuses. Pour ces composés, les constantes absolues des vitesses de piégeage, à 25°C, sont: $(1{,}97 \pm 0{,}10) \times 10^6$, $(3{,}82 \pm 0{,}32) \times 10^7$, $(8{,}11 \pm 0{,}47) \times 10^7$, et $(1{,}14 \pm 0{,}07) \times 10^8$ dm^3 mol^{-1} s^{-1} alors que les énergies d'activation sont respectivement de: 30,7 ± 1,3 (7,5–52,8°C), 40,1 ± 0,7 (8,1–74,5°C), 22,2 ± 0,9 (8,0–39,0°C) et 23,8 ± 0,8 (5,4–67,7°C) kJ mol^{-1}. Des mesures de cinétiques compétitives ont permis d'établir que plus de 95% de la réaction des atomes ·H avec la butan-2-one se fait par enlèvement.

[Traduit par la rédaction]

Introduction

Radioactive iodine is generally recognized as the most hazardous fission product that could be released to the environment in the event of a severe nuclear accident (1). Although most iodine is released as the soluble, non-volatile iodide, the high radiation fields expected following a reactor accident have been shown to significantly affect the iodine chemistry that occurs (2, 3). Of particular concern are the reactions that lead to volatile products, such as low molecular weight iodoalkanes (4).

In an attempt to understand the process of iodoalkane formation, a systematic investigation has been initiated (5) using irradiated aqueous iodide solutions containing 2-butanone (MEK) as a prototypical organic impurity. The steady-state irradiation of aqueous MEK solutions produces a large number of product species (6); thus to ensure a complete understanding of proposed mechanisms, computer modelling is required. Such modelling is dependent on having accurate rate constant data available for the aqueous radiolysis species reactions with MEK and its subsequent degradation products.

Unfortunately no kinetic data could be found in the literature for the radiation chemistry of MEK itself, or for one of its breakdown products, propionaldehyde (propanal). In a recent investigation (7), rate constants and activation energies were determined for hydrated electron and hydroxyl radical reaction with these carbonyls, using the techniques of pulsed electron radiolysis and absorption spectroscopy. However, the pulse radiolysis of these compounds in acidic solutions containing *t*-butanol showed no change in the visible or near-uv absorption spectrum, and thus no measurement of their reaction rate constant with the hydrogen atom was possible at that time.

This paper reports our direct measurement of rate constants and activation energies for the reaction of hydrogen atoms with propanal and MEK in aqueous solution. For comparative purposes, values for butyraldehyde and acetone have also been determined. Because of its great specificity, direct EPR detection of the decay of the ·H atom following electron pulse radiolysis was the monitoring method of choice (8, 9). The pulsed EPR-based free induction decay (FID) attenuation method (10–15) used in this study has been demonstrated to be particularly advantageous for such rate constant measurements because of the simple pseudo-first-order scavenging kinetics generally obtained.

Experimental

The experimental procedure for determining ·H atom reaction rate constants has been described in great detail in several previous publications (10–13), and thus only a short description shall be given here. Hydrogen atoms were generated in aqueous solution by pulse radiolysis, using 3 MeV electrons from a Van de Graaff accelerator. A 35 ns microwave probe pulse was applied to the sample immediately after irradiation, and the resulting free induction decay of the ·H atom low-field ($m_I = +\frac{1}{2}$) EPR transition was recorded on a digital oscilloscope. Typically 500–2000 shots were averaged to measure each FID, at a repetition rate of 120 Hz.

Stock acid solutions were prepared by addition of $HClO_4$ (Mallinkrodt, A.R. Grade, 69.05%) to Millipore filtered water, to give pH 0.0, 1.0, and 2.0 standards. Actual acid concentrations were determined by standardization of the concentrated acid against 1.029 N HCl (Aldrich, Volumetric Standard). A total aqueous sample of ~190 mL was recirculated through a flat cell within an EPR cavity at a high flow rate, such that the actual volume irradiated in each pulse was less than 0.10 mL.

Scavenging experiments were performed by the successive injection of known volumes of acetone (Aldrich, HPLC grade, 99.5%+), butyraldehyde (Aldrich, 99%), MEK (Aldrich, HPLC grade, 99.5%+),

[1]Work at Argonne performed under the auspices of the Office of Basic Energy Sciences, Division of Chemical Science, US-DOE, under contract W-31-109-ENG-38.

[2]Author to whom correspondence should be addressed.

Can. J. Chem. Downloaded from www.nrcresearchpress.com by 85.192.166.187 on 09/08/12
For personal use only.

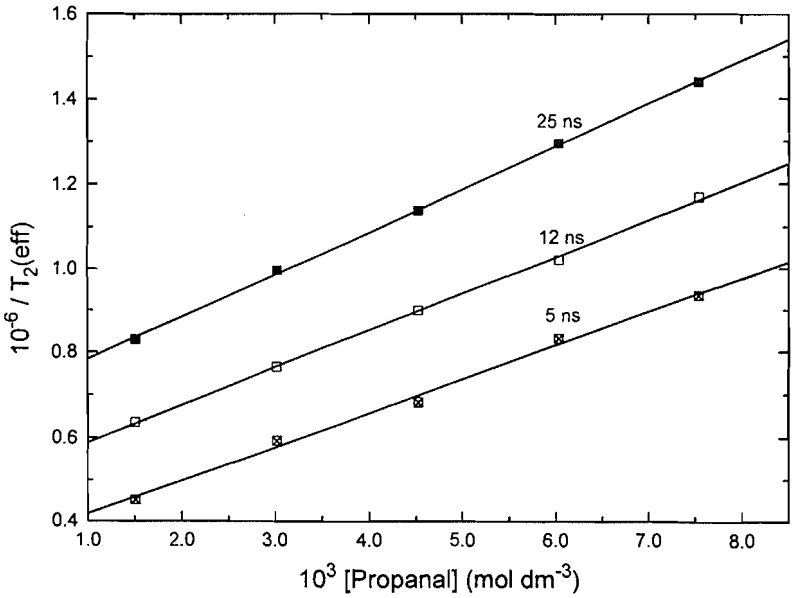

FIG. 1. Dose dependence of the hydrogen atom scavenging rate constants for propanal at pH 1.0 and 22.4°C obtained by using the 25, 12, and 5 ns pulses from the Van de Graaff accelerator.

Can. J. Chem. Downloaded from www.nrcresearchpress.com by 85.192.166.187 on 09/08/12
For personal use only.

or propanal (Aldrich, 99%+) to an initial known volume of solution that had been fully de-oxygenated by bubbling with argon. Accuracy of these concentrations is estimated to be better than 3%.

The measured scavenging rate constants for all four systems of this study were found to have a slight dependence on radiation dose. A typical result for hydrogen atom scavenging of propanal at 22.4°C and pH 1.0 is shown in Fig. 1. The general expression of the effective damping rate of the FID in these experiments is given by (10–13).

$$[1] \quad \frac{1}{T_2\,(\text{eff})} = \frac{1}{T_2^0} + k_s[S] + \Sigma k_{ex}^i\,[R_i]$$

where $k_s[S]$ is the ·H atom scavenging rate, and $\Sigma k_{ex}^i[R_i]$ represents the spin-dephasing contribution of second-order spin exchange and recombination reactions between ·H atoms and other free radicals. The latter term in eq. [1] is responsible for the shift in intercept seen in Fig. 1, as the total free radical concentration $\Sigma[R_i]$ increases. The scavenging reaction converts hydrogen atoms into other free radicals, and the corresponding change in $k_{ex}{}^i$ during the five microsecond experimental time period is responsible for the small change in the slopes. As explained in a previous publication (14), the positive change in slope with increasing dose implies that the carbon-centred product radicals are more efficient spin-exchange partners for ·H than other ·H atoms. The systematic error due to this second-order chemistry can be avoided by either working with very small initial ·H atom concentrations, or by extrapolation to a "zero dose" limit (14).

The primary technique used in this study was extrapolation to zero dose. For example, for propanal at 22.4°C, actual rate constants of $(1.02 \pm 0.01) \times 10^8$, $(8.79 \pm 0.14) \times 10^7$, and $(7.97 \pm 0.32) \times 10^7$ dm^3 mol^{-1} s^{-1} were obtained for the 25, 12, and 5 ns pulses used respectively (see Fig. 1). These pulse widths corresponded to relative doses of 11.2, 5.3, and 1.4, where an absolute dose of ca. 3.0 kRad/pulse was estimated for the 25 ns pulse. These relative values were simply the measurement of the average beam current on a shutter positioned before the irradiation cell, and were assumed to be proportional to the actual dose given to the sample. The beam current values were monitored frequently to correct for any slight drift.

The extrapolation of these dose-dependent values to zero dose is shown in Fig. 2. An excellent linear relationship is obtained, and a limiting, zero dose, value of $(7.65 \pm 0.54) \times 10^7$ dm^3 mol^{-1} s^{-1} was calculated. This behaviour was consistent for all four systems of this study (see values for butyraldehyde at 22.4°C also in Fig. 2).

In an attempt to improve the precision of these extrapolated values, and to minimize the total dose delivered to low carbonyl concentrations, some single point experiments were also performed at very reduced doses (typically about 50% of the normal 5 ns pulse). Excellent agreement was obtained between these two methods. The single point measurements for butyraldehyde at 25.9°C of $(1.21 \pm 0.11) \times 10^8$ dm^3 mol^{-1} s^{-1} is in excellent agreement with the extrapolated value at 25.5°C of $(1.14 \pm 0.07) \times 10^8$ dm^3 mol^{-1} s^{-1}.

Both techniques were used to obtain dose-corrected scavenging rate constants for each compound over a range of temperature, with individual values given in Table 1. The corresponding Arrhenius plots are shown in Fig. 3.

To determine the fractions of addition and abstraction for hydrogen atom reaction with MEK, total hydrogen yield measurements were performed. Stock solutions of 0.10 mol dm^{-3} $HClO_4$ were saturated with argon before adding the required amounts of 2-propanol (Aldrich, 99.5% HPLC grade) or 2-propanol-d_8 (Aldrich, 99.7 atom %D) and MEK by direct injection. Aliquots of these solutions (10.00 mL) were sealed in a 50.0 mL flask and then irradiated (56 kRad) in a ^{60}Co Gammacell at ~28°C. The gas analyses, for H_2 and HD respectively, were performed using a VG Instruments MM 8-80 magnetic sector mass spectrometer, calibrated using standard H_2/HD gas mixtures.

·H atom reaction with acetone

The reaction of aqueous hydrogen atoms with acetone

$$[2] \quad \cdot H + CH_3COCH_3 \rightarrow \text{products}$$

was chosen for study in order to provide a comparison with the MEK data, and also because reaction rate constants have been determined previously, both by EPR (16) and chemical (17–19) methods. Rate constants in this study were determined using 1.0 mol dm^{-3} $HClO_4$ solution, as the fast reaction of acetone with hydrated electrons, k = 6.5×10^9 dm^3 mol^{-1} s^{-1} (20), caused a major reduction in the ·H atom yield for less acidic conditions.

The literature room temperature rate constants are somewhat scattered, with reported values ranging from 0.8 to 2.8×10^6 dm^3 mol^{-1} s^{-1} (16–19). The corrected, zero-dose, rate constant for hydrogen atom reaction with acetone at 23.7°C in this study is $(1.71 \pm 0.11) \times 10^6$ dm^3 mol^{-1} s^{-1}. The individual extrapolated values over the temperature range 7.5–52.8°C are given in Table 1, with the Arrhenius plot (Fig. 3) well described by the equation

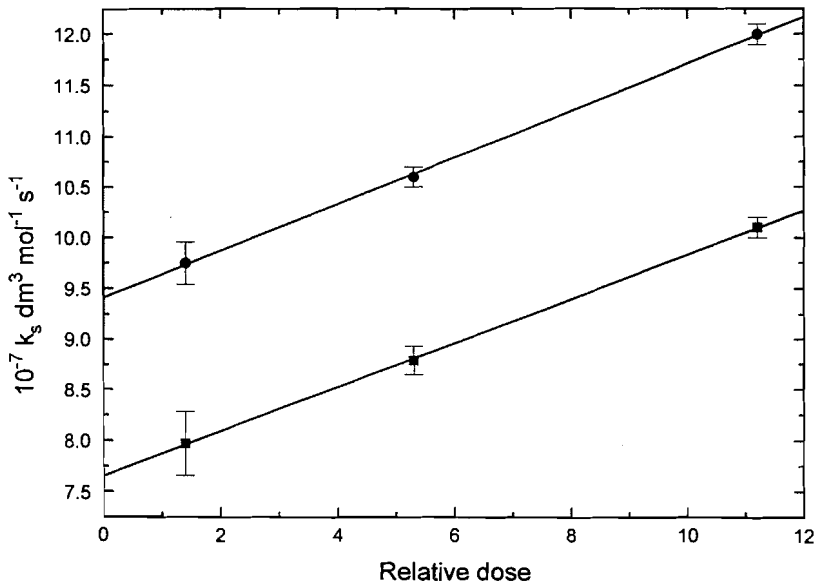

FIG. 2. Rate constant extrapolations to zero dose for propanal (■) at pH 1.0 and 22.4°C, and butyraldehyde (●), pH 1.0 and 22.4°C.

TABLE 1. Summary of the dose-corrected, temperature-dependent scavenging rate constants for hydrogen atom reaction with acetone, MEK, propanal, and butyraldehyde

Species	Temperature °C	Scavenging rate constant dm^3 mol^{-1} s^{-1}
Acetone	7.5	$(9.78 \pm 0.31) \times 10^5$
	16.8	$(1.32 \pm 0.06) \times 10^6$
	23.7	$(1.71 \pm 0.11) \times 10^6$
	25.7	$(1.97 \pm 0.10) \times 10^6$
	42.9	$(4.10 \pm 0.29) \times 10^6$
	52.8	$(5.68 \pm 0.59) \times 10^6$
MEK	8.1	$(1.48 \pm 0.19) \times 10^7$
	16.8	$(2.52 \pm 0.36) \times 10^7$
	25.0	$(3.82 \pm 0.32) \times 10^7$
	44.1	$(1.10 \pm 0.13) \times 10^8$
	74.5	$(3.86 \pm 0.27) \times 10^8$
Propanal	8.0	$(4.59 \pm 0.41) \times 10^7$
	17.0	$(6.13 \pm 0.41) \times 10^7$
	22.4	$(7.65 \pm 0.54) \times 10^7$
	25.0	$(8.11 \pm 0.47) \times 10^7$
	39.0	$(1.17 \pm 0.12) \times 10^8$
Butyraldehyde	5.4	$(5.60 \pm 0.23) \times 10^7$
	22.4	$(9.41 \pm 0.49) \times 10^7$
	25.5	$(1.14 \pm 0.07) \times 10^8$
	25.9	$(1.21 \pm 0.11) \times 10^8$
	39.6	$(1.80 \pm 0.19) \times 10^8$
	54.8	$(2.54 \pm 0.19) \times 10^8$
	67.7	$(3.71 \pm 0.23) \times 10^8$

[3] $\ln k_2 = (26.9 \pm 0.5) - (3690 \pm 160)/T$

with k_2 and T in units of dm^3 mol^{-1} s^{-1} and K respectively. This corresponds to an activation energy of 30.7 ± 1.3 kJ mol^{-1}.

It has previously been shown that there are two possible pathways for hydrogen atom to react with acetone (17, 21), either by abstraction of a methyl hydrogen atom, or by addition to the carbonyl bond. At room temperature, a branching ratio of 2.0:1 in favour of hydrogen atom abstraction has been determined (21). Unfortunately no branching ratios have been determined at other temperatures, and thus the individual activation energies for each process in acetone could not be established.

·H atom reaction with MEK

An identical procedure was followed for the measurement of the rate constant for hydrogen atoms reaction with MEK,

[4] $\cdot H + CH_3CH_2COCH_3 \rightarrow$ products

where in pH 2.0 solution at 25.0°C an extrapolated, limiting dose, value of $(3.82 \pm 0.32) \times 10^7$ dm^3 mol^{-1} s^{-1} was obtained. Similar measurements were performed over the temperature range 8.1–74.5°C (see Table 1). The calculated Arrhenius plot for all data is shown in Fig. 3, and for this compound, the temperature-dependent rate constant is given by

[5] $\ln k_4 = (33.7 \pm 0.3) - (4820 \pm 80)/T$

corresponding to an activation energy of 40.1 ± 0.7 kJ mol^{-1}.

This activation energy is significantly higher than determined for acetone, but at the same time, the MEK reaction is much faster due to a very large pre-exponential factor, 4.3×10^{14} dm^3 mol^{-1} s^{-1}. For MEK it can be assumed that the hydrogen atom reaction of abstraction from the terminal methyl groups would be similar to that for acetone. Thus the factor of twenty increase in the room temperature rate constant suggests that 95% or more of the hydrogen atom reaction with MEK consists of abstraction from the additional methylene group or addition to the carbonyl bond.

To establish the reaction mechanism the addition/abstraction ratio was determined at 28°C, using the competition technique established previously for acetone (21). It was found that the measured molecular hydrogen yield from an irradiated aqueous solution containing 1.0×10^{-3} mol dm^{-3} 2-propanol at pH 1.0 was unchanged upon the addition of $(0.2–1.0) \times 10^{-3}$ mol dm^{-3} MEK. Furthermore, when these experiments were repeated using fully deuterated 2-propanol, the decrease in the measured HD yield was concomitant with an increase in the H_2 yield. Analysis of these changes using standard competition kinetics indicated that more than 95% of the hydrogen atom reaction with MEK was by ·H atom abstraction to give H_2. As the rate constants for hydrogen atom reaction with MEK are far larger than those for acetone over the entire temperature range studied, the 40.1 kJ mol^{-1} activation energy measured essentially corresponds to only the abstraction process.

Can. J. Chem. Downloaded from www.nrcresearchpress.com by 85.192.166.187 on 09/08/12
For personal use only.

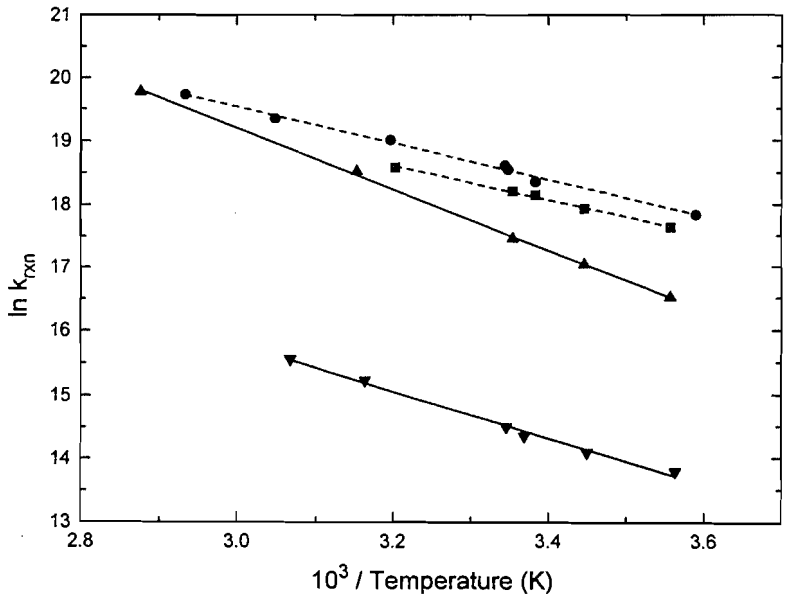

FIG. 3. Arrhenius plots of ln k_s vs. $1/T$ for propanal (■), MEK (▲), butyraldehyde (●), and acetone (▼). Lines correspond to calculated values of equations given in text.

This result is very surprising, because one typically expects faster abstractions from methylene than from methyl groups due to the weaker C—H bonds (22–24). Thus we expect roughly 10 kJ mol^{-1} lower activation energy for abstraction from MEK than from acetone. This ordering is indeed observed in the gas phase ·H abstractions by the methyl radical, where the activation energies are 40.5 kJ mol^{-1} for acetone, 31 kJ mol^{-1} for MEK, and 30 kJ mol^{-1} for diethyl ketone (23). One should consider the possible involvement of the hydrated and enol forms for the ketone. In room temperature water, the enol fraction of MEK is only 3×10^{-8} (25), while the hydrated form is believed to be less than 10^{-3} (22, 26). In order for either form to dominate the overall measured reaction rate, their ·H scavenging reactions would need to be orders of magnitude greater than diffusion-controlled, an obviously impossible situation. The possibility of an impurity that dominates the scavenging by virtue of its diffusion-limited rate can likewise be dismissed. The diffusional activation energy for ·H atoms is approximately 15 kJ mol^{-1} (27), so again we would expect an activation energy lower than that observed for the acetone reaction.

In order to explain the anomalously high activation energy for the MEK reaction with ·H atoms, we are forced to postulate some specific effect of solvation, which provides a large degree of entropic compensation for the higher energy abstraction process. We can suggest two possible concerted reactions. One possibility is that abstraction at the methylene position stimulates the hydration of the carbonyl bond. Hydration of substituted acetones has been shown to occur with overall positive entropy change (28), as required to account for the large pre-exponential factor. A second possibility is suggested by consideration of the enol structure of MEK, which converts the terminal methyl groups into allylic positions, with much weaker C—H bonds (23, 24). One can imagine an abstraction from the terminal methyl group, aided by a simultaneous keto–enol conversion process involving a water molecule in the solvation shell. Further investigation of this MEK scavenging reaction is clearly needed to establish the reaction pathway. Time-resolved EPR detection of the product radicals is planned.

·H atom reaction with propanal

The overall ·H atom scavenging rate constants at pH 1.0 and 22.4°C for the reaction

[6] $\cdot H + CH_3CH_2CHO \rightarrow$ products

were measured for temperatures over the range 8.0–39.0°C (Table 1). The temperature-dependent rate constant behaviour (Fig. 3) of reaction [6] is given by

[7] $\ln k_6 = (27.1 \pm 0.3) - (2670 \pm 100)/T$

This corresponds to an activation energy of 22.2 ± 0.9 kJ mol^{-1}.

This activation energy is much lower than that obtained for either of the ketones studied, suggesting a new reaction channel is available. Previous room temperature studies of ·H atom reaction with aldehydes (21, 29) have identified abstraction of the aldehydic hydrogen as the dominant (>90%) reaction channel. If we take our room temperature MEK rate constant of 3.8×10^7 dm^3 mol^{-1} s^{-1}, and add it to 3.4×10^7 dm^3 mol^{-1} s^{-1}, the rate constant reported for acetaldehyde (21) (aldehydic abstraction), we obtain a number very close to the 8.1×10^7 dm^3 mol^{-1} s^{-1} determined for propanal.

The lower measured activation energy for the overall hydrogen atom reaction with propanal implies that the abstraction from the aldehydic group has a much lower activation energy than abstraction at the methylene or methyl groups. Unfortunately no branching ratios for these two reactions have been determined. If the rate constant for hydrogen atom abstraction from the rest of the molecule (assumed to be the value from MEK) is subtracted from the measured values for propanal, the resulting Arrhenius plot gives an activation energy of ~12 kJ mol^{-1} for the aldehydic abstraction process.

·H atom reaction with butyraldehyde

The measurement of Arrhenius parameters for the reaction

[8] $\cdot H + CH_3CH_2CH_2CHO \rightarrow$ products

at pH 1.0 was performed as a comparison to the propanal system, to allow extension of the temperature range of these measurements, and because experimental difficulties (i.e. low boiling points) prevented determination of rate constants for either the formaldehyde or acetaldehyde systems using equipment on hand. The Arrhenius plot for butyraldehyde is also shown in Fig. 3, and is well characterized by the equation

[9] $\ln k_8 = (28.1 \pm 0.3) - (2870 \pm 95)/T$

This activation energy of 23.8 ± 0.8 kJ mol^{-1} is in very good agreement with the value for propanal, indicating that the same mechanisms of hydrogen atom abstraction also occur for butyraldehyde.

Can. J. Chem. Downloaded from www.nrcresearchpress.com by 85.192.166.187 on 09/08/12
For personal use only.

In summary, the rate constants and competition measurements have shown that the dominant mechanism of hydrogen atom reaction with MEK and propanal is by abstraction. The surprising difference in activation energies between MEK and acetone scavenging leaves some doubt as to the preferred position of ·H atom abstraction in the longer chain carbonyl compounds. We plan an EPR study of these free radical products in order to establish the reaction mechanism and branching ratios as a function of temperature.

Acknowledgements

The authors would like to thank Dr. David Werst for his assistance in operating and maintaining the Van de Graaff accelerator. We would also like to thank Dr. K.P. Madden for helpful discussions during the course of this study, and Mr. R. MacFarlane and Mr. H.G. Delaney for performing the H_2 and HD measurements.

1. T.J. Thompson and J.G. Beckerley (*Editors*). The technology of nuclear reactor safety. MIT Press, Cambridge. 1973.
2. A.C. Vikis (*Editor*). Proceedings of the 2nd CSNI workshop on iodine chemistry in reactor safety. AECL Research Report, AECL-9923. 1989.
3. K. Ishigure, M. Saeki, K. Soda, and J. Sugimoto (*Editors*). Proceedings of the 3rd CSNI workshop on iodine chemistry in reactor safety. JAE Research Report, JAERI-M 92-012. 1992.
4. J. Paquette and B.L. Ford. Radiat. Phys. Chem. **36**, 353 (1990).
5. C.A. Chuaqui and J.M. Ball. 4th Meeting of the European Severe Accident Chemistry Group ENEL/CRTN, Milano, December 1992.
6. S.M.S. Akhtar, R.J. Woods, and J.A.E. Bardwell. Int. J. Radiat. Phys. Chem. **7**, 603 (1975).
7. S.P. Mezyk. Can. J. Chem. **72**, 1116 (1994).
8. R.W. Fessenden and N.C. Varma. Faraday Discuss. Chem. Soc. **63**, 104 (1977).
9. D.M. Bartels, M.T. Craw, P. Han, and A.D. Trifunac. J. Phys. Chem. **93**, 2412 (1989).
10. P. Han and D.M. Bartels. Chem. Phys. Lett. **159**, 538 (1989).
11. P. Han and D.M. Bartels. J. Phys. Chem. **94**, 7294 (1990).
12. P. Han and D.M. Bartels. J. Phys. Chem. **96**, 4899 (1992).
13. E. Roduner and D.M. Bartels. Ber. Bunsen-Ges. Phys. Chem. **96**, 1037 (1992).
14. D.M. Bartels and S.P. Mezyk. J. Phys. Chem. **97**, 4101 (1993).
15. S.P. Mezyk, R.M. MacFarlane, and D.M. Bartels. J. Phys. Chem. In press.
16. P. Neta, R.W. Fessenden, and R.H. Schuler, J. Phys. Chem. **75**, 1654 (1971).
17. P. Neta, G.R. Holdren, and R.H. Schuler. J. Phys. Chem. **75**, 449 (1971).
18. A. Appleby, G. Scholes, and M. Simic. J. Am Chem. Soc. **85**, 3891 (1963).
19. S. Nehari and J. Rabani. J. Phys. Chem. **67**, 1609 (1963).
20. G.V. Buxton, C.L. Greenstock, W.P. Helman, and A.B. Ross. J. Phys. Chem. Ref. Data, **17**, 513 (1988).
21. R.A. Witter and P. Neta. J. Org. Chem. **38**, 484 (1973).
22. J. March. Advanced organic chemistry. 3rd ed. Wiley, New York, NY. 1985.
23. J.A. Kerr and M.J. Parsonage. Evaluated kinetic data on gas phase hydrogen transfer reactions of methyl radicals. Butterworths, London. 1976.
24. J.A. Kerr. Chem. Rev. **66**, 465 (1966).
25. J.R. Keefe, A.J. Kresge, and N.P. Schepp. J. Am. Chem. Soc. **110**, 1993 (1988).
26. R.P. Bell and J.C. Clunie. Trans. Faraday Soc. **48**, 439 (1952).
27. P. Han and D.M. Bartels. *In* AIP Proceedings 298: Ultrafast reaction dynamics and solvent effects. *Edited by* Y. Gauduel and P.J. Rossky. AIP Press, New York. 1994. p. 72.
28. R.P. Bell and A.O. McDougall. Trans. Faraday Soc. **56**, 1281 (1960).
29. P. Neta. Chem. Rev. **72**, 533 (1972).

Can. J. Chem. Downloaded from www.nrcresearchpress.com by 85.192.166.187 on 09/08/12
For personal use only.

The anomeric effect in anionic systems XH_m-CH_2-NH^- and XH_m-CH_2-CH_2^-, with XH_m = F, OH, NH_2 and CH_3

CAMILLA SCOTT AND FRIEDRICH GREIN[1]

Department of Chemistry, University of New Brunswick, Bag Service No. 45222, Fredericton, NB E3B 6E2 Canada

Received June 10, 1994

CAMILLA SCOTT and FRIEDRICH GREIN. Can. J. Chem. **72**, 2521 (1994).

Ab initio geometry optimizations were performed at the RHF/6-31+G* level on anionic acetal-like systems of the form XH_m-CH_2-NH^- and XH_m-CH_2-CH_2^-, with XH_m = F, OH, NH_2, and CH_3. Using Fourier analysis combined with energy decomposition methods, the electronic part of the anomeric stabilization, *e*, has been evaluated. For the NH^- systems, e_N- was calculated to be –16.5 for F, –5.2 for OH, –2.7 for NH_2, and –1.0 for CH_3. For the CH_2^- systems the e_C- values are –8.1 for F, –5.3 for OH, –3.0 for NH_2 and –1.2 for CH_3. The units are kcal/mol. Comparing the trends in calculated energies, bond distances, and charges with those obtained for the model compounds CH_2-NH and CH_2-CH_2, the anomeric effect can be understood as the tendency of the anion to form a π-bond in the CH_2-NH^- or CH_2-CH_2^- portion of the molecule, caused by charge transfer from this portion to XH_m. The CH_3-CH_2-NH^- and CH_3-CH_2-CH_2^- systems form an exception.

CAMILLA SCOTT et FRIEDRICH GREIN. Can. J. Chem. **72**, 2521 (1994).

On a effectué des optimisations *ab initio* de géométries au niveau RHF/6-31+G* sur des systèmes ressemblant à des acétals des formes XH_m-CH_2-NH^- et XH_m-CH_2-CH_2^- dans lesquelles XH_m = F, OH, NH_2 et CH_3. Faisant appel à une analyse de Fourier combinée avec des méthodes de décomposition d'énergie, on a évalué la partie anomérique de la stabilisation, *e*. Pour les systèmes NH^-, on a évalué que les valeurs de e_N- sont –16,5 pour F, –5,2 pour OH, –2,7 pour NH_2 et –1,0 pour CH_3. Pour les systèmes CH_2^- les valeurs de e_C- sont –8,1 pour F, –5,3 pour OH, –3,0 pour NH_2 et –1,2 pour CH_3. Les unités sont les kcal/mol. Une comparaison des tendances dans les énergies, les longueurs de liaisons et les charges calculées avec les valeurs correspondantes obtenues pour les composés modèles CH_2-NH et CH_2-CH_2, on peut comprendre l'effet anomérique comme une tendance de l'anion à former une liaison π dans les portions CH_2-NH^- ou CH_2-CH_2^- des molécules, provoquée par un transfert de charge de cette portion au XH_m. Les systèmes CH_3-CH_2-NH^- et CH_3-CH_2-CH_2^- forment une exception.

[Traduit par la rédaction]

1. Introduction

Over the past 30 years the anomeric effect (ae) has been studied for many different systems of molecules. Recently, papers by Grein and Deslongchamps, to be referred to as papers I (1) and II (2), considered systems of neutral and protonated acetals. In a third paper, III, Grein (3) combined the energy decomposition model first outlined in paper II with the Fourier analysis model given in paper I. In the present study, previous work is extended to include anionic acetal-like systems XH_m-CH_2-YH_n^-, with XH_m = F, OH, NH_2, and CH_3, and YH_n^- = NH^- and CH_2^-.

The main purpose of the energy decomposition method is to separate the electronic part of the anomeric stabilization from the steric and electrostatic contributions. In the Fourier analysis, the rotation of the YH_n hydrogens of compounds XH_m-CH_2-YH_n about the C–Y axis is broken down into V_1, V_2, and V_3 components corresponding to the first three terms in the Fourier series, having periods of 360°, 180°, and 120°, respectively. The electronic part of the anomeric stabilization energy is seen to be related to the V_2 component. The combination of these two methods allows for an assessment of the potential for the occurrence and strength of the anomeric effect in a molecule.

The electronegativity differences between the X and Y atoms in XH_m-CH_2-OH, XH_m-CH_2-NH_2, and corresponding protonated systems are essential to the understanding of the anomeric effect. The more electronegative XH_m is, compared to OH or NH_2, the greater the electronic stabilization from the anomeric effect due to OH or NH_2. For example, in the NH_2 systems, the very electronegative XH_m = F system had an electronic parameter e_N of –3.6 kcal/mol compared to the XH_m = NH_2 system for which e_N was –1.0 kcal/mol.

The anionic XH_m-CH_2-CH_2^- systems are commonly referred to as carbanions. Despite the fact that a large number of organic reactions involve carbanions as reactive intermediates, they are not well understood. Carbanions act as strong bases or nucleophiles in reactions such as electrophilic substitutions. They are an interesting class of compounds because, unlike other molecules, they are destabilized by ethyl and other electron-donating groups. Usually, carbanions acting as intermediates in organic reactions are bonded to groups that stabilize through inductive effects or resonance.

The fact that the XH_m-CH_2-CH_2^- ions studied here are not stabilized indicates that if they exist they are not as common as other carbanions. For example, F-CH_2-CH_2^- is not stable due to β-elimination of the fluorine atom. The *n*-propyl anion CH_3-CH_2-CH_2^- is actually known and exists as an ion pair with such species as Li^+. NH_2-CH_2-CH_2^- is more stable than OH-CH_2-CH_2^- due to the acidities of the other hydrogens. Experimental chemists are presently working on possible OR-CH_2-CH_2^- systems.

A number of theoretical studies have previously been performed on anionic acetal-like systems (4–9). For example, Schleyer and Kos (4) investigated cases with X = F, O, and N, in connection with assessing the importance of negative hyperconjugation. For such systems, negative hyperconjugation is the interaction of a filled *p* orbital on the carbon in CH_2^- with the C—X bonding and antibonding orbitals. The extent of this interaction is dependent on the electronegativity of X. For example, with F this orbital interaction is large and there is a great amount of stabilization, accompanied by a shortening of the C—C bond and lengthening of the C—X bond. Negative (or anionic) hyperconjugation is equivalent to the anomeric effect in anionic systems. Theoreticians studying the negative hyperconjugation effect (4–6) and related topics (7, 9) in anionic acetals compared the energies of the 180° conformer, in which

[1]Author to whom correspondence may be addressed. Telephone: (506) 403-4776. Fax: (506) 453-4599. Bitnet:FRITZ@UNB.CA

Can. J. Chem. Downloaded from www.nrcresearchpress.com by 85.192.166.187 on 09/08/12
For personal use only.

Can. J. Chem. Downloaded from www.nrcresearchpress.com by 85.192.166.187 on 09/08/12
For personal use only.

negative hyperconjugation is at a maximum (lone pair on CH_2^- antiperiplanar to the C—X bond), with that of the 90° conformer where negative hyperconjugation is turned off (lone pair on CH_2^- rotated 90° relative to C—X bond).

The paper by Schleyer and Kos (4) was written in response to a controversy over whether the stabilizing effect seen in $F\text{-}CH_2\text{-}CH_2^-$ was due to negative hyperconjugation or to polarization. Streitweiser et al. (5) supported the polarization idea by showing that there was no charge transfer involved. In reply to this, Schleyer and Kos (4) disagreed with the conclusions of Streitweiser et al. and stated that the definition of hyperconjugation is the interaction of orbitals, independent of charge transfer, but that both charge transfer and polarization can be the result of hyperconjugation. Discrepancies in their findings from those of Streitweiser et al. were shown to result from restrictions placed on geometries. For example, Streitweiser et al. used fixed bond lengths and angles whereas Schleyer and Kos did not. Schleyer and Kos found the energy difference between the 180° conformer (negative hyperconjugation) and the 90° conformer (no negative hyperconjugation) to be 10.2 kcal/mol for $F\text{-}CH_2\text{-}CH_2^-$ (4-31+G) and 6.5 kcal/mol for $NH_2\text{-}CH_2\text{-}CH_2^-$ (3-21+G). Apeloig and Rapporport (7) obtained energy differences of 10.1 and 4.8 kcal/mol, respectively, calculated at the STO-3G level.

An interesting result obtained by Schleyer and Kos (4), which was reviewed by Reed and Schleyer (8), was that in $F\text{-}CH_2\text{-}CH_2^-$ β-elimination occurs, leading to dissociation into F^- and ethylene. This 1,2 elimination in $F\text{-}CH_2\text{-}CH_2^-$ had previously been studied by Bach, Badger, and Lang (9).

The main objective of this paper is to demonstrate that the anomeric effect applies to anionic acetal-like systems as well as to their neutral and protonated counterparts, and to obtain estimates of the stabilization energies, in particular their electronic components.

2. Methods

Geometry optimizations were carried out at the SCF level with the 3-21G* and 6-31+G* basis sets, using the GAUSSIAN 86 program (10). Only the values obtained from 6-31+G* calculations are reported. In our previous studies on the anomeric effect, the 6-31G** and 6-31+G* basis sets were employed. For the anionic systems to be treated in this paper, diffuse basis functions (+) are essential.

For the anionic acetal-like systems $XH_m\text{-}CH_2\text{-}YH_n^-$, with X = F, O, N, and C, and Y = N and C, the dihedral angles of the XH_m and YH_n^- hydrogens were held at certain values while the other parameters, bond lengths, bond angles, and remaining dihedral angles, were optimized. For purposes of the energy decomposition method the hydrogen dihedral angles were fixed to obtain the correct geometry for 0, 1, and 2 anomeric effects (0ae, 1ae, 2ae). Examples are shown in structures **1–4** for the $OH\text{-}CH_2\text{-}NH^-$ system. For use in the Fourier analysis method

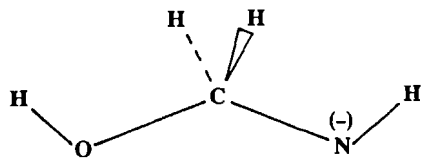

0 ae

1

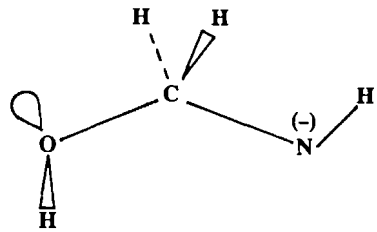

1 ae(O)

2

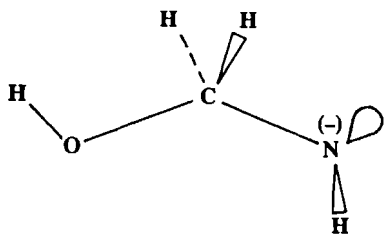

1 ae(N)

3

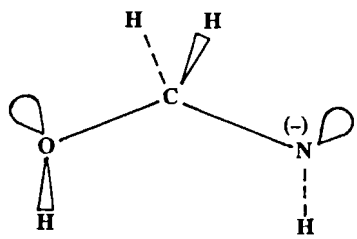

2 ae

4

the XH_m hydrogens were fixed anti (a) for OH and staggered (s) for NH_2 and CH_3 relative to the $CH_2\text{-}YH_n$ fragment of the molecule. The term anti refers to a dihedral angle of 0° for the OH hydrogen, whereas staggered refers to dihedral angles of ±120° for the NH_2 hydrogens and 0°, ±120° for the CH_3 hydrogens. All dihedral angles refer to the plane XCZ, where Z is shown in structure **5**. With the XH_m hydrogens held in these positions the NH^- (CH_2^-) hydrogens were rotated about the C—N (C—C) bond. Calculations were performed at dihedral angles ϕ of 0° (±60°), 60° (0°, 120°), 120° (60°, 180°), and 180° (±120°) referring to the plane XCZ. Numbers in parentheses refer to the CH_2^- systems. Examples are given in structures **5–12**.

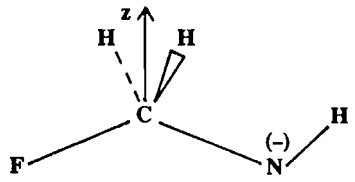

F-CH_2-NH^-, 0°

5

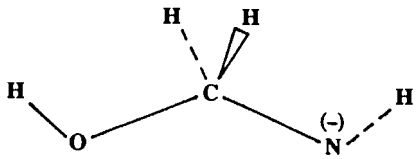

a-OH-CH_2-NH^-, 60°

6

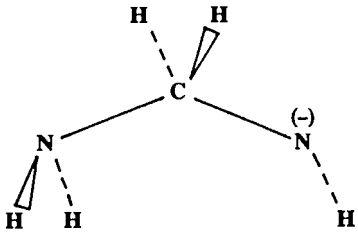

s-NH_2-CH_2-NH^-, 120°

7

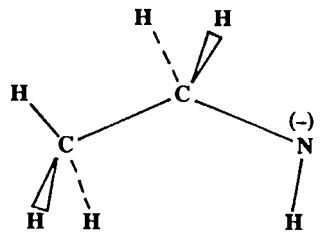

s-CH_3-CH_2-NH^-, 180°

8

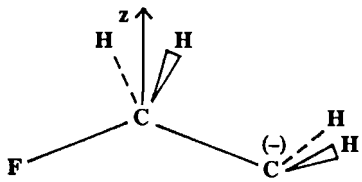

F-CH_2-CH_2^-, 0°

9

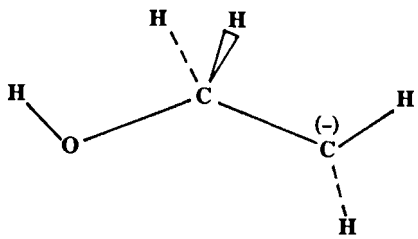

a-OH-CH_2-CH_2^-, 60°

10

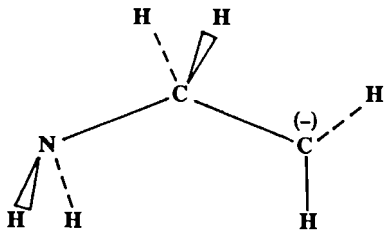

s-NH_2-CH_2-CH_2^-, 120°

11

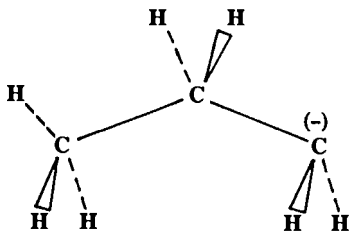

s-CH_3-CH_2-CH_2^-, 180°

12

3. Results for energy analysis model

3.1 The XH_m-CH_2-NH^- systems

In the simple picture of lone pairs (*l*p) of electrons located in sp^3 positions, the anomeric effect is caused be a lone pair antiperiplanar (app) to the C—X or C—Y bond. Therefore, in structure **1** there is 0ae, whereas **2**, **3**, and **4** have 1ae(O), 1ae(N), and 2ae's, respectively.

In Table 1, energies relative to the most stable conformer as well as optimized C—N and C—X distances are given for the 0ae, 1ae, and 2ae conformers of F-CH_2-NH^-, and OH-CH_2-NH^-, NH_2-CH_2-NH^-. As seen from the relative energies, 1ae is more stable than the corresponding 0ae, and 2ae is more stable than 1ae. The 2ae conformer of F-CH_2-NH^- forms a complex (a loosely bound structure of type F^-...CH_2NH), with a long

Can. J. Chem. Downloaded from www.nrcresearchpress.com by 85.192.166.187 on 09/08/12
For personal use only.

TABLE 1. Relative energies ΔE in kcal/mol (first line) and optimized C—N/C—X distances in Å (second line), obtained by 6-31+G* optimizations on systems XH_m-CH_2-NH^-

XH_m-CH_2-NH^-	0ae	1ae(X)	1ae(N)	2ae
F-CH_2-NH^-		26.94 1.3872/1.4205		0.00 1.2638/2.8178
OH-CH_2-NH^-	13.84 1.3965/1.4393	6.61 1.4067/1.4306	6.20 1.3752/1.4923	0.00 1.3856/1.4808
NH_2-CH_2-NH^-	6.84 1.4140/1.4748	1.24 1.4216/1.4693	1.65 1.4013/1.5032	0.00 1.4122/1.5005
CH_3-CH_2-NH^-	0.02 1.4278/1.5318		0.00 1.4249/1.5500	

C—F distance of 2.82 Å. The energy lowerings for CH_3-CH_2-NH^- are essentially zero, which illustrates the point that the anomeric effect is not applicable to this system. The trends in bond lengths are as expected, with an ae from N causing the C—N bond to shorten and the C—X bond to lengthen.

Following the procedures outlined in papers II and III, an energy analysis was carried out for the XH_m-CH_2-NH^- systems. The energy differences between various conformers are described by certain parameters, such as the electronic component, called *e*; 1,3-diaxial H–H repulsions, labelled *r*; 1,3-diaxial *l*p–*l*p repulsions, labelled *l*; and intramolecular "hydrogen bonding" (1,3-diaxial H-*l*p interactions), labelled *h*. The 1,2 hydrogens and bonds are staggered for all of the conformers, so these interactions do not need to be included in the analysis.

The values of the parameters *r*, *l*, and *h* have to be estimated in order to obtain the value of *e* from the calculated energy differences. The 6-31+G* energy difference between g,g-OH-CH_2-NH^-, **13***a*, and g,g*-OH-CH_2-NH^-, **13***b*, is 3.85 kcal/mol. For NH_2-CH_2-NH^- the sterically favoured 1ae(N^-) conformer, **14***a*, is 3.75 kcal/mol (6-31+G*) more stable than the 1ae(N^-) conformer, **14***b*. For both systems the energy difference is given by the formula $\Delta E = l + r - 2h$. For the methoxy

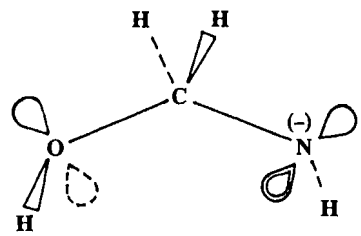

$e_O + e_{N^-} + 2h$

13*a*

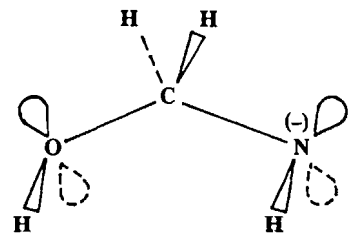

$e_O + e_{N^-} + r + l$

13*b*

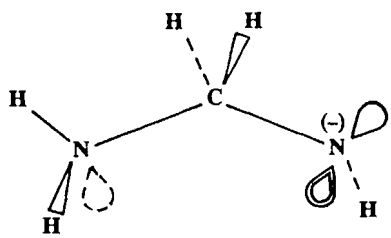

$e_{N^-} + 2h$

14*a*

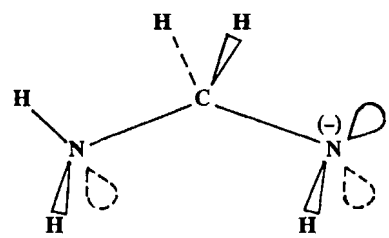

$e_{N^-} + l + r$

14*b*

system discussed in paper II, *h* was estimated to be about −1 kcal/mol. Using this value for *h*, $l + r$ is approximately equal to 2 kcal/mol. To make this method more applicable, only half or whole integers (in kcal/mol) will be used, so $l = r = 1$ kcal/mol will be assumed as in our previous work.

Applying this model to the systems given in Table 1 allows for an estimate of the electronic contribution *e* to the anomeric effect. This is the anomeric stabilization energy (difference between $\phi = 0°$ and $\phi = 120°$) after steric and electrostatic components were removed. The procedure is outlined in paper II. The value of e_{N^-} is –25 for the X = F, –5 for the X = O, –3 for the X = N, and –2 for the X = C system. In e_{N^-} the subscript indicates that the electronic portion of the anomeric effect is due to electron donation from (the formal) N^-. As well, values of $e_N \cong$

Can. J. Chem. Downloaded from www.nrcresearchpress.com by 85.192.166.187 on 09/08/12
For personal use only.

TABLE 2. Relative energies ΔE in kcal/mol (first line) and optimized C—C/C—X distances in Å (second line), obtained by 6-31+G* geometry optimizations on systems XH_m-CH_2-CH_2^-

XH_m-CH_2-CH_2^-	0ae	1ae(X)	1ae(C^-)	2ae
F-CH_2-CH_2^-	10.56 1.4957/1.4236		0.00 1.4496/1.5300	
OH-CH_2-CH_2^-	10.82 1.5043/1.4401	3.56 1.4805/1.4825	2.50 1.5072/1.4342	0.00 1.4863/1.4794
NH_2-CH_2-CH_2^-	3.44 1.5149/1.4749	1.92 1.4751/1.5213	2.51 1.5033/1.5024	0.00 1.5068/1.5026
CH_3-$CH_2CH_2^-$	0.42 1.5282/1.5336		0.00 1.5229/1.5506	

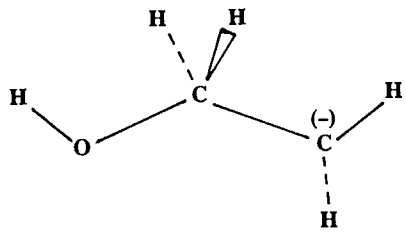

0 ae

15

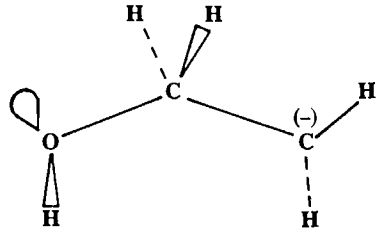

1 ae(O)

16

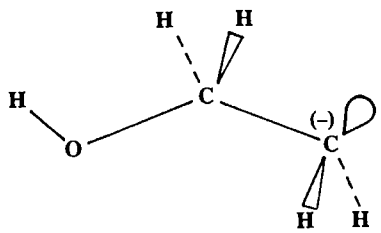

1 ae(C^-)

17

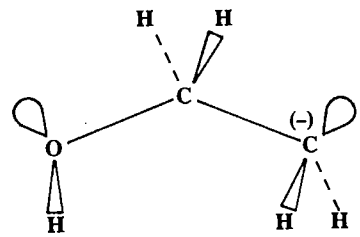

2 ae

18

Can. J. Chem. Downloaded from www.nrcresearchpress.com by 85.192.166.187 on 09/08/12
For personal use only.

–3.5 for the NH_2-CH_2-NH^- system and $e_O \cong -4.5$ for the OH-CH_2-NH^- system were calculated (all in kcal/mol).

3.2 The XH_m-CH_2-CH_2^- systems

For the systems XH_m-CH_2-CH_2^-, with XH_m = F, OH, NH_2, and CH_3, the simple definition for the anomeric effect as given in the previous section yields 0ae for structure **15**, 1ae(O) for **16**, 1ae(C^-) for 17, and 2ae for **18**.

In Table 2, relative energies and optimized C—C and C—X distances are given for the 0ae, 1ae, and 2ae conformers of the various XH_m-CH_2-CH_2^- systems. From the relative energies it can be seen that again the 1ae conformer is more stable than the 0ae conformer and, in turn, 2ae is more stable than 1ae. The energy lowerings for all systems are significant except for CH_3-CH_2-CH_2^-, as expected.

The 6-31+G* energy difference between the 1ae(O) conformation of OH-CH_2-CH_2– and the sterically hindered 1ae(O) is 5.17 kcal/mol. For NH_2-CH_2-CH_2^-, the energy difference (6-31+G*) between the staggered 0ae conformer and its eclipsed version is 4.77 kcal/mol. For both of these systems $\Delta E = l + r - 2h$. Using a value of –1 kcal/mol for the h parameter, $l + r$ is equal to about 3 kcal/mol. Using only half or whole integers, l and r are best fitted to be 1.5 kcal/mol each.

This model applied to the systems listed in Table 2 gives e_{C^-} values of about –8 for F, –5 for OH, –4 for NH_2, and –2 for the CH_3 system (kcal/mol). Also, values of $e_O \cong -6$ kcal/mol for the OH-CH_2-CH_2^- system and $e_N \cong -4.5$ kcal/mol for NH_2-CH_2-CH_2^- are obtained.

The trend for the e_{C^-} values is as expected, with the highest e_{C^-} obtained for the F system, decreasing to the OH, the NH_2, and finally the CH_3 system. It is interesting to note that for the OH system e_O is more negative than e_{C^-}, and a similar situation applies to the NH_2 system. This means that for the a-OH-CH_2-CH_2^- system a lone pair on O donating into C^- is more stabilizing than lone pair donation the other way around (or C^- is more electronegative than O).

Schleyer and Kos (4) reported that under the restraint of C_s symmetry, F-CH_2-CH_2^- optimized to a planar C_{2v} complex, with a large C—F distance. The 1ae (C_s) conformer studied here, however, had the dihedral angles of the CH_2 hydrogens

Can. J. Chem. Downloaded from www.nrcresearchpress.com by 85.192.166.187 on 09/08/12
For personal use only.

TABLE 3. Relative energies ΔE in kcal/mol (first line), optimized C—N/C—X distances in Å (second line), and Mulliken charges on NH^-/XH_m (third line), obtained by 6-31+G* geometry optimizations on XH_m-CH_2-NH^- for NH^- dihedral angles of 0°, 60°, 120°, and 180°

XH_m-CH_2-NH^-	0°	60°	120°	180°
F-CH_2-NH^-	0.00	−7.21	−26.94	−1.06
	1.3872/1.4205	1.3502/1.5389	1.2638/2.8178	1.3828/1.4589
	−0.855/−0.443	−0.741/−0.504	−0.308/−0.963	−0.852/−0.521
a-OH-CH_2-NH^-	0.00	−3.85	−7.64	−1.06
	1.3965/1.4393	1.3831/1.4807	1.3752/1.4923	1.3956/1.4615
	−0.860/−0.296	−0.808/−0.279	−0.783/−0.337	−0.860/−0.378
s-NH_2-CH_2-NH^-	0.00	−0.03	−1.24	4.07
	1.4216/1.4693	1.4168/1.4914	1.4122/1.5005	1.4245/1.4860
	−0.855/−0.173	−0.820/−0.085	−0.796/−0.204	−0.863/−0.300
s-CH_3-CH_2-NH^-	0.00	1.43	−0.02	3.31
	1.4278/1.5318	1.4314/1.5444	1.4249/1.5500	1.4372/1.5407
	−0.844/0.064	−0.827/0.162	−0.837/−0.168	−0.881/−0.272

TABLE 4. Fourier constants V_1–V_3, in kcal/mol, for NH rotation in systems XH_m-CH_2-NH^-, obtained from relative energies of Table 2

XH_m-CH_2-NH^-	V_1	V_2	V_3
F-CH_2-NH^-	−13.86	−22.06	12.80
a-OH-CH_2-NH^-	−3.23	−6.95	2.17
s-NH_2-CH_2-NH^-	1.91	−3.55	2.16
s-CH_3-CH_2-NH^-	1.24	−1.27	2.07

fixed at ±120°, and therefore a planar complex could not be formed. The same situation applies to the 180° conformer of F-CH_2-CH_2^-, which is identical in structure. Due to the restrictions on dihedral angles imposed in this study, β-elimination, leading to F^- + C_2H_4, could not take place.

4. Results for the Fourier analysis model

4.1 The XH_m-CH_2-NH^- systems

In this study the NH^- hydrogen of XH_m-CH_2-NH^- was rotated around the C—N bond, with the XH_m hydrogens held at fixed dihedral angles relative to the CH_2 hydrogens, as explained earlier. XH_m was chosen to be F (**5**), a-OH (**6**), s-NH_2 (**7**), and s-CH_3 (**8**). Relative energies, optimized C—N and C—X distances, and Mulliken charges on NH^- and XH_m for NH^- dihedral angles φ of 0°, 60°, 120°, and 180° are given in Table 3. The dihedral angle φ = 0° corresponds to the 0ae conformation in the case of the a-OH system and to the 1ae(X) conformation for F and s-NH_2. For φ = 120°, one ae has to be added, resulting in the 1ae conformer for a-OH, and 2ae for F and s-NH_2. Again, the F-CH_2-NH^- system forms a F^-...CH_2NH complex at 120°, corresponding to the 2ae conformer of Table 1.

In Table 4, the Fourier constants V_1–V_3 are given for these systems. The constants are obtained by fitting the relative energy values of Table 3 to the formula:

$$[1]\quad \Delta E(\phi) = (V_1/2)(1 - \cos\phi) + (V_2/2)(1 - \cos 2\phi) + (V_3/2)(1 - \cos 3\phi)$$

At φ = 0° and 360°, ΔE = 0; therefore all of the relative energies of Table 3 were calculated with respect to the energy at φ = 0°. According to eq. [1], V_3 has maxima at 60° and 180° and minima at 0° and 120°. V_3 represents the threefold repulsion the NH^- hydrogen receives when it eclipses the two C—H bonds at 60° and 300° and C—X bond at 180°. Since the NH^- hydrogen is staggered relative to CH_2X at 0°, V_3 is positive. The value of the V_3 parameter is expected to be close to that of the energy difference between the staggered and eclipsed conformers of CH_3NH^-, which was calculated to be 2.00 kcal/mol at the 6-31+G* level. Such is the case for all systems except F-CH_2-NH^-. The large V_3 value of 12.80 kcal/mol for the latter system is due to the formation of a complex at φ = 120° (seen from the bond distances in Table 3). Since this conformer is very stable compared to the 60° and 180° conformers, a very large positive V_3 results.

From eq. [1], V_1 has a maximum at 180° and a minimum at 0°. The sign of V_1 is negative if the 180° conformer is more stable than the 0° conformer. V_1 results from steric (H–H repulsions) and electrostatic effects (*l*p–*l*p repulsions and H–*l*p attractions). Components of V_1 relate to the energy parameters *r*, *l*, and *h* used previously in the energy decomposition model. According to eq. [1], $V_1 = \Delta E(180) - V_3$. For F-$CH_2$-$NH^-$ and a-OH-CH_2-NH^-, $\Delta E(180°)$ is the difference between intramolecular 1,3-hydrogen bonding at 180° (negative) and lone pair repulsions at 0° (positive). This situation causes $\Delta E(180)$ to be negative and hence V_1 to be negative (since V_3 is positive). For F-CH_2-NH^-, V_1 is large and negative due to the fact that $\Delta E(180)$ is small and negative whereas V_3 is large and positive. For s-NH_2 and s-CH_3, $\Delta E(180)$ is the difference between 1,3 H–H repulsions at 180° (+) and 1,3 internal hydrogen bonding at 0° (−), causing $\Delta E(180)$ and V_1 (since $\Delta E(180) > V_3$) to be positive.

According to eq. [1], the V_2 parameter has a maximum at φ = 90° and is zero at 0° and 180°. This term results from the electronic part of the anomeric effect. It is always negative and decreases in magnitude from X = F to X = C. V_2 is exceptionally large for the F system owing to the high stabilization received upon the formation of a complex at φ = 120°.

According to Table 3, anomeric stabilization (i.e., $E(120°)$ is lower than $E(0°)$, or $\Delta E(120°)$ is negative) is received by all of the systems except $XH_m = CH_3$. This situation can be explained on the basis of the Fourier constants. According to eq. [1], $\Delta E(120) = 0.75(V_1 + V_2)$. For the F and a-OH systems both V_1 and V_2 are negative, meaning that φ = 120° is more stable than φ = 0° via the V_1 term (steric and electrostatic) and φ = 90° is more stable than φ = 0° via the V_2 term (electronic stabilization). A combination of negative V_1 and V_2 results in a large sta-

TABLE 5. Comparison of e_{N^-} values in kcal/mol, calculated by Fourier analysis with e_{N^-} values obtained from energy analysis

XH_m-CH_2-NH^-	Fourier e_{N^-}	Energy e_{N^-}
F-CH_2-NH^-	−16.5	−25
a-OH-CH_2-NH^-	−5.2	−5
s-NH_2-CH_2-NH^-	−2.7	−3
s-CH_3-CH_2-NH^-	−1.0	−2

bilization at $\phi = 120°$. Therefore, the anomeric stabilization in these two systems is a combination of favourable electronic as well as steric and electrostatic effects as one rotates from $\phi = 0°$ (0ae) to $\phi = 120°$ (1ae).

For s-NH_2, V_1 is positive and V_2 is negative but the electronic effect V_2 is large enough to compensate for the V_1 value such that there is still considerable stabilization at $\phi = 120°$. For the CH_3 system, V_1 is positive and V_2 negative but in this case the sum $V_1 + V_2$ is close to zero so there is no significant stabilization at 120°. Since $\Delta E_{ae} = \Delta E(120°) = 0.75\ (V_1 + V_2)$, the electronic component of the ae stabilization e_{N^-} can be calculated as $0.75V_2$, which gives −16.5 for F, −5.2 for a-OH, −2.7 for s-NH_2, and −1.0 for s-CH_3 (all in kcal/mol).

In Table 5, the e_{N^-} values found from the Fourier analysis model are given and compared with those found previously by the energy decomposition model. Except for F-CH_2-NH^-, which is characterized by complex formation, the agreement is quite good.

4.2 The XH_m-CH_2-CH_2^- systems

The same analysis was also performed for the systems XH_m-CH_2-CH_2^-, where again XH_m = F (**9**), a-OH (**10**), s-NH_2 (**11**), and s-CH_3 (**12**). For symmetry reasons, $\phi(CH_2) = 0°$ was chosen such that the rotating CH_2 hydrogens have dihedral angles of ±60° relative to the plane CCZ (**9**). For $\phi(CH_2) = 60°$, the dihedral angles are 0°, 120°; for $\phi(CH_2) = 120°$ the dihedral angles are 60°, 180°; and for $\phi(CH_2) = 180°$ they are ±120°. Except for the fixed dihedral angles of the CH_2 and the XH_m hydrogens (as described earlier), all geometry parameters were allowed to optimize.

The calculated energy differences, C—C and C—X distances, and Mulliken charges on CH_2^- and XH_m are given in Table 6. In Table 7 the Fourier constants obtained by fitting the relative energies into eq. [1] are presented. The V_3 parameter describes the threefold repulsion the rotating CH_2^- receives when eclipsing the CH_2X group. At $\phi = 0°$ and 120° CH_2^- is eclipsed relative to CH_2X whereas at $\phi = 60°$ and 180° this steric interaction is minimal, therefore V_3 is negative. The V_3 parameter should have a value close to the energy difference between the eclipsed and staggered forms of CH_3-CH_2^- (−2.39 kcal/mol in 6-31+G*). This holds true, as seen from Table 7 in which V_3 for XH_m-CH_2-CH_2^- ranges from −2.61 to −2.92 kcal/mol.

As before, V_1 represents the steric and electrostatic effects. The V_1 term in eq. [1] has a maximum (or minimum) at 180° and is zero at 0°. For F-CH_2-CH_2^- and a-OH-CH_2-CH_2^-, $\Delta E(180°)$ is the difference between lone pair repulsion at 0° (positive) and intramolecular hydrogen bonding at 180° (negative). Therefore, both $\Delta E(180°)$ and V_1 (= $\Delta E(180) - V_3$) are negative. For s-NH_2 and s-CH_3, $\Delta E(180°)$ is the difference between intramolecular hydrogen bonding at 0° (−) and hydrogen repulsion at 180° (+). The sign of $\Delta E(180°)$ cannot be determined by qualitative means. From Table 6 the values of $\Delta E(180°)$ for the s-NH_2 and s-CH_3 systems are −1.53 and −1.63 kcal/mol, respectively, leading to a positive V_1.

The V_2 parameter, which contains the electronic part of the anomeric effect, is positive and decreases in value starting from the XH_m = F to the XH_m = CH_3 systems. For the XH_m-CH_2-CH_2^- systems the anomeric stabilization is given by $\Delta E_{ae} \equiv E(180°) - \Delta E(60°)$. For the F and a-OH systems V_1 is negative and V_2 positive, therefore both terms stabilize the system when going from 0ae (60°) to 1ae (180°). In other words, the observed energy lowering has electrostatic/steric and electronic components. On the other hand, for s-NH_2 and s-CH_3, V_1 and V_2 are positive. The stabilization of these two systems results from favourable V_2 (electronic), which is counteracted by an unfavourable V_1 (steric/electrostatic).

Calculating e_{C^-} as $-0.75V_2$ gives $e_{C^-} = -8.1$ for F-CH_2-CH_2^-, −5.3 for a-OH-CH_2-CH_2^-, −3.0 for s-NH_2-CH_2-CH_2^-, and −1.2 kcal/mol for s-CH_3-CH_2-CH_2^-. In Table 8 the e_{C^-} values obtained by the Fourier method are given and are compared with the corresponding e_{C^-} values obtained earlier from the energy analysis method. In all cases, the agreement is good.

In the paper by Schleyer and Kos (4), mentioned earlier, the energy difference between the 90° and the 180° conformer for systems XH_m-CH_2-CH_2^- was given as 10.2 and 6.5 kcal/mol for X = F and N, respectively. (For OH-CH_2-CH_2^- the a-OH conformation, chosen here, was not considered.) Using the Fourier series to calculate the energy of the 90° conformer, the corresponding energy differences obtained in this work are 13.9 for X = F, 9.7 for X = O and 4.7 for X = N, in kcal/mol.

5. Application of the π-bonding model

The electronic part of the anomeric effect will now be explained as the tendency of the CH_2-YH_n component of XH_m-CH_2-YH_n^- to form a π bond. To do this the trends in relative energies, bond distances, and Mulliken charges of the XH_m-CH_2-YH_n^- systems will be compared with the corresponding trends of the CH_2=YH_n molecule.

The CH_2 hydrogen dihedral angles in CH_2=NH were held at ±90° (planar) and the HNC angle at 109.5°. In previous cases, the CH_2 group was held in pyramidal position (±60°), in order to better mimic the situation in XH_m-CH_2-NH_2^-. However, the optimization process for some dihedral angles led to badly distorted structures, causing inconsistencies in the calculated energies and C—N bond distances. The NH portion of the molecules was rotated from 0° to 180°, with the same convention as illustrated in structures **5–8**. The resulting bond distances, relative energies, and Mulliken charges from the 6-31+G* geometry optimizations are given in Table 9.

The trend in relative energies for the CH_2=NH molecule is as expected, with the least stable conformer at $\phi = 0°$, increasing in stability to $\phi = 90°$ and then decreasing to $\phi = 180°$. The conformers at $\phi = 180°$ and 60° have the same energies as those of $\phi = 0°$ and 120°, respectively, due to the symmetry of the molecule. For the pyramidal (±60°) conformer of CH_2=NH, the 180° geometry would be at lower energy than for 0° due to steric hindrance between the CH_2 and NH hydrogens at 0°.

Table 3 shows that the F-CH_2-NH^- and a-OH-CH_2-NH^- systems have the same trend in energies as the CH_2=NH molecule. For s-NH_2 the 180° conformer is less stable than the 0° conformer. This is due to the fact that there is steric hindrance between the staggered NH_2 hydrogens and the NH hydrogen at $\phi = 180°$. The trends for the CH_3 systems are quite unlike those

Can. J. Chem. Downloaded from www.nrcresearchpress.com by 85.192.166.187 on 09/08/12
For personal use only.

Can. J. Chem. Downloaded from www.nrcresearchpress.com by 85.192.166.187 on 09/08/12
For personal use only.

TABLE 6. Relative energies ΔE, in kcal/mol (first line), optimized C—C/C—X distances in Å (second line), and Mulliken charges on CH_2^-/XH_m (third line), obtained by 6-31+G* geometry optimizations on XH_m-CH_2-CH_2^- for CH_2^- dihedral angles of 0°, 60°, 120°, and 180°

XH_m-CH_2-CH_2^-	0° (±60°)	60°(0°, 120°)	120°(60°, 180°)	180° (±120°)
F-CH_2-CH_2^-	0.00	4.39	5.57	−6.17
	1.4681/1.4730	1.4957/1.4236	1.5002/1.4441	1.4496/1.5300
	−0.557/−0.415	−0.784/−0.437	−0.797/−0.480	−0.702/−0.497
a-OH-CH_2-CH_2^-	0.00	1.81	3.25	−5.45
	1.4915/1.4628	1.5043/1.4403	1.5122/1.4517	1.4803/1.4828
	−0.586/−0.216	−0.782/−0.296	−0.771/−0.346	−0.718/−0.312
s-NH_2-CH_2-CH_2^-	0.00	0.39	4.01	−1.53
	1.5179/1.4862	1.5213/1.4751	1.5308/1.4832	1.5068/1.5026
	−0.562/−0.003	−0.778/−0.176	−0.839/−0.238	−0.776/−0.151
s-CH_3-CH_2-CH_2^-	0.00	−1.20	1.90	−1.63
	1.5326/1.5408	1.5282/1.5336	1.5376/1.5379	1.5229/1.5506
	−0.786/0.156	−0.860/−0.112	−0.811/−0.218	−0.839/−0.127

TABLE 7. Fourier constants V_1–V_3, in kcal/mol, for CH_2 rotation in systems XH_m-CH_2-CH_2^-, obtained from relative energies of Table 6

XH_m-CH_2-CH_2^-	V_1	V_2	V_3
F-CH_2-CH_2^-	−3.33	10.75	−2.84
a-OH-CH_2-CH_2^-	−2.67	7.01	−2.78
s-NH_2-CH_2-CH_2^-	1.39	3.95	−2.92
s-CH_3CH_2-CH_2^-	0.98	1.55	−2.61

TABLE 8. Comparison of e_{C^-} values in kcal/mol, obtained by Fourier analysis and energy analysis

XH_m-CH_2-CH_2^-	Fourier e_{C^-}	Energy e_{C^-}
F-CH_2-CH_2^-	−8.1[a]	−8.0
OH-CH_2-CH_2^-	−5.3	−5.0
NH_2-CH_2-CH_2^-	−3.0	−4.0
CH_3-CH_2-CH_2^-	−1.2	−2.0

[a]Value is −23.8 kcal/mol when restrictions on dihedral angles are removed for the 180° conformer (see text).

TABLE 9. 6-31+G* results for CH_2=NH with NH rotating about C—N, and CH_2 held in planar position, for NH dihedral angles of 0°, 60°, 90°, 120°, and 180°[a]

ϕ	0°	60°	90°	120°	180°
ΔE (kcal/mol)	0.00	−47.28	−57.06	−47.28	0.00
R_{CN} (Å)	1.2653	1.2572	1.2542	1.2572	1.2653
$Q(CH_2)$	0.360	0.189	0.172	0.189	0.360
Q(NH)	−0.360	−0.189	0.172	−0.189	−0.360

[a]V_2 = −63.04 kcal/mol.

TABLE 10. 6-31+G* results for CH_2=CH_2 with on CH_2 group rotating about C—C, and the other CH_2 group held in pyramidal position, for CH_2 dihedral angles of 0°, 60°, 90°, 120°, and 180°[a]

ϕ	0°	60°	90°	120°	180°
ΔE (kcal/mol)	0.00	30.63	77.39	20.07	−9.88
R_{CC} (Å)	1.3321	1.3356	1.4307	1.3620	1.3436

[a]V_1 = 13.63, V_2 = 40.39, V_3 = 3.75 kcal/mol.

of the π-bonded molecule, which indicates that the ae is not applicable for this system.

The C—N bond length for the CH_2=NH molecule decreases from the conformer at ϕ = 0° to ϕ = 90° and then increases to ϕ = 180°. This trend is the same as found for the F and a-OH systems. For the s-NH_2 system the largest bond distance is obtained at ϕ = 180° instead of at ϕ = 0° due to steric factors. For the s-CH_3 system the C—N distances show no similarity at all to the CH_2=NH molecule.

For studying the π-bonding model in the XH_m-CH_2-CH_2^- systems reference calculations on CH_2=CH_2 were performed. For one CH_2 group the dihedral angles were fixed in pyramidal position (±60°). The hydrogens of the other CH_2 group were rotated, with the ϕ angles defined analogously to structures **9**–**12**. The relative energies and C—C distances of CH_2=CH_2 are given in Table 10.

In comparing the trend in relative energies of the CH_2=CH_2 molecule with those of XH_m-CH_2-CH_2^- (Table 6) it is seen that all systems except CH_3-CH_2-CH_2^- follow the same trend. An increase in relative energy between ϕ = 0° and 120° is followed by a decrease down to ϕ = 180°. The trend in C—C bond lengths shown in Table 6 is also similar to that of CH_2=CH_2, except for CH_3−CH_2-CH_2^-. The bond lengths increase from ϕ = 0° to 120° and then decrease at ϕ = 180°. For CH_2=CH_2 the bond at ϕ = 0° is shorter than at ϕ = 180° but the situation is opposite for the XH_m-CH_2-CH_2^- systems. This difference is considered to be due to steric interaction between CH_2 and XH_m in the XH_m-CH_2-CH_2^- systems. The fact that the CH_2^- portion of XH_m-CH_2-CH_2^- is least negative (most positive) at ϕ = 0° indicates increased π bonding.

The π-bonding model shows clearly that the anomeric effect is not applicable to CH_3−CH_2-CH_2^- since it has no similarities with CH_2=CH_2.

6. Discussion and conclusion

The energy parameters e_{N^-} and e_{C^-} obtained by Fourier analysis are summarized in Table 11. These parameters were designed to capture the electronic part of the anomeric stabilization energy. The anomeric effect occurs when NH^- of XH_m-CH_2-NH^- is rotated from ϕ(NH) = 0° to ϕ(NH) = 120° or CH_2^- of XH_m-CH_2-CH_2 from ϕ(CH_2) = 60° to 180°. The values of e_{N^-} and e_{C^-} were calculated as $0.75V_2$ or $-0.75V_2$, respectively, and are similar to the corresponding values obtained by the energy decomposition model.

TABLE 11. Energy parameters (as obtained by Fourier analysis) e_{N^-} and e_{C^-} in kcal/mol for electronic component of anomeric effect due to N and C, for systems XH_m-CH_2-NH^- and XH_m-CH_2-CH_2^-

XH_m	e_{N^-}	e_{C^-}
F	−16.5[a]	−8.1[b]
a-OH	−5.2	−5.3
s-NH_2	−2.7	−3.0
s-CH_3	−1.0	−1.2

[a]Formation of complex.
[b]Value is −23.8 kcal/mol when restrictions on dihedral angles of 180° conformer are removed (see text).

TABLE 12. Comparison of e_{N^-} values (in kcal/mol) obtained for XH_m-CH_2-NH^- with e_N values obtained in paper III for XH_m-CH_2-NH_2 and XH_{m+1}^+-CH_2-NH_2

XH_m	XH_m-CH_2-NH^-	XH_m-CH_2-NH_2	XH_{m+1}^+-CH_2-NH_2	
F	−16.5	−3.6	(a-FH^+)	−30.6
a-OH	−5.2	−1.9	(s-OH_2^+)	−17.3
s-NH_2	−2.7	−1.0	(s-NH_3^+)	−5.7

One important point illustrated by this analysis is the significance of the relative electronegativities of the X and Y atoms. For an anomeric effect to occur by rotation of YH_n^-, the X atom of XH_m-CH_2-YH_n^- must be more electronegative than Y^-. For the XH_m-CH_2-NH^- systems, it is clear that for XH_m = F, a-OH, and s-NH_2 the X atoms are more electronegative than N^-, and therefore the anomeric effect is applicable. For XH_m = CH_3 the question of anomeric stabilization is not so obvious. The small negative e_{N^-} value of −1.00 kcal/mol for this system indicates no, or only a very small amount of anomeric stabilization. The π-bonding model does not support an anomeric effect in CH_3-CH_2-NH^- (and CH_3-CH_2-CH_2^-).

CH_2^- in the XH_m-CH_2-CH_2^- systems is less electronegative than NH^- in the corresponding XH_m-CH_2-NH^- systems, which should result in larger anomeric effect values when compared to the NH^- systems. Slightly larger values were found for all of the systems except for XH_m = F. In the case of F-CH_2-NH^- the formation of a complex results in an extremely large negative V_2, hence a larger e_{N^-} compared to e_{C^-} of the corresponding CH_2^- system, where no complex is found.

Using both models it has been shown that steric and electrostatic effects can either enhance or reduce the anomeric stabilization caused by the electronic component.

A comparison of e_{N^-} values from this paper with e_N values for the corresponding neutral and protonated systems taken from paper III is given in Table 12. Since the electronegativity difference between NH_2 and XH_m is not as large as between NH^- and XH_m, the anionic systems have much larger electronic components of the anomeric stabilization than the corresponding neutral systems. The e_{N^-} values for the OH and NH_2 systems are about 2.7 times larger than the respective e_N values. For the F system the factor is 4.6, due to formation of a complex for the ϕ = 120° conformer of F-CH_2-NH^-.

A comparison with the e_N values of the protonated systems, where the protonation takes place at the XH_m portion of the molecule, is more difficult, since it is not obvious which combination, XH_m vs. NH^-, or XH_{m+1}^+ vs. NH_2, should have the larger electronegativity difference. The difficulty is compounded by the formation of complexes for a-FH^+ and s-OH_2^+. Considering only the species not affected by complexing, i.e., e_{N^-} of s-NH_2-CH_2-NH^- versus e_N of s-NH_3^+-CH_2-NH_2, one sees that the e_N value of the latter system is about twice as large as the corresponding e_{N^-}. It appears that the larger stabilization goes to the cationic system.

It was mentioned in the Introduction that when optimizing the geometry of F-CH_2-CH_2^- without any restrictions there is no stable minimum, and the anion dissociates to F^- + C_2H_4. Under the restriction of C_s symmetry, this system forms a complex with large CF distance. Due to the additional restrictions placed on the dihedral angles of the CH_2^- hydrogens in this work, no complex is formed here. On the other hand, under very similar conditions, the optimization of F-CH_2-NH^- leads to a complex when the dihedral angle is chosen to be 120°, corresponding to maximal stabilizing interaction of the lone pair on NH^- with the CF bond. The optimized CF distance in the complex is 2.82 Å.

Since the electronegativity difference between F and YH_n^- is larger for the CH_2^- than for the NH^- system, the results obtained here appear to contradict expectations. However, the reason for this behaviour can be seen in the details of the restrictions. For the NH^- system, a planar CH_2=NH can still be formed, since the dihedral angles of the CH_2 hydrogens are free. For the CH_2^- system, however, the hydrogens of CH_2^- (not of CH_2) are held at ±120°, preventing the formation of planar CH_2=CH_2.

The geometry of the planar C_s complex of F-CH_2-CH_2^- was optimized using the 6-31+G* basis set. The CF distance is found to be 2.966 Å (2.93 Å in 3-21+G). Using for F-CH_2-CH_2^- the 180° energy of −37.69 kcal/mol (instead of −6.17 from Table 6), corresponding to the difference between the 0° and the planar 180° conformer, the Fourier constants for this system are recalculated to be V_1 = −24.34, V_2 = 31.77, and V_3 = −13.35 kcal/mol, compared with −3.33, 10.75, and −2.84, kcal/mol, respectively, from Table 7. Therefore, a revised value for e_{C^-} of F-CH_2-CH_2^- is −23.8 kcal/mol, significantly lower than −16.5 kcal/mol obtained for e_{N^-} of F-CH_2-NH^-.

In summary, it has been shown that the anomeric effect in anionic systems of type XH_m-CH_2-NH^- and XH_m-CH_2-CH_2^-, caused by donation of electrons from the formally negative atom, is quite pronounced. The electronic part of the energy stabilization is larger than for corresponding neutral systems, varying from about −3 to −16 kcal/mol for NH_2 to F substituents. These findings should be of interest in the understanding of carbanions, as well as in the design and utilization of other anionic systems.

For systems XH_m-CH_2-YH_n^-, the anomeric effect caused by electronic charge on X being transferred to Y (the opposite to what was done here) is expected to be small or nonexistent, especially if X and Y are confined, as in the present case, to the atoms C, N, O, and F.

Studies on the anomeric effect for first-row/second-row combinations, including neutral, protonated, and anionic systems, have been performed. The results and their analysis following the methods presented here will be published shortly.

Acknowledgements

The authors wish to thank the Natural Sciences and Engineering Research Council of Canada for financial support and Employment and Immigration Canada for awarding Challenge 92 and 93 grants to C.S. Helpful discussions with Professor P. Deslongchamps are gratefully acknowledged.

Can. J. Chem. Downloaded from www.nrcresearchpress.com by 85.192.166.187 on 09/08/12
For personal use only.

1. F. Grein and P. Deslongchamp. Can. J. Chem. **70**, 604 (1992).
2. F. Grein and P. Deslongchamps. Can. J. Chem. **70**, 1562 (1992).
3. F. Grein. ACS Symp. Ser. **539**, 205 (1994).
4. P.v.R. Schleyer and A.J. Kos. Tetrahedron, **39**, 1141 (1983).
5. A. Streitwieser, C.M. Berke, G.W. Schriver, D.G. Grier, and J.B. Collins. Tetrahedron Suppl. 1, **37**, 345 (1981).
6. A. Pross and L. Radom. Aust. J. Chem. **33**, 241 (1980).
7. Y. Apeloig and Z. Rapporport. J. Am. Chem. Soc. **101**, 5095 (1979).
8. A.E. Reed and P.v.R. Schleyer. Inorg. Chem. **27**, 3969 (1988).
9. R.D. Bach, R.C. Badger, and T.L. Lang. J. Am Chem. Soc. **101**, 2845 (1979).
10. M.J. Frisch, J.S. Binkley, K. Raghavachari, C.F. Melius, L. Martin, J.P.P. Stewart, F.W. Bobrowicz, C.M. Rohlfing, L.R. Kahn, D.F. Defrees, R. Seeger, R.A. Whiteside, D.J. Fox, E.M. Fleuder, and J.A. Pople. GAUSSIAN 86. Carnegie-Mellon Quantum Chemistry Publishing Unit, Pittsburgh, Pa. 1984.

Can. J. Chem. Downloaded from www.nrcresearchpress.com by 85.192.166.187 on 09/08/12
For personal use only.

Realistic, detailed images of proteins and tertiary structure elements: *ab initio* quality electron density calculations for bovine insulin

P. DUANE WALKER AND PAUL G. MEZEY[1]

Mathematical Chemistry Research Unit, Department of Chemistry and Department of Mathematics and Statistics, University of Saskatchewan, Saskatoon, SK S7N 0W0, Canada

Received August 15, 1994

P. DUANE WALKER and PAUL G. MEZEY. Can. J. Chem. **72**, 2531 (1994).

Detailed, *ab initio* quality electron density calculations are reported for the elements of the tertiary structure of bovine insulin, a protein containing 773 atoms in 51 residues. The high resolution 3D images of the molecular body and tertiary structure elements of insulin are computed using the new Molecular Electron Density Lego Assembler (MEDLA) method. The high, intermediate, and low electron density images show detailed, intricate shape features not revealed before. The MEDLA technique serves as a *computational microscope* for chemical, biochemical, pharmaceutical, and drug design applications.

P. DUANE WALKER et PAUL G. MEZEY. Can. J. Chem. **72**, 2531 (1994).

On a effectué des calculs *ab initio* détaillés de densité électronique pour les élements de la structure tertiaire de l'insuline bovine, une protéine contenant 773 atomes dans 51 résidus. Pour obtenir des images tridimensionnelles à haute résolution de l'ensemble moléculaire et des éléments de la structure tertiaire de l'insuline, on a fait appel à la nouvelle méthode de l'assembleur légo de la densité électronique moléculaire (MEDLA). Les images à densités électronique élevée, intermédiaire et basse présentent des caractéristique détaillées qui n'avaient pas été révélées antérieurement. La technique MEDLA peut servir de *microscope de calcul* pour des applications chimiques, biochimiques, pharmaceutiques ainsi que dans l'esquisse de médicaments.

[Traduit par la rédaction]

Introduction

For the visualization of the detailed shape features of proteins, the usual fused sphere models, solvent accessible surfaces, and motif patterns can provide a valuable, but only rough representation of the molecular shape features. The fuzzy electronic charge clouds form the actual molecular bodies in reality, therefore, faithful images of these charge clouds provide a valuable tool for chemistry. At present, the resolution of X-ray diffraction techniques is still insufficient for detailed shape analysis of the low density ranges of macromolecules. Up till now, the formidable computational problems have prevented the macromolecular applications of *ab initio* electron density calculations, so successful for small molecules.

The main obstacles of *ab initio* quantum chemical computations of electron densities for macromolecules are now circumvented. Here we report detailed, *ab initio* quality electron density calculations for bovine insulin, a protein of 773 atoms. The new Molecular Electron Density Lego Assembler (MEDLA) method (1), calculating and displaying electron density clouds at high resolution, serves as a *computational microscope* for proteins. No earlier experimental or computational method could generate protein images of similar accuracy and detail for the whole range of chemically important electron densities.

The MEDLA approach is suitable for the construction of inexpensive and reasonably accurate electron densities for large molecules. This method is based on a simple electron density fragment additivity principle and an algorithm described earlier (1). Fuzzy, mutually interpenetrating molecular fragment densities are computed for smaller molecules by an *ab initio* method using a suitable basis set (in our case, 6-31G**). These fragment densities are stored in a data bank and can be used as building blocks for the construction of electron densities of larger molecules, by selecting and arranging the interpenetating fuzzy charge clouds of density fragments so that the nuclear positions match those in the target molecule. If fragment densities are recombined to form the density of the molecule they are derived from, then the reconstuction is *exact* on the given *ab initio* level. The computed electronic density is highly accurate (at the given *ab initio* level) even if the fragment densities are combined to form a new molecule (1, 2). The MEDLA method of building electron densities for large molecules extends the scope of earlier methods for the analysis of global and local shapes of molecules (3).

The MEDLA computation for ordinary proteins uses only 22 types of electron density fragments from our MEDLA density fragment data bank. Several versions of these fragments, within a range of possible distorted nuclear geometries had been previously calculated as fuzzy electron density contributions within some smaller parent molecules, using the Gaussian 90 *ab initio* program and the 6-31G** basis set (4). These parent molecules can be chosen in several distorted configurations. Accordingly, each fragment type is represented by several versions in the data bank, where the versions differ by minor deviations in the local nuclear geometry and/or they are taken from parent molecules with different local surroundings. The best matching version of the fragment is selected from the database in order to mimic the actual nuclear arrangement and the effects of the surroundings of the given fragment in the target molecule. In principle, the direct *ab initio* result of the target molecule can be reproduced at the given basis set level to any desired accuracy by taking each fragment with the exact local nuclear arrangement from a large enough parent molecule where the local surroundings also match within a large enough neighborhood. If a new version of a fragment is required, a direct *ab initio* computation is carried

[1]Author to whom correspondence should be addressed.

Can. J. Chem. Downloaded from www.nrcresearchpress.com by 85.192.166.187 on 09/08/12
For personal use only.

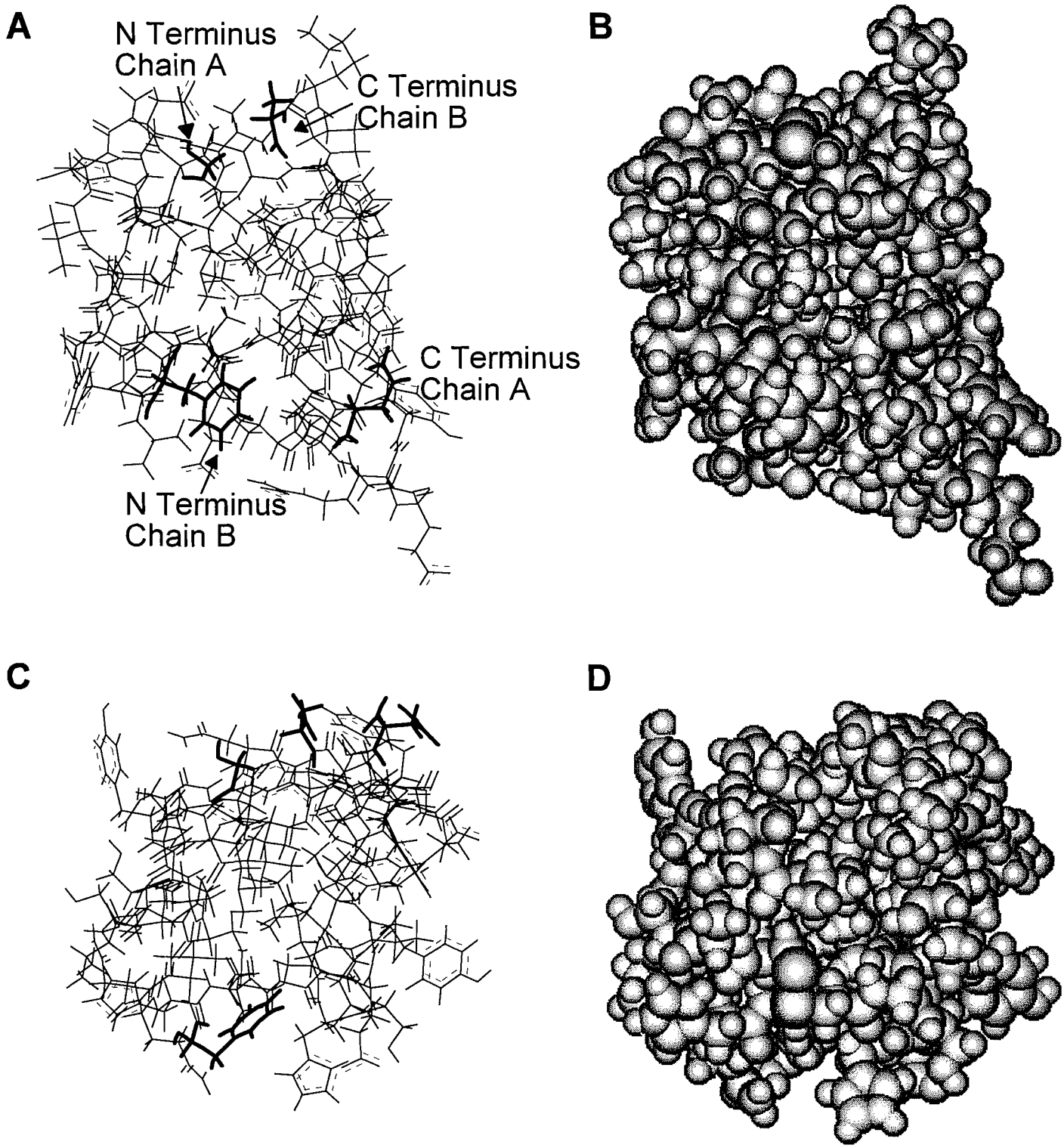

FIG. 1. Two views of the conventional wire frame model of the bonding pattern (A and C) and of the "space filling" fused spheres model (B and D) of the bovine insulin molecule. The second perspective (C and D) is the top view of the first one (A and B). The N and C termini of both chains A and B are indicated. The fused sphere model gives only a crude description of the space-filling properties and shows many artificial features, such as the seams between spheres.

out for a small molecule that contains the fragment with the required local geometry and surroundings, and the new density fragment is added to the MEDLA database. Typical fragment densities are those for the peptide bond moiety, aromatic rings, and the CH_2 group; additional technical details are given in refs. 1 and 2. Test calculations (1, 2) of numerical similarity measures have shown that, for both directly linked and hydrogen-bonded structures, as well as for molecular moieties of density overlap interactions in folded structures, the MEDLA densities are of better quality than densities obtained by direct 3-21G *ab initio* calculations. The differences between the 6-31G** MEDLA and direct 6-31G** *ab initio* electron densities are

Can. J. Chem. Downloaded from www.nrcresearchpress.com by 85.192.166.187 on 09/08/12
For personal use only.

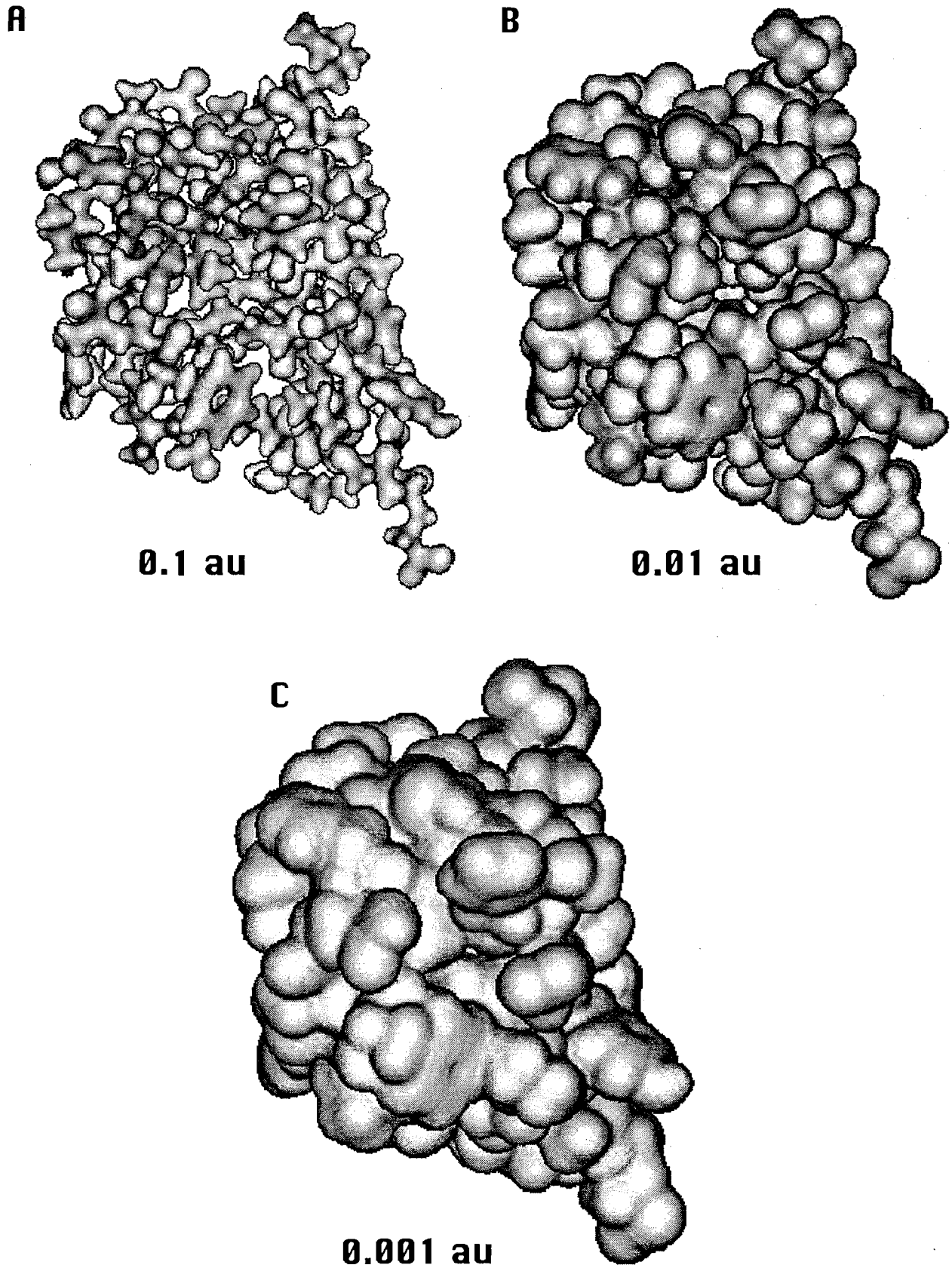

FIG. 2. Realistic views of three MEDLA molecular isodensity contours, MIDCO's A, B, and C, of density thresholds of 0.1 au (au = atomic unit), 0.01 au, and 0.001 au, respectively, are shown for the bovine insulin protein from the first of the two perspectives specified in Fig. 1. Just like a sequence of Russian wooden dolls, isodensity surface C contains B, and B contains A. High density MIDCO's describe the actual bonding pattern as it is generated by the electronic cloud in reality, intermediate density MIDCO's clearly show some additional interactions such as hydrogen bonds, whereas low density MIDCO's describe the realistic space filling shape and size features of the fuzzy, low density electronic charge cloud.

Can. J. Chem. Downloaded from www.nrcresearchpress.com by 85.192.166.187 on 09/08/12
For personal use only.

Can. J. Chem. Downloaded from www.nrcresearchpress.com by 85.192.166.187 on 09/08/12
For personal use only.

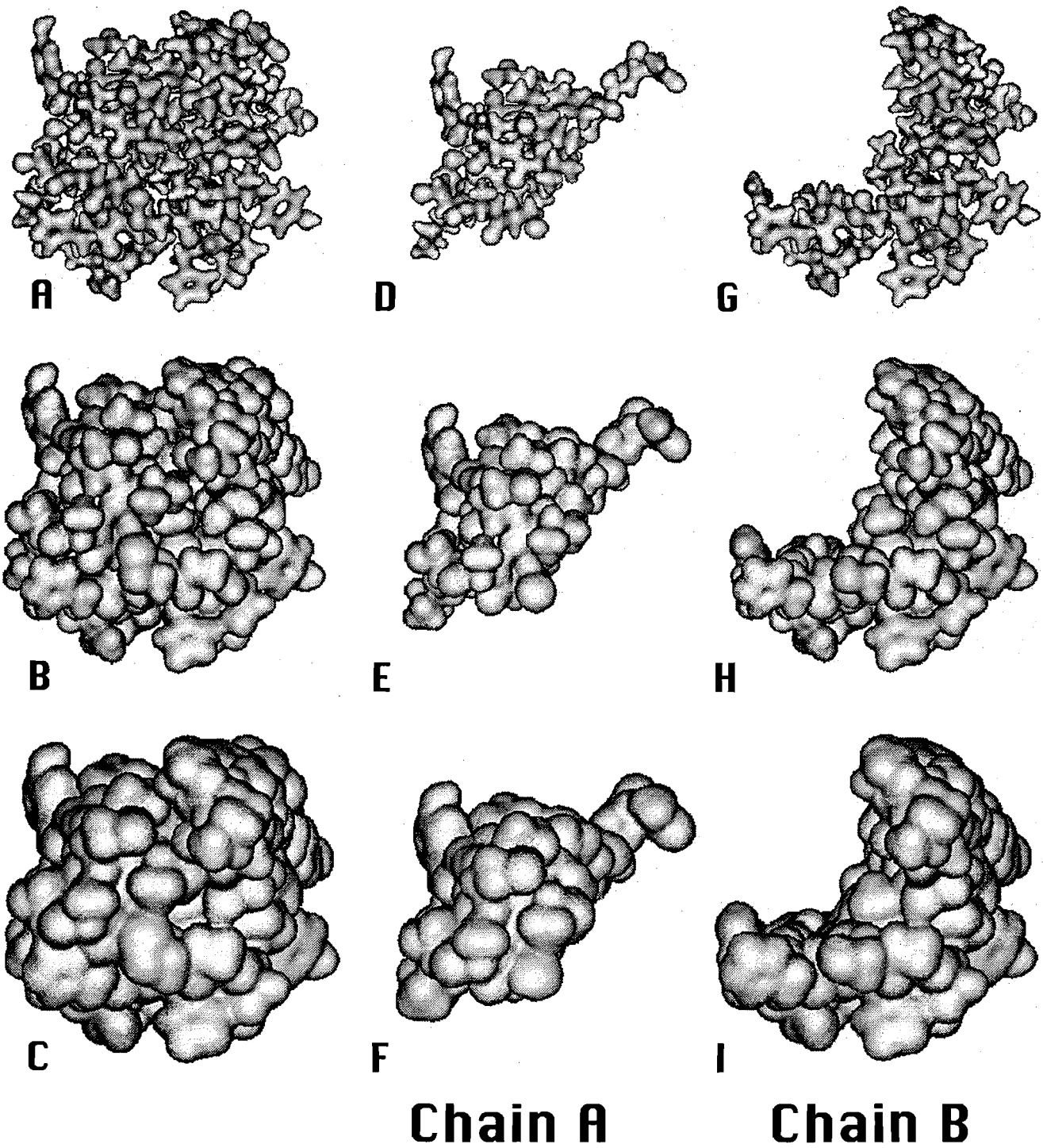

FIG. 3. Views of MEDLA MIDCO's are shown from the second of the two perspectives specified in Fig. 1, for the bovine insulin protein (contours A, B, and C) and for two of its superfragments, chain A (contours D, E, and F), and chain B (contours G, H, and I). MIDCO surfaces of three density thresholds, 0.1 au (contours A, D, and G), 0.01 au (contours B, E, and H), and 0.001 au (contours C, F, and I) are shown.

much less than those between the direct 3-21G and direct 6-31G** *ab initio* electron densities. In fact, the 6-31G** MEDLA and direct 6-31G** *ab initio* results were found visually indistinguishable (1, 2). These tests indicate that the MEDLA results are of better quality than direct 3-21G *ab initio* results, and for shape analysis purposes, 6-31G** *ab initio* and 6-31G** MEDLA are of comparable quality. The electron density calculations can be performed for any desired nuclear geometry, for example, those assumed to occur in any protein folding process. In this study, the crystallographic coordinates of insulin were used; these are available from the Protein Data Bank (5).

At present, the electron density distribution for bovine insulin could not be calculated using conventional *ab initio* techniques, due to the insurmountable RAM memory requirements of storing and retrieving an astronomical number of integrals. Even if these constraints were circumvented, we estimate that a direct calculation would take more than a decade of CPU time

Can. J. Chem. Downloaded from www.nrcresearchpress.com by 85.192.166.187 on 09/08/12
For personal use only.

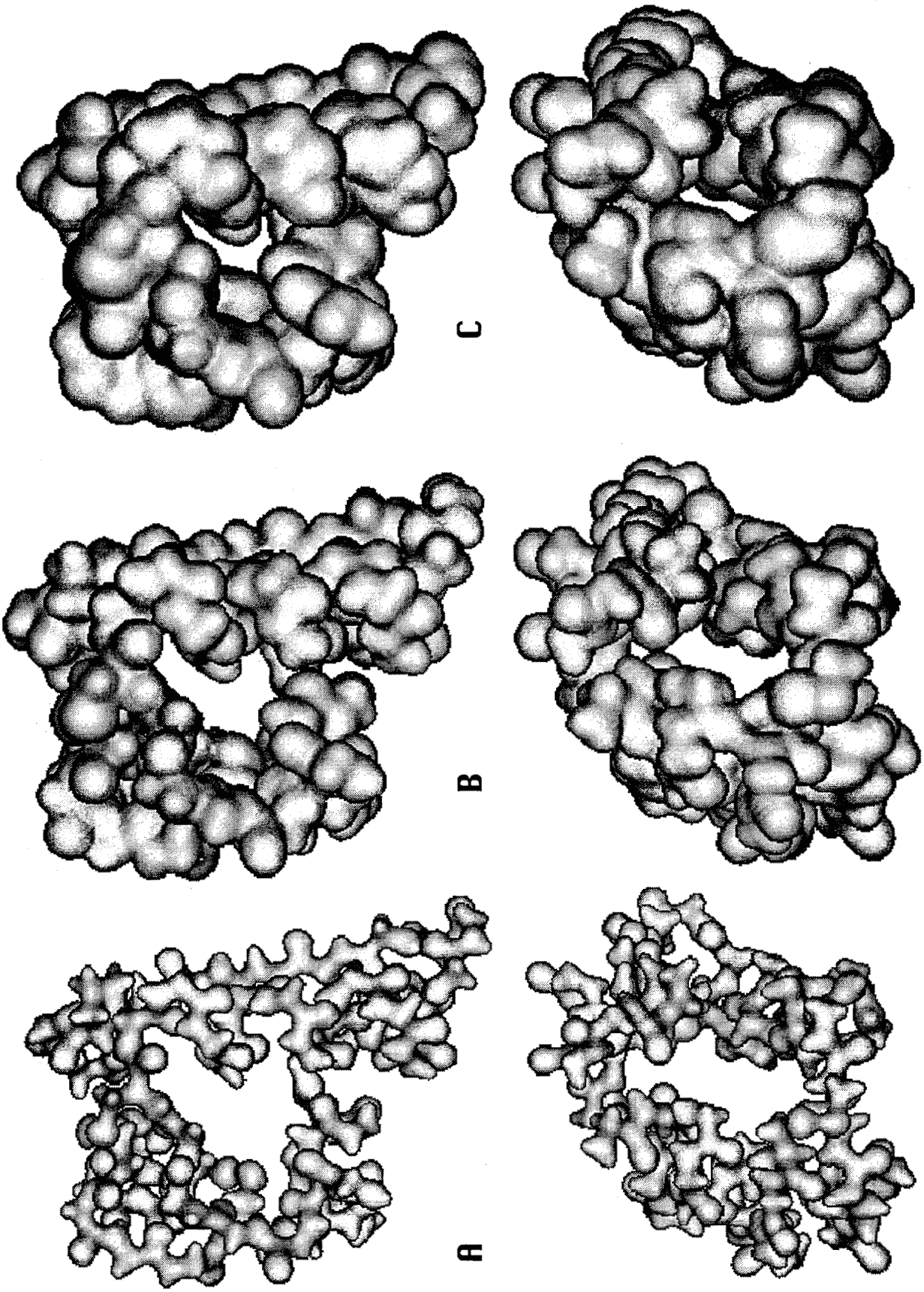

FIG. 4. Views of MEDLA MIDCO's of density thresholds of 0.1 au (contours A and D), 0.01 au (contours B and E), and 0.001 au (contours C and F) are shown for the bare backbone superfragment of the bovine insulin protein from the first (contours A, B, and C) and second (contours D, E, and F) of the perspectives specified in Fig. 1.

on a Cray supercomputer. Using our MEDLA program (6), the entire computation took only 15 min CPU time on a KPC Titan 3000 workstation.

Local regions and structural elements of a protein can be studied in detail: the electron density can be computed for the entire protein or for any "superfragment" (any collection of molecular MEDLA fragments). Bovine insulin is used to illustrate this feature of the method. This protein contains two chains; chain A of 21 amino acids and chain B of 30 amino acids. Two disulfide linkages connect the two chains; a third disulfide bond links two cysteines within chain A. The three superfragments chosen are the individual chains A and B, and the truncated protein backbone without sidechains, clearly showing the secondary structure.

In Fig. 1 two views of the bonding pattern and of a conventional fused sphere model of insulin are shown; the second arrangement is the top view of the first one. The N and C terminals of both chains A and B are identified. The same two perspectives are used for selected MEDLA densities displayed in Figs. 2–4. In Fig. 2, three molecular isodensity contours (MIDCO's), A, B, and C, of density thresholds of 0.1 au (atomic unit), 0.01 au, and 0.001 au respectively, are shown for the complete bovine insulin protein from the first of the two perspectives. In Fig. 3, the top views of the same three MIDCO's are shown, together with the corresponding MIDCO's of the chain A and chain B superfragments. In Fig. 4, both the side and top views of the backbone superfragment are shown for each of the above three density thresholds.

The richness of detail available ftom the MEDLA MIDCO's is evident from these figures. The "tight", (a = 0.1) density threshold MIDCO's in Figs. 2–4 provide a realistic view of the bonding patterns using the actual density domains (3) of the protein and three of its most important superfragments. Neither ball-and-stick models nor fused-sphere van der Waals surfaces or current models of solvent accessible surfaces are able to realistically represent this dense part of the electronic charge cloud, especially in the internuclear regions near the midpoints of formal bonds. The intermediate threshold (a = 0.01 au) images represent MIDCO's where the space filling aspects of globular proteins as well as interactions such as hydrogen bonding become apparent. The bulky, a = 0.001 density threshold MIDCO's are suitable for detailed molecular size considerations, conventionally approached using fused-sphere van der Waals surfaces. These MIDCO's properly represent the size and shape features at a density where mutual interpenetations of charge clouds between neighbor groups not formally linked by direct bonds also occur. Conventional, fused-sphere van der Waals models fail to represent these features. Note that the MEDLA computation generates the entire electronic density for the protein, hence MIDCO's for any other density thresholds, different from 0.1, 0.01, and 0.001 au, can also be displayed.

The fine details of the mutual arrangement of chains A and B are recognizable from the MEDLA MIDCO's. The two chains "hug" each other while surrounding many of their side chains within the space in between them, whereas the backbone superfragment serves as a formal skeleton. In three, mutually perpendicular views of the backbone superfragment (not all shown in Fig. 4), each image shows a central hole, implying that a quasi-cubic cage structure can model the large-scale pattern of the backbone density. This simple, polyhedral representation follows the spirit of the polyhedral models suggested by Murzin and Finkelstein (7), Chothia (8), and Maggiora and co-workers (9).

The MEDLA method describes the shapes of electronic charge density clouds that make up the molecular bodies in reality. The MEDLA approach opens up new possibilities: it can be used as a computational microscope to show accurate images of proteins. The example of bovine insulin illustrates that the MEDLA method is suitable for a detailed description of both global and local shapes of proteins and their structural elements. The speed and accuracy of the method suggests many biochemical, pharmaceutical and drug design applications, where the detailed shapes of structural elements are of importance.

Acknowledgment

This work was supported by NSERC of Canada.

1. P.D. Walker and P.G. Mezey. J. Am. Chem. Soc. **115**, 12423 (1993).
2. P.D. Walker and P.G. Mezey. J. Am. Chem. Soc. In press.
3. P.G. Mezey. *Shape in chemistry: an introduction to molecular shape and topology.* VCH Publishers, New York. 1993.
4. M.J. Frisch, M. Head-Gordon, G.W. Trucks, J.B. Foresman, H.B. Schlegel, K. Raghavachari, M.A. Robb, J.S. Binkley, C. González, D.J. Defrees, D.J. Fox, R.A. Whiteside, R. Seeger, C.F. Melius. J. Baker, R.L. Martin, L.R. Kahn, J.J.P. Stewart, S. Topiol, and J.A. Pople. GAUSSIAN 90. Gaussian Inc., Pittsburgh, PA, 1990.
5. O. Gursky, J. Badger, Y. Li, and D.L.D. Caspar. Biophys. J. **63**, 1210 (1992).
6. P.D. Walker and P.G. Mezey. MEDLA 93. Mathematical Chemistry Research Unit, University of Saskatchewan, Saskatoon, Canada, 1993.
7. A.G. Murzin and A.V. Finkelstein. J. Mol. Biol. **204**, 749 (1988).
8. C. Chothia. Nature, **337**, 204 (1989).
9. G.M. Maggiora, P.G. Mezey, B. Mao, and K.C. Chou. Biopolymers, **30**, 211 (1990).

Can. J. Chem. Downloaded from www.nrcresearchpress.com by 85.192.166.187 on 09/08/12
For personal use only.

A study of the vacuum pyrolysis of 6,6-dihalobicyclo[3.1.0]hexanes with HeI ultraviolet photoelectron spectroscopy

NICK HENRY WERSTIUK,[1] CHANDRA DEO ROY, AND JIANGONG MA
Department of Chemistry, McMaster University, Hamilton, ON L8S 4M1, Canada

Received July 15, 1994

NICK HENRY WERSTIUK, CHANDRA DEO ROY, and JIANGONG MA. Can. J. Chem. **72**, 2537 (1994).

To establish the utility of using a high-power CW (continuous wave) CO_2 laser as a directed heat source for preparing organic transients targeted for gas-phase ultraviolet photoelectron spectroscopic studies, we studied the vacuum pyrolysis of 6,6-dibromobicyclo[3.1.0]hexane (**1***a*), 6,6-dichlorobicyclo[3.1.0]hexane (**1***b*), and *exo*-6-bromo-*endo*-6-chlorobicyclo[3.1.0]hexane (**1***c*). While it has already been established that **1***a* and **1***b* rearrange to the 2,3-dihalocyclohexenes **3***a* and **3***b*, respectively, when heated in the condensed phase, upon vacuum pyrolysis **1***a* and **1***b* readily eliminate HX — not the dihalogens — and give the 2-halo-1,3-cyclohexadienes **2***a* and **2***b* in high yield. That 2,3-dibromocyclohexene (**3***a*) does not eliminate HBr at the laser power used to pyrolyze **1***a* and **1***b* and that bromochloro compound **1***c* selectively loses HCl to form **2***a* suggests that the 1,3-elimination of HX occurs in a concerted fashion without isomerization of the cyclopropane.

NICK HENRY WERSTIUK, CHANDRA DEO ROY et JIANGONG MA. Can. J. Chem. **72**, 2537 (1994).

Afin de déterminer l'utilité de l'usage de laser au CO_2 CW à haute énergie comme source de chaleur dirigée pour la préparation d'espèces organiques transitoires nécessaires pour des études de spectroscopie photoélectronique ultraviolette en phase gazeuse, on a étudié la pyrolyse sous vide des 6,6-dibromobicyclo[3.1.0]hexane (**1***a*), 6,6-dichlorobicyclo[3.1.0]hexane (**1***b*) et *exo*-6-bromo-*endo*-6-chlorobicyclo[3.1.0]hexane (**1***c*). Alors qu'il a déjà été établi que les composés **1***a* et **1***b* se réarrangent en 2,3-dihalocyclohexènes (**3***a* et **3***b* respectivement) lorsqu'on les chauffe en phase condensée, leur pyrolyse sous vide conduit plutôt à une élimination de HX — et non pas à une élimination de dihalogène — et à une formation des 2-halocyclohexa-1,3-diènes, avec d'excellents rendements. Le fait que le 2,3-dibromocyclohexène (**3***a*) n'élimine pas de HBr avec le puissant laser utilisé pour effectuer la pyrolyse des composés **1***a* et **1***b* et que le composé bromochloro **1***c* perde sélectivement du HCl pour former le composé **2***a* suggère qu'une élimination-1,3 de HX se produit d'une façon concertée, sans isomérisation en cyclopropane.

[Traduit par la rédaction]

When combined with semiempirical or ab initio calculations of molecular orbital eigenvalues (orbital energies) and eigenvectors, ultraviolet photoelectron (pe) spectroscopy gives information about the electronic structure and bonding of stable compounds and transient species that is provided by no other experimental technique. Up to the present, transient species studied with pe spectroscopy were prepared pyrolytically by passing labile precursors through electrically heated furnaces centimeters in length (1, 2). To facilitate the preparation and detection of a wide range of organic transients in the gas phase, we interfaced a tunable, 50-W CW CO_2 laser[2] with a recently modified, locally built pe spectrometer (3) in order to use the focussed laser beam as a directed heat source to produce a short (2–3 mm), very hot, contact zone whose temperature is readily altered by tuning the laser to a suitable line. Our interest in preparing and detecting the highly reactive distorted cyclical allene 1,2-cyclohexadiene led us to the CO_2 laser – pes apparatus, its first application to research in the field of organic transients, to study the vacuum pyrolysis of 6,6-dihalobicyclo[3.1.0]hexanes **1***a*, **1***b*, and **1***c*. We chose to study these compounds because cleavage of the C1—C5 bond followed by extrusion of dihalogen (the reaction could be concerted) is a possible route to 1,2-cyclohexadiene (Scheme 1), which is generated in solution (7) and apparently can be trapped and detected at low temperature using the matrix isolation method (8, 9). This communication documents the results of a study of the vacuum pyrolysis of **1***a*, **1***b*, and **1***c* with pe spectroscopy.

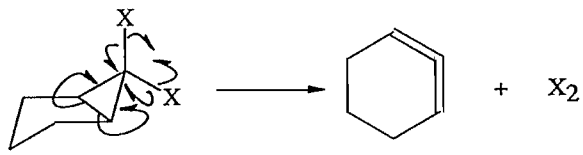

SCHEME 1

Figure 1 displays the pe spectra obtained in this study.[3] Fig-

[1]Author to whom correspondence may be addressed.

[2]Several examples of the application of CO_2 lasers in the field of pe spectroscopy have been documented in the chemical literature. Allen et al. obtained the gas-phase pe spectra of KCl, KBr, and KI by vaporizing the compounds (a stainless steel reservoir was used to hold the samples) with the focussed beam of a 50-W laser (4). Using a 50-W laser to vaporize CdSe contained in a boron nitride sample holder, Streets and Berkowitz obtained the pe spectrum of Se_2 (5). We thank a referee for bringing the work of Allen and Berkowitz to our attention. Using a 50-W CO_2 laser as a directed heat source to heat a nozzle, Bartell et al. obtained highly vibrationally excited stable molecules (6). In addition to heating a nozzle, we plan to use the focussed CO_2 laser beam to thermolyze molecules directly should they absorb strongly in the region of 1100–1000 cm^{-1}, to generate transients by vaporizing solid organic targets suspended in the source, and to carry out sensitized pyrolysis of compounds in the presence of infrared sensitizers such as CO_2, NH_3, or CH_3F.

[3]The 7 mm diameter laser beam is focussed to a 2 mm diameter beam with a convex ZnSe lens and directed through a ZnSe window in the source housing to impinge on a nozzle located on the tip of a probe. A 3 mm o.d. quartz tube constricted to an i.d. of 1 mm was used as the nozzle because quartz has a high melting point and, more importantly, it exhibits a very low lateral thermal conductivity. This produces a high-temperature zone that is approximately 2 mm in length. Measurements with a thermocouple placed in contact with the inner wall of the nozzle showed that even at 26 W the temperature of the hot zone is in the region of 500 ± 50°C. At the highest power level (>60 W), the tightly focussed beam of the Edinburgh Instruments model PL5 CW CO_2 laser in this study vaporizes quartz. The gas-phase pyrolysis reactions were carried out at a source pressure of (3–3.5) × 10^{-3} Torr (1 Torr = 133.3 Pa) with 20–50 mg of liquid sample placed in a 10-mL Pyrex reservoir attached to the external section of the probe.

Can. J. Chem. Downloaded from www.nrcresearchpress.com by 85.192.166.187 on 09/08/12
For personal use only.

Can. J. Chem. Downloaded from www.nrcresearchpress.com by 85.192.166.187 on 09/08/12
For personal use only.

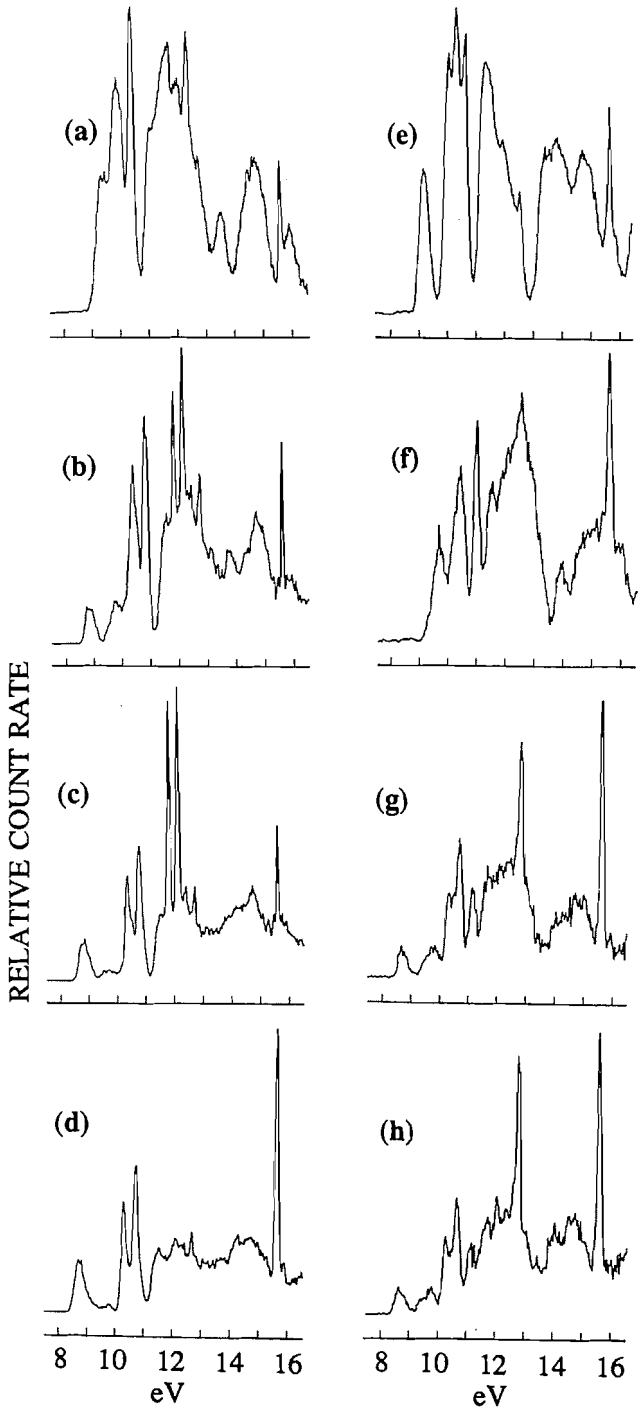

FIG. 1. (*a*) HeI ultraviolet photoelectron spectrum of 6,6-dibromobicyclo[3.1.0]hexane (**1***a*) at ambient temperature; (*b*) pe spectrum of the pyrolyzate at a laser power of 26 W; (*c*) pe spectrum at 35 W; (*d*) pe spectrum of 2-bromo-1,3-cyclohexadiene (**2***a*) at ambient temperature; (*e*) pe spectrum of 2,3-dibromocyclohexene (**3***a*) at ambient temperature; (*f*) pe spectrum of *anti*-6-bromo-*syn*-6-chlorobicyclo[3.1.0]hexane (**1***c*) at ambient temperature; (*g*) pe spectrum of the pyrolyzate at a laser power of 26 W; (*h*) pe spectrum at 42 W. The peak at 15.6 eV in each spectrum is the low-IP peak of N_2, which is used as the calibrant.

ure 1(*a*) is the spectrum of **1***a* acquired at ambient temperature without heating the nozzle. At a laser power of 26 W, the spectrum (Fig. 1(*b*)) exhibits a new broad band at 8.9 eV along with a pair of sharp peaks centered at 12 eV. When the temperature of

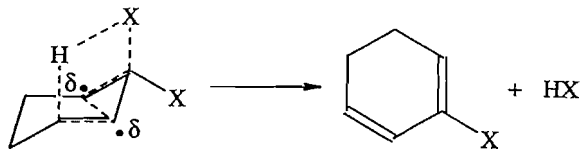

SCHEME 2

the quartz nozzle is increased by tuning the laser to a 35-W line, the intensities of the bands at 8.9 and 12 eV increase and there is a concomitant decrease in the relative intensities of the starting material peaks (Fig. 1(*c*)). The sharp bands centered at 12 eV are due to HBr (10) and the remaining peaks correspond exactly to the pe spectrum (Fig. 1(*d*)) of an authentic sample of 2-bromo-1,3-cyclohexadiene (**2***a*). Dichloro compound **1***b* pyrolyzes under the same conditions yielding HCl and 2-chloro-1,3-cyclohexadiene (**2***b*) (spectra not shown). At higher power levels (>40 W), **1***a* and **1***b* yield benzene, which was identified on the basis of a pe spectrum of an authentic sample.[4] To establish that **2***a* is not formed by 1,2-elimination of HBr from 2,3-dibromocyclohexene (**3***a*), known to be the product of thermal rearrangement of **1***a* in the condensed phase (11), we prepared **3***a* (the pe spectrum is shown in Fig. 1(*e*)) and studied its pyrolysis at 26 and 42 W. Unlike **1***a*, which readily loses HBr at 26 W and pyrolyzes completely at 35 W, the pyrolysis of **3***a* is incomplete even at 42 W (spectrum not shown), indicating that it is not an intermediate in the pyrolysis of **1***a*. To study the stereochemistry of the 1,3-elimination of HX, we prepared (12) and pyrolyzed bromochloro compound **1***c*. The pe spectrum of **1***c* acquired at ambient temperature is displayed in Fig. 1(*f*). As seen in Fig. 1(*g*), **1***c*, like **1***a*, pyrolyzes at 26 W. The peaks at 8.8, 10.3, and 10.7 eV are assigned to **2***a*[5] and the sharp peak at 12.8 eV corresponds precisely to the lowest ionization potential (IP) peak of HCl (10). As indicated by the weak peaks centered at 12 eV (Fig. 1(*h*)), a small amount of HBr is only formed at 42 W, the power level that produces a nozzle temperature sufficient to produce benzene from **2***a*;[4] the lowest-IP band of benzene is seen as part of the overlapped peak at 9.3 eV. At 60 W (spectrum not shown), approximately 50% of **2***a* is converted to benzene, which is recognizable from a peak at 9.3 eV and broad bands centered at 12 and 14.5 eV (10). The results of this study indicate that the three-membered ring of **1***a*, **1***b*, and **1***c* undergoes a disrotatory opening and initiates the cleavage of the *endo* C—X bond, which leads to 1,3-elimination of HX (Scheme 2). This study also establishes that the CO_2 laser – pes apparatus will be generally useful for studying the vacuum pyrolysis of organic compounds.

To block 1,3-elimination of HX and perhaps force the extrusion of X_2, we plan to synthesize and thermolyze 6,6-dibromo-

[4]Isomerization of the 2-halo-1,3-cyclohexadienes to the 5-halo-1,3-cyclohexadienes via consecutive 1,5-hydrogen shifts followed by a facile four-centered 1,2-elimination of HX is the most probable route to benzene.

[5]The orbital energies of the three highest occupied MOs of **2***a* (the torsional angle between the double bonds is 7.9°) calculated with AM1 are 9.01, 10.67, and 11.03 eV, respectively. The HOMO (9.01 eV) is predominately the π_- combination of the diene unit mixed with the π-type group orbitals of the methylene groups and to a smaller extent with n_{Br} The HOMO-1 (10.67 eV) is the π_+ combination of the diene heavily mixed with n_{Br} HOMO-2 is mostly n_{Br} mixed with the σ orbitals of the diene unit. That HOMO-2 has more n_{Br} character than HOMO-1 is supported by the fact that the peak at 10.7 eV (Fig. 1(*d*)) is sharper than the peak at 10.3 eV.

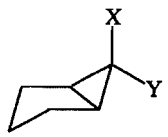

1

a, X=Y=Br
b, X=Y=Cl
c, X=Cl; Y=Br

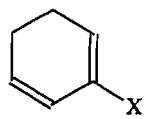

2

a, X=Br
b, X=Cl

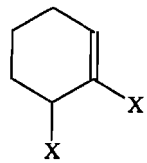

3

a, X=Br
b, X=Cl

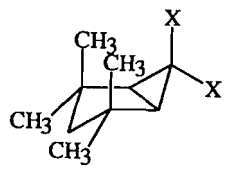

4

a, X=Br
b, X=Cl

2,2,4,4-tetramethylbicyclo[3.1.0]hexane (**4***a*) and 6,6-dichloro-2,2,4,4-tetramethylbicyclo[3.1.0]hexane (**4***b*). Because geminal dihalocyclopropanes are easily synthesized by dihalocarbene addition to alkenes, we also plan to carry out pyrolyses with a preparative-scale apparatus to determine the scope and limitations of the gas-phase 1,3-elimination of HX as a synthetic route to a wide range of cyclic and acyclic 2-halogenated 1,3-dienes.

Acknowledgement

We thank the Natural Sciences and Engineering Research Council of Canada for financial support.

1. R. Schulz and A. Schweig. *In* Structure and reactivity. *Edited by* J.F. Liebman and A. Greenberg. VCH Publishers Inc., New York. 1988. Chap. 8.
2. N.P.C. Westwood. Chem. Soc. Rev. **18**, 317 (1989).
3. N.H. Werstiuk, D.N. Butler, and E. Shahid. Can. J. Chem. **65**, 760 (1986).
4. J.D. Allen, Jr., G.W. Boggess, T.D. Goodman, A.S. Wachtel, Jr., and G.K. Schweitzer. J. Electron Spectrosc. Relat. Phenom. **2**, 289 (1973).
5. D.G. Streets and J. Berkowitz. Chem. Phys. Lett. **9**, 269 (1976).
6. L.S. Bartell, M.A. Kacner, and S.R. Goates. J. Chem. Phy. **75**, 2730 (1981).
7. W.R. Moore and W.R. Moses. J. Am. Chem. Soc. **92**, 5469 (1970).
8. C. Wentrup, G. Gross, A. Maguestiau, and R. Flammang. Angew. Chem. Int. Ed. Engl. **22**, 542 (1983).
9. A. Runge and W. Sander. Tetrahedron Lett. **27**, 5835 (1986).
10. K. Kimura, S. Katsumata, Y. Achiba, T. Yamazaki, and S. Iwata. *In* The handbook of HeI photoelectron spectra of fundamental organic molecules: ionization energies, ab initio assignments and valence electronic structure of 200 molecules. Japan Scientific Societies Press, Tokyo. 1981.
11. J. Sonnenberg and S. Winstein. J. Org. Chem. **27**, 748 (1962).
12. S.R. Sandler. J. Org. Chem. **35**, 2023 (1970).

Can. J. Chem. Downloaded from www.nrcresearchpress.com by 85.192.166.187 on 09/08/12
For personal use only.

Br^+ Transfer to reactive alkenes from the bromonium ion of adamantylideneadamantane

A.A. Neverov and R.S. Brown[1]

Department of Chemistry, University of Alberta, Edmonton, AB T6G 2G2, Canada

Received September 8, 1994

A.A. Neverov and R.S. Brown. Can. J. Chem. **72**, 2540 (1994).

The transfer of Br^+ from the bromonium ion of adamantylideneadamantane (**1**-$Br^+/CF_3SO_3^-$) to the reactive alkenes cyclohexene, ω-alken-1-ols, **3***a–c*, and 4-pentenoic acid, **4**, in 1,2-dichloroethane at 25°C has been investigated. ^1H NMR analysis of the reactions of equimolar **1**-$Br^+/CF_3SO_3^-$ and olefin indicates the products to be the expected cyclic ones in the cases of **3***a–c* and **4**, and *trans*-2-bromocyclohexyltrifluoromethane sulfonate in the case of cyclohexene, along with adamantylideneadamantane (Ad=Ad). Detailed kinetic analysis shows that the reaction rates are suppressed by the addition of free Ad=Ad, suggestive of a common species rate depression. In the case of certain of the cyclization reactions such as that of 4-penten-1-ol, **3***a*, the cyclization reaction is bimolecular in acceptor olefin. A primary deuterium kinetic isotope effect of 2.0 on the cyclization of **3***a*-OH relative to **3***a*-OD exists. The role of the second molecule appears to be that of a general base in assisting the cyclization of an intermediate ω-hydroxy cyclic bromonium ion. A general mechanistic scheme for Br^+ transfer from **1**-Br^+ to the reactive alkenes is proposed.

A.A. Neverov et R.S. Brown. Can. J. Chem. **72**, 2540 (1994).

On a étudié le transfert du Br^+ de l'ion bromonium de l'adamantylidèneadamantane (**1**-$Br^+/CF_3SO_3^-$) à des alcènes réactifs, comme le cyclohexène, les ω-alcèn-1-ols (**3***a–c*) et l'acide pent-4-ènoïque (**4**), dans le 1,2-dichloroéthane, à 25°C. Une analyse par RMN du ^1H des réactions équimolaires du (**1**-$Br^+/CF_3SO_3^-$) avec les oléfines indique que les produits sont, en plus de l'adamantylidèneadamantane (Ad=Ad), les dérivés cycliques attendus dans les cas **3***a–c* et **4** et le sulfonate du *trans*-2-bromocyclohexyltrifluorométhane dans le cas du cyclohexène. Une étude cinétique détaillée montre que les vitesses de réactions sont supprimées par l'addition de Ad=Ad libre; ceci suggère une diminution de vitesse par une espèce commune. Dans le cas de certaines réactions de cyclisation, tel que celle du pent-4-èn-1-ol (**3***a*), la réaction de cyclisation est bimoléculaire en oléfine accepteur. Il existe un effet isotopique cinétique primaire du deutérium de 2,0 lors de la cyclisation du **3***a*-OH par rapport à celle du **3***a*-OD. La deuxième molécule semble jouer le rôle d'une base générale qui assiste la cyclisation d'un ion ω-hydroxy bromonium cyclique intermédiaire. On propose un mécanisme général pour le transfert de Br^+ du **1**-Br^+ à des alcènes réactifs.

[Traduit par la rédaction]

Early studies by Wynberg and co-workers (1*a*) and Olah et al. (1*b*) indicated that the bromonium ion/tribromide salts of adamantylideneadamantane (**1**-Br^+/Br_3^-) were capable of irreversible Br_2 transfer to acceptor olefins such as cyclohexene or 2,3-dimethyl-2-butene to form the corresponding *trans* dibromides. However, subsequent studies (2) made it likely that the actual brominating species was free Br_2 since it was shown that when **1**-Br^+/Br_3^- is dissolved, a complex equilibrium between olefin **1**, Br_2, the Br_2:**1** charge transfer complex, and **1**-Br^+/Br_3^- is instantly established. We have recently shown that the triflate salts of **1**-Br^+ and **1**-I^+ undergo an extremely fast direct X^+ exchange with the parent olefin (eq. [1]) (3).

[1] 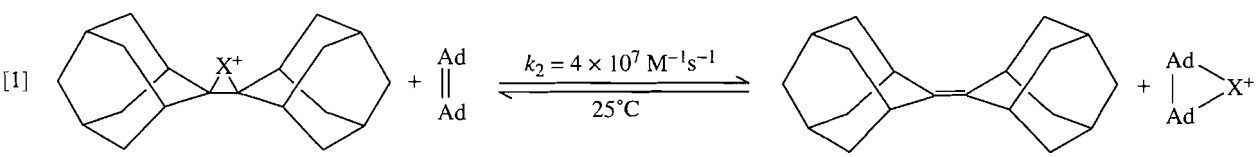

1-Br^+
1-I^+ **1**

The facility of this process suggests that three-membered halonium-ion/olefin exchanges might be a general but heretofore overlooked phenomenon. In support of this latter speculation, it is of note that communication between a bromonium ion of an *n*-pentenyl or *n*-hexenyl glucoside and the two parent olefins has been recently demonstrated by Rodebaugh and Fraser-Reid (4). Herein we report that the use of **1**-$Br^+/CF_3SO_3^-$ as a Br^+ transfer agent allows unusual insight into the mechanism of bromocyclization of ω-alkene-1-ols.

The Ad=Ad bromonium triflate (**1**-$Br^+/CF_3SO_3^-$) is relatively stable at 25°C in non-nucleophilic solvents such as chlorinated hydrocarbons or CH_3CN. We have studied preliminarily

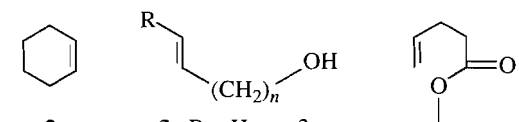

2 **3***a* R = H, *n* = 3; *b* R = H, *n* = 4; *c* R = CH_3, *n* = 3 **4**

the Br^+ transfer from cf. **1**-$Br^+/CF_3SO_3^-$ to a number of olefins, monitoring the reaction progress at equimolar concentration by ^1H NMR. Representative olefins include cyclohexene, **2**, the ω-alken-1-ols, **3***a–c*, and 4-pentenoic acid, **4**, and the products formed in essentially quantitative yield (by ^1H NMR) are the expected ones (4) given in Table 1.

The kinetics of the various transfer reactions were monitored in 1,2-dichloroethane (DCE) at 25°C by determining the initial

[1]Author to whom correspondence may be addressed. Telephone: (403) 492-3254. FAX: (403) 492-8231.

Can. J. Chem. Downloaded from www.nrcresearchpress.com by 85.192.166.187 on 09/08/12
For personal use only.

Can. J. Chem. Downloaded from www.nrcresearchpress.com by 85.192.166.187 on 09/08/12
For personal use only.

TABLE 1. Reaction products formed from reaction of equimolar **1**-$Br^+/CF_3SO_3^-$ and various olefins in $ClCD_2CD_2Cl$

Olefin	Product	Olefin	Product
3*a*	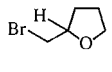	**3***c*	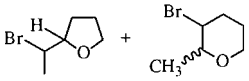
Cyclohexene	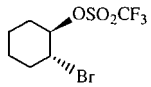	**4**	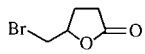
3*b*	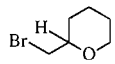		

rate of loss of absorbance at 260 nm of 3.5×10^{-4} M solutions of **1**-$Br^+/CF_3SO_3^-$ in the presence of various concentrations of the above olefins.[2,3] The so-determined rate constants (k_{obs}) are given as Supplementary Material.[4] There are three general observations of note. First, in all cases added Ad=Ad significantly slows the reaction. In some cases, as shown for **3***a* in Fig. 1, plots of k_{obs} vs. [Ad=Ad] at a given concentration of **3***a* asymptotically approach the *X*-axis, signifying an absence of reaction at high Ad=Ad concentration. In other cases (**3***b*, *c*, cyclohexene), the added Ad=Ad does not suppress the reaction completely: rather, the rate reaches some limiting value at high [Ad=Ad] as shown in Fig. 1 for **3***c*. Second, in most cases, the cyclization reactions in DCE have a second-order dependence on concentration of acceptor olefin. Third, in the case we investigated in the most detail (cyclization of **3***a*), there is a significant primary deuterium kinetic isotope effect (*D*kie) on the cyclization reaction for **3***a*-OH relative to **3***a*-OD.

All the above observations can be accommodated by the general mechanism given in Scheme 1 from which can be derived the kinetic expression given in eq. [2] assuming a steady state in the nascent bromonium ion **6**. In the scheme there are three channels for product formation; namely, (*a*) direct collapse of an ol:**1**-Br^+ complex, **5**;[5] (*b*) dissociation of this complex into free Ad=Ad and **6**, the latter undergoing spontaneous cyclization; or (*c*) a similar dissociation to **6** with the latter's cyclization being promoted by a second molecule of ol. The fact that Ad=Ad suppresses the rate is attributable to a common species rate depression where Ad=Ad reacts with free **6** to revert to the starting materials or complex **5**. The observation that in some cases added Ad=Ad cannot fully suppress the reaction requires

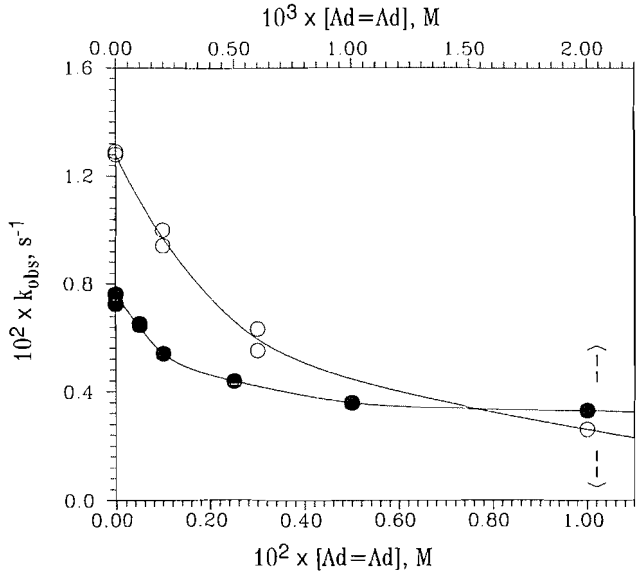

FIG. 1. Plots of k_{obs} vs. [Ad=Ad] for Br^+ transfer from **1**-$Br^+/CF_3SO_3^-$ to **3***a* (○) and **3***c* (●) in DCE at 25°C; [**3***a*] = 0.004 M; [**3***c*] = 0.0002 M.

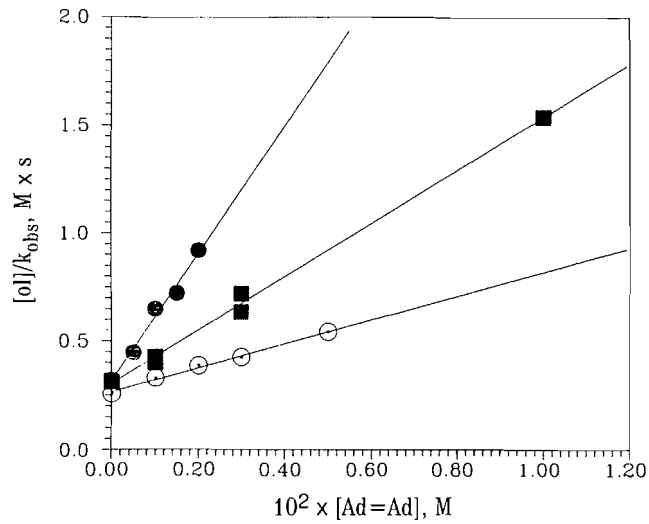

FIG. 2. Plots of [ol]/k_{obsd} vs. [Ad=Ad] for Br^+ transfer from **1**-$Br^+/CF_3SO_3^-$ to various [**3***a*] in DCE at 25°C; ● [**3***a*] = 0.0016 M; ■ [**3***a*] = 0.004 M; ○ [**3***a*] = 0.008 M.

that there be some ol:**1**-Br^+ complex that is not driven backward by external Ad=Ad, but can produce cyclized products. It seems most reasonable to suggest that putative complex **5**[5] is on the reaction pathway for forming free Ad=Ad and **6**.

$$[2] \quad k_{obs} = k_3K_{eq}[ol] + \frac{k_1K_{eq}[ol](k_2'[ol] + k_2)}{k_{-1}[Ad{=}Ad] + (k_2'[ol] + k_2)}$$

We deal first with an example (cyclization of **3***a*) that allows considerable simplification of eq. [2]. Since a high added Ad=Ad concentration completely suppresses the reaction (Fig. 1), k_3K_{eq}[ol] in eq. [2] is not kinetically significant. This allows linearization of eq. [2] into the form of eq. [3] so that a plot of [ol]/k_{obs} vs. [Ad=Ad] yields a straight line, the intercept of which refers to k_1K_{eq}, the slope relating to the partitioning of the intermediate between product formation and reversal. Shown in Fig. 2 are the linear plots for Br^+ transfer from **1**-$Br^+/CF_3SO_3^-$

[2]Using an OLIS® modified Cary 17 UV–visible spectrophotometer, k_{obs} determined by initial rate methods monitoring ΔAbs for the initial 5–10% of the reaction:

$$k_{obs} = \frac{(\Delta Abs/\Delta t)}{([\mathbf{1}\text{-}Br^+/CF_3SO_3^-]_i \cdot \epsilon_{260})}$$

[3]**1**-$Br^+/CF_3SO_3^-$ exhibits a strong but featureless UV band between 300 nm and the solvent cutoff (240 nm in $ClCH_2CH_2Cl$), ϵ_{260} = 3200 M^{-1} cm^{-1}.

[4]Tables of primary kinetic data for transfer of Br^+ from **1**-$Br^+/CF_3SO_3^-$ to acceptor olefins **3***a–c*, **4**, and cyclohexene are available as supplementary material and can be purchased from: The Depository of Unpublished Data, Document Delivery, CISTI, National Research Council Canada, Ottawa, ON K1A 0S2, Canada.

[5]Such a complex has been determined to be energetically favored by the theoretical calculations for the ethylene bromonium ion/ethylene system (3).

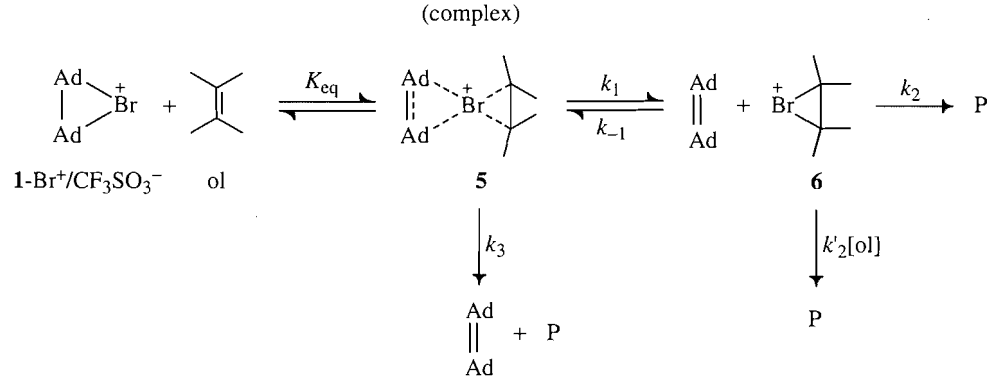

(ol = acceptor olefins such as **3**, **4**, or cyclohexene)

SCHEME 1

TABLE 2. Kinetic parameters for Br^+ transfer reactions from **1**-$Br^+/CF_3SO_3^-$ to various acceptor olefins in $ClCH_2CH_2Cl$ at 25°C[a]

Olefin	$k_1 K_{eq}$ ($M^{-1} s^{-1}$)	$k_3 K_{eq}$ ($M^{-1} s^{-1}$)	k_2'/k_{-1} (or k_2/k_{-1})
3*a*	3.5 ± 0.3	—	0.63 ± 0.04[b]
3*a*-OD	3.0 ± 0.2	—	0.33 ± 0.03[b]
4-Pentenoic acid (**4**)	$(7.2 \pm 0.6) \times 10^{-2}$	—	$(7.1 \pm 0.4) \times 10^{-4}$[c]
Cyclohexene	$(6.0 \pm 0.1) \times 10^{-1}$	$(5.2 \pm 0.1) \times 10^{-1}$	$(5 \pm 2) \times 10^{-3}$[d]
3*b*	$(2.7 \pm 0.3) \times 10^{-1}$	$(8.0 \pm 2.0) \times 10^{-2}$	0.33 ± 0.05[b]
3*c*	$(2.3 \pm 0.3) \times 10^{1}$	$(1.1 \pm 0.3) \times 10^{1}$	0.32 ± 0.07[b]

[a]Determined from initial rate methods (see footnote 2).
[b]Refers to k_2'/k_{-1} (Scheme 1); unitless.
[c]Refers to k_2/k_{-1}; no second order in [4-pentenoic acid] dependence of reaction rate observed; units M.
[d]Refers to k_2/k_{-1}; no second order in [cyclohexene] dependence of reaction rate observed; units M assuming $CF_3SO_3^-$ ion pair collapse.

to **3***a* at various concentrations of the latter. The inverse dependence of the slopes on **3***a* concentration indicates that a second molecule of **3***a* is required to promote product formation from the nascent bromonium ion **6** (i.e., k_2' [ol] >0 in Scheme 1). Numerical evaluation of the partitioning of **6** is allowed by plotting the intercept/slope ratio vs. [ol] as in eq. [4]. For **3***a* the k_2'/k_{-1} ratio is 0.57 ± 0.1, while the k_2/k_{-1} is indistinguishable from zero: thus spontaneous breakdown of **6** to product is kinetically insignificant under these reaction conditions, and such breakdown can only occur via the involvement of a second molecule of **3***a*.

$$[3] \quad \frac{[ol]}{k_{obs}} = \frac{k_{-1}[Ad{=}Ad]}{k_1 K_{eq}(k_2'[ol] + k_2)} + \frac{1}{k_1 K_{eq}}$$

$$[4] \quad \text{intercept/slope} = \frac{k_2'[ol]}{k_{-1}} + \frac{k_2}{k_{-1}}$$

The second molecule appears to function as a general base as in eq. [5] wherein its OH group removes the proton of **6** (4) during the cyclization.

Consistent with this is the fact that 1-pentanol promotes the cyclization reaction of **3***a* and **1**-Br^+. A plot of k_{obs} vs. [1-pentanol] (1.6×10^{-3} M **3***a*, 2×10^{-3} M Ad=Ad, 3.5×10^{-4} M **1**-Br^+) shows a saturation behavior such that at high concentration of 1-pentanol the rate-limiting step becomes formation of **6** from **3***a* plus **1**-Br^+. That the k_2' step involves deprotonation of **6** is supported by the primary *D*kie of 2.0 for $(k_2'/k_{-1})_{3a\text{-OH}/3a\text{-OD}}$.

[5] $\xrightarrow[k_{-1}[Ad{=}Ad]]{k_1}$ 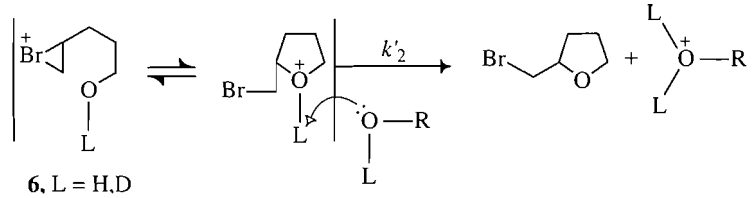

6, L = H,D

For other olefins such as **3***b*, **3***c*, and cyclohexene, added Ad=Ad does not fully suppress the reaction so that $k_3 K_{eq}$[ol] in eq. [2] is kinetically significant, and cyclization occurs directly from complex **5**. For cyclohexene, a second molecule is not required for product formation, so that product formation results from ion-pair collapse, both on and off the complex.

NLLSQ fitting of k_{obs} vs. [Ad=Ad] to eq. [2] yields the parameters $k_1 K_{eq}$, $k_3 K_{eq}$, and k_2'/k_{-1}. These are given in Table 2 along with the comparable parameters for **3***a*-OH and **3***a*-OD derived as above.

There are several important and fundamental points brought to light during this study. Use of **1**-Br^+ as a Br^+ transfer agent allows a much deeper insight into the mechanistic subtleties of the halocyclizations than was previously possible. We previously established that the thermoneutral Br^+ exchange between **1**-Br^+ and Ad=Ad occurs at 4×10^7 $M^{-1} s^{-1}$ at 25°C, the associated $\Delta H^{\ddagger}$ and $\Delta S^{\ddagger}$ being 1.8 kcal mol^{-1} and −21 cal

Can. J. Chem. Downloaded from www.nrcresearchpress.com by 85.192.166.187 on 09/08/12
For personal use only.

K^{-1} mol^{-1} (3). The k_{-1} rate constant for Br^+ transfer from bromonium ions of mono-, di-, and trisubstituted olefins back to Ad═Ad should be as fast or faster than the thermoneutral **1**-Br^+/Ad═Ad transfer since those processes must be exothermic and the transition states somewhat less restrictive in terms of entropy. Indeed, it is the rapidity of the k_{-1} process that competes with, and therefore allows, kinetic assessment of the fast cyclization/deprotonation of **6**.

Acknowledgements

The authors gratefully acknowledge the financial support of the Natural Sciences and Engineering Research Council of Canada and of the University of Alberta.

1. (*a*) J. Strating, J.H. Wieringa, and H. Wynberg. J. Chem. Soc. Chem. Commun. 907 (1969); (*b*) G.A. Olah, P. Schilling, P.W. Westerman, and H.C. Liu. J. Am. Chem. Soc. **96**, 3581 (1974).
2. G. Bellucci, R. Bianchini, C. Chiappe, F. Marioni, R. Ambrosetti, R.S. Brown, and H. Slebocka-Tilk. J. Am. Chem. Soc. **111**, 2640 (1989).
3. (*a*) R.S. Brown, R.W. Nagorski, A.J. Bennet, R.E.D. McClung, G.H.M. Aarts, M. Klobukowski, R. McDonald, and B.D. Santarsiero. J. Am. Chem. Soc. **116**, 2448 (1994); (*b*) A.J. Bennet, R.S. Brown, R.E.D. McClung, M. Klobukowski, G.H.M. Aarts, B.D. Santarsiero, G. Bellucci, and R. Biancini. J. Am. Chem. Soc. **103**, 8532 (1991).
4. R. Rodebaugh and B.J. Fraser-Reid. J. Am. Chem. Soc. **116**, 3155 (1994).
5. A.B. Reitz, S.O. Norley, B.E. Maryanoff, D. Liotta, and R. Monahan. J. Org. Chem. **52**, 4191 (1987), and references therein.

Can. J. Chem. Downloaded from www.nrcresearchpress.com by 85.192.166.187 on 09/08/12
For personal use only.